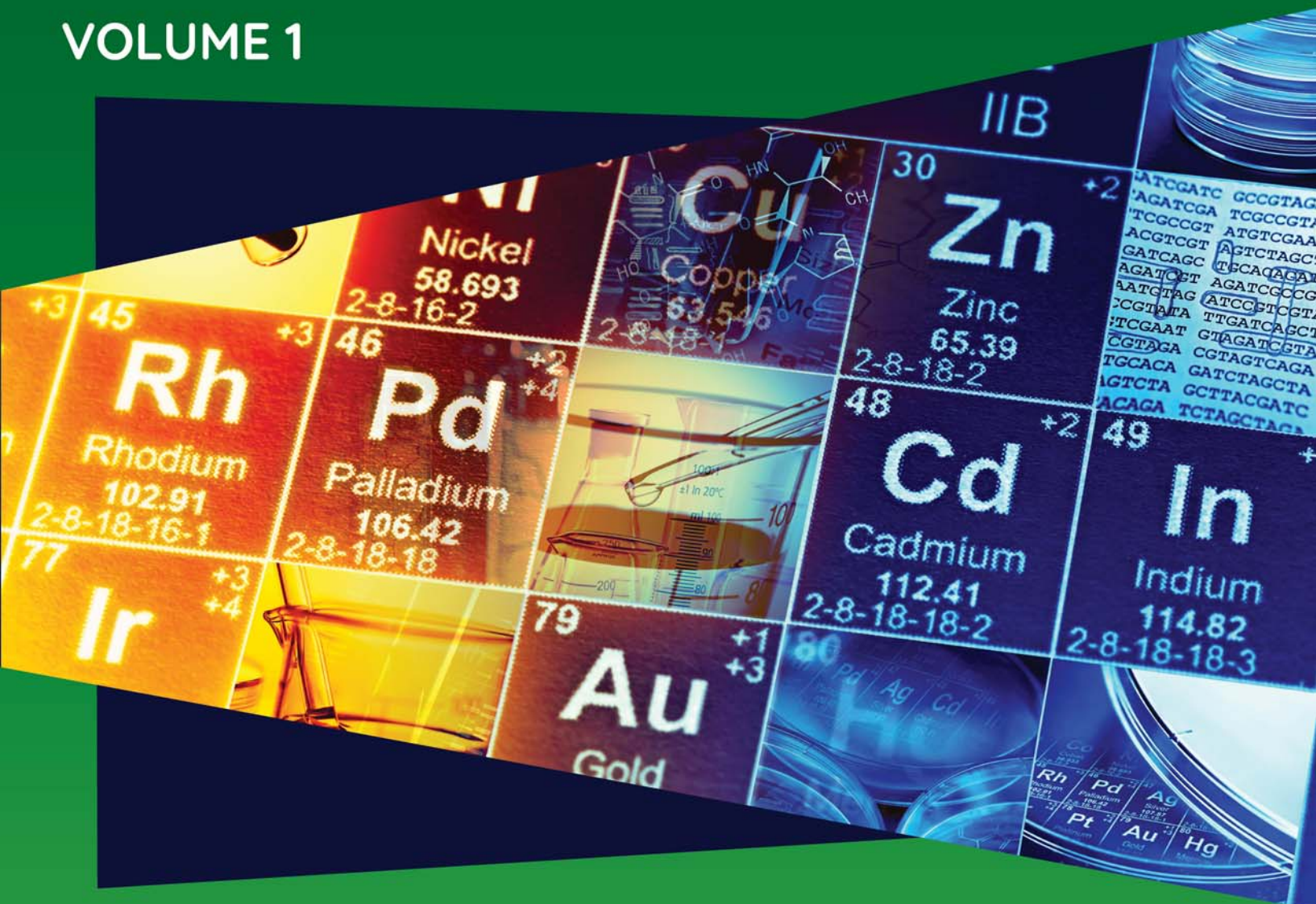


# COMPREHENSIVE INORGANIC CHEMISTRY III

VOLUME 1



EDITORS IN CHIEF  
JAN REEDIJK & KENNETH R. POEPELMEIER

SECTION EDITOR  
RISTO S. LAITINEN



# **COMPREHENSIVE INORGANIC CHEMISTRY III**

---



# COMPREHENSIVE INORGANIC CHEMISTRY III

---

EDITORS IN CHIEF

**Jan Reedijk**

*Leiden Institute of Chemistry, Leiden University, Leiden, the Netherlands*

**Kenneth R. Poeppelmeier**

*Department of Chemistry, Northwestern University, Evanston, IL, United States*

VOLUME 1

## **Synthesis, Structure, and Bonding of Inorganic Molecular Systems**

VOLUME EDITOR

**Risto S. Laitinen**

*Laboratory of Inorganic Chemistry, Environmental and Chemical Engineering,  
University of Oulu, Finland*



Amsterdam • Boston • Heidelberg • London • New York • Oxford  
Paris • San Diego • San Francisco • Singapore • Sydney • Tokyo

Elsevier  
Radarweg 29, PO Box 211, 1000 AE Amsterdam, Netherlands  
The Boulevard, Langford Lane, Kidlington, Oxford OX5 1GB, United Kingdom  
50 Hampshire Street, 5th Floor, Cambridge MA 02139, United States

Copyright © 2023 Elsevier Ltd. All rights reserved

No part of this publication may be reproduced or transmitted in any form or by any means, electronic or mechanical, including photocopying, recording, or any information storage and retrieval system, without permission in writing from the publisher. Details on how to seek permission, further information about the Publisher's permissions policies and our arrangements with organizations such as the Copyright Clearance Center and the Copyright Licensing Agency, can be found at our website: [www.elsevier.com/permissions](http://www.elsevier.com/permissions).

This book and the individual contributions contained in it are protected under copyright by the Publisher (other than as may be noted herein).

#### Notices

Knowledge and best practice in this field are constantly changing. As new research and experience broaden our understanding, changes in research methods, professional practices, or medical treatment may become necessary.

Practitioners and researchers may always rely on their own experience and knowledge in evaluating and using any information, methods, compounds, or experiments described herein. In using such information or methods they should be mindful of their own safety and the safety of others, including parties for whom they have a professional responsibility.

To the fullest extent of the law, neither the Publisher nor the authors, contributors, or editors, assume any liability for any injury and/or damage to persons or property as a matter of products liability, negligence or otherwise, or from any use or operation of any methods, products, instructions, or ideas contained in the material herein.

#### Library of Congress Cataloging-in-Publication Data

A catalog record for this book is available from the Library of Congress

#### British Library Cataloguing-in-Publication Data

A catalogue record for this book is available from the British Library

ISBN 978-0-12-823144-9

For information on all publications visit our website at  
<http://store.elsevier.com>



*Publisher:* Oliver Walter  
*Acquisitions Editors:* Clodagh Holland-Borosh and Blerina Osmanaj  
*Content Project Manager:* Pamela Sadhukhan  
*Associate Content Project Manager:* Abraham Lincoln Samuel  
*Designer:* Victoria Pearson Esser

# CONTENTS OF VOLUME 1

---

<i>Editor Biographies</i>	<i>vii</i>
<i>Volume Editors</i>	<i>ix</i>
<i>Contributors to Volume 1</i>	<i>xv</i>
<i>Preface</i>	<i>xix</i>
1.01 Introduction: Significance of molecular inorganic chemistry <i>Risto S Laitinen</i>	1
<b>SECTION 1: STRUCTURE, BONDING, AND REACTIVITY IN INORGANIC MOLECULAR SYSTEMS</b>	
1.02 Main group metal coordination chemistry <i>Catherine E Housecroft and Edwin C Constable</i>	19
1.03 Low-coordinate compounds of heavier group 14–16 elements <i>Takahiro Sasamori, Vladimir Lee, Noriyoshi Nagahora, and Shogo Morisako</i>	118
1.04 Biradicals in main group chemistry: Synthesis, electronic structure, and application in small-molecule activation <i>Jonas Bresien, Liesa Eickhoff, Axel Schulz, and Edgar Zander</i>	165
1.05 Nonclassical carbenes as noninnocent ligands <i>Daniela I Bezuidenhout, George Kleinhans, and Aino J Karhu</i>	234
1.06 Frustrated lewis pairs in catalysis <i>Katarina Stefkova, Jamie L Carden, and Rebecca L Melen</i>	315
1.07 Chemistry with weakly coordinating aluminates $[\text{Al}(\text{OR}^{\text{F}})_4]^-$ and borates $[\text{B}(\text{OR}^{\text{F}})_4]^-$ : From fundamentals to application <i>Antoine Barthélemy, Philipp Dabringhaus, Eike Jacob, Hendrik Koger, David Röhner, Manuel Schmitt, Malte Sellin, and Krossing Ingo</i>	378
1.08 Noble-gas chemistry <i>Hélène PA Mercier, Mark R Bortolus, and Gary J Schrobilgen</i>	439
1.09 Syntheses and molecular structures of cyclic selenoethers and their derivatives <i>Raija Oilunkaniemi and Risto S Laitinen</i>	527
1.10 [FeFe]-Hydrogenase mimics containing heavy p block elements <i>Hassan Abul-Futouh and Wolfgang Weigand</i>	556



**SECTION 2: INTERMOLECULAR INTERACTIONS**

- 1.11 Computational modeling and characterization of secondary bonding in compounds of late p-block elements 572  
*Ignacio Vargas-Baca*
- 1.12 Halogen-bonded halogen(I) ion complexes 586  
*Jas S Ward, Khai-Nghi Truong, Mate Erdélyi, and Kari Rissanen*
- 1.13 Chalcogen bonding in supramolecular structures, anion recognition, and catalysis 602  
*Simon Kolb, Gwyndaf A Oliver, and Daniel B Werz*
- 1.14 Supramolecular chemistry of p-block elements 652  
*DS Wright and H-C Niu*
- 1.15 Metallophilic interactions 665  
*Linda H Doerrler, Cathlene Del Rosario, and Alice Fan*

**SECTION 3: INORGANIC CHAINS, RINGS, AND CAGES**

- 1.16 Molecular boron clusters 740  
*Igor B Sivaev*
- 1.17 Chain, ring, and cluster compounds of heavy group 13 elements (Al, Ga, In, Tl) 778  
*Gerald Linti and Michael Gast*
- 1.18 Aromatic compounds bearing heavy group 14 atoms in their molecular frameworks 843  
*Masaichi Saito*
- 1.19 Chain, ring, and cluster compounds of group 15 elements (P, As, Sb, Bi) 863  
*Martyn P Coles*
- 1.20 Zintl chemistry: From zintl ions to zintl clusters 903  
*Lei Qiao, John E McGrady, and Zhong-Ming Sun*
- 1.21 Polychalcogen molecules, ligands, and ions Part 1: Homo- and heteronuclear chalcogen rings 934  
*Risto S Laitinen, Raija Oilunkaniemi, Liam McGeachie, Paul F Kelly, and Roberto SP King*
- 1.22 Polychalcogen molecules, ligands, and ions Part 2: Catenated acyclic molecules, ions, and p-block element derivatives 970  
*Risto S Laitinen, Raija Oilunkaniemi, Tristram Chivers, Liam McGeachie, Paul F Kelly, and Roberto SP King*
- 1.23 Catenated compounds in group 17—polyhalides 1021  
*Lars Kloo*
- 1.24 Synthesis, carbon-polymetal bonding and applications of organometallic clusters 1050  
*Kui Xiao and Liang Zhao*

# EDITOR BIOGRAPHIES

---

## Editors in Chief

### Jan Reedijk



**Jan Reedijk** (1943) studied chemistry at Leiden University where he completed his Ph.D. (1968). After a few years in a junior lecturer position at Leiden University, he accepted a readership at Delft University of Technology in 1972. In 1979 he accepted a call for Professor of Chemistry at Leiden University. After 30 years of service, he retired from teaching in 2009 and remained as an emeritus research professor at Leiden University. In Leiden he has acted as Chair of the Department of Chemistry, and in 1993 he became the Founding Director of the Leiden Institute of Chemistry.

His major research activities have been in Coordination Chemistry and Bioinorganic Chemistry, focusing on biomimetic catalysis, molecular materials, and medicinal inorganic chemistry. Jan Reedijk was elected member of the Royal Netherlands Academy of Sciences in 1996 and he was knighted by the Queen of the Netherlands to the order of the Dutch Lion (2008). He is also lifetime member of the Finnish Academy of Sciences and Letters and of Academia Europaea. He has held visiting professorships in Cambridge (UK), Strasbourg (France), Münster (Germany), Riyadh (Saudi Arabia), Louvain-la-Neuve (Belgium), Dunedin (New Zealand), and Torun (Poland). In 1990 he served as President of the Royal Netherlands Chemical Society.

He has acted as the Executive Secretary of the International Conferences of Coordination Chemistry (1988–2012) and served IUPAC in the Division of Inorganic Chemistry, first as a member and later as (vice/past) president between 2005 and 2018. After his university retirement he remained active as research consultant and in IUPAC activities, as well as in several editorial jobs. For Elsevier, he acted as Editor-in-Chief of the *Reference Collection in Chemistry* (2013–2019), and together with Kenneth R. Poeppelmeier for *Comprehensive Inorganic Chemistry II* (2008–2013) and *Comprehensive Inorganic Chemistry III* (2019–present). From 2018 to 2020, he co-chaired the worldwide celebrations of the International Year of the Periodic Table 2019.

Jan Reedijk has published over 1200 papers (1965–2022; cited over 58000 times;  $h = 96$ ). He has supervised 90 Ph.D. students, over 100 postdocs, and over 250 MSc research students.

### Kenneth R. Poeppelmeier



**Kenneth R. Poeppelmeier** (1949) completed his undergraduate studies in chemistry at the University of Missouri (1971) and then volunteered as an instructor at Samoa College—United States Peace Corps in Western Samoa (1971–1974). He completed his Ph.D. (1978) in Inorganic Chemistry with John Corbett at Iowa State University (1978).

He joined the catalysis research group headed by John Longo at Exxon Research and Engineering Company, Corporate Research–Science Laboratories (1978–1984), where he collaborated with the reforming science group and Exxon Chemicals to develop the first zeolite-based light naphtha reforming catalyst. In 1984 he joined the Chemistry Department at Northwestern University and the recently formed Center for Catalysis and Surface Science (CCSS). He is the Charles E. and Emma H. Morrison Professor of Chemistry at Northwestern University and a NAISE Fellow joint with Northwestern University and the Chemical Sciences and Engineering Division, Argonne National Laboratory. Leadership positions held include Director, CCSS, Northwestern University; Associate Division Director for Science, Chemical Sciences and Engineering Division, Argonne National Laboratory; President of the Chicago Area Catalysis Club; Associate Director, NSF Science and Technology Center for Superconductivity; and Chairman of the ACS Solid State Subdivision of the Division of Inorganic Chemistry.

His major research activities have been in Solid State and Inorganic Materials Chemistry focusing on heterogeneous catalysis, solid state chemistry, and materials chemistry. His awards include National Science Council of Taiwan Lecturer (1991); Dow Professor of Chemistry (1992–1994); AAAS Fellow, the American Association for the Advancement of Science (1993); JSPS Fellow, Japan Society for the Promotion of Science (1997); Natural Science Foundation of China Lecturer (1999); National Science Foundation Creativity Extension Award (2000)

and 2022); Institut Universitaire de France Professor (2003); Chemistry Week in China Lecturer (2004); Lecturer in Solid State Chemistry, China (2005); Visitantes Distinguidos, Universidad Complutense Madrid (2008); Visiting Professor, Chinese Academy of Sciences (2011); 20 years of Service and Dedication Award to Inorganic Chemistry (2013); Elected foreign member of Spanish National Academy: Real Academia de Ciencia, Exactas, Fisicas y Naturales (2017); Elected Honorary Member of the Royal Society of Chemistry of Spain (RSEQ) (2018); and the TianShan Award, Xinjiang Uygur Autonomous Region of China (2021).

He has organized and was Chairman of the Chicago Great Lakes Regional ACS Symposium on Synthesis and Processing of Advanced Solid State Materials (1987), the New Orleans National ACS Symposium on Solid State Chemistry of Heterogeneous Oxide Catalysis, Including New Microporous Solids (1987), the Gordon Conference on Solid State Chemistry (1994) and the First European Gordon Conference on Solid State Chemistry (1995), the Spring Materials Research Society Symposium on Environmental Chemistry (1995), the Advisory Committee of Intense Pulsed Neutron Source (IPNS) Program (1996–1998), the Spring Materials Research Society Symposium on Perovskite Materials (2003), the 4th International Conference on Inorganic Materials, University of Antwerp (2004), and the Philadelphia National ACS Symposium on Homogeneous and Heterogeneous Oxidation Catalysis (2004).

He has served on numerous Editorial Boards, including *Chemistry of Materials*, *Journal of Alloys and Compounds*, *Solid State Sciences*, *Solid State Chemistry*, and *Science China Materials*, and has been a co-Editor for *Structure and Bonding*, an Associate Editor for *Inorganic Chemistry*, and co-Editor-in-Chief with Jan Reedijk for *Comprehensive Inorganic Chemistry II* (published 2013) and *Comprehensive Inorganic Chemistry III* (to be published in 2023). In addition, he has served on various Scientific Advisory Boards including for the World Premier International Research Center Initiative and Institute for Integrated Cell-Material Sciences Kyoto University, the European Center SOPRANO on Functional Electronic Metal Oxides, the Kyoto University Mixed-Anion Project, and the Dresden Max Planck Institute for Chemistry and Physics.

Kenneth Poeppelmeier has published over 500 papers (1971–2022) and cited over 28000 times (h-index = 84). He has supervised over 200 undergraduates, Ph.D. students, postdocs, and visiting scholars in research.



## VOLUME EDITORS

---

Risto S. Laitinen



**Risto S. Laitinen** is Professor Emeritus of Chemistry at the University of Oulu, Finland. He received the M.Sc and Ph.D. degrees from Helsinki University of Technology (currently Aalto University). His research interests are directed to synthetic, structural, and computational chemistry of chalcogen compounds focusing on selenium and tellurium. He has published 250 peer-reviewed articles and 15 book chapters and has edited 2 books: *Selenium and Tellurium Reagents: In Chemistry and Materials Science* with Raija Oilunkaniemi (Walther de Gruyter, 2019) and *Selenium and Tellurium Chemistry: From Small Molecules to Biomolecules and Materials* with Derek Woollins (Springer, 2011). He has also written 30 professional and popular articles in chemistry. He is the Secretary of the Division of Chemical Nomenclature and Structure Representation, International Union of Pure and Applied Chemistry, for the term 2016–2023. He served as Chair of the Board of Union of Finnish University Professors in 2007–2010. In 2017, Finnish Cultural Foundation (North Ostrobothnia regional fund) gave him an award for excellence in his activities for science and music. He has been a member of Finnish Academy of Science and Letters since 2003.

Vincent L. Pecoraro



**Professor Vincent L. Pecoraro** is a major contributor in the fields of inorganic, bioinorganic, and supramolecular chemistries. He has risen to the upper echelons of these disciplines with over 300 publications (an h-index of 92), 4 book editorships, and 5 patents. He has served the community in many ways including as an Associate Editor of *Inorganic Chemistry* for 20 years and now is President of the Society of Biological Inorganic Chemistry. Internationally, he has received a Le Studium Professorship, Blaise Pascal International Chair for Research, the Alexander von Humboldt Stiftung, and an Honorary PhD from Aix-Marseille University. His many US distinctions include the 2016 ACS Award for Distinguished Service in the Advancement of Inorganic Chemistry, the 2021 ACS/SCF FrancoAmerican Lectureship Prize, and being elected a Fellow of the ACS and AAAS. He also recently cofounded a Biomedical Imaging company, VIEWaves. In 2022, he was ranked as one of the world's top 1000 most influential chemists.

Zijian Guo



**Professor Zijian Guo** received his Ph.D. from the University of Padova and worked as a postdoctoral research fellow at Birkbeck College, the University of London. He also worked as a research associate at the University of Edinburgh. His research focuses on the chemical biology of metals and metallodrugs and has authored or co-authored more than 400 peer-reviewed articles on basic and applied research topics. He was awarded the First Prize in Natural Sciences from Ministry of Education of China in 2015, the Luigi Sacconi Medal from the Italian Chemical Society in 2016, and the Outstanding Achievement Award from the Society of the Asian Biological Inorganic Chemistry in 2020. He founded Chemistry and Biomedicine Innovation Center (ChemBIC) in Nanjing University in 2019, and is serving as the Director of ChemBIC since then. He was elected to the Fellow of the Chinese Academy of Sciences in 2017. He served as Associated Editor of *Coord. Chem. Rev* and an editorial board member of several other journals.

Daniel C. Fredrickson



**Daniel C. Fredrickson** is a Professor in the Department of Chemistry at the University of Wisconsin-Madison. He completed his BS in Biochemistry at the University of Washington in 2000, where he gained his first experiences with research and crystals in the laboratory of Prof. Bart Kahr. At Cornell University, he then pursued theoretical investigations of bonding in intermetallic compounds, the vast family of solid state compounds based on metallic elements, under the mentorship of Profs. Stephen Lee and Roald Hoffmann, earning his Ph.D. in 2005. Interested in the experimental and crystallographic aspects of complex intermetallics, he then carried out postdoctoral research from 2005 to 2008 with Prof. Sven Lidin at Stockholm University. Since starting at UW-Madison in 2009, his research group has created theory-driven approaches to the synthesis and discovery of new intermetallic phases and understanding the origins of their structural features. Some of his key research contributions are the development of the DFT-Chemical Pressure Method, the discovery of isolobal bonds for the generalization of the 18 electron rule to intermetallic phases, models for the emergence of incommensurate modulations in these compounds, and various design strategies for guiding complexity in solid state structures.

Patrick M. Woodward



**Professor Patrick M. Woodward** received BS degrees in Chemistry and General Engineering from Idaho State University in 1991, an MS in Materials Science, and a Ph.D. in Chemistry from Oregon State University (1996) under the supervision of Art Sleight. After a postdoctoral appointment in the Physics Department at Brookhaven National Laboratory (1996–1998), he joined the faculty at Ohio State University in 1998, where he holds the rank of Professor in the Department of Chemistry and Biochemistry. He is a Fellow of the American Chemical Society (2020) and a recipient of an Alfred P. Sloan Fellowship (2004) and an NSF Career Award (2001). He has co-authored two textbooks: *Solid State Materials Chemistry* and the popular general chemistry textbook, *Chemistry: The Central Science*. His research interests revolve around the discovery of new materials and understanding links between the composition, structure, and properties of extended inorganic and hybrid solids.

**P. Shiv Halasyamani**

**Professor P. Shiv Halasyamani** earned his BS in Chemistry from the University of Chicago (1992) and his Ph.D. in Chemistry under the supervision of Prof. Kenneth R. Poeppelmeier at Northwestern University (1996). He was a Postdoctoral Fellow and Junior Research Fellow at Christ Church College, Oxford University, from 1997 to 1999. He began his independent academic career in the Department of Chemistry at the University of Houston in 1999 and has been a Full Professor since 2010. He was elected as a Fellow of the American Association for the Advancement of Science (AAAS) in 2019 and is currently an Associate Editor of the ACS journals *Inorganic Chemistry* and *ACS Organic & Inorganic Au*. His research interests involve the design, synthesis, crystal growth, and characterization of new functional inorganic materials.

**Ram Seshadri**

**Ram Seshadri** received his Ph.D. in Solid State Chemistry from the Indian Institute of Science (IISc), Bangalore, working under the guidance of Professor C. N. R. Rao FRS. After some years as a Postdoctoral Fellow in Europe, he returned to IISc as an Assistant Professor in 1999. He moved to the Materials Department (College of Engineering) at UC Santa Barbara in 2002. He was recently promoted to the rank of Distinguished Professor in the Materials Department and the Department of Chemistry and Biochemistry in 2020. He is also the Fred and Linda R. Wudl Professor of Materials Science and Director of the Materials Research Laboratory: A National Science Foundation Materials Research Science and Engineering Center (NSF-MRSEC). His work broadly addresses the topic of structure–composition–property relations in crystalline inorganic and hybrid materials, with a focus on magnetic materials and materials for energy conversion and storage. He is Fellow of the Royal Society of Chemistry, the American Physical Society, and the American Association for the Advancement of Science. He serves as Associate Editor of the journals, *Annual Reviews of Materials Research* and *Chemistry of Materials*.

**Serena Cussen**

**Serena Cussen** née Corr studied chemistry at Trinity College Dublin, completing her doctoral work under Yuri Gun'ko. She then joined the University of California, Santa Barbara, working with Ram Seshadri as a postdoctoral researcher. She joined the University of Kent as a lecturer in 2009. She moved to the University of Glasgow in 2013 and was made Professor in 2018. She moved to the University of Sheffield as a Chair in Functional Materials and Professor in Chemical and Biological Engineering in 2018, where she now serves as Department Head. She works on next-generation battery materials and advanced characterization techniques for the structure and properties of nanomaterials. Serena is the recipient of several awards including the *Journal of Materials Chemistry* Lectureship of the Royal Society of Chemistry. She previously served as Associate Editor of Royal Society of Chemistry journal *Nanoscale* and currently serves as Associate Editor for the Institute of Physics journal *Progress in Energy*.



Rutger A. van Santen



**Rutger A. van Santen** received his Ph.D. in 1971 in Theoretical Chemistry from the University of Leiden, The Netherlands. In the period 1972–1988, he became involved with catalysis research when employed by Shell Research in Amsterdam and Shell Development Company in Houston. In 1988, he became Full Professor of Catalysis at the Technical University Eindhoven. From 2010 till now he is Emeritus Professor and Honorary Institute Professor at Technical University Eindhoven. He is a member of Royal Dutch Academy of Sciences and Arts and Foreign Associate of the United States National Academy of Engineering (NAE). He has received several prestigious awards: the 1981 golden medal of the Royal Dutch Chemical Society; in 1992, the F.G. Chiappetta award of the North American Catalysis Society; in 1997, the Spinoza Award from the Dutch Foundation for Pure and Applied Research; and in 2001, the Alwin Mittasch Medal Dechema, Germany, among others. His main research interests are computational heterogeneous catalysis and complex chemical systems theory. He has published over 700 papers, 16 books, and 22 patents.

Emiel J. M. Hensen



**Emiel J. M. Hensen** received his Ph.D. in Catalysis in 2000 from Eindhoven University of Technology, The Netherlands. Between 2000 and 2008, he worked at the University of Amsterdam, Shell Research in Amsterdam, and Eindhoven University of Technology on several topics in the field of heterogeneous catalysis. Since July 2009, he is Full Professor of Inorganic Materials and Catalysis at TU/e. He was a visiting professor at the Katholieke Universiteit Leuven (Belgium, 2001–2016) and at Hokkaido University (Japan, 2016). He is principal investigator and management team member of the gravitation program Multiscale Catalytic Energy Conversion, elected member of the Advanced Research Center Chemical Building Blocks Consortium, and chairman of the Netherlands Institute for Catalysis Research (NIOK). Hensen was Head of the Department of Chemical Engineering and Chemistry of Eindhoven University of Technology from 2016 to 2020. Hensen received Veni, Vidi, Vici, and Casmir grant awards from the Netherlands Organisation for Scientific Research. His main interests are in mechanism of heterogeneous catalysis combining experimental and computation studies. He has published over 600 papers, 20 book chapters, and 7 patents.

Artem M. Abakumov



**Artem M. Abakumov** graduated from the Department of Chemistry at Moscow State University in 1993, received his Ph.D. in Chemistry from the same University in 1997, and then continued working as a Researcher and Vice-Chair of Inorganic Chemistry Department. He spent about 3 years as a postdoctoral fellow and invited professor in the Electron Microscopy for Materials Research (EMAT) laboratory at the University of Antwerp and joined EMAT as a research leader in 2008. Since 2015 he holds a Full Professor position at Skolkovo Institute of Science and Technology (Skoltech) in Moscow, leading Skoltech Center for Energy Science and Technology as a Director. His research interests span over a wide range of subjects, from inorganic chemistry, solid state chemistry, and crystallography to battery materials and transmission electron microscopy. He has extended experience in characterization of metal-ion battery electrodes and electrocatalysts with advanced TEM techniques that has led to a better understanding of charge–discharge mechanisms, redox reactions, and associated structural transformations in various classes of cathode materials on different spatial scales. He has published over 350 papers, 5 book chapters, and 12 patents.

Keith J. Stevenson



**Keith J. Stevenson** received his Ph.D. in 1997 from the University of Utah under the supervision of Prof. Henry White. Subsequently, he held a postdoctoral appointment at Northwestern University (1997–2000) and a tenured faculty appointment (2000–2015) at the University of Texas at Austin. At present, he is leading the development of a new graduate level university (Skolkovo Institute for Science and Technology) in Moscow, Russia, where he is Provost and the former Director of the Center for Energy Science and Technology (CEST). To date he has published over 325 peer-reviewed publications, 14 patents, and 6 book chapters in this field. He is a recipient of Society of Electroanalytical Chemistry Charles N. Reilly Award (2021).

Evgeny V. Antipov



**Evgeny V. Antipov** graduated from the Department of Chemistry at Moscow State University in 1981, received his Ph.D. in Chemistry in 1986, DSc degree in Chemistry in 1998, and then continued working at the same University as a Researcher, Head of the Laboratory of Inorganic Crystal Chemistry, Professor, Head of Laboratory of fundamental research on aluminum production, and Head of the Department of Electrochemistry. Since 2018 he also holds a professor position at Skolkovo Institute of Science and Technology (Skoltech) in Moscow. Currently his research interests are mainly focused on inorganic materials for application in batteries and fuel cells. He has published more than 400 scientific articles and 14 patents.

Vivian W.W. Yam



**Professor Vivian W.W. Yam** is the Chair Professor of Chemistry and Philip Wong Wilson Wong Professor in Chemistry and Energy at The University of Hong Kong. She received both her B.Sc (Hons) and Ph.D. from The University of Hong Kong. She was elected to Member of Chinese Academy of Sciences, International Member (Foreign Associate) of US National Academy of Sciences, Foreign Member of Academia Europaea, Fellow of TWAS, and Founding Member of Hong Kong Academy of Sciences. She was Laureate of 2011 L'Oréal-UNESCO For Women in Science Award. Her research interests include inorganic and organometallic chemistry, supramolecular chemistry, photophysics and photochemistry, and metal-based molecular functional materials for sensing, organic optoelectronics, and energy research.

Also see: <https://chemistry.hku.hk/wwym>.

David L. Bryce



**David L. Bryce** (B.Sc (Hons), 1998, Queen's University; Ph.D., 2002, Dalhousie University; postdoctoral fellow, 2003–04, NIDDK/NIH) is Full Professor and University Research Chair in Nuclear Magnetic Resonance at the University of Ottawa in Canada. He is the past Chair of the Department of Chemistry and Biomolecular Sciences, a Fellow of the Royal Society of Chemistry, and an elected Fellow of the Royal Society of Canada. His research interests include solid-state NMR of low-frequency quadrupolar nuclei, NMR studies of materials, NMR crystallography, halogen bonding, mechanochemistry, and quantum chemical interpretation of NMR interaction tensors. He is the author of approximately 200 scientific publications and co-author of 1 book. He is the Editor-in-Chief of *Solid State Nuclear Magnetic Resonance* and Section Editor (Magnetic Resonance and Molecular Spectroscopy) for the *Canadian Journal of Chemistry*. He has served as the Chair of Canada's National Ultrahigh-Field NMR Facility for Solids and is a past co-chair of the International Society for Magnetic Resonance conference and of the Rocky Mountain Conference on Magnetic Resonance Solid-State NMR Symposium. His work has been recognized with the Canadian Society for Chemistry Keith Laidler Award and with the Gerhard Herzberg Award of the Canadian Association of Analytical Sciences and Spectroscopy.

Paul R. Raithby



**Paul R. Raithby** obtained his B.Sc (1973) and Ph.D. (1976) from Queen Mary College, University of London, working for his Ph.D. in structural inorganic chemistry. He moved to the University of Cambridge in 1976, initially as a postdoctoral researcher and then as a faculty member. In 2000, he moved to the University of Bath to take up the Chair of Inorganic Chemistry when he remains to the present day, having been awarded an Emeritus Professorship in 2022. His research interests have spanned the chemistry of transition metal cluster compounds, platinum acetylide complexes and oligomers, and lanthanide complexes, and he uses laboratory and synchrotron-based X-ray crystallographic techniques to determine the structures of the complexes and to study their dynamics using time-resolved photocrystallographic methods.

Angus P. Wilkinson



**Angus P. Wilkinson** completed his bachelors (1988) and doctoral (1992) degrees in chemistry at Oxford University in the United Kingdom. He spent a postdoctoral period in the Materials Research Laboratory, University of California, Santa Barbara, prior to joining the faculty at the Georgia Institute of Technology as an assistant professor in 1993. He is currently a Professor in both the Schools of Chemistry and Biochemistry, and Materials Science and Engineering, at the Georgia Institute of Technology. His research in the general area of inorganic materials chemistry makes use of synchrotron X-ray and neutron scattering to better understand materials synthesis and properties.



# CONTRIBUTORS TO VOLUME 1

---

Hassan Abul-Futouh

*Faculty of Science, Department of Chemistry, The Hashemite University, Zarqa, Jordan*

Antoine Barthélemy

*Albert-Ludwigs-Universität Freiburg, Institut für Anorganische und Analytische Chemie and Freiburg Materials Research Center FMF, Freiburg, Germany*

Daniela I Bezuidenhout

*Laboratory of Inorganic Chemistry, Environmental and Chemical Engineering, University of Oulu, Oulu, Finland*

Mark R Bortolus

*Department of Chemistry, McMaster University, Hamilton, Ontario, Canada*

Jonas Bresien

*Institute of Chemistry, University of Rostock, Rostock, Germany*

Jamie L Carden

*Cardiff Catalysis Institute, School of Chemistry, Cardiff University, Cardiff, United Kingdom*

Tristram Chivers

*Department of Chemistry, University of Calgary, Calgary, AB, Canada*

Martyn P Coles

*School of Chemical and Physical Sciences, Victoria University of Wellington, Wellington, New Zealand*

Edwin C Constable

*Department of Chemistry, University of Basel, Basel, Switzerland*

Philipp Dabringhaus

*Albert-Ludwigs-Universität Freiburg, Institut für Anorganische und Analytische Chemie and Freiburg Materials Research Center FMF, Freiburg, Germany*

Cathlene Del Rosario

*Department of Chemistry, Boston University, Boston, MA, United States*

Linda H Doerrer

*Department of Chemistry, Boston University, Boston, MA, United States*

Liesa Eickhoff

*Institute of Chemistry, University of Rostock, Rostock, Germany*

Mate Erdélyi

*Department of Chemistry - BMC, Uppsala University, Uppsala, Sweden*

Alice Fan

*Department of Chemistry, Boston University, Boston, MA, United States*

Michael Gast

*Ruprecht-Karls-Universität Heidelberg, Anorganisch-Chemisches Institut, Heidelberg, Germany*

Catherine E Housecroft

*Department of Chemistry, University of Basel, Basel, Switzerland*

Krossing Ingo

*Albert-Ludwigs-Universität Freiburg, Institut für Anorganische und Analytische Chemie and Freiburg Materials Research Center FMF, Freiburg, Germany*

Eike Jacob

*Albert-Ludwigs-Universität Freiburg, Institut für Anorganische und Analytische Chemie and Freiburg Materials Research Center FMF, Freiburg, Germany*

Aino J Karhu

*Laboratory of Inorganic Chemistry, Environmental and Chemical Engineering, University of Oulu, Oulu, Finland*

Paul F Kelly

*Department of Chemistry, Loughborough University, Loughborough, Leicestershire, United Kingdom*

Roberto SP King

*Foster + Freeman Ltd, Evesham, United Kingdom*

George Kleinhans

*Laboratory of Inorganic Chemistry, Environmental and Chemical Engineering, University of Oulu, Oulu, Finland*

Lars Kloo

*Applied Physical Chemistry, Department of Chemistry, KTH Royal Institute of Technology, Stockholm, Sweden*

Hendrik Koger

*Albert-Ludwigs-Universität Freiburg, Institut für Anorganische und Analytische Chemie and Freiburg Materials Research Center FMF, Freiburg, Germany*

Simon Kolb

*Technische Universität Braunschweig, Institute of Organic Chemistry, Braunschweig, Germany*

Risto S Laitinen

*Laboratory of Inorganic Chemistry, Environmental and Chemical Engineering, University of Oulu, Oulu, Finland*

Vladimir Lee

*Division of Chemistry, Faculty of Pure and Applied Sciences, University of Tsukuba, Tsukuba, Japan*

Gerald Linti

*Ruprecht-Karls-Universität Heidelberg, Anorganisch-Chemisches Institut, Heidelberg, Germany*

Liam McGeachie

*Laboratory of Inorganic Chemistry, Environmental and Chemical Engineering, University of Oulu, Oulu, Finland*

John E McGrady

*Department of Chemistry, University of Oxford, Oxford, United Kingdom*

Rebecca L Melen

*Cardiff Catalysis Institute, School of Chemistry, Cardiff University, Cardiff, United Kingdom*

Hélène PA Mercier

*Department of Chemistry, McMaster University, Hamilton, Ontario, Canada*

Shogo Morisako

*Division of Chemistry, Faculty of Pure and Applied Sciences, University of Tsukuba, Tsukuba, Japan; and Tsukuba Research Center for Energy Materials Sciences (TREMS), University of Tsukuba, Tsukuba, Japan*

Noriyoshi Nagahora

*Department of Chemistry, Faculty of Science, Fukuoka University, Fukuoka, Japan*

H-C Niu

*Yusuf Hamied Department of Chemistry, University of Cambridge, Cambridge, United Kingdom*

Raija Oilunkaniemi

*Laboratory of Inorganic Chemistry, Environmental and Chemical Engineering, University of Oulu, Oulu, Finland*

Gwyndaf A Oliver

*Technische Universität Braunschweig, Institute of Organic Chemistry, Braunschweig, Germany*

Lei Qiao

*School of Materials Science and Engineering, State Key Laboratory of Elemento-Organic Chemistry, Nankai University, Tianjin, China*

Kari Rissanen

*Department of Chemistry, University of Jyväskylä, Jyväskylä, Finland*

David Röhner

*Albert-Ludwigs-Universität Freiburg, Institut für Anorganische und Analytische Chemie and Freiburg Materials Research Center FMF, Freiburg, Germany*

Masaichi Saito

*Department of Chemistry, Graduate School of Science and Engineering, Saitama University, Saitama, Saitama, Japan*

Takahiro Sasamori

*Division of Chemistry, Faculty of Pure and Applied Sciences, University of Tsukuba, Tsukuba, Japan; and Tsukuba Research Center for Energy Materials Sciences (TREMS), University of Tsukuba, Tsukuba, Japan*

Manuel Schmitt

*Albert-Ludwigs-Universität Freiburg, Institut für Anorganische und Analytische Chemie and Freiburg Materials Research Center FMF, Freiburg, Germany*

Gary J Schrobilgen

*Department of Chemistry, McMaster University, Hamilton, Ontario, Canada*

Axel Schulz

*Institute of Chemistry, University of Rostock, Rostock, Germany*

Malte Sellin

*Albert-Ludwigs-Universität Freiburg, Institut für Anorganische und Analytische Chemie and Freiburg Materials Research Center FMF, Freiburg, Germany*

Igor B Sivaev

*A.N. Nesmeyanov Institute of Organoelement Compounds, Russian Academy of Sciences, Moscow, Russia*

Katarina Stefkova  
*Cardiff Catalysis Institute, School of Chemistry, Cardiff University, Cardiff, United Kingdom*

Zhong-Ming Sun  
*School of Materials Science and Engineering, State Key Laboratory of Elemento-Organic Chemistry, Nankai University, Tianjin, China*

Khai-Nghi Truong  
*Department of Chemistry, University of Jyväskylä, Jyväskylä, Finland*

Ignacio Vargas-Baca  
*Department of Chemistry and Chemical Biology, McMaster University, Hamilton, ON, Canada*

Jas S Ward  
*Department of Chemistry, University of Jyväskylä, Jyväskylä, Finland*

Wolfgang Weigand  
*Institut für Anorganische und Analytische Chemie, Friedrich-Schiller-Universität Jena, Jena, Germany*

Daniel B Werz  
*Technische Universität Braunschweig, Institute of Organic Chemistry, Braunschweig, Germany*

DS Wright  
*Yusuf Hamied Department of Chemistry, University of Cambridge, Cambridge, United Kingdom*

Kui Xiao  
*Key Laboratory of Bioorganic Phosphorus Chemistry and Chemical Biology (Ministry of Education), Department of Chemistry, Tsinghua University, Beijing, China*

Edgar Zander  
*Institute of Chemistry, University of Rostock, Rostock, Germany*

Liang Zhao  
*Key Laboratory of Bioorganic Phosphorus Chemistry and Chemical Biology (Ministry of Education), Department of Chemistry, Tsinghua University, Beijing, China*

# PREFACE

---

Comprehensive Inorganic Chemistry III is a new multi-reference work covering the broad area of Inorganic Chemistry. The work is available both in print and in electronic format. The 10 Volumes review significant advances and examines topics of relevance to today's inorganic chemists with a focus on topics and results after 2012.

The work is focusing on new developments, including interdisciplinary and high-impact areas. Comprehensive Inorganic Chemistry III, specifically focuses on main group chemistry, biological inorganic chemistry, solid state and materials chemistry, catalysis and new developments in electrochemistry and photochemistry, as well as on NMR methods and diffractions methods to study inorganic compounds.

The work continues our 2013 work Comprehensive Inorganic Chemistry II, but at the same time adds new volumes on emerging research areas and techniques used to study inorganic compounds. The new work is also highly complementary to other recent Elsevier works in Coordination Chemistry and Organometallic Chemistry thereby forming a trio of works covering the whole of modern inorganic chemistry, most recently COMC-4 and CCC-3. The rapid pace of developments in recent years in all areas of chemistry, particularly inorganic chemistry, has again created many challenges to provide a contemporary up-to-date series.

As is typically the challenge for Multireference Works (MRWs), the chapters are designed to provide a valuable long-standing scientific resource for both advanced students new to an area as well as researchers who need further background or answers to a particular problem on the elements, their compounds, or applications. Chapters are written by teams of leading experts, under the guidance of the Volume Editors and the Editors-in-Chief. The articles are written at a level that allows undergraduate students to understand the material, while providing active researchers with a ready reference resource for information in the field. The chapters are not intended to provide basic data on the elements, which are available from many sources including the original CIC-I, over 50-years-old by now, but instead concentrate on applications of the elements and their compounds and on high-level techniques to study inorganic compounds.

## **Vol. 1: Synthesis, Structure, and Bonding in Inorganic Molecular Systems; Risto S. Laitinen**

In this Volume the editor presents an historic overview of Inorganic Chemistry starting with the birth of inorganic chemistry after Berzelius, and a focus on the 20th century including an overview of "inorganic" Nobel Prizes and major discoveries, like inert gas compounds. The most important trends in the field are discussed in an historic context. The bulk of the Volume consists of 3 parts, i.e., (1) Structure, bonding, and reactivity in inorganic molecular systems; (2) Intermolecular interactions, and (3) Inorganic Chains, rings, and cages. The volume contains 23 chapters.

Part 1 contains chapters dealing with compounds in which the heavy p-block atom acts as a central atom. Some chapters deal with the rich synthetic and structural chemistry of noble gas compounds, low-coordinate p-block elements, biradicals, iron-only hydrogenase mimics, and macrocyclic selenoethers. Finally, the chemistry and application of weakly coordinating anions, the synthesis, structures, and reactivity of carbenes containing non-innocent ligands, frustrated Lewis pairs in metal-free catalysis are discussed. Part 2 discusses secondary bonding interactions that play an important role in the properties of bulk materials. It includes a chapter on the general theoretical considerations of secondary bonding interactions, including halogen and chalcogen bonding. This section is concluded by the update of the host-guest chemistry of the molecules of p-block elements and by a comprehensive review of closed-shell metallophilic interactions. The third part of the Volume is dedicated to chain, ring and cage (or cluster) compounds in molecular inorganic chemistry. Separate

chapters describe the recent chemistry of boron clusters, as well as the chain, ring, and cage compounds of Group 13 and 15, and 16 elements. Also, aromatic compounds bearing heavy Group 14 atoms, polyhalogenide anions and Zintl-clusters are presented.

### **Vol. 2: Bioinorganic Chemistry and Homogeneous Biomimetic Inorganic Catalysis; Vincent L. Pecoraro and Zijian Guo**

In this Volume, the editors have brought together 26 chapters providing a broad coverage of many of the important areas involving metal compounds in biology and medicine. Readers interested in fundamental biochemistry that is assisted by metal ion catalysis, or in uncovering the latest developments in diagnostics or therapeutics using metal-based probes or agents, will find high-level contributions from top scientists. In the first part of the Volume topics dealing with metals interacting with proteins and nucleic acids are presented (e.g., siderophores, metallophores, homeostasis, biomineralization, metal-DNA and metal-RNA interactions, but also with zinc and cobalt enzymes). Topics dealing with iron-sulfur clusters and heme-containing proteins, enzymes dealing with dinitrogen fixation, dihydrogen and dioxygen production by photosynthesis will also be discussed, including bioinspired model systems.

In the second part of the Volume the focus is on applications of inorganic chemistry in the field of medicine: e.g., clinical diagnosis, curing diseases and drug targeting. Platinum, gold and other metal compounds and their mechanism of action will be discussed in several chapters. Supramolecular coordination compounds, metal organic frameworks and targeted modifications of higher molecular weight will also be shown to be important for current and future therapy and diagnosis.

### **Vol. 3: Theory and Bonding of Inorganic Non-molecular Systems; Daniel C. Fredrickson**

This volume consists of 15 chapters that build on symmetry-based expressions for the wavefunctions of extended structures toward models for bonding in solid state materials and their surfaces, algorithms for the prediction of crystal structures, tools for the analysis of bonding, and theories for the unique properties and phenomena that arise in these systems. The volume is divided into four parts along these lines, based on major themes in each of the chapters. These are: Part 1: Models for extended inorganic structures, Part 2: Tools for electronic structure analysis, Part 3: Predictive exploration of new structures, and Part 4: Properties and phenomena.

### **Vol. 4: Solid State Inorganic Chemistry; P. Shiv Halasyamani and Patrick M. Woodward**

In a broad sense the field of inorganic chemistry can be broken down into substances that are based on molecules and those that are based on extended arrays linked by metallic, covalent, polar covalent, or ionic bonds (i.e., extended solids). The field of solid-state inorganic chemistry is largely concerned with elements and compounds that fall into the latter group. This volume contains nineteen chapters covering a wide variety of solid-state inorganic materials. These chapters largely focus on materials with properties that underpin modern technology. Smart phones, solid state lighting, batteries, computers, and many other devices that we take for granted would not be possible without these materials. Improvements in the performance of these and many other technologies are closely tied to the discovery of new materials or advances in our ability to synthesize high quality samples. The organization of most chapters is purposefully designed to emphasize how the exceptional physical properties of modern materials arise from the interplay of composition, structure, and bonding. Not surprisingly this volume has considerable overlap with both Volume 3 (Theory and Bonding of Inorganic Non-molecular Systems) and Volume 5 (Inorganic Materials Chemistry). We anticipate that readers who are interested in this volume will find much of interest in those volumes and vice versa

### **Vol. 5: Inorganic Materials Chemistry; Ram Seshadri and Serena Cussen**

This volume has adopted the broad title of Inorganic Materials Chemistry, but as readers would note, the title could readily befit articles in other volumes as well. In order to distinguish contributions in this volume from



those in other volumes, the editors have chosen to use as the organizing principle, the role of synthesis in developing materials, reflected by several of the contributions carrying the terms “synthesis” or “preparation” in the title. It should also be noted that the subset of inorganic materials that are the focus of this volume are what are generally referred to as functional materials, i.e., materials that carry out a function usually through the way they respond to an external stimulus such as light, or thermal gradients, or a magnetic field.

### **Vol. 6: Heterogeneous Inorganic Catalysis; Rutger A. van Santen and Emiel J. M. Hensen**

This Volume starts with an introductory chapter providing an excellent discussion of single sites in metal catalysis. This chapter is followed by 18 chapters covering a large part of the field. These chapters have been written with a focus on the synthesis and characterization of catalytic complexity and its relationship with the molecular chemistry of the catalytic reaction. In the 1950s with the growth of molecular inorganic chemistry, coordination chemistry and organometallic chemistry started to influence the development of heterogeneous catalysis. A host of new reactions and processes originate from that time. In this Volume chapters on major topics, like promoted Fischer-Tropsch catalysts, structure sensitivity of well-defined alloy surfaces in the context of oxidation catalysis and electrocatalytic reactions, illustrate the broadness of the field. Molecular heterogeneous catalysts rapidly grew after high-surface synthetic of zeolites were introduced; so, synthesis, structure and nanopore chemistry in zeolites is presented in a number of chapters. Also, topics like nanocluster activation of zeolites and supported zeolites are discussed. Mechanistically important chapters deal with imaging of single atom catalysts. An important development is the use of reducible supports, such as  $\text{CeO}_2$  or  $\text{Fe}_2\text{O}_3$  where the interaction between the metal and support is playing a crucial role.

### **Vol. 7: Inorganic Electrochemistry; Keith J. Stevenson, Evgeny V. Antipov and Artem M. Abakumov**

This volume bridges several fields across chemistry, physics and material science. Perhaps this topic is best associated with the book “Inorganic Electrochemistry: Theory, Practice and Applications” by Piero Zanello that was intended to introduce inorganic chemists to electrochemical methods for study of primarily molecular systems, including metallocenes, organometallic and coordination complexes, metal complexes of redox active ligands, metal-carbonyl clusters, and proteins. The emphasis in this Volume of CIC III is on the impact of inorganic chemistry on the field of material science, which has opened the gateway for inorganic chemists to use more applied methods to the broad areas of electrochemical energy storage and conversion, electrocatalysis, electroanalysis, and electrosynthesis. In recognition of this decisive impact, the Nobel Prize in Chemistry of 2019 was awarded to John B. Goodenough, M. Stanley Whittingham, and Akira Yoshino for the development of the lithium-ion battery.

### **Vol. 8: Inorganic Photochemistry; Vivian W. W. Yam**

In this Volume the editor has compiled 19 chapters discussing recent developments in a variety of developments in the field. The introductory chapter overviews the several topics, including photoactivation and imaging reagents. The first chapters include a discussion of using luminescent coordination and organometallic compounds for organic light-emitting diodes (OLEDs) and applications to highlight the importance of developing future highly efficient luminescent transition metal compounds. The use of metal compounds in photo-induced bond activation and catalysis is highlighted by non-sacrificial photocatalysis and redox photocatalysis, which is another fundamental area of immense research interest and development. This work facilitates applications like biological probes, drug delivery and imaging reagents. Photochemical  $\text{CO}_2$  reduction and water oxidation catalysis has been addressed in several chapters. Use of such inorganic compounds in solar fuels and photocatalysis remains crucial for a sustainable environment. Finally, the photophysics and photochemistry of lanthanoid compounds is discussed, with their potential use of doped lanthanoids in luminescence imaging reagents.

**Vol. 9: NMR of Inorganic Nuclei; David L. Bryce**

Nuclear magnetic resonance (NMR) spectroscopy has long been established as one of the most important analytical tools at the disposal of the experimental chemist. The isotope-specific nature of the technique can provide unparalleled insights into local structure and dynamics. As seen in the various contributions to this Volume, applications of NMR spectroscopy to inorganic systems span the gas phase, liquid phase, and solid state. The nature of the systems discussed covers a very wide range, including glasses, single-molecule magnets, energy storage materials, bioinorganic systems, nanoparticles, catalysts, and more. The focus is largely on isotopes other than  $^1\text{H}$  and  $^{13}\text{C}$ , although there are clearly many applications of NMR of these nuclides to the study of inorganic compounds and materials. The value of solid-state NMR in studying the large percentage of nuclides which are quadrupolar (spin  $I > \frac{1}{2}$ ) is apparent in the various contributions. This is perhaps to be expected given that rapid quadrupolar relaxation can often obfuscate the observation of these resonances in solution.

**Vol. 10: X-ray, Neutron and Electron Scattering Methods in Inorganic Chemistry; Angus P. Wilkinson and Paul R. Raithby**

In this Volume the editors start with an introduction on the recent history and improvements of the instrumentation, source technology and user accessibility of synchrotron and neutron facilities worldwide, and they explain how these techniques work. The modern facilities now allow inorganic chemists to carry out a wide variety of complex experiments, almost on a day-to-day basis, that were not possible in the recent past. Past editions of Comprehensive Inorganic Chemistry have included many examples of successful synchrotron or neutron studies, but the increased importance of such experiments to inorganic chemists motivated us to produce a separate volume in CIC III dedicated to the methodology developed and the results obtained.

The introduction chapter is followed by 15 chapters describing the developments in the field. Several chapters are presented covering recent examples of state-of-the-art experiments and refer to some of the pioneering work leading to the current state of the science in this exciting area. The editors have recognized the importance of complementary techniques by including chapters on electron crystallography and synchrotron radiation sources. Chapters are present on applications of the techniques in e.g., spin-crossover materials and catalytic materials, and in the use of time-resolved studies on molecular materials. A chapter on the worldwide frequently used structure visualization of crystal structures, using PLATON/PLUTON, is also included. Finally, some more specialized studies, like Panoramic (in beam) studies of materials synthesis and high-pressure synthesis are present. Direct observation of transient species and chemical reactions in a pore observed by synchrotron radiation and X-ray transient absorption spectroscopies in the study of excited state structures, and ab initio structure solution using synchrotron powder diffraction, as well as local structure determination using total scattering data, are impossible and unthinkable without these modern diffraction techniques.

Jan Reedijk, *Leiden, The Netherlands*  
Kenneth R. Poeppelmeier, *Illinois, United States*  
March 2023

## 1.01 Introduction: Significance of molecular inorganic chemistry

Risto S. Laitinen, Laboratory of Inorganic Chemistry, Environmental and Chemical Engineering, University of Oulu, Oulu, Finland

© 2023 Elsevier Ltd. All rights reserved.

1.01.1	Birth of inorganic chemistry	1
1.01.2	Inorganic chemistry in the 20th century	3
1.01.3	Current trends in molecular inorganic chemistry	5
1.01.3.1	General	5
1.01.3.2	Multiple bonding in p-block compounds	6
1.01.3.3	Secondary bonding interactions	8
1.01.3.4	Small-molecule activation	9
1.01.3.5	Weakly coordinating anions	12
1.01.3.6	Biradicals and biradicaloids	13
1.01.4	Volume 1 of Comprehensive Inorganic Chemistry III	15
References		17

### Abstract

Whereas inorganic substances have been known and studied since the antiques, it is only during the 19th century that inorganic chemistry was born as an independent scientific discipline. The advances during the 20th, which have been made in inorganic molecular chemistry, have had an impact in the development of the whole field of chemistry and physical sciences. Several species with novel bonding arrangements, unprecedented structures, and unusual reactivities have been prepared comprising also compounds, which at the time were regarded impossible. The current driving force in chemical research arises from demands of materials science to establish the relationship of the molecular and electronic structures with the bulk properties of the materials. Molecular level understanding is needed to develop further electrical conductors, semiconductors, insulators, coatings, ceramics, catalysts, nanotubes, polymers, and thin films, all of which play a significant role in modern technology. The need to replace fossil fuels demands the development of environmentally friendlier energy sources in which molecular inorganic chemistry plays one of the a key roles. This chapter briefly outlines some important developments in bonding and reactivity of molecular inorganic compounds comprising (a) multiple bonding in p-block compounds, (b) secondary bonding interactions, (c) small-molecule activation, (d) weakly coordinating anions, and (e) biradicals and biradicaloids. This list is not exhaustive but serves as an introduction to the 23 chapters in Volume 1 of *Comprehensive Inorganic Chemistry III*. These chapters describe the spectacular progress in their respective fields during the recent decades.

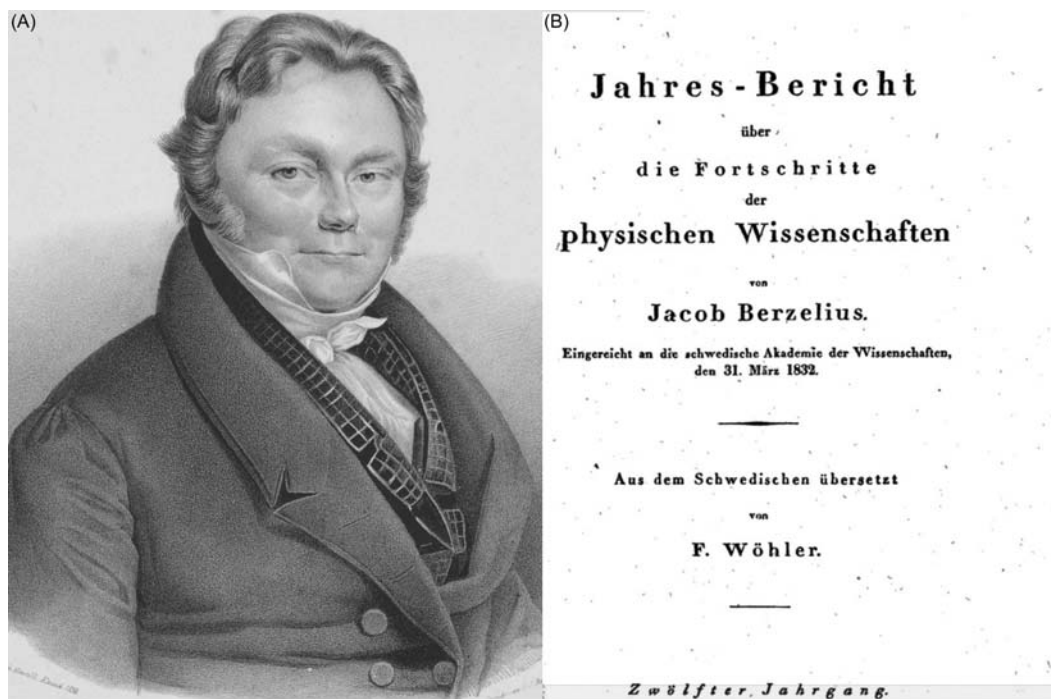
### 1.01.1 Birth of inorganic chemistry

It is generally considered that the last person, who could fully handle and understand the whole field of chemistry, was Jöns Jacob Berzelius (1779–1848) (see Fig. 1A). Between 1822 and 1841, he published annually “Jahresbericht über die Fortschritte der physischen Wissenschaften” to review the progress in physical sciences. This series is probably the first regularly appearing review publication in chemistry (Fig. 1B).

After Berzelius, chemistry was subdivided into inorganic and organic chemistry and was gradually further divided into physical and analytical chemistry, and biochemistry. While inorganic materials have been known and investigated since the antiques, the birth of inorganic chemistry as an independent subdiscipline took place in the late 18th and early 19th century. While there are numerous scientists, who have contributed to this process, possibly the main protagonists are Antoine Lavoisier (1743–94), John Dalton (1766–1844), Friedrich Wöhler (1800–1882), Dmitri Mendeleev (1834–1907), and Alfred Werner (1866–1919).

Lavoisier [see Fig. 2A] was a co-discoverer of oxygen together with Joseph Priestley (1733–1804) and Carl Wilhelm Scheele (1742–1786). The dispute about the discovery of oxygen is well-described in the play “Oxygen” by Carl Djerassi and Roald Hoffmann.<sup>1</sup> Lavoisier repeated the experiments of Priestley and showed that “air” is composed of two components, one of which combines with metals, sustains combustion, and is the source of acidity. The names “oxygen” (Greek for acid-former) and azote (Greek for no life) for the two components in “air” are also given by Lavoisier. In 1789 Lavoisier published a book “*Traité Élémentaire de Chimie, présenté dans un ordre nouveau et d’après les découvertes modernes,*” which is considered the first textbook of modern chemistry [see Fig. 2B].

John Dalton is famous for his atomic theory of 1807 and Friedrich Wöhler for showing that the organic compound, urea ( $(\text{H}_2\text{N})_2\text{CO}$ ), can be synthesized by heating of an inorganic compound, ammonium cyanate  $(\text{NH}_4)(\text{OCN})$ , thus refuting the concept of vitalism of organic compounds. Both scientists have also made other significant advances in chemistry. For instance, Wöhler discovered several elements, such as crystalline boron and silicon. The Periodic Table that was presented by Dmitri Mendeleev in 1869 is the corner stone of modern chemistry.



**Fig. 1** (A) Jöns Jacob Berzelius (1779–1848), lithography portrait from 1836 by P.H. van den Heuvel. (B) The title page of the 1832 issue of the "Jahresbericht über die Fortschritte der physischen Wissenschaften." (A) Reproduced under the terms of the CC 0 license <https://creativecommons.org/publicdomain/zero/1.0/>.



**Fig. 2** (A) Antoine Laurent Lavoisier (1743–1794) and his wife Marie Anne Pierrette Paulze (1758–1836). Portrait by Jacques-Louis David. Metropolitan Museum of Art, USA. (B) Title page of the textbook by Lavoisier. (A) Reproduced under the terms of the CC 0 license <https://creativecommons.org/publicdomain/zero/1.0/>.



**Fig. 3** Alfred Werner (1866–1919). ETH-Bibliothek Zürich, Bildarchiv. Reproduced under the terms of the CC BY-Sa 3.0 license <https://creativecommons.org/licenses/by-sa/3.0/>.

Alfred Werner (see Fig. 3) is considered to be the father of inorganic chemistry. His main contribution is in the creation of coordination chemistry. Werner prepared numerous molecular complexes and inferred their structures. There are 228 publications credited to him in Scifinder during the years 1890–1919. He also established that complexes containing different ligands might show isomerism. His work on metal complexes culminated in the discovery of optically active isomers in octahedral complexes. He was awarded Nobel prize in 1913. A more detailed biography of his life and accomplishments has been presented in Nobel Prize lectures.<sup>2</sup>

### 1.01.2 Inorganic chemistry in the 20th century

The development of inorganic chemistry in the 20th century has been excellently reviewed by McCleverty.<sup>3</sup> As he notes, the progress often rests on the shoulders of the discoveries made in other disciplines. For instance, the advance on modern instrumental methods of analysis in the latter half of 20th century, and the birth of the digital age with the development of ever more powerful computing facilities had enabled the study of unstable species and provided for new understanding on chemical bonding and intermolecular interactions, as well as chemical reactions thus leading to materials with new functions and applications. McCleverty<sup>3</sup> has divided the 20th century highlights to those, which have been recognized by the Nobel prize, and to those, which have not.

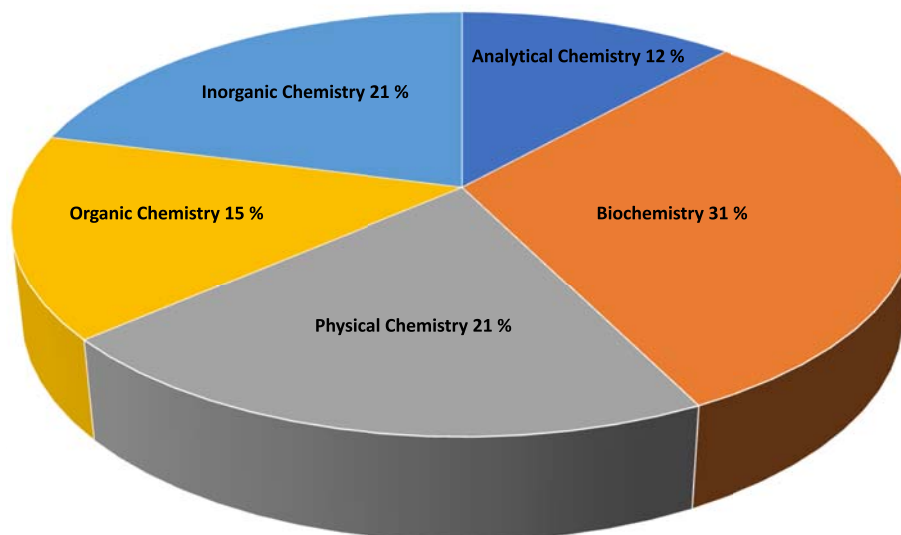
During the history of the Nobel prize in chemistry from 1901, every major field of chemistry has seen recognition by the Nobel committee, though it is naturally a matter of opinion, how research on individual prizes should be categorized in different subdisciplines (Fig. 4).

It is important to note that development of chemistry relies significantly on the progress in Physics. The electronic structures of atoms, molecules, and materials, which form the basis of all current-day chemistry, is based on the work by the so-called Quantum ten (N. Bohr, M. Born, L. de Broglie, P. Dirac, P. Ehrenfest, A. Einstein, W. Heisenberg, P. Jordan, W. Pauli, E. Schrödinger). With the exception of Ehrenfest and Jordan, they all won Nobel prizes in physics. The early history of quantum mechanics and the key players have been reported several times (see, for instance refs. 4, 5). Their collaborations, discussions, and disagreements laid the foundation to the high-level quantum chemical computations that are currently routinely used to understand bonding and reactivity of chemical substances.

The most important discovery for inorganic chemistry has been the use of X-ray diffraction for the crystal structure determinations (M. von Laue, Nobel Prize in 1914; W. H. Bragg and W. L. Bragg, Nobel prize in 1915). The two Nobel prizes for superconductivity (H. Kamerlingh-Onnes for the discovery of superconductivity in 1913) and J. G. Bednorz and K. A. Müller for the superconductivity in ceramic materials 1987), M. Siegbahn for his work on X-ray spectroscopy (1924), J. Chadwick for the discovery of neutron (1935), and C. J. Davisson and G. P. Thomson for the discovery of electron diffraction (1937) also had a significant impact on inorganic chemistry.

The Nobel prizes in chemistry that are directly concerned with inorganic chemistry or have impact on it are shown in Table 1. The early awards involved discovery of radioactive elements and progress in nuclear physics (M. Curie in 1911, and F. Joliot and I.





**Fig. 4** The classification of Nobel prizes in different subdisciplines of chemistry.<sup>3</sup>

Joliot-Curie in 1935). The chemical interpretation of bonding and its significance in molecular structures were awarded to A. Werner (1913), L. Pauling (1954), and G. Herzberg (1971). W. N. Lipscomb received his prize in 1976 for the model of 3c-2e bonding in boranes and other electron-deficient substances. Grignard (1912) and Wittig (1979) reagents as well as the use of boron and silicon hydrides in synthetic chemistry have applications, which go beyond inorganic chemistry. The increasing computer power enabled rapid progress in the techniques of X-ray crystallography (H. A. Hauptman and J. Karle 1985), and the development of high-resolution multinuclear NMR spectroscopy (F. Bloch and E. M. Purcell 1952, and R. R. Ernst 1991). The computational methods and techniques involving molecular orbitals and density functional theory (W. Kohn and J. A. Pople 1998) have become commonplace in understanding structures and bonding of molecules and chemical reactions. Several Nobel prizes in the latter half of 20th century have been awarded for synthetic chemistry and exploration of reaction mechanisms (see **Table 1**). The advent of metallocenes (E. O. Fischer and G. Wilkinson 1973) and the routine use of the working techniques using protective atmosphere in Schlenk lines or glove boxes have been part of the rise of organometallic chemistry. The Nobel prize of Ziegler and Natta (1963) together with the discovery of organometallic catalysts have opened new vistas for the study and industrial applications of polymers.

There are several important main-group discoveries in the 20th century, which have not been awarded the Noble prize, but may have resulted in awarding Nobel prizes in a later stage, as discussed by McCleverty<sup>3</sup> and Chivers and Konu.<sup>7</sup> This is exemplified by crown-ethers<sup>8</sup> and their s-block metal complexes,<sup>9</sup> which paved the way to the Noble prize of Cram, Lehn, and Pedersen about 20 years later.

The oxidation of O<sub>2</sub> by N. Bartlett using the very reactive gas PtF<sub>6</sub> unexpectedly resulted in the formation of (O<sub>2</sub>)[PtF<sub>6</sub>].<sup>10</sup> Since the first ionization energies of O<sub>2</sub> and Xe are similar, Bartlett assumed that xenon could be oxidized using PtF<sub>6</sub>. His experiment of mixing colorless xenon and red PtF<sub>6</sub> to form immediately yellow solid is well described by him<sup>11</sup> and is shown in **Fig. 5**. This pioneering synthesis opened a rich and versatile chemistry of noble gases, which had been considered completely inert till then. It has also forced the chemists to look at the chemical bonding with new eyes. The discovery of noble-gas compound would certainly have merited the Nobel prize.

Electron counting has become a useful tool to predict and rationalize molecular structures. One of the oldest tools is VSEPR (Valence Shell Electron Pair Repulsion) model<sup>13</sup> originally formulated by Gillespie and Nyholm<sup>14</sup> based on the paper by Sidgwick and Powel.<sup>15</sup> While VSEPR is powerful in predicting molecular geometries of main group compounds, its theoretical basis has not been clear. Gillespie<sup>16</sup> has utilized the AIM approach to rationalize the justification of electron density distribution around atoms on which the geometries of the molecules are dependent. He also extended electron-counting principles to main group rings, chains, and cages, which are electron-precise or electron-rich.<sup>17</sup>

Wade's rules provide another approach to utilize electron-counting principles to deduce molecular geometry.<sup>18</sup> This methodology is best applied to so-called electron-deficient compounds and has been originally formulated for boranes. Wade's rules serve to complement Gillespie's rules for classical and electron-rich cages. While Wade's rules work also well for carboranes<sup>19</sup> and transition metal clusters,<sup>20</sup> Gillespie's rule rationalize best the p-block element cages at the right end of the Periodic Table.

Whereas main group chemistry was the principal theme in inorganic chemistry in the first half of the 20th century, the latter half saw the rapid rise of coordination chemistry of transition metal complexes followed by the advent of organometallic chemistry and supramolecular chemistry in 1980s, and bioinorganic chemistry in 1990s. Main group chemistry has, however, been and continues to be the source of fundamental discoveries that has impact in other fields of chemistry.



**Table 1** Nobel prizes awarded in themes involving inorganic chemistry.<sup>6</sup>

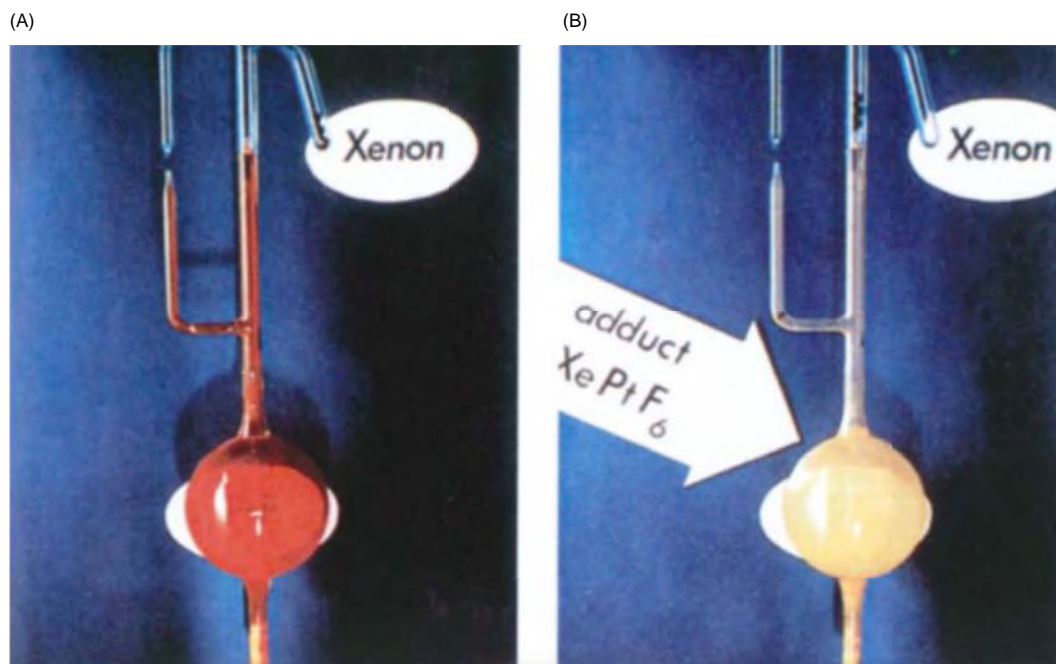
<i>Year</i>	<i>Nobel-prize winners</i>	<i>Justification</i>
1904	Sir W. Ramsay	Inert gaseous elements in air and their place in periodic system
1906	H. Moissan	Isolation of fluorine
1911	M. Curie	Discovery and study of radium and polonium
1912	V. Grignard P. Sabatier	Discovery of Grignard reagent Method of hydrogenating organic compounds
1913	A. Werner	Linkage of atoms of molecules
1918	F. Haber	Ammonia synthesis from the elements
1934	H. C. Urey	Discovery of heavy hydrogen
1935	F. Joliot and I. Joliot-Curie	Synthesis of new radioactive elements
1944	O. Hahn	Discovery of fission of heavy nuclei
1951	E. M. McMillan and G. T. Seaborg	Discoveries in chemistry of transuranium elements
1954	L. Pauling	The nature of the chemical bond
1963	K. Ziegler and G. Natta	Chemistry and technology of high polymers
1965	R. B. Woodward	Outstanding achievements in the art of organic synthesis
1966	R. S. Mulliken	Chemical bonds by the molecular orbital method
1971	G. Herzberg	Electronic structure and geometry of molecules; free radicals
1973	E. O. Fischer and G. Wilkinson	Chemistry of the organometallic sandwich complexes
1976	W. N. Lipscomb	Structure of boranes illuminating problems of chemical bonding
1979	H. C. Brown and G. Wittig	The use of boron- and phosphorus-containing compounds in organic synthesis
1981	K. Fukui and R. Hoffmann	Theories concerning the course of chemical reactions
1982	A. Klug	Development of crystallographic electron microscopy
1983	H. Taube	Mechanism of electron transfer reactions, especially in metal complexes
1984	R. B. Merrifield	Chemical synthesis on a solid matrix
1985	H. A. Hauptman and J. Karle	Direct methods for the determination of crystal structures
1986	D. R. Herschbach, Y. T. Lee, and J. C. Polanyi	Dynamics of chemical elementary processes
1987	D. J. Cram, J.-M. Lehn, and C. J. Pedersen	Molecules with structure-specific interactions of high selectivity
1991	R. R. Ernst	High-resolution NMR spectroscopy
1992	R. A. Marcus	Theory of electron transfer reactions in chemical systems
1994	G. A. Olah	Carbocation chemistry
1995	P. J. Crutzen, M. J. Molina, and F. S. Rowland	Formation and decomposition of ozone
1996	R. F. Curl Jr., Sir H. W. Kroto, and R. E. Smalley	Discovery of fullerenes
1998	W. Kohn J. A. Pople	Development of DFT method Development of computational methods in quantum chemistry
2000	A. J. Heeger, A. G. MacDiarmid, and H. Shirakawa	Discovery and development of conductive polymers
2005	Y. Chauvin, R. H. Grubbs, and R. R. Schrock	Methathesis in organic synthesis
2011	D. Shechtman	Quasicrystals

### 1.01.3 Current trends in molecular inorganic chemistry

#### 1.01.3.1 General

The important opinion papers by Chivers and Konu,<sup>7</sup> Power,<sup>21</sup> and Yam<sup>22</sup> discuss the current state of molecular inorganic chemistry. Several species with novel bonding arrangements, unprecedented structures, and unusual reactivities have been prepared comprising also syntheses, which were earlier regarded impossible.

Chivers and Konu<sup>7</sup> have discussed the future trends in main group chemistry. The main points they enumerate are shown in **Table 2**. Some of the entries listed in the table are discussed in more detail below, as they have relevance to Volume 1 of Comprehensive Inorganic Chemistry III. There are also other emerging features of molecular inorganic chemistry that have not been mentioned by Chivers and Konu.<sup>7</sup> Some of them will also be introduced below, since they are discussed in Volume 1 of Comprehensive Inorganic Chemistry III.



**Fig. 5** Oxidation of xenon by platinum hexafluoride.<sup>12</sup> (A) Xenon and platinum hexafluoride before mixing of the two gases. (B) Yellow solid product after the mixing. Reproduced with permission from Bartlett, N., in Banks, R. E. (ed.), *Fluorine Chemistry at the Millenium, Fascinated by Fluorine*, Elsevier: Amsterdam, 2000, pp. 29–55. © Elsevier 2000.

**Table 2** Future trends in main group chemistry.<sup>7</sup>

<i>New aspects of bonding</i>	<i>New reagents in synthesis</i>	<i>Alternative energy sources</i>	<i>New materials</i>	<i>Catalysis</i>	<i>Medicinal chemistry</i>
<ul style="list-style-type: none"> <li>- Multiply bonded compounds</li> <li>- Biradicals</li> <li>- Homoconjugation and homoaromaticity</li> <li>- Metal-metal bonding in s-block metals</li> </ul>	<ul style="list-style-type: none"> <li>- Bimetallic reagents</li> <li>- Weakly coordinating anions</li> <li>- Ligand-stabilized polycations of isolated p-block elements</li> <li>- Low-coordinate main group element centers</li> <li>- Activation of small molecules</li> </ul>	<ul style="list-style-type: none"> <li>- Hydrogen storage</li> <li>- Solar and thermoelectric energy</li> </ul>	<ul style="list-style-type: none"> <li>- Electronics industries</li> <li>- Nanomaterials</li> <li>- Inorganic polymers</li> <li>- Chemical sensors</li> </ul>	<ul style="list-style-type: none"> <li>- Lactic polymerization</li> <li>- Organic synthesis</li> </ul>	<ul style="list-style-type: none"> <li>- Chemotherapy</li> <li>- Radionuclide therapy</li> <li>- Contact lenses</li> </ul>

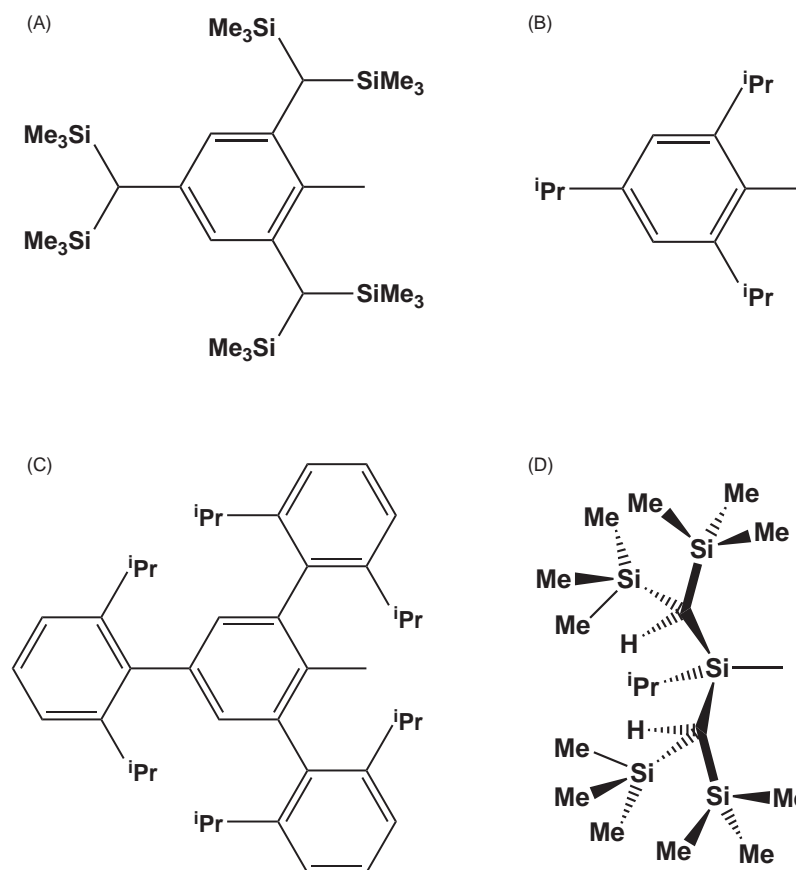
### 1.01.3.2 Multiple bonding in p-block compounds

It was long considered that heavy p-block elements do not form stable multiple bonds due to the poor  $np(\pi)-np(\pi)$  ( $n \geq 3$ ) overlap. In 1981, however, West et al.<sup>23</sup> and Yoshifuji et al.<sup>24</sup> reported the preparations of tetramesityldisilene and bis(2,4,6-tri-*tert*-butylphenyl)diphosphene, respectively. Since then, the chemistry of multiply-bonded heavy Group 13–15 compounds have seen active research interest, and their preparations, structures, bonding, and reactivities have been reviewed several times, as exemplified by some of the most recent reviews.<sup>25–30</sup> The progress in this chemistry is strongly dependent on the application of sterically bulky protective groups, such as 2,4,6-tris[bis(trimethylsilyl)methyl]phenyl<sup>31</sup> and 2,4,6-tris(2-propyl)phenyl<sup>32</sup> [see **Chart 1A** and **B**].

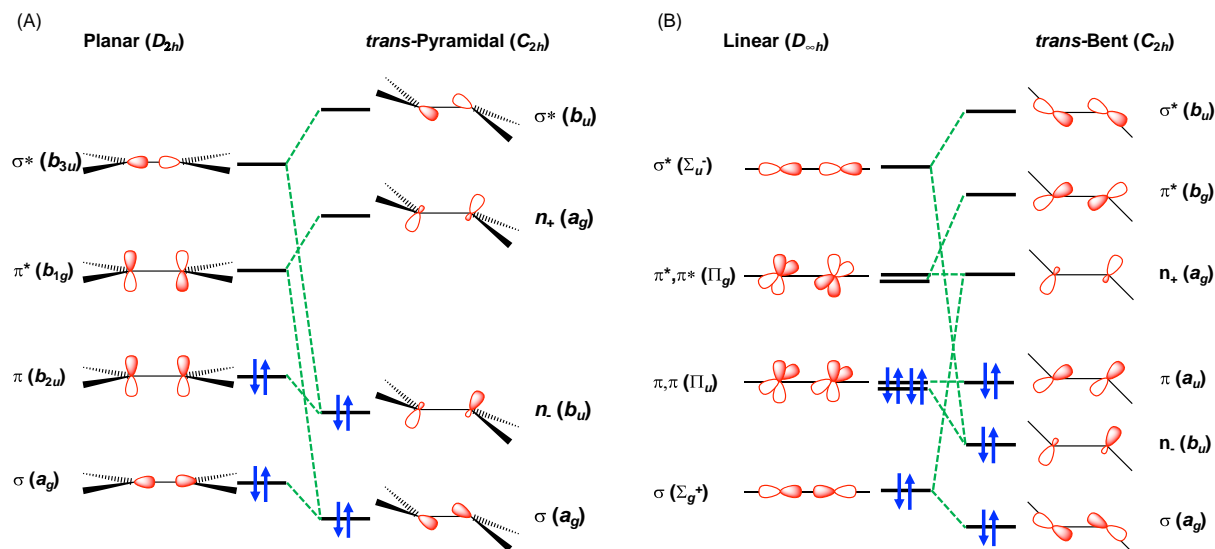
Heavy Group 14 element analogs of alkynes ( $RMMR$ ;  $M = Si, Ge, Sn, Pb$ ) have also been prepared and structurally characterized.<sup>27</sup> Their stabilization requires an even bulkier protective groups, such as terphenyl derivatives [see example in **Chart 1C**] or silyl derivatives with a very bulky substituent [see **Chart 1D**].

By contrast to the ethene derivatives in which the  $>C=C<$  moiety is planar, the  $M$  atoms in  $R_2M=MR_2$  ( $M = Si, Ge, Sn, Pb$ ;  $R =$  is the protective organic group) show pyramidal bonding geometry. In the similar fashion, while  $-C\equiv C-$  is linear, the higher congeners are bent. These differences in the bonding environments have been discussed in terms of Jahn-Teller effect<sup>27</sup> and are shown in **Fig. 6**.

In case of the heavy Group 14 elements, the distortion of the geometry from the planar ( $R_2MMR_2$ ) or the linear ( $RMMR$ ) structure can be explained by the mixing of molecular orbitals, which have different symmetries in the undistorted structures but the same symmetries in the pyramidal or bent structures. In case of disilenes, digermenes, stannenes, and plumbenes, these energy

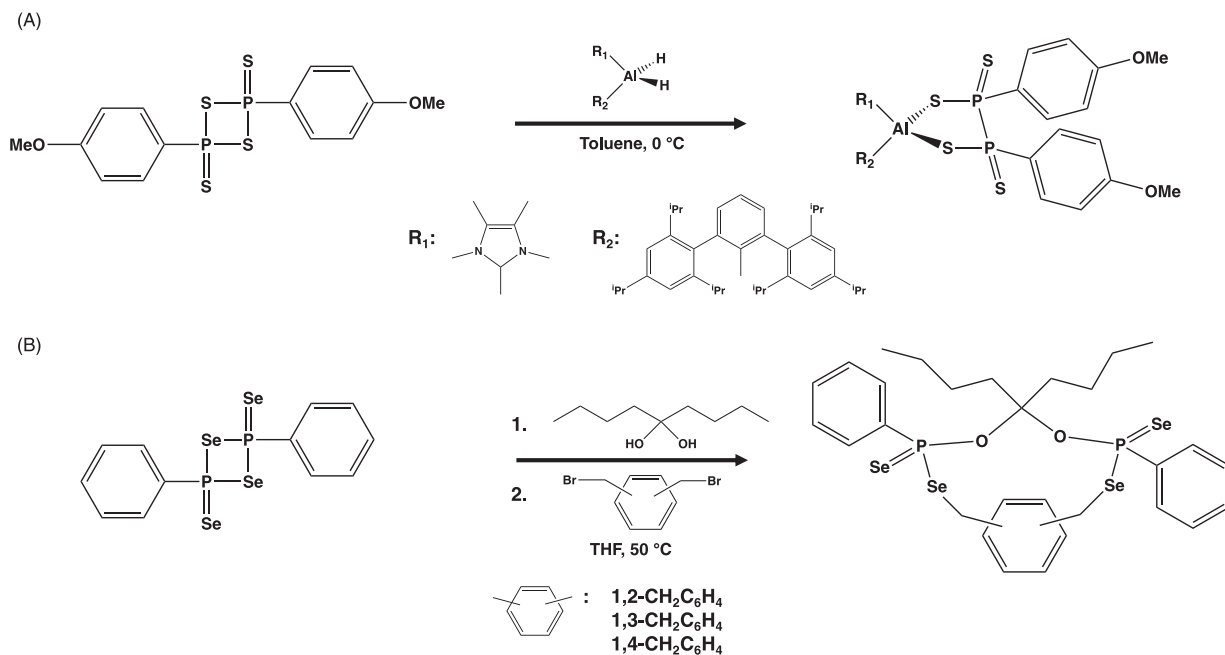


**Chart 1** Protective organic groups in the synthesis of reactive multiply-bonded p-block compounds. (A) 2,4,6-bis[bis(trimethylsilyl)methyl]phenyl,<sup>31</sup> (B) 2,4,6-tris(2-propyl)phenyl,<sup>32</sup> (C) 2,4,6-tris[2,6-bis(2-propyl)phenyl]phenyl,<sup>33</sup> and (D) (2-propyl)bis[bis(trimethylsilyl)silyl].<sup>34</sup>



**Fig. 6** The orbital interactions upon distortion of (A) the planar structure ( $D_{2h}$ ) to *trans*-pyramidal ( $C_{2h}$ ), and (B) the linear structure ( $D_{\infty h}$ ) to *trans*-bent structure ( $C_{2h}$ ).<sup>27</sup>

levels in the planar geometry are sufficiently close to each other due to the weak bonding to enable their mixing, which leads to the lowering of energy and thus to the distortion of the structure. Since the original  $\sigma$  bonds of  $a_g$  symmetry are also weakened by the distortions, and the distortion increases, when going down the Periodic Table, the alkene analog of lead is not stable and dissociates into two monomers. The triple bond, which in organic alkynes is composed of a  $\sigma$  bond and two  $\pi$  bonds, ultimately becomes two



**Scheme 1** Examples of use of (A) Lawesson's reagent as a sulfur-transfer reagent<sup>35</sup> and (B) Woollins' reagent as a selenium-transfer reagent.<sup>36</sup>

lone pair orbitals mostly of 6s character and the Group 14 elements in this case are only linked by a single  $\sigma$ -bond. The behavior of heavy Group 15 elements is analogous to that of Group 14 elements.

Heavier Group 14 and Group 15 atoms form multiple bonds with chalcogen atoms. Lawesson's and Woollins' reagents are important members in this class of compounds. They are efficient sulfur- and selenium-transfer reagents, respectively (see **Scheme 1**).

### 1.01.3.3 Secondary bonding interactions

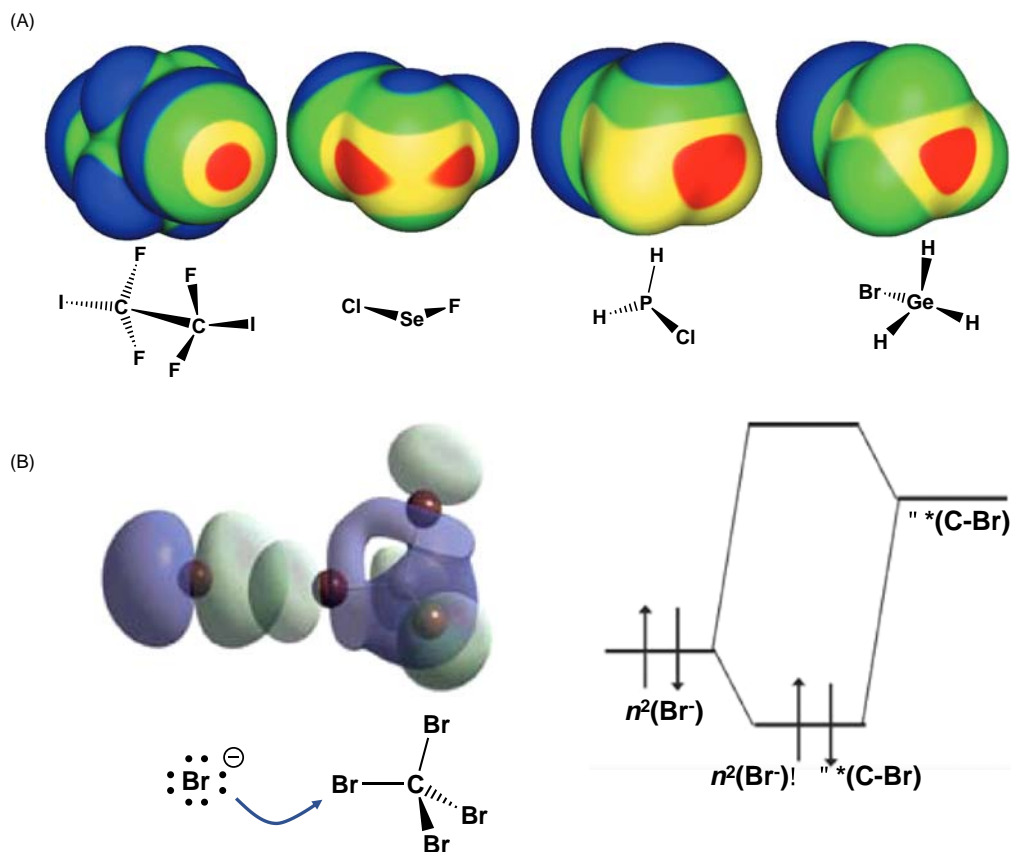
Secondary bonding interactions (SBIs) describe interatomic interactions, which are longer than covalent single bonds but shorter than the sums of the van der Waals radii. The term was originally coined by Alcock.<sup>37</sup> They have also been called soft-soft, closed-shell, nonbonding, semi-bonding, non-covalent, weakly bonding, or  $\sigma$ -hole interactions. In specific case of halogen, chalcogen, pnictogen (or pnicogen), and tetrel atoms, they are also known as halogen, chalcogen, pnictogen, and tetrel bonds, respectively. The SBIs are most significant in case of the heaviest p-block elements in the Periodic Table.

The halogen bond is the best-studied secondary bonding interaction of the compounds involving p-block elements<sup>38–41</sup> and has been defined by IUPAC as an attractive interaction between a positive region in the electrostatic surface potential of a halogen atom and a nucleophile.<sup>42</sup> Chalcogen bonds have also recently been defined by IUPAC<sup>43</sup> and have been reviewed on several occasions.<sup>44–47</sup> Pnictogen and tetrel bonds have seen lesser attention, but the secondary bonding interactions are important also in the solid-state lattices of heavy Group 15 and 14 compounds.<sup>48–51</sup>

Whereas halogen bonds can mainly be rationalized in terms of electrostatic  $\sigma$ -hole interactions [see **Fig. 7A**], they and, more significantly, the chalcogen bonds must be understood as combinations of orbital interactions and dispersion contributions in addition the electrostatic interactions [see **Fig. 7B**]. The covalent aspects of the secondary bonding interactions can be described as donor-acceptor interactions  $n^2(D) \rightarrow \sigma^*(E-X)$  with the lone pair orbital of the electron donor atom D overlapping with the antibonding  $\sigma^*$  orbital of the E-X bond (E = heavy p-block element; X = an electronegative atom). The strength of this 3c-4e arrangement varies from a very weak interaction to that of a hypervalent single bond. The heaviest p-block elements show strongest SBIs, because the energy difference between the  $\sigma(E-X)$  and  $\sigma^*(E-X)$  orbitals diminishes when going down the Periodic Table. At the same time, the orbital overlap diminishes, since the orbitals become more diffuse. The dispersion effects become more significant with increasing periodic number and play the major role in the interactions between the heaviest p-block elements.

SBIs affect the solid-state structures, solution behavior, and reactivities of the bulk materials. Interest in these interactions have given birth to new research areas in chemistry, such as supramolecular chemistry and crystal engineering. Since the weak intermolecular forces play an essential role in the material properties, their study has become an important emerging trend, which will also have an impact on the future research activities in inorganic chemistry.

Metallophilic interactions can also be considered to belong to the class of secondary bonding interactions. They are now well-established in chemistry with numerous reviews of different homonuclear and heteronuclear metal combinations (for some recent examples, see refs. 53–55). The complexes are generally dinuclear, but polynuclear species are also known. Their characterization relies mainly on X-ray diffraction, but currently the use of solution and solid-state spectroscopic techniques, and in particular, high-



**Fig. 7** (A) Surface electrostatic potentials of 1,2-I<sub>2</sub>(CF)<sub>2</sub>, SeFCl, PH<sub>2</sub>Cl, and GeH<sub>3</sub>Br.<sup>41,52</sup> The positive region is denoted in red, the negative region in blue, and the transition region in green/yellow. (B) Example of the charge-transfer  $n^2 \rightarrow \sigma^*$  interaction between the Lewis base Br<sup>-</sup> and the formal Lewis acid CBr<sub>4</sub>.<sup>41</sup> (A) Adapted with permission from Politzer, P.; Murray, J. S.; Clark, T., *Phys. Chem. Chem. Phys.* **2013**, *15*, 11178–11189. © 2013, RSC. (B) Adapted with permission from Gilday, L. C.; Robinson, S. W.; Barendt, T. A.; Langton, M. J.; Mullaney, B. R.; Beer, P. D., *Chem. Rev.* **2015**, *115*, 7118–7195. © ACS. 2015.

level MO calculations have increased the understanding of these interactions. Early literature on theoretical calculations is reviewed by Pyykkö<sup>56</sup> with more recent literature discussed by Zheng et al.<sup>57</sup>

The metallophilic interactions involve neither conventional covalent bonds nor metal-metal bonds with delocalized electrons in the conduction band. The neighboring metal centers, however, lie closer to each other than the sum of their van der Waals radii. The formal metal electron configurations in these interactions are closed-shell  $d^{10}-d^{10}$  [M(I) in Group 11 or M(II) in Group 12],  $s^2-s^2$  [M(I) in Group 13, M(II) in Group 14, or M(III) in Group 15] or  $d^8-d^8$  [M(0) in Group 8, M(I) in Group 9, or M(II) in Group 10]. The metallophilic interactions are therefore also called closed-shell interactions. A few typical examples are shown in Fig. 8.

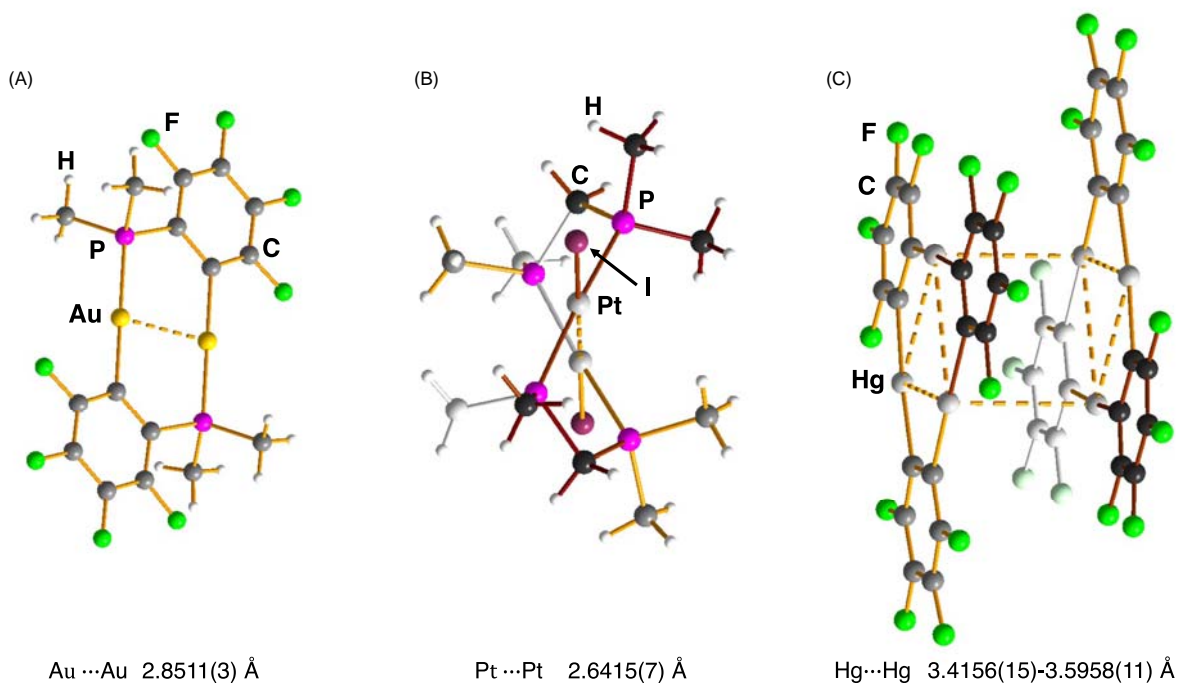
It has been suggested that the bite size of the bridging ligands (donor atom-donor atom distance) correlates with  $M \cdots M$  distance. It can be seen from Fig. 9 for dinuclear silver complexes containing nitrogen-donor ligands that there is indeed a loose correlation between the  $Ag \cdots Ag$  distance and the  $N \cdots N$  bite size. However, short  $M \cdots M$  contacts are also found in cases, when the bite size is large, as shown in Fig. 9. The metal-metal distance may also be short in case of monodentate ligands, as shown by two illustrative examples for the ligand-unsupported complexes.

The stabilization due to the close-shell  $d^{10}-d^{10}$  interaction can be explained by the simplified molecular orbital description, which is shown in Fig. 10.<sup>65</sup> The mixing of the empty  $(n+1)s$  orbital with the filled  $d$  orbitals leads to the stabilization of the bonding  $1\sigma$  orbital and to a smaller extent of the antibonding  $2\sigma$  orbital. It can be seen from Fig. 10 that the  $(n+1)s$  contribution to the  $1\sigma$  orbital is 11.0, 8.8, and 2.6% for Cu, Au, and Ag, respectively.

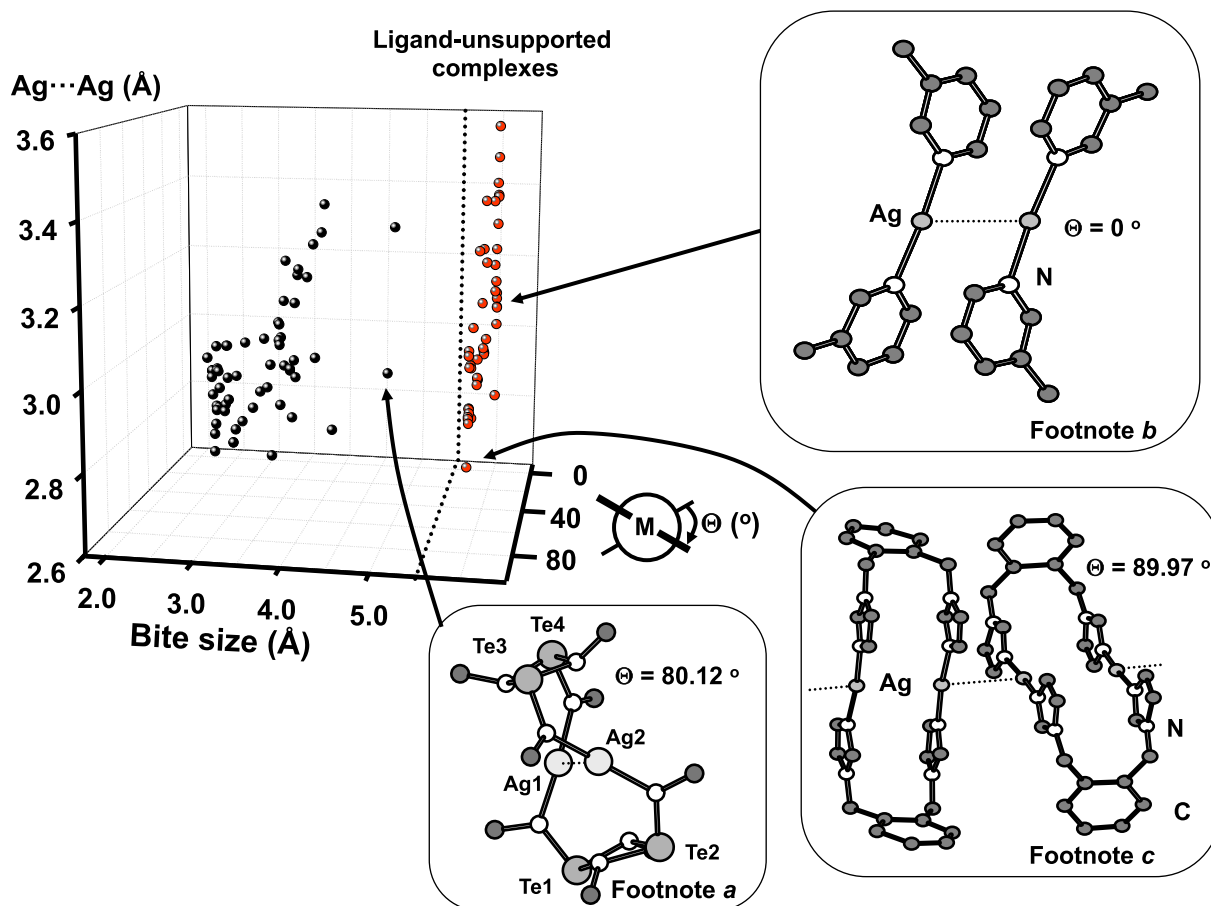
#### 1.01.3.4 Small-molecule activation

Power<sup>21</sup> has noted that the third-row or heavier p-block elements differ significantly from their second-row congeners. It has gradually been realized that the properties of their compounds are closer to those of the transition metal complexes. For instance, H<sub>2</sub> is activated under mild conditions in the same fashion by the germanium or tin analogs of alkynes as by the transition metal

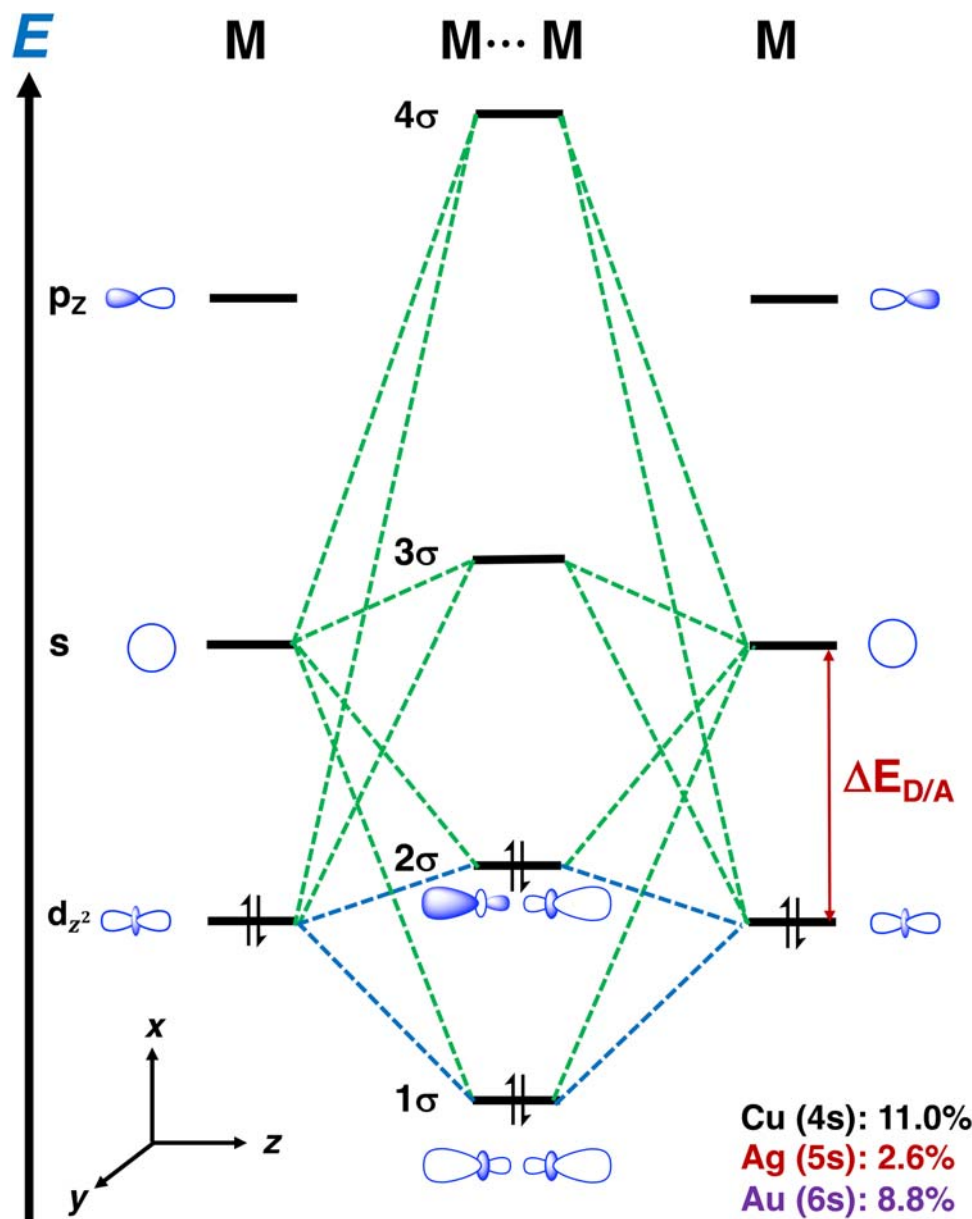




**Fig. 8** Examples of metallophilic interactions in (A)  $[\text{AuPMe}_2(\text{C}_6\text{F}_4)]_2$ ,<sup>58</sup> (B)  $[\text{PtI}(\mu\text{-(PMe}_2)_2\text{CH}_2)]_2$ ,<sup>59</sup> and (C)  $[\text{Hg}_3(\mu\text{-C}_6\text{F}_4)_3]_2$ .<sup>60</sup>



**Fig. 9** The survey of the dependence of the  $\text{M} \cdots \text{M}$  distance on the bite size  $\text{N} \cdots \text{N}$  and the deviation of the  $\text{N}_2\text{Ag} \cdots \text{AgN}_2$  fragment from planarity (angle  $\Theta$ ).<sup>61</sup> <sup>a</sup> Ref. 62. <sup>b</sup> Ref. 63. <sup>c</sup> Ref. 64. Adapted with permission from Risto, M.; Takaluoma, T. T.; Bajorek, T.; Oilunkaniemi, R.; Laitinen, R. S.; Chivers, T., *Inorg. Chem.* **2009**, *48*, 6271–6279. © 2009. ACS.

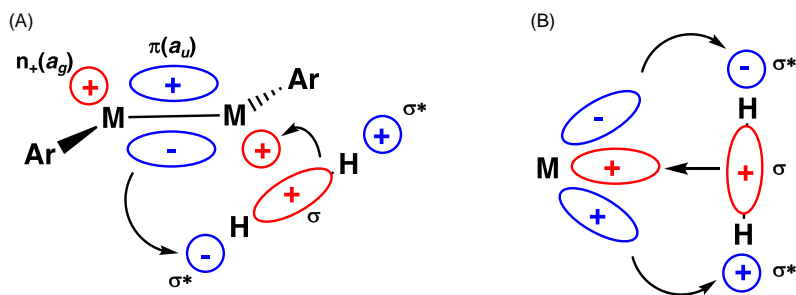


**Fig. 10** Simplified molecular orbital diagram for the formation of  $M \cdot \cdot \cdot M$  metallophilic interactions.<sup>65</sup> The contribution of the vacant s-orbitals of Cu, Ag, and Au are also indicated in the figure. Adapted with permission from Brands, M. B.; Nitsch, J.; Guerra, C. F., *Inorg. Chem.* **2018**, *57*, 2603–2608. © 2018 ACS.

complexes.<sup>66</sup> The initial step in both activations involves oxidative addition (see Fig. 11). It was argued by Power<sup>21</sup> that this is a consequence of the small energy separation between the HOMO and LUMO in the heavy p-block compounds.

Spikes et al.<sup>66</sup> have shown that  $\text{ArGeGeAr}$   $\{\text{Ar} = [2,6\text{-}^i\text{Pr}_2(\text{C}_6\text{H}_3)]_2\text{C}_6\text{H}_5\}$  reacted with  $\text{H}_2$  at ambient temperature and pressure to afford  $\text{ArHGeGeAr}$ ,  $\text{ArH}_2\text{GeGeArH}_2$ , and  $\text{ArGeH}_3$ . Their relative yields depend on the initial molar ratios of the reactants. The related reaction with  $\text{ArSnSnAr}$  gives exclusively  $\text{ArSn}(\mu\text{-H})_2\text{SnAr}$ .<sup>67</sup> Alkenes and alkynes can also be activated by multiply-bonded Group 14 compounds (for a review, see ref. 68).

Singlet carbenes can also mimic the behavior of transition metal complexes. Frey et al.<sup>69</sup> have shown that while electrophilic diaminocarbenes are inert towards molecular hydrogen, the more nucleophilic alkylaminocarbenes activate  $\text{H}_2$  under mild conditions probably involving oxidative addition in the similar manner to that in  $\text{ArMMAr}$  or in transition metal complexes (c.f. Fig. 11). Because of the higher nucleophilicity of these carbenes compared to transition metals, they have been shown to activate also ammonia affording a primary amine.<sup>69</sup>



**Fig. 11** (A) The interaction of  $\sigma(\text{H-H})$  (HOMO) of  $\text{H}_2$  with  $n_x$  (LUMO) of  $\text{ArMMAr}$  ( $M = \text{Ge}, \text{Sn}$ ;  $\text{Ar} =$  moderately bulky aromatic group), and the back-donation from  $\pi$ (HOMO) of  $\text{ArMMAr}$  to  $\sigma^*(\text{H-H})$  (LUMO) of  $\text{H}_2$ . (B) The related interaction of  $\text{H}_2$  with the d orbitals of the transition metal.<sup>21</sup> Reproduced with permission from Power, P. P., *Nature* **2010**, 463, 171–177. © 2010 McMillan Publishers Limited.

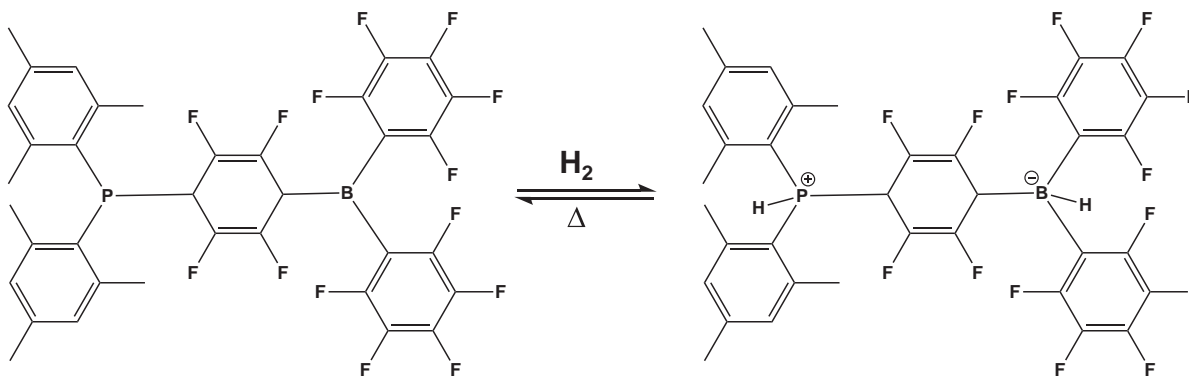
In 2006, Welch et al.<sup>70</sup> reported the first metal-free reversible activation of  $\text{H}_2$  under mild conditions by involving a bulky phosphinoborane (see **Scheme 2**). In this connection, Stephan coined the term frustrated Lewis pair to describe a situation, where due to steric reasons the Lewis acid and base cannot form an adduct.<sup>70</sup>

The orbital interaction between the FLP and  $\text{H}_2$  is shown schematically in **Fig. 12**.

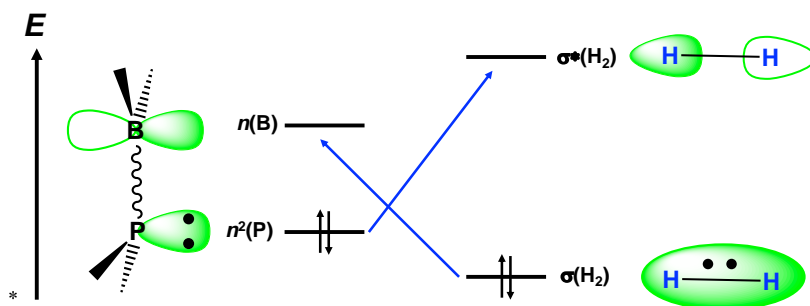
The lone pair on phosphorus can donate electron density to the antibonding  $\sigma^*$  orbital of  $\text{H}_2$ , and the empty p orbital on boron can accept electron density from the bonding  $\sigma$  orbital of  $\text{H}_2$  resulting in the cleavage of the  $\text{H-H}$  bond and the formation of both  $\text{P-H}$  and  $\text{B-H}$  bonds. FLPs have opened a rapidly expanding field of transition-metal free catalysts. While hydrogenation reactions continue to play an important part in FLP reactivity, new applications involve the reduction of other small molecules such as  $\text{CO}$  and  $\text{CO}_2$ , as well as the generation of solid-state FLP catalysts, as reviewed recently.<sup>71</sup>

### 1.01.3.5 Weakly coordinating anions

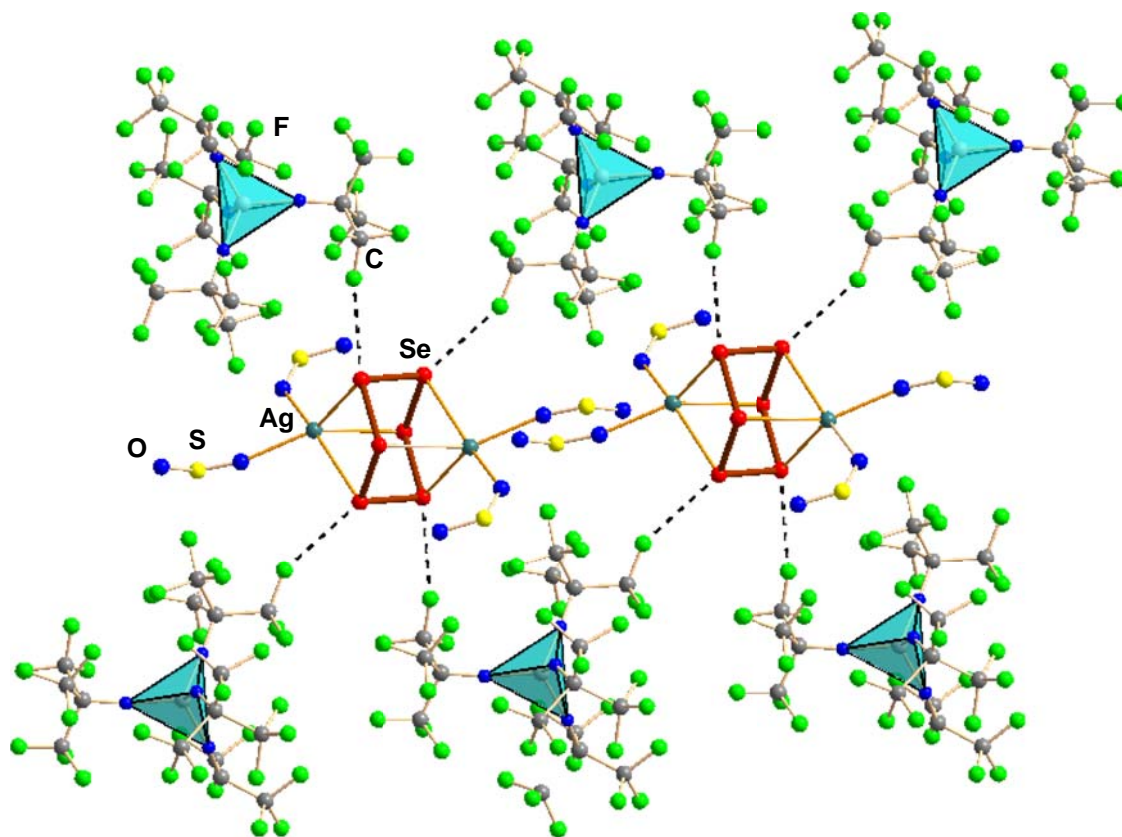
p-Block elements can form polyatomic cations, such as  $\text{E}_4^{2+}$  or  $\text{E}_8^{2+}$  ( $\text{E} = \text{S}, \text{Se}, \text{Te}$ ), but they are highly electrophilic and therefore they can be isolated only by use of the anions of very strong acids like  $\text{SO}_3\text{F}^-$  or  $\text{MF}_6^-$  ( $\text{M} = \text{As}, \text{Sb}$ ) (for two reviews, see refs. 72, 73). The advent of weakly coordinating anions (WCAs) stems from the search of “noncoordinating” anions<sup>74</sup> to improve the stability of



**Scheme 2** Reversible metal-free activation of  $\text{H}_2$ .<sup>70</sup>



**Fig. 12** Simplified hypothetical orbital interactions and charge transfer in the activation of  $\text{H}_2$  by a FLP.



**Fig. 13** Crystal structure of  $[\text{Ag}_2(\text{Se}_6)(\text{O}_2\text{S})_4][\text{Al}(\text{OC}(\text{CF}_3)_3)_4]_2$ .<sup>75</sup>

materials containing such cations. However, WCAs have also had impact on areas like olefin polymerization, lithium battery technology, and ionic liquids.<sup>7</sup>  $[\text{Ag}_2(\text{Se}_6)(\text{O}_2\text{S})_4][\text{Al}(\text{OC}(\text{CF}_3)_3)_4]_2$  is an example of the use of WCAs in stabilization of otherwise unstable cations (see Fig. 13).

Krossing and Raabe<sup>74</sup> have discussed the potential candidates for WCAs. They define the requirements as chemical robustness towards electrophiles and oxidizing agents, minimal tendency for coordination, high solubility in non-polar media, pseudo gas-phase conditions in the solid state or solution, and the stabilization of weakly-bound and low-charged complexes. Several classes of compounds have been considered (see Table 3).

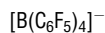
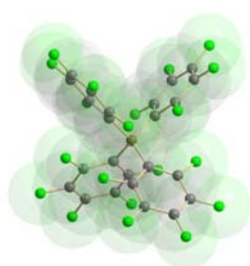
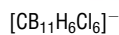
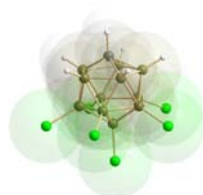
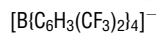
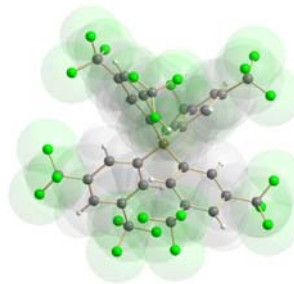
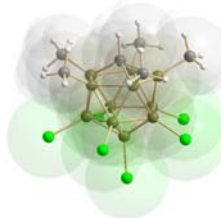
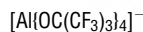
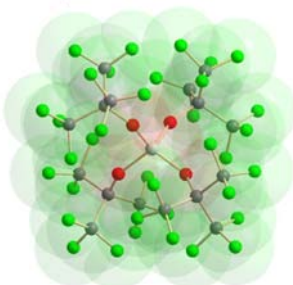
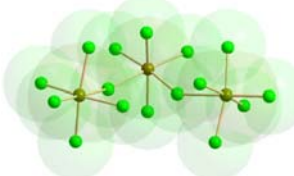
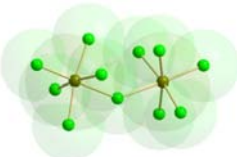
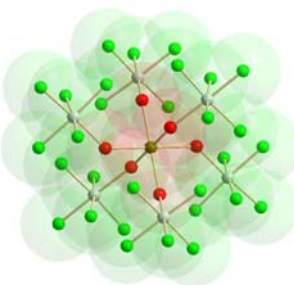
The number of applications of WCAs is rapidly increasing. In addition to the stabilization of low-stability cations, they can act to enhance solubility of s.c. naked  $\text{Li}^+$ -ions in non-polar solvents, which is important in  $\text{Li}^+$ -ion catalyzed organic transformations, such as in Diels-Alder reactions. Air- and moisture-stable  $[\text{Ag}(\text{PPh}_3)]^+[\text{CB}_{11}\text{H}_6\text{Br}_6]^-$  is considered to be the best catalyst for hetero Diels-Alder reactions.<sup>[76]</sup> The use of WCAs in supporting electrolytes in cyclic voltammetry enhances the solubility of the polycationic products and hinders inadvertent oxidation.<sup>[74]</sup> Other applications for salts containing WCAs include their use in low-viscosity ionic liquids, and in extraction of electrophilic metal ions.

### 1.01.3.6 Biradicals and biradicaloids

Radicals are molecular species containing an unpaired electron. They are often only transient species in the course of a chemical reaction. A radical is called stable, if the species can be isolated and stored for an extended period of time under an inert atmosphere in ambient temperature. The persistent radical is long-lived under the conditions of its generation (For a review of the stable and persistent radicals of the Group 13–17 elements, see ref. 77).

In addition to persistent radicals, biradicals have attracted increasing research attention in recent decades.<sup>74</sup> They contain two unpaired electrons in two nearly degenerate non-bonding orbitals. In the ground state, the biradicals show either the singlet or triplet spin states. While organic biradicals are very short-lived species, some related main-group biradicals may be isolated and structurally characterized by X-ray diffraction.<sup>77,78</sup> The increased stability, however, leads to the reduction of the biradical character. These kinds of species are designated as biradicaloids.<sup>78–80</sup>

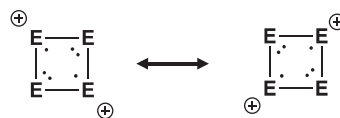
The biradicaloid nature is exemplified by  $(\text{RBPR}'_2)_2$  (see Table 4).<sup>81</sup>  $(\text{PhBP}^i\text{Pr}_2)_2$  and  $(^t\text{BuBP}^i\text{Pr}_2)_2$  both have 22 valence electrons. Their  $\text{B}_2\text{P}_2$  rings are planar and the molecules show singlet biradical character with unpaired electrons localized in the two boron centers. The respective transannular  $\text{B} \cdots \text{B}$  distances of 2.563(2) and 2.559(2) Å are significantly longer than the B–B single bonds. Upon controlled modification of the substituents on boron and phosphorus, it was observed that the four-membered  $\text{B}_2\text{P}_2$  ring is folded and the transannular  $\text{B} \cdots \text{B}$  becomes shorter (see Table 4). The B–B distance is the shortest in

**Table 3** Some examples of commonly used weakly coordinating anions.<sup>74</sup>**Borate-based anions****Carborane-based anions****Fluorinated alkoxytellurates****Tellurate-based anions****Anions from Lewis acid-base reaction**

the case of  $(\text{PhBPPPh}_2)_2$  [1.835(2)] approaching that of the single bond. At the same time the folding is the most pronounced. Scheschkewitz et al.<sup>81</sup> have discussed the factors affecting the folding.

The electronic structures of the four-membered cyclic molecule  $\text{S}_2\text{N}_2$  and its isoelectronic cations  $\text{E}_4^{2+}$  ( $\text{E} = \text{S}, \text{Se}, \text{Te}$ ) have been under extensive discussion.  $\text{S}_2\text{N}_2$  is formally a  $6\pi$  aromatic molecule, but it has been shown to be only a  $2\pi$  aromatic system.<sup>82</sup> Several reports conclude that the ground-state wavefunction of  $\text{S}_2\text{N}_2$  has singlet biradical character, but there is a wide range of estimates of the weight of the contribution of the singlet biradical character in the wavefunction.<sup>83</sup>

The situation in the square-planar  $\text{E}_4^{2+}$  ( $\text{E} = \text{S}; \text{Se}, \text{Te}$ ) cation is somewhat different with that in  $\text{S}_2\text{N}_2$ . The positive charge is delocalized over all chalcogen atoms, and the two main biradical structures.

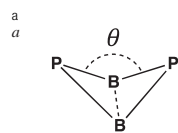


contribute equally to the wavefunction.<sup>83</sup> It was inferred that the biradical character of these cations are comparable to that of  $\text{O}_3$ .



**Table 4** The influence of the substituents on boron and phosphorus on the biradical nature of (RBPR'<sub>2</sub>)<sub>2</sub>.<sup>81</sup>

Compound	$r_{BP}$ (Å)	$\theta$ (°) <sup>a</sup>	$B \cdots B$ (Å)	$P \cdots P$ (Å)
(PhBP <sup>i</sup> Pr <sub>2</sub> ) <sub>2</sub>	1.8915(16)-1.8942(16)	180.00(8)	2.563(2)	2.7861(6)
( <sup>t</sup> BuBP <sup>i</sup> Pr <sub>2</sub> ) <sub>2</sub>	1.8904(14)-1.8933(17)	180.00(9)	2.559(2)	2.7868(6)
[(2,3,5,6-Me <sub>4</sub> C <sub>6</sub> H)BP <sup>i</sup> Pr <sub>2</sub> ] <sub>2</sub>	1.8879(10)-1.8891(11)	133.38(4)	2.2405(17)	2.7924(3)
( <sup>t</sup> BuBPPH <sub>2</sub> ) <sub>2</sub>	1.8859(17)-1.8956(17)	115.50(5)	1.989(2)	2.7498(6)
[(2,3,5,6-Me <sub>4</sub> C <sub>6</sub> H)BPt <sub>2</sub> ] <sub>2</sub>	1.8910(19)-1.8952(18)	114.72(8)	1.892(3)	2.7615(6)
(PhBPPH <sub>2</sub> ) <sub>2</sub>	1.893(5)-1.897(4)	114.07(18)	1.835(8)	2.7833(16)



### 1.01.4 Volume 1 of Comprehensive Inorganic Chemistry III

The first edition of Comprehensive Inorganic Chemistry<sup>84</sup> contained five volumes and discussed the chemistry of the elements according to their position in the Periodic Table. First two volumes concentrated on main group chemistry, volume three described transition metals, and volumes four and five treated the chemistry of lanthanoids and actinoids. The style and approach in this five-volume book were close to that in an extended textbook. For a long time, it was the key authority in inorganic chemistry.

The second edition (CIC II) was published in 2013.<sup>85</sup> Its connection to the Periodic Table as a directing tool was looser than in the first edition. Each of the nine volumes has a specific thematic issue, as shown in Table 5. This nine-volume set was less of a textbook and resembled more closely a review publication, but it still aimed at providing a comprehensive overview on the then present state in inorganic chemistry.

The current, third edition, *Comprehensive Inorganic Chemistry III* (CIC III) continues the same topical approach to the current mainstream in inorganic chemistry as the previous version. This edition contains 10 volumes. Their topics are listed in Table 6.

**Table 5** Themes of the nine volumes in Comprehensive Inorganic Chemistry II (CIC II).<sup>84</sup>

Volume	Theme
1	Main-group elements, including noble gases
2	Transition elements, lanthanides and actinides
3	Bioinorganic fundamentals and applications: Metals in natural living systems and metals in toxicology and medicine
4	Solid-state materials, including ceramics and minerals
5	Porous materials and nanomaterials
6	Homogeneous catalytic applications
7	Surface inorganic chemistry and heterogeneous catalysis
8	Coordination and organometallic chemistry
9	Theory and methods

**Table 6** Themes in Comprehensive Inorganic Chemistry III.

Volume	Theme
1	Synthesis structure and bonding of inorganic molecular systems
2	Bioinorganic chemistry and homogeneous biomimetic inorganic catalysis
3	Theory and bonding of inorganic non-molecular systems
4	Solid-state inorganic chemistry including supramolecular
5	Inorganic materials chemistry
6	Heterogeneous inorganic catalysis
7	Inorganic electrochemistry
8	Inorganic photochemistry
9	NMR of inorganic nuclei
10	Xray, neutron and electron scattering methods in inorganic chemistry

Topics in Volume 1 of the current edition follow logically those of Volume 1 in the 2nd edition. While the principal theme in the 2nd edition was main group chemistry, the current volume of the 3rd edition addresses molecular systems as they appear both in main group and transition metal chemistry. Many themes in the 2nd edition 9 years ago are still relevant today, and many chapters provide the update of the progress during the past years, though not forgetting to give sufficient historical overview for the reader to appreciate the advent and development in any given topic. There were 40 chapters in *Comprehensive Inorganic Chemistry II* (CIC II), but the current Volume 1 contains only 23 chapters. Each chapter in CIC III therefore describes a wider range of topics than those in CIC II. The distribution of themes in the different volumes of CIC III is also different compared to CIC II. This has also affected the choice of actual chapters in any of the 10 volumes.

There are three sections in Volume 1 of CIC III:

- (1) Structure, bonding, and reactivity in inorganic molecular systems
- (2) Intermolecular interactions
- (3) Inorganic chains, rings, and cages

Section 1 contains nine chapters. There is a very comprehensive review of coordination chemistry of complexes in which the heavy p-block atom acts as a central atom. This is a vast field. Therefore, the discussion has been restricted to single-donor ligands. There are also chapters reviewing recent progress in the rich synthetic and structural chemistry of noble gas compounds, low-coordinate p-block elements, biradicals, [Fe,Fe]-hydrogenase mimics, and macrocyclic selenoethers. There has been a very rapid progress in the chemistry and application of weakly coordinating anions, and Volume 1 of CIC III provides a thorough review of the development since the publication of CIC-II. Two last chapters (*see chapters 1.08 and 1.09*) in this Section treat the preparation, structures, and reactivity of carbenes containing non-innocent ligands, and the application of frustrated Lewis pairs in metal-free catalysis.

Section 2 is concerned with secondary bonding interactions (SBI), which play an important role in the properties of bulk materials. The term SBI was originally coined by Alcock in 1960s, but nowadays this term starts to be superseded by more popular expressions like halogen, chalcogen, pnictogen (or pnicogen), and tetrel bonding. Section 2 of Volume 1 contains a separate chapter on the general theoretical considerations of the secondary bonding interactions, and then more specialized treatments of halogen and

chalcogen bonding. This section is concluded by the update of the host-guest chemistry of the molecules of p-block elements and by a comprehensive review of closed-shell  $d^{10}$ - $d^{10}$ ,  $d^8$ - $d^8$ , and  $s^2$ - $s^2$  metallophilic interactions.

Catenation continues to be one of the key characteristics in compounds of p-block elements. The third Section of Volume 1 is therefore dedicated to chain, ring, and cage (also called cluster) compounds in molecular inorganic chemistry. Separate chapters describe the recent chemistry of boron clusters, as well as the chain, ring, and cage compounds of Group 13 and 15, and 16 elements. A more specialized treatise is given on the aromatic compounds bearing heavy Group 14 atoms, Zintl-anions and -clusters, and a comprehensive account on polyhalogenide anions. This Section will be concluded by a review on organometallic clusters.

The driving force in chemical research arises from demands of materials science to develop new materials with innovative functionalities. It is important to establish the relationship of the molecular and electronic structures with the properties in the bulk material. Both new and old materials based on main group compounds show virtually unlimited number of interesting applications. Electrical conductors, semiconductors, insulators, coatings, ceramics, catalysts, nanotubes, polymers, and thin films all play a significant role in the current research in chemistry as well as in the modern technology. The increasing need to replace fossil fuels demands the development of environmentally friendlier energy sources in which molecular inorganic compounds are poised to play an important role due to their high availability and low manufacturing costs.

## References

- Djerassi, C.; Hoffmann, R. *Oxygen*, Wiley-VCH: Weinham-New York-Chichester-Brisbane-Singapore-Tokio, 2001; p 119.
- Nobel Lectures. *Chemistry 1901–1921*, Elsevier Publishing Company: Amsterdam, 1966.
- McCleverty, J. A. *Annu. Rep. Prog. Chem., Sect. A* **2004**, *100*, 3–13.
- Jones, S. *Quantum Ten: A Story of Passion, Tragedy, Ambition, and Science*, Thomas Allen Publishers: Toronto, 2008; p 323.
- Kumar, M. *Quantum: Einstein, Bohr, and the Great Debate about the Nature of Reality*, W. N. Norton & Company: New York-London, 2008; p 448.
- NobelPrize.org. *Nobel Prizes in Chemistry*. Nobel Prize Outreach AB. <https://www.nobelprize.org/prizes/lists/all-nobel-prizes-in-chemistry>, 2022.
- Chivers, T.; Konu, J. *Comments Inorg. Chem.* **2009**, *30*, 131–176.
- Pedersen, C. J. *J. Am. Chem. Soc.* **1967**, *89*, 7017–7036.
- Gokel, G. W.; Negin, S.; Catwell, R. In *Comprehensive Supramolecular Chemistry II*; Atwood, J. L., Gokel, G. W., Barbour, L. J., Eds.; vol. 3; Elsevier: Amsterdam, 2017; pp 3–48 (and references therein).
- Bartlett, N.; Lohmann, D. H. *Proc. Chem. Soc.* **1962**, 115–116.
- Bartlett, N. In *Fluorine Chemistry at the Millenium*, Fascinated by Fluorine; Banks, R. E., Ed., Elsevier: Amsterdam, 2000; pp 29–55.
- Bartlett, N. *Proc. Chem. Soc.* **1962**, 218.
- Gillespie, R. J. *Coord. Chem. Rev.* **2008**, *252*, 1315–1327.
- Gillespie, R. J.; Nyholm, R. S. *Quart. Rev. Chem. Soc.* **1957**, *11*, 339–481.
- Sidgwick, N. V.; Powell, H. E. *Proc. Royal Soc. A* **1940**, *176*, 153–180.
- Gillespie, R. J. *Can. J. Chem.* **1992**, *70*, 742–750.
- Gillespie, R. J. *Chem. Soc. Rev.* **1979**, *8*, 315–352.
- Wade, K. *Adv. Inorg. Chem. Radiochem.* **1976**, *18*, 1–66.
- Williams, R. E. *Adv. Inorg. Chem. Radiochem.* **1976**, *18*, 67–142.
- Mingos, D. M. P. *Pure Appl. Chem.* **1991**, *63*, 807–812.
- Power, P. P. *Nature* **2010**, *463*, 171–177.
- Yam, V. W.-W. *Angew. Chem. Int. Ed.* **2015**, *54*, 8304–8305.
- West, R.; Fink, M. J.; Michl, J. *Science* **1981**, *214*, 1343–1344.
- Yoshifuji, M.; Shima, I.; Inamoto, N. *J. Am. Chem. Soc.* **1981**, *103*, 4587–4589.
- Balázs, L.; Breunig, H. J. *Coord. Chem. Rev.* **2004**, *248*, 603–621.
- Kira, M.; Iwamoto, T. *Adv. Organomet. Chem.* **2006**, *54*, 73–148.
- Fischer, R. C.; Power, P. P. *Chem. Rev.* **2010**, *110*, 3877–3923.
- Rammo, A.; Scheschkevit, D. *Chem. Eur. J.* **2018**, *24*, 6866–6885.
- Weetman, C. *Chem. Eur. J.* **2021**, *27*, 1941–1954.
- Yoshifuji, M. *Molecules* **2022**, *27*, 1557.
- Tokitoh, N.; Aral, Y.; Okazaki, R.; Nagase, S. *Science* **1997**, *277*, 78–80.
- Okazaki, R.; Tokitoh, N. *Acc. Chem. Res.* **2000**, *33*, 625–630.
- Rivard, E.; Power, P. P. *Inorg. Chem.* **2007**, *46*, 10047–10064.
- Sekiguchi, A.; Kinjo, R.; Ichinohe, M. *Science* **2004**, *305*, 1755–1757.
- Xu, H.; Weetman, C.; Hanusch, F.; Inoue, S. *Chem. Eur. J.* **2022**, *28*, e202104042.
- Hua, G.; Du, J.; Slawin, A. M. Z.; Woollins, J. D. *Chem. Eur. J.* **2016**, *22*, 7782–7791.
- Alcock, N. W. *Adv. Inorg. Chem. Radiochem.* **1972**, *15*, 1–58.
- Cavallo, G.; Metrangolo, P.; Milani, R.; Pilati, T.; Priimagi, A.; Resnati, G.; Terraneo, G. *Chem. Rev.* **2016**, *116*, 2478–2601.
- Gilday, L. C.; Robinson, S. W.; Barendt, T. A.; Langton, M. J.; Mullaney, B. R.; Beer, P. D. *Chem. Rev.* **2015**, *115*, 7118–7195.
- Kolář, M. H.; Hobza, P. *Chem. Rev.* **2016**, *116*, 5155–5187.
- Wang, H.; Wang, W.; Jin, W. J. *Chem. Rev.* **2016**, *116*, 5072–5104.
- Desiraju, G. R.; Ho, P. S.; Kloo, L.; Legon, A. C.; Marquardt, R.; Metrangolo, P.; Politzer, P.; Resnati, G.; Rissanen, K. *Pure Appl. Chem.* **2013**, *85*, 1711–1713.
- Aakeroy, C. B.; Bryce, D. L.; Desiraju, G. R.; Frontera, A.; Legon, A. C.; Nicotra, F.; Rissanen, K.; Scheiner, S.; Terraneo, G.; Metrangolo, P.; Resnati, G. *Pure Appl. Chem.* **2019**, *91*, 1889–1892.
- Kolb, S.; Oliver, G. A.; Werz, D. B. *Angew. Chem. Int. Ed.* **2020**, *59*, 22306–22310.
- Gleiter, R.; Haberhauer, G.; Werz, D. B.; Rominger, F.; Bleiholder, C. *Chem. Rev.* **2018**, *118*, 2010–2041.
- Chivers, T.; Laitinen, R. S. *Chem. Soc. Rev.* **2015**, *44*, 1725–1739.
- Cozzolino, A. F.; Elder, P. J. W.; Vargas-Baca, I. *Coord. Chem. Rev.* **2011**, *255*, 1426–1438.
- Juanes, M.; Saragi, R. T.; Caminati, W.; Lesarri, A. *Chem. Eur. J.* **2019**, *25*, 11402–11411.
- Grabowski, S. J. *Struct. Chem.* **2019**, *30*, 1141–1152.

50. Scilabra, P.; Kumar, V.; Ursini, M.; Resnati, G. *J. Mol. Mod.* **2018**, *24*, 1–18.
51. Scilabra, P.; Terraneo, G.; Resnati, G. *J. Fluorine Chem.* **2017**, *203*, 62–74.
52. Politzer, P.; Murray, J. S.; Clark, T. *Phys. Chem. Chem. Phys.* **2013**, *15*, 11178–11189.
53. Doerrner, L. H. *Comments Inorg. Chem.* **2008**, *29*, 93–127.
54. Zheng, J.; Lu, Z.; Wu, K.; Ning, G.-H.; Li, D. *Chem. Rev.* **2020**, *120*, 9675–9742.
55. Kolay, S.; Bain, D.; Maity, S.; Devi, A.; Patra, A.; Antoine, R. *Nanomaterials* **2022**, *12*, 544.
56. Pyykkö, P. *Chem. Rev.* **1997**, *97*, 597–636.
57. Zheng, Q.; Borsley, S.; Nichol, G. S.; Duarte, F.; Cockroft, S. L. *Angew. Chem. Int. ed.* **2019**, *58*, 12617–12623.
58. Müller, F.; Wickenmeyer, L.; Schwabedissen, J.; Erti, M.; Neumann, B.; Stammer, G.; Monkowius, U.; Mitzel, N. W. *Dalton Trans.* **2022**, *51*, 1955–1967.
59. Brunecker, C.; Arrowsmith, M.; Müssig, J. H.; Böhnke, J.; Stoy, A.; Heß, M.; Hofmann, A.; Lenczyk, C.; Lichtenberg, C.; Ramler, J.; Rempel, A.; Braunschweig, H. *Dalton Trans.* **2021**, *50*, 3506–3515.
60. Haneline, M. R.; Gabbai, F. P. *Angew. Chem. Int. Ed.* **2004**, *43*, 5471–5474.
61. Risto, M.; Takaluoma, T. T.; Bajorek, T.; Oilunkaniemi, R.; Laitinen, R. S.; Chivers, T. *Inorg. Chem.* **2009**, *48*, 6271–6279.
62. Chivers, T.; Parvez, M.; Schatte, G. *Angew. Chem. Int. Ed.* **1999**, *38*, 2217–2219.
63. Wu, H.; Dong, X.-W.; Ma, J.-F. *Acta Crystallogr. Sect E* **2006**, *62*, m1227–m1228.
64. Tan, H.-Y.; Zhang, H.-X.; Ou, H.-D.; Kang, B.-S. *Inorg. Chim. Acta* **2004**, *357*, 869–874.
65. Brands, M. B.; Nitsch, J.; Guerra, C. F. *Inorg. Chem.* **2018**, *57*, 2603–2608 (and references therein).
66. Spikes, G. H.; Fettingner, J. C.; Power, P. P. *J. Am. Chem. Soc.* **2005**, *127*, 12232–12233.
67. Peng, Y.; Brynda, M.; Ellis, B. D.; Fettingner, J. C.; Rivard, E.; Power, P. P. *Chem. Commun.* **2008**, 6042–6044.
68. Power, P. P. *Organometallics* **2007**, *26*, 4362–4372.
69. Frey, G. D.; Lavallo, B.; Donnadiu, B.; Schoeller, W. W.; Bertrand, G. *Science* **2007**, *316*, 439–441.
70. Welch, G. C.; San Juan, R. R.; Masuda, J. D.; Stephan, D. W. *Science* **2006**, *314* (5802), 1124–1126.
71. Stephan, D. W. *J. Am. Chem. Soc.* **2021**, *143*, 20002–20014.
72. Kelly, P. F.; King, R. S. P. In *Comprehensive Inorganic Chemistry II*; Reedijk, J., Poeppelmeier, K., Eds., 2nd edn.; vol. 1; Elsevier: Amsterdam, 2013; pp 179–196.
73. Laitinen, R. S.; Oilunkaniemi, R. In *Comprehensive Inorganic Chemistry II*; Reedijk, J., Poeppelmeier, K., Eds., 2nd ed.; vol. 1; Elsevier: Amsterdam, 2013; pp 197–231.
74. Krossing, I.; Raabe, I. *Angew. Chem. Int. Ed.* **2004**, *43*, 2066–2090.
75. Aris, D.; Beck, J.; Decken, A.; Dionne, I.; Schmedt auf der Günne, J.; Hoffbauer, W.; Köchner, T.; Krossing, I.; Passmore, J.; Rivard, E.; Steden, F.; Wang, X. *Dalton Trans.* **2011**, *40*, 5865–5880.
76. Patmore, N. J.; Hague, C.; Cotgreave, J. H.; Mahon, M. F.; Frost, C. G.; Weller, A. S. *Chem. Eur. J.* **2002**, *8*, 2088–2098.
77. Chivers, T.; Konu, J. In *Comprehensive Inorganic Chemistry II*; Reedijk, J., Poeppelmeier, K., Eds., 2nd ed.; vol. 1; Elsevier: Amsterdam, 2013; pp 349–373.
78. Stuyver, T.; Chen, B.; Zeng, T.; Geerlings, P.; De Proft, F.; Hoffmann, R. *Chem. Rev.* **2019**, *119*, 11291–11351.
79. Breher, F. *Coord. Chem. Rev.* **2007**, *251*, 1007–1043.
80. González-Gallardo, S.; Breher, F. In *Comprehensive Inorganic Chemistry II*; Reedijk, J., Poeppelmeier, K., Eds., 2nd edn; vol. 1; Elsevier: Amsterdam, 2013; pp 413–455.
81. Scheschke, D.; Amii, H.; Gornitzka, H.; Schoeller, W. W.; Bourissou, D.; Bertrand, G. *Angew. Chem. Int. Ed.* **2004**, *43*, 585–587.
82. Jung, Y.; Heine, T.; Schleyer, P. v. R.; Head-Gordon, M. *J. Am. Chem. Soc.* **2004**, *126*, 3132–3138.
83. Braida, B.; Lo, A.; Hiberty, P. C. *ChemPhysChem* **2012**, *13* (3), 811–819.
84. Bailar, J. C. Jr., Emeléus, H. J., Nyholm, R., Trotman-Dickenson, A. F., Eds.; *Comprehensive Inorganic Chemistry*; vols. 1–5; Pergamon Press: Oxford-New York-Toronto-Sydney-Braunschweig, 1973.
85. Reedijk, J., Poeppelmeier, K., Eds.; *Comprehensive Inorganic Chemistry II*, 2nd edn; vols. 1–9; Elsevier, 2013. Amsterdam.

## 1.02 Main group metal coordination chemistry

Catherine E. Housecroft and Edwin C. Constable, Department of Chemistry, University of Basel, Basel, Switzerland

© 2023 Elsevier Ltd. All rights reserved.

<b>1.02.1</b>	<b>Introduction</b>	<b>23</b>
<b>1.02.2</b>	<b>Nitrogen-donor ligands</b>	<b>23</b>
1.02.2.1	Monodentate ligands	23
1.02.2.1.1	NH <sub>3</sub> , RNH <sub>2</sub> , R <sub>3</sub> N	23
1.02.2.1.2	R <sub>2</sub> N <sup>-</sup> , RHN <sup>-</sup> , RN <sup>2-</sup>	27
1.02.2.1.3	Nitriles	31
1.02.2.1.4	N <sub>3</sub> , N-bonded CN <sup>-</sup> , NCO <sup>-</sup> , NCS <sup>-</sup> , NCS <sup>e-</sup>	32
1.02.2.1.5	Monodentate heterocyclic ligands	39
<b>1.02.2.2</b>	<b>Bidentate ligands</b>	<b>44</b>
1.02.2.2.1	Diamines	44
1.02.2.2.2	Imidoamidate and guanidinate ligands	46
1.02.2.2.3	β-Diketiminates	50
1.02.2.2.4	Triazenide ligands	52
1.02.2.2.5	2,2'-Bipyridine and 1,10-phenanthroline	53
<b>1.02.2.3</b>	<b>Tridentate ligands</b>	<b>53</b>
1.02.2.3.1	Triamines: Open-chain	53
1.02.2.3.2	Triamines: Tripodal ligands and tris(pyrazolyl)borates	54
1.02.2.3.3	Pincer ligands	57
1.02.2.3.4	2,2':6',2''-Terpyridines	58
1.02.2.4	Polydentate open-chain, macrocyclic and cage ligands	58
<b>1.02.3</b>	<b>Phosphorus-donor ligands</b>	<b>61</b>
<b>1.02.3.1</b>	<b>Monodentate ligands</b>	<b>61</b>
1.02.3.1.1	RPH <sub>2</sub> , R <sub>2</sub> PH, R <sub>3</sub> P including P,P-ligands in monodentate or bridging modes	61
1.02.3.1.2	R <sub>2</sub> P <sup>-</sup> , RPH <sup>-</sup> , RP <sup>2-</sup>	62
1.02.3.1.3	PCO <sup>-</sup> , PCS <sup>-</sup>	63
1.02.3.2	[P <sub>n</sub> ] <sup>x-</sup> ligands derived from P <sub>4</sub>	64
<b>1.02.3.3</b>	<b>Bidentate ligands</b>	<b>65</b>
1.02.3.3.1	Chelating bisphosphanes	65
1.02.3.3.2	PXP (X = P, CR) ligands with delocalized backbone	66
1.02.3.3.3	Heterocyclics: Reduced 2,2'-biphosphinine	66
1.02.3.4	Tris(phosphane) ligands: Open-chain and tripodal	66
<b>1.02.4</b>	<b>Arsenic-donor ligands</b>	<b>67</b>
<b>1.02.4.1</b>	<b>Monodentate ligands</b>	<b>67</b>
1.02.4.1.1	R <sub>3</sub> As	67
1.02.4.1.2	R <sub>2</sub> As <sup>-</sup>	67
1.02.4.1.3	AsCO <sup>-</sup>	67
1.02.4.2	Bidentate ligands: Chelating R <sub>2</sub> As(X)AsR <sub>2</sub>	67
1.02.4.3	Tridentate: Tripod ligands	68
<b>1.02.5</b>	<b>Antimony-donor ligands</b>	<b>68</b>
<b>1.02.5.1</b>	<b>Monodentate ligands</b>	<b>68</b>
1.02.5.1.1	R <sub>3</sub> Sb	68
1.02.5.1.2	R <sub>2</sub> Sb <sup>-</sup>	68
<b>1.02.6</b>	<b>Oxygen-donor ligands</b>	<b>68</b>
<b>1.02.6.1</b>	<b>Monodentate ligands: Simple coordination compounds</b>	<b>68</b>
1.02.6.1.1	H <sub>2</sub> O (restricted to simple aqua complexes)	68
1.02.6.1.2	ROH, R <sub>2</sub> O	70
1.02.6.1.3	RO <sup>-</sup>	70
1.02.6.1.4	NCO <sup>-</sup> and PCO <sup>-</sup>	71
1.02.6.1.5	R <sub>3</sub> PO	71
1.02.6.1.6	Monodentate heterocyclic ligands	73
1.02.6.1.7	Monodentate acetato ligands	75
<b>1.02.6.2</b>	<b>Bidentate ligands</b>	<b>75</b>
1.02.6.2.1	1,2-Dimethoxyethane	75
1.02.6.2.2	Diol and diolato ligands	76
1.02.6.2.3	β-Diketonates	77



1.02.6.2.4	Carboxylates: Bidentate and bridging	78
1.02.6.2.5	Oxalate	80
1.02.6.2.6	<i>N,N</i> -Dioxides of 2,2'-bpy (bpy) and 4,4'-bpy	82
1.02.6.3	Tridentate (open-chain)	83
1.02.6.4	Polydentate (open-chain)	84
1.02.6.5	Macrocyclic ligands	85
<b>1.02.7</b>	<b>Sulfur-donor ligands</b>	<b>85</b>
1.02.7.1	Monodentate ligands	85
1.02.7.1.1	R <sub>2</sub> S	85
1.02.7.1.2	S <sub>n</sub> <sup>2-</sup> (bridging modes)	85
1.02.7.1.3	S-Bonded NCS <sup>-</sup>	86
1.02.7.1.4	Heterocyclic ligands	87
1.02.7.2	Bidentate: [S(CH <sub>2</sub> ) <sub>2</sub> S] <sup>2-</sup> and RS(X)SR	88
1.02.7.3	Tridentate	88
1.02.7.4	Macrocyclic ligands (S only donors)	88
<b>1.02.8</b>	<b>Selenium-donor ligands</b>	<b>89</b>
1.02.8.1	Monodentate and bidentate ligands	89
1.02.8.1.1	R <sub>2</sub> Se	89
1.02.8.1.2	Heterocyclics	90
1.02.8.1.3	RSe(X)SeR	90
1.02.8.2	Tridentate ligands	91
1.02.8.3	Macrocyclic ligands (Se only donors)	91
<b>Acknowledgments</b>		<b>92</b>
<b>References</b>		<b>92</b>

### Abbreviations

<b>8Se2</b>	1,5-Diselenacyclooctane
<b>9S3</b>	1,4,7-Trithiacyclononane
<b>10S3</b>	1,4,7-Trithiacyclodecane
<b>12S4</b>	1,4,7,10-Tetrathiacyclododecane
<b>14S4</b>	1,4,8,11-Tetrathiacyclotetradecane
<b>16S4</b>	1,5,9,13-Tetrathiacyclohexadecane
<b>16Se4</b>	1,5,9,13-Tetraselenacyclohexadecane
<b>18S6</b>	1,4,7,10,13,16-Hexathiacyclooctadecane
<b>24Se6</b>	1,5,9,13,17,21-Hexaselenacyclotetracosane
<b>24S8</b>	1,4,7,10,13,16,19,22-Octathiacyclotetracosane
<b>AcOH</b>	Acetic acid
<b>amgu</b>	Aminoguanidine
<b>Bz18-crown-6</b>	6,7,9,10,17,18,20,21-Octahydrodibenzo[b,k][1,4,7,10,13,16]hexaoxacyclooctadecine
<b>[BAR<sup>F</sup><sub>4</sub>]<sup>-</sup></b>	[{3,5-(CF <sub>3</sub> ) <sub>2</sub> C <sub>6</sub> H <sub>3</sub> } <sub>4</sub> B] <sup>-</sup>
<b>bbp</b>	2,6-Bis(benzimidazol-2-yl)pyridine
<b>bpy</b>	2,2'-Bipyridine
<b>bpydo</b>	2,2'-Bipyridine <i>N,N'</i> -dioxide
<b>4,4'-bpy</b>	4,4'-Bipyridine
<b>4,4'-bpydo</b>	4,4'-Bipyridine <i>N,N'</i> -dioxide
<b><sup>t</sup>Bu<sub>2</sub>acac</b>	2,2,6,6-Tetramethyl-3,5-heptanedione
<b><sup>t</sup>BuOacac</b>	<i>tert</i> -Butyl 3-oxobutanoate
<b><sup>t</sup>BuO<sub>2</sub>acac</b>	Di- <i>tert</i> -butyl malonate/di- <i>tert</i> -butyl propanedione
<b>Bz</b>	Benzyl
<b>4-ClC<sub>6</sub>H<sub>4</sub>tpy</b>	4'-(4-Chlorophenyl)-2,2':6',2''-terpyridine
<b>CMA</b>	Calcium magnesium acetate
<b>CN</b>	Coordination number
<b>4-HO<sub>2</sub>Cpy</b>	Pyridine-4-carboxylic acid
<b>CVD</b>	Chemical vapor deposition

Cy Cyclohexyl  
**dab** 1,4-Diaminobutane  
**dabco** 1,4-Diazabicyclo[2.2.2]octane  
**dgm** Bis(2-methoxyethyl) ether (or diglyme)  
**Dipp** 2,6-<sup>i</sup>Pr<sub>2</sub>C<sub>6</sub>H<sub>3</sub>  
**depe** 1,2-Bis(diethylphosphano)ethane  
**depeO<sub>2</sub>** 1,2-Bis(diethylphosphano)ethane dioxide  
**dien** *N*<sup>1</sup>-(2-Aminoethyl)ethane-1,2-diamine (or diethylenediamine)  
**diox** 1,4-Dioxane  
**dith** 1,4-Dithiane  
**dmap** 4-Dimethylaminopyridine  
**dme** 1,2-Dimethoxyethane  
**dmpbz** 1,2-Bis(dimethylphosphano)benzene  
**dmpe** 1,2-Bis(dimethylphosphano)ethane  
**dpae** 1,2-Bis(diphenylarsano)ethane  
**dpp-bian** 1,2-Bis{(2,6-diisopropylphenyl)imino}acenaphthene  
**dppb** 1,4-Bis(diphenylphosphano)butane  
**dppbO<sub>2</sub>** 1,4-Bis(diphenylphosphano)butane dioxide  
**dppbz** 1,2-Bis(diphenylphosphano)benzene  
**dppe** 1,2-Bis(diphenylphosphano)ethane  
**dppeO<sub>2</sub>** 1,2-Bis(diphenylphosphano)ethane dioxide  
**dppeeO<sub>2</sub>** 1,2-Bis(diphenylphosphano)ethene dioxide  
**dppm** Bis(diphenylphosphano)methane  
**dppmO** Bis(diphenylphosphano)methane monoxide  
**dppmO<sub>2</sub>** Bis(diphenylphosphano)methane dioxide  
**en** Ethane-1,2-diamine  
**Hacac** 2,4-Pentanedione  
**[HBpz<sub>3</sub>]<sup>-</sup>** Tris(pyrazolyl)borate  
**[emim]<sup>+</sup>** 1-Ethyl-3-methylimidazolium  
**HGu** Guanidine  
**Hhfacac** 1,1,1,5,5,5-Hexafluoropentane-2,4-dione  
**Him** Imidazole  
**MeHim** 1-Methyl-1H-imidazole  
**Hinz** Indazole  
**hmpa** Hexamethylphosphoramide (hexamethylphosphoric triamide)  
**Hppy** 2-Phenylpyridine  
**Hpz** Pyrazole  
**Hpz-3,5-Me<sub>2</sub>** 3,5-Dimethylpyrazole  
**Hpz-3,5-Ph<sub>2</sub>** 3,5-Diphenylpyrazole  
**Hpz-4-CO<sub>2</sub>H** 1H-Pyrazole-4-carboxylic acid  
**Hpz-4-SO<sub>3</sub>H** 1H-Pyrazole-4-sulfonic acid  
**Hpz-5-th** 5-(2-Thienyl)pyrazole  
**H(4-Meppy)** 2-(4-Methylphenyl)pyridine  
**HRtfacac** 1-R-4,4,4-Trifluorobutane-1,3-dione (substituent R is specified in the text)  
**Htfacac** 1,1,1-Trifluoropentane-2,4-dione  
**H<sup>t</sup>Butfacac** 1,1,1-Trifluoro-5,5-dimethyl-2,4-hexanedione  
**H<sub>2</sub>adip** Adipic acid (hexanedioic acid)  
**H<sub>2</sub>boa** 4-(Carboxymethoxy)benzoic acid  
**H<sub>2</sub>edt** Ethane-1,2-dithiol  
**H<sub>2</sub>iQ** 1,2-Dihydroisoquinoline  
**4-H<sub>2</sub>Npy** 4-Aminopyridine  
**H<sub>2</sub>pc** Phthalocyanine  
**H<sub>2</sub>pin<sup>F</sup>** 2,3-Bis(trifluoromethyl)perfluorobutane-2,3-diol  
**H<sub>4</sub>tabht** 2,10-Dioxo-1,4,8,11-tetraazabicyclo[11.4.0]1,12-heptadeca-1 (12),14,16-triene

**Htmp** 2,2,6,6-Tetramethylpiperidine  
**H<sub>2</sub>tmtaa** 5,14-Dihydro-6,8,15,17-tetramethyldibenzo[b,i][1,4,8,11] tetraazacyclotetradecine  
**H<sub>2</sub>tpp** 5,10,15,20-Tetraphenylporphyrin  
**H<sub>2</sub>tppBr** 5,10,15,20-Tetrakis(4-bromophenyl)porphyrin  
**H<sub>2</sub>tpp<sup>t</sup>Bu** 5,10,15,20-Tetrakis(4-<sup>t</sup>butylphenyl)porphyrin  
**iQ** Isoquinoline  
**Me<sub>3</sub>tacd** 1,4,7-Trimethyl-1,4,7,10-tetraazacyclododecane  
**Me<sub>4</sub>tacd** 1,4,7,10-Tetramethyl-1,4,7,10-tetraazacyclododecane  
**Me<sub>6</sub>trien** 1,1,4,7,10,10-Hexamethyltriethylenetetramine  
**5,5'-Me<sub>2</sub>bpy** 5,5'-Dimethyl-2,2'-bipyridine  
**2,9-Me<sub>2</sub>phen** 2,9-Dimethyl-1,10-phenanthroline  
**2-Mepy** 2-Methylpyridine  
**4-Mepy** 4-Methylpyridine  
**3,5-Me<sub>2</sub>py** 3,5-Dimethylpyridine  
**MeO<sub>2</sub>acac** Dimethyl malonate/dimethyl propanedione  
**4,4'-(MeO)<sub>2</sub>bpy** 4,4'-Dimethoxy-2,2'-bipyridine  
**Mes** Mesityl  
**NBO** Natural bond orbital  
**NLO** Non-linear optical  
**pentagm** 2,5,8,11,14,17-Hexaoxaoctadecane  
**phen** 1,10-Phenanthroline  
**Ph<sub>2</sub>acac** 1,3-Diphenylpropane-1,3-dione  
**pip** Piperidine  
**pipz** Piperazine  
**pmdeta** *N*<sup>1</sup>-(2-*N,N*-Dimethylaminoethyl)-*N*<sup>1</sup>,*N*<sup>2</sup>,*N*<sup>2</sup>-trimethylethane-1,2-diamine (*N,N,N',N'',N''*-pentamethyldiethylenetriamine)  
**pn** Propane-1,3-diamine  
**py** Pyridine  
**pym** Pyrimidine  
**pyz** Pyrazene  
**quin** Quinuclidine  
**salen** *N,N*-Bis(salicylidene)ethylenediamine  
**seth** Selenanthrene  
**tacd** 1,4,7,10-Tetraazacyclododecane  
**tacn** 1,4,7-Triazacyclononane  
**teg** 2,2'-((Oxybis(ethane-2,1-diyl))bis(oxy))bis(ethan-1-ol)  
**tetraen** (*N,N*-Bis(2-((2-aminoethyl)amino)ethyl)amine)  
**tetragm** 2,5,8,11,14-Pentaoxapentadecane  
**TFSI** Bis(trifluoromethanesulfonyl)imide  
**tgm** 2,5,8,11-Tetraoxadodecane  
**THF** Tetrahydrofuran  
**3-(Thiophen-2'-yl)phen** 3-(Thiophen-2'-yl)-1,10-phenanthroline  
**thp** Thiophene  
**tht** Tetrahydrothiophene  
**tmbp** 4,4',5,5'-Tetramethyl-2,2'-biphosphinine  
**tmeda** 1,2-Bis(dimethylamino)ethane  
**tmpda** 1,3-Bis(dimethylamino)propane  
**tpy** 2,2':6',2''-Terpyridine  
**trien** *N*<sup>1</sup>,*N*<sup>1'</sup>-(ethane-1,2-diyl)bis(ethane-1,2-diamine)  
**tripodSe<sub>3</sub>** 1,1,1-Tris(methylselenomethyl)ethane  
**Tripp** 2,4,6-<sup>t</sup>Pr<sub>3</sub>C<sub>6</sub>H<sub>2</sub>  
**TROP** [5*H*]Dibenzo[*a,d*]cyclohepten-5-yl  
**tth** Thianthrene

## Abstract

This article surveys the coordination chemistry of the main group metals (s- and p-block metals) published during the period 2000–2021. Within the p-block, metallic elements include Al–Tl for group 13, Ge–Pb for group 14, Sb and Bi for group 15, and Te for group 16. The lighter elements in groups 15 (N, P, As) and 16 (O, S, Se) typically behave as donor atoms in ligands. However, the distinction is blurred, and As(III) is included as a metal center with, for example, S- and Se-donor ligands, and Al(III) and Ga(III) complexes containing Sb-donor ligands are included. The aim of the review is to provide as comprehensive as coverage as possible so as to demonstrate different bonding modes of ligands, and the range of metal centers to which they coordinate. At the same time, the number of structurally characterized main group metal complexes is so extensive that a totally comprehensive survey has not been possible within the page constraints.

### 1.02.1 Introduction

This chapter deals with the coordination chemistry of the main group elements and covers coordination compounds of metals in group 1 (Li–Cs), group 2 (Be–Ba) and group 13 (Al–Tl), and of metals or semi-metals in group 14 (Ge–Pb), group 15 (Sb, Bi), and group 16 (Te). The lighter elements in groups 15 (N, P, As) and 16 (O, S, Se) typically behave as donor atoms in ligands. Although *Comprehensive Inorganic Chemistry II* (CIC II) was published in 2013, it did not include a chapter dealing with main group coordination chemistry and, therefore, this article covers the literature from the year 2000 to date. A number of reviews published since 2000 complement the present survey of metal coordination compounds: group 1 and 2 metals including thermodynamic aspects and metal ion sensors,<sup>1–14</sup> aluminum including speciation in solution and under physiological conditions,<sup>15–34</sup> group 13 metals Ga–Tl including precursors for chemical vapor deposition (CVD) materials,<sup>26,30–47</sup> group 14,<sup>34,48–58</sup> group 15,<sup>59–63</sup> and tellurium-centered compounds.<sup>64–67</sup> With an emphasis on ligand-types, the following reviews cover the coordination chemistry of the main group elements with phosphane, arsane and stibane ligands,<sup>68</sup> with amidinate and guanidinate ligands,<sup>69</sup> with tripodal amido ligands,<sup>70</sup> with ligands derived from (XPR<sub>2</sub>)(YPR'<sub>2</sub>)NH acids (X, Y = O, S, Se; R, R' = alkyl, aryl, OR),<sup>71</sup> with  $\alpha$ -diimine ligands,<sup>72</sup> with semicarbazone and thiosemicarbazone ligands,<sup>73,74</sup> with anionic scorpionate ligands,<sup>75</sup> with boraamidinate ligands,<sup>76</sup> with imido ligands,<sup>77–79</sup> with nitrido ligands,<sup>80</sup> with ene-diamido ligands,<sup>9</sup> with formazanate ligands (formazan = Ar<sup>1</sup>-NH-N=CR-N=N-Ar<sup>2</sup>),<sup>81</sup> with amidoborane ligands,<sup>13</sup> with bis(phosphinimino)methanide ligands,<sup>82</sup> with N-heterocyclic imines<sup>83</sup> and N-heterocyclic carbenes,<sup>84,85</sup> and with sterically demanding monodentate amide ligands.<sup>86</sup> Tan and García have reviewed the use of mechanochemical methods in main group metal chemistry.<sup>87</sup>

The literature concerning the coordination chemistry of main group elements is very extensive and we have focused our attention on compounds that are structurally characterized, and on single donor ligands. The primary source of data was the Cambridge Structural Database (CSD)<sup>88,89</sup> with searches made using Conquest v. 2021.3.0 and v. 2022.1.0<sup>88</sup> and figures drawn using Mercury 2021.3.0 and v. 2022.1.0.<sup>90</sup> We have also sourced data from the Inorganic Crystal Structure Database (ICSD, v. 4.7.1, data release 2021.2).<sup>91</sup> Coordination compounds are organized in the following sections by ligand type, with binary metal halide and hydride complexes excluded. The latter have been detailed in several reviews.<sup>92–95</sup> Compounds which include M–C bonds, including metallocene units, have been excluded. Our aim has been to provide an overview that illustrates structure-types rather than a comprehensive coverage since the latter is neither possible within the page-extent available, nor of help to the reader.

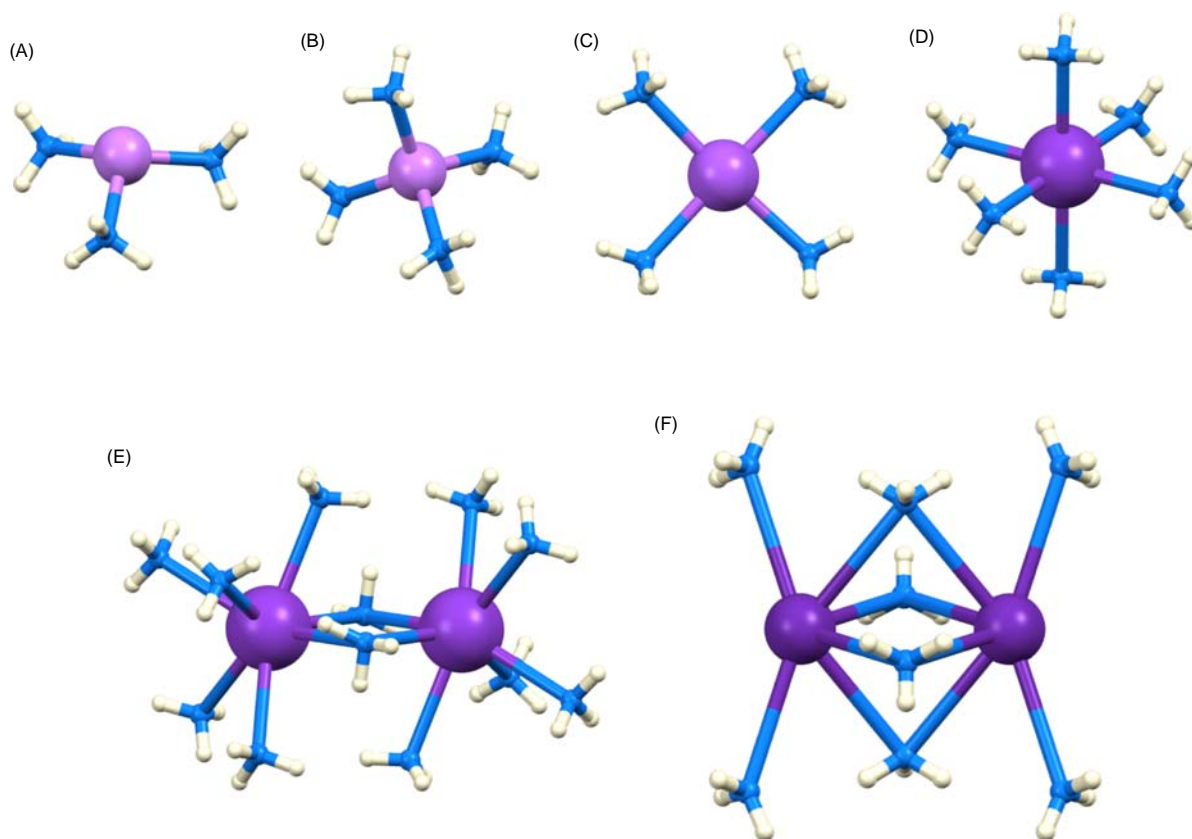
After considerable debate, we have decided not to ‘standardize’ ligand names and abbreviations to IUPAC recommendations. In part, this represents a desire to retain the nomenclature associated with the original publications and the intimate community. Ligand abbreviations used in this review are listed at the beginning of the article.

### 1.02.2 Nitrogen-donor ligands

#### 1.02.2.1 Monodentate ligands

##### 1.02.2.1.1 NH<sub>3</sub>, RNH<sub>2</sub>, R<sub>3</sub>N

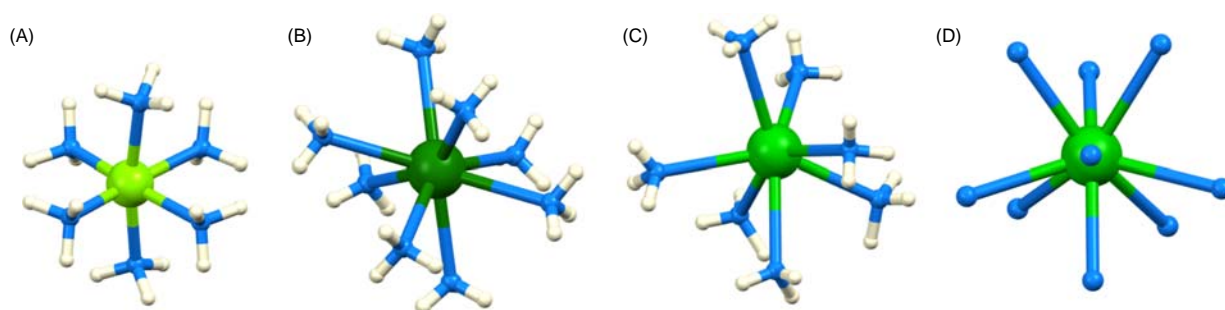
Homoleptic main-group metal ammine complexes are restricted to the s-block (groups 1 and 2) metals and aluminum. One motivation for investigations of these complexes is their potential for hydrogen storage, e.g., using [Mg(NH<sub>3</sub>)<sub>6</sub>]Cl<sub>2</sub>, it is possible to store 9.1% hydrogen by weight in the form of ammonia.<sup>96</sup> The use of liquid NH<sub>3</sub> as a solvent, for example, in reactions to form Zintl ions or hydroborate clusters, is also a method by which s-block metal ammine complexes are accessed. **Fig. 1** illustrates the structures of the group 1 metal complex cations [Li(NH<sub>3</sub>)<sub>3</sub>]<sup>+</sup>,<sup>97</sup> [Li(NH<sub>3</sub>)<sub>4</sub>]<sup>+</sup>,<sup>97–102</sup> [Na(NH<sub>3</sub>)<sub>4</sub>]<sup>+</sup>,<sup>102</sup> [K(NH<sub>3</sub>)<sub>6</sub>]<sup>+</sup>,<sup>103</sup> [K<sub>2</sub>(NH<sub>3</sub>)<sub>10</sub>( $\mu$ -NH<sub>3</sub>)<sub>2</sub>]<sup>2+</sup>,<sup>104</sup> and [Rb<sub>2</sub>(NH<sub>3</sub>)<sub>4</sub>( $\mu$ -NH<sub>3</sub>)<sub>4</sub>]<sup>2+</sup>.<sup>100</sup> The increase in coordination number with size of metal ion is as expected. The 3-coordinate [Li(NH<sub>3</sub>)<sub>3</sub>]<sup>+</sup> occurs (along with [Li(NH<sub>3</sub>)<sub>4</sub>]<sup>+</sup>) in the salt Li<sub>2</sub>B<sub>12</sub>H<sub>12</sub>·7NH<sub>3</sub> and is stabilized by additional Li··H–B contacts in the solid state.<sup>97</sup> In contrast to Li<sub>2</sub>B<sub>12</sub>H<sub>12</sub>·7NH<sub>3</sub>,<sup>97</sup> Li<sub>2</sub>B<sub>12</sub>H<sub>12</sub>·10NH<sub>3</sub> contains tetrahedral [Li(NH<sub>3</sub>)<sub>4</sub>]<sup>+</sup> and NH<sub>3</sub> solvate,<sup>100</sup> and the tetrahedral [Li(NH<sub>3</sub>)<sub>4</sub>]<sup>+</sup> ion is more usual than [Li(NH<sub>3</sub>)<sub>3</sub>]<sup>+</sup>. The square-planar structure of [Na(NH<sub>3</sub>)<sub>4</sub>]<sup>+</sup> is found in the indenyl salt [Na(NH<sub>3</sub>)<sub>4</sub>][In] which forms a layered structure, in contrast to the non-layered [Li(NH<sub>3</sub>)<sub>4</sub>][In] which contains tetrahedral



**Fig. 1** Structures of group 1 metal ammine complexes: (A)  $[\text{Li}(\text{NH}_3)_3]^+$  (CSD refcode XUNYAH), (B)  $[\text{Li}(\text{NH}_3)_4]^+$  (refcode COVLUV), (C)  $[\text{Na}(\text{NH}_3)_4]^+$  (refcode XICMED), (D)  $[\text{K}(\text{NH}_3)_6]^+$  (refcode QOTQOH), (E)  $[\text{K}_2(\text{NH}_3)_{10}(\mu\text{-NH}_3)_2]^{2+}$  (refcode XEJWAL), and (F)  $[\text{Rb}_2(\text{NH}_3)_4(\mu\text{-NH}_3)_4]^{2+}$  (refcode VIHGQU).

$[\text{Li}(\text{NH}_3)_4]^+$  ions.<sup>102</sup> Ammine complexes of  $\text{K}^+$  are represented by the octahedral  $[\text{K}(\text{NH}_3)_6]^+$  and the dinuclear  $[\text{K}_2(\text{NH}_3)_{10}(\mu\text{-NH}_3)_2]^{2+}$  (Fig. 1E) in which  $\text{K}^+$  is 7-coordinate; the K–N distances for the bridging  $\text{NH}_3$  ligands are only slightly longer (3.087(2) Å) than the terminal bonds (2.933(2)–2.998(2) Å).<sup>104</sup> The  $[\text{K}(\text{NH}_3)_7]^+$  ion has also been structurally characterized (see later).<sup>105</sup> The  $[\text{Rb}_2(\text{NH}_3)_4(\mu\text{-NH}_3)_4]^{2+}$  ion (Fig. 1F) is present in  $\text{Rb}_2[\text{B}_{12}\text{H}_{12}] \cdot 8\text{NH}_3$ , whereas in  $\text{Cs}_2[\text{B}_{12}\text{H}_{12}] \cdot 6\text{NH}_3$ , the  $\text{Cs}^+$  ion is bound by only two  $\text{NH}_3$  molecules ( $\text{Cs}–\text{N} = 3.259(2)$  and  $3.125(2)$  Å) with  $\text{Cs} \cdots \text{H}–\text{B}$  contacts completing the  $\text{Cs}^+$  coordination sphere.<sup>100</sup> The competition between M– $\text{NH}_3$  coordinate bond formation and  $\text{M} \cdots \text{H}–\text{B}$  interactions is often seen in the solid-state structures of ammine s-block metal borohydride salts, and further examples are found in  $\text{Li}_2\text{B}_{12}\text{H}_{12} \cdot 4\text{NH}_3$ ,  $\text{Na}_2\text{B}_{12}\text{H}_{12} \cdot 2\text{NH}_3$  and  $\text{NaB}_{12}\text{H}_{12} \cdot 3\text{NH}_3$ ,<sup>106</sup> and in  $\text{Na}_2\text{B}_{10}\text{H}_{10} \cdot 2\text{NH}_3$  and  $\alpha\text{-Na}_2\text{B}_{10}\text{H}_{10} \cdot \text{NH}_3$ .<sup>107</sup>

As in group 1, the increased size of the group 2 metal ion on descending the group leads to higher coordination numbers (CNs). The tetrahedral  $[\text{Be}(\text{NH}_3)_4]^{2+}$  ion is present in  $[\text{Be}(\text{NH}_3)_4]_2\text{Cl}_4 \cdot 17\text{NH}_3$ . The isolation and structural characterization of this compound in 2012 by Kraus et al. provided valuable insight into similarities and differences between aqua and ammine chemistry of the  $\text{Be}^{2+}$  ion.<sup>108</sup> Fig. 2A shows the octahedral  $[\text{Mg}(\text{NH}_3)_6]^{2+}$  ion characterized in  $\text{Li}_2\text{Mg}(\text{BH}_4)_4 \cdot 6\text{NH}_3$ .<sup>109</sup> The  $[\text{Ca}(\text{NH}_3)_7]^{2+}$  ion



**Fig. 2** Structures of group 2 metal ammine complexes: (A)  $[\text{Mg}(\text{NH}_3)_6]^{2+}$  (CSD refcode HIPFIX), (B)  $[\text{Sr}(\text{NH}_3)_8]^{2+}$  (refcode IFUZE0), (C)  $[\text{Ba}(\text{NH}_3)_7]^{2+}$  (refcode NUSVAY), and (D)  $[\text{Ba}(\text{NH}_3)_9]^{2+}$  (H atoms omitted, refcode EBOYOJ).



is present in  $[\text{NH}_4(\text{NH}_3)_4][\text{Ca}(\text{NH}_3)_7]\text{As}_3\text{S}_6 \cdot 2\text{NH}_3$  which was prepared by the reduction of  $\text{As}_4\text{S}_4$  using Ca in liquid  $\text{NH}_3$ . The coordination geometry of  $[\text{Ca}(\text{NH}_3)_7]^{2+}$  is a monocapped trigonal prism,<sup>110</sup> and is structurally similar to that reported by Kolis and coworkers in  $[\text{Ca}(\text{NH}_3)_7][\text{S}_6]$ .<sup>111</sup> Heavier group 2 metal ammine complexes include those associated with the syntheses of fullerene anions in liquid  $\text{NH}_3$  by reduction of  $\text{C}_{60}$  or  $\text{C}_{70}$  with a group 2 metal. The coordination geometries of the  $[\text{Sr}(\text{NH}_3)_8]^{2+}$  ion in different salts are described as a distorted, bicapped trigonal prism (Fig. 2B)<sup>112</sup> or distorted tetragonal anti-prism.<sup>113</sup> Ammine complexes of the heavy group 2  $\text{M}^{2+}$  ions are rather sparse. The structure of  $[\text{Ba}(\text{NH}_3)_7]^{2+}$  (Fig. 2C) in  $[\text{Ba}(\text{NH}_3)_7][\text{C}_{60}] \cdot \text{NH}_3$  is a mono-capped trigonal antiprism,<sup>105,114</sup> and this coordination geometry is replicated in  $[\text{K}(\text{NH}_3)_7]^+$  and  $[\text{Sr}(\text{NH}_3)_7]^{2+}$ .<sup>105</sup> The highest CN of nine is found in  $[\text{Ba}(\text{NH}_3)_9]^{2+}$  which adopts a distorted, tricapped trigonal prismatic structure (Fig. 2D).<sup>115</sup>

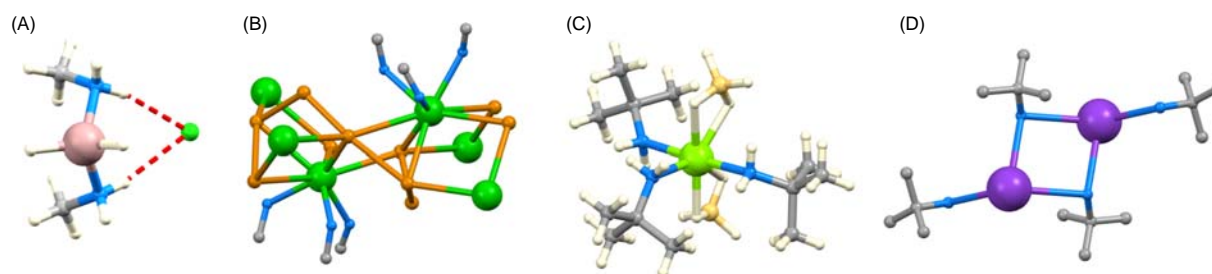
In addition to their relevance for hydrogen storage, group 13 ammine complexes are of interest as precursors for III-V semiconducting materials, and are represented by the octahedral  $[\text{Al}(\text{NH}_3)_6]^{3+}$  and  $[\text{Ga}(\text{NH}_3)_6]^{3+}$  ions.<sup>116–118</sup>

Examples of main group metal complexes incorporating monodentate amino ligands are restricted to simple ligands and include complexes with bridging ethane-1,2-diamine (en), i.e., en in a bis(monodentate) bonding mode. Simple methylamine complexes include  $[\text{Pb}(\text{MeNH}_2)_6]\text{I}_2$  and  $[\text{Pb}(\text{MeNH}_2)_4]\text{I}$  formed from  $\text{PbI}_2$  in liquid  $\text{MeNH}_2$ ; the former has a cubic anti- $\text{K}_2\text{PtCl}_6$  structure. In  $[\text{Pb}(\text{MeNH}_2)_4]\text{I}$ , the  $\text{I}^-$  ion essentially fills the sixth coordination site of the Pb(II) center, but with a long Pb–I distance of 3.8801(4) Å.<sup>119</sup> Interest in these systems stems from relationships to  $\text{MeNH}_3\text{PbI}_3$  perovskite materials. Reactions of  $\text{LiGaH}_4$  with the hydrochloride of  $\text{MeNH}_2$  or  ${}^i\text{PrNH}_2$  lead to  $[\text{Ga}(\text{RNH}_2)_2\text{H}_2]\text{Cl}$  which are structurally similar,<sup>120</sup> and  $[\text{Ga}({}^t\text{BuNH}_2)_2\text{H}_2]\text{Cl}$  has also been reported.<sup>121</sup>  $[\text{Ga}(\text{MeNH}_2)_2\text{H}_2]\text{Cl}$  exhibits short N–H...Cl<sup>-</sup> contacts in the solid state (Fig. 3A).  $[\text{Ga}({}^t\text{PrNH}_2)_2\text{H}_2]^+$  reacts with  $\text{LiGaH}_4$  to yield a trigallium amino complex.<sup>120</sup>  $[\text{Ba}(\text{MeNH}_2)_3\text{Te}_3]_n$  has the layer structure shown in Fig. 3B in which the methylamine ligands protrude above and below the sheet.<sup>122</sup> A study of solvates of  $\text{Mg}(\text{BH}_4)_2$  includes  $[\text{Mg}({}^t\text{BuNH}_2)_3(\text{BH}_4)_2]$  in which the  $\text{Mg}^{2+}$  center can be described as being in a distorted trigonal bipyramidal coordination sphere with bidentate  $[\text{BH}_4]^-$  ligands bound in the axial sites (Fig. 3C); a similar structure is found for  $[\text{Mg}(\text{pip})_3(\text{BH}_4)_2]$  (pip = piperidine). When the solvent was benzylamine ( $\text{BzNH}_2$ ), the  $[\text{BH}_4]^-$  ions were non-coordinated and the octahedral  $[\text{Mg}(\text{BzNH}_2)_6]^{2+}$  cation was formed.<sup>123</sup> In  $[\text{In}(\text{BzNH}_2)_3(\text{PhCH}_2\text{CO}_2)_3]$ , the In(III) center is octahedral with a *fac*-arrangement of  $\text{BzNH}_2$  ligands.<sup>124</sup> The  $[\text{K}_2({}^t\text{BuNH}_2)_4]^{2+}$  ion (Fig. 3D) was isolated in a paramagnetic salt with the 3-oxyl-4,4,5,5-tetramethyl-2-oxoimidazolidin-1-olate anion.<sup>125</sup> Complexes of aniline are represented by  $[\text{Li}(\text{PhNH}_2)_3(\text{BH}_4)]$  which contains a tetrahedral  $\text{Li}^+$  center with a tridentate  $\text{BH}_4^-$  ion occupying one of the four coordination sites.<sup>126</sup> Mixtures of 2,6-dimethylaniline ( $\text{DmpNH}_2$ ) and  $\text{SbCl}_3$  in toluene yielded a co-crystalline mixture of  $[\text{SbCl}_3(\text{DmpNH}_2)_2]$  and  $[\text{SbCl}_3(\text{DmpNH}_2)]$  in which the Sb atoms are in square-based pyramidal and see-saw (disphenoidal) geometries, respectively.<sup>127</sup>

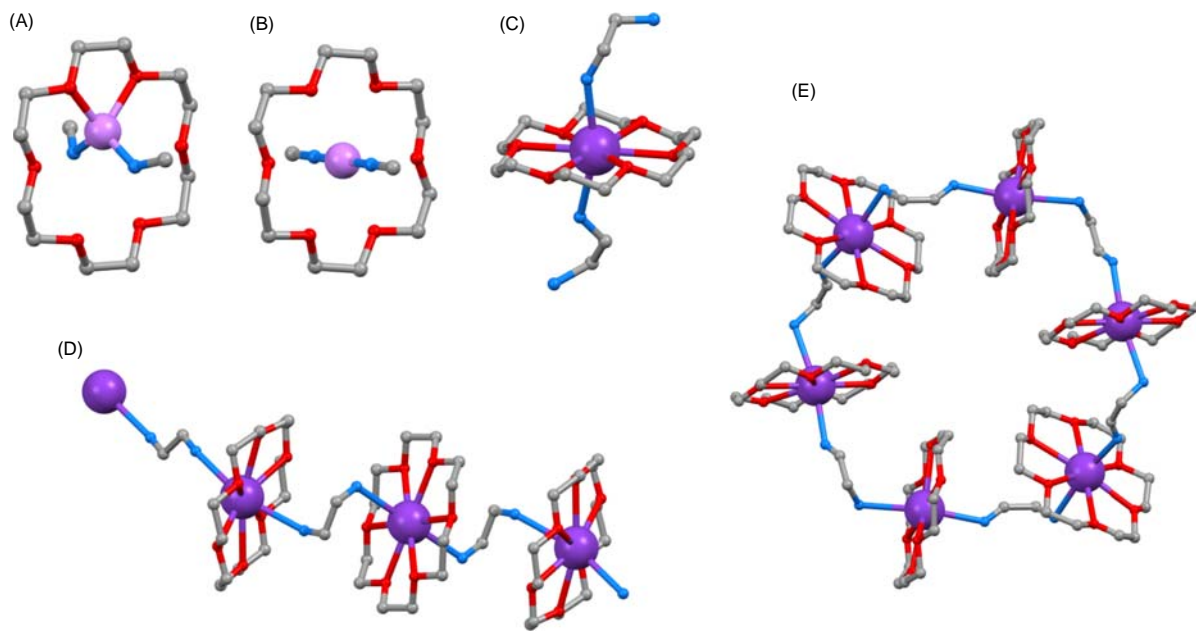
Monodentate, terminal en ligands coordinating to main group metal centers are found in  $[\text{Be}(\text{en})_3]\text{Cl}_2$  and  $[\text{Be}(\text{en})_3]\text{Br}_2$  (one chelating and two monodentate en). A change to  $\text{BeF}_2$  leads to a polymeric structure (see later).<sup>128</sup>

Group 1 metal complexes with  $\{\text{M}(\text{RNH}_2)_2(18\text{-crown-6})\}^+$  motifs are well represented, both with terminal and bridging amino ligands. In 1993, Dye et al. reported the sodide ( $\text{Na}^-$ ) salts  $[\text{Li}(\text{MeNH}_2)_2(18\text{-crown-6})][\text{Na}]$  and  $[\text{Li}(\text{MeNH}_2)_2(18\text{-crown-6})][\text{Na}] \cdot 3(18\text{-crown-6})$ . In the former, the  $\text{Li}^+$  ion is tetrahedrally sited with Li–N distances of 2.021 and 1.955 Å (Fig. 4A) while in the latter, the  $\text{Li}^+$  ion sits centrally in the ring (Fig. 4B) with unusually short Li–N distances of 1.733 Å and an apparently linear Li–N–C unit; a model with a three-fold disorder was suggested but residual electron density did not support the model.<sup>129</sup> While  $\text{Li}^+$  is not size-compatible with the cavity in 18-crown-6, the latter is ideally suited for  $\text{K}^+$ , as illustrated in Fig. 4C with the structure of  $[\text{K}(\text{en})_2(18\text{-crown-6})]^+$ .<sup>130</sup>  $\{\text{K}(18\text{-crown-6})\}^+$  domains connected by bridging en ligands are exemplified in 1D-polymers and cyclic arrays. The chain shown in Fig. 4D is one of two independent chains present in the salt of the  $[\text{Ge}_{16}\text{Sb}_2]^{4-}$  Zintl ion,<sup>131</sup> and other studies of Zintl ions give rise to examples of  $\{\text{K}(18\text{-crown-6})(\mu\text{-en})\}$  units in which the en ligand bridges two  $\text{K}^+$  centers or one  $\text{K}^+$  and a second metal ion.<sup>132–134</sup> A hexanuclear cyclic array (Fig. 4E) has also been structurally characterized.<sup>135</sup>

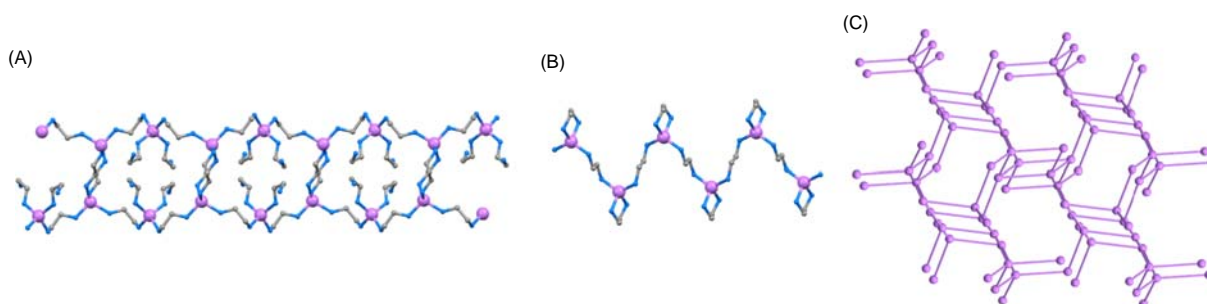
The use of en as a solvent and Li metal as a reductant in reactions to give Chevrel-like clusters has led to the assembly of an  $[\text{Li}_4(\text{en})_{10}]_n^{4n+}$  network comprising sheets of double layers (Fig. 5A) which host the Chevrel clusters.<sup>136</sup> In contrast, a 1D-coordination polymer with both bridging and chelating en ligands (Fig. 5B) is present in  $\{[\text{Li}(\text{en})_2][\text{BH}_4]\}_n$ .<sup>126</sup> Other examples of 1D- and 2D-assemblies with en ligands connecting  $\text{Li}^+$  centers have been described by Dehnen et al.<sup>137</sup> and Thiele et al.<sup>138</sup> In  $\{\text{K}_2[\text{Li}_4(\text{en})_8][\text{Ge}_{18}]\}_n$ , each  $\text{Li}^+$  center acts as a 4-connecting node to give a 3D (sra) net (Fig. 5C).<sup>139</sup> The reduction of red P by



**Fig. 3** (A) The structure of  $[\text{Ga}(\text{MeNH}_2)_2\text{H}_2]\text{Cl}$  (CSD refcode RITRUI) showing short N–H...Cl<sup>-</sup> contacts. (B) Part of one 2D-layer in  $[\text{Ba}(\text{MeNH}_2)_3\text{Te}_3]_n$  with 8-coordinate  $\text{Ba}^{2+}$ , terminal  $\text{MeNH}_2$  ligands and bridging  $\text{Te}_3^{2-}$  units (H atoms omitted, refcode JEQNAX). (C) The structure of  $[\text{Mg}({}^t\text{BuNH}_2)_3(\text{BH}_4)_2]$  (refcode LUVMAQ). (D) The  $[\text{K}_2({}^t\text{BuNH}_2)_4]^{2+}$  ion (H atoms omitted, refcode TICWIM).



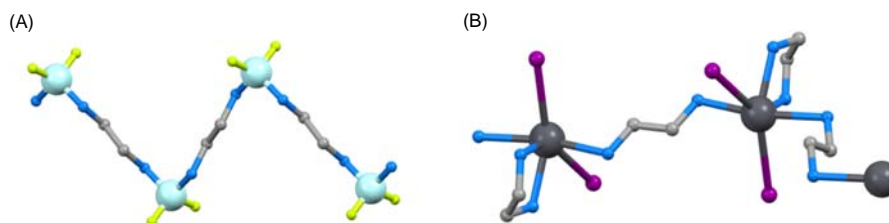
**Fig. 4** The cations in (A)  $[\text{Li}(\text{MeNH}_2)_2(18\text{-crown-6})]^+ \text{Na}^-$  (CSD refcode COJDIO), (B)  $[\text{Li}(\text{MeNH}_2)_2(18\text{-crown-6})]^+ \text{Na}^- \cdot 3(18\text{-crown-6})$  (refcode COJFAI), and (C)  $[\text{K}(\text{en})_2(18\text{-crown-6})]^+$  (refcode HEVTOS). (D) Part of one chain in  $[\text{K}(18\text{-crown-6})(\mu\text{-en})]_n^+$  (refcode EWAVII), and (E) the metallohexacycle  $[\text{K}(18\text{-crown-6})(\mu\text{-en})]_6^+$  (refcode FAPLIU).



**Fig. 5** (A) Part of one sheet in the  $[\text{Li}_4(\text{en})_{10}]_n^{4n+}$  network in  $[\text{Li}_4(\text{en})_{10}][\text{Pd}_6(\mu_3\text{-Te})_8]$  (CSD refcode ZOYNOS). (B) Part of one 1D- $[\text{Li}(\text{en})_2]_n^+$  chain in the borohydride salt (refcode UBEVOM). (C) Part of the *sra* net in  $[\text{K}_2[\text{Li}_4(\text{en})_8][\text{Ge}_{18}]]_n$  represented with only the 4-connecting Li nodes; each  $\text{Li}\cdots\text{Li}$  edge is bridged by an en ligand (refcode OHUWEW).

Na in en gave  $[\text{Na}_4(\text{en})_6\text{P}_{14}]_n$  in which all en ligands bridge between pairs of  $\text{Na}^+$  centers and  $\text{P}_{14}^{4-}$  units are also interconnected by  $\text{Na}^+$  ions; each  $\text{Na}^+$  center is bound by three N and two P donors.<sup>140</sup>

Although a few examples of groups 2 and 13–15 metal complexes with bridging en ligands were reported prior to 2000,<sup>141–144</sup> structurally characterized examples in the period covered by this review are limited. An investigation of the use of liquid en as a solvent in Be coordination chemistry led to the characterization of  $[\text{Be}(\text{en})_3]\text{Cl}_2$  and  $[\text{Be}(\text{en})_3]\text{Br}_2$  (see above), and to the 1D-polymer  $[\text{BeF}_2(\text{en})]_n$  (Fig. 6A).<sup>128</sup> Moving to group 14, lead(II) complexes with bridging en ligands are illustrated by  $[\text{PbI}_2(\text{en})_2]_n$  (Fig. 6B),<sup>145</sup> and  $[\text{PbCl}_2(\text{en})_2]_n$  which is structurally similar to the iodido derivative.<sup>146</sup> The bromido analog was reported in 1996.<sup>147</sup>

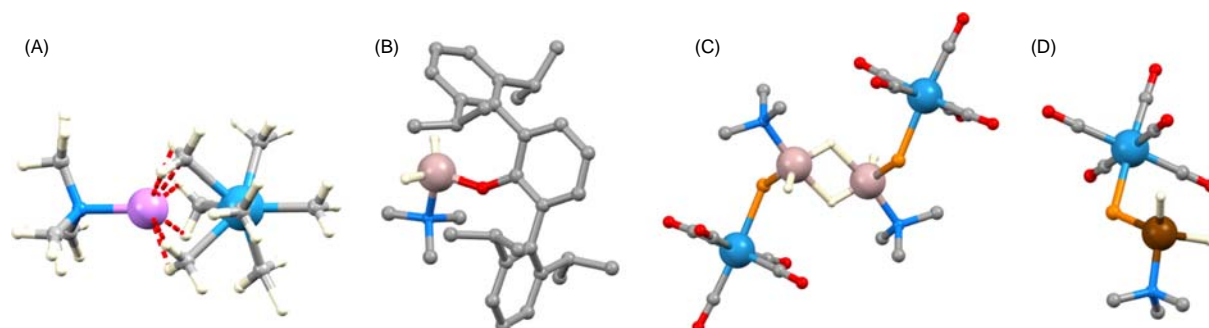


**Fig. 6** Part of one 1D-chain in (A)  $[\text{BeF}_2(\text{en})]_n$  (CSD refcode IRUHOV), (B)  $[\text{PbI}_2(\text{en})_2]_n$  (refcode NOCZOV).

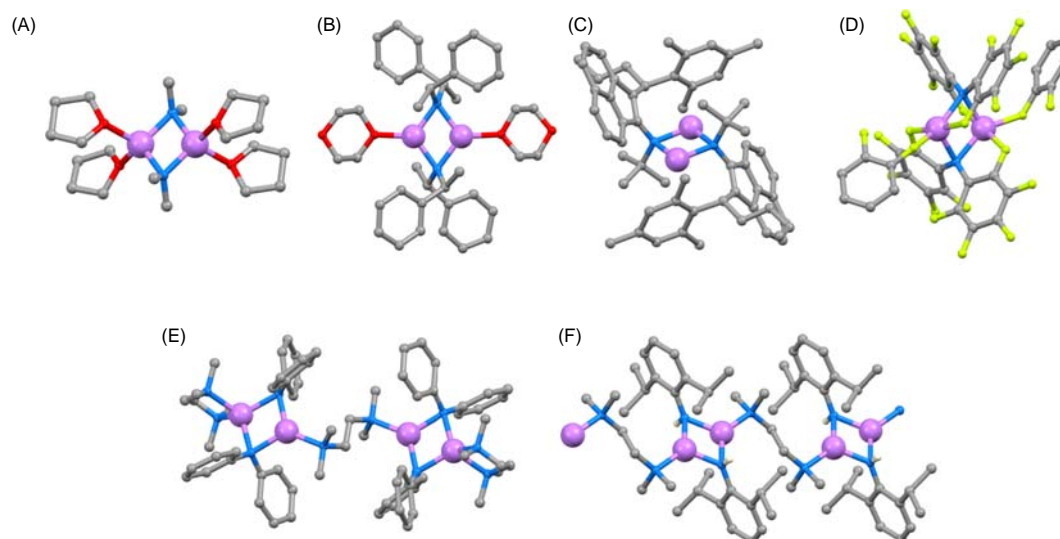
Our discussion of main group metal complexes with tertiary amino ligands is restricted to selected examples of those containing  $\text{Me}_3\text{N}$  and  $\text{Et}_3\text{N}$ , for which group 13 derivatives dominate. Tetrahedral  $\text{M}(\text{III})$  is typical in  $\text{R}_3\text{MNMe}_3$  ( $\text{M}$  = group 13 metal) compounds, but these organometallic derivatives, of which there are many examples, are outside the scope of this article.  $[\text{Li}(\text{NMe}_3)][\text{WMe}_7]$  is worthy of note because of the unusual environment of the  $\text{Li}^+$  ion (Fig. 7A).<sup>148</sup> Examples of group 13 coordination complexes with  $\text{Me}_3\text{N}$  or  $\text{Et}_3\text{N}$  ligands published after 2000 include  $[\text{2,6-(Dipp)}_2\text{C}_6\text{H}_3\text{OAlH}_2(\text{NMe}_3)]$  (Fig. 7B,  $\text{Al-N} = 2.0009(16) \text{ \AA}$ ),<sup>149</sup>  $[\{\text{W}(\text{CO})_5\}(\text{H}_2\text{P})\text{AlH}_2(\text{NMe}_3)]$  (Fig. 7C,  $\text{Al-N} = 2.036(3) \text{ \AA}$ ), and  $[\{\text{W}(\text{CO})_5\}(\text{H}_2\text{P})\text{GaH}_2(\text{NMe}_3)]$  (Fig. 7D,  $\text{Ga-N} = 2.039(7) \text{ \AA}$ ). The latter complexes were designed to stabilize the otherwise elusive simple phosphanylalane and -gallane. In the solid state,  $[\{\text{W}(\text{CO})_5\}(\text{H}_2\text{P})\text{AlH}_2(\text{NMe}_3)]$  exists as a monomer whereas the analogous aluminum compound is dimeric, with asymmetric  $\text{Al-H-Al}$  bridges (Fig. 7E,  $\text{Al-H} = 1.553$  and  $2.053 \text{ \AA}$ ).<sup>150</sup> A  $\text{GaH}(\text{NEt}_3)$  unit has been incorporated into the cyclosiloxane  $[(\text{OPh}_2\text{SiOSiPh}_2\text{OSiPh}_2\text{O})\text{GaH}(\text{NEt}_3)]$ .<sup>151</sup>

#### 1.02.2.1.2 $\text{R}_2\text{N}^-$ , $\text{RHN}^-$ , $\text{RN}^{2-}$

In this section, we survey main group metal complexes incorporating simple amido ( $\text{R}_2\text{N}^-$  and  $\text{RHN}^-$ ) and imido ( $\text{RN}^{2-}$ ) ligands, many of which exhibit an  $\{\text{M}_2(\mu\text{-N})_2\}$  core. There is a wide range of complexes with  $\{\text{Li}_2(\mu\text{-NR}_2)_2\}$  or  $\{\text{Li}_2(\mu\text{-NRH})_2\}$  units,<sup>152-173</sup> and Figs. 8A-C illustrate examples that exhibit 4-, 3- and 2-coordinate lithium.<sup>152,153,174</sup> The use of the sterically demanding ligands to stabilize the  $\{\text{Li}_2(\mu\text{-NR}_2)_2\}$  core without the need for terminal ligands (Fig. 8C) is notable and is observed in several examples.<sup>174,175</sup> Fig. 8D shows the structure of  $[\text{Li}_2(1,2\text{-C}_6\text{F}_2\text{H}_4)_2(\mu\text{-N}(\text{C}_6\text{F}_5)_2)_2]$  in which there are short  $\text{Li}\cdots\text{F}$  contacts ( $2.038\text{-}2.139 \text{ \AA}$ ); this increases the coordination number of  $\text{Li}$  from 4 to 6.<sup>176</sup> A related motif is found in  $[\text{Na}_2(\text{OEt}_2)_2(\mu\text{-N}(\text{C}_6\text{F}_5)_2)_2]$ , but in this case, the structure in the solid state extends into a 1D-coordination polymer by virtue of additional  $\text{Na-F-C}$  contacts;



**Fig. 7** (A) One ion pair in the solid-state structure of  $[\text{Li}(\text{NMe}_3)][\text{WMe}_7]$  (CSD refcode RETNIN). The structures of (B)  $[\text{2,6-(Dipp)}_2\text{C}_6\text{H}_3\text{OAlH}_2(\text{NMe}_3)]$  (refcode OGONAA), (C)  $[\{\text{W}(\text{CO})_5\}(\text{H}_2\text{P})\text{AlH}_2(\text{NMe}_3)]$  (refcode MIHGOZ), and (D)  $[\{\text{W}(\text{CO})_5\}(\text{H}_2\text{P})\text{GaH}_2(\text{NMe}_3)]$  (refcode MIHGUF). In (B), (C), (D), only the  $\text{M-H}$  atoms are shown; in (C) and (D), each  $\text{P}$  is a  $\text{PH}_2$  unit.



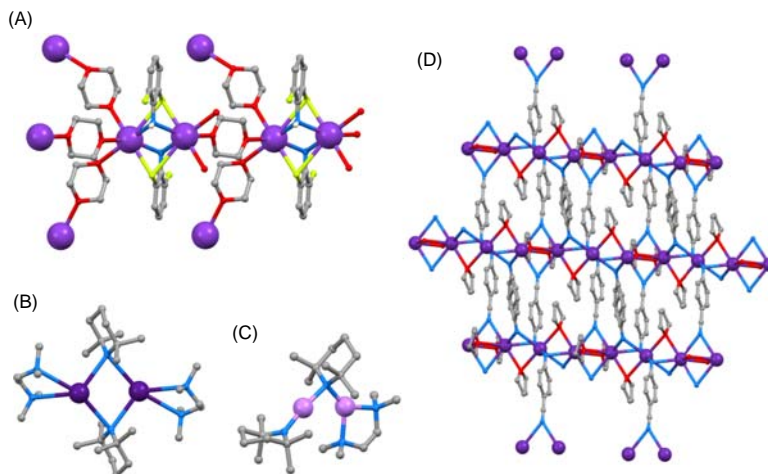
**Fig. 8** Structures of (A)  $[\text{Li}_2(\text{THF})_4(\mu\text{-NMe}_2)_2]$  (CSD refcode PAHCIO), and (B)  $[\text{Li}_2(\text{diox})_2(\mu\text{-N}(\text{CHMePh})_2)_2]$  (refcode CAZLIB). (C) Use of a sterically demanding amido ligand to stabilize 2-coordinate  $\text{Li}^+$  (refcode JOKSIM). (D) The structure of  $[\text{Li}_2(1,2\text{-C}_6\text{F}_2\text{H}_4)_2(\mu\text{-N}(\text{C}_6\text{F}_5)_2)_2]$  (refcode VUHREY). (E) The tetralithium complex  $[\text{Li}_4(\mu\text{-tmeda})_2(\mu\text{-NPh}_2)_2(\mu\text{-tmeda})]$  (refcode COBZUQ). (F) Part of the 1D-chain in  $[\{\text{Li}_2(\mu\text{-NHDipp})_2(\mu\text{-tmeda})\}_n]$  (refcode RUMRAT). Carbon-attached H atoms are omitted.

this is not discussed in the original work but is evident from inspection of the structural data (CSD refcode WIRYED).<sup>177</sup> Related to the homonuclear species described above are  $[\text{LiNa}(\text{THF})_2(\mu\text{-N}(\text{CHMePh})_2)_2]$ ,<sup>153</sup> and associated heterometallic species.<sup>178</sup> Extended systems incorporating  $\{\text{Li}_2(\mu\text{-NR}_2)_2\}$  units include  $\{[\text{Li}_2(\text{tmeda})(\mu\text{-NPh}_2)_2]_2(\mu\text{-tmeda})\}$  (Fig. 8E, tmeda = 1,2-bis(dimethylamino)ethane),<sup>179</sup> and  $\{[\text{Li}_2(\mu\text{-NHDipp})_2]_2(\mu\text{-tmeda})\}_n$  (Fig. 8F).<sup>180</sup> The use of 1,3-bis((2,6-di-isopropylphenyl)amido)methyl)benzene has led to the formation of a metallomacrocyclic containing two  $\{\text{Li}_2(\mu\text{-NR}_2)_2\}$  units.<sup>181</sup>

Complexes containing  $\{\text{Na}_2(\mu\text{-NR}_2)_2\}$  or  $\{\text{Na}_2(\mu\text{-NRH})_2\}$  units (NR<sub>2</sub> includes non-aromatic heterocycles) belonging to the same families as those described above for Li have also been reported,<sup>156,163,182–184</sup> as have potassium-based dimers.<sup>183,185–188</sup> The complex  $[\text{K}_2(\text{diox})_3(\mu\text{-NH}(2,6\text{-C}_6\text{F}_2\text{H}_3))_2]_n$  is worthy of particular note. Firstly, short K–F–C contacts (Fig. 9A) involving the fluorinated arene ring are observed which mirror those seen in  $[\text{Li}_2(\mu\text{-NHDipp})_2]_2(\mu\text{-tmeda})_n$  (Fig. 8F). Secondly, the increase in ionic radius on descending group 1 allows the accommodation of three 1,4-dioxane ligands and these, in turn, lead to the assembly of a 3D-network.<sup>189</sup> Rubidium and cesium derivatives with  $\{\text{M}_2(\mu\text{-NR}_2)_2\}$  motifs are rarer than their lighter group 1 metal analogs.  $[\text{Rb}_2(\text{tmeda})_2(\mu\text{-tmp})_2]$  (Fig. 9B) and  $[\text{Cs}_2(\text{tmeda})_2(\mu\text{-tmp})_2]$ <sup>190</sup> are structurally similar to their Na and K homologs,<sup>185</sup> but differ from that of the tmeda-solvated Li(tmp) derivative which, in the solid state, exists as  $[\text{Li}_2(\text{tmeda})(\text{tmp})(\mu\text{-tmp})]$  (Fig. 9C) with only one bridging amido ligand; note the low coordination numbers of the  $\text{Li}^+$  centers (Fig. 9C).<sup>191</sup> The reaction of Rb metal with 4-aminobenzonitrile in THF results in the formation of  $[\text{Rb}(\mu\text{-THF})_2(\mu\text{-NH}(4\text{-NCC}_6\text{H}_4))]_n$  which possesses an unusual 3D-network. Both THF and amido ligands bridge pairs of adjacent Rb atoms, and the network can be considered in terms of layers, interconnected by  $[(4\text{-NCC}_6\text{H}_4)\text{NH}]^-$  ligands which coordinate to  $\text{Rb}^+$  both through RCN and RHN<sup>−</sup> donors (Fig. 9D).<sup>166</sup>

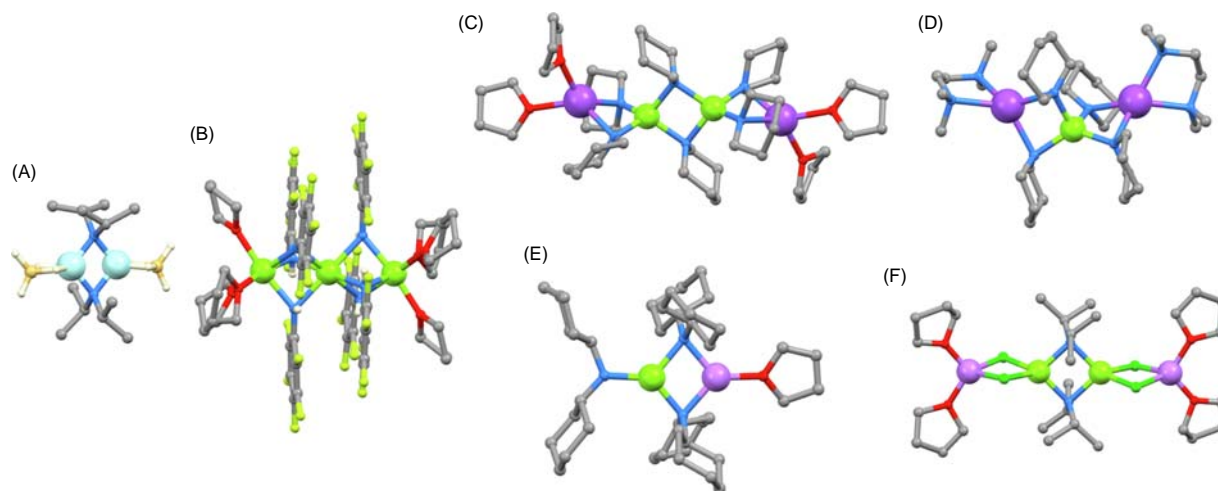
Moving now to group 2, and the ubiquitous  $\{\text{M}_2(\mu\text{-NR}_2)_2\}$  unit is observed in  $[\text{Be}_2(\mu\text{-BH}_4)_2(\mu\text{-N}^i\text{Pr}_2)_2]$  (Fig. 10A).<sup>192</sup> However, amido beryllium derivatives remain scarce, and those of magnesium are dominant.<sup>193–209</sup> Among these examples are trimagnesium and heterometallic species. In  $[\text{Mg}_3(\text{THF})_6(\mu\text{-NHC}_6\text{F}_5)_6]$ , pairs of Mg atoms are triply bridged by amido ligands (Fig. 10B) and each  $\text{Mg}^{2+}$  ion is 6-coordinate. Interestingly, in contrast to examples described earlier in this review, e.g.,  $[\text{Li}_2(1,2\text{-C}_6\text{F}_2\text{H}_4)_2(\mu\text{-N}(\text{C}_6\text{F}_5)_2)_2]$ , there are no short  $\text{M}\cdots\text{F}$  contacts in  $[\text{Mg}_3(\text{THF})_6(\mu\text{-NHC}_6\text{F}_5)_6]$ .<sup>209</sup> On the other hand, short  $\text{Mg}\cdots\text{F}$  contacts are found in the solid-state structure of  $[\text{Mg}_2(\mu\text{-N}(\text{C}_6\text{F}_5)_2)_2(\text{N}(\text{C}_6\text{F}_5)_2)_2]$ .<sup>205</sup> Interest in alkali metal-magnesium complexes lies in their use as cooperative dimetallic catalysts, with  $^i\text{PrNMgCl}\cdot\text{LiCl}$  being described as the ‘turbo Grignard reagent.’<sup>210</sup> Examples include  $[\text{Na}_2(\text{THF})_4\text{Mg}_2(\mu\text{-Npip})_6]$  (Fig. 10C) and  $[\text{Na}_2(\text{tmeda})_2\text{Mg}(\mu\text{-Npip})_4]$  (Fig. 10D). In both, each metal ion is tetrahedrally sited and the Na–N distances are noticeably long (av. 2.46(1) Å in the former and av. 2.432(3) Å in the latter) and are described as ‘ancillary bonds.’<sup>199</sup> Related group 1–2 dimetallic species include  $[\text{Li}(\text{THF})\text{Mg}(\mu\text{-NCy}_2)_2(\text{NCy}_2)]$  in which Na and Mg are both 3-coordinate (Fig. 10E),<sup>200</sup>  $[\text{Na}(\text{tmeda})\text{Mg}(\mu\text{-N}^i\text{Pr}_2)_2(\text{N}^i\text{Pr}_2)]$ ,<sup>204</sup> and  $[\text{Li}_2(\text{THF})_4\text{Mg}_2(\mu\text{-Cl})_4(\mu\text{-N}^i\text{Pr}_2)_2]$  (Fig. 10F) which dissociates in THF solution to give  $[\text{Li}(\text{THF})_4]^+$  and  $^i\text{Pr}_2\text{NMgCl}$ -containing species.<sup>203</sup>

Amido complexes of  $\text{Ca}^{2+}$  reveal the metal in a range of coordination environments. The use of a sterically demanding β-diketimate co-ligand leads to 4-coordinate  $\text{Ca}^{2+}$  in  $[\text{Ca}_2(\text{L})_2(\mu\text{-NHBz})_2]$  (HL and the complex are shown in Fig. 11).<sup>211</sup>  $\text{CaH}_2$  reduction of isoquinoline (iQ) results in the formation of *trans*- $[\text{Ca}(\text{HiQ})_2(\text{iQ})_4]$  ( $\text{H}_2\text{iQ} = 1,2\text{-dihydroisoquinoline}$ ) and  $[\text{Ca}_3(\text{iQ})_6(\mu\text{-HiQ})_6]$  which contains a linear  $\{\text{Ca}_3(\mu\text{-NR}_2)_6\}$  core with 6-coordinate  $\text{Ca}^{2+}$ .<sup>212</sup> A similar linear  $\{\text{Ca}_3(\mu\text{-NHR})_6\}$  core is present in  $[\text{Ca}_3(\text{THF})_6(\mu\text{-NHMe})_6]$  (Mes = mesityl) which was formed by reaction of  $\text{K}[\text{MesNH}]$  with  $\text{CaI}_2$  in THF. In contrast, a change from  $\text{K}[\text{MesNH}]$  to  $\text{K}[2,6\text{-F}_2\text{C}_6\text{H}_3\text{NH}]$  resulted in the formation of the dinuclear complex  $[\text{Ca}_2(\text{THF})_5(2,6\text{-F}_2\text{C}_6\text{H}_3\text{NH})(\mu\text{-NH}(2,6\text{-F}_2\text{C}_6\text{H}_3))_3]$  (Fig. 11B).<sup>189</sup> There are no short  $\text{Mg}\cdots\text{F}$  contacts in the latter, while in  $[\text{Ca}_4(\text{N}(\text{SiMe}_3)_2)_2(\mu\text{-N}(2\text{-FC}_6\text{H}_4)_2)_6]$  (Fig. 11C),  $\text{Ca}\cdots\text{F}$  interactions are key in stabilizing a low-coordinate group 2 metal complex; related  $\text{Ba}^{2+}$

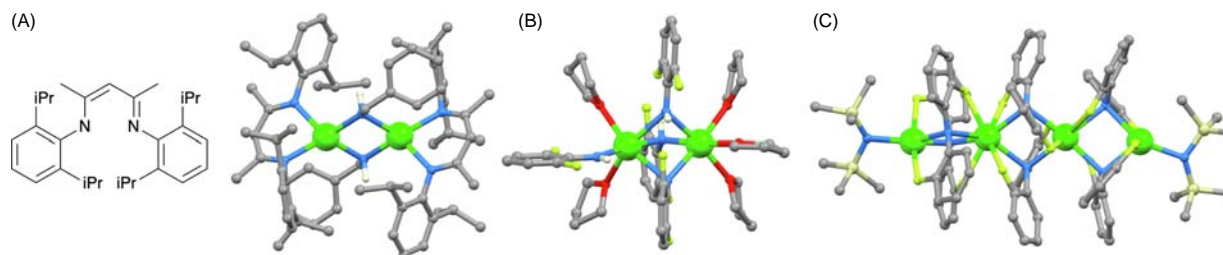


**Fig. 9** (A) Two repeating units in  $[\text{K}_2(\text{diox})_3(\mu\text{-NH}(2,6\text{-C}_6\text{F}_2\text{H}_3))_2]_n$  (CSD refcode NOBQEB). The structures of (B)  $[\text{Cs}_2(\text{tmeda})_2(\mu\text{-tmp})_2]$  (refcode VEBLEV) and (C)  $[\text{Li}_2(\text{tmeda})(\text{tmp})(\mu\text{-tmp})]$  (refcode YAPCOH). (D) Part of the 3D-network in  $[\text{Rb}(\mu\text{-THF})_2(\mu\text{-NH}(4\text{-NCC}_6\text{H}_4))]_n$  (all H atoms omitted, refcode FEXLIE).





**Fig. 10** The structures of (A)  $[\text{Be}_2(\mu\text{-BH}_4)_2(\mu\text{-N}^i\text{Pr}_2)_2]$  (only H atoms in  $[\text{BH}_4]^-$  ligands are shown, CSD refcode AQADAX), (B)  $[\text{Mg}_3(\text{THF})_6(\mu\text{-NHC}_6\text{F}_5)_6]$  (only amido H atoms are shown, refcode YOHTOF), (C)  $[\text{Na}_2(\text{THF})_4\text{Mg}_2(\mu\text{-Npip})_6]$  (refcode POFREK), (D)  $[\text{Na}_2(\text{tmeda})_2\text{Mg}(\mu\text{-Npip})_4]$  (refcode POFRIO), (E)  $[\text{Li}(\text{THF})\text{Mg}(\mu\text{-NCy}_2)_2(\text{NCy}_2)]$  (refcode QOLFEC) and (F)  $[\text{Li}_2(\text{THF})_4\text{Mg}_2(\mu\text{-Cl})_4(\mu\text{-N}^i\text{Pr}_2)_2]$  (refcode TUYGUQ).



**Fig. 11** The structures of (A) the  $\beta$ -diketimine HL, and  $[\text{Ca}_2(\text{L})_2(\mu\text{-NHBz})_2]$  (only amido H atoms are shown, CSD refcode LIYYUO), (B)  $[\text{Ca}_2(\text{THF})_5(2,6\text{-F}_2\text{C}_6\text{H}_3\text{NH})(\mu\text{-NH}(2,6\text{-F}_2\text{C}_6\text{H}_3))_3]$  (only amido H atoms shown, refcode NOBQUR), and (C)  $[\text{Ca}_4(\text{N}(\text{SiMe}_3)_2)_2(\mu\text{-N}(2\text{-FC}_6\text{H}_4)_2)_6]$  (refcode POJXAQ).

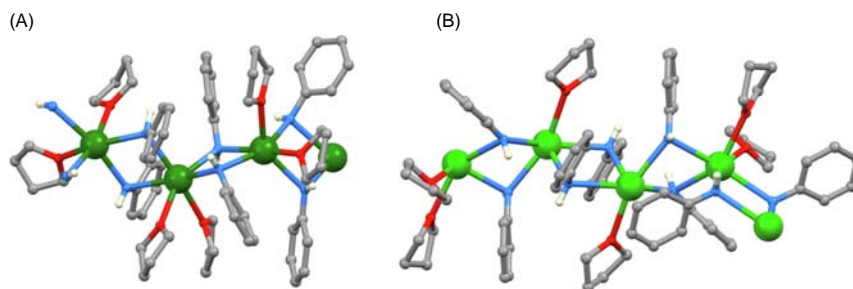
complexes were also reported.<sup>213</sup> The tendency for higher coordination numbers is seen in  $[\text{Ca}_4(\text{THF})_8(\mu\text{-NHPH})_8]$  which contains 6-coordinate  $\text{Ca}^{2+}$  centers in a  $\{(\text{THF})_3\text{Ca}(\mu\text{-N})_3\text{Ca}(\text{THF})(\mu\text{-N})_2\text{Ca}(\text{THF})(\mu\text{-N})_3\text{Ca}(\text{THF})_3\}$  motif.<sup>214</sup> Related strontium and barium derivatives  $[\text{Sr}(\text{THF})_2(\mu\text{-NHPH})_2]_n$  (Fig. 12A) and  $[\text{Ba}_2(\text{THF})_3(\mu\text{-NHPH})_4]_n$  (Fig. 12B) are polymeric with 6-coordinate metal ions and increasing interactions to the phenyl ring  $\pi$ -systems with increasing size of the group 2 metal.<sup>214</sup>

For group 13, we again see complexes based on dimetallic  $\{\text{M}_2(\mu\text{-NR}_2)_2\}$  cores with Al-containing species predominating over complexes of the heavier metals.<sup>215–228</sup> There are many simple dinuclear complexes in the  $[\text{M}_2\text{X}_4(\mu\text{-NR}_2)_2]$  and  $[\text{M}_2\text{X}_4(\mu\text{-NHR})_2]$  families, and their typical structures are illustrated by that of  $[\text{Al}_2\text{Cl}_4(\mu\text{-NEt}_2)_2]$  (Fig. 13A). An interesting related complex is  $[\text{Al}_2\text{H}_2(\text{NHDipp})(\text{NMe}_2\text{Et})(\mu\text{-NHDipp})(\mu\text{-NDipp})]$  in which both amido and imido ligands bridge the  $\text{Al}_2$ -unit (Fig. 13B). This was prepared by reaction of  $\text{H}_3\text{Al}\cdot\text{NMe}_2\text{Et}$  with  $\text{DippNH}_2$ , and is one of a series of associated compounds reported by Bauer et al.<sup>215</sup> Chivers reported a series of heterometallic compounds formed from reactions of  $\text{MAlH}_4$  ( $\text{M} = \text{Li}, \text{Na}$ ) with  $\text{RH}_2\text{N}$  ( $\text{R} = ^i\text{Bu}, ^i\text{Pr}, 4\text{-tolyl}$ ).  $[\text{LiAl}(\text{NH}^i\text{Pr})_4]_n$  and  $[\text{NaAl}(\text{NH}^i\text{Pr})_4]_n$  (Fig. 13C) are 1D-polymers in the solid state, while  $[\text{Li}(\text{THF})_4][\text{Al}(\text{NH}(4\text{-tolyl}))_4]$  contains discrete ions.<sup>229</sup>

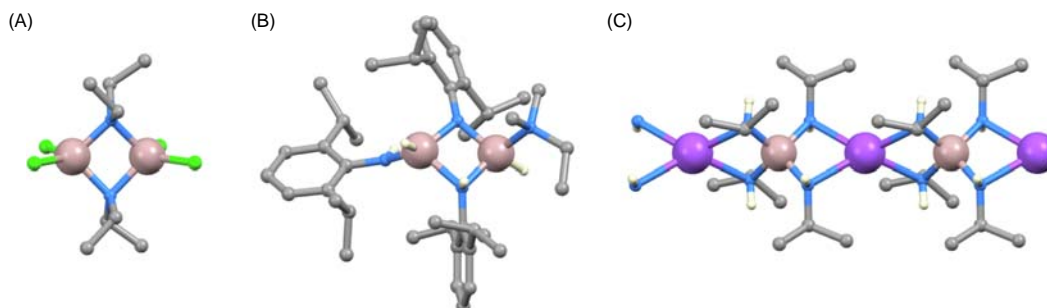
Chloroamides of low-valence group 14 elements include monomers and cyclic products with bridging chlorido and amido ligands. In 2007, Khrustalev et al. reported the thermally stable metal(II) complexes  $[\text{Ge}_2\text{Cl}_2(\mu\text{-NEt}_2)_2]$  (Fig. 14A) and  $[\text{Sn}_2\text{Cl}_2(\mu\text{-NMe}_2)_2]$  which were the first crystallographically characterized group 14 metal(II) chlorides with small alkylamino ligands. The Ge(II) and Sn(II) derivatives are structurally similar. However, the  $\text{Sn}_2\text{N}_2$  rhombus is planar (crystallographically imposed) whereas the  $\text{Ge}_2\text{N}_2$  rhombus has a butterfly configuration with internal dihedral angle of  $167^\circ$ ; Ge–N bond lengths are 2.034(2) and 2.073(2) Å, and Sn–N = 2.267(4) and 2.229(4) Å.<sup>230</sup> In  $[\text{Ge}_2\text{Cl}_2(\mu\text{-NEt}_2)_2]$  and  $[\text{Sn}_2\text{Cl}_2(\mu\text{-NMe}_2)_2]$ , the chlorido ligands are in a mutually *anti* arrangement.<sup>230</sup> In contrast, they are in a *syn*-arrangement in  $[\text{Sn}_2\text{Cl}_2(\mu\text{-NHDipp})_2]$ ,<sup>231</sup> and in  $[\text{Pb}_2\text{Cl}_2(\mu\text{-NHDipp})_2]$ .<sup>232</sup> Other examples of tin(II) amido complexes include  $[\text{Sn}_2\text{L}_2(\mu\text{-NMe}_2)_2]$  (HL is a salicylaldimine, e.g., Fig. 14B) which have been investigated for use in *rac*-lactide polymerization,<sup>233</sup>  $[\text{Sn}_2(\text{Me}_2\text{NC}(\text{S})\text{NPh})_2(\mu\text{-NMe}_2)_2]$  (Fig. 14C) which acts as a single source precursor for the deposition of phase-pure films of  $\text{SnS}$ ,<sup>234</sup> and  $[\text{Sn}_2(\text{OR})_2(\mu\text{-NMe}_2)_2]$  complexes (e.g., Fig. 14D) which have been applied to the synthesis of  $\text{SnO}_x$  nanowires.<sup>235</sup>

The first Sb(III) aziridinides were reported in 2017. The reaction between  $\text{Sb}(\text{NMe}_2)_3$  and aziridine ( $\text{HAzn}$ ) yielded  $[\text{Sb}_2(\text{Azn})_4(\mu\text{-NAzn})_2]$  (Fig. 15A) which exhibits a ‘weak’ dimeric structure in the solid state (for the bridging ligands, Sb–N = 2.084(1) and

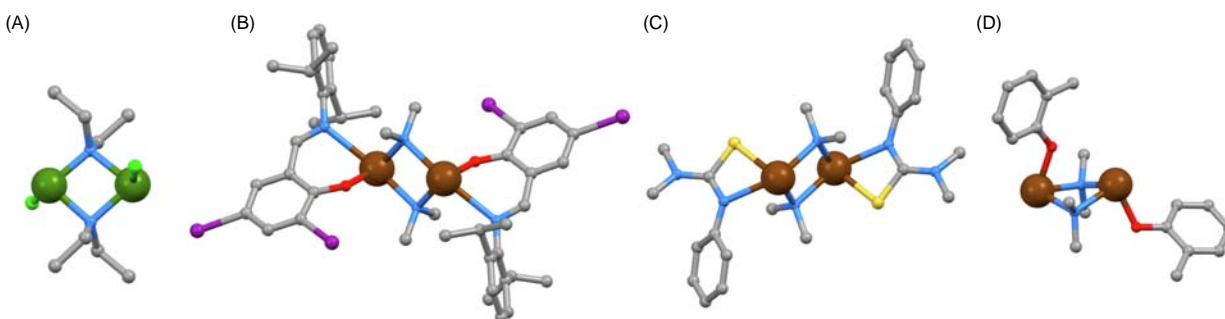




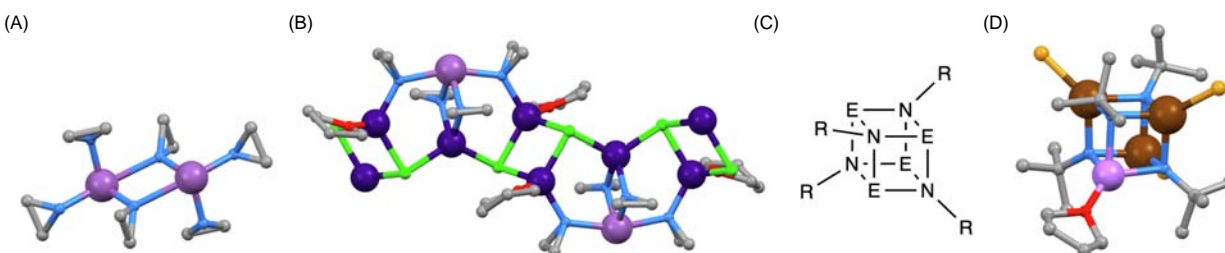
**Fig. 12** Parts of the 1D-polymer chains in (A)  $[\text{Sr}(\text{THF})_2(\mu\text{-NHPh})_2]_n$  (CSD refcode VIMYOG) and (B)  $[\text{Ba}_2(\text{THF})_3(\mu\text{-NHPh})_4]_n$  (CSD refcode VIMYOG). H atoms omitted except for NH.



**Fig. 13** Structures of (A)  $[\text{Al}_2\text{Cl}_4(\mu\text{-NEt}_2)_2]$  (refcode SUDKUZ), and (B)  $[\text{Al}_2\text{H}_2(\text{NHDipp})(\text{NMe}_2\text{Et})(\mu\text{-NHDipp})(\mu\text{-NDipp})]$  (CSD refcode PUZSOS). (C) Part of one 1D-polymer chain in  $[\text{NaAl}(\text{NH}'\text{Pr})_4]_n$  (refcode PEGZAD).



**Fig. 14** The structures of (A)  $[\text{Ge}_2\text{Cl}_2(\mu\text{-NEt}_2)_2]$  (CSD refcode KIJVAB), (B) an example of a  $[\text{Sn}_2\text{L}_2(\mu\text{-NMe}_2)_2]$  (refcode DUGHIX) complex where HL is a salicylalimine, (C)  $[\text{Sn}_2(\text{Me}_2\text{NC}(\text{S})\text{NPh})_2(\mu\text{-NMe}_2)_2]$  (refcode RACPET), (D)  $[\text{Sn}_2(\text{O}(2\text{-MeC}_6\text{H}_4))_2(\mu\text{-NMe}_2)_2]$  (refcode VAYRIY). All H atoms are omitted.



**Fig. 15** The structures of (A)  $[\text{Sb}_2(\text{Azn})_4(\mu\text{-NAzn})_2]$  (CSD refcode HAPSEZ) and (B) part of the 1D-polymer in  $[\text{Li}_3\text{Sb}(\mu_3\text{-Cl})_2(\mu\text{-Azn})_4(\text{THF})_2]_n$  (Li, dark purple, Sb, pale purple; refcode HAPSAV). (C) General structure of an  $\text{E}_4(\mu_3\text{-NR})_4$  cubane, and (D) the cubane  $[\text{Sn}_3\text{Se}_3\text{Li}(\text{THF})(\mu_3\text{-N}^t\text{Bu})_4]^-$  (refcode FERVEE). H atoms are omitted.

2.534(2) Å).  $[\text{Sb}_2(\text{Az}_n)_4(\mu\text{-NAz}_n)_2]$  could not be accessed by reacting  $\text{SbCl}_2$  with  $\text{Li}[\text{Az}_n]$ , but instead, a reaction in THF produced the polymeric  $[\text{Li}_3\text{Sb}(\mu_3\text{-Cl})_2(\mu\text{-Az}_n)_4(\text{THF})_2]_n$  (Fig. 15B).<sup>236</sup> Neutral bismuth amides, e.g.,  $\text{Bi}(\text{N}(\text{SiMe}_3)_2)_3$ , and a bismuth thioamide were investigated as volatile Bi-containing precursors for bismuth oxide materials.<sup>237</sup> Cationic Bi amido derivatives  $[\text{Bi}(\text{NR}_2)_2\text{L}_n]^+$  ( $\text{R}=\text{Me}$ ,  $^i\text{Pr}$ ,  $\text{Ph}$ ;  $\text{L}$  = neutral ligand) have also been described. However, in the  $[\text{BPh}_4]^-$  salts, transfer of  $\text{Ph}$  from  $\text{Bi}$  to  $\text{Bi}$  was observed; use of fluorinated tetraarylborate counterions yielded more stable cationic bismuth amides.<sup>238</sup>

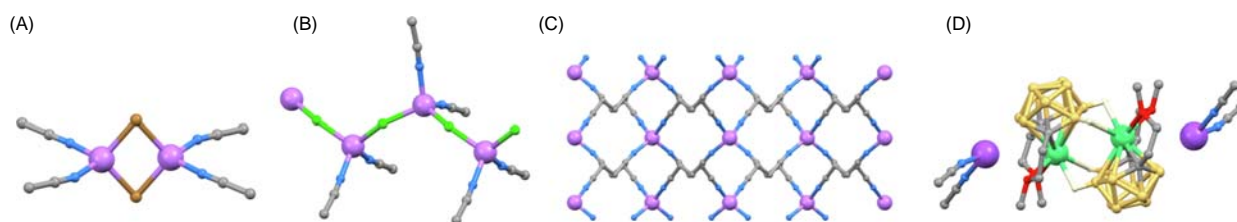
The imido ( $\text{RN}^{2-}$ ) group is isoelectronic with an oxido  $\text{O}^{2-}$  ligand, and main group metal clusters involving  $\text{M}-\text{NR}-\text{M}$  bridging units are well represented and reviewed.<sup>77-79</sup> Although strictly organometallic,  $[\text{Sb}_2\text{Ph}_2(\mu\text{-N}^t\text{Bu})_2]$  is a representative example of a simple imido complex.<sup>239</sup> Imido cubanes  $[\text{E}_4(\mu_3\text{-NR})_4]$  (Fig. 15C) are represented by  $[\text{M}_4(\mu_3\text{-NGeMe}_3)_4]$  ( $\text{M} = \text{Ge}$ ,  $\text{Sn}$ ,  $\text{Pb}$ ) and  $[\text{Sn}_4(\mu_3\text{-NSnMe}_3)_4]$ ,<sup>240</sup>  $[\text{Sn}_3\text{Mg}(\mu_3\text{-N}^t\text{Bu})_4]$  and  $[\text{Sn}_3\text{Li}(\mu_3\text{-N}^t\text{Bu})_4]^-$ ,<sup>241</sup> and  $[\text{Sn}_3\text{X}_3\text{Li}(\text{THF})(\mu_3\text{-N}^t\text{Bu})_4]^-$  ( $\text{X} = \text{Se}$ ,  $\text{Te}$ ; Fig. 15D).<sup>242</sup>

### 1.02.2.1.3 Nitriles

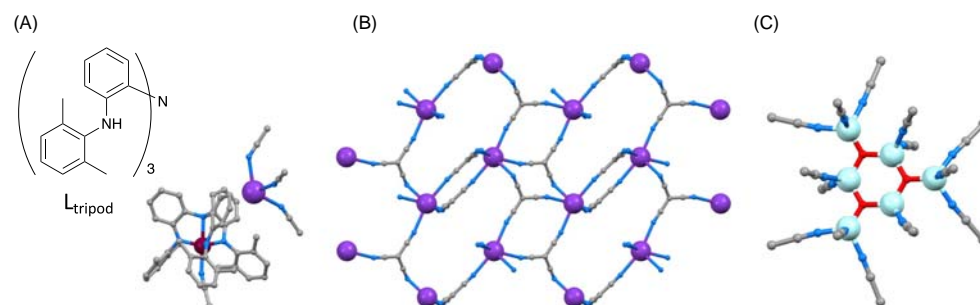
We have restricted our discussion of nitrile ( $\text{RC}\equiv\text{N}$ ) complexes to homoleptic compounds and other simple species. For  $\text{Li}^+$ , tetrahedral coordination is typical, e.g., in salts of  $[\text{Li}(\text{NCMe})_4]^+$ ,<sup>243-247</sup> in  $[\text{Li}_2(\text{NCMe})_4(\mu\text{-Br})_2]$  (Fig. 16A),<sup>248</sup> and in the 1D-coordination polymer  $[\text{Li}(\text{NCMe})_2(\mu\text{-Cl})]_n$  (Fig. 16B).<sup>249,250</sup>  $\{[\text{Li}(\mu\text{-NCCH}_2\text{CH}_2\text{CN})_2][\text{N}(\text{SO}_2\text{F})_2]\}_n$  is an example of a network built up from  $\text{Li}^+$  and a dinitrile (Fig. 16C); the compound is of interest for its high Li-ion conductivity.<sup>251</sup> The coordination environments of  $\text{Na}^+$  in apparently simple complex cations with  $\text{MeCN}$  ligands are surprisingly varied. Both octahedral  $[\text{Na}(\text{NCMe})_6]^+$ ,<sup>252</sup> and 5-coordinate  $[\text{Na}(\text{NCMe})_5]^+$  ions have been structurally characterized.<sup>253-255</sup> The  $\text{Na}^+$  ion displays a square-planar coordination geometry in  $\text{trans-}[\text{Na}(\text{NCMe})_2(\text{OEt}_2)]^+$ <sup>256</sup>; note that this complements the square-planar  $[\text{Na}(\text{NH}_3)_4]^+$  ion described earlier. An unusual  $[\text{Na}(\text{NCMe})_2]^+$  cation with a non-linear geometry has been reported in  $[\text{Na}(\text{NCMe})_2][\eta^7\text{-(MeOCH}_2\text{CH}_2)_2\text{C}_2\text{B}_{10}\text{H}_{10}\text{Er}]_2$ , but as Fig. 16D illustrates, the  $\text{Na}^+$  ion is also closely associated with the carbaborane counterion.<sup>257</sup> Just as  $[\text{Na}(\text{NCMe})_2]^+$  deceptively displays  $\text{CN} = 2$ , the 3-coordinate  $\text{K}^+$  ion present in the tripodal cobalt(II) complex depicted in Fig. 17A exhibits close contacts to arene rings in the complex anion.<sup>258</sup> This and the octahedral  $[\text{K}(\text{NCMe})_6]^+$  ion<sup>259</sup> are among the few structurally characterized homoleptic acetonitrile complexes of  $\text{K}^+$ . A further example in which the low coordination number of the group 1 metal ion is ambiguous is  $[\text{Cs}_2(\mu\text{-CNMe})_2]^{2+}$  where the apparently open coordination sites of  $\text{Cs}^+$  are occupied by virtue of close  $\text{Cs}\cdots\text{Cl}$  or  $\text{Cs}\cdots\text{Br}$  contacts with the counterion.<sup>260</sup>

A number of  $[\text{M}\{\text{C}(\text{CN})_3\}_2]_n^{n-}$  coordination networks containing the group 1 metals have been reported. They possess metal-ocene counterions and are notable for melting in a range 102–239 °C; the dimensionality of the net depends on the size of the organometallic cation. An example is shown in Fig. 17B.<sup>261</sup>

Simple acetonitrile complexes of all the group 2 metals are represented. Tetrahedral coordination prevails in  $\text{RCN}$  complexes of beryllium, exemplified by  $[\text{BeBr}_2(\text{NCMe})_2]$ ,<sup>262</sup>  $[\text{Be}(\text{OSO}_2\text{CF}_3)_2(\text{NCMe})_2]$ ,<sup>263</sup> and  $[\text{BeCl}_2(\text{NCPh})_2]$ .<sup>264</sup> Treatment of  $\text{Be}$  powder with  $\text{I}_2$  in  $\text{MeCN}$  led to the formation of  $[\text{Be}_3(\mu_3\text{-O})_3(\text{MeCN})_6\{\text{Be}(\text{MeCN})_3\}_3]\text{I}_6$  and an active role of trace amounts of  $\text{BeO}$  in this reaction has been suggested. The cation has an essentially planar  $\text{Be}_6\text{O}_3$ -core (Fig. 17C).<sup>265</sup> On going to  $\text{Mg}^{2+}$ , octahedral coordination



**Fig. 16** (A) The structure of  $[\text{Li}_2(\text{NCMe})_4(\mu\text{-Br})_2]$  (CSD refcode SAWSUE01). (B) Part of the 1D-chain in  $[\text{Li}(\text{NCMe})_2(\mu\text{-Cl})]_n$  (refcode XENHAZ01). (C) Part of the 3D-network (viewed down the  $a$ -axis) in the  $[\text{N}(\text{SO}_2\text{F})_2]^-$  salt of  $[\text{Li}(\mu\text{-NCCH}_2\text{CH}_2\text{CN})_2]_n^+$  (refcode FAHDUR). (D) The  $[\text{Na}(\text{NCMe})_2]^+$  cations in  $[\text{Na}(\text{NCMe})_2][\eta^7\text{-(MeOCH}_2\text{CH}_2)_2\text{C}_2\text{B}_{10}\text{H}_{10}\text{Er}]_2$  with only B–H–Er H atoms shown (refcode IRIZEO).



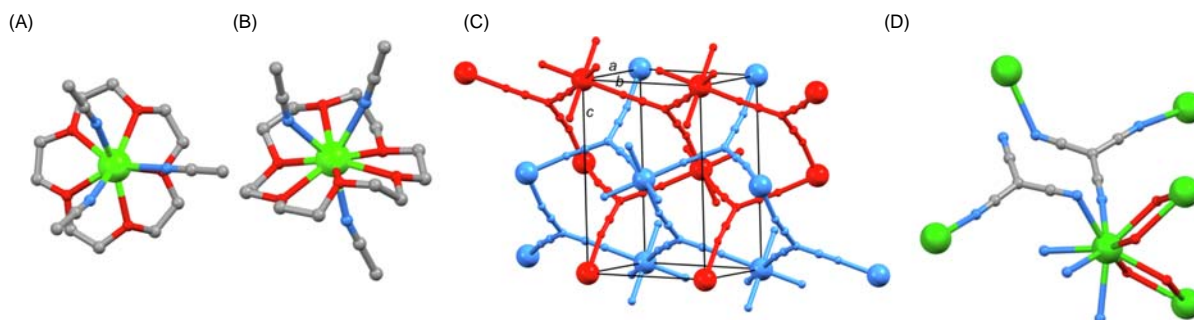
**Fig. 17** (A) The ion-pair in  $[\text{K}(\text{NCMe})_3]^+[\text{Co}(\text{NCMe})(\text{L-tripod})]^-$  (CSD refcode GIGGUW) and the structure of  $\text{H}_3\text{L-tripod}$ . (B) Part of the  $[\text{K}(\text{C}(\text{CN})_3)_2]_n^-$  3D-net in the  $[\text{CpRu}(\text{C}_6\text{H}_5\text{Me})]^+$  salt (refcode LOMZEV). (C) The structure of the  $[\text{Be}_3(\mu_3\text{O})_3(\text{MeCN})_6\{\text{Be}(\text{MeCN})_3\}_3]^{6+}$  cation (refcode INILUN).

dominates as in  $[\text{Mg}(\text{NCMe})_6]^{2+}$ ,<sup>266–272</sup> and *trans*- $[\text{Mg}(\text{OH}_2)_4(\text{NCMe})_2]^{2+}$ .<sup>273</sup> Higher CNs are expected on descending group 2 and are indeed observed in  $[\text{Ca}(\text{NCMe})_8]^{2+}$  (CN = 8),<sup>268</sup>  $[\text{Ca}(\text{NCS})_2(\text{NCMe})_5]$  (CN = 7),<sup>274</sup>  $[\text{Ca}(\text{NCMe})_2(\text{OH}_2)_5]^{2+}$  (CN = 7),<sup>275</sup>  $[\text{Ca}(\text{NCMe})_3(15\text{-crown-5})]^{2+}$  (CN = 8, Fig. 18A),<sup>276</sup>  $[\text{Ca}(\text{NCMe})_2(18\text{-crown-6})]^{2+}$  (CN = 8),<sup>277</sup>  $[\text{Ca}(\text{NCMe})_3(18\text{-crown-6})]^{2+}$  (CN = 9, Fig. 18B),<sup>278</sup>  $[\text{Ca}(\text{NCMe})_4(\text{THF})_4]^{2+}$  (CN = 8),<sup>278</sup>  $[\text{Sr}(\text{NCMe})_8]^{2+}$  (CN = 8),<sup>268</sup>  $[\text{Sr}(\text{NCMe})_3(18\text{-crown-6})]^{2+}$  (CN = 9),<sup>278</sup> and  $[\text{Ba}(\text{NCMe})_8(\text{OH}_2)]^{2+}$  (CN = 9).<sup>260</sup> Fig. 17B showed part of the  $[\text{K}\{\text{C}(\text{CN})_3\}_2]_n^{n-}$  3D-net in which cavities are occupied by cations. In contrast, the neutral  $[\text{Ca}\{\text{C}(\text{CN})_3\}_2]_n$  forms an interpenetrating 3D-network (Fig. 18C) with octahedral  $\text{Ca}^{2+}$  centers connected by  $[\text{C}(\text{CN})_3]^-$  ligands. On going from  $[\text{Ca}\{\text{C}(\text{CN})_3\}_2]_n$  to  $[\text{Ba}\{\text{C}(\text{CN})_3\}_2(\text{OH}_2)_2]_n$ , the coordination number of the group 2 metal increases from 6 to 9 (a capped tetragonal antiprism). The 3D-network is unusual, with  $\text{Ba}^{2+}$  ions linked both by trinitrile and aqua ligands (Fig. 18D).<sup>279</sup>

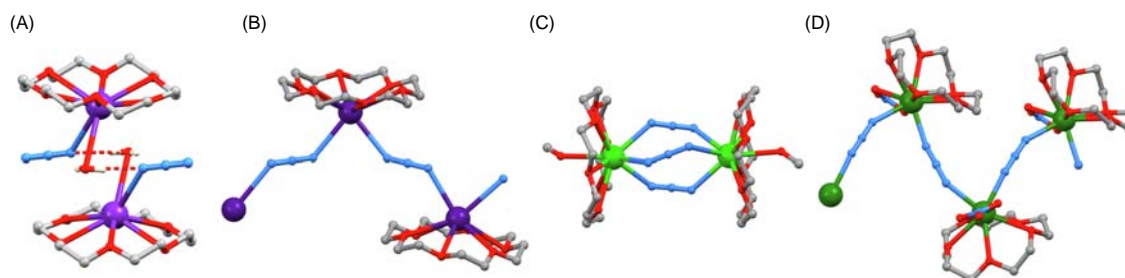
Group 13 metal complexes with simple nitrile ligands are restricted to those of aluminum, if organometallics are excluded. A number of examples of octahedral  $[\text{Al}(\text{NCMe})_5\text{X}]^{2+}$  complexes with X = Cl or Br have been reported since 1979,<sup>280–287</sup> but these dications have been described as being ‘rather uncommon.’<sup>286</sup> The  $\text{Al}^{3+}$  center retains octahedral coordination in  $[\text{Al}_2(\mu\text{-OH})_2(\text{NCPH})_8]^{4+}$ ,<sup>284</sup> and  $[\text{Al}_2(\mu\text{-OH})(\mu\text{-O}_2\text{C}^t\text{Bu})_2(\text{NCPH})_6]^{3+}$ .<sup>288</sup> For the later main groups, examples of simple nitrile metal complexes reported since 2000 are relatively few: *cis*- $[\text{Ge}(\text{NCCH}_2\text{F})_2\text{F}_4]$ ,<sup>289</sup> *cis*- $[\text{Sn}(\text{NCMe})_2\text{Cl}_4]$ ,<sup>290,291</sup> *cis*- $[\text{Sn}(\text{NCMe})_2\text{Br}_4]$ ,<sup>292</sup> *cis*- $[\text{Sn}(\text{NCMe})_2\text{Cl}_4]$ ,<sup>290</sup> *cis*- $[\text{Sn}(\text{NC}^i\text{Pr})_2\text{Cl}_4]$ ,<sup>290</sup>  $[\text{Sn}(\text{NCMe})_6]^{2+}$ ,<sup>293</sup>  $[\text{Sn}(\text{NCMe})_5]^{2+}$ ,<sup>176</sup> and *cis*- $[\text{Te}(\text{NCMe})_2\text{Cl}_4]$ .<sup>294</sup> In the case of  $[\text{Sn}(\text{NCMe})_5]^{2+}$  and  $[\text{Sn}(\text{NCMe})_6]^{2+}$ , such examples of tin(II) dications without close contacts to the counterion are uncommon.<sup>176,293</sup>

#### 1.02.2.1.4 $\text{N}_3^-$ , N-bonded $\text{CN}^-$ , $\text{NCO}^-$ , $\text{NCS}^-$ , $\text{NCSe}^-$

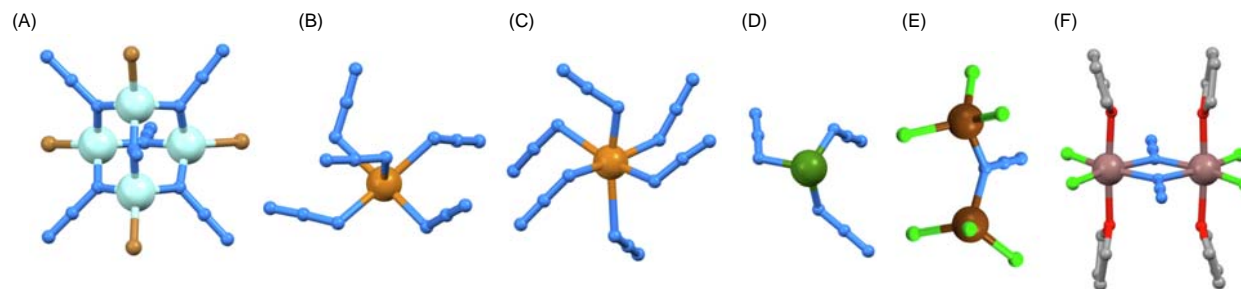
As in previous sections, we focus on homoleptic main group metal complexes and other simple derivatives to give an overview of typical bonding modes of  $\text{N}_3^-$ ,  $\text{CN}^-$ ,  $\text{NCO}^-$ ,  $\text{NCS}^-$  and  $\text{NCSe}^-$ . We first consider azido complexes, investigations of which are motivated by their classification as high-energy materials. For groups 1 and 2, a number of crown ether complexes incorporate axial  $\text{N}_3^-$  ligands as exemplified by  $[\text{Li}(12\text{-crown-4})(\text{N}_3)]$  (with a linear Li–N–N–N unit),<sup>295</sup>  $[\text{Rb}(18\text{-crown-6})(\text{N}_3)(\text{OH}_2)]$  (with an Rb–N–N angle of  $134.7(2)^\circ$  and hydrogen-bonded pairs of molecules, Fig. 19A),<sup>295</sup>  $[\text{Cs}_2(18\text{-crown-6})_2(\mu\text{-N}_3)_2]$ ,<sup>295</sup>  $[\text{Cs}(18\text{-crown-6})(\mu\text{-N}_3)]_n$  (Fig. 19B),<sup>295</sup>  $[\text{K}(18\text{-crown-6})(\text{N}_3)(\text{OPPh}_3)]$ ,<sup>296</sup>  $[\text{Ba}_2(18\text{-crown-6})_2(\text{MeOH})_2(\mu\text{-N}_3)_3]$  (10-coordinate  $\text{Ba}^{2+}$ , Fig. 19C),<sup>297</sup>  $[\text{Sr}(15\text{-crown-5})(\text{N}_3)_2]$ ,<sup>297</sup> and  $[\text{Sr}(15\text{-crown-5})(\text{NO}_3\text{-}\kappa^2)(\mu\text{-N}_3)]_n$  (9-coordinate  $\text{Sr}^{2+}$ , Fig. 19C).<sup>297</sup> In  $[\text{K}(18\text{-crown-6})(\mu\text{-N}_3)]_n$  the azido ligand forms a near-linear bridge between the two metal atoms (K–N–N =  $174.3^\circ$ , U–N–N =  $167.8^\circ$ ).<sup>298</sup> This is one representative example of an  $\text{N}_3^-$  bridging ligand linking a group 1 metal ion to a second metal; in



**Fig. 18** The structures of (A)  $[\text{Ca}(\text{NCMe})_3(15\text{-crown-5})]^{2+}$  (CSD refcode CIPFOZ) and (B)  $[\text{Ca}(\text{NCMe})_3(18\text{-crown-6})]^{2+}$  (refcode FUDCAJ). (C) Part of the interpenetrating nets in  $[\text{Ca}\{\text{C}(\text{CN})_3\}_2]_n$  (refcode DOJVUU). (D) The coordination environment of  $\text{Ba}^{2+}$  in  $[\text{Ba}\{\text{C}(\text{CN})_3\}_2(\text{OH}_2)_2]_n$  (refcode DOJWAB).



**Fig. 19** (A) Structure of one hydrogen-bonded pair of  $[\text{Rb}(18\text{-crown-6})(\text{N}_3)(\text{OH}_2)]$  molecules (CSD refcode TEDKUJ). (B) Part of the 1D-coordination polymer in  $[\text{Cs}(18\text{-crown-6})(\mu\text{-N}_3)]_n$ .<sup>295</sup> (C) Structure of  $[\text{Ba}_2(18\text{-crown-6})_2(\text{MeOH})_2(\mu\text{-N}_3)_3]$  (refcode WIZCEO) and (D) part of the 1D-chain in  $[\text{Sr}(15\text{-crown-5})(\text{NO}_3)(\mu\text{-N}_3)]_n$  (refcode WIZCAK).



**Fig. 20** Structures of (A)  $[\text{Be}_4\text{Br}_4(\mu\text{-N}_3)_6]^{2-}$  (CSD refcode TANHAS), (B)  $[\text{Te}(\text{N}_3)_5]^-$  (refcode BELZUO), (C)  $[\text{Te}(\text{N}_3)_6]^{2-}$  (refcode BEMBAX), (D)  $[\text{Ge}(\text{N}_3)_3]^-$  (refcode JUCROQ), (E)  $[\text{Ga}_2\text{Cl}_6(\mu\text{-N}_3)]^-$  (refcode LUHRIQ), and (F)  $[\text{In}_2\text{Cl}_4(\text{THF})_4(\mu\text{-N}_3)_2]$  (refcode LOFVAD).

some cases the azido unit bridges the two metals as shown in Fig. 19C, while in others, it binds to both metal centers through one terminal N atom.<sup>299–308</sup>

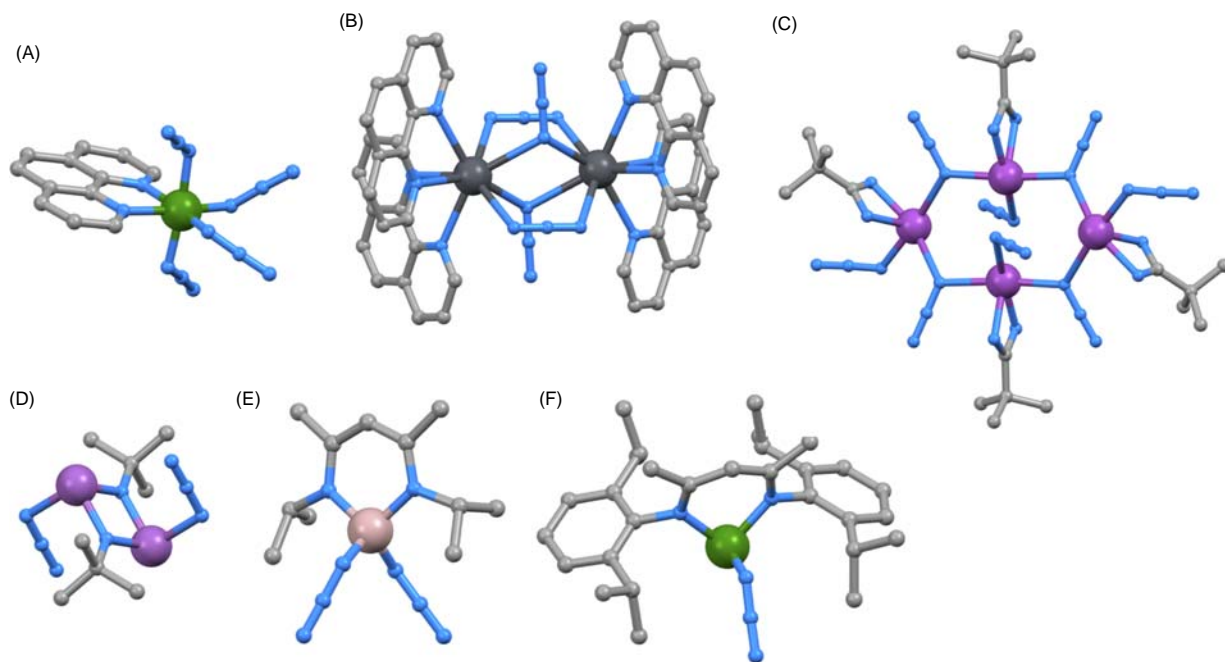
In group 2, in addition to the tetrahedral  $[\text{Be}(\text{N}_3)_4]^{2-}$  ion which was the first structurally characterized homoleptic beryllium azide,<sup>309</sup> Be offers a number of interesting azido complexes. The dimer  $[\text{Be}_2(\text{N}_3)_4(\mu\text{-OSiMe}_3)_2]^{2-}$  contains terminal  $\text{N}_3^-$  ligands with the typical bent geometry ( $\text{Be-N-N} = 134.5(4)$  and  $120.0(4)^\circ$ )<sup>310</sup> which is also observed in  $[\text{BeCl}(\text{N}_3)\text{L}]$  where  $\text{L} = (\text{R,R})\text{-N,N'}$ -di-isopropylcyclohexyl-1,2-diamine.<sup>311</sup>  $[\text{Be}_4\text{Cl}_4(\mu\text{-N}_3)_6]^{2-}$  and  $[\text{Be}_4\text{Br}_4(\mu\text{-N}_3)_6]^{2-}$  (Fig. 20A) are isostructural and contain tetrahedral  $\text{Be}_4$  units, edge-bridged by azido ligands.<sup>312,313</sup> As we move into the p-block, the number of simple azido complexes reported since 2000 increases on moving from group 13 to 15. It is noteworthy that neutral  $[\text{As}(\text{N}_3)_5]$  and  $[\text{Sb}(\text{N}_3)_5]$  were reported for the first time in 2004 and were prepared by treatment of  $\text{AsF}_5$  or  $\text{SbF}_5$  in  $\text{SO}_2$  with excess  $\text{Me}_3\text{SiN}_3$ .<sup>314</sup> Limited examples of non-organometallic compounds are found in group 16, and these include the homoleptic complexes  $[\text{Se}(\text{N}_3)_6]^{2-}$ ,<sup>315</sup>  $[\text{Te}(\text{N}_3)_5]^-$  (Fig. 20B),<sup>316</sup> and  $[\text{Te}(\text{N}_3)_6]^{2-}$  (Fig. 20C).<sup>317</sup> A summary of homoleptic group 15 polyazides was provided in 2013 by Haiges et al.<sup>318</sup> Homoleptic azides of the p-block metals that have been isolated and characterized since 2000 are  $[\text{M}(\text{N}_3)_3]$  ( $\text{M} = \text{Ga}, \text{In}, \text{Tl}$ ),<sup>319</sup>  $[\text{Ga}(\text{N}_3)_5]^{2-}$ ,<sup>319</sup>  $[\text{M}(\text{N}_3)_6]^{3-}$  ( $\text{M} = \text{In}, \text{Tl}$ ),<sup>319</sup> coordinatively unsaturated metal(II)  $[\text{M}(\text{N}_3)_3]^-$  ( $\text{M} = \text{Ge}, \text{Sn}$ ) (Fig. 20D),<sup>320,321</sup> octahedral  $[\text{Ge}(\text{N}_3)_6]^{2-}$ ,<sup>322</sup> octahedral  $[\text{Sn}(\text{N}_3)_6]^{2-}$ ,<sup>323</sup> octahedral  $[\text{As}(\text{N}_3)_6]^-$ ,<sup>324,325</sup> octahedral  $[\text{Sb}(\text{N}_3)_6]^-$ ,<sup>314,325,326</sup> octahedral  $[\text{Bi}(\text{N}_3)_6]^{3-}$ ,<sup>327,328</sup> square-based pyramidal  $[\text{Sb}(\text{N}_3)_5]^{2-}$ ,<sup>326</sup> square-based pyramidal  $[\text{Bi}(\text{N}_3)_5]^{2-}$ ,<sup>327</sup> and  $[\text{Bi}(\text{N}_3)_4]^-$  which forms a chain structure by virtue of weak intermolecular  $\text{Bi}\cdots\text{N}$  interactions.<sup>327</sup> While retaining a see-saw (disphenoidal) coordination geometry at As or Sb, the structures of  $[\text{As}(\text{N}_3)_4]^-$  and  $[\text{Sb}(\text{N}_3)_4]^-$  are cation dependent and show variations in the azido ligand conformations.<sup>318,329</sup> Haiges et al. state that ‘the experimental observation of five distinct single conformers for the same type of anion is unprecedented’. The differences arise from small changes in packing energies and cation–anion interactions in the solid state.<sup>318</sup> Salts of both  $[\text{As}(\text{N}_3)_4]^+$  and  $[\text{Sb}(\text{N}_3)_4]^+$  with As(V) and Sb(V) have been reported; while kinetically stable, they explode violently under conditions of thermal shock. In contrast, the As(III) and Sb(III) compounds  $[\text{Me}_4\text{N}][\text{As}(\text{N}_3)_4]$  and  $[\text{Ph}_4\text{P}][\text{Sb}(\text{N}_3)_4]$  exhibit relatively high stabilities.<sup>325</sup>

Additional simple azido complexes include  $[\text{M}(\text{N}_3)_3(\text{NCMe})]$  ( $\text{M} = \text{Ga}, \text{In}$  with tetrahedral metal center),<sup>319</sup>  $[\text{Ga}_2\text{Cl}_6(\mu\text{-N}_3)]^-$  (Fig. 20E),<sup>330</sup> tetrahedral  $[\text{GaH}_2(\text{N}_3)(\text{qu})]$  ( $\text{qu} = \text{quinuclidine}$ ),<sup>331</sup>  $[\text{In}_2\text{Cl}_4(\text{THF})_4(\mu\text{-N}_3)_2]$  (Fig. 20F),<sup>332</sup> trigonal bipyramidal  $[\text{Ga}(\text{N}_3)_2\{(\text{Et}_2\text{NCH}_2\text{CH}_2)_2\text{N}\}]$  used as a CVD precursor to GaN,<sup>333</sup> octahedral  $[\text{InCl}(\text{N}_3)_2\text{py}_3]$  with a *trans*-arrangement of azido ligands,<sup>334</sup> octahedral  $[\text{Ge}(\text{N}_3)_4(\text{phen})]$  (Fig. 21A),<sup>322,335</sup> octahedral  $[\text{GeCl}_2(\text{N}_3)_2(\text{tmeda})]$  with a *trans*-arrangement of azido ligands,<sup>336</sup> and octahedral *trans*- $[\text{Sn}(\text{N}_3)_4(\text{py})_2]$  and  $[\text{Sn}(\text{N}_3)_4(\text{phen})]$ .<sup>323</sup> Like lead(II) azide, tin(II) azide is shock sensitive and explosive. However, the adducts  $[\text{Sn}(\text{N}_3)_2(\text{py})_2]$  and  $[\text{Sn}(\text{N}_3)_2(4\text{-Mepy})_2]$  (4-Mepy = 4-methylpyridine) are shock- and friction-insensitive and are stable at 298 K under an atmosphere of the respective Lewis base. They possess see-saw (disphenoidal) geometries with azido ligands in the equatorial sites.<sup>321</sup> The dinuclear complex  $[\text{Pb}_2(\text{phen})_4(\mu\text{-N}_3)_4]$  with 8-coordinate Pb(II) exhibits two different azido bridging modes (Fig. 21B) with  $\text{Pb-N-N}$  angles in the range  $104.8\text{--}121.9^\circ$ ,<sup>337</sup> whereas in  $[\text{Pb}_2(\text{phen})_4(\text{NCS})_2(\mu\text{-N}_3)_2]$ , each bridging azido ligand binds to two Pb(II) centers through one terminal N-atom.<sup>338</sup> The Pb(II) coordination sphere suggests the presence of a sterically active lone-pair.<sup>339–342</sup>

The octahedral As(V) and Sb(V) complexes  $[\text{M}(\text{dmap})(\text{N}_3)_5]$  ( $\text{M} = \text{As}, \text{Sb}$ ) have been isolated and it was established that formation of the base adducts led to kinetic stabilization of highly explosive main group metal polyazides.<sup>343</sup> The As(III) and Sb(III) complexes  $[\text{AsCl}(\text{N}_3)_2\text{py}]$  and  $[\text{SbCl}_2(\text{N}_3)(\text{py})_2]$  have disphenoidal and square-based pyramidal geometries, respectively.<sup>344</sup> The homoleptic polyazides  $\text{As}(\text{N}_3)_3$ ,  $\text{Sb}(\text{N}_3)_3$  and  $\text{Bi}(\text{N}_3)_3$  are stabilized by anion formation (as described above) or by the formation of adducts such as  $[\text{As}(\text{bpy})(\text{N}_3)_3]$ ,  $[\text{Sb}(\text{bpy})(\text{N}_3)_3]$ ,  $[\text{Bi}(\text{bpy})(\text{N}_3)_5]^{2-}$  and  $[\text{Bi}_2(\text{bpy})_4(\text{N}_3)_4(\mu\text{-N}_3)_2]$ .<sup>327</sup> The Bi(III) center in  $[\text{Bi}(\text{N}_3)_5(\text{dmsO})]^{2-}$  is octahedrally sited.<sup>329</sup> Fig. 21C shows the structure of  $[\text{Bi}_4\{^t\text{BuC}(\text{PrN})_2\}_4(\text{N}_3)_4(\mu\text{-N}_3)_4]$  which features both terminal and bridging azido ligands; this is one in a series of amidinatobismuth(III) diazides  $[\text{LBi}(\text{N}_3)_2]$  made by reactions between  $\text{LBiX}_2$  ( $\text{X} = \text{Cl}, \text{I}$ ) and  $\text{AgN}_3$ .<sup>345</sup> In  $[\text{Sb}_2(\text{N}_3)_2(\mu\text{-N}^t\text{Bu})_2]$ , each Sb(III) center is in a trigonal pyramidal environment and the azido ligands are directed over the  $\text{Sb}_2\text{N}_2$  rhombus (Fig. 21D).<sup>346</sup>

$\beta$ -Diketimate derivatives include tetrahedral  $[\text{Al}(\text{N}_3)_2\{\text{HC}(\text{CMeN}^i\text{Pr})_2\}]$  (Fig. 21E)<sup>347</sup>  $[\text{Ga}(\text{N}_3)_2\{\text{HC}(\text{CMeN}^i\text{Pr})_2\}]$ <sup>348</sup> and  $[\text{Ga}(\text{N}_3)_2\{\text{HC}(\text{CMeNPh})_2\}]$ ,<sup>349</sup> and the 3-coordinate metal(II) species  $[\text{Ge}(\text{N}_3)\text{L}]$  ( $\text{HL} = \text{H}_2\text{C}(\text{CMeNDipp})_2$ ) (Fig. 21F),<sup>350</sup> and  $[\text{Sn}(\text{N}_3)\text{L}]$  ( $\text{HL}$  with  $\text{Ar} = \text{Mes}$ ).<sup>351</sup>



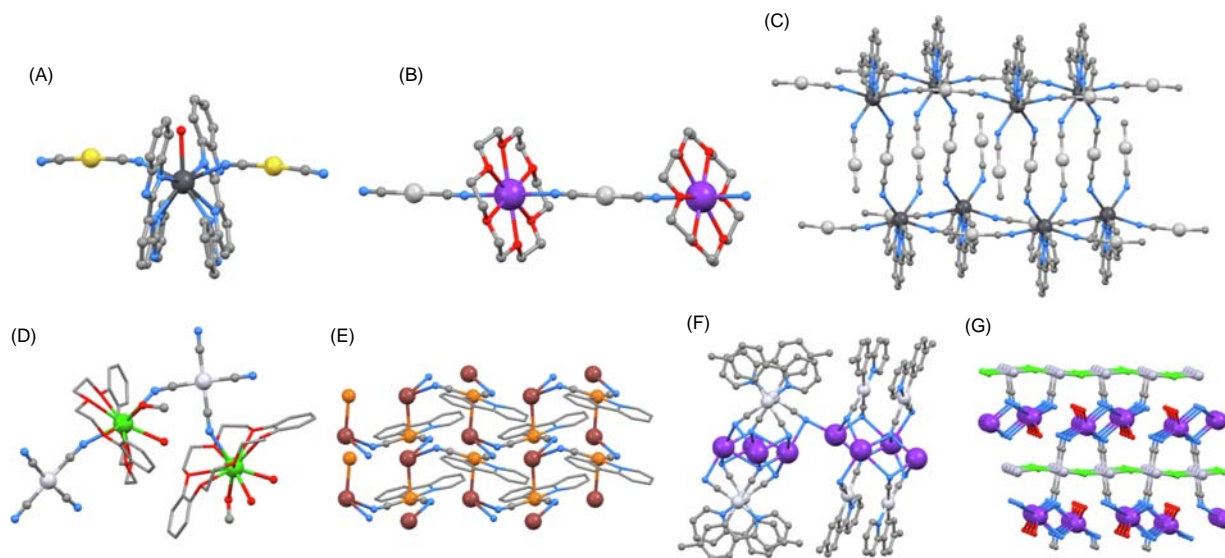


**Fig. 21** Structures of (A)  $[\text{Ge}(\text{N}_3)_4(\text{phen})]$  (refcode BUHQOM), (B)  $[\text{Pb}_2(\text{phen})_4(\mu\text{-N}_3)_4]$  (refcode MUMBUS), (C)  $[\text{Bi}_4\text{t}^{\text{BuC}}(\text{PrN})_2)_4(\text{N}_3)_4(\mu\text{-N}_3)_4]$  with the amidinato 'Pr substituents omitted for clarity (refcode CEJTOC), (D)  $[\text{Sb}_2(\text{N}_3)_2(\mu\text{-N}^{\text{tBu}})_2]$  (refcode RANBUD), (E)  $[\text{Al}(\text{N}_3)_2(\text{HC}(\text{CMeN}^{\text{Pr}})_2)]$  (GSD refcode LUCKEC), and (F)  $[\text{Ge}(\text{N}_3)_4\text{L}]$  (HL =  $\text{H}_2\text{C}(\text{CMeNDipp})_2$ , refcode OHUXIZ).

We now move to N-bonded cyanido ligands. There are few, if any, simple examples containing monodentate N-bonded cyanido ligands coordinated to main group metals. However, there is an extremely interesting subclass of compounds containing cyanido-metallate ligands which can act as monodentate or polydentate N-donors to main group metals, and thus contain bridging CN ligands with the C typically bonded to a d-block metal center. This class of compound will not be discussed extensively, but we present examples of  $\{\text{M}(\text{CN})_n\}$  metalloligands of various denticities coordinated to main group metal centers. Monodentate metalloligands coordinating to main group metal centers are less well represented than higher denticity analogs. An investigation of copper(I)-catalyzed silylation reactions with silyboranes has given rise to the isolation of  $[\text{K}(18\text{-crown-6})][\text{Cu}(\text{CN})(\text{SiMe}_2\text{Ph})]$  in which the cation and anion interact through a bent  $\text{K}-\text{N}\equiv\text{C}-\text{Cu}$  bridge ( $\text{K}-\text{N} = 2.830(4) \text{ \AA}$ ,  $\text{K}-\text{N}\equiv\text{C} = 112.7(3)^\circ$  for one of two independent ion pairs); a change in crystallization conditions leads to a dimer in which the  $\text{K}-\text{N}\equiv\text{C}-\text{Cu}$  bridge is less bent ( $\text{K}-\text{N}\equiv\text{C} = 151.5(2)^\circ$ ).<sup>352</sup> Bidentate metalloligands include linear  $[\text{Ag}(\text{CN})_2]^-$  and  $[\text{Au}(\text{CN})_2]^-$ , although a monodentate mode is observed in  $[\text{Pb}(\text{OH}_2)(\text{bbp})_2\{\text{Au}(\text{CN})_2\}_2]$  (Fig. 22A).<sup>353</sup>  $[\text{Ag}(\text{CN})_2]^-$  coordinates in a bidentate manner to  $\text{Li}^+$  in  $[\text{Li}(\text{NCMe})_2(\mu\text{-Ag}(\text{CN})_2)]_n$ ,<sup>354</sup>  $\text{K}^+$  in  $[\text{K}(18\text{-crown-6})(\mu\text{-Ag}(\text{CN})_2)]_n$  (Fig. 22B),<sup>355</sup> and  $\text{Pb}^{2+}$  in  $[\text{Pb}(\text{tpy})(\mu\text{-Ag}(\text{CN})_2)_2]_n$  (Fig. 22C);  $[\text{Pb}(\text{tpy})(\mu\text{-Au}(\text{CN})_2)_2]_n$  is structurally analogous to the Ag(I) complex.<sup>356</sup> Other examples incorporating bridging  $[\text{Au}(\text{CN})_2]^-$  include  $[\text{Pb}(\text{bpy})_2(\mu\text{-Au}(\text{CN})_2)_2]_n$ ,<sup>356</sup>  $[\text{Pb}(\text{phen})_2(\mu\text{-Au}(\text{CN})_2)_2]_n$ ,<sup>356</sup> and  $[\text{K}(\mu\text{-bpy})(\mu\text{-Au}(\text{CN})_2)_2]_n$  which has a layered structure.<sup>357</sup> Numerous examples of square-planar Au(III), Pd(II) and Pt(II) cyanido derivatives acting as metalloligands to main group metals are known. With L = dibenzo-18-crown-6,  $[\text{Ba}_2\text{L}_2(\text{OH}_2)_3(\text{MeOH})_2\{\text{Pt}(\text{CN})_4\}_2]$  is a discrete molecule (Fig. 22D) featuring one monodentate and one bridging  $[\text{Pt}(\text{CN})_4]^{2-}$ .<sup>358</sup> Other examples of hypodentate  $[\text{Pt}(\text{CN})_4]^{2-}$  ligands are found in the 1D-polymer  $[\text{Ba}(18\text{-crown-6})(\text{OH}_2)_2(\mu\text{-Pt}(\text{CN})_4)]_n$  (bidentate  $[\text{Pt}(\text{CN})_4]^{2-}$ ),<sup>359</sup> the discrete molecule  $[\text{K}_2(18\text{-crown-6})_2(\mu\text{-Pt}(\text{CN})_4)]$  (bidentate  $[\text{Pt}(\text{CN})_4]^{2-}$  with a *trans*-arrangement of  $\text{K}^+$  ions),<sup>360</sup> and the 2D-network  $[\text{Ba}(\text{azacrown})(\mu_3\text{-Pt}(\text{CN})_4)]_n$  where the azacrown is 1,4,10,13-tetraoxa-7,16-diazacyclooctadecane (tridentate  $[\text{Pt}(\text{CN})_4]^{2-}$ ).<sup>361</sup> Tridentate  $[\text{M}(\text{CN})_4]^{2-}$  connecting  $\text{Ba}^{2+}$  or  $\text{Sr}^+$  centers is observed in  $[\text{Ba}(\text{DMF})_4(\mu_3\text{-Ni}(\text{CN})_4)]_n$ ,  $[\text{Sr}(\text{DMF})_4(\mu_3\text{-Ni}(\text{CN})_4)]_n$ ,  $[\text{Sr}(\text{DMF})_4(\mu_3\text{-Pd}(\text{CN})_4)]_n$ , and  $[\text{Sr}(\text{DMF})_4(\mu_3\text{-Pt}(\text{CN})_4)]_n$ . In contrast, in  $[\text{Ba}(\text{DMF})_3(\mu_4\text{-Pd}(\text{CN})_4)]_n$  and  $[\text{Ba}(\text{DMF})_3(\mu_4\text{-Pt}(\text{CN})_4)]_n$ ,  $[\text{M}(\text{CN})_4]^{2-}$  is tetradentate.<sup>362</sup> We return to tetradentate metalloligands later.

Bidentate cyanido metalloligands are further represented by  $[\text{Pd}(\text{ppy})(\text{CN})_2]^-$  which coordinates to Tl(I) in  $[\text{TlPd}(\text{ppy})(\text{CN})_2]_n$  to produce a 2D-network featuring Pd–Tl donor–acceptor metal–metal bonds (Fig. 22E); the  $\text{Tl}-\text{N}\equiv\text{C}$  angles are  $149.8(9)$  and  $110.5(7)^\circ$ .<sup>363</sup> Related to  $[\text{Pd}(\text{ppy})(\text{CN})_2]^-$  is  $[\text{Pt}(4\text{-Meppy})(\text{CN})_2]^-$  which acts as a bidentate ligand, binding  $\text{K}^+$  to give the motif shown in Fig. 22F; the structure propagates into a sheet with additional coordinated  $\text{H}_2\text{O}$  and acetone, and the  $\{\text{Pt}(4\text{-Meppy})(\text{CN})_2\}$  units are arranged in stacked pairs (Fig. 22F) with a  $\text{Pt}\cdots\text{Pt}$  separation of  $3.2785(7) \text{ \AA}$ .<sup>364</sup> The discrete molecule  $[\text{Pb}_2(\text{HBpz}_3)_2(\text{OCMe}_2)_2(\mu\text{-Pt}(\text{CN})_2(4\text{-MeC}_6\text{H}_4\text{C}\equiv\text{C}))_2]$  features a near-linear  $\text{Pb}-\text{N}\equiv\text{C}-\text{Pt}-\text{C}\equiv\text{N}-\text{Pb}$  unit.<sup>365</sup> In  $[\text{K}(\mu\text{-OH}_2)\{\mu\text{-AuCl}_2(\text{CN})_2\}_2]_n$ , *trans*- $[\text{AuCl}_2(\text{CN})_2]^-$  binds  $\text{K}^+$  ions to give a network with both short  $\text{K}-\text{NC}$  and  $\text{K}-\text{Cl}$  contacts; related bromido and iodido compounds also form extended structures by virtue of  $\text{K}-\text{NC}$  coordinate bonds and with additional weak  $\text{X}\cdots\text{X}$  contacts between  $[\text{AuX}_2(\text{CN})_2]^-$  units.<sup>366</sup> On moving from Au(III) to Hg(II), the square-planar metal environment is retained but the





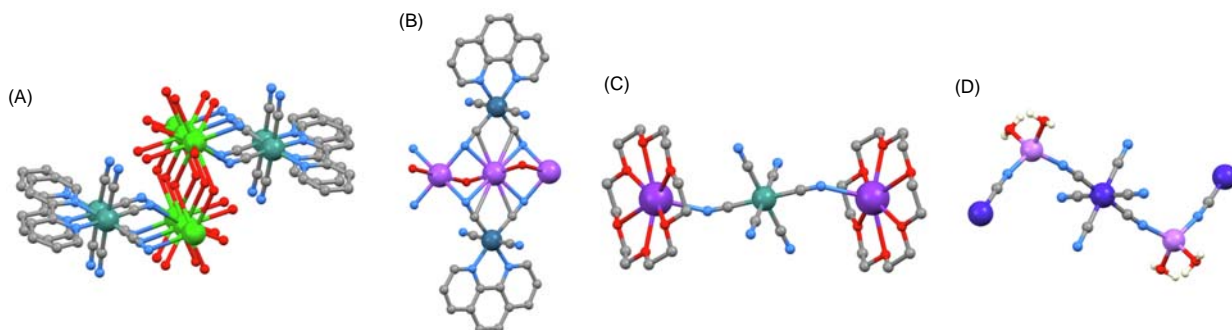
**Fig. 22** (A) The structure of  $[\text{Pb}(\text{OH}_2)(\text{bbp})_2\{\text{Au}(\text{CN})_2\}_2]$  (CSD refcode CAFREJ), (B) part of the 1D-chain in  $[\text{K}(18\text{-crown-6})(\mu\text{-Ag}(\text{CN})_2)]_n$  (refcode EJELUA), and (C) the building block in the 2D-network in  $[\text{Pb}(\text{tpy})(\mu\text{-Ag}(\text{CN})_2)]_n$  (refcode KISDUM). (D) The structure of  $[\text{Ba}_2\text{L}_2(\text{OH}_2)_3(\text{MeOH})_2\{\text{Pt}(\text{CN})_4\}_2]$  (L = dibenzo-18-crown-6) with the crown ether shown in stick representation for clarity (refcode EBALUR). (E) Part a 2D-net in  $[\text{TlPd}(\text{ppy})(\text{CN})_2]_n$  (refcode REJHOF). (F) The building block in the 2D-sheet in solvated  $[\text{KPt}(4\text{-Meppy})(\text{CN})_2]$  (refcode AHIGUV). (g) Part of the 3D-assembly in  $[\text{K}(\mu\text{-OH}_2)\{\mu\text{-HgCl}(\text{CN})_2\}]_n$  (refcode HAYHAT).

propensity for Cl–Hg–Cl bridges leads to an extended array in  $[\text{K}(\mu\text{-OH}_2)\{\mu\text{-HgCl}(\text{CN})_2\}]_n$  comprising alternating  $\{\text{Hg}(\mu\text{-Cl})\}_n$  and K-containing sheets interconnected by bridging  $\text{CN}^-$  ligands (Fig. 22G).<sup>367</sup>

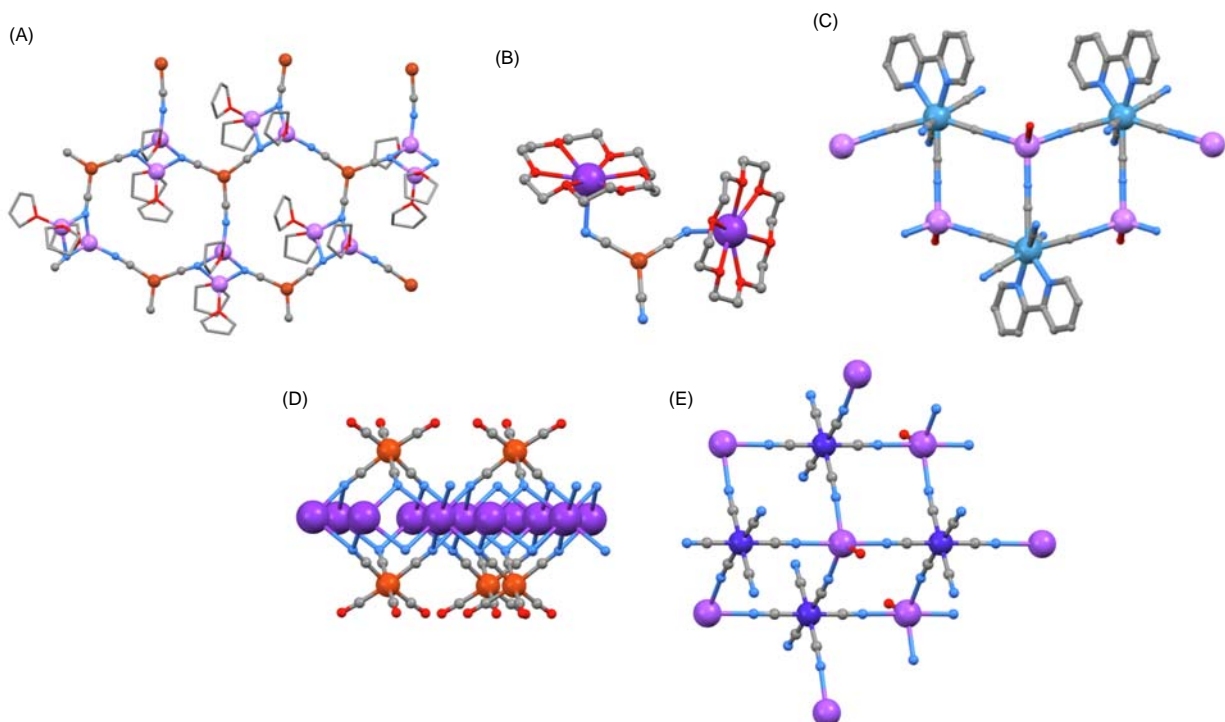
Many hypodentate  $[\text{M}(\text{CN})_n]^{x-}$  and related ligands act in a bidentate mode toward main group metals. Representative examples are the discrete molecular  $[\text{K}_2(18\text{-crown-6})_2\{\mu\text{-Rh}(\text{CN})_3(\text{CO})\}]$  with a *trans*-arrangement of coordinated  $\{\text{K}(18\text{-crown-6})\}^+$  units,<sup>368</sup> and the 1D-coordination polymer  $[\text{Ba}(\text{OH}_2)_5(\mu\text{-OH}_2)\{\mu\text{-Ru}(\text{bpy})(\text{CN})_4\}]_n$  which features a central  $\{\text{Ba}(\mu\text{-OH}_2)\}_n$  chain decorated with bridging  $\{\text{Ru}(\text{bpy})(\text{CN})_4\}$  units (Fig. 23A). The latter heterometallic complex was one of a series investigated to evaluate the effect that the interaction of the *cis*-cyanido ligands with different metal cations has on the <sup>3</sup>MLCT luminescence of  $[\text{Ru}(\text{bpy})(\text{CN})_4]^{2-}$ .<sup>369</sup> Similarly, binding of metal cations to the cyanido ligands of  $[\text{Os}(\text{diimine})(\text{CN})_4]^{2-}$  complexes enhances the emission;  $[\text{Na}(\mu\text{-OH}_2)\{\mu\text{-Os}(\text{phen})(\text{CN})_4\}]_n^{n-}$  (Fig. 23B) is an example of the resulting polynuclear assemblies.<sup>370</sup> With a goal of devising structural models for the iron subsite in  $[\text{NiFe}]$ -hydrogenases, Whaley et al. reported the structure of  $[\text{K}_2(18\text{-crown-6})_2\{\mu\text{-HfFe}(\text{CN})_3(\text{CO})_2\}]$  in which *trans*-cyanido ligands in  $[\text{HfFe}(\text{CN})_3(\text{CO})_2]^{2-}$  link two  $\text{K}^+$  centers.<sup>371</sup> The following assemblies incorporate octahedral  $[\text{M}(\text{CN})_6]^{x-}$  or  $[\text{M}(\text{CN})_5\text{NO}]^{x-}$  metalloligands in bridging modes between two metal centers:  $[\text{K}_2(18\text{-crown-6})_2\{\mu\text{-Ru}(\text{CN})_6\}]^-$  (Fig. 23C) and its Os(III) analog,<sup>372</sup>  $[\text{Li}(\text{OH}_2)_2\{\mu\text{-Co}(\text{CN})_6\}]_n^{2n-}$  (Fig. 23D),<sup>373</sup>  $[\text{Ba}(\text{phen})_3(\text{OH}_2)\{\mu\text{-Fe}(\text{CN})_5\text{NO}\}]$  (in which  $\text{Ba}^{2+}$  and  $\text{Fe}^{2+}$  centers are linked into a 1D-coordination polymer via *trans* CN and NO ligands),<sup>374</sup>  $[\text{Ca}_2(\text{phen})_4(\text{OH}_2)_6\{\mu\text{-Fe}(\text{CN})_6\}]^+$ ,<sup>375</sup>  $[\text{Sr}_2(\text{phen})_4(\text{O}_2\text{CCF}_3)(\text{OH}_2)_3\{\mu\text{-Fe}(\text{CN})_6\}]$  and  $[\text{Ca}_2(\text{phen})_4(\text{O}_2\text{CCF}_3)_2(\text{OH}_2)_2\{\mu\text{-Co}(\text{CN})_6\}]$ .<sup>376</sup>

Trigonal planar  $[\text{Cu}(\text{CN})_3]^{2-}$  is a rare example of a tridentate, but not hypodentate, metalloligand binding to main group metals.  $[\text{Li}_2(\text{THF})_3\{\mu_3\text{-Cu}(\text{CN})_3\}]_n$  possesses the 2D-network shown in Fig. 24A; both the  $\text{Cu}^+$  ions and  $\{\text{Li}_2\}^{2+}$  units are 3-connecting nodes in the net.<sup>377</sup> In  $[\text{K}_2(18\text{-crown-6})_2\{\mu\text{-Cu}(\text{CN})_3\}]$ , the  $[\text{Cu}(\text{CN})_3]^{2-}$  ligand is bidentate (Fig. 24B).<sup>352</sup> Examples in which hypodentate ligands act in a tridentate mode include  $[\text{K}(\text{OH}_2)\{\mu_3\text{-AuCl}_4\}]_n$  (3D-network),<sup>378</sup>  $\{\text{Li}|\text{Li}(\text{O}_2\text{H})(\mu_3\text{-W}(\text{CN})_6(\text{bpy}))\}_n$  (Fig. 24C),<sup>379</sup>  $[\text{K}\{\mu_3\text{-Fe}(\text{CN})_3(\text{CO})_3\}]_n$  (Fig. 24D) and  $[\text{Na}(\text{OH}_2)\{\mu_3\text{-Co}(\text{CN})_6\}]_n^{2n-}$  (both with layer structures).<sup>380,381</sup>

Examples of  $[\text{M}(\text{CN})_4]^{2-}$  and  $[\text{M}(\text{CN})_6]^{n-}$  ions that act as tetradentate ligands are found in  $[\text{K}_2(\text{phen})_2\{\mu_4\text{-Pt}(\text{CN})_4\}]_n$  (2D-sheet),<sup>382</sup>  $[\text{K}_2\{\mu_4\text{-Zn}(\text{CN})_4\}]_n$  (in which  $\text{K}^+$  has CN = 8),<sup>383</sup>  $[\text{Ba}(\text{DMF})_3\{\mu_4\text{-Pd}(\text{CN})_4\}]_n$  (2D-sheet),<sup>362</sup> the imidazolium salt of  $[\text{Na}(\text{OH}_2)\{\mu_4\text{-Co}(\text{CN})_6\}]_n^{2n-}$  (with non-coordinated cyanides being mutually *trans*),<sup>384</sup> the pyridinium salt of  $[\text{Na}(\text{OH}_2)\{\mu_4\text{-Co}(\text{CN})_6\}]_n^{2n-}$  (with non-coordinated cyanides *cis*, Fig. 24E), and  $[\text{Me}_3\text{NOH}]_2[\text{KCo}(\text{CN})_6]$  (a perovskite material in which the  $\{\text{Co}^{\text{III}}(\text{CN})_6\}$  unit is in a  $\mu_4$ -mode).<sup>385</sup> In a second phase of the latter, the  $[\text{Co}(\text{CN})_6]^{3-}$  metalloligand is hexadentate and  $[\text{Me}_3\text{NOH}]^+$  ions are hosted within a 3D-network of cubic cages.<sup>385</sup> Pentadentate metalloligands are observed in the  $[\text{Me}_2\text{NH}_2]^+$  salt of  $[\text{Na}\{\mu_5\text{-Fe}(\text{CN})_5(\text{NO})\}]_n^{n-}$  (3D-network and a hybrid high-temperature ferroelectric material),<sup>386</sup> and the  $[\text{MeNH}_3]^+$  salt of  $[\text{Na}(\text{OH}_2)\{\mu_5\text{-Fe}(\text{CN})_5(\text{NO})\}]_n^{n-}$  (2D-double sheets, Fig. 25A).<sup>387</sup> There are many examples in which  $[\text{M}(\text{CN})_6]^{n-}$  ions act as hexadentate ligands forming 3D-networks with exploitable dielectric, ferroelectric or magnetic properties. Representative examples are the  $[\text{MeNH}_3]^+$  salt of  $[\text{Na}\{\mu_6\text{-Co}(\text{CN})_6\}]_n^{2n-}$ ,<sup>388</sup> salts of  $[\text{K}\{\mu_6\text{-Co}(\text{CN})_6\}]_n^{2n-}$ ,<sup>385,389,390</sup> and  $[\text{Rb}\{\mu_6\text{-Co}(\text{CN})_6\}]_n^{2n-}$  (Fig. 25B),<sup>391</sup> salts of  $[\text{K}\{\mu_6\text{-Fe}(\text{CN})_6\}]_n^{2n-}$  (Fig. 25C),<sup>392–394</sup> the mixed valence Co(II)/Co(III)  $[\text{KCo}_2(\text{ox})(\text{OH}_2)_3\{\mu_6\text{-Co}(\text{CN})_6\}]_n$ ,<sup>395</sup> the Prussian blue analog  $[\text{Ga}\{\mu_6\text{-Fe}(\text{CN})_6\}]_n$ ,<sup>396</sup> the guanidinium salt of  $[\text{Ca}\{\mu_6\text{-Co}(\text{CN})_6\}]_n^{n-}$ ,<sup>397</sup> the  $[\text{H}_3\text{O}]^+$  salt of



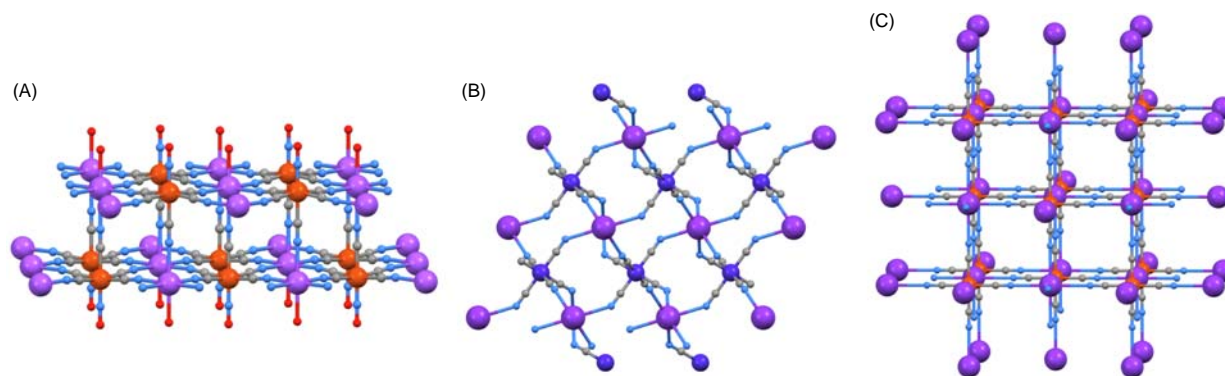
**Fig. 23** The structures of (A) part of the 1D-chain in  $[\text{Ba}(\text{OH}_2)_5(\mu\text{-OH}_2)\{\mu\text{-Ru}(\text{bpy})(\text{CN})_4\}]_n$  (CSD refcode RIBUCUD), (B) part of the 1D-chain in  $[\text{Na}(\mu\text{-OH}_2)\{\mu\text{-Os}(\text{phen})(\text{CN})_4\}]_n^{n-}$  (refcode QITCUS), (C)  $[\text{K}_2(18\text{-crown-6})_2\{\mu\text{-Ru}(\text{CN})_6\}]_n^{-}$  (refcode OSINOU), and (D) part of the 1D-polymer chain in  $[\text{Li}(\text{OH}_2)_2\{\mu\text{-Co}(\text{CN})_6\}]_n^{2n-}$  (refcode PODFEV).



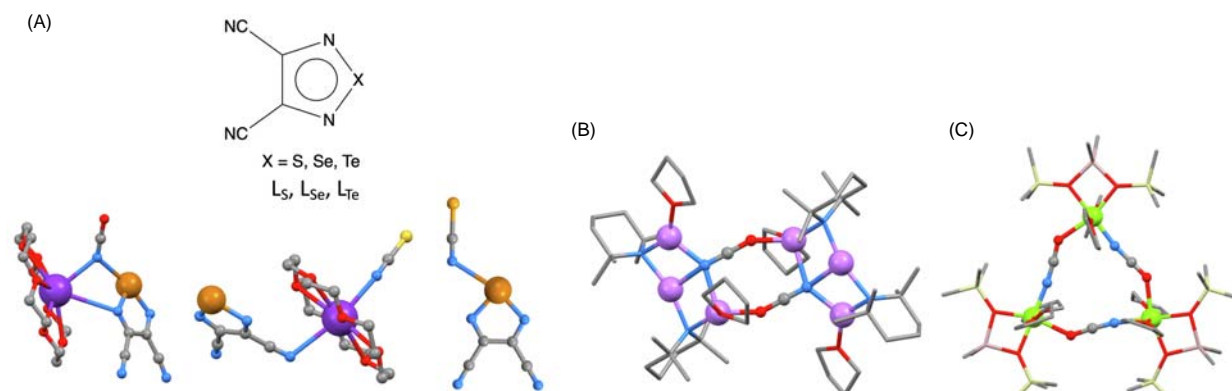
**Fig. 24** (A) Part of the 2D-network in  $[\text{Li}_2(\text{THF})_3\{\mu\text{-Cu}(\text{CN})_3\}]_n$  (CSD refcode GOKXIP); for clarity, the THF molecules are depicted in stick representation. The structures of (B)  $[\text{K}_2(18\text{-crown-6})_2\{\mu\text{-Cu}(\text{CN})_3\}]_n$  (refcode HAXZEO), (C) part of the anionic 2D-net in  $[\text{Li}][\text{Li}(\text{O}_2\text{H})\{\mu_3\text{-W}(\text{CN})_6(\text{bpy})\}]_n$  (refcode BUNJIG), (D) part of a 2D-sheet in  $[\text{K}\{\mu_3\text{-Fe}(\text{CN})_3(\text{CO})_3\}]_n$  (refcode CADYAI), and (E) part of a 2D-sheet in  $[\text{Na}(\text{OH}_2)\{\mu_4\text{-Co}(\text{CN})_6\}]_n^{n-}$  (refcode QUGCECO1).

$[\text{Ca}(\text{OH}_2)_2\{\mu_6\text{-Co}(\text{CN})_6\}]_n^{n-}$ ,<sup>398</sup> the  $[\text{NH}_4]^+$  salts of  $[\text{Sr}\{\mu_6\text{-Fe}(\text{CN})_6\}]_n^{2n-}$ ,<sup>399</sup> and  $[\text{Sr}(\text{OH}_2)_2\{\mu_6\text{-Fe}(\text{CN})_6\}]_n^{2n-}$ ,<sup>400</sup> the  $[\text{NH}_4]^+$  salt of  $[\text{Ba}(\text{OH}_2)_3\{\mu_6\text{-Fe}(\text{CN})_6\}]_n^{2n-}$ ,<sup>401</sup> and salts of  $[\text{K}\{\mu_6\text{-Cr}(\text{CN})_6\}]_n^{2n-}$ .<sup>402,403</sup> The guanidinium salt of  $[\text{K}_2(\text{OH}_2)_6\{\mu_6\text{-Fe}(\text{CN})_6\}]_n^{2n-}$  possesses a 2D-structure with a central layer of  $\{\text{Fe}^{\text{III}}(\text{CN})_6\}$  units interconnecting peripheral *fac*- $\{\text{K}(\text{OH}_2)_3\}$  units.<sup>404</sup>

The final group of pseudo-halides that we consider are  $\text{NCO}^-$ ,  $\text{NCS}^-$  and  $\text{NCSe}^-$  ligands, and we include examples of terminally N-bonded, bridging N-bonded, and bridging N,X-bound ( $\text{X} = \text{O}, \text{S}, \text{Se}$ ) ligands. The structure of  $\text{Cs}[\text{NCO}]$  is related to that of  $\text{KN}_3$  with disordered  $\text{NCO}^-$  ligands in  $\text{Cs-NCO/OCN-Cs}$  bridging sites.<sup>405</sup> Reactions between 3,4-dicyano-1,2,5-chalcogenadiazoles ( $\text{L}_\text{S}$ ,  $\text{L}_\text{Se}$  and  $\text{L}_\text{Te}$ , Fig. 26A) and pseudohalides  $\text{XCN}^-$  ( $\text{X} = \text{O}, \text{S}, \text{Se}, \text{Te}$ ) produced a series of donor-acceptor complexes demonstrating both terminal and bridging modes of the ligands to and between main group metals. These include  $[\text{K}(18\text{-crown-6})(\text{L}_\text{Te})(\mu\text{-NCO})]$ ,  $[\text{K}(18\text{-crown-6})(\text{L}_\text{Te})(\text{NCS})]$  and  $[\text{K}(\text{L}_\text{Te})(\text{NCSe})]$  (Fig. 26A).<sup>406</sup> An investigation of *ortho*-cupration using non cyanide reagents looked at the reaction of  $\text{CuOCN}$  with  $\text{Li}[\text{tmp}]$ . Both lithiocuprates and lithium-only complexes were characterized, and Fig. 26B shows the structure of  $[\text{Li}_6(\text{THF})_4(\text{tmp})_4(\mu\text{-NCO})_2]$  in which the N of each  $\text{NCO}^-$  interacts with three Li centers.<sup>407</sup> Group 2 metal complexes are represented by  $[\text{Mg}(\text{tpp})(\text{NCO})]^-$  (with a terminally N-bound ligand),<sup>408</sup> *trans*- $[\text{Mg}(\text{py})_4(\text{NCO})_2]$  (terminally N-bound  $\text{NCO}^-$ ),<sup>409,410</sup> and a trimer containing a cyclic  $\{\text{Mg}_3(\mu\text{-NCO})_3\}$  core (Fig. 26C).<sup>411</sup>



**Fig. 25** (A) Part of one double sheet in the  $[\text{MeNH}_3]^+$  salt of  $[\text{Na}(\text{OH}_2)\{\mu_5\text{-Fe}(\text{CN})_5(\text{NO})\}]_n^-$  (CSD refcode EHEBOL). Part of the 3D-nets in (B) the  $[\text{MeNH}_3]^+$  salt of  $[\text{Rb}\{\mu_6\text{-Co}(\text{CN})_6\}]_n^-$  (refcode AXUDII), and (C) the  $[\text{Me}_3\text{NOH}]^+$  salt of  $[\text{K}\{\mu_6\text{-Fe}(\text{CN})_6\}]_n^-$  (refcode CATXED).

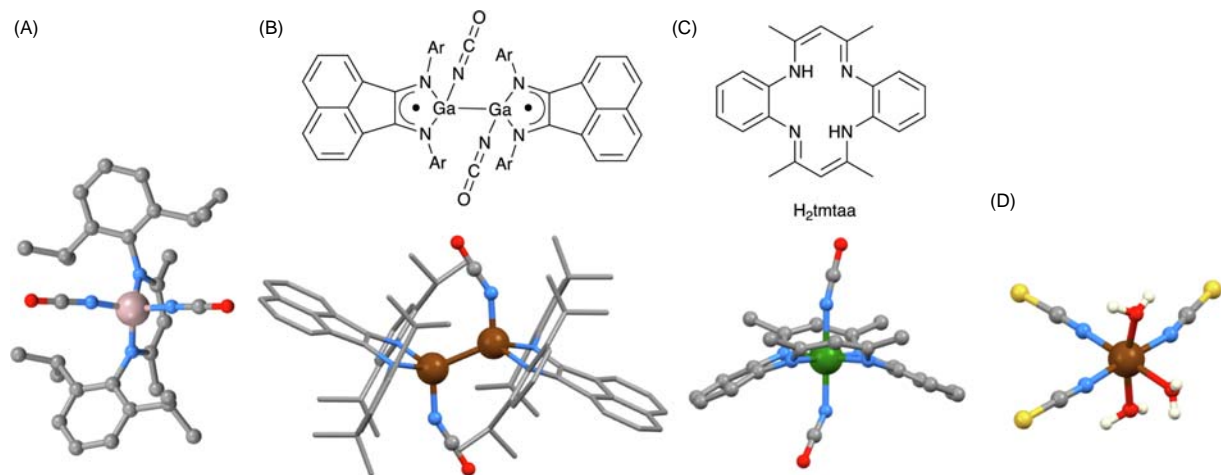


**Fig. 26** (A) Top: ligands  $L_S$ ,  $L_{Se}$  and  $L_{Te}$ ; bottom, left to right: structures of  $[\text{K}(18\text{-crown-6})(L_{Te})(\mu\text{-NCO})]$  (CSD refcode BIHQOB),  $[\text{K}(18\text{-crown-6})(L_{Te})(\text{NCS})]$  (refcode BIQUH) and  $[L_{Te}(\text{NCS})]^-$  in the  $\text{K}^+$  salt (refcode BIHRES). (B) The structure of  $[\text{Li}_6(\text{THF})_4(\text{tmp})_4(\mu\text{-NCO})_2]$  (refcode HASKUK). (C) The structure of  $[\text{Me}_2\text{Al}(\mu\text{-OSiMe}_3)_2\text{Mg}(\text{THF})_2(\mu\text{-NCO})_3]$  (refcode WEJREJ); the  $\text{NCO}^-$  ligands are disordered and only one site for each is shown.

Moving to the p-block and compounds exhibiting N-bound terminal  $\text{NCX}^-$  ligands include the  $\beta$ -ketiminate derivative  $[\text{Al}\{\text{OCMeCHCMeNDipp}\}_2(\text{NCO})]$ ,<sup>412</sup> the tetrahedral  $[\text{LAlX}_2]$  complexes in which  $\text{HL} = \text{HC}\{\text{MeC}(\text{NDipp})\}_2$ ,  $\text{X} = \text{NCO}$  or  $\text{NCS}$  (the first examples of species in which two pseudohalide ligands are bound to  $\text{Al}^{3+}$ , Fig. 27A).<sup>413</sup> Note that in 1996, Assmann et al. reported  $[\text{In}(\text{pc})(\text{NCO})_2]^-$  with two terminal  $\text{NCO}^-$  ligands bound to  $\text{In}^{3+}$ .<sup>414</sup> In the centrosymmetric  $[\text{Ga}_2(\text{dpp-bian})_2(\text{NCO})_2]$  (which contains *dpp-bian* radicals, Fig. 27B), the  $\text{Ga-N-C}$  angle is  $149.2(4)^\circ$ ,<sup>415</sup> compared to  $167.9(1)$  and  $171.8(1)^\circ$  in  $[\text{Al}\{\text{OCMeCHCMeNDipp}\}_2(\text{NCO})]$ . A *trans*-arrangement of  $\text{NCO}^-$  ligands is found in  $[\text{Ge}(\text{tmtaa})(\text{NCO})_2]$  (*H*<sub>2</sub>tmtaa is defined in Fig. 27C) in which the  $\text{Ge-N-C}$  angles are  $160.9(2)$  and  $136.7(2)^\circ$ .<sup>416</sup> Similarly, bent geometries are observed in related  $\text{Ge}(\text{IV})$  complexes,<sup>417</sup> and in *trans*- $[\text{Sn}(\text{pc})(\text{NCO})_2]^{2-}$  ( $\text{Sn-N-C} = 140.9^\circ$ ).<sup>418</sup>

Large numbers of N-bonded thiocyanato derivatives of main group metals are known and we focus on selected examples reported after 2000. Angles designated  $\text{M-N-C}$  refer to terminally attached  $\text{NCS}^-$  ligands. Lithium is tetrahedrally sited in  $[\text{Li}(2,9\text{-Me}_2\text{phen})(\text{NCS})(\text{MeOH})]$  (the  $\text{LiNCS}$  unit is close to linear),<sup>419</sup> while the  $\text{Na}^+$  center in  $[\text{Na}(2,9\text{-Me}_2\text{phen})_2(\text{NCS})]$  is in a distorted trigonal bipyramidal environment; the  $\text{Na-N-C}$  angle is  $156.5(3)^\circ$ .<sup>420</sup> In  $[\text{Na}(18\text{-crown-6})(\text{THF})(\text{NCS})]$ , the  $\text{NaNCS}$  unit is approximately linear, while in  $[\text{Na}(15\text{-crown-5})(\text{NCS})]$ , the  $\text{Na-N-C}$  angle is  $133.6(5)^\circ$ .<sup>421</sup> In  $[\text{Li}(18\text{-crown-6})(\text{OH}_2)(\text{NCS})]$ , the  $\text{Li}^+$  binds to three of the six O-donors of the crown ether and is 5-coordinate<sup>422</sup>; this contrasts with the tetrahedral environment found in  $[\text{Li}(\text{MeNH}_2)_2(18\text{-crown-6})]^+$  (Fig. 4A). Examples with group 2 metals include the tetrahedral  $[\text{Be}(\text{NCS})_4]^{2-}$  anion (linear  $\text{BeNCS}$  units),<sup>423</sup> octahedral *trans*- $[\text{Mg}(\text{THF})_4(\text{NCS})_2]$  ( $\text{Mg-N-C} = 163.6^\circ$ ),<sup>424</sup> octahedral *cis*- $[\text{Mg}(\text{phen})_2(\text{NCS})_2]$  ( $\text{Mg-N-C} = 165.63(16)^\circ$ ),<sup>425</sup> octahedral  $[\text{Ca}(\text{NCS})_6]^{4-}$  (*ca.* linear  $\text{CaNCS}$ ),<sup>426</sup> octahedral *cis*- $[\text{Ca}(\text{OH}_2)_2(\text{NCS})_4]^{2-}$  (*ca.* linear  $\text{CaNCS}$ ),<sup>427</sup>  $[\text{Ca}(\text{N-CMe})_5(\text{NCS})_2]$  and  $[\text{Ca}(\text{OH}_2)(\text{dme})_2(\text{NCS})_2]$  with close to linear  $\text{CaNCS}$  units,<sup>274</sup>  $[\text{Ca}(\text{dme})_3(\text{NCS})_2]$  ( $\text{Ca-N-C} = 156.9(2)^\circ$ ),<sup>274</sup> and the 9-coordinate barium complex  $[\text{Ba}(L_{\text{diazacrown}})(\text{OH}_2)(\text{NCS})_2]$  ( $L_{\text{diazacrown}} = N,N'$ -bis(4-aminobenzyl)-4,13-diaza-18-crown-6) with a  $\text{Ba-N-C}$  angle of  $132.0^\circ$ .<sup>428</sup> Thiocyanato complexes of group 13 metals include octahedral  $[\text{Al}(\text{NCS})_6]^{3-}$  (*ca.* linear  $\text{AlNCS}$  units),<sup>429</sup> *mer*- $[\text{Ga}(\text{OH}_2)_3(\text{NCS})_3]$  (which co-crystallizes with 18-crown-6 and has approximately linear  $\text{GaNCS}$  units, Fig. 27D),<sup>430</sup> *trans*- $[\text{Ga}(\text{iQ})_2(\text{NCS})_4]^-$  (*ca.* linear  $\text{GaNCS}$ ),<sup>431</sup> octahedral  $[\text{In}(\text{NCS})_6]^{3-}$  ( $\text{In-N-C}$  angles in the range  $162.7\text{--}176.2^\circ$ ),<sup>432</sup> and *cis*- $[\text{In}(\text{OH}_2)_4(\text{NCS})_2]^+$  and *trans*- $[\text{In}(\text{OH}_2)_2(\text{NCS})_4]^-$  which occur in the salt

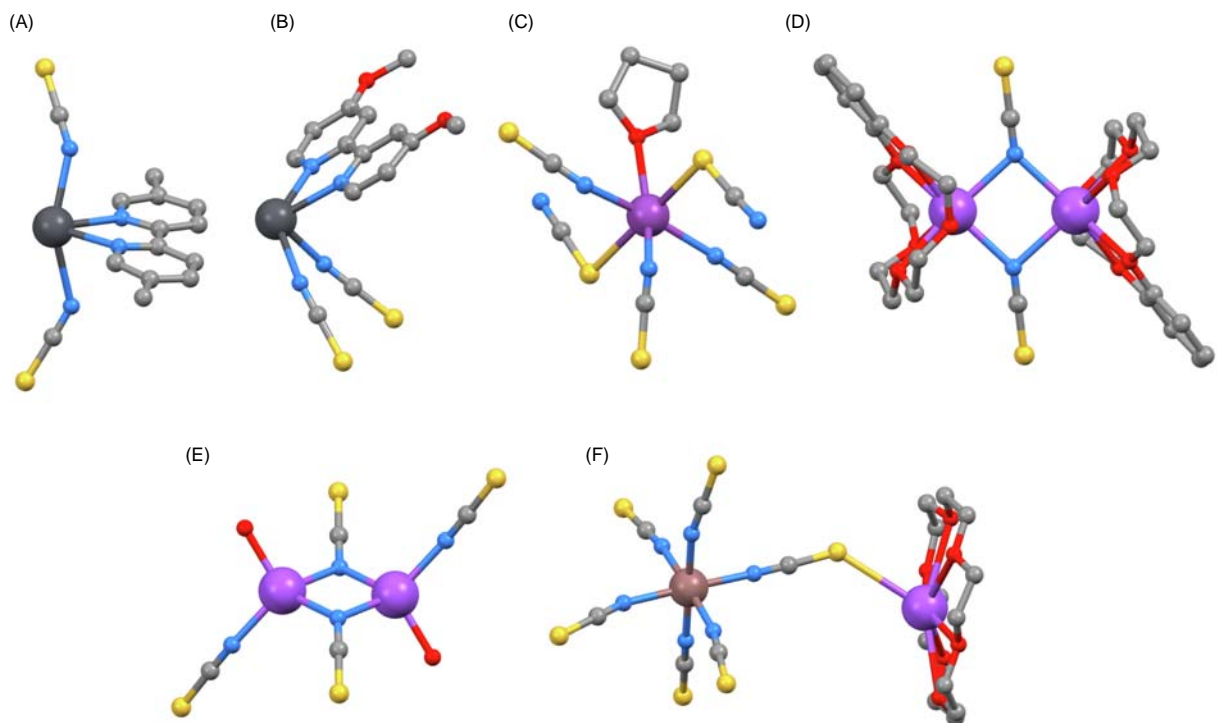




**Fig. 27** (A) Structure of  $[\text{LaI}(\text{NCO})_2]$  where  $\text{HL} = \text{HC}(\text{MeC}(\text{NDipp}))_2$  (CSD refcode QIGWIP). (B) Schematic diagram and structure of  $[\text{Ga}_2(\text{dpp-bian})_2(\text{NCO})_2]$  (refcode XEWMIY). (C) Structures of  $\text{H}_2\text{tmtaa}$  and the  $\text{Ge}(\text{IV})$  complex  $[\text{Ge}(\text{tmtaa})(\text{NCO})_2]$  (refcode DABHEU). (D) The structure of *mer*- $[\text{Ga}(\text{OH}_2)_3(\text{NCS})_3]$  (refcode EFOSAU).

$[\text{In}(\text{OH}_2)_4(\text{NCS})_2][\text{In}(\text{OH}_2)_2(\text{NCS})_4]^-$ .<sup>433</sup> The anion *trans*- $[\text{In}(\text{OH}_2)_2(\text{NCS})_4]^-$  has also been characterized in the 4,4'-bipyridinium salt.<sup>434</sup>

Group 14 germanium and tin complexes are represented by the  $\text{NCS}^-$  analog of  $[\text{Ge}(\text{tmtaa})(\text{NCO})_2]$  (see Fig. 27C),<sup>435</sup> and the trigonal pyramidal  $[\text{SnCl}(\text{NCS})_2]^-$  ( $\text{Sn}-\text{N}-\text{C} = 149.5(4)$  and  $139.5(4)^\circ$ ).<sup>436</sup> Lead(II) thiocyanate derivatives are exemplified by  $[\text{Pb}(\text{18-crown-6})(\text{NCS})_2]^+$  ( $\text{Pb}-\text{N}-\text{C} = 130.8(7)^\circ$ ),<sup>437</sup>  $[\text{Pb}(\text{phen})(\text{NCS})(\text{NO}_2-\kappa^2)]$ ,<sup>438</sup> and  $[\text{Pb}(5,5'\text{-Me}_2\text{bpy})(\text{NCS})_2]$  (Fig. 28A) and  $[\text{Pb}(4,4'\text{-(MeO)}_2\text{bpy})(\text{NCS})_2]$  (Fig. 28B) both of which show four 'normal'  $\text{Pb}-\text{N}$  bonds and three weak  $\text{Pb}\cdots\text{S}$  contacts to adjacent molecules in the solid state.<sup>439</sup> The coordination geometries for  $\text{Pb}(\text{II})$  (Fig. 28A and B) are indicative of the presence of a stereochemically active lone pair,<sup>439</sup> and this is, in general, a much discussed topic for  $\text{Pb}(\text{II})$ .<sup>339-342</sup> Terminal  $\text{NCS}^-$  ligands in



**Fig. 28** The structures of (A)  $[\text{Pb}(5,5'\text{-Me}_2\text{bpy})(\text{NCS})_2]$  (CSD refcode RAXGUU), (B)  $[\text{Pb}(4,4'\text{-(MeO)}_2\text{bpy})(\text{NCS})_2]$  (refcode RAXHAB), (C)  $[\text{Bi}(\text{THF})(\text{NCS})_5]^{2-}$  (refcode CIYKED), (D)  $[\text{K}_2(\text{benzo-15-crown-5})_2(\mu\text{-NCS})_2]$  (refcode FIXJOM), (E)  $[\text{Na}_2(\text{NCS})_2(\text{OH}_2)_2(\mu\text{-NCS})_2]^{2-}$  (refcode LACDOJ), and (F)  $[\text{K}(\text{18-crown-6})(\mu\text{-SCN})\text{In}(\text{NCS})_5]^{2-}$  (refcode RUDTIU).

[Pb<sub>2</sub>(phen)<sub>4</sub>(NCS)<sub>2</sub>(μ-N<sub>3</sub>)<sub>2</sub>] exhibit Pb–N–C angles of 147.1(3)°. In contrast to the N-bonded NCS<sup>−</sup> ligands in the complexes above, Saghatforoush et al. observe S-bonded thiocyanates in [Pb(4-ClC<sub>6</sub>H<sub>4</sub>tpy)(SCN)<sub>2</sub>].<sup>440</sup>

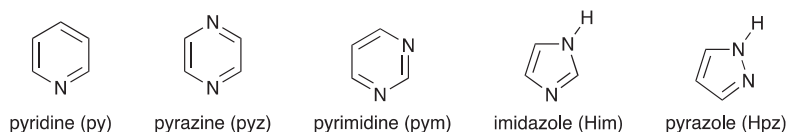
Homoleptic Sb(NCS)<sub>3</sub> and Bi(NCS)<sub>3</sub> are formed in reactions of SbF<sub>3</sub> or BiF<sub>3</sub> with Me<sub>3</sub>Si(SCN) and were crystallized as THF adducts. The thiocyanato ligands are N-bonded in [Sb(THF)(NCS)<sub>3</sub>]. In [(Ph<sub>3</sub>P)<sub>2</sub>N]<sub>2</sub>[Sb(NCS)<sub>5</sub>], the [Sb(NCS)<sub>5</sub>]<sup>2−</sup> ion has a square-pyramidal structure with N-bonded NCS<sup>−</sup> ligands (Sb–N–C angles are in the range 140.1(3)–169.1(3)°). Both N- and S-bonded thiocyanato ligands occur in the [(Ph<sub>3</sub>P)<sub>2</sub>N]<sup>+</sup> salt of [Bi(THF)(NCS)<sub>5</sub>]<sup>2−</sup> (Fig. 28C) with Bi–N–C angles of 173.8(5), 123.9(5) and 159.5(5)°.<sup>441</sup>

Different modes of bonding are observed for bridging thiocyanates, paralleling the modes described above for bridging NCO<sup>−</sup>. An N-bound mode (referring to either terminal or bridging NCO<sup>−</sup>) is seen, for example, in [K<sub>2</sub>(benzo-15-crown-5)<sub>2</sub>(μ-NCS)] (Fig. 28D),<sup>442</sup> and [Na<sub>2</sub>(NCS)<sub>2</sub>(OH<sub>2</sub>)<sub>2</sub>(μ-NCS)]<sup>2−</sup> with both terminal and bridging NCS<sup>−</sup> (Fig. 28E). In [K(18-crown-6)(μ-SCN)In(NCS)<sub>5</sub>]<sup>2−</sup>, one thiocyanate ligand bridges between K<sup>+</sup> and In<sup>3+</sup> centers, S-bound to K and N-bound to In (Fig. 28F).<sup>443</sup> Doubly bridged pairs of Pb(II) centers are seen in the 1D-coordination polymer [PbL<sub>2</sub>(μ-SCN)<sub>2</sub>]<sub>n</sub> (L = 5,6-bis(furan-2-yl)-3-(pyridin-2-yl)-1,2,4-triazine).<sup>444</sup> Further examples of bridging NCS<sup>−</sup> ligands that coordinate through both N- and S-donors are detailed in Section 1.02.7.1.3.

Complexes containing NCSe<sup>−</sup> ligands are far less well represented than their NCO<sup>−</sup> and NCS<sup>−</sup> counterparts. Selenocyanate-containing species related to those shown in Fig. 26A have been reported by Semenov et al.<sup>406</sup> The tetrahedral complex [Be(DMF)<sub>2</sub>(NCSe)<sub>2</sub>] (angle Be–N–C = 176.8(5)°) was the first example of a structurally characterized selenium-containing beryllium compound; it was prepared by reaction of BeCl<sub>2</sub> and KSeCN in DMF/THF.<sup>445</sup> [In(Me<sub>2</sub>NCH<sub>2</sub>CMe<sub>2</sub>S)<sub>2</sub>(NCSe)] is trigonal bipyramidal with the NCSe<sup>−</sup> ligand in an equatorial site, and the linear In–N–C–Se unit is crystallographically imposed; this and related compounds are of interest as single precursors for indium chalcogenides.<sup>446</sup>

### 1.02.2.1.5 Monodentate heterocyclic ligands

The variety of heterocyclic ligands is vast, and for an introduction to their main group metal coordination compounds, we focus only on pyridine (py), pyrazine (pyz), pyrimidine (pym), imidazole (Him) and pyrazole (Hpz) ligands (Scheme 1), exemplified by homoleptic and other simple species. Heterocyclic ligands also feature in other complexes considered in this review but where



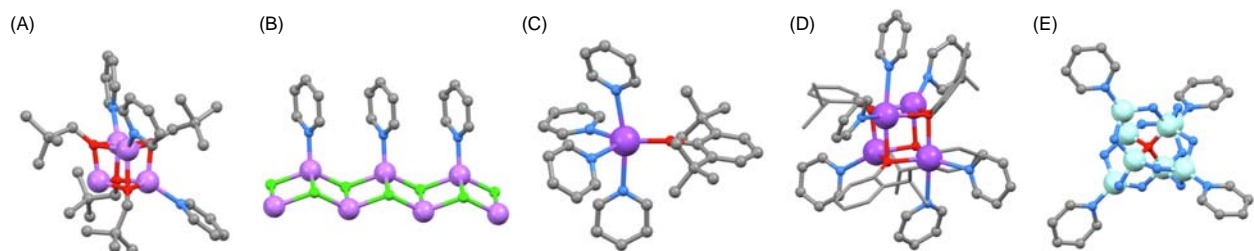
**Scheme 1** Heterocyclic ligands discussed in this section.

the emphasis of the discussion is on a different ligand. The section is organized by heterocyclic ligand, starting with pyridine.

#### 1.02.2.1.5.1 Pyridine

Pyridine often occurs as an axial ligand in main group metal complexes in which macrocyclic ligands occupy the equatorial sites, e.g., [Na(18-crown-6)(py)<sub>2</sub>]<sup>+</sup>,<sup>447–454</sup> [K(18-crown-6)(py)<sub>2</sub>]<sup>+</sup>,<sup>455–457</sup> [Mg(15-crown-5)(py)<sub>2</sub>]<sup>2+</sup>,<sup>458</sup> porphyrinato complexes,<sup>459–468</sup> phthalocyanato complexes,<sup>469,470</sup> corrole derivatives,<sup>471–485</sup> corphycene derivatives,<sup>486</sup> or complexes in which tetradentate Schiff base ligands define a plane in the coordination sphere of the metal.<sup>487</sup>

The role of pyridine as a solvent probably explains the large number of derivatives of the main group metals. Simple pyridine complexes of lithium are represented by tetrahedral [Li(py)<sub>4</sub>]<sup>+</sup>,<sup>488–494</sup> tetrahedral [Li(OH<sub>2</sub>)<sub>2</sub>(py)<sub>2</sub>]<sup>+</sup>,<sup>495</sup> tetrahedral [Li(OH<sub>2</sub>)Cl(py)<sub>2</sub>],<sup>496</sup> trigonal planar [Li(py)<sub>2</sub>{N(SiMe<sub>3</sub>)(SiPh<sub>3</sub>)}],<sup>497</sup> the dimer [Li<sub>2</sub>(py)<sub>4</sub>(μ-NHPh)<sub>2</sub>],<sup>171</sup> tetrahedral [Li(py)<sub>3</sub>(PHR)] adducts and related dimers [Li<sub>2</sub>(py)<sub>2</sub>(μ-PHR)<sub>2</sub>] with 3-coordinate Li<sup>+</sup>,<sup>498</sup> and dimeric [Li<sub>2</sub>(py)<sub>4</sub>(μ-OAr)<sub>2</sub>] e.g., Ar = various arene substituents.<sup>499,500</sup> When the reaction of LiN(SiMe<sub>3</sub>)<sub>2</sub> and HOCH<sub>2</sub><sup>t</sup>Bu was carried out in pyridine, the cubane [Li<sub>4</sub>(py)<sub>3</sub>(μ<sub>3</sub>-OCH<sub>2</sub><sup>t</sup>Bu)<sub>4</sub>] was

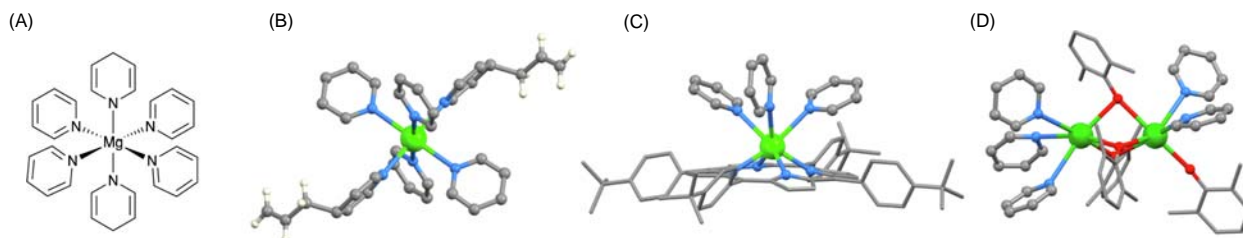


**Fig. 29** The structures of (A) [Li<sub>4</sub>(py)<sub>3</sub>(μ<sub>3</sub>-OCH<sub>2</sub><sup>t</sup>Bu)<sub>4</sub>] (CSD refcode ACIYAM), (B) part of the 1D-polymer chain in [LiCl(py)]<sub>n</sub> (refcode L1CLPY02), (C) [Na(py)<sub>4</sub>]O(2,6-<sup>t</sup>Bu<sub>2</sub>C<sub>6</sub>H<sub>3</sub>) (refcode FIKJUG), (D) the cubane [Na<sub>4</sub>(py)<sub>6</sub>(μ<sub>3</sub>-OC<sub>6</sub>H<sub>4</sub>Pr)<sub>4</sub>] (refcode FIKKIV), and the 2-<sup>t</sup>PrC<sub>6</sub>H<sub>4</sub> groups drawn in stick representation for clarity, and (E) the [Be<sub>8</sub>(py)<sub>4</sub>(μ-NH<sub>2</sub>)<sub>12</sub>(μ<sub>4</sub>-O)]<sup>2+</sup> cation in the iodide salt (refcode DUJYAL).

isolated in which one Li was not solvated due to steric hindrance (Fig. 29A).<sup>501</sup> This contrasts with cubanes such as  $[\text{Li}_4(\text{py})_4(\mu_3\text{-OC}_6\text{H}_4\text{OMe})_4]$  in which all four Li atoms carry a terminal py ligand.<sup>500</sup> Also worthy of note is the 1D-polymeric structure of  $[\text{LiCl}(\text{py})]_n$  (Fig. 29B).<sup>488</sup> There have been few reports since 2000 of homoleptic  $[\text{M}(\text{py})_n]^+$  ( $\text{M} = \text{Na}, \text{K}, \text{Rb}, \text{Cs}$ ) complexes. In terms of simple complexes,  $[\text{Na}(18\text{-crown-6})(\text{py})_2]^+$  and  $[\text{K}(18\text{-crown-6})(\text{py})_2]^+$  are ubiquitous (see above). An apparently low CN is found in  $[\text{Na}(\text{py})_2]^+$  but the vacant coordination sites are occupied by  $\text{B-H}\cdots\text{Na}$  interactions with a carbaborane cluster<sup>502</sup>; this mirrors ambiguous low CNs discussed earlier in this review. A distorted octahedral  $[\text{K}(\text{py})_6]^+$  ion has been reported, but in a composite environment associated with a dicerium-based, so-called, 'letter-box' complex.<sup>503</sup>  $\text{NaBH}_4$  crystallizes from pyridine as the 5-coordinate  $[\text{Na}(\text{py})_3(\text{BH}_4\text{-}\kappa^2)]$  although association of these units via additional  $\text{Na-H-B}$  bridges leads to the assembly of a 1D-chain in the solid state.<sup>449</sup> Related to this is a  $\{\text{Na}(\text{py})_4(\text{BH}_4)\}$  unit in which the  $\text{BH}_4^-$  ion is part of an extended  $\{\text{BH}_4\text{-U}(\mu\text{-BH}_4)\text{-U-BH}_4\}$  motif.<sup>504</sup> Members of the series  $[\text{Na}(\text{py})_x(\text{OAr})]_n$  have been studied in detail.  $[\text{Na}(\text{py})_4\{\text{O}(2,6\text{-}^t\text{Bu}_2\text{C}_6\text{H}_3)\}]$  is trigonal pyramidal (Fig. 29C),<sup>505</sup> and  $\{\text{Na}_4\text{O}_4\}$  cubanes with Na-coordinated py ligands are of different types:  $[\text{Na}_4(\text{py})_4(\mu_3\text{-OR})_4]$  with 4-coordinate Na and  $[\text{Na}_4(\text{py})_6(\mu_3\text{-OR})_4]$  with 4- and 5-coordinate Na (Fig. 29D).<sup>505</sup>

Moving to group 2, beryllium forms a number of simple complexes with pyridine and examples with tetrahedral Be environments are  $[\text{Be}(\text{py})_4]^{2+}$ ,<sup>506,507</sup>  $[\text{BeCl}_3(\text{py})]^-$ ,<sup>508</sup>  $[\text{BeCl}_2(\text{py})_2]$ ,<sup>264</sup>  $[\text{BeBr}(\text{py})_3]^+$ ,<sup>509</sup> and  $[\text{BeCl}(\text{py})(\text{NHPPH}_3)_2]^+$ .<sup>510</sup> An investigation of Be(II) species formed in acidic liquid ammonia led to the isolation of  $[\text{Be}_8(\text{py})_4(\mu\text{-NH}_2)_{12}(\mu_4\text{-O})]_2$  and confirmed that the  $\{\text{Be}_4(\mu_4\text{-O})\}^{6+}$  unit can be stabilized without bidentate  $\text{O}, \text{O}'$ -ligands; Fig. 29E illustrates the structure of the unusual  $[\text{Be}_8(\text{py})_4(\mu\text{-NH}_2)_{12}(\mu_4\text{-O})]^{2+}$  cluster.<sup>511</sup> While CN = 6 is common in simple pyridine-containing complexes of  $\text{Mg}^{2+}$ , lower CNs are also encountered, for example, in trigonal planar  $[\text{Mg}\{\text{N}(\text{SiMe}_3)(\text{SiMe}_2^t\text{Bu})\}_2(\text{py})]$ ,<sup>512</sup> tetrahedral  $[\text{Mg}\{\text{N}(\text{SiMe}_3)_2\}_2(\text{py})_2]$ ,<sup>200</sup> tetrahedral  $[\text{Mg}\{\text{N}(\text{SiMe}_3)(\text{Mes})\}_2(\text{py})_2]$ ,<sup>512</sup> the tetrahedral bis(diphenylphosphanyl)amido complex  $[\text{Mg}\{\text{N}(\text{PPh}_2)_2\}_2(\text{py})_2]$ ,<sup>513</sup> and the 5-coordinate  $[\text{Mg}\{\text{O}(2,6\text{-Me}_2\text{C}_6\text{H}_3)\}_2(\text{py})_3]$  which contains sterically demanding  $\text{ArO}^-$  ligands.<sup>514</sup> The compound  $[\text{Mg}(\text{py})_6][\text{BH}_4]_2$  crystallizes as *trans*- $[\text{Mg}(\text{BH}_4\text{-}\kappa^2)_2(\text{py})_4] \cdot 2\text{py}$ .<sup>123</sup> Taking each  $[\text{BH}_4\text{-}\kappa^2]^-$  ligand as occupying a single coordination site, this can be considered to belong to a well-established family of octahedral Mg(II) complexes which includes *trans*- $[\text{MgCl}_2(\text{py})_4]$ ,<sup>515,516</sup> *trans*- $[\text{Mg}(\text{O}_2\text{CCF}_3)_2(\text{py})_4]$ ,<sup>517</sup> and *trans*- $[\text{Mg}(\text{NCO})_2(\text{py})_4]$ .<sup>409,410</sup> The octahedral *trans*- $[\text{Mg}(\text{NC}_5\text{H}_6)_2(\text{py})_4]$  (Fig. 30A) was formed by treating  $[\text{Mg}(\text{SiPh}_3)_2(\text{THF})_2]$  with neat pyridine,<sup>518</sup> and a related bis(4-allylpyridin-1(4H)-yl) derivative of Ca (Fig. 30B) was formed by reacting bis(allyl)calcium with an excess of py.<sup>519</sup> Simple octahedral complexes of  $\text{Ca}^{2+}$  include *trans*- $[\text{CaBr}_2(\text{py})_4]$ ,<sup>520</sup> and *trans*- $[\text{Ca}\{\text{Si}(\text{SiHMe}_2)_3\}_2(\text{py})_4]$ ,<sup>521</sup> while in  $[\text{Ca}(\text{S}_2\text{COEt-}\kappa^2)_2(\text{py})_3]$ , the  $\text{Ca}^{2+}$  center is 7-coordinate.<sup>522</sup> Lower CNs are represented by the tetrahedral  $[\text{Ca}\{\text{N}(\text{SiMe}_3)(\text{SiMe}_2^t\text{Bu})\}_2(\text{py})_2]$  which contains very bulky amido ligands.<sup>523</sup> Earlier we pointed to the role of py as an axial ligand in  $[\text{ML}(\text{py})_2]$  or  $[\text{ML}(\text{py})]$  species where L is a macrocyclic ligand. The structure of  $[\text{Ca}(\text{tpp}^t\text{Bu})(\text{py})_3]$  is interesting in having three py ligands bound to a  $\text{Ca}^{2+}$  center which resides above the porphyrin  $\text{N}_4$ -donor set (Fig. 30C).<sup>459</sup> Simple complexes of pyridine and the later group 2 metals are represented by the 5-coordinate  $[\text{M}\{\text{O}(2,6\text{-}^t\text{Bu}_2\text{C}_6\text{H}_3)\}_2(\text{py})_3]$  for  $\text{M} = \text{Sr}$  or  $\text{Ba}$ ,<sup>524</sup> the distorted octahedral *trans*- $[\text{Sr}\{\text{O}(2,6\text{-}^t\text{Bu}_2\text{C}_6\text{H}_3)\}_2(\text{py})_4]$  and *trans*- $[\text{M}\{\text{ODipp}\}_2(\text{py})_4]$  ( $\text{M} = \text{Sr}, \text{Ba}$ ),<sup>524</sup>  $[\text{Sr}_2(\text{py})_6\{\text{O}(2,6\text{-Me}_2\text{C}_6\text{H}_3)\}_2\{\mu\text{-O}(2,6\text{-Me}_2\text{C}_6\text{H}_3)\}_2]$ ,<sup>524</sup>  $[\text{Ba}_2(\text{py})_5\{\text{O}(2,6\text{-Me}_2\text{C}_6\text{H}_3)\}_2\{\mu\text{-O}(2,6\text{-Me}_2\text{C}_6\text{H}_3)\}_3]$  (Fig. 30D),<sup>524</sup> and  $[\text{Ba}_3(\text{py})_6\{\mu\text{-O}(2,6\text{-Me}_2\text{C}_6\text{H}_3)\}_6]$  in which each Ba has CN = 6.<sup>524</sup>

Restricting the discussion to non-organometallic complexes leaves a relatively small number of simple complexes of group 13 metals with pyridine ligands. Examples of monomeric species include tetrahedral  $[\text{AlCl}_3(\text{py})]$ ,<sup>525</sup>  $[\text{AlBr}_3(\text{py})]$ ,<sup>526</sup>  $[\text{GaX}_3(\text{py})]$  ( $\text{X} = \text{Cl}, \text{Br}, \text{I}$ ),<sup>526</sup>  $[\text{GaHCl}_2(\text{py})]$  and related derivatives with substituted py ligands,<sup>527</sup>  $[\text{GaCl}_2(\text{py})\{\text{N}(\text{SiMe}_3)_2\}]$ ,<sup>528</sup>  $[\text{InBr}_3(\text{py})]$ ,<sup>529</sup> trigonal bipyramidal  $[\text{M}(\text{CN})_3(\text{py})_2]$  ( $\text{M} = \text{Ga}, \text{Tl}$ ) with axial py ligands,<sup>530</sup> 5-coordinate  $[\text{In}(\text{py})_2(\text{SeC}_6\text{F}_5)_3]$  with axial py ligands,<sup>531</sup> and octahedral *trans*- $[\text{AlF}_2(\text{py})_4]^+$ ,<sup>525,532</sup> *trans*- $[\text{AlCl}_2(\text{py})_4]^+$ ,<sup>284</sup> *trans*- $[\text{AlBr}_2(\text{py})_4]^+$ ,<sup>532</sup> and *trans*- $[\text{AlCl}_4(\text{py})_2]^-$ .<sup>284</sup> The octahedral cation *trans*- $[\text{AlH}_2(\text{py})_4]^+$  has been isolated in the salt  $[\text{Al}(\text{NC}_5\text{H}_6)_4][\text{AlH}_2(\text{py})_4]$  in which  $\text{C}_5\text{H}_6\text{NH}$  is 1,4-dihydropyridine; however, each Al-H site in the anion is disordered with an approximately 0.15 Al-OH superimposition.<sup>533</sup> Examples for the heavier group 13 metals in octahedral environments are  $[\text{GaF}_3(\text{py})_2(\text{OH}_2)]$  with a *trans*-arrangement of py ligands,<sup>534</sup> *mer*- $[\text{InBr}_3(\text{py})_3]$ ,<sup>529</sup> *mer*- $[\text{InI}_3(\text{py})_3]$ ,<sup>535</sup>  $[\text{InCl}(\text{N}_3)_2(\text{py})_3]$ ,<sup>334</sup> and *mer*- $[\text{In}(\text{CN})_3(\text{py})_3]$ .<sup>530</sup> Dimeric species are represented by  $[\text{Al}_2\text{Cl}_2(\text{py})_2(\mu\text{-PSi}^t\text{Pr}_3)_2]$  with an  $\text{Al}_2\text{Cl}_6$ -type structure,<sup>536</sup> and  $[\text{In}_2\text{Br}_4(\text{py})_4(\mu\text{-Br})_2]$  with octahedral In(III) centers and *trans*-py ligands.<sup>529</sup> The compounds  $\text{GaEX}$  ( $\text{E} = \text{S}, \text{Se}$  and  $\text{X} = \text{Cl}, \text{Br}$ ) have been prepared from  $\text{Ga}_2\text{E}_3$  and  $\text{Ga}_2\text{X}_6$ , and cyclic trimers  $[\text{Ga}_3\text{X}_3(\mu\text{-E})_3]$  have been isolated from pyridine solutions of  $\text{GaEX}$ ; each Ga(III) center in a trimer is tetrahedrally sited.<sup>537</sup>



**Fig. 30** Structures of (A) *trans*- $[\text{Mg}(\text{NC}_5\text{H}_6)_2(\text{py})_4]$ , (B) *trans*- $[\text{Ca}(\text{NC}_5\text{H}_5\text{R})_2(\text{py})_4]$  with  $\text{R} = \text{allyl}$  (refcode GUYQEX; for clarity, H atoms are only shown in the allyl group), (C)  $[\text{Ca}(\text{tpp}^t\text{Bu})(\text{py})_3]$  (CSD refcode QIVGIL; for clarity, the porphyrin framework is shown in stick representation), and (D)  $[\text{Ba}_2(\text{py})_5\{\text{O}(2,6\text{-Me}_2\text{C}_6\text{H}_3)\}_2\{\mu\text{-O}(2,6\text{-Me}_2\text{C}_6\text{H}_3)\}_3]$  (refcode FEMCEH).



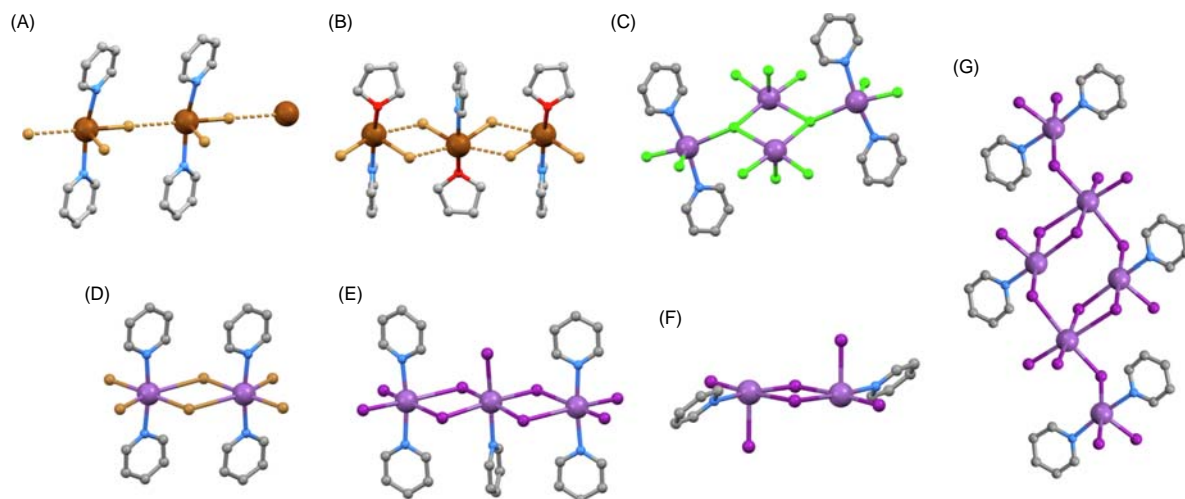
Moving to group 14, the tin(IV) compound *trans*-[Sn(N<sub>3</sub>)<sub>4</sub>(py)<sub>2</sub>] was one of the first charge-neutral Lewis base adducts of Sn(N<sub>3</sub>)<sub>4</sub> and is stable in air over a period of days. It is noteworthy for having (in 2015) the highest temperature (305 °C) of onset of exothermic deposition of any group 14 polyazide, including Pb(N<sub>3</sub>)<sub>2</sub>.<sup>323</sup> Other M(IV) complexes include *trans*-[GeF<sub>4</sub>(py)<sub>2</sub>].<sup>538,539</sup> The metal(II) derivatives [SnBr<sub>2</sub>(py)<sub>2</sub>],<sup>540</sup> [Sn(NCO)<sub>2</sub>(py)<sub>2</sub>],<sup>541</sup> [Sn(N<sub>3</sub>)<sub>2</sub>(py)<sub>2</sub>],<sup>321</sup> [Sn(py)<sub>2</sub>(SeC<sub>6</sub>F<sub>5</sub>)<sub>2</sub>] and [Pb(py)<sub>2</sub>(SeC<sub>6</sub>F<sub>5</sub>)<sub>2</sub>],<sup>531</sup> [Pb(py)<sub>2</sub>(SePh)<sub>2</sub>],<sup>542</sup> [Pb(py)<sub>2</sub>{S(2,6-Me<sub>2</sub>C<sub>6</sub>H<sub>3</sub>)<sub>2</sub>}<sub>2</sub>],<sup>543</sup> and [Pb(py)<sub>2</sub>(SC<sub>6</sub>F<sub>5</sub>)<sub>2</sub>],<sup>544</sup> have disphenoidal (see-saw) geometries with axial py ligands. Interest in some of these lead(II) complexes is as precursors to PbE (E = chalcogen) materials. In [SnBr<sub>2</sub>(py)<sub>2</sub>], close Sn⋯Br contacts (3.65 Å) interconnect molecules into 1D-chains (Fig. 31A). In this case, the Sn–Br⋯Sn angle is close to 180°, and this contrasts with the weak bridging interactions in the related [SnBr<sub>2</sub>(py)(THF)] (Fig. 31B).<sup>540</sup> [Pb(μ-Cl)<sub>2</sub>(py)<sub>2</sub>]<sub>n</sub> comprises infinite 1D-chains in the solid state with octahedral Pb(II).<sup>545</sup>

Octahedral [SbCl<sub>5</sub>(py)] is one of only a limited number of adducts of SbCl<sub>5</sub>.<sup>546</sup> For M(III), examples are the octahedral [BiCl<sub>5</sub>(py)]<sup>2-</sup>,<sup>547</sup> [BiI<sub>5</sub>(py)]<sup>2-</sup>,<sup>548</sup> and [BiBr<sub>4</sub>I<sub>2</sub>(py)]<sup>2-</sup> with disordering of the Br and I sites.<sup>549</sup> Bi(III) appears to be in a square-based pyramidal environment in [Bi(py)<sub>2</sub>(SC<sub>6</sub>Cl<sub>5</sub>)<sub>3</sub>]. However, this last description is ambiguous due to the presence of a third py ligand with a long Bi⋯N distance of 3.983(9) Å, and a similar {5 + 1} coordination pattern is observed in [Bi(py)<sub>3</sub>(SC<sub>6</sub>F<sub>5</sub>)<sub>3</sub>].<sup>550</sup> No such short contacts occur in the crystal structure of [SbCl<sub>2</sub>(N<sub>3</sub>)(py)<sub>2</sub>] which is square-based pyramidal with py ligands mutually *cis* in the basal plane. The latter was prepared by reaction of SbCl<sub>3</sub>, Me<sub>3</sub>SiN<sub>3</sub> and py, while in a similar reaction using AsCl<sub>3</sub>, the isolated product was the 4-coordinate [AsCl(N<sub>3</sub>)<sub>2</sub>(py)].<sup>344</sup> Reactions of SbCl<sub>3</sub> and pyridine under vacuum resulted in the formation of compounds formulated as [(SbCl<sub>3</sub>)<sub>4</sub>(py)<sub>4</sub>] and [(SbCl<sub>3</sub>)<sub>3</sub>(py)<sub>5</sub>]. In the solid state, the former comprises {SbCl<sub>2</sub>(py)<sub>2</sub>} units bridged by an {Sb<sub>2</sub>Cl<sub>6</sub>(μ-Cl)<sub>2</sub>} motif (Fig. 31C). ‘[(SbCl<sub>3</sub>)<sub>3</sub>(py)<sub>5</sub>]’ consists of two 5-coordinate [SbCl<sub>3</sub>(py)<sub>2</sub>] complexes and [SbCl<sub>3</sub>(py)] with a disphenoidal geometry; the three molecules associate through Sb⋯Cl interactions.<sup>551</sup> Prokudina et al. reported a series of [Sb<sub>x</sub>Br<sub>y</sub>py<sub>z</sub>] complexes containing 5-coordinate Sb(III) complexes in which the sixth coordination site is occupied by an additional Sb⋯Br contact. The simplest of these is the dimer shown in Fig. 31D (Sb–N = 2.384(6) and 2.395(6) Å) with asymmetric Br–Sb⋯Br bridges.<sup>552</sup> The analogous iodo-bridged dimer has also been reported and a related complex is [Sb<sub>3</sub>I<sub>9</sub>(py)<sub>4</sub>] (Fig. 31E).<sup>553</sup> These compounds were prepared from pyridine and SbI<sub>3</sub> under vacuum, and other members of the series are the disphenoidal (see-saw) shaped [SbI<sub>2</sub>(py)<sub>2</sub>]<sup>+</sup> cation (the counterion for which is [Sb<sub>2</sub>I<sub>7</sub>(py)]<sub>n</sub><sup>-</sup> comprising a 1D-chain), [Sb<sub>2</sub>I<sub>6</sub>(py)<sub>2</sub>] (Fig. 31F), and [Sb<sub>6</sub>I<sub>18</sub>(py)<sub>6</sub>] (Fig. 31G).<sup>553</sup> A CN of 7 is found in [BiCl<sub>3</sub>(py)<sub>4</sub>]; in the pentagonal bipyramidal structure, the py ligands occupy equatorial sites.<sup>554</sup> Seven-coordinate Bi(III) is also found in the 1D-polymeric [Bi(N<sub>3</sub>)(py)<sub>2</sub>(μ-N<sub>3</sub>)<sub>2</sub>]<sub>n</sub>.<sup>555</sup>

Complexes in which pyridine is coordinated to Se and Te include pyramidal [SeO<sub>2</sub>(py)],<sup>556</sup> disphenoidal [Te(py)<sub>2</sub>(<sup>t</sup>BuNCHMeCHMeN<sup>t</sup>Bu)]<sup>2+</sup>. The latter was the first example of a monodentate pyridine-type donor coordinated to Te(IV).<sup>557</sup>

#### 1.02.2.1.5.2 Pyrazine and pyrimidine

Pyrazine (pyz) and pyrimidine (pym) are isomers (Scheme 1) and coordination complexes of the main group metals with pyz reported since 2000 far exceed those with pym. The spatial arrangement of the two nitrogen lone pairs in pyrazine contribute to its ubiquitous choice as a bridging ligand, and the examples included in this section are representative of its coordination to main group metal ions. Some comparisons with analogous pyridine species by reference to the previous section may be helpful to the reader. Like pyridine, pyrazine may occur as an axial ligand in porphyrinato complexes,<sup>558</sup> but it is more often associated with the assembly of 1D-coordination polymers with [M(porph)] (H<sub>2</sub>porph = general porphyrin) building blocks.<sup>559–561</sup> In the



**Fig. 31** The structures of (A) [SnBr<sub>2</sub>(py)<sub>2</sub>] with intermolecular Sn⋯Br contacts (CSD refcode VUTTAG), (B) [SnBr<sub>2</sub>(py)(THF)] showing intermolecular Sn⋯Br contacts (refcode VUTSUZ), (C) [(SbCl<sub>3</sub>)<sub>4</sub>(py)<sub>4</sub>] (refcode MIQMOR), (D) [Sb<sub>2</sub>Br<sub>6</sub>(py)<sub>4</sub>] (refcode XAFQEE), (E) [Sb<sub>3</sub>I<sub>9</sub>(py)<sub>4</sub>] (refcode UNAHAV), (F) [Sb<sub>2</sub>I<sub>6</sub>(py)<sub>2</sub>] (refcode UNAGEY), and (G) [Sb<sub>6</sub>I<sub>18</sub>(py)<sub>6</sub>] (refcode UNAGIC).

discussion below, the preferences for the formation of discrete molecular species in which pyz is terminally bound, discrete oligomeric complexes, or polymeric assemblies are highlighted.

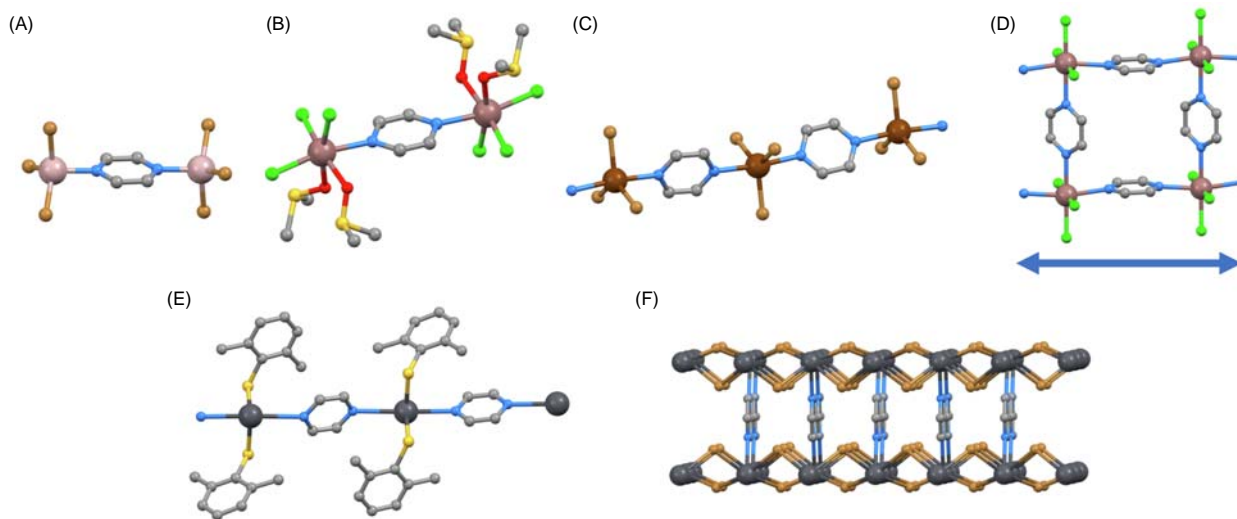
For the s-block metals, complexes with pyz and pym are represented by the 3D-network  $[\text{Na}(\mu_4\text{-ClO}_4)(\mu\text{-pyz})]_n$  (consisting of  $\{\text{Na}(\mu_4\text{-ClO}_4)\}_n$  sheets interconnected by bridging pyz ligands),<sup>562</sup> and heterometallic assemblies in which pyz bridges between  $\text{Na}^+$  and  $\text{Re(V)}$ ,<sup>563</sup> or  $\text{Na}^+$  and  $\text{Ru(III)}$ ,<sup>564</sup> and pym bridges between  $\text{Na}^+$  and  $\text{Ru(III)}$ .<sup>565</sup> As part of a wider investigation of series of  $[\text{BH}_4]^-$ -containing coordination polymers, Kadota et al. reported the 2D-networks present in  $[\text{M}(\text{BH}_4\text{-}\kappa^2)(\mu\text{-pyz})_2]_n$  ( $\text{M} = \text{Mg, Ca}$ ); a (4,4) net is defined by 4-connecting  $\text{Mg}^{2+}$  or  $\text{Ca}^{2+}$  nodes linked by pyz ligands, and terminal  $[\text{BH}_4]^-$  ligands complete the octahedral coordination at each metal.<sup>566</sup> Other  $\text{Mg}^{2+}$  pyrazine complexes involve  $[\text{Mg}(\text{porph})]$  units (see above).

We turn now to the p-block metals. Timoshkin and coworkers<sup>567</sup> have investigated the solid-state structures of group 13 metal halide complexes with pyz and have structurally characterized  $[\text{Al}_2\text{Br}_6(\mu\text{-pyz})]$  (Fig. 32A),  $[\text{Ga}_2\text{Cl}_6(\mu\text{-pyz})]$  (with tetrahedral M), and the 1D-polymers  $[\text{AlBr}_3(\mu\text{-pyz})]_n$  and  $[\text{GaCl}_3(\mu\text{-pyz})]_n$  in which the M(III) center is 5-coordinate.<sup>567,568</sup> The analogous polymer  $[\text{GaBr}_3(\mu\text{-pyz})]_n$  (Fig. 32C) has also been reported.<sup>568</sup>  $\text{GaI}_3$  (which is a weaker Lewis acid than  $\text{AlBr}_3$ ,  $\text{GaCl}_3$  or  $\text{GaBr}_3$ ) forms the tetrahedral monomer  $[\text{GaI}_3(\text{pyz})]$ .<sup>567</sup> A structure related to  $[\text{Al}_2\text{Br}_6(\mu\text{-pyz})]$  (Fig. 32A) is found for  $[\text{In}_2\text{Cl}_6(\text{DMSO})_4(\mu\text{-pyz})]$  (Fig. 32B) but the higher CN of 6 for In vs 4 for Al allows additional DMSO coordination. If DMSO solvent is replaced by aqueous EtOH, reaction of  $\text{InCl}_3$  and pyz yields a 1D-ladder (Fig. 32D) with octahedral In(III) and a *mer*-arrangement of N-donors.<sup>569</sup> A similar polymer was confirmed for  $[\text{Tl}_2\text{Cl}_6(\mu\text{-pyz})_3]_n$ .<sup>568</sup> An interesting comparison is in the products of the reactions of  $\text{InX}_3$  ( $\text{X} = \text{Cl, Br}$ ) and pyrimidine or pyrazine in EtOH. The former leads to the discrete octahedral *mer*- $[\text{InCl}_3(\text{OH})(\text{Hpym})_2]^+$  (hydroxide salt), while for pyz, the 1D-polymer  $[\text{InBr}_3(\text{OH}_2)(\mu\text{-pyz})]_n$  was isolated.<sup>568</sup>

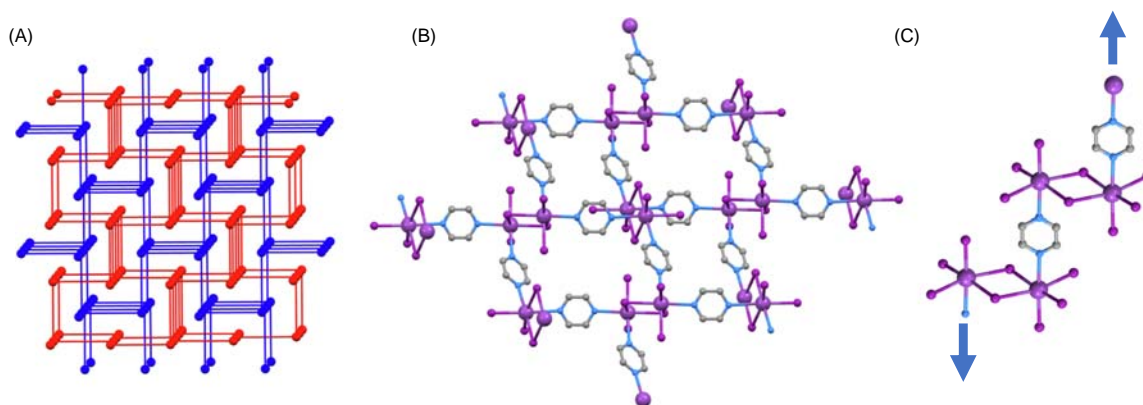
Krossing and coworkers have succeeded in isolating gallium(I) species with monodentate pyz; use of the sterically demanding and weakly coordinating  $[\text{Al}(\text{OR}^f)_4]^-$  anion ( $\text{R}^f = \text{C}(\text{CF}_3)_3$ ) was a key factor. The trigonal pyramidal  $[\text{Ga}(\text{pyz})_3]^+$  was the first 3-coordinate, non-chelated, homoleptic N-donor complex of Ga(I). The addition of one equivalent of pyz to  $[\text{Ga}(\text{pyz})_3][\text{Al}(\text{OR}^f)_4]$  led, unexpectedly, to the isolation of  $\{[\text{Ga}(\mu\text{-pyz})_2(\text{pyz})][\text{Al}(\text{OR}^f)_4]\}_n$ . The formation of monomer or polymer is dependent upon both the concentration of pyz and the temperature of crystallization.<sup>570</sup>

The tin(IV) complex *trans*- $[\text{SnCl}_4(\text{pyz})_2]$  is a discrete molecular species in the solid state.<sup>571</sup> The  $[\text{Sn}(\text{NCMe})_6]^{2+}$  cation was mentioned in Section 1.02.2.1.3, and use of the  $[\text{Al}(\text{OR}^f)_4]^-$  anion led to the tin(II) cation being relatively isolated from the counterion in the solid state. Two MeCN ligands in  $[\text{Sn}(\text{NCMe})_6]^{2+}$  can be replaced by pyz to give *cis*- $[\text{Sn}(\text{pyz})_2(\text{NCMe})_4]^{2+}$  ( $\text{Sn-N}_{\text{pyz}} = 2.373(4)$  and  $2.421(3)$  Å) with three of the MeCN ligands being only weakly bound ( $\text{Sn-N} = 2.713(4)$ – $2.863(4)$  Å).<sup>293</sup>  $[\text{Pb}\{\text{S}(2,6\text{-Me}_2\text{C}_6\text{H}_3)\}_2(\mu\text{-pyz})]_n$  forms a 1D-coordination polymer (Fig. 32G),<sup>543</sup> while in  $[\text{Pb}_2(\mu\text{-Br})_4(\mu\text{-pyz})]_n$  all ligands are in bridging modes giving a double-layer structure (Fig. 32H); each Pb(II) center is in a square-based pyramidal environment.<sup>572</sup>  $[\text{Pb}(\mu\text{-I})_2(\mu\text{-pyz})]_n$  comprises a (4,4) net with Pb(II) acting as 4-connecting nodes; alternate edges of each  $\text{Pb}_4$  rhombus are bridged by pyz or two  $\text{I}^-$  ligands.<sup>573</sup>

Pyrazine complexes of the group 15 metals focus on Sb and Bi. In addition to the discrete molecule  $[\text{Sb}_2\text{F}_{10}(\mu\text{-pyz})]$ ,<sup>574</sup> group 15 metal(III) halides form a number of extended arrays with pyz.  $[\text{SbCl}_3(\mu\text{-pyz})]_n$  is a 1D-chain with Sb(III) in a square-pyramidal environment, indicative of a stereochemically active lone pair. In contrast, the compounds  $[\text{Sb}_2\text{X}_6(\mu\text{-pyz})_3]_n$  ( $\text{X} = \text{Cl, I}$ ) assemble into 3D-networks with each Sb(III) center (*fac*-arrangement of N-donors) acting as a 3-connecting node. The structures are described as ‘dense frameworks’<sup>575</sup>; inspection of the crystallographic data (CDS refcodes KUNXUP and KUNYAW) reveals that both  $[\text{Sb}_2\text{X}_6(\mu\text{-pyz})_3]_n$  ( $\text{X} = \text{Cl, I}$ ) have interpenetrating 3D-nets (Fig. 33A). The reaction between  $\text{BiI}_3$  and pyz yields  $[\text{Bi}(\mu\text{-I})_3(\mu\text{-pyz})]_n$ .



**Fig. 32** Structures of (A)  $[\text{Al}_2\text{Br}_6(\mu\text{-pyz})]$  (CSD refcode HIJBOT), (B)  $[\text{In}_2\text{Cl}_6(\text{DMSO})_4(\mu\text{-pyz})]$  (refcode NIBLOA). (C) Part of the 1D-chain in  $[\text{GaBr}_3(\mu\text{-pyz})]_n$  (refcode NIWTIX). (D) Part of the 1D-ladder in  $[\text{In}_2\text{Cl}_6(\mu\text{-pyz})_3]_n$  (refcode NIBMAN) indicating the direction of chain propagation. Part of (E) a 1D-chain in  $[\text{Pb}\{\text{S}(2,6\text{-Me}_2\text{C}_6\text{H}_3)\}_2(\mu\text{-pyz})]_n$  (refcode GAGXOC), and (F) one double-layer in  $[\text{Pb}_2(\mu\text{-Br})_4(\mu\text{-pyz})]_n$  (refcode MOTSET).



**Fig. 33** (A) The interpenetrating networks in  $[\text{Sb}_2\text{Cl}_6(\mu\text{-pyz})_3]_n$  (CSD refcode KUNXUP) showing only the 3-connecting Sb nodes; the diagram was constructed using Mercury 2021.3.0.<sup>90</sup> (B) Part of the 2D-net in  $[\text{Bi}(\mu\text{-l})_3(\mu\text{-pyz})]_n$  (refcode VUPMAX). (C) Part of the  $[\text{Bi}_2\text{Cl}_6(\mu\text{-Cl})_2(\mu\text{-pyz})]_n^{2n-}$  1D-chain (refcode KEKTIG); the direction of chain propagation is clarified with the arrows.

$\text{pyz})]_n$  with the 2D-network shown in **Fig. 33B**; the (4,4) net is defined by nodes at the centers of the  $\{\text{Bi}_2\text{I}_6\}$  units.<sup>576</sup> In contrast, the reaction between  $\text{BiI}_3$ ,  $\text{Bu}_4\text{NI}$  and  $\text{pyz}$  produces the  $[\text{Bu}_4\text{N}]^+$  salt of 1D-polymer  $[\text{Bi}_2\text{Cl}_6(\mu\text{-Cl})_2(\mu\text{-pyz})]_n^{2n-}$  (**Fig. 33C**).<sup>577</sup>

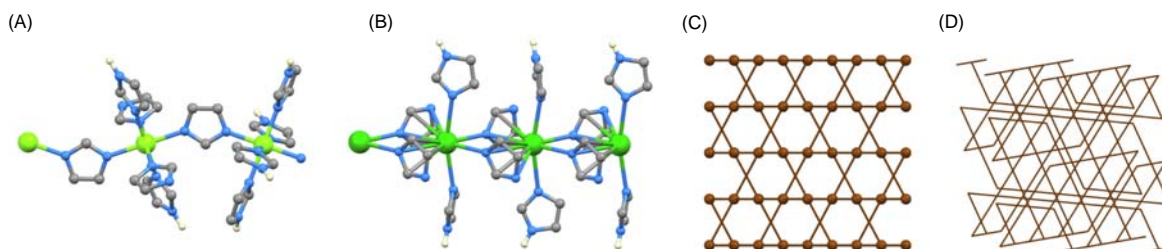
#### 1.02.2.1.5.3 Imidazole

Imidazole (**Scheme 1**) complexes of the s-block metal ions are represented by octahedral  $[\text{Mg}(\text{Him})_6]^{2+}$  and *trans*- $[\text{Mg}(\text{Him})_4(\text{OH}_2)_2]^{2+}$ , the structures of which have been determined from powder X-ray diffraction data using full-profile Rietveld refinement methods.<sup>578</sup> The single crystal structure of *trans*- $[\text{Mg}(\text{Him})_4(\text{OH}_2)_2]\text{Cl}_2$  has also been reported ( $\text{Mg-N} = 2.2281(10)$  and  $2.1611(10)$  Å).<sup>579</sup> Using solvent-free conditions, Zurawski et al. prepared the group 2 coordination polymers  $[\text{Mg}(\text{im})_2(\text{Him})_3]_n$  and  $[\text{M}(\text{im})_2(\text{Him})_2]_n$  ( $\text{M} = \text{Ca}, \text{Sr}, \text{Ba}$ ) with structural dependence on the size of the metal ion. In the Mg and Ca complexes, metal ions are octahedrally sited, but whereas  $[\text{Mg}(\text{im})_2(\text{Him})_3]_n$  (**Fig. 34A**) is a 1D-polymer,  $[\text{Ca}(\text{im})_2(\text{Him})_2]_n$  and  $[\text{Sr}(\text{im})_2(\text{Him})_2]_n$  form (4,4) nets with each  $\text{M}^{2+}$  ion coordinated to *trans*-terminal Him ligands and four bridging  $\text{im}^-$  ligands. A  $\text{CN} > 6$  is favored for  $\text{Ba}^{2+}$  and metal ions are connected into a 1D-chain by bridging  $\text{im}^-$  ligands which coordinate in an  $\eta^5$ -manner to one  $\text{Ba}^{2+}$  and via an  $\text{M-N}$   $\sigma$ -bond to the next (**Fig. 34B**).<sup>580</sup> Note the presence of Him as a terminal ligand, but the conjugate base in bridging sites. Imidazole also occurs as an axial ligand in  $[\text{Mg}(\text{porph})]$  complexes, for example,  $[\text{Mg}(\text{tppBr})(\text{Him})]$ ,<sup>581</sup> in  $[\text{Mg}_2(\text{Him})_4(\text{HOAc})_2(\mu\text{-OAc})_2(\mu\text{-O})]$ ,<sup>582</sup> *fac*- $[\text{Ca}(\text{Him})(\text{OH}_2)_3(\text{O}_2\text{CC}_6\text{H}_4\text{NO}_2)_2]$  and *trans*- $[\text{Ca}(\text{Him})_2(\text{OH}_2)_2(\text{O}_2\text{CC}_6\text{H}_4\text{NO}_2)_2]$ .<sup>583</sup>

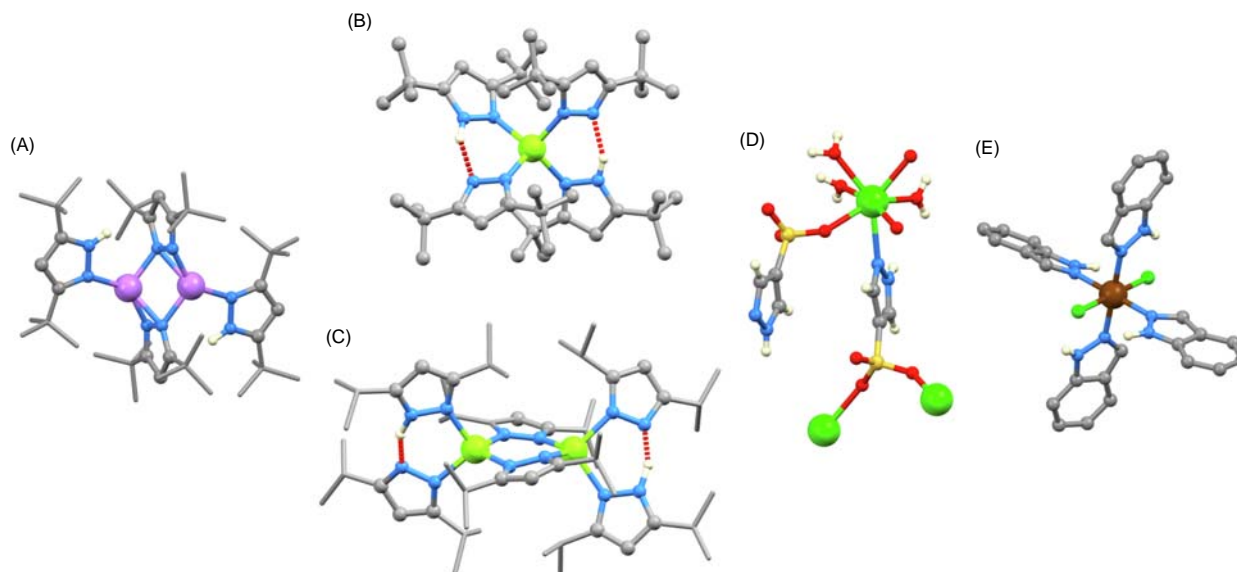
As part of an investigation of Him as a structure-directing agent in the assembly of metal-organic frameworks (MOFs), the octahedral  $[\text{In}(\text{Him})_6]^{3+}$  (as the nitrate salt) was isolated.<sup>584</sup> An interesting approach to MOF synthesis capitalizes on the fact that both gallium metal and imidazole are low melting. Thus  $[\text{Ga}_2(\text{Him})(\text{im})_6]_n$  was isolated from a melt with Ga being oxidized to Ga(III) during the reaction.  $[\text{Ga}_2(\text{Him})(\text{im})_6]_n$  comprises a 3D-network, with two independent, octahedral Ga(III) centers, in  $\{\text{Ga}(\text{im})_6\}$  and  $\{\text{Ga}(\text{im})_5(\text{Him})\}$  environments, respectively. The net has a (3,6) topology constructed from two Kagomé nets which share connectivity points (**Figs. 34C** and **D**).

#### 1.02.2.1.5.4 Pyrazole

In this section, we consider main group metal complexes with  $\text{Hpz}$  (**Scheme 1**) or  $\text{pz}^-$  ligands. Complexes with tris(pyrazolyl) borate ligands are described in **Section 1.02.2.3**. As for imidazole complexes, there is a dominance of s-block and group 13 metal complexes rather than the later main group metals. There is a range of 1H-pyrazole-3-carboxylate and 1H-pyrazole-3,5-



**Fig. 34** Parts of the 1D-chains in (A)  $[\text{Mg}(\text{im})_2(\text{Him})_3]_n$  (CSD refcode CAVTEA) and (B)  $[\text{Ba}(\text{im})_2(\text{Him})_2]_n$  (refcode CAVTUQ); only the N–H hydrogen atoms are shown. (C) The 3D-network in  $[\text{Ga}_2(\text{Him})(\text{im})_6]_n$  (view down the  $a$ -axis) showing only the Ga nodes, and (D) the same lattice viewed to show the two interconnected Kagomé nets (refcode YUWHOO).



**Fig. 35** Structures of (A)  $[\text{Li}_2(\text{Hpz-3,5-}^t\text{Bu}_2)_2\{\mu\text{-(pz-3,5-}^t\text{Bu}_2)_2\}]$  (CSD refcode YEBBOX, only the NH H atoms displayed), (B)  $[\text{Mg}(\text{Hpz-3,5-}^t\text{Bu}_2)(\text{pz-3,5-}^t\text{Bu}_2)_2]$  and (C)  $[\text{Mg}_2(\text{Hpz-3,5-}^i\text{Pr}_2)_2(\text{pz-3,5-}^i\text{Pr}_2)_2\{\mu\text{-(pz-3,5-}^i\text{Pr}_2)_2\}]$  showing intramolecular hydrogen bonds (refcodes MIRMEF and XETXAW, only the NH H atoms are shown). (D) The building block in  $[\text{Ca}(\text{OH}_2)_3(\text{Hpz-4-SO}_3)_2]_n$  (refcode OLITIM). (E) Structure of  $\text{trans-}[\text{GaCl}_2(\text{Hinz})_4]^+$  (refcode TAHPAV, with only NH H atoms shown).

dicarboxylate ligands that act as N,O-chelates to main group metal ions,<sup>585–595</sup> but in this section, we focus on N-bonded pyrazole ligands in simple complexes.

The  $\text{Li}^+$  ion in  $[\text{Li}(\text{Hpz-4-CO}_2)(\text{OH}_2)_3]$  is tetrahedrally sited, with N-bound  $[\text{Hpz-4-CO}_2]^-$ .<sup>596</sup> In  $[\text{Li}_2(\text{Hpz-3,5-}^t\text{Bu}_2)_2\{\mu\text{-(pz-3,5-}^t\text{Bu}_2)_2\}]$ , the bridging pyrazolato ligands exhibit different bonding modes to the two  $\text{Li}^+$  centers as depicted in Fig. 35A. This is one of a series of complexes formed in reactions of  $\text{Hpz-3,5-Me}_2$  or  $\text{Hpz-3,5-}^t\text{Bu}_2$  with  $\text{RLi}$ ,  $\text{Na}$  or  $\text{K}$ .<sup>597</sup> The reaction between  $\text{BeCl}_2$  and  $\text{Hpz}$  in  $\text{Et}_2\text{O}$  produced tetrahedral  $[\text{BeCl}_2(\text{Hpz})(\text{OEt}_2)]$  ( $\text{Be-N} = 1.717(4) \text{ \AA}$ ); with two equivalents of  $\text{Hpz}$ , the isolated product was  $[\text{Be}_2(\text{Hpz})_2\text{Cl}_2(\mu\text{-OEt}_2)_2]$ .<sup>264</sup> An interesting feature of the sterically crowded tetrahedral  $[\text{Mg}(\text{Hpz-3,5-}^t\text{Bu}_2)_2(\text{pz-3,5-}^t\text{Bu}_2)_2]$  is the presence of hydrogen bonds between pairs of  $\text{Hpz-3,5-}^t\text{Bu}_2$  and  $[\text{pz-3,5-}^t\text{Bu}_2]^-$  ligands (Fig. 35B,  $\text{N-H}\cdots\text{N} = 2.7448(17) \text{ \AA}$ , angle  $\text{N-H}\cdots\text{N} = 153(3)^\circ$ ).<sup>598</sup> A similar feature occurs in  $[\text{Mg}_2(\text{Hpz-3,5-}^i\text{Pr}_2)_2(\text{pz-3,5-}^i\text{Pr}_2)_2\{\mu\text{-(pz-3,5-}^i\text{Pr}_2)_2\}]$  (Fig. 35C).<sup>599</sup> Octahedral group 2 metal complexes include  $[\text{Mg}(\text{Hpz-5-th})_4(\text{pz-5-th})_2]$ ,<sup>600</sup>  $[\text{Ca}(\text{Hpz-3,5-Me}_2)_4(\text{pz-3,5-Me}_2)_2]$ ,<sup>601</sup> and  $[\text{Sr}(\text{Hpz-3,5-Me}_2)_4(\text{pz-3,5-Me}_2)_2]$ .<sup>601</sup> Reactions of pyrazole-4-sulfonic acid ( $\text{Hpz-4-SO}_3\text{H}$ ) with  $\text{Na}_2\text{CO}_3$ ,  $\text{K}_2\text{CO}_3$ ,  $\text{CaCO}_3$  and  $\text{BaCO}_3$  under aqueous conditions lead to metal sulfonate networks (the first containing  $\text{Hpz-4-SO}_3^-$ ) which consist of inorganic–organic layered structures. For example, in  $[\text{Ca}(\text{OH}_2)_3(\text{Hpz-4-SO}_3)_2]_n$ , one  $[\text{Hpz-4-SO}_3]^-$  ligand is N-bound and the other O-bound; the structure propagates through additional O–Ca bonds with each  $\text{Ca}^{2+}$  being 7-coordinate (Fig. 35D).<sup>602</sup> This study is complemented by assemblies between  $\text{Hpz-4-SO}_3\text{H}$  and  $\text{Rb}^+$ ,  $\text{Cs}^+$ ,  $\text{Mg}^{2+}$  and  $\text{Sr}^{2+}$ .<sup>603</sup>

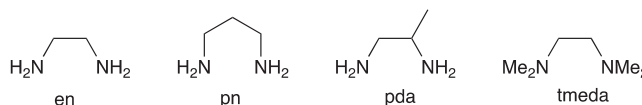
Complexes with group 13 metal ions are illustrated by tetrahedral  $[\text{GaCl}_3(\text{Hpz-3,5-Ph}_2)_2]$ ,<sup>604</sup> octahedral  $\text{trans-}[\text{GaCl}_2(\text{Hpz})_4]^+$ ,<sup>605</sup>  $\text{trans-}[\text{AlCl}_2(\text{Hinz})_4]^+$  and  $\text{trans-}[\text{GaCl}_2(\text{Hinz})_4]^+$  (Fig. 35E)<sup>606</sup>; we include these indazole derivatives because of their close relationship to their pyrazole analogs.

## 1.02.2.2 Bidentate ligands

### 1.02.2.2.1 Diamines

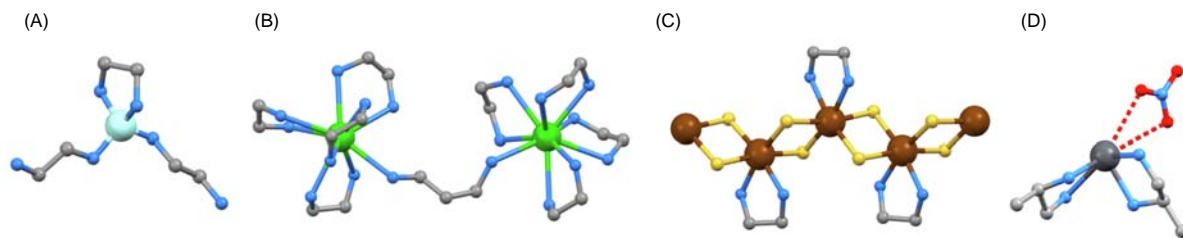
We restrict our discussion of main group metal complexes containing chelating diamine ligands to those with *en*, *pn*, *pda*, *tmeda* and *tmpda* ligands (Scheme 2). Complexes featuring bridging or monodentate *en* were covered in Section 1.02.2.1.1. The use of *tmeda* as a solvent results in its incorporation as a ligand into a wide range of complexes, in particular those of the s-block metals. In 2021, Buchner and Müller investigated the use of *en* as an alternative solvent to liquid  $\text{NH}_3$  in beryllium chemistry.<sup>128</sup>

Homoleptic  $[\text{ML}_x]^{n+}$  are represented by tetrahedral  $[\text{Be}(\text{en})_2]^{2+}$  and  $[\text{Be}(\text{en})(\text{en-N})_2]^{2+}$  (Fig. 36A),<sup>128</sup> octahedral  $[\text{Mg}(\text{en})_3]^{2+}$ ,<sup>607–611</sup>  $[\text{Ca}(\text{en})_3]^{3+}$ ,<sup>612,613</sup>  $[\text{In}(\text{en})_3]^{3+}$ ,<sup>614–616</sup>  $[\text{Tl}(\text{en})_3]^{3+}$ ,<sup>617</sup> and  $[\text{Ge}(\text{en})_3]^{2+}$ .<sup>618,619</sup> In contrast to a CN of 6 in



**Scheme 2** Chelating diamines included in Section 1.02.2.2.1.



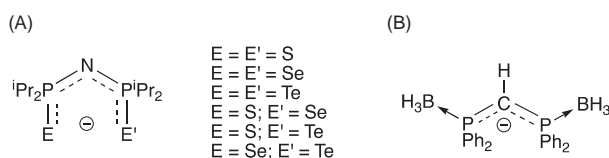


**Fig. 36** Structures of (A) the  $[\text{Be}(\text{en})(\text{en}-M)_2]^{2+}$  cation in the chloride salt (CSD refcode IRUJIR), and (B) the  $[\text{Ba}_2(\text{en})_4(\mu\text{-pn})]^{4+}$  cation with 9-coordinate  $\text{Ba}^{2+}$  (refcode TOMTOG). (C) Part of the 1D-chain in  $[\text{Sn}(\text{en})(\mu\text{-S})_2]_n$  (refcode QUKPUI). (D) In  $[\text{Pb}(\text{pda})_2][\text{NO}_3]_2$ , one  $\text{NO}_3^-$  ion interacts with the cation ( $\text{Pb}\cdots\text{O} = 3.177(3), 3.090(3)$  Å, refcode FAKYUN).

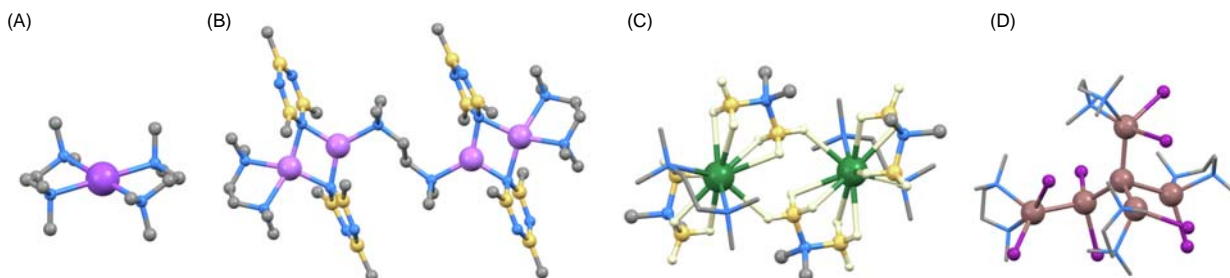
$[\text{Mg}(\text{en})_3]^{2+}$ , the larger  $\text{Ca}^{2+}$  ion forms the 8-coordinate  $[\text{Ca}(\text{en})_4]^{2+}$ . The latter was formed with selenium-based anions under superheated and supercritical solvothermal conditions in en.<sup>620</sup> A further increase in CN is observed on going to  $[\text{Ba}_2(\text{en})_4(\mu\text{-pn})]^{4+}$  (Fig. 36B).<sup>621</sup> Mixed amine/halido and related complexes are illustrated by tetrahedral  $[\text{AlBr}_2(\text{en})]^+$ ,  $[\text{AlI}_2(\text{en})]^+$  and  $[\text{GaI}_2(\text{en})]^+$ ,<sup>622</sup> octahedral *cis*- $[\text{In}(\text{OAc})_2(\text{en})_2]^+$  with monodentate acetate ligands,<sup>623</sup> and octahedral  $[\text{Ge}(\text{en})(\text{OH})_4]$ .<sup>618</sup> The centrosymmetric  $[\text{In}_2(\text{en})_4(\mu\text{-S})_2]^{2+}$ ,<sup>608</sup>  $[\text{In}_2(\text{en})_4(\mu\text{-Se})_2]^{2+}$ ,<sup>624</sup>  $[\text{In}_2(\text{en})_4(\mu\text{-Te})_2]^{2+}$ ,<sup>625</sup> and  $[\text{In}_2(\text{en})_4(\mu\text{-OH})_2]^{4+}$ ,<sup>626</sup> contain octahedrally sited In(III). The  $[\text{Pb}(\text{en})_2]^{2+}$ ,  $[\text{Pb}(\text{pda})_2]^{2+}$ , and  $[\text{Pb}(\text{tmeda})_2]^{2+}$  cations were isolated in salts containing  $[\text{Ag}_2\text{I}_6]^{4-}$  anions with cation $\cdots$ anion interactions through  $\text{Pb}\cdots\text{I}$  contacts. Note the lower CN in  $[\text{Pb}(\text{tmeda})]^{2+}$  vs  $[\text{Pb}(\text{en})_2]^{2+}$  caused by the greater steric hindrance of tmeda.<sup>627</sup> In the solid-state structure of  $[\text{Pb}(\text{en})(\text{NO}_3)(\text{MeCO}_2\text{-}\kappa^2)]$ , the Pb(II) center is 5-coordinate with a geometry that suggests the presence of a stereochemically active lone pair; there are also close  $\text{Pb}\cdots\text{O}$  contacts to the coordinated  $\text{NO}_3^-$  ligand of an adjacent molecule.<sup>628</sup> 1D-coordination polymers featuring interconnected  $\{\text{M}(\text{en})\}$ ,  $\{\text{M}(\text{en})\text{X}_2\}$  or  $\{\text{M}(\text{en})_2\}$  units are represented by  $[\text{Li}(\text{en})_2]_n^{n+}$  with both bridging and chelating en (Fig. 5B),<sup>126</sup>  $[\text{Tl}(\text{en})_2(\mu\text{-CN})]_n^{2n+}$  with a *trans* arrangement of bridging cyanido ligands,<sup>629</sup>  $[\text{Sn}(\text{en})(\mu\text{-S})_2]_n$  (Fig. 36C),<sup>630</sup>  $[\text{Pb}(\text{en})_2(\mu\text{-en})]_n$  (Fig. 6B),<sup>145</sup>

Perhaps surprisingly, simple main group metal complexes containing chelating pn (Scheme 2) are very limited in number, with one of the few structurally characterized examples being octahedral  $[\text{Mg}(\text{pn})\text{L}_2]$  in which  $\text{HL} = 2,2,6,6$ -tetramethylheptane-3,5-dione.<sup>631</sup> There are significantly more examples of complexes with pda (Scheme 2), and this is most likely indicative of a preference for 5- over 6-membered chelate rings. However, few homoleptic complexes have been reported.  $[\text{Pb}(\text{pda})_2]^{2+}$  in salts with  $[\text{Ag}_2\text{I}_6]^{4-}$  anions was mentioned above.<sup>627</sup> Fig. 36D depicts the structure of the  $[\text{Pb}(\text{pda})_2]^{2+}$  cation in the nitrate salt. The ubiquitous ‘gap’ in the coordination sphere for lead(II) is partly occupied by weak contacts to one nitrate ion.<sup>632</sup>

A wide variety of coordination and organometallic compounds is formed between tmeda and the s- and p-block metals, in particular  $\text{Li}^+$ . Some  $\{\text{Li}(\text{tmeda})\}^+$  complexes which also incorporate amido and imido ligands were described in Section 1.02.2.1.2. The steric hindrance imparted by the  $\text{NMe}_2$  units in tmeda does not preclude the formation of tetrahedral  $[\text{Li}(\text{tmeda})_2]^+$  (representative examples are cited),<sup>633–649</sup> while in  $[\text{Li}(\text{tmeda})\{\text{N}(\text{CHMePh})_2\}]$ <sup>153</sup>  $[\text{Li}(\text{tmeda})\{\text{O}(2,6\text{-tBu}_2\text{-4-MeC}_6\text{H}_2)\}]$ ,<sup>650</sup> and  $[\text{Li}(\text{tmeda})\{\text{NPh}(\text{CH}^i\text{Pr}_2)\}]$ ,<sup>651</sup> Li is in a trigonal planar environment. An investigation of dichalcogenidoimidodiphosphinate anions (Scheme 3a) has included structural data for  $[\text{Li}(\text{tmeda})\{\text{N}(\text{tPr}_2\text{PSe})_2\}]$  and  $[\text{Li}(\text{tmeda})\{\text{N}(\text{tPr}_2\text{PTe})_2\}]$  as well as the mixed



**Scheme 3** (A) General families of dichalcogenidoimidodiphosphinate anions.<sup>652</sup> (B) Structure of the  $[\text{Ph}_2\text{PCH}(\text{BH}_3)\text{P}(\text{BH}_3)\text{Ph}_2]^-$  ligand.



**Fig. 37** Structures of (A)  $[\text{Na}(\text{tmeda})_2]^+$  (CSD refcode CIVWIO), (B)  $[\text{Li}_4(\text{tmeda})_2(\mu\text{-tmeda})(\mu\text{-B}_3\text{Me}_2\text{N}_3\text{H}_2)_4]$  (refcode CAPTAP), (C)  $[\text{Sr}_2(\text{tmeda})_2(\text{Me}_2\text{N}(\text{BH}_3)_2)_2]$  (refcode TAHWOS), and (D)  $[\text{In}_6\text{I}_8(\text{tmeda})_4]$  (refcode XIQWAW). In (C) and (D), tmeda is shown in stick representation for clarity.

S/Te and Se/Te analogs; the Li<sup>+</sup> ion is tetrahedrally sited.<sup>652</sup> The [Na(tmeda)<sub>2</sub>]<sup>+</sup> ion appears to have first been structurally characterized in 1983,<sup>653</sup> and the Na<sup>+</sup> ion is in a planar environment (Fig. 37A).<sup>654,655</sup> This mirrors the structural preference found in, for example, [Na(NH<sub>3</sub>)<sub>4</sub>]<sup>+</sup> (Fig. 1C). The axial sites are occupied by MeCN ligands in *trans*-[Na(tmeda)<sub>2</sub>(NC<sup>t</sup>Bu)<sub>2</sub>]<sup>+</sup>.<sup>656</sup> A similar coordination environment is found in [K(tmeda)<sub>2</sub>(Ph<sub>2</sub>PCH(BH<sub>3</sub>)P(BH<sub>3</sub>)Ph<sub>2</sub>)<sub>n</sub>] (see Scheme 3B for the ligand); the axial sites of the {K(tmeda)<sub>2</sub>}<sup>+</sup> unit are occupied by B–H–K interactions to produce a 1D-polymeric structure in the solid state.<sup>657</sup> The K<sup>+</sup> ion is large enough to accommodate three chelating tmeda ligands; [K(tmeda)<sub>3</sub>]<sup>+</sup> has a distorted octahedral structure.<sup>658</sup>

Tetrahedral [M(tmeda)X<sub>2</sub>] derivatives include [Be(tmeda)X<sub>2</sub>] (X = Br, I),<sup>509,659</sup> [M(tmeda){N(SiMe<sub>3</sub>)<sub>2</sub>}<sub>2</sub>] (M = Mg, Sr),<sup>660</sup> [Mg(tmeda)(BH<sub>4</sub>-κ<sup>3</sup>)<sub>2</sub>] (pseudo-tetrahedral with tridentate BH<sub>4</sub><sup>−</sup> ligands),<sup>661</sup> [Mg(tmeda)(NHSi<sup>t</sup>Pr<sub>3</sub>)<sub>2</sub>] (which has large Mg–N–Si bond angles of 139.2(1)<sup>o</sup>),<sup>662</sup> [Mg(tmeda){O(2,6-<sup>t</sup>Bu<sub>2</sub>C<sub>6</sub>H<sub>3</sub>)<sub>2</sub>}<sub>2</sub>],<sup>195</sup> [Ca(tmeda){N(SiMe<sub>3</sub>)<sub>2</sub>}<sub>2</sub>],<sup>663</sup> [Ca(tmeda)(N<sup>t</sup>Pr<sub>2</sub>)<sub>2</sub>],<sup>663</sup> [Ba(tmeda){N(SiMe<sub>3</sub>)<sub>2</sub>}<sub>2</sub>],<sup>664</sup> [AlBr<sub>2</sub>(tmeda)]<sup>+</sup>,<sup>622</sup> and [GaCl<sub>2</sub>(tmeda)]<sup>+</sup>.<sup>622</sup>

Complexes with CN = 5 are exemplified by the square-based pyramidal [K(tmeda)<sub>2</sub>{Si(SiMe<sub>3</sub>)<sub>3</sub>}],<sup>665</sup> trigonal bipyramidal [Mg(tmeda)Br<sub>2</sub>(THF)],<sup>666</sup> [Sr(tmeda)(NPh<sup>t</sup>Pr)<sub>2</sub>(THF)],<sup>667</sup> [In(tmeda)I<sub>3</sub>],<sup>668</sup> and [Sb(tmeda)F<sub>3</sub>]<sup>669</sup>; the latter is unstable unless at low temperatures under inert conditions. Examples of octahedral species include *trans*-[MgBr<sub>2</sub>(tmeda)<sub>2</sub>],<sup>670</sup> *trans*-[CaI<sub>2</sub>(tmeda)<sub>2</sub>],<sup>671</sup> *trans*-[AlH<sub>2</sub>(tmeda)<sub>2</sub>]<sup>+</sup>,<sup>672</sup> [In(tmeda)Cl<sub>4</sub>],<sup>668</sup> [Ge(tmeda)X<sub>4</sub>] (X = F, Cl, Br),<sup>336,538</sup> and [Ge(tmeda)Cl<sub>2</sub>(N<sub>3</sub>)<sub>2</sub>] (with *trans* azido ligands).<sup>336</sup>

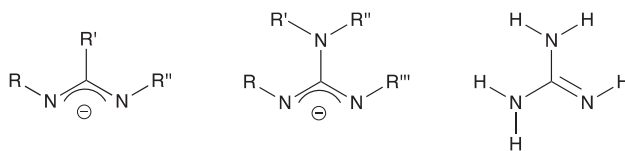
Dimers with {M<sub>2</sub>(tmeda)<sub>2</sub>(μ-X)} motifs are represented by [Li<sub>2</sub>(tmeda)<sub>2</sub>(μ-Cl)<sub>2</sub>],<sup>250</sup> [Li<sub>2</sub>(tmeda)<sub>2</sub>(μ-Br)<sub>2</sub>],<sup>673,674</sup> [Li<sub>2</sub>(tmeda)<sub>2</sub>(μ-OMes)<sub>2</sub>] (note there is a change to a monomer when the ArO<sup>−</sup> ligand is more bulky, see above),<sup>650</sup> a series of [Li<sub>2</sub>(tmeda)<sub>2</sub>{μ-OSArR}<sub>2</sub>] dimers (prepared by lithiation of ArRS=O by <sup>n</sup>BuLi in tmeda),<sup>675</sup> [Li<sub>2</sub>(tmeda)<sub>2</sub>(μ-E<sup>n</sup>Bu)<sub>2</sub>] (E = Se, Te),<sup>676</sup> [M<sub>2</sub>(tmeda)<sub>2</sub>(μ-HBEt<sub>3</sub>)<sub>2</sub>] (M = Na, K),<sup>677</sup> [Na<sub>2</sub>(tmeda)<sub>2</sub>(μ-NPh<sup>t</sup>Pr)<sub>2</sub>],<sup>183</sup> [Rb<sub>2</sub>(tmeda)<sub>2</sub>{μ-N(SiMe<sub>3</sub>)<sub>2</sub>}<sub>2</sub>],<sup>660</sup> and [Ge<sub>2</sub>(tmeda)<sub>2</sub>Cl<sub>2</sub>(μ-Cl)<sub>2</sub>] (in which Ge(II) is in a trigonal pyramidal environment with asymmetrical Ge–Cl⋯Ge bridges).<sup>678</sup>

A number of other species are worthy of note. Reaction of the borazine B<sub>3</sub>Ph<sub>3</sub>N<sub>3</sub>H<sub>3</sub> with LiMe/Li/tmeda in Et<sub>2</sub>O leads to [Li(tmeda)(μ-Ph<sub>3</sub>B<sub>3</sub>N<sub>3</sub>H<sub>2</sub>)Li](tmeda).<sup>679</sup> Similarly, trimethylborazine is deprotonated when treated with BuLi in tmeda giving rise to [Li<sub>4</sub>(tmeda)<sub>2</sub>(μ-tmeda)(μ-B<sub>3</sub>Me<sub>2</sub>N<sub>3</sub>H<sub>2</sub>)<sub>4</sub>] (Fig. 37B).<sup>680</sup> The reactions of Li, Na or K with MesPCL<sub>2</sub> yields MPHMe<sub>s</sub>; for M = Na, the tmeda adduct is the 1D-coordination polymer [Na(tmeda)(μ-PHMe<sub>s</sub>)<sub>n</sub>].<sup>681</sup> An [Mg<sub>3</sub>Cl<sub>5</sub>]<sup>+</sup> unit is stabilized by tmeda in the triangular [Mg<sub>3</sub>(tmeda)<sub>3</sub>(μ-Cl)<sub>3</sub>(μ<sub>3</sub>-Cl)<sub>2</sub>]<sup>+</sup>.<sup>682,683</sup> Sr<sup>2+</sup> is 11-coordinate in [Sr<sub>2</sub>(tmeda)<sub>2</sub>{Me<sub>2</sub>N(BH<sub>3</sub>)<sub>2</sub>}<sub>2</sub>] (Fig. 37C) and was characterized as part of an investigation of complexes of Sr for use as CVD precursors.<sup>684</sup> The [Me<sub>2</sub>N(BH<sub>3</sub>)<sub>2</sub>]<sup>−</sup> ligand coordinates to Ba<sup>2+</sup> through four B–H–Ba interactions in the 10-coordinate [Ba(tmeda){Me<sub>2</sub>N(BH<sub>3</sub>)<sub>2</sub>}<sub>2</sub>].<sup>685</sup> The dissolution of solid indium(I) iodide in a mixture of toluene and tmeda led to the isolation of crystals of [In<sub>6</sub>I<sub>8</sub>(tmeda)<sub>4</sub>] (Fig. 37D) which is the first example of a neutral indium sub-halide cluster complex; thermal decomposition of the latter gave [In<sub>2</sub>I<sub>4</sub>(tmeda)<sub>2</sub>].<sup>686</sup> Dissolving InBr in toluene/tmeda produced [In<sub>2</sub>Br<sub>4</sub>(tmeda)<sub>2</sub>], the transformation being reversible; storing the solution at low temperature resulted in crystals of [InBr(tmeda)] which, in the solid state, associates as a weakly bound dimer with an In⋯In = 3.678(2) Å.<sup>687</sup> Reaction of Pb(SAr)<sub>2</sub> with (Ar = 2,6-Me<sub>2</sub>C<sub>6</sub>H<sub>3</sub>) with tmeda leads to [Pb(tmeda)(SAr)][Pb(SAr)<sub>3</sub>] in which there are close S⋯Pb contacts between the two units.<sup>688</sup>

### 1.02.2.2 Imidoamidate and guanidinate ligands

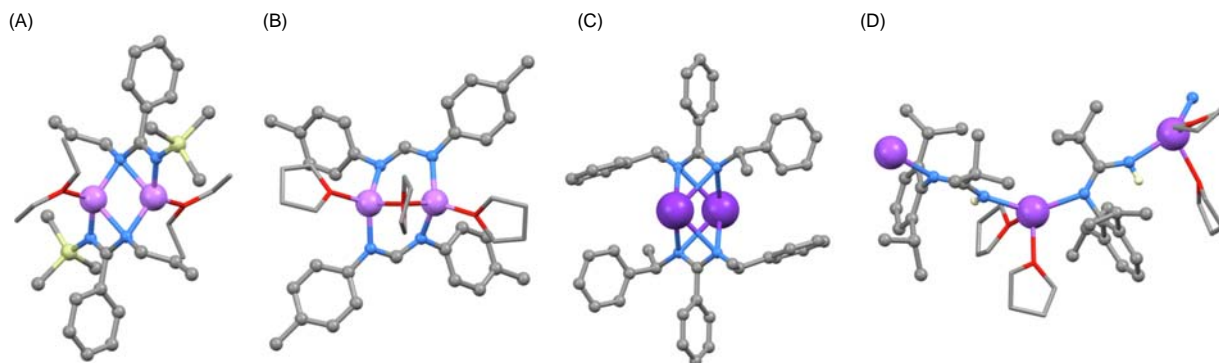
The general structures of imidoamidate and guanidinate anions are shown in Scheme 4. As in previous sections, we can only provide selected examples of their main group metal complexes, and we focus on relatively simple structures with compounds containing M–C bonds being excluded. Many imidoamidate and guanidinate complexes are of interest for their catalytic properties.<sup>69,689,690</sup>

Scheme 4 suggests that imidoamidates are pre-designed as chelating ligands and of the very many such complexes, examples with group 2 metals are tetrahedral [Mg{<sup>t</sup>BuC(NMes)<sub>2</sub>}<sub>2</sub>],<sup>691</sup> 5-coordinate [Mg(THF){HC(NDipp)<sub>2</sub>}<sub>2</sub>],<sup>692</sup> distorted octahedral *cis*-[Ca(THF)<sub>2</sub>{BzC(N<sup>t</sup>Bu)<sub>2</sub>}<sub>2</sub>],<sup>693</sup> *trans*-[Mg(THF)<sub>2</sub>{MeC(NCy)<sub>2</sub>}<sub>2</sub>],<sup>694</sup> and the dimer [Mg<sub>2</sub>(OEt<sub>2</sub>)<sub>2</sub>{MesC(NCy)<sub>2</sub>}<sub>2</sub>(μ-Br)<sub>2</sub>].<sup>695</sup> However, it is important to recognize that a range of other bonding modes is also possible, and we illustrate these with complexes of the s-block metals; a monodentate mode is exemplified in [GaH<sub>2</sub>(quin){HC(NDipp)<sub>2</sub>}]<sup>696</sup> which is discussed later. A combination of chelation and bridging is found in [Li<sub>2</sub>(OEt<sub>2</sub>)<sub>2</sub>{μ-PhC(NSiMe<sub>3</sub>)(N<sup>n</sup>Pr)}<sub>2</sub>] (Fig. 38A)<sup>697</sup> and in a range of other dilithium species.<sup>698–703</sup> A simple bridging mode is exemplified in the dilithium complexes [Li<sub>2</sub>(THF)<sub>2</sub>{μ-THF}{μ-HC(N(4-MeC<sub>6</sub>H<sub>4</sub>))<sub>2</sub>}<sub>2</sub>] (Fig. 38B) and [Li<sub>2</sub>{μ-HC(N(4-MeC<sub>6</sub>H<sub>4</sub>))<sub>2</sub>}<sub>3</sub>],<sup>704</sup> while in [Li<sub>2</sub>(THF)<sub>2</sub>{μ-HC(N(2-FC<sub>6</sub>H<sub>4</sub>))<sub>2</sub>}<sub>2</sub>], the imidoamidate bridging mode is supplemented by CF–Li interactions similar to those depicted in Fig. 8D.<sup>705</sup> The dimer [Mg<sub>2</sub>{MeC(N<sup>t</sup>Pr)<sub>2</sub>}<sub>2</sub>{μ-MeC(N<sup>t</sup>Pr)<sub>2</sub>}<sub>2</sub>] exhibits both chelating and bridging imidoamidates.<sup>706</sup> Fig. 38C depicts an example of another bridging motif, illustrated with the structure of [K<sub>2</sub>{μ-PhC(NCHMePh)<sub>2</sub>}<sub>2</sub>].<sup>707</sup> In the coordination polymer [Na(THF)<sub>2</sub>{μ-<sup>t</sup>BuC(NH)(NDipp)}<sub>n</sub>], the imidoamidate anion acts as a ditopic ligand (Fig. 38D),<sup>708</sup> and a similar structure is observed in [Li(THF)<sub>2</sub>{μ-PhC(NH)(N(2-<sup>t</sup>PrC<sub>6</sub>H<sub>4</sub>))}]<sub>n</sub>.<sup>709</sup>



**Scheme 4** The general structures of imidoamidate (also called amidinate, left) and guanidinate (middle) ligands, and the structure of guanidine (H<sub>5</sub>Gu).

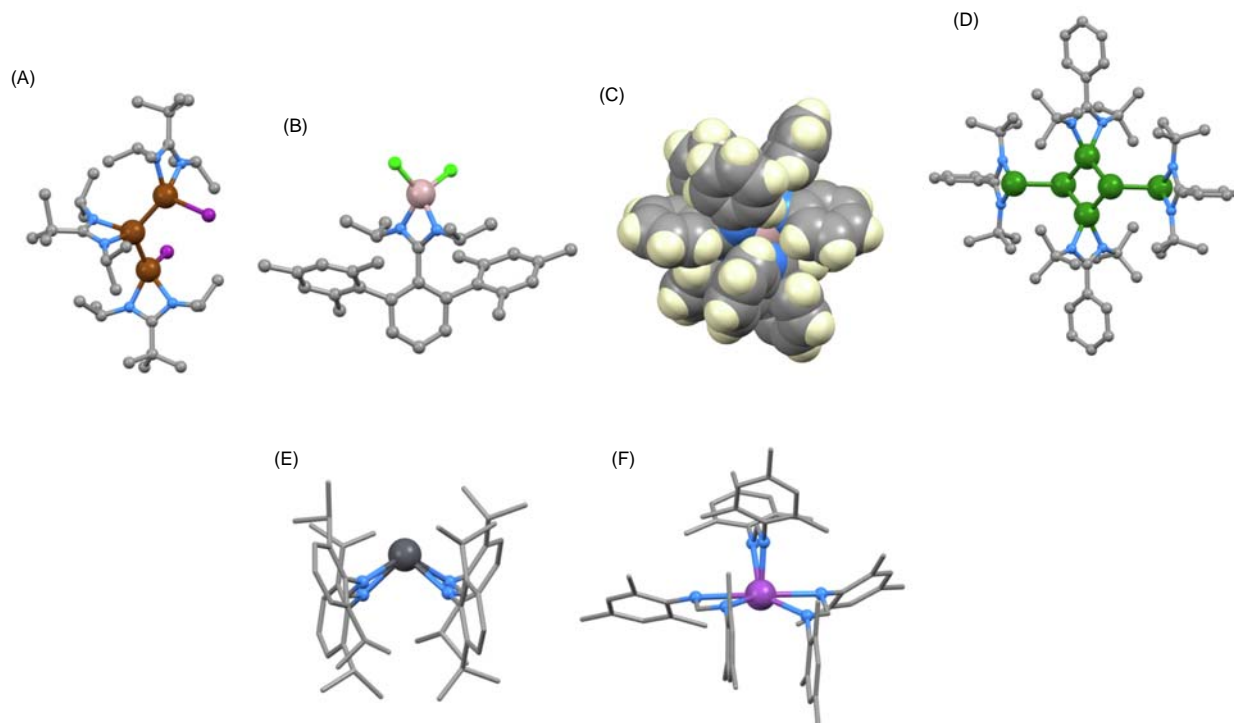




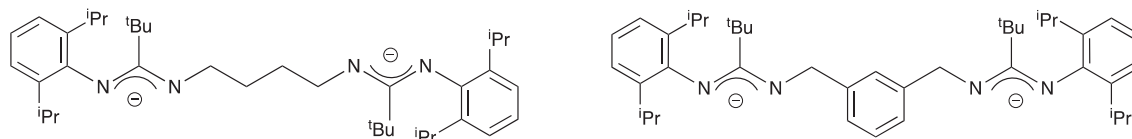
**Fig. 38** Structures of (A)  $[\text{Li}_2(\text{OEt}_2)_2\{\text{PhC}(\text{NSiMe}_3)(\text{N}^i\text{Pr})_2\}]_2$  (CSD refcode AGOJOV; Et<sub>2</sub>O shown in stick representation for clarity), (B)  $[\text{Li}_2(\text{THF})_2(\mu\text{-THF})\{\text{HC}(\text{N}(4\text{-MeC}_6\text{H}_4))_2\}]_2$  (refcode AGONAL; THF shown in stick representation), (C)  $[\text{K}_2\{\mu\text{-PhC}(\text{NCHMePh})_2\}]_2$  (refcode AQISAV), (D) part of a chain in  $[\text{Na}(\text{THF})_2\{\mu\text{-}^t\text{BuC}(\text{NH})(\text{NDipp})\}]_n$  (refcode AROXUC, THF in stick representation, and only NH H atoms shown).

Other s-block metal complexes with imidoamidate ligands which demand attention include  $[\text{Mg}\{(4\text{-MeC}_6\text{H}_4)\text{C}(\text{NDipp})_2\}]_2$ . This is a rare example of square-planar  $\text{Mg}^{2+}$  which is not imposed by a porphyrinato environment<sup>710</sup>; a further example of square-planar  $\text{Mg}^{2+}$  is the guanidinate complex  $[\text{Mg}\{(\text{C}_2\text{N})\text{C}(\text{NMe}_5)_2\}]_2$ .<sup>711</sup> Beryllium complexes with imidoamidate ligands are sparse, and are represented by the tetrahedral  $[\text{BeCl}_2\{\text{PhC}(\text{NSiMe}_3)_2\}]_2$ ,<sup>508</sup> and  $[\text{Be}\{\text{EtC}(\text{NDipp})_2\}]_2$ ,<sup>712</sup> and the centrosymmetric dimer  $[\text{Be}_2(\mu\text{-OEt})_2\{^t\text{BuC}(\text{NDipp})_2\}]_2$ .<sup>712</sup>

Lithio derivatives are typical precursors to p-block metal complexes. For example, treatment of  $[\text{Li}\{\text{PhC}(\text{NSiMe}_3)_2\}]$  with  $\text{GeCl}_2$  leads to  $[\text{GeCl}\{\text{PhC}(\text{NSiMe}_3)_2\}]$ ,<sup>713</sup> reaction of  $[\text{Li}\{(4\text{-}^t\text{BuC}_6\text{H}_4)\text{C}(\text{NDipp})_2\}]$  with  $\text{SnCl}_2$  yields  $[\text{SnCl}\{(4\text{-}^t\text{BuC}_6\text{H}_4)\text{C}(\text{NDipp})_2\}]$ ,<sup>714</sup> and reaction of  $\text{SnCl}_2$  with  $[\text{Li}\{^m\text{BuC}(\text{NCy})_2\}]$  gives  $[\text{SnCl}\{^m\text{BuC}(\text{NCy})_2\}]$ .<sup>715</sup> In each case, the imidoamidate ligand is chelating. Reaction of  $[\text{Li}\{^t\text{BuC}(\text{N}^i\text{Pr})_2\}]$  with  $\text{GaI}_3$  produces  $[\text{GaI}_2\{^t\text{BuC}(\text{N}^i\text{Pr})_2\}]$ , while with  $\text{GaI}$ , the product is the trigallium species shown in Fig. 39A; replacing the C<sup>t</sup>Bu unit in the imidoamidate ligand by CMe redirects the assembly to a tetragallium complex.<sup>716</sup>



**Fig. 39** Structures of (A)  $[\text{Ga}_3\text{I}_2\{^t\text{BuC}(\text{N}^i\text{Pr})_2\}]_3$  (CSD refcode FUBHES), (B)  $[\text{AlCl}_2\{\text{DippC}(\text{N}^i\text{Pr})_2\}]$  (refcode AGEMUU), (C)  $[\text{Al}\{\text{PhC}(\text{NPh})_2\}]_3$  (refcode QETBAS, in space-filling representation), (D)  $[\text{Ge}_6\{\text{PhC}(\text{N}^t\text{Bu})_2\}]_4$  (refcode GIHZOO), (E)  $[\text{Pb}\{\text{HC}(\text{NDipp})_2\}]_2$  (refcode GODWUS), and (F)  $[\text{Bi}\{\text{HC}(\text{NMe}_5)_2\}]_3$  (refcode PIHHYI). In (E) and (F), ligands are shown in stick representation for clarity.



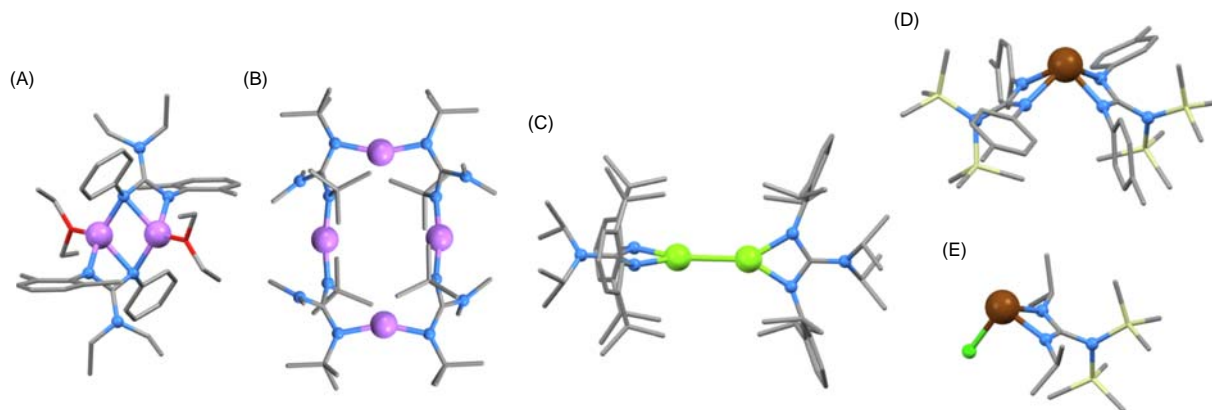
**Scheme 5** Examples of imidoamidates with two metal-binding domains.

Derivatives of group 13 metals are well represented. The use of sterically demanding Dipp substituents which provide 'bowl-shaped' ligands (e.g., in the Al(III) complex shown in Fig. 39B) has been described by Arnold.<sup>717</sup> The same tetrahedral  $\{\text{AlCl}_2\text{N}_2\}$  motif is found in  $[\text{AlCl}_2\{\text{PhC}(\text{N}^t\text{Pr})_2\}_2]$ , and this derivative has been used as a precursor for the synthesis via salt metathesis of complexes with Al–M bonds.<sup>718</sup> Cole et al. showed that the reaction of  $[\text{GaH}_3(\text{quin})]$  with one equivalent of  $\text{H}_2\text{C}(\text{NDipp})_2$  resulted in the formation of tetrahedral  $[\text{GaH}_2(\text{quin})\{\text{HC}(\text{NDipp})_2\}]$  in which the imidoamidate ligand is monodentate; the fact that the quin ligand is not displaced is explained in terms of its strong Lewis basicity.<sup>696</sup> Examples of 5-coordinate  $\{\text{MX}(\text{imidoamidate})_2\}$  complexes include  $[\text{AlH}\{\text{PhC}(\text{N}^t\text{Bu})_2\}_2]$ ,<sup>719</sup>  $[\text{InX}\{\text{PhC}(\text{N}^t\text{Bu})_2\}_2]$  (X = Cl, Br),<sup>720</sup> and  $[\text{InCl}\{\text{MeC}(\text{N}^t\text{Pr})_2\}_2]$ .<sup>721</sup> With less sterically crowded ligands, octahedral tris-chelates can be accommodated, e.g., in  $[\text{Al}\{\text{MeC}(\text{N}^t\text{Pr})_2\}_3]$ ,<sup>722</sup>  $[\text{M}\{\text{HC}(\text{NSiMe}_3)_2\}_3]$  (M = Al, Ga),<sup>723</sup> and  $[\text{In}\{\text{MeC}(\text{N}^t\text{Pr})_2\}_3]$ .<sup>721</sup> Interestingly, even with the relatively sterically encumbered  $[\text{PhC}(\text{NPh})_2]^-$  ligand, interlocking of the phenyl substituents (Fig. 39C) allows three ligands to be accommodated in  $[\text{Al}\{\text{PhC}(\text{NPh})_2\}_3]$ .<sup>724</sup> Ligands such as those shown in Scheme 5 allow the formation of dinuclear complexes, e.g., coordinating to two  $\{\text{AlX}_2\}$  units.<sup>725</sup>

Imidoamidate complexes of Ge(II) and Sn(II) are well established, and examples prepared from lithium derivatives were mentioned earlier. Many feature halido or amido ligands and possess 3-coordinate molecular structures, e.g.,  $[\text{GeCl}\{\text{PhC}(\text{N}^t\text{Bu})_2\}]$ ,<sup>726</sup>  $[\text{SnCl}\{\text{PhC}(\text{N}^t\text{Bu})_2\}]$ ,<sup>727</sup> and  $[\text{M}\{\text{N}(\text{SiMe}_3)_2\}\{\text{PhC}(\text{N}^t\text{Bu})_2\}]$  with M = Ge or Sn (which are catalysts for phenyl isocyanate cyclization).<sup>728</sup> Reduction of  $[\text{GeCl}\{\text{PhC}(\text{N}^t\text{Bu})_2\}]$  by K in THF results in the formation of  $[\text{Ge}_2\{\text{PhC}(\text{N}^t\text{Bu})_2\}_2]$  which contains an unsupported Ge–Ge bond.<sup>726</sup> In  $[\text{Ge}(\mu\text{-O}_3\text{SCF}_3)\{\text{PhC}(\text{N}^t\text{Bu})_2\}]_n$ , the triflate ions bridge between pairs of Ge centers to give a 1D-polymer decorated with chelating imidoamidate ligands.<sup>727</sup> Yeong et al. reported two interesting complexes with  $\text{Ge}_2\text{Sn}_2$  and  $\text{Ge}_4$  cores supported by imidoamidate ligands and bearing low-valent  $\text{Ge}\{\text{PhC}(\text{N}^t\text{Bu})_2\}$  substituents (Fig. 39D); a theoretical investigation confirmed planar charge-separated core-structures.<sup>729</sup> With the use of the sterically demanding  $[\text{RC}(\text{NDipp})_2]^-$  ligands (R = H, <sup>t</sup>Bu), it has been possible to isolate the thermally stable Pb(II) complexes  $[\text{Pb}\{\text{HC}(\text{NDipp})_2\}_2]$  (with a geometry indicative of a stereochemically active lone pair on Pb, Fig. 39E) and  $[\text{PbCl}\{\text{BuC}(\text{NDipp})_2\}]_2$  (in which pairs of molecules are weakly associated through  $\text{Pb}\cdots\text{Cl}$  interactions,  $\text{Pb}\cdots\text{Cl} = 2.571(2)$ ,  $\text{Pb}\cdots\text{Cl} = 3.260(2)$  Å).<sup>730</sup>

Imidoamidate complexes of the heavier group 15 elements are represented by  $[\text{SbCl}_2\{\text{BuC}(\text{N}^t\text{Pr})_2\}]$ ,  $[\text{SbCl}_2\{\text{BuC}(\text{NCy})_2\}]$ ,  $[\text{SbCl}_2\{\text{BuC}(\text{NDipp})_2\}]$ ,  $[\text{BiCl}_2\{\text{BuC}(\text{NDipp})_2\}]$  and  $[\text{Bi}_2\text{Cl}_2(\mu\text{-Cl})_2\{\text{BuC}(\text{N}^t\text{Pr})_2\}_2]$  and this series illustrates the influence of both the metal and ligand on the coordination geometry.<sup>731</sup> In  $[\text{Bi}\{\text{HC}(\text{NMes})_2\}_3]$  (Fig. 39F), two NC(H)N units are roughly coplanar while the third lies perpendicular to this plane, leaving a vacant coordination site below the plane.<sup>732</sup>

Guanidates (Scheme 3) offer the same donor set as imidoamidates with the peripheral  $\text{NR}_2$  (R ≠ H) unit remaining non-coordinated. Similar families of metal complexes with the two ligands types are thus expected and are observed. Within group 1, we observe mononuclear complexes with simple chelating guanidinate ligands,<sup>733</sup> as well as dinuclear species in which the guanidinate acts simultaneously in chelating and bridging modes (e.g., Fig. 40A).<sup>169,702,734–741</sup> A simple bridging mode of a guanidinate ligand is illustrated in  $[\text{Li}_2(\text{THF})_2\{\mu\text{-Me}_2\text{NC}(\text{NPh})(\text{NSiMe}_3)\}_2]$ .<sup>741</sup> In the solid state and in the absence of a donor solvent, [Li



**Fig. 40** Structures of (A)  $[\text{Li}_2(\text{OEt}_2)_2\{\text{Et}_2\text{NC}(\text{NPh})(\text{N}(2,6\text{-Me}_2\text{C}_6\text{H}_3)\}_2)]_2$  (CSD refcode CUHQUT), (B)  $[\text{Li}\{\text{Me}_2\text{NC}(\text{N}^t\text{Bu})_2\}_4]$  (refcode HATZAF), (C)  $[\text{Mg}_2\{\text{Pr}_2\text{NC}(\text{NDipp})_2\}_2]$  (refcode JISWIS), (D)  $[\text{Sn}\{(\text{Me}_3\text{Si})_2\text{NC}(\text{N}(4\text{-Me}_6\text{C}_6\text{H}_4)\}_2)]_2$  (refcode APIHUE), and (E)  $[\text{SnCl}\{(\text{Me}_3\text{Si})_2\text{NC}(\text{N}^t\text{Pr})_2\}]$  (refcode HUKQAI).

$\{\text{Me}_2\text{NC}(\text{N}^t\text{Bu})_2\}$ ] exists as the tetramer shown in Fig. 40B in which each guanidinate acts as a ditopic ligand, bridging two Li centers.<sup>737</sup>

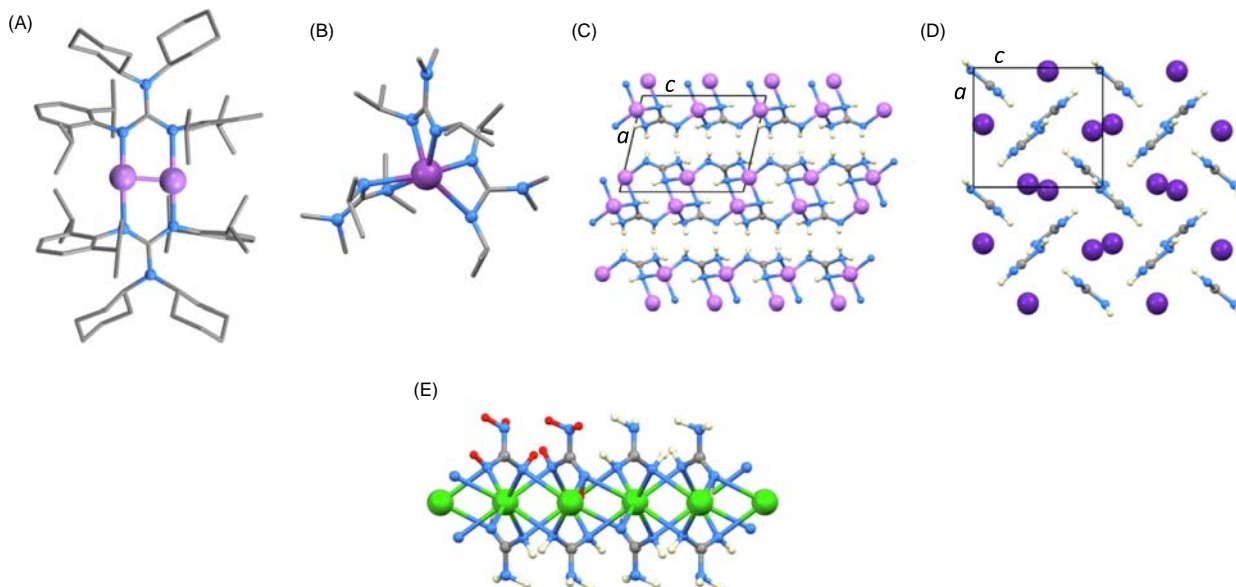
Just as with imidoamidates, there is a variety of group 2 metal complexes of guanidinate with CN = 5 or 6. These include  $[\text{M}(\text{OEt})_2\{\text{(Me}_3\text{Si)}_2\text{NC}(\text{NCy})_2\}_2]$  (M = Ca, Sr),<sup>742</sup>  $[\text{Mg}(\text{THF})\{\text{(Me}_3\text{Si)}_2\text{NC}(\text{N}^i\text{Pr})_2\}_2]$ ,<sup>743</sup> and the dimer  $[\text{Mg}_2(\text{THF})_2\{\text{(Me}_3\text{Si)}_2\text{NC}(\text{NCy})_2\}_2(\mu\text{-Cl})_2]$ .<sup>744</sup> Green et al. have demonstrated that the reduction of  $[\text{Mg}_2(\text{OEt})\{\text{Pr}_2\text{NC}(\text{NDipp})_2\}_2(\mu\text{-I})_2]$  (which contains sterically demanding Dipp substituents) with metallic K results in the formation of the Mg(I) complex  $[\text{Mg}_2\{\text{Pr}_2\text{NC}(\text{NDipp})_2\}_2]$  with an unsupported Mg–Mg bond (Fig. 40C, Mg–Mg = 2.8508(12) Å).<sup>745</sup> The sterically crowded  $[\text{Pr}_2\text{NC}(\text{NDipp})_2]^-$  forms severely distorted 4-coordinate  $[\text{ML}_2]$  complexes with  $\text{Ca}^{2+}$  and  $\text{Sr}^{2+}$ .<sup>746</sup> Kays and coworkers have reported the formation of a series of Mg(II) complexes incorporating the sterically demanding ligand  $[\text{Cy}_2\text{NC}(\text{NMe}_s)_2]^-$ . These include  $[\text{MgI}\{\text{Cy}_2\text{NC}(\text{NMe}_s)_2\}]$  which was isolated in the form of the cubane  $[\text{Mg}_4\{\text{Cy}_2\text{NC}(\text{NMe}_s)_2\}_4(\mu_3\text{-I})_4]$  and the dimer  $[\text{Mg}_2\{\text{Cy}_2\text{NC}(\text{NMe}_s)_2\}_2(\text{OEt})_2(\mu\text{-I})_2]$ .<sup>711</sup> Of particular note is  $[\text{Mg}\{\text{(Cy}_2\text{N})\text{C}(\text{NMe}_s)_2\}_2]$  with sterically demanding ligands with surround a square-planar  $\text{Mg}^{2+}$  center. Significantly, this preference is not wholly due to steric constraints because the 5-coordinate THF adduct  $[\text{Mg}(\text{THF})\{\text{Cy}_2\text{NC}(\text{NMe}_s)_2\}_2]$  has also been structurally characterized. Moving to the larger group 2 metals allows the CN to increase to 6 in  $[\text{M}(\text{THF})_2\{\text{Cy}_2\text{NC}(\text{NMe}_s)_2\}_2]$  (M = Ca, Sr), while for  $\text{Ba}^{2+}$ , there is a preference for  $\text{Ba}^{2+} \cdots \pi_{\text{arene}}$  interactions in  $[\text{Ba}\{\text{Cy}_2\text{NC}(\text{NMe}_s)_2\}_2]$ .<sup>711</sup> A CN of 6 is also exemplified in *cis*- $[\text{M}(\text{THF})_2\{\text{Ph}_2\text{NC}(\text{N}^i\text{Pr})_2\}_2]$  (M = Ca, Sr) and *trans*- $[\text{Ca}(\text{THF})_2\{\text{(Me}_3\text{Si)}_2\text{NC}(\text{NCy})_2\}_2]$ .<sup>747</sup>

Tetrahedral group 13 metal  $[\text{MX}_2(\text{guanidinate})]$  complexes are represented by  $[\text{AlCl}_2\{\text{Pr}_2\text{NC}(\text{NCy})_2\}]$ ,<sup>718</sup>  $[\text{GaCl}_2\{\text{Pr}_2\text{NC}(\text{N}^i\text{Pr})_2\}]$ ,<sup>736</sup>  $[\text{Al}\{\text{NHDipp}\}_2\{\text{(Me}_3\text{Si)}_2\text{NC}(\text{NCy})_2\}]$ ,<sup>748</sup> and  $[\text{GaI}_2\{\text{Cy}_2\text{NC}(\text{NDipp})_2\}]$ .<sup>749</sup> The dimer  $[\text{Al}_2\text{Cl}_4\{\mu\text{-}\{\text{Me}_2\text{NC}(\text{NMe})_2\}\}_2]$  is an interesting example in which the guanidinate ligand adopts a bridging mode in preference to the halide ligands.<sup>750</sup> Five-coordinate complexes of the type  $[\text{MX}(\text{guanidinate})_2]$  (M = Al, Ga; X = H, halide,  $\text{NR}_2$ ) with square-pyramidal structures have been detailed.<sup>734,736,751,752</sup> In group 13, octahedral tris(chelates) are found for sterically non-congested ligands,<sup>753,754</sup> and have been assessed as precursors for  $\text{In}_2\text{O}_3$  thin films.<sup>753,754</sup> By using the sterically congested guanidinate ligands  $[\text{Cy}_2\text{NC}(\text{NDipp})_2]^-$  and  $[\text{Pr}_2\text{NC}(\text{NDipp})_2]^-$ , Jones et al. were able to isolate the air-sensitive, but thermally stable, Ga(I) and In(I)  $[\text{ML}]$  complexes; DFT calculations reveal that these complexes should behave as good  $\sigma$ -donor and weak  $\pi$ -acceptor metalloligands.<sup>749,755</sup>

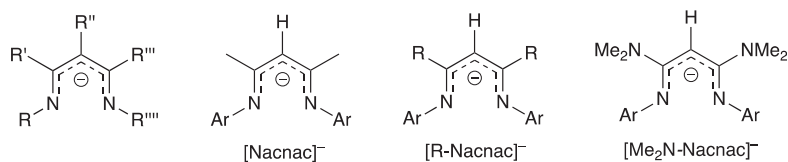
Group 14 metal(II) complexes include 4- and 3-coordinate Sn(II) guanidinate formed, respectively, from reactions of  $\text{R-N}=\text{C}=\text{N-R}'$  with  $[\text{Sn}\{\text{N}(\text{SiMe}_3)_2\}_2]$  or  $[\text{SnCl}\{\text{N}(\text{SiMe}_3)_2\}]$ ; Fig. 40D shows the structure of  $[\text{Sn}\{\text{(Me}_3\text{Si)}_2\text{NC}(\text{N}(4\text{-MeC}_6\text{H}_4))_2\}_2]$  as an example.<sup>756</sup> Similar structures are found for  $[\text{Sn}\{\text{(Me}_3\text{Si)}_2\text{NC}(\text{N}^i\text{Pr})_2\}_2]$ ,<sup>757</sup>  $[\text{Sn}\{\text{(Me}_3\text{Si)}_2\text{NC}(\text{NCy})_2\}_2]$ ,<sup>757</sup>  $[\text{Sn}\{\text{Me}_2\text{NC}(\text{NCy})_2\}_2]$ ,<sup>758</sup> and  $[\text{Sn}\{\text{CyHNC}(\text{NCy})_2\}_2]$ .<sup>759</sup> This structure type is also represented in Sn(II) complexes with one amidinate and one guanidinate ligand, the first example of which appeared in 2014.<sup>760</sup> The structure of  $[\text{SnCl}\{\text{(Me}_3\text{Si)}_2\text{NC}(\text{N}^i\text{Pr})_2\}]$  (Fig. 40E)<sup>757</sup> is typical of  $[\text{MX}(\text{guanidinate})]$  complexes (M<sup>II</sup> = Ge, Sn, Pb).<sup>758,761–763</sup> The oxidative addition of  $\text{Ph}_2\text{E}_2$  (E = S, Se, Te) to  $[\text{Sn}\{\text{Me}_2\text{NC}(\text{NCy})_2\}_2]$  results in the formation of Sn(IV) complexes, e.g.,  $[\text{Sn}(\text{TePh})_2\{\text{Me}_2\text{NC}(\text{NCy})_2\}_2]$ , which have been applied as precursors to SnE nanocrystals.<sup>764</sup> Reactions between elemental S or Se with  $[\text{Sn}^{\text{II}}\{\text{Me}_2\text{NC}(\text{NCy})_2\}_2]$  also result in oxidative addition to yield  $[\text{Sn}^{\text{IV}}(\text{E}_4)\{\text{Me}_2\text{NC}(\text{NCy})_2\}_2]$  in which  $\text{S}_4^{2-}$  or  $\text{Se}_4^{2-}$  ligands adopt chelating modes.<sup>758</sup> Reactions of  $[\text{Ge}^{\text{II}}(\text{N}(\text{SiMe}_2)_2)\{\text{Pr}_2\text{NC}(\text{N}(2,6\text{-Me}_2\text{C}_6\text{H}_3))_2\}_2]$  with elemental S or Se yield the tetrahedral  $[\text{Ge}^{\text{IV}}\text{E}(\text{N}(\text{SiMe}_2)_2)\{\text{Pr}_2\text{NC}(\text{N}(2,6\text{-Me}_2\text{C}_6\text{H}_3))_2\}_2]$  containing  $\text{E}^{2-}$  (E = S, Se) ligands, whereas analogous reactions with the Sn(II) analogs lead to  $[\text{Ge}^{\text{IV}}(\text{E}_4)(\text{N}(\text{SiMe}_2)_2)\{\text{Pr}_2\text{NC}(\text{N}(2,6\text{-Me}_2\text{C}_6\text{H}_3))_2\}_2]$  with chelating  $\text{E}_4^{2-}$  as described above.<sup>765</sup> Treatment of  $\text{SnCl}_4$  with triisopropylguanidine yields  $[\text{SnCl}_2\{\text{PrHNC}(\text{N}^i\text{Pr})_2\}]$  which adopts the expected tetrahedral geometry.<sup>759</sup> Earlier in this section, we described the use of sterically demanding  $[\text{RC}(\text{NDipp})_2]^-$  ligands (R = H,  $^t\text{Bu}$ ) to isolate thermally stable imidoaminate Pb(II) complexes. Related to this are the dimers  $[\text{PbCl}\{\text{DippHNC}(\text{NDipp})_2\}_2]$  and  $[\text{PbCl}\{\text{Cy}_2\text{NC}(\text{NDipp})_2\}_2]$ .<sup>730</sup>

For the group 15 metals, 4-coordinate  $[\text{M}^{\text{III}}\text{X}_2(\text{guanidinate})]$  complexes are represented by  $[\text{MCl}_2\{\text{Cy}_2\text{NC}(\text{NDipp})_2\}]$  (M = As, Sb), and  $[\text{SbI}_2\{\text{Cy}_2\text{NC}(\text{NDipp})_2\}]$ , all with distorted disphenoidal structures, consistent with a stereochemically active lone pair on the metal center.<sup>766</sup> Reduction of  $[\text{AsCl}_2\{\text{Cy}_2\text{NC}(\text{NDipp})_2\}]$  using  $\text{KC}_8$  yielded the dimeric  $[\text{As}_2\{\mu\text{-}\{\text{Cy}_2\text{NC}(\text{NDipp})_2\}_2\}]$  with a planar  $\text{As}_2\text{N}_4$  framework (Fig. 41A).<sup>766</sup> The tris(chelate)  $[\text{Bi}\{\text{Me}_2\text{NC}(\text{N}^i\text{Pr})_2\}_3]$  has the structure shown in Fig. 41B with the coordination sphere consistent with the presence of a stereochemically active lone pair.<sup>767</sup>

Before leaving guanidinate metal complexes, we should mention s-block metal complexes which incorporate conjugate bases of guanidine ( $\text{H}_5\text{Gu}$ ). The very strong basicity of  $[\text{H}_4\text{Gu}]^-$  coupled with moisture sensitivity of its compounds have served as barriers to the isolation of group 1 metal salts.<sup>768</sup>  $[\text{Li}(\text{H}_4\text{Gu})]_n$  was the last of the alkali metal guanidates to be isolated (from guanidine and Li in liquid  $\text{NH}_3$  under pressure, or from solid guanidine and LiH) and structurally characterized. Each  $\text{Li}^+$  center is tetrahedrally bound by one  $\text{NH}_2$  and three  $\text{NH}$  units.<sup>768</sup>  $[\text{Na}(\text{H}_4\text{Gu})]_n$  and  $[\text{K}(\text{H}_4\text{Gu})]_n$  have been prepared from  $\text{H}_5\text{Gu}$  and either Na or K in liquid  $\text{NH}_3$  at  $P \approx 10$  atm and ambient temperature. In the  $\text{Na}^+$  salt, each metal center is tetrahedrally sited, whereas  $\text{K}^+$  coordination environments in  $[\text{K}(\text{H}_4\text{Gu})]_n$  are irregular.<sup>769</sup> While the structures of  $[\text{Li}(\text{H}_4\text{Gu})]_n$  and  $[\text{Na}(\text{H}_4\text{Gu})]_n$  are similar, they differ in that 1D-chains of linked  $\text{LiN}_4$ -tetrahedra are found in the latter contrasting with what are described as ‘edge-sharing tetrahedra’ in the  $\text{Li}^+$  salt; analysis of the structure illustrates an overall sheet assembly (Fig. 41C).<sup>768</sup> Crystalline  $[\text{Rb}(\text{H}_4\text{Gu})]_n$  and  $[\text{Cs}(\text{H}_4\text{Gu})]_n$  (prepared using the liquid  $\text{NH}_3$  route described above) possess the same structure type (Fig. 41D).<sup>770</sup> Group 2 metal guanidates are represented by  $[\text{Ca}(\text{H}_3\text{Gu})]_n$  (prepared in liquid  $\text{NH}_3$  by a similar strategy as described above) and  $[\text{Sr}(\text{H}_3\text{Gu})]_n$  which are isostructural<sup>771</sup>; note that in each compound, guanidine is doubly-deprotonated. In contrast, the barium compound  $[\text{Ba}(\text{H}_4\text{Gu})_2]_n$  contains the  $[\text{H}_4\text{Gu}]^-$  ligand. A liquid ammonia route in an autoclave was again used and precise stoichiometric amounts of reactants are essential for the isolation of phase-pure  $[\text{Ba}(\text{H}_4\text{Gu})_2]_n$ ; each  $\text{Ba}^{2+}$  ion is 8-coordinate and the assembly extends to give a 2D-sheet structure. In Fig. 41E, the different *syn* and *anti*-conformations of the  $[\text{H}_4\text{Gu}]^-$  ligands are highlighted in red.<sup>772</sup>



**Fig. 41** Structures of (A)  $[\text{As}_2\{\mu\text{-}(\text{Cy}_2\text{NC}(\text{NDipp})_2)_2\}]_2$  (CSD refcode JEWRUZ) and (B)  $[\text{Bi}(\text{Me}_2\text{NC}(\text{N}'\text{Pr})_2)_3]$  (refcode OSENEI). (C) Part of the sheet structure of  $[\text{Li}(\text{H}_4\text{Gu})]_n$  viewed down the crystallographic  $b$ -axis (refcode KUTFEQ). (D) Part of the 3D-structure of  $[\text{Rb}(\text{H}_4\text{Gu})]_n$  viewed down the  $b$ -axis (refcode XUNJEX). (E) Part of one sheet in  $[\text{Ba}(\text{H}_4\text{Gu})]_n$  viewed down the  $c$ -axis, and emphasizing in red that both *syn*- and *anti*-conformations of the ligand are present (refcode VUDKAJ01).

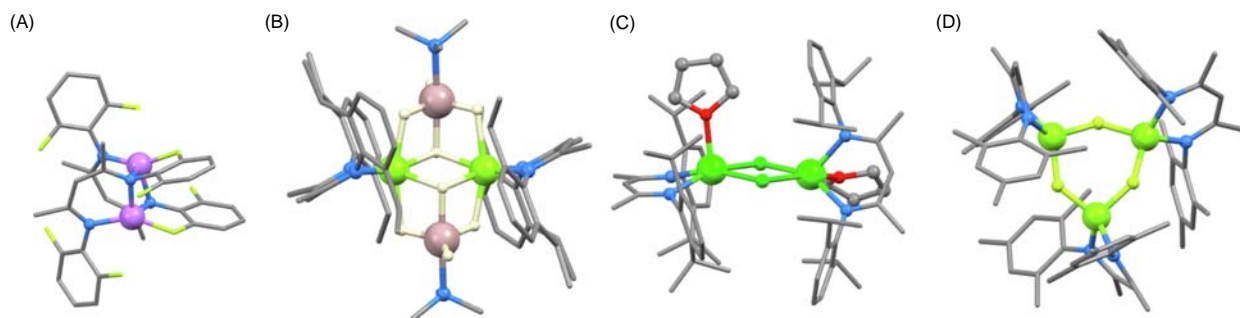


**Scheme 6** General structures of  $\beta$ -diketiminato ligands. The abbreviation  $[\text{Nacnac}]^-$  and  $[\text{Me}_2\text{N-Nacnac}]^-$  are used in the text (here and in later sections) with Ar specified.

### 1.02.2.2.3 $\beta$ -Diketiminates

$\beta$ -Diketiminato ligands are widely used both in main group coordination and organometallic compounds, and a number of derivatives have already been included in earlier sections. The examples below are necessarily selective, and have been chosen to illustrate (i) coordination to metals from each of the s- and p-block groups, and (ii) structural dependence on the size of the N-substituents. The general  $\beta$ -diketiminato structure is shown in **Scheme 6**;  $[\text{Nacnac}]^-$  is commonly used as an abbreviation for the general class shown at the right of **Scheme 6**, and sterically demanding  $[\text{Nacnac}]^-$  ligands are employed to kinetically stabilize extremely reactive low-oxidation state main group metal complexes.<sup>773</sup>

Lithiation of  $\text{HNacnac}$  (Ar = 2,6- $\text{F}_2\text{C}_6\text{H}_3$ ) in  $\text{Et}_2\text{O}$  or THF yields the 3-coordinate  $[\text{Li}(\text{OEt}_2)(\text{Nacnac})]$  or  $[\text{Li}(\text{THF})(\text{Nacnac})]$ , respectively, whereas reaction in pentane leads to the dinuclear complex shown in **Fig. 42A**. In this dimer, each  $[\text{Nacnac}]^-$  ligand



**Fig. 42** Structures of (A)  $[\text{Li}_2(\text{Nacnac})_2]$  with Ar = 2,6- $\text{F}_2\text{C}_6\text{H}_3$  (CSD refcode HEFSUI), (B)  $[\text{Mg}_2(\text{Nacnac})_2(\mu\text{-AIH}_4\text{NMe}_3)_2]$  (refcode FEGJUJ), (C)  $[\text{Ca}_2(\text{THF})_2(\text{Nacnac})_2(\mu\text{-Cl})_2]$  (Ar = Dipp) (refcode DIVTEI), and (D)  $[\text{Mg}_3(\text{Nacnac})_2(\mu\text{-F})_3]$  (Ar = Mes, refcode HEMGOY).

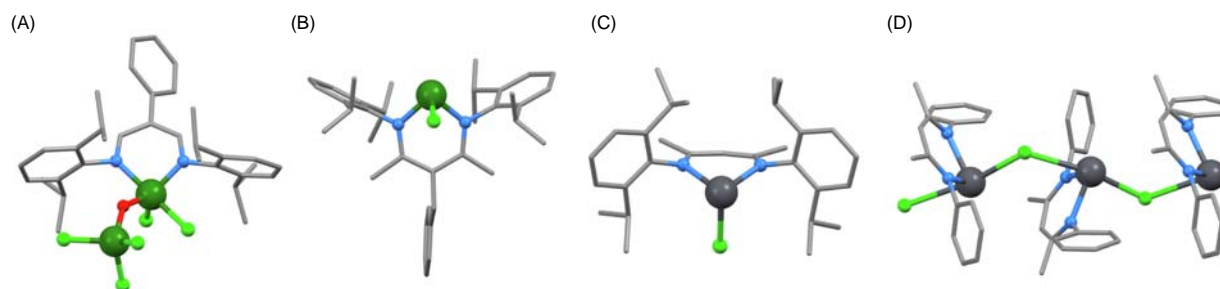


is in both chelating and bridging modes, and one F atom of each ligand forms an F $\cdots$ Li interaction, reminiscent of similar interactions described earlier (e.g., Fig. 8D).<sup>774</sup>

Beryllium  $\beta$ -diketiminate complexes are represented by the trigonal planar [BeX(Nacnac)] (Ar = Mes; X = Br, I),<sup>659</sup> trigonal planar [BeBr(-Nacnac)] (Ar = Dipp),<sup>659</sup> trigonal planar [BeX{HC(CPh)<sub>2</sub>(NDipp)<sub>2</sub>}] (X = Cl, I),<sup>775</sup> and tetrahedral [BeBr(OEt<sub>2</sub>)(Nacnac)] (Ar = Ph).<sup>659</sup> THF reacts with [BeI{HC(CPh)<sub>2</sub>(NDipp)<sub>2</sub>}] in a ring-opening insertion reaction to yield [Be(O(CH<sub>2</sub>)<sub>4</sub>I){HC(CPh)<sub>2</sub>(NDipp)<sub>2</sub>}].<sup>775</sup> The extremely bulky TROP substituent (derived from tropone) has been incorporated into [Nacnac]<sup>-</sup> (Ar = TROP) and the asymmetric [Nacnac]<sup>-</sup> (Ar<sub>1</sub> = TROP, Ar<sub>2</sub> = Dipp). Complexes of Li<sup>+</sup> exhibit a 1:1 stoichiometry, and reactions of the two [Li(Nacnac)] complexes with MgI<sub>2</sub> in Et<sub>2</sub>O led to the 3-coordinate [MgI(Nacnac)] (Ar = TROP) and the highly distorted 4-coordinate [MgI(OEt<sub>2</sub>)(Nacnac)] (Ar<sub>1</sub> = TROP, Ar<sub>2</sub> = Dipp).<sup>776</sup> Tetrahedral Mg(II) complexes with  $\beta$ -diketiminate ligands include [MgCl(THF)(Nacnac)] (Ar = Dipp),<sup>777</sup> and [MgI(OEt<sub>2</sub>)(Nacnac)] with an asymmetric  $\beta$ -diketiminate (Ar<sub>1</sub> = CHMePh, Ar<sub>2</sub> = Dipp).<sup>778</sup> In contrast to the mononuclear [MgCl(THF)(Nacnac)] (Ar = Dipp)<sup>777</sup> and [MgIL(Nacnac)] (Ar = Mes, L = THF, OEt<sub>2</sub>),<sup>779</sup> dimeric structures are found for [Mg<sub>2</sub>(Nacnac)<sub>2</sub>( $\mu$ -I)<sub>2</sub>] (Ar = Mes),<sup>779</sup> [Mg<sub>2</sub>(Nacnac)<sub>2</sub>( $\mu$ -Cl)<sub>2</sub>] (Ar = 2,6-Et<sub>2</sub>C<sub>6</sub>H<sub>3</sub>),<sup>780</sup> and [Mg<sub>2</sub>(Nacnac)<sub>2</sub>( $\mu$ -Cl)<sub>2</sub>] (Ar = Dipp).<sup>781</sup> Bonyhady et al. made a detailed study of the varying steric effects of the N-Ar groups in the  $\beta$ -diketiminate ligands in these latter families of complexes.<sup>779</sup> [Mg<sub>2</sub>(Nacnac)<sub>2</sub>( $\mu$ -Cl)<sub>2</sub>] (Ar = 2,6-Et<sub>2</sub>C<sub>6</sub>H<sub>3</sub>) reacts with NaAlH<sub>4</sub> in Et<sub>2</sub>O to produce [Mg<sub>2</sub>(OEt<sub>2</sub>)<sub>2</sub>(Nacnac)<sub>2</sub>( $\mu$ -AlH<sub>4</sub>)<sub>2</sub>], and with AlH<sub>3</sub>(NMe<sub>3</sub>) to yield [Mg<sub>2</sub>(Nacnac)<sub>2</sub>( $\mu$ -AlH<sub>4</sub>NMe<sub>3</sub>)<sub>2</sub>] (Fig. 42B).<sup>780</sup> The calcium analog of [MgCl(THF)(Nacnac)] is a dimer (Fig. 42C) and is structurally similar to the F<sup>-</sup> and I<sup>-</sup> derivatives, and to [Ca<sub>2</sub>(NH<sub>3</sub>)<sub>4</sub>(Nacnac)<sub>2</sub>( $\mu$ -NH<sub>2</sub>)<sub>2</sub>] (Ar = Dipp). The common precursor to these compounds is [Ca(NSiMe<sub>3</sub>)(THF)(Nacnac)] (Ar = Dipp).<sup>782</sup> Hydrodehalogenation of aromatic halides using [Sr<sub>2</sub>(THF)<sub>2</sub>(Nacnac)<sub>2</sub>( $\mu$ -H)<sub>2</sub>] (Ar = 2,6-(3-pentyl)<sub>2</sub>C<sub>6</sub>H<sub>3</sub>) is a route to the halido derivatives [Sr<sub>2</sub>(THF)<sub>2</sub>(Nacnac)<sub>2</sub>( $\mu$ -X)<sub>2</sub>] with X = F, Cl, Br, I.<sup>783</sup> Earlier, we described the Mg(I) imidoaminate complex [Mg<sub>2</sub>{<sup>i</sup>Pr<sub>2</sub>NC(NDipp)<sub>2</sub>}<sub>2</sub>] which possesses an Mg-Mg bond (Fig. 40C); Green et al. have also prepared analogous complexes containing [Nacnac]<sup>-</sup> ligands with sterically demanding Ar groups.<sup>745</sup> Addition of a C-F bond across the Mg-Mg bond in [Mg<sub>2</sub>(Nacnac)<sub>2</sub>] occurs rapidly in solution to produce a new family of F-containing Grignard reagents<sup>784,785</sup>; among the compounds isolated was the trimer shown in Fig. 42D.<sup>785</sup>

A wide range of tetrahedral [MX<sub>2</sub>( $\beta$ -diketiminate)] complexes is known in which M(III) = Al, Ga, or In, and representative examples include [MF<sub>2</sub>(Nacnac)] (Ar = Dipp, M = Al or Ga),<sup>786</sup> [AlI<sub>2</sub>{HC(CR)<sub>2</sub>(NMe)<sub>2</sub>}] (R = Me, <sup>i</sup>Pr),<sup>787</sup> [GaCl<sub>2</sub>(Nacnac)] and [GaCl(OSiMe<sub>3</sub>)(Nacnac)] (Ar = Dipp),<sup>788</sup> [GaCl<sub>2</sub>{HC(CPh)<sub>2</sub>(NPh)<sub>2</sub>}],<sup>789</sup> [Ga<sub>2</sub>(Nacnac)] (Ar = 2,6-Me<sub>2</sub>C<sub>6</sub>H<sub>3</sub>),<sup>790</sup> [InI<sub>2</sub>(Nacnac)] (Ar = Ph),<sup>791</sup> [AlCl<sub>2</sub>{PhC(CH)<sub>2</sub>(NDipp)<sub>2</sub>}] and related Al, Ga and In complexes,<sup>792</sup> [AlBr<sub>2</sub>{PhC(CPh)<sub>2</sub>(NDipp)<sub>2</sub>}] and related compounds,<sup>793</sup> [AlCl<sub>2</sub>{Ph<sub>2</sub>PC(CMe)<sub>2</sub>(NDipp)<sub>2</sub>}],<sup>794</sup> [GaCl(NR)(Nacnac)] (Ar = Dipp),<sup>795</sup> and [InI<sub>2</sub>(Nacnac)] (Ar = Dipp) and related derivatives.<sup>796</sup> The reaction of [AlCl<sub>2</sub>(Nacnac)] (Ar = C<sub>6</sub>F<sub>5</sub>) with BCl<sub>3</sub> followed by H<sub>2</sub>O produced the first example of a stable oxoborane monomer [O=B(Nacnac)] which is stabilized by B=O  $\rightarrow$  AlCl<sub>3</sub> adduct formation.<sup>797</sup>  $\beta$ -Diketimidate analogs of the ligands shown in Scheme 5 have been used to access dimetallic species in the families [AlX<sub>2</sub>{bis( $\beta$ -diketiminate)}] (X = Cl, Br, I).<sup>798</sup> The hydrolysis of [AlClI(Nacnac)] (Ar = Dipp) led first to [Al<sub>2</sub>Cl<sub>2</sub>(Nacnac)<sub>2</sub>( $\mu$ -OH)<sub>2</sub>] and then to [Al(OH)<sub>2</sub>(Nacnac)].<sup>799</sup> Oxidative addition of SiBr<sub>4</sub> to the Ga(I) derivative [Ga(Nacnac)] (Ar = Dipp) gives [GaBr(SiBr<sub>3</sub>)(Nacnac)]; at 60 °C, the product was [GaBr(Nacnac)]<sub>2</sub>SiBr<sub>2</sub>, while in the presence of CO, [GaBr(Nacnac)]<sub>2</sub>Si(CO)] (a silylene carbonyl that is stable at room temperature) was isolated.<sup>800</sup> Compounds incorporating a non-bridged M-M bond include [In<sub>2</sub>Cl<sub>2</sub>(Nacnac)<sub>2</sub>] (Ar = Dipp, In-In = 2.8343(7) Å),<sup>801</sup> [In<sub>2</sub>Br<sub>2</sub>(Nacnac)<sub>2</sub>] (Ar = Mes),<sup>720</sup> and [In<sub>2</sub>Cl<sub>2</sub>{PhC(CH)<sub>2</sub>(NDipp)<sub>2</sub>}<sub>2</sub>].<sup>792</sup>

The Ge(IV) compound [GeCl<sub>2</sub>{PhC(CH)<sub>2</sub>(NDipp)<sub>2</sub>}(OGeCl<sub>3</sub>)] (Fig. 43A) is formed in the reaction of the lithium  $\beta$ -diketiminate and (GeCl<sub>3</sub>)<sub>2</sub>O.<sup>802</sup> [SnBr<sub>3</sub>(Nacnac)] and [SnI<sub>3</sub>(Nacnac)] (Ar = Dipp) possess square-based pyramidal structures with the  $\beta$ -diketiminate ligand occupying two basal sites.<sup>803</sup> We move now to low oxidation state complexes of the group 14 metals. A combination of structural and calculational data suggest that [GeX(Nacnac)] (Ar = Ph; X = Cl, I, OMe) is best described by a structure comprising [Ge(Nacnac)]<sup>+</sup> weakly coordinated with the X<sup>-</sup> unit.<sup>804</sup> Sterically demanding N-bonded aryl groups such as 2,6-<sup>i</sup>Pr<sub>2</sub>C<sub>6</sub>H<sub>3</sub> (Dipp) are often used to stabilize low oxidation state group 14 metal  $\beta$ -diketiminate complexes,<sup>805-814</sup> and Fig. 43B and C illustrate two examples. [GeX(Nacnac)] and [SnX(Nacnac)] complexes with less sterically demanding NAr units (e.g., Ar = Mes, Ph) are also known.<sup>351,815</sup> Tam et al. showed that the reactions of Li[Nacnac] (Ar = Ph, 4-<sup>i</sup>PrC<sub>6</sub>H<sub>4</sub> or 2,6-Me<sub>2</sub>C<sub>6</sub>H<sub>3</sub>) with PbCl<sub>2</sub> yielded the corresponding [PbCl(Nacnac)] complexes, and that, in the solid state, [PbCl(Nacnac)] with



**Fig. 43** Structures of (A) [GeCl<sub>2</sub>{PhC(CH)<sub>2</sub>(NDipp)<sub>2</sub>}(OGeCl<sub>3</sub>)] (CSD refcode IHIRIB), (B) [GeCl{BzC(CMe)<sub>2</sub>(NDipp)<sub>2</sub>}] (refcode ACEPIJ), and (C) [PbCl(Nacnac)] with Ar = Dipp (refcode CIJQES). (D) Part of the 1D-chain in [PbCl(Nacnac)]<sub>n</sub> (Ar = Ph, refcode DABCIV).



Ar = Ph exists as a 1D-polymer (Fig. 43D). In contrast, intermolecular  $\text{Pb}\cdots\pi$  contacts are observed in  $[\text{PbCl}(\text{Nacnac})]$  with Ar = 2,6-Me<sub>2</sub>C<sub>6</sub>H<sub>3</sub>.<sup>816</sup>

Representative  $\beta$ -diketiminate complexes of the heavier group 15 elements include  $[\text{AsI}_2\{\text{PhC}(\text{CH})_2(\text{NDipp})_2\}]$ ,<sup>817</sup>  $[\text{SbX}_2\{\text{PhC}(\text{CH})_2(\text{NDipp})_2\}]$  (X = Cl, Br; each structure is derived from a square-based pyramid with a stereochemically active lone pair in one basal site),<sup>818</sup>  $[\text{SbCl}_2(\text{Nacnac})]$  (Ar = Mes; disphenoidal geometry with axial Cl),<sup>819</sup>  $[\text{Bi}_2\text{X}_2(\text{THF})\{\text{PhC}(\text{CH})_2(\text{NDipp})_2\}(\mu\text{-X})_2]$  (X = Cl, Br),<sup>820</sup> and  $[\text{Bi}_2\text{I}_2\{\text{PhC}(\text{CH})_2(\text{NDipp})_2\}(\mu\text{-I})_2]$ .<sup>820</sup>

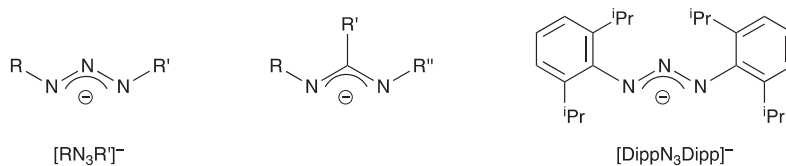
### 1.02.2.2.4 Triazenide ligands

In Section 1.02.2.2.2, we considered metal complexes of imidoamidate ligands (Scheme 3). Replacement of the central CR unit by a (formally) isoelectronic N leads to the family of triazenide ligands (Scheme 7). Gyton et al. have made a direct comparison of the structures and physical properties of a series of s-, p- and d-block metal complexes containing  $[\text{DippN}_3\text{Dipp}]^-$  and  $[\text{DippN}(\text{CH})\text{NDipp}]^-$ ; this detailed study provides an excellent base from which to develop an understanding of the similarities and differences of triazenide and imidoamidate complexes of a given metal ion.<sup>821</sup>

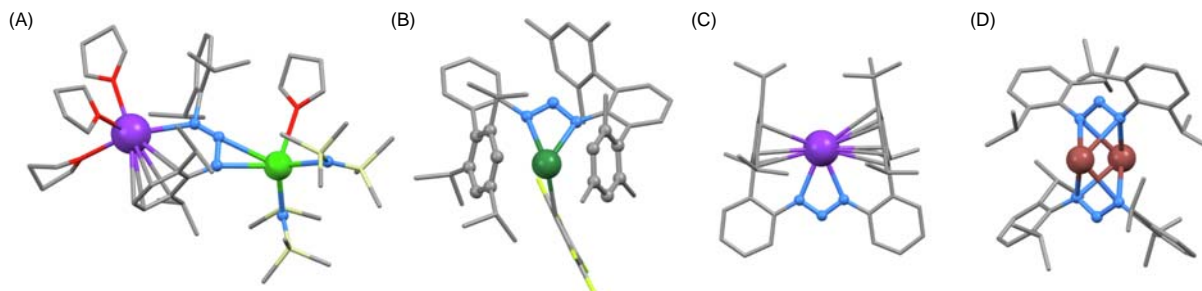
Many complexes of symmetrical  $[\text{RN}_3\text{R}]^-$  ligands with the alkali metals have unexceptional structures which feature chelating  $[\text{RN}_3\text{R}]^-$ , with CN increasing with the size of the metal ion. Examples include  $[\text{Li}(\text{OEt}_2)\{(2,6\text{-Mes}_2\text{C}_6\text{H}_3)\text{N}_3(2,6\text{-Mes}_2\text{C}_6\text{H}_3)\}]$  (trigonal planar),<sup>822</sup>  $[\text{Li}(\text{OEt}_2)_2\{(2,6\text{-Mes}_2\text{C}_6\text{H}_3)\text{N}_3(3\text{-MeC}_6\text{H}_4)\}]$  (tetrahedral),<sup>823</sup>  $[\text{Li}(\text{OEt}_2)_2(\text{DippN}_3\text{Dipp})]$  and  $[\text{Li}(\text{THF})_2(\text{DippN}_3\text{Dipp})]$  (both tetrahedral),<sup>821</sup>  $[\text{Na}(\text{THF})_3(\text{DippN}_3\text{Dipp})]$  (CN = 5),<sup>821</sup>  $[\text{M}(\text{dme})_2(\text{DippN}_3\text{Dipp})]$  (M = Na, K; CN = 6),<sup>821</sup>  $[\text{Na}(15\text{-crown-5})(\text{PhN}_3\text{Ph})]$  (CN = 7),<sup>824</sup>  $[\text{Na}(15\text{-crown-5})(\text{DippN}_3\text{Dipp})]$  (CN = 7),<sup>821</sup> and  $[\text{K}(18\text{-crown-6})(\text{DippN}_3\text{Dipp})]$  (CN = 8).<sup>821</sup> Of particular note is  $[\text{Li}(\text{ArN}_3\text{Ar})]$  (Ar = 2,6-Mes<sub>2</sub>C<sub>6</sub>H<sub>3</sub>) in which there are no additional donors bound to Li<sup>+</sup> and the metal ion is sandwiched between two mesityl rings; similar complexes with heavier alkali metal ions have also been reported.<sup>825</sup> Metal  $\cdots\pi$  interactions feature in a number of triazenide complexes with very bulky aryl substituents, and we discuss these further below.

A departure from monomeric group 1 metal complexes is found in the 1D-coordination polymer  $[\text{K}_2(\text{THF})_3(\text{DippN}_3\text{Dipp})_2]_n$  in which the triazenide ligand is in a bridging mode and the arene ring is involved in  $\text{K}^+\cdots\pi$  interactions; the crystal structure suffers from a complicated disorder/desolvation phenomenon.<sup>821</sup> However, the bonding mode of  $[\text{DippN}_3\text{Dipp}]^-$  in  $[\text{K}_2(\text{THF})_3(\text{DippN}_3\text{Dipp})_2]_n$  is similar to that observed in the heterometallic complex  $[\text{K}(\text{THF})_3(\mu\text{-DippN}_3\text{Dipp})\text{Ba}(\text{THF})\{\text{N}(\text{SiMe}_3)_2\}_2]$  (Fig. 44A).<sup>826</sup> As with imidoamidates and guanidates (Figs. 38A and 40A), triazenides may act both in chelating and bridging modes within the same dilithium species.<sup>827</sup> In contrast, in  $[\text{K}_2(\text{THF})_4(\mu\text{-MesN}_3\text{Mes})_2]$  and  $[\text{K}_2(\text{dme})_2(\mu\text{-MesN}_3\text{Mes})_2]$ , each N<sub>3</sub>-unit symmetrically bridges a K<sub>2</sub>-unit ( $\text{K}\cdots\text{K} = 3.5613(8)$  and  $3.4678(5)$  Å, respectively), coordinating through the outer N atoms to each K<sup>+</sup> to form an octahedral K<sub>2</sub>N<sub>4</sub>-core.<sup>828</sup>

As with group 1, chelating  $[\text{RN}_3\text{R}]^-$  and a general increase in CN on descending the group are seen for the group 2 metals. In the following examples, sterically demanding substituents play an important stabilizing role, and the ability of the 2-(2,4,6-<sup>i</sup>Pr<sub>3</sub>C<sub>6</sub>H<sub>2</sub>)C<sub>6</sub>H<sub>4</sub> and other aryl substituents to participate in  $\text{M}\cdots\pi$  interactions should be noted (see below): tetrahedral  $[\text{Mg}(\text{THF})(\text{ArN}_3\text{Ar}')]^-$  (Ar = 2,6-Mes<sub>2</sub>C<sub>6</sub>H<sub>3</sub>, Ar' = 2-(2,4,6-<sup>i</sup>Pr<sub>3</sub>C<sub>6</sub>H<sub>2</sub>)C<sub>6</sub>H<sub>4</sub>),<sup>829</sup> square-based pyramidal  $[\text{Mg}(\text{OEt}_2)(\text{DippN}_3\text{Dipp})_2]$ ,<sup>830</sup> octahedral *trans*- $[\text{Mg}(\text{THF})_2(\text{MesN}_3\text{Mes})_2]$ ,<sup>828</sup>  $[\text{Ca}(\text{THF})_2\{\text{N}(\text{SiMe}_3)_2\}(\text{DippN}_3\text{Dipp})]$  (CN = 5),<sup>826</sup> *trans*-



**Scheme 7** Structure of a general triazenide ligand  $[\text{RN}_3\text{R}]^-$  which is isoelectronic with an imidoamidate ligand (center). Right: structure of the sterically hindered triazenide ligand  $[\text{DippN}_3\text{Dipp}]^-$ .



**Fig. 44** Structures of (A)  $[\text{K}(\text{THF})_3(\mu\text{-DippN}_3\text{Dipp})\text{Ba}(\text{THF})\{\text{N}(\text{SiMe}_3)_2\}_2]$  (CSD refcode AGEGOJ), (B)  $[\text{Sr}(\text{C}_6\text{F}_5)(\text{ArN}_3\text{Ar}')]^-$  (Ar = 2,6-Mes<sub>2</sub>C<sub>6</sub>H<sub>3</sub>, Ar' = 2-(2,4,6-<sup>i</sup>Pr<sub>3</sub>C<sub>6</sub>H<sub>2</sub>)C<sub>6</sub>H<sub>4</sub>; refcode KAVNOL), (C)  $[\text{K}(\text{ArN}_3\text{Ar})]$  with Ar = 2-(2,4,6-<sup>i</sup>Pr<sub>3</sub>C<sub>6</sub>H<sub>2</sub>)C<sub>6</sub>H<sub>4</sub> (refcode MELPEZ), (D)  $[\text{Ti}_2(\text{DippN}_3\text{Dipp})_2]$  (refcode NADQOC).

[Ca(THF)<sub>2</sub>(MesN<sub>3</sub>Mes)<sub>2</sub>] (a distortion in the coordination sphere is caused by intramolecular face-to-face  $\pi$ -stacking),<sup>828</sup> [Ca<sub>2</sub>(THF)<sub>4</sub>{N(SiMe<sub>3</sub>)<sub>2</sub>}(DippN<sub>3</sub>Dipp)<sub>2</sub>( $\mu$ -I)<sub>2</sub>] (CN = 6),<sup>826</sup> [Sr(THF)<sub>3</sub>{N(SiMe<sub>3</sub>)<sub>2</sub>}(DippN<sub>3</sub>Dipp)] (CN = 6),<sup>826</sup> [Sr(THF)<sub>2</sub>(DippN<sub>3</sub>Dipp)<sub>2</sub>] (CN = 6), and [Sr(tmeda)(MesN<sub>3</sub>Mes)<sub>2</sub>] (CN = 6).<sup>828</sup> Vinduš and Niemeyer have made an extensive study of hetero and homoleptic Mg<sup>2+</sup> triazenides, and among these is [Mg(ArN<sub>3</sub>Ar)<sub>2</sub>] (Ar = 2,6-(3,5-Me<sub>2</sub>C<sub>6</sub>H<sub>3</sub>)<sub>2</sub>C<sub>6</sub>H<sub>3</sub>) in which Mg<sup>2+</sup> is in a square-planar environment.<sup>831</sup> Niemeyer and coworkers have designed sterically hindered triazenides incorporating the 2-(2,4,6-*i*-Pr<sub>3</sub>C<sub>6</sub>H<sub>2</sub>)C<sub>6</sub>H<sub>4</sub> substituent; such a ligand envelops the metal ion to which it is coordinated. A critical factor is the design of the 2-(2,4,6-*i*-Pr<sub>3</sub>C<sub>6</sub>H<sub>2</sub>)C<sub>6</sub>H<sub>4</sub> substituent with the pendant aryl unit oriented so as to facilitate the M $\cdots\pi$  contacts. [MgI(THF)(ArN<sub>3</sub>Ar')] (Ar = 2,6-Mes<sub>2</sub>C<sub>6</sub>H<sub>3</sub>, Ar' = 2-(2,4,6-*i*-Pr<sub>3</sub>C<sub>6</sub>H<sub>2</sub>)C<sub>6</sub>H<sub>4</sub>) was mentioned above,<sup>829</sup> and a related complex is [MgI(OEt<sub>2</sub>)(ArN<sub>3</sub>Ar')].<sup>831</sup> The ligand also encloses Ca<sup>2+</sup>, Sr<sup>2+</sup> or Ba<sup>2+</sup> in a cavity with stabilizing M $\cdots\pi$  interactions as depicted for [Sr(C<sub>6</sub>F<sub>5</sub>)(ArN<sub>3</sub>Ar')] (Ar = 2,6-Mes<sub>2</sub>C<sub>6</sub>H<sub>3</sub>, Ar' = 2-(2,4,6-*i*-Pr<sub>3</sub>C<sub>6</sub>H<sub>2</sub>)C<sub>6</sub>H<sub>4</sub>) in Fig. 44B; although these pentafluorophenyl derivatives are organometallic, we include them because of the innovative triazenide ligand design strategy.<sup>829</sup> Similar M $\cdots\pi$  interactions also feature in [K(ArN<sub>3</sub>Ar)], [Cs(ArN<sub>3</sub>Ar)] and [Tl(ArN<sub>3</sub>Ar)] with Ar = 2-(2,4,6-*i*-Pr<sub>3</sub>C<sub>6</sub>H<sub>2</sub>)C<sub>6</sub>H<sub>4</sub> (Fig. 44C).<sup>827,832</sup>

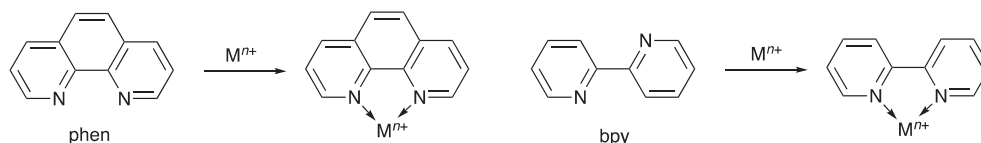
Typical group 13 M(III) triazenide complexes are 5-coordinate and include [AlH(MesN<sub>3</sub>{2,6-(4-MeC<sub>6</sub>H<sub>4</sub>)<sub>2</sub>C<sub>6</sub>H<sub>3</sub>})<sub>2</sub>],<sup>833</sup> and [MX(DippN<sub>3</sub>Dipp)<sub>2</sub>] (M = Ga, In, Tl; X = Cl, Br, I, H).<sup>821</sup> The dihydrido derivative [AlH<sub>2</sub>(THF){MesN<sub>3</sub>(2,6-Mes<sub>2</sub>C<sub>6</sub>H<sub>3</sub>)}] is stabilized by the extreme steric demands of the ligand.<sup>833</sup> [Ga<sub>2</sub>I<sub>2</sub>(DippN<sub>3</sub>Dipp)<sub>2</sub>] contains a Ga–Ga bond and is formally a gallium(II) compound.<sup>821</sup> Trischelates can be accessed using non-sterically crowded substituents, for example, [In(PhN<sub>3</sub>Ph)<sub>3</sub>].<sup>834</sup> Reaction of TlOEt and H[DippN<sub>3</sub>Dipp] yields [Tl(DippN<sub>3</sub>Dipp)] which has a dimeric structure in the solid state (Fig. 44D, Tl $\cdots$ Tl = 3.4612(5) Å)<sup>821</sup>; this motif is seen regularly for thallium(I) triazenide complexes.

Triazenide complexes of the group 14 and 15 metals are relatively sparse. The M(II) derivatives [M(DippN<sub>3</sub>Dipp)<sub>2</sub>] (M = Ge, Sn, Pb)<sup>835</sup> are structurally similar to their imidoamidate analogs, and the sterically demanding [MesN<sub>3</sub>Mes]<sup>−</sup> was used to stabilize [MCl(MesN<sub>3</sub>Mes)] and [MH(MesN<sub>3</sub>Mes)] (M = Ge, Sn).<sup>836</sup>

#### 1.02.2.2.5 2,2'-Bipyridine and 1,10-phenanthroline

Main group metal complexes of bpy and phen, especially the former, are abundant. Whereas phen is preorganized for chelation, bpy must undergo a conformational change (Scheme 8); the resulting 5-membered chelate ring is highly favored.

We have recently surveyed the structural diversity of main group metal complexes containing bpy, phen and tpy,<sup>837</sup> and also bpy complexes of the group 1 metals.<sup>838</sup> Rather than repeat this discussion here, we refer the reader to these reviews.

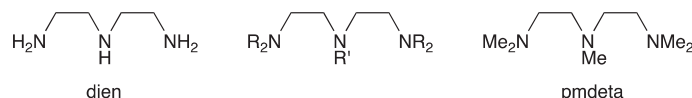


**Scheme 8** The ligand phen is preorganized for chelation, but bpy undergoes a conformational change to form a chelate ring.

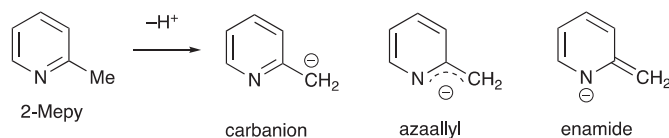
#### 1.02.2.3 Tridentate ligands

##### 1.02.2.3.1 Triamines: Open-chain

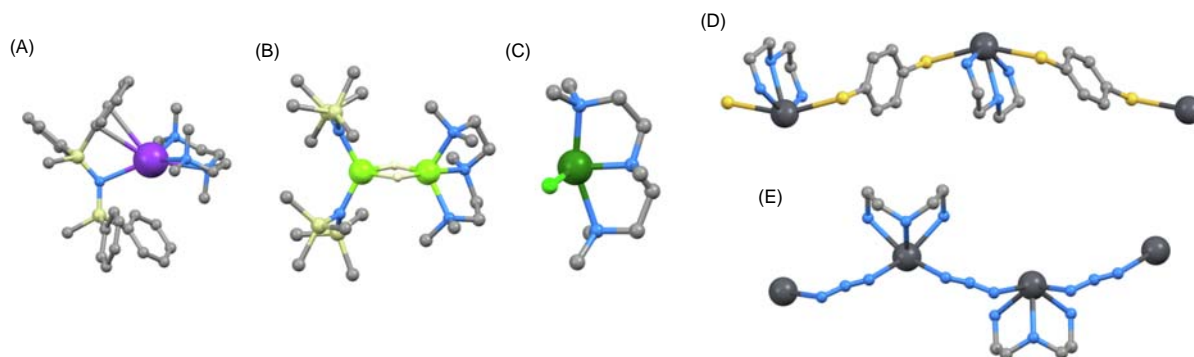
Open-chain tridentate N-donor ligands are typified by those in Scheme 9 which depicts the parent amine N<sup>1</sup>-(2-aminoethyl) ethane-1,2-diamine (dien), a general derivative, and the commonly encountered N<sup>1</sup>-(2-*N,N*-dimethylaminoethyl)-N<sup>1</sup>,N<sup>2</sup>,N<sup>2</sup>-trimethylethane-1,2-diamine (pmdeta). Upon coordination, the formation of 5-membered chelate rings is favored and the large numbers of main group metal complexes containing this family of amines precludes all but a brief overview. Complexes of the s-block metals, in particular lithium, are especially numerous.



**Scheme 9** Typical open-chain tridentate N-donor ligands. The abbreviations derive from the non-IUPAC names diethylenediamine and *N,N,N',N'*-pentamethyldiethylenetriamine.



**Scheme 10** Forms of the conjugate base of 2-methylpyridine, abbreviated to [2-Mepy-H]<sup>−</sup>.



**Fig. 45** Structures of (A)  $[K(\text{pmdeta})(\text{N}(\text{SiMe}_2\text{Ph})_2)_2]$  (CSD refcode HUXPIA), (B)  $[\text{Mg}_2(\text{pmdeta})(\text{N}(\text{SiMe}_3)_2)_2(\mu\text{-H})_2]$  (refcode GOWHOS, only the  $\mu\text{-H}$  atoms are shown), and (C)  $[\text{GeCl}(\text{pmdeta})]^+$  (refcode FULZUI). Parts of the 1D-chains in (D)  $[\text{Pb}(\text{dien})(\mu\text{-S}_2\text{C}_6\text{H}_4)]_n$  (refcode HAVDAL) and (E)  $[\text{Pb}(\text{dien})(\mu\text{-N}_3)]_n$  (refcode HPEXHIK).

Lithium typically exhibits CN = 4 or 5 in complexes with bichelating *pmdeta*. Representative examples are  $[\text{Li}(\text{pmdeta})(\text{NH}\text{-Dipp})]$ ,<sup>180</sup>  $(R,R)\text{-}[\text{Li}(\text{pmdeta})\{\text{N}(\text{CHMePh})_2\}]$ ,<sup>839</sup>  $[\text{Li}(\text{pmdeta})(2\text{-Mepy-H})]$  (see **Scheme 10**),<sup>840</sup>  $[\text{Li}(\text{pmdeta})(\text{THF})]^+$ ,<sup>646</sup>  $[\text{Li}(\text{pmdeta})\{\text{O}(2,6\text{-}^i\text{Bu}_2\text{-4-MeC}_6\text{H}_2)\}]$ ,<sup>650</sup>  $[\text{Li}(\text{pmdeta})\{\text{N}(\text{SnMe}_3)_2\}]$ ,<sup>841</sup>  $[\text{Li}(\text{pmdeta})(\text{TFSI-}\kappa^2)]$ ,<sup>842</sup>  $[\text{Li}(\text{pmdeta})(\text{BH}_4\text{-}\kappa^2)]$ ,<sup>843</sup>  $[\text{Li}_2(\text{pmdeta})_2(\mu\text{-Cl})_2]$ ,<sup>680,844</sup> and  $[\text{Li}_2(\text{pmdeta})_2(\mu\text{-O}_3\text{SCF}_3\text{-}1\kappa\text{O}^1\text{:}2\kappa\text{O}^2)_2]$ .<sup>845</sup>

For sodium, a CN = 5 is illustrated by  $[\text{Na}_2(\text{pmdeta})_2(\mu\text{-OH}_2)_2]^{2+}$ ,<sup>846</sup> and CN = 6 is seen in, for example,  $[\text{Na}(\text{pmdeta})_2]^+$ .<sup>847</sup> In contrast to the tetrahedral  $[\text{Li}(\text{pmdeta})(2\text{-Mepy-H})]$  with N-bound  $[2\text{-Mepy-H}]^-$ , the  $\text{K}^+$  analog is a dimer with bridging  $[2\text{-Mepy-H}]^-$  ligands tending to an azaallylic (**Scheme 10**) mode of coordination.<sup>840</sup> As we have noted earlier in this review (e.g., **Fig. 44A** and C),  $\text{M}^+\cdots\pi$  interactions may influence the structures of complexes of the heavier s-block elements. Such is the case in  $[\text{K}(\text{pmdeta})\{\text{N}(\text{SiMe}_2\text{Ph})_2\}_2]$  (**Fig. 45A**).<sup>848</sup>

Tetrahedral coordination for  $\text{Be}^{2+}$  is exemplified in  $[\text{BeX}(\text{pmdeta})]^+$  ( $\text{X} = \text{Cl}, \text{I}$ ).<sup>509,849</sup> In related halide derivatives,  $\text{Mg}^{2+}$  exhibits a CN = 5 in  $[\text{MgBr}_2(\text{pmdeta})]$ <sup>850</sup> and  $[\text{Mg}(\text{OMes})_2(\text{pmdeta})]$ .<sup>851</sup> Whereas the reaction of  $[\text{Mg}\{\text{N}(\text{SiMe}_3)_2\}_2]$  with  $\text{PhSiH}_3$  yields a poorly defined precipitate, the addition of neutral ligands such as *pmdeta* leads to well-defined complexes; **Fig. 45B** shows one example in which the  $\text{Mg-H}$  bonding is largely ionic in character.<sup>852</sup> As expected, the metal ion coordination number increases down group 2, and an example of CN = 7 is found in  $[\text{Sr}(\text{pmdeta})\{\text{HC}(\text{CO}_2\text{Me})_2\}_2]$ .<sup>853</sup>

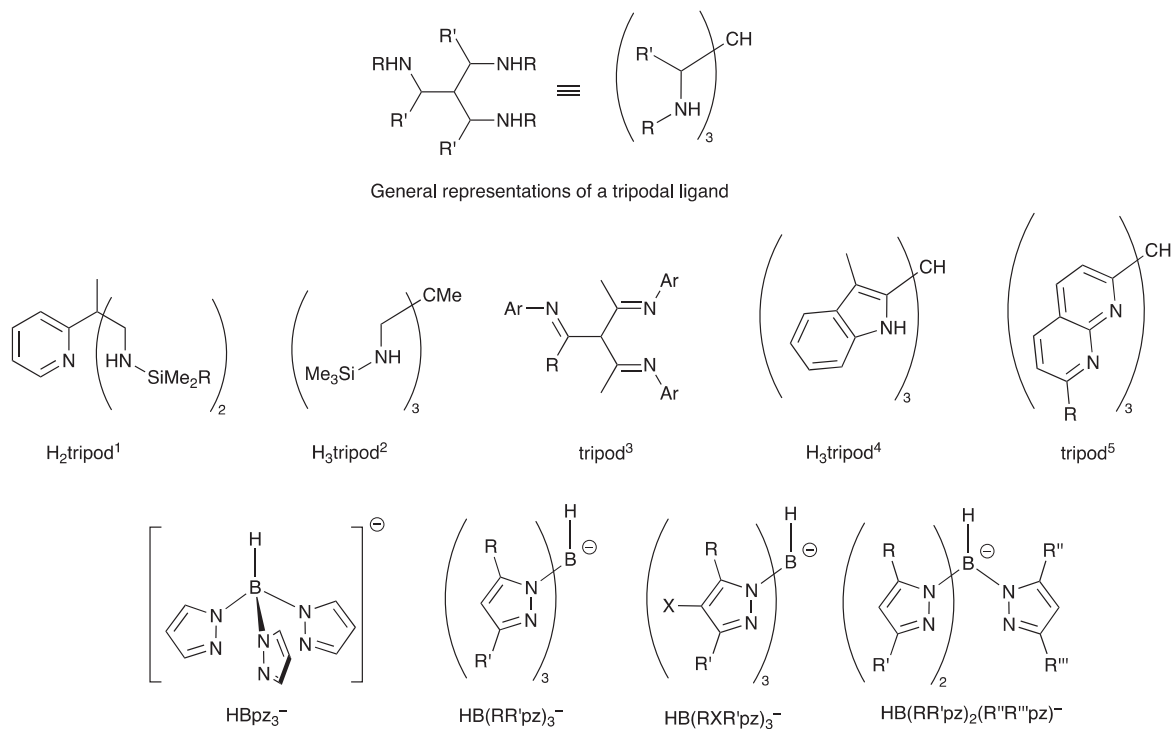
Group 13 metal complexes with dien and *pmdeta* include the trigonal bipyramidal  $[\text{AlH}_2(\text{pmdeta})]^+$ ,<sup>854</sup> and octahedral *fac*- $[\text{M}(\text{dien})_2]^{3+}$  ( $\text{M} = \text{In}, \text{Tl}$ ).<sup>855,856</sup> Group 14  $\text{M}(\text{II})$  complexes include  $[\text{GeCl}(\text{pmdeta})]^+$  (**Fig. 45C**) and its bromido analog.<sup>678</sup> In the 1D-coordination polymer  $[\text{Pb}(\text{dien})(\mu\text{-S}_2\text{C}_6\text{H}_4)]_n$  (**Fig. 45D**), the  $\text{PbN}_3$ -unit is close to planar and the thiolate ligands are mutually *trans*,<sup>857</sup> whereas in  $[\text{Pb}(\text{dien})(\mu\text{-N}_3)]_n$  (**Fig. 45E**), the dien ligand can be described as binding in a *fac*-mode and the azido ligands are *cis*.<sup>858</sup> Note that this description is based upon a pseudo-octahedral  $\text{Pb}(\text{II})$  with a stereochemically active lone pair (**Figs. 45D** and E). A comparison of the five structures in **Fig. 45** illustrates the conformational flexibility of the dien and *pmdeta* ligands.

### 1.02.2.3.2 Triamines: Tripodal ligands and tris(pyrazolyl)borates

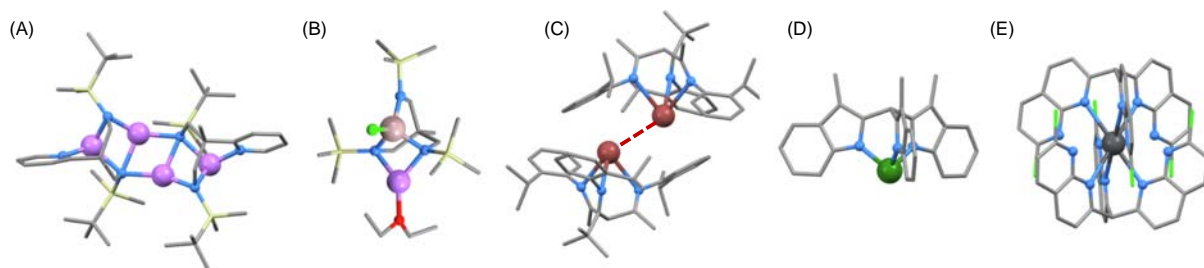
In addition to a general representation of a tripodal-type ligand, **Scheme 11** defines the tripodal ligands described in this section. It also shows the structure of the tris(pyrazolyl)borate ( $\text{HBpz}_3^-$ ) ligand and defines a general substituted tris(pyrazolyl)borate ligand. Typically, tripodal ligands coordinate in a *fac*-mode with all three 'arms' involved in binding a metal ion. Note that such chelating donors are also known as scorpionate ligands, and in 2015, Reglinski and Spicer reviewed their p-block metal coordination compounds.<sup>75</sup> Thallium(I) and potassium salts of tris(pyrazolyl)borate ligands are commonly encountered, and a recent study has highlighted the use of  $^{11}\text{B}$  NMR spectroscopy to follow the synthesis of  $\text{K}^+$  salts and determine compound purity.<sup>859</sup>

The reaction of  $\text{H}_2\text{tripod}^1$  ( $\text{R} = \text{Me}$  or  $^i\text{Bu}$ , **Scheme 11**) with  $^i\text{BuLi}$  produces lithium amides which exhibit dimeric structures in the solid state; the  $\text{Li}_4\text{N}_4$  core possesses a ladder-like assembly (**Fig. 46A**).<sup>860</sup> The ability of amido ligands to bridge between metal centers facilitates the formation of heterometallic species, illustrated by  $[\text{Li}(\text{OEt}_2)\text{AlCl}(\text{tripod}^1)]$  (**Fig. 46B**).<sup>861</sup> Reaction of  $[\text{Li}_4(\text{tripod}^1)_2]$  ( $\text{R} = \text{Me}$ ) with  $\text{TlCl}$  led to  $[\text{Tl}_2(\text{tripod}^1)]$  and in the solid state, pairs of molecules associate through a weak  $\text{Tl}\cdots\text{Tl}$  interaction ( $\text{Tl}\cdots\text{Tl} = 3.500(2)$  Å).<sup>860</sup> Thallium(I) derivatives have also been formed directly. For example, the ligands  $\text{tripod}^3$  with  $\text{R} = \text{Me}$  or  $^i\text{Bu}$ ,  $\text{Ar} = 2\text{-}^i\text{PrC}_6\text{H}_4$  react with  $\text{Tl}[\text{BAR}^{\text{F}}_4]$  to give the  $[\text{BAR}^{\text{F}}_4]^-$  salt of  $[\text{Tl}(\text{tripod}^3)]^+$ . There are no short cation $\cdots$ anion contacts in the solid state, and the cation forms dimers with  $\text{Tl}\cdots\text{Tl}$  distances of 3.649(4) Å ( $\text{R} = \text{Me}$ ) and 3.7862(2) Å ( $\text{R} = ^i\text{Bu}$ , **Fig. 46C**).<sup>862</sup>

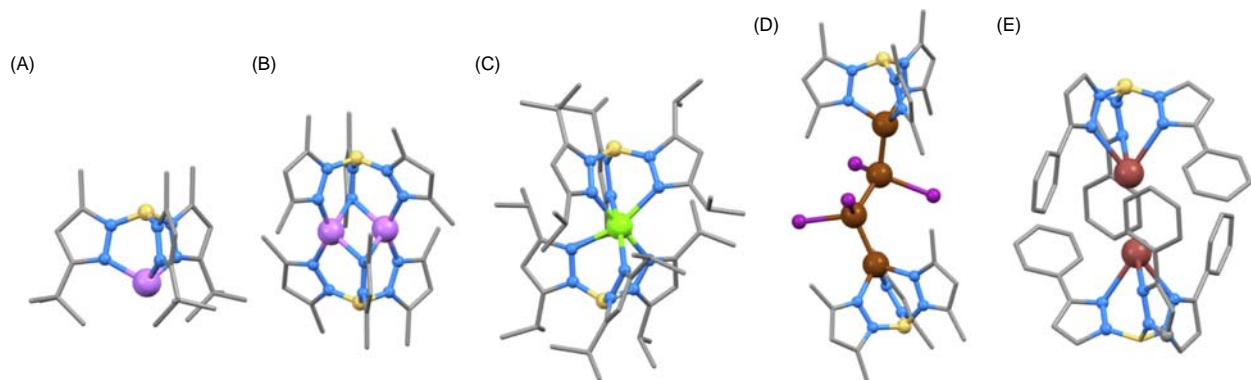
The  $\text{Ge}(\text{II})$  complex  $[\text{Ge}(\text{tripod}^4)]^-$  (**Fig. 46D**) was structurally characterized as the  $[\text{Na}(\text{THF})_5]^+$  salt;  $[\text{Ge}(\text{tripod}^4)]^-$  utilizes its Ge-centered lone pair to act as a ligand to metal centers such as  $\text{Cu}(\text{I})$  and  $\text{Fe}(0)$ .<sup>863</sup> The larger  $\text{Pb}(\text{II})$  can accommodate two  $\text{tripod}^5$  (**Scheme 11**) ligands as shown in **Fig. 46E**, with the metal center in a distorted octahedral environment.<sup>864</sup> Examples from the group 15 metals include  $[\text{Sb}(\text{tripod}^4)]$  with a structure similar to  $[\text{Ge}(\text{tripod}^4)]^-$  (**Fig. 46D**); the compound crystallizes as a benzene solvate and a  $\text{C}_6\text{H}_6$  molecule sits between the  $\text{Sb}$  atoms of two adjacent  $[\text{Sb}(\text{tripod}^4)]$  molecules ( $\text{Sb}\cdots\text{benzene}_{\text{centroid}} =$



**Scheme 11** General types of tripodal ligands. The substituents are specified in the text with reference to these general structures.



**Fig. 46** Structures of (A) [Li<sub>4</sub>(tripod<sup>1</sup>)<sub>2</sub>] with R = <sup>t</sup>Bu (CDS refcode QAQXEL), (B) [Li(OEt<sub>2</sub>)AlCl(tripod<sup>2</sup>)] (refcode RIQGAA), (C) [Ti<sub>2</sub>(tripod<sup>3</sup>)<sub>2</sub>]<sup>2+</sup> (R = <sup>t</sup>Bu, Ar = 2-<sup>i</sup>PrC<sub>6</sub>H<sub>4</sub>; refcode BIKGAF), (D) [Ge(tripod<sup>4</sup>)]<sup>-</sup> (refcode FISGOG), and (E) [Pb(tripod<sup>5</sup>)<sub>2</sub>]<sup>2+</sup> (refcode OTEDOH).



**Fig. 47** Structures of (A) [Li{HB(RR'pz)<sub>3</sub>}] (R = Me, R' = <sup>t</sup>Bu; CSD refcode CEZSOR), (B) [Li<sub>2</sub>{HB(RR'pz)<sub>3</sub>}<sub>2</sub>] (R = R' = Me; refcode IYIQOY), (C) [Mg{HB(RR'pz)<sub>3</sub>}<sub>2</sub>] (R = R' = <sup>i</sup>Pr) (refcode EKOTIK), (D) [HB(RR'pz)<sub>3</sub>]Ga(Gal)<sub>2</sub>Ga[HB(RR'pz)<sub>3</sub>] (R = R' = Me; refcode KAJWID), and (E) the weakly associated dimer [Ti{HB(RR'pz)<sub>3</sub>}<sub>2</sub>] with R = H, R' = Ph (refcode ASADAZ).



3.648 Å). [Sb(tripod<sup>4</sup>)] was used as a building block in conjunction with pyridine-based ligands to produce a number of supramolecular assemblies.<sup>865</sup>

Complexes with tetrahedral Li<sup>+</sup> bound by one tris(pyrazolyl)borate and one other monodentate donor include [Li{HB(RR'pz)<sub>3</sub>}(Hpz-3,5-Me<sub>2</sub>)] (R = R' = Me, see **Scheme 11**),<sup>866</sup> [Li{HB(RR'pz)<sub>3</sub>}(OH<sub>2</sub>)] (R = H or Me, R' = 'Bu),<sup>867</sup> [Li{HB(RR'pz)<sub>3</sub>}(NCMe)] (R = Me, R' = 'Bu),<sup>867</sup> and [Li{HB(RR'pz)<sub>3</sub>}(THF)] (R = H, R' = Me).<sup>868</sup> Less common is 3-coordinate Li<sup>+</sup> as found in [Li{HB(RR'pz)<sub>3</sub>}] (R = Me or H, R' = 'Bu; **Fig. 47A**).<sup>867</sup> A departure from these monomeric assemblies occurs in [Li<sub>2</sub>{HB(RR'pz)<sub>3</sub>}]<sub>2</sub> (R = R' = Me) in which two pz arms of each ligand coordinate to different Li<sup>+</sup> centers, and the third pz unit is in a bridging mode (**Fig. 47B**); each Li<sup>+</sup> maintains a tetrahedral geometry.<sup>869</sup> A further structural variation is achieved by using *B*-fluorenyl substituted tris(pyrazolyl)borates; in [Li(RBpz<sub>3</sub>)<sub>2</sub>] (R = fluorenyl), two pz rings of each ligand coordinate to Li<sup>+</sup> (giving a tetrahedral geometry) leaving a pendant third arm.<sup>870</sup> With bulky substituents in the 3-positions of the pz rings, Na<sup>+</sup> also tends to form 4-coordinate complexes, for example, [Na{HB(RR'pz)<sub>3</sub>}L] (R = Ph; R' = CF<sub>3</sub>; L = H<sub>2</sub>O, THF),<sup>871</sup> [Na{HB(RR'pz)<sub>3</sub>}(OEt<sub>2</sub>)] (R = R' = CF<sub>3</sub>),<sup>871</sup> and [Na{HB(RR'pz)<sub>3</sub>}(THF)] (R = Me, R' = <sup>n</sup>C<sub>3</sub>F<sub>7</sub>),<sup>872</sup> although CN = 5 with a square-based pyramidal arrangement of donors is found in [Na<sub>2</sub>{HB(RR'pz)<sub>3</sub>}]<sub>2</sub>(μ-OH<sub>2</sub>)<sub>2</sub> (R = Me; R' = CF<sub>3</sub>).<sup>871</sup> Two tris(pyrazolyl)borate ligands can be accommodated if the pyrazole 3-substituents are not sterically demanding, e.g., in [Na{HB(RR'pz)<sub>3</sub>}]<sub>2</sub><sup>-</sup> (R = R' = Me).<sup>873</sup> Octahedral Na<sup>+</sup> is also observed in [Na<sub>2</sub>{HB(RR'pz)<sub>3</sub>}]<sub>2</sub>(μ-OCMe<sub>2</sub>)<sub>3</sub> (R = R' = Me) with bridging acetone ligands,<sup>874</sup> and a similar structural motif is found in [K<sub>2</sub>{HB(RR'pz)<sub>3</sub>}]<sub>2</sub>(μ-OH<sub>2</sub>)<sub>3</sub> (R = R' = Me, X = Cl; see **Scheme 11**).<sup>875</sup> We noted above the monomeric structure of [Na{HB(RR'pz)<sub>3</sub>}(THF)] (R = Me, R' = <sup>n</sup>C<sub>3</sub>F<sub>7</sub>). In contrast, in [Cs{HB(RR'pz)<sub>3</sub>}]<sub>n</sub> (R = Me, R' = <sup>n</sup>C<sub>3</sub>F<sub>7</sub>), the perfluoropropyl substituents engage in Cs⋯F contacts (range 3.10–3.72 Å) producing a 1D-chain in the solid state; this was the first structurally characterized tris(pyrazolyl)borate of cesium.<sup>872</sup> The single crystal structure of [K{HB(RR'pz)<sub>3</sub>}(NCMe)<sub>3</sub>] (R = H, R' = Ph) reveals an apparent vacancy in the coordination sphere of K<sup>+</sup> and inspection of the structural data (CSD refcode USUSIN) shows that molecules are aligned into chains with K⋯HB separations of 3.47 Å.<sup>859</sup>

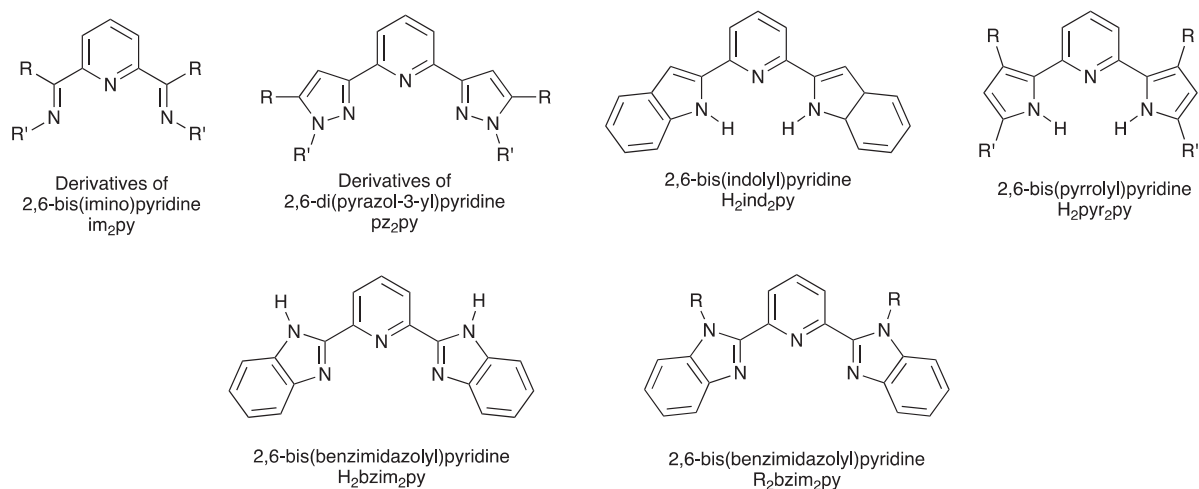
Moving to group 2, beryllium complexes of tris(pyrazolyl)borates are exemplified by tetrahedral [BeX(HBpz<sub>3</sub>)] (X = F, Cl, Br, I),<sup>876</sup> and [Be(THF)(HBpz<sub>3</sub>)].<sup>877</sup> The Mg<sup>2+</sup> ion is large enough to accommodate two tris(pyrazolyl)borate ligands (**Scheme 11**), as exemplified in [Mg(HBpz<sub>3</sub>)<sub>2</sub>],<sup>878–880</sup> [Mg{(4-Br-C<sub>6</sub>H<sub>4</sub>)Bpz<sub>3</sub>}]<sub>2</sub>,<sup>881</sup> [Mg{HB(RR'pz)<sub>3</sub>}]<sub>2</sub> (R = R' = Me),<sup>880</sup> [Mg{HB(RR'pz)<sub>3</sub>}]<sub>2</sub> (R = R' = Me, X = Cl; see **Scheme 11**),<sup>880</sup> and [Mg{HB(RR'pz)<sub>3</sub>}]<sub>2</sub> (R = R' = 'Pr) (**Fig. 47C**).<sup>882</sup> However, incorporating sterically demanding substituents adjacent to the metal-binding site typically prevents the coordination of two tripodal ligands to Mg<sup>2+</sup>, for example, in [MgX{HB(RR'pz)<sub>3</sub>}] (R = Me, R' = 'Bu; X = F, Cl, Br, I).<sup>883</sup> The Ca, Sr and Ba analogs of [Mg{HB(RR'pz)<sub>3</sub>}]<sub>2</sub> (R = R' = 'Pr) (**Fig. 47C**) have also been structurally characterized,<sup>882</sup> as have [Sr(HBpz<sub>3</sub>)<sub>2</sub>] and [M{HB(RR'pz)<sub>3</sub>}]<sub>2</sub> (M = Ca, Sr, Ba; R = R' = Et).<sup>884</sup> Complexation of [HBpz<sub>3</sub>]<sup>-</sup> with Ba<sup>2+</sup> leads to the unusual dimer [Ba<sub>2</sub>(HBpz<sub>3</sub>)<sub>4</sub>] in which two ligands bind in the typical *fac*-mode and two are bridging with a combination of σ- and η<sup>5</sup>-pz-Ba interactions.<sup>884</sup> In [Ca{HB(RR'pz)<sub>3</sub>}]<sub>2</sub> (R = Me, R' = 'Bu), the steric bulk of the 'Bu groups results in a 5-coordinate Ca<sup>2+</sup> with one ligand arm non-coordinated<sup>885</sup>; the same coordination behavior is seen in [Ca{HB(RR'pz)<sub>3</sub>}]<sub>2</sub> (R = H, R' = 'Bu).<sup>886</sup> Interestingly, in [Ca{HB(RR'pz)<sub>3</sub>}]<sub>2</sub> (R = Me, R' = Ph), the spatially demanding phenyl rings engage in inter-ligand face-to face π-interactions and octahedral coordination is retained.<sup>887</sup> Both [Ca{HB(RR'pz)<sub>3</sub>}]<sub>2</sub>(N(SiMe<sub>3</sub>)<sub>2</sub>) (R = H, R' = 'Bu),<sup>888</sup> and [Ca{HB(RR'pz)<sub>3</sub>}(ODipp)] (R = H, R' = 'Bu) contain tetrahedral Ca<sup>2+</sup>.<sup>889</sup> One interest in such species is their activity in lactide ring-opening polymerization.<sup>889</sup> Thermolysis of [Ca(H<sub>2</sub>Bpz<sub>2</sub>)<sub>2</sub>(THF)<sub>2</sub>] leads to the formation of [Ca(HBpz<sub>3</sub>)<sub>2</sub>] and [Ca(HBpz<sub>3</sub>)(BH<sub>4</sub>)]; the latter reacts with THF to give *fac*-[Ca(HBpz<sub>3</sub>)(THF)<sub>2</sub>(BH<sub>4</sub>)] and a tetranuclear [Ca<sub>4</sub>(HBpz<sub>3</sub>)<sub>4</sub>(THF)<sub>4</sub>(μ-BH<sub>4</sub>)<sub>4</sub>] with the Ca centers forming a rhomboid.<sup>890</sup>

Among the many contributions from Parkin and coworkers to the field of tris(pyrazolyl)borate coordination chemistry is a series of compounds containing Ga–Ga bonds. These include [Ga<sub>2</sub>{HB(RR'pz)<sub>3</sub>}]<sub>2</sub> (R = R' = Me), [{HB(RR'pz)<sub>3</sub>}Ga–GaX<sub>3</sub>] (X = Cl, I; R = R' = Me) and [{HB(RR'pz)<sub>3</sub>}Ga(GaI<sub>2</sub>)<sub>2</sub>Ga{HB(RR'pz)<sub>3</sub>}] (R = R' = Me; **Fig. 47D**); the octahedral [Ga{HB(RR'pz)<sub>3</sub>}]<sub>2</sub><sup>+</sup> (R = R' = Me) has also been structurally characterized.<sup>891</sup> In the Ga(III) complex [GaH{HB(RR'pz)<sub>3</sub>}]<sub>2</sub><sup>+</sup> (R = Me, R' = 'Bu), the hydrido ligand is protected within a sheath of 'Bu substituents.<sup>892</sup> Monomeric In(I) complexes are exemplified by [In{HB(RR'pz)<sub>3</sub>}] (R = R' = Me; R = Me, R' = 'Bu).<sup>892</sup> The coordination chemistry of tris(pyrazolyl)borate thallium(I) species is an extensive area which was reviewed by Janiak in 1997,<sup>893</sup> and is included in a 2015 review by Reglinski and Spicer.<sup>75</sup> The following examples are necessarily selective. Thallium(I) complexes of [HB(RR'pz)<sub>3</sub>]<sup>-</sup> with R = H, R' = Ph and [HB(RR'pz)<sub>2</sub>(R''R''pz)]<sup>-</sup> (see **Scheme 11**) with R = R'' = R''' = Me, R' = Ph, possess dimeric structures in the solid state. The former dimer (**Fig. 47E**) is supported by a weak Tl⋯Tl interaction (3.853(1) Å), and in both complexes weak CH⋯π contacts are important packing interactions. This investigation also includes a comparison of previously reported tris(pyrazolyl)borate complexes of thallium(I), giving a useful entry into this area.<sup>894</sup> The incorporation of bulky substituents in the pyrazole 3-position prevents the formation of Tl⋯Tl close contacts in the solid state, e.g., in [Tl{HB(RR'pz)<sub>3</sub>}] (R = Me, R' = Bz),<sup>895</sup> [Tl{HB(RR'pz)<sub>3</sub>}] (R = 'Bu, R' = 4-MeC<sub>6</sub>H<sub>4</sub>),<sup>896</sup> [Tl{HB(RR'pz)<sub>3</sub>}] (R = H, R' = CHPh<sub>2</sub>),<sup>897</sup> [Tl{HB(RR'pz)<sub>3</sub>}] (R = H, R' = Mes),<sup>898</sup> and [Tl{HB(RR'pz)<sub>3</sub>}] (R = 'Pr, R' = adamantan-1-yl).<sup>899</sup>

Group 14 metal(IV) complexes are represented by [Ge{HB(RR'pz)<sub>3</sub>}(N<sub>3</sub>)<sub>3</sub>] (R = R' = Me) (which was prepared by oxidation of [Ge{HB(RR'pz)<sub>3</sub>}(N<sub>3</sub>)] using HN<sub>3</sub>),<sup>900</sup> and octahedral [SnCl<sub>3</sub>{HB(RR'pz)<sub>3</sub>}] (R = R' = Me).<sup>901</sup> The use of sterically non-demanding ligands proved critical in the formation of lead(II) compounds, exemplified by the dimer [Pb<sub>2</sub>{HB(RR'pz)<sub>3</sub>}]<sub>2</sub>(μ-NCS)<sub>2</sub>] (R = R' = Me) and the 2D-coordination network [Pb(HBpz<sub>3</sub>)<sub>2</sub>(μ-NCS)]<sub>n</sub>.<sup>902</sup>

A combination of the size of Bi(III) and lack of steric hindrance in the unsubstituted [HBpz<sub>3</sub>]<sup>-</sup> allows the formation of the 8-coordinate [BiCl(HBpz<sub>3</sub>)<sub>2</sub>(pz)]. This was the first example of a pyrazolylborate complex of a group 15 metal.<sup>903</sup> In [BiCl<sub>2</sub>{HB(RR'pz)<sub>3</sub>}] (R = R' = Me), the Bi(III) center is in square-based pyramidal environment with dimer assembly by virtue





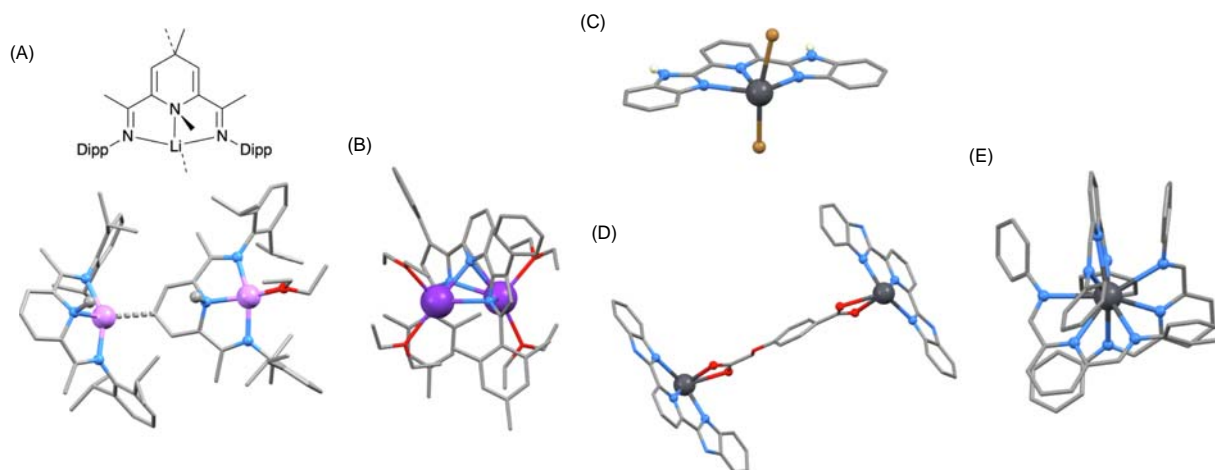
**Scheme 12** General structures of representative pincer-type ligands with three N-donors.

of long Bi...Cl interactions (3.234(3) Å); the highly electrophilic  $[\text{Bi}\{\text{HB}(\text{RR}'\text{pz})_3\}]^{2+}$  cation is an active catalyst for alkene hydro-silylation.<sup>904</sup> Tris(pyrazolyl)borates are tridentate  $\sigma$ -donor ligands, and have been used to investigate the *trans*-influence in Bi(III) compounds in the presence of other ligands with different nucleophilicities. Among the series of complexes studied are  $[\text{Bi}\{\text{HB}(\text{RR}'\text{pz})_3\}_2]$  ( $\text{R} = \text{R}' = \text{Me}$ ),  $[\text{BiCl}_3\{\text{HB}(\text{RR}'\text{pz})\}]$  ( $\text{R} = \text{R}' = \text{Me}$ ), and  $[\text{Bi}_2\text{Cl}_2\{\text{HB}(\text{RR}'\text{pz})\}_2(\mu\text{-O}_3\text{SCF}_3\text{-}1\kappa\text{O}^1\text{:}2\kappa\text{O}^2)]$  ( $\text{R} = \text{R}' = \text{Me}$ ).<sup>905</sup>

### 1.02.2.3.3 Pincer ligands

Typical pincer ligand families are shown in **Scheme 12**. However, it should be noted that the ligands are redox active allowing access to a multiplicity of oxidation- and charge-states. The examples in this section are necessarily selective and aim to provide an entry into the relevant literature.

The reaction of MeLi with  $\text{im}_2\text{py}$  ( $\text{R} = \text{Me}$ ,  $\text{R}' = \text{Dipp}$ ) unexpectedly resulted in methylation of the pyridine N atom to give 'Li  $\{\text{im}_2(\text{C}_5\text{H}_3\text{NMe})\}'$ ; the structure of the crystallized product reveals two different units, one with Li-bound THF and one with a Li...C contact as shown in **Fig. 48A**. The methylation is reversible upon heating, and characterization of  $[\text{Li}(\text{im}_2\text{py})(\text{THF})]$  confirmed  $\text{Li}^+$  in a distorted square-planar environment.<sup>906</sup> In  $[\text{K}_2(\text{OEt}_2)_4(\text{pyr}_2\text{py})]$  ( $\text{R} = \text{Ph}$ ,  $\text{R}' = \text{Mes}$ , see **Scheme 12**), two  $\{\text{K}(\text{OEt}_2)_2\}$  units are bridged by an  $[\text{pyr}_2\text{py}]^{2-}$  ligand as shown in **Fig. 48B**.<sup>907</sup> Jones and coworkers have reported a series of group 2 metal complexes of  $\text{im}_2\text{py}$  with  $\text{R} = \text{Ph}$ ,  $\text{R}' = \text{Dipp}$  (see **Scheme 12**) in which the  $\text{im}_2\text{py}$  ligand is neutral, singly or doubly reduced. These complexes include  $[\text{MgI}_2(\text{im}_2\text{py})]$ ,  $[\text{CaI}_2(\text{im}_2\text{py})]$  and  $[\text{MgI}(\text{im}_2\text{py})]$  (with a radical anion ligand and approximately square-planar  $\text{Mg}^{2+}$ ).<sup>908</sup> Marks and coworkers have reported  $[\text{MgCl}_2(\text{im}_2\text{py})]$  ( $\text{R} = \text{Me}$ ,  $\text{R}' = \text{ferrocenyl}$ ) along with analogous d-block



**Fig. 48** Structures of (A)  $[\text{Li}_2\{\text{im}_2(\text{C}_5\text{H}_3\text{NMe})\}_2(\text{THF})]$  (CSD refcode CALSOY) with a schematic of 'Li  $\{\text{im}_2(\text{C}_5\text{H}_3\text{NMe})\}'$ , (B)  $[\text{K}_2(\text{OEt}_2)_4(\text{pyr}_2\text{py})]$  (refcode GOYNOA), (C)  $[\text{PbBr}_2(\text{H}_2\text{Bzim}_2\text{py})]$  (only the NH H atoms are shown; refcode CAFQEI), (D)  $[\text{Pb}_2(\text{HBzim}_2\text{py})_2(\mu\text{-boa})]$  (refcode EHEYOG), and (E)  $[\text{Pb}(\text{im}_2\text{py})_3]$  ( $\text{R} = \text{H}$ ,  $\text{R}' = \text{Ph}$ ; refcode HOXQER).

metal compounds; combined experimental and computational data indicate that coordination of the im<sub>2</sub>py ligand results in mixing of the ferrocenyl d-orbitals with the π\* orbitals of the im<sub>2</sub>py unit.<sup>909</sup>

Trigonal bipyramidal group 13 metal M(III) complexes containing pincer ligands of the general type [MX<sub>2</sub>(pincer)] with X<sup>-</sup> ligand in equatorial sites are exemplified by [MCl<sub>2</sub>(im<sub>2</sub>py)] (M = Al, Ga; R = Ph, Me, R' = Dipp),<sup>910,911</sup> and [GaCl<sub>2</sub>(R<sub>2</sub>bzim<sub>2</sub>py)] (R = Bz, CH<sub>2</sub>CH=CH<sub>2</sub>).<sup>911</sup> In the blue-emitting complex [InCl<sub>2</sub>(OH<sub>2</sub>)(Hbzim<sub>2</sub>py)],<sup>912</sup> and [InCl(O<sub>3</sub>SCF<sub>3</sub>)<sub>2</sub>(im<sub>2</sub>py)] (R = Ph, R' = 2,6-Me<sub>2</sub>C<sub>6</sub>H<sub>3</sub>),<sup>913</sup> the In(III) center is octahedrally sited. Berden and coworkers have reported bis(imino)pyridine ligand-based mixed valent (MV) complexes of Al(III) which feature electron donating and electron withdrawing substituents on the ligands, allowing access to species with [Al(L<sup>-</sup>)(L<sup>2-</sup>)] and [Al(L<sup>2-</sup>)(L<sup>3-</sup>)] charge states,<sup>914</sup> and related water-stable MV compounds have been prepared by reactions of reduced bis(imino)pyridine ligands with Al(III), Ga(III) and In(III) salts.<sup>915</sup> Related to this is a reaction of [(pz<sub>2</sub>py)AlCl<sub>2</sub>(THF)]<sup>+</sup> (R = CH<sub>2</sub><sup>i</sup>Pr, R' = <sup>i</sup>Pr, see **Scheme 12**) involving 2-electron reduction and single-ligand protonation to give [(pz<sub>2</sub>py)AlCl<sub>2</sub>]; each electron- and H<sup>+</sup>-transfer process is ligand-centered.<sup>916</sup> An attempt to form Ga(I) coordination compounds using the sterically demanding bis(imino)pyridine ligands im<sub>2</sub>py (R = Ph, R' = Dipp or 2,5-<sup>t</sup>Bu<sub>2</sub>C<sub>6</sub>H<sub>3</sub>) resulted instead in the Ga(III) complexes [Ga<sub>2</sub>(im<sub>2</sub>py)][Ga<sub>4</sub>]; the neutral radical [Ga<sub>2</sub>(im<sub>2</sub>py)] was also isolated.<sup>917</sup>

For group 14 M(II), the familiar (see earlier discussions) geometry with a stereochemically active lone pair is illustrated for pincer-type ligands by [GeCl(im<sub>2</sub>py)]<sup>+</sup> (R = Me, R' = Dipp),<sup>918,919</sup> [MCl(im<sub>2</sub>py)]<sup>+</sup> (M = Ge, Sn; R = H, R' = ferrocenyl),<sup>920</sup> [SnCl(im<sub>2</sub>py)]<sup>+</sup> (R = Me, R' = Dipp),<sup>921,922</sup> [SnBr(im<sub>2</sub>py)]<sup>+</sup> (R = H, R' = Dipp),<sup>923</sup> [SnX(im<sub>2</sub>py)]<sup>+</sup> (X = Cl, Br; R = Ph, R' = 2,5-<sup>t</sup>Bu<sub>2</sub>C<sub>6</sub>H<sub>3</sub>),<sup>924</sup> and [Pb(NCS)(im<sub>2</sub>py)]<sup>+</sup> (R = Me, R' = 2,6-Me<sub>2</sub>C<sub>6</sub>H<sub>3</sub>).<sup>902</sup> The reduction of [GeCl(im<sub>2</sub>py)]<sup>+</sup> (R = Me, R' = Dipp) with KC<sub>8</sub> yielded the 3-coordinate Ge(0) derivative [GeCl(im<sub>2</sub>py)] which possesses a singlet ground state and partial Ge–N multiple-bond character.<sup>918</sup> In the triflate salt of [SnCl(im<sub>2</sub>py)]<sup>+</sup>, there is ion pairing in the solid state with an Sn<sub>cat</sub>–O<sub>triflate</sub> separation of 3.042(2) Å, and in [Sn(O<sub>3</sub>SCF<sub>3</sub>)<sub>2</sub>(im<sub>2</sub>py)], both triflate ions coordinate to the Sn(II) center.<sup>921</sup> In a detailed study of Ge(II) and Sn(II) complexes, Flock et al. observed that the triflate salt of [Sn(im<sub>2</sub>py)]<sup>2+</sup> (R = H, R' = Dipp) crystallizes with two independent, neutral molecules in the asymmetric unit; one has CN = 5 (as just described), and the second is 6-coordinate with an additional THF ligand.<sup>923</sup> The same coordination geometry as in [Sn(O<sub>3</sub>SCF<sub>3</sub>)<sub>2</sub>(im<sub>2</sub>py)] is observed in [PbBr<sub>2</sub>(H<sub>2</sub>Bzim<sub>2</sub>py)] (**Fig. 48C**, see **Scheme 12** for the ligand); the latter is one of a series of H<sub>2</sub>Bzim<sub>2</sub>py derivatives of Pb(II) reported by Thompson et al. which has included a correlation of structural parameters with the <sup>207</sup>Pb NMR chemical shift span parameter, Ω.<sup>353</sup> A similar coordination environment is found in [Pb<sub>2</sub>(ONO<sub>2</sub>)<sub>2</sub>(H<sub>2</sub>Bzim<sub>2</sub>py)<sub>2</sub>(μ-adip)], although each CO<sub>2</sub><sup>-</sup> unit of the bridging ligand is bidentate, giving a CN of 7 for each Pb(II).<sup>925</sup> In contrast, in [Pb<sub>2</sub>(HBzim<sub>2</sub>py)<sub>2</sub>(μ-boa)] (**Fig. 48D**) which contains monodeprotonated [HBzim<sub>2</sub>py]<sup>-</sup> ligands, the outer axial site of each Pb(II) center is occupied by a stereochemically active lone pair.<sup>926</sup> Reactions of lead(II) triflate with im<sub>2</sub>py (R = H, R' = Ph) in MeCN solution produced [Pb(im<sub>2</sub>py)<sub>x</sub>] (x = 1–3) while crystal growth by layering produced only [Pb(im<sub>2</sub>py)<sub>3</sub>] with 9-coordinate Pb(II) (**Fig. 48E**); the ligands are arranged so that there is efficient inter-ligand π-stacking of phenyl substituents. Interestingly, when im<sub>2</sub>py (R = H, R' = Ph) was replaced by im<sub>2</sub>py (R = H, R' = 4-HOC<sub>6</sub>H<sub>4</sub>), only single crystals of [Pb(O<sub>3</sub>SCF<sub>3</sub>)<sub>2</sub>(im<sub>2</sub>py)] were obtained.<sup>927</sup>

Group 15 metal(III) complexes with pincer ligands are represented by [BiI(pyr<sub>2</sub>py)] (R = R' = <sup>t</sup>Bu, or R = Ph, R' = Mes) and [SbI(pyr<sub>2</sub>py)] (R = Ph, R' = Mes) in which the 3-coordinate M(III) is protected by sterically hindered substituents <sup>t</sup>Bu or Mes; Turner has reported a detailed study of the reduction of these species with strong metal reductants.<sup>907</sup> Low oxidation compounds include the 3-coordinate As(I) complex [As(im<sub>2</sub>py)]<sup>+</sup> (R = Me, R' = Dipp).<sup>928</sup> The first diiminopyridine complexes of S, Se and Te have been reported; the triflate salts of [Se(im<sub>2</sub>py)]<sup>2+</sup> and [Te(im<sub>2</sub>py)]<sup>2+</sup> (R = H, R' = Dipp) are air-stable, and notably, the analogous sulfur complex was also isolated.<sup>929</sup> Reactions of group 16 element halides with im<sub>2</sub>py (R = H, R' = Dipp) have also been reported, and include the structures of salts of the square-planar [SeX(im<sub>2</sub>py)]<sup>+</sup> (X = Cl, Br) cations.

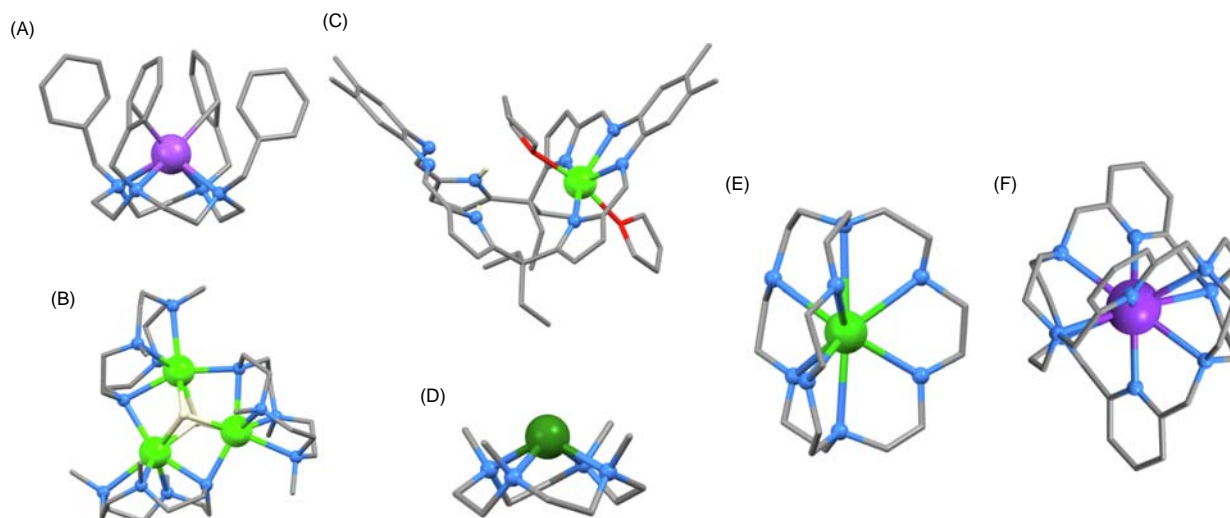
### 1.02.2.3.4 2,2':6',2''-Terpyridines

For a coverage of the coordination chemistry of main group metal complexes containing 2,2':6',2''-terpyridine (tpy) ligands, we direct the reader to our recent review of the field.<sup>837</sup>

### 1.02.2.4 Polydentate open-chain, macrocyclic and cage ligands

Main group metal complexes of polydentate open-chain, macrocyclic and cryptand N-donor ligands are plentiful, and for the open-chain ligands, we have restricted the overview to compounds that can be regarded as representative 'parent' ligands. **Scheme 13** shows ligand types that are included. The macrocyclic tetraamine tacn (**Scheme 13**) is the building block for a wide range of mixed donor polydentate ligands including DOTA (1,4,7,10-tetraazacyclododecane-1,4,7,10-tetraacetic acid) and related ligands, metal complexes of which have significant applications in, for example, biomedical imaging.<sup>41,930,931</sup> Porphyrinato and phthalocyanato main group metal complexes have been adequately reviewed elsewhere.<sup>53,932–938</sup>

Use of the tetradentate ligand Me<sub>6</sub>trien (**Scheme 13**) directs a *cis* configuration in [Ca(Me<sub>6</sub>trien)(PPh<sub>2</sub>)<sub>2</sub>]; this is very air and moisture sensitive, and as a result, *cis*-[Ca(Me<sub>6</sub>trien)(PPh<sub>2</sub>)(OPPh<sub>2</sub>)] was also isolated.<sup>939</sup> In [Sr(tetraen)(<sup>t</sup>Bu<sub>2</sub>acac)<sub>2</sub>], the Sr<sup>2+</sup> ion has CN = 9; this is one of a series of Sr(II) related complexes containing both polyamine and β-diketonate ligands.<sup>940</sup> Examples of group 13 M(III) complexes include the 6-coordinate [In<sub>2</sub>(trien)<sub>2</sub>(μ-Se)<sub>2</sub>]<sup>2+</sup>,<sup>624</sup> [In<sub>2</sub>(trien)<sub>2</sub>(μ-Te)<sub>2</sub>]<sup>2+</sup>,<sup>625</sup> and *cis*-[Tl(trien)(CN)<sub>2</sub>]<sup>+</sup>.<sup>629</sup> In [Pb(tetraen)][Ag<sub>2</sub>L<sub>4</sub>]<sub>n</sub>, the Pb<sup>2+</sup> center is bound by the pentadentate tetraen ligand (**Scheme 13**) and has three Pb⋯I cation⋯anion contacts giving an overall CN of 8.<sup>627</sup>



**Fig. 49** Structures of (A)  $[\text{Na}(\text{R}_4\text{tacd})]^+$  ( $\text{R} = \text{Bz}$ ; CSD refcode JOTRAO), (B)  $[\text{Ca}_3(\text{Me}_3\text{tacd-H})_2(\mu_3\text{-H})_2]^+$  (refcode FAXCOY), (C)  $[\text{Ca}(\text{THF})_2(\text{H}_2\text{L}_{\text{compart}})]^+$  (refcode KAFHAD, only the pyrrole H atoms are shown), (D)  $[\text{Ge}(\text{Me}_4\text{tacd})]^{2+}$  (only the hydrido H atoms are shown; refcode DUSKEJ), (E)  $[\text{Ba}(\text{H}_5\text{aza}(2.2.2)\text{crypt})]^+$  (refcode HAGNOT), and (F)  $[\text{K}(\text{N}_9\text{-azacrypt})]^+$  (refcode HIFCIL).

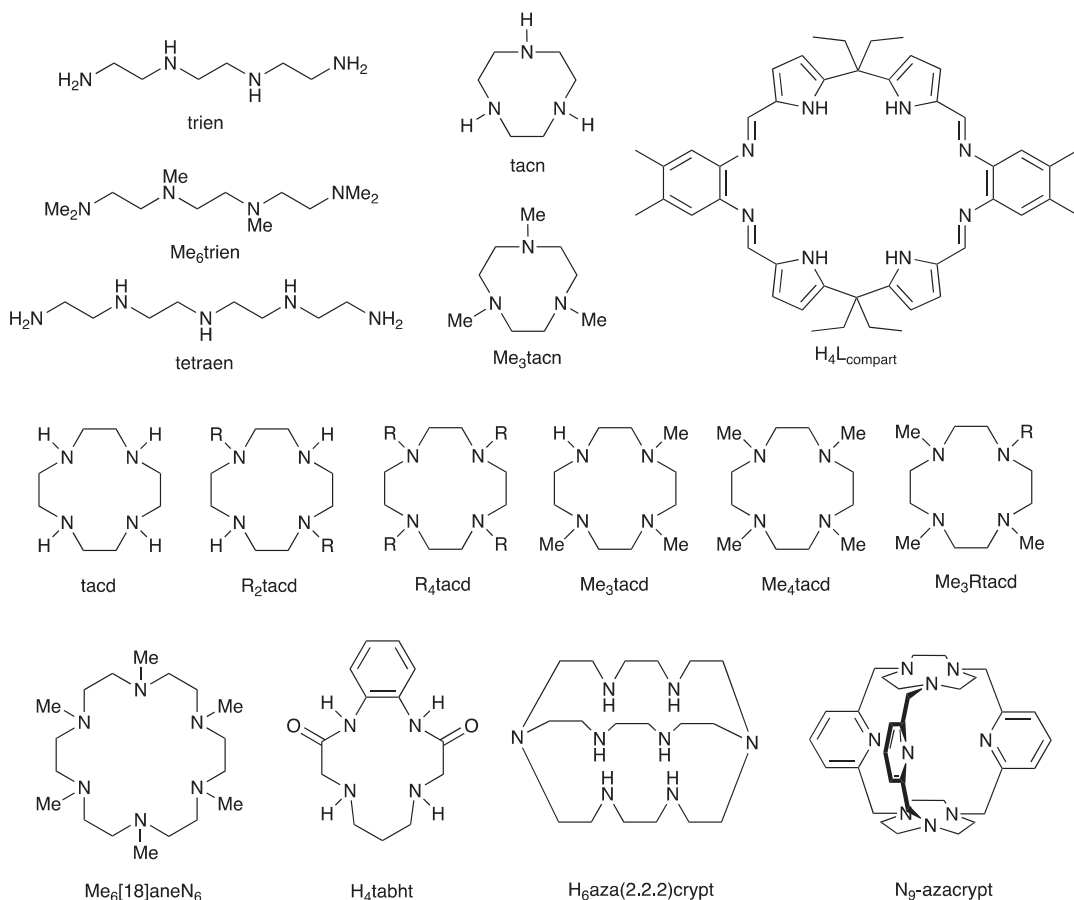
Moving on to the macrocyclic ligands shown in **Scheme 13**, and group 1 metal complexes are exemplified by  $[\text{Li}(\text{THF})(\text{Me}_4\text{tacd})]$  with 5-coordinate  $\text{Li}^+$ ,<sup>941</sup>  $[\text{M}(\text{THF})_n(\text{Me}_3\text{Rtacd})]$  ( $\text{M} = \text{Li}, \text{Na}, n = 1$ ;  $\text{M} = \text{K}, n = 2$ ) containing the hypervalent  $\text{R} = \text{SiH}_2\text{Ph}_2$  group,<sup>942</sup> the peroxolato complexes  $[\text{Li}(\text{O}_2\text{CMe}_2\text{Ph})(\text{Me}_4\text{tacd})]$ ,  $[\text{K}(\text{O}_2\text{CMe}_2\text{Ph})(\text{PhCMe}_2\text{OOH})_2(\text{Me}_4\text{tacd})]$  and  $[\text{K}(\text{O}_2\text{CMe}_2\text{Ph})(\text{PhCMe}_2\text{OOH})_3(\text{Me}_4\text{tacd})]$  (which are stabilized in the solid state by strong hydrogen bonds from  $\text{PhCMe}_2\text{OOH}$  solvate molecules),<sup>943</sup> and the square-based pyramidal  $[\text{Na}(\text{Me}_3\text{tacd})]$ .<sup>944</sup> The trisodium complex  $[\text{Na}_3(\text{Me}_3\text{tacd-H})_3]$  is structurally related to  $[\text{Ca}_3(\text{Me}_3\text{tacd-H})_3(\mu_3\text{-H})_2]^+$  described below.<sup>942</sup> In  $[\text{Na}(\text{R}_4\text{tacd})]^+$  with  $\text{R} = \text{Bz}$ , the benzyl substituents provide a caged environment for the  $\text{Na}^+$  ion with  $\text{Na}^+ \cdots \pi$  contacts (**Fig. 49A**).<sup>945</sup> While the  $[\text{K}(18\text{-crown-6})]^+$  cation is ubiquitous, analogous N-donor ligands (i.e., O atoms in 18-crown-6 replaced by NH or NR) have been much less studied. In 2015, Reid and coworkers reported the preparation and structures of  $[\text{K}\{\text{Me}_6[18]\text{aneN}_6\}]^+$  as well as the  $\text{Li}^+$ ,  $\text{Na}^+$ ,  $\text{Rb}^+$  and  $\text{Cs}^+$  congeners. In  $[\text{K}\{\text{Me}_6[18]\text{aneN}_6\}]^+$ , the  $\text{K}^+$  ion sits within the plane of the six N-donors, while in  $[\text{Rb}\{\text{Me}_6[18]\text{aneN}_6\}]^+$ , the  $\text{Rb}^+$  ion is displaced from the plane; the macrocycle adopts a puckered conformation in  $[\text{Li}\{\text{Me}_6[18]\text{aneN}_6\}]^+$  with  $\text{Li}^+$  in a distorted octahedral environment. This investigation also includes the structures of  $[\text{Na}(\text{THF})(\text{Me}_4\text{tacd})]^+$  (square-based pyramidal  $\text{Na}^+$ ) and  $[\text{K}(\text{Me}_3\text{tacd})_2]^+$  ( $\text{K}^+$  octahedrally sited).<sup>946</sup>

Group 2 metal complexes include the square-based pyramidal  $[\text{Mg}(\text{BH}_4)(\text{Me}_4\text{tacd})]^+$ ,<sup>947</sup>  $[\text{MgCl}(\text{Me}_4\text{tacd})]^+$  (formed by treating  $[\text{Mg}_2(\text{Me}_4\text{tacd})_2(\mu\text{-H})_2]^{2+}$  with  $[\text{NEt}_3\text{H}]\text{Cl}$ ),<sup>948</sup>  $[\text{M}\{\text{N}(\text{SiMe}_3)_2\}(\text{Me}_3\text{tacd-H})]$  ( $\text{M} = \text{Mg}, \text{Ca}$ ),<sup>949</sup>  $[\text{Mg}(\text{pyridin-1}(4\text{H})\text{-yl})(\text{Me}_3\text{tacd})]$ ,<sup>518</sup> and the 7-coordinate  $[\text{Ca}(\text{THF})_2\text{I}(\text{Me}_4\text{tacd})]^+$ .<sup>950</sup> Reaction of  $\text{Me}_3\text{tacd}$  (**Scheme 13**) with  $[\text{Ca}\{\text{N}(\text{SiMe}_3)_2\}_2(\text{THF})_2]$  followed by treatment with  $\text{Ph}_2\text{SiH}_2$  resulted in the formation of  $[\text{Ca}_3(\text{Me}_3\text{tacd-H})_3(\mu_3\text{-H})_2]^+$  (**Fig. 49B**) in which  $[\text{Me}_3\text{tacd-H}]^-$  is the conjugate base of  $\text{Me}_3\text{tacd}$ ; this was the first example of a cationic calcium hydride and was found to be active in the catalytic hydrosilylation and hydrogenation of 1,1-diphenylethene.<sup>951</sup> Related complexes are  $[\text{Sr}_3(\text{Me}_3\text{tacd-H})_3(\mu_3\text{-H})_2]^+$ ,<sup>952</sup>  $[\text{Ca}_2(\text{Me}_4\text{tacd})_2(\mu\text{-H})_3]^+$ ,<sup>953</sup> and  $[\text{Ca}_2(\text{THF})(\text{Me}_4\text{tacd})_2(\mu\text{-H})_2]^{2+}$ .<sup>950,954</sup> The hydrido ligands in  $[\text{Ca}_2(\text{THF})(\text{Me}_4\text{tacd})_2(\mu\text{-H})_2]^{2+}$  exhibit nucleophilic behavior and the complex is a precursor to a series of dicalcium derivatives retaining  $\{\text{Ca}(\text{Me}_4\text{tacd})\}$  units.<sup>950</sup> Mukherjee et al. have reported a series of  $\text{Mg}^{2+}$ ,  $\text{Ca}^{2+}$ , and  $\text{Sr}^{2+}$  silylamide complexes assembled upon an  $\text{Me}_3\text{tacd}$  framework.<sup>955</sup> The Schiff base compartmental ligand  $\text{H}_4\text{L}_{\text{compart}}$  shown in **Scheme 13** accommodates one or two  $\text{Ca}^{2+}$  ions in  $\text{N}_4$ -donor sites in the complexes  $[\text{Ca}(\text{THF})_2(\text{H}_2\text{L}_{\text{compart}})]^+$  (**Fig. 49C**) and  $[\text{Ca}_2(\text{THF})_2(\mu\text{-THF})(\text{L}_{\text{compart}})]$ , as well as one  $\text{Ca}^{2+}$  and one  $\text{Li}^+$  in  $[\text{LiCa}(\text{THF})(\mu\text{-THF})(\text{HL}_{\text{compart}})]$ ; the bowl-shaped conformation of the ligand is noteworthy.<sup>956</sup>

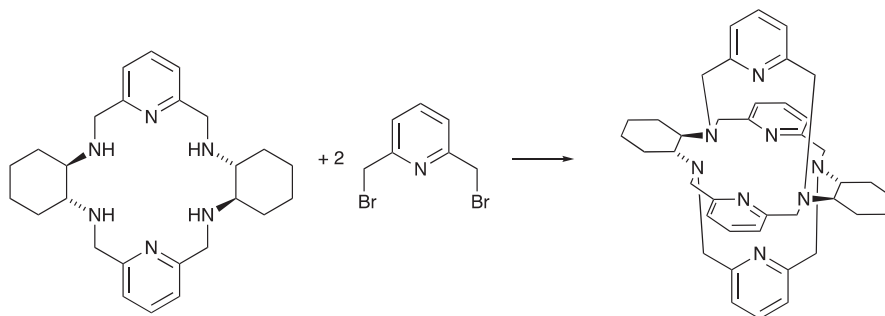
Group 13 metal *tacd* derivatives include the octahedral  $[\text{GaCl}_2(\text{tacd})]^+$  in which the *tacd* ligand directs a *cis* configuration.<sup>957</sup> The reaction of  $[\text{AlH}_2(\text{Me}_3\text{tacd-H})]$  with  $\text{BPh}_3$  in THF gave  $[\text{Al}(\text{O}^t\text{Bu})(\text{Me}_3\text{tacd-H})][\text{HBPh}_3]$  by ring-opening of THF.<sup>958</sup> In  $[\text{GaCl}(\text{H}_2\text{-tabht})]$  (see **Scheme 13** for  $\text{H}_4\text{tabht}$ ), the Ga(III) center is in a square-based pyramidal environment.<sup>959</sup>

Everett et al. have explored reactions of  $[\text{GeCl}_2(\text{diox})]$  with neutral azamacrocyclic ligands, and  $[\text{Ge}(\text{Me}_4\text{tacd})]^{2+}$  is representative of the structurally characterized products; **Fig. 49D** shows that the Ge(II) atom lies above the plane of the four N donors in  $[\text{Ge}(\text{Me}_4\text{tacd})]^{2+}$ ,<sup>960</sup> and a similar coordination geometry is seen for the Pb(II) center in  $[\text{Pb}(\text{R}_2\text{tacd})]^{2+}$  ( $\text{R} = \text{Bz}$ ; see **Scheme 13** for  $\text{R}_2\text{tacd}$ ).<sup>961</sup>

The introduction into macrocyclic ligands such as *tacd* of pendant arms bearing N-donor domains provides a means of increasing the CN of a metal ion bound within the ligand cavity and thereby enhances the stability of the complex with respect to ligand dissociation. The following references give selected examples of such main group metal complexes incorporating purely N-donor ligands.<sup>962–968</sup>



**Scheme 13** Representative 'parent' open-chain, macrocyclic and caging polydentate ligands. In the text, deprotonated Me<sub>3</sub>tacc is represented as Me<sub>3</sub>tacc-H, etc.



**Scheme 14** Formation of the cryptand derivative reported by Gerus et al.<sup>972</sup>

Finally in this section, we consider representative examples of s-block metal ions encapsulated within caging ligands with an emphasis on azacryptands. Cryptands including azacryptands play a crucial role in the synthesis of alkali and electrides.<sup>969</sup> The first barium sodide [Ba{H<sub>5</sub>aza(2.2.2)crypt}]<sup>+</sup>Na<sup>-</sup> was prepared from Ba, Na, and H<sub>6</sub>aza(2.2.2)crypt (**Scheme 13**) in NH<sub>3</sub>-MeNH<sub>2</sub> solution; **Fig. 49E** shows the [Ba{H<sub>5</sub>aza(2.2.2)crypt}]<sup>+</sup> complex.<sup>970</sup> Alkali metal cations template the assembly of the N<sub>9</sub>-azacryptand (N<sub>9</sub>-azacrypt, **Scheme 13**), and the Pb(II) complex has also been described; **Fig. 49F** shows the structure of [K(N<sub>9</sub>-azacrypt)]<sup>+</sup>.<sup>971</sup> The reactions of the hexaazamacrocycle shown in **Scheme 14** with 2,6-bis(bromomethyl)pyridine or 2,6-bis[(tosyloxy)methyl]pyridine in the presence of Na<sub>2</sub>CO<sub>3</sub> or K<sub>2</sub>CO<sub>3</sub> under basic conditions yielded enantiopure azacryptates of Na<sup>+</sup> or K<sup>+</sup>.<sup>972</sup>

## 1.02.3 Phosphorus-donor ligands

### 1.02.3.1 Monodentate ligands

#### 1.02.3.1.1 RPH<sub>2</sub>, R<sub>2</sub>PH, R<sub>3</sub>P including P,P-ligands in monodentate or bridging modes

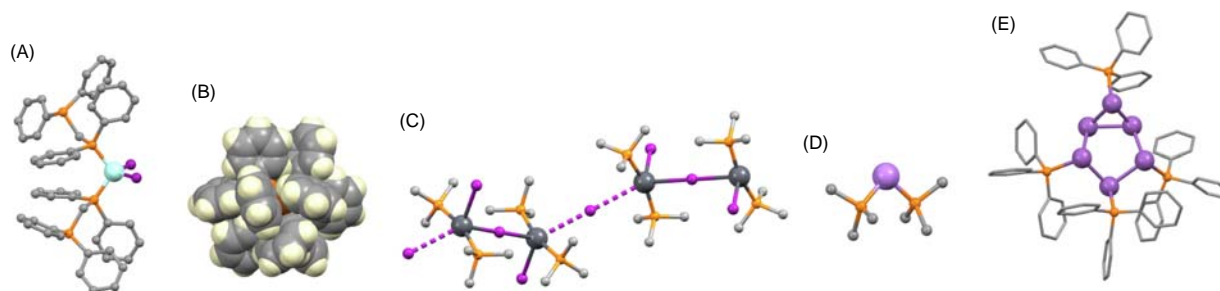
In this section, monodentate phosphane ligands belonging to the classes RPH<sub>2</sub>, R<sub>2</sub>PH, and R<sub>3</sub>P will be discussed along with ditopic ligands such as R<sub>2</sub>PCH<sub>2</sub>CH<sub>2</sub>PR<sub>2</sub> which can coordinate in a monodentate manner to a metal center. The latter category includes those with ligands which bridge between two main group metals. Complexes of main group metals with RPH<sub>2</sub> ligands are restricted to organometallic species and are outside the scope of this review. Simple derivatives of p-block metals containing R<sub>2</sub>PH ligands are also sparse. Group 13 M(III) compounds with R<sub>2</sub>PH ligands are represented by [MBr<sub>3</sub>(PH<sup>t</sup>Bu<sub>2</sub>)] (M = Al, Ga, In),<sup>973</sup> and complexes featuring a Ga–Ga bond include [Ga<sub>2</sub>Br<sub>4</sub>(PHCy<sub>2</sub>)<sub>2</sub>] (formed from [GaBr(THF)<sub>n</sub>] and PHCy<sub>2</sub>),<sup>974</sup> and [Ga<sub>2</sub>I<sub>4</sub>(PHR<sub>2</sub>)<sub>2</sub>] (R = Cy, <sup>t</sup>Bu).<sup>975</sup> Although one could argue that phosphane selenides are not metal coordination compounds, we include them because, in this review, we treat Se as a semimetal. In SePHPh<sub>2</sub><sup>976,977</sup> and SePH<sup>t</sup>Bu<sub>2</sub>,<sup>978</sup> P–H⋯Se hydrogen bonds dominate packing interactions in the solid state, but are not observed in SePH(CH<sub>2</sub>CH<sub>2</sub>Ph)<sub>2</sub>.<sup>979</sup>

Compared to those with RPH<sub>2</sub> and R<sub>2</sub>PH ligands, coordination compounds with tertiary phosphanes are more abundant, and complexes of the p-block metals predominate over those in the s-block. Buchner et al. have reported the synthesis and crystal structure of tetrahedral [BeCl<sub>2</sub>(PMe<sub>3</sub>)<sub>2</sub>] which has been used as a precursor to <sup>n</sup>Bu<sub>2</sub>Be.<sup>980</sup> While reaction of [BeI<sub>2</sub>(OEt<sub>2</sub>)<sub>2</sub>] with dppm yielded [BeI<sub>2</sub>(dppm-κ<sup>1</sup>)<sub>2</sub>] (Fig. 50A),<sup>659</sup> that with dppe led to the 1D-coordination polymer [BeI<sub>2</sub>(μ-dppe)]<sub>n</sub>.<sup>981</sup> A similar structure to that shown in Fig. 50A is also found for [BeCl<sub>2</sub>(dppm-κ<sup>1</sup>)<sub>2</sub>].<sup>982</sup>

The reactions of AlX<sub>3</sub> (X = Cl, Br, I) with PMe<sub>3</sub> lead to the formation of [AlX<sub>3</sub>(PMe<sub>3</sub>)] or [AlX<sub>3</sub>(PMe<sub>3</sub>)<sub>2</sub>] depending on the ratio of reagents used; with the bisphosphane Cy<sub>2</sub>PCH<sub>2</sub>CH<sub>2</sub>PCy<sub>2</sub>, dinuclear [AlCl<sub>3</sub>]<sub>2</sub>(μ-Cy<sub>2</sub>PCH<sub>2</sub>CH<sub>2</sub>PCy<sub>2</sub>) was the sole product while with the less sterically demanding Me<sub>2</sub>PCH<sub>2</sub>CH<sub>2</sub>PMe<sub>2</sub> (dmpe), the formation of [AlCl<sub>3</sub>]<sub>2</sub>(μ-dmpe) competed with *trans*-[AlCl<sub>2</sub>(dmpe)<sub>2</sub>] containing chelating ligands. All products are extremely moisture sensitive.<sup>983</sup> A series of tetrahedral [InX<sub>3</sub>(PR<sub>3</sub>)] and trigonal bipyramidal *trans*-[InX<sub>3</sub>(PR<sub>3</sub>)<sub>2</sub>] complexes with X = Cl, Br, I; R = Ph or various MeO-substituted phenyl) have been structurally characterized and studied in detail by solid-state <sup>115</sup>In and <sup>31</sup>P NMR spectroscopies.<sup>984</sup> [Ga(PPh<sub>3</sub>)<sub>3</sub>]<sup>+</sup> was the first structurally characterized homoleptic gallium–phosphane complex and has a trigonal pyramidal structure; it was isolated by use of the weakly coordinating [Al(O<sup>t</sup>Bu<sup>F</sup>)<sub>4</sub>]<sup>−</sup> anion (<sup>t</sup>Bu<sup>F</sup> = perfluoro-*tert*-butyl).<sup>985</sup> This work was followed by the isolation of the 2-coordinate [M(P<sup>t</sup>Bu<sub>3</sub>)<sub>2</sub>]<sup>+</sup> (M = Ga, In) and 3-coordinate [In(PPh<sub>3</sub>)<sub>3</sub>]<sup>+</sup>.<sup>986</sup> Phosphane adducts of InH<sub>3</sub> have been prepared by reactions of PR<sub>3</sub> (R = Cy, Ph or cyclopentyl) with [InH<sub>3</sub>(NMe<sub>3</sub>)] in 1:1 or 2:1 M ratios, and the crystal structure of [InH<sub>3</sub>(PCy<sub>3</sub>)<sub>2</sub>] reveals a trigonal bipyramidal structure with a *trans*-arrangement of PCy<sub>3</sub> ligands.<sup>987</sup>

Group 14 M(IV) complexes are illustrated by [SnF<sub>4</sub>(PCy<sub>3</sub>)<sub>2</sub>],<sup>988</sup> *trans*-[SnCl<sub>4</sub>(PMe<sub>3</sub>)<sub>2</sub>],<sup>989</sup> *trans*-[SnCl<sub>3</sub>(PMe<sub>3</sub>)<sub>2</sub>]<sup>+</sup>,<sup>989</sup> and [SnCl<sub>2</sub>(PMe<sub>3</sub>)<sub>2</sub>]<sup>2+</sup> (which has close Sn⋯Cl contacts with [AlCl<sub>4</sub>]<sup>−</sup> counterions),<sup>989</sup> as well as octahedral [SnCl<sub>3</sub>(O<sub>3</sub>SCF<sub>3</sub>)(PMe<sub>3</sub>)<sub>2</sub>] with *trans*-PMe<sub>3</sub> groups, and trigonal bipyramidal [SnCl<sub>2</sub>(PEt<sub>3</sub>)<sub>3</sub>] with equatorial phosphanes. The latter are representative of a series of neutral and cationic phosphane and arsane complexes of tin(IV) halides reported in 2019 by Reid and coworkers.<sup>990</sup> Germanium(II) cations containing neutral, soft-donor ligands are rare, and Reid and coworkers reported [Ge(PMe<sub>3</sub>)<sub>3</sub>][CF<sub>3</sub>SO<sub>3</sub>]<sub>2</sub> in 2021; [Ge(PMe<sub>3</sub>)<sub>3</sub>]<sup>2+</sup> has a trigonal pyramidal structure with a stereochemically active lone pair.<sup>991</sup> Tin(II) is large enough to accommodate four PPh<sub>3</sub> ligands in [Sn(PPh<sub>3</sub>)<sub>4</sub>]<sup>2+</sup>; the space-filling diagram in Fig. 50B shows the extent of intra-cation CH⋯π contacts.<sup>992</sup> Lead(II) complexes are illustrated by the tetrahedral [PbI<sub>2</sub>(PPh<sub>3</sub>)<sub>2</sub>],<sup>993</sup> the structure of which contrasts with that of [PbI<sub>2</sub>(PMe<sub>3</sub>)<sub>2</sub>] in which [Pb<sub>2</sub>I<sub>2</sub>(PMe<sub>3</sub>)<sub>4</sub>(μ-I)]<sup>+</sup> units are connected via short contacts through the I<sup>−</sup> counterion (Pb⋯I = Fig. 50C).<sup>994</sup>

A noteworthy reaction in group 15 coordination chemistry is that of [(η<sup>5</sup>-Cp\*)As(toluene)]<sup>2+</sup> with PMe<sub>3</sub> which yields [As(PMe<sub>3</sub>)<sub>2</sub>]<sup>+</sup> (Fig. 50D) isolated as the [B(C<sub>6</sub>F<sub>5</sub>)<sub>4</sub>]<sup>−</sup> salt.<sup>995</sup> This unusual As(I) species has also been reported by Burford and coworkers, but (as the triflate salt) could not be isolated.<sup>996</sup> The reaction of PMe<sub>3</sub> with SbCl<sub>3</sub> in the presence of Me<sub>3</sub>SiOSO<sub>2</sub>CF<sub>3</sub> leads to the [CF<sub>3</sub>SO<sub>3</sub>]<sup>−</sup> salt of [SbCl<sub>2</sub>(PMe<sub>3</sub>)<sub>2</sub>]<sup>+</sup> with the PMe<sub>3</sub> ligands in the equatorial sites of a distorted see-saw (disphenoidal) structure; comparisons were made with the structures and <sup>31</sup>P NMR spectra for related complexes with chelating bisphosphanes.<sup>997</sup> In a complementary study, SbF<sub>3</sub> was reacted with Me<sub>3</sub>SiOSO<sub>2</sub>CF<sub>3</sub>; phosphane coordination to Sb(III) was expected but redox processes between Sb and P ultimately led to *cyclo*-[Sb<sub>4</sub>(PMe<sub>3</sub>)<sub>4</sub>]<sup>4+</sup>.<sup>998</sup> A series of [SbCl<sub>n</sub>(PR<sub>3</sub>)<sub>m</sub>]<sup>(3-n)+</sup> (R = Me, Ph, Cy; n = 1–4, m = 1, 2) has been reported and the structures analyzed in detail. The group 15 metal center can behave as a Lewis acceptor despite



**Fig. 50** Structures of (A) [BeI<sub>2</sub>(dppm-κ<sup>1</sup>)<sub>2</sub>] (CSD refcode TIVJIU), (B) [Sn(PPh<sub>3</sub>)<sub>4</sub>]<sup>2+</sup> highlighting intra-cation CH⋯π contacts (refcode RELKOJ), (C) [Pb<sub>2</sub>I<sub>2</sub>(PMe<sub>3</sub>)<sub>4</sub>(μ-I)]<sup>+</sup> (refcode ZUBWIF), (D) [As(PMe<sub>3</sub>)<sub>2</sub>]<sup>+</sup> (refcode FONTOU), and (E) (refcode QUCWIW).



the presence of a lone pair, and by considering the substituents and ligands, Burford has defined the relative *trans*-labilizing influence as lone-pair < PPh<sub>3</sub> ≤ Cl<sup>-</sup> < PCy ≈ PMe < Ar<sup>-</sup>.<sup>272</sup> Burford and coworkers have also reported the reaction of Ph<sub>3</sub>P with SbF(O<sub>3</sub>SCF<sub>3</sub>)<sub>2</sub> and the 5-coordinate [SbF(O<sub>3</sub>SCF<sub>3</sub>)<sub>2</sub>(PPh<sub>3</sub>)<sub>2</sub>] was isolated; reductive elimination of [Ph<sub>3</sub>PF]<sup>+</sup> (as the triflate salt) occurs and, after a redox process, the unusual bicyclic [Sb<sub>6</sub>(PPh<sub>3</sub>)<sub>4</sub>]<sup>4+</sup> cation (Fig. 50E) resulted.<sup>999</sup>

### 1.02.3.1.2 R<sub>2</sub>P<sup>-</sup>, RPH<sup>-</sup>, RP<sup>2-</sup>

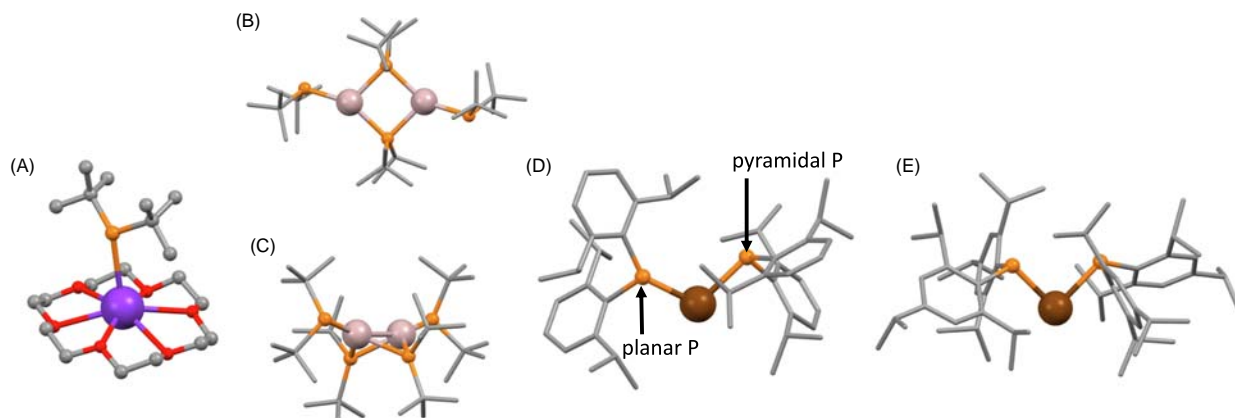
Upon going from neutral phosphanes to anionic phosphide ligands, we see a significant increase in the number of s-block metal complexes, and sterically demanding substituents such as Dipp are typically employed. We provide selected examples which serve as an entry into this area of coordination chemistry. Mixed donor ligands are not included. Lithium phosphides [LiPR<sub>2</sub>] are precursors to a range of main group metal phosphides as exemplified throughout this section.

The reaction of Dipp<sub>2</sub>PH with <sup>n</sup>BuLi in THF leads to the tetrahedral [Li(THF)<sub>3</sub>{P(Dipp)<sub>2</sub>}], while reactions between Dipp<sub>2</sub>PH and BzNa or BzK in THF result in the formation of [Na<sub>2</sub>(THF)<sub>4</sub>{μ-P(Dipp)<sub>2</sub>}<sub>2</sub>] or [K(THF)<sub>4</sub>{P(Dipp)<sub>2</sub>}], respectively. Under vacuum, loss of THF yields new solvates, including [Li(THF)<sub>2</sub>{P(Dipp)<sub>2</sub>}] which undergoes a dynamic monomer–dimer equilibrium in solution.<sup>1000</sup> An analogous reaction to that above is that of Ph{(Me<sub>3</sub>Si)<sub>2</sub>CH}PH with <sup>n</sup>BuLi which leads to [Li(OEt<sub>2</sub>)<sub>n</sub>{PPh(CH(SiMe<sub>3</sub>)<sub>2</sub>)}] or [Li(THF)<sub>3</sub>{PPh(CH(SiMe<sub>3</sub>)<sub>2</sub>)}]. The etherate can be converted to the Na<sup>+</sup> and K<sup>+</sup> derivatives; [K(OEt<sub>2</sub>)<sub>n</sub>(PPhR)] (R = CH(SiMe<sub>3</sub>)<sub>2</sub>) is a precursor to [Ge<sub>2</sub>(PPhR)<sub>2</sub>(μ-PPhR)<sub>2</sub>], while reaction between [Li(PPhR)] and SnCl<sub>2</sub> followed by crystallization from THF leads to [Li(THF)<sub>4</sub>][Sn(PPhR)<sub>3</sub>] in which Sn(II) is in a trigonal pyramidal environment.<sup>1001</sup> In the sterically crowded [Li(THF)<sub>2</sub>{PPh(2,6-Mes<sub>2</sub>C<sub>6</sub>H<sub>3</sub>)}], the Li<sup>+</sup> is 3-coordinate but with additional Li⋯π contacts to one Mes group; the Li–P distance is relatively short (2.478(4) Å). Treatment of [Li(THF)<sub>2</sub>{PPh(2,6-Mes<sub>2</sub>C<sub>6</sub>H<sub>3</sub>)}] with SnCl<sub>2</sub> yielded [Sn{PPh(2,6-Mes<sub>2</sub>C<sub>6</sub>H<sub>3</sub>)}]<sub>2</sub>.<sup>1002</sup> Lithium complexes derived from (Dipp)PH(CH<sub>2</sub>)<sub>n</sub>PH(Dipp) with n = 1–5 have been reported, and structures are dependent upon n; for n = 1 and 3, discrete monomers with Li<sub>2</sub>P<sub>2</sub> cores were found, whereas for n = 4, the complex [(THF)<sub>3</sub>Li{μ-(Dipp)P(CH<sub>2</sub>)<sub>4</sub>P(Dipp)}Li(THF)<sub>3</sub>] was isolated with each Li<sup>+</sup> being tetrahedrally sited. Detailed NMR spectroscopic studies give insight into the solution behavior of these species.<sup>1003</sup>

Recrystallization of an Et<sub>2</sub>O solution containing 18-crown-6 and KP<sup>t</sup>Bu<sub>2</sub> leads to [K(18-crown-6)(P<sup>t</sup>Bu<sub>2</sub>)] (Fig. 51A); the rather long K–P distance of 3.239(1) Å indicates that the K and P centers possess significant Lewis acidity and basicity, respectively, and indeed, the compound reacts with CO via nucleophilic attack by the basic phosphide.<sup>1004</sup> We have noted earlier (e.g., Figs. 44A, C, 45A) that M<sup>+</sup>⋯π interactions may play an important role in the solid-state structures of complexes of the heavier s-block elements, and this is again observed in [KPPH<sub>2</sub>]. The structure is complicated, and exhibits cyclic K<sub>2</sub>P<sub>2</sub> and K<sub>3</sub>P<sub>3</sub> motifs as well as extensive K<sup>+</sup>⋯π<sub>phenyl</sub> interactions.<sup>1005</sup>

In the group 2 metal complexes [M(18-crown-6)(PPh<sub>2</sub>)<sub>2</sub>] (M = Ca, Ba), the phosphido ligands are axially bound,<sup>1006</sup> and a *trans*-arrangement is also found in [M(THF)<sub>4</sub>(PPh<sub>2</sub>)<sub>2</sub>] (M = Ca, Sr)<sup>1006,1007</sup> and [Ba(THF)<sub>5</sub>(PPh<sub>2</sub>)<sub>2</sub>].<sup>1007</sup> However, *trans*–*cis* isomerism in [Ca(THF)<sub>4</sub>(PPh<sub>2</sub>)<sub>2</sub>] can occur.<sup>939</sup> Note the increase from CN = 6 to 7 on going from Ca<sup>2+</sup> and Sr<sup>2+</sup> to M = Ba<sup>2+</sup>. However, in [Ba(THF)<sub>4</sub>(PMes<sub>2</sub>)<sub>2</sub>] with the bulkier Mes<sub>2</sub>P<sup>-</sup> ligands, a CN = 6 is observed.<sup>1007</sup> Di-, tri- and hexanuclear calcium complexes have been obtained from combinations of PH<sub>2</sub>(Si<sup>t</sup>Bu<sub>3</sub>) and [Ca(THF)<sub>2</sub>]{N(SiMe<sub>3</sub>)<sub>2</sub>}]; in the Ca<sub>2</sub> and Ca<sub>3</sub> species, [PH(Si<sup>t</sup>Bu<sub>3</sub>)]<sup>-</sup> ligands bridge between pairs of Ca<sup>2+</sup> centers, while the hexanuclear cluster is supported by μ-[PH(Si<sup>t</sup>Bu<sub>3</sub>)]<sup>-</sup> and μ<sub>3</sub>-[P(Si<sup>t</sup>Bu<sub>3</sub>)]<sup>2-</sup> ligands.<sup>1008</sup> Westerhausen et al. have also characterized Sr<sub>6</sub>P<sub>8</sub>-clusters which are structurally related to their calcium congeners.<sup>1009</sup> Reaction of SrI<sub>2</sub> with K[PHPh] in THF yields the 1D-coordination polymer [Sr(THF)<sub>2</sub>(μ-PHPh)<sub>2</sub>]<sub>n</sub> with octahedrally sited Sr<sup>2+</sup>; this is one of a series of related group 2 metal assemblies with [PHPh]<sup>-</sup> ligands.<sup>1010</sup>

The Ga(III) complex [Ga(P<sup>t</sup>Bu<sub>2</sub>)<sub>3</sub>] (trigonal planar Ga) results from the reaction of GaCl<sub>3</sub> with 3 or more equivalents of Li [P<sup>t</sup>Bu<sub>2</sub>], while a 1:1 reaction followed by protolysis produced the [P<sup>t</sup>Bu<sub>2</sub>PH<sub>2</sub>]<sup>+</sup> salt of [Li{P<sup>t</sup>Bu<sub>2</sub>P(GaCl<sub>3</sub>)<sub>2</sub>}]<sup>-</sup> in which Li is



**Fig. 51** Structures of (A) [K(18-crown-6)(P<sup>t</sup>Bu<sub>2</sub>)] (CSD refcode TIVLUI), (B) the diradical [Al<sub>2</sub>(P<sup>t</sup>Bu<sub>2</sub>)<sub>4</sub>] (refcode LUNMUD), (C) the diamagnetic [Al<sub>2</sub>(P<sup>t</sup>Bu<sub>2</sub>)<sub>4</sub>] (refcode LUNNAK), (D) [Sn<sub>2</sub>(P(Dipp))<sub>2</sub>] highlighting different P environments (refcode DAGQEK), and (E) [Sn<sub>2</sub>(P(Tripp))<sub>2</sub>] (refcode DAGQOU).

octahedrally sited between two  ${}^t\text{Bu}_2\text{P}(\text{GaCl}_3)_2$  units with Ga–Cl–Li bridges.<sup>1011</sup> An intriguing investigation from Henke et al. starts with the premise that highly energetic  $[\text{Al}(\text{P}^t\text{Bu}_2)_2]$  radicals should dimerize via an intermediate biradical with a long Al $\cdots$ Al distance. The addition of Li $[\text{P}^t\text{Bu}_2]$  to a solution containing the metastable AlCl produced green crystals of  $[\text{Al}_2(\text{P}^t\text{Bu}_2)_4]$  (Fig. 51B) with Al $\cdots$ Al = 3.508 Å. In contrast, replacing AlCl by AlBr resulted in the isolation of yellow crystals of  $[\text{Al}_2(\text{P}^t\text{Bu}_2)_4]$  (Fig. 51C) with Al $\cdots$ Al = 2.587 Å. The structural elucidations were supported by computational investigations, and the differences were explained in terms of the isolation of a high-energy triplet molecule (green compound) in contrast to a stable butterfly structure (yellow crystals).<sup>1012</sup>  $[\text{Ga}_8\text{Cl}_2(\text{P}^i\text{Pr}_2)_2(\mu\text{-P}^i\text{Pr}_2)_6]$  is a representative example of group 13 metal clusters supported by  $\text{R}_2\text{P}^-$  ligands.<sup>1013</sup> Other phosphido  $\text{Al}_n$  and  $\text{Ga}_n$  clusters have also been described.<sup>1014–1021</sup> Treatment of  $[\text{Ge}_9\{\text{Si}(\text{SiMe}_3)_3\}_3]^-$  or  $[\text{Ge}_9\{\text{Si}(\text{SiMe}_3)_3\}_2]^{2-}$  with  $\text{R}_2\text{P}^-$  (R = Cy,  ${}^i\text{Pr}$ ,  ${}^t\text{Bu}$ ) yielded the first Zintl clusters carrying  $\text{R}_2\text{P}$ -substituents; one example is  $[\text{Ge}_9\{\text{Si}(\text{SiMe}_3)_3\}_3(\text{PCy}_2)]$ ,<sup>1022</sup> and related  $\text{Ge}_9$ -clusters have been reported.<sup>1023</sup>

Group 14 M(IV) derivatives with  $\text{R}_2\text{P}^-$  ligands include the tetrahedral  $[\text{GeCl}\{\text{N}(\text{SiMe}_3)_2\}_2(\text{PEt}_2)]$ .<sup>1024</sup> The use of  $[\text{Li}(\text{PPhR})]$  (R = CH(SiMe<sub>3</sub>)<sub>2</sub>) to access  $[\text{Ge}_2(\text{PPhR})_2(\mu\text{-PPhR})_2]$  and  $[\text{Sn}(\text{PPhR})_3]^-$  was detailed earlier in this section,<sup>1001</sup> and we also described the synthesis of  $[\text{Sn}\{\text{PPh}(2,6\text{-Mes}_2\text{C}_6\text{H}_3)\}_2]$ .<sup>1002</sup>  $[\text{Sn}\{\text{P}(\text{Dipp})_2\}_2]$  is noteworthy for being the first example of a compound with a crystallographically confirmed P=Sn bond, arising from a P–Sn  $\pi$ -interaction involving a lone pair on a planar P center (Fig. 51C) and the vacant p-orbital on Sn; the analogous Ge(II) complex has also been fully characterized.<sup>1025,1026</sup> Izod et al. point out that if both P environments were planar, a weaker P–Sn or P–Ge  $\pi$ -interaction would result and this would not compensate for the energy required to rehybridize both P atoms. Significantly, in  $[\text{Sn}\{\text{P}(\text{Tripp})_2\}_2]$ , both P atoms are pyramidal (Fig. 51E), indicating the absence of the Sn–P  $\pi$ -bond.<sup>1026</sup> In the related  $[\text{M}\{\text{P}(\text{Dipp})(\text{Mes})_2\}_2]$  and  $[\text{M}\{\text{P}(\text{Dipp})\{\text{CH}(\text{SiMe}_3)_2\}_2\}_2]$  (M = Ge, Sn) derivatives, Izod et al. have assessed the roles of both P–Ge or P–Sn  $\pi$ -interactions and Ge $\cdots$ arene or Sn $\cdots$ arene interactions.<sup>1027</sup> The first example of an  $[\text{As}(\text{PR}_2)_2]^+$  cation was reported in 2019 in the salt  $[\text{As}\{\text{P}(\text{Dipp})_2\}_2][\text{Al}\{\text{OC}(\text{CF}_3)_3\}_4]$ ; as in the isoelectronic Ge(II) and Sn(II) species above, stabilization of  $[\text{As}\{\text{P}(\text{Dipp})_2\}_2]^+$  is due to a P–As  $\pi$ -interaction.<sup>1028</sup> In addition to the carbene-analogs mentioned above, phosphido complexes of the heavier group 15 elements are exemplified by the trigonal pyramidal  $[\text{AsCl}\{\text{P}(\text{Dipp})_2\}_2]$ .<sup>1028</sup>

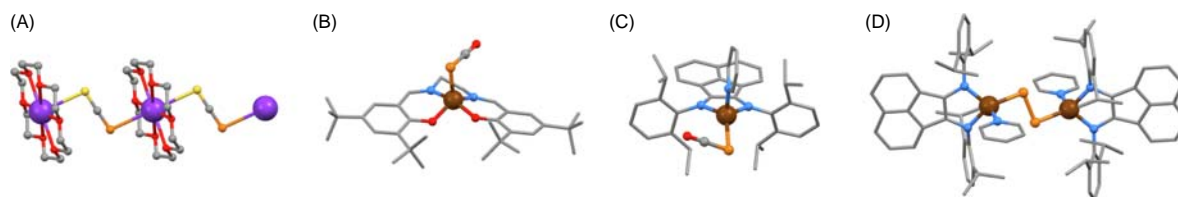
In Section 1.02.2.2.3, we discussed main group metal complexes containing  $\beta$ -diketiminato ligands (see Scheme 6 for ligand abbreviations). Complexes which combine  $\beta$ -diketiminato and phosphide ligands include  $[\text{M}(\text{THF})(\text{Nacnac})(\text{PPh}_2)]$  (M = Mg, Ca; Ar = Dipp, see Scheme 6 for definition of Ar),<sup>1029,1030</sup>  $[\text{AlH}(\text{Nacnac})(\text{PPh}_2)]$  (Ar = Dipp),<sup>1031</sup>  $[\text{Ge}(\text{Nacnac})(\text{PPh}_2)]$  (Ar = Dipp),<sup>1032</sup>  $[\text{M}(\text{Nacnac})(\text{PR}_2)]$  (M = Ge, Sn, Pb; Ar = Dipp; R = Ph, Cy),<sup>1033</sup> and the Ge(IV) derivative  $[\text{Ge}(\text{E})(\text{Nacnac})(\text{PCy}_2)]$  (Ar = Dipp; E = S, Se).<sup>1034,1035</sup>

### 1.02.3.1.3 $\text{PCO}^-$ , $\text{PCS}^-$

In Section 1.02.2.1.4, we surveyed main group metal complexes with N-bonded  $\text{NCO}^-$  and  $\text{NCS}^-$  ligands, and we noted terminally N-bonded, bridging N-bonded, and bridging N,X-bound (X = O, S) modes. Now we consider complexes containing P-bonded  $\text{PCO}^-$  and  $\text{PCS}^-$  ligands. These are less common than their nitrogen counterparts. The  $\text{PCO}^-$  and  $\text{PCS}^-$  anions were first reported in 1992 and 1994, respectively, with structurally characterized  $[\text{Li}(\text{dme})_2(\text{PCO-O})]$  and  $[\text{Li}(\text{dme})_3][\text{PCS}]$  (with non-coordinated  $[\text{PCS}]^-$  ion).<sup>1036,1037</sup> Since 2000, the structures of  $\text{Na}(\text{PCO})$  (a 3D-network with P,O-bonded bridging ligands),<sup>1038</sup>  $[\text{Na}_2(\text{dme})_4(\mu\text{-OCP})_2]$  (with Na–O–Na bridges),<sup>1039</sup>  $[\text{Na}(\text{OCP-O})(\text{THF})(\text{Bz}18\text{-crown-6})]$ ,<sup>1040</sup> and the 1D-coordination polymers  $[\text{K}(18\text{-crown-6})(\text{PCO})]_n$ ,<sup>1041</sup>  $[\text{Na}(18\text{-crown-6})(\text{PCS})]_n$ ,<sup>1042</sup> and  $[\text{K}(18\text{-crown-6})(\text{PCS})]_n$  (Fig. 52A),<sup>1042</sup> all with P,X-bonded (X = O, S) bridging ligands have been described. Note the variation in bonding modes across this series of alkali metal compounds, with only the bridging ligands (as in Fig. 52A) being strictly relevant to this section (see Section 1.02.6.1.4 for O-bonded  $\text{PCO}^-$ ).

Group 2 metal complexes with  $[\text{PCO}]^-$  ligands appear to be sparse; one example is *trans*- $[\text{Mg}(\text{PCO})_2(\text{THF})_4]$ , but with O-bonded  $\text{PCO}^-$ .<sup>1040</sup>

The first  $\text{PCO}$ -adducts of Al and Ga were reported in 2019, when Mei et al. demonstrated the use of a sterically hindered salen-type framework to stabilize  $\{\text{Al}^{\text{III}}\text{-OCP}\}$  and  $\{\text{Ga}^{\text{III}}\text{-PCO}\}$  units. Note the change in coordination mode with selective P-coordination to the softer Ga(III) center (angle Ga–P–C = 88.43(11)°, Fig. 52B).<sup>1043</sup> A similar coordination mode is observed in the Ge(II) compound  $[\text{Ge}(\text{Me}_2\text{N-Nacnac})(\text{PCO})]$  in which  $[\text{Me}_2\text{N-Nacnac}]^-$  is an amino-functionalized  $\beta$ -diketiminato ligand (Scheme 6 with Ar = Dipp),<sup>1044</sup> and in  $[\text{Ge}(\text{Nacnac})(\text{PCO})]$  (Ar = 2-Ph<sub>2</sub>PC<sub>6</sub>H<sub>4</sub>).<sup>1045</sup> The Ge–P–C angles in these two complexes are 87.29(16) and 91.7(3)° respectively. The tin(II) analog of the latter has also been characterized,<sup>1045</sup> and a related structure is found in  $[\text{As}(\text{DippNCH}_2\text{CH}_2\text{NDipp})(\text{PCO})]$ .<sup>1046</sup>  $[\text{Sn}(\text{NRR}')(\text{PCO})]$  with R = Si(4- ${}^t\text{Bu}$ C<sub>6</sub>H<sub>4</sub>)<sub>3</sub> and R' = 2,6-



**Fig. 52** (A) Part of the 1D-chain in  $[\text{K}(18\text{-crown-6})(\text{PCS})]_n$  (CSD refcode QUZWOZ; the S and P sites are disordered). (B) An example of a salen-supported  $\{\text{Ga}^{\text{III}}\text{-PCO}\}$  unit (refcode VOBCEX). Structures of (C)  $[\text{Ga}(\text{py})(\text{dpp-bian})(\text{PCO})]$  (refcode SUZJJJ) and (D)  $[\text{Ga}_2(\text{py})_2(\text{dpp-bian})_2(\mu\text{-P}_2)]$  (refcode SUZLIL).

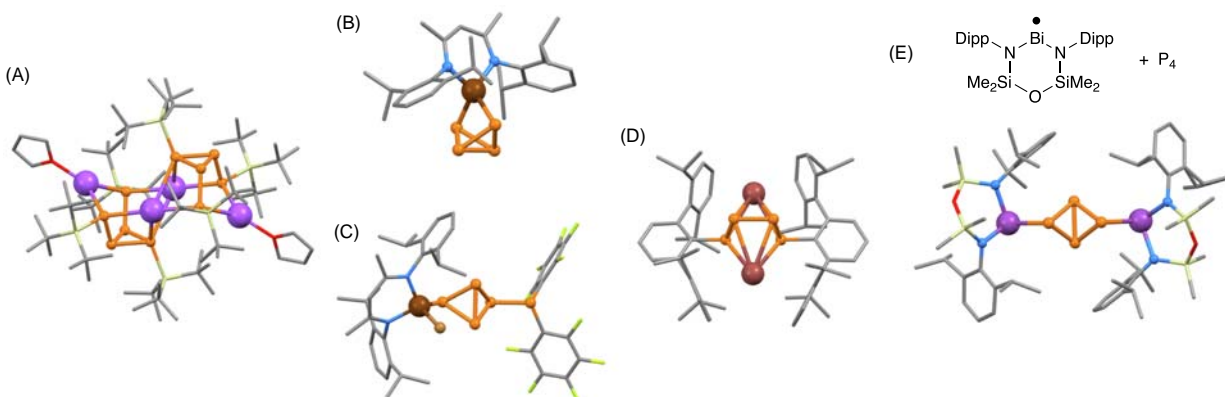
$\{\text{CH}(3,5\text{-}^t\text{Bu}_2\text{C}_6\text{H}_3)_2\}_2\text{-4-MeC}_6\text{H}_2$  is one of a series of Sn(II) and Ge(II) species in which the steric congestion of the amido ligand stabilizes 2-coordinate M(II) in a mononuclear complex.<sup>1047</sup>

One of the interesting aspects of {MPCO}-containing compounds is their potential for the loss of CO and formation of an {M≡P} unit. This has been realized starting from the  $\beta$ -diketiminato complex [Ge(R-Nacnac)(PCO)] (see Scheme 6, Ar = Dipp, R = H) which loses CO upon irradiation and, via an {Ge≡P}-containing intermediate, forms the dimer [Ge<sub>2</sub>(R-Nacnac)<sub>2</sub>( $\mu$ -P)<sub>2</sub>] (Ge–P = 2.2550(6) and 2.2673(6) Å, indicative of some double-bond character).<sup>1048</sup> The work of Goicoechea is prominent in the field of [PCO]<sup>−</sup> complexes. This group has reported the preparation and structure of [Ga(py)(dpp-bian)(PCO)] (Fig. 52C; note the related complex [Ga<sub>2</sub>(dpp-bian)<sub>2</sub>(NCO)<sub>2</sub>], Fig. 27B) and its photolysis with loss of CO to yield [Ga<sub>2</sub>(py)<sub>2</sub>(dpp-bian)<sub>2</sub>( $\mu$ -P<sub>2</sub>)] (Fig. 52D).<sup>1049</sup>

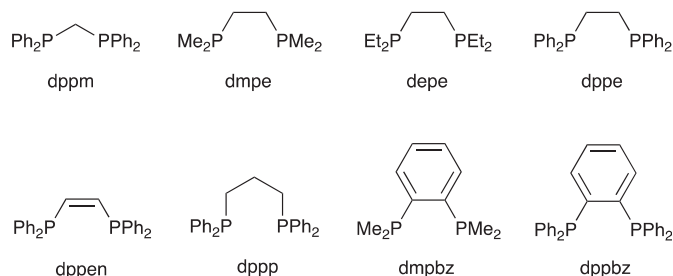
### 1.02.3.2 [P<sub>n</sub>]<sup>x−</sup> ligands derived from P<sub>4</sub>

Chain, ring and cluster species of the group 15 elements P, As, Sb and Bi are covered in a separate section of this reference work.<sup>1050</sup> A themed issue of *Dalton Trans.* ('Phosphorus chemistry: discoveries and advances')<sup>1051</sup> includes a number of papers relevant to the topic. An area of specific interest is the activation of P<sub>4</sub> under mild conditions and a review by Scheer<sup>1052</sup> coupled with papers from Inoue<sup>1053</sup> and Power<sup>1054</sup> give a good entry into this field. In this section we use a few selected examples to illustrate the coordination of small [P<sub>n</sub>]<sup>x−</sup> ligands to main group metals and we focus on activation of P<sub>4</sub>. Many complexes contain M–C bonds, e.g., [Ge(Dipp)<sub>2</sub>(P<sub>4</sub>- $\kappa^2$ )],<sup>1055</sup> and fall outside the scope of this review.

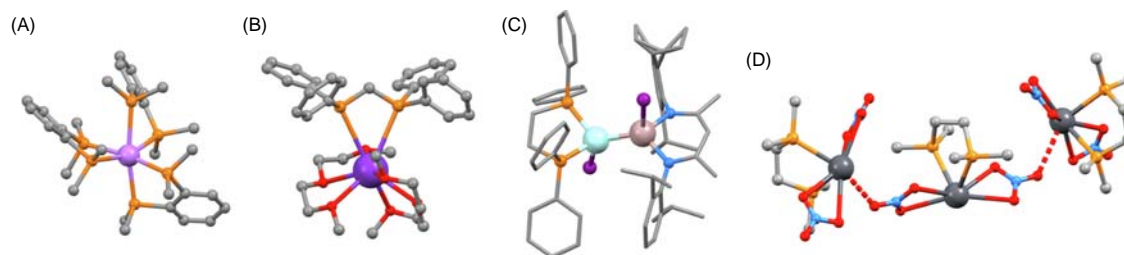
The activation of P<sub>4</sub> by LiSi<sup>t</sup>Bu<sub>3</sub> leads to P<sub>4</sub>(Si<sup>t</sup>Bu<sub>3</sub>)<sub>2</sub>, P<sub>7</sub>(Si<sup>t</sup>Bu<sub>3</sub>)<sub>3</sub>, [Li<sub>3</sub>P(PSi<sup>t</sup>Bu<sub>3</sub>)<sub>3</sub>] and [LiP<sub>5</sub>], while in the presence of LiOSi<sup>t</sup>Bu<sub>3</sub>, the product was [LiP<sub>7</sub>(Si<sup>t</sup>Bu<sub>3</sub>)<sub>2</sub>].<sup>1056</sup> The reaction between P<sub>4</sub> and NaSi<sup>t</sup>Bu<sub>3</sub> produces the dimer [(<sup>t</sup>Bu<sub>3</sub>Si)<sub>3</sub>P<sub>5</sub>Na<sub>2</sub>(THF)]<sub>2</sub> in which the Na atoms have CN = 3 or 4 (Fig. 53A).<sup>1057</sup> A wide range of Ga(III) polyphosphane complexes, the simplest of which is [Ga(Nacnac)(P<sub>4</sub>- $\kappa^2$ )], (Fig. 53B) have been isolated from the reaction of [Ga(Nacnac)] (Ar = Dipp, see Scheme 6) and white phosphorus.<sup>1038</sup> Reactions of [Ga(Nacnac)(P<sub>4</sub>- $\kappa^2$ )] with Cy<sub>2</sub>PCL, Ph<sub>2</sub>PCL, Mes<sub>2</sub>PCL or (C<sub>6</sub>H<sub>5</sub>)<sub>2</sub>PBr have led to compounds containing P<sub>5</sub> units with [GaBr(Nacnac){P<sub>5</sub>(C<sub>6</sub>H<sub>5</sub>)<sub>2</sub>}] as a representative complex (Fig. 53C); kinetics data offer insight into the reaction mechanism.<sup>1058</sup> Power and coworkers have shown that P<sub>4</sub> reacts with Tl<sub>2</sub>(2,6-Dipp<sub>2</sub>C<sub>6</sub>H<sub>3</sub>)<sub>2</sub> with transfer of the aryl groups to phosphorus and formation of [Tl<sub>2</sub>{P<sub>4</sub>(2,6-Dipp<sub>2</sub>C<sub>6</sub>H<sub>3</sub>)<sub>2</sub>}] (Fig. 53D).<sup>1059</sup> Coordination compounds of bismuth with [P<sub>n</sub>]<sup>x−</sup> ligands have proved rather elusive, and innovative work from Coles and coworkers demonstrates the activation of P<sub>4</sub> by an isolated Bi(II) radical (Fig. 53E).<sup>1060</sup>



**Fig. 53** Structures of (A) [(<sup>t</sup>Bu<sub>3</sub>Si)<sub>3</sub>P<sub>5</sub>Na<sub>2</sub>(THF)]<sub>2</sub> (CSD refcode CAQHUY), (B) [Ga(Nacnac)(P<sub>4</sub>- $\kappa^2$ )] (refcode SEGFUI), (C) [GaBr(Nacnac)(P<sub>5</sub>(C<sub>6</sub>H<sub>5</sub>)<sub>2</sub>)] (refcode SAYKAH), and (D) [Tl<sub>2</sub>{P<sub>4</sub>(2,6-Dipp<sub>2</sub>C<sub>6</sub>H<sub>3</sub>)<sub>2</sub>}] (refcode CEDBET). (E) The product of the activation of P<sub>4</sub> by an isolated Bi(II) radical (refcode AYUXEZ).



**Scheme 15** Chelating bisphosphanes included in Section 1.02.3.3.1.



**Fig. 54** Structures of (A)  $[\text{Li}(\text{dmpbz})_3]^+$  (CSD refcode LUDXUF), (B)  $[\text{K}(\text{dppm-H})(\text{diglyme})_2]$  (refcode NISKAD), (C)  $[\text{I}(\text{dppe})\text{BeAl}(\text{Nacac})\text{I}]$  with  $\text{Ar}_{\text{Nacac}} = \text{Dipp}$  (refcode ASIBIQ), and (D)  $[\text{Pb}(\text{dmpe})(\text{O}_2\text{NO-}\kappa^2)_2]$  showing intermolecular  $\text{O}\cdots\text{Pb}$  contacts (refcode MUJMIP).

### 1.02.3.3 Bidentate ligands

#### 1.02.3.3.1 Chelating bisphosphanes

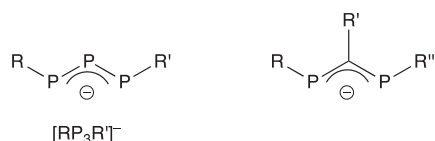
As in Section 1.02.2.2.1 for chelating diamines, we restrict our coverage of main group metal complexes containing chelating bisphosphanes to selected and common ligands (Scheme 15).

Metal complexes from the s-block are relatively sparse. Reid and coworkers have realized the formation of homoleptic  $[\text{Li}(\text{dmpe})_3]^+$ ,  $[\text{Li}(\text{dmpbz})_3]^+$  (Fig. 54A),  $[\text{Na}(\text{dmpe})_3]^+$  and  $[\text{Na}(\text{dmpbz})_3]^+$  cations by using the very weakly coordinating  $[\text{Al}\{\text{OC}(\text{CF}_3)_3\}_4]^-$  and  $[\text{B}\{3,5-(\text{CF}_3)_2\text{-C}_6\text{H}_3\}_4]^-$  anions.<sup>1061</sup> Lithium bis(diphenylphosphanyl)methanide,  $[\text{Li}(\text{dppm-H})]$ , is well established.<sup>1062</sup> In  $[\text{Li}(\text{dppm-H})(\text{tmeda})]$ , the  $\text{Li}^+$  center is tetrahedrally sited with  $\text{Li-P}$  distances of 2.537(4) and 2.568(4) Å,<sup>1063</sup> whereas in  $[\text{Li}(\text{THF})(\text{dppm-H})(\text{tmeda})]$ , the  $\text{Li-P}$  distances of 2.653(4) and 3.018(4) Å indicate preferential coordination of THF and only one principal  $\text{Li-P}$  interaction.<sup>1064</sup> In contrast, in  $[\text{Li}(\text{dppm-H})(\text{dme})_2]$ , both  $\text{Li-P}$  distances are long (2.896(3) Å) suggesting that the species should be considered as a contact ion-pair.<sup>1065</sup> The  $\text{K}^+$  center is 8-coordinate in  $[\text{K}(\text{dppm-H})(\text{dgm})_2]$  (Fig. 54B); this complex can be accessed by treating polymeric  $[\text{K}(\text{dppm-H})(\text{OEt}_2)_{0.5}]_n$  with diglyme.<sup>1066</sup> The conjugate base of dppm also appears in  $[\text{Ca}(\text{THF})_3(\text{dppm-H})_2]$ , which was prepared by treatment of dppm with  $^t\text{BuLi}$ , followed by  $\text{KO}^t\text{Bu}$  and the  $\text{CaI}_2$  in  $\text{Et}_2\text{O}/\text{THF}$ .<sup>1064</sup> A rare example of a Be-Al bonded compound is found in  $[\text{I}(\text{dppe})\text{BeAl}(\text{Nacac})\text{I}]$  with  $\text{Ar} = \text{Dipp}$  (see Scheme 6); the structure (Fig. 54C) features a Be-Al bond distance of 2.368(2) Å.<sup>981</sup>

Octahedral group 13 M(III) coordination environments are found in  $\text{trans-}[\text{AlCl}_2(\text{dmpe})_2]^+$ ,<sup>983</sup>  $\text{trans-}[\text{AlCl}_2(\text{dmpbz})_2]^+$ ,<sup>983</sup>  $\text{trans-}[\text{AlCl}_2(\text{dppbz})_2]^+$ ,<sup>983</sup>  $\text{trans-}[\text{GaX}_2(\text{dmpe})_2]^+$  ( $\text{X} = \text{Cl}, \text{Br}, \text{I}$ ),<sup>1067</sup>  $\text{trans-}[\text{GaX}_2(\text{dmpbz})_2]^+$  ( $\text{X} = \text{Cl}, \text{Br}, \text{I}$ ),<sup>1068</sup>  $\text{trans-}[\text{InX}_2(\text{dmpbz})_2]^+$  ( $\text{X} = \text{Br}, \text{I}$ ),<sup>1069</sup> and  $[\text{In}_2\text{Cl}_4(\text{dmpbz})_2(\mu\text{-Cl})_2]$ .<sup>1069</sup> Tetrahedral M(III) coordination compounds which have been structurally characterized include  $[\text{GaCl}_2(\text{dppbz})]^+$ ,<sup>1068</sup> and  $[\text{InX}_2(\text{dmpbz})]^+$  ( $\text{X} = \text{Br}, \text{I}$ ).<sup>1069</sup>

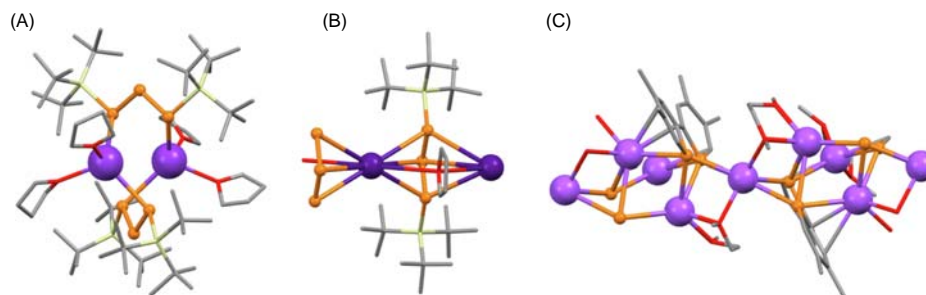
The Reid group in particular has been active in the area of group 14 metal bisphosphane complexes. Octahedral group 14 metal(IV) complexes include  $[\text{GeF}_4(\text{dppe})]$ ,<sup>1070</sup>  $[\text{GeF}_4(\text{dmpbz})]$ ,<sup>1070</sup>  $[\text{SnF}_4(\text{depe})]$ ,<sup>988</sup> and  $[\text{SnCl}_4(\text{dppen})]$ .<sup>1071</sup> In group 14, structurally characterized Ge(II) complexes with chelating bisphosphanes are exemplified by  $[\text{GeX}_2(\text{dmpbz})]$  and  $[\text{GeX}_2(\text{dmpe})]$  ( $\text{X} = \text{Cl}, \text{Br}, \text{I}$ ; disphenoidal geometries), and  $[\text{GeX}_2(\text{dppbz})]$  ( $\text{X} = \text{Cl}, \text{Br}$ ; with an asymmetrically bound dppbz ligand); other complexes in this series have also been described.<sup>1072</sup> The  $[\text{GeCl}(\text{dppp})]^+$  cation has a trigonal pyramidal structure; its synthesis as  $[\text{GeCl}_3]^-$  and triflate salts, was part of a detailed investigation from Béland et al. focusing on reductive dehalogenation of a zwitterionic Ge(II) species to produce a Ge(I) dimer.<sup>1073</sup> An insightful comparison between complexation of  $\text{SnF}_2$  and  $\text{SnCl}_2$  with bisphosphanes concludes that an underlying problem with  $\text{SnF}_2$  is its insolubility in weak donor solvents and, therefore, the lack of soluble molecular precursors with readily displaced ligands.<sup>1074</sup> Reid and coworkers have reported rare examples of phosphane complexes of lead(II).  $[\text{Pb}(\text{dmpe})(\text{O}_2\text{NO-}\kappa^2)_2]$  is a representative example, and Fig. 54D illustrates that intermolecular  $\text{O}\cdots\text{Pb}$  contacts extend the structure in the solid state; a CN = 8 is achieved by additional contacts not shown in Fig. 54F.<sup>1075</sup>

Phosphane complexes of the heavier group 15 M(III) elements include  $[\text{Sb}(\text{dppm})(\text{O}_3\text{SCF}_3)_3(\text{NCMe})]$  (distorted octahedral) and  $[\text{Bi}(\text{dppm})(\text{O}_3\text{SCF}_3)_3]$ ; in contrast to analogous complexes with monodentate phosphane ligands, the latter (along with related complexes with tridentate triphosphanes) are stable with respect to ligand oxidation.<sup>1076</sup> A coordination number of 3 occurs in  $[\text{SbCl}(\text{dppe})]^{2+}$  and  $[\text{SbCl}(\text{dppm})]^{2+}$ , and 4-coordinate geometries occur in  $[\text{SbCl}_2(\text{dmpe})]^+$  (disphenoidal, axial Cl) and  $[\text{SbCl}_2(\text{dppe})]^+$  (disphenoidal, axial Cl); in  $[\text{SbCl}_2(\text{dppm})]^+$  the dppm ligand is asymmetrically bound with Sb-P distances of 2.6011(4) and 3.0272(4) Å.<sup>997</sup> The Bi(III) compounds  $[\text{BiX}_2(\text{O}_3\text{SCF}_3)(\text{dmpe})]$  ( $\text{X} = \text{Cl}, \text{Br}$ ) and  $[\text{BiCl}(\text{O}_3\text{SCF}_3)_2(\text{dmpe})]$  readily decompose in solution giving elemental Bi; in the solid state, all three complexes are dimers supported either by  $\mu\text{-X}$  or  $\mu\text{-O}_3\text{SCF}_3$  ligands.<sup>1077</sup>



**Scheme 16** Ligand types included in Section 1.02.3.3.2.





**Fig. 55** Structures of (A)  $[K_2\{^tBu_3SiPPPSi^tBu_3\}_2(THF)_4]$  (CSD refcode DAKQOW), (B) part of the 1D-chain in  $[Cs\{^tBu_3SiPPPSi^tBu_3\}_2(THF)]_n$  (refcode BIVZAI), and (C) part of the 1D-chain in  $[Na_2(dme)_{1.5}(tmbp)]_n$  (refcode EFAFIA).

In group 16,  $[Se(dppe)][CF_3SO_3]_2$  and  $[Te(dppe)][CF_3SO_3]_2$  provide rare examples of homoleptic P  $\rightarrow$  chalcogen coordination compounds; in the solid state,  $Se \cdots O$  or  $Te \cdots O$  contacts exist but the interaction is considered to be ionic.<sup>1078</sup>

### 1.02.3.3.2 PXP (X = P, CR) ligands with delocalized backbone

In Section 1.02.2.2.4, we surveyed complexes containing  $[RN_3R']^-$  and  $[RNC(R')NR']^-$  ligands (Scheme 7) and in this section, we look at their P-analogs (Scheme 16) which are rather sparse. Note the distinction between  $[dppm-H]^-$  (discussed in the previous section) and  $[RPC(R')PR']^-$  which possesses a delocalized backbone.

Lerner et al. have investigated the reaction of  $P_4$  with  $^tBu_3SiK$  in detail, and  $K\{^tBu_3SiPPPSi^tBu_3\}$  was among the products reported. The structure of the THF adduct (Fig. 55A) exhibits short P–P bond lengths (2.0721(16) Å) consistent with  $\pi$ -character.<sup>1079</sup> The same group has demonstrated that  $Cs\{^tBu_3SiPPPSi^tBu_3\}$  is more stable than the  $Li^+$ ,  $Na^+$  and  $K^+$  homologs. In the solid state,  $[Cs\{^tBu_3SiPPPSi^tBu_3\}_2(THF)]_n$  possesses a 1D-polymer (Fig. 55B) and P–P bond lengths of 2.090(3) Å.<sup>1080</sup> Although an organometallic compound, we include  $[Al^tBu_2\{ArPCHPAR\}]$  ( $Ar = 2,4,6\text{-}^tBu_3C_6H_2$ )<sup>1081</sup> as a representative of the second ligand type shown in Scheme 16.

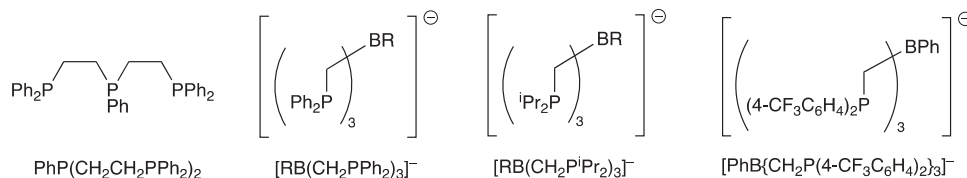
### 1.02.3.3.3 Heterocyclics: Reduced 2,2'-biphosphinine

There are no examples of main group metal complexes containing neutral 2,2'-biphosphinine, i.e., the P analog of 2,2'-bipyridine. However, the reduction of 4,4',5,5'-tetramethyl-2,2'-biphosphinine (tmbp) by lithium naphthalene or sodium naphthalene in dme has been investigated, and  $[Na_2(dme)_{1.5}(tmbp)]_n$  was isolated and structurally characterized. A 1D-chain assembles (Fig. 55C) with the  $[tmbp]^{2-}$  ligand chelating to one  $Na^+$  and forming P–Na contacts to two additional  $Na^+$  centers; there are also weak  $Na^+ \cdots \pi$  contacts.<sup>1082</sup>

### 1.02.3.4 Tris(phosphane) ligands: Open-chain and tripodal

Main group metal complexes of tris(phosphane) ligands, both open-chain and tripodal, are limited and Scheme 17 displays the structures of the ligands included in this section. Coordination compounds incorporating the open-chain ligand  $PhP(CH_2CH_2PPh_2)_2$  are illustrated by Sb(III) and Bi(III) complexes. In *fac*- $[Sb\{PhP(CH_2CH_2PPh_2)_2\}(O_3SCF_3)_3]$ , the Sb(III) center is octahedrally sited, although two Sb–O interactions are longer than the third (2.808(3) and 2.746(3) Å vs 2.589(3) Å).<sup>1076</sup>

The reaction between  $TlPF_6$  and  $[Li\{tmeda\}\{PhB(CH_2PPh_2)_3\}]$  leads to  $[Tl\{PhB(CH_2PPh_2)_3\}]$  which, in the solid state is a dimer, but is a monomer in solution.<sup>1083</sup> Significantly, the  $^iPr$  analog  $[Tl\{PhB(CH_2P^iPr_2)_3\}]$  is monomeric in the crystal and this is attributed to the  $^iPr$  substituents forming a protective sheath around the Tl atom.<sup>1084</sup> The compounds  $[Tl\{(3,5-(CF_3)_2C_6H_3)B(CH_2P^iPr_2)_3\}]$  and  $[Tl\{(3,5-Me_2C_6H_3)B(CH_2P^iPr_2)_3\}]$  are distinct in their solid-state structures; in the latter, there are two Tl(I) environments, one engaging in weak intermolecular  $\pi$ -interactions and the other involving a Tl–Tl interaction. In contrast,  $[Tl\{(3,5-(CF_3)_2C_6H_3)B(CH_2P^iPr_2)_3\}]$ <sup>1085</sup> and  $[Tl\{PhB\{CH_2P(4-CF_3C_6H_4)_2\}_3\}]$ <sup>1086</sup> are monomeric in the solid state. The change in the P-substituents on going from  $[Tl\{PhB(CH_2PPh_2)_3\}]$  to  $[Tl\{PhB\{CH_2P(4-CF_3C_6H_4)_2\}_3\}]$  enhances the electrophilic character at the metal center.<sup>1086</sup>



**Scheme 17** Tris(phosphane) ligands; R is an arene, often Ph.



## 1.02.4 Arsenic-donor ligands

### 1.02.4.1 Monodentate ligands

#### 1.02.4.1.1 $R_3As$

Main group metal complexes containing  $R_3As$  ligands are dominated by metals from the p-block. This section covers monodentate  $R_3As$  ligands, as well as  $R_2As(CH_2)_nAsR_2$  ligands bridging two metal centers and tripodal ligands in which each of one or more 'arms' coordinate to a single metal atom.

Tetrahedral group 13 M(III) complexes are illustrated by  $[AlX_3(AsPh_3)]$  ( $X = Cl, I$ ),<sup>1087</sup>  $[GaCl_3(AsPh_3)]$ ,<sup>1087</sup>  $[GaX_3(AsMe_3)]$  ( $X = Cl, Br, I$ ),<sup>1068</sup>  $[GaCl_3(AsEt_3)]$ ,<sup>1088</sup> and  $[InCl_3(AsEt_3)]$ .<sup>1088</sup> The In(III) center can also accommodate two  $AsEt_3$  ligands as in the trigonal bipyramidal *trans*- $[InCl_3(AsEt_3)_2]$ .<sup>1088</sup>  $Ph_3As$  is among the ligands that forms a donor-acceptor adduct with the Lewis superacid  $Al(OR^F)_3$  ( $R^F = C(CF_3)_3$ ).<sup>1089</sup> In  $[Ga_2I_6(\mu-dpae)]$ , each Ga is tetrahedrally sited.<sup>1068</sup> Rather than coordinate to a single Ga(III) center, the tripodal ligand  $MeC(CH_2AsMe_2)_3$  reacts with  $GaX_3$  ( $X = Cl, I$ ) to yield  $[MeC(CH_2AsMe_2)_3]\{GaX_3\}$  when sufficient  $GaX_3$  is available; with a 1:1 M ratio of reactants,  $[MeC(CH_2AsMe_2)_3]\{GaCl_2\}[GaCl_4]$  was isolated.<sup>1090</sup>

Germanium(IV) and tin(IV) complexes incorporating tertiary arsane ligands include *trans*- $[GeCl_4(AsEt_3)_2]$ ,<sup>1070</sup> *trans*- $[SnX_4(AsEt_3)_2]$  ( $X = Cl, Br$ ),<sup>990</sup> *trans*- $[SnCl_3(OS_3CF_3)(AsEt_3)_2]$ ,<sup>990</sup>  $[SnCl_5(AsEt_3)]^-$ ,<sup>990</sup> and *trans*- $[SnCl_4(AsPh_3)_2]$ .<sup>1091</sup> In contrast to the latter octahedral complex, the bromido analog crystallizes as  $[SnBr_4(AsPh_3)] \cdot AsPh_3$  with the non-coordinated arsane molecule showing a close  $As \cdots Br_{axial}$  contact (3.567(3) Å).<sup>1091</sup> Tetrahedral Ge(II) complexes with arsane ligands are exemplified by  $[Ge(AsMe_3)_2(O_3SCF_3)_2]$ . Reid and coworkers were not able to isolate a tris(trimethylarsane) complex from reactions of  $[GeCl_2(diox)]$  with  $Me_3As$  followed by  $CF_3SO_3SiMe_3$  even when using excess  $Me_3As$ ; this behavior differs from that with  $Me_3P$  and was attributed to the weaker  $\sigma$ -donor power of  $Me_3As$  vs  $Me_3P$ .<sup>991</sup>

Compounds containing Sb-As or Bi-As coordinate bonds remain rare.  $[SbCl_3(AsEt_3)]$ ,  $[SbCl_2(AsPh_3)][O_3SCF_3]$  and  $[BiCl_2(AsPh_3)][O_3SCF_3]$  were reported in 2009; in the triflate salts the  $Sb \cdots O$  and  $Bi \cdots O$  distances are 2.965(2) and 2.726(3) Å, respectively, suggesting ion pairs rather than coordinated  $[CF_3SO_3]^-$  ligands.<sup>1092</sup>

#### 1.02.4.1.2 $R_2As^-$

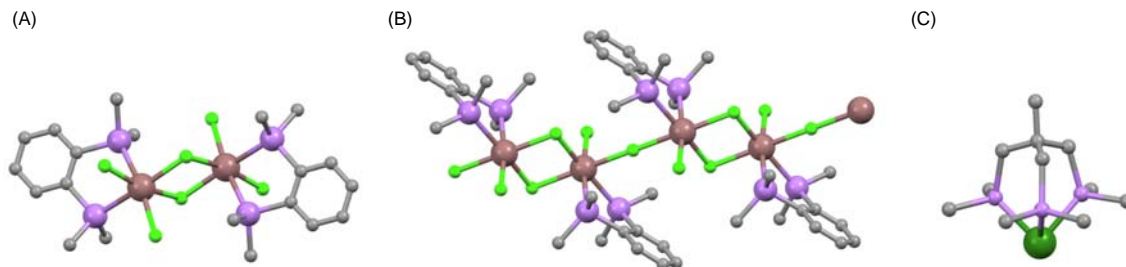
Few non-organometallic complexes involving  $R_2As^-$  ligands have been reported since 2000. The tetrahedral  $[Li(THF)_{2.75}(OEt_2)_{0.25}(AsDipp_2)]$  was used as a precursor to  $[Ge(AsDipp_2)_2]$  and  $[Sn(AsDipp_2)_2]$ . Stabilization by As-Ge/Sn  $\pi$ -interactions is prevented by a high energy barrier to planarization at the As center, and Ge/Sn  $\cdots$ arene interactions are important instead.<sup>1093</sup> The dimer  $[Ge_2Cl_2(AsMes_2)_2(\mu-NPh)_2]$  was observed as one product of the reaction of  $GeCl_2 \cdot diox$  and  $[(Mes_2AsNPh)\{Li(OEt_2)_2\}]$ .<sup>1094</sup>

#### 1.02.4.1.3 $AsCO^-$

In Sections 1.02.2.1.4 and 1.02.3.1.3 we introduced main group metal complexes containing  $NCO^-$  and  $PCO^-$ . The analogous  $AsCO^-$  ligand is little documented. In 2017, Yao et al. published a one-pot synthesis of  $[Na(OCAs)(diox)_x]$ , and used this as a precursor to  $[Ge(AsCO)(Nacnac)]$  ( $Ar = Dipp$ , see Scheme 6 for the  $\beta$ -diketiminate ligand  $[Nacnac]^-$ ). The  $AsCO^-$  ligand coordinates to Ge(II) through As ( $Ge-As = 2.635(1)$  Å,  $Ge-As-C = 84.5^\circ$ ). Loss of CO occurs readily to yield  $[Ge(\equiv As)(Nacnac)]$ .<sup>1095</sup> Results from the Goicoechea group also open up the coordination chemistry of  $AsCO^-$ , e.g., with the organometallic derivative  $[Sn(AsCO)(2,6-Mes_2C_6H_3)_2]^-$ .<sup>1096</sup>

### 1.02.4.2 Bidentate ligands: Chelating $R_2As(X)AsR_2$

Within main group metal coordination chemistry, the most popular chelating  $R_2As(X)AsR_2$  ligand appears to be the preorganized 1,2-bis(dimethylarsino)benzene (dmabz), the arsenic analog of dmpbz, Scheme 15), and complexes from the heavier p-block metals are dominant. Typical examples from group 13 are the tetrahedral  $[GaX_2(dmabz)]^+$  ( $X = Cl, I$ ) and  $[InI_2(dmabz)]^+$ ,<sup>1069</sup> and the dimer  $[In_2Cl_4(dmabz)_2(\mu-Cl)_2]$  (Fig. 56A).<sup>1069</sup> The structure of  $[In_2Cl_2(dmabz)_2(\mu-Cl)_3]^{n+}$  is related to that of  $[In_2Cl_4(dmabz)_2(\mu-Cl)_2]$  but with two terminal In-Cl units converted into In-Cl-In bridges (Fig. 56B).<sup>1069</sup>  $[Bi_2Cl_4(dmabz)_2(\mu-Cl)_2]$ <sup>1097</sup> is structurally related to  $[In_2Cl_4(dmabz)_2(\mu-Cl)_2]$ . Complexes of group 14 M(II) include  $[GeCl(dmabz)]^+$ ,<sup>1072</sup> and



**Fig. 56** Structures of (A)  $[In_2Cl_4(dmabz)_2(\mu-Cl)_2]$  (CSD refcode QOKMIN), (B) part of the 1D-chain in  $[In_2Cl_2(dmabz)_2(\mu-Cl)_3]^{n+}$  in the  $[InCl_4]^-$  salt (refcode QOKMOT), and (C)  $[Ge\{MeC(CH_2AsMe_2)_3\}_2]^{2+}$  (refcode UZEHEP).

$[\text{SnCl}(\text{dmabz})]^+$ ,<sup>1074</sup> which have trigonal pyramidal structures. In  $[\text{Ge}_2(\text{dmabz})]$ , there are significant  $\text{Ge}\cdots\text{I}$  contacts in the solid state which result in a polymeric assembly.<sup>1072</sup>

### 1.02.4.3 Tridentate: Tripod ligands

In Section 1.02.4.1.1, we included  $[\{\text{MeC}(\text{CH}_2\text{AsMe}_2)_3\}(\text{GaX}_3)_3]$  and  $[\{\text{MeC}(\text{CH}_2\text{AsMe}_2)_3\}(\text{GaCl}_2)^+]$  in which the tripodal ligand coordinated to three or one Ga(III) centers, respectively.<sup>1090</sup> Bidentate  $\text{MeC}(\text{CH}_2\text{AsMe}_2)_3$  is also seen in  $[\text{SnBr}_4\{\text{MeC}(\text{CH}_2\text{AsMe}_2)_3-\kappa^2\}]$ .<sup>988</sup> However, in the triflate salt of  $[\text{Ge}\{\text{MeC}(\text{CH}_2\text{AsMe}_2)_3\}]^{2+}$ , the ligand binds a single Ge(II) center (Fig. 56C) in the classical tripodal manner.<sup>991</sup>

## 1.02.5 Antimony-donor ligands

### 1.02.5.1 Monodentate ligands

#### 1.02.5.1.1 $R_3\text{Sb}$

As with main group metal complexes containing  $R_3\text{As}$  ligands, those with monodentate stibanes are relatively few in number if one excludes organometallic species.  $[\text{GaCl}_3(\text{SbPh}_3)]$  has the expected tetrahedral structure ( $\text{Sb}-\text{Ga} = 2.654 \text{ \AA}$ ),<sup>1098</sup> as do  $[\text{GaCl}_3(\text{SbMe}_3)]$ ,<sup>1099</sup>  $[\text{AlI}_3(\text{Sb}^i\text{Pr}_3)]$ ,<sup>1100</sup>  $[\text{GaX}_3(\text{Sb}^i\text{Pr}_3)]$  ( $X = \text{Cl}, \text{I}$ ),<sup>1100</sup>  $[\text{GaBr}_3(\text{SbEt}_3)]$ ,<sup>1100</sup>  $[\text{InX}_3(\text{SbR}_3)]$  ( $X = \text{Cl}, \text{I}$ ;  $R = \text{Et}, ^i\text{Pr}$ ),<sup>1100</sup> and  $[\text{InX}_3(\text{Sb}^n\text{Bu}_3)]$  ( $X = \text{Cl}, \text{Br}$ ).<sup>1088</sup>

#### 1.02.5.1.2 $R_2\text{Sb}^-$

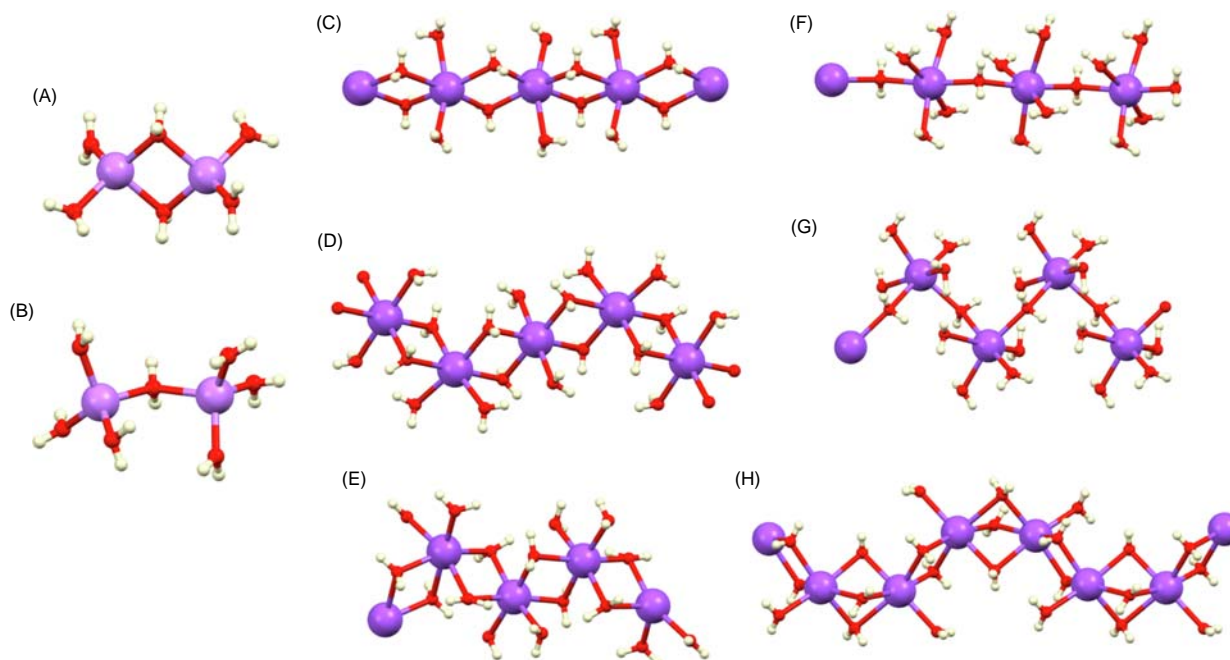
Just as for  $R_2\text{As}^-$  (Section 1.02.4.1.2), non-organometallic main group metal complexes with  $R_2\text{Sb}^-$  ligands are sparse. The reaction of  $[\text{Al}(\text{Nacnac})]$  ( $\text{Ar}$  in  $\text{Nacnac} = \text{Dipp}$ , see Scheme 6) with  $\text{Sb}_2\text{Et}_4$  results in  $\text{Sb}-\text{Sb}$  cleavage and the formation of  $[\text{Al}(\text{SbEt}_2)_2(\text{Nacnac})]$ ; an analogous reaction with  $\text{Bi}_2\text{Et}_4$  follows a similar route,<sup>1101</sup> and related complexes of Ga(III) have also been reported.<sup>1102</sup>

## 1.02.6 Oxygen-donor ligands

### 1.02.6.1 Monodentate ligands: Simple coordination compounds

#### 1.02.6.1.1 $\text{H}_2\text{O}$ (restricted to simple aqua complexes)

Because of the ubiquitous nature of the aqua ligand, we have restricted the discussion to homoleptic aqua complexes of the main group metal ions; additionally, we have included the structures of several hydrated metal halides and perchlorates. Note that for commonly encountered ions such as  $[\text{Li}(\text{OH}_2)_4]^+$ ,  $[\text{Na}(\text{OH}_2)_6]^+$ ,  $[\text{Mg}(\text{OH}_2)_6]^{2+}$ , only selected literature citations are given.



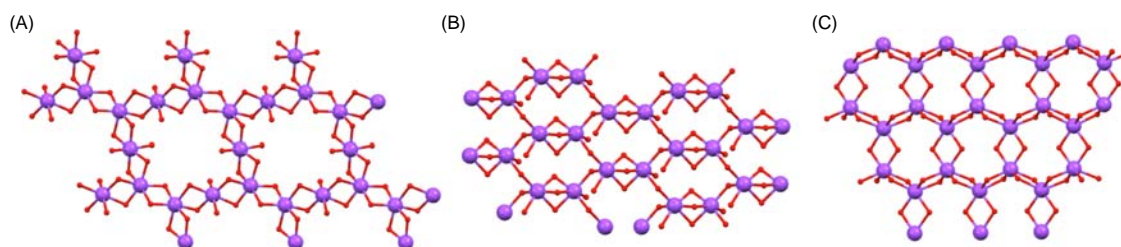
**Fig. 57** Structures of (A)  $[\text{Li}_2(\text{OH}_2)_4(\mu\text{-OH}_2)_2]^{2+}$  (CSD refcode CUSWES01) and (B)  $[\text{Li}_2(\text{OH}_2)_6(\mu\text{-OH}_2)_2]^{2+}$  (refcode SODLEE). Parts of the 1D-chains in (C) *trans*- $[\text{Na}(\text{OH}_2)_2(\mu\text{-OH}_2)_2]_n^{n+}$  (refcode ASABEB), (D)  $[\text{Na}(\text{OH}_2)_2(\mu\text{-OH}_2)_2]_n^{n+}$  with both *trans* and *cis*-arrangements of terminal aqua ligands (refcode OSURUR02), (E) *cis*- $[\text{Na}(\text{OH}_2)_2(\mu\text{-OH}_2)_2]_n^{n+}$  (refcode DARNIU), (F) *trans*- $[\text{Na}(\text{OH}_2)_4(\mu\text{-OH}_2)]_n^{n+}$  (refcode CUPQIO), (G) *cis*- $[\text{Na}(\text{OH}_2)_4(\mu\text{-OH}_2)]_n^{n+}$  (refcode PEPNUU), and (H)  $[\text{Na}_2(\text{OH}_2)_2(\mu\text{-OH}_2)_5]_n^{2n+}$  (refcode LULSAN).

For the group 1  $M^+$  ions, we expect the coordination number to typically increase as the group is descended. However, although CN = 4 is most typical for  $Li^+$ , tetrahedral  $[Li(OH_2)_4]^+$ ,<sup>1103–1111</sup> square-based pyramidal or trigonal bipyramidal  $[Li(OH_2)_5]^+$ ,<sup>1112,1113</sup> and octahedral  $[Li(OH_2)_6]^+$ ,<sup>1114</sup> have all been structurally characterized. Dinuclear aqua complexes of lithium are represented by  $[Li_2(OH_2)_4(\mu-OH_2)_2]^{2+}$  (Fig. 57A),<sup>1115,1116</sup> and  $[Li_2(OH_2)_6(\mu-OH_2)]^{2+}$  (Fig. 57B).<sup>1117,1118</sup>

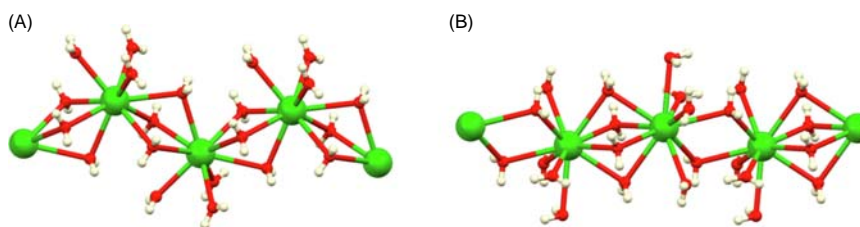
For  $Na^+$ , the octahedral hexaqua ion is common,<sup>1119–1127</sup> with octahedral coordination also seen in  $[Na_2(OH_2)_8(\mu-OH_2)_2]^{2+}$ ,<sup>1128–1134</sup> and  $[Na_4(OH_2)_{12}(\mu-OH_2)_6]^{4+}$ .<sup>1131</sup> The variety of 1D-polymeric assemblies based upon interconnected  $\{Na(OH_2)_6\}$  units is fascinating and these include  $[Na(\mu-OH_2)_3]_n^{n+}$  (face-sharing octahedra),<sup>370</sup>  $[Na(OH_2)_2(\mu-OH_2)_2]_n^{n+}$  with *trans*-terminal aqua ligands (Fig. 57C),<sup>1135–1143</sup>  $[Na(OH_2)_2(\mu-OH_2)_2]_n^{n+}$  with  $Na^+$  centers along the 1D-chain having alternating *cis*- and *trans*-terminal aqua ligands (Fig. 57D),<sup>1144–1146</sup>  $[Na(OH_2)_2(\mu-OH_2)_2]_n^{n+}$  with *cis*-terminal aqua ligands (Fig. 57E),<sup>1147–1149</sup>  $[Na(OH_2)_4(\mu-OH_2)]_n^{n+}$  with a *trans*-arrangement of  $\mu-OH_2$  (Fig. 57F),<sup>1150</sup>  $[Na(OH_2)_4(\mu-OH_2)]_n^{n+}$  with a *cis*-arrangement of  $\mu-OH_2$  (Fig. 57G),<sup>1151</sup> and  $[Na_2(OH_2)_2(\mu-OH_2)_5]_n^{2n+}$  (Fig. 57H).<sup>1152</sup> Such 1D-polymeric assemblies, especially isomers of  $[Na(OH_2)_2(\mu-OH_2)_2]_n^{n+}$ , are well established, but there is also the possibility of extension into a 2D-network as observed in, for example, a layered structure which contains  $[Na_4(OH_2)_{14}]_n^{4n+}$  sheets (Fig. 58A) alternating with layers of Lindqvist heteropolyanions,<sup>1153</sup> the hydrate of sodium (*E*)-2-(2-fluorobenzylidene) butanoate in which  $[Na_2(OH_2)_7]_n^{2n+}$  2D-sheets feature octahedral  $\{Na(OH_2)_6\}$  units connected as shown in Fig. 58B,<sup>1154</sup> and in  $[Na(OH_2)_3]_n^{n+}$  in which all the aqua ligands are in a bridging mode and each  $Na^+$  center is in a distorted trigonal pyramidal rather than octahedral environment.<sup>1155</sup> A departure from CN = 6 is found in  $[Na_2(OH_2)_{12}(\mu-OH_2)]^{2+}$  in which each  $Na^+$  is bound to six terminal and one bridging aqua ligand,<sup>1156</sup> and in the 1D-polymeric  $[Na_4(OH_2)_{14}]_n^{4n+}$  in which both 5- and 6-coordinate  $Na^+$  are observed.<sup>1157</sup> Higher CN values are typical for the heavier group 1 metals, for example,  $[K(OH_2)_7]^+$ ,<sup>1158</sup>  $[K(OH_2)_8]^+$ ,<sup>1159</sup>  $[Rb(OH_2)_9]^+$ ,<sup>1112</sup> and  $[Cs(OH_2)_{10}]^+$ .<sup>1112</sup> However, the diversity of extended chains and networks found for  $Na^+$  (Figs. 57 and 58) is not reproduced for the later alkali metals.

In group 2, the same general trend as in group 1 is observed with a CN = 4 in  $[Be(OH_2)_4]^{2+}$ ,<sup>265,1160,1161</sup> and CN = 6 in the ubiquitous  $[Mg(OH_2)_6]^{2+}$  (only a few examples of *ca.* 430 structures in the CSD between 2000 and 2022 are given).<sup>1140,1162–1175</sup> Calcium shows a wider range of CNs than  $Mg^{2+}$ , starting with CN = 6 in  $[Ca(OH_2)_6]^{2+}$ ,<sup>1140,1176</sup> CN = 7 in  $[Ca(OH_2)_7]^{2+}$ ,<sup>1150,1177–1179</sup> and CN = 8 in  $[Ca(OH_2)_8]^{2+}$ .<sup>1175</sup> A CN of 6 is seen in the 1D-polymer  $[Ca(OH_2)_4(\mu-OH_2)_2]_n^{2n+}$ .<sup>1180</sup> In  $[Ca_2(OH_2)_8(\mu-OH_2)_3]^{4+}$ , each  $Ca^{2+}$  is 7-coordinate,<sup>1181</sup> while a CN of 8 is found in  $[Ca_2(OH_2)_{12}(\mu-OH_2)_2]^{4+}$ .<sup>1167,1182</sup> Crystalline  $CaBr_2 \cdot 9H_2O$ ,  $CaI_2 \cdot 8H_2O$ ,  $CaI_2 \cdot 7H_2O$  and  $CaI_2 \cdot 6.5H_2O$  contain the  $[Ca(OH_2)_8]^{2+}$ ,  $[Ca_2(OH_2)_{12}(\mu-OH_2)_2]^{4+}$ ,  $[Ca_2(OH_2)_{12}(\mu-OH_2)_2]^{4+}$ , and  $[Ca_2(OH_2)_{10}(\mu-OH_2)_3]^{4+}$  cations, respectively, each with CN = 8 (distorted antiprism).<sup>1183</sup> Hennings et al. have also reported the structures of  $Ca(ClO_4)_2 \cdot 4H_2O$  and  $Ca(ClO_4)_2 \cdot 6H_2O$ ; these contain the neutral polymer  $[Ca(OH_2)_4(\mu-ClO_4-1\kappa O^1:2\kappa O^2)]_n$  and discrete  $[Ca(OH_2)_6(ClO_4-\kappa^1)]^+$  cations, respectively.<sup>1184</sup>

For the heaviest group 2 metals, values of CN  $\geq 8$  are common, for example, in  $[Sr(OH_2)_8]^{2+}$  (CN = 8),<sup>1175,1179</sup>  $[Sr_2(OH_2)_{10}(\mu-OH_2)_4]^{4+}$  (CN = 9),<sup>1185</sup>  $[Ba_2(OH_2)_{14}(\mu-OH_2)_2]^{4+}$  (CN = 9),<sup>1186</sup>  $[Ba_2(OH_2)_{10}(\mu-OH_2)_4]^{4+}$  (CN = 9),<sup>1185</sup>  $[Ba(OH_2)_3(\mu-OH_2)_3]_n^{2n+}$  (CN = 9, Fig. 59A),<sup>1187</sup>  $[Ba_2(OH_2)_{10}(\mu-OH_2)_4]_n^{4n+}$  (CN = 10),<sup>1188</sup> and  $[Ba_2(OH_2)_8(\mu-OH_2)_6]_n^{4n+}$  (CN = 10, Fig. 59B).<sup>1189</sup> It is also worth noting that the structures of  $Sr(ClO_4)_2 \cdot 3H_2O$ ,  $Sr(ClO_4)_2 \cdot 4H_2O$  and  $Sr(ClO_4)_2 \cdot 9H_2O$  have been studied by Hennings et al., complementing the investigations of the calcium halides and perchlorates described above.  $Sr(ClO_4)_2 \cdot 3H_2O$  and  $Sr(ClO_4)_2 \cdot 4H_2O$  assemble into 3D-networks with aqua ligands in both terminal and bridging modes, and



**Fig. 58** (A) Part of an  $[Na_4(OH_2)_{14}]_n^{4n+}$  2D-net in a layered structure which also contains Lindqvist heteropolyanions (CSD refcode LAYCAQ), and (B) part of the  $[Na_2(OH_2)_7]_n^{2n+}$  sheet in the hydrate of sodium (*E*)-2-(2-fluorobenzylidene) butanoate (refcode PEHSEC). (C) Part of the  $[Na(OH_2)_3]_n^{n+}$  2D-net with all bridging aqua ligands (refcode SOQZAA).



**Fig. 59** Parts of the 1D-chains in (A)  $[Ba(OH_2)_3(\mu-OH_2)_3]_n^{2n+}$  (CSD refcode LINYEB), and (B)  $[Ba_2(OH_2)_8(\mu-OH_2)_6]_n^{4n+}$  (refcode TEDWAC).

perchlorate ions in  $\mu\text{-ClO}_4\text{-}1\kappa\text{O}^1\text{:}2\kappa\text{O}^2$  bonding modes. In contrast,  $\text{Sr}(\text{ClO}_4)_2\cdot 9\text{H}_2\text{O}$  crystallizes with discrete  $[\text{Sr}(\text{OH}_2)_7(\text{ClO}_4\text{-}\kappa^1)_2]$  complexes and  $\text{H}_2\text{O}$  solvate molecules.<sup>1190</sup>

The octahedral  $[\text{Al}(\text{OH}_2)_6]^{3+}$  ion is found in the solid-state structures of, for example,  $[\text{Al}(\text{OH}_2)_6]_2[\text{C}_6(\text{CO}_2)_6]\cdot 4\text{H}_2\text{O}$ ,<sup>1191</sup>  $[\text{Al}(\text{OH}_2)_6][\text{MeSO}_3]_3$ ,<sup>1192</sup>  $[4\text{-H}_2\text{NpyH}][\text{Al}(\text{OH}_2)_6][\text{SO}_4]_2\cdot 4\text{H}_2\text{O}$ ,<sup>1171</sup> and  $[2\text{-H}_2\text{NpyH}][\text{Al}(\text{OH}_2)_6][\text{SO}_4]_2\cdot 4\text{H}_2\text{O}$ ,<sup>1193</sup>  $[\text{pipzH}_2]_{0.5}[\text{Al}(\text{OH}_2)_6][\text{SO}_4]_2\cdot 4\text{H}_2\text{O}$ ,<sup>1194</sup>  $[\text{Al}(\text{OH}_2)_6][\text{NO}_3]_3\cdot (15\text{-crown-}5)\cdot 4\text{H}_2\text{O}$ ,<sup>1195</sup> and  $[\text{H}_2\text{im}][\text{Al}(\text{OH}_2)_6][\text{SO}_4]_2$ .<sup>1196</sup> Octahedral hexaqua ions of Ga(III) and In(III) have also been structurally characterized in the solid state,<sup>1197–1199</sup> and  $[\text{Me}_4\text{N}]_6[\text{In}(\text{OH}_2)_6][\text{InF}_6]_3\cdot 18\text{H}_2\text{O}$  contains octahedral  $[\text{In}(\text{OH}_2)_6]^{3+}$  cations which form strong  $\text{O}\cdots\text{H}\cdots\text{F}$  hydrogen bonds with the  $[\text{InF}_6]^{3-}$  anions ( $\text{O}\cdots\text{F} = 2.472(1)\text{ \AA}$ ).<sup>1200</sup>

The crystal structure of  $[\text{Bi}(\text{H}_2\text{O})_9][\text{CF}_3\text{SO}_3]_3$  was reported in 2000 (a redetermination); the conversion of the hydrated Bi(III) ion to  $[\text{Bi}_6\text{O}_4(\text{OH})_4]^{6+}$  was prevented by using solutions containing a large excess of  $\text{HClO}_4$  or  $\text{CF}_3\text{SO}_3\text{H}$  (1.0–2.0 mol  $\text{dm}^{-3}$ ). The  $[\text{Bi}(\text{H}_2\text{O})_9]^{3+}$  ion has a tricapped trigonal prismatic structure.<sup>1201</sup>

### 1.02.6.1.2 ROH, R<sub>2</sub>O

The use of coordinating alcohols and ethers as solvents in reactions results in their pervasive incorporation into coordination compounds, either to occupy otherwise vacant coordination sites or preferential coordination in place of other ligands present in a reaction mixture. As in many sections in this review, we have therefore had to be selective in the examples included in this discussion. We have chosen to focus on homoleptic complexes in which ROH or R<sub>2</sub>O is the ligand of focus rather than a secondary ligand, and in this section we deal only with monodentate ligands. As we saw with aqua ligands, the hard O-donor in alcohols and ethers is most compatible with hard metal ions, either s-block or M<sup>3+</sup> from the p-block.

Tetrahedral coordination for Li<sup>+</sup> is seen in  $[\text{Li}(\text{HOME})_4]^+$ ,<sup>1202–1207</sup>  $[\text{Li}(\text{HO}^i\text{Pr})_4]^+$  (in  $[\text{LiO}^i\text{Pr}]\cdot 5i\text{PrOH}$  with a hydrogen-bonded chain structure),<sup>1208</sup> and  $[\text{Li}_2(\text{HOME})_4(\mu\text{-HOME})_2]^{2+}$ .<sup>1209</sup> Two series of <sup>t</sup>BuOH solvates of LiX (X = Cl, Br, I) have been reported with LiX:<sup>t</sup>BuOH ratios of 1:4 and 1:6; in both, Li<sup>+</sup> is 4-coordinate and structurally characterized complexes are  $[\text{Li}(\text{HO}^t\text{Bu})_4]\text{X}$  (X = Cl, I) and  $[\text{Li}(\text{HO}^t\text{Bu})_4]\text{X}\cdot 2^t\text{BuOH}$  (X = Cl, Br, I).<sup>1210</sup> The  $[\text{Na}(\text{HOME})_5]^+$  ion in  $[\text{Na}(\text{HOME})_5]_2[\text{Mo}_6(\mu_3\text{-Br})_8(\text{OME})_6]$  has a square-based pyramidal structure.<sup>1211</sup> The  $[\text{K}(\text{HOME})_4]^+$  ion has been described, with the four O-donors in a plane and the K<sup>+</sup> center disordered above and below this plane.<sup>1212</sup>

Homoleptic group 2 metal complexes with alcohol ligands include  $[\text{Mg}(\text{HOME})_6]^{2+}$ ,<sup>1213–1216</sup>  $[\text{Mg}(\text{HOEt})_6]^{2+}$ ,<sup>1213,1217</sup> and  $[\text{Ca}(\text{HOME})_6]^{2+}$ .<sup>1218</sup> Additionally, there is a range of complexes with alcohols and simple anionic ligands. These are represented by *trans*- $[\text{MgCl}_2(\text{HOEt})_4]$  and  $[\text{Mg}_2\text{Cl}_2(\text{HOEt})_6(\mu\text{-Cl})_2]$  (compounds of interest as precursors for Ziegler-Natta polymerization catalysts),<sup>1219</sup> *trans*- $[\text{Mg}(\text{OH}_2)_2(\text{HOEt})_4]^{2+}$ ,<sup>1220</sup> *trans*- $[\text{Mg}(4\text{-O}_2\text{Cpy})_2(\text{HOME})_4]$ ,<sup>1221</sup> *cis*- $[\text{Ca}(\text{OH}_2)_2(\text{HOME})_4]^{2+}$ ,<sup>1222</sup> and *trans*- $[\text{Ca}(\text{O}_3\text{SCF}_3\text{-}\kappa^1)_2(\text{HOME})_4]$ .<sup>1223</sup>

The cyclic aluminophosphonate  $[\text{Al}_2(\text{HO}^n\text{Bu})_8(\mu\text{-PhHPO}_2\text{-}1\kappa\text{O}^1\text{:}2\kappa\text{O}^2)]^{4+}$  has been isolated and structurally characterized as a chloride salt; a detailed solid-state NMR spectroscopic study was carried out.<sup>1224</sup>

We move now to main group metal complexes containing ether ligands, focusing again only on homoleptic complexes and other simple species. Low CNs for Li<sup>+</sup> are seen in  $[\text{Li}(\text{OEt}_2)_2]^+$  (angle O–Li–O = 113.4(4)°,<sup>672</sup> trigonal planar  $[\text{Li}(\text{OEt}_2)_3]^+$ ,<sup>1225</sup> tetrahedral  $[\text{Li}(\text{OH}_2)_2(\text{THF})_2]^+$ ,<sup>1226</sup> tetrahedral  $[\text{Li}(\text{OEt}_2)_4]^+$ ,<sup>1227–1230</sup> and tetrahedral  $[\text{Li}(\text{OEt}_2)(\text{THF})_3]^+$ .<sup>1231–1236</sup> Cubanes containing  $\{\text{Li}(\text{OEt}_2)\}$  units are illustrated by  $[\text{Li}_4(\text{OEt}_2)_4(\mu_3\text{-Br})_4]$ .<sup>1237</sup>

In line with the structures of a number of Na<sup>+</sup> complexes described earlier in this review, a square-planar geometry is found in *trans*- $[\text{Na}(\text{OEt}_2)_2(\text{NCMe})_2]^+$ .<sup>256</sup> This contrasts with the tetrahedral or distorted tetrahedral structures reported for  $[\text{Na}(\text{OEt}_2)_4]^+$  combined with various complex anions.<sup>177,1238,1239</sup> Na<sup>+</sup> also forms the 5-coordinate cation  $[\text{Na}(\text{OEt}_2)(\text{THF})_4]^+$ .<sup>1240</sup> Four-coordinate K<sup>+</sup> is observed in  $[\text{K}(\text{OEt}_2)_4]^+$ ,<sup>1241–1243</sup> but higher CNs are also observed, for example, in  $[\text{K}(\text{OEt}_2)(\text{THF})_5]^+$ .<sup>1244</sup> Simple complexes containing monodentate ether ligands are not prevalent for Rb<sup>+</sup> and Cs<sup>+</sup>. Examples of structurally simple group 2 metal complexes containing monodentate ether ligands are tetrahedral  $[\text{Be}(\text{O}^n\text{Bu}_2)_2(\text{O}_3\text{SCF}_3\text{-}\kappa^1)_2]$ ,<sup>1245</sup>  $[\text{Be}_2(\text{OEt}_2)_2\text{Cl}_2(\mu\text{-Cl})_2]$ ,<sup>1246</sup> *trans*- $[\text{Mg}(\text{OEt}_2)_4(\text{GaH}_4\text{-}\kappa^1)_2]$ ,<sup>1247</sup> *trans*- $[\text{Ca}_2(\text{OEt}_2)_4]$ ,<sup>671</sup> and  $[\text{Mg}_3(\text{OEt}_2)_6(\mu\text{-Cl})_3(\mu_3\text{-Cl})_2]$ .<sup>1248</sup> As in group 1, complexes containing only monodentate ether ligands are not well represented for the heaviest metals in group 2.

Within the p-block, structurally characterized simple complexes containing monodentate ether ligands include  $[\text{AlCl}_3(\text{OEt}_2)]$ .<sup>1249</sup> Mitzel et al. reported the isolation and structure of *trans*- $[\text{GeF}_4(\text{OEt}_2)_2]$ ,<sup>1250</sup> and the tin(IV) complex *trans*- $[\text{Sn}(\text{O}_2\text{CCF}_3\text{-}\kappa^1)_4(\text{OEt}_2)_2]$  was described as part of a detailed investigation of tin trifluoroacetates as vapor phase single-source precursors for F-doped SnO<sub>2</sub>.<sup>1251</sup>

### 1.02.6.1.3 RO<sup>−</sup>

The field of main group metal compounds containing alkoxide or aryloxide ligands is large, and is often motivated by the search for precursors to metal oxide films and materials or the development of catalysts, e.g., for polymerization. Because of the extent of the literature, we have decided to confine this section to citations of the most pertinent reviews which have appeared within the past 20 years. The following topics (organized according to periodic group) should provide entries into the area:

- lithium double metal alkoxides<sup>1252</sup>;
- Mg(II) alkoxides and aryloxides as promoters of chemical transformations of lactic acid<sup>1253</sup>;
- dinuclear catalysts for the ring opening polymerization of lactide<sup>1254</sup>;
- relevant to Mg(II): precursors of polymerization catalysts and new materials<sup>1255</sup>;
- main group metal complexes as catalysts or initiators for polymerization of lactides<sup>1256</sup>;



- heterometallic alkoxides (includes both main group and transition metals)<sup>1257</sup>;
- Ga(III) and In(III) alkoxides and aryloxides<sup>37</sup>;
- molecular precursors for gallium and indium oxide thin films<sup>38</sup>;
- precursors for semiconducting materials (includes Sn and Sb alkoxides)<sup>40</sup>;
- precursors to bismuth oxide-based materials.<sup>1258</sup>

#### 1.02.6.1.4 NCO<sup>-</sup> and PCO<sup>-</sup>

Main group metal complexes with N-bonded NCO<sup>-</sup> ligands were described in Section 1.02.2.1.4, and this also covered bridging N,O-bound ligands, examples of which will not be repeated here. Examples of main group metal complexes containing terminal O-bonded NCO<sup>-</sup> appear to be sparse, and are represented by [K(18-crown-6)(OPPh<sub>3</sub>)(OCN)],<sup>296</sup> and [Sn(tpp)(OH)(OCN)] (which shows a substitutional disorder of the axial OH<sup>-</sup> and OCN<sup>-</sup> ligands).<sup>1259</sup> Group 1 metal complexes containing O-bound or P,O-bridging PCO<sup>-</sup> were included in Section 1.02.3.1.3.<sup>1036,1038–1042</sup> We also described the use of a sterically demanding salen-type framework to stabilize {Al<sup>III</sup>-OCP}; in contrast, the Ga(III) analog exhibits a P-bound PCO<sup>-</sup> ligand (Fig. 52B).<sup>1043</sup>

#### 1.02.6.1.5 R<sub>3</sub>PO

Phosphane oxide ligands are popular, with their metal complexes sometimes being the result of adventitious oxidation of the corresponding phosphane. The large numbers of main group metal complexes incorporating R<sub>3</sub>PO ligands means that in this section, we focus only on selected coordination compounds. Of the 324 hits in the CSD between 2000 and 2022 for terminal R<sub>3</sub>PO–M units (M = group 1 (Li–Cs), 2 (Be–Ba), group 13 (Al–Tl), group 14 (Ge–Pb), 15 (As–Bi)), the distribution of M–O–P angles is shown in Fig. 60; the search was made using Conquest v. 2022.1.0.<sup>88</sup>

Homoleptic complexes of the group 1 metals include tetrahedral [Li(OPPh<sub>3</sub>)<sub>4</sub>]<sup>+</sup>,<sup>1260–1263</sup> and [Na(OPPh<sub>3</sub>)<sub>4</sub>]<sup>+</sup> (in the PF<sub>6</sub><sup>-</sup> salt),<sup>1264</sup> and related structures are found in [Na(OPPh<sub>3</sub>)<sub>3</sub>(THF)]<sup>+</sup>,<sup>1265</sup> and [Na(OPPh<sub>3</sub>)<sub>3</sub>(O<sub>3</sub>SCF<sub>3</sub>-κ<sup>2</sup>)].<sup>1266</sup> [KI(OPPh<sub>3</sub>)(18-crown-6)] crystallizes in the trigonal space group R3c and the K–O–P bond angle is 180°<sup>1267</sup>; this is one of several examples of linear M–O–P units (Fig. 60) found in [KX(OPPh<sub>3</sub>)(18-crown-6)] complexes, in which crystallographic symmetry is associated with the M–O–P linearity.<sup>296,1268–1271</sup> Reaction of LiBr and dppeO<sub>2</sub> in THF led to the assembly of [Li<sub>2</sub>(dppeO<sub>2</sub>)<sub>3</sub>Br<sub>2</sub>]<sub>n</sub> which has a 2D-network with (6,3) topology; each Li<sup>+</sup> is tetrahedrally sited and is bound to one Br<sup>-</sup> and three O atoms of three different dppeO<sub>2</sub> ligands making the Li a 3-connecting node (Fig. 61A).<sup>1272</sup> An extended assembly is also observed in [Li(dppeO<sub>2</sub>)<sub>2</sub>]<sub>n</sub><sup>+</sup> (isolated as the [CuClBr]<sup>-</sup> salt) in which tetrahedral Li<sup>+</sup> centers are linked by pairs of bridging dppeO<sub>2</sub> ligands into a 1D-coordination polymer

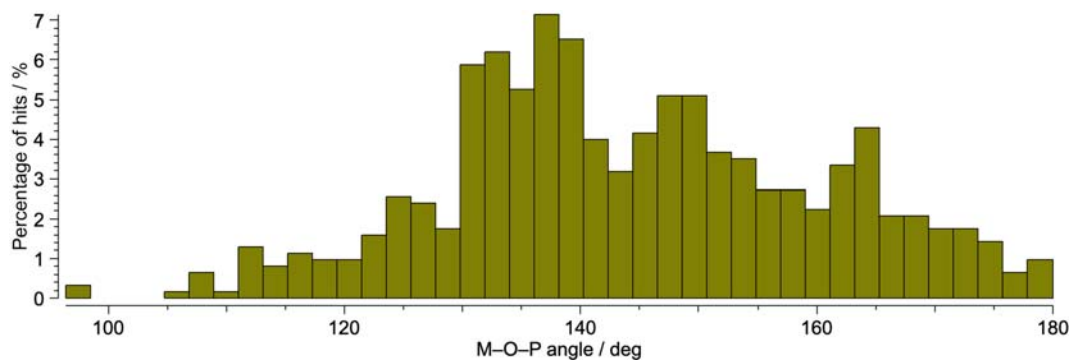


Fig. 60 Distribution of M–O–P angles for terminal R<sub>3</sub>PO–M units (see text for search details).

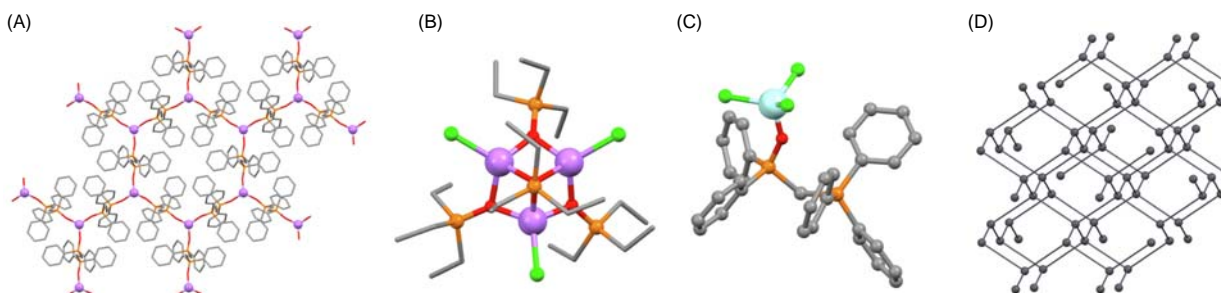


Fig. 61 Structures of (A) part of one (6,3) net in [Li<sub>2</sub>(dppeO<sub>2</sub>)<sub>3</sub>Br<sub>2</sub>]<sub>n</sub> (CSD refcode LAPGIT), (B) [Li<sub>3</sub>Cl<sub>3</sub>(μ-OPEt<sub>3</sub>)<sub>3</sub>(μ<sub>3</sub>-OPEt<sub>3</sub>)] (refcode MISGIF), (C) [BeCl<sub>3</sub>(OPPh<sub>2</sub>CH<sub>2</sub>PPh<sub>3</sub>)] (refcode CAGXEP), and (D) part of the 3D-network in [Pb(dppeO<sub>2</sub>)<sub>2</sub>(NO<sub>3</sub>-κ<sup>2</sup>)<sub>2</sub>]<sub>n</sub> showing only the 4-connecting Pb(II) nodes (refcode MUJNEM).



with a double-loop-like structure.<sup>1273</sup> A few multinuclear lithium clusters provide examples of R<sub>3</sub>PO ligands in  $\mu$ - and  $\mu_3$ -bonding modes, and these are illustrated by [Li<sub>3</sub>Cl<sub>3</sub>( $\mu$ -OPET<sub>3</sub>)<sub>3</sub>( $\mu_3$ -OPET<sub>3</sub>)] (Fig. 61B).<sup>1274</sup>

The zwitterion [BeCl<sub>3</sub>(OPPh<sub>2</sub>CH<sub>2</sub>PPh<sub>3</sub>)] (Fig. 61C) contains an interesting example of a monodentate phosphane oxide formally related to dppm,<sup>1275</sup> and [AlBr<sub>3</sub>(OPPh<sub>2</sub>CH<sub>2</sub>PPh<sub>3</sub>)] adopts an analogous structure.<sup>1276</sup> It is relevant, therefore, to comment that the doubly oxidized form of dppm forms a trigonal prismatic complex with Na<sup>+</sup> in [Na(dppmO<sub>2</sub>- $\kappa^2$ )<sub>3</sub>]Cl.<sup>1277</sup> Note that the corresponding [Mg(dppmO<sub>2</sub>- $\kappa^2$ )<sub>3</sub>]<sup>2+</sup> complex is octahedral.<sup>1278</sup> Octahedral coordination is also seen in [Mg(OPPh<sub>3</sub>)<sub>2</sub>(NO<sub>3</sub>- $\kappa^2$ )<sub>2</sub>].<sup>1279</sup> Ph<sub>3</sub>PO binds as an axial ligand to [Mg(pc)].<sup>1261</sup> Combinations of MCl<sub>2</sub> (M = Mg, Ca, Sr, Ba), Ph<sub>3</sub>PO and SbCl<sub>5</sub> in solution conditions led to [SbCl<sub>6</sub>]<sup>-</sup> salts of distorted tetrahedral [M(OPPh<sub>3</sub>)<sub>4</sub>]<sup>2+</sup> for M = Mg, Ca, Sr, and to [Ba(OPPh<sub>3</sub>)<sub>5</sub>]<sup>2+</sup>; this investigation also included reactions with chelating bis(phosphane) dioxides.<sup>1280</sup> Tetrahedral [MgCl<sub>2</sub>(OPPh<sub>3</sub>)<sub>2</sub>] has also been reported.<sup>1281,1282</sup> Although only 2 equivalents of Ph<sub>3</sub>PO were used in the reaction of CaI<sub>2</sub> in THF, the product was *mer*-[CaI<sub>2</sub>(OPPh<sub>3</sub>)<sub>3</sub>(THF)], while the use of 4 equivalents gave *trans*-[CaI<sub>2</sub>(OPPh<sub>3</sub>)<sub>4</sub>]. Salts of the octahedral [Ca(OP<sup>n</sup>Pr<sub>3</sub>)<sub>5</sub>]<sup>+</sup> and [Ba(OPPh<sub>3</sub>)<sub>5</sub>]<sup>+</sup> were also isolated.<sup>1283</sup> The crystal structure of *trans*-[CaCl<sub>2</sub>(OPPh<sub>3</sub>)<sub>4</sub>] has been reported,<sup>1284</sup> as have the structures of octahedral *cis*-[Ca(OH)<sub>2</sub>(OPPh<sub>3</sub>)<sub>4</sub>]<sup>2+</sup>,<sup>1285</sup> and *fac*-[Ca(OH)<sub>3</sub>(OPPh<sub>3</sub>)<sub>3</sub>]<sup>2+</sup> (as the [AuCl<sub>4</sub>]<sup>-</sup> salt).<sup>1286</sup> [Ca(OPPh<sub>3</sub>)<sub>2</sub>{N(SiMe<sub>3</sub>)<sub>2</sub>}]<sub>2</sub> has a distorted tetrahedral structure with angles O–Ca–O = 95.74(4)° and N–Ca–N = 129.44(5)°; the structure was compared with those of several related compounds.<sup>1287</sup> As part of an investigation of cationic Lewis base-free  $\beta$ -diketimate complexes of Mg<sup>2+</sup> and Ca<sup>2+</sup> (isolated as their [B(C<sub>6</sub>F<sub>5</sub>)<sub>4</sub>]<sup>-</sup> salts), the tetrahedral complexes [Mg(Nacnac)(OPET<sub>3</sub>)<sub>2</sub>]<sup>+</sup> and [Mg(Nacnac)(OPET<sub>3</sub>)(FC<sub>6</sub>H<sub>5</sub>)]<sup>+</sup> (Ar = Dipp in [Nacnac]<sup>-</sup>, see Scheme 6) have been described.<sup>1288</sup> The centrosymmetric strontium complex [Sr<sub>2</sub>(OPPh<sub>3</sub>)<sub>2</sub>( $\mu$ -OH)<sub>2</sub>(Nacnac)<sub>2</sub>] (Ar = Dipp, see Scheme 6) contains 5-coordinate Sr, and is prepared by Ph<sub>3</sub>PO-for-THF ligand substitution from a related dimer.<sup>1289</sup>

Moving on to group 13 metals, and the tetrahedral compound [Al(OPET<sub>3</sub>)(OR)<sub>3</sub>] (R = C(C<sub>6</sub>F<sub>5</sub>)<sub>3</sub>) is an adduct of the thermally stable Lewis superacid Al{OC(C<sub>6</sub>F<sub>5</sub>)<sub>3</sub>}.<sup>1290</sup> The Al(I) compound [Al(Nacnac)] (Ar = Dipp, see Scheme 6) reacts with Ph<sub>3</sub>PO or Et<sub>3</sub>PO with cleavage of the P=O bond and formation of hydroxyl species, along with deprotonation of one Me group in [Nacnac]<sup>-</sup> to yield [Al(Nacnac–H)(OH)(OPR<sub>3</sub>)]; the reaction is proposed to proceed through an intermediate {R<sub>3</sub>PO → Al(Nacnac)} species.<sup>1291</sup> Gallium(III) complexes are illustrated with tetrahedral [GaCl<sub>3</sub>(OPMe<sub>3</sub>)], [GaI<sub>2</sub>(OPMe<sub>3</sub>)<sub>2</sub>]<sup>+</sup> and [(GaBr<sub>3</sub>)<sub>2</sub>{ $\mu$ -1,2-(OPPh<sub>2</sub>CH<sub>2</sub>)<sub>2</sub>C<sub>6</sub>H<sub>4</sub>}] in which the bisphosphane dioxide is monodentate to two GaBr<sub>3</sub> units.<sup>1292</sup> The In(III) complexes *trans*-[InX<sub>2</sub>(OPPh<sub>3</sub>)<sub>4</sub>]<sup>+</sup> (X = Cl, Br) were prepared by halide transfer reactions involving Te(IV) compounds and were isolated as the [PhTeX<sub>4</sub>]<sup>-</sup> salts,<sup>1293</sup> and the structure of *fac*-[InCl<sub>3</sub>(OH)<sub>2</sub>(OPMe<sub>3</sub>)<sub>2</sub>] has also been reported.<sup>1294</sup> In the 5-coordinate [InI<sub>3</sub>{OP(4-MeOC<sub>6</sub>H<sub>4</sub>)<sub>3</sub>}]<sub>2</sub>, the phosphane oxide ligands are mutually *trans*; this is one of a series of complexes studied by solid-state <sup>115</sup>In NMR spectroscopy.<sup>1295</sup> Thallium(I) forms a trigonal pyramidal complex [Tl(OPPh<sub>3</sub>)<sub>3</sub>]<sup>+</sup>.<sup>1268</sup>

Complexes of Ge(IV) and Sn(IV) include octahedral *trans*-[GeF<sub>4</sub>(OPR<sub>3</sub>)<sub>2</sub>] (R = Me, Et, Ph),<sup>1296</sup> *trans*-[SnF<sub>4</sub>(OPMe<sub>3</sub>)<sub>2</sub>] and related complexes with chelating bis(phosphane) dioxides,<sup>1297</sup> *trans*-[SnF<sub>4</sub>(OPPh<sub>3</sub>)<sub>2</sub>],<sup>988</sup> *trans*-[SnI<sub>4</sub>{OP(4-MeC<sub>6</sub>H<sub>4</sub>)<sub>3</sub>}]<sub>2</sub>,<sup>1298</sup> *cis*-[SnCl<sub>4</sub>(OPPh<sub>3</sub>)<sub>2</sub>],<sup>1299</sup> *cis*-[SnI<sub>4</sub>(OPPh<sub>3</sub>)<sub>2</sub>],<sup>1300</sup> *fac*-[GeCl<sub>3</sub>(OPMe<sub>3</sub>)<sub>3</sub>]<sup>+</sup>,<sup>1296</sup> *cis*-[GeX<sub>2</sub>(OPMe<sub>3</sub>)<sub>4</sub>]<sup>2+</sup> (X = Cl, Br),<sup>1296</sup> and the zwitterions [SnF<sub>5</sub>(OPR<sub>2</sub>CH<sub>2</sub>PHR<sub>2</sub>)] (R = Ph, Cy).<sup>1301</sup> In the anionic complex [(SnCl<sub>5</sub>)<sub>2</sub>( $\mu$ -dppeeO<sub>2</sub>)]<sup>2-</sup>, each Sn(IV) center is octahedrally sited.<sup>1302</sup> Moving on to group 14 M(II) compounds takes us to the ylide-containing complex [SnCl<sub>2</sub>(OPPh<sub>2</sub>CHPPH<sub>3</sub>)] in which the Sn(II) center is in a trigonal pyramidal environment,<sup>1303</sup> and to 4-coordinate [SnCl<sub>2</sub>(OPMe<sub>3</sub>)<sub>2</sub>] which possesses a disphenoidal structure with one axial Me<sub>3</sub>PO and one equatorial Me<sub>3</sub>PO.<sup>1074</sup> Under solvothermal conditions (MeCN/EtOH), PbI<sub>2</sub>, KI, I<sub>2</sub> and dppe react to give the 3D-network [Pb<sub>3</sub>( $\mu$ -I)<sub>6</sub>( $\mu$ -dppeeO<sub>2</sub>)<sub>3</sub>]<sub>n</sub>·nEtOH, and in the presence of H<sub>2</sub>O<sub>2</sub>, the product was [Pb<sub>2</sub>( $\mu$ -I)<sub>2</sub>( $\mu_3$ -I)<sub>2</sub>( $\mu$ -dppeeO<sub>2</sub>)<sub>n</sub>]; the former compound contains discrete {Pb<sub>3</sub>( $\mu$ -I)<sub>6</sub>} units connected by bridging dppeeO<sub>2</sub> ligands, while the latter contains [Pb<sub>2</sub>( $\mu$ -I)<sub>2</sub>( $\mu_3$ -I)<sub>2</sub>]<sub>n</sub> 1D-chains interconnected by dppeeO<sub>2</sub> ligands.<sup>1304</sup> Levason and coworkers investigated reactions of Pb(NO<sub>3</sub>)<sub>2</sub> with various bisphosphanes, and the presence of adventitious O<sub>2</sub> resulted in the formation of [Pb( $\mu$ -depeO<sub>2</sub>)<sub>2</sub>(NO<sub>3</sub>- $\kappa^2$ )<sub>2</sub>]<sub>n</sub> in which each Pb(II) has CN = 8 but acts as a 4-connecting node as shown in Fig. 61D.<sup>1075</sup>

Within the group 15 metals, a series of Sb(III) complexes has been described by Bamford et al.: [SbX<sub>3</sub>(OPCy<sub>3</sub>)] (X = F, Cl) with disphenoidal geometry, and [SbCl<sub>3</sub>(OPCy<sub>3</sub>)<sub>2</sub>] with a square-based pyramidal structure.<sup>1305</sup> Octahedral coordination is found in [Bi<sub>2</sub>I<sub>4</sub>( $\mu$ -I)<sub>2</sub>(OPPh<sub>3</sub>)<sub>4</sub>] (Fig. 62A) and this compound is one of a series representing a new class of semiconducting materials.<sup>1306</sup>

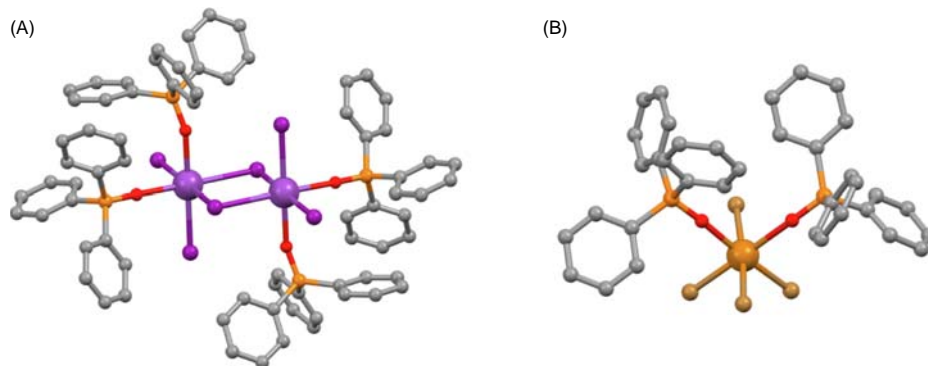


Fig. 62 The structures of (A) [Bi<sub>2</sub>I<sub>4</sub>( $\mu$ -I)<sub>2</sub>(OPPh<sub>3</sub>)<sub>4</sub>] (CSD refcode TPOBII11), and (B) [TeBr<sub>4</sub>(OPPh<sub>3</sub>)<sub>2</sub>] (refcode QUHKOU).

Examples of phosphane oxide coordination to Te(IV) include  $[\text{TeF}_4(\text{OPPh}_3)]$ ,<sup>1307</sup>  $[\text{TeF}_4(\text{OPMe}_3)]$ ,<sup>1307</sup> and *cis*- $[\text{TeBr}_4(\text{OPPh}_3)_2]$  (Fig. 62B).<sup>1308</sup>

### 1.02.6.1.6 Monodentate heterocyclic ligands

There is a wealth of main group complexes incorporating monodentate heterocyclic ligands and THF is ubiquitous, undoubtedly because of its use as a solvent. Many examples have been included in previous sections in this review and here, we focus only on homoleptic complexes containing THF, furan and 1,4-dioxane and on simple halido and aqua derivatives which also contain these heterocyclic ligands. Note that, in many cases and especially for the s-block metals, the complexes detailed below are not the main focus of the original literature work and their structures have often received scant discussion.

Tetrahedral  $[\text{Li}(\text{THF})_4]^+$  is extremely well documented and a few of the very many examples are given in the following references.<sup>1233,1309–1323</sup> Despite the ubiquitous nature of  $[\text{Li}(\text{THF})_4]^+$ , it is noteworthy that trigonal bipyramidal  $[\text{Li}(\text{THF})_5]^+$ ,<sup>1324</sup> and octahedral  $[\text{Li}(\text{THF})_6]^+$  with long Li–O bond lengths (2.16–2.17 Å)<sup>1325,1326</sup> have also been reported. Complexes of  $\text{Li}^+$  containing THF and halido ligands are illustrated by  $[\text{LiBr}(\text{THF})_3]$  and  $[\text{Li}_2(\text{THF})_4(\mu\text{-Br})_2]$ ,<sup>1327</sup> and  $[\text{Li}_2(\text{THF})_6(\mu\text{-Cl})]^+$  which is interesting in that the dimer is supported by a single bridging chlorido ligand (Fig. 63A, angle Li–Cl–Li ranging from 124–174° in different salts)<sup>1328–1331</sup>; the bromido and iodido analogs of the latter are also known (angle Li–Br–Li = 159–168° in different salts, Li–I–Li = 155.9° or 180° which is symmetry-imposed, CSD refcode ZEKCOK).<sup>1016,1332–1334</sup> Other intriguing species include  $[\text{Li}_3(\text{THF})_9(\mu_3\text{-Cl})]^{2+}$  (Fig. 63B)<sup>1335</sup>  $[\text{Li}_4(\text{THF})_{10}(\mu_3\text{-Cl})_2]^{2+}$ ,<sup>1336</sup> and  $[\text{Li}_4(\text{THF})_{10}(\mu_3\text{-Br})_2]^{2+}$ .<sup>1337</sup>

Although both tetrahedral and square-planar  $[\text{Na}(\text{THF})_4]^+$  ions have been structurally characterized,<sup>1338,1339</sup> the CN typically increases on descending group 1. Both trigonal bipyramidal and square-based pyramidal  $[\text{Na}(\text{THF})_5]^+$  have been observed<sup>208,863,1340–1348</sup> with octahedral  $[\text{Na}(\text{THF})_6]^+$  being more typical as illustrated by selected examples.<sup>1349–1364</sup>

Potassium commonly forms the octahedral  $[\text{K}(\text{THF})_6]^+$ ,<sup>503,1240,1309,1365–1372</sup> but in addition  $[\text{K}(\text{THF})_4]^+$ ,<sup>1373</sup>  $[\text{K}(\text{THF})_5]^+$ ,<sup>1374–1376</sup> and  $[\text{K}(\text{THF})_7]^+$ ,<sup>503,1377</sup> have been observed. Cesium exhibits a 7-coordinate complex in  $[\text{Cs}(\text{THF})_7][\text{B}\{3,5\text{-}(\text{CF}_3)_2\text{C}_6\text{H}_3\}_4]^-$ .<sup>1111</sup>

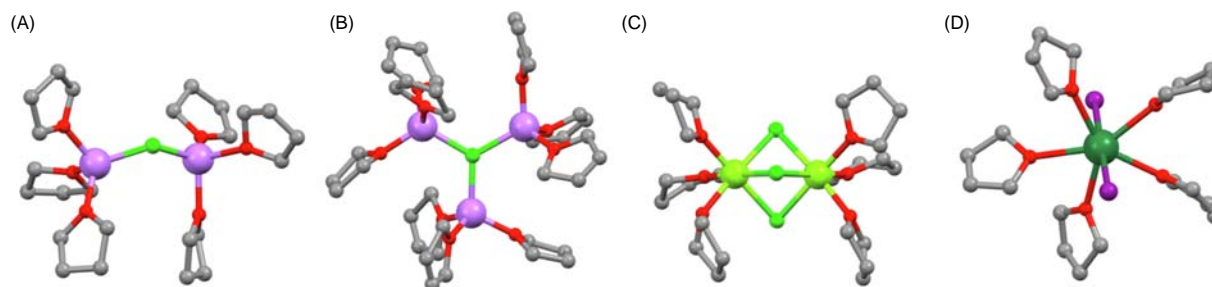
Square-planar  $[\text{Mg}(\text{THF})_4]^{2+}$  in the  $[\text{Ph}\{\text{CH}(\text{SiMe}_3)_2\}\text{P}(\text{BH}_3)_2]^-$  salt adds to the examples of this coordination environment (see earlier) in complexes where the geometry is not imposed by, for example, a porphyrinato ligand. However in this complex, there are close  $\text{Mg}\cdots\text{H}\text{-B}$  contacts, and a similar situation arises in the  $\text{Ca}^{2+}$  and  $\text{Sr}^{2+}$  analogs.<sup>1378</sup> The trigonal bipyramidal  $[\text{Mg}(\text{THF})_5]^{2+}$  ion has been structurally characterized.<sup>1379</sup> Octahedral  $[\text{Mg}(\text{THF})_6]^{2+}$  is well established,<sup>1315,1378,1380–1388</sup> and a CN of 6 is also found in *trans*- $[\text{Mg}(\text{OH}_2)_2(\text{THF})_4]^{2+}$ ,<sup>1389</sup>  $[\text{MgCl}(\text{THF})_5]^+$ ,<sup>683,1390</sup>  $[\text{MgBr}(\text{THF})_5]^+$ ,<sup>1385,1391–1393</sup> *trans*- $[\text{MgCl}_2(\text{THF})_4]$ ,<sup>1394,1395</sup> *trans*- $[\text{MgBrCl}(\text{THF})_4]$ ,<sup>1396</sup> *trans*- $[\text{MgBr}_2(\text{THF})_4]$ ,<sup>1396–1398</sup>  $[\text{Mg}_2(\text{THF})_6(\mu\text{-Cl})_3]^+$  (Fig. 63C, relevant to electrolyte solutions used in rechargeable Mg-containing batteries)<sup>682,1390,1399–1407</sup> and  $[\text{Mg}_2(\text{THF})_6(\mu\text{-Br})_3]^+$ .<sup>1408,1409</sup>

Calcium forms the  $[\text{Ca}(\text{THF})_6]^{2+}$  ion,<sup>1380,1410–1417</sup> and octahedral coordination is also observed in *trans*- $[\text{Ca}(\text{OH}_2)_2(\text{THF})_4]^{2+}$ ,<sup>1418</sup> *trans*- $[\text{CaBr}_2(\text{THF})_4]$ ,<sup>671,1419,1420</sup>  $[\text{CaI}(\text{THF})_5]^+$ ,<sup>1416,1417,1421</sup> *trans*- $[\text{CaI}_2(\text{THF})_4]$ ,<sup>1422</sup>  $[\text{Ca}_2(\text{THF})_8(\mu\text{-Br})_2]^{2+}$ ,<sup>1380</sup> The octahedral  $[\text{Sr}(\text{THF})_6]^{2+}$  ion has been observed in  $[\text{Sr}(\text{THF})_6][\text{VMes}_4]_2$ ,<sup>1417</sup> but a CN of seven is consistent with the increased size of the ion compared to the lighter group 2 metal ions and is found in  $[\text{Sr}(\text{THF})_7]^{2+}$ ,<sup>1417</sup> and *trans*- $[\text{SrI}_2(\text{THF})_5]$  (a pentagonal bipyramidal structure, Fig. 63D).<sup>1423</sup> For  $\text{Ba}^{2+}$ , a CN = 8 is exemplified in  $[\text{Ba}(\text{THF})_8]^{2+}$ .<sup>1424</sup> As part of their investigation of heterobimetallic compounds with complex cations of the group 2 metals coupled with organic anions of M(III) (M = B, Al, Ga, and V), Langer et al. have demonstrated the increased CN with size of metal ion in  $[\text{M}(\text{THF})_n]^{2+}$  (M = Ca, Sr, Ba) with a series of related salts.<sup>1417</sup>

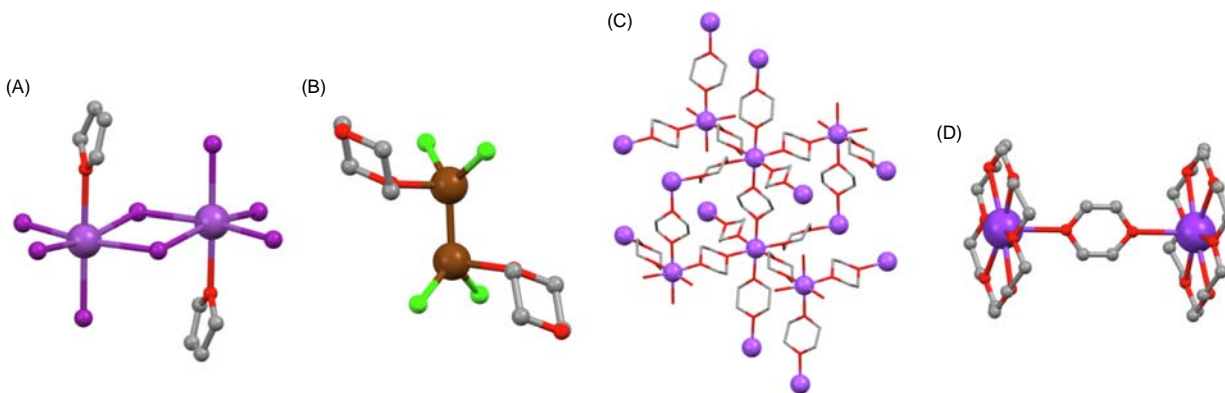
Examples of simple complexes (homoleptic, THF/halido, THF/aqua being the criteria for ‘simple’) of the p-block metals with THF ligands are sparse compared to those of the s-block metals. For aluminum, examples include *trans*- $[\text{AlCl}_2(\text{THF})_4]^+$ ,<sup>1425–1428</sup> and *trans*- $[\text{AlBr}_2(\text{THF})_4]^+$ .<sup>1429</sup> For the group 16 metals, a representative complex is  $[\text{TeCl}_5(\text{THF})]^-$ .<sup>1426</sup>

Moving from THF to furan has a dramatic effect on the number of structurally characterized main group metal complexes. Excluding metallated compounds leaves  $[\text{Bi}_2(\text{furan})_2\text{I}_6(\mu\text{-I})_2]^{2-}$  (Fig. 64A)<sup>1430,1431</sup> as an example of a complex containing non-substituted furan ligands.

The disposition of the O-donors in 1,4-dioxane leads to its role as a bridging ligand, although it can also be found terminally bound to main group metal atoms. Examples of discrete molecular complexes containing monodentate diox include the tetrahedral  $[\text{Li}(\text{diox})_4]^+$ ,<sup>1432,1433</sup>  $[\text{Na}(\text{diox})_4(\text{SiPh}_2\text{SiHPh}_2)]$  (square-based pyramidal),<sup>1434</sup>  $[\text{Na}(\text{diox})_2(\text{dme})(\text{THF})]^+$  (CN = 5),<sup>1435</sup>



**Fig. 63** Structures of (A)  $[\text{Li}_2(\text{THF})_6(\mu\text{-Cl})]^+$  (CSD refcode AXATOI), (B)  $[\text{Li}_3(\text{THF})_9(\mu_3\text{-Cl})]^{2+}$  (refcode MEFKUD), (C)  $[\text{Mg}_2(\text{THF})_6(\mu\text{-Cl})_3]^+$  (refcode AVIXAF), (D) *trans*- $[\text{SrI}_2(\text{THF})_5]$  (refcode IJAVAR).



**Fig. 64** Structures of (A)  $[\text{Bi}_2(\text{furan})_2]_6(\mu\text{-l})_2]^{2-}$  (CSD refcode AZORUE), and (B)  $[\text{Ga}_2\text{Cl}_4(\text{diox})_2]$  (refcode DOXGAC01). (C) Part of the 3D-net in  $[\text{Na}(\mu\text{-diox})_3]_n^{n+}$  (refcode JIGQOI). (D) Structure of the  $[\text{K}_2(18\text{-crown-6})_2(\mu\text{-diox})]^{2+}$  unit found in the  $[(\text{C}_{13}\text{H}_8)\text{CPh}_2(\text{C}_5\text{H}_4)\text{Nd}(\text{BH}_4)_2]^-$  salt (refcode UBUZIA).

octahedral *trans*- $[\text{Na}(\text{OH}_2)_2(\text{diox})_4]^+$  (not discussed in the original work, CSD refcode UKEJEB),<sup>1436</sup> *trans*- $[\text{K}(18\text{-crown-6})(\text{diox})_2]^+$ ,<sup>1437,1438</sup> the 7-coordinate  $[\text{Ca}(\text{diox})_3(\text{NCMe})_4]^{2+}$  and  $[\text{Ca}(\text{diox})_2(\text{NCMe})_3(\text{OH}_2)_2]^{2+}$ .<sup>1410</sup> The cation  $[\text{Li}_2(\text{diox})_6(\mu\text{-diox})]^{2+}$  features both monodentate and bridging diox ligands with each  $\text{Li}^+$  tetrahedrally sited.<sup>1439</sup>  $[\text{Na}_2(\text{MeOC}_6\text{H}_5)_6(\mu\text{-diox})]^{2+}$  is another example of a discrete species with a bridging diox ligand.<sup>1440</sup>

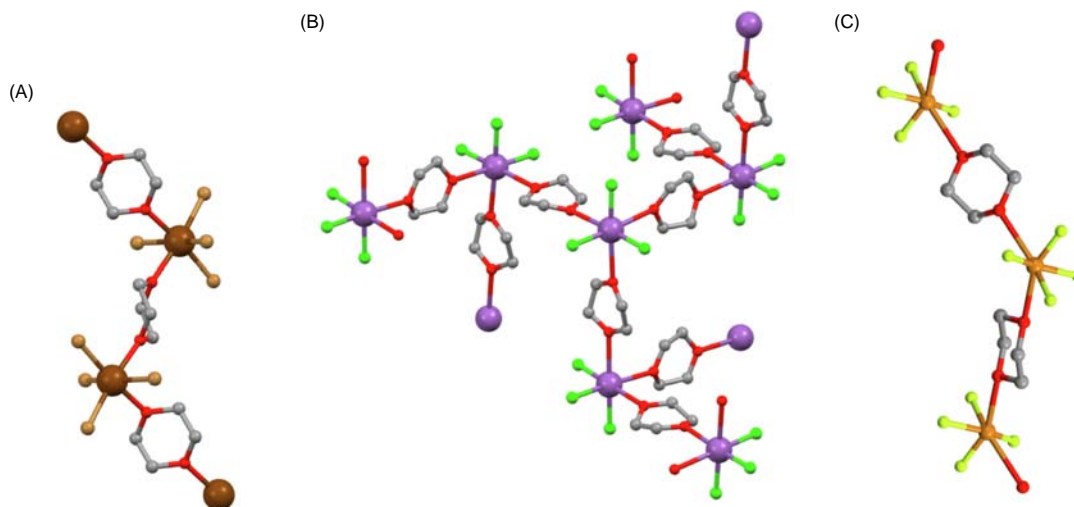
A new polymorph of  $[\text{Ga}_2\text{Cl}_4(\text{diox})_2]$  was reported in 2017; the vacant coordination site in the pseudo-trigonal bipyramidal coordination sphere of Ga (Fig. 64B) is occupied by a long-distance contact to a diox ligand in an adjacent molecule in the lattice.<sup>1441</sup>

Polymeric assemblies supported by bridging diox ligands are illustrated by the following examples from group 1. A redetermination of the structure of  $[\text{Li}(\mu\text{-Cl})(\mu\text{-diox})]_n$  is consistent with a diamondoid network with 4-connecting  $\{\text{LiO}_2\text{Cl}_2\}$ -nodes,<sup>1442</sup> and this has also been described by Jin et al.<sup>1443</sup> In contrast, in  $[\text{Li}_2(\mu\text{-Cl})(\mu\text{-diox})_3]_n^{2n+}$  (isolated as the  $[\text{TaCl}_6]^{2-}$  salt), the 3D-assembly is a puckered hexagonal net with 4-connecting  $\{\text{LiO}_3\text{Cl}\}$ -nodes (distorted tetrahedral, Li–O in the range 1.888(12) to 1.960(10) Å and O–Li–O angles of 101.3(5) to 115.0(6)°).<sup>1444</sup> In  $[\text{Li}_2(\text{O}_3\text{S}^n\text{C}_4\text{F}_9)_2(\mu\text{-diox})]_n$ , each tetrahedrally sited  $\text{Li}^+$  is coordinated by O-donors of three different  $[\text{C}_4\text{F}_9\text{SO}_3]^-$  and one diox; the latter bridge between pairs of  $\text{Li}^+$  and a 2D-sheet assemblies, decorated on the outer surfaces with  ${}^n\text{C}_4\text{F}_9$  chains in extended conformations.<sup>1445</sup> In  $[\text{Na}(\text{H}_3\text{BNHETtBH}_3)(\mu\text{-diox})]_n$ , an intricate network assembles by virtue of a combination of bridging diox ligands and Na–H–B bridges.<sup>1446</sup>  $[\text{Na}(18\text{-crown-6})(\mu\text{-diox})]_n^{n+}$  forms a 1D-coordination polymer,<sup>447,1447</sup> while  $[\text{Na}(\mu\text{-diox})_3]_n^{n+}$  assembles into a 3D-network (Fig. 64C) with diox ligands connecting octahedrally sited  $\text{Na}^+$  ions.<sup>447</sup> The 3D  $[\text{Na}(\mu\text{-diox})_3]_n^{n+}$  network is also found in the  $[\text{PCO}]^-$  salt.<sup>1038</sup> In  $[\text{Na}(\text{diox})_{1.5}][\text{BARF}_4]$ , the  $\text{Na}^+$  ions are octahedrally sited, bound by *trans*-monodentate diox, *trans*-bridging diox (to give an infinite  $\{\text{Na}(\mu\text{-diox})\}_n$  chain) and *trans*- $\text{F}^{\text{BARF}_4}$  contacts; the  $[\text{BARF}_4]^-$  anions act as bridging ligands between the 1D-chains.<sup>1448</sup>

The  $[\text{K}_2(18\text{-crown-6})_2(\mu\text{-diox})]^{2+}$  motif shown in Fig. 64D is observed in the  $[(\text{C}_{13}\text{H}_8)\text{CPh}_2(\text{C}_5\text{H}_4)\text{Nd}(\text{BH}_4)_2]^-$  salt; the vacant coordination site on each  $\text{K}^+$  ion is occupied by a weak  $\eta^2$ -interaction with the fluorene unit in the complex anion.<sup>1449</sup> In the 1D-polymer  $[\text{K}(\text{OH}_2)_4(\mu\text{-diox})]_n^{n+}$ , the bridging diox ligands are mutually *trans* within an octahedral  $\text{K}^+$  coordination sphere.<sup>1450</sup> The reaction of  $(\text{Me}_3\text{Si})_3\text{P}$ , CsF and  $\text{Mes}^*\text{COCl}$  ( $\text{Mes}^* = 2,4,6\text{-}t\text{-Bu}_3\text{C}_6\text{H}_2$ ) in 1,4-dioxane led to a series of products including tri- and tetraphosphides; in the diox adduct of  $[\text{Cs}\{\text{P}(\text{SiMe}_3)\}]$ , a 2D-network supported by  $\{\text{Cs}(\mu\text{-diox})\text{Cs}\}$  units assembles.<sup>1451</sup>

Many examples of Mg(II) complexes containing diox ligands are organometallic, and diox is often used to precipitate magnesium halides from Grignard solutions. An investigation of structure–solubility relationships in these systems also includes the characterization of  $[\text{MgX}_2(\mu\text{-diox})_2]_n$  ( $X = \text{Cl}, \text{Br}$ ) which form (4,4) nets with 4-connecting *trans*- $\{\text{MgX}_2\text{O}_4\}$  units.<sup>1452</sup> The  $\text{AlH}_3$  adduct  $[\text{AlH}_3(\mu\text{-diox})]_n$  contains trigonal bipyramidal Al(III) centers with axial diox ligands and the structure propagates into a 1D-polymer,<sup>1453</sup> and  $[\text{GaCl}_3(\mu\text{-diox})]_n$  is structurally similar.<sup>1454</sup> In group 14, the 1D-coordination polymer  $[\text{SnBr}_4(\mu\text{-diox})]_n$ , each Sn(IV) has a *cis*-arrangement of diox ligands (Fig. 65A).<sup>1455</sup>

Extended assemblies of the heavier group 15 elements are represented by  $[\text{Sb}_2\text{Cl}_6(\mu\text{-diox})_3]_n$  which forms an interpenetrating 3D-network with each Sb(III) center acting as a 3-connecting node; part of one network is shown in Fig. 65B.<sup>1456</sup> A diox adduct of  $\text{SeO}_3$  has been reported, although reactions of  $\text{SeO}_3$  with 1,4-dioxane were fraught with risk of explosion. Nonetheless,  $[\text{SeO}_3(\text{-diox})]_n$  was isolated and structurally characterized; the diox ligands connect planar  $\{\text{SeO}_3\}$  units into 1D-chains but interestingly, there are two crystallographically independent chains, one with symmetrically bound axial diox ligands ( $\text{Se}-\text{O}_{\text{diox}} = 2.314$  Å) and one with  $\text{Se}-\text{O}_{\text{diox}}$  bond lengths of 2.189 and 2.460 Å.<sup>1457</sup> Fig. 65C shows part of the 1D-polymer found in  $[\text{TeF}_4(\mu\text{-diox})]_n$  ( $\text{Te}-\text{O} = 2.686$  Å); this structural study is part of a wider investigation of the gas phase structures of  $\text{TeF}_4$  and  $\text{TeCl}_4$ , and of the solid-state structures of a series of their adducts.<sup>294</sup>



**Fig. 65** (A) Part of a 1D-chain in  $[\text{SnBr}_4(\mu\text{-diox})]_n$  (CSD refcode XUMQEB). (B) Part of the 3D-net in  $[\text{Sb}_2\text{Cl}_6(\mu\text{-diox})_3]$ ; the overall structure is an interpenetrating network (refcode BEKHUV01). (C) Part of a 1D-chain in  $[\text{TeF}_4(\mu\text{-diox})]_n$  (refcode HUQNUD).

### 1.02.6.1.7 Monodentate acetato ligands

We discuss the different modes of bonding of acetato ligands in detail in Section 1.02.6.2.4. In the present section, we provide selected examples of complexes (excluding those with M–C bonds) containing monodentate acetato ligands in which the second O-donor is clearly remote from the metal center.

In the 1D-coordination polymer  $[\text{Na}_2(\mu\text{-OH}_2)_4(\text{OAc})_2(\text{OH}_2)_2]_n$ , the chain is supported by bridging aqua ligands and each  $\text{Na}^+$  is octahedrally sited. The structure is related to that of  $[\text{Na}(\text{OH}_2)_2(\mu\text{-OH}_2)_2]_n^{n+}$  shown in Fig. 57E; in  $[\text{Na}_2(\mu\text{-OH}_2)_4(\text{OAc})_2(\text{OH}_2)_2]_n$ , each  $\text{Na}^+$  carries terminal aqua and acetato ligands in a *cis*-arrangement.<sup>1458</sup> In the octahedral *trans*- $[\text{Mg}(\text{OAc})_2(\text{OH}_2)_4]$ , the acetato ligands are monodentate with Mg–O and Mg $\cdots$ O distances of 2.0811 and 3.3261 Å; this is a redetermination of the structure.<sup>1459</sup> Scheurell et al. have described a family of magnesium acetate solvates and their hydrates and these include  $[\text{Mg}(\text{OAc})_2(\text{OH}_2)_3(\text{EtOH})]$  (with *cis*-AcO<sup>−</sup> ligands) and  $[\text{Mg}(\text{OAc})_2(\text{HOAc})_2(\text{OH}_2)_2]$  (with *trans*-AcO<sup>−</sup> ligands); the second O atom of each monodentate AcO<sup>−</sup> is involved in intermolecular hydrogen bonding.<sup>1460</sup> An investigation of the structural nature of calcium magnesium acetate (CMA) road deicers includes a redetermination of the structure of  $[\text{Ca}(\text{OAc})_2(\text{OH}_2)] \cdot n\text{AcOH}$  which is better written as  $[\text{Ca}_2(\mu\text{-OAc})_3(\text{OAc})(\text{HOAc})(\text{OH}_2)_2]_n \cdot n\text{AcOH}$  and incorporates both monodentate and bridging acetato ligands.<sup>1459</sup>

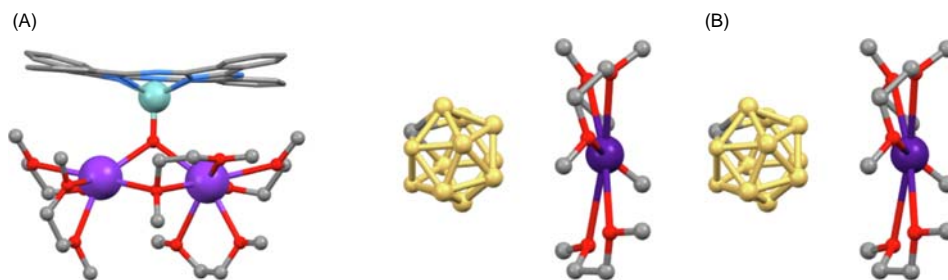
Within the p-block,  $[\text{Ge}(\text{OAc})_3]^-$  is an example of a homoleptic complex with monodentate acetato ligands; it possesses a trigonal pyramidal structure and was isolated as the thermally stable  $[\text{Ph}_3\text{PrP}]^+$  salt.<sup>1461</sup> The Pb(II) containing salt  $[\text{emim}]_2[\text{Pb}(\text{OAc})_4]$  was isolated during the course of the preparation of the ionic liquid 1-ethyl-3-methylimidazolium acetate. The  $[\text{Pb}(\text{OAc})_4]^{2-}$  ion contains one chelating and three monodentate ligands and was the first example of a homoleptic 5-coordinate Pb(II) carboxylate complex with a stereochemically active lone pair.<sup>1462</sup> In  $[\text{Sb}(\mu\text{-O}_2\text{C}_2\text{H}_4)(\text{OAc})]_n$ , a 1D-polymer assembles by virtue of the ethane-1,2-diolato ligands. Each chelates to one Sb(III) center and each O atom of the ethane-1,2-diolato then bridges between two metal atoms; a CN = 5 for the Sb atom is completed by a monodentate acetato ligand.<sup>1463</sup>  $[\text{SeO}_2(\text{OAc})_2]$  was the first example of a selenonyl carboxylate; the Se(VI) center is in a distorted tetrahedral environment, with Se–O<sub>AcO</sub> bond lengths of 1.770(1) and 1.751(1) Å, and an O<sub>AcO</sub>–Se–O<sub>AcO</sub> = 96.5(1)°; the monodentate bonding mode of the AcO<sup>−</sup> ligands is defined by the long contacts to the second O atoms (Se $\cdots$ O<sub>AcO</sub> = 2.933(1) and 2.787(1) Å).<sup>1464</sup>

## 1.02.6.2 Bidentate ligands

### 1.02.6.2.1 1,2-Dimethoxyethane

A variety of coordination compounds incorporating dme are described in other sections in this review. Here, we focus only on homoleptic complexes. For the group 1 metals, such complexes are typically counterions and receive only passing mention in published work. Despite the ubiquitous nature of ions such as  $[\text{Li}(\text{THF})_4]^+$ , the tetrahedral  $[\text{Li}(\text{dme})_2]^+$  ion<sup>1465–1468</sup> is less common than the 6-coordinate  $[\text{Li}(\text{dme})_3]^+$ , and this is presumably a consequence of the presence of chelating rather than monodentate ligands. In some cases, short contacts between the  $\{\text{Li}(\text{dme})_2\}^+$  moiety and, for example, N,<sup>1469</sup> Se,<sup>1470</sup> or Cl<sup>1471–1474</sup> atoms in the complex anion lead to an expansion of the coordination sphere.  $[\text{Li}(\text{dme})_3][\text{PCS}]$  with discrete ions was mentioned earlier in the review,<sup>1036,1037</sup> and the octahedral  $[\text{Li}(\text{dme})_3]^+$  cation is well established, with 217 hits since 2000 in the CSD. Selected examples are found in the following references.<sup>704,1475–1481</sup> Octahedral  $[\text{Na}(\text{dme})_3]^+$  is also ubiquitous, with 82 structurally characterized examples reported since 2000; selected references are given.<sup>1482–1489</sup> For K<sup>+</sup>, the larger size of the metal ion leads to CN ≥ 6, with octahedral  $[\text{K}(\text{dme})_3]^+$ ,<sup>1490</sup>  $[\text{K}(\text{dme})_3]^+$  with close contacts to the complex anion increasing the coordination sphere,<sup>1491</sup>





**Fig. 66** (A) Structure of  $[\text{Nb}(\text{pc})\text{K}_2(\text{dme})_4(\mu\text{-dme})(\mu_3\text{-O})]$  (CSD refcode XAHZIR). (B) Linear arrangement of  $[\text{Cs}(\text{dme})_3]^+$  and  $[\text{CB}_{11}\text{H}_{12}]^-$  ions in  $[\text{Cs}(\text{dme})_3][\text{CB}_{11}\text{H}_{12}]$ ; H atoms are omitted for clarity (refcode WIBKUQ).

$[\text{K}(\text{dme})_4]^+$  (CN = 7 with one monodentate dme)<sup>1491</sup> and  $[\text{K}(\text{dme})_4]^+$  (CN = 8)<sup>1492–1500</sup> being reported. The compound  $[\text{Nb}(\text{pc})\text{K}_2(\text{dme})_4(\mu\text{-dme})(\mu_3\text{-O})]$  deserves inclusion because of the  $\{\text{K}_2(\text{dme})_4(\mu\text{-dme})\}$  unit shown in Fig. 66A.<sup>1501</sup> In  $[\text{Cs}(\text{dme})_3][\text{CB}_{11}\text{H}_{12}]$ , the cations and anions are arranged in alternate positions along the crystallographic *c*-axis (Fig. 66B) and the CN of  $\text{Cs}^+$  is expanded by short interaction between  $\text{Cs}^+$  and BH or CH units (the carborane cages are disordered).<sup>1502</sup>

Homoleptic and other simple complexes of the group 2 metals with dme ligands are relatively well exemplified. Octahedral coordination is observed in  $[\text{Mg}(\text{dme})_3]^{2+}$ ,<sup>1503–1505</sup> *cis*- $[\text{Mg}(\text{dme})_2(\text{O}_3\text{SCF}_3\text{-}\kappa^1)_2]$ ,<sup>1506</sup> and  $[\text{Mg}_2(\text{dme})_4(\mu\text{-Cl})_2]$ .<sup>1405,1507</sup> As with  $[\text{Mg}_2(\text{THF})_6(\mu\text{-Cl})_3]$  (Fig. 63C), these compounds are of interest in studies of electrolytes in rechargeable Mg-containing batteries. The octahedral *cis*- $[\text{MgBr}_2(\text{dme})_2]$  is of relevance to the preparation of chiral Grignard reagents.<sup>670</sup> The variability of CN for the heavier metal ions in group 2 is illustrated by the following: octahedral *cis*- $[\text{Ca}(\text{dme})_2(\text{NPh}_2)_2]$ ,<sup>1508</sup> octahedral *cis*- $[\text{Sr}(\text{dme})_2(\text{N}^i\text{PrPh})_2]$ ,<sup>667</sup>  $[\text{Ca}(\text{OH}_2)_3(\text{dme})_2]^{2+}$  and  $[\text{Ca}(\text{OH}_2)_4(\text{dme})_2]^{2+}$  (CNs = 7 and 8, respectively),<sup>1509</sup>  $[\text{CaBr}(\text{OH}_2)_2(\text{dme})_2]^+$  (CN = 7),<sup>1510</sup> coordination numbers of 7 and 8 in  $[\text{Ca}(\text{OH}_2)_2(\text{dme})_2(\text{NCS})_2]$  and  $[\text{Ca}(\text{dme})_3(\text{NCS})_2]$ , respectively,<sup>274</sup>  $[\text{Ca}(\text{dme})_4]^{2+}$  (CN = 8),<sup>1417,1511</sup>  $[\text{SrI}_2(\text{THF})(\text{dme})_2]$  (CN = 7),<sup>1512</sup>  $[\text{SrI}_2(\text{dme})_3]$  (CN = 8),<sup>1513</sup>  $[\text{SrI}_2(\text{THF})_2(\text{dme})_2]$  (CN = 8),<sup>1423</sup> and  $[\text{BaI}_2(\text{THF})_2(\text{dme})_2]$  and  $[\text{BaI}_2(\text{dme})_3]$  (CN = 8).<sup>1512</sup>

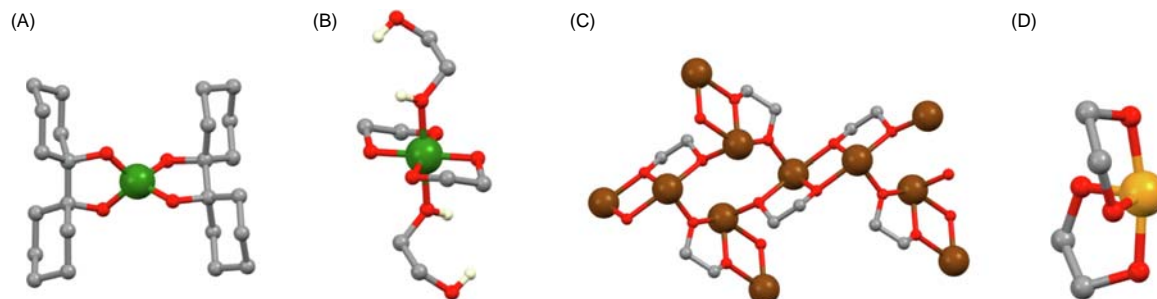
The octahedral *cis*- $[\text{AlCl}_2(\text{dme})_2]^+$  is one of the few examples of simple dme coordination compounds of the p-block metals.

### 1.02.6.2.2 Diol and diolato ligands

Examples in this section are restricted to ethane-1,2-diol, ethane-1,2-diolate and related ligands. Ethane-1,2-diol (ethylene glycol) is often a non-innocent solvent, forming a range of s-block metal complexes. These include octahedral  $[\text{Li}(\text{HOCH}_2\text{CH}_2\text{OH})_3]^+$  and  $[\text{Na}(\text{HOCH}_2\text{CH}_2\text{OH})_3]^+$ ,<sup>1514</sup> and the 8-coordinate  $[\text{Ba}(\text{HOCH}_2\text{CH}_2\text{OH})_4]^{2+}$ .<sup>1515</sup> Tonouchi et al. have studied a series of alkali metal fluoride-diol complexes. While  $[\text{CsF}(\text{HOCH}_2\text{CH}_2\text{OH})]_n$  has a 2D-sheet structure,  $[(\text{MF})_5(\text{HOCH}_2\text{CH}_2\text{OH})_4]_n$  (M = K, Rb) form columnar structures; the effects of increasing the  $C_n$  chain within the diol were also investigated.<sup>1516</sup>

Diolato ligands feature in the cluster complex  $[\text{Al}_{10}(\mu\text{-OAc})_{20}(\mu\text{-O}_2\text{C}_2\text{H}_4)_4(\mu\text{-F})_2]$  described in Section 1.02.6.2.4, and in propane-1,2-diolato and butane-1,2-diolato analogs.<sup>1517</sup> Although the 'brown-ring' test has been an analytical tool for over 100 years, full characterization of the  $[\text{Fe}(\text{OH}_2)_5(\text{NO})]^{2+}$  cation has remained elusive. In 2019, the crystal structures of hydrates of  $[\text{Fe}(\text{OH}_2)_5(\text{NO})][\text{M}(\text{pin}^F)_2(\text{OH}_2)_2]$  (M = Ga<sup>III</sup>, Fe<sup>III</sup>) were reported, and the square-based pyramidal  $[\text{Ga}(\text{pin}^F)_2(\text{OH}_2)]^-$  ion is relevant to this review.<sup>1518</sup>

In 2007, Klüfers et al. commented that only *ca.* 24 germanium complexes containing 1,2-diolate ligands had been structurally characterized, and that spiro-germanes of the type  $[\text{Ge}(\text{diolato})_2]$  were surprisingly absent. A detailed investigation of reactions of  $\text{GeCl}_4$  or  $\text{Ge}(\text{OMe})_4$  with different diols revealed that tetrahedrally sited Ge(IV) in crystalline  $[\text{Ge}(\text{diolato})_2]$  compounds was limited to sterically demanding substituents as exemplified in Fig. 67A. With ethane-1,2-diol, for example, the 6-coordinate



**Fig. 67** Structures of (A) bis(1,1'-bicyclohexyl-1,1'-diolato)germanium(IV) (CSD refcode GICLUA) and (B) *trans*- $[\text{Ge}(\text{O}_2\text{C}_2\text{H}_4)_2(\text{HOCH}_2\text{CH}_2\text{OH})_2]$  (refcode GICMIP, only the OH H atoms are shown). (C) Part of a 2D-sheet in  $\beta\text{-Sn}(\text{O}_2\text{C}_2\text{H}_4)$  (refcode BIVHET01). (D) Structure of the see-saw shaped  $[\text{Se}(\text{O}_2\text{C}_2\text{H}_4)_2]$  (Se–O distances = 1.874(2), 1.780(2), 1.863(2), 1.791(2) Å; refcode HOCBAD).



*trans*-[Ge(O<sub>2</sub>C<sub>2</sub>H<sub>4</sub>)<sub>2</sub>(HOC<sub>2</sub>H<sub>4</sub>OH)<sub>2</sub>] (Fig. 67B) forms.<sup>1519</sup> In [Ge<sub>2</sub>(O<sub>2</sub>C<sub>2</sub>H<sub>4</sub>)<sub>2</sub>(μ-O<sub>2</sub>C<sub>2</sub>H<sub>4</sub>)<sub>2</sub>], each Ge(IV) is 5-coordinate, with one O donor of two diolate ligands in bridging mode.<sup>1520</sup>

1,2-Ethanediolate complexes of Sn(II) and Pb(II) exhibit polymorphism; α- and β-Sn(O<sub>2</sub>C<sub>2</sub>H<sub>4</sub>) can be selectively prepared by controlling the reaction times when tin(II) oxalate reacts with 1,2-ethanediol, while α- and β-Pb(O<sub>2</sub>C<sub>2</sub>H<sub>4</sub>) were obtained by controlling the quantities of NaOH and/or water used in the preparations. In β-Sn(O<sub>2</sub>C<sub>2</sub>H<sub>4</sub>), each Sn(II) center is in a disphenoidal (see-saw) environment and the structure extends into a 2D-sheet (Fig. 67C). Thermal decomposition of both α- and β-Sn(O<sub>2</sub>C<sub>2</sub>H<sub>4</sub>) yields nanocrystalline SnO<sub>2</sub>.<sup>1521</sup> The reaction of Sn(O<sup>t</sup>Bu)<sub>4</sub> with H<sub>2</sub>pin<sup>F</sup> results in the formation of [Sn(pin<sup>F</sup>)<sub>3</sub>]<sup>2-</sup> (isolated as the Et<sub>3</sub>NH<sup>+</sup> salt) which possesses a distorted trigonal prismatic structure; the Sn(II) complex [Sn(pin<sup>F</sup>)<sub>2</sub>]<sup>2-</sup> was also reported.<sup>1522</sup> The Pb(II) coordination network [Pb<sub>4</sub>I<sub>4</sub>(μ<sub>4</sub>-O<sub>2</sub>C<sub>2</sub>H<sub>4</sub>)<sub>2</sub>]<sub>n</sub> is a rare example of a 3D-oxyiodoplumbate assembled from neutral 2D-[Pb<sub>2</sub>I<sub>4</sub>]<sub>n</sub> sheets.<sup>1523</sup>

Fig. 67D shows the structure of [Se(O<sub>2</sub>C<sub>2</sub>H<sub>4</sub>)<sub>2</sub>]; an NBO analysis revealed that the Se–O bonds possess heteropolar character and the Se lone pair exhibits predominantly *s*-character.<sup>1524</sup>

### 1.02.6.2.3 β-Diketonates

The number of main group metal coordination compounds containing β-diketonate ligands is vast, and once again, we have had to define strict criteria for the selection of complexes for coverage. We focus mainly on homoleptic compounds, and those with halido, pseudo-halido or other simple co-ligands.

Mononuclear group 1 metal complexes are illustrated by tetrahedral [Li(OH<sub>2</sub>)<sub>2</sub>(Rtfacac)] (R = 4-BrC<sub>6</sub>H<sub>4</sub>),<sup>1525</sup> and 6-coordinate [Na(hfacac)<sub>3</sub>]<sup>2-</sup> (which was included in a study of hydrophobic ionic liquids with strongly coordinating anions).<sup>1526</sup> [Li(<sup>t</sup>Butfacac)]<sub>n</sub> and [K(18-crown-6)(hfacac)]<sub>n</sub> illustrate different ways in which CF<sub>3</sub>-derivatives of [acac]<sup>-</sup> can produce polymeric structures with group 1 metals. In [Li(<sup>t</sup>Butfacac)]<sub>n</sub>, each O-donor of a [<sup>t</sup>Butfacac] ligand bridges between a pair of Li<sup>+</sup> ions resulting in a 1D-coordination polymer.<sup>1527</sup> In [K(18-crown-6)(hfacac)], the [hfacac]<sup>-</sup> ligand acts as a chelate to one K<sup>+</sup> center and then connects [K(18-crown-6)(hfacac)] units into a 1D-chain through K–F interactions (K–F = 3.081(6) Å for one of two disordered positions).<sup>1528</sup> [Na<sub>3</sub>(μ-acac)<sub>3</sub>(μ-<sup>i</sup>PrOH)]<sub>n</sub> and [Na<sub>3</sub>(μ-acac)<sub>3</sub>(py)]<sub>n</sub> also form 1D-coordination polymers.<sup>1529,1530</sup> [Rb<sub>2</sub>(Rtfacac)<sub>2</sub>(OH<sub>2</sub>)<sub>2</sub>]<sub>n</sub> (R = Ph) assembles into a 2D-sheet with the [Phtfacac]<sup>-</sup> ligand acting both as O,O'-chelate and as an F-donor.<sup>1531</sup> [Cs(μ-<sup>t</sup>BuO<sub>2</sub>acac)]<sub>n</sub> possesses a 2D-network with octahedrally sited Cs<sup>+</sup> ions (Fig. 68A); the ligand coordinates through both the β-diketonate unit and the <sup>t</sup>BuO units. The structure is not discussed in detail in the original work which is focused upon a synergistic ion-binding strategy for asymmetric catalysis of anionic sigmatropic rearrangements.<sup>1532</sup>

Group 2 metal complexes include the tetrahedral [Be(Ph<sub>2</sub>acac)<sub>2</sub>],<sup>1533</sup> octahedral [Mg(hfacac)<sub>3</sub>]<sup>-</sup> (which may be prepared using hydrophobic [hfacac]<sup>-</sup>-containing ionic liquids),<sup>1534–1536</sup> *trans*-[Mg(acac)<sub>2</sub>(3,5-Me<sub>2</sub>py)<sub>2</sub>],<sup>1537</sup> [Mg(<sup>t</sup>Bu<sub>2</sub>acac)<sub>2</sub>(tmeda)],<sup>1538</sup> *trans*-[Mg(tfacac)<sub>2</sub>(OH<sub>2</sub>)<sub>2</sub>],<sup>1539</sup> and *trans*-[Mg(hfacac)<sub>2</sub>(OH<sub>2</sub>)<sub>2</sub>].<sup>1540</sup> The bis(2-methoxyethyl) ether adduct of [Mg(hfacac)<sub>2</sub>(OH<sub>2</sub>)<sub>2</sub>] has been used as an MOCVD precursor to thin films of MgF<sub>2</sub>.<sup>1540</sup> β-Diketonates can act as axial ligands in [M(18-crown-6)(β-diketonate)<sub>2</sub>] (M = Sr, Ba) complexes; related [M(18-crown-6)(β-diketonate)<sub>2</sub>] (*cis* relationship between the β-diketonates), [M(18-crown-6)(OH<sub>2</sub>)(β-diketonate)]<sup>+</sup> and [M(15-crown-5)(β-diketonate)<sub>2</sub>] species have also been reported.<sup>1541–1546</sup> Davies et al. have described the tetramer [Mg(<sup>t</sup>Bu<sub>2</sub>acac)(μ<sub>3</sub>-OMe)(MeOH)]<sub>4</sub> which possesses a cubane structure with each Mg<sup>2+</sup> center coordinated by a chelating β-diketonate, a terminal MeOH, and three μ<sub>3</sub>-methoxy ligands; using THF solutions of the complex, liquid-injection MOCVD has been applied to deposit thin films of MgO.<sup>1547</sup> [Mg(acac)(μ<sub>3</sub>-OMe)(MeOH)]<sub>4</sub> is closely related to [Mg(<sup>t</sup>Bu<sub>2</sub>acac)(μ<sub>3</sub>-OMe)(MeOH)]<sub>4</sub>.<sup>1548</sup> Calcium is 6-coordinate in *trans*-[Ca(Ph<sub>2</sub>acac)<sub>2</sub>(THF)<sub>2</sub>], but exhibits a CN of 7 in [Ca(Ph<sub>2</sub>acac)<sub>2</sub>(tgm)].<sup>1549</sup> The larger Sr<sup>2+</sup> can accommodate four chelating β-diketonates as exemplified by [Sr(Rtfacac)<sub>4</sub>]<sup>2-</sup> (R = Ph), while in [Sr(<sup>t</sup>Bu<sub>2</sub>acac)<sub>2</sub>(OH<sub>2</sub>)<sub>2</sub>(EtOH)], a CN = 7 is observed.<sup>1550</sup> A CN of 8 is observed in [Sr(<sup>t</sup>Bu<sub>2</sub>acac)<sub>2</sub>(<sup>t</sup>PrOH)<sub>4</sub>].<sup>1551</sup>

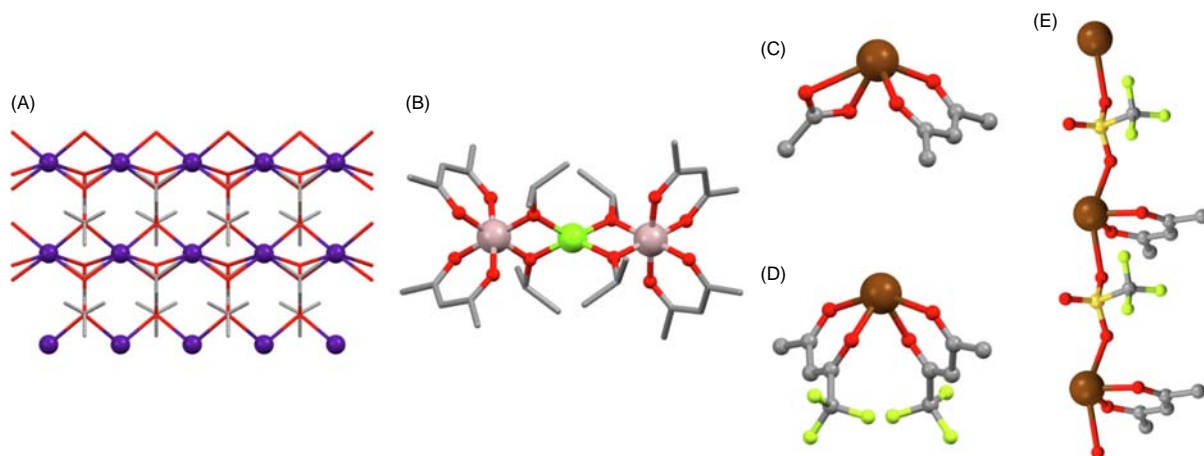


Fig. 68 Structures of (A) part of one 2D-sheet in [Cs(μ-<sup>t</sup>BuO<sub>2</sub>acac)]<sub>n</sub> (CSD refcode FAQQEW), (B) [Al(acac)<sub>2</sub>]<sub>2</sub>[Mg(μ-<sup>i</sup>Pr)<sub>4</sub>] (refcode GUVHEK), (C) [Sn(acac)(OAc)] (refcode BIDWIV), (D) [Sn(tfacac)<sub>2</sub>] (refcode BAMWOE), and (E) [Sn(acac)(μ-O<sub>3</sub>SCF<sub>3</sub>-1κO<sup>1</sup>:2κO<sup>2</sup>)]<sub>n</sub> (refcode BULBIU).

The trinuclear species  $[\{Al(acac)_2\}_2\{Mg(\mu-O^iPr)_4\}]$  (Fig. 68B) makes an appropriate transition in our discussion from group 2 to group 13 metal complexes.<sup>1552</sup> Group 13 metal(III) complexes include tetrahedral  $[Ga(acac)Cl_2]$  and  $[Ga(^tBu_2acac)Cl_2]$ ,<sup>1553</sup> and the octahedral  $[Al(acac)_3]$ ,<sup>1554,1555</sup>  $[Al(^tBuOacac)_3]$ ,<sup>1556</sup>  $[Al(MeO_2acac)_3]$ ,<sup>1557</sup>  $[Al(^tBuO_2acac)_3]$ ,<sup>1557</sup>  $[Al(Rtfacac)_3]$  (R = MeO),<sup>1558</sup>  $[Al(hfacac)_3]$ ,<sup>1559</sup>  $[Al(^tBu_2acac)_3]$ ,<sup>1560,1561</sup>  $[Ga(acac)_3]$ ,<sup>1562</sup>  $[Ga(acac)_2(Hacac)]^+$ ,<sup>1562</sup>  $[Ga(^tBu_2acac)_3]$ ,<sup>1560</sup>  $[Ga(Ph_2acac)_3]$ ,<sup>1563</sup> *trans*- $[Ga(acac)_2(THF)_2]^+$ ,<sup>1553</sup>  $[In(acac)_3]$ ,<sup>1564</sup>  $[In(^tBu_2acac)_3]$ ,<sup>1560,1565</sup> and  $[In(acac)Br_2(THF)_2]$  (with *trans*-THF).<sup>1566</sup>  $[Ga(acac)_3]$  has been introduced into perovskite precursor solutions to create a core-shell structure to protect perovskite crystallites.<sup>1562</sup> Dinuclear group 13 metal species are illustrated by  $[Al_2(hfacac)_4(\mu-OH)_2]$  and  $[Al_2(hfacac)_4(\mu-O^iPr)_2]$  (CN = 6),<sup>1559</sup>  $[Al_2(^tBu_2acac)_2(O^t-Bu)_2(\mu-O^tBu)_2]$  (CN = 5),<sup>1567</sup>  $[Ga_2(Ph_2acac)_4(\mu-OMe)_2]$  (CN = 6),<sup>1568</sup> and  $[In_2(Ph_2acac)_4(\mu-OO^tBu)_2]$  (CN = 6).<sup>1569</sup> The dimers  $[Ga_2Cl_2(acac)_2]$  and  $[Ga_2Cl_2(^tBu_2acac)_2]$  are supported by direct Ga–Ga bonds (2.396(3) and 2.391(2) Å, respectively).<sup>1570</sup> The crystal structure of  $[Tl(acac)]$  reveals that units interact through weak Tl...Tl contacts, the distance of 3.8553(5) Å being approximately twice the van der Waals radius of Tl, leading to an infinite assembly.<sup>1571</sup> A change to  $[Ph_2acac]^-$  results in the formation of dimeric  $[Tl_2(Ph_2acac)_2]$  in the solid state, and close contacts occur between these units.<sup>1572</sup>

Group 14 metal(IV) derivatives are represented by  $[Ge(acac)_3]^+$ ,<sup>1573</sup> *cis*- $[Ge(N_3)_2(acac)_2]$ ,<sup>1574</sup> *cis*- $[SnCl_2(acac)_2]$ ,<sup>1575</sup> *cis*- $[SnCl_2(Ph_2acac)_2]$ ,<sup>1576</sup> *fac*- $[SnCl_3(acac)(OH_2)]$ ,<sup>1577</sup> and *cis*- $[Sn(OEt)_2(acac)_2]$ .<sup>1578</sup> In the trimer  $[Sn_3(acac)_6(\mu-O)_3]$ , the three Sn(IV) centers are in a triangular array and each metal is 6-coordinate, being bound by two chelating  $[acac]^-$  and two bridging oxido ligands.<sup>1579</sup> Mono  $[acac]^-$  derivatives of tin(II) are uncommon. In  $[Sn(acac)(O_2Ac)]$  (in which one Sn–O<sub>acetato</sub> bond is noticeably long, 2.607(5) Å), the coordination geometry (Fig. 68C) reflects the role of the stereochemically active lone pair on Sn(II).<sup>1580</sup> A similar coordination geometry is found in the CVD precursor  $[Sn(hfacac)_2]$ ,<sup>1581</sup> in  $[Sn(^tBu_2acac)_2]$ ,<sup>1582</sup> and in  $[Sn(tfacac)_2]$  (Fig. 68D), although here, the molecules are organized into chains with Sn...Sn distances of 4.290 and 4.299 Å; this compound was used as a precursor to SnO<sub>2</sub> thin films.<sup>1583</sup>  $[Pb(acac)_2]$  is monomeric in the solid state and adopts a structure consistent with the presence of a stereochemically active lone pair; however, in addition to the four Pb–O bonds (range 2.32–2.37 Å), each Pb(II) center exhibits four short Pb...O contacts (3.01–3.26 Å).<sup>1584</sup> In bis(1,1,1-trifluoro-5-methoxy-5-methyl-hexane-2,4-dionato)lead(II), molecules associate into dimers through a Pb...Pb interaction (4.112 Å) and dimers are maintained in the vapor phase.<sup>1585</sup>  $[Sn(acac)(\mu-O_3SCF_3-1\kappa O^1:2\kappa O^2)]_n$  is a second example of a mono  $[acac]^-$  derivative of Sn(II) and assembles as a 1D-coordination polymer (Fig. 68E); adjacent chains exhibit Sn...Sn contacts (4.282 Å).<sup>1586</sup> In  $[Pb(hfacac)_2(18-crown-6)]$ , the Pb(II) center is 8-coordinate with a chelating  $[hfacac]^-$  ligand sited above and below the macrocyclic ligand.<sup>1587,1588</sup>

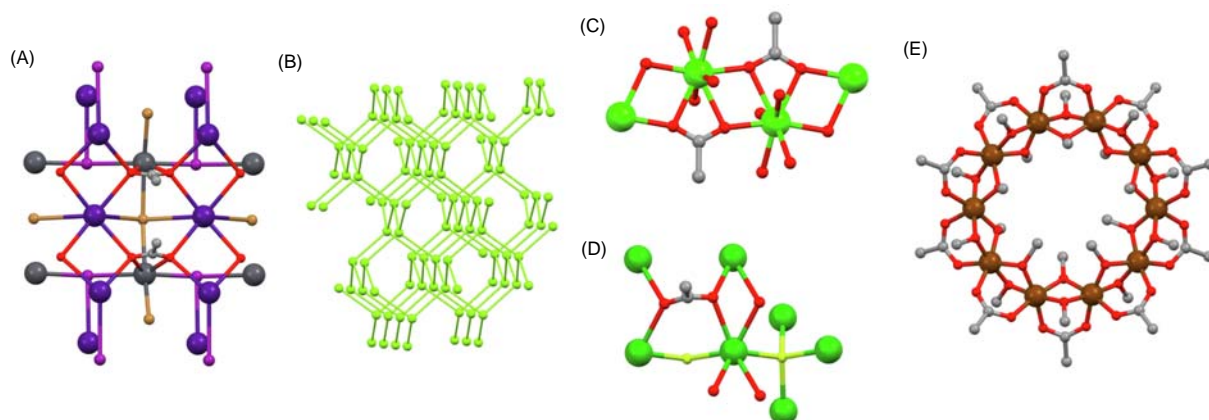
For the heavier elements in group 15, examples of  $\beta$ -diketonate complexes include  $[Sb(^tBu_2acac)_3]$  which exhibits a distorted 6-coordinate structure with three chelating ligands and a stereochemically active lone pair.<sup>1589,1590</sup>  $[Sb(^tBu_2acac)_2(OEt)]$  is square-based pyramidal with the ethoxy ligand in the axial site.<sup>1589</sup>  $[Bi(acac)_3]$  is atypical of Bi(III)  $\beta$ -diketonate complexes in that it is polymeric in the solid state, with 7-coordinate Bi(III) coordinated by one chelating/bridging and two chelating  $[acac]^-$  ligands.<sup>1591</sup> In  $[Bi_2(hfacac)_6]$ <sup>1592</sup> and  $[Bi_2(Ph_2acac)_6]$ ,<sup>1593</sup> each Bi(III) is bound by three chelating ligands, and two O-donors of two of the ligands also bridge between the metal atoms; the latter complex has been used as a precursor for Pt–Bi<sub>2</sub>O<sub>3</sub> thin films.

#### 1.02.6.2.4 Carboxylates: Bidentate and bridging

Carboxylates are ubiquitous ligands for s- and p-block metal ions, and thus, we can only include highly selected examples of carboxylate complexes. Oxalato complexes are covered separately in Section 1.02.6.2.5. Many coordination networks are directed by multifunctional ligands bearing two, three or more  $-CO_2^-$  donor groups. This area of coordination chemistry is too extensive to be covered here, and the reader is directed to pertinent reviews.<sup>3,51,61,1594,1595</sup> In this section, we have chosen to limit the discussion to complexes containing acetato ligands in order to give a broad picture of the different possible bonding modes. Rather than use strict IUPAC nomenclature to describe the bonding modes, we refer to them by the notation in Scheme 18. Complexes containing well-defined monodentate acetato ligands (mode I, Scheme 18) were described in Section 1.02.6.1.7. Modes I–III in Scheme 18 make the transition from monodentate to chelating ligands bound to a single metal center, while modes IV–XIV illustrate different bridging modes, examples of which are given below. Note that modes V and VII are the same in terms of connectivity but we make a distinction based upon the spatial positions of the metal atoms; mode V is best known in  $\{M_2(\mu-O_2CR)_4\}$ -paddle-wheel motifs.

For the group 1 metals, increased CN is observed, as expected, on descending the group. In  $[Li(\mu-OAc)(\mu-OH_2)]_n$ , Li<sup>+</sup> is tetrahedrally sited and 1D-chains assemble from alternating  $\{Li_2(\mu-OAc)_2\}$  and  $\{Li_2(\mu-OH_2)_2\}$  motifs; the OAc<sup>−</sup> ligand adopts mode V (Scheme 18). This investigation deals more widely with polymorphs of anhydrous LiOAc and its hydrate.<sup>1596</sup>  $[Li_9(\mu-OAc)_9(\mu-OH_2)]_n \cdot nTHF$  also contains 4-coordinate Li<sup>+</sup> and the complicated 3D-network combines different modes of acetato bonding including V, IX, and XI.<sup>1597</sup> Different polymorphs of NaOAc are known and the structures of two new polymorphs have been determined by Ditttrich et al.<sup>1598</sup> The structure of  $[Na_4(\mu-OAc)_3(\mu_4-ClO_4)]_n$  is described by Hannon and coworkers as comprising 'sodium acetate planes linked together by sodium perchlorate cylinders'; each AcO<sup>−</sup> ligand is in bonding mode XIII (Scheme 18), and the crystal lattice contains MeOH-filled channels running along the *c*-axis.<sup>1599</sup>  $[K(\mu-OAc)(\mu-AcOH)]_n$  assembles into a 2D-sheet, with the acetato ligands adopting bridging mode XII (Scheme 18); hydrogen-bonded interactions link the coordinated AcOH and AcO<sup>−</sup> ligands.<sup>1600</sup> In both  $[K(18-crown-6)(OAc)] \cdot 2H_2O$  and  $[K(18-crown-6)(OAc)(OH_2)] \cdot HOAc$ , the AcO<sup>−</sup> ion is in a chelating mode. In the former, K<sup>+</sup> is 8-coordinate and AcO<sup>−</sup> adopts bonding mode III (Scheme 18) with K–O = 2.6992(11) and 2.8861(11) Å; a mode closer to II is found in  $[K(18-crown-6)(OAc)(OH_2)] \cdot HOAc$ , but the increase in the CN to 9 causes elongation of the K–O bonds to 2.9562(16) and 3.0303(19) Å.<sup>1601</sup>

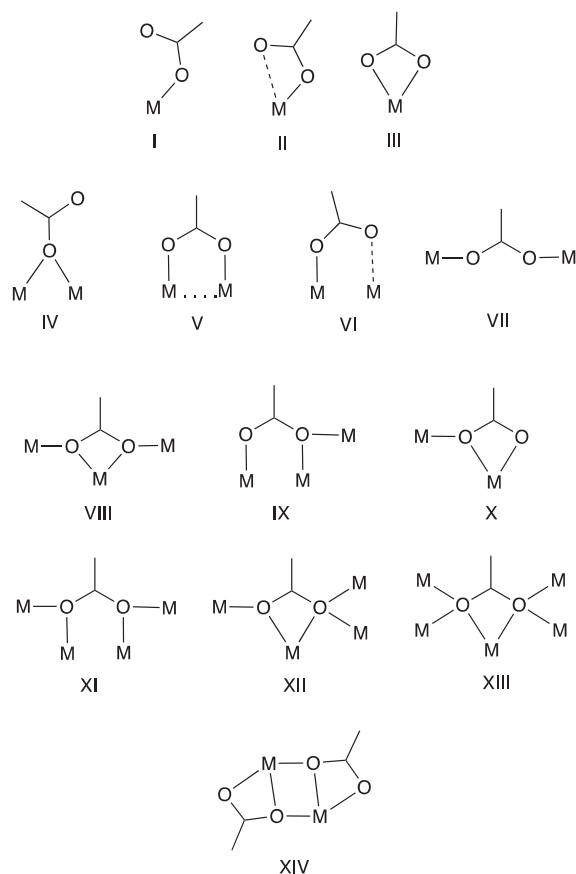
The mixed halido species  $[Cs_3Br_2Pb_2(\mu-OAc)_2(\mu_4-Br)(\mu_3-I)]_n$  is of interest for its NLO properties; part of the 3D-structure is shown in Fig. 69A and the acetato ligands chelate to Pb(II) and bridge between Cs<sup>+</sup> centers (mode VIII in Scheme 18).<sup>1602</sup> The



**Fig. 69** (A) Part of the 3D-network (viewed down the  $c$ -axis) in  $[\text{Cs}_3\text{Br}_2\text{Pb}_2(\mu\text{-OAc})_2(\mu_4\text{-Br})(\mu_3\text{-I})]_n$  (CSD refcode PARNEF). (B) Part of the 3D-net in  $[\text{Mg}_3(\mu\text{-OAc})_6(\mu\text{-MeOH})_6]_n$ , showing only the 4-connecting Mg(II) nodes (refcode BELYIC). (C) Part of the 1D-chain in  $\{[\text{Ca}(\text{OH})_2(\mu\text{-OAc})]\text{Cl}\}_n \cdot n\text{H}_2\text{O}$  (refcode CALCLA02). (D)  $\text{F}^-$  and  $\text{AcO}^-$  bridging modes in  $[\text{BaF}(\text{OAc})]_n$  (refcode IQICOD). (E) Structure of  $[\text{Ga}_{10}(\mu\text{-OAc})_{10}(\mu\text{-OMe})_{20}]$  (refcode CESGAJ).

related NLO compounds  $[\text{Cs}_3\text{Pb}_2(\text{OAc})_2\text{I}_5]$  and  $[\text{Rb}_3\text{Pb}_2(\text{OAc})_2\text{X}_5]$  with  $\text{X} = \text{Br}, \text{Cl}$  have similar structures to that shown in Fig. 69A.<sup>1603,1604</sup>

The group 2 metals, in particular  $\text{Mg}^{2+}$  and  $\text{Ca}^{2+}$ , offer a wealth of carboxylate complexes. The dimer  $[\text{Mg}_2(\text{OH})_6(\mu\text{-OAc})_3]^+$  (6-coordinate Mg) offers an example of bridging mode V (Scheme 18),<sup>1605</sup> and this mode, combined with mode X bridging ligands, is also seen in  $[\text{Mg}_3(\text{OH})_2(\text{AcOH})_2(\mu\text{-OAc})_6]$  which has a linear  $\text{Mg}_3$ -core.<sup>1460,1606</sup> The work of Miller et al. on the structural



**Scheme 18** Different modes of coordination of  $\text{MeCO}_2^-$  to main group metal centers. Formal C–O bond orders are not specified. The dotted line in mode V signifies that the M atoms are close but does not imply M–M bonding.

properties of CMA road deicers is an instructive entry into the area.<sup>1459</sup> In Section 1.02.6.1.7, we illustrated examples of Mg(II) complexes containing monodentate  $\text{AcO}^-$  as part of a wider study of magnesium acetate solvates and their hydrates. In  $[\text{Mg}_3(\mu\text{-OAc})_6(\mu\text{-MeOH})_6]_n$ , a 3D-network is formed with 6-coordinate  $\text{Mg}^{2+}$  (CN includes two terminal MeOH) linked by bridging (mode VII) acetato ligands. Each Mg(II) acts as a 4-connecting node and Fig. 69B shows part of the 3D-net. In  $[\text{Mg}(\text{OAc})_2(\text{HOAc})]_n \cdot 1.8n\text{AcOH}$ , the coordinated AcOH molecules are terminally bonded, while the  $\text{AcO}^-$  ligands adopt two different modes (IV or IX, Scheme 18), leading to 1D-chains.<sup>1460</sup> Scheurell et al. have also reported that the dehydration of  $\text{Mg}(\text{OAc})_2 \cdot 4\text{H}_2\text{O}$  produces basic magnesium acetate which has a porous network; the structures of  $[\text{Mg}_5(\mu_3\text{-OH})_2(\text{OAc})_8] \cdot 2\text{EtOH}$  and  $[\text{Mg}_5(\mu_3\text{-OH})_2(\text{OAc})_8] \cdot 1.19\text{H}_2\text{O}$  were also determined. Within this series of structures,  $\text{AcO}^-$  ligands are found in bonding modes V, VII, IX, and XI.<sup>1607</sup> Thermal dehydration of  $\text{Ca}(\text{OAc})_2 \cdot \text{H}_2\text{O}$  at 300 °C yields anhydrous  $\alpha\text{-Ca}(\text{OAc})_2$  which exhibits low- and high-temperature forms; during the phase transition, the coordination mode of an  $\text{AcO}^-$  ligand switches from monodentate to bidentate.<sup>1608</sup>  $\{[\text{Ca}(\text{OH}_2)_4(\mu\text{-OAc})\text{Cl}]_n \cdot n\text{H}_2\text{O}\}$  possesses a 1D-polymeric structure with the bridging  $\text{AcO}^-$  is mode VIII (Fig. 69C) and a CN = 8 for  $\text{Ca}^{2+}$ .<sup>1609</sup> As part of a study of the ternary system  $\text{Ca}(\text{OAc})_2\text{-Ca}(\text{O}_2\text{CH})_2\text{-H}_2\text{O}$ , Bette et al. reported the structures of  $[\text{Ca}_3(\mu\text{-OAc})_4(\text{O}_2\text{CH})_2(\text{OH}_2)_4]_n$  (which contains terminal formate ligands and  $\text{AcO}^-$  in bonding mode VIII, Scheme 18) and  $[\text{Ca}(\mu\text{-OAc})(\mu\text{-O}_2\text{CH})(\text{OH}_2)]_n$  (containing bridging formates and  $\text{AcO}^-$  in mode X).<sup>1610</sup>

The Sr(II) complex  $[\text{Sr}(\text{OAc})_3]^-$  has been isolated as the [emim]<sup>+</sup> salt as part of an investigation of dialkylimidazolium acetate ionic liquids with relevance to nuclear fuel recycling. The 1D-polymer  $[\text{Sr}(\mu\text{-OAc})_3]_n^{n-}$  contains 9-coordinate Sr(II) in a severely distorted tricapped trigonal prismatic geometry; the bridging  $\text{AcO}^-$  ligands that support the chain adopt bonding mode X (Scheme 18).<sup>1611</sup>  $[\text{Ba}(\text{OAc})(\mu\text{-OAc})(\text{OH}_2)_3]_n$  is a 1D-polymer with CN = 9 for  $\text{Ba}^{2+}$ ; three aqua and one chelating  $\text{AcO}^-$  occupy five coordination sites, and  $\text{Ba}^{2+}$  ions are linked into a chain by mode VIII (Scheme 18) bridging  $\text{AcO}^-$  ligands, similar to the arrangement shown in Fig. 69C.<sup>1612</sup> The compounds  $[\text{MF}(\text{OAc})]_n$  (M = Sr, Ba) assemble into 2D-networks, details of which were elucidated from powder X-ray diffraction data. Each M(II) is in a *cis*- $\{\text{MF}_2\text{O}_4\}$  environment (Fig. 69D), with the  $\text{AcO}^-$  ligands in bridging mode XI (Ba–O = 2.61(7)–2.92(4) Å, Sr–O = 2.54(2)–2.8(2) Å), and each F in a  $\mu_4$ -mode (Ba–F = 2.65(5), 2.71(5) Å, Sr–F = 2.4(2), 2.6(2) Å).<sup>1613</sup>  $[\text{Ba}_9(\text{OAc})_{14}(\text{ClO}_4)_4]_n$  forms an unusual 3D-network in which the building block is a  $\text{Ba}_9$ -cluster with a 'body-centered cubic' (bcc) geometry. Each face of the cube is bridged by  $\text{AcO}^-$  in mode XIII (i.e., also bound to the central Ba of the bcc unit) and  $\text{Ba}_9$  units are then linked by a combination of bridging  $\text{OAc}^-$  and  $\text{ClO}_4^-$  ions. The structure is best appreciated by viewing in 3D (CSD refcode LUHZUI).<sup>1614</sup>

Moving to group 13, and examples of 1D-coordination polymers include  $[\text{M}(\mu\text{-OAc})_2(\mu\text{-OH})]_n$  with M = Ga or In in which the metal is 6-coordinate and pairs of M(III) centers are bridged by two  $\text{AcO}^-$  (bridging mode V) and a hydroxido ligand,<sup>1615,1616</sup> and  $[\text{In}(\mu\text{-OAc})_3]_n$ , the first example of a group 13  $\text{M}(\text{OAc})_3$  compound with an infinite chain in the solid state.<sup>1617</sup> Within group 13, there are a number of examples of discrete high nuclearity species exhibiting mode V (Scheme 18) bridging acetates. These are represented by the cyclic  $[\text{Al}_{10}(\mu\text{-OAc})_{10}(\mu\text{-OEt})_{20}]$ ,  $[\text{Al}_{10}(\mu\text{-OAc})_{10}(\mu\text{-OMe})_{20}]$ , and  $[\text{Al}_{10}(\mu\text{-OAc})_{20}(\mu\text{-O}_2\text{C}_2\text{H}_4)_4(\mu\text{-F})_2]$ ,<sup>1517</sup> and  $[\text{Ga}_{10}(\mu\text{-OAc})_{10}(\mu\text{-OMe})_{20}]$  (described as a 'gallic wheel,' Fig. 69E).<sup>1618</sup>

In the solid state, tin(II) acetate assembles into 1D-chains in groups of four chains, with the Sn(II) centers within the group facing one another (Sn...Sn = 4.171 and 4.189 Å) to generate columns which follow the *c*-axis. Along each 1D-chain, the bonding mode of the  $\text{AcO}^-$  ligand resembles mode X (Scheme 18), although the Sn–O distances in the chelate rings are 2.170(6) and 2.293(7) Å, and 2.207(6) and 2.372(8) Å, making a description of between modes V and X more realistic.<sup>1619</sup>  $[\text{Sn}(\text{acac})(\text{OAc})]_n$  (Fig. 68C), the acetato ligand adopts mode II (Scheme 18) with Sn– $\text{O}_{\text{AcO}}$  distances of 2.165(4) and 2.607(5) Å.<sup>1580</sup> In 2016, the structures of two enantiotropic polymorphs of anhydrous  $\text{Pb}(\text{OAc})_2$  were determined for the first time. In both the  $\alpha$ - and  $\beta$ -forms, the extended arrays are supported by bridging ligands which adopt modes VIII and X (Scheme 18). This work also includes a series of lead(II) acetate derivatives which illustrate a variety of bonding  $\text{AcO}^-$  modes in 1D- and 2D-assemblies.<sup>1620</sup> A related infinite assembly  $[\text{Pb}_2(\mu\text{-OAc})_4(\mu\text{-2,5-dimethylbenzene-1,4-diol})]_n$  has also been described.<sup>1621</sup> Reactions of carboxylic acids with Pb are relevant to the corrosion of lead and lead-tin alloys. One of the corrosion products is  $[\text{Pb}_6(\mu_4\text{-O})_4(\mu\text{-OAc})_2(\text{OAc})_2]_n \cdot n\text{H}_2\text{O}$ , and the solid-state structure consists of interconnected double chains; half of the  $\text{AcO}^-$  ligands adopt mode VI (Scheme 18) within a chain, while the other  $\text{AcO}^-$  groups are in bridging mode VII (Scheme 18) and link adjacent chains, leading to 2D-sheets.<sup>1622</sup>  $[\text{Pb}(\text{OAc})(\mu\text{-OAc})(\text{thiourea})]_n$  is a 1D-coordination polymer in which each Pb(II) center is bound by two  $\text{AcO}^-$  ligands in modes III and X, respectively. However, the Pb–O bond lengths for the chelating units (2.489(3), 2.483(3), 2.520(2) and 2.990(2) Å) indicate that one interaction is weak; the thiourea S-atoms are also involved in Pb...S interactions.<sup>1623</sup> Fig. 69D illustrated part of the 2D-sheet in  $[\text{BaF}(\text{OAc})]_n$ , highlighting the bridging modes of the ligands; analogous coordination modes are observed in  $[\text{PbF}(\text{OAc})]_n$ .<sup>1613</sup>

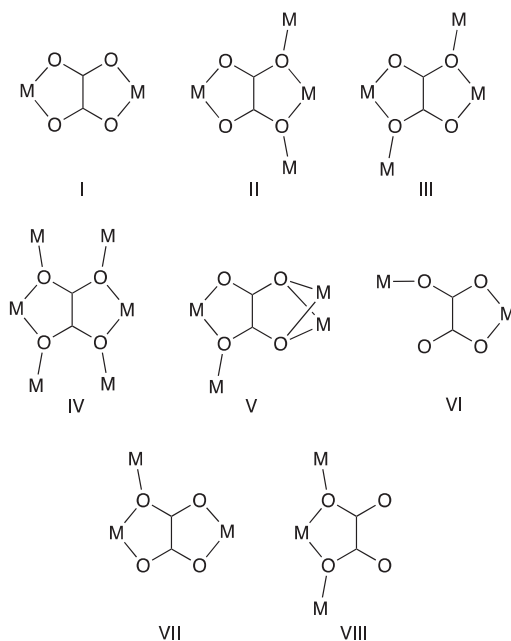
The Bi(III) complex  $[\text{Bi}(\text{OAc})_2(\text{THF})_4]^+$  was characterized in the salt  $[\text{Bi}(\text{OAc})_2(\text{THF})_4]_3[\text{Bi}_7\text{I}_{24}]$ , and contains 8-coordinate Bi.<sup>1624</sup>

### 1.02.6.2.5 Oxalate

The oxalate dianion is widely used as a bridging motif in coordination assemblies and is a building block in numerous coordination networks. However, it also appears as a bidentate, chelating ligand in, for example, the octahedral  $[\text{Al}(\text{ox})_3]^{3-}$ .<sup>1625</sup> As in previous sections, we limit the discussion to homoleptic complexes and those with simple co-ligands. We refer to the different bridging modes of  $\text{ox}^{2-}$  using the notation in Scheme 19, rather than applying strict IUPAC nomenclature.

In compounds such as sodium oxalate, the cation–anion interactions are essentially electrostatic,<sup>1626</sup> and we choose not to consider the structures in terms of oxalate bonding modes. However, it is pertinent to include reference to an investigation of the influence of hydrostatic pressure on the crystal structure of  $\text{Na}_2[\text{ox}]$ .<sup>1626</sup> Group 2 metal oxalates are well represented. In

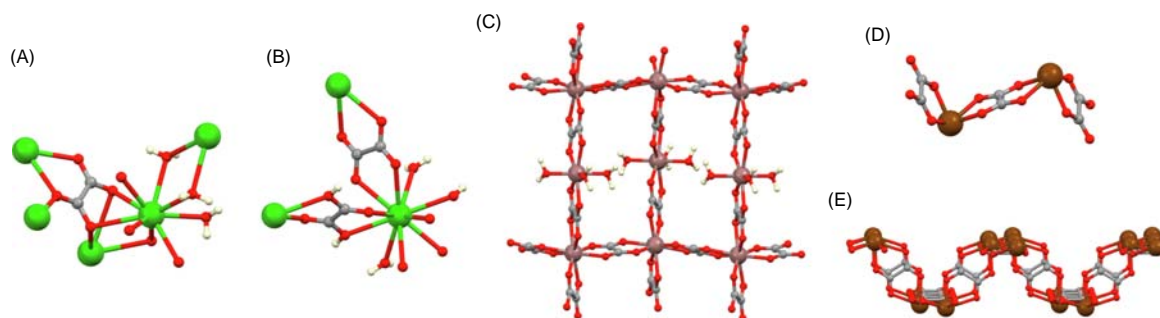




**Scheme 19** Different bridging modes of the  $\text{ox}^{2-}$  anion. The same notations are used for  $\text{H}_2\text{ox}$  and  $\text{Hox}^-$  ligands.

$[\text{Mg}(\text{OH}_2)_2(\mu\text{-ox})]_n$ ,  $\text{Mg}^{2+}$  is in a  $\{\text{trans-Mg}(\text{OH}_2)(\text{ox})_2\}$  environment with the  $\text{ox}^{2-}$  ligands in mode I (Scheme 19), connecting the units into 1D-chains; in 2008, this represented a new polymorph of  $\text{Mg}(\text{ox}) \cdot 2\text{H}_2\text{O}$ .<sup>1627</sup> In  $[\text{H}_2\text{dab}][\text{Mg}_2(\text{ox})_3]$ ,  $[\text{Mg}_2(\mu\text{-ox})_3]_n^{2n-}$  sheets consist of octahedrally sited  $\text{Mg}^{2+}$  connected by bridging  $\text{ox}^{2-}$  ligands in mode I (Scheme 19); this gives rise to a honeycomb-like layered structure.<sup>1628</sup> A similar local  $\{\text{Mg}(\text{ox})_3\}$  coordination environment is also observed in the salt  $[\text{H}_2\text{dabco}][\text{Mg}(\text{ox})_2] \cdot 3\text{H}_2\text{O}$ ; however, only two of the three ligands per  $\text{Mg}^{2+}$  are in bridging modes, leading to the assembly of 1D-chains. This latter compound is one of a series investigated for their structural phase transitions between 203 and 217 K.<sup>1629</sup> Pastoro et al. reported a method of trapping  $\text{CO}_2$  which involved reduction (using vitamin C as a sacrificial reductant) and precipitation as crystalline  $\text{Ca}(\text{ox}) \cdot 2\text{H}_2\text{O}$  (the mineral weddellite) with the  $\text{ox}^{2-}$  ligand adopting mode II (Scheme 19).<sup>1630</sup> The phase transitions between the calcium oxalates whewellite ( $\text{Ca}(\text{ox}) \cdot \text{H}_2\text{O}$ ), weddellite and caoxite ( $\text{Ca}(\text{ox}) \cdot 3\text{H}_2\text{O}$ ) have been studied by Izatulina et al. and bonding modes I, II, III and IV (Scheme 19) are all represented.<sup>1631</sup> The  $\text{ox}^{2-}$  ligand is found in mode IV (Scheme 19) in  $[\text{Ca}_2(\mu\text{-ox})(\mu\text{-Cl})_2(\mu\text{-OH}_2)_2]_n$  (synthetic novgorodovaite) in which 2D-sheets are linked by bridging aqua ligands. On going from the dihydrate to the heptahydrate, coordinated chlorido ligands are replaced by aqua ligands with an associated change to a 2D-sheet structure with hydrogen-bonded  $\text{Cl}^-$  ions and  $\text{H}_2\text{O}$  molecules between the sheets.<sup>1632</sup>

'Acid strontium oxalate',  $\text{Sr}_2(\text{Hox})_2(\text{ox}) \cdot 2\text{H}_2\text{O}$ , possesses a 3D-assembly with the  $\text{Hox}^-$  and  $\text{H}_2\text{O}$  ligands bridging between different pairs of  $\text{Sr}^{2+}$  centers, and the  $\text{ox}^{2-}$  ligand adopting mode III (Scheme 19).<sup>1633</sup> Barium oxalates offer a wide range of structural motifs. The discrete molecular ion  $[\text{Ba}(\text{OH}_2)_2(\text{Hox})_4]^{2-}$  (CN = 10) contains chelating  $\text{Hox}^-$  ligands and a *trans*-arrangement of aqua ligands.<sup>1634</sup>  $[\text{Ba}_2(\text{ox})_2(\text{OH}_2)]_n$  precipitated from aqueous solutions of  $\text{BaCl}_2$  and  $(\text{NH}_4)_2\text{ox}$  possesses a 3D-network with 9-coordinate  $\text{Ba}^{2+}$ , terminal aqua ligand and  $\text{ox}^{2-}$  ligands in bonding mode IV (Scheme 19).<sup>96</sup> Borel et al. described the 3D-networks in  $[\text{Ba}(\text{ox})(\text{OH}_2)(\mu\text{-OH}_2)_2]_n$ ,  $[\text{Ba}(\text{ox})(\text{H}_2\text{ox})(\text{OH}_2)_2]_n$  and  $[\text{Ba}_2(\text{ox})(\text{Hox})_2(\text{OH}_2)_2]_n$ . The repeat unit in  $[\text{Ba}(\text{ox})(\text{OH}_2)(\mu\text{-OH}_2)_2]_n$  is



**Fig. 70** The repeat units in (A)  $[\text{Ba}(\text{ox})(\text{OH}_2)(\mu\text{-OH}_2)_2]_n$  (CSD refcode BAOXAL03), (B)  $[\text{Ba}(\text{ox})(\text{H}_2\text{ox})(\text{OH}_2)_2]_n$  (refcode BAHOXH13). (C) Part of one sheet in  $[\text{In}_2(\text{ox})_3(\text{OH}_2)_3]_n \cdot 7n\text{H}_2\text{O}$  with solvent in the channels omitted (refcode BAPMIP). (D) The structure of the dinuclear complex  $[\text{Sn}_2(\text{ox})_3]^{2-}$  (refcode CIXSIM). (E) Part of one  $[\text{Sn}_2(\text{ox})_3]_n^{2n-}$  sheet in  $\text{Sn}_2(\text{NH}_4)_2(\text{ox})_3 \cdot 3\text{H}_2\text{O}$  (refcode BAHRAE).



shown in Fig. 70A with the  $\text{ox}^{2-}$  ligand adopting mode V (Scheme 19). In contrast, in  $[\text{Ba}(\text{ox})(\text{H}_2\text{ox})(\text{OH}_2)_2]_n$  (Fig. 70B), bridging mode I is found for both  $\text{ox}^{2-}$  and  $\text{H}_2\text{ox}$ , while in  $[\text{Ba}_2(\text{ox})(\text{Hox})_2(\text{OH}_2)_2]_n$  (CN = 9),  $\text{ox}^{2-}$  and  $\text{Hox}^-$  adopt modes III and I, respectively.<sup>1635</sup> In the 2,4,6-trinitrophenolate salt of  $[\text{Ba}_2(\text{ox})(\text{OH}_2)_4(\mu\text{-OH}_2)_4]^{2+}$ , 2D-sheets are present with the  $\text{ox}^{2-}$  ligand adopting mode III (Scheme 19) and  $\text{Ba}^{2+}$  having a CN = 9.<sup>1636,1637</sup>

Group 13 metal oxalato complexes in which  $\text{ox}^{2-}$  ligands are bidentate include  $[\text{Al}(\text{ox})_3]^{3-}$ ,<sup>1625,1638,1639</sup> and  $[\text{Ga}(\text{ox})_3]^{3-}$ ,<sup>1640-1642</sup> Dinuclear complexes are represented by  $[\text{Ga}_2(\text{ox})_4(\mu\text{-ox})]^{4-}$  (bridging mode I).<sup>1643,1644</sup> In the 1D-polymer  $[\text{Ga}(\mu\text{-F})(\text{ox})_2]_n^{2n-}$  (isolated as the  $[\text{H}_2(4,4'\text{-bpy})]^{2+}$  salt), the oxalates are in a chelating mode and each Ga(III) is octahedrally sited with  $\{\text{trans-GaF}_2(\text{ox})_2\}$  units.<sup>1645</sup> Feng, Bu and coworkers have demonstrated the use of linear ligands ( $\text{ox}^{2-}$  in mode I, Scheme 19) for the preparation of zeolite type-structures with RHO, GIS, and ABW (defined in reference 1646) topologies.<sup>1647</sup> In  $\{[\text{H}_2\text{en}][\text{In}_2(\text{ox})_4]\}_n \cdot 4n\text{H}_2\text{O}$ , each In(III) has CN = 8 and is bound by four  $\text{ox}^{2-}$  ligands (mode I, Scheme 19) to assemble a porous 3D-network.<sup>1648</sup> Further examples of extended indium oxalate structures include  $[\text{In}_2(\text{ox})_3(\text{OH}_2)_3]_n \cdot 7n\text{H}_2\text{O}$  which possesses a layer structure with mode I  $\text{ox}^{2-}$  ligands and both 7- and 8-coordinate In(III) (Fig. 70C); thermal decomposition of this material yielded nanocrystalline  $\text{In}_2\text{O}_3$ .<sup>1649</sup> The 2D-layer structure of  $[\text{In}_2(\mu\text{-ox})_3(\text{OH}_2)_4]_n \cdot 2n\text{H}_2\text{O}$  contains 7-coordinate In(III) connected by bridging  $\text{ox}^{2-}$  ligands which adopt either mode I or VI (Scheme 19); the pentagonal bipyramidal coordination sphere also contains axial aqua ligands.<sup>1650</sup> A CN of 7 is also found in the 1D-polymer  $[\text{In}(\mu\text{-ox})(\text{OH}_2)_3]^+$  in which the oxalate ligand adopts mode I (Scheme 19).<sup>1651</sup> The hydrothermal reaction of  $\text{In}_2\text{O}_3$  and oxalic acid in the presence of boric acid produces  $[\text{In}_3(\mu\text{-OH})_3(\mu\text{-ox})_3(\text{OH}_2)_3]_n \cdot n\text{H}_2\text{O}$  which has an open, 3D-network; the  $\text{ox}^{2-}$  ligands adopt mode I (Scheme 19) and links In(III) centers into chains which are interconnected by bridging hydroxido ligands.<sup>1652</sup> Audebrand et al. have reported a series of mixed metal oxalates which includes  $[\text{InK}(\text{ox})_2(\text{OH}_2)_4]_n$  with a 3D-network in which each In(III) is 8-coordinate bound by four chelating  $\text{ox}^{2-}$ ; taking the  $\text{O}\cdots\text{K}$  contacts into account, each  $\text{ox}^{2-}$  adopts mode III, binding two In(III) and two  $\text{K}^+$  (CN = 8).<sup>1644</sup>

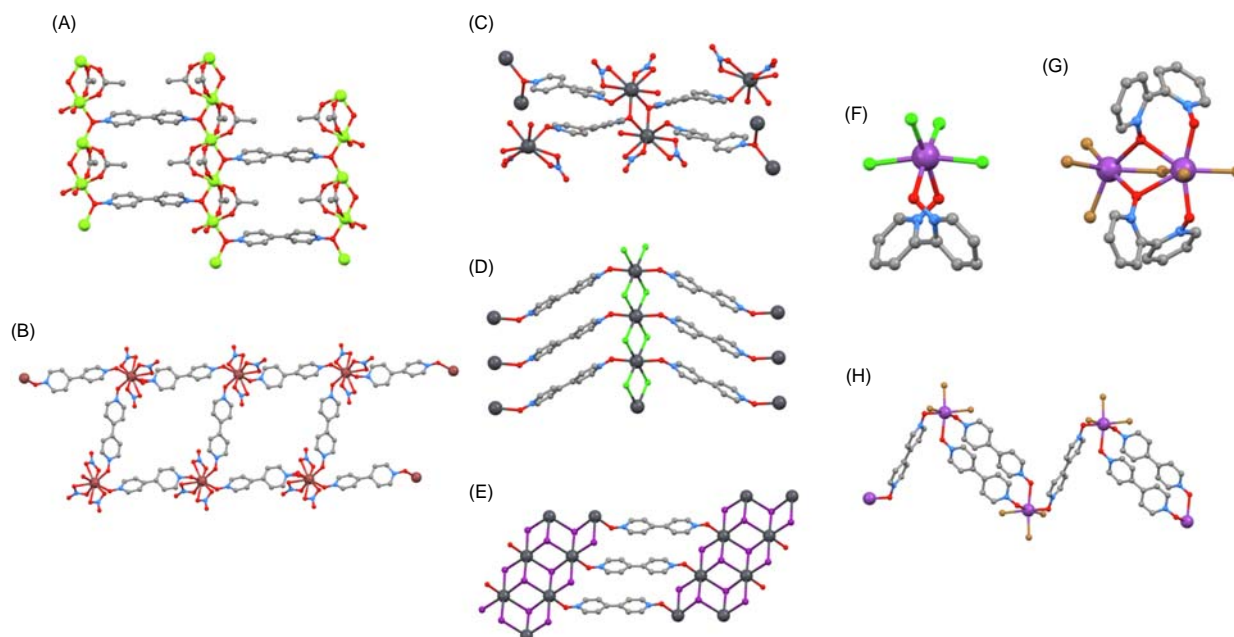
Mononuclear complexes of the group 14 M(IV) metals are illustrated by the octahedral  $[\text{Ge}(\text{ox})_3]^{2-}$ ,<sup>1653-1656</sup> *cis*- $[\text{Ge}(\text{O}-\text{H})_2(\text{ox})_2]^{2-}$ ,<sup>1657</sup>  $[\text{SnCl}_4(\text{ox})]^{2-}$ ,<sup>1658,1659</sup> *fac*- $[\text{SnCl}_3(\text{OH}_2)(\text{ox})]^-$ ,<sup>1660,1661</sup> *cis*- $[\text{SnCl}_2(\text{ox})_2]^{2-}$ ,<sup>1662</sup> and *cis*- $[\text{SnI}_2(\text{ox})_2]^{2-}$ .<sup>1663</sup> A CN = 8 is found for Sn(IV) in  $[\text{PrNH}_2]_4[\text{Sn}(\text{ox})_4]$ .<sup>1664</sup> Mononuclear oxalato complexes containing a group 14 M(II) metal center are represented by the 4-coordinate  $[\text{Sn}(\text{ox})_2]^{2-}$  which exhibits two bidentate ligands and a stereochemically active lone pair.<sup>1665,1666</sup> A similar coordination environment is found in  $[\text{Sn}_2(\text{ox})_3]^{2-}$  (Fig. 70D).<sup>1665-1667</sup> In  $[\text{NH}_4]_2[\text{Sn}_2(\text{ox})_3] \cdot 3\text{H}_2\text{O}$ , there is a 2D-network of formula  $[\text{Sn}_2(\text{ox})_3]_n^{2n-}$  in which ligands adopt mode I (Scheme 19); Fig. 70E illustrates the corrugated nature of the sheet and the role of the stereochemically active lone pair at each Sn(II) center.<sup>1668</sup>  $[\text{NH}_4][\text{SnF}(\text{ox})]$  is one of a series of low dimensional tin(II)-containing materials reported by Oliver and coworkers; it contains  $[\text{SnF}(\text{ox})]_n^{n-}$  chains with the  $\text{ox}^{2-}$  ligand coordinated to three Sn(II) centers (mode VIII, Scheme 19).<sup>1669</sup> In the dihydrate of the  $[\text{H}_2\text{en}]^{2+}$  salt,  $[\text{SnF}(\text{ox})]_n^{n-}$  1D-chains are again present, but the  $\text{ox}^{2-}$  ligand adopts mode VI (Scheme 19), leaving one O-donor uncoordinated.<sup>1667</sup> An example of a Pb(II) species is the 1D-polymer  $[\text{Pb}(\text{phen})_2(\mu\text{-ox})]_n \cdot 5n\text{H}_2\text{O}$  (CN = 8,  $\text{ox}^{2-}$  bonding mode I).<sup>1670</sup>

Oxalato complexes of the heavier group 15 elements include  $[\text{Sb}(\mu\text{-OH})(\mu\text{-ox})]_n$  for which powder diffraction data and refinement by the Rietveld method have been reported. The  $\text{ox}^{2-}$  ligands adopt mode I (Scheme 19) and each Sb(III) center is in a pentagonal pyramidal environment (plus a stereochemically active lone pair), being coordinated by two bridging  $\text{ox}^{2-}$  and two bridging hydroxido ligands to produce a 3D-network.<sup>1671</sup> The birefringent material  $[\text{Hamgu}]_2[\text{Sb}_2(\text{ox})\text{F}_4] \cdot \text{H}_2\text{O}$  contains 1D-coordination polymer chains  $[\text{Sb}_2(\mu\text{-ox})\text{F}_4]_n^{2n-}$  supported by bridging  $\text{ox}^{2-}$  ligands in mode I (Scheme 19); the 6-coordinate Sb(III) center carries a stereochemically active lone pair.<sup>1672</sup> Bismuth oxalates include  $[\text{Bi}_2(\text{ox})_3] \cdot 6\text{H}_2\text{O}$  and  $[\text{Bi}_2(\text{ox})_3] \cdot 8\text{H}_2\text{O}$  which exhibit similar 3D-networks with Bi(III) centers connected by bridging  $\text{ox}^{2-}$  in modes I and VII (Scheme 19); each Bi(III) additionally binds two  $\text{H}_2\text{O}$  ligands leading to a CN of 9, with the lone pair on Bi(III) being stereochemically inactive.<sup>1673</sup> The 3D-network in  $[\text{NH}_4][\text{Bi}(\text{ox})_2] \cdot 3.72\text{H}_2\text{O}$  comprises 8-coordinate Bi(III) coordinated by four  $\text{ox}^{2-}$  ligands in mode I (Scheme 19).<sup>1674</sup> A hydrothermal synthesis was used to form  $\{[\text{Hpy}]_2[\text{Bi}_2(\text{OH}_2)_2(\text{ox})_4]\}_n \cdot 2n\text{H}_2\text{O}$  and  $\{[\text{NH}_4][\text{Bi}(\text{ox})_2]\}_n \cdot 3n\text{H}_2\text{O}$ , in which the Bi(III) centers have CN = 9 and 8, respectively, the difference being a coordinated aqua ligand in the former compound. The  $\text{ox}^{2-}$  ligands adopt mode I (Scheme 19) to connect the Bi atoms into 3D-networks which are thermally stable up to 200 °C.<sup>1675</sup> The structure of  $[\text{Bi}(\mu\text{-ox})(\mu\text{-OH})]_n$  comprises a 3D-network, in which 1D- $\{\text{Bi}(\mu\text{-ox})\}_n$  chains with the  $\text{ox}^{2-}$  ligand in mode I are interconnected by bridging hydroxido ligands.<sup>1676</sup>

### 1.02.6.2.6 *N,N'*-Dioxides of 2,2'-bpy (bpy) and 4,4'-bpy

In this section, we use the abbreviation bpy to refer to 2,2'-bipyridine, while its isomer 4,4'-bipyridine is abbreviated to 4,4'-bpy; their *N,N'*-dioxides are bpydo and 4,4'-bpydo, respectively. The coordination of bpydo in a chelating mode leads to a noticeably twisted bpy unit, as illustrated below. Like 4,4'-bpy, 4,4'-bpydo is a common building block in coordination polymers and networks, and a range of examples is included in this section. We focus only on compounds in which the *N,N'*-dioxides are the main feature of interest.

For the group 1 metals, structural characterization of salts of  $[\text{K}(4,4'\text{-bpydo})_2]_n^{n+}$ ,  $[\text{Rb}(4,4'\text{-bpydo})_2]_n^{n+}$  and  $[\text{Cs}(4,4'\text{-bpydo})_2]_n^{n+}$  reveal similar 3D-networks in the space group  $P4/ncc$  in which anions occupy channels which follow the *c*-axis.<sup>1677-1680</sup> With the aim of designing porous coordination networks with cheap and non-toxic metals, and which show selective or high adsorption capacity, Noro et al. have focused on combinations of  $\text{Mg}^{2+}$  or  $\text{Ca}^{2+}$  with 4,4'-bpydo. Reaction of  $\text{Mg}(\text{OAc})_2 \cdot 4\text{H}_2\text{O}$  with 4,4'-bpydo gave  $[\text{Mg}_2(\mu\text{-OAc})_4(\mu_4\text{-}4,4'\text{-bpydo})]_n$  which has the 2D-network shown in Fig. 71A; each 4,4'-bpydo ligand binds four  $\text{Mg}^{2+}$  centers. 3D-Architectures are accessed by employing 1,4-benzenedicarboxylic acid as a co-ligand.<sup>1681</sup> A 3D-network is exhibited by  $[\text{Ca}_2(\text{OH}_2)_2(\mu\text{-}4,4'\text{-bpydo})_6]_n^{4n+}$ , isolated as the  $[\text{Bi}_2\text{I}_8]^{2-}$  salt; there are two



**Fig. 71** (A) Part of one 2D-sheet in  $[\text{Mg}_2(\mu\text{-OAc})_4(\mu_4\text{-}4,4'\text{-bpydo})]_n$  (CSD refcode MOTRAQ). (B) Part of the 1D-polymer in  $[\text{Tl}_2(\text{NO}_3)_6(\mu\text{-}4,4'\text{-bpydo})_3]_n \cdot 2n\text{CH}_2\text{Cl}_2$  (refcode DEFYUJ). (C) Pb(II) coordination environment in the 2D-sheets in  $[\text{Pb}(\text{NO}_3)_2(\mu\text{-}4,4'\text{-bpdo})(\text{OH}_2)]_n$  (refcode WARFIF). Part of one 2D-sheet in (D)  $[\text{Pb}(\mu\text{-Cl})_2(\mu\text{-}4,4'\text{-bpdo})]_n$  (refcode DEYYEM) and (E)  $[\text{Pb}_2(\mu\text{-Cl})_2(\mu_3\text{-Cl})_2(\mu\text{-}4,4'\text{-bpdo})]_n$  (refcode MIZKUC). The structures of (F)  $[\text{BiCl}_4(\text{bpydo})]^-$  (refcode AKAFOK), (G)  $[\text{Bi}_2\text{Br}_4(\mu\text{-Br})_2(\text{bpydo})_2]$  in the MeCN solvate (refcode ISOYEX), and (H) part of a 1D-chain in  $[\text{Bi}_2\text{Br}_6(4,4'\text{-bpydo})_3]_n$  (refcode GAFKIL).

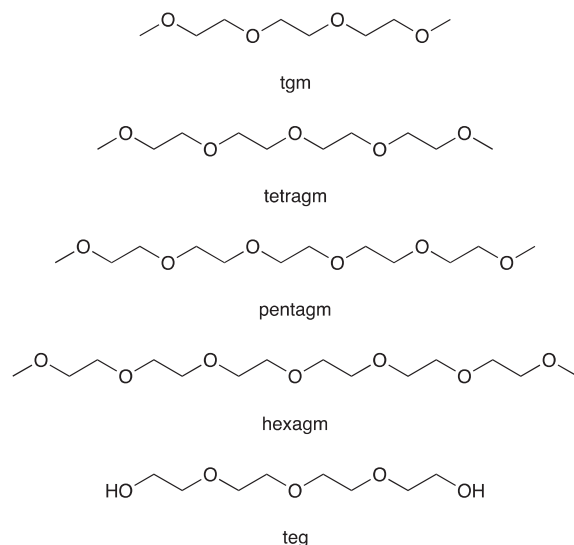
crystallographically independent  $\text{Ca}^{2+}$  centers, one with a *trans*-arrangement of aqua ligands (a 4-connecting node) and one bound by six different bridging 4,4'-bpydo ligands.<sup>1682</sup>

Moving to the p-block, and the reaction between  $\text{Tl}(\text{NO}_3)_3$  and 4,4'-bpydo yielded a ladder-type coordination polymer in which the Tl(III) center has CN = 9; the 4,4'-bpydo ligands form both the 'rungs' and 'rails' of the ladder (Fig. 71B).<sup>1683</sup> A combination of  $\text{Pb}(\text{NO}_3)_2 \cdot 2\text{H}_2\text{O}$  and 4,4'-bpdo produces  $[\text{Pb}(\text{NO}_3)_2(\mu\text{-}4,4'\text{-bpdo})(\text{OH}_2)]_n$  which has a 2D-network in which each Pb(II) center is bound by three 4,4'-bpdo, two chelating  $\text{NO}_3^-$  and one aqua ligand. As Fig. 71C shows, one O-donor of each 4,4'-bpydo ligand coordinates to two Pb(II) centers resulting in  $\{\text{Pb}_2\text{O}_2\}$  units within the network.<sup>1684</sup> In  $[\text{Pb}(\mu\text{-Cl})_2(\text{bpdo})]_n$ , 1D- $\{\text{Pb}(\mu\text{-Cl})_2\}_n$  chains are decorated by chelating bpydo ligands, the latter having the typical twisted conformation; each Pb(II) center is 6-coordinate.<sup>1685</sup> Crystallization of  $\text{PbX}_2$  ( $\text{X} = \text{Cl}, \text{Br}, \text{I}$ ) with 4,4'-bpdo led to the assembly of isostructural 2D-networks in which 4,4'-bpdo ligands connect infinite  $\{\text{PbX}_2\}_n$  chains; Fig. 71D illustrates part of one sheet in  $[\text{Pb}(\mu\text{-Cl})_2(\mu\text{-}4,4'\text{-bpdo})]_n$ .<sup>1686</sup> A related assembly is found in  $[\text{Pb}_2(\mu\text{-Cl})_2(\mu_3\text{-Cl})_2(\mu\text{-}4,4'\text{-bpdo})]_n$  (Fig. 71E).<sup>1685</sup>

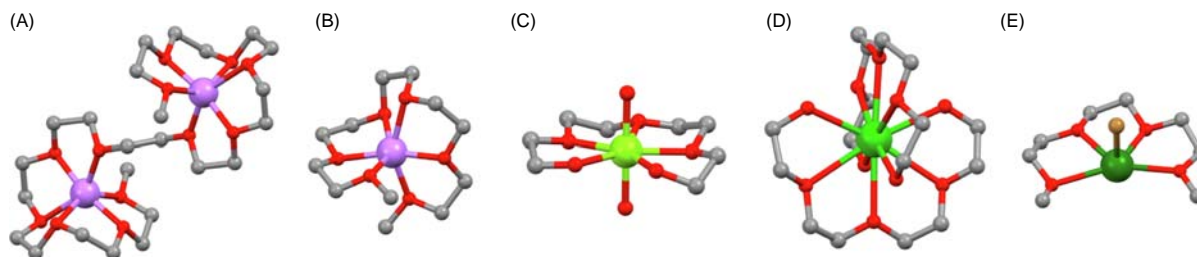
Interest in several bismuth(III) complexes with bpydo or 4,4'-bpydo is, in part, motivated by their photophysical properties. Fig. 71F shows the structure of  $[\text{BiCl}_4(\text{bpydo})]^-$ , highlighting the twisted bpy unit,<sup>1687</sup> which is again seen in the dimer  $[\text{Bi}_2\text{Br}_4(\mu\text{-Br})_2(\text{bpydo})_2]$ . Interestingly, on going to the solvated compound  $[\text{Bi}_2\text{Br}_4(\mu\text{-Br})_2(\text{bpydo})_2] \cdot 0.5\text{MeCN}$ , a second isomer of  $[\text{Bi}_2\text{Br}_5(\mu\text{-Br})(\text{bpydo})_2]$  is observed with the bpydo ligands adopting the unusual bridging mode shown in Fig. 71G.<sup>1688</sup> The 1D-coordination polymer  $[\text{Bi}_2\text{Br}_6(\mu\text{-}4,4'\text{-bpydo})_3]_n$  contains octahedrally sited Bi(III) with a *fac*-arrangement of bromido ligands and O-donors; Fig. 71H illustrates the bridging roles of 4,4'-bpydo ligands.<sup>1689</sup>

### 1.02.6.3 Tridentate (open-chain)

To illustrate open-chain, tridentate  $O, O', O''$ -ligands in main group metal complexes, we have restricted the discussion to bis(2-methoxyethyl) ether (dgm, the abbreviation stemming from the non-IUPAC name diglyme). The bis(chelating) mode is ubiquitous. Both  $[\text{Li}(\text{dgm})_2]^+$  and  $[\text{Na}(\text{dgm})_2]^+$  (CN = 6) are well established, and only selected references are given.<sup>1479,1480,1690,1691</sup> Other examples for the s-block metals include  $[\text{Li}_2(\text{dgm})_2(\mu\text{-O}_3\text{SCF}_3 \cdot 1\kappa\text{O}^1:2\kappa\text{O}^2)_2]$  (CN = 5),<sup>1692</sup>  $[\text{K}(\text{dgm})_3]^+$  (CN = 9),<sup>1693</sup>  $[\text{K}(\text{dppm-H})(\text{dgm})_2]$  (CN = 8, Fig. 54B),<sup>1066</sup>  $[\text{Cs}(\text{dgm})_3]^+$  (CN = 9),<sup>1693</sup>  $[\text{Mg}(\text{dgm})_2]^{2+}$  (CN = 6),<sup>1694</sup>  $[\text{Mg}_2\text{Cl}_2(\mu\text{-Cl})_2(\text{dgm})_2]$  (CN = 6),<sup>1402</sup>  $[\text{CaI}(\text{dgm})_2]^+$  (CN = 7),<sup>1695</sup>  $[\text{Ca}(\text{dgm})_2(\text{OH}_2)_2]^{2+}$  (CN = 8),<sup>1696</sup>  $[\text{Ba}(\text{dgm})_2(\text{OH}_2)_3]^{2+}$  (CN = 9),<sup>1696</sup> and *trans*- $[\text{BaI}_2(\text{dgm})_2]$  (CN = 8).<sup>1512</sup> Simple complexes incorporating p-block metals are poorly represented and are illustrated by  $[\text{SnCl}(\text{dgm})]^+$  (CN = 4 with a stereochemically active lone pair).<sup>1697</sup>



**Scheme 20** Open-chain ligands discussed in Section 1.02.6.4.



**Fig. 72** Structures of (A)  $[\text{Li}_2(\text{undecaglyme})]^+$  (CSD refcode GOFMAQ), (B)  $[\text{Li}(\text{pentagm})]^+$  (refcode LUQHAL), (C)  $[\text{Mg}(\text{OH}_2)_2(\text{teg})]^{2+}$  (refcode BAHTEL), (D)  $[\text{Ba}(\text{teg})_2]^{2+}$  (refcode DACRIM), and (e)  $[\text{GeBr}(\text{tgm})]^+$  (refcode IDUCIW).

### 1.02.6.4 Polydentate (open-chain)

The coverage of coordination compounds containing polydentate open-chain ligands is restricted to the ligands shown in Scheme 20; the abbreviations tgm, tetragm, pentagm and teg originate from the non-IUPAC names triglyme, tetraglyme, pentaglyme and tetraethyleneglycol, respectively. As expected, complexes of the s-block metals dominate over those of the p-block, and coordination of the ligands to produce multiple chelate rings is the norm. For small ions such as  $\text{Li}^+$ , this typically leads to the formation of polynuclear species as shown in Fig. 72A. Group 1 metal complexes containing PEG (polyethylene glycol) or long-chain polyglyme ligands (e.g.,  $[\text{Li}_2(\text{undecaglyme})]^+$ , Fig. 72A) are of interest as polymer electrolytes.<sup>1698–1700</sup>

Group 1 metal complexes are exemplified by  $[\text{Li}(\text{pentagm})]^+$  (CN = 6, Fig. 72B),<sup>1701</sup>  $[\text{Na}(\text{tgm})_2]^+$  (CN = 8),<sup>1702,1703</sup> the 1D-polymer  $[\text{Na}(\text{tetragm})_2(\mu\text{-O}_3\text{SCF}_3\text{-}1\kappa\text{O}^1\text{:}2\kappa\text{O}^2)]_n$  (CN = 7),<sup>1704</sup>  $[\text{Na}(\text{tetragm})(\text{ClO}_4\text{-}\kappa^2)]$  (CN = 7),<sup>1705</sup>  $[\text{Na}(\text{pentagm})(\text{OClO}_3)]$  (CN = 7 although three independent molecules in the asymmetric unit show subtly different bonding modes for the perchlorate ion),<sup>1705</sup>  $[\text{Na}(\text{pentagm})(\text{PF}_6)]$  (CN = 7),<sup>1705</sup>  $[\text{K}(\text{tgm})_2]^+$  (CN = 8),<sup>1706</sup> the 1D-coordination polymer  $[\text{K}(\text{pentagm})(\mu\text{-PF}_6)]_n$  (CN = 8),<sup>1701</sup>  $[\text{K}(\text{pentagm})(\text{O}_3\text{SCF}_3\text{-}\kappa^2)]$ ,<sup>1707</sup> (CN = 8),  $[\text{K}(\text{hexagm})(\text{PF}_6\text{-}\kappa^2)]$  (CN = 9),<sup>1701</sup> and  $[\text{Cs}(\text{tetragm})_2]^+$  (CN = 10).<sup>1708</sup> As expected, these complexes illustrate an increase in the CN as the group is descended.

Group 2 metal complexes are well represented. Octahedral coordination is observed in *cis*- $[\text{MgBr}_2(\text{tgm})]$  and  $[\text{Mg}_2(\text{tgm})_2(\mu\text{-Br})_2]^{2+}$  which feature in an investigation of chiral Grignard reagents.<sup>670</sup> A pentagonal bipyramidal coordination sphere is found in  $[\text{Mg}(\text{OH}_2)_2(\text{teg})]^{2+}$  (Fig. 72C),<sup>1709</sup>  $[\text{MgBr}_2(\text{tetragm})]^{2+}$ ,<sup>1710</sup> and  $[\text{Mg}(\text{MeHim})_2(\text{tetragm})]^{2+}$ ,<sup>1711</sup> while the larger  $\text{Ca}^{2+}$  ion can accommodate a CN of 7 and 8 in  $[\text{Ca}(\text{OH}_2)_2(\text{teg})]^{2+}$  (CN = 7),<sup>1709</sup>  $[\text{Ca}(\text{OH}_2)_3(\text{teg})]^{2+}$  (CN = 8),<sup>1709</sup>  $[\text{Ca}(\text{OH}_2)_4(\text{tgm})]^{2+}$  (CN = 8),<sup>1509,1696</sup> and  $[\text{Ca}(\text{tgm})(\text{hfacac})_2]$  (CN = 8).<sup>1712</sup> Strontium(II) complexes are exemplified by  $[\text{Sr}(\text{tgm})_2]^{2+}$  (CN = 8),<sup>1713</sup>  $[\text{Sr}(\text{tgm})(\text{hfacac})_2]$  (CN = 8),<sup>1712</sup> and  $[\text{Sr}(\text{OH}_2)_4(\text{teg})]^{2+}$  (CN = 9).<sup>1709</sup> The complex  $[\text{Ba}_2(\text{dme})(\text{tgm})]$  has a CN = 8 and a *trans*-arrangement of iodido ligands, while in the 9-coordinate  $[\text{Ba}_2(\text{dme})(\text{tetragm})]$ , the  $\text{I}^-$  ligands are mutually *cis*.<sup>1714</sup> A CN of 9 is observed in  $[\text{Sr}(\text{tgm})_2]^+$ ,<sup>1512</sup> and  $[\text{Ba}(\text{tgm})_2(\text{THF})]^{2+}$ .<sup>1715</sup> 10-Coordinate metal centers are observed in  $[\text{Sr}(\text{teg})_2]^{2+}$ ,<sup>1709</sup>  $[\text{Ba}(\text{teg})_2]^{2+}$  (Fig. 72D),<sup>1709,1716,1717</sup>  $[\text{Sr}(\text{tetragm})_2]^{2+}$ ,<sup>1718</sup>  $[\text{Ba}(\text{tetragm})_2]^{2+}$ ,<sup>1714,1719</sup>  $[\text{Ba}(\text{tgm})_2(\text{OCMe}_2)_2]^{2+}$ ,<sup>1719</sup> and  $[\text{Ba}(\text{OH}_2)(\text{tgm})_2]^+$ .<sup>1696</sup>

Within group 14,  $[\text{GeBr}(\text{tgm})]^+$  (Fig. 71E),  $[\text{SnBr}(\text{tgm})]^+$ ,  $[\text{GeBr}(\text{tetragm})]^+$  and  $[\text{SnBr}(\text{tetragm})]^+$  have similar structures with a stereochemically active lone pair.<sup>1720</sup> Macdonald et al. reported a series of tin(II) triflate and chloride salts incorporating open-

chain and macrocyclic polyether ligands; these include  $[\text{Sn}(\text{tgm})(\text{O}_3\text{SCF}_3)_2]$  (CN = 6) and  $[\text{Sn}(\text{tetragm})(\text{O}_3\text{SCF}_3)_2]$  (CN = 7).<sup>1721</sup> Coordination compounds of the group 15 metals are limited in number, and a representative example is the 8-coordinate  $[\text{BiCl}_3(\text{tetragm})]$ .<sup>1722</sup>

### 1.02.6.5 Macrocyclic ligands

The field of crown ether ligands is vast, and we are not able to overview it here in depth. Many examples have been given in earlier sections, e.g., Sections 1.02.2.1.1, 1.02.2.1.3, 1.02.2.1.4, 1.02.2.1.5.1, 1.02.3.1.2, 1.02.3.1.3, 1.02.6.1.4 and 1.02.6.2.3, and Figs. 4, 18, 19, 22–24, 26, 28, 51, 52 and 64. Pertinent reviews cover alkali metals,<sup>1723</sup> lithium (with a focus on optical lithium sensors),<sup>1724</sup> thallium,<sup>46</sup> and group 13 and 14 metal ions.<sup>34</sup>

## 1.02.7 Sulfur-donor ligands

### 1.02.7.1 Monodentate ligands

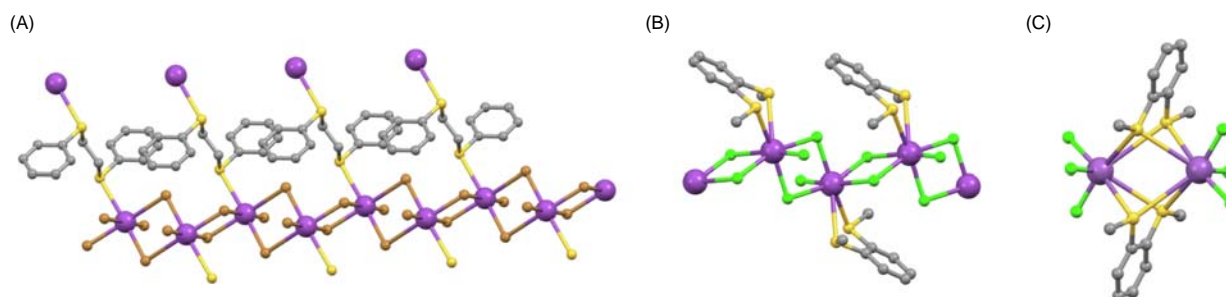
#### 1.02.7.1.1 $R_2S$

Main group metal complexes containing simple thioethers are restricted in number. Dimethyl sulfide appears in the tetrahedral  $[\text{BeX}_2(\text{SMe}_2)_2]$  ( $X = \text{Cl}, \text{Br}, \text{I}$ ) and the dimers  $[\text{Be}_2\text{X}_2(\text{SMe}_2)_2(\mu\text{-X})_2]$  ( $X = \text{Cl}, \text{Br}, \text{I}$ )<sup>1725</sup>; the authors note that the Be–S bond is relatively weak which makes thioether adducts suitable precursors to, for example, beryllium alkyl species. The versatility of  $[\text{BeBr}_2(\text{SMe}_2)_2]$  as a precursor has also been reported by Krossing.<sup>1726</sup> Within the p-block,  $\text{Me}_2\text{S}$  derivatives are illustrated by *trans*- $[\text{SnCl}_4(\text{SMe}_2)_2]$ ,<sup>1727</sup> and  $[\text{SbCl}_3(\text{SMe}_2)]$  (disphenoidal geometry).<sup>1728</sup> In  $[\text{BiBr}_3\{\mu\text{-MeS}(\text{CH}_2)_3\text{SMe}\}]_n$ ,  $\text{MeS}(\text{CH}_2)_3\text{SMe}$  ligands coordinate to Bi(III) in a monodentate and bridging fashion, linking  $\{\text{Bi}_2\text{Br}_4(\mu\text{-Br})_2\}$ -units into a 2D-sheet. In contrast,  $[\text{Bi}_2\text{Br}_6\{\text{PhS}(\text{CH}_2)_2\text{SPh}\}]_n$  contains infinite  $\{\text{Bi}_2\text{Br}_6\}_n$  chains interconnected by thioether ligands (Fig. 73A).<sup>1729</sup> Both  $[(\text{GaCl}_3)_2\{\mu\text{-MeS}(\text{CH}_2)_2\text{SMe}\}]$  and  $[(\text{GaCl}_3)_2\{\mu\text{-PhS}(\text{CH}_2)_2\text{SPh}\}]$  possess discrete molecular structures.<sup>1730</sup>

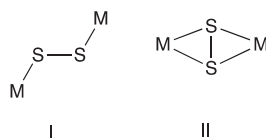
1,2-Bis(methylsulfanyl)benzene ( $1,2\text{-(MeS)}_2\text{C}_6\text{H}_4$ ) reacts with  $\text{BiCl}_3$  to produce the 1D-polymer  $[\text{BiCl}_3\{1,2\text{-(MeS)}_2\text{C}_6\text{H}_4\}]_n$  with chelating thioether ligands (Fig. 73B). In contrast,  $[\text{Sb}_2\text{Cl}_6\{1,2\text{-(MeS)}_2\text{C}_6\text{H}_4\}_2]_n$  contains dimeric units (Fig. 73C) which are then connected via Sb–Cl–Sb bridges into chains; the bonding mode of the  $1,2\text{-(MeS)}_2\text{C}_6\text{H}_4$  ligand is unusual and features long Sb⋯S contacts. This study extends to a wider range of Sb(III) and Bi(III) complexes containing arene-centered thioether ligands. On going from  $1,2\text{-(MeS)}_2\text{C}_6\text{H}_4$  to  $1,2\text{-(MeSCH}_2)_2\text{C}_6\text{H}_4$ , the tendency for chelation is reduced, leading to bridging modes.<sup>1731</sup> This is also seen in the discrete gallium(III) compound  $[(\text{GaCl}_3)_2\{\mu\text{-}(1,2\text{-(MeSCH}_2)_2\text{C}_6\text{H}_4)\}]$ ,<sup>1730</sup> and an analogous structure is observed for  $[(\text{AlCl}_3)_2\{\mu\text{-}(1,2\text{-(EtSCH}_2)_2\text{C}_6\text{H}_4)\}]$ .<sup>1732</sup>

#### 1.02.7.1.2 $S_n^{2-}$ (bridging modes)

In this section, we first consider coordination compounds containing  $S_2^{2-}$  ligands, followed by those with longer polysulfide anions. The section is organized by bonding mode rather than by periodic group. Modes of bonding of  $S_2^{2-}$  are summarized in Scheme 21, and examples of homometallic main group metal compounds are sparse. Bonding mode I of the  $S_2^{2-}$  ligand is exemplified in the structure of  $[\text{MeNH}_3]_2[\text{Sb}_8\text{S}_{14}]$  which contains pairs of chains supported by sulfide bridges linked by bridging  $S_2^{2-}$  ligands to produce double chains (Fig. 74A); further association occurs through longer Sb⋯S contacts.<sup>1733</sup> The network is retained

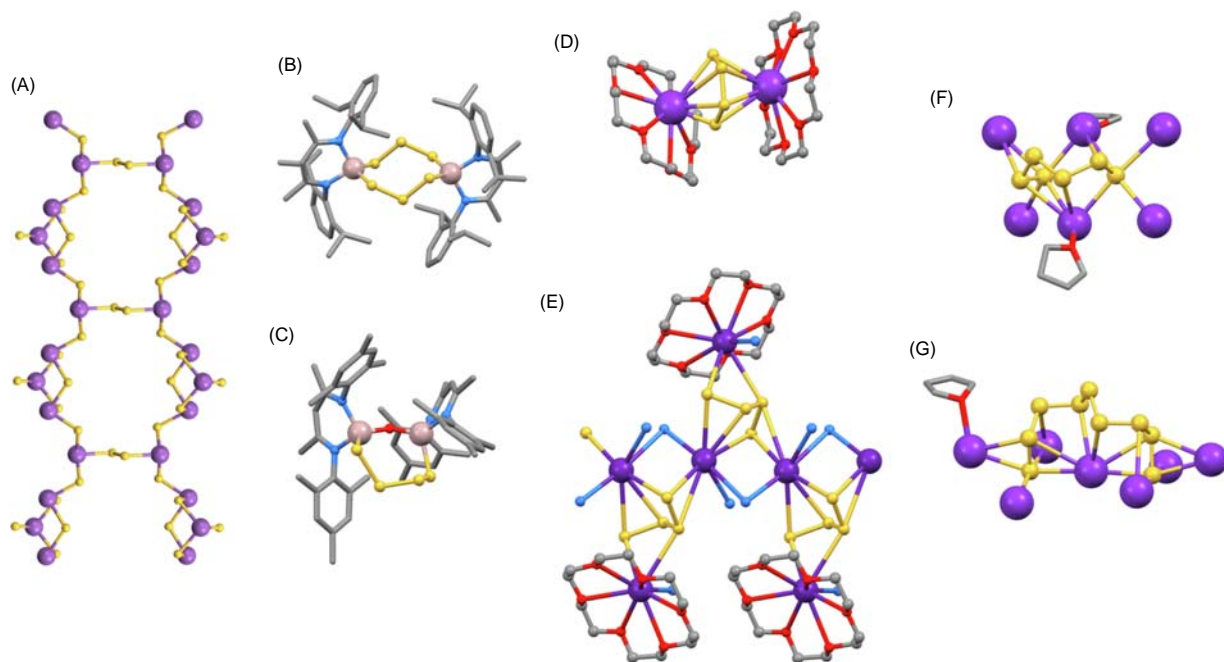


**Fig. 73** (A) Part of the 2D-sheet in  $[\text{Bi}_2\text{Br}_6\{\text{PhS}(\text{CH}_2)_2\text{SPh}\}]_n$  (CSD refcode KIGFAH). (B) Part of the 1D-chain in  $[\text{BiCl}_3\{1,2\text{-(MeS)}_2\text{C}_6\text{H}_4\}]_n$  (refcode WALZUG). (C) A  $[\text{Sb}_2\text{Cl}_6\{1,2\text{-(MeS)}_2\text{C}_6\text{H}_4\}_2]_n$  unit in the 1D-polymer  $[\text{Sb}_2\text{Cl}_6\{1,2\text{-(MeS)}_2\text{C}_6\text{H}_4\}_2]_n$  (refcode WAMBAP).



**Scheme 21** Modes of bonding of the  $S_2^{2-}$  ligand.





**Fig. 74** (A) Part of a double chain in  $[\text{Sb}_8\text{S}_{14}]_n^{2n-}$  (CSD refcode DAYBUB). Structures of (B)  $[\text{Al}_2(\text{Nacnac})_2(\mu\text{-S}_3)_2]$  (refcode FAQCUW) and (C)  $[\text{Al}_2(\text{Nacnac})_2(\mu\text{-O})(\mu\text{-S}_4)]$  (refcode CEYSEG) (both with  $\text{R} = \text{Dipp}$  in  $[\text{Nacnac}]^-$ , see **Scheme 6**). (D) Structure of  $[\{\text{K}(18\text{-crown-6})\}_2(\eta_4\text{-S}_4)]$  (refcode QOXJOE). (E) Part of the 1D-chain in  $[\{\text{Rb}(18\text{-crown-6})\}_2(\text{NH}_3)_2(\mu\text{-NH}_3)(\mu_3\text{-S}_4)]_n$  (refcode QOZLAT). Bonding modes of (F) the  $\text{S}_6^{2-}$  ligand in  $[\text{K}_2(\mu_6\text{-S}_6)(\text{THF})_2]_n$  (refcode JEXCEV) and (G) the  $\text{S}_9^{2-}$  ligand in  $[\text{K}_2(\mu_7\text{-S}_9)(\text{THF})]_n$  (refcode JEXCIZ).

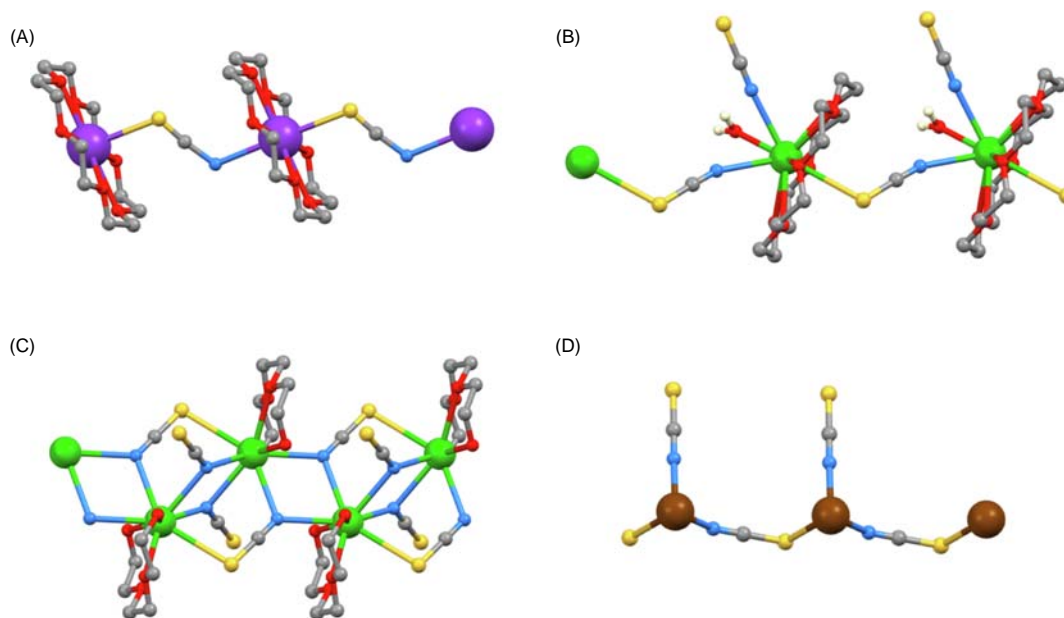
upon going to the  $[\text{H}_3\text{N}(\text{CH}_2)_3\text{NH}_3]^{2+}$  salt.<sup>1734</sup> Bonding mode II occurs in  $[\text{Mg}_2(\text{THF})_2(\text{Nacnac})_2(\mu\text{-S}_2)]$  ( $\text{R} = \text{Dipp}$  in  $[\text{Nacnac}]^-$ , see **Scheme 6**).<sup>1735</sup>

The  $\text{S}_3^{2-}$  ligand occurs in a bridging mode in  $[\text{Al}_2(\text{Nacnac})_2(\mu\text{-S}_3)_2]$  ( $\text{R} = \text{Dipp}$  in  $[\text{Nacnac}]^-$ , see **Scheme 6**) in which each Al(III) is tetrahedrally sited (**Fig. 74B**); the  $\text{Al}_2\text{S}_6$  ring has a crown conformation analogous to that in  $\text{S}_8$ .<sup>1736</sup> A bridging  $\text{S}_3^{2-}$  ligand also occurs as one of the products obtained when  $\text{S}_8$  reacts with reduced Bi(II) species.<sup>1737</sup> (Note, however, that the most important finding of this communication is the structural characterization of a dimeric Bi complex of the tetrasulfide radical anion  $\text{S}_4^-$ ; this was the first report of the structure of a complex (main group or transition metal) of a polysulfido radical anion.) With an increase in the chain length to  $\text{S}_4^{2-}$ , the formation of a favorable 5-membered chelate ring becomes viable, as is observed in  $[\text{Al}(\text{Nacnac})(\text{S}_4)]$  ( $\text{R} = \text{Dipp}$  in  $[\text{Nacnac}]^-$ , see **Scheme 6**) which is a rare example of an aluminum polysulfide; the related  $[\text{Al}(\text{Nacnac})(\text{S}_6)]$  with chelating  $\text{S}_6^{2-}$  was also isolated.<sup>1738</sup> The Sn(IV) compounds  $[\text{Sn}\{\text{Me}_2\text{NC}(\text{NCy})_2\}_2(\text{S}_4)]$  and  $[\text{Sn}\{\text{Me}_2\text{NC}(\text{NCy})_2\}_2(\text{S}_6)]$  exhibit chelating  $\text{S}_n^{2-}$  ligands and are members of a series of guanidinato complexes that have been assessed for use as single-source precursors for Sn and SnS thin films.<sup>758</sup> A related derivative is  $[\text{Sn}\{\text{Et}_2\text{NC}(\text{NCy})_2\}\{\text{N}(\text{SiMe}_3)_2\}(\text{S}_4)]$ .<sup>765</sup> The  $\text{S}_4^{2-}$  ligand can adopt varying bridging modes. In  $[\text{Al}_2(\text{Nacnac})_2(\mu\text{-O})(\mu\text{-S}_4)]$  ( $\text{R} = \text{Dipp}$  in  $[\text{Nacnac}]^-$ , see **Scheme 6**), the sulfide is monodentate with respect to each Al(III) center (**Fig. 74C**).<sup>1739</sup> **Fig. 74D** and **E** illustrate additional bridging modes in alkali metal derivatives. Reaction of  $\text{S}_8$  and 18-crown-6- with  $\text{KC}_8$  produced  $[\{\text{K}(18\text{-crown-6})\}_2(\eta_4\text{-S}_4)]$  (**Fig. 74D**) in which all S atoms are within a similar distance of the two  $\text{K}^+$  centers; the range of K–S distances is 3.191(8)–3.334(9) Å.<sup>1740</sup>  $[\{\text{Rb}(18\text{-crown-6})\}_2(\text{NH}_3)_2(\mu\text{-NH}_3)(\mu_3\text{-S}_4)]_n$  was a by-product in the reaction of Rb metal,  $\text{Si}_2$  and 18-crown-6 in liquid  $\text{NH}_3$ , and assembles into a 1D-coordination polymer; the  $\text{S}_4^{2-}$  ligands supports the polymer backbone and also binds the peripheral  $\{\text{Rb}(18\text{-crown-6})(\text{NH}_3)\}$  units (**Fig. 74E**).<sup>1741</sup> The  $\text{S}_6^{2-}$  ligand interacts with six  $\text{K}^+$  centers in  $[\text{K}_2(\mu_6\text{-S}_6)(\text{THF})_2]_n$  which forms a 2D-network; the bonding mode is highlighted in **Fig. 74F**. Increasing the polysulfide chain length to  $\text{S}_9^{2-}$  leads to the formation of the 2D-network  $[\text{K}_2(\mu_7\text{-S}_9)(\text{THF})]_n$ , and **Fig. 74G** displays the bonding mode of the ligand.<sup>1742</sup>

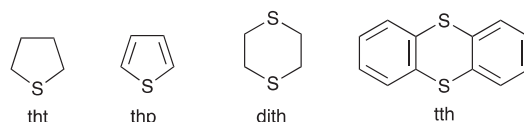
### 1.02.7.1.3 S-Bonded $\text{NCS}^-$

In **Section 1.02.2.1.4**, we surveyed main group metal complexes containing N-bonded  $\text{NCS}^-$  ligands. This ambidentate ligand also offers a range of compounds in which it is coordinated through the S atom, although s- and p-block metal coordination compounds in which the  $\text{SCN}^-$  ligand is terminally bound appear to be rare. A related complex is  $[\text{GaCl}_3(\text{SCNSiMe}_3)]$ .<sup>1743</sup> We have already described  $[\text{K}(18\text{-crown-6})(\mu\text{-SCN})\text{In}(\text{NCS})_5]^{2-}$  which contains an  $\text{NCS}^-$  ligand which is S-bound to  $\text{K}^+$  and N-bound to In(III) (**Fig. 28F**).<sup>443</sup> This kind of bridging mode is relatively well represented (the  $\text{NCS}^-$  bridge often suffering from crystallographic disorder), and other examples are  $[\text{Li}(\mu\text{-SCN})(\mu\text{-hmpa})]_n$  (a 1D-polymer with alternate pairs of  $\text{Li}^+$  centers bridged by two  $\text{SCN}^-$  or two hmpa ligands),<sup>1744</sup>  $[\text{K}(18\text{-crown-6})(\mu\text{-SCN})]_n$  (**Fig. 75A**),<sup>1745</sup>  $[\text{Mg}(\mu\text{-SCN})_2(\text{THF})_2]_n$  (a 1D-chain with octahedral  $\text{Mg}^{2+}$  centers bearing *trans*-THF ligands and connected by pairs of bridging  $\text{NCS}^-$  ligands),<sup>1746</sup>  $[\text{Ca}(\mu\text{-OH}_2)_2(\mu\text{-SCN})_2]_n$  (a 2D-





**Fig. 75** Part of the 1D-chains in (A)  $[K(18\text{-crown-6})(\mu\text{-SCN})]_n$  (CSD refcode KTHOXD05), (B)  $[Ba(OH_2)(NCS)(18\text{-crown-6})(\mu\text{-SCN})]_n$  (refcode GOKKUO, only aqua H atoms are shown), (C)  $[Ba\{HO(CH_2O)_3H\}(\mu\text{-SCN})_2]_n$  (refcode TADQEY), and (D)  $[Sn(NCS)(\mu\text{-SCN})]_n$  (refcode WIXLEX).



**Scheme 22** Structures of the heterocyclic ligands tetrahydrothiophene (tht), thiophene (thp), 1,4-dithiane (dith) and thianthrene (tth).

network with  $\{Ca(\mu\text{-OH}_2)_2\}_n$  chains interconnected by bridging  $SNC^-$  ligands,<sup>1747</sup>  $[Ba(OH_2)(NCS)(18\text{-crown-6})(\mu\text{-SCN})]_n$  (Fig. 75B,  $Ba-S = 3.335(1) \text{ \AA}$ ),<sup>1748</sup> and  $[Ba(NCS)\{HO(CH_2O)_3H\}(\mu\text{-SCN})]_n$  (with a structure related to that in Fig. 75C,  $Ba-S = 3.3307(6) \text{ \AA}$ ).<sup>1749</sup> In  $[Ba\{HO(CH_2O)_3H\}(\mu\text{-SCN})_2]_n$  (Fig. 75C),  $NCS^-$  ligands adopt two different bridging modes, one through the N-donor and one through both N- and S-donors.<sup>1750</sup>

Structurally simple complexes of the p-block metals include  $[Sn(NCS)(\mu\text{-SCN})]_n$  (a 1D-chain supported by bridging  $SCN^-$  ligands, Fig. 75D),<sup>1751</sup> and  $[Bi(THF)(\mu\text{-SCN})_3]_n$  (which forms a 2D-network with adjacent Bi(III) centers bridged by two  $NCS^-$  ligands).<sup>441</sup>

#### 1.02.7.1.4 Heterocyclic ligands

Main group metal coordination compounds with monodentate S-heterocyclic ligands are not extensive and we have restricted the coverage to the ligands shown in Scheme 22, and the soft nature of sulfur naturally leads to a dominance of heavier p-block metals. Complexes containing tht are limited to a few p-block metal species, illustrated by the square-planar *trans*- $[SeCl_2(tht)_2]$  and *trans*- $[TeCl_2(tht)_2]$ ,<sup>1752</sup> octahedral *trans*- $[TeX_4(tht)_2]$  ( $X = Cl, Br$ ),<sup>1307</sup> and the dimer  $[Te_2Br_6(tht)_2(\mu\text{-Br})_2]$ .<sup>1307</sup> In reactions of  $[AuCl(tht)]$  with  $Sn\{N(SiMe_3)_2\}_2$ , the tht ligand is transferred from gold to tin resulting in the formation of  $[Au\{SnCl(NR_2)_2\}\{Sn(tht)(NR_2)_2\}]$  and  $[Au\{Sn(NR_2)_3\}\{Sn(tht)(NR_2)\}]$  ( $R = SiMe_3$ ).<sup>1753</sup> Searches of the CSD for complexes of the main group metals (post 2000) that incorporate non-functionalized thiophene ligands generated no hits, but there are a few examples in which a thiophen-2-yl unit is present.  $[Na(3\text{-}(thiophen\text{-}2\text{-}yl)phen)(BF_4)]$  forms dimeric units by virtue of bridging  $BF_4^-$  ligands, and these further associate through weak  $Na \cdots S$  interactions ( $Na-S = 3.383(5) \text{ \AA}$ ).<sup>1754</sup> Reactions between tris(thiophen-2-yl)methanol (HL) and NaH or KH in THF produced cubanes  $[M_4L_4(THF)_2]$  ( $M = Na, K$ ) in which each  $L^-$  ligand coordinates through the O- and three S-donors.<sup>1755</sup>

The few examples of p-block metal complexes containing 1,4-dithiane ligands illustrate different bonding modes. The ligand is ideally suited as a linker in coordination polymers, and this is exemplified in  $[SnBr_4(\mu\text{-dith})]_n$  which contains *trans*- $\{SnBr_4S_2\}$  coordination spheres ( $Sn-S = 2.6546(6) \text{ \AA}$ ).<sup>1756</sup> 1,4-Dithiane binds to Sb(III) in  $[SbCl_2(dith-\kappa^2)]^+$ ; the dith ligand adopts a boat conformation and coordinates through both S-donors but in an asymmetric manner ( $Sb-S = 2.694(1)$  and  $3.003(2) \text{ \AA}$ ); additional 1,4-dithiane molecules link the  $[SbCl_2(dith-\kappa^2)]^+$  units into 1D-chains although the interactions are rather weak ( $Sb-S = 3.023(2) \text{ \AA}$ ).<sup>1757</sup>

The reaction of tth with  $\text{AlCl}_3$  in a melt yields tetrahedral  $[\text{AlCl}_3(\text{tth})]$  with one non-coordinated S-donor. Note that oxidation of tth is a competitive process and a by-product was  $[\text{tth}_3][\text{Al}_2\text{Cl}_7]_2$  containing  $[\text{tth}_3]^{2+}$  cations.<sup>1758</sup>

### 1.02.7.2 Bidentate: $[\text{S}(\text{CH}_2)_2\text{S}]^{2-}$ and $\text{RS}(\text{X})\text{SR}$

In Section 1.02.7.1.1, we included the coordination of  $\text{RS}(\text{CH}_2)_n\text{SR}$  and 1,2-(MeS) $_2\text{C}_6\text{H}_4$ , 1,2-(MeSCH $_2$ ) $_2\text{C}_6\text{H}_4$  and 1,2-(EtSCH $_2$ ) $_2\text{C}_6\text{H}_4$ . Although the emphasis was on bridging modes (i.e., monodentate to a given metal center), chelation was also illustrated (e.g., see Fig. 73B). We now consider bidentate ligands which show a preference for chelating modes.

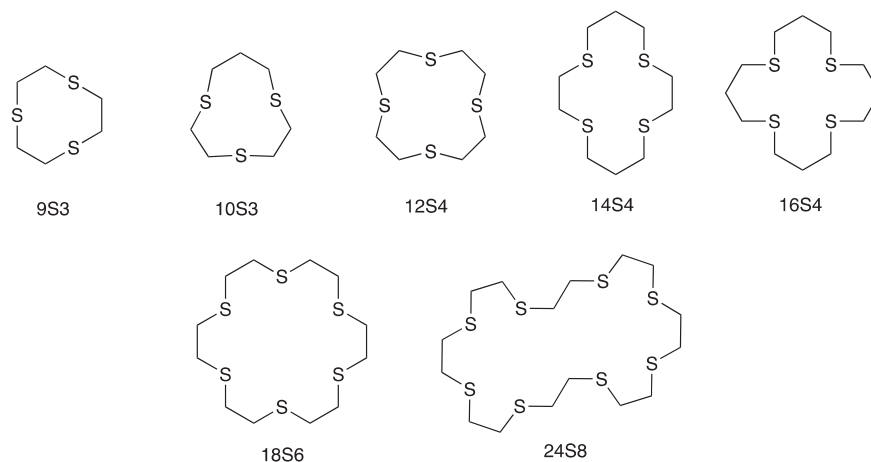
Coordination to a single metal center by  $[\text{S}(\text{CH}_2)_2\text{S}]^{2-}$  or  $\text{RS}(\text{CH}_2)_2\text{SR}$  ligands leads to a favorable 5-membered chelate ring. Structurally simple complexes containing the ethane-1,2-dithiolato ligand,  $\text{edt}^{2-}$ , are exemplified by  $[\text{GaCl}_2(\text{edt})]^-$  (tetrahedral),<sup>1759</sup>  $[\text{Ga}(\text{edt})_2]^-$  (tetrahedral),<sup>1759</sup>  $[\text{Ge}(\text{edt})_2]$  (tetrahedral),<sup>1760</sup>  $[\text{AsX}(\text{edt})]$  (X = Cl, I; trigonal pyramidal),<sup>1761</sup>  $[\text{As}_2(\text{edt})_2(\mu\text{-edt})]$  (trigonal pyramidal),<sup>1761</sup> and  $[\text{SbCl}(\text{edt})]$  (trigonal pyramidal).<sup>1762</sup> Complexes containing neutral, chelating  $\text{RS}(\text{CH}_2)_2\text{SR}$  ligands include *cis*- $[\text{AlI}_2\{\text{MeS}(\text{CH}_2)_2\text{SMe}\}_2]^+$  (octahedral),<sup>1732</sup> *trans*- $[\text{AlCl}_2\{\text{MeS}(\text{CH}_2)_2\text{SMe}\}_2]^+$  (octahedral),<sup>1732</sup> *trans*- $[\text{InX}_2\{\text{PrS}(\text{CH}_2)_2\text{S}^i\text{Pr}\}_2]^+$  (X = Cl, Br; octahedral),<sup>1763</sup>  $[\text{GeF}_4\{\text{RS}(\text{CH}_2)_2\text{SR}\}]$  (R = Me, Et; octahedral),<sup>1764</sup>  $[\text{SnF}_4\{\text{RS}(\text{CH}_2)_2\text{SR}\}]$  (R = Et, <sup>i</sup>Pr; octahedral),<sup>1764</sup>  $[\text{As}_2\text{I}_4\{\text{MeS}(\text{CH}_2)_2\text{SMe}\}_2(\mu\text{-I})_2]$  (octahedral As),<sup>1765</sup>  $[\text{BiBr}_3\{\text{MeS}(\text{CH}_2)_2\text{SMe}\}_2]$  (CN = 7),<sup>1729</sup>  $[\text{TeX}_4\{\text{MeS}(\text{CH}_2)_2\text{SMe}\}]$  (X = Cl, Br; octahedral Te(IV)),<sup>1766</sup> and  $[\text{TeCl}\{\text{PrS}(\text{CH}_2)_2\text{S}^i\text{Pr}\}]^+$  (*ca.* planar Te(II) with a weak Te...Cl contact to the  $[\text{Te}_2\text{Cl}_9]^-$  anion).<sup>1766</sup> Six-membered chelate rings are observed in the octahedral  $[\text{SnCl}_4\{\text{PhS}(\text{CH}_2)_3\text{SPh}\}]$ ,<sup>1767</sup> and  $[\text{TeCl}_4\{\text{MeS}(\text{CH}_2)_3\text{SMe}\}_2]$ .<sup>1307</sup>

### 1.02.7.3 Tridentate

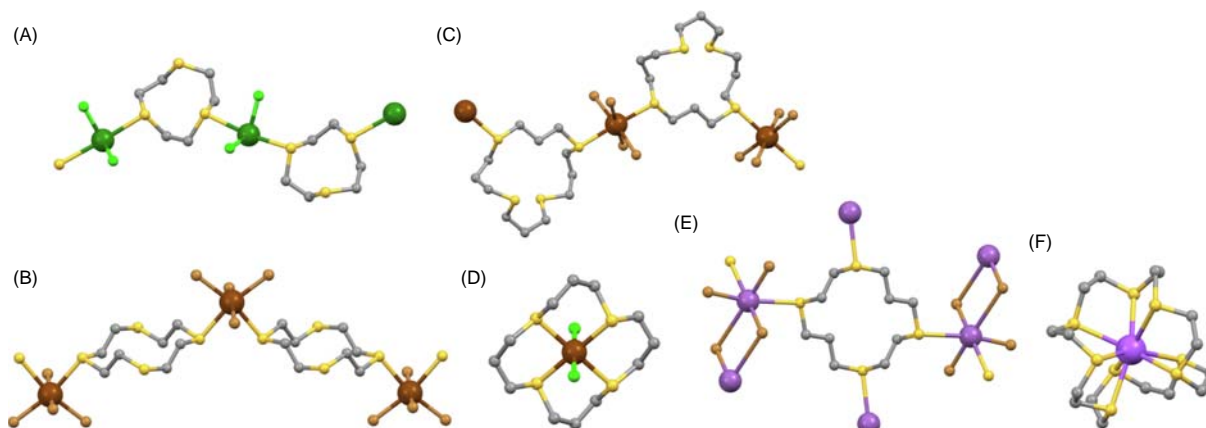
Main group metal coordination compounds incorporating simple tridentate S,S',S''-ligands are not so well represented, and we focus on the few complexes of the p-block metals containing the conjugate base of 2,2'-thiobis(ethane-1-thiol).  $[\text{Sn}(\text{edt})\{\text{S}(\text{CH}_2\text{CH}_2\text{S})_2\}]$  has a trigonal bipyramidal structure with the  $\{\text{S}(\text{CH}_2\text{CH}_2\text{S})_2\}$  facially-bound.<sup>1768</sup> The Sb(II) center in  $[\text{SbI}\{\text{S}(\text{CH}_2\text{CH}_2\text{S})_2\}]$  exhibits a disphenoidal (see-saw) coordination environment with the I<sup>-</sup> ligand in an axial site.<sup>1769</sup> In  $[\text{Ge}\{\text{S}(\text{CH}_2\text{CH}_2\text{S})_2\}(1\text{-HN-2-SC}_6\text{H}_4)]$ , the Ge(IV) center can be described as 5-coordinate, although it exhibits one long Ge-S contact to the central S of the tridentate ligand (3.055(1) Å vs 2.214(1) and 2.2154(9) Å).<sup>1770</sup>

### 1.02.7.4 Macrocyclic ligands (S only donors)

The sulfur-containing macrocyclic ligands incorporated into coordination compounds of the main group metals and reported since 2000 are shown in Scheme 23. The section is organized by ring size, starting with 1,4,7-trithiacyclononane (9S3) for which tridentate (to one metal center) and bridging modes are illustrated.  $\text{Na}[\text{BAr}^{\text{F}}_4]$  was used as a source of 'naked'  $\text{Na}^+$  to prepare  $[\text{Na}(9\text{S3})(\text{THF})_2][\text{BAr}^{\text{F}}_4]$  and  $[\text{Na}(24\text{S8})][\text{BAr}^{\text{F}}_4]$  (see below); severe crystallographic disorder in the  $[\text{Na}(9\text{S3})(\text{THF})_2]^+$  ion militates against discussion of the bond parameters.<sup>1771</sup> In *fac*- $[\text{AsCl}_3(9\text{S3})]$ , the As(III) center is octahedrally sited.<sup>1765</sup> In 2008, Levason, Reid and coworkers reported the first validated chalcogenoether complexes of Ge(II) and these included  $[\text{GeCl}_2(\mu\text{-}9\text{S3})]_n$  (Fig. 76A); the Ge-S bonds are relatively long (range 2.697(3) to 2.782(3) Å for three independent Ge(II) centers in the crystal structure).<sup>1772</sup> Like 9S3, 10S3 may coordinate in a tridentate mode to a single metal center. This is observed in  $[\text{Pb}(10\text{S3})(\text{OClO}_3\text{-}\kappa^2)_2(\text{OH}_2)]$  which exhibits a stereochemically active lone pair; however, the perchlorate ions are only weakly bound to Pb(II).<sup>1773</sup>



**Scheme 23** Structures and acronyms of the sulfur-containing macrocyclic ligands discussed in Section 1.02.8.3. Note that another common method of abbreviation used in the literature is of the form, e.g., [9]aneS3, [10]aneS3, and so on.



**Fig. 76** Part of the 1D-chains in (A)  $[\text{GeCl}_2(9\text{S}3)]_n$  (CSD refcode QOMBAW), (B)  $[\text{SnBr}_4(\mu\text{-}12\text{S}4)]_n$  (refcode AQARAL), (C)  $[\text{SnBr}_4(\mu\text{-}16\text{S}4)]_n$  (refcode AQARIT). (D) The structure of  $\text{trans-}[\text{GaCl}_2(16\text{S}4)]^+$  (refcode CAXJOC). (E) Coordination of 14S4 in  $[\text{Sb}_2\text{Br}_4(\mu\text{-}Br)_2(\mu\text{-}14\text{S}4)]_n$  which extend into a 3D-network (refcode QOFLUS). (F) Structure of the  $[\text{Na}(24\text{S}8)]^+$  ion (refcode JUCGOF).

The 12S4 ligand occurs in a bridging mode in  $[\text{SnBr}_4(\mu\text{-}12\text{S}4)]_n$  (Fig. 76B) and this is one of a series of related Sn(IV) complexes reported by Levason et al. The compounds  $[\text{SnBr}_4(\mu\text{-}14\text{S}4)]_n$  and  $[\text{SnBr}_4(\mu\text{-}16\text{S}4)]_n$  (Fig. 76C) are also 1D-polymers, but with a *trans*-arrangement of S-donors.<sup>1774</sup> For group 13 metal complexes of stoichiometry  $\text{MCl}_3(14\text{S}4)$ , a structural change is observed on going from Al to Ga.  $[\text{AlCl}_2(14\text{S}4)][\text{AlCl}_4]$  contains  $[\text{AlCl}_2(14\text{S}4)]^+$  cations with a tridentate ligand,<sup>1732</sup> whereas  $[\text{GaCl}_3(\mu\text{-}14\text{S}4)]_n$  is a 1D-coordination polymer with trigonal bipyramidal Ga(III) with S-donors in the axial sites.<sup>1775</sup> In contrast,  $\text{trans-}[\text{GaCl}_2(16\text{S}4)]$  is a discrete molecular complex (Fig. 76D).<sup>1775</sup> Earlier, we described the 1D-coordination polymer  $[\text{GeCl}_2(\mu\text{-}9\text{S}3)]_n$ . With 14S4, a 2D-sheet assembles with each 14S4 ligand binding four Ge(II) centers in  $[\text{Ge}_2\text{Cl}_4(\mu\text{-}14\text{S}4)]_n$ . In contrast,  $[\text{GeBr}_2(\mu\text{-}14\text{S}4)]_n$  is a 1D-polymer with only two S-donors per macrocycle involved in coordination; chains are interconnected through weak  $\text{Ge}\cdots\text{Br}$  contacts. A similar structure is found for  $[\text{GeBr}_2(\mu\text{-}16\text{S}4)]_n$ .<sup>1772</sup> As opposed to the discrete molecular *fac*- $[\text{AsCl}_3(9\text{S}3)]$  (see above), 14S4 combines with  $\text{AsCl}_3$  to give  $[\text{AsCl}_2(\mu\text{-}Cl)(\mu\text{-}14\text{S}4)]_n$ ; this is a 2D-network containing octahedrally sited As(III).<sup>1765</sup> Note that while  $\text{AsCl}_3$  and 14S4 give a 1:1 adduct even in the presence of an excess of  $\text{AsCl}_3$ ,  $\text{SbX}_3$  and 14S4 combine to give a 2:1 species exclusively. In  $[\text{Sb}_2\text{Br}_4(\mu\text{-}Br)_2(\mu\text{-}14\text{S}4)]_n$ , the macrocyclic ligand coordinates through all four S-donors (Fig. 76E) and a 3D-network results; however, note that one Sb–Br contact is weak (3.497(2) Å compared to 2.535(2), 2.548(2) and 2.609(2) Å).<sup>1776</sup> In Section 1.02.7.1.4, we described the structure of  $[\text{TeX}_4(\text{tht})_2]$  (X = Cl, Br). Hector et al. also investigated reactions of  $\text{TeX}_4$  with [14]aneS4. Although this typically yielded mixed products as insoluble solids, it was possible to isolate the 1D-polymer  $[\text{TeCl}_4(\mu\text{-}14\text{S}4)]_n$  which exhibits octahedral Te(IV) with a *cis*-arrangement of S-donors.<sup>1307</sup>

The macrocycle 18S6 is the S-analog of 18-crown-6, the coordination chemistry of which was described in numerous sections in this review (see Section 1.02.6.5). Germanium(II) forms the complex  $[\text{GeCl}(18\text{-crown-}6)]^+$  in which the  $\text{GeCl}^+$  unit is bound by four of the six S-donors.<sup>1777</sup> Reid and coworkers have investigated the effects of replacing some or all of the O- by S-donors.<sup>1778</sup> Relevant to this section is the reaction of  $[\text{GeCl}_2(\text{diox})]$  with 18S6 which yields the 1D-polymer  $[\text{GeCl}_2(\mu\text{-}18\text{S}6)]_n$  with a structure similar to that of  $[\text{GeCl}_2(\mu\text{-}9\text{S}3)]$  (Fig. 76A).<sup>1778</sup>

The preparation of  $[\text{Na}(24\text{S}8)][\text{BAR}^F_4]$  was mentioned above; the conformational flexibility of the ligand allows it to encapsulate the  $\text{Na}^+$  ion as shown in Fig. 76F with Na–S bond distances in the range 2.9561(15)–3.0524(15) Å.<sup>1771</sup>

## 1.02.8 Selenium-donor ligands

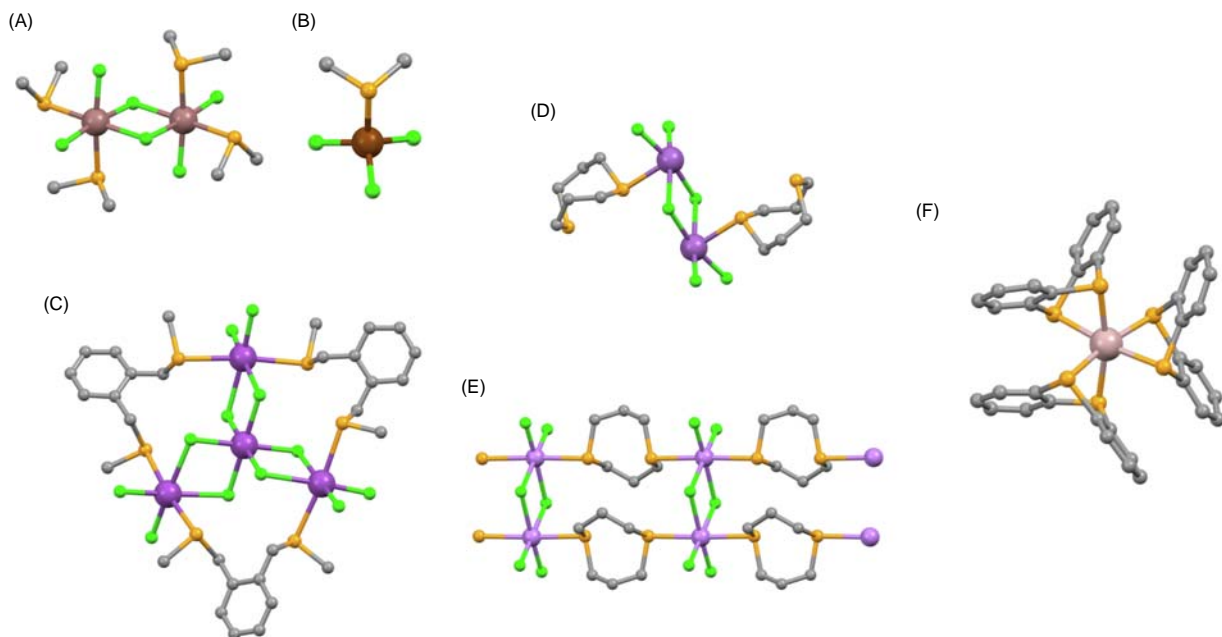
### 1.02.8.1 Monodentate and bidentate ligands

#### 1.02.8.1.1 $R_2\text{Se}$

On going from S- to Se-donor ligands, the number of structurally characterized main group metal complexes is significantly reduced. In keeping with hard–soft metal–ligand principles, complexes of the heavier p-block elements are dominant.

Mishra et al. investigated  $\text{Me}_2\text{Se}$  coordination compounds of gallium and indium halides as potential precursors for Se-containing semiconducting materials. As part of this study, tetrahedral  $[\text{GaI}_3(\text{SeMe}_2)]$ , trigonal bipyramidal  $[\text{InI}_3(\text{SeMe}_2)_2]$ , *fac*- $[\text{InCl}_3(\text{OH}_2)_2(\text{SeMe}_2)]$ ,  $[\text{In}_2\text{Cl}_4(\text{SeMe}_2)_4(\mu\text{-}Cl)_2]$  (Fig. 77A) were isolated and structurally characterized.<sup>1779</sup> Related compounds are tetrahedral  $[\text{AlCl}_3(\text{SeMe}_2)]$ ,<sup>1732</sup>  $[\text{GaCl}_3(\text{SeMe}_2)]$  (Fig. 77B),<sup>1730</sup> and  $[\text{InBr}_3(\text{SeMe}_2)]$ .<sup>1763</sup> *trans*- $[\text{SnCl}_4(\text{SeEt}_2)_2]$  is representative of complexes of the group 14 metals.<sup>1780</sup> Coordination of  $R_2\text{Se}$  to the heavier group 16 congener Te is illustrated by *trans*- $[\text{TeCl}_4(\text{-} \text{SeMe}_2)_2]$  and *trans*- $[\text{TeBr}_4(\text{SeMe}_2)_2]$ .<sup>1307</sup>

As we saw for  $\text{RS(X)SR}$  ligands, a number of  $\text{RSe(X)SeR}$  ligands are found in bridging modes and are monodentate with respect to a single metal center. This bonding mode is illustrated in the solid-state structure of the Ga(III) complex  $[(\text{GaCl}_3)_2\{\mu\text{-}^t\text{BuSe}(\text{CH}_2)_2\text{Se}^t\text{Bu}\}]$ ,<sup>1730</sup> and in the Tl(I) compound  $[\text{Tl}\{\mu\text{-}Me\text{Se}(\text{CH}_2)_3\text{SeMe}\}][\text{PF}_6]$  which contains 1D- $[\text{Tl}\{\mu\text{-}$



**Fig. 77** Structures of (A)  $[\text{In}_2\text{Cl}_4(\text{SeMe}_2)_4(\mu\text{-Cl})_2]$  (CSD refcode BUPTM), and (B)  $[\text{GaCl}_3(\text{SeMe}_2)]$  (refcode XOHNUH). (C) The  $[\text{Bi}_4(\text{Cl}_6)(\mu\text{-Cl}_6)(\mu\text{-1,2-(MeSe)}_2\text{C}_6\text{H}_4)_3]$  molecule is one motif found in  $[(\text{BiCl}_3)_4\{1,2\text{-(MeSe)}_2\text{C}_6\text{H}_4\}_3]$  (refcode WAMCAQ). (D) Structure of  $[\text{Sb}_2\text{Cl}_4(\mu\text{-Cl})_2(8\text{Se}_2)_2]$  (refcode EWIWAI). (E) Part of the 1D-polymer  $[\text{As}_2\text{Cl}_4(\mu\text{-Cl})_2(8\text{Se}_2)_2]_n$  (refcode EWIVUB). (F) Structure of the  $[\text{Al}(\text{seth})_3]^{3+}$  cation (refcode NEFREX).

$\text{MeSe}(\text{CH}_2)_3\text{SeMe}]_n^{n+}$  chains. Shortening the spacer in this last ligand results in a switch to a 3D-network, with each Tl(I) center bound by four Se atoms from different  $\text{MeSe}(\text{CH}_2)_2\text{SeMe}$  ligands; the coordination geometry is distorted tetrahedral with Tl–Se bond lengths in the range 3.2769(8)–3.5058(8) Å. These two compounds represented the first thallium(I) selenoether complexes.<sup>1781</sup>

$[(\text{SbCl}_3)_2\{\mu\text{-MeSe}(\text{CH}_2)_3\text{SeMe}\}_2]$  contains dimeric units which associate into 1D-chains through weak  $\text{Sb}\cdots\text{Cl}$  interactions ( $\text{Sb}\text{---}\text{Cl} = 3.236(3)$  Å). In the bromido-analog, the  $\text{MeSe}(\text{CH}_2)_3\text{SeMe}$  ligands are again in a bridging mode but a 2D-sheet assembles with each  $\{\text{SbBr}_3\text{Se}_3\}$  having a *fac*-arrangement of ligands.<sup>1782</sup> Moving down the group to Bi(III) leads to the formation of  $[\text{BiCl}_3\{\mu\text{-MeSe}(\text{CH}_2)_3\text{SeMe}\}]_n$  with a 2D-network based on  $\{\text{Bi}_2\text{Cl}_4(\mu\text{-Cl})_2\}$  subunits linked by bridging  $\text{MeSe}(\text{CH}_2)_3\text{SeMe}$  ligands, and  $[\text{BiBr}_3\{\mu\text{-MeSe}(\text{CH}_2)_3\text{SeMe}\}]_n$  has a similar solid-state structure.<sup>1729</sup> Levason et al. also reported a compound of stoichiometry  $[(\text{BiCl}_3)_4\{1,2\text{-(MeSe)}_2\text{C}_6\text{H}_4\}_3]$ , the solid-state structure of which contains two tetrabismuth(III) units in the asymmetric unit. One consists of the molecular  $[\text{Bi}_4(\text{Cl}_6)(\mu\text{-Cl}_6)\{\mu\text{-1,2-(MeSe)}_2\text{C}_6\text{H}_4\}_3]$  motif shown in Fig. 77C, while the second can be considered in terms of these same units linked by  $\text{Bi}\cdots\text{Cl}$  interactions into an infinite polymer.<sup>1731</sup>

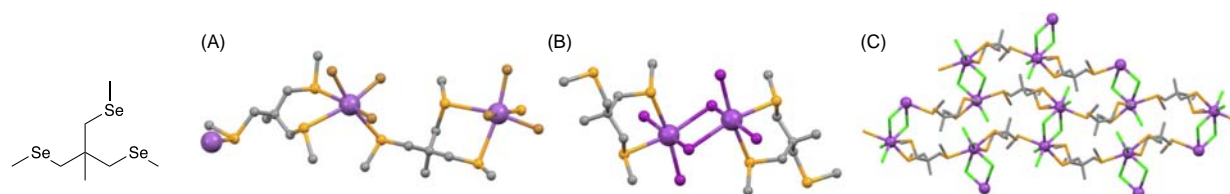
### 1.02.8.1.2 Heterocyclics

1,5-Diselenacyclooctane (8Se2) and selenanthrene (seth, the Se-analog of tth, Scheme 22) act as monodentate, bridging, and bidentate ligands in the following examples. The first examples of Ge(II) complexes of selenoether ligands were reported in 2011 by Levason, Reid and coworkers. These included  $[\text{GeCl}_2(\mu\text{-}8\text{Se}_2)]_n$  which has a 1D-polymeric structure with bridging 8Se2 ligands, each in a boat-conformation; each Ge(II) center is in a disphenoidal (see-saw) environment with S-donors in the axial sites.<sup>1778</sup> Whereas  $[\text{Sb}_2\text{Cl}_4(\mu\text{-Cl})_2(8\text{Se}_2)_2]$  is a discrete dimer in the solid state with monodentate 8Se2 ligands (Fig. 77D), an As(III) complex with the same stoichiometry forms a 1D ladder-like coordination polymer supported by bridging 8Se2 ligands (Fig. 77E). The molecules of  $[\text{Sb}_2\text{Cl}_4(\mu\text{-Cl})_2(8\text{Se}_2)_2]$  associate through weak  $\text{Se}\cdots\text{Sb}$  contacts into infinite chains. In both compounds, 8Se2 adopts a boat conformation.<sup>1783</sup> On going to Bi(III), the ladder polymer is again observed in  $[\text{Bi}_2\text{Cl}_4(\mu\text{-Cl})_2(8\text{Se}_2)_2]_n$ .<sup>1784</sup>

The reaction of selenanthrene with neat  $\text{AlCl}_3$  in 3:7 molar ratio yielded  $[\text{Al}(\text{seth})_3][\text{Al}_2\text{Cl}_7]_3$  which contains the octahedral  $[\text{Al}(\text{seth})_3]^{3+}$  cation (Fig. 77F) with chelating ligands (Al–Se bond lengths are in the range 2.588(2)–2.598(2) Å).<sup>1758</sup>

### 1.02.8.1.3 RSe(X)SeR

In Section 1.02.8.1.1, we considered compounds in which  $\text{RSe}(\text{X})\text{SeR}$  ligands were in bridging modes, acting as monodentate ligands to each metal center. Now we examine  $\text{RSe}(\text{X})\text{SeR}$  ligands in chelating modes. As part of a wider investigation of chalcogeno ether complexes of Al(III) halides, George et al. reported *trans*- $[\text{AlCl}_2\{\text{MeSe}(\text{CH}_2)_2\text{SeMe}\}_2]$  (Al–Se = 2.5950(13), and 2.6232(13) Å).<sup>1732</sup>  $[\text{SnCl}_4(\text{BuSe}(\text{CH}_2)_2\text{Se}^n\text{Bu})]$  has a discrete molecular structure containing octahedral tin(IV), and was used as a precursor for CVD deposition of  $\text{SnSe}_2$  thin films.<sup>1785</sup> Complexes of the soft, heavy group 15 metals are represented by the dimer  $[\text{In}_2\text{Cl}_4(\mu\text{-Cl})_2\{\text{MeSe}(\text{CH}_2)_2\text{SeMe}\}_2]$  and the octahedral complex *trans*- $[\text{InBr}_2\{\text{MeSe}(\text{CH}_2)_2\text{SeMe}\}_2]$ .<sup>1763</sup> In  $[\text{BiCl}_3\{1,2\text{-(MeSe)}_2\text{C}_6\text{H}_4\}]$ , Bi(III) is in a square-based pyramidal environment and the chelating 1,2-( $\text{MeSe}$ )<sub>2</sub>C<sub>6</sub>H<sub>4</sub> ligand occupies basal sites. However, the Bi–Se bonds are long (3.1376(13) Å) and are described as being weak interactions; weak  $\text{Bi}\cdots\text{Cl}$  contacts link the molecules into chains.<sup>1731</sup>



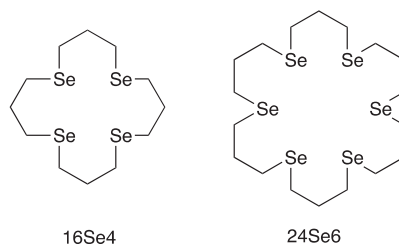
**Fig. 78** Inset: The structure of the tripodal ligand tripodSe<sub>3</sub>. (A) Part of the 1D-chain in [SbBr<sub>3</sub>(μ-tripodSe<sub>3</sub>)]<sub>n</sub> (refcode QOFLQM). (B) Structure of [Bi<sub>2</sub>I<sub>4</sub>(μ-I)<sub>2</sub>(tripodSe<sub>3</sub>-κ<sup>2</sup>)<sub>2</sub>] (CSD refcode KIGGUC). (C) Part of the 2D-network in [BiCl<sub>2</sub>(μ-Cl)(μ-tripodSe<sub>3</sub>)]<sub>n</sub> (refcode KIGGIQ).

### 1.02.8.2 Tridentate ligands

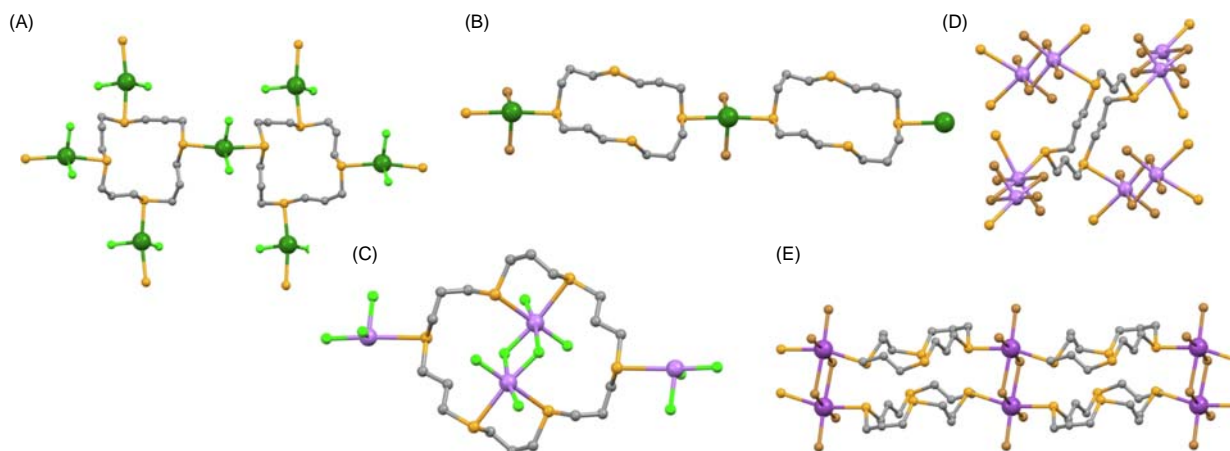
There are a few examples of group 15 metal complexes containing 1,1,1-tris(methylselenomethyl)ethane (tripodSe<sub>3</sub>, Fig. 78). A combination of tripodSe<sub>3</sub> and SbBr<sub>3</sub> leads to a 1D-coordination polymer; Sb(III) is in an octahedral site and each tripodSe<sub>3</sub> ligand is in a bridging mode as shown in Fig. 78A.<sup>1776</sup> Reactions of BiX<sub>3</sub> (X = Cl or I) with tripod Se<sub>3</sub> give rise to products which, in the solid state, are not isostructural. [Bi<sub>2</sub>I<sub>4</sub>(μ-I)<sub>2</sub>(tripodSe<sub>3</sub>-κ<sup>2</sup>)<sub>2</sub>] is a discrete dimer (Fig. 78B) with one Se-atom non-coordinated; the chelate ring exhibits Bi–Se bond lengths of 2.96(1) and 3.19(1) Å. In contrast, the chlorido analog contains 7-coordinate Bi(III) and the tripodal ligand chelates to one Bi(III) and is monodentate to an adjacent Bi(III). The structure propagates into a 2D-sheet, part of which is shown in Fig. 78C.<sup>1729</sup> It is interesting to note that although there are examples of tripodSe<sub>3</sub> acting as a typical tripodal ligand to several d-block metal ions (e.g., in [Ru(tripodSe<sub>3</sub>)<sub>2</sub>]<sup>2+</sup>),<sup>1786</sup> there are no such examples featuring main group metals in the CSD.

### 1.02.8.3 Macrocyclic ligands (Se only donors)

In comparison to the sulfur-containing macrocyclic ligands shown in Scheme 23, those containing selenium and found in structurally characterized p-block metal coordination compounds reported since 2000 are restricted to 16Se4 and 24Se6 (Scheme 24). The smaller 8Se2 was included in Section 1.02.8.1.2 as a heterocyclic ligand.



**Scheme 24** Selenium-macrocyclic ligands.



**Fig. 79** (A) Part of the 2D-sheet in [(GeCl<sub>2</sub>)<sub>2</sub>(16Se<sub>4</sub>)]<sub>n</sub> (CSD refcode ILIHUH). (B) Part of the 1D-chain in [GeBr<sub>2</sub>(16Se<sub>4</sub>)]<sub>n</sub> (refcode ILIJAP). (C) The molecular structure of [(AsCl<sub>3</sub>)<sub>4</sub>(24Se<sub>6</sub>)]<sub>n</sub> (refcode QUTLIA). (D) Building block in the 3D-network of [(AsBr<sub>3</sub>)<sub>2</sub>(μ<sub>4</sub>-16Se<sub>4</sub>)]<sub>n</sub> (refcode MIYZAV). (E) Part of the 1D-ladder in [Bi<sub>2</sub>Br<sub>4</sub>(μ-Cl)<sub>2</sub>(16Se<sub>4</sub>)<sub>2</sub>]<sub>n</sub> (refcode MEMSIG).



The reactions of GaCl<sub>3</sub> or InCl<sub>3</sub> with 16Se<sub>4</sub> yield [MCl<sub>2</sub>(16Se<sub>4</sub>)] [MCl<sub>4</sub>] (M = Ga, In) in which the cations display *trans*-octahedral coordination spheres.<sup>1775</sup> In contrast to Ga(III), Ge(II) shows a preference for *exocyclic*-coordination with the formation of [(GeCl<sub>2</sub>)<sub>2</sub>(16Se<sub>4</sub>)]<sub>n</sub>, [GeBr<sub>2</sub>(16Se<sub>4</sub>)]<sub>n</sub> and [(GeI<sub>2</sub>)<sub>2</sub>(16Se<sub>4</sub>)]<sub>n</sub>. While the chlorido and iodo derivatives have similar 2D-networks (Fig. 79A), the bromido complex assembles into a 1D-chain (Fig. 79B). Note that [(GeI<sub>2</sub>)<sub>2</sub>(16Se<sub>4</sub>)]<sub>n</sub> co-crystallizes with GeI<sub>4</sub> and is only a minor product of the reaction of GeI<sub>2</sub> with 16Se<sub>4</sub> in anhydrous MeCN.<sup>1778</sup>

The first macrocyclic selenoether complex of As(III), [(AsCl<sub>3</sub>)<sub>4</sub>(24Se<sub>6</sub>)], was described in 2001 by Barton et al. The complex has a discrete molecular structure featuring both *endo*- and *exocyclic* bonding modes (Fig. 79C).<sup>1787</sup> The structures of [(AsCl<sub>3</sub>)<sub>2</sub>(μ<sub>4</sub>-16Se<sub>4</sub>)]<sub>n</sub> and [(AsBr<sub>3</sub>)<sub>2</sub>(μ<sub>4</sub>-16Se<sub>4</sub>)]<sub>n</sub> comprise similar 3D-networks based on weakly associated {As<sub>2</sub>X<sub>4</sub>(μ-X)<sub>2</sub>} dimers which are interconnected by 16Se<sub>4</sub> molecules. Fig. 79D depicts the building block in [(AsBr<sub>3</sub>)<sub>2</sub>(μ<sub>4</sub>-16Se<sub>4</sub>)]<sub>n</sub> focusing on the coordination environment of the macrocycle.<sup>1765</sup> Fig. 77D illustrated the ladder-like structure of [As<sub>2</sub>Cl<sub>4</sub>(μ-Cl)<sub>2</sub>(8Se<sub>2</sub>)<sub>2</sub>]<sub>n</sub>. A similar structure is observed for [Bi<sub>2</sub>Br<sub>4</sub>(μ-Br)<sub>2</sub>(16Se<sub>4</sub>)<sub>2</sub>]<sub>n</sub> (Fig. 79E), and attempts to utilize the non-coordinated Se donors by treatment with BiBr<sub>3</sub> in MeCN solution were unsuccessful.<sup>1784</sup> Reid and coworkers have reported [BiX<sub>3</sub>(24Se<sub>6</sub>)], but no structural data appear to be available.<sup>1784</sup>

## Acknowledgments

We are extremely grateful to Dr. Mariia Becker for proofreading this article.

## References

- Daniele, P. G.; Foti, C.; Gianguzza, A.; Prenesti, E.; Sammartano, S. *Coord. Chem. Rev.* **2008**, *252*, 1093–1107.
- Banerjee, D.; Parise, J. B. *Cryst. Growth Des.* **2011**, *11*, 4704–4720.
- Fromm, K. M. *Coord. Chem. Rev.* **2008**, *252*, 856–885.
- Fromm, K. M. *Coord. Chem. Rev.* **2020**, *408*, 213193.
- Inthasot, A.; Tung, S. T.; Chiu, S. H. *Acc. Chem. Res.* **2018**, *51*, 1324–1337.
- Noor, A. *Top. Curr. Chem.* **2021**, *379*, 6.
- Zang, Y.; Li, L.-K.; Zang, S.-Q. *Coord. Chem. Rev.* **2021**, *440*, 213955.
- Torvisco, A.; O'Brien, A. Y.; Ruhlandt-Senge, K. *Coord. Chem. Rev.* **2011**, *255*, 1268–1292.
- Bai, Y.; Chen, W.; Li, J.; Cui, C. *Coord. Chem. Rev.* **2019**, *383*, 132–154.
- Yin, J.; Hu, Y.; Yoon, J. *Chem. Soc. Rev.* **2015**, *44*, 4619–4644.
- Liu, J.; Xie, D.; Shi, W.; Cheng, P. *Chem. Soc. Rev.* **2020**, *49*, 1624–1642.
- Hamilton, G. R.; Sahoo, S. K.; Kamila, S.; Singh, N.; Kaur, N.; Hyland, B. W.; Callan, J. F. *Chem. Soc. Rev.* **2015**, *44*, 4415–4432.
- Stennett, T. E.; Harder, S. *Chem. Soc. Rev.* **2016**, *45*, 1112–1128.
- Mulvey, R. E. *Acc. Chem. Res.* **2009**, *42*, 743–755.
- Li, B.; Yang, Y.; Zhu, H.; Roesky, H. W. *Coord. Chem. Rev.* **2021**, *429*, 213625.
- Liu, Y.; Li, J.; Ma, X.; Yang, Z.; Roesky, H. W. *Coord. Chem. Rev.* **2018**, *374*, 387–415.
- Exley, C. *Coord. Chem. Rev.* **2012**, *256*, 2142–2146.
- Exley, C.; Schneider, C.; Doucet, F. J. *Coord. Chem. Rev.* **2002**, *228*, 127–135.
- Samokhvalov, A. *Coord. Chem. Rev.* **2018**, *374*, 236–253.
- Berthon, G. *Coord. Chem. Rev.* **2002**, *228*, 319–341.
- Williams, R. J. P. *Coord. Chem. Rev.* **2002**, *228*, 93–96.
- Thompson, K. H.; Barta, C. A.; Orvig, C. *Chem. Soc. Rev.* **2006**, *35*, 545–556.
- Petrou, A. L. *Coord. Chem. Rev.* **2002**, *228*, 153–162.
- Swaddle, T. W. *Coord. Chem. Rev.* **2001**, *219–221*, 665–686.
- Bodor, A.; Bányai, I.; Tóth, I. *Coord. Chem. Rev.* **2002**, *228*, 175–186.
- Harris, W. R.; Messori, L. *Coord. Chem. Rev.* **2002**, *228*, 237–262.
- Crisponi, G.; Nurchi, V. M.; Bertolasi, V.; Remelli, M.; Faa, G. *Coord. Chem. Rev.* **2012**, *256*, 89–104.
- Sanz-Medel, A.; Soldado Cabezuelo, A. B.; Milačić, R.; Bantan Polak, T. *Coord. Chem. Rev.* **2002**, *228*, 373–383.
- Yokel, R. A. *Coord. Chem. Rev.* **2002**, *228*, 97–113.
- Neumüller, B.; Iravani, E. *Coord. Chem. Rev.* **2004**, *248*, 817–834.
- Aguirre-Díaz, L. M.; Reinares-Fisac, D.; Iglesias, M.; Gutiérrez-Puebla, E.; Gándara, F.; Snejko, N.; Monge, M.Á. *Coord. Chem. Rev.* **2017**, *335*, 1–27.
- Müller, J. *Coord. Chem. Rev.* **2002**, *235*, 105–119.
- Grabowski, S. J. *Coord. Chem. Rev.* **2020**, *407*, 213171.
- Swidan, A.; Macdonald, C. L. *Chem. Soc. Rev.* **2016**, *45*, 3883–3915.
- Bloor, L. G.; Carmalt, C. J.; Pugh, D. *Coord. Chem. Rev.* **2011**, *255*, 1293–1318.
- Knapp, C. E.; Carmalt, C. J. *Chem. Soc. Rev.* **2016**, *45*, 1036–1064.
- Carmalt, C.; King, S. *Coord. Chem. Rev.* **2006**, *250*, 682–709.
- Marchand, P.; Carmalt, C. J. *Coord. Chem. Rev.* **2013**, *257*, 3202–3221.
- Carmalt, C. J. *Coord. Chem. Rev.* **2001**, *223*, 217–264.
- Malik, M. A.; Afzaal, M.; O'Brien, P. *Chem. Rev.* **2010**, *110*, 4417–4446.
- Bandoli, G.; Dolmella, A.; Tisato, F.; Porchia, M.; Refosco, F. *Coord. Chem. Rev.* **2009**, *253*, 56–77.
- Beraldo, H. *Coord. Chem. Rev.* **2020**, *419*, 213375.
- Hanack, M. *Coord. Chem. Rev.* **2001**, *219–221*, 235–258.
- Caminade, A.-M.; Hameau, A.; Turrin, C.-O.; Laurent, R.; Majoral, J.-P. *Coord. Chem. Rev.* **2021**, *430*, 213739.
- Akhbari, K.; Morsali, A. *Coord. Chem. Rev.* **2010**, *254*, 1977–2006.
- Bochmann, M. *Coord. Chem. Rev.* **2009**, *253*, 2000–2014.

47. Chen, Y.; Hanack, M.; Araki, Y.; Ito, O. *Chem. Soc. Rev.* **2005**, *34*, 517–529.
48. Khan, A.; Foucher, D. *Coord. Chem. Rev.* **2016**, *312*, 41–66.
49. Levason, W.; Reid, G.; Zhang, W. *Coord. Chem. Rev.* **2011**, *255*, 1319–1341.
50. Izod, K. *Coord. Chem. Rev.* **2012**, *256*, 2972–2993.
51. dos Santos, C. G.; de Lima, G. M. *Coord. Chem. Rev.* **2020**, *410*, 213236.
52. Bauzá, A.; Seth, S. K.; Frontera, A. *Coord. Chem. Rev.* **2019**, *384*, 107–125.
53. Arnold, D. P.; Blok, J. *Coord. Chem. Rev.* **2004**, *248*, 299–319.
54. Dias, H. V. R.; Wang, Z.; Jin, W. *Coord. Chem. Rev.* **1998**, *176*, 67–86.
55. Davidovich, R. L.; Stavila, V.; Whitmire, K. H. *Coord. Chem. Rev.* **2010**, *254*, 2193–2226.
56. Hu, M.-L.; Morsali, A.; Aboutorabi, L. *Coord. Chem. Rev.* **2011**, *255*, 2821–2859.
57. Davidovich, R. L.; Stavila, V.; Marinin, D. V.; Voit, E. I.; Whitmire, K. H. *Coord. Chem. Rev.* **2009**, *253*, 1316–1352.
58. Sigel, H. *Coord. Chem. Rev.* **2001**, *219–221*, 435–461.
59. Garje, S. S.; Jain, V. K. *Coord. Chem. Rev.* **2003**, *236*, 35–56.
60. Greenacre, V. K.; Levason, W.; Reid, G. *Coord. Chem. Rev.* **2021**, *432*, 213698.
61. Wang, Z.; Zeng, Z.; Wang, H.; Zeng, G.; Xu, P.; Xiao, R.; Huang, D.; Chen, S.; He, Y.; Zhou, C.; Cheng, M.; Qin, H. *Coord. Chem. Rev.* **2021**, *439*, 213902.
62. Yang, N.; Sun, H. *Coord. Chem. Rev.* **2007**, *251*, 2354–2366.
63. Stavila, V.; Davidovich, R. L.; Gulea, A.; Whitmire, K. H. *Coord. Chem. Rev.* **2006**, *250*, 2782–2810.
64. Tiekink, E. R. T.; Zukerman-Schpector, J. *Coord. Chem. Rev.* **2010**, *254*, 46–76.
65. Cozzolino, A. F.; Elder, P. J. W.; Vargas-Baca, I. *Coord. Chem. Rev.* **2011**, *255*, 1426–1438.
66. Chivers, T.; Laitinen, R. S. *Chem. Soc. Rev.* **2015**, *44*, 1725–1739.
67. Chivers, T.; Ritch, J. S.; Robertson, S. D.; Konu, J.; Tuononen, H. M. *Acc. Chem. Res.* **2010**, *43*, 1053–1062.
68. Burt, J.; Levason, W.; Reid, G. *Coord. Chem. Rev.* **2014**, *260*, 65–115.
69. Chlupatý, T.; Růžička, A. *Coord. Chem. Rev.* **2016**, *314*, 103–113.
70. Gade, L. H. *Acc. Chem. Res.* **2002**, *35*, 575–582.
71. Silvestru, C.; Drake, J. E. *Coord. Chem. Rev.* **2001**, *223*, 117–216.
72. Zhang, R.; Wang, Y.; Zhao, Y.; Redshaw, C.; Fedushkin, I. L.; Wu, B.; Yang, X. J. *Dalton Trans.* **2021**, *50*, 13634–13650.
73. Casas, J. S.; Garcia-Tasende, M. S.; Sordo, J. *Coord. Chem. Rev.* **2000**, *209*, 197–261.
74. Casas, J. S.; Garcia-Tasende, M. S.; Sordo, J. *Coord. Chem. Rev.* **2001**, *213*, 331 (Corrigendum).
75. Reglinski, J.; Spicer, M. D. *Coord. Chem. Rev.* **2015**, *297–298*, 181–207.
76. Fedorchuk, C.; Copesey, M.; Chivers, T. *Coord. Chem. Rev.* **2007**, *251*, 897–924.
77. Aspinall, G. M.; Copesey, M. C.; Leedham, A. P.; Russell, C. A. *Coord. Chem. Rev.* **2002**, *227*, 217–232.
78. Timoshkin, A. Y. *Coord. Chem. Rev.* **2005**, *249*, 2094–2131.
79. Wolf, B. M.; Anwander, R. *Chem. A Eur. J.* **2019**, *25*, 8190–8202.
80. Dehnicke, K.; Wellera, F.; Strähle, J. *Chem. Soc. Rev.* **2001**, *30*, 125–135.
81. Gilroy, J. B.; Otten, E. *Chem. Soc. Rev.* **2020**, *49*, 85–113.
82. Panda, T. K.; Roesky, P. W. *Chem. Soc. Rev.* **2009**, *38*, 2782–2804.
83. Ochiai, T.; Franz, D.; Inoue, S. *Chem. Soc. Rev.* **2016**, *45*, 6327–6344.
84. Nesterov, V.; Reiter, D.; Bag, P.; Frisch, P.; Holzner, R.; Porzelt, A.; Inoue, S. *Chem. Rev.* **2018**, *118*, 9678–9842.
85. Bellemin-Lapornaz, S.; Dagorne, S. *Chem. Rev.* **2014**, *114*, 8747–8774.
86. Kays, D. L. *Chem. Soc. Rev.* **2016**, *45*, 1004–1018.
87. Tan, D.; Garcia, F. *Chem. Soc. Rev.* **2019**, *48*, 2274–2292.
88. Bruno, I. J.; Cole, J. C.; Edgington, P. R.; Kessler, M.; Macrae, C. F.; McCabe, P.; Pearson, J.; Taylor, R. *Acta Crystallogr.* **2002**, *B58*, 389–397.
89. Groom, C. R.; Bruno, I. J.; Lightfoot, M. P.; Ward, S. C. *Acta Crystallogr.* **2016**, *B72*, 171–179.
90. Macrae, C. F.; Sovago, I.; Cottrell, S. J.; Galek, P. T. A.; McCabe, P.; Pidcock, E.; Platings, M.; Shields, G. P.; Stevens, J. S.; Towler, M.; Wood, P. A. *J. Appl. Cryst.* **2020**, *53*, 226–235.
91. <https://icsd.karlsruhe.de>.
92. Roy, M. M. D.; Omaña, A. A.; Wilson, A. S. S.; Hill, M. S.; Aldridge, S.; Rivard, E. *Chem. Rev.* **2021**, *121*, 12784–12965.
93. Englert, U. *Coord. Chem. Rev.* **2010**, *254*, 537–554.
94. Adonin, S. A.; Sokolov, M. N.; Fedin, V. P. *Coord. Chem. Rev.* **2016**, *312*, 1–21.
95. Adonin, S. A.; Sokolov, M. N.; Fedin, V. P. *Coord. Chem. Rev.* **2018**, *367*, 1–17.
96. Christensen, C. H.; Sørensen, R. Z.; Johannessen, T.; Quaade, U. J.; Honkala, K.; Elmøe, T. D.; Köhler, R.; Nørskov, J. K. *J. Mater. Chem.* **2005**, *15*, 4106–4108.
97. Huang, Z.; Gallucci, J.; Chen, X.; Yisgedu, T.; Lingam, H. K.; Shore, S. G.; Zhao, J.-C. *J. Mater. Chem.* **2010**, *20*, 2743–2745.
98. Panda, M.; Hofmann, K.; Prosenic, M. H.; Albert, B. *Dalton Trans.* **2008**, 3956–3958.
99. Michel, R.; Herbst-Irmer, R.; Stalke, D. *Organometallics* **2010**, *29*, 6169–6171.
100. Kraus, F.; Panda, M.; Müller, T.; Albert, B. *Inorg. Chem.* **2013**, *52*, 4692–4699.
101. Wiesler, K.; Korber, N. Z. *Kristallogr.* **2005**, *220*, 188–191.
102. Michel, R.; Nack, T.; Neufeld, R.; Dieterich, J. M.; Mata, R. A.; Stalke, D. *Angew. Chem. Int. Ed.* **2013**, *52*, 734–738.
103. Benda, C. B.; Waibel, M.; Fässler, T. F. *Angew. Chem. Int. Ed.* **2015**, *54*, 522–526.
104. Wiesler, K.; Suchentrunk, C.; Korber, N. *Helv. Chim. Acta* **2006**, *89*, 1158–1168.
105. Daniels, J.; Weigend, F.; Jansen, M. *Z. Anorg. Allg. Chem.* **2021**, *647*, 1132–1138.
106. Hansen, B. R. S.; Tumanov, N.; Santoru, A.; Pisticida, C.; Bednarcik, J.; Klassen, T.; Dornheim, M.; Filinchuk, Y.; Jensen, T. R. *Dalton Trans.* **2017**, *46*, 7770–7781.
107. Jørgensen, M.; Hansen, B. R. S.; Lee, Y.-S.; Cho, Y. W.; Jensen, T. R. *J. Phys. Chem. C* **2019**, *123*, 20160–20166.
108. Kraus, F.; Baer, S. A.; Buchner, M. R.; Karttunen, A. J. *Chem. A Eur. J.* **2012**, *18*, 2131–2142.
109. Yang, Y.; Liu, Y.; Wu, H.; Zhou, W.; Gao, M.; Pan, H. *Phys. Chem. Chem. Phys.* **2014**, *16*, 135–143.
110. Rossmeyer, T.; Reil, M.; Korber, N. *Inorg. Chem.* **2004**, *43*, 2206–2212.
111. Schimek, G. L.; Drake, G. W.; Kolis, J. W.; Gács, I.; Liptay, G.; Mattinen, J.; Senning, A.; Yao, X.-K.; Wang, H.-G.; Tuchagues, J. P.; Ögren, M. *Acta Chem. Scand.* **1999**, *53*, 145–148.
112. Wedig, U.; Brumm, H.; Jansen, M. *Chem. A Eur. J.* **2002**, *8*, 2769–2774.
113. Panthöfer, M.; Wedig, U.; Brumm, H.; Jansen, M. *Solid State Sci.* **2004**, *6*, 619–624.
114. Himmel, K.; Jansen, M. *Inorg. Chem.* **1998**, *37*, 3437–3439.
115. Brumm, H.; Peters, E.; Jansen, M. *Angew. Chem. Int. Ed.* **2001**, *40*, 2069–2071.
116. Tang, Z.; Tan, Y.; Wu, H.; Gu, Q.; Zhou, W.; Jensen, C. M.; Yu, X. *Acta Mater.* **2013**, *61*, 4787–4796.
117. Guo, Y.; Wu, H.; Zhou, W.; Yu, X. *J. Am. Chem. Soc.* **2011**, *133*, 4690–4693.

118. Zhang, S.; Hintze, F.; Schnick, W.; Niewa, R. *Eur. J. Inorg. Chem.* **2013**, *2013*, 5387–5399.
119. Daub, M.; Hillebrecht, H. *Eur. J. Inorg. Chem.* **2021**, *2021*, 1490–1497.
120. Tang, C. Y.; Cowley, A. R.; Downs, A. J.; Marchant, S.; Parsons, S. *Eur. J. Inorg. Chem.* **2008**, *2008*, 737–744.
121. Tang, C. Y.; Downs, A. J.; Greene, T. M.; Marchant, S.; Parsons, S. *Inorg. Chem.* **2005**, *44*, 7143–7150.
122. Kysliak, O.; Beck, J. Z. *Anorg. Allg. Chem.* **2014**, *640*, 856–862.
123. Bremer, M.; Nöth, H.; Warchhold, M. *Eur. J. Inorg. Chem.* **2003**, *2003*, 111–119.
124. Gary, D. C.; Petrone, A.; Li, X.; Cossairt, B. M. *Chem. Commun.* **2016**, *53*, 161–164.
125. Tretyakov, E.; Fokin, S.; Romanenko, G.; Ikorskii, V.; Ovcharenko, V. *Inorg. Chem.* **2007**, *26*, 7143–7150.
126. Giese, H. H.; Habereeder, T.; Knizek, J.; Nöth, H.; Warchhold, M. *Eur. J. Inorg. Chem.* **2001**, *2001*, 1195–1205.
127. Burford, N.; Edelstein, E.; Landry, J. C.; Ferguson, M. J.; McDonald, R. *Chem. Commun.* **2005**, 5074–5076.
128. Buchner, M. R.; Müller, M. *Dalton Trans.* **2021**, *50*, 7246–7255.
129. Dye, J. L.; Huang, R. H. *Pure Appl. Chem.* **1993**, *65*, 435–440.
130. Dai, F.-R.; Xu, L. *Jiegou Huaxue* **2007**, *26*, 45–48.
131. Gillett-Kunnath, M. M.; Oliver, A. G.; Sevov, S. C. *J. Am. Chem. Soc.* **2011**, *133*, 6560–6562.
132. Hauptmann, R.; Fässler, T. F. Z. *Kristallogr. NCS* **2003**, *218*, 370–372.
133. Hauptmann, R.; Fässler, T. F. Z. *Kristallogr. NCS* **2003**, *218*, 455–457.
134. Zhang, C.; Morgan, H. W. T.; Wang, Z. C.; Liu, C.; Sun, Z. M.; McGrady, J. E. *Dalton Trans.* **2019**, *48*, 15888–15895.
135. Li, Z.; Ruan, H.; Wang, L.; Liu, C.; Xu, L. *Dalton Trans.* **2017**, *46*, 3453–3456.
136. Thiele, G.; You, Z.; Dehnen, S. *Inorg. Chem.* **2015**, *54*, 2491–2493.
137. Dehnen, S.; Zimmermann, C.; Anson, C. E. Z. *Anorg. Allg. Chem.* **2002**, *628*, 279–288.
138. Thiele, G.; Lichtenberger, N.; Tonner, R.; Dehnen, S. Z. *Anorg. Allg. Chem.* **2013**, *639*, 2809–2815.
139. Zavaliij, P. Y.; Li, A.-M.; Eichhorn, B. W. *CSD Communication*, 2020. refcode OHUWEW.
140. Miluykov, V.; Kataev, A.; Sinyashin, O.; Lönnecke, P.; Hey-Hawkins, E. Z. *Anorg. Allg. Chem.* **2006**, *632*, 1728–1732.
141. Sheldrick, W. S.; Kaub, J. Z. *Naturforsch.* **1985**, *B40*, 1020–1022.
142. Waters, A. F.; White, A. H. *Aust. J. Chem.* **1996**, *49*, 61–72.
143. Zagler, R.; Eisenmann, B.; Schäfer, H. Z. *Naturforsch.* **1987**, *B42*, 151–156.
144. Du, H.; Chen, J.; Pang, W.; Yu, J.; Williams, I. D. *Chem. Commun.* **1997**, 781–782.
145. Yamanaka, H.; Hihara, G.; Miyamae, H. *Anal. Sci.: X-Ray Struct. Anal. Online*; pp X121–X122.
146. Cho, Y.; Kim, S.; Pyo, S.; Park, Y. S.; Kim, S.-J.; Yun, H.; Do, J. *Polyhedron* **2010**, *29*, 2105–2110.
147. Harrowfield, J. M.; Miyamae, H.; Shand, T. M.; Skelton, B. W.; Soudi, A. A.; White, A. H. *Aust. J. Chem.* **1996**, *49*, 1043–1050.
148. Pfennig, V.; Seppelt, K.; Robertson, N. *Angew. Chem. Int. Ed.* **1997**, *36*, 1350–1352.
149. Shekar, S.; Taylor, M. M.; Twamley, B.; Wehmschulte, R. J. *Dalton Trans.* **2009**, 9322–9326.
150. Vogel, U.; Timoshkin, A. Y.; Scheer, M. *Angew. Chem. Int. Ed.* **2001**, *40*, 4409–4412.
151. Veith, M.; Vogelgesang, H.; Huch, V. *Organometallics* **2002**, *21*, 380–388.
152. Seymen, A.; Oppen, U.; Voß, A.; Brieger, L.; Otte, F.; Unkelbach, C.; O'Shea, D. F.; Strohmman, C. *Angew. Chem. Int. Ed.* **2020**, *59*, 22500–22504.
153. Border, E. C.; Maguire, M.; MacLellan, J. G.; Andrews, P. C. *Organometallics* **2017**, *36*, 1496–1504.
154. Fürstner, A.; Mathes, C.; Lehmann, C. W. *Chem. A Eur. J.* **2001**, *7*, 5299–5317.
155. Hampe, D.; Günther, W.; Görls, H.; Anders, E. *Eur. J. Org. Chem.* **2004**, *2004*, 4357–4372.
156. Kennedy, A. R.; Klett, J.; O'Hara, C. T.; Mulvey, R. E.; Robertson, G. M. *Eur. J. Inorg. Chem.* **2009**, *2009*, 5029–5035.
157. Kamps, I.; Bojer, D.; Hayes, S.; Berger, R.; Neumann, B.; Mitzel, N. *Chem. A Eur. J.* **2009**, *15*, 11123–11127.
158. Andrews, P. C.; Blair, V. L.; Border, E. C.; Peatt, A. C.; MacLellan, J. G.; Thompson, C. D. *Organometallics* **2013**, *32*, 7509–7519.
159. Andrews, P. C.; Minopoulos, M.; Roberston, E. G. *Eur. J. Inorg. Chem.* **2006**, *2006*, 2865–2870.
160. Cole, M. L.; Jones, C.; Junk, P. C. *New J. Chem.* **2002**, *26*, 89–93.
161. Wiklund, T.; Olsson, S.; Lennartson, A. *Monats. Chem.* **2011**, *142*, 813–819.
162. Gessner, V. H.; Koller, S. G.; Strohmman, C.; Hogan, A. M.; O'Shea, D. F. *Chem. A Eur. J.* **2011**, *17*, 2996–3004.
163. Armstrong, D. R.; García-Álvarez, P.; Kennedy, A. R.; Mulvey, R. E.; Robertson, S. D. *Chem. A Eur. J.* **2011**, *17*, 6725–6730.
164. Fairley, M.; Bole, L. J.; Mulks, F. F.; Main, L.; Kennedy, A. R.; O'Hara, C. T.; García-Álvarez, J.; Hevia, E. *Chem. Sci.* **2020**, *11*, 6500–6509.
165. Fan, Z.; Wang, P.; Wu, C.; Liu, Z.; Chen, X. *Eur. J. Inorg. Chem.* **2020**, *2020*, 400–406.
166. von Bulow, R.; Deuerlein, S.; Stey, T.; Herbst-Irmer, R.; Gornitzka, H.; Stalke, D. Z. *Naturforsch.* **2004**, *59B*, 1471–1479.
167. Su, C.; Guang, J.; Williard, P. G. *J. Org. Chem.* **2014**, *79*, 1032–1039.
168. Braun, U.; Habereeder, T.; Nöth, H.; Piotrowski, J.; Warchhold, M. *Eur. J. Inorg. Chem.* **2002**, *2002*, 1132–1145.
169. Chlupatý, T.; Nevoralová, J.; Růžičková, Z.; Růžička, A. *Inorg. Chem.* **2020**, *59*, 10854–10865.
170. Yuan, S.; Wei, X.; Tong, H.; Zhang, H.; Liu, D.; Sun, W.-H. *Organometallics* **2010**, *29*, 2085–2092.
171. Clegg, W.; Horsburgh, L.; Liddle, S. T.; Mackenzie, F. M.; Mulvey, R. E.; Robertson, A. J. *Chem. Soc. Dalton Trans.* **2000**, 1225–1231.
172. Liebing, P.; Merzweiler, K. Z. *Anorg. Allg. Chem.* **2015**, *641*, 1911–1917.
173. Tang, Y.; Zakharov, L. N.; Rheingold, A. L.; Kemp, R. A. *Inorg. Chim. Acta* **2006**, *359*, 775–781.
174. Skatova, A. A.; Fedushkin, I. L.; Maslova, O. V.; Hummert, M.; Schumann, H. *Russ. Chem. Bull.* **2007**, *56*, 2284–2289.
175. Wright, R. J.; Steiner, J.; Beaini, S.; Power, P. P. *Inorg. Chim. Acta* **2006**, *359*, 1939–1946.
176. Schorpp, M.; Heizmann, T.; Schmucker, M.; Rein, S.; Weber, S.; Krossing, I. *Angew. Chem. Int. Ed.* **2020**, *59*, 9453–9459.
177. Yin, H.; Lewis, A. J.; Carroll, P.; Schelter, E. J. *Inorg. Chem.* **2013**, *52*, 8234–8243.
178. Armstrong, D. R.; Kennedy, A. R.; Mulvey, R. E.; Robertson, S. D. *Chem. A Eur. J.* **2011**, *17*, 8820–8831.
179. Clegg, W.; Edwards, A. J. *CSD Communication*, 2014. refcode COBZUQ.
180. Clegg, W.; Graham, D. V.; Herd, E.; Hevia, E.; Kennedy, A. R.; McCall, M. D.; Russo, L. *Inorg. Chem.* **2009**, *48*, 5320–5327.
181. Daniele, S.; Hitchcock, P. B.; Lappert, M. F.; Nile, T. A.; Zdanski, C. M. *J. Chem. Soc. Dalton Trans.* **2002**, 3980–3984.
182. Kennedy, A. R.; Leenhouts, S. M.; Liggat, J. J.; Martínez-Martínez, A. J.; Miller, K.; Mulvey, R. E.; O'Hara, C. T.; O'Keefe, P.; Steven, A. *Chem. Commun.* **2014**, *50*, 10588–10591.
183. Glock, C.; Görls, H.; Westerhausen, M. *Eur. J. Inorg. Chem.* **2011**, *2011*, 5288–5298.
184. Stevens, M. A.; Hashim, F. H.; Gwee, E. S. H.; Izgorodina, E. I.; Mulvey, R. E.; Blair, V. L. *Chem. A Eur. J.* **2018**, *24*, 15669–15677.
185. Armstrong, D. R.; Graham, D. V.; Kennedy, A. R.; Mulvey, R. E.; O'Hara, C. T. *Chem. A Eur. J.* **2008**, *14*, 8025–8034.
186. Glock, C.; Younis, F. M.; Ziemann, S.; Görls, H.; Imhof, W.; Kriek, S.; Westerhausen, M. *Organometallics* **2013**, *32*, 2649–2660.
187. Andrews, P. C.; Armstrong, D. R.; Raston, C. L.; Roberts, B. A.; Skelton, B. W.; White, A. H. *J. Chem. Soc. Dalton Trans.* **2001**, 996–1006.
188. Platonova, E. O.; Bochkarev, L. N.; Samsonov, M. A.; Fukin, G. K. *Russ. J. Coord. Chem.* **2013**, *39*, 758–763.
189. Gärtner, M.; Görls, H.; Westerhausen, M. *Dalton Trans.* **2008**, 1574–1582.

190. Clegg, W.; Kennedy, A. R.; Klett, J.; Mulvey, R. E.; Russo, L. *Eur. J. Inorg. Chem.* **2012**, *2012*, 2989–2994.
191. Williard, P. G.; Liu, Q. Y. *J. Am. Chem. Soc.* **1993**, *115*, 3380–3381.
192. Nöth, H.; Schlosser, D. *Eur. J. Inorg. Chem.* **2003**, *2003*, 2245–2254.
193. Tuscher, L.; Wolper, C.; Schulz, S. *CSD Communication*, 2020. refcode IHAMEM.
194. Kennedy, A. R.; Klett, J.; McGrath, G.; Mulvey, R. E.; Robertson, G. M.; Robertson, S. D.; O'Hara, C. T. *Inorg. Chim. Acta* **2014**, *411*, 1–4.
195. Henderson, K. W.; Honeyman, G. W.; Kennedy, A. R.; Mulvey, R. E.; Parkinson, J. A.; Sherrington, D. C. *Dalton Trans.* **2003**, 1365–1372.
196. Bole, L. J.; Davin, L.; Kennedy, A. R.; McLellan, R.; Hevia, E. *Chem. Commun.* **2019**, *55*, 4339–4342.
197. Neufeld, R.; Teuteberg, T. L.; Herbst-Irmer, R.; Mata, R. A.; Stalke, D. *J. Am. Chem. Soc.* **2016**, *138*, 4796–4806.
198. Yang, K.-C.; Chang, C.-C.; Huang, J.-Y.; Lin, C.-C.; Lee, G.-H.; Wang, Y.; Chiang, M. Y. *J. Organomet. Chem.* **2002**, *648*, 176–187.
199. Davin, L.; Hernán-Gómez, A.; McLaughlin, C.; Kennedy, A. R.; McLellan, R.; Hevia, E. *Dalton Trans.* **2019**, *48*, 8122–8130.
200. Forbes, G. C.; Kennedy, A. R.; Mulvey, R. E.; Rodger, P. J. A.; Rowlings, R. B. *J. Chem. Soc. Dalton Trans.* **2001**, 1477–1484.
201. Freitag, B.; Elsen, H.; Pahl, J.; Ballmann, G.; Herrera, A.; Dorta, R.; Harder, S. *Organometallics* **2017**, *36*, 1860–1866.
202. Armstrong, D. R.; Clegg, W.; Mulvey, R. E.; Rowlings, R. B. *J. Chem. Soc. Dalton Trans.* **2001**, 409–413.
203. Armstrong, D. R.; García-Alvarez, P.; Kennedy, A. R.; Mulvey, R. E.; Parkinson, J. A. *Angew. Chem. Int. Ed.* **2010**, *49*, 3185–3188.
204. Hevia, E.; Kenley, F.; Kennedy, A.; Mulvey, R.; Rowlings, R. *Eur. J. Inorg. Chem.* **2003**, *2003*, 3347–3353.
205. Fischer, C. A.; Rösch, A.; Elsen, H.; Ballmann, G.; Wiesinger, M.; Langer, J.; Färber, C.; Harder, S. *Dalton Trans.* **2019**, *48*, 6757–6766.
206. Jones, D. D. L.; Douair, I.; Maron, L.; Jones, C. *Angew. Chem. Int. Ed.* **2021**, *60*, 7087–7092.
207. Barrett, A. G.; Casely, J.; Crimmin, M. R.; Hill, M. S.; Lachs, J. R.; Mahon, M. F.; Procopiou, P. A. *Inorg. Chem.* **2009**, *48*, 4445–4453.
208. De Tullio, M.; Hernán-Gómez, A.; Livingstone, Z.; Clegg, W.; Kennedy, A. R.; Harrington, R. W.; Antiñolo, A.; Martínez, A.; Carrillo-Hermosilla, F.; Hevia, E. *Chem. A Eur. J.* **2016**, *22*, 17646–17656.
209. Rood, J. A.; Hinman, S. E.; Noll, B. C.; Henderson, K. W. *Eur. J. Inorg. Chem.* **2008**, *2008*, 3935–3942.
210. Bao, R. L.; Zhao, R.; Shi, L. *Chem. Commun.* **2015**, *51*, 6884–6900.
211. Barrett, A. G.; Crimmin, M. R.; Hill, M. S.; Kociok-Köhn, G.; Lachs, J. R.; Procopiou, P. A. *Dalton Trans.* **2008**, 1292–1294.
212. Intemann, J.; Bauer, H.; Pahl, J.; Maron, L.; Harder, S. *Chem. A Eur. J.* **2015**, *21*, 11452–11461.
213. Roueindeji, H.; Ratsifitahina, A.; Roisnel, T.; Dorcet, V.; Kahlal, S.; Saillard, J. Y.; Carpentier, J. F.; Sarazin, Y. *Chem. A Eur. J.* **2019**, *25*, 8854–8864.
214. Gärtner, M.; Görls, H.; Westerhausen, M. *Inorg. Chem.* **2007**, *46*, 7678–7683.
215. Bauer, T.; Schulz, S.; Hupfer, H.; Nieger, M. *Organometallics* **2002**, *21*, 2931–2939.
216. Tang, C. Y.; Downs, A. J.; Greene, T. M.; Parsons, S. *Dalton Trans.* **2003**, 540–543.
217. Hansmann, M. M.; Melen, R. L.; Wright, D. S. *Chem. Sci.* **2011**, *2*, 1554–1559.
218. Sandig-Predzymirska, L.; Ortmeyer, J.; Wagler, J.; Brendler, E.; Habermann, F.; Anders, M.; Felderhoff, M.; Mertens, F. *Dalton Trans.* **2020**, *49*, 17689–17698.
219. Rheingold, A. L.; Hampden-Smith, M. *CSD Communication*, 2015. refcode DUSNAI.
220. Rheingold, A. L.; Hampden-Smith, M. *CSD Communication*, 2015. refcode DUSNUC.
221. Hatnean, J. A.; Thomson, J. W.; Chase, P. A.; Stephan, D. W. *Chem. Commun.* **2014**, *50*, 301–303.
222. Walgenbach, A.; Veith, M.; Huch, V.; Kohlmann, H. *Z. Anorg. Allg. Chem.* **2015**, *641*, 394–399.
223. Veith, M.; Walgenbach, A.; Huch, V.; Kohlmann, H. *Z. Anorg. Allg. Chem.* **2017**, *643*, 1233–1239.
224. Reddy, N.; Kumar, S.; Roesky, H.; Vidovic, D.; Magull, J.; Noltemeyer, M.; Schmidt, H. *Eur. J. Inorg. Chem.* **2003**, *2003*, 442–448.
225. Luo, B.; Pink, M.; Gladfelter, W. L. *Inorg. Chem.* **2001**, *40*, 307–311.
226. Luo, B.; Gladfelter, W. L. *J. Organomet. Chem.* **2004**, *689*, 666–671.
227. Chivers, T.; Fedorchuk, C.; Schatte, G.; Parvez, M. *Inorg. Chem.* **2003**, *42*, 2084–2093.
228. Carmalt, C. J.; Mileham, J. D.; White, A. J. P.; Williams, D. J. *Dalton Trans.* **2003**, 4255–4260.
229. Eisler, D. J.; Chivers, T. *Can. J. Chem.* **2006**, *84*, 443–452.
230. Khrustalev, V. N.; Glukhov, I. V.; Borisova, I. V.; Zemlyansky, N. N. *Appl. Organomet. Chem.* **2007**, *21*, 551–556.
231. Padělková, Z.; Havlík, A.; Švec, P.; Nechaev, M. S.; Růžická, A. *J. Organomet. Chem.* **2010**, *695*, 2651–2657.
232. Harris, L. A.; Tam, E. C.; Coles, M. P.; Fulton, J. R. *Dalton Trans.* **2014**, *43*, 13803–13814.
233. Nimitsirwat, N.; Gibson, V. C.; Marshall, E. L.; Elsegood, M. R. *Dalton Trans.* **2009**, 3710–3715.
234. Ahmet, I. Y.; Hill, M. S.; Johnson, A. L.; Peter, L. M. *Chem. Mater.* **2015**, *27*, 7680–7688.
235. Boyle, T. J.; Doan, T. Q.; Steele, L. A.; Apblett, C.; Hoppe, S. M.; Hawthorne, K.; Kalinich, R. M.; Sigmund, W. M. *Dalton Trans.* **2012**, *41*, 9349–9364.
236. Harmgarth, N.; Liebing, P.; Zörner, F.; Silinskas, M.; Burte, E. P.; Edelmann, F. T. *Inorg. Chem.* **2017**, *56*, 4267–4270.
237. Vehkamäki, M.; Hatanpää, T.; Ritala, M.; Leskelä, M. *J. Mater. Chem.* **2004**, *14*, 3191–3197.
238. Dengel, H.; Lichtenberg, C. *Chem. A Eur. J.* **2016**, *22*, 18465–18475.
239. Briand, G. G.; Chivers, T.; Parvez, M. *Can. J. Chem.* **2003**, *81*, 169–174.
240. Eichler, J. F.; Just, O.; Rees, W. S. *Inorg. Chem.* **2006**, *45*, 6706–6712.
241. Eisler, D. J.; Chivers, T. *Chem. A Eur. J.* **2006**, *12*, 233–243.
242. Chivers, T.; Eisler, D. J. *Angew. Chem. Int. Ed.* **2004**, *43*, 6686–6689.
243. Seo, D. M.; Boyle, P. D.; Henderson, W. A. *Acta Crystallogr.* **2011**, *E67*, m1148.
244. Seo, D. M.; Boyle, P. D.; Borodin, O.; Henderson, W. A. *RSC Adv.* **2012**, *2*, 8014–8019.
245. Suzuki, Y.; Ishida, S.; Sato, S.; Isobe, H.; Iwamoto, T. *Angew. Chem. Int. Ed.* **2017**, *56*, 4593–4597.
246. Breunig, J. M.; Wietelmann, U.; Lerner, H.-W.; Bolte, M. *Acta Crystallogr.* **2013**, *E69*, m253.
247. Ebner, F.; Greb, L. *J. Am. Chem. Soc.* **2018**, *140*, 17409–17412.
248. Weinert, C. S.; Rheingold, A. L. *CSD Communication*, 2008. refcode SAWSUE01.
249. Chivers, T.; Downard, A.; Parvez, M.; Schatte, G. *Inorg. Chem.* **2001**, *40*, 1975–1977.
250. Chitsaz, S.; Pauls, J.; Neumüller, B. *Z. Naturforsch.* **2001**, *B56*, 245–248.
251. Tanaka, K.; Tago, Y.; Kondo, M.; Watanabe, Y.; Nishio, K.; Hitosugi, T.; Moriya, M. *Nano Lett.* **2020**, *20*, 8200–8204.
252. Müller, U.; Noll, A. Z. *Kristallogr. NCS* **2000**, *215*, 191–192.
253. Arbaoui, A.; Redshaw, C.; Elsegood, M. R.; Wright, V. E.; Yoshizawa, A.; Yamato, T. *Chem. Asian J.* **2010**, *5*, 621–633.
254. Ceriotti, A.; Daghetta, M.; El Afeey, S.; Lenco, A.; Longoni, G.; Manca, G.; Mealli, C.; Zacchini, S.; Zarra, S. *Inorg. Chem.* **2011**, *50*, 12553–12561.
255. Redshaw, C.; Walton, M. J.; Lee, D. S.; Jiang, C.; Elsegood, M. R.; Michiue, K. *Chem. A Eur. J.* **2015**, *21*, 5199–5210.
256. Zhao, Q.; Harris, T. D.; Betley, T. A. *J. Am. Chem. Soc.* **2011**, *133*, 8293–8306.
257. Cheung, M.-S.; Chan, H.-S.; Xie, Z. *Organometallics* **2004**, *23*, 517–526.
258. Bagchi, V.; Raptopoulos, G.; Das, P.; Christodoulou, S.; Wang, Q.; Ai, L.; Choudhury, A.; Pitsikalis, M.; Paraskevopoulou, P.; Stavropoulos, P. *Polyhedron* **2013**, *52*, 78–90.
259. Dame, A. N.; Bharara, M. S.; Barnes, C. L.; Walensky, J. R. *J. Coord. Chem.* **2015**, *68*, 3718–3726.
260. Asmis, K. R.; Beele, B. B.; Jenne, C.; Kawa, S.; Knorke, H.; Nierstenhöfer, M. C.; Wang, X. B.; Warneke, J.; Warneke, Z.; Yuan, Q. *Chem. A Eur. J.* **2020**, *26*, 14594–14601.



261. Kimata, H.; Mochida, T. *Chem. A Eur. J.* **2019**, *25*, 10111–10117.
262. Neumüller, B.; Dehnicke, K. *Z. Anorg. Allg. Chem.* **2010**, *636*, 1438–1440.
263. Spang, N.; Müller, M.; Augustinov, W.; Buchner, M. R. *Z. Naturforsch.* **2020**, *B75*, 939–949.
264. Dressel, M. P.; Nogal, S.; Berger, R. J. F.; Schmidbaur, H. *Z. Naturforsch.* **2003**, *B58*, 173–182.
265. Puchta, R.; Neumüller, B.; Dehnicke, K. *Z. Anorg. Allg. Chem.* **2011**, *637*, 67–74.
266. Rabe, S.; Müller, U. *Z. Naturforsch.* **2000**, *B55*, 553.
267. Keyzer, E. N.; Glass, H. F.; Liu, Z.; Bayley, P. M.; Dutton, S. E.; Grey, C. P.; Wright, D. S. *J. Am. Chem. Soc.* **2016**, *138*, 8682–8685.
268. Levason, W.; Pugh, D.; Purkis, J. M.; Reid, G. *Dalton Trans.* **2016**, *45*, 7900–7911.
269. Cheung, M.-S.; Chan, H.-S.; Xie, Z. *Organometallics* **2005**, *24*, 4468–4474.
270. Veyasov, G.; Matsumoto, K.; Hagiwara, R. *Dalton Trans.* **2016**, *45*, 2810–2813.
271. Rödl, C.; Schwedtmann, K.; Weigand, J. J.; Wolf, R. *Chem. A Eur. J.* **2019**, *25*, 6180–6188.
272. Chitnis, S. S.; Burford, N.; McDonald, R.; Ferguson, M. J. *Inorg. Chem.* **2014**, *53*, 5359–5372.
273. Weatherford-Pratt, J. T.; Dickie, D. A.; Harman, W. D. *CSD Communication*, 2019. refcode BOYCAW.
274. Bakker, J. M.; Deacon, G. B.; Forsyth, C. M.; Junk, P. C.; Wiecko, M. *Eur. J. Inorg. Chem.* **2010**, *2010*, 2813–2825.
275. Stavila, V.; Her, J.-H.; Zhou, W.; Hwang, S.-J.; Kim, C.; Ottley, L. A. M.; Udovic, T. J. *J. Solid State Chem.* **2010**, *183*, 1133–1140.
276. Keyzer, E. N.; Matthews, P. D.; Liu, Z.; Bond, A. D.; Grey, C. P.; Wright, D. S. *Chem. Commun.* **2018**, *54*, 12271.
277. Farina, P.; Levason, W.; Reid, G. *Dalton Trans.* **2013**, *42*, 89–99.
278. Verma, A.; Guino-o, M.; Gillett-Kunnath, M.; Teng, W.; Ruhlandt-Senge, K. *Z. Anorg. Allg. Chem.* **2009**, *635*, 903–913.
279. Bessler, K. E.; Gatto, C. C.; Romualdo, L. L.; Ellena, J. A.; Sales, M. J. D. A. *Z. Naturforsch.* **2008**, *B63*, 285–288.
280. Beattie, I. R.; Jones, P. J.; Howard, J. A. K.; Smart, L. E.; Gilmore, C. J.; Akitt, J. W. *J. Chem. Soc. Dalton Trans.* **1979**, 528–535.
281. Gao, Y.; Guery, J.; Jacoboni, C. *Acta Crystallogr.* **1993**, *C49*, 147–151.
282. Troyanov, S. I.; Kharisov, B. I. *Koord. Khim.* **1992**, *18*, 238–242.
283. Junk, P. C.; Skelton, B. W.; White, A. H. *Acta Crystallogr.* **2003**, *C59*, m289–m290.
284. Junk, P. C.; Skelton, C. L.; Skelton, B. W.; White, A. H. *Aust. J. Chem.* **2004**, *57*, 503–506.
285. Zhu, X.; Li, G.; Xu, F.; Zhang, Y.; Xue, M.; Shen, Q. *Tetrahedron* **2017**, *73*, 1451–1458.
286. Dartsch, I.; König, J.; Köckerling, M. *J. Cluster Sci.* **2018**, *29*, 319–323.
287. Li, K.; Choudhary, H.; Mishra, M. K.; Rogers, R. D. *ACS Catalysis* **2019**, *9*, 9789–9793.
288. Bury, W.; Chwojnowska, E.; Justyniak, I.; Lewiński, J.; Affek, A.; Zygadło-Monikowska, E.; Bąk, J.; Florjańczyk, Z. *Inorg. Chem.* **2012**, *51*, 737–745.
289. Waller, A. W.; Weiss, N. M.; Decato, D. A.; Phillips, J. A. *J. Mol. Struct.* **2017**, *1130*, 984–993.
290. Koutsantonis, G. A.; Morien, T. S.; Skelton, B. W.; White, A. H. *Acta Crystallogr.* **2003**, *C59*, m361–m365.
291. Parsons, S.; Maley, I.; Pulham, C.; Wood, P. A. *CSD Communication*, 2004. refcode EKEHAD01.
292. Gully, T. A.; Sonnenberg, K.; Bader, J.; Riedel, S. *Inorg. Chem.* **2021**, *60*, 8093–8102.
293. Schleep, M.; Hettich, C.; Kratzert, D.; Scherer, H.; Krossing, I. *Chem. Commun.* **2017**, *53*, 10914–10917.
294. Shlykov, S. A.; Giricheva, N. I.; Titov, A. V.; Szwak, M.; Lentz, D.; Girichev, G. V. *Dalton Trans.* **2010**, *39*, 3245–3255.
295. Brown, M. D.; Dyke, J. M.; Ferrante, F.; Levason, W.; Ogden, J. S.; Webster, M. *Chem. A Eur. J.* **2006**, *12*, 2620–2629.
296. Kessenich, E.; Polborn, K.; Schulz, A. *Z. Anorg. Allg. Chem.* **2001**, *627*, 2506–2510.
297. Brown, M.; Davis, M.; Dyke, J.; Ferrante, F.; Levason, W.; Ogden, J.; Webster, M. *Chem. A Eur. J.* **2008**, *14*, 2615–2624.
298. Camp, C.; Pécaut, J.; Mazzanti, M. *J. Am. Chem. Soc.* **2013**, *135*, 12101–12111.
299. Bénaud, O.; Berthet, J. C.; Thuéry, P.; Ephritikhine, M. *Chem. Commun.* **2011**, *47*, 9057–9059.
300. Fortier, S.; Wu, G.; Hayton, T. W. *Dalton Trans.* **2010**, *39*, 352–354.
301. Toumi, H.; Amiri, N.; Belkhiria, M. S.; Daran, J. C.; Nasri, H. *Acta Crystallogr.* **2012**, *E68*, m1557–m1558.
302. Ma, M.; Wang, H.; Wang, J.; Shen, L.; Zhao, Y.; Xu, W.-H.; Wu, B.; Yang, X.-J. *Dalton Trans.* **2019**, *48*, 2295–2299.
303. Zhou, W.; McKearney, D.; Leznoff, D. B. *Chem. A Eur. J.* **2020**, *26*, 1027–1031.
304. Maity, A. K.; Murillo, J.; Metta-Magaña, A. J.; Pinter, B.; Fortier, S. *J. Am. Chem. Soc.* **2017**, *139*, 15691–15700.
305. Ge, C.-M.; Zhang, S.-H.; Feng, C.; Wang, Y.-G.; Li, W. *Z. Anorg. Allg. Chem.* **2011**, *637*, 112–116.
306. Roy, S.; Halder, S.; Dey, A.; Harms, K.; Ray, P. P.; Chattopadhyay, S. *New J. Chem.* **2020**, *44*, 1285–1293.
307. Moore, B. F.; Emge, T. J.; Brennan, J. G. *Inorg. Chem.* **2013**, *52*, 6021–6027.
308. Zhang, S.-H.; Zhao, R.-X.; Li, G.; Zhang, H.-Y.; Zhang, C.-L.; Muller, G. *RSC Adv.* **2014**, *4*, 54837–54846.
309. Naglav, D.; Tobey, B.; Lyhs, B.; Römer, B.; Bläser, D.; Wölper, C.; Jansen, G.; Schulz, S. *Angew. Chem. Int. Ed.* **2017**, *56*, 8559–8563.
310. Neumüller, B.; Dehnicke, K. *Z. Anorg. Allg. Chem.* **2006**, *632*, 931–933.
311. Neumüller, B.; Dehnicke, K. *Z. Anorg. Allg. Chem.* **2007**, *633*, 2262–2267.
312. Neumüller, B.; Dehnicke, K. *Z. Anorg. Allg. Chem.* **2004**, *630*, 347–349.
313. Neumüller, B.; Dehnicke, K. *Z. Anorg. Allg. Chem.* **2004**, *630*, 1374–1376.
314. Haiges, R.; Boatz, J. A.; Vij, A.; Vij, V.; Gerken, M.; Schneider, S.; Schroer, T.; Yousuffuddin, M.; Christe, K. O. *Angew. Chem. Int. Ed.* **2004**, *43*, 6676–6680.
315. Klapötke, T. M.; Krumm, B.; Scherr, M.; Haiges, R.; Christe, K. O. *Angew. Chem. Int. Ed.* **2007**, *46*, 8686–8690.
316. Klapötke, T. M.; Krumm, B.; Mayer, P.; Schwab, I. *Angew. Chem. Int. Ed.* **2003**, *42*, 5843–5846.
317. Haiges, R.; Boatz, J. A.; Vij, A.; Gerken, M.; Schneider, S.; Schroer, T.; Christe, K. O. *Angew. Chem. Int. Ed.* **2003**, *42*, 5847–5851.
318. Haiges, R.; Rahm, M.; Christe, K. O. *Inorg. Chem.* **2013**, *52*, 402–414.
319. Haiges, R.; Boatz, J. A.; Williams, J. M.; Christe, K. O. *Angew. Chem. Int. Ed.* **2011**, *50*, 8828–8833.
320. Peerless, B.; Keane, T.; Meijer, A. J.; Portius, P. *Chem. Commun.* **2015**, *51*, 7435–7438.
321. Campbell, R.; Konar, S.; Hunter, S.; Pulham, C.; Portius, P. *Inorg. Chem.* **2018**, *57*, 400–411.
322. Filippou, A. C.; Portius, P.; Neumann, D. U.; Wehrstedt, K.-D. *Angew. Chem. Int. Ed.* **2000**, *39*, 4333–4336.
323. Campbell, R.; Davis, M. F.; Fazakerley, M.; Portius, P. *Chem. A Eur. J.* **2015**, *21*, 18690–18698.
324. Klapötke, T. M.; Nöth, N.; Schutt, T.; Warchhold, M. *Angew. Chem. Int. Ed.* **2000**, *39*, 2108–2109.
325. Karaghiosoff, K.; Klapötke, T. M.; Krumm, B.; Nöth, H.; Schütt, T.; Suter, M. *Inorg. Chem.* **2002**, *41*, 170–179.
326. Lyhs, B.; Jansen, G.; Bläser, D.; Wölper, C.; Schulz, S. *Chem. A Eur. J.* **2011**, *17*, 11394–11398.
327. Haiges, R.; Rahm, M.; Dixon, D. A.; Garner, E. B.; Christe, K. O. *Inorg. Chem.* **2012**, *51*, 1127–1141.
328. Villinger, A.; Schulz, A. *Angew. Chem. Int. Ed.* **2010**, *49*, 8017–8020.
329. Schulz, A.; Villinger, A. *Chem. A Eur. J.* **2012**, *18*, 2902–2911.
330. Schulz, A.; Villinger, A. *Inorg. Chem.* **2009**, *48*, 7359–7367.
331. Luo, B.; Young, V. G.; Gladfelter, W. L. *Inorg. Chem.* **2000**, *39*, 1705–1709.
332. Steffek, C.; McMurrin, J.; Pleune, B.; Kouvetakis, J.; Concolino, T. E.; Rheingold, A. L. *Inorg. Chem.* **2000**, *39*, 1615–1617.
333. Sussek, H.; Stark, O.; Devi, A.; Pritzkow, H.; Fischer, R. A. *J. Organomet. Chem.* **2000**, *602*, 29–36.



334. Claesener, M.; Jansen, M. *Z. Kristallogr. NCS* **2010**, *225*, 67–68.
335. Filippou, A. C.; Portius, P.; Neumann, D. U.; Wehrstedt, K.-D.; Kociok-Köhn, G.; Ziemer, B.; Neubauer, P. *CSD Communication*, 2015. refcode BUHQOM.
336. Eifler, J.; Szafer, S.; Jiao, H.; Sobota, P. *New J. Chem.* **2002**, *26*, 803–805.
337. Zhu, L.-H.; Zeng, M.-H.; Shen, X.-C.; Ng, S. W. *Main Group Met. Chem.* **2008**, *31*, 103–104.
338. Mohammadnezhad, G.; Ghanbarpour, A. R.; Amini, M. M.; Ng, S. W. *Acta Crystallogr.* **2010**, *E66*, m1120.
339. Walsh, A.; Watson, G. W. *J. Solid State Chem.* **2005**, *178*, 1422–1428.
340. Gao, X. S.; Dai, H. J.; Ding, M. J.; Pei, W. B.; Ren, X. M. *Inorg. Chem.* **2019**, *58*, 6772–6780.
341. Shimoni-Livny, L.; Glusker, J. P.; Bock, C. W. *Inorg. Chem.* **1998**, *37*, 1853–1867.
342. Harrowfield, J.; Thuéry, P. *Dalton Trans.* **2017**, *46*, 11533–11536.
343. Lyhs, B.; Bläser, D.; Wölper, C.; Schulz, S.; Jansen, G. *Inorg. Chem.* **2012**, *51*, 5897–5902.
344. Klapötke, T. M.; Nöth, H.; Schutt, T.; Suter, M. *Eur. J. Inorg. Chem.* **2002**, *2002*, 2511–2517.
345. Lyhs, B.; Bläser, D.; Wölper, C.; Haack, R.; Jansen, G.; Schulz, S. *Eur. J. Inorg. Chem.* **2012**, *2012*, 4350–4355.
346. Haagenson, D. C.; Stahl, L.; Staples, R. J. *Inorg. Chem.* **2001**, *40*, 4491–4493.
347. Rheingold, A. L.; Theopold, K. H. *CSD Communication*, 2019. refcode LUCKEC.
348. Rheingold, A. L.; Theopold, K. H. *CSD Communication*, 2019. refcode LUCKOM.
349. Rheingold, A. L.; Theopold, K. H. *CSD Communication*, 2019. refcode LOVLEQ.
350. Jana, A.; Roesky, H. W.; Schulzke, C. *Dalton Trans.* **2010**, 132–138.
351. Ayers, A. E.; Klapötke, T. M.; Dias, H. V. R. *Inorg. Chem.* **2001**, *40*, 1000–1005.
352. Plotzicka, J.; Kleeberg, C. *Inorg. Chem.* **2017**, *56*, 6671–6680.
353. Thompson, J. R.; Snider, D.; Wren, J. E. C.; Kroeker, S.; Williams, V. E.; Leznoff, D. B. *Eur. J. Inorg. Chem.* **2017**, *2017*, 88–98.
354. Klapötke, T. M.; Krumm, B.; Mayer, P.; Scherr, M.; Schwab, I. *Acta Crystallogr.* **2006**, *E62*, m2666–m2667.
355. Schlueter, J. A.; Geiser, U. *Acta Crystallogr.* **2003**, *C59*, m325–m327.
356. Katz, M. J.; Kaluarachchi, H.; Batchelor, R. J.; Bokov, A. A.; Ye, Z. G.; Leznoff, D. B. *Angew. Chem. Int. Ed.* **2007**, *46*, 8804–8807.
357. Döring, C.; Strey, M.; Jones, P. G. *Acta Crystallogr.* **2017**, *C73*, 1104–1108.
358. M.M. Olmstead and C.M. Beavers, CSD Communication refcode EBALUR, 2016.
359. Olmstead, M. M.; Lee, M. A.; Stork, J. R. *Acta Crystallogr.* **2005**, *E61*, m1048–m1050.
360. Sellin, M.; Malischewski, M. *Acta Crystallogr.* **2019**, *E75*, 1871–1874.
361. Olmstead, M. M.; Beavers, C. M.; Paw, U. L. *Acta Crystallogr.* **2009**, *E65*, m408–m409.
362. Ding, E.; Sturgeon, M. R.; Rath, A.; Chen, X.; Keane, M. A.; Shore, S. G. *Inorg. Chem.* **2009**, *48*, 325–330.
363. Sicilia, V.; Forníés, J.; Fuertes, S.; Martín, A. *Inorg. Chem.* **2012**, *51*, 10581–10589.
364. Ogawa, T.; Yoshida, M.; Ohara, H.; Kobayashi, A.; Kato, M. *Chem. Commun.* **2015**, *51*, 13377–13380.
365. Berenguer, J. R.; Fernández, J.; Lalinde, E.; Sánchez, S. *Chem. Commun.* **2012**, *48*, 6384–6386.
366. Ovens, J. S.; Truong, K. N.; Leznoff, D. B. *Dalton Trans.* **2012**, *41*, 1345–1351.
367. Bernhardt, E.; Bernhardt-Pitchougina, V.; Jenne, C. *Inorg. Chem.* **2017**, *56*, 5465–5470.
368. Whaley, C. M.; Rauchfuss, T. B.; Wilson, S. R. *Acta Crystallogr.* **2005**, *E61*, m1918–m1919.
369. Lazarides, T.; Easun, T. L.; Veyne-Marti, C.; Alsindi, W. Z.; George, M. W.; Deppermann, N.; Hunter, C. A.; Adams, H.; Ward, M. D. *J. Am. Chem. Soc.* **2007**, *129*, 4014–4027.
370. Baca, S. G.; Adams, H.; Grange, C. S.; Smith, A. P.; Sazanovich, I.; Ward, M. D. *Inorg. Chem.* **2007**, *46*, 9779–9789.
371. Whaley, C. M.; Rauchfuss, T. B.; Wilson, S. R. *Inorg. Chem.* **2009**, *48*, 4462–4469.
372. Vostríkova, K. E.; Peresyphkina, E. V. *Eur. J. Inorg. Chem.* **2011**, *2011*, 811–815.
373. Shao, X. D.; Yu, C. H. *Acta Crystallogr.* **2014**, *C70*, 603–605.
374. Sun, Y.-M.; Dong, F.-Y.; Wang, D.-Q.; Li, Y.-T.; Dou, J.-M. *J. Inorg. Organomet. Polym. Mater.* **2010**, *20*, 657–665.
375. Datta, A.; Golzar Hossain, G. M.; Karan, N. K.; Abdul Malik, K. M.; Mitra, S. *Inorg. Chem. Comm.* **2003**, *6*, 266–269.
376. Samanta, B.; Chakraborty, J.; Karan, N. K.; Singh, R. K. B.; Yap, G. P. A.; Marschner, C.; Baumgartner, J.; Mitra, S. *Struct. Chem.* **2006**, *17*, 139–147.
377. Lutz, M.; Speck, A. L.; Kronenburg, C. M. P.; van Koten, G. *CSD Communication*, 2010. refcode GOKXIP.
378. Matsushita, N.; Noguchi, W.; Tanaka, R. *IUCrData* **2017**, *2*, x170382.
379. Hodorowicz, M.; Szklarzewicz, J.; Jurowska, A. *CrstEngComm* **2020**, *22*, 3991–3998.
380. Jiang, J.; Koch, S. A. *Inorg. Chem.* **2002**, *41*, 158–160.
381. Xu, W. J.; Zeng, Y.; Yuan, W.; Zhang, W. X.; Chen, X. M. *Chem. Commun.* **2020**, *56*, 10054–10057.
382. Stojanovic, M.; Robinson, N. J.; Ngo, T.; Sykora, R. E. *J. Chem. Crystallogr.* **2011**, *41*, 1425–1432.
383. Werker, M.; Ruschewitz, U. *Z. Naturforsch.* **2020**, *B75*, 97–103.
384. Shi, C.; Gong, Z.-X.; Wang, Q.-W.; Han, X.-B.; Zhang, W. *CrstEngComm* **2020**, *22*, 1848–1852.
385. Rok, M.; Cizman, A.; Zarychta, B.; Zareba, J. K.; Trzebiatowska, M.; Mączka, M.; Stroppa, A.; Yuan, S.; Phillips, A. E.; Bator, G. *J. Mater. Chem. C* **2020**, *8*, 17491–17501.
386. Xu, W. J.; Romanyuk, K.; Martinho, J. M. G.; Zeng, Y.; Zhang, X. W.; Ushakov, A.; Shur, V.; Zhang, W. X.; Chen, X. M.; Kholkin, A.; Rocha, J. *J. Am. Chem. Soc.* **2020**, *142*, 16990–16998.
387. Li, Y. X.; Wang, X. L.; Li, Y.; Sato, O.; Yao, Z. S.; Tao, J. *Inorg. Chem.* **2021**, *60*, 380–386.
388. Shi, C.; Yu, C.-H.; Zhang, W. *Angew. Chem. Int. Ed.* **2016**, *19*, 5798–5802.
389. Rok, M.; Zarychta, B.; Moskwa, M.; Dziuk, B.; Medycki, W.; Bator, G. *Dalton Trans.* **2020**, *49*, 1830–1838.
390. Qian, K.; Shao, F.; Yan, Z.; Pang, J.; Chen, X.; Yang, C. *CrstEngComm* **2016**, *18*, 7671–7674.
391. Shi, C.; Han, X.-B.; Wang, Y.; Zhang, W. *Inorg. Chem. Front.* **2016**, *3*, 1604–1608.
392. Xu, W. J.; Li, P. F.; Tang, Y. Y.; Zhang, W. X.; Xiong, R. G.; Chen, X. M. *J. Am. Chem. Soc.* **2017**, *139*, 6369–6375.
393. Xu, W.-J.; Xie, K.-P.; Xiao, Z.-F.; Zhang, W.-X.; Chen, X.-M. *Cryst. Growth Des.* **2016**, *16*, 7212–7217.
394. Xu, W. J.; Chen, S. L.; Hu, Z. T.; Lin, R. B.; Su, Y. J.; Zhang, W. X.; Chen, X. M. *Dalton Trans.* **2016**, *45*, 4224–4229.
395. Rodríguez-Diéguez, A.; Kivekäs, R.; Sakiyama, H.; Deboudi, A.; Colacio, E. *Dalton Trans.* **2007**, 2145–2149.
396. Gao, Q.; Shi, N.; Sun, Q.; Sanson, A.; Milazzo, R.; Camera, A.; Zhu, H.; Lapidus, S. H.; Ren, Y.; Huang, Q.; Chen, J.; Xing, X. *Inorg. Chem.* **2018**, *57*, 10918–10924.
397. Liu, Y. L.; Zhang, W. *Dalton Trans.* **2017**, *47*, 45–48.
398. Wang, Z.; Yu, B.; Alamri, H.; Yarabarla, S.; Kim, M. H.; Huang, S. D. *Angew. Chem. Int. Ed.* **2018**, *57*, 2214–2218.
399. Duyker, S. G.; Hill, J. A.; Howard, C. J.; Goodwin, A. L. *J. Am. Chem. Soc.* **2016**, *138*, 11121–11123.
400. Medina Córdoba, L.; Morán, J. A.; Santos, S.; Piro, O. E.; Gómez, M. I. *J. Chem. Crystallogr.* **2011**, *41*, 1280.
401. Córdoba, L. M.; Echeverría, G. A.; Piro, O. E.; Gómez, M. I. *J. Therm. Anal. Calorim.* **2015**, *120*, 1827–1834.
402. Rok, M.; Bator, G.; Zarychta, B.; Dziuk, B.; Repeć, J.; Medycki, W.; Zamponi, M.; Usevičius, G.; Šimėnas, M.; Banyš, J. *Dalton Trans.* **2019**, *48*, 4190–4202.
403. Rok, M.; Bator, G.; Zarychta, B.; Dziuk, B.; Skalecki, D. K.; Medycki, W.; Zamponi, M. *Cryst. Growth Des.* **2019**, *19*, 4526–4537.
404. Wei, B.; Shang, R.; Zhang, X.; Shao, X. D.; Yao, Y. F.; Wang, Z. M.; Xiong, R. G.; Zhang, W. *Chem. A Eur. J.* **2014**, *20*, 8269–8273.

405. Reckweg, O.; Schulz, A.; DiSalvo, F. J. *Z. Naturforsch.* **2020**, *B75*, 129–133.
406. Semenov, N. A.; Gorbunov, D. E.; Shakhova, M. V.; Salnikov, G. E.; Bagryanskaya, I. Y.; Korolev, V. V.; Beckmann, J.; Gritsan, N. P.; Zibarev, A. V. *Chem. A Eur. J.* **2018**, *24*, 12983–12991.
407. Peel, A. J.; Ackroyd, R.; Wheatley, A. E. H. *Chem. Sci.* **2017**, *8*, 4904–4916.
408. Ezzayani, K.; Denden, Z.; Najmudin, S.; Bonifácio, C.; Saint-Aman, E.; Loiseau, F.; Nasri, H. *Eur. J. Inorg. Chem.* **2014**, *2014*, 5348–5361.
409. Kemp, R. A.; Saria, J.; Duesler, E. *CSD Communication*, 2007. refcode IFOXIL.
410. Kemp, R. A.; Felix, A. M. *CSD Communication*, 2007. refcode MINBOB.
411. Phull, H.; Alberti, D.; Korobkov, I.; Gambarotta, S.; Budzelaar, P. H. M. *Angew. Chem. Int. Ed.* **2006**, *45*, 5331–5334.
412. Kuo, P.; Chen, I.; Chang, J.; Lee, M.; Hu, C.; Hung, C.; Lee, H.; Huang, J. *Eur. J. Inorg. Chem.* **2004**, *2004*, 4898–4906.
413. Sinhababu, S.; Kundu, S.; Paesch, A. N.; Herbst-Irmer, R.; Stalke, D.; Roesky, H. W. *Eur. J. Inorg. Chem.* **2018**, *2018*, 2237–2240.
414. Assmann, B.; Franken, A.; Homborg, H. *Z. Naturforsch.* **1996**, *B51*, 325–332.
415. Fedushkin, I. L.; Dodonov, V. A.; Skatova, A. A.; Sokolov, V. G.; Piskunov, A. V.; Fukin, G. K. *Chem. A Eur. J.* **2018**, *24*, 1877–1889.
416. Shen, X.; Nakashima, A.; Sakata, K.; Hashimoto, M. *Synth. React. Inorg. Met.-Org. Chem.* **2004**, *34*, 211–222.
417. Sharma, M. K.; Sinhababu, S.; Yadav, D.; Mukherjee, G.; Rajaraman, G.; Nagendran, S. *Chem. Asian J.* **2018**, *13*, 1357–1365.
418. Konarev, D. V.; Kuzmin, A. V.; Shestakov, A. F.; Khasanov, S. S.; Lyubovskaya, R. N. *Dalton Trans.* **2019**, *48*, 4961–4972.
419. Buttery, J. H. N.; Effendy; Mutrofin, S.; Plackett, N. C.; Skelton, B. W.; Whitaker, C. R.; White, A. H. *Z. Anorg. Allg. Chem.* **2006**, *632*, 1809–1828.
420. Buttery, J. H. N.; Effendy; Koutsantonis, G. A.; Mutrofin, S.; Plackett, N. C.; Skelton, B. W.; Whitaker, C. R.; White, A. H. *Z. Anorg. Allg. Chem.* **2006**, *632*, 1829–1838.
421. Nöth, H.; Warchhold, M. *Eur. J. Inorg. Chem.* **2004**, *2004*, 1115–1124.
422. Fu, S.; Fu, B.; Zhao, Z.; Liu, X. *Z. Naturforsch.* **2018**, *B73*, 85–89.
423. Neumüller, B.; Dehnicke, K. *Z. Anorg. Allg. Chem.* **2010**, *636*, 1206–1211.
424. Saria, J. A.; Duesler, E. N.; Dickie, D. A.; Kemp, R. A. *CSD Communication*, 2016. refcode UZAJIQ.
425. Zhao, D.; Li, F. F.; Sha, J. *Acta Crystallogr.* **2010**, *E66*, m988.
426. Chekhlov, A. N. *Russ. J. Coord. Chem.* **2002**, *28*, 454–460.
427. Chekhlov, A. N. *Russ. J. Coord. Chem.* **2002**, *28*, 163–169.
428. Chan, S. H.; Wong, W. T.; Chan, W. K. *Chem. Mater.* **2001**, *13*, 4635–4641.
429. Gumbriš, E. G.; Peresyphkina, E. V.; Virovets, A. V.; Cherkasova, T. G. *Russ. J. Inorg. Chem.* **2012**, *57*, 337–342.
430. Petrosyants, S. P.; Ilyukhin, A. B. *Russ. J. Coord. Chem.* **2007**, *33*, 734–740.
431. Hervé, K.; Cador, O.; Golhen, S.; Costuas, K.; Halet, J.-F.; Shirahata, T.; Muto, T.; Imakubo, T.; Miyazaki, A.; Ouahab, L. *Chem. Mater.* **2006**, *18*, 790–797.
432. Ilyukhin, A.; Petrosyants, S. *CSD Communication*, 2017. refcode OCEMAN.
433. Petrosyants, S. P.; Ilyukhin, A. B. *Russ. J. Coord. Chem.* **2009**, *35*, 302–306.
434. Petrosyants, S. P.; Ilyukhin, A. B.; Ketsko, V. A. *Russ. J. Inorg. Chem.* **2008**, *53*, 879–883.
435. Shen, X.; Sakata, K.; Hashimoto, M. *Polyhedron* **2002**, *21*, 969–973.
436. Karoui, S.; Kamoun, S.; Jouini, A. *J. Solid State Chem.* **2013**, *197*, 60–68.
437. Kong, L.-Q.; Dou, J.-M.; Li, C.-J.; Li, D.-C.; Wang, D.-Q. *Acta Crystallogr.* **2006**, *E62*, m1030–m1032.
438. Morsali, A.; Mahjoub, A. R. *Solid State Sci.* **2005**, *7*, 1429–1437.
439. Marandi, F.; Sartaji, J.; Bruno, G.; Rudbari, H. A. *J. Coord. Chem.* **2012**, *65*, 1872–1881.
440. Saghatforoush, L.; Sahin, E.; Babaei, S.; Bakhtiari, A.; Nasimian, A.; Çelik, Ö.; Zabiollahi, Z. *J. Coord. Chem.* **2014**, *67*, 1463–1477.
441. Arit, S.; Harloff, J.; Schulz, A.; Stoffers, A.; Villinger, A. *Inorg. Chem.* **2019**, *58*, 5305–5313.
442. He, Y.; Li, D.-C.; Liu, Y.; Dou, J.-M.; Wang, D.-Q. *Z. Kristallogr. NCS* **2004**, *219*, 443–444.
443. Kong, L. *Acta Crystallogr.* **2009**, *E65*, m1312.
444. Marandi, F.; Moeni, K.; Mardani, Z.; Krautscheid, H. *Acta Crystallogr.* **2019**, *C75*, 1023–1030.
445. Hanay, W.; Böhlend, H.; Noltemeyer, M.; Schmidt, H.-G. *Microchim. Acta* **2000**, *133*, 197–201.
446. Park, J.-H.; Chung, T.-M.; Park, B. K.; Kim, C. G. *Inorg. Chim. Acta* **2020**, *505*, 119504.
447. Tambornino, F.; Hinz, A.; Köppe, R.; Goicoechea, J. M. *Angew. Chem. Int. Ed.* **2018**, *57*, 8230–8234.
448. Hinz, A.; Goicoechea, J. M. *Angew. Chem. Int. Ed.* **2016**, *55*, 8536–8541.
449. Gálvez Ruiz, J. C.; Nöth, H.; Warchhold, M. *Eur. J. Inorg. Chem.* **2008**, *2008*, 251–266.
450. Hervé, A.; Thuéry, P.; Ephritikhine, M.; Berthet, J.-C. *Organometallics* **2014**, *33*, 2088–2098.
451. Roger, M.; Arliguie, T.; Thuery, P.; Ephritikhine, M. *CSD Communication*, 2019. refcode COLLAT.
452. Roger, M.; Arliguie, T.; Thuéry, P.; Fourmigué, M.; Ephritikhine, M. *Inorg. Chem.* **2005**, *44*, 594–600.
453. Roger, M.; Arliguie, T.; Thuéry, P.; Fourmigué, M.; Ephritikhine, M. *Inorg. Chem.* **2005**, *44*, 584–593.
454. Camp, C.; Mougél, V.; Horeglad, P.; Pécaut, J.; Mazzanti, M. *J. Am. Chem. Soc.* **2010**, *132*, 17374–17377.
455. Tripepi, G.; Young, V. G.; Ellis, J. E. *J. Organomet. Chem.* **2000**, *593–594*, 354–360.
456. Bogart, J. A.; Lewis, A. J.; Medling, S. A.; Piro, N. A.; Carroll, P. J.; Booth, C. H.; Schelter, E. J. *Inorg. Chem.* **2013**, *52*, 11600–11607.
457. Bogart, J. A.; Lewis, A. J.; Boreen, M. A.; Lee, H. B.; Medling, S. A.; Carroll, P. J.; Booth, C. H.; Schelter, E. J. *Inorg. Chem.* **2015**, *54*, 2830–2837.
458. Jaenschke, A.; Paap, J.; Behrens, U. *Z. Anorg. Allg. Chem.* **2008**, *634*, 461–469.
459. Bonomo, L.; Lehaire, M.-L.; Solari, E.; Scopelliti, R.; Floriani, C. *Angew. Chem. Int. Ed.* **2001**, *40*, 771–774.
460. Meininger, D. J.; Arman, H. D.; Tonzetich, Z. J. *CSD Communication*, 2016. refcode INOVAK.
461. Wu, G.; Wong, A.; Wang, S. *Can. J. Chem.* **2003**, *81*, 275–283.
462. Devillers, C. H.; Dimé, A. K. D.; Cattet, H.; Lucas, D. C. *R. Chim.* **2013**, *16*, 540–549.
463. Bohle, D. S.; Dodd, E. L. *Inorg. Chem.* **2012**, *51*, 4411–4413.
464. Saltsman, I.; Goldberg, I.; Gross, Z. *Tetrahedron Lett.* **2003**, *44*, 5669–5673.
465. Enakieva, Y. Y.; Volostnykh, M. V.; Nefedov, S. E.; Kirakosyan, G. A.; Gorbunova, Y. G.; Tsvadze, A. Y.; Bessmertnykh-Lemeune, A. G.; Stern, C.; Guillard, R. *Inorg. Chem.* **2017**, *56*, 3055–3070.
466. Cissell, J. A.; Vaid, T. P.; Yap, G. P. A. *J. Am. Chem. Soc.* **2007**, *129*, 7841–7847.
467. Ogumi, K.; Nakagawa, T.; Okada, H.; Sakai, R.; Wang, H.; Matsuo, Y. *J. Mater. Chem. A* **2017**, *5*, 23067–23077.
468. Garcia, T. Y.; Olmstead, M. M.; Fetting, J. C.; Balch, A. L. *Inorg. Chem.* **2008**, *47*, 11417–11422.
469. Janczak, J.; Kubiak, R. *Polyhedron* **2001**, *20*, 2901–2909.
470. Kucinska, M.; Skupin-Mrugalska, P.; Szczolko, W.; Sobotta, L.; Sciepora, M.; Tykarska, E.; Wierchowski, M.; Teubert, A.; Fedoruk-Wyszomirska, A.; Wyszko, E.; Gdaniec, M.; Kaczmarek, M.; Goslinski, T.; Mielcarek, J.; Murias, M. *J. Med. Chem.* **2015**, *58*, 2240–2255.
471. Bendix, J.; Dmochowski, I. J.; Gray, H. B.; Mahammed, A.; Simkhovich, L.; Gross, Z. *Angew. Chem. Int. Ed.* **2000**, *39*, 4048–4051.
472. Simkhovich, L.; Goldberg, I.; Gross, Z. *J. Inorg. Biochem.* **2000**, *80*, 235–238.
473. Vestfrid, J.; Botoshansky, M.; Palmer, J. H.; Durrell, A. C.; Gray, H. B.; Gross, Z. *J. Am. Chem. Soc.* **2011**, *133*, 12899–12901.
474. Vestfrid, J.; Goldberg, I.; Gross, Z. *Inorg. Chem.* **2014**, *53*, 10536–10542.

475. Ooi, S.; Tanaka, T.; Osuka, A. *Inorg. Chem.* **2016**, *55*, 8920–8927.
476. Zhan, X.; Yadav, P.; Diskin-Posner, Y.; Fridman, N.; Sundararajan, M.; Ullah, Z.; Chen, Q.-C.; Shimon, L. J. W.; Mahammed, A.; Churchill, D. G.; Baik, M.-H.; Gross, Z. *Dalton Trans.* **2019**, *48*, 12279–12286.
477. Vale, L. S. H. P.; Barata, J. F. B.; Neves, M. G. P. M. S.; Faustino, M. A. F.; Tomé, A. C.; Silva, A. M. S.; Paz, F. A. A.; Cavaleiro, J. A. S. *Tetrahedron Lett.* **2007**, *48*, 8904–8908.
478. Vale, L. S. H. P.; Barata, J. F. B.; Santos, C. I. M.; Neves, M. G. P. M. S.; Faustino, M. A. F.; Tomé, A. C.; Silva, A. M. S.; Paz, F. A. A.; Cavaleiro, J. A. S. *J. Porphyrins Phthalocyanines* **2009**, *13*, 358–368.
479. Saltsman, I.; Mahammed, A.; Goldberg, I.; Tkachenko, E.; Botoshansky, M.; Gross, Z. *J. Am. Chem. Soc.* **2002**, *124*, 7411–7420.
480. Sorasaene, K.; Taqavi, P.; Henling, L. M.; Gray, H. B.; Tkachenko, E.; Mahammed, A.; Gross, Z. *J. Porphyrins Phthalocyanines* **2007**, *11*, 189–197.
481. Ueta, K.; Tanaka, T.; Osuka, A. *Chem. Lett.* **2018**, *47*, 916–919.
482. Chen, Q.; Sharma, V.; Saltsman, I.; Fridman, N.; Gross, Z. *CSD Communication*, 2020. refcode QUMJAM.
483. Basumatary, B.; Reddy, R. V. R.; Bhandary, S.; Sankar, J. *CSD Communication*, 2015. refcode QURRUS.
484. Ooi, S.; Tanaka, T.; Osuka, A. *J. Porphyrins Phthalocyanines* **2016**, *20*, 274–281.
485. Chen, Q. C.; Soll, M.; Mizrahi, A.; Saltsman, I.; Fridman, N.; Saphier, M.; Gross, Z. *Angew. Chem. Int. Ed.* **2018**, *57*, 1006–1010.
486. Fowler, C. J.; Sessler, J. L.; Lynch, V. M.; Waluk, J.; Gebauer, A.; Lex, J.; Heger, A.; Zuniga-y-Rivero, F.; Vogel, E. *Chem. A Eur. J.* **2002**, *8*, 3485–3496.
487. Boyle, T. J.; Sears, J. M.; Greathouse, J. A.; Perales, D.; Cramer, R.; Staples, O.; Rheingold, A. L.; Coker, E. N.; Roper, T. M.; Kemp, R. A. *Inorg. Chem.* **2018**, *57*, 2402–2415.
488. Jailil, A.; Clymer, R. N.; Hamilton, C. R.; Vaddypally, S.; Gau, M. R.; Zdilla, M. J. *Acta Crystallogr.* **2017**, *C73*, 264–269.
489. Hoefelmeyer, J. D.; Gabbai, F. P. *Organometallics* **2002**, *21*, 982–985.
490. Nöth, H.; Warchhold, M. *Z. Naturforsch.* **2003**, *B58*, 123–126.
491. Parsons, S.; Stumpf, T.; Pulham, C.; Wood, P. A. *CSD Communication*, 2004. refcode DAVJEP01.
492. Villiers, C.; Thuéry, P.; Ephritikhine, M. *Chem. Commun.* **2006**, 392–394.
493. Wacker, A.; Yan, C. G.; Kaltenpoth, G.; Ginsberg, A.; Arif, A. M.; Ernst, R. D.; Pritzkow, H.; Siebert, W. *J. Organomet. Chem.* **2002**, *641*, 195–202.
494. Rotter, C.; Schuster, M.; Kidik, M.; Schön, O.; Klapötke, T. M.; Karaghiosoff, K. *Inorg. Chem.* **2008**, *47*, 1663–1673.
495. Thuéry, P.; Takemura, H. *Acta Crystallogr.* **2003**, *C59*, m384–m386.
496. Skelton, B. W. *CSD Communication*, 2017. refcode FEGCEC.
497. Tang, Y.; Zakharov, L. N.; Rheingold, A. L.; Kemp, R. A. *Polyhedron* **2005**, *24*, 1739–1748.
498. Rabe, G. W.; Guzei, I. A.; Rheingold, A. L. *Inorg. Chim. Acta* **2001**, *315*, 254–257.
499. Boyle, T. J.; Pedrotty, D. M.; Alam, T. M.; Vick, S. C.; Rodriguez, M. A. *Inorg. Chem.* **2000**, *39*, 5133–5146.
500. MacDougall, D. J.; Noll, B. C.; Kennedy, A. R.; Henderson, K. W. *Dalton Trans.* **2006**, 1875–1884.
501. Boyle, T. J.; Alam, T. M.; Peters, K. P.; Rodriguez, M. A. *Inorg. Chem.* **2001**, *40*, 6281–6286.
502. Zi, G.; Li, H.-W.; Xie, Z. *Organometallics* **2002**, *21*, 3464–3470.
503. Arnold, P. L.; Wang, K.; Gray, S. J.; Moreau, L. M.; Booth, C. H.; Curcio, M.; Wells, J. A. L.; Slawin, A. M. Z. *Dalton Trans.* **2020**, *49*, 877–884.
504. Arnold, P. L.; Stevens, C. J.; Farnaby, J. H.; Gardiner, M. G.; Nichol, G. S.; Love, J. B. *J. Am. Chem. Soc.* **2014**, *136*, 10218–10221.
505. Boyle, T. J.; Velazquez, A. T.; Yonemoto, D. T.; Alam, T. M.; Moore, C.; Rheingold, A. L. *Inorg. Chim. Acta* **2013**, *405*, 374–386.
506. Neumüller, B.; Dehnicke, K. Z. *Anorg. Allg. Chem.* **2010**, *636*, 515–517.
507. Hohl, T.; Sinn, T.; Hoch, C. Z. *Naturforsch.* **2020**, *B75*, 509–516.
508. Neumüller, B.; Dehnicke, K. Z. *Anorg. Allg. Chem.* **2003**, *629*, 2529–2534.
509. Paparo, A.; Smith, C. D.; Jones, C. *Angew. Chem. Int. Ed.* **2019**, *58*, 11459–11463.
510. Neumüller, B.; Dehnicke, K. Z. *Anorg. Allg. Chem.* **2004**, *630*, 369–376.
511. Müller, M.; Karttunen, A. J.; Buchner, M. R. *Chem. Sci.* **2020**, *11*, 5415–5422.
512. Tang, Y.; Zakharov, L. N.; Rheingold, A. L.; Kemp, R. A. *Organometallics* **2005**, *24*, 836–841.
513. Kemp, R. A.; Dickie, D. A.; Felix, A. M. *CSD Communication*, 2007. refcode MINCES.
514. Zechmann, C. A.; Boyle, T. J.; Rodriguez, M. A.; Kemp, R. A. *Polyhedron* **2000**, *19*, 2557–2564.
515. Layfield, R. A.; Bullock, T. H.; Garcia, F.; Humphrey, S. M.; Schüller, P. *Chem. Commun.* **2006**, 2039–2041.
516. Zegke, M.; Zhang, X.; Pidchenko, I.; Hlina, J. A.; Lord, R. M.; Purkis, J.; Nichol, G. S.; Magnani, N.; Schreckenbach, G.; Vitova, T.; Love, J. B.; Arnold, P. L. *Chem. Sci.* **2019**, *10*, 9740–9751.
517. Boyle, T. J.; Pratt, H. D.; Alam, T. M.; Rodriguez, M. A.; Clem, P. G. *Polyhedron* **2007**, *26*, 5095–5103.
518. Lemmerz, L. E.; Spaniol, T. P.; Okuda, J. *Dalton Trans.* **2018**, *47*, 12553–12561.
519. Jochmann, P.; Dols, T. S.; Spaniol, T. P.; Perrin, L.; Maron, L.; Okuda, J. *Angew. Chem. Int. Ed.* **2010**, *49*, 7795–7798.
520. Skelton, B. W.; White, A. H.; Waters, A. F. *CSD Communication*, 2017. refcode ZZZAVA01.
521. Lampland, N. L.; Pindwal, A.; Yan, K.; Ellem, A.; Sadow, A. D. *Organometallics* **2017**, *36*, 4546–4557.
522. Kubiak, P. S.; Johnson, A. L.; Cameron, P. J.; Kociok-Köhn, G. *Eur. J. Inorg. Chem.* **2019**, *2019*, 3962–3969.
523. Tang, Y.; Zakharov, L. N.; Kassel, W. S.; Rheingold, A. L.; Kemp, R. A. *Inorg. Chim. Acta* **2005**, *358*, 2014–2022.
524. Boyle, T. J.; Steele, L. A. M.; Saad, A. *Inorg. Chim. Acta* **2013**, *394*, 259–268.
525. Dimitrov, A.; Heidemann, D.; Kemnitz, E. *Inorg. Chem.* **2006**, *45*, 10807–10814.
526. Timoshkin, A. Y.; Bodensteiner, M.; Sevastianova, T. N.; Lisovenko, A. S.; Davydova, E. I.; Scheer, M.; Graßl, C.; Butlak, A. V. *Inorg. Chem.* **2012**, *51*, 11602–11611.
527. Nogai, S.; Schriewer, A.; Schmidbaur, H. *Dalton Trans.* **2003**, 3165–3171.
528. Seo, W. S.; Park, J. E.; Lee, K.; Choi, Z.-H.; Park, J. T. *CSD Communication*, 2005. refcode NALTUQ.
529. Kazakov, I. V.; Bodensteiner, M.; Lisovenko, A. S.; Suvorov, A. V.; Scheer, M.; Balázs, G.; Timoshkin, A. Y. *Inorg. Chem.* **2013**, *52*, 13207–13215.
530. Haiges, R.; Deokar, P.; Vasiliu, M.; Stein, T. H.; Dixon, D. A.; Christe, K. O. *Chem. A Eur. J.* **2017**, *23*, 9054–9066.
531. Holligan, K.; Rogler, P.; Rehe, D.; Pamula, M.; Kornienko, A. Y.; Emge, T. J.; Krogh-Jespersen, K.; Brennan, J. G. *Inorg. Chem.* **2015**, *54*, 8896–8904.
532. Dimitrov, A.; Heidemann, D.; Kallow, K. I.; Kemnitz, E. *Inorg. Chem.* **2012**, *51*, 11612–11622.
533. Less, R. J.; Simmonds, H. R.; Wright, D. S. *Dalton Trans.* **2014**, *43*, 5785–5792.
534. Bhalla, R.; Burt, J.; Hector, A. L.; Levason, W.; Luthra, S. K.; McRobbie, G.; Monzittu, F. M.; Reid, G. *Polyhedron* **2016**, *106*, 65–74.
535. Pardoe, J. A.; Cowley, A. R.; Downs, A. J.; Greene, T. M. *Acta Crystallogr.* **2005**, *C61*, m200–m202.
536. von Hänisch, C. Z. *Anorg. Allg. Chem.* **2003**, *629*, 1496–1500.
537. Nogai, S. D.; Schier, A.; Schmidbaur, H. *Z. Naturforsch.* **2001**, *B56*, 711–718.
538. Cheng, F.; Davis, M. F.; Hector, A. L.; Levason, W.; Reid, G.; Webster, M.; Zhang, W. *Eur. J. Inorg. Chem.* **2007**, *2007*, 4897–4905.
539. Tran, D. T.; Zavalij, P. Y.; Oliver, S. R. J. *Acta Crystallogr.* **2002**, *E58*, m742–m743.
540. Pacher, A.; Schrenk, C.; Schnepf, A. *J. Organomet. Chem.* **2010**, *695*, 941–944.
541. Saria, J. A.; Duesler, E. N.; Dickie, D. A.; Kemp, R. A. *CSD Communication*, 2016. refcode UZAJEM.
542. Vartak, P. B.; Wang, Z.; Groy, T. L.; Trovitch, R. J.; Wang, R. Y. *ACS Omega* **2020**, *5*, 1949–1955.

543. Appleton, S. E.; Briand, G. G.; Decken, A.; Smith, A. S. *Dalton Trans.* **2004**, 3515–3520.
544. Appleton, S. E.; Briand, G. G.; Decken, A.; Smith, A. S. *Acta Crystallogr.* **2011**, E67, m714.
545. Kennedy, A. R.; Reglinski, J. *CSD Communication*, 2006. refcode LESJID.
546. Davydova, E. I.; Virovets, A. V.; Peresyppkina, E. V.; Kazakov, I. V.; Timoshkin, A. Y. *Russ. Chem. Bull.* **2020**, 69, 84–90.
547. James, S. C.; Lawson, Y. G.; Norman, N. C.; Orpen, A. G.; Quayle, M. J. *Acta Crystallogr.* **2000**, C56, 427–429.
548. Sharutin, V. V.; Egorova, I. V.; Sharutina, O. K.; Boyarkina, E. A. *Russ. J. Coord. Chem.* **2008**, 34, 461–465.
549. Sharutin, V. V.; Egorova, I. V.; Klepikov, N. N.; Boyarkina, E. A.; Sharutina, O. K. *Russ. J. Inorg. Chem.* **2009**, 54, 1768–1778.
550. Anderson, K. M.; Baylies, C. J.; Jahan, A. H. M. M.; Norman, N. C.; Orpen, A. G.; Starbuck, J. *Dalton Trans.* **2003**, 3270–3277.
551. Davydova, E. I.; Virovets, A.; Peresyppkina, E.; Pomogaeva, A. V.; Timoshkin, A. Y. *Polyhedron* **2019**, 158, 97–101.
552. Prokudina, Y. V.; Davydova, E. I.; Virovets, A.; Stöger, B.; Peresyppkina, E.; Pomogaeva, A. V.; Timoshkin, A. Y. *Chem. A Eur. J.* **2020**, 26, 16338–16348.
553. Pomogaeva, A. V.; Khoroshilova, O. V.; Davydova, E. I.; Suslonov, V. V.; Timoshkin, A. Y. *Z. Anorg. Allg. Chem.* **2021**, 647, 687–695.
554. Murphy, J. N.; Kerton, F. M.; Dawe, L. N. *J. Chem. Crystallogr.* **2014**, 44, 108–114.
555. Schulz, S.; Lyhs, B.; Jansen, G.; Bläser, D.; Wölper, C. *Chem. Commun.* **2011**, 47, 3401–3403.
556. Toužín, J.; Neplechová, K.; Zák, Z.; Cerník, M. *Collect. Czech. Chem. Commun.* **2002**, 67, 577–586.
557. Dutton, J. L.; Ragogna, P. J. *Chem. A Eur. J.* **2010**, 16, 12454–12461.
558. Amiri, N.; Ben Taheur, F.; Chevreux, S.; Rodrigues, C. M.; Dorcet, V.; Lemerrier, G.; Nasri, H. *Inorg. Chim. Acta* **2021**, 525, 120466.
559. Ikkal, S. A.; Dhamija, A.; Rath, S. P. *Chem. Commun.* **2015**, 51, 14107–14110.
560. Ikkal, S. A.; Brahma, S.; Rath, S. P. *Inorg. Chem.* **2012**, 51, 9666–9676.
561. Khelifa, A. B.; Ezzayani, K.; Guergueb, M.; Loiseau, F.; Saint-Aman, E.; Nasri, H. *J. Mol. Struct.* **2021**, 1227, 129508.
562. Plackett, N. C.; Kerton, F. M.; Skelton, B. W.; White, A. H. *CSD Communication*, 2017. refcode ZEBHOG.
563. Iengo, E.; Zangrando, E.; Mestroni, S.; Fronzoni, G.; Stener, M.; Alessio, E. *J. Chem. Soc. Dalton Trans.* **2001**, 1338–1346.
564. Anderson, C. M.; Herman, A.; Rochon, F. D. *Polyhedron* **2007**, 26, 3661–3668.
565. Ferrara, S.; Kreider-Mueller, A.; Tanski, J. M.; Anderson, C. M. *Acta Crystallogr.* **2011**, E67, m756–m757.
566. Kadota, K.; Duong, N. T.; Nishiyama, Y.; Sivaniah, E.; Kitagawa, S.; Horike, S. *Chem. Sci.* **2019**, 10, 6193–6198.
567. Sevastianova, T. N.; Bodensteiner, M.; Lisovenko, A. S.; Davydova, E. I.; Scheer, M.; Susliakova, T. V.; Krasnova, I. S.; Timoshkin, A. Y. *Dalton Trans.* **2013**, 42, 11589.
568. Samanamú, C. R.; Lococo, P. M.; Richards, A. F. *Inorg. Chim. Acta* **2007**, 360, 4037–4043.
569. Samanamú, C. R.; Richards, A. F. *Polyhedron* **2007**, 26, 923–928.
570. Lichtenthaler, M. R.; Stahl, F.; Kratzert, D.; Benkmil, B.; Wegner, H. A.; Krossing, I. *Eur. J. Inorg. Chem.* **2014**, 2014, 4335–4341.
571. Grigsby, W. A.; Morien, T. S.; Raston, C. L.; Skelton, B. W.; White, A. H. *Aust. J. Chem.* **2004**, 57, 507–508.
572. Shi, Y.-J.; Chen, X.-T.; Cai, C.-X.; Zhang, Y.; Xue, Z.; You, X.-Z.; Peng, S.-M.; Lee, G.-H. *Inorg. Chem. Comm.* **2002**, 5, 621–624.
573. Aslani, A.; Morsali, A. *Inorg. Chim. Acta* **2009**, 362, 5012–5016.
574. Sham, I. H. T.; Patrick, B. O.; von Ahsen, B.; von Ahsen, S.; Willner, H.; Thompson, R. C.; Aubke, F. *Solid State Sci.* **2002**, 4, 1457–1463.
575. Sorg, J. R.; Schäfer, T. C.; Schneider, T.; Müller-Buschbaum, K. *Z. Anorg. Allg. Chem.* **2020**, 646, 507–513.
576. Usoltsev, A. N.; Adonin, S. A.; Novikov, A. S.; Sokolov, M. N.; Fedin, V. P. *Russ. J. Coord. Chem.* **2020**, 46, 23–27.
577. Kelly, A. W.; Wheaton, A. M.; Nicholas, A. D.; Barnes, F. H.; Patterson, H. H.; Pike, R. D. *Eur. J. Inorg. Chem.* **2017**, 2017, 4990–5000.
578. Masciocchi, N.; Garlaschelli, L.; Peli, G. *Powder Diffr.* **2008**, 23, 286–291.
579. Kayalvizhi, M.; Vasuki, G.; Kaabi, K.; Ben Nasr, C. *Acta Crystallogr.* **2013**, E69, m481.
580. Zurawski, A.; Rybak, J. C.; Meyer, L. V.; Matthes, P. R.; Stepanenko, V.; Dannenbauer, N.; Würthner, F.; Müller-Buschbaum, K. *Dalton Trans.* **2012**, 41, 4067–4078.
581. Amiri, N.; Taheur, F. B.; Chevreux, S.; Wenger, E.; Lemerrier, G.; Nasri, H. *Tetrahedron* **2017**, 73, 7011–7016.
582. Stadie, N. P.; Sanchez-Smith, R.; Groy, T. L. *Acta Crystallogr.* **2007**, E63, m2153–m2154.
583. Srinivasan, B. R.; Sawant, J. V.; Raghavaiah, P. *J. Chem. Sci.* **2007**, 119, 11–20.
584. Sinnwell, M. A.; Miller, Q. R. S.; Palys, L.; Barpaga, D.; Liu, L.; Bowden, M. E.; Han, Y.; Ghose, S.; Sushko, M. L.; Schaeff, H. T.; Xu, W.; Nyman, M.; Thallapally, P. K. *J. Am. Chem. Soc.* **2020**, 142, 17598–17606.
585. Sen, R.; Saha, D.; Koner, S. *Chem. A Eur. J.* **2012**, 18, 5979–5986.
586. Wang, L.-D.; Tao, F.; Cheng, M.-L.; Liu, Q.; Han, W.; Wu, Y.-J.; Yang, D.-D.; Wang, L.-J. *J. Coord. Chem.* **2012**, 65, 923–933.
587. Chen, L.; Tao, F.; Wang, L.; Hong, J.; Jia, X.; Bao, J.; Ji, Y.; Cheng, M.; Liu, Q. *Z. Anorg. Allg. Chem.* **2013**, 639, 552–557.
588. Rong, N.; Qiu, T.; Qian, R.; Lü, L.; Huang, X.; Ma, Z.; Cui, C. *Inorg. Chem. Comm.* **2017**, 86, 98–104.
589. Saha, D.; Maity, T.; Das, S.; Koner, S. *Dalton Trans.* **2013**, 42, 13912–13922.
590. Simões, A. B.; Figueira, F.; Mendes, R. F.; Barbosa, J. S.; Rocha, J.; Paz, F. A. A. *Acta Crystallogr.* **2019**, E75, 1607–1612.
591. Cheng, M.-L.; Han, W.; Liu, Q.; Bao, J.-T.; Li, Z.-F.; Chen, L.-T.; Sun, X.-Q.; Xi, H.-T. *J. Coord. Chem.* **2014**, 67, 215–226.
592. Song, Y.-J.; Han, Z.-B.; He, Y.-K.; Zhang, P. *J. Chem. Crystallogr.* **2008**, 38, 891–894.
593. Song, Y.; Tian, C.-B.; Wu, Z.-F.; Huang, X.-Y. *New J. Chem.* **2018**, 42, 5096–5101.
594. An, C.; Lu, Y.; Shang, Z.; Zhang, Z. *Inorg. Chim. Acta* **2008**, 361, 2721–2730.
595. Pan, L.; Frydel, T.; Sander, M. B.; Huang, X.; Li, J. *Inorg. Chem.* **2001**, 40, 1271–1283.
596. Starosta, W.; Leciejewicz, J. *Acta Crystallogr.* **2013**, E69, m438.
597. Cortés-Llamas, S. A.; Hernández-Lamonedá, R.; Velázquez-Carmona, M. A.; Muñoz-Hernández, M. A.; Toscano, R. A. *Inorg. Chem.* **2006**, 45, 286–294.
598. Mosch-Zanetti, N. C.; Ferbinteanu, M.; Magull, J. *Eur. J. Inorg. Chem.* **2002**, 2002, 950–956.
599. Hitzbleck, J.; Deacon, G. B.; Ruhlandt-Senge, K. *Eur. J. Inorg. Chem.* **2007**, 2007, 592–601.
600. Müller, C.; Koch, A.; Görls, H.; Krieck, S.; Westerhausen, M. *Inorg. Chem.* **2015**, 54, 635–645.
601. Hitzbleck, J.; O'Brien, A. Y.; Forsyth, C. M.; Deacon, G. B.; Ruhlandt-Senge, K. *Chem. A Eur. J.* **2004**, 10, 3315–3323.
602. Mezei, G.; Raptis, R. G. *New J. Chem.* **2003**, 27, 1399–1407.
603. Fernando, I. R.; Daskalakis, N.; Demadis, K. D.; Mezei, G. *New J. Chem.* **2010**, 34, 221–235.
604. Yu, Z.; Korolev, A. V.; Heeg, M. J.; Winter, C. H. *Polyhedron* **2002**, 21, 1117–1123.
605. Nogai, S.; Schier, A.; Schmidbaur, H. *Z. Naturforsch.* **2002**, B57, 183–186.
606. Cortés-Llamas, S. A.; García-Hernández, Z.; Rufino-Felipe, E.; López-Cardoso, M.; Muñoz-Hernández, M.-Á. *Inorg. Chim. Acta* **2010**, 363, 3959–3965.
607. Quiroga-González, E.; Näther, C.; Bensch, W. *Z. Naturforsch.* **2009**, B64, 1312–1318.
608. Quiroga-González, E.; Kienle, L.; Näther, C.; Chakravadhanula, V. S. K.; Lühmann, H.; Bensch, W. *J. Solid State Chem.* **2010**, 183, 2805–2812.
609. Chen, J.; Chua, Y. S.; Wu, H.; Xiong, Z.; He, T.; Zhou, W.; Ju, X.; Yang, M.; Wu, G.; Chen, P. *Int. J. Hydrogen Energy* **2015**, 40, 412–419.
610. Turner, D. L.; Stone, K. H.; Stephens, P. W.; Vaid, T. P. *Dalton Trans.* **2010**, 39, 5070–5073.
611. Chen, X.; Yao, Z.-Y.; Xue, C.; Yang, Z.-X.; Liu, J.-L.; Ren, X.-M. *CrystEngComm* **2018**, 20, 356–361.
612. Zhang, Q.; Malliakas, C. D.; Kanatzidis, M. G. *Inorg. Chem.* **2009**, 48, 10910–10912.
613. Blachnik, R.; Fehliker, A.; Reuter, H. *Z. Kristallogr. NCS* **2001**, 216, 221–222.
614. Chen, R.; Zhou, J.; Liu, X.; Hu, F.; An, L.; Kan, Y.; Xue, C.-J. *Inorg. Chem. Comm.* **2013**, 28, 55–59.



615. Zhang, Q.; Chung, I.; Jang, J. I.; Ketterson, J. B.; Kanatzidis, M. G. *Chem. Mater.* **2009**, *21*, 12–14.
616. Xiao, L.-L.; Wang, N.; Zheng, B.; Yu, J.-M.; Yu, J.-P.; Wang, H.; Xu, Q.; Cheng, F.-F.; Xiong, W.-W. *J. Solid State Chem.* **2021**, *298*, 122109.
617. Ma, G.; Ilyukhin, A.; Glaser, J.; Tóth, I.; Zékány, L. *Inorg. Chim. Acta* **2001**, *320*, 92–100.
618. Gándara, F.; Medina, M. E.; Snejko, N.; Gómez-Lor, B.; Iglesias, M.; Gutiérrez-Puebla, E.; Monge, M. A. *Inorg. Chem.* **2008**, *47*, 6791–6795.
619. Powell, A. V.; Mackay, R. J. *Solid State Chem.* **2011**, *184*, 3144–3149.
620. Menezes, P. W.; Fässler, T. F. *Z. Anorg. Allg. Chem.* **2012**, *638*, 1109–1113.
621. Thiele, G.; Santner, S.; Donsbach, C.; Assmann, M.; Müller, M.; Dehnen, S. Z. *Kristallogr. Cryst. Mater.* **2014**, *229*, 489–495.
622. Trinh, C.; Bodensteiner, M.; Virovets, A. V.; Peresypkina, E. V.; Scheer, M.; Matveev, S. M.; Timoshkin, A. Y. *Polyhedron* **2010**, *29*, 414–424.
623. Sullivan, M. T.; Senaratne, N. K.; Eichhorn, D. M. *Polyhedron* **2016**, *114*, 152–155.
624. Li, C.-Y.; Zhou, J.; Zhang, Y.; Lei, Z.-X.; Bian, G.-Q.; Dai, J. *Z. Anorg. Allg. Chem.* **2009**, *635*, 151–155.
625. Li, C. Y.; Chen, X. X.; Zhou, J.; Zhu, Q. Y.; Lei, Z. X.; Zhang, Y.; Dai, J. *Inorg. Chem.* **2008**, *47*, 8586–8588.
626. Junk, P. C.; Skelton, B. W.; White, A. H. *Aust. J. Chem.* **2006**, *59*, 147–154.
627. Shen, Y.; Lu, J.; Tang, C.; Fang, W.; Jia, D.; Zhang, Y. *Dalton Trans.* **2014**, *43*, 9116–9125.
628. Morsali, A.; Abedini, J. *J. Coord. Chem.* **2004**, *57*, 1629–1636.
629. Ma, G.; Fischer, A.; Ilyukhin, A.; Glaser, J. *Inorg. Chim. Acta* **2003**, *344*, 117–122.
630. Pada Nayek, H.; Lin, Z.; Dehnen, S. *Z. Anorg. Allg. Chem.* **2009**, *635*, 1737–1740.
631. Vikulova, E. S.; Rikhter, E. A.; Piryazev, D. A.; Zherikova, K. V.; Morozova, N. B. *J. Struct. Chem.* **2020**, *61*, 1405–1413.
632. Hakimi, M.; Kukovec, B.-M.; Schuh, E.; Normohammadzadeh, Z.; Mohr, F. *J. Chem. Crystallogr.* **2012**, *42*, 180–185.
633. Deacon, G. B.; Delbridge, E. E.; Fallon, G. D.; Jones, C.; Hibbs, D. E.; Hursthouse, M. B.; Skelton, B. W.; White, A. H. *Organometallics* **2000**, *19*, 1713–1721.
634. Hill, M. S.; Hitchcock, P. B. *Organometallics* **2002**, *21*, 220–225.
635. Breunig, H. J.; Ghesner, M. E.; Lork, E. *Z. Anorg. Allg. Chem.* **2005**, *631*, 851–856.
636. von Hänisch, C.; Hampe, O.; Weigend, F.; Stahl, S. *Angew. Chem. Int. Ed.* **2007**, *46*, 4775–4779.
637. Melero, C.; Guijarro, A.; Yus, M. *Dalton Trans.* **2009**, 1286–1289.
638. García, F.; Less, R. J.; Naseri, V.; McPartlin, M.; Rawson, J. M.; Wright, D. S. *Angew. Chem. Int. Ed.* **2007**, *46*, 7827–7830.
639. Seidel, F. W.; Tomizawa, I.; Nozaki, K. *Angew. Chem. Int. Ed.* **2020**, *59*, 22591–22601.
640. Guo, Z.; Wang, Y.; Cao, W.; Chao, J.; Wei, X. *Dalton Trans.* **2017**, *46*, 2765–2769.
641. Dixon, L. S. H.; Hanf, S.; Waters, J. E.; Bond, A. D.; Wright, D. S. *Organometallics* **2018**, *37*, 4465–4472.
642. Alberti, D.; Goddard, R.; Ruffiniska, A.; Pörschke, K.-R. *Organometallics* **2003**, *22*, 4025–4029.
643. Kotsch, M.; Glenger, C.; Schrenk, C.; Schnepf, A. *Z. Anorg. Allg. Chem.* **2016**, *642*, 670–675.
644. Greer, J. A.; Blair, V. L.; Thompson, C. D.; Andrews, P. C. *Dalton Trans.* **2016**, *45*, 10887–10890.
645. Klink, R.; Schrenk, C.; Schnepf, A. *Dalton Trans.* **2014**, *43*, 16097–16104.
646. Less, R. J.; Allen, L. K.; Steiner, A.; Wright, D. S. *Dalton Trans.* **2015**, *44*, 4141–4147.
647. Wang, Y.; Xie, Y.; Abraham, M. Y.; Gilliard, R. J.; Wei, P.; Campana, C. F.; Schaefer, H. F.; Schleyer, P.; Robinson, G. H. *Angew. Chem. Int. Ed.* **2012**, *51*, 10173–10176.
648. Uhl, W.; Rösener, C.; Layh, M.; Hepp, A. *Z. Anorg. Allg. Chem.* **2012**, *638*, 1746–1754.
649. Sattler, E.; Matern, E.; Rothenberger, A.; Okrut, A.; Bombicz, P.; Fernández, I.; Kovács, I. *Eur. J. Inorg. Chem.* **2014**, *2014*, 221–232.
650. Cousins, D. M.; Davidson, M. G.; García-Vivó, D.; Mahon, M. F. *Dalton Trans.* **2010**, *39*, 8203–8209.
651. Dyer, P. W.; Fawcett, J.; Griffith, G. A.; Hanton, M. J.; Olivier, C.; Patterson, A. R.; Suhard, S. *Chem. Commun.* **2005**, 3835–3837.
652. Robertson, S. D.; Chivers, T. *Dalton Trans.* **2008**, 1765–1772.
653. Pörschke, K. R.; Kleimann, W.; Wilke, G.; Claus, K. H.; Krüger, C. *Angew. Chem. Int. Ed.* **1983**, *22*, 991–992.
654. Armstrong, D. R.; Clegg, W.; Dale, S. H.; García-Alvarez, J.; Harrington, R. W.; Hevia, E.; Honeyman, G. W.; Kennedy, A. R.; Mulvey, R. E.; O'Hara, C. T. *Chem. Commun.* **2008**, 187–189.
655. Francos, J.; Fleming, B. J.; García-Álvarez, P.; Kennedy, A. R.; Reilly, K.; Robertson, G. M.; Robertson, S. D.; O'Hara, C. T. *Dalton Trans.* **2014**, *43*, 14424–14431.
656. Clegg, W.; Dale, S. H.; Hevia, E.; Hogg, L. M.; Honeyman, G. W.; Mulvey, R. E.; O'Hara, C. T.; Russo, L. *Angew. Chem. Int. Ed.* **2008**, *47*, 731–734.
657. Langer, J.; Pálfi, V. K.; Görls, H.; Reiher, M.; Westerhausen, M. *Chem. Commun.* **2013**, *49*, 1121–1123.
658. Carrella, L. M.; Förster, C.; Kennedy, A. R.; Klett, J.; Mulvey, R. E.; Rentschler, E. *Organometallics* **2010**, *29*, 4756–4758.
659. Paparo, A.; Jones, C. *Chem. Asian J.* **2019**, *14*, 486–490.
660. Schüler, P.; Görls, H.; Westerhausen, M.; Kriech, S. *Dalton Trans.* **2019**, *48*, 8966–8975.
661. Soloveichik, G. L.; Andrus, M.; Lobkovsky, E. B. *Inorg. Chem.* **2007**, *46*, 3790–3791.
662. Westerhausen, M.; Bollwein, T.; Makropoulos, N.; Piotrowski, H. *Inorg. Chem.* **2005**, *44*, 6439–6444.
663. Glock, C.; Görls, H.; Westerhausen, M. *Inorg. Chim. Acta* **2011**, *374*, 429–434.
664. Müller, C.; Kriech, S.; Görls, H.; Westerhausen, M. *Eur. J. Inorg. Chem.* **2016**, *2016*, 4637–4642.
665. Teng, W.; Ruhlandt-Senge, K. *Chem. A Eur. J.* **2005**, *11*, 2462–2470.
666. Xue, F.; Zhao, J.; Hor, T. S. A. *Dalton Trans.* **2013**, *42*, 5150–5158.
667. Loh, C.; Glock, C.; Ziemann, S.; Görls, H.; Kriech, S.; Westerhausen, M. *Z. Naturforsch.* **2013**, *B68*, 518–532.
668. Chitsaz, S.; Breyhan, T.; Pauls, J.; Neumüller, B. *Z. Anorg. Allg. Chem.* **2002**, *628*, 956–964.
669. Alič, B.; Štefančič, A.; Tavčar, G. *Dalton Trans.* **2017**, *46*, 3338–3346.
670. Vestergren, M.; Eriksson, J.; Håkansson, M. *J. Organomet. Chem.* **2003**, *681*, 215–224.
671. Langer, J.; Kriech, S.; Fischer, R.; Görls, H.; Westerhausen, M. *Z. Anorg. Allg. Chem.* **2010**, *636*, 1190–1198.
672. Bashkurov, R.; Kratish, Y.; Mokhtarzadeh, C. C.; Fridman, N.; Bravo-Zhivotovskii, D.; Romero, P. E.; Clendenning, S. B.; Apeloig, Y. *Inorg. Chem.* **2020**, *59*, 17488–17496.
673. Nelkenbaum, E.; Kapon, M.; Eisen, M. S. *Organometallics* **2005**, *24*, 2645–2659.
674. Muller, M.; Lerner, H.-W.; Bolte, M. *CSD Communication*, 2006. refcode SAJVEE02.
675. Ludwig, G.; Ruffer, T.; Hoppe, A.; Walther, T.; Lang, H.; Ebbinghaus, S. G.; Steinborn, D. *Dalton Trans.* **2015**, *44*, 5323–5330.
676. Clegg, W.; Davies, R. P.; Snaith, R.; Wheatley, A. E. H. *Eur. J. Inorg. Chem.* **2001**, *2001*, 1411–1413.
677. Haywood, J.; Wheatley, A. E. H. *Eur. J. Inorg. Chem.* **2009**, *2009*, 5010–5016.
678. Cheng, F.; Dyke, J. M.; Ferrante, F.; Hector, A. L.; Levason, W.; Reid, G.; Webster, M.; Zhang, W. *Dalton Trans.* **2010**, *39*, 847–856.
679. Nöth, H.; Troll, A. *Eur. J. Inorg. Chem.* **2005**, *2005*, 3524–3535.
680. Nöth, H.; Rojas-Lima, S.; Troll, A. *Eur. J. Inorg. Chem.* **2005**, *2005*, 1895–1906.
681. Jevtovikj, I.; Herrero, R.; Gómez-Ruiz, S.; Lönnecke, P.; Hey-Hawkins, E. *Inorg. Chem.* **2013**, *52*, 4488–4493.
682. Brouillet, E. V.; Kennedy, A. R.; Koszinowski, K.; McLellan, R.; Mulvey, R. E.; Robertson, S. D. *Dalton Trans.* **2016**, *45*, 5590–5597.
683. Bedford, R. B.; Brenner, P. B.; Carter, E.; Cogswell, P. M.; Haddow, M. F.; Harvey, J. N.; Murphy, D. M.; Nunn, J.; Woodall, C. H. *Angew. Chem. Int. Ed.* **2014**, *53*, 1804–1808.
684. Dunbar, A. C.; Joseph Lastowski, R.; Girolami, G. S. *Inorg. Chem.* **2020**, *59*, 16893–16904.
685. Daly, S. R.; Bellott, B. J.; Nesbit, M. A.; Girolami, G. S. *Inorg. Chem.* **2012**, *51*, 6449–6459.

686. Green, S. P.; Jones, C.; Stasch, A. *Angew. Chem. Int. Ed.* **2007**, *46*, 8618–8621.
687. Green, S. P.; Jones, C.; Stasch, A. *Chem. Commun.* **2008**, 6285–6287.
688. Rossini, A. J.; Macgregor, A. W.; Smith, A. S.; Schatte, G.; Schurko, R. W.; Briand, G. G. *Dalton Trans.* **2013**, *42*, 9533–9546.
689. Hobson, K.; Carmalt, C. J.; Bakewell, C. *Inorg. Chem.* **2021**, *60*, 10958–10969.
690. Edelmann, F. T. *Adv. Organomet. Chem.* **2013**, *61*, 55–374.
691. Xia, A.; El-Kaderi, H. M.; Jane Heeg, M.; Winter, C. H. *J. Organomet. Chem.* **2003**, *682*, 224–232.
692. Cole, M. L.; Junk, P. C. *Z. Anorg. Allg. Chem.* **2015**, *641*, 2624–2629.
693. Anga, S.; Bhattacharjee, J.; Banerjee, I.; Nayek, H. P.; Panda, T. K. *ChemistrySelect* **2016**, *1*, 2014–2020.
694. Chlupatý, T.; Bílek, M.; Merna, J.; Brus, J.; Růžicková, Z.; Strassner, T.; Růžicka, A. *Dalton Trans.* **2019**, *48*, 5335–5342.
695. Day, B. M.; Knowelden, W.; Coles, M. P. *Dalton Trans.* **2012**, *41*, 10930–10933.
696. Cole, M. L.; Jones, C.; Junk, P. C.; Kloth, M.; Stasch, A. *Chem. A Eur. J.* **2005**, *11*, 4482–4491.
697. Boyd, C. L.; Tyrrell, B. R.; Mountford, P. *Acta Crystallogr.* **2002**, *E58*, m597–m598.
698. Sroor, F.; Hrib, C.; Edelmann, F. *Inorganics* **2015**, *3*, 429–447.
699. Hitchcock, P. B.; Lappert, M. F.; Merle, P. G. *Dalton Trans.* **2007**, 585–594.
700. Knapp, C.; Lork, E.; Watson, P. G.; Mews, R. *Inorg. Chem.* **2002**, *41*, 2014–2025.
701. Novotný, M.; Švec, P.; Růžicková, Z.; Růžicka, A. *J. Organomet. Chem.* **2017**, *828*, 68–74.
702. Liebing, P.; Harmgarth, N.; Lorenz, V.; Zörner, F.; Hilfert, L.; Busse, S.; Edelmann, F. T. *Z. Anorg. Allg. Chem.* **2019**, *645*, 440–446.
703. Fan, M.; Yang, Q.; Tong, H.; Yuan, S.; Jia, B.; Guo, D.; Zhou, M.; Liu, D. *RSC Adv.* **2012**, *2*, 6599–6605.
704. Cole, M. L.; Junk, P. C.; Louis, L. M. *J. Chem. Soc. Dalton Trans.* **2002**, 3906–3914.
705. Cole, M. L.; Evans, D. J.; Junk, P. C.; Smith, M. K. *Chem. A Eur. J.* **2003**, *9*, 415–424.
706. Sadique, A. R.; Heeg, M. J.; Winter, C. H. *Inorg. Chem.* **2001**, *40*, 6349–6355.
707. Benndorf, P.; Preuß, C.; Roesky, P. W. *J. Organomet. Chem.* **2011**, *696*, 1150–1155.
708. Kalden, D.; Oberheide, A.; Loh, C.; Görls, H.; Kriek, S.; Westerhausen, M. *Chem. A Eur. J.* **2016**, *22*, 10944–10959.
709. Bai, S.-D.; Guo, J.-P. *Acta Crystallogr.* **2005**, *E61*, m2726–m2727.
710. Boeré, R. T.; Cole, M. L.; Junk, P. C. *New J. Chem.* **2005**, *29*, 128–134.
711. Moxey, G. J.; Blake, A. J.; Lewis, W.; Kays, D. L. *Eur. J. Inorg. Chem.* **2015**, *2015*, 5892–5902.
712. Bayram, M.; Naglav, D.; Wölper, C.; Schulz, S. *Organometallics* **2017**, *36*, 467–473.
713. Matioszek, D.; Kadir, N.; Saffon, N.; Castel, A. *Organometallics* **2010**, *29*, 3039–3046.
714. Jones, C.; Bonyhady, S. J.; Holzmann, N.; Frenking, G.; Stasch, A. *Inorg. Chem.* **2011**, *50*, 12315–12325.
715. Chlupatý, T.; Padělková, Z.; Lyčka, A.; Brus, J.; Růžicka, A. *Dalton Trans.* **2012**, *41*, 5010–5019.
716. Zessin, T.; Anton, J.; Linti, G. *Z. Anorg. Allg. Chem.* **2013**, *639*, 2224–2232.
717. Schmidt, J. A. R.; Arnold, J. *Organometallics* **2002**, *21*, 2306–2313.
718. Riddlestone, I. M.; Urbano, J.; Phillips, N.; Kelly, M. J.; Vidovic, D.; Bates, J. I.; Taylor, R.; Aldridge, S. *Dalton Trans.* **2013**, *42*, 249–258.
719. Zhong, M.; Liu, Y.; Kundu, S.; Graw, N.; Li, J.; Yang, Z.; Herbst-Irmer, R.; Stalke, D.; Roesky, H. W. *Inorg. Chem.* **2019**, *58*, 10625–10628.
720. Banerjee, S.; Dutta, S.; Sarkar, S. K.; Graw, N.; Herbst-Irmer, R.; Koley, D.; Stalke, D.; Roesky, H. W. *Dalton Trans.* **2020**, *49*, 14231–14236.
721. Gebhard, M.; Hellwig, M.; Kroll, A.; Rogalla, D.; Winter, M.; Mallick, B.; Ludwig, A.; Wiesing, M.; Wieck, A. D.; Grundmeier, G.; Devi, A. *Dalton Trans.* **2017**, *46*, 10220–10231.
722. Scheiper, C.; Blaser, D.; Wolper, C.; Schulz, S. *CS D Communication*, 2015. refcode TUQSOP.
723. Ritter, C.; Chizmeshya, A. V. G.; Gray, T. L.; Kouvetakis, J. *Appl. Organomet. Chem.* **2007**, *21*, 595–600.
724. Davies, R. P.; Linton, D. J.; Schooler, P.; Snaith, R.; Wheatley, A. E. H. *Eur. J. Inorg. Chem.* **2001**, *2001*, 619–622.
725. Rösch, A.; Seifert, F.; Vass, V.; Görls, H.; Kretschmer, R. *New J. Chem.* **2021**, *45*, 972–981.
726. Nagendran, S.; Sen, S. S.; Roesky, H. W.; Koley, D.; Grubmüller, H.; Pal, A.; Herbst-Irmer, R. *Organometallics* **2008**, *27*, 5459–5463.
727. Sen, S. S.; Kritzler-Kosch, M. P.; Nagendran, S.; Roesky, H. W.; Beck, T.; Pal, A.; Herbst-Irmer, R. *Eur. J. Inorg. Chem.* **2010**, *2010*, 5304–5311.
728. Foley, S. R.; Zhou, Y.; Yap, G. P.; Richeson, D. S. *Inorg. Chem.* **2000**, *39*, 924–929.
729. Yeong, H. X.; Xi, H. W.; Li, Y.; Kunnappilly, S. B.; Chen, B.; Lau, K. C.; Hirao, H.; Lim, K. H.; So, C. W. *Chem. A Eur. J.* **2013**, *19*, 14726–14731.
730. Stasch, A.; Forsyth, C. M.; Jones, C.; Junk, P. C. *New J. Chem.* **2008**, *32*, 829–834.
731. Lyhs, B.; Schulz, S.; Westphal, U.; Bläser, D.; Boese, R.; Bolte, M. *Eur. J. Inorg. Chem.* **2009**, *2009*, 2247–2253.
732. Brym, M.; Forsyth, C. M.; Jones, C.; Junk, P. C.; Rose, R. P.; Stasch, A.; Turner, D. R. *Dalton Trans.* **2007**, 3282–3288.
733. Wong, G. F.; Yeung, L. F.; Tsoi, H. Y.; Chan, H.; Chiang, M.; Lee, H. K. *Eur. J. Inorg. Chem.* **2019**, *2019*, 98–109.
734. Han, H.-F.; Zhang, S.-F.; Guo, Z.-Q.; Tong, H.-B.; Wei, X.-H. *Polyhedron* **2015**, *99*, 71–76.
735. Jin, G.; Jones, C.; Junk, P. C.; Lippert, K.-A.; Rose, R. P.; Stasch, A. *New J. Chem.* **2009**, *33*, 64–75.
736. Melen, R. L.; Simmonds, H. R.; Wadepohl, H.; Wood, P. T.; Gade, L. H.; Wright, D. S. *Aust. J. Chem.* **2014**, *67*, 1030–1036.
737. Willcocks, A. M.; Robinson, T. P.; Roche, C.; Pugh, T.; Richards, S. P.; Kingsley, A. J.; Lowe, J. P.; Johnson, A. L. *Inorg. Chem.* **2012**, *51*, 246–257.
738. Rudolf, D.; Kaifer, E.; Himmel, H. *Eur. J. Inorg. Chem.* **2010**, *2010*, 4952–4961.
739. Ong, T.-G.; O'Brien, J. S.; Korobkov, I.; Richeson, D. S. *Organometallics* **2006**, *25*, 4728–4730.
740. Fernández-Galán, R.; Antiñolo, A.; Carrillo-Hermosilla, F.; López-Solera, I.; Otero, A.; Serrano-Laguna, A.; Villaseñor, E. *J. Organomet. Chem.* **2012**, *711*, 35–42.
741. Zhou, M.; Tong, H.; Wei, X.; Liu, D. *J. Organomet. Chem.* **2007**, *692*, 5195–5202.
742. Feil, F.; Harder, S. *Eur. J. Inorg. Chem.* **2005**, *2005*, 4438–4443.
743. Schwamm, R. J.; Coles, M. P. *Organometallics* **2013**, *32*, 5277–5280.
744. Cheng, J. *Acta Crystallogr.* **2011**, *E67*, m987.
745. Green, S. P.; Jones, C.; Stasch, A. *Science* **2007**, *318*, 1754–1757.
746. Glock, C.; Loh, C.; Görls, H.; Kriek, S.; Westerhausen, M. *Eur. J. Inorg. Chem.* **2013**, *2013*, 3261–3269.
747. Barrett, A. G. M.; Crimmin, M. R.; Hill, M. S.; Hitchcock, P. B.; Lomas, S. L.; Mahon, M. F.; Procopiou, P. A. *Dalton Trans.* **2010**, *39*, 7393–7400.
748. Koller, J.; Bergman, R. G. *Organometallics* **2010**, *29*, 3350–3356.
749. Jin, G.; Jones, C.; Junk, P. C.; Stasch, A.; Woodul, W. D. *New J. Chem.* **2008**, *32*, 835.
750. Brazeau, A. L.; DiLabio, G. A.; Kreisler, K. A.; Monillas, W.; Yap, G. P. A.; Barry, S. T. *Dalton Trans.* **2007**, 3297–3304.
751. Brazeau, A. L.; Wang, Z.; Rowley, C. N.; Barry, S. T. *Inorg. Chem.* **2006**, *45*, 2276–2281.
752. Kenney, A. P.; Yap, G. P. A.; Richeson, D. S.; Barry, S. T. *Inorg. Chem.* **2005**, *44*, 2926–2933.
753. Gebhard, M.; Hellwig, M.; Parala, H.; Xu, K.; Winter, M.; Devi, A. *Dalton Trans.* **2014**, *43*, 937–940.
754. Barry, S. T.; Gordon, P. G.; Ward, M. J.; Heikkilä, M. J.; Monillas, W. H.; Yap, G. P. A.; Ritala, M.; Leskelä, M. *Dalton Trans.* **2011**, *40*, 9425–9430.
755. Jones, C.; Junk, P. C.; Platts, J. A.; Stasch, A. *J. Am. Chem. Soc.* **2006**, *128*, 2206–2207.
756. Chlupatý, T.; Padělková, Z.; DeProft, F.; Willem, R.; Růžicka, A. *Organometallics* **2012**, *31*, 2203–2211.
757. Ungpittagul, T.; Wongmahasirikun, P.; Phomphrai, K. *Dalton Trans.* **2020**, *49*, 8460–8471.

758. Ahmet, I. Y.; Hill, M. S.; Raithby, P. R.; Johnson, A. L. *Dalton Trans.* **2018**, 47, 5031–5048.
759. Foley, S. R.; Yap, G. P. A.; Richeson, D. S. *Polyhedron* **2002**, 21, 619–627.
760. Chlupatý, T.; Padělková, Z.; Růžička, A. *Main Group Met. Chem.* **2014**, 37, 49–52.
761. Jones, C.; Rose, R. P.; Stasch, A. *Dalton Trans.* **2008**, 2871–2878.
762. Green, S. P.; Jones, C.; Junk, P. C.; Lippert, K.-A.; Stasch, A. *Chem. Commun.* **2006**, 3978–3980.
763. Brym, M.; Francis, M. D.; Jin, G.; Jones, C.; Mills, D. P.; Stasch, A. *Organometallics* **2006**, 25, 4799–4807.
764. Ahmet, I. Y.; Thompson, J. R.; Johnson, A. L. *Eur. J. Inorg. Chem.* **2018**, 2018, 1670–1678.
765. Barman, M. K.; Nembenna, S. *RSC Adv.* **2016**, 6, 338–345.
766. Green, S. P.; Jones, C.; Jin, G.; Stasch, A. *Inorg. Chem.* **2007**, 46, 8–10.
767. Rheingold, A. L. *CSD Communication*, 2021. refcode OSENEI.
768. Sawinski, P. K.; Deringer, V. L.; Dronskowski, R. *Dalton Trans.* **2013**, 42, 15080–15087.
769. Sawinski, P. K.; Dronskowski, R. *Inorg. Chem.* **2012**, 51, 7425–7430.
770. Hoepfner, V.; Jacobs, P.; Sawinski, P. K.; Houben, A.; Reim, J.; Dronskowski, R. *Z. Anorg. Allg. Chem.* **2013**, 639, 1232–1236.
771. Ogutu, G.; Kozar, E.; Stoffel, R. P.; Houben, A.; Dronskowski, R. *Z. Anorg. Allg. Chem.* **2020**, 646, 180–183.
772. Benz, S.; Missong, R.; Ogutu, G.; Stoffel, R. P.; Englert, U.; Torii, S.; Miao, P.; Kamiyama, T.; Dronskowski, R. *ChemistryOpen* **2019**, 8, 327–332.
773. Jones, D. D. L.; Watts, S.; Jones, C. *Inorganics* **2021**, 9, 72.
774. Liu, J.; Vieille-Petit, L.; Linden, A.; Luan, X.; Dorta, R. *J. Organomet. Chem.* **2012**, 719, 80–86.
775. Arrowsmith, M.; Crimmin, M. R.; Hill, M. S.; Kociok-Köhn, G. *Dalton Trans.* **2013**, 42, 9720–9726.
776. Martin, J.; Langer, J.; Wiesinger, M.; Elsen, H.; Harder, S. *Eur. J. Inorg. Chem.* **2020**, 2020, 2582–2595.
777. Bailey, P.; Parsons, S.; Messenger, D.; Liddle, S. *CSD Communication*, 2005. refcode CARWEY.
778. de Bruin-Dickason, C. N.; Rosengarten, C. A.; Deacon, G. B.; Jones, C. *Chem. Commun.* **2021**, 57, 1599–1602.
779. Bonyhady, S. J.; Jones, C.; Nembenna, S.; Stasch, A.; Edwards, A. J.; McIntyre, G. J. *Chem. A Eur. J.* **2010**, 16, 938–955.
780. Bonyhady, S. J.; Holzmann, N.; Frenking, G.; Stasch, A.; Jones, C. *Angew. Chem. Int. Ed.* **2017**, 56, 8527–8531.
781. Dove, A. P.; Gibson, V. C.; Hornmriun, P.; Marshall, E. L.; Segal, J. A.; White, A. J. P.; Williams, D. J. *Dalton Trans.* **2003**, 3088–3097.
782. Ruspic, C.; Harder, S. *Inorg. Chem.* **2007**, 46, 10426–10433.
783. Wiesinger, M.; Rösch, B.; Knüpfel, C.; Mai, J.; Langer, J.; Harder, S. *Eur. J. Inorg. Chem.* **2021**, 2021, 3731–3741.
784. Bakewell, C.; White, A. J.; Crimmin, M. R. *J. Am. Chem. Soc.* **2016**, 138, 12763–12766.
785. Bakewell, C.; Ward, B. J.; White, A. J. P.; Crimmin, M. R. *Chem. Sci.* **2018**, 9, 2348–2356.
786. Singh, S.; Ahn, H. J.; Stasch, A.; Jancik, V.; Roesky, H. W.; Pal, A.; Biadene, M.; Herbst-Irmer, R.; Noltemeyer, M.; Schmidt, H. G. *Inorg. Chem.* **2006**, 45, 1853–1860.
787. Kuhn, N.; Fuchs, S.; Steimann, M. *Z. Anorg. Allg. Chem.* **2002**, 628, 458–462.
788. Chisholm, M. H.; Navarro-Llobet, D.; Gallucci, J. *Inorg. Chem.* **2001**, 40, 6506–6508.
789. Ito, S.; Hirose, A.; Yamaguchi, M.; Tanaka, K.; Chujo, Y. *J. Mater. Chem. C* **2016**, 4, 5564–5571.
790. Laubenstein, R.; Ahrens, M.; Braun, T. *Z. Anorg. Allg. Chem.* **2017**, 643, 1723–1729.
791. Saur, I.; Garcia Alonso, S.; Gornitzka, H.; Lemierre, V.; Chrostowska, A.; Barrau, J. *Organometallics* **2005**, 24, 2988–2996.
792. Cheng, Y.; Dong, D. J.; Hitchcock, P. B.; Lappert, M. F. *Dalton Trans.* **2006**, 4449–4460.
793. Wang, X.; Meng, Y.; Hou, L.; Wang, Y.; Wang, W. *Tetrahedron Lett.* **2021**, 68, 152942.
794. Burford, N.; D'eon, M.; Raggona, P. J.; McDonald, R.; Ferguson, M. J. *Inorg. Chem.* **2004**, 43, 734–738.
795. Solis-Ibarra, D.; Gómora-Figueroa, A. P.; Zavala-Segovia, N.; Jancik, V. *Eur. J. Inorg. Chem.* **2009**, 2009, 4564–4571.
796. Stender, M.; Eichler, B. E.; Hardman, N. J.; Power, P. P.; Prust, J.; Noltemeyer, M.; Roesky, H. W. *Inorg. Chem.* **2001**, 40, 2794–2799.
797. Vidovic, D.; Moore, J. A.; Jones, J. N.; Cowley, A. H. *J. Am. Chem. Soc.* **2005**, 127, 4566–4567.
798. Desat, M. E.; Kretschmer, R. *Inorg. Chem.* **2019**, 58, 16302–16311.
799. Zhu, H.; Chai, J.; He, C.; Bai, G.; Roesky, H. W.; Jancik, V.; Schmidt, H.-G.; Noltemeyer, M. *Organometallics* **2005**, 24, 380–384.
800. Ganesamoorthy, C.; Schoening, J.; Wölper, C.; Song, L.; Schreiner, P. R.; Schulz, S. *Nat. Chem.* **2020**, 12, 608–614.
801. Stender, M.; Power, P. P. *Polyhedron* **2002**, 21, 525–529.
802. Doyle, D. J.; Hitchcock, P. B.; Lappert, M. F.; Li, G. *J. Organomet. Chem.* **2009**, 694, 2611–2617.
803. Räke, B.; Zülch, F.; Ding, Y.; Prust, J.; Roesky, H. W.; Noltemeyer, M.; Schmidt, H.-G. *Z. Anorg. Allg. Chem.* **2001**, 627, 836–840.
804. Saur, I.; Miqueu, K.; Rima, G.; Barrau, J.; Lemierre, V.; Chrostowska, A.; Sotiropoulos, J.-M.; Pfister-Guillouzo, G. *Organometallics* **2003**, 22, 3143–3149.
805. Xiong, Y.; Yao, S.; Driess, M. *Chem. Asian J.* **2012**, 7, 2145–2150.
806. Wang, X.; Liu, J.; Yu, J.; Hou, L.; Sun, W.; Wang, Y.; Chen, S.; Li, A.; Wang, W. *Inorg. Chem.* **2018**, 57, 2969–2972.
807. Chen, M.; Fulton, J. R.; Hitchcock, P. B.; Johnstone, N. C.; Lappert, M. F.; Protchenko, A. V. *Dalton Trans.* **2007**, 2770–2778.
808. Yu, J.; Qin, Y.; Tan, G.; Wang, H.; Cheng, H.; Wang, W.; Li, A. *Inorg. Chem.* **2019**, 58, 5688–5694.
809. Driess, M.; Yao, S.; Brym, M.; van Wüllen, C. *Angew. Chem. Int. Ed.* **2006**, 45, 4349–4352.
810. Pahar, S.; Swamy, V. S. V. S. N.; Das, T.; Gonnade, R. G.; Vanka, K.; Sen, S. S. *Chem. Commun.* **2020**, 56, 11871–11874.
811. Wu, Y.; Liu, L. L.; Su, J.; Yan, K.; Wang, T.; Zhu, J.; Gao, X.; Gao, Y.; Zhao, Y. *Inorg. Chem.* **2015**, 54, 4423–4430.
812. Ding, Y.; Hao, H.; Roesky, H. W.; Noltemeyer, M.; Schmidt, H.-G. *Organometallics* **2001**, 20, 4806–4811.
813. Jana, A.; Schwab, G.; Roesky, H. W.; Stalke, D. *Inorg. Chim. Acta* **2010**, 363, 4408–4410.
814. Woodul, W. D.; Richards, A. F.; Stasch, A.; Driess, M.; Jones, C. *Organometallics* **2010**, 29, 3655–3660.
815. Akkari, A.; Byrne, J. J.; Saur, I.; Rima, G.; Gornitzka, H.; Barrau, J. *J. Organomet. Chem.* **2001**, 622, 190–198.
816. Tam, E. C. Y.; Coles, M. P.; Smith, J. D.; Fulton, J. R. *Polyhedron* **2015**, 85, 284–294.
817. Hitchcock, P. B.; Lappert, M. F.; Li, G.; Protchenko, A. V. *Chem. Commun.* **2009**, 428–429.
818. Hitchcock, P. B.; Lappert, M. F.; Li, G.; Coles, M. P. *Dalton Trans.* **2009**, 7820–7826.
819. Lesikar, L. A.; Richards, A. F. *J. Organomet. Chem.* **2006**, 691, 4250–4256.
820. Hitchcock, P. B.; Lappert, M. F.; Li, G. *Inorg. Chim. Acta* **2010**, 363, 1230–1235.
821. Gyton, M. R.; Leverett, A. R.; Cole, M. L.; McKay, A. I. *Dalton Trans.* **2020**, 49, 5653–5661.
822. Hinz, A.; Schulz, A.; Villinger, A.; Wolter, J.-M. *J. Am. Chem. Soc.* **2015**, 137, 3975–3980.
823. Beweries, T.; Reiß, F.; Rothe, J.; Schulz, A.; Villinger, A. *Eur. J. Inorg. Chem.* **2019**, 2019, 1993–1998.
824. Lego, C.; Neumüller, B. *Z. Anorg. Allg. Chem.* **2011**, 637, 1784–1789.
825. McKay, A. I.; Cole, M. L. *Dalton Trans.* **2019**, 48, 2948–2952.
826. Barrett, A. G. M.; Crimmin, M. R.; Hill, M. S.; Hitchcock, P. B.; Kociok-Köhn, G.; Procopiou, P. A. *Inorg. Chem.* **2008**, 47, 7366–7376.
827. Lee, H. S.; Niemeyer, M. *Inorg. Chem.* **2006**, 45, 6126–6128.
828. Kalden, D.; Kriech, S.; Görls, H.; Westerhausen, M. *Dalton Trans.* **2015**, 44, 8089–8099.
829. Hauber, S.-O.; Lissner, F.; Deacon, G. B.; Niemeyer, M. *Angew. Chem. Int. Ed.* **2005**, 44, 5871–5875.

830. Nimitsiriwat, N.; Gibson, V. C.; Marshall, E. L.; Takolpuckdee, P.; Tomov, A. K.; White, A. J.; Williams, D. J.; Elsegood, M. R.; Dale, S. H. *Inorg. Chem.* **2007**, *46*, 9988–9997.
831. Vinduš, D.; Niemeyer, M. *Inorganics* **2017**, *5*, 33.
832. Lee, H. S.; Hauber, S. O.; Vinduš, D.; Niemeyer, M. *Inorg. Chem.* **2008**, *47*, 4401–4412.
833. Alexander, S. G.; Cole, M. L.; Forsyth, C. M.; Furfari, S. K.; Konstas, K. *Dalton Trans.* **2009**, 2326–2336.
834. Uhl, W.; El-Hamdan, A.; Lawerenz, A. *Eur. J. Inorg. Chem.* **2005**, *2005*, 1056–1062.
835. Flanagan, K. R.; Parish, J. D.; Fox, M. A.; Johnson, A. L. *Inorg. Chem.* **2019**, *58*, 16660–16666.
836. Leverett, A. R.; Diachenko, V.; Cole, M. L.; McKay, A. I. *Dalton Trans.* **2019**, *48*, 13197–13204.
837. Constable, E. C.; Housecroft, C. E. *Aust. J. Chem.* **2020**, *73*, 390–398.
838. Constable, E. C. *Adv. Inorg. Chem.* **2022**, *79*, 105–145.
839. Andrews, P. C.; Duggan, P. J.; Maguire, M.; Nichols, P. J. *Chem. Commun.* **2001**, 53–54.
840. Kennedy, A. R.; Mulvey, R. E.; Urquhart, R. I.; Robertson, S. D. *Dalton Trans.* **2014**, *43*, 14265–14274.
841. Neumann, C.; Seifert, T.; Storch, W.; Vosteen, M.; Wrackmeyer, B. *Angew. Chem. Int. Ed.* **2001**, *40*, 3405–3407.
842. Davidson, M.; Raithby, P.; Johnson, A.; Bolton, P. *Eur. J. Inorg. Chem.* **2003**, *2003*, 3445–3452.
843. Clegg, W. *CSD Communication*, 2016. refcode DEQNIW01.
844. Tagne Kuate, A. C.; Daniliuc, C. G.; Jones, P. G.; Tamm, M. *Eur. J. Inorg. Chem.* **2012**, *2012*, 1727–1733.
845. Clegg, W.; O'Neil, P. A. *CSD Communication*, 2005. refcode SAWXAQ.
846. Jeanneau, E.; Mishra, S.; Hubert-Pfalzgraf, L. G. *Acta Crystallogr.* **2005**, *E61*, m1528–m1530.
847. Graham, D. V.; Hevia, E.; Kennedy, A. R.; Mulvey, R. E.; O'Hara, C. T.; Talmard, C. *Chem. Commun.* **2006**, 417–419.
848. Torvisco, A.; Decker, K.; Uhlig, F.; Ruhlandt-Senge, K. *Inorg. Chem.* **2009**, *48*, 11459–11465.
849. Neumüller, B.; Dehnicke, K. *Z. Anorg. Allg. Chem.* **2005**, *631*, 1029–1031.
850. Yousef, R. I.; Walfort, B.; Rüffer, T.; Wagner, C.; Schmidt, H.; Herzog, R.; Steinborn, D. J. *Organomet. Chem.* **2005**, *690*, 1178–1191.
851. Teng, W.; Guino-o, M.; Hitzbleck, J.; Englich, U.; Ruhlandt-Senge, K. *Inorg. Chem.* **2006**, *45*, 9531–9539.
852. Wiesinger, M.; Maitland, B.; Elsen, H.; Pahl, J.; Harder, S. *Eur. J. Inorg. Chem.* **2019**, *2019*, 4433–4439.
853. Bae, B.-J.; Park, J. T.; Suh, I.-H. *J. Organomet. Chem.* **2002**, *648*, 214–219.
854. Skelton, B. W.; Raston, C. L. *CSD Communication*, 2020. refcode KOLLOM01.
855. Liu, G.-Z.; Zhang, H.-X.; Lin, Z.-E.; Zheng, S.-T.; Zhang, J.; Zhao, J.-T.; Wang, G.-M.; Yang, G.-Y. *Chem. Asian J.* **2007**, *2*, 1230–1239.
856. Kritikos, M.; Ma, G.; Bodor, A.; Glaser, J. *Inorg. Chim. Acta* **2002**, *331*, 224–231.
857. Turner, D. L.; Stone, K. H.; Stephens, P. W.; Walsh, A.; Singh, M. P.; Vaid, T. P. *Inorg. Chem.* **2012**, *51*, 370–376.
858. Marandi, F.; Mirtamizdoust, B.; Soudi, A. A.; Fun, H.-K. *Inorg. Chem. Comm.* **2007**, *10*, 174–177.
859. Thomas, J. R.; Sulway, S. A. *RSC Adv.* **2021**, *11*, 16158–16160.
860. Galka, C. H.; Trosch, D. J. M.; Schubart, M.; Gade, L. H.; Radojevic, S.; Scowen, I. J.; McPartlin, M. *Eur. J. Inorg. Chem.* **2000**, 2577–2583.
861. Zhu, H.; Chen, E. Y.-X. *Organometallics* **2007**, *26*, 5395–5405.
862. Cullinane, J.; Jolleys, A.; Mair, F. S. *Dalton Trans.* **2013**, *42*, 11971–11975.
863. Witterman, L.; van Beek, C. B.; van Veenhuizen, O. N.; Lutz, M.; Moret, M.-E. *Organometallics* **2019**, *38*, 231–239.
864. Gan, X.; Chi, S. M.; Mu, W. H.; Yao, J. C.; Quan, L.; Li, C.; Bian, Z. Y.; Chen, Y.; Fu, W. F. *Dalton Trans.* **2011**, *40*, 7365–7374.
865. Moaven, S.; Andrews, M. C.; Polaske, T. J.; Karl, B. M.; Unruh, D. K.; Bosch, E.; Bowling, N. P.; Cozzolino, A. F. *Inorg. Chem.* **2019**, *58*, 16227–16235.
866. Hernández, L.; Taboada, S.; D'Ornelas, L.; González, T.; Atencio, R. *Acta Crystallogr.* **2004**, *E60*, m979–m981.
867. Chakrabarti, N.; Sattler, W.; Parkin, G. *Polyhedron* **2013**, *58*, 235–246.
868. Álvarez, M.; Álvarez, E.; Fructos, M. R.; Urbano, J.; Pérez, P. J. *Dalton Trans.* **2016**, *45*, 14628–14633.
869. Sambade, D.; Parkin, G. *Polyhedron* **2017**, *125*, 219–229.
870. Bieller, S.; Bolte, M.; Lerner, H.-W.; Wagner, M. *J. Organomet. Chem.* **2005**, *690*, 1935–1946.
871. Dias, H. V. R.; Goh, T. K. H. *Polyhedron* **2004**, *23*, 273–282.
872. King, W. A.; Yap, G. P. A.; Incarvito, C. D.; Rheingold, A. L.; Theopold, K. H. *Inorg. Chim. Acta* **2009**, *362*, 4493–4499.
873. Plasseraud, L.; Cattley, H. *Main Group Metal Chem.* **2020**, *43*, 102–110.
874. Plasseraud, L.; Cattley, H. *Z. Naturforsch.* **2014**, *B69*, 793–798.
875. Joshi, H. K.; Arvin, M. E.; Durivage, J. C.; Gruhn, N. E.; Carducci, M. D.; Westcott, B. L.; Lichtenberger, D. L.; Enemark, J. H. *Polyhedron* **2004**, *23*, 429–438.
876. Naglav, D.; Bläser, D.; Wölper, C.; Schulz, S. *Inorg. Chem.* **2014**, *53*, 1241–1249.
877. Naglav, D.; Tobey, B.; Dzialkowski, K.; Bläser, D.; Wölper, C.; Jansen, G.; Schulz, S. *Dalton Trans.* **2018**, *47*, 12511–12515.
878. Wiederkehr, J.; Wolper, C.; Schulz, S. *CSD Communication*, 2020. refcode IHENER.
879. Ballinas-López, M. G.; Padilla-Martínez, I. I.; Martínez-Martínez, F. J.; Höpfl, H.; García-Báez, E. V. *Acta Crystallogr.* **2006**, *C62*, m132–m135.
880. Marchetti, F.; Pettinari, C.; Pettinari, R.; Skelton, B. W.; White, A. H. *Inorg. Chim. Acta* **2009**, *362*, 4480–4485.
881. Zagermann, J.; Kuchta, M. C.; Merz, K.; Metzler-Nolte, N. *Eur. J. Inorg. Chem.* **2009**, *2009*, 5407–5412.
882. Liebing, P.; Harmgarth, N.; Yang, Y.; McDonald, R.; Engelhardt, F.; Kühling, M.; Edelman, F. T.; Takats, J. *Inorg. Chem.* **2021**, *60*, 1877–1884.
883. Rauch, M.; Ruccolo, S.; Mester, J. P.; Rong, Y.; Parkin, G. *Chem. Sci.* **2016**, *7*, 142–149.
884. Saly, M. J.; Heeg, M. J.; Winter, C. H. *Inorg. Chem.* **2009**, *48*, 5303–5312.
885. Wolf, B. M.; Stuhl, C.; Maichle-Mössmer, C.; Anwander, R. *J. Am. Chem. Soc.* **2018**, *140*, 2373–2383.
886. Harder, S.; Brettar, J. *Angew. Chem. Int. Ed.* **2006**, *45*, 3474–3478.
887. Michel, O.; Dietrich, H. M.; Litlabø, R.; Törnroos, K. W.; Maichle-Mössmer, C.; Anwander, R. *Organometallics* **2012**, *31*, 3119–3127.
888. Wolf, B. M.; Stuhl, C.; Maichle-Mössmer, C.; Anwander, R. *Organometallics* **2019**, *38*, 1614–1621.
889. Chisholm, M. H.; Gallucci, J.; Phomphrai, K. *Chem. Commun.* **2003**, 48–49.
890. Saly, M. J.; Li, J.; Heeg, M. J.; Winter, C. H. *Inorg. Chem.* **2011**, *50*, 7385–7387.
891. Yurkerwich, K.; Parkin, G. *J. Cluster Sci.* **2010**, *21*, 225–234.
892. Yurkerwich, K.; Rong, Y.; Parkin, G. *Acta Crystallogr.* **2013**, *C69*, 963–967.
893. Janiak, C. *Coord. Chem. Rev.* **1997**, *163*, 107–216.
894. Ciunik, Z.; Ruman, T.; Lukaszewicz, M.; Wolowicz, S. *J. Mol. Struct.* **2004**, *690*, 175–180.
895. Rheingold, A. L.; Zakharov, L. N.; Trofimenko, S. *Inorg. Chem.* **2003**, *42*, 827–833.
896. Rheingold, A.; Liable-Sands, L.; Golan, J.; Trofimenko, S. *Eur. J. Inorg. Chem.* **2003**, *2003*, 2767–2773.
897. Rheingold, A. L.; Liable-Sands, L. M.; Golen, J. A.; Yap, G. P. A.; Trofimenko, S. *Dalton Trans.* **2004**, 598–604.
898. Michiue, K.; Jordan, R. F. *Organometallics* **2004**, *23*, 460–470.
899. Fujisawa, K.; Takisawa, H. *Acta Crystallogr.* **2013**, *C69*, 986–989.
900. Filippou, A. C.; Portius, P.; Kociok-Köhn, G.; Albrecht, V. *J. Chem. Soc. Dalton Trans.* **2000**, 1759–1768.
901. Oshiki, T.; Mashima, K.; Kawamura, S.-I.; Tani, K.; Kitaura, K. *Bull. Chem. Soc. Jpn.* **2000**, *73*, 1735–1748.



902. Reger, D. L.; Wright, T. D.; Smith, M. D.; Rheingold, A. L.; Kassel, S.; Concolino, T.; Rhagitan, B. *Polyhedron* **2002**, *21*, 1795–1807.
903. Dodds, C. A.; Kennedy, A. R.; Reglinski, J.; Spicer, M. D. *Inorg. Chem.* **2004**, *43*, 394–395.
904. Balasubramaniam, S.; Kumar, S.; Andrews, A. P.; Varghese, B.; Jemmis, E. D.; Venugopal, A. *Eur. J. Inorg. Chem.* **2019**, *2019*, 3265–3269.
905. Balasubramaniam, S.; Kumar, S.; Andrews, A. P.; Jemmis, E. D.; Venugopal, A. *Eur. J. Inorg. Chem.* **2020**, *2020*, 2530–2536.
906. Khorobkov, I.; Gambarotta, S.; Yap, G. P. A.; Budzelaar, P. H. M. *Organometallics* **2002**, *21*, 3088–3090.
907. Turner, Z. R. *Inorg. Chem.* **2019**, *58*, 14212–14227.
908. Dawkins, M. J. C.; Simonov, A. N.; Jones, C. *Dalton Trans.* **2020**, *49*, 6627–6634.
909. Carter, C.; Kratish, Y.; Jurca, T.; Gao, Y.; Marks, T. J. *J. Am. Chem. Soc.* **2020**, *142*, 18715–18729.
910. Bass, T. M.; Carr, C. R.; Sherbow, T. J.; Fettingner, J. C.; Berben, L. A. *Inorg. Chem.* **2020**, *59*, 13517–13523.
911. Swidan, A.; Binder, J. F.; Onge, B. J. S.; Suter, R.; Burford, N.; Macdonald, C. L. B. *Dalton Trans.* **2019**, *48*, 1284–1291.
912. Liu, S.-G.; Zuo, J.-L.; Li, Y.-Z.; You, X.-Z. *J. Mol. Struct.* **2004**, *705*, 153–157.
913. Jurca, T.; Korobkov, I.; Yap, G. P. A.; Gorelsky, S. I.; Richeson, D. S. *Inorg. Chem.* **2010**, *49*, 10635–10641.
914. Arnold, A.; Sherbow, T. J.; Bohanon, A. M.; Saylor, R. I.; Britt, R. D.; Smith, A. M.; Fettingner, J. C.; Berben, L. A. *Chem. Sci.* **2021**, *12*, 675–682.
915. Arnold, A.; Sherbow, T. J.; Saylor, R. I.; Britt, R. D.; Thompson, E. J.; Muñoz, M. T.; Fettingner, J. C.; Berben, L. A. *J. Am. Chem. Soc.* **2019**, *141*, 15792–15803.
916. Sherbow, T. J.; Fettingner, J. C.; Berben, L. A. *Inorg. Chem.* **2017**, *56*, 8651–8660.
917. Jurca, T.; Dawson, K.; Mallov, I.; Burchell, T.; Yap, G. P.; Richeson, D. S. *Dalton Trans.* **2010**, *39*, 1266–1272.
918. Chu, T.; Belding, L.; van der Est, A.; Dudding, T.; Korobkov, I.; Nikonov, G. I. *Angew. Chem. Int. Ed.* **2014**, *53*, 2711–2715.
919. Singh, A. P.; Roesky, H. W.; Carl, E.; Stalke, D.; Demers, J.-P.; Lange, A. *J. Am. Chem. Soc.* **2012**, *134*, 4998–5003.
920. Magdzinski, E.; Gobbo, P.; Workentin, M. S.; Ragogna, P. J. *Inorg. Chem.* **2013**, *52*, 11311–11319.
921. Bouška, M.; Dostál, L.; Lutter, M.; Glowacki, B.; Ruzickova, Z.; Beck, D.; Jambor, R.; Jurkschat, K. *Inorg. Chem.* **2015**, *54*, 6792–6800.
922. Novák, M.; Bouška, M.; Dostál, L.; Lutter, M.; Jurkschat, K.; Turek, J.; De Proft, F.; Růžicková, Z.; Jambor, R. *Eur. J. Inorg. Chem.* **2017**, *2017*, 1292–1300.
923. Flock, J.; Steller, B.; Unger, P.; Gerke, B.; Pöttgen, R.; Fischer, R. C. *Z. Naturforsch.* **2017**, *B72*, 883–894.
924. Jurca, T.; Hiscock, L. K.; Korobkov, I.; Rowley, C. N.; Richeson, D. S. *Dalton Trans.* **2014**, *43*, 690–697.
925. Wei, L. Q.; Zeng, M. H.; Ng, S. W. *Acta Crystallogr.* **2009**, *E66*, m56.
926. Yu, X.-Y.; Zou, H.-H.; Wei, L.-Q.; Zeng, M.-H. *Inorg. Chem. Comm.* **2010**, *13*, 1137–1139.
927. Barboiu, M.; Dumitru, F.; Legrand, Y. M.; Petit, E.; van der Lee, A. *Chem. Commun.* **2009**, 2192–2194.
928. Reeske, G.; Cowley, A. H. *Chem. Commun.* **2006**, 1784–1786.
929. Martin, C. D.; Le, C. M.; Ragogna, P. J. *J. Am. Chem. Soc.* **2009**, *131*, 15126–15127.
930. Kubiček, V.; Havlíčková, J.; Kotecký, J.; Tircsó, G.; Hermann, P.; Tóth, É.; Lukeš, I. *Inorg. Chem.* **2010**, *49*, 10960–10969.
931. Holub, J.; Meckel, M.; Kubiček, V.; Rösch, F.; Hermann, P. *Contrast Media Mol. Imaging* **2015**, *10*, 122–134.
932. Lemon, C. M.; Brothers, P. J.; Boitrel, B. *Dalton Trans.* **2011**, *40*, 6591–6609.
933. Nyokong, T. *Coord. Chem. Rev.* **2007**, *251*, 1707–1722.
934. Zarrabi, N.; Poddutoori, P. K. *Coord. Chem. Rev.* **2021**, *429*, 213561.
935. Klein, A. In *Spectroelectrochemistry*; Kaim, W., Klein, A., Eds., RSC: Cambridge, 2008; pp 91–122.
936. Tripathy, U.; Steer, R. P. *J. Porphyrins Phthalocyanines* **2007**, *11*, 228–243.
937. Arnold, J. *Porphyrin Handb.* **2000**, *3*, 113–127.
938. Langford, S. J.; Lau, V.-L.; Lee, M. A. P.; Lygris, E. *J. Porphyrins Phthalocyanines* **2002**, *6*, 748–756.
939. Langer, J.; Al-Shboul, T. M. A.; Younis, F. M.; Görls, H.; Westerhausen, M. *Eur. J. Inorg. Chem.* **2011**, *2011*, 3002–3007.
940. Park, J. W.; Kim, J. T.; Koo, S. M.; Kim, C. G.; Kim, Y. S. *Polyhedron* **2000**, *19*, 2547–2555.
941. Osseili, H.; Mukherjee, D.; Spaniol, T. P.; Okuda, J. *Chem. A Eur. J.* **2017**, *23*, 14292–14298.
942. Schuhknecht, D.; Leich, V.; Spaniol, T. P.; Okuda, J. *Chem. A Eur. J.* **2018**, *24*, 13424–13427.
943. Osseili, H.; Truong, K. N.; Spaniol, T. P.; Mukherjee, D.; Englert, U.; Okuda, J. *Chem. A Eur. J.* **2017**, *23*, 17213–17216.
944. Standfuss, S.; Spaniol, T. P.; Okuda, J. *Eur. J. Inorg. Chem.* **2010**, *2010*, 2987–2991.
945. Schettini, R.; D'Amato, A.; Pierri, G.; Tedesco, C.; Della Sala, G.; Motta, O.; Izzo, I.; De Riccardis, F. *Org. Lett.* **2019**, *21*, 7365–7369.
946. Dyke, J.; Levason, W.; Light, M. E.; Pugh, D.; Reid, G.; Bhakhoa, H.; Ramasami, P.; Rhyman, L. *Dalton Trans.* **2015**, *44*, 13853–13866.
947. Lemmerz, L. E.; Mukherjee, D.; Spaniol, T. P.; Wong, A.; Ménard, G.; Maron, L.; Okuda, J. *Chem. Commun.* **2019**, *55*, 3199–3202.
948. Lemmerz, L. E.; Wong, A.; Ménard, G.; Spaniol, T. P.; Okuda, J. *Polyhedron* **2020**, *178*, 114331.
949. Buffet, J.-C.; Davin, J. P.; Spaniol, T. P.; Okuda, J. *New J. Chem.* **2011**, *35*, 2253–2257.
950. Schuhknecht, D.; Spaniol, T. P.; Yang, Y.; Maron, L.; Okuda, J. *Inorg. Chem.* **2020**, *59*, 9406–9415.
951. Jochmann, P.; Davin, J. P.; Spaniol, T. P.; Maron, L.; Okuda, J. *Angew. Chem. Int. Ed.* **2012**, *51*, 4452–4455.
952. Mukherjee, D.; Höllner, T.; Leich, V.; Spaniol, T. P.; Englert, U.; Maron, L.; Okuda, J. *J. Am. Chem. Soc.* **2018**, *140*, 3403–3411.
953. Leich, V.; Spaniol, T. P.; Maron, L.; Okuda, J. *Angew. Chem. Int. Ed.* **2016**, *55*, 4794–4797.
954. Höllner, T.; Schuhknecht, D.; Mistry, A.; Spaniol, T. P.; Yang, Y.; Maron, L.; Okuda, J. *Chem. A Eur. J.* **2021**, *27*, 3002–3007.
955. Mukherjee, D.; Shirase, S.; Beckerle, K.; Spaniol, T. P.; Mashima, K.; Okuda, J. *Dalton Trans.* **2017**, *46*, 8451–8457.
956. Connolly, E. A.; Leeland, J. W.; Love, J. B. *Inorg. Chem.* **2016**, *55*, 840–847.
957. Wang, N.; Lei, H.; Zhang, Z.; Li, J.; Zhang, W.; Cao, R. *Chem. Sci.* **2019**, *10*, 2308–2314.
958. Mukherjee, D.; Osseili, H.; Truong, K.-N.; Spaniol, T. P.; Okuda, J. *Chem. Commun.* **2017**, *53*, 3493–3496.
959. Barnard, P. J.; Holland, J. P.; Bayly, S. R.; Wadas, T. J.; Anderson, C. J.; Dilworth, J. R. *Inorg. Chem.* **2009**, *48*, 7117–7126.
960. Everett, M.; Jolleys, A.; Levason, W.; Light, M. E.; Pugh, D.; Reid, G. *Dalton Trans.* **2015**, *44*, 20898–20905.
961. Correia, B. B.; Brown, T. R.; Reibenspies, J. H.; Lee, H.; Hancock, R. D. *Eur. J. Inorg. Chem.* **2018**, *2018*, 3736–3747.
962. Koppour, H.; Khanmohammadi, H.; Wainwright, K. P.; Taylor, M. R. *Inorg. Chim. Acta* **2004**, *357*, 1283–1291.
963. Masaki, H.; Miyake, H.; Shinoda, S.; Tsukube, H. *Inorg. Chem.* **2009**, *48*, 11921–11928.
964. Khanmohammadi, H.; Amani, S.; Lang, H.; Rüeffer, T. *Inorg. Chim. Acta* **2007**, *360*, 579–587.
965. Botana, L.; Bastida, R.; Macías, A.; Pérez-Lourido, P.; Valencia, L. *Inorg. Chem. Comm.* **2009**, *12*, 249–251.
966. Liberato, A.; Aguinaco, A.; Clares, M. P.; Delgado-Pinar, E.; Pitarch-Jarque, J.; Blasco, S.; Basallote, M. G.; García-España, E.; Verdejo, B. *Dalton Trans.* **2017**, *46*, 6645–6653.
967. Ito, H.; Tsukube, H.; Shinoda, S. *Chem. A Eur. J.* **2013**, *19*, 3330–3339.
968. Marnett, M.; Aragoni, M. C.; Arca, M.; Atzori, M.; Bencini, A.; Bazzicalupi, C.; Blake, A. J.; Caltagirone, C.; Devillanova, F. A.; Garau, A.; Hursthouse, M. B.; Isaia, F.; Lippolis, V.; Valtancoli, B. *Inorg. Chem.* **2009**, *48*, 9236–9249.
969. Dye, J. L.; Redko, M. Y.; Huang, R. H.; Jackson, J. E. *Prog. Inorg. Chem.* **2007**, *59*, 205–231.
970. Redko, M. Y.; Huang, R. H.; Jackson, J. E.; Harrison, J. F.; Dye, J. L. *J. Am. Chem. Soc.* **2003**, *125*, 2259–2263.
971. Brown, A.; Bunchuay, T.; Crane, C. G.; White, N. G.; Thompson, A. L.; Beer, P. D. *Chem. A Eur. J.* **2018**, *24*, 10434–10442.
972. Gerus, A.; Ślepokura, K.; Panek, J.; Turek, A.; Lisowski, J. *J. Org. Chem.* **2018**, *83*, 6748–6753.

973. Dornhaus, F.; Scholz, S.; Sanger, I.; Bolte, M.; Wagner, M.; Lerner, H.-W. *Z. Anorg. Allg. Chem.* **2009**, *635*, 2263–2272.
974. Mayo, D. H.; Peng, Y.; Zavali, P.; Bowen, K. H.; Eichhorn, B. W. *Acta Crystallogr.* **2012**, *E68*, m1245.
975. Baker, R.; Bettenrup, H.; Jones, C. *Eur. J. Inorg. Chem.* **2003**, *2003*, 2446–2451.
976. Dornhaus, F.; Lerner, H.-W.; Bolte, M. *Acta Crystallogr.* **2007**, *E63*, o4917.
977. Tinnemans, P.; Accordini, P. *CSD Communication*, 2019. refcode NIQSEM01.
978. Jones, P. G.; Daniliuc, C. G.; du Mont, W.-W. *CSD Communication*, 2015. refcode DUDRAX.
979. Sukhov, B. G.; Gusarova, N. K.; Ivanova, N. I.; Bogdanova, M. V.; Kazheva, O. N.; Aleksandrov, G. G.; D'yachenko, O. A.; Sinegovskaya, L. M.; Malysheva, S. F.; Trofimov, B. A. *J. Struct. Chem.* **2005**, *46*, 1066–1071.
980. Buchner, M. R.; Muller, M.; Rudel, S. S. *Angew. Chem. Int. Ed.* **2017**, *56*, 1130–1134.
981. Paparo, A.; Matthews, A. J. R.; Smith, C. D.; Edwards, A. J.; Yuvaraj, K.; Jones, C. *Dalton Trans.* **2021**, *50*, 7604–7609.
982. Frenking, G.; Holzmann, N.; Neumuller, B.; Dehnicke, K. *Z. Anorg. Allg. Chem.* **2010**, *636*, 1772–1775.
983. Burt, J.; Levason, W.; Light, M. E.; Reid, G. *Dalton Trans.* **2014**, *43*, 14600–14611.
984. Chen, F.; Ma, G.; Bernard, G. M.; Cavell, R. G.; McDonald, R.; Ferguson, M. J.; Wasylishen, R. E. *J. Am. Chem. Soc.* **2010**, *132*, 5479–5493.
985. Slattery, J.; Higelin, A.; Bayer, T.; Krossing, I. *Angew. Chem. Int. Ed.* **2010**, *49*, 3228–3231.
986. Higelin, A.; Sachs, U.; Keller, S.; Krossing, I. *Chem. A Eur. J.* **2012**, *18*, 10029–10034.
987. Cole, M. L.; Hibbs, D. E.; Jones, C.; Smithies, N. A. *J. Chem. Soc. Dalton Trans.* **2000**, 545–550.
988. Davis, M. F.; Clarke, M.; Levason, W.; Reid, G.; Webster, M. *Eur. J. Inorg. Chem.* **2006**, *2006*, 2773–2782.
989. MacDonald, E.; Doyle, L.; Chitnis, S. S.; Werner-Zwanziger, U.; Burford, N.; Decken, A. *Chem. Commun.* **2012**, *48*, 7922–7924.
990. Greenacre, V. K.; King, R. P.; Levason, W.; Reid, G. *Dalton Trans.* **2019**, *48*, 17097–17105.
991. King, R. P.; Greenacre, V. K.; Levason, W.; Dyke, J. M.; Reid, G. *Inorg. Chem.* **2021**, *60*, 12100–12108.
992. Parsons, S.; Resouly, S.; Bailey, P.; Oswald, I.; Johnstone, R. *CSD Communication*, 2006. refcode RELKOJ.
993. Hu, C. T.; Liu, Y.; Ward, M. D. *CSD Communication*, 2020. refcode ZOYQUC.
994. Hu, C. T.; Liu, Y.; Ward, M. D. *CSD Communication*, 2020. refcode ZUBWIF.
995. Zhou, J.; Liu, L. L.; Cao, L. L.; Stephan, D. W. *Angew. Chem. Int. Ed.* **2019**, *58*, 5407–5412.
996. Chitnis, S. S.; Robertson, A. P. M.; Burford, N.; Patrick, B. O.; McDonald, R.; Ferguson, M. J. *Chem. Sci.* **2015**, *6*, 6545–6555.
997. Chitnis, S. S.; Peters, B.; Conrad, E.; Burford, N.; McDonald, R.; Ferguson, M. J. *Chem. Commun.* **2011**, *47*, 12331–12333.
998. Chitnis, S. S.; Carpenter, Y. Y.; Burford, N.; McDonald, R.; Ferguson, M. J. *Angew. Chem. Int. Ed.* **2013**, *52*, 4863–4866.
999. Chitnis, S. S.; Burford, N.; Weigand, J. J.; McDonald, R. *Angew. Chem. Int. Ed.* **2015**, *54*, 7828–7832.
1000. Izod, K.; Evans, P.; Waddell, P. G. *Dalton Trans.* **2017**, *46*, 13824–13834.
1001. Izod, K.; Stewart, J.; Clark, E. R.; Clegg, W.; Harrington, R. W. *Inorg. Chem.* **2010**, *49*, 4698–4707.
1002. Rivard, E.; Sutton, A. D.; Fettingler, J. C.; Power, P. P. *Inorg. Chim. Acta* **2007**, *360*, 1278–1286.
1003. Izod, K.; Evans, P.; Downie, T. H.; McFarlane, W.; Waddell, P. G. *Inorg. Chem.* **2018**, *57*, 14733–14747.
1004. Xu, M.; Jupp, A. R.; Stephan, D. W. *Angew. Chem. Int. Ed.* **2019**, *58*, 3548–3552.
1005. Avent, A. G.; Bonafoux, D.; Eaborn, C.; Hill, M. S.; Hitchcock, P. B.; Smith, J. D. *J. Chem. Soc. Dalton Trans.* **2000**, 2183–2190.
1006. Crimmin, M. R.; Barrett, A. G. M.; Hill, M. S.; Hitchcock, P. B.; Procopiou, P. A. *Inorg. Chem.* **2007**, *46*, 10410–10415.
1007. Gartner, M.; Gorls, H.; Westerhausen, M. *Z. Anorg. Allg. Chem.* **2007**, *633*, 2025–2031.
1008. Westerhausen, M.; Krofta, M.; Mayer, P. *Z. Anorg. Allg. Chem.* **2000**, *626*, 2307–2312.
1009. Westerhausen, M.; Birg, C.; Krofta, M.; Mayer, P.; Seifert, T.; Noth, H.; Pfitzner, A.; Nilges, T.; Deiseroth, H.-J. *Z. Anorg. Allg. Chem.* **2000**, *626*, 1073–1080.
1010. Gartner, M.; Gorls, H.; Westerhausen, M. *Inorg. Chem.* **2008**, *47*, 1397–1405.
1011. Lerner, H.-W.; Sanger, I.; Schodel, F.; Bolte, M.; Wagner, M. *Z. Naturforsch.* **2011**, *B66*, 695–699.
1012. Henke, P.; Pankewitz, T.; Klopper, W.; Breher, F.; Schnockel, H. *Angew. Chem. Int. Ed.* **2009**, *48*, 8141–8145.
1013. Hartig, J.; Steiner, J.; Stosser, A.; Schnockel, H. *Chem. A Eur. J.* **2007**, *13*, 4475–4482.
1014. Henke, P.; Schnockel, H. *Chem. A Eur. J.* **2009**, *15*, 13391–13398.
1015. Mayo, D. H.; Peng, Y.; DeCarlo, S.; Li, X.; Lightstone, J.; Zavali, P.; Bowen, K.; Schnockel, H.; Eichhorn, B. *Z. Anorg. Allg. Chem.* **2013**, *639*, 2558–2560.
1016. Steiner, J.; Stosser, G.; Schnockel, H. *Angew. Chem. Int. Ed.* **2004**, *43*, 302–305.
1017. Steiner, J.; Stosser, G.; Schnockel, H. *Z. Anorg. Allg. Chem.* **2004**, *630*, 1879–1882.
1018. Steiner, J.; Schnockel, H. *Chem. A Eur. J.* **2006**, *12*, 5429–5433.
1019. Steiner, J.; Stosser, G.; Schnockel, H. *Angew. Chem. Int. Ed.* **2003**, *42*, 1971–1974.
1020. Steiner, J.; Stosser, G.; Schnockel, H. *Angew. Chem. Int. Ed.* **2004**, *43*, 6549–6552.
1021. Henke, P.; Huber, M.; Steiner, J.; Bowen, K.; Eichhorn, B.; Schnockel, H. *J. Am. Chem. Soc.* **2009**, *131*, 5698–5704.
1022. Geitner, F. S.; Dums, J. V.; Fassler, T. F. *J. Am. Chem. Soc.* **2017**, *139*, 11933–11940.
1023. Wallach, C.; Geitner, F. S.; Klein, W.; Fassler, T. F. *Chem. A Eur. J.* **2019**, *25*, 12349–12356.
1024. West, J. K.; Stahl, L. *Inorg. Chem.* **2017**, *56*, 12728–12738.
1025. Izod, K.; Rayner, D. G.; El-Hamruni, S. M.; Harrington, R. W.; Baisch, U. *Angew. Chem. Int. Ed.* **2014**, *53*, 3636–3640.
1026. Izod, K.; Evans, P.; Waddell, P. G.; Probert, M. R. *Inorg. Chem.* **2016**, *55*, 10510–10522.
1027. Izod, K.; Evans, P.; Waddell, P. G. *Inorg. Chem.* **2020**, *59*, 863–874.
1028. Izod, K.; Evans, P.; Waddell, P. G. *Angew. Chem. Int. Ed.* **2019**, *58*, 11007–11012.
1029. Crimmin, M. R.; Barrett, A. G. M.; Hill, M. S.; Hitchcock, P. B.; Procopiou, P. A. *Organometallics* **2007**, *26*, 2953–2956.
1030. Taylor, M. J.; Coles, M. P.; Fulton, J. R. *Aust. J. Chem.* **2015**, *68*, 635–640.
1031. Chu, T.; Korobkov, I.; Nikonov, G. I. *J. Am. Chem. Soc.* **2014**, *136*, 9195–9202.
1032. Yang, Y.; Zhao, N.; Wu, Y.; Zhu, H.; Roesky, H. W. *Inorg. Chem.* **2012**, *51*, 2425–2431.
1033. Tam, E. C.; Maynard, N. A.; Apperley, D. C.; Smith, J. D.; Coles, M. P.; Fulton, J. R. *Inorg. Chem.* **2012**, *51*, 9403–9415.
1034. Tam, E. C.; Harris, L. M.; Borren, E. S.; Smith, J. D.; Lein, M.; Coles, M. P.; Fulton, J. R. *Chem. Commun.* **2013**, *49*, 10278–10280.
1035. Harris, L. M.; Tam, E. C.; Cummins, S. J.; Coles, M. P.; Fulton, J. R. *Inorg. Chem.* **2017**, *56*, 3087–3094.
1036. Becker, G.; Schwarz, W.; Seidler, N.; Westerhausen, M. *Z. Anorg. Allg. Chem.* **1992**, *612*, 72–82.
1037. Becker, G.; Hubler, K. *Z. Anorg. Allg. Chem.* **1994**, *620*, 405–417.
1038. Hennersdorf, F.; Frotchel, J.; Weigand, J. J. *J. Am. Chem. Soc.* **2017**, *139*, 14592–14604.
1039. Puschmann, F. F.; Stein, D.; Heift, D.; Hendriksen, C.; Gal, Z. A.; Grutzmacher, H. F.; Grutzmacher, H. *Angew. Chem. Int. Ed.* **2011**, *50*, 8420–8423.
1040. Gilliard, R. J.; Heift, D.; Benko, Z.; Keiser, J. M.; Rheingold, A. L.; Grutzmacher, H.; Protasiewicz, J. D. *Dalton Trans.* **2018**, *47*, 666–669.
1041. Jupp, A. R.; Goicoechea, J. M. *Angew. Chem. Int. Ed.* **2013**, *52*, 10064–10067.
1042. Jupp, A. R.; Geeson, M. B.; McGrady, J. E.; Goicoechea, J. M. *Eur. J. Inorg. Chem.* **2016**, *2016*, 639–648.
1043. Mei, Y.; Borger, J. E.; Wu, D. J.; Grutzmacher, H. *Dalton Trans.* **2019**, *48*, 4370–4374.
1044. Do, D. C. H.; Protchenko, A. V.; Vasko, P.; Campos, J.; Kolychev, E. L.; Aldridge, S. *Z. Anorg. Allg. Chem.* **2018**, *644*, 1238–1242.

1045. Bestgen, S.; Mehta, M.; Johnstone, T. C.; Roesky, P. W.; Goicoechea, J. M. *Chem. A Eur. J.* **2020**, *26*, 9024–9031.
1046. Mehta, M.; McGrady, J. E.; Goicoechea, J. M. *Chem. A Eur. J.* **2019**, *25*, 5445–5450.
1047. Hinz, A.; Goicoechea, J. M. *Chem. A Eur. J.* **2018**, *24*, 7358–7363.
1048. Yao, S.; Xiong, Y.; Szilvási, T.; Grützmacher, H.; Driess, M. *Angew. Chem. Int. Ed.* **2016**, *55*, 4781–4785.
1049. Wilson, D. W. N.; Myers, W. K.; Goicoechea, J. M. *Dalton Trans.* **2020**, *49*, 15249–15255.
1050. Coles, M. P. *Reference Module in Chemistry, Molecular Sciences and Chemical Engineering*, 2021, Elsevier.
1051. Waterman, R. *Dalton Trans.* **2016**, *45*, 1801–1803.
1052. Scheer, M.; Balázs, G.; Seitz, A. *Chem. Rev.* **2010**, *110*, 4236–4256.
1053. Sarkar, D.; Weetman, C.; Munz, D.; Inoue, S. *Angew. Chem. Int. Ed.* **2021**, *60*, 3519–3523.
1054. Graham, C. M. E.; Macdonald, C. L. B.; Power, P. P.; Brown, Z. D.; Ragogna, P. J. *Inorg. Chem.* **2017**, *56*, 9111–9119.
1055. Dube, J. W.; Graham, C. M.; Macdonald, C. L.; Brown, Z. D.; Power, P. P.; Ragogna, P. J. *Chem. A Eur. J.* **2014**, *20*, 6739–6744.
1056. Sänger, I.; Breunig, J.; Schödel, F.; Bolte, M.; Lerner, H.-W. *Z. Naturforsch.* **2016**, *B71*, 135–139.
1057. Lerner, H.; Margraf, G.; Kaufmann, L.; Bats, J. W.; Bolte, M.; Wagner, M. *Eur. J. Inorg. Chem.* **2005**, *2005*, 1932–1939.
1058. Hennesdorf, F.; Weigand, J. *Angew. Chem. Int. Ed.* **2017**, *56*, 7858–7862.
1059. Fox, A. R.; Wright, R. J.; Rivard, E.; Power, P. P. *Angew. Chem. Int. Ed.* **2005**, *44*, 7729–7733.
1060. Schwamm, R. J.; Lein, M.; Coles, M. P.; Fitchett, C. M. *Angew. Chem. Int. Ed.* **2016**, *55*, 14798–14801.
1061. Carravetta, M.; Concistre, M.; Levason, W.; Reid, G.; Zhang, W. *Chem. Commun.* **2015**, *51*, 9555–9558.
1062. Issleib, K.; Abicht, H. P. *J. Prakt. Chem.* **1970**, *312*, 456–465.
1063. Izod, K.; Wills, C.; Anderson, E.; Harrington, R. W.; Probert, M. R. *Organometallics* **2014**, *33*, 5283–5294.
1064. Langer, J.; Wimmer, K.; Görls, H.; Westerhausen, M. *Dalton Trans.* **2009**, 2951–2957.
1065. Langer, J.; Fabra, M. J.; García-Orduña, P.; Lahoz, F. J.; Görls, H.; Oro, L. A.; Westerhausen, M. *Dalton Trans.* **2010**, *39*, 7813–7821.
1066. Langer, J.; Geitner, R.; Görls, H. *Eur. J. Inorg. Chem.* **2014**, *2014*, 1413–1420.
1067. Gray, P. A.; Saville, J. W.; Krause, K. D.; Burford, N.; McDonald, R.; Ferguson, M. J. *Can. J. Chem.* **2017**, *95*, 346–350.
1068. Cheng, F.; Hector, A. L.; Levason, W.; Reid, G.; Webster, M.; Zhang, W. *Inorg. Chem.* **2007**, *46*, 7215–7223.
1069. Cheng, F.; Friend, S. I.; Hector, A. L.; Levason, W.; Reid, G.; Webster, M.; Zhang, W. *Inorg. Chem.* **2008**, *47*, 9691–9700.
1070. Davis, M. F.; Levason, W.; Reid, G.; Webster, M. *Dalton Trans.* **2008**, 2261–2269.
1071. Ebrahim, M. M.; Stoeckli-Evans, H.; Panchanatheswaran, K. *J. Organomet. Chem.* **2007**, *692*, 2168–2174.
1072. Cheng, F.; Hector, A. L.; Levason, W.; Reid, G.; Webster, M.; Zhang, W. *Inorg. Chem.* **2010**, *49*, 752–760.
1073. Béland, V. A.; Wang, Z.; Macdonald, C. L. B.; Sham, T. K.; Ragogna, P. J. *Chem. A Eur. J.* **2019**, *25*, 14790–14800.
1074. Gurnani, C.; Hector, A. L.; Jager, E.; Levason, W.; Pugh, D.; Reid, G. *Dalton Trans.* **2013**, *42*, 8364–8374.
1075. Burt, J.; Grantham, W.; Levason, W.; Reid, G. *Dalton Trans.* **2015**, *44*, 11533–11541.
1076. Chitnis, S. S.; Vos, K. A.; Burford, N.; McDonald, R.; Ferguson, M. J. *Chem. Commun.* **2016**, *52*, 685–688.
1077. Chitnis, S. S.; Burford, N.; Decken, A.; Ferguson, M. J. *Inorg. Chem.* **2013**, *52*, 7242–7248.
1078. Dube, J. W.; Hänninen, M. M.; Dutton, J. L.; Tuononen, H. M.; Ragogna, P. J. *Inorg. Chem.* **2012**, *51*, 8897–8903.
1079. Lerner, H.-W.; Bolte, M.; Karaghiosoff, K.; Wagner, M. *Organometallics* **2004**, *23*, 6073–6076.
1080. Lerner, H.-W.; Sänger, I.; Schödel, F.; Lorbach, A.; Bolte, M.; Wagner, M. *Dalton Trans.* **2008**, 787–792.
1081. Styra, S.; Radius, M.; Moos, E.; Bihlmeier, A.; Breher, F. *Chem. A Eur. J.* **2016**, *22*, 9508–9512.
1082. Rosa, P.; Mezañiles, N.; Ricard, L.; Mathey, F.; Le Floch, P. *Angew. Chem. Int. Ed.* **2001**, *40*, 4476–4479.
1083. Shapiro, I. R.; Jenkins, D. M.; Thomas, J. C.; Day, M. W.; Peters, J. C. *Chem. Commun.* **2001**, 2152–2153.
1084. Betley, T. A.; Peters, J. C. *Inorg. Chem.* **2003**, *42*, 5074–5084.
1085. Fischer, P. J.; Senthil, S.; Stephan, J. T.; Swift, M. L.; Storie, M. D.; Chan, E. T.; Vollmer, M. V.; Young, V. G. *Dalton Trans.* **2018**, *47*, 6166–6176.
1086. Arenas, I.; Fuentes, M.Á.; Alvarez, E.; Díaz, Y.; Caballero, A.; Castellón, S.; Pérez, P. J. *Inorg. Chem.* **2014**, *53*, 3991–3999.
1087. Conrad, E.; Pickup, J.; Burford, N.; McDonald, R.; Ferguson, M. J. *Can. J. Chem.* **2010**, *88*, 797–803.
1088. Cairns, K. R.; Greenacre, V. K.; Grose, L. A.; Levason, W.; Reid, G.; Robinson, F. J. *Organomet. Chem.* **2020**, *912*, 121176.
1089. Kraft, A.; Possart, J.; Scherer, H.; Beck, J.; Himmel, D.; Krossing, I. *Eur. J. Inorg. Chem.* **2013**, *2013*, 3054–3062.
1090. Cheng, F.; Hector, A. L.; Levason, W.; Reid, G.; Webster, M.; Zhang, W. *Dalton Trans.* **2007**, 2207–2210.
1091. Mahon, M. F.; Moldovan, N. L.; Molloy, K. C.; Muresan, A.; Silaghi-Dumitrescu, I.; Silaghi-Dumitrescu, L. *Dalton Trans.* **2004**, 4017–4021.
1092. Conrad, E.; Burford, N.; McDonald, R.; Ferguson, M. J. *J. Am. Chem. Soc.* **2009**, *131*, 5066–5067.
1093. Izod, K.; Evans, P.; Waddell, P. G. *Chem. Commun.* **2018**, *54*, 2526–2529.
1094. Chen, X.; Simler, T.; Yadav, R.; Garner, M. T.; Köppe, R.; Roesky, P. W. *Chem. Commun.* **2019**, *55*, 9315–9318.
1095. Yao, S.; Grossheim, Y.; Kostenko, A.; Ballester-Martinez, E.; Schutte, S.; Bispinghoff, M.; Grützmacher, H.; Driess, M. *Angew. Chem. Int. Ed.* **2017**, *56*, 7465–7469.
1096. Hinz, A.; Goicoechea, J. M. *Angew. Chem. Int. Ed.* **2016**, *55*, 15515–15519.
1097. Genge, A. R. J.; Hill, N. J.; Levason, W.; Reid, G. *J. Chem. Soc. Dalton Trans.* **2001**, 1007–1012.
1098. Heeg, M. J.; Kudrat, M.; Winter, C. H. *CSD Communication*, 2010. refcode DAFYUG.
1099. Hering, C.; Lehmann, M.; Schulz, A.; Villinger, A. *Inorg. Chem.* **2012**, *51*, 8212–8224.
1100. Greenacre, V. K.; Levason, W.; Reid, G. *Organometallics* **2018**, *37*, 2123–2135.
1101. Ganesamoorthy, C.; Bläser, D.; Wölper, C.; Schulz, S. *Angew. Chem. Int. Ed.* **2014**, *53*, 11587–11591.
1102. Ganesamoorthy, C.; Krüger, J.; Glöckler, E.; Helling, C.; John, L.; Frank, W.; Wölper, C.; Schulz, S. *Inorg. Chem.* **2018**, *57*, 9495–9503.
1103. Rajković, S.; Živković, M. D.; Waržajtis, B.; Rychlewska, U.; Djuran, M. I. *Polyhedron* **2016**, *117*, 367–376.
1104. Raabe, I.; Wagner, K.; Santiso-Quiñones, G.; Krossing, I. *Z. Anorg. Allg. Chem.* **2009**, *635*, 513–517.
1105. Loiseau, T.; Beitone, L.; Huguenard, C.; Taulelle, F.; Henry, M.; Férey, G. *J. Phys. Chem. B* **2004**, *108*, 20011–20019.
1106. Kirillova, M. V.; Kirillov, A. M.; Martins, A. N.; Graiff, C.; Tiripicchio, A.; Pombeiro, A. J. *Inorg. Chem.* **2012**, *51*, 5224–5234.
1107. Imada, Y.; Nakano, H.; Furukawa, K.; Kishi, R.; Nakano, M.; Maruyama, H.; Nakamoto, M.; Sekiguchi, A.; Ogawa, M.; Ohta, T.; Yamamoto, Y. *J. Am. Chem. Soc.* **2016**, *138*, 479–482.
1108. Steyl, G. *Acta Crystallogr.* **2007**, *E63*, m2343.
1109. Jassal, A. K.; Sran, B. S.; Mandal, K.; Mukhopadhyay, P.; Hundal, G. *Cryst. Growth Des.* **2018**, *18*, 4737–4748.
1110. Quarez, É.; Deunf, É.; Cadiou, V.; Gutel, T.; Boucher, F.; Guyomard, D.; Dolhem, F.; Poizot, P. *CrstEngComm* **2017**, *19*, 6787–6796.
1111. Carreras, L.; Rovira, L.; Vaquero, M.; Mon, I.; Martin, E.; Benet-Buchholz, J.; Vidal-Ferran, A. *RSC Adv.* **2017**, *7*, 32833–32841.
1112. Srivastava, A. K.; Vijayakanth, T.; Divya, P.; Praveenkumar, B.; Steiner, A.; Boomishankar, R. *J. Mater. Chem. C* **2017**, *5*, 7352–7359.
1113. Ge, Z.-Y.; Zhu, Z.-B.; Deng, Z.-P.; Huo, L.-H.; Gao, S. *CrstEngComm* **2018**, *20*, 2968–2979.
1114. Hou, Y.; Rodríguez, M. A.; Nyman, M. *Cryst. Growth Des.* **2012**, *12*, 1422–1431.
1115. Srinivasan, B. R.; Shetgaonkar, S. Y.; Dhavskar, K. T.; Sundar, J. K.; Natarajan, S. *Indian J. Chem.* **2012**, *A51*, 564–570.
1116. Drukenmüller, I. E.; Klapötke, T. M.; Morgenstern, Y.; Rusan, M.; Stierstorfer, J. *Z. Anorg. Allg. Chem.* **2014**, *640*, 2139–2148.

1117. Dash, S. P.; Panda, A. K.; Pasayat, S.; Dinda, R.; Biswas, A.; Tiekink, E. R.; Patil, Y. P.; Nethaji, M.; Kaminsky, W.; Mukhopadhyay, S.; Bhutia, S. K. *Dalton Trans.* **2014**, *43*, 10139–10156.
1118. Heczko, M.; Sumińska, E.; Sieklucka, B.; Nowicka, B. *CrstEngComm* **2019**, *21*, 5067–5075.
1119. Xu, Y.; Gao, Y.; Wei, W.; Wang, Z.; Li, S.; Hu, C. *Dalton Trans.* **2013**, *42*, 5228–5231.
1120. Sabaté, C. M.; Delalu, H.; Jeanneau, E. *Chem. Asian J.* **2012**, *7*, 1085–1095.
1121. Bailey, P. J.; Lanfranchi, M.; Marchiò, L.; Parsons, S. *Inorg. Chem.* **2001**, *40*, 5030–5035.
1122. Somov, N. V.; Chausov, F. F.; Lomova, N. V.; Vorobyov, V. L.; Zakirova, R. M.; Petrov, V. G.; Shumilova, M. A.; Zhiro, D. K. *J. Struct. Chem.* **2019**, *60*, 1385–1395.
1123. Philippopoulos, A. I.; Terzis, A.; Raptopoulou, C. P.; Catalano, V. J.; Falaras, P. *Eur. J. Inorg. Chem.* **2007**, *2007*, 5633–5644.
1124. Benetollo, F.; Bombieri, G.; Calabi, L.; Aime, S.; Botta, M. *Inorg. Chem.* **2003**, *42*, 148–157.
1125. Gerasimchuk, N. N.; Dalley, N. K. *J. Coord. Chem.* **2004**, *57*, 1431–1445.
1126. Salcedo, I. R.; Colodrero, R. M. P.; Bazaga-García, M.; Vasileiou, A.; Papadaki, M.; Olivera-Pastor, P.; Infantes-Molina, A.; Losilla, E. R.; Mezei, G.; Cabeza, A.; Demadis, K. D. *CrstEngComm* **2018**, *20*, 7648–7658.
1127. Guo, L.-Y.; Zeng, S.-Y.; Jagličić, Z.; Hu, Q.-D.; Wang, S.-X.; Wang, Z.; Sun, D. *Inorg. Chem.* **2016**, *55*, 9006–9011.
1128. Li, G. B.; Yang, S. H.; Xiong, M.; Lin, J. H. *Acta Crystallogr.* **2004**, *C60*, m612–m614.
1129. Al-Fayaad, H. A.; Arachchige, K. S. A.; Clegg, J. K. *CrstEngComm* **2020**, *22*, 5310–5315.
1130. Konieczny, K.; Bgkowicz, J.; Turowska-Tyrk, I. *Acta Crystallogr.* **2015**, *C71*, 410–414.
1131. Li, Z.; Zhang, J.; Lin, L. D.; Liu, J. H.; Li, X. X.; Zheng, S. T. *Chem. Commun.* **2019**, *55*, 11735–11738.
1132. King, P.; Clérac, R.; Anson, C. E.; Powell, A. K. *Dalton Trans.* **2004**, 852–861.
1133. Miyamoto, K.; Saito, M.; Tsuji, S.; Takagi, T.; Shiro, M.; Uchiyama, M.; Ochiai, M. *J. Am. Chem. Soc.* **2021**, *143*, 9327–9331.
1134. Angeloski, A.; Hook, J. M.; Bhabhade, M.; Baker, A. T.; McDonagh, A. M. *CrstEngComm* **2016**, *18*, 7070–7077.
1135. Biesemeier, F.; Harms, K.; Müller, U. *Z. Kristallogr. NCS* **2004**, *219*, 39–40.
1136. Ma, S.-Y.; Zheng, Z.-B.; Li, J.-K. *Acta Crystallogr.* **2008**, *E64*, m92.
1137. Freisinger, E.; Schimanski, A.; Lippert, B. *J. Biol. Inorg. Chem.* **2001**, *6*, 378–389.
1138. Tounsi, N.; Dupont, L.; Mohamadou, A.; Guillon, E.; Aplincourt, M.; Rogez, G. *Polyhedron* **2008**, *27*, 3674–3682.
1139. Mautner, F. A.; Goher, M. A. S.; Moustafa, H. E.; Abu-Youssef, M. A. M.; Öhrström, L. *Polyhedron* **2007**, *26*, 2703–2712.
1140. Kennedy, A. R.; Kirkhouse, J. B.; McCarney, K. M.; Puissegur, O.; Smith, W. E.; Staunton, E.; Teat, S. J.; Cherryman, J. C.; James, R. *Chem. A Eur. J.* **2004**, *10*, 4606–4615.
1141. Huang, W.; Xie, X.; Cui, K.; Gou, S.; Li, Y. *Inorg. Chim. Acta* **2005**, *358*, 875–884.
1142. Wang, Y.; Song, Y.; Pan, Z.-R.; Shen, Y.-Z.; Hu, Z.; Guo, Z.-J.; Zheng, H.-G. *Dalton Trans.* **2008**, 5588–5592.
1143. Abrahams, B. F.; Commons, C. J.; Hudson, T. A.; Sanchez Arlt, R.; White, K. F.; Chang, M.; Jackowski, J. J.; Lee, M.; Lee, S. X.; Liu, H. D.; Mei, B. M.; Meng, J. E.; Poon, L.; Xu, X.; Yu, Z. *Acta Crystallogr.* **2021**, *C77*, 340–353.
1144. Narvekar, K. U.; Dessai, P. P. G.; Verenkar, V. M. S.; Srinivasan, B. R. *CSD Communication*, 2020. refcode OSURUR02.
1145. Marino, N.; Vortherms, A. R.; Hoffman, A. E.; Doyle, R. P. *Inorg. Chem.* **2010**, *49*, 6790–6792.
1146. Gainsford, G. J.; Kemmitt, T.; Higham, C. *Acta Crystallogr.* **2008**, *E64*, i24–i25.
1147. Yi, X. Y.; Liu, B.; Jiménez-Aparicio, R.; Urbanos, F. A.; Gao, S.; Xu, W.; Chen, J. S.; Song, Y.; Zheng, L. M. *Inorg. Chem.* **2005**, *44*, 4309–4314.
1148. Hao, H.-J.; Lin, C.-W.; Yin, X.-H.; Hu, F.-L.; Zhuang, Y. *Acta Crystallogr.* **2010**, *E66*, m113.
1149. Betz, R.; Gerber, T. *Acta Crystallogr.* **2011**, *E67*, m898.
1150. Kennedy, A.; Andrikopoulos, P.; Arlin, J.-B.; Armstrong, D.; Duxbury, N.; Graham, D.; Kirkhouse, J. *Chem. A Eur. J.* **2009**, *15*, 9494–9504.
1151. Cammidge, A. N.; Goddard, V. H. M.; Gopee, H.; Harrison, N. L.; Hughes, D. L.; Schubert, C. J.; Sutton, B. M.; Watts, G. L.; Whitehead, A. J. *Org. Lett.* **2006**, *8*, 4071–4074.
1152. Li, Z.; Liu, S.; Wu, J.; Li, G. *Huaxue Yanjiu* **2008**, *19*, 51–52.
1153. Kaezer França, M. C.; Eon, J.-G.; Fournier, M.; Payen, E.; Menétré, O. *Solid State Sci.* **2005**, *7*, 1533–1541.
1154. Iqbal, M.; Ali, S.; Muhammad, N.; Parvez, M.; Langer, P.; Villinger, A. *J. Organomet. Chem.* **2013**, *723*, 214–223.
1155. Wang, L.; Chu, Z.; Huang, W.; Gou, S. *Inorg. Chem. Comm.* **2009**, *12*, 4–7.
1156. Srivastava, S.; Aggarwal, H.; Gupta, R. *Cryst. Growth Des.* **2015**, *15*, 4110–4122.
1157. Kinnibrugh, T. L.; Garcia, N.; Clearfield, A. *J. Solid State Chem.* **2012**, *187*, 149–158.
1158. Liu, Y.; Qi, X.; Zhang, W.; Yin, P.; Cai, Z.; Zhang, Q. *Org. Lett.* **2021**, *23*, 734–738.
1159. Srivastava, A. K.; Praveenkumar, B.; Mahawar, I. K.; Divya, P.; Shalini, S.; Boomishankar, R. *Chem. Mater.* **2014**, *26*, 3811–3817.
1160. Fischer, N.; Klapötke, T. M.; Peters, K.; Rusan, M.; Stierstorfer, J. *Z. Anorg. Allg. Chem.* **2011**, *637*, 1693–1701.
1161. Yasodha, V.; Govindarajan, S.; Low, J. N.; Glidewell, C. *Acta Crystallogr.* **2007**, *C63*, m207–m215.
1162. Yisgedu, T. B.; Chen, X.; Lingam, H. K.; Huang, Z.; Highley, A.; Maharey, S.; Behrens, R.; Shore, S. G.; Zhao, J.-C. *J. Phys. Chem. C* **2011**, *115*, 11793–11802.
1163. Didlot, E.; Sadikin, Y.; Łodziana, Z.; Černý, R. *Solid State Sci.* **2019**, *90*, 86–94.
1164. TianLi, L.; Jianlong, W.; Lizhen, C.; DuanLin, C.; ZhiYan, L.; NaNa, W. *Z. Kristallogr. NCS* **2019**, *234*, 933–934.
1165. Shang, W.; Schlam, R. F.; Hickey, M. B.; Zhou, J.; Wheeler, K. A.; de Delgado, G. C. D.; Chen, C.-H.; Snider, B. B.; Foxman, B. M. *Cryst. Growth Des.* **2021**, *21*, 663–682.
1166. Morgant, G.; d'Angelo, J.; Desmaële, D.; Dichì, E.; Sghaier, M.; Fraisse, B.; Retailleau, P.; Brumas, V.; Fiallo, M. M. L.; Tomas, A. *Polyhedron* **2008**, *27*, 2097–2104.
1167. Wang, Y.; Yang, X.; Hu, J.; Li, H.; Li, Z.; Zhang, T. *New J. Chem.* **2020**, *44*, 19054–19060.
1168. Xu, X.; Lu, Y.; Hu, F.; Xu, L.; Shuai, Q. *J. Coord. Chem.* **2016**, *69*, 3294–3302.
1169. Zhang, W.; Chen, Y. T. *Acta Crystallogr.* **2009**, *E65*, m1549.
1170. Tai, X.-S.; Jie, Y. *Crystals* **2015**, *5*, 294–301.
1171. Bednarchuk, T. J.; Kinzybalo, V.; Bednarchuk, O.; Pietraszko, A. *J. Mol. Struct.* **2016**, *1120*, 138–149.
1172. Fujita, M.; Kazerouni, A. M.; Bacsá, J. *Acta Crystallogr.* **2016**, *C72*, 627–633.
1173. Serezhkin, V. N.; Grigoriev, M. S.; Abdulmyanov, A. R.; Fedoseev, A. M.; Savchenkov, A. V.; Serezhkina, L. B. *Inorg. Chem.* **2016**, *55*, 7688–7693.
1174. Tiritiris, I.; Schleid, T. *Z. Anorg. Allg. Chem.* **2004**, *630*, 541–546.
1175. Xanthopoulos, K.; Anagnostou, Z.; Chalkiadakis, S.; Choquesillo-Lazarte, D.; Mezei, G.; Zareba, J. K.; Zoń, J.; Demadis, K. D. *Crystals* **2019**, *9*, 301.
1176. Klapötke, T. M.; Stierstorfer, J. *J. Am. Chem. Soc.* **2009**, *131*, 1122–1134.
1177. Yoshida, R.; Ogasahara, S.; Akashi, H.; Shibahara, T. *Inorg. Chim. Acta* **2012**, *383*, 157–163.
1178. Mateus, P.; Wicher, B.; Ferrand, Y.; Huc, I. *Chem. Commun.* **2017**, *53*, 9300–9303.
1179. Black, D. T.; Kennedy, A. R.; Lobato, K. M. *Acta Crystallogr.* **2019**, *C75*, 633–642.
1180. Amo-Ochoa, P.; Rodríguez-Tapiador, M. I.; Castillo, O.; Olea, D.; Guijarro, A.; Alexandre, S. S.; Gómez-Herrero, J.; Zamora, F. *Inorg. Chem.* **2006**, *45*, 7642–7650.
1181. Mikuriya, M.; Nagao, N.; Kurahashi, S.; Tabuchi, A.; Tomohara, S.; Tsuboi, M.; Yoshioka, D.; Sakiyama, H.; Fuyuhiko, A. *Chem. J. Moldova* **2014**, *9*, 100–105.
1182. Hammerl, A.; Holl, G.; Klapötke, T. M.; Mayer, P.; Nöth, H.; Piotrowski, H.; Warchhold, M. *Eur. J. Inorg. Chem.* **2002**, 834–845.
1183. Hennings, E.; Schmidt, H.; Voigt, W. *Acta Crystallogr.* **2014**, *C70*, 876–881.
1184. Hennings, E.; Schmidt, H.; Voigt, W. *Acta Crystallogr.* **2014**, *E70*, 489–493.



1185. Murugavel, R.; Kuppuswamy, S.; Randoll, S. *Inorg. Chem.* **2008**, *47*, 6028–6039.
1186. Xu, X.; Hu, F.; Shuai, Q. *New J. Chem.* **2017**, *41*, 13319–13326.
1187. Nichol, G. S.; Clegg, W. *Acta Crystallogr.* **2007**, *E63*, m1135–m1137.
1188. Zhang, Z.-T.; Wang, Q.-Y.; Li, W.-W.; Meng, Q.-H.; Zhang, X.-L. *CrstEngComm* **2012**, *14*, 5042–5052.
1189. Huang, H.; Zhou, Z.; Liang, L.; Song, J.; Wang, K.; Cao, D.; Bian, C.; Sun, W.; Xue, M. *Z. Anorg. Allg. Chem.* **2012**, *638*, 392–400.
1190. Hennings, E.; Schmidt, H.; Voigt, W. *Acta Crystallogr.* **2014**, *E70*, 510–514.
1191. Plater, M. J.; Harrison, W. T. A. *J. Chem. Res.* **2015**, *39*, 279–281.
1192. Trella, T.; Frank, W. *Acta Crystallogr.* **2012**, *E68*, m1136–m1137.
1193. Bednarchuk, T. J.; Kinzhybalov, V.; Pietraszko, A. *Acta Crystallogr.* **2016**, *C72*, 432–441.
1194. Bataille, T. *Acta Crystallogr.* **2003**, *C59*, m459–m461.
1195. Sieglér, M. A.; Prewitt, J. H.; Kelley, S. P.; Parkin, S.; Selegue, J. P.; Brock, C. P. *Acta Crystallogr.* **2010**, *B66*, 213–221.
1196. Zarychta, B.; Czaplá, Z.; Przeslawski, J.; Szklarz, P. *Acta Crystallogr.* **2021**, *B77*, 225–231.
1197. Gerasko, O. A.; Mainicheva, E. A.; Naumov, D. Y.; Kuratieva, N. V.; Sokolov, M. N.; Fedin, V. P. *Inorg. Chem.* **2005**, *44*, 4133–4135.
1198. Dalgarno, S. J.; Hardie, M. J.; Raston, C. L. *Cryst. Growth Des.* **2004**, *4*, 227–234.
1199. Tian, Y.-Q.; Cai, C.-X.; Yuan, X.-J.; Li, Y.-Z.; Wang, T.-W.; You, X.-Z. *Chem. Lett.* **2003**, *32*, 796–797.
1200. Davidovich, R. L.; Gerasimenko, A. V.; Voit, E. I.; Logvinova, V. B. *J. Fluor. Chem.* **2019**, *226*, 109343.
1201. Näslund, J.; Persson, I.; Sandström, M. *Inorg. Chem.* **2000**, *39*, 4012–4021.
1202. Son, S. U.; Reingold, J. A.; Kim, S. B.; Carpenter, G. B.; Sweigart, D. A. *Angew. Chem. Int. Ed.* **2005**, *44*, 7710–7715.
1203. Kaib, T.; Bron, P.; Haddadpour, S.; Mayrhofer, L.; Pastewka, L.; Järvi, T. T.; Moseler, M.; Røling, B.; Dehnen, S. *Chem. Mater.* **2013**, *25*, 2961–2969.
1204. Kaib, T.; Haddadpour, S.; Kaptein, M.; Bron, P.; Schröder, C.; Eckert, H.; Røling, B.; Dehnen, S. *Chem. Mater.* **2012**, *24*, 2211–2219.
1205. Albrecht, M.; Baumert, M.; Klankermayer, J.; Kogej, M.; Schalley, C. A.; Fröhlich, R. *Dalton Trans.* **2006**, 4395–4400.
1206. Dodds, C. A.; Garner, M.; Reglinski, J.; Spicer, M. D. *Inorg. Chem.* **2006**, *45*, 2733–2741.
1207. Yamada, M.; Gandhi, M. R.; Akimoto, K.; Hamada, F. *Acta Crystallogr.* **2018**, *E74*, 575–579.
1208. Mehring, M.; Berkei, M.; Schurmann, M. *Z. Anorg. Allg. Chem.* **2002**, *628*, 1975–1978.
1209. Nanjo, M.; Matsudo, K.; Mochida, K. *Inorg. Chem. Comm.* **2003**, *6*, 1065–1067.
1210. Buttery, J. H. N.; Plackett, N. C.; Skelton, B. W.; Whitaker, C. R.; White, A. H. *Z. Anorg. Allg. Chem.* **2006**, *632*, 1870–1873.
1211. Brnićević, N.; Bašić, I.; Hoxha, B.; Planinić, P.; McCarley, R. E. *Polyhedron* **2003**, *22*, 1553–1559.
1212. Wei, M.; Xu, H.; Sun, R. *J. Coord. Chem.* **2009**, *62*, 1989–2002.
1213. Didelot, E.; Łodziana, Z.; Murgia, F.; Černý, R. *Crystals* **2019**, *9*, 372.
1214. Okamura, T.-A.; Nakagawa, J. *Inorg. Chem.* **2013**, *52*, 10812–10824.
1215. Schröder, F.; Köckerling, M. *Z. Anorg. Allg. Chem.* **2021**, *647*, 1625–1632.
1216. Chen, X.; Liu, Y. H.; Alexander, A. M.; Gallucci, J. C.; Hwang, S. J.; Lingam, H. K.; Huang, Z.; Wang, C.; Li, H.; Zhao, Q.; Ozkan, U. S.; Shore, S. G.; Zhao, J. C. *Chem. A Eur. J.* **2014**, *20*, 7325–7333.
1217. Vervasov, G.; Harinaga, U.; Matsumoto, K.; Hagiwara, R. *Eur. J. Inorg. Chem.* **2017**, *2017*, 1087–1099.
1218. Boyle, T. J.; Ottley, L. A.; Alam, T. M.; Rodriguez, M. A.; Yang, P.; McIntyre, S. K. *Polyhedron* **2010**, *29*, 1784–1795.
1219. Malizia, F.; Fait, A.; Cruciani, G. *Chem. A Eur. J.* **2011**, *17*, 13892–13897.
1220. Deng, J.-H.; Wen, Y.-Q.; Luo, J.; Huang, Z.-Q.; Zhong, D.-C. *J. Mol. Struct.* **2017**, *1142*, 211–216.
1221. He, Y.-C.; Guo, J.; Zhang, H.-M.; Yang, J.; Liu, Y.-Y.; Ma, J.-F. *CrstEngComm* **2014**, *16*, 4210–4214.
1222. Koch, E.-C.; Klapötke, T. M.; Radies, H.; Lux, K.; Hahma, A. *Z. Naturforsch.* **2011**, *B66*, 378–386.
1223. Barboiu, M.; van der Lee, A. *Acta Crystallogr.* **2003**, *C59*, m366–m368.
1224. Azais, T.; Bonhomme-Courty, L.; Vaissermann, J.; Bertani, P.; Hirsinger, J.; Maquet, J.; Bonhomme, C. *Inorg. Chem.* **2002**, *41*, 981–988.
1225. Mane, A.; Wagner, C.; Merzweiler, K. *Z. Anorg. Allg. Chem.* **2012**, *638*, 136–140.
1226. Jiang, X.-D.; Yamamoto, Y. *J. Organomet. Chem.* **2010**, *695*, 740–746.
1227. Chivers, T.; Fedorchuk, C.; Parvez, M. *Inorg. Chem.* **2004**, *43*, 2643–2653.
1228. Nukazawa, T.; Iwamoto, T. *Organometallics* **2021**, *40*, 3511–3515.
1229. Sazama, G. T.; Betley, T. A. *Inorg. Chem.* **2014**, *53*, 269–281.
1230. Köhnein, H.; Purath, A.; Klemp, C.; Baum, E.; Krossing, I.; Stösser, G.; Schnöckel, H. *Inorg. Chem.* **2001**, *40*, 4830–4838.
1231. Scheschke, D.; Hofmann, M.; Ghaffari, A.; Amseis, P.; Präsaug, C.; Mesbah, W.; Geiseler, G.; Massa, W.; Berndt, A. *J. Organomet. Chem.* **2002**, *646*, 262–270.
1232. Woodman, T. J.; Schormann, M.; Hughes, D. L.; Bochmann, M. *Organometallics* **2004**, *23*, 2972–2979.
1233. Zheng, Y.; Cao, C.-S.; Ma, W.; Chen, T.; Wu, B.; Yu, C.; Huang, Z.; Yin, J.; Hu, H.-S.; Li, J.; Zhang, W.-X.; Xi, Z. *J. Am. Chem. Soc.* **2020**, *142*, 10705–10714.
1234. Ho, L. P.; Körner, L.; Bannenberg, T.; Tamm, M. *Dalton Trans.* **2020**, *49*, 13207–13217.
1235. Schrenk, C.; Neumaier, M.; Schnepf, A. *Inorg. Chem.* **2012**, *51*, 3989–3995.
1236. Matson, E. M.; Forrest, W. P.; Fanwick, P. E.; Bart, S. C. *Organometallics* **2012**, *31*, 4467–4473.
1237. Spring, D. R.; Krishnan, S.; Blackwell, H. E.; Schreiber, S. L. *J. Am. Chem. Soc.* **2002**, *124*, 1354–1363.
1238. Berndt, A.; Hofmann, M.; Scheschke, D.; Ghaffari, A.; Geiseler, G.; Massa, W.; Schaefer, H. F., III. *J. Mol. Model.* **2000**, *6*, 257–271.
1239. Lancaster, S. J.; Rodriguez, A.; Lara-Sanchez, A.; Hannant, M. D.; Walker, D. A.; Hughes, D. H.; Bochmann, M. *Organometallics* **2002**, *21*, 451–453.
1240. Evans, W. J.; Lee, D. S.; Rego, D. B.; Perotti, J. M.; Kozimor, S. A.; Moore, E. K.; Ziller, J. W. *J. Am. Chem. Soc.* **2004**, *126*, 14574–14582.
1241. Ding, E.; Du, B.; Shore, S. G. *J. Organomet. Chem.* **2007**, *692*, 2148–2152.
1242. Ding, E.; Du, B.; Liu, F. C.; Liu, S.; Meyers, E. A.; Shore, S. G. *Inorg. Chem.* **2005**, *44*, 4871–4878.
1243. Bernsdorf, A.; Brand, H.; Hellmann, R.; Köckerling, M.; Schulz, A.; Villinger, A.; Voss, K. *J. Am. Chem. Soc.* **2009**, *131*, 8958–8970.
1244. Huh, D. N.; Roy, S.; Ziller, J. W.; Furche, F.; Evans, W. J. *J. Am. Chem. Soc.* **2019**, *141*, 12458–12463.
1245. Müller, M.; Buchner, M. R. *Kristallogr. Cryst. Mater.* **2020**, *235*, 263–268.
1246. Paparo, A.; de Bruin-Dickason, C. N.; Jones, C. *Aust. J. Chem.* **2020**, *73*, 1144–1148.
1247. Veith, M.; Burkhart, M.; Huch, V. *Angew. Chem. Int. Ed.* **2006**, *45*, 5544–5546.
1248. Zhang, W.; Hu, J.-P.; Ding, X.-F.; Wu, Y.-J.; Ye, Z.-W. *Inorg. Chem. Commun.* **2003**, *6*, 1185–1187.
1249. Hubener, L.; Lerner, H.-W.; Bolte, M. *Acta Crystallogr.* **2003**, *E59*, m929–m930.
1250. Mitzel, N. W.; Losehand, U.; Vojinovic, K. *Inorg. Chem.* **2001**, *40*, 5302–5303.
1251. Bačić, G.; Rankine, C. D.; Masuda, J. D.; Wann, D. A.; Barry, S. T. *Inorg. Chem.* **2020**, *59*, 996–1005.
1252. Mäntymäki, M.; Ritala, M.; Leskelä, M. *Coord. Chem. Rev.* **2012**, *256*, 854–877.
1253. Petrus, R.; Sobota, P. *Coord. Chem. Rev.* **2019**, *396*, 72–88.
1254. Kremer, A. B.; Mehrhodavandi, P. *Coord. Chem. Rev.* **2019**, *380*, 35–57.
1255. Sobota, P. *Coord. Chem. Rev.* **2004**, *248*, 1047–1060.
1256. Wu, J.; Yu, T.; Chen, C.; Lin, C. *Coord. Chem. Rev.* **2006**, *250*, 602–626.

1257. Singh, A.; Mehrotra, R. C. *Coord. Chem. Rev.* **2004**, *248*, 101–118.
1258. Mehring, M. *Coord. Chem. Rev.* **2007**, *251*, 974–1006.
1259. Ben Moussa, I.; Belkhiria, M. S.; Najmudin, S.; Bonifacio, C.; Nasri, H. *Acta Crystallogr.* **2011**, *E67*, m903–m904.
1260. Hashem, E.; McCabe, T.; Schulzke, C.; Baker, R. J. *Dalton Trans.* **2014**, *43*, 1125–1131.
1261. Huckstadt, H.; Jaouen, C.; Goldner, M.; Cornelissen, U.; Tutass, A.; Homborg, H. Z. *Anorg. Allg. Chem.* **2000**, *626*, 671–678.
1262. Schuster, O.; Schmidbauer, H. Z. *Naturforsch.* **2006**, *B61*, 956–960.
1263. Rheingold, A. L.; Theopold, K. H. *CSD Communication*, 2019. refcode LUCJUR.
1264. Trzeciak, A. M.; Lis, T.; Wojtkow, W.; Ziolkowski, J. J. *Bull. Pol. Acad. Sci. Chem.* **2002**, *50*, 27–35.
1265. Fedushkin, I.; Lukoyanov, A.; Tishkina, A.; Fukin, G.; Lyssenko, K.; Hummert, M. *Chem. A Eur. J.* **2010**, *16*, 7563–7571.
1266. Siffredi, G.; Berthet, J. C.; Thuery, P.; Ephritikhine, M. *CSD Communication*, 2013. refcode ZIXSUW.
1267. Bataineh, E. M.; Doerrer, L. H.; Golen, J. A.; Rheingold, A. L. *CSD Communication*, 2006. refcode JUXPOH01.
1268. Seifert, T. P.; Knoefel, N. D.; Feuerstein, T. J.; Reiter, K.; Lebedkin, S.; Gamer, M. T.; Boukis, A. C.; Weigend, F.; Kappes, M. M.; Roesky, P. W. *Chem. A Eur. J.* **2019**, *25*, 3799–3808.
1269. Chekhlov, A. N. *Zh. Neorg. Khim.* **2005**, *50*, 967–972.
1270. Chekhlov, A. N. *Koord. Khim.* **2005**, *31*, 868–872.
1271. Chekhlov, A. N. *Koord. Khim.* **2008**, *34*, 586–590.
1272. Liu, X.; Guo, Liu, B.; Chen, W.-T.; Huang, J.-S. *Cryst. Growth Des.* **2005**, *5*, 841–843.
1273. Skelton, B. W.; Somers, N.; White, A. H. *CSD Communication*, 2019. refcode YORKEY.
1274. Domanska-Babul, W.; Baranowska, K.; Pikies, J. *Acta Crystallogr.* **2008**, *C64*, m20–m22.
1275. Petz, W.; Dehnicke, K.; Neumüller, B. Z. *Anorg. Allg. Chem.* **2011**, *637*, 1761–1768.
1276. Petz, W.; Kutschera, C.; Tschan, S.; Weller, F.; Neumüller, B. Z. *Anorg. Allg. Chem.* **2003**, *629*, 1235–1244.
1277. Ding, Y.; Fanwick, P. E.; Walton, R. A. *Inorg. Chim. Acta* **2000**, *309*, 159–162.
1278. Stieler, R.; Bubltz, F.; Schulz Lang, E. Manzoni de Oliveira, G. *Polyhedron* **2012**, *31*, 596–600.
1279. Davis, M. F.; Levason, W.; Ratnani, R.; Reid, G.; Webster, M. *New J. Chem.* **2006**, *30*, 782–790.
1280. Hursthouse, M. B.; Levason, W.; Ratnani, R.; Reid, G.; Stainer, H.; Webster, M. *Polyhedron* **2005**, *24*, 121–128.
1281. Kucera, B. E.; Olmstead, M. M.; Tanke, R. S.; Kauzlarich, S. M. *Acta Crystallogr.* **2003**, *E59*, m359–m360.
1282. Belaj, F.; Peschel, L. M.; Mosch-Zanetti, N. C. *CSD Communication*, 2021. refcode ELEVEZ.
1283. Fitts, L. S.; Bierschenck, E. J.; Hanusa, T. P.; Rheingold, A. L.; Pink, M.; Young, V. G. *New J. Chem.* **2016**, *40*, 8229–8238.
1284. Nieger, M. *CSD Communication*, 2019. refcode WOJJOX.
1285. Evtushok, D. V.; Vorotnikova, N. A.; Logvinenko, V. A.; Smolentsev, A. I.; Brylev, K. A.; Plyusnin, P. E.; Pishchur, D. P.; Kitamura, N.; Mironov, Y. V.; Solovieva, A. O.; Efremova, O. A.; Shestopalov, M. A. *New J. Chem.* **2017**, *41*, 14855–14861.
1286. Courtney, B. H.; Fronczek, F. R. *CSD Communication*, 2020. refcode HUZJUK.
1287. Barrett, A. G. M.; Crimmin, M. R.; Hill, M. S.; Kociok-Köhn, G.; MacDougall, D. J.; Mahon, M. F.; Procopiou, P. A. *Organometallics* **2008**, *27*, 3939–3946.
1288. Pahl, J.; Brand, S.; Elsen, H.; Harder, S. *Chem. Commun.* **2018**, *54*, 8685–8688.
1289. Sarish, S.; Nembenna, S.; Nagendran, S.; Roesky, H. W.; Pal, A.; Herbst-Irmer, R.; Ringe, A.; Magull, J. *Inorg. Chem.* **2008**, *47*, 5971–5977.
1290. Kögel, J. F.; Timoshkin, A. Y.; Schröder, A.; Lork, E.; Beckmann, J. *Chem. Sci.* **2018**, *9*, 8178–8183.
1291. Chu, T.; Vyboishchikov, S. F.; Gabidullin, B. M.; Nikonov, G. I. *Inorg. Chem.* **2017**, *56*, 5993–5997.
1292. Cheng, F.; Codgbrook, H. L.; Hector, A. L.; Levason, W.; Reid, G.; Webster, M.; Zhang, W. *Polyhedron* **2007**, *26*, 4147–4155.
1293. Peppe, C.; Mello, M. D. A.; Wiopplod, T. A.; Lang, E. S. J. *Organomet. Chem.* **2012**, *718*, 52–56.
1294. Skelton, B. W. *CSD Communication*, 2017. refcode KEKMUI01.
1295. Chen, F.; Ma, G.; Cavell, R. G.; Terskikh, V. V.; Wasylshen, R. E. *Chem. Commun.* **2008**, 5933–5935.
1296. Cheng, F.; Davis, M. F.; Hector, A. L.; Levason, W.; Reid, G.; Webster, M.; Zhang, W. *Eur. J. Inorg. Chem.* **2007**, *2007*, 2488–2495.
1297. Davis, M. F.; Levason, W.; Reid, G.; Webster, M. *Polyhedron* **2006**, *25*, 930–936.
1298. Hitosugi-Levesque, M.; Tanski, J. M. *Acta Crystallogr.* **2008**, *E64*, m1107.
1299. Szymanska-Buzar, T.; Glowiak, T.; Czelusniak, I. *Main Group Met. Chem.* **2001**, *24*, 821–822.
1300. Wlazlak, E.; Macyk, W.; Nitek, W.; Szacilowski, K. *Inorg. Chem.* **2016**, *55*, 5935–5945.
1301. Batsanov, A. S.; Deng, R. M. K.; Dillon, K. B.; Goeta, A. E.; Howard, J. A. K.; Meldrum, J.; Monks, P. K.; Puschmann, H.; Shepherd, H. J. *Heteroat. Chem.* **2009**, *20*, 136–143.
1302. Barnham, R. J.; Deng, R. M. K.; Dillon, K. B.; Goeta, A. E.; Howard, J. A. K.; Puschmann, H. *Heteroat. Chem.* **2001**, *12*, 501–510.
1303. Petz, W.; Öxler, F.; Aicher, K.; Neumüller, B. Z. *Anorg. Allg. Chem.* **2010**, *636*, 1751–1759.
1304. Huang, Z.-J.; Cheng, H.-J.; Dai, M.; Ni, C.-Y.; Li, H.-X.; Hou, K.-P.; Ren, Z.-G.; Lang, J.-P. *Inorg. Chem. Comm.* **2013**, *31*, 33–36.
1305. Bamford, K. L.; Robertson, A. P. M.; Jenkins, H. A.; Patrick, B. O.; Burford, N. *Can. J. Chem.* **2015**, *93*, 375–379.
1306. Wlazlak, E.; Kalinowska-Tluszcik, J.; Przyczyna, D.; Zawal, P.; Szacilowski, K. *J. Mater. Chem. C* **2020**, *8*, 6136–6148.
1307. Hector, A. L.; Jolleys, A.; Levason, W.; Reid, G. *Dalton Trans.* **2012**, *41*, 10988–10999.
1308. Levason, W.; Reid, G.; Victor, M.; Zhang, W. *Polyhedron* **2009**, *28*, 4010–4016.
1309. Matsuo, Y.; Nakamura, E. *J. Am. Chem. Soc.* **2005**, *127*, 8457–8466.
1310. Jones, P. G.; Freytag, M.; Fecker, A. C.; Walter, M. D. *CSD Communication*, 2021. refcode AJURIJ.
1311. Prat, J. R.; Gaggioli, C. A.; Cammarota, R. C.; Bill, E.; Gagliardi, L.; Lu, C. C. *Inorg. Chem.* **2020**, *59*, 14251–14262.
1312. Sandl, S.; Maier, T. M.; van Leest, N. P.; Kröncke, S.; Chakraborty, U.; Demeshko, S.; Koszinowski, K.; de Bruin, B.; Meyer, F.; Bodensteiner, M.; Herrmann, C.; Wolf, R.; von Wangelin, A. J. *ACS Catal.* **2019**, *9*, 7596–7606.
1313. Zhu, X.; Guo, D.; Zhang, Y.; Wei, Y.; Zhou, S.; Xu, M.; Wang, S.; Yang, Y.; Qi, Y. *Organometallics* **2020**, *39*, 4584–4591.
1314. Serrano, C. B.; Less, R. J.; McPartlin, M.; Naseri, V.; Wright, D. S. *Organometallics* **2010**, *29*, 5754–5756.
1315. Boronski, J. T.; Doyle, L. R.; Woolles, A. J.; Seed, J. A.; Liddle, S. T. *Organometallics* **2020**, *39*, 1824–1831.
1316. Burckhardt, U.; Casty, G. L.; Gavenonis, J.; Tilley, T. D. *Organometallics* **2002**, *21*, 3108–3122.
1317. Riedlberger, F.; Seidl, M.; Scheer, M. *Chem. Commun.* **2020**, *56*, 13836–13839.
1318. Fischer, R.; Görts, H.; Suxdorf, R.; Westerhausen, M. *Organometallics* **2020**, *39*, 3892–3905.
1319. Trageser, T.; Bolte, M.; Lerner, H. W.; Wagner, M. *Angew. Chem. Int. Ed.* **2020**, *59*, 7726–7731.
1320. Copesey, M. C.; Jeffery, J. C.; Russell, C. A.; Slattery, J. M.; Straughan, J. A. *Chem. Commun.* **2003**, 2356–2357.
1321. Stokes, F. A.; Kloo, L.; Lv, Y.; Harford, P. J.; Wheatley, A. E. H.; Wright, D. S. *Chem. Commun.* **2012**, *48*, 11298–11300.
1322. Stokes, F. A.; Vincent, M. A.; Hillier, I. H.; Ronson, T. K.; Steiner, A.; Wheatley, A. E.; Wood, P. T.; Wright, D. S. *Dalton Trans.* **2013**, *42*, 13923–13930.
1323. Jones, C.; Mills, D. P.; Stasch, A. *Main Group Metal Chem.* **2009**, *32*, 161–164.
1324. Zhang, X.-Q.; Lin, M.-S.; Hu, B.; Chen, W.-Q.; Zheng, L.-N.; Wu, J.; Chen, Y.-M.; Zhou, F.-Y.; Li, Y.-H.; Li, W. *Polyhedron* **2012**, *33*, 273–279.
1325. Schenk, C.; Schnepf, A. *Angew. Chem. Int. Ed.* **2007**, *46*, 5314–5316.

1326. Schenk, C.; Henke, F.; Santiso-Quiñones, G.; Krossing, I.; Schnepf, A. *Dalton Trans.* **2008**, 4436–4441.
1327. Nurdin, L.; Spasyuk, D. M.; Fairburn, L.; Piers, W. E.; Maron, L. *J. Am. Chem. Soc.* **2018**, *140*, 16094–16105.
1328. Dubé, T.; Gambarotta, S.; Yap, G. P. A.; Conoci, S. *Organometallics* **2000**, *19*, 115–117.
1329. Bickley, J. F.; Copesey, M. C.; Jeffery, J. C.; Leedham, A. P.; Russell, C. A.; Stalke, D.; Steiner, A.; Stey, T.; Zacchini, S. *Dalton Trans.* **2004**, 989–995.
1330. Alonso, P. J.; Forniés, J.; García-Monforte, M. A.; Martín, A.; Menjón, B.; Rillo, C. *Chem. A Eur. J.* **2002**, *8*, 4056–4065.
1331. Qian, Q.; Tan, Y.; Zhao, B.; Feng, T.; Shen, Q.; Yao, Y. *Org. Lett.* **2014**, *16*, 4516–4519.
1332. Schnepf, A.; Stösser, G.; Schnöckel, H. *J. Am. Chem. Soc.* **2000**, *122*, 9178–9181.
1333. Latendresse, T. P.; Bhuvanesh, N. S.; Nippe, M. *J. Am. Chem. Soc.* **2017**, *139*, 14877–14880.
1334. Liu, J. F.; Min, X.; Lv, J. Y.; Pan, F. X.; Pan, Q. J.; Sun, Z. M. *Inorg. Chem.* **2014**, *53*, 11068–11074.
1335. Rosa, P.; Mézailles, N.; Ricard, L.; Mathey, F.; Le Floch, P. *Angew. Chem. Int. Ed.* **2000**, *39*, 1823–1826.
1336. Radtke, J.; Møllerup, S. K.; Bolte, M.; Lerner, H.-W.; Wang, S.; Wagner, M. *Org. Lett.* **2018**, *20*, 3966–3970.
1337. Schnepf, A.; Stösser, G.; Schnöckel, H. *Angew. Chem. Int. Ed.* **2002**, *41*, 1882–1884.
1338. Söhner, T.; Braun, F.; Over, L. C.; Mehlhose, S.; Rominger, F.; Straub, B. F. *Green Chem.* **2014**, *16*, 4696–4707.
1339. Ma, M.; Shen, X.; Wang, W.; Li, J.; Yao, W.; Zhu, L. *Eur. J. Inorg. Chem.* **2016**, *2016*, 5057–5062.
1340. von Hänisch, C.; Rolli, B. *Z. Anorg. Allg. Chem.* **2004**, *630*, 1987–1990.
1341. Malkowsky, I. M.; Fröhlich, R.; Griesbach, U.; Pütter, H.; Waldvogel, S. R. *Eur. J. Inorg. Chem.* **2006**, *2006*, 1690–1697.
1342. Linti, G.; Çoban, S.; Dutta, D. *Z. Anorg. Allg. Chem.* **2004**, *630*, 319–323.
1343. Brown, S. D.; Peters, J. C. *J. Am. Chem. Soc.* **2005**, *127*, 1913–1923.
1344. Cole, M. L.; Junk, P. C. *Chem. Commun.* **2005**, 2695–2697.
1345. Brown, S. D.; Mehn, M. P.; Peters, J. C. *J. Am. Chem. Soc.* **2005**, *127*, 13146–13147.
1346. Armstrong, D. R.; Clegg, W.; Hernán-Gómez, A.; Kennedy, A. R.; Livingstone, Z.; Robertson, S. D.; Russo, L.; Hevia, E. *Dalton Trans.* **2014**, *43*, 4361–4369.
1347. Chen, W.; Zhao, Y.; Xu, W.; Su, J. H.; Shen, L.; Liu, L.; Wu, B.; Yang, X. J. *Chem. Commun.* **2019**, *55*, 9452–9455.
1348. Jin, P.; Zhai, Y.; Yu, K.; Wimpenny, R. E. P.; Zheng, Y. *Angew. Chem. Int. Ed.* **2020**, *59*, 9350–9354.
1349. Corbey, J. F.; Woen, D. H.; Palumbo, C. T.; Fieser, M. E.; Ziller, J. W.; Furche, F.; Evans, W. J. *Organometallics* **2015**, *34*, 3909–3921.
1350. Evans, W. J.; Giarikos, D. G.; Workman, P. S.; Ziller, J. W. *Inorg. Chem.* **2004**, *43*, 5754–5760.
1351. Setty, V. N.; Zhou, W.; Foxman, B. M.; Thomas, C. M. *Inorg. Chem.* **2011**, *50*, 4647–4655.
1352. Creutz, S. E.; Krummenacher, I.; Clough, C. R.; Cummins, C. C. *Chem. Sci.* **2011**, *2*, 2166–2172.
1353. Zhao, Y.; Liu, Y.; Li, Q.-S.; Su, J.-H. *Dalton Trans.* **2016**, *45*, 246–252.
1354. Yuan, C.; Xu, X.; Zhang, Y.; Ji, S. *Chin. J. Chem.* **2012**, *30*, 1474–1478.
1355. Delgado, E.; Hernández, E.; Perez, M.; Perles, J. *CSD Communication*, 2018. refcode AFUTUT.
1356. Tsoureas, N.; Kilpatrick, A. F. R.; Inman, C. J.; Cloke, F. G. N. *Chem. Sci.* **2016**, *7*, 4624–4632.
1357. Adamczyk, T.; Li, G.; Linti, G.; Pritzkow, H.; Seifert, A.; Zessin, T. *Eur. J. Inorg. Chem.* **2011**, *2011*, 3480–3492.
1358. Semproni, S. P.; Knobloch, D. J.; Millsman, C.; Chirik, P. J. *Angew. Chem. Int. Ed.* **2013**, *52*, 5372–5376.
1359. Ebner, A.; Wachter, J.; Zabel, M. *J. Cluster Sci.* **2004**, *15*, 163–174.
1360. Dubé, T.; Ganesan, M.; Conoci, S.; Gambarotta, S.; Yap, G. P. A. *Organometallics* **2000**, *19*, 3716–3721.
1361. Li, L.; Clarkson, G. J.; Lees, M. R.; Howson, S. E.; Tan, S.; Turner, S. S.; Scott, P. *Organometallics* **2015**, *34*, 2543–2549.
1362. Castillo, O.; Delgado, E.; Hernández, E.; Pérez, M.; Zamora, F. *Cryst. Growth Des.* **2020**, *20*, 4573–4584.
1363. Kückmann, T. I.; Schödel, F.; Sängler, I.; Bolte, M.; Wagner, M.; Lerner, H.-W. *Organometallics* **2008**, *27*, 3272–3278.
1364. Wrede, M.; Ganza, V.; Kannenberg, G.; Rominger, F.; Straub, B. F. *Inorg. Chim. Acta* **2011**, *369*, 71–75.
1365. Shen, H.; Chan, H.-S.; Xie, Z. *Organometallics* **2008**, *27*, 5309–5316.
1366. Zhao, M.; Wang, L.; Li, P.; Ma, J.; Zheng, W. *Dalton Trans.* **2016**, *45*, 11172–11181.
1367. Evans, W. J.; Fang, M.; Zucchi, G.; Furche, F.; Ziller, J. W.; Hoekstra, R. M.; Zink, J. I. *J. Am. Chem. Soc.* **2009**, *131*, 11195–11202.
1368. Kaese, T.; Budy, H.; Bolte, M.; Lerner, H.-W.; Wagner, M. *Angew. Chem. Int. Ed.* **2017**, *56*, 7546–7550.
1369. Gehrhus, B.; Hitchcock, P. B.; Zhang, L. *Angew. Chem. Int. Ed.* **2004**, *43*, 1124–1126.
1370. Matsuo, Y.; Tahara, K.; Nakamura, E. *Chem. Lett.* **2005**, *34*, 1078–1079.
1371. Matsuo, Y.; Isobe, H.; Tanaka, T.; Murata, Y.; Murata, M.; Komatsu, K.; Nakamura, E. *J. Am. Chem. Soc.* **2005**, *127*, 17148–17149.
1372. Pick, F. S.; Leznoff, D. B.; Fryzuk, M. D. *Dalton Trans.* **2018**, *47*, 10925–10931.
1373. Kuehl, C. J.; Simpson, C. K.; John, K. D.; Sattelberger, A. P.; Carlson, C. N.; Hanusa, T. P. *J. Organomet. Chem.* **2003**, *683*, 149–154.
1374. Allaud, I.; Collin, J.; Duhayon, C.; Guillot, R.; Lyubov, D.; Schulz, E.; Trifonov, A. *Chem. A Eur. J.* **2008**, *14*, 2189–2200.
1375. Chan, Z. K.; Wu, Y. Y.; Chen, J. D.; Yeh, C. Y.; Wang, C. C.; Tsai, Y. F.; Wang, J. C. *Dalton Trans.* **2005**, 985–990.
1376. Nakanishi, Y.; Ishida, Y.; Kawaguchi, H. *Angew. Chem. Int. Ed.* **2017**, *56*, 9193–9197.
1377. Becker, M.; Förster, C.; Franzen, C.; Hartrath, J.; Kirsten, E.; Knuth, J.; Klinkhammer, K. W.; Sharma, A.; Hinderberger, D. *Inorg. Chem.* **2008**, *47*, 9965–9978.
1378. Izod, K.; Watson, J. M.; Harrington, R. W.; Clegg, W. *Dalton Trans.* **2021**, *50*, 1019–1024.
1379. Berthet, J.-C.; Thuéry, P.; Ephritikhine, M. *Angew. Chem. Int. Ed.* **2008**, *47*, 5586–5589.
1380. Harder, S.; Feil, F.; Repo, T. *Chem. A Eur. J.* **2002**, *8*, 1991–1999.
1381. Forniés, J.; Martín, A.; Martín, L. F.; Menjón, B.; Zhen, H.; Bell, A.; Rhodes, L. F. *Organometallics* **2005**, *24*, 3266–3271.
1382. Jaenschke, A.; Olbrich, F.; Behrens, U. *Z. Anorg. Allg. Chem.* **2009**, *635*, 2550–2557.
1383. Paparo, A.; Silvia, J. S.; Spaniol, T. P.; Okuda, J.; Cummins, C. C. *Chem. A Eur. J.* **2018**, *24*, 17072–17079.
1384. Doyle, L. R.; Wooles, A. J.; Liddle, S. T. *Angew. Chem. Int. Ed.* **2019**, *58*, 6674–6677.
1385. Braunschweig, H.; D'Andola, G.; Welton, T.; White, A. J. P. *Chem. Commun.* **2004**, 1738–1739.
1386. Standfuss, S.; Abinet, E.; Spaniol, T. P.; Okuda, J. *Chem. Commun.* **2011**, *47*, 11441–11443.
1387. Michel, O.; Meermann, C.; Törnroos, K. W.; Anwender, R. *Organometallics* **2009**, *28*, 4783–4790.
1388. Bond, A. D.; Layfield, R. A.; MacAllister, J. A.; McPartlin, M.; Rawson, J. M.; Wright, D. S. *Chem. Commun.* **2001**, 1956–1957.
1389. Olmstead, M. M.; Kauzlarich, S. M.; Pettigrew, K. A.; Power, P. P. *CSD Communication*, 2002. refcode THFMGB01.
1390. Pour, N.; Gofer, Y.; Major, D. T.; Aurbach, D. *J. Am. Chem. Soc.* **2011**, *133*, 6270–6278.
1391. Stabenow, F.; Saak, W.; Weidenbruch, M. *Chem. Commun.* **2003**, 2342–2343.
1392. Braunschweig, H.; D'Andola, G.; Welton, T.; White, A. J. *Chem. A Eur. J.* **2005**, *12*, 600–606.
1393. Basiak, D.; Wojciechowski, T.; Rzepiński, P.; Dobrzycki, Ł.; Wojewódzka, A.; Monikowska, D.; Zygadło-Monikowska, E.; Ziemkowska, W. *Appl. Organomet. Chem.* **2020**, *34*, e5751.
1394. Bolte, M.; Scholz, S.; Lerner, W. *CSD Communication*, 2002. refcode DOVGAW02.
1395. Fischer, R.; Walther, D.; Gebhardt, P.; Görls, H. *Organometallics* **2000**, *19*, 2532–2540.
1396. Stern, D.; Granitzka, M.; Schulz, T.; Stalke, D. *Z. Naturforsch.* **2010**, *B65*, 719–724.
1397. Lorbach, A.; Lerner, H. W.; Bolte, M. *Acta Crystallogr.* **2007**, *C63*, m174–m176.

1398. Boddie, T. E.; Carpenter, S. H.; Baker, T. M.; DeMuth, J. C.; Cera, G.; Brennessel, W. W.; Ackermann, L.; Neidig, M. L. *J. Am. Chem. Soc.* **2019**, *141*, 12338–12345.
1399. Muldoon, J.; Bucur, C. B.; Oliver, A. G.; Sugimoto, T.; Matsui, M.; Kim, H. S.; Allred, G. D.; Zajicek, J.; Kotani, Y. *Energ. Environ. Sci.* **2012**, *5*, 5941–5950.
1400. Nelson, E. G.; Kampf, J. W.; Bartlett, B. M. *Chem. Commun.* **2014**, *50*, 5193–5195.
1401. Guo, Y.; Zhang, F.; Yang, J.; Wang, F.; NuLi, Y.; Hirano, S. *Energ. Environ. Sci.* **2012**, *5*, 9100–9106.
1402. Zhao-Karger, Z.; Mueller, J. E.; Zhao, X.; Fuhr, O.; Jacob, T.; Fichtner, M. *RSC Adv.* **2014**, *4*, 26924–26927.
1403. Pan, B.; Zhang, J.; Huang, J.; Vaughney, J. T.; Zhang, L.; Han, S. D.; Burrell, A. K.; Zhang, Z.; Liao, C. *Chem. Commun.* **2015**, *51*, 6214–6217.
1404. Pan, B.; Huang, J.; He, M.; Brombosz, S. M.; Vaughney, J. T.; Zhang, L.; Burrell, A. K.; Zhang, Z.; Liao, C. *ChemSusChem* **2016**, *9*, 595–599.
1405. Du, A.; Zhang, Z.; Qu, H.; Cui, Z.; Qiao, L.; Wang, L.; Chai, J.; Lu, T.; Dong, S.; Dong, T.; Xu, H.; Zhou, X.; Cui, G. *Energ. Environ. Sci.* **2017**, *10*, 2616–2625.
1406. Carter, T. J.; Mohtadi, R.; Arthur, T. S.; Mizuno, F.; Zhang, R.; Shirai, S.; Kampf, J. W. *Angew. Chem. Int. Ed.* **2014**, *53*, 3173–3177.
1407. Liu, T.; Shao, Y.; Li, G.; Gu, M.; Hu, J.; Xu, S.; Nie, Z.; Chen, X.; Wang, C.; Liu, J. *J. Mater. Chem. A* **2014**, *2*, 3430–3438.
1408. Schnurr, A.; Samigullin, K.; Breunig, J. M.; Bolte, M.; Lerner, H.-W.; Wagner, M. *Organometallics* **2011**, *30*, 2838–2843.
1409. Dornhaus, F.; Bolte, M. *CSD Communication*, 2012. refcode UXAGAC01.
1410. Perruchas, S.; Simon, F.; Uriel, S.; Avarvari, N.; Boubekur, K.; Batail, P. *J. Organomet. Chem.* **2002**, *643–644*, 301–306.
1411. Lichtenberg, C.; Jochmann, P.; Spaniol, T. P.; Okuda, J. *Angew. Chem. Int. Ed.* **2011**, *50*, 5753–5756.
1412. Deacon, G. B.; Forsyth, C. M.; Jaroschik, F.; Junk, P. C.; Kay, D. L.; Maschmeyer, T.; Masters, A. F.; Wang, J.; Field, L. D. *Organometallics* **2008**, *27*, 4772–4778.
1413. Harder, S.; Müller, S.; Hübner, E. *Organometallics* **2004**, *23*, 178–183.
1414. Fedushkin, I.; Lukoyanov, A.; Dechert, S.; Schumann, H. *Eur. J. Inorg. Chem.* **2004**, *2004*, 2421–2424.
1415. Krieck, S.; Görls, H.; Westerhausen, M. *Inorg. Chem. Comm.* **2008**, *11*, 911–913.
1416. Krieck, S.; Görls, H.; Westerhausen, M. *Organometallics* **2008**, *27*, 5052–5057.
1417. Langer, J.; Krieck, S.; Görls, H.; Kreisel, G.; Seidel, W.; Westerhausen, M. *New J. Chem.* **2010**, *34*, 1667–1677.
1418. Fromm, K. M.; Bernardinelli, G.; Mayor-Lopez, M.-J.; Weber, J.; Goesmann, H. Z. *Anorg. Allg. Chem.* **2000**, *626*, 1685–1691.
1419. Gärtner, M.; Görls, H.; Westerhausen, M. *J. Organomet. Chem.* **2008**, *693*, 221–227.
1420. Beattie, J. W.; White, D. S.; Bheemaraju, A.; Martin, P. D.; Groyzman, S. *Dalton Trans.* **2014**, *43*, 7979–7986.
1421. Krieck, S.; Görls, H.; Westerhausen, M. *Chem. Asian J.* **2010**, *5*, 272–277.
1422. Henderson, K. W.; Rood, J. A.; Noll, B. C. *Acta Crystallogr.* **2005**, *E61*, m2006–m2007.
1423. Langer, J.; Görls, H.; Westerhausen, M. *Organometallics* **2010**, *29*, 2034–2039.
1424. Michel, O.; Kaneko, H.; Tsurugi, H.; Yamamoto, K.; Törnroos, K. W.; Anwender, R.; Mashima, K. *Eur. J. Inorg. Chem.* **2012**, *2012*, 998–1003.
1425. Sluka, R.; Nečas, M.; Šindelář, P. *Acta Crystallogr.* **2004**, *E60*, m447–m448.
1426. Boese, R.; Haas, A.; Hoppmann, E.; Merz, K.; Olteanu, A. Z. *Anorg. Allg. Chem.* **2002**, *628*, 673–680.
1427. Sypień, J. K.; Zevaco, T. A.; Flicker, A.; Walter, O.; Dinjus, E. *Inorg. Chem. Comm.* **2013**, *30*, 69–73.
1428. Nieger, M.; Fuchs, A. *CSD Communication*, 2001. refcode FEYAJ02.
1429. Knabel, K.; Nöth, H. Z. *Naturforsch.* **2005**, *B60*, 1027–1035.
1430. Sharutin, V. *CSD Communication*, 2016. refcode AZORUE.
1431. Sharutin, V. V.; Sharutina, O. K.; Khisamov, R. M.; Senchurin, V. S. *Russ. J. Inorg. Chem.* **2017**, *62*, 766–776.
1432. García-Álvarez, J.; Hevia, E.; Kennedy, A. R.; Klett, J.; Mulvey, R. E. *Chem. Commun.* **2007**, 2402–2404.
1433. Chadwick, F. M.; Cooper, R. T.; O'Hare, D. *Organometallics* **2016**, *35*, 2092–2100.
1434. Xie, W.; Park, S. W.; Jung, H.; Kim, D.; Baik, M. H.; Chang, S. *J. Am. Chem. Soc.* **2018**, *140*, 9659–9668.
1435. Bonomo, L.; Stern, C.; Solari, E.; Scopelliti, R.; Floriani, C. *Angew. Chem. Int. Ed.* **2001**, *40*, 1449–1452.
1436. Bilyachenko, A. N.; Yalymov, A. I.; Korlyukov, A. A.; Long, J.; Larionova, J.; Guari, Y.; Vologzhanina, A. V.; Eskova, M. A.; Shubina, E. S.; Levitsky, M. M. *Dalton Trans.* **2016**, *45*, 7320–7327.
1437. Govor, E. V.; Lysenko, A. B.; Quiñero, D.; Rusanov, E. B.; Chernega, A. N.; Moellmer, J.; Staudt, R.; Krautscheid, H.; Frontera, A.; Domasevitch, K. V. *Chem. Commun.* **2011**, *47*, 1764–1766.
1438. Kameo, H.; Hashimoto, Y.; Nakazawa, H. *Organometallics* **2012**, *31*, 3155–3162.
1439. Schiefer, M.; Reddy, N. D.; Ahn, H. J.; Stasch, A.; Roesky, H. W.; Schlicker, A. C.; Schmidt, H. G.; Noltemeyer, M.; Vidovic, D. *Inorg. Chem.* **2003**, *42*, 4970–4976.
1440. Maddock, L. C. H.; Mu, M.; Kennedy, A. R.; Garcia-Melchor, M.; Hevia, E. *Angew. Chem. Int. Ed.* **2021**, *60*, 15296–15301.
1441. Yang, L.; Bourque, J. L.; McLeod, J. A.; Shen, P.; Baines, K. M.; Liu, L. *Inorg. Chem.* **2017**, *56*, 2985–2991.
1442. Morris, J. J.; Noll, B. C.; Henderson, K. W. *Acta Crystallogr.* **2005**, *E61*, m351–m353.
1443. Jin, L.; Liu, C.; Liu, J.; Hu, F.; Lan, Y.; Batsanov, A. S.; Howard, J. A.; Marder, T. B.; Lei, A. *J. Am. Chem. Soc.* **2009**, *131*, 16656–16657.
1444. Hasche, S.; Mock, C.; Otto, J.; Schweppe, F.; Kirschbaum, K.; Krebs, B.; Pinkerton, A. A. *Inorg. Chim. Acta* **2000**, *298*, 9–15.
1445. Brüdgam, I.; Lentz, D.; Vorbrüggen, H. *CrystEngComm* **2010**, *12*, 795–800.
1446. Daly, S. R.; Bellott, B. J.; Kim, D. Y.; Girolami, G. S. *J. Am. Chem. Soc.* **2010**, *132*, 7254–7255.
1447. Sazonov, P. K.; Artamkina, G. A.; Khrustalev, V. N.; Antipin, M. Y.; Beletskaya, I. P. *J. Organomet. Chem.* **2003**, *681*, 59–69.
1448. McKay, A. I.; Martínez-Martínez, A. J.; Griffiths, H. J.; Rees, N. H.; Waters, J. B.; Weller, A. S.; Krämer, T.; Macgregor, S. A. *Organometallics* **2018**, *37*, 3524–3532.
1449. Qian, C.; Nie, W.; Sun, J. *J. Organomet. Chem.* **2001**, *626*, 171–175.
1450. Wang, G.; Lu, T.; Fan, G.; Li, C.; Yin, H.; Chen, F. X. *Chem. Asian J.* **2018**, *13*, 3718–3722.
1451. Ionkin, A. S.; Marshall, W. J.; Fish, B. M.; Marchione, A. A.; Howe, L. A.; Davidson, F.; McEwen, C. N. *Eur. J. Inorg. Chem.* **2008**, *2008*, 2386–2390.
1452. Fischer, R.; Görls, H.; Meisinger, P. R.; Suxdorf, R.; Westerhausen, M. *Chem. A Eur. J.* **2019**, *25*, 12830–12841.
1453. Humphries, T. D.; Munroe, K. T.; Decken, A.; McGrady, G. S. *Dalton Trans.* **2013**, *42*, 6953–6964.
1454. Bolte, M.; Wagner, M.; Lerner, H.-W. *CSD Communication*, 2000. refcode COHPEU01.
1455. Bauer, M.; Kouvetakis, J.; Groy, L. Z. *Kristallogr. NCS* **2002**, *217*, 421–422.
1456. Rheingold, A. L. *CSD Communication*, 2016. refcode BEKHUV01.
1457. Richtera, L.; Jancik, V.; Martínez-Otero, D.; Pokluda, A.; Zak, Z.; Taraba, J.; Touzin, J. *Inorg. Chem.* **2014**, *53*, 6569–6577.
1458. Fronczek, F. R.; Li, S.-Z.; Hammer, R. P. *CSD Communication*, 2004. refcode NAACET05.
1459. Miller, J. R.; LaLama, M. J.; Kusnic, R. L.; Wilson, D. E.; Kiraly, P. M.; Dickson, S. W.; Zeller, M. *J. Solid State Chem.* **2019**, *270*, 1–10.
1460. Scheurell, K.; Könik, R.; Troyanov, S. I.; Kemptz, E. Z. *Anorg. Allg. Chem.* **2012**, *638*, 1265–1273.
1461. Khurstalev, V. N.; Antipin, M. Y.; Zemlyansky, N. N.; Borisova, I. V.; Ustyuyuk, Y. A.; Lunin, V. V.; Izod, K. *Appl. Organomet. Chem.* **2005**, *19*, 360–362.
1462. Hamill, J. T.; Hardacre, C.; Nieuwenhuyzen, M.; Seddon, K. R.; Thompson, S. A.; Ellis, B. *Chem. Commun.* **2000**, 1929–1930.
1463. Birus, S. M.; Bridgewater, B. M.; Villeges-Estrada, A.; Tanski, J. M.; Parkin, G. *Inorg. Chem.* **2002**, *41*, 4051–4057.
1464. Richtera, L.; Jancik, V.; Barroso-Flores, J.; Nykel, P.; Touzin, J.; Taraba, J. *Eur. J. Inorg. Chem.* **2015**, *2015*, 2923–2927.
1465. Lorenz, V.; Schmiede, B. M.; Hrib, C. G.; Ziller, J. W.; Edelmann, A.; Blaurock, S.; Evans, W. J.; Edelmann, F. T. *J. Am. Chem. Soc.* **2011**, *133*, 1257–1259.
1466. Wang, S.; Yang, Q.; Mak, T. C. W.; Xie, Z. *Organometallics* **2000**, *19*, 334–343.
1467. Liu, D.; Shen, H.; Wang, Y.; Cai, Y.; Xie, Z. *Chem. Asian J.* **2011**, *6*, 628–637.
1468. Ebner, F.; Wadepohl, H.; Greb, L. *J. Am. Chem. Soc.* **2019**, *141*, 18009–18012.



1469. Bonomo, L.; Solari, E.; Scopelliti, R.; Floriani, C.; Re, N. *J. Am. Chem. Soc.* **2000**, *122*, 5312–5326.
1470. Ordyszweska, A.; Szykiewicz, N.; Ponikiewski, Ł.; Scheer, M.; Pikies, J.; Grubba, R. *Inorg. Chem.* **2019**, *58*, 7905–7914.
1471. Dulong, F.; Bathily, O.; Thuéry, P.; Ephritikhine, M.; Cantat, T. *Dalton Trans.* **2012**, *41*, 11980–11983.
1472. Ordoñez, O.; Yu, X.; Wu, G.; Autschbach, J.; Hayton, T. W. *Inorg. Chem.* **2021**, *60*, 12436–12444.
1473. Hayes, C. E.; Gill, D. E.; Brown, M. L.; Leznoff, D. B. *Eur. J. Inorg. Chem.* **2014**, *2014*, 3690–3700.
1474. Vidjayacoumar, B.; Ilango, S.; Ray, M. J.; Chu, T.; Kolpin, K. B.; Andreychuk, N. R.; Cruz, C. A.; Emslie, D. J.; Jenkins, H. A.; Britten, J. F. *Dalton Trans.* **2012**, *41*, 8175–8189.
1475. Iwasaki, T.; Miyata, Y.; Akimoto, R.; Fujii, Y.; Kuniyasu, H.; Kambe, N. *J. Am. Chem. Soc.* **2014**, *136*, 9260–9263.
1476. Budy, H.; Kaese, T.; Bolte, M.; Lerner, H. W.; Wagner, M. *Angew. Chem. Int. Ed.* **2021**, *60*, 19397–19405.
1477. Kaniewska, K.; Ponikiewski, Ł.; Szykiewicz, N.; Ciešlik, B.; Pikies, J.; Krzystek, J.; Dragulescu-Andrasi, A.; Stoian, S. A.; Grubba, R. *Dalton Trans.* **2020**, *49*, 10091–10103.
1478. Pedrick, E. A.; Hrobárik, P.; Seaman, L. A.; Wu, G.; Hayton, T. W. *Chem. Commun.* **2016**, *52*, 689–692.
1479. Wombacher, T.; Goddard, R.; Lehmann, C. W.; Schneider, J. J. *Dalton Trans.* **2017**, *46*, 14122–14129.
1480. Spisak, S. N.; Zabula, A. V.; Ferguson, M. V.; Filatov, A. S.; Petrukina, M. A. *Organometallics* **2013**, *32*, 538–543.
1481. Franz, D.; Haghiri Ilkhechi, A.; Bolte, M.; Lerner, H.; Wagner, M. *Eur. J. Inorg. Chem.* **2011**, *2011*, 5414–5421.
1482. Estrada, J.; Lavallo, V. *Angew. Chem. Int. Ed.* **2017**, *56*, 9906–9909.
1483. Myers, T. W.; Holmes, A. L.; Berben, L. A. *Inorg. Chem.* **2012**, *51*, 8997–9004.
1484. Thomas-Hargreaves, L. R.; Giansiracusa, M. J.; Gregson, M.; Zanda, E.; O'Donnell, F.; Wooles, A. J.; Chilton, N. F.; Liddle, S. T. *Chem. Sci.* **2021**, *12*, 3911–3920.
1485. Liu, D.; Wang, Y.; Chan, H.-S.; Tang, Y.; Xie, Z. *Organometallics* **2008**, *27*, 5295–5302.
1486. Piskunov, A. V.; Meshcheryakova, I. N.; Fukin, G. K.; Shayrin, A. S.; Cherkasov, V. K.; Abakumov, G. A. *Dalton Trans.* **2013**, *42*, 10533–10539.
1487. Suter, R.; Wagner, M.; Querci, L.; Conti, R.; Benkő, Z.; Grützmacher, H. *Dalton Trans.* **2020**, *49*, 8201–8208.
1488. Korobkov, I.; Gorelsky, S.; Gambarotta, S. *J. Am. Chem. Soc.* **2009**, *131*, 10406–10420.
1489. Rosenthal, A. J.; Vogt, M.; de Bruin, B.; Grützmacher, H. *Eur. J. Inorg. Chem.* **2013**, *2013*, 5831–5835.
1490. Kawaguchi, H.; Matsuo, T. *J. Organomet. Chem.* **2005**, *690*, 5333–5345.
1491. Harriman, K. L. M.; Murillo, J.; Suturina, E. A.; Fortier, S.; Murugesu, M. *Inorg. Chem. Front.* **2020**, *7*, 4805–4812.
1492. Fortier, S.; González-del Moral, O.; Chen, C. H.; Pink, M.; Le Roy, J. J.; Murugesu, M.; Mindiola, D. J.; Caulton, K. G. *Chem. Commun.* **2012**, *48*, 11082–11084.
1493. Cai, I. C.; Lipschutz, M. I.; Tilley, T. D. *Chem. Commun.* **2014**, *50*, 13062–13065.
1494. Piesch, M.; Graßl, C.; Scheer, M. *Angew. Chem. Int. Ed.* **2020**, *59*, 7154–7160.
1495. Pöcheim, A.; Marschner, C.; Baumgartner, J. *Inorg. Chem.* **2021**, *60*, 8218–8226.
1496. Yao, S.; Lindenmaier, N.; Xiong, Y.; Inoue, S.; Szilvási, T.; Adelhardt, M.; Sutter, J.; Meyer, K.; Driess, M. *Angew. Chem. Int. Ed.* **2015**, *54*, 1250–1254.
1497. Ali, S. H.; Deacon, G. B.; Junk, P. C.; Hamidi, S.; Wiecko, M.; Wang, J. *Chem. A Eur. J.* **2018**, *24*, 230–242.
1498. Harman, W. H.; Chang, C. J. *J. Am. Chem. Soc.* **2007**, *129*, 15128–15129.
1499. Du, J.; King, D. M.; Chatelain, L.; Lu, E.; Tuna, F.; McInnes, E. J. L.; Wooles, A. J.; Maron, L.; Liddle, S. T. *Chem. Sci.* **2019**, *10*, 3738–3745.
1500. Pribanic, B.; Trincado, M.; Eiler, F.; Vogt, M.; Comas-Vives, A.; Grützmacher, H. *Angew. Chem. Int. Ed.* **2020**, *59*, 15603–15609.
1501. Wong, E. W. Y.; Walsby, C. J.; Storr, T.; Leznoff, D. B. *Inorg. Chem.* **2010**, *49*, 3343–3350.
1502. Hepp, A.; Labbow, R.; Reiß, F.; Schulz, A.; Villinger, A. *Eur. J. Inorg. Chem.* **2018**, *2018*, 2905–2914.
1503. Zhao-Karger, Z.; Gil Bardaji, M. E.; Fuhr, O.; Fichtner, M. *J. Mater. Chem. A* **2017**, *5*, 10815–10820.
1504. Yandulov, D. V.; Schrock, R. R.; Rheingold, A. L.; Ceccarelli, C.; Davis, W. M. *Inorg. Chem.* **2003**, *42*, 796–813.
1505. McArthur, S. G.; Jay, R.; Geng, L.; Guo, J.; Lavallo, V. *Chem. Commun.* **2017**, *53*, 4453–4456.
1506. Nguyen, D.-T.; Eng, A. Y. S.; Ng, M.-F.; Kumar, V.; Sofer, Z.; Handoko, A. D.; Subramanian, G. S.; Seh, Z. W. *Cell Rep. Phys. Sci.* **2020**, *1*, 100265.
1507. Cheng, Y.; Stolley, R. M.; Han, K. S.; Shao, Y.; Arey, B. W.; Washton, N. M.; Mueller, K. T.; Helm, M. L.; Sprenkle, V. L.; Liu, J.; Li, G. *Phys. Chem. Chem. Phys.* **2015**, *17*, 13307–13314.
1508. Gärtner, M.; Fischer, R.; Langer, J.; Görls, H.; Walther, D.; Westerhausen, M. *Inorg. Chem.* **2007**, *46*, 5118–5124.
1509. Fromm, K. M.; Goemann, H.; Bernardinelli, G. *Polyhedron* **2000**, *19*, 1783–1789.
1510. Belli Dell'Amico, D.; Bradicich, C.; Labella, L.; Marchetti, F. *Inorg. Chim. Acta* **2006**, *359*, 1659–1665.
1511. Li, Z.; Fuhr, O.; Fichtner, M.; Zhao-Karger, Z. *Energ. Environ. Sci.* **2019**, *12*, 3496–3501.
1512. Maudez, W.; Fromm, K. M. *Z. Anorg. Allg. Chem.* **2012**, *638*, 1810–1819.
1513. Weber, F.; Wolmershäuser, G.; Sitzmann, H. *Acta Crystallogr.* **2005**, *E61*, m512–m513.
1514. Ali, A.; Langer, M.; Lorenz, V.; Hrib, C. G.; Hilfert, L.; Edelmann, F. T. *J. Organomet. Chem.* **2015**, *776*, 163–169.
1515. Köferstein, R.; Jäger, L.; Lorenz, V.; Abicht, H.-P.; Woltersdorf, J.; Pippel, E.; Görls, H. *Solid State Sci.* **2005**, *7*, 1280–1288.
1516. Tonouchi, Y.; Matsumoto, K.; Nagata, T.; Katahira, M.; Hagiwara, R. *Inorg. Chem.* **2020**, *59*, 6631–6639.
1517. Geng, L.; Li, Q. H.; Wang, S. T.; Liu, Y. J.; Fang, W. H.; Zhang, J. *Chem. Commun.* **2021**, *57*, 2085–2088.
1518. Monsch, G.; Klüfers, P. *Angew. Chem. Int. Ed.* **2019**, *58*, 8566–8571.
1519. Klüfers, P.; Vogler, C. *Z. Anorg. Allg. Chem.* **2007**, *633*, 908–912.
1520. Pathak, M.; Bohra, R.; Mehrotra, R. C.; Lorenz, I.-P.; Piotrowski, H. *J. Chem. Res.* **2004**, *377*–380.
1521. Teichert, J.; Block, T.; Pöttgen, R.; Doert, T.; Ruck, M. *Eur. J. Inorg. Chem.* **2019**, *2019*, 3820–3831.
1522. Elinburg, J. K.; Hyre, A. S.; McNeely, J.; Alam, T. M.; Klenner, S.; Pöttgen, R.; Rheingold, A. L.; Doerrer, L. H. *Dalton Trans.* **2020**, *49*, 13773–13785.
1523. Xiao, H.; Zhou, J.; Hu, F. *Dalton Trans.* **2018**, *47*, 8442–8447.
1524. Betz, R.; Pfister, M.; Reichviser, M. M.; Klüfers, P. *Z. Anorg. Allg. Chem.* **2008**, *634*, 1393–1396.
1525. Zhang, L. *CSD Communication*, 2020. refcode JUMMEM.
1526. Mehdi, H.; Binemans, K.; Van Hecke, K.; Van Meervelt, L.; Nockemann, P. *Chem. Commun.* **2010**, *46*, 234–236.
1527. Filatov, E. S.; Baidina, I. A.; Igumenov, I. K. *J. Struct. Chem.* **2006**, *47*, 484–488.
1528. Evans, W. J.; Rego, D. B.; Ziller, J. W. *Polyhedron* **2006**, *25*, 2691–2697.
1529. Tsybarenko, D. M.; Korsakov, I. E.; Lyssenko, K. A.; Troyanov, S. I. *Polyhedron* **2015**, *92*, 68–76.
1530. Salmon, L.; Thuéry, P.; Ephritikhine, M. *Acta Crystallogr.* **2006**, *E62*, m1250–m1251.
1531. Kochelakov, D. V.; Vikulova, E. S.; Kuratieva, N. V. *J. Struct. Chem.* **2020**, *61*, 439–448.
1532. Kennedy, C. R.; Guidera, P. A.; Jacobsen, E. N. *ACS Cent. Sci.* **2016**, *2*, 416–423.
1533. Raymond, O.; Brothers, P. J.; Buchner, M. R.; Lane, J. R.; Müller, M.; Spang, N.; Henderson, W.; Plieger, P. G. *Inorg. Chem.* **2019**, *58*, 6388–6398.
1534. Lethesh, K. C.; Øien-Ødegaard, S.; Jayasayee, K.; Fiksdahl, A. *Dalton Trans.* **2019**, *48*, 982–988.
1535. Vikulova, E. S.; Piryazev, D. A.; Zherikova, K. V.; Alferova, N. I.; Morozova, N. B.; Igumenov, I. K. *J. Struct. Chem.* **2013**, *54*, 883–889.
1536. Wang, L.; Yang, Y.; Ni, J.; Stern, C. L.; Marks, T. J. *Chem. Mater.* **2005**, *17*, 5697–5704.
1537. Kinzhybalov, V.; Kubiak, R.; Janczak, J. *Polyhedron* **2016**, *115*, 142–154.
1538. Hatanpää, T.; Kansikas, J.; Mutikainen, I.; Leskelä, M. *Inorg. Chem.* **2001**, *40*, 788–794.

1539. Kuratieva, N. V.; Vikulova, E. S.; Zherikova, K. V. *J. Struct. Chem.* **2018**, *59*, 131–135.
1540. Fragalà, M. E.; Toro, R. G.; Rossi, P.; Dapporto, P.; Malandrino, G. *Chem. Mater.* **2009**, *21*, 2062–2069.
1541. Polyanskaya, T. M.; Chistyakov, M. A.; Simonenko, E. P.; Sevastyanov, V. G.; Kuznetsov, N. T. *Inorg. Chim. Acta* **2009**, *362*, 5133–5138.
1542. Pochekutova, T. S.; Khamylov, V. K.; Kurskii, Y. A.; Fukin, G. K.; Petrov, B. I. *Polyhedron* **2010**, *29*, 1381–1386.
1543. Pochekutova, T. S.; Khamylov, V. K.; Fukin, G. K.; Petrov, B. I.; Shavrin, A. S.; Arapova, A. V.; Lazarev, N. M.; Faerman, V. I.; Kulikova, T. I.; Baranov, E. V.; Khamaletdinova, N. M. *Polyhedron* **2020**, *177*, 114263.
1544. Pochekutova, T. S.; Khamylov, V. K.; Fukin, G. K.; Kurskii, Y. A.; Petrov, B. I.; Shavrin, A. S.; Arapova, A. V. *Polyhedron* **2011**, *30*, 1945–1952.
1545. Khamylov, V. K.; Pochekutova, T. S.; Petrov, B. I.; Fukin, G. K.; Lukina, S. P. *Russ. J. Coord. Chem.* **2008**, *34*, 884–890.
1546. Ilyukhin, A.; Ivanov, S. *CSD Communication*, 2017. refcode OCELOA.
1547. Davies, H. O.; Jones, A. C.; Leedham, T. J.; Crosbie, M. J.; Wright, P. J.; Boag, N. M.; Thompson, J. R. *Chem. Vap. Depos.* **2000**, *6*, 71–75.
1548. Kessler, V. G.; Gohil, S.; Kritikos, M.; Korsak, O. N.; Knyazeva, E. E.; Moskovskaya, I. F.; Romanovsky, B. V. *Polyhedron* **2001**, *20*, 915–922.
1549. El Habra, N.; Benetollo, F.; Casarin, M.; Bolzan, M.; Sartori, A.; Rossetto, U. *Dalton Trans.* **2010**, *39*, 8064–8070.
1550. Marchetti, F.; Pettinari, C.; Pettinari, R.; Cingolani, A.; Gobetto, R.; Chierotti, M. R.; Drozdov, A.; Troyanov, S. I. *Inorg. Chim. Acta* **2006**, *45*, 3074–3085.
1551. Davies, H. O.; Brooks, J. J.; Jones, A. C.; Leedham, T. J.; Bickley, J. F.; Steiner, A.; O'Brien, P.; White, A. J. P.; Williams, D. J. *Polyhedron* **2001**, *20*, 2397–2403.
1552. Kessler, V. G.; Gohil, S.; Parola, S. *Dalton Trans.* **2003**, 544–550.
1553. Beachley, O. T.; Gardinier, J. R.; Churchill, M. R. *Organometallics* **2003**, *22*, 1145–1151.
1554. Fahlman, B. D.; Bott, S. G.; Barron, A. R. *J. Chem. Crystallogr.* **2000**, *30*, 65–67.
1555. von Chranowski, L. S.; Lutz, M.; Spek, A. L. *Acta Crystallogr.* **2007**, *C63*, m129–m134.
1556. Dharmaprakash, M. S.; Thamotharan, S.; Neelgund, G. M.; Shivashankar, S. A. *Acta Crystallogr.* **2006**, *E62*, m434–m436.
1557. Lichtenberger, R.; Baumann, S. O.; Bendova, M.; Puchberger, M.; Schubert, U. *Monatsh. Chem.* **2010**, *141*, 717–727.
1558. Reimann, S.; Knöpke, L. R.; Spannenberg, A.; Brückner, A.; Kühn, O.; Langer, P.; Bentrup, U. *Tetrahedron* **2013**, *69*, 3338–3347.
1559. Bouyahy, M.; Roisnel, T.; Carpentier, J.-F. *Organometallics* **2010**, *29*, 491–500.
1560. Ahmed, M. A. K.; Fjellvåg, H.; Kjekshus, A.; Wragg, D. S. *Z. Anorg. Allg. Chem.* **2013**, *639*, 770–778.
1561. Nikolaeva, A.; Nygaard, R.; Martynova, I.; Tsybarensko, D. *Polyhedron* **2020**, *180*, 114373.
1562. Li, W.; Zhang, C.; Ma, Y.; Liu, C.; Fan, J.; Mai, Y.; Schropp, R. E. I. *Energ. Environ. Sci.* **2018**, *11*, 286–293.
1563. Yang, C.-J.; Sheng, T.-L.; Cao, Q.-Y.; Zou, D.-C.; Yi, C.; Gao, X.-C. *Inorg. Chim. Acta* **2007**, *360*, 1593–1598.
1564. Maslov, D. A.; Bukhtenko, O. V.; Yakushev, I. A.; Tsodikov, M. V. *Russ. Chem. Bull.* **2020**, *69*, 815–818.
1565. Pugh, D.; Bloor, L. G.; Sathasivam, S.; Parkin, I. P.; Carmalt, C. J. *Eur. J. Inorg. Chem.* **2011**, *2011*, 1953–1960.
1566. Tyrre, W.; Wickleder, M. S. *J. Organomet. Chem.* **2003**, *677*, 28–34.
1567. Jana, B.; Honaker, C.; Uhl, W. *J. Organomet. Chem.* **2018**, *856*, 78–86.
1568. Abbati, G. L.; Brunel, L. C.; Casalta, H.; Cornia, A.; Fabretti, A. C.; Gatteschi, D.; Hassan, A. K.; Jansen, A. G.; Maniero, A. L.; Pardi, L.; Paulsen, C.; Segre, U. *Chem. A Eur. J.* **2001**, *7*, 1796–1807.
1569. Uhl, W.; Jana, B. *Eur. J. Inorg. Chem.* **2009**, *2009*, 3942–3947.
1570. Beachley, O. T.; Gardinier, J. R.; Churchill, M. R. *Organometallics* **2000**, *19*, 4544–4549.
1571. Fernández, E. J.; Laguna, A.; López-de-Luzuriaga, J. M.; Monge, M.; Montiel, M.; Olmos, M. E.; Pérez, J. *Organometallics* **2004**, *23*, 774–782.
1572. Askarinejad, A.; Morsali, A.; Zhu, L.-G. *Solid State Sci.* **2006**, *8*, 537–540.
1573. Mertens, R. T.; Parkin, S.; Awuah, S. G. *Inorg. Chim. Acta* **2020**, *503*, 119375.
1574. Koroteev, P. S.; Egorov, M. P.; Nefedov, O. M.; Aleksandrov, G. G.; Nefedov, S. E.; Eremenko, I. L. *Russ. Chem. Bull.* **2000**, *49*, 1800–1801.
1575. Shahzadi, S.; Ali, S.; Jin, G. X. *J. Iran. Chem. Soc.* **2006**, *3*, 323–326.
1576. Thy, C. K.; Lo, K. M.; Ng, S. W. *Acta Crystallogr.* **2010**, *E66*, m992.
1577. Briois, V.; Belin, S.; Chalaça, M. Z.; Santos, R. H. A.; Santilli, C. V.; Pulcinelli, S. H. *Chem. Mater.* **2004**, *16*, 3885–3894.
1578. Verdenelli, M.; Parola, S.; Hubert-Pfalzgraf, L. G.; Lecocq, S. *Polyhedron* **2000**, *19*, 2069–2075.
1579. Verdenelli, M.; Parola, S.; Lecocq, S.; Hubert-Pfalzgraf, L. G. *Z. Kristallogr. NCS* **2001**, *216*, 305–306.
1580. Reuter, H. Z. *Kristallogr. NCS* **2004**, *219*, 109–110.
1581. Sevastyanov, V. G.; Simonenko, E. P.; Ignatov, P. A.; Popov, V. S.; Churakov, A. V.; Kuznetsov, N. T.; Sergienko, V. S. *Mendeleev Commun.* **2012**, *22*, 239–241.
1582. Barry, M. C.; Lieberman, C. M.; Wei, Z.; Clérac, R.; Filatov, A. S.; Dikarev, E. V. *Inorg. Chim. Acta* **2018**, *57*, 2308–2313.
1583. Popov, V. S.; Ignatov, P. A.; Churakov, A. V.; Simonenko, E. P.; Simonenko, N. P.; Ignatova, N. N.; Sevastyanov, V. G.; Kuznetsov, N. T. *Russ. J. Inorg. Chem.* **2016**, *61*, 545–553.
1584. Lyczko, K.; Narbutt, J.; Paluchowska, B.; Maurin, J. K.; Persson, I. *Dalton Trans.* **2006**, 3972–3976.
1585. Krisyuk, V. V.; Baidina, I. A.; Turgambaeva, A. E.; Urkasymkyzy, S.; Korolkov, I. V.; Koretskaya, T. P.; Igumenov, I. K. *J. Organomet. Chem.* **2016**, *819*, 115–119.
1586. Nechaev, M. S.; Chernov, O. V.; Portnyagin, I. A.; Khrustalev, V. N.; Aysin, R. R.; Lunin, V. V. *J. Organomet. Chem.* **2010**, *695*, 365–369.
1587. Chistyakov, M. A.; Simonenko, E. P.; Sevostyanov, V. G.; Kuznetsov, N. T. *Russ. J. Coord. Chem.* **2006**, *32*, 693–700.
1588. Sevastyanov, V. G.; Chistyakov, M. A.; Simonenko, E. P.; Fukin, G. K.; Kuznetsov, N. T. *Russ. J. Coord. Chem.* **2008**, *34*, 157–166.
1589. Horley, G. A.; Mahon, M. F.; Mazhar, M.; Molloy, K. C.; Haycock, P. W.; Myers, C. P. *J. Chem. Soc. Dalton Trans.* **2002**, 4416–4421.
1590. Hatanpää, T. *CSD Communication*, 2016. refcode YUJYEV01.
1591. Moniz, S. J. A.; Pugh, D.; Blackman, C. S.; Tang, J.; Carmalt, C. J. *Cryst. Growth Des.* **2016**, *16*, 3818–3825.
1592. Dikarev, E. V.; Zhang, H.; Li, B. *J. Am. Chem. Soc.* **2005**, *127*, 6156–6157.
1593. Moniz, S. J. A.; Bhachu, D.; Blackman, C. S.; Cross, A. J.; Elouali, S.; Pugh, D.; Quesada Cabrera, R.; Vallejos, S. *Inorg. Chim. Acta* **2012**, *380*, 328–335.
1594. Barszcz, B.; Masternak, J.; Kowalik, M. *Coord. Chem. Rev.* **2021**, *443*, 213935.
1595. A. Morsali and L. Hashemi, *Main Group Metal Coordination Polymers*, 2017, John Wiley and Sons, Hoboken.
1596. Martínez Casado, F. J.; Ramos Riesco, M.; Redondo, M. I.; Choquesillo-Lazarte, D.; López-Andrés, S.; Cheda, J. A. R. *Cryst. Growth Des.* **2011**, *11*, 1021–1032.
1597. Rheingold, A. L.; Jankins, T. *CSD Communication*, 2017. refcode MEGVAY.
1598. Dittrich, B.; Bergmann, J.; Roloff, P.; Reiss, G. *Crystals* **2018**, *8*, 213.
1599. Lavalette, A.; Lawrance, G.; Alcock, N.; Hannon, M. *Eur. J. Inorg. Chem.* **2004**, *2004*, 3981–3983.
1600. Courtney, B. H.; Fronczek, F. R. *CSD Communication*, 2005. refcode KHACET02.
1601. Liebing, P.; Zaeni, A.; Olbrich, F.; Edelmann, F. T. *Acta Crystallogr.* **2016**, *E72*, 1757–1761.
1602. Shui, Q. R.; Fu, R. B.; Zhou, Z. Q.; Ma, Z. J.; Tang, H. X.; Wu, X. T. *Chem. A Eur. J.* **2022**, *28*, e202103687.
1603. Shui, Q.; Fu, R.; Tang, H.; Fang, Y.; Ma, Z.; Wu, X. *Inorg. Chem.* **2021**, *60*, 5290–5296.
1604. Shui, Q. R.; Tang, H. X.; Fu, R. B.; Fang, Y. B.; Ma, Z. J.; Wu, X. T. *Angew. Chem. Int. Ed.* **2021**, *60*, 2116–2119.
1605. Müller-Bunz, H.; Vetter, A. C.; Nikitin, K. *CSD Communication*, 2020. refcode KUSCUZ.
1606. Coker, E. N.; Boyle, T. J.; Rodríguez, M. A.; Alam, T. M. *Polyhedron* **2004**, *23*, 1739–1747.
1607. Scheurell, K.; Troyanov, S. I.; Kernitz, E. Z. *Anorg. Allg. Chem.* **2015**, *641*, 1106–1109.
1608. Bette, S.; Eggert, G.; Emmerling, S.; Etter, M.; Schleid, T.; Dinnebier, R. E. *Cryst. Growth Des.* **2020**, *20*, 5346–5355.

1609. Kennedy, C. R.; Hooper, D. *CSD Communication*, 2016. refcode CALCLA02.
1610. Bette, S.; Müller, M. X.; Eggert, G.; Schleid, T.; Dinnebier, R. E. *Dalton Trans.* **2019**, 48, 16062–16073.
1611. Smetana, V.; Kelley, S. P.; Titi, H. M.; Hou, X.; Tang, S. F.; Mudring, A. V.; Rogers, R. D. *Inorg. Chem.* **2020**, 59, 818–828.
1612. Freire, E.; Baggio, R. *Acta Crystallogr.* **2008**, C64, m164–m166.
1613. Zänker, S.; Scholz, G.; Heise, M.; Emmerling, F.; Kemnitz, E. *CrstEngComm* **2020**, 22, 2772–2780.
1614. Dong, G.; Bing-guang, Z.; Chun-ying, D.; Ke-liang, P.; Qing-jin, M. *J. Chem. Soc. Dalton Trans.* **2002**, 3783–3784.
1615. Mensinger, Z. L.; Zakharov, L. N.; Johnson, D. W. *Inorg. Chem.* **2009**, 48, 3505–3507.
1616. Janczak, J.; Kubiak, R. *Inorg. Chim. Acta* **2011**, 376, 28–35.
1617. Churakov, A. V.; Vinokurov, A. A.; Znamekov, K. O.; Mordvinova, N. E.; Gippius, A. A.; Zhurenko, S. V.; Baenitz, M.; Istomin, S. Y. *Polyhedron* **2019**, 160, 42–45.
1618. King, P.; Stammatatos, T. C.; Abboud, K. A.; Christou, G. *Angew. Chem. Int. Ed.* **2006**, 45, 7379–7383.
1619. Stafeeva, V. S.; Mitiaev, A. S.; Abakumov, A. M.; Tsirlin, A. A.; Makarevich, A. M.; Antipov, E. V. *Polyhedron* **2007**, 26, 5365–5369.
1620. Martínez-Casado, F. J.; Ramos-Riesco, M.; Rodríguez-Cheda, J. A.; Cucinotta, F.; Matesanz, E.; Miletto, I.; Gianotti, E.; Marchese, L.; Matěj, Z. *Inorg. Chim. Acta* **2016**, 55, 8576–8586.
1621. Lyczko, K.; Bak, J. *Acta Crystallogr.* **2008**, E64, m1341–m1342.
1622. Mauck, C. M.; van den Heuvel, T. W.; Hull, M. M.; Zeller, M.; Oertel, C. M. *Inorg. Chem.* **2010**, 49, 10736–10743.
1623. Zouihri, H.; Ait Mouha, M.; Ba Mohamed, B.; Yamni, K.; Tijani, N. *IUCrData* **2016**, 1, x161892.
1624. Monakhov, K. Y.; Gourlaouen, C.; Pattacini, R.; Braunstein, P. *Inorg. Chem.* **2012**, 51, 1562–1568.
1625. Aouri, A.; Dridi, R.; Jouffret, L.; Zid, M. F. *Cryst. Struct. Theory Appl.* **2019**, 8, 29–43.
1626. Boldyreva, E. V.; Ahsbahs, H.; Chernyshev, V. V.; Ivashevskaya, S. N.; Oganov, A. R. Z. *Kristallogr. Cryst. Mater.* **2006**, 221, 186–197.
1627. Chen, X. A.; Song, F. P.; Chang, X. A.; Zang, H. G.; Xiao, W. Q. *Acta Crystallogr.* **2008**, E64, m863.
1628. Sadakiyo, M.; Yamada, T.; Kato, K.; Takata, M.; Kitagawa, H. *Chem. Sci.* **2016**, 7, 1349–1356.
1629. Pasińska, K.; Ciupa, A.; Pikul, A.; Gągor, A.; Pietraszko, A.; Cizman, A. *J. Mater. Chem. C* **2020**, 8, 6254–6263.
1630. Pastero, L.; Curretti, N.; Orteni, M. A.; Schiavoni, M.; Destefanis, E.; Pavese, A. *Sci. Total Environ.* **2019**, 666, 1232–1244.
1631. Izatulina, A. R.; Gurzhiy, V. V.; Krzhizhanovskaya, M. G.; Kuzmina, M. A.; Leoni, M.; Frank-Kamenetskaya, O. V. *Cryst. Growth Des.* **2018**, 18, 5465–5478.
1632. Piro, O. E.; Echeverría, G. A.; González-Baró, A. C.; Baran, E. J. *Phys. Chem. Miner.* **2018**, 45, 185–195.
1633. Vanhoyland, G.; Bourée, F.; Van Bael, M. K.; Mullens, J.; Van Poucke, L. C. J. *Solid State Chem.* **2001**, 157, 283–288.
1634. Iveson, S. J.; Johnston, C. B.; Harrison, W. T. A. *Crystals* **2011**, 1, 59–68.
1635. Borel, C.; Ghazzali, M.; Langer, V.; Öhrström, L. *Inorg. Chem. Commun.* **2009**, 12, 105–108.
1636. Hong, P.-Z.; Song, W.-D.; Wu, Z.-H. *Acta Crystallogr.* **2007**, E63, m2296.
1637. Hong, P. Z.; Song, W. D.; Wu, Z. H. *Acta Crystallogr.* **2008**, E64, e12.
1638. Martin, L.; Turner, S. S.; Day, P.; Guionneau, P.; Howard, J. A.; Hibbs, D. E.; Light, M. E.; Hursthouse, M. B.; Uruichi, M.; Yakushi, K. *Inorg. Chem.* **2001**, 40, 1363–1371.
1639. Mouchaham, G.; Roques, N.; Khodja, W.; Duhayon, C.; Coppel, Y.; Brandès, S.; Fodor, T.; Meyer, M.; Sutter, J.-P. *Chem. A Eur. J.* **2017**, 23, 11818–11826.
1640. Akutsu, H.; Akutsu-Sato, A.; Turner, S. S.; Day, P.; Canadell, E.; Firth, S.; Clark, R. J.; Yamada, J.; Nakatsuji, S. *Chem. Commun.* **2004**, 18–19.
1641. Akutsu-Sato, A.; Akutsu, H.; Turner, S. S.; Day, P.; Probert, M. R.; Howard, J. A.; Akutagawa, T.; Takeda, S.; Nakamura, T.; Mori, T. *Angew. Chem. Int. Ed.* **2004**, 44, 292–295.
1642. Prokhorova, T.; Yagubskii, E.; Zorina, L.; Simonov, S.; Zverev, V.; Shibaeva, R.; Buravov, L. *Crystals* **2018**, 8, 92.
1643. Wu, J.; Lou, L.; Han, Y.; Xu, Y.; Zhang, X.; Wang, Z. *RSC Adv.* **2020**, 10, 41720–41726.
1644. Audebrand, N.; Jeanneau, E.; Bataille, T.; Raitte, S.; Louër, D. *Solid State Sci.* **2004**, 6, 579–591.
1645. Wu, J.; Lou, L.; Sun, H.; Tao, C.; Li, T.; Wang, Z.; Zhang, X.; Li, J. *CrstEngComm* **2020**, 22, 1078–1085.
1646. <http://www.iza-structure.org/databases/>.
1647. Yi, F.; Yang, H.; Zhao, X.; Feng, P.; Bu, X. *Angew. Chem. Int. Ed.* **2019**, 58, 2889–2892.
1648. Sun, Q.; Liu, Y.; Li, H.; Luo, Z. *Acta Crystallogr.* **2009**, E65, m394–m395.
1649. Audebrand, N.; Raitte, S.; Louër, D. *Solid State Sci.* **2003**, 5, 783–794.
1650. Chen, Z.; Zhou, Y.; Weng, L.; Zhang, H.; Zhao, D. *J. Solid State Chem.* **2003**, 173, 435–441.
1651. Zhong, Y.; Chen, C.; Zhang, C.; Xu, D.; Lin, Z. *Inorg. Chem. Commun.* **2017**, 84, 186–189.
1652. Yang, S.; Li, G.; Tian, S.; Liao, F.; Lin, J. *J. Solid State Chem.* **2005**, 178, 3703–3707.
1653. Seiler, O.; Burschka, C.; Penka, M.; Tacke, R. *Z. Anorg. Allg. Chem.* **2002**, 628, 2427–2434.
1654. Cunha-Silva, L.; Shi, F.-N.; Almeida Paz, F. A.; Hardie, M. J.; Klinowski, J.; Trindade, T.; Rocha, J. *Inorg. Chim. Acta* **2009**, 362, 263–270.
1655. Lopez, J. R.; Akutsu, H.; Martin, L. *Synth. Met.* **2015**, 209, 188–191.
1656. Martin, L.; Day, P.; Nakatsuji, S.; Yamada, J.-I.; Akutsu, H.; Horton, P. N. *Bull. Chem. Soc. Jpn.* **2010**, 83, 419–423.
1657. Shi, F.-N.; Cunha-Silva, L.; Paz, F. A. A.; Hardie, M. J.; Klinowski, J.; Rocha, J.; Trindade, T. *Inorg. Chem. Commun.* **2008**, 11, 283–287.
1658. Sarr, M.; Diasse-Sarr, A.; Diallo, W.; Plasseraud, L.; Cattet, H. *Acta Crystallogr.* **2013**, E69, m473–m474.
1659. Sow, Y.; Diop, L.; Kociok-Köhn, G.; Molloy, K. C. *Main Group Met. Chem.* **2010**, 33, 205–208.
1660. Diop, M. B.; Diop, L.; Plasseraud, L.; Maris, T. *Acta Crystallogr.* **2015**, E71, 520–522.
1661. Sow, Y.; Diop, L.; Molloy, K. C.; Kociok-Köhn, G. *Acta Crystallogr.* **2013**, E69, m106–m107.
1662. Sarr, B.; Mbaye, A.; Diop, C. A. K.; Sidibe, M.; Rousselin, Y. *Acta Crystallogr.* **2019**, E75, 742–745.
1663. Sarr, B.; Diop, C. A. K.; Sidibe, M.; Rousselin, Y. *Acta Crystallogr.* **2018**, E74, 502–504.
1664. Gueye, N.; Diop, L.; Stoeckli-Evans, H. *Acta Crystallogr.* **2014**, E70, m49–m50.
1665. Ramaswamy, P.; Datta, A.; Natarajan, S. *Eur. J. Inorg. Chem.* **2008**, 2008, 1376–1385.
1666. Li, Y.; Wu, Y.; Mei, D.; Doert, T. *Z. Anorg. Allg. Chem.* **2020**, 646, 288–295.
1667. Kokunov, Y. V.; Gorbunova, Y. E.; Detkov, D. G. *Zh. Neorg. Khim.* **2004**, 49, 1094–1100.
1668. Audebrand, N.; Vaillant, M.-L.; Auffrédic, J.-P.; Louër, D. *Solid State Sci.* **2001**, 3, 483–494.
1669. Salami, T. O.; Marouchkin, K.; Zavilij, P. Y.; Oliver, S. R. *J. Chem. Mater.* **2002**, 14, 4851–4857.
1670. Zhu, L.-H.; Zeng, M.-H.; Ye, B.-H.; Chen, X.-M. *Z. Anorg. Allg. Chem.* **2004**, 630, 952–955.
1671. Kaduk, J. A.; Toft, M. A.; Golab, J. T. *Powder Diffract.* **2010**, 25, 19–24.
1672. Chen, Y.; Zhu, T.; Xiong, Z.; Zhou, Y.; Li, Y.; Ding, Q.; Liu, Y.; Chen, X.; Zhao, S.; Luo, J. *Chem. Commun.* **2021**, 57, 6668–6671.
1673. Kolitsch, U. *Acta Crystallogr.* **2003**, C59, m501–m504.
1674. Yang, J.-Y.; Fu, Y.-L.; Chu, J.; Ng, S. W. *Acta Crystallogr.* **2006**, E62, m2310–m2312.
1675. Chen, X.; Cao, Y.; Zhang, H.; Chen, Y.; Chen, X.; Chai, X. J. *Solid State Chem.* **2008**, 181, 1133–1140.
1676. Rivenet, M.; Roussel, P.; Abraham, F. *J. Solid State Chem.* **2008**, 181, 2586–2590.
1677. Li, H.; Wang, D.; Chen, Z.; Lin, X.; Wang, Y.; Zhao, L. *CSD Communication*, 2017. refcode TEKWUE.
1678. Li, H.; Wang, D.; Chen, Z.; Lin, X.; Wang, Y.; Zhao, L. *CSD Communication*, 2017. refcode TEKXAL.
1679. Li, H.; Wang, D.; Chen, Z.; Lin, X.; Wang, Y.; Zhao, L. *CSD Communication*, 2017. refcode TEKXEP.

1680. Li, H.; Wang, D.; Chen, Z.; Lin, X.; Wang, Y.; Zhao, L. *GSD Communication*, 2017. refcode TEKXIT.
1681. Noro, S.; Mizutani, J.; Hijikata, Y.; Matsuda, R.; Sato, H.; Kitagawa, S.; Sugimoto, K.; Inubushi, Y.; Kubo, K.; Nakamura, T. *Nat. Commun.* **2015**, *6*, 5851.
1682. Li, H.; Wang, D.; Chen, Z.; Lin, X.; Wang, Y.; Zhao, L. *GSD Communication*, 2017. refcode TEPREO.
1683. Moitsheki, L. J.; Bourne, S. A.; Nassimbeni, L. R. *Acta Crystallogr.* **2006**, *E62*, m542–m544.
1684. Xu, Y.; Yuan, D.; Han, L.; Ma, E.; Wu, M.; Lin, Z.; Hong, M. *Eur. J. Inorg. Chem.* **2005**, *2005*, 2054–2059.
1685. Wang, Y. J.; Li, H. H.; Chen, Z. R.; Huang, C. C.; Huang, X. H.; Feng, M.; Lin, Y. *CrstEngComm* **2008**, *10*, 770–777.
1686. Bourne, S. A.; Moitsheki, L. J. *J. Chem. Crystallogr.* **2007**, *37*, 359–367.
1687. Jin, J.-C.; Lin, Y.-P.; Wu, Y.-H.; Gong, L.-K.; Shen, N.-N.; Song, Y.; Ma, W.; Zhang, Z.-Z.; Du, K.-Z.; Huang, X.-Y. *J. Mater. Chem. C* **2021**, *9*, 1814–1821.
1688. Jin, J.-C.; Lin, Y.-P.; Lin, L.-F.; Xiao, C.; Song, Y.; Shen, N.-N.; Gong, L.-K.; Zhang, Z.-Z.; Du, K.-Z.; Huang, X.-Y. *CrstEngComm* **2021**, *23*, 3744–3752.
1689. Toma, O.; Mercier, N.; Allain, M.; Meinardi, F.; Forni, A.; Botta, C. *Cryst. Growth Des.* **2020**, *20*, 7658–7666.
1690. Bock, H.; Havlas, Z.; Gharagozloo-Hubmann, K.; Holl, S.; Sievert, M. *Angew. Chem. Int. Ed.* **2003**, *42*, 4385–4389.
1691. Wagner, H.; Baumgartner, J.; Marschner, C. *Organometallics* **2005**, *24*, 4649–4653.
1692. Rhodes, C. P.; Frech, R. *Macromolecules* **2001**, *34*, 2660–2666.
1693. Spisak, S. N.; Zhou, Z.; Liu, S.; Xu, Q.; Wei, Z.; Kato, K.; Segawa, Y.; Itami, K.; Rogachev, A. Y.; Petrukhina, M. A. *Angew. Chem. Int. Ed.* **2021**, *60*, 25445–25453.
1694. Luo, J.; Bi, Y.; Zhang, L.; Zhang, X.; Liu, T. L. *Angew. Chem. Int. Ed.* **2019**, *58*, 6967–6971.
1695. Langer, J.; Köhler, M.; Hildebrand, J.; Fischer, R.; Görl, H.; Westerhausen, M. *Angew. Chem. Int. Ed.* **2013**, *52*, 3507–3510.
1696. Fromm, K. M. *Chem. A Eur. J.* **2001**, *7*, 2236–2244.
1697. Shapovalov, S. S.; Pasyanskii, A. A.; Torubaev, Y. V.; Skabitskii, I. V.; Scheer, M.; Bodensteiner, M. *Russ. J. Coord. Chem.* **2014**, *40*, 131–137.
1698. Zhang, C.; Gamble, S.; Ainsworth, D.; Slawin, A. M. Z.; Andreev, Y. G.; Bruce, P. G. *Nat. Mater.* **2009**, *8*, 580–584.
1699. Henderson, W. A.; Brooks, N. R.; Young, V. G. *J. Am. Chem. Soc.* **2003**, *125*, 12098–12099.
1700. Zhang, C.; Lilley, S. J.; Ainsworth, D.; Staunton, E.; Andreev, Y. G.; Slawin, A. M. Z.; Bruce, P. G. *Chem. Mater.* **2008**, *20*, 4039–4044.
1701. Mandai, T.; Yoshida, K.; Tsuzuki, S.; Nozawa, R.; Masu, H.; Ueno, K.; Dokko, K.; Watanabe, M. *J. Phys. Chem. B* **2015**, *119*, 1523–1534.
1702. Geysens, P.; Rangasamy, V. S.; Thayumanasundaram, S.; Robeyns, K.; Van Meervelt, L.; Locquet, J. P.; Franssaer, J.; Binnemans, K. *J. Phys. Chem. B* **2018**, *122*, 275–289.
1703. Mishra, S.; Ledoux, G.; Jeanneau, E.; Daniele, S.; Joubert, M. F. *Dalton Trans.* **2012**, *41*, 1490–1502.
1704. Rhodes, C. P.; Khan, M.; Frech, R. *J. Phys. Chem. B* **2002**, *106*, 10330–10337.
1705. Mandai, T.; Nozawa, R.; Tsuzuki, S.; Yoshida, K.; Ueno, K.; Dokko, K.; Watanabe, M. *J. Phys. Chem. B* **2013**, *117*, 15072–15085.
1706. Brennessel, W. W.; Ellis, J. E. *Inorg. Chem.* **2012**, *51*, 9076–9094.
1707. Mandai, T.; Tsuzuki, S.; Ueno, K.; Dokko, K.; Watanabe, M. *Phys. Chem. Chem. Phys.* **2015**, *17*, 2838–2849.
1708. Matsumoto, K.; Haruki, Y.; Sawada, S.; Yamada, S.; Konno, T.; Hagiwara, R. *Inorg. Chem.* **2018**, *57*, 14882–14889.
1709. Gschwind, F.; Fromm, K. M. *Z. Anorg. Allg. Chem.* **2011**, *637*, 1871–1879.
1710. Mantey, S.; Liebenow, C.; Hecht, E. Z. *Anorg. Allg. Chem.* **2001**, *627*, 128–130.
1711. Mandai, T.; Tatesaka, K.; Soh, K.; Masu, H.; Choudhary, A.; Tateyama, Y.; Ise, R.; Imai, H.; Takeguchi, T.; Kanamura, K. *Phys. Chem. Chem. Phys.* **2019**, *21*, 12100–12111.
1712. Tsybarentko, D. M.; Makarevich, A. M.; Shchukin, A. E.; Malkerova, I. P.; Alikhanyan, A. S.; Kuzmina, N. P. *Polyhedron* **2017**, *134*, 246–256.
1713. Clegg, W.; Elsegood, M. R. J. *CSD Communication*, 2020. refcode JUXROM.
1714. Mishra, S.; Pfalzgraf, L. G. H.; Jeanneau, E. *Polyhedron* **2007**, *26*, 66–72.
1715. Clegg, W.; Elsegood, M. R. J. *CSD Communication*, 2020. refcode DABPEF.
1716. Rogers, R. *CSD Communication*, 2020. refcode DACRIM.
1717. Rogers, R. *CSD Communication*, 2020. refcode DACROS.
1718. Clegg, W.; Elsegood, M. R. J. *CSD Communication*, 2020. refcode DABQAC.
1719. Mishra, S.; Jeanneau, E.; Ledoux, G.; Daniele, S. *Inorg. Chem.* **2014**, *53*, 11721–11731.
1720. Secara, A. M.; Binder, J. F.; Swidan, A.; Macdonald, C. L. B. *Can. J. Chem.* **2018**, *96*, 570–577.
1721. Macdonald, C. L.; Bandyopadhyay, R.; Cooper, B. F.; Friedl, W. W.; Rossini, A. J.; Schurko, R. W.; Eichhorn, S. H.; Herber, R. H. *J. Am. Chem. Soc.* **2012**, *134*, 4332–4345.
1722. Rogers, R. *CSD Communication*, 2019. refcode SORGIS.
1723. Steed, J. W. *Coord. Chem. Rev.* **2001**, *215*, 171–221.
1724. Villemain, E.; Raccurt, O. *Coord. Chem. Rev.* **2021**, *435*, 213801.
1725. Buchner, M. R.; Thomas-Hargreaves, L. R.; Kreuzer, L. K.; Spang, N.; Ilev, S. I. *Eur. J. Inorg. Chem.* **2021**, *2021*, 4990–4997.
1726. Himmel, D.; Krossing, I. *Z. Anorg. Allg. Chem.* **2006**, *632*, 2021–2023.
1727. Ruth, K.; Lerner, H.-W.; Bolte, M. *Acta Crystallogr.* **2005**, *E61*, m1852–m1853.
1728. Rheingold, A. L. *CSD Communication*, 2021. refcode ERETED.
1729. Barton, A. J.; Genge, A. R. J.; Levason, W.; Reid, G. *J. Chem. Soc. Dalton Trans.* **2000**, 859–865.
1730. Gurmani, C.; Levason, W.; Ratnani, R.; Reid, G.; Webster, M. *Dalton Trans.* **2008**, 6274–6282.
1731. Levason, W.; Maheshwari, S.; Ratnani, R.; Reid, G.; Webster, M.; Zhang, W. *Inorg. Chem.* **2010**, *49*, 9036–9048.
1732. George, K.; Jura, M.; Levason, W.; Light, M. E.; Reid, G. *Dalton Trans.* **2014**, *43*, 3637–3648.
1733. Lees, R. J.; Powell, A. V.; Chippindale, A. M. *Acta Crystallogr.* **2005**, *C61*, m516–m518.
1734. Puls, A.; Näther, C.; Bensch, W. *Acta Crystallogr.* **2006**, *E62*, m1045–m1047.
1735. Ren, W.; Gu, D. *Inorg. Chem.* **2016**, *55*, 11962–11970.
1736. Peng, Y.; Fan, H.; Jancik, V.; Roesky, H. W.; Herbst-Irmer, R. *Angew. Chem. Int. Ed.* **2004**, *43*, 6190–6192.
1737. Schwamm, R. J.; Lein, M.; Coles, M. P.; Fitchett, C. M. *J. Am. Chem. Soc.* **2017**, *139*, 16490–16493.
1738. Li, B.; Li, J.; Roesky, H. W.; Zhu, H. *J. Am. Chem. Soc.* **2015**, *137*, 162–164.
1739. Hidalgo-Bonilla, S.; Peyrot, R.; Jancik, V.; Barroso-Flores, J.; Reyes-Lezama, M.; Moya-Cabrera, M. *Eur. J. Inorg. Chem.* **2013**, *2013*, 2849–2857.
1740. Smiles, D. E.; Wu, G.; Hayton, T. W. *Inorg. Chem.* **2014**, *53*, 12683–12685.
1741. Meier, M.; Korber, N. Z. *Anorg. Allg. Chem.* **2009**, *635*, 764–767.
1742. Dornhaus, F.; Bolte, M.; Wagner, M.; Lerner, H.-W. *Z. Anorg. Allg. Chem.* **2007**, *633*, 425–428.
1743. Bläsing, K.; Bresien, J.; Maurer, S.; Schulz, A.; Villinger, A. *Eur. J. Inorg. Chem.* **2021**, *2021*, 1913–1920.
1744. Clegg, W.; Liddle, S. T. *CSD Communication*, 2016. refcode UQUJIB.
1745. Pushkarevsky, N. A.; Chulanova, E. A.; Shundrin, L. A.; Smolentsev, A. I.; Salnikov, G. E.; Pritchina, E. A.; Genaev, A. M.; Irtegov, I. G.; Bagryanskaya, I. Y.; Konchenko, S. N.; Gritsan, N. P.; Beckmann, J.; Zibarev, A. V. *Chem. A Eur. J.* **2019**, *25*, 806–816.
1746. Joos, M.; Conrad, M.; Merkle, R.; Schleid, T.; Maier, J.; Dinnebier, R. E.; Bette, S. *Dalton Trans.* **2021**, *50*, 6949–6961.
1747. Wickleder, C.; Larsen, P. Z. *Naturforsch.* **2002**, *B57*, 1419–1426.
1748. Ilyukhin, A.; Petrosyants, S. *CSD Communication*, 2011. refcode GOKKUO.
1749. Rogers, R. *CSD Communication*, 2020. refcode TADQAU.



1750. Rogers, R. *CSD Communication*, 2020. refcode TADQEY.
1751. Wechwithayakhlung, C.; Packwood, D. M.; Chaopaknam, J.; Worakajit, P.; Ittisanronnachai, S.; Chanlek, N.; Promarak, V.; Kongpatpanich, K.; Harding, D. J.; Pattanasattayavong, P. *J. Mater. Chem. C* **2019**, *7*, 3452–3462.
1752. Jolleys, A.; Levason, W.; Reid, G. *Dalton Trans.* **2013**, *42*, 2963–2972.
1753. Cabeza, J. A.; Fernández-Colinas, J. M.; García-Álvarez, P.; Polo, D. *Inorg. Chem.* **2012**, *51*, 3896–3903.
1754. Qian, H.-F.; Liu, Y.; Tao, T.; Gu, K.-H.; Yin, G.; Huang, W. *Inorg. Chim. Acta* **2013**, *405*, 1–8.
1755. Veith, M.; Belot, C.; Huch, V.; Guyard, L.; Knorr, M.; Khatyr, A.; Wickleder, C. *Z. Anorg. Allg. Chem.* **2010**, *636*, 2262–2275.
1756. Reuter, H.; Röwekamp-Krugley, N.; Imwalle, M.; Keil, S.; Reichelt, M. *Acta Crystallogr.* **2015**, *E71*, m267–m268.
1757. Freudenmann, D.; Feldmann, C. *Z. Naturforsch.* **2013**, *B68*, 1090–1094.
1758. Tjahjanto, R. T.; Peintinger, M. F.; Bredow, T.; Beck, J. *Eur. J. Inorg. Chem.* **2012**, *2012*, 3625–3635.
1759. Han, Y.-G.; Xu, C.; Duan, T.; Zhang, Q.-F. *Inorg. Chim. Acta* **2011**, *365*, 414–418.
1760. García-Montalvo, V.; Granados-Ortiz, M.; Guevara-García, A. A.; Lomeli, V.; González-Gallardo, S.; de Velasco, D. O.-G.; Cea-Olivares, R.; Hernández-Ortega, S.; Toscano, R. A. *Polyhedron* **2011**, *30*, 1095–1102.
1761. Shaikh, T. A.; Bakus, R. C.; Parkin, S.; Atwood, D. A. *J. Organomet. Chem.* **2006**, *691*, 1825–1833.
1762. Li, Z.; Du, S. *CSD Communication*, 2016. refcode RALKIB.
1763. Gurmani, C.; Jura, M.; Levason, W.; Ratnani, R.; Reid, G.; Webster, M. *Dalton Trans.* **2009**, 1611–1619.
1764. Davis, M. F.; Levason, W.; Reid, G.; Webster, M.; Zhang, W. *Dalton Trans.* **2008**, 533–538.
1765. Hill, N. J.; Levason, W.; Reid, G. *Inorg. Chem.* **2002**, *41*, 2070–2076.
1766. Gurmani, C.; Jura, M.; Levason, W.; Ratnani, R.; Reid, G.; Webster, M. *Dalton Trans.* **2009**, 4122–4128.
1767. Marsh, R. E. *Acta Crystallogr.* **2004**, *B60*, 252–253.
1768. Zhang, J.-J.; Du, W.-X.; Hu, S.-M.; Xia, S.-Q.; Wang, L.-S.; Wu, X.-T. *Inorg. Chem. Comm.* **2003**, *6*, 387–388.
1769. Kociok-Köhn, G.; Molloy, K. C.; Rodríguez-Castro, J. *Inorg. Chem. Comm.* **2008**, *11*, 599–603.
1770. de Velasco, D. O.-G.; Sánchez-Jiménez, R.; Hernández-Ortega, S.; Toscano, R. A.; García-Montalvo, V. *Polyhedron* **2010**, *29*, 2435–2439.
1771. Champion, M. J. D.; Dyke, J. M.; Levason, W.; Light, M. E.; Pugh, D.; Bhakhoa, H.; Rhyman, L.; Ramasami, P.; Reid, G. *Inorg. Chem.* **2015**, *54*, 2497–2499.
1772. Cheng, F.; Hector, A. L.; Levason, W.; Reid, G.; Webster, M.; Zhang, W. *Chem. Commun.* **2008**, 5508–5510.
1773. Helm, M. L.; Loveday, K. D.; Combs, C. M.; Bentzen, E. L.; VanDerveer, D. G.; Rogers, R. D.; Grant, G. J. *J. Chem. Crystallogr.* **2003**, *33*, 447–455.
1774. Levason, W.; Matthews, M. L.; Patel, R.; Reid, G.; Webster, M. *New J. Chem.* **2003**, *27*, 1784–1788.
1775. George, K.; Jura, M.; Levason, W.; Light, M. E.; Ollivere, L. P.; Reid, G. *Inorg. Chem.* **2012**, *51*, 2231–2240.
1776. Barton, A. J.; Hill, N. J.; Levason, W.; Reid, G. *J. Chem. Soc. Dalton Trans.* **2001**, 1621–1627.
1777. Rupar, P.; Bandyopadhyay, R.; Cooper, B.; Stinchcombe, M.; Ragona, P.; Macdonald, C.; Baines, K. *Angew. Chem. Int. Ed.* **2009**, *48*, 5155–5158.
1778. Hector, A. L.; Levason, W.; Reid, G.; Webster, M.; Zhang, W. *Dalton Trans.* **2011**, *40*, 694–700.
1779. Mishra, S.; Jeanneau, E.; Daniele, S. *Polyhedron* **2010**, *29*, 500–506.
1780. Reid, S. D.; Hector, A. L.; Levason, W.; Reid, G.; Waller, B. J.; Webster, M. *Dalton Trans.* **2007**, 4769–4777.
1781. Hill, N. J.; Levason, W.; Light, M. E.; Reid, G. *Chem. Commun.* **2003**, 110–111.
1782. Barton, A. J.; Hill, N. J.; Levason, W.; Patel, B.; Reid, G. *Chem. Commun.* **2001**, 95–96.
1783. Hill, N. J.; Levason, W.; Patel, R.; Reid, G.; Webster, M. *Dalton Trans.* **2004**, 980–981.
1784. Barton, A. J.; Genge, A. R. J.; Levason, W.; Reid, G. *J. Chem. Soc. Dalton Trans.* **2000**, 2163–2166.
1785. de Groot, C. H. K.; Gurmani, C.; Hector, A. L.; Huang, R.; Jura, M.; Levason, W.; Reid, G. *Chem. Mater.* **2012**, *24*, 4442–4449.
1786. Levason, W.; Orchard, S. D.; Reid, G. *Chem. Commun.* **1999**, 1071–1072.
1787. Barton, A. J.; Hill, N. J.; Levason, W.; Reid, G. *J. Am. Chem. Soc.* **2001**, *123*, 11801–11802.

## 1.03 Low-coordinate compounds of heavier group 14–16 elements

Takahiro Sasamori<sup>a,b</sup>, Vladimir Lee<sup>a</sup>, Noriyoshi Nagahora<sup>c</sup>, and Shogo Morisako<sup>a,b</sup>, <sup>a</sup> Division of Chemistry, Faculty of Pure and Applied Sciences, University of Tsukuba, Tsukuba, Japan; <sup>b</sup> Tsukuba Research Center for Energy Materials Sciences (TREMS), University of Tsukuba, Tsukuba, Japan; and <sup>c</sup> Department of Chemistry, Faculty of Science, Fukuoka University, Fukuoka, Japan

© 2023 Elsevier Ltd. All rights reserved.

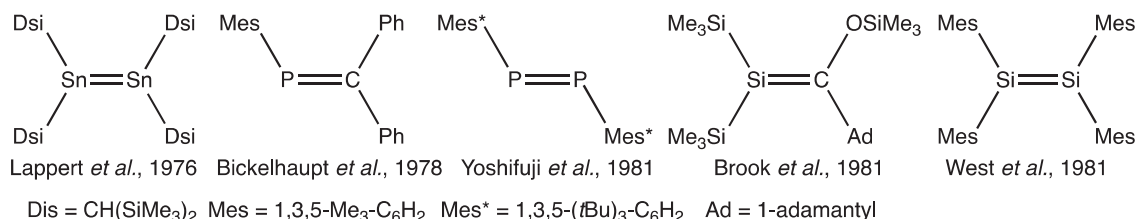
<b>1.03.1</b>	<b>Introduction</b>	<b>118</b>
<b>1.03.2</b>	<b>Theoretical aspects</b>	<b>119</b>
<b>1.03.3</b>	<b>Low-coordinate compounds of heavier group 14 elements</b>	<b>125</b>
1.03.3.1	Introduction	125
1.03.3.2	Doubly bonded derivatives	125
1.03.3.2.1	Alkene analogues	125
1.03.3.2.2	1,3-Diene analogues	139
1.03.3.2.3	Allene analogues	140
1.03.3.2.4	Vinylidene analogues	141
1.03.3.2.5	E(O)=E(O): Derivatives (E=Si, Ge, Sn)	143
1.03.3.3	Triply bonded derivatives	144
1.03.3.3.1	Homonuclear derivatives –E≡E– (E=Si, Ge, Sn, Pb)	144
1.03.3.3.2	Heteronuclear derivatives –E≡C– and –E≡P	145
<b>1.03.4</b>	<b>Low-coordinate compounds of heavier group 15 elements</b>	<b>145</b>
1.03.4.1	Introduction	145
1.03.4.2	Diphosphene derivatives	145
1.03.4.3	Heavier dipnictene derivatives	151
<b>1.03.5</b>	<b>Low-coordinate compounds of heavier group 16 elements</b>	<b>153</b>
1.03.5.1	Multiple bonds between group 13 element and heavier group 16 element	153
1.03.5.2	Multiple bonds between group 14 element and heavier group 16 element	155
1.03.5.3	Multiple bonds between group 15 element and heavier group 16 element	156
1.03.5.4	Multiple bonds between group 16 element and heavier group 16 element	157
<b>1.03.6</b>	<b>Summary</b>	<b>157</b>
<b>References</b>		<b>158</b>

### Abstract

Multiple bond compounds between heavier main group elements should be of great interest, especially due to their unique structures arising from their weak  $\pi$  bonds and the resulting reactivity towards small organic compounds. In order to accommodate the weak  $\pi$ -bond energies of these multiple bonds of heavier main group elements, the bonding situation should be substantially perturbed, i.e., the second order Jahn-Teller effect, which results in unique physical and chemical properties. This update describes the recent outcomes on the synthesis of multiple bond compounds between heavier main group elements published between 2013 and 2021. Those before 2013 have been published in the previous contributions in *Comprehensive Inorganic Chemistry II*, Ed. Jan Reedijk and Kenneth Poepelmeier, Elsevier B.V., 2013 (ISBN: 978-0-08-096529-1).

### 1.03.1 Introduction

Since silicon represents the next homologue to carbon in the periodic table, the question about the analogy between carbon and silicon has been thought for a long time. Many chemists have studied the chemical similarities and differences between them, because “carbon” is a central element in organic chemistry, and “silicon” is a representative main group element in inorganic chemistry. Low-coordinate species of the second-row main group elements, such as olefins ( $>C=C<$ ), carbonyl compounds ( $>C=O$ ), imines ( $>C=N-$ ), aromatic compounds (e.g., benzene, naphthalene), azo compounds ( $-N=N-$ ), carbenes ( $>C:$ ), etc. play very important roles in organic chemistry. Conversely, the chemistry of heavier elements homologues of these low-coordinate species has been undeveloped so far most probably due to their extremely high reactivity and inherent instability under ambient conditions, while these unsaturated compounds have been postulated in many reactions as reactive intermediates. Prior to the 1970s, all attempts at synthesizing the low-coordinate species of elements of the third period and downward (namely, heavier main group elements) proved unsuccessful, leading to the formation of cyclic oligomers or polymers containing only single covalent bonds even under the conditions without any oxygen and water.<sup>1</sup> Therefore, it became believed that “elements having a principal quantum



**Chart 1** The first double-bond compounds of heavier main group elements.

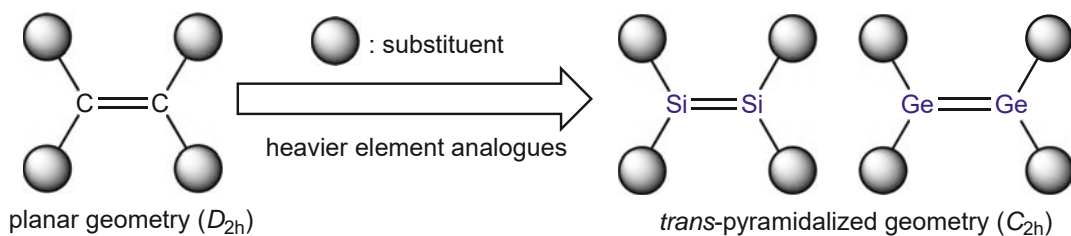
number greater than two should not be able to form a  $\pi$ -bond, i.e., so called “double bond rule”.<sup>2</sup> It should be most likely interpreted in terms of the poor overlap of  $p$  orbitals, due to either large distance between the two bonding atoms or poor size match (e.g., Si–C bond), precluding favorable bonding interactions. However, this rule came to be doubted during the 1970s with the reports on the preparations of such low-coordinate compounds of heavier main group elements in the gas phase and the trapping reactions of them at low temperature. Then, the first distannene (Sn=Sn, 1976),<sup>3</sup> phosphaalkene (P=C, 1978),<sup>4</sup> diphosphene (P=P, 1981),<sup>5</sup> silene (Si=C, 1981),<sup>6</sup> and disilene (Si=Si, 1981)<sup>7</sup> were successfully synthesized as stable compounds by utilizing sterically demanding substituents, disproving the “double bond rule” (Chart 1). These compounds are significant landmarks in the chemistry of kinetically stabilized low-coordinate compounds of heavier main group elements. Since then, several numbers of isolable low-coordinate compounds of heavier main group elements have been reported and their chemical and physical properties have been investigated in detail.<sup>8</sup>

For the stabilization of highly reactive compounds such as low-coordinate compounds of heavier main group elements, two established methodologies are well known, i.e., thermodynamic and kinetic stabilization. The former is defined as stabilization of the ground state by the resonance effect of neighboring heteroatoms, that is, introduction of an electron-donating or -withdrawing substituents, and/or intermolecular complexation with donor molecules and/or Lewis acids such as transition metals. The latter is stabilization resulting from raising the transition state by taking advantage of steric protection using bulky groups, which suppress self-oligomerization and side-reactions with other molecules. Kinetic stabilization is superior to thermodynamic stabilization from viewpoint of investigation into the intrinsic bonding nature, since the thermodynamic stabilization perturbs the intrinsic nature of the species to a greater extent than the kinetic stabilization. Since several review articles are now available on the chemistry of low-coordinate heavier main group elements, which are kinetically and thermodynamically stabilized,<sup>8–10</sup> the contents in this section will be restricted to deal with the synthesis and properties of multiple-bond compounds of heavier group 14, 15 and 16 elements, i.e., unsaturated compounds such as cationic species (R<sub>3</sub>Si<sup>+</sup>, R<sub>2</sub>P<sup>+</sup>, etc.), tetrylene (>Si: etc.), pnictinidene (–P: etc.), and those thermodynamically stabilized with intra- and inter donor coordination are not included. In addition, this update describes only the recent outcomes on the synthesis of multiple bond compounds between heavier main group elements published between 2013 and 2021, because those before 2013 have been published in the previous contributions in *Comprehensive Inorganic Chemistry II*, Ed. Jan Reedijk and Kenneth Poepelmeier, Elsevier B.V., 2013 (ISBN: 978-0-08-096529-1).

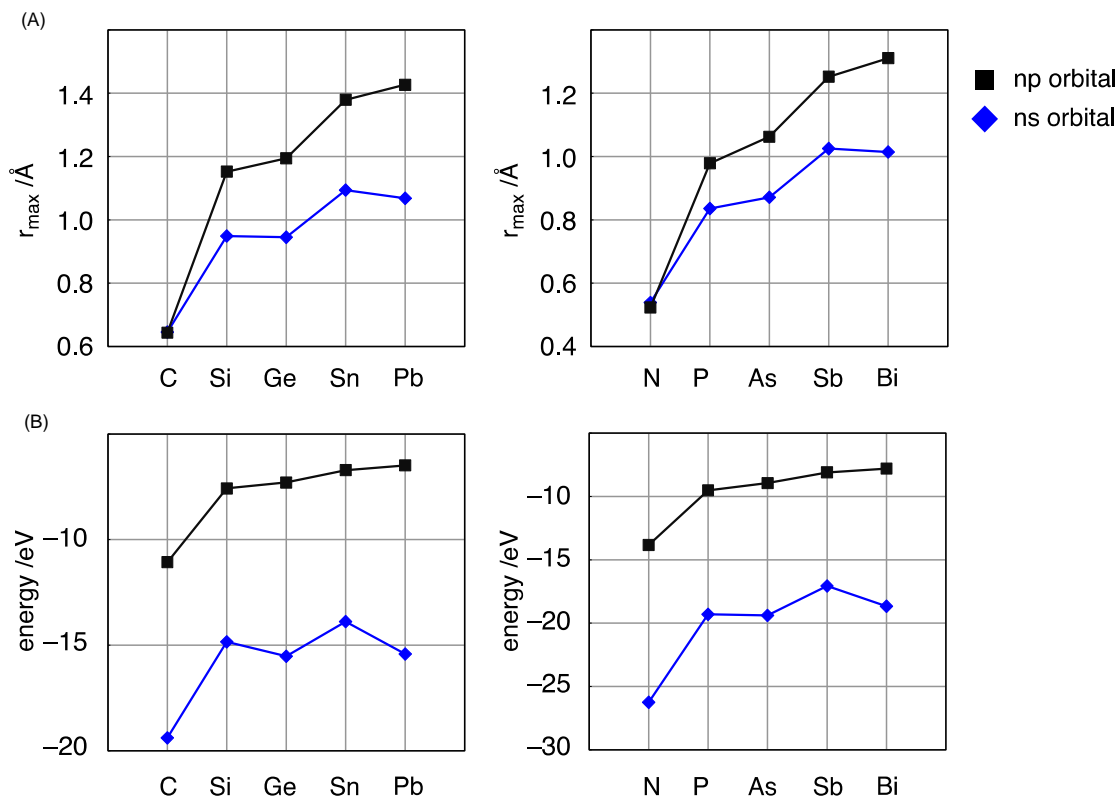
### 1.03.2 Theoretical aspects

Since several  $\pi$ -bonding systems of heavier main group elements have been created by utilizing kinetic stabilization, their structural characters have been thoroughly investigated based on the experimental and theoretical insights.<sup>8–10</sup> For example, although H<sub>2</sub>C=CH<sub>2</sub> is known to exhibit a planar structure around the C=C  $\pi$ -bonding (D<sub>2h</sub>), the planar structures of the heavier analogues, H<sub>2</sub>E = EH<sub>2</sub> (E=Si, Ge, Sn, Pb), are unexpectedly not an energy minimum but a transition state in contrast to the carbon case. The minimum structures of H<sub>2</sub>E = EH<sub>2</sub> were computed as *trans*-bent structure (C<sub>2h</sub>) (Fig. 1).<sup>11</sup> Actually, most of the isolated double bond compounds between heavier group 14 elements, R<sub>2</sub>E = ER<sub>2</sub> (diterpenes), were found to exhibit *trans*-pyramidalized (*trans*-bent) structures as well as the first isolated disilene, Mes<sub>2</sub>Si=SiMes<sub>2</sub>.<sup>7</sup> The intrinsic nature of a diterpene having a *trans*-bent structure can be interpreted in either (i) double donor-acceptor bonds based on the valence bond theory, or (ii) a pseudo (2nd-order) Jahn-Teller effect with mixing of  $\sigma^*$  orbital with the  $\pi$  orbital.<sup>11,12</sup>

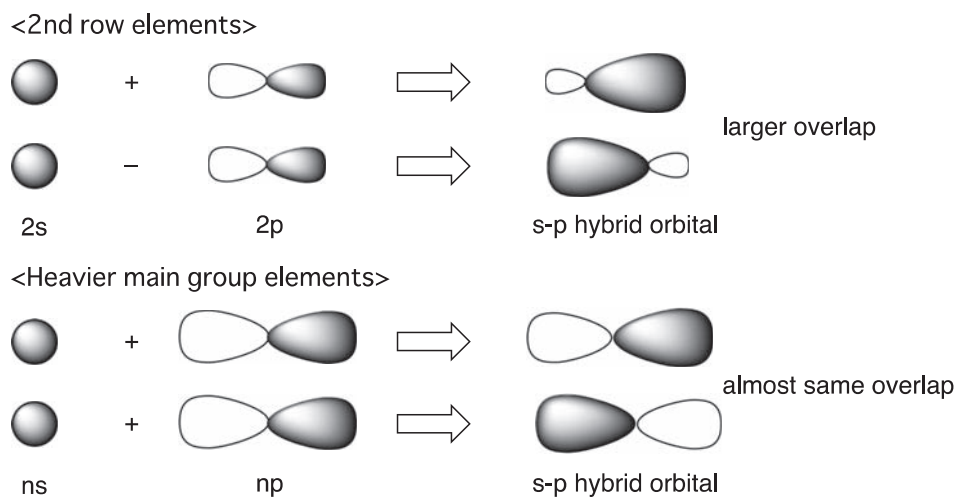
In Fig. 2 are shown the radii of the valence atomic orbitals (maximal electron-density) and the corresponding orbital levels, which are calculated for group 14 and 15 elements.<sup>13</sup> It should be noted that the valence  $ns$  and  $np$  atomic orbitals show great difference in their sizes for the heavier atoms (Si, Ge, Sn, Pb), though the size of the  $2s$  atomic orbital of carbon is almost equal to that of the  $2p$  atomic orbitals due to the absence of inner-shell  $p$  electrons. The tendency of the size of  $ns$  and  $np$  orbitals can be applied not only to group 14 elements but also to other groups. The size-difference between the  $ns$  and  $np$  orbitals increases on going down the row in the periodic table. Thus, the heavier atoms have a lower tendency to form  $s$ - $p$  hybrid orbitals with high  $p$  character and they prefer to preserve the valence  $s$  electrons as core-like electrons with keeping their original  $ns$ - $np$  valence electronic configuration, on the contrary to the case of 2nd row elements. The core-like characters of the valence  $s$  electrons cause the inert lone pair in heavier elements. Conversely, the second-row elements such as carbon prefer to promote one of two valence  $2s$  electrons into the vacant  $2p$  orbital to form  $s$ - $p$  hybrid orbitals. The mixing of the  $2s$  and  $2p$  orbitals, which exhibit almost the same size, can yield the  $s$ - $p$  hybrid orbital as spreading in the direction of bonding (Fig. 3). Thus, the orbital overlapping should be greater in the use of the hybridized



**Fig. 1** Heavier analogues of an alkene.



**Fig. 2** (A) Sizes and (B) energy levels of valence ns and np orbitals for group 14 and 15 elements.



**Fig. 3** Mixing of s and p orbitals.



orbitals to form strong bonds. Accordingly, the resulting gain of the bonding energy can sufficiently compensate the loss of energy for the electron promotion from 2s orbital to 2p orbital.

For the bonding situation of the  $\pi$  bond in heavier diterpenes ( $\text{H}_2\text{E}=\text{EH}_2$ , Si, Ge, Sn, Pb), the orbital interactions between the  $\text{H}_2\text{E}$  units should be considered on the basis of the valence bond theory.<sup>8</sup> Because the heavier group 14 elements prefer to retain their  $ns^2np^2$  valence electronic configuration as described above, the ground state of the tetrylene unit ( $\text{H}_2\text{E}$ ) should be singlet with the s-character lone pair, in contrast to a carbene ( $\text{H}_2\text{C}$ ), which exhibits triplet ground state. Indeed, the singlet-triplet energy difference ( $\Delta E_{\text{ST}}$ ) of the tetrylene ( $\text{H}_2\text{E}$ ) increases  $\Delta E_{\text{ST}} = 16.7$  ( $\text{H}_2\text{Si}$ ), 21.8 ( $\text{H}_2\text{Ge}$ ), 24.8 ( $\text{H}_2\text{Sn}$ ), and 34.8 ( $\text{H}_2\text{Pb}$ ) kcal/mol, though that of  $\text{H}_2\text{C}$  is estimated as  $-14.0$  kcal/mol.<sup>14</sup> Because of the intrinsic nature of tetrylenes, the relative stability of the singlet species of  $\text{R}_2\text{E}$  ( $\text{E}=\text{C}, \text{Si}, \text{Ge}, \text{Sn}, \text{Pb}$ ;  $\text{R} = \text{alkyl or aryl}$ ) as compared with the corresponding dimer,  $\text{R}_2\text{E}=\text{ER}_2$ , are estimated to increase as the element row descends,  $\text{C} < \text{Si} < \text{Ge} < \text{Sn} < \text{Pb}$ . Accordingly, one can expect that a divalent organolead compound (plumbylene) may be isolable as a stable compound. Because there have been huge numbers of stable stannylenes and plumbylene with heteroatom substituents, tetrylenes and those thermodynamically stabilized with intra- and inter donor coordination are not included in this review in the following sections.<sup>10</sup> However, tetrylenes without any electronic and steric stabilization effect were known to be thermally unstable to undergo facile disproportionation. Thus, it should be difficult to isolate tetrylenes as stable compounds under ambient conditions, since tetrylenes generally exhibit extremely high reactivity due to their considerable electrophilicity. Tetrylenes have the singlet ground state with a vacant p-orbital and an s-character lone pair as valence orbitals. The extremely high reactivity of tetrylenes should be due to their vacant p-orbitals, since their 6 valence electrons are less than 8 electrons from the viewpoint of octet rule and the lone pair of the tetrylenes should be inert due to its high s-character. In order to stabilize such tetrylenes enough to be isolated as stable compounds, thermodynamic and/or kinetic stabilization should be afforded towards the reactive vacant p-orbital. Thus, several numbers of “isolable” tetrylenes have been synthesized by using the thermodynamic stabilization of heteroatoms such as N, O, and P, etc., and/or the kinetic stabilization utilizing bulky substituents (Fig. 4).<sup>10</sup> Thus, the number of the valence electrons should be very important to know the property of the low-coordinate species of main group elements.

Carbon substituents on a tetrylene should affect less electronic perturbation as compared with the heteroatom substituents such as N, O, and P, which can stabilize the vacant p-orbital of a tetrylene (Fig. 4). The intrinsic nature of tetrylenes should be obscured in the cases of heteroatom-substituted tetrylenes due to the electronic effects of the heteroatom substituents, i.e., intramolecular coordination of the heteroatom, and hapticity of the ligands. Thus, sterically demanding carbon-substituents on a tetrylene should be effective to suppress the electronic perturbation towards its vacant p-orbital from intra- and intermolecular coordination. That is the reason why some carbon substituted tetrylenes have been isolated with sterically demanding substituents, and they exhibit high reactivity due to their vacant p orbitals even though they would be kinetically stabilized. When the steric hindrance of the carbon-substituted tetrylene is insufficient, the tetrylene ( $\text{R}_2\text{E}$ ) would undergo self-dimerization or oligomerization leading to the formation of the corresponding dimer, i.e., double-bond compounds ( $\text{R}_2\text{E}=\text{ER}_2$ ), oligomer, or polymer. Thus, the bonding situation of a double-bond between heavier group 14 elements can be interpreted in terms of a dimer of a tetrylenes.<sup>8,9</sup>

It can be concluded that, in the case of heavier group 14 elements, a tetrylene exhibits singlet ground state with  $ns^2np^2$  configuration, and has a vacant p-orbital and s-character lone pair. Because a tetrylene is highly reactive towards self-oligomerization and/or electrophilic reactions due to its vacant p-orbital, it can be isolated as a monomeric form only when sterically demanding or heteroatom substituent would be introduced on the tetrylene center. When it has only small substituents, it should undergo facile oligomerization giving the corresponding oligomer/polymer. On the other hand, a tetrylene with “moderately” bulky substituent, which would sufficiently suppress the facile oligomerization, but insufficient to keep its monomeric form, should undergo dimerization to give the corresponding double bond compound, a diterpene, as a dimer of tetrylenes (Fig. 5).

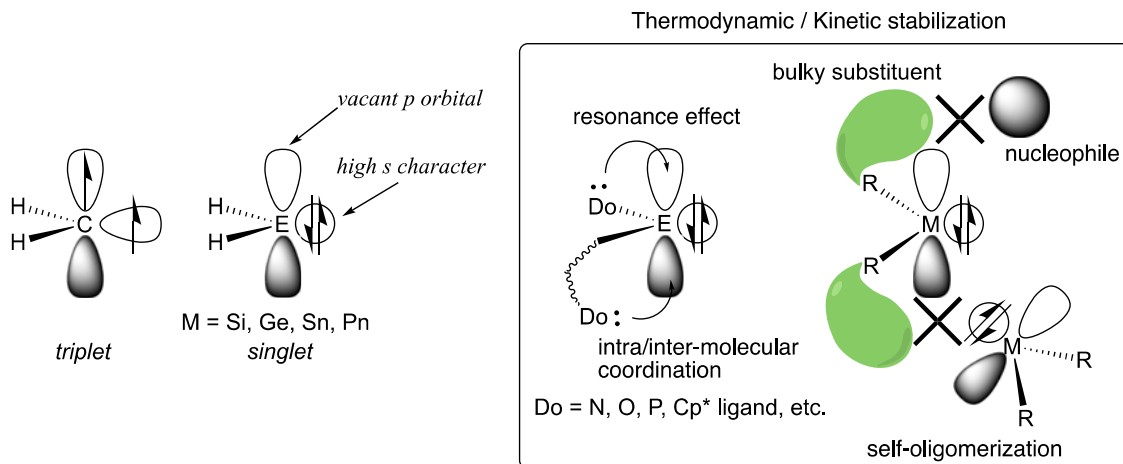
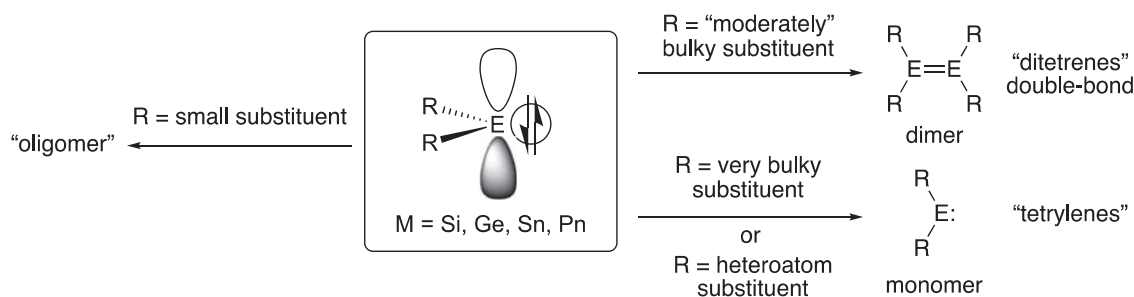


Fig. 4 Thermodynamic and kinetic stabilization for tetrylenes ( $\text{R}_2\text{E}$ ;  $\text{E}=\text{Si}, \text{Ge}, \text{Sn}, \text{Pb}$ ).

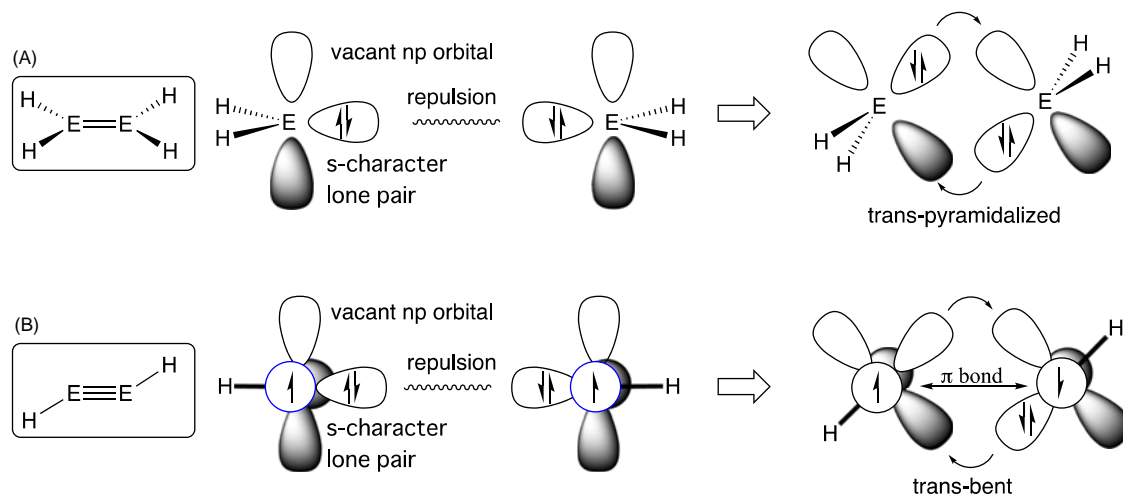


**Fig. 5** Fate of a tetrylene ( $R_2E$ ,  $E=Si, Ge, Sn, Pb$ ) depending on the substituents.

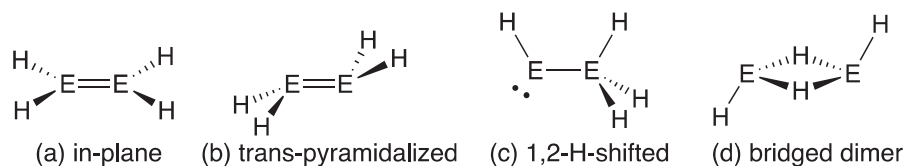
On the consideration of above-mentioned feature of a tetrylene, one can see severe repulsion between the closed-shell orbitals of two  $H_2E$  units would prevent dimerization leading to the formation of a dimer,  $H_2E=EH_2$ , in the planar form as shown in Fig. 6. Accordingly, two  $H_2E$  units can form a double bond not only elongated to avoid the repulsion but also in *trans*-pyramidalized configuration, where each  $H_2E$  unit donates a lone pair of electrons to an empty  $p$  orbital of the other to form double donor-acceptor bonds as shown in Fig. 6.

In addition, much heavier elements of Sn and Pb atoms are very reluctant to form a distinct double-bond,  $H_2Sn=SnH_2$  and  $H_2Pb=PbH_2$ , and the bridged dimer of  $H_2E$  and 1,2-H-shifted isomer,  $HE-EH_3$ , are the more stable isomers (Fig. 7),<sup>14</sup> since at least one atom in these isomers can maintain  $ns^2np^2$  valence electronic configuration as divalent species without hybridization of orbitals leading to the formation of tetravalent species. Thus, two tetrylenes ( $H_2E$ ) can form a double bond as a *trans*-pyramidalized geometry based on (i) valence bond theory. According to the bending from the planar geometry ( $D_{2h}$ ) to the *trans*-pyramidalized geometry ( $C_{2h}$ ), the occupied  $\pi$  ( $b_u$ ) orbital is mixing with the vacant  $\sigma^*$  ( $b_u$ ) to form stabilized slipped- $\pi$  orbital ( $b_u$ ) from the viewpoint of (ii) a pseudo Jahn-Teller effect (Fig. 8).<sup>12</sup>

As in the case of double-bond compounds of heavier group 14 elements, a triple-bond compound of heavier group 14 elements, a ditetryne ( $HE\equiv EH$ ), exhibits the *trans*-bent structure ( $D_{2h}$ ) in contrast to an alkyne, which has an undistorted linear geometry ( $D_{\infty h}$ ).<sup>9,15</sup> Their *trans*-bent structures can be explained by consideration of the bonding interaction between the HE components as well. In all cases of group 14 elements (C, Si, Ge, Sn, Pb), HC and HE exhibit doublet ground states, and their lowest excited states should be quartet.<sup>16</sup> However, those of the heavier element cases, HE ( $E=Si, Ge, Sn, Pb$ ), are much larger than that of HC. Thus, CH can exhibit its excited quartet state with small promotion energy to form one  $s$ -bond and two  $\pi$  bonds between the two HC units in linear geometry of  $HC\equiv CH$  (Fig. 6B), where the gain of triple-bond energies can compensate sufficiently the loss of promotion energy.<sup>15,16</sup> Conversely, two HE units prefer to retain their original electron configurations as doublet states as forming a triple bond, since the large promotion energies cannot be compensated by forming weak ( $\sigma + 2\pi$ ) bonds. Thus, the coupling of doublet HE units could occur as shown in Fig. 4B to form the  $HE\equiv EH$  triple bond with two donor-acceptor bonds and one  $\pi$  bond. From viewpoint of a pseudo Jahn-Teller effect, the *trans*-bent structure can also be explained by  $\pi$ - $\sigma^*$  mixing as in the case of diterpenes (Fig. 9).<sup>15</sup> The linear structure of  $HE\equiv EH$  has occupied valence orbitals of one  $\sigma$  ( $\sigma_g$ ) and two  $\pi$  orbitals ( $\pi_u$ ). According to the *trans*-bending of  $HE\equiv EH$ , one of the  $\pi$  orbitals, in-plane  $\pi_{in}$  orbital, can be mixing with the low-lying  $\sigma^*$  ( $\sigma_u$ ) orbital due to the same symmetry to form slipped  $\pi_{in} + \sigma^*$  orbital ( $b_u$ ). The orbital stabilization due to the mixing of  $\pi$  and

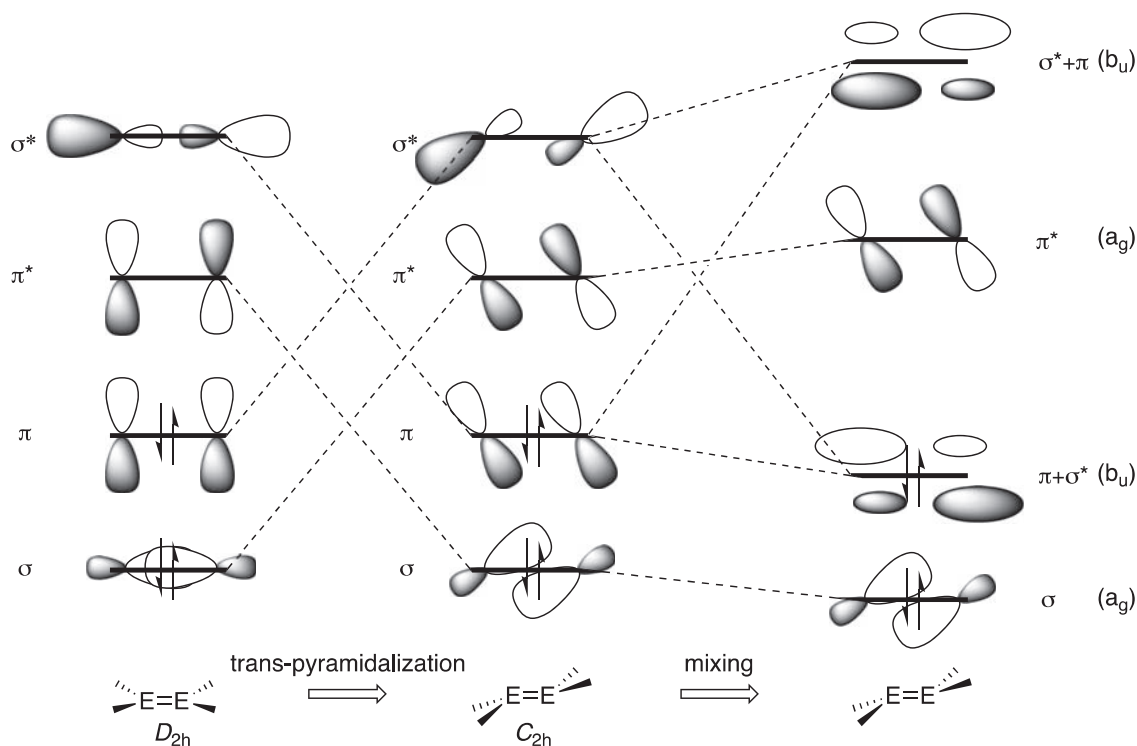


**Fig. 6** Interaction between (A)  $H_2E$  moieties in  $H_2E=EH_2$  and (B) HE moieties in  $HE\equiv EH$ .



M	energy of isomers
C	(a)
Si, Ge	(b) < (c) < (d)
Sn, Pb	(d) < (c) < (b)

**Fig. 7** Isomers of  $\text{H}_2\text{E}=\text{EH}_2$  (E = group 14 elements).

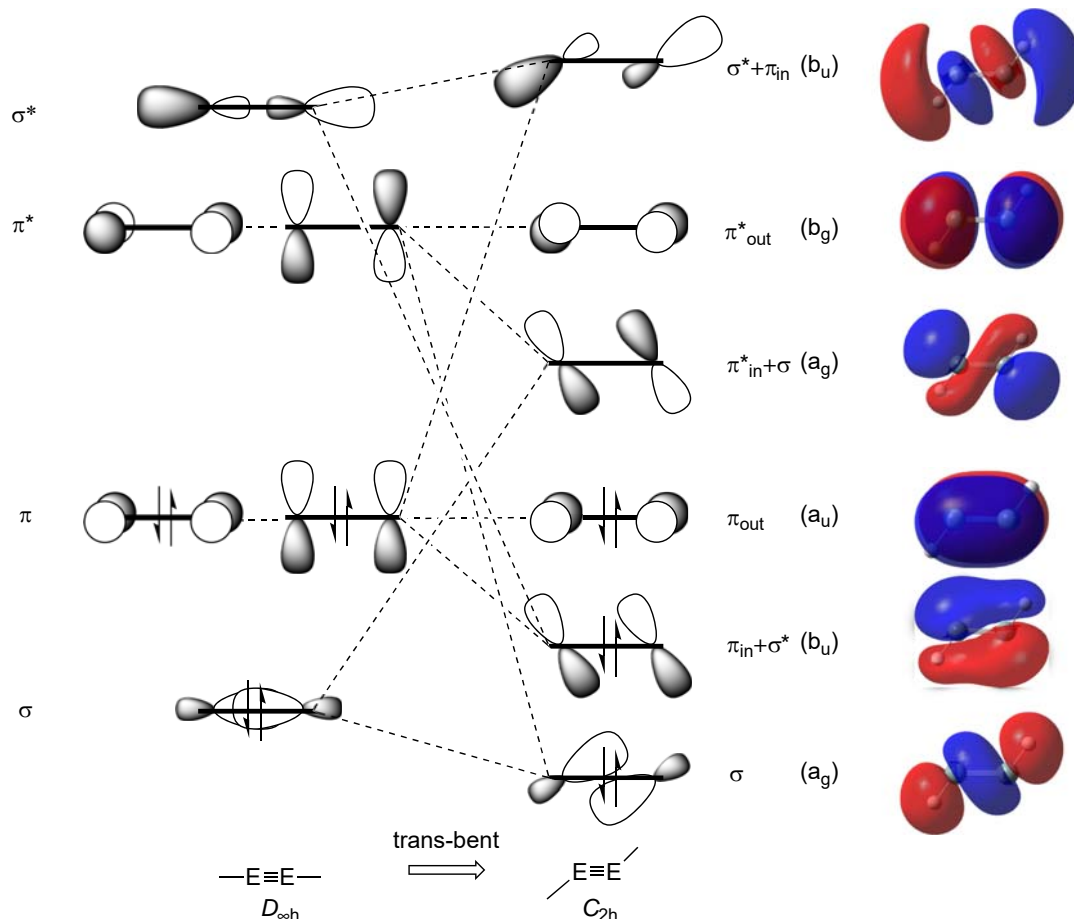


**Fig. 8** Pseudo (2nd-order) Jahn-Teller effect with mixing of  $\sigma^*$  orbital with the  $\pi$  orbital of  $\text{H}_2\text{E}=\text{EH}_2$  upon *trans*-pyramidalization.

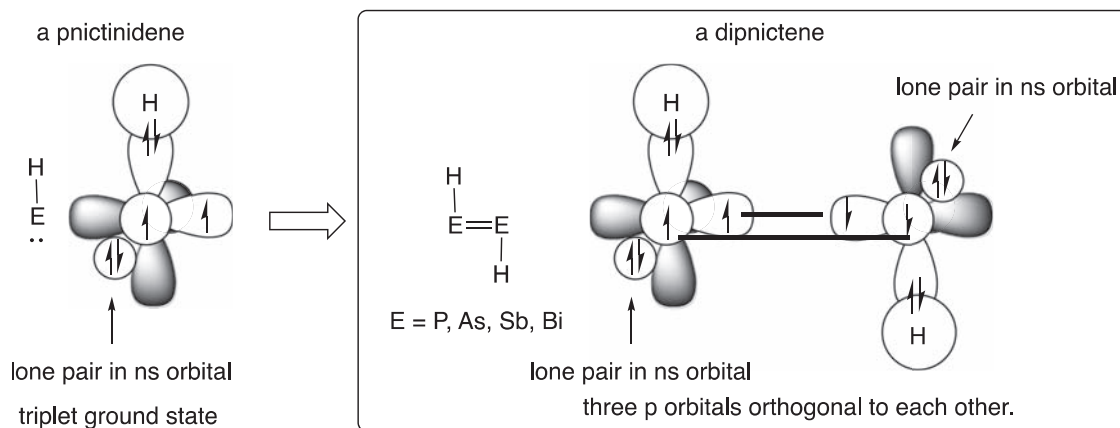
$\sigma^*$  orbitals via the *trans*-bending in  $\text{HE}\equiv\text{EH}$  should be much effective relative to those in  $\text{H}_2\text{E}=\text{EH}_2$ , because the  $\pi_{\text{in}}-\sigma^*$  energy difference in  $\text{HE}\equiv\text{EH}$  should be much smaller than that in  $\text{H}_2\text{E}=\text{EH}_2$ .

The  $\pi$ -bonding situation in heavier group 15 elements is very different from that in heavier group 14 elements.<sup>8,9b,d</sup> When thinking about the bonding situation, it is important to consider the number of valence p electrons. Pnictogen atoms (group 15 elements) have the  $ns^2np^3$  electron configuration, i.e., have one more valence p electron than group 14 atoms ( $ns^2np^2$  electron configuration). On the consideration of the  $ns^2np^3$  electron configuration of pnictogens, the monovalent heavier group 15 element species, a pnictinidene ( $-\text{P}$ : etc.), should have a triplet ground state (Fig. 10). Accordingly, one can understand that it is very difficult to isolate monovalent species of group 15 elements, pnictidenes, as stable compounds because of their triplet ground states with very reactive half-occupied p-orbitals, as compared with the cases of divalent species of heavier group 14 elements, tetrylenes. Instead of the high reactivity/instability of the monovalent species, a dimer of a pnictinidene, a dipnictene, can form a clear double bond without s-p orbital hybridization with the orthogonal np atomic orbitals as shown in Fig. 10. Indeed, it was found that the  $\text{R}-\text{Pn}=\text{Pn}$  angles should be approaching 90 degrees upon descending the elemental row from N to Bi, because the heavier elements reluctant to form s-p hybrid orbitals as described above.<sup>8,9b,d,13</sup>

As well, chalcogen atoms with  $ns^2np^4$  electron configuration can also form a clear double bond with group 14 elements as heavier elements analogues of carbonyl compounds ( $>\text{E}=\text{Ch}$ ),<sup>9c</sup> because chalcogens can form two chemical bonds with the orthogonal np atomic orbitals  $ns^2np^4$  electron configuration. Difficulty in the isolation of such heavier analogues of carbonyl



**Fig. 9** Pseudo (2nd-order) Jahn-Teller effect with mixing of  $\sigma^*$  orbital with the  $\pi$  orbital of  $\text{HE}\equiv\text{EH}$  upon *trans*-bending.



**Fig. 10** Electronic structure of a dipnictene ( $\text{HE}=\text{EH}$ ,  $\text{E}=\text{P, As, Sb, Bi}$ ).

compounds should be the thermal stability. That is, since no further substituent can be introduced on the doubly bonded chalcogen atom, the heavier analogues of a carbonyl compound would undergo facile oligomerization due to the lack of kinetic stability. Conversely, chalcogen cation ( $\text{Ch}^+$ ) can form a double bond bearing substituents,  $\text{RCh}^+=\text{Ch}^+\text{R}$  as well as a dipnictene despite the cationic charge repulsion, because its electron configuration is same as a pnictogen,  $ns^2np^3$ .

Thus, it can be concluded that, when the bonding situation of heavier main group elements would be considered, it should be very important to understand two key points: (i) heavier elements are reluctant to form s-p hybrid orbital, and the large promotion



energy should be required on forming an s-p hybrid orbital, and (ii) the bond formation situation should depend on the number of valence p electrons.

### 1.03.3 Low-coordinate compounds of heavier group 14 elements

#### 1.03.3.1 Introduction

The field of low-coordinate derivatives is one of the mainstreams of the contemporary chemistry of heavy tetrels (tetrel = element of the group 14). Likewise, within the realm of the low-coordinate compounds of the heavy group 14 elements, the field of the multiply bonded derivatives is arguably among the most popular topics of interest. Accordingly, the literature covering this field is vast with an uncountable number of examples of such unsaturated compounds reported to date. However, since the last edition of the *Comprehensive Inorganic Chemistry*, which included our contribution on the multiply bonded derivatives of the group 14 elements, was published in 2013,<sup>17</sup> in this chapter the literature coverage will start from 2013. We will limit our discussion to the range of compounds featuring double and triple bonds involving the heavy group 14 elements, whereas aromatic derivatives representing special and independent class of the unsaturated organometallics will be outside the framework of this chapter.

Moreover, numerous compounds in which the low-coordinate tetrel centers are intramolecularly (by *n*-donor substituents, most frequently, by N-groups) or intermolecularly (by the external donor ligands, typically, by NHC) coordinated and supported, were reported. However, in such compounds electronic support and accordingly thermodynamic stabilization occurs at the expense of the intrinsic nature of unsaturation, often to such a great extent that the electronic perturbation caused by the electron donation almost completely nullify the low-coordinate nature of the compounds in question. It is very problematic and highly risky to classify such compounds as truly low-coordinate species, although some authors still claim them as “doubly bonded”, “triply bonded”, etc., even though in many cases they are best described as the “singly bonded” species. In our chapter, such intramolecularly coordinated derivatives, in which the very presence of the multiple bond is somewhat doubtful, will be excluded from our consideration. As the only exception, intermolecularly coordinated (typically, by NHC) compounds, which cannot be otherwise stabilized to be isolated, will be discussed in our chapter. They include vinylidene derivatives  $>E=E(NHC)$ : and compounds of the type:  $E^0(NHC)=E^0(NHC)$ : ( $E=Si, Ge, Sn$ ), both classes being ultimately stabilized by the strong NHC-coordination. Considering each class of unsaturated compounds, we will start discussion with the brief mentioning of the historically important first stable representatives and will then consider other examples published since 2013. For more comprehensive reading on the multiple bonds to the heavy group 14 elements, we address readers to one of our previous overviews.<sup>18</sup>

#### 1.03.3.2 Doubly bonded derivatives

##### 1.03.3.2.1 Alkene analogues

###### 1.03.3.2.1.1 Homonuclear derivatives, $E=E$ ( $E=Si, Ge, Sn, Pb$ )

###### 1.03.3.2.1.1.1 Disilenes $>Si=Si<$

Although disilenes were not the first reported stable heavy group 14 element alkene analogues (the first were distannenes, *vide infra*), they are undoubtedly most popular, and accordingly the number of publications on isolable disilenes is by far exceeding those of any other class of alkene analogues of the heavy tetrels. The very first, historically most important, isolable disilene  $Mes_2Si=SiMes_2$  ( $Mes=2,4,6-Me_3-C_6H_2$ ), was reported by West and coworkers in 1981.<sup>7</sup> Since then, an overwhelming number of other stable disilenes was reported in the literature, however as mentioned in the Introduction, in this overview we will briefly discuss only papers published in or after 2013. Disilenes, as well as other heavy tetrel analogues, are characterized by the following most important spectral and structural parameters: (a)  $^{29}Si$  NMR chemical shift of the doubly bonded Si atoms,  $\delta(^{29}Si)$  (in ppm) (typically, low-field shifted), (b) length of the Si=Si bond,  $r_{SiSi}$  (in Å) (typically, short), (c) geometry of the substituents at the Si=Si bond defined by either bent angle  $\theta$  (in °) or by the sum of the bond angles around the  $sp^2$ -Si atoms,  $\Sigma$  (in °); (d) twisting of the Si=Si bond,  $\tau$  (in °) (typically, Si=Si bond is planar (non-twisted)) (Chart 2). Accordingly, below for the disilenes in question we will discuss their structures based on these parameters.

Although many groups are actively involved in disilene chemistry, one of the major players in the field is the research group of Iwamoto who made an important contribution within the last decade. Thus, a range of disilenes was synthesized by the functionalization disilene potassium derivatives with organic or heteroatom halides. In such way, “push-pull” disilene  $N-Si=Si-B$  featuring both donating (amino) and accepting (boryl) groups was prepared exhibiting the characteristics typical for disilenes: (1)  $\delta(^{29}Si) = 142.4$  (N- $sp^2$ -Si) and  $-33.0$  (B- $sp^2$ -Si) ppm; (2)  $r_{Si=Si} = 2.2146(6)$  Å; (3)  $\Sigma = 358.1/359.7^\circ$  (planar geometry around

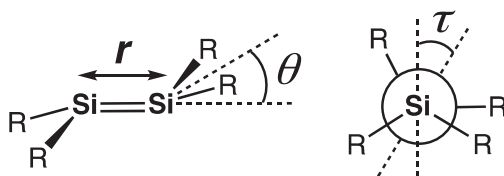


Chart 2 Bent angles of a disilene.

the  $sp^2$ -Si atoms).<sup>19</sup> The structural and computational studies revealed an important contribution of the  $N^+ = Si-Si=B^-$  resonance form caused by the electronic directions of substituents. A series of heteroaryl(thienyl)- and aryl(anthracenyl, acridinyl)-disilenes was also prepared from the potassium disilenide.<sup>20</sup> All of them uniformly displayed deshielded Si nuclei [ $\delta = 44.2$ – $141.5$  ppm], short Si=Si bonds [ $r_{Si=Si} = 2.1669(5)$ – $2.1846(5)$  Å], and *trans*-bent geometry [ $\theta = 11.9$ – $26.0^\circ$ ]. Interestingly, such disilenes showed absorption bands with contribution of intramolecular charge transfer (ICT),  $p(Si=Si) - p^*(aryl)$ . Applying this synthetic approach, Iwamoto and coworkers synthesized disilenes featuring endocyclic Si=Si bonds functionalized at the  $sp^2$ -Si atoms by aryl and silyl substituents.<sup>21</sup> Spectral and structural features of these disilenes were similar to those of acyclic disilenes: low-field shifted resonances of the  $sp^2$ -Si nuclei [ $\delta = 74.9$ – $134.2$  ppm], short Si=Si bonds [ $r_{Si=Si} = 2.1525(7)$ – $2.1915(5)$  Å], and unremarkable *trans*-bent geometry [ $\theta = 0.1$ – $22.5^\circ$ ]. Mono- and bis-borylated cyclic disilenes were also readily available by the above-mentioned synthetic route, showing typical characteristics: highly deshielded  $sp^2$ -Si nuclei [ $\delta = 128.7$ – $187.2$  ppm], relatively short Si=Si bonds [ $r_{Si=Si} = 2.1990(8)$ – $2.2114(5)$  Å], small *trans*-bending [ $\theta = 4.4$ – $9.8^\circ$ ] and twisting [ $\tau = 16.7$ – $19.3^\circ$ ] of the Si=Si bond.<sup>22</sup> The remarkable red-shift on going from mono- to bis-boryl disilene testifies for the effective conjugation between the Si=Si bond and the vacant  $2p$ -orbital of the B atom.

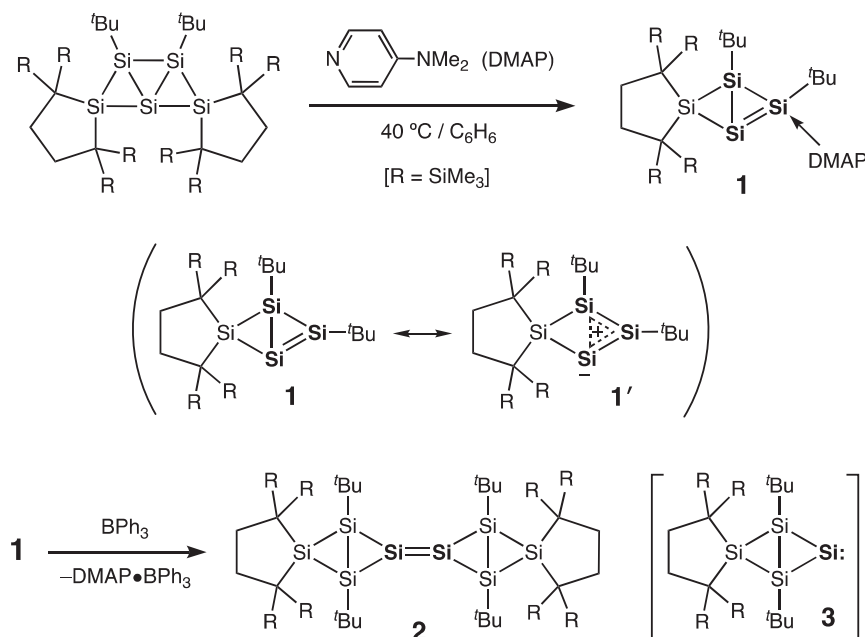
Another approach to disilenes adopted by Iwamoto group was based on the reductive dehalogenation of 1,2-dihalodisilanes  $>SiX-SiX<$  with potassium graphite. Using this method, they recently prepared disilenes which silyl substituents were unexpectedly joined into the polycyclic scaffolds.<sup>23</sup> Unusual polycyclic structures, however, did not greatly affect the structural features of these disilenes, which were characterized by the low-field resonances of the doubly bonded Si atoms [ $\delta = 133.4$ – $146.7$  ppm], short Si=Si bonds [ $r_{Si=Si} = 2.1665(14)$ – $2.2020(6)$  Å], and *trans*-bending of the Si=Si bonds [ $\theta = 5.5$ – $38.2^\circ$ ].

Silicon cluster containing two exocyclic Si=Si bonds at the edges of the tricyclo[2.2.0.0<sup>2,5</sup>]hexasilane framework was unexpectedly isolated from the mixture of several products formed upon the thermolysis of Si<sub>8</sub>-siliconoid cluster.<sup>24</sup> Both Si=Si bonds in this compound are rather short:  $r = 2.1570(12)$  and  $2.1641(12)$  Å.

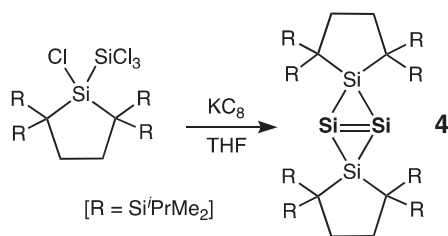
The most spectacular achievement of Iwamoto group was definitely isolation of the tricyclic compound **1** as the silicon analogue of the smallest bridgehead alkene that was stabilized by the 4-(*N,N*-dimethylamino)pyridine (DMAP) base.<sup>25</sup> **1** was selectively formed upon the thermolysis of tricyclo[2.1.0.0<sup>1,3</sup>]pentasilane in the presence of excess DMAP (Scheme 1). Although the resonance of the naked  $sp^2$ -Si atom was not observed (signal of the DMAP-coordinated  $sp^2$ -Si atom was found at +84.5 ppm), structure of **1** was unequivocally established by its X-ray diffraction. The central Si<sub>4</sub>-bicyclo[1.1.0]butane fragment is expectedly folded ( $127.04(2)^\circ$ ), and the bridgehead Si–Si bond is very long (2.6215(6) Å). The endocyclic Si=Si bond of 2.2906(6) Å is quite long for the standard double bond, and DMAP-coordinated  $sp^2$ -Si atom is remarkably pyramidalized. Based on the crystallographic data and computational studies, the real structure of **1** is best described as a zwitterion **1'** containing a (tetrasil)homocyclopropenylum ion and a silyl anion, rather than a bicyclic structure with a localized Si=Si double bond (Scheme 1).

Interestingly, when treated with BPh<sub>3</sub>, **1** underwent elimination of the DMAP-BPh<sub>3</sub> complex and formation of the disilene **2** as a dimer of the hypothetical silylene **3**, which is an isomer of **1** (Scheme 1). The exocyclic Si=Si bond in **2** is relatively long (2.248(2) Å) and expectedly *trans*-bent ( $54^\circ$ ).

Another very interesting disilene, bicyclo[1.1.0]tetrasil-1(3)-ene **4** (as a silicon analogue of non-existing bicyclo[1.1.0]but-1(3)-ene) containing a formal double bond between the bridgehead silicones in an inverted tetrahedral configuration, was recently



Scheme 1



Scheme 2

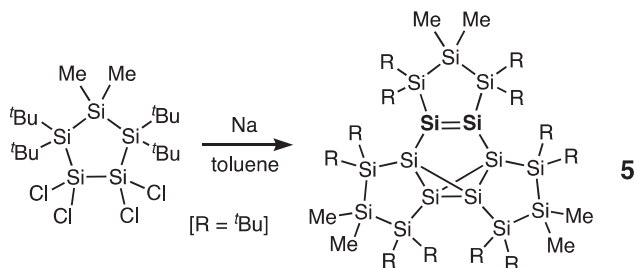
reported by Iwamoto and coworkers.<sup>26</sup> This compound was prepared by the reductive dechlorination of the  $>\text{Si}(\text{Cl})\text{SiCl}_3$ -precursor with  $\text{KC}_8$  (Scheme 2). The doubly bonded Si nuclei resonated at +217.0 ppm, which value is substantially low-field shifted compared to other known acyclic and cyclic silyl-substituted disilenes. Such exceptional deshielding of the  $\text{sp}^2$ -Si atoms suggests, that in contrast to other disilenes, **4** contains a higher-lying  $s$ -orbital and lower-lying  $\pi^*$ -orbital between the bridgehead Si atoms. The central  $\text{Si}=\text{Si}$  bond in **4** is exceptionally long, 2.4716(11) Å, being much longer than the typical  $\text{Si}=\text{Si}$  bond and even longer than the standard  $\text{Si}-\text{Si}$  single bonds, testifying for a rather unusual nature of this bond. Based on the results of DFT calculations, the authors concluded that this bridgehead  $\text{Si}=\text{Si}$  bond consists of a  $\sigma$ -bond with an inverted tetrahedral geometry and a  $\pi$ -bond.

Schschkewitz group reacted their disilyllithium derivative  $\text{Tip}_2\text{Si}=\text{Si}(\text{Tip})\text{Li}$  (Tip = 2,4,6- $\text{Pr}_3\text{-C}_6\text{H}_2$ ) with aryl halides and dihalides to prepare a range of novel (tetraaryl)disilenes  $\text{Tip}_2\text{Si}=\text{Si}(\text{Tip})\text{Ar}$  (Ar = 2,4,6-(MeO)<sub>3</sub>-C<sub>6</sub>H<sub>2</sub>; 2,4,6-Me<sub>3</sub>-C<sub>6</sub>H<sub>2</sub>; 2,3,5,6-Me<sub>4</sub>-C<sub>6</sub>H<sub>2</sub>; naphthalen-2-yl; anthracen-9-yl) and conjugated bisdisilenes  $\text{Tip}_2\text{Si}=\text{Si}(\text{Tip})\text{-[LU]-Si}(\text{Tip})=\text{SiTip}_2$  [LU (linking unit) = -C<sub>6</sub>H<sub>4</sub>-C<sub>6</sub>H<sub>4</sub>-; -C<sub>6</sub>H<sub>4</sub>-C≡C-C<sub>6</sub>H<sub>4</sub>-; 2,6-naphthalene; 9,10-anthracene].<sup>27</sup> As is characteristic for aryl disilenes, all these compounds exhibited moderately deshielded silicon nuclei [ $\delta = 52.7\text{--}71.5$  ppm], short  $\text{Si}=\text{Si}$  bonds [ $r_{\text{Si}=\text{Si}} = 2.1424(7)\text{--}2.1622(6)$  Å], nearly planar geometry around the  $\text{sp}^2$ -Si atoms [ $\Sigma = 357.4\text{--}360.0^\circ$ ], and unremarkable *trans*-bending [ $\theta = 0.0\text{--}15.3^\circ$ ] and twisting [ $\tau = 0.5\text{--}11.4^\circ$ ] along the  $\text{Si}=\text{Si}$  bond. The photophysical and computational data provide evidence for the extended  $p$ -conjugation through the entire backbone of these disilenes. Accordingly, tetrasiladienes  $\text{Tip}_2\text{Si}=\text{Si}(\text{Tip})\text{-[LU]-Si}(\text{Tip})=\text{SiTip}_2$  exhibited room temperature-fluorescence in the solid state and in a hexane solution. Moreover, anthryl-bridged tetrasiladiene represents a first example of a room temperature near infrared-emissive  $\text{Si}=\text{Si}$  derivatives.

Tamao and Matsuo group synthesized a series of disilenes  $\text{EindSi}(\text{Ar})=\text{Si}(\text{Ar})\text{Eind}$  (Ar = 1-naphthyl, phenyl, 1-pyrenyl, thiofen-2-yl, 2,2'-bithiophene-5-yl) stabilized by the very bulky (Eind)-group (Eind = 1,1,3,3,5,5,7,7-octaethyl-*s*-hydrindacen-4-yl) and prepared by a standard reductive dehalogenation of the dibromide precursors  $\text{Eind}(\text{Ar})\text{SiBr}_2$  with lithium naphthalenide.<sup>28</sup> All disilenes uniformly exhibited *trans*-configuration of substituents, with the only exception of 1-pyrenyl-substituted disilene, in which an attractive  $p$ - $p$  interaction between the pyrenyl groups was considered as the factor determining the stereochemistry of the reaction. Novel disilenes were characterized by unremarkably deshielded silicon atoms [ $\delta = 51.5\text{--}63.4$  ppm], short  $\text{Si}=\text{Si}$  bonds [ $r_{\text{Si}=\text{Si}} = 2.1584(9)\text{--}2.1718(6)$  Å], essentially planar geometry of the  $\text{Si}=\text{Si}$  bond with some *trans*-bending [ $\theta = 0.6\text{--}19.1^\circ$ ] and quite negligible twisting [ $\tau = 0.0\text{--}2.8^\circ$ ]. Most of these disilenes exhibited room-temperature intramolecular charge-transfer (ICT) fluorescence, both in the solid state and in solution, caused by the extended  $p$ -conjugation between the  $\text{Si}=\text{Si}$  bonds and aromatic  $\pi$ -electron systems.

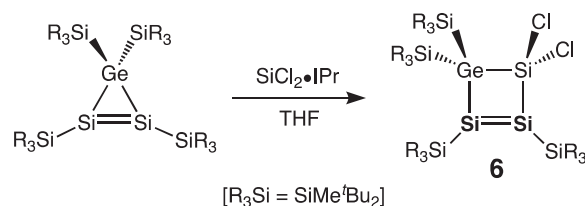
An interesting tetraphospha-substituted disilene  $(\text{Mes}_2\text{P})_2\text{Si}=\text{Si}(\text{PMes}_2)_2$  was recently synthesized by Izod and coworkers by the reaction of  $\text{SiBr}_4$  with 4 eqv. of  $\text{Mes}_2\text{PLi}$ .<sup>29</sup> The <sup>29</sup>Si NMR (CP MAS) chemical shift was observed at +111.7 ppm, that is in the typical range for disilenes. The  $\text{Si}=\text{Si}$  bond of 2.1901(12) Å is also normal for disilenes, although *trans*-bending was unusually high for disilenes ( $\theta = 40.6^\circ$ ).

Other examples of the recently reported disilenes include those in which  $\text{Si}=\text{Si}$  bond is incorporated into the cyclic or polycyclic framework.<sup>30</sup> Thus, in **5** the skeletal  $\text{Si}=\text{Si}$  bond is a part of the cyclopentasilane-fused hexasilabenzvalene, the central core of which represents a valence isomer of elusive hexasilabenzene (Scheme 3). The  $\text{sp}^2$ -Si atoms in **5** are strongly deshielded ( $\delta = 187.3$  ppm), the length of the  $\text{Si}=\text{Si}$  bond is normal for the double bond ( $r_{\text{Si}=\text{Si}} = 2.212(2)$  Å). Because of its highly rigid fused cyclic skeleton, **5** exhibited strongly *trans*-bent and highly twisted  $\text{Si}=\text{Si}$  bond:  $\theta = 36.5/42.5^\circ$  and  $\tau = 16.2^\circ$ , respectively.<sup>30a</sup>



Scheme 3

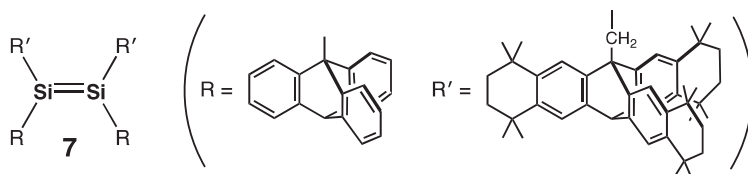
In  $^1\Delta$ -1,2,3,4-trisilagermetene **6**, prepared by the ring expansion reaction of 1-disilagermirene with  $\text{Cl}_2\text{Si-IPr}$  complex (IPr = 1,3-bis(2,6-diisopropylphenyl)-2*H*-imidazol-2-ylidene), both doubly bonded Si atoms were found in the region typical for the four-membered ring cyclic disilenes, +168.0 and +176.9 ppm (Scheme 4).<sup>30b</sup> The  $\text{GeSi}_3$ -ring in **6** is folded ( $24.2^\circ$ ), and the  $\text{Si}=\text{Si}$  bond of 2.199(9) Å conforms to the standards for the double bonds.



Scheme 4

The tetralkyldisilene **7** with exceptionally bulky triptycenylyl substituents was also recently reported (Scheme 5).<sup>30c</sup> Reflecting extraordinary high steric hindrances around the double bond, **7** exhibited a (*Z*)-configuration, elongated  $\text{Si}=\text{Si}$  bond [ $r_{\text{Si}=\text{Si}} = 2.223(1)$  Å], pyramidalization at  $\text{sp}^2$ -Si atoms ( $\Sigma = 351^\circ$ ), and rather important twisting about the  $\text{Si}=\text{Si}$  bond ( $\tau = 34^\circ$ ). The doubly bonded Si atoms resonated in low-field at +115.6 ppm.

Some disilenes, although isolated and spectroscopically characterized, were lacking X-ray structural determination. They include cyclopentasilene,<sup>31</sup> tetrasilyldisilene  $(\text{Me}_3\text{Si})_2\text{Si}=\text{Si}(\text{SiMe}_3)\text{Si}^t\text{Bu}_3$  existing in equilibrium with the isomeric bis(silyl)silylene



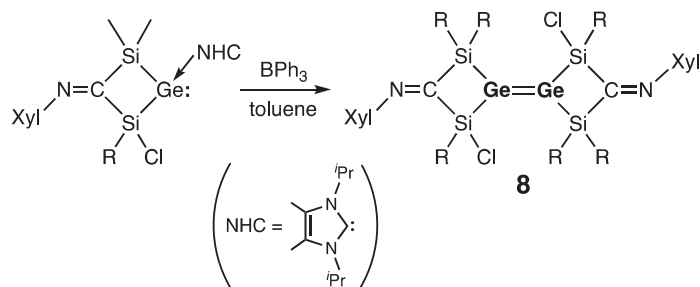
Scheme 5

$(\text{Me}_3\text{Si})_3(^t\text{Bu}_3\text{Si})\text{Si}$ <sup>32</sup>; bis(boryl)disilene (boryl)PhSi=SiPh(boryl) (boryl = *cyclo*[−BN(Ar)CH=CHN(Ar)−]).<sup>33</sup>

In recently reported diimino(disilyl)disilene  $[(\text{Me}_3\text{Si})_3\text{Si}(\text{NHI})\text{Si}=\text{Si}(\text{NHI})[\text{Si}(\text{SiMe}_3)_3]$  (NHI = *N*-heterocyclic imine)<sup>34</sup> and diamino(diaryl)disilene featuring intramolecular coordination of imino-groups on  $\text{sp}^2$ -Si atoms,<sup>35</sup> the silicon-silicon interatomic distances are very long (2.3124(7) Å)<sup>34</sup> or exceptionally long (2.623(1) Å).<sup>35</sup> Accordingly, classification of such compounds as disilenes is somewhat debatable, as they can be alternatively (and even better) viewed as very weak donor-acceptor adducts of two silylenes (rather than the true disilenes).

#### 1.03.3.2.1.1.2 Digermenes >Ge=Ge<

The first stable digermenes [tetra(alkyl)digermenes] were prepared and structurally characterized by Lappert and coworkers in 1976.<sup>36</sup> Since 2013, several remarkable examples of isolable digermenes were synthesized by different synthetic approaches. Thus, Scheschkewitz group prepared their digermene **8** by dimerization of the cyclic germylene generated from its NHC complex (Scheme 6).<sup>37</sup> The  $\text{Ge}=\text{Ge}$  bond in **8** of 2.2944(4) Å is typical for such double bonds, and as is expected for the heavy Group 14 element derivatives, both Ge atoms are strongly pyramidalized ( $\Sigma = 334.5^\circ$ ) and substituents are *trans*-bent ( $\theta = 37.7^\circ$ ). In solution,  $\text{Ge}=\text{Ge}$  double bond retained its structural integrity.



Scheme 6

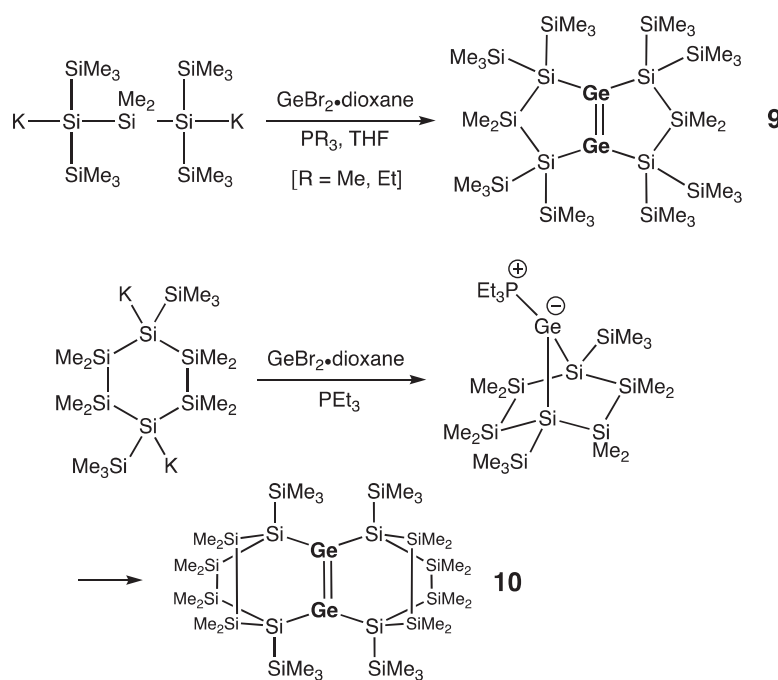


In 2018, the same group reported an interesting example of the first isolable digermene  $\text{Tip}_2\text{Ge}=\text{Ge}(\text{Tip})\text{Li}$  prepared by the simple reduction of  $\text{Tip}_2\text{GeCl}_2$  precursor with metallic lithium.<sup>38a</sup> The Ge=Ge bond is typical for digermenes [ $r_{\text{Ge}=\text{Ge}} = 2.284(6)$  Å], being also unremarkably *trans*-bent ( $\theta = 7.1/12.8^\circ$ ) and twisted ( $\tau = 19.9^\circ$ ). This digermene is synthetically useful and can be functionalized at the anionic Ge center, thus giving access to novel digermenes  $\text{Tip}_2\text{Ge}=\text{Ge}(\text{Tip})\text{R}$  (R=SiMe<sub>3</sub>, SiPhMe<sub>2</sub>, SiPh<sub>3</sub>, SiMe<sub>2</sub>Cl, SiMePhCl, SiPh<sub>2</sub>Cl), and even the first persistent acyldigermenes  $\text{Tip}_2\text{Ge}=\text{Ge}(\text{Tip})[\text{C}(\text{O})\text{R}]$  (R = <sup>t</sup>Bu, 2-methylbutan-2-yl, 1-adamantyl) are accessible via this synthetic route.<sup>38</sup>

Utilizing highly effective (Eind)-substituent, the groups of Matsuo and Sasamori prepared 1,2-dihalodigermenes  $\text{Eind}(\text{X})\text{Ge}=\text{Ge}(\text{X})\text{Eind}$  (X=Cl, Br) by the reaction of germylene  $\text{Eind}_2\text{Ge}$ : with  $\text{GeX}_2$ -dioxane complex.<sup>39</sup> As is typical for digermenes featuring electronegative substituents, dihalodigermenes exhibited strongly *trans*-bent ( $\theta = 43.3$  and  $44.3^\circ$ ) and pyramidal configuration ( $\Sigma = 337.1$  and  $335.9^\circ$ ) at the  $\text{sp}^2$ -Ge atoms. The Ge=Ge bonds are rather long [ $r_{\text{Ge}=\text{Ge}} = 2.4145(3)$  and  $2.4119(5)$  Å] indicative of the weak bonding between the Ge atoms, which was further substantiated by the observation of ready dissociation of the Ge=Ge bond. Thus, in solution dihalodigermenes  $\text{Eind}(\text{X})\text{Ge}=\text{Ge}(\text{X})\text{Eind}$  exist as halogermynes  $\text{Eind}(\text{X})\text{Ge}$ .

Another approach to stable digermenes was demonstrated by Sasamori, Tokitoh and coworkers, who reacted their stable digermene  $\text{BbtGe}\equiv\text{GeBbt}$  (Bbt = 2,6-[(Me<sub>3</sub>Si)<sub>2</sub>CH]<sub>2</sub>-4-[(Me<sub>3</sub>Si)<sub>3</sub>C]-C<sub>6</sub>H<sub>2</sub>) (see Section 1.03.3.1) with ethylene.<sup>40</sup> The corresponding [2 + 2] cycloadduct, 1,2-digermacyclobutene featuring endocyclic Ge=Ge double bond stabilized by the bulky Bbt substituents, revealed folded four-membered ring, *trans*-bent geometry of substituents at the Ge=Ge bond ( $\theta = 39.5$  and  $39.7^\circ$ ), and notably long Ge=Ge bond [ $r_{\text{Ge}=\text{Ge}} = 2.4132(5)$  Å], similar to the one described in the above paragraph. Stretching and weakness of the Ge=Ge bond was attributed to the ring strain and *trans*-bending effects.

Unusual digermenes in which endocyclic Ge=Ge units bridge polycyclic scaffolds were reported by Marschner group.<sup>41</sup> Thus, reaction of 1,3-dipotassiotsilane with  $\text{GeBr}_2$ -dioxane and  $\text{PEt}_3$  unexpectedly produced bicyclic digermene **9**, whereas analogous reaction of 1,4-dipotassiocyclohexasilane with  $\text{GeBr}_2$ -dioxane and  $\text{PEt}_3$  gave tetracyclic digermene **10** (Scheme 7). Both digermenes



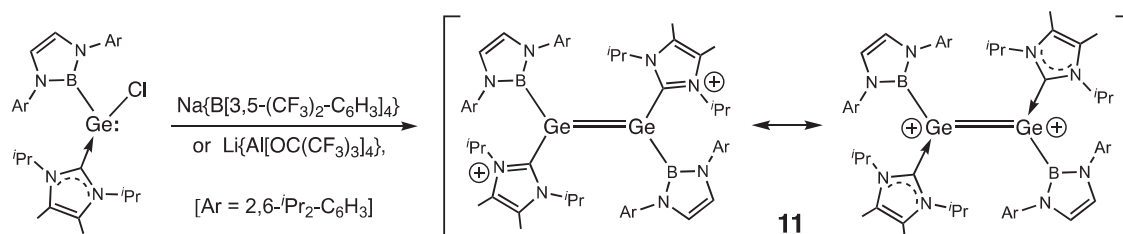
**Scheme 7**

**9** and **10** showed similar structural characteristics typical for the cyclic digermenes, namely, shortened Ge=Ge bonds ( $r_{\text{Ge}=\text{Ge}} = 2.2663(9)$  and  $2.2896(6)$  Å), negligible *trans*-bending ( $\theta = 2.5$  and  $2.1/8.3^\circ$ ), and small twisting ( $\tau = 16.2$  and  $5.2^\circ$ ). According to CV measurements, digermene **9** revealed two reversible reduction waves corresponding to formation of anion-radical and dianion, respectively, whereas cation-radical formed upon one-electron oxidation of **9** was unstable.

By contrast, both oxidation and reduction of the (tetrasilyl)digermene (<sup>t</sup>Bu<sub>2</sub>MeSi)<sub>2</sub>Ge=Ge(SiMe<sup>t</sup>Bu<sub>2</sub>)<sub>2</sub> were fully reversible in *o*-dichlorobenzene with the potentials  $E_{1/2}(\text{ox}) = 0.38$  V and  $E_{1/2}(\text{red}) = -1.5$  V, respectively.<sup>42</sup> This digermene was prepared by Lee, Sekiguchi and coworkers by the reduction of the (<sup>t</sup>Bu<sub>2</sub>MeSi)<sub>2</sub>GeCl<sub>2</sub> precursor with potassium graphite.<sup>42</sup> The length of the Ge=Ge bond is normal for digermenes [ $r_{\text{Ge}=\text{Ge}} = 2.346(2)$  Å] and both Ge centers are essentially planar ( $\Sigma = 358.8$  and  $359.2^\circ$ ). Although this digermene does not dissociate into germynes in solution, which was supported by UV measurements, it exhibited extraordinarily long wavelength UV absorption at 618 nm [ $\pi$  (HOMO)- $\pi^*$  (LUMO) transition]. This fact, along with

the exceptionally great twisting about the Ge=Ge double bond ( $\tau = 52.8^\circ$ ), provides experimental evidence for the remarkably reduced  $4p_\pi(\text{Ge})-4p_\pi(\text{Ge})$  orbital overlap resulting in the partial breaking of the Ge–Ge  $\pi$ -bond, and accordingly causing very important contribution of biradical character to the Ge=Ge bond.

Reacting their NHC-coordinated chlorogermylene with either  $\text{Na}\{\text{B}[3,5-(\text{CF}_3)_2-\text{C}_6\text{H}_3]_4\}$  or  $\text{Li}\{\text{Al}[\text{OC}(\text{CF}_3)_3]_4\}$ , Aldridge and coworkers prepared dicationic species **11**, which can be viewed as a digermene featuring cationic imidazolium substituents (Scheme 8).<sup>43</sup> The length of the Ge=Ge bond in **11** is consistent with its formulation as a double bond [ $r_{\text{Ge}=\text{Ge}} = 2.300(2) \text{ \AA}$ ], and Ge atoms are only insignificantly pyramidalized ( $\Sigma = 353.1$  and  $353.6^\circ$ ). Replacing NHC-substituents on Ge atoms in **11** with  $\text{Me}_4\text{-NHC}$ , and



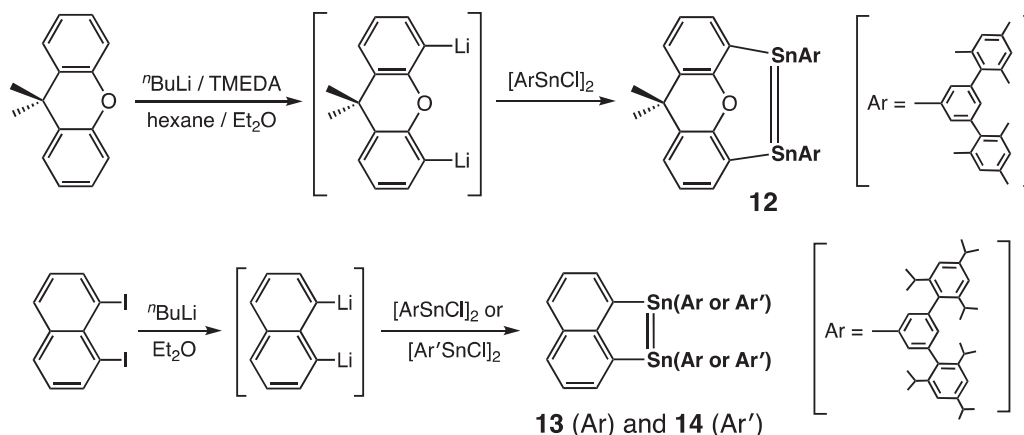
Scheme 8

boryl substituents with  $[2,6\text{-Mes}_2\text{-C}_6\text{H}_3]$  ( $\text{Mes} = 2,4,6\text{-Me}_3\text{-C}_6\text{H}_2$ ), the same authors synthesized another dicationic digermene featuring slightly longer Ge=Ge distance of  $2.380(1) \text{ \AA}$ .<sup>44</sup>

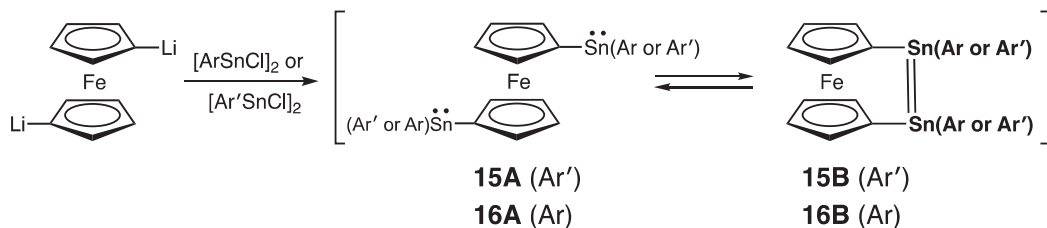
The exciting possibility of the digermene metathesis, as the germanium version of alkene metathesis, was very recently demonstrated by Scheschkewitz group.<sup>45</sup> They heated unsymmetrically substituted digermene  $\text{Tip}_2\text{Ge}=\text{Ge}(\text{Tip})[\text{SiR}_2\text{Dma}]$  ( $\text{R} = \text{Me}, \text{Ph}$ ;  $\text{Dma} = 2\text{-}N,N\text{-dimethylanilino}$  group) to afford a mixture of  $\text{Tip}_2\text{Ge}=\text{GeTip}_2$  and *trans*- $[\text{DmaR}_2\text{Si}](\text{Tip})\text{Ge}=\text{Ge}(\text{Tip})[\text{SiR}_2\text{Dma}]$  ( $\text{Ge}=\text{Ge}$  for  $\text{R} = \text{Me}$ :  $r_{\text{Ge}=\text{Ge}} = 2.2576(5) \text{ \AA}$ ,  $\theta = 21.5^\circ$ ,  $\tau = 0^\circ$ ). Most importantly, this approach was successfully applied towards the development of ADMET (Acyclic Diene METathesis) of digermenes. Thus, thermolysis (benzene,  $60^\circ\text{C}$ , 48 h) of a diene featuring terminal digermene units connected by a *p*-phenylene bridge,  $\text{Tip}_2\text{Ge}=\text{Ge}(\text{Tip})\text{-SiMe}_2\text{-1,4-[2,5-(Me}_2\text{N)}_2\text{-C}_6\text{H}_2]\text{-SiMe}_2\text{-Ge}(\text{Tip})=\text{GeTip}_2$  ( $\text{Ge}=\text{Ge}$ :  $r_{\text{Ge}=\text{Ge}} = 2.3038(4) \text{ \AA}$ ,  $\theta = 24.9/31.9^\circ$ ,  $\tau = 18.0^\circ$ ), yielded the corresponding ADMET-polyene  $\text{Tip}_2\text{Ge}=\{\text{Ge}(\text{Tip})\text{-SiMe}_2\text{-1,4-[2,5-(Me}_2\text{N)}_2\text{-C}_6\text{H}_2]\text{-SiMe}_2\text{-Ge}(\text{Tip})=\}_n\text{-GeTip}_2$  with the number-average degree of polymerization = 23, mass-average degree of polymerization = 45, and dispersity index = 1.95.

### 1.03.3.2.1.1.3 Distannenes $>\text{Sn}=\text{Sn}<$

The first stable distannenes [tetra(alkyl)distannenes] were synthesized and structurally characterized by Lappert group in the same year 1976, as isostructural digermenes.<sup>3,36b</sup> After 2013, several interesting distannenes were synthesized and structurally characterized. Thus, Wesemann reported a range of distannenes **12–14** in which the  $\text{Sn}=\text{Sn}$  double bond is incorporated into the polycyclic aromatic skeleton.<sup>46</sup> They were uniformly prepared by a straightforward procedure, namely, reaction of bulky aryl(chloro)stannylenes  $\text{Ar}(\text{Cl})\text{Sn}$ : ( $\text{Ar} = 2,6\text{-Mes}_2\text{-C}_6\text{H}_3$ ) and  $\text{Ar}'(\text{Cl})\text{Sn}$ : ( $\text{Ar}' = 2,6\text{-Tip}_2\text{-C}_6\text{H}_3$ ) with dilithium arene-diides (Scheme 9). Spectral and structural features of distannenes **12** and **13/14** are distinctly different,  $\text{Sn}=\text{Sn}$ :  $\delta(^{119}\text{Sn}) = 862$  and  $396/412$  ppm,  $r_{\text{Sn}=\text{Sn}} = 3.0009(7)$  and  $2.7299(3)/2.7688(2) \text{ \AA}$ ,  $\theta = 45/59$  and  $55/(46/49)^\circ$ , respectively. However, the longest UV-absorptions (HOMO-LUMO transition) were very similar for all distannenes **12–14**, appearing near 600 nm. Applying this synthetic route,



Scheme 9

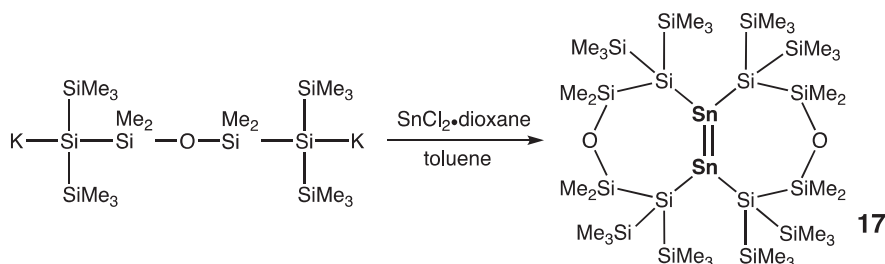


Scheme 10

the same authors prepared also distannene, in which the Sn=Sn bond is bridged by an acenaphthene unit and the substituents at the Sn atoms are 2,6-Mes<sub>2</sub>-C<sub>6</sub>H<sub>3</sub> groups.<sup>47</sup> Similar to distannenes 13 and 14, the new compound featured the following characteristics for its Sn=Sn double bond:  $\delta(^{119}\text{Sn}) = 375$  ppm,  $r_{\text{Sn}=\text{Sn}} = 2.7838(2)$  Å,  $\theta = 43/65^\circ$ , and  $\tau = 65^\circ$ .

A very interesting example of the distannene-stannylene equilibrium was recently reported by Wesemann and coworkers.<sup>48</sup> They simply reacted 1,1'-dilithioferrocene with either Ar(Cl)Sn: (Ar = 2,6-Mes<sub>2</sub>-C<sub>6</sub>H<sub>3</sub>) or Ar'(Cl)Sn: (Ar' = 2,6-Tip<sub>2</sub>-C<sub>6</sub>H<sub>3</sub>) (Scheme 10). Despite the similarity of the starting stannylenes, the outcome of the reaction strongly depends on the steric bulk of aryl substituent at tin. Thus, with bulkier Ar' group, there was an equilibrium between the bis(stannylene) 15A and distannene 15B structures, with the former being favored in the solid state and in solution at high temperatures and the latter being favored in solution at low temperatures ( $-80^\circ\text{C}$ ) (Scheme 10). By contrast, when smaller aryl group Ar was applied, the corresponding distannene derivative 16B was by far predominant structure both in the solid state and in solution, and its chemical shift  $d(^{119}\text{Sn})$  of 449 ppm did not change significantly in the temperature range from  $-80^\circ\text{C}$  [ $\delta(^{119}\text{Sn}) = 437$  ppm] to  $100^\circ\text{C}$  [ $\delta(^{119}\text{Sn}) = 468$  ppm] which implies retaining of the structural integrity of the Sn=Sn bond in solution at these temperatures (Scheme 8). Accordingly, no evidences for the existence of the monomeric stannylenes 16A were found in both solution and in the solid. The reduced bulkiness of the aryl group (Ar vs. Ar') in 16 was attributed to the higher stability of the Sn=Sn bond in 16B (in contrast to 15B).

A bicyclic distannene, as a tin analogue of the above-described bicyclic digermene 9 (see Scheme 7),<sup>41</sup> was prepared by Marschner and coworkers by the reaction of 1,3-dipotassiotrisilane with SnCl<sub>2</sub> in the presence of appropriate Lewis base (PMe<sub>3</sub>, PEt<sub>3</sub>, Me<sub>4</sub>-NHC).<sup>49</sup> This distannene revealed <sup>119</sup>Sn NMR chemical shift of 730.7 ppm that was low-field shifted compared with other silylated distannenes, although its longest UV-absorption of 558 nm was blue-shifted compared to the silylated distannenes. The Sn=Sn double bond is short, measuring only 2.6162(11) Å, being also *trans*-bent ( $\theta = 36.0^\circ$ ) and twisted ( $\tau = 22.6^\circ$ ). Likewise, reacting dipotassium salt of oligosilylanylene-1,5-diide with SnCl<sub>2</sub>·dioxane Marschner group isolated another bicyclic distannene 17 featuring two seven-membered rings fused by the bridging Sn=Sn unit (Scheme 11).<sup>50</sup> 17 showed typical for distannenes <sup>119</sup>Sn NMR chemical shift of 636.9 ppm, and rather long Sn=Sn double bond of 2.7409(9) Å which has a *trans*-bent ( $\theta = 31.1^\circ$ ) and twisted ( $\tau = 17.0/81.6^\circ$ , for two seven-membered rings which have very different conformations) geometry.



Scheme 11

Several stable distannenes were reported by Power and coworkers. Thus, reaction of the Sn(II) hydrides  $[\text{Ar}^{i\text{Pr}_6}\text{Sn}(m\text{-H})]_2$  and  $[\text{Ar}^{i\text{Pr}_4}\text{Sn}(m\text{-H})]_2$  [ $\text{Ar}^{i\text{Pr}_6} = 2,6\text{-}(2,4,6\text{-}^i\text{Pr}_3\text{-C}_6\text{H}_2)\text{-C}_6\text{H}_3$ ,  $\text{Ar}^{i\text{Pr}_4} = 2,6\text{-}(2,6\text{-}^i\text{Pr}_2\text{-C}_6\text{H}_3)\text{-C}_6\text{H}_3$ ] with ethylene and (*tert*-butyl)ethylene afforded distannenes  $\text{Ar}^{i\text{Pr}_6}(\text{CH}_3\text{CH}_2)\text{Sn}=\text{Sn}(\text{CH}_2\text{CH}_3)\text{Ar}^{i\text{Pr}_6}$  18 and  $\text{Ar}^{i\text{Pr}_4}(\text{tBuCH}_2\text{CH}_2)\text{Sn}=\text{Sn}(\text{CH}_2\text{CH}_2\text{tBu})\text{Ar}^{i\text{Pr}_4}$  19.<sup>51</sup> In solution, distannene 18 dissociates into monomeric stannylenes as was evidenced by the low-field <sup>119</sup>Sn NMR resonance observed at 1908 ppm (at 330 K), whereas on cooling down to 250 K two signals were found at 289 and 2915 ppm indicating existence of both distannene and stannylene species in solution. Likewise, distannene 19 also is in solution equilibrium with the corresponding stannylstannylenes: <sup>119</sup>Sn NMR resonances observed at 320 and 1875 ppm. Both 18 and 19 displayed similar structural characteristics:  $r_{\text{Sn}=\text{Sn}} = 2.732(5)$  and  $2.714(2)$  Å,  $\theta = 57.4$  and  $55.5^\circ$ , and  $\Sigma = 335.2$  and  $339.3^\circ$ . Reaction of diarylstannylene  $(\text{Ar}^{i\text{Pr}_4})_2\text{Sn}$ : [ $\text{Ar}^{i\text{Pr}_4} = 2,6\text{-}(2,6\text{-}^i\text{Pr}_2\text{-C}_6\text{H}_3)\text{-C}_6\text{H}_3$ ] with toluene, *m*-xylene and mesitylene at  $80^\circ\text{C}$  provided distannenes  $\text{Ar}^{i\text{Pr}_4}(\text{ArCH}_2)\text{Sn}=\text{Sn}(\text{CH}_2\text{Ar})\text{Ar}^{i\text{Pr}_4}$  (Ar = C<sub>6</sub>H<sub>5</sub>, 3-Me-C<sub>6</sub>H<sub>4</sub>, 3,5-Me<sub>2</sub>-C<sub>6</sub>H<sub>3</sub>) as C–H metathesis products.<sup>52</sup> All of them dissociated in solution into the monomeric aryl(alkyl)stannylenes  $\text{Ar}^{i\text{Pr}_4}(\text{ArCH}_2)\text{Sn}$ ; which was evidenced by their low-field <sup>119</sup>Sn NMR resonances found at 1660–1671 ppm (typical for stannylenes). In the solid-state, however, these compounds exist as the dimeric

distannenes, as can be clearly seen from their crystallographic data:  $r_{\text{Sn}=\text{Sn}} = 2.782(3)$  and  $2.787(1)$  Å,  $\theta = 41.2$  and  $43.0^\circ$ , and  $\Sigma = 330.7$  and  $338.3^\circ$ .

#### 1.03.3.2.1.1.4 Diplumbenes $>\text{Pb}=\text{Pb}<$

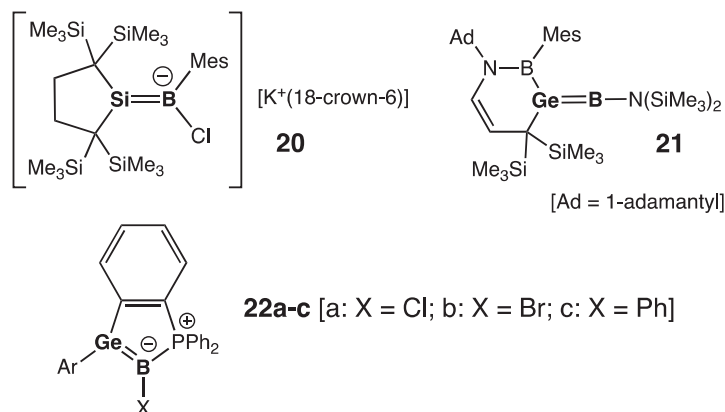
The first stable diplumbene  $\text{Tip}_2\text{Pb}=\text{PbTip}_2$ , that exists in an equilibrium with the corresponding plumbylene  $\text{Tip}_2\text{Pb}$ ·, was reported much later than its lighter analogues (disilene, digermene, and distannene), in 1999, by Weidenbruch and coworkers.<sup>53</sup> Since 2013, little progress has been made into the field of stable diplumbenes with only one report from Power group.<sup>54</sup> They reacted diarylplumbylene  $(\text{Ar}^{\text{Me6}})_2\text{Pb}$ :  $[\text{Ar}^{\text{Me6}} = 2,6-(2,4,6-\text{Me}_3-\text{C}_6\text{H}_2)-\text{C}_6\text{H}_3]$  with  $\text{Me}_3\text{M}$  ( $\text{M}=\text{Al}, \text{Ga}$ ) to afford aryl(methyl) diplumbene  $\text{Ar}^{\text{Me6}}(\text{Me})\text{Pb}=\text{Pb}(\text{Me})\text{Ar}^{\text{Me6}}$  as the result of substituents scrambling reaction, and thus representing a new synthetic route to diplumbenes. Given its remarkably low-field shifted  $^{207}\text{Pb}$  NMR resonance of 8248 ppm, the solution structure of this compound was attributed to that of the monomeric plumbylene  $\text{Ar}^{\text{Me6}}(\text{Me})\text{Pb}$ ·. The  $\text{Pb}=\text{Pb}$  double bond is rather long [ $3.2866(5)$  Å] and Pb centers are notably pyramidalized [ $\Sigma = 325.3^\circ$ ].

#### 1.03.3.2.1.2 Heteronuclear derivatives, $\text{E}=\text{E}'$ ( $\text{E}=\text{Si}, \text{Ge}, \text{Sn}, \text{Pb}$ )

##### 1.03.3.2.1.2.1 $>\text{E}=\text{E}'$ ( $\text{E} = \text{Group 14 element}, \text{E}' = \text{Group 13 element}$ )

The transient sila- and germaborenes  $[(^t\text{Bu}_2\text{MeSi})_2\text{E}=\text{B}-\text{Mes}]$  ( $\text{E}=\text{Si}, \text{Ge}$ ) were reported in 2005 by Sekiguchi and coworkers,<sup>55a</sup> and the first stable silaborene  $[(^t\text{Bu}_2\text{MeSi})_2\text{E}=\text{B}-\text{R}]$  ( $\text{R} = 2,2,6,6\text{-tetramethylpiperidino}$ ) was prepared in 2006 by the same group.<sup>55a</sup>

As the latest advances in the field, one can mention a new silaborene-chloride adduct **20** reported by Iwamoto and coworkers,<sup>56</sup> and the first germaborenes independently prepared and very recently reported by Kinjo (germaborene **21** with an exocyclic  $\text{Ge}=\text{B}$  bond)<sup>57</sup> and Wesemann (germaborene **22** with an endocyclic  $\text{Ge}=\text{B}$  bond) research groups<sup>58</sup> (Scheme 12). In all cases, formation of the  $>\text{E}=\text{B}-$  ( $\text{E}=\text{Si}, \text{Ge}$ ) bond was uniformly accomplished by the reduction of the corresponding dihalo-precursors  $>\text{E}(\text{X})-\text{B}(\text{X})-\text{X}$  ( $\text{X}=\text{Cl}, \text{Br}$ ) with either potassium graphite or magnesium.



Scheme 12

The silaborene-chloride adduct **20** (Scheme 12) features the following spectral and structural parameters of the  $\text{Si}=\text{B}$  fragment:  $r = 1.859(2)$  Å (short bond),  $\Sigma = 359.3(\text{Si})$  and  $360.0(\text{B})^\circ$  (planar geometry around these atoms),  $\delta[^{29}\text{Si}(\text{sp}^2)] = 56.8$  and  $\delta[^{11}\text{B}(\text{sp}^2)] = 38.0$  ppm. Experimental and computational data strongly suggest that **20** is best represented as an anionic silaborene [ $>\text{Si}=\text{B}^-<$ ] rather than (boryl)silyl anion resonance form [ $>\text{Si}^--\text{B}<$ ].

The first two stable germaborenes were published face-to-face in the same issue of *Angew. Chem. Int. Ed.* in 2020. Kinjo germaborene **21** exhibits low-field  $^{11}\text{B}$  NMR chemical shift of the doubly bonded B atom at 94.5 ppm, rather short  $\text{Ge}=\text{B}$  bond ( $r = 1.911(7)$  Å), pyramidal geometry at the Ge center ( $340^\circ$ ), and remarkably bent  $\text{Ge}-\text{B}-\text{N}$  fragment (bond angle =  $158.6^\circ$ ) (Scheme 12).<sup>57</sup> The  $\text{Ge}=\text{B}$  double bond character in **21** was further supported by computations,  $\text{WBI}_{\text{Ge}=\text{B}} = 1.67$ . Likewise, Wesemann germaborenes **22a** ( $\text{X}=\text{Cl}$ ) and **22b** ( $\text{X}=\text{Br}$ ) were characterized by even shorter  $\text{Ge}=\text{B}$  bonds [ $r = 1.886(2)$  Å (for **22a**) and  $1.895(3)$  Å (for **22b**)], trigonal-planar geometry around the  $\text{sp}^2$ -atoms [ $\Sigma = 359.6/359.6^\circ$  (Ge, for **22a/22b**) and  $359.8/360.0^\circ$  (B, for **22a/22b**)], chemical shifts  $\delta(^{11}\text{B})$  as a doublet at 17.3 ppm ( $^1J_{\text{P,B}} = 132$  Hz) (for **22a**) and 10.3 ppm ( $^1J_{\text{P,B}} = 134$  Hz) (for **22b**) (Scheme 12).<sup>58a</sup> The NBO calculations revealed 1.94e-occupancy for the  $\text{Ge}-\text{B}$  s-bond and 1.67e-occupancy for the  $\text{Ge}-\text{B}$  p-bond, which leads to the  $\text{WBI}_{\text{Ge}=\text{B}}$  of 1.51. According to the Natural Resonance Theory (NRT) calculations, the dominating Lewis structure (NRT weights = 29.0% for **22a** and 28.7% for **22b**) is the one with the  $\text{Ge}=\text{B}$  double bond, thus implying formulation of **22a,b** as the germaborenes. Applying the same synthetic strategy, Wesemann group prepared also Ph-substituted germaborene **22c** ( $\text{X}=\text{Ph}$ ) (Scheme 12).<sup>58b</sup> The spectral and structural features of the novel germaborene **22c** are similar to those of the previously reported **22a,b**, namely:  $\delta(^{11}\text{B}) = 16.2$  ppm,  $r_{\text{Ge}=\text{B}} = 1.899(3)$  Å.

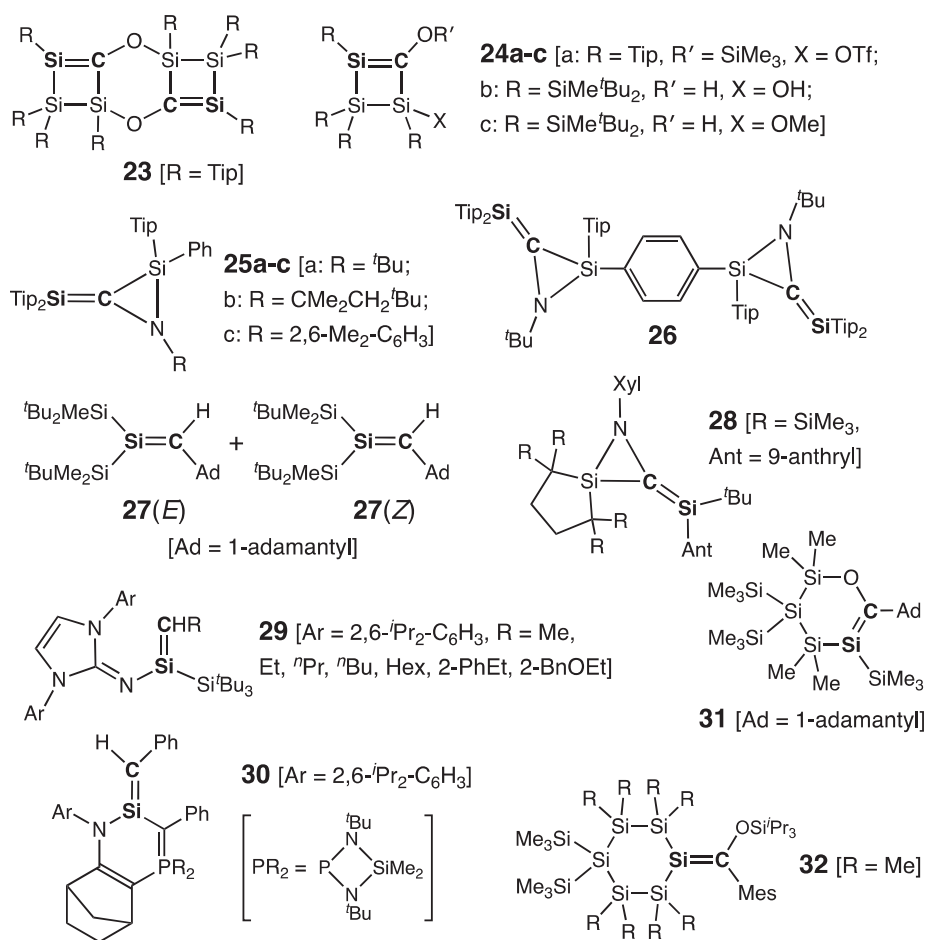


As for the doubly bonded “group 13” = “group 14” combinations, including group 13 elements heavier than boron, we can mention only 1,3-disila-2-gallata- and -indataallenic anionic derivatives  $[(^t\text{Bu}_2\text{MeSi})_2\text{Si}-\text{E}-\text{Si}(\text{SiMe}^t\text{Bu}_2)_2]^- [\text{Li}(\text{thf})_4]^+$  (E=Ga, In), featuring the first structurally authenticated Si=Ga and Si=In double bonds, respectively, and reported by Sekiguchi and coworkers in 2004.<sup>59a</sup> This was then followed by the synthesis of the 1,3-digerma-2-gallata- and -indataallenic anionic derivatives  $[(^t\text{Bu}_2\text{MeSi})_2\text{Ge}-\text{E}-\text{Ge}(\text{SiMe}^t\text{Bu}_2)_2]^- [\text{Li}(\text{thf})_4]^+$  (E=Ga, In) as the first compounds with Ge=Ga and Ge=In double bonds, synthesized by the same authors.<sup>59b</sup> Since then, no progress has been made to this field.

### 1.03.3.2.1.2.2 $>\text{E}=\text{E}'<$ (E, E' = Group 14 element)

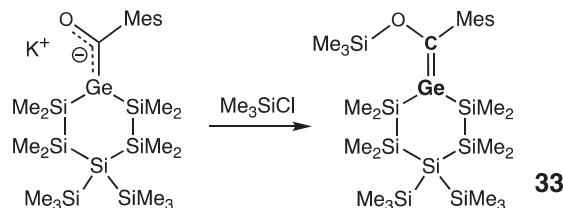
The stable silenes (or silaethenes)  $>\text{Si}=\text{C}<$  are the first isolable doubly bonded derivatives involving Si atoms. The very first stable silene was prepared by Brook<sup>6</sup> and coworkers and reported in the same year 1981 when West reported his disilene  $>\text{Si}=\text{Si}<$ .<sup>7</sup>

Since 2013, several remarkable isolable silenes were reported in the literature, and their structures and peculiar features are discussed below (Scheme 13). Thus, Scheschkewitz and coworkers synthesized a series of silenes with both *endo*- and *exocyclic* Si=C bonds. They include tricyclic Brook-type bis(silene) **23** [ $r_{\text{Si}=\text{C}} = 1.771(4) \text{ \AA}$ ],<sup>60</sup> Brook-type four-membered ring cyclic silenes **24a-c** [ $r_{\text{Si}=\text{C}} = 1.761(3) \text{ \AA}$  (for **24a**) and  $r_{\text{Si}=\text{C}} = 1.7638(16) \text{ \AA}$  (for **24c**)],<sup>60</sup> silaaziridines **25a-c** with exocyclic Si=C double bonds [ $r_{\text{Si}=\text{C}} = 1.735(2) \text{ \AA}$  (for **25a**)],<sup>61</sup> and *para*-phenylene bridged bis(silaaziridine) **26** [ $r_{\text{Si}=\text{C}} = 1.726(4)/1.743(4) \text{ \AA}$ ].<sup>61</sup> Apeloig recently reported reversible (*Z* → *E/E* → *Z*)-isomerization of his silene **27**, originally obtained as a 95:5 (*E/Z*)-mixture, which in the absence of crystallographic data was characterized by the low-field resonances of the doubly bonded Si and C atoms at 72.3 ppm and 181.1 ppm, respectively. Activation barrier for the (*Z* → *E*)-isomerization was determined from kinetic measurements as  $24.4 \pm 1.2 \text{ kcal/mol}$ , and that for the reverse (*E* → *Z*)-isomerization as  $24.3 \pm 1.2 \text{ kcal/mol}$ .<sup>62</sup> Iwamoto and coworkers also synthesized silaaziridine derivative **28** with an exocyclic Si=C double bond [ $r_{\text{Si}=\text{C}} = 1.730(5) \text{ \AA}$ ].<sup>63</sup> Reacting their iminosilylsilanone with Wittig reagents, Inoue and coworkers succeeded in the olefination of the former to produce a series of (*Z*)- or (*E*)-silenes **29** as the products of sila-Wittig reaction.<sup>64</sup> Kato, Bacciredo and their coworkers prepared a tricyclic silene **30** with an exocyclic Si=C double bond, featuring rather peculiar substitution pattern at the doubly bonded Si center which leads to a partial delocalization of the double bond [ $r_{\text{Si}=\text{C}} = 1.725(2) \text{ \AA}$ ].<sup>65</sup> Haas, Stueger and coworkers reported Brook-type silenes **31** and **32** featuring *endocyclic* and *exocyclic* Si=C double bonds, respectively [ $r_{\text{Si}=\text{C}} = 1.786(2) \text{ \AA}$  (for **31**) and  $r_{\text{Si}=\text{C}} = 1.767(2) \text{ \AA}$  (for **32**)].<sup>66</sup>



Scheme 13

The first stable germenes were independently reported in 1987 by the research groups of Berndt<sup>67</sup> and Escudié.<sup>68</sup> Since 2013, only one novel example was reported, namely, the first isolable Brook-type germene **33** with an exocyclic Ge=C double bond, synthesized by Haas and coworkers.<sup>69</sup> This *O*-silylated germene **33** was readily available by the reaction of the stable germenolate (almost exclusively exhibiting the character of acyl germyl anion with a negatively charged Ge atom, a Ge–C single bond, and a C=O double bond) with Me<sub>3</sub>SiCl (Scheme 14). Germene **33** shows a characteristic low-field signal for its doubly bonded C atom at 210.0 ppm, and a Ge=C distance of 1.835(2) Å that is typical for germenes. Nevertheless, the Ge=C double bond in **33** is notably



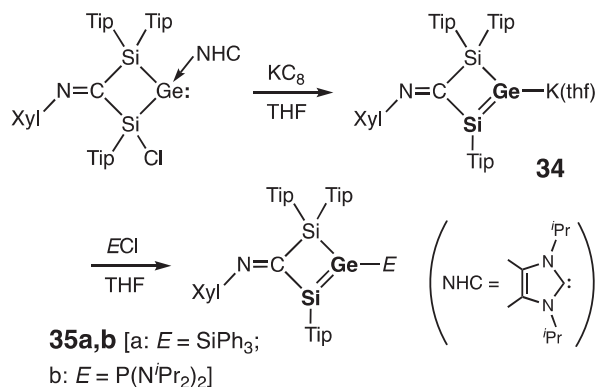
Scheme 14

distorted, as was evidenced by its twisting and pyramidalization at the Ge center ( $\Sigma = 351.7^\circ$ ).

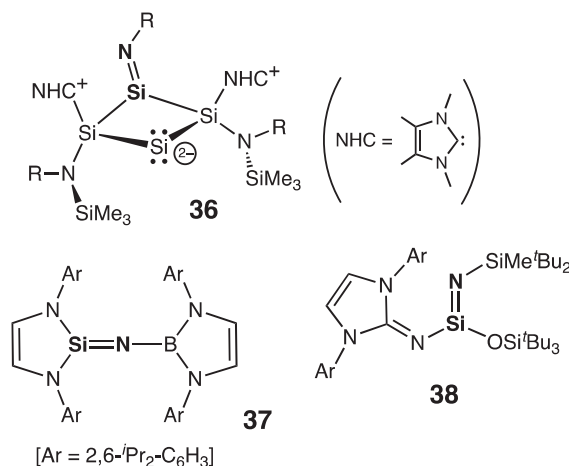
As for the doubly bonded derivatives  $>E = E' <$  consisting of the different heavier group 14 elements, several combinations are possible. Of them, the lightest one is silagermene  $>Si = Ge <$ . The first metastable silagermene Me<sub>2</sub>Si=GeMe<sub>2</sub> was reported by Baines and coworkers in 1992, however this compound was stable only at low temperatures (below  $-70^\circ\text{C}$ ) isomerizing at higher temperatures into the mesityl(silyl)germylene Mes(Mes<sub>3</sub>Si)Ge<sup>70</sup>. The first room temperature-stable silagermene, 2-disilagermirene with an endocyclic Si=Ge double bond, was synthesized and isolated by Lee, Sekiguchi and coworkers in 2000.<sup>71</sup> This was followed by the subsequent report from the same authors on the first structurally authenticated silagermene, namely, 1,2-disila-3-germacyclopenta-2,4-diene with an endocyclic Si=Ge–C=C diene fragment.<sup>72</sup>

Since 2013, only one remarkable example of isolable silagermenes, potassium silagermenide **34** as a Si=Ge analogue of a vinyl anion, was reported by Scheschkewitz and coworkers and prepared by the reduction of the germylene precursor with KC<sub>8</sub> (Scheme 15).<sup>73</sup> The resonance of the doubly bonded Si atom in **34** was found in the characteristic low-field at 142.9 ppm (in C<sub>6</sub>D<sub>6</sub>) and 138.5 ppm (in THF-*d*<sub>8</sub>). In **34**, the Si=Ge double bond length of 2.2590(3) Å well agrees with those earlier reported for other silagermenes, and the GeSi<sub>2</sub>C-four-membered ring is nearly planar with a folding of  $1.9^\circ$ . Based on its X-ray and UV data, a significant extent of  $\pi$ -conjugation between the Si=Ge and C=N double bonds in **34** was assumed, and accordingly the  $\pi_{Si=Ge}\pi^*_{C=N}$  interaction energy was calculated as 23.6 kcal/mol. Silagermenide **34** can be functionalized at the anionic Ge atom to form neutral Ge-substituted silagermenes **35a,b** (Scheme 15). Both (silyl)silagermene **35a** (R=SiPh<sub>3</sub>) and (phosphanyl)silagermene **35b** [R=P(N<sup>*i*</sup>Pr<sub>2</sub>)<sub>2</sub>] revealed low-field shifted <sup>29</sup>Si NMR resonances [singlet at 136.6 ppm and doublet at 104.5 ppm ( $^2J_{Si-P} = 9.8$  Hz), respectively], and short Si=Ge double bonds [2.2020(2) and 2.2252(4) Å, respectively]. In addition, in **35a**, the GeSi<sub>2</sub>C-four-membered ring is almost planar with a quite negligible folding of  $0.2^\circ$ , and the Ge atom is slightly pyramidalized ( $\Sigma = 357.3^\circ$ ).

Among the hybrid  $>Sn = E <$  systems comprising sp<sup>2</sup>-Sn atom, the stanene  $>Sn = C <$  was prepared and structurally characterized for the first time by Berndt and coworkers in 1987.<sup>74</sup> The first, and still the only known, silastannene, namely (tBu<sub>2</sub>MeSi)<sub>2</sub>Si=SnTip<sub>2</sub>, was synthesized in 2002 by Sekiguchi and coworkers.<sup>75</sup> The first germastannenes Tip<sub>2</sub>Ge=SnTip<sub>2</sub> and (tBu<sub>2</sub>MeSi)<sub>2</sub>Ge=SnTip<sub>2</sub>/[(*E*)-(tBu<sub>2</sub>MeSi)(Tip)Ge=Sn(Tip)(SiMe'Bu<sub>2</sub>)] were independently reported in 2003 by the research groups of Weidenbruch<sup>76</sup> and Sekiguchi,<sup>77</sup> respectively. The only known cyclic germastannene, disilagermastannetene, incorporating an endocyclic Ge=Sn double bond into the four-membered ring skeleton, was reported by Lee, Sekiguchi and coworkers in 2004.<sup>78</sup> Since then,



Scheme 15



Scheme 16

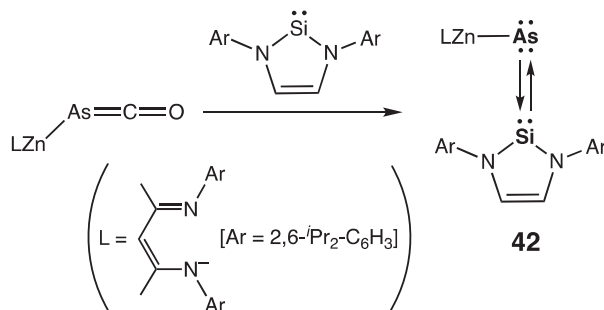
there were no new entries to the field of  $>Sn=E<$  type compounds. Heteronuclear derivatives containing Pb atoms,  $>Pb=E<$  ( $E=C-Sn$ ), still remain unknown.

### 1.03.3.2.1.2.3 $>E=E'-$ ( $E = \text{group 14 element}$ , $E' = \text{group 15 element}$ )

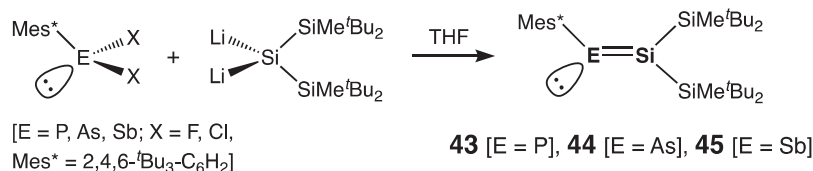
The very first silaimines, that is compounds featuring  $Si=N$  double bond, were independently reported by Klingebiel ( ${}^i\text{Pr}_2\text{Si}=\text{N}-\text{Mes}^*$ ,  $\text{Mes}^* = 2,4,6\text{-}^t\text{Bu}_3\text{-C}_6\text{H}_2$ )<sup>79</sup> and Wiberg ( ${}^t\text{Bu}_2\text{Si}=\text{N}-\text{Si}^t\text{Bu}_3$ )<sup>80</sup> groups in 1986. Since 2013, three stable silaimines **36–38** were synthesized by the research groups of Lips,<sup>81</sup> Jones,<sup>82</sup> and Inoue<sup>83</sup> (Scheme 16). Lips silaimine **36** features rather peculiar  $Si_4$ -ring structure with an exocyclic  $Si=N$  double bond [ $\delta(^{29}\text{Si}) = -65.7$  ppm,  $r_{\text{SiN}} = 1.625(2)$  Å], Jones silaimine **37** manifests a  $Si=N$  double bond where Si is a part of the *N*-heterocyclic silylene unit and N has an *N*-heterocyclic boryl substituent [ $\delta(^{29}\text{Si}) = -48.0$  ppm,  $r_{\text{SiN}} = 1.502(2)$  Å], and Inoue silaimine **38** features *N*-heterocyclic imino (NHI) and silyloxy-substituents at Si and silyl substituent at N [ $\delta(^{29}\text{Si}) = -50.1$  ppm,  $r_{\text{SiN}} = 1.573(2)$  Å].

Phosphasilenes  $>Si=P-$  are known since 1987 when Bickelhaupt and coworkers reported synthesis of the first room temperature stable phosphasilenes,<sup>84</sup> followed by the first crystallographic authentication of the  $Si=P$  bond by Niecke in 1993.<sup>85</sup> Since 2013, two stable phosphasilenes **39–40** were reported by Scheschkewitz and coworkers.<sup>86</sup> Phosphasilene  $\text{Tip}_2(\text{Me}_2\text{N})\text{Si}-(\text{Tip})\text{Si}=\text{P}-\text{NMe}_2$  **39** was isolated as *E/Z*-isomeric mixture (*E/Z* = 95/5) upon the reaction of disilenide  $\text{Tip}_2\text{Si}=\text{Si}(\text{Tip})\text{Li}$  with  $\text{ClP}(\text{NMe}_2)_2$  followed by the isomerization of the initially formed  $\text{Tip}_2\text{Si}=\text{Si}(\text{Tip})[\text{P}(\text{NMe}_2)_2]$  to **39**.<sup>86a</sup> Phosphasilene **39** revealed characteristic low-field resonances for both P and Si atoms [for *E*-isomer:  $\delta(^{31}\text{P}) = 344.8$  ppm ( ${}^1J_{\text{P-Si}} = 186.5$  Hz) and  $\delta(^{29}\text{Si}) = 103.5$  ppm ( ${}^1J_{\text{SiP}} = 186.5$  Hz)] and typical for phosphasilenes short  $Si=P$  double bond [ $r_{\text{SiP}} = 2.1187(7)$  Å]. Calculation of the Mulliken charges in the model **39** clearly shows “inverse” polarization of the  $Si^{\delta-}=\text{P}^{\delta+}$  bond:  $-0.095$  (Si) and  $+0.169$  (P). Reacting **39** with  $\text{MesLi}$ , Scheschkewitz and coworkers prepared *P*-mesityl-phosphasilene  $\text{Tip}_2(\text{Me}_2\text{N})\text{Si}-(\text{Tip})\text{Si}=\text{P}-\text{Mes}$  **40** isolated as *E/Z*-mixture (*E/Z* = 84/16).<sup>86b</sup> **40** exhibited the following spectral and structural features (for *E*-isomer):  $\delta(^{31}\text{P}) = 234.4$  ppm ( ${}^1J_{\text{P-Si}} = 193.9$  Hz) and  $\delta(^{29}\text{Si}) = 193.9$  ppm,  $r_{\text{SiP}} = 2.0923(6)$  Å.

Arsasilenes  $>Si=As-$  were first synthesized<sup>87a</sup> and subsequently structurally characterized<sup>87b</sup> by Driess and coworkers in 1992 and 1995, respectively. Driess recently additionally contributed to the field by the synthesis of arsinidene-silylene complex **42** which alternatively can be viewed as arsilene (Scheme 17).<sup>88</sup> **42** showed the following physico-chemical characteristics:  $\delta(^{29}\text{Si}) = 65.9$  ppm,  $r_{\text{Si-As}} = 2.1661(6)$  Å, and its  $Si=As$  bond order was calculated as 1.72 (Wiberg bond index, WBI) and 1.66 (Mayer bond order, MBO).



Scheme 17



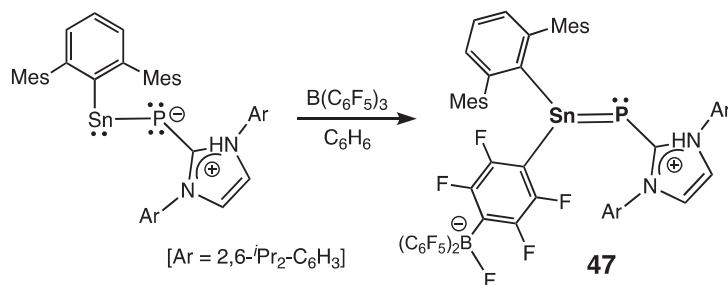
Scheme 18

Lee, Sekiguchi and coworkers applied a different synthetic approach towards stable  $>\text{Si}=\text{E}-$  (E = heavy group 15 element) derivatives, namely, by the reaction of their isolable 1,1-dilithiosilane derivative (<sup>t</sup>Bu<sub>2</sub>MeSi)<sub>2</sub>SiLi<sub>2</sub> with the group 15 halides Mes\*EX<sub>2</sub> (E=P, As, Sb) (Scheme 18).<sup>89</sup> In such way, a series of isostructural phosphasilene (<sup>t</sup>Bu<sub>2</sub>MeSi)<sub>2</sub>Si=P–Mes\* **43**, arsilene (<sup>t</sup>Bu<sub>2</sub>MeSi)<sub>2</sub>Si=As–Mes\* **44**, and stibasilene (<sup>t</sup>Bu<sub>2</sub>MeSi)<sub>2</sub>Si=Sb–Mes\* **45** were prepared and fully characterized, with the latter being the first compound featuring a Si=Sb bond and as such representing the “heaviest” double bond between the silicon and pnictogen element. All these compounds feature particular *push-pull* substitution pattern (electron donors on silicon and electron acceptor on pnictogen), resulting in the relaxation of the natural polarity (and thus high reactivity) of the Si<sup>δ+</sup>=E<sup>δ-</sup> (E=P–Sb) bond, caused by the differing electronegativity of silicon and pnictogen atoms. All these compounds uniformly displayed low-field shifted resonances of the doubly bonded Si atoms:  $\delta(^{29}\text{Si}) = 201.2$  ppm (for **43**, doublet with  $^1J_{\text{Si-P}} = 171.3$  Hz;  $\delta(^{31}\text{P}) = 389.3$  ppm), 214.1 ppm (for **44**), and 215.2 ppm (for **45**). In all **43–45**, the Si=E (E=P–Sb) bond is: (a) remarkably shortened [ $r_{\text{Si-P}} = 2.1114(7)$  Å (**43**),  $r_{\text{Si-As}} = 2.2164(14)$  Å (**44**),  $r_{\text{Si-Sb}} = 2.4146(7)$  Å (**45**)]; (b) practically undistorted [**43–45**:  $\Sigma_{\text{Si}} = 360.0^\circ$  and  $\tau = 0.6\text{--}2.3^\circ$ ]. The Si=E **43–45** is best described as covalent (rather than ionic or donor-acceptor) interactions, given notably low values for the natural ionicity of their double bonds  $I_{\text{Si}=\text{E}}$ : 0.14 ( $\sigma$ -bond) and 0.18 ( $\pi$ -bond) (for phosphasilene **43**), 0.11 ( $\sigma$ -bond) and 0.14 ( $\pi$ -bond) (for arsilene **44**), 0.07 ( $\sigma$ -bond) and 0.06 ( $\pi$ -bond) (for stibasilene **45**). The frontier molecular orbitals of **43–45** are uniformly represented by the Si=E  $\pi$ -orbital (HOMO) and  $\pi^*$ -orbital (LUMO), respectively, whereas HOMO-1 is represented by the pnictogen lone pair  $n$ -orbital.

Among the germanium derivatives of the type  $>\text{Ge}=\text{E}-$  (E = group 15 element), the first reported were germainines  $>\text{Ge}=\text{N}-$ , synthesized and structurally characterized in 1991 by Meller and coworkers.<sup>90</sup> Their heavier congeners, phosphagermenes  $>\text{Ge}=\text{P}-$ , were prepared for the first time<sup>91a</sup> and crystallographically identified<sup>91b</sup> by Escudié and coworkers. No other representatives of the stable germainines and phosphagermenes were reported within the last decade.

The “heaviest” currently known doubly bonded combination between the germanium and group 15 element is arsagermene  $>\text{Ge}=\text{As}-$ . The first (and still the only) example of such compounds, arsagermene (<sup>t</sup>Bu<sub>2</sub>MeSi)<sub>2</sub>Ge=As–Mes\* **46** was recently synthesized by Lee, Sekiguchi and coworkers.<sup>92</sup> **46** was readily available by the simple coupling of 1,1-dilithiogermane derivative (<sup>t</sup>Bu<sub>2</sub>MeSi)<sub>2</sub>GeLi<sub>2</sub> and Mes\*AsF<sub>2</sub>. The Ge=As double bond in **46** is quite short [ $r_{\text{Ge=As}} = 2.2727(8)$  Å] and practically planar, like the C=C bond in alkenes ( $\Sigma_{\text{Ge}} = 360.0^\circ$  and  $\tau_{\text{Ge=As}} = 0.1^\circ$ ). The calculated Ge=As bond order is 1.79 (WBI) and 1.93 [Natural Resonance Theory (NRT) bond order, with 92% NRT covalent character]. The Natural Population Analysis (NPA) charges for the Ge and As atoms are rather similar (+0.08 and +0.14, respectively), indicative of the very small polarization of the double bond in accord with the relaxation of the natural polarity of the Ge<sup>δ+</sup>=As<sup>δ-</sup> bond caused by the peculiar *push-pull* substitution pattern in **46**. As is typical for such compounds, the HOMO and LUMO are represented by the bonding ( $\pi$ ) and antibonding ( $\pi^*$ ) orbitals of the Ge=As double bond, whereas HOMO-1 is the lone pair orbital at the As atom.

For the doubly bonded combinations of tin of the type  $>\text{Sn}=\text{E}-$  (E = group 15 element), only stannaimines  $>\text{Sn}=\text{N}-$  and phosphastannenes  $>\text{Sn}=\text{P}-$  are synthesized, with no examples of the isolable arsastannenes  $>\text{Sn}=\text{As}-$  and stibastannenes  $>\text{Sn}=\text{Sb}-$  known to date. The first stannaimine [(Me<sub>3</sub>Si)<sub>2</sub>N]<sub>2</sub>Sn=N–Ar (Ar = 2,6-<sup>i</sup>Pr<sub>2</sub>-C<sub>6</sub>H<sub>3</sub>) was prepared by Meller group,<sup>93</sup> whereas the first phosphastannene [(Me<sub>3</sub>Si)<sub>2</sub>CH]<sub>2</sub>Sn=P–Mes\* (Mes\* = 2,4,6-<sup>t</sup>Bu<sub>3</sub>-C<sub>6</sub>H<sub>2</sub>) was synthesized by Escudié and coworkers.<sup>94</sup> The latest report on the isolable phosphastannene **47**, with rather unusual substituents at both Sn and P atoms, came from Inoue group.<sup>95</sup> **47** was prepared by the reaction of the precursor (stannylene-phosphinidene NHC complex) with B(C<sub>6</sub>F<sub>5</sub>)<sub>3</sub> in the attempted removal of NHC ligand from P atom (Scheme 19). Due to its specific zwitterionic *push-pull* structure, **47** displayed significantly shielded P and Sn nuclei:  $\delta(^{31}\text{P}) = -93.1$  ppm [ $^1J(^{31}\text{P}-^{117/119}\text{Sn}) = 2919/3046$  Hz] and  $\delta(^{119}\text{Sn}) =$



Scheme 19



152.2 ppm [ $^1J(^{119}\text{Sn}-^{31}\text{P}) = 3069$  Hz]. The Sn=P double bond in **47** is planar ( $\Sigma_{\text{Sn}} = 359.9^\circ$ ) and very short [2.3450(10) Å], being the shortest tin-phosphorus interatomic distance reported to date.

#### 1.03.3.2.1.2.4 $>E=E'$ ( $E = \text{group 14 element}$ , $E' = \text{group 16 element}$ )

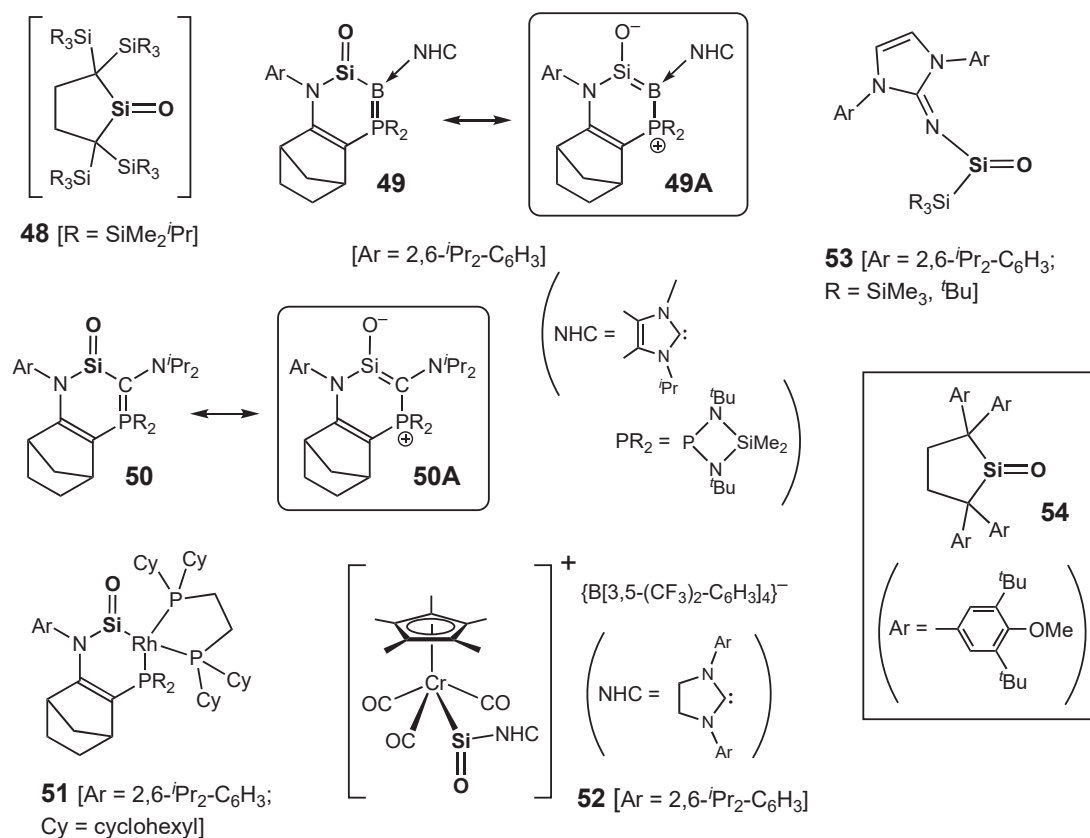
Among all the title compounds, with no doubts, by far most difficult-to-realize and accordingly most synthetically challenging are silanones  $>\text{Si}=\text{O}$ , which are sometimes coined as “Kipping’s dream”. Before 2013, there were several reports from Driess group on the isolable organosilicon compounds featuring Si–O bond possessing some extent of the doubly bonded character, including silanoic ester<sup>96a</sup> and NHC-supported silanone.<sup>96b</sup>

Since 2013, several research groups closely approached the “silanone problem,” uniformly applying the reaction of the corresponding stable silylenes with  $\text{N}_2\text{O}$  as the synthetic method of choice. In 2015, Iwamoto group reported persistent cyclic dialkylsilanone **48** [ $\delta(^{29}\text{Si}_{\text{Si}=\text{O}}) = 128.7$  ppm] that was stable in toluene solution below  $-80^\circ\text{C}$  rapidly isomerizing at higher temperatures (by the 1,3-migration of  $\text{Me}_3\text{Si}$ -group from C to O) to the corresponding siloxysilene (Scheme 20).<sup>97</sup>

In 2017, Kato and coworkers described several compounds which were classified as cyclic silanones, namely, (amino)(phosphonium bora-ylide)silanone **49**<sup>98a</sup> and its carbon analogue, (amino)(phosphonium-ylide)silanone **50**<sup>98b</sup> (the latter is stable below  $-50^\circ\text{C}$ ) (Scheme 20). However, based on their peculiar spectral and structural features [ $\delta(^{29}\text{Si}) = 71.3/38.4$  ppm and  $r_{\text{Si}-\text{O}} = 1.5432(12)/1.533(1)$  Å, for **49/50**, respectively], and also on the computational data, the electronic situation in these compounds is best described by the canonical structures **49A** and **50A** (but not by the silanone resonance form),<sup>98</sup> manifesting Si=B or Si=C double bonds and bora-ylide or phosphonium-ylide moiety, respectively (Scheme 20). Later, the same authors reported also a room temperature stable *N*-hetero-Rh<sup>1</sup>-metallic silanone **51**, featuring their traditional tricyclic framework incorporating Rh atom [ $\delta(^{29}\text{Si}) = 81.5$  ppm and  $r_{\text{Si}-\text{O}} = 1.540(3)$  Å] (Scheme 20).<sup>99</sup>

Filippou and coworkers also contributed to the stable silanone field by preparation of acyclic ionic metallasilanone **52** featuring  $\text{Cr}(\text{Cp}^*)(\text{CO})_3$ -fragment ( $\text{Cp}^* = \text{C}_5\text{Me}_5$ ) as a rather unusual substituent at the  $\text{sp}^2$ -Si atom [ $\delta(^{29}\text{Si}) = 169.6$  ppm,  $r_{\text{Si}-\text{O}} = 1.526(3)$  Å,  $\Sigma_{\text{Si}} = 359.9^\circ$ ] (Scheme 20).<sup>100</sup> According to DFT calculations, the Si–O bond in **52** is expectedly strongly polarized towards oxygen [85% NBO density on O atom; NPA charges: +1.77 (Si) and –1.21 (O); ionic contribution (1.30) is remarkably greater than the covalent contribution (0.56)], thus indicating a crucial contribution of the zwitterionic resonance structure  $\text{Si}^+-\text{O}^-$ .

Inoue and his group made a step closer to the authentic silanone by synthesis of their stable neutral acyclic silanone **53**, featuring  $p$ -donating *N*-heterocyclic imino (NHI) and  $s$ -donating silyl group as substituents at the  $\text{sp}^2$ -Si atom [for  $\text{R}=\text{tBu}$ :  $\delta(^{29}\text{Si}) = 28.8$  ppm,  $r_{\text{Si}-\text{O}} = 1.537(3)$  Å,  $\Sigma_{\text{Si}} = 360.0^\circ$ ] (Scheme 20).<sup>101</sup> Computational analysis of **53** clearly indicated the critical



Scheme 20

importance of the  $p$ -donation from the NHI ligand to electron-deficient Si atom (seen in HOMO-10) and also  $\sigma$ -donation from the silyl substituent to the  $sp^2$ -Si ( $\sigma_{\text{Si-C}} \rightarrow \pi^*_{\text{Si=O}}$ , seen in LUMO+4) for the overall stabilization of otherwise highly reactive Si=O bond. On the other hand, such stabilization occurs at the expense of diminishing Si=O double bond character, as an alternative zwitterionic resonance form (with the Si=N double bond, positive charge on N and negative charge on O atom) begins to operate and contribute to the overall structure of 53.

The long-term quest for the stable silanones was finally culminated in the recent publication from Iwamoto group on the synthesis of their neutral cyclic dialkylsilanone 54 containing electronically unperturbed Si=O double bond (Scheme 20).<sup>102</sup> 54 does not feature coordination of any internal or external Lewis base or Lewis acid to its Si=O double bond, thus lacking any electronically perturbing  $\sigma$ - and  $\pi$ -conjugation stabilizing effects and therefore representing the first example of a genuine silanone. For its Si=O double bond, silanone 54 exhibited low-field <sup>29</sup>Si NMR chemical shift of 90.0 ppm, planar geometry around the  $sp^2$ -Si atom ( $\Sigma_{\text{Si}} = 360.0^\circ$ ), and exceptionally short Si=O bond distance of 1.518(2) Å, the shortest one among all  $>\text{Si=O}$  derivatives reported to date. DFT calculations of 54 revealed the HOMO-13, LUMO, and HOMO-8 as  $\pi_{\text{Si=O}}$ ,  $\pi^*_{\text{Si=O}}$ , and the lone pair orbital of the  $\text{O}_{\text{Si=O}}$  atom. NPA analysis clearly disclosed the presence of a highly polar  $\text{Si}^{\delta+}=\text{O}^{\delta-}$  double bond in 54: +2.08 (Si) and -1.10 (O), that implies intrinsically high electrophilicity of the silicon center and high nucleophilicity of the O center of the genuine Si=O double bond.

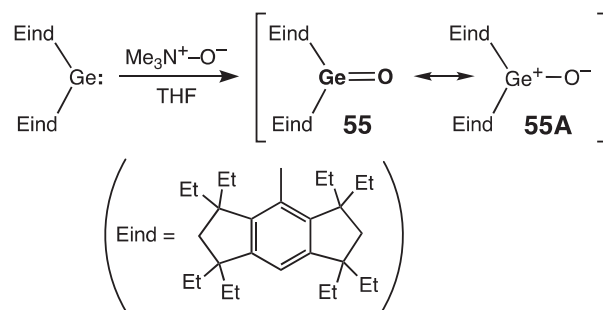
The synthesis of the heavier analogues of silanones, that is (diaryl)silanethiones  $>\text{Si=S}$ , (diaryl)silaneselones  $>\text{Si=Se}$ , and (diaryl)silanetellones  $>\text{Si=Te}$ , was pioneered by Tokitoh group.<sup>103</sup> These achievements were followed by the report from Iwamoto, Kira and coworkers on the synthesis of the stable dialkylsilane-thione, -selone, and -tellone.<sup>104</sup> No further progress has been made to this field since 2013.

The first generation of the stabilized germanone  $>\text{Ge=O}$  complexes, [NHC  $\rightarrow$  germanone]<sup>105a</sup> and [DMAP  $\rightarrow$  germanone]<sup>105b</sup> (DMAP = 4-dimethylaminopyridine), was reported by Driess and coworkers. The major breakthrough to the field of stable germanones was achieved when Matsuo, Tamao and coworkers published their seminal paper on the isolable dirarylgermanone (Eind)<sub>2</sub>Ge=O (Eind = 1,1,3,3,5,5,7,7-octaethyl-*s*-hydrindacen-4-yl) 55 (Scheme 21).<sup>106</sup>

Germanone 55 is stabilized only kinetically by means of its exceptionally bulky Eind substituents, lacking highly perturbing thermodynamic stabilization effects (both inductive and resonance) and thus representing a closest approach towards the genuine germanone. In 55, the Ge=O double bond features a trigonal-planar  $sp^2$ -Ge atom ( $\Sigma_{\text{Ge}} = 359.8^\circ$ ) and a very short Ge=O bond [ $r_{\text{Ge=O}} = 1.6468(5)$  Å]. As is typical for heavy ketones, the Ge=O bond in 55 is highly polarized [NPA charges: +1.798 (Ge) and -1.046 (O); WBI = 1.252], thus being better represented by a charge-separated, *germylene oxide*, resonance form (Eind)<sub>2</sub>Ge<sup>+</sup>-O<sup>-</sup> 55A, rather than the charge-free, *germanone*, resonance extreme (Eind)<sub>2</sub>Ge=O 55.

The first representatives of the heavier analogues of germanones, namely, germanethiones  $>\text{Ge=S}$ , germaneselones  $>\text{Ge=Se}$ , and germanetellones  $>\text{Ge=Te}$ , were all prepared by Tokitoh and coworkers: (Tbt(*Tip*))Ge=S (Tbt = 2,4,6-[(Me<sub>3</sub>Si)<sub>2</sub>CH]<sub>3</sub>-C<sub>6</sub>H<sub>2</sub>), Tbt(*Tip*))Ge=Se, and Tbt(*Tip*))Ge=Te/Tbt(*Dis*))Ge=Te [Dis=CH(SiMe<sub>3</sub>)<sub>2</sub>].<sup>107</sup> Since 2013, there is only one new report on the stable germanethione, namely, (Eind)<sub>2</sub>Ge=S 56, synthesized by Matsuo and coworkers by the reaction of stable germylene (Eind)<sub>2</sub>Ge: with elemental sulfur S<sub>8</sub>, similar to the above case of germanone 55 (see Scheme 21).<sup>108</sup> Although germanethione 56 revealed structural features similar to those of the previously reported germanone 55<sup>106</sup> [trigonal-planar Ge ( $\Sigma_{\text{Ge}} = 360.0^\circ$ ) and short Ge=S bond ( $r_{\text{Ge=S}} = 2.0569(9)$  Å)], its Ge<sup>δ+</sup>=S<sup>δ-</sup> bond is remarkably less polarized compared to the Ge<sup>+</sup>-O<sup>-</sup> bond in germanone 55. This was evidenced by the accompanying computations on the Ge=S bond in 56, NPA charges: +1.336 (Ge) and -0.613 (S) [*vs.* +1.821 (Ge) and -1.039 (O), in 55], WBI = 1.635 [*vs.* 1.263, in 55].

As for the tin containing derivatives of the type  $>\text{Sn=E}$  (E=O-Te), the lightest and most challenging stannanones  $>\text{Sn=O}$  are still unknown. The first stannanthione Tbt(*Tip*))Sn=S,<sup>109a</sup> stannaneselone Tbt(*Ar*))Sn=Se [Ar = 2,6-(2-<sup>i</sup>Pr-C<sub>6</sub>H<sub>4</sub>)<sub>2</sub>-C<sub>6</sub>H<sub>3</sub>],<sup>109b,c</sup> and stannanetellone Bbt(*Ar'*))Sn=Te [Bbt = 2,6-[(Me<sub>3</sub>Si)<sub>2</sub>CH]<sub>2</sub>-4-[(Me<sub>3</sub>Si)<sub>3</sub>C]-C<sub>6</sub>H<sub>2</sub>, Ar' = 2,6-(2,4-<sup>i</sup>Pr<sub>2</sub>-C<sub>6</sub>H<sub>3</sub>)<sub>2</sub>-C<sub>6</sub>H<sub>3</sub>],<sup>109d</sup> were all prepared and characterized by Tokitoh and coworkers. No new compounds of the type  $>\text{Sn=E}$  (E=S-Te) were reported since 2013.



Scheme 21

### 1.03.3.2.2 1,3-Diene analogues

#### 1.03.3.2.2.1 Homonuclear derivatives $>E=E-E=E<$ ( $E=Si, Ge$ )

The very first isolable tetrasilabuta-1,3-diene  $Tip_2Si=(Tip)Si-Si(Tip)=SiTip_2$ <sup>110a</sup> and tetragermabuta-1,3-diene  $Tip_2Ge=(Tip)Ge-Ge(Tip)=GeTip_2$ <sup>110b</sup> were reported by Weidenbruch in 1997 and 2000, respectively, uniformly prepared by the metalation of the disilene  $Tip_2Si=SiTip_2$  or digermene  $Tip_2Ge=GeTip_2$  with metallic lithium followed by the reaction of intermediate vinyl-lithium derivative  $[Tip_2E=E(Tip)Li]$  ( $E=Si, Ge$ ) with MesBr.

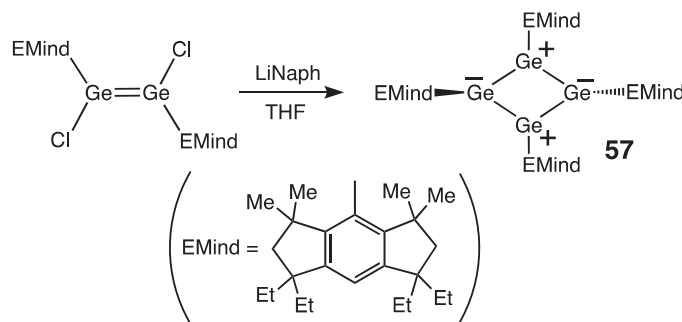
Since 2013, a couple of other 1,3-diene derivatives were reported. The first one, tetragermacyclobutadiene  $Ge_4[EMind]_4$  ( $EMind = 1,1,7,7$ -tetraethyl-3,3,5,5-tetramethyl-*s*-hydrindacen-4-yl) **57** (as the germanium version of the previously reported remarkable tetrasilacyclobutadiene), was synthesized by Matsuo and coworkers.<sup>111</sup> **57** was prepared by the reduction of dichloro-digermene  $[EMind](Cl)Ge=Ge(Cl)[EMind]$  with lithium naphthalenide (Scheme 22). In contrast to its silicon congener, **57** was quite thermally stable, and exhibited UV-absorptions at 458 ( $\epsilon = 15000$ ), 510 ( $\epsilon = 7400$ ), and 836 nm ( $\epsilon = 150$ ). The  $Ge_4$ -ring has a planar (sum of the internal bond angles =  $360^\circ$ ) rhombic shape with  $Ge-Ge$  bonds = 2.430 Å (av.). Two germanium atoms exhibit  $sp^2$ -like trigonal-planar geometry ( $\Sigma = 360.0^\circ$ ), whereas the other two feature  $sp^3$ -like pyramidal configuration ( $\Sigma = 334.0$  and  $327.7^\circ$ , respectively) with the *trans*-bending of substituents at these germanium atoms ( $\theta = 37.9$  and  $40.6^\circ$ , respectively). Computational studies disclosed the  $Ge-Ge$  bond orders in **57** to be 1.08–1.09 (Wiberg bond indices, WBI). The natural population analysis (NPA) clearly showed charge separation within the  $Ge_4$ -ring: two Ge atoms are only slightly positively charged (+0.146 and +0.151), whereas the other two Ge atoms are strongly positively charged (+0.602 and +0.573). All these data suggest the important contribution of the alternately charge-separated resonance form  $cyclo-[Ge^+-Ge^--Ge^+-Ge^-]$ , as was also the case of the previously reported tetrasilacyclobutadiene. Overall, the polar Jahn-Teller distortion causes relaxation of the intrinsic  $4p$ -electron antiaromaticity of the tetragermacyclobutadiene **57** to form a planar rhombic-shaped charge-separated singlet structure, which has nonaromatic character (according to NICS calculations).

The second example, tetrasilabuta-1,3-diene **58**, was reported by Iwamoto group, being prepared starting from  $Me_3Si(Tip)Si=Si(Tip)SiMe_3$  by its reduction with <sup>t</sup>BuOK generating potassium disilene  $[Me_3Si(Tip)Si=Si(Tip)-K]$ , which was subsequently oxidized with 1,2-dibromoethane to form finally **58**,  $Me_3Si(Tip)Si=Si(Tip)-Si(Tip)=Si(Tip)SiMe_3$ .<sup>112</sup> Both *antiperiplanar* (**58<sub>ap</sub>**) and *synclinal* (**58<sub>sc</sub>**) conformations of **58** were separately crystallized as the purple and red crystals, respectively. The  $Si=Si$  bonds in **58<sub>ap</sub>** (2.1599(12)–2.1755(12) Å, for three independent molecules) are marginally longer than those of **58<sub>sc</sub>** (2.1592(7)/2.1617(7) Å), all being within the range of the typical  $Si=Si$  double bonds. The central  $Si-Si$  bond between the two  $Si=Si$  double bonds is notably shorter in **58<sub>ap</sub>** compared to that of **58<sub>sc</sub>**: 2.2801(12)–2.2862(11) Å and 2.2902(2) Å. These structural features provide evidence for the better *p*-conjugation between the two  $Si=Si$  double bonds in **58<sub>ap</sub>**. Such conclusion was further supported by the observation of the longest wavelength absorption of **58** (537 nm) that was remarkably red-shifted compared to that of the starting disilene  $Me_3Si(Tip)Si=Si(Tip)SiMe_3$  (394 nm). Interestingly, **58** can be functionalized at its terminal Si atoms by the metalation with <sup>t</sup>BuOK to generate intermediate tetrasilabutadienyl anion salt  $[Me_3Si(Tip)Si=Si(Tip)-Si(Tip)=Si(Tip)-K]$  (stable below  $-50^\circ C$ ), which readily reacts with  $Et_3SiCl$  at  $-50^\circ C$  forming novel unsymmetrically substituted tetrasiladiene  $Me_3Si(Tip)Si=Si(Tip)-Si(Tip)=Si(Tip)-SiEt_3$ .

#### 1.03.3.2.2.2 Heteronuclear derivatives $>E=E'-E''=E'''<$ ( $E, E', E'', E''' = \text{group 14 element}$ )

The compounds of this type, featuring formally conjugated 1,3-diene moieties  $>E=E'-C=C<$  ( $E, E'=Si, Ge$ ), were first reported by Lee and Sekiguchi in 2000,<sup>113</sup> followed by the report from Power group in 2004.<sup>114</sup> In the first case,<sup>113</sup> the  $>Si=Ge-C=C<$  fragment was incorporated into the cyclopentadiene skeleton in which no noticeable conjugation between the  $Si=Ge$  and  $C=C$  bonds was found, whereas in the second one<sup>114</sup> the  $>Ge=Ge-C=C<$  unit constituted a  $Ge_2C_2$ -cyclobutadiene scaffold.

The structural analogue of the above-described Power digermacyclobutadiene,<sup>114</sup> namely, 1,2-Tbb-3,4-diphenyl-1,2-digermacyclobutadiene ( $Tbb = 4$ -<sup>t</sup>Bu-2,6-[( $Me_3Si$ )<sub>2</sub>CH]<sub>2</sub>-C<sub>6</sub>H<sub>2</sub>) **59**, was recently reported by Sasamori and coworkers, prepared by the [2 + 2] cycloaddition of isolable digermene  $TbbGe=GeTbb$  and diphenylacetylene.<sup>115</sup> **59** featured nearly planar  $Ge_2C_2$ -ring with the endocyclic  $Ge=Ge$  and  $C=C$  double bonds of 2.4160(5) and 1.362(5) Å, respectively [ $Ge-C$  bond length: 2.022(2) Å].

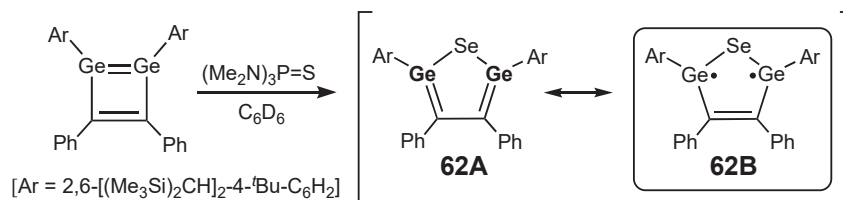


Scheme 22

Two other recently reported examples of the title compounds were of the  $>C=Si-Si=C<$  types. The first one,  $cAAC=Si(Cl)-Si(Cl)=cAAC$  ( $cAAC$ : cyclic alkyl(amino) carbene,  $cyclo-[C-CMe_2-CH_2-CMe_2-N(2,6-^iPr_2-C_6H_3)]$ ) **60**, was synthesized by Roesky and coworkers by the reduction of ( $cAAC$ :  $\rightarrow SiCl_4$ ) complex with  $KC_8$ .<sup>116</sup> The doubly bonded Si atoms in **60** resonated at 25.6 ppm, and both of them featured pyramidal configuration ( $\Sigma = 325.3$  and  $328.0^\circ$ ). The Si=C and Si-Si bond lengths were measured as 1.823(3)/1.826(3) Å and 2.3058(13) Å, the former being elongated compared with the standard Si=C double bonds whereas the latter being shortened compared with the typical Si-Si single bonds. Although such structural peculiarities might be explained by the partial conjugation within the C=Si-Si=C diene system, the authors stated that the conjugation is not effective because C-Si-Si-C unit is not planar but twisted (due to the steric hindrances) which results in the elongation of the C=Si bonds.

By contrast, 2,3-disilabuta-1,3-diene  $Ad=Si(SiMe_2^tBu)-Si(SiMe_2^tBu)=Ad$  ( $Ad = 2$ -adamantylidene) **61**, prepared by Iwamoto and coworkers by the reaction of 1,2-dilithiodisilane ( $^tBuMe_2Si$ )<sub>2</sub>Si(Li)-Si(Li)(SiMe<sub>2</sub><sup>t</sup>Bu)<sub>2</sub> with 2-adamantanone, exhibited significant interaction between the two Si=C units in solution.<sup>117</sup> This was evidenced by the important red-shift of the longest wavelength UV-absorption in **61** of 371 nm, compared with other structurally similar silenes. Likewise, the <sup>29</sup>Si and <sup>13</sup>C NMR resonances of the Si=C unit were found in the region typical for the structurally similar silenes: 41.2 and 197.3 ppm, respectively. The C=Si-Si=C unit adopts a synclinal conformation with the dihedral angle of 76.8°, and the geometries around the doubly bonded Si and C atoms were essentially planar:  $\Sigma = 359.8$  and  $360.0^\circ$ , respectively. The Si=C bond of 1.748(2) Å in **61** is notably shorter than that in Roesky 1,3-diene **60**, whereas the central Si-Si bond of 2.3149(13) Å in **61** is marginally longer than that in **60**.

The reaction of the above-described 1,2-digermacyclobutadiene **59**<sup>115</sup> with  $(Me_2N)_3P=Se$  afforded 2,5-digermaselenophene **62** via the intermediate formation of the "houseen"-type selenadigermirane followed by its valence isomerization to **62**, as reported by Sasamori and coworkers (Scheme 23).<sup>118</sup> Based on the structural data of its cyclic skeleton [ $r_{C-C} = 1.921(3)/1.922(3)$  Å,



Scheme 23

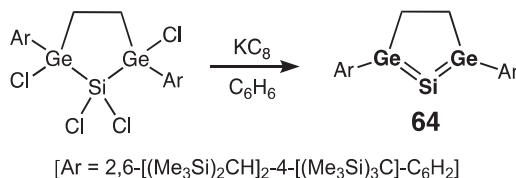
$r_{C-C} = 1.375(4)$  Å,  $\theta_{Tbb} = 7.8^\circ$  (*trans*), nonplanar SeGe<sub>2</sub>C<sub>2</sub> five-membered ring] and computational studies, the structure of **62** is best described as a singlet (digerma)biradicaloid resonance form **62B** whereas classical Lewis structure **62A** is of a minor importance (Scheme 23). Nevertheless, **62** showed some appreciable extent of aromaticity, as its NICS(1) was notably negative ( $-8.0$ ), comparable to that of the parent organic selenophene. The <sup>77</sup>Se NMR resonance of **62** was found in the low-field at 481.8 ppm, thus suggesting that **62** retains its *trans*-pyramidalized structure in solution as well.

### 1.03.3.2.3 Allene analogues

#### 1.03.3.2.3.1 Group 14 element derivatives $>E=E'=E<$ ( $E, E'=C, Si, Ge, Sn$ )

The first compound of this type, namely, tristannaallene ( $^tBu_3Si$ )<sub>2</sub>Sn=Sn=Sn( $Si^tBu_3$ )<sub>2</sub>, was reported by Wiberg and coworkers in 1999.<sup>119</sup> Several years later (in 2003), a milestone trisilaallene  $R_2Si=Si=SiR_2$  was prepared by Kira's group,<sup>120a</sup> followed by the synthesis of its heavier homologues, trigermaallene  $R_2Ge=Ge=GeR_2$  and 1,3-digerma-2-silaallene  $R_2Ge=Si=GeR_2$ , and 2-germa-1,3-disilaallene  $R_2Si=Ge=SiR_2$  (everywhere,  $R_2 = [cyclo-(Si-C(SiMe_3)_2-CH_2-CH_2-C(SiMe_3)_2-)]$ ).<sup>120</sup>

In the last decade, there was only one report on the synthesis of title compounds. In 2017, Sasamori, Tokitoh and coworkers synthesized 1,3-digerma-2-silaallene **64** in which the allenic  $>Ge=Si=Ge<$  moiety is a part of the cyclic system.<sup>121</sup> **64** was prepared by the exhaustive reductive dechlorination of tetrachloro-2,5-digerma-1-silacyclopentane with  $KC_8$  (Scheme 24). The SiGe<sub>2</sub>C<sub>2</sub>-ring in **64** is planar, and the Ge=Si bond lengths of 2.2681(18) and 2.2900(18) Å are typical for the Ge=Si double bonds. However, the <sup>29</sup>Si NMR chemical shift of the allenic Si atom in **64** was found at unusually high-field ( $-16.5$  ppm), thus being exceptionally shielded compared to that of Kira 1,3-digerma-2-silallene (236.6 ppm).<sup>120b</sup> This points to a crucial contribution of the  $[>Ge: \rightarrow Si^0 \leftarrow :Ge<]$  "silylone" resonance form of **64** featuring Si<sup>0</sup> character for its central silicon atom, caused by rather acute Ge-Si-Ge bond angle ( $80.1^\circ$ ) as a result of Ge-Si-Ge unit incorporation into the rigid five-membered ring skeleton. This was



Scheme 24



further backed by computations which showed highly polarized  $\text{Ge}^{d+}\text{-Si}^{d-}$  bonds with clear charge separation (NPA charges):  $-0.27$  (for Si) and  $+0.90/+0.91$  (for Ge), implying a significant s-donation from the germanium atoms to the silicon atom.

Compounds of the type  $>\text{E}=\text{C}=\text{C}<$  ( $\text{E}=\text{Si, Ge}$ ), that is 1-sila- and 1-germaallenes, are known since 1993 when West and coworkers reported the very first 1-silaallene.<sup>122</sup> This was followed by the synthesis of the first stable 1-germaallene by the same research group,<sup>123</sup> and a new 1-silaallene by Pietschnig and coworkers.<sup>124</sup>

As the recent development in the field, one can mention anionic lithium 1-silaallenolate [ ${}^t\text{Bu}_2\text{MeSi}({}^t\text{BuMe}_2\text{Si})\text{C}=\text{C}=\text{Si}(\text{SiMe}{}^t\text{Bu}_2)\text{OLi}$ ] **65** synthesized by Apeloig and coworkers by the reaction of  ${}^t\text{Bu}_2\text{MeSi}({}^t\text{BuMe}_2\text{Si})\text{C}=\text{C}=\text{Si}(\text{SiMe}{}^t\text{Bu}_2)\text{Li}$  with carbon monoxide.<sup>125</sup> As is typical for allenes, the  $\text{Si}-\text{C}-\text{C}$  bond angle of  $175.0^\circ$  only very slightly deviate from the required linearity ( $180^\circ$ ), whereas the  $\text{Si}=\text{C}$  and  $\text{C}=\text{C}$  bond lengths of  $1.711(5)$  and  $1.324(3)$  Å, respectively, are normal for 1-silaallenes. The allenic atoms in **65** resonated in the expected fields, at 50.0 ppm (for  $\text{Si}=\text{C}=\text{C}$ ), 301.7 ppm (for  $\text{Si}=\text{C}=\text{C}$ ), and 160.6 ppm (for  $\text{Si}=\text{C}=\text{C}$ ). Featuring an anionic moiety, **65** can still be functionalized at O atom: thus, reaction of **65** with  $\text{Me}_3\text{SiCl}$  produced a novel 1-silaallene  ${}^t\text{Bu}_2\text{MeSi}({}^t\text{BuMe}_2\text{Si})\text{C}=\text{C}=\text{Si}(\text{SiMe}{}^t\text{Bu}_2)\text{OSiMe}_3$  [NMR chemical shifts ( $\delta$ ): 61.7 ppm ( $\text{Si}=\text{C}=\text{C}$ ), 282.3 ppm ( $\text{Si}=\text{C}=\text{C}$ ), and 165.2 ppm ( $\text{Si}=\text{C}=\text{C}$ )].

#### 1.03.3.2.3.2 Hybrid group 14/group 15 element derivatives $>\text{E}=\text{E}'=\text{E}''-$ ( $\text{E, E}' = \text{group 14 element, E}'' = \text{group 15 element}$ )

Grützmacher and coworkers were the first to report such derivative, stannaketenimine  $\text{R}_2\text{Sn}=\text{C}=\text{NMe}_s$  [ $\text{R} = 2,4,6\text{-}(\text{CF}_3)_3\text{-C}_6\text{H}_2$ ] which exists in equilibrium with the stannylene  $\text{R}_2\text{Sn}$ : and isocyanide:  $\text{C}=\text{NMe}_s$ .<sup>126</sup> The first silaketenimines featuring true  $>\text{Si}=\text{C}=\text{N}-$  allenic character were synthesized by Kira and Iwamoto,<sup>127</sup> and this was followed by the report from Sekiguchi group on the synthesis of bis(silaketenimine).<sup>128</sup>

Unusual silaketenimine anionic derivatives **66** were reported by Cui and coworkers.<sup>129</sup> Both **66a** and **66b** were uniformly prepared from a masked lithiosilylene with isocyanides RNC: ( $\text{R} = 2,6\text{-}{}^i\text{Pr}_2\text{-C}_6\text{H}_3$ , 1-adamantyl) (**Scheme 25**). The allenic atoms resonated at very high-field for silicon nucleus reflecting its negatively-charged nature [ $\delta(^{29}\text{Si}) = -144.0/-162.4$  ppm], and at very low-field for carbon nucleus [ $\delta(^{13}\text{C}) = +235.7/+227.0$  ppm]. The  $\text{Si}=\text{C}$  and  $\text{C}=\text{N}$  bonds in **66a,b** were relatively short and relatively long:  $1.725(4)/1.730(2)$  Å and  $1.285(4)/1.279(3)$  Å, respectively. The  $\text{Si}-\text{C}-\text{N}$  bond angles of  $160.6/157.4^\circ$  in **66a,b** are remarkably smaller than the one required for the classical allenic system ( $180^\circ$ ). Based on the structural and computational data, the authors described their compounds **66a,b** as allenic systems  $\text{B}-\text{Si}=\text{C}=\text{N}-\text{R}$ .

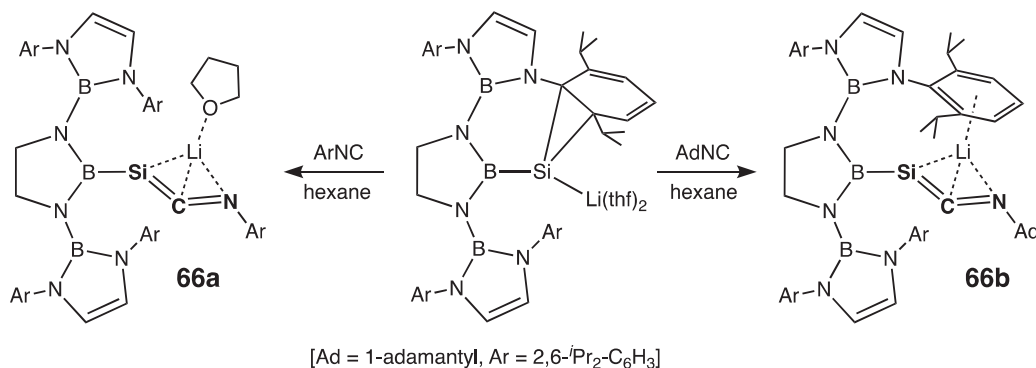
Allenic systems with phosphorus atoms of the type  $>\text{E}=\text{C}=\text{P}-$  ( $\text{E}=\text{Si, Ge, As}$ ) were all prepared by Escudié and coworkers by dehalogenation of the corresponding precursors: phosphasilaallene  $\text{Tip}(\text{Ph})\text{Si}=\text{C}=\text{PMes}^*$  ( $\text{Mes}^* = 2,4,6\text{-}{}^t\text{Bu}_3\text{-C}_6\text{H}_2$ ) stable below  $-30^\circ\text{C}$ ,<sup>130a</sup> phosphagermaallene  $\text{Tip}({}^t\text{Bu})\text{Ge}=\text{C}=\text{PMes}^*$  stable at room temperature,<sup>130b</sup> and arsagermaallene  $\text{Tip}({}^t\text{Bu})\text{Ge}=\text{C}=\text{AsMes}^*$  also stable at room temperature.<sup>130c</sup> Since then and to date, no further progress to the field has been made.

Despite some recent reports on the generation of donor/acceptor-stabilized 1-silaketenes  $>\text{C}=\text{Si}=\text{O}$ ,<sup>131</sup> isolable derivatives of this type, free from the high electronic perturbation caused by the intra/intermolecular donor/acceptor coordination, are still elusive, thus remaining to be the next highly attractive challenge.

#### 1.03.3.2.4 Vinylidene analogues

Vinylidenes  $\text{R}_2\text{C}=\text{C}$ : are the valence isomers of alkynes  $\text{RC}\equiv\text{CR}$  featuring a naked terminal carbon atom (substituents-free) being as such extraordinarily reactive. To stabilize this low-coordinate center, use of external base, such as NHC, is particularly effective, and therefore almost all examples of the isolated heavy group 14 analogues of vinylidenes of the type  $\text{R}_2\text{E}=\text{E}'$ : ( $\text{E, E}' = \text{heavy group 14 elements}$ ), except for the digermavinylidenes, were stabilized in this way by the external NHC-coordination.

The first breakthrough in the field came from the Scheschkewitz group who reported the very first isolable compound of this type, namely, NHC-stabilized silagermenylidene  $\text{Tip}_2\text{Si}=\text{Ge}:(\leftarrow\text{NHC})$  ( $\text{NHC} = 1,3\text{-diisopropyl-4,5-dimethylimidazol-2-ylidene}$ ) **67** prepared by the co-reduction of  $\text{Tip}_2\text{SiCl}_2$  and NHC  $\rightarrow \text{GeCl}_2$  complex with lithium naphthalenide.<sup>132</sup> The  $\text{sp}^2\text{-Si}$  center of **67** is expectedly deshielded [ $\delta(^{29}\text{Si}) = 158.9$  ppm], the  $\text{Si}=\text{Ge}$  bond is short [ $r_{\text{Si}=\text{Ge}} = 2.2521(5)$  Å] well-fitting within the range



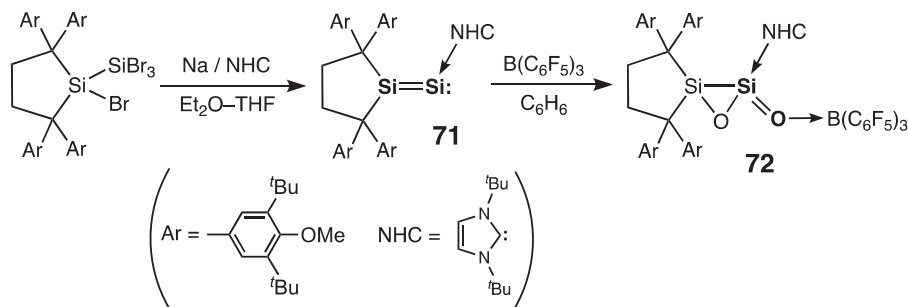
Scheme 25

of the typical silagermenes, and the Si atom has planar configuration ( $\Sigma = 359.8^\circ$ ). The Si=Ge bond is nearly undistorted ( $\tau = 3.1^\circ$ ) thus allowing for an effective  $p_\pi-p_\pi$  orbital overlap, and the NHC-ligand coordinates to Ge center in nearly orthogonal manner ( $C_{\text{NHC}}-\text{Ge}-\text{Si}$  bond angle =  $98.9^\circ$ ) to maximize their  $n_{\text{lone pair NHC}}-p_{\text{Ge}}$  orbital interaction. Following their original report, the same group subsequently synthesized another NHC-stabilized silagermenylidene  $\text{Tip}_2\text{ClSi}-(\text{Tip})\text{Si}=\text{Ge}:(\leftarrow \text{NHC})$  (NHC = 1,3-diisopropyl-4,5-dimethylimidazol-2-ylidene) **68**.<sup>133</sup> Being structurally similar to **67**, **68** manifested spectral and structural characteristics that were reminiscent to those of **67**, namely:  $\delta(^{29}\text{Si}) = 162.5$  ppm,  $r_{\text{Si}=\text{Ge}} = 2.2757(10)$  Å,  $C_{\text{NHC}}-\text{Ge}-\text{Si}$  bond angle =  $101.9^\circ$ .

Silicon analogues of **67** and **68**, that is disilavinylidenes were reported by Filippou and coworkers. The first one,  $\text{Tbb}(\text{Br})\text{Si}=\text{Si}:(\leftarrow \text{NHC})$  (NHC = 1,3-bis(2,6-diisopropylphenyl)imidazoline-2-ylidene) **69** was prepared by the reduction of NHC-stabilized bromo(silyl)silylene  $\text{Tbb}(\text{Br}_2)\text{Si}-(\text{Br})\text{Si}:(\leftarrow \text{NHC})$  with  $\text{KC}_8$ .<sup>134</sup> The  $sp^2$ -Si atoms resonated at 34.6 and 86.0 ppm, the disilavinylidene core was almost planar with the sum of the bond angles around the tricoordinate Si atom of  $360.0^\circ$  and the twist angle about the Si=Si bond of  $2.7^\circ$ , and NHC coordinated to the Si=Si bond nearly orthogonally with the  $C_{\text{NHC}}-\text{Si}-\text{Si}$  bond angle =  $97.6^\circ$ . The Si=Si bond in **69** of 2.167(2) Å was very short corroborating the presence of the genuine double bond, which was further supported by the NBO and NRT calculations (Si=Si: WBI = 1.79, NRT bond order = 1.91). The presence of a stereochemically active lone pair (77% s-character) at the naked Si atom was confirmed by the NBO calculations.

Applying this synthetic approach, the same group succeeded also in the synthesis of the NHC-stabilized phosphasilenyldiene  $\text{Mes}^*\text{P}=\text{Si}:(\leftarrow \text{NHC})$  **70** (NHC is the same as the one in the above paragraph) available by the reaction of  $\text{Cl}_2\text{Si}:(\leftarrow \text{NHC})$  with  $\text{LiP}(\text{Mes}^*)\text{SiMe}_3$  ( $\text{Mes}^* = 2,4,6\text{-}t\text{Bu}_3\text{-C}_6\text{H}_2$ ).<sup>135</sup> **70** displayed structural features that are typical for vinylidene systems, namely: short  $r_{\text{Si}=\text{P}}$  bond of 2.1188(7) Å that is typical for phosphasilenes, acute  $C_{\text{NHC}}-\text{Si}-\text{P}$  bond angle of  $92.7^\circ$ , planar Si=P bond with the twist angle of only  $1.9^\circ$ . Spectroscopic data for **70** are also in line with its formulation as phosphasilenyldiene: both Si and P nuclei are strongly deshielded being observed at 267.3 and 402.4 ppm, respectively. The  $^1J(^{29}\text{Si}-^{31}\text{P})$  coupling constant of 170.4 Hz is large, expectedly for the Si=P doubly bonded system, which was further supported by the NBO calculations (WBI for Si-P bond is 1.68).

The latest example of isolable disilavinylidene, compound **71**, was reported by Iwamoto group. **71** was synthesized by the co-reduction of a mixture of their tetrabromodisilane and NHC (NHC = 1,3-di-*tert*-butylimidazol-2-ylidene) with metallic sodium (Scheme 26).<sup>136</sup> The doubly bonded Si atoms resonated at 160.8 and 65.0 ppm, for the tricoordinate silicon and NHC-



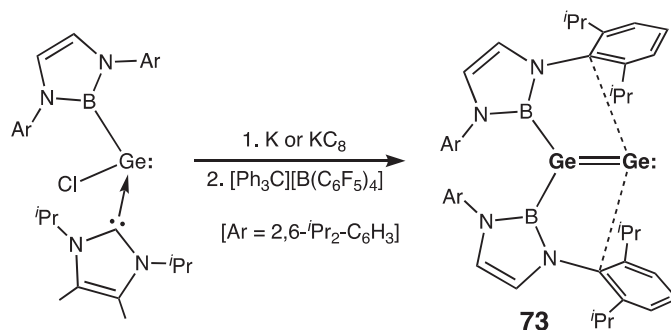
Scheme 26

coordinated terminal silicon nuclei, respectively. As is typical for disilavinylidenes, the Si=Si bond in **71** is short [ $r_{\text{Si}=\text{Si}} = 2.1787(8)$  Å], tricoordinate silicon has a planar geometry ( $\Sigma = 359.7^\circ$ ), and Si=Si bond is only slightly twisted ( $\tau = 7.2^\circ$ ). Interestingly, when **71** was treated with  $\text{N}_2\text{O}$  followed by  $\text{B}(\text{C}_6\text{F}_5)_3$ , unique disilaacetolactone **72** was formed in which the Si=O bond is *push-pull* coordinated to NHC (for Si) and  $\text{B}(\text{C}_6\text{F}_5)_3$  (for O) (Scheme 26).<sup>136</sup>

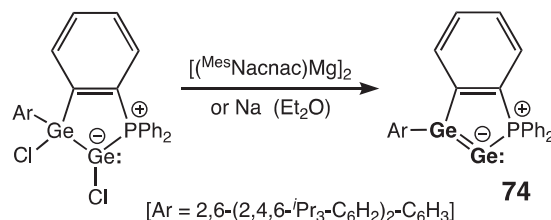
The first digermavinylidene **73** reported by Aldridge group in 2016 is remarkable because it is free from any external NHC-coordination, unlike the case of the above-described NHC-supported silagermenylidenes and disilavinylidenes (*vide supra*).<sup>137</sup>

Digermavinylidene **73** was synthesized by the reaction of the NHC-stabilized boryl(chloro)germylene with K or  $\text{KC}_8$  followed by the oxidation of the intermediate dianionic species by  $[\text{Ph}_3\text{C}][\text{B}(\text{C}_6\text{F}_5)_4]$  (Scheme 27). The Ge=Ge double bond in **73** is practically planar, as the four atoms (two Ge and two B atoms) lie within a single plane. The Ge=Ge distance of 2.312(1) Å is reasonably short to formulate it as a double bond. In the solid state, there are also weak stabilizing interactions between one of the flanking aryl  $\pi$ -systems of each of the boryl substituent and the vacant *in-plane*  $\pi$ -orbital at the one-coordinate Ge atom. The HOMO of **73** is represented by the Ge-Ge  $\pi$ -bond, whereas the HOMO-1 is mostly naked Ge atom lone pair. The longest wavelength UV-absorption in **73** at 460 nm corresponds to a Ge=Ge double bond  $\pi-\pi^*$  electronic transition.

Another digermavinylidene **74** was very recently reported by Wesemann and coworkers.<sup>138</sup> **74** was available by the reduction of intramolecularly phosphine-stabilized chloro(germyl)germylene with  $[(^{\text{Mes}}\text{Nacnac})\text{Mg}]_2$  ( $^{\text{Mes}}\text{Nacnac} = \{[(2,4,6\text{-Me}_3\text{-C}_6\text{H}_2)\text{N}(\text{Me})\text{C}_2\text{CH}\}^-]$ ) or metallic sodium (Scheme 28). The Ge=Ge bond of 2.3060(2) Å is marginally shorter than that in Aldridge digermavinylidene **73**, being in the range of the typical Ge=Ge double bonds. Except for the substituents, the bicyclic molecule is nearly planar, and the tricoordinate Ge atom manifests practically planar geometry ( $\Sigma = 358.8^\circ$ ). Formulation of the germanium-



Scheme 27



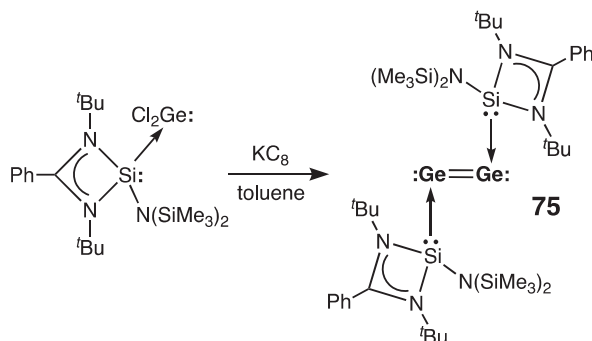
Scheme 28

germanium interaction in 74 as a double bond was further supported by consideration of its frontier orbitals: HOMO and LUMO represent bonding and antibonding  $\pi$ - and  $\pi^*$ -orbitals of the  $Ge=Ge$  double bond. However, alternatively the bonding situation in 74 can be interpreted as a double Lewis base-stabilized Ge atom in the formal oxidation state 0, that is,  $Ge^0$ . As such, digermavinylidene 74 can serve as a source for a single  $Ge^0$  atom transfer by the germanium atom abstraction reactions.

#### 1.03.3.2.5 $E(0)=E(0)$ : Derivatives ( $E=Si, Ge, Sn$ )

This exciting class of low-coordinate group 14 element derivatives, featuring central elements E in their formal oxidation state 0, has emerged recently. The first milestone report in the field was published by Robinson and coworkers in 2008, describing  $[NHC \rightarrow Si^0=Si^0 \leftarrow NHC]$  ( $NHC = 1,3\text{-}(2,6\text{-}iPr_2\text{-}C_6H_3)_2\text{-imidazol-2-ylidene}$ ).<sup>139</sup> This breakthrough was quickly followed by the synthesis of its heavier analogues,  $[NHC \rightarrow Ge^0=Ge^0 \leftarrow NHC]$  ( $NHC = 1,3\text{-}(2,6\text{-}iPr_2\text{-}C_6H_3)_2\text{-imidazol-2-ylidene}$  or  $1,3\text{-}(2,4,6\text{-}Me_3\text{-}C_6H_2)_2\text{-imidazol-2-ylidene}$ ) and  $[NHC \rightarrow Sn^0=Sn^0 \leftarrow NHC]$  ( $NHC = 1,3\text{-}(2,6\text{-}iPr_2\text{-}C_6H_3)_2\text{-imidazol-2-ylidene}$ ), by Jones and coworkers.<sup>140</sup>

As the most recent development in the field, one can mention *N*-heterocyclic silylene(NHSi)-stabilized digermanium(0) complex 75, prepared by So and coworkers by the reduction of  $NHSi-GeCl_2$  complex with  $KC_8$  (Scheme 29).<sup>141</sup> NHSi-ligands in 75 coordinate to the:  $Ge=Ge$ : moiety almost perpendicularly ( $Si-Ge-Ge$  bond angle  $92.0^\circ$ ), and the  $Ge=Ge$  bond of  $2.3518(16)$  Å is still in the range of the typical  $Ge=Ge$  double bonds in digermenes. In contrast to the above-described  $[NHC \rightarrow Ge^0=Ge^0 \leftarrow NHC]$ ,<sup>140a</sup> 75 features *p*-back-bonding interaction of the  $Ge=Ge$   $\pi$ -bond and vacant *p*(Si)-orbital of the NHSi ligand stabilizing the whole molecule, as was evidenced by the frontier molecular orbital (HOMO) and AIM analyses.



Scheme 29

## 1.03.3.3 Triply bonded derivatives

## 1.03.3.3.1 Homonuclear derivatives –E≡E– (E=Si, Ge, Sn, Pb)

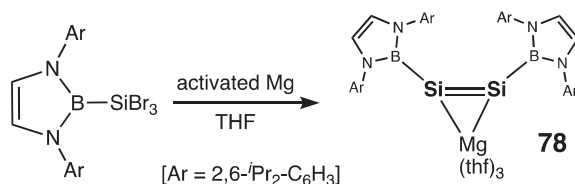
## 1.03.3.3.1.1 Disilynes –Si≡Si–

The quest for the stable alkyne analogues of the heavy group 14 elements has a long history dating back to the early 1990s when Masamune and coworkers described disilyne R–Si≡Si–R among the greatest challenges for silicon chemists in their seminal review.<sup>142</sup> However, it took more than a decade when the first isolable disilynes R<sub>3</sub>Si–Si≡Si–SiR<sub>3</sub> were independently reported by Wiberg (R<sub>3</sub>Si=SiMe(Si<sup>*t*</sup>Bu)<sub>2</sub>)<sup>143</sup> and Sekiguchi (R<sub>3</sub>Si=Si<sup>*i*</sup>Pr[CH(SiMe<sub>3</sub>)<sub>2</sub>]<sub>2</sub>)<sup>144</sup> groups in 2004. These historical achievements were followed by the subsequent synthesis of a couple of other stable disilynes, unsymmetrically substituted bis(silyl)disilyne R<sub>3</sub>Si–Si≡Si–SiR'<sub>3</sub> (R<sub>3</sub>Si=Si<sup>*i*</sup>Pr[CH(SiMe<sub>3</sub>)<sub>2</sub>]<sub>2</sub>, R'<sub>3</sub>Si=Si(CH<sub>2</sub><sup>*t*</sup>Bu)[CH(SiMe<sub>3</sub>)<sub>2</sub>]<sub>2</sub>)<sup>145</sup> by Sekiguchi and coworkers and diaryldisilyne Bbt–Si≡Si–Bbt (Bbt = 2,6-[(Me<sub>3</sub>Si)<sub>2</sub>CH]<sub>2</sub>-4-[(Me<sub>3</sub>Si)<sub>3</sub>C]-C<sub>6</sub>H<sub>2</sub>)<sup>146</sup> by Tokitoh and coworkers.

Since 2013, a few other examples of the stable disilynes were reported. As a remarkable new entry to the stable disilynes family, Iwamoto group reported the first dialkyldisilyne R–Si≡Si–R [R=C(SiMe<sub>3</sub>)<sub>2</sub>(CH<sub>2</sub><sup>*t*</sup>Bu)] **76**.<sup>147</sup> As is uniform for disilynes, **76** was prepared by the exhaustive dehalogenation of the tetrabromodisilane precursor R–SiBr<sub>2</sub>–SiBr<sub>2</sub>–R with KC<sub>8</sub>. The triply bonded Si atoms in **76** resonated at 31.8 ppm, that is at higher field compared to those in bis(silyl)disilynes (89.9 ppm<sup>144</sup> and 62.6/106.3 ppm<sup>145</sup>) but at lower field than that in diaryldisilyne (18.7 ppm).<sup>146</sup> The Si≡Si triple bond in **75** of 2.0863(13) Å is in-between those of bis(silyl)disilynes (2.0622(9) Å<sup>165</sup> and 2.0569(12) Å<sup>145</sup>) and diaryldisilyne (2.108(5) Å<sup>90</sup>). The *trans*-bent angle C–Si≡Si in **76** of 132.1° is again intermediate between those of bis(silyl)disilynes (137.4°<sup>144</sup> and 137.9/138.8°<sup>145</sup>) and diaryldisilyne (133.0°<sup>146</sup>).

The second diaryldisilyne Tbb–Si≡Si–Tbb (Tbb = 2,6-[(Me<sub>3</sub>Si)<sub>2</sub>CH]<sub>2</sub>-4-<sup>*t*</sup>Bu-C<sub>6</sub>H<sub>2</sub>) **77** was synthesized by Sasamori and coworkers by the reduction of 1,2-dibromodisilene precursor (*E*)-Tbb(Br)Si=Si(Br)Tbb with KC<sub>8</sub>.<sup>148</sup> **77** manifested spectral and structural features that are typical for disilynes, namely: <sup>29</sup>Si NMR resonance at 16.2 ppm, short Si≡Si bond of 2.1050(15) Å, and a notable *trans*-bending angle C<sub>aryl</sub>–Si≡Si of 131.4°.

An interesting three-membered ring MgSi<sub>2</sub> compound **78**, featuring cyclic Si=Si double bond (magnesium disilacyclopropene) and as such considered as the doubly reduced disilyne derivative, was recently reported by Cui and coworkers.<sup>149</sup> This dianionic disilyne magnesium complex **78** was available by the reduction of (NHBoryl)tribromosilane with activated magnesium (Scheme 30). The anionic Si atoms in **78** expectedly resonated in very low-field at 204.1 ppm, as is characteristic for disilenides. The Si=Si



Scheme 30

bond of 2.223(17) Å in **78** is also in line with its formulation as a double bond, and both Si atoms have nearly planar geometry ( $\Sigma = 355.7$  and  $359.9^\circ$ ). The dianionic character of the Si<sub>2</sub>-core in **78** was further confirmed by the NPA charge calculations: –0.61 and –0.63 (for Si atoms) and +1.59 (for Mg atom).

## 1.03.3.3.1.2 Digermyne –Ge≡Ge–

The first isolable digermene Ar–Ge≡Ge–Ar [Ar = 2,6-(2,6-<sup>*i*</sup>Pr<sub>2</sub>-C<sub>6</sub>H<sub>3</sub>)<sub>2</sub>-C<sub>6</sub>H<sub>3</sub>] was reported by Power group in 2002,<sup>150</sup> and this was followed by the synthesis of another stable diaryldigermyne Bbt–Ge≡Ge–Bbt (Bbt = 2,6-[(Me<sub>3</sub>Si)<sub>2</sub>CH]<sub>2</sub>-4-[(Me<sub>3</sub>Si)<sub>3</sub>C]-C<sub>6</sub>H<sub>2</sub>) by Tokitoh and coworkers.<sup>151</sup>

A couple of other stable digermynes were reported since 2013. The first one, bis(amido)digermyne R–Ge≡Ge–R {R = N(Si<sup>*i*</sup>Pr<sub>3</sub>)[2,6-(CHPh<sub>2</sub>)<sub>2</sub>-4-<sup>*i*</sup>Pr-C<sub>6</sub>H<sub>2</sub>]} **79**, was synthesized by Jones and coworkers by the reduction of the monomeric germylene R(Cl)Ge: with [(<sup>*Me*</sup>Nacnac)Mg]<sub>2</sub>.<sup>152</sup> However, given the Ge–Ge bond distance of 2.3568(3) Å in **79** that is much longer than those of previously reported diaryldigermynes (2.2850(6) Å<sup>150</sup> and 2.2060(7)/2.2260(7) Å<sup>151</sup>), the very formulation of **79** as a digermene casts some doubts on it. It is very likely that **79** is better viewed as a digermene derivative (WBI = 1.75),<sup>152</sup> rather than a digermene one.

By contrast, triply bonded constitution of another digermene Tbb–Ge≡Ge–Tbb (Tbb = 2,6-[(Me<sub>3</sub>Si)<sub>2</sub>CH]<sub>2</sub>-4-<sup>*t*</sup>Bu-C<sub>6</sub>H<sub>2</sub>) **80** prepared by the reduction of 1,2-dibromodigermene (*E*)-Tbb(Br)Ge=Ge(Br)Tbb with KC<sub>8</sub> as reported by Sasamori, Tokitoh and coworkers, was firmly established.<sup>153</sup> **80** has short Ge≡Ge bond of 2.2410(9)/2.2221(9) Å and *trans*-bent C<sub>aryl</sub>–Ge–Ge angle of 130.5/130.7°.

## 1.03.3.3.1.3 Distannyne –Sn≡Sn–

The first stable distannyne Ar–Sn≡Sn–Ar [Ar = 2,6-(2,6-<sup>*i*</sup>Pr<sub>2</sub>-C<sub>6</sub>H<sub>3</sub>)-C<sub>6</sub>H<sub>3</sub>] was reported by Power group in the same year 2002, when the first digermene was reported by the same group.<sup>150</sup> Since then, several bis(amido)-substituted ditin derivatives were

claimed as distannynes.<sup>155</sup> However, again, based on their exceptionally long Sn–Sn separations of 3.1429(7) Å<sup>155a</sup> and 3.0638(7) Å<sup>155b</sup> (cf.: 2.6675(4) Å in Power distannyne<sup>154</sup>), these compounds should be classified as the singly bonded bis(stannylenes), and therefore their formulation as distannynes is somewhat misleading.

Power group has recently authenticated another diaryldistannyne Ar–Sn≡Sn–Ar [Ar = 2,6-(2,4,6-*i*Bu<sub>3</sub>-C<sub>6</sub>H<sub>2</sub>)<sub>2</sub>-C<sub>6</sub>H<sub>3</sub>] **81** prepared by the standard procedure, namely, by the reduction of the corresponding chlorostannylene Ar(Cl)Sn: with KC<sub>8</sub>.<sup>156</sup> The Sn≡Sn bond in **81** is short (2.7621(6) Å) although being the longest one observed in distannynes, and the C<sub>aryl</sub>–Sn–Sn *trans*-bending angle is narrow (119.1/119.8°) being comparable to that in the first Power distannyne (125.2°).<sup>154</sup> No solution <sup>119</sup>Sn NMR resonance for the triply bonded Sn atoms in **81** were observed due to the anisotropy of the chemical shift tensor, as in the case of other distannynes.

#### 1.03.3.3.1.4 Diplumbyne –Pb≡Pb–

The first diplumbyne Ar–Pb≡Pb–Ar [Ar = 2,6-(2,4,6-*i*Pr<sub>3</sub>-C<sub>6</sub>H<sub>2</sub>)-C<sub>6</sub>H<sub>3</sub>], which was actually the very first example of the formal heavy group 14 element alkyne analogues, was reported by Power and coworkers in 2000.<sup>157</sup> However, given its peculiar structural features (very long Pb–Pb separation of 3.1881(1) Å and nearly orthogonal arrangement of the aryl substituents in relation to the Pb–Pb bond with the C<sub>aryl</sub>–Pb–Pb bond angle of 94.3°), the compound was formulated as the *trans*-bent singly bonded diplumbylene Ar–Pb:–Pb:–Ar, rather than the triply bonded diplumbyne Ar–Pb≡Pb–Ar.

Very recently, Power group reported a series of novel “diplumbynes” ArPbPbAr [Ar = 2,6-(2,6-*i*Pr<sub>2</sub>-C<sub>6</sub>H<sub>3</sub>)<sub>2</sub>-C<sub>6</sub>H<sub>3</sub>, 2,6-(2,4,6-*i*Pr<sub>3</sub>-C<sub>6</sub>H<sub>2</sub>)<sub>2</sub>-3,5-*i*Pr<sub>2</sub>-C<sub>6</sub>H, 2,6-(2,4,6-*i*Bu<sub>3</sub>-C<sub>6</sub>H<sub>2</sub>)<sub>2</sub>-C<sub>6</sub>H<sub>3</sub>, 2,6-(2,6-*i*Pr<sub>2</sub>-C<sub>6</sub>H<sub>3</sub>)<sub>2</sub>-4-SiMe<sub>3</sub>-C<sub>6</sub>H<sub>2</sub>].<sup>158</sup> These compounds were prepared by the reduction of aryl(bromo)plumbylene dimers {Ar(*m*-Br)Pb:}<sub>2</sub> with (<sup>t</sup>Bu<sub>2</sub>AlH)<sub>2</sub> forming intermediate hydrides [{Ar(*H*)Pb:}]<sub>2</sub> which subsequently eliminate H<sub>2</sub> thus forming ArPbPbAr, or alternatively by the reduction of [Ar(*m*-Br)Pb:]<sub>2</sub> with [(<sup>Mes</sup>Nacnac)Mg]<sub>2</sub>. All diplumbynes (except for the one with the bulkiest Ar substituent, 2,6-(2,4,6-*i*Pr<sub>3</sub>-C<sub>6</sub>H<sub>2</sub>)<sub>2</sub>-3,5-*i*Pr<sub>2</sub>-C<sub>6</sub>H) are unstable, surviving only at the temperatures as low as –20 °C/–30 °C. The Pb–Pb separation in these diplumbynes was in the range 3.0382(6)–3.2439(9) Å, with the shorter bonds being still notably longer than the typical Pb–Pb single bonds in diplumbanes but rather comparable to the Pb=Pb double bonds in diplumbenes. The *trans*-bending angles C<sub>aryl</sub>–Pb–Pb were in the range 95.2–116.0°.

#### 1.03.3.3.2 Heteronuclear derivatives –E≡C– and –E≡P

Heteronuclear heavy alkyne analogues featuring different group 14 elements of the type –E≡E'– (E, E' = C–Pb) were the subject of permanently high interest of the main group chemists. However, despite many research efforts, no such stable derivatives were isolated to date. The closest approach to the compounds of interest is represented by the metastable silyne –Si≡C– (stable in solution only below –30 °C), which has rather peculiar substituents pattern and in which the intramolecularly phosphine-stabilized Si≡C bond is very short (1.667(3) Å) being notably shorter than the conventional Si=C double bonds. This compound was reported by Kato, Baccaredo and coworkers in 2010.<sup>159</sup>

An equal, if not even more, attractive synthetic challenge are hybrid group 14/15 element alkyne analogues of the type R–E≡E' (E = group 14 element, E' = group 15 element). Accordingly, the search for the room-temperature stable compounds of this type, first of all, of the heavy nitriles R–E≡N and heavy phosphalkynes R–E≡P types (E = heavy group 14 element), intrigued Main Group elements community for at least a couple of last decades. However, stabilization of such fascinating species appeared to be exceptionally challenging, especially given that only ONE substituent R is available for stabilization (both thermodynamic and kinetic) of otherwise exceptionally reactive E≡N and E≡P triple bonds. The extraordinary difficulties in stabilization of such species was recently experimentally verified by the research of Hinz and Goicoechea, who attempted synthesis of the phosphagermyne R–Ge≡P and phosphastannyne R–Sn≡P derivatives.<sup>160</sup> Accordingly, to date, there is no success in the field of compounds of the type R–E≡E' (E/E' = group 14/group 15 elements), but one can expect progress in this field in the future.

### 1.03.4 Low-coordinate compounds of heavier group 15 elements

#### 1.03.4.1 Introduction

The chemistry of low-coordinate compounds of heavier Group 15 elements has seen remarkable progress. As for low-coordinate compounds of heavier Group 15 elements, the field of the multiple bonded compounds correspond to one of the most popular categories. Up to date, numerous literatures for heteroaromatics such as phosphole (C<sub>4</sub>H<sub>5</sub>P) and phosphine (PC<sub>5</sub>H<sub>5</sub>) derivatives, multiple bonded systems, e.g., phosphalkenes (>C=P–), phosphalkynes (–C≡P), and diphosphenes (–P=P–), have been reported together with their heavier analogues. In this chapter, we will discuss the synthesis and structural features of diphosphenes and related heavier analogues between 2016 and 2020.

#### 1.03.4.2 Diphosphene derivatives

Remarkable advances have been made in low-valent main-group chemistry, providing new insights into bond making and breaking processes. Among heavier Group 15 elements, dipnictenes have attracted considerable attention. Since the preparation of the first stable diphosphene Mes\*–P=P–Mes\* (Mes\* = 2,4,6-*i*Bu<sub>3</sub>-C<sub>6</sub>H<sub>2</sub>) by Yoshifuji and coworkers in 1981,<sup>5</sup> the field of low-coordinate



**Table 1** Selected structural parameters of diphosphene derivatives.

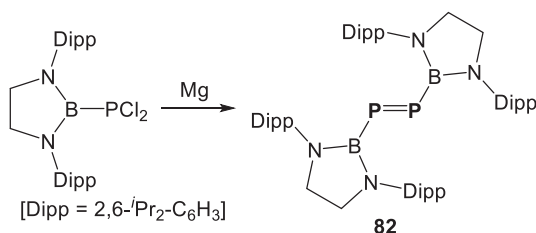
Compounds	Bond lengths/Å		Bond angle/degree
	P=P	E-P	
<b>82</b>	2.0655(17)	1.936(3)	95.83(9)
<b>83</b>	2.026(1)	1.926(2)	97.02(4)
<b>84</b>	2.0210(6)	C-P 1.8778(12)	102.88(4)
<b>85</b>	2.0351(7)		97.72(6)–103.07(4)
<b>86</b>	2.0611(7)	C-P; 1.821(2) P-N; 1.6411(17)	P-P-N; 105.66(6) C-P-P; 94.32(6)
<b>87</b>	2.038(1)	C-P; 1.834(2) P-C; 1.854(4)	C-P-P; 105.0(1) P-P-C; 95.1(1)
<b>88</b>	2.1897(4)	1.7502(11), 1.7488(11)	
<b>89</b>	2.0530(5)	1.832(2)	101.54(5)
<b>90</b>	2.0565(9)	1.824(2), 1.833(2)	
<b>91a</b>	2.0453(6)	C-P 1.854(2)	104.45(5)
<b>91b</b>	2.041(1)	1.864(3)	105.9(1)
<b>92a</b>	2.062(1)	1.785(1)	103.0(1)
<b>92b</b>	2.055(1)	1.797(1)	102.6(1)
<b>93</b>	2.0369(5), 2.0423(4)	1.8853(8), 1.8853(8)	106.10(3), 106.56(3)
<b>94</b>	1.997(6)		
<b>95</b>	2.045(1)	2.439(1)	95.43(4)
<b>96b</b>	2.053(2)		73.54(4)
<b>97a</b>	2.1684(7)		
<b>97b</b>	2.1340(12)		
<b>98a</b>	2.1826(7)	1.8548(13)	108.39(5)
<b>98b</b>	2.1699(5)	1.8548(13), 1.8495(13)	108.88(4), 112.53(4)
<b>99</b>	2.037(1)	2.340(1)	99.04(3)

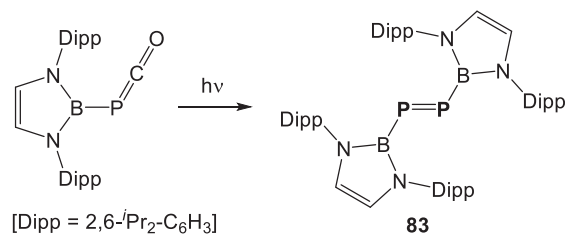
compounds of heavier Group 15 elements has rapidly expanded by using steric protection of bulky substituents. Thus, the concept of kinetic stabilization by sterically demanding substituents provided a breakthrough in the field of multiple bonded compounds based on heavier Group 15 elements. This section covers recent progress for substantial synthesis of diphosphenes and their structural information as summarized in **Table 1**.

The first stable boryl-substituted diphosphene derivative was successfully synthesized by Yamashita and coworkers.<sup>161</sup> Reductive coupling reaction of boryldichlorophosphine precursor with magnesium metal afforded boryl-substituted diphosphene **82** in 47% yield. In the <sup>31</sup>P NMR spectrum in C<sub>6</sub>D<sub>6</sub>, two magnetically equivalent phosphorus nuclei were observed at +605 ppm, which are comparable, albeit slightly low-field-shifted, to the resonances of carbon-substituted *trans*-diphosphenes (477–600 ppm). Furthermore, the solid-state structure of **82** was determined by single-crystal X-ray diffraction analysis. The P–P bond of 2.0655(17) Å is slightly longer than those of previously reported carbon-substituted diphosphenes (1.985–2.051 Å). The five-membered rings containing a boron atom are oriented almost perpendicular to the planar B–P=P–B moiety (**Scheme 31**).

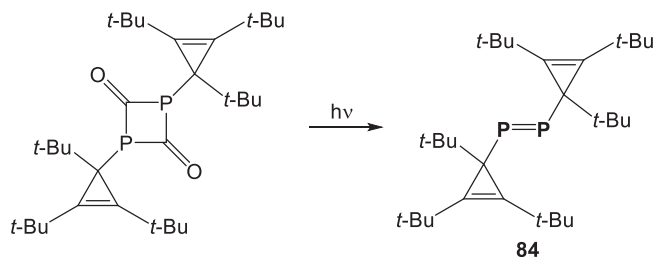
Goicoechea and coworkers reported that photolysis converted boryl-substituted phosphaketene to 2,3-dihydro-1*H*-1,3,2-diazaboryl-substituted diphosphene **83**.<sup>162</sup> The <sup>31</sup>P NMR spectrum showed a singlet resonance at 596.0 ppm. Orange crystals of **83** suitable for single crystal X-ray diffraction could be obtained by cooling a concentrated hexane solution of the product. The single crystal X-ray structural analysis reveals a diphosphene with a relatively short P–P bond distance of 2.027(1) Å, which is in line with the expected distance for a P=P double bond (**Scheme 32**).

Slootweg reported that diphosphetanedione derivative is converted to cyclopropenyl-substituted diphosphene **84** in 99% yield upon UV irradiation.<sup>163</sup> The <sup>31</sup>P NMR spectrum exhibited a signal at +585.3 ppm. The molecular structure of **84**, determined by

**Scheme 31**



Scheme 32

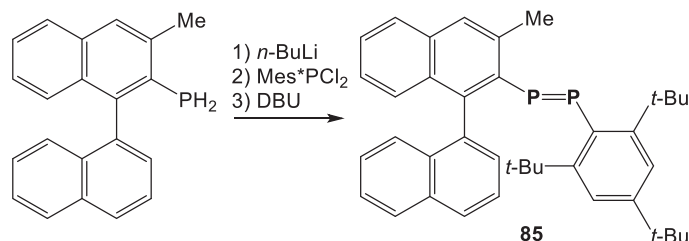


Scheme 33

a single-crystal X-ray analysis, shows a centrosymmetric diphosphene with the P–P and P–C bond lengths of 2.0210(6) and 1.8778(12) Å, respectively (Scheme 33).

Tsurusaki and Kamikawa reported that diphosphene **85** possessing an axially chiral 1,1'-binaphthyl moiety was synthesized.<sup>164</sup> Enantiomerically pure substrate can be converted into diphosphene **85** without any loss of enantiomeric purity (Scheme 34).

Bertrand and co-workers demonstrated that bis-phosphinidene unit stabilized by imidazol-2-yl carbene could be isolated.<sup>165</sup> Since then, persistent unsaturated species with *N*-heterocyclic carbenes based on heavier Group 15 elements have been synthesized.

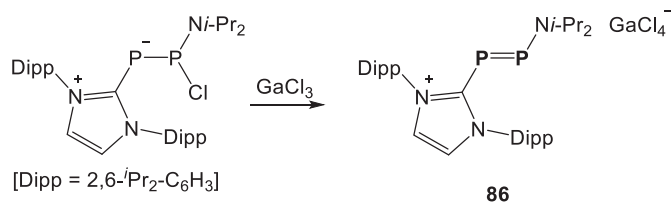


Scheme 34

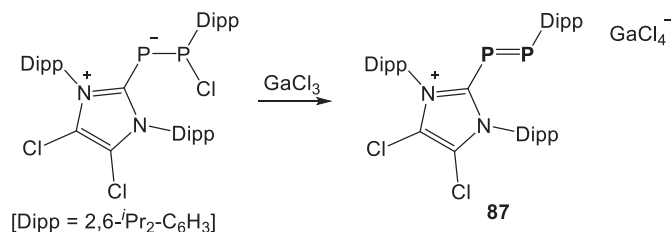
Grützmacher<sup>166</sup> and Weigand<sup>167</sup> independently reported synthesis and structural characterization of NHC-substituted diphosphenes **86** and **87**, respectively. They succeeded in the formation of a P=P double bond via a chloride abstraction of the corresponding chlorodiphosphanide precursor. Treatment of precursors with GaCl<sub>3</sub> afforded diphosphene **86** or **87**, respectively. The <sup>31</sup>P NMR spectrum of diisopropylamino-substituted diphosphene **86** showed two coupled doublets (*J* = 525 Hz) at 492.1 and 158.1 ppm. In the molecular structure of **86**, the P–P distance of **86** was 2.0611(7) Å, being slightly longer than those of previously reported carbon-substituted diphosphenes. In the case of **87**, the <sup>31</sup>P NMR spectrum showed an AX spin system at 398.1 (P<sub>A</sub>) and 605.8 (P<sub>X</sub>) ppm with <sup>1</sup>*J*<sub>PP</sub> = –577.9 Hz. The P<sub>A</sub> and P<sub>X</sub> can be assigned to the imidazoliumyl- and the imidazolyl-substituted phosphorus atoms, respectively. The molecular structure of **87** revealed, the P–P bond length (2.038(1) Å) typical for diphosphenes. The C–P–P angle involving the imidazoliumyl-substituent (C–P–P: 105.0(1)1°) is larger than that involving the Dipp-substituent (C–P–P 95.1(1)1°). This might be a result of a higher degree of π-bonding interactions involving the more electron withdrawing imidazoliumyl-group, or the large steric demand of the imidazoliumyl-substituent (Schemes 35 and 36).

*N*-Heterocyclic carbene coordinated diphosphene **88** was also prepared by chloride abstraction from the corresponding singly-bonded derivative with GaCl<sub>3</sub>.<sup>168</sup> The <sup>31</sup>P NMR spectrum of **88** exhibited a higher-order AB spin system at 438.5 and 440.1 ppm with 543 Hz. The solid-state structure of diphosphene **88** was confirmed by X-ray crystallographic analysis. The P–P bond length of 2.1897(4) Å falls in a range for the reported diphosphenes (Scheme 37).

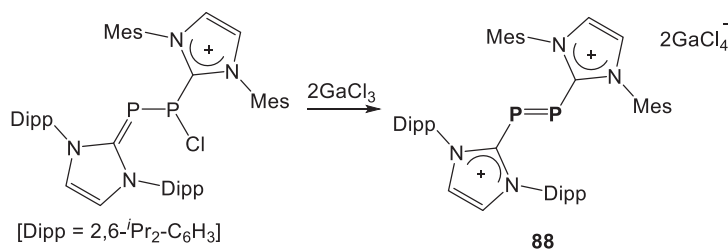
Tamm and coworkers reported that diphosphenes **89** and **90** bearing *N*-heterocyclic carbenes were synthesized by a chloride abstraction by the reduction with magnesium powder or by Lewis acid, respectively.<sup>169,170</sup> The <sup>31</sup>P NMR spectrum of **89** revealed a broad signal at very low field (+434 ppm), which is characteristic of sterically protected diaryldiphosphenes. In the solid-state structure, diphosphene **89** exhibit the typical (*E*)-geometry with the P–P bond length of 2.0530(5) Å. In the case of **90**, The <sup>31</sup>P



Scheme 35



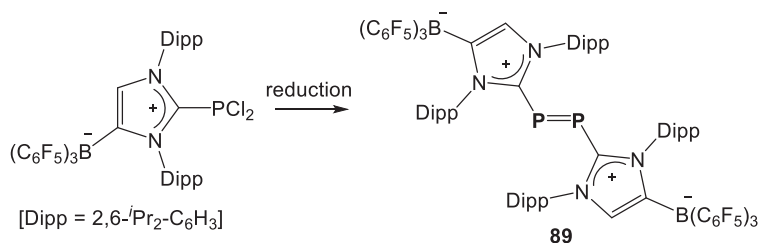
Scheme 36



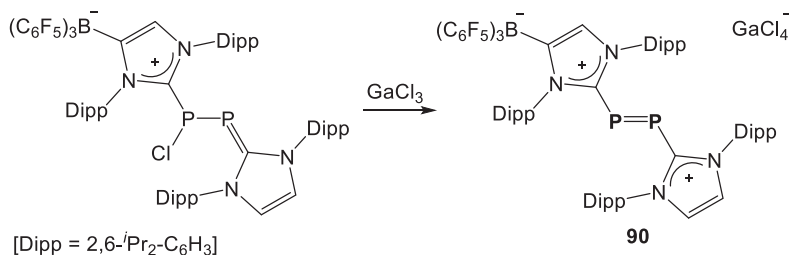
Scheme 37

NMR spectrum in  $\text{THF-}d_8$  showed two doublets at 403 and 456 ppm ( $J = 554$  Hz). The molecular structure for **90** was determined by XRD analysis. The P–P length is 2.0565(9) Å, which is comparable to those of reported diphosphenes (Schemes 38 and 39).

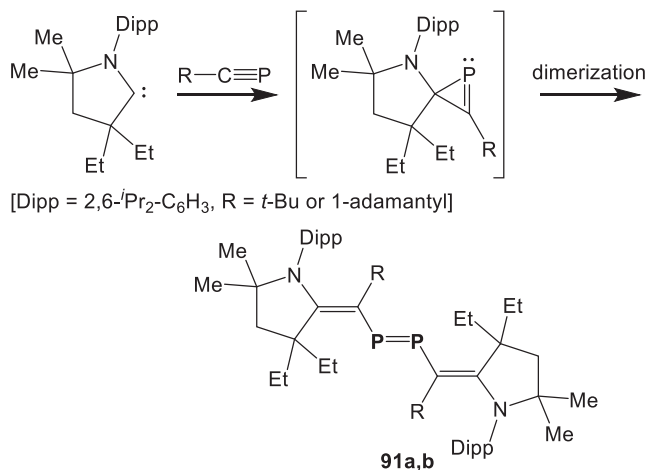
Stephan reported that reaction of a *N*-heterocyclic carbene with three equivalents of *t*-Bu-substituted phosphalkyne afforded vinyl-substituted diphosphenide **91a** as purple crystals in 74% yield.<sup>171</sup> In the case of the reaction with 1-adamantyl-substituted



Scheme 38



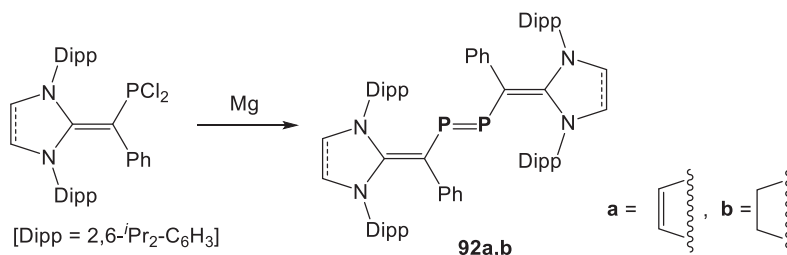
Scheme 39



Scheme 40

phosphaalkyne, diphosphene **91b** was also isolated as pink powder in 68% yield. The <sup>31</sup>P NMR spectra of **91a** and **91b** in CDCl<sub>3</sub> exhibited resonances at 530.1 and 524.0 ppm, respectively. The molecular structures were unambiguously confirmed by single crystal X-ray diffraction. The P–P bond lengths of **91a** and **91b** exhibited 2.0453(6) and 2.041(1) Å, respectively, which are in the typical range of diphosphenes (Scheme 40).

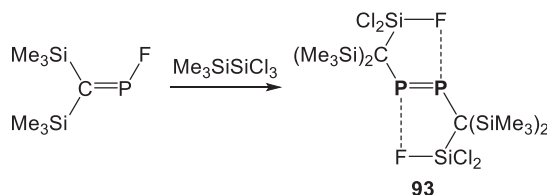
Ghadwal and coworkers reported synthesis and characterization of new divinylidiphosphene compounds.<sup>172</sup> Reduction of dichlorovinylphosphanes with magnesium leads to the formation of divinylidiphosphenes **92a** and **92b** as crystalline solids. The <sup>31</sup>P{<sup>1</sup>H} NMR spectrum of each of **92a** (+380 ppm) and **92b** (+414 ppm) exhibits a signal characteristic for the reported diphosphenes. Molecular structures of **92a** and **92b** were determined by single-crystal X-ray diffraction studies, which reveal their *trans*-configurations along the P=P bonds. The P–P bond lengths of 2.062(1) (92a) and 2.055(1) Å (92b), which are in the typical range of diphosphenes (Scheme 41).



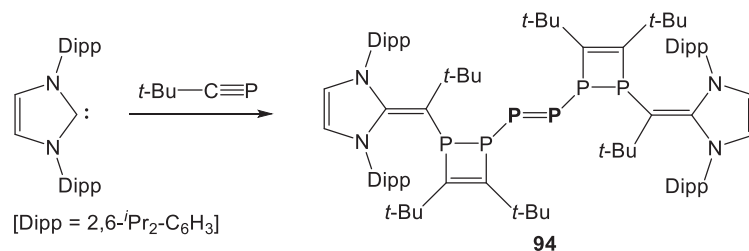
Scheme 41

New *C*-dichlorofluorosilyl-functionalized dialkyldiphosphene was also synthesized by Jones, du Mont and coworkers.<sup>173</sup> Treatment of fluorophosphaalkene with 1,1,1-trichloro-2,2,2-trimethylsilane in pentane at 40 °C finally afforded diphosphene **93** bearing silylmethyl groups. The <sup>31</sup>P NMR spectrum of **93** exhibited four lines at +560.1 ppm as an AA'XX' system with *J*<sub>PF</sub> = 100.3 Hz. The solid-state structure of **93** exhibited intramolecular P⋯F–Si contacts. The P–P bond lengths of **93** are 2.0369(5) and 2.0423(4) Å, which are in a range of those for the reported carbon-substituted diphosphenes (Scheme 42).

Stephan and coworkers synthesized a new di-1,2-dihydro-1,2-diphosphete-substituted diphosphene by oligomerization of phosphalkynes mediated by bulky *N*-heterocyclic carbenes.<sup>174</sup> Reaction of a phosphalkyne with *N*-heterocyclic carbene afforded di-1,2-dihydro-1,2-diphosphete-substituted diphosphene **94** as purple crystals (Scheme 43).

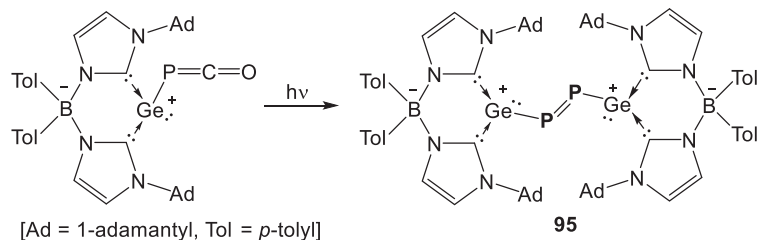


Scheme 42



Scheme 43

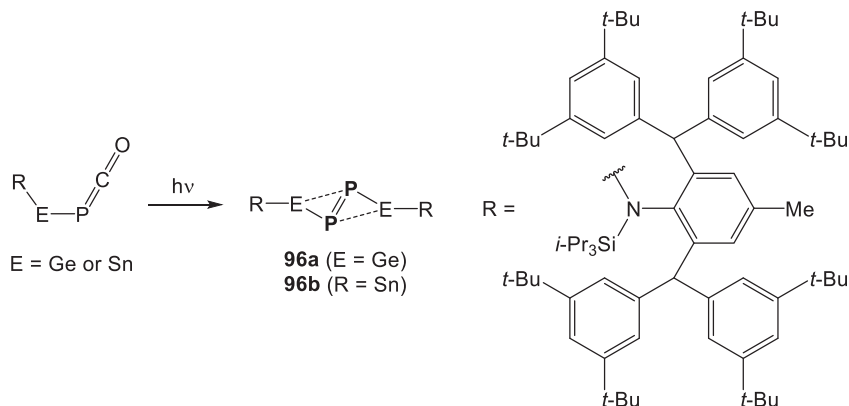
A germyliumylidene-substituted diphosphene was synthesized by Driess and coworkers.<sup>175</sup> Photolysis of phosphaketonylgermyliumylidene borate with UV for 2 h at room temperature afforded bis(germyliumylidene)diphosphene **95** as deep red crystals in 10% yield. Diphosphene **95** is insoluble in common organic solvents and no solution NMR data could be obtained. In the solid-state, <sup>31</sup>P NMR spectrum of **95** exhibited a singlet signal at 903.5 ppm, which is strongly shifted downfield compared with those of other reported diphosphene species. The observed low-field shift indicates strong electron-withdrawing property of the germyliumylidene moieties of **95**. The molecular structure of **95** was determined by single-crystal X-ray diffraction analysis. The P–P bond length is 2.045(1) Å, which is slightly longer than those of previously reported carbon-substituted diphosphenes (1.985–2.051 Å) (Scheme 44).



Scheme 44

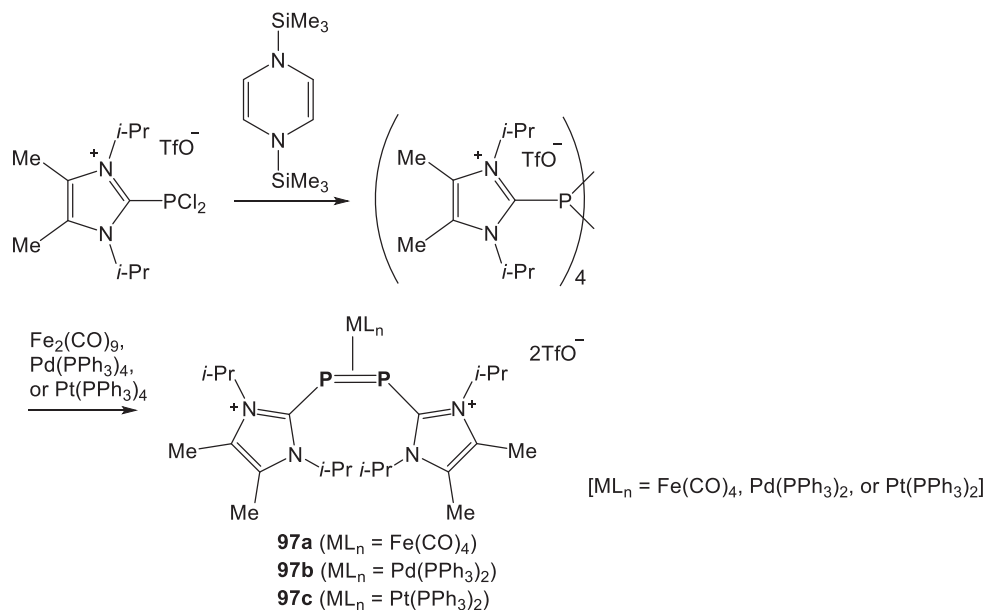
Photolysis of germylenyl- and stannylenyl-phosphaketenes stabilized with sterically hindered groups afforded diphosphenes **96a** and **96b**, respectively.<sup>160</sup> The <sup>31</sup>P NMR resonances were found at +745.7 (**96a**) and +797.8 ppm (**96b**), which are characteristically downfield shifted as is typical for diphosphene derivatives. The single crystal diffraction experiment of **96b** confirmed the presence of a diphosphene-type structure with a typical short P–P distance of 2.053(2) Å (Scheme 45).

New diphosphene-iron, palladium, and platinum complexes were also synthesized by Weigand and coworkers.<sup>176</sup> A sequence of reduction of dichlorophosphine precursor and reaction with transition metal complexes such as Fe<sub>2</sub>(CO)<sub>9</sub>, Pd(PPh<sub>3</sub>)<sub>4</sub>, and Pt(PPh<sub>3</sub>)<sub>4</sub> afforded diphosphene-metal complexes **97a–c**. The molecular structures of **97a–c** were confirmed by X-ray crystallographic analysis. In the solid-state, the η<sup>2</sup>-coordination of the corresponding metal by the diphosphene ligand is observed. In the cases of **97b** and **97c**, Pd/Pt atoms are in a distorted square-planar bonding environment. In addition, complexes **97a–c** reveal that the imidazoliumyl-substituents of the diphosphene ligand are arranged in a *trans*-configuration with the C–P–P–C of



Scheme 45

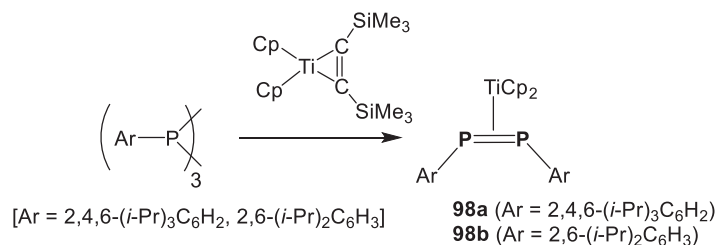




Scheme 46

149.205(1)° (**97a**)/148.393° (**97b**)/147.088° (**97c**). The P–P bond lengths are only marginally shorter (2.1340(12) Å for **97b** and 2.1562(9) Å for **97c**) compared to that of complex **97a** (2.1684(7) Å) (Scheme 46).

In 2019, new  $\eta^2$ -diphosphene titanocene complex was synthesized from a cyclic triphosphane precursor.<sup>177</sup> Diphosphene–titanium complexes **98a** and **98b** were prepared by the reaction of the corresponding triphosphane with titanium bis(trimethylsilyl) acetylene complex in benzene. In  $C_6D_6$  solution, the  $^{31}P$  NMR spectra of **98a** and **98b** showed signals at 290.7 and 283.8 ppm, respectively, which are high-field shifted as compared with that of *trans*-diphosphene Tip–P=P–Tip (Tip = 2,4,6-*i*Pr<sub>3</sub>C<sub>6</sub>H<sub>2</sub>) (517.4 ppm, in  $C_6D_6$ ).<sup>177</sup> In the crystal structures, the aryl groups of **98a**/**98b** are oriented in a *trans*-conformation. Complexes **98a** and **98b** showed the P–P distance of 2.1826(7) and 2.1699(5) Å, respectively, which are intermediate between the typical P–P single and double bonds. This structural feature can be explained by the  $\pi$ -back-donation from d-orbitals of the metal into the  $\pi^*$ -orbital of the P=P unit (Scheme 47).



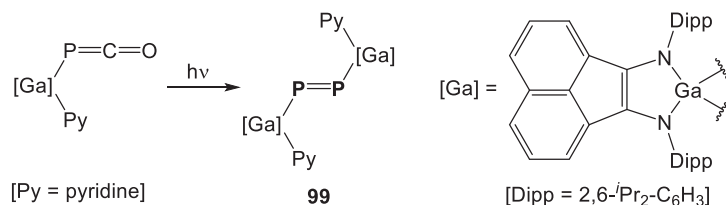
Scheme 47

Goicoechea and co-workers reported that gallium carbenoid-substituted diphosphene **99** was synthesized by UV-promoted decarbonylation of phosphaketene derivative using a 600 W broadband UV lamp.<sup>178</sup> Diphosphene **99** displayed a  $^{31}P$  NMR resonance at +596.2 ppm. The solid-state structure showed that the P–P bond distance of 2.037(1) Å is in the expected range of a double bond and the Ga–P distance of 2.340(1) Å is consistent with a single bond. The Ga–P–P bond angle of 99.04(3)° is comparable to that of boryl-substituted diphosphene **84** (Scheme 48).

### 1.03.4.3 Heavier dipnictene derivatives

In this section, examples of stable diphosphene and their heavier congeners such as arsaphosphene, diarsene, distibene and dibismuthene are discussed.

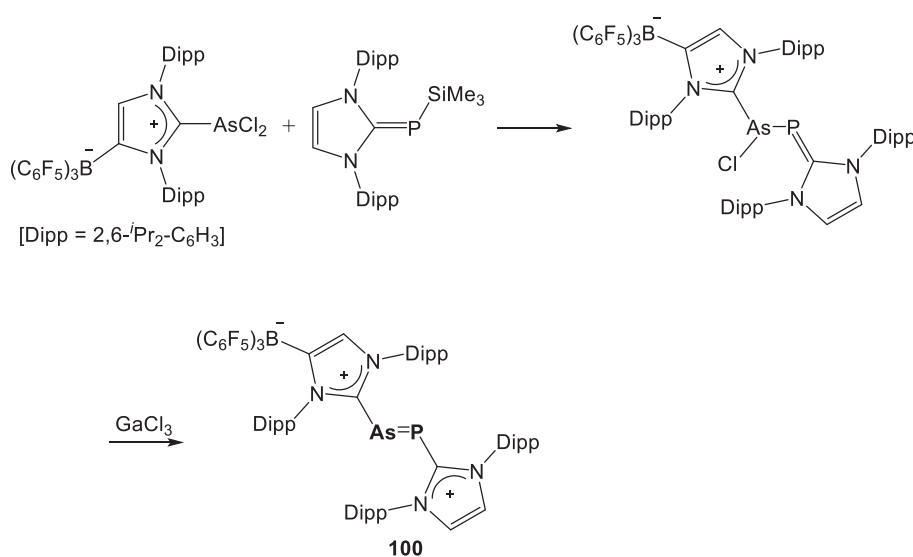
New arsaphosphene **100** bearing *N*-heterocyclic carbenes was prepared by chloride abstraction from the corresponding As–P single bond derivative with GaCl<sub>3</sub>.<sup>170</sup> The  $^{31}P$  NMR spectrum of **100** exhibited a broad singlet at 456 ppm. The  $^1H$  NMR spectrum



Scheme 48

of **100** showed signals at 7.78 and 8.64 ppm for the protons of the *N*-heterocyclic carbene units. The solid-state structures of arsa-phosphene **100** were confirmed by X-ray crystallographic analysis. The As–P bond length of 2.1577(7) Å falls in a range for the reported arsa-phosphenes such as Mes\*–P=As–Mes\* (2.141(5) Å, Mes\* = 2,4,6-*t*Bu<sub>3</sub>-C<sub>6</sub>H<sub>2</sub>), Mes–P=As–(2,6-Tip<sub>2</sub>C<sub>6</sub>H<sub>3</sub>) (2.134(2) Å), and Mes\*–P=As–CH(SiMe<sub>3</sub>)<sub>2</sub> (2.125(1) Å) (Scheme 49).

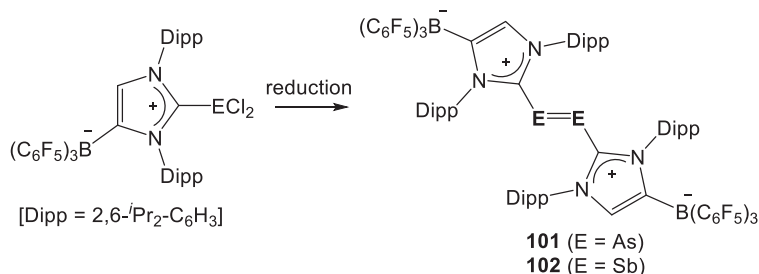
Diarsene **101** and distibene **102** bearing *N*-heterocyclic carbenes were also synthesized by Tamm and co-workers.<sup>169</sup> Dihalogenated compounds were employed for the preparation of the corresponding diarsene and distibene species by reductive coupling



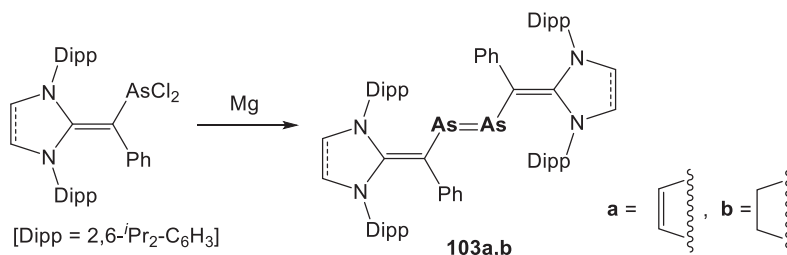
Scheme 49

reaction. The molecular structures of **101** and **102**, were established by X-ray diffraction analysis, and they exhibited the typical (*E*)-geometry. The As–As and Sb–Sb bond lengths are 2.2882(8) and 2.6632(3) Å, which are in good agreement with known diarsene and distibene compounds such as Mes\*–As=As–Mes\* (2.2634(3) Å), (2,6-Mes<sub>2</sub>C<sub>6</sub>H<sub>3</sub>)–E=E–(2,6-Mes<sub>2</sub>C<sub>6</sub>H<sub>3</sub>) (2.276(3) Å; E=As, 2.668(2) Å; E=Sb), (2,6-Trip<sub>2</sub>C<sub>6</sub>H<sub>3</sub>)E=E(2,6-Trip<sub>2</sub>C<sub>6</sub>H<sub>3</sub>) (2.285(3) Å; E=As, 2.668(2) Å; E=Sb), Tbt–Sb=Sb–Tbt (2.642(1) Å, Tbt = 2,4,6-[(Me<sub>3</sub>Si)<sub>2</sub>CH]<sub>3</sub>C<sub>6</sub>H<sub>2</sub>), and Tbb–Sb=Sb–Tbb (2.6677(3) Å, Tbb = 4-*t*Bu-2,6-[(Me<sub>3</sub>Si)<sub>2</sub>CH]<sub>3</sub>C<sub>6</sub>H<sub>2</sub>) (Scheme 50).

Ghadwal reported synthesis of the first divinyl-diarsenes **103a,b** by magnesium reduction of the corresponding dichloroarsines.<sup>179</sup> The molecular structures of **103a,b** were established by X-ray diffraction analysis. Both exhibit a *trans*-geometry along



Scheme 50



Scheme 51

the As=As double bond and the C–As–As–C unit is planar. The As=As bond lengths of **103a** (2.296(3) Å) and **103b** (2.290(1) Å) compare well with those of the known diarsenes (2.276(3)–2.358(4) Å).

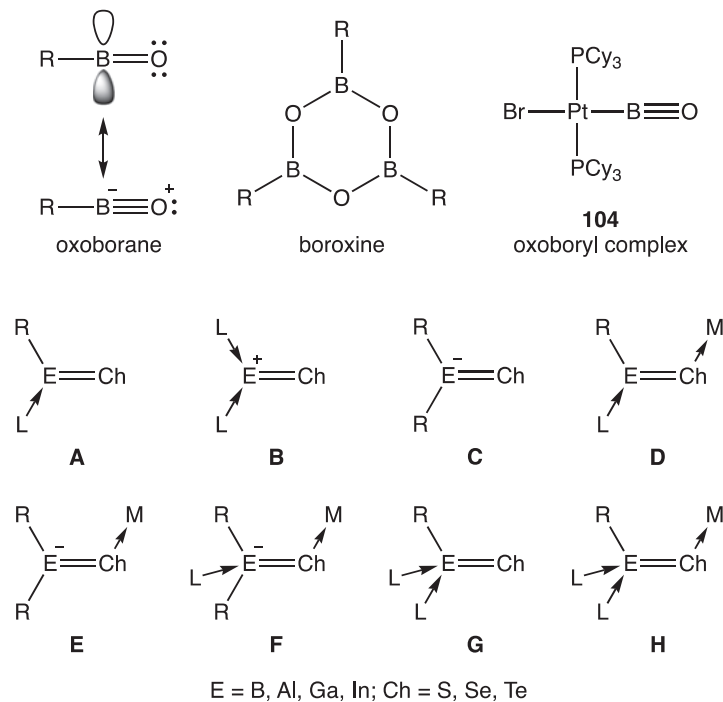
Since 2016, many research groups approached diphosphenes and their heavier analogues possessing a doubly-bonded system, new dipnictenes were involved in the field of chemistry of low-coordinate heavier Group 15 elements, which will be linked to the discovery of new applications (Scheme 51).

### 1.03.5 Low-coordinate compounds of heavier group 16 elements

Heavier group 16 elements in nature mainly bound to metal atoms in minerals. Elemental sulfur is produced as a volcanic product. Elemental selenium and tellurium are produced as by-products of metal refining. Besides, there are numerous organic sulfur, selenium, and tellurium compounds, and they have a wide range of applications. For example, thiourea with a double bond between carbon and sulfur atoms is an excellent synthetic raw material for resins, pharmaceuticals, and agricultural chemicals. In addition, the elemental heavier group 16 elements are widely used for trapping reaction of low-valent p-block element species to afford polarized double bonds such as  $E^{\delta+}=Ch^{\delta-}$  (Ch=S, Se, Te). Herein, we will discuss the synthesis and structural features of p-block element species containing multiple bonding to heavier group 16 elements.

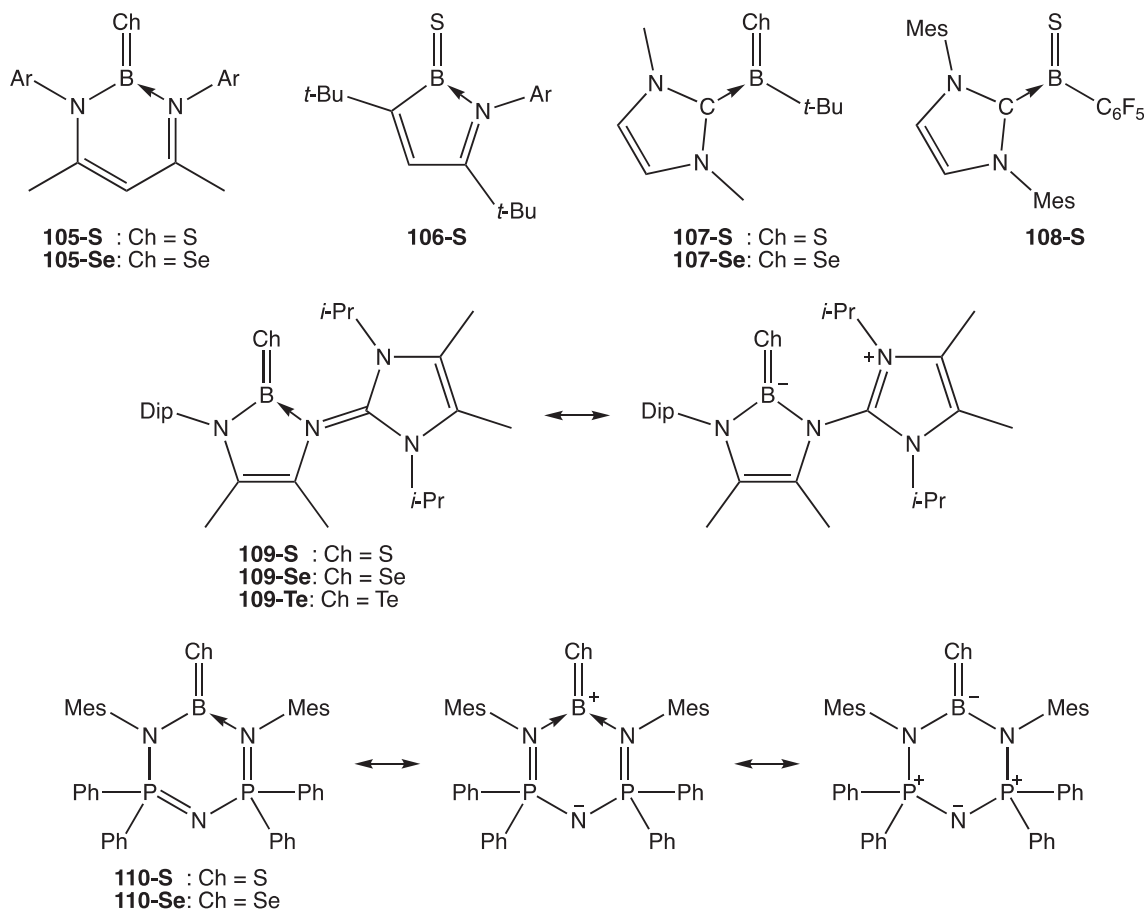
#### 1.03.5.1 Multiple bonds between group 13 element and heavier group 16 element

The multiple bonds between group 13 element and group 16 element are highly polarized due to the large difference in their electronegativities, providing aggregates to balance the polarity. Monomeric oxoboranes (R–B=O, R = monoanionic substituent) and



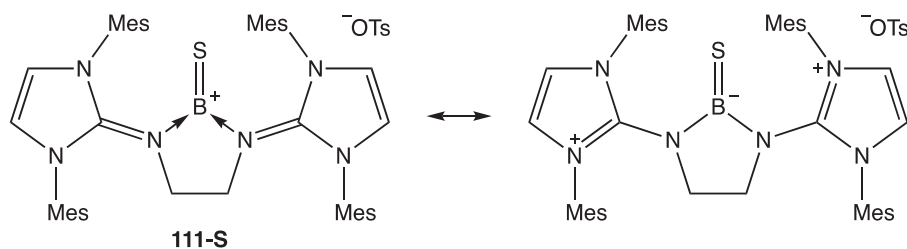
Scheme 52

their heavy analogues ( $R-B=Ch$ ,  $Ch=S$ ,  $Se$ ,  $Te$ ) are labile and elusive under normal laboratory conditions.<sup>180</sup> Only platinum oxoboryl complexes ( $[Pt]-B=O$ , **104**, **Scheme 52**) are structurally characterized as  $R-B=X$  ( $X=O$ ,  $S$ ,  $Se$ ,  $Te$ ) monomers.<sup>181</sup> Because heavier analogues  $R-E=Ch$  ( $E=B$ ,  $Al$ ,  $Ga$ ,  $In$ ) of oxoboranes also easily dimerize/oligomerize, the isolation of their monomeric states requires fine molecular design. Fundamental concepts for the isolation of  $R-E=Ch$  monomers containing multiple bonds between group 13 element and group 16 element are illustrated in **Scheme 52**.<sup>182</sup> Lewis base ligand(s) ( $L$ ) on group 13 element center complement the electron deficiency on the element ( $A$ ,  $B$ ,  $D$ ,  $F$ ,  $G$ , and  $H$ ). Metals, Lewis acids, and Brønsted acids ( $M$ ) quench the negative charge on chalcogen atoms ( $D$ ,  $E$ ,  $F$ , and  $H$ ). Sterically hindered and/or electron-donor groups attached on group 13 element also contribute to prevent the aggregation of  $R-E=Ch$  monomers. Types  $F-H$  have been especially applied for the combination of heavier group 13 and group 16 element.<sup>183–185</sup> In this section, types  $A-C$  containing multiple bonds between group 13 element and heavier group 16 element are focused on, where group 13 element possess the trigonal-planar geometry and only chalcogen atoms bound for group 13 element.



**Scheme 53** Examples of neutral  $R-E=Ch$  monomers. Ar = 2,6-Me<sub>2</sub>C<sub>6</sub>H<sub>3</sub>; Mes = 2,4,6-Me<sub>3</sub>C<sub>6</sub>H<sub>2</sub>.

Types  $A$ ,  $B$ , and  $C$  are classified into neutral,<sup>186</sup> cationic,<sup>187</sup> and anionic<sup>188</sup>  $R-E=Ch$ , respectively. In 2010, Cui and coworkers reported the first isolable monomeric thioxo- and selenoxoboranes **105** with type  $A$  form (**Scheme 53**).<sup>186a</sup> The bond lengths of  $B-S$  (1.741(2) Å) and  $B-Se$  (1.896(4) Å) were significantly shorter than those of  $B-S$  and  $B-Se$  single bonds. The  $B$  atoms had trigonal-planar geometries. The  $B=S$  double bond character was supported by theoretical calculations. Thioxoborane **106** was prepared by desulfurization of boron polysulfides.<sup>186b</sup> The <sup>11</sup>B NMR signal was observed at 50.3 ppm which was downfield-shifted relative to **105-S** (36.79 ppm), indicating the increase of  $B$  and  $S$  bond order due to decreasing the number of  $\pi$ -donor ligands on  $B$  atom. This trend was also observed for carbene coordinated acyclic thioxo- and selenoxoboranes **107**. The  $B-S$  (1.739(2) Å, **107-S**) and  $B-Se$  (1.876(4) Å, **107-Se**) bonds were slightly shorter than those of **105-S** and **105-Se**, and the <sup>11</sup>B NMR signals were observed at 66.4 and 73.5 ppm for **107-S** and **107-Se**, respectively.<sup>186c</sup> For **108-S**, the  $B-S$  bond length was shortened to 1.714(2) Å.<sup>186d</sup> Strong  $\pi$ -donating  $N$ -heterocyclic imine (NHI) ligand stabilized neutral  $R-B=Ch$  in Lewis acid absent form (**109**), shifting their <sup>11</sup>B NMR signals to 35.2 (**109-S**) and 35.8 (**109-Se**).<sup>186e,g</sup> For compound **109**, both of canonical structures

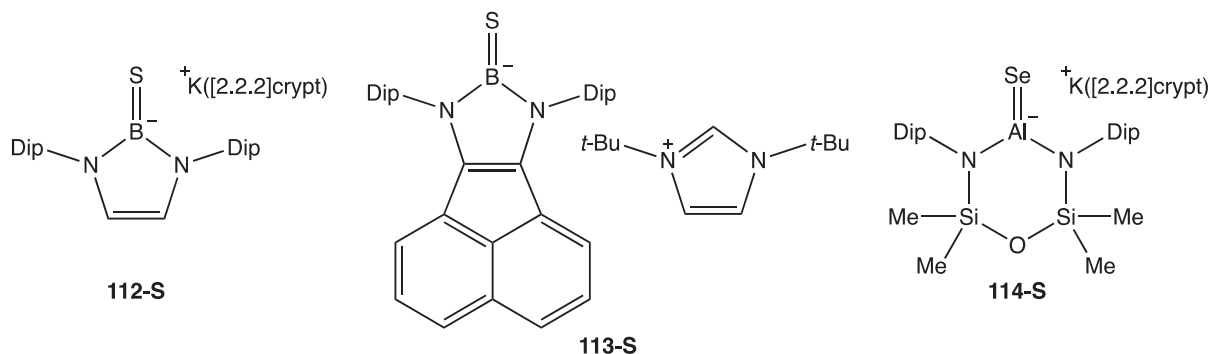


**Scheme 54** An example of cationic R–E=Ch monomer.

corresponding to types A and C can be considered. Multiple canonical structures (types A–C) were considered for **110** bearing bis(phosphinimino)amide ligand.<sup>186f</sup>

In 2014, Inoue and co-workers reported cationic thioxoborane **111-S** by using NHI ligands, which complied with stabilization type B and C (**Scheme 54**).<sup>187</sup> The B–S (1.710(5) Å) bond length was comparable to that of **108-S**, in contrast, the <sup>11</sup>B NMR signal was observed at 33.9 ppm which was up-field-shifted relative to that of **109-S** bearing one NHI ligand.

Anionic R–E=Ch monomers (type C in **Scheme 52**) were obtained in their separated ion-pair form (**Scheme 55**). Thioxoborane anion **112-S**, isoelectronic with thiourea, was reported by Aldridge and co-workers.<sup>188a</sup> The B–S (1.774(1) Å) bond was longer than

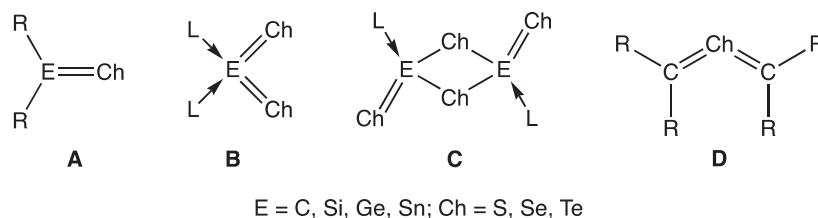


**Scheme 55** Examples of anionic R–E=Ch monomers. Crypt = cryptand; Dip = 2,6-*t*-Pr<sub>2</sub>C<sub>6</sub>H<sub>3</sub>.

those found in neutral and cationic thioxoborane monomers (**Schemes 53 and 54**). The <sup>11</sup>B NMR signals was observed at 33.1 ppm which was comparable to **111-S**. For thioxoborane anion **113-S**, bearing the acenaphthene-annulated 1,3,2-diazaborole skeletal, the B–S bond length was shortened to 1.7682(17) Å, and the <sup>11</sup>B NMR signals was observed at 36.3 ppm.<sup>188b</sup> The heavier analogue of carbonyl moiety containing an Al–Se bond was reported by Coles and coworkers (**114-Se**).<sup>188c</sup> The Al–Se (2.2032(6) Å) bond length was comparable to the calculated value for the sum of the covalent molecular double bond radii,  $r_2$  ( $\sum(r_2) = 2.20$  Å),<sup>189</sup> and significantly shorter than those of Al–(μ-Se)–Al group (2.319(1) Å) in which Al atoms had trigonal-planar geometries.<sup>190</sup> The <sup>77</sup>Se NMR signal (–563 ppm) was up-field-shifted relative to those of **105-Se** (–195.6 ppm),<sup>186a</sup> terminal Al–SeH (–419 to –339 ppm),<sup>191</sup> and Al–(μ-Se)–Al group (–535 to –414 ppm) in which Al atom had tetrahedral geometry.<sup>191</sup>

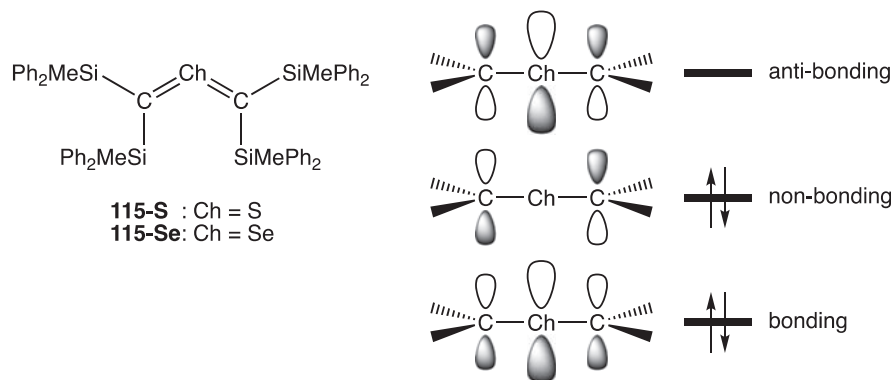
### 1.03.5.2 Multiple bonds between group 14 element and heavier group 16 element

Oxidation of low-valent group 14 species by elemental chalcogens provides multiple bonds between group 14 elements and heavier group 16 elements, and the multiply bonded species have been isolated even if no metals and Lewis acids are attached on terminal group 16 elements (**Scheme 2, A–D**).



**Scheme 56**



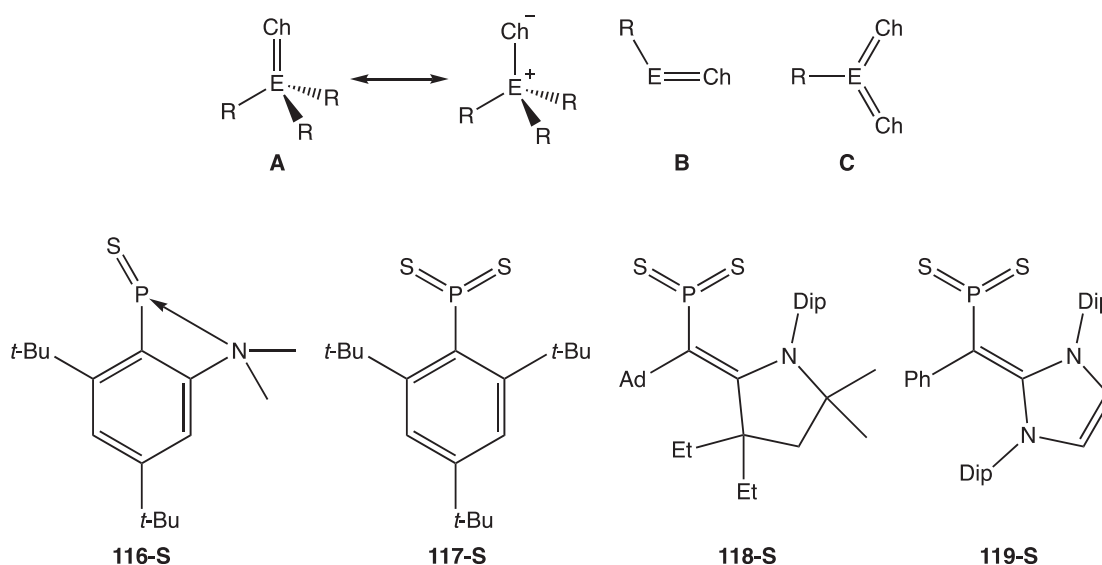


Scheme 57

Heavier analogues  $\text{R}_2\text{E}=\text{Ch}$  ( $\text{E}=\text{C}, \text{Si}, \text{Ge}, \text{Sn}$ ;  $\text{Ch}=\text{S}, \text{Se}, \text{Te}$ ; **Scheme 56, A**) of carbonyl compound ( $>\text{C}=\text{O}$ ) can be obtained by trapping reaction of in situ generated tetrylene ( $>\text{E}$ ) with elemental chalcogens.<sup>192,193</sup> For examples, a variety of chalcogenour-eas have been prepared from N-heterocyclic carbenes (NHC) and elemental chalcogens, which have been applied as a ligand for main-group elements and transition metals.<sup>192,194</sup> It is worth noting that the  $\pi$ -acceptor properties of carbenes can be experimentally estimated by measuring the  $^{77}\text{Se}$  NMR chemical shifts of their selenium adducts.<sup>194,195</sup> In contrast, there are still a few reports on isolable heavier ketone analogues consisting of heavier group 14 and heavier group 16 elements, the details are described in **Section 1.03.3** and recent review papers.<sup>192,193</sup> Oxidation of zero-valent heavier group 14 species afford B and C, which can be viewed as heavier congeners of  $\text{SiO}_2$  monomers and dimers, respectively (**Scheme 56**).<sup>196–198</sup> Heterocumulenes  $\text{R}_2\text{C}=\text{Ch}=\text{CR}_2$  ( $\text{Ch}=\text{S}, \text{Se}$ ) containing heavier group 16 elements have been also obtained from the reaction of carbenoid and elemental chalcogens (**Scheme 56, D**).<sup>199</sup> Sugamata and coworkers reported heterocumulenes 115 containing internal  $\text{C}=\text{Ch}=\text{C}$  multiple bonds with bent geometries (**Scheme 57**). The multiple bond characters were caused by the three-center four-electron ( $3c-4e$ )  $\pi$ -bond. The heterocumulenes 115 reacted with  $\text{AuCl}(\text{SMe}_2)$  to afford dinuclear (chalcogeno)(silyl)carbene gold(I) complexes with an accompanying elimination of  $\text{MePh}_2\text{SiCl}$ .<sup>199c</sup>

### 1.03.5.3 Multiple bonds between group 15 element and heavier group 16 element

Covalently bonded compounds of heavier group 15 element and heavier group 16 element have been investigated as molecular precursors of binary materials  $\text{E}_2\text{Ch}_3$  ( $\text{E}=\text{Sb}, \text{Bi}$ ;  $\text{Ch}=\text{S}, \text{Se}, \text{Te}$ ).<sup>200</sup> The multiply bonded heavier group 15 and 16 compounds can be classified into types A–C as monomers (**Scheme 58**). The compounds of type A are well-known and can be obtained by the reaction of  $\text{R}_3\text{E}$  ( $\text{E}=\text{P}, \text{As}, \text{Sb}, \text{Bi}$ ) with elemental chalcogen to afford  $\text{R}_3\text{E}=\text{X}$  ( $\text{E}=\text{P}, \text{As}, \text{Sb}$ ;  $\text{X}=\text{O}, \text{S}, \text{Se}, \text{Te}$ ), in which the double bonds  $\text{R}_3\text{E}=\text{X}$  are (partially) polarized  $\text{R}_3\text{E}^+-\text{X}^-$ .<sup>201</sup> The multiply bonded group 15 and 16 compounds  $\text{R}-\text{E}=\text{Ch}$  (type B) are labile and elusive. In 1993, Yoshifuji and coworkers reported phosphinothioylidene 116-S by using the bulky substituent and

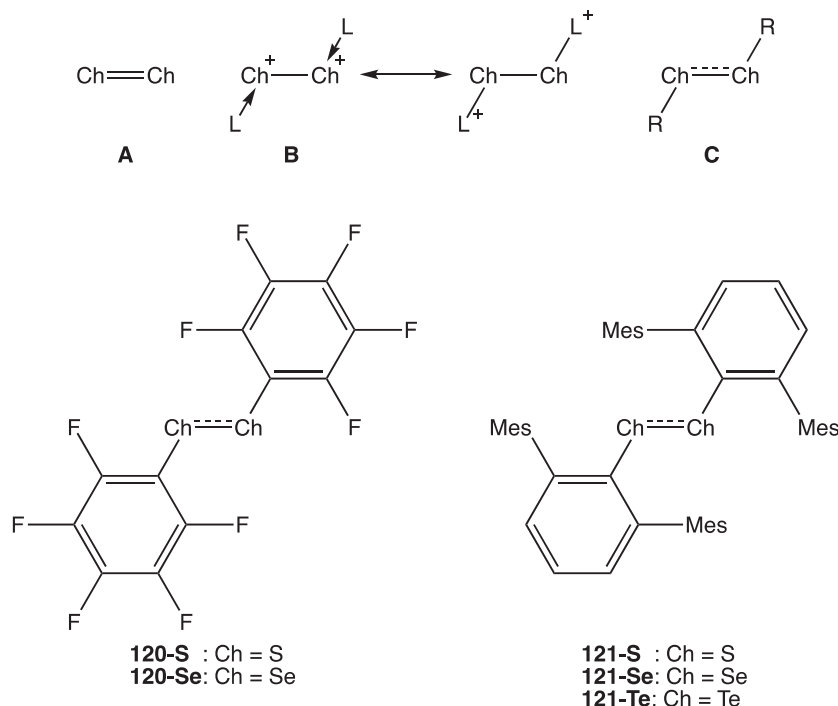


Scheme 58

the intramolecular coordination to P center.<sup>202</sup> Pincer type ligands have also been applied to stabilize R–E=Ch form as monomers.<sup>203</sup> Organodithioxophosphoranes R–P(=S)<sub>2</sub> (type C) were isolated without ligand coordination(s) (117-S, 118-S, and 119-S).<sup>204</sup> In contrast, for Se analogues, only ligand-coordinated (L)R–P(=Se)<sub>2</sub> have been isolated and structurally determined.<sup>205</sup> These differences are most likely due to polarization of  $\pi$ -bond caused by poor  $\pi$ -overlap between P and Se atoms.

### 1.03.5.4 Multiple bonds between group 16 element and heavier group 16 element

Elemental chalcogens form several allotropes in Ch<sub>n</sub> (Ch=S, Se, Te) states. Although multiply bonded diatomic Ch=Ch



**Scheme 59**

compound is the smallest unit (**Scheme 59**, A), their electronic and structural characteristics are difficult to elucidate experimentally. In 1981, Stang and Maas reported the oxidation of thioureas to afford NHC-coordinated dicationic disulfides [(L)Ch–Ch(L)]<sup>2+</sup> (type B).<sup>206</sup> Se analogues were reported by Devillanova and coworkers in 1996.<sup>207</sup> Te analogues were recently discovered by Ishii, Nakata, and coworkers.<sup>208</sup> It is noteworthy that two chalcogen moieties maintain the  $\sigma$ (Ch–Ch) bond despite charge repulsion. For diatomic radical cations (type C), the Ch–Ch bonds were shorter than Ch–Ch single bonds. Beckmann and coworkers reported one-electron oxidation of dichalcogenides ArCh–ChAr to provide the corresponding radical cations **120** and **121**.<sup>209</sup> The Ch–Ch bonds (**120-S**, 1.998(2) Å; **121-S**, 2.014(3) Å), Se–Se (**120-Se**, 2.289(1) Å; **121-Se**, 2.289(7) Å), and Te–Te (**121-Te**, 2.662(1) Å) were shorter than those of corresponding neutral dichalcogenides, as well as significantly shorter than those of NHC-coordinated dicationic disulfides. The Wiberg bond indices of Ch–Ch bonds were between 1.216 and 1.315 for the [(PhCh)<sub>2</sub>]<sup>+</sup> (Ch=S, Se, Te) and between 1.176 and 1.282 for the [(C<sub>6</sub>F<sub>5</sub>Ch)<sub>2</sub>]<sup>+</sup> (Ch=S, Se, Te). The singly occupied molecular orbital of [(C<sub>6</sub>F<sub>5</sub>Se)<sub>2</sub>]<sup>+</sup> was predominantly represented by the  $\pi^*$ (Se–Se) and  $\pi$ (C<sub>6</sub>F<sub>5</sub>) orbitals. For radical cations **120** and **121**, these insights resulted in the double bond characters in Ch–Ch bonds (odd-electron  $\pi$ -bonds).

### 1.03.6 Summary

Combination of experimental and theoretical approaches to low-coordinate compounds with a multiple bond between heavier main group elements revealed essential properties of their chemical bondings. Summarizing the findings described in this chapter leads to the following conclusion: the classical multiple-bond indicators in organic chemistry, e.g., the shorter bond lengths and higher bonding energies, have almost no meanings for the multiple bonds between heavier atoms and they are valid for only 2nd-row elements such as carbon. The bonding characters of multiple bonds of heavier main group elements described above are reasonably interpreted in terms of unfavorable *s-p* hybridization of the heavier atoms. The understanding of the feature of heavier atoms suggested that sterically demanding substituents should be required in order to kinetically stabilize and isolate

the heavier multiply-bonded compounds. Indeed, the concept of kinetic stabilization using bulky substituents led to the significant progress in the chemistry of unsaturated compounds with heavier main group elements. However, important synthetic targets remain in main group element chemistry. For example, a hexasilabenzene ( $R_6Si_6$ ), a silicon-analogue of a benzene, should be one of the important targets, for establishment of a concept of “aromaticity” of heavier main group elements. It is expected that the combination of “organic chemistry”, “transition metal chemistry”, and “main group element chemistry” will open up a new field of chemistry by the use of the characters of every element in the periodic table.

## References

- (a) Köhler, H.; Michaelis, A. Über Phenylphosphin Und Phosphobenzol (Diphosphenyl). *Ber. Dtsch. Chem. Ges.* **1877**, *10*, 807–814; (b) Daly, J. J.; Maier, L. Molecular Structure of Phosphobenzene. *Nature* **1964**, *203*, 1167–1168.
- Pitzer, K. S. Repulsive Forces in Relation to Bond Energies, Distances and Other Properties. *J. Am. Chem. Soc.* **1948**, *70*, 2140–2145.
- Goldberg, D. E.; Harris, D. H.; Lappert, M. F.; Thomas, K. M. New Synthesis of Divalent Group 4b Alkyls  $M[Ch(SiMe_3)_2]_2$  ( $M = Ge$  or  $Sn$ ), and Crystal and Molecular-Structure of Tin Compound. *J. Chem. Soc. Chem. Commun.* **1976**, 261–262.
- Klebach, T. C.; Lourens, R.; Bickelhaupt, F. Synthesis of P-Mesityldiphenylmethylenephosphine—Stable Compound with a Localized  $P=C$  Bond. *J. Am. Chem. Soc.* **1978**, *100*, 4886–4888.
- Yoshifuji, M.; Shima, I.; Inamoto, N.; Hirotsu, K.; Higuchi, T. Synthesis and Structure of Bis(2,4,6-Tri-Tert-Butylphenyl)Diphosphene—Isolation of a True Phosphobenzene. *J. Am. Chem. Soc.* **1981**, *103*, 4587–4589.
- (a) Brook, A. G.; Abdesaken, F.; Gutekunst, B.; Gutekunst, G.; Kallury, R. K. A Solid Silaethene—Isolation and Characterization. *J. Chem. Soc. Chem. Commun.* **1981**, 191–192; (b) Brook, A. G.; Nyberg, S. C.; Abdesaken, F.; Gutekunst, B.; Gutekunst, G.; Kallury, R. K. M. R.; Poon, Y. C.; Chang, Y.-M.; Wong-Ng, W. Stable Solid Silaethylenes. *J. Am. Chem. Soc.* **1982**, *104*, 5667–5672.
- West, R.; Fink, M. J.; Michl, J. Tetramesityldisilene, a Stable Compound Containing a Silicon-Silicon Double-Bond. *Science* **1981**, *214*, 1343–1344.
- (a) Fischer, R. C.; Power, P. P.  $\pi$ -Bonding and the Lone Pair Effect in Multiple Bonds Involving Heavier Main Group Elements: Developments in the New Millennium. *Chem. Rev.* **2010**, *110*, 3877–3923; (b) Nagase, S. Theory and Calculations of Molecules Containing Heavier Main Group Elements and Fullerenes Encaging Transition Metals: Interplay with Experiment. *Bull. Chem. Soc. Jpn.* **2014**, *87*, 167–195.
- (a) Raabe, G.; Michl, J. Multiple Bonding to Silicon. *Chem. Rev.* **1985**, *85*, 419–509 (For examples of reviews on multiple bond compounds of heavier main group elements); (b) Weber, L. The Chemistry of Diphosphenes and Their Heavy Congeners—Synthesis, Structure, and Reactivity. *Chem. Rev.* **1992**, *92*, 1839–1906; (c) Okazaki, R.; Tokitoh, N. Heavy Ketones, the Heavier Element Congeners of a Ketone. *Acc. Chem. Res.* **2000**, *33*, 625–630; (d) Sasamori, T.; Tokitoh, N. Doubly Bonded Systems Between Heavier Group 15 Elements. *Dalton Trans.* **2008**, 1395–1408; (e) Guo, J.-D.; Sasamori, T. Activation of Small Molecules by Compounds that Contain Triple Bonds Between Heavier Group-14 Elements. *Chem. Asian J.* **2018**, *13*, 3800–3817; (f) Majhi, P. K.; Sasamori, T. Tetrylones: An Intriguing Class of Mono Valent Group 14 Compounds. *Chem. A Eur. J.* **2018**, *24*, 9441–9455; (g) Agarwal, A.; Bose, S. K. Bonding Relationship between Silicon and Germanium With Group 13 and Heavier Elements of Groups 14–16. *Chem. Asian J.* **2020**, *15*, 3784–3806; (h) Hanusch, F.; Groll, L.; Inoue, S. Recent Advances of Group 14 Dimetallenes and Dimetalynes in Bond Activation and Catalysis. *Chem. Sci.* **2021**, *12*, 2001–2015.
- (a) Mizuhata, Y.; Sasamori, T.; Tokitoh, N. Stable Heavier Carbene Analogues. *Chem. Rev.* **2009**, *109*, 3479–3511 (For examples of reviews on heavy element analogues of a carbene); (b) Bayat, M.; Soltani, E. Stabilization of Group 14 Tetrylene Compounds by N-Heterocyclic Carbene: A Theoretical Study. *Polyhedron* **2017**, *123*, 39–46; (c) Fujimori, S.; Inoue, S. Small Molecule Activation by Two-Coordinate Acyclic Silylenes. *Eur. J. Inorg. Chem.* **2020**, *2020*, 3131–3142.
- Wedler, H. B.; Wendelboe, P.; Tantilto, D. J.; Power, P. P. Second Order Jahn-Teller Interactions at Unusually High Molecular Orbital Energy Separations. *Dalton Trans.* **2020**, *49*, 5175–5182.
- (a) Kira, M. Distortion Modes of Heavy Ethylenes and their Anions:  $\pi$ - $\sigma^*$  Orbital Mixing Model. *Organometallics* **2011**, *30*, 4459–4465; (b) Nori-Shargh, D.; Mousavi, S. N.; Boggs, J. E. Pseudo Jahn-Teller Effect and Natural Bond Orbital Analysis of Structural Properties of Tetrahydridodimetallenes  $M_2H_4$ , ( $M = Si, Ge, \text{ and } Sn$ ). *J. Phys. Chem. A* **2013**, *117*, 1621–1631; (c) Nori-Shargh, D.; Weinhold, F. Natural Bond Orbital Theory of Pseudo-Jahn-Teller Effects. *J. Phys. Chem. A* **2018**, *122*, 4490–4498.
- (a) Desclaux, J. P. Relativistic Dirac-Fock Expectation Values for Atoms With  $Z = 1$  to  $Z = 120$ . *At. Data Nucl. Data Tables* **1973**, *12*, 311–406; (b) Nagase. In *The Transition State: A Theoretical Approach*; Fueno, T., Ed., Kodansha: Tokyo, 1999; pp 147–162.
- (a) Trinquier, G. Double-Bonds and Bridged Structures in the Heavier Analogs of Ethylene. *J. Am. Chem. Soc.* **1990**, *112*, 2130–2137; (b) Jacobsen, H.; Ziegler, T. Nonclassical Double-Bonds in Ethylene Analogs—Influence of Pauli Repulsion on Trans Bending and  $\pi$ -Bond Strength—A Density-Functional Study. *J. Am. Chem. Soc.* **1994**, *116*, 3667–3679; (c) Driess, M.; Grützmacher, H. Main Group Element Analogues of Carbenes, Olefins, and Small Rings. *Angew. Chem. Int. Ed. Engl.* **1996**, *35*, 829–856.
- (a) Power, P. P. Silicon, Germanium, Tin and Lead Analogues of Acetylenes. *Chem. Commun.* **2003**, 2091–2101; (b) Power, P. P. Bonding and Reactivity of Heavier Group 14 Element Alkyne Analogues. *Organometallics* **2007**, *26*, 4362–4372; (c) Guo, J.-D.; Liptrot, D. J.; Nagase, S.; Power, P. P. The Multiple Bonding in Heavier Group 14 Elementalkene Analogues Is Stabilized Mainly by Dispersionforce Effects. *Chem. Sci.* **2015**, *6*, 6235–6244.
- (a) Lein, M.; Krapp, A.; Frenking, G. Why Do the Heavy-Atom Analogues of Acetylene  $E_2H_2$  ( $E = Si-Pb$ ) Exhibit Unusual Structures? *J. Am. Chem. Soc.* **2005**, *127*, 6290–6299; (b) Landis, C. R.; Weinhold, F. Origin of Trans-Bent Geometries in Maximally Bonded Transition Metal and Main Group Molecules. *J. Am. Chem. Soc.* **2006**, *128*, 7335–7345; (c) Jacobsen, H. Shifting Paradigms: Electrostatic Interactions and Covalent Bonding. *Chem. A Eur. J.* **2010**, *16*, 976–987; (d) Ploshnik, E.; Danovich, D.; Hiberty, P. C.; Shaik, S. The Nature of the Idealized Triple Bonds Between Principal Elements and the Sigma Origins of Trans-Bent Geometries-A Valence Bond Study. *J. Chem. Theory Comput.* **2011**, *7*, 955–968.
- Lee, V. Y.; Sekiguchi, A. Multiply Bonded Compounds of the Heavy Group 14 Elements. In *Comprehensive Inorganic Chemistry II*; Reedijk, J., Poeppelmeier, K., Chivers, T., Eds.; vol. 1; Elsevier: Oxford, 2013; pp 289–324. ch. 1.11.
- Lee, V. Y.; Sekiguchi, A. Heavy Analogs of Alkenes, 1,3-Dienes, Allenes and Alkynes: Multiply Bonded Derivatives of Si, Ge, Sn and Pb. In *Organometallic Compounds of Low-Coordinate Si, Ge, Sn and Pb: From Phantom Species to Stable Compounds*, Wiley: Chichester, 2010 (ch. 5).
- Kosai, T.; Iwamoto, T. Stable Push–Pull Disilene: Substantial Donor–Acceptor Interactions through the  $Si=Si$  Double Bond. *J. Am. Chem. Soc.* **2017**, *139*, 18146–18149.
- Kosai, T.; Ishida, S.; Iwamoto, T. Heteroaryl disilenes: Heteroaryl Groups Serve as electron Acceptors for  $Si=Si$  Double Bonds in Intramolecular Charge Transfer Transitions. *Dalton Trans.* **2017**, *46*, 11271–11281.
- Akasaka, N.; Tanaka, K.; Ishida, S.; Iwamoto, T. Synthesis and Functionalization of a 1,2-Bis(trimethylsilyl)-1,2-disilacyclohexene That Can Serve as a Unit of cis-1,2-Dialkylidasilene. *Inorganics* **2018**, *6*, 21.
- Tanaka, K.; Akasaka, N.; Kosai, T.; Honda, S.; Ushijima, Y.; Ishida, S.; Iwamoto, T. Dialkylboryl-Substituted Cyclic Disilenes Synthesized by Desilylation-Borylation of Trimethylsilyl-Substituted Disilenes. *Molecules* **2021**, *26*, 1632.
- Yokouchi, Y.; Ishida, S.; Iwamoto, T. Facile Skeletal Rearrangement of Polycyclic Disilenes with Bicyclo[1.1.1]pentasilanyl Groups. *Chem. A Eur. J.* **2018**, *24*, 11393–11401.
- Akasaka, N.; Ishida, S.; Iwamoto, T. Transformative  $Si_8R_8$  Siliconoids. *Inorganics* **2018**, *6*, 107.

25. Iwamoto, T.; Ishida, N. A. S. A Heavy Analogue of the Smallest Bridgehead Alkene Stabilized by a Base. *Nat. Commun.* **2014**, *5*, 5353.
26. Iwamoto, T.; Abe, T.; Sugimoto, K.; Hashizume, D.; Matsui, H.; Kishi, R.; Nakano, M.; Ishida, S. ATetrasilicon Analogue of Bicyclo[1.1.0]but-1(3)-ene Containing a Si=Si Double Bond With an Inverted Geometry. *Angew. Chem. Int. Ed.* **2019**, *58*, 4371–4375.
27. (a) Meltzer, A.; Majumdar, M.; White, A. J. P.; Huch, V.; Scheschke, D. Potential Protecting Group Strategy for Disila Analogues of Vinylolithiums: Synthesis and Reactivity of a 2,4,6-Trimethoxyphenyl-Substituted Disilene. *Organometallics* **2013**, *32*, 6844–6850; (b) Obeid, N. M.; Maus, L. K. D.; Zimmer, M.; Jeck, J.; Bejan, I.; White, A. J. P.; Huch, V.; Jung, G.; Scheschke, D. (Oligo)aromatic Species With One or Two conjugated SiVSi Bonds: Near-IR Emission of Anthracenyl-Bridged Tetrasiladiene. *Dalton Trans.* **2017**, *46*, 8839–8848.
28. (a) Kobayashi, M.; Hayakawa, N.; Nakabayashi, K.; Matsuo, T.; Hashizume, D.; Fueno, H.; Tanaka, K.; Tamao, K. Highly Coplanar (E)-1,2-Di(1-Naphthyl)Disilene Involving a Distinct CH– $\pi$  Interaction with the Perpendicularly Oriented Protecting End Group. *Chem. Lett.* **2014**, *43*, 432–434; (b) Li, L.; Matsuo, T.; Hashizume, D.; Fueno, H.; Tanaka, K.; Tamao, K. Coplanar Oligo(P-Phenylenedisilylene)S as Si=Si Analogues of Oligo(P-Phenylenesilylene)S: Evidence for Extended  $\pi$ -Conjugation through the Carbon and Silicon  $\pi$ -Frameworks. *J. Am. Chem. Soc.* **2015**, *137*, 15026–15035; (c) Kobayashi, M.; Hayakawa, N.; Matsuo, T.; Li, B.; Fukunaga, T.; Hashizume, D.; Fueno, H.; Tanaka, K.; Tamao, K. (Z)-1,2-Di(1-Pyrenyl)Disilene: Synthesis, Structure, and Intramolecular Charge-Transfer Emission. *J. Am. Chem. Soc.* **2016**, *138*, 758–761; (d) Hayakawa, N.; Nishimura, S.; Kazusa, N.; Shintani, N.; Nakahodo, T.; Fujihara, H.; Hoshino, M.; Hashizume, D.; Matsuo, T.  $\pi$ -Conjugation between a Si=Si Double Bond and Thiophene Rings: Synthesis, Structural Characteristics, and Photophysical Properties of 1,2-Bis(Thiophen-2-Yl)Disilene and 1,2-Bis(2,2'-Bithiophen-5-Yl)Disilene. *Organometallics* **2017**, *36*, 3226–3233.
29. Izod, K.; Evans, P.; Waddell, P. G. A Fully Phosphane-Substituted Disilene. *Angew. Chem. Int. Ed.* **2017**, *56*, 5593–5597.
30. (a) Tsurusaki, A.; Iizuka, C.; Otsuka, K.; Kyushin, S. Cyclopentasilane-Fused Hexasilabenzvalene. *J. Am. Chem. Soc.* **2013**, *135*, 16340–16343; (b) Lee, V. Y.; Horiguchi, S.; Sekiguchi, A.; Gapurenko, O. A.; Gribanova, T. N.; Minkin, V. I.; Gornitzka, H. Tuning Philycity of Dichlorosilylene: Nucleophilic Behavior of the Dichlorosilylene–NHC Complex  $\text{Cl}_2\text{Si}-\text{IPr}$ . *ACS Omega* **2019**, *4*, 2902–2906; (c) Yukimoto, M.; Minoura, M. The Synthesis of a Novel Bulky Primary Alkyl Group and Its Application toward the Kinetic Stabilization of a Tetraalkyldisilene. *Bull. Chem. Soc. Jpn.* **2018**, *91*, 585–587.
31. Haas, M.; Knoechl, A.; Wiesner, T.; Torvisco, A.; Fischer, R.; Jones, C. Attempted Synthesis of a Homocyclic Bis(Silyl)Silylene Leads to the Formation of a Tricyclo[3,1,1,1,2<sup>4</sup>]Octasilane. *Organometallics* **2019**, *38*, 4158–4170.
32. Reiter, D.; Holzner, R.; Porzelt, A.; Altmann, P. J.; Frisch, P.; Inoue, S. Disilene–Silylene Interconversion: A Synthetically Accessible Acyclic Bis(silyl)silylene. *J. Am. Chem. Soc.* **2019**, *141*, 13536–13546.
33. Liu, Z.; Zhang, J.; Yang, H.; Cui, C. Synthesis of Boryl-Substituted Disilane, Disilene, and Silyl Cation. *Organometallics* **2020**, *39*, 4164–4168.
34. Wendel, D.; Szilvási, T.; Jandl, C.; Inoue, S.; Rieger, B. Twist of a Silicon–Silicon Double Bond: Selective Anti-Addition of Hydrogen to an Iminodisilene. *J. Am. Chem. Soc.* **2017**, *139*, 9156–9159.
35. Kostenko, A.; Driess, M. Geometrically Compelled Disilene with  $\lambda^4$ -Coordinate  $\text{Si}^{\text{II}}$  Atoms. *J. Am. Chem. Soc.* **2018**, *140*, 16962–16966.
36. (a) Davidson, P. J.; Harris, D. H.; Lappert, M. F. Subvalent Group 4B Metal Alkyls and Amides. Part I. The Synthesis and Physical Properties of Kinetically Stable Bis[Bis(trimethylsilyl)methyl]-Germanium(II), –Tin(II), and –Lead(II). *J. Chem. Soc. Dalton Trans.* **1976**, 2268–2274; (b) Goldberg, D. E.; Hitchcock, P. B.; Lappert, M. F.; Thomas, K. M.; Thorne, A. J.; Fjeldberg, T.; Haaland, A.; Schilling, B. E. R. Subvalent Group 4B Metal Alkyls and Amides. Part 9. Germanium and Tin Alkene Analogues, the Dimetalenes  $\text{M}_2\text{R}_4$  [M = Ge or Sn, R = CH(SiMe<sub>3</sub>)<sub>2</sub>]; X-Ray Structures, Molecular Orbital Calculations for  $\text{M}_2\text{H}_4$ , and Trends in the Series  $\text{M}_2\text{R}'_4$  [M = C, Si, Ge, or Sn; R' = R, Ph, C<sub>6</sub>H<sub>2</sub>Me<sub>3</sub>–2,4,6, or C<sub>6</sub>H<sub>3</sub>Et<sub>2</sub>–2,6]. *J. Chem. Soc. Dalton Trans.* **1986**, 2387–2394.
37. Jana, A.; Huch, V.; Rzepa, H. S.; Scheschke, D. A Multiply Functionalized Base-Coordinated Ge<sup>II</sup> Compound and its Reversible Dimerization to the Digermene. *Angew. Chem. Int. Ed.* **2015**, *54*, 289–292.
38. (a) Nieder, D.; Klemmer, L.; Kaiser, Y.; Huch, V.; Scheschke, D. Isolation and Reactivity of a Digerma Analogue of Vinylolithiums: A Lithium Digermenide. *Organometallics* **2018**, *37*, 632–635; (b) Klemmer, L.; Kaiser, Y.; Huch, V.; Zimmer, M.; Scheschke, D. Persistent Digermenes with Acyl and  $\alpha$ -Chlorosilyl Functionalities. *Chem. A Eur. J.* **2019**, *25*, 12187–12195.
39. Hayakawa, N.; Sugahara, T.; Numata, Y.; Kawaai, H.; Yamatani, K.; Nishimura, S.; Goda, S.; Suzuki, Y.; Tanikawa, T.; Nakai, H.; Hashizume, D.; Sasamori, T.; Tokitoh, N.; Matsuo, T. 1,2-Dihalodigermenes Bearing Bulky End Groups: Synthesis, Characterization, and Conversion to Halogermolenoids. *Dalton Trans.* **2018**, *47*, 814–822.
40. Sasamori, T.; Sugahara, T.; Agou, T.; Sugamata, K.; Guo, J.-D.; Nagase, S.; Tokitoh, N. Reaction of a Diaryldigermyne with Ethylene. *Chem. Sci.* **2015**, *6*, 5526–5530.
41. Hlina, J.; Baumgartner, J.; Marschner, C.; Albers, L.; Müller, T.; Jouikov, V. V. Formation and Properties of a Bicyclic Silylated Digermene. *Chem. A Eur. J.* **2014**, *20*, 9357–9366.
42. Lee, V. Y.; McNiece, K.; Ito, Y.; Sekiguchi, A.; Geinik, N.; Becker, J. Y. Tetrakis(di-tert-butylmethylsilyl)digermene: Synthesis, Structure, Electrochemical Properties, and Reactivity. *Heteroatom Chem.* **2014**, *25*, 313–319.
43. Mangan, R. J.; Rit, A.; Sindlinger, C. P.; Tirfoin, R.; Campos, J.; Hicks, J.; Christensen, K. E.; Niu, H.; Aldridge, S. Activation of Protic, Hydridic and Apolar E–H Bonds by a Boryl-Substituted Ge<sup>II</sup> Cation. *Chem. A Eur. J.* **2020**, *26*, 306–315.
44. Mangan, R. J.; Davies, A. R.; Hicks, J.; Sindlinger, C. P.; Thompson, A. L.; Aldridge, S. Synthesis, Structure and Reactivity of Terphenyl-Substituted Germylium-Ylidene Cations. *Polyhedron* **2021**, *196*, 115006.
45. Klemmer, L.; Thömmes, A.-L.; Zimmer, M.; Huch, V.; Morgenstern, B.; Scheschke, D. Metathesis of Ge=Ge Double Bonds. *Nat. Chem.* **2021**, *13*, 373–377.
46. Henning, J.; Eichele, K.; Fink, R. F.; Wesemann, L. Structural and Spectroscopic Characterization of Tin–Tin Double Bonds in Cyclic Distannenes. *Organometallics* **2014**, *33*, 3904–3918.
47. Schneider, J.; Henning, J.; Edrich, J.; Schubert, H.; Wesemann, L. Reversibility in Reactions of Linker-Bridged Distannenes with Terminal Alkynes at Ambient Temperature. *Inorg. Chem.* **2015**, *54*, 6020–6027.
48. Heno, J.; Auch, A.; Diab, F.; Eichele, K.; Schubert, H.; Sirsch, P.; Block, T.; Pöttgen, R.; Wesemann, L. Cyclic Distannene or Bis(Stannylenes) with a Ferrocenyl Backbone: Synthesis, Structure, and Coordination Chemistry. *Inorg. Chem.* **2018**, *57*, 4135–4145.
49. Walewska, M.; Hlina, J.; Gaderbauer, W.; Wagner, H.; Baumgartner, J.; Marschner, C. NHC Adducts of Disilylated Germylenes and Stannylenes and their Coordination Chemistry with Group 11 Metals. *Z. Anorg. Allg. Chem.* **2016**, *642*, 1304–1313.
50. Zitz, R.; Pöcheim, A.; Baumgartner, J.; Marschner, C. A 1,5-Oligosilylanyl Dianion as Building Block for Oligosiloxane Containing Cages, Ferrocenophanes, and Cyclic Germylenes and Stannylenes. *Molecules* **2020**, *25*, 1322.
51. Wang, S.; McCrea-Hendrick, M. L.; Weinstein, C. M.; Caputo, C. A.; Hoppe, E.; Fetting, J. C.; Olmstead, M. M.; Power, P. P. Dynamic Behavior and Isomerization Equilibria of Distannenes Synthesized by Tin Hydride/Olefin Insertions: Characterization of the Elusive Monohydrido Bridged Isomer. *J. Am. Chem. Soc.* **2017**, *139*, 6586–6595.
52. Lai, T. Y.; Fetting, J. C.; Power, P. P. Facile C–H Bond Metathesis Mediated by a Stannylenes. *J. Am. Chem. Soc.* **2018**, *140*, 5674–5677.
53. Stürmann, M.; Saak, W.; Marsmann, H.; Weidenbruch, M. Tetrakis(2,4,6-triisopropylphenyl)diplumbene: A Molecule with a Lead–Lead Double Bond. *Angew. Chem. Int. Ed.* **1999**, *38*, 187–189.
54. Erickson, J. D.; Fetting, J. C.; Power, P. P. Reaction of a Germylene, Stannylenes, or Plumbylene with Trimethylaluminum and Trimethylgallium: Insertion into Al–C or Ga–C Bonds, a Reversible Metal–Carbon Insertion Equilibrium, and a New Route to Diplymbenes. *Inorg. Chem.* **2015**, *54*, 1940–1948.
55. (a) Nakata, N.; Izumi, R.; Lee, V. Y.; Ichinohe, M.; Sekiguchi, A. Reaction of Diiithiosilane  $\text{R}_2\text{SiLi}_2$  and Diiithiogermene  $\text{R}_2\text{GeLi}_2$  (R = SiMe<sub>2</sub>Bu<sub>2</sub>) with MesBCl<sub>2</sub> (Mes = 2,4,6-Trimethylphenyl): Evidence for the Formation of Silaborene  $\text{R}_2\text{Si}=\text{BMe}_2$  and Germborene  $\text{R}_2\text{Ge}=\text{BMe}_2$ . *Chem. Lett.* **2005**, *34*, 582–583; (b) Nakata, N.; Sekiguchi, A. A Stable Silaborene: Synthesis and Characterization. *J. Am. Chem. Soc.* **2006**, *128*, 422–442.
56. Suzuki, Y.; Ishida, S.; Sato, S.; Isobe, H.; Iwamoto, T. An Isolable Potassium Salt of a Borasilene–Chloride Adduct. *Angew. Chem. Int. Ed.* **2017**, *56*, 4593–4597.
57. Rao, B.; Kirjoo, R. Crystalline Boragermenes. *Angew. Chem. Int. Ed.* **2020**, *59*, 3147–3150.

58. (a) Raiser, D.; Sindlinger, C. P.; Schubert, H.; Wesemann, L. Ge=B  $\pi$ -Bonding: Synthesis and Reversible [2+2] Cycloaddition of Germaborenes. *Angew. Chem. Int. Ed.* **2020**, *59*, 3151–3155; (b) Raiser, D.; Schubert, H.; Bettinger, H. F.; Wesemann, L. Germaborenes: Borylene Transfer Agents for the Synthesis of Iminoboranes. *Chem. A Eur. J.* **2021**, *27*, 1981–1983.
59. (a) Nakata, N.; Izumi, R.; Lee, V. Y.; Ichinohe, M.; Sekiguchi, A. 1,3-Disila-2-Gallata- and -Indataallenic Anions [ $>SiMSi<$ ] $^-Li^+$  (M = Ga, In): Compounds Featuring Double Bonds between Elements of Groups 13 and 14. *J. Am. Chem. Soc.* **2004**, *126*, 5058–5059; (b) Nakata, N.; Izumi, R.; Lee, V. Y.; Ichinohe, M.; Sekiguchi, A. 1,3-Digerma-2-Gallata- and -Indataallenic Anions: The First Compounds with Ge=Ga or Ge=In Double Bonds. *Chem. Lett.* **2008**, *37*, 1146–1147.
60. Cowley, M. J.; Ohmori, Y.; Huch, V.; Ichinohe, M.; Sekiguchi, A.; Scheschkewitz, D. Carbonylation of Cyclotrisilenes. *Angew. Chem. Int. Ed.* **2013**, *52*, 13247–13250.
61. Majumdar, M.; Huch, V.; Bejan, I.; Meltzer, A.; Scheschkewitz, D. Reversible, Complete Cleavage of Si=Si Double Bonds by Isocyanide Insertion. *Angew. Chem. Int. Ed.* **2013**, *52*, 3516–3520.
62. Zborovsky, L.; Kostenko, A.; Bravo-Zhivotovskii, D.; Apeloig, Y. Mechanism of the Thermal Z $\Rightarrow$ E Isomerization of a Stable Silene; Experiment and Theory. *Angew. Chem. Int. Ed.* **2019**, *58*, 14524–14528.
63. Iwamoto, T.; Ohnishi, N.; Akasaka, N.; Onno, K.; Ishida, S. Anthryl-Substituted 3-Silylene-2-Silaaziridine Obtained by Isomerization of Disilacyclopropanimine: An Exocyclic Silene Showing a Distinct Intramolecular Charge Transfer Transition. *J. Am. Chem. Soc.* **2013**, *135*, 10606–10609.
64. Reiter, D.; Frisch, P.; Szilvási, T.; Inoue, S. Heavier Carbonyl Olefination: The Sila-Wittig Reaction. *J. Am. Chem. Soc.* **2019**, *141*, 16991–16996.
65. Nakata, N.; Rodriguez, R.; Traodec, T.; Saffon-Merceron, N.; Sotiropoulos, J.-M.; Baceiredo, A.; Kato, T. A Stable Silene Substituted by Strong  $\pi$ -Donors at the Silicon Center. *Angew. Chem. Int. Ed.* **2013**, *52*, 10840–10844.
66. (a) Haas, M.; Radebner, J.; Winkler, C.; Fischer, R.; Torvisco, A.; Stueger, H. Isolable Endocyclic Silenes by Thermal Brook Rearrangement. *J. Organomet. Chem.* **2017**, *830*, 131–140; (b) Haas, M.; Fischer, R.; Flock, M.; Mueller, S.; Rausch, M.; Saf, R.; Torvisco, A.; Stueger, H. Stable Silenolates and Brook-Type Silenes with Exocyclic Structures. *Organometallics* **2014**, *33*, 5956–5959.
67. Meyer, H.; Baum, G.; Massa, W.; Berndt, A. Stable Germaethenes. *Angew. Chem. Int. Ed. Engl.* **1987**, *26*, 798–799.
68. (a) Couret, C.; Escudié, J.; Satgé, J.; Lazraq, M. The First Stable Germene: A Compound with a Germanium-Carbon Double Bond. *J. Am. Chem. Soc.* **1987**, *109*, 4411–4412; (b) Lazraq, M.; Escudié, J.; Couret, C.; Satgé, J.; Dräger, M.; Dammal, R. (Mesityl) $_2$ Ge(flourenylidene)-Stabilization of a Ge-C Double Bond by Charge Transfer into an Aromatic System. *Angew. Chem. Int. Ed. Engl.* **1988**, *27*, 828–829.
69. Haas, M.; Leybold, M.; Schnalzer, D.; Torvisco, A.; Stueger, H. Stable Germenolates and Germenes with Exocyclic Structures. *Organometallics* **2015**, *34*, 5291–5297.
70. Baines, K. M.; Cooke, J. A. Tetramesitylgermasilene: The First Relatively Stable Germasilene and its Rearrangement to a Silylgermylene. *Organometallics* **1992**, *11*, 3487–3488.
71. Lee, V. Y.; Ichinohe, M.; Sekiguchi, A.; Takagi, N.; Nagase, S. The First Three-Membered Unsaturated Rings Consisting of Different Heavier Group 14 Elements: 1-Disilagermirene with a Si=Si Double Bond and its Isomerization to a 2-Disilagermirene with a Si=Ge Double Bond. *J. Am. Chem. Soc.* **2000**, *122*, 9034–9035.
72. Lee, V. Y.; Ichinohe, M.; Sekiguchi, A. The First Metalladiene of Group 14 Elements with a Silole-Type Structure with Si=Ge and C=C Double Bonds. *J. Am. Chem. Soc.* **2000**, *122*, 12604–12605.
73. Majhi, P. K.; Huch, V.; Scheschkewitz, D. A Mixed Heavier Si=Ge Analogue of a Vinyl Anion. *Angew. Chem. Int. Ed.* **2021**, *60*, 242–246.
74. Meyer, H.; Baum, G.; Massa, W.; Berger, S.; Berndt, A. A Stable Stannaethene. *Angew. Chem. Int. Ed. Engl.* **1987**, *26*, 546–548.
75. Sekiguchi, A.; Izumi, R.; Lee, V. Y.; Ichinohe, M. The First Silastannene  $>Si=Sn<$ : A New Doubly-Bonded System of Heavier Group 14 Elements. *J. Am. Chem. Soc.* **2002**, *124*, 14822–14823.
76. Schäfer, A.; Saak, W.; Weidenbruch, M. Tetraarylstannagermene: A Molecule with a Ge=Sn Double Bond. *Organometallics* **2003**, *22*, 215–217.
77. Sekiguchi, A.; Izumi, R.; Lee, V. Y.; Ichinohe, M. R $_2$ Ge=SnR' $_2$  and RR'GeSnRR' (R = SiMe $_2$ BU $_2$ , R' = 2,4,6-iPr $_3$ C $_6$ H $_3$ ): The New Stable Germastannenes. *Organometallics* **2003**, *22*, 1483–1486.
78. Lee, V. Y.; Takashashi, K.; Nakamoto, M.; Sekiguchi, A.  $^3\Delta$ -1,2,3,4-Disilagermastannene: The First Cyclic Germastannene. *Russ. Chem. Bull., Int. Ed.* **2004**, *53*, 1102–1104.
79. Hesse, M.; Klingebiel, U. Diisopropyl(2,4,6-Tri-Tert-Butylphenylimino)Silane—A Very Stable, Free Silaimine. *Angew. Chem. Int. Ed. Engl.* **1986**, *25*, 649–650.
80. Wiberg, N.; Schurz, K.; Reber, G.; Müller, G. Preparation and Structure of a Stable Molecule Containing a Silicon Nitrogen Double Bond and of its Tetrahydrofuran Adduct. *J. Chem. Soc. Chem. Commun.* **1986**, 591–592.
81. Keuter, J.; Hepp, A.; Mück-Lichtenfeld, C.; Lips, F. Facile Access to an NHC-Coordinated Silicon Ring Compound with a Si=N Group and a Two-Coordinate Silicon Atom. *Angew. Chem. Int. Ed.* **2019**, *58*, 4395–4399.
82. Yuvaraj, K.; Jones, C. Synthesis and Reactivity of Boryl Substituted Silaimines. *Dalton Trans.* **2019**, *48*, 11961–11965.
83. Reiter, D.; Frisch, P.; Wendel, D.; Hörmann, F. M.; Inoue, S. Oxidation Reactions of a Versatile, Two-Coordinate, Acyclic Iminosiloxy-silylene. *Dalton Trans.* **2020**, *49*, 7060–7068.
84. Smit, C. N.; Bickelhaupt, F. Phosphasilenes: Synthesis and Spectroscopic Characterization. *Organometallics* **1987**, *6*, 1156–1163.
85. Bender, H. R. G.; Niecke, E.; Nieger, M. The First x-Ray Structure of a Phosphasilene: 1,3,4-Triphospha-2-Sila-1-Butene. *J. Am. Chem. Soc.* **1993**, *115*, 3314–3315.
86. (a) Willmes, P.; Cowley, M. J.; Hartmann, M.; Zimmer, M.; Huch, V.; Scheschkewitz, D. From Disilene (Si=Si) to Phosphasilene (Si=P) and Phosphacumulene (P=C=N). *Angew. Chem. Int. Ed.* **2014**, *53*, 2216–2220; (b) Willmes, P.; Junk, L.; Huch, V.; Yildiz, C. B.; Scheschkewitz, D. Diverse Reactivity of an Electrophilic Phosphasilene towards Anionic Nucleophiles: Substitution or Metal–Amino Exchange. *Angew. Chem. Int. Ed.* **2016**, *55*, 10913–10917.
87. (a) Driess, M.; Pritzkow, H. An Arsanilydensilane (“Arsasilene”) and its Derivatization with Tellurium and Benzophenone. *Angew. Chem. Int. Ed. Engl.* **1992**, *31*, 316–319; (b) Driess, M.; Rell, S.; Pritzkow, H. First Structural Characterization of Silicon–Arsenic and Silicon–Phosphorus Multiple Bonds in Silylated Silylidene-Arsanes and -Phosphanes; X-Ray Structure of a Tellura-Arsasilirane Derivative. *J. Chem. Soc. Chem. Commun.* **1995**, 253–254.
88. Ballester-Martinez, E.; Hadlington, T. J.; Szilvási, T.; Yao, S.; Driess, M. From Zinco(ii) Arsanetenes to Silylene-Stabilised Zinco Arsinidene Complexes. *Chem. Commun.* **2018**, *54*, 6124–6127.
89. Lee, V. Y.; Aoki, S.; Kawai, M.; Meguro, T.; Sekiguchi, A. Stibasilene Sb=Si and its Lighter Homologues: A Comparative Study. *J. Am. Chem. Soc.* **2014**, *136*, 6243–6246.
90. Meller, A.; Ossig, G.; Maringgele, W.; Stalke, D.; Herbst-Irmer, R.; Freitag, S.; Sheldrick, G. M. Synthesis and X-Ray Crystal Structure of Germaimines. *J. Chem. Soc. Chem. Commun.* **1991**, 1123–1124.
91. (a) Escudié, J.; Couret, C.; Satgé, J.; Andrianarison, M.; Andriamizaka, J.-D. 2,2-Dimesityl-1-(2,4,6-Tri-Tert-Butylphenyl)Germaphosphene: The First Stable Compound with a Germanium-Phosphorus Double Bond. *J. Am. Chem. Soc.* **1985**, *107*, 3378; (b) Dräger, M.; Escudié, J.; Couret, C.; Ranaivonjatovo, H.; Satgé, J. Structure of the Stable Germaphosphene Mes $_2$ Ge:PAR. A Ge:P Connection With the Geometry of a True Double Bond. *Organometallics* **1988**, *7*, 1010–1013.
92. Lee, V. Y.; Kawai, M.; Gapurenko, O. A.; Minkin, V. I.; Gornitzka, H.; Sekiguchi, A. Arsanergermene, a Compound with an –As=Ge< Double Bond. *Chem. Commun.* **2018**, *54*, 10947–10949.
93. Ossig, G.; Meller, A.; Freitag, S.; Herbst-Irmer, R. Synthesis and X-Ray Crystal Structure of a Stannaimine. *J. Chem. Soc. Chem. Commun.* **1993**, 497–499.
94. Couret, C.; Escudié, J.; Satgé, J.; Raharinirina, A.; Andriamizaka, J. D. A Compound with a Tin-Phosphorus Double Bond: The First Stable Stannaphosphene. *J. Am. Chem. Soc.* **1985**, *107*, 8280–8281.
95. Nesterov, V.; Baiertl, R.; Hanusch, F.; Ferao, A. E.; Inoue, S. N-Heterocyclic Carbene-Stabilized Germanium and Tin Analogues of Heavier Nitriles: Synthesis, Reactivity, and Catalytic Application. *J. Am. Chem. Soc.* **2019**, *141*, 14576–14580.
96. (a) Yao, S.; Xiong, Y.; Brym, M.; Driess, M. An Isolable Silanoic Ester by Oxygenation of a Stable Silylene. *J. Am. Chem. Soc.* **2007**, *129*, 7268–7269; (b) Xiong, Y.; Yao, S.; Driess, M. An Isolable NHC-Supported Silanone. *J. Am. Chem. Soc.* **2009**, *131*, 7562–7563.



97. Ishida, S.; Abe, T.; Hirakawa, F.; Kosai, T.; Sato, K.; Kira, M.; Iwamoto, T. Persistent Dialkylsilanone Generated by Dehydrobromination of Dialkylbromosilanol. *Chem. A Eur. J.* **2015**, *21*, 15100–15103.
98. (a) Rosas-Sánchez, A.; Alvarado-Beltran, I.; Baceiredo, A.; Saffon-Merceron, N.; Massou, S.; Hashizume, D.; Branchadell, V.; Kato, T. Cyclic (Amino)(Phosphonium Bora-Ylide) Silanone: A Remarkable Room-Temperature-Persistent Silanone. *Angew. Chem. Int. Ed.* **2017**, *56*, 15916–15920; (b) Alvarado-Beltran, I.; Rosas-Sánchez, A.; Baceiredo, A.; Saffon-Merceron, N.; Branchadell, V.; Kato, T. A Fairly Stable Crystalline Silanone. *Angew. Chem. Int. Ed.* **2017**, *56*, 10481–10485.
99. Takahashi, S.; Nakaya, K.; Frutos, M.; Baceiredo, A.; Saffon-Merceron, N.; Massou, S.; Nakata, N.; Hashizume, D.; Branchadell, V.; Kato, T. Synthesis of a Stable N-Hetero-Rh-Metallacyclic Silanone. *Angew. Chem. Int. Ed.* **2020**, *59*, 15937–15941.
100. Filippou, A. C.; Baars, B.; Chernov, O.; Lebedev, Y. N.; Schnakenburg, G. Silicon–Oxygen Double Bonds: A Stable Silanone With a Trigonal-Planar Coordinated Silicon Center. *Angew. Chem. Int. Ed.* **2014**, *53*, 565–570.
101. Wendel, D.; Reiter, D.; Porzelt, A.; Altmann, P. J.; Inoue, S.; Rieger, B. Silicon and Oxygen's Bond of Affection: An Acyclic Three-Coordinate Silanone and Its Transformation to an Iminosiloxysilylene. *J. Am. Chem. Soc.* **2017**, *139*, 17193–17198.
102. Kobayashi, R.; Ishida, S.; Iwamoto, T. An Isolable Silicon Analogue of a Ketone that Contains an Unperturbed Si=O Double Bond. *Angew. Chem. Int. Ed.* **2019**, *58*, 9425–9428.
103. (a) Suzuki, H.; Tokitoh, N.; Nagase, S.; Okazaki, R. The First Genuine Silicon-Sulfur Double-Bond Compound: Synthesis and Crystal Structure of a Kinetically Stabilized Silanethione. *J. Am. Chem. Soc.* **1994**, *116*, 11578–11579; (b) Tokitoh, N.; Sadahiro, T.; Hatano, K.; Sasaki, T.; Takeda, N.; Okazaki, R. Synthesis of Kinetically Stabilized Silaneselone and Silanetellone. *Chem. Lett.* **2002**, *31*, 34–35.
104. Iwamoto, T.; Sato, K.; Ishida, S.; Kabuto, C.; Kira, M. Synthesis, Properties, and Reactions of a Series of Stable Dialkyl-Substituted Silicon–Chalcogen Doubly Bonded Compounds. *J. Am. Chem. Soc.* **2006**, *128*, 16914–16920.
105. (a) Yao, S.; Xiong, Y.; Driess, M. From NHC-Germynes to Stable NHC-Germanone Complexes. *Chem. Commun.* **2009**, 6466–6468; (b) Yao, S.; Xiong, Y.; Wang, W.; Driess, M. Synthesis, Structure, and Reactivity of a Pyridine-Stabilized Germanone. *Chem. A Eur. J.* **2011**, *17*, 4890–4895.
106. Li, L.; Fukawa, T.; Matsuo, T.; Hashizume, D.; Fueno, H.; Tanaka, K.; Tamao, K. A Stable Germanone as the First Isolated Heavy Ketone with a Terminal Oxygen Atom. *Nat. Chem.* **2012**, *4*, 361–365.
107. (a) Tokitoh, N.; Matsumoto, T.; Manmaru, K.; Okazaki, R. Synthesis and Crystal Structure of the First Stable Diarylgermanethione. *J. Am. Chem. Soc.* **1993**, *115*, 8855–8856; (b) Matsumoto, T.; Tokitoh, N.; Okazaki, R. Synthesis and Structure of the First Stable Germaneselone. *Angew. Chem. Int. Ed. Engl.* **1994**, *33*, 2316–2318; (c) Tokitoh, N.; Matsumoto, T.; Okazaki, R. First Stable Germanetellones: Syntheses and Crystal Structures of the Heaviest Germanium–Chalcogen Double-Bond Compound. *J. Am. Chem. Soc.* **1997**, *119*, 2337–2338; (d) Matsumoto, T.; Tokitoh, N.; Okazaki, R. The First Kinetically Stabilized Germanethiones and Germaneselones: Syntheses, Structures, and Reactivities. *J. Am. Chem. Soc.* **1999**, *121*, 8811–8824.
108. Fujita, N.; Li, L.; Lentz, N.; Konaka, S.; Kuroda, A.; Ohno, R.; Hayakawa, N.; Tamao, K.; Madec, D.; Kato, T.; Rosas-Sánchez, A.; Hashizume, D.; Matsuo, T. Comparison of the Chemical Bonding in (Eind)<sub>2</sub>Ge=E (E = O and S): Synthesis and Characterization of Germanethione Bearing Bulky Eind Groups. *Chem. Lett.* **2020**, *49*, 141–144.
109. (a) Tokitoh, N.; Saito, M.; Okazaki, R. The First Stable Stannanethione in Solution Derived from a Kinetically Stabilized Diarylstannylene. *J. Am. Chem. Soc.* **1993**, *115*, 2065–2066; (b) Saito, M.; Tokitoh, N.; Okazaki, R. The First Kinetically Stabilized Stannaneselone and Diselenastannirane: Synthesis by Deselenation of a Tetraselenastannolane and Structures. *J. Am. Chem. Soc.* **1997**, *119*, 11124–11125; (c) Saito, M.; Tokitoh, N.; Okazaki, R. Tin–Chalcogen Double-Bond Compounds, Stannanethione and Stannaneselone: Synthesis, Structure, and Reactivities. *J. Am. Chem. Soc.* **2004**, *126*, 15572–15582; (d) Tajima, T.; Takeda, N.; Sasamori, T.; Tokitoh, N. *Organometallics* **2006**, *25*, 3552–3553.
110. (a) Weidenbruch, M.; Willms, S.; Saak, W.; Henkel, G. Hexaaryltetrasilabuta-1,3-Diene: A Molecule with Conjugated Si-Si Double Bonds. *Angew. Chem. Int. Ed. Engl.* **1997**, *36*, 2503–2504; (b) Schäfer, H.; Saak, W.; Weidenbruch, M. Hexaaryltetragermabuta-1,3-Diene: A Molecule With Conjugated Ge–Ge Double Bonds. *Angew. Chem. Int. Ed.* **2000**, *39*, 3703–3705.
111. (a) Suzuki, K.; Matsuo, T.; Hashizume, D.; Fueno, H.; Tanaka, K.; Tamao, K. A Planar Rhombic Charge-Separated Tetrasilacyclobutadiene. *Science* **2011**, *331*, 1306–1309; (b) Suzuki, K.; Numata, Y.; Fujita, N.; Hayakawa, N.; Tanikawa, T.; Hashizume, D.; Tamao, K.; Fueno, H.; Tanaka, K.; Matsuo, T. A Stable Free Tetragermacyclobutadiene Incorporating Fused-Ring Bulky EMind Groups. *Chem. Commun.* **2018**, *54*, 2200–2203.
112. Akasaka, N.; Fujieda, K.; Garoni, E.; Kamada, K.; Matsui, H.; Nakano, M.; Iwamoto, T. Synthesis and Functionalization of a 1,4-Bis(Trimethylsilyl)Tetrasil-1,3-Diene through the Selective Cleavage of Si(sp<sup>2</sup>)–Si(sp<sup>3</sup>) Bonds under Mild Reaction Conditions. *Organometallics* **2018**, *37*, 172–175.
113. Lee, V. Y.; Ichinohe, M.; Sekiguchi, A. The First Metalladiene of Group 14 Elements with a Silole-Type Structure with SiGe and CC Double Bonds. *J. Am. Chem. Soc.* **2000**, *122*, 12604–12605.
114. Cui, C.; Olmstead, M. M.; Power, P. P. Reactivity of Ar'GeGeAr' (Ar' = C<sub>6</sub>H<sub>3</sub>-2,6-Dipp, Dipp = C<sub>6</sub>H<sub>3</sub>-2,6-Pr<sub>2</sub>) toward Alkynes: Isolation of a Stable Digermacyclobutadiene. *J. Am. Chem. Soc.* **2004**, *126*, 5062–5063.
115. Sugahara, T.; Guo, J.-D.; Sasamori, T.; Karatsu, Y.; Furukawa, Y.; Ferao, A. E.; Nagase, S.; Tokitoh, N. Reaction of a Stable Digermyne with Acetylenes: Synthesis of a 1,2-Digermacyclobutadiene and a 1,4-Digermacyclobutadiene. *Bull. Chem. Soc. Jpn.* **2016**, *89*, 1375–1384.
116. Mondal, K. C.; Roesky, H. W.; Holzmann, N.; Hermann, M.; Frenking, G.; Meents, A. Formation of a 1,4-Diamino-2,3-Disila-1,3-Butadiene Derivative. *J. Am. Chem. Soc.* **2013**, *135*, 15990–15993.
117. Motomatsu, D.; Ishida, S.; Ohno, K.; Iwamoto, T. Isolable 2,3-Disila-1,3-Butadiene from a Double Sila-Peterson Reaction. *Chem. A Eur. J.* **2014**, *20*, 9424–9430.
118. Sugahara, T.; Sasamori, T.; Tokitoh, N. 2,5-Digermaselenophenes: Germanium Analogues of Selenophenes. *J. Am. Chem. Soc.* **2018**, *140*, 11206–11209.
119. Wiberg, N.; Lerner, H.-W.; Vasisht, S.-K.; Karaghiospif, K.; Nöth, H.; Ponikvar, W. Tetrasupersilyl-Tristannaallene and -Tristannacyclopentene (tBu<sub>3</sub>-Si)<sub>4</sub>Sn<sub>3</sub>—Isomers With the Shortest Sn=Sn Double Bonds to Date. *Eur. J. Inorg. Chem.* **1999**, 1211–1218.
120. (a) Ishida, S.; Iwamoto, T.; Kabuto, C.; Kira, M. A Stable Silicon-Based allene Analogue with a Formally Sp-Hybridized Silicon Atom. *Nature* **2003**, *421*, 725–727; (b) Iwamoto, T.; Masuda, H.; Kabuto, C.; Kira, M. Trigermaallene and 1,3-Digermasilaallene. *Organometallics* **2005**, *24*, 197–199; (c) Iwamoto, T.; Abe, T.; Kabuto, C.; Kira, M. A Missing allene of Heavy Group 14 Elements: 2-Germadisilaallene. *Chem. Commun.* **2005**, 5190–5192.
121. Sugahara, T.; Sasamori, T.; Tokitoh, N. Highly Bent 1,3-Digerma-2-silaallene. *Angew. Chem. Int. Ed.* **2017**, *56*, 9920–9923.
122. Miracle, G. E.; Ball, J. L.; Powell, D. R.; West, R. The First Stable 1-Silaallene. *J. Am. Chem. Soc.* **1993**, *115*, 11598–11599.
123. Eichler, B. E.; Powell, D. R.; West, R. Synthesis and Structure of a 1-Germapropadiene. *Organometallics* **1998**, *17*, 2147–2148.
124. Spirk, S.; Belaj, F.; Albering, J. H.; Pietschnig, R. Formation of a Silylated 1-Silaallene Via an Intermediate 1-Chloro-1-Silaallene. *Organometallics* **2010**, *29*, 2981–2986.
125. Kratish, Y.; Pinchuk, D.; Kaushanskii, A.; Molev, V.; Tumanskii, B.; Bravo-Zhivotovskii, D.; Apeloig, Y. The Reactions of Carbon Monoxide with Silyl and Silenyl Lithium—Synthesis and Isolation of the First Stable Tetra-Silyl Di-Ketyl Biradical and 1-Silaallenolate Lithium. *Angew. Chem. Int. Ed.* **2019**, *58*, 18849–18853.
126. Grützmacher, H.; Freitag, S.; Herbst-Irmer, R.; Sheldrick, G. S. Investigations of the Structure and Reactivity of a Stannaketimine. *Angew. Chem. Int. Ed. Engl.* **1992**, *31*, 437–438.
127. Abe, T.; Iwamoto, T.; Kabuto, C.; Kira, M. Synthesis, Structure, and Bonding of Stable Dialkylsilaketimines. *J. Am. Chem. Soc.* **2006**, *128*, 4228–4229.
128. Takeuchi, K.; Ichinohe, M.; Sekiguchi, A. Reactivity of the Disilyne RSi≡SiR (R = SiPr[CH(SiMe<sub>3</sub>)<sub>2</sub>]) toward Silylcyanide: Two Pathways to Form the Bis-Adduct [RSi-SiR(CNSiMe<sub>3</sub>)<sub>2</sub>] with Some Silaketimine Character and a 1,4-Diaza-2,3-Disilabenzene Analogue. *J. Am. Chem. Soc.* **2008**, *130*, 16848–16849.
129. Zhu, L.; Zhang, J.; Yang, H.; Cui, C. Synthesis of Silaketimine Anion and its Coupling with Isocyanide. *J. Am. Chem. Soc.* **2019**, *141*, 19600–19604.
130. (a) Rigon, L.; Ranaivonjatovo, H.; Escudié, J.; Dubourg, A.; Declercq, J.-P. ArP=C=Si(Ph)Tip: The First Allenic Compound with Doubly Bonded Phosphorus and Silicon. *Chem. A Eur. J.* **1999**, *5*, 774–781; (b) Harouch, Y. E.; Gornitzka, H.; Ranaivonjatovo, H.; Escudié, J. The First Stable 3,1-Germaphosphaallene Tip(T-Bu)Ge=C=PAr. *J. Organomet. Chem.* **2002**, *643-644*, 202–208; (c) Ghereg, D.; Saffon, N.; Escudié, J.; Miqueu, K.; Sotiropoulos, J.-M. 1-Arsa-3-Germaallene Tip(T-Bu)Ge=C=AsMes\*: The Heaviest Mixed Group 14 and 15 Heteroallenic Compound. *J. Am. Chem. Soc.* **2011**, *133*, 2366–2369.

131. (a) Troadec, T.; Reyes, M. L.; Rodriguez, R.; Baceiredo, A.; Saffon-Merceron, N.; Branchadell, V.; Kato, T. Donor-Stabilized Silacyclobutanone: A Precursor of 1-Silaketene Via Retro-[2 + 2]-Cycloaddition Reaction at Room Temperature. *J. Am. Chem. Soc.* **2016**, *138*, 2965–2968; (b) Reyes, M. L.; Troadec, T.; Rodriguez, R.; Baceiredo, A.; Saffon-Merceron, N.; Branchadell, V.; Kato, T. Donor/Acceptor-Stabilized 1-Silaketene: Reversible [2 + 2] Cycloaddition with Pyridine and Evolution by an Olefin Metathesis Reaction. *Chem. A Eur. J.* **2016**, *22*, 10247–10253.
132. Jana, A.; Huch, V.; Scheschkewitz, D. NHC-Stabilized Silagermenyldiene: A Heavier Analogue of Vinylidene. *Angew. Chem. Int. Ed.* **2013**, *52*, 12179–12182.
133. Jana, A.; Majumdar, M.; Huch, V.; Zimmer, M.; Scheschkewitz, D. NHC-Coordinated Silagermenyldiene Functionalized in Allylic Position and its Behaviour as a Ligand. *Dalton Trans.* **2014**, *43*, 5175–5181.
134. Ghana, P.; Arz, M. I.; Das, U.; Schnakenburg, G.; Filippou, A. C. Si=Si Double Bonds: Synthesis of an NHC-Stabilized Disilavinylidene. *Angew. Chem. Int. Ed.* **2015**, *54*, 9980–9985.
135. Geiss, D.; Arz, M. I.; Strassmann, M.; Schnakenburg, G.; Filippou, A. C. Si=P Double Bonds: Experimental and Theoretical Study of an NHC-Stabilized Phosphasilenyldiene. *Angew. Chem. Int. Ed.* **2015**, *54*, 2739–2744.
136. Kobayashi, R.; Ishida, S.; Iwamoto, T. Synthesis of an NHC-Coordinated Dialkyldisilavinylidene and its Oxidation Providing a Silicon Analog of an Acetolactone. *Organometallics* **2021**, *40*, 843–847.
137. Rit, A.; Campos, J.; Niu, H.; Aldridge, S. A Stable Heavier Group 14 Analogue of Vinylidene. *Nat. Chem.* **2016**, *8*, 1022–1026.
138. Krebs, K. M.; Hanselmann, D.; Schubert, H.; Wurst, K.; Scheele, M.; Wesemann, L. Phosphine-Stabilized Digermaniyldiene. *J. Am. Chem. Soc.* **2019**, *141*, 3424–3429.
139. Wang, Y.; Xie, Y.; Wei, P.; King, R. B.; Schaefer, H. F., 3rd; Schleyer, P. V. R.; Robinson, G. H. A Stable Silicon(O) Compound with a Si=Si Double Bond. *Science* **2008**, *321*, 1069–1071.
140. (a) Sidiropoulos, A.; Jones, C.; Stasch, A.; Klein, S.; Frenking, G. N-Heterocyclic Carbene Stabilized Digermanium(O). *Angew. Chem. Int. Ed.* **2009**, *48*, 9701–9704; (b) Jones, C.; Sidiropoulos, A.; Holzmann, N.; Frenking, G.; Stasch, A. An N-Heterocyclic Carbene Adduct of Diatomic Tin: Sn=Sn. *Chem. Commun.* **2012**, *48*, 9855–9857.
141. Shan, Y.-L.; Yim, W.-L.; So, C.-W. An N-Heterocyclic Silylene-Stabilized Digermanium(O) Complex. *Angew. Chem. Int. Ed.* **2014**, *53*, 13155–13158.
142. Tsumuraya, T.; Batcheller, S. A.; Masamune, S. Strained-Ring and Double-Bond Systems Consisting of the Group 14 Elements Si, Ge, and Sn. *Angew. Chem. Int. Ed. Engl.* **1991**, *30*, 902–930.
143. Wiberg, N.; Vasisht, S. K.; Fischer, G.; Mayer, P.; Disilynes. III [1] A Relatively Stable Disilyne RSi≡SiR (R = SiMe(Si<sup>t</sup>Bu)<sub>2</sub>). *Z. Anorg. Allg. Chem.* **2004**, *630*, 1823–1828.
144. Sekiguchi, A.; Kinjo, R.; Ichinohe, M. A Stable Compound Containing a Silicon-Silicon Triple Bond. *Science* **2004**, *305*, 1755–1757.
145. Murata, Y.; Ichinohe, M.; Sekiguchi, A. Unsymmetrically Substituted Disilyne Dsi2iPrSi≡Si≡Si-SiNpDsi2 (Np = CH2tBu): Synthesis and Characterization. *J. Am. Chem. Soc.* **2010**, *132*, 16768–16770.
146. Sasamori, T.; Hironaka, K.; Sugiyama, Y.; Takagi, N.; Nagase, S.; Hosoi, Y.; Furukawa, Y.; Tokitoh, N. Synthesis and Reactions of a Stable 1,2-Diaryl-1,2-Dibromodisilene: A Precursor for Substituted Disilenes and a 1,2-Diaryldisilyne. *J. Am. Chem. Soc.* **2008**, *130*, 13856–13857.
147. Ishida, S.; Sugawara, R.; Misawa, Y.; Iwamoto, T. Palladium and Platinum η<sup>2</sup>-Disilyne Complexes Bearing an Isolable Dialkyldisilyne as a Ligand. *Angew. Chem. Int. Ed.* **2013**, *52*, 12869–12873.
148. Sugahara, T.; Guo, J.-D.; Hashizume, D.; Sasamori, T.; Nagase, S.; Tokitoh, N. The Selective Formation of a 1,2-Disilabenzene from the Reaction of a Disilyne with Phenylacetylene. *Dalton Trans.* **2018**, *47*, 13318–13322.
149. Tian, M.; Zhang, J.; Yang, H.; Cui, C. Isolation of a 1-Magnesium-2,3-Disilacyclopropene and a Related Bis(Disilene). *J. Am. Chem. Soc.* **2020**, *142*, 4131–4135.
150. Stender, M.; Phillips, A. D.; Wright, R. J.; Power, P. P. Synthesis and Characterization of a Digermanium Analogue of an Alkyne. *Angew. Chem. Int. Ed.* **2002**, *41*, 1785–1787.
151. Sugiyama, Y.; Sasamori, T.; Hosoi, Y.; Furukawa, Y.; Takagi, N.; Nagase, S.; Tokitoh, N. Synthesis and Properties of a New Kinetically Stabilized Digermyne: New Insights for Germanium Analogue of an Alkyne. *J. Am. Chem. Soc.* **2006**, *128*, 1023–1031.
152. Hadlington, T. J.; Hermann, M.; Li, J.; Frenking, G.; Jones, C. Activation of H<sub>2</sub> by a Multiply Bonded Amido-Digermyne: Evidence for the Formation of a Hydrido-Germylene. *Angew. Chem. Int. Ed.* **2013**, *52*, 10199–10203.
153. Sasamori, T.; Sugahara, T.; Agou, T.; Guo, J.-D.; Nagase, S.; Streubel, R.; Tokitoh, N. Synthesis and Characterization of a 1,2-Digermabenzene. *Organometallics* **2015**, *34*, 2106–2109.
154. Phillips, A. D.; Wright, R. J.; Olmstead, M. M.; Power, P. P. Synthesis and Characterization of 2,6-Dipp<sub>2</sub>-H<sub>3</sub>C<sub>6</sub>SnSnC<sub>6</sub>H<sub>3</sub>-2,6-Dipp<sub>2</sub> (Dipp = C<sub>6</sub>H<sub>3</sub>-2,6-Pr<sub>2</sub>): A Tin Analogue of an Alkyne. *J. Am. Chem. Soc.* **2002**, *124*, 5930–5931.
155. (a) Hadlington, T. J.; Jones, C. A Singly Bonded Amido-Distannyne: H<sub>2</sub> Activation and Isocyanide Coordination. *Chem. Commun.* **2014**, *50*, 2321–2323; (b) Kelly, J. A.; Juckel, M.; Hadlington, T. J.; Fernández, I.; Frenking, G.; Jones, C. Synthesis and Reactivity Studies of Amido-Substituted Germanium(I)/Tin(I) Dimers and Clusters. *Chem. A Eur. J.* **2019**, *25*, 2773–2785.
156. Perla, L. G.; Kulenkampf, J. M.; Fetting, J. C.; Power, P. P. Steric and Electronic Properties of the Bulky Terphenyl Ligand Ar<sup>tBu6</sup> (Ar<sup>tBu6</sup> = C<sub>6</sub>H<sub>3</sub>-2,6-(C<sub>6</sub>H<sub>2</sub>-2,4,6-tBu<sub>3</sub>)<sub>2</sub>) and Synthesis of its Tin Derivatives Ar<sup>tBu6</sup>SnCl, Ar<sup>tBu6</sup>SnSn(H)<sub>2</sub>Ar<sup>tBu6</sup>, and Ar<sup>tBu6</sup>SnSnAr<sup>tBu6</sup>: A New Route to a Distannyne Via Thermolysis of the Asymmetric Hydride Ar<sup>tBu6</sup>SnSn(H)<sub>2</sub>Ar<sup>tBu6</sup>. *Organometallics* **2018**, *37*, 4048–4054.
157. Pu, L.; Twamley, B.; Power, P. P. Synthesis and Characterization of 2,6-Trip<sub>2</sub>-H<sub>3</sub>C<sub>6</sub>PbPbC<sub>6</sub>H<sub>3</sub>-2,6-Trip<sub>2</sub> (Trip = C<sub>6</sub>H<sub>2</sub>-2,4,6-I-Pr<sub>3</sub>): A Stable Heavier Group 14 Element Analogue of an Alkyne. *J. Am. Chem. Soc.* **2000**, *122*, 3524–3525.
158. Queen, J. D.; Bursch, M.; Seibert, J.; Maurer, L. R.; Ellis, B. D.; Fetting, J. C.; Grimme, S.; Power, P. P. Isolation and Computational Studies of a Series of Terphenyl Substituted Diplumbynes with Ligand Dependent Lead–Lead Multiple-Bonding Character. *J. Am. Chem. Soc.* **2019**, *141*, 14370–14383.
159. Gau, D.; Kato, T.; Saffon-Merceron, N.; Cózar, A. D.; Cossio, F. P.; Baceiredo, A. Synthesis and Structure of a Base-Stabilized C-Phosphino-Si-Amino Silyne. *Angew. Chem. Int. Ed.* **2010**, *49*, 6585–6588.
160. Hinz, A.; Goicoechea, J. M. Limitations of Steric Bulk: Towards Phospha-Germynes and Phospha-Stannyne. *Chem. A Eur. J.* **2018**, *24*, 7358–7363.
161. Asami, S.-S.; Okamoto, M.; Suzuki, K.; Yamashita, M. A Boryl-Substituted Diphosphene: Synthesis, Structure, and Reaction with N-Butyllithium to Form a Stabilized Adduct by π-π Interaction. *Angew. Chem. Int. Ed.* **2016**, *55*, 12827–12831.
162. Wilson, D. W. N.; Franco, M. P.; Myers, W. K.; McGrady, J. E.; Goicoechea, J. M. Base Induced Isomerisation of a Phosphaethynolato-Borane: Mechanistic Insights into Boryl Migration and Decarbonylation to Afford a Triplet Phosphinidene. *Chem. Sci.* **2020**, *11*, 862–869.
163. Krachko, T.; Ehlers, A. W.; Nieger, M.; Lutz, M.; Slootweg, J. C. Synthesis and Reactivity of the Phosphorus Analogues of Cyclopentadienone, Tricyclopentanone, and Housene. *Angew. Chem. Int. Ed.* **2018**, *57*, 1683–1687.
164. Tsurusaki, A.; Ura, R.; Kamikawa, K. A Gold(I) Complex with a 1,1'-Binaphthyl-Substituted Diphosphene: Synthesis, Structure, and Catalytic Application to Intramolecular Hydroarylation Reactions. *Dalton Trans.* **2018**, *47*, 4437–4441.
165. Back, O.; Donnadiou, B.; Parameswaran, P.; Frenking, G.; Bertrand, G. Isolation of Crystalline Carbene-Stabilized P<sub>2</sub>-Radical Cations and P<sub>2</sub>-Dications. *Nat. Chem.* **2010**, *2*, 369–373.
166. Beil, A.; Gilliard, R. J., Jr.; Grützmacher, H. From the Parent Phosphinidene-Carbene Adduct NHC=PH to Cationic P<sub>4</sub>-Rings and P<sub>2</sub>-Cycloaddition Products. *Dalton Trans.* **2016**, *45*, 2044–2052.
167. Schwedtmann, K.; Holthausen, M. H.; Sala, C. H.; Hengersdorf, F.; Fröhlich, R.; Weigand, J. J. [(<sup>C</sup>Im<sup>Dipp</sup>)P=P(Dipp)][GaCl<sub>4</sub>]: A Polarized, Cationic Diphosphene. *Chem. Commun.* **2016**, *52*, 1409–1412.
168. Doddi, A.; Bockfeld, D.; Zaretzke, M.-K.; Kleeberg, C.; Bannenberg, T.; Tamm, M. A Modular Approach to Carbene-Stabilized Diphosphorus Species. *Dalton Trans.* **2017**, *46*, 15859–15864.

169. Ho, L. P.; Nasr, A.; Jones, P. G.; Altun, A.; Neese, F.; Bistoni, G.; Tamm, M. London Dispersion Interactions in Pnictogen Cations  $[ECl_2]^+$  and  $[E=E]^2+$  ( $E=P, As, Sb$ ) Supported by Anionic N-Heterocyclic Carbenes. *Chem. A Eur. J.* **2018**, *24*, 18922–18932.
170. Ho, L. P.; Zaretsky, M.-K.; Bannenberg, T.; Tamm, M. Heteroleptic Diphosphenes and Arsphosphenes Bearing Neutral and Anionic N-Heterocyclic Carbenes. *Chem. Commun.* **2019**, *55*, 10709–10712.
171. Liu, L. L.; Cao, L. L.; Zhou, J.; Stephan, D. W. Facile Cleavage of the P=P Double Bond in Vinyl-Substituted Diphosphenes. *Angew. Chem. Int. Ed.* **2019**, *58*, 273–277.
172. Rottschäfer, D.; Sharma, M. K.; Neumann, B.; Stammler, H.-G.; Andradra, D. M.; Ghadwal, R. S. A Modular Access to Divinyldiphosphenes with a Strikingly Small HOMO–LUMO Energy Gap. *Chem. A Eur. J.* **2019**, *25*, 8127–8134.
173. Mitrofan, C.; Gust, T.; Zanin, A.; Birzoi, R. M.; Jones, P. G.; du Mont, W.-W.; Hayashi, S.; Nakanishi, W.; Marsmann, H. C. Dichlorosilylene Transfer to a P-Fluorophosphaalkene: The Route to a C-Dichlorofluorosilyl-Functionalized Diallyldiphosphene. *Eur. J. Inorg. Chem.* **2017**, 1526–1536.
174. Liu, L. L.; Zhou, J.; Kim, Y.; Cao, L. L.; Stephan, D. W. Oligomerization of Phosphaalkynes Mediated by Bulky N-Heterocyclic Carbenes: Avenues to Novel Phosphorus Frameworks. *Dalton Trans.* **2019**, *48*, 14242–14245.
175. Xiong, Y.; Yao, S.; Szilvási, T.; Ballester-Martínez, E.; Grützmacher, H.; Driess, M. Unexpected Photodegradation of a Phosphaketonyl-Substituted Germlyumylidene Borate Complex. *Angew. Chem. Int. Ed.* **2017**, *56*, 4333–4336.
176. Schwedtman, K.; Haberstroh, J.; Roediger, S.; Bauzá, A.; Frontera, A.; Hennersdorf, F.; Weigand, J. J. Formation of an Imidazolium-Substituted  $[(L_2)_4P_4]^{4+}$  Tetracation and Transition Metal Mediated Fragmentation and Insertion Reaction ( $L_C = NHC$ ). *Chem. Sci.* **2019**, *10*, 6868–6875.
177. Schumann, A.; Reiß, F.; Jiao, H.; Rabeah, J.; Siewert, J.-E.; Krummenacher, I.; Braunschweig, H.; Hering-Junghans, C. A Selective Route to Aryl-Triphosphiranes and their Titanocene-Induced Fragmentation. *Chem. Sci.* **2019**, *10*, 7859–7867.
178. Wilson, D. W. N.; Myers, W. K.; Goicochea, J. M. Synthesis and Decarbonylation Chemistry of Gallium Phosphaketenes. *Dalton Trans.* **2020**, *49*, 15249–15255.
179. Sharma, M. K.; Blomeyer, S.; Neumann, B.; Stammler, H.-G.; Ghadwa, R. S. Crystalline Divinyldiarsenes and Cleavage of the As=As Bond. *Chem. A Eur. J.* **2019**, *25*, 8249–8253.
180. (a) Paetzold, P.; Neyses, S.; Géret, L. Oxo(trisilyl)boran ( $Me_3Si)_3C-B \equiv O$  als Zwischenstufe. *Z. Anorg. Allg. Chem.* **1995**, *621*, 732–736. R–B=O, Ar–B=S, and Ar–B=Se are highly reactive and easily oligomerized; (b) Groteklaes, M.; Paetzold, P. Oxo(Tri-Tert-Butylphenyl)Boran  $ArB \equiv O$  Als Zwischenstufe. *Chem. Ber.* **1988**, *121*, 809–810; (c) Tokitoh, N.; Ito, M.; Okazaki, R. Formation and Reactions of a Thioxoborane, a Novel Boron–Sulfur Double-bond Compound. *Tetrahedron Lett.* **1996**, *37*, 5145–5148; (d) Ito, M.; Tokitoh, N.; Kawashima, T.; Okazaki, R. Formation of a Borylene by Photolysis of an Overcrowded Bis(Methylseleno)Borane. *Tetrahedron Lett.* **1999**, *40*, 5557–5560.
181. (a) Braunschweig, H.; Radacki, K.; Schneider, A. Oxoboryl Complexes: Boron–Oxygen Triple Bonds Stabilized in the Coordination Sphere of Platinum. *Science* **2010**, *328*, 345–347; (b) Braunschweig, H.; Radacki, K.; Schneider, A. Reactivity of an Oxoboryl Complex toward Fluorinated Aryl Boron Reagents. *Chem. Commun.* **2010**, *46*, 6473–6475.
182. (a) Franz, D.; Inoue, S. Advances in the Development of Complexes that Contain a Group 13 Element Chalcogen Multiple Bond. *Dalton Trans.* **2016**, *45*, 9385–9397; (b) Borthakur, R.; Chandrasekhar, V. Boron-Heteroelement (B–E; E = Al, C, Si, Ge, N, P, As, Bi, O, S, Se, Te) Multiply Bonded Compounds: Recent Advances. *Coord. Chem. Rev.* **2021**, *431*, 213647; (c) Weber, L. Recent Progress in 1,3,2-Diazaborole Chemistry. *Coord. Chem. Rev.* **2021**, *431*, 213667.
183. (a) Neculai, D.; Roesky, H. W.; Neculai, A. M.; Magull, J.; Walfort, B.; Stalke, D. Formation and Characterization of the First Monoaluminum,  $AlI-B(C_6F_5)_3$ . *Angew. Chem. Int. Ed.* **2002**, *41*, 4294–4296; (b) Franz, D.; Szilvási, T.; Irran, E.; Inoue, S. A Monotopic Aluminum Telluride with an Al=Te Double Bond Stabilized by N-Heterocyclic Carbenes. *Nat. Commun.* **2015**, *6*, 10037; (c) Chu, T.; Vyboishchikov, S. F.; Gabidullin, B.; Nikonov, G. I. Oxidative Cleavage of C=S and P=S Bonds at an Al<sup>I</sup> Center: Preparation of Terminally Bound Aluminum Sulfides. *Angew. Chem. Int. Ed.* **2016**, *55*, 13306–13311; (d) Evans, M. J.; Anker, M. D.; McMullin, C. L.; Rajabi, N. A.; Coles, M. P. Double Insertion of CO<sub>2</sub> into an Al–Te Multiple Bond. *Chem. Commun.* **2021**, *57*, 2673–2676.
184. (a) Kuchta, M. C.; Parkin, G. Terminal Chalcogenido Complexes of Gallium Supported by Tris(3,5-di-tert-butylpyrazolyl)hydroborato Ligand:  $[Tp^{Bu_2}]GaE$  (E = Se, Te). *Inorg. Chem.* **1997**, *36*, 2492–2493; (b) Kuchta, M. C.; Parkin, G. Synthesis and Structural Characterization of  $[Tp^{Bu_2}]GaS$ : A Terminal Gallium Sulfido Complex in a System for which the Indium Counterpart Is a Tetrasulfido Derivative,  $[Tp^{Bu_2}]In(\eta^2-S_4)$ . *J. Chem. Soc. Dalton Trans.* **1998**, 2279–2280.
185. Kuchta, M. C.; Parkin, G. Multiple Bonding to Indium: The Synthesis and Structure of  $[Tp^{Bu_2}]InSe$ , a Terminal Selenido Complex Supported by Tris(3,5-di-tert-butylpyrazolyl)hydroborato Ligand. *J. Am. Chem. Soc.* **1995**, *117*, 12651–12652.
186. (a) Wang, H.; Zhang, J.; Hu, H.; Cui, C. Access to B=S and B=Se Double Bonds Via Sulfur and Selenium Insertion into a B–H Bond and Hydrogen Migration. *J. Am. Chem. Soc.* **2010**, *132*, 10998–10999; (b) Chen, P.; Cui, C. Isolable Boron Persulfide: Activation of Elemental Sulfur with a 2-Chloro-Azaborolyl Anion. *Chem. A Eur. J.* **2016**, *22*, 2902–2905; (c) Liu, S.; Légaré, M.-A.; Hofmann, A.; Braunschweig, H. A Boraditellurirane and a Boraditellurirane: Isolable Heavy Analogs of Dioxiranes and Dithiranes. *J. Am. Chem. Soc.* **2018**, *140*, 11223–11226; (d) Chen, C.; Daniliuc, C. G.; Mück-Lichtenfeld, C.; Kehr, G.; Erker, G. A BH Borenum-Derived Thioxoborane, its Persulfide, and their Li + -Induced Reactions with Alkynes and with Carbon Dioxide. *J. Am. Chem. Soc.* **2020**, *142*, 19763–19771; (e) Dolati, H.; Denker, L.; Trzaskowski, B.; Frank, R. Superseding  $\beta$ -Diketiminato Ligands: An Amido Imidazoline-2-Imine Ligand Stabilizes the Exhaustive Series of B=X Boranes (X=O, S, Se, Te). *Angew. Chem. Int. Ed.* **2021**, *60*, 4633–4639; (f) Jaiswal, K.; Prashanth, B.; Ravi, S.; Shamasundar, K. R.; Singh, S. Reactivity of a Dihydroboron Species: Synthesis of a Hydroborenum Complex and an Expedient Entry into Stable Thio- and Seleno-Boranes. *Dalton Trans.* **2015**, *44*, 15779–15785; (g) Martínez, J. P.; Trzaskowski, B. Structural and Electronic Properties of Boranes Containing Boron-Chalcogen Multiple Bonds and Stabilized by Amido Imidazoline-2-Imine Ligands. *Chem. A Eur. J.* **2022**, *28*, e202103997.
187. Franz, D.; Irran, E.; Inoue, S. Isolation of a Three-Coordinate Boron Cation with a Boron–Sulfur Double Bond. *Angew. Chem. Int. Ed.* **2014**, *53*, 14264–14268.
188. (a) Loh, Y. K.; Porteous, K.; Fuentes, M.A.; Do, D. C. H.; Hicks, J.; Aldridge, S. An Acid-Free Anionic Oxoborane Isoelectronic with Carbonyl: Facile Access and Transfer of a Terminal B=O Double Bond. *J. Am. Chem. Soc.* **2019**, *141*, 8073–8077; (b) Liu, R.; Gao, F.; Liu, J.; Wei, J.; Hou, L.; Xie, G.; Chen, S.; Zeng, F.; Li, A.; Wang, W. Anionic Oxoborane and Thioxoborane Molecules Supported by a 1,2-Bis(Imino)Acenaphthene Ligand. *Dalton Trans.* **2021**, *50*, 6797–6801; (c) Anker, M. D.; Coles, M. P. Isoelectronic Aluminium Analogues of Carbonyl and Dioxirane Moieties. *Angew. Chem. Int. Ed.* **2019**, *58*, 13452–13455.
189. Pyykkö, P.; Atsumi, M. Molecular Double-Bond Covalent Radii for Elements Li–E112. *Chem. A Eur. J.* **2009**, *15*, 12770–12779.
190. Uhl, W.; Gerding, R.; Hahn, I.; Pohl, S.; Saak, W.; Reuter, H. The Insertion of Chalcogen Atoms into Al–Al and Ga–Ga Bonds: Monomeric Compounds with Al–Se–Al, Ga–S–Ga and Ga–Se–Ga Groups. *Polyhedron* **1996**, *15*, 3987–3992.
191. (a) Cui, C.; Roesky, H. W.; Hao, H.; Schmidt, H.-G.; Noltemeyer, M. The First Structurally Characterized Metal–SeH Compounds:  $[Al(SeH)_2]$  and  $[L(HSe)AlSeAl(SeH)_L]$ . *Angew. Chem. Int. Ed.* **2000**, *39*, 1815–1817; (b) González-Gallardo, S.; Cruz-Zavala, A. S.; Jancik, V.; Cortés-Guzmán, F.; Moya-Cabrera, M. Preparation of Telluro- and Selenoaluminum Analogues Under Mild Conditions. *Inorg. Chem.* **2013**, *52*, 2793–2795.
192. Agarwal, A.; Bose, S. K. Bonding Relationship Between Silicon and Germanium With Group 13 and Heavier Elements of Groups 14–16. *Chem. Asian J.* **2020**, *15*, 3784–3806.
193. Ritch, J. S. Synthesis and Coordination Chemistry of Cyclic Seleno- and Telluroureas. *Phys. Sci. Rev.* **2019**, *4*, 20170128.
194. Saab, M.; Nelson, D. J.; Tzouras, N. V.; Bayraktar, A. C. A.; Nolan, S. P.; Nahra, F.; Van Hecke, K. Straightforward Access to Chalcogenoureas Derived from N-Heterocyclic Carbenes and Their Coordination Chemistry. *Dalton Trans.* **2020**, *49*, 12068–12081.
195. Liske, A.; Verlinden, K.; Buhl, H.; Schaper, K.; Ganter, C. Determining the  $\pi$ -Acceptor Properties of N-Heterocyclic Carbenes by Measuring the <sup>77</sup>Se NMR Chemical Shifts of Their Selenium Adducts. *Organometallics* **2013**, *32*, 5269–5272.
196. Yao, S.; Xiong, Y.; Saddington, A.; Driess, M. Entering New Chemical Space with Isolable Complexes of Single, Zero-Valent Silicon and Germanium Atoms. *Chem. Commun.* **2021**, *57*, 10139–10153.
197. (a) Xiong, Y.; Yao, S.; Müller, R.; Kaupp, M.; Driess, M. From Silylone to an Isolable Monomeric Silicon Disulfide Complex. *Angew. Chem. Int. Ed.* **2015**, *54*, 10254–10257; (b) Xiong, Y.; Yao, S.; Karni, M.; Kostenko, A.; Burchert, A.; Apeloig, Y.; Driess, M. Heavier Congeners of CO and CO<sub>2</sub> as Ligands: From Zero-Valent Germanium (‘Germlyone’) to Isolable Monomeric GeX and GeX<sub>2</sub> Complexes (X = S, Se, Te). *Chem. Sci.* **2016**, *7*, 5462–5469.

198. (a) Mohapatra, C.; Mondal, K. C.; Samuel, P. P.; Keil, H.; Niepötter, B.; Herbst-Irmer, R.; Stalke, D.; Dutta, S.; Koley, D.; Roesky, H. W. A Stable Dimer of SiS<sub>2</sub> Arranged between Two Carbene Molecules. *Chem. A Eur. J.* **2015**, *21*, 12572–12576; (b) Mondal, K. C.; Roy, S.; Dittrich, B.; Maity, B.; Dutta, S.; Koley, D.; Vasa, S. K.; Linsler, R.; Dechert, S.; Roesky, H. W. A Soluble Molecular Variant of the Semiconducting Silicondiselenide. *Chem. Sci.* **2015**, *6*, 5230–5234.
199. (a) Sugamata, K.; Hashizume, D.; Suzuki, Y.; Sasamori, T.; Ishii, S. Synthesis and Structure of a Stable Bis(Methylene)- $\lambda^4$ -Sulfane. *Chem. A Eur. J.* **2018**, *24*, 6922–6926; (b) Sugamata, K.; Urao, Y.; Minoura, M. A Stable Bis(Methylene)- $\lambda^4$ -Selane with a  $>C=Se=C<$  Bond Containing Se(IV). *Chem. Commun.* **2019**, *55*, 8254–8257; (c) Sugamata, K.; Urao, Y.; Minoura, M. (Thio)(Silyl)Carbene and (Seleno)(Silyl)Carbene Gold(I) Complexes From the Reaction of Bis(Methylene)- $\lambda^4$ -Sulfane and Bis(Methylene)- $\lambda^4$ -Selane With Chloro(Dimethylsulfide)Gold(I). *Dalton Trans.* **2020**, *49*, 7688–7691.
200. Schulz, S. Covalently Bonded Compounds of Heavy Group 15/16 Elements—Synthesis, Structure and Potential Application in Material Sciences. *Coord. Chem. Rev.* **2015**, *297–298*, 49–76.
201. (a) Heimann, S.; Bläser, D.; Wölper, C.; Haack, R.; Jansen, G.; Schulz, S. The Bonding Situation in Triethylchalcogenostiboranes—Polarized Single Bonds vs. Double Bonds. *Dalton Trans.* **2014**, *43*, 14772–14777; (b) Nordheider, A.; Woolins, J. D.; Chivers, T. Organophosphorus—Tellurium Chemistry: From Fundamentals to Applications. *Chem. Rev.* **2015**, *115*, 10378–10406.
202. Yoshifuji, M.; Sangu, S.; Hirano, M.; Toyota, K. A Stabilized Phosphinothioylidene Generated by Deselenation of a Selenoxothioxophosphorane. *Chem. Lett.* **1993**, *22*, 1715–1718.
203. Jambor, R. The Pincer Complexes of Group 13–15 Elements: Recent Developments. In *Pincer Compounds*; Dostál, L., Morales-Morales, D., Eds., Elsevier, 2018; pp 47–65. ch. 3.
204. (a) Appel, R.; Knoch, F.; Kunze, H. The First Organodithioxophosphorane. *Angew. Chem. Int. Ed. Engl.* **1983**, *22*, 1004–1005; (b) Liu, L. L.; Cao, L. L.; Zhou, J.; Stephan, D. W. Facile Cleavage of the P=P Double Bond in Vinyl-Substituted Diphosphenes. *Angew. Chem. Int. Ed.* **2019**, *58*, 273–277; (c) Rottschäfer, D.; Sharma, M. K.; Neumann, B.; Stammler, H.; Andrada, D. M.; Ghadwal, R. S. A Modular Access to Divinyldiphosphenes with a Strikingly Small HOMO–LUMO Energy Gap. *Chem. A Eur. J.* **2019**, *25*, 8127–8134.
205. (a) Yoshifuji, M.; Sangu, S.; Kamijo, K.; Toyota, K. 2,4-Di-Tert-Butyl-6-Piperidinophenyl as a Sterically and Electronically Stabilizing Group and X-Ray Analysis of the Corresponding Diselenoxophosphorane. *J. Chem. Soc. Chem. Commun.* **1995**, *3*, 297–298; (b) Reznicek, T.; Dostál, L.; Růžicka, A.; Jirásko, R.; Jambor, R. Synthesis of Organophosphorus Compounds Containing Different Y,C,Y-Chelating Ligands. Crystal Structure of P←N Intramolecularly Coordinated Diselenoxophosphorane. *Inorg. Chim. Acta* **2010**, *363*, 3302–3307; (c) Kornev, A. N.; Daza, D. F. D.; Sushev, V. V.; Panova, Y. S.; Galperin, V. E.; Fukin, G. K.; Baranov, E. V.; Abakumov, G. A. Reactions of Cyclohexene-Annulated 3a,6a-Diaza-1,4-Diphosphapentalene With Sulfur, Selenium, and CS<sub>2</sub>: Structural Features of Zwitterionic Products. *Russ. Chem. Bull.* **2018**, *67*, 114–120.
206. Maas, G.; Stang, P. J. Dication Disulfides by Reaction of Thioureas and Related Compounds With Trifluoromethanesulfonic Anhydride. The Role of Triflic Anhydride as an Oxidizing Agent. *J. Org. Chem.* **1981**, *46*, 1606–1610.
207. Bigoli, F.; Demartin, F.; Deplano, P.; Devillanova, F. A.; Isaia, F.; Lippolis, V.; Mercuri, M. L.; Pellinghelli, M. A.; Trogu, E. F. Synthesis, Characterization, and Crystal Structures of New Dications Bearing the –Se–Se– Bridge. *Inorg. Chem.* **1996**, *35*, 3194–3201.
208. Nakata, N.; Kawauchi, F.; Takahashi, S.; Ishii, A. Dicationic Ditelluride Salts Stabilized by N-Heterocyclic Carbene. *New J. Chem.* **2019**, *43*, 10894–10898.
209. Mallow, O.; Khanfar, M. A.; Malischewski, M.; Finke, P.; Hesse, M.; Lork, E.; Augenstein, T.; Breher, F.; Harmer, J. R.; Vasilieva, N. V.; Zibarev, A.; Bogomyakov, A. S.; Seppelt, K.; Beckmann, J. Diaryldichalcogenide Radical Cations. *Chem. Sci.* **2014**, *6*, 497–504.



## 1.04 Biradicals in main group chemistry: Synthesis, electronic structure, and application in small-molecule activation

Jonas Bresien, Liesa Eickhoff, Axel Schulz, and Edgar Zander, Institute of Chemistry, University of Rostock, Rostock, Germany

© 2023 Elsevier Ltd. All rights reserved.

<b>1.04.1</b>	<b>Introduction</b>	<b>165</b>
<b>1.04.2</b>	<b>Theoretical description of biradicals</b>	<b>168</b>
1.04.2.1	Scope of this section	168
1.04.2.2	Dynamic vs. non-dynamic correlation	168
1.04.2.3	Two electrons in two orbitals	169
1.04.2.4	Two degenerate frontier orbitals	169
1.04.2.5	Energetic ordering of the biradical states	170
1.04.2.6	Chemical interpretation of the biradical states	172
1.04.2.7	Two nearly degenerate frontier orbitals	175
1.04.2.8	More orbital transformations	180
1.04.2.9	Non-symmetric biradicals	183
1.04.2.10	Biradical character	184
1.04.2.11	Different classifications of biradicals	187
<b>1.04.3</b>	<b>Main group biradicals</b>	<b>188</b>
1.04.3.1	General aspects	188
1.04.3.2	Main group analogs of cyclobutane-1,3-diyls	189
1.04.3.2.1	Niecke's 1,3-diphospha-cyclobutane-2,4-diyl	190
1.04.3.2.2	Hetero-cyclobutane-1,3-diyls with radical centers on elements of group 13	190
1.04.3.2.3	Hetero-cyclobutane-1,3-diyls with radical centers on elements of group 14	193
1.04.3.2.4	Hetero-cyclobutane-1,3-diyls with radical centers on elements of group 15	202
1.04.3.2.5	Hetero-cyclobutane-1,3-diyls with radical centers on elements of group 16	208
1.04.3.3	Main group 15 analogs of cyclopentane-1,3-diyls	210
1.04.3.3.1	Hetero-cyclopentane-1,3-diyls with radical centers on elements of group 14	210
1.04.3.3.2	Hetero-cyclopentane-1,3-diyls with radical centers on elements of group 15	213
<b>1.04.4</b>	<b>Applications of biradicals as molecular switches</b>	<b>221</b>
<b>1.04.5</b>	<b>Outlook: Beyond four and five-membered heterocyclic biradicals</b>	<b>224</b>
<b>References</b>		<b>224</b>
<b>Further reading</b>		<b>232</b>
<b>Relevant websites</b>		<b>233</b>

### Abstract

In this article, we review the concept of biradical(oid)s from a theoretical as well as experimental perspective. In particular, we analyze the “two electrons in two orbitals” model, which is frequently used to describe the electronic structure of biradical(oid)s, with special emphasis on systems with a small HOMO-LUMO gap, so-called open-shell singlet biradicals or singlet biradicaloids. We then revise the chemistry of main group analogs of cyclobutane-1,3-diyls and cyclopentane-1,3-diyls as typical examples of singlet biradical(oid)s. Lastly, it is shown how some of these biradicals can be applied as molecular switches by switching the biradical character on and off.

### 1.04.1 Introduction

To be radical is to grasp things by the root.

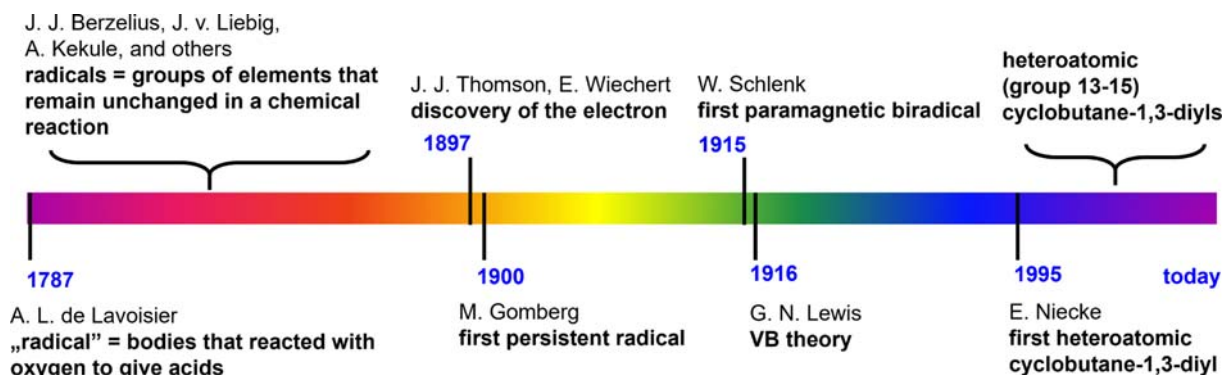
Karl Marx in Critique of Hegel's Philosophy of Right (1844).<sup>1</sup>

The word “radical” is borrowed from the Latin word *radix* (English: root) and originally meant “going to the origin, essential.” The word appeared in several European languages at the end of the 14th century, mostly in a philosophical context. The “root sign” of mathematics was introduced in the 1680s.<sup>2</sup> In chemistry, the word appears for the first time at the end of the 18th century, when

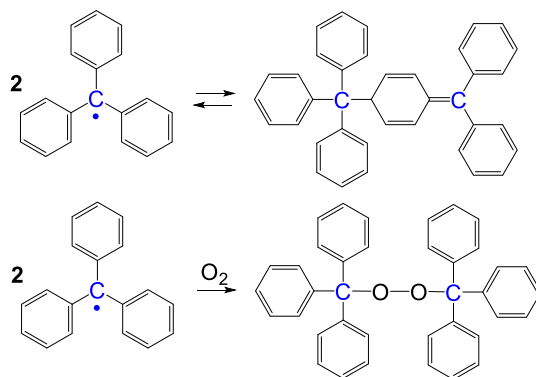


Lavoisier spoke of organic compounds as “oxides of radicals” (components of an acid).<sup>3</sup> The meaning of the word changed over time in everyday language (radical = extreme) as well as in chemistry. Let’s look a little closer at the historical development of the term radical in chemistry.<sup>4</sup> Lavoisier used the term radical for an atom or a group of atoms bound to oxygen in oxygen compounds (Fig. 1), “the residue of a body freed from oxygen.” Sulfur and phosphorus were the radicals of sulfuric acid and phosphoric acid. Moreover, he called organic compounds “oxides of radicals” composed of at least two elements, and according to Berzelius the main difference in composition between inorganic and organic compounds seemed to be that the former contained simple, the latter compound radicals. This concept was given a more definite and real form by investigations into cyanogenic compounds, above all by those carried out by Gay-Lussac in 1815,<sup>5,6</sup> from which it emerged that the radical composed of carbon and nitrogen (cyanogen) behaves entirely like an element and passes from one compound into the other, and can even be deposited in free form. At that time, however, cyanogenic compounds had not yet found their proper place among organic compounds. This radical concept gave rise to the first comprehensive theory for the inner composition of organic compounds which was mainly introduced by Liebig and Wöhler in 1832.<sup>7</sup> It should be noted that the word “radical” has two meanings in chemistry today, which, however, developed at different times.<sup>8</sup> On the one hand, it is understood to mean the part of a molecule that remains unchanged during a chemical transformation (e.g., an alkyl or aryl group); on the other hand, certain fragments of molecules that occur as intermediates in chemical reactions are called “free radicals.”<sup>3</sup> Today, according IUPAC Gold Book,<sup>9</sup> a radical is “a molecular entity such as  $\cdot\text{CH}_3$ ,  $\cdot\text{SnH}_3$ ,  $\text{Cl}\cdot$  possessing an unpaired electron.” With respect to the two meanings, as mentioned above, it is recommended: “In the past, the term “radical” was used to designate a substituent group bound to a molecular entity, as opposed to “free radical,” which nowadays is simply called radical. The bound entities may be called groups or substituents, but should no longer be called radicals.”<sup>9</sup>

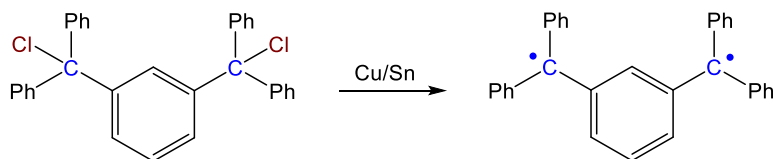
Interestingly, the term “radical” was introduced long before a corresponding theoretical basis, so it is not surprising that the original meaning referred to an atomic group in the sense of a substituent. The electron was not discovered until 1897. Shortly afterwards, Gomberg<sup>10</sup> published his work on the first persistent radical (Scheme 1), while the first paramagnetic biradical was synthesized by Schlenk in 1915 (Scheme 2).<sup>11</sup> Furthermore, Gomberg’s groundbreaking work also showed the typical reaction behavior of radicals, such as dimerization at lower temperatures or the reaction with oxygen to give a peroxide (Scheme 1). This is all the more astonishing because the birth of a modern bond theory or a theoretical basis for today’s radical definition was only laid in 1916 by Lewis<sup>12</sup> with the introduction of the valence-bond (VB) method. In terms of VB theory, a biradical bond situation is in some ways the opposite of a bond. If you break a bond in a molecule, you have a biradical or at least its relative, a zwitterion (see below).



**Fig. 1** Timeline of important dates leading to the modern description of biradicals.



**Scheme 1** Gomberg's persistent radical.



**Scheme 2** Schlenk's paramagnetic biradical.

What's in a name? That which we call a rose by any other name would smell as sweet.

William Shakespeare in *Romeo and Juliet* (1597).<sup>13</sup>

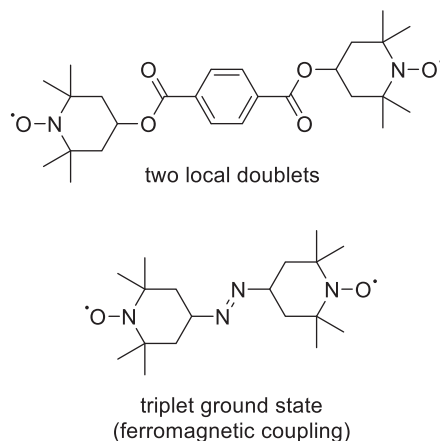
Unfortunately, there are many names and classifications for biradicals; even the IUPAC does not offer a consistent definition.<sup>14–16</sup> According to the “Gold Book,” a “biradical”<sup>14</sup> is a molecule with two radical centers that act nearly independently of each other, i.e., singlet and triplet state are nearly degenerate. In the case of a particularly weak interaction between the two electrons, such species are best described as a pair of radicals (two local doublets) that are connected by a linker of some sort (**Scheme 3**). In case of a significant interaction between the radical centers (here: antiferromagnetic coupling), the term “biradicaloid” is proposed. Conversely, a “diradical”<sup>15</sup> is a molecule with two “unpaired electrons,” in which a distinct singlet (electron-paired) and triplet (electron-unpaired) state can be identified. Hence, the electrons display antiferromagnetic (or ferromagnetic) coupling, respectively. According to the above definitions, the terms “diradical” and “biradicaloid” could be regarded as synonyms.

To make matters more complicated, a different definition by the IUPAC exists,<sup>16</sup> stating that the terms “biradical” and “diradical” are to be considered synonymous and describe an “even-electron molecular entity with two (possibly delocalized) radical centers,” whereas the terms “biradicaloid” and “diradicaloid” are synonyms for “species in which the two radical centers interact significantly.”

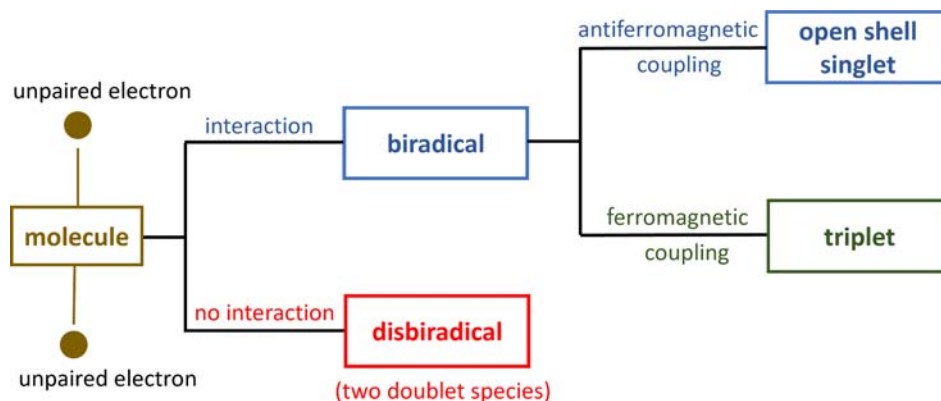
In the literature, we often find yet another definition<sup>18–20</sup>: While the expressions “biradical” or “diradical” are used to indicate species with degenerate frontier molecular orbitals (e.g., dioxygen or trimethylenemethane), the terms “biradicaloid” or “diradicaloid” refer to species with a small HOMO–LUMO gap, which may be regarded as somewhere in between an open-shell biradical and a closed-shell singlet species. While this classification is of course equally valid, it is worthy to note that the various definitions presented here rely on different properties of the electronic structure of biradical(oid)s, so they are not always identical.

To use a uniform notation, we recently proposed to use the term “disbiradical”<sup>21</sup> (using the Latin prefix “dis-”: asunder, apart) for the two-doublet species (almost no coupling) and “(singlet/triplet) biradical” for all other cases. As stated above, ferromagnetic coupling between the two electrons leads to a triplet biradical, whereas antiferromagnetic coupling results in an (open-shell) singlet biradical (**Scheme 4**). Since there is no defined limit to the degree of interaction, there is no real need to use the term “di-/biradicaloid” unless theory presents us with a clear dividing line. In fact, the transitions between biradical → biradicaloid → closed-shell singlet species are smooth in terms of electronic interaction.<sup>22</sup> For this reason, a corresponding distinction between (singlet) biradicals and biradicaloids is not made in this text.

Nonetheless, we will explore the electronic structure of biradicals in detail and point out various descriptors that help to understand the nature of different “types” of biradicals. This includes, but is not limited to, the HOMO–LUMO gap, the singlet–triplet gap (ST gap), the bonding situation (e.g., with regard to the conjugation of  $\pi$  bonds), whether the radical sites are localized or



**Scheme 3** Examples of biradicals according to the “Gold Book” definition. Adapted from Abe, M. *Diradicals*. Chem. Rev. 2013, 113 (9), 7011–7088.



**Scheme 4** Definition for biradicals and disbiradicals used in this article.

delocalized, etc. The different types and classifications of biradicals are discussed in detail throughout [Section 1.04.2](#) and, particularly, in [Sections 1.04.2.10](#) and [1.04.2.11](#).

In [Section 1.04.3](#), we will discuss cyclic four-membered and five-membered biradicals, namely so-called **cyclobutane-1,3-diyls** and **cyclopentane-1,3-diyls**,<sup>21</sup> for which there are experimental studies and in which at least one of the carbon atoms of the central ring fragment is substituted by a main group heteroatom. Furthermore, the radical centers should be centered within the four- and five-membered ring system, respectively, and be in 1,3-position to each other. Cyclic triplet carbenes, which can be understood as 1,1-diyls, are therefore not part of the present work. Cyclic heavier analogs containing double bonds, such as the disilene<sup>23</sup> investigated by Glasovac et al., which can be regarded as 1,2-diyls, are also not discussed. Furthermore, cage compounds that can formally be derived from cyclobutanediyls, such as [1.1.1]propellane derivatives,<sup>22,24,25</sup> are also not included in our review. We will discuss why the classes of compounds presented are biradicals and describe the synthesis and reactivity of these special molecules.

In [Section 1.04.4](#), the application of heterocyclopentane-1,3-diyls as molecular switches is shortly discussed. This very recent field of research offers new possibilities to control chemical equilibria by outside stimuli such as irradiation with visible light.

## 1.04.2 Theoretical description of biradicals

### 1.04.2.1 Scope of this section

This section aims to convey a principal understanding of the electronic structure of biradicals and is targeted at readers who have a basic understanding of Hartree-Fock (HF) and Density Functional Theory (DFT). First, we will cover fundamentals such as two-configuration wavefunctions, and then discuss implications of the theoretical description on our understanding of biradicals, especially regarding their classification in different subsets. Lastly, we will shortly discuss the popular “broken-symmetry” approach, which may be used to describe biradicals using UHF/UKS wavefunctions, and its connection to multireference wavefunctions.

The discussion presented in this section is partly adapted from the excellently worked-out analyses of Salem/Rowland,<sup>18</sup> Bonačić/Koutecký/Michl,<sup>19,26</sup> Lineberger/Borden,<sup>27</sup> Stuyver/Chen/Zeng/Hoffmann<sup>20</sup> and their co-workers.

### 1.04.2.2 Dynamic vs. non-dynamic correlation

Before we start our exploration of the electronic structure of biradicals, a quick revision of the concept of “electron correlation” is in order<sup>28</sup>. Electron correlation describes the instantaneous interaction of each electron with all other electrons of a many-electron wavefunction. Consequently, it cannot be described by a single molecular orbital (MO) configuration, such as a Hartree-Fock (HF) Slater determinant. Remember that in HF self-consistent field (SCF) calculations, the MOs are variationally optimized as one-electron eigenfunctions of the Fock operator and include only the averaged repulsion with the mean field of all other electrons/orbitals (expressed as a sum over Coulomb integrals  $J_{ij}$ ) as well as the exchange interaction (which is a correlation effect between same-spin electrons as a result of the antisymmetrized Slater determinant, expressed as a sum over exchange integrals  $K_{ij}$ ). Thus, the correlation energy can be defined as the difference between the HF limit ( $E_{\text{HF}}$ , i.e., the HF-SCF energy at the basis set limit) and the true ground state energy ( $E_{\text{exact}}$ , i.e., the exact solution of the non-relativistic Schrödinger equation):

$$E_{\text{corr}} = E_{\text{exact}} - E_{\text{HF}} \quad (1)$$

To include electron correlation and thus lower the energy of a given system, it is necessary to express the wavefunction  $\Psi$  not as a single Slater determinant, but as a linear combination of several Slater determinants  $\Psi_i$ :

$$\Psi = c_1\Psi_1 + c_2\Psi_2 + c_3\Psi_3 + \dots \quad (2)$$

This linear combination is, in general, called a “configuration interaction” (CI) wavefunction, with CI coefficients  $c_i$  defining the contribution of each determinant to the CI expansion. Note if  $\langle \Psi_i | \Psi_j \rangle = \delta_{ij}$  (i.e., if the Slater determinants are orthonormal, which is typically the case), then  $\sum c_i^2 = 1$ .

For many molecular systems, the leading contribution  $\Psi_1$  is the HF wavefunction  $\Psi_{\text{HF}}$  (also called HF reference in this context). Even though the correlation might be large, it is usually composed of a sum of individually small contributions from all other determinants, that is,  $c_1$  is much larger than all other coefficients. (The other determinants  $\Psi_2, \Psi_3$ , etc. are then typically generated by “exciting” one or more electrons from occupied to unoccupied HF orbitals.) This type of electron correlation is called “dynamic correlation,” and the wavefunction can still be approximately described using a single configuration.

There are, however, instances in which two (or more) coefficients  $c_i$  in Eq. (2) are much larger than the other coefficients. In these cases, a single electronic configuration is unsuitable to describe the wavefunction of the system! Thus, the HF reference is an insufficient approximation, and we must use two-configurational (or multireference) wavefunctions for a qualitatively correct representation of the electronic structure. This type of electron correlation is called “non-dynamic” or “static correlation” and is key to the understanding of biradicals (or polyradicals).

For readers who are unfamiliar with the concept of two-configurational or multireference wavefunctions, the idea that several configurations are needed to describe the electronic wavefunction of a molecule might be astounding. Thus, we must stress once more that the representation of the wavefunction as a single electronic configuration (i.e., a single Slater determinant) is the central approximation of HF theory, and as such simply does not hold for every molecular system. As the variational principle of quantum mechanics allows us to express the electronic wavefunction in arbitrary form, it is mathematically justified to use linear combinations of determinants as in Eq. (2) if this lowers the total energy of the system.<sup>28</sup> Two-configurational or multireference wavefunctions follow that logic and use two or several determinants to describe non-dynamic correlation that single determinants fail to represent.

In the next sections, we will learn when and why multireference wavefunctions are needed, as we begin our journey of the electronic structure of biradicals.

### 1.04.2.3 Two electrons in two orbitals

As indicated by the discussion of the term “biradical” in Section 1.04.1, several properties of biradicals need to be considered to gain an understanding of their electronic structure. First and foremost, it is important to realize that the interaction between the radical electrons (ferromagnetic/antiferromagnetic coupling) dictates the spin multiplicity of the electronic ground state<sup>29</sup> (spin-dipole and spin-orbit couplings will be ignored for the sake of simplicity). Thus, biradicals may adopt either a singlet or a triplet ground state. Yet, as the extent of the interaction between the radical centers is directly linked to the singlet-triplet energy gap ( $\Delta E_{\text{ST}}$ ), both singlet and triplet state must be considered to understand the electronic structure, as these two states ultimately define the reactivity of a biradical.<sup>20</sup> In this vein, “disbiradicals” could be regarded as a special case, where the lack of magnetic coupling between the unpaired electrons results in degenerate singlet and triplet states. Typical examples of disbiradicals are dihydrogen ( $\text{H}_2$ ) at its dissociation limit (see below) or bisnitroxides with long linkers as depicted in Scheme 3.

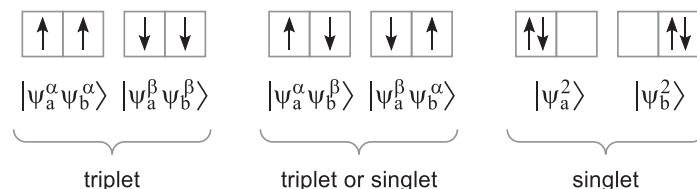
From an MO viewpoint, a prerequisite and characteristic feature of biradicals is the (near) degeneracy of the frontier molecular orbitals (FMOs), as opposed to classical closed-shell species with typically large HOMO-LUMO gaps. The electronic structure of biradicals is therefore best described by the “two electrons in two orbitals” picture<sup>20,27</sup>. The two “radical electrons” can be distributed among the two (nearly) degenerate orbitals  $\psi_a$  and  $\psi_b$ , in six different ways; that is, there are six possible determinants that need to be considered for the description of the different electronic states of biradicals (Fig. 2; note that all orbitals outside the two-orbital “active space” are omitted for clarity).

### 1.04.2.4 Two degenerate frontier orbitals

Initially, we will assume that the two orbitals are exactly degenerate (by symmetry). Note that the first two determinants in Fig. 2,  $|\psi_a^\alpha \psi_b^\alpha\rangle$  and  $|\psi_a^\beta \psi_b^\beta\rangle$ , correspond to the  $M_S = \pm 1$  configurations of a triplet (T):

$$\Psi_{T_{+1}} = |\psi_a^\alpha \psi_b^\alpha\rangle \quad (3)$$

$$\Psi_{T_{-1}} = |\psi_a^\beta \psi_b^\beta\rangle \quad (4)$$



**Fig. 2** When distributing two electrons among two degenerate orbitals  $\psi_a$  and  $\psi_b$ , six different SLATER determinants need to be considered.

The last two determinants  $|\psi_a^2\rangle$  and  $|\psi_b^2\rangle$  are closed-shell singlet configurations. Due to the degeneracy of  $\psi_a$  and  $\psi_b$ , however, neither one of these configurations alone is sufficient to describe the corresponding singlet states, but linear combinations of the two configurations must be formed:

$$\Psi_{S_{TC+}} = \frac{1}{\sqrt{2}} (|\psi_a^2\rangle + |\psi_b^2\rangle) \quad (5)$$

$$\Psi_{S_{TC-}} = \frac{1}{\sqrt{2}} (|\psi_a^2\rangle - |\psi_b^2\rangle) \quad (6)$$

Note that  $\Psi_{S_{TC+}}$  and  $\Psi_{S_{TC-}}$  are two-configuration (TC) wavefunctions and the formally paired electrons are therefore strongly (non-dynamically) correlated. Thus, the wavefunction cannot be accurately described using single-determinantal methods such as HF or post-HF methods relying on a single HF reference. (The same applies to typical Kohn-Sham DFT methods; however, this also depends on the approximation used for the exchange-correlation functional as discussed in [Section 1.04.2.10](#)) One could argue that the inability of HF theory to properly describe the wavefunction of singlet biradicals is one of their defining features! In this context, it is worthy to note that triplet biradicals *can* be described using a single determinant as evidenced by Eqs. (3) and (4), so the “problem” of non-dynamic correlation due to the degeneracy of the orbitals  $\psi_a$  and  $\psi_b$  only arises in the case of singlet biradicals.

Lastly, the two determinants at the center of [Fig. 2](#),  $|\psi_a^\alpha\psi_b^\beta\rangle$  and  $|\psi_a^\beta\psi_b^\alpha\rangle$ , do not correspond to pure spin states, but their linear combinations define the  $M_S = 0$  configuration of the triplet state (antisymmetric spatial wavefunction, symmetric spin wavefunction) and the so-called “open-shell” singlet configuration (symmetric spatial wavefunction, antisymmetric spin wavefunction):

$$\Psi_{T_0} = \frac{1}{\sqrt{2}} (|\psi_a^\alpha\psi_b^\beta\rangle + |\psi_a^\beta\psi_b^\alpha\rangle) = \frac{1}{2} [\psi_a(1)\psi_b(2) - \psi_b(1)\psi_a(2)] [\alpha(1)\beta(2) + \beta(1)\alpha(2)] \quad (7)$$

$$\Psi_{S_{OS}} = \frac{1}{\sqrt{2}} (|\psi_a^\alpha\psi_b^\beta\rangle - |\psi_a^\beta\psi_b^\alpha\rangle) = \frac{1}{2} [\psi_a(1)\psi_b(2) + \psi_b(1)\psi_a(2)] [\alpha(1)\beta(2) - \beta(1)\alpha(2)] \quad (8)$$

The three triplet configurations  $\Psi_{T_{+1}}$ ,  $\Psi_{T_0}$ , and  $\Psi_{T_{-1}}$  are, of course, degenerate in the absence of a magnetic field when neglecting the small spin-dipole coupling between the unpaired electrons. Thus, usually only  $\Psi_{T_{+1}}$  is considered in MO calculations. On the other hand, the three singlet configurations  $\Psi_{S_{TC+}}$ ,  $\Psi_{S_{TC-}}$ , and  $\Psi_{S_{OS}}$  are, in general, not degenerate. Thus, these three singlet states and the triplet state define the four lowest energy states of every biradical ([Fig. 3](#)). Their relative ordering and especially the singlet-triplet gap  $\Delta E_{ST} = E_S - E_T$  between the lowest-lying singlet and triplet state define some of the most important characteristics of biradicals.

### 1.04.2.5 Energetic ordering of the biradical states

The energy of the triplet state is given by the usual expression

$$E_T = \langle \Psi_T | H | \Psi_T \rangle = h_a + h_b + J_{ab} - K_{ab} \quad (9)$$

where  $h_a$  and  $h_b$  are the one-electron energies of the orbitals  $\psi_a$  and  $\psi_b$  exclusive of the interelectronic interaction, and  $J_{ab}$  as well as  $K_{ab}$  are the Coulomb and exchange integrals

$$J_{ab} = (aa|bb) = \iint \psi_a^2(1) \frac{1}{r_{12}} \psi_b^2(2) dr_1 dr_2 \quad (10)$$

$$K_{ab} = (ab|ab) = \iint \psi_a(1)\psi_b(1) \frac{1}{r_{12}} \psi_a(2)\psi_b(2) dr_1 dr_2 \quad (11)$$

which arise from the interelectronic repulsion term  $\sum_{ij} 1/r_{ij}$  of the Hamiltonian acting on the determinantal wavefunction (all expressions in atomic units). Eq. (9) implies that the Coulomb repulsion energy  $J_{ab}$  between the two spin-unpaired electrons is



**Fig. 3** The four lowest energy states of a biradical are expressed as linear combinations of the six determinants in [Fig. 2](#). Note that all singlet states of a biradical are linear combinations of two determinants; thus, they cannot be described by single-determinantal methods such as HF. Normalization constants omitted for clarity.



reduced by the exchange interaction energy  $K_{ab}$  (which is always positive).<sup>30</sup> This circumstance is usually interpreted in terms of the so-called “Fermi hole” around each electron, which means that electrons of equal spin tend to avoid each other, thus reducing their mutual repulsion in the triplet state.

The situation is different for the singlet states. In HF theory, we learn that there is no exchange interaction between opposite-spin electrons.<sup>28</sup> However, this is a result of the single-determinantal nature of the HF wavefunction! When evaluating the interelectronic repulsion operator for the two-determinantal singlet wavefunction  $\Psi_{S_{OS}}$ , one can easily show that the exchange interaction between the two electrons leads to an increase of the interelectronic repulsion:

$$\begin{aligned} \langle \Psi_{S_{OS}} | \frac{1}{r_{12}} | \Psi_{S_{OS}} \rangle &= J_{ab} + K_{ab} \\ \Rightarrow E_{S_{OS}} = \langle \Psi_{S_{OS}} | H | \Psi_{S_{OS}} \rangle &= h_a + h_b + J_{ab} + K_{ab} \end{aligned} \quad (12)$$

Thus, the electrons of opposite spin tend to localize in the same region of space, i.e., their movement is strongly correlated, resulting in a larger repulsive term. In consequence, the triplet state  $\Psi_T$  is  $2K_{ab}$  lower in energy than the open-shell singlet  $\Psi_{S_{OS}}$ , if (and only if!) the optimal MOs for singlet and triplet state are identical. Moreover, note that dynamic electron correlation (which is neglected in our derivation) may also impact the energy difference between open-shell (OS) singlet and triplet.<sup>29</sup>

The energies of the two-configurational (TC) singlet states may be derived in a similar manner, resulting in the following expression:

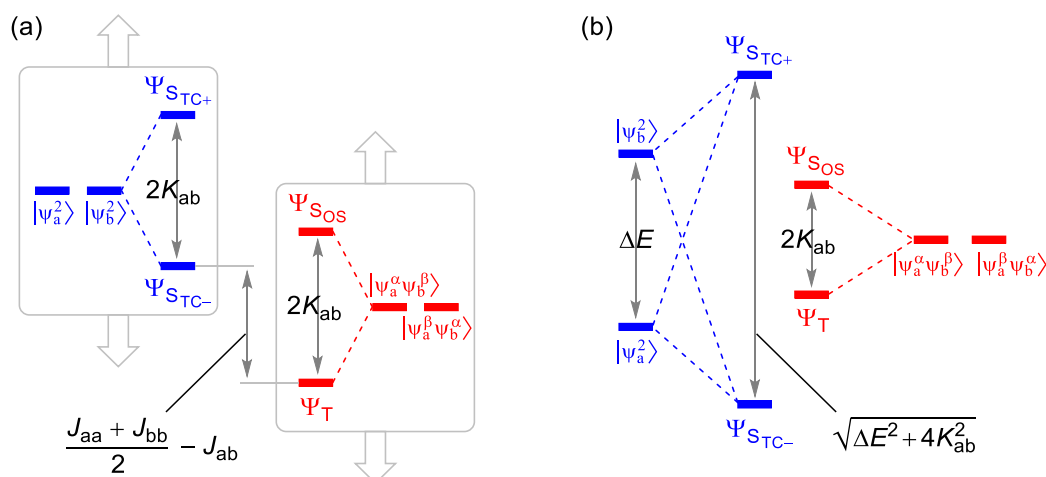
$$E_{S_{TC\pm}} = \langle \Psi_{S_{TC\pm}} | H | \Psi_{S_{TC\pm}} \rangle = h_a + h_b + \frac{J_{aa} + J_{bb}}{2} \pm K_{ab} \quad (13)$$

Thus, the energy of the singlet state  $\Psi_{S_{TC-}}$  is  $2K_{ab}$  lower than the energy of the  $\Psi_{S_{TC+}}$  state. Moreover, the energy difference between the singlet  $\Psi_{S_{TC-}}$  and triplet  $\Psi_T$  can be expressed solely in terms of the one-site and two-site Coulomb integrals:

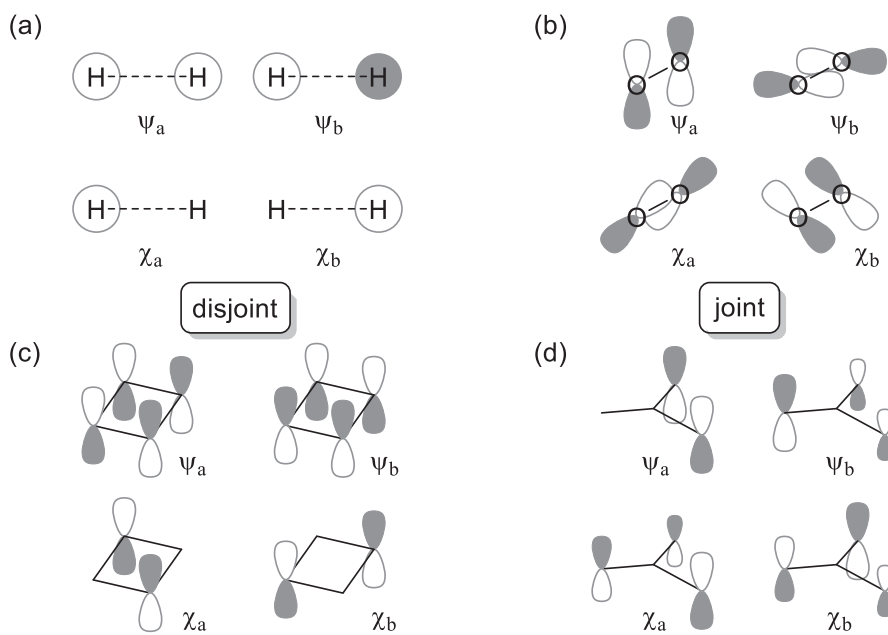
$$E_{S_{TC-}} - E_T = \frac{J_{aa} + J_{bb}}{2} - J_{ab} \quad (14)$$

Again, note that these considerations are only valid under the approximation that the same set of orbitals can be used to describe all four electronic states. As pointed out by Stuyver et al.,<sup>20</sup> it is then obvious that the four electronic states can be grouped in two pairs, namely  $\Psi_T/\Psi_{S_{OS}}$  and  $\Psi_{S_{TC-}}/\Psi_{S_{TC+}}$  (Fig. 4A). The two states in each pair have a constant energy separation of  $2K_{ab}$ , while the energetic position of the two pairs relative to each other is determined by Eq. (14). Thus, the final order of the states depends on the magnitude of the Coulomb and exchange integrals.

According to Hund’s rule, the triplet state is usually the ground state of a biradical with a set of degenerate frontier orbitals. To decide whether the singlet-triplet (ST) gap is small or large, let us take a closer look at the nature of the two orbitals  $\psi_a$  and  $\psi_b$ . We started our discussion by assuming that the two orbitals are a degenerate set of MOs, such as the two  $\pi^*$  valence orbitals of the  $O_2$  molecule, or the  $\sigma$  and  $\sigma^*$  orbitals of  $H_2$  stretched to the dissociation limit (Fig. 5). However, this is not the only acceptable choice! As the two-configurational wavefunctions discussed here are of the “complete active space” (CAS) type (i.e., all possible configurations of two electrons in the two “active” orbitals are considered, basically a full-CI within the active space), they are invariant to arbitrary orbital rotations within the active space (the CI coefficients being rotated accordingly). Thus, any normalized set of linear



**Fig. 4** Relative energy levels of the four electronic states of a biradical. (A) Two degenerate orbitals  $\psi_a$  and  $\psi_b$ . The position of the formal closed-shell (blue) and open-shell (red) states depends on the Coulomb and exchange integrals. (B) Small energy gap between orbitals  $\psi_a$  and  $\psi_b$  ( $\Psi_{S_{TC-}} = c_1|\psi_a^2\rangle - c_2|\psi_b^2\rangle$ , cf. Section 1.04.2.7). Adapted from Stuyver, T.; Chen, B.; Zeng, T.; Geerlings, P.; De Proft, F.; Hoffmann, R. Do Diradicals Behave Like Radicals? *Chem. Rev.* **2019**, *119* (21), 11291–11351.



**Fig. 5** Examples of MOs and corresponding GVB orbitals. (A) H<sub>2</sub> orbitals at the dissociation limit ( $r_{\text{HH}} \rightarrow \infty$ ). Due to zero overlap of the atomic 1s orbitals, the MOs  $\psi_a$  and  $\psi_b$  are degenerate. (B) Degenerate set of  $\pi^*$  orbitals in the O<sub>2</sub> molecule. The GVB orbitals correspond to a 45° rotation of the MO set. (C) Although the GVB orbitals of square cyclobutadiene ( $D_{4h}$ ) are not localized on single atoms, both are localized on different sets of atoms and therefore do not share a considerable region of space. (D) The MOs of trimethylmethylene (TMM) cannot be localized in the GVB picture.<sup>20,27</sup>

combinations of the orbitals  $\psi_a$  and  $\psi_b$  is an equally acceptable choice. We may therefore define a different set of orthogonal, degenerate orbitals

$$\chi_a = \frac{1}{\sqrt{2}}(\psi_a + \psi_b), \chi_b = \frac{1}{\sqrt{2}}(\psi_a - \psi_b) \quad (15)$$

which is also referred to as “generalized valence bond” (GVB) orbitals.<sup>20,27,31</sup> This orbital transformation has important implications for the chemical interpretation of the different electronic states, as we will discuss in a moment. First, note that the transformed orbitals  $\chi_a$  and  $\chi_b$  might be localized on different atoms (as in case of H<sub>2</sub>, Fig. 5A) or still be delocalized (as in case of O<sub>2</sub>, Fig. 5B). If the transformed orbitals are localized, the biradical is a so-called “disjoint” biradical<sup>17,20</sup> and the ST gap is generally small, that is,  $\Psi_{\text{SIC}}$  and  $\Psi_{\text{T}}$  have similar energies. Thus, the interaction between the radical centers is weak (cf. Section 1.04.2.10). If, however, the orbitals cannot be localized, the biradical belongs to the group of so-called “joint” or “non-disjoint” biradicals.<sup>17,20</sup> They exhibit a large ST gap, and the triplet state is the ground state according to Hund’s rule (see also Section 1.04.2.6). The radical centers of these biradicals are therefore said to be ferromagnetically coupled.

We need to stress again that dynamic electron correlation (including orbitals/electrons outside the “active space” of two electrons in two orbitals) may also influence the ordering of the states (as is the case, for example, in square cyclobutadiene which possesses a singlet ground state).<sup>32–34</sup> This phenomenon has been dubbed “dynamic spin polarization” and/or “dynamic charge polarization” by different authors, and the reader is referred to the literature for an in-depth analysis of these correlation effects.<sup>27,29,32,33</sup>

#### 1.04.2.6 Chemical interpretation of the biradical states

Let us now consider the orbital transformation laid out in Eq. (15) in more detail. It should be clear that we can equivalently write

$$\psi_a = \frac{1}{\sqrt{2}}(\chi_a + \chi_b) \quad (16)$$

$$\psi_b = \frac{1}{\sqrt{2}}(\chi_a - \chi_b) \quad (17)$$

Substituting Eqs. (16) and (17) in Eq. (6) yields

$$\begin{aligned}
 \Psi_{S_{TC-}} &= \frac{1}{\sqrt{2}} (|\psi_a^2\rangle - |\psi_b^2\rangle) \\
 &= \frac{1}{2} [\psi_a(1)\psi_a(2) - \psi_b(1)\psi_b(2)] [\alpha(1)\beta(2) - \beta(1)\alpha(2)] \\
 &= \frac{1}{2} [\chi_a(1)\chi_b(2) + \chi_b(1)\chi_a(2)] [\alpha(1)\beta(2) - \beta(1)\alpha(2)] \\
 &= \frac{1}{\sqrt{2}} (|\chi_a^\alpha\chi_b^\beta\rangle - |\chi_a^\beta\chi_b^\alpha\rangle) = \Psi'_{S_{OS}}
 \end{aligned} \tag{18}$$

that is, the closed-shell, two-configurational singlet wavefunction  $\Psi_{S_{TC-}}$  transforms into an open-shell singlet wavefunction  $\Psi_{S_{OS}}$  in the GVB basis!<sup>20,27</sup> Conversely, the open-shell singlet wavefunction  $\Psi_{S_{OS}}$  in the MO basis transforms into a closed-shell, two configurational singlet wavefunction  $\Psi_{S_{TC-}}$  in the GVB basis, as evidenced by substituting Eqs. (16) and (17) in Eq. (8):

$$\begin{aligned}
 \Psi_{S_{OS}} &= \frac{1}{\sqrt{2}} (|\psi_a^\alpha\psi_b^\beta\rangle - |\psi_b^\beta\psi_a^\alpha\rangle) \\
 &= \frac{1}{2} [\psi_a(1)\psi_b(2) + \psi_b(1)\psi_a(2)] [\alpha(1)\beta(2) - \beta(1)\alpha(2)] \\
 &= \frac{1}{2} [\chi_a(1)\chi_a(2) - \chi_b(1)\chi_b(2)] [\alpha(1)\beta(2) - \beta(1)\alpha(2)] \\
 &= \frac{1}{\sqrt{2}} (|\chi_a^2\rangle - |\chi_b^2\rangle) = \Psi'_{S_{TC-}}
 \end{aligned} \tag{19}$$

Thus,  $\Psi_{S_{TC-}}$  and  $\Psi_{S_{OS}}$  have exchanged their character upon orbital transformation. The assignment of a singlet state as “closed-shell” or “open-shell” is therefore dependent on the orbital basis, and the latter must be specified if the terms “closed-shell” and “open-shell” singlet are to be used to describe the electronic structure of any biradical.<sup>27</sup> Arguably, any two-configurational singlet could be regarded as “open-shell” singlet<sup>18,19</sup> due to the ambiguity of the wavefunction depending on the orbital basis.

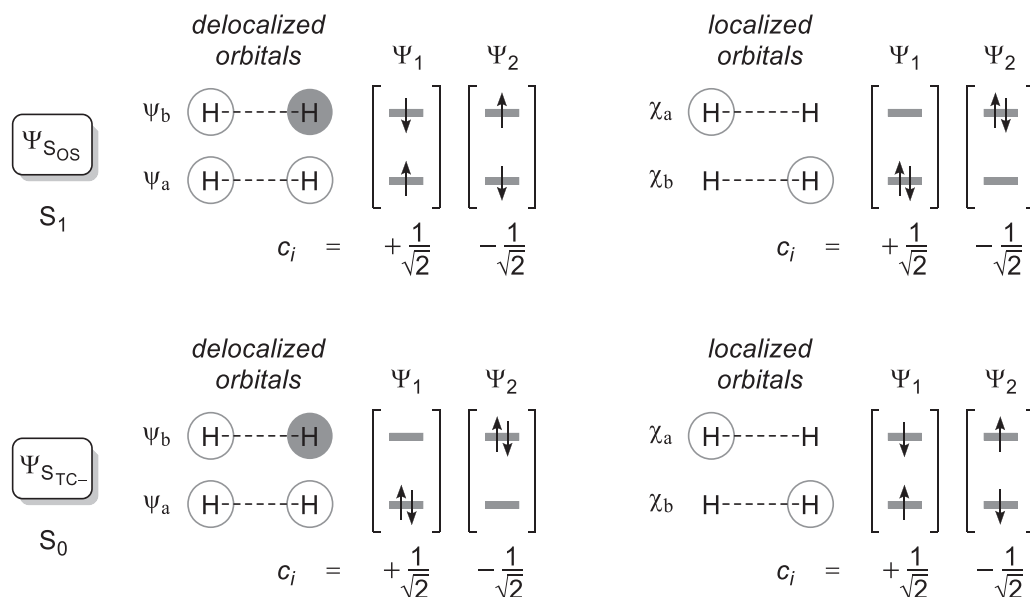
Now, one may ask why this change of character is remarkable, especially when we noted before that the choice of orbital basis is arbitrary. Yet, the transformed orbitals  $\chi_a$  and  $\chi_b$  are often localized on different atoms of a molecule (i.e., they can be regarded as “localized orbitals” in many instances) and therefore guide us to a chemical interpretation of the wavefunction. The two-configurational wavefunction  $\Psi_{S_{TC-}}$ , which has two electrons in either of the two delocalized MOs  $\psi_a$  and  $\psi_b$ , can thus be viewed as a “biradical” state, as we find one electron in each of the localized orbitals  $\chi_a$  and  $\chi_b$ . By localizing on two different sites, the two non-dynamically correlated electrons avoid each other. *It is exactly this correlated movement of the electrons that results in biradical character.* In contrast, the formal open-shell wavefunction  $\Psi_{S_{OS}}$ , which has one electron in each of the delocalized MOs, is actually a zwitterionic state, since the two electrons will always occupy the same orbital,  $\chi_a$  or  $\chi_b$ , in the localized picture.<sup>18</sup>

Let us once again consider dihydrogen ( $H_2$ ) at its dissociation limit as an example:  $\Psi_{S_{TC-}}$  is the lowest-energy singlet ( $S_0$ ) wavefunction and the two formally spin-paired electrons are distributed equally across the two delocalized MOs  $\psi_a$  and  $\psi_b$  (Fig. 6, bottom). This electronic situation is chemically hard to interpret. In the localized picture, however, one electron is localized in each of the two hydrogenic 1s orbitals ( $\chi_a$  and  $\chi_b$ ), in agreement with our anticipation that we find two H radicals at the dissociation limit. (Notice that in this special example, singlet and triplet state are degenerate, resulting in a true “disbiradical.”) Conversely, the first excited singlet state ( $S_1$ ) is described by  $\Psi_{S_{OS}}$ , which corresponds to the ionic dissociation limit as shown by the orbital transformation to the localized orbital basis (Fig. 6, top). The localized picture therefore offers a straightforward description of the electronic structure in a sense that it is often easier to understand in chemical terms. We must stress, though, that neither orbital basis (MO or GVB) is more “right” or “wrong” than the other; they merely represent different sides of the same coin.

As mentioned before, the transformed orbitals are not always nicely localized (cf. joint biradicals, Fig. 5). In such cases, an interpretation of the wavefunction is more difficult; however, one can still choose the more localized set of orbitals (i.e.,  $\chi_a$  and  $\chi_b$ ) to decide whether an electronic state has larger biradical or zwitterionic character. There will, however, always remain an ambiguity with respect to the biradical and zwitterionic nature of the singlet states of joint biradicals.<sup>20</sup> Note that  $O_2$  is a special case; here, the GVB orbitals correspond to a 45° rotation of the molecule around the O–O axis; thus, the GVB and MO description are equivalent. Consequently,  $\Psi_{S_{TC-}}$  and  $\Psi_{S_{OS}}$  are degenerate by symmetry and it is no longer possible to classify these states as biradical or zwitterionic states. The situation is similar for TMM in  $D_{3h}$  symmetry.<sup>20,27</sup>

The attentive reader will have noticed that we have not yet discussed the remaining two states of a biradical,  $\Psi_{S_{TC+}}$  and  $\Psi_T$ . These states do not change their character upon orbital transformation:

$$\begin{aligned}
 \Psi_{S_{TC+}} &= \frac{1}{\sqrt{2}} (|\psi_a^2\rangle + |\psi_b^2\rangle) \\
 &= \frac{1}{2} [\psi_a(1)\psi_a(2) + \psi_b(1)\psi_b(2)] [\alpha(1)\beta(2) - \beta(1)\alpha(2)] \\
 &= \frac{1}{2} [\chi_a(1)\chi_a(2) + \chi_b(1)\chi_b(2)] [\alpha(1)\beta(2) - \beta(1)\alpha(2)]
 \end{aligned}$$



**Fig. 6** H<sub>2</sub> at its dissociation limit in the delocalized (MO) and localized (GVB) orbital picture. The CAS-Cl wavefunctions are given by  $\Psi = \sum c_i \Psi_i$ . Note that the orbitals  $\psi_a$  and  $\psi_b$  as well as  $\chi_a$  and  $\chi_b$  are degenerate.

$$= \frac{1}{\sqrt{2}} (|\chi_a^2\rangle + |\chi_b^2\rangle) = \Psi'_{S_{TC+}} \quad (20)$$

$$\begin{aligned} \Psi_T &= |\psi_a^\alpha \psi_b^\alpha\rangle \\ &= \frac{1}{\sqrt{2}} [\psi_a(1)\psi_b(2) - \psi_b(1)\psi_a(2)][\alpha(1)\alpha(2)] \\ &= \frac{1}{\sqrt{2}} [\chi_b(1)\chi_a(2) - \chi_a(1)\chi_b(2)][\alpha(1)\alpha(2)] \\ &= |\chi_b^\alpha \chi_a^\alpha\rangle = \Psi'_T \end{aligned} \quad (21)$$

Therefore, the triplet wavefunction  $\Psi_T = \Psi'_T$  corresponds to a biradical state, whereas the singlet wavefunction  $\Psi_{S_{TC+}} = \Psi_{S_{TC+}}'$  is zwitterionic.

Let us finally come back to the ordering of the states as depicted in Fig. 4A. We already mentioned that disjoint and joint biradicals differ in that they display small or large ST gaps, respectively. This is intuitively understandable; if the orbitals are localized in different regions of space, the interaction between the electrons and thus the ST gap will be small. Conversely, if the orbitals cannot be localized, the interaction between the electrons and thus the ST gap will be large. Still, we have not yet answered the question whether  $\Psi_{S_{Os}}$  or  $\Psi_{S_{TC-}}$  is lower in energy and therefore defines the ST gap.

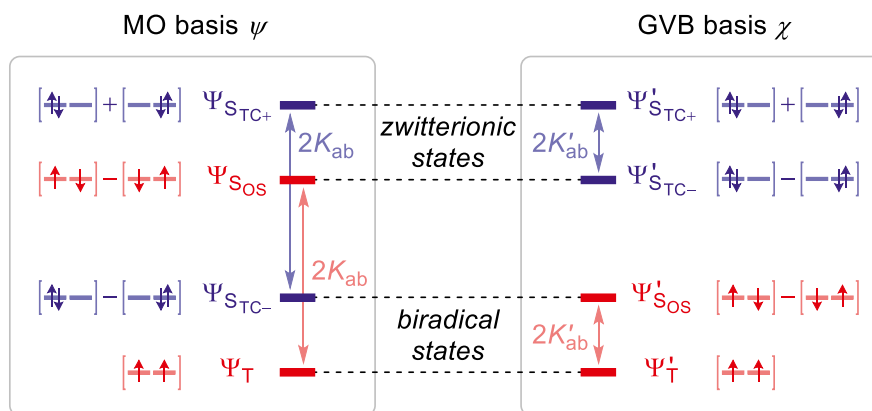
Once again, considering the (possibly localized) GVB orbitals gives us an easy answer. Notice that, as we did not make any restrictions to the choice of orbitals in our derivation of the biradical states in Sections 1.04.2.4 and 1.04.2.5, the same energetic relations apply within the sets of the “original” and “transformed” states, i.e., regardless of whether we use MOs  $\psi$  or GVB orbitals  $\chi$  (Fig. 7). However, recall that  $\Psi_{S_{TC-}}$  (using orbitals  $\psi$ ) equals  $\Psi_{S_{Os}}'$  (using orbitals  $\chi$ ) and vice versa, so the Coulomb and exchange integrals will, of course, have different magnitudes depending on the orbital basis. If we now consider a disjoint biradical (with orbitals  $\chi_a$  and  $\chi_b$  localized on different sites), the exchange integral  $K_{ab}'$  between those two orbitals will typically be small. Thus, the energy difference between  $\Psi_{S_{Os}}'$  and  $\Psi'_T$

$$E'_{S_{Os}} - E'_T = 2K'_{ab} \quad (22)$$

will also be small. Conversely, the energy splitting between  $\Psi_{S_{TC-}}'$  and  $\Psi'_T$  as given by Eq. (14)

$$E'_{S_{TC-}} - E'_T = \frac{J'_{aa} + J'_{bb}}{2} - J'_{ab} \quad (23)$$

will be large, since the one-site Coulomb integrals  $J'_{aa}$  and  $J'_{bb}$  will be much larger than the two-site Coulomb integral  $J'_{ab}$ . Therefore, the formal “open-shell” singlet  $\Psi_{S_{Os}}'$  will be the lowest-energy singlet state, and the ST gap will be determined by Eq. (22).



**Fig. 7** The four biradical states expressed in the (fully delocalized) MO basis and the (possibly localized) GVB basis. The states that are formed from open-shell determinants are printed in red, those that are formed from closed-shell determinants are printed in blue. If the GVB orbitals are localized,  $K_{ab}'$  is small. Otherwise,  $K_{ab}'$  is larger, but generally smaller than  $K_{ab}$ . Note that  $H_2$  at its dissociation limit and  $O_2$  can be regarded as “extreme” cases of disjoint and joint biradicals: For dissociated  $H_2$ ,  $K_{ab}' = 0$  (i.e.,  $\Delta E_{ST} = 0$ ), whereas for  $O_2$ ,  $K_{ab}' = K_{ab}$  (i.e.,  $E_{S_{TC-}} = E_{S_{OS}}$ ).

Transforming the orbitals back to the delocalized MOs  $\psi_a$  and  $\psi_b$ , it becomes clear that  $\Psi_{S_{TC-}} = \Psi_{S_{OS}}'$  will be the lowest-energy singlet state, and the ST gap will be given by Eq. (14). Hence,

$$\Delta E_{ST} = 2K_{ab}' = \frac{J_{aa} + J_{bb}}{2} - J_{ab} \quad (24)$$

that is, the exchange integral in the GVB basis is related to the Coulomb integrals in the MO basis and vice versa.

The same reasoning holds true for joint biradicals. Even if the transformed orbitals  $\chi_a$  and  $\chi_b$  are not perfectly localized on different sites, the exchange integral  $K_{ab}'$  between the localized orbitals will generally be smaller than the exchange integral  $K_{ab}$  between the delocalized orbitals, because the localized orbitals only share a smaller region of space.<sup>19,20</sup> Therefore,  $\Psi_{T}'$  and  $\Psi_{S_{OS}}'$  will generally be lower in energy than  $\Psi_{S_{TC-}}'$  and  $\Psi_{S_{TC+}}'$ , the former being assigned biradical and the latter being assigned zwitterionic character as discussed before (Fig. 7).

#### 1.04.2.7 Two nearly degenerate frontier orbitals

Up to this point, we have assumed that the two orbitals  $\psi_a$  and  $\psi_b$  are exactly degenerate (thus, the resulting biradicals have a biradical character of 100%, cf. Section 1.04.2.10). This degeneracy is often induced by symmetry, but there are numerous examples of biradicals with lower symmetry than  $D_{2d}$  or  $C_3$ , that is, these systems do not possess orbital degeneracy required by symmetry. Therefore, many (if not the majority of) biradicals possess at least a small energy gap between the two orbitals  $\psi_a$  and  $\psi_b$ , which are then typically referred to as HOMO and LUMO, the so-called frontier molecular orbitals (FMOs). These species with a small HOMO-LUMO gap are also referred to as “di-/biradicaloids” in the literature<sup>17–20,22,24–26,35–37</sup> (see also our discussion of different designations of biradicals in Section 1.04.1).

In the following discussion, we assume that the radical centers are, just as before, connected by some symmetry operation, such as inversion or rotation (this has been dubbed the “homosymmetric” case by Salem and Rowland),<sup>18</sup> that is, the orbitals  $\psi_a$  and  $\psi_b$  are typically derived from symmetry-adapted linear combinations (SALCs) of atomic orbitals (basis functions) at the radical sites. Thus, the orbitals are perfectly delocalized (Fig. 8). When the energy gap between  $\psi_a$  and  $\psi_b$  is increased ( $h_a < h_b$ ), the configuration  $|\psi_a^2\rangle$  with two electrons in the lower-energy orbital  $\psi_a$  becomes energetically favored, considering that all other configurations place at least one electron in the higher-energy orbital  $\psi_b$ . In the limiting case of a large HOMO-LUMO gap, a closed-shell singlet ground state is expected, i.e., the configuration  $|\psi_a^2\rangle$  alone is sufficient to describe the ground state wavefunction (when disregarding dynamic correlation, of course). Thus, increasing the HOMO-LUMO gap results in a decreasing biradical character (cf. Section 1.04.2.10), until a closed-shell species is obtained (Fig. 9).

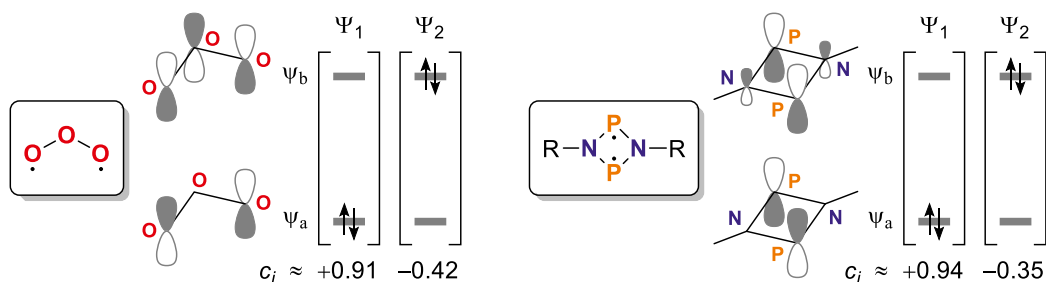
Obviously, this means that the mixing (i.e., the “interaction”) of the configurations  $|\psi_a^2\rangle$  and  $|\psi_b^2\rangle$  in  $\Psi_{S_{TC-}}$  (Eq. 6) must decrease when the HOMO-LUMO gap is increased, up to the point where the contribution of  $|\psi_b^2\rangle$  can be neglected and a closed-shell species is obtained. To account for varying HOMO-LUMO separations, we therefore introduce the CI coefficients  $c_1$  and  $c_2$ ,

$$\Psi_{S_{TC-}} = c_1 |\psi_a^2\rangle - c_2 |\psi_b^2\rangle \quad (25)$$

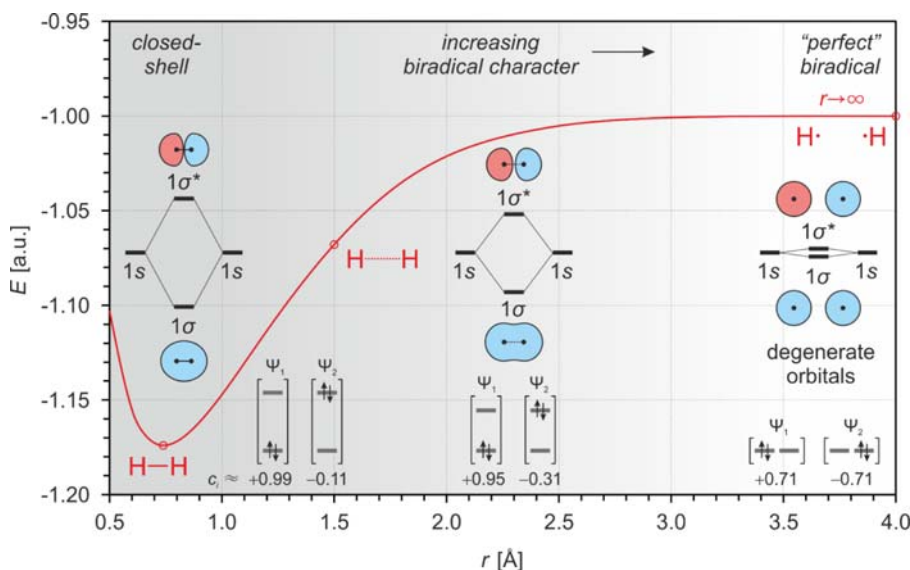
where  $c_1 \geq c_2 > 0$  and  $c_1^2 + c_2^2 = 1$  for normalization of the wavefunction. (Notice that by this definition, we explicitly state that the second term on the r.h.s. of Eq. (25) is negative. In a general CI expansion of the type  $\Psi = \sum c_i \Psi_i$ , the value of  $c_2$  of  $\Psi_{S_{TC-}}$  would have a negative sign, cf. Figs. 8 and 9) Conversely,

$$\Psi_{S_{TC+}} = c_2 |\psi_a^2\rangle + c_1 |\psi_b^2\rangle \quad (26)$$





**Fig. 8** Examples of symmetric biradicals with a small HOMO-LUMO gap. The CAS-Cl wavefunctions are given by  $\Psi = \sum c_i \Psi_i$ , where  $\Psi_1 = |\psi_a^2\rangle$  and  $\Psi_2 = |\psi_b^2\rangle$ .



**Fig. 9** Dissociation of  $\text{H}_2$ . The CAS-Cl wavefunctions of the different structures along the dissociation curve are given by  $\Psi = \sum c_i \Psi_i$ . At its equilibrium structure,  $\text{H}_2$  is a typical “closed-shell” molecule ( $c_2 \approx -0.1$ , so the contribution of the second determinant  $\Psi_2$  would be considered dynamic correlation). When the H-H distance  $r$  is increased, the overlap of the atomic  $1s$  orbitals decreases, and so does the HOMO-LUMO gap. For  $r \rightarrow \infty$ , the overlap integral between the atomic orbitals vanishes, so the MOs  $1\sigma$  and  $1\sigma^*$  become degenerate and a “perfect” biradical is obtained. Notice that there is no clear distinction between closed-shell and biradical(oid); the biradical character increases smoothly with increasing  $r$ .

that is, the second term on the r.h.s. of Eq. (26) is always positive. In case of  $c_1 = c_2 = 1/\sqrt{2}$ , we have the limiting case of degenerate orbitals  $\psi_a$  and  $\psi_b$  as discussed in the previous sections, and in case of  $c_1 = 1$  and  $c_2 = 0$ , a closed-shell species is obtained:

$$\Psi_{\text{S}_{\text{TC}^-}} = |\psi_a^2\rangle$$

$$\Psi_{\text{S}_{\text{TC}^+}} = |\psi_b^2\rangle$$

Thus, if the quotient  $c_1/c_2$  is large, the system resembles a closed-shell system, and if  $c_1/c_2$  approaches unity, the molecule becomes more biradical-like.<sup>20</sup>

The formal open-shell wavefunctions  $\Psi_{\text{T}}$  and  $\Psi_{\text{S}_{\text{OS}}}$  remain, of course, unaffected by the HOMO-LUMO energy gap, as one electron is placed in each orbital, irrespective of the relative orbital energies.

Let us once again look at the energies of the four biradical states. To simplify the mathematical description, we first introduce the energies  $H_{aa}$  and  $H_{bb}$  of the configurations  $|\psi_a^2\rangle$  and  $|\psi_b^2\rangle$ , respectively.<sup>20</sup>

$$H_{aa} = \langle \psi_a^2 | H \psi_a^2 \rangle = 2h_a + J_{aa} \quad (27)$$

$$H_{bb} = \langle \psi_b^2 | H \psi_b^2 \rangle = 2h_b + J_{bb} \quad (28)$$

In Eqs. (27) and (28),  $h_a$  and  $h_b$  are the one-electron energies of the orbitals  $\psi_a$  and  $\psi_b$  exclusive of the interelectronic repulsion, and  $J_{aa}$  as well as  $J_{bb}$  are the one-site Coulomb integrals (as discussed above). It is straightforward to show that the energy  $E_{\text{S}_{\text{TC}^-}}$  of the two-configurational wavefunction  $\Psi_{\text{S}_{\text{TC}^-}}$  as defined in Eq. (25) is given by

$$\begin{aligned}
 E_{S_{TC-}} &= \langle \Psi_{S_{TC-}} | H | \Psi_{S_{TC-}} \rangle \\
 &= c_1^2 \cdot \langle \psi_a^2 | H | \psi_a^2 \rangle + c_2^2 \cdot \langle \psi_b^2 | H | \psi_b^2 \rangle - c_1 c_2 \cdot \langle \psi_a^2 | H | \psi_b^2 \rangle - c_2 c_1 \cdot \langle \psi_b^2 | H | \psi_a^2 \rangle \\
 &= c_1^2 H_{aa} + c_2^2 H_{bb} - 2c_1 c_2 K_{ab}
 \end{aligned} \tag{29}$$

where  $K_{ab} = \langle \psi_a^2 | H | \psi_b^2 \rangle = \langle \psi_b^2 | H | \psi_a^2 \rangle$  is the exchange integral between orbitals  $\psi_a$  and  $\psi_b$ . In case that  $c_1 = c_2 = 1/\sqrt{2}$  (i.e., if the orbitals are degenerate), Eq. (29) reduces to

$$\begin{aligned}
 E_{S_{TC-}} &= \frac{1}{2} H_{aa} + \frac{1}{2} H_{bb} - K_{ab} \\
 &= h_a + h_b + \frac{J_{aa} + J_{bb}}{2} - K_{ab}
 \end{aligned}$$

which is identical to the expression derived in Eq. (13). Similarly, the energy of the wavefunction  $\Psi_{S_{TC+}}$  amounts to

$$E_{S_{TC+}} = \langle \Psi_{S_{TC+}} | H | \Psi_{S_{TC+}} \rangle = c_2^2 H_{aa} + c_1^2 H_{bb} + 2c_1 c_2 K_{ab} \tag{30}$$

The energies of  $\Psi_T$  and  $\Psi_{S_{OS}}$  remain the same as those given in Eqs. (9) and (12), respectively:

$$E_T = \langle \Psi_T | H | \Psi_T \rangle = h_a + h_b + J_{ab} - K_{ab}$$

$$E_{S_{OS}} = \langle \Psi_{S_{OS}} | H | \Psi_{S_{OS}} \rangle = h_a + h_b + J_{ab} + K_{ab}$$

Clearly, for a system with non-degenerate orbitals  $\psi_a$  and  $\psi_b$  (i.e.,  $c_1 > c_2$ ), Eqs. (27) and (29) show that the energy of  $\Psi_{S_{TC-}}$  is dominated by the energy  $H_{aa}$ , and thus the one-electron energy  $h_a$  of orbital  $\psi_a$ . In contrast, as shown by Eqs. (9) and (12), the energies of  $\Psi_T$  and  $\Psi_{S_{OS}}$  are dependent on the formal average of the one-electron energies  $h_a$  and  $h_b$ , whereas the energy of  $\Psi_{S_{TC+}}$  is a function of the one-electron energy  $h_b$ , as demonstrated by Eq. (30). Given that orbital  $\psi_a$  is the lower-energy orbital, the singlet state  $\Psi_{S_{TC-}}$  is usually the ground state, followed by the triplet state  $\Psi_T$  and the “open-shell” singlet  $\Psi_{S_{OS}}$ , while  $\Psi_{S_{TC+}}$  is the highest-energy state of the four states of a biradical (Fig. 4B).

The energy difference between the two “closed-shell” states  $\Psi_{S_{TC-}}$  and  $\Psi_{S_{TC+}}$  amounts to

$$E_{S_{TC+}} - E_{S_{TC-}} = (c_1^2 - c_2^2) \cdot (H_{bb} - H_{aa}) + 4c_1 c_2 K_{ab} \tag{31}$$

which reduces to  $2K_{ab}$  for  $c_1 = c_2 = 1/\sqrt{2}$ . The energy difference between the two “open-shell” states  $\Psi_T$  and  $\Psi_{S_{OS}}$  is  $2K_{ab}$  as discussed before.

Let us now consider Eqs. (29) and (30) in more detail. The integrals  $H_{aa}$ ,  $H_{bb}$ , and  $H_{ab} = H_{ba} = K_{ab}$  (if real orbitals are used, which is normally the case) are the matrix elements of a CI matrix with double substitutions in the active space (i.e., orbitals  $\psi_a$  and  $\psi_b$ ).<sup>28</sup> To find an optimal set of coefficients  $c_i$ , the energy of the system must be minimized ( $\partial E / \partial c_i = 0$ ).<sup>28,38</sup> Thus, we need to solve for the energy eigenvalues  $E$  of the matrix equation

$$\mathbf{H}\mathbf{c} = E\mathbf{S}\mathbf{c} \tag{32}$$

where  $\mathbf{H}$  is the CI matrix

$$\mathbf{H} = \begin{pmatrix} H_{aa} & H_{ab} \\ H_{ba} & H_{bb} \end{pmatrix} \tag{33}$$

$\mathbf{S}$  (here  $S_{ij} = \delta_{ij}$ ) is the overlap matrix, and  $\mathbf{c}$  are the eigenvectors associated with the CI coefficients  $c_i$  of the general two-configuration CI wavefunction

$$\Psi = c_1 |\psi_a^2\rangle + c_2 |\psi_b^2\rangle \tag{34}$$

Note that in Eq. (34),  $c_2 < 0$  for  $\Psi_{S_{TC-}}$ . The energy eigenvalues are obtained by diagonalizing the CI matrix, that is, by solving the corresponding secular equation,<sup>28</sup>

$$\begin{vmatrix} H_{aa} - E & H_{ab} \\ H_{ba} & H_{bb} - E \end{vmatrix} = 0 \tag{35}$$

$$\begin{aligned}
 (H_{aa} - E)(H_{bb} - E) - K_{ab}^2 &= 0 \\
 \Rightarrow E_{\pm} &= \frac{H_{aa} + H_{bb}}{2} \pm \frac{1}{2} \sqrt{(H_{bb} - H_{aa})^2 + 4K_{ab}^2}
 \end{aligned} \tag{36}$$

where  $E_- = E_{S_{TC-}}$  and  $E_+ = E_{S_{TC+}}$ . It becomes evident from Eq. (36) that  $E_- = H_{aa}$  if  $K_{ab} = 0$ , and consequently,  $E_- < H_{aa}$  if  $K_{ab} > 0$ . Thus,  $\Psi_{S_{TC-}}$  is typically lower in energy than the single configuration  $|\psi_a^2\rangle$ , but certainly never higher in energy. That is, the two-configurational wavefunction  $\Psi_{S_{TC-}}$  improves upon the single-determinantal description of the RHF wavefunction, and the

energy lowering is directly connected to the magnitude of  $K_{ab}$ . Similarly,  $\Psi_{S_{TC+}}$  is generally higher in energy than the single configuration  $|\psi_b^2\rangle$  (cf. Fig. 4B).

Using Eq. (36), we can now express the energy difference between the two “closed-shell” states  $\Psi_{S_{TC-}}$  and  $\Psi_{S_{TC+}}$  as

$$E_{S_{TC+}} - E_{S_{TC-}} = \sqrt{(H_{bb} - H_{aa})^2 + 4K_{ab}^2} \quad (37)$$

whereas the singlet-triplet energy gap  $\Delta E_{ST}$  amounts to

$$\begin{aligned} \Delta E_{ST} &= E_{S_{TC-}} - E_T \\ &= 2K'_{ab} + K_{ab} - \frac{1}{2}\sqrt{(H_{bb} - H_{aa})^2 + 4K_{ab}^2} \end{aligned} \quad (38)$$

with

$$2K'_{ab} = \frac{J_{aa} + J_{bb}}{2} - J_{ab} \quad (39)$$

by analogy with Eq. (24). Thus, the singlet-triplet gap depends on the exchange integral, the one- and two-site Coulomb integrals, as well as the energy difference between the configurations  $|\psi_a^2\rangle$  and  $|\psi_b^2\rangle$ , which again is related to the HOMO-LUMO gap (Fig. 10).

As indicated above, the CI coefficients  $c_i$  of the two-configuration wavefunction are typically computed as eigenvectors  $\mathbf{c}$  of the CI matrix  $\mathbf{H}$ . For the sake of our discussion, though, it is advantageous to re-write the CI wavefunction in Eq. (34) as

$$\Psi_\tau = \cos(\tau)|\psi_a^2\rangle + \sin(\tau)|\psi_b^2\rangle \quad (40)$$

where

$$\cos(\tau) = c_1 \quad (41)$$

$$\sin(\tau) = c_2 \quad (42)$$

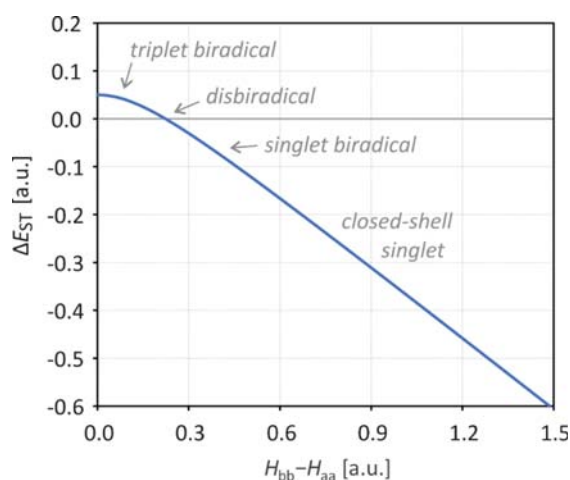
Note that  $\cos^2(\tau) + \sin^2(\tau) = 1$  for any value of  $\tau$ , that is, the normalization condition is always fulfilled. The energy of the wavefunction in Eq. (40) is then given by

$$E = \langle \Psi_\tau | H \Psi_\tau \rangle = \cos^2(\tau)H_{aa} + \sin^2(\tau)H_{bb} + \sin(2\tau)K_{ab} \quad (43)$$

Note that  $\sin(2\tau) = 2 \cos(\tau) \sin(\tau)$ . We can calculate  $\tau$  by minimizing the energy,  $\partial E / \partial \tau = 0$ ,

$$\tan(2\tau) = -\frac{2K_{ab}}{H_{bb} - H_{aa}} \quad (44)$$

$$\Rightarrow \tau_n = -\frac{1}{2} \arctan\left(\frac{2K_{ab}}{H_{bb} - H_{aa}}\right) + \frac{n\pi}{2} \quad (45)$$



**Fig. 10** Singlet-triplet gap  $\Delta E_{ST}$  as a function of  $H_{bb} - H_{aa}$ . The exchange integral is arbitrarily fixed at  $K_{ab} = 0.1 E_h$ . The quantity  $K_{ab}'$ , which corresponds to the exchange integral between the localized orbitals  $\phi_a$  and  $\phi_a$  (cf. Section 1.04.2.8), is set to  $K_{ab}' = 0.025 E_h$ . If  $\Delta E_{ST} > 0$ , the triplet state is the ground state; if  $\Delta E_{ST} < 0$ , the ground state is a singlet. In the region where  $\Delta E_{ST} \approx 0$ , the species is best described as a “disbiradical”, i.e., a molecule with two independent radical sites. When the difference  $H_{bb} - H_{aa}$  increases, the singlet ground state is stabilized, and the molecule gradually becomes a closed-shell species.

where  $n \geq 0$  is an integer (even  $n$  correspond to  $\Psi_{S_{TC-}}$ , odd  $n$  to  $\Psi_{S_{TC+}}$ ).<sup>19</sup> Thus, the CI coefficients  $c_i$  as defined in Eqs. (41) and (42) depend on the energy difference  $H_{bb} - H_{aa}$ , which is related to the HOMO-LUMO gap, as well as the exchange integral  $K_{ab}$ , which depends on the shape of the orbitals (whether or not they share a significant region of space).<sup>19</sup> In particular, the multireference character of the wavefunction is significant (i.e.,  $c_1 \approx -c_2 \approx 1/\sqrt{2}$ ) when the quotient on the r.h.s. of Eq. (44) becomes large, that is, when the exchange integral  $K_{ab}$  is large and the energy difference between  $H_{aa}$  and  $H_{bb}$  is small. However, notice that in case of a vanishing exchange integral,

$$\begin{aligned} \lim_{K_{ab} \rightarrow 0} \tau_0 &= 0 \\ \Rightarrow c_1 &= \cos(\tau_0) = 1 \\ c_2 &= \sin(\tau_0) = 0 \end{aligned}$$

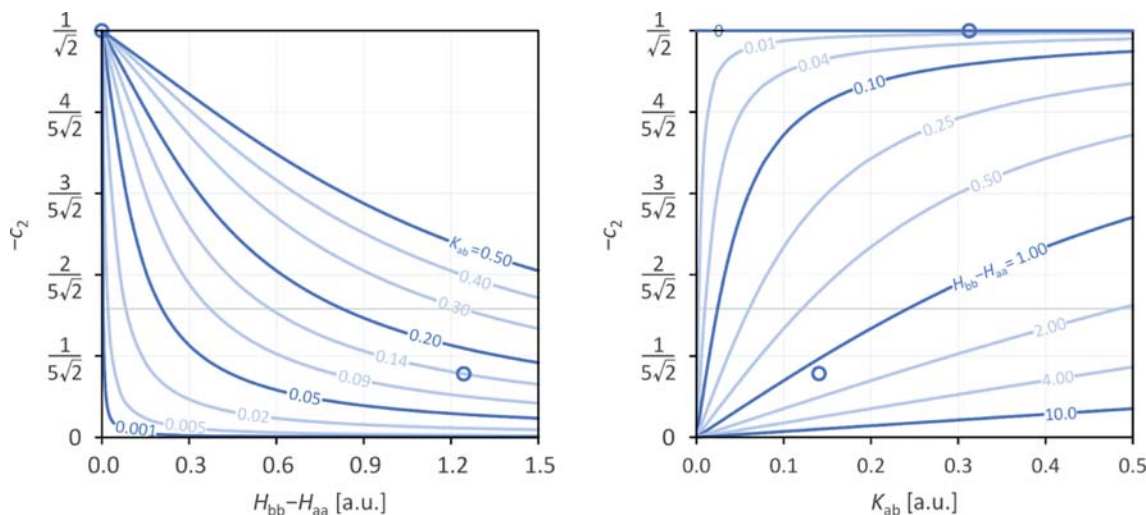
a closed-shell wavefunction is obtained, even if the HOMO-LUMO gap is small. While this usually does not occur in “homo-symmetric” species (here, the orbitals  $\psi_a$  and  $\psi_b$  share a significant region of space due to symmetry), it may well be the case in non-symmetric species (cf. Section 1.04.2.9), e.g., if the HOMO is localized on a ligand and the LUMO is localized on a metal center.

In case of a vanishing energy difference  $\Delta E = H_{bb} - H_{aa}$ , we have

$$\begin{aligned} \lim_{\Delta E \rightarrow 0} \tau_0 &= -\frac{\pi}{4} \\ \Rightarrow c_1 &= \cos(\tau_0) = +\frac{1}{\sqrt{2}} \\ c_2 &= \sin(\tau_0) = -\frac{1}{\sqrt{2}} \end{aligned}$$

which is, of course, a biradical with degenerate orbitals  $\psi_a$  and  $\psi_b$ . Clearly, as it has already been implied throughout this section, the CI coefficients can be taken as a measure of biradical character, seeing that the limiting cases  $c_2 = 0$  and  $c_2 = -1/\sqrt{2}$  correspond to a “pure” closed-shell species and a “pure” biradical, respectively. While we will postpone our discussion of different measures of biradical character to Section 1.04.2.10, it is still worthy to appreciate the interrelation between  $c_2$  and the biradical character of the wavefunction  $\Psi_{S_{TC-}}$  at this stage. In Fig. 11, the evolution of  $c_2$  (and thus the biradical character) is plotted as a function of the energy difference  $H_{bb} - H_{aa}$  and the exchange integral  $K_{ab}$  according to Eqs. (42) and (45). The plots nicely demonstrate that the contribution of  $|\psi_b^2\rangle$  to the wavefunction (34) decreases with an increasing HOMO-LUMO gap, even more so when  $K_{ab}$  is small (Fig. 11, left). Conversely, as the exchange integral  $K_{ab}$  becomes larger, the multireference character of the wavefunction grows (Fig. 11, right). This is in line with the typical observation that two orbitals  $\psi_a$  and  $\psi_b$  correlate most strongly when they are a pair of bonding and antibonding MOs,<sup>20</sup> because they have a large exchange integral  $K_{ab}$  due to their localization in the same region of space.<sup>19</sup>

Allow us to make a last comment on Eq. (45): It is worthy to note that  $\cos(\tau_0) = \sin(\tau_1)$  and  $\sin(\tau_0) = -\cos(\tau_1)$ . Thus, if we define  $\cos(\tau_0) = c_1$  and  $\sin(\tau_0) = -c_2$ , we get



**Fig. 11** Dependence of the CI coefficient  $c_2 = \sin(\tau_0)$  of  $\Psi = c_1|\psi_a^2\rangle + c_2|\psi_b^2\rangle$  on the energy difference  $\Delta E = H_{bb} - H_{aa}$  and exchange integral  $K_{ab}$  (note that  $c_2 < 0$ , i.e.,  $\Psi = \Psi_{S_{TC-}}$ ). Left:  $c_2$  vs.  $\Delta E$ , with isolines for different values of  $K_{ab}$ . The contribution of the second determinant  $|\psi_b^2\rangle$  decreases with an increasing energy difference, especially if  $K_{ab}$  is small. Right:  $c_2$  vs.  $K_{ab}$ , with isolines for different values of  $\Delta E$ . In case of a small energy difference, the contribution of  $|\psi_b^2\rangle$  rises quickly even for small values of  $K_{ab}$ . The circles indicate  $H_2$  at its equilibrium structure ( $-c_2 = 0.111$ ,  $\Delta E = 1.24 E_h$ ,  $K_{ab} = 0.14 E_h$ ) and dissociation limit ( $-c_2 = 1/\sqrt{2}$ ,  $\Delta E = 0$ ,  $K_{ab} = 0.31 E_h$ ).<sup>39</sup> The horizontal gray line indicates  $2c_2^2 = 0.1$ , i.e., a biradical character of 10%.

$$\Psi_{S_{TC-}} = \cos(\tau_0)|\psi_a^2\rangle + \sin(\tau_0)|\psi_b^2\rangle = c_1|\psi_a^2\rangle - c_2|\psi_b^2\rangle$$

$$\Psi_{S_{TC+}} = \cos(\tau_1)|\psi_a^2\rangle + \sin(\tau_1)|\psi_b^2\rangle = c_2|\psi_a^2\rangle + c_1|\psi_b^2\rangle$$

which proves our previous statement in Eqs. (25) and (26).

#### 1.04.2.8 More orbital transformations

We now understand the effect of a small HOMO-LUMO gap on the energies of the four biradical states, and how an increasing HOMO-LUMO gap leads us to the limiting case of a closed-shell species. However, we have only discussed the case of delocalized orbitals  $\psi_a$  and  $\psi_b$  so far, yet for a chemical interpretation of the electronic structure, localized orbitals are the preferred choice.

For reasons of simplicity, let us continue to discuss a homosymmetric biradical. We can then use a similar approach as discussed in the previous sections for orbital localization. However, since the MOs  $\psi_a$  and  $\psi_b$  are no longer degenerate, some additional considerations must be made. Let us re-consider the orthogonal orbital transformation scheme laid out in Eq. (15), i.e.

$$\chi_a = \frac{1}{\sqrt{2}}(\psi_a + \psi_b), \chi_b = \frac{1}{\sqrt{2}}(\psi_a - \psi_b)$$

As discussed in Section 1.04.2.5, the transformed orbitals  $\chi_a$  and  $\chi_b$  correspond to the generalized valence bond (GVB) orbitals if (and only if) the orbitals  $\psi_a$  and  $\psi_b$  are degenerate. In case of non-degenerate orbitals  $\psi_a$  and  $\psi_b$ , the GVB transformation<sup>20,31</sup> depends on the CI coefficients  $c_i$  of the wavefunction

$$\Psi_{S_{TC-}} = c_1|\psi_a^2\rangle - c_2|\psi_b^2\rangle$$

and is given by

$$\chi_a = k_1\psi_a + k_2\psi_b, \quad \chi_b = k_1\psi_a - k_2\psi_b \quad (46)$$

where

$$k_1 = \sqrt{\frac{c_1}{c_1 + c_2}}, k_2 = \sqrt{\frac{c_2}{c_1 + c_2}}$$

Thus, in case of  $c_1 = c_2 = 1/\sqrt{2}$ , Eq. (46) is identical to Eq. (15). When applying the GVB transformation in Eq. (46) to  $\Psi_{S_{TC-}}$  we get

$$\begin{aligned} \Psi_{S_{TC-}} &= c_1|\psi_a^2\rangle - c_2|\psi_b^2\rangle \\ &= \frac{1}{\sqrt{2}}[c_1\psi_a(1)\psi_a(2) - c_2\psi_b(1)\psi_b(2)][\alpha(1)\beta(2) - \beta(1)\alpha(2)] \\ &= \frac{c_1 + c_2}{\sqrt{2}} \cdot \frac{1}{2}[\chi_a(1)\chi_b(2) + \chi_b(1)\chi_a(2)][\alpha(1)\beta(2) - \beta(1)\alpha(2)] \\ &= \frac{c_1 + c_2}{\sqrt{2}} \cdot \frac{1}{\sqrt{2}}(|\chi_a^\alpha\chi_b^\beta\rangle - |\chi_b^\beta\chi_a^\alpha\rangle) = \Psi'_{S_{OS}} \end{aligned} \quad (47)$$

where the prefactor  $(c_1 + c_2)/\sqrt{2}$  is required for normalization (since  $\chi_a$  and  $\chi_b$  are, in general, no longer orthogonal). Thus,  $\Psi_{S_{TC-}}$  transforms into an open-shell wavefunction in the GVB basis, and in the limiting case  $c_1 = c_2 = 1/\sqrt{2}$ , we obtain the same result as in Eq. (18).

Thus, in principle, we can draw the same conclusions as before:  $\Psi_{S_{TC-}}$  is generally a biradical state, and the system can be classified either as disjoint biradical if the GVB orbitals are localized on different atoms, or as joint biradical if they cannot be localized. In the latter case, it is less straightforward to assign biradical or ionic character to the wavefunction, as discussed before.

Notice how the overlap between  $\chi_a$  and  $\chi_b$  depends on the CI coefficients (and thus on the HOMO-LUMO gap, cf. Section 1.04.2.7):

$$\langle\chi_a|\chi_b\rangle = \frac{c_1 - c_2}{c_1 + c_2} \quad (48)$$

In the limiting case of a “perfect” biradical ( $c_1 = c_2 = 1/\sqrt{2}$ ), we have  $\langle\chi_a|\chi_b\rangle = 0$ , i.e., the orbitals are orthogonal (and, in case of a disjoint biradical, perfectly localized). Conversely, a “perfect” closed-shell species ( $c_1 = 1$  and  $c_2 = 0$ ) has an overlap integral  $\langle\chi_a|\chi_b\rangle = 1$ , i.e.,  $\chi_a$  and  $\chi_b$  are identical and correspond to the delocalized HOMO  $\chi_a$  according to Eq. (46). Thus, with an increasing HOMO-LUMO gap, the GVB orbitals gradually become more and more delocalized across the radical centers (Fig. 12), which makes chemical interpretation of the wavefunction in terms of “biradical” and “ionic” contributions impractical in the GVB basis. In fact, it is exactly this delocalization of the GVB orbitals that describes the ionic contributions that are inherent to any covalent bond.<sup>31</sup> (In the closed-shell limit, i.e., using a single determinant to describe a closed-shell wavefunction, the wavefunction has 50% covalent and 50% ionic character, see below.)<sup>18</sup>



To overcome the “problem” of the partly delocalized GVBs in biradicals with non-degenerate frontier orbitals  $\psi_a$  and  $\psi_b$ , different localization methods may be used, such as Foster-Boys localization.<sup>40,41</sup> In the case of homosymmetric species, this is equivalent to

$$\phi_a = \frac{1}{\sqrt{2}}(\psi_a + \psi_b), \phi_b = \frac{1}{\sqrt{2}}(\psi_a - \psi_b)$$

which is mathematically identical to the orbital transformation laid out in Eq. (15). Note that due to the non-degeneracy of  $\psi_a$  and  $\psi_b$ , the transformed orbitals  $\phi_a$  and  $\phi_b$  are no longer the GVB orbitals, but rather orthonormal, (semi-)localized orbitals (Fig. 12) that minimize the exchange integral  $K_{ab}$ .<sup>19</sup> Applying this orbital transformation to the singlet wavefunction  $\Psi_{S_{TC-}}$  yields

$$\begin{aligned} \Psi_{S_{TC-}} &= c_1 |\psi_a^2\rangle - c_2 |\psi_b^2\rangle \\ &= \frac{1}{\sqrt{2}} [c_1 \psi_a(1)\psi_a(2) - c_2 \psi_b(1)\psi_b(2)] [\alpha(1)\beta(2) - \beta(1)\alpha(2)] \\ &= \frac{c_1 + c_2}{\sqrt{2}} \cdot \frac{1}{2} [\phi_a(1)\phi_b(2) + \phi_b(1)\phi_a(2)] [\alpha(1)\beta(2) - \beta(1)\alpha(2)] \\ &\quad + \frac{c_1 - c_2}{\sqrt{2}} \cdot \frac{1}{2} [\phi_a(1)\phi_a(2) + \phi_b(1)\phi_b(2)] [\alpha(1)\beta(2) - \beta(1)\alpha(2)] \\ &= \frac{c_1 + c_2}{\sqrt{2}} \cdot \frac{1}{\sqrt{2}} (|\phi_a^\alpha \phi_b^\beta\rangle - |\phi_a^\beta \phi_b^\alpha\rangle) + \frac{c_1 - c_2}{\sqrt{2}} \cdot \frac{1}{\sqrt{2}} (|\phi_a^2\rangle + |\phi_b^2\rangle) \end{aligned} \quad (49)$$

Thus, the wavefunction can be written as

$$\Psi_{S_{TC-}} = c_{cov} |\Psi_{cov}\rangle + c_{ion} |\Psi_{ion}\rangle \quad (50)$$

with

$$\frac{c_1 + c_2}{\sqrt{2}} = c_{cov}, \frac{c_1 - c_2}{\sqrt{2}} = c_{ion} \quad (51)$$

Using the localized orbitals  $\phi_a$  and  $\phi_b$ , it becomes clear that the singlet ground state wavefunction  $\Psi_{S_{TC-}}$  possesses covalent (biradical) and ionic character, if the delocalized frontier orbitals  $\psi_a$  and  $\psi_b$  are non-degenerate. In fact, in the limiting case of a “perfect” biradical (i.e.,  $c_1 = c_2 = 1/\sqrt{2}$ ) we have  $c_{cov} = 1$  and  $c_{ion} = 0$ , whereas the limiting case of a “perfect” closed-shell with an infinite HOMO-LUMO gap (i.e.,  $c_1 = 1$  and  $c_2 = 0$ ) is defined by  $c_{cov} = c_{ion} = 1/\sqrt{2}$ . Thus, the wavefunction varies from purely covalent in the “perfect” biradical limit to 50% covalent and 50% ionic in the closed-shell limit.

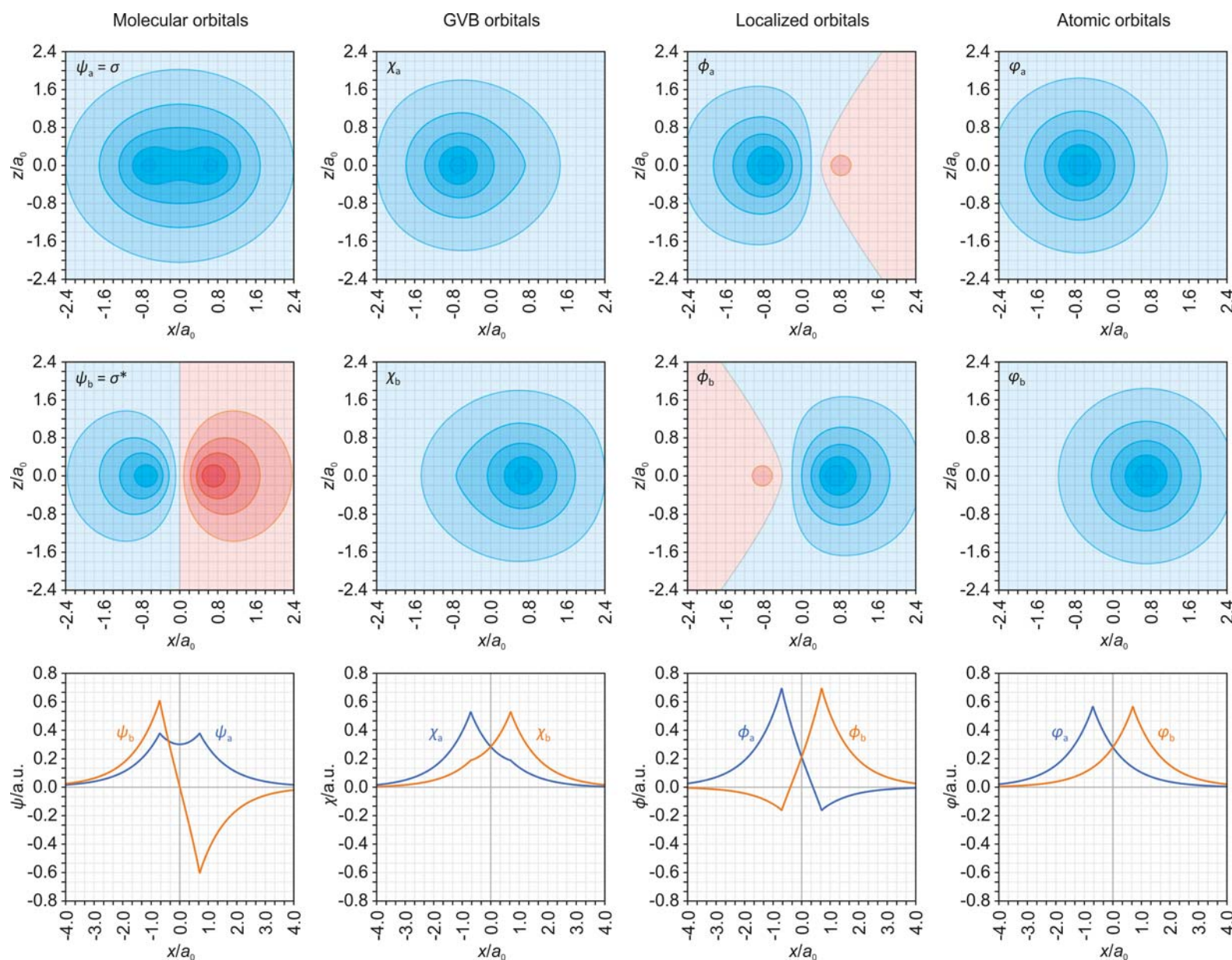
In case the radical centers can be fully localized on two single atoms, it is also possible to use atomic (hybrid) orbitals  $\varphi_a$  and  $\varphi_b$  as localized orbitals (Fig. 12).<sup>18</sup> Again assuming a homosymmetric system, the MOs can then be expressed as linear combinations

$$\psi_a = \frac{1}{\sqrt{2 + 2S_{ab}}}(\varphi_a + \varphi_b), \psi_b = \frac{1}{\sqrt{2 - 2S_{ab}}}(\varphi_a - \varphi_b) \quad (52)$$

where the prefactor  $1/\sqrt{2 + 2S_{ab}}$  ensures normalization of the MOs, and  $S_{ab} = \langle \varphi_a | \varphi_b \rangle$  is the overlap integral between the atomic orbitals  $\varphi_a$  and  $\varphi_b$  (notice that the atomic orbitals are, in general, not orthogonal to each other). It is straightforward to show that

$$\begin{aligned} \Psi_{S_{TC-}} &= c_1 |\psi_a^2\rangle - c_2 |\psi_b^2\rangle \\ &= \frac{1}{\sqrt{2}} [c_1 \psi_a(1)\psi_a(2) - c_2 \psi_b(1)\psi_b(2)] [\alpha(1)\beta(2) - \beta(1)\alpha(2)] \\ &= \left[ \frac{c_1}{2 + 2S_{ab}} + \frac{c_2}{2 - 2S_{ab}} \right] \frac{1}{\sqrt{2}} [\varphi_a(1)\varphi_b(2) + \varphi_b(1)\varphi_a(2)] [\alpha(1)\beta(2) - \beta(1)\alpha(2)] \\ &\quad + \left[ \frac{c_1}{2 + 2S_{ab}} - \frac{c_2}{2 - 2S_{ab}} \right] \frac{1}{\sqrt{2}} [\varphi_a(1)\varphi_a(2) + \varphi_b(1)\varphi_b(2)] [\alpha(1)\beta(2) - \beta(1)\alpha(2)] \\ &= \left[ \frac{c_1}{2 + 2S_{ab}} + \frac{c_2}{2 - 2S_{ab}} \right] (|\varphi_a^\alpha \varphi_b^\beta\rangle - |\varphi_a^\beta \varphi_b^\alpha\rangle) + \left[ \frac{c_1}{2 + 2S_{ab}} - \frac{c_2}{2 - 2S_{ab}} \right] (|\varphi_a^2\rangle + |\varphi_b^2\rangle) \end{aligned} \quad (53)$$

Thus, the wavefunction is composed of covalent and ionic contributions just as in case of the orthogonal, localized orbitals  $\phi_a$  and  $\phi_b$ . Note, however, that due to the non-orthogonality of the atomic orbitals  $\varphi_a$  and  $\varphi_b$ , the covalent and ionic contributions to the wavefunction are also not orthogonal and a partitioning scheme is needed to assign their overlaps either to the covalent or the ionic contribution.<sup>20</sup> Also note that Eq. (53) is mathematically equivalent to the valence bond (VB) wavefunction of the system.



**Fig. 12** Molecular orbitals of  $\text{H}_2$  ( $r = 1.4$  a.u.,  $\Psi = 0.994|\psi_a^2\rangle - 0.111|\psi_b^2\rangle$ ).<sup>39</sup> Top and middle row: Contour plots of the orbitals in the  $xz$  plane. Bottom row: Section of the orbitals along the  $x$ -axis (i.e.,  $y = z = 0$ ). Left column: Canonical (delocalized) MOs  $\psi_a$  and  $\psi_b$ . Center left column: GVB orbitals  $\chi_a$  and  $\chi_b$ . The two electrons are mainly located at opposite nuclei, demonstrating their correlated motion. However, notice the small (positive) cusp at the position of the second H atom, indicating that the orbitals are still somewhat delocalized and there is a certain probability of finding both electrons at the same nucleus. Center right column: Orthogonal localized orbitals  $\phi_a$  and  $\phi_b$ . The negative cusps are the so-called “orthogonalization tails,” ensuring that  $\langle\phi_a|\phi_b\rangle = 0$ . Right column: Atomic orbitals  $\varphi_a$  and  $\varphi_b$ . Like the GVB orbitals, the atomic orbitals are not orthogonal. At infinite separation of the H nuclei (i.e., a “perfect” biradical), GVB orbitals, localized orbitals, and atomic orbitals are identical.

In fact, as we have not made any mathematical restrictions on the orbitals  $\varphi_a$  and  $\varphi_b$ , the orbital transformation in Eq. (52) holds true for *any* choice of (semi-)localized orbitals, so Eq. (53) is valid for *all* the cases discussed above. For example, if  $S_{ab} = 0$  (i.e., if the orbitals  $\varphi_a$  and  $\varphi_b$  are orthogonal), we obtain the same solution as in Eq. (49). Moreover, if the overlap integral is

$$S_{ab} = \frac{2c_1}{c_1 + c_2} - 1 = 1 - \frac{2c_2}{c_1 + c_2} \quad (54)$$

Eq. (53) transforms into Eq. (47), i.e., the GVB wavefunction.

#### 1.04.2.9 Non-symmetric biradicals

Up to this point, we have restricted our discussion to “homosymmetric” biradicals (radical centers localized on symmetry equivalent sites). If, however, the radical centers are inequivalent, the singlet ground state wavefunction (in the basis of the canonical molecular orbitals  $\psi_a$  and  $\psi_b$ ) takes the general form

$$\Psi_S = c_1 |\psi_a^2\rangle - c_2 |\psi_b^2\rangle + c_3 \cdot \frac{1}{\sqrt{2}} \left( |\psi_a^\alpha \psi_b^\beta\rangle - |\psi_a^\beta \psi_b^\alpha\rangle \right) \quad (55)$$

where the last term on the r.h.s. of Eq. (55) is responsible for distributing the electrons unevenly between the two radical sites; that is,  $c_3 = 0$  for homosymmetric and  $c_3 > 0$  for non-symmetric species. In the basis of localized orbitals  $\phi_a$  and  $\phi_b$ , this will result in two different ionic contributions, since the probabilities of finding both electrons at either radical site “a” or “b” will, in general, not be the same<sup>20</sup>:

$$\Psi_S = c_{\text{cov}} \cdot \frac{1}{\sqrt{2}} \left( |\phi_a^\alpha \phi_b^\beta\rangle - |\phi_a^\beta \phi_b^\alpha\rangle \right) + c_{\text{ion},1} |\phi_a^2\rangle + c_{\text{ion},2} |\phi_b^2\rangle \quad (56)$$

with

$$\phi_a = \cos(\alpha) \cdot \psi_a + \sin(\alpha) \cdot \psi_b$$

$$\phi_b = \sin(\alpha) \cdot \psi_a - \cos(\alpha) \cdot \psi_b$$

where  $\alpha$  is the “rotation angle” that transforms the MOs  $\psi_a$  and  $\psi_b$  into the localized orbitals  $\phi_a$  and  $\phi_b$  (for homosymmetric species,  $\alpha = 45^\circ$ ). The different ionic terms in Eq. (56) are typically due to different electronegativities of the atoms involved, i.e.,  $\phi_a$  might have a lower orbital energy than  $\phi_b$  (and thus higher occupation number), resulting in an overall polarization.

In this regard, we see fit to introduce another type of delocalized orbitals which is often used to represent multiconfigurational wavefunctions, the so-called natural orbitals (NOs)  $\omega_i$ . These are often the default orbitals in CASSCF-type calculations, and are defined as the eigenfunctions of the 1-electron reduced density operator  $\Gamma$ ,<sup>20,42,43</sup>

$$\Gamma \omega_i = n_i \omega_i \quad (57)$$

with eigenvalues  $n_i$  that correspond to the occupation numbers of the NOs, and the density operator being defined as

$$\Gamma = |\Psi\rangle\langle\Psi| \quad (58)$$

For the wavefunction in Eq. (55), the density operator is

$$\Gamma = (2c_1^2 + c_3^2) |\psi_a\rangle\langle\psi_a| + (2c_2^2 + c_3^2) |\psi_b\rangle\langle\psi_b| + \sqrt{2}(c_1c_3 - c_2c_3) (|\psi_a\rangle\langle\psi_b| + |\psi_b\rangle\langle\psi_a|) \quad (59)$$

with the corresponding density matrix

$$\rho = \begin{pmatrix} 2c_1^2 + c_3^2 & \sqrt{2}(c_1c_3 - c_2c_3) \\ \sqrt{2}(c_1c_3 - c_2c_3) & 2c_2^2 + c_3^2 \end{pmatrix} \quad (60)$$

The diagonal elements correspond to the occupancy of orbitals  $\psi_a$  and  $\psi_b$ , while the off-diagonal elements indicate the “bond order” between these orbitals<sup>19</sup> (clearly, this value makes more sense if the density matrix is constructed for localized orbitals). The NOs diagonalize the density matrix, so all off-diagonal elements become zero in the NO basis.

Note that for a homosymmetric biradical ( $c_3 = 0$ ), all off-diagonal elements of the density matrix in the MO basis are zero, so the density matrix is already diagonalized<sup>20</sup>:

$$\rho = \begin{pmatrix} 2c_1^2 & 0 \\ 0 & 2c_2^2 \end{pmatrix}$$

$$\Gamma = 2c_1^2 |\psi_a\rangle\langle\psi_a| + 2c_2^2 |\psi_b\rangle\langle\psi_b|$$

Thus, the NOs of a homosymmetric biradical are just the regular canonical MOs. In all other cases, though, the NOs are distinctly different (but often similar in shape). By diagonalizing the density matrix, the NO basis offers the most compact representation of any multireference state, i.e., the wavefunction in Eq. (55) becomes

$$\begin{aligned}\Psi_S &= c_1|\psi_a^2\rangle - c_2|\psi_b^2\rangle + c_3 \cdot \frac{1}{\sqrt{2}} \left( |\psi_a^\alpha\psi_b^\beta\rangle - |\psi_a^\beta\psi_b^\alpha\rangle \right) \\ &= c'_1|\omega_a^2\rangle - c'_2|\omega_b^2\rangle\end{aligned}\quad (61)$$

Hence, only two determinants are needed to express the singlet ground state wavefunction in the NO basis, irrespective of molecular symmetry.

#### 1.04.2.10 Biradical character

Our discussion up to this point has already hinted several times at a fundamental concept of biradicals, namely the quantification of the biradical character. There are a lot of different ways to do so; thus, discussing all different indices lies outside the scope of this article. Nonetheless, we are going to cover some of the most fundamental approaches and give some selected examples.

In **Section 1.04.2.7**, we have already discussed that the CI coefficients can act as a measure of biradical character: Using delocalized orbitals (usually the MOs or NOs), that is,

$$\Psi_{S_{TC-}} = c_1|\psi_a^2\rangle - c_2|\psi_b^2\rangle \quad (62)$$

the limit of a “perfect” biradical is given by  $c_1 = c_2 = 1/\sqrt{2}$ , whereas the closed-shell limit is defined by  $c_1 = 1$  and  $c_2 = 0$ . Thus, if we find a function that normalizes  $c_2$  in the limit of a “perfect” biradical, it can serve as a measure of biradical character that ranges from 0 to 1. However, while the end points of such a scale are clearly defined, it remains unclear how to interpolate between these values.<sup>20</sup>

Conversely, using localized orbitals  $\phi_a$  and  $\phi_b$ , we find

$$\Psi_{S_{TC-}} = c_{cov}|\Psi_{cov}\rangle + c_{ion}|\Psi_{ion}\rangle \quad (63)$$

where  $c_{cov}$  and  $c_{ion}$  can be derived from  $c_1$  and  $c_2$  as described in Eq. (51). Here, the “perfect” biradical limit is defined by  $c_{cov} = 1$  and  $c_{ion} = 0$ , while the closed-shell limit is given by  $c_{cov} = c_{ion} = 1/\sqrt{2}$ .

Using these limits, one can devise many different normalized indicators of biradical character, such as

$$\gamma = \sqrt{2} \cdot c_2 = c_{cov} - c_{ion} \quad (64)$$

$$d = 2c_1c_2 = c_{cov}^2 - c_{ion}^2 \quad (65)$$

$$\beta = 2c_2^2 = (c_{cov} - c_{ion})^2 \quad (66)$$

The first indicator in Eq. (64)<sup>44</sup> simply measures the amplitude of the configuration  $|\psi_b^2\rangle$ , which corresponds to the excess of the covalent amplitude relative to the ionic contribution. To understand the second indicator in Eq. (65), we note that when using orthonormal orbitals (which is usually the case), the configurations  $|\psi_a^2\rangle$  and  $|\psi_b^2\rangle$  or  $|\Psi_{cov}\rangle$  and  $|\Psi_{ion}\rangle$  are also orthonormal, and thus  $\sum c_i^2 = 1$ . Therefore, the squared CI coefficients correspond to the relative weight (i.e., the probability) of each contribution to the CI expansion. Thus, the indicator in Eq. (65)<sup>45</sup> describes the difference between the probabilities of the covalent and ionic contributions. The last indicator in Eq. (66)<sup>43</sup> is directly related to the probability of  $|\psi_b^2\rangle$ , which (if natural orbitals are used, see below) also corresponds to the occupation number of  $\psi_b$ .

The indices in Eqs. (65) and (66) were also modified for general CI wavefunctions that contain more than two coefficients<sup>45,46</sup>:

$$\Psi = \sum_{i=1}^N c_i \Psi_i = c_1 \Psi_1 + \underbrace{c_2 \Psi_2 + \dots + c_N \Psi_N}_{\sqrt{c_1^2 + c_2^2} \cdot \Psi_{S_{TC\pm}}} \quad (67)$$

This may be the case if the active space is chosen larger than the simple “two electrons in two orbitals” [i.e., CAS(2,2)] model discussed here, or even within the CAS(2,2) picture if the biradical is non-symmetric [cf. Eq. (56)]. The coefficients  $c_3 \dots c_N$  are typically small and describe dynamic electron correlation. Note that the notation used in Eq. (67) implies that  $c_2 < 0$  for the singlet ground state.

Due to the inclusion of dynamic correlation, the relative contribution of the original two-configuration wavefunction  $\Psi_{S_{TC-}}$  to the total CI wavefunction is  $c_1^2 + c_2^2$ . Thus, the factor  $1/(c_1^2 + c_2^2)$  is introduced in Eqs. (65) and (66) to normalize the biradical character:

$$d = 2 \sqrt{\frac{c_1^2 c_2^2}{c_1^2 + c_2^2}} \quad (68)$$

$$\beta = \frac{2c_2^2}{c_1^2 + c_2^2} \quad (69)$$

The different biradical indicators are depicted in Fig. 13. It becomes clear that  $\beta$  predicts the smallest, while  $d$  predicts the highest numerical values of biradical character.

Notice that in the localized picture, i.e., when considering the covalent and ionic coefficients  $c_{\text{cov}}$  and  $c_{\text{ion}}$ , all biradical indicators discussed above depend on *both* coefficients. This is noteworthy insofar as the “covalent” and “ionic” structures  $|\Psi_{\text{cov}}\rangle$  and  $|\Psi_{\text{ion}}\rangle$  can be translated to the valence bond (VB) picture, where the “covalent” structure is usually drawn as a dot-dot structure. However, this should not be regarded solely as a biradical contribution, as  $|\Psi_{\text{cov}}\rangle$  clearly describes a purely “bonding” situation in the closed-shell limit. Thus, even though one might draw a Lewis structure with two dots at the radical centers, the weight of this structure (i.e.,  $c_{\text{cov}}^2$ ) alone is not a suitable measure of biradical character.

A last note of caution: As we have discussed in quite some detail in the previous sections, the CI coefficients depend on the choice of orbitals, thus they are not uniquely defined! There are many more possible choices than those we have discussed,<sup>19</sup> and therefore it is not necessarily straightforward to compare the biradical character of different molecules, especially among different publications by different authors, who might have used different computational methods and orbital bases.

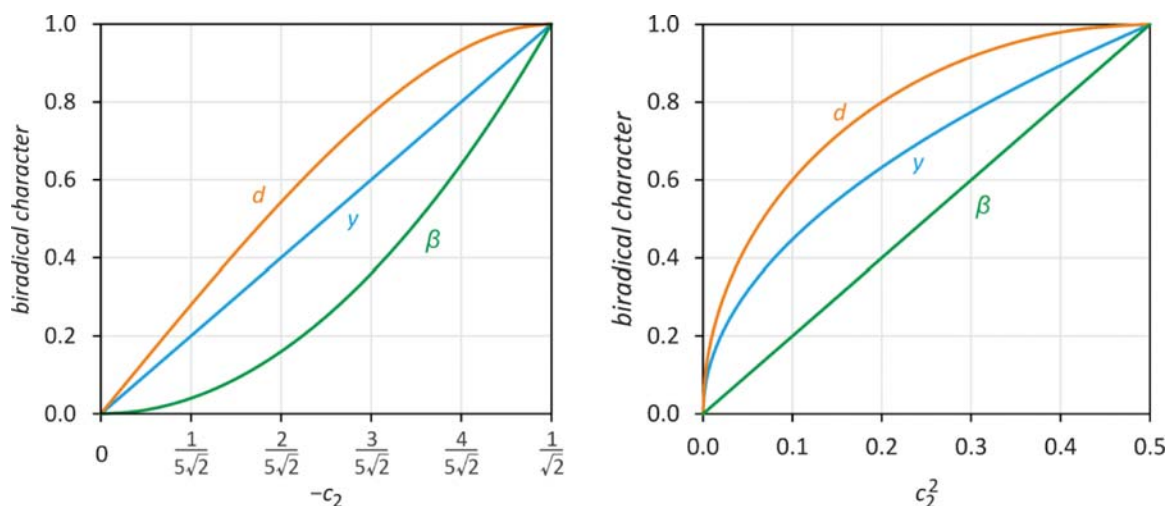
Another popular indicator of biradical character is derived from the occupation numbers of the natural orbitals (NOs). The NOs are uniquely defined for a given system (cf. Section 1.04.2.9), independently of the orbitals that were used to derive the multireference wavefunction. If NOs are used to represent the CAS(2,2) wavefunction, the occupancy of the lowest unoccupied NO (LUNO) is equal to  $2c_2^2$ , as the NOs diagonalize the density matrix. Thus, its occupancy varies from 0 in the closed-shell limit to 1 in the limit of a “perfect” biradical and it is therefore a natural indicator of biradical character. The occupancy of the HONO (highest occupied NO), on the other hand, varies from 2 to 1, with  $n_{\text{HONO}} = 2 - x$  and  $n_{\text{LUNO}} = x \leq 1$ , and thus  $n_{\text{HONO}} + n_{\text{LUNO}} = 2$ .

In a general CI wavefunction, i.e., using larger active spaces than (2,2), the LUNO is the orbital with the highest occupation number smaller than 1, while the HONO corresponds to the orbital with the smallest occupation number larger than 1. Orbitals with smaller occupancy than the LUNO, in the order of decreasing occupation numbers, are called LUNO+1, LUNO+2, ..., while orbitals with increasing occupancy are named HONO-1, HONO-2, etc.<sup>20</sup> Typically, each pair of HONO- $i$  and LUNO+ $i$  corresponds to a pair of delocalized bonding and anti-bonding orbitals. The equality  $n_{\text{HONO}-i} + n_{\text{LUNO}+i} = 2$  holds strictly for “broken-symmetry” UHF or UDFT calculations (see below), while it is approximately satisfied for general multireference wavefunctions.<sup>20</sup> In this vein, the occupation numbers can be generalized to polyradical indicators, the occupancy of the LUNO indicating biradical character as explained above, the occupancy of LUNO+1 indicating tetradical character and so on. Note that apart from non-dynamic correlation, dynamic correlation in highly correlated calculations (e.g., when using large active spaces or a multireference configuration interaction (MRCI) approach) can also influence the occupation numbers.

One advantage of NOs is certainly that they can be calculated using almost all computational methods, especially UHF or UDFT, which come with a much smaller computational cost than CI methods. Using the “broken-symmetry” formalism, one can approximately describe a multiconfigurational wavefunction by single-determinantal methods. For instance, the “broken-symmetry” UHF wavefunction of a singlet biradical (ignoring all paired electrons) is given by

$$\Psi_{\text{BS}} = |\chi_a^\alpha \chi_b^\beta\rangle \quad (70)$$

where the orbitals  $\chi_a$  and  $\chi_b$  are the GVB orbitals localized at the radical sites “a” and “b” as defined in Eq. (46):



**Fig. 13** Examples of biradical indicators based on the CI coefficients. While  $y$  is proportional to the amplitude  $c_2$ ,  $\beta$  is proportional to the probability  $c_2^2$ . Note that both  $y$  and  $d$  predict a significant biradical character for  $|c_2| = 0.1$ , which is typically considered dynamic correlation ( $y = 14\%$ ,  $d = 20\%$ ,  $\beta = 2\%$ ; cf.  $\text{H}_2$  at  $r_{\text{eq}} = 1.4$  a. u.,  $\Psi = 0.994|\psi_a^2\rangle - 0.111|\psi_b^2\rangle$ ).<sup>39</sup> Thus, numerical values of the different indicators cannot be compared directly.



$$\chi_a = k_1\psi_a + k_2\psi_b, \chi_b = k_1\psi_a - k_2\psi_b$$

As discussed above,  $\psi_a$  and  $\psi_b$  are the delocalized frontier orbitals, and the coefficients  $k_1 = \cos \theta$ ,  $k_2 = \sin \theta$ .

Obviously, the wavefunction in Eq. (70) is physically wrong, since it introduces unphysical spin polarization. The correct wavefunction using the GVB orbitals would, of course, be given by Eq. (47). In fact, using the GVB orbital transformation we can show that

$$\Psi_{\text{BS}} = \underbrace{\cos^2\theta|\psi_a^2\rangle - \sin^2\theta|\psi_b^2\rangle}_{\Psi_{\text{SIC-}}} + \sin\theta \cos\theta \cdot \underbrace{\left(|\psi_b^\alpha\psi_a^\beta\rangle + |\psi_b^\beta\psi_a^\alpha\rangle\right)}_{\Psi_{\text{T}}} \quad (71)$$

Hence, the “broken-symmetry” UHF wavefunction is really a mixture of singlet and triplet wavefunctions, leading to the well-known problem of spin contamination.<sup>20,28,47</sup> It changes from a closed-shell singlet in the limit  $\theta = 0$

$$\Psi_{\text{BS}} = |\psi_a^2\rangle$$

to an equal mixture of singlet and triplet in the limit  $\theta = \pi/4$  (i.e., a “perfect” biradical)

$$\Psi_{\text{BS}} = \frac{1}{2}(|\psi_a^2\rangle - |\psi_b^2\rangle) + \frac{1}{2}\left(|\psi_b^\alpha\psi_a^\beta\rangle + |\psi_b^\beta\psi_a^\alpha\rangle\right)$$

The density operator of the UHF wavefunction is given by

$$\begin{aligned} \Gamma &= |\chi_a\rangle\langle\chi_a| + |\chi_b\rangle\langle\chi_b| \\ &= |\cos\theta\cdot\psi_a + \sin\theta\cdot\psi_b\rangle\langle\cos\theta\cdot\psi_a + \sin\theta\cdot\psi_b| \\ &\quad + |\cos\theta\cdot\psi_a - \sin\theta\cdot\psi_b\rangle\langle\cos\theta\cdot\psi_a - \sin\theta\cdot\psi_b| \\ &= 2\cos^2\theta\cdot|\psi_a\rangle\langle\psi_a| + 2\sin^2\theta\cdot|\psi_b\rangle\langle\psi_b| \end{aligned}$$

Thus,  $\psi_a$  and  $\psi_b$  are the natural orbitals of the UHF wavefunction with occupancies  $n_{\text{HONO}}$  and  $n_{\text{LUNO}}$ :

$$n_{\text{HONO}} = 2\cos^2\theta = 1 + \langle\chi_a|\chi_b\rangle$$

$$n_{\text{LUNO}} = 2\sin^2\theta = 1 - \langle\chi_a|\chi_b\rangle$$

The latter, however, is not a good indicator of biradical character, since it suffers from spin contamination. This can be remedied by projecting out the spin-contaminants, as proposed by Yamaguchi<sup>47</sup>:

$$\gamma_0 = n_{\text{LUNO}}^{\text{p}} = \frac{n_{\text{LUNO}}^2}{1 + \langle\chi_a|\chi_b\rangle^2} = \frac{2n_{\text{LUNO}}^2}{n_{\text{HONO}}^2 + n_{\text{LUNO}}^2} \quad (72)$$

Here,  $n_{\text{LUNO}}^{\text{p}}$  is the spin-projected occupation number of the LUNO. The occupation number of other NOs can also be corrected using a generalized version of Eq. (72):

$$\gamma_i = n_{\text{LUNO}+i}^{\text{p}} = \frac{2n_{\text{LUNO}+i}^2}{n_{\text{HONO}-i}^2 + n_{\text{LUNO}+i}^2} \quad (73)$$

There are many more bi- and polyradical indicators based on natural occupancies. The interested reader is referred to the excellent review of Stuyver/Chen/Zeng/Hoffmann and co-workers.<sup>20</sup>

Lastly, the biradical character is often also related to the singlet-triplet gap  $\Delta E_{\text{ST}}$ ,<sup>48,49</sup> which in turn is related to the magnetic coupling between the two radical sites. The magnetic coupling between two electrons can be described by the phenomenological Heisenberg-Dirac-van-Vleck Hamiltonian<sup>29,45,49,50</sup>

$$H_{\text{HDvV}} = -2J_{ij} S_i \cdot S_j \quad (74)$$

where  $J_{ij}$  is the magnetic exchange coupling constant (not to be confused with the Coulomb integral  $J_{\text{ab}}$ ) and  $S_i$  and  $S_j$  are the local spin operators on radical sites “i” and “j”. Note that some authors also use the definition  $H_{\text{HDvV}} = -J_{ij} S_i \cdot S_j$ ,<sup>29,51</sup> which changes the magnitude of  $J_{ij}$  by a factor of two. When comparing values between different publications, it is therefore paramount to check which definition was used! We will continue to use the definition in Eq. (74).

The exchange coupling constant  $J_{ij}$  can be computed from  $\Delta E_{\text{ST}}$ :

$$\Delta E_{\text{ST}} = E_{\text{S}} - E_{\text{T}} = 2J_{ij} \quad (75)$$

Thus, if  $\Delta E_{\text{ST}} \approx 0$ , there is no magnetic coupling between the electrons, and the species is best understood as a disbiradical, i.e., a molecule with two independent radical sites. If  $\Delta E_{\text{ST}} > 0$  (and thus  $J_{ij} > 0$ ), the electrons are ferromagnetically coupled and the ground state is a triplet. Conversely, if  $\Delta E_{\text{ST}} < 0$  (i.e.,  $J_{ij} < 0$ ), the electrons are antiferromagnetically coupled and the ground state is a singlet. Depending on the magnitude of the coupling constant  $J_{ij}$ , it may either be a singlet biradical (in the weak coupling region) or a closed-shell singlet in the limit of strong coupling. Note that for a “perfect biradical,” we have

$$\Delta E_{\text{ST}} = 2K'_{\text{ab}} = 2J_{ij} \quad (76)$$

that is, the magnetic exchange coupling constant  $J_{ij}$  is equal to the exchange integral  $K'_{\text{ab}}$  between the localized orbitals  $\chi_{\text{a}}$  and  $\chi_{\text{b}}$ .

While the ST gap  $\Delta E_{\text{ST}}$  is most accurately computed using multireference methods that include dynamic correlation,<sup>29,32-34</sup> it may also be inferred from “broken-symmetry” UDFT (or UHF) calculations.<sup>52,53</sup> In the latter case, it is typically necessary to correct the computed ST gap using spin-projection to account for the spin-contamination of the “broken-symmetry” singlet wavefunction  $\Psi_{\text{BS}}$ . While several schemes for spin projection exist, we only want to discuss the most generally applicable formula here<sup>49,50,54</sup>:

$$J_{ij} = \frac{E_{\text{BS}} - E_{\text{T}}}{\langle S^2 \rangle_{\text{T}} - \langle S^2 \rangle_{\text{BS}}} \quad (77)$$

$E_{\text{BS}}$  and  $E_{\text{T}}$  are the SCF energies of the “broken-symmetry” singlet and triplet state, respectively, while  $\langle S^2 \rangle_{\text{T}}$  and  $\langle S^2 \rangle_{\text{BS}}$  are the expectation values of the  $S^2$  operator, *viz*

$$\langle S^2 \rangle_{\text{T}} = \langle \Psi_{\text{T}} | S^2 | \Psi_{\text{T}} \rangle$$

$$\langle S^2 \rangle_{\text{BS}} = \langle \Psi_{\text{BS}} | S^2 | \Psi_{\text{BS}} \rangle$$

Typically,  $\langle S^2 \rangle_{\text{T}} \approx 2$ , whereas  $\langle S^2 \rangle_{\text{BS}}$  may range from 0 in the closed-shell limit to 1 in the limit of a “perfect” biradical. Remember that in the biradical limit,  $\Psi_{\text{BS}}$  is a 50:50 mixture of singlet and triplet; thus,  $\langle S^2 \rangle_{\text{BS}}$  is then also the average of the actual eigenvalues of a singlet (0) and a triplet (2). In consequence, the ST gap  $\Delta E_{\text{ST}} = 2J_{ij}$  is twice the difference  $E_{\text{BS}} - E_{\text{T}}$  in the case of a “perfect” biradical, while in the closed-shell limit, it is just the normal difference  $E_{\text{BS}} - E_{\text{T}} = E_{\text{S}} - E_{\text{T}}$ .

On a final note, some care should be taken when using the “broken-symmetry” formalism to detect biradical character. As implied by our discussion above, biradical character will induce “symmetry-breaking” of the Hartree-Fock or Kohn-Sham wavefunction (i.e., the non-dynamic correlation is represented by localization of the  $\alpha$  and  $\beta$  spin orbitals in different regions of space). However, DFT methods are typically able to describe biradicals with small to moderate biradical character (depending on the choice of density functional) using a restricted approach,<sup>20,28,55</sup> as the electron correlation is incorporated into an effective potential. Thus, “symmetry-breaking” of Kohn-Sham wavefunctions usually only occurs when the biradical character is already quite significant. Therefore, when comparing the biradical character of different molecules, it is imperative to use consistent indices and electronic structure methods!

#### 1.04.2.11 Different classifications of biradicals

Lastly, we wish to give a few more notes on the classification of biradicals in addition to what is written in the introduction as well as in Section 1.04.2.5, where the distinction between disjoint and non-disjoint (or joint) biradicals is discussed in some detail. There are, however, other possibilities to classify different types of biradicals.

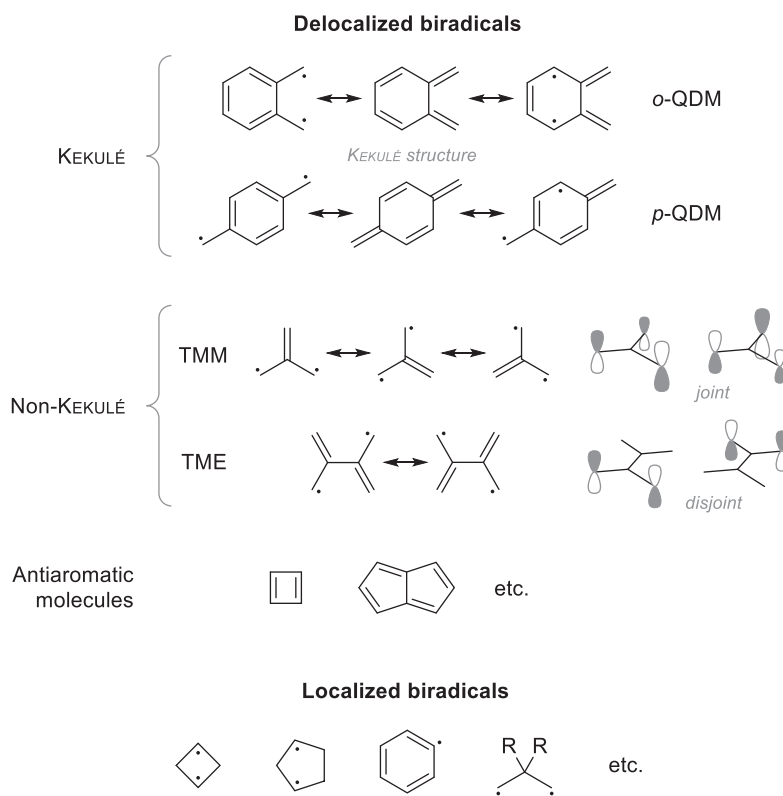
Typically,  $\pi$ -conjugated biradicals are categorized as either “Kekulé” or “non-Kekulé” molecules, depending on whether a classical Kekulé structure (i.e., a structure without radical electrons) can be drawn in the Lewis representation. For example, *o*- and *p*-quinodimethane (QDM, Scheme 5) are typical Kekulé molecules, whereas trimethylenemethane (TMM) or tetramethyleneethane (TME) are archetypical examples of Non-Kekulé structures. Note that TMM is a joint biradical, while TME is a disjoint biradical.

Often, the term “non-Kekulé biradicals” is used synonymously with “delocalized biradicals,”<sup>22,24</sup> because the radical sites cannot be localized on a single set of two atoms. Moreover, Kekulé molecules can also be regarded as delocalized biradicals, since it is usually possible to draw different resonance structures where the radical sites are localized at different atoms (Scheme 5).<sup>17</sup> Additionally, antiaromatic compounds can also be classified as delocalized biradicals. (Note that planar, highly symmetric structures of antiaromatic compounds often correspond to an excited triplet state, which distorts in the singlet ground state due to a second-order Jahn-Teller effect. A typical example is cyclobutadiene, which has a rectangular equilibrium structure.)<sup>56</sup> The term “localized” biradicals, on the other hand, refers to molecules whose radical sites are not conjugated by a classical  $\pi$  system, so each radical electron can be localized at a single atom.<sup>17,24</sup> Typical examples of localized biradicals are cyclobutane-1,3-diyl and cyclopentane-1,3-diyl (Scheme 5).

Another important classification is based on the orbital symmetry of the frontier orbitals, specifically regarding their bonding and antibonding character. Usually (at least in most closed-shell molecules), the bonding orbital is lower in energy than the corresponding anti-bonding orbital. However, depending on the relative strengths of the so-called “through-space” and “through-bond” interactions in cyclic biradicals,<sup>17,22</sup> the transannular antibonding orbital can be the HOMO, whereas the bonding orbital is the LUMO (Fig. 14), effectively inverting the typical order of the orbitals. Abe classified biradicals with a bonding HOMO and anti-bonding LUMO as “type-1 biradicals,” whereas those with an anti-bonding HOMO and bonding LUMO were classified as “type-2 biradicals.”<sup>17</sup>

It should be noted that, when the two radical centers are on the same atom, the species are most often referred to by their generic names: carbenes, nitrenes, etc. rather than biradicals.

As we have discussed in detail, the transition between closed-shell, biradical(oid)s and “perfect” biradicals is continuous. Thus, biradicals can, depending on their biradical character, singlet-triplet gap, orbital symmetry etc. undergo typical radical reactions (i.e., stepwise reactions, or reactions that take place solely at one radical site) as well as typical closed-shell reactions (i.e., concerted reactions that involve both radical centers). While closed-shell reactivity is confined to the singlet energy surface, (bi-)radical reactivity



**Scheme 5** Classification of biradicals as localized, delocalized, Kekulé and non-Kekulé biradicals.

can take place both on the singlet as well as triplet energy surface. Less coupling between the electrons (i.e., stronger non-dynamic correlation) will lead to more radical-like reactivity and vice versa. This has very recently been thoroughly reviewed by Stuyver/Chen/Zeng/Hoffmann,<sup>20</sup> so we will not further discuss the matter here but refer the interested reader to that excellent review article.

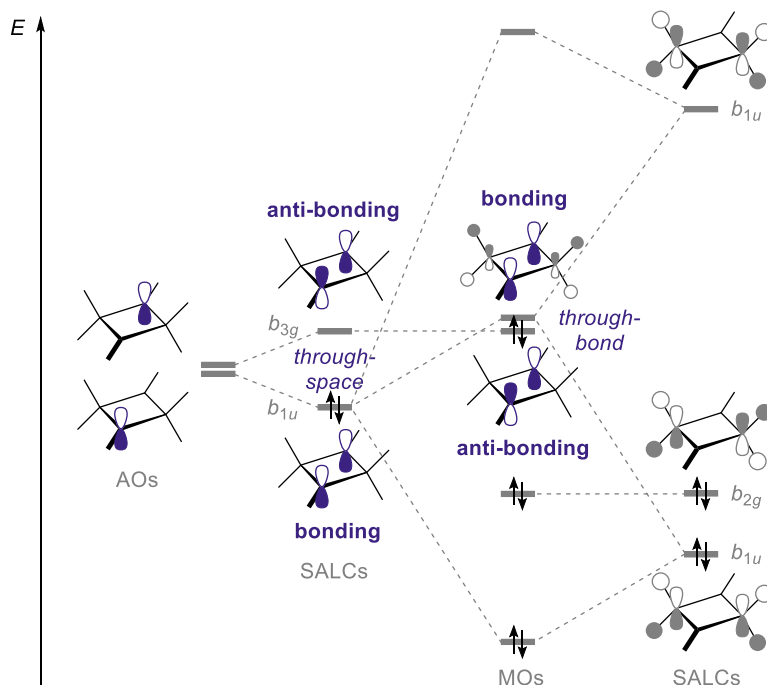
Nonetheless, the following sections will showcase various reactions of heterocyclobutane-1,3-diyls as well as heterocyclopentane-1,3-diyls that give a good impression of the versatility of biradical reactivity.

### 1.04.3 Main group biradicals

#### 1.04.3.1 General aspects

In main group molecular chemistry, the activation of small molecules plays a central role. In recent years, many new concepts have been introduced for this, e.g., the utilization of bulky substituents to introduce kinetic stabilization,<sup>57–74</sup> weakly coordinating anions,<sup>75–84</sup> as well as unusual reaction media,<sup>85</sup> such as ionic liquids,<sup>86–91</sup> neat (Brønsted and Lewis) acids (e.g.,  $\text{SO}_2$ ,<sup>92,93</sup> oleum<sup>94,95</sup>) and bases (e.g.,  $\text{NH}_3$ <sup>96–101</sup>). However, the generation of unusual bonding situations such as in frustrated Lewis acid/Lewis base pairs (FLPs),<sup>102–105</sup> *N*-heterocyclic carbene stabilized fragments,<sup>106–114</sup> adducts<sup>115</sup> with large substituents (e.g.,  $\text{B}(\text{C}_6\text{F}_5)_3$ ),<sup>116–119</sup> low-valent main group species<sup>120</sup> with open coordination sites, persistent radicals<sup>120</sup> or the use of biradicals led to new ways in molecular activation. The latter concept of biradicals was introduced in a series of publications by Niecke, who can be considered a pioneer in this field, in the 1990s. Beyond the exact definition of the different bonding situations in biradicals (cf. Section 1.04.2), the use of such open-shell species for molecule activation can or should also be understood as a *concept*.

The concept of the open-shell singlet biradicals is sometimes met with doubt and questions are raised as to how an open-shell singlet biradical can be identified spectroscopically. There is no such defined experiment (unless there is a very low-lying triplet state), but there are indicators that can be derived from both theory and experiment. Theoretically derived biradical indicators are (see also Section 1.04.2.10): (1) a restricted Hartree-Fock  $\rightarrow$  unrestricted Hartree-Fock wavefunction instability, i.e., no closed shell wavefunction is found, (2) a small singlet-triplet gap ( $\Delta E_{\text{S-T}}$ ), (3)  $\beta$  value<sup>46</sup>  $> 15\%$  and (4) biradical and zwitterionic Lewis representations in the valence bond description, e.g., obtained from NRT calculations (NRT = natural resonance theory). Experimentally, rather long bonds, unusual chemistry (molecular activation such as reversible  $\text{H}_2$  addition) and molecular switching behavior are often observed. Moreover, such biradicals can be easily oxidized to persistent (mono)radicals or reduced to anions. In addition, biradicals also usually exhibit a small splitting between their lowest energy and first excited singlet states ( $\Delta E_{\text{S1-S0}}$ ). Biradicals often occur when bonds are formed or broken and can therefore also be regarded as compounds with an extraordinarily stretched bond, which also results in the unusual observed reactivity. The latter aspect plays an essential role when it comes to



**Fig. 14** Schematic MO diagram of cyclobutane-1,3-diyl.<sup>17,22,25</sup> The singly occupied atomic orbitals (left) are combined to a bonding and anti-bonding symmetry adapted linear combination (SALC, sometimes also referred to as “group orbital”). The bonding orbital is somewhat lower in energy due to the orbital interaction (the “through-space” interaction). The  $b_{1u}$  SALC interacts with the SALCs of corresponding symmetry at the  $CR_2$  bridges (depicted on the far right), which are part of the formal  $\sigma(C-R)$  bonding system (thus, this interaction is called “through-bond” interaction). In consequence, the transannular bonding orbital is raised in energy, and depending on the magnitude of the different interactions, it may lie above or below the anti-bonding orbital. (For reasons of clarity, the C–H anti-bonding  $b_{2g}$  orbital is not depicted.)

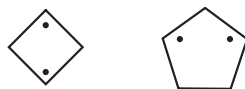
molecular switching properties as found for the pnictogen-centered cyclopentane-1,3-diyl analogs (cf. Sections 1.04.3.3.2 and 1.04.4).

In this book chapter we will mainly focus on main group analogs of cyclobutane-1,3-diyls and cyclopentane-1,3-diyls. Both localized biradical species have two well-defined radical substructures that are not conjugated by a  $\pi$ -system (Scheme 6).

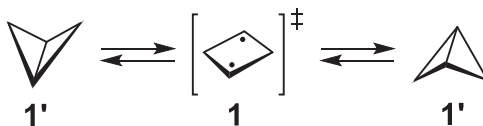
### 1.04.3.2 Main group analogs of cyclobutane-1,3-diyls

Cyclobutane-1,3-diyls (**1**) are very unstable compounds. Singlet cyclobutanediyls were predicted as extremely short-lived transition states for the ring inversion of bicyclo[1.1.0]butanes (Scheme 7). For a long time, experimental observation was not possible. The singlet state of **1** is quantum chemically predicted as the transition state of the inversion reaction from bicyclo[1.1.0]butane **1'** by homolytic cleavage of the transannular bond (Scheme 7). The calculated activation barrier for the inversion is between  $46 \text{ kcal mol}^{-1}$  and  $52 \text{ kcal mol}^{-1}$ , depending on the method and basis set used.<sup>121</sup> According to calculations by Dougherty et al., the singlet ground state of **1** is  $1.7 \text{ kcal mol}^{-1}$  higher than the triplet state (CASSCF(2,2)).<sup>122</sup> In 1984, Dougherty et al. reported the detection of the first cyclobutanediyl derivative (**1Me**), which was substituted with methyl groups at the radical centers, by EPR spectroscopy (electron paramagnetic resonance). This triplet molecule was generated by irradiating the diazo compound in a solid matrix below 25 K (Scheme 8).<sup>123</sup>

In the following years, further derivatives of **1** could be observed (Scheme 8).<sup>124</sup> However, the unsubstituted parent compound **1H** could not be detected so far.<sup>125</sup> The triplet species **1R** are very short-lived and react via formation of a transannular bond to the bicyclic isomers **1'R** and to other products.<sup>124,125</sup> On the way to stable cyclobutane-1,3-diyls, attempts were made to enlarge the transannular bond in bicyclo[1.1.0]butane by introducing substituents, thereby possibly forcing the system into the planar, biradical form.<sup>126,127</sup> Calculations by Schleyer et al. show that the exchange of the hydrogen atoms on the geminal carbon atoms in bicyclo[1.1.0]butane for heteroatoms leads to a significant lengthening of the transannular carbon-carbon bond. However, the resulting compounds are still preferentially angled and feature weak elongated bonds.<sup>128</sup>



**Scheme 6** Left: Cyclobutane-1,3-diyl, right: cyclopentane-1,3-diyl.



**Scheme 7** Inversion of bicyclo[1.1.0]butane **1'** via a planar transition state that represents a planar biradical.

### 1.04.3.2.1 Niecke's 1,3-diphospha-cyclobutane-2,4-diyl

In 1995, Niecke published his first report on a main group analog of cyclobutane-1,3-diyl,  $[\text{Cl-C}(\mu\text{-P-Mes}^*)]_2$ , which was a landmark in main group as well as biradical chemistry (cf. [Section 1.04.3.2.2](#)).<sup>129</sup> The reactivity of 1,3-diphospha-cyclobutane-2,4-diyls has been studied in detail by the Niecke group and later by Ito et al., who introduced air-tolerant 1,3-diphospha-cyclobutane-2,4-diyls obtained by direct arylation ([Section 1.04.3.2.2](#)).<sup>37,130</sup> It should be noted that probably the first heteroatom-substituted cyclobutanediyl derivative to be synthesized is 4-membered cyclic disulfur-dinitride ( $\text{S}_2\text{N}_2$ ), however the biradical character of  $\text{S}_2\text{N}_2$  was/is heavily discussed in the literature ([Section 1.04.3.2.4](#)).<sup>131</sup>

Ever since the discovery of Niecke's biradical, cyclobutane-2,4-diyl analogs have been intensively studied,<sup>16,17,20–22,24,25,29,35,132–138</sup> which we will also systematically describe in more detail below. Before we begin, however, we want to shed light on the "intrinsic" reactivity, i.e., what possibilities such biradical systems themselves have to avoid a biradical electronic structure. We would like to discuss this using  $[\text{E}^2(\mu\text{-E}^1\text{R})]_2$  ( $\text{E}^{1,2}$  = pnictogen, [Scheme 9](#)) as an example.

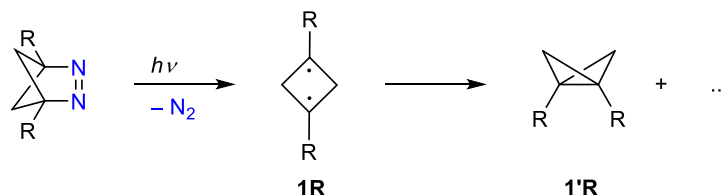
Species such as  $[\text{E}^2(\mu\text{-E}^1\text{R})]_2$  are easily generated by reduction of  $[\text{Cl-E}^2(\mu\text{-E}^1\text{R})]_2$  with e.g., magnesium chips forming either a planar 4-membered heterocycle featuring open-shell biradical character or a closed-shell, non-planar butterfly species with a transannular bond ([Scheme 9](#)). Both species are singlet species, that is, the spin density is precisely zero at each and every point in space (i.e., both are NMR active but EPR silent). If a bond is formed across the ring, one obtains a puckered butterfly molecule that has no radical character at all. Interestingly, according to calculations, when  $\text{E}^1$  is a nitrogen atom, the planar  $6\pi$ -electronic biradical is always energetically favored, while in all other cases the closed-shell bicyclic butterfly species are the global minima on the energy surface.<sup>139,140</sup> Such butterfly species, e.g., with four phosphorus atoms,<sup>141</sup> have been known for more than 30 years and exhibit a normal transannular covalent bond.<sup>142</sup>

The question now arises, what is the origin of these structural and electronic differences? Essentially, three things are important: (i) first, better delocalisation of the  $6\pi$ -electrons in the case of nitrogen favors a planar situation.<sup>143–146</sup> (ii) second, and Ugalde et al. have drawn attention to this, is the fact that angular strain is reduced in the case of the nitrogen species in the planar structure because nitrogen prefers a larger bond angle. Therefore, the angular strain is not compensated by the  $\text{E}^2\text{-E}^2$  bond across the ring, as is the case in the butterfly structure ([Scheme 9](#)).<sup>140</sup> When nitrogen is replaced by heavier pnictogen atoms (P–Bi), the angular strain of the bond is reduced, a transannular bond is formed and the butterfly compound becomes the most stable isomer.<sup>142</sup> (iii) When a small substituent is used, oligomerisation—mainly dimerization—occurs, leading to the formation of different types of dimers, as shown in [Scheme 9](#).<sup>145–147</sup> Therefore, to protect the four-membered biradical from oligomerisation, kinetic protection must be provided (e.g., by a terphenyl = Ter = 2,6-bis(2,4,6-trimethylphenyl)-phenyl, Bbp = 2,6-bis[bis(trimethylsilyl)methyl]phenyl, hypersilyl = Hyp = bis-tris(trimethylsilyl)silyl group). Besides the buried volume,<sup>69,108,148,149</sup> the cone angle<sup>71,72</sup> is a good measure of the steric hindrance introduced by the bulky substituent on the nitrogen atom. For example, the cone angle decreases along the series  $232^\circ$  (terphenyl),  $230^\circ$  (Bbp) to  $213^\circ$  (hypersilyl).<sup>58</sup> The smallest cone angle for kinetic stabilization of biradicals of the type  $[\text{E}^2(\mu\text{-E}^1\text{R})]_2$  is about  $200^\circ$ . Even for the hypersilyl-substituted biradical, dimerization occurs slowly in polar solvents (forming the  $\alpha$ -cage dimer), but can be suppressed if nonpolar solvents are used.<sup>145,146</sup> Furthermore, the charge transfer of the substituent into the four-membered ring plays a crucial role in reactivity, e.g., it increases for  $[\text{P}(\mu\text{-NR})]_2$  (R = Ter, Bbp, Hyp) from the terphenyl- ( $0.4e$ ) to the hypersilyl-substituted ( $1.2e$ ) species, which is the most reactive species among these three compounds.

### 1.04.3.2.2 Hetero-cyclobutane-1,3-diyls with radical centers on elements of group 13

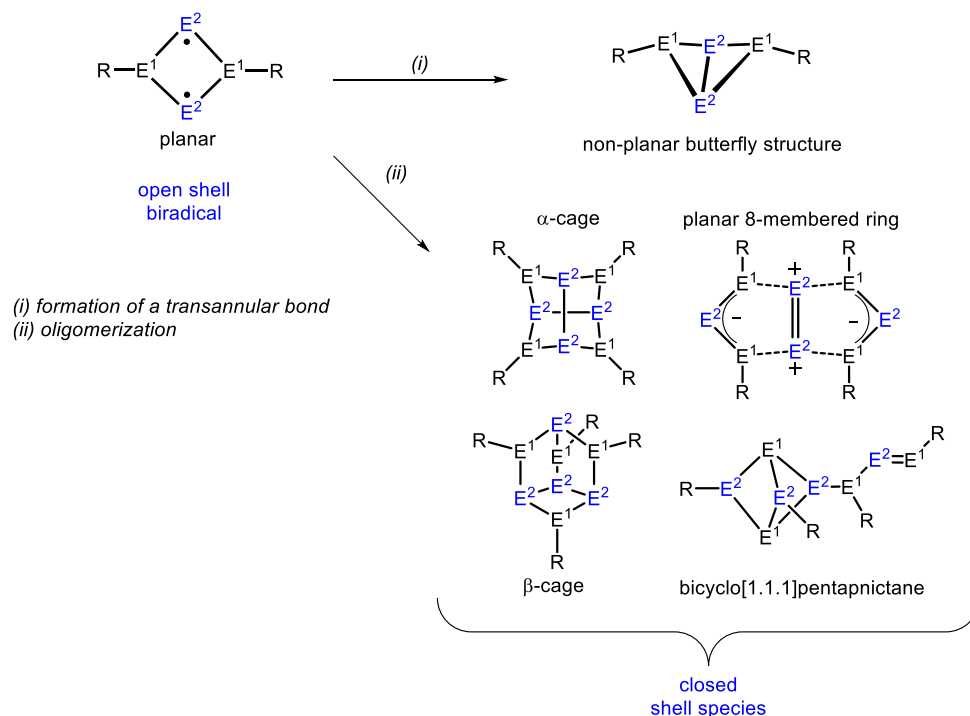
#### 1.04.3.2.2.1 Boron centered biradicals: $[\text{R}^1_2\text{P}(\mu\text{-BR}^2)_2\text{PR}^1_2]$

The first 1,3-diphospha-2,4-dibora-cyclobutane-2,4-diyl,  $2\text{-}^t\text{Bu-}^t\text{Bu}$ , was synthesized in 2002 by the group of Bertrand,<sup>150</sup> starting from correspondingly substituted 1,2-dichlorodiboranes ([Scheme 10](#), path a).<sup>150</sup> The biradical is formed by the addition of two equivalents of lithium diisopropyl phosphide to the diborane. Investigations of the mechanism suggest that the chlorine



**Scheme 8** Generation of triplet cyclobutanediyl **1R** by photolysis of an  $\text{N}_2$  bridged precursor.



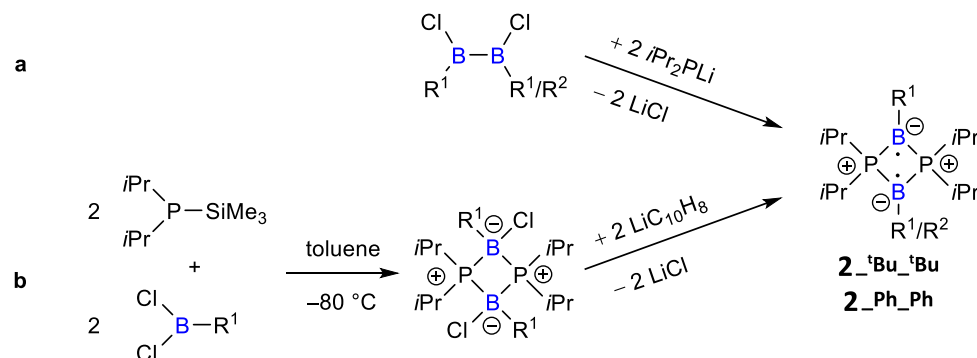


**Scheme 9** Oligomerization and transannular bond formation in  $[E^2(\mu-E^1R)]_2$  depending on the size of R and the element E ( $E^{1,2} = \text{pnictogen}$ ).

substituents on the diborane are first replaced by diisopropyl phosphane groups through the elimination of LiCl. The resulting *trans*-butadiene structure subsequently isomerizes to form the four-membered ring.<sup>151</sup>

Quantum chemical calculations for  $2\text{-}^t\text{Bu-}^t\text{Bu}$  are interpreted differently in the literature. Calculations by Bertrand's group confirm the singlet state as the energetic minimum ((U)B3LYP/6-31G\*). If the substituents on the boron and phosphorus atoms are replaced by protons, the planar structure is no longer an energetic minimum, but the transition state of the inversion of the bicyclic compound (B3LYP/6-31++G\*\*).<sup>150</sup> It is noteworthy that for the molecule  $2\text{-}^t\text{Bu-}^t\text{Bu}$  the formal HOMO describes the transannular bonding situation and the LUMO the corresponding antibonding one. This is true for all 1,3-diphospha-2,4-diboracyclobutane-2,4-diyls, but the reverse is true for the other heteroatomic cyclobutanediyl analogs described in this article (see Sections 1.04.3.2 and 1.04.3.3).<sup>150,153,154</sup> Cramer et al. calculated a singlet-triplet gap of  $-23.4 \text{ kcal mol}^{-1}$  (B3LYP/6-31G(d)) for  $2\text{-}^t\text{Bu-}^t\text{Bu}$ , as well as the occupation numbers of the HONO (1.81) and the LUNO (0.19) (GVVB(2,2)/6-31G(d)).<sup>154</sup> Jung and Head-Gordon determined a singlet-triplet gap of  $-33.7 \text{ kcal mol}^{-1}$  (SF-TD-DFT/TDA/6-31G(d)) and an occupation number of the LUNO of 0.17 electrons (UB3LYP/6-31G(d)). They conclude that  $2\text{-}^t\text{Bu-}^t\text{Bu}$  is clearly below known organic biradicals in terms of biradical character, but above normal closed-shell compounds.<sup>155</sup> Cheng and Hu conclude from their calculations (taking into account a singlet triplet gap of  $-28.4 \text{ kcal mol}^{-1}$ , B3LYP/6-31G\*) that 1,3-diphospha-2,4-diboracyclobutane-2,4-diyls are not biradicals but have a long  $\pi$ -bond between the boron atoms.<sup>156</sup>

According to Bertrand et al. the biradical character of  $2\text{-}^t\text{Bu-}^t\text{Bu}$  is clearly shown by its reactivity. With  $\text{CDCl}_3$ , one chlorine atom is added to each of the radical centers in a reaction over 3 days at room temperature. This produces a mixture of the *cis* and *trans*



**Scheme 10** Syntheses of  $2\text{-}^t\text{Bu-}^t\text{Bu}$  (route a,  $R^1 = ^t\text{Bu}$ ) and  $2\text{-Ph-Ph}$  (route b,  $R^1 = \text{Ph}$ ).<sup>150,152,153</sup>

compound (ratio 3:1). A spontaneous reaction takes place with  $\text{HSnMe}_3$  and leads to the *trans*-2,4 adduct. With elemental selenium, the two radical centers are bridged by a selenium atom, resulting in a [1.1.1]bicycle.<sup>157</sup>

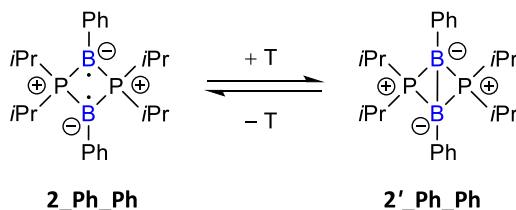
In addition to the *t*Bu-substituted biradical **2\_’Bu\_’Bu**, the phenyl-substituted compound **2\_Ph\_Ph** was also synthesized in the group of Bertrand.<sup>152</sup> Here, in contrast to **2\_’Bu\_’Bu**, the diborane is not used as the starting material, but a cyclic 2,4-dichloro-substituted compound, generated from P1 and B1 building blocks (**Scheme 10**, route **b**), in which the four-membered ring is pre-formed. The chlorine atoms are abstracted by reduction with lithium naphthalide and the violet biradical **2\_Ph\_Ph** is formed. Like **2\_’Bu\_’Bu**, this is sensitive to air, but stable in the solid state in the absence of air. In solution, an equilibrium can be observed between the open-shell form **2\_Ph\_Ph** and the closed-shell variant **2’\_Ph\_Ph** (**Scheme 11**).<sup>152</sup>

With the help of NMR investigations, it could also be determined that at high temperatures the closed-shell (transannular bonded) species is preferred (room temperature, ratio 7:1 [**2’\_Ph\_Ph**:**2\_Ph\_Ph**]) and at low temperatures the open-shell species ( $-145\text{ }^\circ\text{C}$ , ratio 1:3). The trend is confirmed by temperature-dependent UV-vis investigations. It is crucial to note that the bicyclic **2’\_Ph\_Ph** is colorless in contrast to the violet biradical **2\_Ph\_Ph**. The observed absorption decreases with increasing temperature. The bond formation at higher temperatures is explained by entropy effects, since, for example, the phenyl substituents in the closed-shell species are freely rotatable; in the biradical they lie co-planar to the four-membered ring.<sup>152</sup>

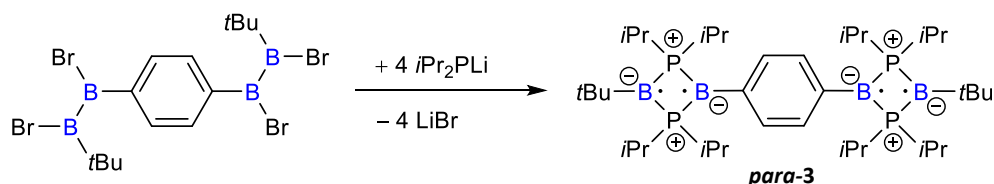
In addition to the “monomeric” biradical compounds **2\_’Bu\_’Bu** and **2\_Ph\_Ph**, Bertrand et al. succeeded in linking two biradical units via a phenyl linker and thus synthesizing the formal tetraradical *para*-3.<sup>158</sup> The synthesis is similar to route **a** shown in **Scheme 10**, again utilizing a diborane. However, here two diborane units are already linked to each other via a phenyl ring in the *para* position. Bromine serves as leaving group on the boron atoms. Hence, the violet, phenyl linked biradical *para*-3 is obtained by reaction with lithium diisopropylphosphide (**Scheme 12**).<sup>158</sup>

In the solid state, only the open-shell species is observed. The phenyl ring lies in one plane with the two four-membered rings. In solution, however, as with **2\_Ph\_Ph**, an equilibrium is formed between the open-shell form *para*-3 and the closed-shell compound *para*-3’ (**Scheme 13**). Here, too, the open-shell compound is preferentially present at low temperatures, and the closed-shell compound at high temperatures.<sup>158</sup>

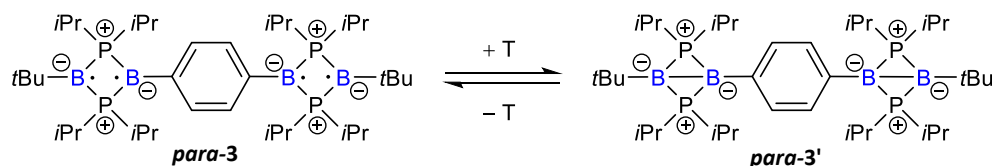
The synthesis as shown in **Scheme 12** can also be carried out with the two diborane groups in the *meta* position. In this case, however, the open-shell tetraradical *meta*-3 is not obtained, but only the closed-shell isomer *meta*-3’, both in solution and in the solid state.<sup>158</sup> This difference is attributed to the fact that *meta*-phenyl is a ferromagnetic linker, whereas *para*-phenyl is an anti-ferromagnetic linker. Antiferromagnetic linkers favor a coupling between radical centers more strongly than ferromagnetic ones.<sup>159</sup> In the *para*-substituted compound, the coupling or “communication” between the individual biradical units is therefore stronger than in the *meta*-substituted isomer. This argument is supported by further experimental findings of Bertrand et al. The asymmetrically substituted biradicals **2’\_’Bu\_Ph** (cf. **Scheme 10**, route **a**:  $\text{R}^1 = \text{’Bu}$ ,  $\text{R}^2 = \text{Ph}$ ) and **2’\_’Bu\_Npht** (cf. **Scheme 10**, route **a**:  $\text{R}^1 = \text{’Bu}$ ,  $\text{R}^2 = \text{Npht}$ ; Npht = 2-naphthyl) exist in solution and in the solid state only as closed-shell compounds.<sup>160</sup> From this observation it was concluded that the combination of a *t*Bu substituent and an aromatic radical does not sufficiently stabilize the open-shell species. In order to exclude the possibility that the electronic effect of the second  $\text{P}_2\text{B}_2$  unit on the phenyl ring in



**Scheme 11** Equilibrium between open-shell species **2\_Ph\_Ph** and bicyclic **2’\_Ph\_Ph** in solution, as a function of temperature.<sup>152</sup>



**Scheme 12** Synthesis of *para*-3.<sup>158</sup>



**Scheme 13** Equilibrium between open-shell form *para*-3 and closed-shell form *para*-3’ in solution, as a function of temperature.<sup>158</sup>

*para*-3 alone is decisive for the stabilization of the biradical form, a methyl group was introduced on the linking phenyl ring in the *ortho*-position of one or both P<sub>2</sub>B<sub>2</sub> units. The result is a closed-shell system. Through steric interactions, the methyl groups prevent the phenyl ring from lying co-planar to the P<sub>2</sub>B<sub>2</sub> units, which means that communication via the π-system is no longer possible. These results indicate an existing communication between the biradical units in *para*-3, which is essential for the stabilization of the open-shell singlet species.<sup>160</sup>

#### 1.04.3.2.2.2 Aluminum centered biradical: [R<sup>1</sup>P(μ-AIR<sup>2</sup>)<sub>2</sub>PR<sup>1</sup>]

The synthesis of the 1,3-diphospha-2,4-dialumina-cyclobutane-2,4-diyl (**4**) was published in 2009 by Schnöckel et al.<sup>161</sup> For the formation of **4**, a LiP(<sup>t</sup>Bu)<sub>2</sub> solution in toluene is overlaid with an AlCl solution in a toluene-diethyl ether mixture (Scheme 14). As AlCl is metastable, elemental aluminum and AlCl<sub>3</sub> are formed over time by disproportionation reactions. The reactive intermediate is thought to be Al<sub>3</sub>Cl<sub>7</sub>(OEt<sub>2</sub>)<sub>5</sub>.<sup>161</sup>

Biradical **4** is only obtained in low yields in the form of green crystals. Additionally, colorless by-products are formed. The low yield can be attributed to the instability of the biradical compound **4**, both in the solid state and in solution. Characterization of **4** was only possible by X-ray crystal structure analysis. Further investigations (including EPR spectroscopy) were not carried out due to the complex synthesis and low yields, therefore further conclusions could only be drawn from quantum chemical calculations.<sup>161</sup> The open-shell character of biradical **4** was confirmed by calculations of UV-vis spectra (BP86/def2-TZVP). It is assumed that green colored **4** is a triplet biradical that is stabilized by reaching the singlet state through spin reversal, which results in the direct formation of the transannular Al–Al bond to give **4'**.<sup>162</sup> Stabilization through dimerization is not possible due to steric hindrance (see Section 1.04.3.2). The singlet state is between 1.0 and 1.4 kcal mol<sup>-1</sup> lower in energy than the triplet state (vertical energy gap at the triplet structure), depending on the methods and basis sets used for the calculations (CASSCF(2,2); MRCI).<sup>162</sup> The adiabatic singlet-triplet gap ranges between –16.3 and –18.3 kJ/mol depending on the method (PB86, TPSS, B3LYP with def2-TZVP basis). Thus, **4'** with a transannular Al–Al bond is the equilibrium ground state structure.<sup>161</sup>

#### 1.04.3.2.3 Hetero-cyclobutane-1,3-diyls with radical centers on elements of group 14

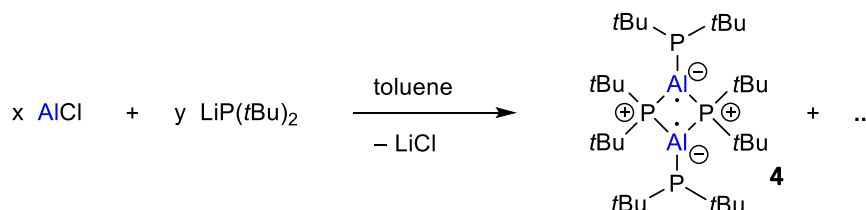
##### 1.04.3.2.3.1 Carbon centered biradicals: [R<sup>1</sup>P(μ-CR<sup>2</sup>)<sub>2</sub>PR<sup>1</sup>]

1,3-Diphospha-cyclobutane-2,4-diyl, Niecke's biradical (Scheme 15),<sup>163</sup> was the first carbon centered biradical within a [P<sub>2</sub>C<sub>2</sub>]-four-membered heterocycle and, in a sense, the prototype for the chemistry of the four-membered biradicals that followed in the subsequent period of time. Starting from Mes\*P=CCL<sub>2</sub> (Mes\* = 2,4,6-<sup>t</sup>Bu<sub>3</sub>C<sub>6</sub>H<sub>2</sub>), the biradical 5<sub>Cl</sub>Cl is obtained when reacted with half an equivalent of <sup>n</sup>BuLi and LiCl is eliminated.

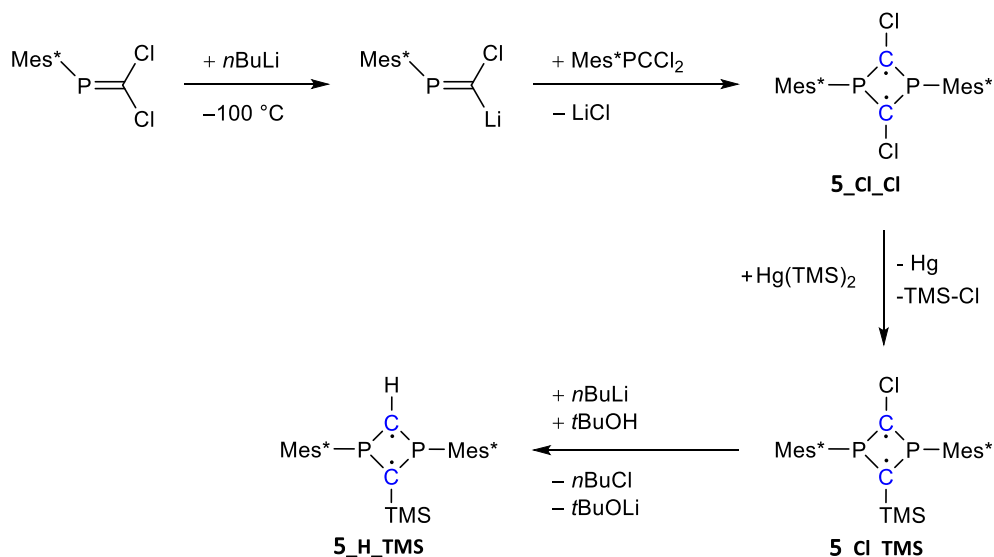
Further biradicals of a similar structure can be synthesized through subsequent reactions starting from 5<sub>Cl</sub>Cl. In this case, the phosphorus atoms are always substituted with Mes\*, however, different substituents can be attached to the carbon atoms. By adding Hg(TMS)<sub>2</sub>, the exchange of a chlorine substituent for a TMS group is achieved leading to 5<sub>Cl</sub>TMS (Scheme 15). The second chlorine substituent can be abstracted with <sup>n</sup>BuLi. Addition of <sup>t</sup>BuOH yields the hydrogen-substituted biradical 5<sub>H</sub>TMS as a red, crystalline solid.<sup>164</sup> 5<sub>H</sub>TMS is thermally very stable under inert conditions. However, when a solution of 5<sub>H</sub>TMS is irradiated with a mercury vapor lamp at –25 °C, the closed-shell isomer 5'<sub>H</sub>TMS with a transannular C–C bond is formed (Scheme 16). When this bicyclus in solution is heated to 150 °C, ring opening and formation of a butadiene derivative occurs (Scheme 16).<sup>164</sup>

By adding LDA (lithium diisopropylamide) to the protonated biradical 5<sub>H</sub>TMS, the likewise red, deprotonated anion [5<sub>TMS</sub>]<sup>–</sup> is generated (Scheme 16). In the solid state, under inert atmosphere, the lithium salt of [5<sub>TMS</sub>]<sup>–</sup> is stable. In THF solution, however, the protonated species is re-formed within 1 day.<sup>165</sup> During the reaction of [5<sub>TMS</sub>]<sup>–</sup> with AlCl<sub>3</sub>, the water-sensitive Lewis acid adduct [5<sub>AlCl<sub>3</sub>TMS</sub>]<sup>–</sup> is formed (Scheme 16). The proton in 5<sub>H</sub>TMS can be replaced by another TMS group after reaction with two equivalents of LDA and subsequent addition of TMS-Cl. This leads to the symmetrically substituted biradical 5<sub>TMS</sub>TMS. Irradiation of this compound, however, does not cause the formation of a transannular bond to give 5'<sub>TMS</sub>TMS (cf. 5<sub>H</sub>TMS); instead, homolytic cleavage of the bond between a phosphorus atom and a Mes\* substituent occurs.<sup>166</sup>

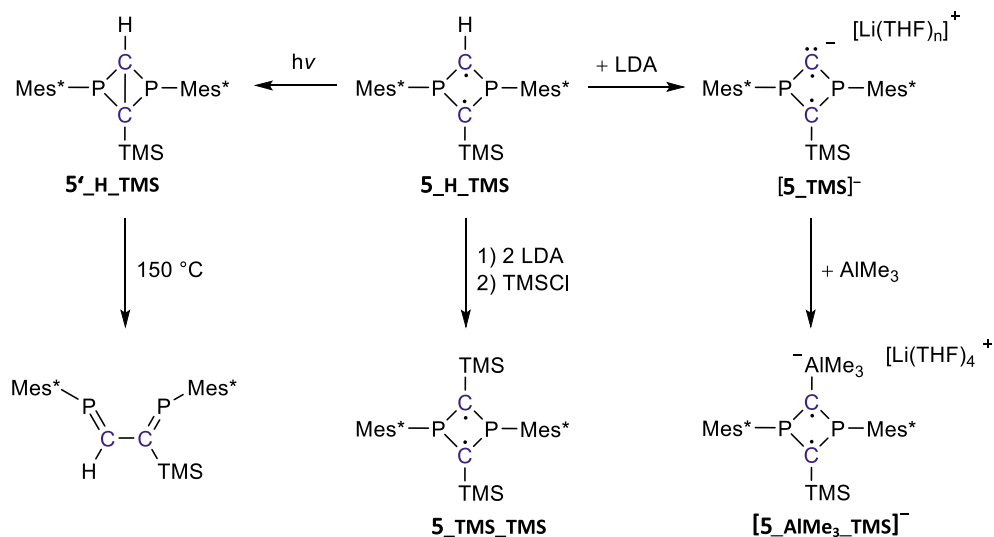
Yoshifuji and Ito have expanded the class of 1,3-diphospha-cyclobutane-2,4-diyl compounds by being able to introduce a wide variety of substituents at the P atom, starting from phospho-alkynes,<sup>167</sup> in contrast to Niecke's biradicals, which are limited to the Mes\* substituent at the P atom (cf. Scheme 15 compound 5 and Scheme 17 compound 6). Thus, the 1,3-diphospha-cyclobutane-2,4-diyls synthesized in the working groups of Yoshifuji and Ito differ from those of Niecke by the arrangement of the substituents (Scheme 17, compound 6), that is, in Yoshifuji's and Ito's biradicals the carbon atoms are always Mes\*-substituted, since Mes\*-CP is always utilized in the synthesis. Until today, various substitution patterns are known for the phosphorus atoms. This diversity is



Scheme 14 Synthesis of **4**.

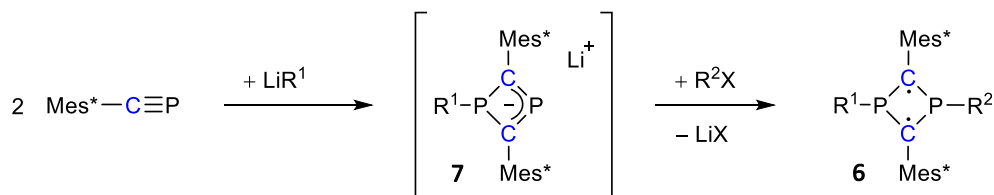


**Scheme 15** Synthesis of **5\_Cl\_Cl**, **5\_Cl\_TMS** und **5\_H\_TMS** ( $\text{Mes}^* = 2,4,6\text{-}t\text{Bu}_3\text{C}_6\text{H}_2$ ,  $\text{TMS} = \text{SiMe}_3$ ).<sup>163,164</sup>



**Scheme 16** Reactivity of **5\_H\_TMS** and synthesis of **5\_TMS\_TMS**, **[5\_TMS]<sup>-</sup>** as well as **[5\_AlMe<sub>3</sub>\_TMS]<sup>-</sup>**.<sup>164–166</sup>

made possible by the new synthesis route (**Scheme 17**), which allows the introduction of the substituents at the phosphorus atoms in two successive steps. The phosphalkyne,  $\text{Mes}^*\text{CP}$ , is reacted with half an equivalent of the lithium compound of the first substituent ( $\text{LiR}^1$ ). This leads to the formation of the anionic  $[\text{C}_2\text{P}_2]$ -four-membered ring **7**, which subsequently reacts with an alkyl-halogenide ( $\text{R}^2\text{-X}$ ,  $\text{X} = \text{halogen}$ ) of the desired second substituent ( $\text{R}^2$ ) to form the biradical **6** (**Scheme 17**). The majority of the examples of compound class **6** were generated by this two-step reaction pathway. However, some compounds are obtained only by subsequent reactions at the substituent  $\text{R}^2$ .<sup>168–170</sup> If  $\text{R}^2$  is an aromatic substituent (**Table 2**),  $\text{R}^2$  is introduced via the intermediate



**Scheme 17** General synthesis route of compound class **6** according to YOSHIFUJI and ITO.<sup>167</sup>

formation of an arine.<sup>171</sup> Almost all biradicals of this type and synthesized by this procedure can be handled in air, and some are stable in air for more than 6 months.<sup>37,167–170,172–180</sup>

The first example of this class of biradicals was 6-<sup>t</sup>Bu-Me. To prepare 6-<sup>t</sup>Bu-Me, the phosphalkyne, Mes\*CP, was reacted with <sup>t</sup>BuLi and MeI according to the synthetic route shown in Scheme 17, resulting in the formation of a deep blue-purple solution of biradical 6-<sup>t</sup>Bu-Me.<sup>167</sup> This biradical shows extremely high stability. It can be handled in air and decomposes only after some time after treatment with water, which is explained by kinetic stabilization due to the steric hindrance of the Mes\* substituents.<sup>167</sup> In contrast to the 1,3-diphospha-cyclobutane-2,4-diyl 5-H-TMS of Niecke, no reaction is observed when 6-<sup>t</sup>Bu-Me is irradiated with a mercury lamp.<sup>167</sup> Numerous examples are known of compounds of type 6. For an overview, the biradicals are divided into categories depending on their substituents R<sup>1</sup> and R<sup>2</sup> and listed in Tables 1–4. The reactivity of the biradicals is summarized below using selected examples.

The reactivity of diphospha-cyclobutanediyls is strongly dependent on the substituents at the phosphorus atoms. In the following, selected examples are presented that reflect the most important reactivities of this class of compounds. Despite the exceptional stability of the biradicals synthesized by Yoshifuji and Ito et al., decomposition of the compounds is observed upon prolonged heating in solution. Depending on the nature of the substituents, the starting material Mes\*-CP is released again or ring expansion occurs (Scheme 18).<sup>177,181</sup>

In the case of the heteroatom-substituted biradical 6-N<sup>i</sup>Pr<sub>2</sub>-Me, reaction with TEMPO (2,2,6,6-tetramethylpiperidinyloxy) under irradiation leads to the transfer of an oxygen atom to the methyl-substituted phosphorus atom (Scheme 19). This reactivity is not observed with the aliphatically substituted biradical 6-<sup>t</sup>Bu-Me.<sup>181</sup> The reaction of 6-N<sup>i</sup>Pr<sub>2</sub>-Me with elemental sulfur leads to the analogous product with a sulfur atom on the methyl-substituted phosphorus atom (Scheme 19).<sup>176</sup> Again, also this reaction with the aliphatically substituted biradical 6-<sup>t</sup>Bu-Me is not observed.

The reaction of 6 with LiAlH<sub>4</sub> can lead to different products. Depending on the substituents, either a hydride ion is transferred to a phosphorus atom so that the cyclic anion 8 is formed (Scheme 20) or the cyclic anion 7 is formed by eliminating a hydrogenated substituent R<sup>2</sup>H (Scheme 21).<sup>168,183</sup> Both reactions can be observed for compounds 6-<sup>t</sup>Bu-CH<sub>2</sub>CH=CMe<sub>2</sub> and 6-<sup>t</sup>Bu-CH<sub>2</sub>-(E)-CH=CHPh.<sup>168</sup>

In the case of the hydrogenated four-membered ring 8, protonation can then take place by adding methanol. The proton is added to the second phosphorus atom affording 9 (Scheme 20). Formally, the reaction product 9 can be seen as the addition of molecular hydrogen. However, the hydrogen atoms are not bound to the carbon atoms where the radical electrons were previously located, but to the phosphorus atoms. According to Yoshifuji and Ito et al., the reaction with molecular hydrogen was attempted in a 1:1 stoichiometry as well as under increased pressure, but this has not yet been further elaborated in the literature.<sup>183</sup>

For numerous other compounds of class 6, the reaction with LiAlH<sub>4</sub> leads to the cleavage of a substituent, whereby the anion 7 is obtained, which also occurs as an intermediate in the synthesis of the biradicals. When MeI is added, this reacts to form a biradical with a methyl substituent. In the overall reaction, R<sup>2</sup> is exchanged for a methyl group (Scheme 21, cf. Scheme 17).<sup>168</sup>

Some compounds of type 6 add hydrogen fluoride, HF, reversibly yielding 10 (Scheme 22). Different HF sources are possible. Reactions were carried out with HF · NEt<sub>3</sub> and the mixture of C<sub>5</sub>F<sub>5</sub>N and HNEt<sub>2</sub>, among others. As in the reaction with LiAlH<sub>4</sub> and the subsequent protonation (Scheme 20), the hydrogen and fluorine atoms are transferred to the two phosphorus atoms, although the radical centers are located on the carbon atoms. The elimination of HF takes place in each case by the addition of NaH and crown ether (15-crown-5).<sup>171,182</sup>

In contrast to the biradicals presented above, 6-<sup>t</sup>Bu-C(O)Ph reacts with HF with the addition of the fluorine atom to the <sup>t</sup>Bu-substituted phosphorus atom and of the hydrogen atom to a carbon atom.<sup>182</sup> In addition to the reactions presented so far, different reactivities of various representatives of 6 towards <sup>t</sup>BuLi have been observed.<sup>169</sup> In the context of an EPR study, the groups of Yoshifuji and Ito have also succeeded in oxidizing the biradical 6-<sup>t</sup>Bu-Me with tris(4-bromophenyl)ammonium hexachloridoantimonate to a radical cation.<sup>184</sup> Some derivatives have also been investigated with regard to their suitability as semiconductors in field-effect transistors.<sup>173,185</sup>

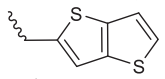
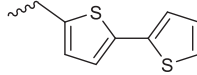
In addition to the numerous biradicals summarized in Tables 1–4, biradical compounds of type 6 were also synthesized in which two or three biradical units are linked (Scheme 23). The synthesis does not deviate significantly from the route shown in Scheme 17. The anion 7 is reacted with a di- or tri-brominated linker (Scheme 23, bromine atoms instead of the biradical units R). For some derivatives, it is necessary to react a still brominated intermediate with the anion 7 again. The resulting tetra- or hexaradicals are summarized in Table 5.<sup>175,178,180</sup> The tetra- and hexaradicals isolated by Yoshifuji and Ito et al. have non-conjugated moieties as linkers (Scheme 23). This means that no communication of the biradical units via a conjugated π-system is possible, but only covalent and electrostatic “communication.” An equilibrium between the biradical and the closed-shell isomer with a transannular bond (as depicted in Scheme 9) is also not observed in contrast to Bertrand’s boron centered biradical 2.

#### 1.04.3.2.3.2 Silicon centered biradicals: [R<sup>1</sup>N(μ-SiR<sup>2</sup>)<sub>2</sub>NR<sup>1</sup>]

The silicon-centered biradical, a 1,3-diaza-2,4-disilacyclobutane-2,4-diyl derivative (11), was presented by Sekiguchi’s group in 2011. The synthesis was achieved by reacting a disilyne with an azo compound (Scheme 24).<sup>186</sup> The violet biradical 11 is sensitive to air and water. The biradical character was derived from the planarity of the central four-membered ring and the increased Si-Si distance in the X-ray structure as well as the absence of a bond-critical point between the silicon atoms in AIM (atoms in molecules) calculations on a model system (phenyl groups at N, TMS groups at Si, RB3LYP/6-31G(d)). The calculated singlet-triplet gap of the model compound of 12.8 kcal mol<sup>-1</sup>, the absence of an EPR signal and the smooth recording of NMR spectra indicate the singlet character of the biradical.<sup>186</sup>



**Table 1** 1,3-Diphospha-cyclobutane-2,4-diyls according to Yoshifuji and Ito et al. (Scheme 17) in which the substituents R<sup>1</sup> and R<sup>2</sup> are linked to the phosphorus atoms via non-aromatic carbon atoms.

Entry	R <sup>1</sup>	R <sup>2</sup>	References
1	Me	Me	176
2	Me	Et	179
3	Et	Et	179
4	<sup>t</sup> Pr	<sup>t</sup> Pr	169
5	<sup>t</sup> Pr	<sup>t</sup> Bu	169
6	<sup>t</sup> Bu	Me	167
7	<sup>n</sup> Bu	<sup>n</sup> Bu	176
8	<sup>s</sup> Bu	<sup>s</sup> Bu	180
9	<sup>s</sup> Bu	CH <sub>2</sub> Ph	180
10	<sup>s</sup> Bu	CH <sub>2</sub> -( <i>o</i> )-C <sub>6</sub> H <sub>4</sub> CH <sub>2</sub> Br	180
11	<sup>t</sup> Bu	<sup>t</sup> Bu	176
12	<sup>t</sup> Bu	C <sub>18</sub> H <sub>37</sub>	176
13	<sup>t</sup> Bu	<sup>t</sup> Pen	168
14	<sup>t</sup> Bu	C <sub>3</sub> F <sub>7</sub>	176
15	<sup>t</sup> Bu	CH <sub>2</sub> OMe	179
16	<sup>t</sup> Bu	CH <sub>2</sub> C( <i>O</i> )OMe	168
17	<sup>t</sup> Bu	CH <sub>2</sub> CH=CMe <sub>2</sub>	168
18	<sup>t</sup> Bu	CH <sub>2</sub> Ph	177
19	<sup>t</sup> Bu	(CH <sub>2</sub> ) <sub>2</sub> Ph	169
20	<sup>t</sup> Bu	C( <i>O</i> )Ph	181
21	<sup>t</sup> Bu	CH <sub>2</sub> -( <i>E</i> )-CH=CHPh	168
22	<sup>t</sup> Bu	CH <sub>2</sub> C≡CH	168
23	<sup>t</sup> Bu	CH <sub>2</sub> -( <i>p</i> )-C <sub>6</sub> H <sub>4</sub> C≡CPh	168
24	<sup>t</sup> Bu	CH <sub>2</sub> -( <i>p</i> )-C <sub>6</sub> H <sub>4</sub> Br	168
25	<sup>t</sup> Bu	CH <sub>2</sub> -( <i>p</i> )-C <sub>6</sub> H <sub>4</sub> I	168
26	<sup>t</sup> Bu	CH <sub>2</sub> -( <i>p</i> )-C <sub>6</sub> H <sub>4</sub> OMe	168
27	<sup>t</sup> Bu	CH <sub>2</sub> -( <i>p</i> )-C <sub>6</sub> H <sub>4</sub> CH <sub>2</sub> OH	168
28	<sup>t</sup> Bu	CH <sub>2</sub> -( <i>p</i> )-C <sub>6</sub> H <sub>4</sub> C( <i>O</i> )OMe	168
29	<sup>t</sup> Bu	(CH <sub>2</sub> ) <sub>4</sub> O(SiMe <sub>3</sub> ) <sub>3</sub>	169
30	<sup>t</sup> Bu	(CH <sub>2</sub> ) <sub>4</sub> O(SiMe <sub>2</sub> <sup>t</sup> Bu) <sub>3</sub>	169
31	CH <sub>2</sub> Ph	(CH <sub>2</sub> ) <sub>4</sub> O(SiMe <sub>2</sub> <sup>t</sup> Bu) <sub>3</sub>	169
32	(CH <sub>2</sub> ) <sub>4</sub> O(SiMe <sub>2</sub> <sup>t</sup> Bu) <sub>3</sub>	(CH <sub>2</sub> ) <sub>4</sub> O(SiMe <sub>2</sub> <sup>t</sup> Bu) <sub>3</sub>	169
33	<sup>t</sup> Bu	CH <sub>2</sub> -1-naphtyl	173
34	<sup>t</sup> Bu	CH <sub>2</sub> -2-naphtyl	173
35	<sup>t</sup> Bu	CH <sub>2</sub> -2-antraceny	173
36	<sup>t</sup> Bu		173
37	<sup>t</sup> Bu		173
38	<sup>t</sup> Bu	CH <sub>2</sub> -2-thienyl	168
39	<sup>t</sup> Bu	CH <sub>2</sub> -3-thienyl	168

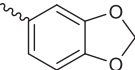
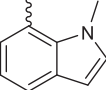
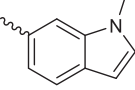
If **11** is reacted with methanol, the *cis* addition product is formed in which one silicon atom is additionally substituted with a hydrogen atom and the other with a methoxy group (**12**). With CCl<sub>4</sub>, both silicon atoms are chlorinated forming the *trans* isomer (**13**, Scheme 25).<sup>186</sup>

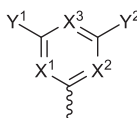
#### 1.04.3.2.3.3 Silicon centered biradicals: [R<sup>1</sup><sub>2</sub>C(μ-SiR<sup>2</sup>)<sub>2</sub>CR<sup>1</sup><sub>2</sub>]

The synthesis and characterization of a singlet delocalised 2,4-diimino-1,3-disila-cyclobutane-1,3-diyl, [LSi(μ-CNAr)<sub>2</sub>SiL] (**14a**), and a silylenyl-sila-imine, [LSi(=NAr)SiL] (**14b**), were published by So et al. (Scheme 26, L = PhC(N<sup>t</sup>Bu)<sub>2</sub>, Ar = 2,6-<sup>i</sup>Pr<sub>2</sub>C<sub>6</sub>H<sub>3</sub>).<sup>187</sup> The reaction of three equivalents of the disilylene [LSiSiL] with two equivalents of Ar-N=C=N-Ar in toluene at room temperature for 12 h gave biradical **14a** and [LSi(=NAr)SiL] (**14b**) in a ratio of 1:2. Compounds **14a** and **14b** were characterized by NMR spectroscopy and X-ray crystallography.

Pure **14a** was found in the form of dichromic yellow-brown crystals in 25.7% yield. Compounds **14a** and **14b** are stable in solution or in the solid state at room temperature under inert atmosphere. They are soluble in toluene and THF. The four-membered Si<sub>2</sub>C<sub>2</sub> ring in **14a** is planar. The Si–C bonds (1.834(5)–1.829(5) Å) are almost identical and are between the Si–C single (1.87 Å)

**Table 2** 1,3-Diphospha-cyclobutane-2,4-diyls according to Yoshifuji and Ito et al. with aromatic R<sup>1</sup> and/or R<sup>2</sup>.

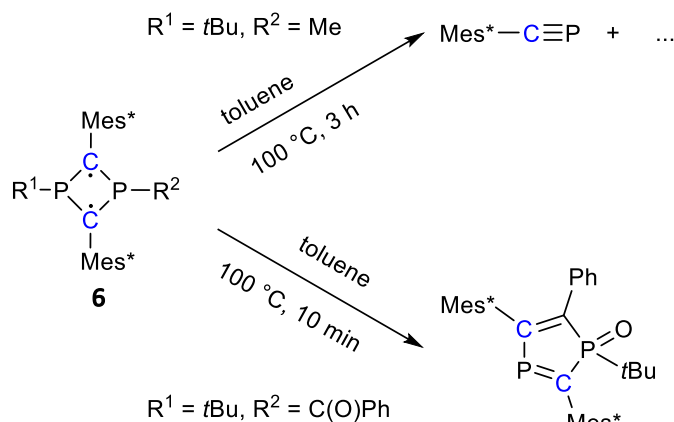
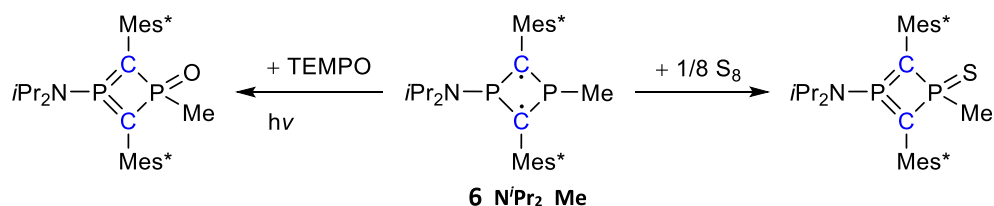
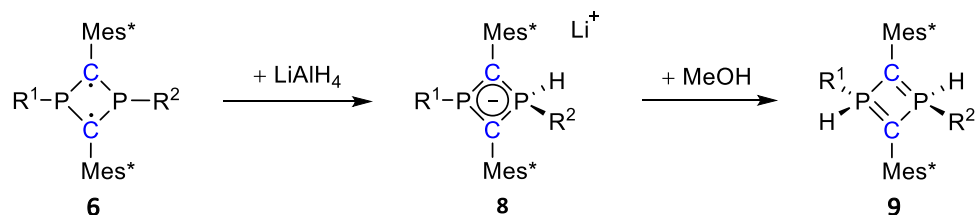
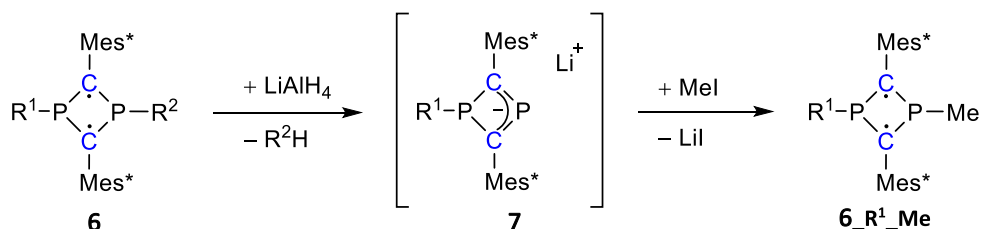
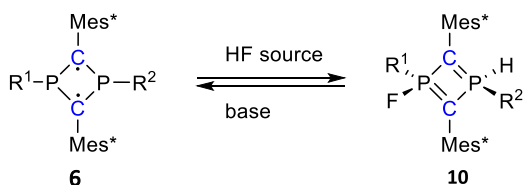
Entry	R <sup>1</sup>	R <sup>2</sup>	References
1	Ph	Me	168
2	<sup>t</sup> Bu	Ph	171
3	Ph	Ph	170
4	<sup>t</sup> Bu	( <i>o</i> )-C <sub>6</sub> H <sub>4</sub> I	171
5	<sup>t</sup> Bu	1-Naphtyl	171
6	<sup>t</sup> Bu	2-Naphtyl	171
7	<sup>t</sup> Bu	3,4-Dimethylphenyl	171
8	<sup>t</sup> Bu	( <i>m</i> )-C <sub>6</sub> H <sub>4</sub> OMe	171
9	<sup>t</sup> Bu		171
10	<sup>t</sup> Bu		171
11	<sup>t</sup> Bu		171

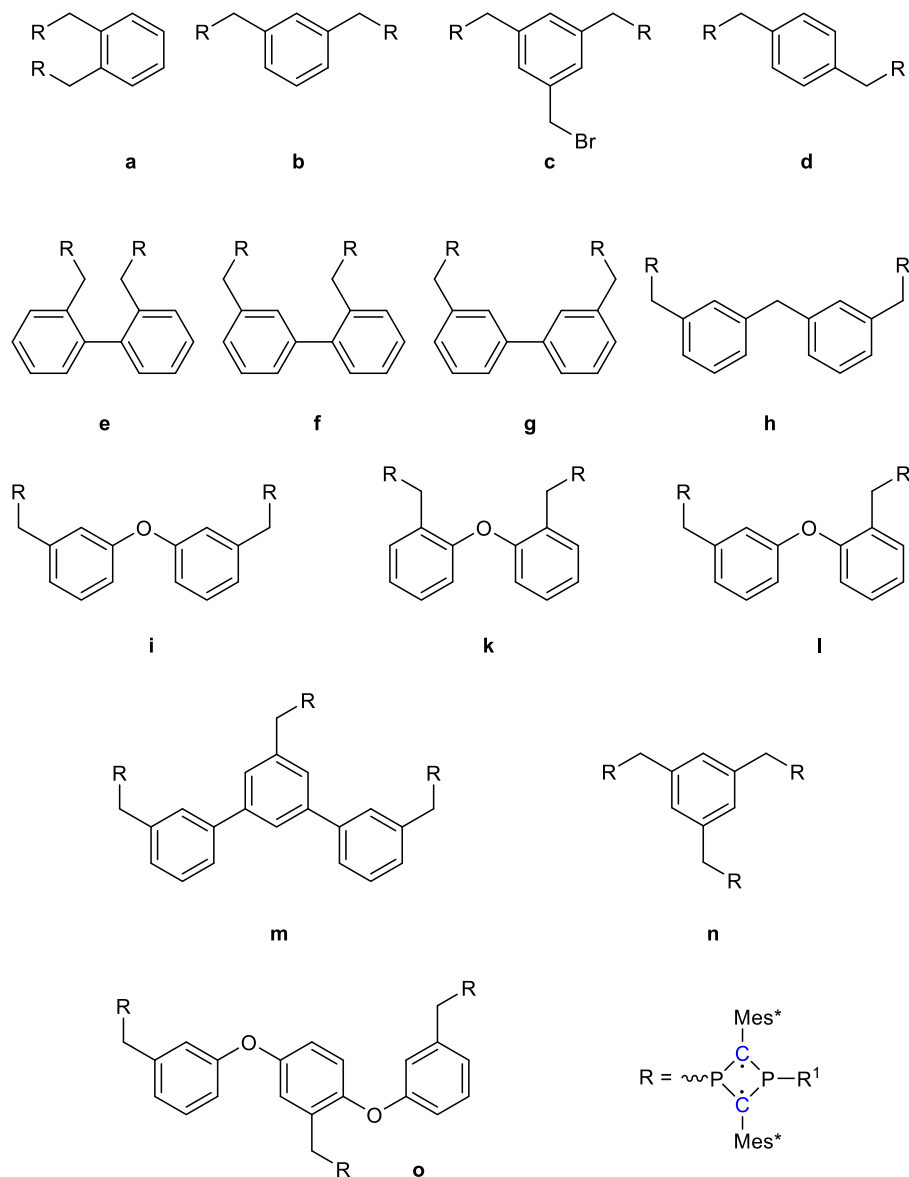
**Table 3** 1,3-Diphospha-cyclobutane-2,4-diyls according to Yoshifuji and Ito et al. in which a phosphorus atom is directly linked to a heterocycle (R<sup>2</sup>).


Entry	R <sup>1</sup>	X <sup>1</sup>	X <sup>2</sup>	X <sup>3</sup>	Y <sup>1</sup>	Y <sup>2</sup>	References
1	<sup>t</sup> Bu	CF	CF	N	F	F	170
2	<sup>t</sup> Bu	CF	CF	N	Ph	Ph	170
3	<sup>t</sup> Bu	N	N	N	Cl	Cl	170
4	<sup>t</sup> Bu	N	N	N	Ph	Ph	170
5	<sup>t</sup> Bu	N	N	N	O <sup>t</sup> Bu	O <sup>t</sup> Bu	170
6	<sup>t</sup> Bu	N	N	N	NEt <sub>2</sub>	NEt <sub>2</sub>	170
7	<sup>t</sup> Bu	N	N	N	N(H) <i>n</i> Bu	N(H) <i>n</i> Bu	170
8	<sup>t</sup> Bu	N	N	N	Me	Me	170
9	<sup>t</sup> Bu	N	N	N	C≡CTMS	C≡CTMS	170
10	<sup>t</sup> Bu	N	N	N	N <sub>3</sub>	N <sub>3</sub>	182
11	<sup>t</sup> Bu	CCl	N	N	F	F	182
12	<sup>t</sup> Bu	CCl	N	N	F	NEt <sub>2</sub>	182
13	<sup>t</sup> Bu	CCl	N	N	O <sup>t</sup> Bu	O <sup>t</sup> Bu	37
14	<sup>t</sup> Bu	CCl	N	N	NEt <sub>2</sub>	NEt <sub>2</sub>	182

**Table 4** 1,3-Diphospha-cyclobutane-2,4-diyls according to Yoshifuji and Ito et al. in which a phosphorus atom is substituted with a heteroatom (R<sup>2</sup>).

Entry	R <sup>1</sup>	R <sup>2</sup>	References
1	Me	N <sup>i</sup> Pr <sub>2</sub>	181
2	Ph	N <sup>i</sup> Pr <sub>2</sub>	174
3	CH <sub>2</sub> Ph	N <sup>i</sup> Pr <sub>2</sub>	174
4	<sup>t</sup> Bu	SMe	172
5	<sup>t</sup> Bu	S-( <i>p</i> )-C <sub>6</sub> H <sub>4</sub> Me	172

**Scheme 18** Decomposition of biradicals **6** <sup>*t*Bu</sup><sub>Me</sub> and **6** <sup>*t*Bu</sup><sub>C(O)Ph</sub> in solution by elevated temperature.<sup>177,181</sup>**Scheme 19** Reactivity of **6** <sup>*N'*Pr<sub>2</sub></sup><sub>Me</sub> towards TEMPO and sulfur.<sup>176,181</sup> (The Lewis representation of the products was taken from the original publication. Possibly, the reaction products are also biradicals, but this was not discussed by the authors.)**Scheme 20** Reactivity of compound class **6** ( $R^1 = {}^t\text{Bu}, R^2 = \text{Me}, {}^i\text{Pen}, \text{CH}_2\text{CH}=\text{CMe}_2, \text{CH}_2\text{-}(E)\text{-CH}=\text{CHPh}; R^1 = \text{Ph}, R^2 = \text{Me}$ ) with  $\text{LiAlH}_4$ .<sup>168,183</sup>**Scheme 21** Reactivity of compound class **6** ( $R^1 = {}^t\text{Bu}, R^2 = \text{CH}_2\text{C}(\text{O})\text{OMe}, \text{CH}_2\text{CH}=\text{CMe}_2, \text{CH}_2\text{-}(E)\text{-CH}=\text{CHPh}, \text{CH}_2\text{C}\equiv\text{CH}, \text{CH}_2\text{Ph}, \text{CH}_2\text{-}(p)\text{-C}_6\text{H}_4\text{Br}, \text{CH}_2\text{-}(p)\text{-C}_6\text{H}_4\text{I}, \text{CH}_2\text{-}(p)\text{-C}_6\text{H}_4\text{OMe}, \text{CH}_2\text{-}(p)\text{-C}_6\text{H}_4\text{C}\equiv\text{CPh}$ , s. **Table 1**, entries 36, 37) with  $\text{LiAlH}_4$ .<sup>168</sup>**Scheme 22** Reversible reaction of representatives of compound **6** (see **Table 3**: entries 7, 11, 12; **Table 2**: entry 7) with HF.<sup>171,182</sup>



**Scheme 23** Linkers for connecting two or three biradical units ( $R$  = biradical group;  $R^1$  =  $t$ Bu,  $s$ Bu).<sup>175,178,180</sup>

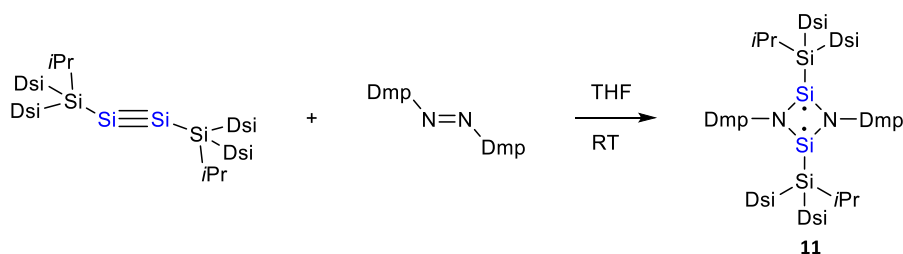
and double (1.70 Å) bond lengths. The Si...Si distance (2.553(2) Å) is significantly longer than a typical Si–Si single bond ( $\Sigma r_{\text{cov}}(\text{Si}–\text{Si}) = 2.32$  Å).<sup>188</sup> Theoretical studies show that compound **14a** has a singlet biradical character with extensive electronic delocalisation via the  $\text{Si}_2\text{C}_2$  four-membered ring and exocyclic  $\text{C}=\text{N}$  bonds. The energy difference between the singlet and triplet states of **14a** was calculated at the B3PW91/6-31G(d) level with the singlet state being more stable than the triplet state by 30.1 kcal mol<sup>-1</sup>. The complete active space self-consistent field CASSCF(4,6) calculations show that there are two dominant contributions to the configuration interaction (CI) wave function for the <sup>1</sup>A state with occupation numbers of 1.86 in the HONO and of 0.13 in the LUNO, clearly indicating open-shell singlet biradical character for **14a**.<sup>187</sup>

#### 1.04.3.2.3.4 Silicon centered biradicals: $[\text{R}_2^1\text{Si}(\mu\text{-SiR}^2)_2\text{SiR}_2^3]$

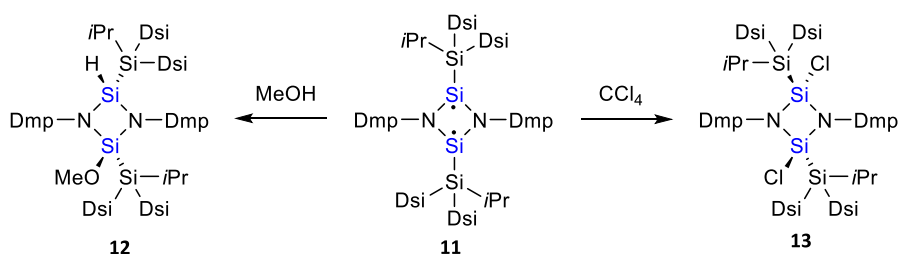
In 2020, Scheschkewitz et al. reported on the isolation and characterization of all-silicon cyclobutane-1,3-diyls as singlet species (**15**) obtained from the reversible reactions of cyclotrisilene,  $\text{cycloSi}_3\text{Tip}_4$  (Tip = 2,4,6-triisopropylphenyl) with the heterocyclic silylenes  $\text{cyclo}[(\text{CR}_2\text{CH}_2)(\text{N}^t\text{Bu})_2]\text{Si}$ : ( $R$  = H or methyl) with saturated backbones (**Scheme 27**).<sup>189</sup> At elevated temperature, tetrasilacyclobutenes are obtained from these equilibrium mixtures. However, in the first reaction step biradical **15** is formed upon treatment of cyclotrisilene with one equivalent of heterocyclic silylene in toluene at room temperature yielding a red-brown solution. Storage of such a concentrated solution in toluene gave dark purple single crystals of **15** ( $R$  = H) in 63% yield. Dissolution of single crystals of **15** re-establishes the equilibrium (**Scheme 27**). An X-ray diffraction study of the crystals revealed the structure of the homonuclear biradical **15** with a cyclic  $\text{Si}_4$  subunit. The four-membered ring is essentially planar with a strikingly

**Table 5** Bis- and tris-1,3-diphosphacyclobutane-2,4-diyls according to Yoshifuji and Ito et al. in which two or three biradical units (R) are linked together via a linker (Scheme 23).

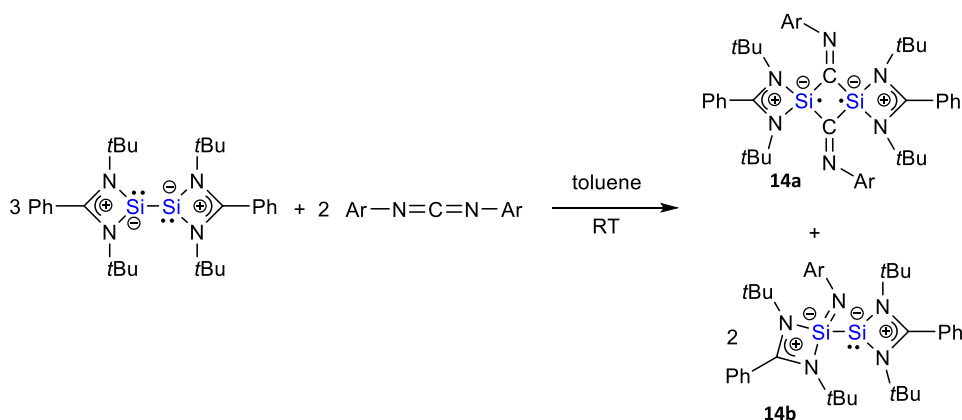
Entry	linker	R <sup>1</sup>	References
1	a	<sup>s</sup> Bu	180
2	b	<sup>s</sup> Bu	180
3	d	<sup>s</sup> Bu	180
4	m	<sup>s</sup> Bu	180
5	b	<sup>t</sup> Bu	178
6	c	<sup>t</sup> Bu	178
7	d	<sup>t</sup> Bu	178
8	e	<sup>t</sup> Bu	175
9	f	<sup>t</sup> Bu	175
10	g	<sup>t</sup> Bu	175
11	h	<sup>t</sup> Bu	175
12	i	<sup>t</sup> Bu	175
13	k	<sup>t</sup> Bu	175
14	l	<sup>t</sup> Bu	175
15	m	<sup>t</sup> Bu	178
16	n	<sup>t</sup> Bu	175
17	o	<sup>t</sup> Bu	175



**Scheme 24** Synthesis of **11** (Dsi = SiH(Me)<sub>2</sub>; Dmp = 3,5-Me<sub>2</sub>C<sub>6</sub>H<sub>3</sub>).<sup>186</sup>



**Scheme 25** Reactivity of **11** towards methanol and CCl<sub>4</sub>.



**Scheme 26** Synthesis of **14** (Ar = 2,6-*i*-Pr<sub>2</sub>C<sub>6</sub>H<sub>3</sub>).



long distance between the three-coordinated silicon atoms ( $\text{Si}\cdots\text{Si}$  2.871(1) Å), which is significantly longer than, for example, the very long Si–Si bond length in  ${}^t\text{Bu}_3\text{Si-Si}^t\text{Bu}_3$  with 2.697 Å<sup>190</sup> (cf.  $\Sigma r_{\text{cov}}(\text{Si-Si}) = 2.32$  Å),<sup>188</sup> suggesting a very weak interaction.

The singlet ground state of **15** is confirmed by the well-resolved NMR spectra at low temperature and by the absence of an EPR signal at RT, 193 K and in the frozen state in toluene solution.<sup>189</sup> This is confirmed by DFT calculations, which determine the singlet state of **15** to be 8.4 kcal mol<sup>-1</sup> lower in energy than the triplet (B3LYP-D3(bj)/6-311G(d,p)/SCRF = toluene). The calculated HOMO-LUMO energy gap is 2.21 eV, where the HOMO can be associated with a weak transannular  $\pi$ -bond (bond order 0.57) over the two silicon centers. Already Fischer and Frenking *et al.* identified such transannular  $\pi$ -bond, which is not supported by an underlying  $\sigma$ -bond, in a cyclic  $\text{Ge}_2\text{Ga}_2$  biradical (see biradical **18**).<sup>191</sup>

Time-resolved electron paramagnetic resonance (TR-EPR) spectra recorded after pulse laser excitation of **15** in frozen solution at 80 K together with a spectral simulation revealed a broad signal centered at about 340 mT, a value that compares well with reported silicon-centered biradicals.<sup>189</sup> A dipolar coupling between two unpaired electrons in a triplet state is assumed. Furthermore, the shape of the signal suggests that this triplet state is not in Boltzmann equilibrium, but rather spin-polarized. Spectra with these properties indicate the formation of a triplet state through intersystem crossing from an excited singlet state after photoexcitation.<sup>189</sup>

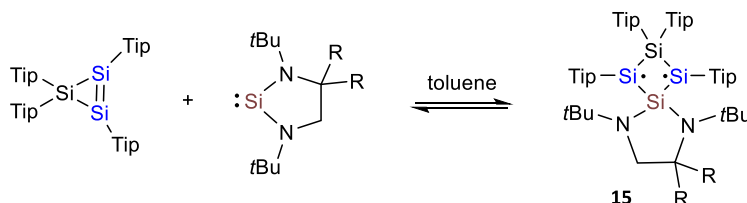
#### 1.04.3.2.3.5 Germanium centered biradicals: $[\text{R}^1\text{N}(\mu\text{-GeR}^2)_2\text{NR}^1]$

The germanium-centered biradical, a 1,3-diaza-2,4-digermacyclobutane-2,4-diyl derivative (**16**) was first synthesized by the Power group in 2004.<sup>192</sup> The heavy analog of Sekiguchi's silicon biradical with two germanium atoms is obtained when a sterically very demanding digerma-alkyne is reacted with trimethylsilyl azide (Scheme 28). The resulting biradical **16** has a deep violet color and is very sensitive to air and water. With solvents, it reacts within a few days, which is evident by decolorisation of the solution.<sup>192</sup> The planarity of the  $\text{N}_2\text{Ge}_2$  ring, the large distance between the germanium atoms, the absence of signals on EPR investigation and the ease of investigation of **16** by NMR spectroscopy indicate a singlet biradical character for the electronic ground state. Using a model system (SiH<sub>3</sub> groups at N, methyl groups at Ge), quantum chemical calculations were performed to characterize **16**. The HOMO of the compound is antibonding with respect to the transannular Ge-Ge interaction, while the LUMO is bonding. A HOMO-LUMO gap of 57.97 kcal mol<sup>-1</sup> and a singlet-triplet gap of 17.51 kcal mol<sup>-1</sup> were determined for the model compound (UB3LYP/6-31G\*, broken symmetry approach).<sup>192</sup>

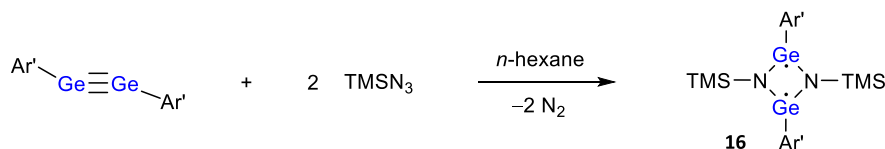
Furthermore, Power *et al.* observed that biradical **16** reacts with molecular hydrogen in solution at room temperature and 1 bar, assuming that the hydrogen is added to the germanium atoms of **16**, which results in two tetravalent Ge atoms as parts of the four-membered ring.<sup>192</sup>

#### 1.04.3.2.3.6 Germanium centered biradicals: $[\text{O}(\mu\text{-GeR}^2)_2\text{NR}^1]$

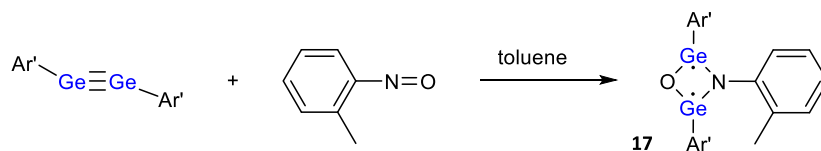
In 2009, Power *et al.* described the synthesis of the first 1-oxa-3-aza-2,4-digerma-cyclobutane-2,4-diyl, a substituted asymmetric biradical (**17**), which is obtained when a bulky digerma-alkyne is treated with a nitroso-arene (Scheme 29).<sup>193</sup> The properties of the resulting biradical are very similar to those of the symmetrical germanium biradical **16** in Scheme 28. Biradical **17** is also violet and highly sensitive to air and water. In the experimental structure, the biradical character is implied by the planarity of the ring system and a large Ge-Ge distance. In addition, there is the measurability of NMR spectra as well as the absence of signals in EPR spectra that indicate the singlet character of the biradical.<sup>193</sup> Quantum chemical calculations of a model system (nitrogen substituted with a hydrogen atom, germanium substituted with methyl groups) show, as for compound **16**, a transannular antibonding HOMO localized at the two germanium atoms in **17**. The HOMO-LUMO gap of the model compound is 55.3 kcal mol<sup>-1</sup> (UB3LYP/6-31G\*<sup>193</sup>).



**Scheme 27** Equilibrium reactions of a cyclotrisilene and a heterocyclic silylenes yielding biradical **15** (R = H or methyl).



**Scheme 28** Synthesis of **16** ( $\text{Ar}' = 2,6\text{-Dipp}_2\text{C}_6\text{H}_3$ ;  $\text{Dipp} = 2,6\text{-}^i\text{Pr}_2\text{C}_6\text{H}_3$ ).<sup>192</sup>



**Scheme 29** Synthesis of **17** ( $\text{Ar}' = 2,6\text{-Dipp}_2\text{C}_6\text{H}_3$ ;  $\text{Dipp} = 2,6\text{-}^i\text{Pr}_2\text{C}_6\text{H}_3$ ).<sup>193</sup>

#### 1.04.3.2.3.7 Germanium centered biradicals: $[\text{R}_2\text{Ga}(\mu\text{-Ge})_2\text{GaR}_2]$

Fischer and Frenking reported on the reduction of  $\text{GeCl}_2$  with  $\text{Ga}(\text{DDP})/\text{KC}_8$  and the properties of a possible biradical  $\text{Ge}_2[\text{Ga}(\text{DPP})]_2$  (**18**) (**Scheme 30**,  $\text{DDP} = \text{HC}(\text{CMeNC}_6\text{H}_3\text{-2,6-}^i\text{Pr}_2)_2$ ) that is formed in the course of this reaction.<sup>191</sup> Compound **18** shows a planar, four-membered  $\text{Ge}_2\text{Ga}_2$  ring with the two  $\text{R}_2\text{Ga}$  moieties in a bridging position. The planar, four-membered  $\text{Ge}\text{--Ga}$  rhombic ring of **18** has two sets of equivalent  $\text{Ga}\text{--Ge}$  bonds of 2.3899(8) and 2.4113(8) Å which are shorter than the sum of the covalent radii (cf.  $\Sigma r_{\text{cov}}(\text{Ga}\text{--Ge}) = 2.45$  Å). The  $\text{Ge}\cdots\text{Ge}$  distance of 2.8714(11) Å, however, is much longer than the value of elemental germanium (2.45 Å) as well the sum of the covalent radii (cf.  $\Sigma r_{\text{cov}}(\text{Ga}\text{--Ge}) = 2.45$  Å).<sup>188</sup> BP86/SVP AIM computations show four  $\text{Ge}\text{--Ga}$  bond paths and one ring critical point but there is no  $\text{Ge}\text{--Ge}$  bond path. The unusual bonding situation in **18** is described in terms of the  $\text{Ge}\cdots\text{Ge}$  interaction by a transannular  $\pi$ -bond but no  $\sigma$ -bonding, which is supported by NBO and ELF (electron localization function) analyzes. Alternatively, the authors describe the bond situation by two unpaired electrons (in p atomic orbitals) at the Ge atoms possessing opposite spin which are weakly coupled.<sup>191</sup> This in turn means **18** can be understood as a singlet biradical (**Scheme 30**).

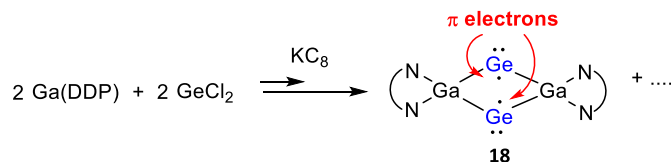
#### 1.04.3.2.3.8 Tin centered biradicals: $[\text{R}^1\text{N}(\mu\text{-SnR}^2)_2\text{NR}^1]$

The Lappert group synthesized 1,3-diaza-2,4-distanna-cyclobutane-2,4-diyl **19** in 2004 (**Scheme 31**).<sup>194</sup> Biradical **19** was isolated from a reaction of a nitrogen-tin precursor,  $[(\text{TMS})_2\text{N-Sn}(\mu\text{-Cl})_2]$ , when treated with silver cyanate. It is assumed that  $\text{Ag}$  and  $\text{CO}_2$  are eliminated. Biradical **19** was shown to be diamagnetic in the crystal and in solution, in accord with computational studies, showing that the singlet ground state is substantially favored over the triplet. The solid-state structure of the colorless compound shows a planar heterocycle. Quantum chemical calculations indicate that **19** can be assumed to be biradical with singlet-triplet gaps of 18.2 kcal mol<sup>-1</sup> (non-relativistic) and 13.6 kcal mol<sup>-1</sup> (relativistic).<sup>194</sup>

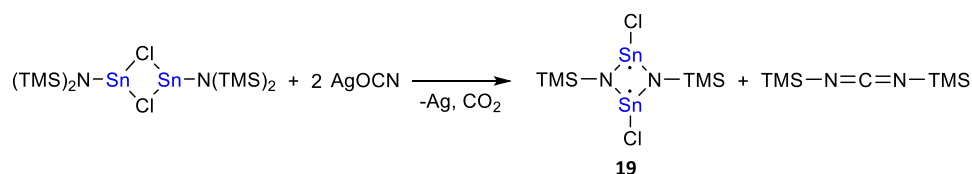
### 1.04.3.2.4 Hetero-cyclobutane-1,3-diyls with radical centers on elements of group 15

#### 1.04.3.2.4.1 Nitrogen/Pnictogen centered biradicals: $[\text{N}(\mu\text{-NR}^2)_2\text{Pn}]$

1,2,3-Triaza-4-pnicta-cyclobutane-2,4-diyls (**20**) have both a nitrogen-centered radical center and a further pnictogen ( $\text{Pn} = \text{P}, \text{As}, \text{Sb}, \text{and Bi}$ ) radical center. They can be prepared starting from terphenyl (Ter)-substituted triazenides. The pnictogen atom is introduced by reaction with the respective pnictogen trichloride affording **21**. Upon reduction of acyclic compound **21** either with magnesium or  $\text{KC}_8$ , the cyclic biradical **20** is formed (**Scheme 32**).<sup>195</sup> The stability of the biradicals **20\_Pn** decreases along the series  $\text{P} > \text{As} > \text{Sb} > \text{Bi}$ . For example, the red biradical **20\_Bi** is only stable for a few minutes in solution, while the other compounds **20\_P** (yellow), **20\_As** (yellow), **20\_Sb** (red) could be isolated in substance and completely characterized. They are sensitive to water and air. X-ray crystal structure analysis shows that all three derivatives have a planar, kite-shaped distorted four-membered ring. The distortion increases with the atomic number of the pnictogen. However, none of the compounds shows reactivity towards small molecules with double or triple bonds, as has been observed with similar compounds (see below). This speaks against a pronounced biradical character of the compounds.<sup>195</sup> Only the reaction of **20\_P** and **20\_As** with the isonitrile  $\text{CN-Dmp}$  leads to the expected



**Scheme 30** Synthesis and schematic description of the bonding situation in the four-membered ring of **18**. Only a Lewis representation with the spin-coupled lone-electrons, describing a transannular  $\pi$  bond, is shown ( $\text{DDP} = \text{HC}(\text{CMeNC}_6\text{H}_3\text{-2,6-}^i\text{Pr}_2)_2$ ).



**Scheme 31** Synthesis of **19**.<sup>194</sup>

insertion of the carbon atom into the four-membered ring. The insertion takes place selectively in the nitrogen-phosphorus or nitrogen-arsenic bond and not in the nitrogen-nitrogen bond (for further information on similar insertion reactions, see below).<sup>196</sup>

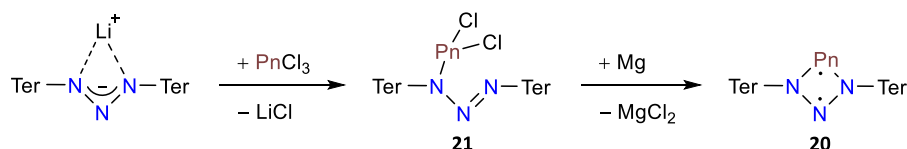
Calculations on model compounds of **20\_Pn** (Ph substituents instead of Ter) show a decrease of the biradical character  $\beta$  from the phosphorus- to the bismuth-containing compound (**20\_P** 15%, **20\_As** 10%, **20\_Sb** 6%, and **20\_Bi** 0%) (M06-2X/aug-cc-pVDZ, CASSCF(2,2)). The larger the atomic number of the pnictogen, the more strongly the bonding situation is described by closed-shell, zwitterionic resonance formulae. Some of the possible Lewis representations within the resonance are illustrated in **Scheme 33**.<sup>195</sup>

#### 1.04.3.2.4.2 Pnictogen centered biradicals: $[\text{Pn}^1(\mu\text{-NR})_2\text{Pn}^2]$ (Pn = P, As, Sb, Bi)

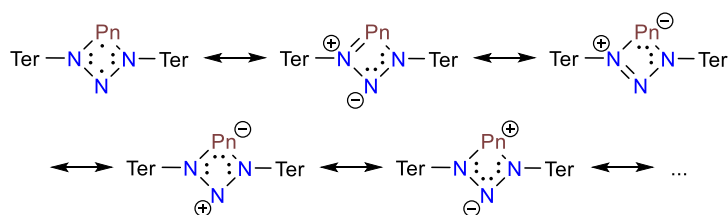
1,3-Diaza-2,4-dipnicta-cyclobutane-2,4-diyls (**22**) of the type  $[\text{Pn}^1(\mu\text{-NR})_2\text{Pn}^2]$  are biradicals with exclusively pnictogen-centered radical sites (notation: **22\_Pn<sup>1</sup>Pn<sup>2</sup>\_R** means  $\text{Pn}^{1,2}$  = pnictogen, R = bulky substituent in  $[\text{Pn}^1(\mu\text{-NR})_2\text{Pn}^2]$ ). All these biradicals with the pnictogen in the oxidation state +II are discussed together here, as are the biradicals with two different pnictogens as radical centers. Due to similar synthetic routes, properties and reaction behavior, 1,3-diaza-2,4-diphosphacyclobutane-2,4-diyls (**22\_PP**), 1,3-diaza-2,4-diarsacyclobutane-2,4-diyls (**22\_AsAs**) and 1,3-diaza-2-phospha-4-arsacyclobutane-2,4-diyls **22\_PAs** are grouped together in this section, all of which were synthesized by us.<sup>21</sup> The first examples of this biradical class to be presented in 2011 were the biradicals **22\_PP\_Ter** and **22\_PP\_Hyp** (Hyp =  $(\text{Me}_3\text{Si})_3\text{Si}$ ), **Scheme 34**.<sup>143</sup>

The synthesis of **22** is possible via two reaction paths, depending on the substituent R, which are shown in **Scheme 34**. The first route starts with the chlorinated heterocycle which can be transformed into the biradical by reduction with magnesium,  $(\text{Cp}_2\text{TiCl})_2$  or  $\text{Cp}_2\text{Ti}(\text{BTMSA})$  (BTMSA = bis(trimethylsilyl)acetylene; **Scheme 34**, route a). This synthetic route can be used for the phosphorus-containing biradicals **22\_PP\_Ter**,<sup>143</sup> **22\_PP\_Hyp**,<sup>143,145</sup> **22\_PP\_CPh<sub>3</sub>**,<sup>197</sup> the arsenic-containing derivative **22\_AsAs\_Ter**<sup>144</sup> and the mixed biradical **22\_PAs\_Ter**.<sup>199</sup> For the substituent Bbp (2,6-bis[bis(trimethylsilyl)methyl]phenyl), a different synthetic route is used. Here, the Bbp amine substituted twice with the pnictogen (phosphorus or arsenic) is reduced with magnesium (**Scheme 34**, route b), which gives access to the symmetrical biradicals **22\_PP\_Bbp** and **22\_AsAs\_Bbp**.<sup>198</sup> Heavier derivatives, i.e., the symmetrical biradicals of antimony and bismuth (**22\_SbSb** and **22\_BiBi**) as well as the asymmetrical phosphorus-antimony biradical (cf. **22\_PsB**), could only be observed *in situ* due to their intrinsic instability. However, their existence could be proven by reaction with trapping reagents such as alkynes.<sup>200,201</sup>

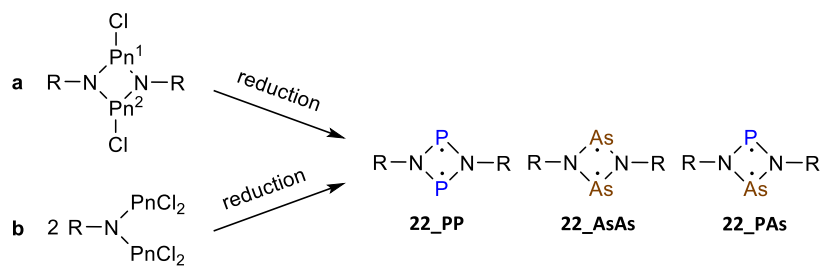
Most of these biradicals show strong coloration: **22\_PP\_Ter** orange, **22\_PP\_Hyp** pink, **22\_PP\_CPh<sub>3</sub>** yellow, **22\_PP\_Bbp** yellow, **22\_AsAs\_Ter** violet, **22\_AsAs\_Bbp** greenish yellow, **22\_PAs\_Ter** violet. All are sensitive to water and air, but are thermally extremely stable ( $> 100^\circ\text{C}$ ) in the solid state under an inert atmosphere. The central heterocycles of all these biradicals are planar and the



**Scheme 32** Synthesis of **20** (Pn = P, As, Sb, Bi; Ter = 2,6-Mes<sub>2</sub>-C<sub>6</sub>H<sub>3</sub>, Mes = 2,4,6-Me<sub>3</sub>C<sub>6</sub>H<sub>2</sub>).<sup>195</sup>



**Scheme 33** Closed-shell, zwitterionic resonance structures of **20** besides a biradical Lewis representation.<sup>195</sup>



**Scheme 34** Synthesis of biradicals **22\_PP**, **22\_AsAs** und **22\_PAs** [route a: R = Ter, Hyp, CPh<sub>3</sub>, Pn<sup>1</sup>, Pn<sup>2</sup> = P, As; route b: R = Bbp, Pn = P, As (Hyp =  $(\text{Me}_3\text{Si})_3\text{Si}$ , Bbp = 2,6-bis[bis(trimethylsilyl)methyl]phenyl)].<sup>143-145,197-199</sup>

transannular pnictogen-pnictogen distance in each case is significantly larger than the sum of the covalent radii of the atoms.<sup>143–145,197–199</sup>

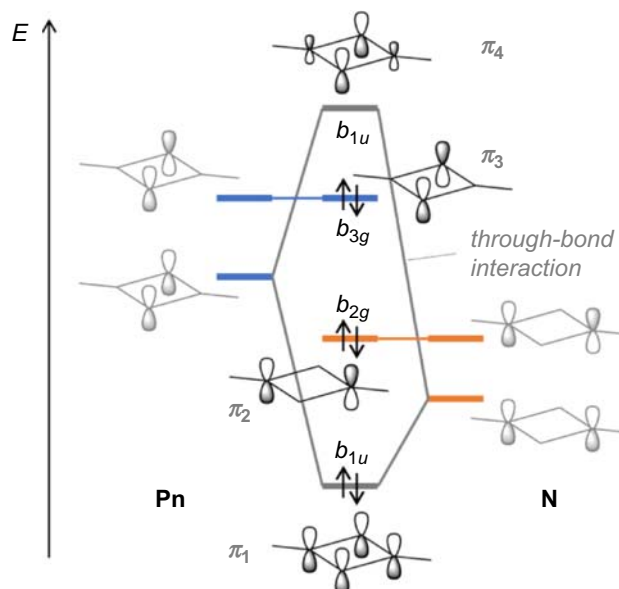
Singlet-triplet gaps of 22.6 and 29.8 kcal mol<sup>-1</sup> were calculated for **22\_PP\_Ter** and **22\_PP\_Hyp**, respectively (UB3LYP/6-311+G(d,p)//6-31G(d)), as well as a LUNO occupation number of 0.3 electrons and a biradical character  $\beta = 25\%$  for **22\_PP\_Ter** (UHF and CASSCF(2,2)/6-31G(d)).<sup>143</sup> For the Bbp-substituted biradicals **22\_PP\_Bbp** and **22\_AsAs\_Bbp**, biradical characters of 23% and 28%, respectively, could be calculated utilizing CASSCF(6,4) computations; also, the occupation numbers of the LUNOs were calculated for **22\_PP\_Bbp** (0.24) and **22\_AsAs\_Bbp** (0.29).<sup>198</sup> The singlet-triplet gap of **22\_AsAs\_Ter** is 19.8 kcal mol<sup>-1</sup> (UB3LYP/6-311+G(d,p)//6-31G(d,p)) and a biradical character of 32% was determined (CASSCF(2,2)/6-31G(d,p)).<sup>144</sup> For the mixed biradical **22\_PAs\_Ter**, the biradical character is 28% and an occupation number of the LUNO of 0.3 electrons [CASSCF(2,2)] was estimated.<sup>199</sup> It should be noted that DFT calculations can only give an estimate of the singlet-triplet gap due to their limitations with respect to multi-configurational systems (cf. Section 1.04.2.10).

The heavier congeners, **22\_SbSb** and **22\_BiBi** possess even higher biradical character (36% and 39%, respectively, for model compounds with R = H). The biradical character of the series **22\_PnPn\_H** was also computed by us using high-level MRCI calculations that include the effect of dynamic correlation on the wavefunction.<sup>198</sup> While the absolute numbers ( $\beta = 17\text{--}30\%$ ) are somewhat smaller than in case of a CASSCF calculation, the MRCI calculations confirm the trend that the biradical character increases with atomic number. This can nicely be rationalized by a change in the through-bond interaction (cf. Section 1.04.2.11) between the radical sites, owing to the increasing size of the heteroatoms (Fig. 15).

Especially the reactivity of the Ter-substituted compounds **22\_PP\_Ter** and **22\_AsAs\_Ter**, but also the reactivity of **22\_PP\_Hyp** and **22\_PAs\_Ter** were studied in detail, paying attention to the activation of small molecules. In the reaction of **22\_PP\_Ter** and **22\_AsAs\_Ter** with a variety of molecules, containing single, double and triple bonds, the addition of the molecules to the phosphorus or arsenic atoms is mostly observed (Scheme 35). For example, molecules with single bonds such as chalcogens (sulfur, selenium and tellurium), with double bonds (e.g., acetone, CS<sub>2</sub>, diphenyl-diazene and diphenyl-diphosphene), and with triple bonds (acetylene, tolane, acetonitrile and various sulfanyl-acetylenes) add easily forming [2.1.1]bicyclic structures (**23**) in almost quantitative yields at ambient temperatures.<sup>144,146,201–205</sup> Molecules with sterically too high demands are not activated. For example, no reaction is observed between **22\_PP\_Ter** and the bulky alkyne BTMSA. Most of the addition reactions can be understood as a formal [2 + 2] reaction (Scheme 35).

Interestingly, if the substituent on the alkyne is small, such as R = H, the addition product (**23**, [2.1.1]bicyclic) slowly isomerizes to a [3.1.0]bicyclic species (**24**, Scheme 35) upon thermal treatment, which is not observed for bulkier substituents (e.g., R = Ph).<sup>202</sup> X-ray structure elucidation shows that the alkyne is inserted into the four-membered Pn<sub>2</sub>N<sub>2</sub> ring and initially forms a six-membered heterocycle, which is also a pnictogen-centered biradical. In this case, however, a transannular covalent bond is formed, giving **24** with a three-membered dipnicta-aziridine and a fused planar five-membered ring that is almost perpendicular to the three-ring.

The addition reaction of molecular hydrogen to **22\_PP\_Ter** takes place under H–H bond breaking yielding exclusively the *cis* product (**25**, Scheme 36). Interestingly, this addition is reversible. At room temperature (and even lower temperatures), dihydrogen



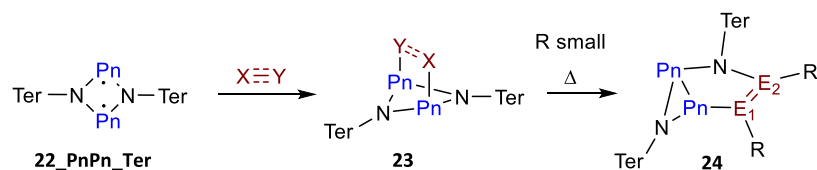
**Fig. 15** Schematic MO diagram of the  $\pi$  orbitals of **22\_PnPn\_H**. Only the configuration with the largest contribution to the CI wavefunction is shown. Due to the through-bond interaction (i.e., the interaction between the two  $b_{1u}$  SALCs; see also Fig. 14), the LUMO  $\pi_4$  is transannular bonding in character. With increasing size of the Pn atom, the overlap between the  $p$  orbitals at the Pn and N atoms (i.e., the  $b_{1u}$  SALCs) decreases, resulting in an energetic lowering of the orbital  $\pi_4$ . Thus, the HOMO-LUMO gap decreases, resulting in an increase in biradical character.<sup>198</sup>

is added to the biradical; at elevated temperatures (above 60 °C), dihydrogen is slowly eliminated again.<sup>206</sup> Regarding the activation of hydrogen, Zhivonitko et al. carried out investigations with *para*-hydrogen to check the potential suitability of **22\_PP\_Ter** for signal amplification via Phip (*para*-hydrogen-induced polarization) in NMR spectroscopy.<sup>207</sup> Indeed, **22\_PP\_Ter**, provides pronounced <sup>1</sup>H and <sup>31</sup>P hyperpolarization while activating the *para*-hydrogen molecules. It was the first time, in general, that a metal-free compound of a biradical structure was shown to produce hyperpolarized nuclear spins, introducing a new class of *para*-hydrogen activators for NMR signal enhancement. This observation also proved that the mechanism of H<sub>2</sub> activation with **22\_PP\_Ter** is pairwise, i.e., the two hydrogen atoms of an H<sub>2</sub> molecule follow each other through all elementary steps of the activation process. An up to 300-fold signal amplification was observed in <sup>31</sup>P NMR spectra of **22\_PP\_Ter**.<sup>207</sup> Similar results were obtained for **22\_PAs\_Ter** and **22\_AsAs\_Ter**.<sup>208</sup>

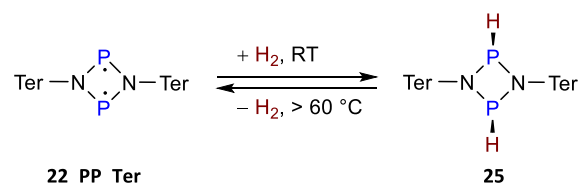
Hydrogen (pseudo)halides HX (X = Cl, CN, NCO, N<sub>3</sub>, PCO) cleanly add to the biradical **22\_PP\_Ter**. Upon addition, the H–X bond is broken, and exclusively the *cis* product is formed (**26**, **Scheme 37**).<sup>209</sup> In the case of HPCO, the addition product isomerizes to a [3.1.1]bicyclic compound (**27**, **Scheme 37**). When **22\_PP\_Ter** is treated with the free acid of a weakly coordinating anion such as Jutzi's acid, H[B(C<sub>6</sub>F<sub>5</sub>)<sub>4</sub>]·2Et<sub>2</sub>O, the biradical is protonated at one phosphorus atom, yielding a (closed-shell) phosphonium cation (**28**). Treating this cation with an X<sup>–</sup> source again results in the formation of the formal HX adduct **26**.<sup>209</sup>

A special reactivity is observed in the reaction of **22\_PP\_Ter** and **22\_PAs\_Ter** with CO or isocyanides. Although these molecules also contain multiple bonds, they do not add to the radical centers as shown in **Scheme 35** (forming a [2.1.1]bicyclic species), but insert into the heterocycle (in the case of **22\_PAs\_Ter** selectively into the nitrogen-arsenic and not into the nitrogen-phosphorus bond, **Scheme 38**). This insertion reaction was also observed for 1,2,3-triaza-4-pnicta-cyclobutane-2,4-diyls (see above).<sup>196,210,211</sup> Both, the insertion of CO and the electronically very similar isocyanides lead to the formation of a five-membered heterocycle (**29**), which is also a biradical, which will be discussed in detail in **Section 1.04.3.3.2**. Since the insertion only takes place via the carbon atom, one can speak of a carbene-like reactivity.

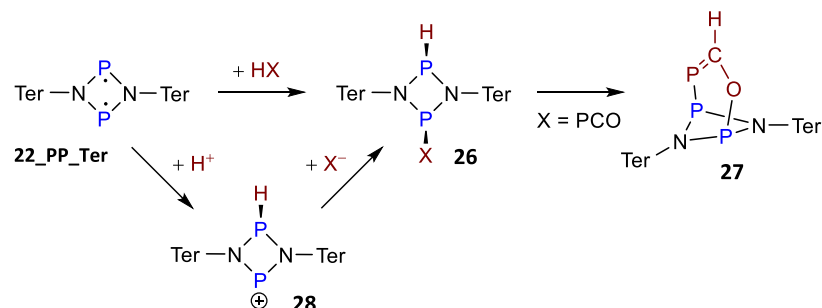
For example, the reaction of **22\_PP\_Ter** with CO at a CO pressure of 60 bar yields the five-membered biradical **29\_PP\_Ter** as the main product. This reacts to a small extent with another equivalent of CO, which bridges the two radical centers with the carbon atom yielding a [2.1.1]bicyclic species (**Scheme 38**, **30\_PP\_Ter**).<sup>210</sup> The reaction of **22\_PP\_Ter** with CN-<sup>t</sup>Bu gives a similar result (see also **Section 1.04.3.3.2**). In all cases, there is an equilibrium between the formal mono-adduct (**29**, i.e., the five-membered biradical) and di-adduct (**30**, i.e., the bridged five-membered ring). On heating, the four-membered biradical **22\_PP\_Ter** can also be observed in the mixture. With CN-Dmp, the reaction is more selective due to a larger steric hindrance of the Dmp



**Scheme 35** Reactivity of **22\_PnPn\_Ter** (Pn = P, As) towards small molecules (XY) containing single, double and triple bonds, and isomerization of alkyne adducts with small substituents R (e.g., XY = R-CC-R).

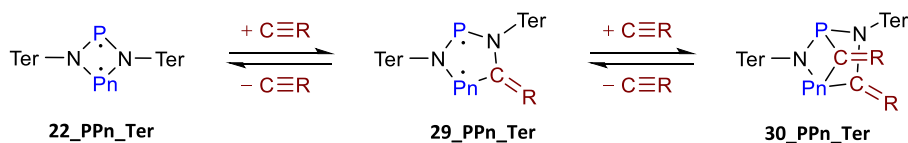


**Scheme 36** Reversible reaction of **22\_PP\_Ter** with molecular hydrogen.<sup>206</sup>



**Scheme 37** Reaction of **22\_PP\_Ter** with Brønsted acids (X = Cl, CN, NCO, N<sub>3</sub>, PCO).<sup>209</sup>





**Scheme 38** Reactivity of **22\_PPn\_Ter** towards CO and isocyanides (Pn = P, As; R = O, N<sup>t</sup>Bu, NDmp).<sup>196,210,211</sup>

substituent. Only the five-membered biradical is formed. No double addition was observed.<sup>211</sup> The reaction with CN-Dmp was also carried out with **22\_PAs\_Ter**. Here, as with **22\_PP\_Ter**, only the insertion of one isocyanide molecule is observed, which, however, selectively inserts into the nitrogen-arsenic bond.<sup>196</sup> In the case of **22\_PP\_Hyp**, the reaction with sterically demanding CN-Ter leads to biradical **29\_PP\_Hyp**, while smaller isocyanides yield a cyclic diene due to migration of one Hyp substituent (see [Section 1.04.3.3.2](#), [Scheme 56](#)).<sup>212</sup>

Furthermore, **22\_PP\_Ter** reacts with molecular oxygen and KMnO<sub>4</sub> yielding not a [2.1.1]bicyclic species as illustrated in [Scheme 39](#), but only one P atom is oxidized. That is, both oxygen atoms are transferred to one phosphorus atom affording **31**.<sup>146</sup> In the reaction with CO<sub>2</sub>, one oxygen atom is transferred to a phosphorus atom and CO is released leading to the formation of **32**. The reaction with ammonia leads to the cleavage of a nitrogen-phosphorus bond. A hydrogen atom is transferred to the nitrogen atom, and an NH<sub>2</sub> group is transferred to the phosphorus atom yielding **33** ([Scheme 39](#)).<sup>206</sup>

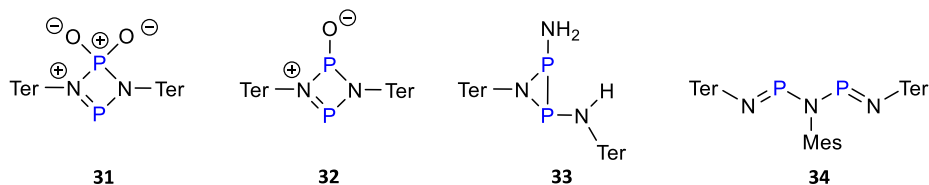
Phosphorus-centered biradicals **22\_PP\_R** (R = Ter, Hyp) were also treated with ionic azides (AgN<sub>3</sub> and Hg(N<sub>3</sub>)<sub>2</sub>), leading to the formation of diazides, [N<sub>3</sub>-P(μ-NR)]<sub>2</sub> (R = Ter), and reduced metal in a redox process, while triaza-diphospha-pentadienes (**34**) could be isolated when covalent azides were added to **22\_PP\_R** (R = Ter, Hyp; [Scheme 39](#)).<sup>213</sup> Theoretical studies of the azide addition reaction showed a very soft potential energy surface with a large number of different isomers. This reaction can be understood as a novel Staudinger reaction. The classical STAUDINGER reaction consists of two steps: (i) the *trans*-azide, RN<sub>3</sub>, attacks the P<sup>III</sup> atom of a phosphane, R<sub>3</sub>P, and forms a chain-like *cis*-intermediate, R<sub>3</sub>P-NNN-R (*cis*-PNNN and *trans*-NNNR unit),<sup>214</sup> and (ii) this intermediate forms a four-membered PN<sub>3</sub> ring, which readily separates into N<sub>2</sub> and R<sub>3</sub>P=NR, forming a P<sup>V</sup> atom. Due to the mostly very flat potential energy surface in the second step, the Staudinger reaction essentially requires one step to release N<sub>2</sub>, which means that mostly no intermediates can be isolated. In contrast, the potential energy surface for the reaction of biradical **22\_PP\_R** with R-N<sub>3</sub> has several reaction channels, including classical Staudinger-type reactions with the formation of four-membered N<sub>3</sub>P rings followed by the release of molecular nitrogen.<sup>213</sup> Since there is also a second P atom present in the molecular skeleton, oxidation to a P<sup>V</sup> species does not take place (in contrast to the classical Staudinger reaction), but rather the formation of a triaza-diphospha-pentadiene (**34**, [Scheme 39](#)) with two P<sup>III</sup> atoms. Since both P atoms are described with the formal oxidation state +II in the biradical, each P atom is oxidized by the loss of one electron. This also means a total loss of two electrons in accordance with the oxidation of P<sup>III</sup> to P<sup>V</sup> in the typical Staudinger reaction when only one P<sup>III</sup> atom is involved. In terms of the oxidation process and mechanism, the reaction of the phosphorus-centered biradical with a covalent azide represents a new variant of the Staudinger reaction.<sup>213</sup>

In addition, **22\_PP\_Ter** can also be used as a radical scavenger. Moreover, since biradicals of the type **22** possess also zwitterionic character they can be utilized in reactions either as Lewis acid and/or base.<sup>215,216</sup> Finally, a short word on **22\_PP\_Hyp**, which takes on a special role as far as reactivity is concerned. First, the dimerization of the biradical to a cage compound is observed here in polar solvents.<sup>145</sup> Such a dimerization is known from reduction reactions with sterically less demanding substituents such as <sup>t</sup>Bu or Dmp (see [Section 1.04.3.2](#), [Scheme 9](#)).<sup>203,217</sup>

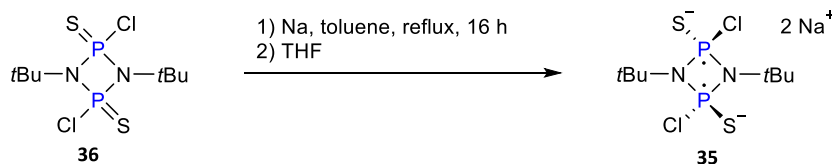
Finally, cyclo-1,3-dipnicta-2,4-diazane-1,3-diyls of the type [Pn(μ-NTer)<sub>2</sub>Pn] (**22**, Pn = P, As) can undergo a one-electron oxidation utilizing silver salts of weakly coordinating anions such as [AgL<sub>n</sub>][B(C<sub>6</sub>F<sub>5</sub>)<sub>4</sub>]<sup>-</sup> (L = donor solvents) to afford the cyclic radical cations, [E(μ-NTer)<sub>2</sub>E]<sup>•+</sup>. The bonding situation in the radical cations features a rare example of a transannular one-electron π-bond without having a σ bond (cf. Frenking's biradical **18**).<sup>218</sup>

#### 1.04.3.2.4.3 Phosphorus centered biradical dianions

The only example so far of a biradical with tetravalent phosphorus atoms (**35**, [Scheme 40](#)) was presented by Wright and co-workers. For its preparation, the four-membered ring **36**, which is already substituted on the phosphorus atoms with sulfur and chlorine, is reduced with sodium, yielding the anionic biradical **35** as *trans* isomer ([Scheme 40](#)). The *cis* isomer (possibly also the *trans* isomer) reacts with polymerization to form a macrocycle. Both reactions run parallel.<sup>219</sup> Biradical salt **35** is a colorless compound. The appearance of sharp NMR signals confirms the singlet character of the biradical. For the model substance of the biradical **35** (R = methyl), occupation numbers of 1.21 *e* for the HONO and 0.79 *e* for the LUNO were calculated (CASSCF(2,2), MRCI methods; base set: aug-cc-pVDZ).<sup>219</sup>



**Scheme 39** Products of the reaction of **22\_PP\_Ter** with O<sub>2</sub> (**31**), CO<sub>2</sub> (**32**), NH<sub>3</sub> (**33**) and Mes-N<sub>3</sub> (**34** as an example).



**Scheme 40** Synthesis of **35**.

#### 1.04.3.2.4.4 NHC stabilized phosphorus centered biradicals

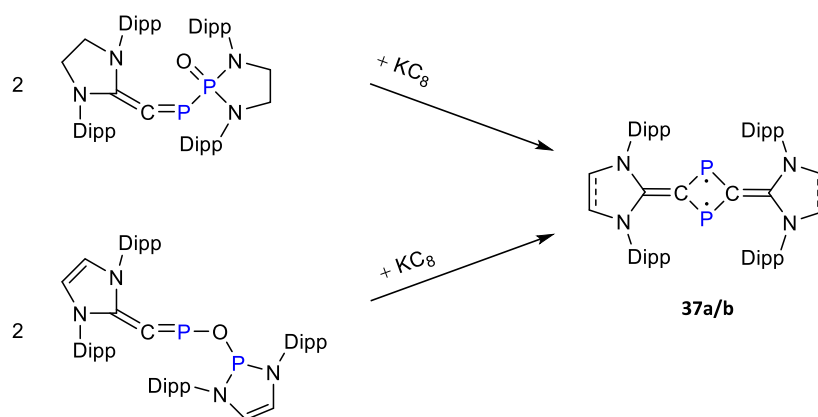
In 2017, two groups independently presented synthesis options for a phosphorus centered biradical **37** (**Scheme 41**), where the  $C_2P_2$  four-membered rings are stabilized by NHC (*N*-heterocyclic carbene) ligands. In contrast to the 1,3-diphosphacyclobutanediyls **5** and **6** synthesized by Niecke and Yoshifuji/Ito et al. biradical **37** also features a  $C_2P_2$  four-membered ring, however, both radical centers are located on both phosphorus instead of on the carbon atoms. The synthesis procedure of the Grützmacher group begins with a phospho-allene, which is reduced by  $KC_8$  (**Scheme 41**). The substituent of the phosphorus atom serves as a leaving group which leaves the molecule upon reduction. The terminal carbon atom of the phospho-allene is part of the *N* heterocycle that stabilizes the biradical after the reaction. The reaction is possible with a saturated backbone in the heterocycle as well as with an unsaturated backbone. This gives rise to the biradicals **37a** and **37b**, which differ by one  $\pi$ -bond in the ligand.<sup>220</sup>

An alternative synthesis for **37a** was developed by Ghadwal et al. (**Scheme 42**). An *N*-heterocyclic olefin is reacted with  $PCl_3$  in the presence of  $NEt_3$ . On elimination of  $HCl$ , a  $C_2P_2$  four-membered ring is formed, which affords, after reduction with  $KC_8$ , the biradical **37a** (see **Scheme 42**).<sup>221</sup>

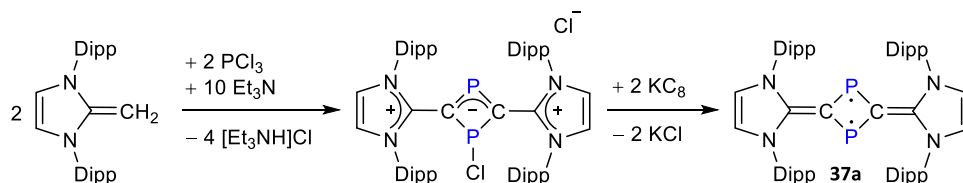
Biradicals of type **37a** and **37b** are sensitive to air and water, but thermally stable under an inert atmosphere. While **37a** has a dark green color, **37b** is yellow. The planarity of the central 4-ring as well as the rather large distance between both phosphorus atoms suggest a biradical character within these species.<sup>220,221</sup> AIM calculations on a model system of **37a** (nitrogen atoms substituted by methyl groups) show a ring-critical point between the phosphorus atoms but no bond-critical point (BP86/def2-TZVPP).<sup>220</sup>

Grützmacher and Li et al. conducted first investigations on the reactivity of biradical **37** (**Scheme 43**).<sup>220</sup> **37** was shown to react with molecular hydrogen at atmospheric pressure yielding an addition product (**38b**) with one hydrogen atom at each phosphorus atom of the biradical. With ferrocenium ions, both biradicals are oxidized to radical cations as illustrated in **Scheme 43**. The positive charge of the cation (**39a/b**) sits in both *N*-heterocycles and the overall positive charge of the radical cation is compensated by the  $BARF^-$  anion.

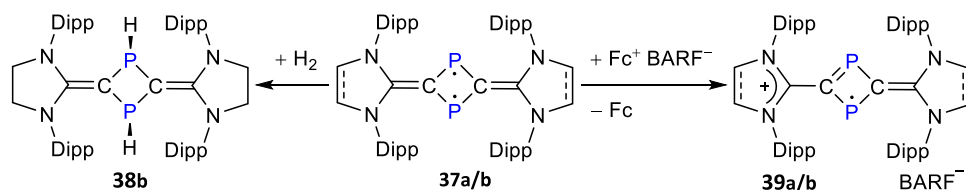
Moreover, biradical **37b** was treated with alkyl iodides, leading to the formation of cyclic phosphonium ions **40**, which can be further reacted with  $Me_2Zn$  to give the dialkyl substituted ring system (**Scheme 44**).<sup>222</sup> The reaction of **37b** with diketones leads to the corresponding [4 + 2] addition products (**41**).<sup>223</sup> Biradical **37b** can also activate C–H, N–H, and O–H bonds, leading to cyclic



**Scheme 41** Synthesis of **37** (**a** = unsaturated backbone, **b** = saturated) according to Grützmacher et al.<sup>220</sup>



**Scheme 42** Synthesis of **37a** according to Ghadwal et al.<sup>221</sup>



**Scheme 43** Reactivity of **37** towards oxidation (Fc = Fe(C<sub>5</sub>H<sub>5</sub>)<sub>2</sub>; BARF<sup>-</sup> = [B(3,5-(CF<sub>3</sub>)<sub>2</sub>C<sub>6</sub>H<sub>3</sub>)<sub>4</sub>]<sup>-</sup>).<sup>220</sup>

products of the type [HP(μ-C(NHC))<sub>2</sub>P-ER] (**42**, E = C, N, O).<sup>224</sup> Lastly, biradicals **37a/b** can act as η<sub>4</sub> ligand in transition metal complexes (**43**).<sup>225</sup>

#### 1.04.3.2.4.5 Pnictogen centered biradical anions: [Pn<sub>4</sub>]<sup>2-</sup>

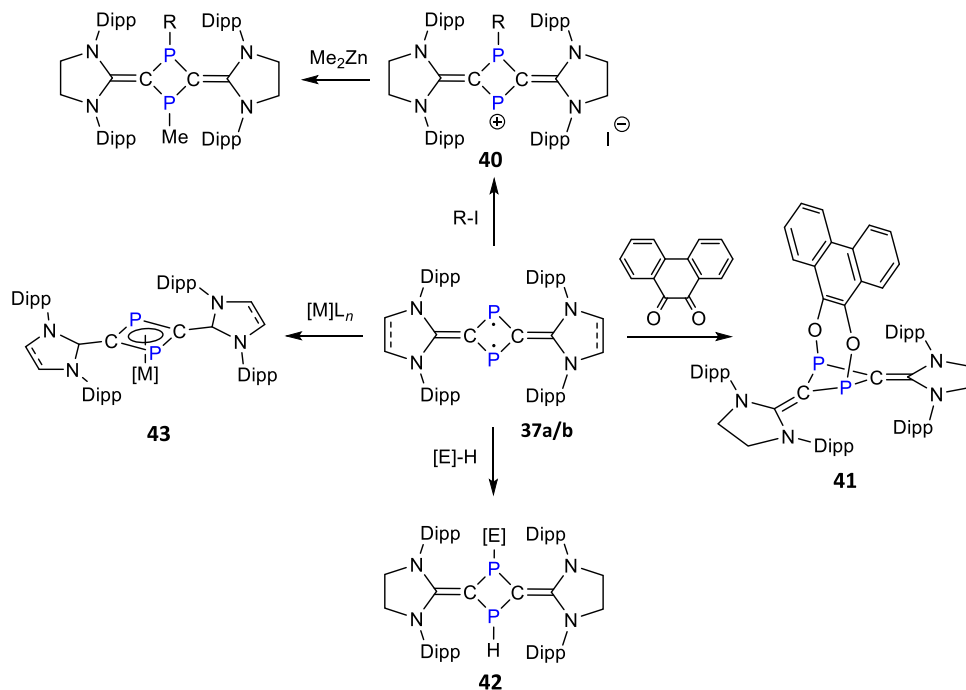
Cyclic tetrapnictide anions of the type [Pn<sub>4</sub>]<sup>2-</sup> can formally be derived from the archetypical inorganic biradicaloid S<sub>2</sub>N<sub>2</sub> (see **Section 1.04.3.2.4**) by substituting the group 16 atoms (i.e., S) with group 15 atoms. The first experimentally characterized derivative was [Bi<sub>4</sub>]<sup>2-</sup> in the salt [K(crypt)]<sub>2</sub>[Bi<sub>4</sub>] (crypt = [2.2.2]cryptand) by Corbett and co-workers in 1977.<sup>226</sup> The same group later also published the Sb derivative [K(crypt)]<sub>2</sub>[Sb<sub>4</sub>].<sup>227</sup> The As and P species were reported in 2002 and 2003, respectively, by Korber et al. as the alkali metal salts [Na(NH<sub>3</sub>)<sub>5</sub>]<sub>2</sub>[As<sub>4</sub>]·3NH<sub>3</sub> and Cs<sub>2</sub>[P<sub>4</sub>]·2NH<sub>3</sub>.<sup>228,229</sup> All compounds were characterized by single-crystal X-ray diffraction. The structure of all four-membered ring systems is nearly ideally square planar, with equal Pn–Pn bond lengths within the uncertainty of the structure elucidation, and Pn–Pn–Pn bond angles of nearly 90° (deviation less than 0.5°).

The biradical character of the tetrapnictide anions was recently investigated by Coburger et al. by means of CASSCF(6,4) calculations.<sup>230</sup> All species possess a medium-low biradical character, with *n*(LUNO) = 0.11 (P), 0.14 (As), 0.16 (Sb) and 0.19 (Bi). Due to the D<sub>4h</sub> symmetry of the anions, there are two biradicaloid Lewis structures with equal weights (A, B in **Scheme 45**), which the authors determined by localizing the active orbitals (cf. **Sections 1.04.2.8 and 1.04.2.10**). In total, the two biradicaloid structures contribute more than 40% to the total wavefunction (P: 41%, As: 43%, Sb: 45%, Bi: 47%).

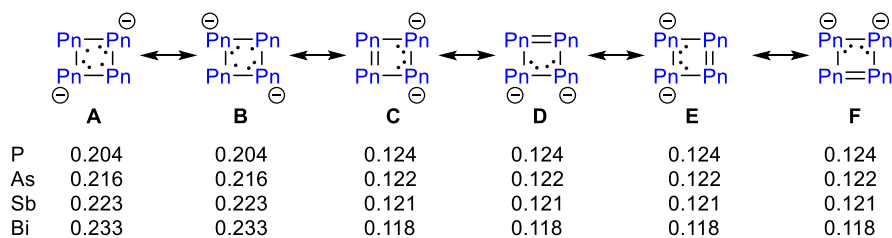
Furthermore, the aromaticity of the [Pn<sub>4</sub>]<sup>2-</sup> anions was investigated on the basis of the Shannon aromaticity index (SAI),<sup>231</sup> revealing a somewhat lower aromaticity than benzene.<sup>230</sup>

#### 1.04.3.2.5 Hetero-cyclobutane-1,3-diyls with radical centers on elements of group 16

In this article on chalcogen-centered cyclobutanediyl analogs, we found only one neutral compound, S<sub>2</sub>N<sub>2</sub>, which could also have been discussed in the section on nitrogen centered biradicals. Although molecular oxygen<sup>232–236</sup> is a triplet radical in its ground state and ozone, O<sub>3</sub>, also shows (open-shell singlet) biradical character,<sup>237,238</sup> there is no compound with oxygen that can be



**Scheme 44** Reactivity of **37** towards alkyl iodides R-I (R = Me, Et, <sup>*i*</sup>Bu),<sup>222</sup> a diketone,<sup>223</sup> compounds with polarized E–H bonds (e.g., Ph-CC-H, 4-NC-C<sub>6</sub>H<sub>4</sub>-NH<sub>2</sub>, 4-F<sub>3</sub>C-C<sub>6</sub>H<sub>4</sub>-NH<sub>2</sub>, MeOH, PhOH),<sup>224</sup> and metal complexes ([M] = Cr(CO)<sub>3</sub>, Mo(CO)<sub>3</sub>, Co(CO)<sub>2</sub>, NiBr<sub>2</sub>).<sup>225</sup>



**Scheme 45** Most important Lewis structures of  $[\text{Pn}_4]^{2-}$  and their corresponding weights in the entire resonance.<sup>230</sup>

regarded as cyclobutenediyl analog, even though  $\text{N}_2\text{O}_2 = 2 \text{NO}$ , which is isovalence electronic to  $\text{S}_2\text{N}_2$ , is of course a radical that, however, does not exist as a ring but only as a NO molecule or as its non-cyclic dimer at lower temperatures.

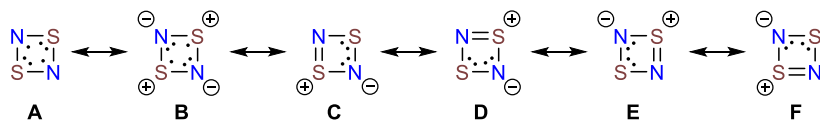
#### 1.04.3.2.5.1 Sulfur-nitrogen centered biradical: $[\text{N}(\mu\text{-S})_2\text{N}]^-$

One of the first heteroatom-substituted cyclobutenediyl derivatives to be synthesized is  $\text{S}_2\text{N}_2$ , disulfurdinitride (**44**, **Scheme 46**), the biradical character of which was/is discussed in the literature.<sup>20,239,240</sup> It can be obtained by decomposing  $\text{S}_4\text{N}_4$  on silver wool, followed by freezing out the product. At room temperature, **44** polymerizes to the chain-like polythiazyl  $(\text{SN})_x$ .<sup>131</sup> By means of single crystal X-ray structural analysis of **44** in 1975, it was shown that the  $\text{S}_2\text{N}_2$  ring is planar.<sup>131</sup> The electronic structure, on the other hand, is still disputed today.<sup>131,239–243</sup> Among other things, the aromatic character of **44** is in question. While the molecule fulfills the criteria of a Hückel aromatic compound due to its formal six  $\pi$ -electrons and planarity, Head-Gordon et al. conclude from their calculations that it is merely a  $2\pi$ -aromatic system.<sup>244</sup> Another point of discussion is the biradical character of **44**. While Head-Gordon et al. do not attribute any significant biradical properties to the molecule,<sup>244</sup> other groups discuss the question of where the radical centers are localized. Gerratt et al. see these at the sulfur atoms (Lewis representation **B**), while Harcourt, Schulz and Klapötke conclude from their calculations a stronger localization at the nitrogen atoms (**A**), which has the advantage that no formal charges are needed.<sup>239,245,246</sup> Furthermore, it is argued that the electronic situation in **44** can only be described properly by resonance between two biradical (Lewis representation **A** and **B**) and further zwitterionic structures (**C–F**, **Scheme 46**). In addition to the resonance forms shown in **Scheme 46**, further formulae can be formulated, utilizing *d*-type orbitals (extension of the electron octet), which, however, have a very small contribution to the description of the ground state.<sup>239,240</sup> In 2012, Hiberty and Braida et al. calculated the contributions of the individual resonance formulae using different methods and concluded that the biradical form with the radical centers on the nitrogen atoms (**A**) has the largest weight. This is followed by the four degenerate, zwitterionic structures (**C–F**). However, the biradical formula with the radical centers on the sulfur atoms (**B**) also has a non-negligible contribution.<sup>240</sup> One further essential statement of this work regarding aromaticity versus biradical character is that the biradical structure indicates that aromaticity and biradical are not mutually exclusive, contrary to what is usually claimed.

Apart from VB-type calculations with localized orbitals, the biradical character of **44** was also estimated on the basis of CI coefficients and the LUNO occupancy (i.e., in the delocalized picture). For example, Tuononen et al. reported comprehensive CAS(22,16) computations, which correlate all orbitals in the valence space.<sup>247,248</sup> They report the CI coefficients  $c_1$  and  $c_2$  from which  $\beta = 7\%$  can be estimated, and they also conclude that resonance structure **A** has the largest weight. More recently, Coburger et al. reported a LUNO occupancy of 0.14 electrons, as derived from CAS(6,4) calculations including all  $\pi$ -type orbitals in the valence space.<sup>230</sup>

#### 1.04.3.2.5.2 Chalcogen biradicals $[\text{E}_4]^{2+}$ (E = S, Se, and Te)

Starting from an isoelectronic substitution of the nitrogen atoms by one  $\text{E}^+$  ion each in  $\text{S}_2\text{N}_2$  leads to the substance class of  $[\text{E}_4]^{2+}$  cations (E = chalcogen = S-Te), which also have  $6\pi$  electrons. Since this substance class has already been described in a large number of reviews,<sup>81,86,249–253</sup> we would like to focus here on its biradical character. To begin with, let us shortly summarize the synthesis of salts bearing these chalcogen polycations. The first synthesis of a chalcogen polycation may have been carried out in 1798, when Klaproth described that tellurium dissolves gradually in sulfuric acid to give a red solution.<sup>254</sup> However, it was Gillespie and Bjerrum et al. who first synthesized and characterized polycations of the type  $[\text{E}_4]^{2+}$ .<sup>249,255</sup> There are a variety of established methods for the synthesis of such polycations, which all use strongly polar media such as  $\text{H}_2\text{SO}_4$ , anhydrous HF,  $\text{HSO}_3\text{F}$ , liquid  $\text{SO}_2$ , molten salts, e.g.,  $\text{Na}[\text{AlCl}_4]$ , or  $\text{GaX}_3$  benzene media (X = Br, Cl).<sup>86</sup> The chalcogens can be transformed into the cations either by oxidation with suitable oxidants such as  $\text{AsF}_5$  or  $\text{SbF}_5$ , or synproportionation reactions in the presence of a strong halide ion acceptor such as  $\text{AlX}_3$  (X = Cl, Br, I). Recently, room-temperature ionic liquids have been used as a new alternative reaction medium



**Scheme 46** Resonance formulae to describe the electronic situation of **44**.<sup>239,240</sup>

for the synthesis of such polycations.<sup>86</sup> In any case, a suitable oxidizing agent is needed to oxidize the chalcogen to the  $[E_4]^{2+}$  ion and a suitable anion, e.g., weakly coordinating anions that can stabilize these cations.<sup>81</sup>

With regard to the electronic situation in the  $[E_4]^{2+}$  ion, it strongly resembles the  $S_2N_2$  biradical. Hiberty and Braida et al. pointed out that for all cations ( $E = S, Se, \text{ and } Te$ ) the cumulative weights of the two possible biradical structures (**Scheme 47**, representations **H** and **I**) are always important and close to 50%, making these molecular cations comparable to ozone in terms of biradical character.<sup>240</sup> As the two biradical structures are degenerate in the  $[E_4]^{2+}$  dications, they have equal weights in contrast to the situation in the neutral and heteroatomic ring  $S_2N_2$ . The biradical character increases slightly with increasing atomic number.

### 1.04.3.3 Main group 15 analogs of cyclopentane-1,3-diyls

The parent system of the five-membered 1,3-diyls is cyclopentane-1,3-diyl (**45**), which is also known as the Closs biradical named after Closs and co-workers who first synthesized it (**Scheme 48**).<sup>256</sup> Biradical **45** was detected as a reaction product after irradiation of 2,3-diazabicyclo[2.2.1]hept-2-ene **46** with UV light at 5.5 K in a cyclohexane matrix by EPR spectroscopy. At 5.5 K, **45** has a half-life of approx. 30 min. The EPR signal behaves almost unchanged in the range from 1.3–20 K, suggesting a triplet ground state,<sup>257</sup> in accord with quantum mechanical studies. On the singlet energy hypersurface (**Fig. 16**), the bicyclo[2.1.0]pentane (housane, **47**) represents a minimum structure, while the planar isomer, which has the same point group as cyclopentane-1,3-diyl, is a transition state.<sup>256,258</sup> By heating the cyclopentane-1,3-diyl **45**, housane **47** can be detected as the main product,<sup>259</sup> as well as a small amount of 0.5% cyclopentene **48** as the Wagner-Meerwein rearrangement product.<sup>260</sup> Kinetic investigations of the formation of cyclopentane-1,3-diyl and its decay were carried out by Engel and co-workers using Raman spectroscopy.<sup>261</sup> Since then, a large number of experimental investigations have been carried out in which the protons of the cyclopentane-1,3-diyl parent system were replaced by organic substituents.<sup>17,262–264</sup> However, to the best of our knowledge, it was never possible to achieve sufficient stabilization solely by substituting the protons to obtain cyclopentane-1,3-diyls that are stable at room temperature. The next section summarizes the experimental investigations in which additional substitutions of the carbon atoms by heteroatoms were carried out to stabilize the corresponding biradicals.

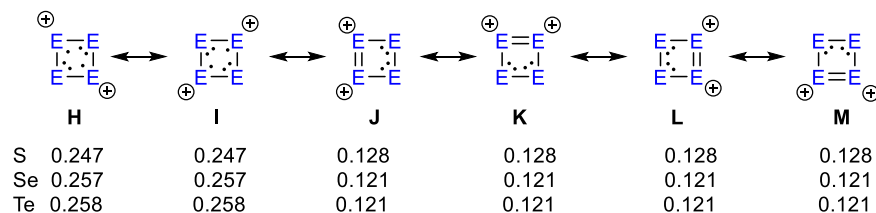
#### 1.04.3.3.1 Hetero-cyclopentane-1,3-diyls with radical centers on elements of group 14

##### 1.04.3.3.1.1 Carbon centered biradicals: 1,2-Diaza-cyclopentane-3,5-diyls

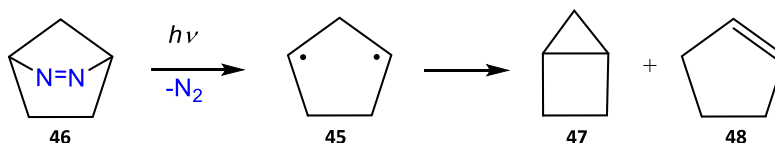
Starting from the parent compound cyclopentane-1,3-diyl **45**, both, the carbon atoms can be substituted by heteroatoms and the protons by other groups. First studies on heteroatom-substituted systems, in which the carbon atoms are substituted in the 4- and 5-position by nitrogen atoms, were carried out by Arnold et al. in the late 1960s.<sup>265–267</sup> In their syntheses, they started from various isopyrazole derivatives **49a–d** and reacted them in a cycloaddition with 4-phenyl-1,2,4-triazoline-3,5-dione (PTAD) **50Ph** yielding **51a–e** (**Scheme 49**). From the reaction products **51a–e**, the transient biradicals **52a–d** can be generated by light-induced  $N_2$  elimination ( $\lambda = 253.7 \text{ nm}$ ).

With **51b** and **51c** in hand, the biradical species **52b** and **52c** could be investigated in solution after previous irradiation at 77 K. The two compounds **52b** and **52c** are green and by means of EPR spectroscopy it could be shown that **52b** and **52c** exist as triplet biradicals in the ground state. At 77 K the biradicals are stable for several hours, but decompose within a short time at 190 K. Compounds **52a** and **52d** are of lower stability and could only be detected as triplet species after previous irradiation at 4 K by EPR spectroscopy.

When irradiation of **51a–e** occurs at room temperature, the biradicals **52a–e** immediately react further with transannular bond formation to form the housane derivatives **52'a–e**. In the case of **52'a** and **52'd**, isolation and extensive characterization of the compounds were successful. Compounds **52'b** and **52'c** could be detected by low-temperature  $^1\text{H}$  NMR spectroscopy or by the trapping reaction with **50Ph** to give **53b** and **53c**. It could be shown by time-dependent  $^1\text{H}$  NMR spectroscopy that the housane

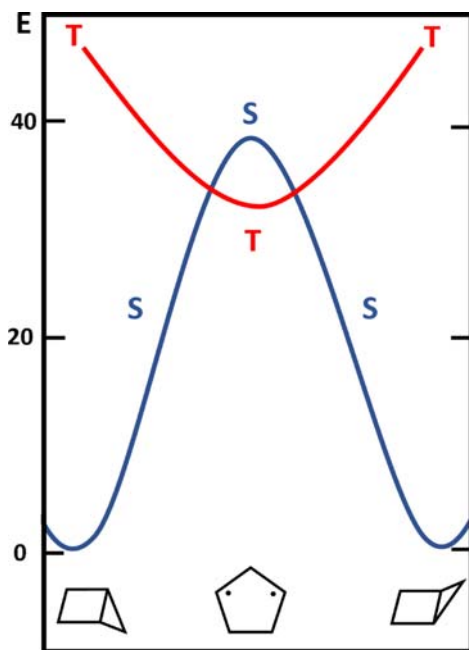


**Scheme 47** Resonance formulae to describe the electronic situation of  $[E_4]^{2+}$  and their weights in the entire resonance.<sup>240</sup>

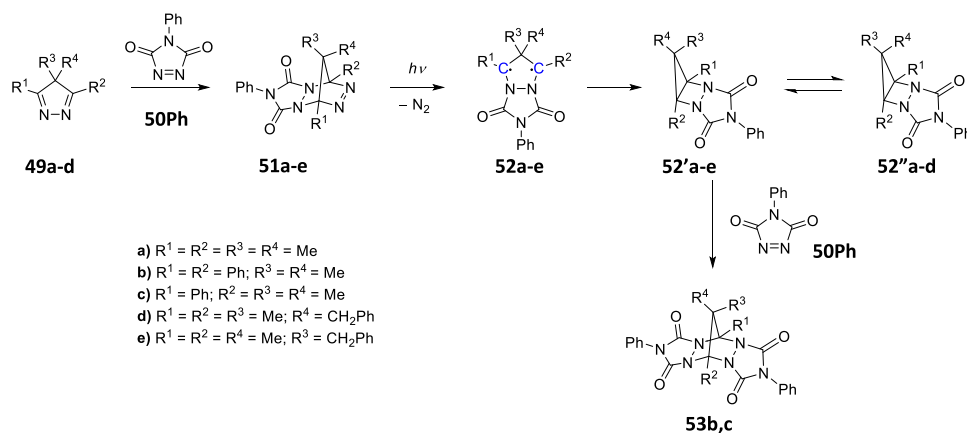


**Scheme 48** Synthesis of cyclopentane-1,3-diyl **45** starting from 2,3-diazabicyclo[2.2.1]hept-2-ene **46**.





**Fig. 16** Schematically depicted potential energy hypersurfaces of the singlet (S) and triplet (T) states of biradical **45** ( $E$  in kcal mol<sup>-1</sup>).



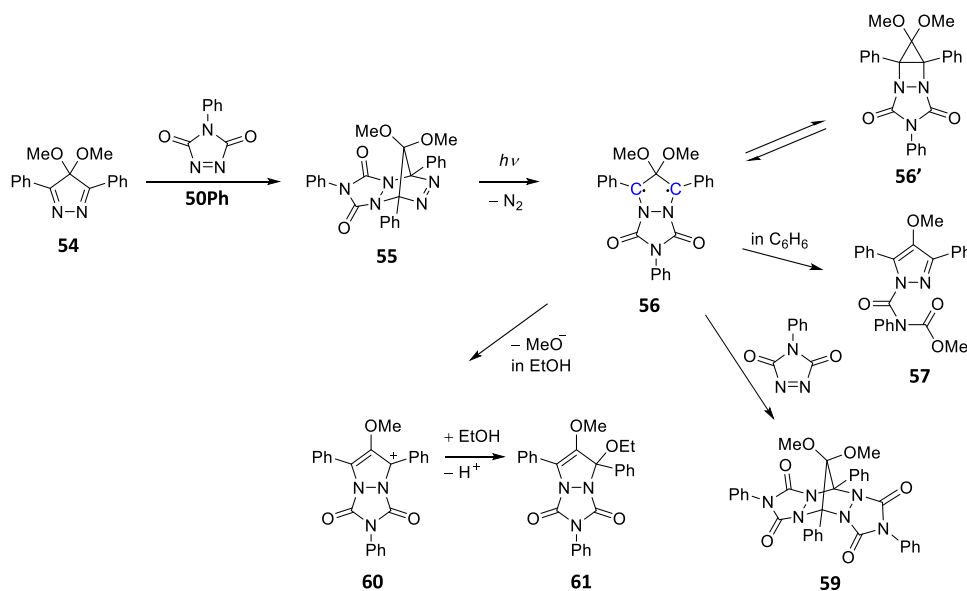
**Scheme 49** Synthesis of **52a-e**.

derivatives **52'a-e** are in thermal equilibrium with the isomers **52''a-d**. In the case of **52'e**, the reaction to **52''e** is irreversible. For the respective conversion between the two isomers, a reaction path via the biradical **52a-e** is discussed.

Abe et al. were able to show with quantum mechanical calculations at the UB3LYP/6-31G(d) level that in the systems studied by Arnold et al. a substitution of the substituents  $R^3$  and  $R^4$  by electron-withdrawing groups (-F, -OH) leads to an energetic lowering of the singlet state and that this singlet state is even more stable than the triplet state.<sup>268,269</sup>

Preparatively, such a modification of the system was carried out in 2006 by Abe et al.<sup>270</sup> Analogous to the work of Arnold et al., the synthesis is based on an isopyrazole derivative **54** (Scheme 50). The difference is that the quaternary carbon of the isopyrazole ring is no longer saturated with alkyl substituents (see **49a-d**), but with electron-withdrawing methoxy groups. The cycloaddition of **54** with **50Ph** leads to the diazoalkane **55**. Irradiation with short-wave light ( $\lambda = 360\text{--}440$  nm) forms the 1,2-diazacyclopentane-3,5-diyl 4,4-dimethoxy-3,5-diphenylpyrazolidine-3,5-diyl **56** as a short-lived compound under  $\text{N}_2$  elimination. Biradical **56** is in rapid thermal equilibrium with **56'** and irreversibly decomposes to **57**.

By laser flash photolysis ( $\lambda_{\text{excitation}} = 355$  nm,  $\lambda_{\text{observation}} = 640$  nm), **58** was shown to have a lifetime of  $9.67 \pm 0.007$  ms in toluene at 298 K and to react in a 1st order reaction to **57**. In contrast to compounds **52a-e** introduced by Arnold et al., **56** is a singlet biradical, as demonstrated by EPR inactivity at 77 K in a 2-methyltetrahydrofuran (MTHF) matrix and quantum mechanical calculations at the UB3LYP/6-31G(d) level. Furthermore, the presence of oxygen leads to no change in the lifetime and with PTAD (**50Ph**) the addition product **59** is formed. The housane species **56'** was also detected by laser flash photolysis and time-resolved IR spectroscopy (TRIR).<sup>271</sup> Using TRIR, rate constants and free enthalpy were determined. In toluene, the formation of



**Scheme 50** Synthesis and reaction behavior of 4,4-dimethoxy-3,5-diphenylpyrazolidine-3,5-diyl (**56**).

**56'** at 293 K is exergonic ( $\Delta G^\circ_{293} = -1.3 \text{ kJ mol}^{-1}$ ), while in acetonitrile it is endergonic ( $\Delta G^\circ_{293} = 0.2 \text{ kJ mol}^{-1}$ ). (BS)-CAM-B3LYP/6-31G(d) calculations show an exergonic reaction course for the formation of **56'** ( $\Delta G^\circ_{293} = -1.4 \text{ kJ mol}^{-1}$ ) for the gas phase. Due to the rapid reaction of **56'** via **56** to **57**, a more comprehensive characterization is not possible. The decay product **57** can be isolated in 70% yield and its structure could be confirmed by 2D NMR spectroscopy (HMBC, HMQC).<sup>270</sup>

In protic solvents, such as ethanol, a different reaction behavior is shown after irradiation of **55**, in which first a cation **60** is formed, with cleavage of a methanolate anion, and then **61** is formed by reaction with the solvent. The lifetime of the cation **60** could be determined by laser flash photolysis and is  $607 \pm 18 \text{ ms}$ . The formal ethanol addition product **61** can be isolated in 48% yield.

#### 1.04.3.3.1.2 Carbon centered biradicals: 1,2-Diaza-4-silacyclopentane-3,5-diyls

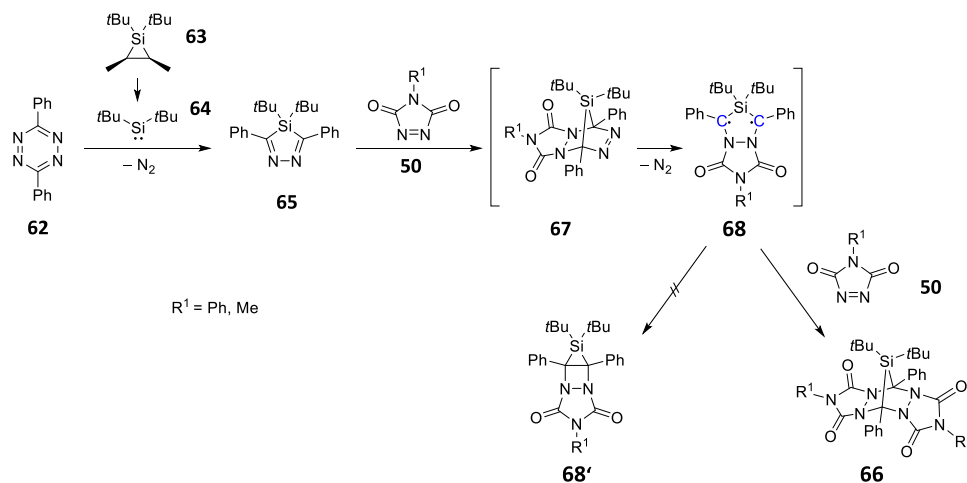
In 2010, Abe et al. found another possibility to stabilize the singlet state with respect to the triplet state by substituting the carbon atom in position 2 by a silicon atom in the 2-position of the cyclopentane-1,3-diyl (**Scheme 51**).<sup>269</sup> The synthesis starts with 3,6-diphenyl-1,2,4,5-tetrazine **62**, which is reacted with the silirane **63** at  $125^\circ\text{C}$  for 3 days.<sup>272</sup> The reaction leads to the formation of silylene **64** in situ, which reacts with **62** under elimination of  $N_2$  to give diazasilol **65**. **65** can be isolated in 27% yield after purification by column chromatography. Reaction of **65** with PTAD (**50Ph**) or 4-methyl-1,2,4-triazoline-3,5-dione (**50Me**) at  $60^\circ\text{C}$  in threefold excess leads to the isolatable compounds **66Ph**, and **66Me** in yields of 53%, and 90%, respectively. During the reaction, the Diels-Alder product, azo compound **67**, could not be observed by NMR spectroscopy. Abe et al. therefore assumed that the denitrogenation of the azo compounds **67Ph** and **67Me** to the biradicals **68Ph** and **68Me** proceeds faster than their formation by the Diels-Alder reaction.

Quantum mechanical calculations for biradical formation at the UB3LYP/6-31G(d) level assume a stepwise elimination of nitrogen with an activation energy of  $22 \text{ kcal mol}^{-1}$ . Furthermore, neither the biradicals **68Ph** and **68Me**, nor the housane derivatives **68'Ph** and **68'Me** derived from the biradicals could be observed by NMR spectroscopy. Since no change in reactivity was observed under  $O_2$  atmosphere and no EPR signals were observed during the reaction, Abe et al. were able to show that **68'Ph** and **68'Me** are singlet biradicals, in accord with quantum mechanical calculations at the UB3LYP/6-31G(d) level.<sup>269</sup>

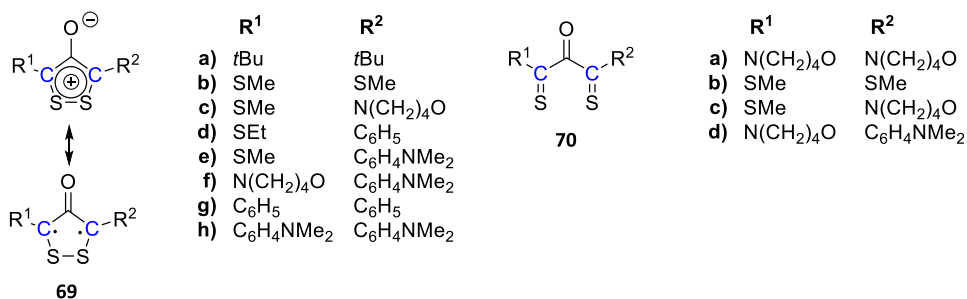
#### 1.04.3.3.1.3 Carbon-centered biradicals: 1,2-Dithiolylium-4-olates

Another substance class with biradicaloid compounds are the 1,2-dithiolylium-4-olates **69** (**Scheme 52**). The synthesis of the first 1,2-dithiolylium-4-olate, the 3,5-diphenyl-1,2-dithiolylium-4-olate **69g** was described in 1969 by Frese et al.<sup>273</sup> However, the authors assumed the presence of the open-chain form, the 1,3-thioxacetone (1,2-diphenyl-1,3-thioxacetone, **70**). An initial formulation of **69g** in its mesoionic, cyclic form was made the following year by Frese et al. as this better explained UV-vis and IR spectra.<sup>274</sup> That is, mesoionic 3,5-diphenyl-1,2-dithiolylium-4-olate was considered a valence isomer of 2-oxo-1,3-dithio-1,3-diphenyl-propane. Using single crystal X-ray structural analysis, the cyclic structure in the solid state was finally established.<sup>275,276</sup>

However, depending on substituents  $R^1$  and  $R^2$ , the open-chain 1,3-thioxacetone **70** rather than the cyclic species, 1,2-dithiolylium-4-olate **69**, can also be stabilized (**Scheme 52**).<sup>276–284</sup> Experimental and theoretical studies on the valence isomeric structure types **69** and **70** have shown that the cyclic biradical structure **69** is preferred by acceptor substituents (and to a lesser extent by phenyl groups), while the acyclic species **70** is energetically preferred by donor substituents.<sup>278</sup> The open-shell singlet biradical nature of the 1,2-dithiolylium-4-olates was studied and established by Fabian et al. for the phenyl-substituted system **69g** and the



**Scheme 51** Preparation and reactivity of in situ generated 1,2-diaza-4-silacyclopentane-3,5-diyls **68Ph** and **68Me**.



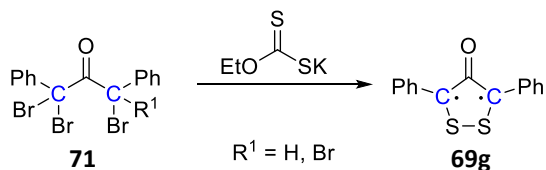
**Scheme 52** Literature known 1,2-dithiolium-4-olates **69**, which possess some biradical character, and 1,3-thioxacetones **70**.

*para*-dimethylaminophenyl-substituted system **69h** using quantum mechanical calculations.<sup>48</sup> Thus, a singlet-triplet splitting energy  $\Delta E_{\text{ST}}$  of 0.88 eV could be calculated in the case of **69g** and of 0.87 eV for **69h** at the B3LYP/6-31G\* level. However, for both systems an expectation value  $\langle S^2 \rangle = 0.0$  was calculated for the  $S^2$  operator at the UB3LYP/6-31G\* level, indicating that the biradical character is small to moderate at most (cf. Section 1.04.2.10). Furthermore, an antiaromatic character in the center of the molecules was calculated with a NICS(0) value of about +10 ppm, in which the authors see a further indication of the biradical character of the compounds. The authors conclude that the compounds have a low biradical character, but this has not been further quantified. Likewise, the authors do not comment on the influence of substituents  $R^1$  and  $R^2$  on the biradical character of 1,2-dithiolium-4-olates **69**.<sup>48</sup>

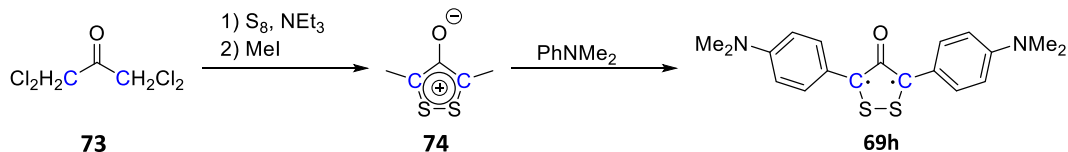
Interestingly, biradicals of the type **69** are very stable. It is remarkable that despite the biradical character present, only a low reactivity of e.g. **69g** towards oxygen was observed.<sup>273</sup> Studies on reactions with alkynes were carried out by White et al. leading to different classes of substances that were obtained as products depending on the alkyne.<sup>275</sup> Preparatively, 1,2-dithiolium-4-olates **69** are accessible via a variety of synthetic routes summarized in the *Science of Synthesis* book series.<sup>285</sup> To give one example, **69g** can be prepared via the reaction of 1,1,3,3-tetrabromo-1,3-diphenylacetone<sup>273,274</sup> (**71Br**) or 1,1,3-tribromo-1,3-diphenylacetone<sup>275</sup> (**72H**) with potassium *O*-ethylthiocarbonate in ethanol at 50–60 °C (Scheme 53). The products **69** can be isolated in yields of 26–50%. It should be noted that White et al. doubt on the basis of experimental data that 1,1,3,3-tetrabromo-1,3-diphenylacetone was really used in the synthesis described by Frese et al.<sup>275</sup> Synthesis of biradical **69h** starts with 1,3-dichloropropane-2-one **73**, which is thiolated in DMF at 0 °C in the presence of triethylamine and then alkylated with methyl iodide (Scheme 54).<sup>278</sup> The resulting 3,5-bis(methylthio)-1,2-dithiolium-4-olate **74** is then converted to the target product with *N,N*-dimethylaniline in boiling acetic acid with 2 eq. of pyridine.<sup>284</sup> The product **69h** can be isolated in 18% yield.

### 1.04.3.3.2 Hetero-cyclopentane-1,3-diyls with radical centers on elements of group 15

Five-membered biradicals with radical centers at atoms of the 15th group were obtained by serendipity when investigating the reaction behavior of pnictogen-centered cyclobutane-1,3-diyl (**22**) with unsaturated compounds (Scheme 38). While the reaction with alkynes and nitriles, for example, leads to bridging of the radical centers (Scheme 35; compound **23**), an insertion reaction was observed in the reaction with carbon monoxide and the isovalence-electronic isonitriles, which in some cases leads to the formation of room-temperature-stable five-membered biradicals as shown by us (Scheme 38, compound **29**).<sup>21</sup>



**Scheme 53** Synthesis of **69g** starting from 1,1,3,3-tetrabromo-1,3-diphenylacetone **71Br** or 1,1,3-tribromo-1,3-diphenylacetone **71H**.<sup>226,227</sup>



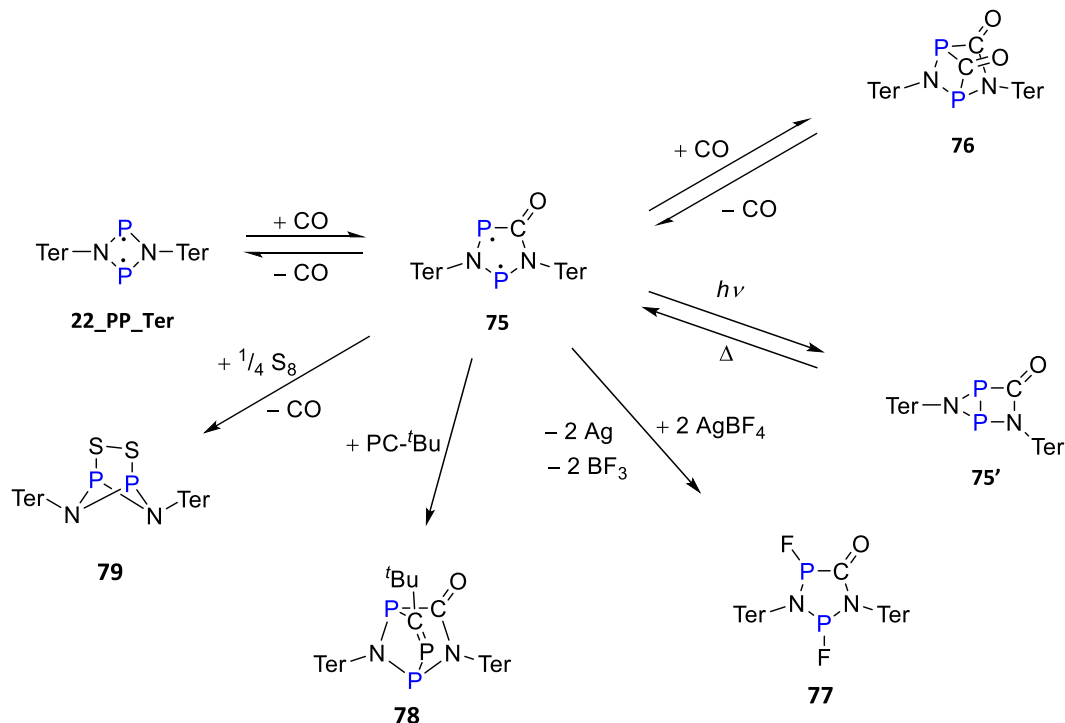
**Scheme 54** Synthesis of **69h**.

#### 1.04.3.3.2.1 Phosphorus-centered heterocyclopentane-1,3-diyls - Generated by CO insertion

The reactivity towards carbon monoxide was investigated with the cyclo-1,3-diphospha-2,4-diazane-1,3-diyl [ $\text{P}(\mu\text{-N}(\text{Ter})_2)_2\text{P}$ ] (**22\_PP\_Ter**, Ter = terphenyl = 2,6-bis(2,4,6-trimethylphenyl)-phenyl).<sup>210</sup> Carbon monoxide reacts completely within 48 h (60 bar, RT) in benzene to give the insertion product **75** derived from cyclopentane-1,3-diyl (**Scheme 55**). Biradical **75** can be obtained with 80% yield in the form of red crystals. The same reaction already takes place at 1 bar CO pressure, but here only a 75% reaction conversion could be observed by  $^{31}\text{P}$  NMR spectroscopy after 24 h reaction time. Single crystal X-ray diffraction revealed a planar  $\text{P}_2\text{N}_2\text{C}$  heterocycle with an exocyclic CO bond. Interestingly, under light the crystal slowly decomposed, which was studied further. UV-vis studies revealed the formation of a housane type species **75'** upon irradiation in accord with quantum mechanical calculations at the PBE/6-31G(d,p) level. A biradical character  $\beta = 22\%$  was calculated for biradical **75** using CASSCF(2,2) calculations according to Xantheas et al.<sup>46</sup>

Biradical **75** exhibits a diverse reaction behavior, which is summarized in **Scheme 55**. For example, the reaction of **75** with CO gives the formal addition product **76** that was only observed as a by-product in the  $^{31}\text{P}$  NMR spectra, but it decomposes rapidly to **75** and CO when the CO pressure drops so that isolation has not yet been possible.<sup>210</sup>

As already mentioned above, a “decomposition” of the biradical under light was observed at very low temperatures ( $-100^\circ\text{C}$ ) on the diffractometer. This led to a detailed investigation, as a result of which it was found that biradical **75** behaves like a molecular



**Scheme 55** Synthesis and reactivity of **75**.

switch (see Section 1.04.4). An intramolecular reaction can be observed when 75 is irradiated with light affording housane 75'. Under decolorisation of the reaction solution, the housane-type isomer 75' with a transannular P–P bond is formed, which reacts back thermally yielding the red-colored biradical 75 again. The reaction can be traced easily by  $^{31}\text{P}$  NMR spectroscopy. The initial assumption of decomposition of biradical 75 under irradiation was therefore not correct, but only showed the molecular switching under the influence of light. Calculations on the structure at the PBE/6-31G(d,p) level show that the bond formation significantly shortens the P–P distance within the five-membered ring of 75', which is now in the range of a typical P–P single bond, and leads to a bending of the planar ring along the P–P bond axis. However, housane species 75' could not be isolated.<sup>210</sup> The reaction of 75 with two equivalents of silver tetrafluoroborate leads to 77, which is accompanied by the loss of the biradical character, and the fluorination of the two P atoms (Scheme 55). Furthermore, elemental silver and gaseous trifluoro borane is formed. Since the two P atoms in 75 are prochiral, several isomers of 77 are conceivable, three of which could be detected by  $^{31}\text{P}$  NMR spectroscopy. Structural evidence was obtained for one of the isomers by single-crystal X-ray diffraction.<sup>210</sup> As depicted in Scheme 55, the reaction of 75 with *tert*-butylphosphaalkyne,  $^t\text{Bu-PC}$ , selectively leads to 78. Only one isomer with respect to the connectivity of the bridge was found by an X-ray structure analysis.<sup>210</sup> Unlike the reactions of 75 presented so far, the reaction with elemental sulfur results in the elimination of CO in the course of the reaction.<sup>210</sup> The resulting  $\text{S}_2$ -bridged product 79 can also be obtained by the direct reaction of 22\_PP\_Ter with elemental sulfur.<sup>146</sup>

#### 1.04.3.3.2.2 Pnictogen-centered heterocyclopentane-1,3-diyls - Generated by isonitrile insertion

Isonitriles, R-NC, that are isovalent to carbon monoxide show a similar reaction behavior, which, however, is strongly dependent on the type of the R-NC species (Scheme 56). Still, this is precisely the advantage of isonitriles over CO, since the former can be modified both sterically and electronically via the R substituent.

With the terphenyl-substituted system  $[\text{P}(\mu\text{-N}^i\text{Ter})]_2$  (22a), it could be shown that the steric demand of the substituent  $\text{R}^2$  on the isonitrile must match the steric demand of the system in order to achieve a selective insertion. For example, no reaction could be observed in the reaction of 22a with the sterically very demanding terphenyl isonitrile, Ter-NC. The sterically less demanding 2,6-dimethylphenylisonitrile (Dmp-NC) selectively inserts with the carbon atom into the phosphorus-nitrogen bond to give the intensely blue colored compound 29a. The reaction of the relatively small  $^t\text{Bu-NC}$  first leads to the insertion into the P–N bond to the blue-green insertion product 29b. Moreover, the addition of another equivalent of  $^t\text{Bu-NC}$  to the two phosphorus atoms takes place to form 30a. The reactions are equilibrium reactions. By using a large excess of  $^t\text{Bu-NC}$ , 30a can be isolated in the form of colorless crystals from a green reaction solution in benzene. However, re-dissolving the colorless crystals again leads to a green solution in which both 29b and 30a were detected by  $^{31}\text{P}$  NMR spectroscopy and even 22a at temperatures above 50 °C. The analogous equilibrium was detected upon insertion of  $\text{Me}_3\text{Si-NC}$  yielding 22a, the simple insertion product 29c, and the bridged derivative 30b.<sup>286</sup>

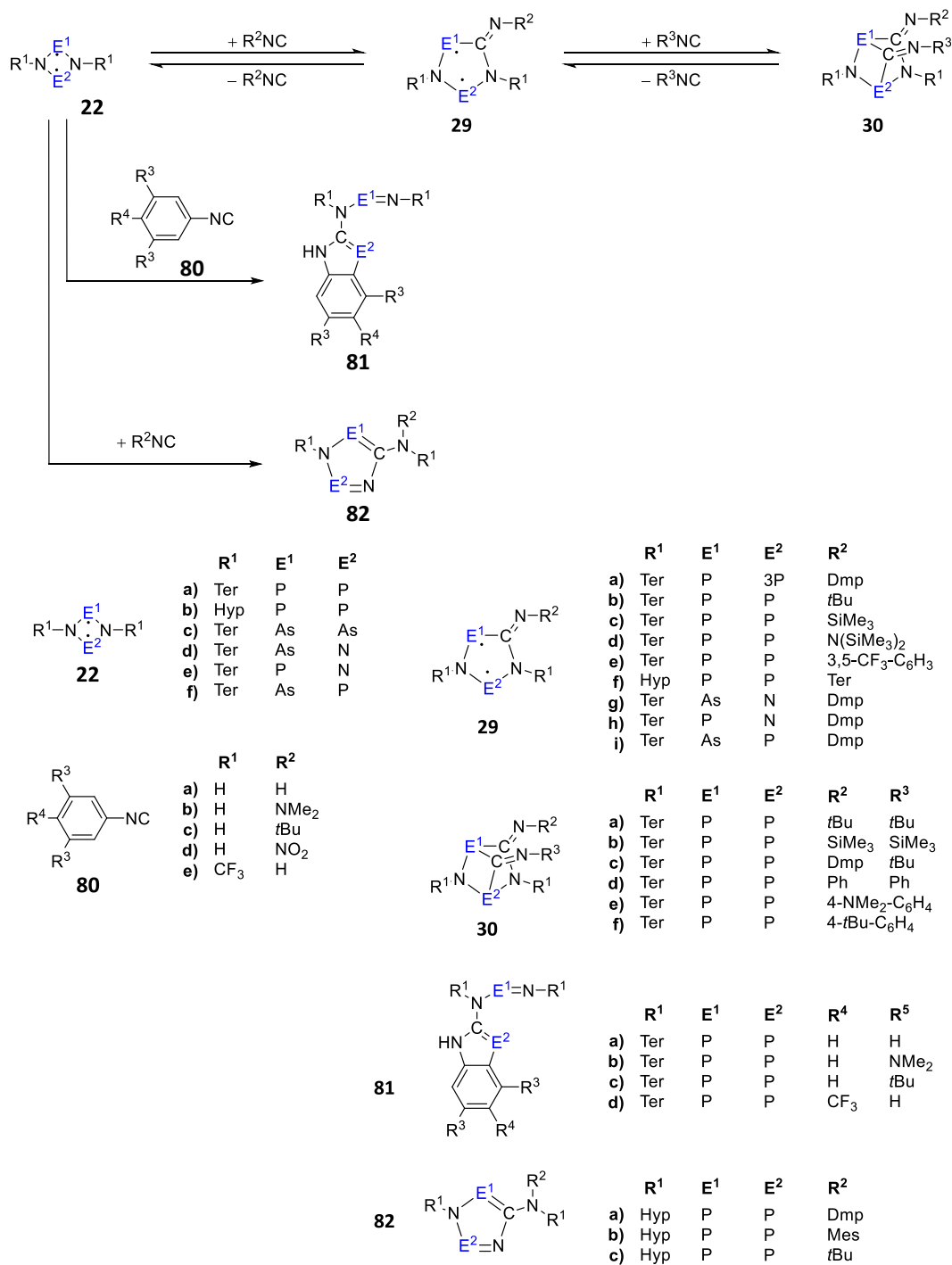
Another factor influencing the equilibrium and product distribution is the stability of the isonitrile. According to  $^{31}\text{P}$  NMR spectroscopic studies, the use of  $(\text{SiMe}_3)_2\text{N-NC}$  led to a large number of products among which the insertion product 29d could only be identified as a by-product.<sup>211</sup>

Further studies were concerned with the reactivity of 22a towards various phenyl isonitriles (80a-e), which, however, do not have substituents in the 2- and 6-position (Scheme 56). The electron-rich isonitriles phenyl-isonitrile (Ph-NC) 80a, *para-N,N*-dimethylaminophenyl-isonitrile 80b, *para-tert*-butylphenyl-isonitrile 80c are activated by equimolar reaction with 22a in the *ortho*-position to the isonitrile function, resulting in the formation of the phospho-indole-derived structures 81a-c. In the case of *para-N,N*-dimethylaminophenyl-isonitrile, crystals could be isolated from which the structure could be clarified beyond doubt by means of single-crystal X-ray diffraction. Interestingly, compounds of the type 30d-f could be detected when the isonitriles were used in excess. Here, the derivative of *para-tert*-butylphenyl-isonitrile 30f could be crystallized. When *para*-nitrophenyl-isonitrile 80d was reacted with  $[\text{P}(\mu\text{-N}^i\text{Ter})]_2$  (22a), a hitherto unknown product formation occurred, which, according to the  $^{31}\text{P}$  NMR data, indicates an oxidized phosphorus species, which could neither be further characterized nor isolated. The reaction of the electron-deficient 3,5-dis(trifluoromethyl)phenyl-isonitrile 80e with  $[\text{P}(\mu\text{-N}^i\text{Ter})]_2$  (22a) initially led to the formation of a mixture in which the heterocyclopentane-1,3-diyl 29e could also be identified by  $^{31}\text{P}$  NMR spectroscopy. Within 48 h, however, the formation of the phospho-indane-like compound 81d also occurred here.<sup>286</sup>

The reaction behavior between the biradical  $[\text{P}(\mu\text{-NR})]_2$  and the isonitriles is not only dependent on the isonitriles but also on the substituent at the nitrogen atom. For example, the hypersilyl-substituted biradical  $[\text{P}(\mu\text{-NHyp})]_2$  (22b, hypersilyl = Hyp = tris(trimethylsilyl)silyl) showed a different reactivity with some isonitriles than the terphenyl-substituted system.<sup>212</sup> In contrast to  $[\text{P}(\mu\text{-N}^i\text{Ter})]_2$ , a reaction of  $[\text{P}(\mu\text{-NHyp})]_2$  with terphenyl-isonitrile Ter-NC could be observed, leading to heterocyclopentane-1,3-diyl 29f. However, isolation failed. When reacting  $[\text{P}(\mu\text{-NHyp})]_2$  with the sterically less demanding isonitriles  $^t\text{Bu-NC}$ , Dmp-NC and Mes-NC (Mes = 2,4,6-trimethylphenyl), heterocyclopentadienes 82a-b are obtained. The latter are formed by migration of the hypersilyl substituent to the nitrogen atom of the isonitrile (Scheme 56). According to our computations, the dienes are the thermodynamically favored products and are best understood as closed-shell species ( $\beta = 10\%$ , CASSCF(8,6)/def2-TZVP).<sup>212</sup>

Another approach to obtain new five-membered biradicals 29 (by insertion of isonitriles starting from the four-membered biradical 22) is to vary the pnictogens within the starting material: Thus, using four-membered biradicals with two identical heavier pnictogens such as 22c<sup>144,201</sup> and with two different pnictogens (22d-f, cf. Section 1.04.3.2.3)<sup>195,199,200</sup> as starting materials, we attempted to synthesize the corresponding five-membered biradicals 29 by insertion of Dmp-NC.<sup>196</sup> The system with two arsenic atoms 22c did not react to form the desired product. Likewise, no insertion reaction with Dmp-NC was observed for the mixed-



**Scheme 56** Reactivity of **22** and **29** towards isonitriles.

centered biradicals with antimony and nitrogen, and with antimony and phosphorus.<sup>196</sup> However, for the lighter triazene derivative **22d** with arsenic and nitrogen as biradical centers, an insertion reaction with Dmp-NC to give **29g** was observed. The product could be isolated in the form of red crystals. Interestingly, X-ray structure analysis revealed two different isomers within the unit cell. A mixture of the expected five-membered biradical **29g** and the corresponding housane structure **29'g** was found. This means that two molecular structures, namely **29g** and **29'g**, were obtained with one measurement on one crystal.<sup>196</sup>

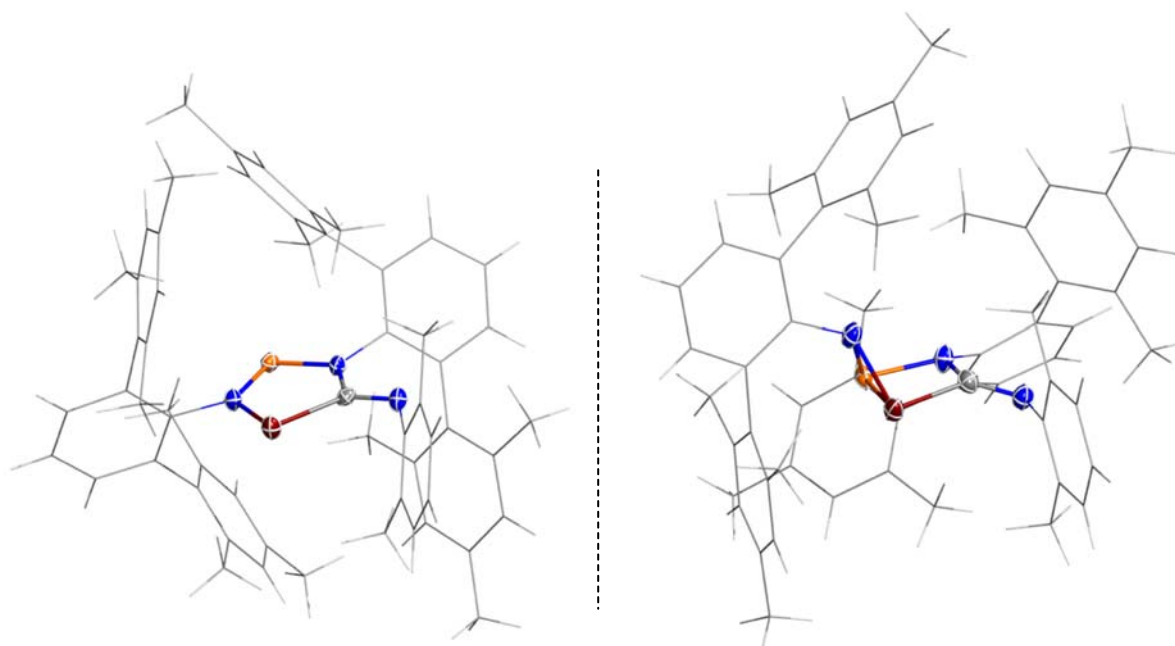
In the reaction of Dmp-NC with the phosphorus- and nitrogen-centered biradical **22e**, the analogous reaction to **29h** was observed. Here, too, structural elucidation by means of single-crystal X-ray structural analyzes was successful, but no partial housane (**29'h**) formation was observed. The same reaction behavior was found for the arsenic- and phosphorus-centered biradical **22f** in

which a selective insertion into the arsenic-phosphorus bond could be observed with the formation of the five-membered biradical **29i**.<sup>196</sup> Here, the isomerisation in the solid state could be investigated by single crystal X-ray structural analysis. In a simple measurement of a crystal, two isomers could be found in a disordered arrangement. The structure is dominated by the heterocyclopentane-1,3-diyl **29i**, which is present to 86%. The housane-like structure **29'i** was found as the second layer of the disorder (Fig. 17).

In all cases, the mixed-centered four-membered biradicals of type **22** (Scheme 56) reacted with the isonitrile to five-membered biradicals **29** in which the insertion of the carbon atom of the isonitrile takes place at the element-nitrogen bond of the heavier pnictogen of the two radical centers. An insertion into the other bond could not be observed. For all biradicals of type **29**, the calculated biradical characters and coefficients of the CASSCF wavefunction (with  $c_i \geq 0.1$ ) are listed in Table 6. These data show that the biradical character of the biradicals **29** ranges between 10 and 33%. Analogous to the five-membered biradical **75**, which is obtained by insertion of CO, the structural isomerism between the heterocyclopentane-1,3-diyl **29** and the housane-like, transannular bonded structure **29'** could also be observed.

When the crystal of **29i** was exposed to light for a longer time on the X-ray diffractometer, a reversal of the ratio between the two isomers was observed. Thus, after 12 h of irradiation, 95% of the crystal exhibited the housane species **29'i**.<sup>196</sup> During the formation of the housane derivative, a structural change occurs within the molecules. The central five-membered ring angles along the phosphorus-arsenic axis and the phosphorus-arsenic distance decreases, forming finally a covalent bond. The structural change leads only to minor changes within the molecular packing, so that only minor stresses occur within the crystal and it remains intact as a single crystal during the transformation and X-ray measurement. In solution, only the heterocyclopentane-1,3-diyl **29i** could be detected by <sup>31</sup>P NMR spectroscopy so far. However, recent studies show that for some biradicals of type **29**, the housane **29'** can be detected by NMR spectroscopy after irradiation with low-energy radiation, such as light in the visible range. More detailed studies on the isomerism between **29** and **29'** were carried out by us using the phosphorus-centered system **29a**.<sup>287</sup> The heterocyclopentane-1,3-diyl **29a** can be isolated in good yields in the form of blue crystals. Using UV-vis spectroscopy and quantum mechanical calculations, it was found that red light leads to a conversion of **29a** to **29a'** ( $\lambda_{\text{max}} = 643 \text{ nm}$ ). Irradiation leads to the formation of the colorless isomer **29a'**, which shows no absorption at 643 nm. After irradiation, a thermally induced reverse reaction occurs. This behavior is also called *molecular switching*, which we will examine in detail in Section 1.04.4. Unlike the arsenic/phosphorus-centered biradical **29i**, for biradical **29a** it was impossible to induce a transformation between the two isomers while maintaining an intact single crystal on the diffractometer. Accordingly, the transformation between the two isomers was accompanied by such large mechanic stress that the crystal split, as can be seen clearly in Fig. 18. Due to this internal stress in the crystal caused by light, the measurement of a complete data set of **29a** was only possible in complete darkness and revealed the planar biradical species. Attempts to crystallize the housane derivative, for example under light, failed.<sup>287</sup>

The reactivity of the heterocyclopentane-1,3-diyls synthesized by insertion of isonitriles was investigated in detail for a large number of molecules utilizing the terphenyl-substituted biradicals (Scheme 57).<sup>196,211</sup> The reaction of *tert*-butylphosphaalkyne with the phosphorus-centered biradicals **29a**<sup>211</sup> and **29b**<sup>211</sup> and the mixed, arsenic/phosphorus-centered derivative<sup>196</sup> **29i** lead to a selective bridging of the two radical centers, whereby bonds to the phosphorus atom and carbon atom of the phosphaalkyne



**Fig. 17** Molecular structures of biradical **29i** (left) and housane **29'i** (right) in the crystal obtained from one irradiated crystal. Color code: blue N, red As, orange P, and gray C.<sup>196</sup>

**Table 6** Computed biradical character of different heterocyclopentane-1,3-diyls.<sup>197</sup>

	<i>Ter</i> <sub>2</sub> <i>N</i> <sub>2</sub> <i>P</i> <sub>2</sub> <i>CO</i> ( <b>75</b> )	<i>Ter</i> <sub>2</sub> <i>N</i> <sub>2</sub> <i>P</i> <sub>2</sub> <i>CNDmp</i> ( <b>29a</b> )	<i>Ter</i> <sub>2</sub> <i>N</i> <sub>2</sub> <i>P</i> <sub>2</sub> <i>CNTBu</i> ( <b>29b</b> )	<i>Ter</i> <sub>2</sub> <i>N</i> <sub>2</sub> <i>P</i> <sub>2</sub> <i>CNN(SiMe<sub>3</sub>)<sub>2</sub></i> ( <b>29d</b> )
C <sub>1</sub>	0.92	0.94	0.93	0.93
C <sub>2</sub>	−0.35	−0.33	−0.34	−0.35
C <sub>3</sub>	−0.13		−0.10	
LUNO	0.25	0.23	0.25	0.25
β	0.25	0.22	0.24	0.24
	<i>Hyp</i> <sub>2</sub> <i>N</i> <sub>2</sub> <i>P</i> <sub>2</sub> <i>CNTer</i> ( <b>29f</b> )	<i>Ter</i> <sub>2</sub> <i>N</i> <sub>3</sub> <i>AsCNDmp</i> ( <b>29g</b> )	<i>Ter</i> <sub>2</sub> <i>N</i> <sub>3</sub> <i>PCNDmp</i> ( <b>29h</b> )	<i>Ter</i> <sub>2</sub> <i>N</i> <sub>2</sub> <i>PAsCNDmp</i> ( <b>29i</b> )
C <sub>1</sub>	0.95	0.96	0.95	0.91
C <sub>2</sub>	−0.33	−0.22	−0.26	−0.40
C <sub>3</sub>		−0.14	−0.15	
LUNO	*	0.10	0.15	0.33
β	29	0.10	0.14	0.33

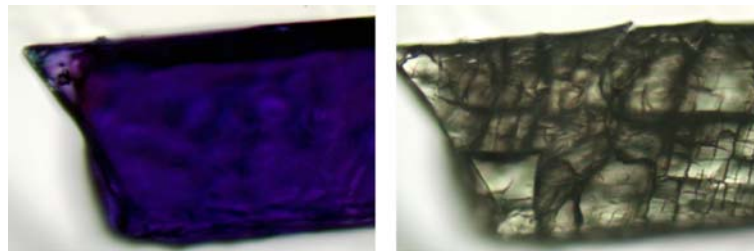
C<sub>1,2,3</sub>: coefficients of the wave function, listed from |c<sub>i</sub>| ≥ 0.1; LUNO: Occupation number of the LUNO according to CASSCF calculation; \*: not listed in the reference.

are formed. In the addition reaction to products **83a**, **83b** and **83c**, complete selectivity was achieved in all cases, with the substituent on the phosphalkyne always localized on the side of the inserted isonitrile. The selectivity could be proven by <sup>31</sup>P NMR spectroscopic data. It was also possible to isolate all compounds in yields between 52% and 70% and to describe the solid state structure by single crystal X-ray diffraction. A reversible loss of the phosphalkyne by prolonged irradiation with light of different wavelengths could not be detected in investigations on **83b**.<sup>288</sup> This speaks for a stronger binding of the phosphalkyne compared to the bridging isonitriles. No reaction was observed when the arsenic/nitrogen-centered derivative **29g** and the phosphorus/nitrogen-centered derivative **29h** was reacted with <sup>t</sup>Bu-PC. This agrees with the comparatively low biradical character of the two compounds (Table 6).

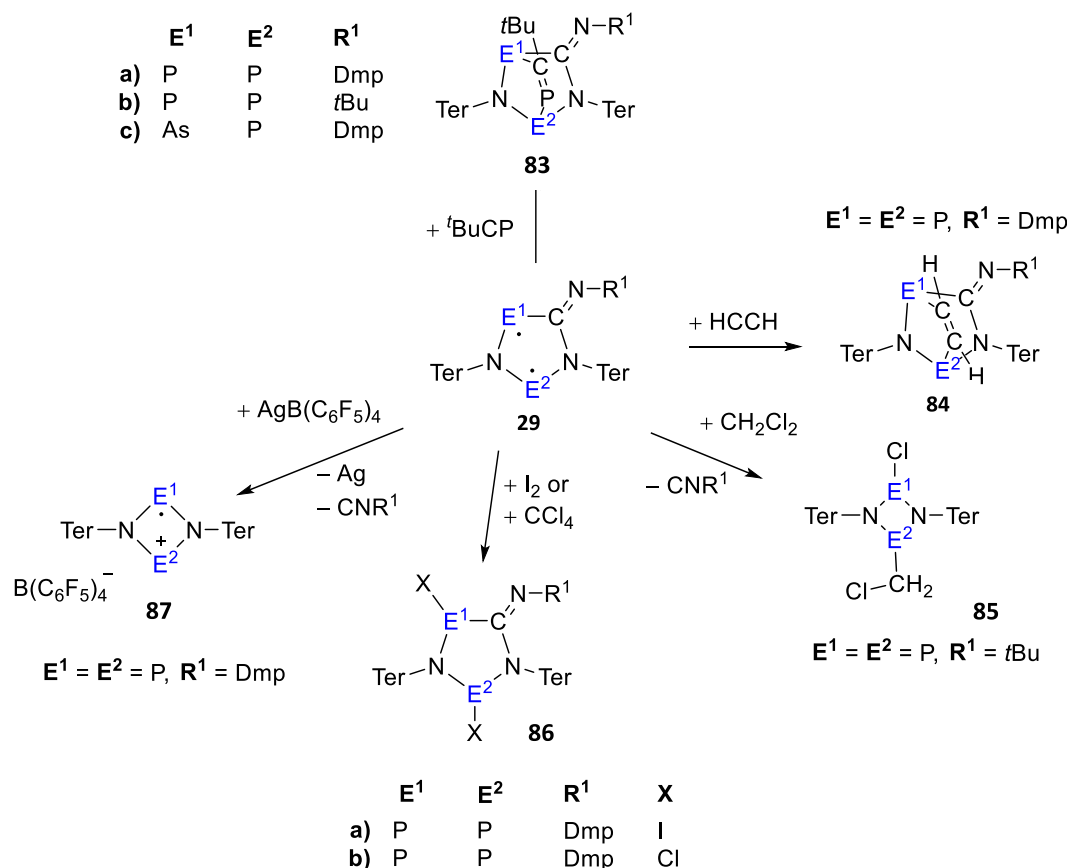
For acetylene, which also contains a triple bond, a similar reactivity towards **29a** was observed as for <sup>t</sup>Bu-NC. Thus, activation of the triple bond occurs with bond formation with the two phosphorus atoms. The product **84** resulting from the reaction could be fully characterized. Whether the addition is reversible as in the case of isonitriles or irreversible as in the case of phosphorus atoms has not been investigated in detail.<sup>211</sup>

By reacting **29b** with dichloromethane, one of the two C–Cl bonds could be activated, forming **85** with elimination of the isonitrile. The same reaction product can be observed when **22a** is reacted with dichloromethane.<sup>211</sup> Halogenation of the phosphorus-centered biradical **29a** was possible with elemental iodine or carbon tetrachloride to form compounds **86a** and **86b**. However, the reaction products could not be isolated, but only detected by mass spectrometry and NMR spectroscopy.<sup>211</sup> The reaction of the one-electron oxidant Ag[B(C<sub>6</sub>F<sub>5</sub>)<sub>4</sub>] with **29a** leads to the formation of the radical cation **87** under elimination of the isonitrile.<sup>211</sup> The same radical cation is generated by the direct reaction of Ag[B(C<sub>6</sub>F<sub>5</sub>)<sub>4</sub>] with **22a**.<sup>218</sup>

Moreover, it was possible to show that a diisonitrile **88** can insert into two four-membered heterocyclobutane-1,3-diyls such as **22a** (Scheme 58) affording tetraradical **89**. Very similar NMR spectroscopic data to **29a** suggest that the two biradical units do not interact significantly with each other, which is not surprising as both phenyl rings are linked by a methylene group. Due to the hindered rotation around the CN double bond, three different isomers for **89** are conceivable, of which only two could be detected in solution. Photoisomerisation could also be observed for **89** after irradiation. In addition to two isomers of the double housane species **89'**, the isomer in which only housane formation took place, could also be detected in the <sup>31</sup>P NMR studies. The tetraradical **89** reacts analogously to the biradicals of type **29** with *tert*-butylphosphalkyne to **90**. Here, an addition to the two biradical centers occurs (Scheme 58). By means of NMR spectroscopy, three different isomers could be detected. Whether the addition is reversible has not yet been investigated.<sup>211</sup>



**Fig. 18** Left: Crystal of **29a** before irradiation with red light; right: the same crystal shortly after irradiation where the blue **29a** was converted to the colorless housane isomer **29'a**.<sup>287</sup>



**Scheme 57** Reactivity of heterocyclopentane-1,3-diyl derivatives **29**.

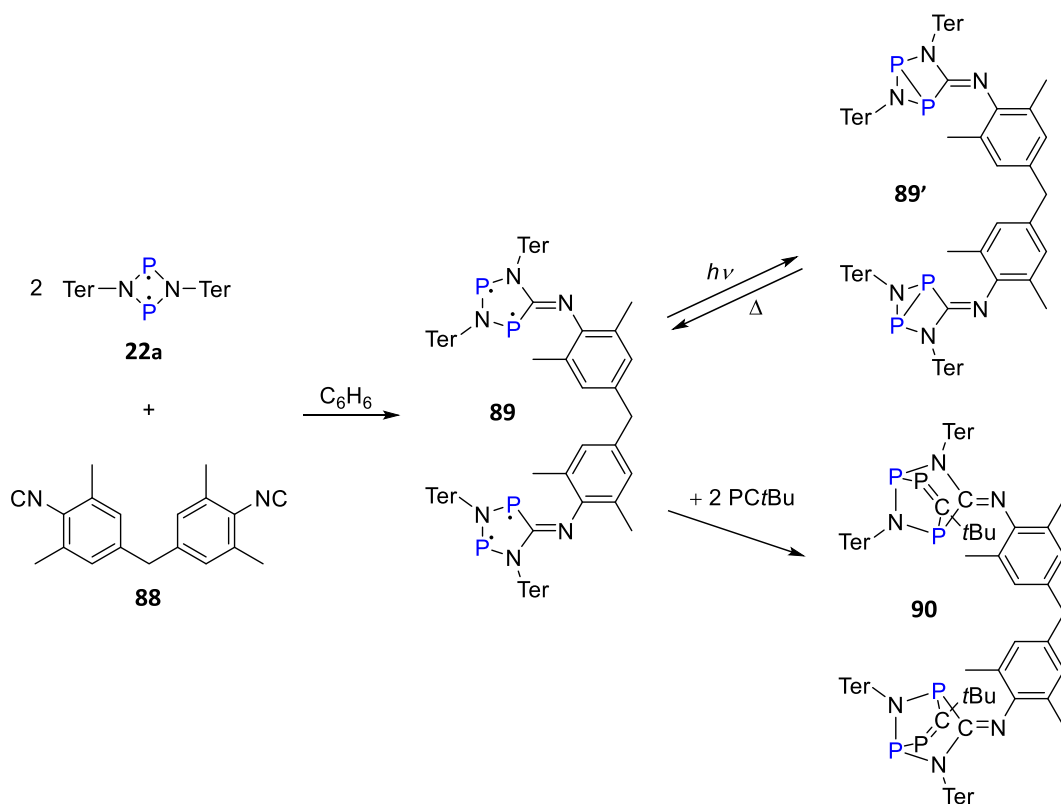
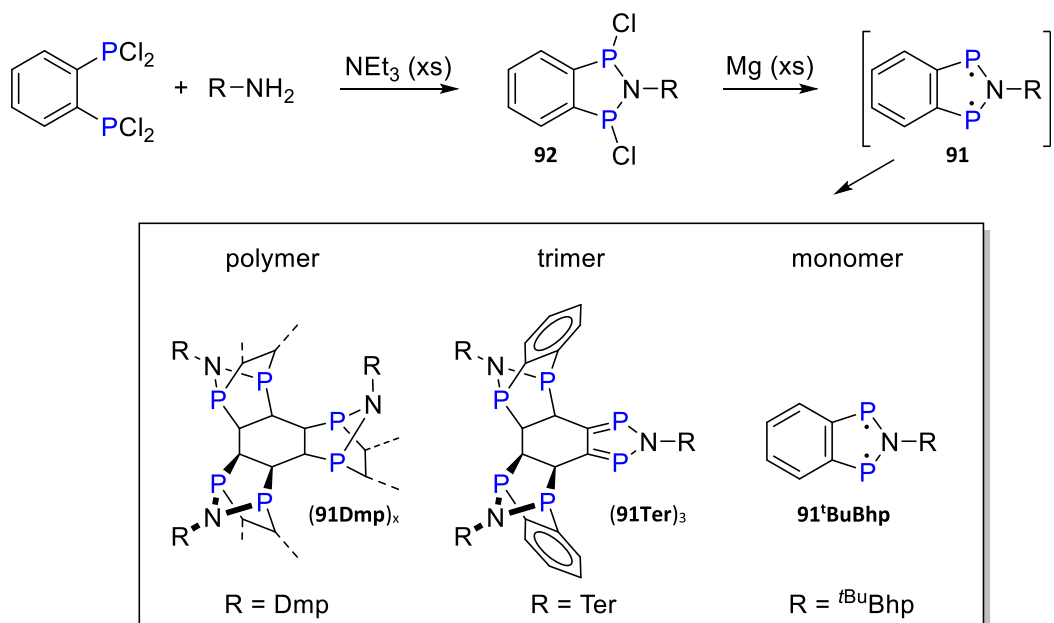
#### 1.04.3.3.2.3 Phosphorus-centered benzo-fused cyclopentane-1,3-diyls

Heterocyclopentane-1,3-diyl derivatives of type **29** often eliminate the isonitrile moiety, R-NC, upon activation of small molecules, reforming the corresponding heterocyclobutane-1,3-diyl (**22**), which was used to synthesize **29**. Therefore, we developed 5-membered phosphorus-centered biradicals that are significantly more stable with regard to an elimination reaction. For this reason, the related benzo-fused cyclopentane-1,3-diyls (i.e., hetero-indanediyls **91**, **Scheme 59**), which also provide aromatic stabilization, were introduced.<sup>289</sup>

The synthesis of biradical **91** was carried out in two steps (**Scheme 59**).<sup>289</sup> In the first step, a suitable precursor (**92**) for the biradical was synthesized: In analogy to the synthesis of **22** (**Scheme 34**), chlorinated azadiphospha-indanes (**92**) were prepared by reacting primary amines with 1,2-bis(dichlorophosphino)benzene under HCl elimination. For different substituents (Dmp, Ter, <sup>t</sup>BuBhp), the *cis* isomer of **92** (*cis* with respect to the Cl atoms) was obtained (<sup>31</sup>P NMR:  $\delta = 147\text{--}149$  ppm). The synthesis of the hetero-indanediyls **91R** (R = Dmp, Ter, <sup>t</sup>BuBhp; <sup>t</sup>BuBhp = 2,6-bis(benzhydryl)-4-*tert*-butylphenyl) was achieved by reduction of **92R** with elemental magnesium. In the course of the reaction, the colorless solutions turned orange, indicating the formation of the desired product. This could be traced by <sup>31</sup>P NMR spectroscopy; all hetero-indanediyls **91R** could be identified by a characteristic singlet resonance ( $\delta = 280\text{--}285$  ppm). However, depending on the steric demand of R, different subsequent reactions were observed (**Scheme 59**, bottom). The biradical **91Dmp** was completely converted to an insoluble red polymer within 1 day, as demonstrated by <sup>31</sup>P NMR spectroscopy. In the case of **91Ter**, selective trimerization to (**91Ter**)<sub>3</sub> was observed. (**91Ter**)<sub>3</sub> is formed by activation of the condensed benzene ring of **91Ter** by two further equivalents of the monomeric biradical. This self-activation process can be regarded as a formal [2 + 2] addition reaction. The sterically most demanding derivative **91<sup>t</sup>BuBhp** is stable in benzene for several weeks, as verified by NMR spectroscopy. **91<sup>t</sup>BuBhp** is intensely yellow and shows absorption maxima at 407 and 424 nm in the UV-vis spectrum. The calculated biradical character (CASSCF(2,2)) of **91<sup>t</sup>BuBhp** is  $\beta = 18\%$ , while the LUNO occupancy amounts to  $n_{\text{LUNO}} = 0.21$  (CASSCF(10,9)/def2-TZVP). This is slightly lower compared to other biradicals such as **22** and **29** ( $\beta = 20\text{--}30\%$ ,  $n_{\text{LUNO}} = 0.2\text{--}0.3$ ). In contrast, the biradical character of (**91Ter**)<sub>3</sub> with 12% ( $n_{\text{LUNO}} = 0.12$ ) is significantly lower, so that it can be better described as diene.

#### 1.04.3.3.2.4 Phosphorus-carbon-centered heterocyclopentane-1,3-diyl

Lips et al. described the addition of phospho-alkyne PC-<sup>t</sup>Bu to an NHC-coordinated trisilacyclopropylidene, Si<sub>3</sub>Mes<sub>4</sub>NHC (**93**), resulting in the formation of a heavier analog (**94'**) of a bicyclo[2.1.0]pentane, a so-called housane.<sup>290</sup> The NHC used was 1,3-diisopropylimidazol-2-ylidene. In housane **94'**, the folding angle is 88.46(2)°, as expected for a housane. Upon irradiation or at

**Scheme 58** Synthesis and reactivity of tetradical **89**.**Scheme 59** Synthesis of differently substituted 2-aza-1,3-diphosphaindane-1,3-diyls **91**. Their stability depends on the sterical demand of the substituent R, as depicted in the box.<sup>289</sup>



temperatures above 60 °C, the housane isomerises to a formal cyclopentenyl anion analog, which can also be regarded as a compound with biradical character (94, Scheme 60). However, Lips et al. describe the bond as a 3c-4e  $\pi$  bond but do not comment on a possible biradical character. Nonetheless, if one looks at the HOMO (transannular antibonding) or the LUMO (transannular bonding, cf. Section 1.04.2), this corresponds exactly to the situation in typical cyclopentane-1,3-diyls such as 29, as discussed above.

#### 1.04.4 Applications of biradicals as molecular switches

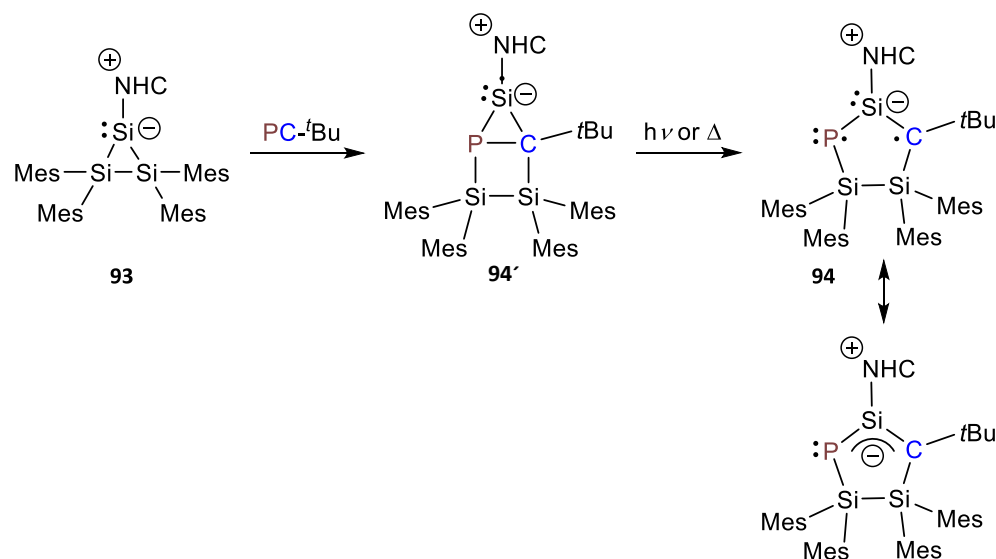
Due to their peculiar electronic structure, biradicals have various (potential) applications; for example, they may be applied in small-molecule activation (see Section 1.04.3), molecular electronics,<sup>291–294</sup> singlet fission,<sup>295–300</sup> non-linear optics,<sup>35,301–303</sup> or as molecular switches.<sup>164,212,264,270,287,303–313</sup>

The concept of **switchable biradicals** is generally that a molecule can exist in two different (meta)stable states, just as is the case for “normal” molecular switches.<sup>314–317</sup> However, the biradical character is often very sensitive towards even small structural changes, so it can effectively be varied by switching the molecule between different isomers. As the biradical character is the source of many of the interesting properties outlined above, these properties can also be modified through the switching behavior. For example, if the switchable biradical is light-activated, the biradical character can effectively be switched “on” and “off” by irradiation (i.e., an outside stimulus). This will then also influence the activation chemistry, non-linear optical properties etc.

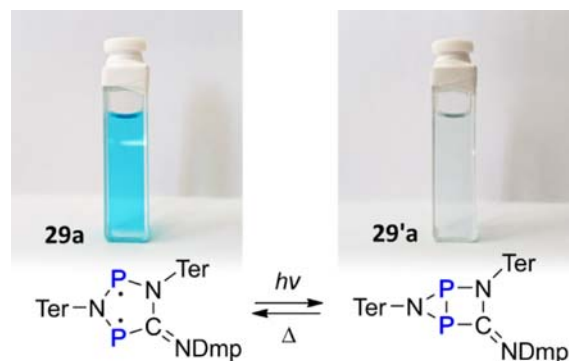
Regarding the cyclobutane-1,3-diyls and cyclopentane-1,3-diyls discussed in this article, the concept of switchable biradicals was demonstrated by us using hetero-cyclopentanediylys of type 29. As indicated in Section 1.04.3.3.2, these five-membered cyclic biradicals can be photoisomerized to housane-type species 29', which do not possess significant biradical character (Fig. 19). Thus, irradiation of biradical 29 effectively quenches the biradical nature of the compound. The housane 29' thermally reverts to the biradical isomer 29. This thermal reverse reaction was studied by variable temperature <sup>31</sup>P NMR spectroscopy,<sup>212,287,310</sup> revealing that the housane possesses a half-life of up to 1 h at ambient temperature, depending on the substituents ( $t_{1/2}$  for 29'a: 7 min, 29'b: 57 min, 29'f: 31 min).<sup>212,287</sup>

The isomerization between biradical 29 and housane isomer 29' can also be traced by UV-vis spectroscopy, as the biradical is intensely blue ( $\lambda_{\max}$  for 29a: 643 nm,<sup>287</sup> 29b: 663 nm,<sup>287</sup> 29c: 675 nm,<sup>286</sup> 29f: 595 nm,<sup>208</sup> 29i: 684 nm<sup>196</sup>), while the housane is colorless (Fig. 19). We studied the ultrafast dynamics of the photoisomerization of 29a using theoretical methods and transient absorption spectroscopy,<sup>311</sup> revealing that the photoisomerization proceeds via the first excited singlet state (Fig. 20). The excited molecules can transfer back to the ground state through a conical intersection without the emission of radiation. The conical intersection between the S<sub>1</sub> and S<sub>0</sub> surfaces is located in the vicinity of the thermal transition state between 29a and 29'a. Approx. 25% of the excited molecules isomerize to the housane isomer (quantum yield 24.6(8)%),<sup>287</sup> while the remaining 75% revert to the biradical isomer. The photoreaction is very fast (exponential time constant  $\tau = 210$  fs),<sup>311</sup> so the thermal reverse reaction does not play a role on this timescale. Thus, it is easily possible to fully convert the biradical 29a to the housane isomer 29'a.<sup>287</sup>

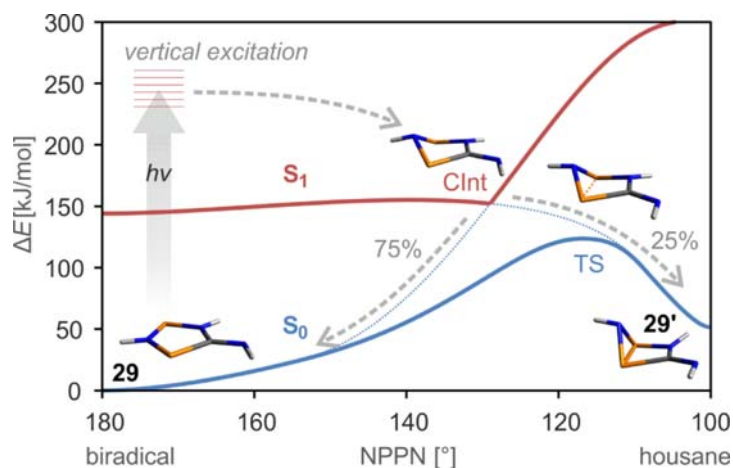
The switching between biradical and (closed-shell) housane isomer was exploited to influence the product formation in a thermal equilibrium reaction (Scheme 61).<sup>287,310</sup> Biradicals of type 29 can activate small molecules such as <sup>t</sup>BuNC (cf. Section 1.04.3.3.2), leading to the formation of addition products of type 30. Depending on the substituents at the biradical, this addition reaction is often an equilibrium reaction, i.e., both product 30 and starting material 29 can be identified in solution. If the biradical 29 is now switched to the housane isomer 29' by irradiation with red (or white) light, the activation chemistry is inhibited (or, to



Scheme 60 Synthesis of 94 and 94'.



**Fig. 19** Sample solution of biradical **29a** before (left) and after illumination (right) with red light. Adapted from Bresien, J.; Kröger-Badge, T.; Lochbrunner, S.; Michalik, D.; Müller, H.; Schulz, A.; Zander, E. A Chemical Reaction Controlled by Light-Activated Molecular Switches Based on Hetero-Cyclopentenediyls. *Chem. Sci.* **2019**, *10* (12), 3486–3493.

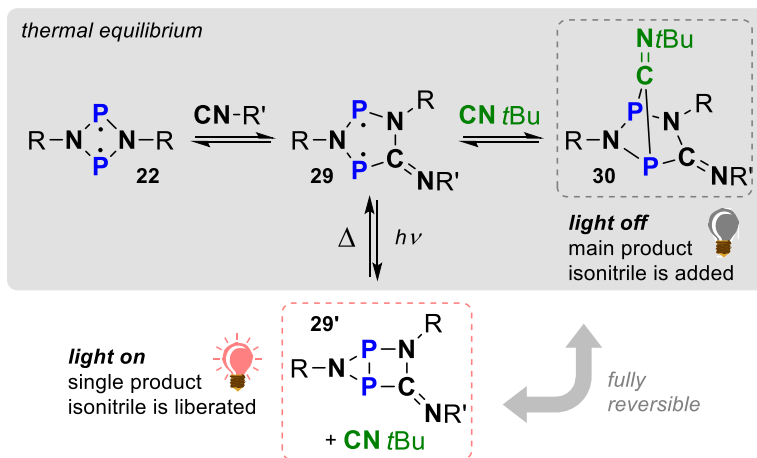


**Fig. 20** Minimum energy paths along the  $S_0$  and  $S_1$  potential energy surface (PES) of biradical **29a** (here a model system with H substituents). After excitation with red light, the excited state deactivates through a conical intersection (CInt), leading to formation of the housane **29'a** with a quantum yield of approx. 25%. The thermal reverse reaction of the housane to the biradical proceeds via a single transition state (TS) in a first-order reaction. Adapted from Völzer, T.; Beer, H.; Schulz, A.; Lochbrunner, S.; Bresien, J. Photoisomerization of a Phosphorus-Based Biradicaloid: Ultrafast Dynamics Through a Conical Intersection. *Phys. Chem. Chem. Phys.* **2021**, *23* (12), 7434–7441.

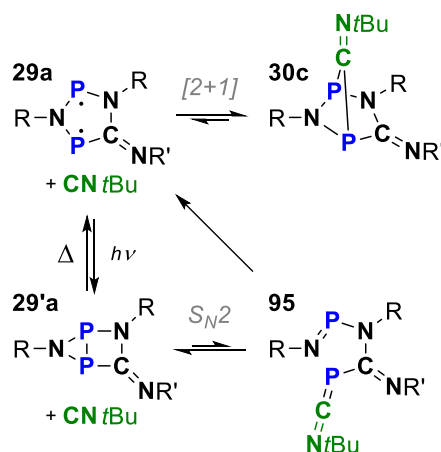
put it in different terms, the biradical **29** is removed from the equilibrium reaction), resulting in quantitative dissociation of the adduct **30**. Once the light is switched off again, the thermal equilibrium is restored, and the adduct **30** is again the main product of the reaction. This switching can be repeated several times without detectable degradation of the mixture.<sup>287,310</sup>

Lastly, it could also be shown that the isonitrile can catalyze the thermal reverse reaction. In the presence of an excess of <sup>t</sup>BuNC, the thermal isomerization of the housane **29'a** to the biradical **29a** is accelerated. The housane **29'a** forms a transient adduct with the isonitrile (95, **Scheme 62**), which quickly decays to the biradical **29a** and free <sup>t</sup>BuNC. The formal addition of the isonitrile to the housane proceeds via an  $S_N2$ -type substitution of the isonitrile at *one* P atom (one P–N bond is broken in the process), as opposed to the reactivity of the biradical, which reacts in a concerted reaction mechanism with *both* P atoms. This observation demonstrates that (i) the thermal reverse reaction can be influenced chemically, and (ii) that switching the biradical character “on” and “off” can open completely different reaction channels using the same reagent.

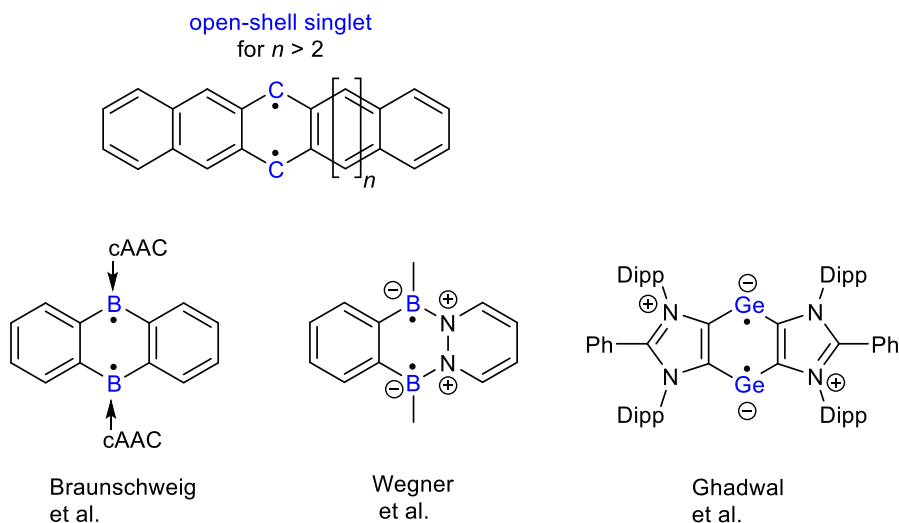
As discussed in **Section 1.04.3.2**, there are also examples of hetero-cyclobutane-1,3-diyls that can be thermally isomerized to a closed-shell butterfly structure. This further underlines the potential of the concept of switchable biradicals. In the future, we expect that more applications of switchable biradicals will be found, for example in the field of molecular electronics or in (metal-free) catalysis.



**Scheme 61** The activation chemistry of biradical **29** can be switched “on” and “off.” This effect has been studied by time-dependent and variable-temperature NMR spectroscopy for **29a** ( $R = \text{Ter}$ ,  $R' = \text{Dmp}$ ) and **29b** ( $R = \text{Ter}$ ,  $R' = {}^t\text{Bu}$ ).<sup>287,310</sup>



**Scheme 62** The two isomers of **29a** react differently with  ${}^t\text{BuNC}$ : The biradical **29a** undergoes a formal [2 + 1] cycloaddition reaction, while the housane **29'a** reacts in an  $S_N2$ -type substitution.<sup>310</sup>



**Scheme 63** Examples of biradicals as part of a six-membered heterocycle containing main group elements (cAAC = cyclic alkylaminocarbene, Dipp = 2,6- $i\text{Pr}_2\text{C}_6\text{H}_3$ ).<sup>333–335,341</sup>

### 1.04.5 Outlook: Beyond four and five-membered heterocyclic biradicals

The biradical chemistry of the main group elements has been enriched by many new molecules in the last decade.<sup>318–332</sup> Besides the cyclobutane-1,3-diyls and cyclopentane-1,3-diyls discussed in this book chapter, there are of course also a large number of biradicals as part of a six-membered heterocycle or even with a cage structure, which are not considered here. A few examples from recent research are shown in **Scheme 63**.<sup>324,333–335</sup>

Still a very interesting strategy for producing new biradicals is the incorporation of main group elements into organic heterocycles, e.g., into so-called acenes, which have been investigated intensively in recent years.<sup>333,336–392</sup> Acenes are an important subclass of polycyclic aromatic hydrocarbons that consist of linearly fused benzene rings (**Scheme 63**).<sup>17,337,340,348,351,363,374,375,391–395</sup> Theoretical studies predicted that (oligo)-acenes from hexacene ( $n = 2$ ) to decacene ( $n = 6$ ) no longer have closed-shell configurations, but open-shell singlet biradical ground states.<sup>17,20,295,329,333,334,396,397</sup> The reason for this is the decreasing HOMO-LUMO gap in these systems, which in turn leads to a smaller singlet-triplet energy gap.<sup>341,343</sup> Acenes larger than dodecacene therefore have polyradical character with an open-shell singlet ground state.<sup>353,355,389</sup> Therefore, as the number of condensed benzene rings increases, the acenes become p-type organic semiconductors, which makes them very relevant for organic electronic applications<sup>336,337,345,354,356,362,373,375</sup> such as field-effect transistors,<sup>374,378</sup> light-emitting diodes,<sup>365,371</sup> organic conductors,<sup>354,362</sup> and solar cells. However, the widespread use of acenes larger than pentacene in such applications is still hampered by major experimental difficulties in synthesizing large amounts of the pure acene compounds due to increasing instability and insolubility.<sup>357,361,377,384</sup> Implementation of heteroatoms such as boron into organic molecules could be another strategy to modify, for example, these pure organic biradicalic acenes.<sup>333,334,346,376,381</sup> Indeed, the implementation of boron atoms into organic molecules proved to be a quite efficient strategy to reduce their HOMO-LUMO gaps, mainly by raising the energy of the HOMO.<sup>333</sup> It is assumed that this approach may also be feasible for acenes or other organic poly-aromatics, allowing the generation of open-shell singlet systems even with a smaller number of condensed benzene rings. A similar approach is the incorporation of a biradical moiety into a stabilizing NHC system or heterocyclic system, e.g., *N*-heterocyclic olefins,<sup>221,289,331,333,335,398</sup> which are also similar in structure to acene-based biradicals. Here, too, the biradical character can be significantly enhanced by the specific incorporation of main group elements in unusual oxidation states (low valent) and chemical environments (low coordinated, bulky substituents).

## References

- Marx, K.; Engels, F. *Zur Kritik Der Hegelschen Rechtsphilosophie in Karl Marx/Friedrich Engels—Werke. (Karl) Dietz Verlag, Berlin*; vol. 1; Berlin: DDR, 1976; pp 378–391.
- Radical: <https://www.etymonline.com/word/radical>.
- Constable, E. C.; Housecroft, C. E. Before Radicals Were Free—The Radical Particulier of de Morveau. *Chemistry* **2020**, *2* (2), 293–304.
- Hjelt, E. *Geschichte Der Organischen Chemie von Ältester Zeit Bis Zur Gegenwart*, Springer, 1916.
- Gay-Lussac, J. L. Recherches sur l'acide prussique. *Ann. Chim.* **1815**, *95*, 136–199.
- Gay-Lussac, J. L.; Gilbert, L. W. Untersuchungen Über Die Blausäure. *Ann. Phys.* **1816**, *53* (6), 138–183.
- Wöhler, F.; von Liebig, J. Untersuchungen Über Das Radikal Der Benzoesäure. *Ann. Pharmacotheor.* **1832**, *3* (3), 249–282.
- Rüchardt, C. Radikale: Eine Chemische Theorie in Historischer Sicht. *Sitzungsber. Heidelb. Akad. Wiss.* **1992**, *1992*, 319–345.
- IUPAC. *IUPAC Compendium of Chemical Terminology, Gold Book, Release 2.3.3*, International Union of Pure and Applied Chemistry (IUPAC): Research Triangle Park, NC, 2012; p 427. <http://goldbook.iupac.org>.
- Gomberg, M. Triphenylmethyl, Ein Fall von Dreiwertigem Kohlenstoff. *Ber. Dtsch. Chem. Ges.* **1900**, *33* (3), 3150–3163.
- Schlenk, W.; Brauns, M. Zur Frage Der Metachinoide. *Ber. Dtsch. Chem. Ges.* **1915**, *48*, 661–669.
- Lewis, G. The Atom and the Molecule. *J. Am. Chem. Soc.* **1916**, *38*, 762–785.
- Shakespeare, W. (1597) *Romeo and Juliet, Act-II, Scene-II, Lines 38–49*.
- Biradical. In *IUPAC Compendium of Chemical Terminology, ("The Gold Book")*; McNaught, A. D., Wilkinson, A., Eds., 2nd ed.; Blackwell Scientific Publications: Oxford, 1997.
- Diradicals. In *IUPAC Compendium of Chemical Terminology, ("The Gold Book")*; McNaught, A. D., Wilkinson, A., Eds., 2nd ed.; Blackwell Scientific Publications: Oxford, 1997.
- Braslavsky, S. E. Glossary of Terms Used in Photochemistry, 3rd Edition (IUPAC Recommendations 2006). *Pure Appl. Chem.* **2007**, *79* (3), 293–465.
- Abe, M. Diradicals. *Chem. Rev.* **2013**, *113* (9), 7011–7088.
- Salem, L.; Rowland, C. The Electronic Properties of Diradicals. *Angew. Chem. Int. Ed. Engl.* **1972**, *11* (2), 92–111.
- Bonačić-Koutecký, V.; Koutecký, J.; Michl, J. Neutral and Charged Biradicals, Zwitterions, Funnels in S<sub>1</sub>, and Proton Translocation: Their Role in Photochemistry, Photophysics, and Vision. *Angew. Chem. Int. Ed. Engl.* **1987**, *26* (3), 170–189.
- Stuyver, T.; Chen, B.; Zeng, T.; Geerlings, P.; De Profijt, F.; Hoffmann, R. Do Diradicals Behave Like Radicals? *Chem. Rev.* **2019**, *119* (21), 11291–11351.
- Schulz, A. Group 15 Biradicals: Synthesis and Reactivity of Cyclobutane-1,3-Diyl and Cyclopentane-1,3-Diyl Analogues. *Dalton Trans.* **2018**, *47* (37), 12827–12837.
- Breher, F. Stretching Bonds in Main Group Element Compounds—Borderlines between Biradicals and Closed-Shell Species. *Coord. Chem. Rev.* **2007**, *251* (7–8), 1007–1043.
- Glasovac, Z.; Antol, I.; Vazdar, M.; Margetić, D. Zwitterionic Structures of Strained Cis-Pyramidalized Disilenes: Fact or Artifact. *Theor. Chem. Accounts* **2009**, *124* (5–6), 421–430.
- Grützmaier, H.; Breher, F. Odd-Electron Bonds and Biradicals in Main Group Element Chemistry. *Angew. Chem. Int. Ed.* **2002**, *41* (21), 4006–4011.
- González-Gallardo, S.; Breher, F. Main Group Biradicaloids. In *Comprehensive Inorganic Chemistry II*; vol. 1; Elsevier, 2013; ; pp 413–455.
- Michl, J.; Bonačić-Koutecký, V. Biradicals and Biradicaloids: A Unified View. *Tetrahedron* **1988**, *44* (24), 7559–7585.
- Lineberger, W. C.; Borden, W. T. The Synergy between Qualitative Theory, Quantitative Calculations, and Direct Experiments in Understanding, Calculating, and Measuring the Energy Differences Between the Lowest Singlet and Triplet States of Organic Diradicals. *Phys. Chem. Chem. Phys.* **2011**, *13* (25), 11792.
- Cramer, C. J. *Essentials of Computational Chemistry: Theories and Models*, John Wiley & Sons, Ltd.: Chichester, UK, 2004.
- Malrieu, J. P.; Caballol, R.; Calzado, C. J.; de Graaf, C.; Guihéry, N. Magnetic Interactions in Molecules and Highly Correlated Materials: Physical Content, Analytical Derivation, and Rigorous Extraction of Magnetic Hamiltonians. *Chem. Rev.* **2014**, *114* (1), 429–492.
- Roothaan, C. C. J. New Developments in Molecular Orbital Theory. *Rev. Mod. Phys.* **1951**, *23* (2), 69–89.

31. Goddard, W. A.; Dunning, T. H.; Hunt, W. J.; Hay, P. J. Generalized Valence Bond Description of Bonding in Low-Lying States of Molecules. *Acc. Chem. Res.* **1973**, *6* (11), 368–376.
32. Kollmar, H.; Staemmler, V. A Theoretical Study of the Structure of Cyclobutadiene. *J. Am. Chem. Soc.* **1977**, *99* (11), 3583–3587.
33. Borden, W. T.; Davidson, E. R.; Hart, P. The Potential Surfaces for the Lowest Singlet and Triplet States of Cyclobutadiene. *J. Am. Chem. Soc.* **1978**, *100* (2), 388–392.
34. Eckert-Maksić, M.; Vazdar, M.; Barbatti, M.; Lischka, H.; Maksić, Z. B. Automerization Reaction of Cyclobutadiene and Its Barrier Height: An Ab Initio Benchmark Multi-reference Average-Quadratic Coupled Cluster Study. *J. Chem. Phys.* **2006**, *125* (6), 064310.
35. Schoeller, W. W. The Niecke Biradicals and Their Congeners—The Journey from Stable Biradicaloids to Their Utilization for the Design of Nonlinear Optical Properties. *Eur. J. Inorg. Chem.* **2019**, *2019* (11–12), 1495–1506.
36. Abe, M.; Ye, J.; Mishima, M. The Chemistry of Localized Singlet 1,3-Diradicals (Biradicals): From Putative Intermediates to Persistent Species and Unusual Molecules With a  $\pi$ -Single Bonded Character. *Chem. Soc. Rev.* **2012**, *41* (10), 3808–3820.
37. Ito, S. Topics of 1,3-Diphosphacyclobutane-2,4-Diyl Derivatives: Structural Aspects and Functionality of Isolable Heavier Congeners of Cyclobutane-1,3-Diyl and the Related Molecules. *Tetrahedron Lett.* **2018**, *59* (1), 1–13.
38. Levine, I. N. *Quantum Chemistry*, 7th ed.; Pearson, 2014.
39. Helgaker, T.; Jørgensen, P.; Olsen, J. *Molecular Electronic-Structure Theory*, John Wiley & Sons, Ltd: Chichester, UK, 2000.
40. Foster, J. M.; Boys, S. F. Canonical Configurational Interaction Procedure. *Rev. Mod. Phys.* **1960**, *32* (2), 300–302.
41. Kleier, D. A.; Halgren, T. A.; Hall, J. H.; Lipscomb, W. N. Localized Molecular Orbitals for Polyatomic Molecules. I. A Comparison of the Edmiston-Ruedenberg and Boys Localization Methods. *J. Chem. Phys.* **1974**, *61* (10), 3905–3919.
42. Löwdin, P.-O. Quantum Theory of Many-Particle Systems. I. Physical Interpretations by Means of Density Matrices, Natural Spin-Orbitals, and Convergence Problems in the Method of Configurational Interaction. *Phys. Rev.* **1955**, *97* (6), 1474–1489.
43. Hayes, E. F.; Siu, A. K. Q. Electronic Structure of the Open Forms of Three-Membered Rings. *J. Am. Chem. Soc.* **1971**, *93* (8), 2090–2091.
44. Bachler, V.; Olbrich, G.; Neese, F.; Wieghardt, K. Theoretical Evidence for the Singlet Diradical Character of Square Planar Nickel Complexes Containing Two O—Semiquinonato Type Ligands. *Inorg. Chem.* **2002**, *41* (16), 4179–4193.
45. Herebian, D.; Wieghardt, K. E.; Neese, F. Analysis and Interpretation of Metal-Radical Coupling in a Series of Square Planar Nickel Complexes: Correlated Ab Initio and Density Functional Investigation of  $[\text{Ni}(\text{LISQ})_2]$  (LISQ = 3,5-Di-Tert-Butyl-O-Diiminobenzosemiquinonate(1-)). *J. Am. Chem. Soc.* **2003**, *125* (36), 10997–11005.
46. Miliordos, E.; Ruedenberg, K.; Xantheas, S. S. Unusual Inorganic Biradicals: A Theoretical Analysis. *Angew. Chem. Int. Ed.* **2013**, *52* (22), 5736–5739.
47. Yamaguchi, K. The Electronic Structures of Biradicals in the Unrestricted Hartree-Fock Approximation. *Chem. Phys. Lett.* **1975**, *33* (2), 330–335.
48. Fabian, J.; Peichert, R. On the Nature of Some Biradicaloid and Antiaromatic Vis/NIR-Chromophores. *J. Phys. Org. Chem.* **2010**, *23* (12), 1137–1145.
49. David, G.; Trinquier, G.; Malrieu, J. Consistent Spin Decontamination of Broken-Symmetry Calculations of Diradicals. *J. Chem. Phys.* **2020**, *153* (19), 194107.
50. Soda, T.; Kitagawa, Y.; Onishi, T.; Takano, Y.; Shigeta, Y.; Nagao, H.; Yoshioka, Y.; Yamaguchi, K. Ab Initio Computations of Effective Exchange Integrals for H–H, H–He–H and  $\text{Mn}_2\text{O}_2$  Complex: Comparison of Broken-Symmetry Approaches. *Chem. Phys. Lett.* **2000**, *319* (3–4), 223–230.
51. Orms, N.; Krylov, A. I. Singlet–Triplet Energy Gaps and the Degree of Diradical Character in Binuclear Copper Molecular Magnets Characterized by Spin-Flip Density Functional Theory. *Phys. Chem. Chem. Phys.* **2018**, *20* (19), 13127–13144.
52. Noodleman, L. Valence Bond Description of Antiferromagnetic Coupling in Transition Metal Dimers. *J. Chem. Phys.* **1981**, *74* (10), 5737–5743.
53. Caballol, R.; Castell, O.; Illas, F.; de PR Moreira, I.; Malrieu, J. P. Remarks on the Proper Use of the Broken Symmetry Approach to Magnetic Coupling. *J. Phys. Chem. A* **1997**, *101* (42), 7860–7866.
54. Malrieu, J.-P.; Trinquier, G. A Recipe for Geometry Optimization of Diradical Singlet States From Broken-Symmetry Calculations. *J. Phys. Chem. A* **2012**, *116* (31), 8226–8237.
55. Malrieu, J.-P.; Trinquier, G. Can a Topological Approach Predict Spin-Symmetry Breaking in Conjugated Hydrocarbons? *J. Phys. Chem. A* **2016**, *120* (48), 9564–9578.
56. Fantuzzi, F.; Cardozo, T. M.; Nascimento, M. A. C. The Nature of the Singlet and Triplet States of Cyclobutadiene as Revealed by Quantum Interference. *ChemPhysChem* **2016**, *17* (2), 288–295.
57. Wolf, R.; Ni, C.; Nguyen, T.; Brynda, M.; Long, G. J.; Sutton, A. D.; Fischer, R. C.; Fetting, J. C.; Hellman, M.; Pu, L.; et al. Substituent Effects in Formally Quintuple-Bonded  $\text{ArCrCrAr}$  Compounds (Ar = Terphenyl) and Related Species. *Inorg. Chem.* **2007**, *46* (26), 11277–11290.
58. Schulz, A. On the Steric Hindrance of Bulky Substituents—Determination of Their Cone Angles. *Z. Anorg. Allg. Chem.* **2014**, *640* (11), 2183–2192.
59. Rivard, E.; Power, P. P. Multiple Bonding in Heavier Element Compounds Stabilized by Bulky Terphenyl Ligands. *Inorg. Chem.* **2007**, *46* (24), 10047–10064.
60. Guidimetta, V. B.; Ma, L.; Washington, M. P.; Payton, J. L.; Cather Simpson, M.; Protasiewicz, J. D. Meta-Terphenyl Phosphaalkenes Bearing Electron-Donating and -Accepting Groups. *Eur. J. Inorg. Chem.* **2010**, *2010* (6), 854–865.
61. Flynn, K. M.; Murray, B. D.; Olmstead, M. M.; Power, P. P. Interaction of Phosphorous Bis(Trimethylsilyl)Amide Dichloride with Carbonylmetalate Dianions of Iron and Chromium: Syntheses and x-Ray Crystal Structures of New Transition Metal Complexes Involving Phosphorus and Arsenic in Multiple Bonding. *J. Am. Chem. Soc.* **1983**, *105* (25), 7460–7461.
62. Power, P. P. Pi-Bonding and the Lone Pair Effect in Multiple Bonds Between Heavier Main Group Elements. *Chem. Rev.* **1999**, *99* (12), 3463–3504.
63. Cyburne, J. A. C.; McMullen, N. Unusual Structures of Main Group Organometallic Compounds Containing M-Terphenyl Ligands. *Coord. Chem. Rev.* **2000**, *210* (1), 73–99.
64. Power, P. P. Persistent and Stable Radicals of the Heavier Main Group Elements and Related Species. *Chem. Rev.* **2003**, *103* (3), 789–810.
65. Fischer, R. C.; Power, P. P. Pi-Bonding and the Lone Pair Effect in Multiple Bonds Involving Heavier Main Group Elements: Developments in the New Millennium. *Chem. Rev.* **2010**, *110* (7), 3877–3923.
66. Gynane, M. J. S. J.; Hudson, A.; Lappert, M. F. F.; Power, P. P.; Goldwhite, H. Bulky Alkyls, Amides, and Aryloxides of Main Group 5 Elements. Part 1. Persistent Phosphinyl and Arsinyl Radicals MRR and Their Chloroprecursors MRRCl and Related Compounds. *J. Chem. Soc. Dalton Trans.* **1980**, (12), 2428.
67. Twamley, B.; Haubrich, S. T.; Power, P. P. In *Advances in Organometallic Chemistry*; West, R., Hill, A. F., Eds.; vol. 44; Elsevier, 1999.
68. Niksch, T.; Görts, H.; Weigand, W. The Extension of the Solid-Angle Concept to Bidentate Ligands. *Eur. J. Inorg. Chem.* **2010**, *2010* (1), 95–105.
69. Cavallo, L.; Correa, A.; Costabile, C.; Jacobsen, H. Steric and Electronic Effects in the Bonding of N-Heterocyclic Ligands to Transition Metals. *J. Organomet. Chem.* **2005**, *690* (24–25), 5407–5413.
70. Tolman, C. A.; Seidel, W. C.; Gosser, L. W. Formation of Three-Coordinate Nickel(0) Complexes by Phosphorus Ligand Dissociation From  $\text{NiL}_4$ . *J. Am. Chem. Soc.* **1974**, *96* (1), 53–60.
71. Tolman, C. A. Steric Effects of Phosphorus Ligands in Organometallic Chemistry and Homogeneous Catalysis. *Chem. Rev.* **1977**, *77* (3), 313–348.
72. Bilbrey, J. A.; Kazez, A. H.; Locklin, J.; Allen, W. D. Exact Ligand Cone Angles. *J. Comput. Chem.* **2013**, *34* (14), 1189–1197.
73. Wright, R. J.; Steiner, J.; Beaini, S.; Power, P. P. Synthesis of the Sterically Encumbering Terphenyl Silyl and Alkyl Amines (R = Me and  $\text{SiMe}_3$ ), Their Lithium Derivatives, and the Tertiary Amine. *Inorg. Chim. Acta* **2006**, *359* (6), 1939–1946.
74. Glöckner, A.; Bauer, H.; Maekawa, M.; Bannenberg, T.; Daniliuc, C. G.; Jones, P. G.; Sun, Y.; Sitzmann, H.; Tamm, M.; Walter, M. D. How Big Is a Cp? Cycloheptatrienyl Zirconium Complexes With Bulky Cyclopentadienyl and Indenyl Ligands. *Dalton Trans.* **2012**, *41* (22), 6614–6624.
75. Zhou, J.; Lancaster, S. J.; Walker, D. A.; Beck, S.; Thornton-Pett, M.; Bochmann, M. Synthesis, Structures, and Reactivity of Weakly Coordinating Anions With Delocalized Borate Structure: The Assessment of Anion Effects in Metallocene Polymerization Catalysts. *J. Am. Chem. Soc.* **2001**, *123* (2), 223–237.
76. Krossing, I.; Raabe, I. Noncoordinating Anions - Fact or Fiction? A Survey of Likely Candidates. *Angew. Chem. Int. Ed. Engl.* **2004**, *43* (16), 2066–2090.
77. Krossing, I.; Raabe, I. Relative Stabilities of Weakly Coordinating Anions: A Computational Study. *Chem. A Eur. J.* **2004**, *10* (20), 5017–5030.
78. LaPointe, R. E.; Roof, G. R.; Abboud, K. A.; Klosin, J. New Family of Weakly Coordinating Anions. *J. Am. Chem. Soc.* **2000**, *122* (39), 9560–9561.



79. Krossing, I. The Facile Preparation of Weakly Coordinating Anions: Structure and Characterisation of Silverpolyfluoroalkoxyaluminates  $\text{Ag}[\text{Al}(\text{OR})_4]$ , Calculation of the Alkoxide Ion Affinity. *Chem. A Eur. J.* **2001**, *7* (2), 490–502.
80. Strauss, S. H. The Search for Larger and More Weakly Coordinating Anions. *Chem. Rev.* **1993**, *93* (3), 927–942.
81. Krossing, I.; Reisinger, A. Chemistry With Weakly-Coordinating Fluorinated Alkoxyaluminate Anions: Gas Phase Cations in Condensed Phases? *Coord. Chem. Rev.* **2006**, *250* (21–22), 2721–2744.
82. Reed, C.; Carboranes, A. A New Class of Weakly Coordinating Anions for Strong Electrophiles, Oxidants, and Superacids. *Acc. Chem. Res.* **1998**, *31* (3), 133–139.
83. Engesser, T. A.; Lichtenthaler, M. R.; Schleep, M.; Krossing, I. Reactive P-Block Cations Stabilized by Weakly Coordinating Anions. *Chem. Soc. Rev.* **2016**, *45* (4), 789–899.
84. Krossing, I.; Raabe, I. Nichtkoordinierende Anionen—Traum Oder Wirklichkeit? Eine Übersicht Zu Möglichen Kandidaten. *Angew. Chem.* **2004**, *116* (16), 2116–2142.
85. Holliday, A. K.; Massey, A. G. *Non-Aqueous Solvents in Inorganic Chemistry*, Pergamon, 1965.
86. Ahmed, E.; Ruck, M. Homo- and Heteroatomic Polycations of Groups 15 and 16. Recent Advances in Synthesis and Isolation Using Room Temperature Ionic Liquids. *Coord. Chem. Rev.* **2011**, *255* (23–24), 2892–2903.
87. Freudenmann, D.; Wolf, S.; Wolff, M.; Feldmann, C. Ionic Liquids: New Perspectives for Inorganic Synthesis? *Angew. Chem. Int. Ed.* **2011**, *50* (47), 11050–11060.
88. Wilkes, J. S. A Short History of Ionic Liquids - From Molten Salts to Neoteric Solvents. *Green Chem.* **2002**, *4* (2), 73–80.
89. Xue, H.; Verma, R.; Shreeve, J. M. Review of Ionic Liquids With Fluorine-Containing Anions. *J. Fluor. Chem.* **2006**, *127* (2), 159–176.
90. Ruß, C.; König, B. Low Melting Mixtures in Organic Synthesis - An Alternative to Ionic Liquids? *Green Chem.* **2012**, *14* (11), 2969.
91. Krossing, I.; Slattery, J. M.; Daguenet, C.; Dyson, P. J.; Oleinikova, A.; Weingärtner, H. Why Are Ionic Liquids Liquid? A Simple Explanation Based on Lattice and Solvation Energies. *J. Am. Chem. Soc.* **2006**, *128* (41), 13427–13434.
92. Ross, J.; Percy, J. H.; Brandt, R. L.; Gebhart, A. I.; Mitchell, J. E.; Yolles, S. Liquid Sulfur Dioxide as Solvent Medium for Chemical Reactions. *Ind. Eng. Chem.* **1942**, *34* (8), 924–926.
93. Decken, A.; Jenkins, H. D. B.; Nikiforov, G. B.; Passmore, J. The Reaction of  $\text{Li}[\text{Al}(\text{OR})_4]$   $\text{R} = \text{OC}(\text{CF}_3)_2\text{Ph}$ ,  $\text{OC}(\text{CF}_3)_3$  With  $\text{NO}/\text{NO}_2$  Giving  $\text{NO}[\text{Al}(\text{OR})_4]$ ,  $\text{Li}[\text{NO}_3]$  and  $\text{N}_2\text{O}$ . The Synthesis of  $\text{NO}[\text{Al}(\text{OR})_4]$  from  $\text{Li}[\text{Al}(\text{OR})_4]$  and  $\text{NO}[\text{SbF}_6]$  in Sulfur Dioxide Solution. *Dalton Trans.* **2004**, (16), 2496–2504.
94. Logemann, C.; Gunzelmann, D.; Klüner, T.; Senker, J.; Wickleder, M. S. Reactions With Oleum Under Harsh Conditions: Characterization of the Unique  $[\text{M}(\text{S}_2\text{O}_7)_3]_2^-$  Ions ( $\text{M} = \text{Si}$ ,  $\text{Ge}$ ,  $\text{Sn}$ ) in  $\text{A}_2[\text{M}(\text{S}_2\text{O}_7)_3]$  ( $\text{A} = \text{NH}_4$ ,  $\text{Ag}$ ). *Chem. A Eur. J.* **2012**, *18* (48), 15495–15503.
95. Bruns, J.; Klüner, T.; Wickleder, M. S. Oxidizing Elemental Platinum With Oleum Under Harsh Conditions: The Unique Tris(Disulfato)Platinate(IV)  $[\text{Pt}(\text{S}_2\text{O}_7)_3]_2^-$  Anion. *Chem. A Eur. J.* **2014**, *20* (24), 7222–7227.
96. DeKock, R. L.; Haddad, M. S. Gas-Phase Reaction of Ammonia With Thionyl Chloride. *Inorg. Chem.* **1977**, *16* (1), 216–217.
97. Appelt, C.; Slootweg, J. C.; Lammertsma, K.; Uhl, W. Die Reaktionen Eines P/Al-Basierten Frustrierten Lewis-Paars Mit Ammoniak, Boran Und Aminboranen: Adduktbildung Und Katalytische Wasserstoffeliminierung. *Angew. Chem.* **2013**, *125* (15), 4350–4353.
98. Kraus, C. A. Reactions and Reagents in Liquid Ammonia. *Chem. Rev.* **1940**, *26* (1), 95–104.
99. Franklin, E. C. Reactions and Reagents in Liquid Ammonia. *Trans. Kans. Acad. Sci.* **1903**, *26* (1), 74–77.
100. Fernelius, W. C.; Watt, G. W. Reactions of Solutions of Metals in Liquid Ammonia. *Chem. Rev.* **1937**, *20* (2), 195–258.
101. Kraus, F. Fluorine Chemistry Meets Liquid Ammonia. *Bioinorg. React. Mech.* **2012**, *8* (1–2).
102. Erker, G. Frustrated Lewis Pairs: Some Recent Developments. *Pure Appl. Chem.* **2012**, *84* (11), 2203–2217.
103. Stephan, D. W. Frustrated Lewis Pairs: A New Strategy to Small Molecule Activation and Hydrogenation Catalysis. *Dalton Trans.* **2009**, 9226 (17), 3129–3136.
104. Stephan, D. W. Frustrated Lewis Pairs. *J. Am. Chem. Soc.* **2015**, *137* (32), 10018–10032.
105. Stephan, D. W.; Erker, G. Frustrated Lewis Pairs: Metal-Free Hydrogen Activation and More. *Angew. Chem. Int. Ed. Engl.* **2010**, *49* (1), 46–76.
106. Bourissou, D.; Guerret, O.; Gabbai, F.; Bertrand, G. Stable Carbenes. *Chem. Rev.* **2000**, *100* (1), 39–92.
107. Hahn, F. E.; Jahnke, M. C. Heterocyclische Carbene - Synthese Und Koordinationschemie. *Angew. Chem.* **2008**, *120* (17), 3166–3216.
108. Hopkinson, M. N.; Richter, C.; Schedler, M.; Glorius, F. An Overview of N-Heterocyclic Carbenes. *Nature* **2014**, *510* (7506), 485–496.
109. Martin, C. D.; Soleilhavou, M.; Bertrand, G. Carbene-Stabilized Main Group Radicals and Radical Ions. *Chem. Sci.* **2013**, *4* (8), 3020–3030.
110. Martin, D.; Soleilhavou, M.; Bertrand, G. Stable Singlet Carbenes as Mimics for Transition Metal Centers. *Chem. Sci.* **2011**, *2* (3), 389–399.
111. Melaimi, M.; Soleilhavou, M.; Bertrand, G. Stable Cyclic Carbenes and Related Species beyond Diaminocarbenes. *Angew. Chem. Int. Ed. Engl.* **2010**, *49* (47), 8810–8849.
112. Schuster, O.; Yang, L.; Raubenheimer, H. G.; Albrecht, M. Beyond Conventional N-Heterocyclic Carbenes: Abnormal, Remote, and Other Classes of NHC Ligands With Reduced Heteroatom Stabilization. *Chem. Rev.* **2009**, *109* (8), 3445–3478.
113. Siemeling, U.; Färber, C.; Bruhn, C.; Leibold, M.; Selent, D.; Baumann, W.; von Hopfgarten, M.; Goedecke, C.; Frenking, G. N-Heterocyclic Carbenes Which Readily Add Ammonia, Carbon Monoxide and Other Small Molecules. *Chem. Sci.* **2010**, *1* (6), 697–704.
114. Soleilhavou, M.; Bertrand, G. Cyclic (Alkyl)(Amino)Carbenes (CAACs): Stable Carbenes on the Rise. *Acc. Chem. Res.* **2015**, *48* (2), 256–266.
115. Davydova, E. I.; Sevastianova, T. N.; Suvorov, A. V.; Timoshkin, A. Y. Molecular Complexes Formed by Halides of Group 4,5,13–15 Elements and the Thermodynamic Characteristics of Their Vaporization and Dissociation Found by the Static Tensimetric Method. *Coord. Chem. Rev.* **2010**, *254* (17–18), 2031–2077.
116. Jacobsen, H.; Berke, H.; Döring, S.; Kehr, G.; Erker, G.; Fröhlich, R.; Meyer, O. Lewis Acid Properties of Tris(Pentafluorophenyl)Borane. Structure and Bonding in  $\text{L}-\text{B}(\text{C}_6\text{F}_5)_3$  Complexes. *Organometallics* **1999**, *18* (9), 1724–1735.
117. Piers, W. E.; Chivers, T. Pentafluorophenylboranes: From Obscurity to Applications. *Chem. Soc. Rev.* **1997**, *26* (5), 345–354.
118. Bläsing, K.; Bresien, J.; Labbow, R.; Schulz, A.; Villinger, A. Stabilisierung Eines Blausäure-Dimers Mit Einer Lewis-Säure. *Angew. Chem.* **2018**, *130* (29), 9311–9316.
119. Labbow, R.; Michalik, D.; Reiß, F.; Schulz, A.; Villinger, A. Isolierung Labiler NSO-Pseudohalogen-Spezies. *Angew. Chem.* **2016**, *128* (27), 7811–7815.
120. Linti, G.; Schnöckel, H. Low Valent Aluminum and Gallium Compounds—Structural Variety and Coordination Modes to Transition Metal Fragments. *Coord. Chem. Rev.* **2000**, *206–207*, 285–319.
121. Nguyen, K. A.; Gordon, M. S.; Boatz, J. A. The Inversion of Bicyclobutane and Bicyclobutane. *J. Am. Chem. Soc.* **1994**, *116* (20), 9241–9249.
122. Goldberg, A. H.; Dougherty, D. A. Effects of Through-Bond and through-Space Interactions on Singlet-Triplet Energy Gaps in Localized Biradicals. *J. Am. Chem. Soc.* **1983**, *105* (2), 284–290.
123. Jain, R.; Snyder, G. J.; Dougherty, D. A. Direct, ESR Observation of the Localized Biradical 1,3-Dimethyl-1,3-Cyclobutadiyl. *J. Am. Chem. Soc.* **1984**, *106* (23), 7294–7295.
124. Jain, R.; Sponsler, M. B.; Corns, F. D.; Dougherty, D. A. Cyclobutanediyls: A New Class of Localized Biradicals. Synthesis and Epr Spectroscopy. *J. Am. Chem. Soc.* **1988**, *110* (5), 1356–1366.
125. Chang, M. H.; Dougherty, D. A. Photochemistry of 2,3-Diazabicyclo[2.1.1]Hex-2-Ene. Beta. Carbon-Carbon Cleavage to a Stereoreandom Triplet Biradical. *J. Am. Chem. Soc.* **1982**, *104* (8), 2333–2334.
126. Hopf, H.; Lipka, H.; Traetteberg, M. Photoisomerization of Highly Alkylated Butadienes. *Angew. Chem. Int. Ed. Engl.* **1994**, *33* (2), 204–205.
127. Saettel, N. J.; Wiest, O. Sterically Crowded Bicyclo[1.1.0]Butane Radical Cations. *J. Org. Chem.* **2003**, *68* (11), 4549–4552.
128. Budzelaar, P. H. M.; Kraka, E.; Cremer, D.; Schleyer, P. v. R. Long Interbridgehead Bonds in Acceptor-Substituted Bicyclobutanes. *J. Am. Chem. Soc.* **1986**, *108* (4), 561–567.
129. Niecke, E.; Fuchs, A.; Baumeister, F.; Nieger, M.; Schoeller, W. W. Ein  $\text{P}_2\text{C}_2$ -Vierring Mit Ungewöhnlicher Bindungssituation - Synthese, Struktur Und Ringöffnung Eines 1,3-Diphosphacyclobutan-2,4-Diyls. *Angew. Chem.* **1995**, *107* (5), 640–642.
130. Ito, S. Study of the Air-Tolerant 1,3-Diphosphacyclobutan-2,4-Diyl Through the Direct Arylation. *Chem. Rec.* **2018**, *18* (4), 445–458.
131. Mikulski, C. M.; Russo, P. J.; Saran, M. S.; MacDiarmid, A. G.; Garito, A. F.; Heeger, A. J. Synthesis and Structure of Metallic Polymeric Sulfur Nitride,  $(\text{SN})_x$ , and Its Precursor, Disulfur Dinitride,  $\text{S}_2\text{N}_2$ . *J. Am. Chem. Soc.* **1975**, *97* (22), 6358–6363.

132. Zipse, H.; Schulz, A. Glossar Zur Theoretischen Organischen Chemie. *Angew. Chem.* **2003**, *115* (24), 2806.
133. Chivers, T.; Manners, I. *Inorganic Rings and Polymers of the P-Block Elements*, Royal Society of Chemistry, 2009.
134. Power, P. P. Main-Group Elements as Transition Metals. *Nature* **2010**, *463* (7278), 171–177.
135. Abe, M.; Furunaga, H.; Ma, D.; Gagliardi, L.; Bodwell, G. J. Stretch Effects Induced by Molecular Strain on Weakening  $\sigma$ -Bonds: Molecular Design of Long-Lived Diradicals (Biradicals). *J. Org. Chem.* **2012**, *77* (17), 7612–7619.
136. He, G.; Shynkaruk, O.; Lui, M. W.; Rivard, E. Small Inorganic Rings in the 21st Century: From Fleeting Intermediates to Novel Isolable Entities. *Chem. Rev.* **2014**, *114* (16), 7815–7880.
137. Kundu, S.; Sinhababu, S.; Chandrasekhar, V.; Roesky, H. W. Stable Cyclic (Alkyl)(Amino)Carbene (CAAC) Radicals With Main Group Substituents. *Chem. Sci.* **2019**, *10* (18), 4727–4741.
138. Grützmacher, H.; Breher, F. Bindungen Mit ungerader Elektronenzahl und Biradikale in der Chemie der Hauptgruppenelemente. *Angew. Chem.* **2002**, *114* (21), 4178–4184.
139. Bresien, J.; Eickhoff, L.; Schulz, A.; Suhrbier, T.; Villinger, A. A Systematic Survey of the Reactivity of Chlorinated  $N_2$ ,  $P_2$ ,  $NP_3$  and  $P_4$  Ring Systems. *Chem. Eur. J.* **2019**, *25* (71), 16311–16319.
140. Grande-Aztatzi, R.; Mercero, J. M.; Ugalde, J. M. The Stability of Biradicaloid versus Closed-Shell  $[E(\mu-XR)]_2$  ( $E = P, As$ ;  $X = N, P, As$ ) Rings. Does Aromaticity Play a Role? *Phys. Chem. Chem. Phys.* **2016**, *18*, 11879–11884.
141. Fluck, E.; Riedel, R.; Hausen, H.-D.; Heckmann, G. Bis(Mes\*)Bicyclotetraphosphan. *Z. Anorg. Allg. Chem.* **1987**, *551*, 85–94.
142. Hinz, A.; Schulz, A.; Villinger, A. Synthesis of Heavy Cyclopidnicatodiphosphanes  $[ClE(\mu-P-Ter)]_2$  ( $E = P, As, Sb, or Bi$ ;  $Ter = 2,6-Bis(2,4,6-Trimethylphenyl)Phenyl$ ). *Inorg. Chem.* **2016**, *55* (7), 3692–3699.
143. Beweries, T.; Kuzora, R.; Rosenthal, U.; Schulz, A.; Villinger, A.  $[P(\mu-NTer)]_2$ : A Biradicaloid That Is Stable at High Temperature. *Angew. Chem. Int. Ed.* **2011**, *50* (38), 8974–8978.
144. Demeshko, S.; Godemann, C.; Kuzora, R.; Schulz, A.; Villinger, A. An Arsenic-Nitrogen Biradicaloid: Synthesis, Properties, and Reactivity. *Angew. Chem. Int. Ed.* **2013**, *52* (7), 2105–2108.
145. Hinz, A.; Kuzora, R.; Rölke, A.-K.; Schulz, A.; Villinger, A.; Wustrack, R. Synthesis of a Silylated Phosphorus Biradicaloid and Its Utilization in the Activation of Small Molecules. *Eur. J. Inorg. Chem.* **2016**, *2016* (22), 3611–3619.
146. Hinz, A.; Kuzora, R.; Rosenthal, U.; Schulz, A.; Villinger, A. Activation of Small Molecules by Phosphorus Biradicaloids. *Chem. A Eur. J.* **2014**, *20* (45), 14659–14673.
147. Hinz, A.; Rothe, J.; Schulz, A.; Villinger, A. Reduction of Dichloro(Diaza-Phospha)Stibanes—Isolation of a Donor-Stabilized Distibonium Dication. *Dalton Trans.* **2016**, *45* (14), 6044–6052.
148. Dröge, T.; Glorius, F. The Measure of All Rings—N-Heterocyclic Carbenes. *Angew. Chem. Int. Ed. Engl.* **2010**, *49* (39), 6940–6952.
149. Vrána, J.; Samsonov, M. A.; Némec, V.; Růžicka, A. Access to the Most Sterically Crowded Anilines via Non-Catalysed C–C Coupling Reactions. *Chem. Commun.* **2020**, *56* (16), 2487–2490.
150. Scheschke, D.; Amii, H.; Gornitzka, H.; Schoeller, W. W.; Bourissou, D.; Bertrand, G. Singlet Diradicals: From Transition States to Crystalline Compounds. *Science* **2002**, *295* (5561), 1880–1881.
151. Bourg, J.-B.; Rodriguez, A.; Scheschke, D.; Gornitzka, H.; Bourissou, D.; Bertrand, G. Thermal Valence Isomerization of 2,3-Diborata-1,4-Diphosphoniabuta-1,3-Dienes to Bicyclo[1.1.0]Butanes and Cyclobutane-1,3-Diyls. *Angew. Chem. Int. Ed.* **2007**, *46* (30), 5741–5745.
152. Rodriguez, A.; Olsen, R. A.; Ghaderi, N.; Scheschke, D.; Tham, F. S.; Mueller, L. J.; Bertrand, G. Evidence for the Coexistence of Two Bond-Stretch Isomers in Solution. *Angew. Chem. Int. Ed.* **2004**, *43* (37), 4880–4883.
153. Soleilhavoup, M.; Bertrand, G. Let's Play With Valence Isomers: The Influence of Different Main Group Elements on Their Relative Stability. *Bull. Chem. Soc. Jpn.* **2007**, *80* (7), 1241–1252.
154. Seierstad, M.; Kinsinger, C. R.; Cramer, C. J. Design Optimization of 1,3-Diphospha-2,4-Diboretane Diradicals. *Angew. Chem. Int. Ed.* **2002**, *41* (20), 3894–3896.
155. Jung, Y.; Head-Gordon, M. How Diradicaloid Is a Stable Diradical? *ChemPhysChem* **2003**, *4* (5), 522–525.
156. Cheng, M. J.; Hu, C. H.  $B_2P$  Rings: Through-Space  $\pi$  Bond or Stable Diradical? A Theoretical Study. *Mol. Phys.* **2003**, *101* (9), 1319–1323.
157. Amii, H.; Vranicar, L.; Gornitzka, H.; Bourissou, D.; Bertrand, G. Radical-Type Reactivity of the 1,3-Dibora-2,4-Diphosphoniocyclobutane-1,3-Diyl. *J. Am. Chem. Soc.* **2004**, *126* (5), 1344–1345.
158. Rodriguez, A.; Tham, F. S.; Schoeller, W. W.; Bertrand, G. Catenation of Two Singlet Diradicals: Synthesis of a Stable Tetraradical (Tetraradicaloid). *Angew. Chem. Int. Ed.* **2004**, *43* (37), 4876–4880.
159. Rajca, A. Organic Diradicals and Polyradicals: From Spin Coupling to Magnetism? *Chem. Rev.* **1994**, *94* (4), 871–893.
160. Rodriguez, A.; Fuks, G.; Bourg, J.-B.; Bourissou, D.; Tham, F. S.; Bertrand, G. 1,3-Diborata-2,4-Diphosphoniocyclobutane-1,3-Diyls Communicate through a Para-Phenylene Linker. *Dalton Trans.* **2008**, (33), 4482.
161. Henke, P.; Pankewitz, T.; Klopper, W.; Breher, F.; Schnöckel, H. Snapshots of the Al–Al  $\sigma$ -Bond Formation Starting From  $\{AlR_2\}$  Units: Experimental and Computational Observations. *Angew. Chem. Int. Ed.* **2009**, *48* (43), 8141–8145.
162. Pankewitz, T.; Klopper, W.; Henke, P.; Schnöckel, H. Isomeric  $Al_2R_4$ ,  $Mg_2R_2$  Species and Oligomerisation Products: Investigation of Al–Al and Mg–Mg  $\sigma$  Bonding. *Eur. J. Inorg. Chem.* **2008**, *2* (31), 4879–4890.
163. Niecke, E.; Fuchs, A.; Baumeister, F.; Nieger, M.; Schoeller, W. W. A  $P_2C_2$  Four-Membered Ring With Unusual Bonding - Synthesis, Structure, and Ring Opening of a 1,3-Diphosphacyclobutane-2,4-Diyl. *Angew. Chem. Int. Ed. Engl.* **1995**, *34* (5), 555–557.
164. Niecke, E.; Fuchs, A.; Nieger, M. Valence Isomerization of a 1,3-Diphosphacyclobutane-2,4-Diyl: Photochemical Ring Closure to 2,4-Diphosphabicyclo[1.1.0]Butane and Its Thermal Ring Opening Togauche-1,4-Diphosphabutadiene. *Angew. Chem. Int. Ed.* **1999**, *38* (20), 3028–3031.
165. Niecke, E.; Fuchs, A.; Nieger, M.; Schmidt, O.; Schoeller, W. W. 1,3-Diphosphacyclobutane-2,4-Diyl-2-Ylidenide: A Unique Carbene and Its Trimethylalane Complex. *Angew. Chem. Int. Ed.* **1999**, *38* (20), 3031–3034.
166. Sebastian, M.; Nieger, M.; Szieberth, D.; Nyulászi, L.; Niecke, E. Synthesis and Structure of a 1,3-Diphosphacyclobutadienediide: An Anionolytic Fragmentation of a 1,3-Diphosphetane-2,4-Diyl in Solution. *Angew. Chem. Int. Ed.* **2004**, *43* (5), 637–641.
167. Sugiyama, H.; Ito, S.; Yoshifuji, M. Synthesis of a 1,3-Diphosphacyclobutane-2,4-Diyl From  $Mes^*C\equiv P$ . *Angew. Chem. Int. Ed.* **2003**, *42* (32), 3802–3804.
168. Ito, S.; Miura, J.; Morita, N.; Yoshifuji, M.; Arduengo, A. J., III Diverse Reactions of Sterically-Protected 1,3-Diphosphacyclobutane-2,4-Diyls With Hydride. *Dalton Trans.* **2010**, *39* (35), 8281.
169. Ito, S.; Ngo, T. T.; Mikami, K. Silyl Effects on 1,3-Diphosphacyclobutane-2,4-Diyl: Ring-Opening of Tetrahydrofuran and Promotion of Reductive P–C Cleavage. *Chem. Asian J.* **2013**, *8* (9), 1976–1980.
170. Ito, S.; Ueta, Y.; Ngo, T. T.; Kobayashi, M.; Hashizume, D.; Nishida, J.; Yamashita, Y.; Mikami, K. Direct Arylations for Study of the Air-Stable P-Heterocyclic Biradical: From Wide Electronic Tuning to Characterization of the Localized Radicalic Electrons. *J. Am. Chem. Soc.* **2013**, *135* (46), 17610–17616.
171. Ueta, Y.; Mikami, K.; Ito, S. Access to Air-Stable 1,3-Diphosphacyclobutane-2,4-Diyls by an Arylation Reaction With Arynes. *Angew. Chem. Int. Ed.* **2016**, *55* (26), 7525–7529.
172. Ito, S.; Miura, J.; Morita, N.; Yoshifuji, M.; Arduengo, A. J. Synthesis and Physicochemical Properties of Stable 1,3-Diphosphacyclobutane-2,4-Diyls Bearing Sulfanyl Groups. *C. R. Chim.* **2010**, *13* (8–9), 1180–1184.
173. Ito, S.; Torihata, Y.; Mikami, K. Exploration of 1-Arylmethyl-1,3-Diphosphacyclobutane-2,4-Diyls as Hole Transfer Materials. *ChemistrySelect* **2016**, *1* (12), 3310–3315.
174. Ito, S.; Ueta, Y.; Ngo, T. T.; Koshino, K.; Mikami, K. Air-Tolerant 1-Amino-1,3-Diphosphacyclobutane-2,4-Diyls Featuring Strong Electron-Donating Properties and Small HOMO-LUMO Gaps. *Eur. J. Inorg. Chem.* **2017**, *2017* (24), 3048–3052.

175. Ito, S.; Kobayashi, M.; Mikami, K. Through-Space Electrostatic Interaction Between the Electron-Donating 1,3-Diphosphacyclobutane-2,4-Diyl Units. *Org. Lett.* **2013**, *15* (13), 3404–3407.
176. Ito, S.; Kikuchi, M.; Sugiyama, H.; Yoshifuji, M. Synthesis and Properties of Air-Stable 1,3-Diphosphacyclobutane-2,4-Diyls and the Related Compounds. *J. Organomet. Chem.* **2007**, *692* (13), 2761–2767.
177. Yoshifuji, M.; Sugiyama, H.; Ito, S. Syntheses and Reactivity of Novel Unsaturated Cyclic Compounds Containing Phosphorus Atoms. *J. Organomet. Chem.* **2005**, *690* (10), 2515–2520.
178. Ito, S.; Miura, J.; Morita, N.; Yoshifuji, M.; Arduengo, A. J. Poly(Biradicals): Oligomers of 1,3-Diphosphacyclobutane-2,4-Diyl Units. *Angew. Chem. Int. Ed.* **2008**, *47* (34), 6418–6421.
179. Ito, S.; Kikuchi, M.; Miura, J.; Morita, N.; Yoshifuji, M. Spectroscopic and Stability Studies on Unsymmetrical 1,3-Dialkyl-1,3-Diphosphacyclobutane-2,4-Diyls. *J. Phys. Org. Chem.* **2012**, *25* (9), 733–737.
180. Ito, S.; Miura, J.; Morita, N.; Yoshifuji, M.; Arduengo, A. J. Catenation of 1,3-Diphosphacyclobutane-2,4-Diyl Units Having 2,4,6-Tri-Tert-Butylphenyl Protecting Groups and a P-Sec-Butyl Group in the Ring. *Z. Anorg. Allg. Chem.* **2009**, *635* (3), 488–495.
181. Sugiyama, H.; Ito, S.; Yoshifuji, M. Preparation and Reactions of 1,3-Diphosphacyclobutane-2,4-Diyls That Feature an Amino Substituent and/or a Carbonyl Group. *Chem. A Eur. J.* **2004**, *10* (11), 2700–2706.
182. Ueta, Y.; Mikami, K.; Ito, S. Chemical Detection of Hydrogen Fluoride by the Phosphorus Congener of Cyclobutane-1,3-Diyl. *Inorg. Chem.* **2015**, *54* (17), 8778–8785.
183. Ito, S.; Miura, J.; Morita, N.; Yoshifuji, M.; Arduengo, A. J. Modeling the Direct Activation of Dihydrogen by a P<sub>2</sub>C<sub>2</sub> Cyclic Biradical: Formation of a Cyclic Bis(P–H λ<sub>5</sub>-Phosphorane). *Inorg. Chem.* **2009**, *48* (17), 8063–8065.
184. Yoshifuji, M.; Arduengo, A. J.; Ill, K.; Konovalova, T. A.; Kispert, L. D.; Kikuchi, M.; Ito, S. Oxidation of 1,3-Diphosphacyclobutane-2,4-Diyl With Ammoniumyl Antimonate and EPR Study of the Corresponding Cation Radical. *Chem. Lett.* **2006**, *35* (10), 1136–1137.
185. Ito, S.; Ueta, Y.; Torihata, Y.; Mikami, K. The Air-Stable P-Heterocyclic Biradical for OFET Devices. *Phosphorus Sulfur Silicon Relat. Elem.* **2015**, *190* (5–6), 854–857.
186. Takeuchi, K.; Ichinohe, M.; Sekiguchi, A. Access to a Stable Si<sub>2</sub>N<sub>2</sub>four-Membered Ring With Non-Kekulé Singlet Biradical Character From a Disilyne. *J. Am. Chem. Soc.* **2011**, *133* (32), 12478–12481.
187. Zhang, S.-H.; Xi, H.-W.; Lim, K. H.; Meng, Q.; Huang, M.-B.; So, C.-W. Synthesis and Characterization of a Singlet Delocalized 2,4-Diimino-1,3-Disilacyclobutanediyl and a Silylenylsilaamine. *Chem. A Eur. J.* **2012**, *18* (14), 4258–4263.
188. Pyykkö, P.; Atsumi, M. Molecular Double-Bond Covalent Radii for Elements Li–E112. *Chem. A Eur. J.* **2009**, *15* (46), 12770–12779.
189. Yildiz, C. B.; Leszczyńska, K. I.; González-Gallardo, S.; Zimmer, M.; Azizoglu, A.; Biskup, T.; Kay, C. W. M.; Huch, V.; Rzepa, H. S.; Scheschke, D. Equilibrium Formation of Stable All-Silicon Versions of 1,3-Cyclobutanediyl. *Angew. Chem. Int. Ed.* **2020**, *59* (35), 15087–15092.
190. Wiber, N.; Schuster, H.; Simon, A.; Peters, K. Hexa-Tert-Butyldisilane—The Molecule With the Longest Si–Si Bond. *Angew. Chem. Int. Ed.* **1986**, *25*, 79–80.
191. Doddi, A.; Gemel, C.; Winter, M.; Fischer, R. A.; Goedecke, C.; Rzepa, H. S.; Frenking, G. Low-Valent Ge(2) and Ge(4) Species Trapped by N-Heterocyclic Gallylene. *Angew. Chem. Int. Ed.* **2013**, *52* (1), 450–454.
192. Cui, C.; Brynda, M.; Olmstead, M. M.; Power, P. P. Synthesis and Characterization of the Non-Kekulé, Singlet Biradicaloid Ar'Ge(μ-NSiMe<sub>3</sub>)<sub>2</sub>GeAr' (Ar' = 2,6-Dipp<sub>2</sub>C<sub>6</sub>H<sub>3</sub>, Dipp = 2,6-I-Pr<sub>2</sub>C<sub>6</sub>H<sub>3</sub>). *J. Am. Chem. Soc.* **2004**, *126* (21), 6510–6511.
193. Wang, X.; Peng, Y.; Olmstead, M. M.; Fetting, J. C.; Power, P. P. An Unsymmetric Oxo/Imido-Bridged Germanium-Centered Singlet Diradicaloid. *J. Am. Chem. Soc.* **2009**, *131* (40), 14164–14165.
194. Cox, H.; Hitchcock, P. B.; Lappert, M. F.; Pierrssens, L. J. M. A 1,3-Diaza-2,4-Distannacyclobutanediide: Synthesis, Structure, and Bonding. *Angew. Chem. Int. Ed.* **2004**, *43* (34), 4500–4504.
195. Hinz, A.; Schulz, A.; Villinger, A.; Wolter, J. M. Cyclo-Pnicta-Triazanes: Biradicaloids or Zwitterions? *J. Am. Chem. Soc.* **2015**, *137* (11), 3975–3980.
196. Hinz, A.; Schulz, A.; Villinger, A. Zwitterionic and Biradicaloid Heteroatomic Cyclopentane Derivatives Containing Different Group 15 Elements. *Chem. Sci.* **2016**, *7* (1), 745–751.
197. Hinz, A. Untersuchungen Zu Gruppe-15-Biradikaloiden, PhD Thesis, Universität Rostock, 2015.
198. Bresien, J.; Schulz, A.; Szych, L. S.; Villinger, A.; Wustrack, R. [E(μ-NBbp)]<sub>2</sub> (E = P, As)—Group 15 Biradicals Synthesized From Acyclic Precursors. *Dalton Trans.* **2019**, *48* (29), 11103–11111.
199. Hinz, A.; Schulz, A.; Villinger, A. A Mixed Arsenic-Phosphorus Centered Biradicaloid. *Angew. Chem. Int. Ed.* **2015**, *54* (2), 668–672.
200. Hinz, A.; Rothe, J.; Schulz, A.; Villinger, A. Reduction of Dichloro(Diaza-Phospha)Stibanes—Isolation of a Donor-Stabilized Distibonium Dication. *Dalton Trans.* **2016**, *45* (14), 6044–6052.
201. Bresien, J.; Hinz, A.; Schulz, A.; Villinger, A. Trapping of Transient, Heavy Pnictogen-Centred Biradicals. *Dalton Trans.* **2018**, *47* (13), 4433–4436.
202. Hinz, A.; Schulz, A.; Seidel, W. W.; Villinger, A. A New Class of Azadipnictiridines Generated by an Unusual Rearrangement Reaction. *Inorg. Chem.* **2014**, *53* (21), 11682–11690.
203. Hinz, A.; Schulz, A.; Villinger, A. New P-N Cage Compounds Generated by Small-Molecule Activation. *Chem. A Eur. J.* **2014**, *20* (14), 3913–3916.
204. Bresien, J.; Hinz, A.; Schulz, A.; Villinger, A. As-N and As-N-P Cage Compounds Generated by [2+2] Addition of Diazenes and Diphosphenes to Diarsadiazanediyls. *Eur. J. Inorg. Chem.* **2018**, *2018* (15), 1679–1682.
205. Chojetzki, L.; Schulz, A.; Villinger, A.; Wustrack, R. Cycloaddition of Alkenes and Alkynes to the P-Centered Singlet Biradical [P(M-Nter)]<sub>2</sub>. *Z. Anorg. Allg. Chem.* **2020**, *646* (13), 614–624.
206. Hinz, A.; Schulz, A.; Villinger, A. Metal-Free Activation of Hydrogen, Carbon Dioxide, and Ammonia by the Open-Shell Singlet Biradicaloid [P(μ-Nter)]<sub>2</sub>. *Angew. Chem. Int. Ed.* **2016**, *55* (40), 12214–12218.
207. Zhivonitko, V. V.; Bresien, J.; Schulz, A.; Koptuyg, I. V. Parahydrogen-Induced Polarization With a Metal-Free P–P Biradicaloid. *Phys. Chem. Chem. Phys.* **2019**, *21* (11), 5890–5893.
208. Zhivonitko, V. V.; Beer, H.; Zakharov, D. O.; Bresien, J.; Schulz, A. Hyperpolarization Effects in Parahydrogen Activation With Pnictogen Biradicaloids: Metal-Free PHP and SABRE. *ChemPhysChem* **2021**, *22* (9), 813–817.
209. Beer, H.; Bläsing, K.; Bresien, J.; Chojetzki, L.; Schulz, A.; Stoer, P.; Villinger, A. Trapping of Brønsted Acids With a Phosphorus-Centered Biradicaloid—Synthesis of Hydrogen Pseudohalide Addition Products. *Dalton Trans.* **2020**, *49* (39), 13655–13662.
210. Hinz, A.; Schulz, A.; Villinger, A. Stable Heterocyclopentane-1,3-Diyls. *Angew. Chem. Int. Ed.* **2015**, *54* (9), 2776–2779.
211. Hinz, A.; Schulz, A.; Villinger, A. Tunable Cyclopentane-1,3-Diyls Generated by Insertion of Isonitriles Into Diphosphadiazanediyls. *J. Am. Chem. Soc.* **2015**, *137* (31), 9953–9962.
212. Beer, H.; Bresien, J.; Michalik, D.; Röike, A.-K.; Schulz, A.; Villinger, A.; Wustrack, R. Heterocyclopentenediyls vs Heterocyclopentadienes: A Question of Silyl Group Migration. *J. Org. Chem.* **2020**, *85* (22), 14435–14445.
213. Schulz, A.; Hinz, A.; Röike, A.; Villinger, A.; Wustrack, R. On New Staudinger Type Reactions of Phosphorus Centered Biradicaloids, [P(μ-NR)]<sub>2</sub> (R = Ter, Hyp), With Ionic and Covalent Azides. *Z. Anorg. Allg. Chem.* **2021**, *647* (4), 245–257.
214. Tian, W. Q.; Wang, Y. A. Mechanisms of Staudinger Reactions Within Density Functional Theory. *J. Org. Chem.* **2004**, *69* (13), 4299–4308.
215. Godemann, C.; Dura, L.; Hollmann, D.; Grabow, K.; Benstrup, U.; Jiao, H.; Schulz, A.; Brückner, A.; Beweries, T. Highly Selective Visible Light-Induced Ti–O Bond Splitting in an Ansa-Titanocene Dihydroxido Complex. *Chem. Commun.* **2015**, *51* (15), 3065–3068.
216. Hinz, A.; Schulz, A.; Villinger, A. On the Behaviour of Biradicaloid [P(μ-Nter)]<sub>2</sub> towards Lewis Acids and Bases. *Chem. Commun.* **2016**, *52* (37), 6328–6331.

217. DuBois, D.; Duesler, E. N.; Paine, R. T. Synthesis and X-Ray Structural Characterization of an Eight-Membered P<sub>4</sub>N<sub>4</sub> Cage Compound Analogue of S<sub>4</sub>N<sub>4</sub> and  $\alpha$ -P<sub>4</sub>S<sub>4</sub>. *J. Chem. Soc. Chem. Commun.* **1984**, 4 (8), 488–489.
218. Brückner, A.; Hinz, A.; Priebe, J. B.; Schulz, A.; Villinger, A. Cyclic Group 15 Radical Cations. *Angew. Chem. Int. Ed.* **2015**, 54 (25), 7426–7430.
219. Bawari, D.; Prashanth, B.; Ravi, S.; Shamasundar, K. R.; Singh, S.; Wright, D. S. Two Different Pathways in the Reduction of [(S=)PCl( $\mu$ -N'Bu)]<sub>2</sub> With Na. *Chem. A Eur. J.* **2016**, 22 (34), 12027–12033.
220. Li, Z.; Chen, X.; Andrada, D. M.; Frenking, G.; Benkő, Z.; Li, Y.; Harmer, J. R.; Su, C.-Y.; Grützmacher, H. (L)<sub>2</sub>C<sub>2</sub>P<sub>2</sub>: Dicarbondiphosphide Stabilized by N-Heterocyclic Carbenes or Cyclic Diamido Carbenes. *Angew. Chem. Int. Ed.* **2017**, 56 (21), 5744–5749.
221. Rottschäfer, D.; Neumann, B.; Stammler, H. G.; Ghadwal, R. S. N-Heterocyclic Vinylidene-Stabilized Phosphorus Biradicaloid. *Chem. A Eur. J.* **2017**, 23 (38), 9044–9047.
222. Chen, X.; Hu, C.; Zhang, X.; Liu, S.; Mei, Y.; Hu, G.; Liu, L. L.; Li, Z.; Su, C.-Y. Reversible Stereoisomerization of 1,3-Diphosphetane Frameworks Revealed by a Single-Electron Redox Approach. *Inorg. Chem.* **2021**, 60 (8), 5771–5778.
223. Chen, X.; Liu, L. L.; Liu, S.; Grützmacher, H.; Li, Z. A Room-Temperature Stable Distonic Radical Cation. *Angew. Chem. Int. Ed.* **2020**, 59 (52), 23830–23835.
224. Zhang, X.; Chen, X.; Zhai, H.; Liu, S.; Hu, C.; Liu, L. L.; Wang, S.; Li, Z. Facile Addition of E–H Bonds to a Dicarbondiphosphide. *Dalton Trans.* **2020**, 49 (19), 6384–6390.
225. Li, Z.; Chen, X.; Liu, L. L.; Schamhölz, M. T.; Grützmacher, H. N-Heterocyclic Carbene Stabilized Dicarbondiphosphides: Strong Neutral Four-Membered Heterocyclic 6 $\pi$ -Electron Donors. *Angew. Chem. Int. Ed.* **2020**, 59 (11), 4288–4293.
226. Cisar, A.; Corbett, J. D. Polybismuth Anions. Synthesis and Crystal Structure of a Salt of the Tetrabismuthide(2-) Ion, Bi<sub>4</sub><sup>2-</sup>. A Basis for the Interpretation of the Structure of Some Complex Intermetallic Phases. *Inorg. Chem.* **1977**, 16 (10), 2482–2487.
227. Critchlow, S. C.; Corbett, J. D. Homopolyatomic Anions of the Post Transition Elements. Synthesis and Structure of Potassium-Crypt Salts of the Tetraantimonide(2-) and Heptaantimonide(3-) Anions, Sb<sub>4</sub><sup>2-</sup> and Sb<sub>7</sub><sup>3-</sup>. *Inorg. Chem.* **1984**, 23 (6), 770–774.
228. Korber, N.; Reil, M. An Isolated Cyclo-Tetraarsendiide: Low Temperature Synthesis and Crystal Structure of Bis-Pentaamminesodium Tetraarsendiide-Ammonia (1/3) [Na(NH<sub>3</sub>)<sub>5</sub>]<sub>2</sub>As<sub>4</sub>·3NH<sub>3</sub>. *Chem. Commun.* **2002**, 41 (1), 84–85.
229. Kraus, F.; Aschenbrenner, J. C.; Korber, N. P<sub>4</sub><sup>2-</sup>: A 6 $\pi$  Aromatic Polyphosphide in Cesium Cyclotetraphosphide-Ammonia (1/2). *Angew. Chem. Int. Ed.* **2003**, 42 (34), 4030–4033.
230. Coburger, P.; Wolf, R.; Grützmacher, H. Isomerism and Biradical Character of Tetrapnictide Dianions: A Computational Study. *Eur. J. Inorg. Chem.* **2020**, 3580–3586.
231. Noorizadeh, S.; Shakerzadeh, E. Shannon Entropy as a New Measure of Aromaticity, Shannon Aromaticity. *Phys. Chem. Chem. Phys.* **2010**, 12 (18), 4742.
232. Bevssek, H. M.; Ahmed, M.; Peterka, D. S.; Cortney Sailes, F.; Suits, A. G. Direct Detection and Spectroscopy of O<sub>4</sub><sup>\*</sup>. *Faraday Discuss.* **1997**, 108, 131–138.
233. Fujihisa, H.; Akahama, Y.; Kawamura, H.; Ohishi, Y.; Shimomura, O.; Yamawaki, H.; Sakashita, M.; Gotoh, Y.; Takeya, S.; Honda, K. O<sub>8</sub> Cluster Structure of the Epsilon Phase of Solid Oxygen. *Phys. Rev. Lett.* **2006**, 97 (8), 085503.
234. Borden, W. T.; Hoffmann, R.; Stuyver, T.; Chen, B. Dioxigen: What Makes This Triplet Diradical Kinetically Persistent? *J. Am. Chem. Soc.* **2017**, 139 (26), 9010–9018.
235. Scemama, A.; Caffarel, M.; Ramírez-Solís, A. Bond Breaking and Bond Making in Tetraoxygen: Analysis of the O<sub>2</sub>(X<sub>3</sub>Sigma(g)) + O<sub>2</sub>(X<sub>3</sub>Sigma(g))  $\rightleftharpoons$  O<sub>4</sub> Reaction Using the Electron Pair Localization Function. *J. Phys. Chem. A* **2009**, 113 (31), 9014–9021.
236. Zhu, L.; Wang, Z.; Wang, Y.; Zou, G.; Mao, H.; Ma, Y. Spiral Chain O<sub>4</sub> Form of Dense Oxygen. *Proc. Natl. Acad. Sci. U. S. A.* **2012**, 109 (3), 751–753.
237. Miliordos, E.; Xanthreas, S. S. On the Bonding Nature of Ozone (O<sub>3</sub>) and Its Sulfur-Substituted Analogues SO<sub>2</sub>, OS<sub>2</sub>, and S<sub>3</sub>: Correlation Between Their Biradical Character and Molecular Properties. *J. Am. Chem. Soc.* **2014**, 136 (7), 2808–2817.
238. Glezakou, V. A.; Elbert, S. T.; Xanthreas, S. S.; Ruedenberg, K. Analysis of Bonding Patterns in the Valence Isoelectronic Series O<sub>3</sub>, S<sub>3</sub>, SO<sub>2</sub>, and OS<sub>2</sub> in Terms of Oriented Quasi-Atomic Molecular Orbitals. *J. Phys. Chem. A* **2010**, 114 (33), 8923–8931.
239. Harcourt, R. D.; Klapötke, T. M.; Schulz, A.; Wolyneć, P. On the Singlet Diradical Character of S<sub>2</sub>N<sub>2</sub>. *J. Phys. Chem. A* **1998**, 102 (10), 1850–1853.
240. Braïda, B.; Lo, A.; Hiberty, P. C. Can Aromaticity Coexist With Diradical Character? An Ab Initio Valence Bond Study of S<sub>2</sub>N<sub>2</sub> and Related 6 $\pi$ -Electron Four-Membered Rings E<sub>2</sub>N<sub>2</sub> and E<sub>4</sub><sup>2+</sup> (E = S, Se, Te). *ChemPhysChem* **2012**, 13 (3), 811–819.
241. Goehring, M.; Voigt, D. Über Die Schwefelnitride (SN)<sub>2</sub> Und (SN)<sub>x</sub>. *Naturwissenschaften* **1953**, 40 (18), 482.
242. Bragin, J.; Evans, M. V. Vibrational Spectra and Structure of S<sub>4</sub>N<sub>4</sub> and S<sub>2</sub>N<sub>2</sub>. *J. Chem. Phys.* **1969**, 51 (1), 268–277.
243. Penotti, F. E.; Cooper, D. L.; Karadakov, P. B. Is the S<sub>2</sub>N<sub>2</sub> Ring a Singlet Diradical? Critical Analysis of Alternative Valence Bond Descriptions. *Int. J. Quantum Chem.* **2018**, e25845.
244. Jung, Y.; Heine, T.; Schleyer, P. v. R.; Head-Gordon, M. Aromaticity of Four-Membered-Ring 6 $\pi$ -Electron Systems: N<sub>2</sub>S<sub>2</sub> and Li<sub>2</sub>C<sub>4</sub>H<sub>4</sub>. *J. Am. Chem. Soc.* **2004**, 126 (10), 3132–3138.
245. Gerratt, J.; McNicholas, S. J.; Karadakov, P. B.; Sironi, M.; Raimondi, M.; Cooper, D. L. The Extraordinary Electronic Structure of N<sub>2</sub>S<sub>2</sub>. *J. Am. Chem. Soc.* **1996**, 118 (27), 6472–6476.
246. Klapötke, T. M.; Li, J.; Harcourt, R. D. Ab Initio Double- $\zeta$  (D95) Valence Bond Calculations for the Ground States of S<sub>2</sub>N<sub>2</sub> and S<sub>4</sub><sup>2+</sup>. *J. Phys. Chem. A* **2004**, 108 (31), 6527–6531.
247. Tuononen, H. M.; Suontamo, R.; Valkonen, J.; Laitinen, R. S. Electronic Structures and Spectroscopic Properties of 6 $\pi$ -Electron Ring Molecules and Ions E<sub>2</sub>N<sub>2</sub> and E<sub>4</sub><sup>2+</sup> (E = S, Se, Te). *J. Phys. Chem. A* **2004**, 108 (26), 5670–5677.
248. Tuononen, H. M.; Suontamo, R.; Valkonen, J.; Laitinen, R. S.; Chivers, T. Electronic Structures and Molecular Properties of Chalcogen Nitrides Se<sub>2</sub>N<sub>2</sub> and SeSN<sub>2</sub>. *J. Phys. Chem. A* **2005**, 109 (28), 6309–6317.
249. Gillespie, R. J.; Passmore, J. Polycations of Group VI. *Acc. Chem. Res.* **1971**, 4 (12), 413–419.
250. Gillespie, R. J. Nyholm Memorial Lecture. Ring, Cage, and Cluster Compounds of the Main Group Elements. *Chem. Soc. Rev.* **1979**, 8 (3), 315.
251. Brownridge, S. Recent Advances in the Understanding of the Syntheses, Structures, Bonding and Energetics of the Homopolyatomic Cations of Groups 16 and 17. *Coord. Chem. Rev.* **2000**, 197 (1), 397–481.
252. Beck, J.; Steden, F.; Reich, A.; Fölsing, H. Synthese, Struktur Und Phasenumwandlung von Te<sub>4</sub>[AsF<sub>6</sub>]<sub>2</sub>·SO<sub>2</sub>. *Z. Anorg. Allg. Chem.* **2003**, 629 (6), 1073–1079.
253. Corbett, J. D. *Homopolyatomic Ions of the Post-Transition Elements-Synthesis, Structure, and Bonding*, Wiley, 2007; pp 129–158.
254. Klaproth, XVIII. Extract from a Memoir on a New Metal Called Tellurium, M. H. *Philos. Mag.* **1798**, 1, 78–82.
255. Bjerrum, N. J.; Smith, G. P. Tellurium in the Formal Electropositive Oxidation State One-Half in Acidic Chloride Media. *J. Am. Chem. Soc.* **1968**, 90 (16), 4472–4473.
256. Conrad, M. P.; Pitzer, R. M.; Schaefer, H. F. Geometrical Structure and Energetics of Closs's Diradical: 1,3-Cyclopentadiyl. *J. Am. Chem. Soc.* **1979**, 101 (8), 2245–2246.
257. Buchwalter, S. L.; Closs, G. L. Electron Spin Resonance Study of Matrix Isolated 1,3-Cyclopentadiyl, a Localized 1,3-Carbon Biradical. *J. Am. Chem. Soc.* **1975**, 97 (13), 3857–3858.
258. Sherrill, C. D.; Seidl, E. T.; Schaefer, H. F. Closs's Diradical: Some Surprises on the Potential Energy Hypersurface. *J. Phys. Chem.* **1992**, 96 (9), 3712–3716.
259. Gassmann, P. G.; Mansfield, K. T. Bicyclo[2.1.0]Pentane. *Organic Synth.* **1969**, 49 (1).
260. Adam, W.; Doerr, M. Wagner-Meerwein Rearrangements of Radical Cations Generated by Triphenylpyrylium Tetrafluoroborate Photosensitized Electron Transfer of Azoalkanes. *J. Am. Chem. Soc.* **1987**, 109 (5), 1570–1572.
261. Adams, J. S.; Weisman, R. B.; Engel, P. S. Photodissociation of a Bicyclic Azoalkane: Time-Resolved Coherent Anti-Stokes Raman Spectroscopy Studies of Vapor-Phase 2,3-Diazabicyclo[2.2.1]Hept-2-Ene. *J. Am. Chem. Soc.* **1990**, 112 (25), 9115–9121.
262. Adam, W.; Sendelbach, J. Denitrogenation of Bicyclic Azoalkanes Through Photosensitized Electron Transfer: Generation and Intramolecular Trapping of Radical Cations. *J. Org. Chem.* **1993**, 58 (20), 5316–5322.
263. Abe, M.; Adam, W.; Nau, W. M. Photochemical Generation and Methanol Trapping of Localized 1,3 and 1,4 Singlet Diradicals Derived From a Spiroepoxy-Substituted Cyclopentane 1,3-Diyl. *J. Am. Chem. Soc.* **1998**, 120 (44), 11304–11310.



264. Adam, W.; Borden, W. T.; Burda, C.; Foster, H.; Heidenfelder, T.; Heubes, M.; Hrovat, D. A.; Kita, F.; Lewis, S. B.; Scheutzw, D.; et al. Transient Spectroscopy of a Derivative of 2,2-Difluoro-1,3-Diphenylcyclopentane-1,3-Diyl Persistent Localized Singlet 1,3-Diradical. *J. Am. Chem. Soc.* **1998**, *120* (3), 593–594.
265. Evin, A. B.; Arnold, D. R. Diels-Alder Reactions of Diazadienes and Chemistry of the Adducts. *J. Am. Chem. Soc.* **1968**, *90* (19), 5330–5332.
266. Arnold, D. R.; Evin, A. B.; Kasal, P. H. Triplet Electron Spin Resonance Signal of 1,3-Diradicals From Bicyclic Azo Compounds. *J. Am. Chem. Soc.* **1969**, *91* (3), 784–785.
267. Arnold, D. R.; Evin, A. B.; Karnischky, L. A.; Strom, E. Chemical and Spectroscopic Studies of the Decomposition of Bicyclic Azo Compounds Derived From Isopyrazoles. *J. Am. Chem. Soc.* **1970**, *92* (21), 6218–6231.
268. Abe, M.; Adam, W.; Borden, W. T.; Hattori, M.; Hrovat, D. A.; Nojima, M.; Nozaki, K.; Wirz, J. Effects of Spiroconjugation on the Calculated Singlet–Triplet Energy Gap in 2,2-Dialkoxy-cyclopentane-1,3-Diyls and on the Experimental Electronic Absorption Spectra of Singlet 1,3-Diphenyl Derivatives. Assignment of the Lowest-Energy Electronic Transition. *J. Am. Chem. Soc.* **2004**, *126* (2), 574–582.
269. Nakamura, T.; Gagliardi, L.; Abe, M. Computational Study of the Cooperative Effects of Nitrogen and Silicon Atoms on the Singlet-Triplet Energy Spacing in 1,3-Diradicals and the Reactivity of Their Singlet States. *J. Phys. Org. Chem.* **2010**, 300–307.
270. Abe, M.; Kubo, E.; Nozaki, K.; Matsuo, T.; Hayashi, T. An Extremely Long-Lived Singlet 4,4-Dimethoxy-3,5-Diphenylpyrazolidine-3,5-Diyl Derivative: A Notable Nitrogen-Atom Effect on Intra- and Intermolecular Reactivity. *Angew. Chem. Int. Ed.* **2006**, *45* (46), 7828–7831.
271. Yoshidomi, S.; Mishima, M.; Seyama, S.; Abe, M.; Fujiwara, Y.; Ishibashi, T. Direct Detection of a Chemical Equilibrium between a Localized Singlet Diradical and Its  $\sigma$ -Bonded Species by Time-Resolved UV/Vis and IR Spectroscopy. *Angew. Chem. Int. Ed.* **2017**, *56* (11), 2984–2988.
272. Nakamura, T.; Takegami, A.; Abe, M. Generation and Intermolecular Trapping of 1,2-Diaza-4-Silacyclopentane-3,5-Diyls in the Denitrogenation of 2,3,5,6-Tetraaza-7-Silabicyclo[2.2.1]hept-2-Ene: An Experimental and Computational Study. *J. Org. Chem.* **2010**, *75* (6), 1956–1960.
273. Schönberg, A.; Frese, E. Synthese Des 1.3-Diphenyl-1.3-Dithio-1.2.3-Triketonen Aus Dibenzylketontetrabromid Und Kaliumxanthogenat. *Tetrahedron Lett.* **1969**, *10* (46), 4063–4064.
274. Schönberg, A.; Frese, E. Mesoionische Aromaten, II. Über Das Mesoionische 3.5-Diphenyl-1.2-Dithiolylium-4-Olat, Ein Valenzisomeres Des 2-Oxo-1.3-Dithio-1.3-Diphenyl-Propans. *Chem. Ber.* **1970**, *103* (12), 3885–3895.
275. Cannon, J. R.; Potts, K. T.; Raston, C. L.; Sierakowski, A. F.; White, A. H. Chemistry and Crystal Structures of L, 3-Bis(4'-Bromophenyl)Propane-L, 2, 3-Trione, 3, 5-Diphenyl-L, 2-Dithiolylium-4-Olate and 4-Hydroxy-3, 5-Diphenyl-L, 2-Dithiolylium Perchlorate. *Aust. J. Chem.* **1978**, *31* (2), 297–311.
276. Barillier, D. Physicochemical Properties and Structural Study of 1,2-Dithiolylium-4-Olates and Isothiazolium-4-Olates. *Phosphorus Sulfur Rel. Elem.* **1980**, *8* (1), 79–85.
277. Fabian, J.; Mayer, R.; Čársky, P.; Zahradnik, R. Quantenchemische Ab-Initio-Berechnungen an Schwefelorganischen Verbindungen: Experimentelle Und Theoretische Untersuchungen an Thioformaldehyd Und Dithioglyoxal. *Z. Chem.* **1985**, *25* (2), 50–61.
278. Mayer, R.; Fabian, J.; Viola, H.; Jakisch, L. Synthesis and Electronic Structure of Potentially Valence Isomeric 1,2-Dithiolylium-4-Olates. *Phosphorus Sulfur Rel. Elem.* **1987**, *31* (1–2), 109–122.
279. Chinone, A.; Inouye, K.; Ohta, M. Syntheses of 1,2-Dithiole Derivatives. *Bull. Chem. Soc. Jpn.* **1972**, *45* (1), 213–215.
280. Inouye, K.; Sato, S.; Ohta, M. Sulfurization of 1,3-Diphenylpropanetrione. *Bull. Chem. Soc. Jpn.* **1970**, *43* (6), 1911.
281. Viola, H.; Jakisch, L.; Mayer, R. 3,5-Di(Alkylthio)-1,2-Dithiolylium-4-Olate - Valenzisomere der Tetrathiohexaäure-dialkylester. *Z. Chem.* **1982**, *22* (11), 405.
282. Potts, K. T.; Singh, U. P. Mesoionic Derivatives of the 1,3-Dithiole System. *J. Chem. Soc. D* **1969**, *9* (11), 569.
283. Hordvik, A.; Jynge, K.; Pedersen, I.; Weidlein, J.; Wahlberg, O. The Crystal and Molecular Structures of 3,5-Diphenyl-1,2-Dithiolylium-4-Olate, 3,5-Di(2-Thienyl)-1,2-Dithiolylium-4-Olate and 3,5-Di(t-Butyl)-1,2-Dithiolylium-4-Olate. *Acta Chem. Scand.* **1981**, *35a*, 607–616.
284. Mann, M.; Fabian, J. Structures and Properties of 1,2-Dithiolylium-4-Methide, 1,2-Dithiolylium-4-Olate and 1,2-Dithiolylium-4-Thiolate: An MO Study at the HF and Post-HF Levels. *J. Phys. Org. Chem.* **1995**, *8* (8), 536–544.
285. Product Class 7: 1,2-Dithiolylium Salts and Related Compounds. In *Category 2, Heterarenes and Related Ring Systems*; Boyd, G. V., Brown, D. W., Fanghänel, E., Gudat, D., Kikelj, D., Klenke, C., Pedersen, C. T., Perst, H., Pfeiffer, W.-D., Sainsbury, M., ; et al. Schaumann, E., Eds., Georg Thieme Verlag: Stuttgart, 2002; pp 125–186.
286. Winkler, J. Untersuchungen Zur Einstellbarkeit von Schaltbaren Hetero-Cyclopentandiolen, Bachelor's Thesis, Universität Rostock, 2018.
287. Bresien, J.; Kröger-Badge, T.; Lochbrunner, S.; Michalik, D.; Müller, H.; Schulz, A.; Zander, E. A Chemical Reaction Controlled by Light-Activated Molecular Switches Based on Hetero-Cyclopentanediylys. *Chem. Sci.* **2019**, *10* (12), 3486–3493.
288. Müller, H. Modifikation von Molekularen Schaltern, Master's Thesis, Universität Rostock, 2018.
289. Bresien, J.; Michalik, D.; Schulz, A.; Villinger, A.; Zander, E. Azadiphosphaindane-1,3-Diyls: A Class of Resonance-Stabilized Biradicals. *Angew. Chem. Int. Ed.* **2021**, *60* (3), 1507–1512.
290. Guddorf, B. J.; Mück-Lichtenfeld, C.; Hepp, A.; Lips, F. Formation of an NHC-Stabilized Heterocyclic Housane and its Isomerization into a Cyclopentenyl Anion Analogue. *Chem. Commun.* **2019**, *55* (86), 12896–12899.
291. Tsuji, Y.; Hoffmann, R.; Strange, M.; Solomon, G. C. Close Relation Between Quantum Interference in Molecular Conductance and Diradical Existence. *Proc. Natl. Acad. Sci.* **2016**, *113* (4), E413–E419.
292. Stuyver, T.; Zeng, T.; Tsuji, Y.; Geerlings, P.; De Proft, F. Diradical Character as a Guiding Principle for the Insightful Design of Molecular Nanowires With an Increasing Conductance With Length. *Nano Lett.* **2018**, *18* (11), 7298–7304.
293. Stuyver, T.; Danovich, D.; Shaik, S. Captodative Substitution Enhances the Diradical Character of Compounds, Reduces Aromaticity, and Controls Single-Molecule Conductivity Patterns: A Valence Bond Study. *J. Phys. Chem. A* **2019**, *123* (32), 7133–7141.
294. Kröncke, S.; Herrmann, C. Designing Long-Range Charge Delocalization From First-Principles. *J. Chem. Theory Comput.* **2019**, *15* (1), 165–177.
295. Smith, M. B.; Michl, J. Singlet Fission. *Chem. Rev.* **2010**, *110* (11), 6891–6936.
296. Minami, T.; Nakano, M. Diradical Character View of Singlet Fission. *J. Phys. Chem. Lett.* **2012**, *3* (2), 145–150.
297. Smith, M. B.; Michl, J. Recent Advances in Singlet Fission. *Annu. Rev. Phys. Chem.* **2013**, *64* (1), 361–386.
298. Zeng, T.; Ananth, N.; Hoffmann, R. Seeking Small Molecules for Singlet Fission: A Heteroatom Substitution Strategy. *J. Am. Chem. Soc.* **2014**, *136* (36), 12638–12647.
299. Casanova, D. Theoretical Modeling of Singlet Fission. *Chem. Rev.* **2018**, *118* (15), 7164–7207.
300. Messelberger, J.; Grünwald, A.; Pinter, P.; Hansmann, M. M.; Munz, D. Carbene Derived Diradicaloids - Building Blocks for Singlet Fission? *Chem. Sci.* **2018**, *9* (28), 6107–6117.
301. Nakano, M.; Champagne, B. Theoretical Design of Open-Shell Singlet Molecular Systems for Nonlinear Optics. *J. Phys. Chem. Lett.* **2015**, *6* (16), 3236–3256.
302. Nakano, M.; Champagne, B. Nonlinear Optical Properties in Open-Shell Molecular Systems. *WIREs Comput. Mol. Sci.* **2016**, *6* (2), 198–210.
303. Alexander Voigt, B.; Steenbock, T.; Herrmann, C. Structural Diradical Character. *J. Comput. Chem.* **2019**, *40* (7), 854–865.
304. Okuno, K.; Shigeta, Y.; Kishi, R.; Nakano, M. Photochromic Switching of Diradical Character: Design of Efficient Nonlinear Optical Switches. *J. Phys. Chem. Lett.* **2013**, *4* (15), 2418–2422.
305. Sun, J.; Wu, Y.; Wang, Y.; Liu, Z.; Cheng, C.; Hartlieb, K. J.; Wasielewski, M. R.; Stoddart, J. F. An Electrochromic Tristable Molecular Switch. *J. Am. Chem. Soc.* **2015**, *137* (42), 13484–13487.
306. Paolino, M.; Gueye, M.; Pieri, E.; Manathunga, M.; Fusi, S.; Cappelli, A.; Latterini, L.; Pannacci, D.; Filatov, M.; Léonard, J.; et al. Design, Synthesis, and Dynamics of a Green Fluorescent Protein Fluorophore Mimic With an Ultrafast Switching Function. *J. Am. Chem. Soc.* **2016**, *138* (31), 9807–9825.
307. Wang, J.-J.; Zhou, Z.-J.; He, H.-M.; Wu, D.; Li, Y.; Li, Z.-R.; Zhang, H.-X. An External Electric Field Manipulated Second-Order Nonlinear Optical Switch of an Electride Molecule: A Long-Range Electron Transfer Forms a Lone Excess Electron Pair and Quenches Singlet Diradical. *J. Phys. Chem. C* **2016**, *120* (25), 13656–13666.
308. Ravat, P.; Šolomek, T.; Häußinger, D.; Blacque, O.; Juríček, M. Dimethylcethrene: A Chiroptical Diradicaloid Photoswitch. *J. Am. Chem. Soc.* **2018**, *140* (34), 10839–10847.
309. Yoshidomi, S.; Abe, M. 1,2-Diazacyclopentane-3,5-Diyl Diradicals: Electronic Structure and Reactivity. *J. Am. Chem. Soc.* **2019**, *141* (9), 3920–3933.



310. Beer, H.; Bresien, J.; Michalik, D.; Schulz, A.; Villinger, A. Reversible Switching between Housane and Cyclopentenediyl Isomers: An Isonitrile-Catalysed Thermal Reverse Reaction. *Dalton Trans.* **2020**, *49*, 13986–13992.
311. Völzer, T.; Beer, H.; Schulz, A.; Lochbrunner, S.; Bresien, J. Photoisomerization of a Phosphorus-Based Biradicaloid: Ultrafast Dynamics Through a Conical Intersection. *Phys. Chem. Chem. Phys.* **2021**, *23* (12), 7434–7441.
312. Gopalakrishna, T. Y.; Zeng, W.; Lu, X.; Wu, J. From Open-Shell Singlet Diradicaloids to Polyradicaloids. *Chem. Commun.* **2018**, *54* (18), 2186–2199.
313. Kita, F.; Adam, W.; Jordan, P.; Nau, W. M.; Wirz, J. 1,3-Cyclopentenediyl Diradicals: Substituent and Temperature Dependence of Triplet–Singlet Intersystem Crossing. *J. Am. Chem. Soc.* **1999**, *121* (40), 9265–9275.
314. Feringa, B. L.; van Delden, R. A.; Koumura, N.; Geertsema, E. M. Chiroptical Molecular Switches. *Chem. Rev.* **2000**, *100* (5), 1789–1816.
315. Feringa, B. L., Ed.; *Molecular Switches*, Wiley-VCH: Weinheim, Germany, 2001.
316. Zhang, J. L.; Zhong, J. Q.; Lin, J. D.; Hu, W. P.; Wu, K.; Xu, G. Q.; Wee, A. T. S.; Chen, W. Towards Single Molecule Switches. *Chem. Soc. Rev.* **2015**, *44* (10), 2998–3022.
317. Bléger, D.; Hecht, S. Visible-Light-Activated Molecular Switches. *Angew. Chem. Int. Ed.* **2015**, *54* (39), 11338–11349.
318. Böhnke, J.; Dellermann, T.; Celik, M. A.; Krummenacher, I.; Dewhurst, R. D.; Demeshko, S.; Ewing, W. C.; Hammond, K.; Heß, M.; Bill, E.; et al. Isolation of Diborenes and Their 90°-Twisted Diradical Congeners. *Nat. Commun.* **2018**, *9* (1), 1197.
319. Mukhopadhyay, D. P.; Schleier, D.; Wirsing, S.; Ramlar, J.; Kaiser, D.; Reusch, E.; Hemberger, P.; Pretschopf, T.; Krummenacher, I.; Engels, B.; et al. Methylbismuth: An Organometallic Bismuthinidene Biradical. *Chem. Sci.* **2020**, *11* (29), 7562–7568.
320. Wang, W.; Chen, C.; Shu, C.; Rajca, S.; Wang, X.; Rajca, A. S = 1 Tetraazacyclophane Diradical Dication With Robust Stability: A Case of Low-Temperature One-Dimensional Antiferromagnetic Chain. *J. Am. Chem. Soc.* **2018**, *140* (25), 7820–7826.
321. Chen, Y.; Li, J.; Zhao, Y.; Zhang, L.; Tan, G.; Zhu, H.; Roesky, H. W. Stable Radical Cation and Dication of a 1,4-Disilabenzene. *J. Am. Chem. Soc.* **2021**, *143* (5), 2212–2216.
322. Tan, G.; Li, S.; Chen, S.; Sui, Y.; Zhao, Y.; Wang, X. Isolable Diphosphorus-Centered Radical Anion and Diradical Dianion. *J. Am. Chem. Soc.* **2016**, *138* (21), 6735–6738.
323. Tang, S.; Zhang, L.; Ruan, H.; Zhao, Y.; Wang, X. A Magnetically Robust Triplet Ground State Sulfur-Hydrocarbon Diradical Dication. *J. Am. Chem. Soc.* **2020**, *142* (16), 7340–7344.
324. Gu, X.; Gopalakrishna, T. Y.; Phan, H.; Ni, Y.; Herg, T. S.; Ding, J.; Wu, J. A Three-Dimensionally  $\pi$ -Conjugated Diradical Molecular Cage. *Angew. Chem. Int. Ed.* **2017**, *56* (48), 15383–15387.
325. Wentrup, C.; Regimbald-Krnel, M. J.; Müller, D.; Comba, P. A Thermally Populated, Perpendicularly Twisted Alkene Triplet Diradical. *Angew. Chem. Int. Ed.* **2016**, *55* (47), 14600–14605.
326. Maskey, R.; Wadepohl, H.; Greb, L. Silicon Tris(Perchloro)Dioxolene: A Neutral Triplet Diradical. *Angew. Chem. Int. Ed.* **2019**, *58* (11), 3616–3619.
327. Lu, R.; Wu, S.; Yang, L.; Gao, W.; Qu, H.; Wang, X.; Chen, J.; Tang, C.; Shi, H.; Cao, X. Stable Diindeno-Fused Corannulene Regioisomers With Open-Shell Singlet Ground States and Large Diradical Characters. *Angew. Chem. Int. Ed.* **2019**, *58* (23), 7600–7605.
328. Rajca, A.; Olankitwanit, A.; Rajca, S. Triplet Ground State Derivative of Aza-M-Xylylene Diradical With Large Singlet–Triplet Energy Gap. *J. Am. Chem. Soc.* **2011**, *133* (13), 4750–4753.
329. Intorp, S. N.; Hodecker, M.; Müller, M.; Tverskoy, O.; Rosenkranz, M.; Dmitrieva, E.; Popov, A. A.; Rominger, F.; Freudenberg, J.; Dreuw, A.; et al. Quinoidal Azaacenes: 99% Diradical Character. *Angew. Chem. Int. Ed.* **2020**, *59* (30), 12396–12401.
330. Zhang, C.; Medina Rivero, S.; Liu, W.; Casanova, D.; Zhu, X.; Casado, J. Stable Cross-Conjugated Tetrathiophene Diradical. *Angew. Chem. Int. Ed.* **2019**, *58* (33), 11291–11295.
331. Sharma, M. K.; Rottschäfer, D.; Glodde, T.; Neumann, B.; Stämmler, H.; Ghadwal, R. S. Ein Offenschaliges Singulett-Sn I -Diradikal Und H<sub>2</sub>-Spaltung. *Angew. Chem.* **2021**, *133* (12), 6485–6489.
332. Shu, C.; Zhang, H.; Olankitwanit, A.; Rajca, S.; Rajca, A. High-Spin Diradical Dication of Chiral  $\pi$ -Conjugated Double Helical Molecule. *J. Am. Chem. Soc.* **2019**, *141* (43), 17287–17294.
333. Saalfrank, C.; Fantuzzi, F.; Kupfer, T.; Ritschel, B.; Hammond, K.; Krummenacher, I.; Bertermann, R.; Wirthensohn, R.; Finze, M.; Schmid, P.; et al. CAAC-Stabilized 9,10-diboraanthracenes—Acenes With Open-Shell Singlet Biradical Ground States. *Angew. Chem. Int. Ed.* **2020**, *59* (43), 19338–19343.
334. Lu, Z.; Quanz, H.; Burghaus, O.; Hofmann, J.; Logemann, C.; Beeck, S.; Schreiner, P. R.; Wegner, H. A. Stable Organic Neutral Diradical via Reversible Coordination. *J. Am. Chem. Soc.* **2017**, *139* (51), 18488–18491.
335. Sharma, M. K.; Ebeler, F.; Glodde, T.; Neumann, B.; Stämmler, H.-G.; Ghadwal, R. S. Isolation of a Ge(II) Diradicaloid and Dihydrogen Splitting. *J. Am. Chem. Soc.* **2021**, *143* (1), 121–125.
336. Clar, E.; Schoental, R. *Polycyclic Hydrocarbons*, Springer: Berlin, 1964.
337. Bendikov, M.; Wudl, F.; Perepichka, D. F. Tetrathiafulvalenes, Oligoacenes, and Their Buckminsterfullerene Derivatives: The Brick and Mortar of Organic Electronics. *Chem. Rev.* **2004**, *104* (11), 4891–4945.
338. Novoselov, K. S.; Geim, A. K.; Morozov, S. V.; Jiang, D.; Zhang, Y.; Dubonos, S. V.; Grigorieva, I. V.; Firsov, A. A. Electric Field in Atomically Thin Carbon Films. *Science* **2004**, *306* (5696), 666–669.
339. Goldmann, C.; Haas, S.; Krellner, C.; Pernstlch, K. P.; Gundlach, D. J.; Batlogg, B. Hole Mobility in Organic Single Crystals Measured by a “Flip-Crystal” Field-Effect Technique. *J. Appl. Phys.* **2004**, *96* (4), 2080–2086.
340. Batail, P. Introduction: Molecular Conductors. *Chem. Rev.* **2004**, 4887–4890.
341. Bendikov, M.; Duong, H. M.; Starkey, K.; Houk, K. N.; Carter, E. A.; Wudl, F. Oligoacenes: Theoretical Prediction of Open-Shell Singlet Diradical Ground States. *J. Am. Chem. Soc.* **2004**, *126* (24), 7416–7417.
342. Aihara, J. I.; Kanno, H. Local Aromaticities in Large Polyacene Molecules. *J. Phys. Chem. A* **2005**, *109* (16), 3717–3721.
343. Portella, G.; Poater, J.; Bofill, J. M.; Alemany, P.; Solà, M. Local Aromaticity of [N]Acenes, [N]Phenacenes, and [N]Helicenes (N = 1–9). *J. Org. Chem.* **2005**, *70* (7), 2509–2521.
344. Poater, J.; Bofill, J. M.; Alemany, P.; Solà, M. Local Aromaticity of the Lowest-Lying Singlet States of [N]Acenes (N = 6–9). *J. Phys. Chem. A* **2005**, *109* (47), 10629–10632.
345. Würthner, F.; Schmidt, R. Electronic and Crystal Engineering of Acenes for Solution-Processible Self-Assembling Organic Semiconductors. *ChemPhysChem* **2006**, *7* (4), 793–797.
346. Baumgartner, T.; Réau, R. Organophosphorus  $\pi$ -Conjugated Materials. *Chem. Rev.* **2006**, *106* (11), 4681–4727.
347. Yoshida, M.; Aihara, J. Ichi. Validity of the Weighted HOMO-LUMO Energy Separation as an Index of Kinetic Stability for Fullerenes With up to 120 Carbon Atoms. *Phys. Chem. Chem. Phys.* **1999**, *1* (2), 227–230.
348. Anthony, J. E. Functionalized Acenes and Heteroacenes for Organic Electronics. *Chem. Rev.* **2006**, *106*, 5028–5048. American Chemical Society.
349. Geim, A. K.; Novoselov, K. S. The Rise of Graphene. *Nat. Mater.* **2007**, *6* (3), 183–191.
350. Dresselhaus, M. S.; Endo, M. Relation of Carbon Nanotubes to Other Carbon Materials. In *Carbon Nanotubes*, Springer: Berlin, Heidelberg, 2007; pp 11–28.
351. Murphy, A. R.; Fréchet, J. M. J. Organic Semiconducting Oligomers for Use in Thin Film Transistors. *Chem. Rev.* **2007**, *107*, 1066–1096. American Chemical Society.
352. Kaur, I.; Jia, W.; Kopeski, R. P.; Selvarasah, S.; Dokmeci, M. R.; Pramanik, C.; McGruer, N. E.; Miller, G. P. Substituent Effects in Pentacenes: Gaining Control Over HOMO-LUMO Gaps and Photooxidative Resistances. *J. Am. Chem. Soc.* **2008**, *130* (48), 16274–16286.

353. Jiang, D. E.; Dai, S. Electronic Ground State of Higher Acenes. *J. Phys. Chem. A* **2008**, *112* (2), 332–335.
354. Anthony, J. E. The Larger Acenes: Versatile Organic Semiconductors. *Angew. Chem. Int. Ed.* **2008**, 452–483.
355. Qu, Z.; Zhang, D.; Liu, C.; Jiang, Y. Open-Shell Ground State of Polyacenes: A Valence Bond Study. *J. Phys. Chem. A* **2009**, *113* (27), 7909–7914.
356. Pron, A.; Gawrys, P.; Zagorska, M.; Djurado, D.; Demadrille, R. Electroactive Materials for Organic Electronics: Preparation Strategies, Structural Aspects and Characterization Techniques. *Chem. Soc. Rev.* **2010**, *39* (7), 2577–2632.
357. Tönshoff, C.; Bettinger, H. F. Photochemische Erzeugung von Octacene Und Nonacene. *Angew. Chem.* **2010**, *122* (24), 4219–4222.
358. Dötz, F.; Brand, J. D.; Ito, S.; Gherghel, L.; Müllen, K. Synthesis of Large Polycyclic Aromatic Hydrocarbons: Variation of Size and Periphery. *J. Am. Chem. Soc.* **2000**, *122* (32), 7707–7717.
359. Tönshoff, C.; Bettinger, H. F. Photogeneration of Octacene and Nonacene. *Angew. Chem. Int. Ed.* **2010**, *49* (24), 4125–4128.
360. Chen, T. A.; Liu, R. S. Synthesis of Polyaromatic Hydrocarbons From Bis(Biaryl)Dynes: Large PAHs With Low Clar Sextets. *Chem. A Eur. J.* **2011**, *17* (29), 8023–8027.
361. Watanabe, M.; Chang, Y. J.; Liu, S. W.; Chao, T. H.; Goto, K.; Islam, M. M.; Yuan, C. H.; Tao, Y. T.; Shinmyozu, T.; Chow, T. J. The Synthesis, Crystal Structure and Charge-Transport Properties of Hexacene. *Nat. Chem.* **2012**, *4* (7), 574–578.
362. Wang, C.; Dong, H.; Hu, W.; Liu, Y.; Zhu, D. Semiconducting  $\pi$ -Conjugated Systems in Field-Effect Transistors: A Material Odyssey of Organic Electronics. *Chem. Rev.* **2012**, *112*, 2208–2267. American Chemical Society.
363. Sun, Z.; Ye, Q.; Chi, C.; Wu, J. Low Band Gap Polycyclic Hydrocarbons: From Closed-Shell Near Infrared Dyes and Semiconductors to Open-Shell Radicals. *Chem. Soc. Rev.* **2012**, *41* (23), 7857–7889.
364. Solà, M. Forty Years of Clar's Aromatic  $\pi$ -Sextet Rule. *Front. Chem.* **2013**, *1*, 22.
365. Roncali, J.; Leriche, P.; Blanchard, P. Molecular Materials for Organic Photovoltaics: Small Is Beautiful. *Adv. Mater.* **2014**, *26* (23), 3821–3838.
366. Bursi, L.; Calzolari, A.; Corni, S.; Molinari, E. Light-Induced Field Enhancement in Nanoscale Systems From First-Principles: The Case of Polyacenes. *ACS Photonics* **2014**, *1* (10), 1049–1058.
367. Chakraborty, H.; Shukla, A. Theory of Triplet Optical Absorption in Oligoacenes: From Naphthalene to Heptacene. *J. Chem. Phys.* **2014**, *141* (16), 164301.
368. Bhattacharya, D.; Panda, A.; Misra, A.; Klein, D. J. Clar Theory Extended for Polyacenes and Beyond. *J. Phys. Chem. A* **2014**, *118* (24), 4325–4338.
369. Dimitrakopoulos, C. D.; Mascaro, D. J. Organic Thin-Film Transistors: A Review of Recent Advances. *IBM J. Res. Dev.* **2001**, *45* (1), 11–27.
370. Li, J.; Zhang, Q. Linearly Fused Azaacenes: Novel Approaches and New Applications beyond Field-Effect Transistors (FETs). *ACS Appl. Mater. Interfaces* **2015**, *7* (51), 28049–28062.
371. Li, J.; Zhao, Y.; Lu, J.; Li, G.; Zhang, J.; Zhao, Y.; Sun, X.; Zhang, Q. Double [4 + 2] Cycloaddition Reaction to Approach a Large Acene With Even-Number Linearly Fused Benzene Rings: 6,9,16,19-Tetraphenyl-1,20,4,5,10,11,14,15-Tetrabenzooctatwistacene. *J. Org. Chem.* **2015**, *80* (1), 109–113.
372. Zhang, L.; Cao, Y.; Colella, N. S.; Liang, Y.; Brédas, J. L.; Houk, K. N.; Briseno, A. L. Unconventional, Chemically Stable, and Soluble Two-Dimensional Angular Polycyclic Aromatic Hydrocarbons: From Molecular Design to Device Applications. *Acc. Chem. Res.* **2015**, *48* (3), 500–509.
373. Ortmann, F.; Radke, K. S.; Günther, A.; Kasemann, D.; Leo, K.; Cuniberti, G. Materials Meets Concepts in Molecule-Based Electronics. *Adv. Funct. Mater.* **2015**, *25* (13), 1933–1954.
374. Xiang, D.; Wang, X.; Jia, C.; Lee, T.; Guo, X. Molecular-Scale Electronics: From Concept to Function. *Chem. Rev.* **2016**, *116*, 4318–4440. American Chemical Society.
375. Miao, Q. *Polycyclic Arenes and Heteroarenes: Synthesis Properties, and Applications*, Wiley-VCH, Weinheim: Weinheim, Germany, 2016.
376. Shameem, M. A.; Orthaber, A. Organophosphorus Compounds in Organic Electronics. *Chem. A Eur. J.* **2016**, *22* (31), 10718–10735.
377. Einholz, R.; Fang, T.; Berger, R.; Grüninger, P.; Früh, A.; Chassé, T.; Fink, R. F.; Bettinger, H. F. Heptacene: Characterization in Solution, in the Solid State, and in Films. *J. Am. Chem. Soc.* **2017**, *139* (12), 4435–4442.
378. Naibi Lakshminarayana, A.; Ong, A.; Chi, C. Modification of Acenes for N-Channel OFET Materials. *J. Mater. Chem. C* **2018**, 3551–3563. Royal Society of Chemistry.
379. Ai, Q.; Jarolimek, K.; Mazza, S.; Anthony, J. E.; Risko, C. Delimited Polyacenes: Edge Topology as a Tool to Modulate Carbon Nanoribbon Structure, Conjugation, and Mobility. *Chem. Mater.* **2018**, *30* (3), 947–957.
380. Schleyer, P. v. R.; Manoharan, M.; Jiao, H.; Stahl, F. The Acenes: Is There a Relationship Between Aromatic Stabilization and Reactivity? *Org. Lett.* **2001**, *3* (23), 3643–3646.
381. Imoto, H.; Fujii, T.; Tanaka, S.; Yamamoto, S.; Mitsuishi, M.; Yumura, T.; Naka, K. As-Heteropentacenes: An Experimental and Computational Study on a Novel Class of Heteroacenes. *Org. Lett.* **2018**, *20* (18), 5952–5955.
382. Clevenger, R. G.; Kumar, B.; Menuet, E. M.; Lee, G. H.; Patterson, D.; Kilway, K. V. A Superior Synthesis of Longitudinally Twisted Acenes. *Chem. A Eur. J.* **2018**, *24* (1), 243–250.
383. Trinquier, G.; David, G.; Malrieu, J. P. Qualitative Views on the Polyradical Character of Long Acenes. *J. Phys. Chem. A* **2018**, *122* (34), 6926–6933.
384. Jancarík, A.; Levet, G.; Gourdon, A. A Practical General Method for the Preparation of Long Acenes. *Chem. A Eur. J.* **2019**, *25* (9), 2366–2374.
385. Dressler, J. J.; Barker, J. E.; Karas, L. J.; Hashimoto, H. E.; Kishi, R.; Zakharov, L. N.; Macmillan, S. N.; Gomez-Garcia, C. J.; Nakano, M.; Wu, J. I.; et al. Late-Stage Modification of Electronic Properties of Antiaromatic and Diradicaloid Indeno[1,2-b]fluorene Analogues Via Sulfur Oxidation. *J. Org. Chem.* **2020**, *85* (16), 10846–10857.
386. Asako, T.; Suzuki, S.; Tanaka, S.; Ota, E. Synthesis of Decaarylthracene With Nine Different Substituents. *J. Org. Chem.* **2020**, *85* (23), 15437–15448.
387. Valdiviezo, J.; Rocha, P.; Polakovsky, A.; Palma, J. L. Nonexponential Length Dependence of Molecular Conductance in Acene-Based Molecular Wires. *ACS Sens.* **2021**, *6* (2), 477–484.
388. Cao, Y.; Zhu, C.; Bartóg, M.; Barker, K. P.; Ji, X.; Kalin, A. J.; Al-Hashimi, M.; Fang, L. Electron-Deficient Polycyclic  $\pi$ -System Fused With Multiple B  $\leftarrow$  N Coordinate Bonds. *J. Org. Chem.* **2021**, *86* (3), 2100–2106.
389. Houk, K. N.; Lee, P. S.; Nendel, M. Polyacene and Cyclacene Geometries and Electronic Structures: Bond Equalization, Vanishing Band Gaps, and Triplet Ground States Contrast with Polyacetylene. *J. Org. Chem.* **2001**, *66* (16), 5517–5521.
390. Dimitrakopoulos, C. D.; Malenfant, P. R. L. Organic Thin Film Transistors for Large Area Electronics. *Adv. Mater.* **14** (2), 2002, 99–117.
391. Randić, M. Aromaticity of Polycyclic Conjugated Hydrocarbons. *Chem. Rev.* **2003**, *103* (9), 3449–3605.
392. Mori, T. Organic Conductors With Unusual Band Fillings. *Chem. Rev.* **2004**, *104* (11), 4947–4969.
393. Watson, M. D.; Fechtenkötter, A.; Müllen, K. Big Is Beautiful - "Aromaticity" Revisited From the Viewpoint of Macromolecular and Supramolecular Benzene Chemistry. *Chem. Rev.* **2001**, *101* (5), 1267–1300.
394. Gomes, J. A.; Mallion, R. B. Aromaticity and Ring Currents. *Chem. Rev.* **2001**, *101* (5), 1349–1383.
395. Shaik, S.; Shurki, A.; Danovich, D.; Hiberty, P. C. A Different Story of Pi-Delocalization - The Distortivity of Pi-Electrons and its Chemical Manifestations. *Chem. Rev.* **2001**, *101* (5), 1501–1539.
396. Lambert, C. Auf dem Weg zu polycyclischen aromatischen Kohlenwasserstoffen mit offenschaligem Singulettgrundzustand. *Angew. Chem.* **2011**, *123* (8), 1794–1796.
397. Dougherty, D. A. Spin Control in Organic Molecules. *Acc. Chem. Res.* **1991**, *24* (3), 88–94.
398. Rottschäfer, D.; Neumann, B.; Stammler, H.-G.; Ghadwal, R. S. N-Heterocyclic Vinylidene-Stabilized Phosphorus Biradicaloid. *Chem. A Eur. J.* **2017**, *23* (38), 9044–9047.

## Further reading

Abe, M. Diradicals. *Chem. Rev.* **2013**, *113* (9), 7011–7088.

- Bonačić-Koutecký, V.; Koutecký, J.; Michl, J. Neutral and Charged Biradicals, Zwitterions, Funnels in S<sub>1</sub>, and Proton Translocation: Their Role in Photochemistry, Photophysics, and Vision. *Angew. Chem. Int. Ed. Engl.* **1987**, *26* (3), 170–189.
- Breher, F. Stretching Bonds in Main Group Element Compounds—Borderlines Between Biradicals and Closed-Shell Species. *Coord. Chem. Rev.* **2007**, *251* (7–8), 1007–1043.
- González-Gallardo, S.; Breher, F. Main Group Biradicaloids. In *Comprehensive Inorganic Chemistry II*; vol. 1; Elsevier, 2013, ; pp 413–455.
- Salem, L.; Rowland, C. The Electronic Properties of Diradicals. *Angew. Chem. Int. Ed. Engl.* **1972**, *11* (2), 92–111.
- Stuyver, T.; Chen, B.; Zeng, T.; Geerlings, P.; De Proft, F.; Hoffmann, R. Do Diradicals Behave Like Radicals? *Chem. Rev.* **2019**, *119* (21), 11291–11351.

### Relevant websites

<https://www.schulz.chemie.uni-rostock.de/> —Institute of Chemistry, University of Rostock.

## 1.05 Nonclassical carbenes as noninnocent ligands

Daniela I. Bezuidenhout, George Kleinhans, and Aino J. Karhu, Laboratory of Inorganic Chemistry, Environmental and Chemical Engineering, University of Oulu, Oulu, Finland

© 2023 Elsevier Ltd. All rights reserved.

<b>1.05.1</b>	<b>Introduction</b>	<b>235</b>
1.05.1.1	Imidazol-4-ylidene	235
1.05.1.2	1,2,3-Triazol-5-ylidene	236
1.05.1.3	Cyclic (alkyl)(amino)carbene	238
<b>1.05.2</b>	<b>Chemical noninnocence</b>	<b>242</b>
1.05.2.1	Group 4 donor functionalized nonclassical carbenes	243
1.05.2.1.1	C-donor functionalized carbenes	243
1.05.2.2	Group 5 donor functionalized nonclassical carbenes	247
1.05.2.2.1	N-donor functionalized carbenes	247
1.05.2.3	Chalcogen donor functionalized nonclassical carbenes	257
1.05.2.3.1	O-donor functionalized carbenes	257
1.05.2.3.2	S-donor functionalized carbenes	261
<b>1.05.3</b>	<b>Redox noninnocence</b>	<b>262</b>
1.05.3.1	Metallocenyl-appended carbenes	263
1.05.3.2	Nonmetal redox active moieties appended to triazolylidenes and imidazol-4-ylidenes	266
<b>1.05.4</b>	<b>Chiral noninnocence</b>	<b>268</b>
<b>1.05.5</b>	<b>Multinuclear cooperativity</b>	<b>275</b>
1.05.5.1	Homonuclear cooperativity	275
1.05.5.2	Heterobimetallic cooperativity	287
1.05.5.3	Metal carbene complex heterogenization	288
1.05.5.3.1	Tethered nonclassical metal carbene complexes	290
1.05.5.3.2	Nonclassical carbene stabilized metal clusters	294
1.05.5.3.3	Metal nanoparticles and surfaces stabilized by nonclassical carbenes	296
<b>1.05.6</b>	<b>Emerging applications of nonclassical carbenes</b>	<b>297</b>
1.05.6.1	Light-harvesting and -emitting applications	297
1.05.6.1.1	Photoactive nonclassical carbene complexes of group 8 transition metals	297
1.05.6.1.2	Photoactive nonclassical carbene complexes of group 9 transition metals	298
1.05.6.1.3	Photoactive nonclassical carbene complexes of group 10 transition metals	299
1.05.6.1.4	Photoactive nonclassical carbene complexes of group 11 transition metals	300
1.05.6.2	Biological and medicinal applications of the nonclassical carbenes	303
<b>1.05.7</b>	<b>Perspective</b>	<b>305</b>
<b>References</b>		<b>305</b>

### Abstract

The introduction of monoheteroatom stabilized cyclic carbenes, less than a decade after the discovery of stable acyclic and *N*-heterocyclic carbenes (NHCs), soon led to the development of complex ligands fulfilling more than a simple spectator role. Particularly the imidazol-4-ylidenes (Im4), cyclic (alkyl)(amino)carbenes (CAACs) and 1,2,3-triazol-5-ylidenes (trz) have emerged as ligands for transition metal complexes that demonstrate a noninnocent role. The advancements of these nonclassical *N*-heterocyclic carbenes as noninnocent ligands are reviewed in this contribution. A short overview of the unique (stereo)electronic features of these classes of carbenes is provided. The focus of this study is however on the impact of Im4, CAACs and trz on the metal complex reactivity in catalytic applications where the ligands exhibit a chemically or a redox noninnocent role in cooperative, bifunctional or redox-switchable catalysis. The introduction of ligand-based chirality and the role played in chiral induction are included, as well as the effect of multinuclear cooperativity in polymetallic complexes of these nonclassical carbenes. The extension of these ligands to macromolecular systems, including surface functionalization for catalytic or material applications, are showcased. Finally, the potential for the nonclassical carbenes as noninnocent ligands in non-catalytic applications, such as light emitting and biological applications, are highlighted.

### 1.05.1 Introduction

Organic transformations mediated by transition metal complexes have historically been dominated by precious metal catalysts following a metal centered reactivity profile.<sup>1–4</sup> Tailored ligand design for coordination to an appropriate metal has increasingly become a methodology that can aid or alter the classical reactivity pattern to further decrease reaction energy requirements or waste produced, or even both.<sup>5</sup> This is achieved by decorating the ligand with various functional groups that can assist in substrate manipulation, lowering the reaction energy barrier and consequently allowing for even milder reaction conditions. Furthermore, the reaction selectivity can be enhanced by using tailored ligands, thereby maximizing atom-economy to ultimately align with environmentally friendly targets. In the context of this work, ligands that do not just play a spectator role, but rather actively participate in the complex reactivity, are generally referred to as noninnocent. The noninnocent class of ligands has cemented itself as a ligand category available to the synthetic chemist towards preparation of targeted coordination compounds.<sup>5–25</sup> Beyond stabilization of reactive metal complexes, the noninnocent ligands assist in the substrate transformation process via a redox event, a multifunctional mode of action, or a chemically or light induced response, among others.

Another tool available to synthetic chemists, used generally as ligands during the preparation of organometallic compounds, is the now ubiquitous *N*-heterocyclic carbenes (NHCs).<sup>26–28</sup> These compounds, originally viewed as ‘laboratory curiosities,’ have demonstrated wide and versatile application over the past 30 years.<sup>5,29</sup> A subset of the classical NHCs that has also firmly established itself as a ligand of choice during the preparation of targeted organometallic complexes over the past two decades, is the cyclic monoheteroatom-stabilized carbenes, or nonclassical carbenes with increased basicity as a result of carbene stabilization imparted by only one nitrogen atom adjacent to the carbene carbon and not two as in the case of classical NHCs.<sup>30–51</sup> Of these nonclassical carbenes, the abnormal or mesoionic carbenes (MICs)<sup>30–44</sup> including imidazol-4-ylidenes (Im4) and 1,2,3-triazol-5-ylidenes (trz), and the cyclic (alkyl)(amino)carbene (CAAC)<sup>45–51</sup> class of carbene ligands have received growing attention compared to other nonclassical carbenes (Fig. 1). This can be attributed to the characteristic donor properties of the carbene ligands, in addition to their ease of preparation and ligand modification that allow for facile tailoring of the ligand’s electronic and steric properties. Accordingly, the merging of a nonclassical carbene with a noninnocent ligand role is not surprising, and these multifunctional, strong donor ligands have already exceeded expectations.

This chapter aims to highlight the impact of noninnocent nonclassical carbene ligands on metal complexes and their resultant reactivity. This includes a short overview of the stereoelectronic properties of the different types of nonclassical carbenes (Im4, trz and CAACs), as their electronic properties have been the subject of several recent reviews.<sup>1,2,33,35,37,38,47–49</sup> For the sake of brevity, only the five-membered cyclic (alkyl)(amino)carbenes will be reviewed, and not their derivatives such as the bicyclic CAACs (BiCAACs), cyclic (aryl)aminocarbenes (CAArCs), etc. Important also towards the foundation of this chapter, is the brief discussion with regards to the carbenes’ inherent noninnocent and stabilizing attributes. The advent of noninnocent ligand behavior of coordinated nonclassical carbenes is showcased by a non-exhaustive account of recent topical developments. Various case studies are used as examples to illustrate the state of the art of the advancements made within this topic, while the developments with possible emerging noninnocent roles in applications beyond catalysis are highlighted.

#### 1.05.1.1 Imidazol-4-ylidene

The explosive growth witnessed within the field of nonclassical carbenes, specifically for Im4, trz and CAACs, can be traced back to their early reports detailing either the preparation of a stable coordination compound or the free carbene.<sup>52–56</sup> Manifestation of an unusual bonding mode during classical NHC metal complex preparation evidenced the first example of an abnormally bound imidazolylidene, the imidazol-4-ylidene.<sup>52</sup> Abnormal C4 coordination, instead of the classical C2 mode of bonding, yielded the iridium carbene complex **2** with carbene stabilization imparted by only one heteroatom adjacent to the carbene carbon (Scheme 1, i). This was followed a few years later by the first example of a free abnormal carbene obtained by blocking of the other ring positions and C4 deprotonation of the imidazolium salt **3**, yielding **4** (Scheme 1, ii).<sup>53</sup> The electronic properties of the abnormal carbenes have been extensively investigated and reviewed to confirm increased electron donation to a metal when compared to classical NHCs.<sup>33,35,38–40,44,57</sup> The lack of a second heteroatom adjacent to the carbene carbon imparts increased electron donation towards the metal, a result of modifications to the  $\sigma$ -pull/ $\pi$ -push properties of the heterocycle.

The Im4 five-membered heterocycle has been described as more than just a spectator ligand, tasked with aiding the metal during bond manipulation processes.<sup>39,58,59</sup> It is the unique electronic structure of Im4 that permits a possible cooperative mode of action<sup>35,38–40,57–59</sup> to render the nonclassical carbene with an in-built/inherent noninnocent character. Albrecht et al. proposed a mechanism by which the Im4 could mediate a cooperative strategy. Intramolecular charge separation within

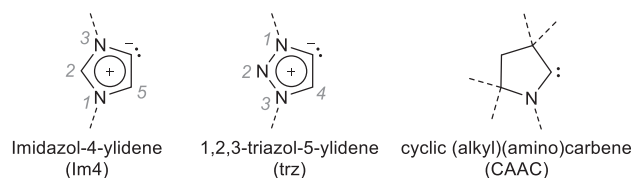
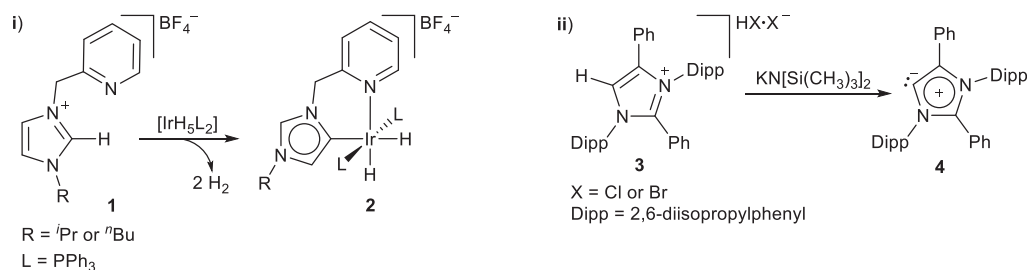


Fig. 1 Nonclassical carbenes highlighted in this contribution.





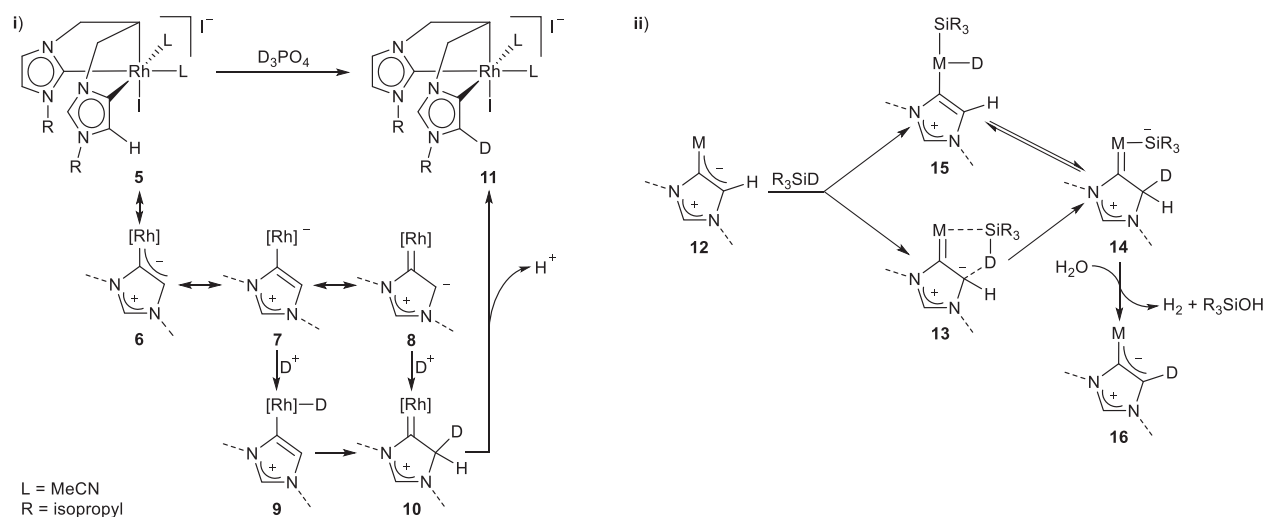
**Scheme 1** The first Im4 metal complex and free Im4.

the five-membered heterocycle would result in a vinylic metal-bound C–C fragment and a cationic amidinium unit (**Scheme 2**).<sup>35,39,58,59</sup> The vinylic M=C fragment would then be susceptible to electrophilic attack, as postulated for the treatment of a bisimidazol-4-ylidene coordinated rhodium(III) complex with D<sub>3</sub>PO<sub>4</sub>, yielding the C5 deuterated complex (**Scheme 2**, i).<sup>59,60</sup> Deuteration was observed to occur only at the C4 bound carbene of **5**, and not the classical C2 bound carbene, which results in formation of **11** when treated with D<sub>3</sub>PO<sub>4</sub> (**Scheme 2**, i). Additional mechanistic investigations, in this case using Et<sub>3</sub>SiD, supported the proposed intramolecular charge separation within the imidazol-4-ylidene heterocycle (**Scheme 2**, ii).<sup>39,58</sup> Im4 deuteration at the C5 position was noted once more, with its formation again postulated to involve the vinylic M=C fragment resulting from intramolecular charge separation.<sup>58</sup> A ligand-assisted Si–D heterolytic bond cleavage across the metal-vinylic moiety, followed by hydrolysis due to the presence of a small amount of water, yields the deuterated complex **16**. An alternative mechanism was also proposed for the reaction between **12** and Et<sub>3</sub>SiD, namely the oxidative addition of the hydrosilane across the metal, leading to formation of the intermediate rhodium(V) complex **15** (**Scheme 2**, ii), only accessible due to the donor characteristics of the nonclassical carbene.<sup>58</sup> Im4 has been suggested to stabilize metals in both low and high oxidation states, also ascribed to be a consequence of the intramolecular charge separation.<sup>33,35,38–40,44,57</sup> Subsequent tautomerization and rehybridization results in the C5 deuterated rhodium complex **14**, leading to **16** after hydrolysis (**Scheme 2**, ii).<sup>58</sup>

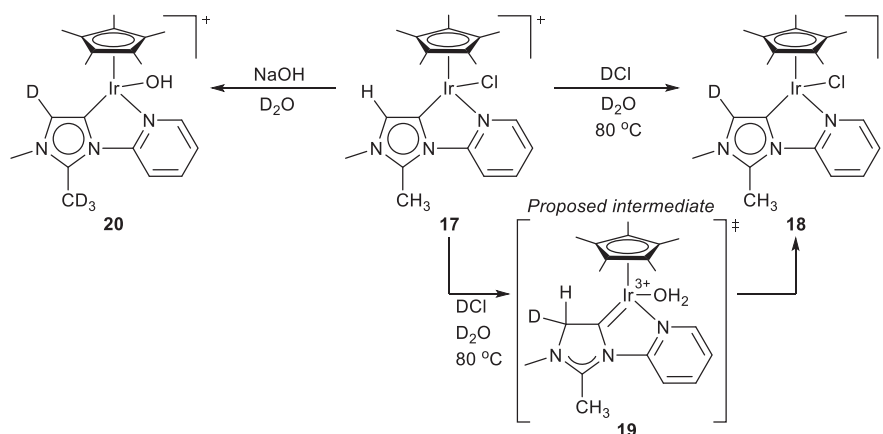
In yet another corroboration of the postulated intramolecular charge separation, selective C5 deuteration was evidenced under both acidic and basic conditions.<sup>61</sup> Treatment of the iridium Im4 complex **17** with DCl in D<sub>2</sub>O at 80 °C yielded the expected deuterated complex **18** (**Scheme 3**). The formation of the intermediary metalla-allyl anionic fragment **19** was postulated to account for the observed reactivity. Subjecting **17** to basic conditions also yielded the C5 deuterated product **20**, in addition to deuteration on the C2 substituted methyl group (**Scheme 3**). In the presence of NaOH and D<sub>2</sub>O, fast deuteration of the methyl group was noted, with C5 deuteration completed only after 2 days.

### 1.05.1.2 1,2,3-Triazol-5-ylidene

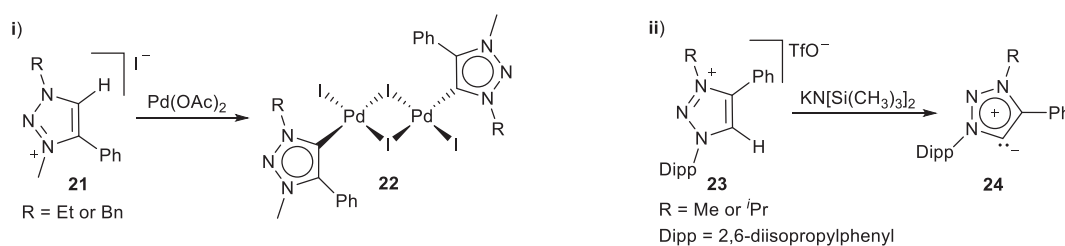
The first trz coordinated complex was reported by Albrecht and co-workers (**Scheme 4**, i),<sup>54</sup> while the deprotonated free trz **24** was reported 2 years later by Bertrand and co-workers (**Scheme 4**, ii).<sup>55</sup> The carbene carbon atom is flanked by one of the three nitrogen atoms in the five-membered heterocycle where the C2 carbon of the imidazolylidene is substituted with another nitrogen.<sup>30,33–38,42</sup>



**Scheme 2** Im4 heterocyclic intramolecular charge separation.



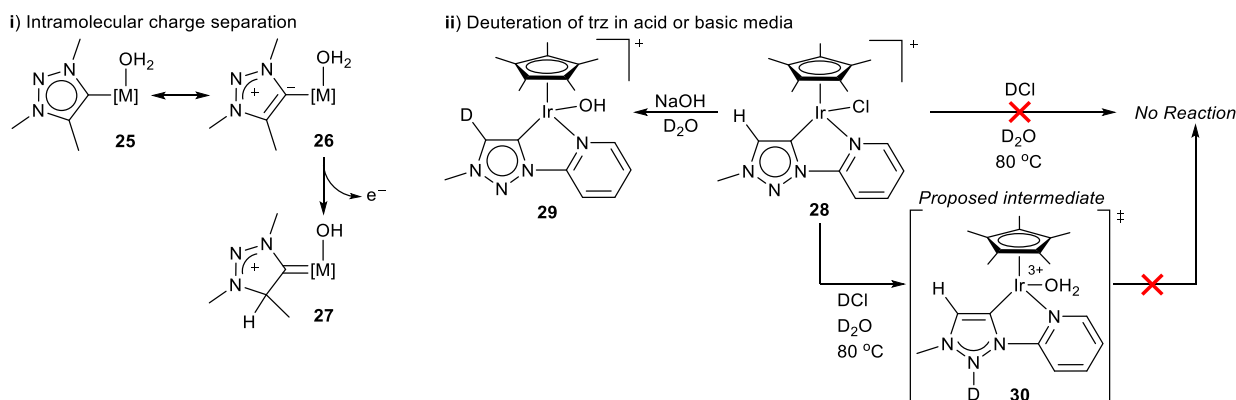
**Scheme 3** IrM4 deuteration in acidic or basic reaction media.



**Scheme 4** The first examples of (i) coordinated and (ii) free 1,2,3-triazol-5-ylidenes.

As for Im4, the donor properties of trz have also been extensively evaluated as stronger compared to classical NHCs, but are weaker when compared against Im4.<sup>33,37,38</sup>

In the case of trz, the intramolecular charge separation derived from the mesoionic nature of the heterocycle leads to the formation of the anionic M=C and the cationic NNN<sup>+</sup> fragments (**Scheme 5, i**) which facilitate bond manipulation processes cooperatively.<sup>37,39,62</sup> The intramolecular charge separation has indeed been linked to the observed water oxidation reactivity of ruthenium and iridium complexes coordinated by trz (vide infra).<sup>37,39,62,63</sup> An alternative cooperative mode of action involving the second nitrogen in the triazolylidene heterocycle has also been speculated.<sup>61</sup> Deuteration experiments by Albrecht et al. confirmed that, similar to Im4, selective deuteration occurs at the C4 position of the trz heterocycle under basic conditions, with instantaneous deuteration of **28** reported in the presence of NaOH and D<sub>2</sub>O yielding **29** (**Scheme 5, ii**). The authors described the deuteration of both the Im4 and trz heterocycles under basic conditions as reminiscent of a deprotonation followed by deuteration mechanism. This would explain the differences noted in the rate of deuteration, depending on the differences in the acidity of the protons being deprotonated. However, under acidic conditions no deuterium incorporation occurred in contrast to the reactivity displayed by Im4 (**Scheme 5, ii**). The authors described the triazolylidene as exhibiting proton/deuterium scavenging properties, with nitrogen deuteration leading to the formation of intermediate **30** proposed (**Scheme 5, ii**). Deuteration is therefore precluded



**Scheme 5** Triazolylidenes acting as more than simple spectator ligands.

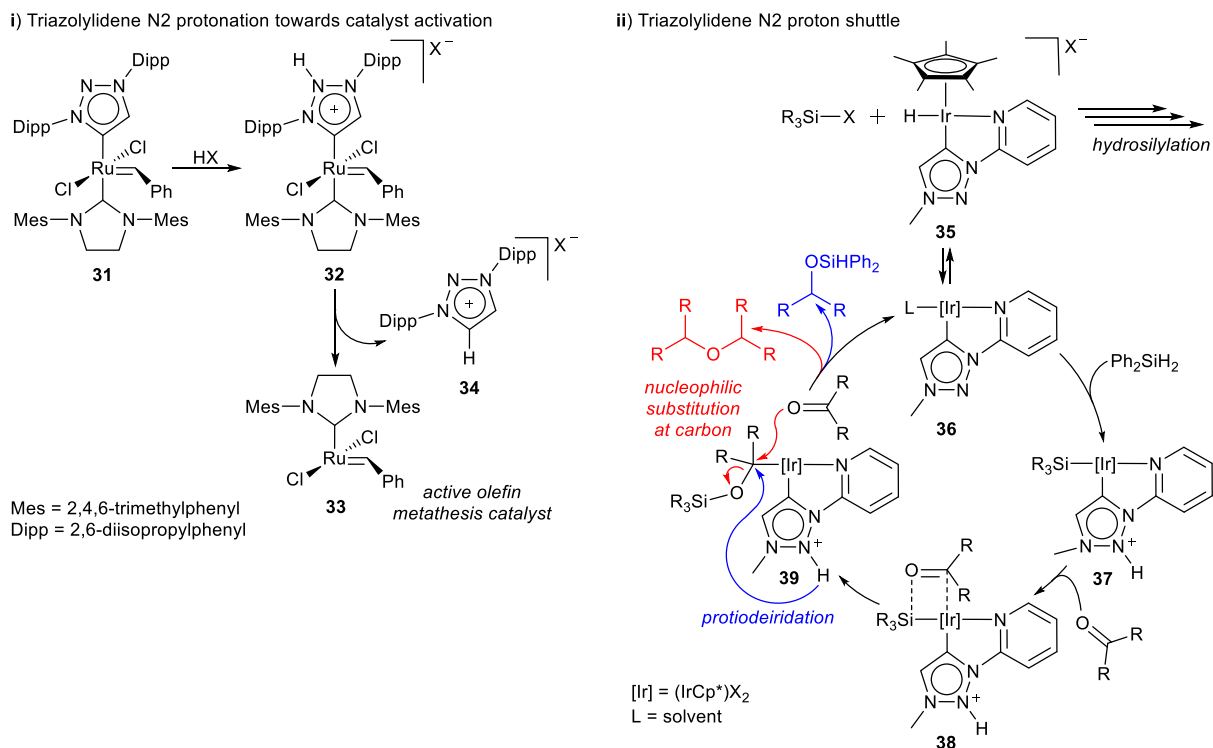
at the carbenic carbon of the heterocycle, illustrating the basicity of the trz central N2.<sup>61</sup> This is similar to reported reactivity of the five-membered heterocycle, with N2 protonation leading to catalyst activation<sup>64</sup> or metal coordination by the second nitrogen,<sup>65</sup> to associate the trz heterocycle with a cooperative mode of action where the proton responsive entity acts as a proton shuttle during bond activation reactions.

Indeed, both the groups of Albrecht<sup>66</sup> and Bertrand, Grubbs and co-workers<sup>64</sup> exploited the proton scavenging ability of the trz during catalytic processes. Bertrand and Grubbs prepared the olefin metathesis catalyst **31** substituted with a trz (Scheme 6, i).<sup>64,67</sup> Catalyst initiation was mediated by the addition of trifluoroacetic acid, hypothesized to protonate the heterocycle at the N2 position with concomitant trz dissociation from **32**. A 1,3-proton shift follows to yield the active catalyst **33** and the triazolium salt **34** (Scheme 6, i).<sup>64</sup> Symmetrical ethers could be accessed very efficiently through the reductive coupling of ketones and aldehydes, employing an iridium catalyst coordinated by a C,N-bidentate trz.<sup>66</sup> The authors suggested that the trz acts as a proton shuttle during the catalytic process. Heterocycle protonation at the N2 position leads to formation of **37**, followed by substrate coordination at **38** with subsequent protodeiridation or nucleophilic substitution, yielding the active catalyst **36** and the targeted product (Scheme 6, ii). The authors also suggest an alternative catalytic mechanism, involving ligand dearomatization, which implies an intramolecular charge separation mechanism within the five-membered heterocycle rather than a proton shuttling process.<sup>66</sup>

### 1.05.1.3 Cyclic (alkyl)(amino)carbene

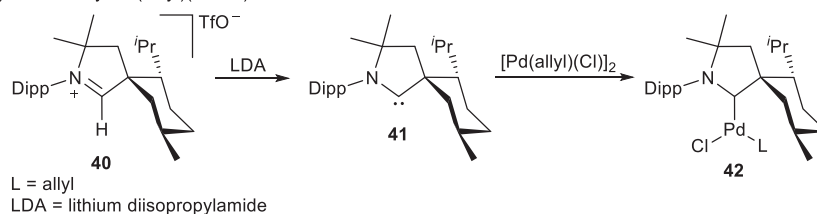
Cyclic (alkyl)(amino)carbenes made their debut in 2005 with the report of both the free carbene **41** and the CAAC coordinated Pd complex **42** (Scheme 7, i).<sup>56</sup> Akin to the Im4 and trz, the CAACs feature only one electronegative and  $\pi$ -donating amino-substituent neighboring the carbene. In a variation of the other nonclassical carbenes discussed, the other position adjacent the carbene carbon is an  $sp^3$ -hybridized carbon.<sup>42,45–51,68–70</sup> This results in increased  $\sigma$ -donating characteristics with negligible  $\pi$ -donating attributes from said  $\alpha$ -position. CAACs are both more nucleophilic and more electrophilic than traditional or nonclassical NHCs, as are evident from the HOMO (highest occupied molecular orbital) and LUMO (lowest unoccupied molecular orbital) energies (Scheme 7, ii). The energy gap between the frontier orbitals is smaller compared to other popular donor ligands. This has led to the dubbing of CAACs as ambiphilic carbenes.<sup>71,72</sup> Both the steric environment imparted by the CAAC substituents and the electronic structure of the frontier orbitals bestow unique reactivity profiles to this class of ligands which can be viewed as tantamount to noninnocent ligand behavior.<sup>42,45–51,68–70</sup>

The stabilizing ability of CAACs attendant to the stereoelectronic properties is well-known.<sup>42,45–51,68–70</sup> A direct consequence of the low lying LUMO (Scheme 7, ii) is the ease with which CAACs can stabilize electron-rich main group elements (Scheme 8, ii), low valent transition metals (Scheme 8, iii) and radical species (Scheme 8, iv).<sup>42,45–48,50,51,69</sup> The empty p-orbital of CAACs can accommodate  $\pi$ -electron density (**43**, Scheme 8, i), delocalizing the accumulated  $\pi$ -electron density and increasing the stability

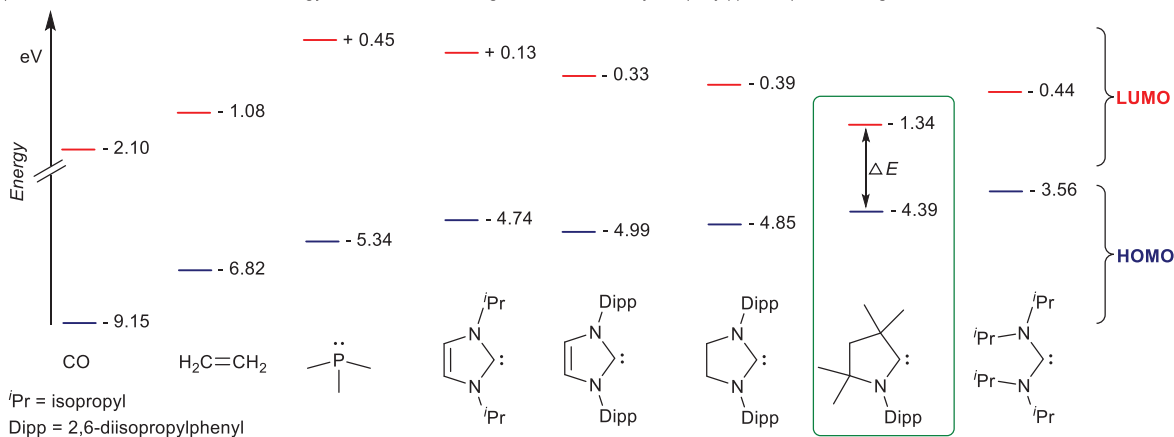


**Scheme 6** The noninnocent role of triazolylidenes towards (i) catalyst activation and (ii) proton transfer processes.

## i) Debut of cyclic (alkyl)(amino)carbenes

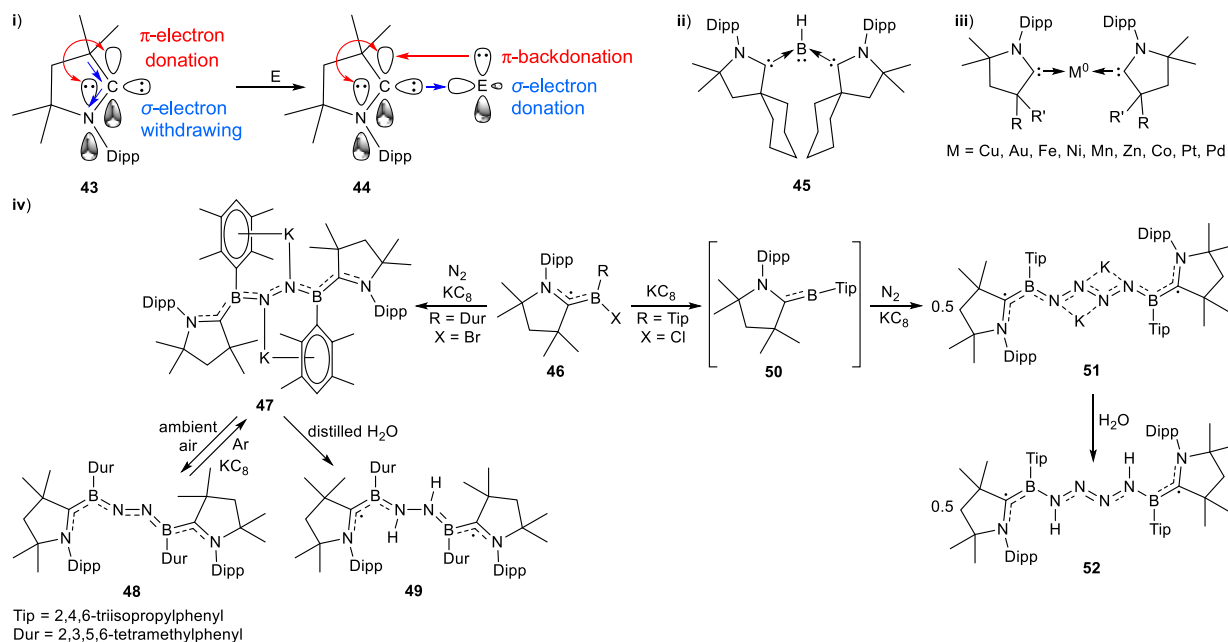


## ii) Calculated HOMO and LUMO energy levels of common ligands and of the cyclic (alkyl)(amino)carbene ligand



**Scheme 7** Cyclic (alkyl)(amino)carbenes' (i) debut and (ii) calculated HOMO and LUMO energy level.<sup>48</sup> Modified from Paul, U. S. D.; Radius, U. *Eur. J. Inorg. Chem.* **2017**, 2017, 3362–3375.

of the species investigated (44, **Scheme 8**, i).<sup>46,50,51,73</sup> This attribute was irrefutably illustrated by Bertrand and co-workers, who disclosed the first example of a nucleophilic neutral trivalent boron derivative 45 that is isoelectronic with amines (**Scheme 8**, ii).<sup>74</sup> Calculations confirmed the delocalization of the boron's lone pair of electrons into the HOMO of 45, as an overlap of the boron p( $\pi$ )-orbital with the carbene atomic p( $\pi$ )-orbital (**Scheme 8**, ii). The groups of Bertrand, Roesky and others extended the range of well-defined isolable reactive species by utilizing CAACs.<sup>42,45–48,50,51,69</sup> This includes stabilization of radicals, again possible due to the vacant p( $\pi$ )-orbital of the carbene to accommodate additional electron density through conjugated electron



**Scheme 8** Stabilization of reactive species by CAACs via  $\sigma$ -donation and  $\pi$ -backdonation.

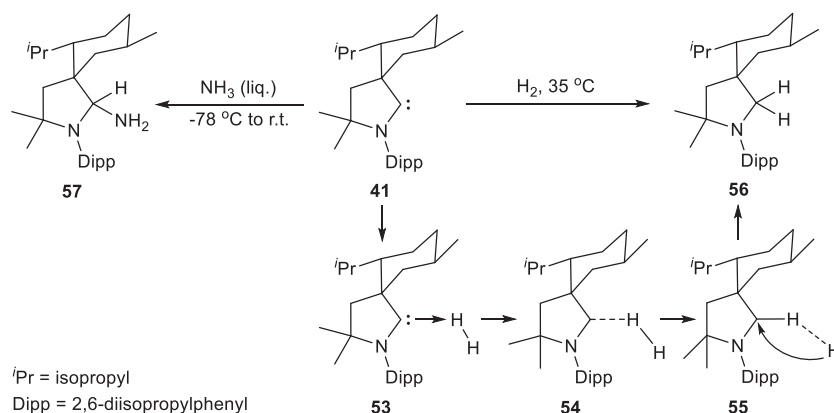
delocalization, while the rigid scaffold prevents rearrangement and subsequent decomposition. This was illustrated very recently by nitrogen fixation<sup>75</sup> and the reductive coupling thereof (Scheme 8, iv).<sup>76</sup> Hydride transfer to and from the CAACs p( $\pi$ )-orbital has also been reported, illustrating the susceptibility of the carbene to nucleophilic hydrogen. Transition metals, and especially coinage metals, have also demonstrated unique reactivities due to the coordination of CAACs (Scheme 8, iii). Diamagnetic and paramagnetic main group elements, persistent radicals and transition metals of varying oxidation states that were previously not accessible, are now available to the chemist via CAAC coordination.<sup>42,45–51,68–70</sup>

The stereoelectronic properties of CAACs allow for reactivity profiles of the metal-free ambiphilic carbenes that mimic the reactivity of transition metals.<sup>47,49,70</sup> This includes the binding and activation of small inert molecules to catalytic transformations. In their seminal contribution, Bertrand and co-workers disclosed the facile activation of hydrogen and ammonia (Scheme 9).<sup>77</sup> The free CAAC 41 was treated with hydrogen, resulting in oxidative addition of H<sub>2</sub> across the carbene, yielding 56. The activation of H<sub>2</sub> was computationally modeled, with nucleophilic attack of the carbene lone pair of electrons into the antibonding orbital of H<sub>2</sub> at 53. This induces H<sub>2</sub> polarization, with the electrophilic hydrogen bonded to the carbene carbon. Subsequent elongation of the H–H bond provides the hydrogen not bound to the carbene carbon with increased hydridic character. After stereochemical inversion, the hydrogen featuring hydridic character coordinates to the carbene at 55 and forms the second C–H bond after H–H cleavage, leading to 56. Accordingly, nucleophilic activation is followed by hydride transfer leading to H<sub>2</sub> activation. Ammonia activation was found to be favorable even at –40 °C. Ammonia activation was reported to be similar to H<sub>2</sub> activation, with bond polarization as the intermediary step towards formation of 57 from 41.<sup>77</sup>

The activation of E–H bonds via oxidative addition across the carbenic carbon<sup>78</sup> was extended to include Si–H, B–H and P–H bonds.<sup>79</sup> Accordingly, facile oxidative addition of primary, secondary and tertiary silanes across the carbene carbon of CAAC 58 was reported (Scheme 10). Similarly, primary and secondary phosphines reacted with 58 leading to the corresponding products (62 and 63, respectively) of oxidative addition. Sterically less encumbered CAACs result in improved reactivity with silanes and phosphines compared to CAACs featuring bulky substituents. Furthermore, the authors disclosed the oxidative addition of pinacolborane across the carbene carbon of 58 yielding 64, while adduct formation was noted upon reacting 58 with BH<sub>3</sub> to yield 65.<sup>79</sup> Radius et al. also described the oxidative addition of diboron leading to the oxidized product 66,<sup>80</sup> while Turner disclosed the activation of C–H and C–F bonds with CAACs, referring to the nonclassical carbenes as chemically noninnocent.<sup>81</sup>

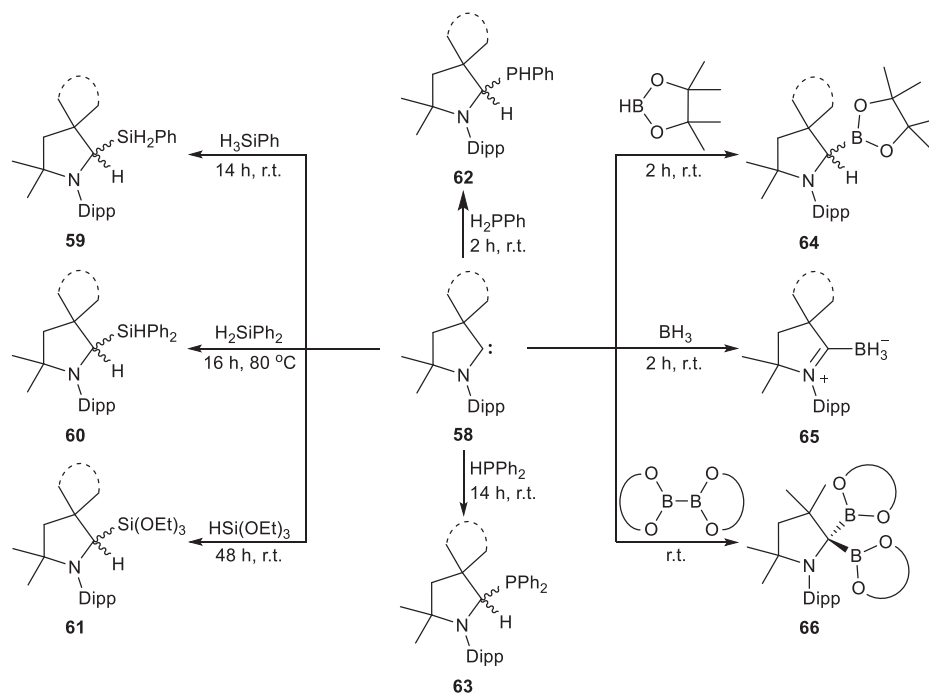
For efficient catalysts and catalytic processes, however, both oxidative addition and reductive elimination reactions should be viable. In support of the transition metal-like reactivity of CAACs, a recent report confirms the feasible reductive elimination at the carbene carbon of CAACs.<sup>82</sup> It was demonstrated that reductive elimination is dependent on the steric environment imposed by the ligand, with sterically encumbered menthyl-CAACs such as 67 favoring reductive elimination (Scheme 11, i). The requirement for the unique electronic properties of the CAAC ligand was verified computationally, with the prediction of the carbene p( $\pi$ )-orbital participating in the reductive elimination reaction (see formation of 41 from 67, Scheme 11, i). The stereoelectronic properties of the CAAC ligand therefore plays a crucial role during both the oxidative addition and reductive elimination processes. Reversible oxidative addition facilitated by CAACs has also been described for the activation of boronates.<sup>83</sup> Addition of arylboronate esters 74 to CAAC 68 resulted in oxidative addition of the boronate across the carbene carbon yielding 75 (Scheme 11, ii). The product of oxidative addition is in equilibrium with the reduced species, an equilibrium affected by heating or cooling of the reaction mixture (Scheme 11, ii). The above discussed examples of oxidative addition and reductive elimination further advances our understanding towards carbene carbon-centered organocatalysis.

In culmination of the work described above, the ambiphilic CAAC was employed as an organocatalyst, with oxidation and reduction reactions key steps toward closing the catalytic loop to access the organic products.<sup>84</sup> Bertrand and co-workers also reported the activation of CO leading to formation of the ketene 76 (Scheme 12, i).<sup>85</sup> The authors exploited the activation of CO with CAACs by promoting carbonylation of *o*-quinone catalytically to yield the corresponding cyclic carbonate.<sup>84</sup> Accordingly, *o*-quinone was converted under 4 atm of CO in the presence of 10 mol% 41. Both stoichiometric and computational investigations support a mechanism that involves first ketene formation through the reaction of CO with the carbene organocatalyst 41. The



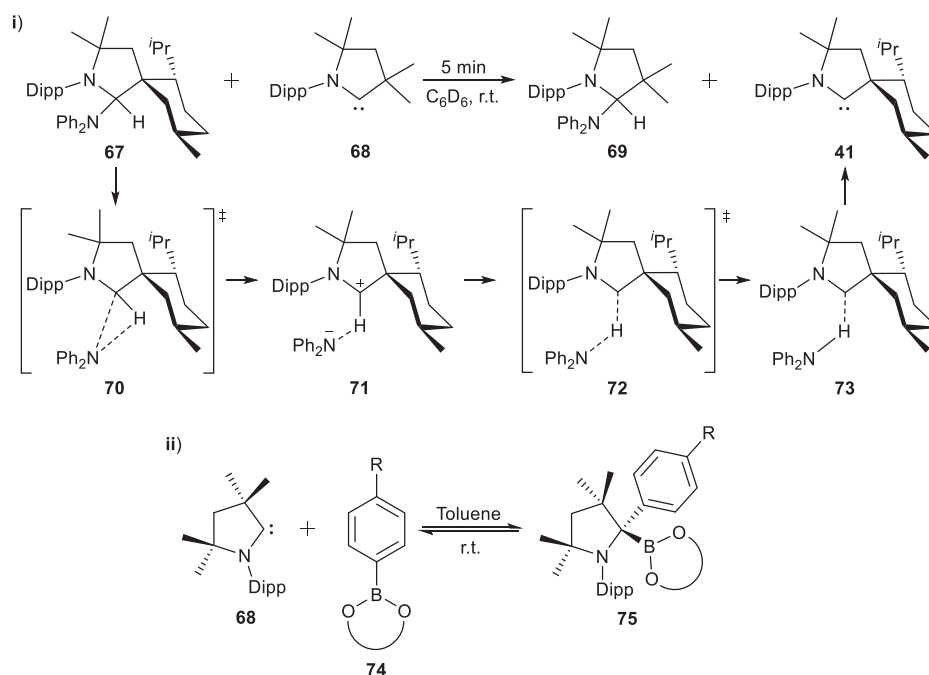
**Scheme 9** Oxidative addition of H<sub>2</sub> and NH<sub>3</sub> via nucleophilic addition with subsequent hydride transfer.



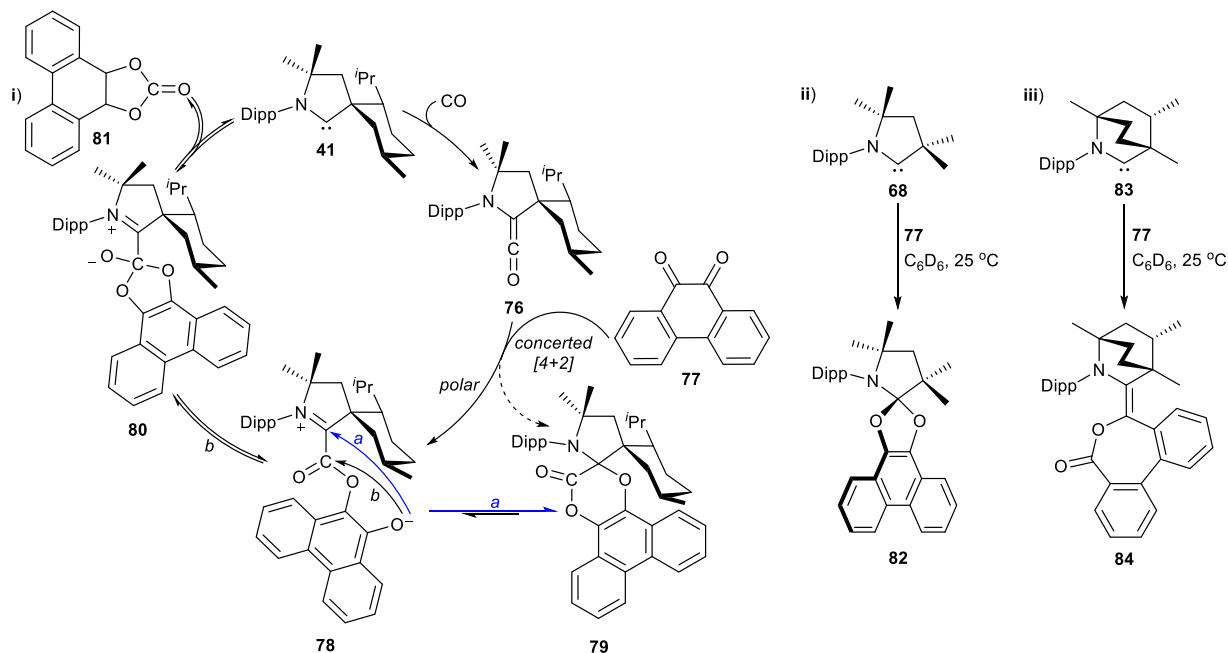


**Scheme 10** Oxidative addition across the carbene carbon of CAACs.

subsequent reaction of ketene **76** with quinone **77** can lead to **78** or **79**, with **79** reported to be the resting state of the catalytic reaction. Reduction of **79** leads to reformation of the catalytically active species **78**. The final step in the catalytic mechanism involves elimination of the targeted cyclic carbonate **81** from **80**, regenerating the free CAAC. A pronounced influence exerted by the stereo-electronic properties of the selected carbene on the catalytic reaction was noted. Reduction of **79** is possible (**Scheme 12**, i), but the analogous compounds **82** (**Scheme 12**, ii) and **84** (**Scheme 12**, iii), obtained when using **68** or **83** as organocatalyst, respectively, demonstrated reluctance towards reduction. Hence, the catalytic reaction is arrested at the resting state when employing **68** or **83** as catalyst.<sup>84</sup>



**Scheme 11** Reductive elimination across the carbene carbon of CAACs.

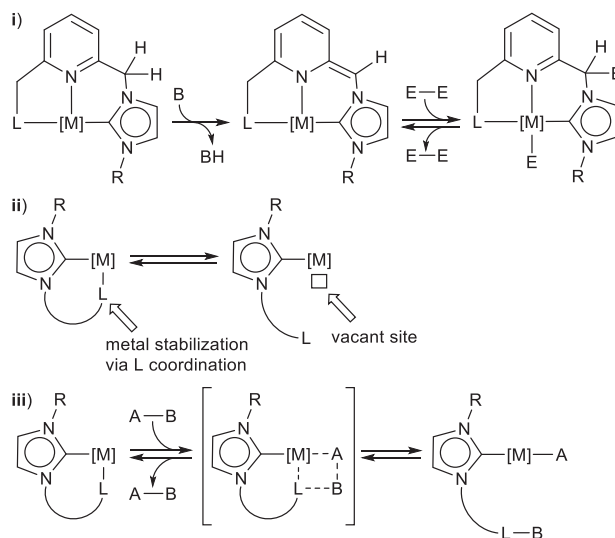


**Scheme 12** Realizing cyclic carbonates via CAAC catalyzed carbonylation of quinone with CO.

### 1.05.2 Chemical noninnocence

Tailored ligand design for noninnocent participation in substrate activation is elegantly exemplified by various strategies, such as the established (de)aromatization process allowing for inert substrate activation.<sup>6–9,20,86–93</sup> Substrate bond manipulation is realized across the metal and the ligand, which is facilitated via aromatization/dearomatization of the ligand, with the metal remaining in the same oxidation state (**Scheme 13**, i). Another approach involves tethering of a hemilabile donor functionality to the coordinating ligand, with coordination/decoordination of the donor moiety either stabilizing the metal complex or vacating a coordination site for substrate binding (**Scheme 13**, ii).<sup>10,11,18,19,21,23,24,94,95</sup> Alternatively, multifunctional ligands containing a reactive site can be used in a Lewis acid-base pair activation strategy. Generally a reactive site such as a Lewis basic donor moiety is included in the ligand structure while the metal fulfills the acceptor role (**Scheme 13**, iii).<sup>9,12–25,87,92,94,96–102</sup>

The amalgamation of a strong donor carbene with an additional functionality to aid substrate bond activation (**Scheme 13**),<sup>5,95,96,103–107</sup> is in most instances achieved when the robust M–C bond acts as the anchor, securing the metal in close proximity to the added noninnocent moiety. Substitution of the classical NHC with a nonclassical NHC allows access to different reactivity



**Scheme 13** Tailored NHC-ligand design towards facile bond manipulation via ligand cooperativity.

profiles, and if tethered to a noninnocent moiety, new complex reactivity could be imagined. Various nonclassical NHC ligands decorated with an auxiliary functional group that manifests the carbene containing ligand as noninnocent, have been developed. These ligand functionalities range from hemilabile pendants, to chemoactive ligands, as well as ligands featuring bifunctionality to actively participate in bond making and bond breaking processes.

The nonclassical carbene ligand of interest in this section, must demonstrate chemical noninnocence, with the noninnocent functionality tethered (see Fig. 2) to the carbene donor group as a prerequisite (i.e. a metal complex coordinated by a trz, Im4 or CAAC and an independent ancillary noninnocent ligand will not be considered). The chemically cooperative nonclassical carbenes are grouped according to the periodic group of the noninnocent moiety participating in the noninnocent strategy (Fig. 2). A broad overview of the developments is presented, with various examples highlighted to emphasize either the importance of the cooperative ligand, or the mechanism by which the noninnocent ligand facilitates bond manipulation strategies, or both.

### 1.05.2.1 Group 4 donor functionalized nonclassical carbenes

#### 1.05.2.1.1 C-donor functionalized carbenes

A popular chelation strategy involves C–H bond activation, generally resulting in cyclometalation and subsequent isolation of the target complex.<sup>108</sup> Accordingly, Mandal and co-workers prepared C,C-cyclometalated complexes via a C–H activation strategy, for use as catalyst mediating various cross-coupling catalyzed reactions.<sup>31</sup> A C,C-chelated nickel complex was prepared, purposed for the catalyzed hydroheteroarylation of vinylarenes, through coordination of the phenyl substituted Im4 **85** to a Ni<sup>0</sup> precursor (Scheme 14).<sup>109</sup> Carbene coordination is followed by isomerization of 1,5-cyclooctadiene to 1,3-cyclooctadiene, with concomitant elimination of one of the cyclooctadiene (cod) ligands (Scheme 14). Subsequent C(aryl)–H bond activation results to C–H oxidative addition and formation of **87**, with ensuing hydride transfer to the remaining cod ligand, yielding the C,C-chelated nickel complex **88** with the cod ligand coordinating in a  $\eta^3$ -allyl fashion (Scheme 14). Decoordination of the phenyl carbon followed by reduction of the Ni<sup>II</sup> precatalyst **88** leads to the formation of the active Ni<sup>0</sup> catalyst **89** (Scheme 14). The postulated reaction mechanism indicates that the succeeding catalytic cycle does not involve cyclometalation of the C(phenyl)–H bond again, and therefore re-coordination of the sp<sup>2</sup> phenyl carbon does not occur during the completion of a catalytic cycle.<sup>109</sup>

In addition, Mandal et al. prepared C,C-cyclometalated dinuclear palladium complexes **91** and **92** (Scheme 15, route i), and investigated the complexes as catalysts in the Suzuki-Miyaura cross-coupling of aryl chlorides with phenylboronic acid.<sup>31,110</sup> High turnover numbers (TONs) were accessed, even when using aryl chlorides substituted with electron donating or electron withdrawing groups. Furthermore, complex **91** was determined to be catalytically active for 10 consecutive catalytic runs, while retaining its catalytic activity. Both crystal structure analysis and DFT calculations suggested a stronger palladium carbene carbon bond compared to the palladium aryl carbon bond.<sup>110</sup> Subsequent addition of excess trifluoroacetic acid (TFA) resulted in C(aryl)–Pd bond cleavage, as reported by the same group, when exploiting the analogous chloro-bridged dimer **93** as a catalyst in the hydroarylation of aromatic C–H bonds (Scheme 15, route ii), in the presence of TFA.<sup>111</sup> The catalytic addition of arenes across alkynes was realized with adequate product yields and preferential selectivity towards the *cis*-adduct. The proposed mechanism commences with substitution of the bridging chloro ligands of **93** with TFA ligands, first leading to the dimer **94**, followed by monomer (**95**) formation after addition of more TFA. Excess TFA then leads to protonation of the palladium-bound aryl carbon of **95**, with

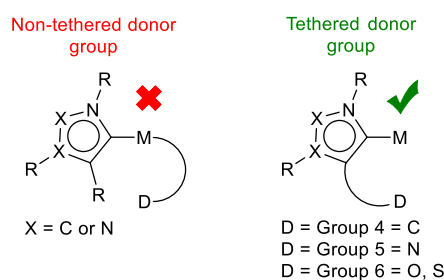
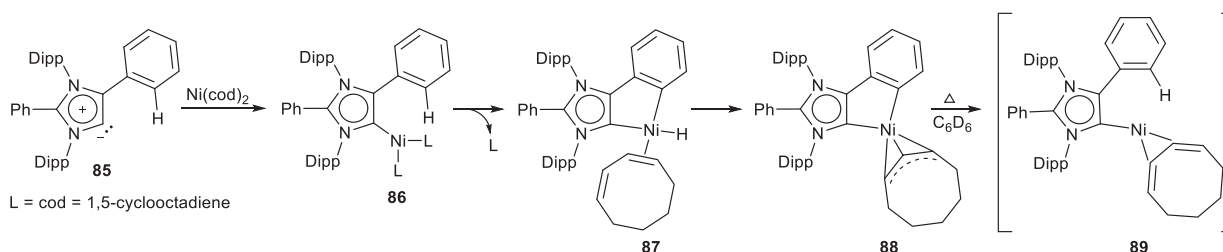
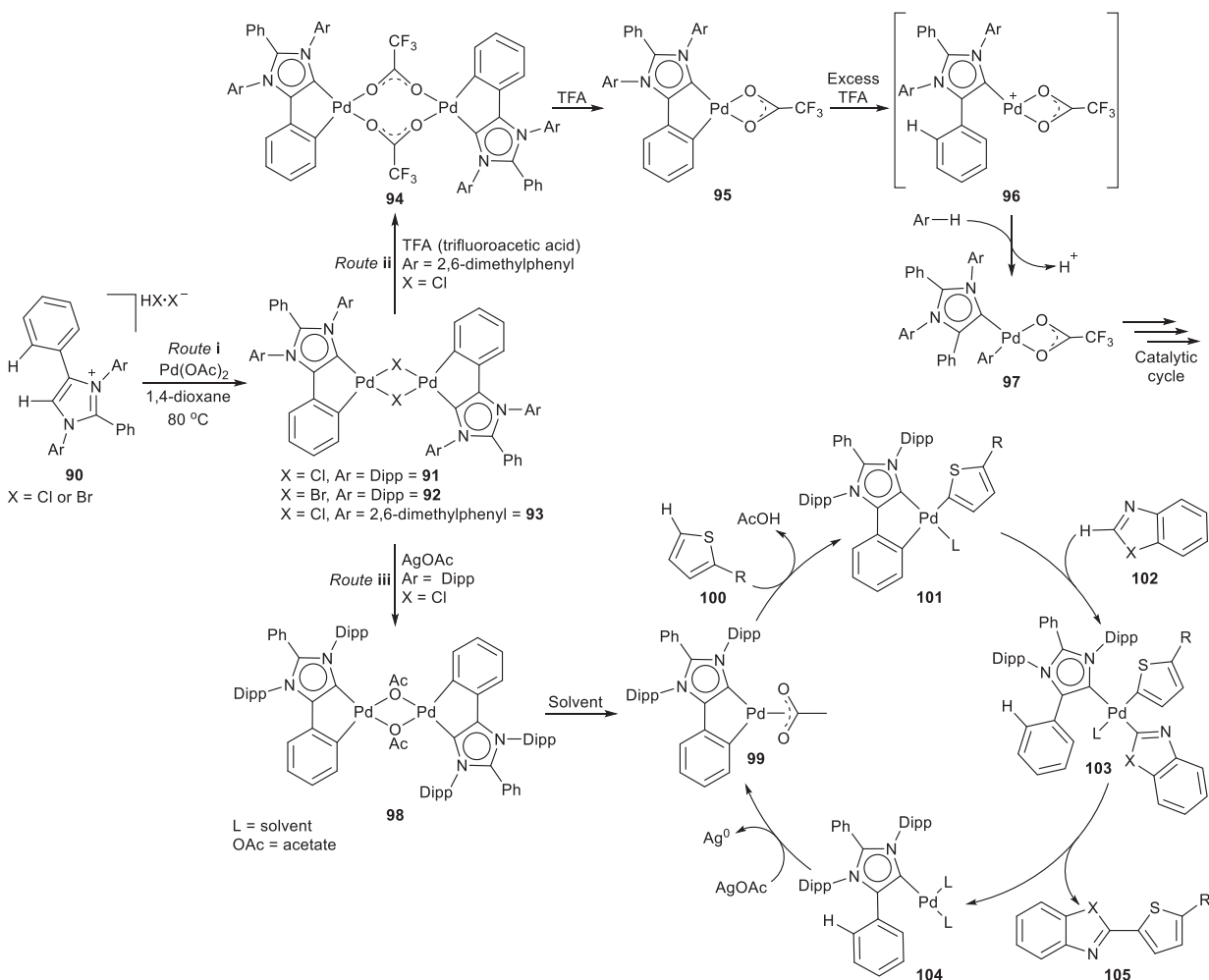


Fig. 2 Nonclassical carbenes containing a tethered functional group towards ligand cooperativity.



Scheme 14 Cyclometalation and phenyl decoordination yields a hydroheteroarylation catalyst.

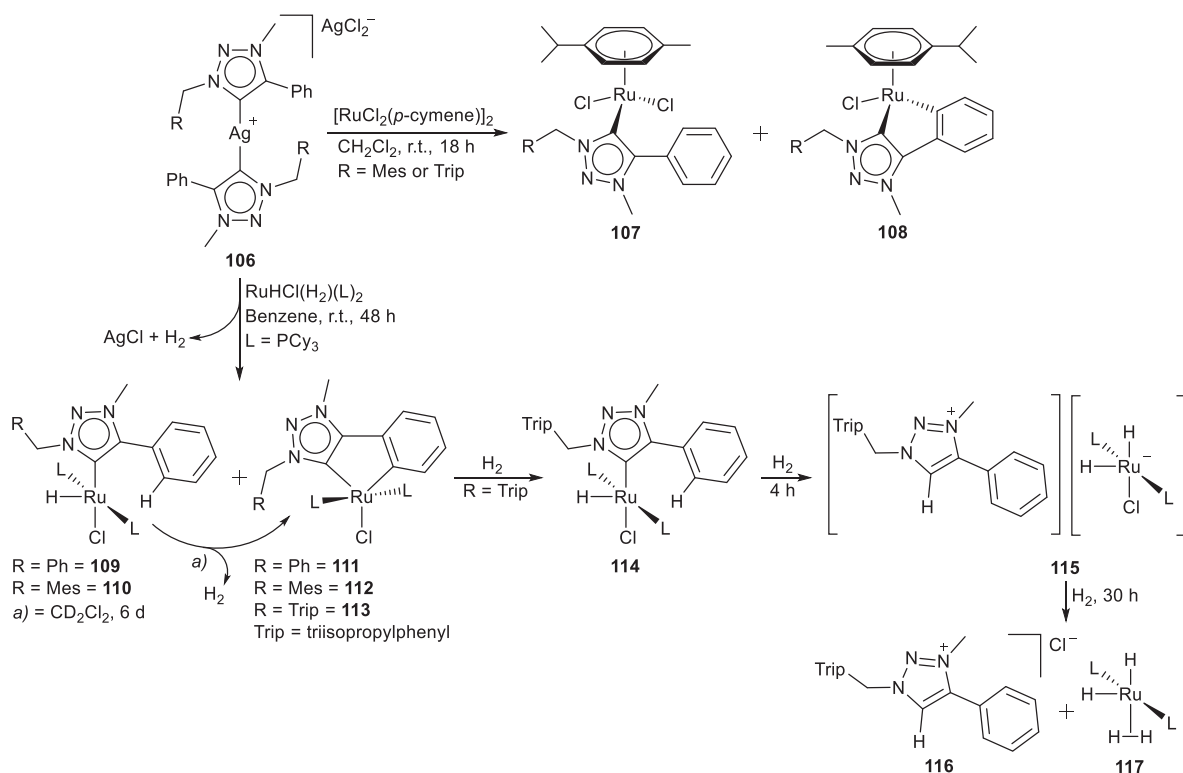


**Scheme 15** C–H activation towards C,C-cyclometalated dinuclear palladium complexes.

subsequent decooordination of the phenyl moiety to yield the catalytically active Pd-TFA species **96** (Scheme 15, route ii). This allows for electrophilic attack on the substrate's aromatic C–H bond, leading to the  $\sigma$ -aryl-Pd complex **97**, reported to be the first step in the catalytic cycle (Scheme 15).<sup>111</sup> The group further demonstrated the multifaceted potential of the dinuclear bridged complex, with an analogous C,C-chelated palladium dimer mediating the oxidative Heck coupling reaction of arylboronic acids with electron rich or electron deficient olefins at ambient conditions, using water as the solvent of the reaction.<sup>112</sup>

The dinuclear palladium complex **91** can additionally be utilized for the catalytic dehydrogenative cross-coupling of heteroarenes (Scheme 15).<sup>113</sup> The complex catalytically mediated the C–H activation of both heteroaryl substrates in the presence of AgOAc as oxidant. A range of stoichiometric experiments allowed insight into a possible reaction mechanism, involving again first the substitution of the chloro-bridging ligands of **91** with acetato-ligands, originating from the addition of silver acetate (Scheme 15, route iii). It was proposed that dimer **98** subsequently dissociates in the presence of solvent, leading to formation of mononuclear complex **99** that is considered to be the catalytically active species.<sup>113</sup> Next, the C–H activation of the first heteroaryl substrate (**100**, Scheme 15) results in formation of the heteroaryl-palladium(II) complex **101** with acetic acid elimination. It is proposed that the second substrate (**102**) inserts across the C(aryl)–Pd bond of **101**, yielding the corresponding phenyl substituted mono-coordinated triazolylidene palladium complex **103** with both heteroaryl substrates coordinated via a carbon-metal bond, in addition to coordination of a solvent molecule (Scheme 15). The authors further postulated that reduction of **103** yields the Pd<sup>0</sup> complex **104** with elimination of the cross-coupled product **105**, followed by oxidation of **104** with silver acetate leading to cyclometalation and the catalytically active species **99** (Scheme 15).

The C–H bond activation methodology was further implemented towards preparation of trz metal complexes.<sup>59,114–122</sup> This process was demonstrated to be reversible in some instances, albeit through the addition of a base effecting cyclometalation, while under acidic conditions, protonation occurred leading to decooordination and subsequent re-formation of the pendant moiety.<sup>123–125</sup> A variant to this is a cyclometalated ruthenium trz complex, demonstrated to activate hydrogen across the C(aryl)–metal bond with accompanying C–H insertion or phenyl decooordination.<sup>126</sup> The group of Stephan et al. prepared a series of ruthenium complexes coordinated by a trz featuring a pendant phenyl group.<sup>126–128</sup> The complexes were prepared via silver transmetalation,

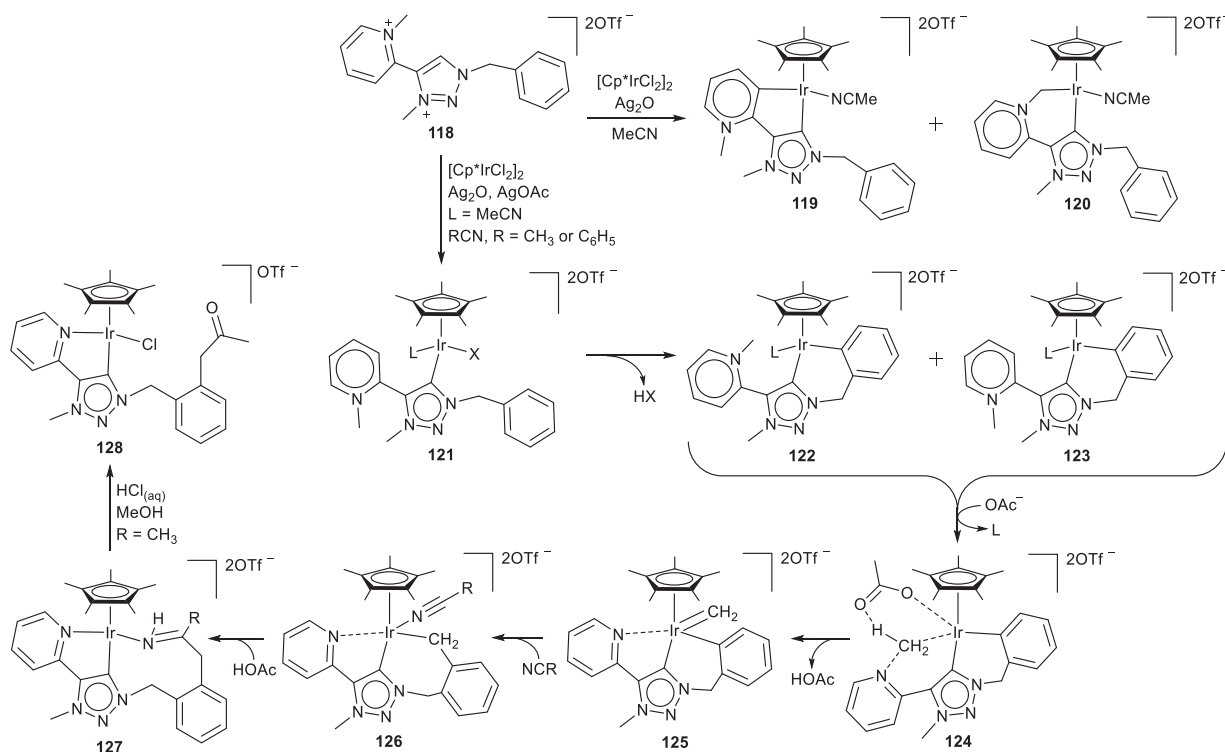


**Scheme 16** Ruthenium triazolylidene complexes accessed via C–H activation.

leading to formation of various products, including the cyclometalated products **108**, **111**, **112** and **113** through phenyl C–H bond activation (Scheme 16).<sup>126,127</sup> The group further demonstrated that stirring a solution of the ruthenium hydride **109** in  $\text{CD}_2\text{Cl}_2$  resulted in hydrogen elimination with concomitant phenyl cyclometallation (Scheme 16).<sup>126</sup> Addition of  $\text{H}_2$  to the cyclometalated product **113** immediately resulted in C(phenyl)–ruthenium bond cleavage, with decooordination of the phenyl pendant and formation of the hydride **114**. Continuous exposure to hydrogen gave rise to trz protonation and dissociation yielding **115**, en route to the triazolium salt **116** and the ruthenium hydride **117**. Due to the observed reactivity, the complexes could be successfully utilized as hydrogenation catalysts. Mechanistic considerations by Stephan et al. shows a catalytic pathway initiated by fast transformation of the cyclometalated species **113** to the corresponding hydride product **114** under a hydrogen gas atmosphere (Scheme 16). The authors further hypothesized the dissociation of a phosphine ligand with olefin coordination and subsequent insertion across the metal hydride bond. Reaction with  $\text{H}_2$  leads to product formation and regeneration of the active catalyst.<sup>126</sup>

Noninnocent ligand behavior was inferred for iridium complexes catalyzing the oxidation of water, with the catalyst facilitating the prevalent process with high TONs.<sup>129</sup> Employing ligand **118** (Scheme 17), the water oxidation catalysts could be accessed through double C–H activation of the ligand salt upon reacting with  $[\text{Cp}^*\text{IrCl}_2]_2$  ( $\text{Cp}^* = \text{pentamethylcyclopentadienyl}$ ), yielding two different C,C-chelated complexes. Pyridinium  $\text{C}(\text{sp}^2)\text{--H}$  bond activation leads to the five-membered metallacycle **119**. Alternatively,  $\text{C}(\text{sp}^3)\text{--H}$  bond activation resulted in formation of an iridium-containing ylide complex **120**, which is unusual as a strong base is generally required to access the ylide in classical pyridinium chemistry.<sup>129</sup> Both experimental and computational investigations elucidated the control effected by the remote substituent on the site of cyclometallation.<sup>130</sup> Of further note is addition of acetate to the reaction mixture during the complexation of the ligand to iridium, leading to N–CH<sub>3</sub> bond activation instead of the  $\text{C}(\text{sp}^2)\text{--H}$  or  $\text{C}(\text{sp}^3)\text{--H}$  bond activation (Scheme 17).<sup>131</sup> Consequent selective methylene transfer from the pyridinium moiety to the benzyl functional group has been paralleled to the methyltransferase activity in biological systems. Based on deuteration experiments followed with NMR spectroscopic analysis, Albrecht et al. proposed a preliminary reaction mechanism illuminating the methyl transfer and insertion process. Formation of **121** through initial carbene coordination is proposed to be followed by cyclometallation, either acetate assisted or via oxidative addition, yielding C,C-chelated complexes **122** and **123** (Scheme 17). Nitrile ligand substitution by the added acetate ensues with formation of **124**. The authors speculated formation of **125** via concerted C–H bond activation and  $\text{N}_{\text{pyr}}\text{--C}$  bond cleavage in **124**, mediated by the coordinating acetate ligand. Methylene insertion across the metal–phenyl bond is then followed by acetonitrile or benzonitrile coordination, with subsequent nitrile activation through nucleophilic addition of the anionic benzyl functionality yielding the imine coordinated complex **127**. Reacting the imine-containing triazolylidene complex with HCl further resulted in immediate dissociation of the imine donor followed by Schiff base reactivity to yield the carbonyl containing complex **128**.<sup>131</sup> Accordingly, the carbonyl oxygen could also potentially act as a noninnocent moiety assisting in bond making and breaking processes.

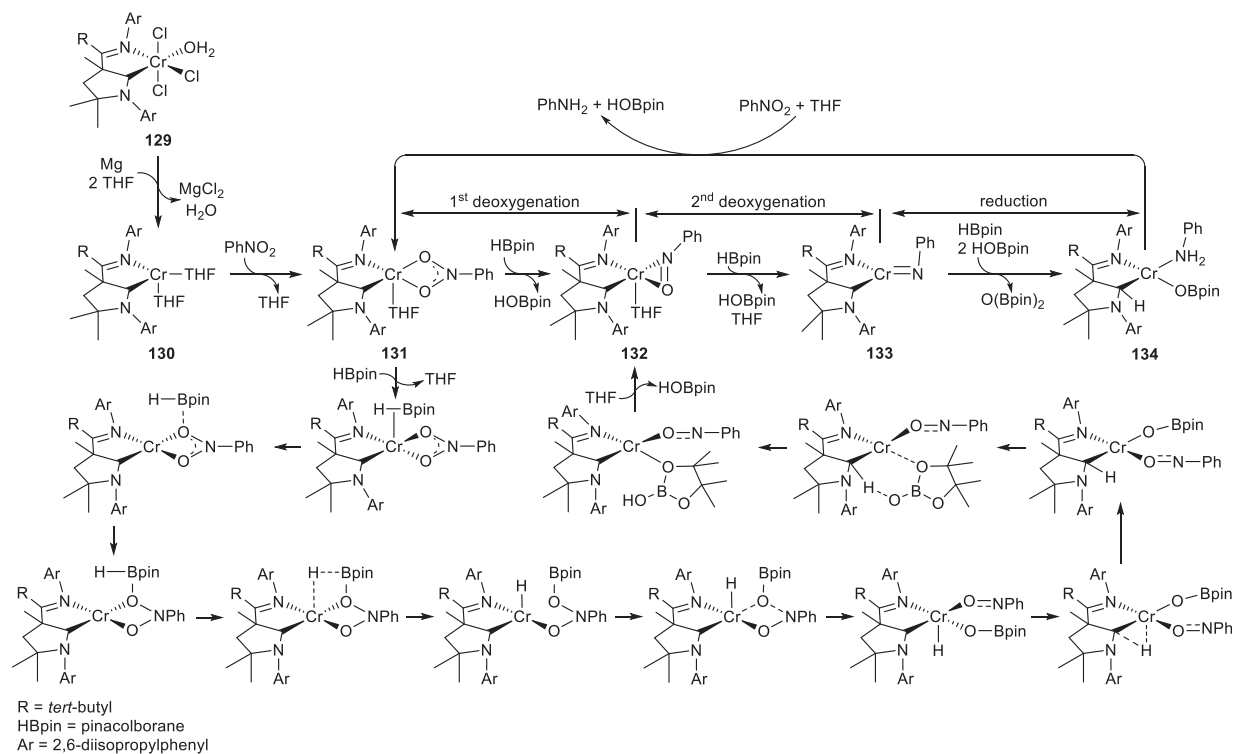




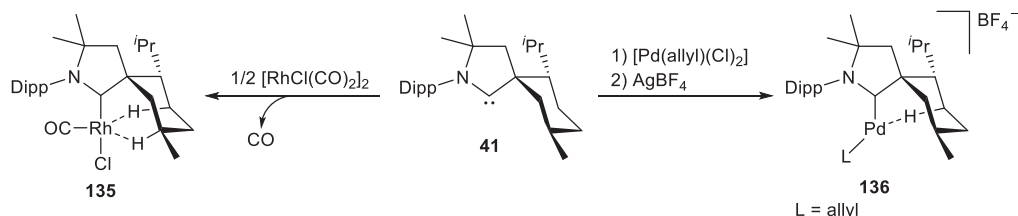
**Scheme 17** Pyridinium-containing trz iridium complexes for water oxidation and methyltransferase activity.

Noninnocent ligand roles of the cyclic (alkyl)(amino)carbene class of the nonclassical carbenes, apart from the inherent noninnocence discussed above, have also been exploited in metal-mediated processes. The unique reactivity of CAAC-metal complexes, compared to metal complexes coordinated by inert ligands, was eloquently demonstrated by a CAAC coordinated chromium complex, reported by Zeng et al.<sup>132</sup> Chromium complexes coordinated by CAAC ligands has previously been reported.<sup>133</sup> A CAAC ligand featuring a hemilabile imine pendant, first reported by Bertrand et al. (vide infra),<sup>134</sup> was coordinated to  $\text{CrCl}_3$  yielding the corresponding C,N-chelated  $\text{Cr}^{\text{III}}$  complex **129** (Scheme 18).<sup>132</sup> Zeng and co-workers determined that the CAAC coordinated chromium complex could mediate the deoxygenative hydroboration of nitro functional groups, yielding the corresponding amine derivatives. The catalytic deoxygenative hydroboration reaction was also realized with an analogous catalyst, such as a chromium complex coordinated by a classical NHC (featuring either an imine pendant or no hemilabile group at all), in addition to a CAAC coordinated chromium complex with no tethered donor functionality on the CAAC ligand. However, diminished catalytic reactivity for these analogous catalysts was reported, highlighting the requirement for the CAAC donor ligand to feature a hemilabile pendant. Various experiments and calculations allowed for insight into the catalytic reaction mechanism (Scheme 18).<sup>132</sup> Reduction of complex **129** from  $\text{Cr}^{\text{III}}$  to the  $\text{Cr}^0$  complex **130** by Mg is marked by a catalyst induction period, which is followed by THF ligand exchange for  $\text{PhNO}_2$  yielding **131**. The oxygen lone pair of  $\text{PhNO}_2$  in **131** can subsequently coordinate the boron from the added HBpin (HBpin = pinacolborane), leading to  $\sigma$ -bond metathesis and formation of the hydride intermediate (Scheme 18). This is followed by N–O bond scission with ensuing Cr–O bond formation. The noninnocent ligand effects the following step involving hydride migration. The hydride is transferred from the metal to the carbene with accompanying reversal of the polarity of the hydride. Proton transfer from the metal-bound carbon to the boron oxygen ensues, regenerating the carbene coordinated complex **132** with concomitant elimination of HOBpin (Scheme 18). This constitutes the first deoxygenation step. The second deoxygenation step yields the chromium nitrene complex **133**, with elimination of another HOBpin molecule (Scheme 18). Both HBpin and HOBpin contribute toward the reduction of the nitrene moiety, ultimately leading to  $\text{O}(\text{Bpin})_2$  elimination and release of the aniline product in a stepwise manner, regenerating the nitro-ligated active catalyst **131** (Scheme 18). Calculations evidenced the carbene's  $\pi$ -accepting attributes to accommodate a Cr unpaired d-type electron in the vacant p-orbital, facilitating the reversible proton transfer event.<sup>132</sup> Hydride transfer from a CAAC-coordinated dinuclear copper complex to the electrophilic carbene carbon has also been reported, albeit as an irreversible migratory process.<sup>135</sup>

Ligand cooperation not only applies for bond making and breaking processes, but also towards stabilization of reactive complexes, as discussed above.<sup>136</sup> Isolation of these reactive species allows insight into transient intermediates in catalysis, facilitating a better understanding of the catalytic processes. Bertrand and co-workers coordinated the menthyl-substituted CAAC ligand **41** to rhodium, resulting to formation of a stable 14-electron T-shaped rhodium complex **135** (Scheme 19). Crystal structure and NMR analysis of the complex in solution confirm two agostic interactions which provide stabilization towards the low-valent metal complex.<sup>136</sup> Furthermore, chloride abstraction of a menthyl-CAAC coordinated palladium complex<sup>56</sup> with a silver salt, yielded



**Scheme 18** Deoxygenative hydroboration catalyzed by a CAAC-Cr complex.



**Scheme 19** Agostic interactions stabilizing low-valent metal complexes.

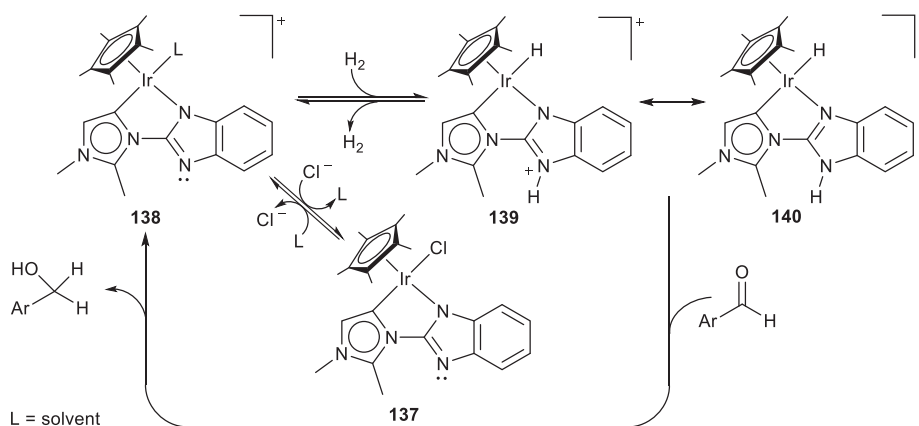
a stable 14-electron cationic palladium complex **136**, featuring an agostic interaction as evidenced by X-ray diffraction and NMR analysis.<sup>136</sup> The corresponding cyclohexyl-substituted CAAC rhodium and palladium complexes could not be isolated.

### 1.05.2.2 Group 5 donor functionalized nonclassical carbenes

#### 1.05.2.2.1 *N*-donor functionalized carbenes

Noninnocent ligand roles of the group 5 atom functionalized nonclassical carbenes predominantly employ N-donors, although examples of P-donor tethered carbenes are known.<sup>137,138</sup> A bifunctional ligand, featuring the strongly donating imidazol-4-ylidene and a benzimidazolato motif, was developed towards facile hydrogenation of various aromatic and aliphatic aldehydes under atmospheric hydrogen pressure, room temperature, and base-free reaction conditions in the presence of water (**Scheme 20**).<sup>139</sup> The authors postulated that the noninnocent Im4 coordinated iridium complex **137** catalyzed this transformation via a rate-determining outer-sphere hydride transfer step, followed by a fast proton transfer event (**Scheme 20**). The two hydrogen transfer steps could be realized due to the bifunctional character of the ligand, with the strong donor Im4 increasing the hydric character of the hydride ligand, resulting to enhanced hydride transfer, while the benzimidazolato functionality mediated the proton transfer step via the basic imino moiety. It was established that the aldehyde hydrogenation reaction could be catalyzed chemoselectively in the presence of various functionalities. The catalytic reaction was shown to be scalable, with a 95% yield obtained for the alcohol at a 5 mmol scale. A plausible reaction mechanism included a 'switch' between the imine nitrogen of complex **139** and an iridium coordinated amine nitrogen in **140**, facilitating the fast proton transfer step and completing the catalytic cycle, regenerating **138** and yielding the targeted product (**Scheme 20**).<sup>139</sup>

Choudhury et al. further exploited the analogous iridium complex towards storage of hydrogen at ambient pressure and subsequent release at 90 °C, via the carbon dioxide-formic acid couple.<sup>140</sup> Development of a homogeneous catalyst facilitating both the



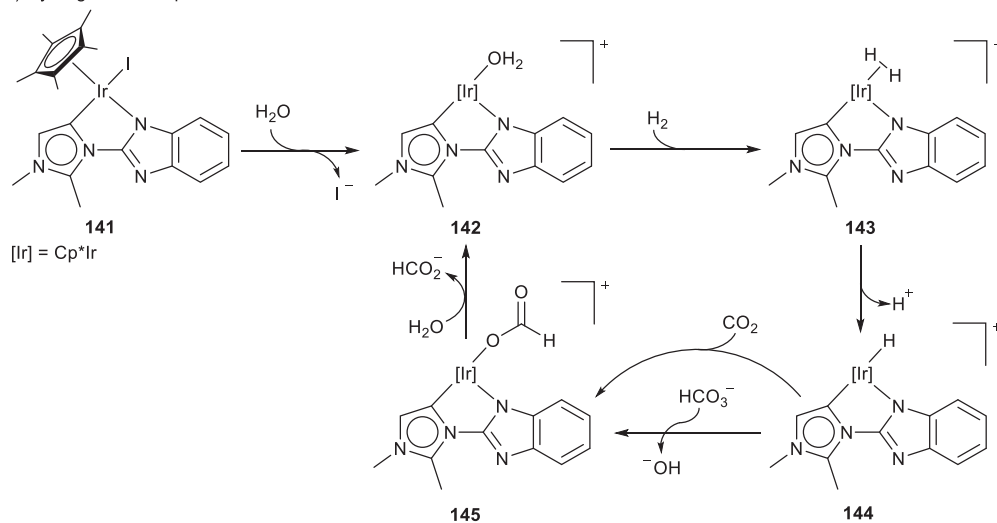
**Scheme 20** Bifunctional imidazol-4-ylidene ligand featuring a benzimidazolato motif.

storage and release of hydrogen from a carrier liquid would contribute towards the advancement of green processes, as it allows for the risk mitigated transport of the volatile substance.<sup>141–143</sup> Accordingly, the iridium complex reported by the group of Choudhury was shown to promote both the hydrogen storage and release reactions, switching between the two processes via pH adjustment (**Scheme 21**).<sup>140</sup> Hydrogen incorporation was catalyzed by the C,N-chelated iridium complex **141** with a solution pH of 8.5, attained through the addition of base (**Scheme 21, i**). Hydrogen coordinates to the metal yielding intermediate **143** from **142**, followed by H<sub>2</sub> cleavage leading to formation of the hydride complex **144**, with base-mediated proton abstraction hypothesized. Iridium formate **145** is obtained after metal-bound hydride transfer from **144** to either CO<sub>2</sub> or in situ generated HCO<sub>3</sub><sup>−</sup>. This leads to formate release and regeneration of the active iridium catalyst **142** upon reacting with aqueous KOH. In contrast to the formation of formate, the liberation of hydrogen occurs under acidic conditions (**Scheme 21, ii**). The mechanism postulated for the release of hydrogen from formate involves the simultaneous protonation of the basic *exo* nitrogen of the benzimidazole moiety with HCO<sub>2</sub>H and coordination of HCO<sub>2</sub><sup>−</sup> to iridium. An equilibrium ensues between the metal bound anionic amido nitrogen **146** and the imino-coordinated iridium complex **147**, after imine protonation (**Scheme 21, ii**),<sup>140</sup> resembling the imine-amine switch in the aldehyde hydrogenation mechanism discussed above (see **139** and **140** in **Scheme 20**).<sup>139</sup> β-Hydride elimination proceeds from the equilibrium, releasing CO<sub>2</sub> and yielding **148** (**Scheme 20, ii**).<sup>140</sup> Presumably, HCO<sub>2</sub>H forms a hydrogen bond with the distal γ-NH of **148** leading to intermediate **149**, followed by formic acid and H<sub>2</sub> formation with subsequent release of H<sub>2</sub> yielding **146** (**Scheme 21, ii**). The noninnocent role of the ligand allows for the hydrogen transfer events, while the significance of the nonclassical carbene was illustrated upon comparison to the analogous benzimidazole tethered pyridinylidene complex which demonstrated poor catalytic performance in both reactions. The increased catalytic performance was attributed to the stronger donor characteristics of the Im4, inducing increased hydride character and a decreased hydride transfer energy barrier. The iridium catalyst was also demonstrated to facilitate the CO<sub>2</sub>-transfer hydrogenation catalysis at ambient pressure using biomass-derived alcohols such as glycerol, as the source of hydrogen.<sup>144</sup> Hydrogen storage and release,<sup>140</sup> as well as the hydrogenation of CO<sub>2</sub>,<sup>144</sup> substantiate the requirement for noninnocent ligand design with stronger donor carbenes, as both case studies demonstrate relevance towards more environmentally friendly processes.

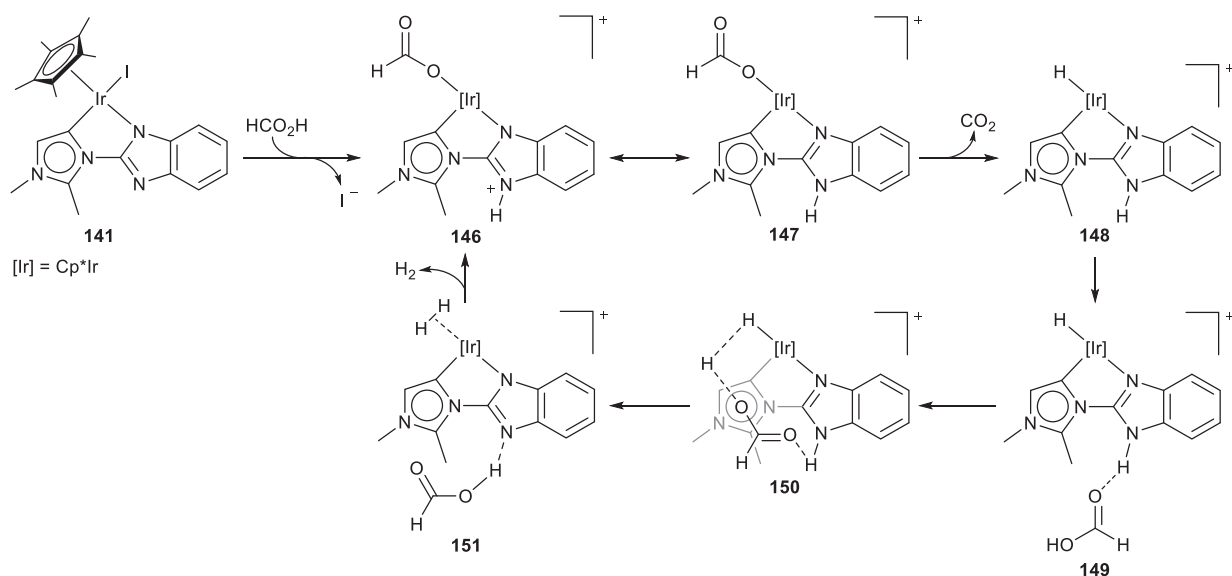
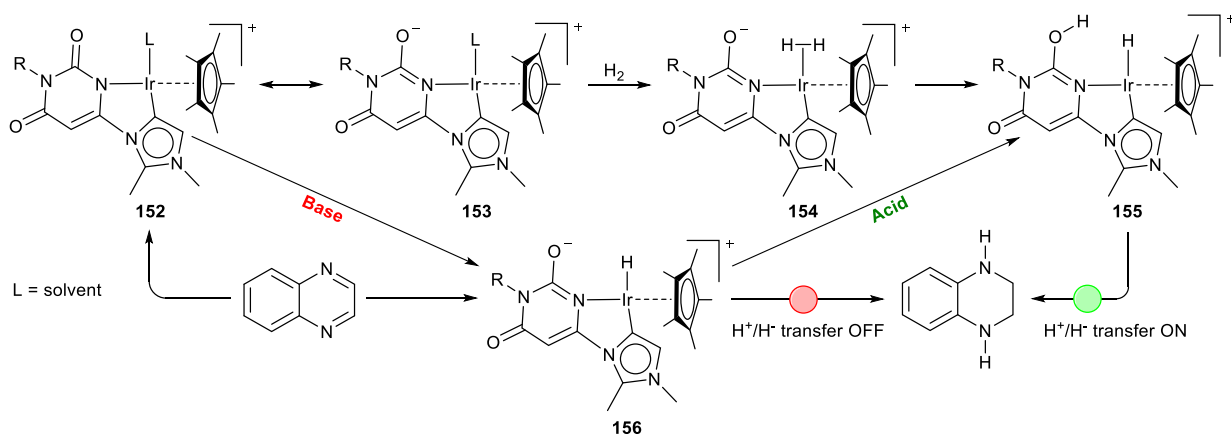
The same group furthered investigations into switchable catalysis, in this case scrutinizing an acid/base-responsive complex towards hydrogenation of quinoxalines.<sup>145</sup> Accordingly, a nonclassical carbene tethered by a uracil motif was coordinated to iridium (**152**, **Scheme 22**). The incorporation of the uracil motif was rationalized by the possible lactam-lactim tautomerization, which would render the ligand noninnocent and subsequently aid in heterolytic H<sub>2</sub> activation towards hydrogenation. Choudhury et al. determined that the complex could catalyze the hydrogenation of quinoxaline with 1 mol% catalyst loading, under atmospheric hydrogen gas pressure at 50 °C in just 90 min. The catalyst could be switched off through the addition of base and switched back on via the addition of HCl (**Scheme 22**). Thus, charging a solution of the neutral analog of **152** (where L = Cl) with H<sub>2</sub>, yielded the corresponding iridium hydride intermediate **155** through heterolytic H<sub>2</sub> cleavage aided by the noninnocent ligand, with protonation of the uracil carbonyl moiety forming the Ir–N=C–OH fragment.<sup>145</sup> Heterolytic cleavage is followed by quinoxaline hydrogenation, which is proposed to occur via an outer-sphere mechanism. Catalysis is however halted by the addition of base, a result of the base capturing H<sup>+</sup> from the heterolytic H<sub>2</sub> cleavage process. Proton transfer to the quinoxaline is therefore ceased, which subsequently inhibits hydride transfer (**Scheme 22**). The catalyst could be switched on again through the addition of HCl, and the catalyst switching process could be repeated several times.

Tethering of a pyridine functionality to a carbene donor ligand allows for the preparation of C,N-chelating ligands, with the possibility of yielding an inert nitrogen-metal bond upon chelation. Alternatively, the coordination/decoordination of the pyridine moiety can affect a hemilabile noninnocent role,<sup>10–12,18,19,21,23,24,94,95</sup> closely resembling the contributions of the pyridine functionality in the well-known PEPPSI-type complexes (PEPPSI = Pyridine Enhanced Precatalyst Preparation Stabilization and Initiation).<sup>146–162</sup> From an electronic point of view, the trz-pyridyl combination results in increased donor strength compared to the pyridine-triazole C,N-chelating derivatives and the analogous bis-triazole and 2,2'-bipyridine N,N-chelating ligands, while lower

i) Hydrogenation at pH ~ 8.5



ii) Dehydrogenation at pH ~ 5.0


**Scheme 21** Hydrogen storage and release facilitated by an iridium catalyst.

**Scheme 22** Acid/base switchable hydrogenation catalyst.

donating capabilities are seen when likened against the bis-trz C,C-chelating ligand<sup>163</sup> (see Fig. 4 for representative examples of the mentioned bidentate ligands). Scrutinizing the  $\pi$ -acceptor properties of the trz-pyridyl ligand reveals that only the 2,2'-bipyridine ligand has improved  $\pi$ -acceptor capabilities, with the abovementioned N,N-bistriazole, C,N- and C,C-chelating ligands demonstrating decreased  $\pi$ -acceptor properties. Arguably, these features provide a balance between donor-acceptor strength of the bidentate trz-pyridyl ligand, while at the same time providing stabilization due to chelation in addition to possible metal coordination/decoordination affecting a bifunctional role. Not surprising then is the number of documented examples of trz ligands featuring a pyridine hemilabile donor.<sup>30,33,35,37</sup>

At the onset of the previous decade, Albrecht et al. reported ruthenium complexes chelated by a trz-pyridyl ligand, with coordination of the nitrogen moiety to the metal (Fig. 3).<sup>62</sup> Similarly, the corresponding C,N-chelated iridium complexes were also disclosed (Fig. 3).<sup>63,164</sup> It was determined that in the presence of sacrificial oxidant, both the ruthenium and iridium complexes catalyzed the oxidation of water,<sup>62,63,165</sup> with the cationic pyridine coordinated ruthenium complexes displaying selectivity towards oxygen (Fig. 3), contrasting to the cymene coordinated ruthenium complexes investigated in the study which formed CO<sub>2</sub> in addition to O<sub>2</sub>.<sup>62</sup> The iridium complexes depicted in Fig. 3 displayed selectivity towards oxygen.<sup>63</sup> However, catalytic activity for the C,N-chelated complexes was still lower compared against the C-bound iridium complexes described above (see Scheme 17).<sup>129</sup> Stable complex formation due to rigid C,C-chelation versus trz-pyridyl chelation could rationalize the difference noted in catalytic activity, similar to the reported example of a trz-thiazole C,N-chelated iridium complex with increased water oxidation catalytic activity compared against an analogous benzoxazole-tethered triazolylidene iridium complex.<sup>166</sup>

The group of Albrecht et al. also described the storage and release of hydrogen from a carrier molecule<sup>167</sup> similar to the trz-pyridyl coordinated iridium complex 141 described above.<sup>140</sup> Hydrogenation and dehydrogenation of N-heteroarenes were mediated by iridium trz-pyridyl catalysts.<sup>167</sup> It was established that the two iridium complexes 164 (Fig. 3) and 177 (Scheme 23) could catalyze both the hydrogenation and the dehydrogenation of quinolines, either in the presence or absence of hydrogen, respectively (Scheme 23, i). The iridium complexes further demonstrated its functional group tolerance with the hydrogenation of a variety of quinolines with varying substituents. The authors' mechanistic consideration proposed a roll-over cyclometalation,<sup>168</sup> which in the presence of hydrogen and D<sub>2</sub>O as solvent<sup>167</sup> results in formation of a C,C-chelated iridium intermediate leading to deuteration of the C6 of the pyridyl pendant, yielding 176 (Scheme 23, ii). Dissociation and coordination of the pyridine nitrogen therefore allows for the deuteration to proceed, with selective deuteration at the C6 position. The proposed mechanism for hydrogen activation by the trz-pyridyl chelated iridium complex 164 in the presence of hydrogen and D<sub>2</sub>O is depicted in Scheme 23. Deuteration at the C6 position of the C,C-chelated complex 177 was also demonstrated. However, for complex 177, deuteration occurred at both the C6 position and the pendant phenyl substituent, with concomitant formation of 178 (Scheme 23, iii).<sup>167</sup>

Another pyridine tethered trz complex, a palladium complex 179, was reported to catalyze the intermolecular hydroamination reaction between anilines and terminal alkynes yielding the corresponding imines.<sup>169</sup> Both the classical NHC as well as the trz containing Pd-PEPSSI complexes showed no reactivity towards the intermolecular hydroamination catalyzed reaction. This clearly illustrated the requirement for both the stronger donor nonclassical carbene in conjunction with the tethered donor moiety to access noninnocent reactivity. Complex stabilization is mediated through pyridine to metal association (Scheme 24, i). Pyridine dissociation from palladium 179 opens the catalytic pocket, exposing a coordination site in the metal's first coordination sphere for subsequent  $\eta^2$ -acetylene coordination via one of the alkyne's  $\pi$ -bonds (Scheme 24, i). The decoordinated pyridine pendant arm was reported to be in close proximity to the Pd center (<5.0 Å), as requisite for successful catalysis (vide supra).<sup>169</sup> The basic nitrogen subsequently facilitates the proton transfer events between the catalyst and the catalytic intermediates, working in tandem with the Pd metal center to furnish the imines at room temperature with exclusive Markovnikov selectivity (Scheme 24, ii). The noninnocent nonclassical carbene containing palladium complex could also catalyze the Sonagashira coupling reaction between an aryl halide and a terminal alkyne.<sup>170,171</sup> This could be achieved either through employing the trz palladium complex as shown,<sup>170</sup> or in conjunction with a second palladium complex coordinated by a phosphine donor ligand.<sup>171</sup>

Sarkar and co-workers demonstrated the  $\sigma$ -donor  $\pi$ -acceptor balance of the trz-pyridyl ligand<sup>163</sup> during both the electrocatalytic H<sub>2</sub> production employing a cobalt catalyst with acetic acid as the proton source (Fig. 4, i),<sup>172</sup> as well as the oxygenation of sp<sup>3</sup> C-H bonds using iridium chelated complexes as catalysts (Fig. 4, ii).<sup>173</sup> The trz-pyridyl ligand was compared

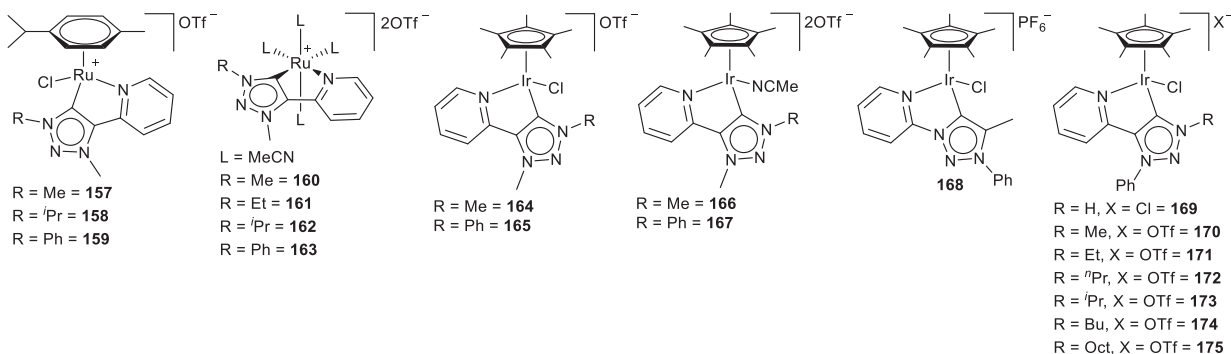
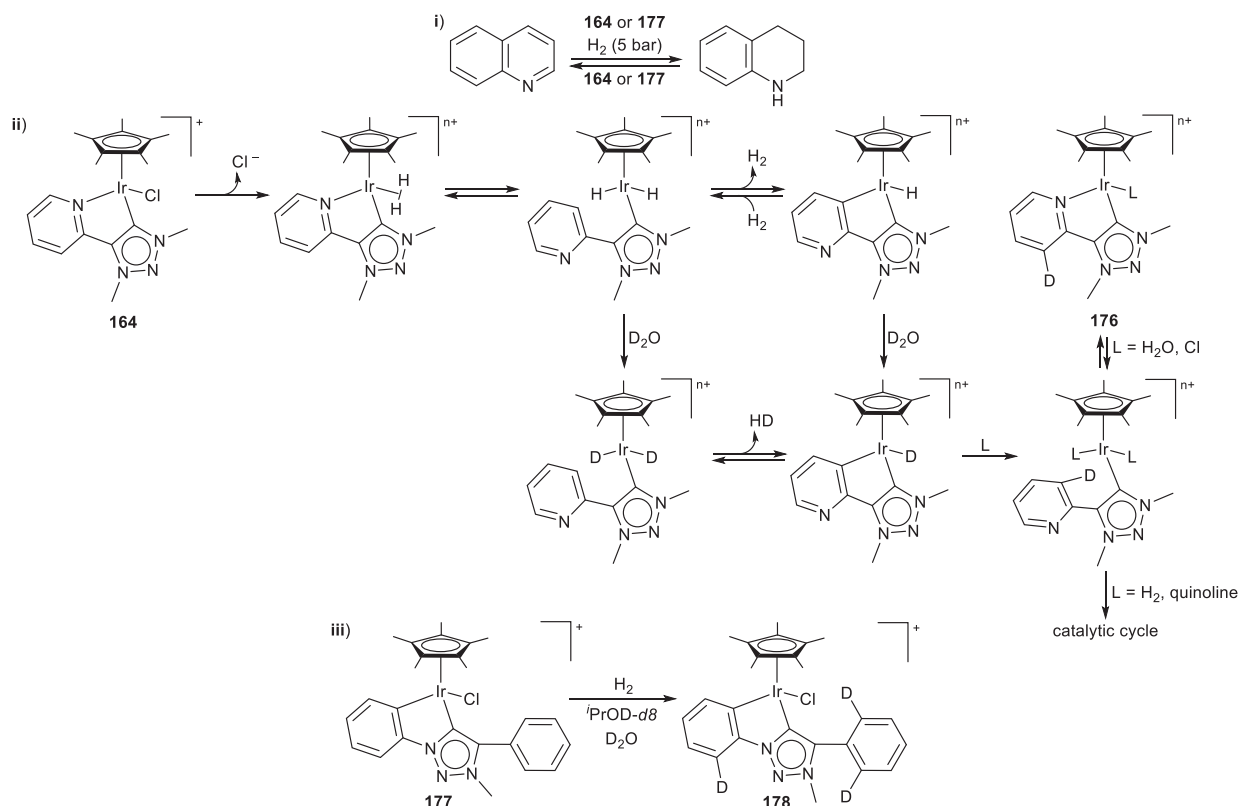


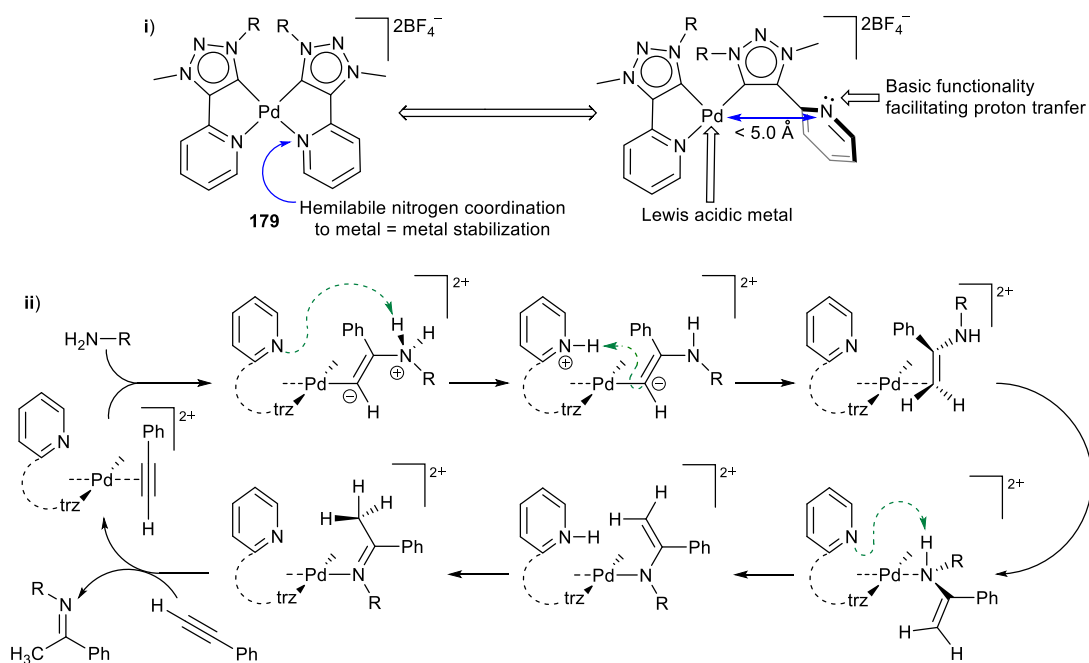
Fig. 3 Water oxidation catalysts featuring trz-pyridyl C,N-chelating ligands.





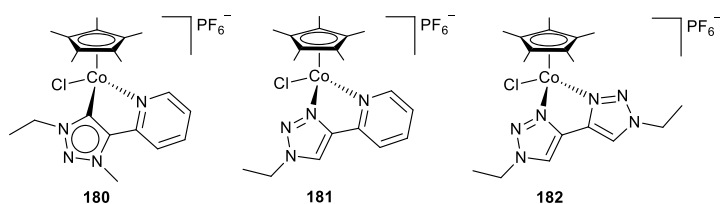
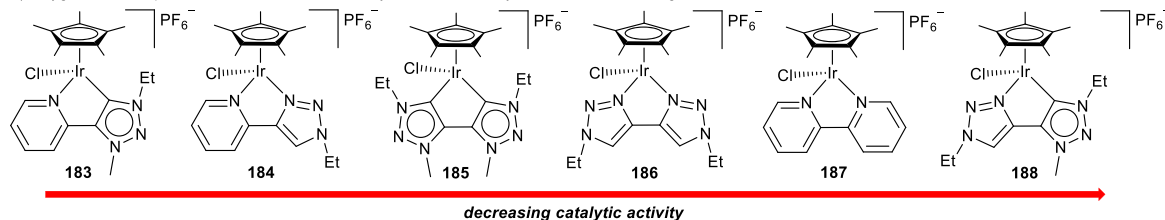
**Scheme 23** Proposed roll-over cyclometalation leading to pendant substituent deuteration.<sup>167</sup> Modified from Vivancos, Á; Beller, M.; Albrecht, M. *ACS Catal.* **2018**, *8*, 17–21.

against C,N-, C,C- and N,N-chelating ligands, displaying superior catalytic activity for the trz-pyridyl chelated metal complexes.<sup>172,173</sup> Košmrlj and Sarkar also investigated the effect of structure variation of the trz-pyridyl ligand, introducing either a methylene spacer between the pyridine and the trz moieties [Fig. 4, iii (a)],<sup>174,175</sup> or a second nitrogen at the pyridine site yielding the corresponding pyrimidine appended trz ligand [Fig. 4, iii (b)].<sup>176</sup> When equated against the analogous

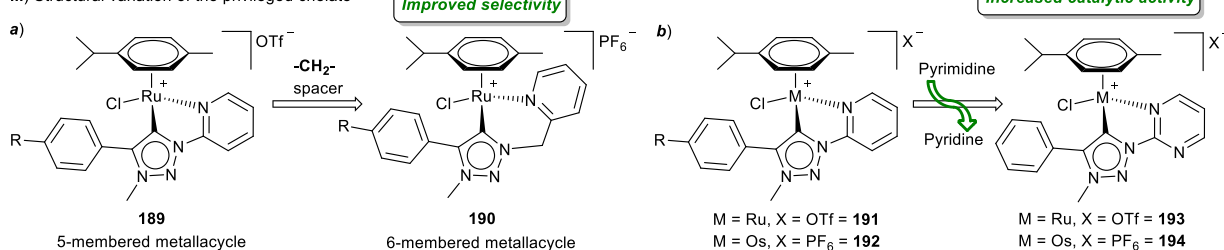


**Scheme 24** Hemilabile pyridine coordination/decoordination enabling catalytic processes.

i) Catalyst used towards electrocatalytic dihydrogen production

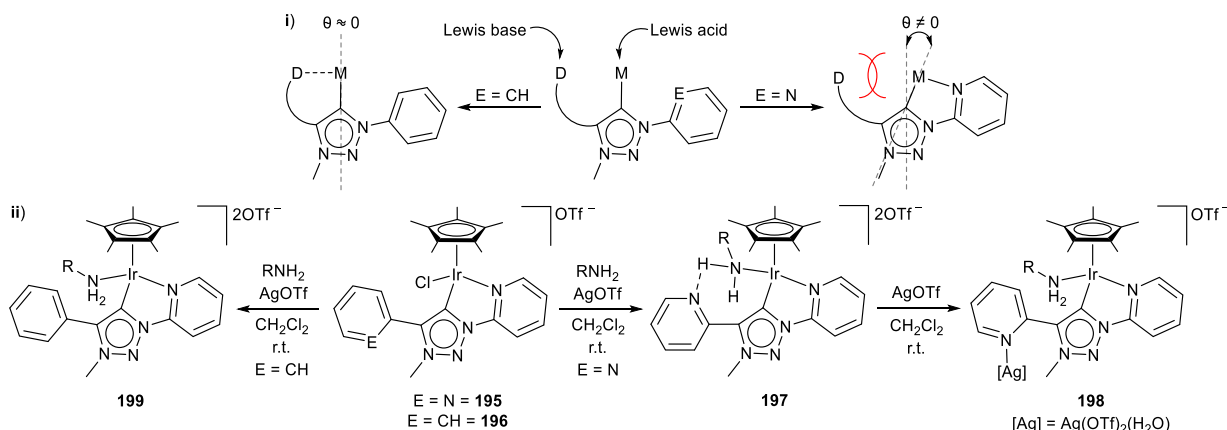
ii) Oxygenation of  $sp^3$  C-H bonds with iridium catalyst coordinated by a neutral bidentate ligand

iii) Structural variation of the privileged chelate

**Fig. 4** Towards improved catalyst with trz-pyridyl and trz-pyrimidine chelating ligands.

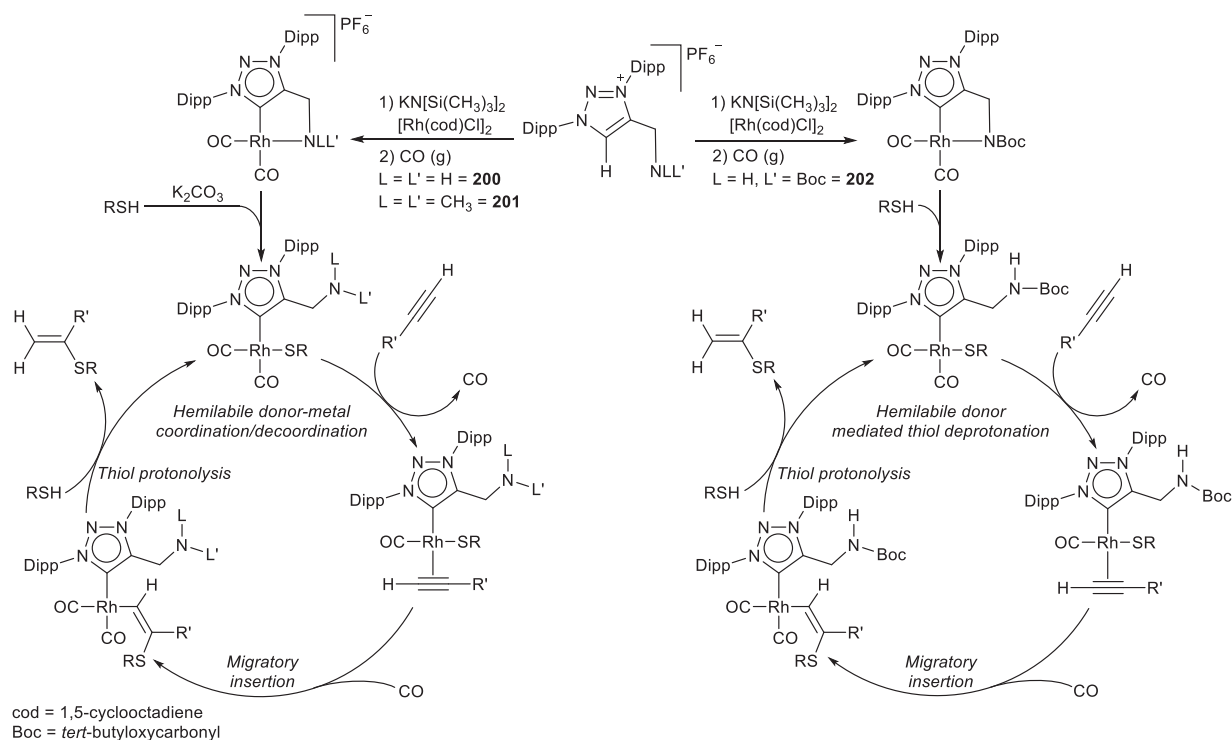
trz-pyridyl metal complexes, improved catalytic performance was observed.<sup>174,176</sup> Enhanced selectivity in the catalyzed alcohol oxidation reaction was noted for the six-membered metallacycle complex, compared against the five-membered trz-pyridyl ruthenium complex derivatives investigated [Fig. 4, iii (a)].<sup>174</sup> Sandoval et al. also reported a similar picolyl tethered trz ruthenium complex, in addition to its catalytic transfer hydrogenation activity.<sup>177</sup> Trz-pyrimidine chelated complexes catalyzed various reduction reactions with increased catalytic activity when compared with the equivalent trz-pyridine complexes, reported to be the effect of pyridine substitution with the pyrimidine pendant [Fig. 4, iii (b)].<sup>176</sup> It is therefore evident that even minor structural variation of the privileged trz-pyridyl chelate can accomplish improved catalytic activity and/or selectivity.<sup>174,176</sup>

A slightly varied ligand design approach utilizes a pendant donor moiety, tethered to a triazolium-pyridyl C,N-bidentate proligand.<sup>178–182</sup> Chelation of the C,N-bidentate ligand results in an increased yaw angle (Scheme 25, i), which disfavors coordination of the pendant donor to the metal center, but at the same time securing the pendant donor in close proximity to the metal.<sup>178,179</sup> Substrate recognition and binding can subsequently be mediated by the noncoordinating Lewis basic pendant. Concomitantly, the metal can complete the catalytic processes while exploiting the attributes imparted by the privileged trz-pyridyl chelate to mediate

**Scheme 25** Functional group tethered trz-pyridine C,N-chelated iridium complexes.

the sought-after process/es. The design methodology centered around the Lewis acidic metal in tandem with the Lewis basic donor group, parallels the well-known frustrated Lewis acid-base pairs.<sup>183–185</sup> Accordingly, Albrecht et al. prepared triazolium-pyridyl C,N-bidentate ligand precursors containing either a phenyl or a second pyridine functionality (Scheme 25, ii).<sup>178</sup> Coordination to iridium formed the corresponding C,N-chelated iridium complexes, with the pyridine 195 or phenyl 196 pendant moiety in close proximity to the metal center, but not coordinating to the iridium coordination sphere. The complexes were determined to be catalytically active in the base- and oxidant-free oxidative dehydrogenation of amines yielding the corresponding imines. The catalytic activity and selectivity were advantageously influenced by the presence of the hemilabile pyridine moiety. Stoichiometric investigations with X-ray diffraction, NMR and IR spectroscopic analysis confirmed the noninnocent behavior of the chelating ligand, exposing the substrate to pyridine hydrogen bond formation upon coordination of an amine substrate in 197, after addition of one equivalent of silver triflate to 195 (Scheme 25, ii). Addition of a second equivalent of silver triflate yielded complex 198, with silver coordinated by the pyridine nitrogen. The use of the phenyl substituted trz-pyridyl complex 196 did not amount to any substrate recognition and binding to the ligand backbone, only substrate coordination to the metal upon addition of silver triflate, yielding 199. The elegance behind the design of the pyridine tethered trz-pyridyl ligand is rooted in the fact that dehydrogenative coupling of amines requires N–H bond activation and elimination of hydrogen. Transition metals are celebrated for mediating  $\beta$ -hydrogen elimination reactions,<sup>3</sup> while N–H bond activation necessitates a Lewis base.<sup>183–185</sup> Complex 195 features both the mentioned requirements.<sup>178</sup>

In addition to the reports above, the group of Albrecht also reported the preparation of nitrogen functionalized hemilabile trz ligand salts for complexation to a gold(I) metal center.<sup>186</sup> Bidentate ligand coordination yielding a chelated mononuclear gold(I) complex was not reported. Instead, dinuclear gold(I) complexes were formed upon ligation, with coordination of the ligand's carbene moiety to a gold atom, while the amine functionality coordinated the second gold center. The chiral biscarbene dinuclear gold(I) complexes were found to be catalytically active in the aldol condensation reaction between various aldehydes and methyl isocanoacetate. However, the catalytically active species in the aldol condensation reactions was attributed to gold nanoparticle formation upon ligand dissociation.<sup>186</sup> The diarylated nitrogen tethered trz ligand analogs were reported a few years later, with nitrogen coordination and formation of bidentate mononuclear rhodium(I) complexes (Scheme 26).<sup>187</sup> The hemilabile donor was varied between either an amine 200, dimethylamine 201 or Boc (*tert*-butyloxycarbonyl) protected amine 202, functional group. The rhodium complexes were investigated as alkyne hydrothiolation catalysts and determined to be highly selective towards the formation of the Markovnikov-type  $\alpha$ -vinyl sulfide product. The catalytic reaction mechanism was described, in the case of the amine or dimethylamine substituted ligand complexes 200 and 201, respectively, as hemilabile coordination/decoordination, stabilizing the metal center when required while yielding an active catalyst upon catalyst initiation. It was determined that the addition of  $K_2CO_3$  was required to ensure selectivity towards the  $\alpha$ -vinyl sulfide product. However, the rhodium complex 202 featuring the NBoc-protected ligand displayed a different reaction mechanism (Scheme 26). Thiol deprotonation was mediated by the Boc-protected amine moiety, yielding the HNBoc-pendant arm as well as the metal thiolate complex. This was followed by alkyne

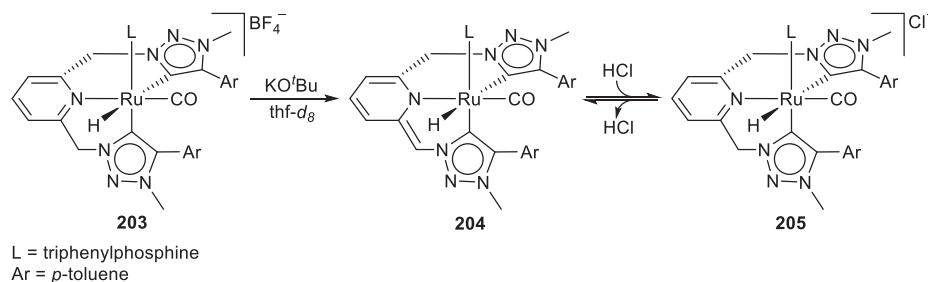


**Scheme 26** Alkyne hydrothiolation catalyzed by nitrogen tethered triazolylidene rhodium complexes.

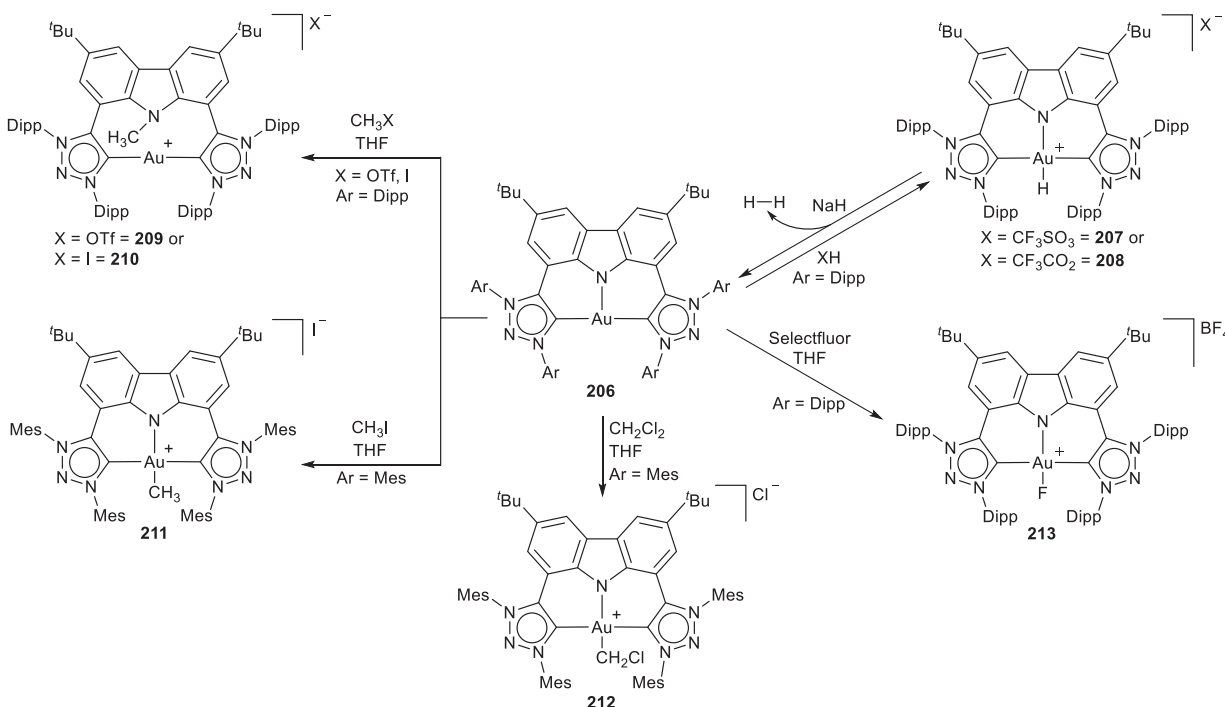
coordination with subsequent migratory insertion and finally, thiol protonolysis yielding the catalytically active intermediate (Scheme 26). The incorporation of the NBoc-protected ligand allowed for catalysis via a non-oxidative addition mechanism, circumventing the formation of  $\text{Rh}^{\text{III}}$  catalytic intermediates,<sup>188,189</sup> while retaining the high selectivity towards the  $\alpha$ -vinyl sulfide product. This again illustrates the importance of ligand design and noninnocent ligands, as the reaction can be completed without the addition of base which allows for an even 'greener' method towards the preparation of vinyl sulfides.<sup>187</sup>

Nonclassical carbenes have also been incorporated into the privileged pincer platform, harnessing the increased electron donating properties of the carbene moieties<sup>33</sup> and combining it with the stability imparted by a tridentate pincer into one ligand scaffold.<sup>190–199</sup> Pincer ligands featuring nonclassical carbenes have been reported,<sup>33,58,59,200–214</sup> albeit only a few exhibit a noninnocent role. One such example reports the combination of trz with the lutidine fragment, as disclosed by van der Vlugt, Elsevier and co-workers.<sup>215</sup> The incorporation of the lutidine backbone is not surprising, as this is a known motif for ligand cooperativity via aromatization/dearomatization (Scheme 13, i).<sup>6–9,20,86–93</sup> Accordingly, alkylation of both triazoles flanking the pyridine moiety yielded the corresponding bistriazolium ligand salt.<sup>215</sup> Subsequent silver transmetalation from the silver carbene complex with a ruthenium metal precursor resulted in formation of the corresponding ruthenium complex 203 (Scheme 27). The pincer ruthenium complexes were demonstrated to catalytically mediate the hydrogenation of carboxylic esters to alcohols, in the presence of base and  $\text{H}_2$ . Stoichiometric experiments involving the addition of base or acid evidenced the sought-after aromatization/dearomatization reactivity, which was postulated to participate in the catalytic hydrogenation process alongside the added base (Scheme 27). Addition of base resulted to the dearomatized complex 204, while adding HCl yielded the aromatized product 205.

Metals that are classically viewed as inert can be coerced to react under mild conditions by effective ligand tailoring. This was demonstrated by the 'remote basicity' imparted by a pincer bis(triazolylidene)carbazole ligand, which rendered a gold(I) metal site nucleophilic (206, Scheme 28).<sup>216</sup> Furthermore, 206 featured an unusual T-shaped geometry around the gold(I) metal, a result



**Scheme 27** Aromatization/dearomatization of a bistriazolylidene-lutidine ruthenium complex.

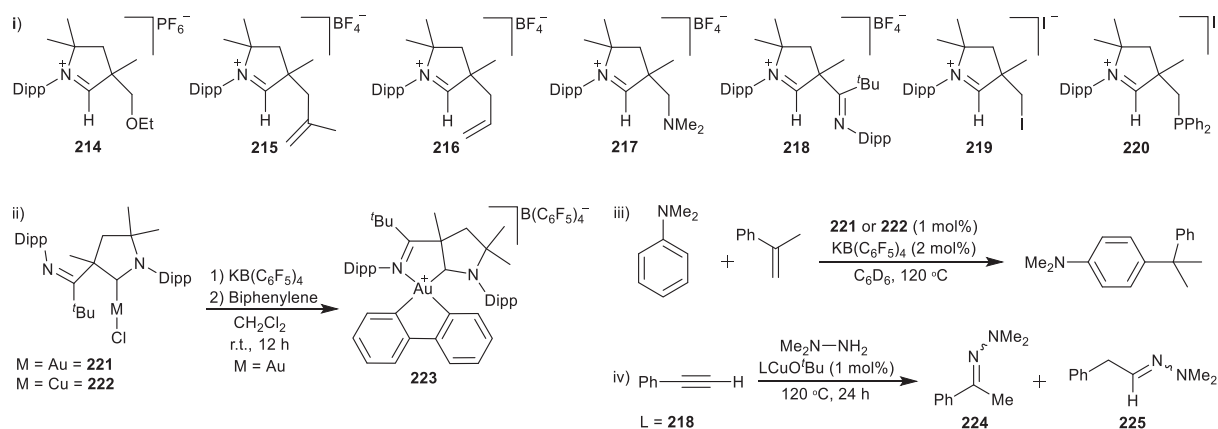


**Scheme 28** Oxidation of T-shaped gold(I) complexes towards square planar gold(III) complexes.

of the tridentate pincer ligand anchoring the metal into a constrained geometry. These main attributes allowed for protonation of the coinage metal **206** followed by mild oxidation, yielding the corresponding cationic gold(III) hydrides **207** or **208**. Protic rather than hydridic character was established for **207** upon stoichiometric treatment with either acid or base. No reactivity was noted for **207** under acidic conditions but **207** reacted cleanly with sodium hydride liberating  $H_2$  and yielding the gold(I) complex **206**. The electrophilic oxidation strategy was extended to include oxidation of the gold(I) pincer complex with electrophilic alkylating reagents (Scheme 28), leading to alkylation of either the amido nitrogen or the gold(I), and subsequent oxidation of the metal yielding the corresponding cationic gold(III) alkyl complex **211**. Reacting the T-shaped gold(I) complex with Selectfluor resulted in the first example of a stable, well-defined monomeric cationic gold(III) fluoride complex **213**.<sup>217</sup> The bis(trz)carbazolide imparts unique, unprecedented reactivity to the gold(I) metal center,<sup>216,217</sup> as an important contribution to the recent realization that mild gold oxidation can be accessed through appropriate ligand design.<sup>218–221</sup>

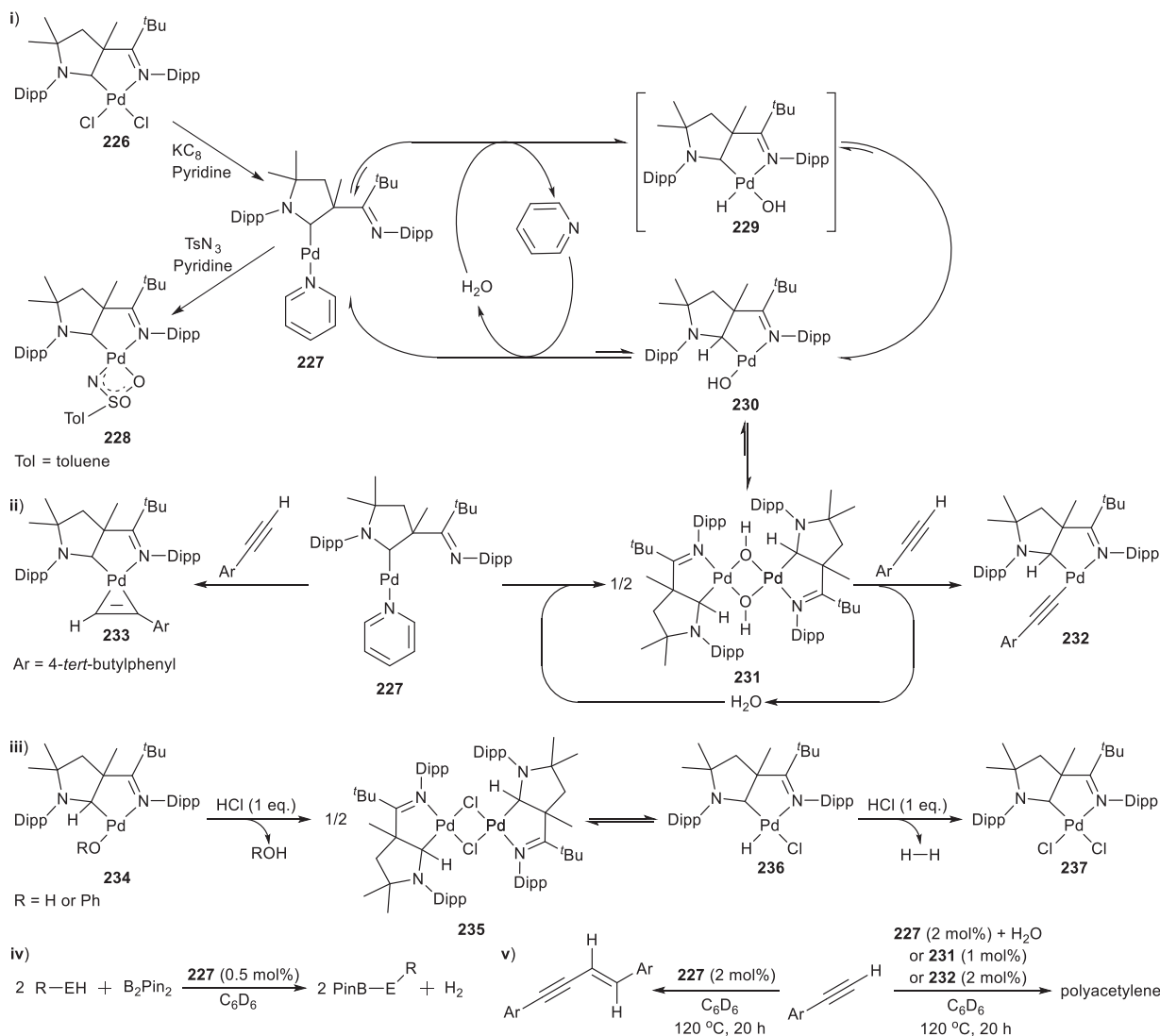
Gold(I) coordination to another noninnocent nonclassical carbene, in this case, a bifunctional CAAC ligand, could likewise accomplish mild oxidation.<sup>134</sup> The group of Bertrand expanded the library of CAACs to comprise a range of hemilabile functional group containing ligand salts (Scheme 29, i). The hemilabile groups consisted of various functionalities, which included an ethoxy **214**, alkenes **215** and **216**, amine **217**, iodo **219** and even a phosphine **220** containing functional group. The imine containing ligand salt **218**<sup>134</sup> introduced above,<sup>132</sup> was again of particular interest. Treatment of the corresponding gold(I) complex **221**<sup>134</sup> with  $KB(C_6F_5)_4$  followed by addition of biphenylene resulted in oxidative addition of the biphenylene substrate across the gold(I) metal, yielding the corresponding cationic gold(III) complex **223** (Scheme 29, ii), similar to the seminal report by Toste et al.<sup>222</sup> The reaction was only successful in the presence of the hemilabile functionality.<sup>134</sup> The gold(I) complex **221** and its copper analog **222** were also found to be catalytically active in the hydroarylation of  $\alpha$ -methylstyrenes with *N,N*-dimethyl aniline (Scheme 29, iii). The reaction is known to involve a proton transfer step, implicating the basic hemilabile functionality in ligand assisted coinage metal catalysis. The copper containing CAAC complex with the imine hemilabile tether (**218**) was further verified to selectively catalyze the hydroamination of phenyl acetylene with dimethylhydrazine, affording the *anti*-Markovnikov product **225** with 96% selectivity (Scheme 29, iv). The pendant imine moiety has a pronounced influence on the outcome of the reaction, as the corresponding copper complex without a tethered pendant catalyzed the aforementioned hydroamination reaction with diminished selectivity.

The imine-containing CAAC ligand **218** (Scheme 29, i)<sup>134</sup> was also coordinated to palladium, allowing for isolation of highly reactive complexes demonstrating unique reactivity.<sup>223</sup> One such reactive and elusive complex is a palladium(II) terminal imido complex (**228**, Scheme 30, i), obtained through reduction of the palladium(II) chloride **226** followed by oxidation of **227** with tosyl azide (Scheme 30, i). Reduction with  $KC_8$  in pyridine was accompanied with decoordination of the imine moiety,<sup>223</sup> yielding the 14-electron pyridine substituted palladium complex **227**.<sup>224</sup> Subsequent oxidation allows re-coordination of the pendant donor and formation of the target complex **228**.<sup>223</sup> In both examples, complex stability could be mediated, in part, by cooperation of the hemilabile pendant which stabilizes the various oxidation states of the metal either via coordination or decoordination. Additionally, it was established that the CAAC supported palladium(0) complex **227** could facilitate the reversible oxidative addition of water, isopropanol, hexafluoroisopropanol, phenol and aniline at room temperature, reactions generally deemed as unfeasible for palladium.<sup>224</sup> Accordingly, the addition of water to **227** resulted in substitution of the pyridine ligand and oxidative addition of  $H_2O$ , with concomitant imine coordination stabilizing the suggested intermediary palladium (hydrido)(hydroxo) complex **229** *en route* to **230** via hydride transfer (Scheme 30, i). Computational analysis elucidated the influence of the pendant imine on the reaction. It was determined that the hemilabile donor moderately stabilizes the transition state during the oxidative addition of water, while trapping the square planar palladium product through coordination after oxidation,<sup>224</sup> akin to the oxidative addition of biphenylene to gold (*vide supra*) (Scheme 29).<sup>134</sup> Hydride migration from the carbene carbon in **229** yields the palladium hydroxo complex **230**, which dimerizes to form the stable palladium dimer **231** (Scheme 30).<sup>224</sup> The palladium(0) complex **227** could be regenerated through the addition of excess pyridine to **230**, resulting in reduction of the dimer complex **231**,



**Scheme 29** Hemilabile substituted cyclic alkyl amino carbenes.<sup>134</sup> Modified from Chu, J.; Munz, D.; Jazzar, R.; Melaimi, M.; Bertrand, G. *J. Am. Chem. Soc.* **2016**, *138*, 7884–7887.





**Scheme 30** Palladium complexes coordinated by a CAAC ligand featuring a hemilabile imine donor.

elimination of water and decoordination of the tethered imine from palladium (**Scheme 30, i**). Reacting the palladium dimer **231** with 4-*tert*-butylphenylacetylene afforded the Pd<sup>II</sup> acetylide complex **232** with hemilabile coordination to the monomeric metal, in addition to water being eliminated from the reaction (**Scheme 30, ii**). However, addition of 4-*tert*-butylphenylacetylene to the Pd<sup>0</sup> complex **227** did not result in oxidative addition. Rather, the  $\pi$ -complex **233** was obtained with coordination of the hemilabile donor to the palladium metal (**Scheme 30, ii**). The reactivity, and outcome thereof, in the presence and absence of water illuminates the requirement of water for oxidative addition of weak C–H bonds to ensue.

The hydridic nature of the hydride migrating to the carbene carbon was evidenced upon treatment of the hydroxo complex **234** with HCl, leading first to formation of **235**, namely the palladium chloride dimer (**Scheme 30, iii**). Addition of another equivalent of HCl was followed by hydride transfer back to the palladium metal, with subsequent H<sub>2</sub> elimination, yielding palladium(II) chloride **237** with imine pendant coordination (**Scheme 30, iii**).<sup>224</sup> This contrasts the hydride transfer step noted above for the analogous chromium complex **129**, where hydride transfer from the metal to the carbene carbon was accompanied with a reversal of the polarity of the hydride ligand, and subsequent proton transfer to the substrate (see **Scheme 18** above).<sup>132</sup> The reversible and facile oxidative addition mediated by **227** was exploited in several catalytic reactions, such as the mild transfer hydrogenation reaction catalyzed without the need for additives, cross-coupling of esters with aniline and borylation of alcohols and amines with bis(pinacolato)diboron (B<sub>2</sub>Pin<sub>2</sub>) (**Scheme 30, iv**).<sup>224</sup> The oxidative addition of water was further utilized as a switch in catalytic activity, with dry reaction conditions mediating the alkyne dimerization reaction yielding enynes, while addition of water resulted to polyacetylene formation from the starting terminal alkyne (**Scheme 30, v**). As is evident from the above examples, combining the inherent noninnocent properties of the CAACs with a noninnocent hemilabile pendant, allows access to highly reactive complexes with atypical or even unknown reactivity patterns. Of particular significance is the multiple noninnocent roles fulfilled by a singular

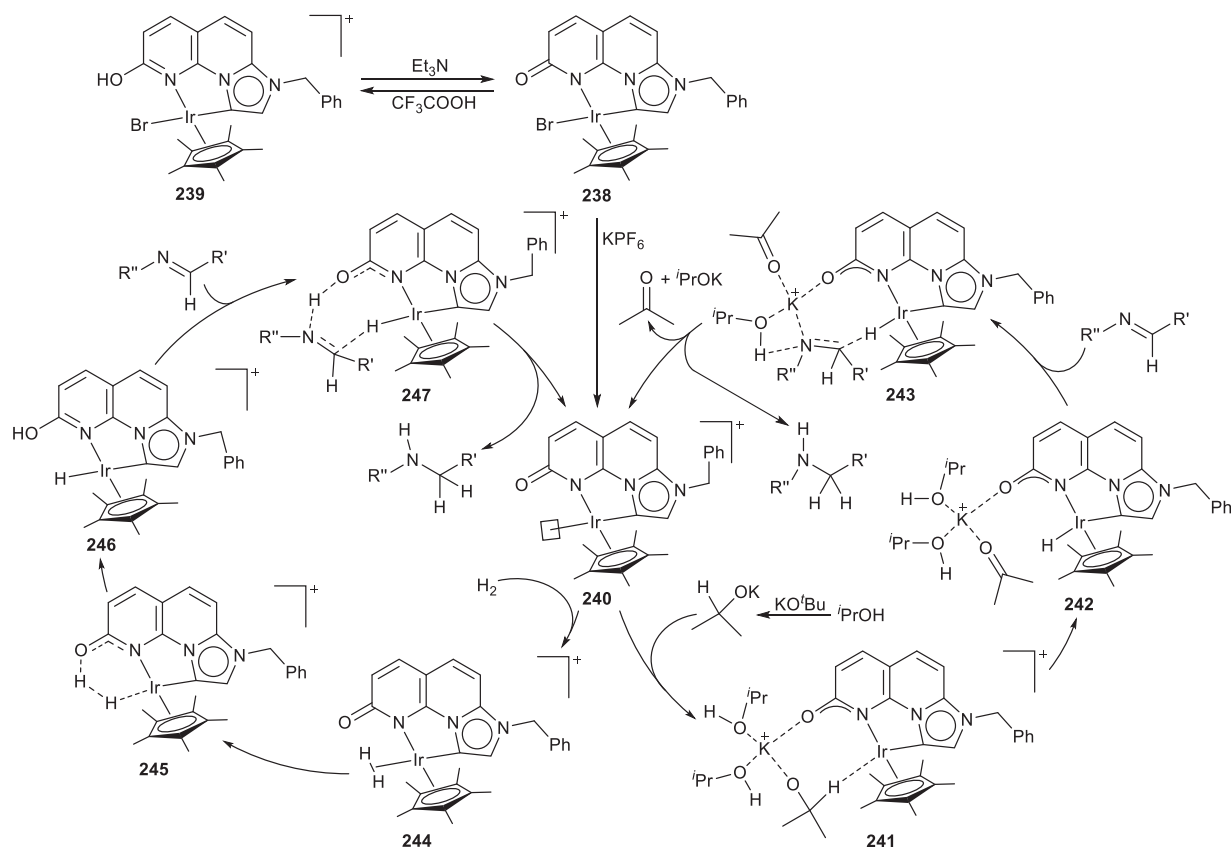
ligand design strategy, with the noninnocent processes facilitated either by the imine pendant,<sup>134</sup> the carbene carbon,<sup>132</sup> or the mid-road taken with either the imine *or* carbene carbon directly involved in the noninnocent role.<sup>223,224</sup>

### 1.05.2.3 Chalcogen donor functionalized nonclassical carbenes

#### 1.05.2.3.1 O-donor functionalized carbenes

Incorporation of oxygen into multifunctional ligands, ultimately towards noninnocent ligand design, has also been investigated.<sup>8,14–16,23,29,97,101,122,225–230</sup> The rationale includes the acid base mismatch, imparted by the use of the hard-basic oxygen donor with the Lewis acidic metal, which constitutes a soft Lewis metal in most examples. Akin to the nitrogen donor functionalized ligands, the presence of the oxygen donor could possibly effect a hemilabile role through coordination/decoordination to the metal or provide a basic site towards electrophilic substrate recognition and binding, followed by substrate activation. Apart from the mentioned multifunctional roles, an alternative noninnocent role imparted by the oxygen donor could also be imagined. Hence, the combination of noninnocent carbenes and oxygen containing moieties are prevalent albeit less explored compared to the nitrogen based multifunctional nonclassical carbenes.

The group of Bera focused on annulated Im4,<sup>231–235</sup> and more specifically, reported on the preparation of an iridium complex coordinated by a hydroxy containing imidazo-naphthyridine ligand (**238**, Scheme 31).<sup>236</sup> It was reasoned that the strong donor characteristics of the nonclassical carbene would mediate improved hydride transfer from the metal to the substrate. Moreover, chelation of the annulated ligand would suppress ligand dissociation, while an extended  $\pi$ -conjugated system should facilitate aromatization/dearomatization processes. Most importantly, the presence of the hydroxyl functionality would mediate a proton responsive role, ensuring metal-ligand cooperativity. Accordingly, the lactam-lactim tautomerization was realized via stoichiometric addition of acid or base, with NMR and UV-vis spectroscopy confirming the reversible aromatization/dearomatization (Scheme 31). The iridium complex **238** was employed in the catalytic reductive amination of aldehydes.<sup>236</sup> It was established that **238** catalyzed the reduction reaction using one of three different hydrogen sources, either molecular hydrogen, *i*PrOH/*KO*<sup>t</sup>Bu combination or an azeotropic mixture of HCOOH/*Et*<sub>3</sub>N in a 5:2 ratio. For the catalyzed reaction utilizing the HCOOH/*Et*<sub>3</sub>N azeotrope, a turnover frequency (TOF) of 645 h<sup>-1</sup> was noted while for the catalyzed reactions using either H<sub>2</sub> or the *i*PrOH/*KO*<sup>t</sup>Bu combination, the TOF was reported to be 33 h<sup>-1</sup> and 1.82 h<sup>-1</sup>, respectively. Of particular note was the different mechanistic considerations, computed or postulated for each of the catalytic systems, depending on the hydrogen source. For the best performing catalytic system, which involved the HCOOH/*Et*<sub>3</sub>N azeotrope, ion-pair decarboxylation results in iridium hydride

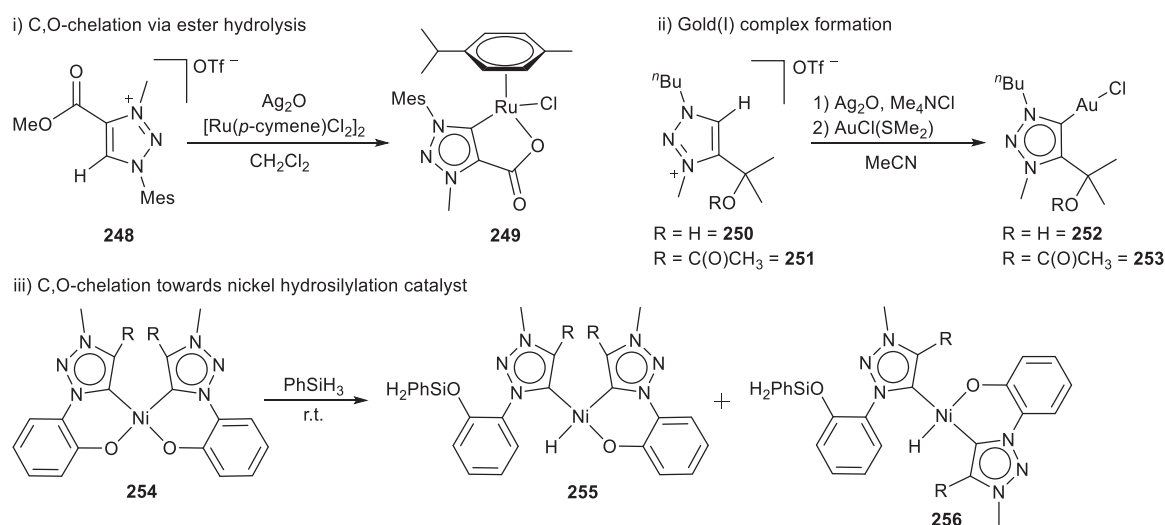


**Scheme 31** Proton responsive nonclassical carbene coordinated iridium complex towards amine preparation from aldehydes.

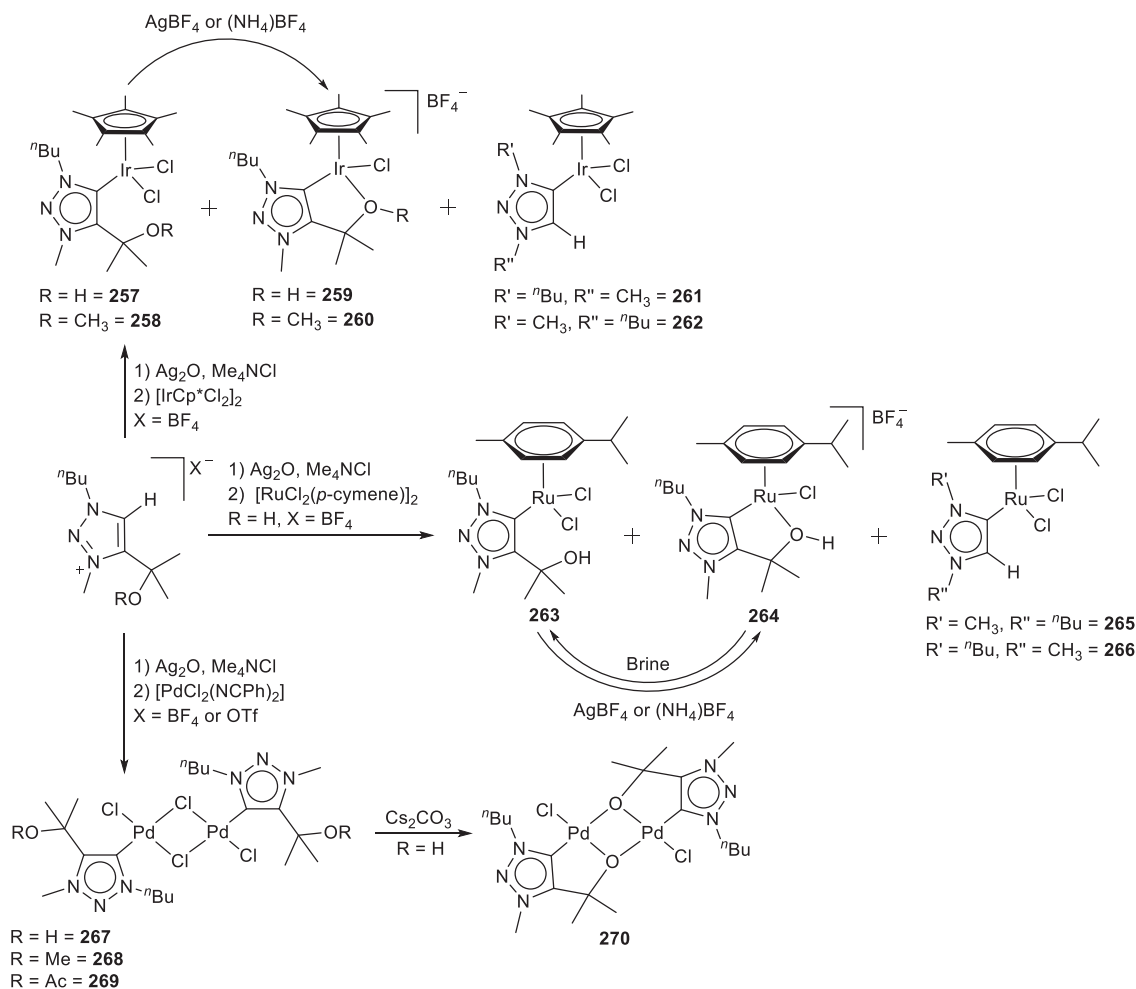
formation, with subsequent outer-sphere hydride transfer to the protonated imine leading to product formation, as supported by calculations. For the transfer hydrogenation exploiting the <sup>t</sup>PrOH/KO<sup>t</sup>Bu combination, Bera et al. proposed the formation of the solvated complex 241 from the cationic active species 240 (Scheme 31), with the anionic form of the ligand stabilized by a solvated potassium ion (241, Scheme 31).<sup>236</sup> This is followed by formation of the metal hydride 242, via an outer-sphere mechanism. Finally, amine formation is speculated to occur through both hydride and proton transfer from the iridium hydride and a proton from a solvent molecule, respectively. Direct hydrogenation was postulated and supported by computational calculations to ensue from the cationic active species 240, first via H<sub>2</sub> coordination yielding intermediate 244 (Scheme 31). Successive heterolytic H<sub>2</sub> cleavage across the metal and the lactam oxygen of 245 leads to ligand aromatization and subsequent lactim and iridium hydride formation, yielding intermediate 246. A synchronous process, involving hydride and proton transfer to the imine substrate, achieves product formation and regeneration of the catalytically active species via the imine H-bonded intermediate 247. The complex is therefore proposed to be able to mediate the catalytic reductive amination through three distinct mechanisms, with the ligand either being inert or facilitating the catalytic reaction via two discrete ligand cooperative pathways.

Albrecht et al. harnessed the electron donating contribution imparted by trz and combined it with an oxygen containing fragment, towards multifunctional ligand design featuring a basic oxygen hemilabile donor.<sup>237</sup> Ruthenation of an ester containing bidentate ligand 248 resulted to C,O-chelation via loss of the methyl group with formation of 249, presumed to have occurred through ester hydrolysis under the basic reaction conditions (Scheme 32, i). The catalytic alcohol dehydrogenation and transfer hydrogenation activity of the C,O-chelated ruthenium complexes were also investigated, and determined to be lower compared against the analogous trz-pyridyl complexes<sup>237</sup> (see Fig. 3). Additionally, gold(I) complexes 252 and 253 coordinated by either an alcohol or an acetate tethered trz carbene, respectively, was also reported by the same group (Scheme 32, ii).<sup>238</sup> It is well-known that coordination compounds of gold(I) generally results in linear complex formation,<sup>218,219</sup> which was also the case with the C,O-functionalized ligands.<sup>238</sup> Further development of the oxygen-tethered trz class of ligands involved coordination of a trz-containing C,O-bidentate ligand to nickel, leading to the isolation of the nickel complex 254 (Scheme 32, iii).<sup>239</sup> The nickel complex catalyzes the hydrosilylation of C=O bonds with a catalytic efficiency comparable to some of the best hydrosilylation catalysts reported to date. Moreover, the nonclassical carbene coordinated nickel complex 254 outperformed the classical NHC supported complex derivatives. The O-pendant introduced cooperativity to the complex, as PhSiH<sub>3</sub> reacted with 254 across the nickel-oxygen bond (Scheme 32, iii). This resulted to cleavage of the metal oxygen bond, yielding the catalytically active nickel hydride species 255 and 256. The contribution of multiple factors, such as the incorporation of nonclassical carbenes imparting increased donor strength to the metal, the stabilizing chelate effect which limits catalyst decomposition as noted for the monodentate nickel complexes,<sup>240</sup> in addition to cooperativity leading to the catalytically active species, again evidence the importance of appropriate ligand design to access highly active catalysts.<sup>239</sup>

Iridium(I),<sup>241</sup> iridium(III)<sup>242</sup> and ruthenium(II)<sup>242</sup> complexes coordinated by C,O-bidentate ligands featuring either an alcohol tether,<sup>242</sup> or an ether pendant<sup>241,242</sup> were also disclosed. Chelation was realized through chloride substitution, either during metalation or via chloride scavenging, yielding C,O-chelated iridium complexes 259 and 260, in addition to ruthenium complex 264 (Scheme 33).<sup>242</sup> Addition of brine to the chelated ruthenium complex 264 resulted in metallacycle ring-opening and re-formation of the hydroxyl tethered complex 263, demonstrating reversible hydroxyl binding and therefore the hemilabile nature of the tether. Transfer hydrogenation catalysis utilizing the iridium complexes proved that the pendant O-donor does have a marked influence on the catalytic activity, as the unfunctionalized complex 261 demonstrated significantly reduced catalytic activity. Furthermore, the iridium complex 257 featuring a hydroxyl pendant was reported to facilitate the hydrogenation with improved catalytic activity when compared against the ether functionalized complex 258 (Scheme 33). Stoichiometric experiments of



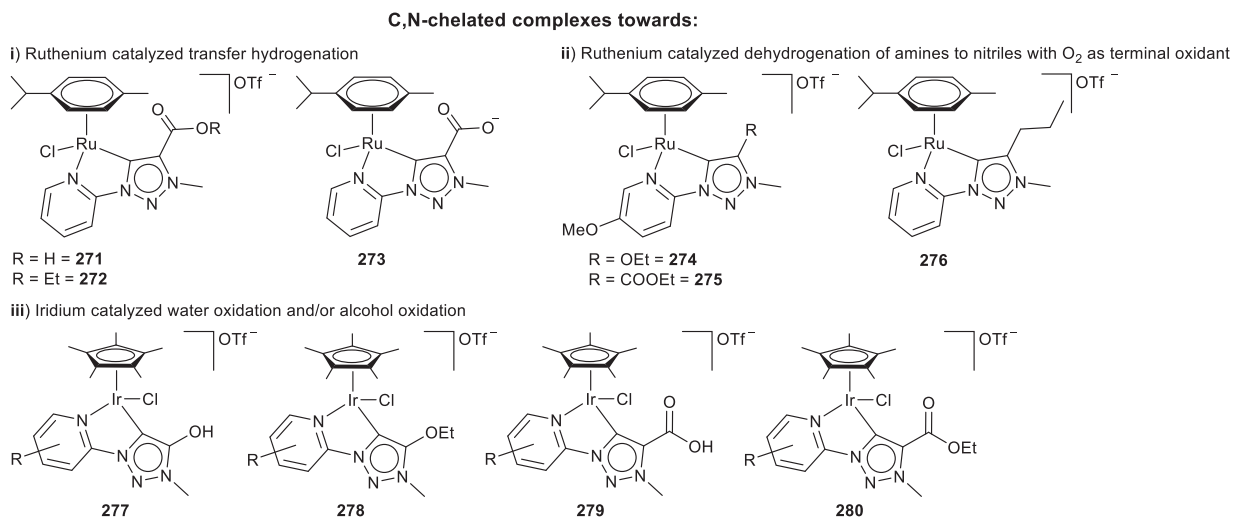
**Scheme 32** Mono- or bidentate complex formation with oxygen tethered triazolylidene ligands.



**Scheme 33** Towards O-donor functionalized hemilabile ligands.

$\text{Cs}_2\text{CO}_3$  addition to 259 evidenced iridium-alkoxide formation. As a consequence, the impact of the hydroxyl functionality was postulated to impart increased electron density to the metal during catalysis upon metal-bound alkoxide bond formation, subsequently increasing the catalytic activity. An alternative role was also hypothesized by the authors, involving dihydrogen abstraction via an outer-sphere mechanism with concomitant hydride and proton transfer to the substrate. The analogous ruthenium complexes demonstrate superior transfer hydrogenation catalytic activity compared to the iridium complexes, with no real difference noted between the ruthenium complexes containing either the O-functionalized pendants or the unfunctionalized ligands. Accordingly, an inner-sphere monohydride mechanism was credited as the reaction mechanism at play during the ruthenium catalyzed hydrogenation reaction. Thus, generalization of ligand cooperativity should be made only with careful consideration.<sup>242</sup> Metalation of the hydroxyl and ether substituted trz proligands, in addition to an ester containing triazolium salt, was also extended to include palladium, rhodium and iridium(I).<sup>243</sup> Oxygen coordination of the ester and ether hemilabile substituent to the trz supported palladium, rhodium and iridium complexes was not reported. However, the presence of the oxygen moiety could still function as a hard-basic site, that can aid catalysis implicating the ligand as noninnocent. On the other hand, addition of  $\text{Cs}_2\text{CO}_3$  to the alcohol containing trz palladium complex 267 resulted to metal-alkoxide bond formation, yielding 270 (Scheme 33). The rhodium and iridium complexes also yielded the corresponding alkoxide products, albeit through in situ deprotonation of the ligand with  $\text{KN}[\text{Si}(\text{CH}_3)_3]$  followed by coordination to the metal precursor, differing from the silver transmetalation strategy employed towards preparation of the aforementioned palladium complexes.<sup>243</sup>

The bidentate chelation strategy towards inhibiting pendant donor coordination to the metal, was again reported by Albrecht and co-workers.<sup>178–182</sup> However, oxygen-containing pendant donor functionalities were used instead of a pyridine tethered to the trz-pyridyl chelate (Fig. 5). The ruthenium trz-pyridyl chelated complexes feature either a carboxylic acid (271), ester (272), or carboxylate (273) pendant. Catalytic transfer hydrogenation activity of these complexes surpassed that of the analogous ruthenium complexes without a pendant donor site (Fig. 5, i).<sup>179</sup> The results indicate that the pendant carboxylate contributes in catalysis, with the noninnocent role of the ligand postulated to mediate either proton shuttling or bond manipulation processes. This necessitates C,N-bidentate chelation which in turn fosters a larger yaw angle, ultimately preventing coordination of the pendant



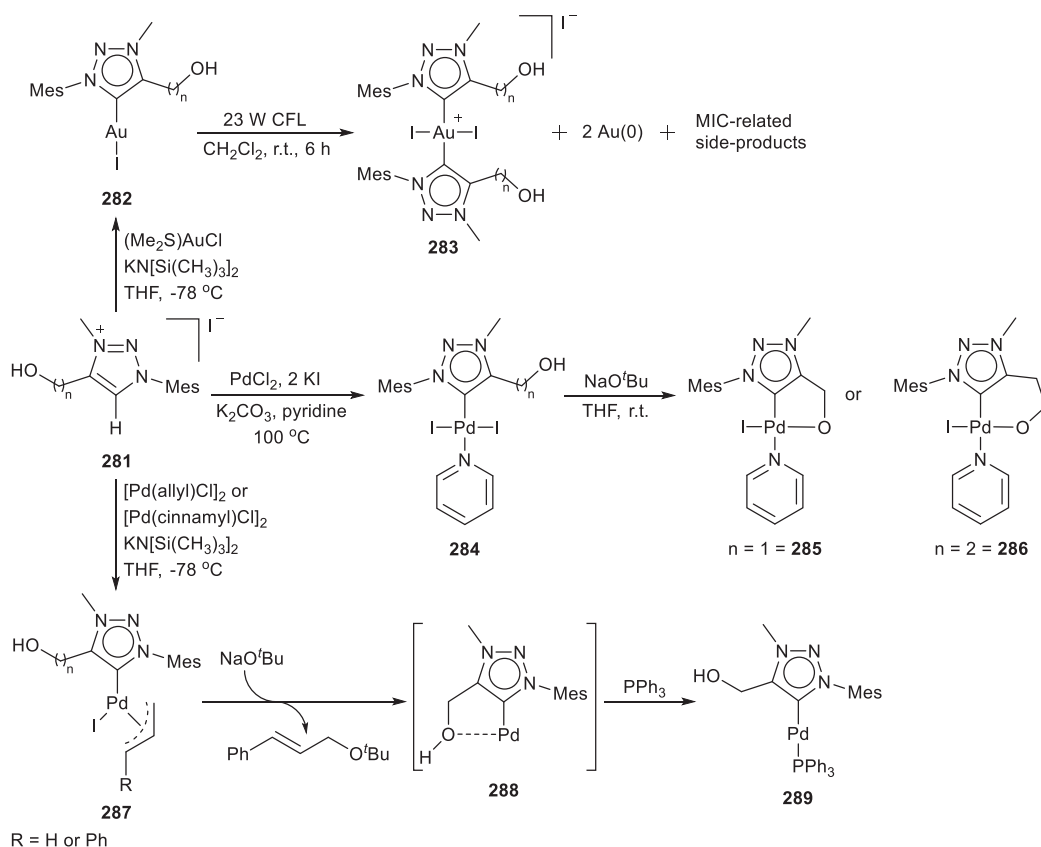
**Fig. 5** C,N-chelated ruthenium (i, ii) and iridium (iii) complexes.

O-donor to the metal center to render it available for substrate recognition and binding. In addition to the transfer hydrogenation, C,N-chelated ruthenium complexes (**Fig. 5, ii**) featuring either an oxygen donor **274** and **275**, or an alkyl group **276** as pendant, were also successfully used towards the catalyzed dehydrogenation of amines to nitriles, using O<sub>2</sub> as terminal oxidant.<sup>182</sup> The range of coordination compounds substituted by the trz-pyridyl ligand framework featuring the oxygen pendant donor, was extended to include iridium(III) as well (**Fig. 5, iii**).<sup>180,181</sup> The complexes **277–280** were prepared towards catalytic water oxidation<sup>180</sup> and alcohol dehydration/dehydrogenation reactions.<sup>181</sup> The C,N-chelated iridium complexes could facilitate the catalytic water oxidation reaction in the presence of cerium(IV) as sacrificial oxidant, or under electrochemical conditions.<sup>180</sup> The presence or absence of HPF<sub>6</sub> allowed for switching between the alcohol dehydration or alcohol dehydrogenation catalyzed reactions, mediated by **278**.<sup>181</sup> In both reports, the remote electronic effect imparted by the presence or absence of the oxygen containing donor moieties was credited for the observed differences in catalytic activity,<sup>180,181</sup> rather than a cooperative role as was postulated for the analogous ruthenium complexes (**Fig. 5**).<sup>179</sup>

A trz ligand featuring a hydroxyl-containing hemilabile pendant was reported in another example of mild gold(I) to gold(III) oxidation, this time mediated by visible light.<sup>244</sup> The group of Mendoza-Espinosa reported on the preparation of a series of triazolium ligand salts featuring a hydroxyl hemilabile moiety with either one, two or three methylene spacer groups between the oxygen donor and the five-membered triazolium heterocycle.<sup>244–246</sup> Coordination of these hemilabile containing ligands allowed for isolation of the corresponding monodentate gold(I) complexes.<sup>244</sup> Exposure of the trz gold(I) complex **282** to visible light (23 W fluorescent light) resulted in oxidation, yielding the biscarbene gold(III) complex **283**, albeit accompanied with gold(0) and MIC-related side-products (**Scheme 34**). The gold(I) and gold(III) complexes efficiently catalyze the hydrohydrazination of terminal alkynes with hydrazine, with the gold(I) complex demonstrating enhanced catalytic activity compared to the gold(III) complex, ascribed to possible reduction of the high oxidation state gold in the presence of a reducing agent. The role of the hemilabile oxygen moiety in both the oxidation and hydrohydrazination catalyzed reactions was not reported. However, subsequent reports by the group of Mendoza-Espinosa shed light on the possible involvement of the hydroxyl hemilabile donor once coordinated to other transition metals. Ligand coordination to palladium in the presence of pyridine yielded the corresponding trz complexes **284**, with pyridine occupying the position *trans* to the carbene (**Scheme 34**). The hydroxyl pendant did not coordinate to the metal,<sup>246</sup> similar to the palladium hydroxyl-trz complexes reported by Sankararaman and co-workers.<sup>247</sup> However, initial Suzuki-Miyaura cross-coupling catalytic investigations indicated that the hydroxyl-tethered trz palladium complexes outperformed ether functionalized derivatives or a commercially available NHC-containing palladium complex (**Scheme 34**).<sup>246</sup> Moreover, it was verified that the complexes featuring either a one or two carbon spacer, respectively, between the OH pendant and the trz heterocycle have higher catalytic activity while the complex featuring three CH<sub>2</sub> moieties displayed diminished catalytic activity.

Stoichiometric investigations allowed insight into the observed differences between the hydroxyl functionalized hemilabile trz complexes.<sup>246</sup> Deprotonation of the pendant arm resulted in stable palladium alkoxide complex formation, in the case of the two complexes featuring either one (**285**) or two (**286**) -CH<sub>2</sub>- spacer groups (**Scheme 34**). The pendant arm featuring three methylene moieties resulted in decomposition after deprotonation, reported to be attributable to formation of an unstable seven-membered palladacycle. The five- and six-membered palladacycles were also found to exhibit high catalytic activity in the abovementioned catalyzed reactions. Resultantly, the hemilabile oxygen donor functionality of complexes **285** and **286** enhance the catalytic reactivity of the palladium complexes, stabilizing the catalytic intermediate and therefore mitigating catalyst decomposition.<sup>246</sup> Similarly, allyl and cinnamyl palladium complexes featuring a hydroxyl hemilabile functional group displayed higher catalytic activity in the cross-coupling catalyzed reaction of phenylboronic acid with *p*-chloroanisole, compared against an analogous palladium complex containing a phenoxy-linked pendant.<sup>245</sup> On the other hand, similar catalytic reactivity was noted when the





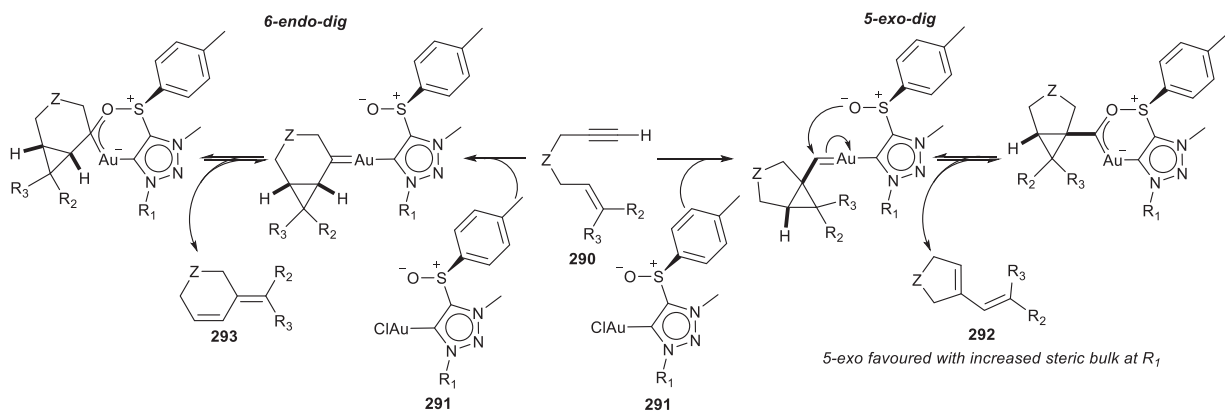
**Scheme 34** O-donor tethered trz gold and palladium complexes.

hydroxyl-functionalized trz was compared against a palladium complex without a hemilabile O-donor group. The observed differences in the catalytic reactivity of the complexes investigated was rather attributed to the presence of cinnamyl versus allyl substituents, with cinnamyl substituted complexes exhibiting higher catalyst activity. The hydroxyl pendant was however implicated in a proposed reaction mechanism for the catalytic reaction, stabilizing the catalytic intermediate during the formation of the catalytically active Pd<sup>0</sup> catalyst, as illustrated in **Scheme 34**.<sup>245</sup>

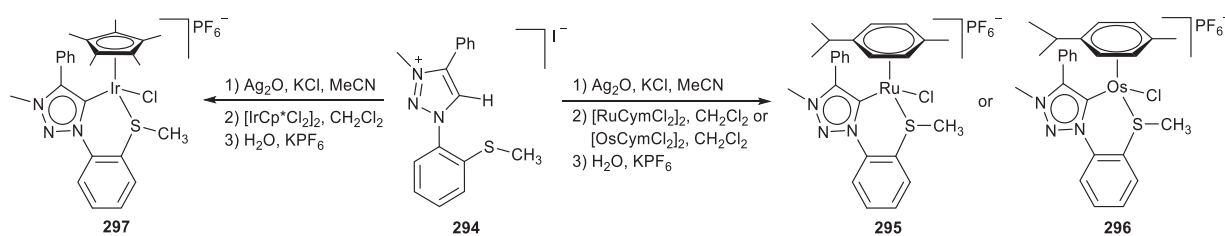
The group of Sierra and Torre prepared a range of triazolium salts featuring a chiral sulfoxide pendant, with subsequent coordination to gold via a silver transmetalation route.<sup>32,248</sup> Selected gold(I) complexes were investigated as enyne cycloisomerization catalysts. It was determined that both the sulfoxide moiety and the gold metal were required for catalysis, as the complex without a sulfoxide functionality or a corresponding silver analogs complex failed to catalyze the cycloisomerization reaction.<sup>248</sup> A hypothesized mechanistic scenario involved terminal alkyne coordination with subsequent cyclization dictated by the steric bulk of the nitrogen substituent, to proceed either via the 5-exo or 6-endo cyclization pathways yielding the corresponding 5-membered or 6-membered cycles (**Scheme 35**).<sup>32,248</sup> A bulkier substituent at the nitrogen favored the 5-exo pathway, and the 5-membered product could therefore be preferentially accessed through simple ligand modification. The authors theorized description of the sulfoxide's influence in the catalytic process is especially noteworthy. It is suggested that the oxygen or the sulfur lone pair coordinates and stabilizes the gold carbenic intermediate, facilitating the reaction towards completion (oxygen coordination and stabilization is depicted in **Scheme 35**, similar to the authors mechanistic proposal).<sup>32</sup> The sulfoxide containing gold catalyst was further shown to mediate the cycloisomerization-dimerization cascade of 1,6-enynes, in addition to the diastereoselective [2+2+2] cycloaddition of 1,6-enynes with benzaldehyde.<sup>249</sup>

### 1.05.2.3.2 S-donor functionalized carbenes

Nonclassical carbenes with a sulfur pendant have also been reported.<sup>250,251</sup> Compared to its oxygen analog, the 'softer' chalcogen is expected to readily dissociate from a metal coordination sphere, vacating a coordination site on the metal.<sup>95,252</sup> Not surprising then, was the introduction of sulfur as a hemilabile pendant tethered to nonclassical carbenes. However, chelation of the sulfur containing carbene ligand was not achieved in every instance, and more specifically, sulfur coordination to copper was not realized.<sup>253</sup> Fortunately, the use of arene-containing ruthenium, osmium or iridium metal precursors allowed for the preparation of the corresponding metal complexes with coordination of the sulfur pendant (**Scheme 36**).<sup>254</sup> The complexes were used as oxidation catalysts, oxidizing benzyl alcohol as well as diphenylmethanol in the presence of *N*-methylmorpholine *N*-oxide. However, catalytic activity of the trz-substituted complexes was markedly lower compared against the analogous triazole *N*-coordinated complexes.



**Scheme 35** Noninnocent ligand mediated enyne cycloisomerization.<sup>32</sup> Modified from Sierra, M. A.; De La Torre, María C. *ACS Omega* **2019**, *4*, 12983–12994.



**Scheme 36** Introducing possible hemilability through C,S-chelation.

A noticeable difference was the selectivity of the complexes in the oxidation of benzyl alcohol, with the trz-coordinated complexes displaying higher selectivity for the targeted benzaldehyde product over the benzoic acid side product.<sup>254</sup>

### 1.05.3 Redox noninnocence

The noninnocent behavior of a ligand class cannot be discussed without referral to the original definition of (redox) noninnocence as the oxidation state ambiguity arising when redox active ligands may contribute as the site of redox processes, thereby leaving the formal metal d-electron count unequivocal.<sup>255</sup> The definition has since evolved and the terminology is nowadays broadly used to refer to the cooperative role that redox active ligands play in controlling metal complex reactivity, often involving additional chemical noninnocent roles e.g. hemilability or reversible dissociation.<sup>256</sup> Categorization of redox noninnocent ligands has been done by various definitions<sup>5,256–258</sup> to describe their roles as electron reservoirs or as radical transfer agents to substrates in both stoichiometric and catalytic conversions.<sup>259,260</sup> In the case of traditional carbene complexes, carbene ligands of the Fischer-type (acyclic heteroatom-stabilized singlet carbenes) are readily reduced in a single electron transfer to yield carbene radical ligands that mediate catalytic C–C bond formation.<sup>259</sup> For redox active NHCs, noninnocent behavior has mostly included redox switchable ligands<sup>5,261–263</sup> often with accompanying structural differences between the distinct redox states. Toggling between the various states, with different activities, selectivities or solubilities, delivers redox switchable catalysts.<sup>263–267</sup> Inherent redox noninnocence of carbenes, such as the radical reactivity displayed by one-electron Fischer-type carbene ligands<sup>259</sup> or N-donor ligands,<sup>268</sup> is lesser known for NHCs.

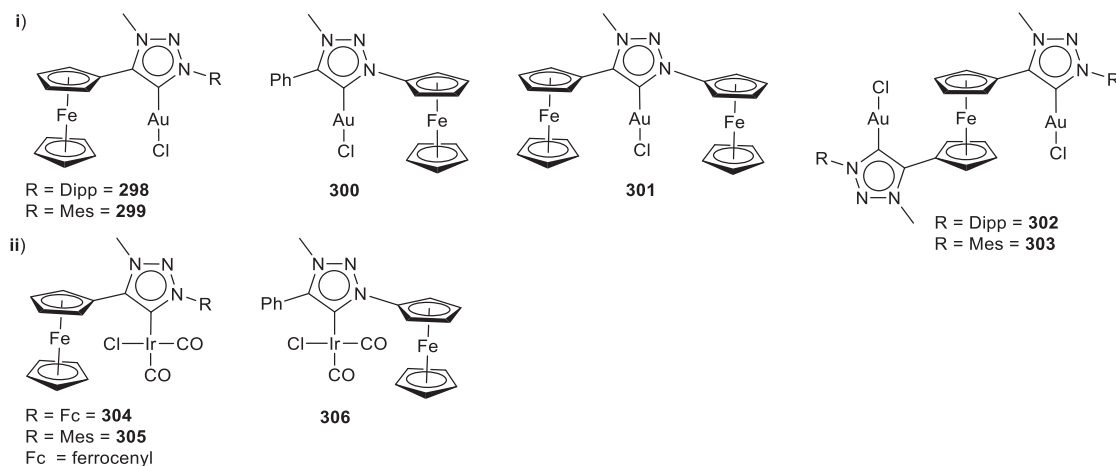
For the non-traditional carbene ligands under review in this chapter, redox noninnocence demonstrated has mostly been focused on one area, namely the introduction of a redox active pendant group on a trz ligand scaffold, that is utilized to tailor the Lewis basicity of the transition metal bonded to the carbene towards switchable catalytic applications. This common theme is well demonstrated for traditional NHCs with ferrocenyl-appended or annulated quinone NHC scaffolds,<sup>261</sup> a strategy also used towards the preparation of chiral ligands for chiral catalysis (vide infra). The other classes of redox noninnocence (including redox switchable hemilabile ligands,<sup>256</sup> where the ligand (i) acts as an electron reservoir, or (ii) a reactive radical involved in bond making/breaking; or (iii) mediates ligand-to-substrate single or two-electron transfer, or (iv) provides for metal-ligand bifunctional homolytic substrate cleavage, as definitively categorized in recent reviews), remains predominantly unexplored.<sup>259,260</sup> The dearth of redox noninnocence reported is especially noticeable for Im4 and CAACs and examples are almost exclusively based on the ability of these nonclassical carbene ligands to stabilize radicals (see [Section 1.05.1](#)).

## 1.05.3.1 Metallocenyl-appended carbenes

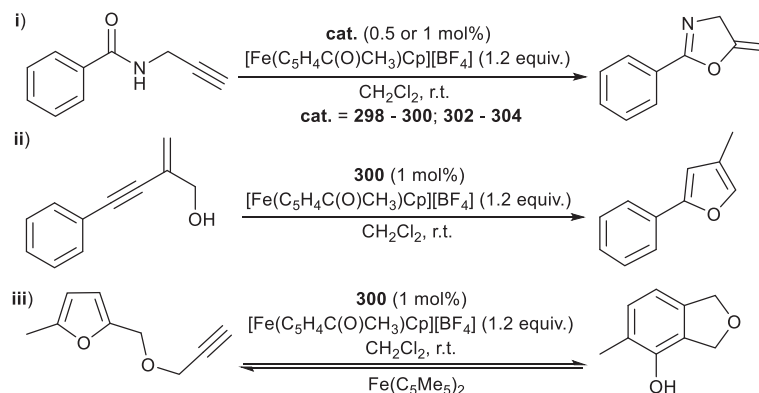
In his initial report, Sarkar et al. describes the use of a trz with a pendant ferrocenyl (Fc) substituted on the C4-position of the heterocycle, to prepare the first examples of heterobimetallic trz complexes of Fe and Au, 298 and 299 (Fig. 6, i).<sup>269</sup> Ferrocene was chosen as the redox active substituent of choice not only due to its reversible one electron anodic behavior, but also because of its ease of functionalization and its known electron-donating ability,<sup>270</sup> while the oxidized ferrocenium moiety is almost as electron-withdrawing as a  $-\text{CF}_3$  substituent.<sup>271</sup> This means that the ligand donor properties can be redox modified for catalyst fine-tuning, for example in gold(I)-mediated alkyne cyclizations where the carbophilic nature of the Lewis acidic, cationic gold(I) carbene underpins the catalytic reactivity: coordination of the unsaturated substrate to the gold center is followed by  $\pi$ -activation of the substrate towards nucleophilic attack.<sup>272–275</sup> The metallocenyl-containing trz precursors were prepared via the copper-catalyzed azide-alkyne click methodology from the accessible ferrocenyl azide and/or ferrocenyl acetylene to yield respectively, the N1-substituted or the C4-substituted Fc-appended triazoles,<sup>276–286</sup> followed by N3-methylation to give the corresponding triazolium salts. In addition, bis(triazolium) salts featuring a bridging 1,1'-ferrocendiyl as a redox active spacer provides the opportunity to prepare multinuclear complexes.<sup>287–290</sup> Taking advantage of these facile modifications, Sarkar expanded his series of metalloligands to prepare gold(I) chloride complexes with the trz containing also an N1-appended Fc, 300;<sup>291</sup> or C4,N1-diferrocenylated trz complex 301,<sup>292</sup> based on a previously reported diferrocenylated complex.<sup>293</sup> The digold complexes 302, 303 with the bridging 1,1'-ferrocendiyl completes the series (Fig. 6, i).<sup>292</sup>

The electrochemical properties of the precursor triazoles, triazolium salts and the corresponding gold(I) complexes 298–303 (Fig. 6, i) were investigated by detailed cyclic voltammetry, UV-Vis-NIR and TD-DFT (time-dependent density functional theory) calculations.<sup>292</sup> As expected, reversible one-electron oxidations are observed in all cases, associated with the ferrocene/ferrocenium couples, while irreversible reductions were found to be trz-based, as confirmed by calculated spin population analyses. A direct comparison of the oxidation potentials of 298–303 to elucidate ligand donor properties is not possible, among others due to different solvents/electrolyte systems employed in the cyclic voltammetry experiments. An indication of increased ligand donor ability is seen when comparing the  $^{13}\text{C}$  NMR carbene carbon chemical shifts, with the trz carbene carbon atoms with N1-bound Fc groups consistently resonating at higher field than the C4-bound Fc-trz carbene. Synthesis of the iridium dicarbonyl chloride trz complexes 304–306 (Fig. 6, ii) containing the diferrocenyl trz with both N1- and C4-bound Fc (304), the C4-bound Fc (305) or the N1-Fc (306), provided the opportunity for using the diagnostic carbonyl ligands as probes to determine the ligand donating properties by calculating the modified Tolman Electronic Parameter (TEP).<sup>294–296</sup> IR spectroelectrochemistry allows for the measurement of the oxidized complexes' carbonyl stretching frequencies so that the TEPs of also the one-electron oxidized trz (and two-electron in the case of 304) could be calculated for comparison with the ligands in their native form. The obtained TEPs confirmed that in general, Fc-trz (TEP = 2045–2047  $\text{cm}^{-1}$ ) are better donors than imidazol-2-ylidene based NHCs, while the one-electron oxidized trz (TEP = 2052–2057  $\text{cm}^{-1}$ ) have donor properties equivalent to phosphine ligands.<sup>294–296</sup> However, no significant increase in the donor ability of the trz with electron-donating Fc substituents compared to other alkylated/arylated trz<sup>54,55,67</sup> are observed. The electron-withdrawing nature of the ferrocenium group is reflected in 7–11  $\text{cm}^{-1}$  increase of the TEPs. Unexpectedly, the highest TEP is obtained for the diferrocenylated trz ligand, and the N1-bound Fc-trz is found to be a weaker donor compared to the C4-bound Fc-trz. For the two-electron oxidized  $[304]^{2+ \bullet\bullet}$ , the corresponding decrease in ligand donor ability is reflected by an increased TEP = 2068.3  $\text{cm}^{-1}$ .<sup>292</sup>

Chemical oxidation of 299 to  $[299]^+ \bullet$  was achieved with acetylferrocenium tetrafluoroborate.<sup>292</sup> To correlate the enhanced Lewis acidity of  $[299]^+ \bullet$  with improved catalytic activity for heterocyclic compound synthesis, the benchmark intramolecular



**Fig. 6** Ferrocenyl-functionalized triazolylidene complexes for application (i) in redox-switchable gold(I) mediated oxazoline synthesis, and (ii) as probes of ligand donor strength.



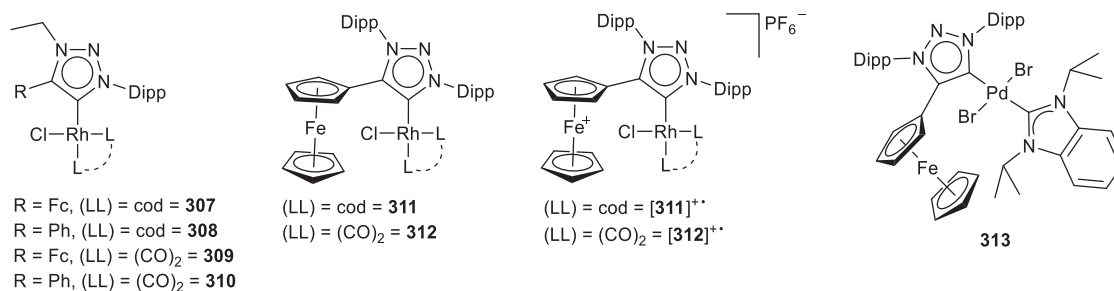
**Scheme 37** Redox switchable catalysis mediated by gold(I) Fc-trz complexes for the preparation of (i) 5-methylene-2-phenyl-4,5-dihydroxazole from *N*(2-propyn-1-yl)benzamide, (ii) 4-methyl-2-phenylfuran from 2-methylene-4-phenylbut-3-yn-1-ol and (iii) 4-methyl-1,3-dihydroisobenzofuran-5-ol from 2-methyl-5-((prop-2-yn-1-yloxy)methyl)furan.

alkyne cyclisation of *N*(2-propyn-1-yl)benzamide to 5-methylene-2-phenyl-4,5-dihydroxazole (Scheme 37, i) was probed. Catalytic conditions including 1 mol% loading of 299 and 1.2 equivalents of oxidant to generate  $[299]^{+\bullet}$  in situ in  $\text{CH}_2\text{Cl}_2$  at room temperature yielded 88% yield of the oxazoline, while only 12% yield was reported in the absence of the oxidant. Notably, no silver salts or other additives were required in the reaction with redox-induced catalyst  $[299]^{+\bullet}$ , as is usually the case for gold(I) trz complexes catalyzing organic transformations.<sup>186,238,248,297–302</sup> Utilizing the same conditions, both the native and the oxidized forms of 298, 300, and 302–304 were screened as catalysts for the reaction. In all cases, the native forms gave significantly lower conversions (0–10% except for 300 where 30% conversion was obtained).<sup>269,292</sup> Full conversion was observed for N3-bound ferroceniumyl trz complex  $[300]^{+\bullet}$  in accordance with its slightly higher TEP ( $2054.3\text{ cm}^{-1}$ ), compared to the C4-bound ferroceniumyl trz  $[299]^{+\bullet}$  (TEP =  $2052.7\text{ cm}^{-1}$ ). However, diferrocenylated-trz 304 yielded significantly lower yields (30% and 40%, respectively for the one- ( $[304]^{+\bullet}$ ) and two-electron ( $[304]^{2+\bullet\bullet}$ ) oxidized complexes), despite their higher TEP values ( $2056.9\text{ cm}^{-1}$  and  $2068.3\text{ cm}^{-1}$ , respectively). This was ascribed to the varying solubility of especially the dicationic complex  $[304]^{2+\bullet\bullet}$ . For the  $[302]^{+\bullet}$ , the excellent activity observed (95% yield with a 0.5 mol% catalyst loading taking the metal molar ratio into account), was similarly accounted for by increased solubility rather than any cooperative catalytic digold effects.

True redox switchable catalysis (RSC) (rather than redox induced) was demonstrated for catalyst 300 whereby the catalytic reaction could be cycled between a ‘switched on’ catalyst (in situ generated  $[300]^{+\bullet}$ ), followed by reduction to the native form 300 (‘switched off’) with the consecutive addition of excess decamethylferrocene as reductant, or vice versa for more than one cycle, as a first in gold(I)-catalysis.<sup>291</sup> No conversion of the substrate in the presence of either the oxidant or reductant *sans* 300 was observed. To test this redox switchability in other gold-mediated cyclizations, both the formation of furan from a  $\beta$ -alkynyl alcohol (Scheme 37, ii) and intramolecular phenol formation from furan with a terminal alkyne (Scheme 37, iii) catalyzed by 300 were investigated. These processes are known to be catalyzed by either gold(I) or gold(III), and notably require activation by a silver(I) or copper(I) salt in the case of the low valent gold, even cationic gold(I) complexes.<sup>275,303</sup>

Utilizing the same reaction conditions reported for the oxazoline synthesis, 300 as catalyst in its native form did not yield any product furan after 24 h, but 40% conversion of the substrate  $\beta$ -alkynyl alcohol was observed after 45 min of addition of  $[\text{Fe}(\text{C}_5\text{H}_4\text{C}(\text{O})\text{CH}_3)\text{Cp}]\text{BF}_4$  (Scheme 37, ii).<sup>291</sup> The reaction is quenched at this point, but addition of excess oxidant restarts the reaction. Although the reasons for reaction quenching are not clear, a conversion of 90% after 24 h can be obtained in this way. The acetyl ferrocenium oxidant itself does not catalyze the reaction, and a ‘switching off’ of the reaction can also be achieved by addition of 1.2 equiv. of decamethylferrocene. The third reaction investigated involves the ring-opening of the substrate furan followed by an intramolecular oxygen migration and rearrangement to the product phenol. Catalyst 300 in its native form catalyzes the reaction but a low conversion of only 12% is observed after 24 h. A marked increase in catalyst activity is achieved by addition of  $[\text{Fe}(\text{C}_5\text{H}_4\text{C}(\text{O})\text{CH}_3)\text{Cp}]\text{BF}_4$ , with full conversion within 5 min. Remarkably, adding reductant not only switches off the reaction, but leads to the back-conversion of phenol to the starting material alkynylfuran. The phenol does not react with decamethylferrocene, nor a mixture of the oxidant/reductant or 300, and the authors ascribe the backwards and forwards switching of the reaction as being inherently linked to the total catalytic mixture. In all three reactions investigated, oxidation of the pendant Fc group on the trz ligand is the trigger to activate the gold(I) center towards catalysis.

Parallel to the efforts of Sarkar et al. in gold(I) RSC, related Fc-trz ligands coordinated to  $\text{Rh}^{\text{I}}$  were similarly investigated for their ability to offer an additional handle on catalyst fine-tuning by influencing the catalytic metal center reactivity in heterobimetallic catalysts for olefin hydroformylation.<sup>304</sup> The series of complexes feature trz with a pendant Fc bound to the trz-C4 position, and either an alkyl (ethyl) (307, 309) or aryl (Dipp = 2,6-diisopropylphenyl) (311, 312) group on the N3-ring position, in addition to the N1-Dipp group, to investigate the effect of the ring-substituent (ethyl vs Dipp). The influence exerted by the Fc in its native



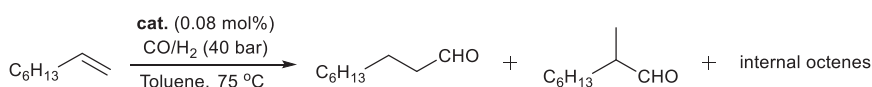
**Fig. 7** Ferrocenyl-functionalized trz rhodium(I) complexes for application in tunable olefin hydroformylation.

state on the donor properties of the ligand coordinated to Rh<sup>I</sup>, was also evaluated by replacing the metallocene with a phenyl substituent (**308**, **310**, Fig. 7).

The cod complexes **307**, **308** and **311** were employed as the catalyst precursors, while the dicarbonyl substituted complexes **309**, **310** and **312** were prepared as probes for ligand donor ability.<sup>304</sup> Unexpectedly, the TEPs<sup>305</sup> calculated for **309**, **310** and **312** were found to be equivalent (2047.0 cm<sup>-1</sup>), also to that of **300**. In an effort to delineate the more subtle ligand effects, the <sup>13</sup>C NMR spectroscopic method of Huynh et al. was applied by the preparation of **313** to probe ligand donicity in terms of the Huynh Electronic Parameter (HEP).<sup>306,307</sup> A chemical shift of <sup>13</sup>C δ162.2 ppm was observed; lower field than any of the previously evaluated N3-alkylated trz (δ157.9–160.6 ppm), with no significant electron donation evident from the proximal Fc group.<sup>304</sup> Catalytic evaluation of **307**, **308** and **311** as catalysts in the hydroformylation of 1-octene was done under optimized conditions of syngas CO/H<sub>2</sub> (1:1) at 40 bar, 75 °C in toluene with 0.08 mol% catalyst loading (Scheme 38). Complex **311** yielded slightly lower conversion (96%) compared to the full conversion reported for the N3-alkylated complexes, **307** and **308**, but gave the highest *n/iso* ratio for the formation of the more desirable linear aldehyde products (2.4 compared to 1.8 for **307** and **308**). This finding is in accord with the findings of improved regioselectivity for less electron donating and sterically more demanding NHCs.<sup>308–313</sup> However, this improved regioselectivity is accompanied with a decrease in chemoselectivity and in the total yield of product aldehyde compared to internal octene formation.<sup>304</sup> In order to maintain the steric bulk of the complex but decrease the donor ability of the N3-arylated Fc-trz ligand, one-electron oxidized complexes [**311**]<sup>+</sup> and [**312**]<sup>+</sup> (Fig. 7) were prepared either by chemical oxidation of the native complexes **311** or **312** by [Fe(C<sub>5</sub>H<sub>4</sub>C(O)CH<sub>3</sub>)Cp]PF<sub>6</sub>, or by oxidation of the precursor triazolium salt, followed by in situ deprotonation of the triazolium and coordination to [Rh(cod)Cl]<sub>2</sub>, and treatment with CO (g). Oxidation to the ferrocenium moiety led to an increase of 10 cm<sup>-1</sup> in the TEP. Performing the catalytic reaction with [**311**]<sup>+</sup> under the same conditions as for the native complexes did improve the total aldehyde yield by 10%, as well as the activity of the catalysts (full conversion and a TOF of 119 h<sup>-1</sup> compared to a TOF of 100 h<sup>-1</sup> for **311**). The effects of solubility in the toluene were not considered. Unfortunately, the regioselectivity is decreased so that the lowest *n/iso* aldehyde ratio for the series of catalysts is seen. Nevertheless, this study is another example of a redox tunable ligand influencing metal-ligand reactivity.

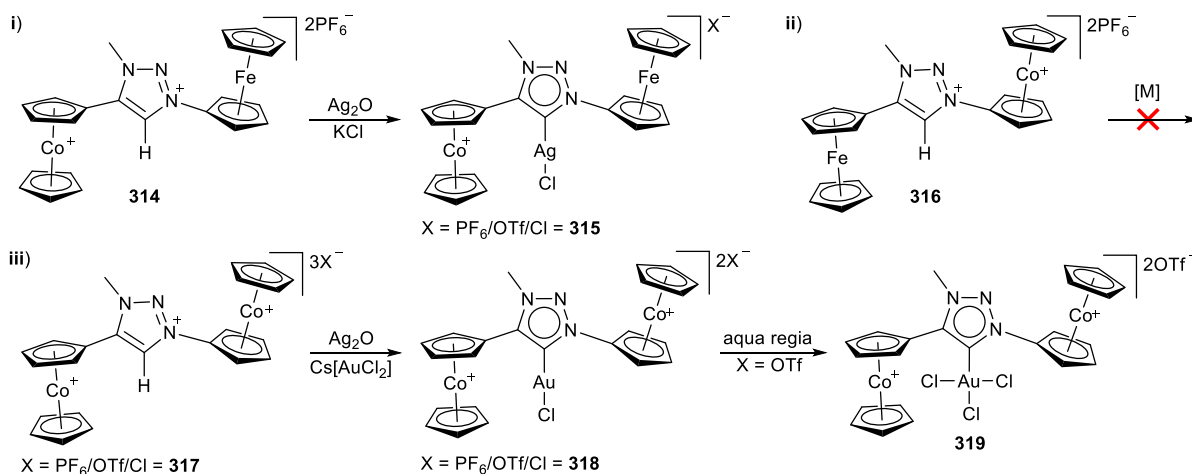
Replacing the Fc-substituent with an isoelectronic cobaltoceniumyl group provides yet another handle on electronic modification of the metal complex as acceptor ligands, while simultaneously altering the solubility of the complex as a result of the inherent cationic charge of the cobaltoceniumyl. Continuing on their previous work of metallocenyl-functionalized trz gold(I) complexes, Sarkar et al. prepared regioisomeric cobaltoceniumyl ferrocenyl triazolium salts with the cobaltoceniumyl bound to the C4-position on the heteroaryl ring, and the Fc bound to the N1-position of the ring (**314**, Scheme 39, i), or vice versa (**316**, Scheme 39, ii).<sup>314</sup> The tricationic triazolium precursor containing cationic cobaltoceniumyl moieties on both C4 and N1-positions was prepared as a highly polar compound with two electron-withdrawing metalloceniumyl substituents (**317**, Scheme 39, iii). Deprotonation and subsequent complexation of the trz ligands were complicated both by the commonly known nucleophilic attack of nucleophilic bases on the cobaltoceniumyl group as well as the steric bulk of the two  $\alpha$ -metallocenyl substituents hindering deprotonation of the triazolium C–H proton. Coordination was therefore not successful for **316** with the least acidic triazolium precursor. In situ deprotonation with Ag<sub>2</sub>O in the presence of excess KCl yielded monocationic silver(I) chloride complex **315** from proligand **314** (Scheme 39, i), while the silver complex from precursor **317** was not isolated, but used as carbene transfer agent in the transmetalation reaction with gold(I) precursor Cs[AuCl<sub>2</sub>] to yield the dicobaltoceniumyl trz gold(I) chloride complex **318** (Scheme 39, iii).<sup>314</sup>

The difficulty associated with the coordination of the deprotonated ligands to transition metals precluded the preparation of rhodium(I) or iridium(I) dicarbonyl complexes for experimental determination of their  $\sigma$ -donor,  $\pi$ -acceptor properties from TEPs derived from their FT-IR spectra.<sup>314</sup> However, DFT calculations were employed to calculate theoretical values for the trz based on precursors **314**, **316** and **317**. The values of 2077.9 cm<sup>-1</sup> (**314**), 2077.1 cm<sup>-1</sup> (**316**) and 2108.7 cm<sup>-1</sup> (**317**), identify these



**Scheme 38** Hydroformylation of 1-octene with trz rhodium(I) complexes.





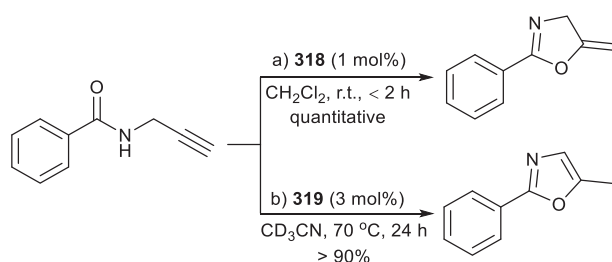
**Scheme 39** Cobaltoceniumyl-ferrocenyl and dicobaltoceniumyl triazolium ligand precursors and the corresponding triazolylidene coinage metal complexes.

carbenes as among the most electrophilic *N*-heterocyclic MICs known.<sup>315,316</sup> Electrochemical characterization of the triazolium salts confirm the expected reversible one-electron oxidation of the Fc moieties in **314** and **316**, while no oxidation processes are observed in their absence (**317**, **318**). The reduction events of the cobaltoceniumyl groups represent two successive one-electron reductions of  $\text{Co}^{\text{III}} \rightarrow \text{Co}^{\text{II}} \rightarrow \text{Co}^{\text{I}}$ . The electrophilic nature of **318** portends to its use in the beforementioned gold-catalyzed oxazoline synthesis (Scheme 40, a). The same reaction conditions were employed as previously optimized for the Fc-trz gold(I) analogs,<sup>269,292</sup> and full conversion in less than 2 h was observed.<sup>314</sup> In this case, no redox induction/additive was required in the presence of these electron-poor dicationic carbene ligands. Redox switchability was potentially demonstrated with reaction termination upon the addition of slight excess cobaltocene. However, addition of oxidant ferrocenium did not result in the back-switching on of the catalytic activity of the system.<sup>314</sup>

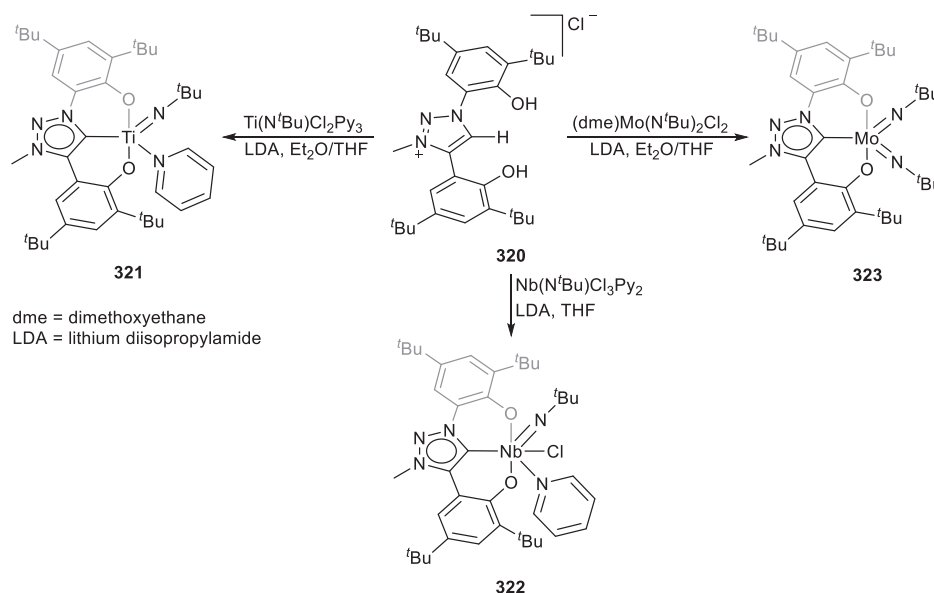
Further utility of this ligand in reaction selectivity was demonstrated shortly thereafter.<sup>317</sup> Oxidative chlorination of **318** was possible simply by stirring overnight in aqua regia at room temperature, to yield dicationic gold(III) trichlorido complex **319** (Scheme 39, iii), without dissociation of the dicobaltoceniumyl trz ligand. More traditional methodology for gold(III) complex formation, e.g. the use of a  $\text{Au}^{\text{III}}$  precursor or halogens as oxidants, proved intractable. Initial attempts at using **319** as catalyst for oxazoline synthesis were discouraging, with no conversion observed under similar reaction conditions even after adding a silver(I) salt. Observation of the reduced solubility of the catalyst in dichloromethane prompted the use of the more polar solvent  $\text{CD}_3\text{CN}$  at elevated temperature. Reaction optimization resulted in conversion of the substrate (more than 90% after 24 h), but notably a different product isomer, 5-methyl-2-phenyloxazole, forms exclusively (Scheme 40, b).<sup>318</sup> This different mechanistic reaction outcomes for  $\text{Au}^{\text{I}}$  vs  $\text{Au}^{\text{III}}$  catalysts are well-known, yet such facile reaction tailoring by post-complexation of a metal-ligand system is striking.

### 1.05.3.2 Nonmetal redox active moieties appended to triazolylidenes and imidazol-4-ylidenes

Reports of redox noninnocent nonclassical carbene ligands beyond these metalloligands are limited, yet new reports of other redox active nonclassical carbenes bode well for the development of further redox switchable catalysts. One such example is the preparation of a bis-phenolate mesoionic carbene ligand that is not only redox active but the dianionic pincer ligand provides excellent stabilization for high-valent early transition metal complexes, as exemplified by the isolation of the titanium (**321**), niobium (**322**) and molybdenum (bis)imido complexes (**323**) from the precursor bisphenol triazolium **320** (Scheme 41).<sup>319</sup>

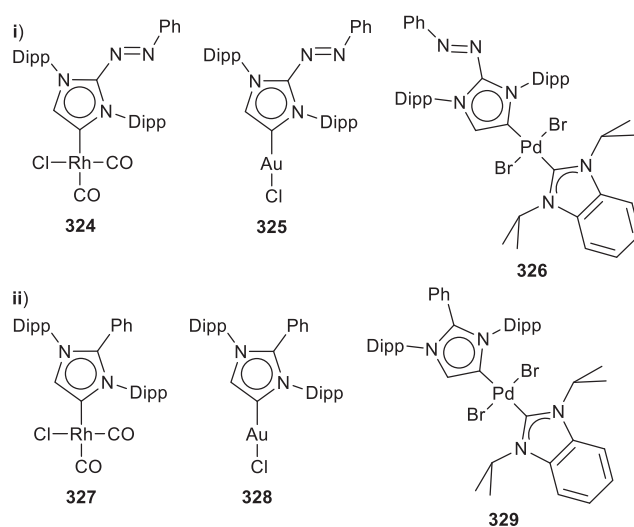


**Scheme 40** Chemoselective oxazole formation catalyzed by gold(I) and gold(III) dicobaltoceniumyl trz complexes.



**Scheme 41** Bis(phenolate)trz salt as precursor to bis(phenolate)trz imido complexes of group 4–6 transition metals.

A recent report by the group of Severin details the strategy of incorporating arylazo-groups on the C2-position of Im4 to modify the electronic properties in such a way that these aNHCs become more CAAC-like.<sup>320</sup> Au<sup>I</sup>, Rh<sup>I</sup> and Pd<sup>II</sup> complexes of these azoimidazolium-based dyes were prepared (324–326, Fig. 8, i), along with a range of C2-phenyl substituted analogs for comparative purposes (327–329, Fig. 8, ii). The aim was to maintain the strong  $\sigma$ -donating ability (i.e. high-lying HOMOs) known for Im4s while increasing the  $\pi$ -acceptor ability (i.e. lowering the LUMO energy levels) to produce complexes with the small singlet-triplet gaps that are responsible for the unique reactivity of CAACs. Experimental spectroscopic methods were employed to evaluate the ligand properties. HEPs measured from 326 (181.1 ppm) and 329 (181.0 ppm) demonstrate the similar  $\sigma$ -donor ability of both Im4. However, the TEP of 324 was determined to be 2045 cm<sup>-1</sup>, both lower than what is observed for normal NHCs (2048–2053 cm<sup>-1</sup>) and higher than typical Im4 (2037–2043 cm<sup>-1</sup>) as an indication of the overall donating ability ( $\sigma$ -donor/ $\pi$ -acceptor) of the ligands.<sup>321</sup> In comparison, TEP = 2039 cm<sup>-1</sup> for 327 falls in the range typical for Im4. From these spectroscopic values it can be inferred that the energy of the LUMO of the azo-Im4 ligand is lowered in comparison to the unfunctionalized carbene, while the HOMO energy levels remain mostly unaffected. This was confirmed by DFT calculations, as well as cyclic voltammetry experiments. The reduction events of 324–326 are unambiguously linked to the presence of the arylazo substituent, and are carbene ligand-centered as a first step in the preparation of Im4 that could potentially stabilize radicals.



**Fig. 8** Azo-Im4 complexes with CAAC-like electronic properties.

## 1.05.4 Chiral noninnocence

Enantiopure chiral products, from achiral organic substrates, can be accessed via asymmetric catalytic transformations using transition metal catalysts featuring a chiral motif on their backbone.<sup>322–327</sup> Accordingly, the use of NHCs featuring a chiral motif which imparts chirality to the corresponding metal complex after metalation, has led to further developments within the field of asymmetric catalysis. The chiral motif can be introduced on the five-membered heterocycle framework, as depicted by 330 and 331 in Fig. 9. Alternatively, the N-side arm can accommodate the chiral motif, with various types of chiral functionalities possible, such as a stereogenic center (332 or 333), or an axial (334) or a planar (335) chiral group (Fig. 9). These chiral motifs impart the required chirality to the corresponding metal complex, which dictates the chirality outcome of catalyzed reaction.<sup>322–327</sup> Not surprising then, is the substitution of NHCs with the even stronger donor abnormal carbenes to access, possibly, a complex catalyst with increased catalytic activity while controlling the stereogenic outcome of the catalyzed reaction. Consequently, the ligand plays more than just a simple spectator role, as it has a direct influence on the outcome of a catalytic reaction.

Chiral trz made their introduction in 2009, with the report of Sankararaman disclosing the palladium complex 336 featuring a chiral motif on the ligand (Fig. 10), obtained from transmetalation of the intermediary silver complex.<sup>328</sup> Similarly, the group of Albrecht reported a triazolium salt with a chiral center on the ligand backbone which was subsequently coordinated to gold, also via a silver transmetalation route 337.<sup>186</sup> PEPPSI type complexes 338 and 339, where the chiral center is situated on the ligand backbone, were reported by the groups of Sankararaman<sup>329</sup> and Sarkar,<sup>330</sup> respectively. Gangwar et al. disclosed the synthesis and isolation of chiral trz-coordinated palladium complex 340, in addition to the PEPPSI-analog.<sup>331</sup> The same group very recently also reported the axially chiral bis(trz)Au(I) complex 341, obtained by means of transmetalation from the corresponding silver complex that was isolated and characterized.<sup>332</sup>

Trz complexes featuring two chiral centers could be accessed via a chirality cascade transfer approach. Hence, Sierra, Torre and co-workers utilized the triazolium ligand salt 342 containing the chiral sulfoxide moiety<sup>248</sup> to prepare the corresponding half-sandwich rhodium and iridium metal complexes with the chirality at the metal influenced by the chirality at the trz ligand (Scheme 42, i).<sup>333</sup> As evidenced in Scheme 42, trz coordination to the metal is followed by C–H-activation in the presence of NaOAc, which affects the chirality transfer leading to the chirality at the metal center being opposite to that of the sulfoxide functional group (Scheme 42, i). Of particular note is the retention of configuration observed upon preparation of either the cationic complex 345 via chloride abstraction with NaPF<sub>6</sub>, or insertion of dimethyl acetylenedicarboxylate across the M–C<sub>phenyl</sub> bond of 344, yielding 346. The authors suggested that retention of configuration at the metal center is a result of the vacant coordination site at the metal center being occupied by the sulfoxide moiety during the dissociation process,<sup>245</sup> akin to the gold carbenic intermediate stabilized by the sulfoxide substituent during the enyne cycloisomerization (vide supra, Scheme 35).<sup>32,248</sup> This implicates the sulfoxide substituted trz ligand as fulfilling both a chiral and a multifunctional ligand noninnocent role (see Scheme 35). Facile insertion of the terminal alkyne methyl propiolate was also reported, with both regioisomers 347 and 348 isolated as enantiomerically pure diastereoisomers (Scheme 42, i).<sup>333</sup> The chiral cascade transfer methodology was exploited towards the preparation of BODIPY-tagged (BODIPY = 4,4-difluoro-4-bora-3a,4a-diaza-s-indacene) luminescent complexes featuring two chiral centers, both at the sulfoxide moiety

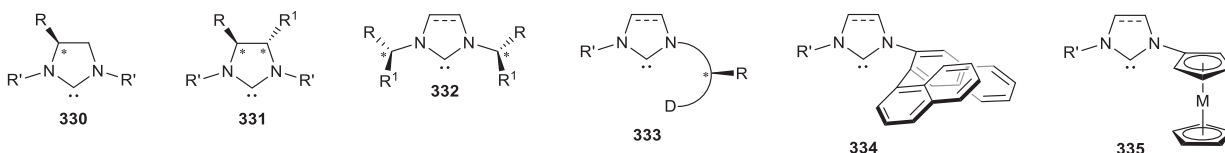


Fig. 9 Various representative classes of chiral functionalized NHCs.

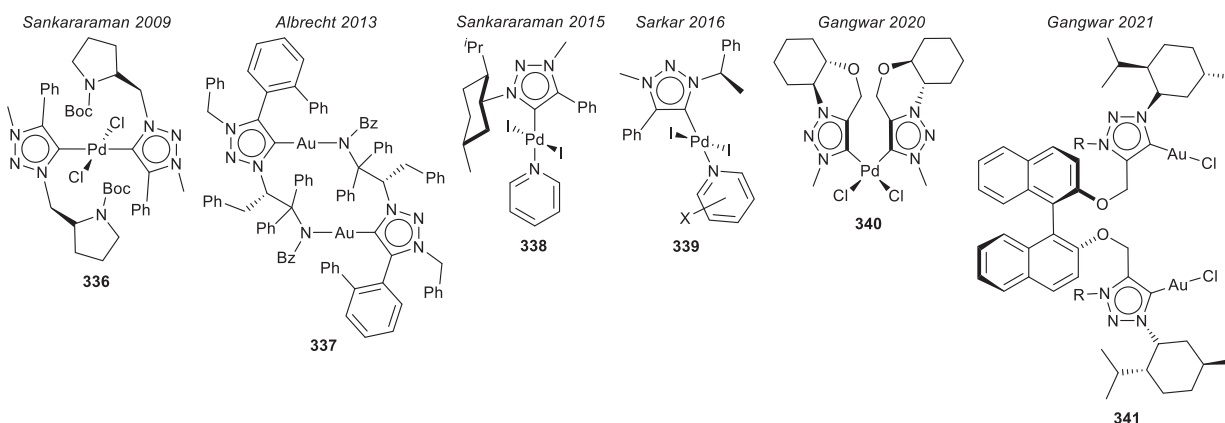
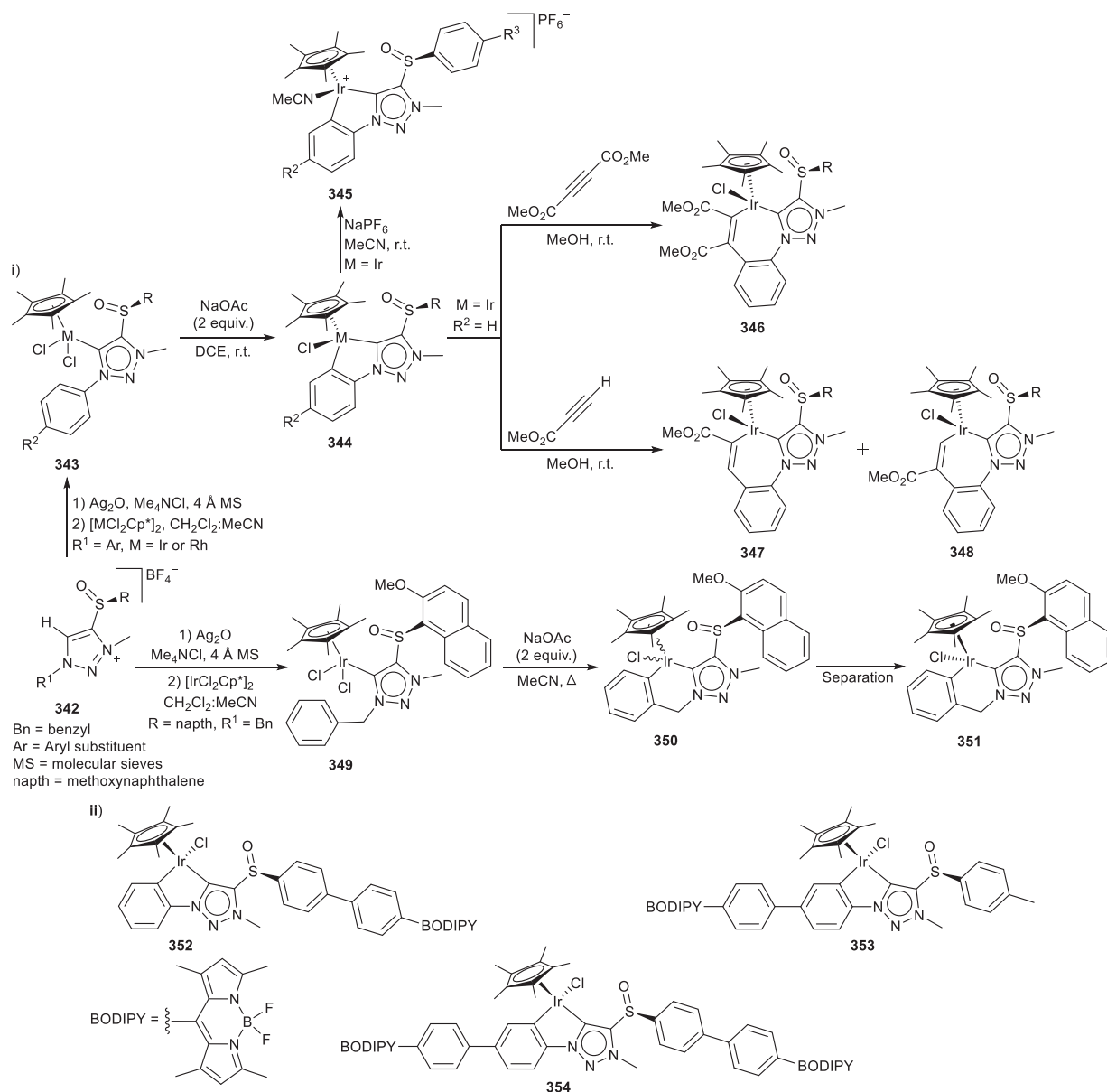


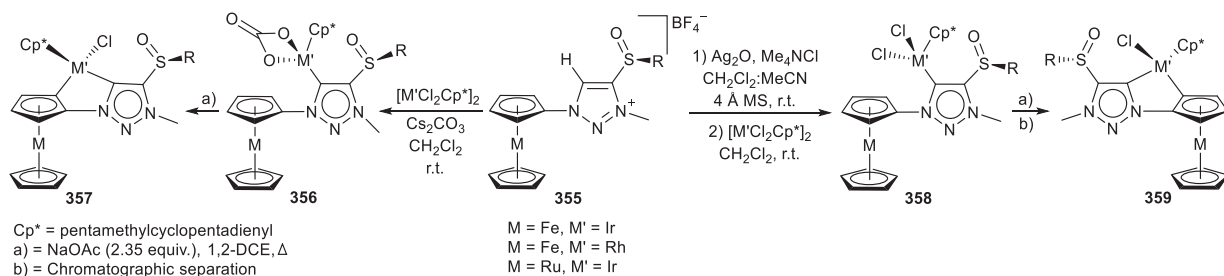
Fig. 10 Selected chiral trz complexes.



**Scheme 42** Chirality cascade leading to enantiomerically pure complexes.

and at the metal center (Scheme 42, ii).<sup>334</sup> Lack of conjugation renders the absorption and emission of the complexes similar to the BODIPY reference. Unfortunately, the circularized polarized emissions, an application of these types of complexes, was met with no avail.<sup>334</sup> However, this illustrates the significance of this synthetic process to allow for preparation of complexes with multiple chiral centers, ultimately for highly specialized applications.

Appending ferrocene to classical NHCs is well documented and predictable (335, Fig. 9), as the combination of the strong donor carbene ligand with the planar chiral ferrocene moiety can lead to chiral catalyst mimicking the expanded field of the  $C_1$ -symmetric Fc phosphine coordinated complex catalyst<sup>335</sup> in addition to its possible redox noninnocence (see Section 1.05.3). Accordingly, Štěpnička et al. prepared a series of trz coordinated  $\text{Pd}^{\text{II}}$  and  $\text{Au}^{\text{I}}$  complexes featuring phosphinoferrocene ligands.<sup>336</sup> Sierra, Torre and co-workers also used the planar chiral element, but in combination with the chirality cascade transfer methodology from their sulfoxide containing trz ligand (355, Scheme 43).<sup>337</sup> They were thus able to prepare enantiopure bimetallic complexes containing three different chiral centers (Scheme 43). The chiral centers are located at the trz sulfoxide moiety and at the metal center, with the third chiral moiety being the planar Fc or ruthenocene substituent. Catalytic applications of these chiral complexes were not disclosed but should prove exploitable in the chiral cascade transfer approach during the preparation of chiral catalyst, especially for a complex catalyst featuring multiple chiral centers for the production of highly selective catalysts.

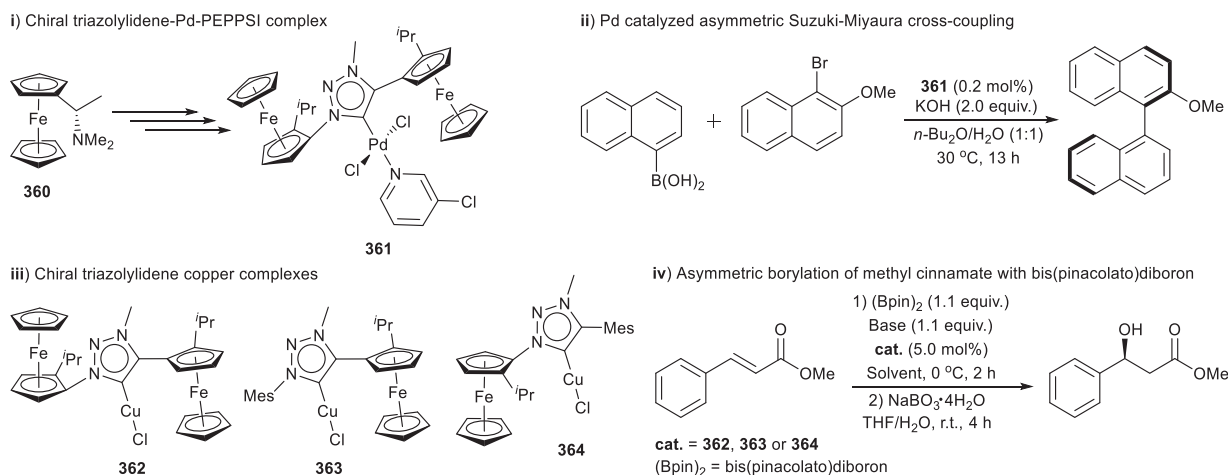


**Scheme 43** Bimetallic complexes with three different elements of chirality.

Direct applicability of Fc-containing nonclassical carbene ligands in chiral catalysis has been demonstrated. Planar chiral ferrocene-based triazolium ligand salts, their coordination to palladium<sup>338</sup> and copper,<sup>339</sup> and consequent asymmetric catalytic activity was reported by Fukuzawa, Haraguchi and co-workers. The chirality imparted by the planar ferrocene allows for the palladium and copper catalysts to mediate the transformation reactions selectively. Thus, the Fc-containing complex **361** was prepared starting from (*S*)-Ugi's amine **360** (Scheme 44, i).<sup>338</sup> It was found that catalyst **361** could furnish the asymmetric Suzuki-Miyaura cross-coupling reaction with good enantioselectivity and appreciable TONs (Scheme 44, ii). Similarly, copper complexes coordinated by a Fc-substituted trz ligand was prepared (Scheme 44, iii) towards the asymmetric borylation of an  $\alpha,\beta$ -unsaturated ester (Scheme 44, iv).<sup>339</sup> Complexes **362**, **363** and **364** catalyzed the borylation of methyl cinnamate with bis(pinacolato)diboron yielding the borylated complex, which further underwent oxidation in the presence of  $\text{NaBO}_3 \cdot 4\text{H}_2\text{O}$  to afford 3-hydroxy-3-phenylpropanoate (Scheme 44, iv).

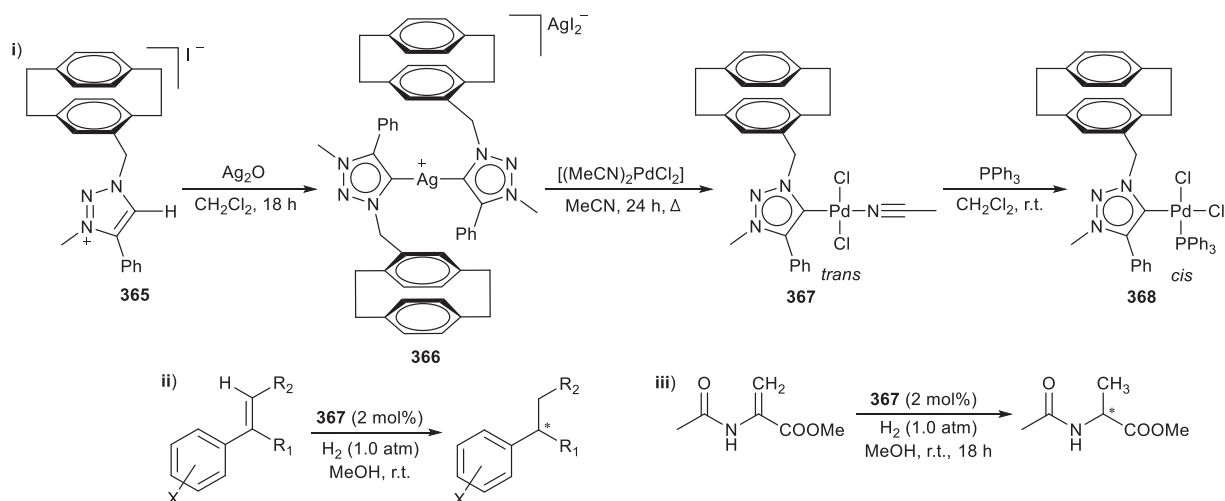
Metalloocene incorporation is not the only method towards introducing planar chirality to a targeted complex featuring a nonclassical carbene, as demonstrated by Sankararaman and co-workers. Catalytic chemoselective olefin hydrogenation as well as enantioselective hydrogenation of prochiral alkenes under ambient conditions and 1 atm of  $\text{H}_2$ , was mediated by the chiral trz palladium complex **367** (Scheme 45, i).<sup>340</sup> The triazolium ligand **365** is substituted with a [2.2]paracyclophane wingtip moiety, which imparts planar chirality to the palladium complex **367**, obtained after transmetalation from the silver complex **366**. Ligand substitution yields the phosphine analog **368** from the acetonitrile complex **367**, accompanied by a *trans* to *cis* isomerization of the chlorido ligands (Scheme 45, i). Olefin hydrogenation catalyzed with 2 mol% **367** yielded the corresponding alkanes with moderate to high enantioselectivities and appreciable yields of the targeted product (Scheme 45, ii and iii). Contrary to this, **368** was determined to be catalytically inactive, attributed to the substitution of the labile acetonitrile ligand for the  $\text{PPh}_3$  donor (Scheme 45, i). Furthermore, it was found that **367** could catalyze the hydrogenation of stilbene, retaining its catalytic activity for 13 consecutive cycles, to reach a TON of 640. The combination of a catalytically active metal and a chiral ligand therefore allows for the realization of a hydrogenation catalyst that selectively hydrogenates olefins at mild conditions.

The 2,2'-diamino-1,1'-binaphthalene (BINAM) motif has been used as the backbone from which bis-triazoles could be prepared, followed by alkylation of the N3 nitrogen.<sup>341,342</sup> This resulted in the preparation of the corresponding bis(triazolium) ligand salts, with axial chirality induced by the ligand backbone. Subsequent metalation of the chiral ligand allowed for the preparation of the corresponding Pd (**370**), Ir (**371**) and Rh (**372**, **373** and **374**) complexes (Scheme 46, i), with the Rh complex **372** found to be catalytically active in the hydrosilylation of aryl ketones, yielding the alcohols with good yield and moderate enantioselectivity (Scheme 46, ii).<sup>341</sup> Similarly, the group of Chen prepared the corresponding gold complexes through coordination of the



**Scheme 44** Fc-trz complexes for asymmetric catalytic applications.



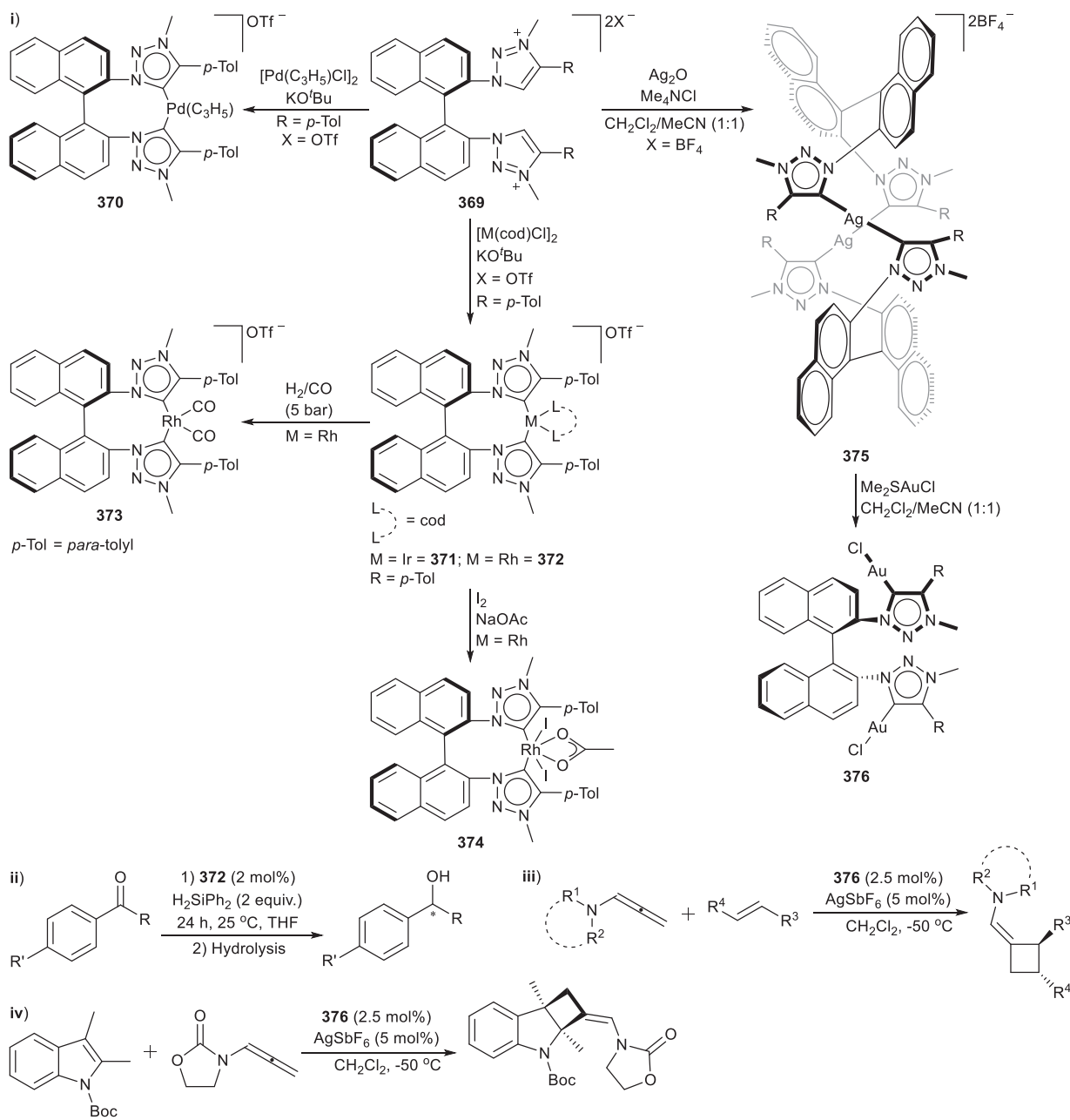


**Scheme 45** [2.2]paracyclophane Pd<sup>II</sup> complex towards selective hydrogenation of various olefins.

bis(triazolium)-BINAM ligand salt **369** to silver yielding **375**, followed by transmetalation with Me<sub>2</sub>SAuCl leading to the coinage metal complex **376** (Scheme 46, i).<sup>342</sup> The chiral gold(I) complex was prepared towards the enantioselective [2+2] cycloaddition of alleneamides with olefins, yielding chiral cyclobutanes (Scheme 46, iii). Moderate to high enantioselectivities could be obtained with **376** as catalyst in the presence of AgSbF<sub>6</sub>, at a reaction temperature of -50 °C in CH<sub>2</sub>Cl<sub>2</sub>. Furthermore, it was shown that the indole functionalized cycloadduct could be obtained with good enantioselectivity when starting from the corresponding indole and the alleneamide (Scheme 46, iv),<sup>342</sup> in an expansion of the structural analogs available of this biologically relevant class of heterocyclic compounds.<sup>343–346</sup>

Suginome et al. described the cyclopropanation of styrene with propargylic ester, yielding the cyclopropane with a 6:1 *cis:trans* ratio (Scheme 47).<sup>347</sup> The reaction was catalyzed by gold(I) complexes **378** or **380** (Scheme 47), prepared via two different strategies. The ligand used towards preparation of gold(I) complex **378** could be obtained either by the copolymerization of a triazole-containing monomer or the post-polymerization CuAAC across an alkyne-functionalized PQX [PQX = poly(quinoxaline-2,3-diyl)s] to yield the precursor **377**. Positive signals obtained in the circular dichroism (CD) spectra indicated the induction of *P*-helical structures via chirality transfer from the triazole group to the polymer main chain. Conversion of the pendant 1,2,3-triazole precursors to trz-Au-Cl complexes **378** as catalyst precursors were achieved by alkylation to yield the triazolium pendants, followed by treatment with silver(I) oxide and transmetalation to AuCl at room temperature (Scheme 47, i). Alternatively, the gold(I) complex **380** was also prepared starting from the monomer triazolium salt **379**, with the bis(trz)-Au<sup>I</sup> complex obtained due to the absence of a rigid polymer chain (Scheme 47, ii). As a proof of concept, **378** and **380** were employed as catalysts after activation with AgSbF<sub>6</sub> to prepare cyclopropane from the reaction of propargylic pivalate with styrene (Scheme 47, iii). Higher yields were obtained for the polymer-supported **378** compared to **380**, but the most notable benefit of the use of **378** vs **380** is the ability to recover **378** from the reaction by precipitating it out with solvent pentane, whereafter it could be reused at least eight times without any loss of catalytic activity.<sup>347</sup>

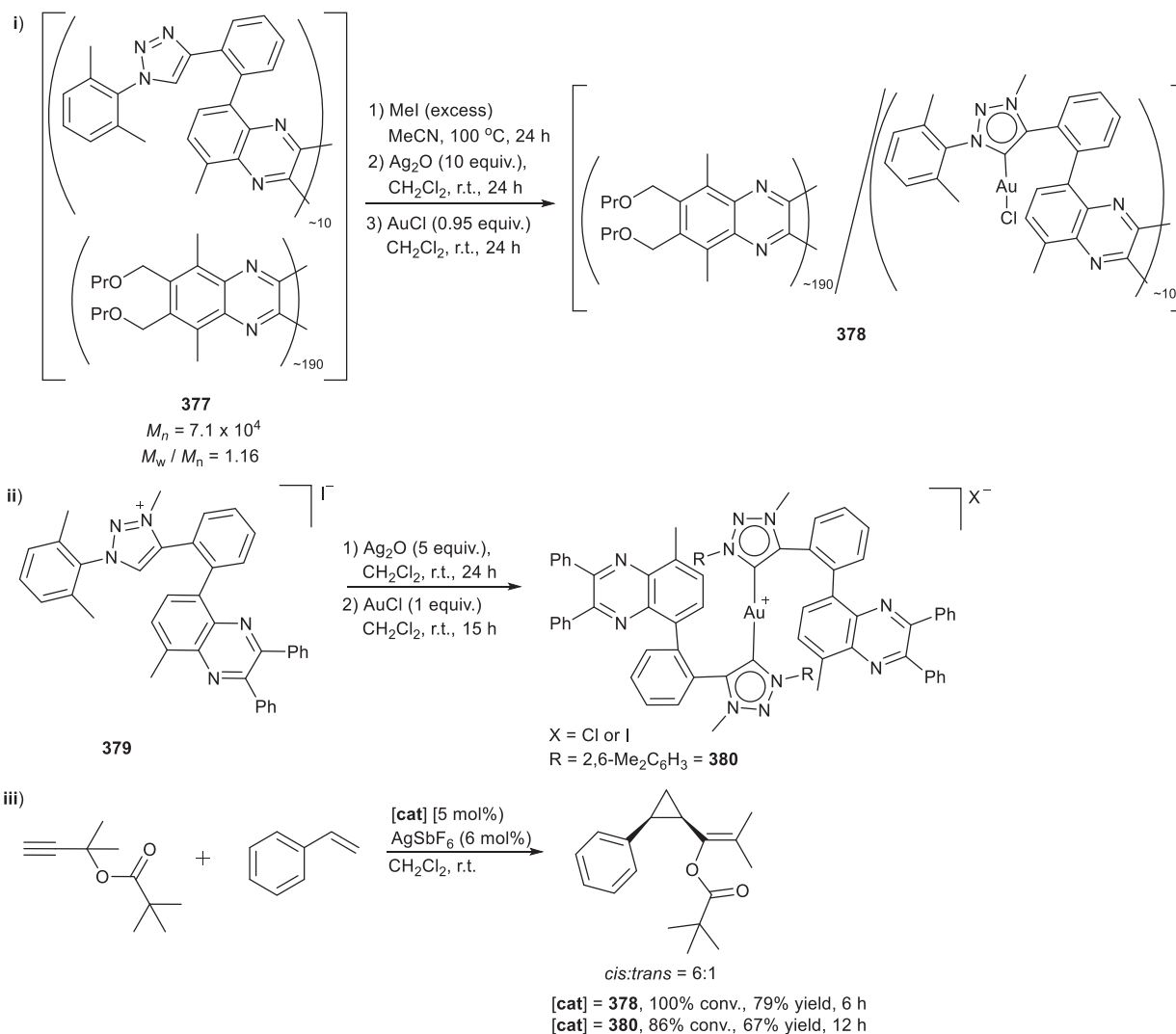
Within the realm of luminescence, circularly polarized light is advantageous towards various optical applications.<sup>348</sup> As mentioned earlier, the BODIPY-tagged trz iridium complexes (Scheme 42, ii) were subjected to circularly polarized light emission studies, albeit without success.<sup>334</sup> However, symmetrical CAAC-CuCl complexes **381** and **382** accessed starting from either (-)-L-Menthol or (+)-D-Menthol, respectively, were described to exhibit circularly polarized luminescence (Scheme 48, i).<sup>348</sup> Photophysical characterization, and more specifically, electronic circular dichroism (ECD) and circularly polarized light experiments, confirmed that **381** and **382** have preferential emission of light in one direction over the other. This could be achieved due to the presence of the simple chiral CAAC ligand inducing the light emission in the left or right direction. Also, of particular importance, is the short timescale coupled with excitation and subsequent emission. Upon application as catalyst, no chiral induction in the catalyzed reaction could be observed. The lack of chirality transfer during the catalytic reaction mediated by **381**, was reported by Bertrand, Jazzar, Mauduit and co-workers to be a result of conformational inversion (Scheme 48, ii).<sup>349</sup> The chiral CAAC-CuCl complex **381** was used to mediate the asymmetric conjugate borylation reaction to prepare the corresponding chiral organoboron products (Scheme 48, iv). However, it was reported that **381** catalyzed the reaction with diminished selectivity, albeit with high catalytic activity. The lack of control over the selectivity outcome was traced back to the energetically accessible conformer of **381**, being **383** (Scheme 48, ii). Conformational inversion leads to the existence of two conformers in solution, hence the lack of selectivity. The authors addressed this problem by introducing increased steric bulk at the quaternary carbon in question, in the form of a 5 $\alpha$ -cholestan-3-one group. The more rigid CAAC would resist conformational changes, ensuring the presence of one conformer in solution. Accordingly, the copper complex **385** could be isolated after deprotonation of the ligand salt **384** with KHMDS followed by metalation with CuCl, with X-ray analysis confirming the absolute stereochemistry of the complex (Scheme 48, iii). Catalyzing the asymmetric conjugate borylation reaction using **385** delivered the chiral organoboron product



**Scheme 46** BINAM-based axially chiral bis(trz) complexes towards enantioselective catalyzed reactions.

with a marked improvement in the enantioselectivities of the targeted product, while retaining the high catalytic activity (**Scheme 48**, iv).

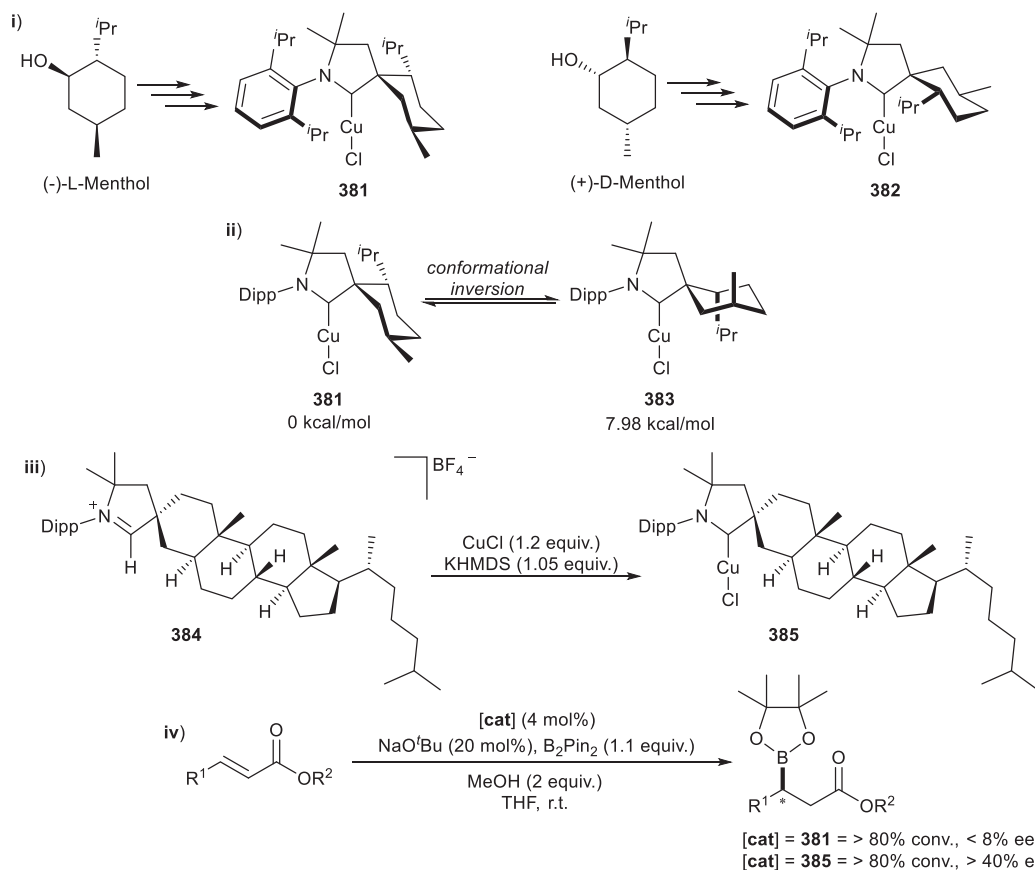
A serendipitous cascade cyclization-rearrangement resulted in a chiral CAAC-gold(I) complex (**387**, **Scheme 49**, i), further established to selectively catalyze the cycloisomerization of allenol, yielding the substituted dihydrofuran as a single diastereomer (**Scheme 49**, iii).<sup>350</sup> The chance synthetic protocol was subsequently utilized to prepare a range of different chiral containing CAAC-gold(I) complexes. From this, a proposed mechanism towards the formation of the gold complexes was elucidated, with the formation of the zwitterionic vinyl-gold complex **390** from the  $\pi$ -coordinated gold intermediate **389** postulated (**Scheme 49**, ii). A [3,3]-sigmatropic rearrangement ensues, leading to iminium **391** which ultimately undergoes a 1,2-silicon migration, resulting in the observed gold complex **393**. An alternative mechanism was also considered, involving the high energy carbene intermediate **394**, from the alkylation on the  $\beta$ -carbon of the vinyl system. The high energy carbene **394** isomerizes via carbon and silicon migrations, yielding the thermodynamically favored product **393** (**Scheme 49**, ii). An independent theoretical investigation confirmed that the pathway following the [3,3]-sigmatropic rearrangement towards **393** is feasible, and also lower in energy compared against the pathway via the high energy carbene intermediate **394** (**Scheme 49**, ii).<sup>351</sup> The gold complex **387** was also



**Scheme 47** Preparation of (i) polymer PQX-supported and (ii) monomer triazolylidene Au<sup>I</sup> complexes as (iii) cyclopropanation catalyst precursors.

found to efficiently catalyze the intramolecular hydroamination of *N*-methyl-2-(2-phenylethynyl)aniline yielding the corresponding indole (**Scheme 49**, iv), in addition to the cycloisomerization (**Scheme 49**, iii).<sup>350</sup> It was further evidenced that the chiral gold complexes exhibited biological properties, with the complexes successfully screened against various cancer cell lines. Hence, the unique cascade cyclization-rearrangement reaction allows for the preparation of chiral containing CAAC-gold(I) complexes, finding application in multiple disciplines.

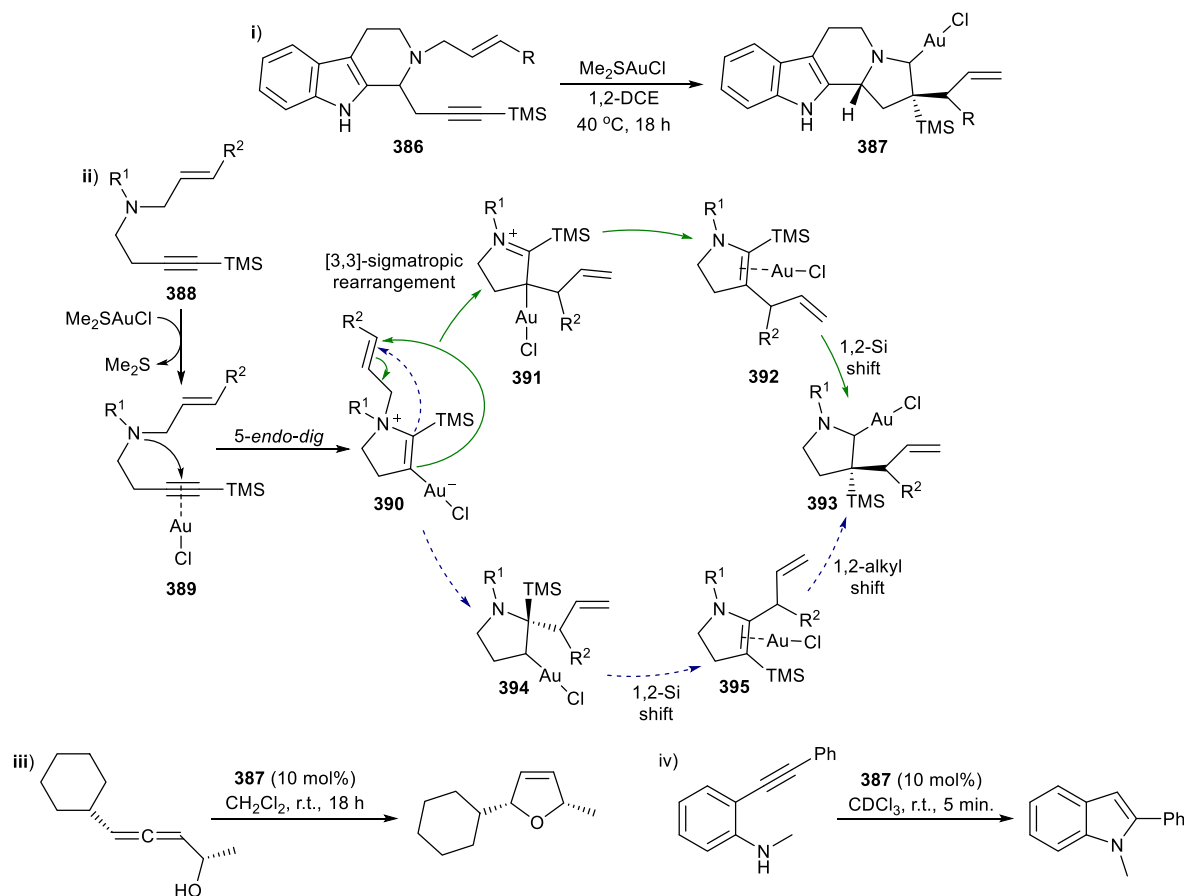
The advancements made in olefin metathesis catalyzed by CAAC coordinate ruthenium complexes was very recently extensively covered in the perspective by Bertrand and co-workers.<sup>352</sup> Only selected milestones are mentioned, of which the recent report by Bertrand et al.<sup>353</sup> regarding a chiral catalyst mediating the metathesis reaction with induced chiral control, is of particular relevance to the current topic. The proliferation of CAAC-Ru complexes for olefin metathesis can be attributed to their exceptional catalytic activity, as opposed to their NHC counterparts.<sup>352</sup> This difference was already noted in 2007 with the first example of a CAAC coordinated ruthenium complex 396 catalyzing the ring-closing metathesis reaction (**Scheme 50**, i).<sup>354</sup> Bertrand, Grubbs and co-workers continued their research, expanding the family of CAAC coordinated ruthenium metathesis complexes to include catalysts with exceptional metathesis catalytic activity.<sup>355</sup> This included the CAAC ruthenium complex 397, catalyzing the ethenolysis of methyl oleate with a TON of 340,000 when using ethylene with a purity of 99.995% at a catalyst loading of 1 ppm, while ethylene with a slightly lower purity gave TONs of 180,000 (**Scheme 50**, ii). Similar olefin metathesis activity could also be achieved with bis(-CAAC)Ru indenylidene complexes of the type 398 (**Scheme 50**, ii), which could catalyze the formation of both terminal and internal olefins.<sup>356</sup> The properties of the CAAC ruthenium complexes allowing for the high metathesis catalytic reactivity was investigated.<sup>357</sup> It was determined that the CAAC-Ru complexes are susceptible to bimolecular coupling but resist  $\beta$ -elimination due to stabilization imparted by the stronger  $\sigma$ -donor carbenes (**Scheme 50**, iii). Decreased complex decomposition through  $\beta$ -elimination allows for lower catalyst loading, which also decreases the propensity towards decomposition via bimolecular coupling. The high



**Scheme 48** Chiral containing CAAC-CuCl complexes towards (i) circularly polarized light emission and (iv) asymmetric conjugate borylation reaction.

catalytic activity and low catalyst loading render these metathesis catalysts industrially applicable,<sup>355</sup> and even more so, with the realization of these catalyzed reactions in continuous flow processes<sup>358,359</sup> or the preparation of the complex catalyst via mechanochemical techniques circumventing the use of solvents (Scheme 50, iv).<sup>360</sup>

Optically pure CAAC ruthenium complexes for asymmetric olefin metathesis was reported by the group of Bertrand, Jazzar and Maduit.<sup>353</sup> The (+)-(R)-Ru 406 and (-)-(S)-Ru 407 could be isolated, obtained through the separation of (*rac*)-Ru 405 with preparative high-performance liquid chromatographic techniques (<sup>Prep</sup>HPLC) (Scheme 51, i). The method allowed for the isolation of the two enantiomers with excellent yields and optical purities, with ECD and XRD characterization confirming the absolute configuration of the complexes. The asymmetric ring-opening cross-metathesis of styrene with norbornenes catalyzed by the chiral ruthenium complexes was investigated. The reaction yielded the products of metathesis with excellent enantiomeric purity. It was further demonstrated that the catalyst (-)-(S)-Ru 407 and the (+)-(R)-Ru 406 yielded the metathesis product with an *S,R*- or *R,S*-configuration, respectively. Both enantiopure catalyst also showed excellent *E/Z* ratios, with the ratio increasing from an *E/Z* ratio of 80:20 to an *E/Z* ratio of 95:5. The authors proposed a preliminary reaction mechanism by which the ruthenium catalyst selectively mediates the metathesis reaction (Scheme 51, ii).<sup>353</sup> A 14 electron-propagating Ru-benzylidene species 409 was suggested, accessed after the addition of excess styrene resulting to the dissociation of the *p*-nitro styrenylether ligand. The *anti*-conformer 409 (calculated 9.9 kcal/mol in energy compared to 407 at 0.0 kcal/mol) is formed that is less stable due to the quaternary chiral center being above the benzylidene fragment (i.e. the benzylidene is apical or *trans* to the *N*-Dipp moiety), resulting to increased steric congestion. Accordingly, calculations support direct rotation of the CAAC ligand around the metal-carbon bond, leading to the more stable *syn*-conformer 410 (calculated 7.2 kcal/mol in energy compared to 407 at 0.0 kcal/mol), with the *N*-Dipp moiety being above the benzylidene fragment (i.e. the benzylidene is apical or *syn* to the quaternary chiral substituent). This results in decreased steric congestion, favoring 410 as the 14e-propagating species (Scheme 51, ii). Subsequent coordination of norbornene was considered to occur *trans* to the carbene carbon and on its *exo* face, leading to 411 and 412 as possible conformers. Coordination of norbornene at 412 positions the phenyl substituent of the chiral carbon at a calculated distance of 3.64 Å and 3.38 Å from the norbornene substituents, which results in an increase in the energy of 412 due to the steric clash between the mentioned substituents. Alternatively, coordination of norbornene at 411 positions the norbornene substituents away from the phenyl substituent, which results in the energy of 411 increasing to 23.6 kcal/mol from 410, calculated to be 7.2 kcal/mol. This results towards formation of the metallacyclobutane 413, while the unfavored pathway leads to formation of metallacyclobutane 414, which ultimately yields 418, the



**Scheme 49** Cascade cyclization-rearrangement leads to chiral CAAC-gold(I) complexes via a [3,3]-sigmatropic shift.

minor product of the reaction. Calculations confirmed that 411 formation is favored, being 4.1 kcal/mol lower in energy compared to 412. This was attributed to a lack of steric clash noted in 411, while 412 experienced steric repulsion. Hence, the chiral center at the CAAC ligand ensures the selectivity transfer from the top down, first dictating the formation of either the *syn* or *anti*-isomer of the propagating species, which subsequently controls the product of insertion, preferentially leading to a single isomer via a lower reaction energy barrier controlled by steric congestion or lack thereof. Subsequent norbornene ring-opening at 415 followed by styrene insertion leads to the targeted product 417 and the catalytically active species 410, via intermediate 416.

### 1.05.5 Multinuclear cooperativity

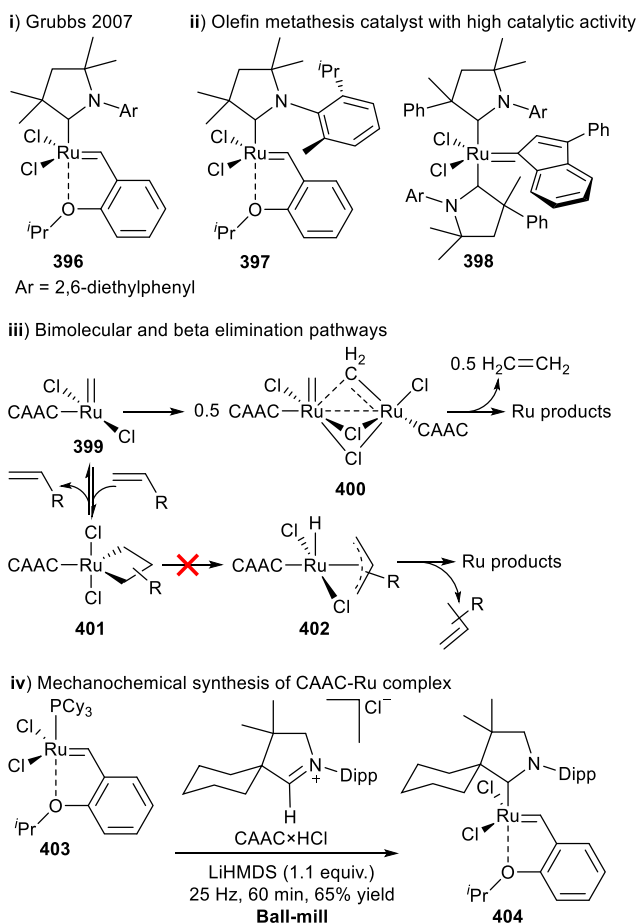
The multinuclearity effect, or cooperative effect, is a term used to describe the synergistic properties, function amplification or integrated multifunctionality attained for metal complexes containing two or more metal atoms/ions within a designated framework to provision for direct metal-metal bonds, or electronically discrete metal centers.<sup>361–363</sup> The approach to design such multinuclear systems are often inspired by metalloenzymes with proximal active sites,<sup>364,365</sup> where the posing of the active metal centers within an effective relevant distance to achieve their desired functions are accomplished by using appropriate ligand scaffolds, i.e. rigid or flexible, allowing for  $\pi$ -communication along the aromatic framework,<sup>366</sup> or enhanced probability of interaction with catalytic substrates due to the three dimensional structural arrangement of metals with appropriate intermetallic distances.<sup>367</sup>

The metal centers employed may be the same, rendering enhanced catalytic performance (more than summative improvement in activity and selectivity) for the homobi- or -multimetallic catalysts compared to the monometallic species or as building blocks for supramolecular assemblies. Incorporation of different transition metals opens up pathways toward multifunctional, tandem or cascade catalysis.<sup>368</sup>

#### 1.05.5.1 Homonuclear cooperativity

Considering the modularity of the 1,2,3-triazol-5-ylidene (trz) backbone via ‘click’-chemistry approaches, it is perhaps not surprising that the examples of bi- to tetranuclear homometallic complexes of this class of non-classical carbenes (vi)–(xii)





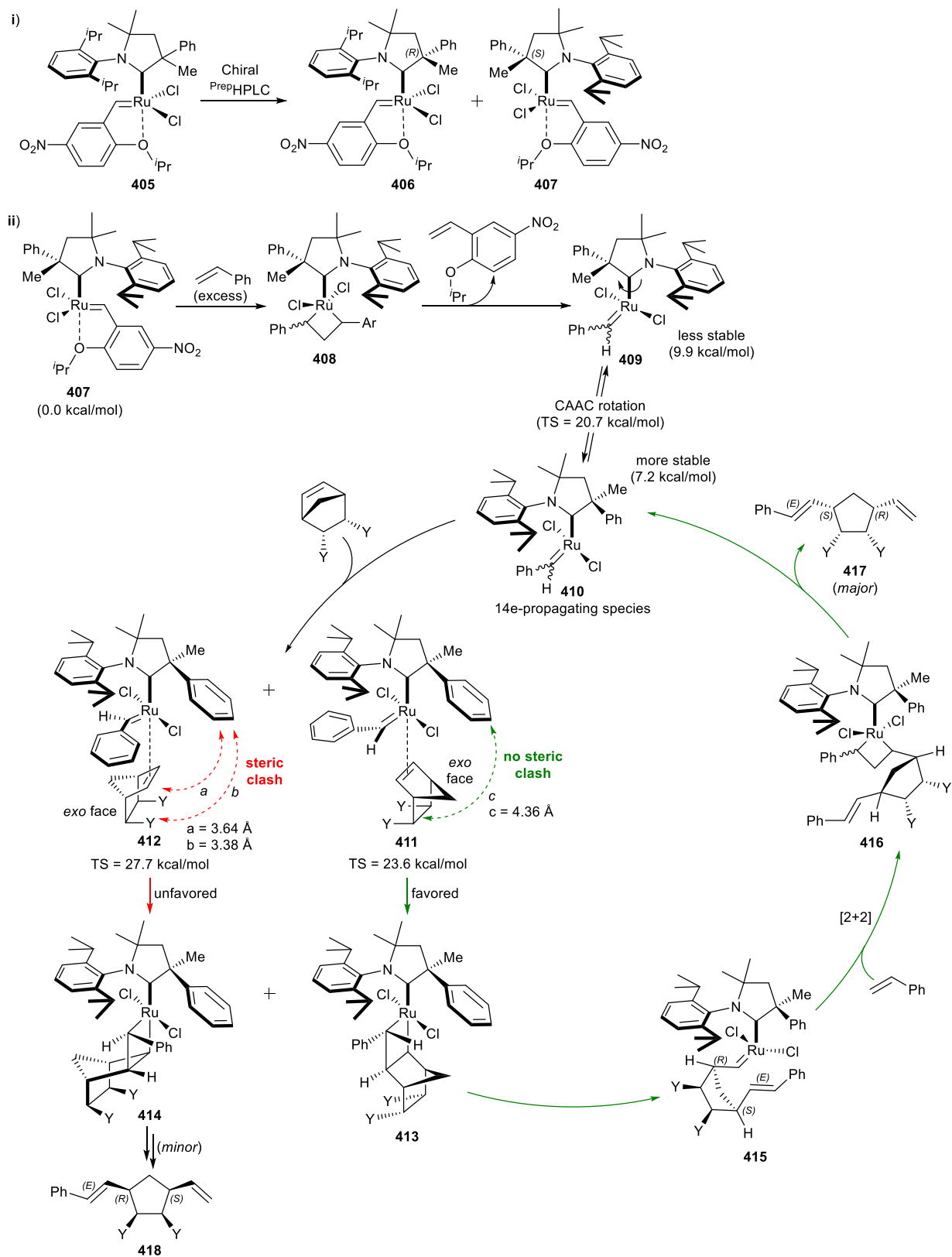
**Scheme 50** CAAC-coordinated ruthenium olefin metathesis catalyst.

outnumber those of Im4 (i) and (xiii) and CAACs (ii)–(v), **Fig. 11**. The bonding modes of homobimetallic complexes of the trz include incorporation of a spacer- or linker group bound to the N1-positions of the two bridged trz rings (vi),<sup>369–372</sup> or the C4-position (viii–xii)<sup>204,300,373,374</sup> to link two trz metal moieties that can accommodate interaction between the homonuclear metal centers. This approach is also the first step for the preparation of cyclometalated complexes where C4-trz substitution with a phenylene linker leads to *ortho* C–H activation (**Fig. 11**, x).<sup>375</sup> Direct coupling of the C4-positions of two trz in the so-called i-bitz (bis(1,2,3-triazol-5-ylidene)) ligands<sup>376</sup> (vii),<sup>377</sup> or introduction of a P-donor site on C4 (**Fig. 11**, ix)<sup>378</sup> yields dinuclear complexes with enforced proximity of the metals leading to direct metal-metal bonds.

In the case of Im4, bimetallic complexes are formed almost exclusively from the bridging of two metal centers by a single ditopic anionic NHC or NHDC (N-heterocyclic dicarbene),<sup>379,380</sup> and very few homonuclear examples are known (**Fig. 11**, i).<sup>118,381–383</sup> For example, the dimetallic palladium(II) complex **421** was prepared by sequential metalation.<sup>381</sup> The C2-imidazolium position of precursor **419** is metalated first via transmetalation from silver(I) to yield monometallic **420**, followed by oxidative addition of the iodide-functionalized C4-imidazolylidene to a different Pd<sup>0</sup> precursor (**Scheme 52**). Although both C2- and C4-ring positions are occupied by Pd<sup>II</sup> in **421**, the asymmetry of the ditopic NHDC leads to electronic inequivalence for potential exploitation of site-specific reactivity and redox activity.<sup>381</sup>

Both directed synthetic routes and serendipitous findings have yielded homobimetallic complexes with a NHDC ligand coordinated to the two metal centers. Transmetalation of an NHDC complex **422** with coordinated Na on the C2- and Zn coordinated on the C4-imidazole to gold(I) with 2 equiv. of (PPh<sub>3</sub>)AuCl yields the neutral digold(I) NHDC complex **423** (**Scheme 53**, i) as an example of targeted homonuclear complex preparation.<sup>382</sup> A PNC-pincer NHC complex of Co<sup>I</sup> (**424**) with a dearomatized phosphine-picoline tethered to the NHC, is unexpectedly converted to a dinuclear dicobalt(I) complex **425** with coordinated N<sub>2</sub> and a second PNC-Co moiety bound to the C4-imidazolylidene group upon reduction with KC<sub>8</sub> in a non-saturated N<sub>2</sub> atmosphere (**Scheme 53**, ii).<sup>383</sup>

If the main group cluster adducts (Si, P, Al, Ga, Ge, Se, etc.) of CAACs are excluded, the number of reported multimetal CAAC complexes are unexpectedly small. Homonuclear bimetallic complexes that feature direct metal-metal bonds (**Fig. 11**, ii),<sup>384</sup> (iii)<sup>385,386</sup> and (iv)<sup>387</sup> or doubly-bridged metal centers (**Fig. 11**, v)<sup>135,388–393</sup> are representative examples. In all cases, the inherent noninnocent behavior of the CAAC ligands (vide supra) stabilize the metals in varying oxidation states, including radical centers,<sup>135</sup>



**Scheme 51**  $C_1$ -Symmetric CAAC ruthenium complexes towards asymmetric olefin metathesis.

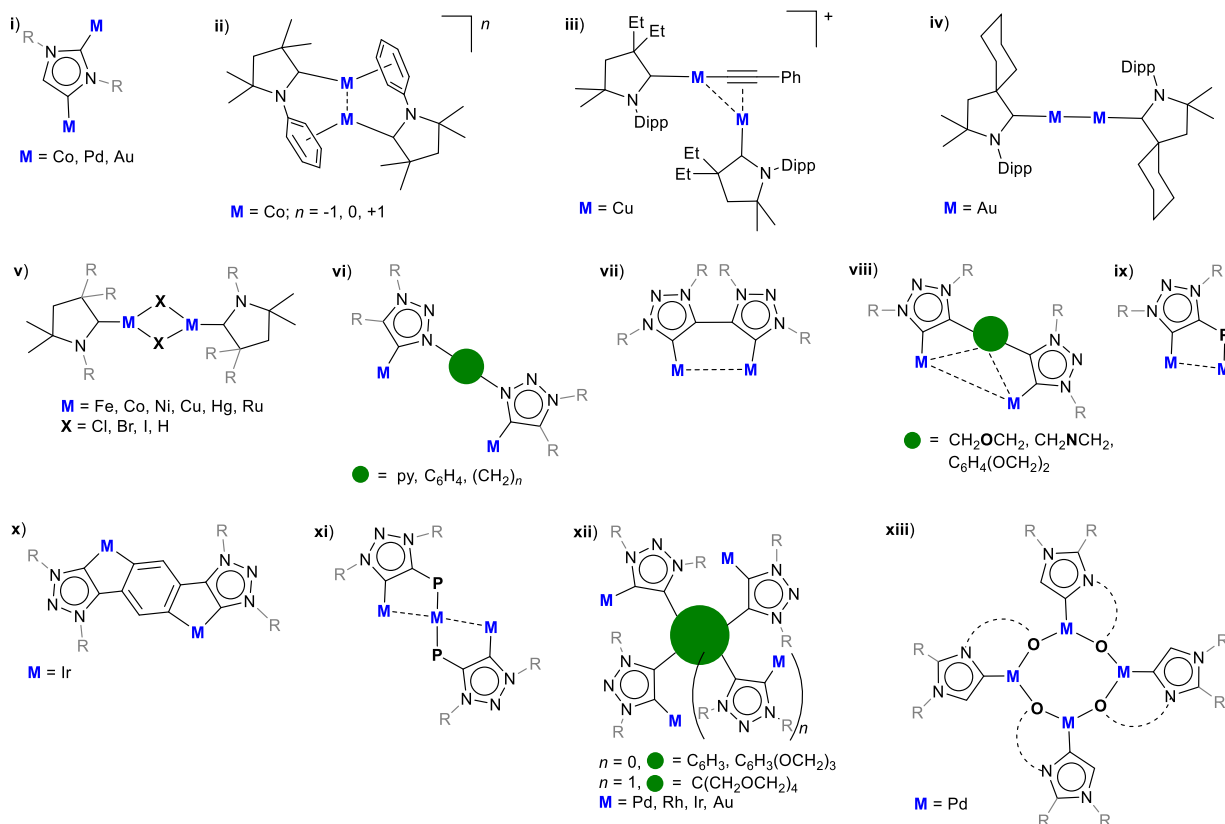
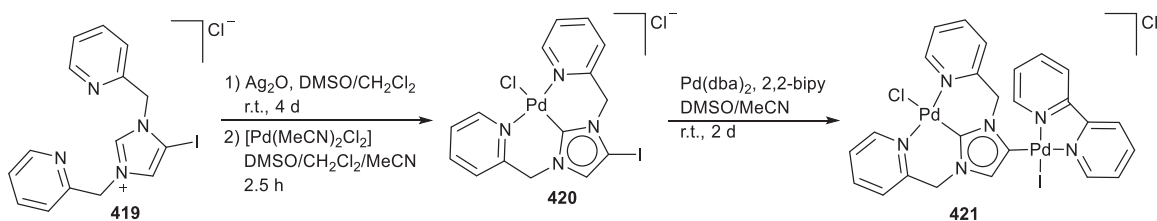
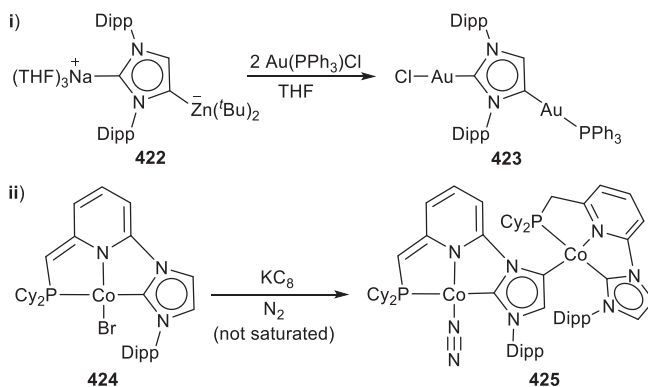


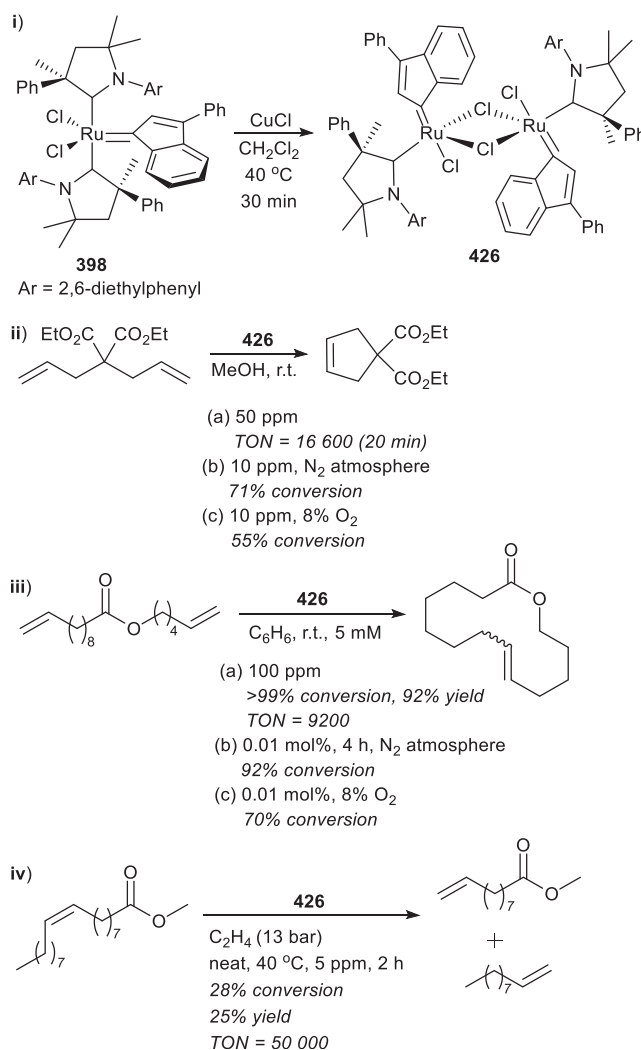
Fig. 11 Common bonding modes for homonuclear multimetallic complexes of the non-classical heteroatom stabilized carbenes.



Scheme 52 Stepwise preparation of homobimetallic NHDC complex of Pd<sup>II</sup>.



Scheme 53 Targeted and unanticipated homobimetallic NHDC complex formation.

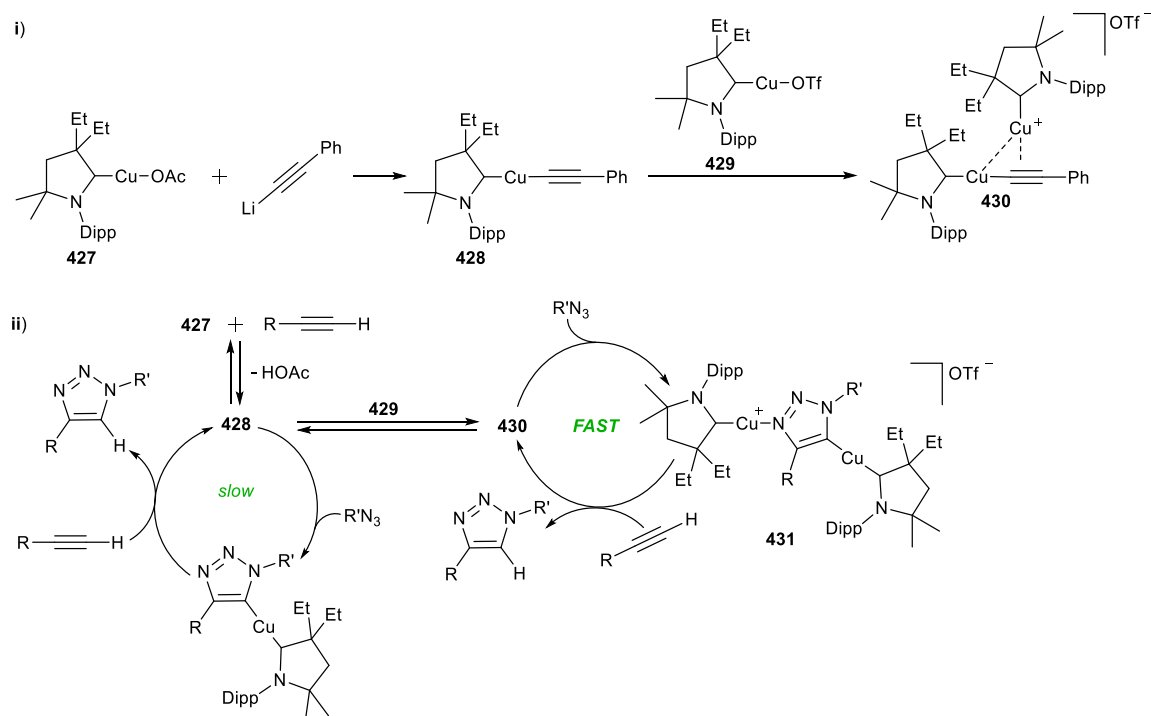


**Scheme 54** (i) Synthesis and application of the Ru(CAAC)(indenylidene) dimer as RCM (ii and iii) and (iv) ethenolysis catalyst precursor.

or maintain proximity of the metals by facilitating metal- $\pi$ -aryl interactions of CAAC-substituent to the transition metal,<sup>384,385</sup> or dimerization with labile bridging halides or hydride X-type ligands.

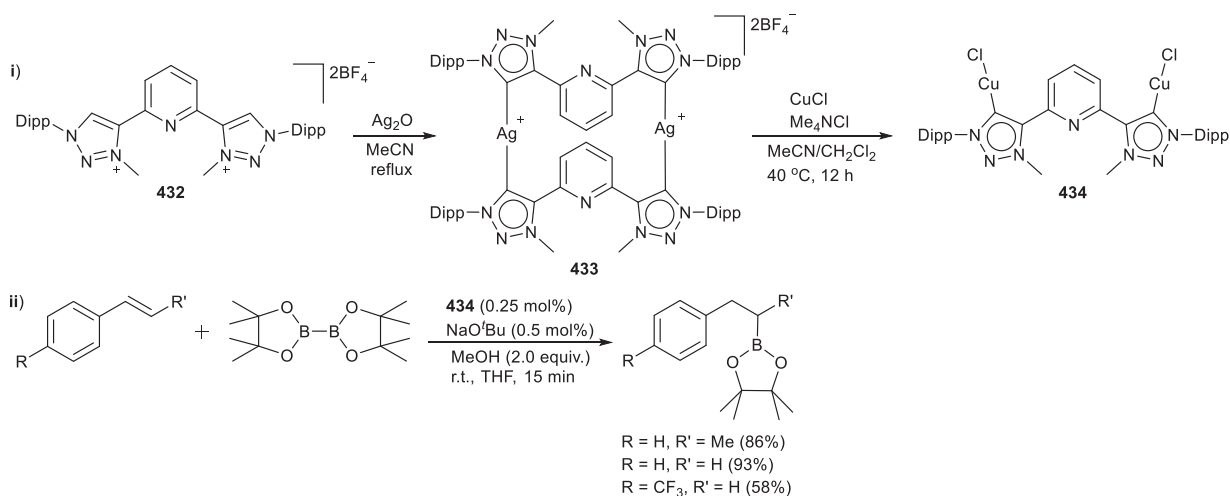
Catalytic applications of the homobimetallic CAAC complexes are limited. One example is the Ru<sup>II</sup> indenylidene CAAC dimer 426 (Scheme 54, i),<sup>389</sup> employed as a Grubbs type olefin metathesis catalyst (see Section 1.05.4 above).<sup>352</sup> The dimer 426 could outperform the monomeric analogs at a very low catalyst loading (0.005%) in the RCM of diallyl malonate (Scheme 54, ii), while excellent selectivity was seen in macro-RCM to yield the exaltolide precursor with no trace of oligomerization (Scheme 54, iii). The increased initiation rate and productivity of these reactions were ascribed to the lability of the bridging chloride, while the stability of the catalyst towards oxygen in these processes was simultaneously attributed to the lack of vacant coordination sites in the dimer.<sup>388</sup> Similarly, the dimer compared favorably with monometallic catalysts for the ethenolysis reaction (Scheme 54, iv), although catalytic activity was demonstrated as being predominantly reliant on ethylene pressure.<sup>389</sup>

Considering the widespread utility of the copper-catalyzed azide-alkyne cycloaddition (CuAAC)<sup>394,395</sup> as the premier example of a 'click' chemistry reaction,<sup>396,397</sup> it is not surprising that copper(I) NHC complexes were explored early on as click catalysts.<sup>398–401</sup> Mechanistic studies by Fokin et al. identified cationic  $\pi,\sigma$ -bis(copper) acetylide complexes as the catalytically active species,<sup>402</sup> but it was not until the group of Bertrand employed a stabilizing CAAC ligand that the isolation of this reactive dinuclear species 430 could be realized from the reaction of the monomeric CAAC-copper(I) acetylide 428 with the related CAAC-copper(I) triflate 429 (Scheme 55, i).<sup>385</sup> They went on to demonstrate that although both monomeric 428 and dinuclear 430 are active in the dipolar cycloaddition catalytic cycle, the 430 cycle is the kinetically favored pathway (Scheme 55, ii). Importantly, though, it was found that the use of the weakly coordinating triflate ligand is key to the observation of the bis(copper) 430 as well as the newly elucidated bis(copper) triazole complex 431 as catalyst resting state (Scheme 55, ii). Incoming substrate alkyne protodemetalates 431 to regenerate 430, as the step in the catalytic cycle that excludes 428 from the preferred pathway.



**Scheme 55** (i) Preparation of active click catalysts **428** and **430**, and (ii) mechanistic pathway elucidated with the isolation of intermediate **431**.

Copper(I) complexes of other nonclassical carbenes, especially  $\text{Cu}^{\text{I}}$  bis(trz) complexes have been increasingly reported for application in molecular catalysis, with the prevalence of metal cooperativity for this coinage metal on the rise. The catalytic applications range widely, extending from catalytic hydroboration of styrene with commercial boranes<sup>373</sup> to the development of new click catalysts.<sup>370,372,377</sup> Synthetic approaches include bonding motifs (vi)–(viii) as shown in Fig. 11. The bistriazolium salt **432** with a bridging 2,6-pyridylene linker attached to the respective C4-positions of the triazoles could be metalated with  $\text{Ag}_2\text{O}$  to yield the homoleptic dinuclear silver(I) dimer **433** (Scheme 56, i).<sup>373</sup> Following transmetalation from the silver(I) complex as carbene transfer agent, the dinuclear dicopper(I) complex **434** could be isolated. Stepwise copper-based oxidation events were observed during cyclic voltammetry experiments as an indication of an expanded  $\pi$ -conjugated triazolylidene ring system of the pyridine-bridged ligand. Utilizing this complex **434** as catalyst in the hydroboration of *trans*- $\beta$ -methylstyrene with bis(pinacolato)diborane allowed for the  $\beta$ -selective formation of 1-methyl-2-phenylethylboronate (Scheme 56, ii), while the reaction with the corresponding *cis*-styrene substrate did not occur. However, despite the electrochemical suggestion of metal-interaction, no evidence for multi-nuclear cooperativity was evidenced in the catalytic reaction.

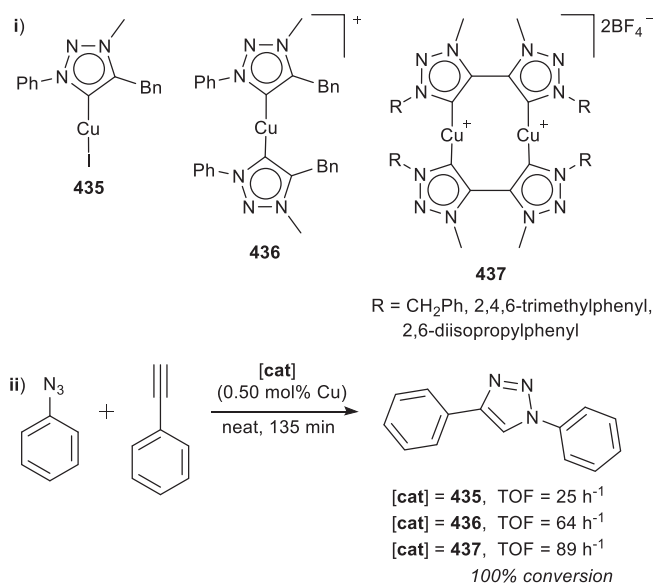


**Scheme 56** (i) Preparation of pyridyl-bridged bistriazolylidene dicopper **434**, and (ii) its application as catalyst for styrene hydroboration.

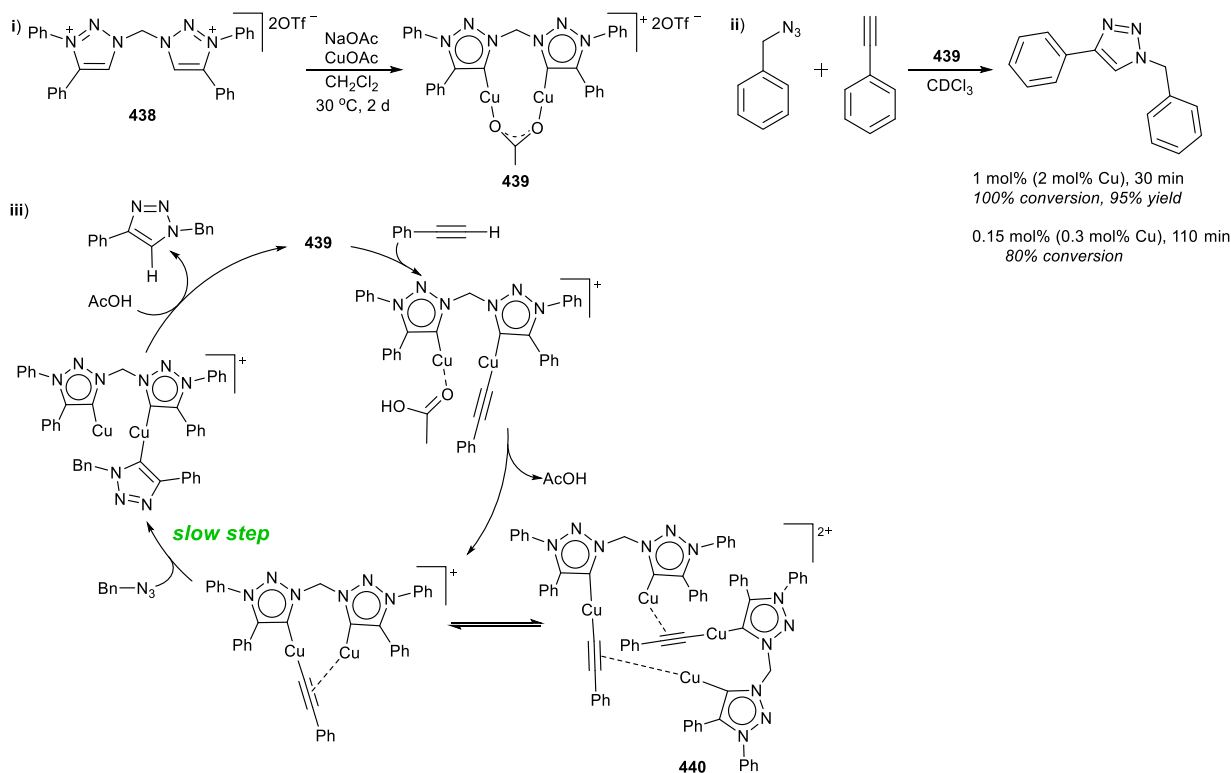


Exploitation of Cu<sup>I</sup> trz complexes as click catalysts progressed a couple of years after the development of the NHC catalysts with comparative activity for the mesoionic carbene catalyst precursors.<sup>253,403–405</sup> However the initial reports focused mostly on mononuclear catalysts and examples of well-defined dicopper catalysts are scarce in the literature, despite the highlighted role played by dinuclear catalytic intermediates.<sup>406</sup> This lack was addressed by Sarkar et al. in preparing a dicopper bis(*i*-bitz) complex **437** for direct comparison with the catalytic activity of the monomeric catalyst precursors, the neutral halido-substituted complex trz-Cu<sup>I</sup> **435** or the cationic bis(trz)-Cu<sup>I</sup> **436** (Scheme 57, i).<sup>377</sup> The use of the *i*-bitz ligand, directly linking the C4-positions of two trz, positions the two copper metal centers in close proximity (2.8–2.9 Å) in the 10-membered metallacycle formed by the bridging of two *i*-bitz ligands. Substrates phenyl azide and phenyl acetylene were employed in the benchmark click reaction to prepare 1,4-diphenyl-1*H*-1,2,3-triazole and the less sterically hindered *N*-benzyl substituted **437** proved to be the most active of the series of dicopper complexes (Scheme 57, ii). Comparison of this catalyst precursor with the monomeric catalysts **435** and **436** under the same conditions (room temperature, neat, with a total metal mol% catalyst loading of 0.50%) demonstrated significantly improved activity, with a TOF of 89 h<sup>-1</sup> for the dicopper **437** after 135 min reaction time, compared to TOF = 25 h<sup>-1</sup> for **435** and 64 h<sup>-1</sup> for **436**. Kinetic NMR experiments were conducted to investigate the indicated metal cooperativity. A reaction order of 1 with respect to the catalyst points to the involvement of a dinuclear species in the catalytic cycle, while the disappearance of the acetylene C–H, and the appearance of the bis(triazolium) acidic C–H proton chemical resonances lead to the hypotheses of Cu–C<sub>carbene</sub> bond breaking for two of the Cu–trz bonds (of the same *i*-bitz ligand), to generate the ligand precursor. The postulated catalytically active species therefore still contains one bridging *i*-bitz ligand linking the two copper(I) metal centers, while the demetalated *i*-bitz acted as an internal base to deprotonate the alkyne to yield the expected Cu-acetylide, in accordance with the known mechanism. The catalytic reaction is efficient for the cycloaddition of a wide range of alkene and azide substrates, with even the most sterically hindered substrates showing improved conversions compared to the known monomeric copper-catalyzed reactions.<sup>404,405</sup>

With the knowledge in hand that Cu–trz bond breaking (× 2) is likely for the cationic dicopper complexes containing two bridging bis(trz) ligands (**437**), as well as the importance of a weakly coordinating acetate ligand for the formation of the proved dicopper catalytic intermediates,<sup>386,406</sup> the group of Sarkar continued their investigations by preparing another trz-supported dicopper click catalyst (Scheme 58, i).<sup>372</sup> A bis(trz) ligand containing an N1-methylene linker (**438**) binds to two copper(I) metal centers, supporting the bridging of the labile acetate ligand that can act as an internal base in complex **439** (Scheme 58, i). The μ-OAc forces the copper metal centers into a spatial arrangement such that the Cu–Cu distance of 2.76 Å is smaller than the sum of the Van der Waals radii of two copper centers, thus the short distance is not necessarily an indication of cuprophilic interactions. The benchmark reaction in this case employs substrate phenyl acetylene again, alongside the less bulky benzyl azide. The complex is a very active catalyst with complete conversion (and 95% isolated yield for the triazole product) in 30 min with 1 mol% catalyst loading. Kinetic experiments for full mechanistic elucidation also indicated the catalyst efficiency, with complete conversion observed with a catalyst loading of 0.15 mol%, and 80% completion within 110 min as tribute to unprecedented efficiency for dilute click reactions. The kinetic NMR measurements demonstrated an overall first order reaction, but yielded an estimated catalyst order of 0.87. Subunity reaction orders are usually attributed to fast and reversible formation of an inactive catalytic intermediate.<sup>407–409</sup> In addition, it was determined that the azide substrate participates in the slowest step of the catalytic cycle, but not the alkyne – contrary to some literature reports.<sup>385,410,411</sup> A modified catalytic cycle was therefore postulated, with equilibration of the σ,π-dicopper acetylide key



**Scheme 57** (i) Synthesis and (ii) benchmark activity of neutral mononuclear, and cationic mono- and dinuclear copper(I) trz complexes as click catalysts for triazole preparation.

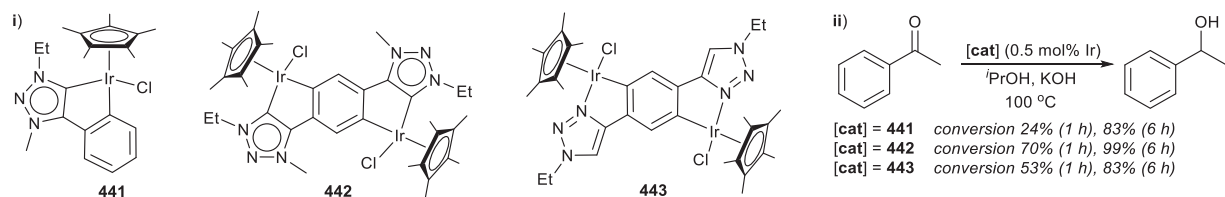


**Scheme 58** (i) Synthesis, (ii) catalytic performance and (iii) postulated mechanism for bis(triazolylidene) dicopper acetate click catalyst precursor.<sup>372</sup> Modified from Beerhues, J.; Fauché, K.; Cisnetti, F.; Sarkar, B.; Gautier, A. *Dalton Trans.* **2019**, *48*, 8931–8936.

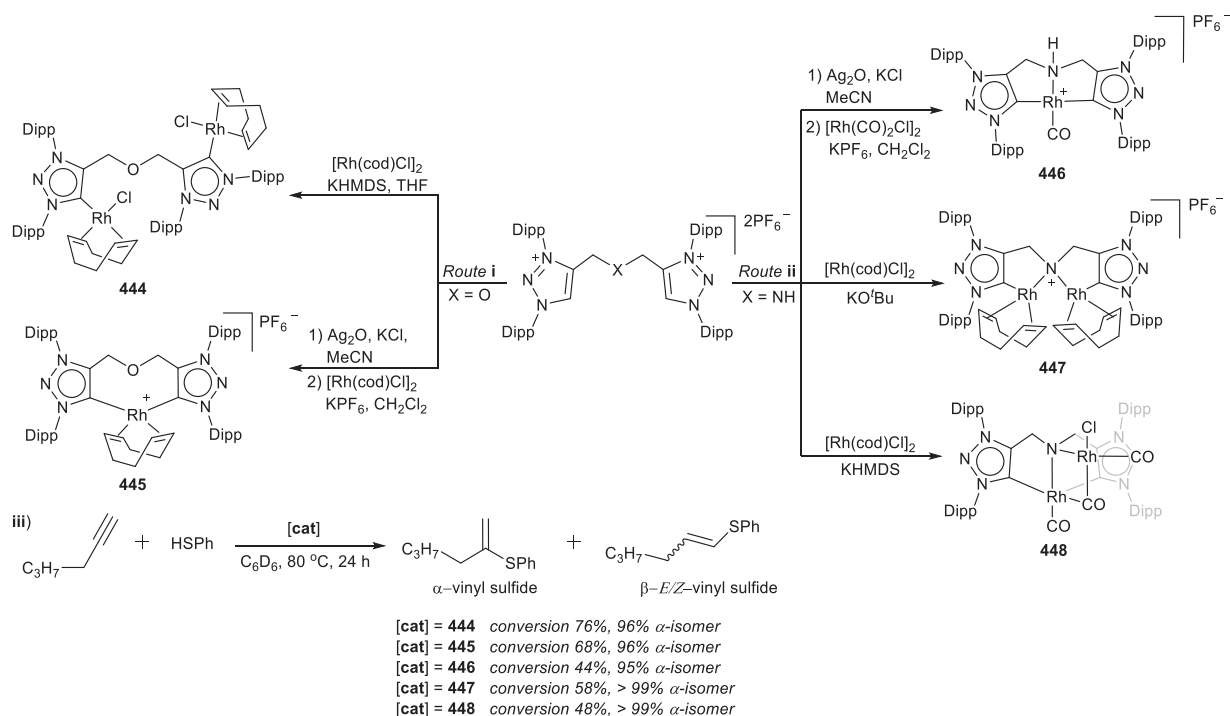
intermediate to an inactive  $\sigma,\pi$ -bis(dicopper acetylide) dimer **440** (Scheme 58, iii). The rate-determining step in this cycle is the formation of the copper-triazolide before the final step of protodemetalation by the acetic acid. Further developments in the click methodology by the same group, namely (di)copper trz complex catalysts for halo-click reactions that utilize halo-alkynes, have on the other hand, been shown not to demonstrate any observable benefit for the incorporation of two metal centers compared to the mononuclear catalyst precursors for this modified click reaction.<sup>370</sup>

The success of cyclometalated trz-Ir complexes as WOCs (see Section 1.05.2) prompted investigation of other catalytic reactions. A C,C-dicyclopentylated Ir<sup>III</sup> complex (**442**) of a bis(trz) ligand featuring a C4,C4-phenylene group was published, together with its mononuclear analog **441** (Scheme 59, i).<sup>375</sup> The central phenylene in **442** both connects the two Ir<sup>III</sup> moieties as a spacer group and facilitates *ortho*-cyclometalation on each iridium center with the addition of sodium acetate during the transmetalation reaction from the Ag<sup>I</sup> precursor to Ir<sup>III</sup> (unlike the bis-C4-phenyl-trz Ir<sup>III</sup> WOC catalysts prepared in the absence of base).<sup>371</sup> The related bis-triazole complex **443** with C,N-dicyclopentylated Ir<sup>III</sup> metal centra was prepared for comparative reasons. Potential cooperativity was investigated in the catalytic transfer hydrogenation of benzaldehyde and acetophenone with sacrificial hydrogen donor isopropanol. For both reactions, the dinuclear C,N-dicyclopentylated complex **443** displayed higher activity than the mononuclear complex **441**, and even higher conversions for the reactions were obtained for the C,C-dimetalated phenylenebis(trz) complex **442** (Scheme 59, ii).

A series of mono- and dinuclear Rh<sup>I</sup> complexes were prepared from a COC- and a CNC-pincer proligand, containing either an ether or amine-linker, respectively. The latter serves as both spacer group and heteroatom-donor in the case of the CNC-bis(trz) ligand (Scheme 60, ii).<sup>204</sup> The complexes displayed diverse coordination modes, ranging from bridged dinuclear (**444**) to chelated dinuclear (**445**) complex geometry for the bidentate COC-ligand, while versatility of the CNC-ligand yielded a mononuclear pincer complex of Rh<sup>I</sup> with a tridentate ligand (**446**), a bischelated dinuclear complex with a tetradentate ligand (**447**), or a pincer Rh<sup>I</sup>



**Scheme 59** (i) Mono- and dinuclear C,C-dicyclopentylated Ir<sup>III</sup> complexes for (ii) transfer hydrogenation of acetophenone.



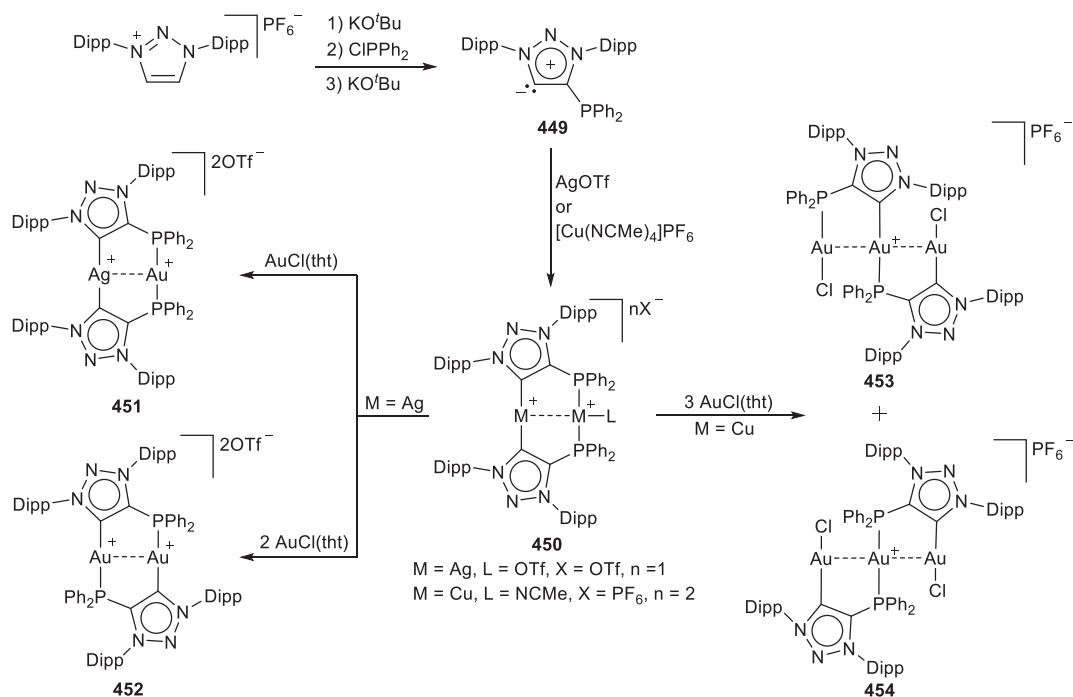
**Scheme 60** Preparation of mono- and homobimetallic Rh<sup>I</sup> complexes with (i) COC- and (ii) CNC-bistriazolylidene ligands, as (iii) selective alkyne hydrothiolation catalysts.

complex bridging a second metal center (**448**). The role of the mono- vs dinuclear complexes, N- vs O-functionalized triazolylidene and chelating vs bridging ligands were investigated for selective alkyne hydrothiolation.<sup>374</sup> In all cases, excellent selectivity (> 95%) for the α-vinyl sulfide product was obtained in the benchmark reaction of thiophenol with 1-hexyne (**Scheme 60**, iii). For the same catalyst (metal) loading, increased conversion was observed for the homobimetallic **444** with an ether-bridge, compared to its chelated mononuclear analog **445**. **444** also outperformed all the CNC-complexes **446–448**, even in the absence of a hemilabile, basic N-donor group that can assist with substrate thiol deprotonation/activation. This result, coupled with the observation that a decrease in selectivity for the α-isomer was observed when the ancillary cod-ligands were substituted with π-acid carbonyls, points to an alternative catalytic mechanism for these complexes as compared to the non-oxidative route (**Scheme 26**, vide supra).<sup>187</sup>

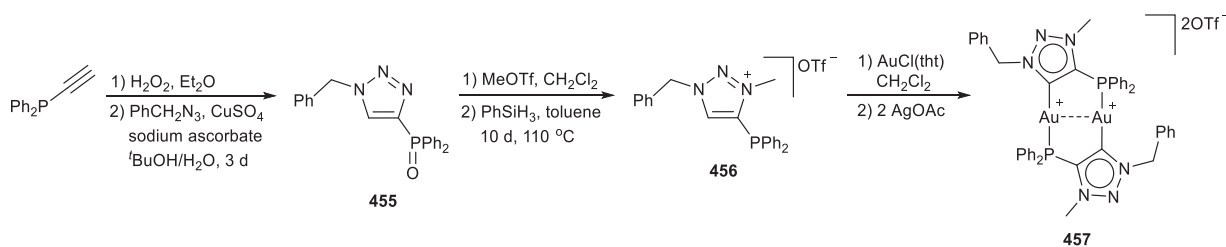
The inclusion of another donor group, namely a phosphino group on the C4-trz position, has also recently been utilized for the preparation of not only homobi- but also heterobi- and trimetallic metal complexes (**Fig. 11**, xi).<sup>378</sup> The 4-phosphino-1,2,3-triazolylidene ligand was found to be thermally stable and could be isolated as the free carbene **449** (**Scheme 61**), in contrast to its normal N-phosphinoimidazol-2-ylidene<sup>412–414</sup> and abnormal imidazol-5-ylidene counterparts.<sup>415</sup> Coordination to the coinage metals (Cu, Ag, Au) afforded not only the formation of the expected head-to-head homobimetallic complexes **450**, but transmetalation to gold(I) from the Ag<sup>I</sup> **450** yielded a heterodinuclear Ag<sup>I</sup>–Au<sup>I</sup> complex **451** or a head-to-tail homobimetallic Au<sup>I</sup> complex **452**, while the corresponding transmetalation from Cu<sup>I</sup> **450** gave rise to trinuclear Au<sup>I</sup> complexes **453** and **454**.<sup>378</sup> In addition, computational studies indicated increased nucleophilicity for both the carbon and the phosphorous atoms of the free carbene ligand **449** by way of increased energy of the occupied frontier orbitals, although this feature is yet to be exploited in catalytic reactions.

The N3-alkylated analog **456** of **449** was prepared by using a bottom-up approach in building a triazole **455** functionalized with the same phosphino group (**Scheme 62**).<sup>416</sup> Metalation with gold(I) led to formation of homobimetallic **457** as analog of **452**, displaying the same supported aurophilic interactions as enforced by the rigid scaffold and spatial proximity of the donor sites,<sup>417</sup> accompanied by yellow phosphorescence that was tentatively assigned to free (or delocalized) excitons related to molecular chain formation in the solid state.

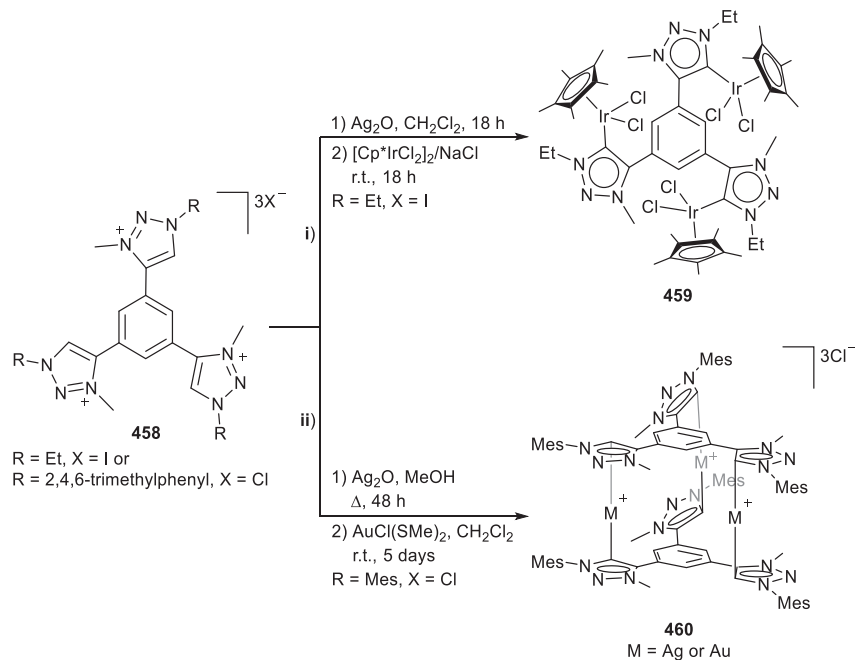
Utilization of a central phenylene-linker as strategy to develop trimetallic complexes is a common alternative to the use of heteroatom-donor to increase complex nuclearity (**Fig. 11**, xii). This route has been followed with success to prepare tris(triazolium)phenyl ligand salts where the triazole is bound to the phenyl spacer on the C4-ring position either directly<sup>418,419</sup> (**Scheme 63**, i and ii), or connected by a methyleneoxy-bridge (**Scheme 64**, i).<sup>300,420,421</sup> The first methodology has been followed to prepare Ir<sup>III</sup> complex **459** for catalytic transfer hydrogenation (**Scheme 63**, i), where di- or trimetallic complexation is dependent on the base employed during synthesis and metalation.<sup>418</sup> However the steric bulk surrounding the central benzene ring precludes the possibility of *ortho*-cyclometalation as seen for the dinuclear derivative **442** (**Scheme 59**, i),<sup>375</sup> and the lack of cooperativity observed in the catalytic reactions was ascribed to the corresponding reduction of electronic interaction of the non-cyclometalated Ir<sup>III</sup> centra of



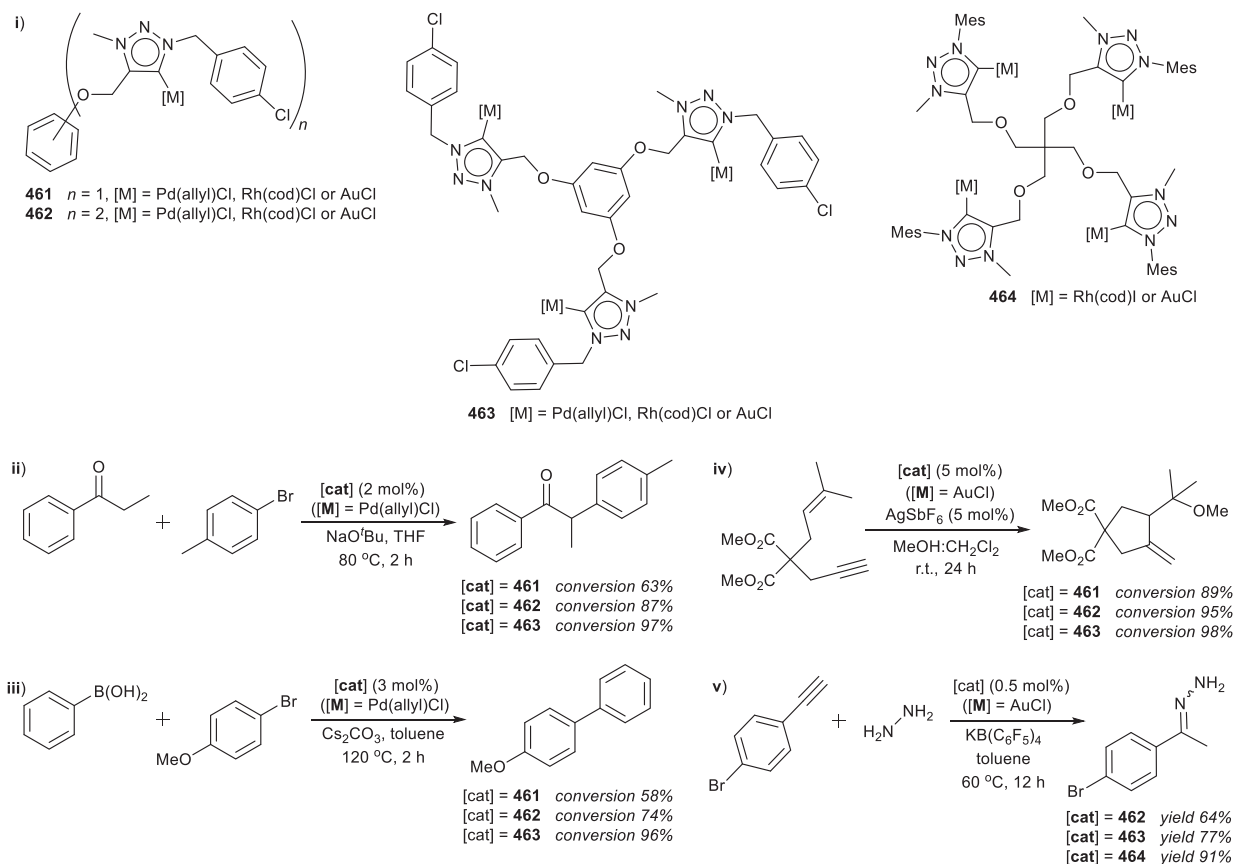
**Scheme 61** Synthesis and versatile coordination of a phosphino-trz for the preparation of di- and trinuclear group 11 metal complexes.



**Scheme 62** Preparation of phosphino-trz gold(I) derivative from a phosphino-alkyne click-precursor.



**Scheme 63** Preparation of trinuclear metal complexes from a tris(triazolium)benzene ligand precursor.



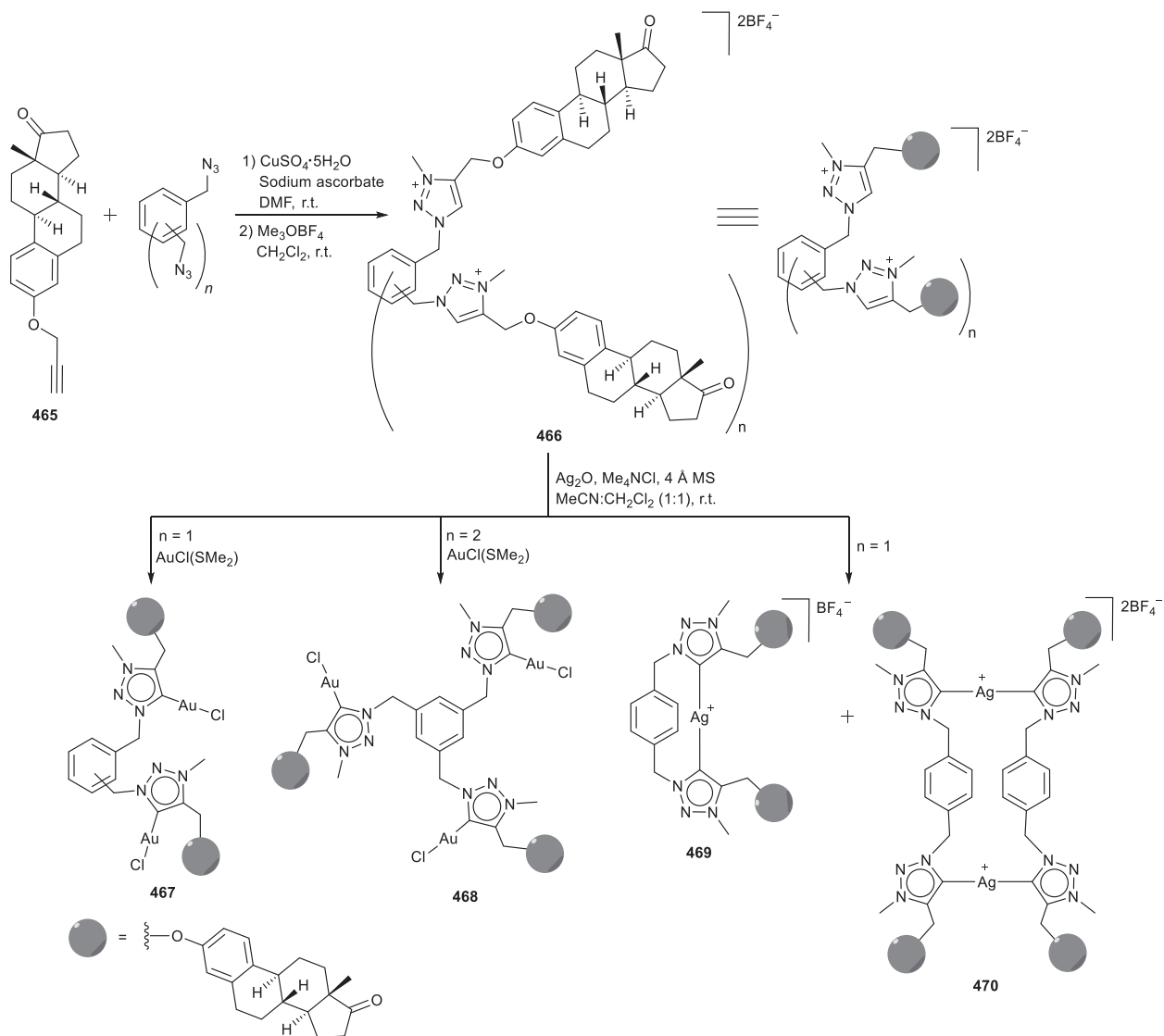
**Scheme 64** (i) Mono- to tetrametallic trz complexes and their comparative catalytic performance in palladium-catalyzed coupling reactions (ii and iii), gold-mediated intramolecular enyne cyclization (iv and v) alkyne hydrohydrazination.

459. Tris(triazolium) salts of this type has also been investigated as potential anion receptors, while reaction with a silver(I) precursor (and subsequent transmetalation with Au<sup>I</sup>) forms a prismatic trinuclear cage with the metal cations sandwiched between two tridentate tris(trz) ligand scaffolds (460, **Scheme 63**, ii).<sup>419</sup> The coordination occurs via a metal-controlled self-assembly to yield exclusively the cylindrical coordination cages 460 as reaction products. The phenoxy-linked trz ligands (**Scheme 64**, i) could be modified by including either one, two or three O-methylene triazolium groups on the phenyl-spacer to prepare the corresponding mono- (461), di- (462) or trinuclear complexes (463) of group 9–11 transition metals.<sup>300</sup> NMR studies indicated complete symmetry for the trinuclear complexes. Synergistic multinuclear effects in catalytic reactions were probed for both palladium-catalyzed carbon-carbon bond formation ( $\alpha$ -arylation of propiophenone with aryl bromides, **Scheme 64** (ii) and Suzuki-Miyaura coupling of aryl bromides and boronic acids, **Scheme 64**, iii), as well as intramolecular alkyne cyclization catalyzed by gold(I) (enyne methoxycyclization, **Scheme 64**, iv). In all cases, enhanced catalytic performance was seen, increasing successively from the mono- to di- to trinuclear catalysts. Replacement of the central rigid aromatic linker with a flexible aliphatic group (central quaternary carbon with four methyleneoxy-connected triazolium rings derived from a pentaerythritol scaffold) provides for extension to tetranuclear complexes 464 (**Scheme 64**, i) to be exploited in Rh<sup>I</sup><sup>422</sup> or Au<sup>I</sup>-mediated catalysis.<sup>423</sup> As for the trinuclear complexes, improved catalyst performance suggestive of cooperative effects was evident for both the rhodium(I) and gold(I) tetrametallic complexes, in benchmark catalytic reactions, e.g. Rh<sup>I</sup>-catalyzed alkyne hydrosilylation or Au<sup>I</sup>-catalyzed alkyne hydrohydrazination (**Scheme 64**, v).

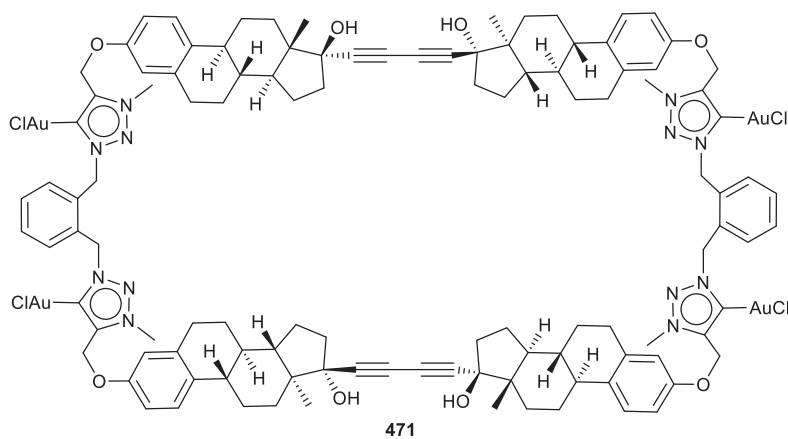
A combination of the preceding construction motifs can be employed to prepare bi- and trimetallic gold(I) or silver(I) steroid-derived trz, or even a tetrametallic trz steroid macrocycle.<sup>424</sup> Click-reaction of 3-O-propargylestrone 465 with a di- or tri-azidomethylene-functionalized benzene followed by triazole alkylation (466) and metalation yield the corresponding symmetrical gold complexes with the central phenylene linker 467 and 468, while biscarbene formation with silver delivers the metallacyclic compounds 469 and 470 (**Scheme 65**). If a functionalized phenylene is not employed as the core but rather a macrocyclic tetrakis-triazolium salt containing four steroidal spacers linked by a dialkyne, then incorporation of four gold carbene functionalities in the framework producing the stereoidal cavity is possible (471, **Fig. 12**) for potential biological and chiral catalytic activity.

Tridentate CNO-pincer ligands were prepared from imidazolium salts as precursors to Im<sub>4</sub> C-donors, with an N-CH<sub>2</sub>C(O)NHPh-OH substituent to provide the pendant N- and O-donor moieties.<sup>227</sup> For the imidazolium salts containing a C2-phenyl substituent, deprotonation and coordination to PdCl<sub>2</sub> proceeded smoothly to yield the unprecedented tetranuclear complexes





**Scheme 65** Polymetallic complexes of steroid-appended trz.<sup>424</sup> Modified from Frutos, M.; de la Torre, María C; Sierra, M. A. *Inorg. Chem.* **2015**, *54*, 11174–11185.

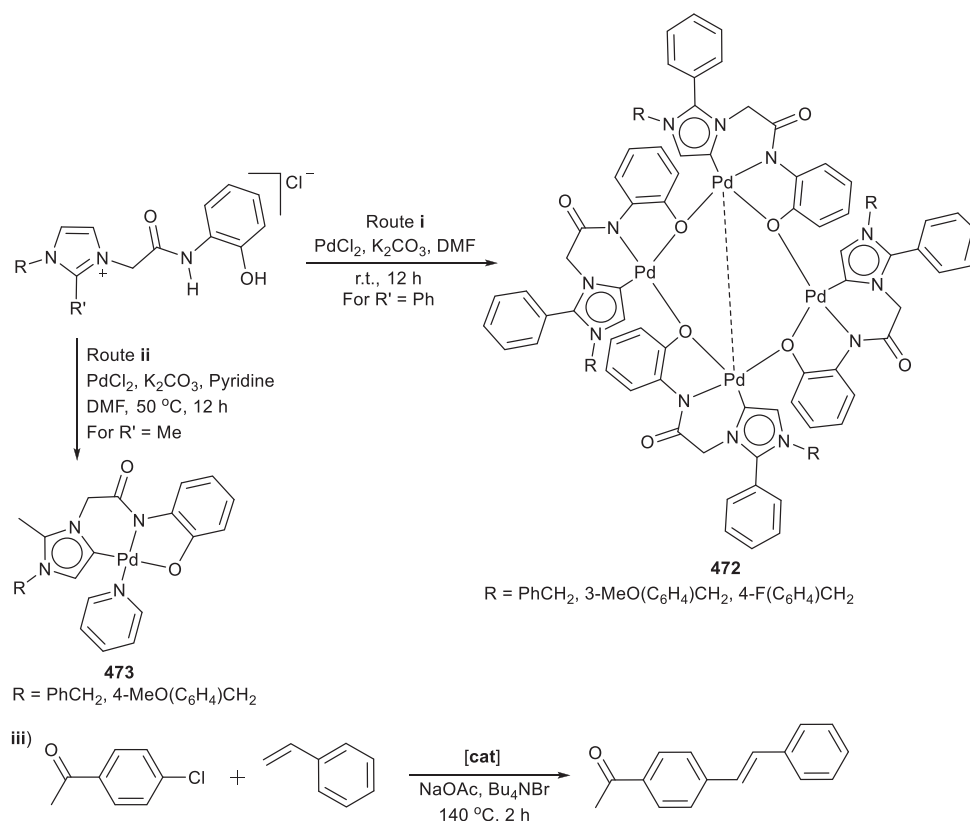


**Fig. 12** Gold trz embedded in a tetrametallic macrocyclic steroidal cavity containing four estrone nuclei.

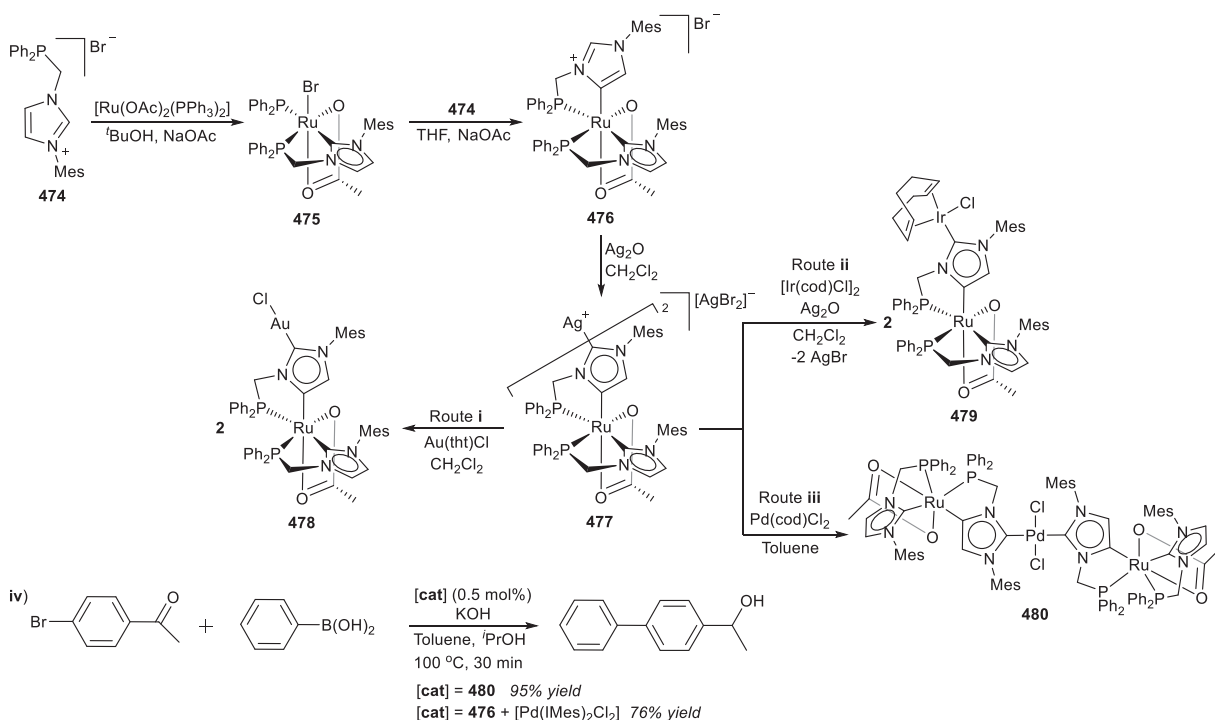
472 (Scheme 66, route i), as a first for Im4 palladium complexes (Fig. 11, xiii). In contrast, for the imidazolium salt containing a C2-Me group, only the mononuclear derivatives 473 were isolated (Scheme 66, route ii). The strongly electron-donating ability of the CNO-ligand is exemplified by the short Pd–C<sub>carbene</sub> bond distance observed (1.9308(8) Å), one of the shortest of those reported for palladium Im4 complexes (ranging from 1.951–2.022 Å).<sup>425,426</sup> Moreover, the  $\mu$ -phenoxide bridge was found to be stable even in the presence of PPh<sub>3</sub>, pyridine or at elevated temperatures.<sup>227</sup> The catalytic activity of the tetra- vs mononuclear complexes was evaluated in the Mizoroki-Heck reaction in ionic liquid medium. Only at very low catalyst loadings (0.1 mol% Pd and lower), did the multinuclear complexes demonstrate superior catalytic activity compared to the mononuclear analogs (Scheme 66, iii).

### 1.05.5.2 Heterobimetallic cooperativity

NHC ligands are an attractive choice as scaffold for the design of multinuclear architectures due to the ability to link not only two or more carbenes as C-donors to different metals separated by a spacer group, but also the ease of introduction of other donor functionalities tethered to either the ring-N or backbone-C to yield so-called hybrid ligands.<sup>427</sup> For imidazol-based heterocycles, these methodologies are very widely explored pertaining to traditional N-heterocyclic carbenes. For nonclassical Im4, incorporation of two different transition metals in a heteronuclear complex most often is based on the backbone metalation of an NHC to yield the formally anionic, ditopic NHDCs.<sup>380,428</sup> Reports detailing coordination of the C4- or C2-imidazolylidene position with non-transition metals (i.e. s- or p-block elements) are relatively common,<sup>429–439</sup> often displaying unpredictable reactivity.<sup>440,441</sup> However, NHDC complexes metalated with only d-block metals are less common, and only the reports by Kühn and Baratta et al. disclose coordination of two different metals.<sup>137,442,443</sup> Such an assembly of two distinct metal centers with varying functionality in electronic contact is of particular interest in cooperative catalysis, but this application is currently limited by the synthetic scope. The complexes are obtained by consecutive reaction of a Ru<sup>II</sup> precursor with two P-functionalized imidazolium salts (474), to coordinate first as an P,C-chelated NHC 475, and then as a P,C-chelated Im4 476 (Scheme 67). Subsequent metalation and transmetalation of the Im4 with silver(I) and then gold(I) precursors, yield the first example of complexes 477 and 478 bearing anionic dicarbene ligands connecting different transition metals (Scheme 67, route i).<sup>442</sup> The Ag/Ru bimetallic derivative 477 could be employed as precursor for transmetalation to iridium(I)<sup>137</sup> or palladium(II)<sup>443</sup> to yield complexes of the type 479 (Scheme 67, route ii) and 480 (Scheme 67, route iii), respectively. Electrochemical studies indicated pronounced metal interactions affecting



**Scheme 66** (i) Synthesis of tetra- and (ii) monopalladium(II) aNHC complexes and (iii) comparative catalytic performance in the Mizoroki-Heck coupling reaction.



**Scheme 67** Preparation (routes i–iii) and application (iv) of heteronuclear NHDC complexes in tandem Suzuki-Miyaura/transfer hydrogenation catalysis.

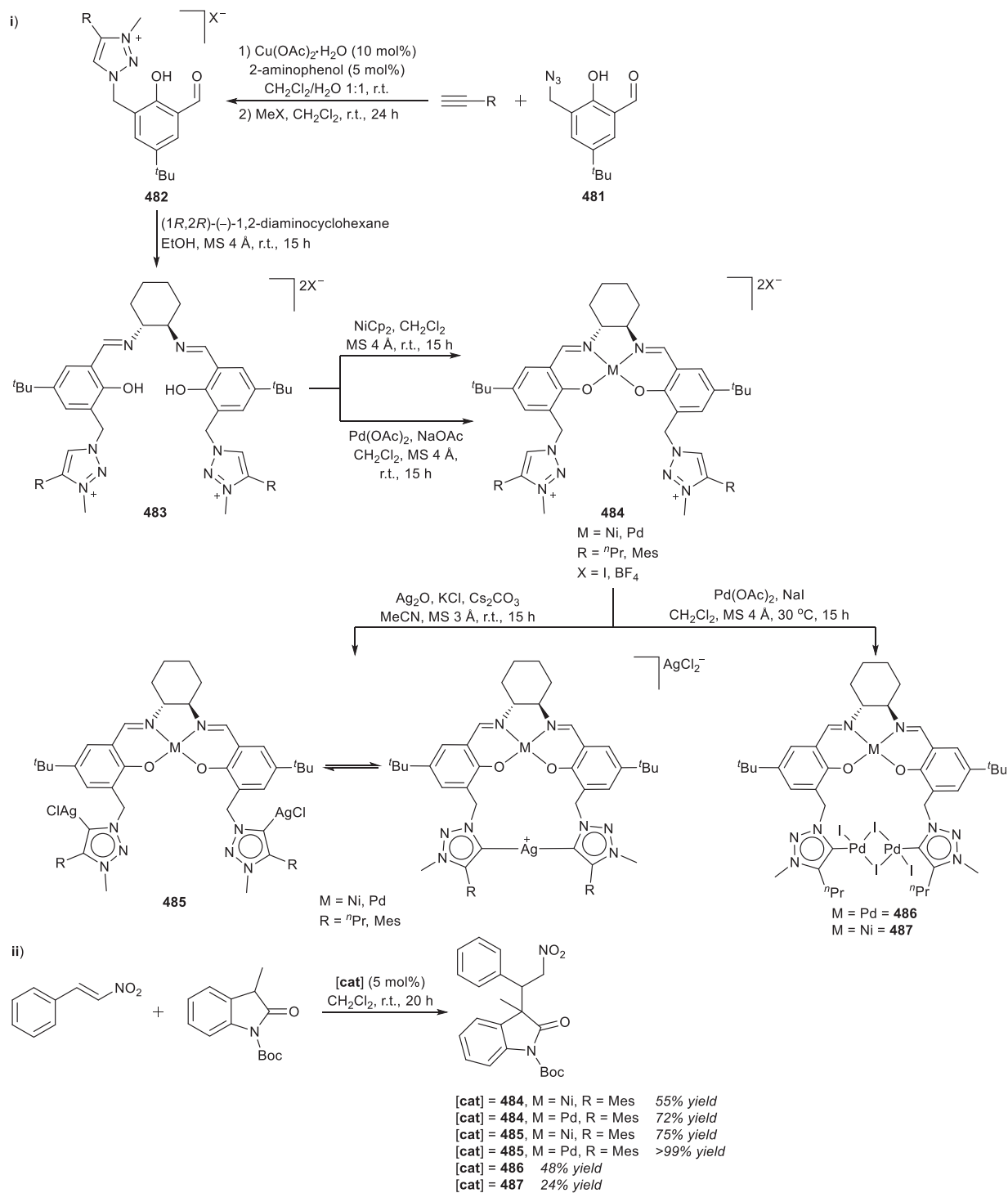
the redox behavior of the  $\text{Ru}^{\text{II}}/\text{Ru}^{\text{III}}$  for  $\text{Ru}/\text{Ir}$  479, however this did not translate to cooperative effects in the catalytic transfer hydrogenation reaction investigated for this heteronuclear complex. Dimeric complex  $\text{Pd}/\text{Ru}$  480, on the other hand, could be employed as a tandem Suzuki-Miyaura/transfer hydrogenation catalyst for bromoacetophenones and boronic acids to yield biphenyl alcohols (Scheme 67, iv). Moreover, 480 demonstrated enhanced catalytic performance compared to a combination of the related mononuclear ruthenium complex 476 and benchmark  $[\text{Pd}(\text{IMes})_2\text{Cl}_2]$  in the tandem catalytic reactions.<sup>443</sup>

Hybrid (multifunctional) ligands incorporating trz are accessible from click-chemistry approaches in a metal coordination sphere, whereby the cycloaddition of *coordinated* alkynes and azides give coordinated triazoles as precursor to the corresponding triazolylidene metal complex,<sup>444,445</sup> and can be extended to bimetallic complexes containing different metals connected to the C4- or N1-positions of the trz.<sup>446</sup> Alternatively, click reactions on functionalized scaffolds of ligand motifs such as salens, well known in homogeneous catalysis, can similarly produce hybrid ligands via consecutive metalations.<sup>447–450</sup> The group of Peters prepared hybrid salen-bis(triazolium) ligand precursors from a benzylic azide 481 and alkyne CuAAC reaction, followed by Schiff base condensation of reaction product 482 to yield proligand 483 (Scheme 68, i).<sup>451</sup> Selective metalation of the  $\text{N}_2\text{O}_2$  salen core (484) followed by sequential carbene metalation can be employed to yield either homo- or hetero- or trinuclear complexes 485–487 (Scheme 68, i). The catalytic 1,4-addition of an oxindole to a nitroolefin was studied in a preliminary investigation of the catalytic application of the hybrid complexes (Scheme 68, ii). The palladium complexes fared better, especially the heterodinuclear  $\text{Pd}/\text{Ag}$  complex 485, but decomposition of the trinuclear complexes 486 and 487 was observed under the given reaction conditions.

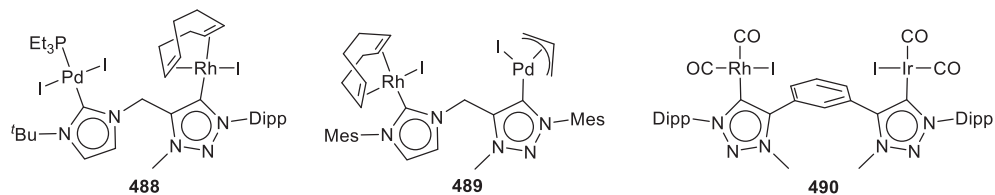
Hybrid NHC-trz ligands with a methylene linker for heterobimetallic complexes with unsymmetrical dicarbene ligands were developed not long after the first reports of trz as MICs, yet surprisingly few examples of these ligands bridging two different metals are known.<sup>452–454</sup> The first of these were reported in 2012 by Cowie et al. utilizing sequential metalations to form first the NHC-anchored/pendant-triazolium complex, after which a second metal center could be coordinated to the trz C4-position to give the  $\text{Pd}/\text{Rh}$  heterobimetallic complexes 488<sup>455</sup> or a more recent example, 489,<sup>456</sup> in addition to the known symmetrical dicarbene bis(trz) ligands that function as heterodinuclear bridge 490 (Fig. 13).<sup>457</sup>

### 1.05.5.3 Metal carbene complex heterogenization

Immobilization and other heterogenization strategies related to multinuclear cooperativity have been increasingly utilized over the past two decades in pushing the boundary of NHC transition metal complex application to heterogeneous catalysis and other material science applications.<sup>458–464</sup> For CAACs, Im4 and trz, these developments have been in the making only during the past 10 years, but interest is surging. The non-classical NHCs here play a role in furnishing a functional metal complex while also providing unique access to immobilization strategies. An example of remarkably improved catalytic performance by abnormal carbene ligand modification is observed when changing a peripheral N1-bound methyl in 170 to an N1-octyl group in 175, for the  $\text{Cp}^*\text{Ir}$



**Scheme 68** (i) Preparation of hybrid bis(trz)-salen mono- to trinuclear complexes and (ii) catalytic application in the 1,4-addition of oxindoles to nitroolefins.



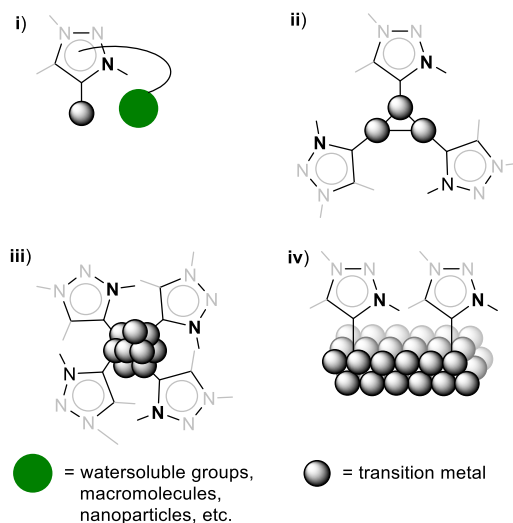
**Fig. 13** Bridging dicarbene ligands for heterobimetallic complexes.

complexes with C,N-cyclometalated trz-pyridyl WOCs (vide infra, Fig. 3).<sup>465</sup> The methyl-substituted complex 170 displays comparative activity in water oxidation to the most active known iridium-based WOCs with a  $\text{TOF}_{\text{max}} = 16\text{--}19 \text{ min}^{-1}$  and rate independence of the catalyst concentration and the nature and concentration of the sacrificial oxidant.<sup>466,467</sup> However, if CAN is employed as sacrificial oxidant with 175, the catalytic activity rate increases up to 10 times that of 170, and is reliant on both concentration of catalyst and oxidant. Kinetic studies revealed a bifurcation time where the activity of 175 increases substantially compared to 170, producing oxygen at a constant rate. Initially, this was presumed to indicate associated processes such as micelle formation facilitated by the amphiphilic nature of the octyl-substituted 175 inducing metal proximity for the rate-limiting O–O bond formation step. Diffusion NMR experiments showed that 175 exhibits only marginally higher self-aggregation tendency than 170, with an equilibrium between monomeric and dimeric species implicated from the measured aggregation numbers  $N = 1.4\text{--}2$ , with 175 having the higher  $N$ -value. If the self-aggregation studies were performed in the presence of the sacrificial oxidant CAN, oxidation of the Cp\* ligand is observed but the C,N-cyclometalated pyridyl-trz ligand remains bound to the iridium, presumably with bridging oxo or hydroxo-moieties as proposed by Crabtree.<sup>468</sup> In this case, larger aggregation numbers are obtained, but the absence of any particles in the 3–500 nm hydrodynamic radius supports the formation of oligomeric aggregates rather than any micellar assemblies. Thus, oxidative transformation of 175 with its longer alkyl chain leads to self-aggregation to yield a catalyst with uncommonly high activity.

In the case of heterogeneous catalysis effected by immobilization methodologies, water-solubilization strategies for biphasic catalysis or solvent precipitation/recyclability has often been implicated,<sup>469–472</sup> or immobilization of the complex metal atom/ion via coordination to a tethered, anchored carbene ligand,<sup>462,464,473,474</sup> or stabilization of elemental allotropes or small metal clusters to metal surfaces with carbene ligands.<sup>459,460,475</sup> The developments are discussed in this section based on the nature of the metal carbene ligand interaction – from molecular complexes with tethered ligands to surface stabilization of infinite metal atom arrays (Fig. 14). However, the carbene ligand commonly serves a stabilizing rather than a noninnocent role, and thus only some striking developments are highlighted here.

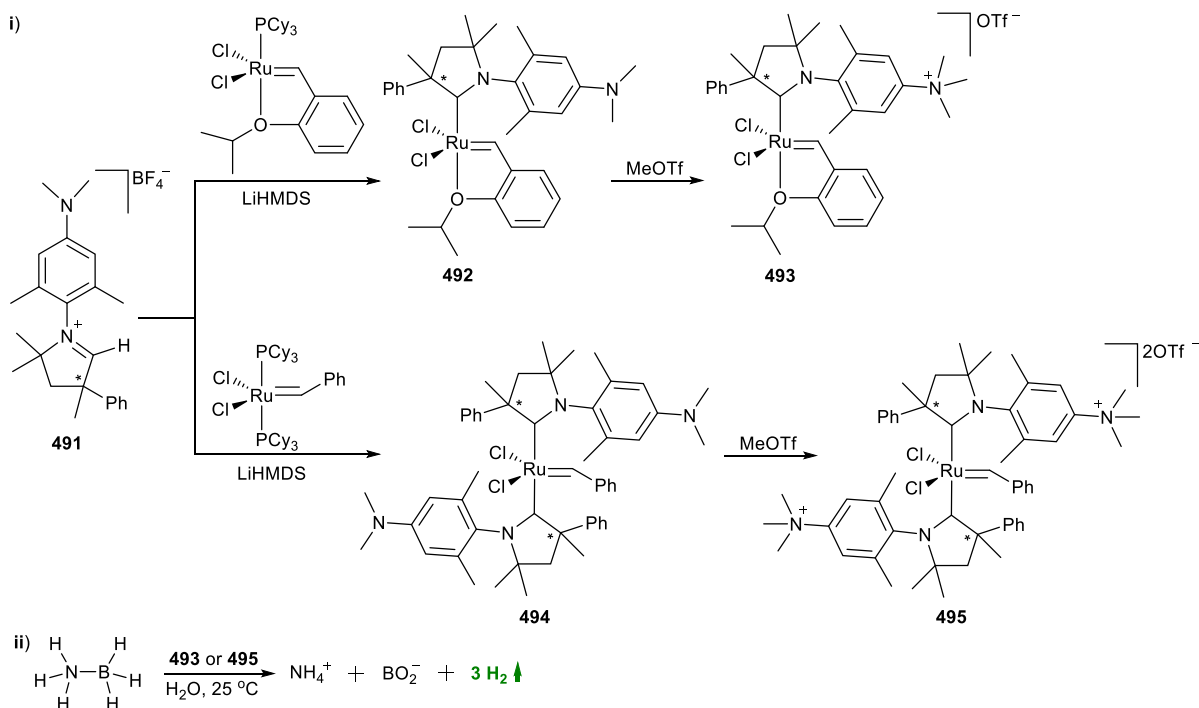
#### 1.05.5.3.1 Tethered nonclassical metal carbene complexes

Surprisingly few reports of the nonclassical carbenes under review describe the inclusion of charged polar groups like sulfonates or carbonates as pendant water-solubilizing moieties for catalytic activity in aqueous media.<sup>476</sup> One such report details the preparation of a CAAC ruthenium complex as biphasic olefin metathesis catalyst.<sup>477</sup> Unlike other CAAC ruthenium olefin metathesis catalysts like 396 and 398 (Scheme 50, i), CAAC salt 491 (Scheme 69, i) was tagged with an electrophilic amino substituent on the backbone. Thus, addition of MeOTf to the CAAC coordinated ruthenium complexes resulted in alkylation of the amino groups and formation of 493 and 495, from 492 and 494, respectively (Scheme 69, i). The highly polar functional groups render the ruthenium catalyst soluble in environmentally benign polar protic solvents, such as methanol, isopropanol, water and a mixture of methanol and water. It was further demonstrated that the ruthenium complexes were stable under atmospheric conditions and could catalyze various metathesis reactions. In the mentioned protic solvents, catalyst 493 and 495 could also furnish the metathesis reactions. Therefore, the synthetic methodology imparts high solubility to catalyst of industrial relevance,<sup>477</sup> and 493 and 495 were even determined to be active in the environmentally significant ammonia borane hydrolytic dehydrogenation yielding hydrogen in neat water.<sup>478</sup> The ammonia borane dehydrogenation reaction was catalyzed with a TON of 86,100, which equates to 1.70 kg H<sub>2</sub> released per 1 g ruthenium metal used (Scheme 69, ii).



**Fig. 14** Immobilization strategies for nonclassical carbenes: (i) Tethering to macromolecules e.g. polymers or solid support, stabilization of (ii) clusters, (iii) nanoparticles and (iv) surfaces.



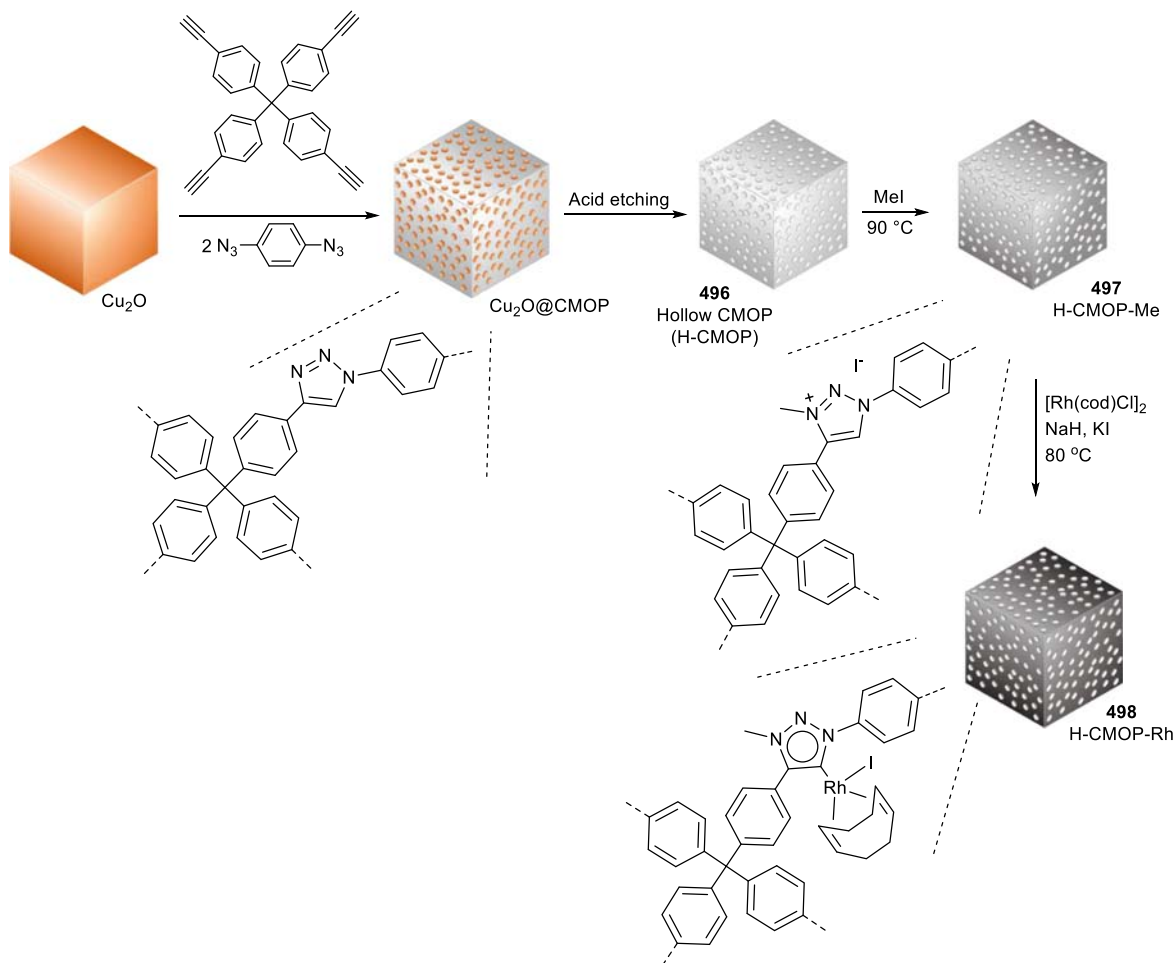


**Scheme 69** Polar functionalized tagged CAAC ruthenium complexes.

Functionalization of the nonclassical carbene ligand framework with (larger) molecular moieties also comprising ancillary applications is a well-known catalyst design strategy, and have included such diverse substituents as chrysin and coumarin<sup>479</sup> and carboranes.<sup>480–482</sup> Trz ligands that render catalytically active metal complexes are especially popular in this heterogenization methodology, as covalent linking facilitated by click-reactions to different support is facile. Tethering of carbene complexes to polymer supports is attractive as an immobilization strategy for scaffolds that are homogeneous in reactions but heterogeneous for recovery.<sup>483–485</sup> Such phase reversibility is mediated by polymers with switchable solubility, as observed for poly(quinoxaline-2,3-diyl)s (PQXs).<sup>486</sup> Moreover, the rigid helical rod-structure of the PQX polymer provides for a highly enantioselective chiral catalyst.<sup>487</sup> These advantages were combined with the ease of preparation and post-polymerization functionalization of macromolecules by CuAAC methodologies to yield macromolecular 1,2,3-triazole precursors to supported triazolydene metal complexes for chiral gold catalysis (see 378 and 380, **Scheme 47**).<sup>347</sup>

Exploitation of the facile CuAAC click reaction was similarly employed in the synthesis of N-doped carbon boxes from microporous organic polymers (MOPs).<sup>488</sup> Microporous organic network (MON) layers are formed on the surface of Cu<sub>2</sub>O nanocubes<sup>489</sup> by click reaction of tetra(4-ethynyl)methane (1 equiv.) with 1,4-diazidobenzene (2 equiv.), utilizing the copper surface of the nanocube as catalyst. The copper is etched out by treatment with hydrochloric acid to form hollow MON boxes 496 bearing triazole rings, which can then be alkylated to yield the corresponding triazolium species H-CMOPs (hollow click-based MOP) 497 (**Scheme 70**). Successive incorporation of rhodium is achieved by metalation of 497 with [Rh(cod)Cl]<sub>2</sub> in the presence of base NaH and KI, to generate H-CMOP-Rh 498 featuring trz coordinated rhodium(I) (2.2 mmol/g trz), as confirmed by NMR and X-ray photoelectron spectroscopy (XPS).<sup>490</sup> N<sub>2</sub> sorption studies showed that the surface area of 498 increases to 310 m<sup>2</sup>/g from 167 m<sup>2</sup>/g for 497, with a pore size volume of 0.55 cm<sup>3</sup>/g. Complex 498 can then be used as heterogeneous catalyst for the stereoselective synthesis of poly(-arylacetylene)s, in a rare example of a Rh-based heterogeneous catalytic system.<sup>491–495</sup> Utilizing an optimized catalyst load of 0.60 mol% 498, yields of 96% (*cis-trans* content 98%) was achieved.<sup>490</sup> If the conventional nonhollow spherical CMOP-Rh was employed, significantly impaired catalytic efficiency is observed due to reduced diffusion pathways of the reagents. The recyclability of 498 was illustrated in catalytic activity maintained for five cycles and is a good indicator for the usefulness of Rh-containing H-CMOPs in other catalytic reactions.

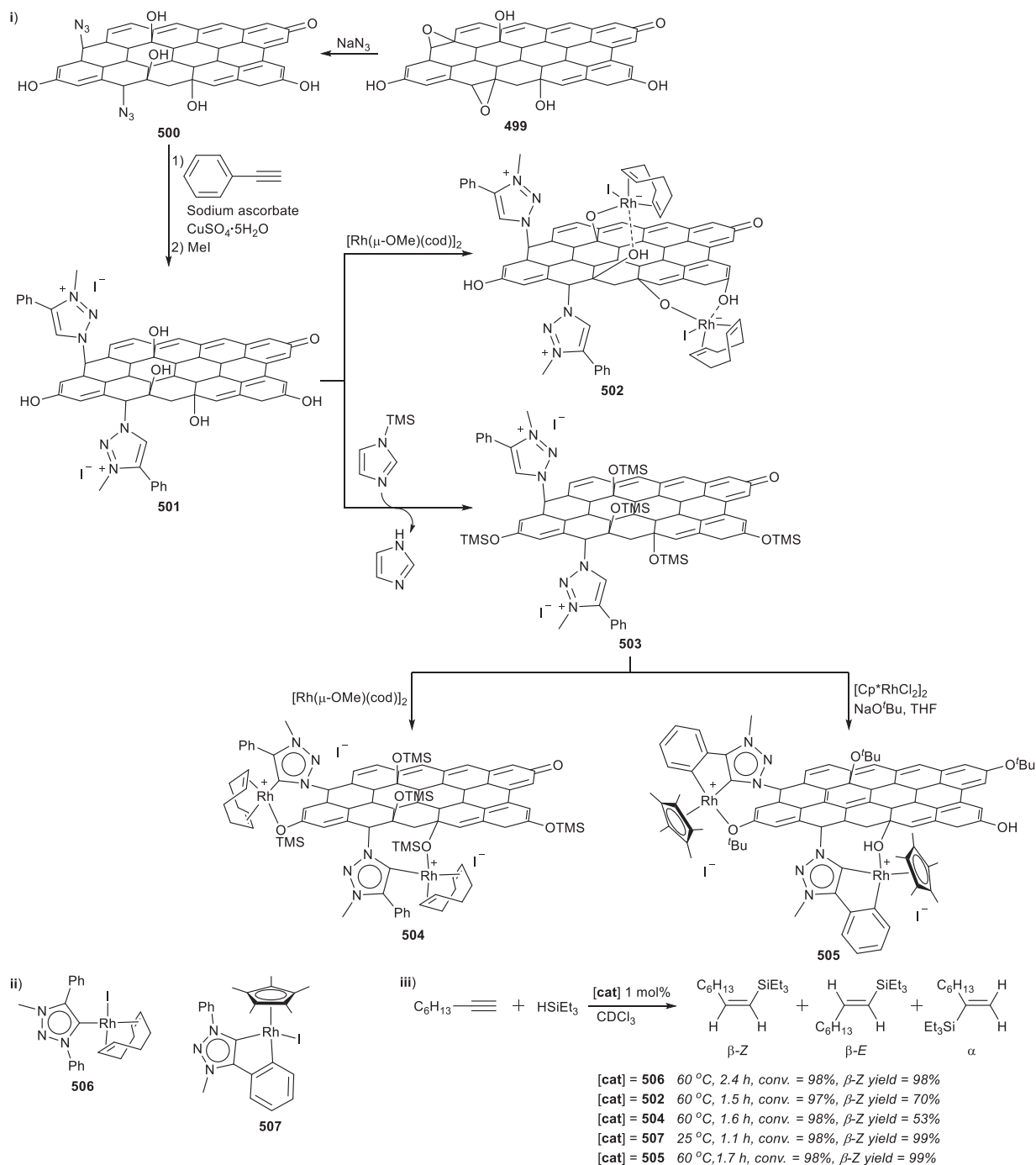
Covalent tethering of a catalytically active metal complex to a graphene material is a heterogenization strategy for designing hybrid catalysts, but is contingent on a simple method of covalent attachment. For nonclassical carbenes based on triazoles, CuAAC click-chemistry presents yet again a facile route towards anchoring triazolium groups on the carbonaceous surface of thermally reduced graphene oxide (TRGO) materials 499 via the abundant epoxy groups situated at the basal planes, as an alternative to functionalization of surface hydroxyl groups.<sup>496</sup> The 1,2-epoxide ring opening is mediated with sodium azide to give the azide-functionalized graphene material 500 which can then be treated with phenylacetylene in the presence of sodium ascorbate and copper(II) sulfate catalyst for the click-reaction (**Scheme 71**, i). The resultant 1,2,3-triazole surface can be reacted with methyl iodide to quaternize the triazol-N1 atoms to yield surface 501 decorated with triazolium groups, in addition to free hydroxyl groups. The amount of ligand introduced in the graphene sheet was quantified as 5.8 wt% by means of TGA. If 501 was directly reacted with



**Scheme 70** Preparation of heterogeneous Rh<sup>I</sup> polymerization catalysts from templated Cu<sub>2</sub>O nanocubes to give hollow click-based microporous organic polymers (H-CMOP-Rh).<sup>490</sup> Modified from Cho, K.; Yang, H.; Lee, I.; Lee, S. M.; Kim, H. J.; Son, S. U. *J. Am. Chem. Soc.* **2021**, *143*, 4100–4105.

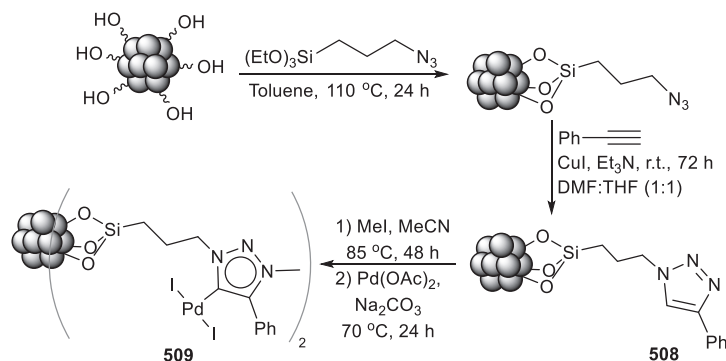
[Rh( $\mu$ -OMe)(cod)<sub>2</sub>], the coordinated methoxy group does not deprotonate the triazolium moieties but rather the rhodium coordinates to the remaining surface hydroxyl groups in metal-functionalized TRGO 502. To circumvent Rh–O bond formation, the hydroxyl groups can be first protected to yield the TRGO material with triazolium and -OTMS surface pendant groups 503. If 503 is treated with [Rh( $\mu$ -OMe)(cod)<sub>2</sub>], then trz coordination is achieved to give anchored 504 Rh(cod)(trz)-complexes on TRGO with 2.6 wt% Rh as determined by means of ICP-MS measurements, with a homogenous distribution of the metal. A reference molecular complex 506 (Scheme 71, ii) as analog to the anchored complexes was also prepared.

Catalytic alkyne hydrosilylation reactions employing 1-octyne and HSiMe<sub>2</sub>Ph or HSiEt<sub>3</sub> as substrates were evaluated with 502, 504, and 506 (Scheme 71, iii). The homogeneous catalysts 506 displayed excellent catalytic performance both in terms of selectivity (for the thermodynamically less stable  $\beta$ -Z vinylsilane isomer),<sup>497</sup> while the hybrid 502 and 504 are active at 60 °C in solvent CDCl<sub>3</sub>, although decreased selectivity is seen for 504 when the more active silane HSiEt<sub>3</sub> is employed as substrate.<sup>496</sup> However the labile Rh–O linkages for hybrid 502 lead to the loss of activity over successive catalytic cycles whereas the heterogeneous 504 with robust Rh–C(trz) covalent bonds can be reused at least six times, even under atmospheric conditions, without loss of activity. Heterogenization of a molecular catalyst utilizing instead of Rh<sup>I</sup> a C,C-cyclometalated Rh<sup>III</sup> anchored to the TRGO material, was probed next as a more  $\beta$ -Z vinylsilane selective hydrosilylation complex catalyst.<sup>498</sup> The Rh<sup>III</sup> complex 507 was prepared containing a C4-phenyl trz ligand (Scheme 71, ii), and proved highly active even at room temperature (Scheme 71, iii). DFT calculated mechanistic routes pointed to a metal-ligand bifunctional mechanism for 507 involving a reversible cyclometalation of the C4-phenyl-trz ligand that is competitive with a noncooperative pathway. The triazolium moiety with a C4-phenyl group was bound to the TRGO surface through a similar strategy as used for 504, whereafter metalation with [RhCp\*Cl<sub>2</sub>]<sub>2</sub> (Cp\* = pentamethylcyclopentadienyl) in the presence of sodium *tert*-butoxide as base yielded the hybrid 505 as immobilized version of the molecular rhodium(III) catalyst 507 (Scheme 71, ii), with the iodo-ligands replaced by Rh–O bonds from the O-functionalities on the carbon wall. 505 only proved active at 60 °C but the hybrid again showed excellent recyclability with exclusive selectivity for the  $\beta$ -Z vinylsilane formation (Scheme 71, iii).



**Scheme 71** (i) Click-preparation of hybrid hydrosilylation catalysts on thermally reduced graphene oxide surfaces<sup>496</sup> and (ii) molecular catalysts for (iii)  $\beta$ -Z selective alkyne hydrosilylation. Modified from Sánchez-Page, B.; Jiménez, M. V.; Pérez-Torrente, J. J.; Passarelli, V.; Blasco, J.; Subias, G.; Granda, M.; Álvarez, P. *ACS Appl. Nano Mater.* **2020**, *3*, 1640–1655.

Click-based covalent connection of trz to nanoparticles is equally attainable, to prepare for example, nanomagnetic catalysts that can be readily recycled with magnetic work-up.<sup>499</sup> Hydroxyl-surface functionalized magnetic nanoparticles (MNPs) prepared via coprecipitation of Fe<sup>III</sup> and Fe<sup>II</sup> at high pH was reacted with 3-azidopropyltriethoxysilane that could be subjected to CuAAC-reaction with phenylacetylene to yield the triazole-functionalized MNPs **508** (Scheme 72). Alkylation followed by metalation with Pd(OAc)<sub>2</sub> result in Pd<sup>II</sup> trz-functionalized MNPs **509** that proved efficient in Suzuki-Miyaura and Mizoroki-Heck cross-coupling reactions under mild conditions. The benefit of the heterogenization was illustrated in catalyst recycling and reuse of up to 10 times without appreciable loss of catalytic activity.

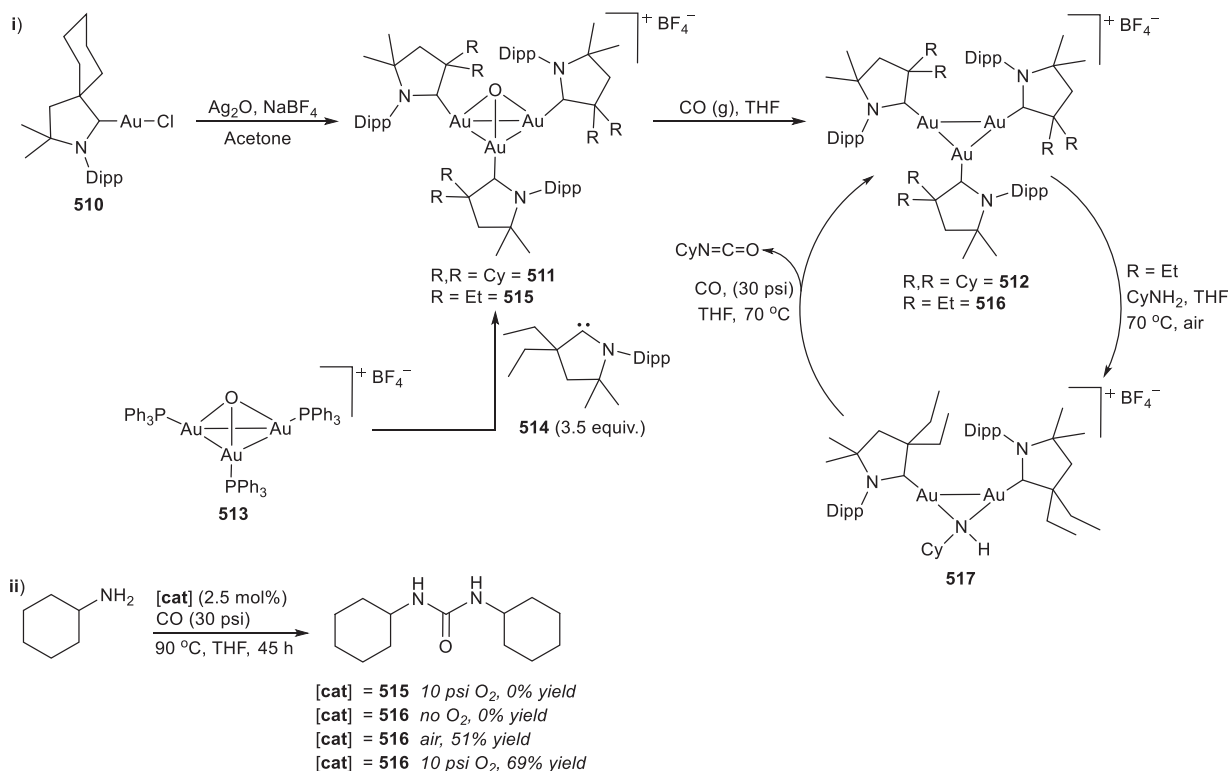


**Scheme 72** Magnetic nanoparticle tethered trz palladium(II).<sup>499</sup> Modified from Kempasiddhaiah, M.; Kandathil, V.; Dateer, R. B.; Sasidhar, B. S.; Patil, S. A.; Patil, S. A. *Appl. Organometal. Chem.* **2019**, *33*, e4846.

### 1.05.5.3.2 Nonclassical carbene stabilized metal clusters

The uncommon stabilizing effect attained from the unique bonding between polymetallic and organic species in organometallic clusters are well-documented, although the cooperative effects of carbon-multimetal bonds in catalytic reactions remain obscure.<sup>500</sup> Especially for carbenes, this can be ascribed to the fact that the exact nature of the carbon-metal bond in clusters is ambiguous, and the redox behavior of the multimetal centers may differ from single metal compounds. The inherent noninnocence of CAACs exemplified by their radical-stabilization capabilities (Section 1.05.1, vide supra) make these nonclassical carbenes the most-explored of the series under review in this work, extended to the stabilization of the p-block elements, allotropes and radicals,<sup>501–505</sup> monomers;<sup>506,507</sup> dimers<sup>508–510</sup> to small molecules<sup>511</sup> and clusters.<sup>512–516</sup> Examples of small metal clusters stabilized by the other monoheteroatom-stabilized carbenes (Im4 and trz) are exceedingly rare and adventitious.<sup>517</sup>

For atomically precise *transition metal* clusters that are ligand-protected (Fig. 14, ii), precedents utilizing nonclassical NHCs are scarce and exclusively implicated for the coinage metals and CAACs, as metal and carbene partners, respectively.<sup>71,518</sup> The interest in these types of cluster compounds lies in their potential to act as mimics for heterogeneous catalysts while maintaining the advantage of possible catalytic reaction intermediate characterization. The initial study of Bertrand et al. detailing the stabilization of electron-rich mono- and dinuclear gold(0) complexes with CAACs<sup>387</sup> was followed by a straightforward synthesis of small gold(I)/gold(0) triangular clusters ligated by three CAACs.<sup>518</sup> The corresponding cyclohexyl-substituted CAAC-gold(I) chloride **510** can be treated with Ag<sub>2</sub>O in the presence of NaBF<sub>4</sub> to yield the μ<sup>3</sup>-oxo **511**, which can be reduced with carbon monoxide to the mixed valent cluster **512** (Scheme 73). Alternatively the readily available phosphine μ<sup>3</sup>-oxo complex **513** can be used as a precursor for reaction of the

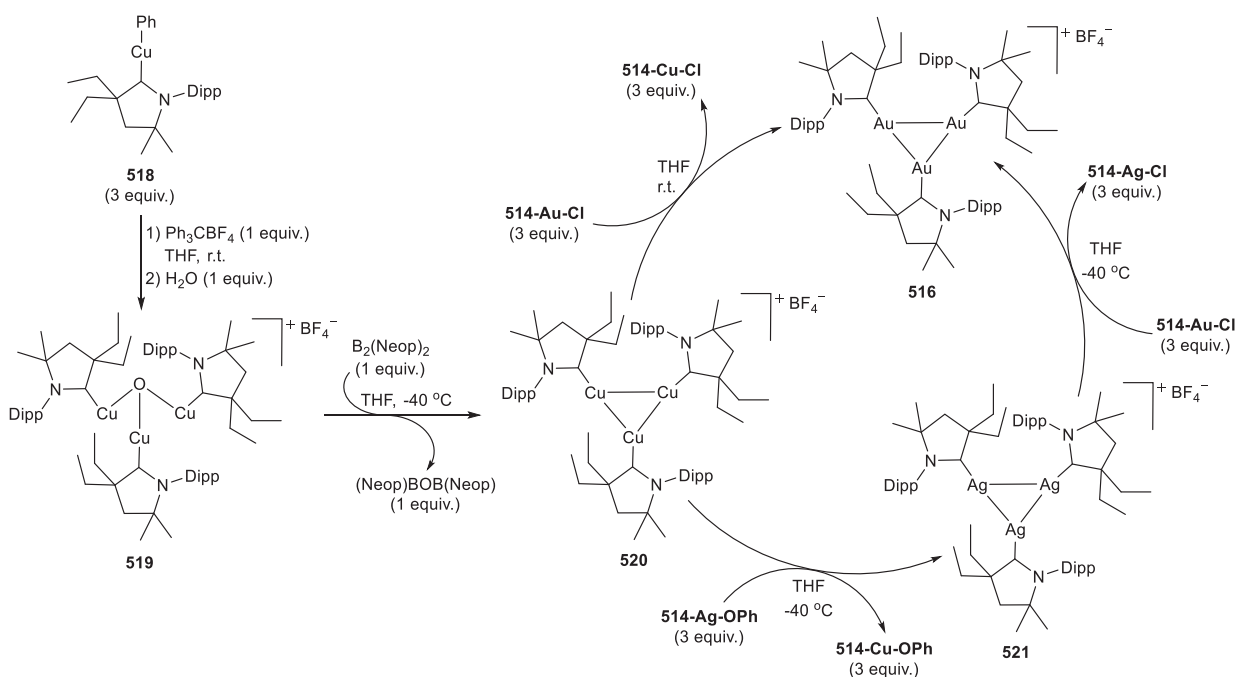


**Scheme 73** (i) CAAC-stabilized Au<sub>2</sub>Au<sup>I</sup> clusters utilized in (ii) catalytic amine carbonylation.

diethyl-substituted CAAC **514** in a ligand substitution reaction to give trinuclear oxo complex **515** before reduction to the characterized  $\text{Au}_2^0\text{Au}^{\text{I}}$  cluster **516**. **516** was shown to be an active catalyst for the catalytic carbonylation of cyclohexylamine to a urea derivative, but not under anaerobic conditions (Scheme 73, ii). Only if the reaction was performed in the air was product formation observed, with a significant improvement under a 10 psi  $\text{O}_2$  atmosphere at  $90^\circ\text{C}$ , while a CAAC- $\text{Au}^{\text{I}}$ -Cl remained inactive and the  $\mu^3$ -oxo bridged **515** much less efficient. Identification of the different reaction steps were possible by the isolation of the reaction intermediates. First, cyclohexylamine reaction with **516** leads to an oxidized dinuclear gold(I)-gold(I) complex **517** with bond distances typical for  $\text{Au}^{\text{I}}-\text{Au}^{\text{I}}$  aurophilic interactions (Scheme 73, i). The requirement for an oxygen atmosphere was presumed to be necessary for the scavenging of the hydrogen atoms. Treatment of **517** with CO (g) reduces the two gold(I) atoms to the recovered **516** and the carbon monoxide is oxidized by two electrons. Trace amounts of cyclohexyl isocyanate and urea formation was also noted in this step.

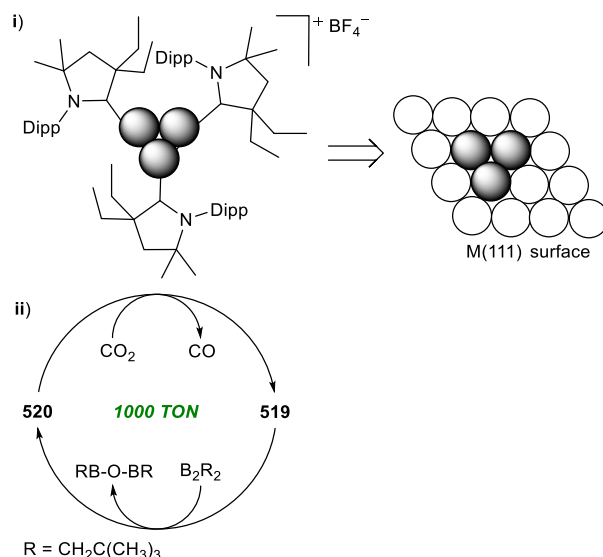
Preparation of the copper-derivative of the  $\text{M}_2^0\text{M}^{\text{I}}$  cluster via reduction of the  $\mu^3$ -oxo complex **519** with carbon monoxide did not proceed as for the gold congener **516**.<sup>71</sup> However, if bis(neopentyl glycolato)diboron was employed as the reducing agent, the corresponding trinuclear  $\text{Cu}_2^0\text{Cu}^{\text{I}}$  cluster **520** was accessible in high yield (Scheme 74). The availability of the copper variant of these trinuclear coinage metal clusters stabilized by the ambiphilic CAACs meant that the concept of galvanic exchange, the redox process between a sacrificial metal template and metal ions in solution to deposit the replacement metal ions on the surface of the template,<sup>519</sup> could be utilized for absolute templating.<sup>71</sup> For copper as the least electronegative of the three coinage metals, the exchange of all the copper in a sacrificial template with silver or gold should be possible. DFT calculations confirmed that the exchange of copper by gold should be exergonic ( $+27.6\text{ kcal mol}^{-1}$ ). Thus **520** could be employed as a template for the clean preparation of **516** from the complex **514-Au-Cl**. Using **514-Ag-OPh** as silver precursor analog, the increased oxophilicity of copper compared to silver could be exploited as driving force of the reaction to prepare also the mixed valent  $\text{Ag}_2^0\text{Ag}^{\text{I}}$  cluster **521**, which in turn could be used as template for **516** preparation from **514-Au-Cl** in a synthetic route that describes the first examples of mixed-valent trinuclear clusters also for silver and copper (Scheme 74).

Computational analyses suggested that the galvanic replacement does not occur through an outer sphere reduction pathway, but rather via an associative addition-elimination. This observation is rationalized by the isolobal analogy of **516** with the triatomic hydrogen cation  $[\text{H}_3]^+$  as  $\sigma$ -aromatic compound.<sup>520</sup> Lewis base reactivity where the delocalized metal-metal bonds mimic the  $\pi$ -aromatic interactions is therefore implicated to form tetranuclear 4-center-2-electron clusters with Lewis acid metals.<sup>521</sup> From these presumptions, it was proposed that galvanic templating occurs incrementally via a transient tetranuclear dicationic alloy cluster to form intermediated trinuclear alloys.<sup>71</sup> The similarity of the spatial arrangements of **516**, **520** and **521** to a M(111) metal surface (see Scheme 75, i), and the M-M bond distances of the clusters that closely resemble the distances observed in the free-standing 2D monolayers, lead to the hypothesis that these clusters could be used as a molecular model for understanding the interaction of small molecule substrates with M(111) metal surfaces. Specifically, for carbon dioxide reduction, surface interaction takes place via charge transfer from the surface to the antibonding orbital of  $\text{CO}_2$ . Formation of a bent radical is then disputed to either dissociate into CO and O, or to facilitate transient carboxyl (COOH) or formate (HCOO) formation.<sup>522</sup> **516** and **521** do not react with  $\text{CO}_2$ , in accordance with computational studies,<sup>523</sup> but **520** reacts cleanly to form **519** with CO formation (Scheme 75, ii).<sup>71</sup>



**Scheme 74** Mixed-valent trinuclear coinage metal cluster formation via absolute templating by galvanic exchange.



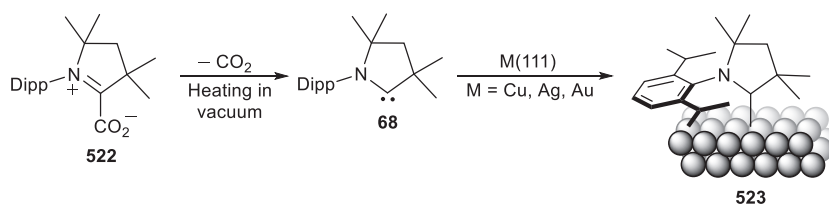


**Scheme 75** Using  $\text{M}_2^0\text{M}^{\text{I}}$  clusters as (i) M(111) molecular model for understanding of (ii)  $\text{CO}_2$  reduction on M(111) surfaces.<sup>71</sup> Modified from Peltier, J. L.; Soleilhavoup, M.; Martin, D.; Jazzar, R.; Bertrand, G. *J. Am. Chem. Soc.* **2020**, *142*, 16479–16485.

With the introduction of a reducing agent to regenerate 520, a TON of 1000 could be obtained without optimization. The use of 520 as a surrogate for Cu(111) means that the hypothesis of reductive  $\text{CO}_2$  dissociation to  $\text{CO} + \text{O}$  by copper surfaces could be supported at the molecular level. The electronic properties of CAACs are also excellently suited to the control of cluster size and composition of coinage metal/chalcogen clusters.<sup>524</sup> This translates to a tunability of the functionality of the clusters in terms of their photophysical properties as the increased  $\sigma$ -donicity and  $\pi$ -acceptor ability lower the metal/chalcogenide-to-ligand charge transfer excited states to impact on the observed photoluminescence.

### 1.05.5.3.3 Metal nanoparticles and surfaces stabilized by nonclassical carbenes

Although the value of metal carbenes in heterogeneous catalysis is well-recognized, the influence of carbene surface attachment has been barely explored.<sup>525–527</sup> Carbene stabilized nanoparticles (NPs) are commonly prepared by ligand exchange of L-NP with NHC, or by controlled selective degradation of the corresponding metal complexes using reducing agents.<sup>528</sup> For classic NHCs, robust self-assembled monolayers on Au(111) surface and nanoparticles (NPs) have been reported as a consequence of the strong, substitutionally inert metal-carbon bond formed.<sup>529</sup> The bonding mode for CAACs on heterogeneous surfaces has been implicated to differ from the single carbene-metal bond found in CAAC complexes.<sup>530</sup> In other, independent studies, it could be shown that Rh-NP formation occurred as a result of Rh-CAAC complex decomposition, as shown independently by the groups of Bullock<sup>531</sup> and Glorius<sup>532</sup> for Rh-catalyzed arene hydrogenations. In both cases, the formed Rh-NPs are stabilized by protonated CAAC species, albeit that these non-carbene CAAC derivatives did play a key role in determining the chemoselectivity of fluorinated arene hydrogenation.<sup>532</sup> Even more recently, a systematic investigation of CAACs on coinage M(111) (M = Cu, Ag, Au) surfaces has been conducted.<sup>533</sup> The dimethyl-CAAC- $\text{CO}_2$  adduct 522 was used as precursor for free carbene 68 formation which could be vacuum-deposited on M(111) surfaces to form 523 (Scheme 76). Confirmation and characterization of the intact-deposited carbene and surface-interaction was achieved with scanning tunneling microscopy (STM), X-ray photoelectron spectroscopy (XPS) and DFT calculations. The 2,6-diisopropylphenyl group is orientated perpendicular to the CAAC ring and parallel to the surface, while the two methyl groups adjacent to the ring-N points upward to minimize steric hindrance. At high coverage, molecular islands with short-range order were observed. The asymmetry and bulk of the substituents flanking the carbene carbon atom prevents self-assembly to a well-ordered, close-packed structure. STM images showed that the CAACs are mobile on the metal surfaces at lower coverage.



**Scheme 76** Deposition of CAACs generated from  $\text{CO}_2$ -adducts on M(111) surface.<sup>533</sup> Modified from Bakker, A.; Freitag, M.; Kolodzeiski, E.; Bellotti, P.; Timmer, A.; Ren, J.; Lammers, B. S.; Moock, D.; Roesky, H. W.; Mönig, H.; Amirjalayer, S.; Fuchs, H.; Glorius, F. *Angew. Chem. Int. Ed.* **2020**, *59*, 13643–13646.

This pioneering study on the coinage metal surfaces paves the way for studies of other nonclassical carbenes on (different) metal surfaces.<sup>525–527</sup>

### 1.05.6 Emerging applications of nonclassical carbenes

In the different categories of ligand noninnocence highlighted in this work, the applications of the metal complexes developed have been predominantly in the arena of molecular catalysis. The nonclassical carbenes are increasingly used also in non-catalytic applications including supramolecular and material chemistry<sup>458–461</sup> (see Section 1.05.5), and in light emitting or harvesting,<sup>458,534–538</sup> and biological or medicinal applications<sup>458,534,539–542</sup> of these carbon-donor ligands. Of relevance to the current work is especially the demonstration of a participatory role of the ligand in the targeted application extending beyond the inherent electronic properties of the ligand, to facilitate the photophysical or biological applications.

#### 1.05.6.1 Light-harvesting and -emitting applications

Transition metal complexes of Pt<sup>II</sup>, Ir<sup>III</sup> and Ru<sup>II</sup> are well-known as triplet emitters for OLED (Organic Light Emitting Diode) applications, as a result of the spin-orbit coupling (SOC) induced by the heavy metal central atom,<sup>543</sup> or as photosensitizer dyes for solar energy conversion based on electrochemiluminescence.<sup>544,545</sup> Cost and availability factors mean that less expensive complexes based on iron, copper, osmium, etc. are attractive alternatives, but the role of the ligand on the photophysical and -chemical properties is an important consideration here. The interest in the photoactivity of the nonclassical carbene complexes is on the rise as a consequence of the stereoelectronic properties of these ligands. Robust metal-carbon bonds that can facilitate stressed geometries are preventative to distortions in the excited state to disfavor nonradiative decay for improved emission.<sup>546</sup> Secondly, strong  $\sigma$ -donor ligands increase the energy levels of the empty d-orbitals as an additional strategy for emissive complex design that avoid the nonradiative metal-centered d-d transitions. The bonding motif of cyclometalated bi- or tridentate C- and/or N-donor luminophores is the most explored one to achieve the objectives above. Based on the success of polypyridine complexes of ruthenium(II) as photosensitizer dyes for dye sensitized solar cells (DSSCs),<sup>545,547,548</sup> this has also been the starting point for research using the nonclassical carbenes as C,N- (or C,C)-cyclometalated  $\sigma$ -donors substituting one or more pyridine sites.

##### 1.05.6.1.1 Photoactive nonclassical carbene complexes of group 8 transition metals

Accordingly, several examples of triazolylidene Ru<sup>II</sup> complexes have been investigated (Fig. 15). The first of these were reported by Albrecht in a series of NHC-py and one trz-py (524) complex,<sup>549</sup> in an improvement to emissionless picolyl-tethered NHC complexes without the CH<sub>2</sub>-spacer.<sup>550</sup> The bidentate i-bitz ligand as C,C- analogs in 528 was compared also to the trz-py C,N-bidentate ligands where the pyridine was linked to either N1 (525) or C4-ring triazol-ring position (527). The significant effect of trz incorporation on ground and excited state redox potentials was demonstrated when comparing emission band positions and excited state lifetimes of the benchmark [Ru(bpy)<sub>3</sub>]<sup>2+</sup> complex emitting from the long-lived triplet metal-to-ligand charge transfer (<sup>3</sup>MLCT) state.<sup>551</sup> Moreover, this was also the first report of Os<sup>II</sup> trz complexes (526, 529, Fig. 15) for photosensitizer applications. Alternatively, C,C-cyclometalating ligands were used to prepare monocationic derivatives 530.<sup>552</sup> Proceeding from the

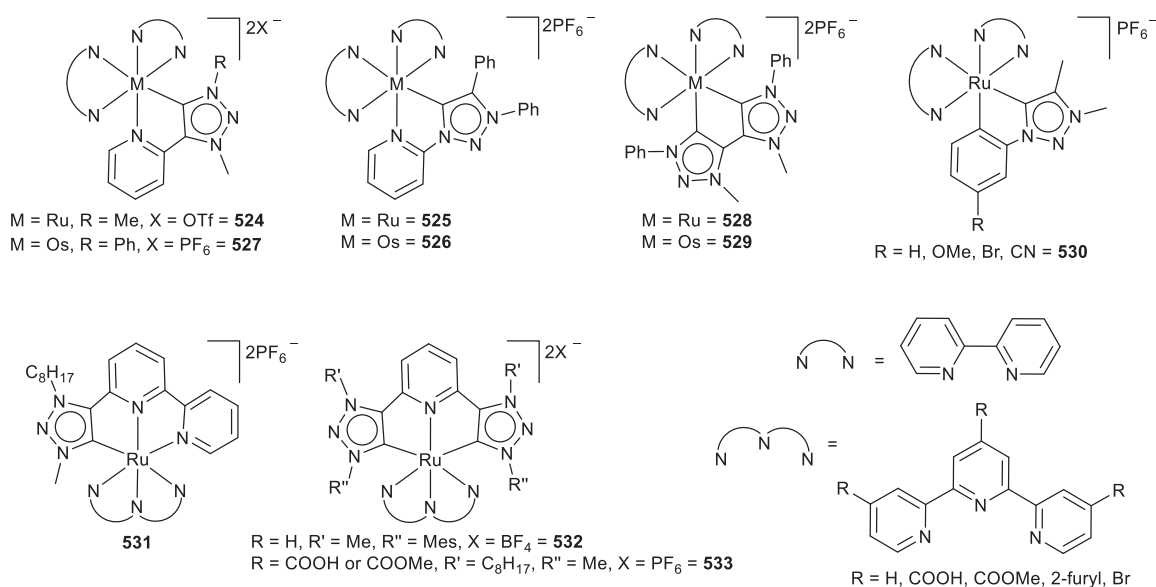


Fig. 15 Photoluminescent tris(bidentate) and bis(tridentate) ruthenium(II) complexes with triazolylidene donor ligands.

tris-bidentate ligand arrangement to a bis-tridentate octahedral Ru<sup>II</sup> was accomplished with CNN-pincer trz-py-py (531, Fig. 15) or CNC-pincer trz-py-trz (532 and 533, Fig. 15) ligands as analogs to the well-known bis(terpyridine) (terpy = 2,2':6',2''-terpyridine) ruthenium(II) complexes.<sup>206–208</sup> The advantages of high stability and isomer-free functionalization of terpy complexes are often offset by short-lived excited states, due to rapid deactivation via energetically low-lying triplet metal-centered (<sup>3</sup>MC) excited state. This is a result of weaker  $\sigma$ -donation of the pyridyl-based ligands with strained bond-angles deviating from ideal octahedral geometry in [Ru(terpy)<sub>2</sub>]<sup>2+</sup>. For the Ru<sup>II</sup> trz complexes listed in Fig. 15, destabilization of the <sup>3</sup>MC state relative to the <sup>3</sup>MLCT state occurs with the introduction of the trz donors, in addition to the expected more positive redox potentials which should facilitate charge separation in the excited state.<sup>550</sup> Radiationless deactivation via <sup>3</sup>MC is thereby suppressed. Also the weaker  $\pi$ -donation from trz ligands facilitates a <sup>3</sup>MLCT–<sup>3</sup>MC separation as well as an increase in the ground state (GS)–<sup>3</sup>MLCT gap to yield complexes displaying photoluminescence emission with longer lived excited states and higher emission quantum yields. The practical functionality of the Ru<sup>II</sup> dyes in DSSCs is proven with the cooperative binding of the complexes to TiO<sub>2</sub> surfaces through the carboxylate- or phosphonate-functionalized terpy-ligands (533). This anchoring method robustly anchors the complex while maintaining charge transfer from the dye into the semiconductor.<sup>208,553</sup>

For the first-row transition metal analog of [Ru(bpy)<sub>3</sub>]<sup>2+</sup> and its polyimine derivatives, the smaller ligand-field splitting of Fe<sup>II</sup> results in high-spin electronic configurations that are characterized by low-lying MC states (quintet <sup>5</sup>MC and triplet <sup>3</sup>MC).<sup>554</sup> The <sup>5</sup>MC state is commonly regarded as the main deactivating state for the photochemically pertinent <sup>3</sup>MLCT state, leading to extremely short excited state lifetimes in the femtosecond range.<sup>555</sup> The use of ligands with higher field strength and  $\sigma$ -donation can effectively destabilize the <sup>5</sup>MC state so that the <sup>3</sup>MLCT state is first intercepted by the <sup>3</sup>MC before the <sup>5</sup>MC surface crosses the <sup>3</sup>MLCT potential energy surface.<sup>556</sup> Employment of the strongly donating bidentate bis(triazolylidene) i-bitz ligand in the heteroleptic complex Fe<sup>II</sup> 534 (Fig. 16), destabilizes both the <sup>5</sup>MC and the <sup>3</sup>MC states so that a long-lived <sup>3</sup>MLCT state (13 ps compared to the 130 fs of [Fe(bpy)<sub>3</sub>]<sup>2+</sup>) is accessible with photophysical behavior resembling that of Ru<sup>II</sup>.<sup>557</sup> The strategy of using the i-bitz ligands to realize longer-lived excited state lifetimes for iron complexes were extended by the same group, to a homoleptic tris(bidentate) complex 535 (Fig. 16) featuring a low-spin Fe<sup>III</sup>.<sup>558</sup> The unique combination of the ground state doublet iron(III) metal center and the three i-bitz ligands promotes the reversal of the charge-transfer excitation direction.<sup>559</sup> A ligand-to-metal charge-transfer (<sup>2</sup>LMCT) excited state is generated, with a groundbreaking lifetime of 100 ps emitting at room temperature. The complex in the double <sup>2</sup>LMCT state retains its ground state geometry so that little energy is lost to molecular rearrangements during the light-induced charge transfer process. Thus the <sup>2</sup>LMCT state provides for spin-allowed fluorescence as it relaxes to the ground state with conservation of electron spin.

Chemical reduction of Fe<sup>III</sup> in 535 by dithionite to Fe<sup>II</sup> yields dicationic 536 (Fig. 16), that displays the expected MLCT as the lowest-energy charge transfer process as observed for 534.<sup>560</sup> However, the homoleptic ligand environment furnishes an unusually strong ligand field for the Fe<sup>II</sup> complex that provides for an unprecedented lifetime of 528 ps for the <sup>3</sup>MLCT state, with a deactivation pathway that excludes energetic access to the <sup>5</sup>MC state.<sup>561</sup> Resonant photoelectron spectroscopy (RPES) provides direct spectroscopic evidence to corroborate the density theory calculations revealing pronounced mixing of the frontier orbitals as MO interactions between the iron(III) 3d-levels and the i-bitz frontier  $\sigma$ - and  $\pi$ -orbitals of 535.<sup>562</sup>

### 1.05.6.1.2 Photoactive nonclassical carbene complexes of group 9 transition metals

The high SOC of the heavy platinum-group metal ions means that rapid intersystem crossing (ISC) takes place in the excited state, so that high quantum efficiencies are reached for the photoluminescent emissions of these triplet emitters in OLED applications.<sup>563</sup> Also in the case of photoluminescent iridium(III) and platinum(II) complexes, the structural motif of bidentate N,N-, N,C- or C,C- ligands employing neutral pyridyl or anionic pyrazolyl derivatives as N-donors and anionic phenyls or neutral NHCs as C-donors for cyclometalation, has been the most common approach. In the case of Ir<sup>III</sup> complexes, these metal-ligand combinations deliver mostly blue and near-UV phosphorescence.<sup>535,564</sup> As for the group 8 metal complexes discussed above, only the trz class of the nonclassical carbenes under review has been explored as even stronger donating C-donors for Ir<sup>III</sup> complexes for OLED applications.

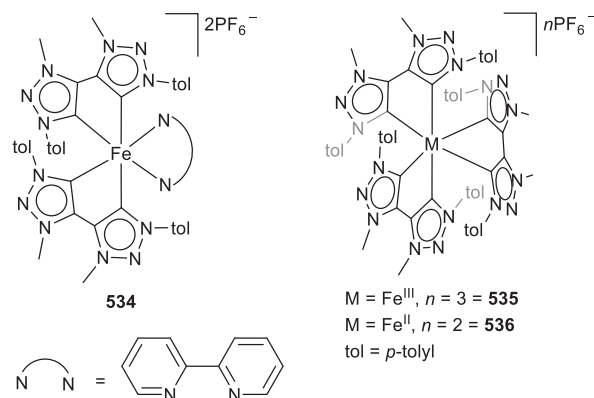


Fig. 16 Photoluminescent iron bis(triazolylidene) complexes.

The use of two trz-pyridyl (C,N) (537),<sup>565</sup> trz-triazolide (C,C) (538),<sup>566</sup> trz-phenyl (C,C) (539),<sup>121</sup> and trz-imidazolylidene (C,C) (540 and 541)<sup>567</sup> bidentate ligands yield phosphorescent Ir<sup>III</sup> complexes emitting in the blue region with microsecond lifetimes ranging from 0.4–3.8  $\mu$ s at room temperature (Fig. 17). Variable quantum efficiencies of 3.1–28.0% for 539,<sup>121</sup> 9–12% for 537,<sup>565</sup> 538<sup>566</sup> and 541,<sup>567</sup> and 50.0–57.4% for 540<sup>567</sup> are achieved, and depend on the ancillary ligands present in the coordination sphere.<sup>568</sup> The expected <sup>3</sup>MLCT state is the major emitting state, although for 537 it was found that ligand-centered (LC) transitions between the two trz present occur. Nevertheless, the moderate  $\pi$ -acceptor and strong  $\sigma$ -donor abilities of the trz are again responsible for stabilizing the emissive complexes due to more stable Ir–C bonds<sup>566</sup> to lower access to the nonradiative deactivation pathway involving low-lying <sup>3</sup>MC states.<sup>568</sup>

### 1.05.6.1.3 Photoactive nonclassical carbene complexes of group 10 transition metals

A series of C,C-cyclometalated platinum(II) complexes featuring phenyl-Im4 (543, Fig. 18)<sup>569</sup> or -trz (544<sup>570</sup> and 545,<sup>571</sup> Fig. 18) with  $\beta$ -diketonate acac (acetylacetonato) auxiliary ligands were reported by Strassner et al. They propose a strongly metal-perturbed intraligand/metal-to-ligand charge transfer (ILCT/MLCT) for the long-lived (27–57  $\mu$ s) room temperature phosphorescence ( $\phi$  = 40–69%) observed for the cyclometalated Im4 complexes 543.<sup>569</sup> Improved quantum yields ( $\phi$  = 67–78% and 70–84%, respectively for 545 and 544) in poly(methyl methacrylate) (PMMA) matrices are paired with shorter excited state lifetimes (18–21  $\mu$ s and 11–15  $\mu$ s, respectively) upon introduction of the trz ring instead of Im4. Modification of the cyclometalating phenyl in 544 to the annulated dibenzofuranyl shifts emission to significantly lower energy,<sup>571</sup> while variation of the N3-aryl from phenyl to mesityl or duryl in 544 (Fig. 18) also affects emission color. The sterically unencumbered N3-phenyl rotates into the molecular plane to enlarge the conjugated system as predicted by theoretical calculations to stabilize the excited state. In contrast, planarization of the mesityl ligand is hindered due to steric demand such that its contribution to the conjugated system is reduced which leads to a blue shift of the emission.<sup>570</sup>

A tridentate CNC-ligand comprising a central pyridine flanked by two trz was used to chelate a platinum(II) metal to give the square planar complexes 542 with variable ancillary ligands (chloride, acetonitrile or cyanido) that only slightly influences emission wavelengths and lifetimes (Fig. 18).<sup>211,572</sup> Only weak green emission was observed ( $\phi$  = 3%) arising from mixed LC and MLCT transitions.<sup>572</sup> If a CNC-pincer like 2,6-di(*p*-tolyl)pyridine is rather used as ancillary chromophoric ligand, cyclometalation of a trz with a phenyl substituent on the N1-position yields complexes 546 and 547, consecutively, with the CNC ligand either acting as a bidentate or tridentate ligand in the octahedral coordination sphere (Fig. 18).<sup>573</sup> Complexes 546 and 547 represent the first examples of Pt<sup>IV</sup> with mesoionic carbenes. At room temperature, weak emission from <sup>3</sup>LC states is observed, but in PMMA matrices quantum efficiencies increase to 71% and 61%, respectively, for 546 and 547. An increase in the energy of deactivating LMCT excited states is ascribed to the aryl-carbene ligand. Fine-tuning of emission color from blue to yellow is accessible by introduction of variable C,N-chelating chromophores into the Pt<sup>IV</sup> coordination sphere (548–549, Fig. 18), with exceptional efficiency reported for the first time for platinum(IV) complexes ( $\phi$  = 97% for 549 and  $\phi$  = 93% for 550).<sup>574</sup> The role of the trz is that of supporting ligand that leads to significantly lower nonradiative decay rates and higher quantum efficiencies, compared to the homologous C2-symmetrical [PtCl<sub>2</sub>(C,N)trz-Ph]. Computational calculations substantiate the effect of the carbene ligands in raising the energies

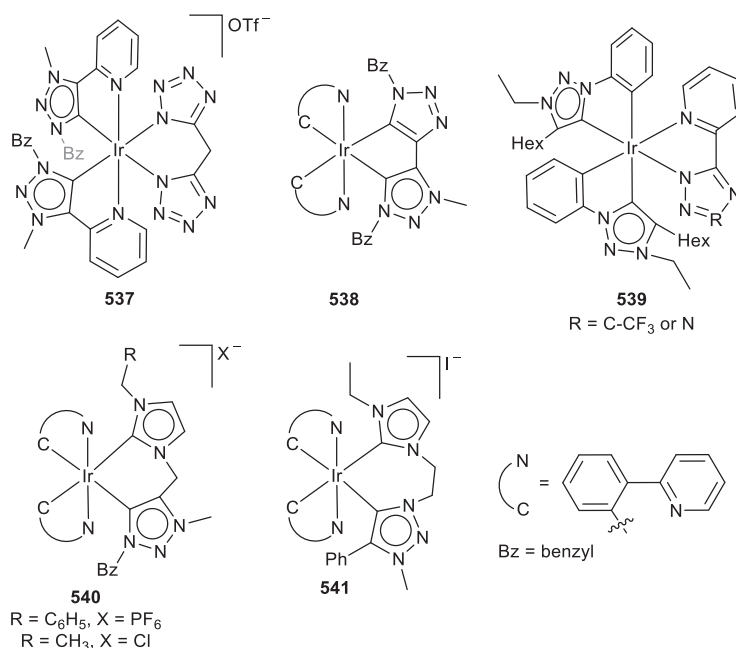
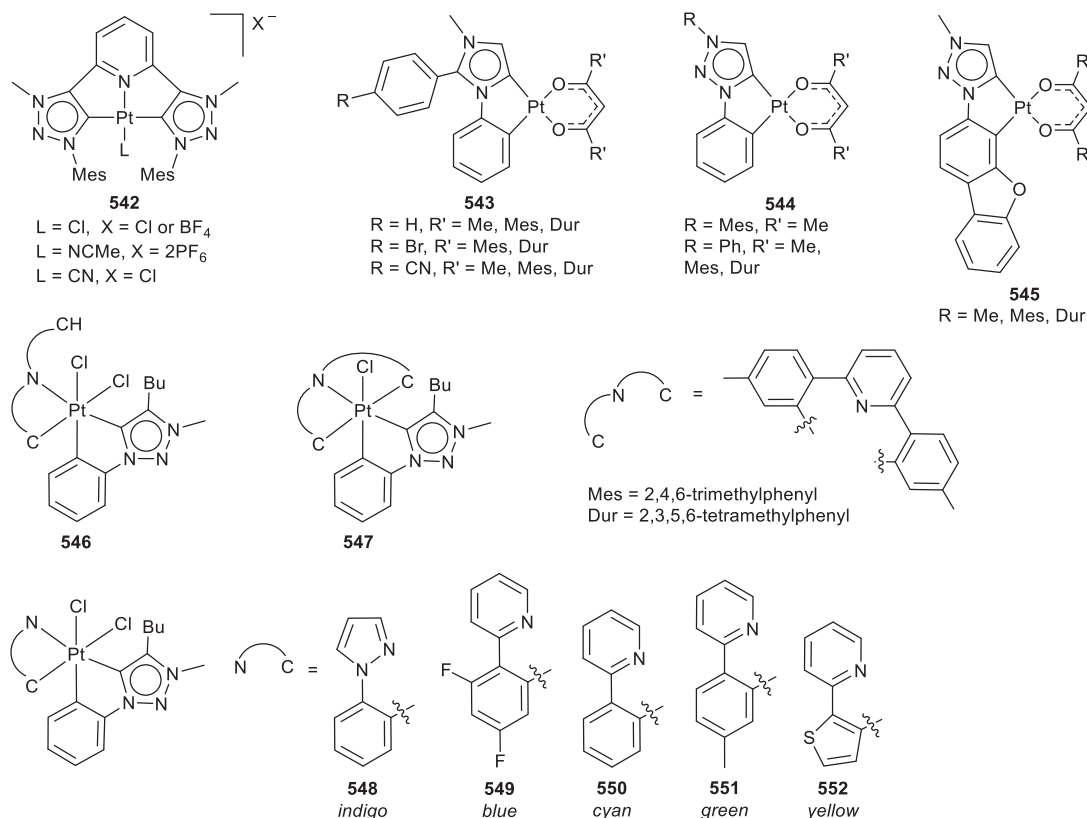


Fig. 17 Phosphorescent iridium(III) trz complexes.



**Fig. 18** Photoluminescent platinum bis(trz) complexes.

of the nonemissive deactivating <sup>3</sup>LMCT states for the OC-6-54 isomers 548–552 shown in Fig. 18. In contrast, the OC-6-42 isomers are not luminescent as they present a <sup>3</sup>LMCT state with long excited state lifetimes.

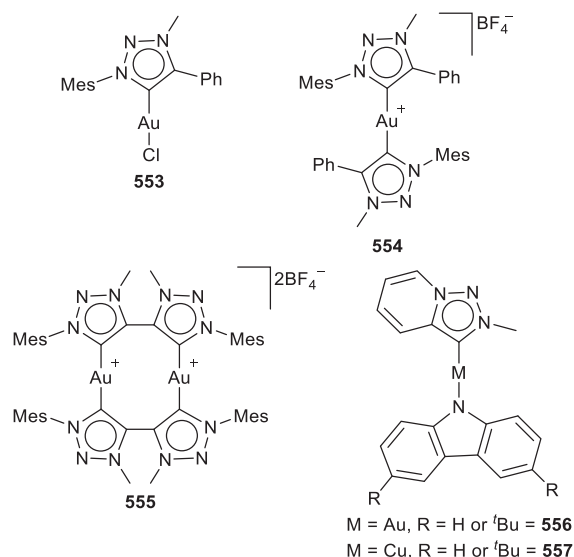
#### 1.05.6.1.4 Photoactive nonclassical carbene complexes of group 11 transition metals

The linear geometry of the coinage metals in oxidation state +1 coordinated by NHC ligands are well-known to produce photoluminescent complexes.<sup>458,535,575,576</sup> The large SOC of the 4d<sup>10</sup> and 5d<sup>10</sup> metals, enhanced by relativistic effects in the case of gold and underscored by aurophilic interactions, facilitates the access to emissive triplet excited states via intersystem crossing.<sup>576</sup> Using simple monodentate trz, either neutral monocarbene Au<sup>I</sup> complex 553 or cationic biscarbene Au<sup>I</sup> complex 554 were prepared, or the dinuclear 555 with a bidentate i-bitz ligand enforcing short Au–Au bond distances (Fig. 19).<sup>577</sup> MLCT and intraligand π–π\* transitions led to the identification of two excited states – a singlet state with weak fluorescence as well as an intense and long-lived phosphorescent triplet state.

For 3d<sup>10</sup> Cu, metal-centered d–d\* transitions are absent to preclude excited state deactivation but SOC is small in comparison to its heavier congeners. High radiative rate constants can nevertheless be achieved by using π-accepting carbenes as monodentate chromophoric ligands that lead to the formation of excited states with large MLCT or LLCT.<sup>578–581</sup> Especially the molecular design strategy of the combination of a donor amide and an acceptor carbene ligand bridged by a d<sup>10</sup> metal (CMA = carbene metal amide) mediates interligand charge transfer (LLCT). In this way, thermally activated reverse intersystem crossing (rISC) from nonemissive triplet states to fluorescent singlet states can be achieved for thermally activated delayed fluorescence (TADF) emitters (vide infra Cu CAAC complexes).<sup>582–584</sup> Fu and Yan et al. utilized the CMA motif in the preparation of linear gold(I) (556) and copper(I) complexes (557, Fig. 19) containing pyridine-fused trz ligands *trans* to either an unfunctionalized carbazolidide or a di(*tert*-butyl)-substituted carbazolidide to hinder π–π interactions.<sup>585</sup> In both cases, head-to-tail intermolecular self-assembly between the carbazolidide and pyridine-fused trz of adjacent molecules also facilitate intermolecular CT. In the absence of triplet-quenching oxygen, a delayed photoluminescent component in both solution and in the solid state is indicative of TADF emitters. Evidence for the existence of a monomer-dimer equilibrium in solution presents dual-emission bands which displays single component multicolor emission. Moreover, emission color could be tuned by variation of excitation wavelength, temperature, degree of concentration and complex concentration.

Photoluminescence is also dependent on the coordination geometry of the d<sup>10</sup> coinage metals, with three coordinate trigonal planar copper(I) complexes demonstrating tunable behavior from pure phosphorescence to TADF depending on the CMA dihedral angles.<sup>582</sup> Limited ligand scaffold possibilities are available for photophysical tuning of the triplet-singlet gap by modification of three coordinate geometries to ground state Jahn Teller-distorted T-shapes.<sup>586</sup> The combination of a carbazolidide with two flanking



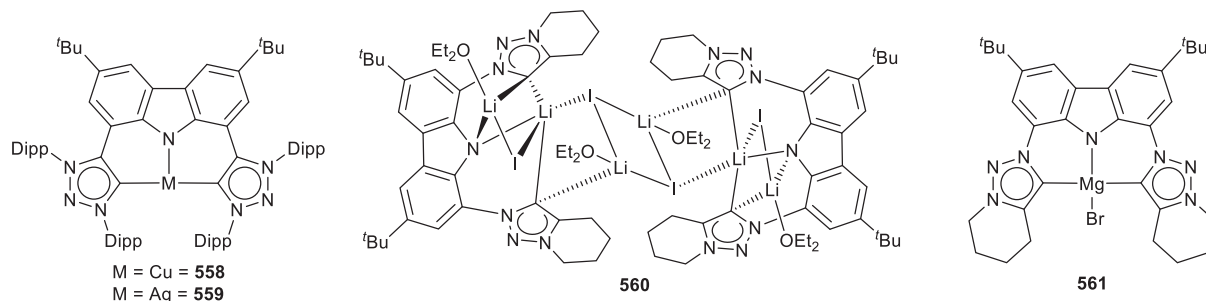


**Fig. 19** Photoactive trz complexes of Au<sup>I</sup> and Cu<sup>I</sup> with linear geometries.

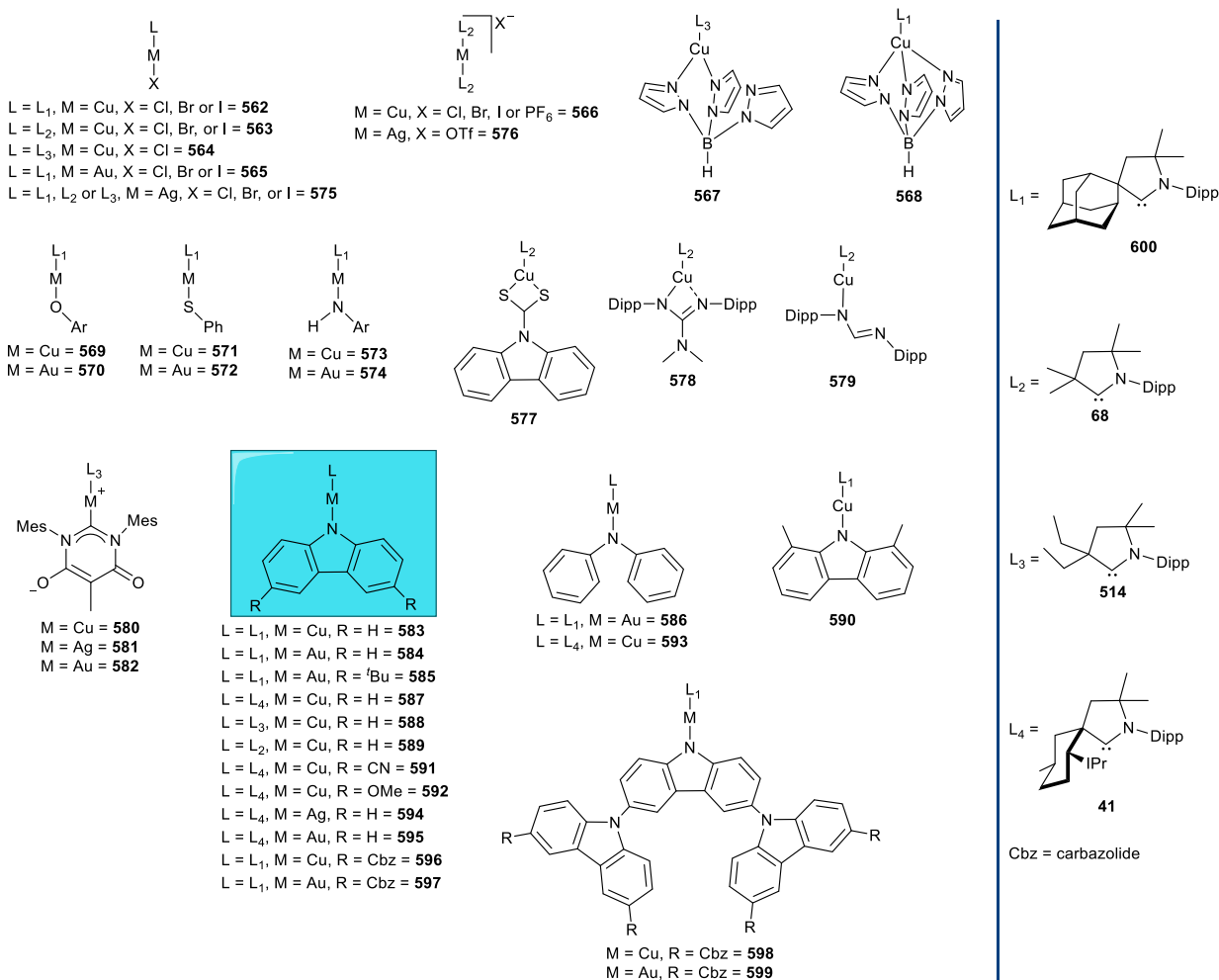
trz yields such T-shape geometries for all three the coinage metals Cu<sup>I</sup> (558),<sup>210</sup> Ag<sup>I</sup> (559, Fig. 20)<sup>217</sup> and Au<sup>I</sup> (206, Scheme 28).<sup>216</sup> The unique reactivity of 206 with electrophiles provides the opportunity to modify the gold(I) complex post-complexation by electrophilic attack either at the amide to yield the cationic linear Au<sup>I</sup> complex 209, or at the nucleophilic metal to furnish the Au<sup>III</sup>-F square planar complex 213 (Scheme 28, Section 1.05.2.2.1).<sup>217</sup> Emissions extending from the blue (copper) to green (gold) to orange (silver) spectrum originate from metal-perturbed  $\pi(\text{carbazolide})-\pi^*(\text{carbene})$  <sup>3</sup>ILCT excited states. The highest quantum yield ( $\phi = 14\%$ ) is observed for the linear Au<sup>I</sup> complex 209. rISC is prohibited by a larger triplet-singlet gap to suppress TADF, with greater phosphorescence contributions to the photoluminescence leading to longer decay times in THF at room temperature. On the other hand, the lifetime of Cu<sup>I</sup> complex 558 is too short (sub-nanosecond) to be determined with certainty, and emission may be fluorescent in nature. For the Ag<sup>I</sup> 559 and Au<sup>I</sup> 206 analogs, decay lifetimes in the microsecond range, increases to millisecond lifetimes upon cooling to 77 K. This increase is in line with the assignment of a change in emission origin from <sup>3</sup>ILCT to <sup>3</sup>IL excited state and may suggest TADF.

Modification of the bis(trz)carbazolide scaffold can be effected by means of the carbazolide-trz connection via the N1-trz atoms instead of the C4-trz atoms, as well as utilization of an intramolecular cyclization as N-alkylation strategy.<sup>587</sup> Employing (earth) alkali metals prevents ligand distortion following excitation to avoid nonradiative deactivation. A lithium dimeric structure bridged by iodo- and lithium iodide adducts (560, Fig. 20) is used also as a precursor for the preparation of the mononuclear magnesium bromide complex 561. Blue-green and intense lime-green luminescence in solution were observed for 560 and 561 ( $\phi = 16\%$  and 14%, respectively) at room temperature.

The recent seminal developments of highly emissive coinage metal complexes of CAACs were initiated by the photophysical investigation of linear copper(I) halido complexes 562, 563 and 564 in Fig. 21, by the groups of Credgington and Bochmann,<sup>588</sup> Steffen,<sup>589</sup> and Bertrand and Thompson,<sup>590</sup> respectively, utilizing adamantyl (AdCAAC) 600, dimethyl (Me<sub>2</sub>CAAC) 68 or diethyl (Et<sub>2</sub>CAAC) 514 substituted CAAC ligands. In contrast to analogous NHC complexes that are almost non-emissive,<sup>589</sup> these complexes displayed excellent quantum efficiencies with values for  $\phi$  of up to 96% achieved for 562 with AdCAAC ligand 600.<sup>588,590</sup> Disproportionation of the neutral linear complexes yield cationic bisCAAC complexes 566. Both these, and the 3- and 4-coordinate Cu<sup>I</sup>-AdCAAC complexes (567, 568, Fig. 21) accommodating bi- or tridentate trispyrazolylborate (Tp) ligands



**Fig. 20** Bis(trz)carbazolide complexes of the coinage and the s-block metals.



**Fig. 21** Photoactive CAAC complexes of the coinage metals.

were found to display much lower quantum yields, associated with radiationless energy loss involving excited structural rearrangements for coordination numbers exceeding two.<sup>590</sup> The complexes are phosphorescent with decay lifetimes ranging from 1 to 32  $\mu$ s and radiative rate constants ( $k_r = 2.6\text{--}3.9 \times 10^4 \text{ s}^{-1}$ ), indicating emission from the triplet  $^3\text{MLCT}$  state, with evidence for aggregation that leads to a red-shift in the emission wavelengths as compared to NHC  $\text{Cu}^I$  complexes.<sup>589,590</sup> The improved  $\sigma$ -donor/ $\pi$ -acceptor properties of the CAACs, compared to the NHCs, allow for participation of the copper d-orbitals in several HOMOs. This yields exceptionally strong SOC mixing of the  $^1\text{MLCT}$  and  $^3\text{MLCT}$  states to ensure efficient ISC, CT and radiative recombination in commercially available OLED host-guest systems.<sup>589</sup>

Copper(I) CAAC complexes with nanosecond photoemissions could be achieved with the incorporation of aryloxy- (569), thiophenol (571) or arylamido- (573) ligands as the second coordinating moiety (Fig. 21).<sup>591</sup> The heavier gold(I) analogs 570, 572 and 574, respectively, were similarly shown to present decay lifetimes varying from 2 to 275 ns. Emission color ranged from blue to yellow, depending on the ancillary ligand, while luminescence intensity was shown to increase with increasing steric bulk of the CAAC employed, as well as the  $M\text{--}O\text{--}C\text{--}C$  torsion angles for 569 and 570. Notably, more than one emission mechanism were found to operate for both the first and third row metals: both a prompt fluorescence emission in the nanosecond range, and a minor component with (sub)microsecond lifetime, depending on the ligand *trans* to the carbene in LMLCT-type delayed emissions. Silver(I) CAAC complexes 575 and 576 similarly displayed such dual emission mechanisms.<sup>592</sup>

Employment of potentially bidentate S,S or N,S-ligands to prepare 3-coordinate copper(I) complexes 577 and 578, as well as linear 579 (Fig. 21) was reported next by Bochmann et al.<sup>593</sup> The two-coordinate 579 proved to be a particularly efficient white phosphorescent emitter, with solid state quantum yield exceeding 96%. On the other hand, the tridentate 577 proved nonemissive, but the complex was found to decompose at 180  $^\circ\text{C}$  with the loss of the coordinating  $\text{CS}_2$  molecule, yielding the first example of a CAAC- $\text{Cu}^I$ -carbazolidene with the CMA-motif (vide supra). The same group also demonstrated the use of *malon*NHCs as anionic 6-membered NHC ligands based on a malonate unit to prepare zwitterionic  $\text{Cu}^I$  (580),  $\text{Ag}^I$  (581) and  $\text{Au}^I$  (582) mixed-carbene complexes (Fig. 21).<sup>579</sup> The two carbene ligands are co-planar which allows LUMO delocalization across the carbene carbon atom of both carbenes. This results in overlap between the HOMO and LUMO, and the large HOMO-LUMO energy gap (as

established electrochemically), gives rise to blue-white phosphorescence with excited state lifetimes (of 50–400  $\mu\text{s}$ ) increasing from the first row to the third row metal, in line with the SOC constants. For these compounds, and the preceding complexes, no strong intermolecular interactions were observed. Ultimately, however, the CMA bonding motif yielded the most successful photoemitters. Both copper (583) and gold (584) AdCAAC carbazolidine (Cbz) complexes were prepared, as well as substituted Cbz-gold(I) 585 and diphenylamide 586 (Fig. 21) for incorporation into OLED devices.<sup>594</sup> Rapid ISC from the triplet state is required to enable higher efficiencies for phosphorescent OLEDs not based on heavy atoms like platinum or iridium, or TADF OLEDs with low exchange energies. In the case of these CMAs 583–585, molecular configurations (depending on the relative dihedral angle of the CAAC (acceptor) and Cbz (donor) planes) that achieve low exchange energies exist. This means that internal quantum efficiencies of near-100% are obtained for the solution-processed OLEDs. Optimization of the Cu<sup>I</sup> CAAC OLED by fine-tuning of the CAAC steric encumbrance (CAAC variation between AdCAAC 600 in complex 583, MenthCAAC 41 in complex 587, Et<sub>2</sub>CAAC 514 in complex 588 and Me<sub>2</sub>CAAC 68 in complex 589, Fig. 21) and electronic properties of substituted Cbz (cyano-substituted 591, methoxy-substituted 592 or methyl-substituted 590) in addition to diphenylamide 593, Fig. 21 demonstrate the requirement of coplanar conformation of the ligands to suppress nonradiative decay associated with structural reorganization to achieve photoluminescence efficiencies > 99% from microsecond lifetime interligand charge transfer (ICT) transition between carbene and amide, and SOC through the metal d orbitals.<sup>595</sup>

In a further investigation of the photophysical properties of linear CAAC coinage metal CMAs (comparing Cu<sup>I</sup> 587, Ag<sup>I</sup> 594 and Au<sup>I</sup> 595, Fig. 21), it was found that the metals are redox innocent in contrast to other d<sup>10</sup> metal centers that emit from MLCT excited states.<sup>580</sup> Instead, the metal modulates electron coupling as a monoatomic electrical conduit between donor Cbz and acceptor CAAC. Delayed fluorescence resulting from thermally promoted rapid ISC arises from long-lived T<sub>1</sub> transition to the S<sub>1</sub> state. The fastest radiative rate is achieved for the silver complex, inversely related to the metal-ligand bond distances of the complexes. Exploitation of the success of the CAAC-based CMA photoemitters is evident from the rapid development of analogous coinage metal photoemitters utilizing e.g. first (596, 597, Fig. 21) and second generation carbazolidine dendrimers (598, 599, Fig. 21),<sup>581,596</sup> or modified CAACs such as the cyclic (aryl)(amino)carbenes (CAArCs)<sup>597</sup> or bicyclic CAACs,<sup>581</sup> with new or improved photophysical properties.

#### 1.05.6.2 Biological and medicinal applications of the nonclassical carbenes

The precedent of NHC metal complexes as chemotherapeutic agents<sup>458,539–542,598</sup> for anticancer, antimicrobial and antibacterial applications, or for biomedical applications<sup>458,540,599,600</sup> like chemosensing, photodynamic therapeutics or cell imaging, is underpinned by the strong metal carbon bond formed, as well as the ease of substituent variation and high functional group tolerance for biological property tuning. For the nonclassical carbene complexes under review, biological applications are being reported with increasing frequency, but remains an area where development is still in its infancy.

Coinage metal carbene complexes are being developed in attempts to minimize the significant side effects of Auranofin, the leading phosphine gold(I) thiolate complex with antitumor activity used clinically. Auranofin, and other gold(I)-based drugs, are thought to operate via a mode of action that includes binding to selenocysteine groups of the Thioredoxin Reductase (TrxR) enzyme active site, which is involved in cell death pathways mediated by Reactive Oxygen Species (ROS).<sup>601</sup> The stronger metal-ligand bond granted by coinage metal CAAC complexes of the type CAAC–M–Cl (562–565, 575; Fig. 21) was therefore thought to be potential cytotoxic agents capable of inhibiting TrxR with improved selectivity, while the cationic biscarbene complexes of the type CAAC–M<sup>+</sup>–CAAC (566, 576; Fig. 21) (M = Cu, Ag, Au) as delocalized lipophilic cations have the potential to target the mitochondria of cancer cells by compounds characterized by elevated partition coefficient values to readily pass lipid membranes.<sup>602</sup> The neutral and cationic CAAC coinage metal complexes were screened against a panel of human cancer cell lines of varying degrees of cisplatin resistance by O'Connell and Bochmann et al., with high cytotoxicity exhibited (the half maximal inhibitory concentration ( $\mu\text{M}$ ) required to inhibit the growth of 50% of cells in the culture, or IC<sub>50</sub> values, are in submicromolar – 100 nanomolar range). Especially the CAAC–M<sup>+</sup>–CAAC complexes proved effective against the cisplatin-insensitive cell lines. The mode-of-action of these complexes could not be unambiguously assigned, but TrxR inhibition and ROS formation were ruled out as primary pathways. A closer inspection of the apparently metal-dependent mode-of-action<sup>602</sup> was done by preparing the Et<sub>2</sub>CAAC–Au<sup>+</sup>–Et<sub>2</sub>CAAC 601 and the CAAC-bound Auranofin analog 602 containing the gluco-pyranosyl-1-thiolate ligand (Fig. 22), and evaluating TrxR and bovine serum albumin (BSA) protein binding.<sup>603</sup> 601 proved even more cytotoxic than Auranofin and is also the least lipophilic of the series but showed the highest cellular uptake. No mitochondrial delocalization occurred and thus the cytotoxicity of 601 is likely cell-based but independent of the mitochondria or the inhibition of related proteins.

The anticancer activity of trz coordinated complexes has also been explored for similar reasons, namely the robust metal-carbon bond that is stable under physiological conditions, while examples of Im4 complexes explored for their cytotoxic activity are exceedingly rare.<sup>202</sup> Ruthenium, osmium (193 and 194, Fig. 4 and 603, Fig. 23),<sup>600,604</sup> and iridium trz complexes (604, Fig. 23)<sup>604</sup> have been reported. All the complexes showed in vitro cytotoxicity for human ovarian cancer cells (e.g. for 603, human ovarian cancer cell lines A2780 and A2780R IC<sub>50</sub> < 50  $\mu\text{M}$ ; or for 604, for ovarian cancer cell line MES\_OV IC<sub>50</sub> = 4.08 ± 0.5  $\mu\text{M}$ ), with a high degree of selectivity towards normal cell lines. No metal dissociation under physiological conditions occurred. Linear coinage metal metallocenyl-trz complexes 315 and 318 (see Scheme 39, i and iii, respectively) have also displayed varying degrees of cytotoxicity but proved non-selective.<sup>314</sup> If Fc-functionalized trz complexes containing C5-alkyl chains (605 and 606, Fig. 23) were prepared, good antibacterial activity against the resistant Gram-negative bacterial *Salmonella* strain was obtained, although higher concentrations were required for the inhibition of *E. coli*.<sup>605</sup> The requirement of both the metal centers (Fe and Au) as well as the cationic

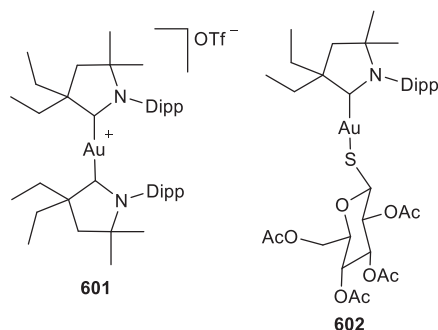


Fig. 22 Cytotoxic CAAC Au<sup>I</sup> complexes.

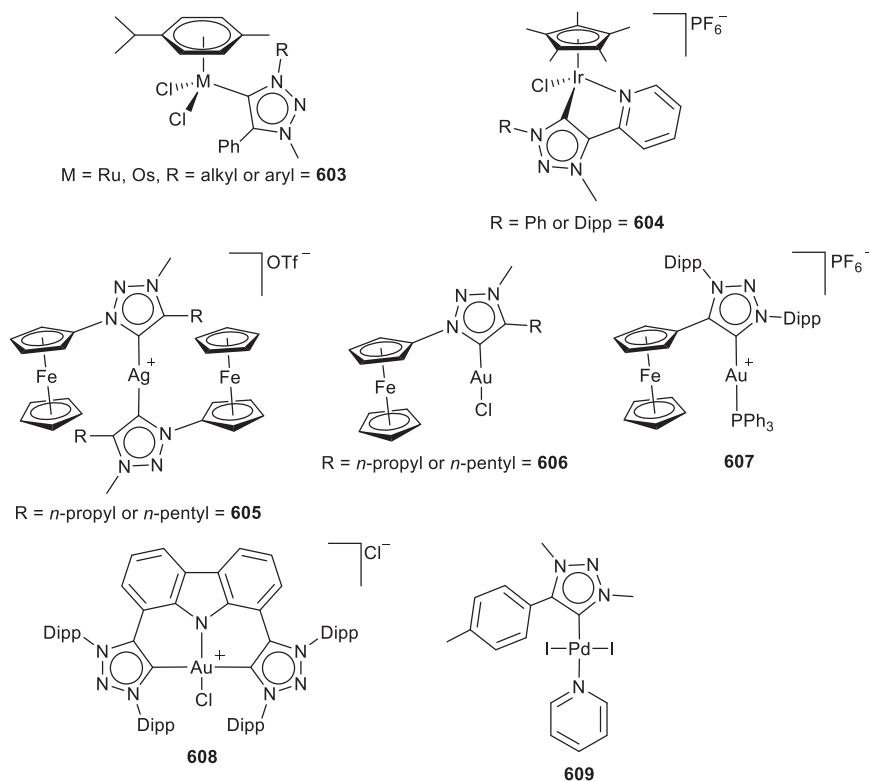


Fig. 23 Trz metal complexes with medicinal or bio-photophysical applications.

charge for cytotoxicity towards lung cancer cell lines A549 and H1975 (with limited cytotoxicity for human embryonic kidney cells HEK-293 as a normal cell model), could be unambiguously proved for a Fc-trz gold(I) phosphine 607 (Fig. 23), although preliminary mode-of-action studies only confirmed apoptotic cell death pathways.<sup>606</sup>

Different cellular targets are available to the harder Au<sup>III</sup> complexes for antitumor activities based on different mechanisms than TrxR inhibition, as viable alternatives to isoelectronic platinum(II)-based drugs. However, the kinetic lability, light sensitivity and the tendency for the Au<sup>III</sup> to reduce to Au<sup>I</sup> or Au<sup>0</sup> under physiological conditions limit the usefulness of Au<sup>III</sup> metal complexes as anticancer agents.<sup>607,608</sup> Modification of the bis(trz)carbazolide ligand scaffold known to favor gold(I) oxidation,<sup>216</sup> yielded a proligand containing an 'unsubstituted' aromatic planar carbazole moiety for potential DNA intercalation. Metalation and subsequent chemical oxidation resulted in a redox stable Au<sup>III</sup> complex 608 (Fig. 23) containing a labile chloride ligand available for covalent DNA-bonding, as a multi-pronged approach to targeting cancer DNA.<sup>609</sup> The complex was found to be notably cytotoxic toward the breast cancer cell line MDA-MB-231 (IC<sub>50</sub> = 2.3 ± 0.8 μM) and behaves as a partial DNA intercalator that can target DNA three-way junctions with good specificity, several other B-DNA forms and Z-DNA *in silico*. Both the redox stability (and inertia towards reaction with intracellular reductant glutathione GSH) and the DNA affinity of 608 might be key factors underlying its cytotoxicity *in vitro*.

One further area of application is the combination of photoactivity in the biological field for cell imaging possibilities. The principle was recently demonstrated by a fluorescent Pd<sup>II</sup> trz complex 609 (Fig. 23) as a non-toxic probe for selectively labelling the

endoplasmic reticulum in live cells,<sup>610</sup> and Ir<sup>III</sup> trz complexes 541 (Fig. 17) as luminescent probes for cell imaging of lung cancer cells.<sup>567</sup> The developments in biological and photophysical applications have been in line with the tunable electronic, steric and stabilizing properties associated with these carbene ligands. The applications are therefore mostly based on the inherent electronic properties of these ligands, rather than specific noninnocent behavior (ligand-based cooperative or multifunctional), with the notable exception of 608.<sup>609</sup>

### 1.05.7 Perspective

In little more than a decade, the deployment of nonclassical carbenes Im4, CAACs and trz as ligands has seen the boundaries of metal-mediated (re)activity pushed to new limits. The distinct (stereo)electronic properties of the different nonclassical carbenes have led to remarkable inherent noninnocent ligand behavior of the heterocycles when compared to classical NHCs and other donor ligands. Exploitation of this feature during ligand design leads to tailored ligands for highly specialized applications, particularly when coupled with the incorporation of a functional group furnishing a multifunctional role for the nonclassical carbene heterocycle in (chiral) catalysis. The potential of switchable carbene ligands that can adopt more than two electronic states, or the combination of two different switchable states, e.g., redox and light switchable, especially warrants future interest. The ancillary roles accessible from these ligands pave the way to multimodal functional compounds. As an illustrative example, the development of theranostic compounds or multitarget therapeutic agents can be anticipated from the preparation of ligands that are cytotoxic, redox- and photoactive. Applications extending beyond the molecular level are still rare, but scaling up to functional macromolecular materials is the next step.

### References

- Chiusoli, G. P.; Maitlis, P. M., Eds.; *Metal-catalysis in Industrial Organic Processes*, The Royal Society of Chemistry: Cambridge, UK, 2006.
- Bullock, R. M., Ed.; *Catalysis Without Precious Metals*, Wiley-VCH Verlag & Co. KGaA: Weinheim, Germany, 2010.
- Hartwig, J. F. *Organotransition Metal Chemistry: From Bonding to Catalysis*, University Science Books: Mill Valley, California, 2010.
- Crabtree, R. H. *The Organometallic Chemistry of the Transition Metals*, Wiley: Hoboken, NJ, 2019.
- Peris, E. *Chem. Rev.* **2018**, *118*, 9988–10031.
- Khusnutdinova, J. R.; Milstein, D. *Angew. Chem. Int. Ed.* **2015**, *54*, 12236–12273.
- Shimabayashi, T.; Fujita, K. *Catalysts* **2020**, *10*, 635.
- Gonçalves, T. P.; Dutta, I.; Huang, K. *Chem. Commun.* **2021**, *57*, 3070–3082.
- Gunanathan, C.; Milstein, D. *Acc. Chem. Res.* **2011**, *44*, 588–602.
- Grützmacher, H. *Angew. Chem. Int. Ed.* **2008**, *47*, 1814–1818.
- Braunstein, P.; Naud, F. *Angew. Chem. Int. Ed.* **2001**, *40*, 680–699.
- Zhao, B.; Han, Z.; Ding, K. *Angew. Chem. Int. Ed.* **2013**, *52*, 4744–4788.
- Dixon, D. J. *Beilstein J. Org. Chem.* **2016**, *12*, 1079–1080.
- Burrows, A. D. *Sci. Prog.* **2002**, *85*, 199–217.
- Higashi, T.; Kusumoto, S.; Nozaki, K. *Chem. Rev.* **2019**, *119*, 10393–10402.
- Zhang, W.; Chien, S. W.; Hor, T. S. A. *Coord. Chem. Rev.* **2011**, *255*, 1991–2024.
- Verhoeven, D. G. A.; Moret, M. *Dalton Trans.* **2016**, *45*, 15762–15778.
- Bouhadir, G.; Bourissou, D. *Chem. Soc. Rev.* **2016**, *45*, 1065–1079.
- Berben, L. A.; De Bruin, B.; Heyduk, A. F. *Chem. Commun.* **2015**, *51*, 1553–1554.
- Annibale, V. T.; Song, D. *RSC Adv.* **2013**, *3*, 11432–11449.
- Crabtree, R. H. *New J. Chem.* **2011**, *35*, 18–23.
- Choudhury, J.; Semwal, S. *Synlett* **2018**, *29*, 141–147.
- Chatterjee, B.; Chang, W.; Jena, S.; Werlé, C. *ACS Catal.* **2020**, *10*, 14024–14055.
- Elsby, M. R.; Baker, R. T. *Chem. Soc. Rev.* **2020**, *49*, 8933–8987.
- Morris, R. H. *Acc. Chem. Res.* **2015**, *48*, 1494–1502.
- Diez-González, S., Ed.; *N-Heterocyclic Carbenes: From Laboratory Curiosities to Efficient Synthetic Tools*; *RSC Catalysis Series*, The Royal Society of Chemistry: Cambridge, UK, 2011.
- Diez-González, S., Ed.; *N-Heterocyclic Carbenes: From Laboratory Curiosities to Efficient Synthetic Tools*; *RSC Catalysis Series* vol. 27; The Royal Society of Chemistry: Cambridge, UK, 2017.
- Cazin, C. S. J., Ed.; *N-Heterocyclic Carbenes in Transition Metal Catalysis and Organocatalysis*; *Catalysis by Metal Complexes* vol. 32; Springer: Dordrecht, 2011.
- Haameury, S.; de Frémont, P.; Braunstein, P. *Chem. Soc. Rev.* **2017**, *46*, 632–733.
- Patil, S. A.; Heras-Martinez, H. M.; Lewis, A. M.; Patil, S. A.; Bugarin, A. *Polyhedron* **2021**, *194*, 114935.
- Sau, S. C.; Hota, P. K.; Mandal, S. K.; Soleilhavoup, M.; Bertrand, G. *Chem. Soc. Rev.* **2020**, *49*, 1233–1252.
- Sierra, M. A.; De La Torre, M. C. *ACS Omega* **2019**, *4*, 12983–12994.
- Vivancos, Á.; Segarra, C.; Albrecht, M. *Chem. Rev.* **2018**, *118*, 9493–9586.
- Guisado-Barrios, G.; Soleilhavoup, M.; Bertrand, G. *Acc. Chem. Res.* **2018**, *51*, 3236–3244.
- Marichev, K. O.; Patil, S. A.; Bugarin, A. *Tetrahedron* **2018**, *74*, 2523–2546.
- Schweinfurth, D.; Hettmanczyk, L.; Suntrup, L.; Sarkar, B. *Z. Anorg. Allg. Chem.* **2017**, *643*, 554–584.
- Donnelly, K. F.; Petronilho, A.; Albrecht, M. *Chem. Commun.* **2013**, *49*, 1145–1159.
- Crabtree, R. H. *Coord. Chem. Rev.* **2013**, *257*, 755–766.
- Krüger, A.; Albrecht, M. *Aust. J. Chem.* **2011**, *64*, 1113–1117.
- Poulain, A.; Iglesias, M.; Albrecht, M. *Curr. Org. Chem.* **2011**, *15*, 3325–3336.
- Melaimi, M.; Soleilhavoup, M.; Bertrand, G. *Angew. Chem. Int. Ed.* **2010**, *49*, 8810–8849.



42. Martin, D.; Melaimi, M.; Soleilhavoup, M.; Bertrand, G. *Organometallics* **2011**, *30*, 5304–5313.
43. Albrecht, M. *Chimia* **2009**, *63*, 105–110.
44. Arnold, P. L.; Pearson, S. *Coord. Chem. Rev.* **2007**, *251*, 596–609.
45. Jazzar, R.; Soleilhavoup, M.; Bertrand, G. *Chem. Rev.* **2020**, *120*, 4141–4168.
46. Kundu, S.; Sinhababu, S.; Chandrasekhar, V.; Roesky, H. W. *Chem. Sci.* **2019**, *10*, 4727–4741.
47. Melaimi, M.; Jazzar, R.; Soleilhavoup, M.; Bertrand, G. *Angew. Chem. Int. Ed.* **2017**, *56*, 10046–10068.
48. Paul, U. S. D.; Radius, U. *Eur. J. Inorg. Chem.* **2017**, *2017*, 3362–3375.
49. Soleilhavoup, M.; Bertrand, G. *Acc. Chem. Res.* **2015**, *48*, 256–266.
50. Chandra Mondal, K.; Roy, S.; Roesky, H. W. *Chem. Soc. Rev.* **2016**, *45*, 1080–1111.
51. Roy, S.; Mondal, K. C.; Roesky, H. W. *Acc. Chem. Res.* **2016**, *49*, 357–369.
52. Gründemann, S.; Kovacevic, A.; Albrecht, M.; Faller, J. W.; Crabtree, R. H. *J. Am. Chem. Soc.* **2002**, *124*, 10473–10481.
53. Aldeco-Perez, E.; Rosenthal, A. J.; Donnadieu, B.; Parameswaran, P.; Frenking, G.; Bertrand, G. *Science* **2009**, *326*, 556–559.
54. Mathew, P.; Neels, A.; Albrecht, M. *J. Am. Chem. Soc.* **2008**, *130*, 13534–13535.
55. Guisado-Barrios, G.; Bouffard, J.; Donnadieu, B.; Bertrand, G. *Angew. Chem. Int. Ed.* **2010**, *49*, 4759–4762.
56. Lavallo, V.; Canac, Y.; Präsaug, C.; Donnadieu, B.; Bertrand, G. *Angew. Chem. Int. Ed.* **2005**, *44*, 5705–5709.
57. Schuster, O.; Yang, L.; Raubenheimer, H. G.; Albrecht, M. *Chem. Rev.* **2009**, *109*, 3445–3478.
58. Krüger, A.; Albrecht, M. *Chem. Eur. J.* **2012**, *18*, 652–658.
59. Krüger, A.; Häller, L. J. L.; Müller-Bunz, H.; Serada, O.; Neels, A.; Macgregor, S. A.; Albrecht, M. *Dalton Trans.* **2011**, *40*, 9911–9920.
60. Krüger, A.; Neels, A.; Albrecht, M. *Chemical Commun.* **2010**, *46*, 315–317.
61. Petronilho, A.; Woods, J. A.; Mueller-Bunz, H.; Bernhard, S.; Albrecht, M. *Chem. Eur. J.* **2014**, *20*, 15775–15784.
62. Bernet, L.; Lalrempuia, R.; Ghattas, W.; Mueller-Bunz, H.; Vigara, L.; Llobet, A.; Albrecht, M. *Chem. Commun.* **2011**, *47*, 8058–8060.
63. Woods, J. A.; Lalrempuia, R.; Petronilho, A.; McDaniel, N. D.; Müller-Bunz, H.; Albrecht, M.; Bernhard, S. *Energy Environ. Sci.* **2014**, *7*, 2316–2328.
64. Keitz, B. K.; Bouffard, J.; Bertrand, G.; Grubbs, R. H. *J. Am. Chem. Soc.* **2011**, *133*, 8498–8501.
65. Tulchinsky, Y.; Kozuch, S.; Saha, P.; Botoshansky, M.; Shimon, L. J. W.; Gandelman, M. *Chem. Sci.* **2014**, *5*, 1253–1662.
66. Petronilho, A.; Vivancos, A.; Albrecht, M. *Catal. Sci. Technol.* **2017**, *7*, 5766–5774.
67. Bouffard, J.; Keitz, B. K.; Tonner, R.; Guisado-Barrios, G.; Frenking, G.; Grubbs, R. H.; Bertrand, G. *Organometallics* **2011**, *30*, 2617–2627.
68. Munz, D. *Organometallics* **2018**, *37*, 275–289.
69. Nesterov, V.; Reiter, D.; Bag, P.; Frisch, P.; Holzner, R.; Porzelt, A.; Inoue, S. *Chem. Rev.* **2018**, *118*, 9678–9842.
70. Martin, D.; Soleilhavoup, M.; Bertrand, G. *Chem. Sci.* **2011**, *2*, 389–399.
71. Peltier, J. L.; Soleilhavoup, M.; Martin, D.; Jazzar, R.; Bertrand, G. *J. Am. Chem. Soc.* **2020**, *142*, 16479–16485.
72. Weinstein, C. M.; Junor, G. P.; Tolentino, D. R.; Jazzar, R.; Melaimi, M.; Bertrand, G. *J. Am. Chem. Soc.* **2018**, *140*, 9255–9260.
73. Mondal, K. C.; Roy, S.; Maity, B.; Koley, D.; Roesky, H. W. *Inorg. Chem.* **2016**, *55*, 163–169.
74. Kinjo, R.; Donnadieu, B.; Ali Celik, M.; Frenking, G.; Bertrand, G. *Science* **2011**, *333*, 610–613.
75. Légaré, M.; Bélanger-Chabot, G.; Dewhurst, R. D.; Welz, E.; Krummenacher, I.; Engels, B.; Braunschweig, H. *Science* **2018**, *359*, 896–900.
76. Légaré, M.; Rang, M.; Bélanger-Chabot, G.; Schweizer, J. I.; Krummenacher, I.; Bertermann, R.; Arrowsmith, M.; Holthausen, M. C.; Braunschweig, H. *Science* **2019**, *363*, 1329–1332.
77. Frey, G. D.; Lavallo, V.; Donnadieu, B.; Schoeller, W. W.; Bertrand, G. *Science* **2007**, *316*, 439–441.
78. Chu, T.; Nikonov, G. I. *Chem. Rev.* **2018**, *118*, 3608–3680.
79. Frey, G. D.; Masuda, J. D.; Donnadieu, B.; Bertrand, G. *Angew. Chem. Int. Ed.* **2010**, *49*, 9444–9447.
80. Eichhorn, A. F.; Kuehn, L.; Marder, T. B.; Radius, U. *Chem. Commun.* **2017**, *53*, 11694–11696.
81. Turner, Z. R. *Chem. Eur. J.* **2016**, *22*, 11461–11468.
82. Tolentino, D. R.; Neale, S. E.; Isaac, C. J.; Macgregor, S. A.; Whittlesey, M. K.; Jazzar, R.; Bertrand, G. *J. Am. Chem. Soc.* **2019**, *141*, 9823–9826.
83. Eichhorn, A. F.; Fuchs, S.; Flock, M.; Marder, T. B.; Radius, U. *Angew. Chem. Int. Ed.* **2017**, *56*, 10209–10213.
84. Peltier, J. L.; Tomás-Mendivil, E.; Tolentino, D. R.; Hansmann, M. M.; Jazzar, R.; Bertrand, G. *J. Am. Chem. Soc.* **2020**, *142*, 18336–18340.
85. Lavallo, V.; Canac, Y.; Donnadieu, B.; Schoeller, W. W.; Bertrand, G. *Angew. Chem. Int. Ed.* **2006**, *45*, 3488–3491.
86. van der Vlugt, J. I. *Eur. J. Inorg. Chem.* **2012**, *2012*, 363–375.
87. Kumar, A.; Gao, C. *Chem CatChem* **2021**, *13*, 1105–1134.
88. Li, H.; Hall, M. B. *ACS Catal.* **2015**, *5*, 1895–1913.
89. Milstein, D. *Phil. Trans. R. Soc. A* **2015**, *373*, 20140189.
90. Li, H.; Zheng, B.; Huang, K. *Coord. Chem. Rev.* **2015**, *293–294*, 116–138.
91. Li, H.; Gonçalves, T. P.; Lupp, D.; Huang, K. *ACS Catal.* **2019**, *9*, 1619–1629.
92. Gunanathan, C.; Milstein, D. *Chem. Rev.* **2014**, *114*, 12024–12087.
93. Milstein, D. *Top. Catal.* **2010**, *53*, 915–923.
94. Pandey, M. K.; Choudhury, J. *ACS Omega* **2020**, *5*, 30775–30786.
95. Flidel, C.; Braustein, P. *J. Organomet. Chem.* **2014**, *751*, 286–300.
96. Kuwata, S.; Ikariya, T. *Chem. Eur. J.* **2011**, *17*, 3542–3556.
97. Conley, B. L.; Pennington-Boggio, M. K.; Boz, E.; Williams, T. J. *Chem. Rev.* **2010**, *110*, 2294–2312.
98. Flynn, S. R.; Wass, D. F. *ACS Catal.* **2013**, *3*, 2574–2581.
99. DuBois, D. L. *Inorg. Chem.* **2014**, *53*, 3935–3960.
100. Yamakawa, M.; Ito, H.; Noyori, R. *J. Am. Chem. Soc.* **2000**, *122*, 1466–1478.
101. Noyori, R.; Yamakawa, M.; Hashiguchi, S. *J. Org. Chem.* **2001**, *66*, 7931–7944.
102. Hale, L. V. A.; Szymczak, N. K. *ACS Catal.* **2018**, *8*, 6446–6461.
103. Ramasamy, B.; Ghosh, P. *Eur. J. Inorg. Chem.* **2016**, *2016*, 1448–1465.
104. Pape, F.; Teichert, J. F. *Eur. J. Org. Chem.* **2017**, *2017*, 4206–4229.
105. Kuwata, S.; Ikariya, T. *Chem. Commun.* **2014**, *50*, 14290–14300.
106. Liddle, S. T.; Edworthy, I. S.; Arnold, P. L. *Chem. Soc. Rev.* **2007**, *36*, 1732–1744.
107. Jahnke, M. C.; Hahn, F. E. *Coord. Chem. Rev.* **2015**, *293–294*, 95–115.
108. Albrecht, M. *Chem. Rev.* **2010**, *110*, 576–623.
109. Vijaykumar, G.; Jose, A.; Vardhanapu, P. K.; Sreejyothi, P.; Mandal, S. K. *Organometallics* **2017**, *36*, 4753–4758.
110. Sau, S. C.; Santra, S.; Sen, T. K.; Mandal, S. K.; Koley, D. *Chem. Commun.* **2012**, *43*, 555–557.
111. Hota, P. K.; Jose, A.; Mandal, S. K. *Organometallics* **2017**, *36*, 4422–4431.
112. Hota, P. K.; Vijaykumar, G.; Pariyar, A.; Sau, S. C.; Sen, T. K.; Mandal, S. K. *Adv. Synth. Catal.* **2015**, *342*, 3162–3170.
113. Sreejyothi, P.; Sau, S. C.; Vardhanapu, P. K.; Mandal, S. K. *J. Org. Chem.* **2018**, *83*, 9403–9411.

114. Saravananakumar, R.; Ramkumar, V.; Sankararaman, S. *Organometallics* **2011**, *30*, 1689–1694.
115. Sureshbabu, B.; Ramkumar, V.; Sankararaman, S. *J. Organomet. Chem.* **2015**, *799–800*, 232–238.
116. Yan, X.; Feng, R.; Yan, C.; Lei, P.; Guo, S.; Huynh, H. V. *Dalton Trans.* **2018**, *47*, 7830–7838.
117. Song, G.; Wang, X.; Li, Y.; Li, X. *Organometallics* **2008**, *27*, 1187–1192.
118. Scheele, U.; Dechert, S.; Meyer, F. *Chem. Eur. J.* **2008**, *14*, 5112–5115.
119. Wolf, J.; Labande, A.; Daran, J.; Poli, R. *Eur. J. Inorg. Chem.* **2008**, *2008*, 3024–3030.
120. Stylianides, N.; Danopoulos, A. A.; Tsoureas, N. *J. Organomet. Chem.* **2005**, *690*, 5948–5958.
121. Topchiy, M. A.; Dzhevakov, P. B.; Kirilenko, N. Y.; Rzhevskiy, S. A.; Aghshina, A. A.; Khrustalev, V. N.; Paraschuk, D. Y.; Bermeshev, M. V.; Nechaev, M. S.; Asachenko, A. F. *Mendeleev Commun.* **2019**, *29*, 128–131.
122. Bhat, I. A.; Avinash, I.; Anantharaman, G. *Organometallics* **2019**, *38*, 1699–1708.
123. Donnelly, K. F.; Lalrempuia, R.; Müller-Bunz, H.; Albrecht, M. *Organometallics* **2012**, *31*, 8414–8419.
124. Petronilho, A.; Rahman, M.; Woods, J. A.; Al-Sayyed, H.; Müller-Bunz, H.; Don MacElroy, J. M.; Bernhard, S.; Albrecht, M. *Dalton Trans.* **2012**, *41*, 13074–13080.
125. Poulain, A.; Canseco-Gonzalez, D.; Hynes-Roche, R.; Müller-Bunz, H.; Schuster, O.; Stoeckli-Evans, H.; Neels, A.; Albrecht, M. *Organometallics* **2011**, *30*, 1021–1029.
126. Bagh, B.; McKinty, A. M.; Lough, A. J.; Stephan, D. W. *Dalton Trans.* **2015**, *44*, 2712–2723.
127. Bagh, B.; McKinty, A. M.; Lough, A. J.; Stephan, D. W. *Dalton Trans.* **2014**, *43*, 12842–12850.
128. Bagh, B.; Stephan, D. W. *Dalton Trans.* **2014**, *43*, 15638–15645.
129. Lalrempuia, R.; McDaniel, N. D.; Müller-Bunz, H.; Bernhard, S.; Albrecht, M. *Angew. Chem. Int. Ed.* **2010**, *49*, 9765–9768.
130. Donnelly, K. F.; Lalrempuia, R.; Müller-Bunz, H.; Clot, E.; Albrecht, M. *Organometallics* **2015**, *34*, 858–869.
131. Lalrempuia, R.; Müller-Bunz, H.; Albrecht, M. *Angew. Chem. Int. Ed.* **2011**, *50*, 9969–9972.
132. Zhao, L.; Hu, C.; Cong, X.; Deng, G.; Liu, L. L.; Luo, M.; Zeng, X. *J. Am. Chem. Soc.* **2021**, *143*, 1618–1629.
133. Samuel, P. P.; Neufeld, R.; Chandra Mondal, K.; Roesky, H. W.; Herbst-Imer, R.; Stalke, D.; Demeshko, S.; Meyer, F.; Rojisha, V. C.; De, S.; Parameswaran, P.; Stückl, A. C.; Kaim, W.; Christian, J. H.; Bindra, J. K.; Dalal, N. S. *Chem. Sci.* **2015**, *6*, 3148–3153.
134. Chu, J.; Munz, D.; Jazsar, R.; Melaimi, M.; Bertrand, G. *J. Am. Chem. Soc.* **2016**, *138*, 7884–7887.
135. Frey, G. D.; Donnadiou, B.; Soleilhavoup, M.; Bertrand, G. *Chem. Asian J.* **2011**, *6*, 402–405.
136. Lavallo, V.; Canac, Y.; DeHope, A.; Donnadiou, B.; Bertrand, G. *Angew. Chem. Int. Ed.* **2005**, *44*, 7236–7239.
137. Pardatscher, L.; Bitzer, M. J.; Jandl, C.; Kück, J. W.; Reich, R. M.; Kühn, F. E.; Baratta, W. *Dalton Trans.* **2019**, *48*, 79–89.
138. Witt, J.; Pöthig, A.; Kühn, F. E.; Baratta, W. *Organometallics* **2013**, *32*, 4042–4045.
139. Garhwal, S.; Maji, B.; Semwal, S.; Choudhury, J. *Organometallics* **2018**, *37*, 4720–4725.
140. Semwal, S.; Kumar, A.; Choudhury, J. *Catal. Sci. Technol.* **2018**, *8*, 6137–6142.
141. Crabtree, R. H. *Energy Environ. Sci.* **2008**, *1*, 134–138.
142. Eberle, U.; Felderhoff, M.; Schüth, F. *Angew. Chem. Int. Ed.* **2009**, *48*, 6608–6630.
143. Teichmann, D.; Arit, W.; Wasserscheid, P.; Freymann, R. *Energy Environ. Sci.* **2011**, *4*, 2767–2773.
144. Kumar, A.; Semwal, S.; Choudhury, J. *ACS Catal.* **2019**, *9*, 2164–2168.
145. Maji, B.; Choudhury, J. *Chem. Commun.* **2019**, *55*, 4574–4577.
146. Shi, S.; Nolan, S. P.; Szostak, M. *Acc. Chem. Res.* **2018**, *51*, 2589–2599.
147. Valente, C.; Çalimsiz, S.; Hoi, K. H.; Mallik, D.; Sayah, M.; Organ, M. G. *Angew. Chem. Int. Ed.* **2012**, *51*, 3314–3332.
148. Kaloglu, N.; Özdemir, I. *Tetrahedron* **2019**, *75*, 2306–2313.
149. Osińska, M.; Gniewek, A.; Trzeciak, A. M. *J. Mol. Catal. A Chem.* **2016**, *418–419*, 9–18.
150. Groombridge, B. J.; Guldop, S. M.; Larrosa, I. *Chem. Commun.* **2015**, *51*, 3832–3834.
151. O'Brien, C. J.; Kantchev, E. A. B.; Valente, C.; Hadei, N.; Chass, G. A.; Lough, A.; Hopkinson, A. C.; Organ, M. G. *Chem. Eur. J.* **2006**, *12*, 4743–4748.
152. Organ, M. G.; Avola, S.; Dubovyk, I.; Hadei, N.; Kantchev, E. A. B.; O'Brien, C. J.; Valente, C. *Chem. Eur. J.* **2006**, *12*, 4749–4755.
153. Organ, M.; Çalimsiz, S.; Sayah, M.; Hoi, K.; Lough, A. *Angew. Chem. Int. Ed.* **2009**, *48*, 2383–2387.
154. Hadei, N.; Achonduh, G. T.; Valente, C.; O'Brien, C. J.; Organ, M. G. *Angew. Chem. Int. Ed.* **2011**, *50*, 3896–3899.
155. Sharif, S.; Rucker, R. P.; Chandrasoma, N.; Mitchell, D.; Rodríguez, M. J.; Froese, R. D. J.; Organ, M. G. *Angew. Chem. Int. Ed.* **2015**, *54*, 9507–9511.
156. Guillet, S. G.; Voloshkin, V. A.; Saab, M.; Bellis, M.; Van Hecke, K.; Nagra, F.; Nolan, S. P. *Chem. Commun.* **2020**, *56*, 5953–5956.
157. Buchspies, J.; Pyle, D. J.; He, H.; Szostak, M. *Molecules* **2018**, *23*, 3134.
158. Atwater, B.; Chandrasoma, N.; Mitchell, D.; Rodríguez, M. J.; Pompeo, M.; Froese, R. D. J.; Organ, M. G. *Angew. Chem. Int. Ed.* **2015**, *54*, 9502–9506.
159. Lei, P.; Meng, G.; Ling, Y.; An, J.; Szostak, M. *J. Org. Chem.* **2017**, *82*, 6638–6646.
160. Shi, S.; Lei, P.; Szostak, M. *Organometallics* **2017**, *36*, 3784–3789.
161. Liu, C.; Li, G.; Shi, S.; Meng, G.; Lalancette, R.; Szostak, R.; Szostak, M. *ACS Catal.* **2018**, *8*, 9131–9139.
162. Li, G.; Shi, S.; Lei, P.; Szostak, M. *Adv. Synth. Catal.* **2018**, *360*, 1538–1543.
163. Suntrup, L.; Klenk, S.; Klein, J.; Sobottka, S.; Sarkar, B. *Inorg. Chem.* **2017**, *56*, 5771–5783.
164. Petronilho, A.; Llobet, A.; Albrecht, M. *Inorg. Chem.* **2014**, *53*, 12896–12901.
165. Corbucci, I.; Zaccaria, F.; Heath, R.; Gatto, G.; Zuccaccia, C.; Albrecht, M.; Macchioni, A. *ChemCatChem* **2019**, *11*, 5353–5361.
166. Mazloomi, Z.; Margalef, J.; Gil-Sepulcre, M.; Romero, N.; Albrecht, M.; Llobet, A.; Sala, X.; Pàmies, O.; Diéguez, M. *Inorg. Chem.* **2020**, *59*, 12337–12347.
167. Vivancos, Á.; Beller, M.; Albrecht, M. *ACS Catal.* **2018**, *8*, 17–21.
168. Butschke, B.; Schwarz, H. *Chem. Sci.* **2012**, *3*, 308–326.
169. Virant, M.; Mihelač, M.; Gazvoda, M.; Cotman, A. E.; Frantar, A.; Pinter, B.; Košmrlj, J. *Org. Lett.* **2020**, *22*, 2157–2161.
170. Gazvoda, M.; Virant, M.; Pevec, A.; Urankar, D.; Bolje, A.; Kočevar, M.; Košmrlj, J. *Chem. Commun.* **2016**, *52*, 1571–1574.
171. Martek, B. A.; Gazvoda, M.; Urankar, D.; Košmrlj, J. *Org. Lett.* **2020**, *22*, 4938–4943.
172. Van Der Meer, M.; Glais, E.; Siewert, I.; Sarkar, B. *Angew. Chem. Int. Ed.* **2015**, *54*, 13792–13795.
173. Hohloch, S.; Kaiser, S.; Duecker, F. L.; Bolje, A.; Maity, R.; Košmrlj, J.; Sarkar, B. *Dalton Trans.* **2015**, *44*, 686–693.
174. Bolje, A.; Hohloch, S.; Urankar, D.; Pevec, A.; Gazvoda, M.; Sarkar, B.; Košmrlj, J. *Organometallics* **2014**, *33*, 2588–2598.
175. Bolje, A.; Košmrlj, J. *Org. Lett.* **2013**, *15*, 5084–5087.
176. Bolje, A.; Hohloch, S.; Košmrlj, J.; Sarkar, B. *Dalton Trans.* **2016**, *45*, 15983–15993.
177. Olguín, J.; Paz-Sandoval, M. A. *J. Organomet. Chem.* **2017**, *848*, 309–317.
178. Valencia, M.; Pereira, A.; Müller-Bunz, H.; Belderrain, T. R.; Pérez, P. J.; Albrecht, M. *Chem. Eur. J.* **2017**, *23*, 8901–8911.
179. Sabater, S.; Müller-Bunz, H.; Albrecht, M. *Organometallics* **2016**, *35*, 2256–2266.
180. Olivares, M.; van der Ham, C. J. M.; Mdluli, V.; Schmidtendorf, M.; Müller-Bunz, H.; Verhoeven, M. W. G. M.; Li, M.; Niemantsveriet, J. W.; Hettterscheid, D. G. H.; Bernhard, S.; Albrecht, M. *Eur. J. Inorg. Chem.* **2020**, *2020*, 801–812.
181. Olivares, M.; Albrecht, M. *J. Organomet. Chem.* **2020**, *920*, 121290.
182. Olivares, M.; Knörr, P.; Albrecht, M. *Dalton Trans.* **2020**, *49*, 1981–1991.
183. Power, P. P. *Nature* **2010**, *463*, 171–177.

184. Stephan, D.; Erker, G. *Angew. Chem. Int. Ed.* **2010**, *49*, 46–76.
185. Scott, D. J.; Fuchter, M. J.; Ashley, A. E. *Chem. Soc. Rev.* **2017**, *46*, 5689–5700.
186. Canseco-Gonzalez, D.; Petronilho, A.; Mueller-Bunz, H.; Ohmatsu, K.; Ooi, T.; Albrecht, M. *J. Am. Chem. Soc.* **2013**, *135*, 13193–13203.
187. Strydom, I.; Guisado-Barrios, G.; Fernández, I.; Liles, D. C.; Peris, E.; Bezuidenhout, D. I. *Chem. Eur. J.* **2017**, *23*, 1393–1401.
188. Castarlenas, R.; Di Giuseppe, A.; Pérez-Torrente, J. J.; Oro, L. A. *Angew. Chem. Int. Ed.* **2013**, *52*, 211–222.
189. Palacios, L.; Meheut, Y.; Galiana-Cameo, M.; Artigas, M. J.; Di Giuseppe, A.; Lahoz, F. J.; Polo, V.; Castarlenas, R.; Pérez-Torrente, J. J.; Oro, L. A. *Organometallics* **2017**, *36*, 2198–2207.
190. Alig, L.; Fritz, M.; Schneider, S. *Chem. Rev.* **2019**, *119*, 2681–2751.
191. Peris, E.; Crabtree, R. H. *Chem. Soc. Rev.* **2018**, *47*, 1959–1968.
192. Valdés, H.; García-Eleno, M. A.; Canseco-Gonzalez, D.; Morales-Morales, D. *ChemCatChem* **2018**, *10*, 3136–3172.
193. Albrecht, M.; Lindner, M. M. *Dalton Trans.* **2011**, *40*, 8733–8744.
194. Choi, J.; MacArthur, A. H. R.; Brookhart, M.; Goldman, A. S. *Chem. Rev.* **2011**, *111*, 1761–1779.
195. Pugh, D.; Danopoulos, A. A. *Coord. Chem. Rev.* **2007**, *251*, 610–641.
196. Mata, J. A.; Poyatos, M.; Peris, E. *Coord. Chem. Rev.* **2007**, *251*, 841–859.
197. Albrecht, M.; van Koten, G. *Angew. Chem. Int. Ed.* **2001**, *40*, 3750–3781.
198. van Koten, G.; Milstein, D., Eds.; *Organometallic Pincer Chemistry; Topics in Organometallic Chemistry* vol. 40; Springer-Verlag: Berlin Heidelberg, 2013.
199. van Koten, G.; Gossage, R. A., Eds.; *The Privileged Pincer-Metal Platform: Coordination Chemistry & Applications; Topics in Organometallic Chemistry* vol. 54; Springer International Publishing, 2016.
200. Schuster, E. M.; Botoshansky, M.; Gandelman, M. *Dalton Trans.* **2011**, *40*, 8764–8767.
201. Farrell, K.; Müller-Bunz, H.; Albrecht, M. *Dalton Trans.* **2016**, *45*, 15859–15871.
202. Lee, J.-Y.; Lee, J.-Y.; Chang, Y.-Y.; Hu, C.-H.; Wang, N. M.; Lee, H. M. *Organometallics* **2015**, *34*, 4359–4368.
203. Zuo, W.; Braunstein, P. *Organometallics* **2012**, *31*, 2606–2615.
204. Tolley, L. C.; Strydom, I.; Louw, W. J.; Fernandes, M. A.; Bezuidenhout, D. I.; Guisado-Barrios, G. *ACS Omega* **2019**, *4*, 6360–6374.
205. Li, L.; Cao, L.; Yan, X. *ChemistrySelect* **2018**, *3*, 10706–10710.
206. Schulze, B.; Escudero, D.; Friebe, C.; Siebert, R.; Görls, H.; Köhn, U.; Altuntas, E.; Baumgaertel, A.; Hager, M. D.; Winter, A.; Dietzek, B.; Popp, J.; González, L.; Schubert, U. S. *Chem. Eur. J.* **2011**, *17*, 5494–5498.
207. Brown, D. G.; Sanguantrakun, N.; Schulze, B.; Schubert, U. S.; Berlinguette, C. P. *J. Am. Chem. Soc.* **2012**, *134*, 12354–12357.
208. Sinn, S.; Schulze, B.; Friebe, C.; Brown, D. G.; Jäger, M.; Altuntas, E.; Kübel, J.; Guntner, O.; Berlinguette, C. P.; Dietzek, B.; Schubert, U. S. *Inorg. Chem.* **2014**, *53*, 2083–2095.
209. Filonenko, G. A.; Cosimi, E.; Lefort, L.; Conley, M. P.; Copéret, C.; Lutz, M.; Hensen, E. J. M.; Pidko, E. A. *ACS Catal.* **2014**, *4*, 2667–2671.
210. Bezuidenhout, D. I.; Kleinhans, G.; Guisado-Barrios, G.; Liles, D. C.; Ung, G.; Bertrand, G. *Chem. Commun.* **2014**, *50*, 2431–2433.
211. Naziruddin, A. R.; Lee, C.; Lin, W.; Sun, B.; Chao, K.; Chang, A. H. H.; Hwang, W. *Dalton Trans.* **2016**, *45*, 5848–5859.
212. Iwasaki, H.; Koga, Y.; Matsubara, K. *Organic. Chem. Current. Res.* **2016**, *5*, 1–5.
213. Iwasaki, H.; Yamada, Y.; Ishikawa, R.; Koga, Y.; Matsubara, K. *Eur. J. Org. Chem.* **2016**, *2016*, 1651–1654.
214. Hollering, M.; Albrecht, M.; Kühn, F. E. *Organometallics* **2016**, *35*, 2980–2986.
215. Sluijter, S. N.; Korstanje, T. J.; van der Vlugt, J. I.; Elsevier, C. J. *J. Organomet. Chem.* **2017**, *845*, 30–37.
216. Kleinhans, G.; Hansmann, M. M.; Guisado-Barrios, G.; Liles, D. C.; Bertrand, G.; Bezuidenhout, D. I. *J. Am. Chem. Soc.* **2016**, *138*, 15873–15876.
217. Kleinhans, G.; Chan, A. K.; Leung, M.; Liles, D. C.; Fernandes, M. A.; Yam, V. W.-W.; Fernández, I.; Bezuidenhout, D. I. *Chem. Eur. J.* **2020**, *26*, 6993–6998.
218. Herrera, R. P.; Gimeno, M. C. *Chem. Rev.* **2021**, *121*, 8311–8363.
219. Rocchigiani, L.; Bochmann, M. *Chem. Rev.* **2021**, *121*, 8364–8451.
220. Joost, M.; Amgoune, A.; Bourissou, D. *Angew. Chem. Int. Ed.* **2015**, *54*, 15022–15045.
221. Teles, J. H. *Angew. Chem. Int. Ed.* **2015**, *54*, 5556–5558.
222. Wu, C.; Horibe, T.; Jacobsen, C. B.; Toste, F. D. *Nature* **2015**, *517*, 449–454.
223. Grünwald, A.; Orth, N.; Scheurer, A.; Heinemann, W.; Pöthig, A.; Munz, D. *Angew. Chem. Int. Ed.* **2018**, *57*, 16228–16232.
224. Grünwald, A.; Heinemann, F. W.; Munz, D. *Angew. Chem.* **2020**, *132*, 21274–21281.
225. Modak, S.; Gangwar, M. K.; Nageswar Rao, M.; Madasu, M.; Kalita, A. C.; Dorcet, V.; Shejale, M. A.; Butcher, R. J.; Ghosh, P. *Dalton Trans.* **2015**, *44*, 17617–17628.
226. Park, D.; Byun, S.; Ryu, J. Y.; Lee, J.; Lee, J.; Hong, S. *ACS Catal.* **2020**, *10*, 5443V5453.
227. Lee, J.; Su, Y.; Wang, Y.; Lee, H. M. *Adv. Synth. Catal.* **2019**, *361*, 4714–4726.
228. Byrne, J. P.; Musembi, P.; Albrecht, M. *Dalton Trans.* **2019**, *48*, 11838–11847.
229. Mollar-Cuni, A.; Byrne, J. P.; Borja, P.; Vicent, C.; Albrecht, M.; Mata, J. A. *ChemCatChem* **2020**, *12*, 3746–3752.
230. Pretorius, R.; Olguin, J.; Albrecht, M. *Inorg. Chem.* **2017**, *56*, 12410–12420.
231. Saha, S.; Daw, P.; Bera, J. K. *Organometallics* **2015**, *34*, 5509–5512.
232. Daw, P.; Petakamsetty, R.; Sarbajna, A.; Laha, S.; Ramapanicker, R.; Bera, J. K. *J. Am. Chem. Soc.* **2014**, *136*, 13987–13990.
233. Tyagi, A.; Reshi, N. U. D.; Daw, P.; Bera, J. K. *Dalton Trans.* **2020**, *49*, 15238–15248.
234. Saha, S.; Yadav, S.; Reshi, N. U. D.; Dutta, I.; Kunnikuruvan, S.; Bera, J. K. *ACS Catal.* **2020**, *10*, 11385–11393.
235. Yadav, S.; Dutta, I.; Saha, S.; Das, S.; Pati, S. K.; Choudhury, J.; Bera, J. K. *Organometallics* **2020**, *39*, 3212–3223.
236. Pandey, P.; Daw, P.; Din Reshi, N. U.; Ehmann, K. R.; Hölscher, M.; Leitner, W.; Bera, J. K. *Organometallics* **2020**, *39*, 3849–3863.
237. Delgado-Rebollo, M.; Canseco-Gonzalez, D.; Hollering, M.; Mueller-Bunz, H.; Albrecht, M. *Dalton Trans.* **2014**, *43*, 4462–4473.
238. Pretorius, R.; Frutos, M. R.; Müller-Bunz, H.; Gossage, R. A.; Pérez, P. J.; Albrecht, M. *Dalton Trans.* **2016**, *45*, 14591–14602.
239. Bertini, S.; Albrecht, M. *Chimia* **2020**, *74*, 483–488.
240. Wei, Y.; Petronilho, A.; Mueller-Bunz, H.; Albrecht, M. *Organometallics* **2014**, *33*, 5834–5844.
241. Mazloomi, Z.; Pretorius, R.; Pàmies, O.; Albrecht, M.; Diéguez, M. *Inorg. Chem.* **2017**, *56*, 11282–11298.
242. Pretorius, R.; Mazloomi, Z.; Albrecht, M. *J. Organomet. Chem.* **2017**, *845*, 196–205.
243. Pretorius, R.; McDonald, A.; Regueira Beltrão Da Costa, L.; Müller-Bunz, H.; Albrecht, M. *Eur. J. Inorg. Chem.* **2019**, *2019*, 4263–4272.
244. Mendoza-Espinosa, D.; Rendón-Nava, D.; Álvarez-Hernández, A.; Angeles-Beltrán, D.; Negrón-Silva, G. E.; Suárez-Castillo, O. R. *Chem. Asian J.* **2017**, *12*, 203–207.
245. De la Fuente-Olvera, A. A.; Suárez-Castillo, O. R.; Mendoza-Espinosa, D. *Eur. J. Inorg. Chem.* **2019**, *2019*, 4879–4886.
246. Rendón-Nava, D.; Álvarez-Hernández, A.; Rheingold, A. L.; Suárez-Castillo, O. R.; Mendoza-Espinosa, D. *Dalton Trans.* **2019**, *48*, 3214–3222.
247. Saravanakumar, R.; Ramkumar, V.; Sankararaman, S. *J. Organomet. Chem.* **2013**, *736*, 36–41.
248. Frutos, M.; Avello, M. G.; Viso, A.; Fernández de la Pradilla, R.; de la Torre, M. C.; Sierra, M. A.; Gornitzka, H.; Hemmert, C. *Org. Lett.* **2016**, *18*, 3570–3573.
249. Álvarez-Pérez, M.; Frutos, M.; Viso, A.; Fernández De la Pradilla, R.; De La Torre, M. C.; Sierra, M. A.; Gornitzka, H.; Hemmert, C. *J. Org. Chem.* **2017**, *82*, 7546–7554.
250. Yuan, D.; Huynh, H. V. *Dalton Trans.* **2011**, *40*, 11698–11703.
251. Xu, X.; Li, L.; Zhang, Z.; Yan, X. *Tetrahedron* **2018**, *74*, 6846–6853.
252. Bierenstiel, M.; Cross, E. D. *Coord. Chem. Rev.* **2011**, *255*, 574–590.

253. Hohloch, S.; Su, C.; Sarkar, B. *Eur. J. Inorg. Chem.* **2011**, *2011*, 3067–3075.
254. Hohloch, S.; Hettmanczyk, L.; Sarkar, B. *Eur. J. Inorg. Chem.* **2014**, *2014*, 3164–3171.
255. Dzik, W. I.; van der Vlugt, J. I.; Reek, J. N. H.; de Bruin, B. *Angew. Chem. Int. Ed.* **2011**, *50*, 3356–3358.
256. Allgeier, A. M.; Mirkin, C. A. *Angew. Chem. Int. Ed.* **1998**, *37*, 894–908.
257. Kaim, W. *Eur. J. Inorg. Chem.* **2012**, *2012*, 343–348.
258. van der Vlugt, J. I. *Chem. Eur. J.* **2019**, *25*, 2651–2662.
259. Dzik, W. I.; Zhang, X. P.; de Bruin, B. *Inorg. Chem.* **2011**, *50*, 9896–9903.
260. Broere, D. L. J.; Plessius, R.; van der Vlugt, J. I. *Chem. Soc. Rev.* **2015**, *44*, 6886–6915.
261. Ryu, Y.; Ahumada, G.; Bielawski, C. W. *Chem. Commun.* **2019**, *55*, 4451–4466.
262. Blanco, V.; Leigh, D. A.; Marcos, V. *Chem. Soc. Rev.* **2015**, *44*, 5341–5370.
263. Lüning, U. *Angew. Chem. Int. Ed.* **2012**, *51*, 8163–8165.
264. McConnell, A. J.; Wood, C. S.; Neelakandan, P. P.; Nitschke, J. R. *Chem. Rev.* **2015**, *115*, 7729–7793.
265. Zhan, G.; Du, W.; Chen, Y. *Chem. Soc. Rev.* **2017**, *46*, 1675–1692.
266. Yağcı, Y.; Reetz, I. *Prog. Polym. Sci.* **1998**, *23*, 1485–1538.
267. Leibfarth, F. A.; Mattson, K. M.; Fors, B. P.; Collins, H. A.; Hawker, C. J. *Angew. Chem. Int. Ed.* **2013**, *52*, 199–210.
268. Suarez, A. I. O.; Lyaskovskyy, V.; Reek, J. N. H.; van der Vlugt, J. I.; de Bruin, B. *Angew. Chem. Int. Ed.* **2013**, *52*, 12510–12529.
269. Hettmanczyk, L.; Manck, S.; Hoyer, C.; Hohloch, S.; Sarkar, B. *Chem. Commun.* **2015**, *51*, 10949–10952.
270. Atkinson, R. C. J.; Long, N. J. In *Ferrocenes: Ligands, Materials and Biomolecules*; Štěpnička, P., Ed., John Wiley & Sons, Ltd: Chichester, UK, 2008; pp 1–32.
271. Hildebrandt, A.; Rüffer, T.; Erasmus, E.; Swarts, J. C.; Lang, H. *Organometallics* **2010**, *29*, 4900–4905.
272. Dorel, R.; Echavarren, A. M. *Chem. Rev.* **2015**, *115*, 9028–9072.
273. Raubenheimer, H. G.; Schmidbaur, H. *J. Chem. Educ.* **2014**, *91*, 2024–2036.
274. Gorin, D. J.; Sherry, B. D.; Toste, F. D. *Chem. Rev.* **2008**, *108*, 3351–3378.
275. Hashmi, A. S. K. *Chem. Rev.* **2007**, *107*, 3180–3211.
276. Badéche, S.; Daran, J.; Ruiz, J.; Astruc, D. *Inorg. Chem.* **2008**, *47*, 4903–4908.
277. Sai Sudhir, V.; Phani Kumar, N. Y.; Chandrasekaran, S. *Tetrahedron* **2010**, *66*, 1327–1334.
278. Lewis, J. E. M.; McAdam, C. J.; Gardiner, M. G.; Crowley, J. D. *Chem. Commun.* **2013**, *49*, 3398–3400.
279. Uppal, B. S.; Zahid, A.; Elliott, P. I. P. *Eur. J. Inorg. Chem.* **2013**, *2013*, 2571–2579.
280. Cao, Q.; Pradhan, T.; Kim, S.; Kim, J. S. *Org. Lett.* **2011**, *13*, 4386–4389.
281. Salmon, A. J.; Williams, M. L.; Wu, Q. K.; Morizzi, J.; Gregg, D.; Charman, S. A.; Vullo, D.; Supuran, C. T.; Poulsen, S. *J. Med. Chem.* **2012**, *55*, 5506–5517.
282. Kumar, K.; Carrère-Kremer, S.; Kremer, L.; Guérardel, Y.; Biot, C.; Kumar, V. *Organometallics* **2013**, *32*, 5713–5719.
283. Verschoor-Kirss, M.; Kreis, J.; Feighery, W.; Reiff, W. M.; Frommen, C. M.; Kirss, R. U. *J. Organomet. Chem.* **2009**, *694*, 3262–3269.
284. Amoah, C.; Obuah, C.; Ainooson, M. K.; Muller, A. J. *Organomet. Chem.* **2021**, *935*, 121664.
285. Yang, B.; Yao, W.; Xia, X.; Wang, D. *Org. Biomol. Chem.* **2018**, *16*, 4547–4557.
286. Zhao, H.; Guo, L.; Chen, S.; Bian, Z. *RSC Adv.* **2013**, *3*, 19929–19932.
287. Langer, J.; Fischer, R.; Görls, H.; Walther, D. *Eur. J. Inorg. Chem.* **2007**, *2007*, 2257–2264.
288. Otón, F.; González, M. D. C.; Espinosa, A.; Tárraga, A.; Molina, P. *Organometallics* **2012**, *31*, 2085–2096.
289. Bezuidenhout, D. I.; van der Westhuizen, B.; Swarts, P. J.; Chaturgoon, T.; Munro, O. Q.; Fernández, I.; Swarts, J. C. *Chem. Eur. J.* **2014**, *20*, 4974–4985.
290. Kaufmann, S.; Radius, M.; Moos, E.; Breher, F.; Roesky, P. W. *Organometallics* **2019**, *38*, 1721–1732.
291. Klenk, S.; Rupf, S.; Suntrup, L.; van der Meer, M.; Sarkar, B. *Organometallics* **2017**, *36*, 2026–2035.
292. Hettmanczyk, L.; Suntrup, L.; Klenk, S.; Hoyer, C.; Sarkar, B. *Chem. Eur. J.* **2017**, *23*, 576–585.
293. Romero, T.; Orenes, R. A.; Tárraga, A.; Molina, P. *Organometallics* **2013**, *32*, 5740–5753.
294. Tolman, C. A. *Chem. Rev.* **1977**, *77*, 313–348.
295. Chianese, A. R.; Li, X.; Janzen, M. C.; Faller, J. W.; Crabtree, R. H. *Organometallics* **2003**, *22*, 1663–1667.
296. Kelly, R. A., III; Clavier, H.; Giudice, S.; Scott, N. M.; Stevens, E. D.; Bordner, J.; Samardjiev, I.; Hoff, C. D.; Cavallo, L.; Nolan, S. P. *Organometallics* **2008**, *27*, 202–210.
297. Rigo, M.; Hettmanczyk, L.; Heutz, F. J. L.; Hohloch, S.; Lutz, M.; Sarkar, B.; Müller, C. *Dalton Trans.* **2017**, *46*, 86–95.
298. Hettmanczyk, L.; Schulze, D.; Suntrup, L.; Sarkar, B. *Organometallics* **2016**, *35*, 3828–3836.
299. Tolentino, D. R.; Jin, L.; Melaimi, M.; Bertrand, G. *Chem. Asian J.* **2015**, *10*, 2139–2142.
300. Mendoza-Espinosa, D.; González-Olvera, R.; Negrón-Silva, G. E.; Angeles-Beltrán, D.; Suárez-Castillo, O. R.; Álvarez-Hernández, A.; Santillan, R. *Organometallics* **2015**, *34*, 4529–4542.
301. Wright, J. R.; Young, P. C.; Lucas, N. T.; Lee, A.; Crowley, J. D. *Organometallics* **2013**, *32*, 7065–7076.
302. Kilpin, K. J.; Paul, U. S. D.; Lee, A.; Crowley, J. D. *Chem. Commun.* **2011**, *47*, 328–330.
303. Echavarren, A. M.; Jiao, N.; Gevorgyan, V. *Chem. Soc. Rev.* **2016**, *45*, 4445–4447.
304. Aucamp, D.; Witteler, T.; Dielmann, F.; Siangwata, S.; Liles, D. C.; Smith, G. S.; Bezuidenhout, D. I. *Eur. J. Inorg. Chem.* **2017**, *2017*, 1227–1236.
305. Dröge, T.; Glorius, F. *Angew. Chem. Int. Ed.* **2010**, *49*, 6940–6952.
306. Huynh, H. V.; Han, Y.; Jothibasur, R.; Yang, J. A. *Organometallics* **2009**, *28*, 5395–5404.
307. Yuan, D.; Huynh, H. V. *Organometallics* **2012**, *31*, 405–412.
308. Gil, W.; Trzeciak, A. M. *Coord. Chem. Rev.* **2011**, *255*, 473–483.
309. Almeida, A. R.; Peixoto, A. F.; Calvete, M. J. F.; Gois, P. M. P.; Pereira, M. M. *Curr. Org. Synth.* **2011**, *8*, 764–775.
310. Díez-González, S.; Marion, N.; Nolan, S. P. *Chem. Rev.* **2009**, *109*, 3612–3676.
311. Praetorius, J. M.; Crudden, C. M. *Dalton Trans.* **2008**, 479–494.
312. Veige, A. S. *Polyhedron* **2008**, *27*, 3177–3189.
313. Peris, E.; Crabtree, R. H. *Coord. Chem. Rev.* **2004**, *248*, 2239–2246.
314. Vanicek, S.; Podewitz, M.; Stubbe, J.; Schulze, D.; Kopacka, H.; Wurst, K.; Müller, T.; Lippmann, P.; Haslinger, S.; Schottenberger, H.; Liedl, K. R.; Ott, I.; Sarkar, B.; Bildstein, B. *Chem. Eur. J.* **2018**, *24*, 3742–3753.
315. Mathew, J.; Suresh, C. H. *Inorg. Chem.* **2010**, *49*, 4665–4669.
316. Nelson, D. J.; Nolan, S. P. *Chem. Soc. Rev.* **2013**, *42*, 6723–6753.
317. Vanicek, S.; Beerhues, J.; Bens, T.; Levchenko, V.; Wurst, K.; Bildstein, B.; Tilset, M.; Sarkar, B. *Organometallics* **2019**, *38*, 4383–4386.
318. Weyrauch, J.; Hashmi, A.; Schuster, A.; Hengst, T.; Schetter, S.; Littmann, A.; Rudolph, M.; Hamzic, M.; Visus, J.; Rominger, F.; Frey, W.; Bats, J. *Chem. Eur. J.* **2010**, *16*, 956–963.
319. Baltrun, M.; Watt, F. A.; Schoch, R.; Wölper, C.; Neuba, A. G.; Hohloch, S. *Dalton Trans.* **2019**, *48*, 14611–14625.
320. Chadwick, F. M.; Curchod, B. F. E.; Scopelliti, R.; Fadaei Tirani, F.; Solari, E.; Severin, K. *Angew. Chem. Int. Ed.* **2019**, *58*, 1764–1767.
321. Ung, G.; Bertrand, G. *Chem. Eur. J.* **2011**, *17*, 8269–8272.
322. Fliedel, C.; Labande, A.; Manoury, E.; Poli, R. *Coord. Chem. Rev.* **2019**, *394*, 65–103.



323. Wang, F.; Liu, L.; Wang, W.; Li, S.; Shi, M. *Coord. Chem. Rev.* **2012**, *256*, 804–853.
324. Perry, M. C.; Burgess, K. *Tetrahedron Asymmetry* **2003**, *14*, 951–961.
325. Gade, L. H.; Bellemin-Laponnaz, S. In *N-Heterocyclic Carbenes in Transition Metal Catalysis*; Glorius, F., Ed.; vol. 21; Springer Berlin Heidelberg: Berlin, Heidelberg, 2007; pp 117–157.
326. César, V.; Bellemin-Laponnaz, S.; Gade, L. H. *Chem. Soc. Rev.* **2004**, *33*, 619–636.
327. Janssen-Müller, D.; Schleppehorst, C.; Glorius, F. *Chem. Soc. Rev.* **2017**, *46*, 4845–4854.
328. Karthikeyan, T.; Sankararaman, S. *Tetrahedron Lett.* **2009**, *50*, 5834–5837.
329. Mohan, A.; Ramkumar, V.; Sankararaman, S. *J. Organomet. Chem.* **2015**, *799–800*, 115–121.
330. Maity, R.; Verma, A.; van der Meer, M.; Hohloch, S.; Sarkar, B. *Eur. J. Inorg. Chem.* **2016**, *2016*, 111–117.
331. Gangwar, M. K.; Butcher, R. J. *J. Organomet. Chem.* **2020**, *930*, 121598.
332. Gangwar, M. K.; Butcher, R. J. *J. Organomet. Chem.* **2021**, *932*, 121626.
333. Avello, M. G.; Frutos, M.; de la Torre, M. C.; Viso, A.; Velado, M.; de la Pradilla, R. F.; Sierra, M. A.; Gornitzka, H.; Hemmert, C. *Chem. Eur. J.* **2017**, *23*, 14523–14531.
334. Avello, M. G.; de la Torre, M. C.; Guerrero-Martínez, A.; Sierra, M. A.; Gornitzka, H.; Hemmert, C. *Eur. J. Inorg. Chem.* **2020**, *2020*, 4045–4053.
335. Yoshida, K.; Yasue, R. *Chem. Eur. J.* **2018**, *24*, 18575–18586.
336. Škoch, K.; Vosáňová, I.; Čisáňová, I.; Štěpnička, P. *Dalton Trans.* **2020**, *49*, 1011–1021.
337. Avello, M. G.; Torre, M. C.; Sierra, M. A.; Gornitzka, H.; Hemmert, C. *Chem. Eur. J.* **2019**, *25*, 13344–13353.
338. Haraguchi, R.; Hoshino, S.; Yamazaki, T.; Fukuzawa, S. *Chem. Commun.* **2018**, *54*, 2110–2113.
339. Haraguchi, R.; Yamazaki, T.; Torita, K.; Ito, T.; Fukuzawa, S. *Dalton Trans.* **2020**, *49*, 17578–17583.
340. Dasgupta, A.; Ramkumar, V.; Sankararaman, S. *RSC Adv.* **2015**, *5*, 21558–21561.
341. Sluijter, N.; Jongkind, L. J.; Elsevier, C. J. *Eur. J. Inorg. Chem.* **2015**, *2015*, 2948–2955.
342. Huang, W.; Zhang, Y.; Jin, R.; Chen, B.; Chen, Z. *Organometallics* **2018**, *37*, 3196–3209.
343. Zhang, M.; Chen, Q.; Yang, G. *Eur. J. Med. Chem.* **2015**, *89*, 421–441.
344. Kumari, A.; Singh, R. K. *Bioorg. Chem.* **2019**, *89*, 103021.
345. Chadha, N.; Silakari, O. *Eur. J. Med. Chem.* **2017**, *134*, 159–184.
346. Jia, Y.; Wen, X.; Gong, Y.; Wang, X. *Eur. J. Med. Chem.* **2020**, *200*, 112359.
347. Zhang, P.; Yamamoto, T.; Sugino, M. *ChemCatChem* **2019**, *11*, 424–429.
348. Deng, M.; Mukthar, N. F. M.; Schley, N. D.; Ung, G. *Angew. Chem. Int. Ed.* **2020**, *59*, 1228–1231.
349. Pichon, D.; Soleilhavoup, M.; Morvan, J.; Junor, G. P.; Vives, T.; Crévisy, C.; Lavallo, V.; Campagne, J.; Mauduit, M.; Jazzar, R.; Bertrand, G. *Chem. Sci.* **2019**, *10*, 7807–7811.
350. Kolundžić, F.; Murali, A.; Pérez-Galán, P.; Bauer, J. O.; Strohmman, C.; Kumar, K.; Waldmann, H. *Angew. Chem. Int. Ed.* **2014**, *53*, 8122–8126.
351. Han, S.; Liu, T.; Yu, Z. *J. Organomet. Chem.* **2016**, *801*, 24–29.
352. Morvan, J.; Mauduit, M.; Bertrand, G.; Jazzar, R. *ACS Catal.* **2021**, *11*, 1714–1748.
353. Morvan, J.; Vermersch, F.; Zhang, Z.; Falivene, L.; Vives, T.; Dorcet, V.; Roisnel, T.; Crévisy, C.; Cavallo, L.; Vanthuyne, N.; Bertrand, G.; Jazzar, R.; Mauduit, M. *J. Am. Chem. Soc.* **2020**, *142*, 19895–19901.
354. Anderson, D.; Lavallo, V.; O’Leary, D.; Bertrand, G.; Grubbs, R. *Angew. Chem. Int. Ed.* **2007**, *46*, 7262–7265.
355. Marx, V. M.; Sullivan, A. H.; Melaimi, M.; Virgil, S. C.; Keitz, B. K.; Weinberger, D. S.; Bertrand, G.; Grubbs, R. H. *Angew. Chem. Int. Ed.* **2015**, *54*, 1919–1923.
356. Gawin, R.; Kozakiewicz, A.; Guńka, P. A.; Dąbrowski, P.; Skowerski, K. *Angew. Chem. Int. Ed.* **2017**, *56*, 981–986.
357. Nascimento, D. L.; Fogg, D. E. *J. Am. Chem. Soc.* **2019**, *141*, 19236–19240.
358. Breen, C. P.; Parrish, C.; Shangguan, N.; Majumdar, S.; Murnen, H.; Jamison, T. F.; Bio, M. M. *Org. Process Res. Dev.* **2020**, *24*, 2298–2303.
359. Park, C. P.; Van Wingerden, M. M.; Han, S.; Kim, D.; Grubbs, R. H. *Org. Lett.* **2011**, *13*, 2398–2401.
360. Mukherjee, N.; Marczyk, A.; Szczepaniak, G.; Sytniczuk, A.; Kajetanowicz, A.; Grela, K. *ChemCatChem* **2019**, *11*, 5362–5369.
361. Nabeshima, T.; Yamamura, M. *Pure Appl. Chem.* **2013**, *85*, 763–776.
362. Zhang, Y.; Chen, Z.; Zhang, X.; Deng, X.; Zhuang, W.; Su, W. *Commun. Chem.* **2020**, *3*, 41.
363. McInnis, J. P.; Delferro, M.; Marks, T. J. *Acc. Chem. Res.* **2014**, *47*, 2545–2557.
364. van der Vlugt, J. I. *Chem. Soc. Rev.* **2010**, *39*, 2302–2322.
365. Albrecht, M.; Bedford, R.; Plietker, B. *Organometallics* **2014**, *33*, 5619–5621.
366. Khoshsefat, M.; Ma, Y.; Sun, W. *Coord. Chem. Rev.* **2021**, *434*, 213788.
367. Park, J.; Hong, S. *Chem. Soc. Rev.* **2012**, *41*, 6931–6943.
368. Shibasaki, M.; Yamamoto, Y., Eds.; *Multimetallic Catalysts in Organic Synthesis*, Wiley-VCH: Weinheim, Germany, 2004.
369. Cai, J.; Yang, X.; Arumugam, K.; Bielawski, C. W.; Sessler, J. L. *Organometallics* **2011**, *30*, 5033–5037.
370. Suntrup, L.; Beerhues, J.; Etzold, O.; Sarkar, B. *Dalton Trans.* **2020**, *49*, 15504–15510.
371. Petronilho, A.; Woods, J. A.; Bernhard, S.; Albrecht, M. *Eur. J. Inorg. Chem.* **2014**, *2014*, 708–714.
372. Beerhues, J.; Fauché, K.; Cisnetti, F.; Sarkar, B.; Gautier, A. *Dalton Trans.* **2019**, *48*, 8931–8936.
373. Iwasaki, H.; Teshima, Y.; Yamada, Y.; Ishikawa, R.; Koga, Y.; Matsubara, K. *Dalton Trans.* **2016**, *45*, 5713–5719.
374. Tolley, L. C.; Fernández, I.; Bezuidenhout, D. I.; Guisado-Barrios, G. *Catal. Sci. Technol.* **2021**, *11*, 516–523.
375. Maity, R.; Hohloch, S.; Su, C.; van der Meer, M.; Sarkar, B. *Chem. Eur. J.* **2014**, *20*, 9952–9961.
376. Guisado-Barrios, G.; Bouffard, J.; Donnadieu, B.; Bertrand, G. *Organometallics* **2011**, *30*, 6017–6021.
377. Hohloch, S.; Suntrup, L.; Sarkar, B. *Inorg. Chem. Front.* **2016**, *3*, 67–77.
378. Cao, L.; Huang, S.; Liu, W.; Yan, X. *Organometallics* **2018**, *37*, 2010–2013.
379. Leow, M.; Ho, C.; Gardiner, M.; Bissember, A. *Catalysts* **2018**, *8*, 620.
380. Waters, J. B.; Goicoechea, J. M. *Coord. Chem. Rev.* **2015**, *293–294*, 80–94.
381. Krüger, A.; Kluser, E.; Müller-Bunz, H.; Neels, A.; Albrecht, M. *Eur. J. Inorg. Chem.* **2012**, *2012*, 1394–1402.
382. Armstrong, D. R.; Baillie, S. E.; Blair, V. L.; Chabloz, N. G.; Diez, J.; Garcia-Alvarez, J.; Kennedy, A. R.; Robertson, S. D.; Hevia, E. *Chem. Sci.* **2013**, *4*, 4259–4266.
383. Simler, T.; Braunstein, P.; Danopoulos, A. A. *Chem. Commun.* **2016**, *52*, 2717–2720.
384. Mondal, K. C.; Samuel, P. P.; Roesky, H. W.; Carl, E.; Herbst-Irmer, R.; Stalke, D.; Schwederski, B.; Kaim, W.; Ungur, L.; Chibotaru, L. F.; Hermann, M.; Frenking, G. *J. Am. Chem. Soc.* **2014**, *136*, 1770–1773.
385. Jin, L.; Tolentino, D. R.; Melaimi, M.; Bertrand, G. *Sci. Adv.* **2015**, *1*, e1500304.
386. Jin, L.; Romero, E. A.; Melaimi, M.; Bertrand, G. *J. Am. Chem. Soc.* **2015**, *137*, 15696–15698.
387. Weinberger, D. S.; Melaimi, M.; Moore, C. E.; Rheingold, A. L.; Frenking, G.; Jerabek, P.; Bertrand, G. *Angew. Chem. Int. Ed.* **2013**, *52*, 8964–8967.
388. Ton, S. J.; Fogg, D. E. *ACS Catal.* **2019**, *9*, 11329–11334.
389. Nascimento, D. L.; Gawin, A.; Gawin, R.; Guńka, P. A.; Zachara, J.; Skowerski, K.; Fogg, D. E. *J. Am. Chem. Soc.* **2019**, *141*, 10626–10631.
390. Zhang, Y.; Mei, T.; Yang, D.; Zhang, Y.; Wang, B.; Qu, J. *Dalton Trans.* **2017**, *46*, 15888–15896.
391. Bawari, D.; Thakur, S. K.; Manar, K. K.; Goswami, B.; Sabari, V. R.; Choudhury, A. R.; Singh, S. *J. Organomet. Chem.* **2019**, *880*, 108–115.



392. Bawari, D.; Goswami, B.; Sabari, V. R.; Thakur, S. K.; Varun Tej, R. V.; Roy Choudhury, A.; Singh, S. *Dalton Trans.* **2018**, *47*, 6274–6278.
393. Pelties, S.; Wolf, R. Z. *Anorg. Allg. Chem.* **2013**, *639*, 2581–2585.
394. Rostovtsev, V. V.; Green, L. G.; Fokin, V. V.; Sharpless, K. B. *Angew. Chem. Int. Ed.* **2002**, *41*, 2596–2599.
395. Tornøe, C. W.; Christensen, C.; Meldal, M. *J. Org. Chem.* **2002**, *67*, 3057–3064.
396. Kolb, H. C.; Finn, M. G.; Sharpless, K. B. *Angew. Chem. Int. Ed.* **2001**, *40*, 2004–2021.
397. Finn, M. G.; Fokin, V. V. *Chem. Soc. Rev.* **2010**, *39*, 1231–1232.
398. Díez-González, S.; Correa, A.; Cavallo, L.; Nolan, S. P. *Chem. Eur. J.* **2006**, *12*, 7558–7564.
399. Díez-González, S.; Stevens, E. D.; Nolan, S. P. *Chem. Commun.* **2008**, 4747–4749.
400. Díez-González, S.; Escudero-Adán, E. C.; Benet-Buchholz, J.; Stevens, E. D.; Slawin, A. M. Z.; Nolan, S. P. *Dalton Trans.* **2010**, *39*, 7595–7606.
401. Díez-González, S.; Nolan, S. *Angew. Chem. Int. Ed.* **2008**, *47*, 8881–8884.
402. Worrell, B. T.; Malik, J. A.; Fokin, V. V. *Science* **2013**, *340*, 457–460.
403. Nakamura, T.; Terashima, T.; Ogata, K.; Fukuzawa, S. *Org. Lett.* **2011**, *13*, 620–623.
404. Hohloch, S.; Sarkar, B.; Nauton, L.; Cisnetti, F.; Gautier, A. *Tetrahedron Lett.* **2013**, *54*, 1808–1812.
405. Hohloch, S.; Scheiffele, D.; Sarkar, B. *Eur. J. Inorg. Chem.* **2013**, *2013*, 3956–3965.
406. Berg, R.; Straub, J.; Schreiner, E.; Mader, S.; Rominger, F.; Straub, B. *Adv. Synth. Catal.* **2012**, *354*, 3445–3450.
407. Kina, A.; Iwamura, H.; Hayashi, T. *J. Am. Chem. Soc.* **2006**, *128*, 3904–3905.
408. Kina, A.; Yasuhara, Y.; Nishimura, T.; Iwamura, H.; Hayashi, T. *Chem. Asian J.* **2006**, *1*, 707–711.
409. Rosner, T.; Le Bars, J.; Pfaltz, A.; Blackmond, D. G. *J. Am. Chem. Soc.* **2001**, *123*, 1848–1855.
410. Nolte, C.; Mayer, P.; Straub, B. *Angew. Chem. Int. Ed.* **2007**, *46*, 2101–2103.
411. Kuang, G.; Guha, P. M.; Brotherton, W. S.; Simmons, J. T.; Stanke, L. A.; Nguyen, B. T.; Clark, R. J.; Zhu, L. *J. Am. Chem. Soc.* **2011**, *133*, 13984–14001.
412. Ai, P.; Danopoulos, A. A.; Braunstein, P.; Monakhov, K. Y. *Chem. Commun.* **2014**, *50*, 103–105.
413. Ai, P.; Mauro, M.; De Cola, L.; Danopoulos, A. A.; Braunstein, P. *Angew. Chem. Int. Ed.* **2016**, *55*, 3338–3341.
414. Ai, P.; Gourlaouen, C.; Danopoulos, A. A.; Braunstein, P. *Inorg. Chem.* **2016**, *55*, 1219–1229.
415. Rottschäfer, D.; Ebeler, F.; Strothmann, T.; Neumann, B.; Stammler, H.; Mix, A.; Ghadwal, R. S. *Chem. Eur. J.* **2018**, *24*, 3716–3720.
416. Veillard, R.; Bernoud, E.; Abdellah, I.; Lohier, J.; Alayrac, C.; Gaumont, A. *Org. Biomol. Chem.* **2014**, *12*, 3635–3640.
417. Seifert, T. P.; Bestgen, S.; Feuerstein, T. J.; Lebedkin, S.; Krämer, F.; Fengler, C.; Gamer, M. T.; Kappes, M. M.; Roesky, P. W. *Dalton Trans.* **2019**, *48*, 15427–15434.
418. Maity, R.; van der Meer, M.; Hohloch, S.; Sarkar, B. *Organometallics* **2015**, *34*, 3090–3096.
419. AL-Shnani, F.; Guisado-Barrios, G.; Sainz, D.; Peris, E. *Organometallics* **2019**, *38*, 697–701.
420. Mendoza-Espinosa, D.; González-Olvera, R.; Osornio, C.; Negrón-Silva, G. E.; Álvarez-Hernández, A.; Bautista-Hernández, C. I.; Suárez-Castillo, O. R. *J. Organomet. Chem.* **2016**, *803*, 142–149.
421. Mendoza-Espinosa, D.; González-Olvera, R.; Osornio, C.; Negrón-Silva, G. E.; Santillan, R. *New J. Chem.* **2015**, *39*, 1587–1591.
422. Rendón-Nava, D.; Vásquez-Pérez, J. M.; Sandoval-Chávez, C. I.; Álvarez-Hernández, A.; Mendoza-Espinosa, D. *Organometallics* **2020**, *39*, 3961–3971.
423. Flores-Jarillo, M.; Mendoza-Espinosa, D.; Salazar-Pereda, V.; González-Montiel, S. *Organometallics* **2017**, *36*, 4305–4312.
424. Frutos, M.; de la Torre, M. C.; Sierra, M. A. *Inorg. Chem.* **2015**, *54*, 11174–11185.
425. Heckenroth, M.; Kluser, E.; Neels, A.; Albrecht, M. *Dalton Trans.* **2008**, 6242–6249.
426. Xu, X.; Xu, B.; Li, Y.; Hong, S. H. *Organometallics* **2010**, *29*, 6343–6349.
427. Evans, K. J.; Mansell, S. M. *Chem. Eur. J.* **2020**, *26*, 5927–5941.
428. Uzelac, M.; Hevia, E. *Chem. Commun.* **2018**, *54*, 2455–2462.
429. Wang, Y.; Xie, Y.; Abraham, M. Y.; Wei, P.; Schaefer, H. F.; Schleyer, P. v. R.; Robinson, G. H. *J. Am. Chem. Soc.* **2010**, *132*, 14370–14372.
430. Waters, J. B.; Goicoechea, J. M. *Dalton Trans.* **2014**, *43*, 14239–14248.
431. Hernán-Gómez, A.; Uzelac, M.; Baillie, S. E.; Armstrong, D. R.; Kennedy, A. R.; Fuentes, M.Á.; Hevia, E. *Chem. Eur. J.* **2018**, *24*, 10541–10549.
432. Wang, Y.; Xie, Y.; Abraham, M. Y.; Gilliard, R. J., Jr.; Wei, P.; Campana, C. F.; Schaefer, H. F., III; Schleyer, P. v. R.; Robinson, G. H. *Angew. Chem. Int. Ed.* **2012**, *51*, 10173–10176.
433. Schnee, G.; Nieto Faza, O.; Specklin, D.; Jacques, B.; Karmazin, L.; Welter, R.; Silva López, C.; Dagorne, S. *Chem. Eur. J.* **2015**, *21*, 17959–17972.
434. Uzelac, M.; Hernán-Gómez, A.; Armstrong, D. R.; Kennedy, A. R.; Hevia, E. *Chem. Sci.* **2015**, *6*, 5719–5728.
435. Waters, J. B.; Tucker, L. S.; Goicoechea, J. M. *Organometallics* **2018**, *37*, 655–664.
436. Maddock, L. C. H.; Cadenbach, T.; Kennedy, A. R.; Borilovic, I.; Aromí, G.; Hevia, E. *Inorg. Chem.* **2015**, *54*, 9201–9210.
437. Musgrave, R. A.; Turberville, R. S. P.; Irwin, M.; Goicoechea, J. M. *Angew. Chem. Int. Ed.* **2012**, *51*, 10832–10835.
438. Arnold, P. L.; Liddle, S. T. *Organometallics* **2006**, *25*, 1485–1491.
439. Schneider, H.; Hock, A.; Bertermann, R.; Radius, U. *Chem. Eur. J.* **2017**, *23*, 12387–12398.
440. Ghadwal, R. S.; Rottschäfer, D.; Andrada, D. M.; Frenking, G.; Schürmann, C. J.; Stammler, H. *Dalton Trans.* **2017**, *46*, 7791–7799.
441. Martínez-Martínez, A. J.; Fuentes, M.Á.; Hernán-Gómez, A.; Hevia, E.; Kennedy, A. R.; Mulvey, R. E.; O'Hara, C. T. *Angew. Chem. Int. Ed.* **2015**, *54*, 14075–14079.
442. Bitzer, M. J.; Pöthig, A.; Jandl, C.; Kühn, F. E.; Baratta, W. *Dalton Trans.* **2015**, *44*, 11686–11689.
443. Bitzer, M. J.; Kühn, F. E.; Baratta, W. *J. Catal.* **2016**, *338*, 222–226.
444. Álvarez, C. M.; García-Escudero, L. A.; García-Rodríguez, R.; Miguel, D. *Chem. Commun.* **2012**, *48*, 7209–7211.
445. Del Castillo, T. J.; Sarkar, S.; Abboud, K. A.; Veige, A. S. *Dalton Trans.* **2011**, *40*, 8140–8144.
446. Clough, M. C.; Zeits, P. D.; Bhuvanesh, N.; Gladysz, J. A. *Organometallics* **2012**, *31*, 5231–5234.
447. Mechler, M.; Latendorf, K.; Frey, W.; Peters, R. *Organometallics* **2013**, *32*, 112–130.
448. Broghammer, F.; Brodbeck, D.; Junge, T.; Peters, R. *Chem. Commun.* **2017**, *53*, 1156–1159.
449. Brodbeck, D.; Broghammer, F.; Meisner, J.; Klepp, J.; Garnier, D.; Frey, W.; Kästner, J.; Peters, R. *Angew. Chem. Int. Ed.* **2017**, *56*, 4056–4060.
450. Latendorf, K.; Mechler, M.; Schamne, I.; Mack, D.; Frey, W.; Peters, R. *Eur. J. Org. Chem.* **2017**, *2017*, 4140–4167.
451. Schmid, J.; Frey, W.; Peters, R. *Organometallics* **2017**, *36*, 4313–4324.
452. Paulose, T. A. P.; Olson, J. A.; Wilson Quail, J.; Foley, S. R. *J. Organomet. Chem.* **2008**, *693*, 3405–3410.
453. Khan, S. S.; Liebscher, J. *Synthesis* **2010**, *15*, 2609–2615.
454. Wang, R.; Jin, C.; Twamley, B.; Shreeve, J. M. *Inorg. Chem.* **2006**, *45*, 6396–6403.
455. Zamora, M. T.; Ferguson, M. J.; McDonald, R.; Cowie, M. *Organometallics* **2012**, *31*, 5463–5477.
456. Mendoza-Espinosa, D.; Álvarez-Hernández, A.; Angeles-Beltrán, D.; Negrón-Silva, G. E.; Suárez-Castillo, O. R.; Vásquez-Pérez, J. M. *Inorg. Chem.* **2017**, *56*, 2092–2099.
457. Zamora, M. T.; Ferguson, M. J.; Cowie, M. *Organometallics* **2012**, *31*, 5384–5395.
458. Mercks, L.; Albrecht, M. *Chem. Soc. Rev.* **2010**, *39*, 1903–1912.
459. Zhukhovitskiy, A. V.; MacLeod, M. J.; Johnson, J. A. *Chem. Rev.* **2015**, *115*, 11503–11532.
460. Smith, C. A.; Narouz, M. R.; Lummis, P. A.; Singh, I.; Nazemi, A.; Li, C.; Crudden, C. M. *Chem. Rev.* **2019**, *119*, 4986–5056.
461. Ibáñez, S.; Poyatos, M.; Peris, E. *Acc. Chem. Res.* **2020**, *53*, 1401–1413.
462. Zhong, R.; Lindhorst, A. C.; Groche, F. J.; Kühn, F. E. *Chem. Rev.* **2017**, *117*, 1970–2058.

463. Ezugwu, C. I.; Kabir, N. A.; Yusubov, M.; Verpoort, F. *Coord. Chem. Rev.* **2016**, *307*, 188–210.
464. Ranganath, K. V. S.; Onitsuka, S.; Kumar, A. K.; Inanaga, J. *Catal. Sci. Technol.* **2013**, *3*, 2161–2181.
465. Corbucci, I.; Petronilho, A.; Müller-Bunz, H.; Rocchigiani, L.; Albrecht, M.; Macchioni, A. *ACS Catal.* **2015**, *5*, 2714–2718.
466. Cao, R.; Lai, W.; Du, P. *Energy Environ. Sci.* **2012**, *5*, 8134–8157.
467. Liu, X.; Wang, F. *Coord. Chem. Rev.* **2012**, *256*, 1115–1136.
468. Hintermair, U.; Sheehan, S. W.; Parent, A. R.; Ess, D. H.; Richens, D. T.; Vaccaro, P. H.; Brudvig, G. W.; Crabtree, R. H. *J. Am. Chem. Soc.* **2013**, *135*, 10837–10851.
469. Velazquez, H. D.; Verpoort, F. *Chem. Soc. Rev.* **2012**, *41*, 7032–7060.
470. Schaper, L.; Hock, S. J.; Herrmann, W. A.; Kühn, F. E. *Angew. Chem. Int. Ed.* **2013**, *52*, 270–289.
471. Levin, E.; Ivry, E.; Diesendruck, C. E.; Lemcoff, N. G. *Chem. Rev.* **2015**, *115*, 4607–4692.
472. De, S.; Udvardy, A.; Czégényi, C. E.; Joó, F. *Coord. Chem. Rev.* **2019**, *400*, 213038.
473. Cazin, C. S. J. *C. R. Chim.* **2009**, *12*, 1173–1180.
474. Sommer, W. J.; Weck, M. *Coord. Chem. Rev.* **2007**, *251*, 860–873.
475. Engel, S.; Fritz, E.; Ravoo, B. J. *Chem. Soc. Rev.* **2017**, *46*, 2057–2075.
476. Azua, A.; Sanz, S.; Peris, E. *Chem. Eur. J.* **2011**, *17*, 3963–3967.
477. Nagyházi, M.; Turczel, G.; Balla, Á.; Szálás, G.; Tóth, I.; Gál, G. T.; Petra, B.; Anastas, P. T.; Tuba, R. *ChemCatChem* **2020**, *12*, 1953–1957.
478. Nagyházi, M.; Turczel, G.; Anastas, P. T.; Tuba, R. *ACS Sustain. Chem. Eng.* **2020**, *8*, 16097–16103.
479. Ruiz-Mendoza, F. J.; Mendoza-Espinosa, D.; González-Montiel, S. *Eur. J. Inorg. Chem.* **2018**, *2018*, 4622–4629.
480. El-Hellani, A.; Lavallo, V. *Angew. Chem. Int. Ed.* **2014**, *53*, 4489–4493.
481. Asay, M. J.; Fisher, S. P.; Lee, S. E.; Tham, F. S.; Borchardt, D.; Lavallo, V. *Chem. Commun.* **2015**, *51*, 5359–5362.
482. Frutos, M.; Gómez-Gallego, M.; Giner, E. A.; Sierra, M. A.; Ramírez de Arellano, C. *Dalton Trans.* **2018**, *47*, 9975–9979.
483. Toy, P. H.; Janda, K. D. *Acc. Chem. Res.* **2000**, *33*, 546–554.
484. Bergbreiter, D. E. *Chem. Rev.* **2002**, *102*, 3345–3384.
485. Bergbreiter, D. E.; Tian, J.; Hongfa, C. *Chem. Rev.* **2009**, *109*, 530–582.
486. Yamamoto, T.; Murakami, R.; Sugimoto, M. *J. Am. Chem. Soc.* **2017**, *139*, 2557–2560.
487. Yoshinaga, Y.; Yamamoto, T.; Sugimoto, M. *ACS Macro Lett.* **2017**, *6*, 705–710.
488. Lee, J.; Choi, J.; Kang, D.; Myung, Y.; Lee, S. M.; Kim, H. J.; Ko, Y.; Kim, S.; Son, S. U. *ACS Sustain. Chem. Eng.* **2018**, *6*, 3525–3532.
489. Uemura, T.; Kitaura, R.; Ohta, Y.; Nagaoka, M.; Kitagawa, S. *Angew. Chem. Int. Ed.* **2006**, *45*, 4112–4116.
490. Cho, K.; Yang, H.; Lee, I.; Lee, S. M.; Kim, H. J.; Son, S. U. *J. Am. Chem. Soc.* **2021**, *143*, 4100–4105.
491. Balcar, H.; Sedláček, J.; Čejka, J.; Vohlídal, J. *Macromol. Rapid Commun.* **2002**, *23*, 32–37.
492. Park, K. H.; Jang, K.; Son, S. U.; Sweigart, D. A. *J. Am. Chem. Soc.* **2006**, *128*, 8740–8741.
493. Abe, S.; Hirata, K.; Ueno, T.; Morino, K.; Shimizu, N.; Yamamoto, M.; Takata, M.; Yashima, E.; Watanabe, Y. *J. Am. Chem. Soc.* **2009**, *131*, 6958–6960.
494. Grimm, A. R.; Sauer, D. F.; Polen, T.; Zhu, L.; Hayashi, T.; Okuda, J.; Schwaneberg, U. *ACS Catal.* **2018**, *8*, 2611–2614.
495. Zhang, L.; Cao, Q.; Gao, F.; Dong, Y.; Li, X. *Polym. Chem.* **2020**, *11*, 2904–2913.
496. Sánchez-Page, B.; Jiménez, M. V.; Pérez-Torrente, J. J.; Passarelli, V.; Blasco, J.; Subias, G.; Granda, M.; Álvarez, P. *ACS Appl. Nano Mater.* **2020**, *3*, 1640–1655.
497. Jiménez, M. V.; Pérez-Torrente, J. J.; Bartolomé, M. I.; Gierz, V.; Lahoz, F. J.; Oro, L. A. *Organometallics* **2008**, *27*, 224–234.
498. Sánchez-Page, B.; Munariz, J.; Jiménez, M. V.; Pérez-Torrente, J. J.; Blasco, J.; Subias, G.; Passarelli, V.; Álvarez, P. *ACS Catal.* **2020**, *10*, 13334–13351.
499. Kempasiddhaiah, M.; Kandathil, V.; Dateer, R. B.; Sasidhar, B. S.; Patil, S. A.; Patil, S. A. *Appl. Organometal. Chem.* **2019**, *33*, e4846.
500. Tang, J.; Zhao, L. *Chem. Commun.* **2020**, *56*, 1915–1925.
501. Martin, C. D.; Soleilhavoup, M.; Bertrand, G. *Chem. Sci.* **2013**, *4*, 3020–3030.
502. Back, O.; Celik, M. A.; Frenking, G.; Melaimi, M.; Donnadieu, B.; Bertrand, G. *J. Am. Chem. Soc.* **2010**, *132*, 10262–10263.
503. Li, Y.; Mondal, K. C.; Samuel, P. P.; Zhu, H.; Orben, C. M.; Panneerselvam, S.; Dittrich, B.; Schwederski, B.; Kaim, W.; Mondal, T.; Koley, D.; Roesky, H. W. *Angew. Chem. Int. Ed.* **2014**, *53*, 4168–4172.
504. Jin, L.; Melaimi, M.; Liu, L.; Bertrand, G. *Org. Chem. Front.* **2014**, *1*, 351–354.
505. Mondal, K. C.; Roesky, H. W.; Schwarzer, M. C.; Frenking, G.; Tkach, I.; Wolf, H.; Kratzert, D.; Herbst-Irmer, R.; Niepötter, B.; Stalke, D. *Angew. Chem. Int. Ed.* **2013**, *52*, 1801–1805.
506. Kinjo, R.; Donnadieu, B.; Bertrand, G. *Angew. Chem. Int. Ed.* **2010**, *49*, 5930–5933.
507. Ruiz, D. A.; Melaimi, M.; Bertrand, G. *Chem. Commun.* **2014**, *50*, 7837–7839.
508. Back, O.; Kuchenbeiser, G.; Donnadieu, B.; Bertrand, G. *Angew. Chem. Int. Ed.* **2009**, *48*, 5530–5533.
509. Kretschmer, R.; Ruiz, D. A.; Moore, C. E.; Rheingold, A. L.; Bertrand, G. *Angew. Chem. Int. Ed.* **2014**, *53*, 8176–8179.
510. Dorsey, C. L.; Mushinski, R. M.; Hudnall, T. W. *Chem. Eur. J.* **2014**, *20*, 8914–8917.
511. Freeman, L. A.; Obi, A. D.; Machost, H. R.; Molino, A.; Nichols, A. W.; Dickie, D. A.; Wilson, D. J. D.; Machan, C. W.; Gilliard, R. J., Jr. *Chem. Sci.* **2021**, *12*, 3544–3550.
512. Masuda, J. D.; Schoeller, W. W.; Donnadieu, B.; Bertrand, G. *J. Am. Chem. Soc.* **2007**, *129*, 14180–14181.
513. Chandra Mondal, K.; Roy, S.; Dittrich, B.; Maity, B.; Dutta, S.; Koley, D.; Vasa, S. K.; Linsler, R.; Dechert, S.; Roesky, H. W. *Chem. Sci.* **2015**, *6*, 5230–5234.
514. Martin, C. D.; Weinstein, C. M.; Moore, C. E.; Rheingold, A. L.; Bertrand, G. *Chem. Commun.* **2013**, *49*, 4486–4488.
515. Chandra Mondal, K.; Roy, S.; Dittrich, B.; Andrada, D. M.; Frenking, G.; Roesky, H. W. *Angew. Chem. Int. Ed.* **2016**, *55*, 3158–3161.
516. Kulkarni, A.; Arumugam, S.; Francis, M.; Reddy, P. G.; Nag, E.; Gorantla, S. M. N. V. T.; Mondal, K. C.; Roy, S. *Chem. Eur. J.* **2021**, *27*, 200–206.
517. Ellul, C.; Mahon, M.; Saker, O.; Whittlesey, M. *Angew. Chem. Int. Ed.* **2007**, *46*, 6343–6345.
518. Jin, L.; Weinberger, D. S.; Melaimi, M.; Moore, C. E.; Rheingold, A. L.; Bertrand, G. *Angew. Chem. Int. Ed.* **2014**, *53*, 9059–9063.
519. da Silva, A. G. M.; Rodrigues, T. S.; Haigh, S. J.; Camargo, P. H. C. *Chem. Commun.* **2017**, *53*, 7135–7148.
520. Robilotto, T. J.; Bacsa, J.; Gray, T. G.; Sadighi, J. P. *Angew. Chem. Int. Ed.* **2012**, *51*, 12077–12080.
521. Wang, Y.; Monfredini, A.; Deyris, P.; Blanchard, F.; Derat, E.; Maestri, G.; Malacria, M. *Chem. Sci.* **2017**, *8*, 7394–7402.
522. Feaster, J. T.; Shi, C.; Cave, E. R.; Hatsukade, T.; Abram, D. N.; Kuhl, K. P.; Hahn, C.; Nørskov, J. K.; Jaramillo, T. F. *ACS Catal.* **2017**, *7*, 4822–4827.
523. Ko, J.; Kim, B.; Han, J. W. *J. Phys. Chem. C* **2016**, *120*, 3438–3447.
524. Polgar, A. M.; Zhang, A.; Mack, F.; Weigend, F.; Lebedkin, S.; Stillman, M. J.; Corrigan, J. F. *Inorg. Chem.* **2019**, *58*, 3338–3348.
525. Mieres-Perez, J.; Lucht, K.; Trosien, I.; Sander, W.; Sanchez-Garcia, E.; Morgenstern, K. *J. Am. Chem. Soc.* **2021**, *143*, 4653–4660.
526. Man, R. W. Y.; Li, C.; Maclean, M. W. A.; Zenkina, O. V.; Zamora, M. T.; Saunders, L. N.; Rousina-Webb, A.; Nambo, M.; Crudden, C. M. *J. Am. Chem. Soc.* **2018**, *140*, 1576–1579.
527. Narouz, M. R.; Osten, K. M.; Unsworth, P. J.; Man, R. W. Y.; Salorinne, K.; Takano, S.; Tomihara, R.; Kaappa, S.; Malola, S.; Dinh, C.; Padmos, J. D.; Ayoo, K.; Garrett, P. J.; Nambo, M.; Horton, J. H.; Sargent, E. H.; Häkkinen, H.; Tsukuda, T.; Crudden, C. M. *Nat. Chem.* **2019**, *11*, 419–425.
528. Richter, C.; Schaepe, K.; Glorius, F.; Ravoo, B. J. *Chem. Commun.* **2014**, *50*, 3204–3207.
529. Crudden, C. M.; Horton, J. H.; Ebralidze, I. I.; Zenkina, O. V.; McLean, A. B.; Drevniok, B.; She, Z.; Kraatz, H.; Mosey, N. J.; Seki, T.; Keske, E. C.; Leake, J. D.; Rousina-Webb, A.; Wu, G. *Nat. Chem.* **2014**, *6*, 409–414.
530. Zhukhovitskiy, A. V.; Mavros, M. G.; Queeney, K. T.; Wu, T.; Voorhis, T. V.; Johnson, J. A. *J. Am. Chem. Soc.* **2016**, *138*, 8639–8652.

531. Tran, B. L.; Fulton, J. L.; Linehan, J. C.; Balasubramanian, M.; Lercher, J. A.; Bullock, R. M. *ACS Catal.* **2019**, *9*, 4106–4114.
532. Moock, D.; Wiesenfeldt, M. P.; Freitag, M.; Muratsugu, S.; Ikemoto, S.; Knitsch, R.; Schneidewind, J.; Baumann, W.; Schäfer, A. H.; Timmer, A.; Tada, M.; Hansen, M. R.; Glorius, F. *ACS Catal.* **2020**, *10*, 6309–6317.
533. Bakker, A.; Freitag, M.; Koldzeiski, E.; Bellotti, P.; Timmer, A.; Ren, J.; Lammers, B. S.; Moock, D.; Roesky, H. W.; Mönig, H.; Amirjalayer, S.; Fuchs, H.; Glorius, F. *Angew. Chem. Int. Ed.* **2020**, *59*, 13643–13646.
534. Elie, M.; Renaud, J. L.; Gaillard, S. *Polyhedron* **2018**, *140*, 158–168.
535. Visbal, R.; Gimeno, M. C. *Chem. Soc. Rev.* **2014**, *43*, 3551–3574.
536. Biffis, A.; Baron, M.; Tubaro, C. In *Advances in Organometallic Chemistry*; Pérez, P. J., Ed.; vol. 63; Academic Press, 2015; pp 203–288.
537. Chábera, P.; Lindh, L.; Rosemann, N. W.; Prakash, O.; Uhlig, J.; Yartsev, A.; Wärmmark, K.; Sundström, V.; Persson, P. *Coord. Chem. Rev.* **2021**, *426*, 213517.
538. Bonfiglio, A.; Mauro, M. *Eur. J. Inorg. Chem.* **2020**, *2020*, 3427–3442.
539. Teyssot, M.; Jarrousse, C.; Manin, M.; Chevry, A.; Roche, S.; Norre, F.; Beaudoin, C.; Morel, L.; Boyer, D.; Mahiou, R.; Gautier, A. *Dalton Trans.* **2009**, 6894–6902.
540. Mora, M.; Gimeno, M. C.; Visbal, R. *Chem. Soc. Rev.* **2019**, *48*, 447–462.
541. Hindi, K. M.; Panzner, M. J.; Tessier, C. A.; Cannon, C. L.; Youngs, W. J. *Chem. Rev.* **2009**, *109*, 3859–3884.
542. Liu, W.; Gust, R. *Coord. Chem. Rev.* **2016**, *329*, 191–213.
543. Lees, A. J. *Chem. Rev.* **1987**, *87*, 711–743.
544. Richter, M. M. *Chem. Rev.* **2004**, *104*, 3003–3036.
545. Hagfeldt, A.; Boschloo, G.; Sun, L.; Kloo, L.; Pettersson, H. *Chem. Rev.* **2010**, *110*, 6595–6663.
546. Li, K.; Ming Tong, G. S.; Wan, Q.; Cheng, G.; Tong, W.; Ang, W.; Kwong, W.; Che, C. *Chem. Sci.* **2016**, *7*, 1653–1673.
547. Grätzel, M. *Nature* **2001**, *414*, 338–344.
548. Nazeeruddin, M. K.; Péchy, P.; Renouard, T.; Zakeeruddin, S. M.; Humphry-Baker, R.; Comte, P.; Liska, P.; Cevey, L.; Costa, E.; Shklover, V.; Spiccia, L.; Deacon, G. B.; Bignozzi, C. A.; Grätzel, M. *J. Am. Chem. Soc.* **2001**, *123*, 1613–1624.
549. Leigh, V.; Ghattas, W.; Lalrempuia, R.; Müller-Bunz, H.; Pryce, M. T.; Albrecht, M. *Inorg. Chem.* **2013**, *52*, 5395–5402.
550. Ghattas, W.; Müller-Bunz, H.; Albrecht, M. *Organometallics* **2010**, *29*, 6782–6789.
551. Suntrup, L.; Stein, F.; Hermann, G.; Kleoff, M.; Kuss-Petermann, M.; Klein, J.; Wenger, O. S.; Tremblay, J. C.; Sarkar, B. *Inorg. Chem.* **2018**, *57*, 13973–13984.
552. Soellner, J.; Čišarová, I.; Strassner, T. *Organometallics* **2018**, *37*, 4619–4629.
553. Brown, D. G.; Schauer, P. A.; Borau-Garcia, J.; Fancy, B. R.; Berlinguette, C. P. *J. Am. Chem. Soc.* **2013**, *135*, 1692–1695.
554. Figgis, B. N.; Hitchman, M. A. *Ligand Field Theory and Its Applications*, Wiley-Vch: New York, 2000; p 376.
555. Cannizzo, A.; Milne, C. J.; Consani, C.; Gawelda, W.; Bressler, C.; van Mourik, F.; Chergui, M. *Coord. Chem. Rev.* **2010**, *254*, 2677–2686.
556. Fredin, L. A.; Pápai, M.; Rozsályi, E.; Vankó, G.; Wärmmark, K.; Sundström, V.; Persson, P. *J. Phys. Chem. Lett.* **2014**, *5*, 2066–2071.
557. Liu, Y.; Kjær, K. S.; Fredin, L. A.; Chábera, P.; Harlang, T.; Canton, S. E.; Lidin, S.; Zhang, J.; Lomoth, R.; Bergquist, K.; Persson, P.; Wärmmark, K.; Sundström, V. *Chem. Eur. J.* **2015**, *21*, 3628–3639.
558. Chábera, P.; Liu, Y.; Prakash, O.; Thyraug, E.; Nahhas, A. E.; Honarfar, A.; Essén, S.; Fredin, L. A.; Harlang, T. C. B.; Kjær, K. S.; Handrup, K.; Ericson, F.; Tatsuno, H.; Morgan, K.; Schnadt, J.; Häggström, L.; Ericsson, T.; Sobkowiak, A.; Lidin, S.; Huang, P.; Styring, S.; Uhlig, J.; Bendix, J.; Lomoth, R.; Sundström, V.; Persson, P.; Wärmmark, K. *Nature* **2017**, *543*, 695–698.
559. Castellano, F. N. *Nature* **2017**, *543*, 627–628.
560. Chábera, P.; Kjær, K. S.; Prakash, O.; Honarfar, A.; Liu, Y.; Fredin, L. A.; Harlang, T. C. B.; Lidin, S.; Uhlig, J.; Sundström, V.; Lomoth, R.; Persson, P.; Wärmmark, K. *J. Phys. Chem. Lett.* **2018**, *9*, 459–463.
561. Tatsuno, H.; Kjær, K. S.; Kunnus, R.; Harlang, T. C. B.; Timm, C.; Guo, M.; Chábera, P.; Fredin, L. A.; Hartscock, R. W.; Reinhard, M. E.; Koroidov, S.; Li, L.; Cordones, A. A.; Gordivska, O.; Prakash, O.; Liu, Y.; Laursen, M. G.; Biasin, E.; Hansen, F. B.; Vester, P.; Christensen, M.; Haldrup, K.; Németh, Z.; Szemes, D. S.; Bajnóczi, É.; Vankó, G.; Van Driel, T. B.; Alonso-Mori, R.; Glownia, J. M.; Nelson, S.; Sikorski, M.; Lemke, H. T.; Sokaras, D.; Canton, S. E.; Dohn, A. O.; Möller, K. B.; Nielsen, M. M.; Gaffney, K. J.; Wärmmark, K.; Sundström, V.; Persson, P.; Uhlig, J. *Angew. Chem. Int. Ed.* **2020**, *59*, 364–372.
562. Temperton, R. H.; Rosemann, N. W.; Guo, M.; Johansson, N.; Fredin, L. A.; Prakash, O.; Wärmmark, K.; Handrup, K.; Uhlig, J.; Schnadt, J.; Persson, P. *J. Phys. Chem. A* **2020**, *124*, 1603–1609.
563. Chi, Y.; Chou, P. *Chem. Soc. Rev.* **2010**, *39*, 638–655.
564. Urinda, S.; Das, G.; Pramanik, A.; Sarkar, P. *Comput. Theor. Chem.* **2016**, *1092*, 32–40.
565. Baschieri, A.; Monti, F.; Matteucci, E.; Mazzanti, A.; Barbieri, A.; Armaroli, N.; Sambri, L. *Inorg. Chem.* **2016**, *55*, 7912–7919.
566. Matteucci, E.; Monti, F.; Mazzoni, R.; Baschieri, A.; Bizzarri, C.; Sambri, L. *Inorg. Chem.* **2018**, *57*, 11673–11686.
567. Karmis, R. E.; Carrara, S.; Baxter, A. A.; Hogan, C. F.; Hulett, M. D.; Barnard, P. J. *Dalton Trans.* **2019**, *48*, 9998–10010.
568. Urinda, S.; Das, G.; Pramanik, A.; Sarkar, P. *J. Phys. Chem. A* **2018**, *122*, 7532–7539.
569. Soellner, J.; Strassner, T. *Chem. Eur. J.* **2018**, *24*, 15603–15612.
570. Soellner, J.; Strassner, T. *Chem. Eur. J.* **2018**, *24*, 5584–5590.
571. Soellner, J.; Strassner, T. *ChemPhotoChem* **2019**, *3*, 554–558.
572. Schulze, B.; Friebe, C.; Jäger, M.; Görls, H.; Birkner, E.; Winter, A.; Schubert, U. S. *Organometallics* **2018**, *37*, 145–155.
573. Vivancos, Á.; Bautista, D.; González-Herrero, P. *Chem. Eur. J.* **2019**, *25*, 6014–6025.
574. Vivancos, A.; Jiménez-García, A.; Bautista, D.; González-Herrero, P. *Inorg. Chem.* **2021**, *60*, 7900–7913.
575. Lin, J. C. Y.; Huang, R. T. W.; Lee, C. S.; Bhattacharyya, A.; Hwang, W. S.; Lin, I. J. B. *Chem. Rev.* **2009**, *109*, 3561–3598.
576. Yam, V. W.; Cheng, E. C. *Chem. Soc. Rev.* **2008**, *37*, 1806–1813.
577. Hettmanczyk, L.; Spall, S. J. P.; Klenk, S.; van der Meer, M.; Hohloch, S.; Weinstein, J. A.; Sarkar, B. *Eur. J. Inorg. Chem.* **2017**, *2017*, 2112–2121.
578. Shi, S.; Collins, L. R.; Mahon, M. F.; Djurovich, P. I.; Thompson, M. E.; Whittlesey, M. K. *Dalton Trans.* **2017**, *46*, 745–752.
579. Chotard, F.; Romanov, A. S.; Hughes, D. L.; Linnolahti, M.; Bochmann, M. *Eur. J. Inorg. Chem.* **2019**, *2019*, 4234–4240.
580. Hamze, R.; Shi, S.; Kapper, S. C.; Muthiah Ravinson, D. S.; Estergreen, L.; Jung, M.; Tadler, A. C.; Haiges, R.; Djurovich, P. I.; Peltier, J. L.; Jazzar, R.; Bertrand, G.; Bradforth, S. E.; Thompson, M. E. *J. Am. Chem. Soc.* **2019**, *141*, 8616–8626.
581. Chotard, F.; Sivchik, V.; Linnolahti, M.; Bochmann, M.; Romanov, A. S. *Chem. Mater.* **2020**, *32*, 6114–6122.
582. Leitl, M. J.; Krylova, V. A.; Djurovich, P. I.; Thompson, M. E.; Yersin, H. *J. Am. Chem. Soc.* **2014**, *136*, 16032–16038.
583. Yersin, H.; Czerwiec, R.; Shafikov, M. Z.; Suleymanova, A. F. *ChemPhysChem* **2017**, *18*, 3508–3535.
584. Föllner, J.; Kleinschmidt, M.; Marian, C. M. *Inorg. Chem.* **2016**, *55*, 7508–7516.
585. Cao, L.; Huang, S.; Liu, W.; Zhao, H.; Xiong, X.; Zhang, J.; Fu, L.; Yan, X. *Chem. Eur. J.* **2020**, *26*, 17222–17229.
586. Barakat, K. A.; Cundari, T. R.; Omary, M. A. *J. Am. Chem. Soc.* **2003**, *125*, 14228–14229.
587. Pinter, P.; Schüßlbauer, C. M.; Watt, F. A.; Dickmann, N.; Herbst-Irmer, R.; Morgenstern, B.; Grünwald, A.; Ullrich, T.; Zimmer, M.; Hohloch, S.; Guldí, D. M.; Munz, D. *Chem. Sci.* **2021**, *12*, 7401–7410.
588. Romanov, A. S.; Di, D.; Yang, L.; Fernandez-Cestau, J.; Becker, C. R.; James, C. E.; Zhu, B.; Linnolahti, M.; Credgington, D.; Bochmann, M. *Chem. Commun.* **2016**, *52*, 6379–6382.
589. Gernert, M.; Müller, U.; Haehnel, M.; Pflaum, J.; Steffen, A. *Chem. Eur. J.* **2017**, *23*, 2206–2216.

590. Hamze, R.; Jazzar, R.; Soleilhavoup, M.; Djurovich, P. I.; Bertrand, G.; Thompson, M. E. *Chem. Commun.* **2017**, *53*, 9008–9011.
591. Romanov, A. S.; Becker, C. R.; James, C. E.; Di, D.; Credgington, D.; Linnolahti, M.; Bochmann, M. *Chem. Eur. J.* **2017**, *23*, 4625–4637.
592. Romanov, A. S.; Bochmann, M. *J. Organomet. Chem.* **2017**, *847*, 114–120.
593. Romanov, A. S.; Chotard, F.; Rashid, J.; Bochmann, M. *Dalton Trans.* **2019**, *48*, 15445–15454.
594. Di, D.; Romanov, A. S.; Yang, L.; Richter, J. M.; Rivett, J. P. H.; Jones, S.; Thomas, T. H.; Abdi Jalebi, M.; Friend, R. H.; Linnolahti, M.; Bochmann, M.; Credgington, D. *Science* **2017**, *356*, 159–163.
595. Hamze, R.; Peltier, J. L.; Sylvinson, D.; Jung, M.; Cardenas, J.; Haiges, R.; Soleilhavoup, M.; Jazzar, R.; Djurovich, P. I.; Bertrand, G.; Thompson, M. E. *Science* **2019**, *363*, 601–606.
596. Romanov, A. S.; Yang, L.; Jones, S. T. E.; Di, D.; Morley, O. J.; Drummond, B. H.; Reponen, A. P. M.; Linnolahti, M.; Credgington, D.; Bochmann, M. *Chem. Mater.* **2019**, *31*, 3613–3623.
597. Gernert, M.; Balles-Wolf, L.; Kerner, F.; Müller, U.; Schmiedel, A.; Holzapfel, M.; Marian, C. M.; Pflaum, J.; Lambert, C.; Steffen, A. *J. Am. Chem. Soc.* **2020**, *142*, 8897–8909.
598. Tong, K.; Hu, D.; Wan, P.; Lok, C.; Che, C. In *Advances in Inorganic Chemistry*; Sadler, P. J., van Eldik, R., Eds.; 75; Academic Press, 2020; pp 87–119.
599. Hemmert, C.; Gornitzka, H. *Dalton Trans.* **2016**, *45*, 440–447.
600. Zou, T.; Hung, F.; Yang, C.; Che, C. In *Luminescent and Photoactive Transition Metal Complexes as Biomolecular Probes and Cellular Reagents*; Lo, K. K., Ed.; vol. 165; Springer Berlin Heidelberg: Berlin, Heidelberg, 2015; pp 181–203.
601. Simon, T. M.; Kunishima, D. H.; Vibert, G. J.; Lorber, A. *Cancer* **1979**, *44*, 1965–1975.
602. Bertrand, B.; Romanov, A. S.; Brooks, M.; Davis, J.; Schmidt, C.; Ott, I.; O'Connell, M.; Bochmann, M. *Dalton Trans.* **2017**, *46*, 15875–15887.
603. Proetto, M. T.; Alexander, K.; Melaimi, M.; Bertrand, G.; Gianneschi, N. C. *Chem. Eur. J.* **2021**, *27*, 3772–3778.
604. Kralj, J.; Bolje, A.; Polančec, D. S.; Steiner, I.; Gržan, T.; Tupek, A.; Stojanović, N.; Hohloch, S.; Urankar, D.; Osmak, M.; Sarkar, B.; Brozovic, A.; Košmrlj, J. *Organometallics* **2019**, *38*, 4082–4092.
605. Hoyer, C.; Schwerek, P.; Suntrup, L.; Beerhues, J.; Nössler, M.; Albold, U.; Denedde, J.; Tedin, K.; Sarkar, B. *Eur. J. Inorg. Chem.* **2021**, *2021*, 1373–1382.
606. Aucamp, D.; Kumar, S. V.; Liles, D. C.; Fernandes, M. A.; Harmse, L.; Bezuidenhout, D. I. *Dalton Trans.* **2018**, *47*, 16072–16081.
607. Shaw, C. F., III *Chem. Rev.* **1999**, *99*, 2589–2600.
608. Shaw, C. F. In *Metal Compounds in Cancer Therapy*; Fricker, S. P., Ed.; Springer Netherlands: Dordrecht, 1994; pp 46–64.
609. van der Westhuizen, D.; Slabber, C. A.; Fernandes, M. A.; Joubert, D. F.; Kleinhans, G.; van der Westhuizen, C. J.; Stander, A.; Munro, O. Q.; Bezuidenhout, D. I. *Chem. Eur. J.* **2021**, *27*, 8295–8307.
610. Verma, S. K.; Kumari, P.; Ansari, S. N.; Ansari, M. O.; Deori, D.; Mobin, S. M. *Dalton Trans.* **2018**, *47*, 15646–15650.

## 1.06 Frustrated lewis pairs in catalysis

Katarina Stefkova, Jamie L. Carden, and Rebecca L. Melen, Cardiff Catalysis Institute, School of Chemistry, Cardiff University, Cardiff, United Kingdom

© 2023 Elsevier Ltd. All rights reserved.

<b>1.06.1</b>	<b>Introduction to frustrated Lewis pairs (FLPs)</b>	<b>315</b>
<b>1.06.2</b>	<b>FLP-mediated catalytic hydrogenation</b>	<b>316</b>
1.06.2.1	FLP-mediated catalytic hydrogenation of polar substrates	316
1.06.2.1.1	Reduction of C–N multiple bonds and silyl enols	317
1.06.2.1.2	Reduction of amides and phosphine oxides	319
1.06.2.1.3	Substrates which also serve as the Lewis basic components of FLPs	320
1.06.2.1.4	Enantioselective reduction of C–N multiple bonds and silyl enols	323
1.06.2.1.5	Reduction of carbonyls	326
1.06.2.1.6	Reductive etherification of carbonyls	330
1.06.2.1.7	Reductive alkylation of amines with carbonyls	330
<b>1.06.2.2</b>	<b>FLP-mediated catalytic hydrogenation of non-polar substrates</b>	<b>332</b>
1.06.2.2.1	Reduction of alkenes and allenes	333
1.06.2.2.2	Reduction of alkynes	336
<b>1.06.2.3</b>	<b>FLP-mediated transfer hydrogenation</b>	<b>338</b>
<b>1.06.2.4</b>	<b>FLP-mediated dehydrogenation</b>	<b>342</b>
<b>1.06.2.5</b>	<b>Unusual FLP systems for catalytic hydrogenation</b>	<b>344</b>
1.06.2.5.1	Boremium cations	344
1.06.2.5.2	Electrophilic phosphonium cations	346
1.06.2.5.3	Inverse FLPs	347
<b>1.06.3</b>	<b>Hydrosilylation</b>	<b>349</b>
1.06.3.1	FLP-mediated hydrosilylation	349
1.06.3.2	Asymmetric FLP-mediated hydrosilylation	352
1.06.3.3	FLP-mediated reduction of amides to amines via hydrosilylation	359
<b>1.06.4</b>	<b>FLP-mediated hydroamination</b>	<b>362</b>
<b>1.06.5</b>	<b>FLP-mediated C–H borylation</b>	<b>363</b>
<b>1.06.6</b>	<b>FLP-mediated cyclization reactions</b>	<b>366</b>
<b>1.06.7</b>	<b>FLP-mediated reduction of CO<sub>2</sub></b>	<b>369</b>
<b>1.06.8</b>	<b>Summary and outlook</b>	<b>373</b>
<b>Acknowledgments</b>		<b>373</b>
<b>Conflicts of Interest</b>		<b>373</b>
<b>References</b>		<b>373</b>

### Abstract

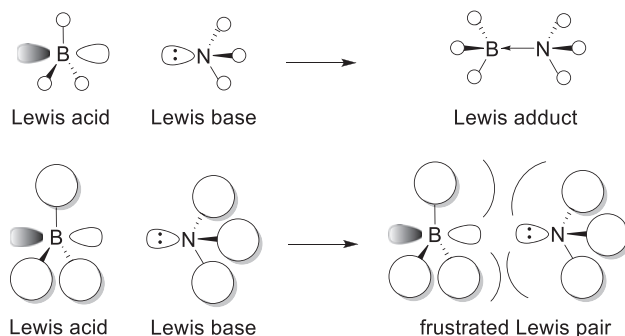
Since frustrated Lewis pairs were first defined in 2006, they have become one of the most exciting areas of main group chemistry. In just 15 years, these systems have gone from chemical curiosities to commonplace catalysts, and many research groups are now exploring their ability to supersede conventional transition metal catalysts. This article aims to discuss the catalytic applicability of frustrated Lewis pairs, with a discussion on hydrogenation catalysis, 1,2-hydrofunctionalization catalysis, cyclization catalysis, and CO<sub>2</sub> reduction catalysis.

### 1.06.1 Introduction to frustrated Lewis pairs (FLPs)

When a Lewis acid and a Lewis base combine, the lone pair of electrons on the base are donated into the empty *p*-orbital of the acid to form a Lewis adduct. In cases where there is segregation between the Lewis acidic and basic sites, an adduct is unable to form and instead a frustrated Lewis pair (FLP) is formed (Fig. 1). FLPs retain the reactivity of the individual Lewis acid and base centers and are thus able to partake in reactions which Lewis adducts are recalcitrant toward.<sup>1</sup>

Whilst the first frustrated Lewis pair was not identified until 2006, unexpected reactivity by Lewis acids and bases that could retrospectively be described as FLP-like in nature can be found as early as 1942.<sup>2–4</sup> In 1996, Piers observed that tris(pentafluorophenyl)borane [B(C<sub>6</sub>F<sub>5</sub>)<sub>3</sub>] was an efficient catalyst toward the hydrosilylation of carbonyls with triphenylsilane, but it was not for a further 12 years that the mechanism was fully elucidated.<sup>5,6</sup> Stephan coined the term ‘frustrated Lewis pair’ following the





**Fig. 1** Formation of Lewis adducts and frustrated Lewis pairs.<sup>1</sup>

seminal discovery of 2006, which reported the first metal-free reversible activation of dihydrogen (**Scheme 1**).<sup>7</sup> The described phosphinoborane exhibited a large steric bulk around the Lewis acidic and basic sites and was able to reversibly activate dihydrogen under mild conditions.<sup>7</sup>

The simplicity of hydrogen activation by frustrated Lewis pairs led to a plethora of interest in their application toward further small molecule activation, and more recently catalysis. Since 2006, the scope of small molecules amenable to activation by FLPs has expanded toward CO<sub>2</sub>, NO<sub>2</sub>, SO<sub>2</sub>, alkenes and N<sub>2</sub>.<sup>8–11</sup> This article aims to explore the catalytic aspect of frustrated Lewis pairs.

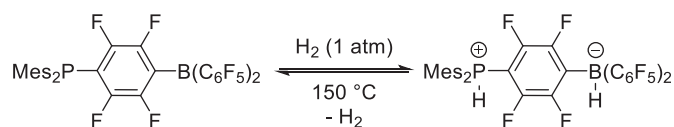
### 1.06.2 FLP-mediated catalytic hydrogenation

The catalytic reduction of unsaturated compounds with dihydrogen is one of the most widely applied processes in industrial and academic settings. In fact, it is estimated that up to 20% of all synthesized chemicals have been subjected to one form of catalytic hydrogenation at one point in development<sup>12</sup>; however, the majority of catalysts used in the hydrogenation transformation contain a transition-metal center, which facilitates the reduction of dihydrogen with its *d*-orbitals. Herein, the filled  $\sigma$  orbital of dihydrogen is able to donate into an empty *d*-orbital of the metal, whilst simultaneously a filled *d*-orbital is able to donate electron density into the dihydrogen's empty  $\sigma^*$  orbital (**Fig. 2**, left).

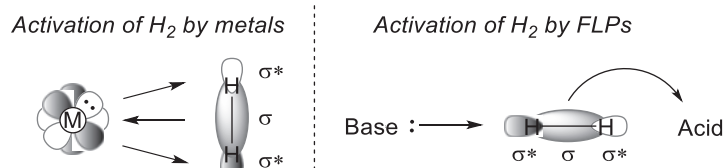
A different process occurs in the activation of hydrogen by FLPs, wherein the basic component is able to donate electron density into the empty  $\sigma^*$  orbital of dihydrogen, whilst the acidic component is able to accept electron density from the filled  $\sigma$  orbital of dihydrogen (**Fig. 2**, right). For many years transition metals dominated the field of hydrogen reduction, with reports of main-group metals utilized in the field significantly rarer.<sup>13</sup> Thus, upon the seminal discovery of frustrated Lewis pairs an exciting new article in metal-free catalytic hydrogenations was launched.

#### 1.06.2.1 FLP-mediated catalytic hydrogenation of polar substrates

The serendipitous discovery by Stephan that a phosphinoborane could reversibly activate H<sub>2</sub> launched an exciting new article within the field of metal-free catalysis.<sup>7</sup> In quick succession, Stephan and other researchers observed that an FLP's ability to mediate reversible dihydrogen activation also granted it the ability to reduce catalytically a range of polar substrates. C–N multiple bonds and silyl



**Scheme 1** First example of reversible activation of dihydrogen by a non-metal complex.<sup>7</sup>



**Fig. 2** Activation of H<sub>2</sub> by metals (left) and FLPs (right).

enol ethers were the first to be reduced; however, it was not long before a more diverse scope of amides, phosphine oxides, and carbonyls were observed to be amenable to FLP-catalyzed hydrogenation.

### 1.06.2.1.1 Reduction of C–N multiple bonds and silyl enols

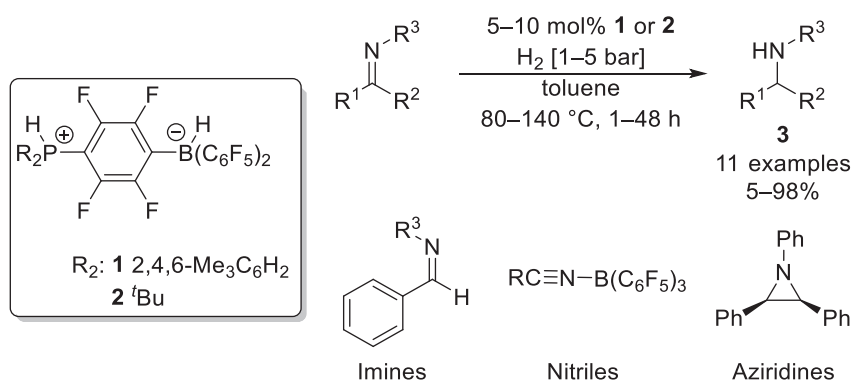
Stephan's seminal work on stoichiometric H<sub>2</sub> activation was swiftly followed with the first example of FLP catalyzed hydrogenation (Scheme 2).<sup>14</sup> Two intramolecular FLPs, **1** and **2**, were demonstrated to catalyze the reduction of a range of eleven sterically demanding unsaturated substrates including imines, protected nitriles and unactivated aziridines into their respective amines **3**, in poor to excellent yield.<sup>14</sup>

Shortly afterwards, Erker reported that phosphonium borate **4** could be employed as an intramolecular FLP toward the reduction of bulky imines. Unlike in previous examples,<sup>14</sup> where elevated temperatures were required for efficient reduction, FLP **4** was capable of reducing five imines under ambient conditions in good to excellent yield. Furthermore, this system also gave the first report of enamine reduction at room temperature (Scheme 3).<sup>15</sup>

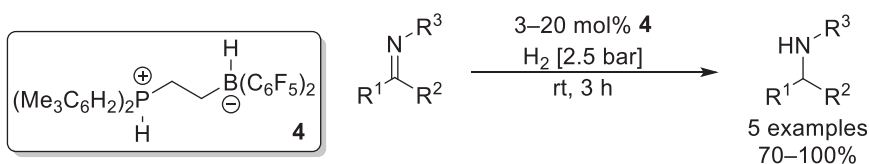
A linked amine-borane FLP **5** termed a 'molecular tweezer' was later developed by Repo (Fig. 3).<sup>16</sup> This new system was reported to reduce imines that the previously known phosphine/borane FLPs had been recalcitrant toward.<sup>14,15</sup> For example, when catalyst **1** was investigated in this reduction, the imine substrate formed a strong amine-borate adduct **6**. The strength of this B–N interaction resulted in inhibition of the boron center, thus only allowing for stoichiometric reductions to occur.<sup>16</sup>

FLP **5** was found to catalyze the reduction of imines at low loadings under relatively ambient conditions, reflux in toluene under 2 bar of hydrogen (Scheme 4). Eight examples were reported, with almost quantitative NMR yields observed for most substrates; however, less sterically demanding imines (**7** and **8**) remained a limitation for this catalytic system, generating their corresponding amine products in a mere 4% yield.<sup>16</sup>

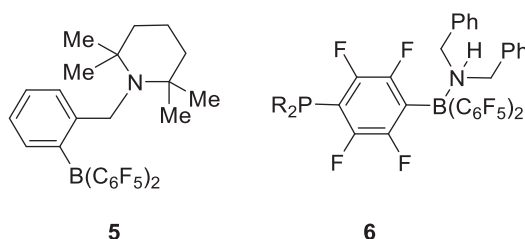
An intermolecular FLP composed of 1,8-bis(diphenylphosphino)naphthalene **9** and B(C<sub>6</sub>F<sub>5</sub>)<sub>3</sub> was reported to catalyze the reduction of five silyl enol ethers into silanes (Scheme 5).<sup>17</sup> Whilst a relatively high catalyst loading was required, very mild conditions and low H<sub>2</sub> pressure was sufficient to catalyze the reduction, forming the desired silanes in high yields; however, for the less sterically demanding enol silyl ether **10**, a much harsher pressure of H<sub>2</sub> was required for the reduction to proceed.<sup>17</sup>



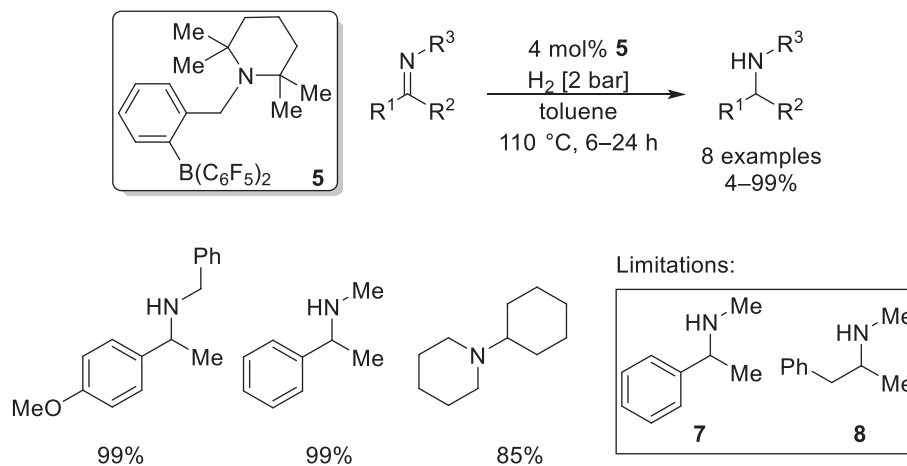
**Scheme 2** The first report of FLP catalyzed hydrogenation with intramolecular FLPs **1** and **2**.<sup>14</sup>



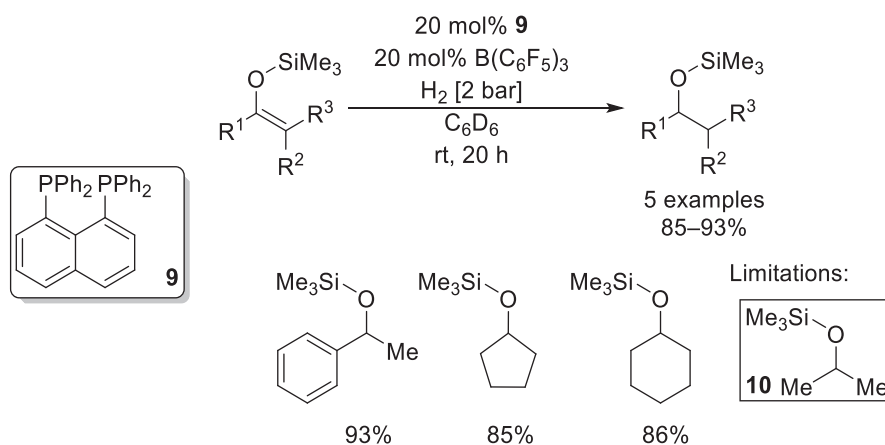
**Scheme 3** FLP catalyzed reduction of imines.<sup>15</sup>



**Fig. 3** Intramolecular FLP **5** for imine reduction (left); amine-borate adduct **6** formed when catalyst **1** used in imine reduction (right).<sup>16</sup>

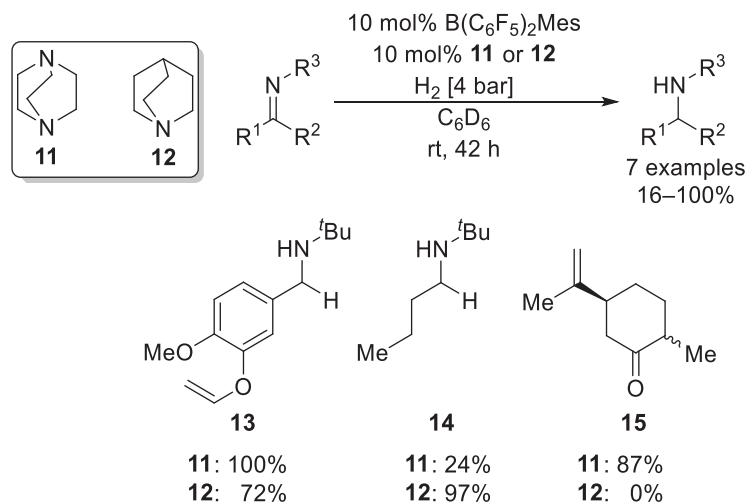


**Scheme 4** Imine reduction catalyzed by FLP **5**.<sup>16</sup>



**Scheme 5** Silyl enol ether reduction catalyzed with a **9**/ $\text{B}(\text{C}_6\text{F}_5)_3$  FLP.<sup>17</sup>

In effort to improve the functional group tolerability for catalytic reduction, novel FLP systems were designed by Soós (**Scheme 6**). A simple modification to the archetypal  $\text{B}(\text{C}_6\text{F}_5)_3$  was employed, wherein a single perfluorinated aryl group on the borane was replaced with a mesitylene substituent. This had the effect of increasing congestion around the boron center, thus preventing the FLP from unwanted reactivity with the olefin functionalities in most cases. With the Lewis acid  $\text{B}(\text{C}_6\text{F}_5)_2\text{Mes}$  in hand, a screening with



**Scheme 6** Catalytic reduction by  $\text{B}(\text{C}_6\text{F}_5)_2\text{Mes}/\mathbf{11}$  and  $\text{B}(\text{C}_6\text{F}_5)_2\text{Mes}/\mathbf{12}$  FLP systems.<sup>18</sup>

various commercially available nitrogen-based Lewis bases was performed toward the reduction of an imine. Here DABCO (1,4-diazabicyclo[2.2.2]octane) **11** and quinuclidine **12** were found to perform the best when combined with  $B(C_6F_5)_2Mes$ , with the DABCO **11** system operating efficiently under ambient conditions.

The novel FLPs comprised of  $B(C_6F_5)_2Mes$  and **11** or **12** were applied toward the reduction of seven imines, with poor to excellent yields observed. Notably, challenging substrates **13** and **14** were also reduced by these FLP systems. In the case of allyloxy derivative **13**, the FLP systems tolerated the allyl and unactivated olefin groups, with only reduction of the imine observed; however, when subjecting the crotyl imine **14** toward the reduction, both the imine and olefin groups were hydrogenated. Finally, carvone **15** was investigated and the  $B(C_6F_5)_2Mes/11$  FLP was observed to reduce selectively the activated olefin within the six-membered ring in the presence of a terminal alkene, whereas the  $B(C_6F_5)_2Mes/12$  FLP was unable to promote any reactivity.<sup>18</sup>

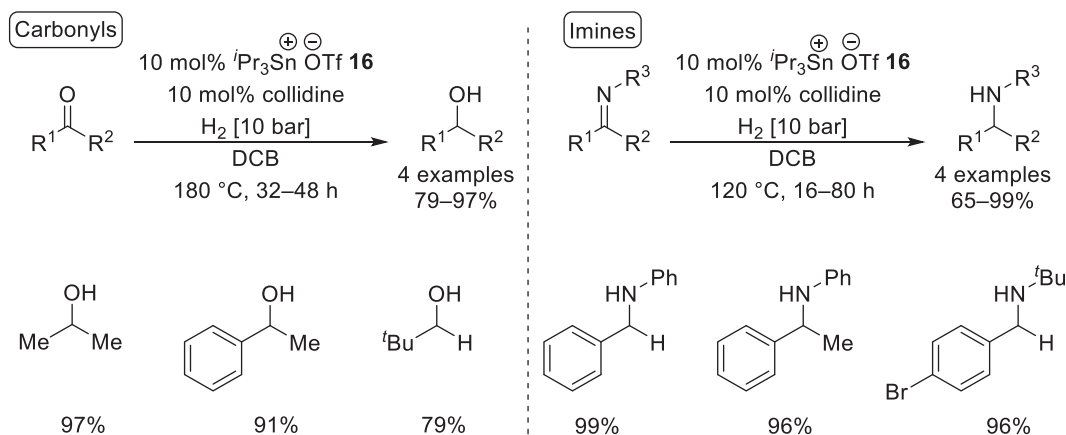
An alternative approach to conventional FLP chemistry was demonstrated by Ashley, who used the softer *p*-block element, tin, rather than boron (Scheme 7).<sup>19</sup> Stannylum salt  ${}^iPr_3SnOTf$  **16** was prepared, of which the ion,  ${}^iPr_3Sn^+$ , can be considered as an isolobal equivalent to a triarylborane. The bulky alkyl groups around the tin center prevent the triflate counterion from interacting with its empty *p*-orbital, thus generating a shielded electrophilic moiety acidic enough to participate in FLP-type reactivity. Here, in combination with various bases, **16** was employed in the reduction of carbonyls and imines under mild conditions in 1,2-dichlorobenzene (DCB), and without the requirement for air sensitive techniques. Four carbonyls and six imines were readily reduced, with product yields strongly dependent on the identity of the base; in most cases the reaction proceeded best with 2,4,6-trimethylpyridine (collidine).<sup>19</sup>

### 1.06.2.1.2 Reduction of amides and phosphine oxides

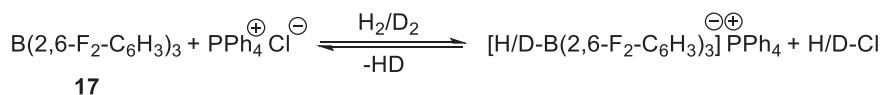
The one-pot reduction of tertiary amides was achieved with a catalytic amount of the weakly Lewis acidic  $B(2,6-F_2C_6H_3)_3$  **17** in combination with an excess of oxalyl chloride  $(COCl)_2$ .<sup>20</sup> Oxalyl chloride served as a deoxygenating agent for the amide, forming chloroiminium chloride **18** in situ. Further reduction yielded the desired amine, which was formed as hydrochloride salt **19** and could be obtained readily by filtration. Through  $H_2/D_2$  isotope scrambling between **17** and tetraphenylphosphonium chloride, it was revealed that the chloride **18** formed in situ served as the Lewis base in the FLP, in what was noted as the first example of a halide acting as a Lewis base in FLP chemistry (Scheme 8).<sup>20</sup>

The reduction protocol with **17** was observed to be versatile across a range of functionalities, with benzoyl, formyl and cyclohexyl derived amides amenable to reduction in good to excellent yield. Moreover, acid-sensitive amides derived from proline **20** or containing a *tert*-butyloxycarbonyl (Boc) group **21** were also reduced adequately; however, acetyl derived amides performed poorly and highly reactive aromatic *N*-heterocycles such as diphenylamine and indole simply decomposed (Scheme 9).<sup>20</sup>

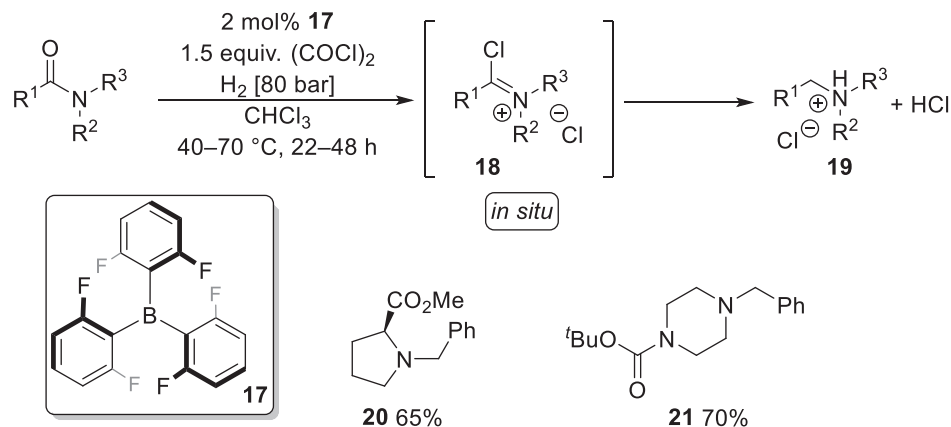
A combination of **17** and oxalyl chloride was also used in the reduction of triaryl phosphine oxides.<sup>21</sup> Here, 2,6-lutidine **22** was initially applied as the Lewis basic component of the FLP. While an optimization found the reduction would work efficiently, forming the desired phosphine in 93% yield, the hydrogen chloride by-product was observed to protonate **22**, thereby deactivating the catalyst. The reduction was also noted to occur quantitatively in the absence of **22**, wherein the phosphine oxide itself served as the Lewis basic component of the FLP (Scheme 10).<sup>21</sup> Further examples of substrates which act as a Lewis base in FLP chemistry can be found in the next section.



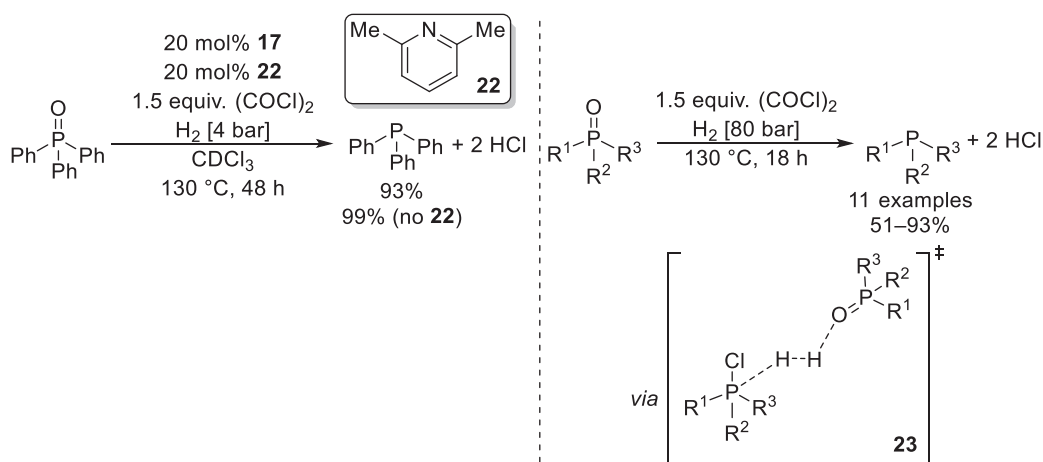
Scheme 7  ${}^iPr_3SnOTf$  **16** catalyzed reduction of carbonyls and imines.<sup>19</sup>



Scheme 8  $H_2/D_2$  isotope scrambling between  $B(2,6-F_2C_6H_3)_3$  **17** and tetraphenylphosphonium chloride.<sup>20</sup>



**Scheme 9** FLP mediated reduction of tertiary amides.<sup>20</sup>



**Scheme 10** FLP mediated reduction of phosphine oxides.<sup>21</sup>

Interestingly, by applying a higher pressure of hydrogen, the reduction of triaryl phosphine oxides could be observed to occur in the absence of the borane altogether, forming the phosphine in 93% yield. Computational studies suggested that this reaction proceeded via  $H_2$  activation by the phosphine oxide and a chlorophosphonium ion **23** (generated *in situ* by reaction between the phosphine oxide and the  $(COCl)_2$  additive) which served as the Lewis basic and Lewis acidic components of a new FLP respectively (Scheme 10).<sup>21</sup>

### 1.06.2.1.3 Substrates which also serve as the Lewis basic components of FLPs

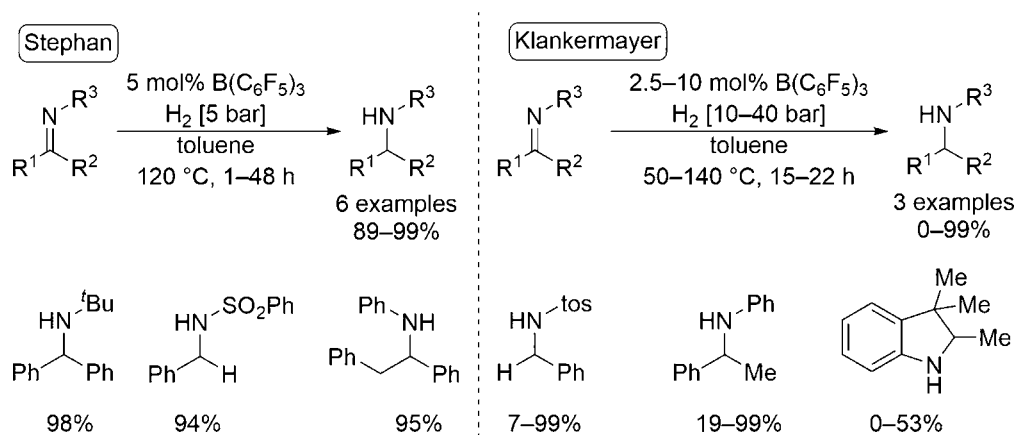
Just 2 years after the discovery of frustrated Lewis pairs, it was recognized that basic substrates could also act as a component in a FLP, negating the use of an external base in the reaction. This was demonstrated simultaneously by Klankermayer and Stephan through the reduction of bulky imines by  $B(C_6F_5)_3$  (Scheme 11).<sup>22,23</sup> Stephan investigated a short scope of six imines, exploring the functional group tolerance with a set of optimized conditions.<sup>23</sup> Meanwhile, Klankermayer optimized the reduction of three imines, optimizing time,  $H_2$  pressure, catalyst loading and temperature.<sup>22</sup>

Stephan further expanded this methodology toward a protected aziridine, forming the corresponding amine in 95% yield (Scheme 12). Nitrile reduction was also attempted; however, it was observed that protected nitriles were not basic enough to extract the proton from the activated  $H_2$  without external assistance. Nonetheless, the addition of an external base, such as  $P(C_6H_2Me_3)_3$ , proved to be sufficient to catalyze the reduction of protected nitriles.<sup>23</sup>

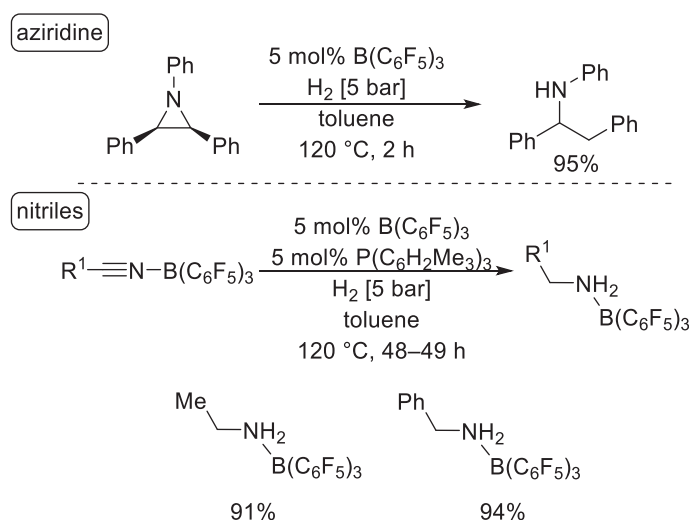
A subsequent report further increased the scope of this system, with the reduction of five *N*-heterocycles such as acridine and substituted quinolines (Scheme 13). Whilst some quinolines required elevated temperatures to undergo reduction, good to excellent yields were observed throughout.<sup>24</sup>

Stephan later detailed that  $B(C_6F_5)_3$  could also catalyze the reduction of indole derivatives into their corresponding dihydroindoles.<sup>25</sup> Whilst the imines and *N*-heterocycles investigated previously were reducible under relatively ambient conditions,<sup>23,24</sup> the indole derivatives required harsher temperatures and pressures (80 °C; 103 bar  $H_2$ ) for sufficient reactivity. High temperatures were

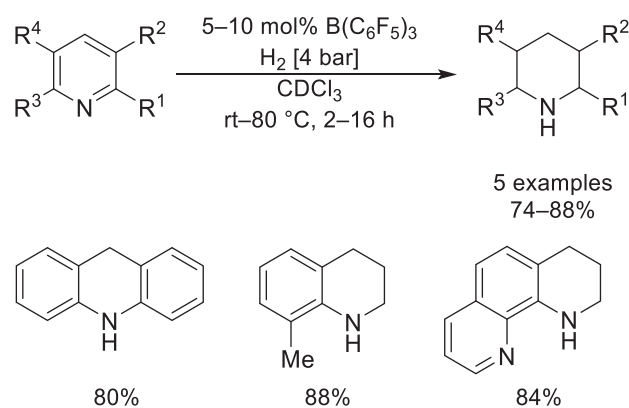




**Scheme 11** Catalytic reduction of imines where the imine acts as both substrate and the basic component of the FLP.<sup>22,23</sup>



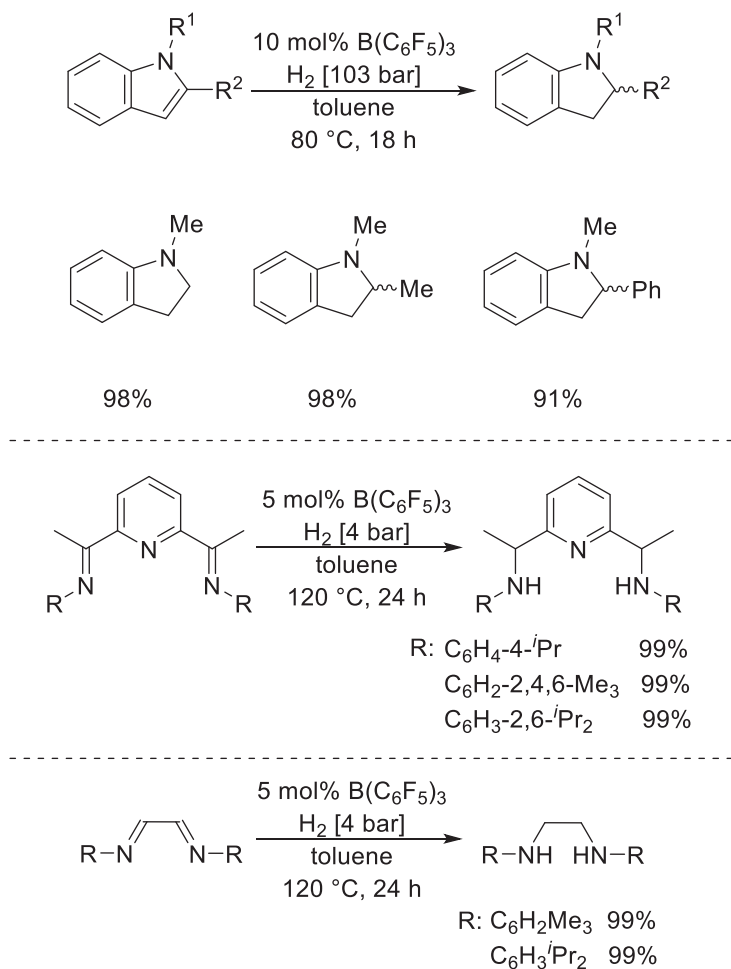
**Scheme 12** Catalytic reduction of aziridine and nitriles with B(C<sub>6</sub>F<sub>5</sub>)<sub>3</sub>.<sup>23</sup>



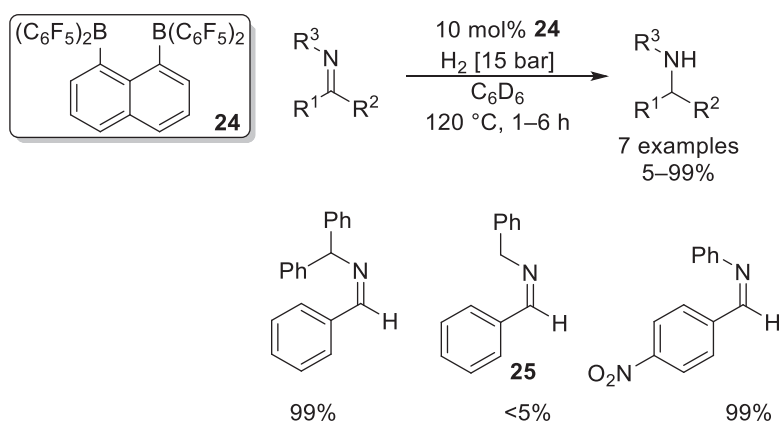
**Scheme 13** Catalytic reduction of *M*-heterocycles with B(C<sub>6</sub>F<sub>5</sub>)<sub>3</sub>.<sup>24</sup>

also required for the reduction of pyridines and diimines, although only 4 bar of H<sub>2</sub> was required. Notably, upon the reduction of pyridine derivatives, the FLP system selectively reduced the imine functionality and not the aromatic pyridine ring (**Scheme 14**).<sup>25</sup>

In 2009, Berke introduced a modified Lewis acid with two acidic centers, 1,8-bis(dipentafluorophenylboryl)naphthalene **24**, which was able to form a FLP with the substrates it was designed to reduce. Seven bulky imines were subjected toward the reduction with this FLP system with 10 mol% loading of **24** (**Scheme 15**). Most substrates were reduced into their respective amines in 99%



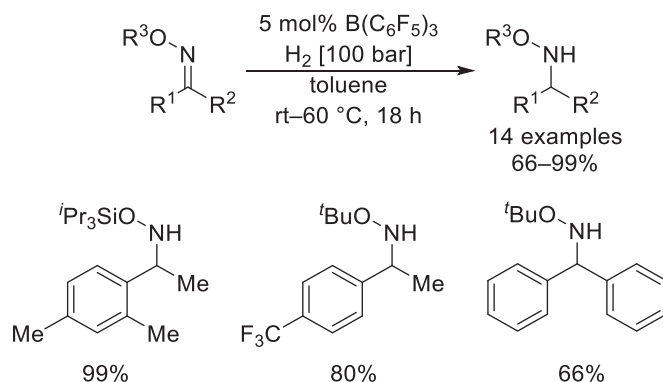
**Scheme 14** Catalytic reduction of indoles, pyridine derivatives and diimines.<sup>25</sup>



**Scheme 15** Catalytic reduction of imines with bisborane **24**.<sup>26</sup>

yield in as little as 6 h; however, a limitation was noted upon the attempted reduction of *N*-benzyl-1-phenylmethanimine **25**, which was resistant toward reaction.<sup>26</sup>

Moreover, the reduction of protected oximes into their corresponding protected hydroxylamines was observed by Oestreich, whilst using a catalytic amount of B(C<sub>6</sub>F<sub>5</sub>)<sub>3</sub> (**Scheme 16**). Good to excellent yields were reported over 14 examples, though the reduction was found to be unsuccessful with unprotected oximes or when the oxime protecting group was not sufficiently bulky. The stable boron-oxime adduct intermediate was observed when a *t*Bu or Si<sup>*i*</sup>Pr<sub>3</sub> protecting group was installed on the oxime; however, the Si<sup>*i*</sup>Pr<sub>3</sub> protecting group was preferred as the free hydroxylamine was obtainable through a simple treatment with



**Scheme 16** Chemoselective reduction of protected oximes with catalytic  $\text{B}(\text{C}_6\text{F}_5)_3$ .<sup>27</sup>

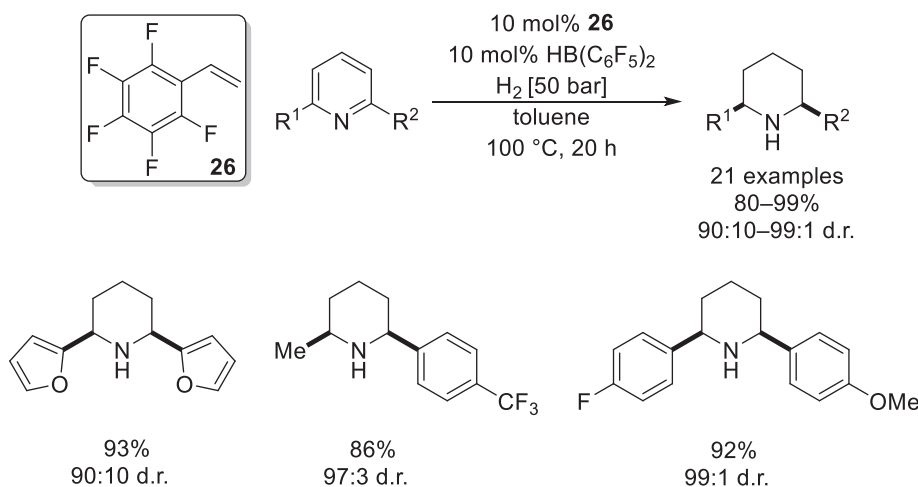
$\text{HF}\cdot\text{pyridine}$ .<sup>27</sup> Moreover, the reduction was observed to be chemoselective, with exclusive reduction of the  $\text{C}=\text{N}$  bond and no  $\text{N}-\text{O}$  bond scission.<sup>27</sup>

Du targeted the direct reduction of pyridines with the use of a borane catalyst formed in situ through the hydroboration of Piers borane  $[\text{HB}(\text{C}_6\text{F}_5)_2]$  with alkene **26** (Scheme 17). A broad range of 21 piperidines were formed through reduction of their corresponding pyridines with excellent *cis* stereoselectivities (up to 99:1 d.r.) and isolated yields (up to 99%). This methodology was also applied toward the synthesis of isosolenopsin A, an anti-HIV drug.<sup>28</sup>

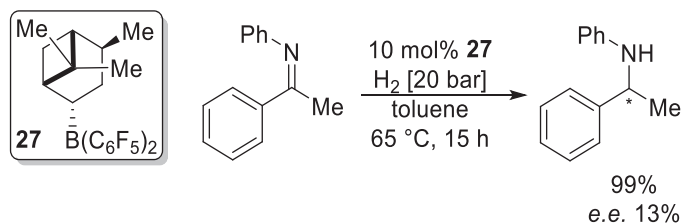
#### 1.06.2.1.4 Enantioselective reduction of C–N multiple bonds and silyl enols

Enantioselective reductions are of high importance to the synthetic chemist. With many biologically active molecules active only as a single enantiomer, there is a great deal of interest in the enantioselective synthesis of compounds. Many enantioselective catalysts are based upon transition metals due to the ease of installing chiral ligands onto the metal center; however, there have been an increasing number of frustrated Lewis pair systems that are viable alternatives for enantioselective reductions.

The first report of a FLP-mediated enantioselective reduction came in 2008, where Klankermayer prepared a chiral borane catalyst capable of reducing imines asymmetrically. This chiral borane was derived from the natural product (+)- $\alpha$ -pinene, which upon hydroboration with Piers borane formed borane **27**. By applying 10 mol% of **27**, heating to 65 °C and applying 20 bar of hydrogen pressure, full conversion of an imine substrate could be observed with 13% *e.e.* (Scheme 18).<sup>22</sup>



**Scheme 17** Catalytic reduction of pyridines with Piers borane and **26**.<sup>28</sup>



**Scheme 18** First report of FLP-mediated enantioselective reduction of imines.<sup>22</sup>

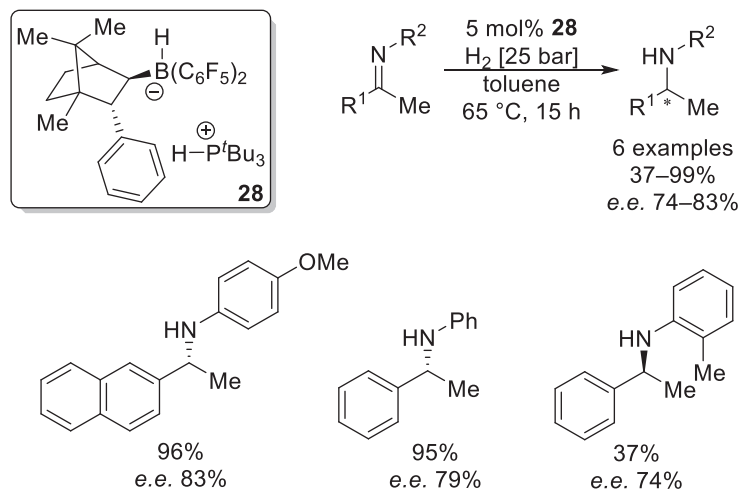
This system was significantly improved just 2 years later with the introduction of a borane derived from a different natural product, (1R)-(+)-camphor. Again, Piers borane was employed to undergo a hydroboration reaction with the natural product to form a chiral borane, which when in the presence of  $P^tBu_3$  would form FLP system **28**. This novel chiral intermolecular FLP system was investigated in a series of pro-chiral ketimine reductions (Scheme 19). Indeed, higher enantioselective reductions of up to 83% *e.e.* were achieved with just 5 mol% catalytic loading of **28**.<sup>29</sup>

An intramolecular version of intermolecular FLP **28** was developed in 2012 (Scheme 20). Here, (1R)-(+)-camphor was initially installed with a phosphine moiety before hydroboration with Piers borane to form the desired chiral borane **29**. **29** was then subjected toward a scope of imines with variously substituted aryl groups, promoting highly enantioselective reductions (up to 76% *e.e.*). Moreover, recyclability of the catalyst was also investigated. It was found that **29** could give reproducible results (>99% conversion, 76% *e.e.*) over four consecutive experiments, confirming the catalyst's effectiveness and stability.<sup>30</sup>

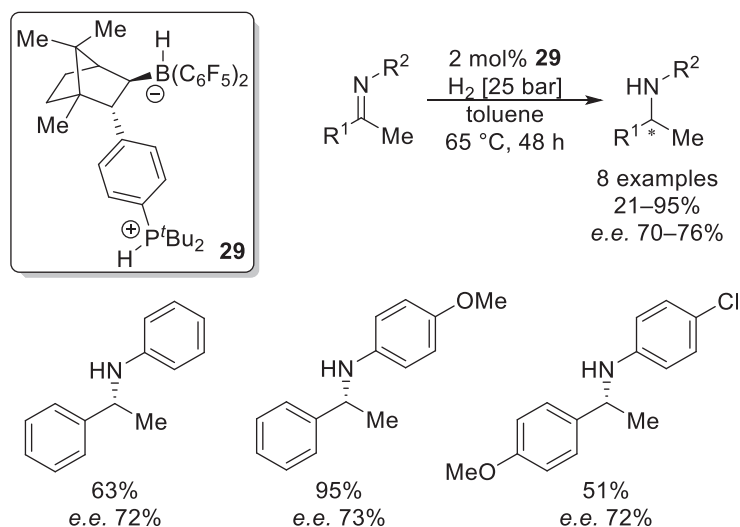
Diastereoselective reduction of chiral ketimines was attempted with  $B(C_6F_5)_3$  to mixed success (Scheme 21). Whilst yields were observed to be satisfactory over nine examples, the success of diastereoselectivity was found to correlate with the distance between the chiral center of the imine and the unsaturated carbon center. For example, the camphor **30** and menthone **31** derived imines performed well under the conditions investigated, whilst phenethylamine **32** did not.<sup>31</sup>

In 2011, Repo prepared a chiral variant **33** of the 'molecular tweezer' FLP **5**,<sup>16</sup> and probed the capability of this novel catalyst in the enantioselective reduction of imines (Fig. 4).<sup>32</sup> However whilst *ansa*-ammonium borate **33** displayed high air and moisture stability it did not show satisfactory results in enantioselective reductions, with a maximum reported *e.e.* of 37%.<sup>32</sup>

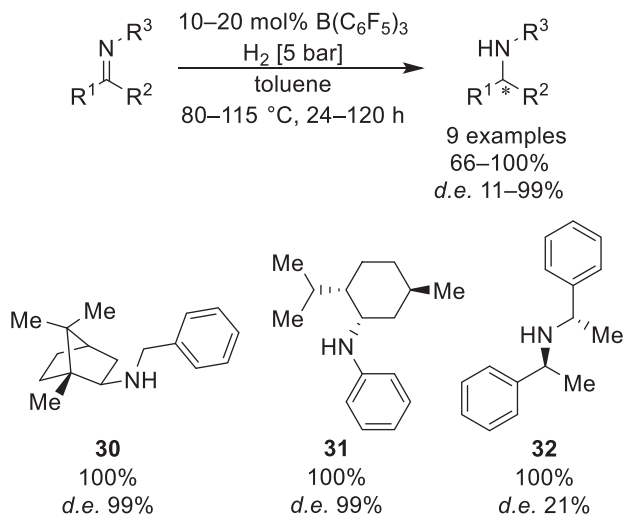
Du established an alternate strategy for asymmetric reduction with catalytically active bisboranes, generated through reaction of chiral dienes or diyenes with Piers borane. Here the chirality imparted upon the catalytic reduction originated from the ligand



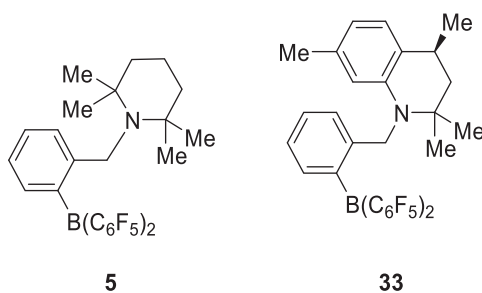
**Scheme 19** Enantioselective reduction of imines with an intermolecular FLP system containing a camphor-based borane.<sup>29</sup>



**Scheme 20** Enantioselective reduction of imines with an intermolecular FLP system containing a camphor-based borane.<sup>30</sup>



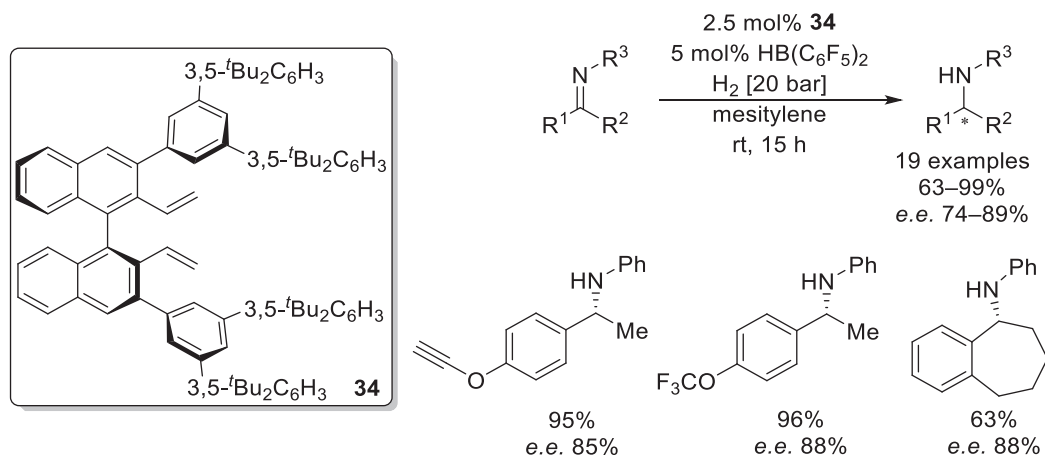
**Scheme 21** Diastereoselective reduction of chiral ketimines with  $\text{B(C}_6\text{F}_5\text{)}_3$ .<sup>31</sup>



**Fig. 4** Chiral variant of FLP 'molecular tweezers'.<sup>32</sup>

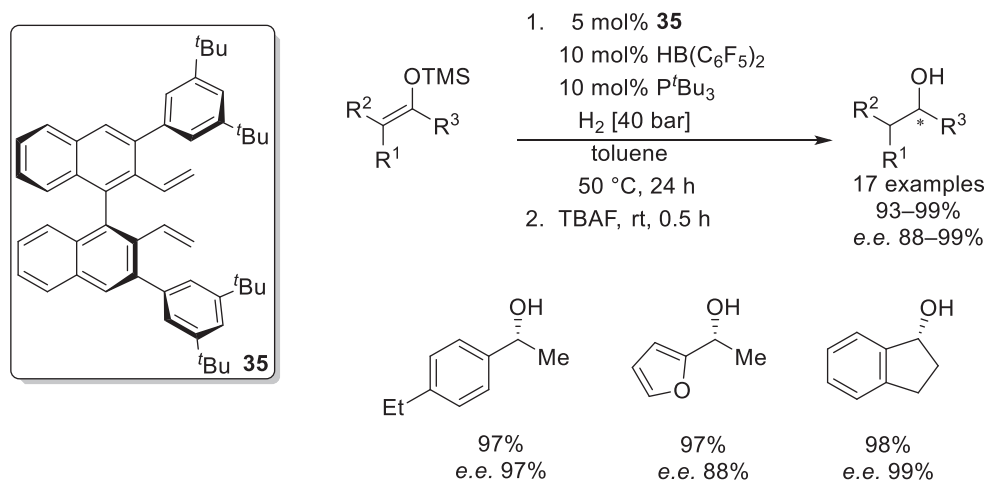
attached to the boron based catalyst.<sup>33–36</sup> The first attempt toward asymmetric reduction was performed with diene **34** (Scheme 22), which when reacted with Piers borane formed a catalytically active chiral bisborane in situ. Various ketimines were subjected toward reduction by this bisborane, with high yields and enantioselectivities observed at room temperature (63–99%, 74–89% *e.e.*). Moreover, various functional groups on the phenyl substituent were tolerated, including an alkyne moiety.<sup>33</sup>

A related chiral diene with modified aryl rings **35** was later developed into a chiral bisborane through hydroboration with Piers borane (Scheme 23). Here, equimolar  $\text{P}^t\text{Bu}_3$  was employed to assist in the asymmetric reduction of silyl enol ethers in excellent yields (up to 99%) and high *e.e.* (up to 99%).<sup>34</sup>



**Scheme 22** Chiral reduction of ketimines with bisborane based upon diene **34**.<sup>33</sup>





**Scheme 23** Chiral reduction of silyl enol ethers with bisborane based upon diene **35**.<sup>34</sup>

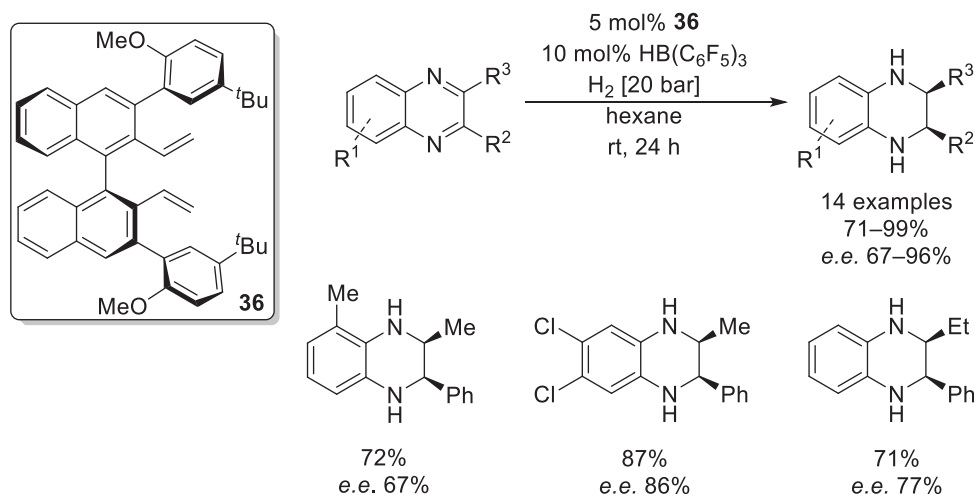
A further, more electron deficient chiral diene **36** was employed in the preparation of a different in situ chiral diphenyl bisborane through reaction with Piers borane for the asymmetric reduction of quinoxalines (**Scheme 24**). Here the quinoxaline was able to act as the Lewis base of the frustrated Lewis pair, leading to 14 enantioselective reductions at room temperature. The formed tetrahydroquinoxalines were highly *cis*-selective (up to 99:1 *d.r.*) and highly enantioselective (67–96% *e.e.*).<sup>35</sup>

The most recent development by Du in chiral reduction was based upon a naphthyl-derived diyne ligand **37** (**Scheme 25**). Such structural change made the chiral borane formed upon hydroboration with Piers borane more rigid, as well as susceptible to electronic tuning upon modification to the naphthyl ring. The chiral bisborane and P<sup>t</sup>Bu<sub>3</sub> were employed in the catalytic reduction of a range of silyl enol ethers, employing the optimized conditions used with the bisborane based upon **35**.<sup>34</sup> The reactions proceeded smoothly, yielding optically active alcohols in up to 99% isolated yields and up to 99% *e.e.*<sup>36</sup>

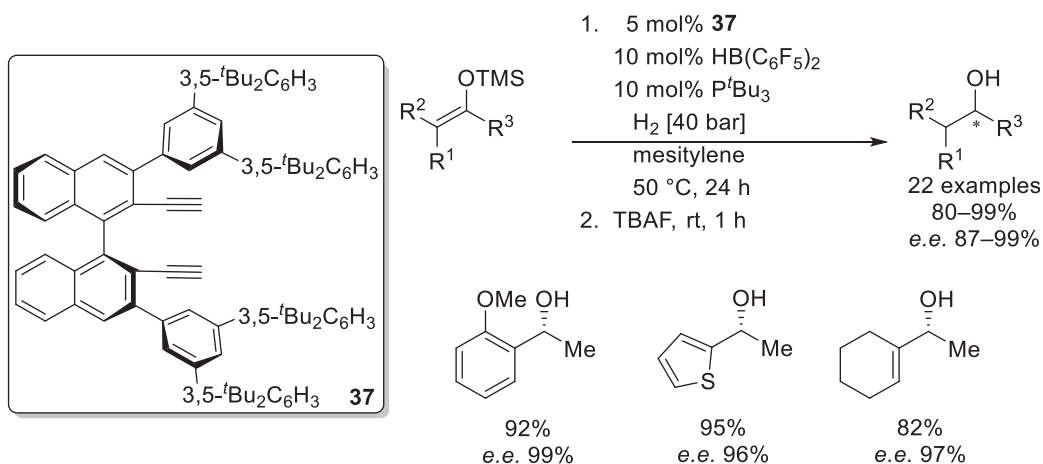
Further effort in imparting chirality by using a binaphthyl scaffold within an FLP was reported with binaphthyl-linked amino-borane **38** (**Scheme 26**). This intramolecular FLP was utilized in the asymmetric reductions of six imines and notably, in the first reported asymmetric reduction of enamines. Under mild conditions, the chiral catalyst was able to reduce various *N*-aryl and *N*-alkyl imines, including imines with non-bulky *N*-substituents such as **39**. Smaller imines tend to be problematic for FLP systems, as they often form strong B–N adducts, thus promoting irreversible catalyst deactivation. The reductions of bulkier imines proceeded with good to excellent yields and *e.e.s* (up to 92% and 83% respectively); however, the *e.e.* was significantly reduced when *N*-alkyl imines were investigated (34% *e.e.*). Symmetric and asymmetric enamines also showed excellent results, displaying up to 99% isolated yields and up to 99% *e.e.s* following reduction.<sup>37</sup>

#### 1.06.2.1.5 Reduction of carbonyls

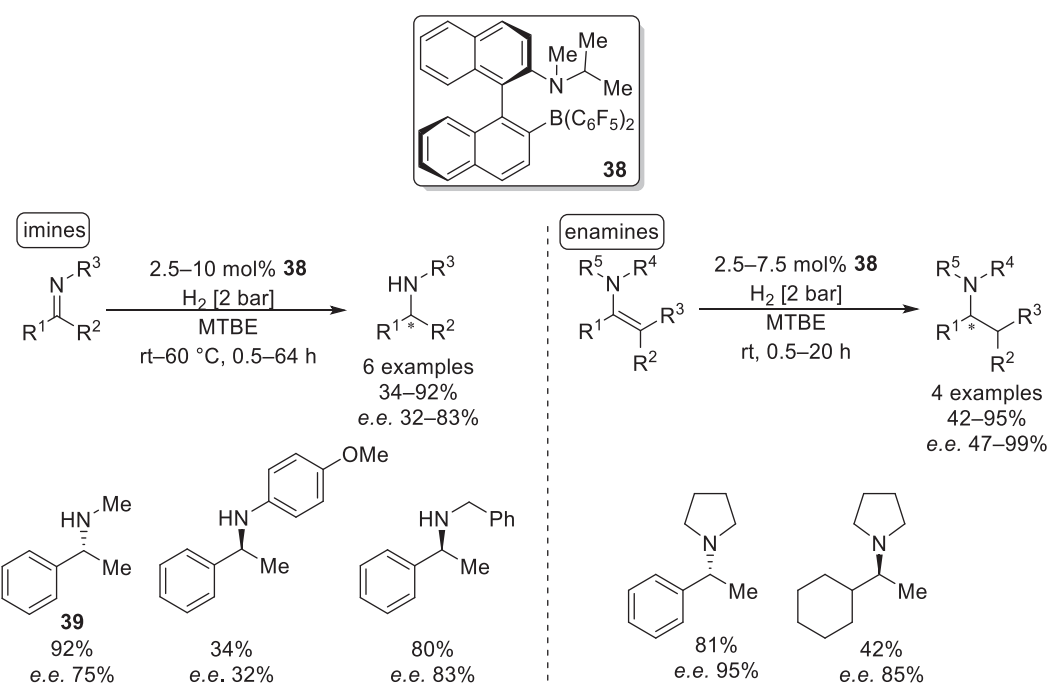
As many FLP systems contain boron-based compounds as their acidic component, the FLP mediated hydrogenation of carbonyl substrates posed a difficult problem for many researchers. Attempts to perform catalytic carbonyl reduction often resulted in the



**Scheme 24** Chiral reduction of ketimines with bisborane based upon diene **36**.<sup>35</sup>



**Scheme 25** Chiral reduction of silyl enol ethers with bisborane based upon diene **37**.<sup>36</sup>

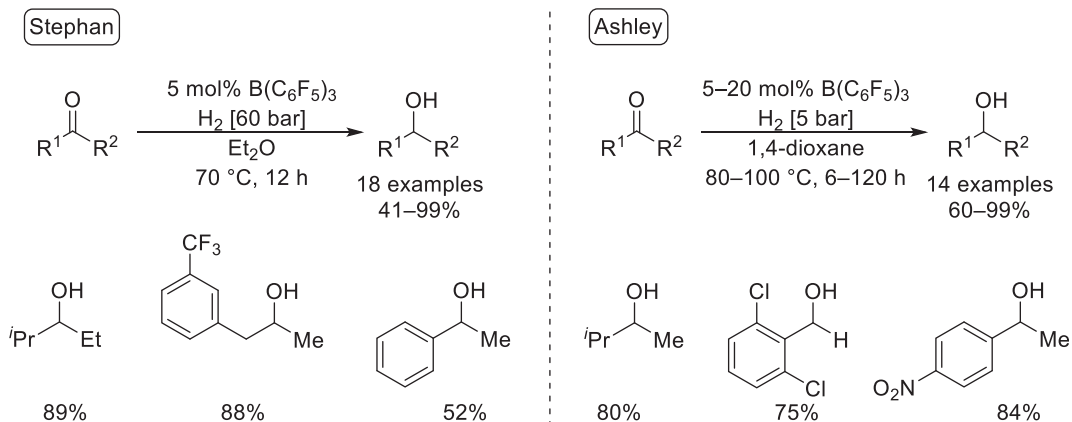


**Scheme 26** Chiral reduction of imines and enamines.<sup>37</sup>

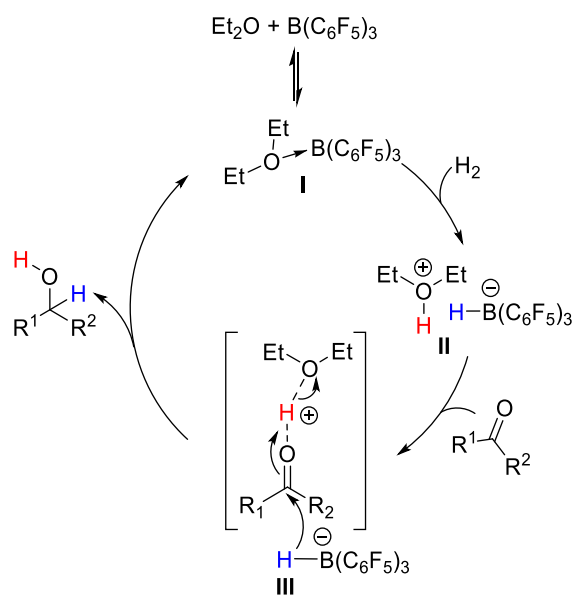
formation of boronic acids rather than the desired alcohols due to the high oxophilicity of the Lewis acids. Despite this complication, the FLP mediated reduction of carbonyls was achieved independently by Stephan and Ashley in 2014, who both utilized  $\text{B}(\text{C}_6\text{F}_5)_3$  as a catalyst in a Lewis basic ethereal solvent (**Scheme 27**).<sup>38,39</sup> Stephan reported the reduction of 18 carbonyls in  $\text{Et}_2\text{O}$ , using a high  $\text{H}_2$  pressure,<sup>38</sup> whereas Ashley reported the reduction of 14 carbonyls in 1,4-dioxane using a milder  $\text{H}_2$  pressure but longer reaction times and higher temperatures.<sup>39</sup>

Mechanistic probes indicated that the reduction of carbonyls bore many similarities to the reduction of imines (**Scheme 28**).<sup>38</sup> The catalytic cycle was initiated upon the co-ordination of the ethereal solvent (depicted below as  $\text{Et}_2\text{O}$ ) to  $\text{B}(\text{C}_6\text{F}_5)_3$ , thereby forming the active FLP catalyst in situ (**Scheme 28, I**). This catalyst was able to activate  $\text{H}_2$  (**Scheme 28, II**), facilitating its heterolytic cleavage between the acidic and basic centers. The resulting protonated solvent was then able to form a hydrogen-bond with the oxygen atom on the carbonyl substrate, thus making the carbonyl carbon more susceptible to attack by the hydride from the  $[\text{HB}(\text{C}_6\text{F}_5)_3]^-$  anion (**Scheme 28, III**). Upon protonation, the alcohol was released and the active FLP catalyst regenerated, closing the catalytic cycle.<sup>38</sup>

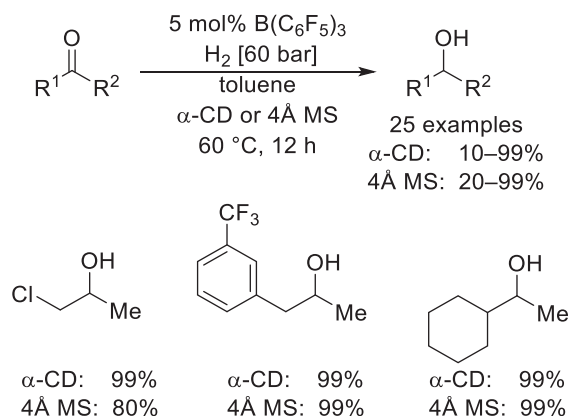
The reduction of ketones and aldehydes was later demonstrated in the non-ethereal solvent toluene, but only in the presence of 4 Å molecular sieves (4 Å MS) or alpha-cyclodextrin ( $\alpha\text{-CD}$ ) (**Scheme 29**). Using these insoluble Lewis bases, a heterogeneous FLP system could be formed upon exposure to  $\text{B}(\text{C}_6\text{F}_5)_3$ . The reduction of 25 carbonyl containing complexes was observed with excellent yields, in up to 99% with both Lewis bases.<sup>40</sup>



**Scheme 27** First reports of FLP mediated reduction of carbonyls.<sup>38,39</sup>



**Scheme 28** Mechanism of carbonyl reduction by  $\text{B(C}_6\text{F}_5)_3$  in an ether solvent.<sup>38</sup>



**Scheme 29** Reduction of carbonyl containing complexes with an FLP comprised of  $\text{B(C}_6\text{F}_5)_3$  and alpha-cyclodextrin ( $\alpha\text{-CD}$ ) or 4 Å molecular sieves (4 Å MS).<sup>40</sup>

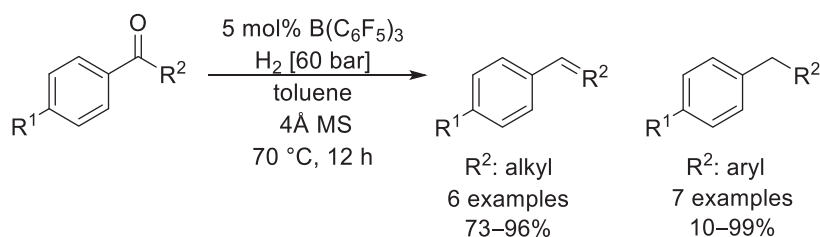
When acetophenone was subjected to reduction, two products were observed. One was the expected phenylethanol, and the other styrene, a product of reductive deoxygenation (Scheme 30). Whilst reductive deoxygenation of carbonyls had previously been reported with stoichiometric  $B(C_6F_5)_3$ ,<sup>41</sup> this was the first FLP catalyzed reaction of its type. Further investigation uncovered a range of aryl ketones, including bicyclic and diaryl ketones, that were amenable toward catalytic reductive deoxygenation, resulting in the formation of their corresponding alkanes or alkenes.<sup>40</sup>

The mechanism was proposed to be analogous to the reduction of carbonyls using ethereal solvents, with the key difference being the identity of the Lewis basic oxygen: whereas previously the oxygen was situated on a basic solvent, forming a homogeneous system, the present system incorporated Lewis basic oxygens on the surface of  $\alpha$ -cyclodextrin or molecular sieves, thereby forming a heterogeneous FLP catalyst (Scheme 31).<sup>40</sup>

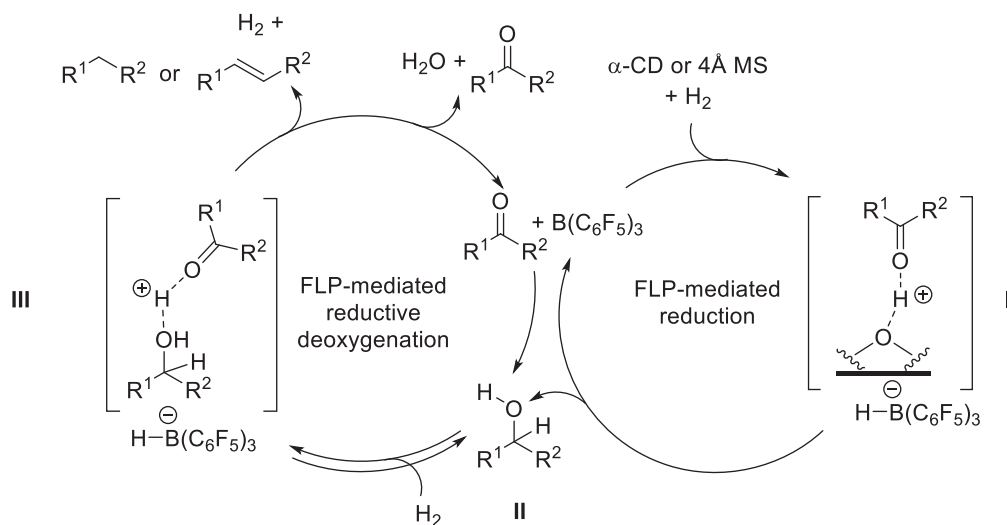
The catalytic cycle initiated when dihydrogen was heterolytically split by the FLP. The protonated basic surface was then able to form a hydrogen bond with the carbonyl's oxygen atom. The activated carbonyl was then susceptible to nucleophilic attack from the borohydride (Scheme 31, I). The generated basic alkoxide anion then accepted the proton from the Lewis basic surface, forming the alcohol product and regenerating the borane catalyst (Scheme 31, II). For most carbonyl compounds, the catalytic cycle terminated at this point; however, in the case of benzylic alcohols, an autocatalytic amount of ketone was able to promote FLP-mediated reductive deoxygenation. Here, an FLP was formed between the ketone and the borane, which heterolytically split  $H_2$ . The protonated ketone then proceeded to activate the C–O bond of the alcohol, leading it to be susceptible to hydride delivery from  $[HB(C_6F_5)_3]^-$  (Scheme 31, III). Subsequent C–O bond cleavage and water liberation formed the alkane or alkene with concomitant loss of  $H_2$ .<sup>40</sup> Molecular sieves served a dual purpose in this mechanism. Not only were they used for the initial reduction, but they also absorbed the water by-product from the reductive deoxygenation, thereby promoting the reaction further.

One inherent problem of using  $B(C_6F_5)_3$  is its moisture sensitivity. Upon exposure to water, the oxophilic boron atom will form a strong adduct, which fills its empty  $p$ -orbital and ultimately prevents the borane's ability to act as a catalyst irreversibly.<sup>42</sup> One method to overcome this is to replace the fluorinated aryl rings of the borane with heavier halogens, which impart more steric shielding around the boron's acidic center, thus shielding it from any water molecules; however, altering the halogen substitution pattern around the triarylborane can cause remarkable effects upon its Lewis acidity and consequentially its catalytic activity.<sup>43</sup>

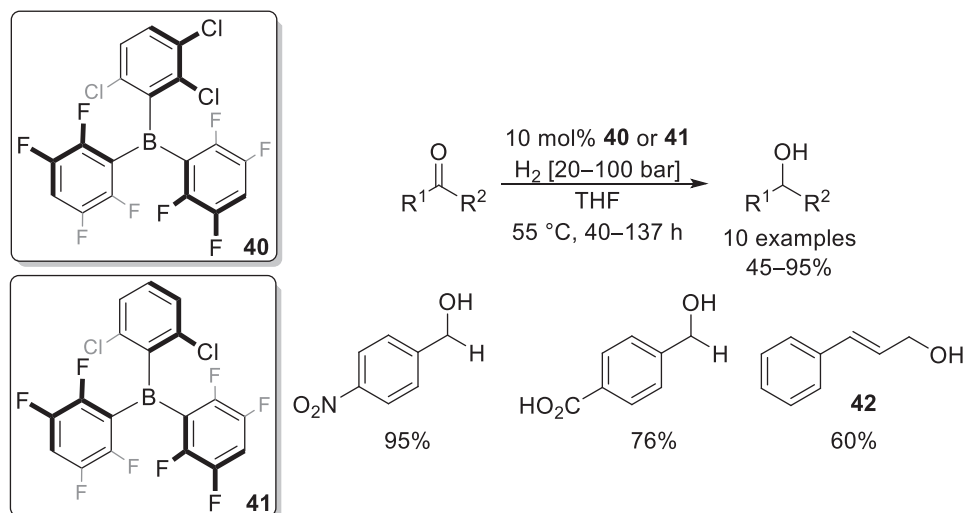
Soós aimed to develop a moisture tolerant, bench stable, and functional group tolerant FLP catalyst in order to make the reduction of carbonyls more accessible through the design of novel triarylboranes 40 and 41 which incorporated chlorine atoms at the *ortho* position of a single aryl ring (Scheme 32). This had the effect of increasing the steric effect around the boron center but also did



**Scheme 30** Reductive deoxygenation of carbonyl containing complexes with an FLP comprised of  $B(C_6F_5)_3$  and 4 Å molecular sieves (4 Å MS).<sup>40</sup>



**Scheme 31** Mechanism of reductive deoxygenation of carbonyl containing complexes with an FLP comprised of  $B(C_6F_5)_3$  and  $\alpha$ -cyclodextrin ( $\alpha$ -CD) or 4 Å molecular sieves (4 Å MS).<sup>40</sup>



**Scheme 32** Moisture tolerant FLPs **40** and **41** for carbonyl reduction.<sup>44</sup>

not decrease the Lewis acidity significantly enough to prevent it from activating dihydrogen. The choice of the water tolerant Lewis base was also important, as strong Lewis bases were known to inhibit hydrogenation through forming hydrogen bonds with water. Thus tetrahydrofuran (THF), a weakly coordinating ethereal solvent was chosen to complete the moisture tolerant FLP design. The reductions were then performed without the use of air sensitive techniques. A scope of 10 carbonyls were readily reduced using this moisture tolerant FLP system. Electron-deficient and electron-rich benzaldehydes were readily tolerated, and chemoselective reactivity was noted upon reduction of cinnamaldehyde **42**, wherein the alkene functional group remained intact.<sup>44</sup>

#### 1.06.2.1.6 Reductive etherification of carbonyls

Further investigation by Soós found that water tolerant borane **40** could also be employed in the reductive etherification of acetals, aldehydes and ketones without the use of air-sensitive techniques (Scheme 33).<sup>45</sup> Initially, the reduction of acetals into ethers was probed, with THF acting as both the reaction medium and the basic component of the FLP. The lower oxophilicity of borane **40** compared to  $B(C_6F_5)_3$  was observed to be important, as neither the alcohol by-product nor the ethereal product were observed to hinder the catalytic activity through binding irreversibly to the boron center. Fifteen examples were given, with good to excellent yields throughout. High functional group tolerance was noted, with satisfactory reactivity even when unactivated olefin **43** or ester moieties were present in the substrate. The protocol was expanded through the reductive etherification of aldehydes and ketones. Here, three equivalents of an alcohol or an *ortho*-ester were required to act as an alkylating agent for the transformation. A wide variety of carbonyls were converted into their corresponding ethers with varying yields. When alcohols were used as the alkylating agent, the resultant ether yields were significantly reduced, due to the competing reduction of the carbonyl reagents into alcohols.<sup>45</sup>

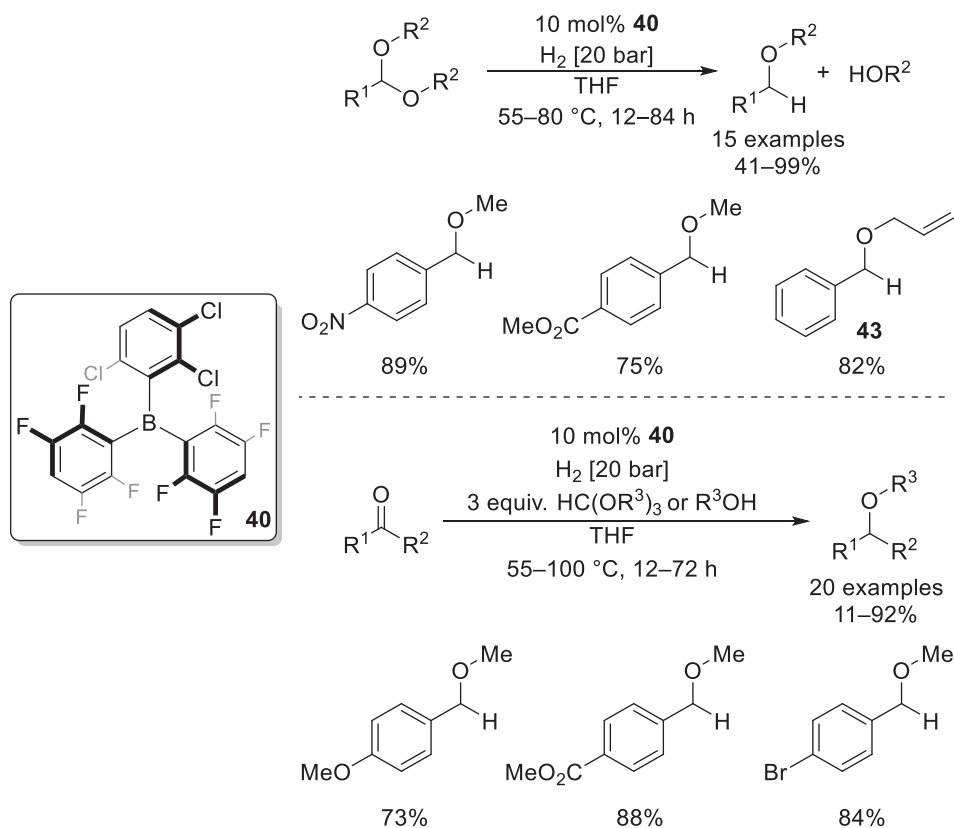
This reductive etherification of carbonyls was termed to operate under 'auto-tandem' catalysis, wherein FLP catalyzed hydrogenation and FLP-assisted Brønsted-Lowry acid catalysis worked synchronously (Scheme 34).<sup>45</sup> The proposed mechanism began with the formation of a FLP between the borane and the THF solvent, followed by FLP-mediated  $H_2$  activation to generate  $H[THF]^+$  and borohydride  $H[BAr_3]^-$  (Scheme 34, I). The carbonyl's oxygen could then be protonated by the Brønsted-Lowry acidic  $H-THF^+$  (Scheme 34, II), thereby activating the carbonyl and making it susceptible to attack by the alkylating agent ( $R^3OH$ ). Upon loss of water and a proton, this generated the acetal intermediate (Scheme 34, III), which was accompanied by release of water. The released proton was then able to acidify another THF molecule, which in turn protonated the acetal (Scheme 34, IV). Expulsion of one  $R^3OH$  group generated the oxocarbenium cation (Scheme 34, V), which was readily reduced into the ether product (Scheme 34, VI) by the previously generated borohydride  $H[BAr_3]^-$ .<sup>45</sup>

#### 1.06.2.1.7 Reductive alkylation of amines with carbonyls

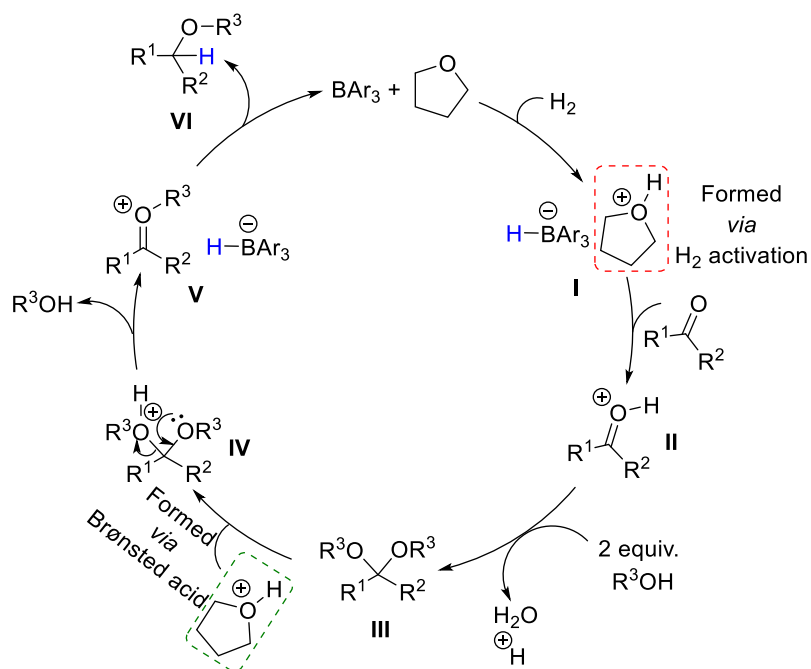
The exceptional moisture tolerance of Soós' boranes **40** and **41** in the reductive etherification of carbonyls inspired Ogoshi to apply borane **41** toward the reductive alkylation of amines with carbonyls and dihydrogen (Scheme 35).<sup>46</sup> The presented system operated under a tandem catalytic procedure, wherein FLP-mediated reductive alkylation and Lewis acid catalyzed intramolecular amidation occurred concurrently. Moisture tolerant borane **41** was crucial to the success of the reaction as water was the sole by-product of secondary amine formation. Whilst other boranes such as  $B(C_6F_5)_3$  were investigated, only the imine intermediate could be isolated as the FLP-mediated reductive alkylation was inhibited, presumably due to the generated water promoting catalyst deactivation.

The presented FLP system operated with 5 mol% of borane **41** and was able to exploit THF as both a solvent and the Lewis basic component of the FLP. 4 Å molecular sieves were inserted into the reaction vessel to absorb the water by-product. Whilst borane **41** was moisture tolerant, the inclusion of molecular sieves reduced reaction time and increased product yields significantly.<sup>46</sup> 34 secondary amines were successfully prepared in good to excellent yields, with functional group tolerance of bulky, carboxyl, and

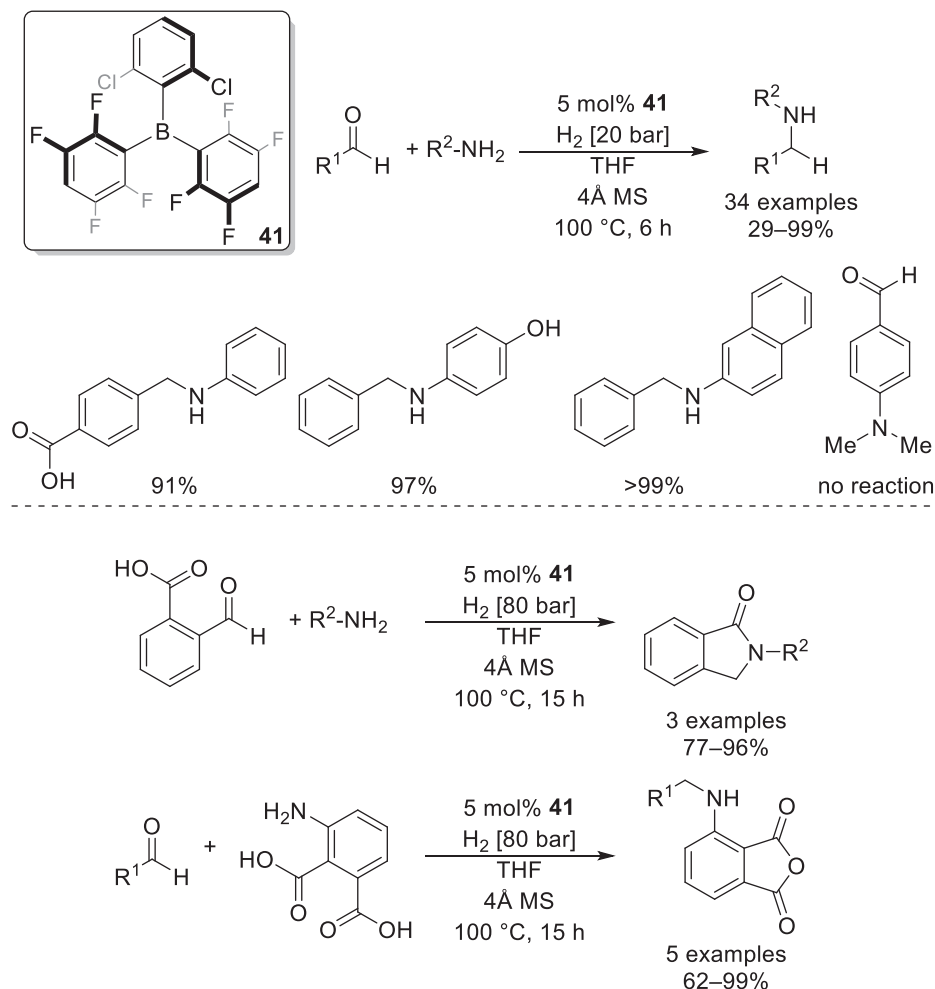




**Scheme 33** FLP catalyzed reductive etherification of acetals, aldehydes and ketones.<sup>45</sup>



**Scheme 34** Mechanism of reductive etherification of acetals, aldehydes and ketones.<sup>45</sup>



**Scheme 35** FLP catalyzed reductive alkylation of amines with carbonyls to form secondary amines, isoindolinones, and 3-aminophthalic anhydrides.<sup>46</sup>

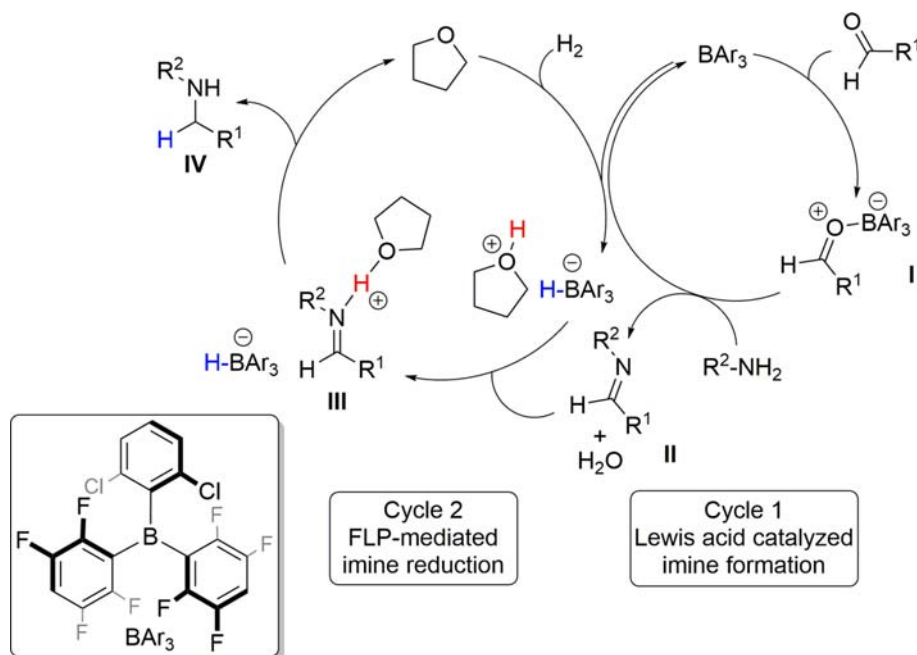
hydroxyl groups (Scheme 35); however, a limitation was noted upon the attempted reductive alkylation of aniline with 4-(dimethylamino)benzaldehyde, wherein the presence of a secondary amino group promoted FLP-mediated-hydrogenation followed by reduction to instead form *N,N*-dimethyl-*p*-toluidine. Moreover, by careful choice of reagents and by applying slightly harsher reaction conditions, the FLP system could catalyze intramolecular cyclizations to form isoindolinones and 3-aminophthalic anhydrides in good to excellent yields (Scheme 35).<sup>46</sup>

A mechanism which was comprised of two tandem catalytic cycles was proposed (Scheme 36). It was suggested that the first catalytic cycle comprised solely of Lewis acid catalysis, wherein the borane initially coordinated to and activated the carbonyl substrate (Scheme 36, I). The activated carbonyl was then susceptible toward nucleophilic attack from the amine, resulting in the formation of the imine intermediate and H<sub>2</sub>O as a by-product (Scheme 36, II). The second catalytic cycle involved FLP-mediated reduction, wherein the THF solvent acted as the Lewis basic component of the FLP. First, the FLP performed heterolytic cleavage of H<sub>2</sub>, which could then be used to reduce the imine (Scheme 36, III) to generate the desired amine (Scheme 36, IV).<sup>46</sup>

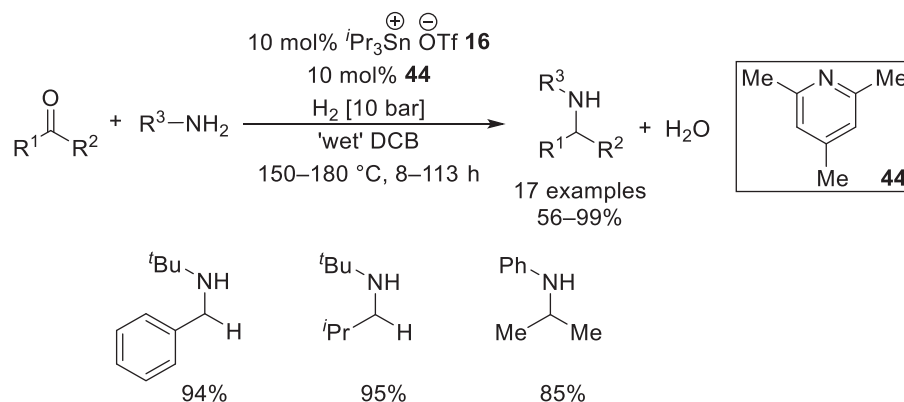
Motivated by previous investigation into the <sup>i</sup>Pr<sub>3</sub>SnOTf 16 catalyzed reduction of carbonyls and imines (Scheme 7),<sup>19</sup> Ashley extended the use of <sup>i</sup>Pr<sub>3</sub>SnOTf toward the reductive amination of carbonyls (Scheme 37). 17 secondary amines were formed in good to excellent yields, with tolerance toward bulky, electron-donating and electron-withdrawing groups. In most cases, the substrates were able to act as the Lewis basic FLP component, but collidine 44 was added to assist reactivity for more difficult substrates. For substrates with lower amine yields, this was attributed to a competing reaction wherein the carbonyl was directly reduced into its corresponding alcohol.<sup>47</sup>

### 1.06.2.2 FLP-mediated catalytic hydrogenation of non-polar substrates

The reduction of unsaturated non-polar substrates such as alkenes, allenes and alkynes presented a large challenge for FLP-based catalysts for many years. The primary factor behind this difficulty was that the generated Brønsted acid from the H<sub>2</sub> activated



**Scheme 36** Mechanism of FLP catalyzed reductive alkylation of amines with carbonyls to form secondary amines.<sup>46</sup>

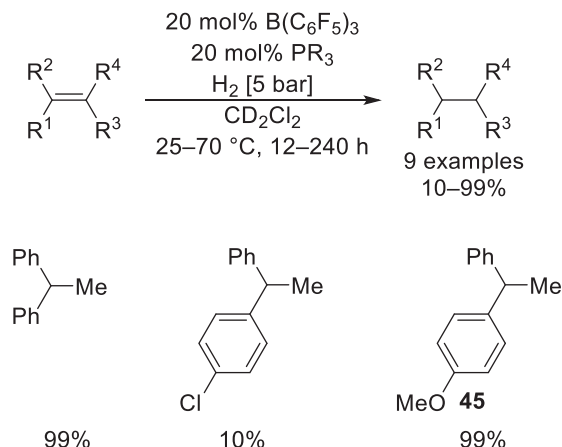


**Scheme 37**  $t\text{Pr}_3\text{SnOTf}$  catalyzed reductive alkylation of amines with carbonyls to form secondary amines.<sup>47</sup>

FLP complex needed to be acidic enough to protonate the substrate to form a carbocation, whilst the base needed to be able to release its hydride so that it could attack this carbocation. Traditional bases used in FLP systems were too strong for effective reduction of non-polar substrates. Hence, modified FLP systems were introduced by increasing the Brønsted acidity of the formed conjugate acid by using a weak Lewis base in the FLP.

#### 1.06.2.2.1 Reduction of alkenes and allenes

The first recorded FLP-mediated reduction of alkenes was reported by Stephan in 2012, who used a system comprised of  $\text{B}(\text{C}_6\text{F}_5)_3$  and the weakly basic phosphine  $\text{Ph}_2\text{P}(\text{C}_6\text{F}_5)$ . Initial evidence that this FLP could activate dihydrogen came from low temperature  $^{31}\text{P}$  NMR studies, wherein a signal at  $\delta = 12.5$  ppm indicated that  $[\text{HP}(\text{C}_6\text{F}_5)_2\text{Ph}]^+$  was generated at  $-80$  °C when mixed with  $\text{B}(\text{C}_6\text{F}_5)_3$  under a dihydrogen atmosphere. A slight increase of temperature to  $-50$  °C revealed that the phosphine could liberate its proton to reform  $\text{H}_2$ , indicating that this FLP system required a very low energy barrier for the reversible activation of  $\text{H}_2$  and confirming that weak bases could participate in FLP reductions.<sup>48</sup> Encouraged by this observation, ten olefins which were capable of forming stable carbocations were subjected toward reduction using gaseous hydrogen and a catalytic amount of FLP, consisting of  $\text{B}(\text{C}_6\text{F}_5)_3$  with various weak phosphine Lewis bases (Scheme 38). Generally, reductions proceeded smoothly; however, the poorest conversions were observed when electron-deficient olefins were subjected to the reaction conditions. This suggested that the FLP's ability to reduce an olefin was strongly dependent on its ability to stabilize the formed carbocation upon the initial protonation by the phosphonium cation. Additionally, methoxy substituted olefin 45 resulted predominantly in the formation of a dimerized



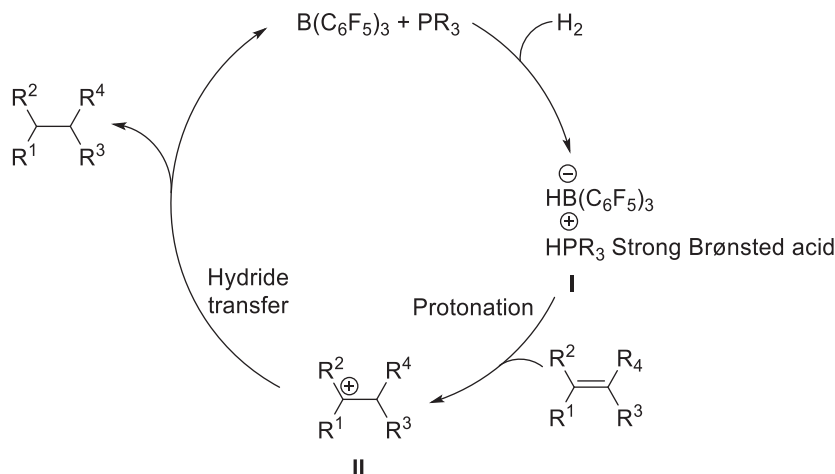
**Scheme 38** First reported example of FLP-mediated olefin reduction.<sup>48</sup>

product. This was attributed to the inefficiency of the hydride transfer step and competing Brønsted acid-catalyzed Friedel-Crafts dimerization. This dimerization could be avoided by applying a diphosphine (GemPhos) as a Lewis base.<sup>48</sup>

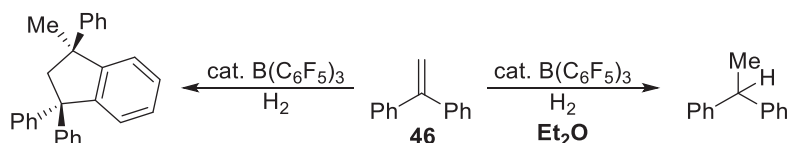
Combined experimental and computational probes were undertaken in order to elucidate the reaction mechanism (**Scheme 39**). It was suggested that the FLP initially activated dihydrogen (**Scheme 39, I**). The conjugate acid  $[\text{HPR}_3]^+$  then attacked the olefin to form a transient carbocation (**Scheme 39, II**). Hydride attack from  $[\text{HB}(\text{C}_6\text{F}_5)_3]^-$  toward this carbocation resulted in the saturated product and regeneration of the FLP.<sup>48</sup>

Further investigation by Stephan found that  $\text{Et}_2\text{O}$  could serve as the Lewis base in an FLP with  $\text{B}(\text{C}_6\text{F}_5)_3$  for the reduction of 1,1-diphenylethene **46** (**Scheme 40**). Notably in this case,  $\text{Et}_2\text{O}$  was added in a catalytic amount to a chlorinated solvent, instead of being used as the reaction medium. Without  $\text{Et}_2\text{O}$  present, the olefin would undergo Friedel-Crafts dimerization in the chlorinated solvent.<sup>49</sup>

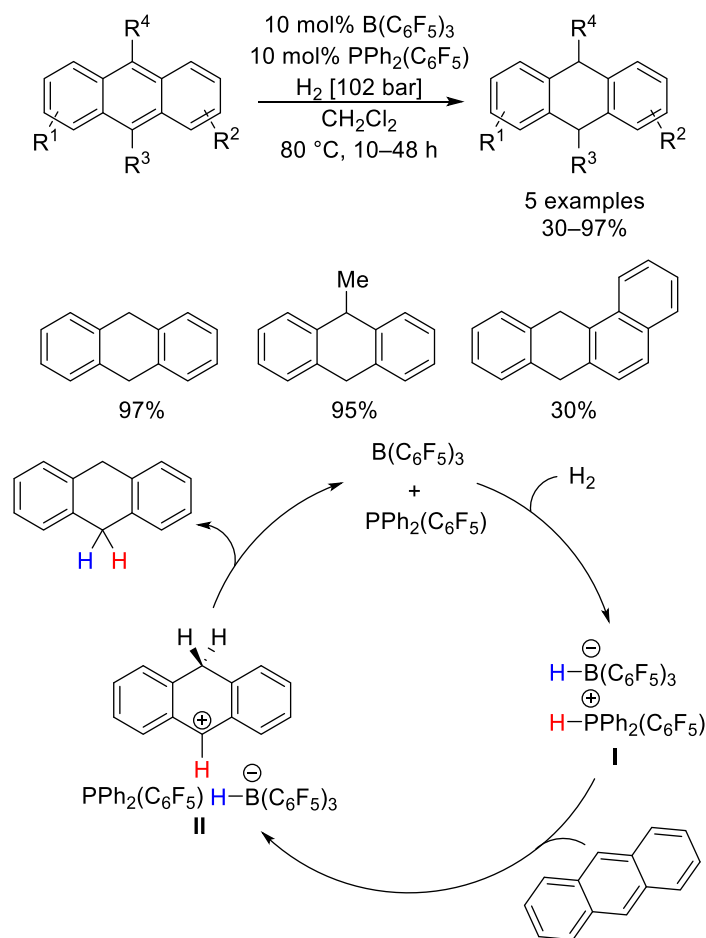
Moreover, the partial reduction of five polycyclic aromatic hydrocarbons was demonstrated with a FLP comprised of  $\text{P}(\text{C}_6\text{F}_5)_2$  and  $\text{B}(\text{C}_6\text{F}_5)_3$ . Harsh conditions were required, but reduction occurred in good to excellent yield (**Scheme 41**).<sup>50</sup> DFT calculations suggested that the mechanism for 1,4-hydrogenation of polycyclic aromatic hydrocarbons operated in a similar fashion to the 1,2-hydrogenation of olefins, through  $\text{H}_2$  activation (**Scheme 41, I**), followed by substrate protonation and subsequent hydride attack (**Scheme 41, II**).<sup>50</sup>



**Scheme 39** Mechanism of FLP-mediated olefin reduction.<sup>48</sup>



**Scheme 40** Reaction of 1,1-diphenylethene **46** with  $\text{B}(\text{C}_6\text{F}_5)_3$  in the presence and absence of  $\text{Et}_2\text{O}$ .<sup>49</sup>



**Scheme 41** FLP-mediated reduction of polycyclic aromatic hydrocarbons.<sup>50</sup>

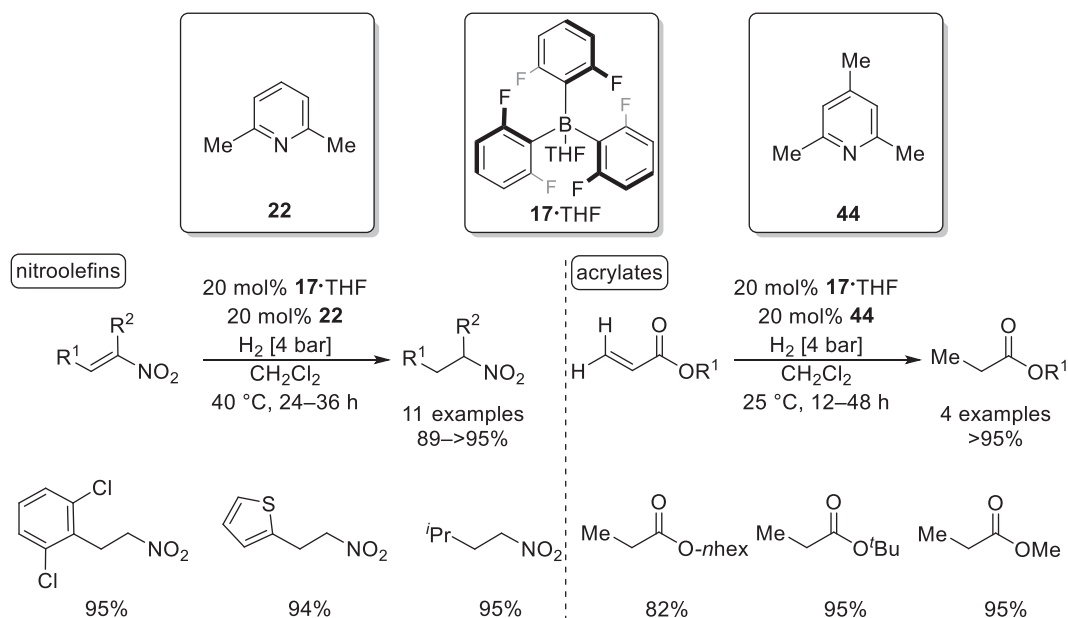
By using a weakly Lewis acidic borane  $B(2,6-F_2C_6H_3)_3$  **17**, the functional group tolerance of FLP-mediated hydrogenation was observed to increase. This was attributed to a greater nucleophilicity of the generated borohydride upon hydrogen activation, thus promoting the hydride attack in olefin reduction. Indeed, when the **17**·THF adduct was combined with the weak Lewis base, 2,6-lutidine **22**, the catalytic reduction of nitro substituted olefins proceeded under mild conditions (Scheme 42). Further substitution to the nitroolefins through the installation of various electron withdrawing and donating groups was not observed to hinder reactivity, with excellent isolated yields of eleven alkanes. Moreover, the scope of reactivity was widened toward  $\alpha,\beta$ -unsaturated esters and acrylates, with collidine **44** used as a Lewis base instead of 2,6-lutidine **22**.<sup>51</sup>

The FLP-mediated diastereoselective hydrogenation of Morita-Baylis-Hillman adducts was also observed with a weak borane, in this instance  $B(2,4,6-F_3C_6H_2)_3$  **47** in combination with DABCO **11**. Over 28 examples, excellent reactivity was noted with good to excellent yields (80–97%) and diastereoselective ratios (up to 89:11 *d.r.*) (Scheme 43). Inspired by these results, the authors explored sequential organo-FLP catalysis for the preparation of  $\beta$ -aminoacid derivatives from readily available starting materials. The first step of this reaction involved a DABCO-catalyzed aza-Morita-Baylis-Hillman reaction of *N*-sulfonyl aldimines with  $\alpha,\beta$ -unsaturated ketones. Sequential addition of the borane and a continuation of reaction under a hydrogen atmosphere allowed for various  $\beta$ -aminoacid derivatives to be obtained in good yields (52–66%) and good diastereoselective ratios (80:20–85:5 *d.r.*).<sup>52</sup>

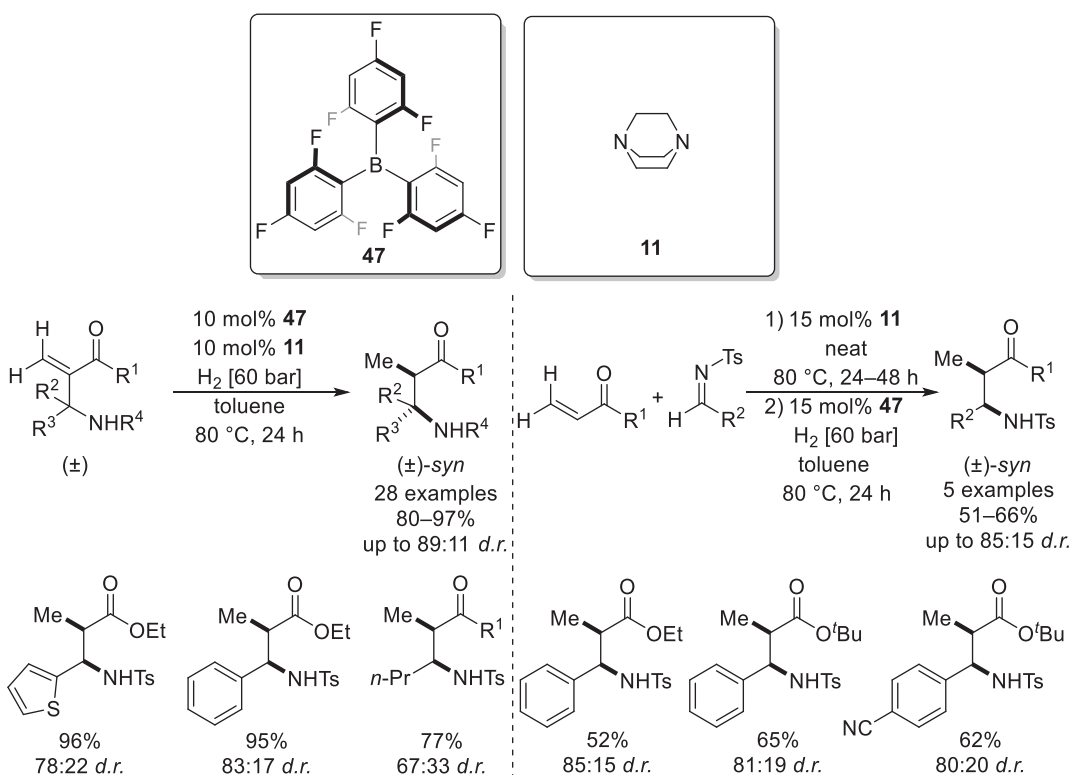
The scope of FLP-mediated reductions was also expanded toward electron-deficient allenes using catalytic DABCO **11** and  $B(C_6F_5)_3$  (Scheme 44). Five variously substituted diethyl 2-vinylidenemalonates were transformed into their respective olefinic products in good to excellent yield (43–94%) using this system; however, deviation from the optimized conditions was observed to lead to Friedel-Crafts alkylation, affording cyclized products. Interestingly, reductions occurred exclusively on the  $C=C$  double bond directly attached to the ester functional group. To study whether the allene moiety was indeed crucial for reductions, alkylidene malonates were also subjected toward the optimized conditions. These substrates were also well tolerated, with reductions operating at a faster rate and lower catalytic loadings of FLP compared to the allenes.<sup>53</sup>

Deuterium labelling studies suggested that instead of a direct protonation of the olefinic moiety, the reaction proceeded through hydrogen bonding between  $[HDABCO]^+$  and the carbonyl moiety of one of the esters (Scheme 45, I). The borohydride could then perform nucleophilic attack on the activated substrate (Scheme 45, II). Protonation by  $[HDABCO]^+$  could then regenerate the unactivated FLP and yield the desired product (Scheme 45).<sup>53</sup>





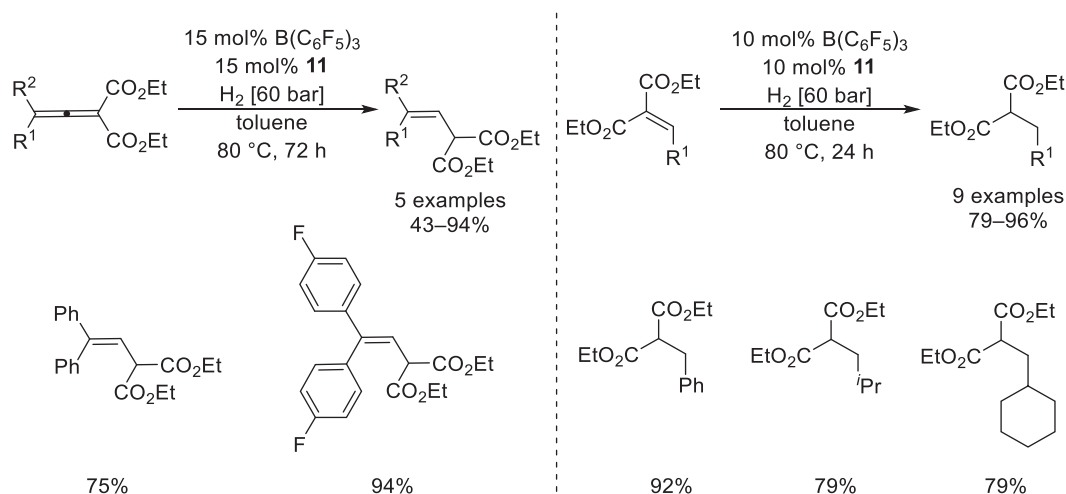
**Scheme 42** B(2,6-F<sub>2</sub>C<sub>6</sub>H<sub>3</sub>)<sub>3</sub> **17·THF** mediated reduction of nitroolefins,  $\alpha,\beta$ -unsaturated esters and acrylates.<sup>51</sup>



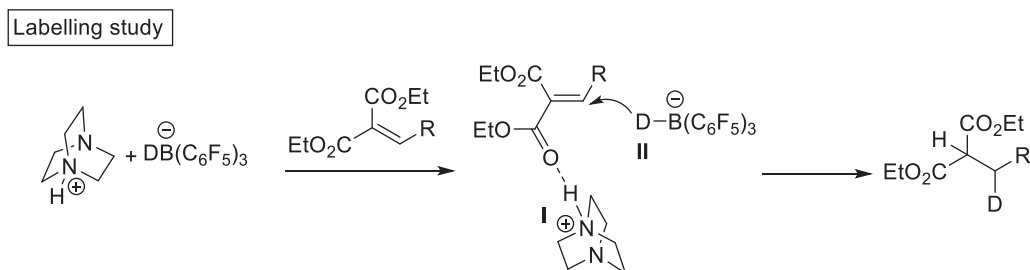
**Scheme 43** FLP-mediated diastereoselective hydrogenation of Morita-Baylis-Hillman adducts (left) and sequential organo-FLP catalysis for the preparation of  $\beta$ -aminoacid derivatives (right).<sup>52</sup>

### 1.06.2.2.2 Reduction of alkynes

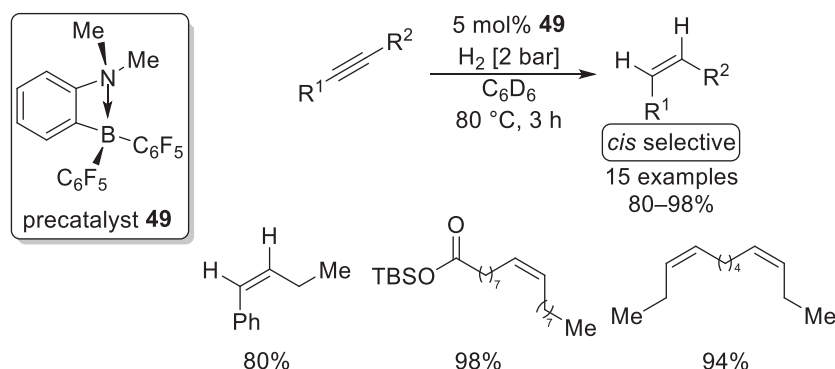
The first FLP-mediated reduction of unactivated internal alkynes was reported in 2013, with the use of intramolecular FLP *ansa*-aminohydroborane **48** as a catalyst. This active hydroborane catalyst was formed in situ via H<sub>2</sub> activation by aminoborane **49** and a subsequent B–C<sub>6</sub>F<sub>5</sub> hydrogenolysis. Various dialkyl-, diaryl-, and arylalkyl-acetylenes were successfully stereoselectively reduced into their respective *cis*-alkenes under mild conditions with no overreduction toward the alkane products (**Scheme 46**). Moreover,



**Scheme 44** FLP mediated reduction of allenes and alkylidene malonates.<sup>53</sup>



**Scheme 45** Deuterium label studies on the FLP mediated reduction of alkylidene malonates.<sup>53</sup>

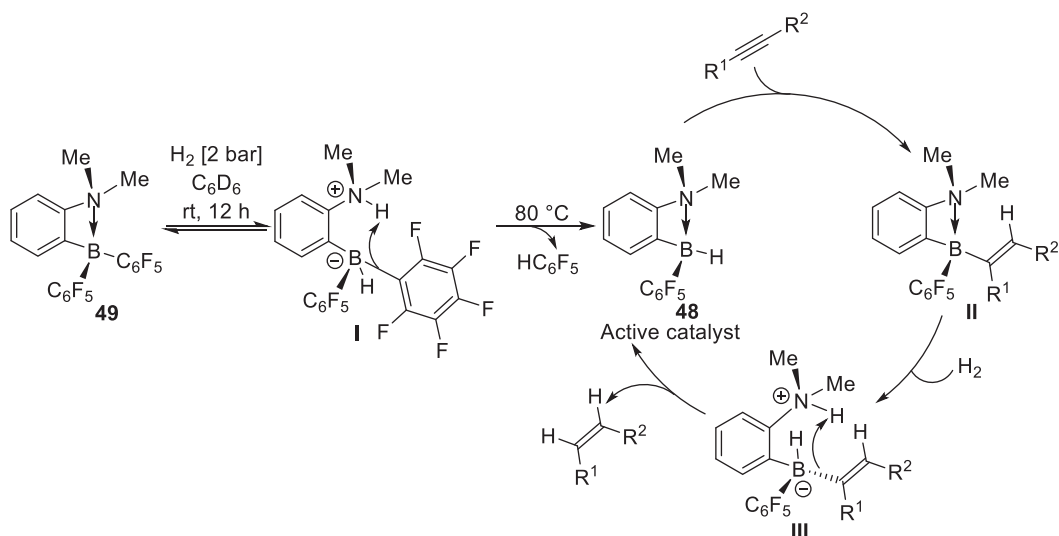


**Scheme 46** FLP-mediated reduction of unactivated internal alkynes.<sup>54</sup>

silyl-protected ynols, esters, and enynes were also observed to undergo chemoselective reductions. Contrarily, terminal alkynes were inert toward the transformation.<sup>54</sup>

Various experimental and computational mechanistic studies were conducted in order to propose a catalytic cycle (**Scheme 47**). First, aminoborane pre-catalyst **49** was exposed to a hydrogen atmosphere to form a borohydride (**Scheme 47, I**), which subsequently performed B–C<sub>6</sub>F<sub>5</sub> protonative cleavage at 80 °C to form the active hydroborane catalyst **48**. The alkyne substrate was then activated via hydroboration with the catalyst, forming a vinylborane (**Scheme 47, II**). The vinylborane then activated H<sub>2</sub>, resulting in the formation of a zwitterionic intermediate (**Scheme 47, III**), which upon intramolecular protonation of the vinyl carbon resulted in the elimination of the *cis*-alkene and a regeneration of the active catalyst.<sup>54</sup>

The stereoselective reduction of alkynes to *Z*-alkenes was later achieved by applying a heterogenous, silica-supported intermolecular borane/phosphine FLP. Importantly, it was demonstrated that the supported catalyst could be recycled by adding one equivalent of the Lewis acid up to a maximum of five times.<sup>55</sup>



**Scheme 47** Mechanism of FLP-mediated reduction of unactivated internal alkynes.<sup>54</sup>

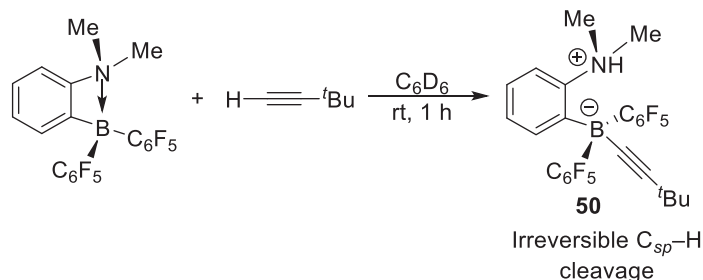
Although the successful reduction of alkynes was a milestone in the continued expansion of FLP-mediated reactivity, terminal alkynes were thought recalcitrant for many years. Rather than reduction, FLPs were observed to react with terminal alkynes via deprotonative borylation through irreversible  $C_{sp}-H$  cleavage. Instead of liberation of an alkene, this yielded alkynylborate adduct 50 thus deactivating the catalyst (**Scheme 48**).<sup>56</sup>

In 2020, the FLP-mediated reduction of terminal alkynes was achieved with intramolecular FLP 51. This novel FLP system exhibited unique behavior after  $H_2$  activation. Following initial formation of the expected  $H_2$ -activated pyridone borane 52, the complex dissociated, resulting in the formation of Piers borane and 6-*tert*-butylpyridone 53. The active catalyst 52 was thus generated in situ, through the coordination of  $HB(C_6F_5)_2$  and 53 under a hydrogen atmosphere. Combined experimental and computational studies revealed that unlike conventional FLP systems, 51 was able to undergo reversible  $C_{sp}-H$  cleavage, allowing for the catalytic reduction of terminal alkynes. Indeed, six terminal alkynes were stereoselectively reduced to their corresponding *cis*-alkenes under mild conditions, with isolated yields of 47–76%. Six internal alkynes were also reduced into their corresponding *cis*-alkenes, displaying the versatility of the catalyst (**Scheme 49**).<sup>57</sup>

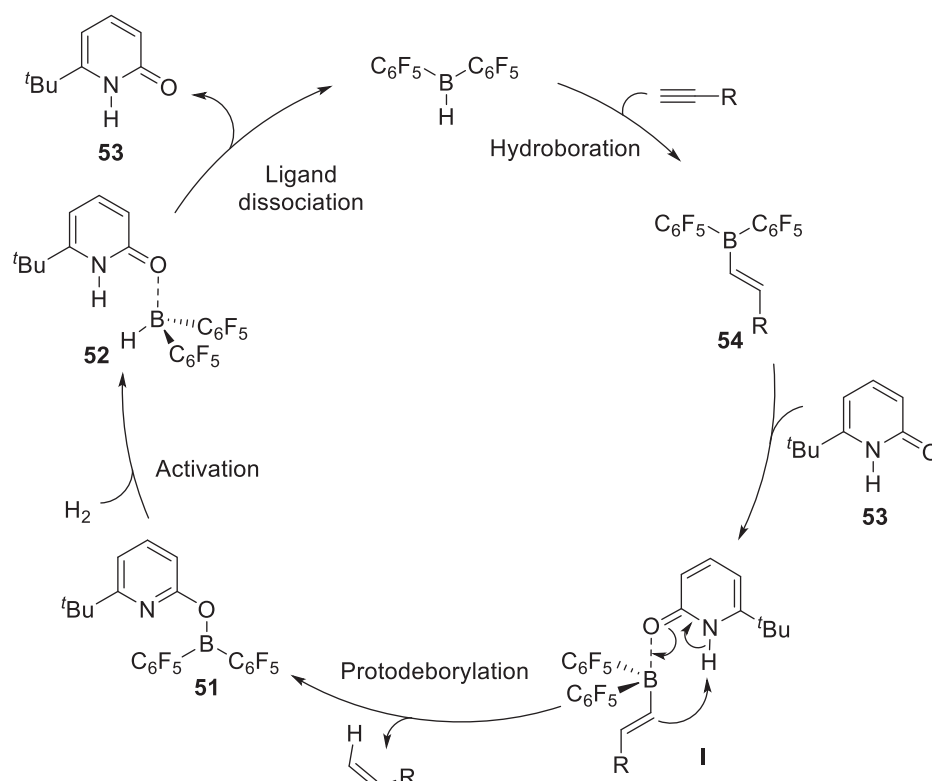
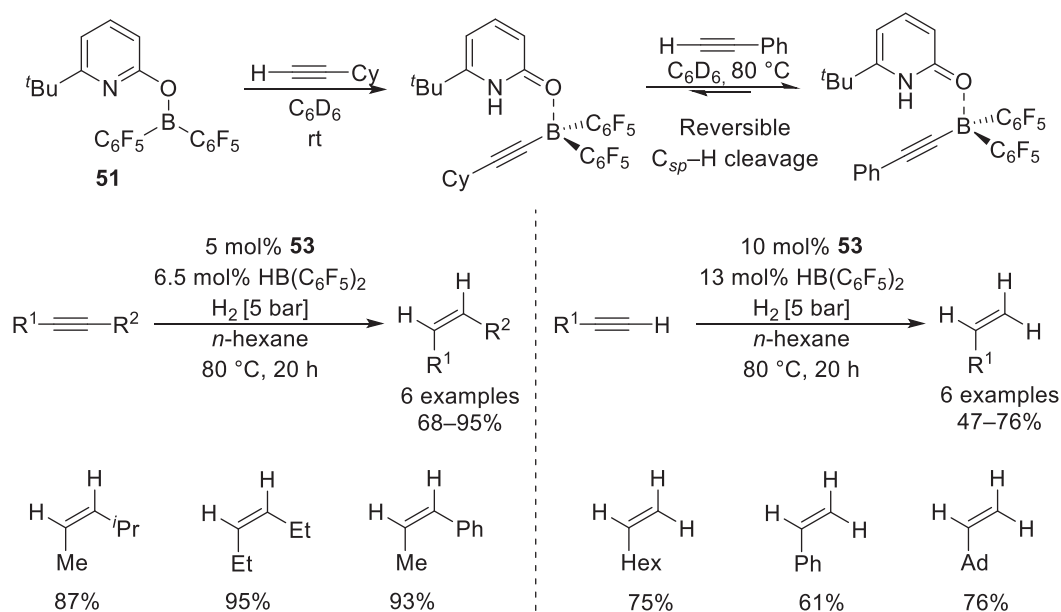
A proposed catalytic cycle suggested that the reduction process initiated with the hydroboration of the terminal alkyne by  $HB(C_6F_5)_2$ , resulting in the formation of alkenyl borane 54. 6-*tert*-butylpyridone 53 then coordinated toward the alkenyl borane (**Scheme 50**, I), which initiated protodeborylation to form the desired *cis*-alkene and boroxypyridine 51. 51, an intramolecular FLP, then activated  $H_2$ , resulting in the formation of the pyridine complex 52, which finally underwent ligand dissociation (53) to regenerate the Piers borane catalyst (**Scheme 50**).<sup>57</sup>

### 1.06.2.3 FLP-mediated transfer hydrogenation

An alternative to the reduction of unsaturated bonds using molecular hydrogen is the use of a surrogate  $H_2$  source, in what is termed as ‘transfer hydrogenation’. The primary advantage of transfer hydrogenation is that it negates the inherent safety risks of working with gaseous  $H_2$ ; however, large quantities of waste are produced from the surrogate, which can reduce the economic benefit and increase the environmental impact of the reaction. The idea of FLP-mediated transfer hydrogenation was initiated from the observation that  $B(C_6F_5)_3$  was able to abstract a hydride from the  $\alpha$ -carbon of secondary or tertiary amines.<sup>58,59</sup> For example: reaction of  $B(C_6F_5)_3$  with  $Et_2NPh$  would form an equilibrium between salt 55 and zwitterion 56 (**Scheme 51**).<sup>58</sup>

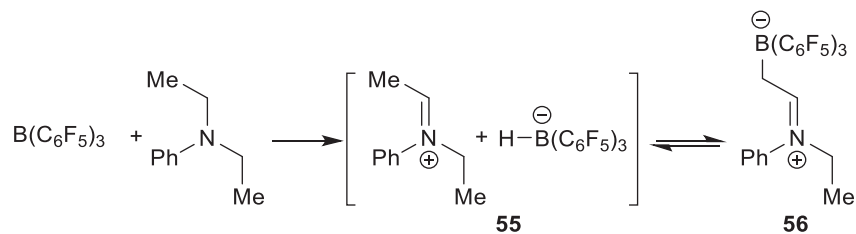


**Scheme 48** Irreversible catalyst deactivation upon attempted terminal alkyne reduction.<sup>56</sup>

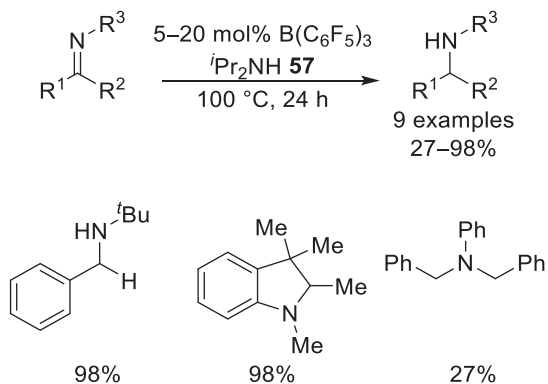


A catalytic example of transfer hydrogenation with FLPs was the reduction of  $C=N$  bond, as part of the catalytic racemization of chiral imines.<sup>60</sup> By applying diisopropylamine **57** as a  $H_2$  surrogate, imines, enamines and  $N$ -heterocycles could be readily reduced (**Scheme 52**). Most imines and enamines were reduced almost quantitatively, whilst  $N$ -heterocycles, such as aziridine and quino-line, were reduced to form amines in lower yields.<sup>60</sup>

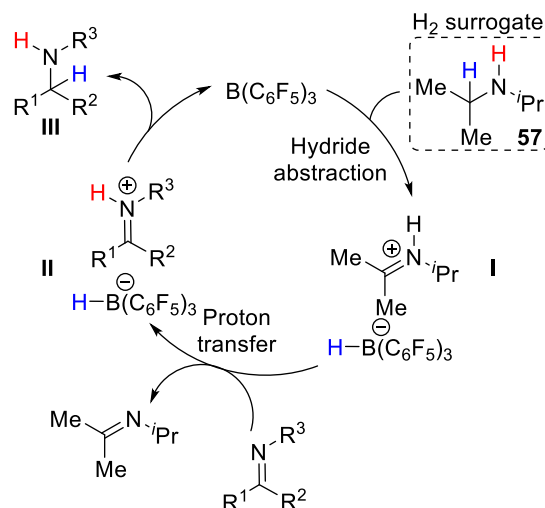
Mechanistic studies found that  $B(C_6F_5)_3$  would not interact with the substrate at first, but instead would abstract a proton from the  $\alpha$  carbon from the diisopropylamine **57**. The formed salt (**Scheme 53**, **I**) was then able to undergo proton transfer with the



**Scheme 51** Ability of  $B(C_6F_5)_3$  to abstract a hydride from the  $\alpha$ -carbon of  $Et_2PhN$ .<sup>58</sup>



**Scheme 52** An example of catalytic transfer hydrogenation.<sup>60</sup>



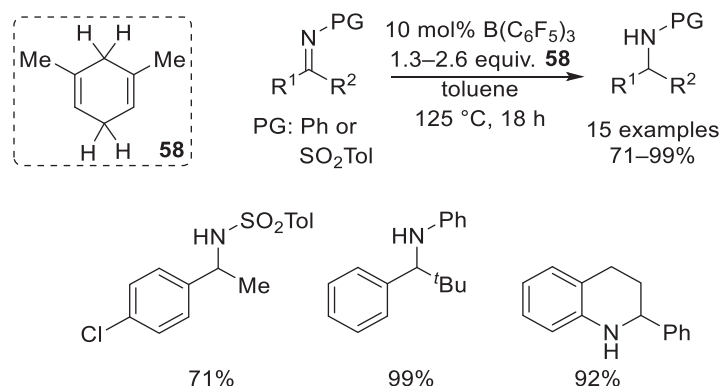
**Scheme 53** Mechanism of catalytic transfer hydrogenation.<sup>60</sup>

chosen substrate to form a second salt consisting of the borohydride and the protonated imine product (**Scheme 53, II**). Upon relinquishing its hydride toward the imine, the desired amine (**Scheme 53, III**) could be formed and the  $B(C_6F_5)_3$  catalyst could be regenerated.<sup>60</sup>

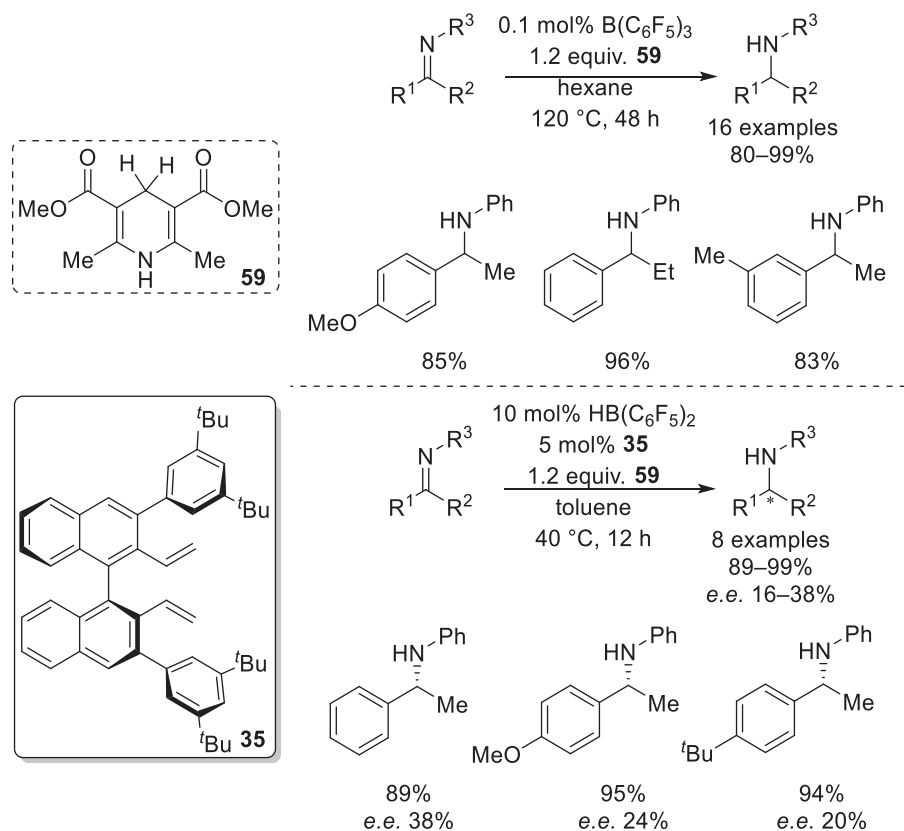
Cyclohexa-1,4-diene **58** was also exploited as a  $H_2$  source in the catalytic hydrogenation of imines and heteroarenes (**Scheme 54**).<sup>61</sup> Whilst good to excellent yields were observed, bulky protecting groups such as Ph or  $SO_2Tol$  were required on the imine substrates in order to be successfully reduced. On the other hand, all heteroarenes probed in the study were reduced almost quantitatively (up to 94%).<sup>61</sup>

Similarly, Hantzsch ester **59** was explored as a  $H_2$  surrogate toward the  $B(C_6F_5)_3$  catalyzed hydrogenation of imines (**Scheme 55**). Under the conditions probed, a notably low catalytic loading of 0.1 mol%  $B(C_6F_5)_3$  proved sufficient to transform 16 imines into their respective amines.<sup>62</sup> Further investigation found that this system could be adapted toward asymmetric imine transfer hydrogenation. The chirality was imparted via chiral diene ligand **35**, which upon hydroboration with Piers borane would form a chiral bisborane in situ. This bisborane was also used for the reduction of silyl enol ethers (**Scheme 23**).<sup>34</sup> This asymmetric variant





**Scheme 54** Transfer hydrogenation with cyclohexa-1,4-diene **58** as a H<sub>2</sub> surrogate.<sup>61</sup>

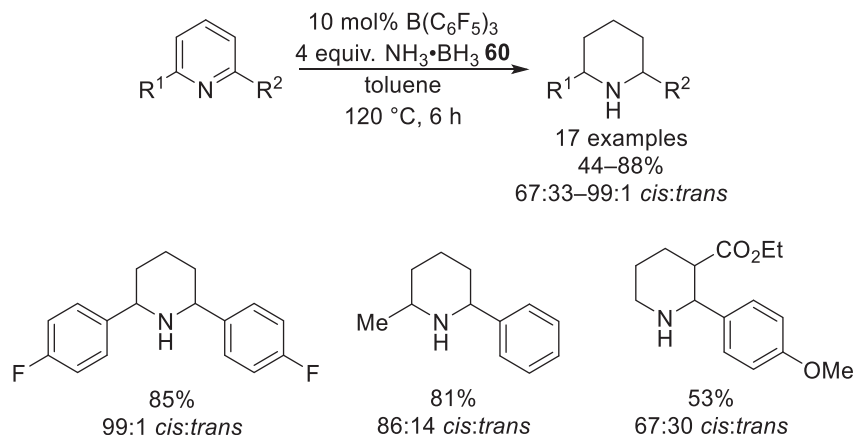


**Scheme 55** Symmetric and asymmetric imine transfer hydrogenation using Hantzsch ester **59** as a H<sub>2</sub> surrogate.<sup>62</sup>

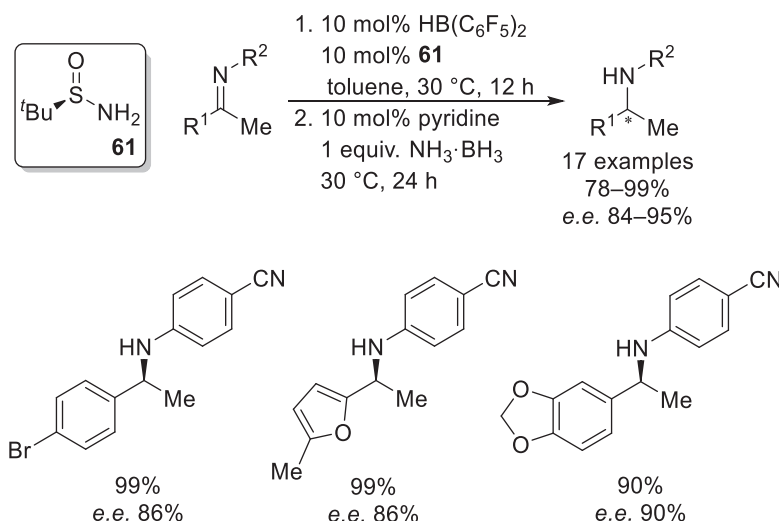
of transfer hydrogenation required higher catalytic loadings; however, excellent yields of amine were reported, along with moderate *e.e.s* of 16–38%.<sup>62</sup>

One significant disadvantage to transfer hydrogenation is the amount of waste generated from the H<sub>2</sub> surrogate. In 2016, Du demonstrated the use of ammonia borane **60** as a hydrogen source in the B(C<sub>6</sub>F<sub>5</sub>)<sub>3</sub> catalyzed reduction of pyridines (**Scheme 56**), wasting significantly fewer atoms than the amines, dienes and Hantzsch ester employed previously. Here, 17 *N*-heterocycles were generated in moderate to excellent yields (44–88%) with great *cis*-selectivities (up to 99:1). Reductions were tolerated with a wide variety of diaryl pyridines, although electron donating groups gave slightly reduced yields. 2-Aryl-6-methyl pyridines were also well tolerated; however, limited conversion and lower *cis*-selectivity was observed with 2,3-disubstituted pyridines.<sup>63</sup>

The use of ammonia borane as a hydrogen surrogate was further incorporated into the enantioselective transfer hydrogenation of imines (**Scheme 57**). Here, Piers borane and (*R*)-*tert*-butylsulfonamide **61** were employed, wherein the sulfonamide served as both the Lewis basic component of the FLP catalyst and as the source of chirality. A pyridine additive was also included to trap any unreacted Piers borane, which would otherwise promote a racemic imine reduction. This system was found to reduce 17 imines in good to excellent yields, and excellent enantioselectivities of up to 95% *e.e.*<sup>64</sup>



**Scheme 56** Transfer hydrogenation employing ammonia borane as the  $H_2$  surrogate.<sup>63</sup>



**Scheme 57** Enantioselective transfer hydrogenation of imines.<sup>64</sup>

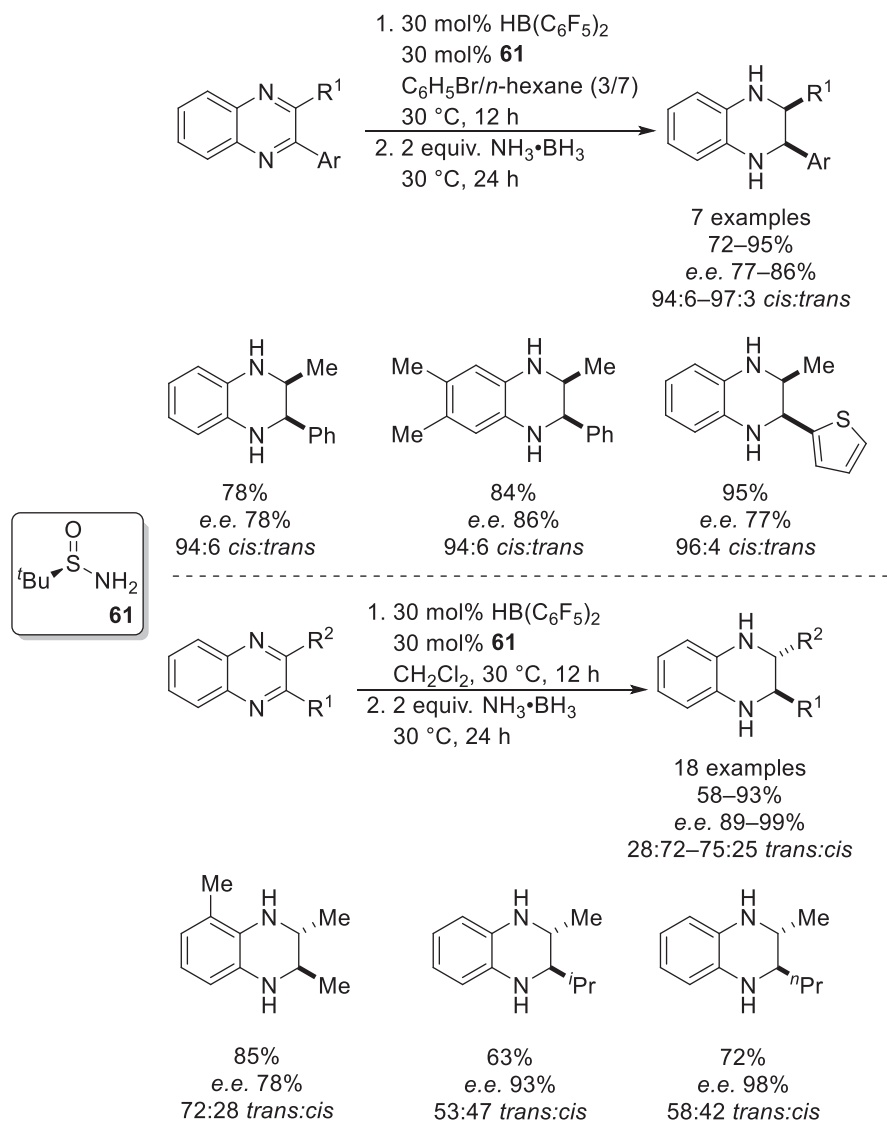
The intermolecular FLP system composed of **61** and Piers borane, coupled with an ammonia borane as a hydrogen surrogate was subsequently employed in the reduction of 2-alkyl-3-arylquinoxalines and 2,3-dialkylquinoxalines (**Scheme 58**).<sup>65</sup> These substrates were initially subjected to the conditions presented in **Scheme 24**, wherein molecular hydrogen was used in an attempt to promote reduction, however no reactivity was observed.<sup>35</sup> Conversely, using a combination of **61** and Piers borane was observed to reduce 25 quinoxalines successfully in up to 99% *e.e.* *Cis*-tetrahydroquinoxalines were generally the predominant isomers formed upon 2-alkyl-3-arylquinoxaline reduction, whilst *trans*-tetrahydroquinoxalines were formed when 2,3-dialkylquinoxalines were used.<sup>65</sup>

The first reported transfer hydrogenation of silyl enol ethers was observed with the use of a FLP system composed of 2,2,6,6-tetramethylpiperidine (TMP) **62** and  $B(C_6F_5)_3$ , and with the widely available  $\gamma$ -terpinene **63** as a source of  $H_2$  (**Scheme 59**). 10 mol% of FLP catalyst was employed with a slight excess of  $\gamma$ -terpinene to mediate the reduction of 29 silyl enol ethers with a wide variety of substituents in excellent yield.<sup>66</sup>

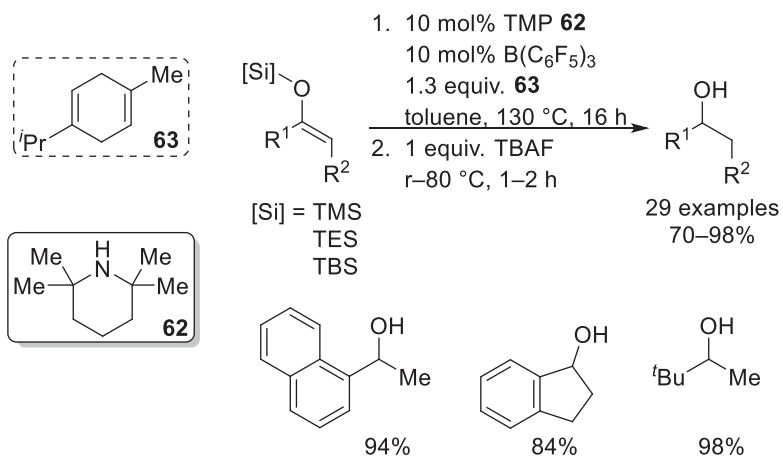
#### 1.06.2.4 FLP-mediated dehydrogenation

As highlighted in the previous section on FLP-mediated transfer hydrogenation, Lewis acidic triarylboranes are capable of  $C_{sp^3}-H$  bond activation via hydride abstraction. This allows for the use of a hydrogen surrogate in catalytic reduction, rather than molecular  $H_2$ . Until 2016, hydride abstraction by boranes was exploited only for transfer hydrogenation; however, simultaneous reports by Paradies and Kanai proved it was possible to reverse the protocol, through the FLP catalyzed dehydrogenation of heterocycles.<sup>67,68</sup>

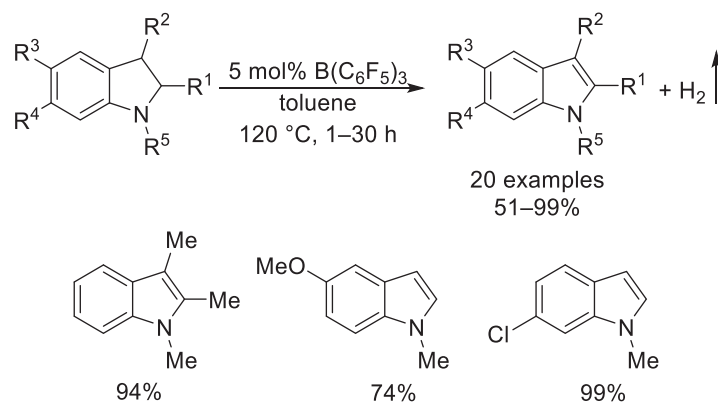
Paradies developed a protocol toward the  $B(C_6F_5)_3$ -catalyzed acceptor-less dehydrogenation of 21 *N*-protected indolines (**Scheme 60**). The resultant indoles were obtained in good to excellent yields; however, when the sterically demanding indoline with a neopentyl *N*-protecting group was subjected toward the reaction conditions, it was not oxidized, indicating that hydride abstraction or transfer can be sterically blocked by the *N*-substituent. Moreover, the protocol was expanded toward other



**Scheme 58** Chiral transfer hydrogenation of 2-alkyl-3-arylquinoxalines and 2,3-dialkylquinoxalines.<sup>65</sup>



**Scheme 59** Transfer hydrogenation of silyl enol ethers.<sup>66</sup>



**Scheme 60**  $B(C_6F_5)_3$ -catalyzed dehydrogenations of *N*-protected indolines.<sup>67</sup>

heterocycles including 1,4-dihydropyridines and thiazoline. Some heterocycles required more forcing conditions to undergo dehydrogenation, but the oxidized product could be isolated in good to excellent yield.<sup>67</sup>

Meanwhile, Kanai reported the  $B(C_6F_5)_3$ -catalyzed dehydrogenation of 23 *N*-heterocycles, with a range of steric and electronic variations (Scheme 61). 5 mol% of  $B(C_6F_5)_3$  catalyst was applied for most substrates; however, a slightly higher temperature of 150 °C was required for efficient dehydrogenation. Notably, the protocol was extended toward the preparation of biologically active pyrazoles, displaying a metal-free alternative toward a precursor to celecoxib, a nonsteroidal painkiller. Good to excellent yield of the oxidized product was noted in all cases.<sup>68</sup>

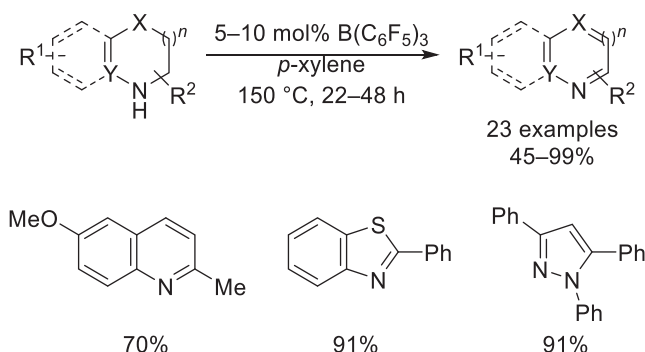
Paradies further explored the mechanism of this dehydrogenation through a combination of kinetic and DFT probes. The reaction was observed to proceed via an initial borane-induced hydride abstraction at the  $C_2$  position of the indole **64**, resulting in the formation of a 3*H*-indolium ion intermediate (Scheme 62, I). A rapid intermolecular proton transfer at the  $C_3$  position of the 3*H*-indolium ion to a second indoline nitrogen atom generated the first equivalent of indole product **65** and an ammonium hydridoborate intermediate (Scheme 62, II). In the rate-determining step, proton-hydride recombination occurred, releasing  $H_2$ , a second equivalent of indole product **65** and regenerating the borane catalyst. Interestingly, the reaction could be accelerated by incorporating an additional 5 mol% of the less Lewis acidic borane  $B(2,4,6-F_3C_6H_2)_3$  **47**, which served as a hydride shuttle. Thus, in the proton-hydride recombination step,  $B(2,4,6-F_3C_6H_2)_3$  **47** generated a stronger hydride donor than  $B(C_6F_5)_3$ , accelerating the final  $H_2$  liberation.<sup>67</sup>

### 1.06.2.5 Unusual FLP systems for catalytic hydrogenation

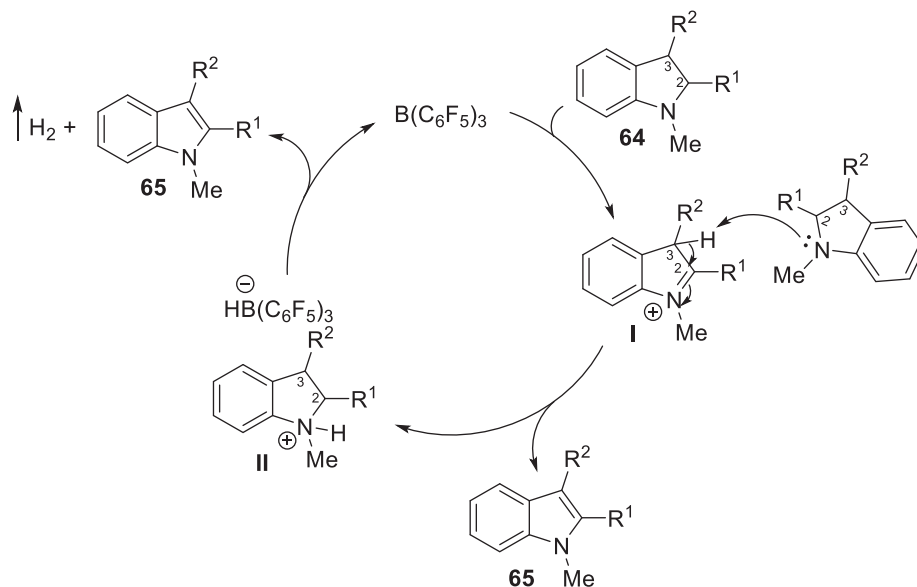
Since the ground-breaking discovery of a phosphinoborane capable of activating dihydrogen, many types of FLPs that are alternate to the conventional phosphinoborane or triarylborane/bulky Lewis base FLPs have been described. Selected examples include: FLPs containing transition metals as the Lewis acidic or Lewis basic component; FLPs based upon polymers and nanoparticles, and FLPs with cationic Lewis acidic centers.<sup>69</sup> This section aims to discuss the less common FLP systems which have been reported to partake in catalytic reductions.

#### 1.06.2.5.1 Borenium cations

Borenium cations are a class of cationic boron compound  $[L \rightarrow BR_2]^+$  which contain only two  $\sigma$ -bound substituents (R) and are partially stabilized by one dative interaction with a ligand (L). This results in a highly electropositive species which acts as a potent



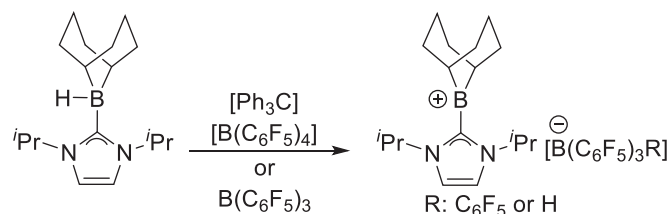
**Scheme 61**  $B(C_6F_5)_3$ -catalyzed dehydrogenations of *N*-protected heterocycles.<sup>68</sup>



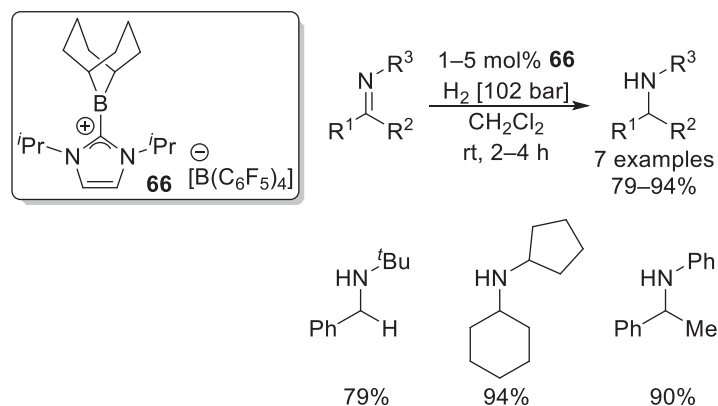
**Scheme 62** Mechanism of FLP-mediated dehydrogenation of indoles.<sup>67</sup>

Lewis acid. In 2012, Stephan reported the first use of these highly acidic species in FLP-mediated reductions, citing them as an attractive smaller alternative to bulky triarylboranes such as  $B(C_6F_5)_3$ . Such borocations are readily available through hydride abstraction with trityl tetrakis(pentafluorophenyl)borate  $[Ph_3C][B(C_6F_5)_4]$  from the appropriate air-stable adduct. Here, Stephan prepared an FLP comprised of the *N*-heterocyclic carbene (NHC) adduct of 9-borabicyclo[3.3.1]nonane (9-BBN) (**Scheme 63**). Initial probes found that this could activate  $H_2$  in the presence of  $P^tBu_3$ .<sup>70</sup>

Further investigation showed the Lewis acid **66** to be highly active toward the catalytic reduction of imines through an FLP mechanism (**Scheme 64**). Catalytic loadings as low as 1 mol% were found to be sufficient to mediate the reduction of seven imines at room temperature, yielding the corresponding amines in good to excellent isolated yields. Whilst the reactions were performed at room temperature, a high dihydrogen pressure of 102 bar was required.<sup>70</sup>



**Scheme 63** Preparation of FLP containing a borenium cation.<sup>70</sup>



**Scheme 64** Catalytic reduction of imines with a borenium cation **66**.<sup>70</sup>

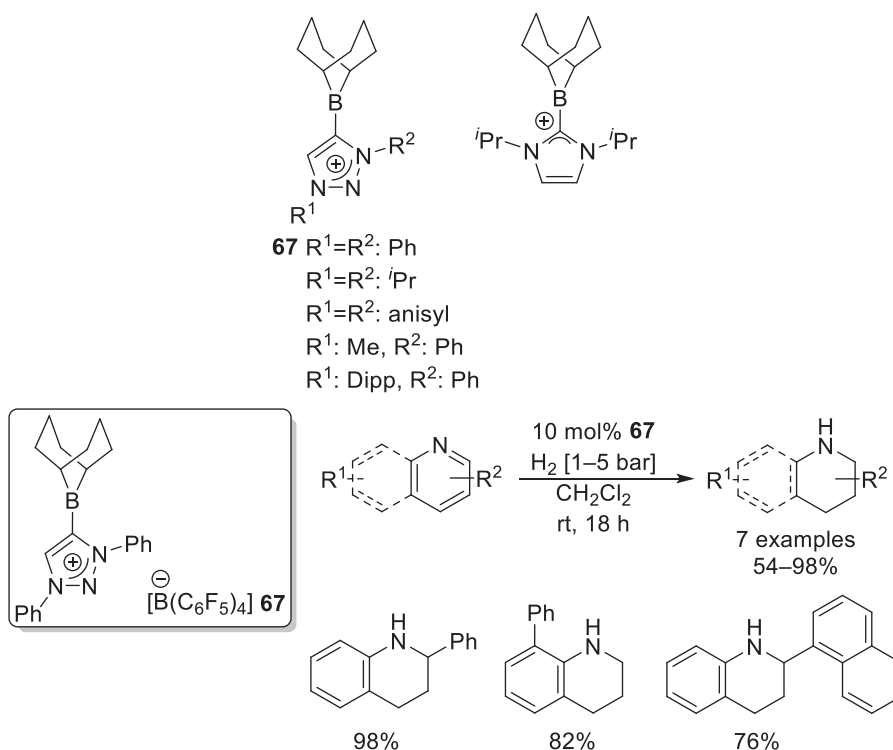


Crudden later expanded the scope of cationic Lewis acids for hydrogenation catalysis toward mesoionic carbene-stabilized boronium ions. A series of 1,2,3-triazolylidene-based mesoionic carbene boranes were prepared from their respective 1,2,3-triazolium salts, a base, and a borane. They were then subjected toward the reduction of *N*,1-diphenylethanamine, wherein catalyst **67** was observed to be most active. Catalyst **67** was then applied toward the reduction of 11 sterically hindered *N*-heterocycles, with only mild conditions required for efficient transformation (Scheme 65).<sup>71</sup>

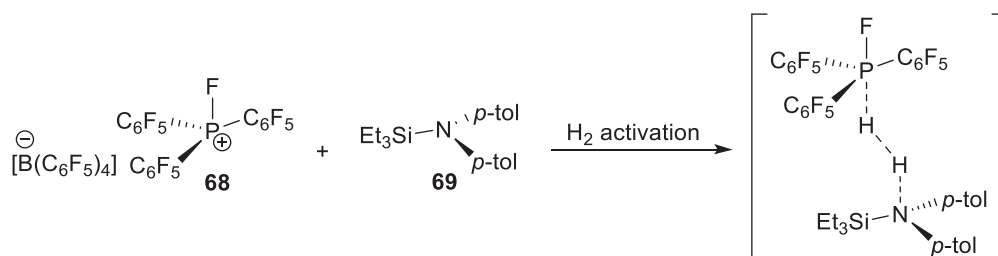
### 1.06.2.5.2 Electrophilic phosphonium cations

A further type of FLP system consisting of electrophilic phosphonium cation (EPC)  $[\text{FP}(\text{C}_6\text{F}_5)_3][\text{B}(\text{C}_6\text{F}_5)_4]$  **68** in combination with bulky silylamine *p*-Tol<sub>2</sub>NSiEt<sub>3</sub> **69** was reported by Stephan for the reduction of alkenes (Scheme 66). EPCs are highly Lewis acidic species, in which reactivity arises from a low lying  $\sigma^*$  orbital. This can be contrasted to traditional Lewis acids, wherein the reactivity originates from an empty *p*-orbital. The formation of an FLP between **68** and **69** which was capable of reversible H<sub>2</sub> activation was proven through H/D isotope scrambling.<sup>72</sup>

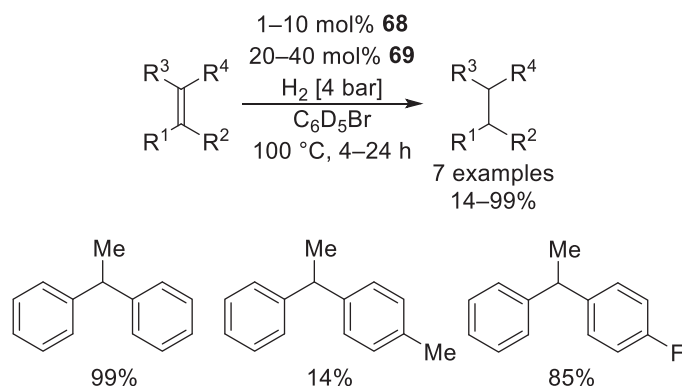
Before a scope of catalytic reductions was performed, a screening of suitable Lewis bases was investigated, which revealed that increased steric hindrance around the Lewis base had an adverse effect upon catalytic efficiency. *p*-Tol<sub>2</sub>NSiEt<sub>3</sub> **69** and *p*-Tol<sub>2</sub>NSi(*i*Pr)<sub>3</sub> were eventually chosen as the most suitable Lewis bases for the catalytic reduction. Previous research by the group on EPCs had found that **68** was capable of catalyzing the dehydrocoupling of *p*-Tol<sub>2</sub>NH with HSiEt<sub>3</sub> to form **69**,<sup>73</sup> and thus the combination of the amine and silane or the silylamine was used interchangeably. With EPC **68** and a choice of silylamine in hand, twelve olefins were reduced to their corresponding alkanes in good to excellent conversion (Scheme 67). A limitation was noted upon the reduction of bulky olefins, which resulted in lower conversions to their respective alkanes.<sup>72</sup>



**Scheme 65** Catalytic reduction of sterically hindered *N*-heterocycles using a 1,2,3-triazolylidene-based mesoionic carbene borane catalyst **67**.<sup>71</sup>



**Scheme 66** Activation of H<sub>2</sub> by an FLP composed of an electrophilic phosphonium cation **68** (EPC) and a bulky silylamine **69**.<sup>72</sup>



**Scheme 67** Catalytic reduction of olefins by an FLP composed of an electrophilic phosphonium cation (EPC) and a bulky silylamine.<sup>72</sup>

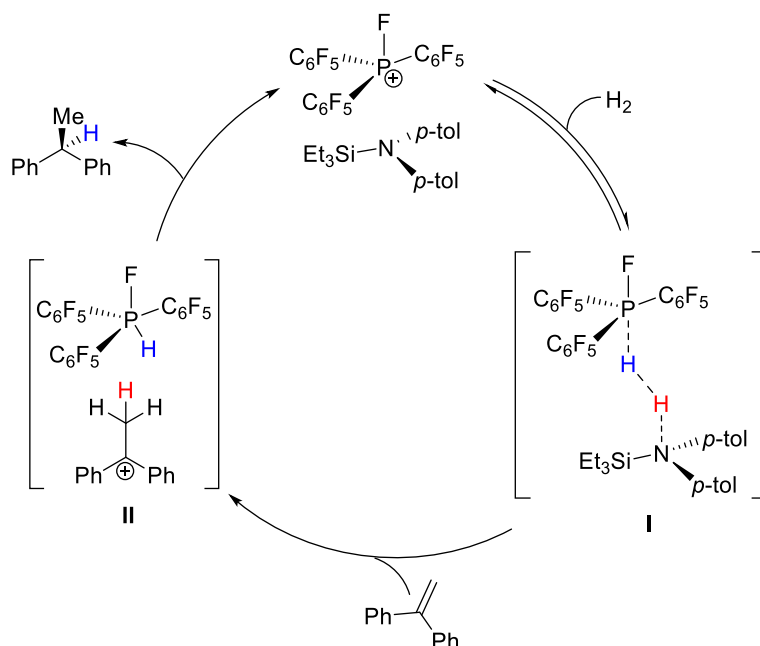
A proposed mechanism was based upon DFT calculations and experimental isotope labelling studies (**Scheme 68**). Initially, the EPC and silylamine activated  $H_2$  to form hydridophosphorane [FP(C<sub>6</sub>F<sub>5</sub>)<sub>3</sub>H] and ammonium cation [*p*-Tol<sub>2</sub>N(H)SiEt<sub>3</sub>]<sup>+</sup> (**Scheme 68, I**). The ammonium cation was then able to protonate the olefin to form a carbocation (**Scheme 68, II**). Subsequent hydride delivery from the hydridophosphorane liberated the alkane product and regenerated the unactivated FLP.<sup>72</sup>

### 1.06.2.5.3 Inverse FLPs

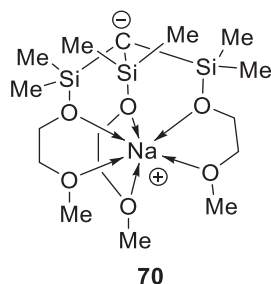
A conventional frustrated Lewis pair is composed of a strong Lewis acid that is unable to form an adduct with a weak-to-medium strength Lewis base, often due to unfavorable steric interactions between the acidic and basic centers. Conversely, an inverse FLP is composed of a bulky Lewis superbase that is unable to form an adduct with weak-to-medium strength Lewis acids.

Krempner has extensively focused upon the use of inverse FLPs toward dihydrogen cleavage and substrate reduction. The first report of an inverse FLP occurred in 2013, inspired by a search to use more readily available and stable Lewis acids for FLP chemistry rather than the expensive triarylborane B(C<sub>6</sub>F<sub>5</sub>)<sub>3</sub>.<sup>74</sup> Initial computational studies suggested that  $H_2$  could be cleaved by a weak Lewis acid in situations where a strong and bulky base was present. Indeed, experimental evidence demonstrated that strongly basic zwitterionic organosodium compound **70** was able to activate  $H_2$  in the presence of weaker Lewis acids, such as BPh<sub>3</sub> or HBMe<sub>2</sub> (**Fig. 5**).<sup>74</sup>

The catalytic potential of inverse FLPs was first demonstrated in the reduction of *N*-benzylidenaniline. Various inverse FLP systems were studied, comprised of phosphazene **71** or Verkade's superbase **72** in combination with a weak Lewis acid. From these observations, it was demonstrated that inverse FLPs **71**/BPh<sub>3</sub> and **72**/9-Hex-BBN were able to catalytically reduce the imine in



**Scheme 68** Mechanism of olefin reduction by an FLP composed of an electrophilic phosphonium cation (EPC) and a bulky silylamine.<sup>72</sup>

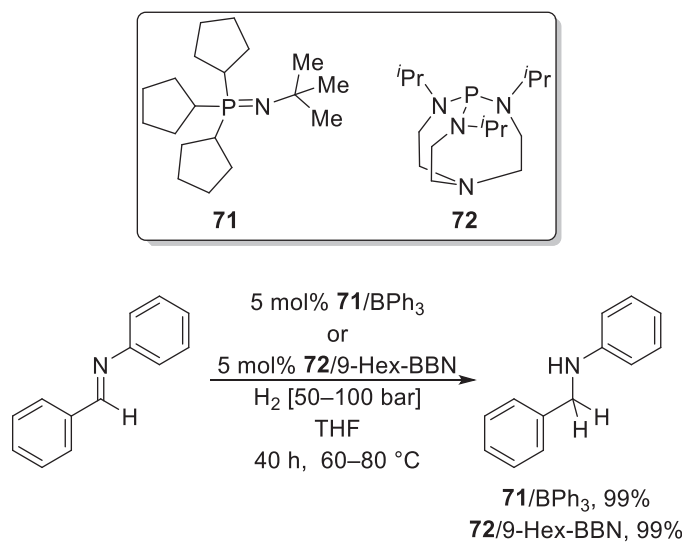


**Fig. 5** First example of a superbases capable of activating  $H_2$  as part of an inverse FLP.<sup>74</sup>

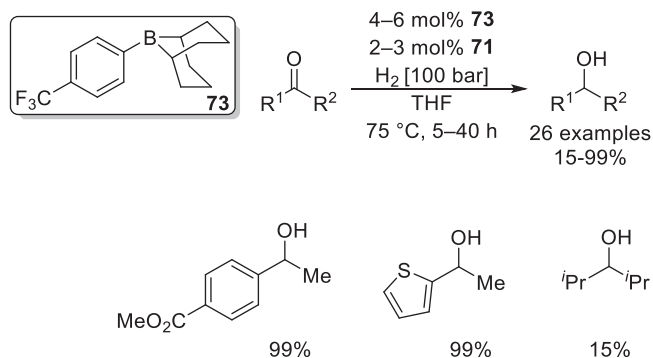
quantitative yields at only 5 mol% loading (**Scheme 69**). However, harsh conditions were required to maximize conversion (60–80 °C, 50–100 bar  $H_2$ ).<sup>75</sup>

Inverse FLPs were later demonstrated to be active toward the catalytic reduction of ketones. The bulky base phosphazene **71** was used in combination with aryl substituted derivatives of 9-BBN (9-(4-X-C<sub>6</sub>H<sub>4</sub>)-BBN) where X could be designated an electron donating or withdrawing group. Both donating and withdrawing groups on the substituted boranes could be used in combination with **71** to perform the selective catalytic reduction of acetophenone with no formation of side products.

Optimal yields were obtained when 9-(4-(F<sub>3</sub>C)-C<sub>6</sub>H<sub>4</sub>)-BBN **73** was used as a Lewis acid, wherein diphenylethanol could be quantitatively prepared from its corresponding ketone after just 5 h. As with the reduction of imines, harsh reaction conditions were required for the reaction to proceed efficiently. Moreover, the speed of reduction was significantly improved when two equivalents of Lewis acid was used per equivalent of base. The presented inverse FLP was observed to be more tolerant toward functional groups than classical FLPs. 26 aliphatic and aromatic ketones, some bearing sensitive amide, amine, thioether, or ester groups were all successfully reduced in excellent yield (**Scheme 70**). Limitation was noted upon the reduction of isopropyl ketone, which



**Scheme 69** First examples of catalytic reduction by inverse FLPs.<sup>75</sup>



**Scheme 70** Catalytic reduction of ketones by an inverse FLP.<sup>76</sup>

proceeded poorly and formed the alcohol in just 15% yield after 40 h, whilst 4-nitroacetophenone and 4-cyanoacetophenone could not be reduced.<sup>76</sup>

Combined DFT and experimental deuteration studies justified the requirement of two acid equivalents per base. A proposed mechanism showed that a highly reactive borohydride species was initially formed via H<sub>2</sub> activation by the inverse FLP (**Scheme 71, I**). This borohydride was then able to react with an additional equivalent of Lewis acid **73** to form a stable, bridged borohydride (**Scheme 71, II**). A subsequent hydride transfer with the carbonyl substrate then yielded alkoxide anion (**Scheme 71, III**), which was then readily protonated by the conjugate acid, releasing the alcohol product and regenerating the inverse FLP. A secondary minor pathway was also suggested, in which the alkoxy anion intermediate (**Scheme 71, III**) acted as the Lewis base in an FLP in combination with Lewis acid **73**. Upon activating H<sub>2</sub>, this FLP formed the bridged borohydride salt (**Scheme 71, II**) upon the release of the alcohol product.<sup>76</sup>

### 1.06.3 Hydrosilylation

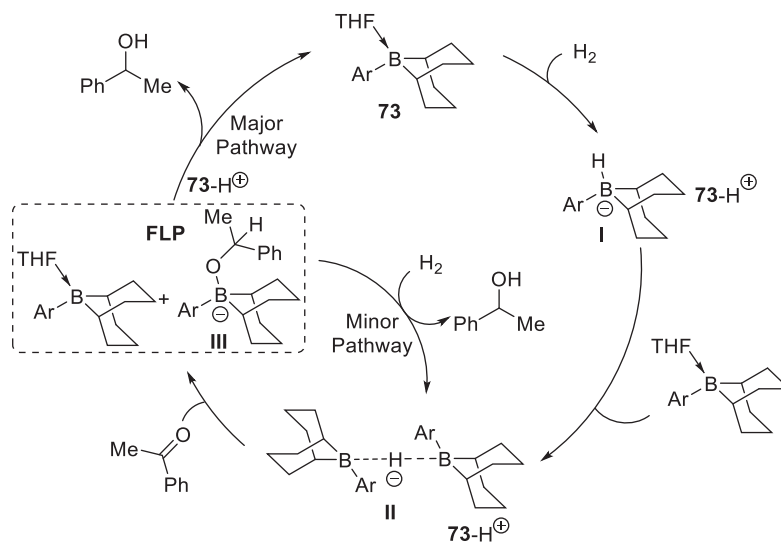
Hydrosilylation is a well-known method of installing synthetically useful silanes onto unsaturated bonds (**Scheme 72**).<sup>77</sup> Classically, this process was performed with platinum based catalysts, such as Speier's catalyst or Karstedt's catalyst; however, with a focus toward sustainable chemistry many research groups have elected to pursue viable alternatives based upon earth abundant metals and main group elements.<sup>77</sup> Recent advances have found that FLP systems can also be used for the process.

#### 1.06.3.1 FLP-mediated hydrosilylation

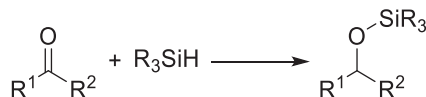
Whilst the term frustrated Lewis pair was not coined until 2006, a decade earlier Piers observed unusual activity during the B(C<sub>6</sub>F<sub>5</sub>)<sub>3</sub> catalyzed hydrosilylation of aromatic aldehydes, ketones and esters with triphenylsilane.<sup>5</sup> Extensive mechanistic probes revealed that the borane did not activate the carbonyl moiety as was the expected reactivity at the time, and instead coordinated to the silane's hydride. A further result that preceded the discovery of frustrated Lewis pairs was that the substrate was required to be sufficiently basic to undergo hydrosilylation.<sup>5</sup>

Twelve years later, Oestreich performed a concerted mechanistic study to reveal conclusively that FLP-type reactivity was present in B(C<sub>6</sub>F<sub>5</sub>)<sub>3</sub>-catalyzed hydrosilylation (**Scheme 73**). It was proved that the hydride abstraction from the silane occurred simultaneously with the coordination of the carbonyl moiety toward the silicon atom to enable hydride abstraction by the borane.<sup>6</sup>

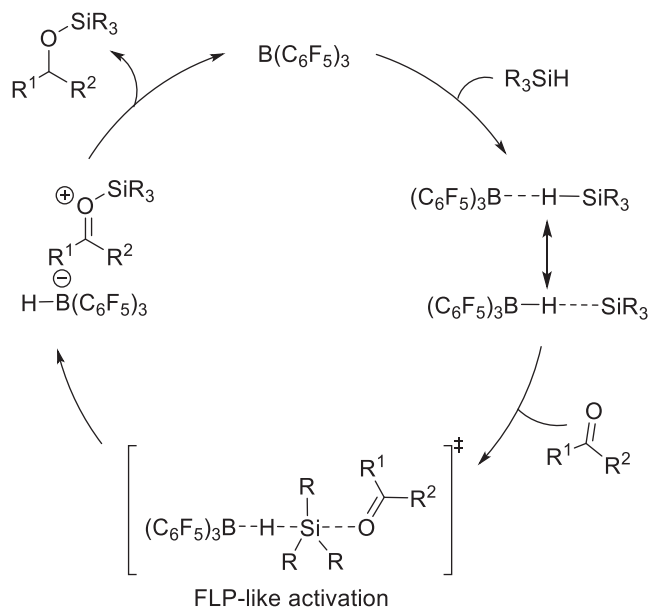
The metal-free hydrosilylation protocol with a B(C<sub>6</sub>F<sub>5</sub>)<sub>3</sub> catalyst was further extended toward imines (**Scheme 74**).<sup>78</sup> Twelve amines were obtained after a base promoted desulfonylation, resulting in moderate to excellent yields (57–97%). In the reaction,



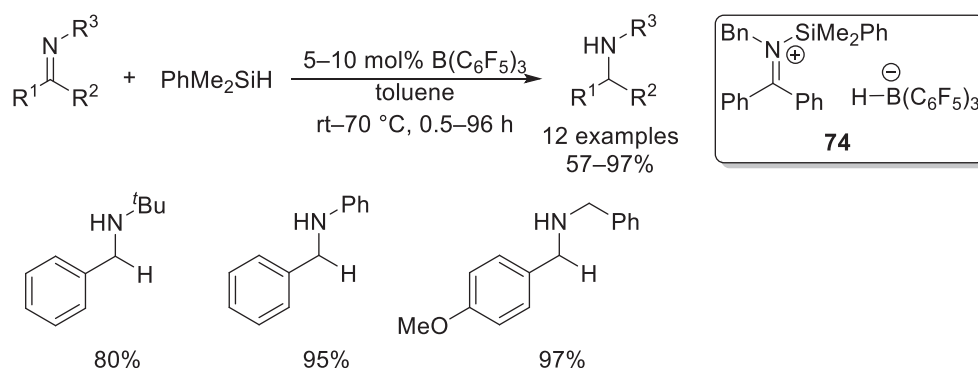
**Scheme 71** Mechanism of reduction of ketones by an inverse FLP.<sup>76</sup>



**Scheme 72** Hydrosilylation of a carbonyl.<sup>77</sup>



**Scheme 73** Mechanism of  $B(C_6F_5)_3$  catalyzed hydrosilylation.<sup>5,6</sup>



**Scheme 74**  $B(C_6F_5)_3$  mediated hydrosilylation of imines.<sup>78</sup>

a silyliminium ion pair intermediate **74** was identified spectroscopically, which suggested that the imine hydrosilylation mechanism was indeed FLP-like in nature.<sup>78</sup>

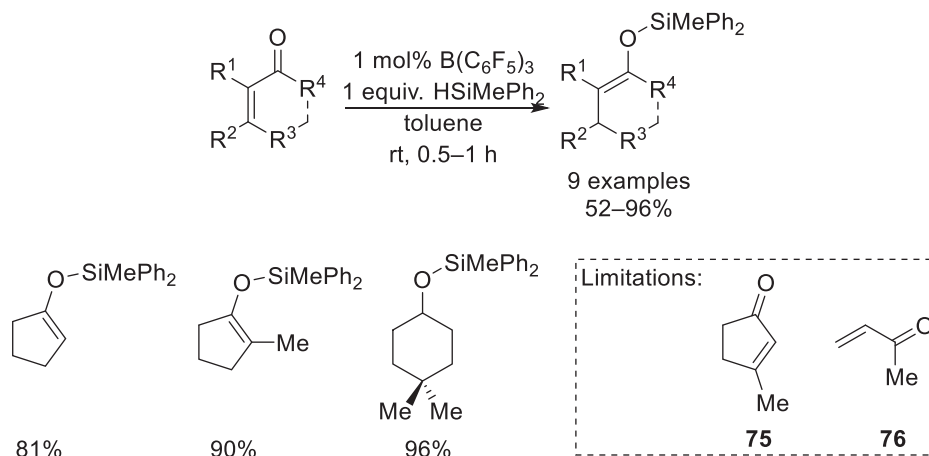
Enones and silyl enol ethers have also been observed to undergo  $B(C_6F_5)_3$ -catalyzed hydrosilylation.<sup>79</sup> Whilst not described as a frustrated Lewis pair as the term had not yet been coined, FLP-like activation was noted in a similar vein to the  $B(C_6F_5)_3$ -catalyzed hydrosilylation of carbonyls.<sup>5</sup> Both cyclic and acyclic enones were observed to participate in 1,4-hydrosilylation in good to high yields (**Scheme 75**); however, certain substrates such as 3-methyl-2-cyclopentenone **75** and methyl vinyl ketone **76** gave complicated mixtures, presumably by participating in competing 1,2-hydrosilylation and oligomerization reactions. Further investigation found that a wide range of silanes could be employed in the hydrosilylation, with only triisopropylsilane recalcitrant toward the reaction with enones.<sup>79</sup>

When the silane was used in excess, the silyl enol ether product from initial hydrosilylation was observed to undergo a secondary hydrosilylation reaction (**Scheme 76**). Such  $\beta$ -silylalkoxy functionalities are known to be susceptible to elimination under acidic or basic conditions, revealing how the hydrosilylation catalysis protocol could transform an enone into an alkene with a vinylic group.<sup>79</sup>

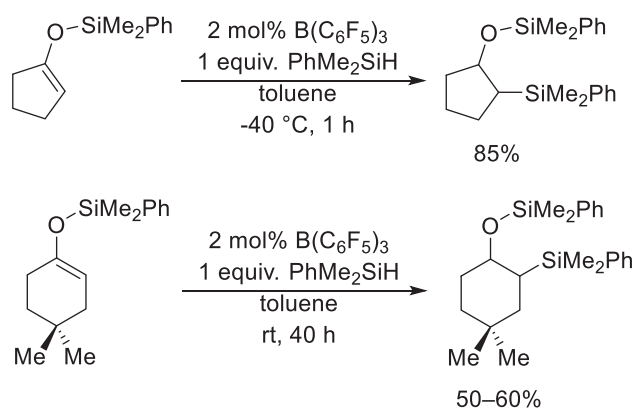
In 2005, the  $B(C_6F_5)_3$ -catalyzed hydrosilylation of thiobenzophenones was reported as a novel synthetic route toward a silicon-sulfur bond (**Scheme 77**). A combination of sterically accessible tertiary hydrosilanes and dihydrosilanes was crucial for such transformation, as when two equivalents of thiobenzophenone were reacted with the more sterically hindered  $(H^tPr_2Si)_2$ , no reactivity was observed after 48 h. Over six examples, the reactions gave quantitative conversions toward the corresponding silyl thioethers with catalytic loadings of  $B(C_6F_5)_3$  as low as 0.004 mol%.<sup>80</sup>

A further observation of a borane-silane adduct which was able to engage in FLP-mediated hydrosilylation was demonstrated with a combination of a boraindene **77** and triethylsilane. Initially the formation of the adduct could not be spectroscopically observed at room temperature; however, variable-temperature  $^{19}F$  and  $^1H$  NMR experiments (following the boraindene and the





**Scheme 75** Hydrosilylation of enones.<sup>79</sup>



**Scheme 76** Hydrosilylation of silyl enol ethers.<sup>79</sup>

silane respectively) clearly revealed the formation of adduct **78**. Subsequently, adduct **78** was further reacted with the nucleophile  $(\text{Ph}_3\text{PNPPH}_3)\text{Cl}$  to form hydridoborate salt **79** and  $\text{Et}_3\text{SiCl}$ . This analogy toward carbonyl nucleophiles once again confirmed the generally accepted FLP mechanism in the process of borane-catalyzed hydrosilylation (**Scheme 78**).<sup>81</sup>

The FLP-mediated hydrosilylation of pentafulvenes into allyl silanes was observed in excellent yield and regioselectivity.<sup>82</sup> Whilst standard Lewis acid catalysis by  $\text{B}(\text{C}_6\text{F}_5)_3$  was observed to promote both hydrosilylation and fulvene oligomerization, the introduction of a sterically hindered base suppressed any oligomerization from occurring. When tris(1-naphthyl)phosphine **80** was employed as the base, the reactions proceeded at room temperature and regioselectively catalyzed 1,2-hydrosilylation at the  $\text{C}_2$  carbon in excellent yields (**Scheme 79**).

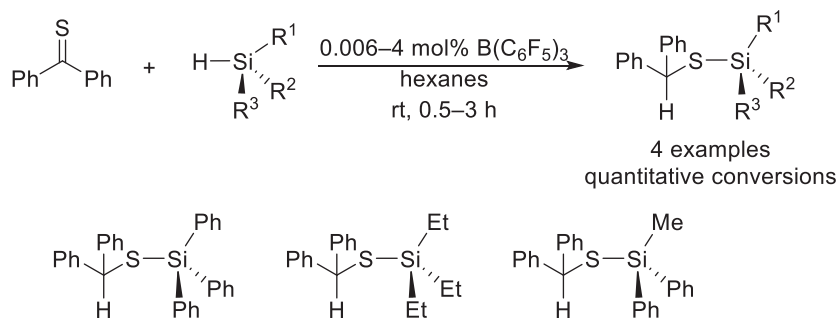
The hydrosilylation of unsymmetrical fulvenes, such as 6-phenyl-6-methylfulvene **81**, yielded two isomers at the  $\text{C}_2$  carbon (*E*) and (*Z*) in a 1.6:1 ratio. Moreover, regioselectivity was drastically decreased when 6,6-dimethylbenzofulvene was subjected toward hydrosilylation, where the formation of two regioisomers **82** and **83** was observed in a 1.2:1 ratio, a result of both Markovnikov and anti-Markovnikov addition (**Scheme 79**).<sup>82</sup>

Electrophilic phosphonium cations have also been observed to partake in FLP-style reactivity during hydrosilylation catalysis. The first example was shown through the hydrosilylation of olefins and alkynes with two EPCs, **68** and **84** (**Scheme 80**).<sup>83</sup> EPC **68** differed from **84** by the replacement of one pentafluorophenyl ring with one phenyl ring, a modification that reduced its electrophilicity substantially. This was reflected in its slower performance when catalyzing the hydrosilylation of hexene with triethylsilane. Nevertheless, good to excellent isolated yields were obtained by employing both **68** and **84** as catalysts for the hydrosilylation of 14 unsaturated C–C bond containing substrates.<sup>83</sup>

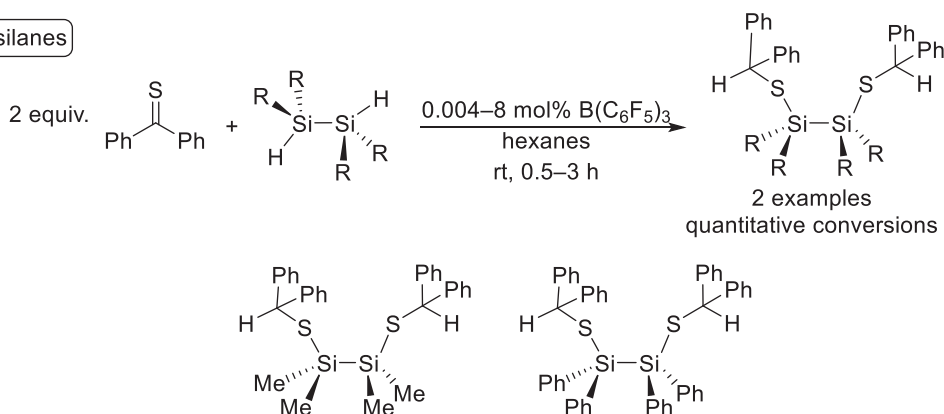
Combined mechanistic and DFT studies suggested that initially the EPC catalyst **68** activated the silane, in a fashion similar to borane catalysts (**Scheme 81, I**). Introduction of the olefin resulted in a polarization of the olefin bond by the electropositive silicon atom (**Scheme 81, II**). 1,2-addition then occurred, whereupon the hydride from the silicon attacked the olefin carbocation in an anti-fashion, leading to addition to the free silane cation (**Scheme 81, III**). This liberated the silylated product and regenerated the EPC catalyst **68** (**Scheme 81**).<sup>83</sup>

The substrate scope, amenable toward hydrosilylation by EPC catalyst **68** was later extended toward ketones, imines, and nitriles (**Scheme 82**).<sup>84</sup> Whilst the ketones and imines formed their corresponding silyl enol ethers and *N*-silylamines respectively, the

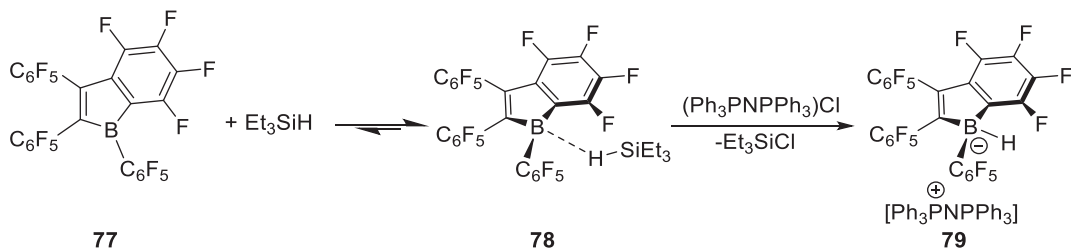
## Silanes



## Disilanes



**Scheme 77**  $B(C_6F_5)_3$ -catalyzed hydrosilylation of thiobenzophenones.<sup>80</sup>



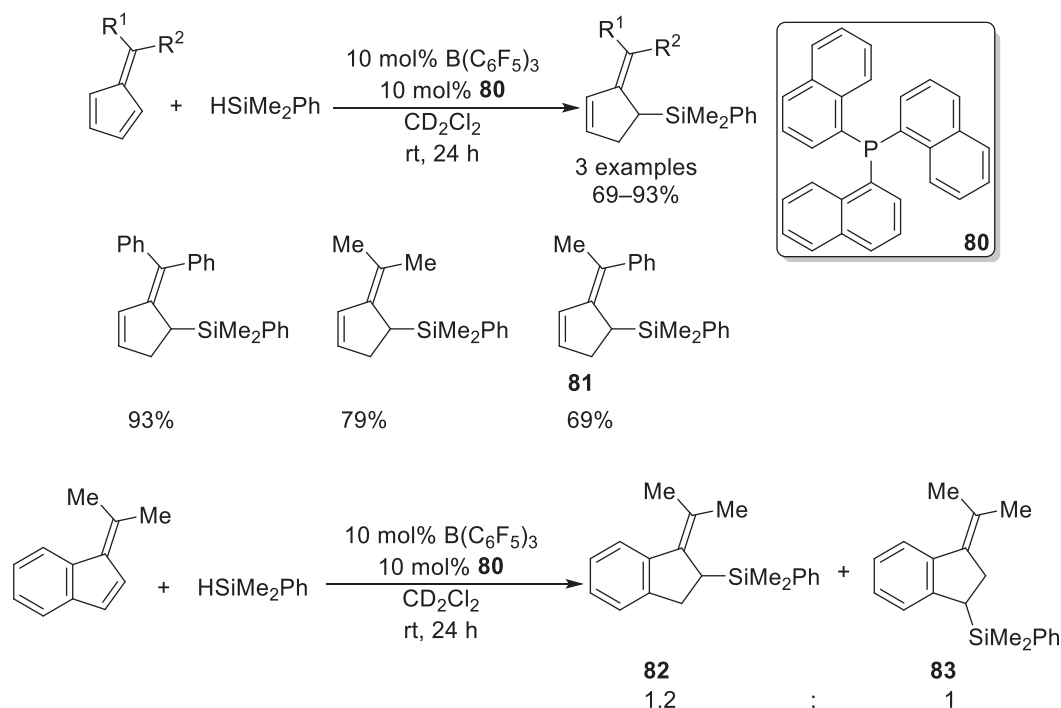
**Scheme 78** Further evidence of a borane-silane adduct participating in FLP-type reactivity.<sup>81</sup>

hydrosilylation of nitriles would either form *N*-silylimines or *N,N*-disilylamines depending on the identity of the substrate. All substrates underwent hydrosilylation in excellent conversion, with the exception of *N*-benzyl-1-phenylmethanimine **25**, presumably as a result of steric hindrance around the basic nitrogen atom precluding reactivity. Competition reactions found that **68** would preferentially catalyze the groups in the order ketone > nitrile > imine > olefin in substrates where multiple functional groups were present.<sup>84</sup>

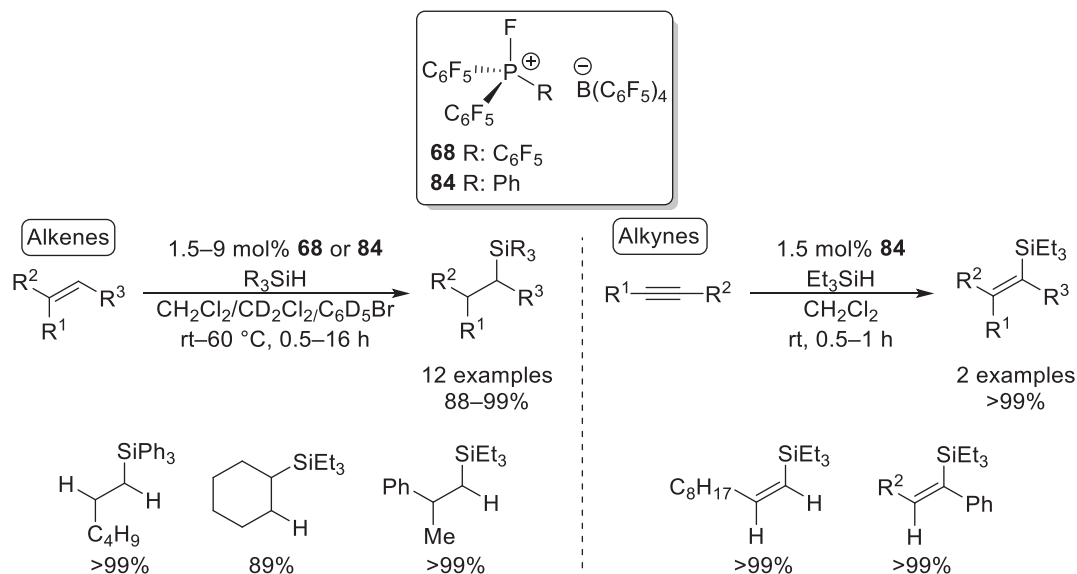
The mechanism of reaction was proposed to be common for ketones, imines and nitriles. DFT and experimental probes suggested that the EPC catalyst **68** initially activated the silane (**Scheme 83, I**). Introduction of the ketone led to an interaction between the basic carbonyl oxygen and the electropositive silicon (**Scheme 83, II**). The carbonyl then attacked the silane, thereby forming a carbocation and forcing the silane hydride to transfer onto the EPC (**Scheme 83, III**). Hydride attack from the EPC to the carbocation liberated the silyl enol ether and thus regenerated the free EPC **68** (**Scheme 83**).<sup>84</sup>

### 1.06.3.2 Asymmetric FLP-mediated hydrosilylation

The first example of asymmetric hydrosilylation was demonstrated with chiral silane (<sup>Si</sup>*R*)-**85** and  $B(C_6F_5)_3$ , as part of the mechanistic study which confirmed the FLP-type reactivity of the hydrosilylation reaction.<sup>6</sup> It was observed that a mixture of (<sup>Si</sup>*R*)-**85** and 5 mol% of  $B(C_6F_5)_3$  would hydrosilylate acetophenone to form hydrosilane (<sup>Si</sup>*R*, *R*) **86** as a scalemic mixture with a *d.r.* ratio of



**Scheme 79** FLP-mediated hydrosilylation of pentafulvenes.<sup>82</sup>

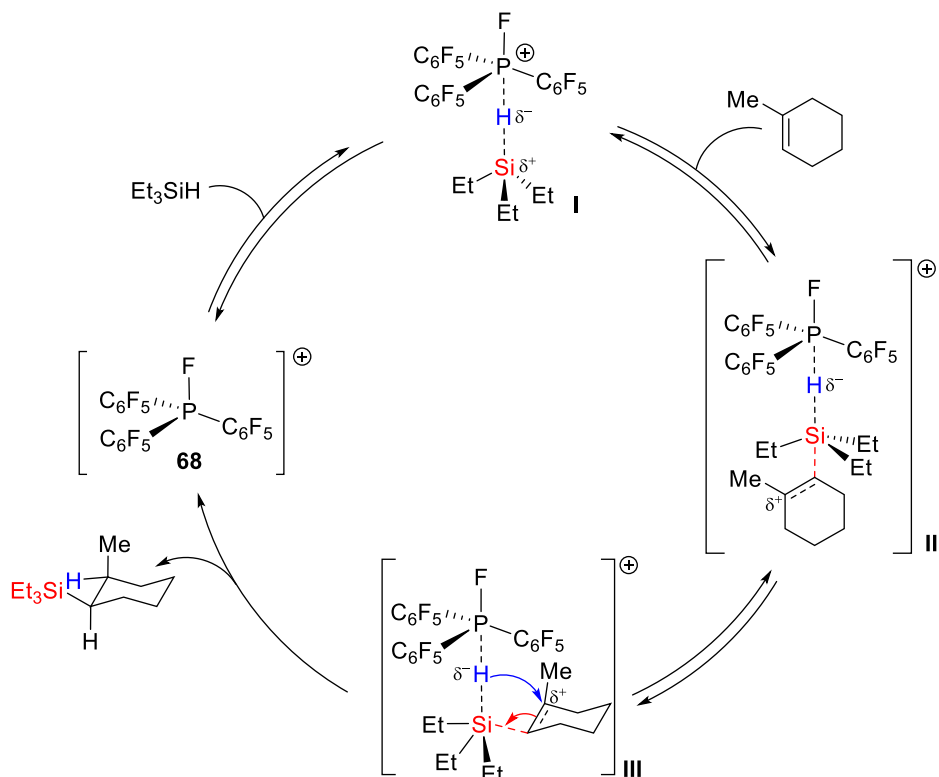


**Scheme 80** Hydrosilylation of olefins and alkynes with an EPC catalyst.<sup>83</sup>

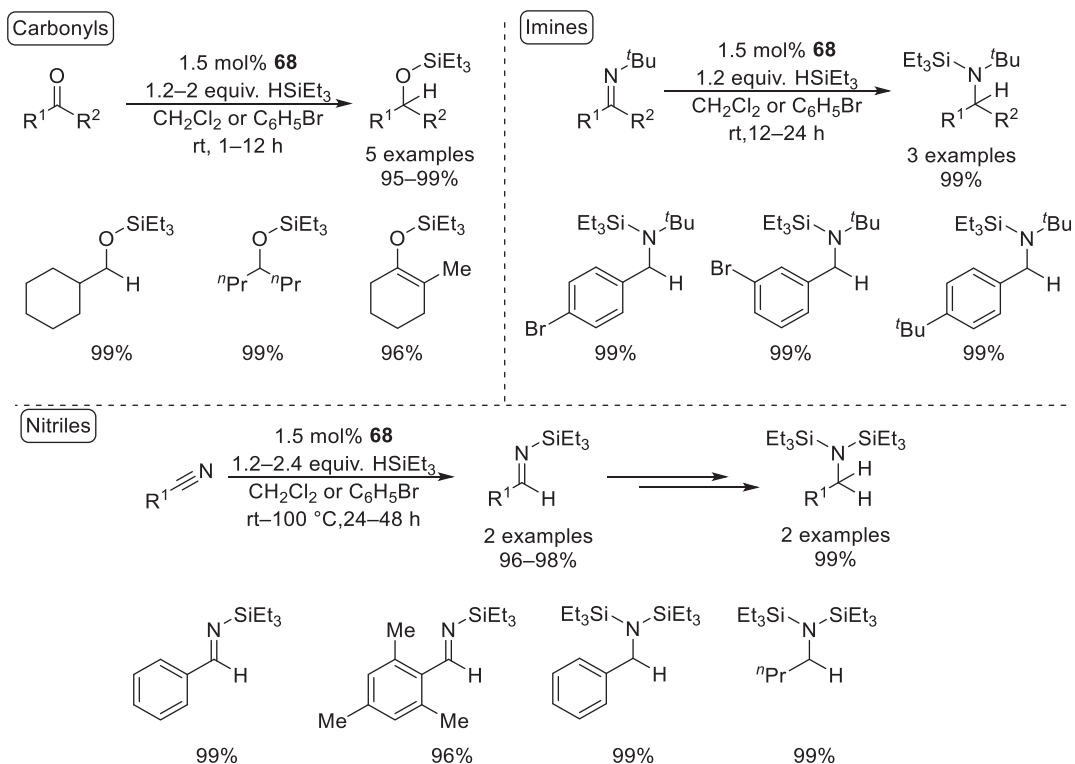
74:26. Following a racemization-free reductive cleavage of (<sup>Si</sup>R, R) **86**, the alcohol **87** was isolated in good yield (68%) and *e.e.* (38%) (**Scheme 84**).<sup>6</sup>

A series of six acyclic methyl ketones were subsequently hydrosilylated in an asymmetric fashion with a racemic mixture of silane **85** (**Scheme 85**).<sup>85</sup> The reactions proceeded at room temperature, with excellent conversions and good diastereoselective ratios (up to 81:19). Unexpectedly, when cyclic ketones (**88**, **89**) were subjected toward the asymmetric hydrosilylation, the reactions were sluggish, and the obtained diastereoselective ratios were low. Additionally, when the same conditions were applied toward the hydrosilylation of imines, good conversions of racemic mixtures were obtained.<sup>85</sup>

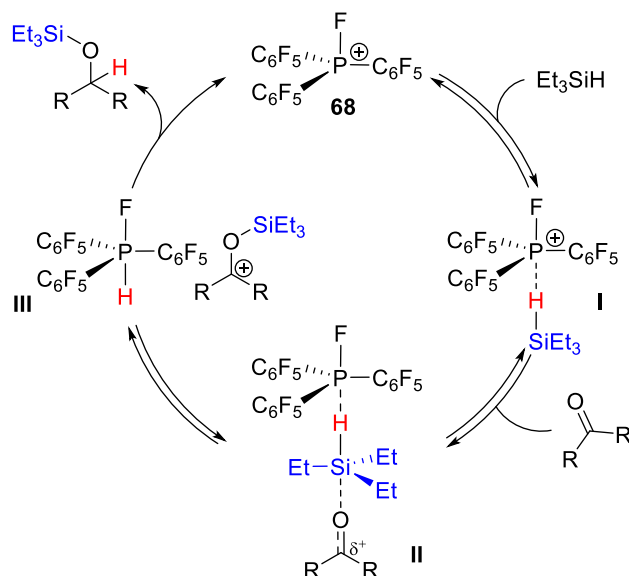
It was suggested that such discrepancy in stereochemical outcome was a result of different hydride transfer pathways (**Fig. 6**). Whilst hydride transfer was able to impart chirality at the silylated carbonyl (**Fig. 6, I**) during the hydrosilylation of carbonyls, when imines were hydrosilylated, hydride transfer would instead occur at the borane-activated imine (**Fig. 6, II**) during a different



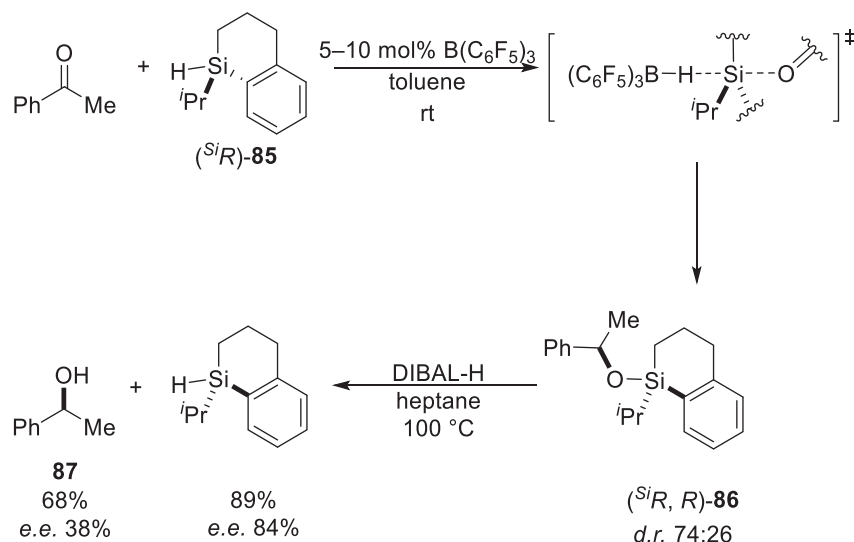
**Scheme 81** Mechanism of hydrosilylation of olefins with an EPC catalyst.<sup>83</sup>



**Scheme 82** Hydrosilylation of ketones, imines and nitriles by an EPC catalyst **68**.<sup>84</sup>



**Scheme 83** Mechanism of hydrosilylation of ketones by an EPC catalyst.<sup>84</sup>



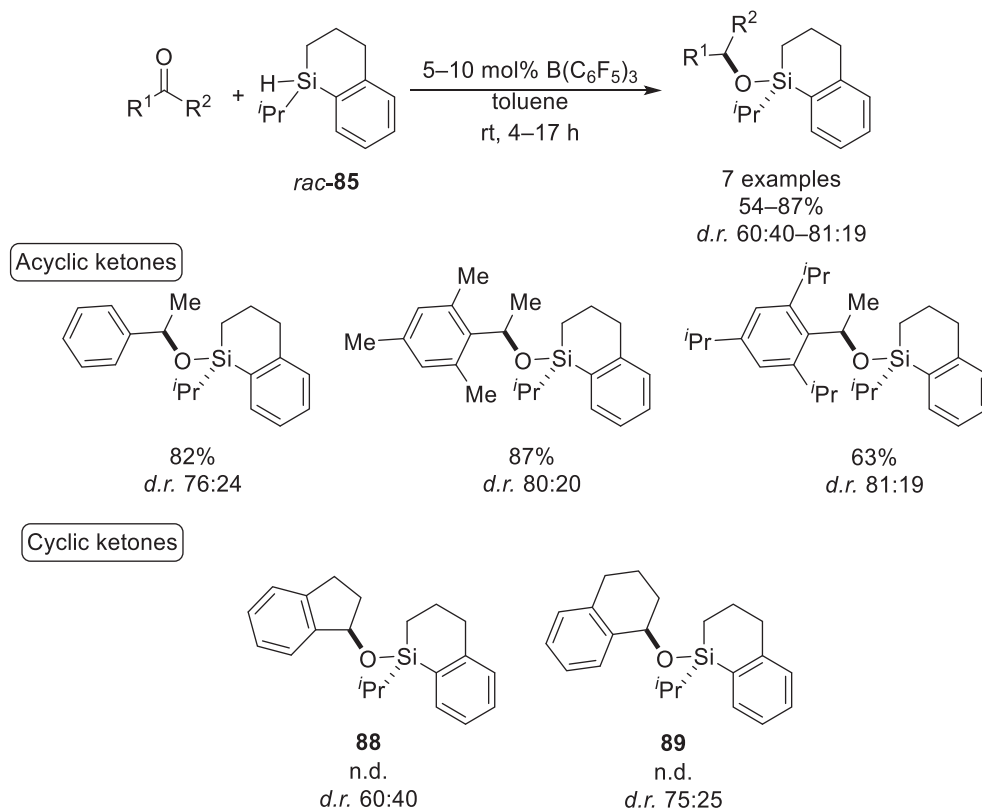
**Scheme 84** First example of FLP-mediated asymmetric hydrosilylation.<sup>6</sup>

stage of the reaction due to the steric encumbrance around the silylated iminium ion intermediate (**Fig. 6, III**) where it had no effect upon stereoselectivity.<sup>85</sup>

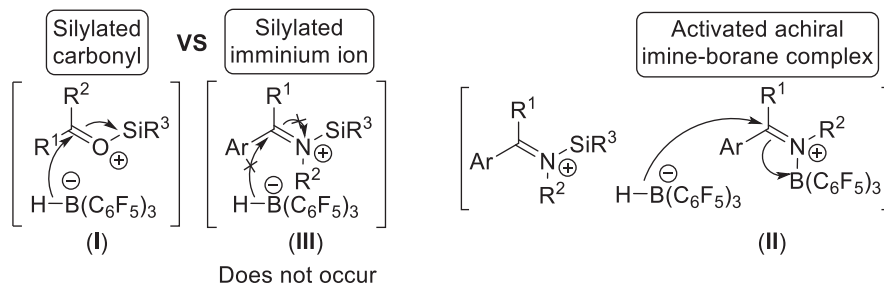
The first highly enantioselective hydrosilylation of imines was achieved by Klankermayer with the use of chiral camphor-derived boranes **28** and **90** (**Scheme 86**). With low catalytic FLP loadings, a range of six acyclic *N*-aryl imines were hydrosilylated and reduced in good to excellent yields and high enantioselective ratios. Limitations were noted upon the attempted reduction of more sterically hindered imines such as 2-methyl-*N*-(1-phenylethylidene)aniline, which gave negligible conversions and imines which contained electron withdrawing groups on the *para* position of their aryl rings, which were formed in low yield but high *e.e.*<sup>86</sup>

The THF adduct of a chiral analogue of  $B(C_6F_5)_3$ , (*S*)-**91**·THF, was developed to probe further asymmetric hydrosilylation reactions. This borane had a lower Lewis acidity when compared to  $B(C_6F_5)_3$ , a result of fewer pentafluorophenyl groups, but the incorporation of a BINOL-like ligand imparted axial chirality upon the molecule (**Scheme 87**). Initially, a series of four imines were asymmetrically hydrosilylated and reduced using  $Me_2PhSiH$  as a hydride source. The (*S*)-borane preferentially catalyzed the formation of (*S*)-amines, resulting in overall moderate *e.e.s* (30–41%). Interestingly, further investigations revealed that when axially chiral silanes (*S*-**92** or *R*-**92**) were used as the hydride source, the amine product would preferentially be the same enantiomer of the chiral silane used rather than the (*S*)-amine that was formed when (*S*)-**91**·THF was employed as a catalyst with a racemic silane.<sup>87</sup>

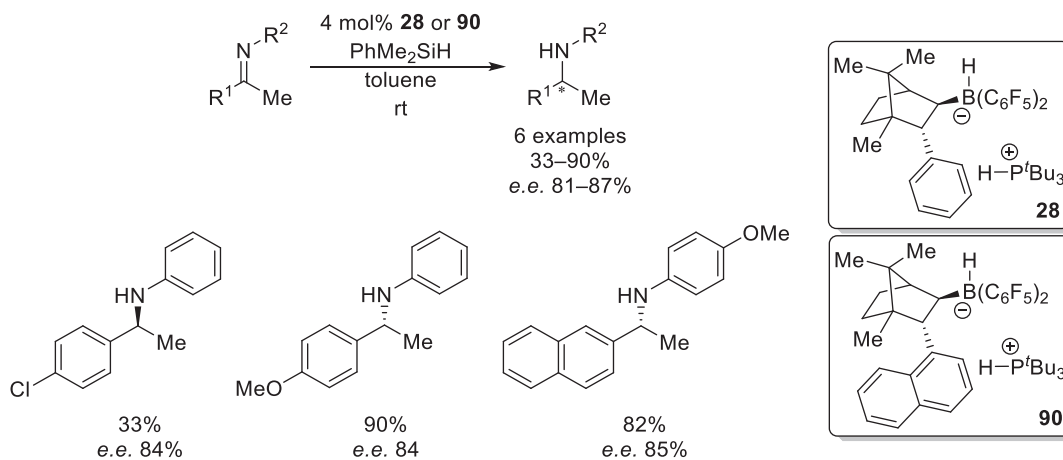




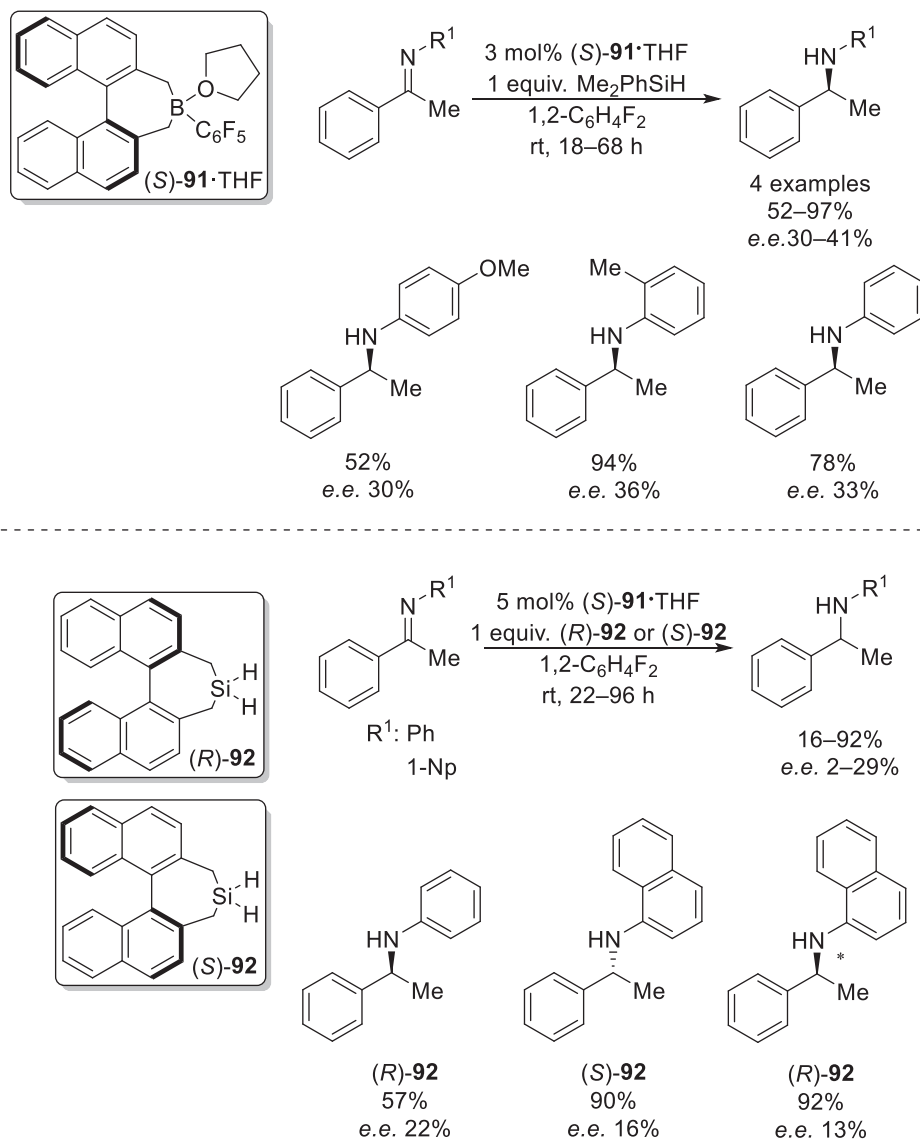
**Scheme 85** Asymmetric hydrosilylation of prochiral ketones.<sup>85</sup>



**Fig. 6** Origin of stereochemical outcomes in the hydrosilylation of ketones and imines.<sup>85</sup>



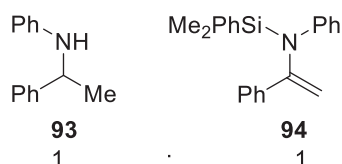
**Scheme 86** First FLP-mediated enantioselective reduction of imines.<sup>86</sup>



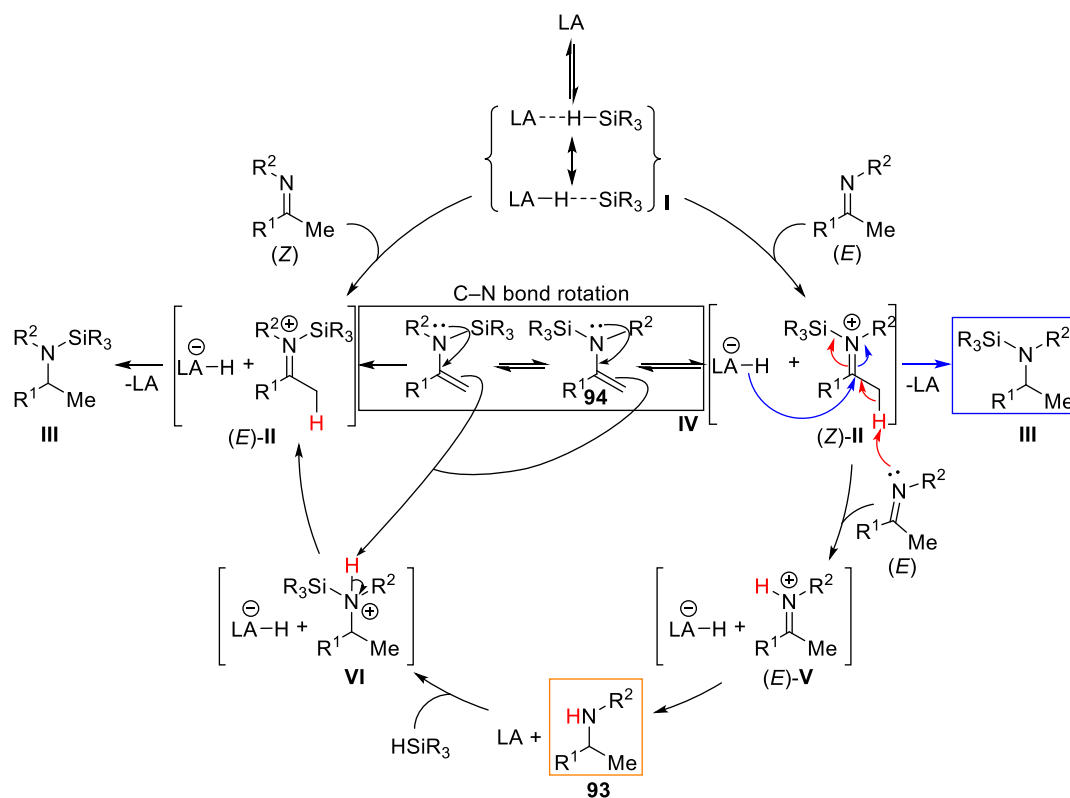
**Scheme 87** Tuneable FLP-mediated asymmetric hydrosilylation.<sup>87</sup>

The hydride transfer pathway for (S)-91·THF catalyzed imine hydrosilylation was later identified using in situ <sup>1</sup>H-NMR studies. An equimolar ratio of the free amine 93 and silylated enamine 94 intermediates were observed during the hydrosilylation process (Fig. 7), along with the expected silylated iminium ion intermediate 95. The presence of these unexpected intermediates suggested that there were competing reaction pathways that introduced further enantioselectivity-determining steps, thus increasing the likelihood that a racemic silyl imine would be formed despite the use of a chiral borane.<sup>88</sup>

The proposed mechanism suggested that the hydrosilane was initially activated by the borane catalyst (Scheme 88, I). A subsequent reaction of an imine with this activated complex formed a silyliminium ion and its ion pair borohydride (Scheme 88, (E)-II or (Z)-II), with the inverted stereochemistry of the silyliminium ion when compared to the imine reagent used. Both silyliminium ions (Scheme 88, (E)-II and (Z)-II) were then susceptible toward the hydride attack from the borohydride, forming their respective



**Fig. 7** Intermediates observed during the (S)-91·THF catalyzed imine hydrosilylation reaction.<sup>88</sup>

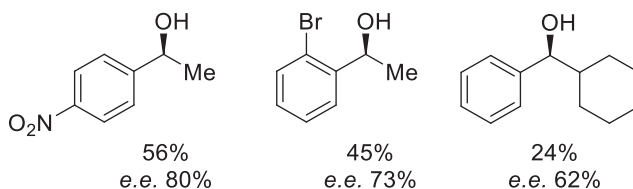
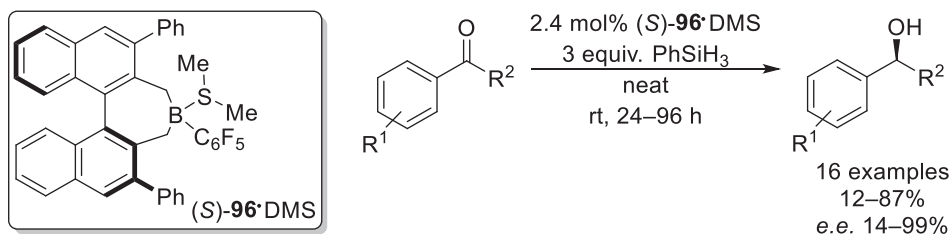


**Scheme 88** Mechanism of imine hydrosilylation catalyzed by (*S*)-**91**·THF.<sup>88</sup>

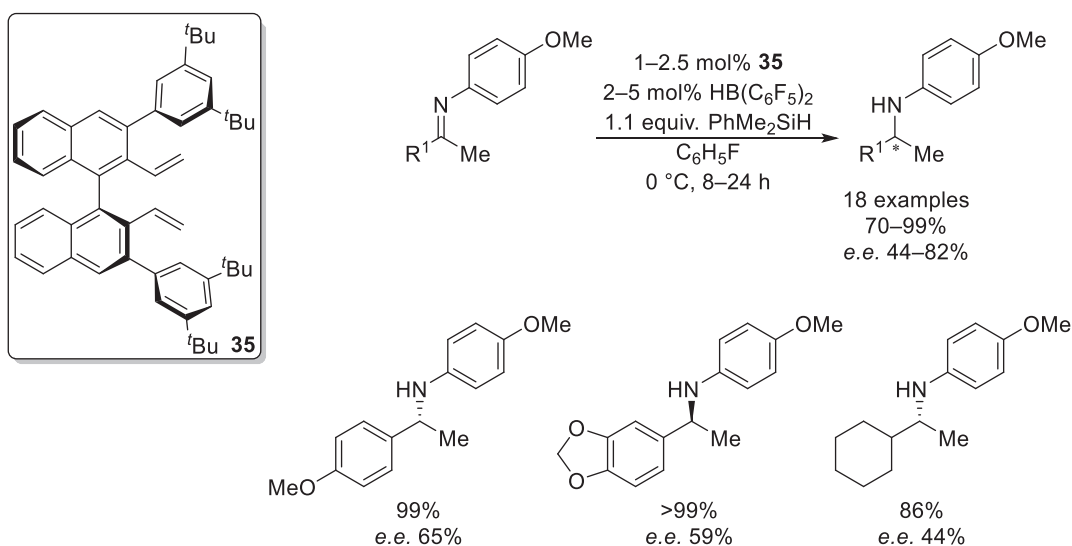
silylamine product (**Scheme 88**, **III**) through loss of the borane. Furthermore, two other mechanisms were also observed to occur. The silyliminium ion (**Scheme 88**, (*E*)-**II** and (*Z*)-**II**) could also be deprotonated by unreacted imines to form a silylated enamine **94**, which was one of the intermediates detected by the initial <sup>1</sup>H NMR study. The silylated enamines were then able to interconvert through C–N bond rotation (**Scheme 88**, **IV**), which resulted in the racemized silylamine product (**Scheme 88**, **III**). The second possible mechanism involved silyliminium ion (**Scheme 88**, (*Z*)-**II**; note, this mechanism could also involve (*E*)-**II**; however, only (*Z*)-**II** is explicitly drawn for clarity), being attacked at the  $\alpha$ -position by a second equivalent of (*E*)-imine to form an ion pair (**Scheme 88**, (*E*)-**V**) through a loss of hydrosilane. Reduction of the iminium cation (**Scheme 88**, (*E*)-**V**) formed the free amine **93**, the other intermediate detected by the initial <sup>1</sup>H NMR study. Upon re-exposure to an equivalent of hydrosilane, an ion pair composed of an ammonium ion and a borohydride was formed (**Scheme 88**, **VI**). Deprotonation of the ammonium cation (**Scheme 88**, **VI**) by the silylated enamine **94** resulted in the formation of silyliminium ion (**Scheme 88**, (*E*)-**II**), which upon hydride attack from the borohydride subsequently resulted in the formation of silylamine (**Scheme 88**, **III**).<sup>88</sup>

A further analogue of (*S*)-**91**·THF was later developed by Oestreich for the enantioselective hydrosilylation of carbonyls. (*S*)-**96**·DMS also contained axial chirality, but it contained extra steric congestion around the boron center from the installation of phenyl groups at the 3 and 3' positions on its binaphthyl rings. Such modification found that THF was too large to co-ordinate to the boron, thus dimethyl sulfide (DMS) was instead employed.<sup>89</sup> With catalyst (*S*)-**96**·DMS in hand, the hydrosilylation of acetophenone was optimized against a range of hydrosilanes. In general, larger monohydrosilanes were more unreactive, which was attributed to their steric hindrance; however, more compact trihydrosilanes such as PhSiH<sub>3</sub> and MeSiH<sub>3</sub>, showed quantitative conversions in up to 87% *e.e.*<sup>89</sup> 16 acetophenone derivatives were then subjected toward hydrosilylation with PhSiH<sub>3</sub> using a catalytic amount of (*S*)-**96**·DMS (**Scheme 89**). Acetophenones containing strongly electron withdrawing groups on the aryl rings caused the reactions to proceed significantly slower, yielding the corresponding alcohols in moderate yields, albeit good *e.e.* Conversely, acetophenones with electron donating groups on the aryl ring underwent full conversion more rapidly, although the resultant *e.e.s* were significantly lower. Additionally, sterically hindered acetophenone derivatives displayed both low reactivity and enantioselectivity.<sup>89</sup>

Chiral bisboranes formed through the hydroboration of binaphthyl-based dienes by Piers borane have already been discussed for their activity in catalytic asymmetric hydrogenations.<sup>33–36</sup> Further studies found that such catalysts could also be extended toward asymmetric hydrosilylations (**Scheme 90**).<sup>90</sup> A range of chiral bisboranes were evaluated for their capability toward imine hydrosilylation, with the bisborane formed from diene **35** being chosen as optimal. The chiral borane was employed in the successful enantioselective hydrosilylation of 18 imines, with excellent yields and *e.e.s* of the corresponding amine observed following reduction. Interestingly, this system did not require an external Lewis base, in contrast to Klankermayer's chiral boranes (**28**, **90**), which racemically reduced the imines in the absence of a Lewis base.<sup>86,90</sup>



**Scheme 89** (S)-96.DMS-mediated hydrosilylation of acetophenones.<sup>89</sup>



**Scheme 90** Asymmetric hydrosilylation catalyzed by a chiral bisborane.<sup>90</sup>

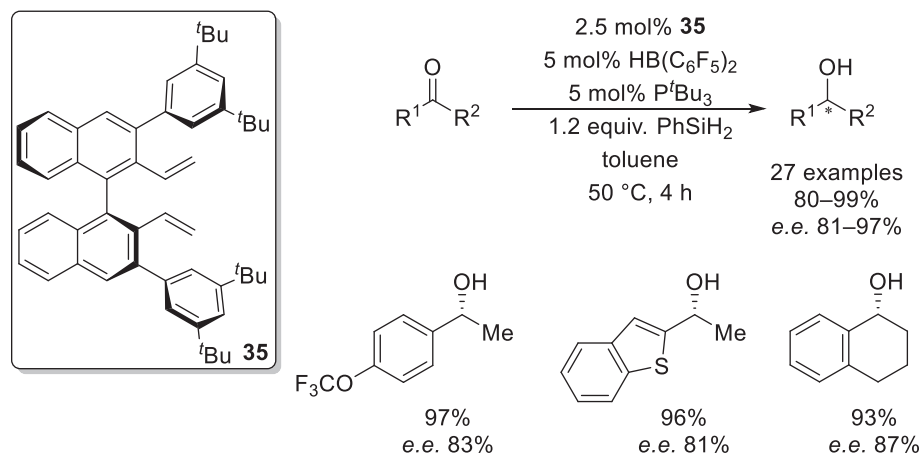
The bisborane formed from hydroboration of **35** with Piers borane was later employed in the asymmetric hydrosilylation of acetophenone derivatives when part of an FLP with P<sup>t</sup>Bu<sub>3</sub>. Employing 5 mol% of the chiral FLP catalyst enabled the hydrosilylation of simple ketones in excellent yields and *e.e.* (**Scheme 91**).<sup>91</sup>

The first example of FLP-mediated diastereoselective hydrosilylation was presented through the B(C<sub>6</sub>F<sub>5</sub>)<sub>3</sub>-catalyzed hydrosilylation and bishydrosilylation of  $\alpha$ -diketones. Interestingly, the relative stereochemistry of the products was determined by the steric bulk of the hydrosilane reagent. When smaller hydrosilanes such as Me<sub>3</sub>SiH were employed, *meso* products were preferentially formed (up to 96 *d.e.*). Conversely, larger silanes such as Ph<sub>3</sub>SiH provided *dl* products preferentially (up to 92 *d.e.*) (**Scheme 92**).<sup>92</sup>

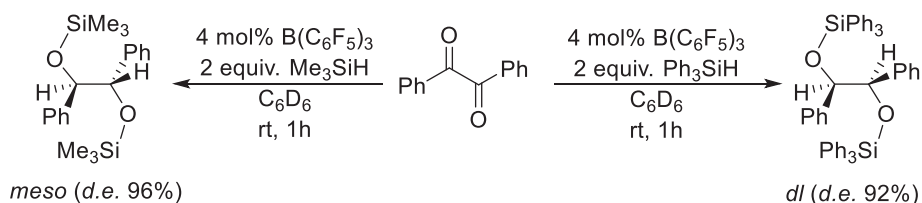
Further diastereoselective hydrosilylation of 1,2-dicarbonyls was demonstrated using a bisborane formed by the hydroboration of diyne **97** with Piers borane.<sup>93</sup> The bisborane was subjected toward the hydrosilylation of a range of 1,2-dicarbonyl compounds to form optically active  $\alpha$ -hydroxy ketones and  $\alpha$ -hydroxy esters in good to excellent isolated yields and *e.e.s* following reduction (**Scheme 93**). A limitation upon the system was noted upon the reduction of smaller substrates; when acetophenone was hydrosilylated and subsequently reduced, 1-phenylethanol was obtained in 95% yield with a mediocre *e.e.* of 42%.<sup>93</sup>

### 1.06.3.3 FLP-mediated reduction of amides to amines via hydrosilylation

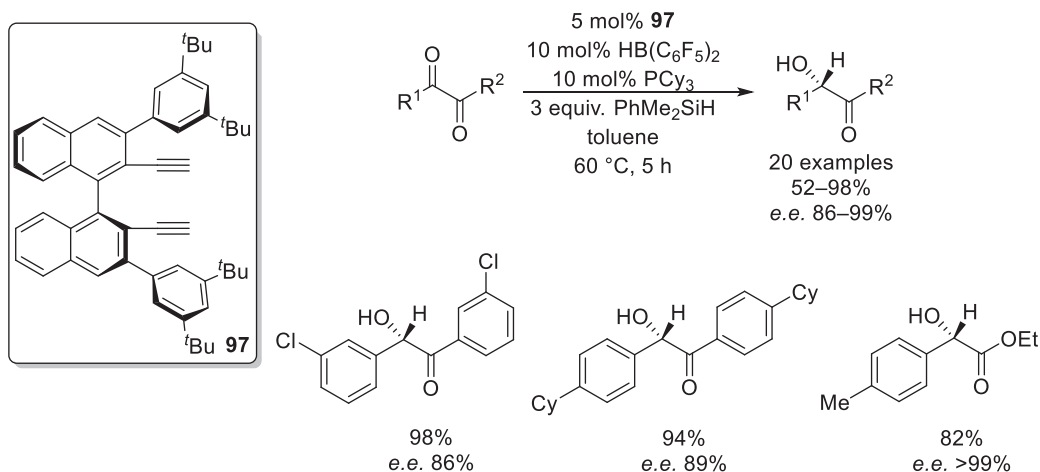
Metal-free amide reduction was classically a challenging transformation; previously, metal-free approaches employed stoichiometric boron hydrides, but a common problem was over-reduction and the resultant formation of unwanted by-products. These issues made the reactions less economically viable and made product purification a more challenging task.<sup>94</sup>



**Scheme 91** FLP-mediated asymmetric hydrosilylation of acetophenones by a chiral bisborane.<sup>91</sup>



**Scheme 92** FLP-mediated diastereoselective hydrosilylation of  $\alpha$ -diketones.<sup>92</sup>

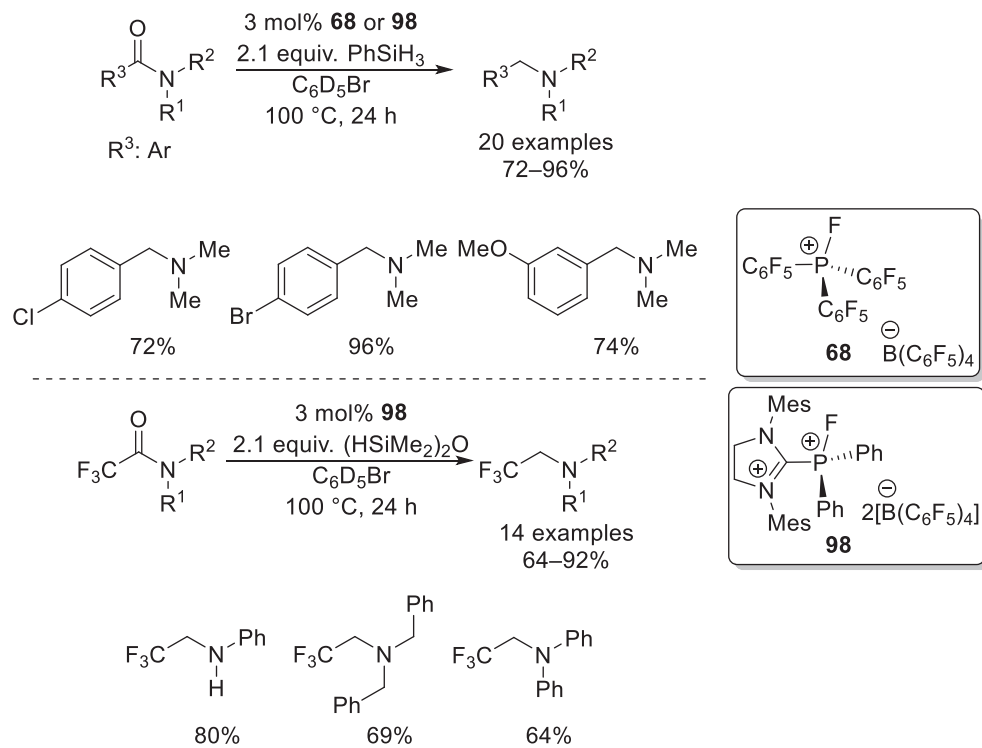


**Scheme 93** FLP-mediated enantioselective hydrosilylation of 1,2-dicarbonyl compounds.<sup>93</sup>

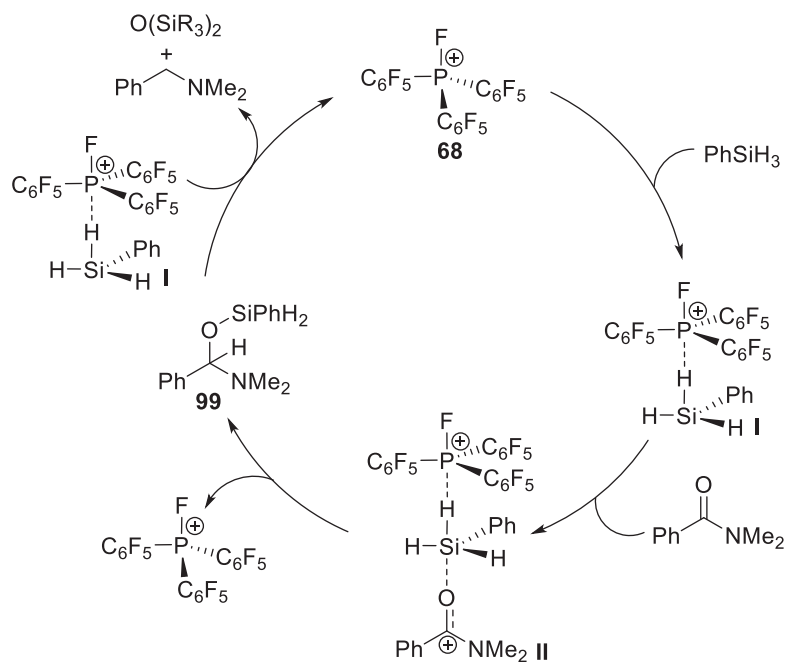
In 2016, it was found that EPC systems could be employed to reduce amides into amines via a hydrosilylated intermediate.<sup>95</sup> Two EPCs **68** and **98** were observed to readily catalyze amide reduction with low catalytic loadings, although harsh reaction conditions and long reaction times were required for quantitative conversions. Moreover, the silane reagent also played a crucial role in the effectiveness of the reaction. Silanes with lower hydricity such as  $\text{HSiMe}_3$  or  $\text{HSiPh}_3$  promoted no reduction of *N,N*-dimethylbenzamide, whereas the more hydridic  $\text{PhSiH}_3$  gave almost quantitative conversion. A wide scope of aliphatic and aromatic amides was subsequently reduced to their corresponding amines in up to 99% conversion with concomitant loss of siloxane (**Scheme 94**). A series of 2,2,2-trifluoroacetamides were also chemoselectively reduced into their respective 2,2,2-trifluoroethyl amines in good to excellent isolated yield; however, limitations on the efficiency of the protocol were observed with highly basic amides, which were recalcitrant toward reduction. This was attributed to irreversible binding of the EPC to the substrate, thus poisoning the catalyst.<sup>95</sup>

The reaction mechanism of the EPC catalyzed amide reductions was based upon previous FLP-like EPC catalyzed hydrosilylations.<sup>83,84,95</sup> It was proposed that upon addition of the silane to the EPC **68**, the Si–H bond was weakened through co-ordination of the hydride with the Lewis acidic phosphorus atom (**Scheme 95, I**). Nucleophilic attack of the amide toward the activated silane





**Scheme 94** FLP-mediated reduction of amides into amines via a hydrosilylated intermediate.<sup>95</sup>



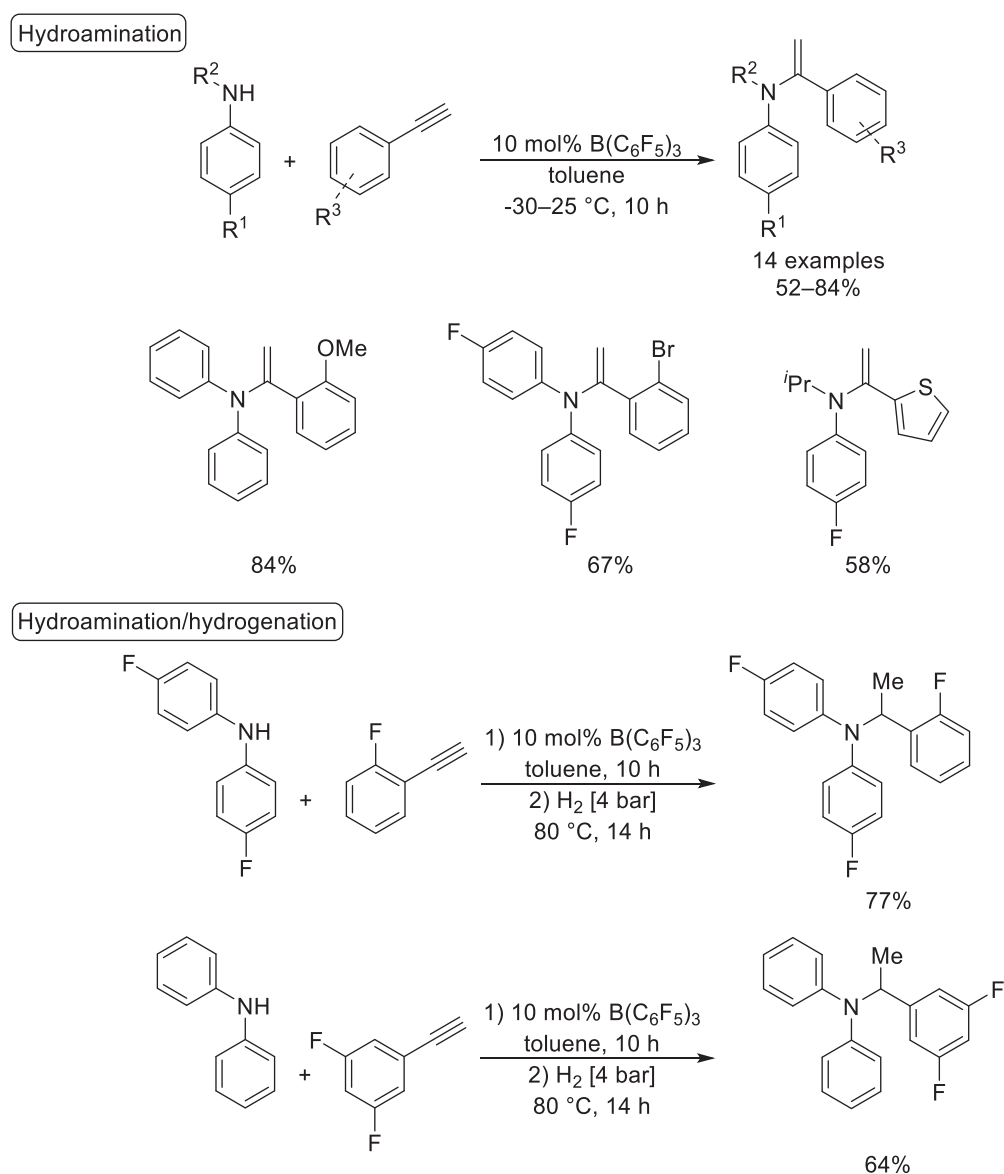
**Scheme 95** Proposed mechanism of FLP-mediated reduction of amides into amines.<sup>95</sup>

then occurred (Scheme 95, II) which formed a silylated intermediate 99. This intermediate further reacted with another equivalent of activated silane (Scheme 95, I) to liberate the amine, the silylether, and the EPC catalyst 68 (Scheme 95).<sup>95</sup>

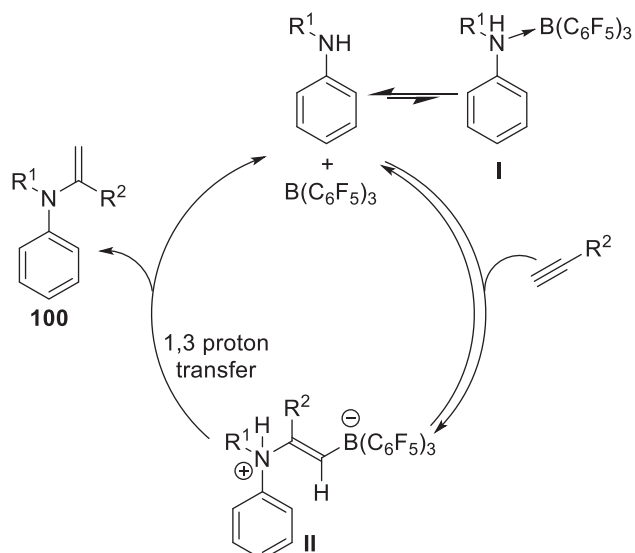
#### 1.06.4 FLP-mediated hydroamination

$B(C_6F_5)_3$  was first adapted for use as a hydroamination catalyst by Stephan in 2013. 14 enamines were formed in good to excellent yield as the Markovnikov addition product, following the  $B(C_6F_5)_3$ -mediated 1,2-addition of a secondary amine to an alkyne. For efficient reactivity, slow addition of the alkyne into the reaction mixture was necessary and low temperatures were required to enhance product yield in certain circumstances (Scheme 96). Inspired by the FLP-like nature of the hydroamination catalysis and the well-established reduction catalysis mediated by FLPs, two examples of one-pot tandem hydroamination/hydrogenation reactions were also demonstrated to directly form tertiary amines in good yield (Scheme 96).<sup>96</sup>

The observed enamine products from Markovnikov addition suggested the reaction to be FLP-like in nature, with the amine substrate also acting as the FLP's Lewis basic component (Scheme 97, I). It was proposed that the alkyne initially coordinated to  $B(C_6F_5)_3$  resulting in an adduct between the terminal alkyne carbon and the Lewis acidic boron atom. Nucleophilic attack by the amine then resulted in the formation of a zwitterionic intermediate (Scheme 97, II) wherein the alkyne was activated between



**Scheme 96**  $B(C_6F_5)_3$  mediated hydroamination of terminal alkynes and  $B(C_6F_5)_3$  mediated tandem hydroamination/hydrogenation of alkynes.<sup>96</sup>



**Scheme 97** Mechanism of  $B(C_6F_5)_3$  mediated hydroamination of terminal alkynes.<sup>96</sup>

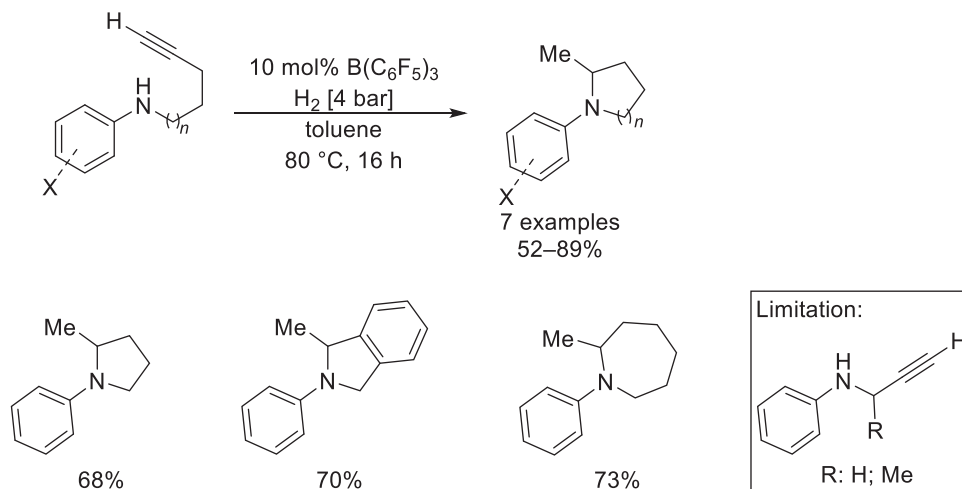
the Lewis acidic and basic centers. A subsequent 1,3-proton transfer furnished the enamine product **100**, whilst regenerating the Lewis acid catalyst (**Scheme 97**).<sup>96</sup>

The  $B(C_6F_5)_3$  catalyzed hydroamination protocol was later extended toward tandem intramolecular hydroamination/hydrogenation reactions for the preparation of cyclic amines.<sup>97</sup> Seven substrates were reported to form their respective *N*-heterocycles in good to high yields using similar conditions reported for the intermolecular reaction.<sup>96</sup> Whilst the preparation of five, six and seven-membered heterocycles was successful, the attempted cyclization of *N*-propynyl-substituted anilines into their respective aziridines could not be achieved under the explored conditions (**Scheme 98**).<sup>97</sup>

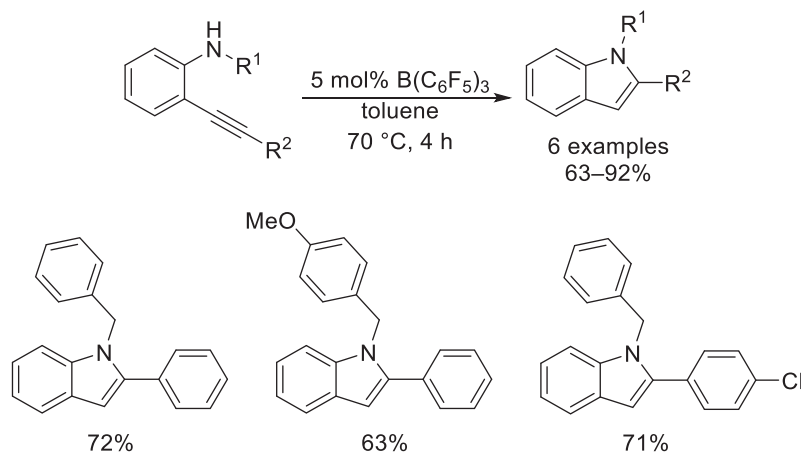
Paradies later applied Lewis acidic boranes toward the synthesis of indoles via intramolecular hydroamination; however, only  $B(C_6F_5)_3$  was able to promote the reaction while neither of weakly Lewis acidic boranes such  $B(2,6-F_2C_6H_3)_3$  **17** or  $B(2,4,6-F_3C_6H_2)_3$  **47** could do so. Six indoles were successfully synthesized in good to excellent yield through 5-*endo*-dig cyclizations (**Scheme 99**). Limitation to the protocol was noted when the nucleophilicity of the nitrogen atom was reduced whereupon no reactivity was observed. Additionally, some substrates were able to form adducts with  $B(C_6F_5)_3$  but decomposed under elevated temperatures without forming the desired indole.<sup>98</sup>

### 1.06.5 FLP-mediated C–H borylation

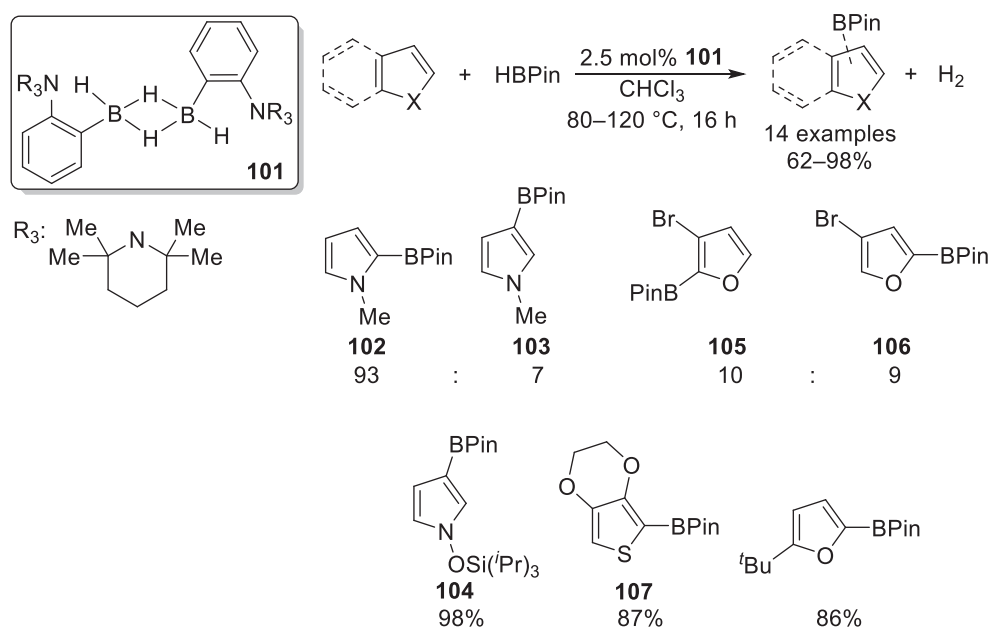
In 2015, Fontaine demonstrated the C–H activation and subsequent borylation of heteroarenes with the use of intramolecular FLP **101** (**Scheme 100**). The intramolecular catalyst was designed specifically for this reaction: the position of the Lewis acidic boron



**Scheme 98**  $B(C_6F_5)_3$  mediated tandem hydroamination/hydrogenation of alkynes.<sup>97</sup>



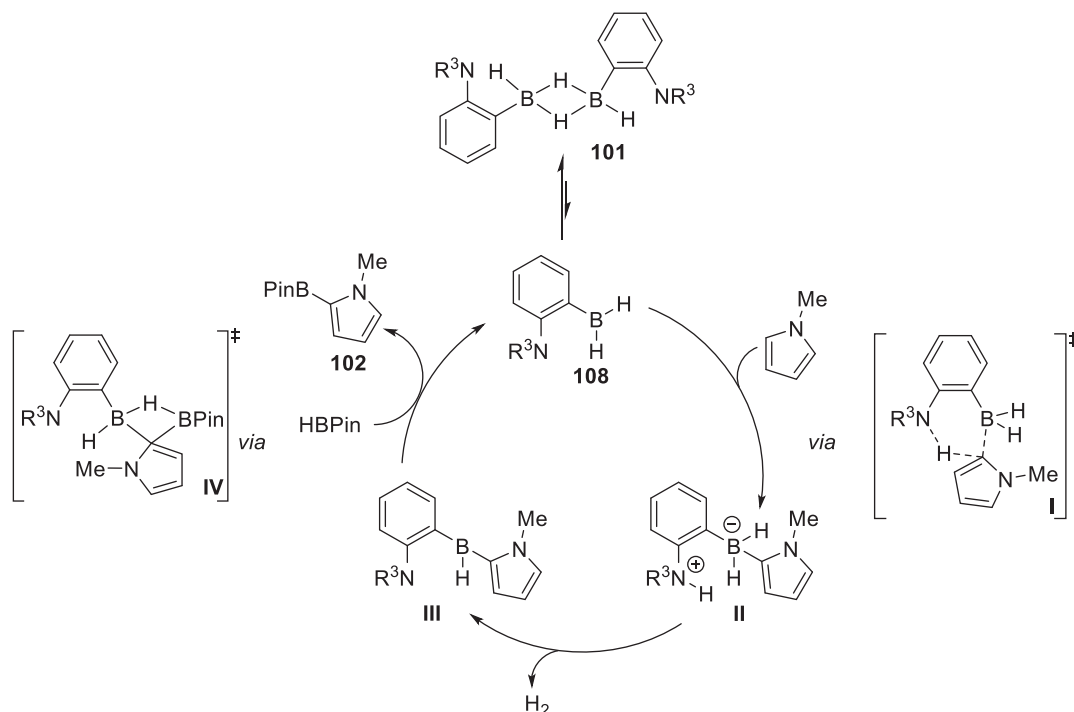
**Scheme 99**  $B(C_6F_5)_3$  catalyzed indole synthesis through intramolecular hydroamination.<sup>98</sup>



**Scheme 100** FLP-mediated borylation of heteroarenes.<sup>99</sup>

atom was constructed to be in close proximity to the heteroarene's nucleophilic carbon, whilst the base was designed to be bulky in order to prevent any possible dimerization which could occur following proton abstraction of the heteroarene. In solution, **101** was observed to be in equilibrium between a monomeric and dimeric form. Catalyst **101** was observed to catalyze the borylation of 13 oxygen, nitrogen and sulfur containing heterocycles in high conversions. The position of borylation was dependent upon the substrate. Initially 1-methylpyrrole was investigated toward borylation, which formed two regioisomers: 2-borylated **102** and 3-borylated **103** in a 93:7 ratio. Bulkier *N*-protecting groups on pyrrole such as triisopropyl silyl ether (TIPS) **104** and trimethylsilyl (TMS) enabled the pyrroles to undergo the borylation specifically at the 3 position, whilst protection with a benzyl group reduced selectivity significantly toward a 3:2 ratio. Electron-rich furan derivatives generally underwent borylation with exclusive selectivity at the C<sub>2</sub> position in high to excellent conversion. Notably, 3-bromofuran required harsher conditions (increased temperature, time and catalytic loading) to undergo borylation. Although selectivity was heavily decreased, yielding **105** and **106** in a 10:9 ratio, 90% overall conversion was observed. Only electrophilic thiophene derivatives were amenable to reaction. 3,4-Ethylenedioxythiophene in particular was observed to form either monoborylated **107** or diborylated products in 87% and 99% yield respectively, depending upon the stoichiometry of HBPin applied.<sup>99</sup>

With the aid of DFT and kinetic studies, a mechanism was proposed for the borylation of 1-methylpyrrole. Initial dissociation of the FLP dimer **101** resulted in the formation of the monomeric active catalyst **108**. In the rate determining step of the cycle, **108** proceeded to activate the C–H bond of the 1-methylpyrrole via a four-membered transition state (**Scheme 101, I**), generating zwitterionic species (**Scheme 101, II**). A subsequent rapid H<sub>2</sub> release from this zwitterionic species formed a borohydride intermediate



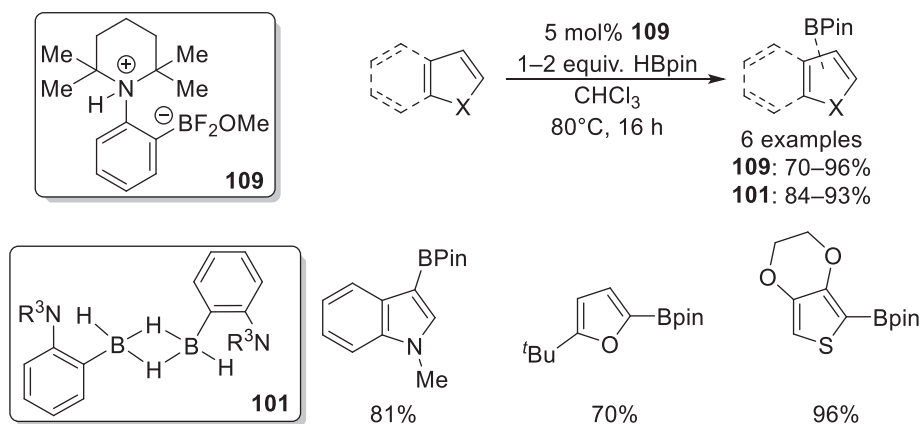
**Scheme 101** Mechanism of FLP-mediated borylation of heteroarenes.<sup>99</sup>

(**Scheme 101, III**), from which product **102** was obtained via a four-center sigma bond metathesis with HBPIn (**Scheme 101, IV**). Activation at the C<sub>2</sub> position was found to require only 0.4 kcal mol<sup>-1</sup> less energy compared to the C<sub>3</sub> position, thus accounting for the formation of two regioisomers.<sup>99</sup>

One year later, Fontaine improved this protocol with the introduction of an oxygen and moisture stable precatalyst **109**, thus precluding the necessity for Schlenk techniques or glove boxes for the catalytic borylation transformation (**Scheme 102**). Precatalyst **109** differed only by the installation of a fluoroborate salt in favor of the dihydroborane group in **101**. Deprotection of **109** to the active dihydroborane catalyst **101** was mediated by the borylating agent HBPIn, thus no other additive was required for the reaction. A brief substrate scope of six heteroarenes found that the catalytic activity of **109** was comparable to **101**, despite the bench-stable nature of the precatalyst.<sup>100</sup>

Repo later discovered that 2-aminophenylboranes were able to catalyze the C–H activation of heteroarenes, as the rigid phenyl bridge between the acidic and basic sites provided an optimal geometry for efficient reactivity. It was demonstrated that the catalyst's reactivity was more affected by steric factors and the Lewis acidity and basicity of its boron and nitrogen atoms, rather than being sensitive to the substituents situated upon the acidic and basic sites.<sup>101</sup>

With these observations in hand, Fontaine subsequently investigated modifications to the amine moiety of catalyst **101**, citing low yields and expensive synthesis as motivation to replace the TMP unit. Thus, smaller and more readily available amine



**Scheme 102** FLP-mediated borylation of heteroarenes with a bench stable pre-catalyst.<sup>100</sup>

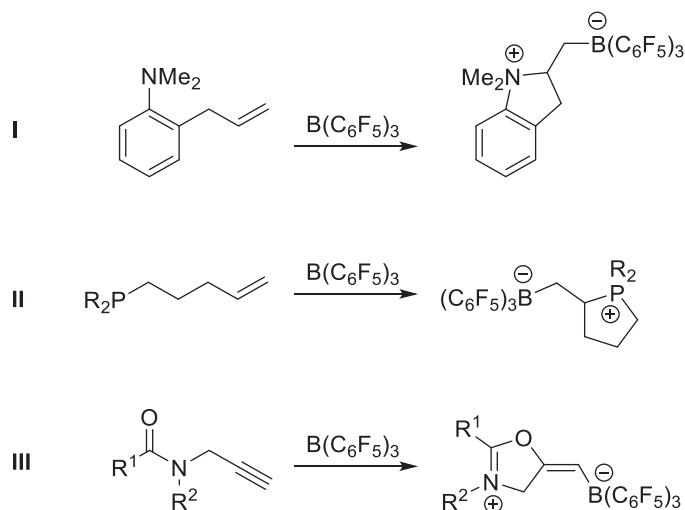


derivatives such as piperidine, diethylamine and dimethylamine were installed onto the intramolecular FLP catalyst. Moreover, it was observed that these smaller FLPs were up to 15 times more reactive than **101**. DFT and kinetic studies revealed this increase in activity was due to the change in the rate determining step; in the presence of smaller amines the rate determining step became the initial dimer dissociation, rather than the C–H activation step observed for **101**.<sup>102</sup>

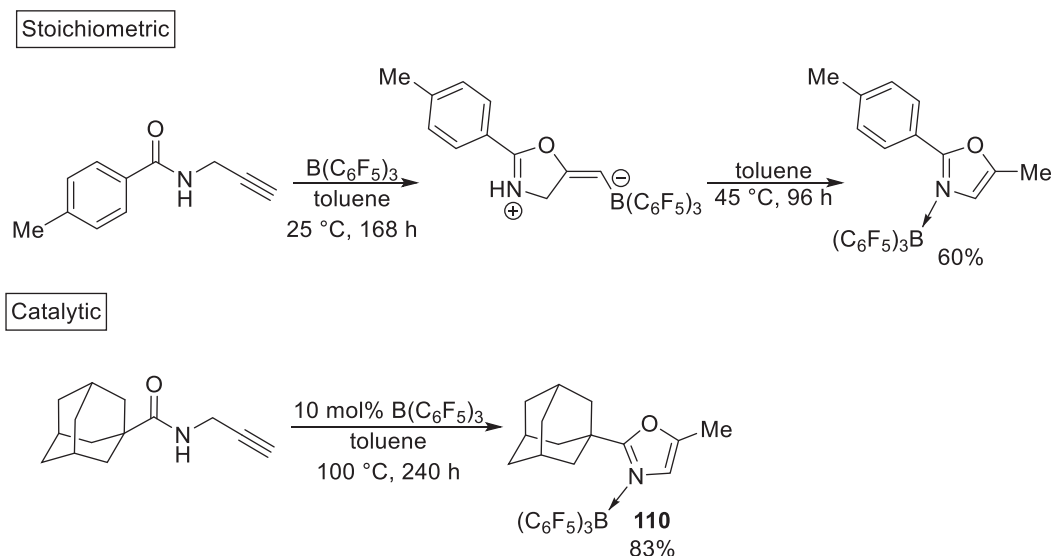
### 1.06.6 FLP-mediated cyclization reactions

Stoichiometric cyclization reactions involving FLPs are well documented. Examples include: intramolecular additions of amines to unsaturated C–C bonds to form zwitterionic nitrogen containing heterocycles (**Scheme 103, I**)<sup>103</sup>; three-component cyclizations of phosphines, boranes and olefins to form zwitterionic phosphorus containing heterocycles (**Scheme 103, II**)<sup>104</sup>; and B(C<sub>6</sub>F<sub>5</sub>)<sub>3</sub> mediated cyclization of propargyl amides to form methylene-oxazolines (**Scheme 103, III**).<sup>105</sup>

Notably, when B(C<sub>6</sub>F<sub>5</sub>)<sub>3</sub> mediated cyclization was performed on N–H propargyl amides with an aryl substituent, the methylene-oxazoline products were observed to isomerize into oxazoles, an important heterocyclic moiety found in anti-bacterial and anti-fungal agents.<sup>105,106</sup> Unfortunately, whilst 16 examples of B(C<sub>6</sub>F<sub>5</sub>)<sub>3</sub> mediated propargyl amide cyclizations into their respective methylene-oxazoline products were reported, only four isomerizations were observed (**Scheme 104**). This isomerization required gentle heating over 4 days, and only one oxazole was isolated out of the four prepared. This reaction was



**Scheme 103** Examples of stoichiometric FLP-mediated cyclizations.<sup>103–105</sup>



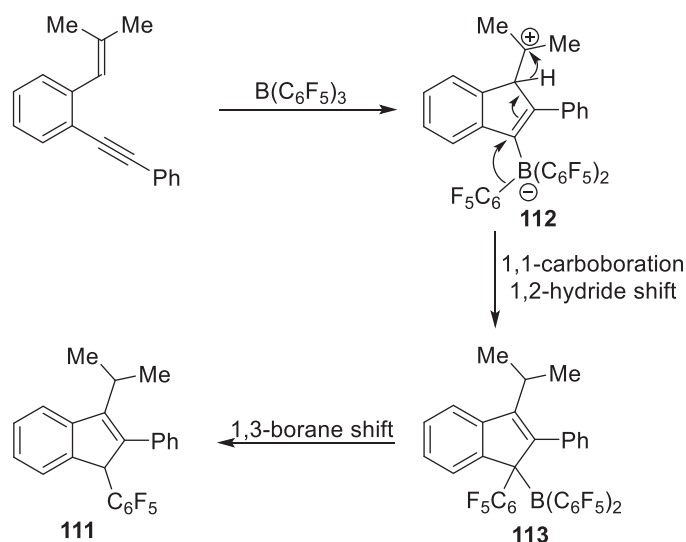
**Scheme 104** B(C<sub>6</sub>F<sub>5</sub>)<sub>3</sub> mediated cyclization and subsequent isomerization of propargyl amides.<sup>105</sup>

initially perceived to be incapable of catalysis as the dative bond  $N \rightarrow B$  in the isolated compound was too strong to permit the release of  $B(C_6F_5)_3$ <sup>105</sup>; however, when the propargyl amide was installed with an adamantyl group, steric frustration was induced in the dative  $N \rightarrow B$  bond prompting the release of the Lewis acid. The formation of oxazole **110** in 83% yield was thus observed from its corresponding propargyl amide when 10 mol% catalytic loading of  $B(C_6F_5)_3$  was applied. Harsh conditions were essential (100 °C, 240 h), but this was the first example of catalytic transition metal-free cyclization of propargyl amides.<sup>105</sup>

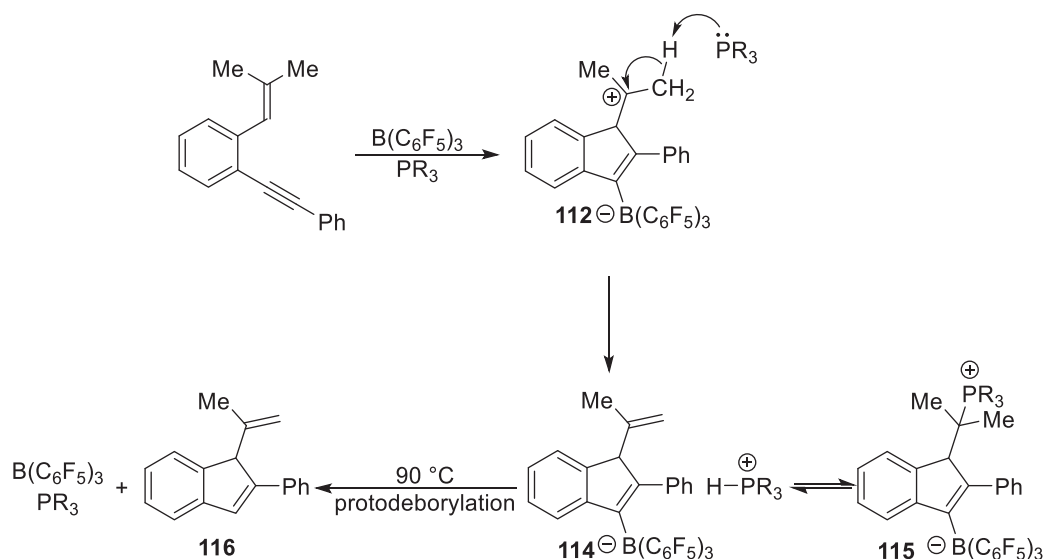
FLPs were later observed to catalyze the cycloisomerization of 1,5-enynes.<sup>107</sup> Initial stoichiometric reactions between 1,5-enyne and  $B(C_6F_5)_3$  resulted in the formation of 5-*endo*-dig cyclized product **111** (Scheme 105). DFT probes suggested that the borane initially activated the alkyne, to form a reactive carbocation. Addition of the olefinic bond to this carbocation resulted in a cyclization and the formation of zwitterionic intermediate **112**. The formed reactive carbocation subsequently rearranged via a 1,1-carbaboration and a 1,2-hydride shift to form intermediate **113**, which upon a final 1,3-borane shift, furnished the stable borane product **111**.<sup>107</sup>

When a phosphine Lewis base was included in the cycloisomerization reaction, the 1,1-carbaboration was prevented. Instead, the phosphine was observed to promote proton abstraction from carbocation intermediate **112**, forming the stable onium borate intermediate **114**, which existed in equilibrium with its addition product **115**. Heating to 90 °C promoted protodeborylation, furnishing the cycloisomerized product **116** and liberating the FLP (Scheme 106).<sup>107</sup>

With proof of catalytic cycloisomerization, the protocol was developed further to variously substituted enynes using 20 mol% catalytic loading of  $B(C_6F_5)_3$  and  $PPh_3$ . Overall, 7 examples were presented with NMR yields ranging from 50% to 98%. Electron



**Scheme 105** Synthesis of 5-*endo*-dig cyclized product **82** from 1,5-enyne and  $B(C_6F_5)_3$ .<sup>107</sup>

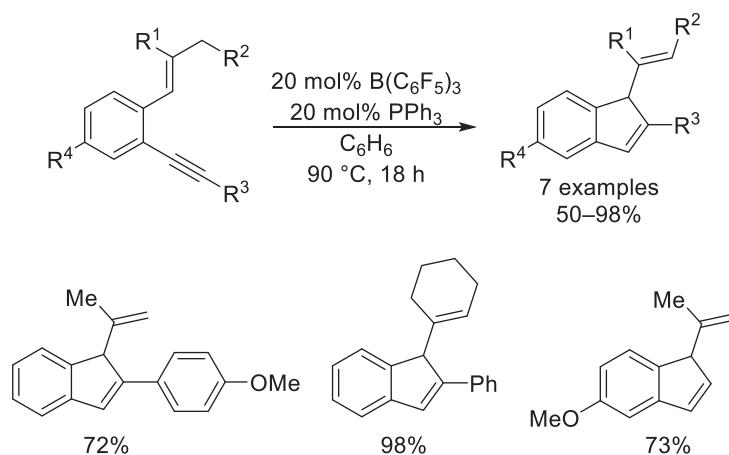


**Scheme 106** Mechanism of FLP-mediated cycloisomerization of 1,5-enynes.<sup>107</sup>

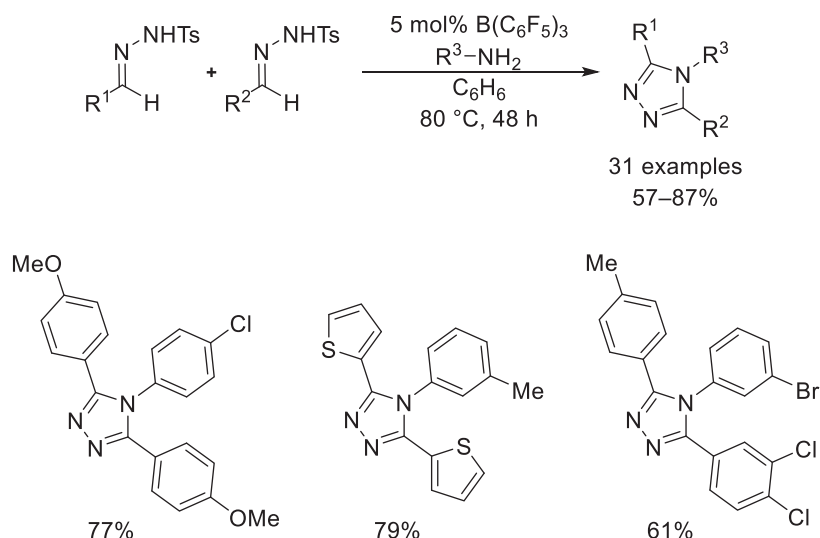
donating substitutions on the alkyne moiety provided better results whereas electron withdrawing and thiophenyl substitutions decreased the yields. Moreover, exchanging the core phenyl ring with heterocyclic furanyl or thiophenyl groups caused the catalytic cyclization to completely cease, presumably due to the increased distance between alkene and alkyne functional groups (**Scheme 107**).<sup>107</sup>

$B(C_6F_5)_3$  was also observed to act as a dual-role catalyst in the preparation of 3,4,5-triaryl-1,2,4-triazoles from *N*-tosylhydrazones and anilines (**Scheme 108**). 3,4,5-triaryl-1,2,4-triazole motifs are found in a range of pharmaceutical drugs, pesticides, and organic photovoltaic cells; however, many of their preparations are restricted by large excesses of reagents or narrow functional group tolerance, thus this one-pot metal-free system was shown to be particularly useful.<sup>108</sup> Symmetrical 1,2,4-triazoles were obtained in good to excellent yield after 48 h, using two equivalents of hydrazone and one equivalent of amine. Additionally, the protocol was extended to asymmetrical 1,2,4-triazoles by using two different hydrazones, yielding the asymmetrical triazole in excellent yield. Due to the potential low selectivity, the two different *N*-tosylhydrazone reagents were required to possess different electronic properties on their aryl groups, otherwise a 1:1:1 ratio between the symmetrical and asymmetrical products was observed.<sup>108</sup>

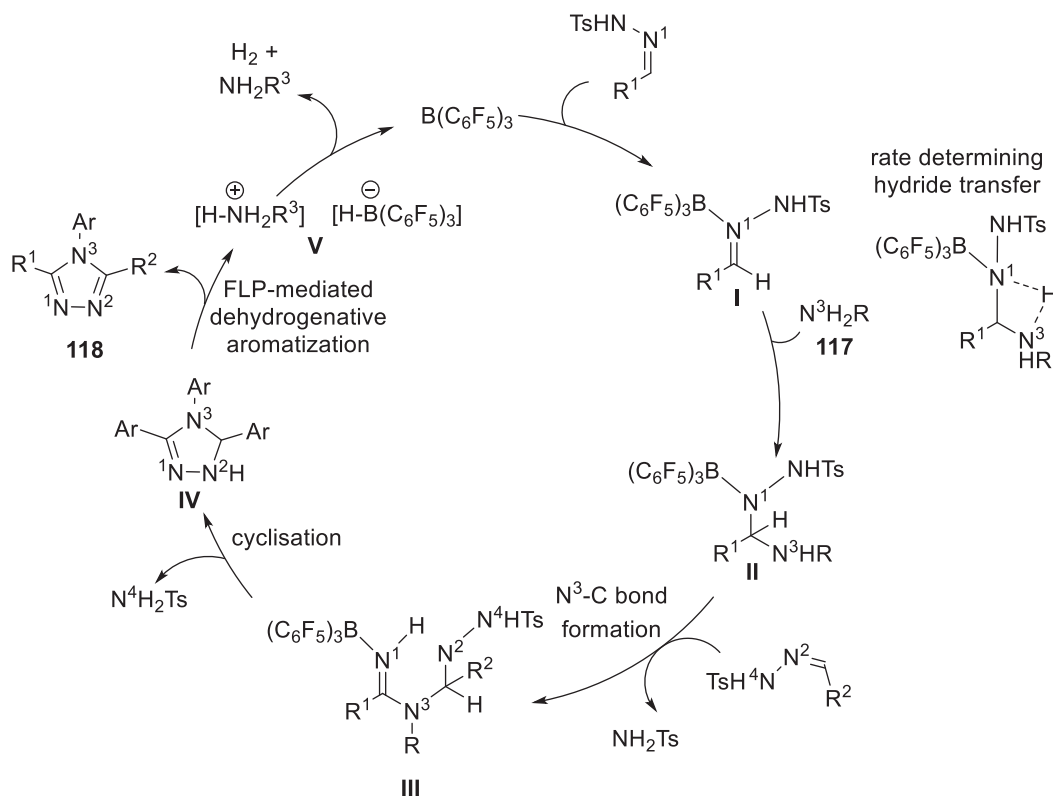
A combined experimental and computational approach allowed for the elucidation of the catalytic cycle, wherein  $B(C_6F_5)_3$  acted as both a Lewis acid catalyst and as the Lewis acidic component of an FLP at different stages. The cycle commenced with the formation of an adduct between  $B(C_6F_5)_3$  and *N*-tosylhydrazone, in which the boron coordinated toward the  $sp^2$ -hybridized nitrogen atom (**Scheme 109, I**). The aniline **117** then coordinated to this adduct, forming a zwitterionic complex which performed a rate-determining intramolecular hydride transfer from  $N^3$  to  $N^1$ , thus furnishing an adduct intermediate (**Scheme 109, II**), which upon reaction with a second equivalent of *N*-tosylhydrazone, resulted in the formation of an unstable intermediate (**Scheme 109, III**) through loss of a  $NH_2Ts$  fragment. Intermediate (**Scheme 109, III**) then rapidly cyclized to form a heterocycle (**Scheme 109, IV**).



**Scheme 107** FLP-mediated cycloisomerization of 1,5-enynes.<sup>107</sup>



**Scheme 108**  $B(C_6F_5)_3$ -mediated synthesis of 3,4,5-triaryl-1,2,4-triazoles.<sup>108</sup>



**Scheme 109** Mechanism of FLP-mediated synthesis of 3,4,5-triaryl-1,2,4-triazoles.<sup>108</sup>

via initial dissociation of the borane from  $N^1$  and subsequent protonation of  $N^4$ , resulting in an intramolecular nucleophilic attack of  $N^2$  to  $N^1$  to form the new N–N bond with concomitant loss of another  $NH_2Ts$  fragment. At this stage  $B(C_6F_5)_3$  switched role from a Lewis acid catalyst to be part of an FLP catalyst, facilitating dehydrogenative aromatization to liberate the triazole product **118** and the zwitterionic FLP (Scheme 109, V). Finally, release of  $H_2$  from this FLP liberated aniline and regenerated the borane catalyst for further turnovers (Scheme 109).<sup>108</sup>

### 1.06.7 FLP-mediated reduction of $CO_2$

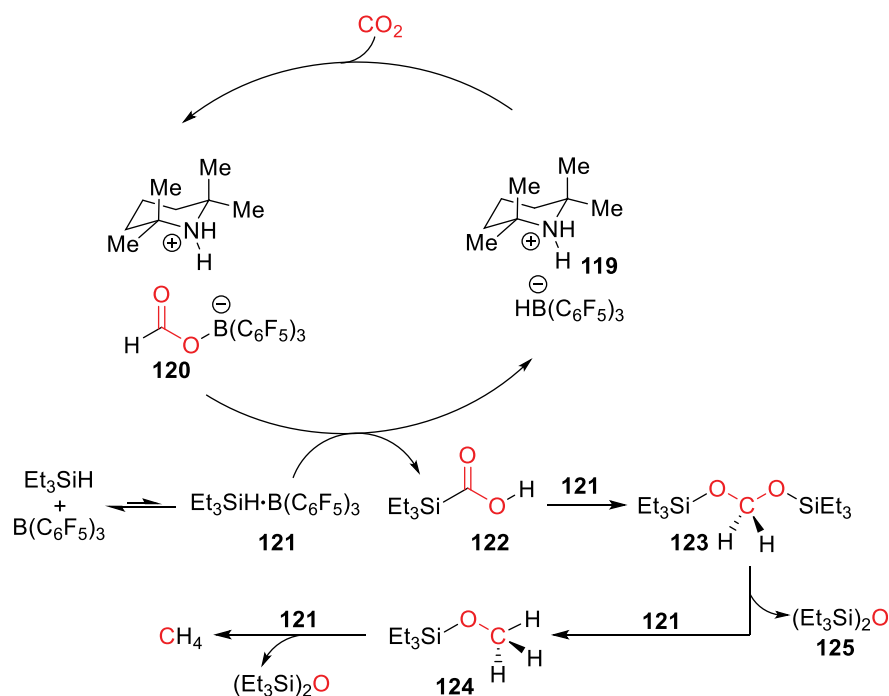
It is well known that increasing levels of carbon dioxide in the Earth's atmosphere is one of the main contributing factors toward global warming. One method to reduce the levels of this greenhouse gas in our atmosphere is to use it as a chemical feedstock. For example,  $CO_2$  can be reduced to form methanol, which can be used for electricity generation in fuel cells and can serve as a precursor for many organic molecules. Such utilization of  $CO_2$  is a challenging task due to its high thermodynamic and kinetic stability, thus harsh conditions and transition-metal catalysts are generally required for the direct reduction of  $CO_2$  into methanol with molecular  $H_2$ .<sup>109</sup> As a result of this, the application of metal-free catalysts toward  $CO_2$  reduction has become an up-and-coming field of research.<sup>110</sup>

Following Stephan and Erker's discovery that an FLP comprised of  $B(C_6F_5)_3$  and  $P^tBu_3$  could reversibly bind to  $CO_2$  under mild conditions,<sup>111</sup> the search for FLPs which are able to promote  $CO_2$  reduction has become a target for main-group chemists worldwide. The first examples of FLP-mediated reduction of  $CO_2$  with gaseous  $H_2$  were stoichiometric. An FLP comprised of TMP **62** and  $B(C_6F_5)_3$  was observed to quantitatively reduce  $CO_2$  into  $CH_3OB(C_6F_5)_2$ , from which methanol could be obtained by vacuum distillation, albeit in low yields of 17–25%.<sup>112</sup> A subsequent report found that stoichiometric FLP-mediated  $CO_2$  reduction into methanol could occur at room temperature when  $BH_3 \cdot NH_3$  was employed as a hydrogen source.<sup>113</sup> A joint publication from the groups of Stephan and Fontaine found an aminoborane FLP capable of activating both  $H_2$  and  $CO_2$ ; however, this system was unable to release the reduced products.<sup>114</sup> The first successful catalytic reduction of  $CO_2$  into methane was reported by Piers; however, catalytic efficiency was low. The intermolecular FLP caused an unfavorably high entropy within the system and 18 equivalents of triethylsilane reductant were required for efficient reaction.<sup>115</sup> A proposed mechanism suggested that  $B(C_6F_5)_3$  would form an FLP with both TMP **62** and an adduct with triethylsilane at different stages in the reaction. Initially, the  $B(C_6F_5)_3 \cdot TMP$  adduct activated hydrogen **119**. This activated complex could then go on to activate  $CO_2$  to form formatoborate intermediate **120**. Meanwhile, the  $B(C_6F_5)_3 \cdot HSiEt_3$  **121** adduct was formed, which was able to hydrosilate formatoborate **120** to form a formatosilane **122**.

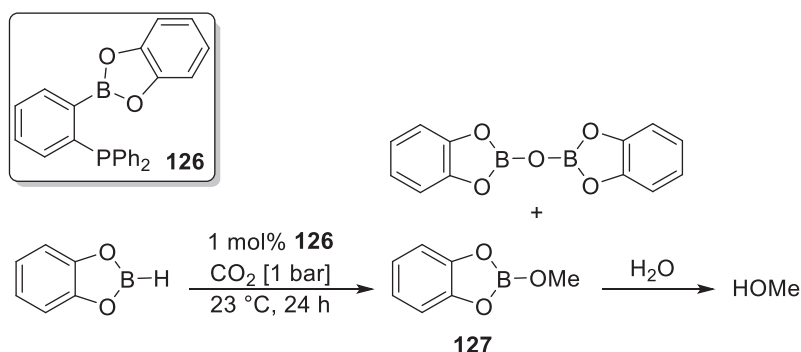
Sequential hydrosilylation of the formatosilane by the adduct **121** resulted in bis(triethylsilyl)acetal **123**, followed by silylether **124** and finally methane through the loss of disiloxane **125** (Scheme 110).<sup>115</sup>

The first highly efficient FLP-catalyzed reduction of CO<sub>2</sub> was reported by Fontaine in 2013, with the use of an air-stable aryl-bridged phosphinoborane FLP **126**. Reaction of catecholborane with CO<sub>2</sub> in the presence of a catalytic amount of **126** was observed to form methoxyborane **127** with concomitant loss of a B–O–B dimer. Hydrolysis of **127** liberated methanol readily. This transformation proceeded under mild conditions, with low CO<sub>2</sub> pressures and catalytic loading, albeit with large amounts of waste per methanol generated (Scheme 111).<sup>116</sup> A recent computational study by Grimme observed that Fontaine's catalytic system was more active than the ensuant systems reported by Stephan,<sup>117</sup> and Cantat.<sup>118,119</sup>

An extensive combined experimental and DFT study elucidated the mechanism of this reaction, revealing that the phosphinoborane did not adhere to conventional FLP-style small molecule activation. Instead, it was observed that the Lewis basic center activated the HBCat reducing agent, whilst the Lewis acidic/basic centers promoted catalysis through assisting the release of the reaction products. It was suggested that the Lewis basic center of the phosphinoborane initially activated the catecholborane, thereby forming an adduct. This resulted in a hydride transfer from the borane to the carbon of CO<sub>2</sub>, thereby forming a formate anion which could co-ordinate to the Lewis acidic center of the phosphinoborane to form intermediate **120**. This intermediate existed in equilibrium with **129**, wherein the nucleophilic catecholborane co-ordinated to the CO<sub>2</sub> rather than the Lewis basic component of the phosphinoborane. Reaction with a second equivalent of catecholborane resulted in intermediate **130**, which was subsequently reduced to form the formaldehyde phosphinoborane adduct **131**. Finally, this species was reduced by another equivalent of catecholborane to form the methoxyborane product **132** (Scheme 112).<sup>120</sup>

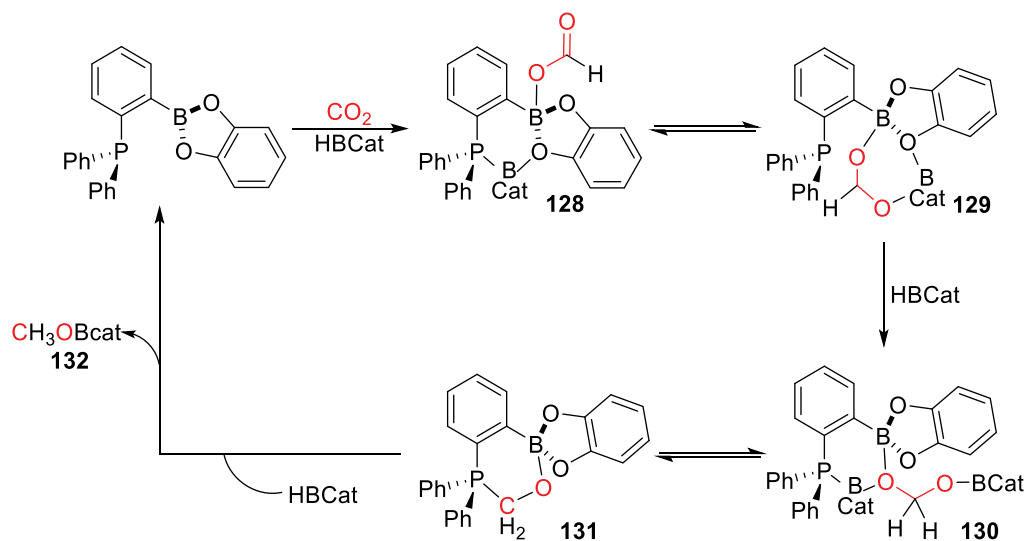


Scheme 110 FLP-mediated reduction of CO<sub>2</sub> into methane.<sup>115</sup>



Scheme 111 FLP-mediated reduction of CO<sub>2</sub> into methanol via a methoxyborane intermediate.<sup>116</sup>

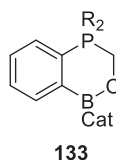




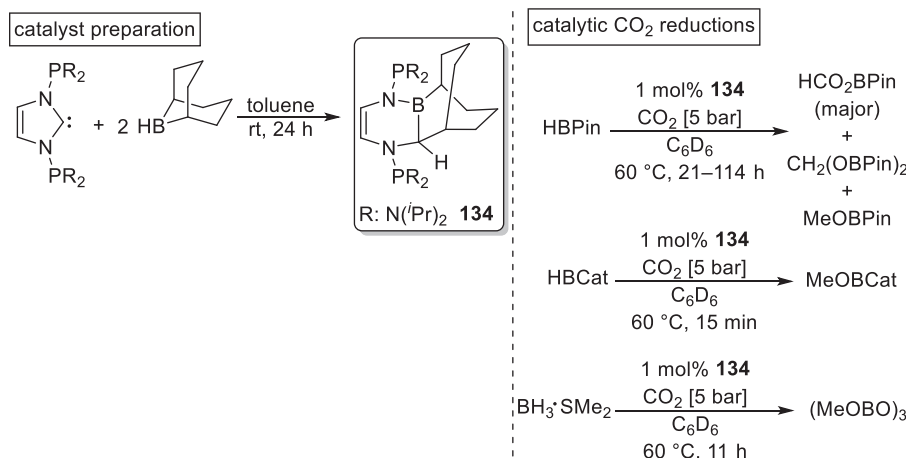
**Scheme 112** Proposed mechanism of FLP-mediated reduction of CO<sub>2</sub> into methanol via a methoxyborane intermediate.<sup>120</sup>

Subsequent spectroscopic and computational mechanistic studies identified that phosphinoborane **126** was a precatalyst and rather, the formaldehyde phosphinoborane adduct **133** (**Fig. 8**) acted as the active catalyst in the reaction. Experimental comparisons and deuteration studies confirmed that adduct **133** was more active toward CO<sub>2</sub> reduction than the phosphinoborane **126** alone.<sup>121</sup>

In 2014, Stephan reported a different intramolecular FLP catalyst **134** for CO<sub>2</sub> reduction (**Scheme 113**). This FLP was generated from reaction of two equivalents of 9-BBN with an *N*-phosphorylated NHC. Catalytic amounts of **134** were observed to promote the reduction of CO<sub>2</sub> by catecholborane under relatively mild conditions to form the corresponding methoxyborane. Notably, the identity of the reductant had a significant effect upon the product or products observed. If HBpin was used, a mixture of HCO<sub>2</sub>Bpin, CH<sub>2</sub>(OBpin)<sub>2</sub> and MeOBpin was formed, whilst when BH<sub>3</sub>·SMe<sub>2</sub> was used as the reductant, exclusively (MeOBO)<sub>3</sub> was generated.<sup>117</sup>



**Fig. 8** Identity of active catalyst in **Schemes 111 and 112**.<sup>121</sup>



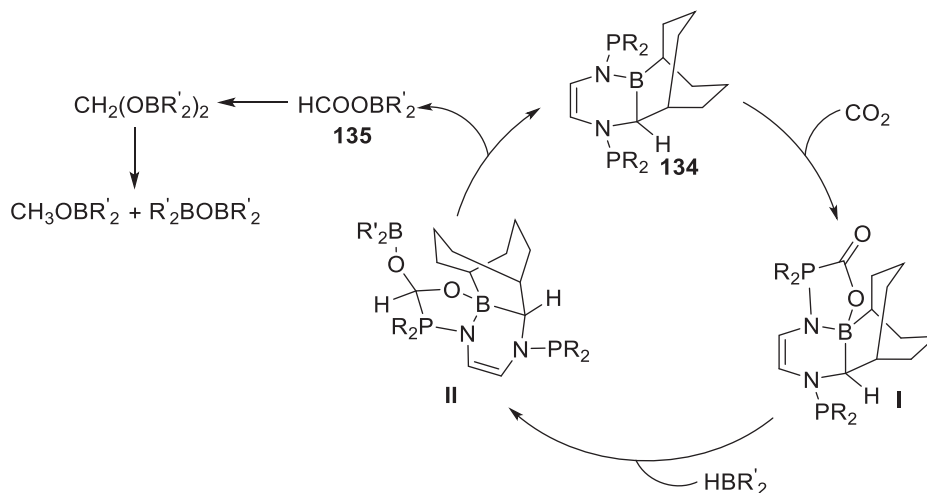
**Scheme 113** Reduction of CO<sub>2</sub> with an NHC-borane FLP **134**.<sup>117</sup>

It was proposed that **134** would initially activate  $\text{CO}_2$  between the boron and one of the phosphorus centers (**Scheme 114, I**). Subsequent reaction with the borane reductant formed cyclic intermediate (**Scheme 114, II**), which liberated the boron formate **135** to regenerate the FLP catalyst. The liberated boron formate could then be further reduced by additional borane reductants to afford the observed mixture of products depending upon which reductant was used.<sup>117</sup>

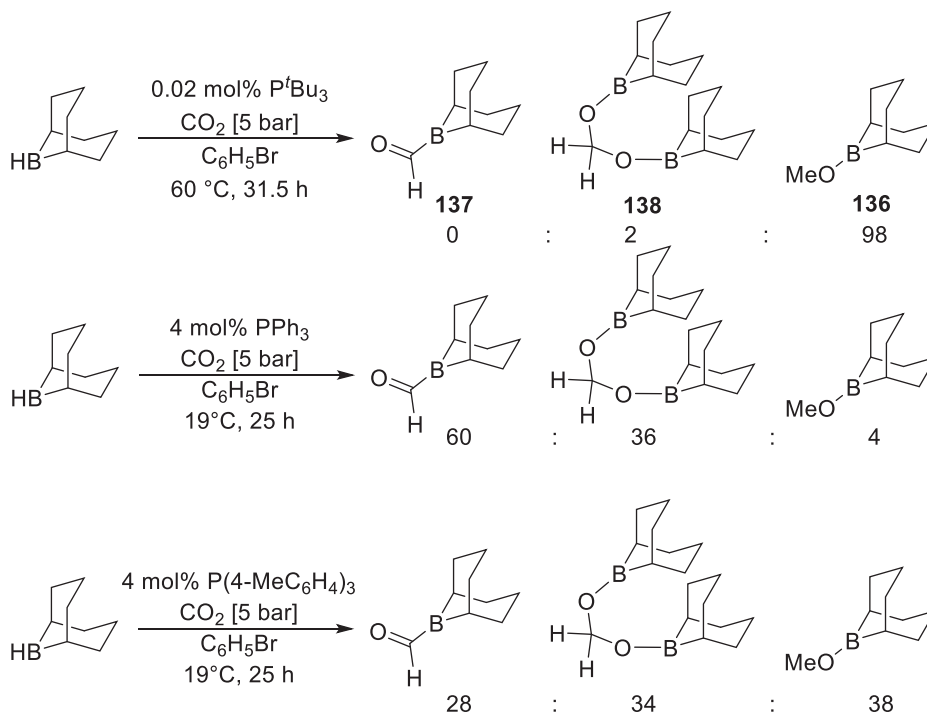
Shortly afterwards, Stephan also probed intermolecular FLP systems comprised of 9-BBN and bulky Lewis basic phosphines for  $\text{CO}_2$  reduction. Here, 9-BBN was used as a reductant, to form its corresponding methoxide product **136** upon  $\text{CO}_2$  reduction. Of the bases probed,  $\text{P}^t\text{Bu}_3$  was observed to be most selective, with other bases promoting the formation of other  $\text{CO}_2$ -reduced products such as boron-bound formate species **137** or diolate-linked compounds **138** (**Scheme 115**).<sup>122</sup>

Silylium cations are isoelectronic to boranes, thus can also be used as the Lewis acidic component of FLPs. Stephan first discussed the application of silylium cation FLPs for  $\text{CO}_2$  activation in 2015; however, these were stoichiometric reactions and formed simple adducts rather than promoting reduction.<sup>123</sup>

Cantat later introduced a base-stabilized silylium species **139**, which was able to readily react with  $\text{CO}_2$  to yield the corresponding FLP· $\text{CO}_2$  adduct salt **140** quantitatively (**Fig. 9**).<sup>118</sup> Salt **140** exhibited a greater stability compared to Stephan's silylium-based



**Scheme 114** Mechanism of  $\text{CO}_2$  reduction with an NHC-borane FLP **134**.<sup>117</sup>



**Scheme 115** Reduction of  $\text{CO}_2$  with 9-BBN.<sup>122</sup>

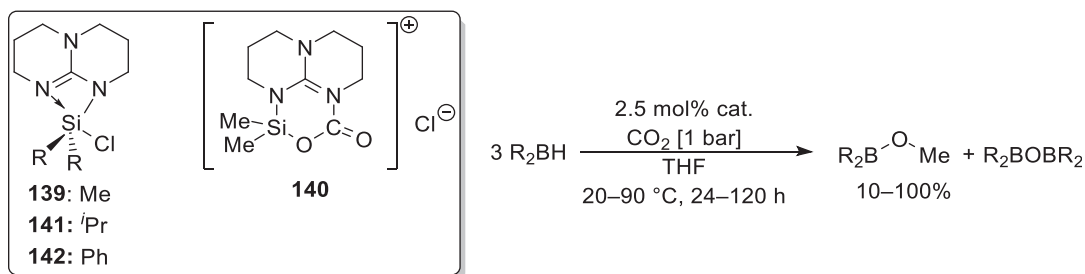


Fig. 9 Silylium cation FLPs for CO<sub>2</sub> activation.<sup>118</sup>

FLP-CO<sub>2</sub> adducts, which had been observed to decompose at room temperature.<sup>123</sup> Moreover, it was demonstrated that steric crowding around the Si<sup>+</sup> center was essential in determining whether the CO<sub>2</sub> adduct could be formed, as <sup>i</sup>Pr 141 and Ph 142 substituted silylium cations were unable to bind to CO<sub>2</sub>. Thus, it was suggested that the FLP·CO<sub>2</sub> adduct was not thermodynamically favorable and therefore could be potentially suitable for catalytic CO<sub>2</sub> reduction.<sup>118</sup> Indeed, a series of base stabilized silylium cation FLPs and their CO<sub>2</sub> adducts were observed to catalytically hydroborate CO<sub>2</sub>, yielding the corresponding methoxide quantitatively.<sup>118</sup>

### 1.06.8 Summary and outlook

In this article, the catalytic applications of frustrated Lewis pairs have been considered. From simple catalytic reduction of substrates with dihydrogen, to complex enantioselective reduction and 1,2-functionalizations, FLPs have been demonstrated to act as excellent alternatives to precious metal catalysts. With such exponential interest in the field over the past decade and a half we predict many more exciting catalytic reactions to be performed by FLPs.

### Acknowledgments

K.S. and R. L. M. would like to acknowledge the EPSRC for an Early Career Fellowship for funding (EP/R026912/1). J. L. C. would like to thank the EPSRC Cardiff/Bristol/Bath CDT in Catalysis for funding (EP/L016443/1).

### Conflicts of Interest

There are no conflicts to declare.

### References

- Stephan, D. W. "Frustrated Lewis Pair" Hydrogenations. *Org. Biomol. Chem.* **2012**, *14*, 5740–5746. <https://doi.org/10.1039/c2ob25339a>.
- Brown, H. C.; Schlesinger, H. I.; Cardon, S. Z. Studies in Stereochemistry. I. Steric Strains as a Factor in the Relative Stability of Some Co-Ordination Compounds of Boron. *J. Am. Chem. Soc.* **1942**, *64* (2), 325–329. <https://doi.org/10.1021/ja01254a031>.
- Wittig, G.; Benz, E. Über Das Verhalten von Dehydrobenzol Gegenüber Nucleophilen Und Elektrophilen Reagenzien. *Chem. Ber.* **1959**, *92* (9), 1999–2013. <https://doi.org/10.1002/cber.19590920904>.
- Tochtermann, W. Structures and Reactions of Organic Ate-Complexes. *Angew. Chem. Int. Ed.* **1966**, *5* (4), 351–371. <https://doi.org/10.1002/anie.196603511>.
- Parks, D. J.; Piers, W. E. Tris(Pentafluorophenyl)Boron-Catalyzed Hydrosilylation of Aromatic Aldehydes, Ketones, and Esters. *J. Am. Chem. Soc.* **1996**, *118* (39), 9440–9441. <https://doi.org/10.1021/ja961536g>.
- Rendler, S.; Oestreich, M. Conclusive Evidence for an S<sub>N</sub>2-Si Mechanism in the B(C<sub>6</sub>F<sub>5</sub>)<sub>3</sub>-Catalyzed Hydrosilylation of Carbonyl Compounds: Implications for the Related Hydrogenation. *Angew. Chem. Int. Ed.* **2008**, *47* (32), 5997–6000. <https://doi.org/10.1002/anie.200801675>.
- Welch, G. C.; San Juan, R. R.; Masuda, J. D.; Stephan, D. W. Reversible, Metal-Free Hydrogen Activation. *Science* **2006**, *314* (5802), 1124–1126. <https://doi.org/10.1126/science.1134230>.
- Stephan, D. W. Frustrated Lewis Pairs: A New Strategy to Small Molecule Activation and Hydrogenation Catalysis. *J. Chem. Soc. Dalton Trans.* **2009**, (17), 3129–3136. <https://doi.org/10.1039/b819621d>.
- Fontaine, F.-G.; Courtemanche, M.-A.; Légaré, M.-A.; Rochette, É. Design Principles in Frustrated Lewis Pair Catalysis for the Functionalization of Carbon Dioxide and Heterocycles. *Coord. Chem. Rev.* **2017**, *334*, 124–135. <https://doi.org/10.1016/j.ccr.2016.05.005>.
- Stephan, D. W.; Erker, G. Frustrated Lewis Pair Chemistry of Carbon, Nitrogen and Sulfur Oxides. *Chem. Sci.* **2014**, *5* (7), 2625–2641. <https://doi.org/10.1039/C4SC00395K>.
- Légaré, M.-A.; Bélanger-Chabot, G.; Dewhurst, R. D.; Welz, E.; Krummenacher, I.; Engels, B.; Braunschweig, H. Nitrogen Fixation and Reduction at Boron. *Science* **2018**, *359* (6378), 896–900. <https://doi.org/10.1126/science.aag1684>.
- Neruzzi, F. Heterogeneous Catalytic Hydrogenation. *Platin. Metals Rev.* **2012**, *56* (4), 236–241. <https://doi.org/10.1595/147106712X654187>.

13. Aldridge, S.; Downs, A. J. Hydrides of the Main-Group Metals: New Variations on an Old Theme. *Chem. Rev.* **2001**, *101* (11), 3305–3365. <https://doi.org/10.1021/cr960151d>.
14. Chase, P. A.; Welch, G. C.; Jurca, T.; Stephan, D. W. Metal-Free Catalytic Hydrogenation. *Angew. Chem. Int. Ed.* **2007**, *46* (42), 8050–8053. <https://doi.org/10.1002/anie.200702908>.
15. Spies, P.; Schwendemann, S.; Lange, S.; Kehr, G.; Fröhlich, R.; Erker, G. Metal-Free Catalytic Hydrogenation of Enamines, Imines, and Conjugated Phosphinoalkenylboranes. *Angew. Chem. Int. Ed.* **2008**, *47* (39), 7543–7546. <https://doi.org/10.1002/anie.200801432>.
16. Sumerin, V.; Schulz, F.; Atsumi, M.; Wang, C.; Nieger, M.; Leskelä, M.; Repo, T.; Pyykkö, P.; Rieger, B. Molecular Tweezers for Hydrogen: Synthesis, Characterization, and Reactivity. *J. Am. Chem. Soc.* **2008**, *130* (43), 14117–14119. <https://doi.org/10.1021/ja806627s>.
17. Wang, H.; Fröhlich, R.; Kehr, G.; Erker, G. Heterolytic Dihydrogen Activation with the 1,8-Bis(Diphenylphosphino) Naphthalene/B(C<sub>6</sub>F<sub>5</sub>)<sub>3</sub> Pair and Its Application for Metal-Free Catalytic Hydrogenation of Silyl Enol Ethers. *Chem. Commun.* **2008**, (45), 5966–5968. <https://doi.org/10.1039/b813286k>.
18. Eros, G.; Mehdi, H.; Pápai, I.; Rokob, T. A.; Király, P.; Tárkányi, G.; Soós, T. Expanding the Scope of Metal-Free Catalytic Hydrogenation through Frustrated Lewis Pair Design. *Angew. Chem. Int. Ed.* **2010**, *49* (37), 6559–6563. <https://doi.org/10.1002/anie.201001518>.
19. Scott, D. J.; Phillips, N. A.; Sapsford, J. S.; Deacy, A. C.; Fuchter, M. J.; Ashley, A. E. Versatile Catalytic Hydrogenation Using A Simple Tin(IV) Lewis Acid. *Angew. Chem. Int. Ed.* **2016**, *55* (47), 14738–14742. <https://doi.org/10.1002/anie.201606639>.
20. Sitte, N. A.; Bursch, M.; Grimme, S.; Paradies, J. Frustrated Lewis Pair Catalyzed Hydrogenation of Amides: Halides as Active Lewis Base in the Metal-Free Hydrogen Activation. *J. Am. Chem. Soc.* **2019**, *141* (1), 159–162. <https://doi.org/10.1021/jacs.8b12997>.
21. Stepen, A. J.; Bursch, M.; Grimme, S.; Stephan, D. W.; Paradies, J. Electrophilic Phosphonium Cation-Mediated Phosphane Oxide Reduction Using Oxalyl Chloride and Hydrogen. *Angew. Chem. Int. Ed.* **2018**, *57* (46), 15253–15256. <https://doi.org/10.1002/anie.201809275>.
22. Chen, D.; Klankermayer, J. Metal-Free Catalytic Hydrogenation of Imines with Tris(Perfluorophenyl) Borane. *Chem. Commun.* **2008**, (18), 2130–2131. <https://doi.org/10.1039/b801806e>.
23. Chase, P. A.; Jurca, T.; Stephan, D. W. Lewis Acid-Catalyzed Hydrogenation: B(C<sub>6</sub>F<sub>5</sub>)<sub>3</sub>-Mediated Reduction of Imines and Nitriles with H<sub>2</sub>. *Chem. Commun.* **2008**, (14), 1701–1703. <https://doi.org/10.1039/b718598g>.
24. Geier, S. J.; Chase, P. A.; Stephan, D. W. Metal-Free Reductions of N-Heterocycles via Lewis Acid Catalyzed Hydrogenation. *Chem. Commun.* **2010**, *46* (27), 4884–4886. <https://doi.org/10.1039/c0cc00719f>.
25. Stephan, D. W.; Greenberg, S.; Graham, T. W.; Chase, P.; Hastie, J. J.; Geier, S. J.; Farrell, J. M.; Brown, C. C.; Heiden, Z. M.; Welch, G. C.; Ullrich, M. Metal-Free Catalytic Hydrogenation of Polar Substrates by Frustrated Lewis Pairs. *Inorg. Chem.* **2011**, *50* (24), 12338–12348. <https://doi.org/10.1021/ci200663v>.
26. Jiang, C.; Blacque, O.; Berke, H. Metal-Free Hydrogen Activation and Hydrogenation of Imines by 1,8-Bis(Dipentafluorophenylboryl)Naphthalene. *Chem. Commun.* **2009**, (37), 5518–5520. <https://doi.org/10.1039/b909620e>.
27. Mohr, J.; Oestreich, M. B(C<sub>6</sub>F<sub>5</sub>)<sub>3</sub>-Catalyzed Hydrogenation of Oxime Ethers without Cleavage of the N–O Bond. *Angew. Chem. Int. Ed.* **2014**, *53* (48), 13278–13281. <https://doi.org/10.1002/anie.201407324>.
28. Liu, Y.; Du, H. Metal-Free Borane-Catalyzed Highly Stereoselective Hydrogenation of Pyridines. *J. Am. Chem. Soc.* **2013**, *135* (35), 12968–12971. <https://doi.org/10.1021/ja406761j>.
29. Chen, D.; Wang, Y.; Klankermayer, J. Enantioselective Hydrogenation with Chiral Frustrated Lewis Pairs. *Angew. Chem. Int. Ed.* **2010**, *49* (49), 9475–9478. <https://doi.org/10.1002/anie.201004525>.
30. Ghattas, G.; Chen, D.; Pan, F.; Klankermayer, J. Asymmetric Hydrogenation of Imines with a Recyclable Chiral Frustrated Lewis Pair Catalyst. *Dalton Trans.* **2012**, *41* (30), 9026–9028. <https://doi.org/10.1039/c2dt30536d>.
31. Heiden, Z. M.; Stephan, D. W. Metal-Free Diastereoselective Catalytic Hydrogenations of Imines Using B(C<sub>6</sub>F<sub>5</sub>)<sub>3</sub>. *Chem. Commun.* **2011**, *47* (20), 5729–5731. <https://doi.org/10.1039/c1cc10438a>.
32. Sumerin, V.; Chernichenko, K.; Nieger, M.; Leskelä, M.; Rieger, B.; Repo, T. Highly Active Metal-Free Catalysts for Hydrogenation of Unsaturated Nitrogen-Containing Compounds. *Adv. Synth. Catal.* **2011**, *353* (11–12), 2093–2110. <https://doi.org/10.1002/adsc.201100206>.
33. Liu, Y.; Du, H. Chiral Dienes as “Ligands” for Borane-Catalyzed Metal-Free Asymmetric Hydrogenation of Imines. *J. Am. Chem. Soc.* **2013**, *135* (18), 6810–6813. <https://doi.org/10.1021/ja4025808>.
34. Wei, S.; Du, H. A Highly Enantioselective Hydrogenation of Silyl Enol Ethers Catalyzed by Chiral Frustrated Lewis Pairs. *J. Am. Chem. Soc.* **2014**, *136* (35), 12261–12264. <https://doi.org/10.1021/ja507536n>.
35. Zhang, Z.; Du, H. A Highly *Cis*-Selective and Enantioselective Metal-Free Hydrogenation of 2,3-Disubstituted Quinoxalines. *Angew. Chem. Int. Ed.* **2015**, *54* (2), 623–626. <https://doi.org/10.1002/anie.201409471>.
36. Ren, X.; Li, G.; Wei, S.; Du, H. Facile Development of Chiral Alkenylboranes from Chiral Diynes for Asymmetric Hydrogenation of Silyl Enol Ethers. *Org. Lett.* **2015**, *17* (4), 990–993. <https://doi.org/10.1021/acs.orglett.5b00085>.
37. Lindqvist, M.; Borre, K.; Axenov, K.; Kótai, B.; Nieger, M.; Leskelä, M.; Pápai, I.; Repo, T. Chiral Molecular Tweezers: Synthesis and Reactivity in Asymmetric Hydrogenation. *J. Am. Chem. Soc.* **2015**, *137* (12), 4038–4041. <https://doi.org/10.1021/ja512658m>.
38. Mahdi, T.; Stephan, D. W. Enabling Catalytic Ketone Hydrogenation by Frustrated Lewis Pairs. *J. Am. Chem. Soc.* **2014**, *136* (45), 15809–15812. <https://doi.org/10.1021/ja508829x>.
39. Scott, D. J.; Fuchter, M. J.; Ashley, A. E. Nonmetal Catalyzed Hydrogenation of Carbonyl Compounds. *J. Am. Chem. Soc.* **2014**, *136* (45), 15813–15816. <https://doi.org/10.1021/ja5088979>.
40. Mahdi, T.; Stephan, D. W. Facile Protocol for Catalytic Frustrated Lewis Pair Hydrogenation and Reductive Deoxygenation of Ketones and Aldehydes. *Angew. Chem. Int. Ed.* **2015**, *54* (29), 8511–8514. <https://doi.org/10.1002/anie.201503087>.
41. Lindqvist, M.; Sarnela, N.; Sumerin, V.; Chernichenko, K.; Leskelä, M.; Repo, T. Heterolytic Dihydrogen Activation by B(C<sub>6</sub>F<sub>5</sub>)<sub>3</sub> and Carbonyl Compounds. *Dalton Trans.* **2012**, *41* (15), 4310–4312. <https://doi.org/10.1039/c2dt12268e>.
42. Fasano, V.; Ingleson, M. Recent Advances in Water-Tolerance in Frustrated Lewis Pair Chemistry. *Synthesis* **2018**, *50* (09), 1783–1795. <https://doi.org/10.1055/s-0037-1609843>.
43. Carden, J. L.; Dasgupta, A.; Melen, R. L. Halogenated Triarylboranes: Synthesis, Properties and Applications in Catalysis. *Chem. Soc. Rev.* **2020**, *49* (6), 1706–1725. <https://doi.org/10.1039/c9cs00769e>.
44. Gyömöre, Á.; Bakos, M.; Földes, T.; Pápai, I.; Domján, A.; Soós, T. Moisture-Tolerant Frustrated Lewis Pair Catalyst for Hydrogenation of Aldehydes and Ketones. *ACS Catal.* **2015**, *5* (9), 5366–5372. <https://doi.org/10.1021/acscatal.5b01299>.
45. Bakos, M.; Gyömöre, Á.; Domján, A.; Soós, T. Auto-Tandem Catalysis with Frustrated Lewis Pairs for Reductive Etherification of Aldehydes and Ketones. *Angew. Chem. Int. Ed.* **2017**, *56* (19), 5217–5221. <https://doi.org/10.1002/anie.201700231>.
46. Hoshimoto, Y.; Kinoshita, T.; Hazra, S.; Ohashi, M.; Ogoshi, S. Main-Group-Catalyzed Reductive Alkylation of Multiply Substituted Amines with Aldehydes Using H<sub>2</sub>. *J. Am. Chem. Soc.* **2018**, *140* (23), 7292–7300. <https://doi.org/10.1021/jacs.8b03626>.
47. Sapsford, J. S.; Scott, D. J.; Allcock, N. J.; Fuchter, M. J.; Tighe, C. J.; Ashley, A. E. Direct Reductive Amination of Carbonyl Compounds Catalyzed by a Moisture Tolerant Tin(IV) Lewis Acid. *Adv. Synth. Catal.* **2018**, *360* (6), 1066–1071. <https://doi.org/10.1002/adsc.201701418>.
48. Greb, L.; Oña-Burgos, P.; Schirmer, B.; Grimme, S.; Stephan, D. W.; Paradies, J. Metal-Free Catalytic Olefin Hydrogenation: Low-Temperature H<sub>2</sub> Activation by Frustrated Lewis Pairs. *Angew. Chem. Int. Ed.* **2012**, *51* (40), 10164–10168. <https://doi.org/10.1002/anie.201204007>.

49. Hounjet, L. J.; Bannwarth, C.; Garon, C. N.; Caputo, C. B.; Grimme, S.; Stephan, D. W. Combinations of Ethers and  $B(C_6F_5)_3$  Function as Hydrogenation Catalysts. *Angew. Chem. Int. Ed.* **2013**, *52* (29), 7492–7495. <https://doi.org/10.1002/anie.201303166>.
50. Segawa, Y.; Stephan, D. W. Metal-Free Hydrogenation Catalysis of Polycyclic Aromatic Hydrocarbons. *Chem. Commun.* **2012**, *48* (98), 11963–11965. <https://doi.org/10.1039/c2cc37190a>.
51. Greb, L.; Daniliuc, C. G.; Bergander, K.; Paradies, J. Functional-Group Tolerance in Frustrated Lewis Pairs: Hydrogenation of Nitroolefins and Acrylates. *Angew. Chem. Int. Ed.* **2013**, *52* (22), 5876–5879. <https://doi.org/10.1002/anie.201210175>.
52. Khan, I.; Manzotti, M.; Tizzard, G. J.; Coles, S. J.; Melen, R. L.; Morrill, L. C. Frustrated Lewis Pair (FLP)-Catalyzed Hydrogenation of Aza-Morita-Baylis-Hillman Adducts and Sequential Organo-FLP Catalysis. *ACS Catal.* **2017**, *7* (11), 7748–7752. <https://doi.org/10.1021/acscatal.7b03077>.
53. Inés, B.; Palomas, D.; Holle, S.; Steinberg, S.; Nicasio, J. A.; Alcarazo, M. Metal-Free Hydrogenation of Electron-Poor Allenes and Alkenes. *Angew. Chem. Int. Ed.* **2012**, *51* (49), 12367–12369. <https://doi.org/10.1002/anie.201205348>.
54. Chernichenko, K.; Madarász, Á.; Pápai, I.; Nieger, M.; Leskelä, M.; Repo, T. A Frustrated-Lewis-Pair Approach to Catalytic Reduction of Alkynes to *Cis*-Alkenes. *Nat. Chem.* **2013**, *5* (8), 718–723. <https://doi.org/10.1038/nchem.1693>.
55. Szeto, K. C.; Sahyoun, W.; Merle, N.; Castelbou, J. L.; Popoff, N.; Lefebvre, F.; Raynaud, J.; Godard, C.; Claver, C.; Delevoye, L.; Gauvin, R. M.; Taoufik, M. Development of Silica-Supported Frustrated Lewis Pairs: Highly Active Transition Metal-Free Catalysts for the Z-Selective Reduction of Alkynes. *Cat. Sci. Technol.* **2016**, *6* (3), 882–889. <https://doi.org/10.1039/c5cy01372k>.
56. Dureen, M. A.; Stephan, D. W. Terminal Alkyne Activation by Frustrated and Classical Lewis Acid/Phosphine Pairs. *J. Am. Chem. Soc.* **2009**, *131* (24), 8396–8397. <https://doi.org/10.1021/ja903650w>.
57. Gellrich, U.; Wech, F.; Hasenbeck, M. Semihydrogenation of Alkynes Catalyzed by a Pyridone Borane Complex: Frustrated Lewis Pair Reactivity and Boron-Ligand Cooperation in Concert. *Chem. A Eur. J.* **2020**. <https://doi.org/10.1002/chem.202001276>.
58. Millot, N.; Santini, C. C.; Fenet, B.; Basset, J. M. Formation and Characterization of Zwitterionic Stereoisomers from the Reaction of  $B(C_6F_5)_3$  and  $NEt_2Ph$ : (E)- and (Z)-[EtPhN<sup>+</sup>=CHCH<sub>2</sub>-B(C<sub>6</sub>F<sub>5</sub>)<sub>3</sub>]. *Eur. J. Inorg. Chem.* **2002**, *2002* (12), 3328–3335. [https://doi.org/10.1002/1099-0682\(200212\)2002:12<3328::AID-EJIC3328>3.0.CO;2-P](https://doi.org/10.1002/1099-0682(200212)2002:12<3328::AID-EJIC3328>3.0.CO;2-P).
59. Sumerin, V.; Schulz, F.; Nieger, M.; Leskelä, M.; Repo, T.; Rieger, B. Facile Heterolytic H<sub>2</sub> Activation by Amines and  $B(C_6F_5)_3$ . *Angew. Chem. Int. Ed.* **2008**, *47* (32), 6001–6003. <https://doi.org/10.1002/anie.200800935>.
60. Farrell, J. M.; Heiden, Z. M.; Stephan, D. W. Metal-Free Transfer Hydrogenation Catalysis by  $B(C_6F_5)_3$ . *Organometallics* **2011**, *30* (17), 4497–4500. <https://doi.org/10.1021/om2005832>.
61. Chatterjee, I.; Oestreich, M.  $B(C_6F_5)_3$ -Catalyzed Transfer Hydrogenation of Imines and Related Heteroarenes Using Cyclohexa-1,4-Dienes as a Dihydrogen Source. *Angew. Chem. Int. Ed.* **2015**, *54* (6), 1965–1968. <https://doi.org/10.1002/anie.201409246>.
62. Wang, Q.; Chen, J.; Feng, X.; Du, H.  $B(C_6F_5)_3$ -Catalyzed Transfer Hydrogenations of Imines with Hantzsch Esters. *Org. Biomol. Chem.* **2018**, *16* (9), 1448–1451. <https://doi.org/10.1039/c8ob00023a>.
63. Zhou, Q.; Zhang, L.; Meng, W.; Feng, X.; Yang, J.; Du, H. Borane-Catalyzed Transfer Hydrogenations of Pyridines with Ammonia Borane. *Org. Lett.* **2016**, *18* (20), 5189–5191. <https://doi.org/10.1021/acs.orglett.6b02610>.
64. Li, S.; Li, G.; Meng, W.; Du, H. A Frustrated Lewis Pair Catalyzed Asymmetric Transfer Hydrogenation of Imines Using Ammonia Borane. *J. Am. Chem. Soc.* **2016**, *138* (39), 12956–12962. <https://doi.org/10.1021/jacs.6b07245>.
65. Li, S.; Meng, W.; Du, H. Asymmetric Transfer Hydrogenations of 2,3-Disubstituted Quinoxalines with Ammonia Borane. *Org. Lett.* **2017**, *19* (10), 2604–2606. <https://doi.org/10.1021/acs.orglett.7b00935>.
66. Khan, I.; Reed-Berendt, B. G.; Melen, R. L.; Morrill, L. C. FLP-Catalyzed Transfer Hydrogenation of Silyl Enol Ethers. *Angew. Chem. Int. Ed.* **2018**, *57* (38), 12356–12359. <https://doi.org/10.1002/anie.201808800>.
67. Maier, A. F. G.; Tussing, S.; Schneider, T.; Flörke, U.; Qu, Z. W.; Grimme, S.; Paradies, J. Frustrated Lewis Pair Catalyzed Dehydrogenative Oxidation of Indolines and Other Heterocycles. *Angew. Chem. Int. Ed.* **2016**, *55* (40), 12219–12223. <https://doi.org/10.1002/anie.201606426>.
68. Kojima, M.; Kanai, M. Tris(Pentafluorophenyl)borane-Catalyzed Acceptorless Dehydrogenation of N-Heterocycles. *Angew. Chem. Int. Ed.* **2016**, *55* (40), 12224–12227. <https://doi.org/10.1002/anie.201606177>.
69. Stephan, D. W. The Broadening Reach of Frustrated Lewis Pair Chemistry. *Science* **2016**, *354*, aaf7229. <https://doi.org/10.1126/science.aaf7229>.
70. Farrell, J. M.; Hatnean, J. A.; Stephan, D. W. Activation of Hydrogen and Hydrogenation Catalysis by a Borenum Cation. *J. Am. Chem. Soc.* **2012**, *134* (38), 15728–15731. <https://doi.org/10.1021/ja307995f>.
71. Eisenberger, P.; Bestvater, B. P.; Keske, E. C.; Crudden, C. M. Hydrogenations at Room Temperature and Atmospheric Pressure with Mesoionic Carbene-Stabilized Borenum Catalysts. *Angew. Chem. Int. Ed.* **2015**, *54* (8), 2467–2471. <https://doi.org/10.1002/anie.201409250>.
72. vom Stein, T.; Peréz, M.; Dobrovetsky, R.; Winkelhaus, D.; Caputo, C. B.; Stephan, D. W. Electrophilic Fluorophosphonium Cations in Frustrated Lewis Pair Hydrogen Activation and Catalytic Hydrogenation of Olefins. *Angew. Chem. Int. Ed.* **2015**, *54* (35), 10178–10182. <https://doi.org/10.1002/anie.201504109>.
73. Pérez, M.; Caputo, C. B.; Dobrovetsky, R.; Stephan, D. W. Metal-Free Transfer Hydrogenation of Olefins via Dehydrocoupling Catalysis. *Proc. Natl. Acad. Sci. U. S. A.* **2014**, *111* (30), 10917–10921. <https://doi.org/10.1073/pnas.1407484111>.
74. Li, H.; Aquino, A. J. A.; Cordes, D. B.; Hung-Low, F.; Hase, W. L.; Krempner, C. A Zwitterionic Carbanion Frustrated by Boranes—Dihydrogen Cleavage with Weak Lewis Acids via an “Inverse” Frustrated Lewis Pair Approach. *J. Am. Chem. Soc.* **2013**, *135* (43), 16066–16069. <https://doi.org/10.1021/ja409330h>.
75. Mummadi, S.; Unruh, D. K.; Zhao, J.; Li, S.; Krempner, C. “Inverse” Frustrated Lewis Pairs—Activation of Dihydrogen with Organosuperbases and Moderate to Weak Lewis Acids. *J. Am. Chem. Soc.* **2016**, *138* (10), 3286–3289. <https://doi.org/10.1021/jacs.5b13545>.
76. Mummadi, S.; Brar, A.; Wang, G.; Kenefake, D.; Diaz, R.; Unruh, D. K.; Li, S.; Krempner, C. “Inverse” Frustrated Lewis Pairs: An Inverse FLP Approach to the Catalytic Metal Free Hydrogenation of Ketones. *Chem. Eur. J.* **2018**, *24* (62), 16526–16531. <https://doi.org/10.1002/chem.201804370>.
77. Obligation, J. V.; Chirik, P. J. Earth-Abundant Transition Metal Catalysts for Alkene Hydrosilylation and Hydroboration. *Nat. Rev. Chem.* **2018**, *2* (5), 15–34. <https://doi.org/10.1038/s41570-018-0001-2>.
78. Blackwell, J. M.; Sonmor, E. R.; Scoccitti, T.; Piers, W. E.  $B(C_6F_5)_3$ -Catalyzed Hydrosilylation of Imines via Silyliminium Intermediates. *Org. Lett.* **2000**, *2* (24), 3921–3923. <https://doi.org/10.1021/ol006695q>.
79. Blackwell, J. M.; Morrison, D. J.; Piers, W. E.  $B(C_6F_5)_3$  Catalyzed Hydrosilylation of Enones and Silyl Enol Ethers. *Tetrahedron* **2002**, *58* (41), 8247–8254. [https://doi.org/10.1016/S0040-4020\(02\)00974-2](https://doi.org/10.1016/S0040-4020(02)00974-2).
80. Harrison, D. J.; McDonald, R.; Rosenberg, L. Borane-Catalyzed Hydrosilylation of Thiobenzophenone: A New Route to Silicon-Sulfur Bond Formation. *Organometallics* **2005**, *24* (7), 1398–1400. <https://doi.org/10.1021/om048993n>.
81. Houghton, A. Y.; Hurmalainen, J.; Mansikkamäki, A.; Piers, W. E.; Tuononen, H. M. Direct Observation of a Borane-Silane Complex Involved in Frustrated Lewis-Pair-Mediated Hydrosilylations. *Nat. Chem.* **2014**, *6* (11), 983–988. <https://doi.org/10.1038/NCHEM.2063>.
82. Tamke, S.; Daniliuc, C. G.; Paradies, J. Frustrated Lewis Pair Catalyzed Hydrosilylation and Hydrosilane Mediated Hydrogenation of Fulvenes. *Org. Biomol. Chem.* **2014**, *12* (45), 9139–9144. <https://doi.org/10.1039/c4ob01346h>.
83. Pérez, M.; Hounjet, L. J.; Caputo, C. B.; Dobrovetsky, R.; Stephan, D. W. Olefin Isomerization and Hydrosilylation Catalysis by Lewis Acidic Organofluorophosphonium Salts. *J. Am. Chem. Soc.* **2013**, *135* (49), 18308–18310. <https://doi.org/10.1021/ja410379x>.



84. Pérez, M.; Qu, Z.-W.; Caputo, C. B.; Podgorny, V.; Hounjet, L. J.; Hansen, A.; Dobrovetsky, R.; Grimme, S.; Stephan, D. W. Hydrosilylation of Ketones, Imines and Nitriles Catalysed by Electrophilic Phosphonium Cations: Functional Group Selectivity and Mechanistic Considerations. *Chem. A Eur. J.* **2015**, *21* (17), 6491–6500. <https://doi.org/10.1002/chem.201406356>.
85. Hog, D. T.; Oestreich, M.  $B(C_6F_5)_3$ -Catalyzed Reduction of Ketones and Imines Using Silicon-Stereogenic Silanes: Stereinduction by Single-Point Binding. *Eur. J. Org. Chem.* **2009**, *2009* (29), 5047–5056. <https://doi.org/10.1002/ejoc.200900796>.
86. Chen, D.; Leich, V.; Pan, F.; Klankermayer, J. Enantioselective Hydrosilylation with Chiral Frustrated Lewis Pairs. *Chem. A Eur. J.* **2012**, *18* (17), 5184–5187. <https://doi.org/10.1002/chem.201200244>.
87. Mewald, M.; Oestreich, M. Illuminating the Mechanism of the Borane-Catalyzed Hydrosilylation of Imines with Both an Axially Chiral Borane and Silane. *Chem. A Eur. J.* **2012**, *18* (44), 14079–14084. <https://doi.org/10.1002/chem.201202693>.
88. Hermeke, J.; Mewald, M.; Oestreich, M. Experimental Analysis of the Catalytic Cycle of the Borane-Promoted Imine Reduction with Hydrosilanes: Spectroscopic Detection of Unexpected Intermediates and a Refined Mechanism. *J. Am. Chem. Soc.* **2013**, *135* (46), 17537–17546. <https://doi.org/10.1021/ja409344w>.
89. Süsse, L.; Hermeke, J.; Oestreich, M. The Asymmetric Piers Hydrosilylation. *J. Am. Chem. Soc.* **2016**, *138* (22), 6940–6943. <https://doi.org/10.1021/jacs.6b03443>.
90. Zhu, X.; Du, H. A Chiral Borane Catalyzed Asymmetric Hydrosilylation of Imines. *Org. Biomol. Chem.* **2015**, *13* (4), 1013–1016. <https://doi.org/10.1039/c4ob02419b>.
91. Liu, X.; Wang, Q.; Han, C.; Feng, X.; Du, H. Chiral Frustrated Lewis Pairs Catalyzed Highly Enantioselective Hydrosilylations of Ketones. *Chin. J. Chem.* **2019**, *37* (7), 663–666. <https://doi.org/10.1002/cjoc.201900121>.
92. Skjel, M. K.; Houghton, A. Y.; Kirby, A. E.; Harrison, D. J.; McDonald, R.; Rosenberg, L. Silane-Controlled Diastereoselectivity in the Tris(Pentafluorophenyl) Borane-Catalyzed Reduction of  $\alpha$ -Diketones to Silyl-Protected 1,2-Diols. *Org. Lett.* **2010**, *12* (2), 376–379. <https://doi.org/10.1021/ol902451h>.
93. Ren, X.; Du, H. Chiral Frustrated Lewis Pairs Catalyzed Highly Enantioselective Hydrosilylations of 1,2-Dicarbonyl Compounds. *J. Am. Chem. Soc.* **2016**, *138* (3), 810–813. <https://doi.org/10.1021/jacs.5b13104>.
94. Gribble, G. W. Sodium Borohydride in Carboxylic Acid Media: A Phenomenal Reduction System. *Chem. Soc. Rev.* **1998**, *27* (6), 395–404. <https://doi.org/10.1039/a827395z>.
95. Augurusa, A.; Mehta, M.; Perez, M.; Zhu, J.; Stephan, D. W. Catalytic Reduction of Amides to Amines by Electrophilic Phosphonium Cations via FLP Hydrosilylation. *Chem. Commun.* **2016**, *52* (82), 12195–12198. <https://doi.org/10.1039/c6cc06914b>.
96. Mahdi, T.; Stephan, D. W. Frustrated Lewis Pair Catalyzed Hydroamination of Terminal Alkynes. *Angew. Chem. Int. Ed.* **2013**, *52* (47), 12418–12421. <https://doi.org/10.1002/anie.201307254>.
97. Mahdi, T.; Stephan, D. W. Stoichiometric and Catalytic Inter- and Intramolecular Hydroamination of Terminal Alkynes by Frustrated Lewis Pairs. *Chem. A Eur. J.* **2015**, *21* (31), 11134–11142. <https://doi.org/10.1002/chem.201501535>.
98. Tussing, S.; Ohland, M.; Wicker, G.; Flörke, U.; Paradies, J. Borane-Catalyzed Indole Synthesis through Intramolecular Hydroamination. *Dalton Trans.* **2017**, *46* (5), 1539–1545. <https://doi.org/10.1039/C6DT04725D>.
99. Légaré, M. A.; Courtemanche, M. A.; Rochette, É.; Fontaine, F. G. Metal-Free Catalytic C-H Bond Activation and Borylation of Heteroarenes. *Science* **2015**, *349* (6247), 513–516. <https://doi.org/10.1126/science.aab3591>.
100. Légaré, M. A.; Rochette, É.; Légaré Lavergne, J.; Bouchard, N.; Fontaine, F. G. Bench-Stable Frustrated Lewis Pair Chemistry: Fluoroborate Salts as Precatalysts for the C-H Borylation of Heteroarenes. *Chem. Commun.* **2016**, *52* (31), 5387–5390. <https://doi.org/10.1039/c6cc01267a>.
101. Chernichenko, K.; Lindqvist, M.; Kótai, B.; Nieger, M.; Sorochkina, K.; Pápai, I.; Repo, T. Metal-Free  $Sp^2$ -C-H Borylation as a Common Reactivity Pattern of Frustrated 2-Aminophenylboranes. *J. Am. Chem. Soc.* **2016**, *138* (14), 4860–4868. <https://doi.org/10.1021/jacs.6b00819>.
102. Légaré Lavergne, J.; Jayaraman, A.; Misal Castro, L. C.; Rochette, É.; Fontaine, F. G. Metal-Free Borylation of Heteroarenes Using Ambiphilic Aminoboranes: On the Importance of Sterics in Frustrated Lewis Pair C-H Bond Activation. *J. Am. Chem. Soc.* **2017**, *139* (41), 14714–14723. <https://doi.org/10.1021/jacs.7b08143>.
103. Voss, T.; Chen, C.; Kehr, G.; Nauha, E.; Erker, G.; Stephan, D. W. Cyclizations via Frustrated Lewis Pairs: Lewis Acid Induced Intramolecular Additions of Amines to Olefins and Alkynes. *Chem. A Eur. J.* **2010**, *16* (10), 3005–3008. <https://doi.org/10.1002/chem.200903483>.
104. McCahill, J. S. J.; Welch, G. C.; Stephan, D. W. Reactivity of “Frustrated Lewis Pairs”: Three-Component Reactions of Phosphines, a Borane, and Olefins. *Angew. Chem. Int. Ed.* **2007**, *46* (26), 4968–4971. <https://doi.org/10.1002/anie.200701215>.
105. Melen, R. L.; Hansmann, M. M.; Lough, A. J.; Hashmi, A. S. K.; Stephan, D. W. Cyclisation versus 1,1-Carbaboration: Reactions of  $B(C_6F_5)_3$  with Propargyl Amides. *Chem. A Eur. J.* **2013**, *19* (36), 11928–11938. <https://doi.org/10.1002/chem.201301899>.
106. Pattenden, G. Synthetic Studies with Natural Oxazoles and Thiazoles. *J. Heterocyclic Chem.* **1992**, *29* (3), 607–618. <https://doi.org/10.1002/jhet.5570290302>.
107. Tamke, S.; Qu, Z.-W.; Sitte, N. A.; Flörke, U.; Grimme, S.; Paradies, J. Frustrated Lewis Pair-Catalyzed Cycloisomerization of 1,5-Enynes via a 5-Endo-Dig Cyclization/Protodeborylation Sequence. *Angew. Chem. Int. Ed.* **2016**, *55* (13), 4336–4339. <https://doi.org/10.1002/anie.201511921>.
108. Guru, M. M.; De, S.; Dutta, S.; Koley, D.; Maji, B.  $B(C_6F_5)_3$ -Catalyzed Dehydrogenative Cyclization of: N-Tosylhydrazones and Anilines via a Lewis Adduct: A Combined Experimental and Computational Investigation. *Chem. Sci.* **2019**, *10* (34), 7964–7974. <https://doi.org/10.1039/c9sc02492a>.
109. Wang, W. H.; Himeda, Y.; Muckerman, J. T.; Manbeck, G. F. Fujita, E.  $CO_2$  Hydrogenation to Formate and Methanol as an Alternative to Photo- and Electrochemical  $CO_2$  Reduction. *Chem. Rev.* **2015**, *129* (36), 12936–12973. <https://doi.org/10.1021/acs.chemrev.5b00197>.
110. Sreejith, P.; Mandal, S. K. From  $CO_2$  Activation to Catalytic Reduction: A Metal-Free Approach. *Chem. Sci.* **2020**, *11* (39), 10571–10593. <https://doi.org/10.1039/d0sc03528a>.
111. Mömring, C. M.; Otten, E.; Kehr, G.; Fröhlich, R.; Grimme, S.; Stephan, D. W.; Erker, G. Reversible Metal-Free Carbon Dioxide Binding by Frustrated Lewis Pairs. *Angew. Chem. Int. Ed.* **2009**, *48* (36), 6643–6646. <https://doi.org/10.1002/anie.200901636>.
112. Ashley, A. E.; Thompson, A. L.; O'Hare, D. Non-Metal-Mediated Homogeneous Hydrogenation of  $CO_2$  to  $CH_3OH$ . *Angew. Chem. Int. Ed.* **2009**, *48* (52), 9839–9843. <https://doi.org/10.1002/anie.200905466>.
113. Ménard, G.; Stephan, D. W. Room Temperature Reduction of  $CO_2$  to Methanol by Al-Based Frustrated Lewis Pairs and Ammonia Borane. *J. Am. Chem. Soc.* **2010**, *132* (6), 1796–1797. <https://doi.org/10.1021/ja9104792>.
114. Courtemanche, M. A.; Pulis, A. P.; Rochette, É.; Légaré, M. A.; Stephan, D. W.; Fontaine, F. G. Intramolecular B/N Frustrated Lewis Pairs and the Hydrogenation of Carbon Dioxide. *Chem. Commun.* **2015**, *51* (48), 9797–9800. <https://doi.org/10.1039/c5cc03072b>.
115. Berkefeld, A.; Piers, W. E.; Parvez, M. Tandem Frustrated Lewis Pair/Tris(Pentafluorophenyl)Borane-Catalyzed Deoxygenative Hydrosilylation of Carbon Dioxide. *J. Am. Chem. Soc.* **2010**, *132* (31), 10660–10661. <https://doi.org/10.1021/ja105320c>.
116. Courtemanche, M. A.; Légaré, M. A.; Maron, L.; Fontaine, F. G. A Highly Active Phosphine-Borane Organocatalyst for the Reduction of  $CO_2$  to Methanol Using Hydroboranes. *J. Am. Chem. Soc.* **2013**, *135* (25), 9326–9329. <https://doi.org/10.1021/ja404585p>.
117. Wang, T.; Stephan, D. W. Carbene-9-BBN Ring Expansions as a Route to Intramolecular Frustrated Lewis Pairs for  $CO_2$  Reduction. *Chem. A Eur. J.* **2014**, *20* (11), 3036–3039. <https://doi.org/10.1002/chem.201304870>.
118. Von Wolff, N.; Lefèvre, G.; Berthet, J. C.; Thuéry, P.; Cantat, T. Implications of  $CO_2$  Activation by Frustrated Lewis Pairs in the Catalytic Hydroboration of  $CO_2$ : A View Using  $N/Si+$  Frustrated Lewis Pairs. *ACS Catal.* **2016**, *6* (7), 4526–4535. <https://doi.org/10.1021/acscatal.6b00421>.
119. Qu, Z.; Zhu, H.; Grimme, S. Frustrated Lewis Pair Catalyzed Reduction of Carbon Dioxide Using Hydroboranes: New DFT Mechanistic Insights. *ChemCatChem* **2020**, *12* (14), 3656–3660. <https://doi.org/10.1002/cctc.202000604>.



120. Courtemanche, M.-A.; Légaré, M.-A.; Maron, L.; Fontaine, F.-G. Reducing CO<sub>2</sub> to Methanol Using Frustrated Lewis Pairs: On the Mechanism of Phosphine–Borane-Mediated Hydroboration of CO<sub>2</sub>. *J. Am. Chem. Soc.* **2014**, *136* (30), 10708–10717. <https://doi.org/10.1021/ja5047846>.
121. Declercq, R.; Bouhadir, G.; Bourissou, D.; Légaré, M. A.; Courtemanche, M. A.; Nahi, K. S.; Bouchard, N.; Fontaine, F. G.; Maron, L. Hydroboration of Carbon Dioxide Using Ambiphilic Phosphine-Borane Catalysts: On the Role of the Formaldehyde Adduct. *ACS Catal.* **2015**, *5* (4), 2513–2520. <https://doi.org/10.1021/acscatal.5b00189>.
122. Wang, T.; Stephan, D. W. Phosphine Catalyzed Reduction of CO<sub>2</sub> with Boranes. *Chem. Commun.* **2014**, *50* (53), 7007–7010. <https://doi.org/10.1039/c4cc02103g>.
123. Weicker, S. A.; Stephan, D. W. Activation of Carbon Dioxide by Silyl Triflate-Based Frustrated Lewis Pairs. *Chem. A Eur. J.* **2015**, *21* (37), 13027–13034. <https://doi.org/10.1002/chem.201501904>.

## 1.07 Chemistry with weakly coordinating aluminates $[\text{Al}(\text{OR}^{\text{F}})_4]^-$ and borates $[\text{B}(\text{OR}^{\text{F}})_4]^-$ : From fundamentals to application

Antoine Barthélemy\*, Philipp Dabringhaus\*, Eike Jacob\*, Hendrik Koger\*, David Röhner\*, Manuel Schmitt\*, Malte Sellin\*, and Krossing Ingo\*, Albert-Ludwigs-Universität Freiburg, Institut für Anorganische und Analytische Chemie and Freiburg Materials Research Center FMF, Freiburg, Germany

© 2023 Elsevier Ltd. All rights reserved.

<b>1.07.1</b>	<b>Introduction</b>	<b>379</b>
1.07.1.1	A brief introduction to weakly coordinating anions	379
1.07.1.2	Fluorinated alkoxyaluminates as WCAs: A comparison to competitors	380
<b>1.07.2</b>	<b>Chemistry with fluorinated alkoxy-aluminates and -borates</b>	<b>383</b>
1.07.2.1	Starting materials to introduce $[\text{M}(\text{OR}^{\text{F}})_4]^-$ aluminates and borates	383
1.07.2.2	Reactive cations stabilized by $[\rho\text{f}]^-$ aluminates	384
1.07.2.2.1	Unusual group 1 $\text{M}^+$ -complexes	387
1.07.2.2.2	Reactive group 2 and related group 12 cations	387
1.07.2.2.3	Reactive group 13 cations: Normal valency and subvalent	389
1.07.2.2.4	Reactive group 14 cations: Carbocations and their heavier homologues	396
1.07.2.2.5	Low valent group 14 cations	398
1.07.2.2.6	Reactive group 15 cations: Phosphorus and some higher homologues	400
1.07.2.2.7	Reactive group 16 cations	406
1.07.2.2.8	Lanthanide and actinoid complexes	406
1.07.2.3	Complexation of weak ligands: Coordination compounds of the transition metals stabilized by $[\rho\text{f}]^-$ aluminates	407
1.07.2.3.1	Complexed olefins and acetylenes	408
1.07.2.3.2	Homoleptic transition metal carbonyl cations (TMCCs)	410
1.07.2.3.3	Transition metal carbonyls as complex ligands	411
1.07.2.3.4	Further transition metal cations with gaseous ligands	411
1.07.2.3.5	Transition metal carbonyl cations as starting materials	411
1.07.2.3.6	Complexed free elemental clusters	412
1.07.2.3.7	Complexed mixed group 15/16 cages	415
1.07.2.3.8	Complexed mixed-transition metal-element clusters	416
1.07.2.3.9	Miscellaneous further transition-metal complexes	419
1.07.2.3.10	Unusual solvent complexes of the Ga-, Cu- and Ag-salts	420
1.07.2.4	Applications in catalysis and polymerization chemistry	421
1.07.2.4.1	Applications in homogenous catalysis	421
1.07.2.4.2	Applications in polymerization chemistry	423
1.07.2.5	Material science and electrochemical applications	425
1.07.2.5.1	As ionic liquids	425
1.07.2.5.2	As supporting electrolytes	427
1.07.2.5.3	As battery electrolytes	428
1.07.2.5.4	As electrolytes for supercapacitors	432
1.07.2.5.5	In organic photovoltaics OPV	432
1.07.2.5.6	In the life sciences as hydrophobic, non-bleaching dyes	432
<b>1.07.3</b>	<b>Conclusion and outlook</b>	<b>432</b>
<b>References</b>		<b>433</b>

### Abstract

Fluorinated alkoxyaluminates  $[\text{Al}(\text{OR}^{\text{F}})_4]^-$ ,  $[(^{\text{F}}\text{RO})_3\text{Al}-\text{F}-\text{Al}(\text{OR}^{\text{F}})_3]^-$  and the related borates  $[\text{B}(\text{OR}^{\text{F}})_4]^-$  ( $\text{R}^{\text{F}}$  stands for a poly- or perfluorinated organic alkyl residue) belong to the class of Weakly Coordinating Anions (WCAs) that made their way over the past decades from a means to stabilize unusual cationic systems of fundamental interest to a well-developed class of materials that help to prepare problem case model compounds similarly to being useful in applied research, e.g.,

\*All authors contributed equally.

for Ionic Liquids (ILs). In this review we briefly sketch the range of known WCAs, before turning mainly to the aluminate class of materials, but, where relevant, also to the related borates. We highlight the synthesis of starting materials, ways to introduce the WCAs to the system, the physical properties they induce and report on their performance in fundamental as well as applied chemistry, i.e. in catalysis, polymerization, electrochemistry, as electrolyte salts for supercaps and secondary batteries.

### 1.07.1 Introduction

Fluorinated alkoxyaluminates  $[\text{Al}(\text{OR}^{\text{F}})_4]^-$  belong to the class of Weakly Coordinating Anions (WCAs) that made their way over the past decades from a means to stabilize unusual cationic systems of fundamental interest to a well-developed class of materials that help to prepare problem case model compounds similarly to being useful in applied research, e.g., for Ionic Liquids (ILs), catalysis, polymerizations, electrochemistry and electrolytes (Fig. 1). In this article  $\text{R}^{\text{F}}$  stands for any poly- or perfluorinated organic residue. The specific abbreviations used for the most common WCAs are delineated in Fig. 2. In the following we briefly sketch the range of known WCAs, before turning mainly to the aluminate  $[\text{Al}(\text{OR}^{\text{F}})_4]^-$  class of materials, but, where relevant, also to the related borates  $[\text{B}(\text{OR}^{\text{F}})_4]^-$ . We highlight the synthesis of starting materials, their physical properties, typical routes to introduce them into a system and report on their performance in fundamental as well as applied chemistry.

This chapter is an update on our 2013 review in this book<sup>1</sup> and covers the literature until end of 2021/beginning of 2022.

#### 1.07.1.1 A brief introduction to weakly coordinating anions

The prime role of WCAs is to suppress strong cation-anion interactions and to replace the few strong electrostatic interactions in classical salts by a multitude of weak interactions. To achieve this goal, the majority of more recent WCAs are rather large and exhibit diameters in the nanometer range; moreover their “surfaces” are often covered by poorly polarizable fluorine atoms that produce a “Teflon”-type coating additionally dampening the efficiency of ion pairing and increasing the (kinetic) inertness and (thermodynamic) stability of these anions against ligand coordination or abstraction as well as oxidation. Overall this leads to improved solubilities of WCA-salts in less or even non-polar solvents, reduces ion pairing in these solvents and ultimately also leads to electric conductivity in these media. Clearly these are favorable properties for a range of applications and accordingly a large group of different WCAs has been prepared over the years. Those were recently reviewed<sup>2,3</sup> and shall not be detailed here, other than mentioning that they are typically built from a very Lewis acidic central atom M that usually bears a range of mainly univalent, chemically robust and often fluorinated ligands L giving the normally univalent ate-complexes  $[\text{M}(\text{L}_{n+1})]^-$  ( $n$  = valency of M) as WCAs. Examples are the classical fluorometallates like  $[\text{BF}_4]^-$  or  $[\text{MF}_6]^-$  and their aggregates like  $[\text{M}_2\text{F}_{11}]^-$  ( $\text{M} = \text{As}, \text{Sb}$ ), poly-fluorinated tetraaryl- or tetraalkylborates  $[\text{B}(\text{R}^{\text{F}})_4]^-$  ( $\text{R}^{\text{F}} = \text{CF}_3, \text{C}_6\text{F}_5, \text{C}_6\text{H}_3(\text{CF}_3)_2$  and others), dimeric borates  $[\text{X}(\text{B}(\text{C}_6\text{F}_5)_3)_2]^-$  ( $\text{X} = \text{CN}, \text{NH}_2$  and others), tetra- or hexateflatometallates  $[\text{M}(\text{OTeF}_5)_n]^-$  ( $n = 4, 6, \text{M} = \text{B}, \text{Al}, \text{Ga}$ ;  $n = 6, \text{M} = \text{As}, \text{Sb}, \text{Bi}, \text{Nb}$ ) but also bis(trifluoromethane-sulfonyl)imides  $[(\text{R}^{\text{F}}\text{SO}_2)_2\text{N}]^-$  or tris(trifluoromethane-sulfonyl)methanides  $[(\text{R}^{\text{F}}\text{SO}_2)_3\text{C}]^-$  and many others. Alternatively, also chemically robust *closo*-clusters may replace the central Lewis acidic atom M. When the periphery of these clusters is halogenated or trifluoromethylated, this leads to the important and chemically very stable, but difficult to prepare class of

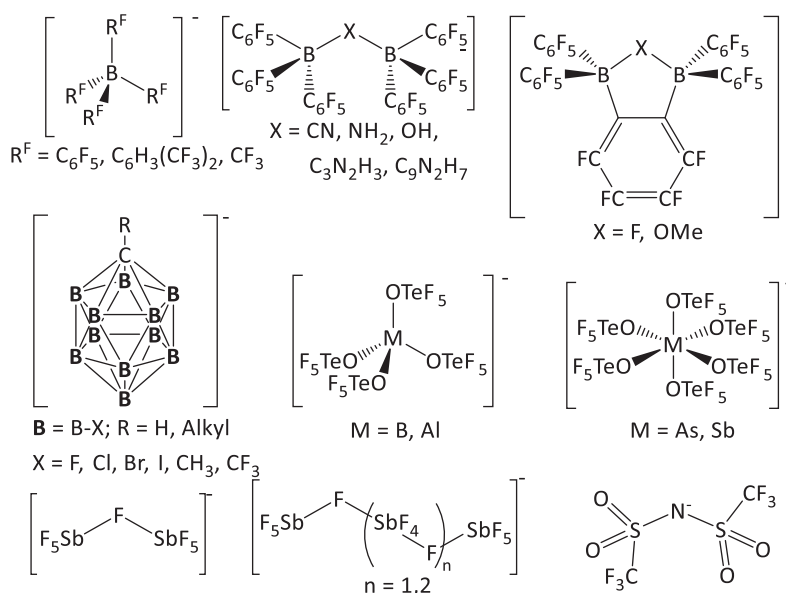
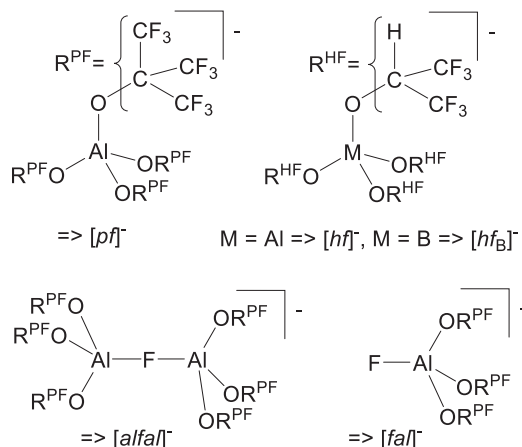


Fig. 1 Overview to common WCAs excluding the simple anions that are common knowledge like  $[\text{ClO}_4]^-$ ,  $[\text{CF}_3\text{SO}_3]^-$ ,  $[\text{BF}_4]^-$ ,  $[\text{MF}_6]^-$  and more.



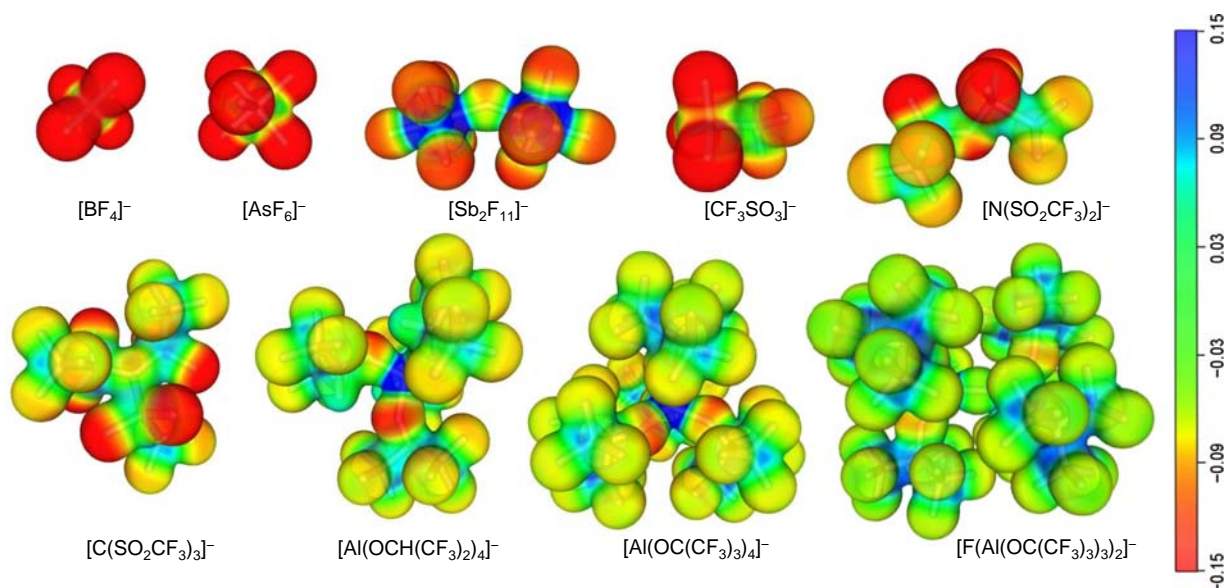
**Fig. 2** Definitions of the acronyms of the most commonly used fluorinated residues and WCAs used in this article.

carborane based WCAs  $[CB_{11}X_nH_{12-n}]^-$  ( $n = 0-12$ ,  $X = F, Cl, Br, I, CH_3, CF_3$ ), which was augmented by the synthetically in larger scale accessible *closo*-dodecaborates  $[B_{12}X_{12}]^{2-}$  ( $X = F, Cl, Br, I$ ). Recent additions include the WCAs  $[M(OTeF_5)_4]^-$  ( $M = Al, Ga$ ), introduced by the Riedel group,<sup>4,5</sup> and  $[Ga(C_2F_5)_4]^-$  prepared by the Hoge group.<sup>6</sup> Fig. 1 shows a personally selected overview on currently used WCAs.

### 1.07.1.2 Fluorinated alkoxyaluminates as WCAs: A comparison to competitors

Among the above mentioned WCAs, the fluorinated alkoxyaluminates  $[Al(OR^F)_4]^-$  are a newer addition that were first published by S. Strauss<sup>7</sup> in 1996 and were complemented by our group since 1999.<sup>8-12</sup> Also several of the related borates  $[B(OR^F)_4]^-$  came into the focus,<sup>13-15</sup> mainly for use in ionic liquids or as electrolyte salts for various batteries. Currently we are aware of about 100 groups worldwide that use the favorable properties of this chemically robust and easily in large scale or even commercially at [www.iolitec.de](http://www.iolitec.de) available WCA class. Importantly, a simple and straight-forward large scale access to the least coordinating fluoride-bridged anion  $[(^{PF}RO)_3Al-F-Al(OR^{PF})_3]^-$  was published<sup>12</sup>; the synthesis routes delineated therein override the ones published in 2004.<sup>16</sup> The simplified nomenclature used to address the most frequent aluminate and borate WCAs described with this work is included with Fig. 2.

With Respect to Coordinating Ability: Since the major purpose of a WCA is to reduce the overall cation-anion interaction, the performance of the coordination ability of the  $[pfo]^-$  and  $[alfal]^-$  aluminate in comparison to other well-known WCAs may best be visualized by from a projection of the BP86/def2-TZVP calculated electrostatic potential onto a  $0.005 e^- \text{ Bohr}^{-3}$  isodensity surface of the aluminate WCA in comparison to classical WCAs (Fig. 3; red coloration indicates high accumulation of negative charge).



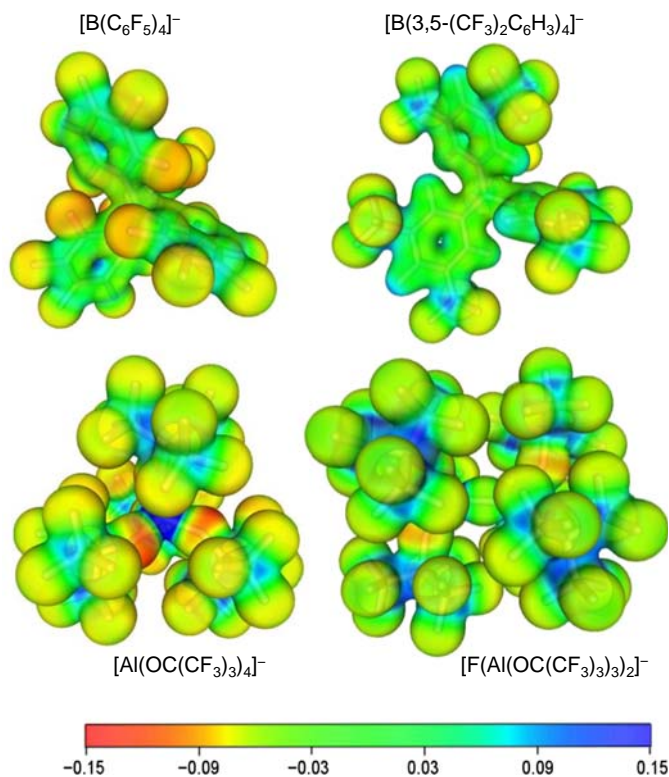
**Fig. 3** Projection of the BP86/def2-TZVP calculated electrostatic potential map onto a  $0.005 e^- \text{ Bohr}^{-3}$  isodensity surface of  $[hfo]^-$ ,  $[pfo]^-$  and  $[alfal]^-$  in comparison to classical WCAs.

When comparing with the often employed fluorinated tetraarylborates (Fig. 4), one also realizes the favorable performance of the aluminates. From this projection also follows that the weak coordination ability of the  $[pf]^-$  and  $[alfal]^-$  aluminates is a result of two effects: electronic deactivation of the most basic oxygen alkoxide atoms by the fluorination (see low  $pK_a$  value of  $\text{HO}-\text{C}(\text{CF}_3)_3$  of 5.4 if compared to non-fluorinated  $\text{HO}-\text{C}(\text{CH}_3)_3$  of 19.3)<sup>8,17</sup> and the steric hindrance introduced by the umbrella effect of the bulky  $\text{C}(\text{CF}_3)_3$  group preventing electrophiles/cations to attack these most basic/negatively charged sites.

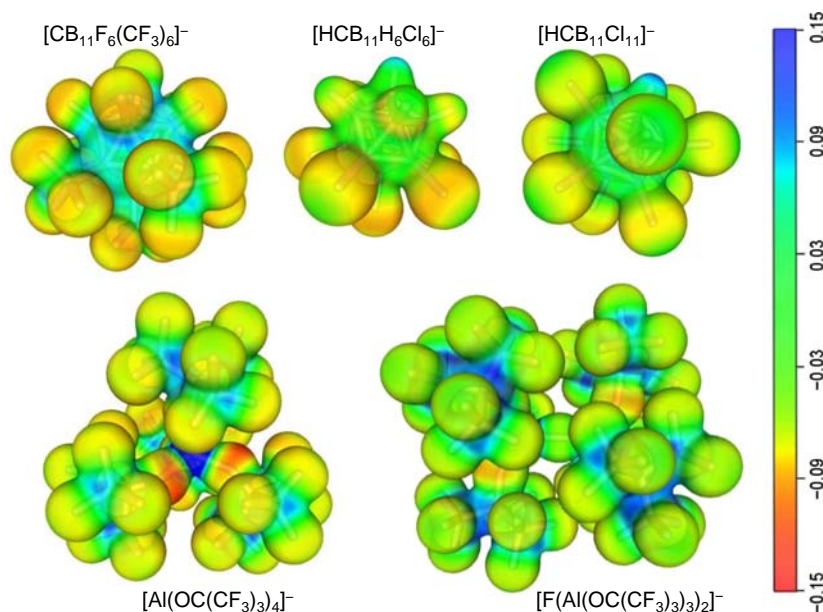
The final Fig. 5 of this series, compares the  $[pf]^-$  and  $[alfal]^-$  aluminates with the difficult to synthesize, but chemically extraordinary robust carborane based WCAs. One realizes from this Fig. 5, that only the most advanced mixed fluorinated-/trifluoromethylated carborane WCAs reach the potential of the  $[pf]^-$  and  $[alfal]^-$  aluminates in terms of for coordination available negatively charged sites. The more common only partially chlorinated carborane based anions exhibit higher and accessible surface charges. In agreement with this, these carborane ions tend to get easily coordinated, but can sustain extreme electrophilicity in such a coordinated state (e.g., they tolerate a coordinated  $\text{AlMe}_2^+$  cation).<sup>18</sup>

In Terms of Thermodynamic WCA-Stability: Little quantitative data is available here, and apart from comparisons on a chemical basis ("This WCA is compatible with this reactive cation, while another WCA does not tolerate this...!"), which may on a personal basis be concluded from the next sections, only few comparative studies on the basis of quantum chemical calculations exist. Larger parts of the following section were adapted from Refs.<sup>2,19</sup> and later addenda.<sup>3,20,21</sup> However, as recently the use of the very reliable DSD-PBEP86(D3BJ)/def2-QZVPP//pbeh3-c/def2-mSVP level of theory as described by Greb et al.<sup>22</sup> was recommended, we have recalculated all data collected in Table 1 at this reliable D3BJ-dispersion corrected double hybrid functional level. With the calculated data, the thermodynamic stability of the WCA's as collected in Table 1 was established based on the following considerations:

- (i) The *Fluoride Ion Affinity FIA*: All anions that are based on Lewis acidic central atoms, are prone to ligand abstraction as a decomposition reaction. A measure for the intrinsic stability of a given WCA is the Lewis acidity of the parent Lewis acid A, i.e., the acid  $\text{B}(\text{C}_6\text{F}_5)_3$  for the anion  $[\text{B}(\text{C}_6\text{F}_5)_4]^-$ . A firmly established measure for Lewis acidity is the fluoride ion affinity *FIA*.<sup>21</sup> The higher the *FIA*-value of the parent Lewis acid A, the more stable is the WCA against ligand abstraction. For recent systematic work by Greb et al. see.<sup>23–25</sup>
- (ii) The *Ligand Affinity LA* of the WCAs. The *LA* is the enthalpy of reaction necessary to remove the anionic ligand  $[\text{L}]^-$  from the anion  $[\text{M}(\text{L})_n]^-$  (Eq. 1):



**Fig. 4** Projection of the BP86/def2-TZVP calculated electrostatic potential onto a  $0.005 \text{ e}^- \text{ Bohr}^{-3}$  isodensity surface of  $[pf]^-$  and  $[alfal]^-$  in comparison to fluorinated tetraarylborates.



**Fig. 5** The  $[\rho f]^-$  aluminates in comparison with the difficult to synthesize, but chemically extraordinary robust carborane based WCAs. Projection of the BP86/def2-TZVP calculated electrostatic potential onto a  $0.005 e^- \text{ Bohr}^{-3}$  isodensity surface.

**Table 1** Calculated properties of WCAs: The *FIA* of the parent Lewis acid, the *LA*, *PD* and *CuD* of the WCA, the position of the HOMO of the WCA in eV and the HOMO-LUMO gap of the WCA in eV.

Anion	Sym.	FIA of the Lewis-Acid [ $\text{kJ mol}^{-1}$ ]	LA [ $\text{kJ mol}^{-1}$ ]	PD [ $\text{kJ mol}^{-1}$ ]	CuD [ $\text{kJ mol}^{-1}$ ]	HOMO [eV]	Gap [eV] <sup>a</sup>
$[\text{BF}_4]^-$	$T_d$	345	<i>b</i>	-1214	-483	-8.13	8.57
$[\text{PF}_6]^-$	$O_h$	380	<i>b</i>	-1180	-448	-9.05	8.99
$[\text{AsF}_6]^-$	$O_h$	437	<i>b</i>	-1122	-391	-9.50	7.05
$[\text{SbF}_6]^-$	$O_h$	493	<i>b</i>	-1066	-335	-9.92	5.85
$[\text{Sb}_2\text{F}_{11}]^-$ vs. $\text{Sb}_2\text{F}_{10}$	$C_7$	536	<i>b</i>	-1024	-292	-11.43	5.13
$[\text{Sb}_3\text{F}_{16}]^-$ vs. $\text{Sb}_3\text{F}_{15}$	$C_i$	555	<i>b</i>	-1004	-273	-12.21	4.83
$[\text{Sb}_4\text{F}_{21}]^-$ vs. $\text{Sb}_4\text{F}_{20}$	$C_{2v}$	562	<i>b</i>	-998	-266	-12.67	4.72
$[\text{B}(\text{OTeF}_5)_4]^-$	$C_1$	502	199	-1090	-422	-10.11	3.57
$[\text{Al}(\text{OTeF}_5)_4]^-$	$S_4$	603	339	-950	-282	-10.63	4.19
$[\text{Ga}(\text{OTeF}_5)_4]^-$	$S_4$	571	325	-964	-296	-10.68	3.98
$[\text{As}(\text{OTeF}_5)_6]^-$	$C_3$	566	275	-1014	-346	-10.71	2.86
$[\text{Sb}(\text{OTeF}_5)_6]^-$	$C_3$	616	334	-954	-287	-11.00	2.53
$[\text{B}(\text{OC}(\text{H})(\text{CF}_3)_2)_4]^-$	$S_4$	391	284	-1164	-446	-8.03	7.04
$[\text{Al}(\text{OC}(\text{H})(\text{CF}_3)_2)_4]^-$	$S_4$	540	413	-1035	-317	-8.36	6.63
$[\rho f]^-$	$S_4$	547	366	-1020	-317	-8.72	7.06
$[\text{Al}(\text{OC}_{10}\text{F}_{15})_4]^-$	$C_1$	600	388	-963	-271	-9.03	4.72 <sup>d</sup>
<i>[alfal]</i> <sup>c</sup>	$S_6$	738 <sup>c</sup>	439	-947	-244	-9.73	7.11 <sup>d</sup>
$[\text{B}(\text{C}_6\text{H}_5)_4]^-$	$S_4$	314	347	-1333	-565	-4.35	4.52
$[\text{B}(\text{C}_6\text{H}_3(\text{CF}_3)_2)_4]^-$	$S_4$	452	419	-1170	-413	-6.23	4.33
$[\text{B}(\text{C}_6\text{F}_5)_4]^-$	$S_4$	441	341	-1164	-442	-5.94	4.40
$[\text{Al}(\text{C}_6\text{F}_5)_4]^-$	$S_4$	546	373	-1132	-410	-6.33	4.44
$[\text{Ga}(\text{C}_6\text{F}_5)_4]^-$	$S_4$	449	350	-1155	-433	-6.33	4.48
$[\text{Ga}(\text{C}_2\text{F}_5)_4]^-$	$S_4$	501	417	-1154	-389	-7.38	7.05
$[\text{B}(\text{CF}_3)_4]^-$	$T$	559	533	-1069	-293	-8.27	9.63

<sup>a</sup>The HOMO-LUMO gaps were calculated with TD-DFT as the first singlet excitation energy at the DSD-PBEP86(D3BJ)/def2-QZVPP level.<sup>26</sup>

<sup>b</sup>LA and FIA are identical.

<sup>c</sup>FIA vs. 2  $\text{Al}(\text{OR})_3$ .

<sup>d</sup>For size restrictions, we had to use the DSD-PBEP86(D3BJ)/def2-TZVP level of theory, which gave for  $[\rho f]^-$  very similar values (i.e., 7.15 (def2-TZVP) vs. 7.06 eV (def2-QZVPP)). Note, the WCAs were selected based on Ref.<sup>2,3,19-21</sup> and the values recalculated at the DSD-PBEP86(D3BJ)/def2-QZVPP//pbeh3-c/def2-mSVP level of theory as described by Greb et al.<sup>22</sup>



The *LA* is always endothermic and the higher the positive *LA*-value in **Table 1**, the more stable is the WCA versus a ligand abstraction. However, a word of caution is needed here: The *LA* also reflects the intrinsic stability of the generated  $[L]^-$  anion. Thus, if  $[L]^-$  is stable such as  $[L]^- = [OC(CF_3)_3]^-$  or  $[OTeF_5]^-$  the *LA* is relatively low compared to less stable anionic ligands such as  $[L]^- = [C_6H_5]^-$  or  $[C_6H_3(CF_3)_2]^-$ .

- (iii) To assess the stability of a WCA towards attack of a hard or soft electrophile and to eliminate the contribution of the intrinsic stability of  $[L]^-$  in (ii), the decomposition reactions of  $[M(L)_n]^-$  with the hard  $H^+$  (Eq. 2) and soft  $Cu^+$  (Eq. 3) electrophiles were calculated:



*PD* stands for *Proton-Decomposition* (Eq. 2) and *CuD* for *Copper-Decomposition* (Eq. 3). Since a gaseous anion and a gaseous cation react giving two neutral species, *PD* and *CuD* are both exothermic. The less negative *PD*- and *CuD*-values in **Table 1** are, the more stable is the WCA against electrophilic attack.

- (iv) The energy of the HOMO of a WCA relates to its resistance towards oxidation. The lower the HOMO energy, the more difficult it is to remove an electron and thus oxidize the WCA.
- (v) The HOMO-LUMO gap in **Table 1** can be associated with the resistance of an anion towards reduction and the larger the gap, the more stable is the anion with respect to reduction. Small gaps in combination with very low HOMOs such as those for  $[Sb_4F_{21}]^-$  or  $[As(OTeF_5)_6]^-$  are an indication of the potentially oxidizing character of these anions that may interfere with counter cations sensitive towards oxidation.

Ligand abstraction and hydrolysis are frequently observed decomposition pathways for WCAs and, therefore, the computational approach to calculate *LA*, *PD* and *CuD* mimics experimental observations (see<sup>2,3</sup>).

However, by calculations only the underlying thermodynamics can be assessed, kinetic barriers against decomposition may additionally stabilize a given WCA. The data included in **Table 1** may not be taken absolute. Yet, since the same methods were used for all computations relative trends will definitely be correct.

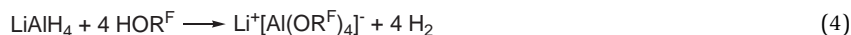
## 1.07.2 Chemistry with fluorinated alkoxy-aluminates and -borates

One of the major advantages of these aluminates is their simple access on a preparative scale: they can be prepared with little synthetic effort on a large scale with high yield within 2 days in common inorganic/organometallic laboratories; many  $[pf]^-$  salts are also commercially available at [www.iolitec.de](http://www.iolitec.de).

### 1.07.2.1 Starting materials to introduce $[M(OR^F)_4]^-$ aluminates and borates

Over the past decade new and optimized syntheses of a wide range of starting materials to introduce the  $[pf]^-$  aluminates into a given system were developed.

*Homoleptic Anions:* The syntheses of all  $[Al(OR^F)_4]^-$  starting materials begin with the preparation of the  $Li^+$ -salts using carefully purified  $LiAlH_4$  and the appropriate commercially available alcohols in heptane (Eq. 4).

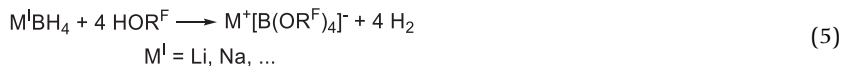


Explicit details for the preparation of these Li-salts were published; we recommend to check the fine details.<sup>11</sup> The related borates work either with  $LiBH_4$ <sup>27</sup> or  $NaBH_4$ <sup>13,14</sup> instead of  $LiAlH_4$ . The alcohols  $(HOC(H)(CF_3)_2)$ ,  $HOC(CH_3)(CF_3)_2$  and  $HOC(CF_3)_3$  were purchased from Apollo Scientific, Fluorochem or ABCR (at 0.1–3 € per gram) and were first degassed, then distilled prior to use. The synthesis of the  $Li[pf]$  salts is done in our group in well over 99% yield within 2 days in scales of up to 250 g.

Most other salts can then be prepared in high yield via metathesis reactions with precipitation of  $LiX$  ( $X = F, Cl, Br, BF_4$ ) or by protonation with e.g., protonated ethers.<sup>28</sup> In addition, the more recent access to (synergistic or innocent) oxidants like  $Ag^+$ ,  $Ag^+$ /

0.5 X<sub>2</sub> (X = Cl, Br, I), NO<sup>+</sup>, NO<sub>2</sub><sup>+</sup> or Phenazin<sup>F+</sup> (cf. sections below) did allow for access to many new materials on deelectronation<sup>a</sup> routes.

The borates may be obtained from both, the Li as well as Na borohydride salts as in Eq. (5):



*Routes to the [alfal]<sup>-</sup> Anion:* The converged and best preps available in multigram scale start from Me<sub>3</sub>Si-F-Al(OR<sup>F</sup>)<sub>3</sub>, including the ion-like bound SiMe<sub>3</sub><sup>+</sup> cation.<sup>12</sup> Its optimized large-scale ‘best synthesis’ is described here, before we turn to the [alfal]<sup>-</sup> preparation. AlEt<sub>3</sub> (15.0 mL, 109 mmol, 93% purity) was dissolved in heptane (120 mL) and cooled to -40 °C. Under vigorous (!) stirring, the first two equivalents of HOR<sup>F</sup> (30.0 mL, 215 mmol, 2.0 eq.) were added dropwise to the reaction mixture, while keeping the cooling bath between -40 °C and -20 °C. During the addition of HOR<sup>F</sup>, gas evolution (C<sub>2</sub>H<sub>6</sub>) was observed, the viscosity of the solution increased and small amounts of precipitate formed. After complete addition of the first HOR<sup>F</sup> portion (typically within 1 h), Me<sub>3</sub>SiF (12.5 g, 136 mmol, 1.2 eq.) was condensed onto the reaction mixture at -40 °C. The solution was stirred for 10 min, and then the third equivalent of HOR<sup>F</sup> (20.0 mL, 143 mmol, 1.3 eq.) was added within 5 min. The cooling bath was removed and the reaction mixture was allowed to reach r.t., which led to dissolution of the precipitate. After 30 min, more HOR<sup>F</sup> (5.0 mL, 36 mmol, 0.3 eq.) was added and the solution was stirred overnight. From the clear solution, slowly a white powder crystallized. For product isolation, simply the solvent and excess alcohol was removed *in vacuo* yielding a white crystalline powder (85.4 g, 103 mmol, 94%). Note: One needs the excess of the fluorinated alcohol, as it is very volatile (b.p. = +45 °C) and the continuous stream of evolving ethane removes the part of the alcohol through the bubbler.

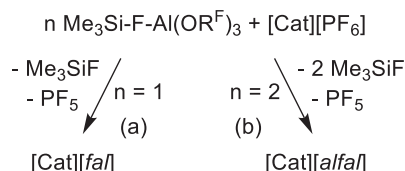
The synthesis of the [alfal]<sup>-</sup> WCA then uses the reaction with many [PF<sub>6</sub>]<sup>-</sup> salts,<sup>12</sup> as the PF<sub>5</sub> is the much weaker Lewis acid if compared to Me<sub>3</sub>Si-F-Al(OR<sup>F</sup>)<sub>3</sub>. Hence, in general Cat<sup>+</sup>[alfal]<sup>-</sup> forms by reaction with Cat[PF<sub>6</sub>] and Cat<sup>+</sup> being K<sup>+</sup>, Ag<sup>+</sup>, NO<sup>+</sup>, NO<sub>2</sub><sup>+</sup>, CPh<sub>3</sub><sup>+</sup> etc. (Fig. 6).

Also the smaller [fal]<sup>-</sup> anion (= F-Al(OC(CF<sub>3</sub>)<sub>3</sub>)<sub>3</sub><sup>-</sup>) can be synthesized in this way. Yet, this includes one coordinating fluoride-tooth. Table 2 gives an overview on useful materials, for which good synthesis routes have been developed.

It should be noted that in contrast to the normally easily hydrolyzed alkoxyaluminates, the [pff]<sup>-</sup> anion is stable in 6 N nitric acid.<sup>8</sup> This stability towards hydrolysis was attributed to steric shielding of the oxygen atoms, provided by the bulky C(CF<sub>3</sub>)<sub>3</sub> groups, as well as to electronic stabilization due to perfluorination. The electron withdrawing effect of the fluorinated ligand can be demonstrated by the increased acidity of the fluorinated HOC(H)(CF<sub>3</sub>)<sub>2</sub> (pK<sub>a</sub> = 9.5) and HOC(CF<sub>3</sub>)<sub>3</sub> (pK<sub>a</sub> = 5.5) alcohols in comparison to the non-fluorinated HOC(CH<sub>3</sub>)<sub>3</sub> (pK<sub>a</sub> = 19.3).<sup>8,17</sup> Thus, perfluoro<sup>b</sup>butanol is 14 orders of magnitude more acidic than non-fluorinated <sup>b</sup>butanol. Therefore, the [pff]<sup>-</sup> anion may be viewed as the complex anion of the H[pff] super acid. This H[pff] acid can be prepared and is capable of directly protonating mesitylene 1,3,5-Me<sub>3</sub>C<sub>6</sub>H<sub>3</sub>.<sup>61</sup> In addition, the redox stability of both, the [pff]<sup>-</sup> and [alfal]<sup>-</sup> anions towards high deelectronation potentials is large and they sustain reversible redox processes in published work<sup>63</sup> that may reach +1.42 V vs. Fc<sup>+</sup>/Fc, but in unpublished work we see that one may even reach +1.9 V vs. Fc<sup>+</sup>/Fc in suitable polar, but weakly basic solvents like 1,2,3,4-F<sub>4</sub>C<sub>6</sub>H<sub>2</sub> (= 4FB). This complies with the reported<sup>64</sup> stability of the [pff]<sup>-</sup> anion in Li<sup>+</sup> ion battery electrolytes of up to 5.5 V vs. Li<sup>+</sup>/Li.

### 1.07.2.2 Reactive cations stabilized by [pff]<sup>-</sup> aluminates

The best choices to stabilize really electrophilic reactive cations with aluminate WCAs, are the [pff]<sup>-</sup> and [alfal]<sup>-</sup> WCAs with the perfluorinated residue OC(CF<sub>3</sub>)<sub>3</sub>; the latter often forms as a decomposition product of the first. Electrophilic limits for anion stability are cations like [CCl<sub>3</sub>]<sup>+</sup> or [P<sub>2</sub>Cl<sub>5</sub>]<sup>+</sup> that are stable in solution at about -20 °C, but have a half-life at RT of about 1–2 h. Small truly



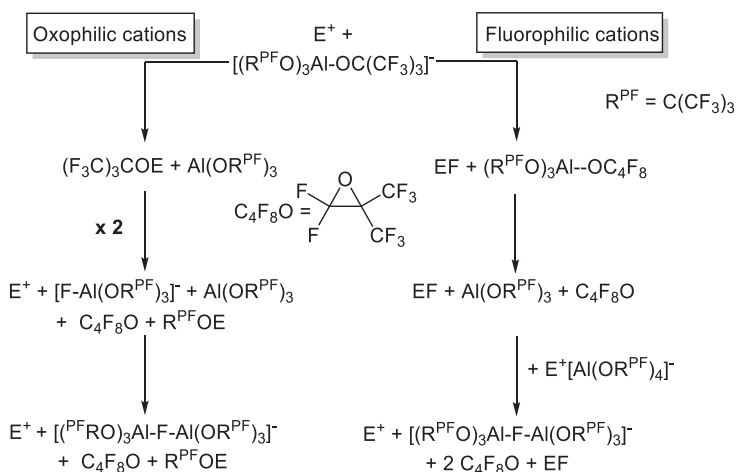
**Fig. 6** Optimized preparation towards Cat<sup>+</sup>[alfal]<sup>-</sup> salts. Frequently used Cat<sup>+</sup> include K<sup>+</sup>, Ag<sup>+</sup>, NO<sup>+</sup>, NO<sub>2</sub><sup>+</sup>, CPh<sub>3</sub><sup>+</sup> etc. Scale is typically done in the 5–10 g product range, the typical solvents include CH<sub>2</sub>Cl<sub>2</sub>, oDFB or SO<sub>2</sub>. Also the smaller [fal]<sup>-</sup> anion (= F-Al(OC(CF<sub>3</sub>)<sub>3</sub>)<sub>3</sub><sup>-</sup>) including one clearly coordinating (Al–)F tooth can be synthesized in this way.

<sup>a</sup>We use the elementary steps *electronation* and *deelectronation* in their strict sense, i.e., addition or removal of e<sup>-</sup>. Thus, a classically termed ‘oxidant’ is addressed as a ‘deelectronator’ and a ‘reductant’ as an ‘electronator’, if only a single electron transfer as the elementary step takes place. This particle-based terminology is related to the acid-base picture, where the terms deprotonation and protonation describe the transfer of a proton between two partners, i.e., deelectronation is the electron-based equivalent to a deprotonation. This terminology has been discussed in ref.<sup>29</sup> and ref.<sup>30</sup> from our work on the protoelectric potential map and is transferred to describe these types of reactions more accurately.

**Table 2** Overview to available starting materials that allow introducing the fluorinated alkoxyaluminates into a system.

Cation	$[hf]^-$ , $R^F: C(H)(CF_3)_2$	$[pf]^-$ , $R^F: C(CF_3)_3$	$[Al(OR^F)_4]^-$ $R^F: misc.$	$[alfal]^-$
'Naked' $M^{+/2+}$	Li <sup>8,11</sup> Cs <sup>9,31</sup> Tl <sup>32</sup>	Li <sup>8,11</sup> ; Na–Cs <sup>9,31</sup> Ga <sup>33</sup> ; In <sup>34,35</sup> ; Tl <sup>32</sup> Sr <sup>36</sup>	Li <sup>8,11,30</sup>	–
$[Cu(L)_n]^+$	Cu <sup>+37</sup>	$[Cu(C_6H_4F_2)_2]^{+37}$ $[Cu(NCMe)_4]^{+38}$	Cu <sup>+37</sup>	–
$[Ag(L)_n]^+$	Ag <sup>+8,11</sup> $[Ag(L)_n]^{+8,11}$	Ag <sup>+11</sup> $[Ag(L)_n]^{+8,11}$ $[Ag(NCMe)_4]^{+39}$	Ag <sup>+8,11</sup> $[Ag(L)_n]^{+8,11}$ $[Ag(NCMe)_4]^{+39}$	$[Ag(CH_2Cl_2)_3]^{+12,16}$
$Ag^+/0.5 X_2$	–	X = Cl, Br, I <sup>40,41</sup>	–	–
$[Au(L)_n]^+$	–	$[Au(NCMe)_2]^{+42}$	–	–
$[M(L)_n]^+$	–	$[Co(oDFB)_2]^{+43}$	–	$[Co(oDFB)_2]^{+43}$
$[M(L)_n]^{2+}$	$[Mg(DME)_3]^{2+,44}$ $[Ca(DME)_4]^{2+}$ $([hf]^-)_2^{45}$	$[Cu(NCMe)_6]^{2+46}$ $[Zn(NCMe)_6]^{2+47}$ $[Mg(NCMe)_6]^{2+48}$ $[Sn(NCMe)_6]^{2+49}$	$[Cu(NCMe)_6]^{2+46}$	–
$[Ln-(NCMe)_n]^{3+}$	–	$n = 9: Nd, Eu, Gd, Dy^{50}$ $n = 8: Tm^{50}$	–	–
$NO^+/NO_2^+$	–	$NO^{+51,52}$ $NO_2^{+52}$	–	$NO^{+12}$ $NO_2^{+12}$
$NS^+/NS_2^+$	–	Pure $NS_2^{+53}$ Impure $NS^{+53}$	–	–
Carbocations	$CPh_3^{+9}$	$CPh_3^{+9}$ $[C_6(CH_3)_6]^{+54}$ $[C_{14}F_8Cl_2]^+$	–	$CPh_3^{+12}$ $[C_6(CH_3)_6]^{+48}$
Ammoniumyl cations	–	$N(C_6H_4-4-Br)_3^{+55}$ Phenazin <sup>F+55</sup>	–	Phenazin <sup>F+56</sup>
$NR_4^+$ (R = Alkyl)	Me, Et, Bu <sup>57</sup>	Me, Et, Bu <sup>57</sup>	Me, Et, Bu <sup>57</sup>	Bu <sup>58</sup>
Ionic Liquid Cations	Many, see Review <sup>59</sup>	Imidazolium <sup>60</sup> Pyrrolidinium <sup>60</sup>	–	–
$[H(L)_n]^+$	Unstable	$H^{+61}$ $OEt_2, THF^{28}$ $1,3,5-Me_3C_6H_3^{61}$ $PR_3^{62}$	–	$1,3,5-Me_3C_6H_3^{61}$

tricoordinate silylium ions like  $[Me_3Si]^+$  are not compatible at room temperature with these WCAs, but still have a reasonable lifetime at lower temperatures. In addition, the coordination of a silane to the silane stabilized  $[R_3Si-H-SiR_3]^+$  ions greatly increases stability.<sup>65,66</sup> Moreover, subvalent silicocenium ions like  $[Cp^*Si]^{+67}$  as well as silylium ions with larger residues like pentamethylphenyl,  $[Si(C_6Me_5)_3]^+$ , are stable with the  $[pf]^-$  WCA.<sup>68</sup> Favorably, it was shown that the  $[pf]^-$  WCA also enables very rapid silylium

**Fig. 7** Different decomposition pathways of the  $[pf]^-$  anion depending on the nature of the electrophilic cation  $E^+$ .

ion based catalysis with in part unprecedented turn over frequencies (hydrosilylation, hydrodefluorination) even if small silane stabilized  $\text{SiR}_3^+$  residues such as  $\text{R} = \text{Me}, \text{Et}$  were used.<sup>65</sup>

**Decomposition Pathways of the  $[pf]^-$  Anion:** To show the (moderate) limitations of these aluminates upfront, we initially sketch repeatedly observed decomposition reactions of  $[pf]^-$ . Larger parts of this section were taken from ref.<sup>10</sup> Generally, two different possibilities exist: the electrophilic cation attacks either the oxygen atom, the most basic site of the anion, or one of the 36 peripheral fluorine atoms (Fig. 7).

Small oxophilic cations such as  $[\text{P}_2\text{Cl}_5]^+$ , or eventually it's dissociation product  $\text{PCl}_2^+$ , initially attack one of the 4 O atoms and abstract an alkoxy group. The resulting  $^{\text{PF}}\text{RO}-\text{PCl}_2$  has been detected in low temperature  $^{31}\text{P}$  NMR studies as a decet.<sup>16</sup> The generated  $\text{Al}(\text{OR}^{\text{F}})_3$  Lewis acid, which can be prepared independently and later was shown to be Lewis superacidic,<sup>20,21,69</sup> then abstracts an  $\text{F}^-$  ion from the  $^{\text{PF}}\text{RO}-\text{PCl}_2$  that is in close proximity. The formed  $[\text{F}-\text{Al}(\text{OR}^{\text{F}})_3]^-$  and  $\text{Al}(\text{OR}^{\text{F}})_3$  then combine to the fluoride bridged anion.

More fluorophilic cations such as  $[\text{SiMe}_3]^+$ ,  $[\text{BX}_2]^+$  ( $\text{X} = \text{Cl}, \text{Br}, \text{I}$ ) abstract one of the peripheral fluorine atoms. This attack is followed by a rearrangement of the alkoxy group and formation of a Lewis acid-base adduct of  $\text{Al}(\text{OR}^{\text{F}})_3$  and the epoxide  $\text{C}_4\text{F}_8\text{O}$ . In the following step the epoxide is replaced by another abstracted fluoride ion from another  $[pf]^-$  anion forming the (known<sup>12</sup>)  $[fal]^-$  anion ( $= [\text{FAl}(\text{OR}^{\text{PF}})_3]^-$ ). This anion may now react with the just formed  $\text{Al}(\text{OR}^{\text{PF}})_3$  by complexation to the stable fluoride bridged  $[alfal]^-$  anion. Alternatively, fluorophilic cations  $\text{E}^+$  like  $\text{SiMe}_3^+$  may prefer direct coordination to the fluoride tooth of  $[\text{FAl}(\text{OR}^{\text{PF}})_3]^-$  and hence give  $\text{Me}_3\text{Si}-\text{F}-\text{Al}(\text{OR}^{\text{PF}})_3$ .<sup>12</sup> Thus, the decomposition may proceed by

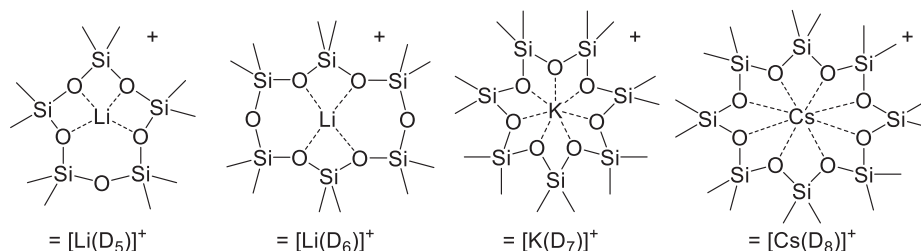
- (i) Ligand ( $\text{R}^{\text{PF}}\text{O}^-$ ) abstraction or
- (ii) Fluoride ion abstraction.

The thermodynamic stability of the  $[pf]^-$  and  $[alfal]^-$  anion with respect to (i) and (ii) are compared in Table 3.

Note that the decomposition reactions were assessed through isodesmic reactions and should therefore be reliable.<sup>10</sup> Which of the two mechanisms proceeds, depends on the steric bulk of the attacking electrophile  $\text{E}^+$ , the bond enthalpies of the formed  $\text{E}-\text{F}$  or  $\text{E}-\text{OR}$  compounds and the strengths of the  $\text{Al}-\text{O}$  or  $\text{C}-\text{F}$  bonds in the  $[pf]^-$  anion.

We note that the formation of the epoxide  $\text{C}_4\text{F}_8\text{O}$  or related ones is a general decomposition pathway of all  $[\text{Al}(\text{OR}^{\text{F}})_4]^-$  anions observed upon thermal treatments<sup>31,70</sup> of the salts or upon collisions<sup>57</sup> inside a mass spectrometer with sufficiently high energies.

Nevertheless, the following sections show that these aluminate WCAs tolerate considerably high electrophilicity and allow the preparation of a wealth of unusual reactive cation salts. For the revision, we have chosen a structure following the position of the reactive cations first in the respective main group, next according to the ligand class in the respective transition metal systems.



**Fig. 8** Examples for known siloxane complexes of group 1 metal cations ( $= (\text{Me}_2\text{SiO})_x$  with  $x = 5-8$ ) generated via reaction of the respective  $\text{M}^+[\text{pf}]^-$  ( $\text{M} = \text{Li}, \text{K}, \text{Cs}$ ) with the siloxane.

**Table 3** Calculated reaction enthalpies and free energies for selected decomposition reactions.

Decomposition reaction	$\Delta_r H^\circ_{(g)}$	$\Delta_r G^\circ_{(g)}$	$\Delta_r G^\circ_{(\text{CH}_2\text{Cl}_2)}$
$[\text{Al}(\text{OR}^{\text{PF}})_4]^- \rightarrow \text{F}^- + \text{C}_4\text{F}_8\text{O} \rightarrow \text{Al}(\text{OR}^{\text{PF}})_3$	603	561	316
$[(\text{R}^{\text{PF}}\text{O})_3\text{Al}-\text{F}-\text{Al}(\text{OR}^{\text{PF}})_3]^- \rightarrow \text{F}^- + \text{C}_4\text{F}_8\text{O} \rightarrow \text{Al}(\text{OR}^{\text{PF}})_2-\text{F}-\text{Al}(\text{OR}^{\text{PF}})_3$	674	645	379
$[\text{Al}(\text{OR}^{\text{PF}})_4]^- + \text{AsF}_5 \rightarrow [\text{AsF}_6]^- + \text{C}_4\text{F}_8\text{O} \rightarrow \text{Al}(\text{OR}^{\text{PF}})_3$	179	180	91
$[(\text{R}^{\text{PF}}\text{O})_3\text{Al}-\text{F}-\text{Al}(\text{OR}^{\text{PF}})_3]^- + \text{AsF}_5 \rightarrow [\text{AsF}_6]^- + \text{C}_4\text{F}_8\text{O} \rightarrow \text{Al}(\text{OR}^{\text{PF}})_2-\text{F}-\text{Al}(\text{OR}^{\text{PF}})_3$	250	264	154
$[\text{Al}(\text{OR}^{\text{PF}})_4]^- \rightarrow \text{Al}(\text{OR}^{\text{PF}})_3 + [\text{OR}^{\text{PF}}]^-$	342		
$[(\text{R}^{\text{PF}}\text{O})_3\text{Al}-\text{F}-\text{Al}(\text{OR}^{\text{PF}})_3]^- \rightarrow \text{Al}_2(\text{OR}^{\text{PF}})_5\text{F} + [\text{OR}^{\text{PF}}]^-$	441/ 363 <sup>a</sup>		

All values are given in  $\text{kJ mol}^{-1}$ .  
<sup>a</sup>Kinetic/thermodynamic value.<sup>10,19</sup>

### 1.07.2.2.1 Unusual group 1 M<sup>+</sup>-complexes

As a consequence of the very weakly coordinating character, also rather nontypical ligands complex to the M<sup>+</sup> cation of the [pfl]<sup>-</sup> anion, in part only discovered by serendipity.

**Almost Planar Li-Siloxane Complexes:** In a reaction designed to give Se<sub>6</sub>Ph<sub>2</sub>([pfl])<sub>2</sub> from Se<sub>4</sub>[AsF<sub>6</sub>]<sub>2</sub>, 2 Li[pfl], and Se<sub>2</sub>Ph<sub>2</sub>, unexpectedly the crystals of Li(D<sub>6</sub>)<sup>+</sup>[pfl]<sup>-</sup> were obtained in the presence of silicone grease. Subsequently, Li(D<sub>5</sub>)<sup>+</sup>[pfl]<sup>-</sup> and Li(D<sub>6</sub>)<sup>+</sup>[pfl]<sup>-</sup> were prepared in high yield by the reaction of Li[pfl] with D<sub>5</sub> or D<sub>6</sub> in CH<sub>2</sub>Cl<sub>2</sub> solution (Fig. 8).<sup>71</sup>

The syntheses of the Li(D<sub>5</sub>)<sup>+</sup>[pfl]<sup>-</sup> and Li(D<sub>6</sub>)<sup>+</sup>[pfl]<sup>-</sup> salts are the first examples of the preparation of host-guest complexes directly from cyclic dimethylsiloxanes, alkali-metal ions, and WCAs. Their structures imply that the cyclic dimethylsiloxanes (D<sub>5</sub> and D<sub>6</sub>) act as pseudo crown ethers and provide rare examples of silicon ethers behaving as Lewis bases.<sup>71</sup> The counterpoise-corrected binding energies for the alkali-metal complexes [MD<sub>6</sub>]<sup>+</sup> exhibit a remarkable similarity to that for [18]crown-6 for both sets of complexes (in the gas phase). The binding energies become less negative with increasing size of the alkali-metal cation. However, the binding affinity of D<sub>6</sub> calculated at the HF/3-21G\* level is approximately 100 kJ mol<sup>-1</sup> less than that of [18]crown-6, reflecting the lower basicity of the siloxanes.

Recently, Hänisch and co-workers (re-)investigated alkali cation-siloxane complex salts. They discovered that while a [Ga<sub>4</sub>]<sup>-</sup> anion is sufficient to prepare respective Li-Rb<sup>+</sup> siloxane complexes, the preparation of novel Rb<sup>+</sup> and Cs<sup>+</sup>-siloxane complexes as well as 2:1 complexes demanded a good WCA, in this case [pfl]<sup>-</sup>.<sup>72</sup> Here, the synthesis of the Cs(D<sub>8</sub>)<sup>+</sup>[pfl]<sup>-</sup>, K(D<sub>7</sub>)<sup>+</sup>[pfl]<sup>-</sup> and Rb(D<sub>8</sub>)<sup>+</sup>[pfl]<sup>-</sup> were reported. Moreover, the synthesis of the first sandwich-type complexes with cyclosiloxane ligands could be isolated in the form of the 2:1 complexes Cs(D<sub>6</sub>)<sub>2</sub><sup>+</sup>[pfl]<sup>-</sup> and K(D<sub>5</sub>)<sub>2</sub><sup>+</sup>[pfl]<sup>-</sup>.

**Lithium-Siloxane-Phosphane-Complex:** The lithium-siloxane-phosphane-complex<sup>73,74</sup> shown in Fig. 8 is related to the siloxane complex in the preceding section: These results showed that cyclosiloxanes can be considered as inorganic analogs of the well-established crown ether ligands. In this respect the cage [P<sub>2</sub>{(Si<sup>i</sup>Pr<sub>2</sub>)<sub>2</sub>O}<sub>2</sub>{Me<sub>2</sub>Si(OSiMe<sub>2</sub>)<sub>2</sub>}] (A) corresponds to a cryptand. This analogy could be confirmed by the synthesis of the lithium complex [Li@A]<sup>+</sup>[pfl]<sup>-</sup> (R<sup>F</sup> = C(CF<sub>3</sub>)<sub>3</sub>; Fig. 9).

**Lithium Phosphane Complexes:** According to HSAB, the small and hard group 1 cations prefer ionic interactions to hard, electro-negative Lewis bases such as water, alkoxides etc. However, homoleptic neutral Li<sup>+</sup>-phosphane complexes could be prepared by simply mixing the phosphane ligands with Li<sup>+</sup>[pfl]<sup>-</sup> in toluene.<sup>75</sup> Structural analysis as well as solid state and solution multinuclear NMR studies, confirm a distorted octahedral coordination at the Lithium cation. The analogous sodium complexes could be synthesized by using Na<sup>+</sup>[B{3,5-(CF<sub>3</sub>)<sub>2</sub>-C<sub>6</sub>H<sub>3</sub>}<sub>4</sub>]<sup>-</sup> as "naked" cation source.

### 1.07.2.2.2 Reactive group 2 and related group 12 cations

#### 1.07.2.2.2.1 Alkaline earth metals

**On the Way to [Cp\*Be]<sup>+</sup>:** Due to the extreme Lewis acidity of the hard Be<sup>2+</sup> cation, the Be<sup>2+</sup> cation in known cationic complexes is stabilized by strong N- or O-donors. Aiming for the isolation of a [Cp\*Be]<sup>+</sup> cation, Ag<sup>+</sup>[pfl]<sup>-</sup> was reacted with Cp\*Be-Br in PhF or 1,2-DFB (Fig. 10).<sup>76</sup> Although AgBr precipitation showed the successful bromide-abstraction, the in situ generated highly Lewis-acidic [Cp\*Be]<sup>+</sup> cation induced the decomposition of the [pfl]<sup>-</sup> anion to form the [fal]<sup>-</sup> adduct Cp\*Be-F-Al(OR<sup>F</sup>)<sub>3</sub>. An ionic dissociation into [Cp\*Be]<sup>+</sup> and [fal]<sup>-</sup> was postulated to be feasible in polar solvents.

**Group 2 cations stabilized by β-diketiminato ligands:** To study interactions of the highly Lewis acidic group 2 cations with various mostly soft nucleophiles, a stabilization of the metal cation by β-diketiminato ligands has proven feasible (Fig. 11). Here, Hill and co-workers reported the synthesis of complexes of [(<sup>Me</sup>BDI)Ae]<sup>+</sup> and [(<sup>tBu</sup>BDI)Ae]<sup>+</sup> (<sup>Me</sup>BDI = HC{(Me)CN-2,6-*i*Pr<sub>2</sub>C<sub>6</sub>H<sub>3</sub>}<sub>2</sub>; <sup>tBu</sup>BDI = HC{(tBu)CN-2,6-*i*Pr<sub>2</sub>C<sub>6</sub>H<sub>3</sub>}<sub>2</sub>) with Ae = Mg or Ca to benzene or toluene.<sup>77</sup> The usage of the weakly-coordinating [pfl]<sup>-</sup> anion precluded ion-pair formation and an η<sup>6</sup>-coordination of Mg and Ca to the aromatic systems could be observed. In contrast, ion

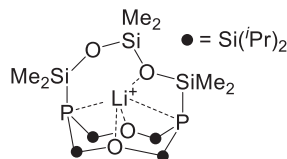


Fig. 9 Reactions of Li<sup>+</sup>[pfl]<sup>-</sup> with the siloxane-phosphane A: Formation of the lithium complex [Li@A]<sup>+</sup>[pfl]<sup>-</sup> (R<sup>F</sup> = C(CF<sub>3</sub>)<sub>3</sub>).

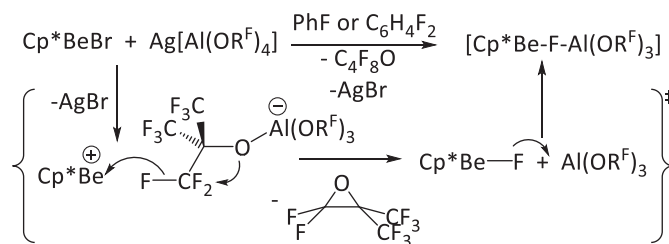
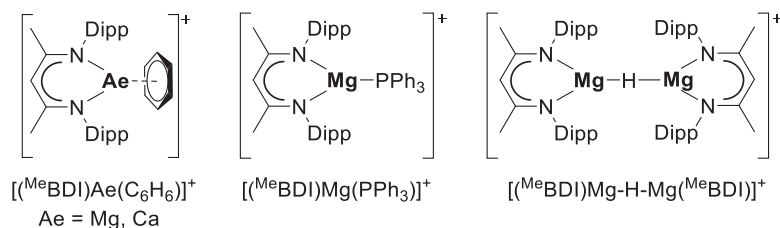


Fig. 10 Preparation of the [fal]<sup>-</sup> adduct of [Cp\*Be]<sup>+</sup> via decomposition of a [pfl]<sup>-</sup> anion.



**Fig. 11** Examples for complexes containing  $[(^{\text{Me}}\text{BDI})\text{Ae}]^+$  ( $^{\text{Me}}\text{BDI} = \text{HC}(\text{Me})\text{CN-2,6-}i\text{Pr}_2\text{C}_6\text{H}_3_2$ ) cations and  $[\text{pf}]^-$  anions.

pairs were reported for the analogous complexes with the  $[\text{B}(\text{C}_6\text{F}_5)_4]^-$  anion, allowing only for an  $\eta^3$ -coordination of benzene in the respective Mg complex.<sup>78</sup> Similar observations have been made for Cp and norbornadiene complexes of  $[(^{\text{Me}}\text{BDI})\text{Mg}]^+$ .<sup>79</sup> Moreover, Hill and co-workers observed formation of the first  $\text{Mg-PPh}_3$  complexes by addition of  $\text{PPh}_3$  to  $[(^{\text{Me}}\text{BDI})\text{Ae}(\text{C}_7\text{H}_8)]^+[\text{pf}]^-$  or  $[(^{\text{tBu}}\text{BDI})\text{Ae}(\text{C}_7\text{H}_8)]^+[\text{pf}]^-$ .<sup>77</sup> In a recent publication, multimetallic hydride derivatives could be obtained via reaction of  $[(^{\text{Me}}\text{BDI})\text{Mg}]^+[\text{pf}]^-$  with  $[(^{\text{Me}}\text{BDI})\text{MgH}]_2$  or  $[(^{\text{Me}}\text{BDI})\text{CaH}]_2$ .<sup>80</sup>

**Dicationic Group 2 Arene Complexes:** Inspired by the reported cationic group 2 arene complexes, we aimed for the isolation of dicationic and highly Lewis acidic group 2 arene complexes. Here, the synthesis of the first unsupported dicationic arene complexes of calcium and strontium could be achieved by reaction of the hexamethylbenzene radical cation  $[\text{HMB}]^+[\text{alfal}]^-$  (*vide infra*) with the elemental metals in 1,2-difluorobenzene.<sup>48</sup> In these complexes, an  $\eta^6$ -HMB coordination to  $\text{Ca}^{2+}$  and  $\text{Sr}^{2+}$  is observed as well as a  $\kappa^2$ -F-coordination of four 1,2-DFB solvent molecules. Unfortunately, in all cases partial decomposition of the  $[\text{alfal}]^-$  anion yielded *fal*-adducts  $[\text{M}(\text{HMB})(1,2\text{-DFB})_n\{\text{fal}\}]^+[\text{alfal}]^-$  ( $n = 2$  for  $\text{M} = \text{Ca}$ ,  $n = 3$  for  $\text{M} = \text{Sr}$ ,  $\text{Ba}$ ). While the *fal*-adduct represented only a minor impurity for the strontium complex, the respective complexes of calcium and barium were the major products in the oxidation reactions.

The reactions of  $[\text{HMB}]^+[\text{alfal}]^-$  with magnesium metal did only proceed after addition of acetonitrile to yield the complex salts  $[\text{Mg}(\text{MeCN})_6]^{2+}([\text{WCA}]^-)_2$  ( $\text{WCA} = [\text{pf}]^-$  or  $[\text{alfal}]^-$ ).

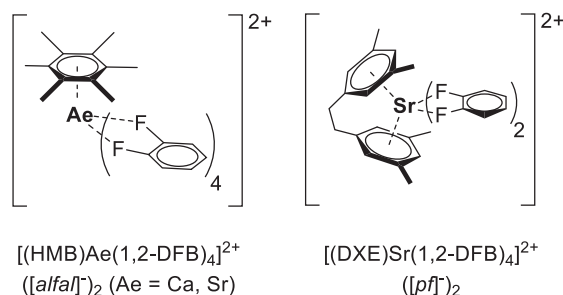
The application of group 2 cations demanded for clean starting materials. Hence, we developed a simple route to a “naked”  $\text{Sr}^{2+}$  synthon  $[\text{Sr}(\text{pf})]^+[\text{pf}]^-$  via salt metathesis between  $\text{Ag}[\text{pf}]$  and  $\text{SrI}_2$  in 1,2-DFB.<sup>36</sup> Here, the strontium dication is coordinated closely by the three oxygen atoms of one *pf*-unit, while the other  $[\text{pf}]^-$  anion only coordinates loosely via the fluorine atoms. Addition of dixylylethylene (DXE) to solutions of  $[\text{Sr}(\text{pf})]^+[\text{pf}]^-$  allowed for the isolation of the dicationic  $\text{Sr}^{2+}$ -ansa-arene complex  $[\text{Sr}(\text{DXE})(1,2\text{-DFB})_2]^{2+}([\text{pf}]^-)_2$  in **Fig. 12**. The high Lewis-acidity of this complex could be unambiguously shown by catalysis of the hydrosilylation of  $\text{CO}_2$  to methane and successful initiation of a controlled isobutene polymerization at high temperatures ( $-12^\circ\text{C}$  and  $0^\circ\text{C}$ ), yielding polyisobutylene with narrow dispersities and high molecular weights.

#### 1.07.2.2.2 Group 12 metals

**Divalent  $\text{Zn}^{\text{II}}$ -Compounds.** Attempts to prepare previously unknown simple and very Lewis acidic  $[\text{RZn}]^+[\text{pf}]^-$  salts from  $\text{ZnR}_2$ ,  $\text{AlR}_3$ , and  $\text{HO-R}^{\text{F}}$  delivered the *ion-like*  $\text{R-Zn}(\text{pf})$  ( $\text{R} = \text{Me}$ ,  $\text{Et}$ ) with a coordinated counterion, but never the ionic compound.<sup>81,82</sup> They were synthesized in a one-pot reaction and fully characterized by single-crystal X-ray diffraction, NMR and vibrational spectroscopy, and by quantum chemical calculations.<sup>81,82</sup> Increasing the steric bulk in  $\text{RZn}^+$  to  $\text{R} = \text{CH}_2\text{CMe}_3$ ,  $\text{CH}_2\text{SiMe}_3$ , or  $\text{Cp}^*$ , thus attempting to induce ionization, failed and led only to reaction mixtures including anion decomposition.

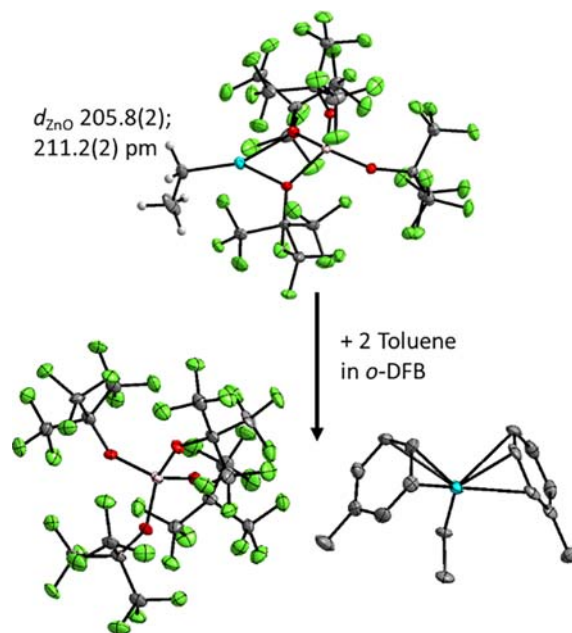
The catalytic activity of *ion-like*  $\text{Et-Zn}(\text{pf})$  in intermolecular hydroamination and in the unusual double hydroamination of anilines and alkynes was investigated.<sup>81</sup> Favorable performance was also found in comparison to the  $\text{Et}_2\text{Zn}/[\text{PhNMe}_2\text{H}]^+[\text{B}(\text{C}_6\text{F}_5)_4]^-$  system generated in situ at lower catalyst loadings of 2.5 mol%.<sup>81</sup>

From these *ion-like* ethylzinc aluminates, the arene complexes  $[\text{EtZn}(\text{arene})_2]^+[\text{pf}]^-$  were accessible as well soluble salts. Ionization yielded the salts with arene = toluene, mesitylene, or *o*-difluorobenzene (*o*DFB)/toluene. In contrast to the known<sup>83</sup> *ion-like*  $\text{EtZn}(\eta^3\text{-C}_6\text{H}_6)(\text{CHB}_{11}\text{Cl}_{11})$  with coordinated counterion, which co-crystallizes with one benzene molecule, the less coordinating nature of the  $[\text{pf}]^-$  anion allowed the ionization and preparation of the purely organometallic  $[\text{EtZn}(\text{arene})_2]^+$  cation (**Fig. 13**).



**Fig. 12** Literature-known dicationic Group 2 arene complexes. DXE = Dixylylethylene.





**Fig. 13** Molecular structures of *ion-like* Et–Zn[*pf*] (top) and [EtZn(toluenes)<sub>2</sub>]<sup>+</sup>[*pf*]<sup>–</sup> (bottom) and synthesis of the second from the first.

These stable *ion-like* organozinc aluminate materials were shown to have further applications, for example, as initiators of isobutene polymerization.<sup>82</sup> DFT calculations to compare the Lewis acidities of the zinc cations to those of a large number of organometallic cations were performed on the basis of the fluoride ion affinity. The complexation energetics of EtZn<sup>+</sup> with arenes and THF was assessed and related to the experiments.<sup>82</sup>

**Univalent Base-stabilized Zn<sub>2</sub><sup>2+</sup> Dication:** A base-stabilized [Zn<sub>2</sub>]<sup>2+</sup> dication, namely [(dmap)<sub>3</sub>Zn–Zn(dmap)<sub>3</sub>]<sup>2+</sup>, was obtained from the reaction of [Cp\*<sub>2</sub>Zn<sub>2</sub>(dmap)<sub>2</sub>] (dmap = 4-dimethylaminopyridine) with two equivalents of [H(OEt<sub>2</sub>)<sub>2</sub>][*pf*] and was structurally characterized for the first time as its [*pf*]<sup>–</sup> salt. It exhibits a Zn–Zn bond lengths of 2.419(1) Å.<sup>84</sup> The low stability of the [Zn<sub>2</sub>]<sup>2+</sup> cation is in marked contrast to that of the intensively studied [Hg<sub>2</sub>]<sup>2+</sup> and [Cd<sub>2</sub>]<sup>2+</sup> cations, which are long-known also with very simple ligands or even in the absence of ligands in Lewis acidic salt melts.

### 1.07.2.2.3 Reactive group 13 cations: Normal valency and subvalent

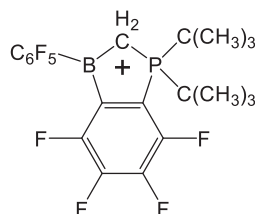
#### 1.07.2.2.3.1 Reactions leading to trivalent group 13 cations

**Cationic Phosphonioborane Lewis Acid:** From a zwitterionic, chloro-substituted phosphonioborate, the Cl atom could be heterolytically cleaved by reaction with Ag[*pf*] giving the cationic Lewis acid shown in Fig. 14.<sup>85</sup>

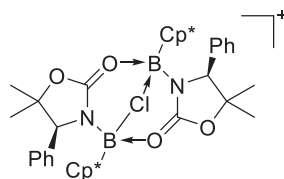
Only when using the silver salt of the good WCA [*pf*]<sup>–</sup>, the free cationic Lewis acid could be generated and was studied also at RT in CH<sub>2</sub>Cl<sub>2</sub> solution. With [PF<sub>6</sub>]<sup>–</sup> as counterion, decomposition through fluoride ion abstraction and formation of the fluoro-substituted phosphonioborate was observed. The more coordinating [CF<sub>3</sub>SO<sub>3</sub>]<sup>–</sup> and [CF<sub>3</sub>COO]<sup>–</sup> anions were bound by the boron atom of the cationic Lewis acid.<sup>85</sup>

**Cationic Borole:** Halide abstraction from a NHC-chloroborole precursor with Li[*pf*] yielded the first cationic borole featuring a high boron-centered Lewis-acidity.<sup>86</sup> The cation is formally antiaromatic, since the boron atom is part of a cyclic 4π electron system. With CO, it reversibly reacts under formation of an extremely rare example of a main group metal carbonyl complex. The C–O stretching frequency at 2128 cm<sup>–1</sup> suggests that backbonding plays a role in this cationic CO complex.<sup>86</sup>

**Chloroborane Masked Chiral Borenium Ion:** Chloroborane masked borenium ions, featuring a symmetrical [B–Cl–B]<sup>+</sup> linkage have been prepared and employed as catalysts in enantioselective Diels-Alder cycloaddition reactions.<sup>87</sup> These cationic complexes



**Fig. 14** Structure of the Cationic Phosphonioborane Lewis Acid.



**Fig. 15** Molecular structure of a chiral chloroborane masked borenium ion. The  $[pf]^-$  counter anions are not shown for clarity.

are available after chloride abstraction with one equivalent  $\text{Li}[pf]$  from  $C_2$ -symmetric cyclic chiral diboron complexes. The substituents of the chiral oxazolidinone ligand (see Fig. 15) control the stereoselectivity, which can be improved by adding  $\text{SnCl}_4$ .<sup>87</sup>

**Chloroborenium Ion:** After chloride abstraction from  $\text{Cp}^*\text{BCl}_2(\text{cAAC})$ , a tricoordinated chloroborenium ion with one  $[\text{Cp}^*]^-$  and one cAAC ligand could be synthesized.<sup>88</sup>  $\text{Ag}[pf]$  had to be employed as the chloride abstracting reagent, since attempts to isolate the product in the analogous reaction with  $\text{TMSOTf}$ , other silver salts or  $\text{AlCl}_3$  were futile.<sup>88</sup>

**Ferrocene-Based Planar-Chiral Borenium Cation:** The first planar chiral, enantiomerically pure ferrocenylborenium cation was obtained as its  $[pf]^-$  salt after halide abstraction from the respective chloroborane adduct using either  $[\text{Ag}(\text{CH}_2\text{Cl}_2)][pf]$  or  $\text{Li}[pf]$ .<sup>89</sup> With acetophenone, the borenium ion forms a Lewis acid-base adduct, which can be isolated and readily reacts with  $\text{HSiEt}_3$ , resulting in the hydrosilylation of acetophenone.<sup>89</sup> This ferrocenylborenium ion catalyzes the stereoselective hydrosilylation of acetophenone, however, with modest enantiomeric excess.<sup>89</sup>

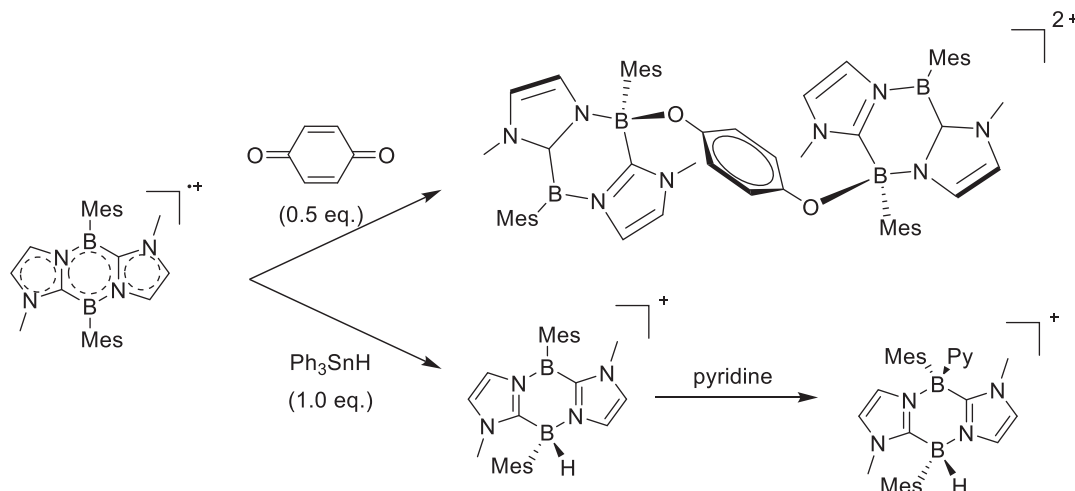
**Borinium Cation:** The synthesis of a highly Lewis acidic borinium cation was recently achieved by chloride-abstraction from  $\text{Cl}(\text{Mes})\text{B-TMP}$  (TMP = tetramethylpiperidine) with  $\text{Ag}[pf]$ . The  $[\text{Mes-B-TMP}]^+$  cation was reported to initiate cyanosilylation and catalyze hydrosilylation of ketones and aldehydes.<sup>90</sup>

**Diazadiborinine Radical Cation:** One-electron oxidation of a neutral 1,4,2,5-diazadiborinine with  $\text{Ag}[pf]$  afforded the respective diazadiborinine radical cation as its  $[pf]^-$  salt.<sup>91</sup> The spin density mainly resides on the B centers, accounting for a boron-centered radical reactivity. This was confirmed by the reactions of the radical cation with *p*-benzoquinone and  $\text{Ph}_3\text{SnH}$ , which furnished a non-radical dicationic complex after B–O bond formation, and a non-radical monocationic species featuring a B–H bond, respectively.<sup>91</sup> The molecular structures of the diazadiborinine radical cation and of the reaction products are shown in Fig. 16.

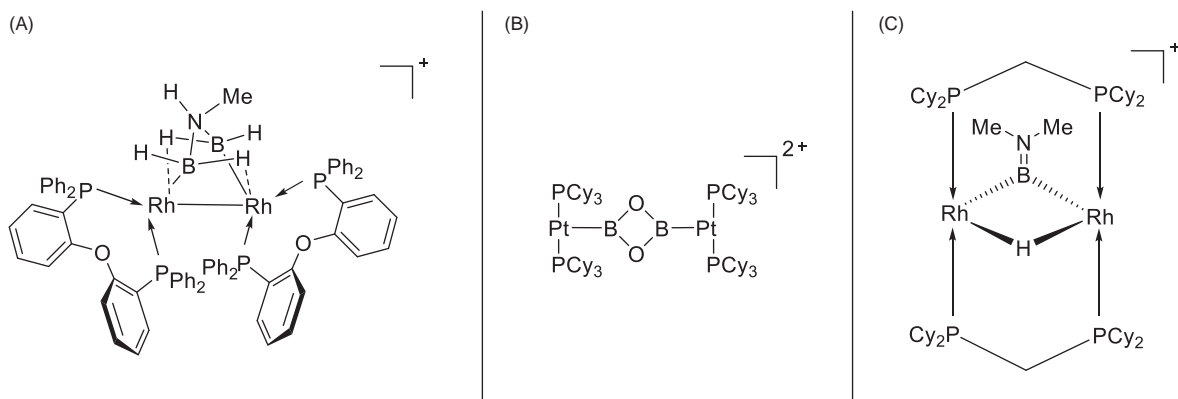
**Borazine Radical Cation:** The radical cation  $[1,2\text{-B}_2\{1,2\text{-(MeN)}_2\text{C}_6\text{H}_4\}_2]^{\bullet+}$  has been synthesized by deelectronation of the neutral, methylated 1,2-bis(diaminobenzene)diborane precursor with  $\text{Ag}[pf]$ .<sup>92</sup> However, unlike in the diazadiborinine radical cation,<sup>91</sup> only a minor contribution of boron-based orbitals to the spin density is observed. Instead, the radical is centered primarily on the two N-heterocycles joined by a  $\text{B}_2$  moiety.<sup>92</sup>

**A boron<sup>III</sup>/oxido-phenalenone Complex:** The isolation of a monocationic complex featuring a central  $\text{B}^{\text{III}}$ , coordinated in a nearly tetrahedral fashion by two chelating 9-oxido-1-phenalenone ligands, has recently been reported.<sup>93</sup>

**Multinuclear, Mixed Boron/Transition Metal Clusters:** The cationic  $[\text{Rh}_2(\kappa^2\text{-P,P-DPEphos})_2(\sigma,\mu\text{-(H}_2\text{B)}_2\text{NHMe})]^+$  complex, which has been shown to act as a catalyst in the dehydropolymerization reaction of  $\text{H}_3\text{B}\cdot\text{NMeH}_2$ , could not be crystallized with borate anion  $[\text{BAR}^{\text{F}}_4]^-$ , but with the  $[pf]^-$  anion (structure A) in Fig. 17.<sup>94</sup> Another unusual cation was obtained from the reaction of a platinum(II)-bis(tricyclohexylphosphine)-bromo-oxoboryl complex with the bromide abstraction agent  $\text{Ag}[pf]$  giving the dinuclear and dicationic platinum(II)-bis(tricyclohexylphosphine) with an unprecedented 1,3,2,4-dioxodiboretane ligand that bridges two cationic bis(tricyclohexylphosphine)platinum(II)-fragments, which have a distorted T-shaped geometry (structure B) in (Fig. 17).<sup>95</sup> The observed cyclodimerization reaction indicates the influence the platinum fragment exerts on the oxoboryl moiety.<sup>95</sup>



**Fig. 16** Reactivity of a diazadiborinine radical cation towards *p*-benzoquinone and  $\text{Ph}_3\text{SnH}$ . The  $[pf]^-$  counter anions are not shown for clarity.



**Fig. 17** Molecular structures of three mixed boron/transition metal complexes. The  $[pf]^-$  counter anions are not shown for clarity.

Additionally, the fluoroarene complex  $[\text{Rh}(\text{dcpm})(\eta^6\text{-1,2,3-F}_3\text{C}_6\text{H}_3)][pf]^-$  (dcpm = *bis*(dicyclohexylphosphino)methane) does not act as an efficient hydrodefluorination catalyst towards  $\text{H}_3\text{B}\cdot\text{NMe}_2\text{H}$ , but instead forms the bimetallic aminoborylene complex  $\{[\text{RhH}(\mu\text{-dcpm})]_2(\mu\text{-H})(\mu\text{-BNMe}_2)\}^+$  (structure c) in Fig. 17.<sup>96</sup> In this cation, a hydride and a borylene moiety act as bridging units (structure C) in Fig. 17).

**Aluminocenium Cation:** The reaction of the protonated ether salt  $[\text{H}(\text{OEt}_2)_2]^+ [pf]^-$  with  $\text{AlCp}_2$  in ether solution leads to the  $[\text{AlCp}_2]^+$ -cation, which is stabilized by the weakly coordinating anion  $[pf]^-$ .<sup>97</sup> In an equilibrium reaction, the aluminocenium cation is coordinated in solution by two diethylether molecules. Depending on the conditions, from this solution crystallize either the free  $[\text{AlCp}_2]^+$ -cation (Fig. 18), characterized for the first time by single crystal XRD, or the coordinated  $[\text{AlCp}_2\cdot 2\text{Et}_2\text{O}]^+$  species.

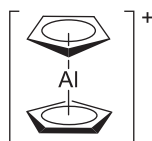
Furthermore, the influence of the counterions  $[pf]^-$  and  $[\text{MeB}(\text{C}_6\text{F}_5)_3]^-$  on the activity of  $[\text{AlCp}_2]^+$  as initiators for the polymerization of isobutene<sup>97,98</sup> was investigated: It appears that the  $[pf]^-$  salt is more active as initiator.

**Chiral Tetra-coordinate Aluminum Cation:** An  $\text{Al}^{\text{III}}$  cation can also be stabilized by chiral amino-alcoholate ligands.<sup>99</sup> It was shown experimentally that the Lewis acidity of this species exceeds that of  $\text{B}(\text{C}_6\text{F}_5)_3$ . As suggested by preliminary catalytic activity studies, the tetra-coordinate aluminum cation is an effective catalyst for hydroboration of ketones, Diels-Alder reactions, and Michael additions. However, the enantioselectivity of these reactions is limited due to the presence of the labile  $\text{N}-\text{Al}$  bond.<sup>99</sup>

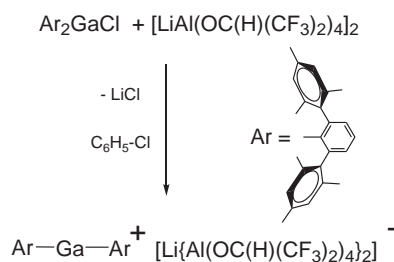
**Cationic Aluminum Carboxylate:** The Lewis acidic trityl cation in  $[\text{Ph}_3\text{C}][pf]^-$  can be used to abstract a formate ligand from a dimeric, N-heterocyclic imino-supported aluminum carboxylate complex.<sup>100</sup> Formate abstraction can also be performed with two equivalents of  $\text{B}(\text{C}_6\text{F}_5)_3$  and yields a dinuclear cationic aluminum complex with one bridging carboxylate ligand.<sup>100</sup>

**Two-coordinate Gallium Cations:**  $[(2,6\text{-Mes}_2\text{C}_6\text{H}_3)_2\text{Ga}]^+ [\text{Li}[hf]_2]^-$  containing a linear two-coordinate gallium cation, was obtained by metathesis reaction of  $(2,6\text{-Mes}_2\text{C}_6\text{H}_3)_2\text{Ga}-\text{Cl}$  with dimeric  $\text{Li}[hf]$  in  $\text{C}_6\text{H}_5-\text{Cl}$  solution at room temperature (Fig. 19).<sup>101,102</sup>

The compound consists of isolated  $[(2,6\text{-Mes}_2\text{C}_6\text{H}_3)_2\text{Ga}]^+$  cations and Lithium-bridged  $[\text{Li}[hf]_2]^-$  anions,<sup>101,102</sup> that were initially observed as the  $[\text{EMIM}]^+$ <sup>17</sup> and  $[\text{CPh}_3]^+$ <sup>9</sup> salts. The  $\text{C}-\text{Ga}-\text{C}$  angle is  $175.69(7)^\circ$  and the  $\text{Ga}-\text{C}$  distances are 191.3(1) and 191.5(2) pm. The compound is remarkably stable and is only a weak Lewis acid that polymerizes cyclohexene oxide. This behavior indicates that in non-basic solvents like  $\text{CH}_2\text{Cl}_2$  or  $\text{C}_6\text{H}_5\text{Cl}$ , only one  $\text{Li}^+$  cation from the dimeric  $\text{Li}[hf]$  that exists in



**Fig. 18** The unsubstituted aluminocenium cation in  $[\text{AlCp}_2]^+ [pf]^-$ .



**Fig. 19** Synthesis of the almost linear  $[\text{Ga}(\text{Ar})_2]^+$  cation.

the solid phase<sup>17</sup> is available and that the Li-bridged  $[\text{Li}(\text{hf})_2]^-$  anion is remarkably more stable<sup>9</sup> than the simple homoleptic  $[\text{hf}]^-$  anion that decomposes with similarly electrophilic cations.

Upon chloride abstraction from  $(^t\text{Bu}_3\text{Si})_2\text{GaCl}$  with  $\text{Ag}[\text{pff}]$ , the salt  $[(^t\text{Bu}_3\text{Si-Ga-Si}^t\text{Bu}_3)[\text{pff}]$  was isolated quantitatively.<sup>103</sup> The highly reactive  $[(^t\text{Bu}_3\text{Si-Ga-Si}^t\text{Bu}_3)^+$  cation features a perfectly linear Si–Ga–Si unit<sup>103</sup> and is isostructural and isoelectronic with neutral  $[(^t\text{Bu}_3\text{Si-Zn-Si}^t\text{Bu}_3)]^{104}$  and anionic  $[(^t\text{Bu}_3\text{Si-Cu-Si}^t\text{Bu}_3)]^{-105}$ .

**A Bridged, Dinuclear Ga<sup>III</sup> Complex:** Reaction of  $\text{IPr-GaCl}_3$  with  $[\text{Ag}(\text{CH}_2\text{Cl}_2)_3][\text{pff}]$  yielded, in the presence of adventitious water, the salt  $\{[\text{IPrGaCl}(\mu\text{-OH})_2]_2 \cdot \text{H}_2\text{O}\}[\text{pff}]_2$  with a dinuclear cationic gallium dihydroxide.<sup>106</sup>

**Disproportionation Reactions of Ga<sup>+</sup> yielding Ga(III)-Complexes:** Subvalent Ga<sup>+</sup> is rather stable as  $[\text{pff}]^-$  salt, as long as weakly basic ligands and solvents are present. Yet, Ga<sup>+</sup> cations disproportionate in the presence of non-innocent reducible ligands, e.g., 2,2'-bipyridine (bipy) and a substituted derivative, 4,4'-(<sup>t</sup>Bu)<sub>2</sub>-bipy (D'Bbipy). Hence, mixing the Ga<sup>I</sup> source  $[\text{Ga}(\text{PhF})_x][\text{pff}]$  with these ligands yielded Ga<sup>0</sup> as well as  $[\text{Ga}^{\text{III}}(\text{D}'\text{Bbipy})_3]^{3+107}$  and  $[\text{Ga}^{\text{III}}\{(\text{bipy})_3\}]^{2+108}$  respectively. The latter includes one radical anionic  $[\text{bipy}]^-$  ligand.

A disproportionation reaction was also observed when mixing  $[\text{Ga}(\text{HMB})][\text{pff}]$ ,  $\text{SbCl}_3$  and a non-innocent bisiminopyridine  $\text{dimpyr}^{\text{dipp}}$ , since, among other products,  $[\text{Ga}^{\text{III}}\text{Cl}_2(\text{dimpyr}^{\text{dipp}})][\text{pff}]$  was isolated.<sup>62</sup>

**Functionalization of a pentaphosphaferrocene:** The reaction of two equivalents of  $[\text{Cp}^*\text{Fe}(\eta^5\text{-P}_5)]$  with  $\text{Ti}[\text{pff}]$  and  $\text{GaI}_3$  afforded the bimetallic compound  $\{[\text{Cp}^*\text{Fe}]_2\{\mu, \eta^{5:5}\text{-}(\text{P}_5)_2\text{GaI}_2\}\}[\text{pff}]$  with the unprecedented  $\{(\text{cycloP}_5)_2\text{GaI}_2\}$  ligand and thus resulted in functionalization of pentaphosphaferrocene.<sup>109</sup> Employing  $\text{BBr}_3$  instead of  $\text{GaI}_3$  furnished  $\{[\text{Cp}^*\text{Fe}]_2\{\mu, \eta^{5:5}\text{-}(\text{P}_5)_2\text{BBr}_2\}\}[\text{pff}]$ , with a structurally analogous cation.<sup>109</sup> However, calculations suggest that the BBr<sub>2</sub>-linker is better described as a borate-bridge, since the B atom shows negative charge accumulation.<sup>109</sup> In contrast to this, the P–Ga bonds in the GaI<sub>2</sub>-bridged cation have a more polar character, accounting for the small positive charge on the Ga atom.<sup>109</sup>

**A Dicationic [H-Ga(PPh<sub>3</sub>)<sub>3</sub>]<sup>2+</sup> Salt:** The dissolved  $[\text{Ga}(\text{HMB})][\text{pff}]^-$  salt reacts with  $[\text{H-PPh}_3]^+$  under formation of the unprecedented dicationic gallium hydride complex  $[\text{H-Ga}(\text{PPh}_3)_3][\text{pff}]_2$ , which may either proceed via a direct oxidative addition of Ga<sup>I</sup> into the H–P bond or via initial protonation of Ga<sup>I</sup>, followed by the subsequent addition of the deprotonated, Lewis basic  $\text{PPh}_3$  (Fig. 20).<sup>62</sup>

**Gallylene Transition-Metal Cations:** The Aldridge group described the syntheses of a series of cationic transition metal complexes with gallylene ligands of the type  $(\text{NacNac})^{\text{dipp}}\text{Ga}$ , underlining the carbene-like character of subvalent gallium.<sup>110,111</sup>

**Gallylene Main Group-Metal Cations:** Halide abstraction of the carbene-coordinated pnictinidenes  $(^{\text{Me}}\text{cAAC})\text{EGa}(\text{Cl})\text{L}$  ( $\text{E} = \text{P},^{112} \text{As}, \text{Sb}$ ,  $^{\text{Me}}\text{cAAC} = [\text{H}_2\text{C}(\text{CMe}_2)_2\text{Ndipp}]\text{C}$ ;  $\text{L} = \text{HC}[\text{C}(\text{Me})\text{Ndipp}]_2$ ) yielded the cationic group 15 compounds  $[(^{\text{Me}}\text{cAAC})\text{EGaL}][\text{pff}]$  ( $\text{E} = \text{P},^{112} \text{As}, \text{Sb}$ ). Quantum chemical calculations suggest that the central pnictogen atom determines the electronic nature of the cations  $[(^{\text{Me}}\text{cAAC})\text{EGaL}]^+$ . In these structures, the heavier pnictogen atoms serve as a trap for the positive charge, resulting in carbene-stabilized heterovinyl-type structures.<sup>113</sup> The cation containing the lighter congener P reacts with ethyl isocyanate under C–C bond formation.<sup>112</sup>

**An In<sup>III</sup>-Crown Ether Complex:** In addition to the [18]crown-6 ether complex of univalent indium<sup>114</sup> (*vide infra*), the isolation of  $[\text{InCl}_2(\{18\}\text{crown-6 ether})][\text{pff}]$  with a linear  $[\text{Cl-In}^{\text{III}}-\text{Cl}]^+$  chain has been reported.<sup>115</sup>

#### 1.07.2.2.3.2 Subvalent group 13 cations: From coordination compounds to clusters

The stability of group 13 elements in their +1 oxidation state increases with increasing atom number, due to the stabilizing “inert pair effect” of the  $ns^2$  electrons.<sup>116,117</sup> Consequently, no successful isolation of cationic B<sup>I</sup> or Al<sup>I</sup> complexes has been reported so far, while cationic Ga<sup>I</sup>, In<sup>I</sup> and Tl<sup>I</sup> compounds are well known.

**Gallium.** Even though subvalent gallium is more stable than subvalent boron or aluminum, classical Ga<sup>I</sup>-sources like “GaI”<sup>118,119</sup> or “GaX<sub>2</sub>”<sup>120–122</sup> still tend to undergo redox reactions like dis- or comproportionation with  $\sigma$ -donating ligands, which hampered systematic studies on the coordination chemistry.<sup>123,124</sup> The susceptibility of Ga<sup>I</sup> to redox chemistry upon the interaction with electron donating ligands or the counter anion is reduced by employing WCAs and  $\pi$ -donating ligands, e.g., arenes.<sup>124</sup> When  $[\text{Ga}[\text{GaX}_4]]$  ( $\text{X} = \text{Cl}, \text{Br}$ ) is dissolved in the presence of chelating arene ligands like cyclophanes, a similar interaction of the weakly accepting Ga<sup>+</sup> ion with three arene ligands may be realized. However, if the chelating cyclophane is replaced by individual arenes, only coordination of up to two arenes per Ga<sup>+</sup> ion was hitherto possible,<sup>125</sup> likely due to the weak complexation of the third arene that competes with stronger interactions with the  $[\text{GaCl}_4]^-$  counterion at 310–370 pm in the  $[\text{Ga}(\text{C}_6\text{H}_6)_2][\text{GaCl}_4]^-$  salt<sup>125</sup> (sum of Ga + Cl van der Waals radii: 370 pm).<sup>126</sup> If the more coordinating  $[\text{GaCl}_4]^-$  counterion is replaced by the less coordinating  $[\text{pff}]^-$  anion, this competition is negligible and the entropically and enthalpically normally disfavored coordination of a third arene becomes now possible, underlining the weakly coordinating nature of the  $[\text{pff}]^-$  anion.<sup>33</sup>

Notably, salts of the type  $[\text{Ga}(\text{arene})_x][\text{pff}]$  (arene = e.g., toluene,<sup>33</sup> *p*-xylene,<sup>127</sup> mesitylene,<sup>128</sup> HMB<sup>127</sup> or oDFB,<sup>33</sup> in most cases  $\text{PhF}^{33,128}$ ,  $x = 2\text{--}3$  and  $x = 1$  for *ansa*-arene ligands<sup>127</sup>) are well-defined and nowadays established starting materials for Ga<sup>I</sup> chemistry, since they are room temperature stable and easily synthesized by oxidizing elemental gallium with the silver salt  $\text{Ag}[\text{pff}]$  in an

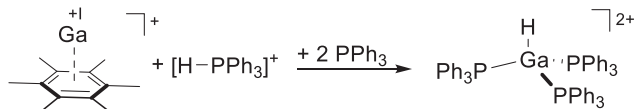


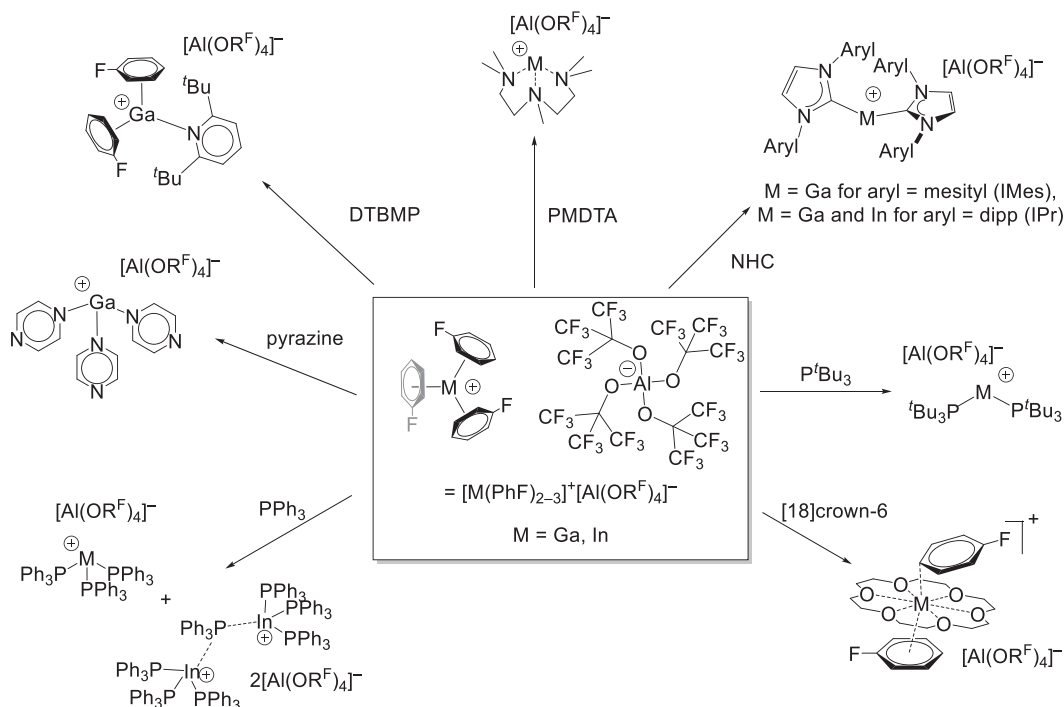
Fig. 20 Oxidative addition of a P–H bond at a subvalent gallium cation.<sup>62</sup>

aromatic solvent by using ultrasound.<sup>33</sup> With the particularly electron rich HMB, isolation of a mono-arene complex has been reported from the HMB radical cation.<sup>54</sup> Consequently, the introduction of  $[\text{Ga}(\text{arene})_x][\text{pf}]$  has allowed for the synthesis of several unusual cationic, subvalent gallium compounds and has led to a better understanding of  $\text{Ga}^{\text{I}}$  chemistry, which was recently reviewed<sup>124</sup> and from which part of the descriptions here are taken. Isolated mononuclear  $\text{Ga}^{\text{I}}$  (and  $\text{In}^{\text{I}}$ ) complexes with the  $[\text{pf}]^-$  counter anion are shown in Fig. 21.

The central  $\text{Ga}^+$  ion may interact with a variety of ligands, ranging from soft (e.g., phosphines, carbenes) to hard (e.g., pyrazine, crown ethers). The steric bulk and denticity of the ligands determine the coordination numbers. Reaction of sterically less demanding  $\text{PPh}_3$ <sup>33</sup> and pyrazine ligands<sup>129</sup> with  $[\text{Ga}(\text{PhF})_x][\text{pf}]$  yielded the respective trigonal-pyramidal gallium complexes (Fig. 21). The coordination mode reflects the electron donation of the ligands in the three empty  $4p$  orbitals at gallium and its formally stereochemical active lone pair. It is interesting to note that each  $\text{Ga}^+$  cation is coordinated in a trigonal-pyramidal fashion by three  $\eta^1$ -donating pyrazine ligands, and that the ligands are not  $\pi$ -coordinated, which would likewise be conceivable.<sup>129</sup> This coordination mode is also observed in 1D coordination polymers of  $[\text{Ga}(\mu\text{-pyrazine})_2(\eta^1\text{-pyrazine})]_n[\text{pf}]_n$  which clearly implies that  $\text{Ga}^+$  cations favor  $\sigma$ - over  $\pi$ -coordination.<sup>129</sup> A  $\text{Ga}^{\text{I}}$  complex with the tridentate, chelating pentamethyldiethylenetriamine (PMDTA) has also been described (Fig. 21).<sup>130</sup> The  $\pi$ -Lewis-acidity of the  $\text{Ga}^+$  cation is significantly diminished upon saturation of all three  $4p$ -orbitals by the ligands.<sup>124</sup> In contrast, the steric bulk of a  $\text{P}(\text{tBu})_3$  ligand allowed only for coordination of two phosphines to the gallium atom (Fig. 21).<sup>34</sup> With  $N$ -heterocyclic carbenes (NHC = IMes, IPr), structurally similar dicoordinate complex cations were isolated and characterized (Fig. 21).<sup>131</sup> An analysis of the crystal structure and of the bonding situation reveals a  $\sigma$ -backdonation of the  $4s^2$  lone pair into the LUMO of the NHCs.<sup>131</sup> Thus, since the Lewis acidity of  $\text{Ga}^+$  is not quenched by the coordination of only two ligands, such dicoordinate gallium complexes may potentially show a metal-centered, ambiphilic, transition-metal like reactivity with a low-valent and low-coordinate main-group cation.<sup>124</sup> With sterically highly demanding 2,6-di-*tert*-butyl-4-methylpyridine (DTBMP), a nonchelated mixed  $\sigma$ - and  $\pi$ -bound complex was obtained, i.e.,  $[\text{Ga}(\text{C}_6\text{H}_5\text{F})_2(\text{DTBMP})]^+$ . As with pyrazine, the aromatic nitrogen base exclusively interacts through its nitrogen lone pair. However, the steric bulk of the DTBMP ligand only allows for one ligand to coordinate to  $\text{Ga}^+$ , while the PhF ligands display their usual  $\pi$ -coordination mode.<sup>129</sup> Moreover, the  $\text{pf}$  salt of a  $[\text{Ga}^{\text{I}}(\text{18crown-6})]^+$  complex with one arene ligand above and below the  $\text{Ga}$ -[18]crown-6 plane, respectively, was reported (Fig. 21).<sup>114</sup> In this complex cation, one arene ring is bound in  $\eta^6$ -fashion to  $\text{Ga}^+$ , while the second arene ligand shows only a  $\eta^1$ -coordination.<sup>114</sup> The  $\eta^6$ -coordination for the second arene ligand is probably prevented by the  $4s^2$  lone pair residing on  $\text{Ga}^{\text{I}}$ , which likely exerts a stereochemical effect.

The mono-arene complex  $[\text{Ga}(\text{HMB})]^+$  can also serve as a starting point for  $\text{Ga}^{\text{I}}$  chemistry. The aromatic HMB ligand can be replaced by the electron rich, chelating and non-innocent *bis*iminopyridine *dimpyr*<sup>dipp</sup> ligand, allowing for the isolation of  $[\text{Ga}(\text{dimpyr}^{\text{dipp}})][\text{pf}]$ .<sup>62</sup>

**A Homoleptic Olefin Main Group Metal Complex:** Employing the very weakly coordinating  $[\text{pf}]^-$  anion also allowed the isolation of the first homoleptic olefin complex of any main-group metal accessible as a bulk compound, i.e.,  $[\text{Ga}^{\text{I}}(\text{COD})_2][\text{pf}]$  ( $\text{COD} = 1,5$ -



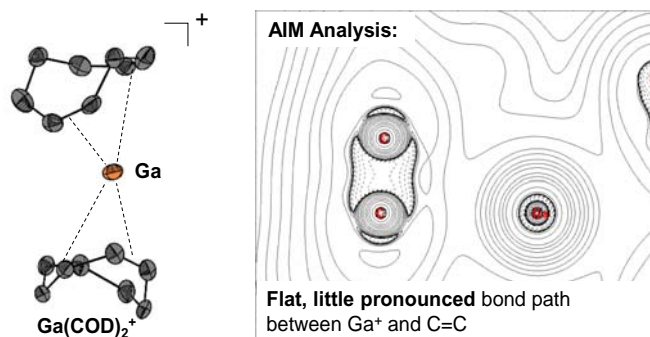
**Fig. 21** Synthesis of cationic  $\text{M}^{\text{I}}$  complexes starting from  $[\text{M}(\text{PhF})_{2-3}][\text{pf}]$  ( $\text{M} = \text{Ga, In}$ ) and  $\sigma$ -donating ligands (mesityl = 2,4,6-( $\text{CH}_3$ )<sub>3</sub> $\text{C}_6\text{H}_2$ ; dipp = 2,6- $\text{Pr}_2\text{C}_6\text{H}_3$ ).<sup>124</sup>

cyclooctadiene).<sup>132</sup> It constitutes an olefin complex of a main-group metal that may adopt different oxidation states, again showing parallels to transition metals and opening potential applications in catalysis. The highly unusual bonding between an olefin and a main-group metal was analyzed in detail and was shown to be a weak bond with mostly electrostatic character.<sup>132</sup> The crystal structure of the cation as well as the Laplacian of the electron density of the bonding interactions between Ga and a carbon-carbon double bond is shown in Fig. 22.

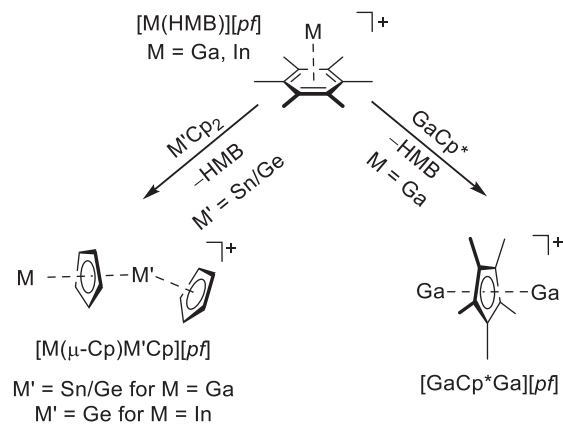
**Indium.** The chemistry of univalent indium is akin to the chemistry of univalent gallium and for this reason included with Fig. 21.<sup>124</sup> In analogy to the  $[pf]^-$  salt of the lighter counterpart,  $[\text{In}(\text{PhF})_x][pf]$  ( $x = 2-3$ ) has proven to be a useful source of  $\text{In}^+$  as it is easily synthesized by oxidizing elemental indium with the silver salt  $\text{Ag}[pf]$  in PhF by using ultrasound.<sup>34,35</sup> Additionally, the *o*DFB complex  $[\text{In}(\text{oDFB})_2]^{+35}$  has also been isolated. With electron rich aromatic ligands, monoarene complexes of the type  $[\text{In}(\text{arene})_1]^+$  (arene = mesitylene, HMB) were prepared after in situ generation of the radical cations with  $\text{I}_2$  and  $\text{Ag}[pf]$ .<sup>54</sup> Starting from  $[\text{In}(\text{PhF})_x][pf]$  ( $x = 2-3$ ), mononuclear  $\text{In}^1$  complexes with PMDTA,<sup>130</sup> IPr,<sup>131</sup> [18]crown-6 ether<sup>114</sup> and  $\text{P}^t\text{Bu}_3$ <sup>34</sup> could be synthesized, as shown in Fig. 21. The molecular structures of these compounds are analogous to the respective  $\text{Ga}^1$  complexes. Employing  $\text{PPh}_3$  leads to two different  $\text{In}^1$  complexes, with the first cation being structurally similar to the  $\text{Ga}^1$  complex. In the second cation, two  $[\text{In}(\text{PPh}_3)_3]^+$  units are linked by a bridging  $\text{PPh}_3$  ligand.<sup>34</sup> However, the  $\text{In}-\text{P}$  bond lengths for the seventh phosphane ligand exceed the sum of their van-der-Waals radii, suggesting that the additional phosphane does not affect the coordination at the indium cations and is located in between the indium centers due to packing effects.<sup>34</sup>

**Binuclear  $\text{Ga}^1$  and  $\text{In}^1$  Complexes:** With  $[\text{Ga}(\text{HMB})][pf]$  and  $\text{GeCp}_2$  or  $\text{SnCp}_2$ , two isostructural binuclear complexes, i.e.,  $[\text{Ga}(\mu\text{-Cp})\text{GeCp}]^+$  and  $[\text{Ga}(\mu\text{-Cp})\text{SnCp}]^+$ , were isolated as their  $pf$  salts, respectively.<sup>133</sup> Instead of obtaining a GaGa-bonded Lewis acid-base adduct, the reaction between  $[\text{Ga}(\text{HMB})][pf]$  and  $\text{GaCp}^*$  only yielded the inverse sandwich cation  $[\text{GaCp}^*\text{Ga}][pf]$  under substitution of neutral HMB.<sup>133</sup> It was concluded that coordination by the formally negatively charged aromatic  $\text{Cp}^*$  moiety is favored over the coordination by the Lewis basic Ga atom.<sup>133</sup> The reaction between  $[\text{In}(\text{HMB})][pf]$  and  $\text{GeCp}_2$  afforded the binuclear complex  $[\text{In}(\mu\text{-Cp})\text{GeCp}]^+$  in an unselective reaction, while the reaction  $\text{SnCp}_2$  resulted in a crude mixture of products.<sup>133</sup> The different reaction outcomes are summarized in Fig. 23.

**Cationic Coordination Polymers:** Starting from  $[\text{In}(\text{HMB})][pf]$  and  $\text{SnCp}_2$  or  $\text{FeCp}_2$ , cationic coordination polymers featuring a chain motif were isolated, i.e.,  $[\{\text{In}(\text{HMB})(\mu\text{-SnCp}_2)\}_n][pf]_n$  and  $[\{\text{In}(\text{HMB})(\mu\text{-FeCp}_2)\}_n][pf]_n$ , respectively.<sup>133</sup>  $\text{FeCp}_2$  reacts

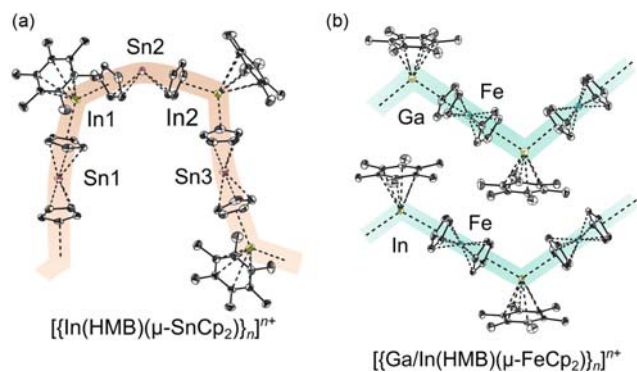


**Fig. 22** Molecular structure of the cation (left; hydrogen atoms are omitted for clarity) as well as the Laplacian of the electron density of the bonding interaction between Ga and a carbon-carbon double bond of a COD ligand (right).<sup>124,132</sup>



**Fig. 23** Reactivity of  $[\text{M}(\text{HMB})][pf]$  ( $\text{M} = \text{Ga, In}$ ) towards  $\text{M}'\text{Cp}_2$  ( $\text{M}' = \text{Sn, Ge}$ ) and  $\text{GaCp}^*$ . Note that the formation of  $[\text{In}(\mu\text{-Cp})\text{GeCp}]^+$  is unselective and accompanied by the side product  $[\text{CpGe}(\mu\text{-Cp})\text{GeCp}][\text{al}fa]$  with a decomposed anion.<sup>133</sup>





**Fig. 24** Molecular structures of the infinite ( $n = \infty$ ) coordination polymers  $\{[\text{In}(\text{HMB})(\mu\text{-SnCp}_2)]_n\}^{n+}$  (shown with  $n = 3$ ; a) and of  $\{[\text{Ga/In}(\text{HMB})(\mu\text{-FeCp}_2)]_n\}^{n+}$  (shown with  $n = 2$ ; b). Thermal displacement ellipsoids drawn at 50% probability,  $[\text{pf}]^-$  counterions are omitted for clarity.<sup>133</sup>

with  $[\text{Ga}(\text{HMB})][\text{pf}]$  under the formation of the isostructural cationic coordination polymer  $\{[\text{Ga}(\text{HMB})(\mu\text{-FeCp}_2)]_n\}^{n+}$ .<sup>133</sup> The molecular structures of these compounds are shown in Fig. 24.

**Multinuclear Complexes of  $\text{Ga}^I$ ,  $\text{In}^I$  and  $\text{Tl}^I$  with  $\text{E}_n$  ( $\text{E} = \text{Group 15}$ ) ligands:** With the sandwich complexes  $[\text{Cp}^*\text{Fe}(\eta^5\text{-E}_5)]$  ( $\text{E} = \text{P, As}$ ) and  $\text{Ga}^+$  or  $\text{In}^+$ , the Scheer group obtained one-dimensional coordination polymers  $[\text{M}(\mu, \eta^5: \eta^1\text{-E}_5\text{FeCp}^*)_3]_n[\text{pf}]_n$  ( $\text{M} = \text{In, Tl}$  for  $\text{E} = \text{As}$ <sup>134</sup>;  $\text{M} = \text{Ga, In}$  and  $\text{Tl}$  for  $\text{E} = \text{P}$ <sup>134,135</sup>). In these compounds, the  $\text{P}_5$  ligands are  $\eta^5$ -bound and show a very weak  $\sigma$ -interactions between one P atom of the ring and the neighbored subvalent group 13 cation, as shown in Fig. 25.<sup>134</sup>

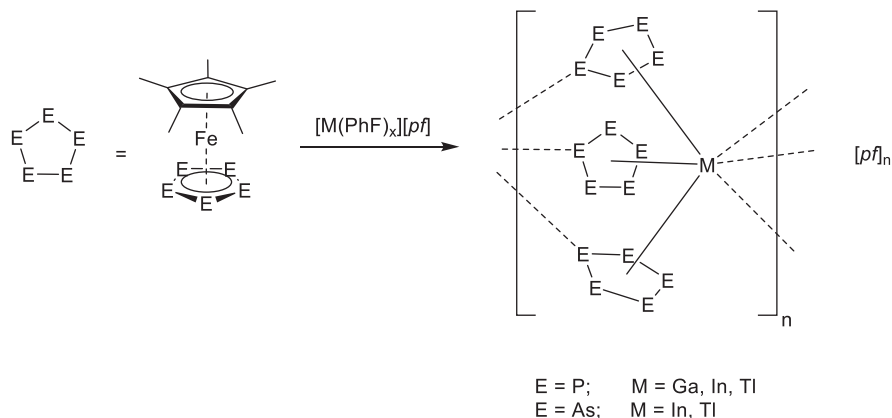
Again using the  $[\text{pf}]^-$  anion, the same group reported the synthesis of a tetracationic indium aggregate including  $\text{P}_2$  ligands<sup>35</sup> as well as the synthesis of polymeric chain compounds of  $\text{In}^+$  ions, bridged by  $[\text{CpM}'(\text{CO})_2(\eta^3\text{-P}_3)]$  units ( $\text{M}' = \text{Cr}$ <sup>35</sup> or  $\text{Mo}$ ).<sup>136</sup>

The reaction of  $\text{Tl}[\text{pf}]$  and  $\{[\text{CpMo}(\text{CO})_2]_2(\text{P}_2)\}$  afforded a dimeric, dicationic  $\text{Tl}^I$  compound, with the two  $\text{Tl}^I$  ions asymmetrically bridged by two  $[\text{CpMo}(\text{CO})_2]_2(\text{P}_2)$  moieties.<sup>135</sup> One dimensional coordination polymers containing  $\text{Tl}^I$  were also obtained starting from  $\text{Tl}[\text{pf}]$  and a mixed  $\text{P}_m\text{Sn}_n$  ligand or  $[\text{CpM}'(\text{CO})_2(\eta^3\text{-P}_3)]$  ( $\text{M}' = \text{Cr, Mo}$ ).<sup>136</sup> Reacting  $[(\text{Cp}^*\text{Mo})_2(\mu, \eta^6: \eta^6\text{-P}_6)]$  with  $\text{Tl}[\text{pf}]$ <sup>137</sup> yielded a two-dimensional coordination network.<sup>138</sup>

**Miscellaneous  $\text{Tl}^I$  Complexes:** As already pointed out, the stability of subvalent Group 13 elements increases with increasing atom number due to the inert pair effect. Thus, the +1 oxidation state is rather common for Tl and relying on WCAs is usually not a prerequisite when investigating  $\text{Tl}^I$  chemistry. Due to the stability of  $\text{Tl}^I$ , it is unsurprising that the solvent-free salts  $\text{Tl}[\text{pf}]$ <sup>137</sup> and  $\text{Tl}[\text{hf}]$ <sup>139</sup> are readily available from the reaction of the respective Li salt and  $\text{TlF}$ . It was shown that, stabilized by a 2,5-bis(2-pyridyl)phosphole ligand, mono- and dimetallic  $\text{Tl}^I$  complexes are obtained with  $\text{Tl}[\text{pf}]$ , while  $[\text{PF}_6]^-$  anions coordinate to  $\text{Tl}^I$  and lead to polymetallic species when working with  $\text{Tl}[\text{PF}_6]$ .<sup>140</sup>

#### 1.07.2.2.3.3 Formation of polycationic group 13 clusters

Since organometallic group 13 element compounds are inherently electron deficient compounds, the vast majority of group 13 metal clusters are neutral or anionic.<sup>141–152</sup> In order to obtain group 13 metal clusters, subvalent cations have to be employed since their  $ns^1$  or  $2$  electrons are required for bond formation. Cationic cluster formation is hampered by the accumulation of positive charge, which has to be overcome using electron rich  $\sigma$ -donating ligands, which delocalize the positive charge. Generally, the disproportionation energetics is much more favored for the lighter group 13 elements, suggesting that polycationic cluster



**Fig. 25** Formation and molecular structure of the one-dimensional coordination polymers that are formed upon reaction of  $\text{cycloE}_5$  ligand complexes with the  $\text{pf}$  salts of monovalent  $\text{Ga}^+$ ,  $\text{In}^+$ , and  $\text{Tl}^+$ .<sup>134,135</sup>

formation is possible with the heavier congeners, i.e., Ga, In and Tl.<sup>108</sup> The energetics underlying either a disproportionation or a cationic cluster formation suggest that cationic cluster formation can only be achieved employing WCAs instead of small anions.<sup>108</sup>

**Gallium Clusters:** Indeed, the formation of tetracationic clusters with a Ga<sub>4</sub> core was observed upon mixing [Ga(PhF)<sub>x</sub>][pfl] and bis(dimethylphosphino)ethane (DMPE)<sup>153</sup> or *tert*-butylisocyanide (CN<sup>t</sup>Bu)<sup>107</sup> as  $\sigma$ -donating ligands. With 4-dimethylaminopyridine (DMAP), even a pentacationic cluster was obtained, representing the first salt with an ionic 1:5 packing.<sup>154</sup> The molecular structures of these cationic Ga<sup>I</sup> clusters are shown in Fig. 26. The CN<sup>t</sup>Bu- and DMAP-supported clusters are essentially planar, while the DMPE-supported cluster is slightly puckered, probably due to steric repulsion of the methyl groups. Quantum chemical calculations and the Ga–Ga bond lengths (246–250.5 pm) suggest that the Ga–Ga bonds are best described as single bonds.<sup>107,153,154</sup>

In the presence of non-innocent, chelating, pyridine-based aromatic ligands, Ga<sup>+</sup> tends to disproportionate. For example, the reaction between [Ga(PhF)<sub>x</sub>][pfl] and phenanthroline (phen) results in the formation of elemental gallium and [Ga<sup>II</sup>(phen)<sub>4</sub>]<sup>4+</sup>, a dimeric tetracation with relatively short Ga<sup>II</sup>–Ga<sup>II</sup> bond (256 pm).<sup>107</sup> With bipy and a substituted derivative, Ga<sup>I</sup> disproportionates to elemental gallium and mononuclear Ga<sup>III</sup> complexes (*vide supra*).<sup>107,108</sup>

**Indium Clusters.** In contrast to the more limited propensity of Ga<sup>+</sup> to aggregate towards clusters, In<sup>+</sup> readily forms cationic clusters with the non-innocent ligands bipy and phen. With [In(PhF)<sub>x</sub>][pfl] and bipy, one rhombohedral, tetracationic and two triangular, tricationic clusters were isolated, depending on the exact crystallization conditions and molar ratios (Fig. 27).<sup>108</sup>

The rhombic In<sub>4</sub> motif was reproduced by employing phen instead of bipy; both contain the shortest known In–In bonds around 259 pm.<sup>108</sup> As a side product, [(phen)<sub>2</sub>In<sup>I</sup>Ag<sup>I</sup>(PhF)]<sup>2+</sup>, the first monomeric and dicationic In–Ag adduct was isolated.<sup>108</sup>

In addition, the synthesis of a tetracationic In<sup>I</sup> cluster was recently reported with DMPE as a ligand.<sup>153</sup> In this polycationic cluster, the In<sub>4</sub> core forms a nearly perfectly planar square, unlike the puckered Ga<sub>4</sub> moiety in the analogous, isostructural gallium cluster (cf. Fig. 26). By contrast, <sup>t</sup>BuNC does not induce the formation of cationic indium clusters, but only of the monocationic pyramidal [In<sup>I</sup>(<sup>t</sup>BuNC)<sub>3</sub>]<sup>+</sup> and, probably due to traces of water, the OH-bridged dimeric [(<sup>t</sup>BuNC)<sub>4</sub>In<sup>III</sup>( $\mu$ -OH)<sub>2</sub>In<sup>III</sup>(CN<sup>t</sup>Bu)<sub>4</sub>]<sup>4+</sup>.<sup>107</sup>

#### 1.07.2.2.4 Reactive group 14 cations: Carbocations and their heavier homologues

##### 1.07.2.2.4.1 Tricoordinate carbenium ions

In the course of our investigations into new arsenic-halogen-cations we fortuitously prepared a simple, but electronically very interesting carbenium ion<sup>155</sup>: the [CS<sub>2</sub>Br<sub>3</sub>]<sup>+</sup> cation, which may be obtained by the quantitative reaction of [AsBr<sub>4</sub>]<sup>+</sup> with CS<sub>2</sub> yielding [CS<sub>2</sub>Br<sub>3</sub>]<sup>+</sup> and a polymeric As<sup>I</sup>Br (Eq. 6).

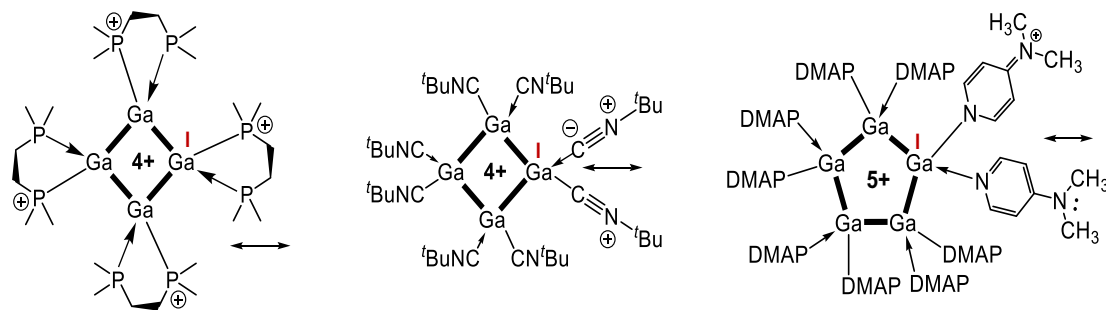


Fig. 26 Molecular structures of polycationic, subvalent Ga<sup>I</sup> clusters that were isolated as their respective [pfl]<sup>−</sup> salts. Only one out of many possible resonance structures is shown, respectively.<sup>107,153,154</sup>

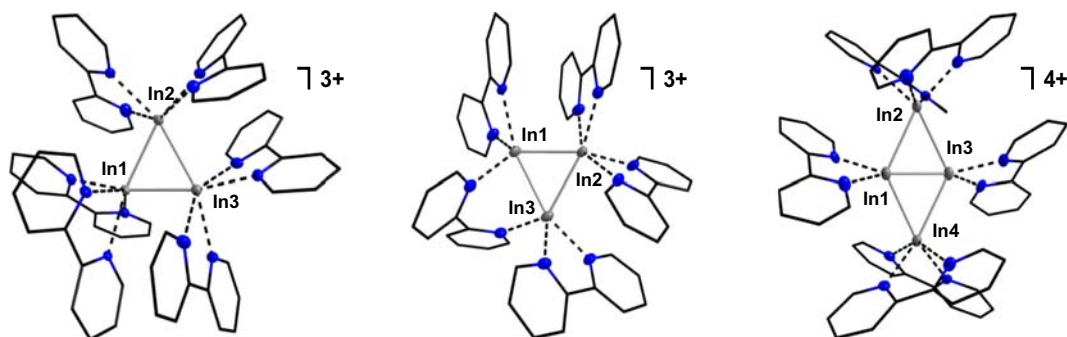
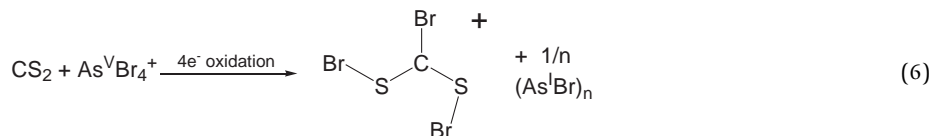
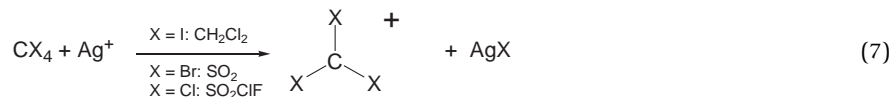


Fig. 27 Molecular structures of selected In<sup>I</sup>-bipy clusters obtained upon mixing [In(PhF)<sub>x</sub>][pfl] and 2,2'-bipyridine, isolated as their respective [pfl]<sup>−</sup> salts.<sup>108</sup>

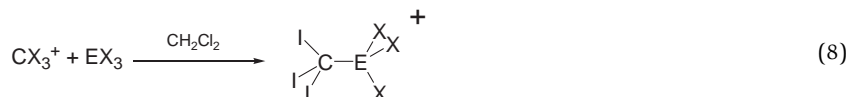


The C–Br bond length in  $[\text{CS}_2\text{Br}_3]^+$  is very close to that expected for the simple  $\text{CBr}_3^+$  cation (181.7 vs. 181.3 pm @MP2/TZVPP) and thus it appeared likely that simple binary carbon-halogen cations such as  $[\text{CX}_3]^+$  may also be accessible by metathesis of  $\text{CX}_4$  with silver aluminates. Therefore, we decided to examine the reaction of  $\text{CX}_4$  ( $X = \text{Cl}, \text{Br}, \text{I}$ ) and  $\text{Ag}[pf]$  or  $\text{Ag}[alfal]$  with the goal to prepare  $[\text{CX}_3]^+$  salts (and  $\text{AgX}$ ). These reactions are successful and quantitative with both anions, but need different solvents for optimal performance (Eq. 7):  $\text{CH}_2\text{Cl}_2$  for  $[\text{Cl}_3]^+$ .<sup>156–158</sup>  $\text{SO}_2$  for  $[\text{CBr}_3]^+$ <sup>159</sup> and  $\text{SO}_2\text{ClF}$  for  $[\text{CCl}_3]^+$ .<sup>159</sup>



For the successful preparation of  $[\text{Cl}_3^+][pf]^-$ , the complete exclusion of light and the use of carefully purified diiodine free  $\text{Cl}_4$  is absolutely necessary. Solutions of  $[\text{Cl}_3]^+$  are stable at RT (exclusion of light), while those of  $[\text{CCl}_3]^+$  decompose at RT with half-lives of about 1–2 h. The solid salts are more robust and survive a few hours at RT without decompositions and may be stored without noticeable decompositions for months at  $-20^\circ\text{C}$ . In the framework of these experimental investigations, also the theoretical aspects of these  $[\text{CX}_3]^+$  salts was thoroughly investigated<sup>160</sup> and compared to the bonding in the isoelectronic boron halides.<sup>161,162</sup>

The  $[\text{Cl}_3]^+$  salts were used for further reactions with the weak nucleophiles  $\text{PX}_3$  ( $X = \text{Cl}, \text{Br}, \text{I}$ ) and  $\text{AsI}_3$  that lead to the formation of the  $[\text{I}_3\text{C-EX}_3]^+$ .<sup>158</sup> with ethane conformation (Eq. 8; but not with the hoped for non-classical structures<sup>162</sup>).

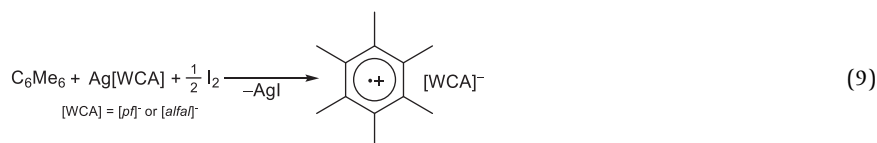


#### 1.07.2.2.4.2 Delocalized carbocations

Dibenzo[*a,e*]pentalene (DBP) is a non-alternant conjugated hydrocarbon with antiaromatic character and ambipolar electrochemical behavior. Upon oxidation, it becomes aromatic. The chemical oxidation of a planar DBP derivative and a bent DBP-*phane* was studied<sup>163</sup> and the molecular structures of its planar dication and cation radical in the solid state demonstrate the gained aromaticity through bond length equalization, which is supported by nucleus independent chemical shift-calculations. EPR spectra on the cation radical confirm the spin delocalization over the DBP framework. This is the first report on structures of a DBP cation radical and dication in the solid state. In addition,<sup>164</sup> the facile gold-mediated skeletal rearrangement of [7]-helicene into a cationic polyaromatic hydrocarbon was published. It reports in-depth studies on the structure and aromaticity of this novel stable cation and proposes a mechanism for its formation.

*Silylated Tetramethylcyclobutenyl Cation:* Instead of yielding the desired non-classical silylium ions, the reactions of different alkenes/alkynes with several  $[\text{Me}_3\text{Si}]^+$ -sources mostly led to oligomerization, or—in the presence of  $\text{Me}_3\text{SiH}$ —hydrosilylation of the alkenes/alkynes.<sup>66</sup> Yet, from the reaction of 2-butyne with ion-like  $\text{Me}_3\text{Si-F-Al}(\text{OR}^{\text{PF}})_3$  the salt of the silylated tetramethylcyclobutenyl cation  $[\text{Me}_4\text{C}_4\text{-SiMe}_3]^+[\text{alfal}]^-$  was obtained in good yield (NMR, scXRD, Raman, and IR).<sup>66</sup> All the experimental and calculated evidence suggest a mechanism in which  $[\text{Me}_4\text{C}_4\text{-SiMe}_3]^+$  was formed via a non-classical silylium ion as an intermediate.

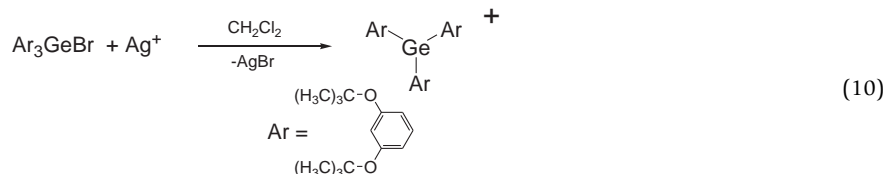
*Delocalized Carbocations as Ligand-forming Oxidants:* Ligand-forming oxidizing agents are designed to oxidize the substrate and directly stabilize the oxidation product. An example of a “soft” ligand-forming oxidant is the hexamethylbenzene (HMB) radical cation, accessible as  $[pf]^-$ <sup>54</sup> or  $[alfal]^-$ <sup>48</sup> salt via oxidation of neutral hexamethylbenzene with  $\text{Ag}[\text{WCA}]/\text{I}_2$  as in Eq. (9) ( $[\text{WCA}]^- = [pf]^-$  and  $[alfal]^-$ ). Although no crystal structure of  $[\text{HMB}]^+[\text{WCA}]^-$  could be obtained, in situ generated red solutions of the radical cation react readily with elemental metals such as Gallium, Indium, Calcium, Strontium and Barium to form the respective cationic HMB-complexes in oxidation states +I (for Ga/In)<sup>54</sup> or +II (for Ca/Sr/Ba).<sup>48</sup>



## 1.07.2.2.4.3 Extensions to heavier homologues

**Silylium Ions:** Attempts to prepare simple  $[\text{Me}_3\text{Si}]^+$  silylium ions were futile: while  $\text{Ag}[pf]$  reacts with  $\text{Me}_3\text{SiCl}$  with formation of  $\text{AgCl}$  and likely the  $[\text{Me}_3\text{Si}]^+[pf]^-$  intermediate, the latter decomposes already at low temperatures with fluoride abstraction and formation of  $\text{Me}_3\text{Si-F-Al}(\text{OR}^F)_3$ .<sup>165</sup> The synthesis of the latter has been scaled up in an alternative direct route to 85 g batches and is now the starting point for the best  $[alfal]^-$  syntheses.<sup>12</sup> Interestingly, silver salts of the halogenated carborane anions were reported not to react with chlorosilanes,<sup>166</sup> probably due to the considerably stronger coordinating nature and thus reduced electrophilicity of their silver salts available for metathesis. See for a recent systematic investigation.<sup>12</sup> However, silylium ions  $[\text{Si}(\text{C}_6\text{Me}_5)_3]^+$  with larger residues like pentamethylphenyl form stable salts with  $[pf]^-$ .<sup>68</sup> Notably, a silylium cation stabilized by a three-center two-electron Si–C–B bond was isolated in the reaction of  $\text{Cl}(\text{Mes})\text{B-N}(\text{TMS})_2$  with  $\text{Ag}[pf]$ .<sup>90</sup> In addition, it was shown that the  $[pf]^-$  anion is very effective in performing silylium ion induced hydrosilylation and hydrodefluorination reactions at very low catalyst loadings down to 0.1 mol%.<sup>65</sup>

**A Stable  $[\text{Ar}_3\text{Ge}]^+[pf]^-$  Salt:** When changing to the larger and less electrophilic Ge atom in combination with larger aromatic ligands, a  $[\text{Ar}_3\text{Ge}]^+[pf]^-$  salt ( $\text{Ar} = 2,6\text{-(OtBu)}_2\text{C}_6\text{H}_3$ ) is straight forward to prepare (Eq. 10)<sup>167</sup>:

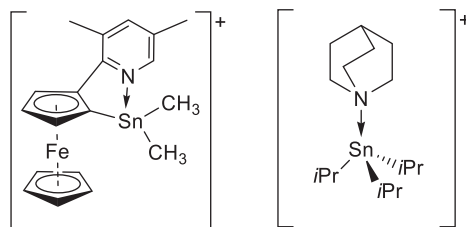


Trying to stabilize tin cations with the less stable  $[hf]^-$  aluminate with the smaller residue  $\text{C}(\text{H})(\text{CF}_3)_2$  led to decomposition by the intermediately prepared tin cation.<sup>168</sup>

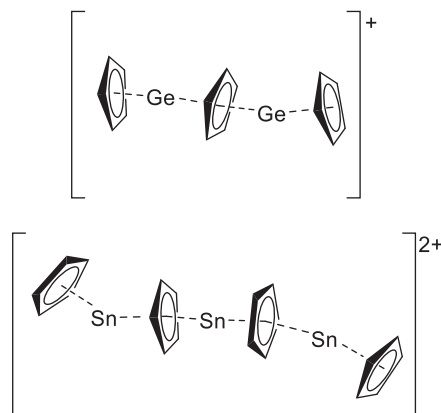
However, a masked  $[\text{R}_3\text{Sn}]^+$  cation was reported by Jäkle in 2013 in which a pyridine donor stabilizes the tin cation intramolecularly (Fig. 28).<sup>169</sup> Moreover, amine-stabilized tin cations  $[(^i\text{Pr})_3\text{Sn}(\text{L})]^+$  ( $\text{L} =$  quinuclidine, 2,4,6-collidine) were synthesized by anion exchange of the coordinating triflate anion in  $[(^i\text{Pr})_3\text{Sn}(\text{OTf})]$  with  $\text{K}[pf]$  in presence of the free amine ligands (Fig. 28).<sup>170</sup>

## 1.07.2.2.5 Low valent group 14 cations

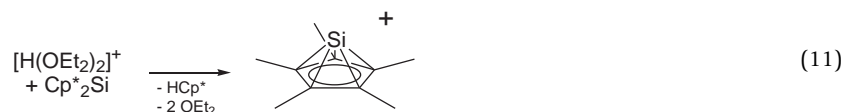
**Jutzi's cation and derivatives:** The reactions of protonated ether  $[\text{H}(\text{OEt}_2)_2]^+$ .<sup>28</sup> with subvalent  $\text{Cp}^*\text{Si}$  and related Cp-derivatives led to the clean and simple formation of the silicocenium  $[\text{SiCp}^*]^+$  *nido*-cluster ion (Eq. 11).<sup>67</sup>



**Fig. 28** Structurally characterized tetra-valent tin cations stabilized with  $[pf]^-$ .



**Fig. 29** Multi-decker cations  $[\text{Sn}_3\text{Cp}_4]^{2+}$  and  $[\text{Ge}_2\text{Cp}_3]^+$  stabilized with  $[pf]^-$  and  $[alfal]^-$  respectively.



For the heavier tetrrels germanium and tin, even the *nido*-clusters  $[\text{MCp}]^+[\text{alfal}]^-$  with the sterically less-encumbering Cp ligands (Cp = C<sub>5</sub>H<sub>5</sub>, M = Sn,<sup>171</sup> Ge<sup>133</sup>) were made accessible by reacting  $\text{MCp}_2$  with 2 equivalents of  $\text{Me}_3\text{Si-F-Al}(\text{OR}^F)_3$  in weakly-coordinating solvents (Fig. 29). Addition of excess  $\text{MCp}_2$  to solutions of  $[\text{MCp}]^+[\text{alfal}]^-$  allowed for isolation of the multi-decker cations  $[\text{Sn}_3\text{Cp}_4]^{2+}[\text{pfl}]_2^-$ <sup>171</sup> and  $[\text{Ge}_2\text{Cp}_3]^+[\text{alfal}]^-$ .<sup>133</sup>

**Two-coordinate M(II) cations:** Two-coordinate M(II) cations (M = Si(II), Ge(II), Sn(II)) are widely investigated due to their diverse reactivity in particular towards small molecules (Fig. 30). An extensively used ligand class are the mono-anionic  $\beta$ -diketiminate ligands. The  $[(^{\text{Me}_2\text{N}}\text{BDI})\text{M}]^+[\text{pfl}]^-$  ( $^{\text{Me}_2\text{N}}\text{BDI} = \text{HC}\{(\text{Me}_2\text{N})\text{CN-2,6-}i\text{Pr}_2\text{C}_6\text{H}_3\}_2$ , M = Si, Ge, Sn) are accessible via chloride abstraction from the  $[(^{\text{Me}_2\text{N}}\text{BDI})\text{MCl}]$ .<sup>172</sup> For these heavier group 14 cations, a different reactivity towards amines was discovered. While the silicon-derivative reacted under oxidative addition into the N–H bonds, the heavier analogs did undergo Werner complex formation. Yet, cleavage of N–H bonds at a Ge cation could be achieved by combination of a cationic Ge<sup>II</sup> metal center with a C,N- and or P,N-ligands containing an amide function.<sup>173</sup> Moreover, the first isolable terphenyl-substituted germylium-ylidenes were reported as complex salts with  $[\text{pfl}]^-$  by Aldridge and co-workers.<sup>174</sup> Depending on the steric bulk of the ligands, the respective monomers or dimers were isolated (Fig. 30).

**Towards reactive one-coordinate M(II) cations:** Mono-coordinate group 14 cations are highly promising synthetic targets in main-group chemistry due to a postulated ambiphilic reactivity (Fig. 31). On the one hand these complexes are highly electrophilic due to the cationic charge and empty p-orbitals at the metal center, on the other hand the lone-pair at the low-valent metal retains an inherent nucleophilicity. On the way to an one-coordinate M(II) cation, Krossing and Jones prepared Ge(II) and Sn(II) cations stabilized by an extremely bulky amido ligand and the  $[\text{pfl}]^-$  anion.<sup>175</sup> Although being highly electropositive, the metal centers exhibit a weak intramolecular  $\eta^2$ -arene interaction (Fig. 31). Showing the high electro positivity of mono-coordinate M(II) cations, Wesemann and co-workers reported the isolation of the benzene-adduct of an terphenyl-ligated Sn(II)-cation (Fig. 31), accessible via reductive elimination of H<sub>2</sub> from the tin-hydride  $[\text{Ar}^*\text{SnH}_2]^+[\text{pfl}]^-$ .<sup>176</sup> In 2019, Hinz introduced a carbazole-ligand combining high bulkiness and electronic non-innocence. Cationic complexes of the carbazole with Ge, Sn and Pb were reported.<sup>177</sup> QTAIM analysis of the obtained complexes revealed a weak interaction between the *ipso*-C atoms of the arene substituents and the tetrrel cations. Finally, Hinz recently achieved the synthesis of the first mono-substituted silicon(II) cation via kinetic stabilization by

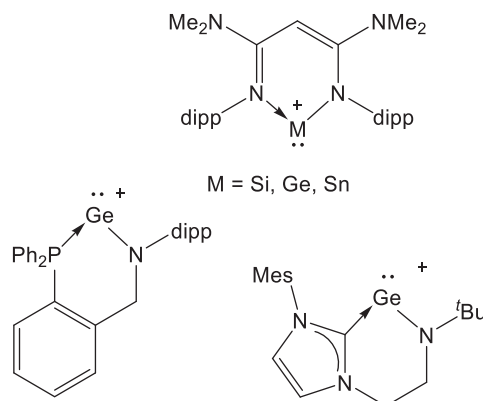


Fig. 30 Examples of two-coordinate M(II) cations stabilized with  $[\text{pfl}]^-$ .

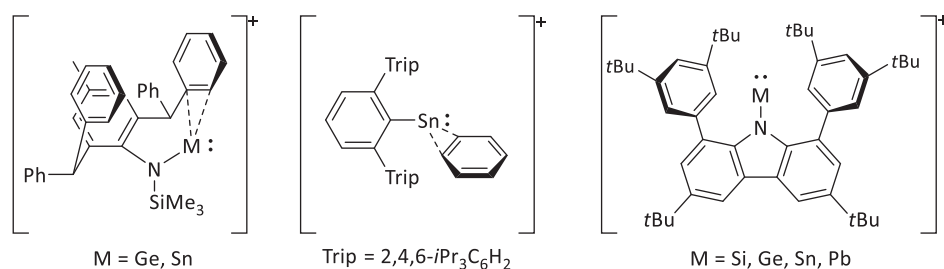


Fig. 31 Examples for highly Lewis-acidic mono-coordinate tetrrel cations or their adducts stabilized with  $[\text{pfl}]^-$ .

a bulky carbazole.<sup>178</sup> The preparation was performed via reduction of the carbazole-SiI<sub>3</sub> adduct with Jones magnesium dimer and subsequent abstraction of the iodide from the halosilylene complex with Ag<sup>+</sup>[pf]<sup>-</sup> (Fig. 31). Reactivity of the isolated “supersilyene” towards <sup>t</sup>BuNH<sub>2</sub> resulted in formation of three bonds at the silicon center, hence confirming its nature as mono-coordinate Si(II) cation.

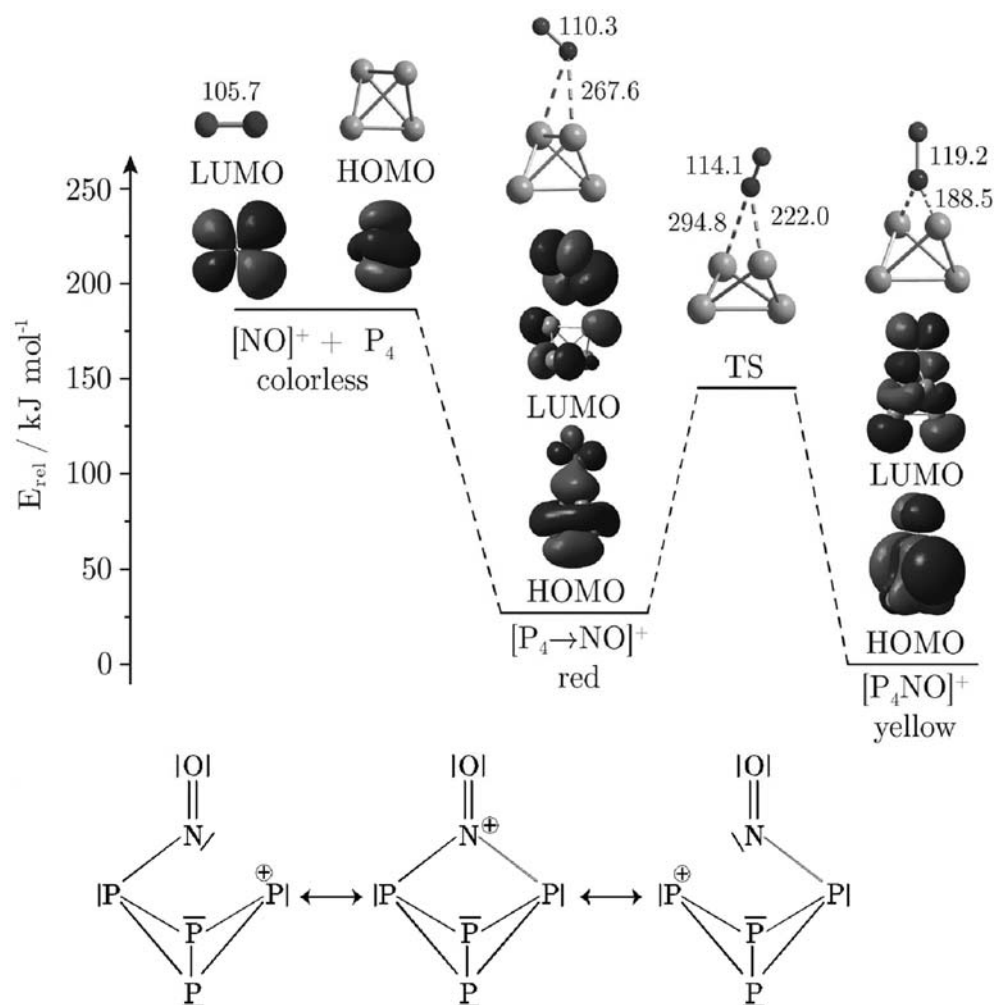
**Dicationic Sn(II) Salts:** Dicationic M(II) complexes stabilized with aluminate anions were hitherto only reported for tin. Here, oxidation of tin metal with NO<sup>+</sup>[pf]<sup>-</sup> in acetonitrile yielded the [Sn(MeCN)<sub>6</sub>]<sup>2+</sup>([pf]<sup>-</sup>)<sub>2</sub> complex.<sup>49</sup> Another route was discovered accidentally when dimethylaminopyridine was added to [SnCp]<sup>+</sup>[pf]<sup>-</sup> and [Sn(dmap)<sub>4</sub>]<sup>2+</sup>([pf]<sup>-</sup>)<sub>2</sub> was isolated.<sup>49</sup> Expanding the oxidation route, the innocent deelectronator [“phenazine”]<sup>+</sup>[pf]<sup>-</sup> (Table 2) was reacted with tin metal in the presence of acetonitrile or a tripyrazolylmethanide ligand to allow for isolation of the respective [Sn(MeCN)<sub>5</sub>]<sup>2+</sup>([pf]<sup>-</sup>)<sub>2</sub> and [Sn(CHpz<sub>3</sub>)<sub>2</sub>]<sup>2+</sup>([pf]<sup>-</sup>)<sub>2</sub>.<sup>55</sup>

### 1.07.2.2.6 Reactive group 15 cations: Phosphorus and some higher homologues

A variety of different homopolyatomic nonmetallic cations have been published and reviewed in detail.<sup>179</sup> Herein we want to highlight and complement cations that have been published using aluminate type WCAs. Phosphorus is an element that occurs in different modifications, although white phosphorus P<sub>4</sub> with its tetrahedral structure represents a frequently used starting point to obtain cations in condensed phase.

**Towards homopolyatomic Phosphorus Cations:** The reaction of [NO]<sup>+</sup> and [NO<sub>2</sub>]<sup>+</sup> salts of the [pf]<sup>-</sup> aluminates with white phosphorus P<sub>4</sub> lead to the [P<sub>4</sub>NO]<sup>+</sup> cage cation; while [NO]<sup>+</sup> inserts directly into P<sub>4</sub>, [NO<sub>2</sub>]<sup>+</sup> is first reduced by P<sub>4</sub> to [NO]<sup>+</sup> and then reacts accordingly in an orbital controlled reaction (Fig. 32).

From the spectroscopic and structural data as well as the first reaction chemistry of the [P<sub>4</sub>NO]<sup>+</sup> cluster cation it followed that only the left and the right phosphonium-structure in Fig. 32 are relevant, but *not* the central iminium structure. In agreement with



**Fig. 32** The orbital controlled pathway to the  $[\text{P}_4\text{NO}]^+$  cation and the primary VB structures accounting for the charge delocalization and further “P<sup>+</sup>” reactivity.<sup>52</sup>



this, the  $[P_4NO]^+$  cluster cation served as a  $P^+$ -source upon reaction with two equivalents of  $PPh_3$  giving exclusively the  $[Ph_3P-P-PPh_3]^+$  triphosphenium cation.<sup>52</sup>

With further equivalents of white phosphorus the first condensed-phase homopolyatomic phosphorus cation  $[P_9]^+$  was prepared using a combination of the oxidant  $[NO]^+$  and weakly coordinating anion.  $[P_9]^+$  consists of two  $P_5$  cages linked by a phosphonium atom to give a  $D_{2d}$ -symmetric Zintl cluster. NMR, Raman, and IR spectroscopy, mass spectrometry, and quantum-chemical calculations confirmed the structure.<sup>180</sup> Recently the conversion of  $P_4$  using  $Ga(Ga_2Cl_7)$  or  $[Co(arene)_2][pf]$  (arene = *o*-difluorobenzene, fluorobenzene) or  $[NO][alfal]$  disclosed new pathways towards  $[P_9]^+$  including its structural characterization. Quantum chemical ccsd(t)-calculations suggest that  $[P_9]^+$  formation from  $[Co(arene)_2]^+$  occurs via the *nido*-type cluster  $[(arene)CoP_4]^+$ , which resembles the isoelectronic elusive  $[P_5]^+$ .<sup>[181]</sup>

**Related *nido*-Cations:** Along similar lines to those intermediates as well as to  $[P_4NO]^+$ , one finds the cationic cages *nido*- $[C_2^tBu_2P_2E]^+$  ( $E = P, As, Sb$ ), which are isolobal to the cyclopentadienyl or the pentaphosphorus cation, to adopt square based pyramidal structures with the heavy pnictogen atom at the apex (Fig. 33). *Inter alia*, they were stabilized by  $[pf]^-$  type WCAs.<sup>182</sup>

NMR and computational methods have been used to probe the dynamic behavior of the complexes. Related to this reaction is the abstraction of a  $Cl^-$  ion from the 1-chlorophospholes  $R_4C_4PCl$  ( $R = Me, Et$ ): It produced the P–P bonded cations  $[R_4C_4P-P(Cl)C_4R_4]^+$ , which undergo nucleophilic substitution with  $PPh_3$  to afford the triphenylphosphine analogs,  $[R_4C_4P-PPh_3]^+$ , isolated as triflate,  $[pf]^-$  aluminate, carbadodecaborate and tetrachlorogallate salts and characterized by XRD. Examination of the  $^{31}P\{^1H\}$  NMR spectrum of  $[Et_4C_4P-PPh_3]^+$  and  $PPh_3$  revealed broadening of the resonances due to both free and coordinated  $PPh_3$ . Second-order kinetics consistent with an unusual  $SN_2$ -type pathway was established. Probably, the high electrophilicity of the phosphorus center in the *nido*- $[Et_4C_4P]^+$  cation, combined with strong pi-pi interactions between the ring and the incoming and outgoing Ph groups of  $PPh_3$ , favors the  $SN_2$ -type over the  $SN_1$ -type pathway in  $[Et_4C_4P-PPh_3]^+$ .<sup>183</sup>

**Mixed Arsenic Phosphorus Cations:** The synthesis of mixed arsenic phosphorus cations was investigated on theoretical and experimental grounds by replacing  $P_4$  with  $AsP_3$  in the known syntheses of  $[P_4NO]^+$  and  $[P_9]^+$ . Calculations of  $[AsP_3NO]^+$  and  $[AsP_8]^+$  showed that 1- $[AsP_3NO]^+$  and 3- $[AsP_8]^+$  should be the most stable isomers. However, 2- $[AsP_3NO]^+$  was prepared by reacting  $[NO]^+[pf]^-$  with  $AsP_3$  with a regioselectivity of 45:1. The kinetic control of this reaction was proven by calculation of the complete reaction mechanism. Examination of the formation energetics of the  $[As_xP_{4-x}NO]^+$  ( $x = 0, 1, 4$ ) and  $[As_xP_{9-x}]^+$  ( $x = 0, 1, 9$ ) cations at the CCSD(T)/complete basis set limit level showed that for  $[As_xP_{4-x}NO]^+$  ( $x = 0, 1, 4$ ), the replacement of phosphorus by arsenic leads to more exergonic formation energetics. For the  $[As_xP_{9-x}]^+$  clusters ( $x = 0, 1, 9$ ), the reaction to  $[AsP_8]^+$  is slightly more exergonic compared to the synthesis of  $[P_9]^+$ . The calculation of the reaction to the homopolyatomic arsenic cation  $[As_9]^+$  suggested that this reaction will at least be very difficult. Attempts to prepare  $[As_xP_{9-x}]^+$  from  $AsP_3$  as well as  $[As_x]^+$  from gray arsenic led to the formation of  $[AsP_3NO]^+$ ,  $[P_4NO]^+$ ,  $[P_9]^+$  and  $P_4$  in case of  $[As_xP_{9-x}]^+$  and decomposition products (e.g., novel  $As(OR^F)_3$ ) for  $[As_x]^+$ .<sup>184</sup>

**Arylphosphine Radical Cations and Dications:**  $[pf]$ -Salts containing triarylphosphine radical cations  $[(Mes)P(Trip)_2]^{\bullet+}$  and  $[P(Trip)_3]^{\bullet+}$  ( $Mes = 2,4,6$ -trimethylphenyl;  $Trip = 2,4,6$ -triisopropyl) have been isolated and characterized by electron paramagnetic resonance (EPR) and UV/Vis absorption spectroscopy as well as scXRD. Radical  $[(Mes)P(Trip)_2]^{\bullet+}$  exhibits a relaxed pyramidal geometry, while radical  $[P(Trip)_3]^{\bullet+}$  becomes fully planar. EPR studies and theoretical calculations showed that the introduction of bulky aryl groups leads to enhanced p character of the singly occupied molecular orbital, and the radicals become less pyramidalized or fully flattened.<sup>185</sup> Furthermore  $[pf]$ -salts of tetraaryldiphosphine radical cation  $[(Trip)_2P=P(Trip)_2]^{\bullet+}$  and dication  $[(Trip)_2P=P(Trip)_2]^{2+}$  have been isolated and were structurally characterized.  $[(Trip)_2P=P(Trip)_2]^{\bullet+}$  has a relaxed pyramidal geometry, while dication  $[(Trip)_2P=P(Trip)_2]^{2+}$  prefers a planar, olefin-like geometry with a two-electron  $\pi$  bond. The alteration of the geometries of the tetraaryldiphosphine upon oxidation is rationalized by the nature of the bonding. The EPR spectrum showed that the spin density of the radical  $[(Trip)_2P=P(Trip)_2]^{\bullet+}$  is mainly localized on phosphorus atoms, which is supported by theoretical calculation.<sup>186</sup>

**Phosphorus-Containing Four-Membered Ring Radical Cations:** Two phosphorus-containing four-membered ring radical cations (Fig. 34) have been isolated and characterized by UV-vis absorption spectroscopy, electron paramagnetic resonance (EPR), and single-crystal X-ray diffraction. Compared with neutral molecules, the radical cation of cyclotetraphosphine has elongated P–P



Fig. 33 The structure of the *nido*- $[C_2^tBu_2P_2]_3^+$  cation.

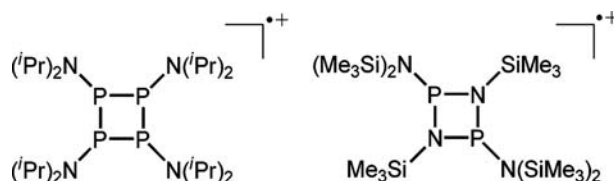


Fig. 34 Radical cations of cyclotetraphosphine and cyclodiphosphazane.

bonds and more pyramidalized phosphorus atoms, while shortened P–N ring distances and larger angles around phosphorus centers are observed for the radical cation of cyclodiphosphazane. EPR studies indicate that for the radical cation of cyclotetraphosphine the spin density mainly resides on the exocyclic nitrogen atoms with very minor contribution from endocyclic phosphorus atoms, while the situation is opposite for the radical of cyclodiphosphazane. Such an inverse spin density distribution is controlled by the exocyclic substituents, which is supported by DFT calculations.<sup>187</sup>

*N,N*-Bis(terphenyl)aminophosphenium Cations: A series of salts that contain the terphenyl-substituted bis(amino)phosphenium cation with different anions including  $[hf]^-$  have been prepared by different synthetic protocols. All of the products have been characterized spectroscopically and by scXRD studies. A detailed analysis of the interionic interactions and their influence on the molecular structure of the phosphenium cation reveals a strong dependence on the capability of the anion to enter the pocket generated by the bulky terphenyl substituents.<sup>188</sup>

*Phosphaalkene radical cations*: Two phosphaalkene radical cations  $[\text{Mes}^*\text{P}=\text{C}(\text{NMe}_2)_2]^{\bullet+}$  and the fluorene based phosphaalkene  $[\text{Mes}^*\text{P}=\text{C}(\text{C}_6\text{H}_3^t\text{Bu}_2)_2]^{\bullet+}$  have been reported with  $[pf]^-$  as counter-ion.  $[\text{Mes}^*\text{P}=\text{C}(\text{NMe}_2)_2]^{\bullet+}$  is stable in the solid state and has been structurally characterized and can be described as phosphorus-centered radical.  $[\text{Mes}^*\text{P}=\text{C}(\text{C}_6\text{H}_3^t\text{Bu}_2)_2]^{\bullet+}$  only remains persistent in solution and has a delocalized radical character with little contribution from phosphorus.<sup>189</sup>

*Phosphonium Cations*: A series of catecholato phosphonium ions, including the first stable bis(catecholato)-substituted derivatives, were isolated and fully characterized. The cations rank among the most potent Lewis acids on the Gutmann-Beckett and ion affinity scales. In contrast to halogenated or multiply charged phosphorus cations, Lewis superacidity is imparted by structural constraints, as disclosed by energy decomposition analyses. The modular access provides a tunable scaffold while maintaining extreme affinities, as demonstrated by the synthesis of a chiral Lewis superacid. The combination of electrophilic phosphorus and basic oxygen substituents leverages new reactivity modes by phosphorus-ligand cooperativity. With this, a phosphorus-mediated C–H bond activation was accomplished.<sup>190</sup>

*Pnictocenium cations*: Complementing the already known pnictocenium salts  $[(\text{Cp}^*)_2\text{Pn}]^+$  (Pn = As,<sup>191</sup> Sb,<sup>192</sup> Bi,<sup>193</sup>), structural characterization of  $[(\text{Cp}^*)_2\text{P}]^+$  has been achieved with the chloride equivalent WCA  $[\text{ClAl}(\text{OR}^{\text{PF}})_3]$  and  $[(\text{R}^{\text{PF}}\text{O})_3\text{Al}-\text{Cl}-\text{Al}(\text{OR}^{\text{PF}})_3]$  via halide abstraction from the respective halopnictines with the Lewis superacid  $\text{PhF}-\text{Al}(\text{OR}^{\text{PF}})_3$ . Furthermore the chloropnictocenium salts  $[\text{Cp}^*\text{P}^+\text{Cl}]^+$ ,  $[\text{Cp}^*\text{As}^+\text{Cl}]^+$  have been prepared with those WCAs. The X-ray crystal structures of these cations established that in the half as well as in the sandwich cations the  $\text{Cp}^*$  rings are attached in an  $\eta^2$ -fashion.<sup>194</sup> Also the antimony analogue  $[(\text{Cp}^*)_2\text{Sb}]^+$  has been synthesized using  $[pf]^-$ .<sup>195</sup>

Stable acyclic arsenium cations like  $[(\text{Cp}^*)_2\text{As}]^+$  are rare in comparison to the corresponding phosphenium cations. The first example of a diphosphaarsenium salt,  $\{[(\text{Dipp})_2\text{P}]_2\text{As}\}[pf]$  exhibits remarkable stability due to the delocalization of a lone pair from a planar phosphorus center into the vacant p-orbital at arsenic; the bonding has been probed by DFT calculations.<sup>196</sup> In 2015 Chloro-pnictocenium cations of the type  $[\text{R}^{\text{Ar}^*}\text{N}(\text{SiMe})\text{ECl}][hf]$  were published ( $\text{R}^{\text{Ar}^*} = 2,6\text{-}(\text{CHPh}_2)\text{-4-R-C}_6\text{H}_4$ , R=Me, *t*Bu; E=Sb, Bi).<sup>197</sup>

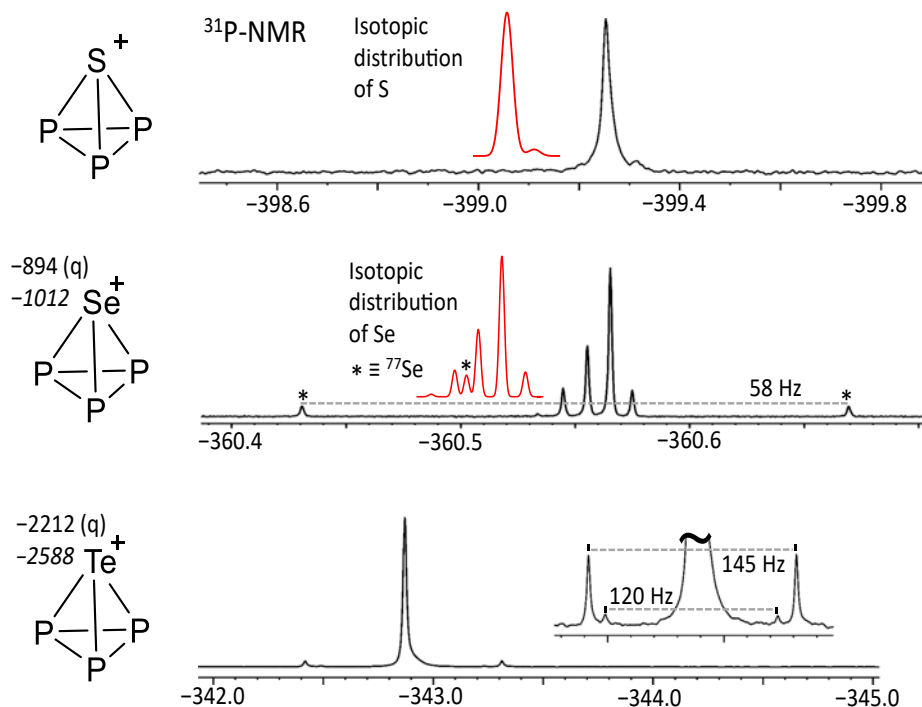


Fig. 35 Structure of the  $[\text{EP}_3]^+$  cations (E = S, Se, Te) and  $^{31}\text{P}$  NMR spectra.

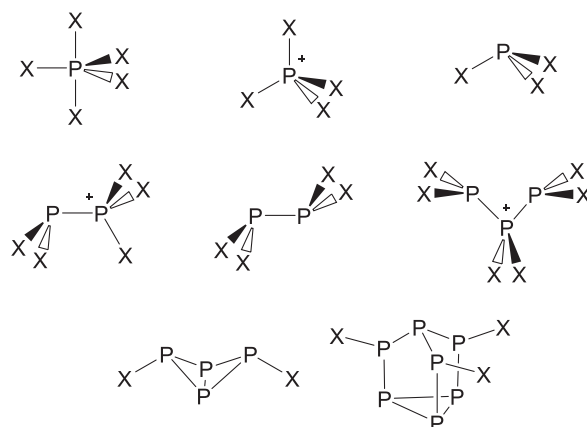
**Binary Phosphorus-Chalcogen Cations and heavier homologues:** While neutral tetrahedral structures ( $P_4$ ,  $AsP_3$ ) are well known, cationic structures remained elusive until first experimental evidence  $[EP_3]^+$  ( $E = S, Se, Te$ ) in the condensed phase was achieved through the reaction of  $ECl_3[A]$  ( $[A] = [pf]^-$  or  $[alfal]^-$ ) with white phosphorus (Fig. 35). Previously,  $[EP_3]^+$  was only known from gas phase MS investigations. By contrast, the reaction of  $ECl_3[A]$  with the known  $[P_3]^{3-}$  synthon  $Na[Nb(ODipp)_3(P_3)]$  (enabling  $AsP_3$  synthesis), led to formation of  $P_4$ . The cations  $[EP_3]^+$  were characterized by multinuclear NMR spectroscopy in combination with high-level quantum chemical calculations. Their bonding situation is described with several approaches including Atoms in Molecules and Natural Bond Orbital analysis.<sup>137</sup>

Another mixed group 15–16 cage cation resembles  $[As_3S_4]^+$  and  $[As_3Se_4]^+$ , which were obtained by the reaction of  $As_4S_4$  with the Lewis acids and oxidants  $AsF_5$  and  $SbF_5$ .<sup>198</sup> Oxidation with  $Ag[pf]$  in *o*DFB resulted in the analogous  $[pf]^-$ -salt.<sup>199</sup> The one-electron deelectronation of main-group heteronuclear species  $Nap(SPh)(P(Mes)_2)$  (1),  $Nap(SePh)(P(Mes)_2)$  (2),  $Nap(-SPh)(As(Mes)_2)$  (3) and  $Nap(SePh)(As(Mes)_2)$  (4) ( $Nap = naphthalin$ ) with  $NO[pf]$  produced persistent radical cations  $1\bullet^+ - 4\bullet^+$  in solution. DFT calculations indicate large amounts of spin densities over heteroatoms and the formation of  $2c-3e^-$   $\sigma$ -bonds between chalcogen and pnictogen atoms.<sup>200</sup>

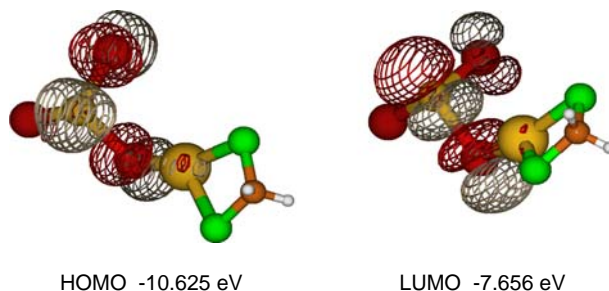
**Binary Phosphorus-Halogen Cations:** In the course of our investigations directed to the preparation of the at that time still unknown homopolyatomic phosphorus cations we—fortuitously—found a simple approach to generate new binary phosphorus halogen cations. When we began our investigations in 2001,<sup>201–203</sup> the knowledge on cationic or neutral binary P-X-species, where X may be F, Cl, Br, I, was sparse and limited to  $P^VX_5$  ( $X = F, Cl$ ),  $[P^VX_4]^+$  ( $X = F-I$ ),  $P^{III}X_3$  ( $X = F-I$ ),  $[P^{III}_2I_5]^+$ ,  $P^{II}X_4$  ( $X = F, Cl, I$ ) and  $P_3X_5$  ( $X = F, I$ ) (Fig. 36).

Solution studies showed the additional existence of small amounts of the phosphorus rich cage molecules  $P_4Br_2$  and  $P_7I_3$  in  $CS_2$  solutions of  $P_4$  and  $X_2$  mixtures ( $X = Br, I$ ). Structural data of the cations was only available for  $[PX_4]^+$  ( $X = Cl-I$ ) and  $[P_2I_5]^+$ .

Binary phosphorus-iodine cations are very electrophilic and  $[P_2I_5]^+$  immediately decomposed the  $[EF_6]^-$  counterions, when prepared from  $P_2I_4$  and  $I_3^+[EF_6]^-$  ( $E = As, Sb$ ) at  $-78^\circ C$ .<sup>204</sup> This kind of decomposition can be avoided by the use of the weakly basic  $[pf]^-$  anion. Thus, a silver-salt metathesis of  $Ag[pf]$  with  $PX_3$  resulted in the formation of the highly reactive “ $[X_2P-X-Ag]^+$ ”—perhaps the closest possible approximation to the still unknown free “ $[PX_2]^+$ ” intermediates—which were previously only investigated in the gas phase. Probably the active ingredient of such reactions is the  $[(CH_2Cl_2)Ag-X-PX_2]^+$  cation shown in Fig. 37.<sup>205</sup>



**Fig. 36** Previously known<sup>201,202</sup> neutral or cationic binary P-X-species ( $X = F, Cl, Br, I$ ) prior to our work in 2001; note that some compounds only exist with one type of X.



**Fig. 37** Frontier orbitals of  $[(CH_2Cl_2)Ag-Br-PBr_2]^+$ —the hypothetical source of the “ $[PX_2]^+$ ” intermediate.

This formal "[PX<sub>2</sub>]<sup>+</sup>" equivalent is a good [PX<sub>2</sub>]<sup>+</sup> source and reacted with X<sub>2</sub>, PX<sub>3</sub> and P<sub>4</sub> to quantitatively give stable but highly electrophilic and soluble [PX<sub>4</sub>]<sup>+</sup>, [P<sub>2</sub>X<sub>5</sub>]<sup>+</sup>, phosphorus rich [P<sub>5</sub>X<sub>2</sub>]<sup>+</sup>, as well as subvalent [P<sub>3</sub>I<sub>6</sub>]<sup>+</sup> salts of the weakly basic [pf]<sup>-</sup> anion (Fig. 38).

Thus, the preparation of [PX<sub>4</sub>]<sup>+</sup>-salts (X = Br, I) with the [pf]<sup>-</sup> counterion is possible.<sup>201</sup> This reaction was extended to the [AsBr<sub>4</sub>]<sup>+</sup>-salt.<sup>206,207</sup> These solid [EX<sub>4</sub>]<sup>+</sup>-salts are stable at room temperature for days. This stability may be contrasted by the absence of experimental evidence for PI<sub>5</sub> and AsBr<sub>5</sub>, while AsCl<sub>5</sub> decomposes already at about -50 °C.<sup>208</sup> Similarly solid PI<sub>4</sub><sup>+</sup>[MF<sub>6</sub>]<sup>-</sup> (M = As, Sb) decomposes already at 0 °C.<sup>209</sup>

Using two equivalents of PX<sub>3</sub> for the reaction, [P<sub>2</sub>X<sub>5</sub>]<sup>+</sup>-salts (X = Br, I) and the mixed [I<sub>2</sub>P-AsI<sub>3</sub>]<sup>+</sup> were prepared.<sup>201,206</sup> Dissolved [P<sub>2</sub>X<sub>5</sub>]<sup>+</sup> is fluxional on the time scale of <sup>31</sup>P NMR spectroscopy and disproportionates for X = I into reduced [P<sub>3</sub>I<sub>6</sub>]<sup>+</sup> and an oxidized species that was assigned as [PI<sub>4</sub>]<sup>+</sup>.<sup>201</sup> [P<sub>2</sub>Br<sub>5</sub>]<sup>+</sup> is even more fluxional than [P<sub>2</sub>I<sub>5</sub>]<sup>+</sup> and is probably in equilibrium with [PBr<sub>2</sub>(CH<sub>2</sub>Cl<sub>2</sub>)]<sup>+</sup> and PBr<sub>3</sub> (Fig. 39).

Due to this equilibrium, [P<sub>2</sub>Br<sub>5</sub>]<sup>+</sup> serves as a "[PBr<sub>2</sub>]<sup>+</sup>" source and reacts with insertion into the P<sub>4</sub> cage to give [P<sub>5</sub>Br<sub>2</sub>]<sup>+</sup> and PBr<sub>3</sub>.<sup>201,202</sup> However, the amount of free [EX<sub>2</sub>]<sup>+</sup> available in the equilibrium in Fig. 39 is highest for the (hypothetical) [As<sub>2</sub>Br<sub>5</sub>]<sup>+</sup>. Therefore, we did not succeed to prepare an [As<sub>2</sub>Br<sub>5</sub>]<sup>+</sup> salt but rather observed the immediate decomposition of the counterion due to the [AsBr<sub>2</sub>(CH<sub>2</sub>Cl<sub>2</sub>)]<sup>+</sup> readily available in the equilibrium.<sup>206,207</sup>

Unlike other oxidative methods, the silver salt metathesis approach also allowed to stabilize reduced subvalent cations. Thus, the interaction of the "[PI<sub>2</sub>]<sup>+</sup>" intermediate with P<sub>2</sub>I<sub>4</sub> results in formation of the subvalent [P<sub>3</sub>I<sub>6</sub>]<sup>+</sup> cation<sup>203</sup> (av. valency: 2.33), a derivative of the poorly characterized P<sub>3</sub>I<sub>5</sub>. The solid-state structure of [P<sub>3</sub>I<sub>6</sub>]<sup>+</sup>[*alal*]<sup>-</sup> (R<sup>F</sup> = C(CF<sub>3</sub>)<sub>3</sub>) is known, [P<sub>3</sub>I<sub>6</sub>]<sup>+</sup>[pf]<sup>-</sup> is only marginally stable in the solid state.

The synthesis of [P<sub>5</sub>X<sub>2</sub>]<sup>+</sup> (X = Cl,<sup>16</sup> Br,<sup>202</sup> I<sup>201,203</sup>) salts with [pf]<sup>-</sup> revealed that the "[PX<sub>2</sub>]<sup>+</sup>" intermediate likely reacts with insertion into the P-P bond of P<sub>4</sub>. The [P<sub>5</sub>X<sub>2</sub>]<sup>+</sup> cations are the first phosphorus rich binary P-X cations known and include a prior

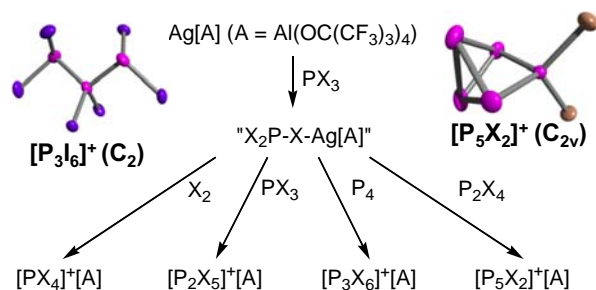


Fig. 38 Reactions of the "[PX<sub>2</sub>]<sup>+</sup>" intermediate. For [P<sub>3</sub>X<sub>6</sub>]<sup>+</sup>, X may be I, for [P<sub>2</sub>X<sub>5</sub>]<sup>+</sup> Br and I, for the rest X = Cl-I.

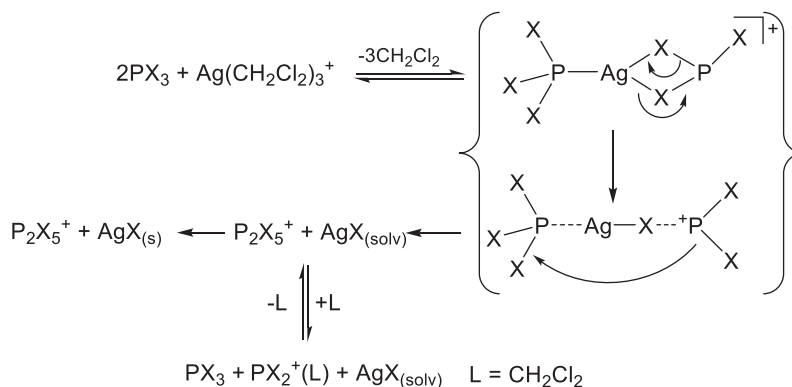


Fig. 39 Proposed mechanism for the formation of the [P<sub>2</sub>X<sub>5</sub>]<sup>+</sup> cations.

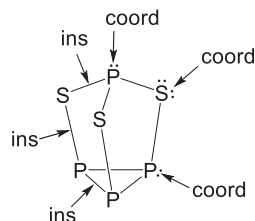


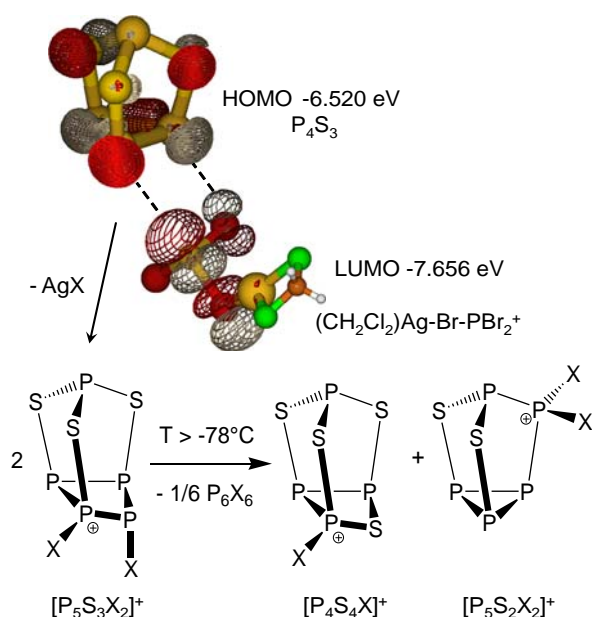
Fig. 40 Possible insertion- or coordination-sites of the P<sub>4</sub>S<sub>3</sub> cage.

unknown  $C_{2v}$ -symmetric  $P_5$ -cage. The solid-state structure of  $[P_5Br_2]^+[pf]^-$  is also known. In the meantime more than 30 structures with this cage are known, mainly by the work of Jan Weigand et al.<sup>210,211</sup>  $[P_5X_2]^+$  resembles a fraction of the known homopolyatomic phosphorus cation  $[P_9]^+$  and contains the hitherto elusive " $[P_5]^+$ ".<sup>180</sup> However, isolobal analogs of this substance class are known (see above).

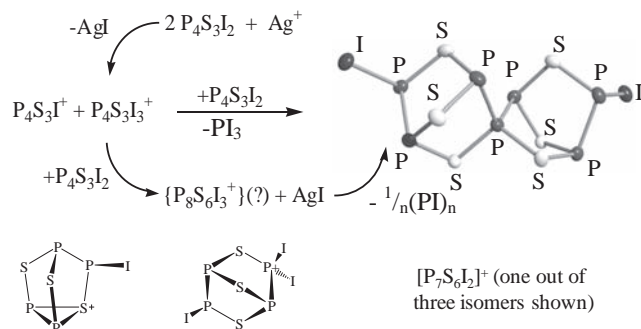
**Ternary Phosphorus Cations:** To further investigate the nature of the formal " $[PX_2]^+$ " equivalent, a substrate with a limited number of bonds eligible for insertion or atoms available for coordination was chosen<sup>205</sup>: The  $P_4S_3$  cage in the nortricyclane-structure. Fig. 40 shows the possible sites for simple insertion and/or coordination.

However, nature rendered these initial thoughts useless: The system apparently prefers the orbital controlled addition of a P–X bond of the formal " $[PX_2]^+$ " equivalent to the basal P–P bond of the  $P_4S_3$  cage giving initially at  $-78^\circ\text{C}$  the  $[P_5S_3X_2]^+$  cation (X = Br, I; Fig. 41).<sup>205</sup>

The  $[P_5S_3X_2]^+$  cation intermediate (NMR) disproportionates upon warming to  $-20^\circ\text{C}$  with separation of tentatively assigned  $P_6X_6$  giving the  $[P_4S_4X]^+$  (NMR, IR, Raman) and the  $[P_5S_2X_2]^+$  (XRD, NMR, IR, Raman) cations.<sup>205</sup> From this work it was clear that mixed P–S–X cations are accessible. Therefore, the reaction of  $P_4S_3I_2$  in its  $\alpha$ - and  $\beta$ -form with the silver aluminates was investigated.<sup>212</sup> The two main group cages may be coupled by a  $Ag^+$  ion:  $P_4S_3I_2$  is ionized by  $Ag^+$  to sulfonium  $[P_4S_3I]^+$  that reacts with another  $P_4S_3I_2$  molecule either to give an iodophosphonium  $[P_4S_3I_3]^+$  (NMR simulated and assigned) and  $P_4S_3$  or to give several isomers of a metastable compound that probably is  $[P_8S_6I_3]^+$ . The intermediate likely loses  $1/n(PI)_n$  and forms the spirocyclic  $P_7S_6I_2^+$  phosphonium cation (Fig. 42), which includes the largest hitherto characterized P–S cage and the first example of main



**Fig. 41** Orbital controlled<sup>205</sup> addition of the P–X bond of the formal " $[PX_2]^+$ " equivalent (=  $[(CH_2Cl_2)Ag-X-PX_2]^+$ ) to the basal P–P bond of the  $P_4S_3$  cage giving initially at  $-78^\circ\text{C}$  the  $[P_5S_3X_2]^+$  cation, which then disproportionates with separation of  $P_6X_6$  giving the  $[P_4S_4X]^+$  and the  $[P_5S_2X_2]^+$  cations (X = Br, I).



**Fig. 42** Reaction of  $Ag^+$  with the  $P_4S_3I_2$  molecules: Intermediate formation of  $[P_4S_3I_x]^+$  (x = 1, 3) and disproportionation to  $[P_7S_6I_2]^+$  (XRD), the largest P–S cage known to date incorporating the first cages that are coupled through a phosphonium center.<sup>212</sup>

group cages connected through a phosphonium center, which was successfully achieved towards homopolyatomic phosphorus cation  $[P_9]^+$  (see above).<sup>180,212</sup>

*Decomposition of the Less Stable Aluminate WCAs:* When using the less stable aluminate  $[hf]^-$  to stabilize phosphazanium cations, the anion reacted with the cation intermediate and served as a clean source of the  $OC(H)(CF_3)_2$  alkoxide.<sup>213</sup>

### 1.07.2.2.7 Reactive group 16 cations

*$[ChX_3]^+$  cations:*  $[ChX_3]^+$  cations (Ch = S, Se, Te) were already reported in 1954.<sup>214</sup> Since they were often obtained via solvothermal syntheses and show poor solubility in many solvents, other counterparts are needed, making these cations suitable starting materials for further chemistry. In 2012  $[TeX_3]^+$  cations (X = Cl, Br, I) were obtained by halide abstraction with  $Ag[pf]$  in liquid  $SO_2$ .<sup>215</sup> Except for  $[SI_3]^+$ , which remained elusive, all  $[ChX_3]^+$  cations (Ch = S, Se) stabilized with  $[pf]^-$  as well as  $[alfal]^-$ .<sup>137</sup>

Upon reacting  $SeCl_4$  with  $Me_3Si-F-Al(OR^F)_3$ , unexpected methylation was observed and the selenonium salt  $SeMeCl_2[alfal]$  was obtained and thoroughly characterized. The only previous example of a salt with the  $[SeMeCl_2]^+$  cation is  $SeMeCl_2[SbCl_6]$ , which was never structurally characterized and is unstable in solution over hours.<sup>216</sup>

*Organic sulfur radical cations and heavier homologues:* Sulfur radical cations are key intermediates in biological processes and organic reactions and claim an important role in materials science. Two different classes are observed, either where the electron is  $\pi$ -delocalized over one or more sulfur atoms containing heterocyclic rings, or where the unpaired electron resides on sulfur 3p-orbitals. To obtain these radical cations a typical starting point is the neutral compound, which is then deelectronated with  $NO[pf]$  or other innocent oxidizers. A series of radical cations respectively their neutral starting molecules I-L that have been published are shown in Fig. 43.

Using silver salts of smaller WCAs ( $[BF_4]^-$ ,  $[SbF_6]^-$ ) to deelectronate  $BP_nT$  ( $n = 1-3$ ) (I) led either to no reaction or to insoluble solids. By contrast, deelectronation with  $Ag[pf]$  resulted in the sought for radical cations, which led in case of  $[BP_2T]^+$  to meso-helical stacking.<sup>217</sup> Also radical cations and dications of tetrathiafulvalene (J) derivatives were obtained via deelectronation with  $Ag[pf]$ .<sup>218,219</sup> With *in-situ* generation of  $NO[pf]$  from  $NO[SbF_6]$  and  $Li[pf]$ , a dithiophene dication that enabled temperature controlled covalent connection and disconnection was obtained.<sup>220</sup>

Also, p-localized sulfur and selenium radical cations are known.  $[Nap(SPh)_2]^+$  formed an unusual sulfur-sulfur three electron  $\sigma$ -bond. In contrast,  $[Nap(SPh)(Se(Ph))]^+$  dimerized in the solid state and formed a S-Se bond (K).<sup>221</sup>

Extension towards tetrachalcogenides (L) showed that two-electron deelectronation formed a closed-shell singlet ground state for sulfur with a quinoidal backbone while for selenium a diradical dication was obtained.<sup>222</sup> Another diradical dication was obtained via deelectronation of a pyrene derivative.<sup>223</sup> Just recently a sulfur tri-cation that contain three radicals resulting in an excited quartet state was published and stabilized with  $[pf]^-$ .<sup>224</sup>

### 1.07.2.2.8 Lanthanide and actinoid complexes

*Synthesis, Structures and Characterizations of Homoleptic Acetonitrile  $Ln^{3+}$  Complexes:* Total halide abstraction from  $LnCl_3$  by  $Ag[pf]/CH_3CN$  yielded  $[Ln(CH_3CN)_n][pf]_3$  ( $n = 9$ ,  $Ln^{3+} = Nd, Eu, Gd, Dy$ ;  $n = 8$ ,  $Ln^{3+} = Tm$ ) complexes.<sup>50</sup> Both in the solid state (X-ray, IR and Raman spectroscopy) and in acetonitrile solution (conductivity, EPR and NMR measurements) the  $[pf]^-$  anion coordinates very weakly to the  $Ln^{3+}$  ions. Lanthanides at the beginning (Nd) and the middle (Eu, Gd, Dy) of the Ln series are typically nine-coordinated, with a mono-capped square antiprismatic arrangement of the N donor atoms around the metal centers. Homoleptic eight-coordinated acetonitrile species are characteristic for those from the end of the series (Tm). Conductivity measurements revealed 3:1 electrolyte types for these species in acetonitrile. EPR and  $^{19}F$  NMR line broadening measurements suggest that the lanthanide complexes are free of any  $[pf]^-$  anion coordinating.<sup>50</sup>

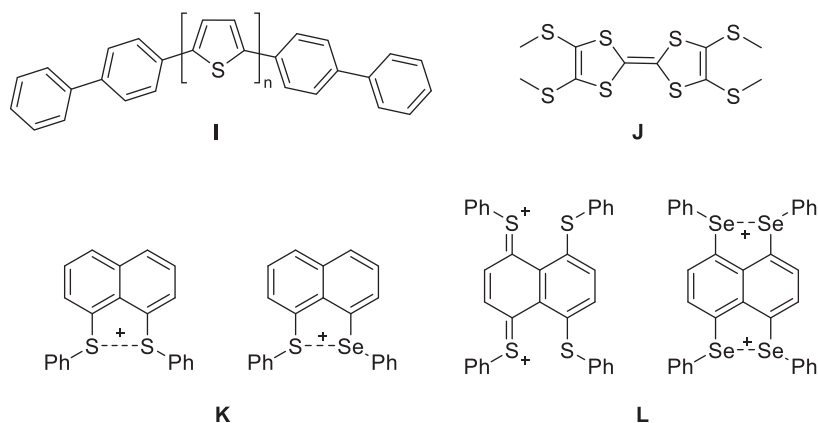
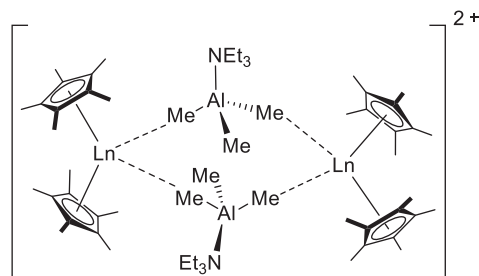


Fig. 43 Selection of different sulfur and selenium compounds and radical cations that have been characterized.





**Fig. 44** Molecular structure of  $[\{\text{Ln}(\text{Cp}^*)_2(\mu\text{-Me}_3\text{AlNEt}_3)_2\}][\text{pf}]_2$  ( $\text{Ln} = \text{Dy}, \text{Y}$ ).<sup>226</sup> The  $[\text{pf}]^-$  counteranions are not shown for clarity.

*A Dysprosium Metallocene Dimer:* Replacing half of the  $[\text{BPh}_4]^-$  anions by  $[\text{pf}]^-$  in the dysprosium metallocene  $\text{DyCp}^*_2\text{BPh}_4$  results in the first example of  $[\text{BPh}_4]^-$  acting as a bridging ligand in 4f metal complexes.<sup>225</sup> The dimer shows improved slow relaxation of the magnetization compared to its mononuclear congener, resulting in waist-restricted hysteresis up to 6.5 K.<sup>225</sup>

*A Double-Dysprosocenium Single-Molecule Magnet:* Weak interactions between  $[\text{Dy}(\text{Cp}^*)_2]^+$  fragments and neutral  $\text{NEt}_3\text{AlMe}_3$  molecules have been observed in a dinuclear dysprosocenium dication with a  $[\text{pf}]^-$  counterion (Fig. 44).<sup>226</sup> These equatorial interactions perturb the axiality of the  $\text{Dy}^{3+}$  crystal fields. A magnetic hysteresis up to 12 K and relatively large effective barrier to magnetization reversal of  $860(60) \text{ cm}^{-1}$  are reported for this compound.<sup>226</sup> The synthesis of an isostructural Yttrium complex has also been reported, along with a doped Y/Dy system.<sup>226</sup>

*A Bis-Monophosphohyl Dysprosium Cation:* Bis-cyclopentadienyl lanthanide sandwich complexes are promising candidates for single-molecule magnets (SMMs) that show magnetic memory at ca. 77 K.<sup>227</sup> However, the relaxation mechanisms mediated by aromatic  $\text{C}_5$  rings are not fully understood yet. A bis-monophosphohyl dysprosium SMM  $[\text{Dy}(\text{Dtp})_2][\text{pf}]$  ( $\text{Dtp} = [\text{P}(\text{C}^i\text{BuCMe})_2]$ ) has been synthesized by the treatment of in situ prepared “ $[\text{Dy}(\text{Dtp})_2(\text{C}_3\text{H}_5)]$ ” with  $[\text{HNEt}_3][\text{pf}]$ .<sup>227</sup> The Dysprosium-*pf* salt shows magnetic hysteresis up to 48 K and an effective barrier to magnetization reversal of 1760 K ( $1223 \text{ cm}^{-1}$ ).<sup>227</sup> The preparation and analysis of this compound allows to improve the understanding of relaxation processes in bis- $\text{C}_5/\text{C}_4\text{P}$  sandwich lanthanide SMMs, which is pivotal for rationally achieving higher magnetic blocking temperatures in these systems.

*A  $\beta$ -diketiminate Uranium Complex:* A homoleptic, octahedral  $\text{U}^{\text{III}}$  complex  $[\text{U}^{\text{III}}(\text{NacNac}^{\text{Ph}})_3]$  ( $\text{NacNac}^{\text{Ph}-} = [\text{PhNC}(\text{CH}_3)_2\text{CH}^-]$ ) was obtained after transmetalation of the alkali metal  $\beta$ -diketiminate salts  $[\text{M}][\text{NacNac}^{\text{Ph}}]$  ( $\text{M}^+ = \text{Na}^+$  or  $\text{K}^+$ ) with  $\text{U}(\text{THF})_4$ . Oxidation with mild oxidants, such as  $[\text{FeCp}_2][\text{pf}]$ , yields the discrete  $\text{U}^{\text{IV}}$  salt  $[\text{U}^{\text{IV}}(\text{NacNac}^{\text{Ph}})_3][\text{pf}]$ .<sup>228</sup>

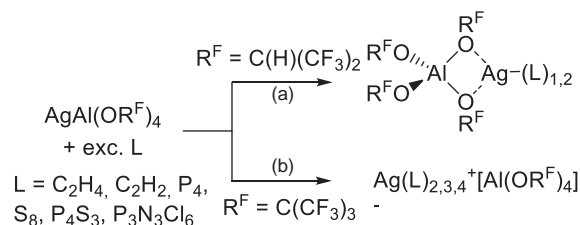
### 1.07.2.3 Complexation of weak ligands: Coordination compounds of the transition metals stabilized by $[\text{pf}]^-$ aluminates

*Anion Effects:* To stabilize weakly-bound Lewis acid-base adducts of the type presented in this section, anion-cation as well as solvent-cation interactions have to be minimized and must be smaller in magnitude than the interaction with the weakly basic ligand. The influence of the counterion may be illustrated by the following series of silver complexes in (i) and (ii); here the univalent silver cation serves as a prototype for any weak acceptor:

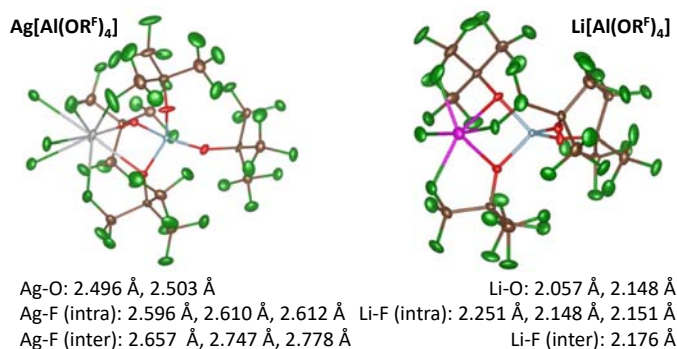
- (i) *role of the counterion:* From the determined solid-state structures it is evident that  $[\text{Al}(\text{OR}^{\text{F}})_4]^-$  anions with  $\text{R}^{\text{F}} = \text{C}(\text{H})(\text{CF}_3)_2$  and  $\text{C}(\text{CH}_3)(\text{CF}_3)_2$  coordinate to the  $\text{Ag}^+$  cation and give molecular compounds like  $(\text{L})_{1,2}\text{Ag}[\text{hf}]$  (Fig. 45a). With the least basic anions,  $[\text{pf}]^-$  and  $[\text{alfal}]^-$ , also the very weak ligands  $\text{C}_2\text{H}_4$ ,  $\text{C}_2\text{H}_2$ ,  $\text{P}_4$ ,  $\text{S}_8$ , etc. are stronger Lewis bases towards the cation than the anion. Consequently, in the analogous reactions the  $\text{Ag}^+$  cation coordinates  $n$  ligands  $\text{L}$  and forms  $[\text{Ag}(\text{L})_n]^+[\text{pf}]^-$  complexes with truly ionic structures ( $n = 2, 3, 4$ ; Fig. 45b).

Similarly, in almost all investigated cases, the fluoride bridged  $[\text{alfal}]^-$  anion remained non-coordinating to any cation, with the only exception of the ion-paired crystal structure of the donor free silver salt  $\text{Ag}[\text{alfal}]$  obtained by crystallization from a solution in extremely non-polar perfluorohexanes (!).<sup>31</sup>

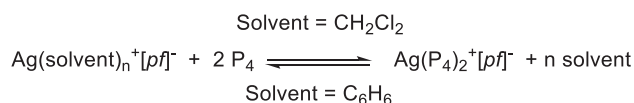
Limiting cases that lead to ion-pairing are the molecular structures of the solvate free compounds  $\text{Li}[\text{pf}]$ ,<sup>40</sup>  $\text{Ag}[\text{pf}]$ <sup>40</sup> and  $\text{Ag}[\text{alfal}]$ ,<sup>31</sup> two of which are included in the next Fig. 46.



**Fig. 45** Counterion dependence of the structures of weakly-bound Lewis acid-base adducts of the silver cation. In addition, we have never observed ion-pairing as in (a) with the least coordinating anion  $[\text{alfal}]^-$  but only salt formation as in (b).



**Fig. 46** Molecular structures of the solvate-free compounds Li[*pf*] and Ag[*pf*] obtained by crystallization from perfluorohexanes.



**Fig. 47** Solvent dependence of the stability of the structures of weakly-bound Lewis acid-base adducts of the silver cation.

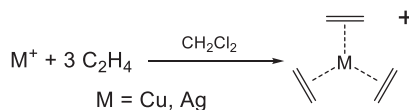
- (ii) *role of the solvent*: When  $\text{Ag}^+[\text{pf}]^-$  and 2  $\text{P}_4$  are mixed in  $\text{CH}_2\text{Cl}_2$  the equilibrium of the reaction shown in Fig. 47 lies completely on the right hand side.<sup>229,230</sup> However, replacing the weakly basic solvent  $\text{CH}_2\text{Cl}_2$  for the more strongly coordinating solvent benzene  $\text{C}_6\text{H}_6$  led to the replacement of  $\text{P}_4$  by  $\text{C}_6\text{H}_6$  in the  $[\text{Ag}(\text{P}_4)_2]^+$  cation to give  $[\text{Ag}(\text{C}_6\text{H}_6)_2]^+$ . Thus, in benzene the equilibrium lies completely on the left side.<sup>229,230</sup>

### 1.07.2.3.1 Complexed olefins and acetylenes

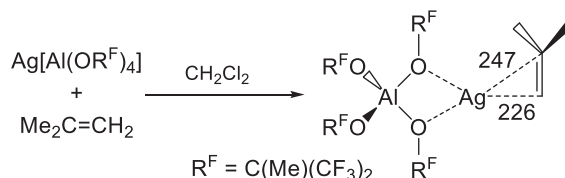
*Parent  $\text{H}_2\text{C}=\text{CH}_2$ -Complexes*: Since the discovery of Zeise's salt  $\text{K}[\text{PtCl}_3(\text{C}_2\text{H}_4)]$  in 1827 the investigation of simple ethene-metal complexes is an area of continuing interest in all fields of chemistry, fueled by the interest in transformations of the coordinated  $\text{C}_2\text{H}_4$  molecule. Several ethene-metal coordination modes including  $\mu$ ,  $\eta^2$ : $\eta^2$  are known. Ethene-silver complexes with very little back bonding served to formulate the Dewar-Chatt-Duncanson model for the binding of olefins to transition metal atoms. Although  $\text{Ag}-\text{C}_2\text{H}_4$  complexes are textbook compounds, experimental information on this system was very limited and only one disordered solid-state structure of a  $[\text{Ag}(\text{C}_2\text{H}_4)_n]^+$  unit was determined prior to our work (see ref.<sup>231</sup> for a literature overview). In the gas phase,  $[\text{Ag}(\text{C}_2\text{H}_4)_n]^+$  cations were already characterized by MS for  $n = 1$  and 2.<sup>232,233</sup>

Using [*pf*]<sup>−</sup> as the WCA, a cationic  $[\text{Ag}(\text{C}_2\text{H}_4)_3]^+$  complex with an ionic lattice in the solid state and an almost planar  $D_{3h}$  symmetric cation in a spoke wheel arrangement was synthesized in 2003 (Fig. 48).<sup>231,234</sup>

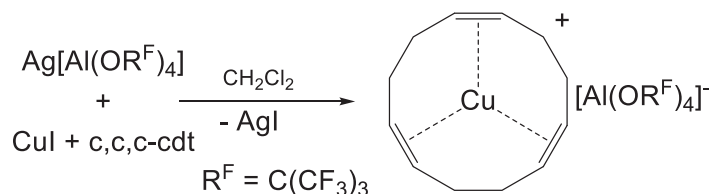
The synthesis and full characterization of  $[\text{Ag}(\text{C}_2\text{H}_4)_3]^+[\text{pf}]^-$  in condensed phases is rather remarkable, especially since initially only  $[\text{Ag}(\text{C}_2\text{H}_4)_n]^+$  complexes with  $n = 1, 2$  were observed in the gas phase. This is probably due to the low (calculated) binding energy of the third  $\text{C}_2\text{H}_4$  molecule of  $\Delta G^\circ = -55 \text{ kJ mol}^{-1}$  in the gas phase (MP2/TZVPP). However, in 2005 the formation of gaseous  $[\text{Ag}(\text{C}_2\text{H}_4)_3]^+$  was reported also with MS. Subsequently also the analogous copper and gold complexes  $[\text{M}(\text{C}_2\text{H}_4)_3]^+$  were prepared ( $\text{M} = \text{Cu}$ ,<sup>236</sup>  $\text{Au}$ <sup>235</sup>). When the more coordinating aluminates  $[\text{Al}(\text{OR}^F)_4]^-$  with  $\text{R}^F = \text{C}(\text{H})(\text{CF}_3)_2$  and  $\text{C}(\text{Me})(\text{CF}_3)_2$  were used, molecular ion pairs  $(\text{C}_2\text{H}_4)_n\text{Ag}[\text{Al}(\text{OR}^F)_4]$  with  $n = 1$  and 2 resulted.<sup>231</sup> A general method for the determination of the C=C bond lengths from the Raman stretch of the coordinated ethene molecule was developed. Structure and



**Fig. 48** Formation of the homoleptic coinage metal-ethene complexes  $[\text{M}(\text{C}_2\text{H}_4)_3]^+[\text{pf}]^-$  ( $\text{M} = \text{Cu, Ag}$ ). Later also  $\text{M} = \text{Au}$  was published.<sup>235</sup>



**Fig. 49** Formation of the asymmetrically bound molecular isobutene complex in  $(\text{C}_4\text{H}_8)\text{Ag}[\text{Al}(\text{OR}^F)_4]$  ( $\text{Ag}-\text{C}$  distances given in pm).



**Fig. 50** Metathesis reaction leading to the trigonal planar  $[\text{Cu}(\text{c,c,c-cdt})]^+[\text{pf}]^-$  complex.

bonding of those ethene complexes and the related isoelectronic but neutral  $\text{M}(\text{C}_2\text{H}_4)_3$  molecules ( $\text{M} = \text{Ni}, \text{Pd}, \text{Pt}$ ) was investigated with experiments and quantum chemical calculations including (theoretical) charge density studies.<sup>231</sup>

*Substituted Olefin Complexes:* Using the aluminate with the more basic  $\text{OC}(\text{Me})(\text{CF}_3)_2$  residue, an interesting asymmetrically bound isobutene complex was obtained (Fig. 49).<sup>231</sup>

This structure, with a short  $\text{Ag}-\text{C}$  bond to the  $\text{CH}_2$ -group and a long  $\text{Ag}-\text{C}$  bond to the  $\text{CMe}_2$ -group, points to the similarity of  $\text{Ag}^+$  and  $\text{H}^+$  in that the silver ion induces the formation of an asymmetric complex, which resembles in a way the Markovnikov-product  $[\text{C}(\text{CH}_3)_3]^+$ .<sup>231</sup>

Also the  $\text{Cu}^{\text{I}}$ -complex of *cis,cis,cis*-1,5,9-cyclododecatriene (*c,c,c-cdt*) was reported.<sup>237</sup> It was prepared in the metathesis reaction of the silver aluminate with  $\text{CuI}$  in the presence of the olefin shown in Fig. 50—a reaction that also proved suitable<sup>236</sup> for the preparation of the related  $[\text{Cu}(\text{C}_2\text{H}_4)_3]^+[\text{pf}]^-$  salt.

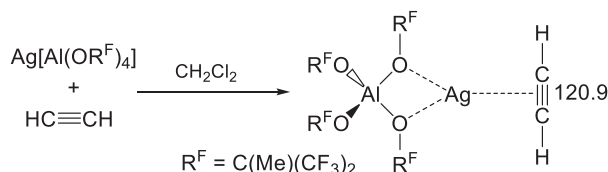
It should be noted that with the smaller and more coordinating  $[\text{BF}_4]^-$  WCA as counterion, tetracoordinate copper ions resulted: either including a coordinated solvent molecule ( $\text{MeOH}$ ) or, in the absence of coordinating solvents, the coordinated anion, i.e.,  $(\text{c,c,c-cdt})\text{Cu}-\text{F}-\text{BF}_3$ . Only with the least coordinating  $[\text{pf}]^-$  WCA access to the truly undistorted and crystallographically almost  $\text{C}_3$ -symmetric  $[\text{Cu}(\text{c,c,c-cdt})]^+$  complex cation was possible.<sup>237</sup>

*A  $[\text{Ni}^{\text{I}}(\text{cod})_2]^+$  Salt:* The straightforward synthesis of the cationic, purely organometallic  $\text{Ni}^{\text{I}}$  salt  $[\text{Ni}(\text{cod})_2]^+[\text{Al}(\text{OR}^{\text{F}})_4]^-$  was realized through a reaction between  $[\text{Ni}(\text{cod})_2]$  and  $\text{Ag}[\text{Al}(\text{OR}^{\text{F}})_4]$  ( $\text{cod} = 1,5$ -cyclooctadiene).<sup>238</sup> Crystal-structure analysis and EPR, XANES, and cyclic voltammetry studies confirmed the presence of a homoleptic  $\text{Ni}^{\text{I}}$  olefin complex. Weak interactions between the metal center, the ligands, and the anion provide a good starting material for further cationic  $\text{Ni}^{\text{I}}$  complexes, i.e. even linear  $[\text{Ni}(\text{P}^t\text{Bu}_3)_2]^+$ .<sup>239,240</sup>

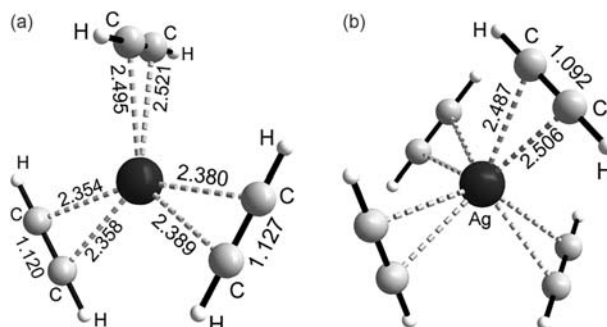
*$\text{HC}\equiv\text{CH}$ -Complexes:* Also the simplest ethyne,  $\text{HC}\equiv\text{CH}$ , may be bound to the weak acceptor  $\text{Ag}^+$  with the suitable counterion.<sup>241</sup> Again, the more coordinating  $[\text{Al}(\text{OR}^{\text{F}})_4]^-$  WCA with  $\text{R}^{\text{F}} = \text{C}(\text{CH}_3)(\text{CF}_3)_2$  forms a molecular complex, which binds only one ethyne per  $\text{Ag}^+$  ion in  $(\text{C}_2\text{H}_2)\text{Ag}[\text{Al}(\text{OR}^{\text{F}})_4]$  (Fig. 51).

Fortunately, the quality of this batch of single crystals was extremely good and so an experimental charge density study at 9 K could be performed on this compound. This revealed for the first time the long theoretically predicted T-shaped bond path for the  $\text{AgC}_2$  plane. This T-shaped bond path with an electron density on the critical point of  $\rho(\mathbf{r})_{\text{TCP}} = 0.47 \text{ e}\text{\AA}^{-3}$ , implied an admixture in-between electrostatic and covalent bonding with almost no back-bonding from the silver ion.

With the much less coordinating  $[\text{pf}]^-$  WCA ( $\text{C}(\text{CF}_3)_3$  residue), homoleptic tris- and tetra-ethyne complexes  $[\text{Ag}(\text{C}_2\text{H}_2)_{3,4}]^+[\text{pf}]^-$  were realized (Fig. 52).



**Fig. 51** Synthesis of the molecular ethyne complex  $(\text{C}_2\text{H}_2)\text{Ag}[\text{Al}(\text{OR}^{\text{F}})_4]$ . The  $\text{C}\equiv\text{C}$  distance, given in pm, stems from the charge density study at 9 K and is considered to be the best experimental  $\text{C}\equiv\text{C}$  distance determined for any ethyne complex. It implies almost no back-bonding.



**Fig. 52** Molecular structures of (a) the  $\text{C}_2$ -symmetric  $[\text{Ag}(\text{C}_2\text{H}_2)_3]^+$  and (b) the  $\text{S}_4$ -symmetric  $[\text{Ag}(\text{C}_2\text{H}_2)_4]^+$  cation in the salts  $[\text{Ag}(\text{C}_2\text{H}_2)_{3,4}]^+[\text{pf}]^-$ .

Here it is interesting to analyze the structure of the  $C_2$ -symmetric  $[\text{Ag}(\text{C}_2\text{H}_2)_3]^+$  cation: From an initial guess one would have expected the cation to exhibit  $D_3$  or even  $D_{3h}$  symmetry, and not  $C_2$  with two ligands in plane and one ligand out of plane. However, DFT and ab initio calculations revealed that in a  $D_{3h}$ -structure the H-atoms come too close and therefore distort the system either to  $D_3$  or alternatively and unexpectedly to  $C_2$ ; both forms are within 1 or 2  $\text{kJ mol}^{-1}$  isoenergetic in the gas phase. This again points to the capability of the least coordinating aluminate WCA to introduce *pseudo gas phase conditions*<sup>2,3,10,242</sup> in the condensed phase.

### 1.07.2.3.2 Homoleptic transition metal carbonyl cations (TMCCs)

Since the discovery of  $\text{Ni}(\text{CO})_4$  by Mond in 1890,<sup>243</sup> transition metal carbonyls were continuously and extensively studied. Especially homoleptic transition metal carbonyls fascinate due to their simplicity, fundamental bonding characteristics and rich substitution and redox chemistry. Transition metal carbonyl often obey the 18-electron rule and their bonding is well described by the Dewar-Chatt-Duncanson model.<sup>244–247</sup> However, compared to their anionic and neutral counterparts, TMCCs exhibit a reduced  $\pi$ -back bonding, which leads to a weaker M–CO bond and usually to blue-shifted CO-stretching frequencies compared to free CO ( $2143 \text{ cm}^{-1}$ )<sup>248</sup> that may reach values up to  $2295 \text{ cm}^{-1}$  in  $[\text{Ir}(\text{CO})_6]^{3+}$ .<sup>249</sup> In the last decades, TMCCs like  $[\text{Au}(\text{CO})_2]^+$ ,<sup>250</sup>  $[\text{Pt}(\text{CO})_4]^{2+}$ ,<sup>251</sup>  $[\text{Co}(\text{CO})_5]^{2+}$ <sup>252</sup> and  $[\text{Fe}(\text{CO})_6]^{2+}$ <sup>253</sup> were mainly generated and stabilized in superacidic media and these compounds were already reviewed elsewhere.<sup>247,249,254,255</sup> However, the superacidic media hampers the access of the TMCCs to a broader community and the investigation of follow-up chemistry. Additionally, the accessible TMCCs were limited by the quality of the  $[\text{SbF}_6]^-$ / $[\text{Sb}_2\text{F}_{11}]^-$  anions as a WCA.

*Access to known TMCCs:* Consequently, a more appropriate WCA like the fluorinated alkoxyaluminates, enables the synthesis of TMCCs in standard organic solvents. This was proven by isolation of a series of coinage metal carbonyl cations including  $[\text{Cu}(\text{CO})_n][\text{pf}]^-$  ( $n > 2$ ),  $[\text{Ag}(\text{CO})_2(\text{hf})]$  and  $[\text{Au}_2(\text{CO})_2\text{Cl}][\text{pf}]^-$  by a metathesis reaction of the corresponding metal halide and  $\text{Li}[\text{pf}]$  in dichloromethane and CO atmosphere<sup>256</sup> and the synthesis of  $[\text{Co}(\text{CO})_5][\text{pf}]^-$  by deelectronation of  $[\text{Co}_2(\text{CO})_8]$  with  $\text{Ag}[\text{pf}]$  in 1,2-difluorobenzene under CO atmosphere.<sup>257</sup> Fortunately, the CO stretching frequency responds noticeably to the interaction of the TMCC with the environment and the observed frequencies of the  $[\text{Cu}(\text{CO})_n]^+$  and  $[\text{Co}(\text{CO})_5]^+$  cations in combination with fluorinated alkoxyaluminates were the most similar to the corresponding gas phase values, which justifies the declaration of pseudo-gas phase conditions.<sup>256,257</sup>

*The first Heptacarbonyls  $[\text{M}(\text{CO})_7]^+$ :* The reaction of  $[\text{M}(\text{CO})_6]^-$  ( $\text{M} = \text{Nb}, \text{Ta}$ ) with two equivalents  $\text{Ag}^+[\text{pf}]^-$  under CO pressure led to stable salts of the first transition metal heptacarbonyls  $[\text{M}(\text{CO})_7]^+$  in the condensed phase. In addition, the reaction of  $[\text{Ta}(\text{CO})_6]^-$  with  $[\text{Ta}(\text{CO})_7]^+$  led to  $\text{Ta}_2(\text{CO})_{12}$  with a long, unsupported Ta–Ta bond.<sup>258</sup>

*Radical Cations  $[\text{M}(\text{CO})_6]^{+\cdot}$ :* Homoleptic carbonyl radical cations are a textbook family of complexes. The 17-electron  $[\text{Cr}(\text{CO})_6]^{+\cdot}$  salt was synthesized by deelectronation of  $\text{Cr}(\text{CO})_6$  with  $[\text{NO}]^+[\text{pf}]^-$  in  $\text{CH}_2\text{Cl}_2$  and removal of the NO gas.<sup>259</sup> In contrast, the higher homologues  $[\text{M}(\text{CO})_6]^{+\cdot}$  ( $\text{M} = \text{Mo}, \text{W}$ ) were not accessible by deelectronation of the respective metal hexacarbonyls with nitrosyl cations and the synergistic  $\text{Ag}^+[\text{pf}]^-/0.5 \text{ I}_2$  system at  $-20 \text{ }^\circ\text{C}$  was necessary for the successful synthesis of the 17 valence electron species.<sup>260</sup>

*Nickel Tetracarbonyl Radical Cation:* With the same  $\text{Ag}^+[\text{pf}]^-/0.5 \text{ I}_2$  system, also the synthesis of the nickel tetracarbonyl radical cation  $[\text{Ni}(\text{CO})_4]^{+\cdot}$  was achieved, as the last missing entry among the structurally characterized TMCCs of Groups 6 to 11.<sup>261</sup>

*Iron Pentacarbonyl Radical Cation:* While the deelectronation of the pentacarbonyl iron failed with common inorganic oxidants, the usage of the innocent deelectronator  $[\text{phenazine}^{\text{F}}]^+[\text{pf}]^-$  has allowed the preparation of the open-shell  $[\text{Fe}(\text{CO})_5]^{+\cdot}[\text{pf}]^-$ . The pentacarbonyl iron radical cation is a novel example of low-valent iron and has thus been fully characterized including Mößbauer and SQUID.<sup>56</sup>

*Homotrinary TMCCs  $[\text{M}_3(\text{CO})_{14}]^{2+}$ :* The use of innocent deelectronations also allows the isolation of the first homotrinary TMCCs  $[\text{M}_3(\text{CO})_{14}]^{2+}([\text{pf}]^-)_2$  ( $\text{M} = \text{Ru}, \text{Os}$ ) through the reaction of  $\text{M}_3(\text{CO})_{12}$  with two equivalents of  $[\text{anthracene}^{\text{Hal}}]^+[\text{pf}]^-$  under a CO atmosphere.<sup>63</sup> The metal atoms are arranged in a linear chain and have each a nearly octahedral coordination geometry. The structural characterization and the DFT calculations as well as vibrational and NMR spectroscopies are indicating the presence of three electronically independent sets of carbonyl ligands, which almost mimic  $\text{M}(\text{CO})_5$ , free CO and even  $[\text{M}(\text{CO})_6]^{2+}$  in one and the same cation.

*Currently Known TMCCs:* All currently known TMCCs are collected in Table 4. Entries marked in bold are only known with a perfluoroalkoxyaluminate anion.

**Table 4** Structurally characterized homoleptic TMCCs.<sup>247,249,254,255</sup>

	5	6	7	8	9	10	11	12
<b>3 d</b>		<b><math>[\text{Cr}(\text{CO})_6]^+</math></b>	$[\text{Mn}(\text{CO})_6]^+$	<b><math>[\text{Fe}(\text{CO})_5]^+</math></b> $[\text{Fe}(\text{CO})_6]^{2+}$	$[\text{Co}(\text{CO})_5]^+$	<b><math>[\text{Ni}(\text{CO})_4]^+</math></b>	$[\text{Cu}(\text{CO})_4]^+$	
<b>4 d</b>	<b><math>[\text{Nb}(\text{CO})_7]^+</math></b>	<b><math>[\text{Mo}(\text{CO})_6]^{+\cdot}</math></b>	$[\text{Tc}(\text{CO})_6]^+$	<b><math>[\text{Ru}_3(\text{CO})_{14}]^{2+}</math></b> $[\text{Ru}(\text{CO})_6]^{2+}$	$[\text{Rh}(\text{CO})_4]^+$	$[\text{Pd}(\text{CO})_4]^{2+}$	$[\text{Ag}(\text{CO})_2]^+$	
<b>5 d</b>	<b><math>[\text{Ta}(\text{CO})_7]^+</math></b>	<b><math>[\text{W}(\text{CO})_6]^{+\cdot}</math></b>	$[\text{Re}(\text{CO})_6]^+$	<b><math>[\text{Os}_3(\text{CO})_{14}]^{2+}</math></b> $[\text{Os}(\text{CO})_6]^{2+}$	$[\text{Ir}(\text{CO})_6]^{3+}$	$[\text{Pt}(\text{CO})_4]^{2+}$	$[\text{Au}(\text{CO})_2]^+$	$[\text{Hg}(\text{CO})_2]^{2+}$ $[\text{Hg}_2(\text{CO})_2]^{2+}$

Entries marked in bold are only known with an perfluoroalkoxyaluminate anion.

### 1.07.2.3.3 Transition metal carbonyls as complex ligands

The reaction of the silver(I)-cation with Transition Metal Carbonyls (TMCs) leads in a few cases to a deelectronation of the TMCCs. However, an often-encountered side-reaction is the formation of a metal-only Lewis-pair (MOLP),<sup>262</sup> in which the Lewis-acidic silver(I) cation is surrounded by Lewis-basic TMCs.

**Fe(CO)<sub>5</sub>-Complexes:** In an attempt to deelectronate pentacarbonyl-iron to its radical-cation with Ag<sup>+</sup>[*pf*]<sup>-</sup> the silver-complex [Ag{Fe(CO)<sub>5</sub>}<sub>2</sub>]<sup>+</sup> formed instead.<sup>263</sup> Inspired by this work, Dias et al. synthesized further silver-complexes with Fe(CO)<sub>5</sub> as ligand and with other WCAs including [B{3,5-(CF<sub>3</sub>)<sub>2</sub>C<sub>6</sub>H<sub>3</sub>}<sub>4</sub>]<sup>-</sup> and [SbF<sub>6</sub>]<sup>-</sup>.<sup>264</sup> A few years later Dias et al. showed, that Fe(CO)<sub>5</sub> reacts also with the other coinage-metals completing the [M{Fe(CO)<sub>5</sub>}<sub>2</sub>]<sup>+</sup> (M = Cu, Ag, Au) triad.<sup>265</sup>

**M(CO)<sub>6</sub>-Complexes:** Although the metal-centers of the group 6 hexacarbonyls seem to be sterically inaccessible for the coordination, molybdenum and tungsten hexacarbonyl form silver(I)-complexes [Ag{M(CO)<sub>6</sub>}<sub>2</sub>]<sup>+</sup> (M = Mo, W) in the same 2:1 stoichiometry as pentacarbonyl iron, while the lightest group 6 silver(I)-complex, [Ag{Cr(CO)<sub>6</sub>}<sub>2</sub>]<sup>+</sup> remained inaccessible.<sup>266</sup>

**Hexacarbonylate Anions as Ligands:** When the group 5 hexacarbonylate anions [M(CO)<sub>6</sub>]<sup>-</sup> (M = Nb, Ta) were treated with silver(I) in absence of uncoordinated monoxide, different clusters, depending on the stoichiometry formed.<sup>267</sup> Those included also large heterobimetallic cluster cores, i.e. a supertetrahedral Ta<sub>4</sub>Ag<sub>6</sub>- or a Ta<sub>5</sub>Ag<sub>6</sub>-core, in which five Ta(CO)<sub>6</sub>-moieties cap the five faces of a Ag<sub>6</sub>-trigonal prisma.

**M<sub>3</sub>(CO)<sub>12</sub>-Complexes:** The trimetal dodecacarbonyls M<sub>3</sub>(CO)<sub>12</sub> (M = Ru, Os) react with silver(I) in the same 2:1 stoichiometry to the respective [Ag{TMC}<sub>2</sub>]<sup>+</sup> complexes. Yet, the trimetal dodecacarbonyls are coordinating over the metal-metal bond to the silver-cation, which leads to an elongation of this bond and strong interaction energies, which surpass the interaction energies of the other metal carbonyls with the silver(I) cation.

### 1.07.2.3.4 Further transition metal cations with gaseous ligands

**Transition Metal Nitrosyl Complexes:** Transition metal nitrosyl complexes exhibit an interesting bonding situation due to the covalency of the M–NO bond.<sup>268,269</sup> Attempts to synthesis TMCCs, like [Cr(CO)<sub>6</sub>]<sup>+</sup>, by deelectronation of a neutral starting material with NO<sup>+</sup> often leads to NO/CO ligand exchange and to a rather scarce family of *pseudo*-ternary mixed carbonyl/nitrosyl cations.<sup>270</sup> Whereas longer reaction times are necessary for the ligand exchange to the thermodynamically more stable 18-electron species [Cr(CO)<sub>5</sub>(NO)]<sup>+</sup>, the higher homologous [M(CO)<sub>5</sub>(NO)]<sup>+</sup> (M = Mo, W) are formed exclusively by reaction of NO<sup>+</sup> with the corresponding metal carbonyl.<sup>259</sup> The non-innocent character of NO<sup>+</sup> as deelectronater was also observed during the deelectronation of nickel powder under CO atmosphere and Fe(CO)<sub>5</sub> resulting in [Ni(CO)<sub>3</sub>(NO)]<sup>+</sup><sup>261</sup> and [Fe(CO)<sub>4</sub>(NO)]<sup>+</sup>.<sup>270</sup> Further addition of NO gas to [Fe(CO)<sub>4</sub>(NO)]<sup>+</sup> yielded [Fe(CO)(NO)<sub>3</sub>]<sup>+</sup>,<sup>270</sup> which completes the series of heteroleptic iron carbonyl/nitrosyl complexes, since the discovery of the anionic [Fe(CO)<sub>3</sub>(NO)<sub>2</sub>]<sup>-</sup><sup>271</sup> and the neutral [Fe(CO)<sub>2</sub>(NO)<sub>2</sub>].<sup>272</sup>

**Homoleptic [Mn(NO)<sub>4</sub>]<sup>+</sup>:** In contrast to the homoleptic TMCCs, only one truly homoleptic transition metal nitrosyl cation is hitherto known. [Mn(NO)<sub>4</sub>][*pf*]<sup>-</sup> and [Mn(NO)<sub>4</sub>][*alfal*]<sup>-</sup> were synthesized from in situ generated “Mn(CO)(NO)<sub>3</sub>” and NO[WCA], which could be used as well-characterized model system for the further investigation of the metal nitrosyl bonding.<sup>273</sup>

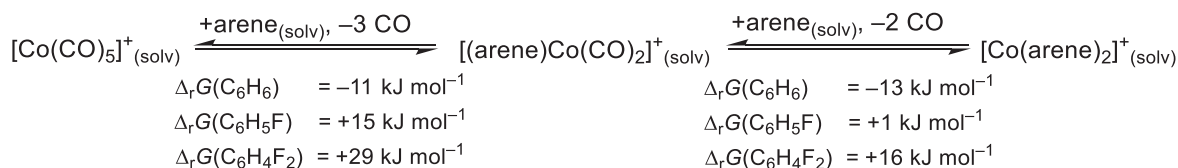
**A Copper-N<sub>2</sub>O-Complex:** Compared to CO and NO, nitrous oxide (N<sub>2</sub>O) is considered an even poorer ligand due to the low dipole moment and weak σ-donor and π-acceptor properties.<sup>274</sup> However, solvent free Cu[*pf*], obtained by oxidation of copper powder with the synergistic Ag<sup>+</sup>[*pf*]<sup>-</sup>/0.5 I<sub>2</sub> system in perfluorinated hexane, is able to reversibly bind N<sub>2</sub>O over the terminal nitrogen atom.<sup>275</sup> [Cu(N<sub>2</sub>O)(*pf*)] is one of only four structurally characterized N<sub>2</sub>O transition metal complexes,<sup>274–276</sup> and exhibits a blue-shifted N–N and N–O vibrational band compared to free N<sub>2</sub>O.<sup>275</sup>

### 1.07.2.3.5 Transition metal carbonyl cations as starting materials

Due to the reduced π-back bonding, the carbonyl ligands in TMCCs are typically only weakly bound to the metal centers, which is why they present excellent starting materials for a rich substitution chemistry.

For instance, [Co(CO)<sub>5</sub>]<sup>+</sup> reacts with different arenes like toluene, benzene or 1,2-difluorobenzene to the cationic two-legged piano-stool complexes [(arene)Co(CO)<sub>2</sub>]<sup>+</sup>.<sup>277</sup> To complete the conversion, the reaction has to be performed under reduced pressure or at elevated temperatures in an open system to obtain the respective [Co(arene)<sub>2</sub>]<sup>+</sup> sandwich complexes.<sup>43</sup> Fortunately, as the gaseous CO can be easily removed from the equilibrium, even sandwich complexes with the weakly Lewis basic 1,2-difluorobenzene are accessible, although the reaction from [Co(CO)<sub>5</sub>]<sup>+</sup> to [Co(*o*DFB)<sub>2</sub>]<sup>+</sup> is endergonic by +45 kJ mol<sup>-1</sup> (Fig. 53).<sup>43,277</sup> The resulting [Co(*o*DFB)<sub>2</sub>]<sup>+</sup> complex can then be utilized as a “Co<sup>+</sup>” synthon leading to complexes like [Co(P<sup>*t*</sup>Bu<sub>3</sub>)<sub>2</sub>]<sup>+</sup>.<sup>43</sup>

Although in part endergonic, the reactions proceed due to the irreversible removal CO at lower pressures.<sup>43,277</sup>



**Fig. 53** Reaction scheme for the synthesis of [(arene)Co(CO)<sub>2</sub>]<sup>+</sup> and [Co(arene)<sub>2</sub>]<sup>+</sup>, together with the calculated Gibbs free energy for different arenes.<sup>43,277</sup>



Similarly, when the  $[M(\text{CO})_7]^+$  ( $M = \text{Nb}, \text{Ta}$ ) cation are dissolved in *o*DFB, they form the  $[(\text{oDFB})M(\text{CO})_4]^+$  piano-stool complexes. In the case of  $[(\text{oDFB})\text{Nb}(\text{CO})_4]^+$ , the reaction is reversible on addition of CO pressure.<sup>258</sup> The deelectronation of the  $\text{Nb}(\text{arene})_2$  (arene = toluene, mesitylene) complexes are yielding the respective 16-valence electron  $[\text{Nb}(\text{arene})_2]^+$  complexes, which react with carbon monoxide to the 18-valence electron  $[(\text{arene})_2\text{Nb}(\text{CO})]^+$  complexes. An excess of carbon monoxide leads to the piano-stool complexes  $[(\text{arene})\text{Nb}(\text{CO})_4]^+$ .<sup>278</sup>

### 1.07.2.3.6 Complexed free elemental clusters

The activation and complexation of small elemental clusters like  $\text{P}_4$ ,  $\text{S}_8$ , etc. has sparked considerable interest over the past decades. However, only by using the least coordinating  $[pf]^-$  and  $[alfal]^-$  aluminates, truly undistorted and even homoleptic  $[\text{M}_n(\text{cluster})_x]^{n+}$  ions could be realized. Those often served as structural model for the complexes that were earlier already observed in the gas phase by one of the advanced mass spectrometry methods. Moreover, direct access to metastable or unknown allotropes of the elements like  $\text{Se}_6$  and  $\text{E}_{12}$  ( $\text{E} = \text{S}, \text{Se}$ ) was provided by the weak complexation. Recent additions are the complexes of the heavier dihalogens  $\text{X}_2$  ( $\text{X} = \text{Cl}, \text{Br}, \text{I}$ ),<sup>40</sup> of which  $\text{I}_2$  showed a diverse coordination chemistry<sup>41</sup> towards  $\text{Ag}^+$ .

**Complexes with  $\text{P}_4$ :** In a pioneering MS study, two binary silver-phosphorus cations were observed:  $[\text{AgP}_4]^+$  and  $[\text{AgP}_8]^+$ . On the basis of this mass spectrometric experiment and initial DFT-calculations a structure with two  $\eta^1$ -bound molecules was predicted. In agreement with this,  $\text{Ag}^+-\text{P}_4$  complexes containing one or two almost undistorted tetrahedral  $\text{P}_4$  units can be formed, i.e., molecular  $(\text{P}_4)\text{AgAl}(\text{OC}(\text{R})(\text{CF}_3)_2)_4$  ( $\text{R} = \text{H}, \text{Me}$ ) and  $[\text{Ag}(\text{P}_4)_2][pf]$ , which contains the first homoleptic metal  $\text{P}_4$  cation (Fig. 54).<sup>229,230</sup> In contrast to the initial computational prediction, the crystal structure determination revealed a  $[\text{Ag}(\text{P}_4)_2]^+$ -cation with  $D_{2h}$ -symmetry and two coplanar  $\eta^2$ -bound  $\text{P}_4$ -molecules. The synthesis of the  $\text{Ag}(\eta^2-\text{P}_4)_2^+$  complex was also carried out using the fluoride bridged  $[alfal]^-$  anion,<sup>16</sup> where the least coordinating character of this anion was employed to clarify the question of the ground state geometry of the  $[\text{Ag}(\eta^2-\text{P}_4)_2]^+$  cation ( $D_{2h}$ ,  $D_2$  or  $D_{2d}$ ?). Calculations showed a very small energy difference of  $5.2 \text{ kJ mol}^{-1}$  between the planar ( $D_{2h}$ ) and tetrahedral ( $D_{2d}$ ) conformation.<sup>16,229,230</sup> According to other calculations, the most favorable structure is of  $D_2$  symmetry.<sup>279</sup> In agreement with this computational data and NMR spectra it could be shown on experimental grounds that several orientations of the  $[\text{Ag}(\eta^2-\text{P}_4)_2]^+$  cation are very close in energy, that the rotation around the  $\text{Ag}-(\text{P}-\text{P}-\text{centroid})$  axis has no barrier and that the finally realized geometry in the solid state clearly depends on packing effects. These effects lead to an almost  $D_{2h}$  symmetric  $[\text{Ag}(\eta^2-\text{P}_4)_2]^+$  cation (0 to  $10.6^\circ$  torsion) for the more symmetrical  $[pf]^-$  anion, but to a  $D_2$  symmetric  $[\text{Ag}(\eta^2-\text{P}_4)_2]^+$  cation with a  $44^\circ$  twist angle of the two  $\text{AgP}_2$  planes for the less symmetrical  $[alfal]^-$  anion (Fig. 54).<sup>16</sup>

In a metathesis reaction from the silver salt,  $\text{CuI}$  and white phosphorus, later also the isostructural  $\text{Cu}(\eta^2-\text{P}_4)_2^+[pf]^-$  salt was prepared.<sup>236</sup> Compared to the silver complex, the bonding to the  $\text{P}_4$  moiety is stronger in  $[\text{Cu}(\eta^2-\text{P}_4)_2]^+$  and accordingly the  $^{31}\text{P}$  NMR chemical shift ( $-460 \text{ ppm}$ ) is by  $36 \text{ ppm}$  more deshielded than that of the homologous silver complex ( $-496 \text{ ppm}$ ), but still very much in the range of a true  $\text{P}_4$ -complex and *not* a coordinated phosphidic tetraphosphabicyclobutane-moiety. To complement the series  $[\text{Au}(\eta^2-\text{P}_4)_2]^+$  has also been reported but only stabilized with  $[\text{GaCl}_4]^-$  ( $\delta = -452 \text{ ppm}$ ).<sup>280</sup> With  $[(\text{NHC})\text{MP}_4][pf]$  ( $\text{M} = \text{Au}, \text{Cu}$ ), functionalization of  $\text{P}_4$  using Aryl lithium compounds was investigated resulting in a doubly complexed  $\text{RP}_4$  butterfly derivative.<sup>281</sup> Since phosphorus is a rather electronegative element, transition metal complexes tend to form a phosphidic tetraphosphabicyclobutane-moiety instead of an intact  $\text{P}_4$  tetrahedron.

For  $[\text{CpFe}(\text{CO})_2(\eta^1-\text{P}_4)]^+[pf]^-$ , strong blue-shifting of the  $\text{P}_4$  vibrational modes vs. neutral  $\text{P}_4$  indicates mainly  $\pi$ -donation with minor  $\pi$ -back donation. This results in an *Umpolung* of the usually more phosphidic character of  $\text{P}_4$  to a phosphonium character, opening up a possibility of  $\text{P}_4$  functionalization via nucleophiles.<sup>282</sup>

**Complexes with  $\text{As}_4$ :** Yellow arsenic is far less stable than  $\text{P}_4$  and polymerizes to gray arsenic within minutes in solid state or in presence of light. Nevertheless, the group of Prof. Manfred Scheer reported side-on coordination of  $\text{As}_4$  tetrahedra  $[\text{Ag}(\eta^2-\text{As}_4)_2]^+[pf]^-$  in analogy to white phosphorus. This salt can be used as  $\text{As}_4$  transfer agent, e.g., generating  $[(\text{PPh}_3)\text{Au}(\eta^2-$

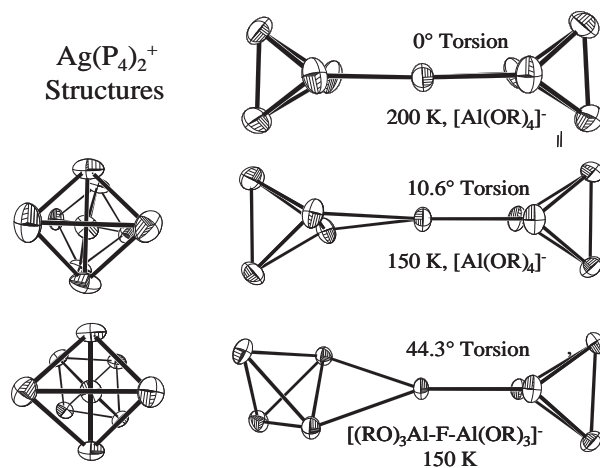
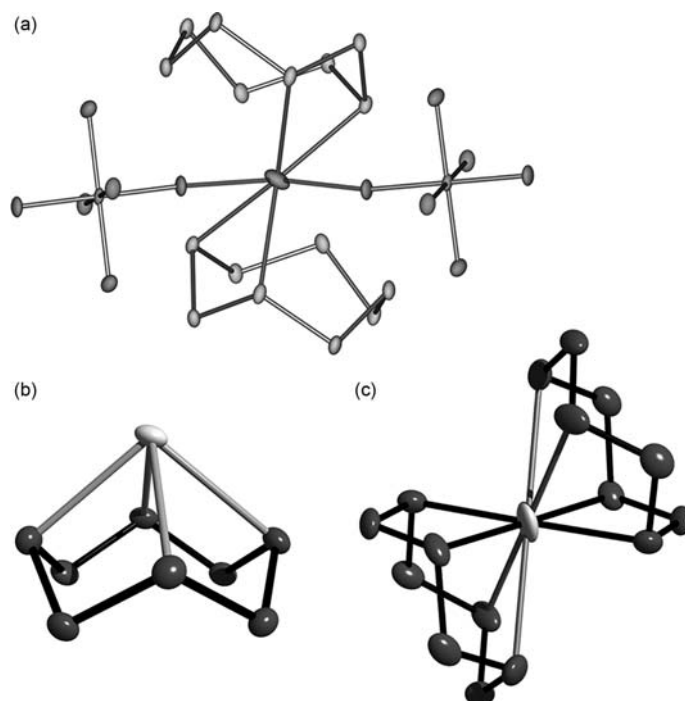


Fig. 54 Temperature and anion dependence of the orientations of the  $[\text{Ag}(\eta^2-\text{P}_4)_2]^+$  cations ( $[pf]^-$  and  $[alfal]^-$  salts).



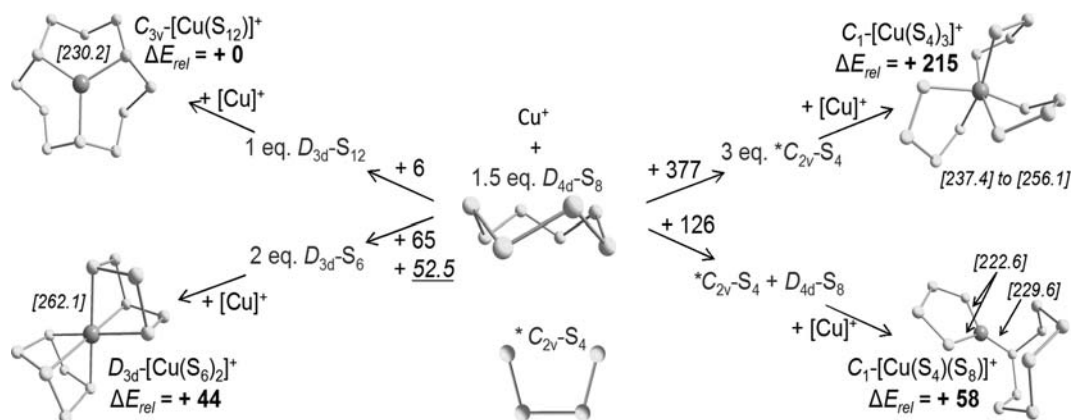


**Fig. 55** (a) Section of the solid-state structure of  $(S_8)_2AgSbF_6$ : coordinated  $[MF_6]^-$  anions that lead to a distortion of the  $[Ag(S_8)_2]^+$  structure. (b)  $(S_8)Ag[hf]$  and (c)  $[Ag(S_8)_2][pf]$  including the undistorted  $[Ag(S_8)]^+$  and  $[Ag(S_8)_2]^+$  cations.

$As_4)]^+[pf]^-$ .<sup>283</sup> The reaction of  $[Ag(\eta^2-As_4)_2]^+[pf]^-$  with  $[Cp^*Ru(dppe)Cl]$  leads to  $[Cp^*Ru(dppe)(\eta^1-As_4)]^+[pf]^-$  with an unprecedented end-on-coordinated  $As_4$  tetrahedron. A second cationic ruthenium complex fragment does not lead to a second end-on coordination but to the cleavage of one basal As–As bond, which differs from its phosphorus analogs.<sup>284</sup>

**Complexes with  $S_8$ :** It has been shown by mass spectrometry that  $Ag^+$  and  $S_8$  give complexes of type  $[Ag(S_8)_x]^+$  ( $x = 1, 2$ ).<sup>285,286</sup> The only available structural model for such complexes was  $(S_8)_2Ag[MF_6]$  ( $M = As, Sb$ ),<sup>242,287</sup> however, due to anion coordination it is unlikely that the gaseous  $[Ag(S_8)_2]^+$  cation will adopt the same geometry (Fig. 55a). Therefore, the larger  $[pf]^-$  anions were used to approximate the still unknown geometries of gaseous  $Ag(S_8)_x^+$ . The compounds  $(S_8)Ag[Al(OC(H)(CF_3)_2)_4]$  and  $[Ag(S_8)_2][pf]$  were obtained<sup>242</sup> and include the first examples of undistorted homoleptic metal  $S_8$ -complexes, i.e., the almost  $C_{4v}$ -symmetric  $[Ag(\eta^4-S_8)]^+$  and the approximately centrosymmetric  $[Ag(\eta^4-S_8)_2]^+$  cations in Fig. 55b and c. As also shown by quantum chemical calculations, they provide the best structural models for the gaseous  $AgS_8^+$  and  $AgS_{16}^+$  cations.

It should be noted that quantum chemical calculations of these cations are rather difficult due to the substantial participation of dispersion in the bonding. Without the experimental structures, it would have been hard to establish the quality of the computation.<sup>242</sup> Weak dispersive Ag–S interactions are structure determining and, therefore, DFT and HF-DFT theory failed to describe the  $Ag(S_8)_x^+$  cations. Only MP2 calculations with a larger basis set (TZVPP) gave minimum geometries close to the experiment. After these initial calculations, we were able to also characterize  $Cu(S_8)$  complexes.<sup>37,288</sup> However, these were only accessible with the



**Fig. 56** Calculated energies (PBE0/TZVPP,  $\Delta H_{(g)}^\circ$ ,  $\text{kJ mol}^{-1}$ ) and experimental values *italics* for the interconversion of cyclooctasulfur into  $S_n$  species and possible  $[Cu(S_x)(S_y)]^+$  ( $x + y = 12$ ) structures. Relative energies to the most favorable complex  $C_{3v}\text{-}[Cu(S_{12})]^+$  **bold**. Cu–S distances [*italics*] given in pm.

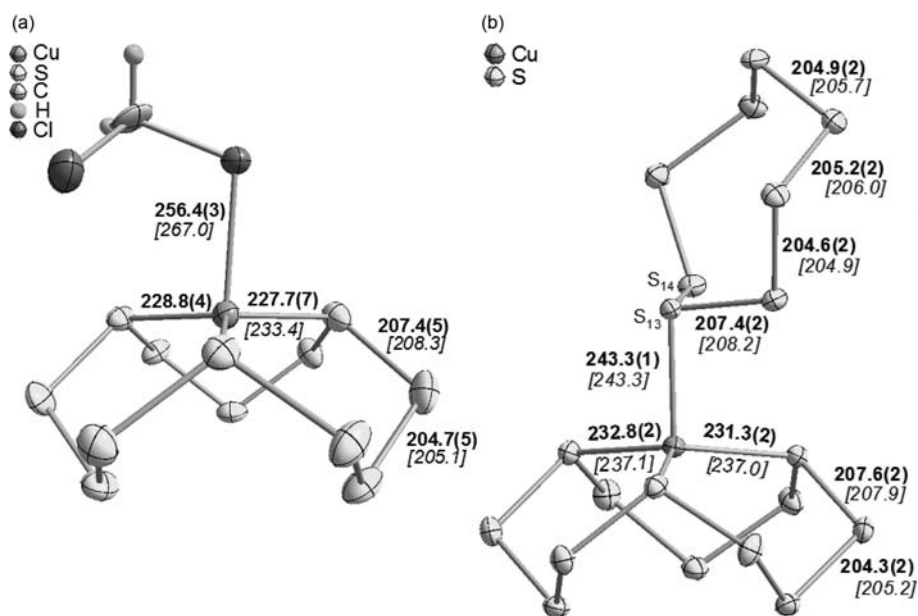
more coordinating  $[\text{Al}(\text{OR}^{\text{F}})_4]^-$  aluminates with  $\text{R}^{\text{F}} = \text{C}(\text{H})(\text{CF}_3)_2$  and  $\text{R}^{\text{F}} = \text{C}(\text{Me})(\text{CF}_3)_2$ ; with the least coordinating  $[\text{pf}]^-$ -aluminate, the formation of  $\text{S}_{12}$ -complexes was observed (v.i.). In the  $\text{Cu}(\text{S}_8)$ -complexes, the  $\text{S}_8$ -molecule may also serve as a bridging ligand.

**Complexes including the  $\text{S}_{12}$  molecule:** Besides  $\text{S}_8$ ,  $D_{3d}$ - $\text{S}_{12}$  is the thermodynamically second most stable allotrope of sulfur. By MS it was shown,<sup>285,286</sup> that the  $\text{Cu}^+$  ion only forms  $\text{S}_8$ -complexes immediately after mixing of the vapors in the MS. Within 10 s, almost all of the  $\text{S}_8$  was transformed into gaseous  $[\text{CuS}_{12}]^+$ . Unfortunately, MS provides no structural information on the nature of the involved sulfur ligands being  $\text{S}_{12}$ , two  $\text{S}_6$ , three  $\text{S}_4$  or even a mix of  $\text{S}_4$  and  $\text{S}_8$ . First insights were gained by DFT calculations that suggested a  $[\text{Cu}(\text{S}_{12})]^+$  complex including the  $D_{3d}$ - $\text{S}_{12}$  molecule to be the global minimum (Fig. 56).

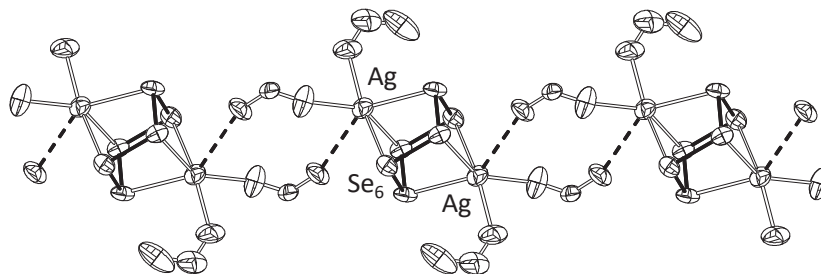
It was therefore interesting to see, as to whether the  $\text{Cu}[\text{pf}]$  starting material<sup>37</sup> including the least coordinating aluminate WCA could induce this reaction also in condensed phases. However, nature always has its surprises, and so two substances could be isolated from the reaction of  $\text{Cu}[\text{pf}]$  and excess  $\text{S}_8$ <sup>37,288</sup>. Depending on the sonication time, single crystals of  $[(\text{S}_8-\eta^1)\text{Cu}(1,5,9-\eta^3-\text{S}_{12})]^+[\text{pf}]^-$  or  $[(\text{CH}_2\text{Cl}_2)\text{Cu}(1,5,9-\eta^3-\text{S}_{12})]^+[\text{pf}]^-$  were repeatedly isolated from several independent reactions. Both copper complexes contain almost undistorted  $D_{3d}$ - $\text{S}_{12}$  and both provide the first examples of any metal- $\text{S}_{12}$  complex. Additionally the  $[(\text{S}_8-\eta^1)\text{Cu}(1,5,9-\eta^3-\text{S}_{12})]^+$  cation is the first example of a metal complex, in which two different ring sizes of an element are bound to a metal (Fig. 57).

Probably the  $[(\text{CH}_2\text{Cl}_2)\text{Cu}(1,5,9-\eta^3-\text{S}_{12})]^+$  cation, containing a very weakly bound  $\text{CH}_2\text{Cl}_2$  molecule, is the best structural approximation of gaseous  $\text{C}_{3v}$ - $[\text{CuS}_{12}]^+$ . It could be shown by DFT calculations that the formation of the  $\text{S}_{12}$ -complexes is thermodynamically driven upon  $\text{S}_8$  complexation to copper.<sup>37,288</sup>

**Complexes with metastable  $\text{Se}_6$ :** The gray, semi-metallic form is the thermodynamically most stable modification of selenium. Red selenium, a mixture of mainly  $\text{Se}_8$  and some  $\text{Se}_6$  with traces of  $\text{Se}_7$  also exists in condensed phases. With considerable effort, pure  $\text{Se}_8$  and pure  $\text{Se}_6$  were prepared. It has been shown that complexation with  $\text{Ag}^+$  and the least coordinating  $[\text{pf}]^-$  WCA leads to the



**Fig. 57** Cation structures of the  $\text{S}_{12}$ -complexes in (a)  $[(\text{CH}_2\text{Cl}_2)\text{Cu}(1,5,9-\eta^3-\text{S}_{12})]^+[\text{pf}]^-$  and (b)  $[(\text{S}_8-\eta^1)\text{Cu}(1,5,9-\eta^3-\text{S}_{12})]^+[\text{pf}]^-$ . Experimental distances are given in pm in bold and PBE0/TZVPP calculated values in brackets in italics.



**Fig. 58** Section of the  $[(\text{SO}_2)_2\text{Ag}]_2(\mu:\eta^3,\eta^3-\text{Se}_6)]^{2+}$  dication stack in  $[(\text{SO}_2)_2\text{Ag}]_2(\text{Se}_6)]^{2+}$  ( $[\text{pf}]^-$ )<sub>2</sub>.

thermodynamically preferred transformation of gray selenium into weakly complexed metastable  $\text{Se}_6$  in the dicationic  $[\text{Ag}_2(\eta^3, \eta^3\text{-Se}_6)]^{2+}$  heterocubane,<sup>289</sup> which is coordinatively saturated on each silver ion by further ligation of two sulfur dioxide molecules. Overall, these  $[(\text{SO}_2)_2\text{Ag}]_2(\eta^3, \eta^3\text{-Se}_6)^{2+}$ -moieties further form slightly aggregated 1D chains, as shown in Fig. 58.

A related isolated structure was observed, when the similarly large and weakly coordinating  $[\text{Sb}(\text{OTeF}_5)_6]^-$  WCA was employed.<sup>290</sup> However, upon changing to the smaller  $[\text{MF}_6]^-$  anions ( $\text{M} = \text{As}, \text{Sb}$ ), aggregated 1D-stacks of composition  $([\text{Ag}(\mu\text{-}\eta^3, \eta^3\text{-Se}_6)]^+)_\infty$  partly also crosslinked by  $\mu\text{-}\eta^1, \eta^1\text{-Ag}$ -ions. But in all cases the thermodynamically preferred complexes of the metastable hexaselenium allotrope formed by reaction of silver ions with gray selenium.<sup>289</sup> It appears that the size of the anions governs the formation of molecular or polymeric structures (see also  $\text{P}_4\text{S}_3$  below).

*A complex of the unknown  $\text{Se}_{12}$  allotrope:* When using red, instead of gray selenium as a starting material, again a dicationic silver-selenium complex resulted:  $[\text{Ag}_2(\text{Se}_{12})]^{2+}([\text{pf}]^-)_2$ .<sup>291</sup> The only other account of  $\text{Se}_{12}$  is a structure as a cocrystal with mixed molybdate  $(\text{NH}_4)_2[(\text{Mo}_3\text{S}_{11.72}\text{Se}_{1.28})(\text{Se}_{12})]$ . Again, complexation with silver leads to the reproducible formation of the unknown modification and also bulk characterization of a salt with the  $D_{3d}$ - $[\text{Ag}_2(\text{Se}_{12})]^{2+}$  dication. To our knowledge this presents a novel 14 cornered closed polyhedron built from six-membered rings in the boat conformation (Fig. 59).

The cross-cluster Ag–Ag separation is with 286 pm weakly bonding and presents a rare example for an argentophilic interaction in a dication. Further research regarding other coinage metals as well as different allotrops of Selenium resulted in the report of a dicationic  $[\text{Cu}_2(\text{Se}_{19})][\text{pf}]_2$  salt. This  $\text{Se}_{19}$  cycle represents the first  $\text{E}_{19}$  cycle of any element.<sup>292</sup>

*Complexes of the Dihalogens  $\text{X}_2$ :* Due to their low Lewis basicity, complexes of dihalogens  $\text{X}_2$  ( $\text{X} = \text{Cl}, \text{Br}, \text{I}$ ) with a Lewis acid are rare. Nevertheless  $\text{Ag}^+[\text{pf}]^-$  forms  $[\text{Ag}(\text{X}_2)][\text{pf}]$  complexes with the respective dihalogens and  $\text{X} = \text{Cl}, \text{Br}, \text{I}$  in non-coordinating solvents like perfluorohexane (Fig. 60).<sup>40,41</sup>

Because the X–X bond length is only slightly perturbed, it is assumed, that the bonding  $\pi(\text{X}_2)$  and  $\pi^*(\text{X}_2)$  orbitals donate electron density towards the silver(I) ion. Also, after the addition of the dihalogens, the silver cation remains ion-paired to the  $[\text{pf}]^-$  anion, therefore these complexes are soluble in perfluorohexanes.

*Silver(I)-Diiodine-Complexes:* Variation of the amount of diiodine leads to different silver(I) diiodine complexes including  $[\text{Ag}_2\text{I}_2]^{2+}([\text{pf}]^-)_2$ ,  $[\text{Ag}_2(\text{I}_2)_4]^{2+}([\text{pf}]^-)_2$  and  $[\text{Ag}_2(\text{I}_2)_6]^{2+}([\text{pf}]^-)_2$ . The first of those is a strong oxidizer, which can oxidize  $\text{P}_4$  into  $\text{P}_9^+$  and pentane into carbocations.<sup>41</sup>

### 1.07.2.3.7 Complexed mixed group 15/16 cages

*Complexes with  $\text{P}_4\text{S}_3$ :* Only few examples on intact, coordinated  $\text{P}_4\text{S}_3$  are reported.<sup>293–295</sup> Normally, the  $\text{P}_4\text{S}_3$  molecule degrades upon coordination to transition metal fragments and phosphide or sulfide groups are incorporated into the complex.<sup>296,297</sup> Therefore, we extended our investigations to the coordination behavior of the  $\text{P}_4\text{S}_3$  cage, with the goal to learn more about the most reactive coordination sites of this molecule. All of them were exclusively bound through the apical P-atom. No coordination of an S-atom or a P-atom of the  $\text{P}_3$  basis was reported, however, S-coordination was postulated as a possible pathway for the sulfidic degradation.<sup>296</sup>

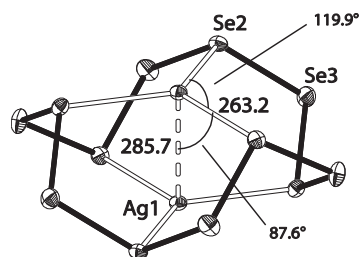
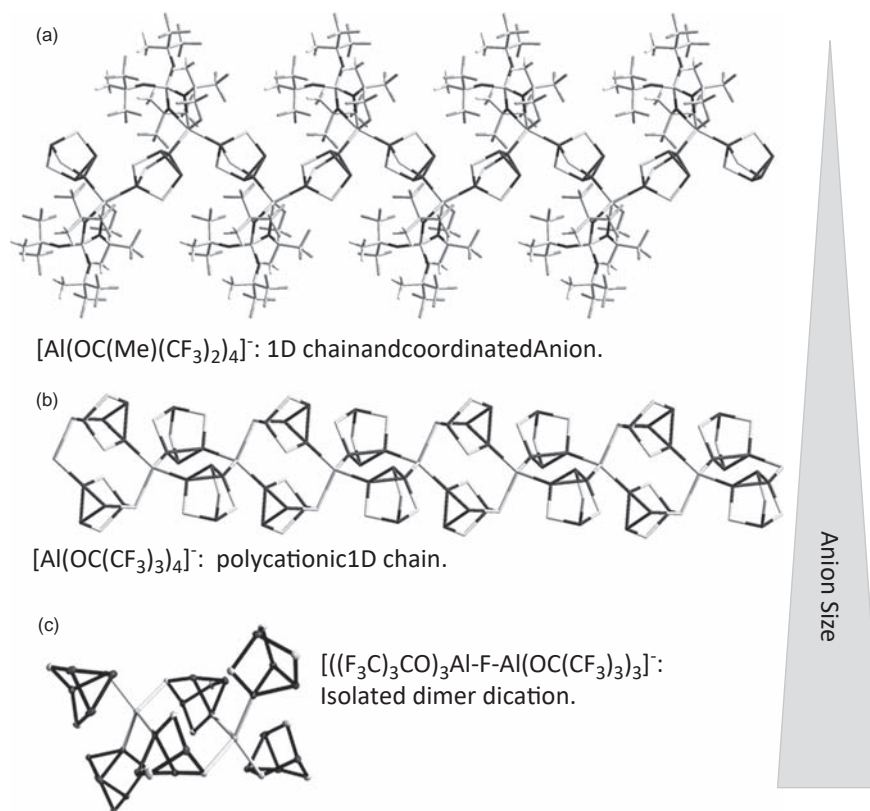


Fig. 59 Molecular structure of the  $[\text{Ag}_2\text{Se}_{12}]^{2+}$  dication in the solid state structure of  $[\text{Ag}_2\text{Se}_{12}][\text{pf}]_2$ . Bond lengths are given in pm.

	$d(\text{X-X})/\text{Å}$	$\nu(\text{X-X})/\text{cm}^{-1}$	$d(\text{Ag-X})/\text{Å}$
$\text{Ag}(\text{Cl}_2)[\text{A}]$	1.985	543 ( $^{35}\text{Cl}_2$ )	2.577
$\text{Cl}_2(\text{g})$	1.988	560 ( $^{35}\text{Cl}_2$ )	$\text{AgCl}: 2.773$
$\text{Ag}(\text{Br}_2)[\text{A}]$	2.277	315	2.610
$\text{Br}_2(\text{g})$	2.281	320	$\text{AgBr}: 2.887$
$\text{Ag}(\text{I}_2)[\text{A}]$	2.663	210	2.663
$\text{I}_2(\text{g})$	2.666	215	$\text{AgI}: 2.81$

With libration correction:  $d(\text{X-X}) \approx$  gaseous  $\text{X}_2$

Fig. 60 Molecular structure of the  $\text{Cl}_2$ -adduct  $(\text{Cl}_2)\text{Ag}[\text{pf}]$  and the principal structural and Raman data of the entire series of characterized  $(\text{X}_2)\text{Ag}[\text{pf}]$  compounds.



**Fig. 61** From polymeric to dimeric structures. Counterion/size effects of the coordination chemistry of the system  $\text{Ag}^+/\text{P}_4\text{S}_3$ .

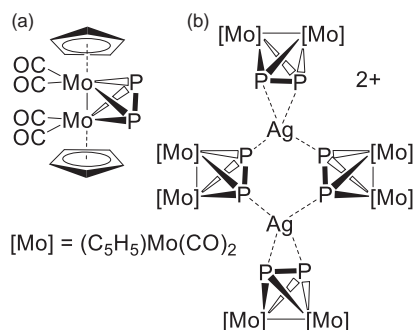
The polymeric  $\text{Ag}(\text{P}_4\text{S}_3)$  complexes with the  $[\text{pf}]^-$  anions include one dimensional chains. With the more basic  $[\text{Al}(\text{OR}^{\text{F}})_4]^-$  anion ( $\text{R}^{\text{F}} = \text{C}(\text{CH}_3)(\text{CF}_3)_2$ ), one anion remained coordinated to the silver atom in addition to one bridging  $\text{P}_4\text{S}_3$  cage (Fig. 61a), however, with the least basic perfluorinated aluminate with  $\text{R}^{\text{F}} = \text{C}(\text{CF}_3)_3$  a cationic polymer of the general formula  $[\text{Ag}(\text{P}_4\text{S}_3)_2]^+_{\infty}$  with no anion contacts formed (Fig. 61b).<sup>298</sup> By application of the even larger fluoride bridged anion  $[\text{alfal}]^-$  one may cut a segment of the composition  $[\text{Ag}_2(\text{P}_4\text{S}_3)_6]^{2+}$  out of this structure. Due to the large size of the counterion, polymerization is inhibited and an isolated dimeric dication formed in the  $\text{AB}_2$  salt  $[\text{Ag}_2(\text{P}_4\text{S}_3)_6]^{2+}([\text{alfal}]^-)_2$  (Fig. 61c).<sup>298</sup>

**Heavier homologues  $\text{P}_4\text{Se}_3$  and  $\text{As}_4\text{S}_3$ :** By reacting  $\text{P}_4\text{Se}_3$  and  $\text{As}_4\text{S}_3$  with  $\text{Ag}[\text{pf}]$  or  $\text{Ag}[\text{hf}]$  in suitable solvents,  $\text{Ag}(\text{P}_4\text{Se}_3)[\text{hf}]$ ,  $\text{Ag}(\text{P}_4\text{Se}_3)_2[\text{pf}]$ ,  $\text{Ag}(\text{P}_4\text{Se}_3)_3[\text{pf}]$ ,  $\text{Ag}_2(\text{As}_4\text{S}_3)_3[\text{pf}]_2$  and  $\text{Ag}(\text{As}_4\text{S}_3)_2[\text{pf}]$  were synthesized and characterized by SC-XRD, Mass spectrometry, Raman spectroscopy as well as solution NMR spectroscopy. Investigations demonstrated, that synthesized structures not only vary with the size of the WCA but also depend significantly on the coordinating ability of the solvent. This leads towards variation in stoichiometry and binding modes of the ligands in these complexes.<sup>299</sup>

**Complexes with  $\text{As}_4\text{S}_4$ :** By reacting  $\text{As}_4\text{S}_4$  with  $\text{Ag}[\text{pf}]$  in  $\text{SO}_2$  or ortho-difluorobenzene (*o*DFB) at room temperature, the compounds  $\text{Ag}(\text{As}_4\text{S}_4)(\text{SO}_2)_2[\text{pf}]$  and  $\text{Ag}_3(\text{As}_4\text{S}_4)_4(\text{oDFB})[\text{pf}]_3$  were obtained and characterized by single-crystal X-ray scXRD, Raman spectroscopy, as well as solution NMR spectroscopy and mass spectrometry.  $\text{Ag}(\text{As}_4\text{S}_4)(\text{SO}_2)_2[\text{pf}]$  aggregates to form a one-dimensional polymer including  $\text{SO}_2$  ligands binding to the metal cation.  $\text{Ag}_3(\text{As}_4\text{S}_4)_4(\text{oDFB})[\text{pf}]_3$  forms a two-dimensional polymer displaying an unprecedented coordination mode of the ligand through one of the arsenic atoms. Experiments as well as orienting DFT calculations suggest that the  $\text{As}_4\text{S}_4$  cage is an inferior ligand, compared to the nortricyclane cages  $\text{P}_4\text{Ch}_3$  ( $\text{Ch} = \text{S}, \text{Se}$ ) and  $\text{As}_4\text{S}_3$ .<sup>199</sup>

### 1.07.2.3.8 Complexed mixed-transition metal-element clusters

Similar to the complexes of the free elemental clusters in the preceding section, also the complexes of transition metal stabilized complexes of mainly the group 15 elemental clusters ( $\text{P}_2$ , cyclo $\text{E}_3$ , cyclo $\text{P}_5$ ;  $\text{E} = \text{P}, \text{As}$ ) profit from the—in these cases—non-coordinating nature of the  $[\text{pf}]^-$  aluminates with  $\text{R}^{\text{F}} = \text{C}(\text{CF}_3)_3$ . The group of Prof. Manfred Scheer in Regensburg has to be acknowledged here as prime contributors. When other anions like halide, nitrate,  $[\text{CF}_3\text{SO}_3]^-$ , etc. are used, in many cases very different, often polymeric structures, incorporating the more coordinating anions were observed. Moreover, the use of the large aluminate WCA allowed for studying the solution equilibrium composition, which was often impossible with the other more coordinating anions, due to the formation of insoluble products. From the available experimental and computational data, it became clear that in the solid state often polymeric compounds, depolymerize in solution with formation of very different isolated molecular structures. In the following we describe the complexes according to increasing size of the coordinated  $\text{E}_n$ -cluster.



**Fig. 62** Drawings of (a)  $[\text{Mo}]$  and (b) the dication of  $[\text{Ag}_2(\text{[Mo]}_4)]^{2+}([\text{pf}]^-)_2$ .

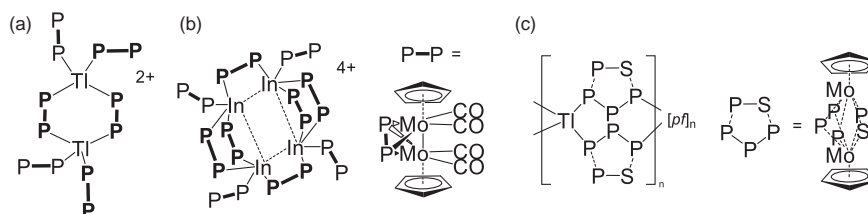
**Complexes of Tetrahedro- $\text{Mo}_2\text{P}_2$ -Units:** This work<sup>300</sup> describes a systematic study on the reaction of  $[\text{Cp}_2\text{Mo}_2(\text{CO})_4(\mu, \eta^2\text{-P}_2)]$  ( $[\text{Mo}]$ ; Cp =  $\text{C}_5\text{H}_5$ ) with a series of the coinage metal salts  $\text{Cu}[\text{PF}_6]$ ,  $\text{Ag}[\text{X}]$  (X =  $\text{BF}_4$ ,  $\text{ClO}_4$ ,  $\text{PF}_6$ ,  $\text{SbF}_6$ ,  $[\text{pf}]^-$ ) and  $[(\text{Ph}_3\text{P})\text{Au}(\text{THF})][\text{PF}_6]$ , respectively. The reactions resulted in the facile formation of the dimer dication  $[\text{M}_2(\text{[Mo]}_4)]^{2+}$  in  $[\text{M}_2(\{\text{Cp}_2\text{Mo}_2(\text{CO})_4(\mu, \eta^2:\eta^2\text{-P}_2)\}_2)(\{\text{Cp}_2\text{Mo}_2(\text{CO})_4(\mu, \eta^2:\eta^1:\eta^1\text{-P}_2)\}_2)][\text{X}]_2$  (M = Cu, Ag, Au). As revealed by X-ray crystallography, all these dimers comprise dicationic moieties that are well-separated from the WCAs in the solid state. However, if  $[\text{Mo}]$  is allowed to react with  $\text{AgNO}_2$  and  $\text{LAuCl}$  (L = CO or tetrahydrothiophene), dimers with coordinated anions at the Group 11 metal centers resulted. Spectroscopic data suggest that the dimers  $[\text{M}_2(\text{[Mo]}_4)]^{2+}$  display dynamic behavior in solution, and this was discussed by using the comprehensive results obtained for  $[\text{Ag}_2(\text{[Mo]}_4)]^{2+}([\text{pf}]^-)_2$  as a basis (Fig. 62).<sup>300</sup> The interpretation of the experimental results was facilitated by DFT calculations on  $[\text{Ag}_2(\text{[Mo]}_4)]^{2+}$  (structures, energetics, NMR shielding tensors). Further investigations using Ag  $[\text{pf}]^-$ ,  $[\text{Mo}]$  and trans-1,2-di(pyridine-4-yl)ethene led to a variety of organometallic-organic hybrid compounds. Depending on reaction conditions two-dimensional networks were obtained.<sup>301</sup>

The diphosphorus half-sandwich molybdenum complex of  $[\text{Cp}_2\text{Mo}_2(\text{CO})_4(\mu, \eta^2\text{-P}_2)]$  (Cp =  $\text{C}_5\text{H}_5$ ) reacts also with the thallium source  $\text{Tl}^+[\text{pf}]^-$  to form the polynuclear thallium-molybdenum complex  $[\text{Tl}_2[\text{Cp}_2\text{Mo}_2(\text{CO})_4(\mu, \eta^1:\eta^2\text{-P}_2)]_4[\text{Cp}_2\text{Mo}_2(\text{CO})_4(\mu^3\text{-}\eta^1:\eta^2:\eta^1\text{-P}_2)]_2][\text{pf}]^-$ ; Fig. 63a.<sup>135</sup>

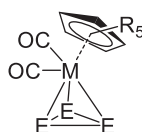
After the initial report on  $\text{Tl}^+$ , the same authors developed a new route to  $\text{In}^+$  salts: the Indium(I) complex  $[(\eta^6\text{-1,2-}\text{F}_2\text{C}_6\text{H}_4)_2\text{In}]^+[\text{pf}]^-$  ( $\text{R}^f = \text{C}(\text{CF}_3)_3$ ) was prepared by reaction of  $\text{InCl}$  with  $\text{Li}[\text{pf}]^-$  in 1,2-difluorobenzene.<sup>35</sup> It is a convenient precursor for the indium-molybdenum diphosphorus-bridged cluster  $[\text{In}_4[\text{Cp}_2\text{Mo}_2(\text{CO})_4\text{P}_2]_8][\text{pf}]_4$  prepared by reaction of the  $\text{In}^+$  salt with  $[\text{Cp}_2(\text{CO})_4\text{Mo}_2(\mu, \eta^2\text{-P}_2)]$  (Fig. 63b).<sup>35</sup>

Additionally the  $\text{Tl}^+$  salt was used to build a polymeric structure with  $[(\text{Cp}^*\text{Mo})_2(\mu, \eta^3:\eta^3\text{-P}_3)(\mu, \eta^2:\eta^2\text{-PS})]$  (Fig. 63c).<sup>302</sup>

**Complexes of Tetrahedro- $\text{Mo}_2\text{As}_2$ -Unit:** With  $\text{Ag}[\text{pf}]^-$  a the heavier pnictogen complex using  $[\text{Cp}_2\text{Mo}_2(\text{CO})_4(\eta^2\text{-As}_2)]$  was used to yield  $[\text{Ag}(\eta^2\text{-}(\text{Cp}_2\text{Mo}_2(\text{CO})_4(\eta^2\text{-As}_2))_3)][\text{pf}]^-$ . Reaction with 2,2'-bipyrimidine then led via a stepwise pathway to the dicationic complex  $\{[(\eta^2\text{-}(\text{Cp}_2\text{Mo}_2(\text{CO})_4(\eta^2\text{-As}_2))_2\text{Ag})]_2(\mu\text{-}(2,2'\text{-bipyrimidine}))\}[\text{pf}]_2$ .<sup>303</sup>



**Fig. 63** Drawings of the cationic part of (a)  $[\text{Tl}_2[\text{Cp}_2\text{Mo}_2(\text{CO})_4(\mu\text{-}\eta^1:\eta^2\text{-P}_2)]_4[\text{Cp}_2\text{Mo}_2(\text{CO})_4(\mu^3\text{-}\eta^1:\eta^2:\eta^1\text{-P}_2)]_2][\text{pf}]^-$ , (b)  $[\text{In}_4[\text{Cp}_2\text{Mo}_2(\text{CO})_4\text{P}_2]_8][\text{pf}]_4$  and (c) coordination polymer formed by the reaction of  $\text{Tl}[\text{pf}]^-$  with  $[(\text{Cp}^*\text{Mo})_2(\mu, \eta^3:\eta^3\text{-P}_3)(\mu, \eta^2:\eta^2\text{-PS})]$ .



R = H, Me; M = Cr, Mo;  
E = P, As

**Fig. 64** An organometallic building block for supramolecular chemistry: cyclo $\text{E}_3$  ligand complexes  $[\text{Cp}^R\text{M}(\text{CO})_2(\eta^3\text{-P}_3)]$  (M = Mo, E = P:  $\text{Cp}^R = \text{C}_5\text{H}_5$  (M),  $\text{C}_5\text{Me}_5$  (N); M = Mo, E = As:  $\text{Cp}^R = \text{C}_5\text{Me}_5$  (O); M = Cr, E = P:  $\text{Cp}^R = \text{C}_5\text{H}_5$  (P)).



*Complexes of Cyclo-E<sub>3</sub>-Units (E = P, As):* The synthesis and characterization of the first supramolecular aggregates incorporating the organometallic cycloP<sub>3</sub> ligand complexes [Cp<sup>R</sup>Mo(CO)<sub>2</sub>(η<sup>3</sup>-P<sub>3</sub>)] (Cp<sup>R</sup> = Cp (C<sub>5</sub>H<sub>5</sub>; M), Cp\* (C<sub>5</sub>Me<sub>5</sub>; N)) as linking units were described (Fig. 64).<sup>304</sup>

The reaction of the Cp derivative M with AgX [X = CF<sub>3</sub>SO<sub>3</sub>, Al(OC(CF<sub>3</sub>)<sub>3</sub>)<sub>4</sub>] yields the 1-dimensional (1D) coordination polymers [Ag{CpMo(CO)<sub>2</sub>(μ,η<sup>3</sup>:η<sup>1</sup>:η<sup>1</sup>-P<sub>3</sub>)<sub>2</sub>]<sub>n</sub>[pf]<sub>n</sub> and [Ag{CpMo(CO)<sub>2</sub>(μ,η<sup>3</sup>:η<sup>1</sup>:η<sup>1</sup>-P<sub>3</sub>)<sub>3</sub>]<sub>n</sub>[X]<sub>n</sub>. The solid-state structures of these polymers were revealed by X-ray crystallography and shown to comprise polycationic chains well-separated from the WCAs. If Ag[CF<sub>3</sub>SO<sub>3</sub>] was used as a silver source, the polymer [Ag{CpMo(CO)<sub>2</sub>(μ,η<sup>3</sup>:η<sup>1</sup>:η<sup>1</sup>-P<sub>3</sub>)<sub>3</sub>]<sub>n</sub>[CF<sub>3</sub>SO<sub>3</sub>]<sub>n</sub> was obtained regardless of reactant stoichiometry. In the case of Ag[pf],<sup>304</sup> reactant stoichiometry plays a decisive role in determining the structure and composition of the resulting product. These polymers are the first examples of homoleptic Ag complexes in which Ag<sup>I</sup> centers are found octahedrally coordinated to six P atoms. The Cp\* derivative N reacts with Ag[pf] to yield the 1-dimensional polymer [Ag{CpMo(CO)<sub>2</sub>(μ,η<sup>3</sup>:η<sup>1</sup>:η<sup>1</sup>-P<sub>3</sub>)<sub>2</sub>]<sub>n</sub>[pf]<sub>n</sub>, the crystal structure of which differs from that of the polymer of the same stoichiometry in the coordination mode of the cycloP<sub>3</sub> ligands<sup>304</sup>: in the first, the Ag<sup>+</sup> cations are bridged by the cycloP<sub>3</sub> ligands in a η<sup>1</sup>:η<sup>1</sup> (edge bridging) fashion whereas in the latter, they are bridged exclusively in a η<sup>2</sup>:η<sup>1</sup> mode (face bridging). Thus, 1/3 of the P atoms in the first compound are not coordinated to Ag, while in 4, all P atoms are engaged in coordination with Ag. Comprehensive spectroscopic and analytical measurements revealed that all described polymers depolymerize extensively upon dissolution and display dynamic behavior in solution, as evidenced in particular by variable temperature <sup>31</sup>P NMR spectroscopy. Solid-state <sup>31</sup>P-MAS-NMR measurements demonstrated that two of the polymers also display dynamic behavior in the solid state at room temperature.<sup>304</sup>

The indium(I) complex [(η<sup>6</sup>-1,2-F<sub>2</sub>C<sub>6</sub>H<sub>4</sub>)<sub>2</sub>In]<sup>+</sup>[pf]<sup>-35</sup> may be used for the synthesis of the indium-chromium polymeric P<sub>3</sub>-bridged half-sandwich [In{CpCr(CO)<sub>2</sub>P<sub>3</sub>}]<sub>n</sub>[pf]<sub>n</sub>, prepared by reaction of the In<sup>+</sup> salt with [CpCr(CO)<sub>2</sub>(η<sup>3</sup>-P<sub>3</sub>)] (O, Fig. 64). Equilibrium constants for substitution of O ligands for CH<sub>2</sub>Cl<sub>2</sub> solvent molecules in the complex were calculated at DFT level in vacuum and in CH<sub>2</sub>Cl<sub>2</sub> solution; according to the value of K<sub>eq</sub>(CH<sub>2</sub>Cl<sub>2</sub>), the complex is mostly decomposed in the solution.<sup>35</sup>

Also the cycloAs<sub>3</sub>-complex [Cp\*Mo(CO)<sub>2</sub>(η<sup>3</sup>-As<sub>3</sub>)] (P) reacted with Ag[pf] to yield a novel dimeric complex featuring the cycloAs<sub>3</sub> ligand in an unusual face-bridging coordination mode.<sup>305</sup> The analytical data and DFT calculations supported the existence of a monomer-dimer equilibrium in solution. O also reacted with CuX (X = Cl, Br, I) to yield insoluble dimers consisting of planar Cu<sub>2</sub>X<sub>2</sub> moieties.<sup>305</sup>

*Dicationic E<sub>4</sub> Chains (E = P, As, Sb, Bi):* The oxidation of [{CpMo(CO)<sub>2</sub>]<sub>2</sub>(μ,η<sup>2</sup>:η<sup>2</sup>-E<sub>2</sub>)] with [Thia]<sup>+</sup> (= [C<sub>12</sub>H<sub>8</sub>S<sub>2</sub>]<sup>+</sup>) results in the selective formation of the dicationic E<sub>4</sub> complexes [{CpMo(CO)<sub>2</sub>]<sub>4</sub>(μ<sup>4</sup>, η<sup>2</sup>:η<sup>2</sup>:η<sup>2</sup>:η<sup>2</sup>-E<sub>4</sub>)]<sup>2+</sup> stabilized by four [CpMo(CO)<sub>2</sub>] fragments. For phosphorus and arsenic, unprecedented [E<sub>4</sub>]<sup>2+</sup> chains were stabilized in the coordination sphere of transition metals, whereas the heavier antimony and bismuth representatives reacted to unprecedented dicationic E<sub>4</sub> cages.<sup>306</sup> Following these investigations, the mixed structures as well as the mixed E<sub>4</sub> dicationic complexes were reported, containing cages, cycles as well as chain structures depending on the pnictogene combination used.<sup>307</sup>

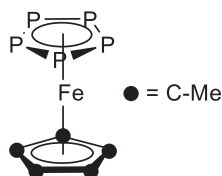
*Complex cations with [(Cp<sup>'''</sup>Co)<sub>2</sub>(μ,η<sup>2</sup>:η<sup>2</sup>-E<sub>2</sub>)]<sub>2</sub> (E = P, As; Cp<sup>'''</sup> = 1,2,4-tri(tert-butyl)cyclopentadienyl):* Investigation of the redox chemistry of [(Cp<sup>'''</sup>Co)<sub>2</sub>(μ,η<sup>2</sup>:η<sup>2</sup>-E<sub>2</sub>)]<sub>2</sub> led *inter alia* to the dications [(Cp<sup>'''</sup>Co)<sub>2</sub>(μ,η<sup>4</sup>:η<sup>4</sup>-E<sub>2</sub>)]<sub>2</sub>[pf]<sub>2</sub>. Deelectronation was accomplished using two equivalents of Ag[pf] and resulted in E-E bond formation which is completely reversible.<sup>308</sup>

*Cationic functionalization by Phosphonium Ion Insertion:* The reaction of [Cp<sup>'''</sup>Ni(η<sup>3</sup>-P<sub>3</sub>)] with in situ generated phosphonium ions [RR'P]<sup>+</sup> yielded the unprecedented polyphosphorus cations of the type [Cp<sup>'''</sup>Ni(η<sup>3</sup>-P<sub>4</sub>R<sub>2</sub>)]<sub>2</sub>[pf] (R = Ph, Mes, Cy, 2,2'-biphen, Me) among other anions and [Cp<sup>'''</sup>Ni(η<sup>3</sup>-P<sub>4</sub>RCl)]<sub>2</sub>[pf] (R = Ph, <sup>t</sup>Bu). Upon reaction of [Cp<sup>'''</sup>Ni(η<sup>3</sup>-P<sub>3</sub>)] with [Br<sub>2</sub>P]<sup>+</sup>, an analogous compound is observed only as an intermediate and the final product is an unexpected dinuclear complex [{Cp<sup>'''</sup>Ni}<sub>2</sub>(μ,η<sup>3</sup>:η<sup>1</sup>:η<sup>1</sup>-P<sub>4</sub>Br<sub>3</sub>)]<sub>2</sub>[pf] that exhibits a unique asymmetrically substituted and distorted P<sub>4</sub> chain stabilized by two {Cp<sup>'''</sup>Ni} fragments.<sup>309</sup>

*Protonation of E<sub>4</sub>-butterfly-complexes:* To investigate the reaction behavior of previously synthesized [{Cp<sup>'''</sup>Fe(CO)<sub>2</sub>]<sub>2</sub>(μ, η<sup>1</sup>:η<sup>1</sup>-P<sub>4</sub>)]<sup>310</sup> protonation with H(OEt<sub>2</sub>)<sub>2</sub>[pf] has been done and resulted in a wing tip protonation of the P<sub>4</sub> butterfly structure, which corroborates the results of DFT calculations.<sup>311</sup>

*Complexes of Cyclo-E<sub>5</sub>-Units (E = P, As):* The pentaphosphaferrocene [Cp\*Fe(η<sup>5</sup>-P<sub>5</sub>)] (Fig. 65) reacts with the WCA salt Ag[pf] to yield a polymer comprising cycloP<sub>5</sub> moieties in an unprecedented 1,2,3-coordination mode. Analytical data and DFT calculations support the existence of a monomer/dimer/oligomer equilibrium in solution, which is entirely in favor of the monomer at room temperature and shifts to the dimer/oligomer at reduced temperatures.<sup>312</sup>

The same [Cp\*Fe(η<sup>5</sup>-P<sub>5</sub>)] complex in Fig. 65 also reacts with the thallium source Tl<sup>+</sup>[pf]<sup>-</sup> to form the polynuclear [Tl{Cp\*Fe(μ-η<sup>5</sup>:η<sup>5</sup>:η<sup>1</sup>-P<sub>5</sub>)]<sub>3</sub>[pf].<sup>135</sup> Optimized geometries were calculated for pentaphosphaferrocene complexes {Tl{Cp\*Fe(μ-η<sup>5</sup>:η<sup>5</sup>:η<sup>1</sup>-P<sub>5</sub>)]<sub>n</sub>}<sup>+</sup> (n = 1-3) and dimer {Tl<sub>2</sub>{Cp\*Fe(μ-η<sup>5</sup>:η<sup>5</sup>:η<sup>1</sup>-P<sub>5</sub>)]<sub>6</sub>}<sup>2+</sup>. In this complex, one of the phosphorus atoms of each cycloP<sub>5</sub> moiety



**Fig. 65** The pentaphosphaferrocene complex [Cp\*Fe(η<sup>5</sup>-P<sub>5</sub>)]: A versatile Ligand for further coordination chemistry with Ag<sup>+</sup> and Tl<sup>+</sup> salts of [pf]<sup>-</sup>.



additionally coordinates to a neighboring  $\text{Tl}^+$  ion to give a one-dimensional polymer. Even at low temperatures, fast rotation of the  $\text{P}_5$  rings was observed in solution and in the solid state.<sup>135</sup>

With copper, a cationic supramolecular structure was reported containing 12  $[\text{Cp}^*\text{Fe}(\eta^5\text{-P}_5)]$  fragments and resulting in  $[(\text{Cp}^*/\text{Fe}(\eta^5\text{-P}_5))_{12}\{\text{CuNCMe}\}_8]^{8+}$  with 2.66 nm in diameter. It was selectively isolated as a salt of  $[\text{pf}]^-$  and characterized by scXRD, pXRD, NMR spectroscopy, and mass spectrometry.<sup>313</sup>

**Mixed TM-P,S-Complex:** The complex  $[(\text{Cp}^*\text{Mo})_2(\mu, \eta^3\text{-P}_3)(\mu, \eta^2\text{-PS})]$  reacts with  $\text{Ag}[\text{pf}]$  to form a linear polymer  $[\text{Ag}[(\text{Cp}^*\text{Mo})_2(\mu^3\text{-}\eta^3\text{:}\eta^3\text{:}\eta^1\text{-P}_3)(\mu, \eta^2\text{-PS})][(\text{Cp}^*\text{Mo})_2(\mu^3\text{-}\eta^3\text{:}\eta^3\text{:}\eta^1\text{-P}_3)(\mu^3\text{-}\eta^2\text{:}\eta^2\text{:}\eta^1\text{-PS})]]_n[\text{pf}]_n$ . Even with X-ray crystallographic data available, the fact that the sulfur atoms in this polymer do not coordinate to the Group 11 metal center could only be established with the help of  $^{31}\text{P}$  MAS NMR spectroscopy.<sup>314</sup>

### 1.07.2.3.9 Miscellaneous further transition-metal complexes

**Methane Complex:** The  $\sigma$ -alkane complexes of transition metals, which contain an essentially intact alkane molecule weakly bound to the metal, have been well established as crucial intermediates in the activation of the strong C–H  $\sigma$ -bonds found in alkanes. Methane, the simplest alkane, binds even more weakly than larger alkanes. Recently, an example of a long-lived methane complex formed by directly binding methane as an incoming ligand to a reactive organometallic complex was published.<sup>315</sup> Photo-ejection of carbon monoxide from a cationic osmium-carbonyl complex dissolved in an inert hydrofluorocarbon solvent saturated with methane at  $-90^\circ\text{C}$  affords the osmium(II) complex,  $[\eta^5\text{-CpOs}(\text{CO})_2(\text{CH}_4)]^+[\text{pf}]^-$ , containing methane bound to the metal centre.<sup>315</sup> Nuclear magnetic resonance (NMR) spectroscopy confirmed the identity of the  $\sigma$ -methane complex and showed that the four protons of the metal-bound methane are in rapid exchange with each other. The methane ligand has a characteristically shielded  $^1\text{H}$  NMR resonance ( $\delta = 2.16$ ), and the highly shielded carbon resonance ( $\delta = 56.3$ ) shows coupling to the four attached protons ( $^1J_{\text{C-H}} = 127$  Hz). The methane complex has an effective half-life of about 13 h at  $-90^\circ\text{C}$ .

**Cationic  $[\text{Ag}(\text{GaDDP})_2]^+$ -Complex:** In this case the  $\text{Ga}^1$  center acts as a ligand, and not as an acceptor. The interaction of two univalent GaDDP molecules with  $\text{Ag}[\text{Al}(\text{OR}^F)_4]$  ( $\text{R}^F = \text{C}(\text{H})(\text{CF}_3)_2$ ) astonishingly does not lead to decoordination of the  $\text{Ga}^1$  complex but to coordination and formation of the linear  $14 e^- [\text{Ag}(\text{GaDDP})_2]^+$  complex cation (Fig. 66).<sup>316</sup>

**A study on chelating phospholes bridging homoatomic  $M_2$ -dimers ( $M = \text{Cu}, \text{Ag}, \text{Au}$ ):** A systematic study investigated the properties of the N,P,N-pincer ligand **Q** (Fig. 67) to stabilize homonuclear dimer-dications of the general formula  $[\text{M}_2(\text{Q})_n]^{2+}$  ( $n = 1, 2, 3$ ) with several weakly coordinating counterions including  $[\text{pf}]^-$ .<sup>317</sup>

A variety of dimetallic coordination complexes of monovalent  $\text{Ag}^1$  and  $\text{Au}^1$  dimers assembled by the 2,5-bis(2-pyridyl)-phosphole **Q** was synthesized. This ligand adopts diverse coordination modes depending on the electronic and steric demands of the bimetallic core. The study nicely underlined the versatility of ligand **Q** for the stabilization of metal dimers and the diversity of bimetallic complexes bearing  $\mu\text{-P}$  donors is now considerably enlarged.<sup>317</sup> To study the undistorted complexes, the use of the very good WCA  $[\text{pf}]^-$  was helpful.

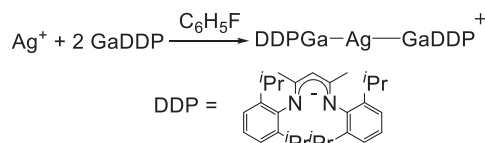


Fig. 66 Synthesis of the homoleptic  $\text{Ag}^1$ -GaDDP complex  $[\text{Ag}(\text{GaDDP})_2]^+[\text{Al}(\text{OR}^F)_4]^-$  ( $\text{R}^F = \text{C}(\text{H})(\text{CF}_3)_2$ ).

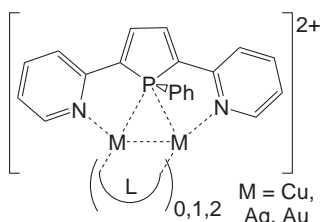


Fig. 67 Variety of coordination modes found for the bridging N,P,N-pincer ligand 2,5-bis(2-pyridyl)-phosphole **Q**.

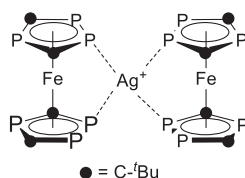
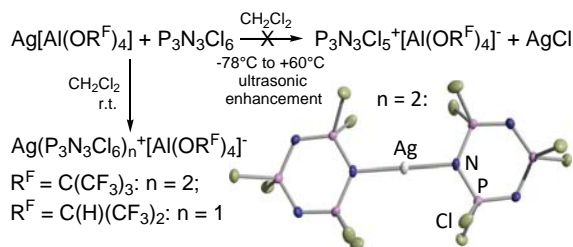


Fig. 68 Cation structure of the homoleptic  $\text{Ag}^1$ -hexaphosphaferrocene complex  $[\text{Ag}^1(\text{Fe}(\eta^5\text{-P}_3\text{C}_2^t\text{Bu}_2)_2)_2][\text{pf}]$ .



**Fig. 69** Reactions of  $\text{Ag}^+[\text{pf}]^-$  with  $\text{P}_3\text{N}_3\text{Cl}_6$ : Formation of the homoleptic  $[\text{Ag}(\text{P}_3\text{N}_3\text{Cl}_6)_2]^+[\text{pf}]^-$  complex instead of ionization and formation of a  $\text{P}_3\text{N}_3\text{Cl}_5^+$  salt. The molecular structure of the  $[\text{Ag}(\text{P}_3\text{N}_3\text{Cl}_6)_2]^+$  cation is shown as an inset.

*A homoleptic silver complex of hexaphosphaferrocene*  $[\text{Fe}(\eta^5\text{-P}_3\text{C}_2^t\text{Bu}_2)_2]$ : The hexaphosphaferrocene complex reacted with  $\text{CuX}$  ( $\text{X} = \text{Cl}, \text{Br}, \text{I}$ ) in a 1:1 stoichiometry to give the isostructural, one-dimensional polymeric compounds, which display a unique sinusoidal  $(\text{CuX})_n$  ladder structure.<sup>318</sup> The reaction of  $[\text{Fe}(\eta^5\text{-P}_3\text{C}_2^t\text{Bu}_2)_2]$  with  $\text{CuX}$  in a 1:2 stoichiometric ratio led only for  $\text{CuCl}$  to the formation of a new, oligomeric compound. Only when reacted with the WCA salt  $\text{Ag}[\text{pf}]$  an isolated, molecular salt  $[\text{Ag}\{\text{Fe}(\eta^5\text{-P}_3\text{C}_2^t\text{Bu}_2)_2\}_2][\text{pf}]$  resulted, which shows dynamic behavior in solution (Fig. 68).<sup>318</sup>

*A homoleptic silver complex of hexachlorocyclotriphosphazene*: The first solid state structures of complexed  $\text{P}_3\text{N}_3\text{X}_6$  ( $\text{X} = \text{halogen}$ ) were reported for  $\text{X} = \text{Cl}$ . The compounds were obtained from  $\text{P}_3\text{N}_3\text{Cl}_6$  and the  $\text{Ag}[\text{pf}]$  silver salts in  $\text{CH}_2\text{Cl}_2/\text{CS}_2$  solution.<sup>319</sup> The very weakly coordinating  $[\text{pf}]^-$  anion led to a  $\text{Ag}(\text{P}_3\text{N}_3\text{Cl}_6)_2^+[\text{pf}]^-$  salt, but the more coordinating  $[\text{hf}]^-$  anion gave a molecular  $(\text{P}_3\text{N}_3\text{Cl}_6)_2\text{Ag}[\text{hf}]$  adduct (Fig. 69). Crystals of  $[\text{Ag}(\text{CH}_2\text{Cl}_2)(\text{P}_3\text{N}_3\text{Cl}_6)_2]^+[\text{pf}]^-$ , in which  $\text{Ag}^+$  coordinates two phosphazene and one  $\text{CH}_2\text{Cl}_2$  ligand, were isolated from  $\text{CH}_2\text{Cl}_2$  solution.<sup>319</sup>

The formation of the complex-cations was calculated to be exergonic by  $\Delta_r G^\circ(\text{CH}_2\text{Cl}_2) = -97, -107$  and  $-27 \text{ kJ mol}^{-1}$ . All prepared complexes are thermally stable; formation of  $\text{P}_3\text{N}_3\text{Cl}_5^+$  and  $\text{AgCl}$  was *not* observed, even at  $60^\circ\text{C}$  in an ultrasonic bath. Therefore, the formation of  $\text{P}_3\text{N}_3\text{Cl}_5^+$ , which was postulated as an intermediate during the polymerization of  $\text{P}_3\text{N}_3\text{Cl}_6$ , was investigated by quantum chemistry.<sup>319</sup>

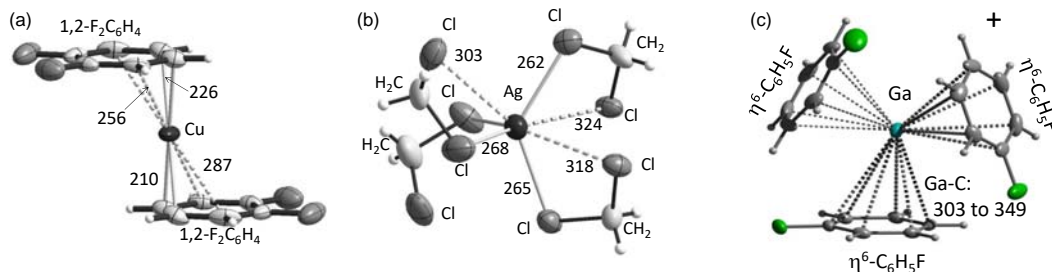
*An argentophilic  $\text{S}_2\text{C}=\text{C}(\text{PPh}_3)_2$ -silver-complex*: The betain-like carbodiphosphorane  $\text{CS}_2$  adduct  $\text{S}_2\text{C}=\text{C}(\text{PPh}_3)_2$  reacts with  $\text{Ag}^+$  salts, which contain WCAs such as  $[\text{BF}_4]^-$  or  $[\text{pf}]^-$  to produce the cluster compounds  $[\text{Ag}_6\{\text{S}_2\text{CC}(\text{PPh}_3)_2\}_4][\text{BF}_4]_6$  and  $[\text{Ag}_4\{\text{S}_2\text{CC}(\text{PPh}_3)_2\}_4][\text{pf}]_4$  respectively.<sup>320</sup> The size of the cluster depends on the WCA size: with the smaller  $[\text{BF}_4]^-$  anion, two of the opposite edges of the tetrahedron are bridged by  $\text{Ag}^+$  ions giving the  $\text{Ag}_6$  core. With the larger  $[\text{pf}]^-$  anion, this extra charge cannot be accommodated and the smaller  $\text{Ag}_4$  unit only forms a tetrahedron. Both clusters are held together by argentophilic interactions, with each sulfur atom being coordinated by three or four silver atoms.

### 1.07.2.3.10 Unusual solvent complexes of the Ga-, Cu- and Ag-salts

A prerequisite to form complexes with all the weak ligands collected in the preceding sections is that the central ions are only weakly coordinated by both, the counter WCA and the solvent. This latter point can be enforced by a selection of crystal structure-sections of the solvated Ga-, Cu- and Ag-monocations shown in Fig. 70. In a way, these solvent complexes are the record holder in terms of weak coordination: The chosen solvents  $\text{CH}_2\text{Cl}_2$  or the fluorinated arenes  $\text{C}_6\text{H}_5\text{F}/1,2\text{-F}_2\text{C}_6\text{H}_4$  coordinate so weakly that almost any ligand added, will coordinate better to the central ion and accordingly form a complex.

$[\text{Cu}(1,2\text{-F}_2\text{C}_6\text{H}_4)_2]^+$ : To the best of our knowledge, only five crystal structures including Cu<sup>I</sup>-arene coordination had been reported and this  $[\text{Cu}(1,2\text{-F}_2\text{C}_6\text{H}_4)_2]^+$  solvent complex was the first homoleptic Cu<sup>I</sup>-arene-complex. The fluorinated arene  $1,2\text{-F}_2\text{C}_6\text{H}_4$  is less basic than the non-fluorinated benzene  $\text{C}_6\text{H}_6$ : It facilitates coordination chemistry with by  $48 \text{ kJ mol}^{-1}$  lower Cu-arene bond energies<sup>37</sup> and a rather high dielectric constant  $\epsilon_r$  of 13.3 at RT indicative for a rather polar solvent (cf.  $\epsilon_r$  of benzene: 2.6).

$[\text{Ag}(\text{Cl}_2\text{CH}_2)_4]^+$ : For a lot of the  $\text{Ag}^{\text{I}}$ -coordination chemistry described above, the frequent solvent choice is  $\text{CH}_2\text{Cl}_2$  (apart from  $o\text{DFB}$ ,  $1,2,3,4\text{-F}_4\text{C}_6\text{H}_2$  and  $\text{SO}_2$ ). As shown by the cation structure in Fig. 70b, the silver ion coordinates only very weakly and with long Ag–Cl separations to up to four  $\text{CH}_2\text{Cl}_2$  solvent molecules. If the silver salt  $\text{Ag}^+[\text{pf}]^-$  is crystallized at RT, entropy only allows



**Fig. 70** Solvated Ga-, Cu- and Ag-monocations: Crystal structure-sections of the  $[\text{Cu}(1,2\text{-F}_2\text{C}_6\text{H}_4)_2]^+$  (a),  $[\text{Ag}(\text{Cl}_2\text{CH}_2)_4]^+$  (b) and  $[\text{Ga}(\eta^6\text{-C}_6\text{H}_5\text{F})_3]^+$  (c) cations from the respective  $[\text{pf}]^-$  salts ( $\text{R}^{\text{F}} = \text{C}(\text{CF}_3)_3$ ). Selected distances are given in pm. Sum of van der Waals radii for comparison:  $\text{Cu} + \text{C}$  310 pm;  $\text{Ag} + \text{Cl}$  350 pm;  $\text{Ga} + \text{C}$  360 pm.

for coordination of three  $\text{CH}_2\text{Cl}_2$  ligands and the complex  $\text{Ag}(\text{Cl}_2\text{CH}_2)_3^+[\text{pf}]^-$  may be isolated (from which two solvent molecules may be easily removed by exposure to a vacuum. The removal of the third  $\text{CH}_2\text{Cl}_2$  requires prolonged exposure to a high vacuum of about 24 h at  $10^{-3}$  mbar). However, if the silver salt is crystallized at  $-80^\circ\text{C}$  and the resulting crystals are mounted at low temperatures, the complex cation shown in Fig. 70b as part of the salt  $\text{Ag}(\text{Cl}_2\text{CH}_2)_4^+[\text{pf}]^-$  resulted. No interaction with a fluorine atom of the counterion below 380 pm was evident from the structure (cf. sum of van der Waals radii  $\text{Ag} + \text{F}$ : 320 pm;  $\text{Ag} + \text{Cl}$ : 350 pm).

#### 1.07.2.4 Applications in catalysis and polymerization chemistry

Why should one invest the extra effort and (often also money) to exchange the counterion in a classical cationic catalyst for a good WCA, e.g., the aluminates or borates  $[\text{M}(\text{OR}^{\text{F}})_4]^- \dots$ ? From a very general point of view, good WCAs should be employed, if the catalysis/polymerization under investigation presents difficulties with classical ions like  $[\text{CF}_3\text{SO}_3]^-$ ,  $[\text{BF}_4]^-$  or  $[\text{PF}_6]^-$ . If the catalysis runs already very well, there is absolutely *no need* to introduce a good WCA.

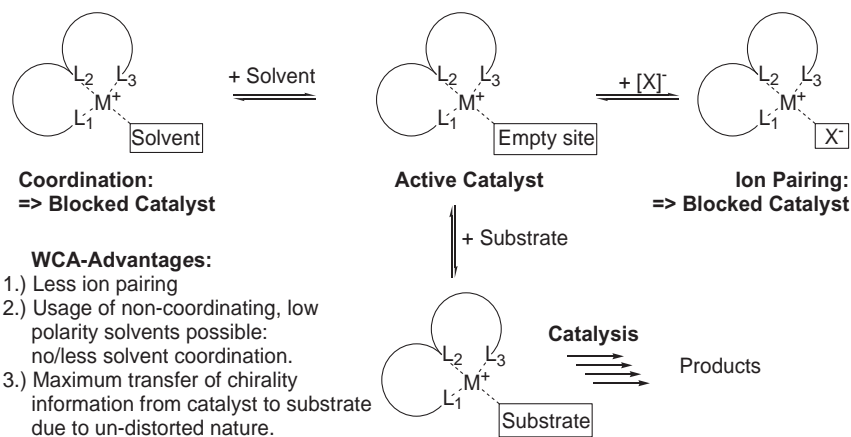
However, if one of the limiting situations shown in Fig. 71 plays a negative role, one should definitely consider employing a catalyst partnered with a good WCA.

Besides reduced ion pairing, especially the greatly improved solubility of WCA-catalysts in low polarity non-coordinating solvents can be used to increase the overall catalyst activity and selectivity.

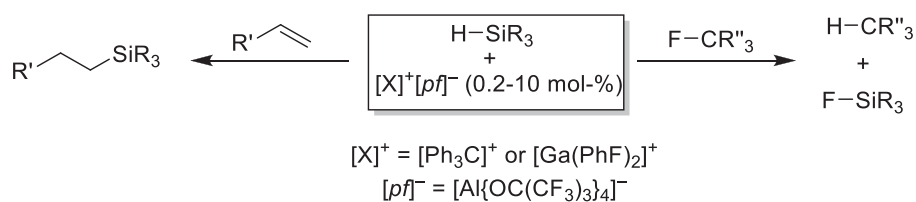
**Gold Affinity and Hydrogen Bonding Basicity Index:** Recently, a gold affinity index (GAI) and hydrogen bonding basicity index (HBI) was developed for several weakly coordinating counterions.<sup>321</sup> This index was used to forecast the reactivity of a series of salts  $[\text{Au}(\text{L})]^+[\text{WCA}]^-$  ( $\text{L} = \text{JohnPhos}$ ) in cationic gold catalysis. The counterion  $[\text{pf}]^-$  always furnished the lowest GAI and HBI entries of zero, while the triflate ion, e.g., gives values of 2.4 (GAI) and 3.4 (HBI).

##### 1.07.2.4.1 Applications in homogenous catalysis

**Hydrodefluorination and Hydrosilylation:** Catalytic amounts of subvalent  $[\text{Ga}(\text{PhF})_2]^+[\text{pf}]^-$  ( $[\text{pf}]^- = [\text{Al}(\text{OR}^{\text{F}})_4]^-$ ,  $\text{R}^{\text{F}} = \text{C}(\text{CF}_3)_3$ ) initiate the hydrosilylation of olefinic double bonds under mild conditions.<sup>65</sup> Reactions with  $\text{HSiMe}_3$  and  $\text{HSiEt}_3$  as substrates efficiently yield *anti*-Markovnikov and *anti*-addition products while  $\text{H}_2$  and metallic  $\text{Ga}^0$  form as side products. Partial anion decomposition to  $\text{R}_3\text{Si-F-Al}(\text{OR}^{\text{F}})_3$  ( $\text{R} = \text{alkyl}$ ) was observed, especially without the addition of olefins. In weakly coordinating, but polar *ortho*-difluorobenzene, univalent  $[\text{Ga}(\text{PhF})_2]^+[\text{pf}]^-$  has a surprisingly high oxidation potential of  $E_{1/2}(\text{Ga}^+/\text{Ga}^0; \text{oDFB}) = +0.26\text{--}0.37$  V vs.  $\text{Fc}^+/\text{Fc}$ , depending on the scan rate. It was concluded that subvalent  $\text{Ga}^+$ , mainly known as a reductant, initially deelectrones the silane and generates a highly electrophilic silylium ion representing the actual catalyst. Consequently, the  $[\text{Ga}(\text{PhF})_2]^+[\text{pf}]^-/\text{HSiEt}_3$  system also hydrodefluorinates  $\text{C}(\text{sp}^3)\text{-F}$  bonds in 1-fluoroadamantane, 1-fluorobutane and  $\text{PhCF}_3$  at



**Fig. 71** How ion pairing and solvent coordination may block catalysis. Both effects may be improved by using good aluminate  $[\text{pf}]^-$  based WCAs.



**Fig. 72** Hydrosilylation of olefinic double bonds and hydrodefluorination of  $\text{C}(\text{sp}^3)\text{-F}$  bonds, initiated by catalytic amounts of  $[\text{Ga}(\text{PhF})_2][\text{pf}]^-$  or, much more efficient,  $[\text{Ph}_3\text{C}][\text{pf}]^-$ .

room temperature. Both the hydrosilylation and the hydrodefluorination reaction may be initiated using only 0.2 mol% of  $[\text{Ph}_3\text{C}]^+[\text{pf}]^-$  as a silylium ion-generating initiator. The reactions are summarized in Fig. 72.

It follows from these results that silylium ion catalysis is possible with the readily accessible weakly coordinating  $[\text{pf}]^-$  anion. Apparently, the kinetics of hydrosilylation and hydrodefluorination successfully compete with that of anion degradation under ambient conditions. These findings open up new windows for main group catalysis, since it was often assumed that the use of carborate or  $[\text{B}(\text{C}_6\text{F}_5)_4]^-$  borate anions is mandatory for silylium ion catalysis.<sup>65</sup> Moreover, it was reported that the dicationic bismuth species  $[(\text{Me}_2\text{NC}_6\text{H}_4)\text{Bi}(\text{L})_3]^{2+}$ , in conjunction with a WCA, e.g.,  $[\text{pf}]^-$ , catalyzes the hydrosilylation of carbonyl compounds.<sup>322</sup> For this reaction, a mechanism involving carbonyl activation at the bismuth center followed by Si–H addition was postulated.<sup>322</sup>

*$\pi$  Acid Catalysis with Alkenes and Alkynes:* Hydroarylation, cycloisomerization and transfer hydrogenation reactions of alkene or alkyne substrates have been performed using low-valent  $\text{Ga}^{\text{I}}$  species.<sup>106</sup>  $[\text{Ga}(\text{PhF})_2]^+[\text{pf}]^-$  proved to be an efficient catalyst for these reactions and showed, compared to other cationic  $\text{Ga}^{\text{III}}$  complexes, a competitive or markedly superior activity.<sup>106</sup>

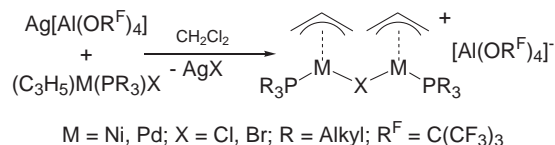
*$\text{Li}^+$  catalyzed reactions:* The compound  $\text{Li}[\text{Al}(\text{OC}(\text{Ph})(\text{CF}_3)_2)_4]$  is an active Lewis acid catalyst<sup>7</sup> in toluene solution for the 1,4-conjugate addition of silyl ketene acetals to  $\alpha,\beta$ -unsaturated carbonyl compounds and for the direct substitution of allylic acetates by silyl ketene acetals. This account<sup>7</sup> was actually the first report of any of the  $[\text{Al}(\text{OR}^{\text{F}})_4]^-$  type WCAs. The structure of this specific lithium salt contains a rare trigonal prismatic coordination-sphere around the  $\text{Li}^+$  cation, with two Li–O(C, Al) bonds and four Li–F(C) bonds.

*Hydrogenation of olefins:* In the asymmetric hydrogenation of unfunctionalized olefins with cationic iridium-phox catalysts (phox = {2-[2-(diphenylphosphanyl)phenyl]-4,5-dihydro-4-isopropylloxazole}), the reaction kinetics and, as a consequence, catalyst activity and productivity depend heavily on the counterion.<sup>323</sup> A strong decrease in the reaction rate was observed in the series  $[\text{pf}]^- > [\text{B}\{3,5-(\text{CF}_3)_2\text{-C}_6\text{H}_3\}_4]^- > [\text{B}(\text{C}_6\text{F}_5)_4]^- > [\text{PF}_6]^- > [\text{BF}_4]^- \approx [\text{CF}_3\text{SO}_3]^-$ . With the first two anions, high rates, turnover frequencies (TOF > 5000  $\text{h}^{-1}$  at 4 °C), and turnover numbers (TONs) of 2000–5000 are routinely achieved. The hexafluorophosphate salt reacts with lower rates, although they are still respectable; however, this salt suffers from deactivation during the reaction and extreme water-sensitivity, especially at low catalyst loading. Triflate and tetrafluoroborate almost completely inhibit the catalyst. In contrast to the hexafluorophosphate salt, catalysts with  $[\text{pf}]^-$ ,  $[\text{B}\{3,5-(\text{CF}_3)_2\text{-C}_6\text{H}_3\}_4]^-$  and  $[\text{B}(\text{C}_6\text{F}_5)_4]^-$  WCAs as counterions do not lose activity during the reaction<sup>323</sup> and remain active, even after all the substrate was consumed. They are much less sensitive to moisture and, in general, rigorous exclusion of water and oxygen is not necessary.

*Asymmetric Cycloisomerization of 1,6-Dienes:* The influence of the counterion on cationic nickel catalysts for asymmetric cycloisomerization of diethyl diallylmalonate (**R**) and *N,N*-diallyltosylamide (**S**) was investigated.<sup>324</sup> The activity of the catalysts formed from  $[\text{Ni}(\eta^3\text{-allyl})(\eta^4\text{-cod})]^+$  salts of WCAs in combination with Wilke's azaphospholene ligand decreases in the order  $[\text{pf}]^- > [\text{B}\{3,5-(\text{CF}_3)_2\text{-C}_6\text{H}_3\}_4]^- > [\text{Al}\{\text{OC}(\text{CF}_3)_2\text{Ph}\}_4]^-$  for **R** and  $[\text{B}\{3,5-(\text{CF}_3)_2\text{-C}_6\text{H}_3\}_4]^- > [\text{Al}\{\text{OC}(\text{CF}_3)_2\text{Ph}\}_4]^- > [\text{pf}]^-$  for **S**, respectively. No significant influence on the enantioselectivity was observed for **R**, whereas a marked increase in *ee* parallel to a decreasing activity was observed for the cyclization of **S**.

*Asymmetric Catalytic Intramolecular Pauson-Khand Reactions with Ir(phox) Catalysts:* Cationic iridium complexes derived from chiral phox ligand (phox = {2-[2-(diphenylphosphanyl)phenyl]-4,5-dihydro-4-isopropylloxazole}) proved to be efficient catalysts for intramolecular Pauson-Khand reactions. For optimal results the various reaction parameters had to be carefully adjusted. The nature of the anion<sup>325</sup> including the WCA  $[\text{pf}]^-$  also proved to be important, as it had a significant influence on the enantioselectivity and yield.

*Olefin oligomerization:* The trimerization and tetramerization of ethylene to 1-hexene and 1-octene with a Cr/PNP/ $\text{AlEt}_3$  catalyst system, in combination with a variety of cocatalysts, was investigated.<sup>326</sup> The cocatalysts  $\text{B}(\text{C}_6\text{F}_5)_3$ ,  $\text{Al}(\text{OC}_6\text{F}_5)_3$ ,  $[(\text{Et}_2\text{O})_2\text{H}][\text{Al}(\text{OC}_6\text{F}_5)_4]$ ,  $[\text{Ph}_3\text{C}][\text{Ta}(\text{OC}_6\text{F}_5)_6]$ ,  $(\text{Et}_2\text{O})\text{Al}\{\text{OCH}(\text{C}_6\text{F}_5)_2\}_3$ ,  $(\text{Et}_2\text{O})\text{-Al}\{\text{OC}(\text{CF}_3)_3\}_3$ ,  $[\text{Ph}_3\text{C}][\text{pf}]$ ,  $[\text{Ph}_3\text{C}][\text{AlF}\{\text{OC}(\text{CF}_3)_3\}_3]$ ,  $[\text{Ph}_3\text{C}][\text{alfal}]$ , and  $[\text{Ph}_3\text{C}][\text{CB}_{11}\text{H}_6\text{Br}_6]$  were evaluated. The relative selectivity to 1-hexene and 1-octene obtained shows a strong dependence on the nature of the cocatalyst, and a range of selectivities from <5% C8 (90% C6) to 72% C8 were observed. The stability of several cocatalysts towards  $\text{AlEt}_3$  has been studied, and the poor performance of  $\text{B}(\text{C}_6\text{F}_5)_3$  and  $\text{Al}(\text{OC}_6\text{F}_5)_3$  was linked to degradation of the cocatalyst through ethyl group exchange with  $\text{AlEt}_3$ . In contrast, the  $[\text{pf}]^-$  anion is much more stable and gives rise to a highly active and longer-lived catalyst. The overall productivity and selectivity of the catalyst is dependent upon both cocatalyst stability and the nature of the anion present, and a reason for this effect was suggested. Selectivity control by the cocatalyst has been ascribed to interaction of the anion with the active Cr center. Subsequently<sup>327</sup> the use of  $\text{AlEt}_3$  (TEA) in combination with  $[\text{Ph}_3\text{C}][\text{pf}]$  for the activation of a range of bis(imino)pyridine complexes of vanadium, chromium, iron, and cobalt was reported. It was shown that this activator combination successfully replaces methylaluminumoxane (MAO), in some cases showing improvements in terms of activity and productivity. Furthermore, when activities and productivities are considered in terms of the aluminum center (MAO vs. TEA), the true cost driver in the commercialization of most catalyst systems, then in nearly all cases a significant improvement is seen. A combination of TEA with  $[\text{Ph}_3\text{C}][\text{B}(\text{C}_6\text{F}_5)_4]$  was one of the most successful examples of this



**Fig. 73** In the absence of additional donors upon halide abstraction by  $\text{Ag}[\text{WCA}]$  initially formed halide bridged  $[(\eta^3\text{-C}_3\text{H}_5)\text{M}(\text{PR}_3)_2(\mu\text{-X})]^+$  cation.

methodology, it has nonetheless suffered from several problems relating to catalyst deactivation: (i) exchange of groups between the trialkylaluminum and the borate, thus destroying the weakly coordinating nature of the borate anion; (ii) transfer of fluorinated aryl groups from the borate to the transition metal center.

The use of fluorinated aluminate  $[pf]^-$  as WCA, offers the advantage of being less coordinating than borates, while displaying increased stability. The use of TEA in combination with  $[Ph_3C][pf]$  was successfully used to replace MAO in the Cr–PNP ethylene tetramerization catalyst system to greatly reduce the amount of aluminum used overall. Later work transferred this methodology to different metals and ligands,<sup>328–331</sup> however, with varying success that resulted from insufficient stability of the cationic catalyst systems under the conditions of true catalysis. However, aluminate degradation was never a problem.

**Allyl-Nickel-/Palladium-Precatalysts:** A systematic publication<sup>332</sup> sheds light on the broadly held opinion that the reaction of  $(\eta^3\text{-allyl})M(\text{PR}_3)X$  complexes ( $M = \text{Ni}, \text{Pd}; X = \text{halide}$ ) with  $\text{Ag}[\text{WCA}]$  or  $\text{TI}[\text{WCA}]$  reagents of very good WCAs like  $[pf]^-$  or  $[\text{B}(\text{C}_6\text{F}_5)_4]^-$  generates coordinatively unsaturated complexes  $\{(\eta^3\text{-allyl})M(\text{PR}_3)\}^+$  (**Fig. 73**).

However, it was shown<sup>332</sup> that under the conditions of such experiments dinuclear ionic complexes  $\{[(\eta^3\text{-C}_3\text{H}_5)M(\text{PR}_3)]_2(\mu\text{-X})\}[\text{WCA}]$  are formed (**Fig. 73**), and these contain a strong central  $M\text{-}(\mu\text{-X})\text{-}M$  linkage that is not cleaved by additional  $\text{Ag}/\text{TI}[\text{WCA}]$  in the absence of donor ligands. More recently it was shown<sup>333</sup> that the Palladium complexes do form isolated mononuclear complexes, given that the phosphane is replaced by a more basic NHC-Ligand (**Fig. 74**). In this case, a  $\text{CH}_2\text{Cl}_2$  donor molecule is bound, which apparently was the first  $\text{Pd}\text{-CH}_2\text{Cl}_2$  complex (**Fig. 74**).

It should be noted that with the more basic  $[\text{BF}_4]^-$  counterion, the solvent-free adduct  $(\eta^3\text{-C}_3\text{H}_5)\text{Pd}(\text{NHC})\text{-F}\text{-BF}_3$  separates directly from  $\text{CH}_2\text{Cl}_2$  solution. Upon evacuation, the  $\text{Pd}\text{-CH}_2\text{Cl}_2$  complex loses all  $\text{CH}_2\text{Cl}_2$ -donor, but it was not clear, whether a truly isolated 14 VE salt or a complex with coordinated  $[pf]^-$  counterion resulted (no sXRD).<sup>333</sup>

**Au(III)-catalyzed tandem nucleophilic substitution-1,5-enyne cycloisomerization process:** The trivalent  $(\text{I}^t\text{Pe})\text{AuBr}_2(\text{N-imidate})$  gold complexes—prepared in high yield by oxidative bromination—are active catalysts for 1,5-enyne cycloisomerization ( $\text{I}^t\text{Pe} = \text{N},\text{N}'\text{-di-tert-pentylimidazol-2-ylidene}$ , N-imidate is N-succinimide, N-tetrafluorosuccinimide, and N-maleimide).<sup>334</sup> An efficient tandem nucleophilic substitution-1,5-enyne cycloisomerization is promoted by these novel  $\text{Au}^{\text{III}}$  precatalysts and a silver salt  $\text{Ag}[\text{WCA}]$ . Typical loads are 4 mol-% precatalyst and silver salt. Catalyst efficacy is affected by the imidate ligand and the counterion of the silver salt used. Best results were achieved with the least coordinating  $[pf]^-$  counterion. The authors<sup>334</sup> anticipated that the Au catalysis field could exploit this very weakly coordinating anion for further highly active Au-catalysis.

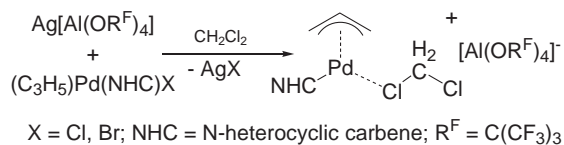
**Copper(II)-based Aziridination:** Acetonitrile ligated copper complexes with  $[pf]^-$  as the weakly coordinating counter anion were successfully synthesized. Aziridination of various olefins with PhINTs catalyzed by the copper(II) complex  $[\text{Cu}(\text{II})(\text{NCCCH}_3)_6][pf]_2$  affords good to excellent yields (up to 96%) and very high turnover frequency (higher than  $5000 \text{ h}^{-1}$ ) under mild conditions.<sup>38</sup>

**Cu(I)-based Monooxygenation:** Three Cu(I) salts with the very weakly coordinating anion  $[pf]^-$  including the unique, linear  $[\text{Cu}(\text{NET}_3)_2]^+$ -cation were synthesized and used as catalysts for the conversion of monophenols to *o*-quinones.<sup>335</sup> 2,4-di-*tert*-butylphenol (DTBP-H) as well as, for the most active catalyst, five additional different monophenols served as substrates. The activities of these Cu(I) salts towards monooxygenation of DTBP-H were compared to those of  $[\text{Cu}(\text{CH}_3\text{CN})_4]X$  salts with classical anions  $X^-$  ( $[\text{BF}_4]^-$ ,  $[\text{OTf}]^-$ ,  $[\text{PF}_6]^-$ ), revealing an *anion effect* on the activity of the catalyst and a *ligand effect* on the reaction rate. A drastic acceleration of the reaction rate was obtained by employing Cu(II)-semiquinone complexes as catalysts, indicating that formation of a Cu(II) complex precedes the actual catalytic cycle. This and further observations indicate that the oxygenation of monophenols in this system did not follow a dinuclear, but mononuclear pathway analogous to that of topaquinone cofactor biosynthesis in amine oxidase.

#### 1.07.2.4.2 Applications in polymerization chemistry

**Photo Acids for Polymerization Chemistry:** Cationic photopolymerization is a powerful method for UV-curing of epoxy, vinyl ether and oxetane monomers. Little attention has been paid to it over the last few decades compared to the corresponding free radical applications due to unsuitable and inefficient photo-acid generators (PAGs) used for photoinitiation. A novel type of PAG based on the  $[pf]^-$  aluminate anion was introduced and in facile preparations, diphenyliodonium and triarylsulfonium salts were synthesized, followed by characterization of absorbance and thermal stability.<sup>336</sup> Comparative photo-differential scanning calorimetry (photo-DSC) studies with common onium salt PAGs showed the advantageous reactivity of the novel aluminate-based cationic photoinitiators. The novel diphenyliodonium PAG was also examined in photosensitization studies for potential use in higher wavelength applications.

**ROP with Protonated Ether<sup>337</sup>:** The cationic ring-opening polymerization (CROP) and copolymerization of 2-ethyl-2-oxazoline and 2-*tert*-butyl-2-oxazoline using the strong cationic Bronsted acid,  $[\text{H}(\text{OEt}_2)_2][pf]$  as an initiator was described. First, various



**Fig. 74** Mononuclear cationic  $\text{Pd}\text{-CH}_2\text{Cl}_2$  complex with the stronger NHC ligand.



poly(2-ethyl-2-oxazoline) (PEtOx) samples were prepared and the living/controlled character of the reaction was demonstrated. The microwave-assisted CROP of EtOx using this initiator system proceeds faster, if compared to classical initiators such as methyl tosylate. Upon extension to the CROP of poly(2-tert-butyl-2-oxazoline) (PtButOx) and to PEtOx/PtButOx, random and block copolymers of different compositions were obtained and fully analyzed.

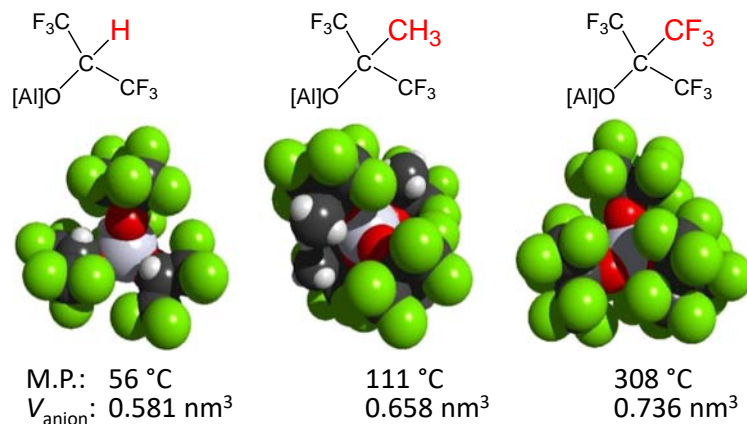
**Catalytic Polymerization of Butadiene in Aqueous Systems with Cationic Nickel(II) Complexes:** The cationic nickel(II) complexes  $[(\eta^3\text{-C}_3\text{H}_5)\text{Ni}(\text{SbPh}_3)_2][\text{WCA}]$  with  $\text{WCA} = [\text{B}(3,5\text{-}(\text{CF}_3)_2\text{C}_6\text{H}_3)_4]^-$  and  $[\text{pf}]^-$  were prepared and their polymerization activities<sup>338</sup> in aqueous systems were compared with  $[(\eta^3\text{-C}_3\text{H}_5)\text{Ni}(\eta^6\text{-BHT})][\text{B}(3,5\text{-}(\text{CF}_3)_2\text{C}_6\text{H}_3)_4]$  (BHT = 3,5-di-tert-butyl-4-hydroxytoluene). *cis*-Polybutadiene formed in non-aqueous solution polymerization. The presence of water decreases activity and polymer molecular weight and increased *trans* incorporation of butadiene units. In emulsion polymerization, stable polymer dispersions were obtained with  $[(\eta^3\text{-C}_3\text{H}_5)\text{Ni}(\text{SbPh}_3)_2][\text{WCA}]$ . The microstructure is strongly altered by comparison to non-aqueous polymerization. *trans*-Polybutadiene is formed with activities of up to  $1.5 \times 10^3 \text{ mol (butadiene) mol (Ni)}^{-1} \text{ h}^{-1}$ . The semicrystalline latex particles have sizes of *ca.* 200 nm, with a monoclinic structure.

**Isobutene Polymerization by  $[M(\text{NC-R})_6]^{2+}$  Salts:** Various transition metal cations  $\text{M}^{2+}$  solvated by nitriles and including  $\text{M} = \text{Mn, Zn, etc.}$  proved to be valuable isobutene polymerization initiators as well as in other catalytic reactions, if partnered with very weakly coordinating counterions like  $[\text{pf}]^-$ . This work was reviewed<sup>339</sup> and is, therefore, only briefly mentioned here. Initially this started with nitrile-ligated zinc(II) complexes incorporating  $[\text{pf}]^-$ -based WCAs. A X-ray crystal structure proved both the octahedral symmetry of the zinc(II) cation  $[\text{Zn}(\text{NC-R})_6]^{2+}$  having six nitrile ligands  $\text{R-CN}$  ( $\text{R} = \text{CH}_3, \text{Ph}$ ) and the non-coordinating nature of the anion. Similar to complexes bearing borate-based WCAs like  $[\text{B}(\text{C}_6\text{F}_5)_4]^-$  and others, the compounds described in this work can be applied to polymerize isobutylene at room temperature resulting in polyisobutylene with a high content of exo double bonds.<sup>47</sup>

**Polymerization of Isobutene by  $[\text{H}(\text{OR}_2)_2]^+[\text{pf}]^-$  salts:** However, the most efficient process to polymerize isobutene, is the use of protonated ether salts  $[\text{H}(\text{OR}_2)_2]^+[\text{pf}]^-$  ( $\text{R} = \text{Et,}^{28} \text{ }^i\text{Pr, } ^n\text{Bu}$ ). Very high efficiency of the polymerization and high content of exo double bonds (92 to 97%) at initiator loads down to the 4  $\mu\text{mol}$ -range for complete polymerization of 20 mL isobutene were achieved.<sup>340</sup> However, for commercialization this process is slightly too expensive, due to the low price of poly-isobutene and the relatively high cost of the initiators  $[\text{H}(\text{OR}_2)_2]^+[\text{pf}]^-$ . Since this process required the initiation by formation of a  $[\text{C}(\text{CH}_3)_3]^+$  cation from isobutene and  $[\text{H}(\text{OR}_2)_2]^+$  and this process is substantially uphill, a recent investigation<sup>30</sup> based on the unified Bronsted acidity scale investigated the situation quantitatively and suggested a protonation degree of the isobutene to be 0.35% in  $\text{CH}_2\text{Cl}_2$  solution which is sufficient for the polymerization.

**Polymerization of Isobutene by  $[\text{Ga}(\text{arene})_n]^+[\text{pf}]^-$  salts:** The scope of univalent gallium salts  $[\text{Ga}(\text{arene})_n]^+[\text{pf}]^-$  ( $\text{arene} = \text{ansa-arene, PhF, mesitylene; } n = 1\text{-}2$ ) was investigated in terms of initiating or catalysing the synthesis of highly reactive polyisobutylene (HR-PIB).<sup>127,128</sup> The univalent gallium salts displayed high efficiency for the polymerization of isobutylene. Polymerization was observed with very low catalyst concentrations of down to 0.002 mol% while working at reaction temperatures of up to  $+15^\circ\text{C}$ .<sup>127</sup> HR-PIB with an  $\alpha$ -content of terminal olefinic double bonds up to 93 mol% and a molecular weight of 1000–3000 was obtained in good yields.<sup>127,128</sup> Obviously, ligand exchange tunes the reactivity of the gallium(I) cations. A coordinative polymerization mechanism, typically invoked for transition metal catalysts, was postulated for this reaction.<sup>128</sup>

**Polymerization of Isobutene by  $[(\text{DXE})\text{Sr}(\text{oDFB})_2]^{2+}([\text{pf}]^-)_2$  salts:** A surprisingly controlled polymerization was achieved with 0.01 mol% of a dicationic strontium *ansa*-arene complex in 1,2,3,4-tetrafluorobenzene. Here, the polymerization reactions yielded medium-to-high molecular weights ( $M_w = 1.30 \times 10^5 \text{ g mol}^{-1}$  and  $M_w = 0.7 \times 10^5 \text{ g mol}^{-1}$ ) and narrow dispersities ( $D = 1.87$  and  $D = 1.69$ ) at elevated temperatures of  $-12^\circ\text{C}$  and  $0^\circ\text{C}$ .<sup>36</sup>



**Fig. 75** Space filling representations and molecular volumes of the  $[\text{Al}(\text{OR}^{\text{F}})_4]^-$  WCAs and comparison to the melting points of their  $[\text{NEt}_4]^+$  salts.



### 1.07.2.5 Material science and electrochemical applications

#### 1.07.2.5.1 As ionic liquids

When partnered with suitable low symmetry organic cations, also the rather large  $[M(OR^F)_4]^-$  WCAs may form low viscosity room temperature Ionic Liquids (ILs) with very advantageous physical properties, see our review.<sup>59</sup> Best in this respect is the  $[hf]^-$  WCA,<sup>14</sup> which appears to include enough structural flexibility to induce a sufficiently high entropy of melting that is decisive for the overall melting point of any salt.<sup>341</sup> This conclusion is also visible from the space filling representations of the usual set of  $[Al(OR^F)_4]^-$  WCAs shown in Fig. 75.

Only with the  $[hf]^-$  aluminate, many new and entropy increasing conformations can be assumed in the liquid state upon melting. The other  $R^F$  residues do not provide enough flexibility (i.e.,  $C(CH_3)(CF_3)_2$ ) or additionally have a too high symmetry (i.e.,  $C(CF_3)_3$ ). This leads to the great melting point differences  $\Delta T_m$  of up to 252 °C between the  $[NEt_4]^+$  salts of the aluminates shown in Fig. 75. According to volume-based thermodynamics,<sup>342–348</sup> the lattice energies of the three WCAs are similar, since their average rather large volume is the same within 12%.

After these initial findings, the perspective to use the  $[M(OR^F)_4]^-$  type of WCAs as counterions was systematically investigated in quite some subsequent work; the full results are reviewed.<sup>59</sup> Hence, here only syntheses and interesting properties are discussed together with some important findings.

*Syntheses:* Similar to most IL classes, the general synthesis schemes towards  $[Cat][M^{III}(OR^F)_4]$  ILs are not very difficult and follow Fig. 76.<sup>59</sup> However, there are minor but important differences between the anions that are used in Fig. 76.

Interestingly, although all IL classes are easily soluble in dichloromethane, the metathesis of the borate anions does only take place in  $Et_2O$  or  $MeCN$ , respectively. In order to remove the alkali metal halide, the acetonitrile in the case of  $[B(Otfe_4)]^-$  ( $tfe = CH_2CF_3$ ) must be exchanged after the reaction with  $CH_2Cl_2$  so that the by-product can precipitate.<sup>14</sup> Yields are in all cases well above 85%, and deviations from a quantitative yield often simply occur due to too short reaction times.

*Physicochemical Data of these ILs:* A large number of—also room temperature—ILs was prepared with these WCAs<sup>13,14,57,59,345,346</sup>; their important physicochemical data,  $T_{melt}$  = melting temperature (°C),  $T_c$  = crystallization temperature (°C),  $T_d$  = decomposition temperature (°C),  $\epsilon_r$  = dielectric constant (Cole-Cole model),  $\eta$  = viscosity (mPa·s),  $\sigma$  = ionic conductivity (mS  $cm^{-1}$ ),  $D$  = diffusion constants ( $10^{-11} m^2 s^{-1}$ ) are collected in Table 5, to give an impression on their performance as ILs.<sup>59</sup>

Moreover, the biodegradability of  $[hf]^-$  ILs was investigated using the closed bottle and the manometric respirometry test; the results of which suggested no particular danger.<sup>349</sup> Temperature-dependent viscosities and conductivities were measured and described by the Vogel-Fulcher-Tammann (VFT) or Arrhenius equation, respectively.<sup>59</sup> In addition, conductivities and viscosities were investigated in the context of the molecular volume,  $V_m$ . Physical property— $V_m$  correlations were provided for different temperatures, and the temperature dependence of the molecular volume was analyzed using crystal structure data and DFT calculations.<sup>59</sup> The IL-ionicity was investigated by Walden plots and especially the  $[hf]^-$  ILs may be classified as “very good to good ILs”; according to this analysis (Fig. 77), many ILs with the  $[hf]^-$  WCA qualify as better ILs than the respective  $[NTf_2]^-$  ILs with the same cation.<sup>59,349,350</sup>

Also the dielectric constants of many  $[hf]^-$  ILs were determined and are unexpectedly high ( $\epsilon_r$  12.5–18.0; Table 5).<sup>351</sup> This was rationalized by additional calculated dipole moments of the structures frozen in the solid-state using DFT.<sup>349</sup> The determination of hydrogen gas solubility in  $[hf]^-$  RTILs by high pressure NMR revealed very high hydrogen solubilities at 25 °C and 1 atm. The hydrogen solubilities are 5 to 6 times higher than those in other ILs and still 2–3 times higher than those in molecular solvents.<sup>349</sup> All the information acquired point to the large potential of this IL class in a manifold of applications.

*$[hf]^-$  ILs compared to the  $[Tf_2N]^-$  Analogs:* ILs containing imidazolium and ammonium cations as well as the medium-sized anion  $[Tf_2N]^-$  ( $0.230 nm^3$ ;  $Tf = CF_3SO_2$ ) and the large anion  $[hf]^-$  ( $0.581 nm^3$ ) were synthesized and characterized.<sup>350</sup> Their temperature-dependent viscosities and conductivities between 25 °C and 80 °C showed typical Vogel-Fulcher-Tammann (VFT) behavior. Ion-specific self-diffusion constants were measured at room temperature by pulsed-gradient stimulated-echo (PGSTE) NMR experiments. In general, self-diffusion constants of both cations and anions in  $[hf]^-$ -based ILs were higher than in  $[Tf_2N]^-$ -based ILs. Ionicities were calculated from self-diffusion constants and measured bulk conductivities, and showed that  $[hf]^-$ -based ILs yield higher ionicities than their  $[Tf_2N]^-$  analogs, the former of which reach values of virtually 100% in some cases. From these observations it was concluded that  $[hf]^-$ -based ILs come close to systems without any interactions, and this hypothesis was underlined with a Hirshfeld analysis.<sup>350</sup> Additionally, a robust, modified Marcus theory quantitatively accounted for the differences between the two anions and yielded a minimum of the activation energy for ion movement at an anion diameter of slightly greater than 1 nm, which fits almost perfectly the size of  $[hf]^-$ . Shallow Coulomb potential wells are responsible for the high mobility of ILs with such anions (Fig. 78).

As a consequence, viscosities (conductivities) of  $[hf]^-$  ILs are typically lower (higher) than those of  $[Tf_2N]^-$  ILs with like cation. Moreover, also ionicities underline this explanation, with  $[hf]^-$  ILs possessing in general explicitly higher ionicities than their  $[Tf_2N]^-$  counterparts.<sup>59,350</sup>

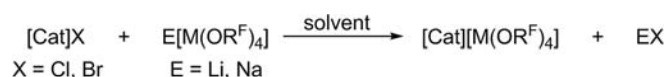


Fig. 76 General metathesis reaction for the formation of ILs with  $[M^{III}(OR^F)_4]^-$  anions.

**Table 5** Comparison of physicochemical data of salts with highly fluorinated  $[M(OR^F)_4]^-$  anions.

IL	$T_{melt}$	$T_c$	$T_d$	$\epsilon_r$	$\eta(40^\circ C)$	$\sigma(40^\circ C)$	$D^+$	$D^-$	ionicity
$[C_2MIm][Al(Ohfip_4)]^{349,350}$	31	<25		12.6	24.4	6.22	1.94	0.80	2.10 <sup>a</sup>
$[C_2MIm][Al(Otfe)_4]^{14}$	35				15.9				
$[C_2MMIm][Al(Ohfip_4)]^{349}$	39	34	172–176	18.0					
$[AllylMIm][Al(Ohfip_4)]^{349,350}$	12	–24		17.0	22.4	6.86	4.77	1.89	0.87
$[AllylMIm][B(Ohfip_4)]^{349,350}$	68	44	172						
$[C_4MIm][Al(Ohfip_4)]^{349,350}$	40	<25		14.5	21.8		2.20	1.30	1.03
$[C_4MIm][B(Ohfip_4)]^{13}$	49	42	198						
$[C_4MMIm][Al(Ohfip_4)]^{349,350}$	0	–35		19.0	23.6	4.08	2.78	1.69	0.83
$[C_4MMIm][B(Ohfip_4)]^{13}$	68	48	221						
$[C_4MMIm][B(Otfe)_4]^{14}$	58								
$[C_6MIm][Al(Ohfip_4)]^{349,350}$	5	–5		17.3	25.3	3.57	2.80	1.80	0.73
$[C_6MIm][B(Ohfip_4)]^{13}$	–25 < $T_{melt}$ < 0				58.9	1.10			
$[C_6MIm][B(Otfe)_4]^{14}$	45								
$[C_6MIm][Al(Opftb)_4]^{59}$	67								
$[C_8MIm][Al(Ohfip_4)]^{350}$	<20				22.0	2.70	2.01	1.46	0.82
$[C_8MIm][B(Otfe)_4]^{14}$	28								
$[C_{10}MIm][Al(Ohfip_4)]^{350}$	<20				25	2.10	1.60	1.29	0.79
$[N_{1111}][Al(Ohfip_4)]^{57}$	61		147						
$[N_{1111}][Al(Ohftb)_4]^{57}$	96		>150						
$[N_{1111}][Al(Opftb)_4]^{57}$	320		>400						
$[N_{1123}][Al(Ohfip_4)]^{350}$	43								
$[N_{1444}][Al(Ohfip_4)]^{350}$	<20				30.4	2.00	1.21	0.97	0.87
$[N_{2222}][Al(Ohfip_4)]^{57}$	56		>130						
$[N_{2222}][Al(Ohftb)_4]^{57}$	111		>230						
$[N_{2222}][Al(Opftb)_4]^{57}$	308		>400						
$[N_{4444}][Al(Ohfip_4)]^{57}$	42		190		49.9				
$[N_{4444}][Al(Ohftb)_4]^{57}$	108		>150						
$[N_{4444}][Al(Opftb)_4]^{57}$	199		>250						
$[N_{2225}][Al(Ohfip_4)]^{350}$	<20	–53 <sup>b</sup>			34.4	2.77	2.10	1.50	0.69
$[N_{2225}][B(Otfe)_4]^{14}$	89								
$[N_{2666}][Al(Ohfip_4)]^{350}$	<20				35	0.92	0.73	0.76	0.80
$[N_{2666}][B(Otfe)_4]^{14}$	68								
$[N_{1888}][Al(Ohfip_4)]^{350}$	<20	–53 <sup>b</sup>			45.7	0.62	0.63	0.75	0.47
$[N_{1888}][B(Otfe)_4]^{14}$	4				161				
$[N_{1888}][Al(Opftb)_4]^{59}$	<20				320.5				
$[C_3MPip][Al(Ohfip_4)]^{349}$	69	58							
$[C_4MPyr][Al(Ohfip_4)]^{349}$	50	39	155	16.6					
$[C_4MMorph][Al(Ohfip_4)]^{349}$	31	6	164	16.5	41.3	1.99			
$[C_4MMorph][B(Ohfip_4)]^{13}$	113 <sup>27</sup>	102	256						
$[C_4Py][Al(Ohfip_4)]^{349}$	36	<25		16.5	25.1				

$T_{melt}$  = melting temperature ( $^\circ C$ ),  $T_c$  = crystallization temperature ( $^\circ C$ ),  $T_d$  = decomposition temperature ( $^\circ C$ ),  $\epsilon_r$  = dielectric constant (Cole-Cole model),  $\eta$  = viscosity (mPa · s),  $\sigma$  = ionic conductivity ( $mS \cdot cm^{-1}$ ),  $D$  = diffusion constants ( $10^{-11} m^2 s^{-1}$ ), hftb =  $C(CF_3)_2(CH_3)$ . Data taken from Ref.<sup>59</sup> The citations to the original publications are included with the IL name.

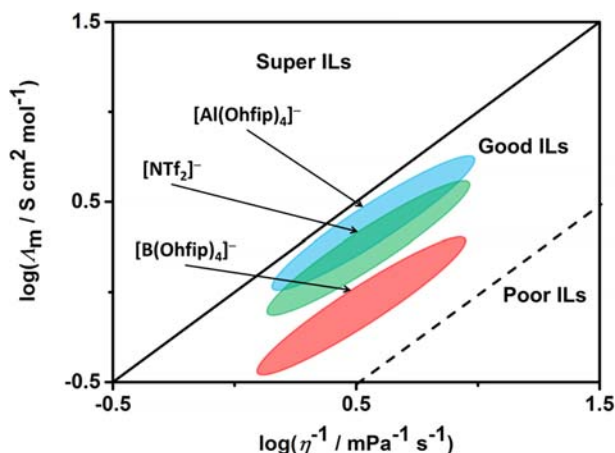
<sup>a</sup>Measured in a highly supercooled state.

<sup>b</sup>Glass transition.

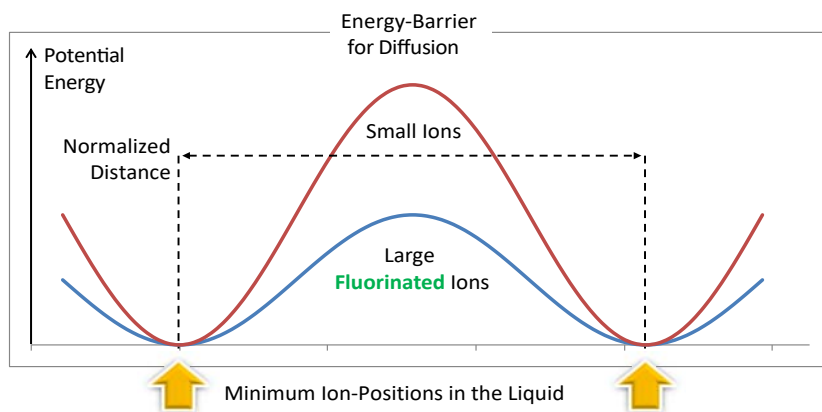
*Siloxane-Functionalized  $[hf]^-$  ILs compared to the  $[Tf_2N]^-$  Analogs:* Two ILs with siloxane-functionalized cations and  $[hf]^-$  counterion were prepared and characterized (Fig. 79).

With melting points below  $0^\circ C$  they qualify as room temperature ILs (RTILs). Their temperature-dependent viscosities and conductivities, together with those of two  $[Tf_2N]^-$  ILs with the same cations and a further siloxane-functionalized  $[Tf_2N]^-$  IL, were measured between  $0$  and  $80^\circ C$ , and all were described by the VFT-equations. We note that the  $[hf]^-$  ILs have lower viscosities than their  $[Tf_2N]^-$  analogs at all measured temperatures and higher conductivities at room temperature.

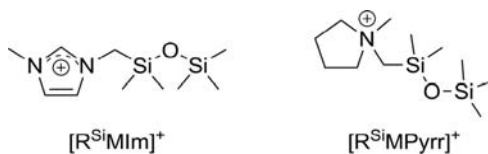
*Mixtures of  $[hf]^-$  and  $[hf_B]^-$  ILs with Dimethylcarbonate (DMC):* The influence of dimethylcarbonate (DMC) on the properties of  $[hf]^-$  and  $[hf_B]^-$  ILs was investigated, with a focus on conductivity, viscosity and diffusion constants.<sup>15</sup> DMC was chosen due to its good electrochemical stability, its low viscosity and its low permittivity of  $\epsilon_r = 3.12$ , which typically would rule out DMC as solvent for salts. Quite in contrast, addition of DMC to the  $[hf]^-$  and  $[hf_B]^-$  ILs with a weak and flat Coulomb potential resulted in a pronounced increase of conductivity and diffusion constants, while viscosity decreased with DMC content.<sup>15</sup>



**Fig. 77** Schematic Walden plot with typical regions of non-functionalized  $[\text{Al}(\text{Ohfip})_4]^-$  and  $[\text{B}(\text{Ohfip})_4]^-$  ILs in comparison to  $[\text{NTf}_2]^-$  ILs.  $\Delta_m$  = molar conductivity.



**Fig. 78** Energy barriers of ions diffusing in an IL.



**Fig. 79** Siloxane-modified cations.

#### 1.07.2.5.2 As supporting electrolytes

In a study of 2009,<sup>57</sup> the  $[\text{NR}_4]^+$  tetraalkylammonium salts of the weakly coordinating fluorinated alkoxyaluminates  $[\text{pf}]^-$ ,  $[\text{hf}]^-$  and  $[\text{Al}(\text{OC}(\text{CH}_3)(\text{CF}_3)_2)_4]^-$  were prepared in order to obtain information on their undisturbed spectral and structural properties, but more importantly to study their electrochemical behavior (i.e., conductivities in non-polar solvents and electrochemical windows). Simple and almost quantitative metathesis reactions yielding these materials in high purity were developed. The  $[\text{NBu}_4]^+$  salts are highly soluble in non-polar solvents (up to  $1.09 \text{ mol L}^{-1}$  are possible for  $[\text{NBu}_4][\text{Al}(\text{OC}(\text{CH}_3)(\text{CF}_3)_2)_4]$  in  $\text{CH}_2\text{Cl}_2$  and  $0.41 \text{ mol L}^{-1}$  for  $[\text{NBu}_4][\text{hf}]$  in  $\text{CHCl}_3$ ) and show higher molar conductivities, if compared to  $[\text{NBu}_4][\text{PF}_6]$ . The electrochemical windows of  $\text{CH}_2\text{Cl}_2$ ,  $\text{CH}_3\text{CN}$  and  $\text{oDFB}$  using the  $[\text{NBu}_4]^+$  aluminate electrolytes are up to  $+0.5 \text{ V}/-0.7 \text{ V}$  larger than those using the standard  $[\text{NBu}_4][\text{PF}_6]$ .<sup>57</sup>

**Instability of Aryl-Borate-WCAs:** It should be noted that, fluorinated tetraaryl borate ( $[\text{BAR}_4^{\text{F}}]^-$ ) salts were not as stable at similarly high positive potentials as the fluorinated alkoxyaluminates and rather the boron bound aryl groups were C–C coupled at potentials higher than 1.25 to 1.78 V vs.  $\text{Fc}^+/\text{Fc}$  in synthetically useful yields to the respective biaryls  $^{\text{F}}\text{Ar-Ar}^{\text{F}}$ .<sup>352</sup>

**Stability of  $[\text{pf}]^-$  Electrolytes:** By contrast, we observed reversible electrochemistry in several suitable solvents up to limiting potentials around 2 V vs.  $\text{Fc}^+/\text{Fc}$  with no decomposition of the supporting electrolyte. Hence, this favorable electrochemical behavior of especially  $[\text{NBu}_4][\text{pf}]$  was used to investigate the redox behavior of organometallic complexes in solution.<sup>353</sup> Anodic voltammetry

and electrolysis of the metallocenes ferrocene, ruthenocene, and nickelocene were studied in dichloromethane, containing two different fluorine-containing anions in the supporting electrolyte. The perfluoroalkoxyaluminate anion  $[pf]^-$  has very low nucleophilicity, as shown by its inertness towards the strong electrophile  $[\text{RuCp}_2]^+$  and by computation of its electrostatic potential in comparison to other frequently used electrolyte anions. The low ion-pairing ability of this anion was shown by the large spread in  $E_{1/2}$  potentials ( $\Delta E_{1/2} = 769$  mV) for the two one-electron deelectronations of bis(fulvalene)dinickel.<sup>353</sup> The hexafluoroarsenate anion  $[\text{AsF}_6]^-$ , on the other hand, reacted rapidly with the ruthenocenium ion and is much more strongly ion-pairing towards deelectronated bis(fulvalene)dinickel ( $\Delta E_{1/2} = 492$  mV). In terms of applications of these two anions to the anodic deelectronation of organometallic sandwich complexes, the behavior of the simple to prepare  $[pf]^-$  is similar or even superior to that of other very good WCAs such as  $[\text{B}(\text{C}_6\text{F}_5)_4]^-$ , whereas that of  $[\text{AsF}_6]^-$  is similar to the more traditional electrolyte anions such as  $[\text{PF}_6]^-$  and  $[\text{BF}_4]^-$ . Additionally, the synthesis and crystal structure of  $[\text{Cp}_2\text{Fe}][pf]$  were reported.

The use of  $[pf]^-$  together with the weakly coordinating  $\text{CH}_2\text{Cl}_2$  made the two redox processes of two cobalt salen centers bridged by non-conjugated linkers distinguishable.<sup>354</sup> The same has been observed for  $N,N'$ -bis(ferrocenoyl)-1,2-diaminoethane.<sup>355</sup>

**Viologens and Bis-viologens:** The weakly coordinating property of  $[pf]^-$  can be seen as the redox couples of viologens and bis-viologens in CV and DPV experiments are shifted towards lower potentials relative to the  $[\text{PF}_6]^-$  electrolyte.<sup>356</sup> For the twice charged, unreduced species and electron richer viologens the shift is more pronounced. The peak potential separation, however, is higher and  $>59$  mV. The values increase with increasing substrate concentration and decreasing electrolyte concentration. This was attributed to the Ohmic drop caused by the high resistance within the WCA-based electrolyte. In particular, for the 0.01 m system, this effect is significant and a proper analysis of the I-E curves at fast scan rates was no longer possible. The enhanced peak separation in the  $[pf]^-$  system compared to the  $[\text{PF}_6]^-$  based electrolyte demonstrates that the WCA increases the communication between the two viologen redox centers. The reduction of one of the viologen units impedes (thermodynamically) the reduction of the second one.

### 1.07.2.5.3 As battery electrolytes

#### 1.07.2.5.3.1 In lithium-based batteries

**Aluminates:** Six lithium salts of tris- and tetrakis(polyfluoroalkoxy)aluminate WCAs were studied for their potential use as battery electrolytes.<sup>64</sup> Four of the six are based on the formula  $\text{Li}[\text{Al}(\text{OC}(\text{R})(\text{CF}_3)_2)_4]$  ( $\text{R} = \text{H}, \text{Me}, \text{CF}_3, \text{Ph}$ ); the other two are  $\text{Li}[\text{Al}(\text{OCH}_2\text{CF}_3)_4]$  and  $\text{Li}[\text{F}-\text{Al}(\text{OC}(\text{Ph})(\text{CF}_3)_2)_3]$ . The thermally stable electrolytes  $\text{Li}[hf]$  and  $\text{Li}[\text{Al}(\text{OC}(\text{Ph})(\text{CF}_3)_2)_4]$  were not oxidized at potentials less than or equal to 5.0 V vs.  $\text{Li}^{+/0}$  in dimethoxyethane (DME) or in 50:50% ethylene carbonate:dimethylcarbonate (EC:DMC). The  $\text{Li}[hf]$  electrolyte was not reduced at 0 V vs.  $\text{Li}^{+/0}$  in DME. Neither  $\text{Li}[hf]$  nor  $\text{Li}[\text{Al}(\text{OC}(\text{Ph})(\text{CF}_3)_2)_4]$  promoted the corrosion of aluminum at 5.0 V vs.  $\text{Li}^{+/0}$ . The electrolyte  $\text{Li}[hf]$  underwent efficient, reversible reductive intercalation of  $\text{Li}^+$  with MCMB carbon or  $\text{LiCoO}_2$  electrodes over the potential ranges 0–2 and 2.4–4.8 V, resp., vs.  $\text{Li}^{+/0}$ , but did not react in any other way with these electrode materials. The conductivities of some of the  $\text{Li}[pf]$  electrolytes in DME or in EC:DMC were high enough for them to be considered as potential replacements for  $\text{Li}[\text{PF}_6]$  in primary and secondary lithium batteries.

After this initial finding, the electrolyte performance of  $\text{Li}[hf]$  was investigated in more detail<sup>357,358</sup>: it was expected to generate a large number of ionic charge carriers in an aprotic solvent, because of its large anion size and structure that promotes delocalization of the anionic charge. The electrolyte properties of  $\text{Li}[hf]$ , were studied in the bulk, in aprotic solvents, and in a polyether.<sup>358</sup> Although the lithium salt melts at the fairly low temperature of 120 °C, it shows poor conductivity even in the molten state because of its strong ionic association. However, in aprotic solvents,  $\text{Li}[hf]$  exhibits a relatively high degree of dissociation, because of the weak coordination ability of the anion towards the cation. This is reflected in the higher ionic conductivity than that of common lithium salts,  $\text{Li}[\text{N}(\text{SO}_2\text{CF}_3)_2]$  and  $\text{Li}[\text{BF}_4]$ , at an identical concentration in the low polar solvents.<sup>358</sup> In polyether, an increase in the glass-transition temperature  $T_g$  of the polymer electrolytes with salt concentration is less marked in the  $\text{Li}[hf]$  system. The lithium salt can be incorporated in the matrix polyether at high concentrations, without a loss in the ionic conductivity. The interface between the polyether electrolyte containing  $\text{Li}[hf]$  and a metallic lithium electrode is statically stable for a long time, and the charge-transfer resistance decreases with increased salt concentration. These results indicate that an increase in  $\text{Li}[hf]$  concentration in the polyether facilitates not only an increase in the ionic conductivity but also a decrease in the interfacial resistance.

Also composite electrolyte solutions of  $\text{Li}[hf]$  were prepared by dispersing different amounts of  $\text{Al}_2\text{O}_3$  nanoparticles in the EC solutions of  $\text{Li}[hf]$ .<sup>357</sup> The composite solutions are hard slurries, however, the ionic conductivity is similar to that of neat solutions. The addition of  $\text{Al}_2\text{O}_3$  particles to polyether electrolytes, i.e., the high molecular weight polymer poly[ethylene oxide-2-(2-methoxyethoxy)ethylglycidyl ether] containing  $\text{Li}[hf]$  resulted in an increase of the mechanical strength, without changing the glass transition temperature,  $T_g$ , of the matrix. The ionic conductivity of the polymer electrolyte passed through a maximum against  $\text{Al}_2\text{O}_3$  composition, at which the conductivity reached  $10^{-4} \text{ S cm}^{-1}$  at 30 °C. The apparent lithium ion transfer number also increased with increasing  $\text{Al}_2\text{O}_3$  content.<sup>357</sup>

**Lithium-Sulfur-Battery:** Lithium-sulfur batteries comprising lightweight elements provide a promising alternative to lithium-ion batteries, but the associated polysulfide shuttle in typical ether-based electrolytes generates loss in capacity and low Coulombic efficiency. A new electrolyte, basing on the unique combination of a relatively hydrophobic  $N,N$ -dimethyl triflamide and  $\text{Li}[hf]$  as a low ion-pairing salt, inhibits the polysulfide shuttle and was presented by Nazar, Krossing et al. This system behaves as a sparingly solvating electrolyte at slightly elevated temperatures (50 °C), where it sustains reversible capacities as high as 1200–1500  $\text{mAh g}^{-1}$  over a wide range of current density (2C–C/5, respectively) when paired with a lithium metal anode. Notably, the Coulombic efficiency was  $>99.7\%$  and this in the absence of any  $\text{LiNO}_3$  additive. This electrolyte is anticipated to be low cost, as the salt is both

inexpensive and comprises a small fraction of the total electrolyte compared to an ionic liquid chelate such as  $[(\text{CH}_3\text{CN})_2\text{Li}(\text{NTf}_2)]$  and suggests substantial mass savings in comparison to the highly concentrated salt-in-solvent electrolytes, which also exhibit reduced polysulfide shuttling. A capacity fade was reported, which appears to be due to gradually increasing electronic isolation of the  $\text{Li}_2\text{S}$  formed on discharge owing to the complexity of dissolution-precipitation chemistry in poorly solvating media, which needs to be further addressed.<sup>359</sup>

**Borates:** The salt<sup>27</sup>  $\text{Li}[\text{B}(\text{OTfe})_4]$  with views to success in electrolytes was synthesized in excellent yields from lithium borohydride with excess 2,2,2-trifluoroethanol (HOTfe) in toluene and at least two equivalents of 1,2-dimethoxyethane (DME). It was obtained in multigram scale without impurities, as long as DME was present during the reaction. It was characterized by heteronuclear magnetic resonance and vibrational spectroscopy (IR and Raman), has high thermal stability ( $T_{\text{dec.}} > 271^\circ\text{C}$ , DSC) and shows long-term stability in water. The concentration-dependent electrical conductivity of  $\text{Li}[\text{B}(\text{OTfe})_4]$  was measured in water, acetone, EC/DMC, EC/DMC/DME, ethyl acetate and THF at RT. In DME ( $0.8\text{ mol L}^{-1}$ ) it is  $3.9\text{ mS cm}^{-1}$ , which is satisfactory for the use in lithium-sulfur batteries (LiSB). Cyclic voltammetry confirmed the electrochemical stability of  $\text{Li}[\text{B}(\text{OTfe})_4]$  in a potential range of 0 to 4.8 V vs.  $q\text{-Li}^+/\text{Li}$ . The performance of  $\text{Li}[\text{B}(\text{OTfe})_4]$  as conducting salt in a  $0.2\text{ mol L}^{-1}$  solution in 1:1 wt% DME/DOL was investigated in LiSB test cells. After the 40<sup>th</sup> cycle, 86% of the capacity remains, with a Coulombic efficiency of around 97% for each cycle. This indicates a considerable performance improvement for LiSB, if compared to the standard  $\text{Li}[\text{NTf}_2]/\text{DOL}/\text{DME}$  electrolyte system.

$\text{Li}[\text{hf}_\text{B}]$  was found as an interesting possible electrolyte for rechargeable lithium batteries and in-depth analysis was provided by Lucia Álvarez Hernandez in her PhD thesis.<sup>360</sup> The synthesis was investigated in different solvents and a series of novel liquid electrolytes using *o*DFB as an electrolyte solvent for the first time was produced. Two unique dicationic crystal structures of solvates of lithium salt were determined and derivatives of the anion, such as  $\text{Li}[\text{B}(\text{C}_2\text{O}_4(\text{Ohfp})_2)]$ , were successfully synthesized and fully characterized. Significant insight into the impact of the anion on the properties of the electrolyte was provided by an extensive comparison of the new salt with the classical lithium salts  $\text{Li}[\text{BF}_4]$ ,  $\text{Li}[\text{PF}_6]$  and  $\text{Li}[\text{NTf}_2]$  in different solvents. Additionally, IR, Raman, quantum chemical calculations, viscosity, ionic conductivity, Walden plots and diffusion NMR measurements have been used to extensively explore the ionic interactions in these electrolytes.<sup>360</sup>

The stoichiometric 1:1 combination of  $\text{LiX}$  ( $X = \text{OCH}_2\text{CF}_3$ ,  $\text{OC}(\text{H})(\text{CF}_3)_2$ ,  $\text{CO}_2\text{CF}_3$ ) with  $\text{BF}_3 \cdot \text{D}^{361,362}$  ( $\text{D} = \text{dimethyl carbonate, ethylene carbonate, ethyl methyl carbonate, propylene carbonate and diethyl ether}$ ) yields electrolytes with a significantly increased conductivity in comparison to pure  $\text{LiX}$  in EC:EMC (3:7 wt%). The combination of  $\text{Li}[\text{CO}_2\text{CF}_3]$  and  $\text{BF}_3 \cdot \text{EC}$  displayed the highest conductivity of all investigated systems, with  $5.8\text{ mS cm}^{-1}$  ( $1.5\text{ mol L}^{-1}$ ), which is higher than that of  $\text{Li}[\text{BF}_4]$  in the same solvent. NMR studies of all composite electrolytes showed the presence of various boron species like  $\text{BX}_3$ ,  $\text{Li}[\text{BF}_3\text{X}]$ ,  $\text{Li}[\text{BF}_2\text{X}_2]$  and  $\text{Li}[\text{BFX}_3]$ , which distribute characteristically for each  $\text{LiX}$ . The investigation of the electrochemical behavior of the composite electrolytes in NCM-111/graphite cells showed a direct relation between cycling behavior, impedance and boron content on CEI/SEI. In the differential plots of the first cycle, an irreversible oxidation was observed for all cells, which was attributed to the formation of the SEI. Ex situ analysis of the electrodes with XPS showed an increase of the boron content on the surface of both electrodes in the order of  $\text{Li}[\text{OC}(\text{H})(\text{CF}_3)_2] < \text{Li}[\text{OCH}_2\text{CF}_3] < \text{Li}[\text{CO}_2\text{CF}_3]$ . This ordering was also found for the growth of the impedance of the cells.<sup>362</sup>

#### 1.07.2.5.3.2 In rechargeable magnesium batteries (RMBs)

Electrolytes for magnesium batteries need to be kinetically or thermodynamically inert towards the highly reductive surface of magnesium metal at plating potentials, as the reduction products usually tend to passivate the metallic electrode. Furthermore, they need to be stable towards positive potentials of the positive electrode to enable the use high-voltage materials for the positive electrode. Non-corrosive and non-nucleophilic behavior is another prerequisite. Additionally, the conductivity of the electrolytes needs to be high, to enable good reaction kinetics. Given the large charge density of  $\text{Mg}^{2+}$ , WCA-based electrolytes with  $[\text{hf}]^-$ , stemming from the laboratory of S. Strauss<sup>363</sup> in 1998 and being augmented by us since 2001,<sup>8</sup> as well as  $[\text{hf}_\text{B}]^-$  stemming from our labs<sup>13</sup> in 2011, are on the rise, addressing all discussed prerequisites.

**Aluminates:** The synthesis and use of  $\text{Mg}[\text{hf}]_2$  electrolytes was described by Arnold et al. in 2016 and independently by Fichtner et al. in 2017.<sup>44,364</sup> Arnold et al. demonstrated the electrolyte as a new class of electrolytes for magnesium-ion battery systems, exhibiting high conductivity and reversible plating of Mg with high efficiencies, as well as its use in full battery cells using prototype cathode materials. With few exceptions, the oxide layer on magnesium metal had limited the scope of research to halide ion-based electrolytes, which help activate the electrode surface but also limit the working voltage window considerably. The synthesis was described via a facile and scalable method proceeding via the mixing of the respective magnesium and aluminum fluoroalkoxides in ethereal solvents. The obtained solutions of the  $\text{Mg}[\text{hf}]_2$  salt can reversibly deposit magnesium metal with near unit efficiency and achieved suitable oxidative stabilities ( $> 3.5\text{ V vs. } q\text{-Mg}^{2+}/\text{Mg}$  on glassy carbon and gold) and conductivities ( $> 6\text{ mS cm}^{-1}$ ). The practical oxidative stability of the electrolyte was probed using chronoamperometric methods on Al electrodes, indicating that anodic dissolution may be inhibited, but is not stopped, by formation of an aluminum fluoride layer. Exploration of this class of anions was described as an important step forward not only in Mg-ion battery chemistry but also for other multivalent ionic systems such as calcium and aluminum.<sup>44</sup> Fichtner et al. described an alternative synthesis of  $\text{Mg}[\text{hf}]_2$  via metathesis of  $\text{MgBr}_2$  with the sodium alkoxy aluminate.<sup>364</sup> As the electrochemical behavior of  $\text{Mg}[\text{hf}]_2$  was already described by Arnold et al., the Fichtner group focused strongly on the borate analogue and no significant additional electrochemical data was published in the discussed article.<sup>44,364</sup> Mandai et al. investigated 2021 the different electrochemical properties and structure-property relationships of the  $\text{Mg}[\text{hf}]_2$  and  $\text{Mg}[\text{hf}_\text{B}]_2$  salts in different glymes (G1–G4) in a comparative study. The bulk physiochemical properties, electrochemical



characteristics and ion-transport behaviors were systematically and comprehensively studied. The concentration dependent ionic conductivity showed no dependence on the type of anion, while the temperature-concentration-conductivity profiled showed distinct dependences for the respective anions, suggesting different ion-transport mechanisms. The respective alkoxyaluminates  $[hf]^-$  showed higher ionic conductivities than their borate counterparts  $[hf_B]^-$  did in all salt/solvent combinations due to their higher charge-carrier diffusivity, leading to better desposition and dissolution activities. The systematic study showed  $Mg[hf]_2$  in diglyme to be the salt/solvent combination exhibiting the best electrochemical activity, exhibiting stable and efficient (99.4% coulombic efficiency), low polarized ( $<\pm 60$  mV) deposition and dissolution cycles. The findings were supported via ab initio molecular dynamic simulation, showing exceptionally high  $Mg^{2+}$  diffusivity, electrochemical impedance spectroscopy, and Vogel-Tammann-Fulcher fitting analysis.<sup>365</sup> Bitenc et al. published single-crystal data accompanied by NMR and IR data for  $[Mg(DME)_3][hf]_2$  (DME = 1,2-dimethoxyethane) proving the hexacoordinated structure of the salt. The performance was investigated in different glymes, confirming diglyme as the optimal solvent. Special attention was given to the influence of water content, showing high tolerance towards the presence of water traces for the salt in diglyme, which would simplify the upscaling of the electrolyte. Under macrocycling conditions, including OCV periods, the addition of  $nBu_2Mg$  and  $MgCl_2$  was shown to be beneficial. The performance was additionally tested using three different positive electrodes (intercalation-type Chevrel phase, organic conversion-type poly(anthraquinone) and inorganic conversion-type sulfur), showing reversible behavior and lower overpotentials than observed for the analogue borate salt. The improved performance establishes  $[Mg(DME)_3][hf]_2$  as a new standard salt for future RMB research.<sup>366</sup>

In 2019, Clare Grey, Dominic Wright et al. reported a series of Mg aluminate salts  $Mg[Al(OR_4)]_2$  ( $R = ^tBu, ^tBu^F, ^iPr^F, Ph$  and  $Ph^F$ ), that were prepared using a general synthetic approach employing  $Mg[AlH_4]_2$  and the respective fluorinated and non-fluorinated alcohols as starting materials, for use in electrolyte systems for Mg batteries. This methodology provided access to Mg aluminates that do not possess  $\beta$ -hydrogens and thereby precluded possible  $\beta$ -hydride elimination decomposition pathways, which have been reported for analogous aluminum-based electrolytes.<sup>44</sup> The cycling of these systems using Au and Mg electrodes was found to be strongly influenced by the presence of chloride that was present due to the synthesis of  $Mg[AlH_4]_2$ . Chloride was found to lower plating/stripping overpotentials and increased Coulombic efficiencies. The Mg aluminates were cycled efficiently in Mg full cells containing a Chevrel phase  $Mo_6S_8$  cathode with good capacity retention.<sup>367</sup>

A lower chloride content for an  $Mg[pf]_2$  salt was reported by Lau et al., in the same year. They hypothesized, that the electrochemical window of Mg salt could be widened by disfavoring the cathodic decomposition pathway of a thermodynamically and anodically stable anion, rendering it kinetically inert towards Mg-mediated reduction. Computational and electrochemical analyses on  $Mg[pf]_2$  supported this hypothesis, and showcased a widened electrochemical window as a result of mitigated cathodic decomposition as well as enhanced anodic stability from electron-withdrawing  $CF_3$  groups. Detailed NMR and IR spectroscopy and scanning electron microscopy/energy-dispersive X-ray spectroscopy further supported, that the weak coordination to  $Mg^{2+}$  in solution is important for maintaining the wide electrochemical window of the Mg salt, as it impedes thermodynamically favorable decomposition pathways of Mg-WCA associates.<sup>368</sup>

The Crossing group showed another, clean and contaminant free route towards  $[Mg(L)_x][pf]_2$  ( $L = MeCN, DME; x = 3, 6$ ) in a 2022 study.<sup>369</sup> Surprisingly, our electrochemical results contradict the findings of Grey/Wright and Lau, as we could not prove magnesium plating and stripping activity of the electrolytes due rapid insulation of the electrodes by solid  $MgF_2$  formed by slight degradation of the anion at the negatively polarized magnesium surface. The findings are supported by calculations and XPS data.

**Borates:** Borate-WCA electrolytes for the application in RMBs are mainly reported for the respective  $[hf_B]^-$  salts by the group of Fichtner and Zhao-Karger. First data was presented in 2017.<sup>364,370</sup> Fichtner et al. presented  $[Mg(DME)_3][hf_B]_2$  as a new class of fluorinated alkoxyborates (yet, they are known from our work<sup>13</sup> since 2011) that is well-suited to be used as conductive salts in Mg electrolytes. Profound chemical and electrochemical characterization of the salt was presented. The solution of  $[Mg(DME)_3][hf_B]_2$  in DME showed most promising electrochemical characteristics among the current state-of-the-art Mg electrolytes in terms of high oxidative stability, high conductivity and excellent Coulombic efficiency of Mg deposition. The good chemical compatibility makes it well-suited for high energy Mg batteries. The use of fluorinated alkoxyborate based electrolytes for Mg-S batteries has been demonstrated. For the first time, a stable cyclability with a nearly theoretical discharge voltage and good Coulombic efficiency was realized for the Mg-S cells. The straightforward, scalable synthesis from the alcoholysis of  $Mg[BH_4]_2$  and the air and water insensitive nature were pointed out to be promising properties.<sup>364</sup> The vast number of publications associated with the application  $[hf_B]^-$  salts of magnesium in RMBs<sup>371-390</sup> shows, that the  $[Mg(DME)_3][hf_B]_2$  has become a new standard electrolyte for magnesium based batteries that use sulfur, intercalation type, and organic positrode materials. Especially, for the validation of new concepts, that are susceptible to chloride induced corrosion of previously utilized electrolytes, this non-corrosive electrolyte has proven to be an important compound, avoiding side effects associated with the nature of the chloride-containing electrolytes and enabling the realistic capabilities of the positrode materials and surface engineering in RMBs. The understanding of the electrode-electrolyte interphase and interface plays an important role, which has been recently studied in a model full-cell. Electrochemical impedance spectroscopy (EIS) was applied to analyze the Mg-electrolyte interaction in a three-electrode system, showing a rapid increase in charge transfer resistance on the anode side with increasing resting time. In contrast a significant drop in the charge transfer impedance was observed upon cycling along with the appearance of an additional semi-circle, which suggested to the development of a solid interphase. X-ray photoelectron spectroscopy (XPS) and Fourier transform infrared spectroscopy (FTIR) corroborated the EIS results and confirmed the solid interphase layer formation, in which  $MgF_2$  was identified as the primary species contributing to its formation.<sup>387</sup> Recently, Fichtner et al. provided an additional in-depth analysis of the structure of  $[Mg(DME)_3][hf_B]_2$  and the interactions generated in the electrolyte among the dissociated ions. The results show a delicate balance between electron-withdrawing effects

and ligand stabilization in the anion, that is crucial for the working principle of the magnesium electrolyte. The group found, that the bulk nature of  $[hf_b]^-$  limits the anion-cation contacts to infrequent interactions through fluorine atoms, which has consequences for ion transport and the decomposition pathways towards the formation of  $MgF_2$ . The study allows for further rational development of new anion structures.<sup>388</sup> In a 2020 paper, Mandai addresses issues concerning the reproducibility of the  $[Mg(DME)_3][hf_b]_2$  synthesis from  $Mg[BH_4]_2$ , reported to be batch dependent and to achieve low yields. An alternative synthetic route using  $Mg(OHfp)_2$ ,  $BH_3$ -THF-adduct and  $HOHfp$  as starting materials was suggested. Despite outstanding performance of the electrolyte salt in 1,2-DME, the electrolyte formulations were found to be unstable against magnesium metal mainly due to decomposition of the polarized coordinating solvent molecules. Non-dendritic short-circuiting was described and analyzed as a function of cycle number, separator thickness and highly localized electrode utilization leading to isolated magnesium particle and continuous magnesium deposition into the separator materials. The overall findings highlighted the need for further research.<sup>391</sup> Following these findings and earlier observations on electrolyte conditioning, the Aurbach-group examined the electrochemical performance of the  $Mg[hf_b]_2/DME$ -system and chemical changes upon prolonged cyclic voltammetric cycling using various electrochemical windows. Stable behavior of the magnesium electrodes was observed after their conditioning pretreatment, stated to remove reactive, passivating contaminants from the electrolyte solutions. All electrochemical parameters, such as current density, coulombic efficiency, overpotential for deposition and deposition morphology were described to be improved by the presented method. Nevertheless, observed potential gaps between the end of deposition and the start of dissolution were observed for all CVs, reflecting inherent kinetic barriers, found likewise in the Fichtner publications. The fundamental nature of the conditioning process was not fully understood and it was concluded that the removal of detrimental impurities, such as traces of water, is supposed to be a consequence of conditioning. In macrocycling experiments a coulombic efficiency not higher than 96.5% was obtained, being lower than the necessary >99.9% for practical battery applications using balanced electrode masses.<sup>392</sup>

Besides the  $Mg[hf_b]_2$  salt, Liu et al. reported on the perfluoro pinacolatoborate salt  $Mg[B(O_2C_2(CF_3)_4)_2]_2$  as a possible RMB electrolyte, that was synthesized from commercially available reagents and fully characterized. The electrolyte delivered good electrochemical performance, specifically, 95% Coulombic efficiency and 197 mV overpotential, enabling reversible Mg deposition, and an anodic stability of up to 4.0 V vs.  $q-Mg^{2+}/Mg$ . The electrolyte was applied to assemble a high voltage, rechargeable  $Mg/MnO_2$  battery with a discharge capacity of 150 mAh  $g^{-1}$ .<sup>393</sup> It must be noted though that the perfluoropinacol, which is a starting material and a possible degradation product of  $Mg[B(O_2C_2(CF_3)_4)_2]_2$ , is an extremely toxic compound (fatal in contact with skin).<sup>394</sup>

#### 1.07.2.5.3.3 In rechargeable calcium batteries

*Aluminates:* Electrolytes or batteries containing aluminates of any alkoxide residue were hitherto *not* reported.<sup>395</sup>

*Borates:* The first electrolytes allowing plating and stripping of metallic calcium were simple borates. For  $Ca[BF_4]_2$  in EC/PC a temperature of 100 °C is necessary.<sup>396</sup>  $Ca[NTf_2]_2$  is a non-functioning electrolyte at these conditions unless the calcium electrode was pretreated with a  $[BF_4]^-$  electrolyte enabling the plating of calcium from this electrolyte and being advantageous to the stripping as well.<sup>397</sup>  $CaBH_4$  used in THF allows plating and stripping at room temperature.<sup>398</sup> The coulomb efficiency is 95% and  $CaH_2$  is continuously formed.

Li et al.<sup>399</sup> and Shyamsunder et al.<sup>400</sup> simultaneously reported solutions of the weakly coordinating alkoxyborate  $[Ca(DME)_4][hf_b]_2$  in DME as an active room temperature electrolyte. It showed coulombic efficiencies of about 80–90% in CV on Pt (0.25 m) and Au (0.5 m) with stripping and plating overpotentials of 300 and 600 mV, respectively. Conditioning cycles were needed. In a symmetrical cell with calcium electrodes, the overpotential is >500 mV. The anodic stability reaches 4.2 V on stainless steel and 4.8 V on aluminum. It could be raised up to 4.9 V on calcium metal by using  $Me_2NTf$  as solvent.<sup>400</sup> The electrode passivates through formation of  $CaF_2$  as a result of anion cleavage possibly through water impurities, which was also correlated to the dendritic Ca deposit.<sup>399</sup> The addition of 0.1 m  $nBu_4NCl$  to the 0.5 m electrolyte enhances the coulombic efficiency (92%) as well as the cycling life.<sup>400</sup> As it is not nucleophilic and offers a great anodic stability, it is the mainly used prototype electrolyte in latest publications. It has been successfully used with  $VS_4$ ,<sup>390</sup> sulfur<sup>45</sup> and polyanthracinon<sup>401</sup> positrodes.

The salt has also been tested in THF and diglyme.<sup>402</sup> The latter improved deposit morphology, reversibility, overpotentials and cycle life in CV experiments and symmetrical  $Ca | Ca$  cells. A full cell using this electrolyte with a  $FePO_4$  positrode was demonstrated.

The ion interactions determining the solvation environments in WCA electrolytes being investigated for their oxidative stability exhibit significant and non-intuitive concentration relationships.<sup>403</sup> This statement is particularly true for electrolytes utilizing reductively stable ethereal solvents due to their low dielectric constants. Solutions of  $[Ca(DME)_4][hf_b]_2$  in the ethereal solvents DME and THF were characterized across a concentration range of several orders of magnitude. The effective salt dissociation has a minimum around 0.01 m and a maximum around 0.2 m. Combined experimental and computational dielectric and X-ray spectroscopic analyses of the changes occurring in the  $Ca^{2+}$  solvation environment across these concentration regimes reveals a progressive transition from well-defined solvent-separated ion pairs to decorrelated free ions. This transition in ion correlation results in improvements in both conductivity and calcium cycling stability with increased salt concentration.

#### 1.07.2.5.3.4 Application in battery electrolytes for zinc ion batteries

Liao et al. report a new zinc salt with the  $[pf]^-$  anion, as a stable electrolyte for nonaqueous systems. The electrochemical and structural properties of this nonaqueous electrolyte was examined in various solvents.<sup>404</sup> The synthesis was derived from the previously reported Mg-salt synthesis.<sup>368</sup>  $Zn[pf]_2$  supported highly reversible Zn deposition and stripping behavior in acetonitrile and ethereal solvents, with up to 91% Coulombic efficiency and anodic stability. The metal deposits on the electrode were determined to be an amorphous layer of zinc metal, along with decomposition products of the fluorinated anion. A variety of analytical techniques was

used to identify the local coordination structure around  $\text{Zn}^{2+}$  in both the crystal phase and the solution phase, providing clear evidence of solvent coordination around the cation. The WCA grants the salt a high-level of ion separation as was shown by X-ray crystallography, and the zinc cations are reported to be fully solvated in organic solvents such as MeCN, THF, and G3. IR measurements suggested the presence of ion association with increased concentration. However, XAS measurement could only distinguish cation-solvent interactions at concentrations up to 0.1 m. It was supposed, that the anion likely persists as a solvent-separated ion pair in the discussed zinc electrolytes.<sup>404</sup>

#### 1.07.2.5.4 As electrolytes for supercapacitors

An electrochemical investigation into ILs based on  $[\text{hf}]^-$  and  $[\text{Tf}_2\text{N}]^-$  anions as electrolytes in supercapacitors was performed.<sup>405</sup> The synthesis of  $[\text{hf}]^-$  ILs was improved to minimize the water content for electrochemical measurements. Several electrodes with different pore sizes from micropores to macropores were prepared. Impedance and cyclic voltammetry studies of eight ILs were conducted with the electrodes and revealed that, despite their close-to-ideal transport properties (cf. Table 5),  $[\text{hf}]^-$  ILs suffer from a sieving effect in the case of micropores, which leads to a sharp drop in capacitance compared with  $[\text{Tf}_2\text{N}]^-$  ILs. When the influence of the size is abrogated at meso- or macroporous electrodes, the aluminate salts become competitive in terms of capacitance and show that, without a sieving effect, their basic properties in principle make them suitable electrolytes as well.

#### 1.07.2.5.5 In organic photovoltaics OPV

*Increasing OPV-Efficiency:* The aluminate anion  $[\text{pf}]^-$  was employed<sup>406</sup> to introduce pseudo-gas-phase conditions to the 2-[5-(1,3-dihydro-1,3,3-trimethyl-2H-indol-2-ylidene)-1,3-pentadien-1-yl]-1,3,3-trimethyl-3H-indolium chromophore. The resulting formation of a photoactive organic-inorganic hybrid salt has led to a highly stabilized excited state of the organic chromophore mainly due to the minimized lattice energy and Coulomb interactions. These highly beneficial features caused by the well dispersed negative charge of the anion have led to an enhanced neat spin-casted film fluorescence intensity, prolonged fluorescence lifetime, smooth thin film surfaces and a record power photovoltaic efficiency of 3.8% when compared to organic salts of this particular chromophore containing anions with localized negative charge. Clear evidence is given that a superweak coordinating anion is an emerging key parameter in cyanine dye photochemistry. This approach can be seen as a general guideline to prepare highly efficient ionic dyes for organic semiconductor applications and was further elaborated in 2022 by using even larger aluminate based anions with the perfluorinated 2-adamantoxo residue.<sup>407</sup>

#### 1.07.2.5.6 In the life sciences as hydrophobic, non-bleaching dyes

The  $[\text{pf}]^-$  counterion was used for enhanced encapsulation and emission of dyes in biodegradable polymer nanoparticles.<sup>408</sup> Hence, dye-loaded polymer nanoparticles, due to their high brightness and potential biodegradability, emerge as a powerful alternative to quantum dots in bioimaging applications. To minimize aggregation-caused quenching of the loaded dyes, the use of cationic dyes with WCAs, which serve as spacers preventing dye  $\pi$ -stacking inside nanoparticles, was recently proposed. However, so far this approach of counterion-enhanced emission inside polymer NPs was limited to tetrakis(pentafluorophenyl)borate (F5-TPB). The authors showed that the counterion-enhanced emission approach is not limited to tetraphenylborates and can be extended to other types of anions, such as the  $[\text{pf}]^-$  anion, which is much easier to scale up, compared to F5-TPB.  $[\text{pf}]^-$  strongly improved the encapsulation efficiency of the octadecyl rhodamine B dye compared to the perchlorate counterion (97.2 vs. 51.2%), being slightly better than F5-TPB (92.4%). Similarly, to F5-TPB,  $[\text{pf}]^-$  can effectively prevent aggregation-caused quenching of rhodamine inside NPs made of the biodegradable polymer, poly(lactide-co-glycolide) (PLGA), even at 50 mM dye loading. According to single-particle microscopy, the obtained NPs are 33-fold brighter than commercial quantum dots QD585 at 532 nm excitation and exhibit complete ON/OFF switching (blinking), as was originally observed for NPs based on F5-TPB. Importantly, NPs loaded with the rhodamine/ $[\text{pf}]^-$  ion pair entered the cells by endocytosis, showing no signs of dye leaching, in contrast to rhodamine perchlorate, which exhibited severe leakage from NPs with characteristic accumulation inside mitochondria. Moreover,  $[\text{pf}]^-$  surpassed the F5-TPB anion in stability of dye-loaded NPs against leaching, which can be attributed to the higher hydrophobicity of the former. Overall, this work shows that counterion-enhanced encapsulation and emission of cationic dyes inside polymer NPs is a general approach for the preparation of stable and highly fluorescent nanomaterials for bioimaging applications.

### 1.07.3 Conclusion and outlook

The preceding sections show that synthetically easily accessible WCAs like the  $[\text{M}(\text{OR}^f)_4]^-$  ( $\text{M} = \text{Al}, \text{B}$ ) class of ions will soon find their way from laboratory curiosities, used to stabilize “crazy” cations, to applications in a multitude of areas like coordination chemistry, ionic liquids, electrolytes, catalysis, polymerization chemistry etc. However, the prerequisite to achieve this is the ready availability of such materials. Here the fluorinated aluminates and several of the borates have made their way: The syntheses of many starting materials to introduce these WCAs were developed and thus nowadays allow preparing almost any set of compounds, given that the cation is compatible with the specific aluminate or borate. Limits for this WCA class are certainly extreme electrophiles, i.e., small silylium ions like  $[\text{SiMe}_3]^+$ . Yet, the ions are compatible with the very strong electrophile  $[\text{CCl}_3]^+$ . In terms of weak coordination ability, there are only less than a handful—much more difficult to prepare—WCAs known, that offer the same quality. Electrochemically, the aluminates are stable in strongly reducing environments (metallic Li), but also very oxidizing conditions (up to +5.5 V vs. Li/Li<sup>+</sup>).

Thus, if there is a need to replace a more common WCA like  $[\text{SO}_3\text{CF}_3]^-$ ,  $[\text{BF}_4]^-$  or  $[\text{PF}_6]^-$  due to problems in the desired application (solubility, stability, ion pairing, etc.), the introduction of the  $[\text{M}(\text{OR}^F)_4]^-$ -type aluminates and borates is certainly a good move. This is facilitated by the commercial availability of many aluminate starting materials through [www.iolitec.de](http://www.iolitec.de) (e.g., Li-, Ag-, CPh<sub>3</sub>-, H(OEt<sub>2</sub>)<sub>2</sub>-salts and more). However, if a system runs well with a conventional smaller WCA, there is usually no need to take the extra effort to introduce these large WCAs.

## References

- Krossing, I. *Comprehensive Inorganic Chemistry II*, Elsevier, 2013; pp 681–705.
- Krossing, I.; Raabe, I. *Angew. Chem. Int. Ed. Engl.* **2004**, *43*, 2066–2090.
- Riddlestone, I. M.; Kraft, A.; Schaefer, J.; Krossing, I. *Angew. Chem. Int. Ed. Engl.* **2018**, *57*, 13982–14024.
- Wiesner, A.; Gries, T. W.; Steinhauer, S.; Beckers, H.; Riedel, S. *Angew. Chem. Int. Ed.* **2017**, *56*, 8263–8266.
- Wiesner, A.; Fischer, L.; Steinhauer, S.; Beckers, H.; Riedel, S. *Chem. A Eur. J.* **2019**, *25*, 10441–10449.
- Niemann, M.; Neumann, B.; Stammeler, H.-G.; Hoge, B. *Angew. Chem. Int. Ed. Engl.* **2019**, *58*, 8938–8942.
- Barbarich, T. J.; Handy, S. T.; Miller, S. M.; Anderson, O. P.; Grieco, P. A.; Strauss, S. H. *Organometallics* **1996**, *15*, 3776–3778.
- Krossing, I. *Chem. A Eur. J.* **2001**, *7*, 490–502.
- Krossing, I.; Brands, H.; Feuerhake, R.; Koenig, S. *J. Fluor. Chem.* **2001**, *112*, 83–90.
- Krossing, I.; Reisinger, A. *Coord. Chem. Rev.* **2006**, *250*, 2721–2744.
- Roesky, H. W.; Kennepohl, D. K.; Lehn, J.-M., Eds.; *Experiments in green and sustainable chemistry: I. Raabe, A. Reisinger, I. Krossing: Efficient syntheses of Li[Al(OR<sup>F</sup>)<sub>4</sub>], Ag[Al(OR<sup>F</sup>)<sub>4</sub>] (R<sup>F</sup> = C(CF<sub>3</sub>)<sub>3</sub>, C(H)(CF<sub>3</sub>)<sub>2</sub>, C(CH<sub>3</sub>)(CF<sub>3</sub>)<sub>2</sub>) and [H(OEt<sub>2</sub>)<sub>2</sub>]<sup>+</sup>[Al(OC(CF<sub>3</sub>)<sub>3</sub>)<sub>4</sub>]<sup>-</sup>*; *Green Chemistry*, Wiley-VCH Verlag GmbH & Co. KGaA, 2009; pp 131–144.
- Martens, A.; Weis, P.; Krummer, M. C.; Kreuzer, M.; Meierhöfer, A.; Meier, S. C.; Bohnenberger, J.; Scherer, H.; Riddlestone, I.; Krossing, I. *Chem. Sci.* **2018**, *9*, 7058–7068.
- Bulut, S.; Klose, P.; Krossing, I. *Dalton Trans.* **2011**, *40*, 8114–8124.
- Rupp, A. B. A.; Klose, P.; Scherer, H.; Krossing, I. *ChemPhysChem* **2014**, *15*, 3729–3731.
- Rupp, A. B. A.; Welle, S.; Klose, P.; Scherer, H.; Krossing, I. *ChemPhysChem* **2015**, *16*, 1940–1947.
- Bihlmeier, A.; Gonsior, M.; Raabe, I.; Trapp, N.; Krossing, I. *Chem. A Eur. J.* **2004**, *10*, 5041–5051.
- Ivanova, S. M.; Nolan, B. G.; Kobayashi, Y.; Miller, S. M.; Anderson, O. P.; Strauss, S. H. *Chem. A Eur. J.* **2001**, *7*, 503–510.
- Kim, K.-C.; Reed, C. A.; Long, G. S.; Sen, A. *J. Am. Chem. Soc.* **2002**, *124*, 7662–7663.
- Krossing, I.; Raabe, I. *Chem. A Eur. J.* **2004**, *10*, 5017–5030.
- Müller, L. O.; Himmel, D.; Stauffer, J.; Steinfeld, G.; Slattery, J.; Santiso-Quinones, G.; Brecht, V.; Krossing, I. *Angew. Chem. Int. Ed. Engl.* **2008**, *47*, 7659–7663.
- Böhrer, H.; Trapp, N.; Himmel, D.; Schleep, M.; Krossing, I. *Dalton Trans.* **2015**, *44*, 7489–7499.
- Erdmann, P.; Greb, L. *ChemPhysChem* **2021**, *22*, 935–943.
- Greb, L. *Chem. A Eur. J.* **2018**, *24*, 17881–17896.
- Erdmann, P.; Leitner, J.; Schwarz, J.; Greb, L. *ChemPhysChem* **2020**, *21*, 987–994.
- Erdmann, P.; Greb, L. *Angew. Chem. Int. Ed. Engl.* **2022**, *61*, e202114550.
- Zhang, G.; Musgrave, C. B. *J. Phys. Chem. A* **2007**, *111*, 1554–1561.
- Rohde, M.; Eiden, P.; Leppert, V.; Schmidt, M.; Garsuch, A.; Semrau, G.; Krossing, I. *ChemPhysChem* **2015**, *16*, 666–675.
- Krossing, I.; Reisinger, A. *Eur. J. Inorg. Chem.* **2005**, 1979–1989.
- Radtke, V.; Himmel, D.; Pütz, K.; Goll, S. K.; Krossing, I. *Chem. A Eur. J.* **2014**, *20*, 4194–4211.
- Himmel, D.; Radtke, V.; Butschke, B.; Krossing, I. *Angew. Chem. Int. Ed. Engl.* **2018**, *57*, 4386–4411.
- Malinowski, P. J.; Jaroń, T.; Domańska, M.; Slattery, J. M.; Schmitt, M.; Krossing, I. *Dalton Trans.* **2020**, *49*, 7766–7773.
- Gonsior, M.; Krossing, I.; Mitzel, N. *Z. Anorg. Allg. Chem.* **2002**, *628*, 1821–1830.
- Slattery, J. M.; Higelin, A.; Bayer, T.; Krossing, I. *Angew. Chem. Int. Ed.* **2010**, *49*, 3228–3231.
- Higelin, A.; Sachs, U.; Keller, S.; Krossing, I. *Chem. A Eur. J.* **2012**, *18*, 10029–10034.
- Welsch, S.; Bodensteiner, M.; Dusek, M.; Sierka, M.; Scheer, M. *Chem. A Eur. J.* **2010**, *16*, 13041–13045.
- Dabringhaus, P.; Schorpp, M.; Scherer, H.; Krossing, I. *Angew. Chem. Int. Ed. Engl.* **2020**, *59* (49), 22023–22027.
- Santiso-Quinones, G.; Higelin, A.; Schaefer, J.; Brueckner, R.; Knapp, C.; Krossing, I. *Chem. A Eur. J.* **2009**, *15*, 6663–6677.
- Li, Y.; Diebl, B.; Raith, A.; Kuehn, F. E. *Tetrahedron Lett.* **2008**, *49*, 5954–5956.
- Li, Y.; Kühn, F. E. *J. Organomet. Chem.* **2008**, *693*, 2465–2467.
- Malinowski, P. J.; Himmel, D.; Krossing, I. *Angew. Chem. Int. Ed. Engl.* **2016**, *55*, 9259–9261.
- Malinowski, P. J.; Himmel, D.; Krossing, I. *Angew. Chem. Int. Ed. Engl.* **2016**, *55*, 9262–9266.
- Engesser, T. A.; Friedmann, C.; Martens, A.; Kratzert, D.; Malinowski, P. J.; Krossing, I. *Chem. A Eur. J.* **2016**, *22*, 15085–15094.
- Meier, S. C.; Holz, A.; Kulenkampff, J.; Schmidt, A.; Kratzert, D.; Himmel, D.; Schmitz, D.; Scheidt, E.-W.; Scherer, W.; Bülow, C.; Timm, M.; Lindblad, R.; Akin, S. T.; Zamudio-Bayer, V.; von Issendorff, B.; Duncan, M. A.; Lau, J. T.; Krossing, I. *Angew. Chem. Int. Ed. Engl.* **2018**, *57*, 9310–9314.
- Herb, J. T.; Nist-Lund, C. A.; Arnold, C. B. *ACS Energy Lett.* **2016**, *1*, 1227–1232.
- Li, Z.; Vinayan, B. P.; Diemant, T.; Behm, R. J.; Fichtner, M.; Zhao-Karger, Z. *Small* **2020**, *16*, e2001806.
- Li, Y.; He, J.; Khankhoje, V.; Herdtweck, E.; Köhler, K.; Storcheva, O.; Cokoja, M.; Kühn, F. E. *Dalton Trans.* **2011**, *40*, 5746–5754.
- Li, Y.; Yeong, H. Y.; Herdtweck, E.; Voit, B.; Kuehn, F. E. *Eur. J. Inorg. Chem.* **2010**, 4587–4590.
- Schorpp, M.; Krossing, I. *Chem. Sci.* **2020**, *11*, 2068–2076.
- Schleep, M.; Hettich, C.; Kratzert, D.; Scherer, H.; Krossing, I. *Chem. Commun.* **2017**, *53*, 10914–10917.
- Bodizs, G.; Raabe, I.; Scopelliti, R.; Krossing, I.; Helm, L. *Dalton Trans.* **2009**, 5137–5147.
- Decken, A.; Jenkins, H. D. B.; Nikiforov, G. B.; Passmore, J. *Dalton Trans.* **2004**, 2496–2504.
- Kochner, T.; Riedel, S.; Lehner, A. J.; Scherer, H.; Raabe, I.; Engesser, T. A.; Scholz, F. W.; Gellrich, U.; Eiden, P.; Schmidt, R. A. P.; Plattner, D. A.; Krossing, I. *Angew. Chem. Int. Ed. Engl.* **2010**, *49*, 8139–8143.
- Knapp, C.; Mailman, A.; Nikiforov, G. B.; Passmore, J. *J. Fluor. Chem.* **2006**, *127*, 916–919.
- Schorpp, M.; Rein, S.; Weber, S.; Scherer, H.; Krossing, I. *Chem. Commun.* **2018**, *54*, 10036–10039.
- Schorpp, M.; Heizmann, T.; Schmucker, M.; Rein, S.; Weber, S.; Krossing, I. *Angew. Chem. Int. Ed. Engl.* **2020**, *59*, 9453–9459.
- Rall, J. M.; Schorpp, M.; Keilwerth, M.; Mayländer, M.; Friedmann, C.; Daub, M.; Richert, S.; Meyer, K.; Krossing, I. *Angew. Chem. Int. Ed. Engl.* **2022**, e202204080.
- Raabe, I.; Wagner, K.; Guttsche, K.; Wang, M.; Grätzel, M.; Santiso-Quinones, G.; Krossing, I. *Chem. A Eur. J.* **2009**, *15*, 1966–1976.
- Krossing, I.; Raabe, I. *Acta Cryst. E* **2007**, *63*, M2144-U1081.
- Rupp, A. B. A.; Krossing, I. *Acc. Chem. Res.* **2015**, *48*, 2537–2546.



60. Timofte, T.; Pitula, S.; Mudring, A.-V. *Inorg. Chem.* **2007**, *46*, 10938–10940.
61. Kraft, A.; Beck, J.; Steinfeld, G.; Scherer, H.; Himmel, D.; Krossing, I. *Organometallics* **2012**, *31*, 7485–7491.
62. Schorpp, M.; Tamim, R.; Krossing, I. *Dalton Trans.* **2021**, *50*, 15103–15110.
63. Sellin, M.; Friedmann, C.; Maylaender, M.; Richert, S.; Krossing, I. *Chem. Sci.* **2022**.
64. Tsujioka, S.; Nolan, B. G.; Takase, H.; Fauber, B. P.; Strauss, S. H. *J. Electrochem. Soc.* **2004**, *151*, A1418–A1423.
65. Barthélemy, A.; Glootz, K.; Scherer, H.; Hanske, A.; Krossing, I. *Chem. Sci.* **2022**, *13*, 439–453.
66. Martens, A.; Kreuzer, M.; Ripp, A.; Schneider, M.; Himmel, D.; Scherer, H.; Krossing, I. *Chem. Sci.* **2019**, *10*, 2821–2829.
67. Jutzi, P.; Mix, A.; Neumann, B.; Rummel, B.; Stämmler, H.-G. *Chem. Commun.* **2006**, 3519–3521.
68. Großekappenberg, H.; Reißmann, M.; Schmidtman, M.; Müller, T. *Organometallics* **2015**, *34*, 4952–4958.
69. Kraft, A.; Trapp, N.; Himmel, D.; Böhler, H.; Schlüter, P.; Scherer, H.; Krossing, I. *Chem. A Eur. J.* **2012**, *18*, 9371–9380.
70. Cameron, T. S.; Nikiforov, G. B.; Passmore, J.; Rautiainen, J. M. *Dalton Trans.* **2010**, *39*, 2587–2596.
71. Decken, A.; Passmore, J.; Wang, X. *Angew. Chem.* **2006**, *118*, 2839–2843.
72. Dankert, F.; Erlemeier, L.; Ritter, C.; von Hänisch, C. *Inorg. Chem. Front.* **2020**, *7*, 2138–2153.
73. von Hänisch, C.; Weigend, F.; Hampe, O.; Stahl, S. *Chem. A Eur. J.* **2009**, *15*, 9642–9646.
74. von Hänisch, C.; Hampe, O.; Weigend, F.; Stahl, S. *Angew. Chem. Int. Ed. Engl.* **2007**, *46*, 4588.
75. Carravetta, M.; Concistre, M.; Levason, W.; Reid, G.; Zhang, W. *Chem. Commun.* **2015**, *51*, 9555–9558.
76. Himmel, D.; Scherer, H.; Kratzert, D.; Krossing, I. *Z. Anorg. Allg. Chem.* **2015**, *641*, 655–659.
77. Garcia, L.; Anker, M. D.; Mahon, M. F.; Maron, L.; Hill, M. S. *Dalton Trans.* **2018**, *47*, 12684–12693.
78. Pahl, J.; Brand, S.; Elsen, H.; Harder, S. *Chem. Commun.* **2018**, *54*, 8685–8688.
79. Thum, K.; Pahl, J.; Eyslein, J.; Elsen, H.; Langer, J.; Harder, S. *Chem. Commun.* **2021**, *57*, 5278–5281.
80. Garcia, L.; Mahon, M. F.; Hill, M. S. *Organometallics* **2019**, *38*, 3778–3785.
81. Petersen, T. O.; Tausch, E.; Schaefer, J.; Scherer, H.; Roesky, P. W.; Krossing, I. *Chem. A Eur. J.* **2015**, *21*, 13696–13702.
82. Petersen, T. O.; Simone, D.; Krossing, I. *Chem. A Eur. J.* **2016**, *22*, 15847–15855.
83. Wehmschulte, R. J.; Wojtas, L. *Inorg. Chem.* **2011**, *50*, 11300–11302.
84. Schulz, S.; Schuchmann, D.; Krossing, I.; Himmel, D.; Blaser, D.; Boese, R. *Angew. Chem. Int. Ed. Engl.* **2009**, *48*, 5748–5751.
85. Schnurr, A.; Vitze, H.; Bolte, M.; Lerner, H.-W.; Wagner, M. *Organometallics* **2010**, *29*, 6012–6019.
86. Heitkemper, T.; Sindlinger, C. P. *Chem. A Eur. J.* **2020**, *26*, 11684–11689.
87. Shih, D.-N.; Boobalan, R.; Liu, Y.-H.; Chein, R.-J.; Chiu, C.-W. *Inorg. Chem.* **2021**, *60*, 16266–16272.
88. Huang, J.-S.; Lee, W.-H.; Shen, C.-T.; Lin, Y.-F.; Liu, Y.-H.; Peng, S.-M.; Chiu, C.-W. *Inorg. Chem.* **2016**, *55*, 12427–12434.
89. Chen, J.; Lalancette, R. A.; Jäkle, F. *Chem. Commun.* **2013**, *49*, 4893–4895.
90. Chen, P.-H.; Hsu, C.-P.; Tseng, H.-C.; Liu, Y.-H.; Chiu, C.-W. *Chem. Commun.* **2021**, *57*, 13732–13735.
91. Wang, B.; Li, Y.; Ganguly, R.; Webster, R. D.; Kinjo, R. *Angew. Chem. Int. Ed.* **2018**, *57*, 7826–7829.
92. Xie, X.; Adams, C. J.; Al-Ibadi, M. A. M.; McGrady, J. E.; Norman, N. C.; Russell, C. A. *Chem. Commun.* **2013**, *49*, 10364–10366.
93. Budanow, A.; Bolte, M.; Wagner, M. CCDC 2159287: Experimental Crystal Structure Determination. CCDC.
94. Adams, G. M.; Ryan, D. E.; Beattie, N. A.; McKay, A. I.; Lloyd-Jones, G. C.; Weller, A. S. *ACS Catal.* **2019**, *9*, 3657–3666.
95. Braunschweig, H.; Radacki, K.; Schneider, A. *Angew. Chem. Int. Ed.* **2010**, *49*, 5993–5996.
96. Colebatch, A. L.; McKay, A. I.; Beattie, N. A.; Macgregor, S. A.; Weller, A. S. *Eur. J. Inorg. Chem.* **2017**, *2017*, 4533–4540.
97. Huber, M.; Kurek, A.; Krossing, I.; Mühlaupt, R.; Schnöckel, H. *Z. Anorg. Allg. Chem.* **2009**, *635*, 1787–1793.
98. Bochmann, M.; Dawson, D. M. *Angew. Chem. Int. Ed.* **1996**, *35*, 2226–2228.
99. Hsu, C.-P.; Liu, Y.-H.; Boobalan, R.; Lin, Y.-F.; Chein, R.-J.; Chiu, C.-W. *Organometallics* **2021**, *40*, 1244–1251.
100. Franz, D.; Jandl, C.; Stark, C.; Inoue, S. *ChemCatChem* **2019**, *11*, 5275–5281.
101. Young, J. D.; Khan, M. A.; Powell, D. R.; Wehmschulte, R. J. *Eur. J. Inorg. Chem.* **2007**, *2007*, 1671–1681.
102. Wehmschulte, R. J.; Steele, J. M.; Young, J. D.; Khan, M. A. *J. Am. Chem. Soc.* **2003**, *125*, 1470–1471.
103. Budanow, A.; Sinke, T.; Tillmann, J.; Bolte, M.; Wagner, M.; Lerner, H. W. *Organometallics* **2012**, *31*, 7298–7301.
104. Wiberg, N.; Amelunxen, K.; Lerner, H.-W.; Nth, H.; Appel, A.; Knizek, J.; Polborn, K. *Z. Anorg. Allg. Chem.* **1997**, *623*, 1861–1870.
105. Lerner, H.-W.; Scholz, S.; Bolte, M. *Organometallics* **2001**, *20*, 575–577.
106. Li, Z.; Thiery, G.; Lichtenthaler, M. R.; Guillot, R.; Krossing, I.; Gandon, V.; Bour, C. *Adv. Synth. Catal.* **2018**, *360*, 544–549.
107. Glootz, K.; Kratzert, D.; Himmel, D.; Kastro, A.; Yassine, Z.; Findeisen, T.; Krossing, I. *Angew. Chem. Int. Ed.* **2018**, *57*, 14203–14206.
108. Lichtenthaler, M. R.; Stahl, F.; Kratzert, D.; Heidinger, L.; Schleicher, E.; Hamann, J.; Himmel, D.; Weber, S.; Krossing, I. *Nat. Commun.* **2015**, *6*, 8288.
109. Riesinger, C.; Balázs, G.; Seidl, M.; Scheer, M. *Chem. Sci.* **2021**, *12*, 13037–13044.
110. Caise, A.; Abdalla, J. A. B.; Tirfoin, R.; Edwards, A. J.; Aldridge, S. *Chem. A Eur. J.* **2017**, *23*, 16906–16913.
111. Abdalla, J. A. B.; Caise, A.; Sindlinger, C. P.; Tirfoin, R.; Thompson, A. L.; Edwards, A. J.; Aldridge, S. *Nat. Chem.* **2017**, *9*, 1256–1262.
112. Li, B.; Wölper, C.; Haberhauer, G.; Schulz, S. *Angew. Chem. Int. Ed.* **2021**, *60*, 1986–1991.
113. Krüger, J.; Wölper, C.; Haberhauer, G.; Schulz, S. *Inorg. Chem.* **2022**, *61*, 597–604.
114. Higelin, A.; Haber, C.; Meier, S.; Krossing, I. *Dalton Trans.* **2012**, *41*, 12011–12015.
115. Higelin, A.; Meier, S.; Krossing, I. CCDC 912610: Experimental Crystal Structure Determination. CCDC.
116. Downs, A. J. *Chemistry of Aluminium, Gallium, Indium and Thallium*, 1st ed.; Blackie Academic & Professional, 1993.
117. Greenwood, N. N.; Earnshaw, A. *Chemistry of the Elements*, 2nd ed.; Elsevier, 1997.
118. Wilkinson, M.; Worrall, I. J. *J. Organomet. Chem.* **1975**, *93*, 39–42.
119. Green, M. L.; Mountford, P.; Smout, G. J.; Speel, S. *Polyhedron* **1990**, *9*, 2763–2765.
120. Garton, G.; Powell, H. M. *J. Inorg. Nucl. Chem.* **1957**, *4*, 84–89.
121. Gerlach, G.; Hönl, W.; Simon, A. *Z. Anorg. Allg. Chem.* **1982**, *486*, 7–21.
122. Hönl, W.; Simon, A.; Gerlach, G. *Z. Naturforsch. B* **1987**, *42*, 546–552.
123. Baker, R. J.; Jones, C. *Dalton Trans.* **2005**, 1341–1348.
124. Dabringhaus, P.; Barthélemy, A.; Krossing, I. *Z. Anorg. Allg. Chem.* **2021**.
125. Schmidbaur, H. *Angew. Chem. Int. Ed.* **1985**, *24*, 893–904.
126. Bondi, A. J. *Phys. Chem.* **1964**, *68*, 441–451.
127. Lichtenthaler, M. R.; Maurer, S.; Mangan, R. J.; Stahl, F.; Mönkemeyer, F.; Hamann, J.; Krossing, I. *Chem. A Eur. J.* **2015**, *21*, 157–165.
128. Lichtenthaler, M. R.; Higelin, A.; Kraft, A.; Hughes, S.; Steffani, A.; Plattner, D. A.; Slattery, J. M.; Krossing, I. *Organometallics* **2013**, *32*, 6725–6735.
129. Lichtenthaler, M. R.; Stahl, F.; Kratzert, D.; Benkmlil, B.; Wegner, H. A.; Krossing, I. *Eur. J. Inorg. Chem.* **2014**, *2014*, 4335–4341.
130. Glootz, K.; Kratzert, D.; Krossing, I. *Z. Anorg. Allg. Chem.* **2020**, *646*, 523–525.
131. Higelin, A.; Keller, S.; Göhringer, C.; Jones, C.; Krossing, I. *Angew. Chem. Int. Ed.* **2013**, *52*, 4941–4944.
132. Glootz, K.; Barthélemy, A.; Krossing, I. *Angew. Chem. Int. Ed.* **2021**, *60*, 208–211.



133. Schorpp, M.; Krossing, I. *Chem. A Eur. J.* **2020**, *26*, 14109–14117.
134. Fleischmann, M.; Welsch, S.; Krauss, H.; Schmidt, M.; Bodensteiner, M.; Peresyphina, E. V.; Sierka, M.; Gröger, C.; Scheer, M. *Chem. A Eur. J.* **2014**, *20*, 3759–3768.
135. Welsch, S.; Gregoriades, L. J.; Sierka, M.; Zabel, M.; Virovets, A. V.; Scheer, M. *Angew. Chem. Int. Ed.* **2007**, *46*, 9323–9326.
136. Fleischmann, M.; Welsch, S.; Gregoriades, L. J.; Gröger, C.; Scheer, M. *Z. Naturforsch. B* **2014**, *69*, 1348–1356.
137. Weis, P.; Röhner, D. C.; Prediger, R.; Butschke, B.; Scherer, H.; Weber, S.; Krossing, I. *Chem. Sci.* **2019**, *10*, 10779–10788.
138. Fleischmann, M.; Dielmann, F.; Gregoriades, L. J.; Peresyphina, E. V.; Virovets, A. V.; Huber, S.; Timoshkin, A. Y.; Balázs, G.; Scheer, M. *Angew. Chem. Int. Ed.* **2015**, *54*, 13110–13115.
139. Gonsior, M.; Krossing, I.; Mitzel, N. *Z. Anorg. Allg. Chem.* **1821**, 2002, 628.
140. Welsch, S.; Lescop, C.; Réau, R.; Scheer, M. *Dalton Trans.* **2009**, 2683–2686.
141. Beachley, O. T.; Blom, R.; Churchill, M. R.; Faegri, K.; Fetting, J. C.; Pazik, J. C.; Victoriano, L. *Organometallics* **1989**, *8*, 346–356.
142. Uhl, W.; Hiller, W.; Layh, M.; Schwarz, W. *Angew. Chem. Int. Ed.* **1992**, *31*, 1364–1366.
143. Schluter, R. D.; Cowley, A. H.; Atwood, D. A.; Jones, R. A.; Atwood, J. L. *J. Coord. Chem.* **1993**, *30*, 25–28.
144. Brothers, P. J.; Hübler, K.; Hübler, U.; Noll, B. C.; Olmstead, M. M.; Power, P. P. *Angew. Chem. Int. Ed.* **1996**, *35*, 2355–2357.
145. Uhl, W.; Jantschak, A.; Saak, W.; Kaupp, M.; Warchow, R. *Organometallics* **1998**, *17*, 5009–5017.
146. Wiberg, N. *J. Organomet. Chem.* **1999**, *574*, 246–251.
147. Wiberg, N.; Blank, T.; Purath, A.; Stöber, G.; Schnöckel, H. *Angew. Chem. Int. Ed.* **1999**, *38*, 2563–2565.
148. Schnepf, A.; Stösser, G.; Schnöckel, H. *J. Am. Chem. Soc.* **2000**, *122*, 9178–9181.
149. Schnepf, A.; Stöber, G.; Köppe, R.; Schnöckel, H. *Angew. Chem. Int. Ed.* **2000**, *39*, 1637–1639.
150. Schnepf, A.; Schnöckel, H. *Angew. Chem. Int. Ed.* **2001**, *40*, 711–715.
151. Donchev, A.; Schnepf, A.; Baum, E.; Stöber, G.; Schnöckel, H. *Z. Anorg. Allg. Chem.* **2002**, *628*, 157–161.
152. Protchenko, A. V.; Urbano, J.; Abdalla, J. A. B.; Campos, J.; Vidovic, D.; Schwarz, A. D.; Blake, M. P.; Mountford, P.; Jones, C.; Aldridge, S. *Angew. Chem. Int. Ed.* **2017**, *56*, 15098–15102.
153. Barthélemy, A.; Scherer, H.; Krossing, I. *Chem. A Eur. J.* **2022**.
154. Gloetz, K.; Himmel, D.; Kratzert, D.; Butschke, B.; Scherer, H.; Krossing, I. *Angew. Chem. Int. Ed.* **2019**, *58*, 14162–14166.
155. Gonsior, M.; Krossing, I. *Chem.-Eur. J.* **2004**, *10*, 5730–5736.
156. Krossing, I.; Bihlmeier, A.; Raabe, I.; Trapp, N. *Angew. Chem. Int. Ed. Engl.* **2003**, *42*, 1531–1534.
157. Raabe, I.; Himmel, D.; Mueller, S.; Trapp, N.; Kaupp, M.; Krossing, I. *Dalton Trans.* **2008**, 946–956.
158. Raabe, I.; Rohr, C.; Krossing, I. *Dalton Trans.* **2007**, 5376–5386.
159. Lehner, A. J.; Trapp, N.; Scherer, H.; Krossing, I. *Dalton Trans.* **2011**, *40*, 1448–1452.
160. Raabe, I.; Himmel, D.; Krossing, I. *J. Phys. Chem. A* **2007**, *111*, 13209–13217.
161. Santiso-Quiniones, G.; Krossing, I. *Z. Anorg. Allg. Chem.* **2008**, *634*, 704–707.
162. Krossing, I.; Raabe, I. *J. Am. Chem. Soc.* **2004**, *126*, 7571–7577.
163. Hermann, M.; Böttcher, T.; Schorpp, M.; Richert, S.; Wassy, D.; Krossing, I.; Esser, B. *Chem.-Eur. J.* **2021**, *27*, 4964–4970.
164. Berger, R. J. F.; Fuchter, M. J.; Krossing, I.; Rzepa, H. S.; Schaefer, J.; Scherer, H. *Chem. Commun.* **2014**, *50*, 5251–5253.
165. Rohde, M.; Mueller, L. O.; Himmel, D.; Scherer, H.; Krossing, I. *Chem. A Eur. J.* **2014**, *20*, 1218–1222.
166. Reed, C. A. *Acc. Chem. Res.* **1998**, *31*, 325–332.
167. Schenk, C.; Drost, C.; Schnepf, A. *Dalton Trans.* **2009**, 773–776.
168. Nechaev, M. S.; Chernov, O. V.; Portnyagin, I. A.; Khrustalev, V. N.; Aysin, R. R.; Lunin, V. V. *J. Organomet. Chem.* **2010**, *695*, 365–369.
169. Chen, J.; Lalancette, R. A.; Jäkle, F. *Organometallics* **2013**, *32*, 5843–5851.
170. Sapsford, J. S.; Csókás, D.; Scott, D. J.; Turnell-Ritson, R. C.; Piascik, A. D.; Pápai, I.; Ashley, A. E. *ACS Catal.* **2020**, *10*, 7573–7583.
171. Schleep, M.; Hettlich, C.; Velazquez Rojas, J.; Kratzert, D.; Ludwig, T.; Lieberth, K.; Krossing, I. *Angew. Chem. Int. Ed. Engl.* **2017**, *56*, 2880–2884.
172. Do, D. C. H.; Protchenko, A. V.; Fuentes, M.Á.; Hicks, J.; Vasko, P.; Aldridge, S. *Chem. Commun.* **2020**, *56*, 4684–4687.
173. Zhou, X.; Vasko, P.; Hicks, J.; Fuentes, M.Á.; Heilmann, A.; Kolychev, E. L.; Aldridge, S. *Dalton Trans.* **2020**, *49*, 9495–9504.
174. Mangan, R. J.; Davies, A. R.; Hicks, J.; Sindlinger, C. P.; Thompson, A. L.; Aldridge, S. *Polyhedron* **2021**, *196*, 115006.
175. Li, J.; Schenk, C.; Winter, F.; Scherer, H.; Trapp, N.; Higelin, A.; Keller, S.; Poettgen, R.; Krossing, I.; Jones, C. *Angew. Chem. Int. Ed.* **2012**, *51*, 9557–9561.
176. Diab, F.; Aicher, F. S. W.; Sindlinger, C. P.; Eichele, K.; Schubert, H.; Wesemann, L. *Chem. A Eur. J.* **2019**, *25*, 4426–4434.
177. Hinz, A. *Chem. A Eur. J.* **2019**, *25*, 3267–3271.
178. Hinz, A. *Angew. Chem. Int. Ed. Engl.* **2020**, *59*, 19065–19069.
179. Engesser, T. A.; Krossing, I. *Coord. Chem. Rev.* **2013**, *257*, 946–955.
180. Koehnert, T.; Engesser, T. A.; Scherer, H.; Plattner, D. A.; Steffani, A.; Krossing, I. *Angew. Chem. Int. Ed. Engl.* **2012**, *51*, 6529–6531. S6529/1–S6529/16.
181. Frötschel-Rittmeyer, J.; Holthausen, M.; Friedmann, C.; Röhner, D.; Krossing, I.; Weigand, J. *J. Sci. Adv.* **2022**, *8*, eabq8613. <https://doi.org/10.1126/sciadv.abq8613>.
182. Fish, C.; Green, M.; Jeffery, J. C.; Kilby, R. J.; Lynam, J. M.; McGrady, J. E.; Pantazis, D. A.; Russell, C. A.; Willans, C. E. *Chem. Commun.* **2006**, 1375–1377.
183. Slattery, J. M.; Fish, C.; Green, M.; Hooper, T. N.; Jeffery, J. C.; Kilby, R. J.; Lynam, J. M.; McGrady, J. E.; Pantazis, D. A.; Russell, C. A.; Willans, C. E. *Chem. A Eur. J.* **2007**, *13*, 6967–6974.
184. Engesser, T. A.; Transue, W. J.; Weis, P.; Cummins, C. C.; Krossing, I. *Eur. J. Inorg. Chem.* **2019**, *2019*, 2607–2612.
185. Pan, X.; Chen, X.; Li, T.; Li, Y.; Wang, X. *J. Am. Chem. Soc.* **2013**, *135*, 3414–3417.
186. Pan, X.; Su, Y.; Chen, X.; Zhao, Y.; Li, Y.; Zuo, J.; Wang, X. *J. Am. Chem. Soc.* **2013**, *135*, 5561–5564.
187. Su, Y.; Zheng, X.; Wang, X.; Zhang, X.; Sui, Y.; Wang, X. *J. Am. Chem. Soc.* **2014**, *136*, 6251–6254.
188. Reiss, F.; Schulz, A.; Villinger, A. *Eur. J. Inorg. Chem.* **2012**, 261–271.
189. Pan, X.; Wang, X.; Zhang, Z.; Wang, X. *Dalton Trans.* **2015**, *44*, 15099–15102.
190. Roth, D.; Stirn, J.; Stephan, D. W.; Greb, L. *J. Am. Chem. Soc.* **2021**, *143*, 15845–15851.
191. Baxter, S. G.; Cowley, A. H.; Mehrotra, S. K. *J. Am. Chem. Soc.* **1981**, *103*, 5572–5573.
192. Jutzi, P.; Wippermann, T.; Kruger, C.; Kraus, H. *J. Angew. Chem. Int. Ed.* **1983**, *22*, 250.
193. Sitzmann, H.; Wolmershäuser, G.; Boese, R.; Bläser, D. *Z. Anorg. Allg. Chem.* **1999**, *625*, 2103–2107.
194. Kraft, A.; Beck, J.; Krossing, I. *Chem. A Eur. J.* **2011**, *17*, 12975–12980.
195. Heini, V.; Balázs, G.; Seidl, M.; Scheer, M. *Chem. Commun.* **2022**, *58*, 2484–2487.
196. Izod, K.; Evans, P.; Waddell, P. G. *Angew. Chem. Int. Ed. Engl.* **2019**, *58*, 11007–11012.
197. Hering-Junghans, C.; Thomas, M.; Villinger, A.; Schulz, A. *Chem. A Eur. J.* **2015**, *21*, 6713–6717.
198. Christian, B. H.; Gillespie, R. J.; Sawyer, J. F. *Inorg. Chem.* **1981**, *20*, 3410–3420.
199. Weis, P.; Kratzert, D.; Krossing, I. *Eur. J. Inorg. Chem.* **2018**, *2018*, 3203–3212.
200. Yang, W.; Wang, W.; Zhang, L.; Zhang, L.; Ruan, H.; Feng, Z.; Fang, Y.; Wang, X. *Chem. Commun.* **2021**, *57*, 5067–5070.
201. Gonsior, M.; Krossing, I.; Müller, L.; Raabe, I.; Jansen, M.; van Wullen, L. *Chem. A Eur. J.* **2002**, *8*, 4475–4492.
202. Krossing, I.; Raabe, I. *Angew. Chem. Int. Ed. Engl.* **2001**, *40*, 4406.

203. Krossing, I. *Dalton Trans.* **2002**, 500–512.
204. Aubauer, C.; Engelhardt, G.; Klapötke, T. M.; Schulz, A. J. *Chem. Soc., Dalton Trans.* **1999**, 1729–1734.
205. Gonsior, M.; Krossing, I.; Matern, E. *Chem.-Eur. J.* **2006**, *12*, 1703–1714.
206. Gonsior, M.; Krossing, I. *Dalton Trans.* **2005**, 1203–1213.
207. Gonsior, M.; Krossing, I. *Dalton Trans.* **2005**, 2022–2030.
208. Haupt, S.; Seppelt, K. Z. *Anorg. Allg. Chem.* **2002**, *628*, 729.
209. Aubauer, C.; Kaupp, M.; Klapötke, T. M.; Nöth, H.; Piotrowski, H.; Schnick, W.; Senker, J.; Suter, M. *Dalton Trans.* **2001**, 1880–1889.
210. Donath, M.; Hennesdorf, F.; Weigand, J. J. *Chem. Soc. Rev.* **2016**, *45*, 1145–1172.
211. Holthausen, M. H.; Weigand, J. J. *Chem. Soc. Rev.* **2014**, *43*, 6639–6657.
212. Gonsior, M.; Krossing, I.; Matern, E. *Chem.-Eur. J.* **2006**, *12*, 1986–1996.
213. Kuprat, M.; Kuzora, R.; Lehmann, M.; Schulz, A.; Villinger, A.; Wustrack, R. J. *Organomet. Chem.* **2010**, *695*, 1006–1011.
214. Gerding, H.; Houtgraaf, H. *Recl. Trav. Chim. Pays-Bas* **1954**, *73*, 737–747.
215. Engesser, T. A.; Hrobarik, P.; Trapp, N.; Eiden, P.; Scherer, H.; Kaupp, M.; Krossing, I. *ChemPlusChem* **2012**, *77*, 643–651.
216. Weis, P.; Scherer, H.; Krossing, I. *Z. Anorg. Allg. Chem.* **2019**, *645*, 64–71.
217. Chen, X.; Ma, B.; Chen, S.; Li, Y.; Huang, W.; Ma, J.; Wang, X. *Chem. Asian J.* **2013**, *8*, 238–243.
218. Gao, F.; Zhu, F.-F.; Wang, X.-Y.; Xu, Y.; Wang, X.-P.; Zuo, J.-L. *Inorg. Chem.* **2014**, *53*, 5321–5327.
219. Li, X.; Liu, Y.-H.; Zhu, G.-Z.; Gao, F. *New J. Chem.* **2020**, *44*, 16959–16964.
220. Yuan, N.; Zhang, Z.; Wang, X.; Wang, X. *Chem. Commun.* **2015**, *51*, 16714–16717.
221. Zhang, S.; Wang, X.; Sui, Y.; Wang, X. *J. Am. Chem. Soc.* **2014**, *136*, 14666–14669.
222. Yang, W.; Zhang, L.; Xiao, D.; Feng, R.; Wang, W.; Pan, S.; Zhao, Y.; Zhao, L.; Frenking, G.; Wang, X. *Nat Comms* **2020**, *11*, 3441.
223. Tang, S.; Zhang, L.; Ruan, H.; Zhao, Y.; Wang, X. *J. Am. Chem. Soc.* **2020**, *142*, 7340–7344.
224. Tang, S.; Ruan, H.; Hu, Z.; Zhao, Y.; Song, Y.; Wang, X. *Chem. Commun.* **2022**, *58*, 1986–1989.
225. Errulat, D.; Gabidullin, B.; Mansikkamäki, A.; Murugesu, M. *Chem. Commun.* **2020**, *56*, 5937–5940.
226. Evans, P.; Reta, D.; Goodwin, C. A. P.; Ortu, F.; Chilton, N. F.; Mills, D. P. *Chem. Commun.* **2020**, *56*, 5677–5680.
227. Evans, P.; Reta, D.; Whitehead, G. F. S.; Chilton, N. F.; Mills, D. P. *J. Am. Chem. Soc.* **2019**, *141*, 19935–19940.
228. Riedhammer, J.; Aguilar-Caldéron, J. R.; Miehlisch, M.; Halter, D. P.; Munz, D.; Heinemann, F. W.; Fortier, S.; Meyer, K.; Mendiola, D. J. *Inorg. Chem.* **2020**, *59*, 2443–2449.
229. Krossing, I. *J. Am. Chem. Soc.* **2001**, *123*, 4603–4604.
230. Krossing, I.; van Wullen, L. *Chem. A Eur. J.* **2002**, *8*, 700–711.
231. Reisinger, A.; Trapp, N.; Knapp, C.; Himmel, D.; Breher, F.; Ruegger, H.; Krossing, I. *Chem. A Eur. J.* **2009**, *15*, 9505–9520. S9505/1–S9505/69.
232. Guo, B. C.; Castleman, A. W. *Chem. Phys. Lett.* **1991**, *181*, 16–20.
233. Deng, H.; Kebarle, P. *J. Phys. Chem. A* **1998**, *102*, 571–579.
234. Krossing, I.; Reisinger, A. *Angew. Chem. Int. Ed. Engl.* **2003**, *42*, 5725–5728.
235. Schaefer, J.; Himmel, D.; Krossing, I. *Eur. J. Inorg. Chem.* **2013**, 2712–2717.
236. Santiso-Quinones, G.; Reisinger, A.; Slattery, J.; Krossing, I. *Chem. Commun.* **2007**, 5046–5048.
237. Chernyshova, E. S.; Goddard, R.; Pörschke, K.-R. *Organometallics* **2007**, *26*, 4872–4880.
238. Schwab, M. M.; Himmel, D.; Kacprzak, S.; Kratzert, D.; Radtke, V.; Weis, P.; Ray, K.; Scheidt, E.-W.; Scherer, W.; de Bruin, B.; Weber, S.; Krossing, I. *Angew. Chem. Int. Ed.* **2015**, *54*, 14706–14709.
239. Schwab, M. M.; Himmel, D.; Kacprzak, S.; Radtke, V.; Kratzert, D.; Weis, P.; Wernet, M.; Peter, A.; Yassine, Z.; Schmitz, D.; Scheidt, E.-W.; Scherer, W.; Weber, S.; Feuerstein, W.; Breher, F.; Higelin, A.; Krossing, I. *Chem. A Eur. J.* **2018**, *24*, 918–927.
240. Schwab, M. M.; Himmel, D.; Kacprzak, S.; Radtke, V.; Kratzert, D.; Yassine, Z.; Weis, P.; Weber, S.; Krossing, I. *Z. Anorg. Allg. Chem.* **2018**, *644*, 50–57.
241. Reisinger, A.; Trapp, N.; Krossing, I.; Altmannshofer, S.; Herz, V.; Presnitz, M.; Scherer, W. *Angew. Chem. Int. Ed. Engl.* **2007**, *46*, 8295–8298.
242. Cameron, T. S.; Decken, A.; Dionne, I.; Fang, M.; Krossing, I.; Passmore, J. *Chem. A Eur. J.* **2002**, *8*, 3386–3401.
243. Mond, L.; Langer, C.; Quincke, F. *J. Chem. Soc. Trans.* **1890**, *57*, 749–753.
244. Chatt, J.; Duncanson, L. A. *J. Chem. Soc.* **1953**, 2939.
245. Frenking, G. *J. Organomet. Chem.* **2001**, *635*, 9–23.
246. Frenking, G.; Loschen, C.; Krapp, A.; Fau, S.; Strauss, S. H. *J. Comput. Chem.* **2007**, *28*, 117–126.
247. Willner, H.; Aubke, F. *Angew. Chem. Int. Ed.* **1997**, *36*, 2403–2425.
248. Bistoni, G.; Rampino, S.; Scafuri, N.; Ciancaleoni, G.; Zuccaccia, D.; Belpassi, L.; Tarantelli, F. *Chem. Sci.* **2016**, *7*, 1174–1184.
249. Xu, Q. *Coord. Chem. Rev.* **2002**, *231*, 83–108.
250. Willner, H.; Schaeb, J.; Hwang, G.; Mistry, F.; Jones, R.; Trotter, J.; Aubke, F. *J. Am. Chem. Soc.* **1992**, *114*, 8972–8980.
251. Willner, H.; Bodenbinder, M.; Bröchlner, R.; Hwang, G.; Rettig, S. J.; Trotter, J.; von Ahsen, B.; Westphal, U.; Jonas, V.; Thiel, W.; Aubke, F. *J. Am. Chem. Soc.* **2001**, *123*, 588–602.
252. Bernhardt, E.; Finze, M.; Willner, H.; Lehmann, C. W.; Aubke, F. *Angew. Chem. Int. Ed.* **2003**, *42*, 2077–2079.
253. Bley, B.; Willner, H.; Aubke, F. *Inorg. Chem.* **1997**, *36*, 158–160.
254. Willner, H.; Aubke, F. *Chem. A Eur. J.* **2003**, *9*, 1668–1676.
255. Willner, H.; Aubke, F. *Organometallics* **2003**, *22*, 3612–3633.
256. Schaefer, J.; Kraft, A.; Reisinger, S.; Santiso-Quinones, G.; Himmel, D.; Trapp, N.; Gellrich, U.; Breit, B.; Krossing, I. *Chem. A Eur. J.* **2013**, *19*, 12468–12485.
257. Meier, S. C.; Himmel, D.; Krossing, I. *Chem. A Eur. J.* **2018**, *24*, 19348–19360.
258. Unkrig, W.; Schmitt, M.; Kratzert, D.; Himmel, D.; Krossing, I. *Nat. Chem.* **2020**, *12*, 647–653.
259. Bohnenberger, J.; Feuerstein, W.; Himmel, D.; Daub, M.; Breher, F.; Krossing, I. *Nat. Comms* **2019**, *10*, 624.
260. Bohnenberger, J.; Schmitt, M.; Feuerstein, W.; Krummenacher, I.; Butschke, B.; Czajka, J.; Malinowski, P. J.; Breher, F.; Krossing, I. *Chem. Sci.* **2020**, *11*, 3592–3603.
261. Schmitt, M.; Mayländer, M.; Goost, J.; Richert, S.; Krossing, I. *Angew. Chem. Int. Ed. Engl.* **2021**, *60*, 14800–14805.
262. Bauer, J.; Braunschweig, H.; Dewhurst, R. D. *Chem. Rev.* **2012**, *112*, 4329–4346.
263. Malinowski, P. J.; Krossing, I. *Angew. Chem. Int. Ed.* **2014**, *53*, 13460–13462.
264. Wang, G.; Ceylan, Y. S.; Cundari, T. R.; Dias, H. V. R. *J. Am. Chem. Soc.* **2017**, *139*, 14292–14301.
265. Pan, S.; Gorantla, S. M. N. V. T.; Parasar, D.; Dias, H. V. R.; Frenking, G. *Chem. A Eur. J.* **2021**, *27*, 6936–6944.
266. Krossing, I.; Frenking, G.; Kratzert, D.; Bohnenberger, J.; Gorantla, S. M. N. V. T.; Pan, S. *Chem. A Eur. J.* **2020**.
267. Unkrig, W.; Kloiber, K.; Krossing, I.; Butschke, B.; Kratzert, D. *Chem. A Eur. J.* **2020**.
268. Klein, J. E. M. N.; Miehlisch, B.; Holzwarth, M. S.; Bauer, M.; Milek, M.; Khusniyarov, M. M.; Knizia, G.; Werner, H.-J.; Plietker, B. *Angew. Chem. Int. Ed. Engl.* **2014**, *53*, 1790–1794.
269. Ampßler, T.; Monsch, G.; Popp, J.; Riggermann, T.; Salvador, P.; Schröder, D.; Klüfers, P. *Angew. Chem. Int. Ed. Engl.* **2020**, *59*, 12381–12386.
270. Bohnenberger, J.; Krossing, I. *Angew. Chem. Int. Ed.* **2020**, *59*, 5581–5585.
271. Hieber, W.; Beutner, K. Z. *Naturforsch. B* **1960**, 323.

272. Anderson, J. S.; Hieber, W.; Mitarbeitern, Z. *Anorg. Allg. Chem.* **1932**, *208*, 238–248.
273. Bohnenberger, J.; Derstine, B.; Daub, M.; Krossing, I. *Angew. Chem. Int. Ed. Engl.* **2019**, *58*, 9586–9589.
274. Gyton, M. R.; Leforestier, B.; Chaplin, A. B. *Angew. Chem. Int. Ed. Engl.* **2019**, *58*, 15295–15298.
275. Zhuravlev, V.; Malinowski, P. J. *Angew. Chem. Int. Ed. Engl.* **2018**, *57*, 11697–11700.
276. Piro, N. A.; Lichterman, M. F.; Harman, W. H.; Chang, C. J. *J. Am. Chem. Soc.* **2011**, *133*, 2108–2111.
277. Meier, S. C.; Holz, A.; Schmidt, A.; Kratzert, D.; Himmel, D.; Krossing, I. *Chem. A Eur. J.* **2017**, *23*, 14658–14664.
278. Unkrig, W.; Zhe, F.; Tamim, R.; Oesten, F.; Kratzert, D.; Krossing, I. *Chem. A Eur. J.* **2021**, *27*, 758–765.
279. Tai, H.-C.; Krossing, I.; Seth, M.; Deubel, D. V. *Organometallics* **2004**, *23*, 2343–2349.
280. Forfar, L. C.; Clark, T. J.; Green, M.; Mansell, S. M.; Russell, C. A.; Sanguramath, R. A.; Slattery, J. M. *Chem. Commun.* **2012**, *48*, 1970–1972.
281. Borger, J. E.; Bakker, M. S.; Ehlers, A. W.; Lutz, M.; Sloatweg, J. C.; Lammertsma, K. *Chem. Commun.* **2016**, *52*, 3284–3287.
282. Riddlestone, I. M.; Weis, P.; Martens, A.; Schorpp, M.; Scherer, H.; Krossing, I. *Chem. A Eur. J.* **2019**, *25*, 10546–10551.
283. Schwarzmaier, C.; Sierka, M.; Scheer, M. *Angew. Chem. Int. Ed. Engl.* **2013**, *52*, 858–861.
284. Schwarzmaier, C.; Timoshkin, A. Y.; Scheer, M. *Angew. Chem. Int. Ed. Engl.* **2013**, *52*, 7600–7603.
285. Dance, I.; Fisher, K.; Willett, G. *Angew. Chem. Int. Ed. Engl.* **1995**, *34*, 201–203.
286. Dance, I. G.; Fisher, K. J.; Willett, G. D. *Inorg. Chem.* **1996**, *35*, 4177–4184.
287. Roesky, H. W.; Thomas, M.; Schimkowiak, J.; Jones, P. G.; Pinkert, W.; Sheldrick, G. M. *J. Chem. Soc.-Chem. Commun.* **1982**, 895–896.
288. Santiso-Quinones, G.; Bruckner, R.; Knapp, C.; Dionne, I.; Passmore, J.; Krossing, I. *Angew. Chem. Int. Ed. Engl.* **2009**, *48*, 1133–1137.
289. Aris, D.; Beck, J.; Decken, A.; Dionne, I.; Schmedt auf der Günne, J.; Hoffbauer, W.; Köchner, T.; Krossing, I.; Passmore, J.; Rivard, E.; Steden, F.; Wang, X. *Dalton Trans.* **2011**, *40*, 5865–5880.
290. Aris, D.; Beck, J.; Decken, A.; Dionne, I.; Krossing, I.; Passmore, J.; Rivard, E.; Steden, F.; Wang, X. P. *Phosphorus, Sulfur Silicon Relat. Elem.* **2004**, *179*, 859–863.
291. Köchner, T.; Trapp, N.; Engesser, T. A.; Lehner, A. J.; Röhr, C.; Riedel, S.; Knapp, C.; Scherer, H.; Krossing, I. *Angew. Chem. Int. Ed.* **2011**, *50*, 11253–11256.
292. Schaefer, J.; Steffani, A.; Plattner, D. A.; Krossing, I. *Angew. Chem. Int. Ed. Engl.* **2012**, *51*, 6009–6012.
293. Di Vaira, M.; Peruzzini, M.; Stoppioni, P. *Inorg. Chem.* **1983**, *22*, 2196–2198.
294. Aubauer, C.; Irran, E.; Klapötke, T. M.; Schnick, W.; Schulz, A.; Senker, J. *Inorg. Chem.* **2001**, *40*, 4956–4965.
295. Cordes, A. W.; Joyner, R. D.; Shores, R. D.; Dill, E. D. *Inorg. Chem.* **1974**, *13*, 132–134.
296. Di Vaira, M.; Stoppioni, P. *Coord. Chem. Rev.* **1992**, *120*, 259–279.
297. Scherer, O. J. *Chemie in Unserer Zeit* **2000**, *34*, 374–381.
298. Adolf, A.; Gonsior, M.; Krossing, I. *J. Am. Chem. Soc.* **2002**, *124*, 7111–7116.
299. Weis, P.; Hettich, C.; Kratzert, D.; Krossing, I. *Eur. J. Inorg. Chem.* **2019**, *2019*, 1657–1668.
300. Scheer, M.; Gregoriades, L. J.; Zabel, M.; Bai, J.; Krossing, I.; Brunklaus, G.; Eckert, H. *Chem.-Eur. J.* **2008**, *14*, 282–295.
301. Attenberger, B.; Peresykina, E. V.; Scheer, M. *Inorg. Chem.* **2015**, *54*, 7021–7029.
302. Fleischmann, M.; Welsch, S.; Peresykina, E. V.; Virovets, A. V.; Scheer, M. *Chem. A Eur. J.* **2015**, *21*, 14332–14336.
303. Elsayed Moussa, M.; Shelyanov, P. A.; Seidl, M.; Peresykina, E.; Berg, N.; Gschwind, R. M.; Balázs, G.; Schiller, J.; Scheer, M. *Chem. A Eur. J.* **2021**, *27*, 5028–5034.
304. Gregoriades, L. J.; Wegley, B. K.; Sierka, M.; Brunner, E.; Gröger, C.; Peresykina, E. V.; Virovets, A. V.; Zabel, M.; Scheer, M. *Chem. Asian J.* **2009**, *4*, 1578–1587.
305. Gregoriades, L. J.; Krauss, H.; Wachter, J.; Virovets, A. V.; Sierka, M.; Scheer, M. *Angew. Chem. Int. Ed.* **2006**, *45*, 4189–4192.
306. Dütsch, L.; Fleischmann, M.; Welsch, S.; Balázs, G.; Kremer, W.; Scheer, M. *Angew. Chem. Int. Ed. Engl.* **2018**, *57*, 3256–3261.
307. Dütsch, L.; Riesinger, C.; Balázs, G.; Seidl, M.; Scheer, M. *Chem. Sci.* **2021**, *12*, 14531–14539.
308. Piesch, M.; Graßl, C.; Scheer, M. *Angew. Chem. Int. Ed. Engl.* **2020**, *59*, 7154–7160.
309. Riesinger, C.; Dütsch, L.; Balázs, G.; Bodensteiner, M.; Scheer, M. *Chem. A Eur. J.* **2020**, *26*, 17165–17170.
310. Scherer, O. J.; Schwarz, G.; Wolmershuser, G. Z. *Anorg. Allg. Chem.* **1996**, *622*, 951–957.
311. Schwarzmaier, C.; Heinel, S.; Balázs, G.; Scheer, M. *Angew. Chem. Int. Ed. Engl.* **2015**, *54*, 13116–13121.
312. Scheer, M.; Gregoriades, L. J.; Virovets, A. V.; Kunz, W.; Neueder, R.; Krossing, I. *Angew. Chem. Int. Ed. Engl.* **2006**, *45*, 5689–5693.
313. Schiller, J.; Peresykina, E.; Virovets, A. V.; Scheer, M. *Angew. Chem. Int. Ed. Engl.* **2020**, *59*, 13647–13650.
314. Gregoriades, L. J.; Balázs, G.; Brunner, E.; Gröger, C.; Wachter, J.; Zabel, M.; Scheer, M. *Angew. Chem. Int. Ed.* **2007**, *46*, 5966–5970.
315. Watson, J. D.; Field, L. D.; Ball, G. E. *Nat. Chem.* **2022**.
316. Prabhusankar, G.; Gonzalez-Gallardo, S.; Doddi, A.; Gemel, C.; Winter, M.; Fischer, R. A. *Eur. J. Inorg. Chem.* **2010**, *2010*, 4415–4418.
317. Welsch, S.; Nohra, B.; Peresykina, E. V.; Lesco, C.; Scheer, M.; Réau, R. *Chem. A Eur. J.* **2009**, *15*, 4685–4703.
318. Schindler, A.; Zabel, M.; Nixon, J. F.; Scheer, M. *Z. Naturforsch. B* **2009**, *64*, 1429–1437.
319. Gonsior, M.; Antonijevic, S.; Krossing, I. *Chem.-Eur. J.* **2006**, *12*, 1997–2008.
320. Petz, W.; Neumüller, B.; Krossing, I. *Z. Anorg. Allg. Chem.* **2006**, *632*, 859–865.
321. Lu, Z.; Han, J.; Okoromoba, O. E.; Shimizu, N.; Amii, H.; Tormena, C. F.; Hammond, G. B.; Xu, B. *Org. Lett.* **2017**, *19*, 5848–5851.
322. Kannan, R.; Balasubramaniam, S.; Kumar, S.; Chamenahalli, R.; Jemmis, E. D.; Venugopal, A. *Chem. A Eur. J.* **2020**, *26*, 12717–12721.
323. Smidt, S. P.; Zimmermann, N.; Studer, M.; Pfaltz, A. *Chem. A Eur. J.* **2004**, *10*, 4685–4693.
324. Böing, C.; Franció, G.; Leitner, W. *Adv. Synth. Catal.* **2005**, *347*, 1537–1541.
325. Lu, Z.-L.; Neumann, E.; Pfaltz, A. *Eur. J. Org. Chem.* **2007**, *2007*, 4189–4192.
326. Rucklidge, A. J.; McGuinness, D. S.; Tooze, R. P.; Slawin, A. M. Z.; Pelletier, J. D. A.; Hanton, M. J.; Webb, P. B. *Organometallics* **2007**, *26*, 2782–2787.
327. Hanton, M. J.; Tenza, K. *Organometallics* **2008**, *27*, 5712–5716.
328. McDyre, L. E.; Hamilton, T.; Murphy, D. M.; Cavell, K. J.; Gabrielli, W. F.; Hanton, M. J.; Smith, D. M. *Dalton Trans.* **2010**, *39*, 7792–7799.
329. Tenza, K.; Hanton, M. J.; Slawin, A. M. Z. *Organometallics* **2009**, *28*, 4852–4867.
330. Dulai, A.; de Bod, H.; Hanton, M. J.; Smith, D. M.; Downing, S.; Mansell, S. M.; Wass, D. F. *Organometallics* **2009**, *28*, 4613–4616.
331. Downing, S. P.; Hanton, M. J.; Slawin, A. M. Z.; Tooze, R. P. *Organometallics* **2009**, *28*, 2417–2422.
332. Alberti, D.; Goddard, R.; Pörschke, K.-R. *Organometallics* **2005**, *24*, 3907–3915.
333. Chernyshova, E. S.; Goddard, R.; Pörschke, K.-R. *Organometallics* **2007**, *26*, 3236–3251.
334. Reeds, J. P.; Whitwood, A. C.; Healy, M. P.; Fairlamb, I. J. S. *Chem. Commun.* **2010**, *46*, 2046–2048.
335. Schneider, R.; Engesser, T. A.; Näther, C.; Tucek, F. *Angew. Chem. Int. Ed. Engl.* **2022**, *61*, e202202562.
336. Kikivits, N.; Knaack, P.; Bomze, D.; Krossing, I.; Liska, R. *Polym. Chem.* **2017**, *8*, 4414–4421.
337. Rudolph, T.; Kempe, K.; Crotty, S.; Paulus, R. M.; Schubert, U. S.; Krossing, I.; Schacher, F. H. *Polym. Chem.* **2013**, *4*, 495–505.
338. Korthals, B.; Berkefeld, A.; Ahlmann, M.; Mecking, S. *Macromolecules* **2008**, *41*, 8332–8338.
339. Rach, S. F.; Kuehn, F. E. *Chem. Rev.* **2009**, *109*, 2061–2080.
340. Hildebrandt, N.; Koenig, H. M.; Hanefeld, P.; Muehlbach, K.; Krossing, I.; Steinfeld, G. W02010139684A1 - Preparation of compound made of protonated aromatic and weakly coordinating anion for polymerization catalyst of isobutene (2010).
341. Preiss, U.; Bulut, S.; Krossing, I. *J. Phys. Chem. B* **2010**, *114*, 11133–11140.
342. Glasser, L.; Jenkins, H. D. B. *Inorg. Chem.* **2008**, *47*, 6195–6202.



343. Glasser, L.; Jenkins, H. D. B. *Inorg. Chem.* **2011**, *50*, 8565–8569.
344. Glasser, L.; Jenkins, H. D. B. *J. Chem. Eng. Data* **2011**, *56*, 874–880.
345. Jenkins, H. D. B.; Roobottom, H. K.; Passmore, J.; Glasser, L. *Inorg. Chem.* **1999**, *38*, 3609–3620.
346. Jenkins, H. D. B.; Krossing, I.; Passmore, J.; Raabe, I. *J. Fluor. Chem.* **2004**, *125*, 1585–1592.
347. Jenkins, H. D. B.; Roobottom, H. K.; Passmore, J. *Inorg. Chem.* **2003**, *42*, 2886–2893.
348. Roobottom, H. K.; Jenkins, H. D. B.; Passmore, J.; Glasser, L. *J. Chem. Educ.* **1999**, *76*, 1570.
349. Bulut, S.; Klose, P.; Huang, M. M.; Weingartner, H.; Dyson, P. J.; Laurency, G.; Friedrich, C.; Menz, J.; Kummerer, K.; Krossing, I. *Chem.-Eur. J.* **2010**, *16*, 13139–13154.
350. Rupp, A.; Roznyatovskaya, N.; Scherer, H.; Beichel, W.; Klose, P.; Sturm, C.; Hoffmann, A.; Tübke, J.; Koslowski, T.; Krossing, I. *Chem. A Eur. J.* **2014**, *20*, 9794–9804.
351. Huang, M. M.; Bulut, S.; Krossing, I.; Weingartner, H. *J. Chem. Phys.* **2010**, *133*, 101101.
352. Bell, S. B.; Möhle, S.; Enders, P.; Waldvogel, S. R. *Chem. Commun.* **2018**, *54*, 6128–6131.
353. Stewart, M. P.; Paradee, L. M.; Raabe, I.; Trapp, N.; Slattery, J. S.; Krossing, I.; Geiger, W. E. *J. Fluor. Chem.* **2010**, *131*, 1091–1095.
354. Speiser, B.; Zitzer, G. *ChemElectroChem* **2021**, *8*, 2888–2902.
355. Janisch, J.; Klinkhammer, R.; Ruff, A.; Schäfer, J.; Speiser, B.; Wolff, C. *Electrochim. Acta* **2013**, *110*, 608–618.
356. Passon, M.; Ruff, A.; Schuler, P.; Speiser, B.; Leis, W. *J. Solid State Electrochem.* **2015**, *19*, 85–101.
357. Tokuda, H.; Watanabe, M. *Electrochim. Acta* **2003**, *48*, 2085–2091.
358. Tokuda, H.; Tabata, S.; Susan, M. A. B. H.; Hayamizu, K.; Watanabe, M. *J. Phys. Chem. B* **2004**, *108*, 11995–12002.
359. Shyamsunder, A.; Beichel, W.; Klose, P.; Pang, Q.; Scherer, H.; Hoffmann, A.; Murphy, G. K.; Krossing, I.; Nazar, L. F. *Angew. Chem. Int. Ed.* **2017**, *56*, 6192–6197.
360. Álvarez Hernández, L. *Li[B(OCH(CF<sub>3</sub>)<sub>2</sub>)<sub>4</sub>] - Synthesis Optimization and Characterization of Its Electrolytes*. Dissertation, Albert-Ludwigs-Universität: Freiburg, 2013. <https://freidok.uni-freiburg.de/data/9771>.
361. Eisele, L.; Laszczynski, N.; Schneider, M.; Lucht, B.; Krossing, I. *J. Electrochem. Soc.* **2020**, *167*, 60514.
362. Eisele, L.; Laszczynski, N.; Görg, M.; Schneider, M.; Burger, S.; Radtke, V.; Lucht, B.; Krossing, I. *J. Electrochem. Soc.* **2020**, *167*, 80507.
363. Barbarich, T. J.; Miller, S. M.; Anderson, O. P.; Strauss, S. H. *J. Mol. Catal. A-Chem.* **1998**, *128*, 289–331.
364. Zhao-Karger, Z.; Gil Bardaji, M. E.; Fuhr, O.; Fichtner, M. *J. Mater. Chem. A* **2017**, *5*, 10815–10820.
365. Mandai, T.; Youn, Y.; Tateyama, Y. *Mater. Adv.* **2021**, *2*, 6283–6296.
366. Pavčnik, T.; Lozinšek, M.; Pimat, K.; Vizintin, A.; Mandai, T.; Aurbach, D.; Dominko, R.; Bitenc, J. *ACS Appl. Mater. Interfaces* **2022**, *14*, 26766–26774.
367. Keyzer, E. N.; Lee, J.; Liu, Z.; Bond, A. D.; Wright, D. S.; Grey, C. P. *J. Mater. Chem. A* **2019**, *7*, 2677–2685.
368. Lau, K.-C.; Seguin, T. J.; Carino, E. V.; Hahn, N. T.; Connell, J. G.; Ingram, B. J.; Persson, K. A.; Zavadil, K. R.; Liao, C. *J. Electrochem. Soc.* **2019**, *166*, A1510–A1519.
369. Schmidt, A.; Koger, H.; Barthélemy, A.; Butschke, B.; Studer, G.; Esser, B.; Krossing, I. *Batter. Supercaps* **2022**, *2022*, e202200340. <https://doi.org/10.1002/batt.202200340>.
370. Fichtner, M.; Zhao-Karger, Z. *Meet. Abstr.* **2017**, 440. MA2017-02.
371. Du, A.; Zhang, Z.; Qu, H.; Cui, Z.; Qiao, L.; Wang, L.; Chai, J.; Lu, T.; Dong, S.; Dong, T.; Xu, H.; Zhou, X.; Cui, G. *Energ. Environ. Sci.* **2017**, *10*, 2616–2625.
372. Zhirong, Z.-K.; Maximilian, F. *MRS Commun.* **2017**, *7*, 770–784.
373. Zhao-Karger, Z.; Liu, R.; Dai, W.; Li, Z.; Diemant, T.; Vinayan, B. P.; Bonatto Minella, C.; Yu, X.; Manthiram, A.; Behm, R. J.; Ruben, M.; Fichtner, M. *ACS Energy Lett.* **2018**, *3*, 2005–2013.
374. Li, Z.; Mu, X.; Zhao-Karger, Z.; Diemant, T.; Behm, R. J.; Kübel, C.; Fichtner, M. *Nat. Commun.* **2018**, *9*, 5115.
375. Li, Z.; Zhao-Karger, Z.; Fichtner, M. *Meet. Abstr.* **2019**, 353. MA2019-01.
376. Li, Z.; Vinayan, B. P.; Jankowski, P.; Njel, C.; Roy, A.; Vegge, T.; Maibach, J.; Lastra, J. M. G.; Fichtner, M.; Zhao-Karger, Z. *Angew. Chem.* **2020**, *132*, 11580–11587.
377. Bhagavathi Parambath, V.; Zhao-Karger, Z.; Diemant, T.; Jäckle, M.; Li, Z.; Scherer, T.; Gross, A.; Behm, R. J.; Fichtner, M. *J. Mater. Chem. A* **2020**, *8*, 22998–23010.
378. Kaland, H.; Håskjold Fagerli, F.; Hadler-Jacobsen, J.; Zhao-Karger, Z.; Fichtner, M.; Wiik, K.; Wagner, N. P. *ChemSusChem* **2021**, *14*, 1864–1873.
379. Ji, Y.; Liu-Théato, X.; Xiu, Y.; Indris, S.; Njel, C.; Maibach, J.; Ehrenberg, H.; Fichtner, M.; Zhao-Karger, Z. *Adv. Funct. Mater.* **2021**, *31*, 2100868.
380. Abouzarí-Loft, E.; Azmi, R.; Li, Z.; Shakouri, S.; Chen, Z.; Zhao-Karger, Z.; Klyatskaya, S.; Maibach, J.; Ruben, M.; Fichtner, M. *ChemSusChem* **2021**, *14*, 1840–1846.
381. Meng, Z.; Li, Z.; Wang, L.; Diemant, T.; Bosubabu, D.; Tang, Y.; Berthelot, R.; Zhao-Karger, Z.; Fichtner, M. *ACS Appl. Mater. Interfaces* **2021**, *13*, 37044–37051.
382. Li, Z.; Diemant, T.; Meng, Z.; Xiu, Y.; Reupert, A.; Wang, L.; Fichtner, M.; Zhao-Karger, Z. *ACS Appl. Mater. Interfaces* **2021**, *13*, 33123–33132.
383. Xiu, Y.; Li, Z.; Bhagavathi Parambath, V.; Ding, Z.; Wang, L.; Reupert, A.; Fichtner, M.; Zhao-Karger, Z. *Batteries & Supercaps* **2021**, *4*, 1850–1857.
384. Drews, J.; Jankowski, P.; Häcker, J.; Li, Z.; Danner, T.; García Lastra, J. M.; Vegge, T.; Wagner, N.; Friedrich, K. A.; Zhao-Karger, Z.; Fichtner, M.; Latz, A. *ChemSusChem* **2021**, *14*, 4820–4835.
385. Drews, J.; Danner, T.; Jankowski, P.; Vegge, T.; García Lastra, J. M.; Liu, R.; Zhao-Karger, Z.; Fichtner, M.; Latz, A. *ChemSusChem* **2020**, *13*, 3599–3604.
386. Bosubabu, D.; Li, Z.; Meng, Z.; Wang, L.-P.; Fichtner, M.; Zhao-Karger, Z. *J. Mater. Chem. A* **2021**, *9*, 25150–25159.
387. Roy, A.; Bhagavathi Parambath, V.; Diemant, T.; Neusser, G.; Kranz, C.; Behm, R. J.; Li, Z.; Zhao-Karger, Z.; Fichtner, M. *Batter. Supercaps* **2022**, *5*, e202100305.
388. Jankowski, P.; Li, Z.; Zhao-Karger, Z.; Diemant, T.; Fichtner, M.; Vegge, T.; Lastra, J. M. G. *Energ. Stor. Mater.* **2022**, *45*, 1133–1143.
389. Wang, L.; Li, Z.; Meng, Z.; Xiu, Y.; Dasari, B.; Zhao-Karger, Z.; Fichtner, M. *Energ. Stor. Mater.* **2022**, *48*, 155–163.
390. Li, Z.; Vinayan, B. P.; Jankowski, P.; Njel, C.; Roy, A.; Vegge, T.; Maibach, J.; Lastra, J. M. G.; Fichtner, M.; Zhao-Karger, Z. *Anwew. Chem., Int. Ed. Engl.* **2020**, *59*, 11483–11490.
391. Mandai, T. *ACS Appl. Mater. Interfaces* **2020**, *12*, 39135–39144.
392. Dlugatch, B.; Mohankumar, M.; Attias, R.; Krishna, B. M.; Elias, Y.; Gofer, Y.; Zitoun, D.; Aurbach, D. *ACS Appl. Mater. Interfaces* **2021**, *13*, 54894–54905.
393. Luo, J.; Bi, Y.; Zhang, L.; Zhang, X.; Liu, T. L. *Angew. Chem. Int. Ed. Engl.* **2019**, *58*, 6967–6971.
394. ECHA (2015) ECHA - European Chemicals Agency. *Substance Infocard: Hexafluoro-2,3-dimethylbutane-2,3-diol*. <https://echa.europa.eu/de/substance-information/-/substanceinfo/100.153.195> (accessed 2022-06-15).
395. Scifinder (2022) *Reference search for structure [Al(OA)<sub>4</sub>] (A = alkoxide) and "calcium" as well as "battery" or "electrolyte" in Abstract/Keywords in CAS Scifinder-n, 2022*. <https://scifinder-n.cas.org/> (accessed 2022-05-27).
396. Ponrouch, A.; Frontera, C.; Bardé, F.; Palacín, M. R. *Nat. Mater.* **2016**, *15*, 169–172.
397. Forero-Saboya, J.; Davoisne, C.; Dedryvère, R.; Yousef, I.; Canepa, P.; Ponrouch, A. *Energ. Environ. Sci.* **2020**, *13*, 3423–3431.
398. Wang, D.; Gao, X.; Chen, Y.; Jin, L.; Kuss, C.; Bruce, P. G. *Nat. Mater.* **2018**, *17*, 16–20.
399. Li, Z.; Fuhr, O.; Fichtner, M.; Zhao-Karger, Z. *Energ. Environ. Sci.* **2019**, *12*, 3496–3501.
400. Shyamsunder, A.; Blanc, L. E.; Assoud, A.; Nazar, L. F. *ACS Energy Lett.* **2019**, *4*, 2271–2276.
401. Bitenc, J.; Scafuri, A.; Pimat, K.; Lozinšek, M.; Jerman, I.; Gradolnik, J.; Fraise, B.; Berthelot, R.; Stievano, L.; Dominko, R. *Batter. Supercaps* **2021**, *4*, 214–220.
402. Nielson, K. V.; Luo, J.; Liu, T. L. *Batter. Supercaps* **2020**, *3*, 766–772.
403. Hahn, N. T.; Self, J.; Driscoll, D. M.; Dandu, N.; Han, K. S.; Murugesan, V.; Mueller, K. T.; Curtiss, L. A.; Balasubramanian, M.; Persson, K. A.; Zavadil, K. R. *PCCP* **2022**, *24*, 674–686.
404. Yang, M.; Driscoll, D. M.; Balasubramanian, M.; Liao, C. *J. Electrochem. Soc.* **2020**, *167*, 160529.
405. Roznyatovskaya, N.; Rupp, A. B. A.; Tübke, J.; Krossing, I. *ChemElectroChem* **2015**, *2*, 829–836.
406. Gesevicius, D.; Neels, A.; Yakunin, S.; Hack, E.; Kovalenko, M. V.; Nüesch, F.; Heier, J. *ChemPhysChem* **2018**, *19*, 3356–3363.
407. Fish, G. C.; Moreno-Naranjo, J. M.; Billion, A.; Kratzert, D.; Hack, E.; Krossing, I.; Nüesch, F.; Moser, J.-E. *PCCP* **2021**, *23*, 23886–23895.
408. Andreiuk, B.; Reisch, A.; Pivovarenko, V. G.; Klymchenko, A. S. *Mater. Chem. Front.* **2017**, *1*, 2309–2316.

## 1.08 Noble-gas chemistry

Hélène P.A. Mercier, Mark R. Bortolus, and Gary J. Schrobilgen, Department of Chemistry, McMaster University, Hamilton, Ontario, Canada

© 2023 Elsevier Ltd. All rights reserved.

<b>1.08.1</b>	<b>Introduction</b>	<b>440</b>
1.08.1.1	Noble-gas chemistry and the periodic table	440
1.08.1.2	Noble-gas chemistry reviews (2012–21)	441
<b>1.08.2</b>	<b>Synthesis and reactivity of XeF<sub>2</sub></b>	<b>441</b>
1.08.2.1	A room-temperature non-irradiative synthesis of XeF <sub>2</sub>	441
1.08.2.2	XeF <sub>2</sub> /fluoride-ion acceptors as versatile one-electron oxidants	441
<b>1.08.3</b>	<b>Xenon(II) and krypton(II) compounds</b>	<b>442</b>
1.08.3.1	Main-group ligand compounds of Xe(II)	442
1.08.3.1.1	C <sub>6</sub> F <sub>5</sub> XeF and C <sub>6</sub> F <sub>5</sub> XeCl	442
1.08.3.1.2	Xe(OSO <sub>2</sub> F) <sub>2</sub>	444
1.08.3.2	Transition-metal coordination complexes of NgF <sub>2</sub> (Ng = Kr, Xe)	444
1.08.3.2.1	[Hg(FKrF) <sub>8</sub> ][AsF <sub>6</sub> ] <sub>2</sub> ·2HF	444
1.08.3.2.2	Hg(FNgF) <sub>1.5</sub> (OTeF <sub>5</sub> ) <sub>2</sub>	445
1.08.3.2.3	NgF <sub>2</sub> · <i>n</i> CrOF <sub>4</sub> , NgF <sub>2</sub> ·MOF <sub>4</sub> , and XeF <sub>2</sub> ·2MOF <sub>4</sub> ( <i>n</i> = 1, 2; M = Mo, W)	447
1.08.3.2.4	[Ln(XeF <sub>2</sub> ) <sub>3</sub> ][BF <sub>4</sub> ] <sub>3</sub> (Ln = La, Ce, Pr, Nd, Sm, Eu, Gd, Tb, Dy, and Y), [Ln(XeF <sub>2</sub> )][BF <sub>4</sub> ] <sub>3</sub> (Ln = La, Ce, Pr, Nd), [La(XeF <sub>2</sub> ) <sub>2</sub> ][BF <sub>4</sub> ] <sub>3</sub> , and [Ln(XeF <sub>2</sub> ) <sub>2</sub> ][BF <sub>4</sub> ] <sub>2</sub> (Ln = La, Nd, Sm, Eu, Gd, Tb, Dy, and Y)	450
1.08.3.3	Main-group coordination complexes of NgF <sub>2</sub>	452
1.08.3.3.1	[O <sub>2</sub> Cl(FXeF) <sub>2</sub> ][AsF <sub>6</sub> ]	452
1.08.3.3.2	[Mg(FKrF) <sub>4</sub> ][AsF <sub>6</sub> ] <sub>2</sub>	452
1.08.3.4	Mixed krypton/xenon compounds	454
1.08.3.4.1	[F <sub>5</sub> Xe(FKrF) <sub><i>n</i></sub> AsF <sub>6</sub> ] <sub><i>n</i></sub> ( <i>n</i> = 1 or 2)	454
1.08.3.4.2	[FKrFXeF][AsF <sub>6</sub> ]·0.5KrF <sub>2</sub> ·2HF, XeF <sub>4</sub> ·NgF <sub>2</sub> , and [(F <sub>5</sub> Xe) <sub>2</sub> (μ-FKrF)][AsF <sub>6</sub> ] <sub>2</sub>	456
1.08.3.5	Xenon(II) cations	460
1.08.3.5.1	[XeOXeOXe][μ-F(ReO <sub>2</sub> F <sub>3</sub> ) <sub>2</sub> ] <sub>2</sub>	460
1.08.3.5.2	[CH <sub>3</sub> CN---XeOXe---NCCH <sub>3</sub> ][AsF <sub>6</sub> ] <sub>2</sub>	462
1.08.3.5.3	[XeF] <sup>+</sup> and [Xe <sub>2</sub> F <sub>3</sub> ] <sup>+</sup> salts of transition-metal fluoro-anions	463
<b>1.08.4</b>	<b>Xenon(IV) compounds</b>	<b>465</b>
1.08.4.1	Xenon oxide fluorides	465
1.08.4.1.1	[H(OXeF <sub>2</sub> ) <sub><i>n</i></sub> ][AsF <sub>6</sub> ] <sub><i>n</i></sub> and [FXe(OXeF <sub>2</sub> ) <sub><i>n</i></sub> ][AsF <sub>6</sub> ] <sub><i>n</i></sub> ( <i>n</i> = 1, 2)	465
1.08.4.2	Xenon fluorides	466
1.08.4.2.1	[F <sub>3</sub> Xe---FH][Sb <sub>2</sub> F <sub>11</sub> ] and [H <sub>5</sub> F <sub>4</sub> ][SbF <sub>6</sub> ] <sub>2</sub> [F <sub>3</sub> Xe---FH][Sb <sub>2</sub> F <sub>11</sub> ]	466
1.08.4.2.2	[C <sub>6</sub> F <sub>5</sub> XeF <sub>2</sub> ][BF <sub>4</sub> ], [C <sub>6</sub> F <sub>5</sub> XeF <sub>2</sub> ][BF <sub>4</sub> ] <sub>2</sub> ·2HF, and [C <sub>6</sub> F <sub>5</sub> XeF <sub>2</sub> ][BF <sub>4</sub> ] <sub>2</sub> ·1.5CH <sub>3</sub> CN	468
<b>1.08.5</b>	<b>Xenon(VI) compounds</b>	<b>473</b>
1.08.5.1	XeF <sub>6</sub> and coordination complexes of XeF <sub>6</sub>	473
1.08.5.1.1	F <sub>6</sub> XeNCCH <sub>3</sub> and F <sub>6</sub> Xe(NCCH <sub>3</sub> ) <sub>2</sub> ·CH <sub>3</sub> CN	473
1.08.5.1.2	Vibrational study of XeF <sub>6</sub> and XeOF <sub>4</sub>	477
1.08.5.2	Salts of [XeF <sub>5</sub> ] <sup>+</sup> and [Xe <sub>2</sub> F <sub>11</sub> ] <sup>+</sup>	478
1.08.5.2.1	Oxyfluoro-anion salts	478
1.08.5.2.2	Fluoro-anion salts	486
1.08.5.3	Chemistry of XeO <sub>3</sub>	496
1.08.5.3.1	Solid-state structures of XeO <sub>3</sub> : α-XeO <sub>3</sub> , β-XeO <sub>3</sub> , and γ-XeO <sub>3</sub>	497
1.08.5.3.2	Xenon trioxide adducts of N- and O-donor ligands	498
1.08.5.3.3	A stable crown ether complex with a noble-gas compound	502
1.08.5.3.4	Stable chloro- and bromoxenate cage anions; [X <sub>3</sub> (XeO <sub>3</sub> ) <sub>3</sub> ] <sup>3-</sup> and [X <sub>4</sub> (XeO <sub>3</sub> ) <sub>4</sub> ] <sup>4-</sup> (X = Cl or Br)	503
<b>1.08.6</b>	<b>Xenon(VIII) compounds</b>	<b>504</b>
1.08.6.1	Infrared spectra of XeO <sub>4</sub> and Na <sub>4</sub> [XeO <sub>6</sub> ] in Ne and Ar matrices	504
1.08.6.2	Photolysis of XeO <sub>4</sub> and formation of (η <sup>2</sup> -O <sub>2</sub> )XeO <sub>3</sub> and its infrared spectra in Ne, Ar, Kr, and F <sub>2</sub> matrices	506
<b>1.08.7</b>	<b>Noble-gas molecules characterized by matrix isolation</b>	<b>507</b>
1.08.7.1	Xenon and krypton hydrides	508
1.08.7.2	<i>bis</i> -Noble-gas hydrides	513
1.08.7.3	Noble-gas insertion compounds	513
1.08.7.4	Gold complexes	515
1.08.7.5	Beryllium complexes	515
1.08.7.6	Xenon van der Waals complexes with aromatic rings	517



<b>1.08.8</b>	<b>High-pressure noble-gas chemistry</b>	<b>517</b>
1.08.8.1	Helium compounds	517
1.08.8.2	Neon compounds	518
1.08.8.3	Argon, xenon, and krypton compounds	518
<b>1.08.9</b>	<b>Perspective and outlook</b>	<b>521</b>
<b>References</b>		<b>521</b>

### Abbreviations

aHF	Anhydrous HF
CN	Coordination number
Cp	C <sub>5</sub> H <sub>5</sub>
DAC	Diamond-anvil cell
EDA	Energy decomposition analysis
ELF	Electron localization function (denoted as $\eta(\mathbf{r})$ )
EP	Electrostatic potential
Et	C <sub>2</sub> H <sub>5</sub>
ETS-NOCV	Extended transition state natural orbitals for chemical valence
FEP	Perfluoroethylene/perfluoropropylene copolymer
FIA	Fluoride-ion affinity
Freon 114	1,2-Dichlorotetrafluoroethane
LT	Low-temperature
Me	CH <sub>3</sub>
MEPS	Molecular electrostatic potential surface
NBO	Natural bond order
NHE	Normal hydrogen electrode
NMR	Nuclear magnetic resonance
NPA	Natural population analysis
PET	Positron emission tomography
Ph	C <sub>6</sub> H <sub>5</sub>
QTAIM	Quantum theory of atoms in molecule
SCE	Saturated calomel electrode
SCXRD	Single-crystal X-ray diffraction
Tf	CF <sub>3</sub> SO <sub>2</sub>
V	Volt
VELP	Valence electron lone pair

### Abstract

The present review covers recent advances (2012–21) in the field of noble-gas chemistry, with emphases on the synthetic and structural characterizations of xenon and krypton compounds that have been formed in macroscopic quantities. The results of gas-phase theoretical calculations are discussed in the light of the experimental structures and spectroscopic findings. Applications of noble-gas compounds to the syntheses of the high-oxidation-state transition-metal fluoride and oxide fluoride species are also featured. The formation of noble-gas species in the gas-phase, in matrices, and at high pressures are also discussed.

## 1.08.1 Introduction

### 1.08.1.1 Noble-gas chemistry and the periodic table

In 2006, Oganessian et al.<sup>1</sup> reported the synthesis of a new noble-gas element, <sup>294</sup>118, based on the observation of three concordant events that resulted from the fusion of <sup>48</sup>Ca with <sup>249</sup>Cf. The discovery of this superheavy element was only validated<sup>2</sup> in January 2016 when element 118 was recognized by the International Union of Pure and Applied Chemistry (IUPAC) and the International Union of Pure and Applied Physics (IUPAP). The discoverers christened it *oganesson* after the Armenian born Russian physicist Yuri T. Oganessian, who led the group at Dubna, Russian Federation that discovered <sup>294</sup>118 and several other of the heaviest transuranium elements. The name and symbol, Og, were approved by IUPAC in November 2016.

Today, the discovery of the last element in row seven of the Periodic Table is undisputed, but its physical properties and chemistry remain unknown owing to the short half-life (< 1 ms) of <sup>294</sup>Og, which decays by  $\alpha$ -emission. High-level calculations have been used to estimate the melting and boiling points of this super-heavy element.<sup>3</sup> The two approaches that were used indicated Og is

solid at ambient conditions with a melting point of  $\sim 325$  K when relativity was included in the calculations, whereas in the non-relativistic limit, a melting point of 220 K was obtained that suggested a gaseous state, as expected for a typical noble-gas element. Thus, relativistic effects shift the solid-to-liquid phase transition by ca. 100 K, and Og is likely not a gas.

The 150<sup>th</sup> anniversary of the Mendeleev's periodic classification of the chemical elements was designated by UNESCO as the International Year of the Periodic Table (IYPT). It is in this context that D. M. P. Mingos edited a two-volume work, *The Periodic Table I<sup>4a</sup> and II<sup>4b</sup>*, wherein an overview is presented of how the Periodic Table, as we now know it, evolved since Mendeleev's conceptualized Periodic Table and how the Periodic Table evolved and guided chemistry research ever since. A chapter dealing with the noble gases, "Chemistry at the Edge of the Periodic Table: The Importance of Periodic Trends on the Discovery of the Noble Gases and the Development of Noble-Gas Chemistry", describes how the discovery of the noble-gas family of elements helped to validate the periodic system and the role the Periodic Table played in the Discovery of noble-gas chemistry.<sup>5</sup> There is no doubt that initial attempts to form noble-gas compounds were prompted, guided, and illuminated by trends within the Periodic Table. Neil Bartlett, the first to synthesize a noble-gas compound,<sup>6</sup> also looked to the Periodic Table for trends among the chemistries of nearby elements to understand the newly discovered chemistries of xenon and krypton.<sup>7–10</sup> Over the past 60 years, the compounds of both elements have continued to fascinate chemists and illustrate periodic behavior in a variety of ways that encompass, for example, oxidative fluorinating properties and pursuant synthetic applications, isoelectronic and hyper-valent species among the main-group elements and their structural relationships, and thermochemical bond energy trends.

### 1.08.1.2 Noble-gas chemistry reviews (2012–21)

During the period 2012–21 (inclusive), a significant number of reviews have appeared that deal with a broad spectrum of topics in noble-gas chemistry: general noble-gas chemistry;<sup>11</sup> the coordination chemistry of the noble gases and noble-gas fluorides;<sup>12</sup> the chemistry of xenon(IV);<sup>13</sup> noble-gas – noble-metal chemistry;<sup>14</sup> developments in the syntheses and structural characterization of noble-gas compounds;<sup>15</sup> the molecular and X-ray crystal structures of noble-gas compounds and their vibrational spectra;<sup>16</sup> matrix-isolated noble-gas molecules characterized by infrared spectroscopy;<sup>17</sup> noble-gas chemistry under high pressure;<sup>18</sup> and theoretical advances in noble-gas chemistry.<sup>14,19,20</sup> The present chapter is a continuation of a prior review in *Comprehensive Inorganic Chemistry II*,<sup>21</sup> which covered the period 2000–2011 (inclusive), and should also be consulted along with the aforementioned reviews.

## 1.08.2 Synthesis and reactivity of XeF<sub>2</sub>

### 1.08.2.1 A room-temperature non-irradiative synthesis of XeF<sub>2</sub>

Developments in Xe(II) chemistry are primarily related to the application and/or derivation of XeF<sub>2</sub>, making its preparation in high yield and purity critically important to noble-gas chemistry.<sup>11,21,22</sup> Xenon difluoride is an accessible and easy-to-handle noble-gas compound that has found important synthetic applications as a gas-phase etchant for microelectromechanical systems<sup>23</sup> and as an electrophilic and oxidative fluorinating agent in <sup>18</sup>F positron emission tomography (PET),<sup>24–26</sup> main-group chemistry,<sup>27–29</sup> transition-metal chemistry,<sup>30–32</sup> and organic chemistry.<sup>33–35</sup>

The reaction conditions for an alternative synthesis of XeF<sub>2</sub> have been optimized which require neither thermal nor irradiative dissociation of F<sub>2</sub>. The work elaborates on a very brief account by Bartlett et al.<sup>36</sup> wherein the authors describe the reaction of Xe (1.26 mmol) with F<sub>2</sub> (1.65 mmol) in anhydrous HF (aHF; 2 mL) in a 42 mL FEP (perfluoroethylene/perfluoropropylene copolymer) reactor under dark conditions at 20 °C for 12 h which gave a 63% yield of XeF<sub>2</sub> (0.134 g, 0.792 mmol).<sup>36</sup> It is clear from this and related studies involving the oxidative fluorination of Xe with <sup>19</sup>F<sub>2</sub><sup>36</sup> and [<sup>18</sup>F]F<sub>2</sub><sup>37</sup> in the presence of aHF and aHF/AsF<sub>5</sub> superacid mixtures that liquid aHF and strong Lewis acid fluoride-ion acceptor AsF<sub>5</sub> activate the F–F bond of F<sub>2</sub> and facilitate its homolytic dissociation at low temperatures and pressures.

A more recent high-yield synthesis of XeF<sub>2</sub> also used liquid aHF to activate F<sub>2</sub> under dark conditions.<sup>38</sup> The reaction conditions were optimized for the syntheses of gram quantities of high-purity XeF<sub>2</sub> at ambient temperature in near quantitative yields (Table 1). It is noteworthy that no reaction occurs between Xe and F<sub>2</sub> under dark conditions when HF is entirely in the gas-phase.

### 1.08.2.2 XeF<sub>2</sub>/fluoride-ion acceptors as versatile one-electron oxidants

Xenon difluoride has a rich history as an oxidative fluorinating agent,<sup>22–35</sup> and its use as such in the presence of fluoride-ion acceptors has been investigated.<sup>39</sup> In an attempt to synthesize [Me<sub>3</sub>Se<sub>3</sub>][BF<sub>4</sub>] by reaction of Me<sub>2</sub>Se<sub>2</sub> with a XeF<sub>2</sub>/BF<sub>3</sub>·OEt<sub>2</sub> mixture, the one-electron oxidation product, [Me<sub>4</sub>Se<sub>4</sub>][BF<sub>4</sub>]<sub>2</sub>, was obtained instead (Scheme 1).<sup>39</sup>

Prior to this study, only two oxidation reactions involving the use of XeF<sub>2</sub>/BF<sub>3</sub> mixtures had been reported.<sup>40,41</sup> Potent one-electron oxidants are important synthetic reagents for the syntheses of reactive cations. This finding provided impetus to further investigate the one-electron oxidation reactions of XeF<sub>2</sub> in the presence of the fluoride-ion acceptors BF<sub>3</sub>, B(C<sub>6</sub>F<sub>5</sub>)<sub>3</sub>, Al{OC(CF<sub>3</sub>)<sub>3</sub>}<sub>3</sub>, TfOSiMe<sub>3</sub>, Tf<sub>2</sub>NSiMe<sub>3</sub>, [Me<sub>3</sub>Si][B(C<sub>6</sub>F<sub>5</sub>)<sub>4</sub>], and [Me<sub>3</sub>Si][CHB<sub>11</sub>Cl<sub>11</sub>]. The XeF<sub>2</sub>/fluoride-ion acceptor mixtures were allowed to react with compounds that have known oxidation potentials (Table 2) and were shown to have oxidation potentials that are at least 2 V vs. the NHE. These mixtures are therefore intermediate in oxidative strength with respect to [NO]<sup>+</sup><sup>42</sup> and [O<sub>2</sub>]<sup>+</sup><sup>42</sup> salts and led to the formation of [BF<sub>4</sub>]<sup>−</sup>, [TfO]<sup>−</sup>, [Tf<sub>2</sub>N]<sup>−</sup>, [FB(C<sub>6</sub>F<sub>5</sub>)<sub>3</sub>]<sup>−</sup>, [FAl{OC(CF<sub>3</sub>)<sub>3</sub>}<sub>3</sub>]<sup>−</sup>, [B(C<sub>6</sub>F<sub>5</sub>)<sub>4</sub>]<sup>−</sup>, and [CHB<sub>11</sub>Cl<sub>11</sub>]<sup>−</sup> salts of the cationic oxidation products [Me<sub>4</sub>E<sub>4</sub>]<sup>2+</sup> (E = Se, Te), [Fe(Cp)<sub>2</sub>]<sup>+</sup>, [2,6-(Me<sub>2</sub>NCH<sub>2</sub>)<sub>2</sub>C<sub>6</sub>H<sub>3</sub>Se]<sup>+</sup>, [C<sub>12</sub>H<sub>8</sub>S<sub>2</sub>]<sup>+</sup>, [2,4-Br<sub>2</sub>C<sub>6</sub>H<sub>3</sub>]<sup>+</sup>, [(H<sub>2</sub>C<sub>2</sub>S<sub>2</sub>C)<sub>2</sub>]<sup>+</sup>, [(H<sub>2</sub>C<sub>2</sub>S<sub>2</sub>C)<sub>2</sub>]<sup>2+</sup>, [tBu<sub>2</sub>C<sub>2</sub>EPH]<sup>+</sup>, [tBu<sub>2</sub>C<sub>2</sub>EPH]<sup>+</sup>, [tBu<sub>2</sub>C<sub>2</sub>EPH]<sup>+</sup>, [C<sub>12</sub>H<sub>15</sub>Se]<sup>+</sup>, [tBu<sub>2</sub>C<sub>2</sub>SPh]<sup>+</sup>, and [tBu<sub>2</sub>C<sub>2</sub>SMe]<sup>+</sup>. The salts were characterized by <sup>11</sup>B, <sup>13</sup>C, <sup>19</sup>F, <sup>77</sup>Se, and <sup>125</sup>Te NMR spectroscopy, electrospray ionization time-of-flight (ESI-TOF), mass spectrometry, and LT SCXRD.

**Table 1** Representative amounts and yields of XeF<sub>2</sub> resulting from the reaction of Xe and F<sub>2</sub> in liquid aHF.<sup>a,b</sup>

Amount				XeF <sub>2</sub> amount		
Xe, mmol	F <sub>2</sub> , mmol	aHF, g	Time, h	g	mmol	% yield <sup>c</sup>
8.03	13.48	2.141	21.0	1.261	7.45	92.8
8.25	14.63	1.151	20.0	1.300	7.68	93.1
8.02	14.89	0.945	8.0	0.786	4.64	57.9
8.21	16.23	0.424	20.0	0.949	5.61	68.3
8.63	15.22	0.143	67.5	0.594	3.51	40.7
8.27	14.87	0.054 <sup>d</sup>	143.5	0.000	0.00	0.0

<sup>a</sup>Reproduced with permission from Ref. 38.<sup>b</sup>All reactions were carried out at ambient temperature (23.5–25.5 °C) under dark conditions.<sup>c</sup>Yields are based on Xe as the limiting reagent.<sup>d</sup>Hydrogen fluoride is in the gas phase.**Scheme 1** Oxidations of Me<sub>2</sub>Se<sub>2</sub>. Reproduced with permission from Poleschner, H.; Seppelt, K. *Angew. Chem. Int. Ed.* **2013**, *52*, 12838–12842.**Table 2** Model compounds to be oxidized, oxidation potentials vs. NHE in Volts.<sup>a,b</sup>

Me <sub>2</sub> S <sub>2</sub> , 1.65	Ph <sub>2</sub> S <sub>2</sub> 1.75	[FeCp <sub>2</sub> ]	[(FeCpS) <sub>4</sub> ]
Me <sub>2</sub> Se <sub>2</sub>	Ph <sub>2</sub> Se <sub>2</sub> 1.59	0.7	<sup>0/+</sup> -0.05,
Me <sub>2</sub> Te <sub>2</sub>	Ph <sub>2</sub> Te <sub>2</sub> 0.99		<sup>+2+</sup> 0.57
	TTF	Thianthrene	1.84
	<sup>0/+</sup> 0.58,	1.56	
	<sup>+2+</sup> 0.95		

<sup>a</sup>Reproduced with permission from Ref. 39.<sup>b</sup>Conversion from SCE to NHE: 0.245 V, Ag/0.1 M AgNO<sub>3</sub>/SCE 0.36 V, [FeCp<sub>2</sub>]<sup>+</sup>/[FeCp<sub>2</sub>]/SCE 0.46 V.

### 1.08.3 Xenon(II) and krypton(II) compounds

#### 1.08.3.1 Main-group ligand compounds of Xe(II)

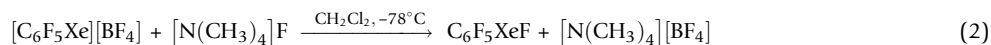
##### 1.08.3.1.1 C<sub>6</sub>F<sub>5</sub>XeF and C<sub>6</sub>F<sub>5</sub>XeCl

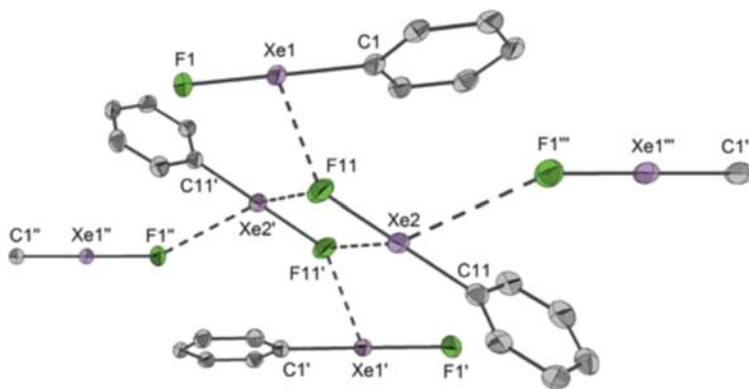
The chemistry of the organylxenonium cation, [C<sub>6</sub>F<sub>5</sub>Xe]<sup>+</sup>, is well documented and has been comprehensively reviewed.<sup>43–45</sup> The related compounds, C<sub>6</sub>F<sub>5</sub>XeY (Y = Cl,<sup>46</sup> Br,<sup>46</sup> NCO,<sup>46</sup> CN,<sup>46–48</sup> CF<sub>3</sub>C(O)O,<sup>46</sup> CF<sub>3</sub>S(O)<sub>2</sub>O,<sup>46</sup> C<sub>6</sub>F<sub>5</sub>,<sup>46–48</sup> 2,3-C<sub>6</sub>H<sub>3</sub>F<sub>2</sub><sup>46</sup>), were previously synthesized by reaction of C<sub>6</sub>F<sub>5</sub>XeF<sup>47,49</sup> with the alkylsilanes R<sub>3</sub>SiY (R = alkyl, Y = Cl) in CH<sub>2</sub>Cl<sub>2</sub> (Eq. 1).



The substrate, C<sub>6</sub>F<sub>5</sub>XeF, was prepared by two routes; (1) the F<sup>-</sup> catalyzed F/C<sub>6</sub>F<sub>5</sub> substitution of Me<sub>3</sub>SiC<sub>6</sub>F<sub>5</sub> with XeF<sub>2</sub>, which yielded a mixture of C<sub>6</sub>F<sub>5</sub>XeF and Xe(C<sub>6</sub>F<sub>5</sub>)<sub>2</sub>,<sup>49</sup> and (2) the slow surface reaction of a [C<sub>6</sub>F<sub>5</sub>Xe]<sup>+</sup> salt with [N(CH<sub>3</sub>)<sub>4</sub>]F in CH<sub>2</sub>Cl<sub>2</sub>.<sup>47</sup> Reactions of [C<sub>6</sub>F<sub>5</sub>Xe][BF<sub>4</sub>] with different sources of nucleophiles ([N(CH<sub>3</sub>)<sub>4</sub>]F, (CH<sub>3</sub>)<sub>3</sub>SiCl and (C<sub>2</sub>H<sub>5</sub>)<sub>3</sub>SiH, and Cd(C<sub>6</sub>F<sub>5</sub>)<sub>2</sub>) in coordinating solvents (C<sub>2</sub>H<sub>5</sub>CN, CH<sub>3</sub>CN, and CD<sub>3</sub>CN) have been explored in greater detail and have led to improved yields for C<sub>6</sub>F<sub>5</sub>XeY.

Reaction of [C<sub>6</sub>F<sub>5</sub>Xe][BF<sub>4</sub>] with [N(CH<sub>3</sub>)<sub>4</sub>]F in C<sub>2</sub>H<sub>5</sub>CN solution afforded nearly complete conversion of [C<sub>6</sub>F<sub>5</sub>Xe][BF<sub>4</sub>] to give C<sub>6</sub>F<sub>5</sub>XeF (95%), C<sub>6</sub>F<sub>5</sub>H (5%), and trace amounts of C<sub>6</sub>F<sub>6</sub>.<sup>50</sup> More rapid reaction rates and improved yields were obtained for a modified literature synthesis of C<sub>6</sub>F<sub>5</sub>XeF in which 1.5 equivalents of [N(CH<sub>3</sub>)<sub>4</sub>]F were allowed to react with [C<sub>6</sub>F<sub>5</sub>Xe][BF<sub>4</sub>] in CH<sub>2</sub>Cl<sub>2</sub> (Eq. 2).



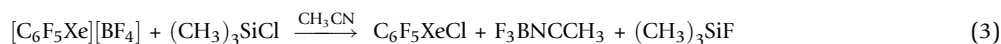


**Fig. 1** The molecular structure of  $C_6F_5XeF$  showing the most significant intermolecular contacts; the fluorine atoms of the  $C_6F_5$  groups are not depicted. The thermal ellipsoids are drawn at the 50% probability level. Reproduced with permission from Bilir, V.; Frohn, H.-J. *Acta Chim. Slov.* **2013**, *60*, 505–512.

Addition of *n*-pentane to  $CH_2Cl_2$  improved reaction yields by promoting  $[N(CH_3)_4]^+$  salt precipitation. Single crystals of  $C_6F_5XeF$  were obtained by slow removal of  $CH_2Cl_2$  solvent under dynamic vacuum and LT SCXRD provided the first structural characterization of  $C_6F_5XeF$  (Fig. 1).

The coordination environment of xenon in the crystal structure of  $C_6F_5XeF$  is an  $AX_2E_3$  VSEPR arrangement in which the C–Xe–F bond angle is near linear ( $178.67(6)$ ,  $179.67(6)^\circ$ ). The Xe–C bond ( $2.128(2)$ ,  $2.132(2)$  Å) is significantly longer than those of the  $[AsF_6]^-$  ( $2.079(6)$  Å),<sup>51</sup>  $[B(CN)_4]^-$  ( $2.081(3)$  Å),<sup>52</sup> and  $[B(CF_3)_4]^-$  ( $2.104(5)$  Å)<sup>52</sup> salts of  $[C_6F_5Xe]^+$  and somewhat longer than those of the  $[B(CN)_4]^-$  and  $[B(CF_3)_4]^-$  salts of the  $CH_3CN$  adduct-cation,  $[C_6F_5Xe \cdots NCCH_3]^+$  ( $2.100(10)$ ,  $2.100(6)$  Å).<sup>52</sup> The terminal Xe–F bond ( $2.172(1)$ ,  $2.182(1)$  Å) is somewhat longer than those of  $XeF_2$  ( $1.999(2)$  Å),<sup>53</sup> but significantly shorter than the Xe $\cdots$ F secondary bonds of the strongly ion-paired  $[C_6F_5Xe]^+$  salts ( $2.672(5)$ – $2.913(4)$  Å),<sup>51,52</sup> and is best described as a highly polar-covalent bond.

The synthesis of  $C_6F_5XeCl$  had previously been achieved by reaction of  $[C_6F_5Xe][AsF_6]$  with  $4-ClC_5H_5N \cdot HCl$  in  $CH_2Cl_2$  solvent at  $-78$  °C,<sup>54</sup> whereas attempts to prepare  $C_6F_5XeCl$  by reaction of  $(CH_3)_3SiCl$  with  $[C_6F_5Xe][AsF_6]$  in  $CH_2Cl_2$  yielded  $[(C_6F_5Xe)_2Cl][AsF_6]$ ,  $(CH_3)_3SiF$ ,  $AsCl_3$ , and  $Cl_2$ .<sup>54</sup> When the latter reaction was carried out in a  $CH_2Cl_2/CH_3CN$  solvent mixture,  $[(C_6F_5Xe)_2Cl][AsF_6]$ ,  $(CH_3)_3SiF$ , and  $F_5As \cdot NCCH_3$  were formed.<sup>54</sup> The reaction of  $[C_6F_5Xe][BF_4]$  with  $(CH_3)_3SiCl$  in  $CH_3CN$  solvent at  $-40$  °C was shown to yield  $C_6F_5XeCl$ ,  $F_3BNCCH_3$ , and  $(CH_3)_3SiF$  in quantitative yields (Eq. 3). When the influence of the reactive  $[C_6F_5Xe]^+$  cation on the formation of  $C_6F_5XeCl$  was studied by reaction of  $[N(n-C_4H_9)_4][BF_4]$  with  $(CH_3)_3SiCl$  under similar reaction conditions, only low yields ( $\sim 17\%$ ) of the desired product,  $N(n-C_4H_9)_4Cl$ , were obtained. This indicated that a highly electrophilic cation such as  $[C_6F_5Xe]^+$  is required for F/Cl substitution. The reaction of  $[C_6F_5Xe][BF_4]$  with  $(C_2H_5)_3SiH$  in  $CD_3CN$  was carried out in an attempt to prepare  $C_6F_5XeH$ , but yielded  $C_6F_5H$ ,  $[C_6F_5C(CD_3)=N(H,D)_2][BF_4]$ ,  $C_6F_5D$ ,  $Xe(C_6F_5)_2$ ,  $(C_6F_5)_2$ , and  $BF_3 \cdot NCCD_3$  instead. Reaction of  $[C_6F_5Xe][BF_4]$  with  $Cd(C_6F_5)_2$  gave  $Xe(C_6F_5)_2$  and  $Cd[BF_4]_2$  in near-quantitative yield.



Both  $C_6F_5XeF$  and  $C_6F_5XeCl$  were characterized by  $^{19}F$  solution NMR spectroscopy and  $C_6X_5XeCl$  was also characterized by  $^{129}Xe$  NMR Spectroscopy (Table 3).

**Table 3** The  $^{19}F$  and  $^{129}Xe$  NMR parameters of  $C_6F_5XeF$  and  $C_6F_5XeCl$ .

	Chem shift ( $\delta$ ) (ppm)				Coupling constant (Hz)			
	$^{129}Xe$	$^{19}F$			$^3J(F_{2,6}-^{129}Xe)$	$^3J(F_{4-}F_{3,5})$	$^4J(F_{4-}F_{2,6})$	$^1J(^{19}F-^{129}Xe)$
		XeF	<i>o</i> - $C_6F_5$	<i>p</i> - $C_6F_5$	<i>m</i> - $C_6F_5$			
$C_6F_5XeF$								
<sup>a</sup>			–129.0 (m)	–146.6 (t)	–156.2 (m)	81	20	
$C_6F_5XeCl$								
<sup>a</sup>			–139.3 (m)	–154.5 (t)	–162.7 (m)		21	
<sup>b</sup>			–130.3 (m)	–146.7 (t)	–156.4 (m)	91	20	3
<sup>c</sup>	–4077 <sup>d</sup>	–2.2 (s) <sup>e</sup>	–131.1 (m)	–147.3 (t)	–157.1 (m)	94	21	4030

<sup>a</sup>In  $CH_2Cl_2/n-C_5H_{12}$ ,  $-80$  °C

<sup>b</sup>In  $CH_3CN$ ,  $-40$  °C.

<sup>c</sup>In  $C_2H_5CN$ ,  $-80$  °C.

<sup>d</sup> $\Delta\nu = 206$  Hz.

<sup>e</sup> $\Delta\nu = 153$  Hz.

### 1.08.3.1.2 Xe(OSO<sub>2</sub>F)<sub>2</sub>

The xenon(II) fluorosulfate, Xe(OSO<sub>2</sub>F)<sub>2</sub>, was initially synthesized in 1969 by the LT reaction of XeF<sub>2</sub> with HSO<sub>3</sub>F.<sup>55</sup> It was shown to be thermodynamically unstable, decomposing to Xe and S<sub>2</sub>O<sub>6</sub>F<sub>2</sub> at RT. It was not until 1972 that further experiments were reported along with key Raman vibrational bands and unit cell parameters<sup>56</sup>; whereas <sup>19</sup>F and <sup>129</sup>Xe NMR spectra were reported in 1974<sup>57</sup> and 1978,<sup>58</sup> respectively. Recently, Xe(OSO<sub>2</sub>F)<sub>2</sub> was synthesized as previously described and single crystals were obtained from HSO<sub>3</sub>F solvent and characterized by SCXRD (Fig. 2).<sup>59</sup>

The primary coordination environment of xenon in Xe(OSO<sub>2</sub>F)<sub>2</sub> is an AX<sub>2</sub>E<sub>3</sub> VSEPR arrangement in which the Xe atom is covalently bound to an O atom of each fluorosulfate group to give a near linear O–Xe–O AX<sub>2</sub>E<sub>3</sub> arrangement, where ∠O–Xe–O = 179.13(4)°. The Xe–O bond lengths (2.1101(13), 2.1225(13) Å) are consistent with Xe–O bonds that are only slightly shorter than in FXeOSO<sub>2</sub>F (2.155(8) Å).<sup>60</sup> The S–O bridge bonds (1.5237(13), 1.5334(13) Å) are significantly longer than the terminal S=O bonds (1.4092(14)–1.4150(14) Å), and are in good agreement with FXeOSO<sub>2</sub>F (1.501(8) Å).

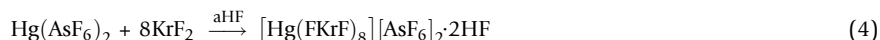
### 1.08.3.2 Transition-metal coordination complexes of NgF<sub>2</sub> (Ng = Kr, Xe)

The ligand behaviors of KrF<sub>2</sub> and XeF<sub>2</sub> are well established and have been described in several reviews.<sup>21,22,61</sup> To stabilize NgF<sub>2</sub> coordination complexes, the fluoride-ion affinity of the acceptor must be closely matched with the fluorobasicity of NgF<sub>2</sub>, and the acceptor must be resistant to oxidative fluorination by the polarized NgF<sub>2</sub> molecule which has enhanced [NgF]<sup>+</sup> character. Xenon difluoride forms coordination complexes with a considerable number of fluoride-ion acceptors which include, but are not limited to, main-group and transition-metal cations (i.e., Li<sup>+</sup>, Mg<sup>2+</sup>, Ca<sup>2+</sup>, Cu<sup>2+</sup>, Zn<sup>2+</sup>, Sr<sup>2+</sup>, Ag<sup>+</sup>, Cd<sup>2+</sup>, Ba<sup>2+</sup>, La<sup>3+</sup>, Nd<sup>3+</sup>, Pb<sup>2+</sup>,<sup>12,21</sup> La<sup>3+</sup>, Ce<sup>3+</sup>, Pr<sup>3+</sup>, Nd<sup>3+</sup>, Sm<sup>3+</sup>, Eu<sup>3+</sup>, Gd<sup>3+</sup>, Tb<sup>3+</sup>, and Dy<sup>3+</sup>, Y<sup>3+</sup><sup>63</sup>), the high-oxidation-state halogen cations [ClO<sub>2</sub>]<sup>+</sup><sup>63</sup> and [BrO<sub>2</sub>]<sup>+</sup>,<sup>64,65</sup> the noble-gas cation [XeF<sub>5</sub>]<sup>+</sup>,<sup>21,66</sup> and the neutral transition-metal oxide tetrafluorides MOF<sub>4</sub> (M = Cr,<sup>67–69</sup> Mo,<sup>69,70</sup> W<sup>69,70</sup>).

In contrast, crystallographically characterized examples of KrF<sub>2</sub> coordination compounds are very rare due to the thermodynamic instability and exceptional oxidative fluorinating strength of KrF<sub>2</sub> and its derivatives. The only KrF<sub>2</sub> coordination complexes that have been structurally characterized by SCXRD are [F<sub>2</sub>OBr(FKrF)<sub>2</sub>AsF<sub>6</sub>],<sup>64</sup> Hg(FKrF)<sub>1.5</sub>(OTeF<sub>5</sub>)<sub>2</sub>,<sup>71</sup> KrF<sub>2</sub>·MOF<sub>4</sub> (M = Cr,<sup>67</sup> Mo,<sup>70</sup> W<sup>70</sup>), KrF<sub>2</sub>·2CrOF<sub>4</sub>,<sup>67</sup> [F<sub>5</sub>Xe(FKrF)<sub>n</sub>AsF<sub>6</sub>] (n = 1, 2),<sup>72</sup> [Mg(FKrF)<sub>4</sub>(AsF<sub>6</sub>)<sub>2</sub>], and [Mg(FKrF)<sub>4</sub>(AsF<sub>6</sub>)<sub>2</sub>].2BrF<sub>5</sub>.<sup>73</sup>

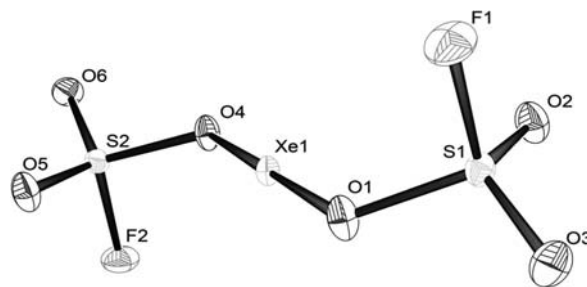
#### 1.08.3.2.1 [Hg(FKrF)<sub>8</sub>][AsF<sub>6</sub>]<sub>2</sub>·2HF

Reaction of Hg(AsF<sub>6</sub>)<sub>2</sub> with approximately 10 equivalents of KrF<sub>2</sub> in aHF solvent yielded the first homoleptic KrF<sub>2</sub> coordination complex of a transition-metal cation as the HF-solvated salt, [Hg(FKrF)<sub>8</sub>][AsF<sub>6</sub>]<sub>2</sub>·2HF, (Eq. 4).<sup>74</sup>



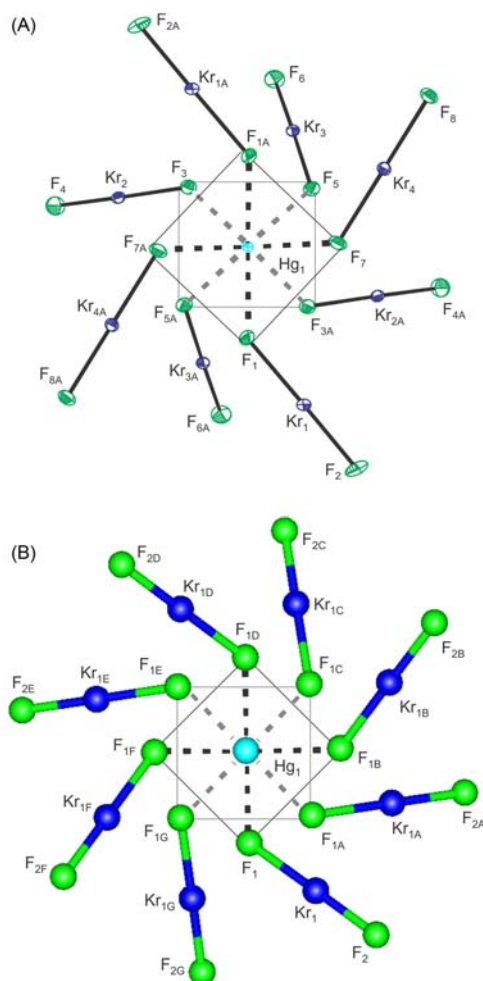
The crystal structure consists of well-isolated [Hg(FKrF)<sub>8</sub>]<sup>2+</sup> dications and [AsF<sub>6</sub>]<sup>−</sup> anions in which the primary coordination sphere of Hg is a distorted square-antiprism consisting of eight terminally coordinated KrF<sub>2</sub> molecules that interact with Hg<sup>2+</sup> through Hg···F<sub>b</sub> bridge bonds (Fig. 3). The Hg coordination sphere is well reproduced by the gas-phase, optimized geometry of [Hg(FKrF)<sub>8</sub>]<sup>2+</sup> (Fig. 3). The Hg···F<sub>b</sub> bridge bonds (2.300(1)–2.412(1) Å) are significantly shorter than the Hg···F<sub>b</sub> bonds of Hg(FKrF)<sub>1.5</sub>(OTeF<sub>5</sub>)<sub>2</sub> (2.664(3) Å). The asymmetric coordination of KrF<sub>2</sub> results from polarized Kr–F bonds that give significantly shorter Kr–F<sub>i</sub> (1.822(1)–1.852(1) Å) and longer Kr–F<sub>b</sub> bonds (1.933(1)–1.957(1) Å) than free KrF<sub>2</sub> (1.894(5) Å).<sup>75</sup> Similar Kr–F bond length differences have been observed for the KrF<sub>2</sub> ligands of [F<sub>5</sub>Xe(FKrF)<sub>n</sub>AsF<sub>6</sub>] (n = 1, 2),<sup>72</sup> [Mg(FKrF)<sub>4</sub>(AsF<sub>6</sub>)<sub>2</sub>], [Mg(FKrF)<sub>4</sub>(AsF<sub>6</sub>)<sub>2</sub>].2BrF<sub>5</sub>,<sup>73</sup> [F<sub>2</sub>OBr(FKrF)<sub>2</sub>AsF<sub>6</sub>],<sup>64</sup> and KrF<sub>2</sub>·MOF<sub>4</sub> (M = Cr,<sup>67</sup> Mo,<sup>70</sup> W<sup>70</sup>). The Hg–F<sub>b</sub>–Kr bond angles are non-linear (124.0(1)–134.3(1)°), which suggests the Hg···F<sub>b</sub> bridge bonds have a degree of covalent character (vide infra).

The Raman spectrum of [Hg(FKrF)<sub>8</sub>][AsF<sub>6</sub>]<sub>2</sub>·2HF was fully assigned with the aid of calculated gas-phase vibrational frequencies and intensities for [Hg(FKrF)<sub>8</sub>]<sup>2+</sup>. Although the calculated vibrational displacements showed no significant intraligand coupling between the Kr–F<sub>i</sub> and Kr–F<sub>b</sub> stretching modes, interligand coupling was observed in the Raman spectrum and subsequently predicted. The coupled Kr–F<sub>i</sub> stretches occur between 540 and 603 cm<sup>−1</sup> (calcd. 584–614 cm<sup>−1</sup>), whereas the coupled Kr–F<sub>b</sub> stretches



**Fig. 2** The molecular structure of Xe(OSO<sub>2</sub>F)<sub>2</sub>; thermal ellipsoids are drawn at the 50% probability level. Reproduced with permission from Malischewski, M.; Seppelt, K. *Acta Crystallogr.* **2015**, *E71*, 363–365.





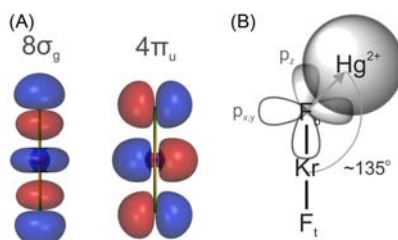
**Fig. 3** The  $[\text{Hg}(\text{FKrF})_8]^{2+}$  cation (A) in the single-crystal X-ray structure of  $[\text{Hg}(\text{FKrF})_8][\text{AsF}_6]_2 \cdot 2\text{HF}$  viewed down the  $C_2$ -axis with thermal ellipsoids drawn at the 50% probability level and (B) calculated ( $S_8$ ) at the B3LYP/def2-TZVPD level of theory and viewed down the  $S_8$ -axis. Dashed lines indicate bonds coming out (black) and going into (grey) the plane of the page. Square faces of square-antiprismatic polyhedron are indicated by narrow lines. Reproduced with permission from DeBackere, J. R.; Schrobilgen, G. J. *Angew. Chem. Int. Ed.* **2018**, *57*, 13167–13171.

were observed at lower frequencies (exptl. 449, 508  $\text{cm}^{-1}$ ; calcd. 413–467  $\text{cm}^{-1}$ ), consistent with their relative degrees of covalency. The vibrational frequencies of these modes are comparable to those of other  $\text{KrF}_2$  complexes.<sup>64,67,70–73,76</sup>

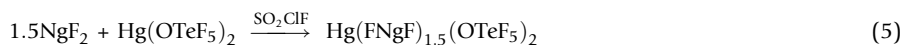
Computational studies indicate that both electrostatic and orbital interactions are involved in metal–ligand bonding and provide insight into the geometry of  $[\text{Hg}(\text{FKrF})_8]^{2+}$  and the nature of its ligand bonding. The NBO analysis of  $[\text{Hg}(\text{FKrF})_8]^{2+}$  indicates that the  $\text{Hg} \cdots \text{F}_b$  bridge bonds have a degree of covalent character, and the NPA charges of the  $\text{KrF}_2$  ligands reveal significantly more negative charge on  $\text{F}_b$  than on  $\text{F}_t$ , consistent with ligand polarization. An energy decomposition analysis (EDA) of the  $\text{Hg} \cdots \text{F}_b$  bridge bonds shows that there are significant orbital ( $\Delta E_{\text{orb}} = -940.1 \text{ kJ mol}^{-1}$ ) and electrostatic ( $\Delta E_{\text{elstat}} = -651.0 \text{ kJ mol}^{-1}$ ) interactions that contribute to the stabilization of  $[\text{Hg}(\text{FKrF})_8]^{2+}$ . A complementary, extended transition state natural orbitals for chemical valence (ETS-NOCV) analysis further partitioned the orbital contributions ( $\Delta E_{\text{orb}}$ ) obtained from the EDA analysis. The analysis showed each  $\text{KrF}_2$  ligand  $\sigma$ -donates electron density from two different fragment orbitals into the unoccupied 6s and 6p orbitals of  $\text{Hg}^{2+}$  (Fig. 4), and accounts for the bent  $\text{Hg} \cdots \text{F}_b \text{--} \text{Kr}$  bond angles observed in the crystal structure of  $[\text{Hg}(\text{FKrF})_8][\text{AsF}_6]_2 \cdot 2\text{HF}$ .

### 1.08.3.2.2 $\text{Hg}(\text{FNgF})_{1.5}(\text{OTeF}_5)_2$

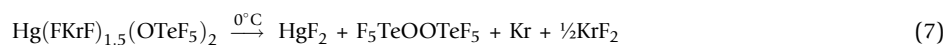
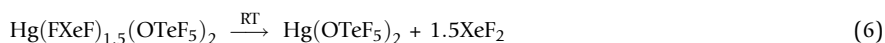
The synthesis of high-purity  $\text{Hg}(\text{OTeF}_5)_2$  has led to its LT structural characterization in the solid state by Raman spectroscopy and SCXRD and in solution by  $^{19}\text{F}$  NMR spectroscopy.<sup>71</sup> The reactions of Lewis acidic  $\text{Hg}(\text{OTeF}_5)_2$  with  $\text{NgF}_2$  ( $\text{Ng} = \text{Xe}, \text{Kr}$ ) in  $\text{SO}_2\text{ClF}$  solvent yielded stable coordination complexes that were also characterized at LT by Raman spectroscopy and SCXRD (Eq. 5).<sup>71</sup> Although the solid  $\text{Hg}(\text{FNgF})_{1.5}(\text{OTeF}_5)_2$  coordination complexes are stable under  $\text{SO}_2\text{ClF}$  solvent and as dry



**Fig. 4** (A) The occupied Kohn-Sham  $8\sigma_g$  and  $4\pi_u$  MOs of  $\text{KrF}_2$ . (B) A simplified diagram showing the interaction of the unoccupied  $6s$  AO of  $\text{Hg}^{2+}$  with the  $F_b$  “ $2p_z$ ” and “ $2p_{x,y}$ ” AO-components of the  $8\sigma_g$  and  $4\pi_u$  MOs, respectively. These interactions, along with those involving the  $6p$  AOs of  $\text{Hg}^{2+}$  (not shown), account for the nonlinear  $\text{Hg}-\text{F}-\text{Kr}$  contact angle ( $\sim 135^\circ$ ). Reproduced with permission from DeBackere, J. R.; Schrobilgen, G. J. *Angew. Chem. Int. Ed.* **2018**, *57*, 13167–13171.



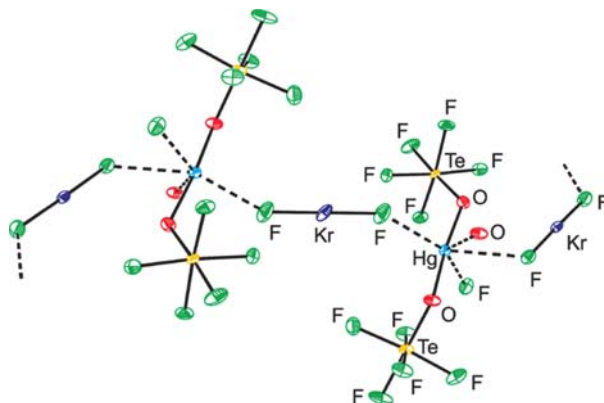
solids at  $-78^\circ\text{C}$ , upon warming to room-temperature (Xe) or  $0^\circ\text{C}$  (Kr), the solid compounds either dissociated (Eq. 6), or underwent redox decomposition (Eq. 7).



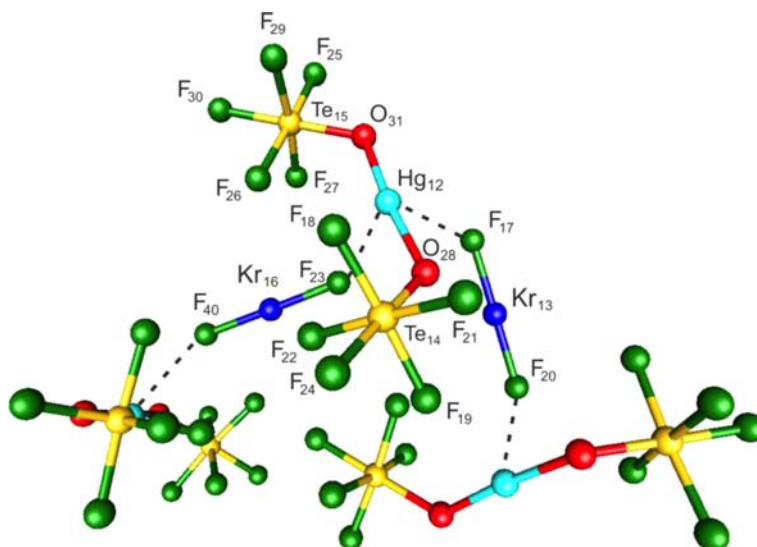
The complexes are isostructural, where the  $\text{Hg}(\text{OTeF}_5)_2$  moieties of  $\text{Hg}(\text{FNgF})_{1.5}(\text{OTeF}_5)_2$  have *gauche*-conformations and are linked by bridging  $\text{NgF}_2$  molecules that result in infinite-chain structures (Fig. 5). The secondary  $\text{Hg}\cdots\text{F}_b$  bonds with  $\text{XeF}_2$  ligands ( $2.606(5)$ – $2.701(5)$  Å) are marginally shorter than those of the  $\text{KrF}_2$  analogue ( $2.664(3)$ – $2.741(3)$  Å), consistent with the greater ionic characters of the  $\text{Xe}-\text{F}$  bonds in the  $\text{XeF}_2$  analogue. There are two crystallographically nonequivalent  $\text{NgF}_2$  molecules in the asymmetric units of  $\text{Hg}(\text{FNgF})_{1.5}(\text{OTeF}_5)_2$ ; one is symmetrically bridged ( $\text{Ng}-\text{F}$ , (Kr)  $1.883(3)$  Å; (Xe)  $1.981(4)$  Å), and the other is asymmetrically bridged ( $\text{Ng}-\text{F}$ , (Kr)  $1.885(3)$ ,  $1.897(3)$  Å; (Xe)  $1.991(4)$ ,  $2.012(4)$  Å). In both cases, the  $\text{Ng}-\text{F}$  bond lengths are equal within  $\pm 3\sigma$  to those of  $\text{NgF}_2$  (Kr,  $1.894(5)$  Å; Xe,  $1.999(4)$  Å). The crystal structures provide the first examples of coordination compounds in which  $\text{NgF}_2$  coordinates to  $\text{Hg}(\text{II})$  in a neutral covalent compound, and the first symmetrically bridged  $\text{KrF}_2$  coordination complex to be structurally characterized.

Calculated gas-phase vibrational frequencies and atomic displacements for the model compounds,  $(\text{F}_5\text{TeO})_2\text{Hg}\cdots(\text{FNgF}\cdots\text{Hg}(\text{OTeF}_5)_2)_2$  (Fig. 6), which well reproduced the experimental values, were used to assign the Raman spectra of  $\text{Hg}(\text{FNgF})_{1.5}(\text{OTeF}_5)_2$ .

The calculated vibrational displacements show that the stretching modes of the bridging  $\text{KrF}_2$  and  $\text{XeF}_2$  ligands are extensively coupled. The bands at  $468$  (Kr)  $\text{cm}^{-1}$  and  $489$ ,  $501$ ,  $508$  (Xe)  $\text{cm}^{-1}$  are assigned to  $\text{NgF}_2$  ligand stretching modes that are derived from the symmetric stretches of free  $\text{NgF}_2$  (Kr:  $464$   $\text{cm}^{-1}$ ; Xe:  $494$   $\text{cm}^{-1}$ ), whereas the bands at  $558$  and  $553$  (Kr)  $\text{cm}^{-1}$  and  $518$  (Xe)  $\text{cm}^{-1}$  are assigned to  $\text{NgF}_2$  ligand stretching modes that are derived from the asymmetric stretches of free  $\text{NgF}_2$  (Kr:  $580$   $\text{cm}^{-1}$ ; Xe:  $555$   $\text{cm}^{-1}$ ). The ligand bending modes are observed at  $237$ ,  $260$   $\text{cm}^{-1}$  (Kr) and at  $223$ ,  $241$   $\text{cm}^{-1}$  (Xe) and are shifted to slightly higher frequencies relative to those of free  $\text{NgF}_2$  (Kr:  $236$   $\text{cm}^{-1}$ ; Xe:  $213$   $\text{cm}^{-1}$ ).



**Fig. 5** The chain structure in the X-ray crystal structure of  $\text{Hg}(\text{OTeF}_5)_2 \cdot 1.5\text{KrF}_2$ , where thermal ellipsoids are drawn at the 50% probability level. Secondary bonding interactions with the F and O atoms of adjacent  $\text{KrF}_2$  and  $-\text{OTeF}_5$  groups to  $\text{Hg}(\text{II})$  are indicated by dashed lines. Reproduced with permission from DeBackere, J. R.; Mercier, H. P. A.; Schrobilgen, G. J. *J. Am. Chem. Soc.* **2014**, *136*, 3888–3903.



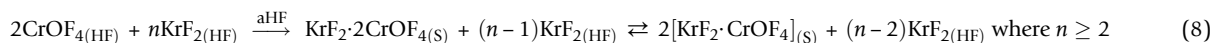
**Fig. 6** The gas-phase, energy-minimized geometry of  $(F_5TeO)_2Hg--(FKrF--Hg(OTeF_5)_2)_2$  ( $C_1$ ) calculated at the PBE1PBE/def2-TZVPP level of theory. The dashed lines designate long contacts between the Hg(II) atom of the central  $Hg(OTeF_5)_2$  unit and the oxygen atoms of two adjacent terminal  $Hg(OTeF_5)_2$  molecules. Reproduced with permission from DeBackere, J. R.; Mercier, H. P. A.; Schrobilgen, G. J. *J. Am. Chem. Soc.* **2014**, *136*, 3888–3903.

Quantum-chemical calculations were used to assess the nature of the Hg--F secondary bond. NBO analyses of the model  $(F_5TeO)_2Hg--(F_bNgF_b--Hg(OTeF_5)_2)_2$  compound show small negative charge transfers from both  $NgF_2$  ligands to the central (Kr,  $-0.038$ ; Xe,  $-0.046$ ) and both terminal (Kr,  $-0.040$ ; Xe,  $-0.046$ )  $Hg(OTeF_5)_2$  units. This, coupled with the small Wiberg bond indices of the secondary Hg--F<sub>b</sub> bonds ( $\sim 0.06$ ), indicates that these interactions are primarily electrostatic,  $\sigma$ -hole type bonds.<sup>77</sup>

#### 1.08.3.2.3 $NgF_2 \cdot nCrOF_4$ , $NgF_2 \cdot MOF_4$ , and $XeF_2 \cdot 2MOF_4$ ( $n = 1, 2$ ; $M = Mo, W$ )

The noble-gas difluorides are moderate strength fluoride-ion donors that form coordination complexes with the Lewis acidic Group 6 oxide tetrafluorides. Until recently, the only example of an  $NgF_2$  complex with  $CrOF_4$  was  $KrF_2 \cdot CrOF_4$ ,<sup>78</sup> which was obtained as an intermediate in the synthesis of  $CrOF_4$  by the oxidative fluorination of  $CrO_2F_2$  with  $KrF_2$  and was structurally characterized by LT Raman and infrared spectroscopies. In addition,  $XeF_2 \cdot WOF_4$  was the only  $NgF_2 \cdot nMOF_4$  ( $n = 1, 2$ ;  $M = Mo, W$ ) complex to have been structurally characterized by SCXRD, albeit at low-precision.<sup>79</sup> Low-temperature solution  $^{19}F$  and  $^{129}Xe$  NMR studies in both  $BrF_5$  and  $SO_2ClF$  solvents showed  $F_tXeF_b--MOF_4$ ,  $F_tXeF_b--M(O_3F)-F_b'--M_t'OF_4$ ,  $F_tXeF_b--M(O_3F)-F_b'--M'(OF_3)-F_b''--M_t''OF_4$ , and  $F_tXeF_b--M(O_3F)-F_b'--M'(OF_3)-F_b''--M''(OF_3)-F_b'''--M_t'''OF_4$  have Xe–F<sub>b</sub>–M bridges and metal-fluorine-metal bridges that are non-labile on the NMR time scale, with structures having *trans*, *trans*-arrangements of the  $M=O$  and  $M_t'=O/M_t''=O/M_t'''=O$  bonds with respect to  $F_b'/F_b''/F_b'''$ .<sup>80</sup> The  $KrF_2 \cdot nMOF_4$  ( $n = 1-3$ ) and  $KrF_2 \cdot WOF_4$  complexes were formed at LT in  $SO_2ClF$  solution.<sup>76</sup> Their solution  $^{19}F$  NMR spectra ( $-121^\circ C$ ) provided definitive proof for the formation of  $F_tKrF_b--MoOF_4$ ,  $F_tKrF_b--WOF_4$ ,  $F_tKrF_b--Mo(O_3F)-F_b'--Mo_t'OF_4$ , and  $F_tKrF_b--Mo(O_3F)-F_b'--Mo'(OF_3)-F_b''--Mo_t''OF_4$  complexes having non-labile Kr–F<sub>b</sub>–Mo/W bridges and metal-fluorine-metal bridges that are assigned *trans*, *trans*-arrangements of the  $Mo=O$  and  $Mo_t'=O/Mo_t''=O$  bonds with respect to  $F_b'/F_b''$ .<sup>76</sup> Several of these complexes ( $F_tNgF_b--MOF_4$  and  $F_tXeF_b--M(O_3F)-F_b'--M_t'OF_4$ , where  $Ng = Kr, Xe$  and  $M = Mo, W$ ) have also been characterized in the solid state by Raman spectroscopy, and their spectra were tentatively assigned based on structures deduced from NMR studies.

Most recently,  $NgF_2 \cdot nCrOF_4$ ,  $NgF_2 \cdot MOF_4$ , and  $XeF_2 \cdot 2MOF_4$  ( $Ng = Kr, Xe$ ;  $M = Mo, W$ ) have been synthesized and structurally characterized by LT Raman spectroscopy and SCXRD.<sup>67,70</sup> Although the synthesis of  $KrF_2 \cdot CrOF_4$  by reaction of  $CrO_2F_2$  with  $KrF_2$  in aHF solvent and its vibrational characterization by IR and Raman spectroscopies had been previously described,<sup>78</sup> the  $KrF_2/CrOF_4/HF$  system was subsequently shown to be more complex than previously thought.<sup>67</sup> Raman spectroscopy and SCXRD showed that the previously undocumented coordination complex,  $KrF_2 \cdot 2CrOF_4$ , (Eq. 8) crystallized from aHF at  $-78^\circ C$  along with small amounts of  $KrF_2 \cdot CrOF_4$  when the initial  $KrF_2:CrO_2F_2$  molar ratios were 1.35:1.00.



The  $KrF_2 \cdot 2CrOF_4$  complex was also the major component in equilibrium mixtures even when an initial 3:1 molar ratio of  $KrF_2:CrOF_4$  was used, demonstrating that equilibrium (8) favored  $KrF_2 \cdot 2CrOF_4$  formation below  $-30^\circ C$ . The  $KrF_2 \cdot 2CrOF_4$  complex also remained the dominant species when HF was removed under dynamic vacuum at  $-65^\circ C$ . Equilibrium (8) favored  $KrF_2 \cdot CrOF_4$  when a solid mixture of one equivalent of  $KrF_2 \cdot 2CrOF_4$  and two equivalents of  $KrF_2$  were fused at  $22^\circ C$  and allowed to crystallize at  $22^\circ C$  over a period of 29 h. Hydrogen fluoride solvation of  $KrF_2$  and the low fluoride-ion affinity of  $CrOF_4$  are likely the most significant factors that favor  $KrF_2 \cdot 2CrOF_4$  formation, whereas  $KrF_2 \cdot CrOF_4$  is exclusively favored in melts in the absence of HF.

The  $\text{XeF}_2\text{-CrOF}_4$ ,  $\text{XeF}_2\cdot 2\text{CrOF}_4$ ,  $\text{NgF}_2\cdot\text{MOF}_4$ , and  $\text{XeF}_2\cdot 2\text{MOF}_4$  ( $M = \text{Mo}, \text{W}$ ) complexes were synthesized by reaction of  $\text{NgF}_2$  with  $\text{CrOF}_4$  or  $\text{MOF}_4$  in either melts or aHF solvent (Eqs. 9 and 10).



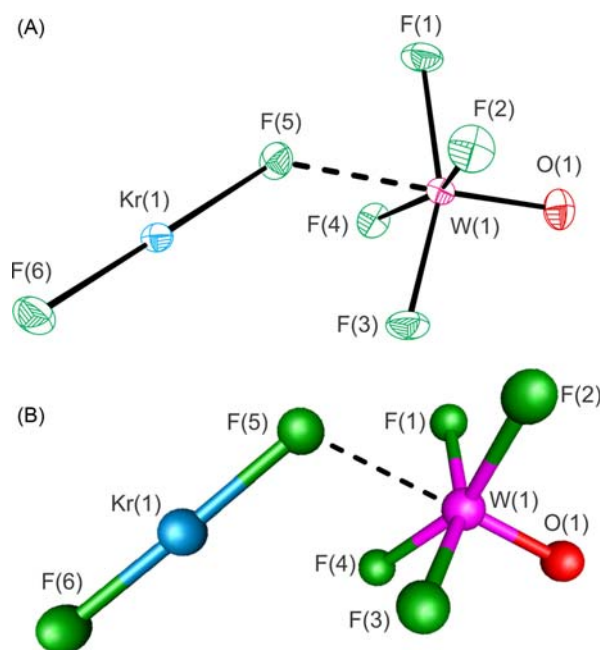
Attempts to synthesize  $\text{KrF}_2\cdot 2\text{MoOF}_4$  in aHF yielded crystalline  $\text{KrF}_2\cdot\text{MoOF}_4$  and the HF solvate,  $[-(\text{F}_4\text{OMo})(\mu_3\text{-F})\text{H}---\text{H}(\mu\text{-F})-]_\infty$ . In contrast, attempts to form the solvated  $\text{WOF}_4$  analogue by dissolution of  $\text{WOF}_4$  in aHF yielded the acidium ion salt,  $[\text{H}_2\text{F}][\text{W}_2\text{O}_2\text{F}_9]$ , consistent with the higher calculated FIA of  $\text{WOF}_4$  ( $-386 \text{ kJ mol}^{-1}$ ) relative to that of  $\text{MoOF}_4$  ( $-355 \text{ kJ mol}^{-1}$ ).<sup>81</sup>

The crystal structures of  $\text{NgF}_2\text{-CrOF}_4$  and  $\text{NgF}_2\cdot\text{MOF}_4$  are best described as coordination complexes in which an F atom of  $\text{NgF}_2$  coordinates into the  $\sigma$ -hole region of Cr or M, that is trans to the  $\text{M}=\text{O}$  bond, to give well isolated  $\text{F}_1\text{-Ng-F}_b---\text{Cr}(\text{O})\text{F}_4$  and  $\text{F}_1\text{-Ng-F}_b---\text{M}(\text{O})\text{F}_4$  structural units (Fig. 7). The  $\text{Ng-F}$  bonds of the  $\text{NgF}_2$  ligand become more polarized as the FIA of the Group 6 oxide tetrafluoride increases ( $\text{CrOF}_4$ ,  $-285$ ;  $\text{MoOF}_4$ ,  $-355$ ;  $\text{WOF}_4$ ,  $-386 \text{ kJ mol}^{-1}$ ),<sup>81</sup> resulting in longer  $\text{Ng-F}_b$  bridge bonds and shorter terminal  $\text{Ng-F}_t$  bonds upon descending Group 6 which is indicative of primarily electrostatic,  $\sigma$ -hole type  $\text{Cr-F}_b/\text{M-F}_b$  bonds. The bent  $\text{Ng-F}_b---\text{Cr}$  and  $\text{Ng-F}_b---\text{M}$  bond angles ( $118.50(8)$ – $150.6(2)^\circ$ ) are similar to those of other terminally coordinated  $\text{NgF}_2$  ( $\text{Ng} = \text{Kr}, \text{Xe}$ ) complexes.<sup>64,65,67,70–73</sup>

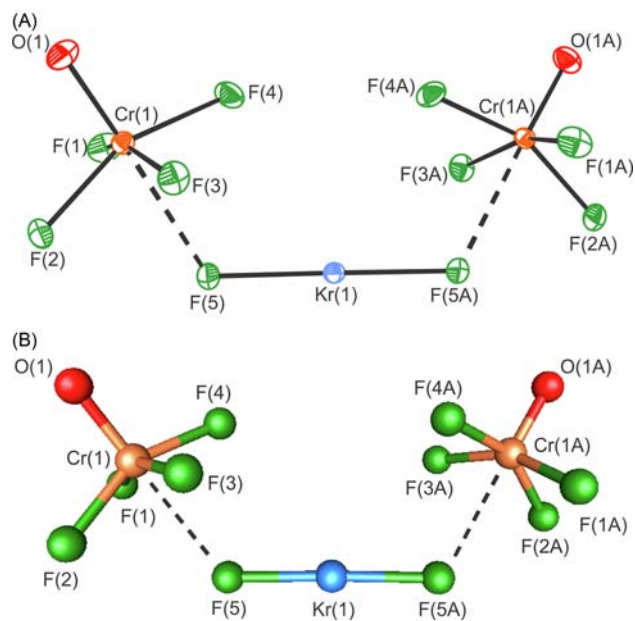
In  $\text{NgF}_2\cdot 2\text{CrOF}_4$ , both fluorine atoms of  $\text{NgF}_2$  coordinate to  $\text{CrOF}_4$  to form  $\text{F}_4(\text{O})\text{Cr}---\text{F}_b\text{-Ng-F}_b---\text{Cr}(\text{O})\text{F}_4$ , where the fluorine bridges are trans to the oxygen atoms and the  $\text{CrOF}_4$  groups are syn to one another (Fig. 8). The  $\text{Kr-F}_b$  ( $1.8882(6) \text{ \AA}$ ) and  $\text{Xe-F}_b$  ( $2.001(1) \text{ \AA}$ ) bond lengths of  $\text{NgF}_2\cdot 2\text{CrOF}_4$  are equal, within  $\pm 3\sigma$ , to those of  $\text{KrF}_2$  ( $1.894(4) \text{ \AA}$ )<sup>75</sup> and  $\text{XeF}_2$  ( $1.999(4) \text{ \AA}$ ),<sup>53</sup> which is indicative of very weak fluorine bridge interactions between  $\text{NgF}_2$  and  $\text{CrOF}_4$ . The structure of  $\text{KrF}_2\cdot 2\text{CrOF}_4$  is only the second example of a bridging  $\text{KrF}_2$  molecule after  $\text{Hg}(\text{FKrF})_{1.5}(\text{OTeF}_5)_2$  (vide supra).<sup>71</sup>

In contrast with  $\text{NgF}_2\cdot 2\text{CrOF}_4$ , one F atom of the  $\text{XeF}_2$  ligand of  $\text{XeF}_2\cdot 2\text{MOF}_4$  ( $M = \text{Mo}, \text{W}$ ) is coordinated to the  $\text{M}(\text{OF}_3)\text{F}_b'$  moiety, where  $\text{F}_b'$  is bridged trans to a second  $\text{M}'\text{OF}_4$  moiety that is, in turn, coordinated trans to the  $\text{M}'=\text{O}$  bond to give the  $\text{F}_t\text{XeF}_b---\text{M}(\text{OF}_3)\text{F}_b'---\text{M}'\text{OF}_4$  arrangement (Fig. 9). The *cis*, *trans*-arrangements of  $\text{M}=\text{O}/\text{M}'=\text{O}$  bonds relative to  $\text{F}_b'$  in the crystal structures contrast with the *trans*, *trans*-arrangements that had been assigned based on prior LT solution  $^{19}\text{F}$  NMR studies.<sup>80</sup>

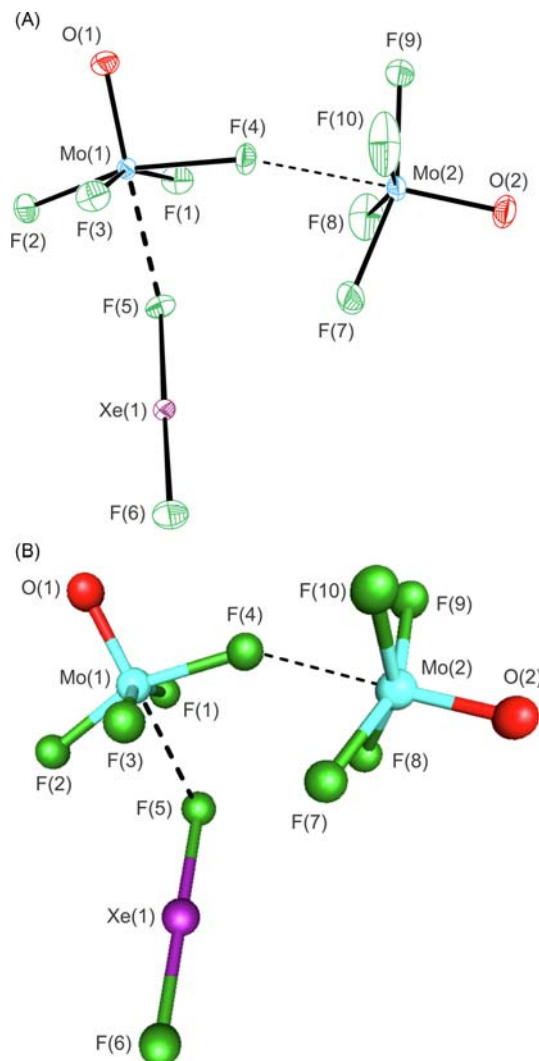
The  $\text{Xe-F}_t$  ( $\text{Mo}, 1.9283(10)$ ;  $\text{W}, 1.922(4) \text{ \AA}$ ) and  $\text{Xe-F}_b$  ( $\text{Mo}, 2.1153(10)$ ;  $\text{W}, 2.136(4) \text{ \AA}$ ) bonds of  $\text{XeF}_2\cdot 2\text{MOF}_4$  ( $M = \text{Mo}, \text{W}$ ) are somewhat shorter and longer, respectively, than those of  $\text{XeF}_2\cdot\text{MOF}_4$  ( $M = \text{Mo}, \text{W}$ ), indicating that  $\text{M}(\text{OF}_3)\text{F}_b'---\text{M}'\text{OF}_4$  is a stronger fluoride-ion acceptor than  $\text{MOF}_4$ . The  $\text{M}---\text{F}_b$  bridge bonds ( $\text{Mo}, 2.1980(9)$ ;  $\text{W}, 2.177(4) \text{ \AA}$ ) are significantly shorter than those of  $\text{XeF}_2\cdot\text{MOF}_4$ , and when combined with the trends observed for  $\text{Xe-F}_t$  and  $\text{Xe-F}_b$  bond lengths, are in accordance with the FIA trend:  $\text{MoOF}_4 < \text{WOF}_4 \approx \text{Mo}(\text{OF}_3)\text{F}_b'---\text{Mo}'\text{OF}_4 < \text{W}(\text{OF}_3)\text{F}_b'---\text{W}'\text{OF}_4$ . The asymmetries of the  $\text{M-F}_b'---\text{M}'$  bridge bonds are consistent with the greater polar covalent characters of the  $\text{M-F}_b'$  bonds ( $\text{Mo-F}_b', 1.9350(10)$ ,  $\text{W-F}_b', 1.929(4) \text{ \AA}$ ) and the primarily electrostatic characters of the  $\text{F}_b'---\text{M}'$  bonds ( $\text{F}_b'---\text{Mo}', 2.2990(10)$ ;  $\text{F}_b'---\text{W}', 2.313(4) \text{ \AA}$ ).



**Fig. 7** (A) The X-ray crystal structure of  $\text{KrF}_2\cdot\text{WOF}_4$  (near-eclipsed conformation) with thermal ellipsoids drawn at the 50% probability level, and (B) its calculated staggered conformation. Reproduced with permission from Bortolus, M. R.; Mercier, H. P. A.; Brock, D. S.; Schrobilgen, G. J. *Chem. Eur. J.* **2022**, *28*, e2021037.



**Fig. 8** (A) The structural unit in the X-ray crystal structure of *syn*- $\text{KrF}_2 \cdot 2\text{CrOF}_4$ , with thermal ellipsoids drawn at the 50% probability level, and (B) the calculated *syn*-conformation of  $\text{KrF}_2 \cdot 2\text{CrOF}_4$ . Reproduced with permission from Mercier, H. P. A.; Breddemann, U.; Brock, D. S.; Bortolus, M. R.; Schrobilgen, G. J. *Chem. Eur. J.* **2019**, *25*, 12105–12119.



**Fig. 9** The X-ray crystal structure of (A)  $\text{XeF}_2 \cdot 2\text{MoOF}_4$  with thermal ellipsoids drawn at the 50% probability level; and (B) its calculated geometry. Reproduced with permission from Bortolus, M. R.; Mercier, H. P. A.; Brock, D. S.; Schrobilgen, G. J. *Chem. Eur. J.* **2022**, *28*, e2021037.



The calculated gas-phase vibrational frequencies and atomic displacements for  $\text{NgF}_2 \cdot \text{MOF}_4$  ( $M = \text{Cr}, \text{Mo}, \text{W}$ ), and  $\text{XeF}_2 \cdot 2\text{MOF}_4$  ( $M = \text{Mo}, \text{W}$ ), and *syn*- $\text{NgF}_2 \cdot 2\text{CrOF}_4$  well reproduced the experimental values and were used to assign their Raman spectra. The  $\nu(\text{Ng}-\text{F}_b)$  and  $\nu(\text{Ng}-\text{F}_t)$  stretching frequencies occur at very similar frequencies for the  $\text{KrF}_2 \cdot \text{MOF}_4$  (566/579 and 462/479 (Mo), and 571/581 and 450/469 (W)  $\text{cm}^{-1}$ ) and  $\text{XeF}_2 \cdot \text{MOF}_4$  (562/567 and 449/466 (Mo) and 571/574 and 437/466 (W)  $\text{cm}^{-1}$ ) complexes.<sup>70</sup> These frequencies are bracketed by those of  $\text{KrF}_2 \cdot \text{CrOF}_4$  (543/550 and 486  $\text{cm}^{-1}$ ) and  $\text{XeF}_2 \cdot \text{CrOF}_4$  (551/562 and 460/465  $\text{cm}^{-1}$ ).<sup>67</sup> Coordination of  $\text{NgF}_2$  to  $\text{MOF}_4$  results in in-plane,  $\delta(\text{F}_b\text{NgF}_t)_{i.p.}$ , and out-of-plane,  $\delta(\text{F}_b\text{NgF}_t)_{o.o.p.}$ , bends that are expected to be very weak, so that only  $\delta(\text{F}_b\text{XeF}_t)_{i.p.}$  (254 (Cr), 277 (Mo) and 274 (W)  $\text{cm}^{-1}$ ) and  $\delta(\text{F}_b\text{XeF}_t)_{o.o.p.}$  (241 (W)  $\text{cm}^{-1}$ ) could be observed in the Raman spectrum.

The Raman spectra of  $\text{XeF}_2 \cdot 2\text{MOF}_4$ , which had been previously assigned to a *trans, trans*-arrangement of  $M=O$  bonds based on solution  $^{19}\text{F}$  NMR studies,<sup>80</sup> were re-assigned based on the *cis, trans*-arrangements of  $M=O$  bonds in their crystal structures.<sup>70</sup> The calculations show no intraligand coupling between  $\nu(\text{Xe}-\text{F}_t)$  and  $\nu(\text{Xe}-\text{F}_b)$ . The bands at 572/574 (Mo) and 582/585 (W)  $\text{cm}^{-1}$  are assigned to  $\nu(\text{Xe}-\text{F}_t)$  and those at 421 (Mo) and 408 (W)  $\text{cm}^{-1}$  are assigned to  $\nu(\text{Xe}-\text{F}_b)$ . Both bending modes,  $\delta(\text{F}_b\text{Xe}_1\text{F}_t)_{i.p.}$  (259, 276 (Mo); 248, 270<sup>80</sup> (W)  $\text{cm}^{-1}$ ) and  $\delta(\text{F}_b\text{Xe}_1\text{F}_t)_{o.o.p.}$  (193/198, 236 (Mo); 193/201, 235/237 (W)  $\text{cm}^{-1}$ ) were observed along with a rocking mode,  $\rho_r(\text{F}_b\text{Xe}_1\text{F}_t)$  (141/146 (Mo); 139/142 (W)  $\text{cm}^{-1}$ ). The torsional bands,  $\rho_r(\text{F}_b\text{Xe}_1\text{F}_t)$ , were too weak to be observed, as in the case of the  $\delta(\text{M}_1\text{F}_b\text{Xe}_1)$  bending modes, are too low in frequency to be observed.

As observed in the Raman spectra of  $\text{Hg}(\text{FNgF})_{1.5}(\text{OTeF}_5)_2$ ,<sup>71</sup> two sets of  $\text{NgF}_2$  stretching bands, derived from the symmetric and asymmetric stretches of the free  $\text{NgF}_2$  molecules are expected for  $\text{NgF}_2 \cdot 2\text{CrOF}_4$  which were observed at 465 and 569  $\text{cm}^{-1}$  (Kr) and 512 and 553  $\text{cm}^{-1}$  (Xe), respectively. The associated deformation bands were predicted to be very weak so that only  $\delta(\text{F}_t\text{KrF}_b)_{i.p.}$  was observed at 246  $\text{cm}^{-1}$ .

Quantum-chemical analyses (QTAIM, ELF, NBO, MEPS, EDA, and ETS-NOCV) were carried out to assess the nature of the bridging interactions, with the MEPS and EDA analyses giving some specific insights into the coordination of  $\text{OF}_4\text{Cr}---\text{FNgF}---\text{CrOF}_4$ <sup>67</sup> and  $\text{XeF}_2 \cdot 2\text{MOF}_4$ .<sup>70</sup> The EP extrema of the  $\text{XeF}_2 \cdot \text{MOF}_4$  MEPS show the fluorine atoms on the metals are significantly more basic than the terminal fluorine of  $\text{XeF}_2$ . Thus, when a second  $\text{M}'\text{OF}_4$  molecule coordinates to  $\text{XeF}_2 \cdot \text{MOF}_4$ , it preferentially coordinates to a more basic fluorine atom of the  $\text{MOF}_4$  moiety of  $\text{F}_t\text{NgF}_b---\text{MOF}_4$  rather than to  $\text{F}_t$  of the  $\text{XeF}_2$  ligand, thereby providing rationales for (1) why coordination of a second  $\text{MOF}_4$  molecule does not result in  $\text{XeF}_2$ -bridged complexes analogous to  $\text{OF}_4\text{Cr}---\text{FNgF}---\text{CrOF}_4$ , and (2) why the O ligands of the  $\text{O}=\text{M}-\text{F}_b'---\text{M}'=\text{O}$  moiety are *cis* to one another and  $\text{XeF}_2$  coordinates *trans* to the  $\text{M}=\text{O}$  bond as in  $\text{XeF}_2 \cdot \text{MOF}_4$ . Energy decomposition analyses of the  $\text{Cr}---\text{F}_b$  and  $\text{M}---\text{F}_b$  bonds for gas-phase  $\text{NgF}_2 \cdot \text{CrOF}_4$ ,  $\text{NgF}_2 \cdot \text{MOF}_4$ ,  $\text{NgF}_2 \cdot 2\text{CrOF}_4$ , and  $\text{XeF}_2 \cdot 2\text{MOF}_4$  ( $\text{Ng} = \text{Kr}, \text{Xe}$ ;  $M = \text{Mo}, \text{W}$ ) show they are primarily electrostatic in nature, with electrostatic contributions ( $\Delta E_{\text{elstat}}$ ) that provide ca. 60–64% of the total attractive interactions between  $\text{NgF}_2$  and  $\text{MOF}_4$ , whereas orbital mixing (covalent) interactions ( $\Delta E_{\text{orb}}$ ) comprise 26–35% of the total bonding interactions. The EDAs show that the  $\text{F}_b'---\text{M}'$  bonds are somewhat weaker than their  $\text{M}---\text{F}_b$  counterparts and the orbital contributions to these bonds account for their non-linear  $\text{M}---\text{F}_b-\text{Xe}$  and  $\text{M}---\text{F}_b'-\text{M}'$  bond angles.

#### 1.08.3.2.4 $[\text{Ln}(\text{XeF}_2)_3][\text{BF}_4]_3$ ( $\text{Ln} = \text{La}, \text{Ce}, \text{Pr}, \text{Nd}, \text{Sm}, \text{Eu}, \text{Gd}, \text{Tb}, \text{Dy}, \text{and Y}$ ), $[\text{Ln}(\text{XeF}_2)][\text{BF}_4]_3$ ( $\text{Ln} = \text{La}, \text{Ce}, \text{Pr}, \text{Nd}$ ), $[\text{La}(\text{XeF}_2)_2][\text{BF}_4]_3$ , and $[\text{Ln}(\text{XeF}_2)]_2[\text{BF}_4]_2$ ( $\text{Ln} = \text{La}, \text{Nd}, \text{Sm}, \text{Eu}, \text{Gd}, \text{Tb}, \text{Dy}, \text{and Y}$ )

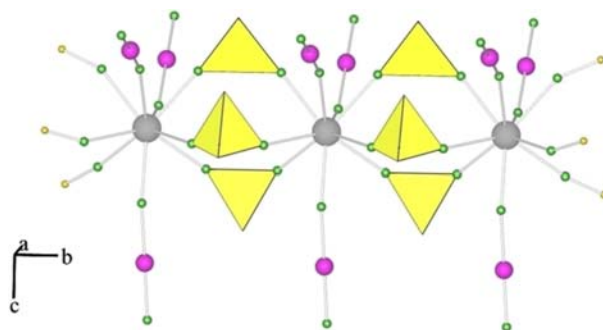
Examples of  $\text{XeF}_2$  coordination complexes having the general formulation,  $[\text{M}^{x+}(\text{XeF}_2)_n][\text{A}^-]_x$ , are known for singly ( $\text{M}^+ = \text{Ag}$ ,<sup>82,83</sup>  $\text{Li}$ <sup>84</sup>), doubly ( $\text{M}^{2+} = \text{Mg}-\text{Ba}, \text{Cu}, \text{Zn}, \text{Cd}, \text{Hg}, \text{Pb}$ ),<sup>85–87</sup> and triply charged ( $\text{M}^{3+} = \text{La}$ ,<sup>88,89</sup>  $\text{Nd}$ <sup>90</sup>) cations. Of these complexes, examples with  $\text{M}^+$  and  $\text{M}^{3+}$  are rarer than those with  $\text{M}^{2+}$ , and  $\text{M}^{3+}$  complexes have only been reported for the lanthanide elements. The Lewis acidity of  $\text{LnF}_3$  increases across the  $\text{La}-\text{Lu}$  row, and early studies of the  $\text{LnF}_3/\text{XeF}_2/\text{BF}_3/\text{aHF}$  ( $\text{Ln} = \text{La}, \text{Nd}, \text{Sm}, \text{Eu}$ ) systems showed clear evidence for the formation of  $\text{XeF}_2$ -containing compounds.<sup>91</sup> However, these species were only characterized by mass balance measurements, thus it was not possible to determine if they were pure compounds or mixtures. Since then, the  $[\text{La}(\text{XeF}_2)_{2.5}][\text{AsF}_6]_3$  and  $[\text{La}(\text{XeF}_2)_3][\text{XF}_6]$  ( $\text{X} = \text{As}, \text{Bi}$ ) complexes have been briefly mentioned in reviews,<sup>88,89</sup> and the syntheses and characterizations of  $[\text{Nd}(\text{XeF}_2)_n][\text{AsF}_6]_3$  ( $n = 2.5$  and 3) have been reported,<sup>90</sup> in which the crystal structure of  $[\text{Nd}(\text{XeF}_2)_{2.5}][\text{AsF}_6]_3$  was described. The coordination chemistries of the lanthanide elements have recently been extended by the syntheses and characterizations of a series of  $\text{XeF}_2$  coordination complexes with  $\text{Ln}$  ( $\text{Ln} = \text{La}, \text{Ce}, \text{Pr}, \text{Nd}, \text{Sm}, \text{Eu}, \text{Gd}, \text{Tb}, \text{Dy}, \text{and Y}$ ). The complexes were obtained by reaction of  $\text{LnF}_3$  with  $\text{XeF}_2$  in  $\text{BF}_3$  acidified *aHF* solvent and were structurally characterized by Raman spectroscopy and single-crystal X-ray diffraction.

Electronic spectra of solutions of  $\text{LnF}_3$  ( $\text{Ln} = \text{Pr}, \text{Nd}$ ) in  $\text{BF}_3/\text{aHF}$  mixtures are known to resemble their respective spectra in aqueous solution,<sup>92</sup> which indicates that the  $\text{Ln}^{3+}$  cations in these systems are present as simple solvated cations with coordination environments that resemble those in water, where  $\text{CN} = 9$ .<sup>93</sup> Removal of volatiles from solutions of  $\text{LnF}_3$  ( $\text{Ln} = \text{La}, \text{Ce}, \text{Pr}, \text{Nd}, \text{Sm}, \text{Eu}, \text{Gd}, \text{Tb}, \text{Dy}, \text{and Y}$ ) in  $\text{BF}_3/\text{aHF}$  mixtures results in  $\text{La}(\text{BF}_4)_3$ ,  $\text{LnF}(\text{BF}_3)_2$  ( $\text{Ln} = \text{La}, \text{Ce}, \text{Pr}, \text{Nd}, \text{Eu}, \text{Gd}, \text{Tb}, \text{Dy}$ ), and  $\text{LnF}_3 \cdot n\text{BF}_3$  side products of unknown composition ( $\text{Ln} = \text{Ho}-\text{Lu}$  and  $\text{Y}$ ).<sup>91,94</sup> In a more recent study, addition of  $\text{XeF}_2$  to  $\text{LnF}_3/\text{BF}_3/\text{aHF}$  ( $\text{Ln} = \text{La}, \text{Ce}, \text{Pr}, \text{Nd}, \text{Sm}, \text{Eu}, \text{Gd}, \text{Tb}, \text{Dy}, \text{and Y}$ ) mixtures yielded a series of coordination complexes having the formulations:  $[\text{Ln}(\text{XeF}_2)_3][\text{BF}_4]_3$  ( $\text{Ln} = \text{La}, \text{Ce}, \text{Pr}, \text{Nd}, \text{Sm}, \text{Eu}, \text{Gd}, \text{Tb}, \text{Dy}, \text{and Y}$ ),  $[\text{Ln}(\text{XeF}_2)][\text{BF}_4]_3$  ( $\text{Ln} = \text{La}, \text{Ce}, \text{Pr}, \text{Nd}$ ),  $[\text{La}(\text{XeF}_2)_2][\text{BF}_4]_3$ , and  $[\text{Ln}(\text{XeF}_2)]_2[\text{BF}_4]_2$  ( $\text{Ln} = \text{La}, \text{Nd}, \text{Sm}, \text{Eu}, \text{Gd}, \text{Tb}, \text{Dy}, \text{and Y}$ ).<sup>62</sup> Raman spectroscopy was the only characterization method for the majority of these salts. Each of the four salt types gave different Raman spectra that had characteristic  $\nu_1(\text{BF}_4)$  and  $\nu(\text{Xe}-\text{F})$  vibrational frequencies which made it possible to distinguish which  $[\text{Ln}(\text{XeF}_2)_n][\text{F}_x\text{BF}_4]_{3-x}$  salts were present in reaction mixtures and whether the coordinated  $\text{XeF}_2$  molecule was terminal or bridging. The Raman spectra of the  $[\text{Ln}(\text{XeF}_2)_n][\text{F}_x\text{BF}_4]_{3-x}$  salts exhibited characteristic bands assigned to  $\text{Xe}-\text{F}_t$  (552–587  $\text{cm}^{-1}$ ) and  $\text{Xe}-\text{F}_b$  (428–485  $\text{cm}^{-1}$ ) stretching bands that were shifted to higher and lower frequencies

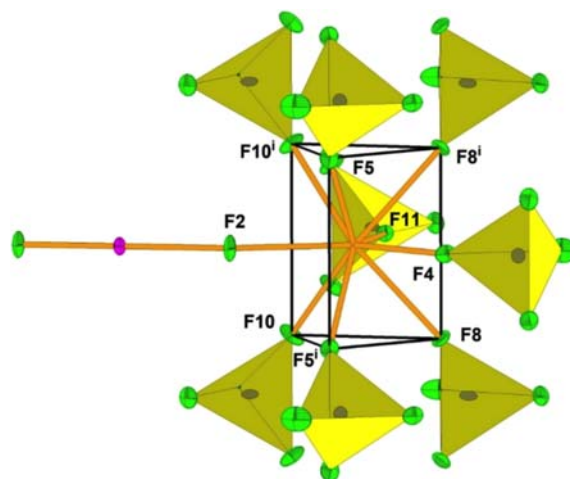
relative to the LT phase of XeF<sub>2</sub> (496 cm<sup>-1</sup>),<sup>22</sup> and consistent with terminal XeF<sub>2</sub> coordination. The crystal structures of [Ln(XeF<sub>2</sub>)<sub>2</sub>](BF<sub>4</sub>)<sub>3</sub> and [Ln(XeF<sub>2</sub>)]F(BF<sub>4</sub>)<sub>2</sub> salts were not obtained, but based on their Raman spectra, the [La(XeF<sub>2</sub>)<sub>2</sub>](BF<sub>4</sub>)<sub>3</sub> salt contains both terminal and bridging XeF<sub>2</sub> ligands, whereas the Raman spectra of [Ln(XeF<sub>2</sub>)]F(BF<sub>4</sub>)<sub>2</sub> (Ln = La, Nd, Sm, Eu, Tb, Dy, Y) showed vibrational bands that can only be assigned to terminal XeF<sub>2</sub> ligands. The Raman spectra also provided evidence for the presence of other compounds that did not contain XeF<sub>2</sub>; among which were LaF(HF)(BF<sub>4</sub>)<sub>2</sub> and LaF(BF<sub>4</sub>)<sub>2</sub>, for which crystal structures were determined. The crystal structures of three XeF<sub>2</sub> coordination complexes; [La(XeF<sub>2</sub>)<sub>3</sub>][BF<sub>4</sub>]<sub>3</sub>, [La(XeF<sub>2</sub>)]<sub>2</sub>[BF<sub>4</sub>]<sub>3</sub>, and [Nd(XeF<sub>2</sub>)]<sub>2</sub>[BF<sub>4</sub>]<sub>3</sub> were determined.<sup>62</sup>

(i) [La(XeF<sub>2</sub>)<sub>3</sub>][BF<sub>4</sub>]<sub>3</sub>. The coordination sphere of the La atom in the crystal structure of [La(XeF<sub>2</sub>)<sub>3</sub>][BF<sub>4</sub>]<sub>3</sub> is best described as a tri-capped trigonal prism (Fig. 10) where La is coordinated to the F atoms of six neighboring [BF<sub>4</sub>]<sup>-</sup> anions (La---F<sub>B</sub>, 2.422(8)–2.474(3) Å) and the F<sub>b</sub> atoms of three crystallographically independent terminally coordinated XeF<sub>2</sub> ligands (La---F<sub>Xe</sub>, 2.391(4)–2.473(6) Å). The [La(XeF<sub>2</sub>)<sub>3</sub>][BF<sub>4</sub>]<sub>3</sub> structural units pack in infinite columns in which the cations and anions are bridged through short ion-pair secondary bonds. The Xe–F<sub>b</sub> bonds (2.058(6), 2.056(4), 2.052(4) Å) are significantly elongated relative to the Xe–F<sub>t</sub> bonds (1.932(7), 1.850(4), 1.825(5) Å), consistent with terminal XeF<sub>2</sub> coordination. The La---F<sub>b</sub>–Xe bond angles are bent (138.8(2), 147.9(5), 152.3(3)°) and are comparable to those observed in other terminally coordinated NgF<sub>2</sub> complexes (vide supra).

(ii) [Ln(XeF<sub>2</sub>)]<sub>2</sub>[BF<sub>4</sub>]<sub>3</sub> (Ln = La, Nd). The crystal structures of [Ln(XeF<sub>2</sub>)]<sub>2</sub>[BF<sub>4</sub>]<sub>3</sub> (Ln = La, Nd) are isotopic and form strongly ion-paired three-dimensional networks of structural units that are interconnected by strong secondary bonds between the Ln<sup>3+</sup> cations and nearby XeF<sub>2</sub> molecules and [BF<sub>4</sub>]<sup>-</sup> anions. As in [La(XeF<sub>2</sub>)<sub>3</sub>][BF<sub>4</sub>]<sub>3</sub>, the coordination sphere of Ln (Fig. 11) is best described as a tri-capped trigonal prism comprised of eight F atoms from neighboring [BF<sub>4</sub>]<sup>-</sup> anions (La---F<sub>B</sub>, 2.437(2)–2.483(3); Nd---F<sub>B</sub>, 2.446(7)–2.511(9) Å) and one F<sub>b</sub> atom from a terminally coordinated XeF<sub>2</sub> molecule (La---F<sub>Xe</sub>, 2.375(4); Nd---F<sub>Xe</sub>, 2.312(7) Å). The XeF<sub>2</sub> ligands in [Ln(XeF<sub>2</sub>)]<sub>2</sub>[BF<sub>4</sub>]<sub>3</sub> (Xe–F<sub>b</sub>, (La) 2.093(4); (Nd) 2.115(6) Å; Xe–F<sub>t</sub>, (La) 1.920(4); (Nd) 1.923(8) Å) are more polarized than in [La(XeF<sub>2</sub>)<sub>3</sub>][BF<sub>4</sub>]<sub>3</sub> (see above), and their Ln---F<sub>b</sub>–Xe bond angles are also bent (La, 154.3(2); Nd, 154.4(4)°).



**Fig. 10** A portion of the infinite column in the crystal structure of [La(XeF<sub>2</sub>)<sub>3</sub>][BF<sub>4</sub>]<sub>3</sub>. Reproduced with permission from Mazej, Z.; Goreshnik, E. *Eur. J. Inorg. Chem.* **2021**, 2669–2681.



**Fig. 11** A portion of the crystal structure of [La(XeF<sub>2</sub>)]<sub>2</sub>[BF<sub>4</sub>]<sub>3</sub> showing the nine-fold coordination sphere of the La atom, where the thermal ellipsoids are drawn at the 50% probability level. Reproduced with permission from Mazej, Z.; Goreshnik, E. *Eur. J. Inorg. Chem.* **2021**, 2669–2681.

### 1.08.3.3 Main-group coordination complexes of NgF<sub>2</sub>

#### 1.08.3.3.1 [O<sub>2</sub>Cl(FXeF)<sub>2</sub>][AsF<sub>6</sub>]

The synthesis and structural characterization of the first Cl(V) coordination complex of XeF<sub>2</sub>, [O<sub>2</sub>Cl(FXeF)<sub>2</sub>][AsF<sub>6</sub>], has been reported.<sup>63</sup> The reaction of  $\alpha$ -[ClO<sub>2</sub>][AsF<sub>6</sub>] with XeF<sub>2</sub> at -78 °C in aHF solvent yielded [O<sub>2</sub>Cl(FXeF)<sub>2</sub>][AsF<sub>6</sub>] (Eq. 11), which provides a rare example of XeF<sub>2</sub> coordination to a halogen Lewis acid center (vide infra).



The low-temperature (LT) phase of  $\beta$ -[ClO<sub>2</sub>][AsF<sub>6</sub>] was also obtained by recrystallization of  $\alpha$ -[ClO<sub>2</sub>][AsF<sub>6</sub>] from aHF solvent at -10 °C. Both compounds were characterized by LT SCXRD (Fig. 12) and LT Raman spectroscopy.

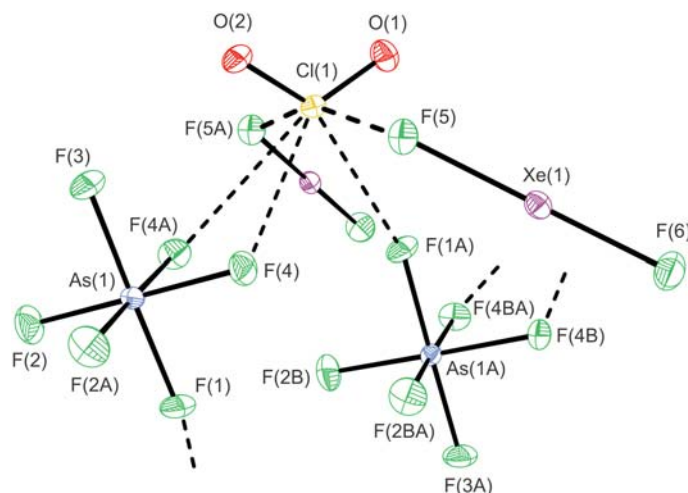
The trajectories of the Cl...F secondary bonds in the crystal structure of [O<sub>2</sub>Cl(FXeF)<sub>2</sub>][AsF<sub>6</sub>] are directed towards regions of high positive electrostatic potential,  $\sigma$ -holes, on the Cl atom. The two shortest Cl...F<sub>Xe</sub> secondary bonds result from terminal coordination of both XeF<sub>2</sub> ligands ( $2 \times 2.4242(10)$  Å) into  $\sigma$ -holes that are located on either side of the triangle defined by the two Cl–O double-bond domains and the VELD domain of Cl. The longest Cl...F secondary bonds are formed with the F atoms of neighboring [AsF<sub>6</sub>]<sup>-</sup> anions (2.6350(13), 3.0307(13), 3.0307(13) Å) that are directed towards  $\sigma$ -holes on Cl that are trans to Cl–O double bond domains. This is presently the only example of seven-coordinate [ClO<sub>2</sub>]<sup>+</sup> (CN<sub>Cl</sub> = 2 + 5) salt, whereas CN<sub>Cl</sub> = 2 + 4 and CN<sub>Cl</sub> = 2 + 6 coordination numbers have been observed for other [ClO<sub>2</sub>]<sup>+</sup> salts.<sup>95</sup>

Terminal coordination of XeF<sub>2</sub> to the Cl atom of [ClO<sub>2</sub>]<sup>+</sup> results in Xe–F<sub>t</sub> bond contraction (1.9721(11) Å) and Xe–F<sub>b</sub> bond elongation (2.0381(10) Å) relative to the Xe–F bonds of XeF<sub>2</sub> (1.999(2) Å).<sup>53</sup> The Xe–F<sub>t</sub> bond is very similar to that of XeF<sub>2</sub>·CrOF<sub>4</sub> (1.969(2) Å),<sup>67</sup> somewhat longer than those of [F<sub>2</sub>OBr(FXeF)<sub>2</sub>][AsF<sub>6</sub>] (1.956(5), 1.960(4) Å),<sup>65</sup> and the Xe–F<sub>b</sub> bonds are somewhat shorter than those of XeF<sub>2</sub>·CrOF<sub>4</sub> (2.057(2) Å) and [F<sub>2</sub>OBr(FXeF)<sub>2</sub>][AsF<sub>6</sub>] (2.052(4), 2.053(4) Å). The Xe–F bonds of the aforementioned complexes are significantly less polarized than those of [XeF][AsF<sub>6</sub>] (Xe–F<sub>t</sub>, 1.888(3) Å; Xe–F<sub>b</sub>, 2.208(3) Å),<sup>53</sup> consistent with a terminally coordinated XeF<sub>2</sub> complex.

Quantum-chemical calculations for the model gas-phase ([O<sub>2</sub>Cl(FXeF)<sub>2</sub>][AsF<sub>6</sub>])<sup>-</sup> anion aided in the assignments of fundamental vibrational frequencies and <sup>35/37</sup>Cl isotopic shifts of [O<sub>2</sub>Cl(FXeF)<sub>2</sub>][AsF<sub>6</sub>] and were employed to assess chemical bonding by use of an NBO analysis. The [O<sub>2</sub>Cl(FXeF)<sub>2</sub>]<sup>+</sup> cations and [AsF<sub>6</sub>]<sup>-</sup> anions of [O<sub>2</sub>Cl(FXeF)<sub>2</sub>][AsF<sub>6</sub>] are intimate ion-pairs with secondary Cl...F<sub>As</sub> and Cl...F<sub>Xe</sub> bonds that are significantly shorter than the sums of the Cl and F van der Waals radii, consistent with primarily electrostatic  $\sigma$ -hole type bonding. MEPS and NBO analyses of the gas-phase [XO<sub>2</sub>]<sup>+</sup> (X = Cl, Br, I) cations suggest the syntheses of other [O<sub>2</sub>X(FNgF)<sub>2</sub>]<sup>+</sup> (Ng = Kr, Xe) coordination complexes should be possible.

#### 1.08.3.3.2 [Mg(FKrF)<sub>4</sub>][AsF<sub>6</sub>]<sub>2</sub>

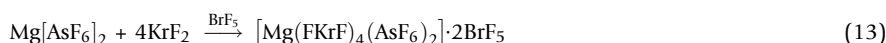
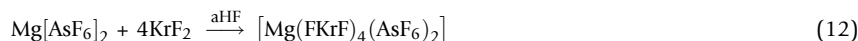
Although numerous XeF<sub>2</sub> coordination complexes that have the general formulation [M<sup>n+</sup>(FXeF)<sub>p</sub>][AF<sub>x</sub>]<sub>n</sub> (M = Li, Ag, Mg–Ba, Cu, Zn–Hg, Pb, La, Pr, Nd; A = B, P, As, Sb, Bi, V, Nb, Ta, Ru) have been synthesized and structurally characterized,<sup>21,22</sup> the only examples of KrF<sub>2</sub> coordination complexes with alkali or alkaline earth metal cations that have been reported are the [M(FKrF)<sub>n</sub>][AuF<sub>6</sub>]<sub>2</sub> (M = Ca, Sr, Ba; n = 1–4) salts, whose solid-state structures are unsubstantiated.<sup>96,97</sup> Structurally well characterized examples of KrF<sub>2</sub> coordination compounds are very rare due to the significant technical challenges associated with handling KrF<sub>2</sub> and its derivatives. In order to stabilize a KrF<sub>2</sub> coordination complex, the Lewis acidity of the acceptor must not only be closely matched with the



**Fig. 12** The structural unit in the crystal structure of [O<sub>2</sub>Cl(FXeF)<sub>2</sub>][AsF<sub>6</sub>]. Thermal ellipsoids are drawn at the 50% probability level and secondary Cl–F bonds are indicated by dashed lines. Reproduced from Bortolus, M. R.; Ellwanger, M.; Haner, J.; Schrobilgen, G. J. *J. Fluorine Chem.* **2021**, *250*, 109814.

fluorobasicity of  $\text{KrF}_2$ , but the Lewis acid site must be resistant to oxidative fluorination. Reactions of  $\text{Mg}[\text{AsF}_6]_2$  with  $\text{XeF}_2$  and  $\text{XeF}_4$  in aHF solvent have previously yielded  $[\text{Mg}(\text{FXeF})_n][\text{AsF}_6]_2$  ( $n = 2$  or  $4$ )<sup>98</sup> and  $[\text{Mg}(\text{FXeF})(\text{XeF}_4)][\text{AsF}_6]_2$ .<sup>99</sup>

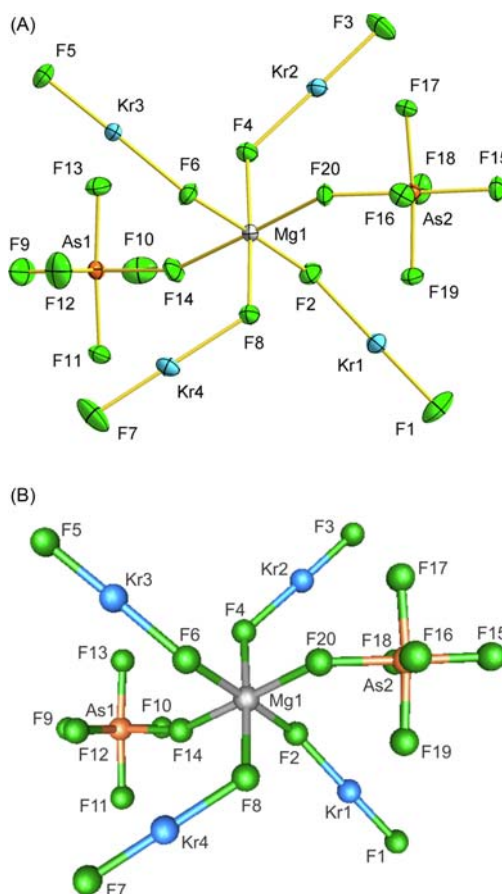
The reactions of  $\text{Mg}[\text{AsF}_6]_2$  and  $\text{KrF}_2$  in HF or  $\text{BrF}_5$  solvent have afforded  $[\text{Mg}(\text{FKrF})_4(\text{AsF}_6)_2]$  and  $[\text{Mg}(\text{FKrF})_4(\text{AsF}_6)_2] \cdot 2\text{BrF}_5$ , respectively, and have provided the first examples of a metal cation coordination complex with  $\text{KrF}_2$  (Eqs. 12 and 13).<sup>73</sup>



The X-ray crystal structures and Raman spectra of both complexes show the  $\text{KrF}_2$  ligands and  $[\text{AsF}_6]^-$  anions are F-coordinated to a  $\text{Mg}^{2+}$  cation (Fig. 13). The geometric parameters of  $[\text{Mg}(\text{FKrF})_4]^{2+}$  and  $[\text{AsF}_6]^-$  in both crystal structures are very similar. The crystal structure of  $[\text{Mg}(\text{FKrF})_4(\text{AsF}_6)_2]$  consists of well-isolated  $[\text{Mg}(\text{FKrF})_4]^{2+}$  dications and  $[\text{AsF}_6]^-$  anions that interact by means of short secondary  $\text{Mg} \cdots \text{F}$  bonds ( $\text{Mg} \cdots \text{F}_{\text{Kr}}, 1.965(2) \text{--} 2.005(2) \text{ \AA}$ ;  $\text{Mg} \cdots \text{F}_{\text{As}}, 1.982(2) \text{--} 2.001(2) \text{ \AA}$ ) that significantly polarize the terminal  $\text{Kr} \text{--} \text{F}$  and  $\text{As} \text{--} \text{F}$  bonds. The  $\text{Mg} \cdots \text{F}_b \text{--} \text{Kr}$  bond angles are bent ( $121.84(7)^\circ \text{--} 144.43(8)^\circ$ ), as observed for the other structurally characterized examples of terminally coordinated  $\text{KrF}_2$  complexes.<sup>64,67,70,72,74</sup>

Calculated vibrational frequencies and vibrational displacements for gas-phase  $[\text{Mg}(\text{FKrF})_4(\text{AsF}_6)_2]$  and  $\text{BrF}_5$  were used to aid in the assignment of the Raman spectra of  $[\text{Mg}(\text{FKrF})_4(\text{AsF}_6)_2]$  and  $[\text{Mg}(\text{FKrF})_4(\text{AsF}_6)_2] \cdot 2\text{BrF}_5$ . Because the cocrystallized  $\text{BrF}_5$  molecules of  $[\text{Mg}(\text{FKrF})_4(\text{AsF}_6)_2] \cdot 2\text{BrF}_5$  very weakly interact with  $[\text{Mg}(\text{FKrF})_4(\text{AsF}_6)_2]$ , the Raman spectrum of the co-crystal was analyzed as a composite of  $[\text{Mg}(\text{FKrF})_4(\text{AsF}_6)_2]$  and  $\text{BrF}_5$  spectra. No intraligand coupling was observed between the  $\text{Kr} \text{--} \text{F}_t$  and  $\text{Kr} \text{--} \text{F}_b$  stretches, whereas significant interligand coupling resulted in four, coupled  $\text{Kr} \text{--} \text{F}_t$  modes ( $558 \text{--} 589$  and  $558 \text{--} 591 \text{ cm}^{-1}$ ) and four coupled  $\text{Kr} \text{--} \text{F}_b$  modes ( $449 \text{--} 495$  and  $451 \text{--} 492 \text{ cm}^{-1}$ ). Similar interligand couplings have been observed for other terminally coordinated  $\text{KrF}_2$  complexes.<sup>64,74</sup>

The NBO analysis of gas-phase  $[\text{Mg}(\text{FKrF})_4][\text{AsF}_6]_2$  is consistent with weak covalent, ligand-metal bonding, where the charge distributions indicate polarization of the  $\text{KrF}_2$  ligands accompanied by a small degree of charge transfer from  $\text{KrF}_2$  to  $\text{Mg}^{2+}$  ( $-0.148$ ) and very small  $\text{Mg} \cdots \text{F}_b$  Wiberg bond indices ( $0.042 \text{--} 0.045$ ) that are consistent with  $\text{Mg} \cdots \text{F}_b$  bonds that are essentially electrostatic in character.



**Fig. 13** The X-ray crystal structure of  $[\text{Mg}(\text{FKrF})_4(\text{AsF}_6)_2]$ ; thermal ellipsoids are drawn at the 50% probability level. (B) Calculated geometry (B3LYP/aug-cc-pVDZ(-PP)). Reproduced with permission from Lozinšek, M.; Mercier, H. P. A.; Schrobilgen, G. J.; Žemva, B. *Angew. Chem. Int. Ed.* **2017**, *56*, 6251–6254.

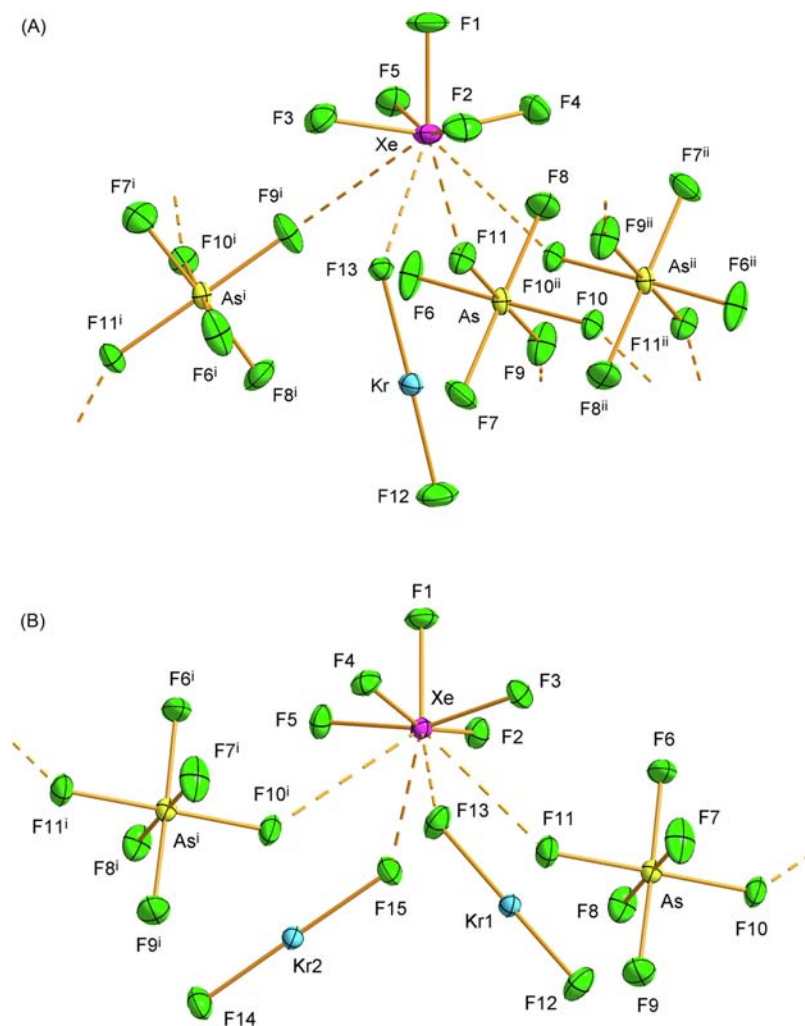
## 1.08.3.4 Mixed krypton/xenon compounds

1.08.3.4.1  $[F_5Xe(FKrF)_nAsF_6]$  ( $n = 1$  or  $2$ )

Although the chemical reactivities of xenon and krypton were discovered 60 years ago,<sup>6,100</sup> no chemically bound species containing both noble-gas elements had been synthesized and isolated in macroscopic amounts. In contrast with xenon, which exhibits formal oxidation states in its compounds of 0, +1/2, +2, +4, +6, and +8, krypton compounds are limited to the +2 oxidation state. The only binary fluoride of krypton that can be prepared in synthetically useful amounts is thermodynamically unstable  $KrF_2$ ,<sup>21,61</sup> from which all other krypton compounds are derived.<sup>21,61,64,67,70,71,73,74</sup> Terminal coordination of  $NgF_2$  to a Lewis-acid acceptor polarizes the  $Ng-F$  bonds, resulting in increased  $[NgF]^+$  character and a concomitant increase in oxidative fluorination strength.<sup>61</sup> The  $[KrF]^+$  cation is the strongest chemical oxidative fluorinating agent known, and thus  $KrF_2$  coordination complexes are prone to undergo redox decomposition by oxidative fluorination of the Lewis acid acceptor.

The  $[XeF_5]^+$  cation is sufficiently Lewis acidic to form coordination complexes with  $KrF_2$ . The positive charge on the cation and the high oxidation state of xenon render  $[XeF_5]^+$  resistant to oxidation by  $Kr(II)$ . The  $XeF_2$  analogues,  $[F_5Xe(FXeF)_nAsF_6]$  ( $n = 0.5, 1, 2$ ), have been prepared by reaction of  $[XeF_5][AsF_6]$  with  $XeF_2$  in aHF solvent and were structurally characterized by Raman spectroscopy<sup>66,101</sup> and SCXRD.<sup>66</sup>

Reactions of  $[XeF_5][AsF_6]$  with  $KrF_2$  at various molar ratios in aHF solvent, yielded the first mixed krypton/xenon coordination compounds,  $[F_5Xe(FKrF)AsF_6]$  and  $[F_5Xe(FKrF)_2AsF_6]$ , which were characterized by LT Raman spectroscopy and LT SCXRD (Fig. 14).<sup>72</sup> In the attempted synthesis of  $[F_5Xe(FKrF)_{0.5}][AsF_6]$ , reaction of a 1.0:1.9 molar ratio of  $KrF_2$  with  $[XeF_5][AsF_6]$  in aHF afforded  $[F_5Xe(FKrF)AsF_6]$  and the previously unknown HF coordination complex,  $[F_5Xe(FH)AsF_6]$ . The  $[F_5Xe(FH)][PnF_6]$  ( $Pn = As, Sb$ ) salts were also prepared by crystallization of  $[XeF_5][PnF_6]$  from aHF, and were characterized by LT Raman



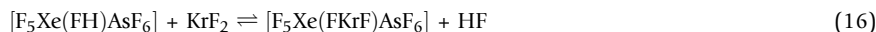
**Fig. 14** The X-ray crystal structure of (A)  $[F_5Xe(FKrF)AsF_6]$  and (B)  $[F_5Xe(FKrF)_2AsF_6]$  where the coordination environments of the Xe atoms are expanded to include symmetry-generated atoms. Thermal ellipsoids are drawn at the 50% probability level. Reproduced with permission from Lozinšek, M.; Mercier, H. P. A.; Schrobilgen, G. J. *Angew. Chem. Int. Ed.* **2021**, *60*, 8149–8156.



spectroscopy and SCXRD (Eq. 14). The 1:1 complex  $[\text{F}_5\text{Xe}(\text{FKrF})\text{AsF}_6]$  was obtained by reaction of a 1.5:1.0 ratio of  $\text{KrF}_2:\text{[XeF}_5\text{]AsF}_6$ , whereas a 3.5:1.0 molar ratio of  $\text{KrF}_2:\text{[XeF}_5\text{]AsF}_6$  yielded  $[\text{F}_5\text{Xe}(\text{FKrF})_2\text{AsF}_6]$  (Eqs. 15–17).



and/or

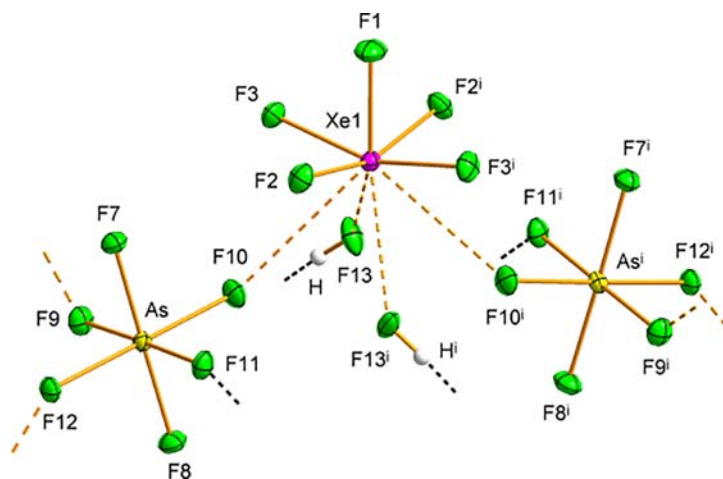


The crystal structure of  $[\text{F}_5\text{Xe}(\text{FKrF})][\text{AsF}_6]$  is isotypic with  $[\text{F}_5\text{Xe}(\text{FXeF})][\text{AsF}_6]$ , whereas  $[\text{F}_5\text{Xe}(\text{FKrF})_2][\text{AsF}_6]$  is not isotypic with  $[\text{F}_5\text{Xe}(\text{FXeF})_2][\text{AsF}_6]$ . The cations and anions interact through primarily electrostatic,  $\sigma$ -hole type  $\text{Xe}\cdots\text{F}_{\text{As}}$  bonds (2.59–3.57 Å) that are equal to or shorter than the sums of the Xe and F van der Waals radii (3.63 Å,<sup>102</sup> 3.52 Å<sup>103</sup>). The  $\text{Xe}\cdots\text{F}_{\text{Kr}}$  secondary bonds (2.5139(9)–2.576(2) Å) are significantly shorter than the  $\text{Xe}\cdots\text{F}_{\text{As}}$  secondary bonds, and are also primarily electrostatic. Coordination of  $\text{KrF}_2$  to  $[\text{XeF}_5]^+$  significantly polarizes the  $\text{Kr}\text{--}\text{F}$  bonds to give slightly elongated bridge bonds ( $\text{Kr}\text{--}\text{F}_{\text{b}}$ , 1.917(2)–1.9367(9) Å) and slightly contracted terminal bonds ( $\text{Kr}\text{--}\text{F}_{\text{t}}$ , 1.8393(12)–1.851(2) Å) relative to those of free  $\text{KrF}_2$ .<sup>75</sup> The bent  $\text{Xe}\cdots\text{F}_{\text{b}}\text{--}\text{Kr}$  bond angles (133.24(5)–141.80(7)°), suggest the  $\text{Xe}\cdots\text{F}_{\text{b}}$  bond possesses a small, but significant degree of covalent character. Similar bond polarization effects and bent fluorine bridge angles have been observed for other  $\text{KrF}_2$  coordination complexes.

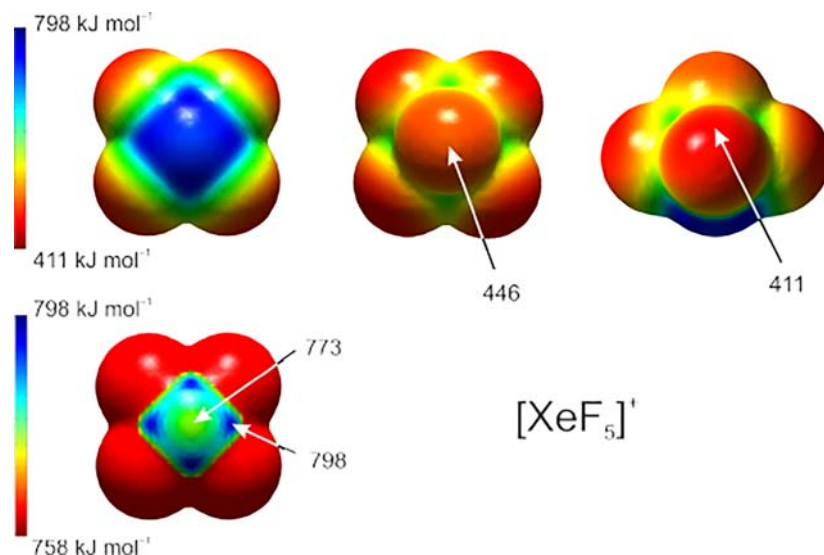
The primary bond lengths and bond angles of the  $[\text{XeF}_5]^+$  cations in the crystal structures of  $[\text{F}_5\text{Xe}(\text{FKrF})_n\text{AsF}_6]$  (Fig. 14) and  $[\text{F}_5\text{Xe}(\text{FH})][\text{PnF}_6]$  (Fig. 15) are comparable to those of fluoro- and oxyfluoro-anion salts of  $[\text{XeF}_5]^+$ .<sup>68,104–112</sup> The  $\text{Xe}\cdots\text{F}_{\text{H}}$  secondary bonding interactions of  $[\text{F}_5\text{Xe}(\text{FH})][\text{PnF}_6]$  (As, 2.656(2) Å; Sb, 2.6501(10) Å) are significantly longer than those of  $[\text{F}_3\text{Xe}(\text{FH})][\text{Sb}_2\text{F}_{11}]$  (2.432(2) Å) and  $[\text{FXe}(\text{FH})][\text{Sb}_2\text{F}_{11}]$  (2.359(4) Å), in accordance with the relative Lewis acidities of the xenon fluorocations:  $[\text{XeF}_5]^+ < [\text{XeF}_3]^+ < [\text{XeF}]^+$ .

The calculated gas-phase optimized geometries of the hypothetical  $\{[\text{F}_5\text{Xe}(\text{FKrF})][\text{AsF}_6]_3\}^{2-}$  and  $\{[\text{F}_5\text{Xe}(\text{FKrF})_2][\text{AsF}_6]_2\}^-$  anions well reproduced the coordination environments of the xenon atoms in  $[\text{F}_5\text{Xe}(\text{FKrF})\text{AsF}_6]$  and  $[\text{F}_5\text{Xe}(\text{FKrF})_2\text{AsF}_6]$ , respectively, and the calculated  $\text{Xe}\cdots\text{F}_{\text{b}}\text{--}\text{Kr}$  bond angles are also bent (121.2–124.71°).<sup>72</sup> The Raman spectra of the 1:1 and 1:2 complexes were fully assigned with the aid of calculated gas-phase vibrational frequencies and intensities for  $\{[\text{F}_5\text{Xe}(\text{FKrF})][\text{AsF}_6]_3\}^{2-}$  and  $\{[\text{F}_5\text{Xe}(\text{FKrF})_2][\text{AsF}_6]_2\}^-$ . Bands observed at 533 and 454  $\text{cm}^{-1}$  in the Raman spectrum of  $[\text{F}_5\text{Xe}(\text{FKrF})\text{AsF}_6]$  are assigned to  $\nu(\text{Kr}\text{--}\text{F}_{\text{t}})$  and  $\nu(\text{Kr}\text{--}\text{F}_{\text{b}})$ , respectively. In the case of  $[\text{F}_5\text{Xe}(\text{FKrF})_2\text{AsF}_6]$ , vibrational coupling occurs, giving rise to additional bands at 543 and 564/567 and 466 and 472/474  $\text{cm}^{-1}$ . The deformation bands,  $\delta(\text{FKrF})_{\text{i.p.}}$ ,  $\delta(\text{FKrF})_{\text{o.o.p.}}$ ,  $\rho_{\text{t}}(\text{FKrF})$ , and  $\rho_{\text{b}}(\text{FKrF})$  were observed at similar frequencies in both complexes ( $[\text{F}_5\text{Xe}(\text{FKrF})\text{AsF}_6]$ ; 294, 255, 143, 130  $\text{cm}^{-1}$ ;  $[\text{F}_5\text{Xe}(\text{FKrF})_2\text{AsF}_6]$ ; 273/278, 251, 145, 110  $\text{cm}^{-1}$ ).

NBO analyses reveal that complex formation significantly reduces the net positive charges on the  $[\text{XeF}_5]^+$  cations of  $\{[\text{F}_5\text{Xe}(\text{FKrF})][\text{AsF}_6]_3\}^{2-}$  and  $\{[\text{F}_5\text{Xe}(\text{FKrF})_2][\text{AsF}_6]_2\}^-$  relative to gas-phase  $[\text{XeF}_5]^+$ , indicating that significant charge transfer from  $[\text{AsF}_6]^-$  and the  $\text{KrF}_2$  ligands to Xe occurs. The small Wiberg bond indices of the  $\text{Xe}\cdots\text{F}_{\text{Kr}}$  bonds (0.037–0.102), indicate that these bonds are primarily electrostatic in nature. ELF analyses of  $\{[\text{F}_5\text{Xe}(\text{FKrF})][\text{AsF}_6]_3\}^{2-}$  and  $\{[\text{F}_5\text{Xe}(\text{FKrF})_2][\text{AsF}_6]_2\}^-$  show that the stereo-active VELP distributions of Xe are perturbed and notably flattened upon complex formation, occupying significantly less volume than the VELP of gas-phase  $[\text{XeF}_5]^+$ . MEPS analyses show four localized regions of positive electrostatic potential maxima (798  $\text{kJ mol}^{-1}$ ) on the Xe atom of the  $[\text{XeF}_5]^+$  cation that are located at the intersections of the equatorial F atom isosurfaces at the base of the square pyramid formed by its axial and equatorial F atoms (Fig. 16). The  $\text{Xe}\cdots\text{F}$  secondary bonds in the crystal



**Fig. 15** The crystal structure of  $[\text{F}_5\text{Xe}(\text{FH})\text{AsF}_6]$ . The coordination environment of Xe1 is expanded to include symmetry-generated atoms. Thermal ellipsoids are drawn at the 50% probability level. Reproduced with permission from Lozinšek, M.; Mercier, H. P. A.; Schrobilgen, G. J. *Angew. Chem. Int. Ed.* **2021**, *60*, 8149–8156.

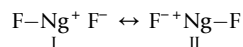


**Fig. 16** The molecular electrostatic potential surface (MEPS) contours calculated at the 0.001  $e\cdot a_0^{-3}$  isosurface of  $[\text{XeF}_5]^+$  and the top 5% of the positive electrostatic potential range (bottom left). The extrema of selected electrostatic potentials are indicated by arrows. The optimized geometries and MEPS were calculated at the APFD/aVDZ(-PP)(Xe)/aVDZ(F) level of theory. Modified from Lozinšek, M.; Mercier, H. P. A.; Schrobilgen, G. J. *Angew. Chem. Int. Ed.* **2021**, *60*, 8149–8156.

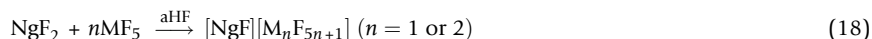
structures of  $[\text{F}_5\text{Xe}(\text{FKrF})][\text{AsF}_6]$ ,  $[\text{F}_5\text{Xe}(\text{FKrF})_2][\text{AsF}_6]$ , and  $[\text{F}_5\text{Xe}(\text{FH})][\text{PnF}_6]$  (Pn = As, Sb) are directed towards these positive regions, consistent with  $\sigma$ -hole type interactions.

#### 1.08.3.4.2 $[\text{FKrFXeF}][\text{AsF}_6] \cdot 0.5\text{KrF}_2 \cdot 2\text{HF}$ , $\text{XeF}_4 \cdot \text{NgF}_2$ , and $[(\text{F}_5\text{Xe})_2(\mu\text{-FKrF})][\text{AsF}_6]_2$

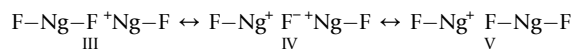
The bonding of  $\text{NgF}_2$  (Ng = Kr, Xe) may be represented by 3c-4e valence bond descriptions in which the Ng valence  $p_z$ -orbitals interact with fluorine  $2p_z$ -orbitals. The resulting  $\sigma$ -bonds have formal bond orders of  $\frac{1}{2}$ , which are represented by resonance Structures I and II. The high ionic characters of the Ng–F bonds of  $\text{NgF}_2$  implied by Structures I and II account for



their fluoro-basicities and fluoride-ion donor behaviors towards strong to moderate strength Lewis acids such as  $\text{MF}_5$  (M = As,<sup>53,61</sup> Sb,<sup>53,61</sup> Bi,<sup>53,61</sup> V,<sup>61</sup> Nb,<sup>61</sup> Ta,<sup>61</sup> Au<sup>61</sup>). These fluoride-ion transfer reactions readily occur in aHF to form  $[\text{NgF}][\text{MF}_6]$  and  $[\text{NgF}][\text{M}'_2\text{F}_{11}]$  (M' = Sb,<sup>53,61</sup> Bi,<sup>53,61</sup> Nb,<sup>61</sup> Ta,<sup>61</sup> Ir,<sup>61</sup> Pt<sup>61</sup>) salts (Eq. 18). Reactions of  $\text{NgF}_2$  with a  $[\text{NgF}]^+$  salt in aHF also yield the V-shaped  $[\text{Ng}_2\text{F}_3]^+$  (Ng = Kr or Xe) cations (Eq. 19).<sup>61,75,113,114</sup>

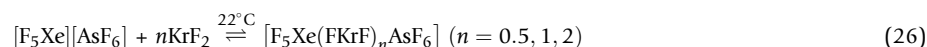
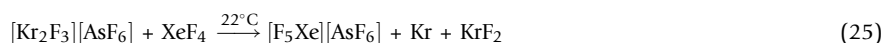
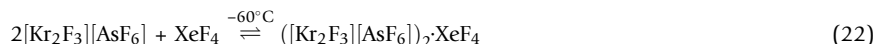
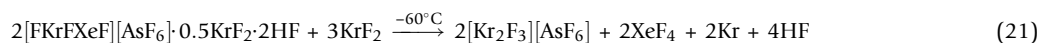
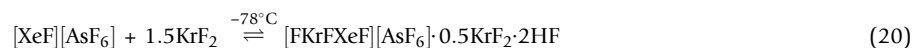


The bonding of  $[\text{Ng}_2\text{F}_3]^+$  may be represented by the 5c-6e valence bond description given by resonance Structures III–V. The formal bond orders of  $[\text{Ng}_2\text{F}_3]^+$  lie between  $\frac{1}{2}$  ( $\text{NgF}_2$ ) and 1  $[\text{NgF}]^+$ , where the central Ng–F<sub>b</sub> bonds are significantly more ionic.



Although a significant number of  $[\text{Ng}_2\text{F}_3]^+$  salts have been synthesized and structurally characterized at LT by SCXRD,<sup>61,75,113,114</sup> Raman spectroscopy,<sup>61,75,113–115</sup> and multi-NMR spectroscopy,<sup>61</sup> the mixed Kr(II)/Xe(II) analogue,  $[\text{FKrFXeF}]^+$ , had not been reported. The isolation and structural characterization of mixed Kr(II)/Xe(II) and Kr(II)/Xe(IV) noble-gas compounds pose a formidable synthetic challenge owing to the ability of  $\text{KrF}_2$ ,  $[\text{KrF}]^+$ , and  $[\text{Kr}_2\text{F}_3]^+$  to oxidize Xe(II) and Xe(IV) to Xe(VI).<sup>5,61</sup>

Reaction of  $[\text{XeF}][\text{AsF}_6]$  with excess  $\text{KrF}_2$  at  $-78^\circ\text{C}$  in aHF yielded the first mixed Kr(II)/Xe(II) noble-gas compound,  $[\text{FKrFXeF}][\text{AsF}_6] \cdot 0.5\text{KrF}_2 \cdot 2\text{HF}$  (Eq. 20), which was characterized by LT Raman spectroscopy and LT SCXRD.<sup>116</sup> The potent oxidative fluorinating properties of  $[\text{FKrFXeF}]^+$  led to redox decomposition at  $-60^\circ\text{C}$  in aHF in the presence of excess  $\text{KrF}_2$ , and resulted in oxidation of Xe(II) to Xe(IV) and the formation of the first mixed Kr(II)/Xe(IV) cocrystals,  $([\text{Kr}_2\text{F}_3][\text{AsF}_6])_2 \cdot \text{XeF}_4$  and  $\text{XeF}_4 \cdot \text{KrF}_2$ , which were characterized by LT Raman spectroscopy and LT SCXRD. The crystal structure of  $([\text{Kr}_2\text{F}_3][\text{AsF}_6])_2 \cdot \text{XeF}_4$  also provides a rare example of a structurally characterized salt of the strong-oxidant  $[\text{Kr}_2\text{F}_3]^+$  cation. Further decomposition at  $22^\circ\text{C}$  resulted in oxidation of Xe(IV) to Xe(VI) to give the Kr(II)/Xe(VI) coordination complexes,  $[\text{F}_5\text{Xe}(\text{FKrF})_n][\text{AsF}_6]$  ( $n = 1$  or  $2$ ),  $[\text{F}_5\text{Xe}][\text{AsF}_6]$ , and a new Kr(II)/Xe(VI) complex,  $[(\text{F}_5\text{Xe})_2(\mu\text{-FKrF})][\text{AsF}_6]_2$ , that was characterized by LT Raman spectroscopy (Eqs. 21–26).

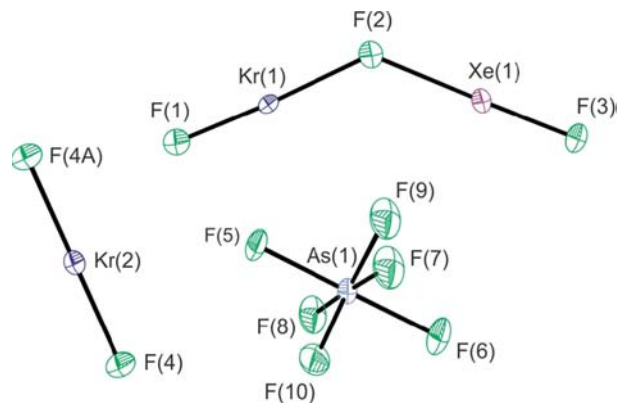


The  $\text{XeF}_4 \cdot \text{NgF}_2$  cocrystals were subsequently synthesized by reaction of  $\text{XeF}_4$  with  $\text{NgF}_2$  in  $\text{CFCl}_3$  solvent and structurally characterized by LT Raman spectroscopy and LT SCXRD. Higher precision, LT SCXRD structures of  $[\text{Xe}_2\text{F}_3][\text{SbF}_6]$ ,  $\text{XeF}_4$ , and  $[\text{F}_5\text{Xe}][\text{AsF}_6]$  were also obtained.

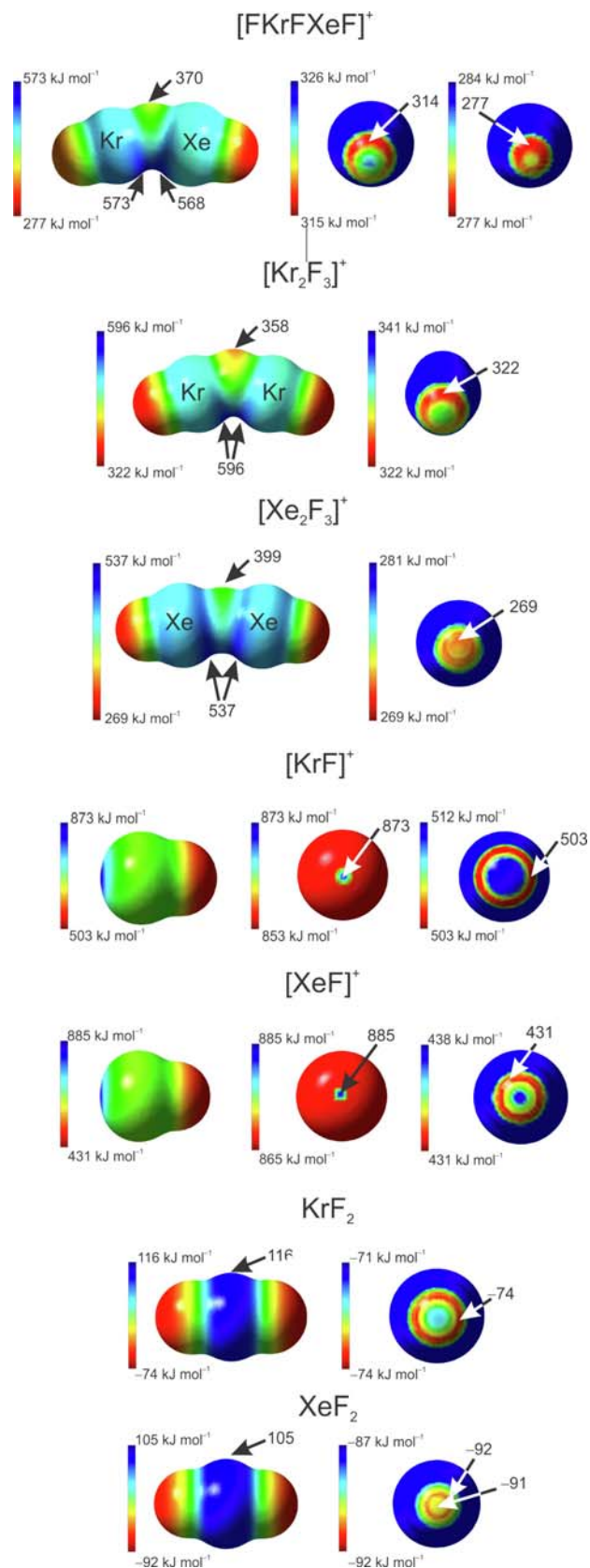
(i)  $[\text{FKrFXeF}]^+$ . The crystal structures of  $[\text{FKrFXeF}][\text{AsF}_6] \cdot 0.5\text{KrF}_2 \cdot 2\text{HF}$  (Fig. 17),  $([\text{Kr}_2\text{F}_3][\text{AsF}_6])_2 \cdot \text{XeF}_4$ , and  $[\text{Xe}_2\text{F}_3][\text{SbF}_6]$  consist of discrete  $[\text{FKrFXeF}]^+$  or  $[\text{Ng}_2\text{F}_3]^+$  ( $\text{Ng} = \text{Kr}, \text{Xe}$ ) cations and  $[\text{MF}_6]^-$  ( $\text{M} = \text{As}, \text{Sb}$ ) anions that are cocrystallized with  $\text{KrF}_2$  or  $\text{XeF}_4$ .<sup>116</sup> The geometric parameters of cocrystallized  $\text{KrF}_2$  and  $\text{XeF}_4$  are equal within  $\pm 3\sigma$  to those of  $\alpha\text{-KrF}_2$  and  $\text{XeF}_4$ , respectively. The  $[\text{FKrFXeF}]^+$  cation also has the V-shaped geometry previously observed for the  $[\text{Ng}_2\text{F}_3]^+$  cations. The  $\text{Ng}-\text{F}_t$  bonds of  $[\text{FKrFXeF}]^+$  ( $\text{Kr}$ , 1.806(4) Å;  $\text{Xe}$ , 1.882(4) Å) are significantly shorter than the  $\text{Ng}-\text{F}_b$  bonds ( $\text{Kr}$ , 2.055(4) Å;  $\text{Xe}$ , 2.172(4) Å), in accordance with Structures III – V. The  $\text{Ng}-\text{F}_b$  bridge bonds of  $[\text{FKrFXeF}]^+$  are significantly shorter than the primarily electrostatic  $\text{Xe}-\text{F}_b$  bonds of  $[\text{F}_5\text{Xe}(\text{FKrF})_n][\text{AsF}_6]$  ( $n = 1$  or  $2$ ). The  $\text{Kr}-\text{F}$  bonds of  $[\text{FKrFXeF}]^+$  are comparable to those of  $[\text{Kr}_2\text{F}_3]^+$  salts.<sup>61,75</sup> In contrast, the terminal  $\text{XeF}$  group of  $[\text{FKrFXeF}]^+$  has greater  $[\text{XeF}]^+$  character and shorter  $\text{Xe}-\text{F}_t$  and  $\text{Xe}-\text{F}_b$  bonds than in  $[\text{Xe}_2\text{F}_3]^+$  salts.<sup>61,113,114</sup> The bond length trends are consistent with the relative electronegativities of  $\text{Kr}$  and  $\text{Xe}$  and with the QTAIM, NBO, MEPS, and ELF analyses of  $[\text{FKrFXeF}]^+$  and  $[\text{Ng}_2\text{F}_3]^+$ .

Raman spectral assignments for the  $[\text{FKrFXeF}]^+$  cation of  $[\text{FKrFXeF}][\text{AsF}_6] \cdot 0.5\text{KrF}_2 \cdot 2\text{HF}$  were made by comparison with the calculated gas-phase vibrational frequencies, vibrational mode displacements, and Raman intensities of the  $[\text{FKrFXeF}]^+$  cation and with the calculated and experimental frequencies of the related  $[\text{Ng}_2\text{F}_3]^+$  cations. All  $[\text{FKrFXeF}]^+$  bands in the Raman spectrum of  $[\text{FKrFXeF}][\text{AsF}_6] \cdot 0.5\text{KrF}_2 \cdot 2\text{HF}$  were split into two components due to factor-group splitting. Significant in- and out-of-phase intra-ionic vibrational coupling between the  $\text{Ng}-\text{F}_t$  and  $\text{Ng}-\text{F}_b$  stretching modes gave four coupled modes,  $[\nu(\text{Kr}-\text{F}_t) \pm \nu(\text{Xe}-\text{F}_t)]$  and  $[\nu(\text{Kr}-\text{F}_b) \pm \nu(\text{Xe}-\text{F}_b)]$ , which were at frequencies that were intermediate with respect to those of the known  $[\text{Ng}_2\text{F}_3]^+$  salts.<sup>61,75,113</sup>

The calculated gas-phase geometries of  $[\text{FKrFXeF}]^+$  and  $[\text{Ng}_2\text{F}_3]^+$  well reproduce the experimental V-shaped geometries of the cations. Quantum-chemical (NBO, QTAIM, ELF, and MEPS) analyses were used to assess the bonding in  $[\text{FKrFXeF}]^+$  and  $[\text{Ng}_2\text{F}_3]^+$ , and are consistent with the 5c-6e valence bond descriptions provided by Structures III–V, where the  $\text{Ng}-\text{F}_t$  bonds have greater covalent character than the  $\text{Ng}-\text{F}_b$  bonds. The analyses confirm that the  $\text{Kr}-\text{F}$  bonds of the  $[\text{FKrFXeF}]^+$  cation have greater degrees of covalent character than their  $\text{Xe}-\text{F}$  counterparts, consistent with the relative electronegativities of  $\text{Kr}$  and  $\text{Xe}$ ,<sup>117,118</sup> and differences in MEPS electrostatic potential maxima among the  $[\text{NgF}]^+$ ,  $[\text{Ng}_2\text{F}_3]^+$ , and  $[\text{FKrFXeF}]^+$  cations (Fig. 18), where EP maxima of  $\text{Kr}$  are greater than those of  $\text{Xe}$ .



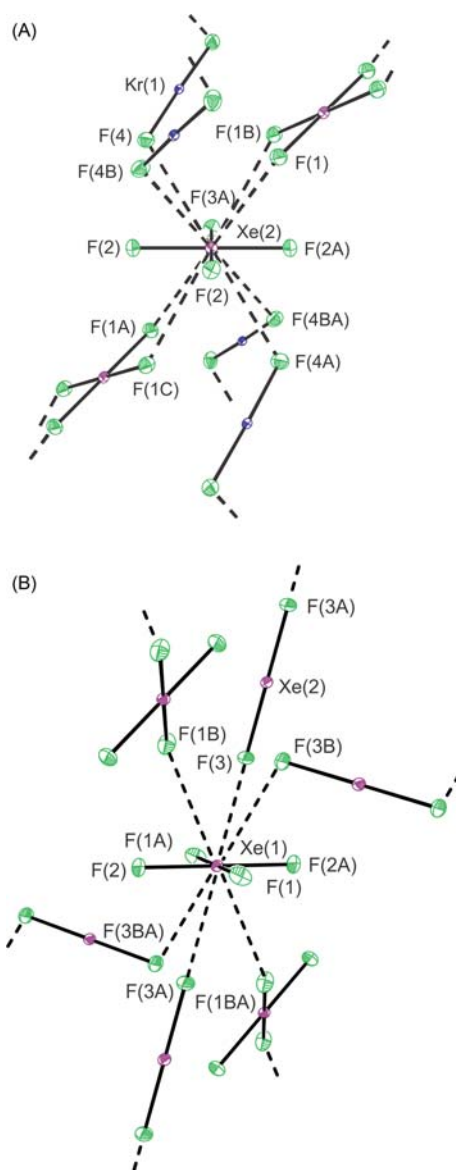
**Fig. 17** The structural unit in the crystal structure of  $[\text{FKrFXeF}][\text{AsF}_6] \cdot 0.5\text{KrF}_2 \cdot 2\text{HF}$ , where one of two orientations of the disordered  $[\text{AsF}_6]^-$  anion is shown. Thermal ellipsoids are drawn at the 50% probability level. Modified from Bortolus, M. R.; Mercier, H. P. A.; Nguyen, B.; Schrobilgen, G. J. *Angew. Chem. Int. Ed.* **2021**, *60*, 23678–23686.



**Fig. 18** Molecular electrostatic potentials of [FKrFXeF]<sup>+</sup>, [Kr<sub>2</sub>F<sub>3</sub>]<sup>+</sup>, [KrF]<sup>+</sup>, and KrF<sub>2</sub> are depicted at their 0.001  $e_a^{-3}$  isosurfaces where extrema are indicated by arrows (B2PLYP-D3/Def2-TZVPD). Reproduced and modified with permission from Bortolus, M. R.; Mercier, H. P. A.; Nguyen, B.; Schrobilgen, G. J. *Angew. Chem. Int. Ed.* **2021**, *60*, 23678–23686.

(ii)  $\text{XeF}_4 \cdot \text{NgF}_2$ . A low-precision, RT SCXRD crystal structure of  $\text{XeF}_4 \cdot \text{XeF}_2$  has been reported without an accompanying structural diagram.<sup>119</sup> High-precision LT SCXRD crystal structures of  $\text{XeF}_4 \cdot \text{KrF}_2$  and  $\text{XeF}_4 \cdot \text{XeF}_2$  have now been obtained.<sup>116</sup> The structures are not isotopic and are best described as cocrystals, where the shortest  $\text{Xe}^{\text{IV}} \cdots \text{F}_\text{b}$  secondary bonding interactions are shorter than the sums of the Xe and F van der Waals radii (3.63 Å,<sup>102</sup> 3.52 Å<sup>103</sup>). The crystal structure of  $\text{XeF}_4 \cdot \text{KrF}_2$  is comprised of two crystallographically inequivalent  $\text{XeF}_4$  molecules that form either six ( $\text{CN}_{\text{Xe}} = 4 + 6$ ) or eight ( $\text{CN}_{\text{Xe}} = 4 + 8$ ) secondary bonds with neighboring  $\text{KrF}_2$  ( $\text{Xe} \cdots \text{F}_{\text{Kr}}$ , 3.083(2)–3.367(2) Å) and  $\text{XeF}_4$  ( $\text{Xe} \cdots \text{F}_{\text{Xe}}$ , 3.341(2)–3.508(2) Å) molecules (Fig. 19A). The crystal structure of  $\text{XeF}_4 \cdot \text{XeF}_2$  consists of one  $\text{XeF}_4$  molecule that forms six ( $\text{CN}_{\text{Xe}} = 4 + 6$ ) secondary bonds with neighboring  $\text{XeF}_2$  ( $\text{Xe} \cdots \text{F}_{\text{Xe}}$ , 3.219(1), 3.290(1) Å) and  $\text{XeF}_4$  ( $\text{Xe} \cdots \text{F}_{\text{Xe}}$ , 3.262(1) Å) molecules (Fig. 19b). The  $\text{KrF}_2$  molecules of  $\text{XeF}_4 \cdot \text{KrF}_2$  are symmetrically bridged, with Kr–F bonds (1.922(2) Å) that are slightly elongated with respect to those of  $\alpha\text{-KrF}_2$  (1.984(5) Å). In contrast, the Xe–F bonds of  $\text{XeF}_2$  in  $\text{XeF}_4 \cdot \text{XeF}_2$  (1.9940(9) Å) are equal within  $\pm 3\sigma$  to those of crystalline  $\text{XeF}_2$  (1.999(4) Å). The geometric parameters of  $\text{XeF}_4$  in both  $\text{XeF}_4 \cdot \text{NgF}_2$  cocrystals are comparable to those of the LT SCXRD structure of  $\text{XeF}_4$ .<sup>116</sup> The LT Raman spectrum of  $\text{XeF}_4 \cdot \text{KrF}_2$  was assigned as a composite of  $\text{XeF}_4$  and  $\text{KrF}_2$  spectra.

(iii)  $[(\text{F}_5\text{Xe})_2(\mu\text{-FKrF})][\text{AsF}_6]_2$ . The solid-state LT Raman spectrum of  $[(\text{F}_5\text{Xe})_2(\mu\text{-FKrF})][\text{AsF}_6]_2$ <sup>116</sup> is very similar to those of  $[\text{F}_5\text{Xe}][\text{AsF}_6]$  and  $[\text{F}_5\text{Xe}(\text{FKrF})_n][\text{AsF}_6]$  ( $n = 1, 2$ ), and contains a strong Kr–F stretching band at  $485 \text{ cm}^{-1}$  that is intermediate with respect to the  $\nu(\text{Kr-F}_\text{t})$  and  $\nu(\text{Kr-F}_\text{b})$  stretching bands of the terminally coordinated ligands in  $[\text{F}_5\text{Xe}(\text{FKrF})_n][\text{AsF}_6]$  ( $n = 1, 2$ ) complexes (Kr–F<sub>t</sub>, 533–564/567  $\text{cm}^{-1}$ ; Kr–F<sub>b</sub>, 454–472/474  $\text{cm}^{-1}$ ), and is shifted to slightly higher frequency than the symmetric



**Fig. 19** The coordination spheres of  $\text{XeF}_4$  in the X-ray crystal structures of (A)  $\text{XeF}_4 \cdot \text{KrF}_2$  and (B)  $\text{XeF}_4 \cdot \text{XeF}_2$ . Thermal ellipsoids are drawn at the 50% probability level. Reproduced with permission from Bortolus, M. R.; Mercier, H. P. A.; Nguyen, B.; Schrobilgen, G. J. *Angew. Chem. Int. Ed.* **2021**, *60*, 23678–23686.

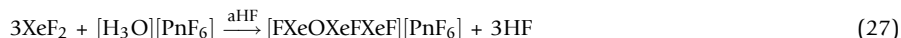


$\nu_s(\text{Kr-F})$  stretches of  $\alpha\text{-KrF}_2$  ( $465\text{ cm}^{-1}$ ) and  $\beta\text{-KrF}_2$  ( $468, 469\text{ cm}^{-1}$ ). The observation of a single  $\nu(\text{Kr-F})$  stretching band in the Raman spectrum of  $[(\text{F}_5\text{Xe})_2(\mu\text{-FKrF})][\text{AsF}_6]_2$  is consistent with a symmetrically bridged  $\text{KrF}_2$  coordination complex and with the xenon analogue,  $[(\text{F}_5\text{Xe})_2(\mu\text{-FXeF})][\text{AsF}_6]_2$ .<sup>66</sup>

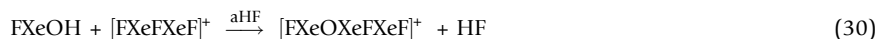
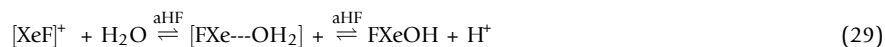
### 1.08.3.5 Xenon(II) cations

Although the oxides of xenon are thermodynamically unstable with respect to decomposition, xenon oxides had been isolated and characterized in macroscopic quantities for every known oxidation state of Xe except  $+\frac{1}{2}$  and  $+2$ .<sup>120</sup> Xenon(II) monoxide,  $\text{XeO}$ , was proposed as an intermediate in several oxidation reactions employing  $\text{XeO}_3$ , and the gas-phase UV and vacuum UV emission spectra of  $\text{XeO}$  have been attributed to emissions from  $\text{Xe}^+\text{O}^-$  ion-pair states.<sup>121,122</sup> Monomeric  $\text{XeO}$  has not been synthesized in macroscopic amounts in the condensed state but it has been isolated in an argon matrix.<sup>123</sup> A subsequent UV spectroscopic study indicated that the matrix-isolated  $\text{XeO}$  monomer is a van der Waals molecule with an unbound ground state.<sup>121,122</sup>

Prior to 2013, the only Xe(II) oxo-species that had been synthesized in macroscopic quantities and structurally characterized was the  $[\text{FXeOXeFXeF}]^+$  cation, which was prepared as the  $[\text{PnF}_6]^-$  ( $\text{Pn} = \text{As}, \text{Sb}$ ) salts by reaction of  $\text{XeF}_2$  with  $[\text{H}_3\text{O}][\text{PnF}_6]$  in aHF solvent at LT (Eq. 27).<sup>124</sup> Mixtures of  $\text{XeF}_2$  and  $[\text{H}_3\text{O}][\text{AsF}_6]$  in aHF solvent at  $-78\text{ }^\circ\text{C}$  were shown to exist



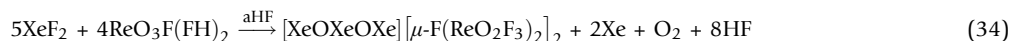
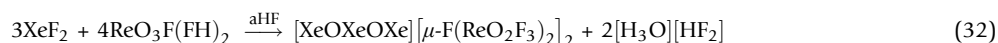
in equilibrium with  $[\text{XeF}][\text{AsF}_6]$  and  $\text{H}_2\text{O}$ . When excess  $\text{XeF}_2$  or  $[\text{XeF}][\text{PnF}_6]$  was employed,  $[\text{Xe}_2\text{F}_3][\text{PnF}_6]$  also formed. A transient  $\text{FXeOH}$  intermediate was postulated to account for the formation of  $[\text{FXeOXeFXeF}][\text{PnF}_6]$  from these mixtures which likely forms by hydrolysis of  $\text{XeF}_2$  or  $[\text{XeF}]^+$  in aHF (Eqs. 28–30).



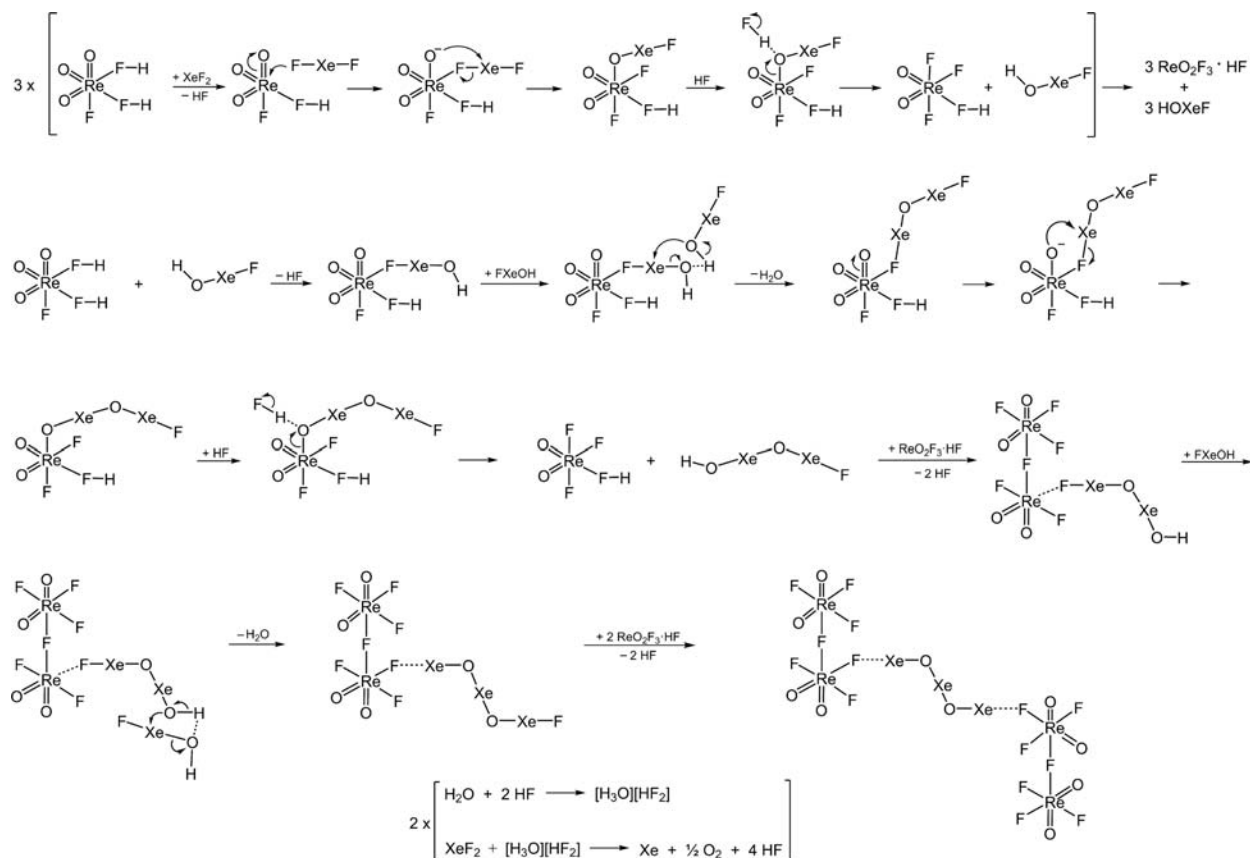
Deep red-orange crystals were obtained for both  $[\text{FXeOXeFXeF}][\text{PnF}_6]$  salts and their X-ray crystal structures were determined which revealed Z-shaped  $[\text{FXeOXeFXeF}]^+$  cations. The Raman spectra of solid  $[\text{FXe}^{16,18}\text{OXeFXeF}][\text{AsF}_6]$  and  $[\text{FXe}^{16}\text{OXeFXeF}][\text{SbF}_6]$  were recorded at ca.  $-160\text{ }^\circ\text{C}$  and confirmed the Z-shaped geometry of  $[\text{FXeOXeFXeF}]^+$ .<sup>124</sup> The  $[\text{FXeOXeFXeF}][\text{PnF}_6]$  salts decompose under aHF solvent above  $-30\text{ }^\circ\text{C}$  with Xe gas evolution.

#### 1.08.3.5.1 $[\text{XeOXeOXe}][\mu\text{-F}(\text{ReO}_2\text{F}_3)_2]_2$

Following a report of the reliable syntheses and isolation of high-purity  $\text{ReO}_3\text{F}$  and  $\text{ReO}_3\text{F}(\text{FH})_2$  from aHF,<sup>125</sup> the reaction of  $\text{ReO}_3\text{F}(\text{FH})_2$  with  $\text{XeF}_2$  in aHF was explored at  $-30\text{ }^\circ\text{C}$  and found to yield the Xe(II) oxo-cation salt,  $[\text{XeOXeOXe}][\mu\text{-F}(\text{ReO}_2\text{F}_3)_2]_2$ .<sup>120</sup> The reaction scheme is given by Eqs. (31)–(34). The  $[\text{XeOXeOXe}]^{2+}$  salt rapidly decomposes to  $\text{XeF}_2$ ,  $\text{ReO}_2\text{F}_3$ , Xe, and  $\text{O}_2$  upon warming the solid or its HF solutions above  $-20\text{ }^\circ\text{C}$ .



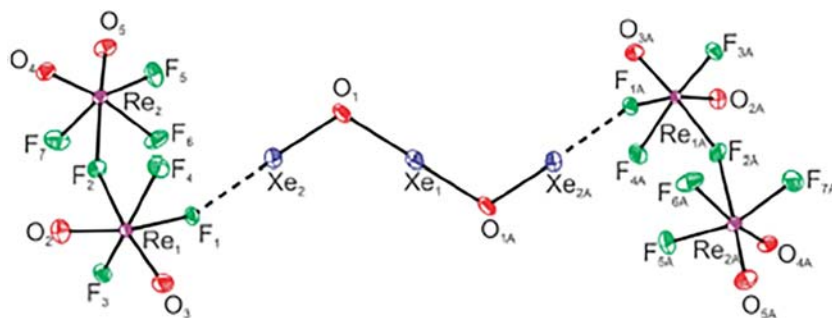
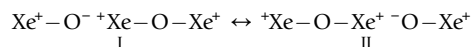
A proposed reaction pathway which leads to  $[\text{XeOXeOXe}][\mu\text{-F}(\text{ReO}_2\text{F}_3)_2]_2$  consists of a series of oxygen/fluorine metathesis reactions that involves  $\text{FXeOH}$  as a transient reaction intermediate (Scheme 2).



**Scheme 2** A proposed reaction pathway leading to the formation of  $[\text{XeOXeOXe}][\mu\text{-F}(\text{ReO}_2\text{F}_3)_2]_2$ . Reproduced with permission from Ivanova, M. V.; Mercier, H. P. A.; Schrobilgen, G. J. *J. Am. Chem. Soc.* **2015**, *137*, 13398–13413.

The synthesis and structural characterization of the  $[\text{XeOXeOXe}]^{2+}$  cation as its  $[\mu\text{-F}(\text{ReO}_2\text{F}_3)_2]^-$  salt provided the first example of a xenon(II) oxo-species and noble-gas oxocation, and a rare example of a noble-gas dication.<sup>120</sup> The crystal structure of  $[\text{XeOXeOXe}][\mu\text{-F}(\text{ReO}_2\text{F}_3)_2]_2$  consists of a planar, zigzag-shaped  $[\text{XeOXeOXe}]^{2+}$  cation ( $C_{2h}$  symmetry) that is fluorine bridged through its terminal xenon atoms to two  $[\mu\text{-F}(\text{ReO}_2\text{F}_3)_2]^-$  anions by means of two, primarily electrostatic, Xe...F secondary bonds (2.392(4) Å) (Fig. 20).

The central Xe...O bonds (2.135(6) Å) are significantly longer and more polar than the terminal Xe...O bonds (1.987(6) Å), in accordance with the dominant resonance Structures I and II, which suggested that the shorter chain Xe(II) oxo-cation,  $[\text{XeOXe}]^{2+}$ , may also exist.



**Fig. 20** The crystal structure of  $[\text{XeOXeOXe}][\mu\text{-F}(\text{ReO}_2\text{F}_3)_2]_2$ . Thermal ellipsoids are drawn at the 50% probability level. Reproduced with permission from Ivanova, M. V.; Mercier, H. P. A.; Schrobilgen, G. J. *J. Am. Chem. Soc.* **2015**, *137*, 13398–13413.

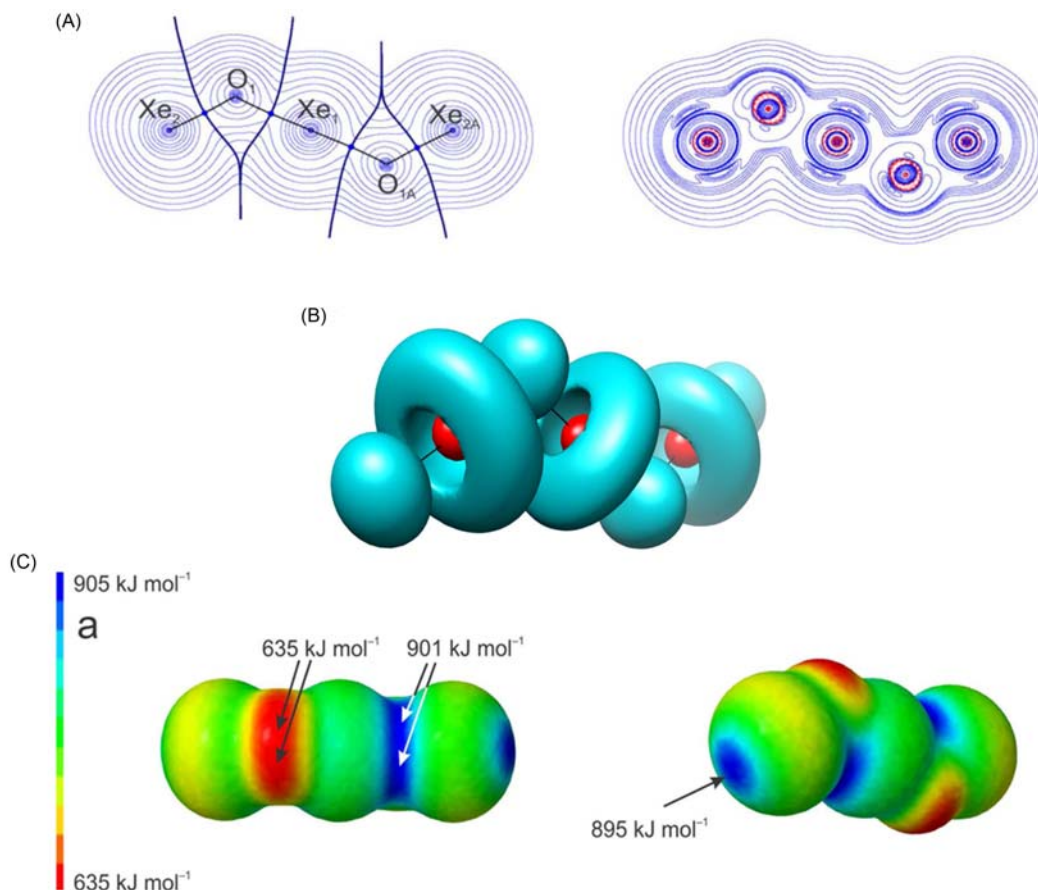
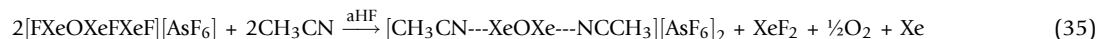
The central Xe–O bonds of  $[\text{XeOXeOxe}]^{2+}$  are equal within  $\pm 3\sigma$  to those of  $\text{Xe}(\text{OTeF}_5)_2$  (2.119(11) Å),<sup>126</sup>  $\text{FXeOSO}_2\text{F}$  (2.155(8) Å),<sup>60</sup> and  $\text{FXeONO}_2$  (2.126(4) Å),<sup>127</sup> whereas the terminal Xe–O bonds are comparable to that of the strongly oxidizing  $[\text{XeOTeF}_5]^+$  cation in  $[\text{XeOTeF}_5][\text{Sb}(\text{OTeF}_5)_6]\cdot\text{SO}_2\text{ClF}$  (1.969(4) Å).<sup>128</sup>

Quantum-chemical calculations were used to aid in the vibrational assignments of  $[\text{Xe}^{16/18}\text{Oxe}^{16/18}\text{Oxe}][\mu\text{-F}(\text{Re}^{16/18}\text{O}_2\text{F}_3)_2]$ .<sup>120</sup> The Raman spectra of the natural abundance and  $^{18}\text{O}$ -enriched  $[\text{XeOXeOxe}]^{2+}$  salts were fully assigned and shown to be consistent with a centrosymmetric ( $C_{2h}$ ) cation geometry. The band at  $581.6\text{ cm}^{-1}$  exhibits a  $^{18}\text{O}$  isotope shift,  $\Delta\nu^{16/18} = \nu(^{18}\text{O}) - \nu(^{16}\text{O}) = -32.3\text{ cm}^{-1}$ , that corresponds to the symmetric out-of-phase  $[\nu(\text{Xe}_1\text{O}_1) + \nu(\text{Xe}_{1A}\text{O}_{1A})] - [\nu(\text{Xe}_2\text{O}_1) + \nu(\text{Xe}_2\text{O}_{1A})]$  stretching mode. The band at  $358.7\text{ cm}^{-1}$ ,  $\Delta\nu^{16/18} = -17.8\text{ cm}^{-1}$ , is assigned to its in-phase counterpart,  $[\nu(\text{Xe}_1\text{O}_1) + \nu(\text{Xe}_1\text{O}_{1A})] + [\nu(\text{Xe}_2\text{O}_1) + \nu(\text{Xe}_{2A}\text{O}_{1A})]$ , and the band at  $92.8\text{ cm}^{-1}$ ,  $\Delta\nu^{16/18} = -2.5\text{ cm}^{-1}$ , corresponds to the symmetric in-phase  $[\delta(\text{Xe}_2\text{O}_1\text{Xe}_1) + \delta(\text{Xe}_{2A}\text{O}_{1A}\text{Xe}_1)]_{i.p.}$  bending mode.

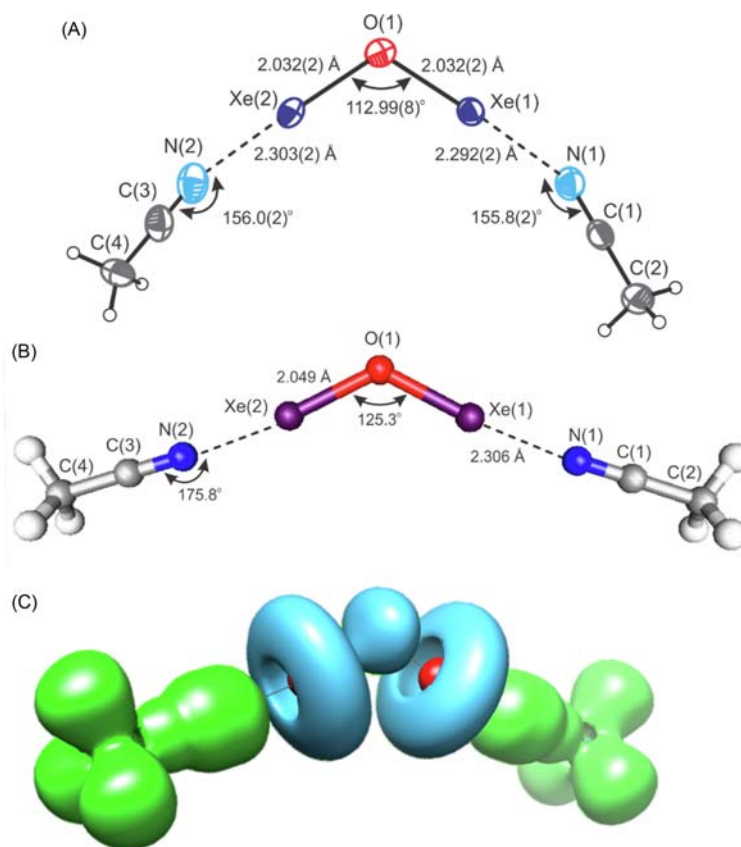
NBO, QTAIM, ELF, and MEPS analyses were used to assess the bonding in  $[\text{XeOXeOxe}]^{2+}$  (Fig. 21), and the hypothetical  $\text{FXe}^{16/18}\text{Oxe}^{16/18}\text{OxeF}$  ( $C_{2h}$ ) molecule was also calculated in order to better assess the nature of the Xe---F bridge bonds in the ion pair.<sup>120</sup> Ion pair interactions occur through  $\text{Re}-\text{F}_{\mu}\text{---Xe}$  bridges, which are predominantly electrostatic in nature and result from polarization of the  $\text{F}_{\mu}$ -atom electron densities by the exposed core charges of the terminal xenon atoms. Each xenon atom is surrounded by a torus of xenon valence electron density comprised of the three VELPs. The positive regions of the terminal xenon atoms and associated fluorine bridge bonds correspond to the positive  $\sigma$ -holes and donor interactions that are associated with “halogen bonding”.

#### 1.08.3.5.2 $[\text{CH}_3\text{CN}\text{---XeOxe}\text{---NCCH}_3][\text{AsF}_6]_2$

Following the synthesis and structural characterization of  $[\text{XeOXeOxe}]^{2+}$ ,<sup>120</sup> the reaction of  $\text{CH}_3\text{CN}$  with  $[\text{FXeOxeFXeF}][\text{AsF}_6]$  at  $-60^\circ\text{C}$  in aHF was investigated and shown to yield the *bis*- $\text{CH}_3\text{CN}$  adduct of the previously unknown  $[\text{XeOxe}]^{2+}$  cation (Eq. 35).<sup>129</sup>



**Fig. 21** (A) A contour map of the charge density showing the bond paths and the intersection of the interatomic surfaces (left) and charge density contour map of the Laplacian distribution (right) in  $[\text{XeOxeOxe}]^{2+}$ ; (B) ELF isosurface plots at  $\eta(r) = 0.60$ ; and (C) calculated MEPS at the 0.001 electron bohr<sup>-3</sup> (B3LYP/aug-cc-pVDZ(-PP)). Reproduced and modified with permission from Ivanova, M. V.; Mercier, H. P. A.; Schrobilgen, G. J. *J. Am. Chem. Soc.* **2015**, *137*, 13398–13413.



**Fig. 22** (A) The  $[\text{CH}_3\text{CN}\cdots\text{XeOXe}\cdots\text{NCCH}_3]^{2+}$  cation in the single-crystal X-ray structure of its  $[\text{AsF}_6]^-$  salt; thermal ellipsoids are drawn at the 50% probability level. (B) The energy-minimized gas-phase geometry ( $C_{2v}$ ) of the  $[\text{CH}_3\text{CN}\cdots\text{XeOXe}\cdots\text{NCCH}_3]^{2+}$  cation calculated at the B3LYP/aug-cc-pVTZ-PP level of theory, and (C) the ELF isosurface plot shown at  $\eta(r) = 0.54$ . Color code: red = xenon core basin, blue = monosynaptic basins (oxygen and Xe VELPs), and green = disynaptic basins. Modified from DeBackere, J. R.; Bortolus, M. R.; Schrobilgen, G. J. *Angew. Chem. Int. Ed.* **2016**, *55*, 11917–11920.

The low-temperature X-ray crystal structure of  $[\text{CH}_3\text{CN}\cdots\text{XeOXe}\cdots\text{NCCH}_3][\text{AsF}_6]_2$  (Fig. 22) consists of a well-isolated adduct-cation that has among the shortest Xe---N bond distances (2.294(2) and 2.304(2) Å) known for an sp-hybridized nitrogen base coordinated to xenon, and provides only the second example of a Xe(II) oxo-species to be structurally characterized. The Xe–O bond lengths (2.032(2) and 2.033(2) Å) are intermediate with respect to the terminal and central Xe–O bonds of  $[\text{XeOXeOXe}]^{2+}$ .<sup>120</sup>

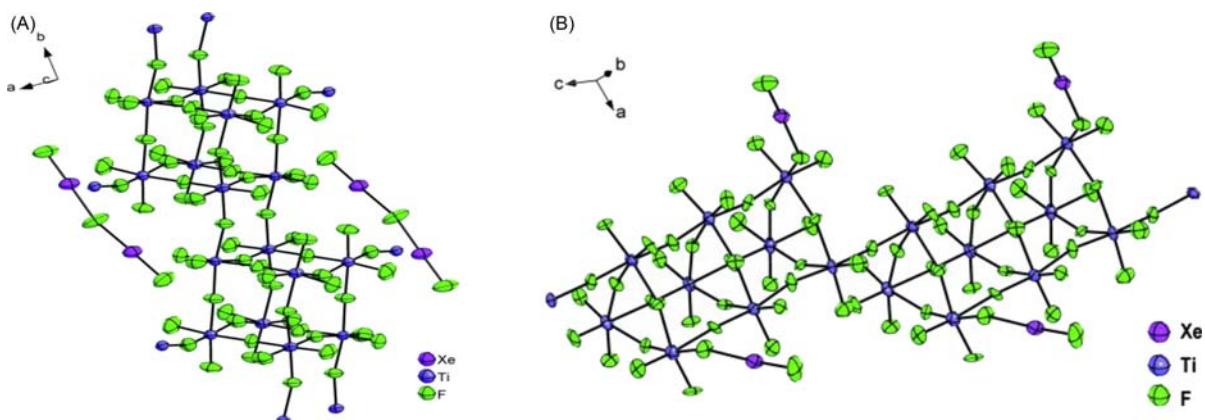
Quantum-chemical (NBO, QTAIM, ELF, and MEPS) analyses show that the Xe–O bonds are polar covalent whereas the Xe---N bonds may be described as primarily electrostatic ( $\sigma$ -hole) interactions. Quantum-chemical calculations were used to aid in the vibrational assignments of  $[\text{CH}_3\text{CN}\cdots\text{XeOXe}\cdots\text{NCCH}_3][\text{AsF}_6]_2$ , along with <sup>18</sup>O-enrichment studies. The spectra were analyzed assuming  $C_{2v}$  symmetry for the adduct-cation. The band at 599.9  $\text{cm}^{-1}$ ,  $\Delta\nu^{16/18} = -31.1 \text{ cm}^{-1}$ , was assigned to the symmetric  $[\nu(\text{Xe}_1\text{O}) - \nu(\text{Xe}_2\text{O})]$  stretching mode and the band at 443.8  $\text{cm}^{-1}$ ,  $\Delta\nu^{16/18} = -15.2 \text{ cm}^{-1}$  was assigned to its in-phase counterpart,  $[\nu(\text{Xe}_1\text{O}) + \nu(\text{Xe}_2\text{O})]$ , and is weakly coupled to the  $\delta(\text{CCN})_{i.p.}$  deformation mode. The band at 263.9  $\text{cm}^{-1}$ ,  $\Delta\nu^{16/18} = -0.2 \text{ cm}^{-1}$ , corresponds to the  $\delta(\text{Xe}_1\text{OXe}_2)_{i.p.}$  bending mode, which is strongly coupled with the in-phase  $\nu(\text{Xe-N})$  stretching modes.

#### 1.08.3.5.3 $[\text{XeF}]^+$ and $[\text{Xe}_2\text{F}_3]^+$ salts of transition-metal fluoro-anions

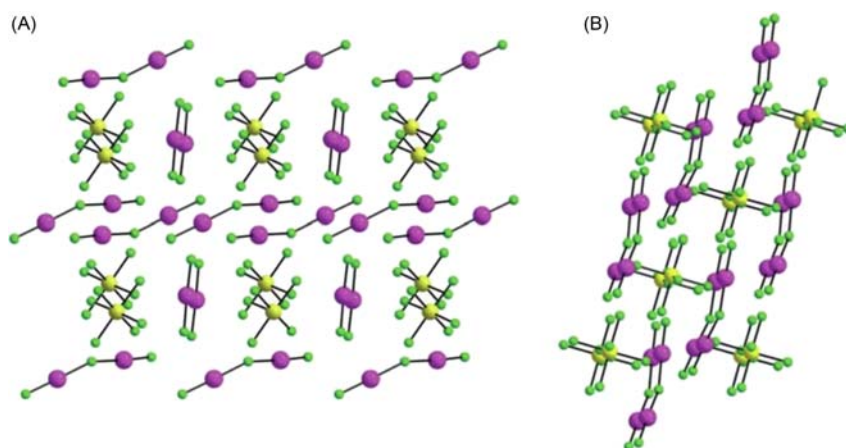
(i)  $[\text{Xe}_2\text{F}_3][\text{Ti}_8\text{F}_{33}]$  and  $[\text{XeF}][\text{Ti}_9\text{F}_{38}]$ . The metal tetrafluorides  $\text{MF}_4$  ( $M = \text{Ti, Cr, Mn, Rh, Pd, Pt, and Sn}$ ) are moderate strength fluoride-ion acceptors. Although their reactions with  $\text{XeF}_2$  were characterized by many different techniques (Ti,<sup>130</sup> Cr,<sup>109,131</sup> Mn,<sup>132,133</sup> Rh,<sup>134</sup> Pd,<sup>135</sup> Pt,<sup>136</sup> and Sn<sup>137</sup>), only the  $\text{XeF}_2\cdot\text{CrF}_4$ <sup>109</sup> and  $\text{XeF}_2\cdot 2\text{CrF}_4$ <sup>131</sup> complexes have been structurally characterized by LT SCXRD. Preliminary work had shown that  $n\text{XeF}_2\cdot\text{TiF}_4$  complexes are formed when  $\text{TiF}_4$  is heated with  $\text{XeF}_2$  at 120 °C.<sup>130</sup> Most recently, the reaction of  $\text{XeF}_2$  with excess  $\text{TiF}_4$  at 135 °C for several hours was shown to yield  $[\text{Xe}_2\text{F}_3][\text{Ti}_8\text{F}_{33}]$  and  $[\text{XeF}][\text{Ti}_9\text{F}_{38}]$ , which were characterized by LT SCXRD.<sup>114</sup> The Xe–F<sub>t</sub> bond lengths are equal within  $\pm 3\sigma$  (1.901(4), 1.905(4) Å), whereas the Xe---F<sub>b</sub> bond length difference is greater (2.158(4), 2.194(4) Å). The Xe---F<sub>b</sub>---Xe bond angle (164.3(3)°) is thus far the largest among the known  $[\text{Xe}_2\text{F}_3]^+$  salts. The structural characterization of  $[\text{XeF}][\text{Ti}_9\text{F}_{38}]$  also provided the first crystal structure of the  $[\text{Ti}_9\text{F}_{38}]^{2-}$  anion (Fig. 23).

The RT Raman spectra of  $[\text{Xe}_2\text{F}_3][\text{Ti}_8\text{F}_{33}]$  and  $[\text{XeF}][\text{Ti}_9\text{F}_{38}]$  show two strong bands at 594 and 612  $\text{cm}^{-1}$ , respectively, that were assigned to the Xe–F<sub>t</sub> stretches of the  $[\text{Xe}_2\text{F}_3]^+$  and  $[\text{XeF}]^+$  cations.





**Fig. 23** Selected fragments from the X-ray crystal structures of (A) [Xe<sub>2</sub>F<sub>3</sub>][Ti<sub>8</sub>F<sub>33</sub>] and (B) [XeF<sub>2</sub>][Ti<sub>9</sub>F<sub>38</sub>]; thermal ellipsoids are drawn at the 50% probability level. Reproduced with permission from Radan, K.; Goreshnik, E.; Žemva, B. *Angew. Chem. Int. Ed.* **2014**, *53*, 13715–13719.



**Fig. 24** A packing diagram showing the X-ray crystal structure of (A) [Xe<sub>2</sub>F<sub>3</sub>][RuF<sub>6</sub>]·XeF<sub>2</sub> and (B) [Xe<sub>2</sub>F<sub>3</sub>][RuF<sub>6</sub>]. Reproduced and modified with permission from Tramšek, M.; Goreshnik, E.; Tavčar, G. *Acta Chim. Slov.* **2016**, *63*, 369–375.

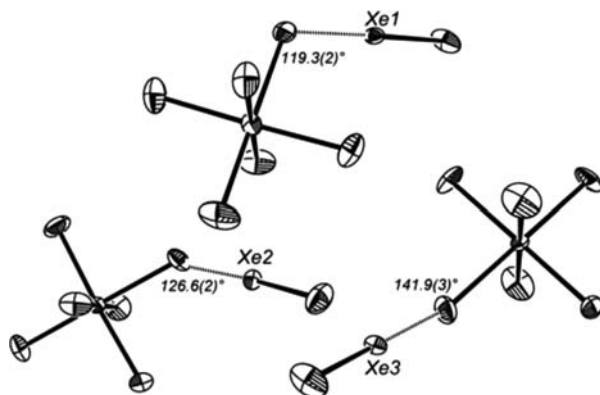
(ii) [Xe<sub>2</sub>F<sub>3</sub>][RuF<sub>6</sub>]·XeF<sub>2</sub>, [Xe<sub>2</sub>F<sub>3</sub>][MF<sub>6</sub>] (M = Ru, Ir). The reaction of M (M = Ir, Ru) powders with excess XeF<sub>2</sub> in aHF solvent were shown to yield [Xe<sub>2</sub>F<sub>3</sub>]<sup>+</sup> salts of the [MF<sub>6</sub>]<sup>-</sup> anions, therein demonstrating the strength and utility of XeF<sub>2</sub> as an oxidative fluorinator.<sup>138</sup> Single crystals of [Xe<sub>2</sub>F<sub>3</sub>][RuF<sub>6</sub>]·XeF<sub>2</sub>, [Xe<sub>2</sub>F<sub>3</sub>][RuF<sub>6</sub>], and [Xe<sub>2</sub>F<sub>3</sub>][IrF<sub>6</sub>] were grown by slow evaporation of the aHF solvent and were characterized by LT SCXRD. The [Xe<sub>2</sub>F<sub>3</sub>]<sup>+</sup> cations are more isolated in the crystal structure of [Xe<sub>2</sub>F<sub>3</sub>][RuF<sub>6</sub>]·XeF<sub>2</sub> (Fig. 24A) than those of [Xe<sub>2</sub>F<sub>3</sub>][RuF<sub>6</sub>] and [Xe<sub>2</sub>F<sub>3</sub>][IrF<sub>6</sub>] (Fig. 24B). Their geometrical parameters differ slightly from those of other [Xe<sub>2</sub>F<sub>3</sub>]<sup>+</sup> salts, an indication of their dependence on the crystal packing and on the nature of the counter anion, e.g., the Xe---F<sub>b</sub>---Xe bond angle (154.3(4)°) of [Xe<sub>2</sub>F<sub>3</sub>][RuF<sub>6</sub>]·XeF<sub>2</sub> is less than that of [Xe<sub>2</sub>F<sub>3</sub>][Ti<sub>8</sub>F<sub>33</sub>] (164.3(3)°); and the respective Xe---F<sub>b</sub> (2.139(7) and 2.152(7) Å) and Xe---F<sub>t</sub> (1.913(8) and 1.919(6) Å) bonds are correspondingly shorter and longer.

The RT Raman spectra of [Xe<sub>2</sub>F<sub>3</sub>][RuF<sub>6</sub>]·XeF<sub>2</sub> and [Xe<sub>2</sub>F<sub>3</sub>][IrF<sub>6</sub>]·XeF<sub>2</sub> were also obtained<sup>138</sup>; the bands at 506/515 cm<sup>-1</sup> (Ru) and 506/516 cm<sup>-1</sup> (Ir) were assigned to the Xe-F stretches of cocrystallized XeF<sub>2</sub>, and bands at 578/586 cm<sup>-1</sup> (Ru) and 578/587 cm<sup>-1</sup> (Ir) were assigned to the Xe-F<sub>t</sub> stretches of the [Xe<sub>2</sub>F<sub>3</sub>]<sup>+</sup> cations by comparison with other salts. The RT Raman spectrum of [Xe<sub>2</sub>F<sub>3</sub>][RuF<sub>6</sub>] was obtained in admixture with [Xe<sub>2</sub>F<sub>3</sub>][RuF<sub>6</sub>]·XeF<sub>2</sub> and/or [XeF][RuF<sub>6</sub>].

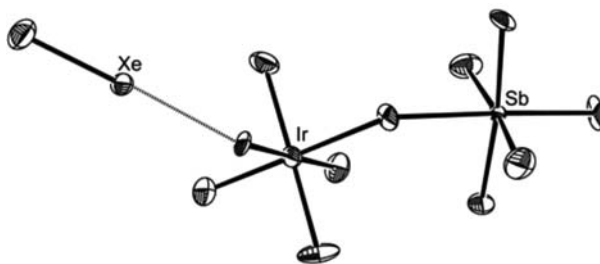
(iii) [XeF][IrF<sub>6</sub>] and [XeF][IrSbF<sub>11</sub>]. Xenon and OsF<sub>6</sub> or IrF<sub>6</sub>, when condensed into a quartz tube and held at -78 °C give intense blue solutions.<sup>139</sup> Similar blue colors have been attributed to [Cl<sub>4</sub>]<sup>+</sup> and [Xe<sub>4</sub>]<sup>+</sup> in the LT reactions of Cl<sub>2</sub> with MF<sub>6</sub> (M = Ir, Os)<sup>139</sup> and Xe with SbF<sub>5</sub>,<sup>139</sup> respectively, however the exact nature of the blue species observed in this study was not determined. Warming to RT resulted in the formation of yellow crystals of [XeF][IrF<sub>6</sub>] (Fig. 25), whereas no further reaction was observed in the case of OsF<sub>6</sub>.<sup>140</sup> The low-temperature reaction of Xe with IrF<sub>6</sub> in the superacid medium, aHF/SbF<sub>5</sub>, rapidly yielded yellow crystals of [XeF][IrSbF<sub>11</sub>] with no evidence for a dark blue species. The SCXRD determination of [XeF][IrSbF<sub>11</sub>] provided the first geometric parameters for the [IrSbF<sub>11</sub>]<sup>-</sup> anion (Fig. 26).<sup>140</sup>

Both [XeF][IrF<sub>6</sub>] and [XeF][IrSbF<sub>11</sub>] are ion-pairs having geometric parameters that are similar to those of [XeF][Sb<sub>2</sub>F<sub>11</sub>]<sup>53</sup> and [XeF][Bi<sub>2</sub>F<sub>11</sub>],<sup>53</sup> with near linear F-Xe---F<sub>b</sub> angles (177.4(2)–179.3(2)° and 178.1(4)°, respectively) and bent Xe---F<sub>b</sub>-Ir angles





**Fig. 25** The X-ray crystal structure of  $[\text{XeF}][\text{IrF}_6]$  with thermal ellipsoids drawn at the 50% probability level. Reproduced with permission from Tamadon, F.; Seidel, S.; Seppelt, K. *Acta Chim. Slov.* **2013**, *60*, 491–494.



**Fig. 26** The X-ray crystal structure of  $[\text{XeF}][\text{IrSbF}_{11}]$  with thermal ellipsoids drawn at the 50% probability level. Reproduced with permission from Tamadon, F.; Seidel, S.; Seppelt, K. *Acta Chim. Slov.* **2013**, *60*, 491–494.

( $119.3(2)$ – $141.9(3)^\circ$  and  $122.0(4)^\circ$ , respectively). The Xe–F ( $1.854(4)$ – $1.867(5)$  Å and  $1.879(10)$  Å) and Xe---F bond lengths ( $2.220(4)$ – $2.272(5)$  Å and  $2.288(8)$  Å, respectively) are similar in both salts.

## 1.08.4 Xenon(IV) compounds

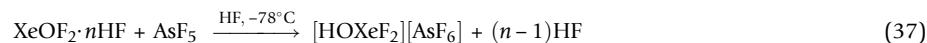
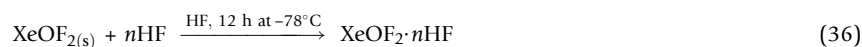
A previous review<sup>13</sup> should be consulted for a comprehensive survey of developments pertaining to the syntheses, properties, structures, and bonding of xenon(IV) compounds that covers the discovery of noble-gas reactivity in 1962 to 2014 inclusive.

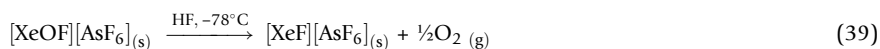
### 1.08.4.1 Xenon oxide fluorides

#### 1.08.4.1.1 $[\text{H}(\text{OXeF}_2)_n][\text{AsF}_6]$ and $[\text{FXe}(\text{OXeF}_2)_n][\text{AsF}_6]$ ( $n = 1, 2$ )

There are far fewer Xe(IV) compounds than Xe(II) or Xe(VI) compounds, which is, in part, due to the propensity of the oxides and oxide fluorides of Xe(IV) to undergo redox elimination and disproportionation to Xe(II) and O<sub>2</sub> or Xe(II) and Xe(VI), respectively.<sup>141–144</sup> Until recently, examples of Xe(IV) cations were limited to  $[\text{XeF}_3]^+$ ,<sup>53,58,145–150</sup>  $[\text{F}_x\text{Xe}(\text{OTeF}_5)_{3-x}]^+$  ( $x = 0–3$ ),<sup>151</sup> and  $[\text{C}_6\text{F}_5\text{XeF}_2]^+$ <sup>152</sup> salts.

Examples of noble-gas hydroxy derivatives are rare, and had been limited to the perxenate anions,  $[\text{H}_3\text{XeO}_6]^-$ ,<sup>153</sup>  $[\text{H}_2\text{XeO}_6]^{2-}$ ,<sup>153</sup> and  $[\text{HXeO}_6]^{3-}$ ,<sup>153</sup> which have yet to be structurally characterized in the solid state. Natural abundance and <sup>18</sup>O- and <sup>2</sup>H-enriched salts of  $[\text{H}(\text{OXeF}_2)_n][\text{AsF}_6]$  and  $[\text{FXe}(\text{OXeF}_2)_n][\text{AsF}_6]$  ( $n = 1, 2$ ) have been synthesized and structurally characterized by Raman spectroscopy.<sup>154</sup> The xenon(IV) oxide fluoride salt,  $[\text{H}(\text{OXeF}_2)_n][\text{AsF}_6]$ , was synthesized by the low-temperature reaction of  $\text{XeOF}_2 \cdot n\text{HF}$  ( $n$  is likely 1, and HF is H-bonded to oxygen) with  $\text{AsF}_5$  in aHF solvent (Eq. 36).<sup>143</sup> The synthesis of this salt requires that  $\text{XeOF}_2 \cdot n\text{HF}$ , prepared from  $\text{F}_2\text{OXeNCCH}_3$ , be fully solvated in aHF to form  $\text{XeOF}_2 \cdot n\text{HF}$  prior to reaction. A prior computational study revealed that the coordinated HF molecule of  $\text{XeOF}_2 \cdot n\text{HF}$  is H-bonded to the oxygen atom of  $\text{XeOF}_2$ .<sup>143</sup> This provides a more fluorobasic site for attack of the fluorine atom of coordinated HF by  $\text{AsF}_5$ . Reactions of  $\text{AsF}_5$  with pure or partially solvated  $\text{XeOF}_2$  result in decomposition, ultimately yielding  $[\text{XeF}][\text{AsF}_6]$  through the formation of the unstable Xe(II) oxyfluoro-cation intermediate,  $[\text{XeOF}]^+$  (Eqs. 37–39).<sup>154</sup> Solid  $[\text{HOXeF}_2][\text{AsF}_6]$  is stable indefinitely at  $-78^\circ\text{C}$ , and rapidly outgases, but not explosively, upon warming to  $-35^\circ\text{C}$ .





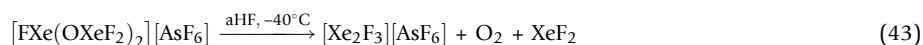
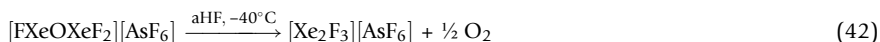
Reaction of  $\text{XeOF}_2 \cdot n\text{HF}$  with trace amounts of water in  $\text{AsF}_5/\text{HF}$  superacid solvent led to the formation of  $[\text{HOXe}(\text{F})_2\text{OXeF}_2][\text{AsF}_6]$ . This salt was also efficiently prepared by reaction of 0.5 equiv. of  $[\text{H}_3\text{O}][\text{AsF}_6]$  with  $\text{XeOF}_2 \cdot n\text{HF}$  in aHF solvent at  $-78^\circ\text{C}$  (Eq. 40). Oxygen isotope scrambling was not observed when  $\text{Xe}^{18}\text{OF}_2 \cdot n\text{HF}$  was allowed to react with  $[\text{H}_3^{16}\text{O}][\text{AsF}_6]$ , indicating that  $[\text{H}_3\text{O}]^+$  only contributes a proton in the reaction. Precipitated  $[\text{HOXe}(\text{F})_2\text{OXeF}_2][\text{AsF}_6]$  is stable at  $-78^\circ\text{C}$  under aHF solvent for several days, but decomposes over a one month period with  $\text{O}_2$  gas evolution to give orange crystals of the known Xe(II) oxyfluorocation,  $[\text{FXeOXeFXeF}]^+$ , as its  $[\text{AsF}_6]^-$  salt.<sup>124</sup>



The basicity of the oxygen atom of  $\text{XeOF}_2$  and the existence of unidentified peaks in the Raman spectrum of  $[\text{HOXeF}_2][\text{AsF}_6]$  led to the attempted synthesis of a  $\text{Xe}^{\text{II}}-\text{O}-\text{Xe}^{\text{IV}}$  bridged cation. The reaction of the Lewis acidic  $[\text{XeF}]^+$  cation with  $\text{XeOF}_2 \cdot n\text{HF}$  yielded  $[\text{FXe}^{\text{II}}(\text{OXe}^{\text{IV}}\text{F}_2)_m][\text{AsF}_6]$  ( $m = 1, 2$ ) (Eq. 41).



The reactions were initially fast, forming pale yellow precipitates within 5–10 min at  $-78^\circ\text{C}$ , but required up to a week or longer to go to completion. Both salts are stable as precipitates under HF solvent and as dry powders for several weeks at  $-78^\circ\text{C}$ , but decompose upon warming to  $-40^\circ\text{C}$  (Eqs. 42 and 43).<sup>154</sup>



Standard enthalpies and Gibbs free energies for the solid-state decompositions of  $[\text{XeOF}][\text{AsF}_6]$ ,  $[\text{HOXeF}_2][\text{AsF}_6]$ ,  $[\text{HOXe}(\text{F})_2\text{OXeF}_2][\text{AsF}_6]$ ,  $[\text{FXeOXeF}_2][\text{AsF}_6]$ ,  $[\text{FXeOXe}(\text{F})_2\text{OXeF}_2][\text{AsF}_6]$ , and the hydrolyses of  $[\text{HOXe}(\text{F})_2\text{OXeF}_2][\text{AsF}_6]$ ,  $[\text{FXeOXeF}_2][\text{AsF}_6]$ , and  $[\text{FXeOXe}(\text{F})_2\text{OXeF}_2][\text{AsF}_6]$  were calculated from Born-Fajans-Haber thermochemical cycles and support the proposed decomposition pathways.

The  $[\text{H}(\text{OXeF}_2)_n][\text{AsF}_6]$  and  $[\text{FXe}(\text{OXeF}_2)_n][\text{AsF}_6]$  ( $n = 1, 2$ ) salts were structurally characterized in the solid-state by LT Raman spectroscopy and quantum-chemical calculations (Fig. 27) were employed to aid in their vibrational frequency assignments.

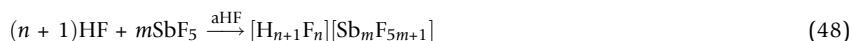
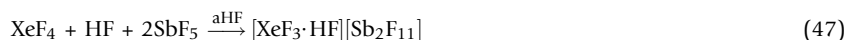
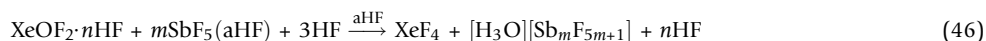
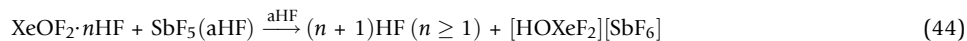
The experimental vibrational frequencies and isotopic shift trends were well reproduced by the calculated gas-phase frequencies at several levels of theory. The cation chains are limited to either one or two  $\text{OXeF}_2$  units which are oxygen-bridged, and strongly ion-paired with their  $[\text{AsF}_6]^-$  anions.

## 1.08.4.2 Xenon fluorides

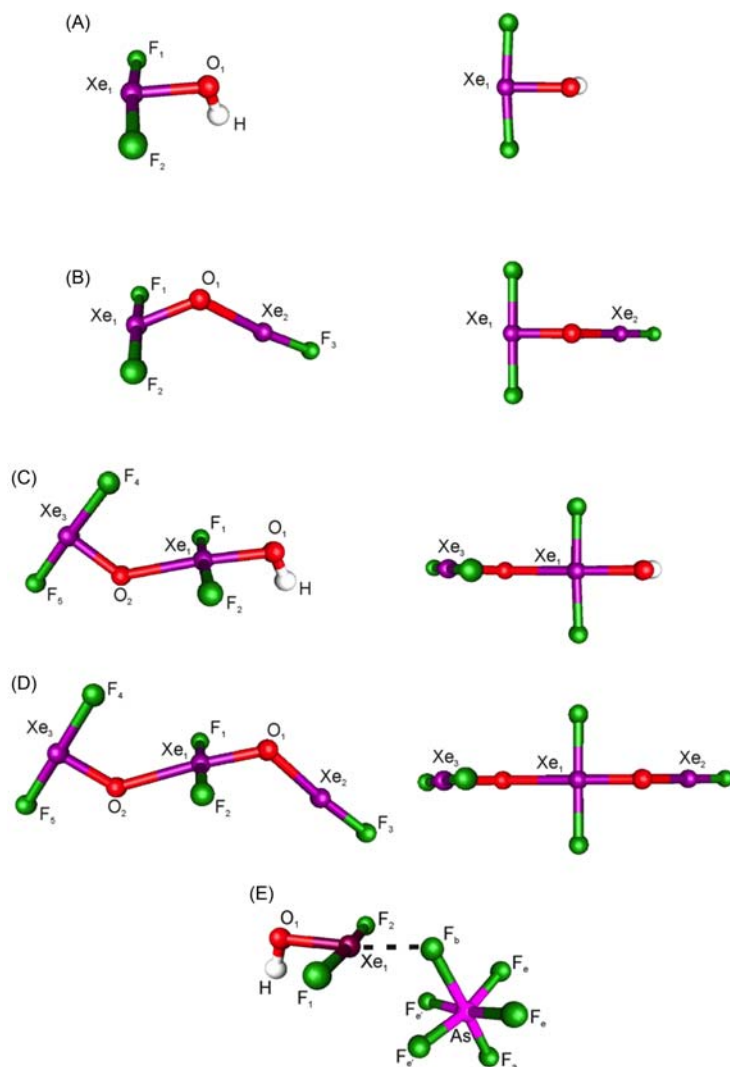
### 1.08.4.2.1 $[\text{F}_3\text{Xe}---\text{FH}][\text{Sb}_2\text{F}_{11}]$ and $[\text{H}_5\text{F}_4][\text{SbF}_6] \cdot 2[\text{F}_3\text{Xe}---\text{FH}][\text{Sb}_2\text{F}_{11}]$

Although examples of HF coordination complexes with cationic metal centers are known,<sup>155</sup> examples of structurally characterized noble-gas coordination complexes of HF were limited to  $[\text{XeF}_5][\text{HF}_2] \cdot \text{HF}$ .<sup>156</sup> The  $[\text{XeF}_3]^+$  cation, a stronger Lewis acid than  $[\text{XeF}_5]^+$ , may therefore be expected to also form coordination complexes with HF. Several  $[\text{SbF}_6]^-$  and  $[\text{Sb}_2\text{F}_{11}]^-$  salts of polyatomic acidium cations,  $[\text{H}_{x+1}\text{F}_x]^+$  ( $x \geq 1$ ) form in the superacid medium, HF/SbF<sub>5</sub>. Of these salts, only  $[\text{H}_2\text{F}][\text{Sb}_2\text{F}_{11}]$ ,<sup>157</sup>  $[\text{H}_3\text{F}_2][\text{Sb}_2\text{F}_{11}]$ ,<sup>157</sup> and  $[\text{H}_7\text{F}_6][\text{SbF}_6]$ <sup>158</sup> had been structurally characterized by SCXRD.

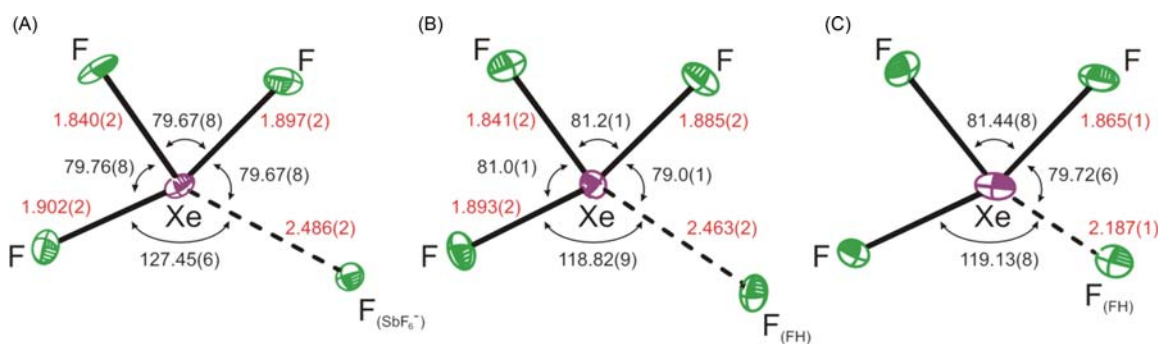
The reaction of  $\text{XeOF}_2 \cdot n\text{HF}$  with an HF/SbF<sub>5</sub> solution yielded a mixture of crystalline  $[\text{H}_5\text{F}_4][\text{SbF}_6] \cdot 2[\text{XeF}_3 \cdot \text{HF}][\text{Sb}_2\text{F}_{11}]$ ,  $[\text{XeF}_3 \cdot \text{HF}][\text{Sb}_2\text{F}_{11}]$ , and  $[\text{XeF}_3][\text{SbF}_6]$ .<sup>154</sup> A plausible reaction pathway leading to the formation of these species involves protonation of the hydroxyl group of  $[\text{HOXeF}_2][\text{SbF}_6]$  by SbF<sub>5</sub>/aHF, which leads to water displacement as soluble  $[\text{H}_3\text{O}]^+$  salts and XeF<sub>4</sub>, which react with SbF<sub>5</sub> (Eqs. 44–48).



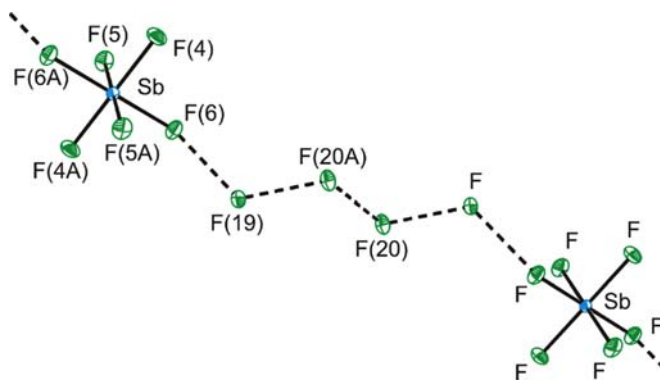
The  $[\text{XeF}_3]^+$  cations display T-shaped primary coordination spheres for the central xenon and three fluorine atoms ( $\text{AX}_3\text{E}_2$  VSEPR arrangements) and secondary contacts to the fluorine atom of HF in  $[\text{H}_5\text{F}_4][\text{SbF}_6] \cdot 2[\text{XeF}_3 \cdot \text{HF}][\text{Sb}_2\text{F}_{11}]$  and  $[\text{XeF}_3 \cdot \text{HF}][\text{Sb}_2\text{F}_{11}]$  and to a fluorine atom of  $[\text{SbF}_6]^-$  in  $[\text{XeF}_3][\text{SbF}_6]$  (Fig. 28).



**Fig. 27** The calculated geometries [B3LYP/aug-cc-pVTZ(-PP)] of (A)  $[\text{HOXeF}_2]^+$ , (B)  $[\text{FXeOXeF}_2]^+$ , (C)  $[\text{HOXe}(\text{F})_2\text{OXeF}_2]^+$ , (D)  $[\text{FXeOXe}(\text{F})_2\text{OXeF}_2]^+$ , and (E)  $[\text{HOXeF}_2][\text{AsF}_6]$ . Reproduced with permission from Brock, D. S.; Mercier, H. P. A.; Schrobilgen, G. J. *J. Am. Chem. Soc.* **2013**, *135*, 5089–5104.



**Fig. 28** The  $[\text{XeF}_3]^+$  cations in the X-ray crystal structures of (A)  $[\text{H}_5\text{F}_4][\text{SbF}_6] \cdot 2[\text{XeF}_3 \cdot \text{HF}][\text{Sb}_2\text{F}_{11}]$ , (B)  $[\text{XeF}_3 \cdot \text{HF}][\text{Sb}_2\text{F}_{11}]$ , and (C)  $[\text{XeF}_3][\text{SbF}_6]$ . Thermal ellipsoids are drawn at the 50% probability level. Reproduced with permission from Brock, D. S.; Mercier, H. P. A.; Schrobilgen, G. J. *J. Am. Chem. Soc.* **2013**, *135*, 5089–5104.



**Fig. 29** The  $[\text{H}_5\text{F}_4][\text{SbF}_6]$  unit in the X-ray crystal structure of  $[\text{H}_5\text{F}_4][\text{SbF}_6] \cdot 2[\text{XeF}_3 \cdot \text{HF}][\text{Sb}_2\text{F}_{11}]$ . Thermal ellipsoids are drawn at the 30% probability level. The hydrogen atoms of  $[\text{H}_5\text{F}_4]^+$  could not be located in the difference map. Reproduced with permission from Brock, D. S.; Mercier, H. P. A.; Schrobilgen, G. J. *J. Am. Chem. Soc.* **2013**, *135*, 5089–5104.

The secondary coordination spheres of xenon in  $[\text{H}_5\text{F}_4][\text{SbF}_6] \cdot 2[\text{XeF}_3 \cdot \text{HF}][\text{Sb}_2\text{F}_{11}]$  and  $[\text{XeF}_3 \cdot \text{HF}][\text{Sb}_2\text{F}_{11}]$  are similar; however, the  $[\text{F}_3\text{Xe} \cdots \text{FH}]^+$  cation of the latter salt is disordered. An additional contact between the  $[\text{XeF}_3]^+$  cation and the  $[\text{SbF}_6]^-$  anion of  $[\text{H}_5\text{F}_4][\text{SbF}_6] \cdot 2[\text{XeF}_3 \cdot \text{HF}][\text{Sb}_2\text{F}_{11}]$  presumably alters the crystal packing sufficiently to give an ordered  $[\text{F}_3\text{Xe} \cdots \text{FH}]^+$  cation and the second example of HF coordinated to a noble-gas center. The latter compound also provides the first report of the  $[\text{H}_5\text{F}_4]^+$  acidium ion, a zigzag  $\text{F}_4$ -chain terminated by H-bonding to  $[\text{SbF}_6]^-$  anions (Fig. 29).

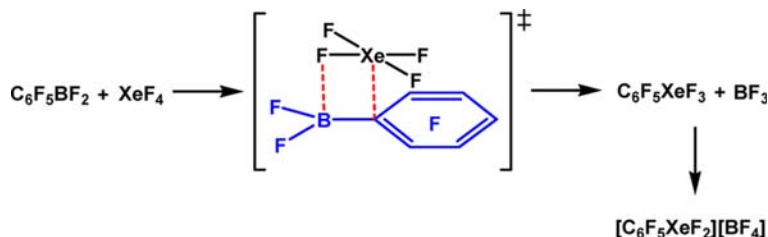
#### 1.08.4.2.2 $[\text{C}_6\text{F}_5\text{XeF}_2][\text{BF}_4]$ , $[\text{C}_6\text{F}_5\text{XeF}_2][\text{BF}_4] \cdot 2\text{HF}$ , and $[\text{C}_6\text{F}_5\text{XeF}_2][\text{BF}_4] \cdot 1.5\text{CH}_3\text{CN}$

Prior developments in Xe(II) chemistry have yielded an impressive number of  $\text{Xe}^{\text{II}}-\text{C}$  bonded species;  $[\text{RXe}][\text{A}]$  (R = aryl,<sup>43–45</sup> alkenyl,<sup>159–161</sup> alkynyl<sup>162–164</sup>; A = a weakly coordinating anion),  $\text{Xe}(\text{C}_6\text{F}_5)_2$ ,<sup>47–49,165</sup> and  $\text{C}_6\text{F}_5\text{XeX}$  (X = F<sup>50</sup> or Cl<sup>54</sup>).

As in the case of  $\text{Xe}^{\text{II}}-\text{C}$  bonded species, the synthesis of a  $\text{Xe}^{\text{IV}}-\text{C}$  bonded species<sup>166</sup> required a ligand group that is sufficiently electronegative and resistant to oxidation by Xe(IV). The  $\text{C}_6\text{F}_5$  group proved to be a viable candidate for the synthesis of a stable  $\text{Xe}^{\text{IV}}-\text{C}$  bonded species and led to the synthesis of  $[\text{C}_6\text{F}_5\text{XeF}_2][\text{BF}_4]$  by reaction of  $\text{XeF}_4$  with  $\text{C}_6\text{F}_5\text{BF}_2$  in  $\text{CH}_2\text{Cl}_2$  at  $-55^\circ\text{C}$  (Eq. 49), which was initially characterized by LT  $^{11}\text{B}$ ,  $^{13}\text{C}$ ,  $^{19}\text{F}$ , and  $^{129}\text{Xe}$  NMR spectroscopy.<sup>152</sup>



The proposed xenodeborylation reaction pathway initially involves polarization of an Xe–F bond by the Lewis acid,  $\text{C}_6\text{F}_5\text{BF}_2$ .<sup>166</sup> The resulting Lewis acid–base interaction enhances the nucleophilic character of the  $\text{C}_6\text{F}_5$  group, which migrates to the highly electrophilic Xe(IV) center to form  $\text{C}_6\text{F}_5\text{XeF}_3$  and  $\text{BF}_3$ . In the final step, fluoride-ion abstraction from  $\text{C}_6\text{F}_5\text{XeF}_3$  by  $\text{BF}_3$  yields  $[\text{C}_6\text{F}_5\text{XeF}_2][\text{BF}_4]$  (Scheme 3). Although  $[\text{C}_6\text{F}_5\text{XeF}_2][\text{BF}_4]$  had been previously characterized by LT multi-NMR spectroscopy, the  $J(^{19}\text{F}-^{19}\text{F})$ ,  $J(^{19}\text{F}-^{129}\text{Xe})$ , and  $J(^{13}\text{C}-^{129}\text{Xe})$  coupling constants of the  $\text{C}_6\text{F}_5$  group had not been reported.<sup>152</sup> Oxidative fluorination reactions of  $[\text{C}_6\text{F}_5\text{XeF}_2][\text{BF}_4]$  with  $\text{P}(\text{C}_6\text{F}_5)_3$ ,  $\text{C}_6\text{F}_5\text{I}$ , and  $\text{I}_2$  in  $\text{CH}_3\text{CN}$  solvent were also investigated and shown to yield  $\text{P}(\text{C}_6\text{F}_5)_3\text{F}_2$ ,  $\text{C}_6\text{F}_5\text{IF}_2$ , and  $\text{IF}_5$ , respectively, by LT multi-NMR spectroscopy.<sup>152</sup>



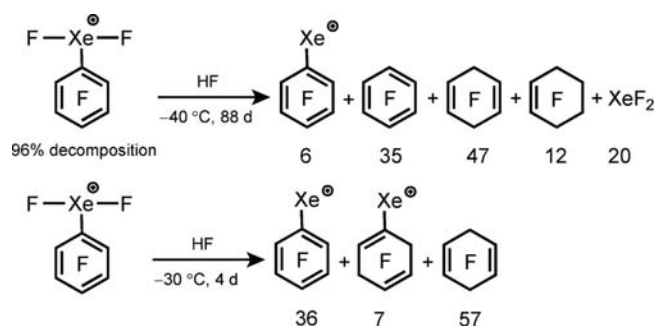
**Scheme 3** Proposed xenodeborylation mechanism for the formation of  $[\text{C}_6\text{F}_5\text{XeF}_2][\text{BF}_4]$ . Reproduced with permission from Koppe, K.; Haner, J.; Mercier, H. P. A.; Frohn, H.-J.; Schrobilgen, G. J. *Inorg. Chem.* **2014**, *53*, 11640–11661.

The synthesis of  $[\text{C}_6\text{F}_5\text{XeF}_2][\text{BF}_4]$  was subsequently improved upon and the syntheses of its  $\text{CH}_3\text{CN}$  and  $\text{HF}$  solvates,  $[\text{C}_6\text{F}_5\text{XeF}_2][\text{BF}_4] \cdot n\text{CH}_3\text{CN}$  ( $n = 1.5, 2$ ) and  $[\text{C}_6\text{F}_5\text{XeF}_2][\text{BF}_4] \cdot 2\text{HF}$ , were structurally characterized by LT Raman and multi-NMR spectroscopies, and LT SCXRD, providing the first and only crystal structures of  $\text{Xe}^{\text{IV}}-\text{C}$  bonded compounds.<sup>166</sup> The improved synthesis of high-purity  $[\text{C}_6\text{F}_5\text{XeF}_2][\text{BF}_4]$  was a modification of the earlier synthesis<sup>152</sup> in which a very narrow concentration range had been employed for the starting materials. Dilute solutions of  $\text{XeF}_4$  ( $\sim 1$  mmol) were required due to its low solubility in  $\text{CH}_2\text{Cl}_2$  at  $-55^\circ\text{C}$  ( $\sim 20 \mu\text{mol mL}^{-1}$ ) and the voluminous nature of the reaction product,  $[\text{C}_6\text{F}_5\text{XeF}_2][\text{BF}_4]$ , which tended to occlude solid

XeF<sub>4</sub> and inhibit its reaction with C<sub>6</sub>F<sub>5</sub>BF<sub>2</sub>. Reactions of partially dissolved XeF<sub>4</sub> with C<sub>6</sub>F<sub>5</sub>BF<sub>2</sub> in CH<sub>2</sub>Cl<sub>2</sub> at -78 °C were slow, but accelerated at -60 °C to give light yellow [C<sub>6</sub>F<sub>5</sub>XeF<sub>2</sub>][BF<sub>4</sub>] as an insoluble precipitate. The reactions were quantitative when equimolar amounts of XeF<sub>4</sub> and C<sub>6</sub>F<sub>5</sub>BF<sub>2</sub> were used and went to completion within 1 h.

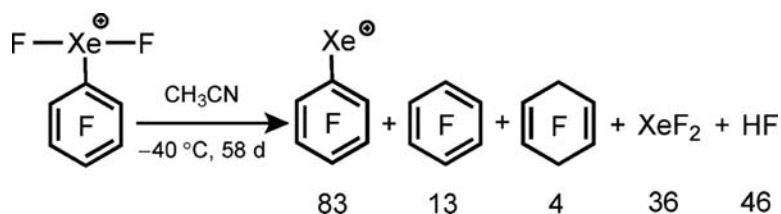
The solution stability of [C<sub>6</sub>F<sub>5</sub>XeF<sub>2</sub>][BF<sub>4</sub>] is dependant on the solvent and on the temperature. The salt is insoluble in the weakly coordinating solvents CH<sub>2</sub>Cl<sub>2</sub>, SO<sub>2</sub>ClF, and 1,1,1,3,3-pentafluorobutane (PFB), however it is stable as a suspension in CH<sub>2</sub>Cl<sub>2</sub> at temperatures below -40 °C. Warming the suspensions from -40 °C to room temperature resulted in rapid gas evolution with the formation of a black suspension comprised of C<sub>6</sub>F<sub>5</sub>H, C<sub>6</sub>F<sub>6</sub>, and C<sub>6</sub>F<sub>5</sub>Cl in a 6:3:1 molar ratio, and the fluorination products of CH<sub>2</sub>Cl<sub>2</sub>, namely CH<sub>2</sub>F<sub>2</sub>, CH<sub>2</sub>ClF, CHF<sub>3</sub>, and HF in a 78:33:7:75 molar ratio.

Crystals of the HF solvate, [C<sub>6</sub>F<sub>5</sub>XeF<sub>2</sub>][BF<sub>4</sub>] $\cdot$ 2HF, were grown by dissolution of [C<sub>6</sub>F<sub>5</sub>XeF<sub>2</sub>][BF<sub>4</sub>] in aHF followed by slow solvent removal under dynamic vacuum at -78 °C. Solutions of [C<sub>6</sub>F<sub>5</sub>XeF<sub>2</sub>][BF<sub>4</sub>] are more stable in aHF than in weakly coordinating solvents, and may be stored for up to 18 d at -78 °C with negligible decomposition. Complete decomposition occurs within 88 d at -40 °C, 4 d at -30 °C, and immediately upon warming to room temperature (Scheme 4). Decomposition in aHF likely occurs by means of heterolysis of the Xe<sup>IV</sup>-C bond by BF<sub>3</sub> acidified aHF, which leads to oxidative fluorination of the C<sub>6</sub>F<sub>5</sub> functional group and formation of Xe<sup>II</sup> and Xe<sup>0</sup> redox decomposition products.



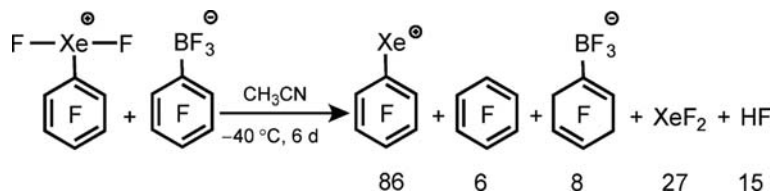
**Scheme 4** The decomposition product distribution of [C<sub>6</sub>F<sub>5</sub>XeF<sub>2</sub>][BF<sub>4</sub>] in aHF. The total weighted <sup>19</sup>F NMR intensities of the C<sub>6</sub>F<sub>5</sub> groups and their derivatives is set equal to 100 mol%. Reproduced with permission from Koppe, K.; Haner, J.; Mercier, H. P. A.; Frohn, H.-J.; Schrobilgen, G. J. *Inorg. Chem.* **2014**, *53*, 11640–11661.

Conversion of the HF solvate [C<sub>6</sub>F<sub>5</sub>XeF<sub>2</sub>][BF<sub>4</sub>] $\cdot$ 2HF back to [C<sub>6</sub>F<sub>5</sub>XeF<sub>2</sub>][BF<sub>4</sub>] was accomplished by dissolution of [C<sub>6</sub>F<sub>5</sub>XeF<sub>2</sub>][BF<sub>4</sub>] $\cdot$ 2HF in CH<sub>3</sub>CN, followed by slow solvent removal at ca. -40 °C under dynamic vacuum. Decomposition of [C<sub>6</sub>F<sub>5</sub>XeF<sub>2</sub>][BF<sub>4</sub>] in CH<sub>3</sub>CN solvent at -40 °C proceeded slowly over 58 d to primarily yield the Xe<sup>II</sup> reduction product, [C<sub>6</sub>F<sub>5</sub>Xe][BF<sub>4</sub>], and small amounts of C<sub>6</sub>F<sub>6</sub>, *c*-C<sub>6</sub>F<sub>8</sub>-1,4, XeF<sub>2</sub>, and HF (Scheme 5). Slow removal of the CH<sub>3</sub>CN solvent under dynamic vacuum at -40 °C afforded crystalline [C<sub>6</sub>F<sub>5</sub>XeF<sub>2</sub>][BF<sub>4</sub>]. The CH<sub>3</sub>CN solvate, [C<sub>6</sub>F<sub>5</sub>XeF<sub>2</sub>][BF<sub>4</sub>] $\cdot$ 1.5CH<sub>3</sub>CN, is only stable at LT (-78 °C) and was synthesized by allowing [C<sub>6</sub>F<sub>5</sub>XeF<sub>2</sub>][BF<sub>4</sub>] to stand at -78 °C in a CH<sub>2</sub>Cl<sub>2</sub>/CH<sub>3</sub>CN solvent mixture for several days, during which time crystals of solvated [C<sub>6</sub>F<sub>5</sub>XeF<sub>2</sub>][BF<sub>4</sub>] $\cdot$ 1.5CH<sub>3</sub>CN deposited from solution. It is possible that excess C<sub>6</sub>F<sub>5</sub>BF<sub>2</sub>, used in the synthesis of [C<sub>6</sub>F<sub>5</sub>XeF<sub>2</sub>][BF<sub>4</sub>], could further react to form [C<sub>6</sub>F<sub>5</sub>XeF<sub>2</sub>][C<sub>6</sub>F<sub>5</sub>BF<sub>3</sub>], which is expected to be less stable than [C<sub>6</sub>F<sub>5</sub>XeF<sub>2</sub>][BF<sub>4</sub>]. The reaction of [C<sub>6</sub>F<sub>5</sub>XeF<sub>2</sub>][BF<sub>4</sub>] with K[C<sub>6</sub>F<sub>5</sub>BF<sub>3</sub>] was therefore explored in CH<sub>3</sub>CN solvent at -40 °C and yielded a mixture of [C<sub>6</sub>F<sub>5</sub>Xe]<sup>+</sup>, C<sub>6</sub>F<sub>6</sub>, [C<sub>6</sub>F<sub>7</sub>BF<sub>3</sub>]<sup>-</sup>, XeF<sub>2</sub>, and HF, in a 86:6:8:27:15 molar ratio, respectively. The decomposition of [C<sub>6</sub>F<sub>5</sub>XeF<sub>2</sub>][BF<sub>4</sub>] was ca. 10 times faster at -40 °C in CH<sub>3</sub>CN when the [C<sub>6</sub>F<sub>5</sub>BF<sub>3</sub>]<sup>-</sup> anion was present (Scheme 6).



**Scheme 5** The product distribution for the decomposition of [C<sub>6</sub>F<sub>5</sub>XeF<sub>2</sub>][BF<sub>4</sub>] in CH<sub>3</sub>CN (cf. Scheme 4). Reproduced with permission from Koppe, K.; Haner, J.; Mercier, H. P. A.; Frohn, H.-J.; Schrobilgen, G. J. *Inorg. Chem.* **2014**, *53*, 11640–11661.





**Scheme 6** The product distribution resulting from the reaction of  $[\text{C}_6\text{F}_5\text{XeF}_2][\text{BF}_4]$  with a suspension of  $\text{K}[\text{C}_6\text{F}_5\text{BF}_3]$  in  $\text{CH}_3\text{CN}$  at  $-40^\circ\text{C}$ . Reproduced with permission from Koppe, K.; Haner, J.; Mercier, H. P. A.; Frohn, H.-J.; Schrobilgen, G. J. *Inorg. Chem.* **2014**, *53*, 11640–11661.

The reactions of  $[\text{C}_6\text{F}_5\text{XeF}_2][\text{BF}_4]$  with  $\text{P}(\text{C}_6\text{F}_5)_3$  and  $\text{C}_6\text{F}_5\text{I}$ <sup>152</sup> were re-examined, and extended to reactions with  $\text{Pn}(\text{C}_6\text{F}_5)_3$  ( $\text{Pn} = \text{P}, \text{As}, \text{or Bi}$ ) and  $\text{C}_6\text{F}_5\text{X}$  ( $\text{X} = \text{Br}$  or  $\text{I}$ ).<sup>166</sup> Oxidative fluorination of  $\text{Pn}(\text{C}_6\text{F}_5)_3$  and  $\text{C}_6\text{F}_5\text{I}$  by  $[\text{C}_6\text{F}_5\text{XeF}_2][\text{BF}_4]$  in  $\text{CH}_3\text{CN}$  solvent at  $-40^\circ\text{C}$  yielded  $\text{Pn}(\text{C}_6\text{F}_5)_3\text{F}_2$  and  $\text{C}_6\text{F}_5\text{IF}_2$ , respectively, after ca. 15 min. No reaction with  $\text{C}_6\text{F}_5\text{Br}$  was observed under similar conditions, and oxidative fluorination was not observed for  $\text{Pn}(\text{C}_6\text{F}_5)_3$  or  $\text{C}_6\text{F}_5\text{I}$  in aHF solvent.

Although the  $^{11}\text{B}$ ,  $^{13}\text{C}$ ,  $^{19}\text{F}$ , and  $^{129}\text{Xe}$  NMR spectra of  $[\text{C}_6\text{F}_5\text{XeF}_2][\text{BF}_4]$  had previously been reported,<sup>152</sup> only the chemical shifts and  $^1J(^{19}\text{F}-^{129}\text{Xe})$  and  $^1J(^{13}\text{C}-^{19}\text{F})$  coupling constants were provided for the  $[\text{C}_6\text{F}_5\text{XeF}_2]^+$  cation. Improved  $^{11}\text{B}$ ,  $^{19}\text{F}$ , and  $^{129}\text{Xe}$  NMR spectra of  $[\text{C}_6\text{F}_5\text{XeF}_2][\text{BF}_4]$  were obtained in aHF solvent at  $-40$  and  $-80^\circ\text{C}$  and were fully assigned, providing the missing  $^1J(^{19}\text{F}-^{19}\text{F})$ ,  $^1J(^{19}\text{F}-^{129}\text{Xe})$ , and  $^1J(^{13}\text{C}-^{129}\text{Xe})$  coupling constants associated with the  $\text{C}_6\text{F}_5$  group (Fig. 30, Table 4).<sup>166</sup>

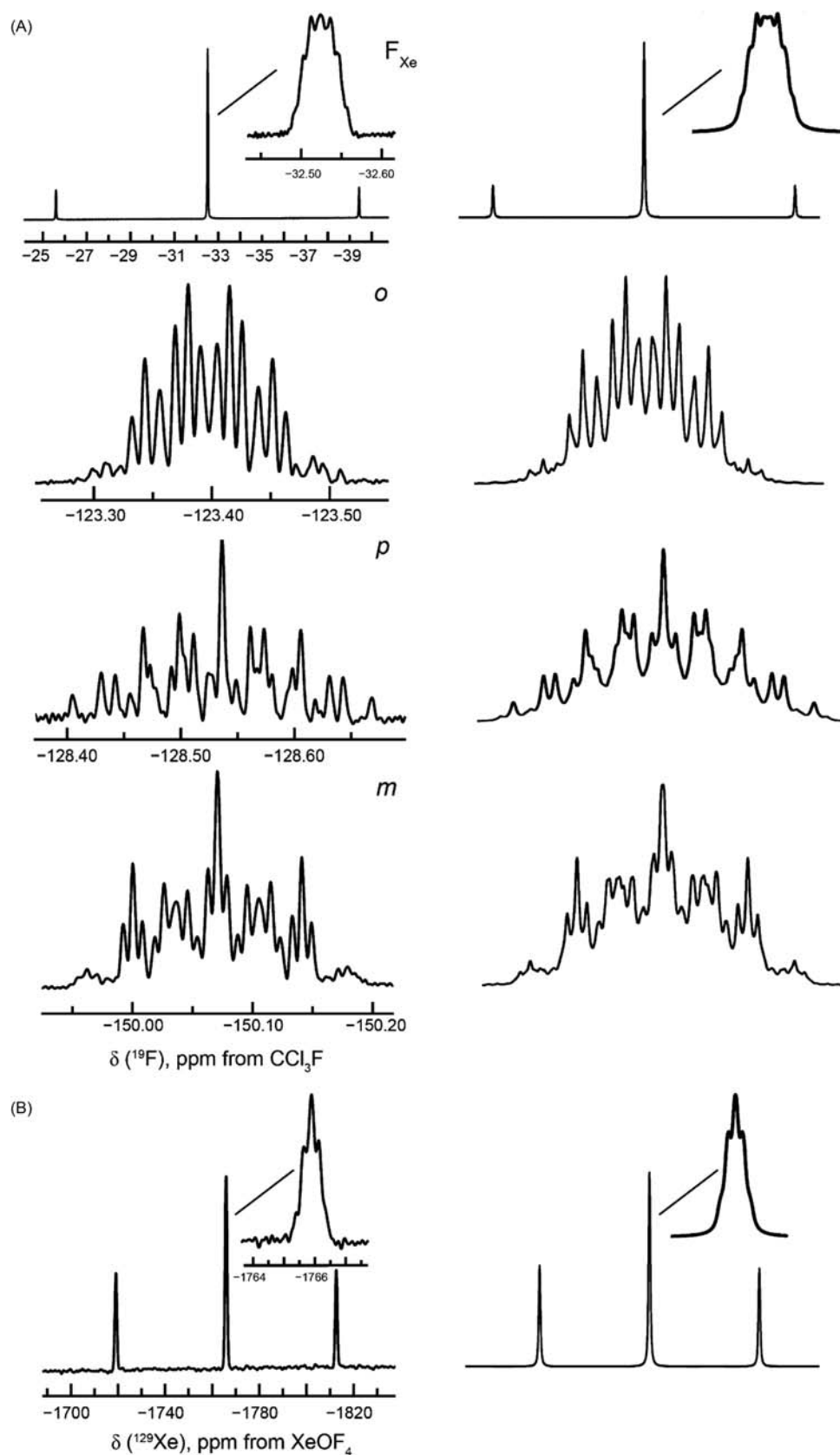
The geometric parameters of the  $[\text{C}_6\text{F}_5\text{XeF}_2]^+$  cations and  $[\text{BF}_4]^-$  anions in the crystal structures of  $[\text{C}_6\text{F}_5\text{XeF}_2][\text{BF}_4]$ ,  $[\text{C}_6\text{F}_5\text{XeF}_2][\text{BF}_4]\cdot 2\text{HF}$ , and  $[\text{C}_6\text{F}_5\text{XeF}_2][\text{BF}_4]\cdot 1.5\text{CH}_3\text{CN}$  are very similar, and those of coordinated  $\text{CH}_3\text{CN}$  and  $\text{HF}$  are in good agreement with other terminally coordinated  $\text{CH}_3\text{CN}$  and  $\text{HF}$  solvates.<sup>166</sup> The primary coordination environments of  $\text{Xe}^{\text{IV}}$  in the crystal structures of  $[\text{C}_6\text{F}_5\text{XeF}_2][\text{BF}_4]$ ,  $[\text{C}_6\text{F}_5\text{XeF}_2][\text{BF}_4]\cdot 2\text{HF}$ , and  $[\text{C}_6\text{F}_5\text{XeF}_2][\text{BF}_4]\cdot 1.5\text{CH}_3\text{CN}$  are T-shaped  $\text{AX}_2\text{YE}_2$  arrangements of three bond pairs and two stereo-active VELPs (Fig. 31). The more electronegative F atoms occupy axial positions, whereas the  $\text{C}_6\text{F}_5$  group and the VELPs occupy equatorial positions.

The  $\text{Xe}^{\text{IV}}-\text{C}$  bonds of the  $[\text{C}_6\text{F}_5\text{XeF}_2]^+$  cations in all three salts (2.058(2)–2.083(5) Å) are somewhat shorter than the  $\text{Xe}^{\text{II}}-\text{C}$  bonds of the structurally characterized  $[\text{C}_6\text{F}_5\text{Xe}]^+$  salts (2.100(6)–2.104(5) Å),<sup>52</sup> and are not significantly affected by  $\text{HF}$  or  $\text{CH}_3\text{CN}$  solvation. The  $\text{Xe}-\text{F}$  bonds (1.925(2)–1.948(2) Å) are significantly longer than the  $\text{Xe}-\text{F}_{\text{ax}}$  bonds of  $[\text{XeF}_3]^+$  salts (1.893(2)–1.901(2) Å),<sup>146,154</sup> and only marginally shorter than the  $\text{Xe}-\text{F}$  bonds of  $\text{XeF}_4$  (1.9449(6) and 1.9509(6) Å).<sup>116</sup> The C, Xe, and  $\text{F}_{\text{ax}}$  atoms of the  $[\text{C}_6\text{F}_5\text{XeF}_2]^+$  cations are coplanar within  $\pm 3\sigma$ , and the  $\text{F}-\text{Xe}-\text{F}$  bond angles are bent towards the  $\text{C}_6\text{F}_5$  group to accommodate electrostatic secondary bonding interactions with  $[\text{BF}_4]^-$ ,  $\text{CH}_3\text{CN}$ , and  $\text{HF}$  in the crystal structures of  $[\text{C}_6\text{F}_5\text{XeF}_2][\text{BF}_4]$ ,  $[\text{C}_6\text{F}_5\text{XeF}_2][\text{BF}_4]\cdot 1.5\text{CH}_3\text{CN}$ , and  $[\text{C}_6\text{F}_5\text{XeF}_2][\text{BF}_4]\cdot 2\text{HF}$ , respectively.

The cations and anions in  $[\text{C}_6\text{F}_5\text{XeF}_2][\text{BF}_4]$ ,  $[\text{C}_6\text{F}_5\text{XeF}_2][\text{BF}_4]\cdot 1.5\text{CH}_3\text{CN}$ , and  $[\text{C}_6\text{F}_5\text{XeF}_2][\text{BF}_4]\cdot 2\text{HF}$  are ion-paired, interacting through short  $\text{Xe}\cdots\text{F}$  secondary bonds (2.686(2)–3.110(3) Å) that avoid the stereochemically active VELPs on  $\text{Xe}^{\text{IV}}$ . The  $[\text{C}_6\text{F}_5\text{XeF}_2]^+$  cations in  $[\text{C}_6\text{F}_5\text{XeF}_2][\text{BF}_4]$  also interact with neighboring cations by means of long  $\text{Xe}\cdots\text{F}_{\text{Xe}}$  secondary bonds to form an infinite, zigzag chain. One or two of the secondary  $\text{Xe}\cdots\text{F}$  bonds in the  $\text{HF}$  and  $\text{CH}_3\text{CN}$  solvates are replaced by bonds to the fluorine atom of  $\text{HF}$  (Fig. 32) or the nitrogen atom of  $\text{CH}_3\text{CN}$  (Fig. 33), so that the crystal structures consist of well-isolated structural units. The  $\text{HF}$  molecules of  $[\text{C}_6\text{F}_5\text{XeF}_2][\text{BF}_4]\cdot 2\text{HF}$  are also H-bonded to F atoms of the  $[\text{BF}_4]^-$  anion, thereby bridging the  $[\text{C}_6\text{F}_5\text{XeF}_2]^+$  cation and  $[\text{BF}_4]^-$  anion. The crystal structure of  $[\text{C}_6\text{F}_5\text{XeF}_2][\text{BF}_4]\cdot 1.5\text{CH}_3\text{CN}$  consists of two structural units,  $[\text{C}_6\text{F}_5\text{XeF}_2][\text{BF}_4]\cdot \text{CH}_3\text{CN}$  and  $[\text{C}_6\text{F}_5\text{XeF}_2][\text{BF}_4]\cdot 2\text{CH}_3\text{CN}$ . The  $\text{Xe}\cdots\text{F}$  (2.959(3)–3.036(3) Å) and  $\text{Xe}\cdots\text{N}$  (2.742(4)–2.868(4) Å) secondary bonds are significantly shorter than the sums of the Xe and F (3.63 Å)<sup>102</sup> and Xe and N (3.71 Å)<sup>102</sup> van der Waals radii, and are consistent with primarily electrostatic,  $\sigma$ -hole interactions.

The LT solid-state Raman spectra of  $[\text{C}_6\text{F}_5\text{XeF}_2][\text{BF}_4]$  and  $[\text{C}_6\text{F}_5\text{XeF}_2][\text{BF}_4]\cdot 2\text{HF}$  have been assigned by comparison with the calculated gas-phase frequencies and vibrational mode descriptions of  $[\text{C}_6\text{F}_5\text{XeF}_2][\text{BF}_4]$  and  $[\text{C}_6\text{F}_5\text{XeF}_2][\text{BF}_4]\cdot 2\text{HF}$ . Overall, the calculated frequencies well reproduce the experimental spectra.<sup>166</sup>

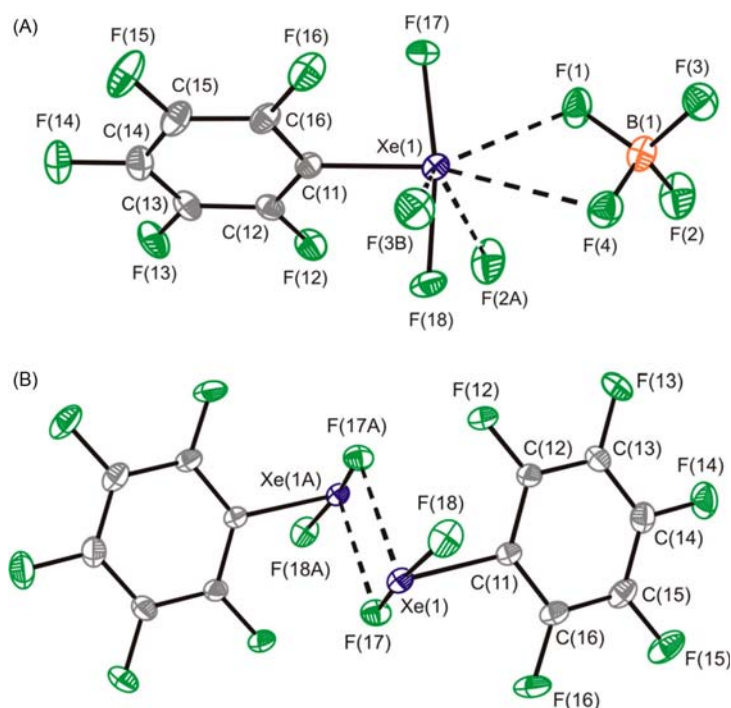
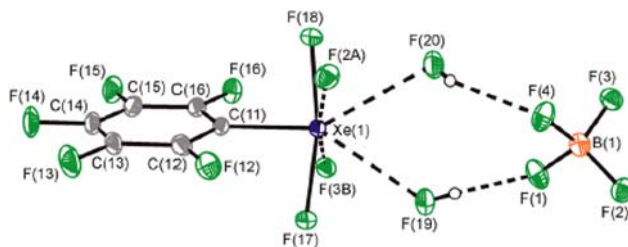
The bonding in  $[\text{C}_6\text{F}_5\text{XeF}_2]^+$ ,  $[\text{C}_6\text{F}_5\text{XeF}_2][\text{BF}_4]$ ,  $[\text{C}_6\text{F}_5\text{XeF}_2][\text{BF}_4]\cdot \text{CH}_3\text{CN}$ ,  $[\text{C}_6\text{F}_5\text{XeF}_2][\text{BF}_4]\cdot 2\text{CH}_3\text{CN}$ , and  $[\text{C}_6\text{F}_5\text{XeF}_2][\text{BF}_4]\cdot 2\text{HF}$  was assessed with the aid of natural bond orbital analyses and molecular orbital calculations.<sup>166</sup> The calculated geometric parameters are in good agreement with experiment, and ion-pairing and coordination of  $\text{CH}_3\text{CN}$  or  $\text{HF}$  was not found to significantly affect the geometry of the  $[\text{C}_6\text{F}_5\text{XeF}_2]^+$  cation. The NBO analyses revealed that the *ipso*-carbon of  $\text{C}_6\text{F}_5$  carried the greatest negative charge, where the atomic charges become more positive in the order  $\text{C}_{\text{ipso}} < \text{C}^{3,5} < \text{C}^{2,6} < \text{C}^4$ , reflecting the strong inductive effect of the high atomic charge of  $\text{Xe}^{\text{IV}}$ . The total  $\text{C}_6\text{F}_5$  group charge of  $[\text{C}_6\text{F}_5\text{XeF}_2]^+$  (0.171) is greater than in  $[\text{C}_6\text{F}_5\text{Xe}]^+$  (0.122) and becomes more negative in the order  $[\text{C}_6\text{F}_5\text{XeF}_2]^+$  (0.171) >  $[\text{C}_6\text{F}_5\text{XeF}_2]^+\cdot \text{CH}_3\text{CN}$  (0.083) >  $[\text{C}_6\text{F}_5\text{XeF}_2]^+\cdot 2\text{CH}_3\text{CN}$  (0.045) >  $[\text{C}_6\text{F}_5\text{XeF}_2][\text{BF}_4]\cdot 2\text{HF}$  (−0.009) >  $[\text{C}_6\text{F}_5\text{XeF}_2][\text{BF}_4]$  (−0.056), which indicates that the total  $\text{C}_6\text{F}_5$  group charge is influenced by both the oxidation state of xenon and the coordination environment of xenon. The  $\text{Xe}^{\text{IV}}-\text{C}$  Mayer bond orders (0.633–0.740) are approximately double those of the more ionic  $\text{Xe}^{\text{IV}}-\text{F}$  bonds (0.360). The  $\text{Xe}^{\text{IV}}-\text{C}$  Wiberg bond order decreases slightly upon complexation ( $[\text{C}_6\text{F}_5\text{XeF}_2]^+$  (0.740) >  $[\text{C}_6\text{F}_5\text{XeF}_2]^+\cdot 2\text{CH}_3\text{CN}$  (0.690) >  $[\text{C}_6\text{F}_5\text{XeF}_2]^+\cdot \text{CH}_3\text{CN}$  (0.667) >  $[\text{C}_6\text{F}_5\text{XeF}_2][\text{BF}_4]\cdot 2\text{HF}$  (0.657) >  $[\text{C}_6\text{F}_5\text{XeF}_2][\text{BF}_4]$  (0.633), consistent with the trends observed among the  $\text{C}_6\text{F}_5$  group charges. The  $\text{Xe}\cdots\text{F}$  and  $\text{Xe}\cdots\text{N}$  secondary bonding interactions have small bond orders (0.078–0.101), in accordance with their description as primarily electrostatic,  $\sigma$ -hole type interactions. Molecular orbital calculations of gas-phase  $[\text{C}_6\text{F}_5\text{XeF}_2]^+$  reveal that the LUMO and LUMO + 1 MOs represent the electrophilic character of the cation and are primarily  $\sigma^*_{\text{Xe}-\text{C}}$  and  $\sigma^*_{\text{Xe}-\text{F}}$  in nature. Consequently, donation of electron density from the Lewis bases,  $\text{CH}_3\text{CN}$  and  $\text{HF}$ , into these MOs results in more ionic  $\text{Xe}-\text{C}$  and  $\text{Xe}-\text{F}$  bonds.

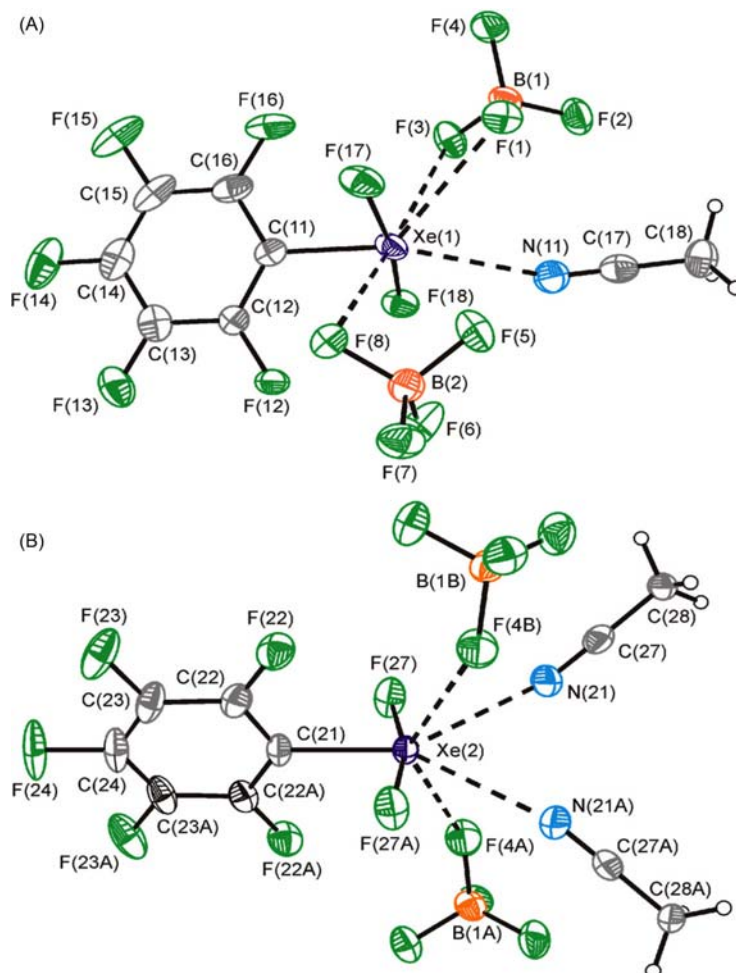


**Fig. 30** (A) The  $^{19}\text{F}$  NMR spectrum (282.40 MHz) (FXe, o-, p-, and m-F) and (B) the  $^{129}\text{Xe}$  NMR spectrum (83.02 MHz) of the  $[\text{C}_6\text{F}_5\text{XeF}_2]^+$  cation in  $[\text{C}_6\text{F}_5\text{XeF}_2][\text{BF}_4]$  (aHF,  $-40^\circ\text{C}$ ). The experimental spectra, resolution-enhanced by Gaussian multiplication (left), and the simulated spectra (right) are shown. Reproduced with permission from Koppe, K.; Haner, J.; Mercier, H. P. A.; Frohn, H.-J.; Schrobilgen, G. J. *Inorg. Chem.* **2014**, *53*, 11640–11661.

**Table 4** Coupling constants (Hz) derived from the simulated  $^{19}\text{F}$  NMR spectra of  $[\text{C}_6\text{F}_5\text{XeF}_2]^+$  and  $[\text{C}_6\text{F}_5\text{Xe}]^+$ .

	$[\text{C}_6\text{F}_5\text{XeF}_2]^+$ <sup>a</sup>	$[\text{C}_6\text{F}_5\text{Xe}]^+$ <sup>b</sup>
$^1J(^{19}\text{F}_{\text{Xe}}-^{129}\text{Xe})$	3902	
$^3J(^{19}\text{F}_{\sigma}-^{129}\text{Xe})$	19.05	67.7
$^4J(^{19}\text{F}_{m}-^{129}\text{Xe})$	21.61	8.8
$^5J(^{19}\text{F}_{p}-^{129}\text{Xe})$	8.23	3.7
$^3J(^{19}\text{F}_{\sigma}-^{19}\text{F}_m) = J_{23}$	-17.24	-20.2
$^4J(^{19}\text{F}_{\sigma}-^{19}\text{F}_p) = J_{24}$	10.38	8.24
$^5J(^{19}\text{F}_{\sigma}-^{19}\text{F}_m) = J_{25}$	-2.71	6.50
$^4J(^{19}\text{F}_{\sigma}-^{19}\text{F}_p) = J_{26}$	-17.01	-9.9
$^3J(^{19}\text{F}_m-^{19}\text{F}_p) = J_{34}$	-19.39	-19.5
$^4J(^{19}\text{F}_m-^{19}\text{F}_m) = J_{35}$	2.50	0.83
$^4J(^{19}\text{F}_{\text{Xe}}-^{19}\text{F}_p) = J_{12}$	3.27	
$^5J(^{19}\text{F}_{\text{Xe}}-^{19}\text{F}_m) = J_{13}$	2.30	
$^6J(^{19}\text{F}_{\text{Xe}}-^{19}\text{F}_p) = J_{14}$	7.50	

<sup>a</sup>ahf (-40 °C). From reference 166.<sup>b</sup>CH<sub>3</sub>CN (-40 °C). From reference 167.**Fig. 31** The structural unit in the crystal structure of  $[\text{C}_6\text{F}_5\text{XeF}_2][\text{BF}_4]$  (A) showing the Xe $\cdots$ F<sub>B</sub> cation–anion contacts. (C) A view showing the  $[\text{C}_6\text{F}_5\text{XeF}_2]_2$  dimer units in  $[\text{C}_6\text{F}_5\text{XeF}_2][\text{BF}_4]$ . Thermal ellipsoids are drawn at the 50% probability level. Reproduced with permission from Koppe, K.; Haner, J.; Mercier, H. P. A.; Frohn, H.-J.; Schrobilgen, G. J. *Inorg. Chem.* **2014**, *53*, 11640–11661.**Fig. 32** The structural unit in the crystal structure of  $[\text{C}_6\text{F}_5\text{XeF}_2][\text{BF}_4]\cdot 2\text{HF}$  showing the contacts, Xe $\cdots$ F<sub>H</sub>, F<sub>B</sub> $\cdots$ H, and Xe $\cdots$ F<sub>B</sub>. Thermal ellipsoids are drawn at the 50% probability level. Reproduced with permission from Koppe, K.; Haner, J.; Mercier, H. P. A.; Frohn, H.-J.; Schrobilgen, G. J. *Inorg. Chem.* **2014**, *53*, 11640–11661.



**Fig. 33** The two solvated cations in the crystal structure of  $[\text{C}_6\text{F}_5\text{XeF}_2][\text{BF}_4] \cdot 1.5\text{CH}_3\text{CN}$ : (A)  $[\text{C}_6\text{F}_5\text{XeF}_2] \cdot \text{CH}_3\text{CN}$  solvate and its Xe...F<sub>B</sub> contacts with two adjacent  $[\text{BF}_4]^-$  anions and (B) one of two crystallographically nonequivalent  $[\text{C}_6\text{F}_5\text{XeF}_2] \cdot 2\text{CH}_3\text{CN}$  solvates and its Xe...F<sub>B</sub> contacts with two adjacent  $[\text{BF}_4]^-$  anions. Thermal ellipsoids are drawn at the 50% probability level. Reproduced with permission from Koppe, K.; Haner, J.; Mercier, H. P. A.; Frohn, H.-J.; Schrobilgen, G. J. *Inorg. Chem.* **2014**, *53*, 11640–11661.

## 1.08.5 Xenon(VI) compounds

### 1.08.5.1 XeF<sub>6</sub> and coordination complexes of XeF<sub>6</sub>

#### 1.08.5.1.1 F<sub>6</sub>XeNCCH<sub>3</sub> and F<sub>6</sub>Xe(NCCH<sub>3</sub>)<sub>2</sub>·CH<sub>3</sub>CN

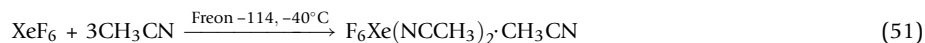
The stereochemical activity of the XeF<sub>6</sub> VELP has been the subject of considerable discussion for almost 60 years. The possible geometries of monomeric gas-phase XeF<sub>6</sub> are an octahedral structure (O<sub>h</sub>) with a stereochemically inactive VELP or a monocapped octahedron (C<sub>3v</sub> or C<sub>2v</sub>) with a stereo-active VELP. The VSEPR model of molecular geometry predicted a monocapped octahedral geometry (C<sub>3v</sub>) for XeF<sub>6</sub> very early in the history of noble-gas chemistry.<sup>134,168</sup> It was subsequently confirmed that the gas-phase structure of monomeric XeF<sub>6</sub> has C<sub>3v</sub> symmetry by electron diffraction,<sup>169–173</sup> and by far-infrared,<sup>174</sup> Raman,<sup>175,176</sup> UV-visible absorption,<sup>176</sup> and photoelectron spectroscopies.<sup>177,178</sup> Coupled-cluster quantum-chemical calculations indicate that the O<sub>h</sub> and C<sub>3v</sub> conformers correspond to local minima, whereas the higher energy C<sub>2v</sub> geometry is a transition state between C<sub>3v</sub> conformers.<sup>179</sup>

Although seven crystalline morphologies of XeF<sub>6</sub> have been characterized by LT SCXRD,<sup>156</sup> none of these phases contain well isolated XeF<sub>6</sub> molecules that have local C<sub>3v</sub> symmetry. Rather, five phases are ionic oligomers of the form (XeF<sub>5</sub><sup>+</sup>F<sup>-</sup>)<sub>n</sub> (n = 4, 6), and two phases contain (XeF<sub>5</sub><sup>+</sup>F<sup>-</sup>)<sub>3</sub>·XeF<sub>6</sub> structural units which may be described as (XeF<sub>5</sub><sup>+</sup>F<sup>-</sup>)<sub>3</sub> trimers that are coordinated to an XeF<sub>6</sub> molecule having C<sub>2v</sub> local symmetry. The LT solution structure of XeF<sub>6</sub> has been shown by <sup>19</sup>F and <sup>129</sup>Xe NMR spectroscopy to be a fluxional tetramer, Xe<sub>4</sub>F<sub>24</sub>, in which the four Xe and 24 F atoms undergo rapid intramolecular exchange on the NMR time scale<sup>58,180</sup> and therefore do not provide definitive stereochemical information about the VELPs of the Xe<sup>VI</sup> atoms in solution. The Xe<sub>4</sub>F<sub>24</sub> structure corresponds to the tetrameric (XeF<sub>5</sub><sup>+</sup>F<sup>-</sup>)<sub>4</sub> units observed in several crystal structures of XeF<sub>6</sub>.

Because the crystal structures of XeF<sub>6</sub> do not contain well-isolated XeF<sub>6</sub> monomers, the stereo-activity of the Xe<sup>VI</sup> VELP of XeF<sub>6</sub> could not be confirmed in the solid-state. Xenon hexafluoride is Lewis acidic and has been shown to react with MF (M = Cs<sup>+</sup>,<sup>181</sup> Rb<sup>+</sup>,<sup>181</sup> and [NO]<sup>+182</sup>) to form M<sub>2</sub>[XeF<sub>8</sub>] salts and with NaF and CsF to form [NF<sub>4</sub>][XeF<sub>7</sub>]<sup>183</sup> and Cs[XeF<sub>7</sub>].<sup>183</sup> The [NF<sub>4</sub>][XeF<sub>7</sub>] salt was prepared from XeF<sub>6</sub> and [NF<sub>4</sub>][HF<sub>2</sub>] and converted to [NF<sub>4</sub>]<sub>2</sub>[XeF<sub>8</sub>] by selective laser photolysis.<sup>183</sup> It may therefore also be expected to react with oxidatively resistant Lewis bases to form coordination complexes. A considerable number of Xe(II)–N

bonded coordination complexes with  $sp$ -,  $sp^2$ -, or  $sp^3$ - hybridized organo-nitrogen bases are known,<sup>184</sup> such as  $\text{CH}_3\text{CN}$  coordination complexes of strong oxidant  $\text{Xe}^{\text{IV}}$  species;  $[\text{C}_6\text{F}_5\text{XeF}_2][\text{BF}_4] \cdot n\text{NCCH}_3$  ( $n = 1$  or  $2$ )<sup>166</sup> and  $\text{F}_2\text{OXeNCCH}_3$ .<sup>143</sup> This provided impetus to attempt the syntheses of the first  $\text{Xe}^{\text{VI}}\text{-N}$  bonded species by the reaction of  $\text{XeF}_6$  with  $\text{CH}_3\text{CN}$ .

Acetonitrile and the potent oxidative fluorinating agent  $\text{XeF}_6$  react at  $-40^\circ\text{C}$  in Freon-114 ( $\text{CF}_2\text{ClCF}_2\text{Cl}$ ) to form the highly energetic, shock-sensitive compounds  $\text{F}_6\text{XeNCCH}_3$  and  $\text{F}_6\text{Xe}(\text{NCCH}_3)_2 \cdot \text{CH}_3\text{CN}$  (Eqs. 50 and 51).<sup>185</sup>

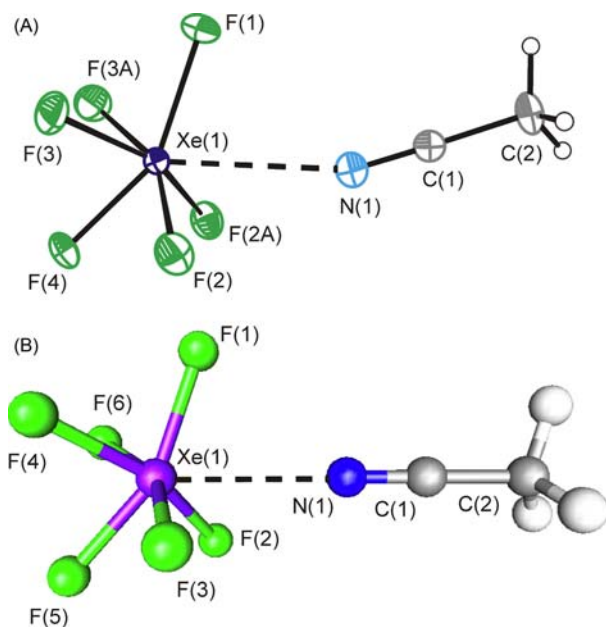


Solid samples of  $\text{F}_6\text{XeNCCH}_3$  and  $\text{F}_6\text{Xe}(\text{NCCH}_3)_2 \cdot \text{CH}_3\text{CN}$  are kinetically stable at  $-78^\circ\text{C}$  but detonate when mechanically shocked at this temperature. Coordinated  $\text{CH}_3\text{CN}$  could be removed under dynamic vacuum at  $-40$  to  $-20^\circ\text{C}$ . Reaction of  $\text{F}_6\text{Xe}(\text{NCCH}_3)_2 \cdot \text{CH}_3\text{CN}$  with an additional equivalent of  $\text{CH}_3\text{CN}$  did not afford  $\text{F}_6\text{Xe}(\text{NCCH}_3)_3$ .

The  $\text{F}_6\text{XeNCCH}_3$  complex was characterized by LT  $^{19}\text{F}$  and  $^{129}\text{Xe}$  NMR spectroscopy in  $\text{SO}_2\text{ClF}$ , but yielded little information regarding its solution structure.<sup>185</sup> Single crystals of  $\text{F}_6\text{XeNCCH}_3$  and  $\text{F}_6\text{Xe}(\text{NCCH}_3)_2 \cdot \text{CH}_3\text{CN}$  were grown from their respective  $\text{SO}_2\text{ClF}$  and  $\text{CH}_3\text{CN}/\text{Freon-114}$  solutions and characterized by LT SCXRD (Figs. 34 and 35).<sup>185</sup>

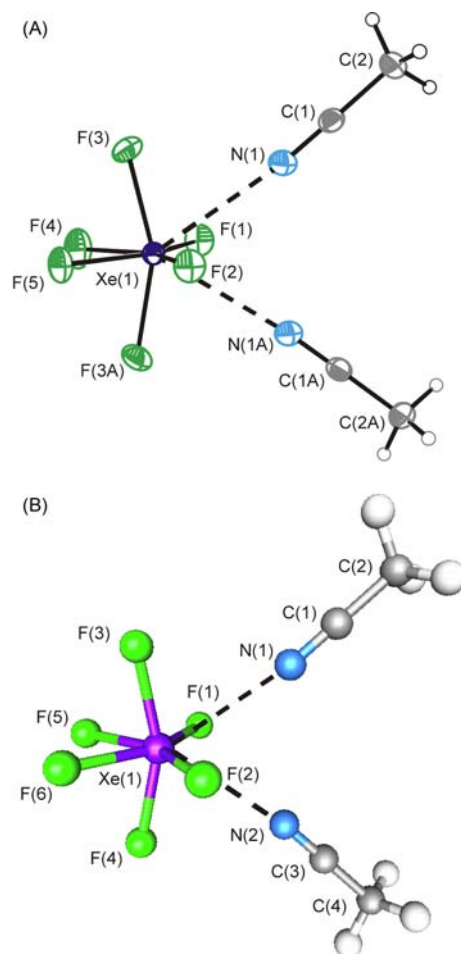
The adducted  $\text{XeF}_6$  molecules of these compounds are the most isolated  $\text{XeF}_6$  moieties thus far encountered in the solid state and have provided the first examples of  $\text{Xe}^{\text{VI}}\text{-N}$  bonds. The geometry of the  $\text{XeF}_6$  moiety in  $\text{F}_6\text{Xe}(\text{NCCH}_3)_3$  is nearly identical to the calculated distorted octahedral ( $C_{3v}$ ) geometry of gas-phase  $\text{XeF}_6$ , whereas the geometry of the  $\text{XeF}_6$  moiety ( $C_{2v}$ ) in  $\text{F}_6\text{Xe}(\text{NCCH}_3)_2 \cdot \text{CH}_3\text{CN}$  resembles the transition state proposed to account for the fluxionality of gas-phase  $\text{XeF}_6$ . The  $\text{Xe}^{\text{VI}}\text{-N}$  bonds (2.762(2) and 2.785(2) Å) are significantly longer than the  $\text{Xe}^{\text{II}}\text{-N}$  bonds of  $[\text{C}_6\text{F}_5\text{XeNCCH}_3]^+$  (2.642(6)–2.610(11) Å),<sup>52</sup> but are comparable to the  $\text{Xe}^{\text{IV}}\text{-N}$  bonds of  $\text{F}_2\text{OXeNCCH}_3$  (2.808(5) and 2.752(5) Å).<sup>143</sup> The  $\text{Xe}^{\text{VI}}\text{-N}$  bonds are therefore best described as primarily electrostatic,  $\sigma$ -hole bonds. The complexes have non-linear  $\text{Xe}\text{-N-C}$  bond angles (160.31(17) and  $170.00(13)^\circ$ ) that are expected to be highly deformable and sensitive to crystal packing. The xenon atom VEMP of  $\text{F}_6\text{XeNCCH}_3$  presumably resides between the  $\text{Xe-F}$  bonds which are proximate to the  $\text{Xe}\text{-N}$  bond and results in larger  $\text{F-Xe-F}$  bond angles ( $105.92(6)^\circ$  and  $115.65(4)^\circ$ ) relative to the  $\text{Xe-F}$  bonds that are opposite to the  $\text{Xe}\text{-N}$  bond(s) ( $79.93^\circ$  and  $82.59^\circ$ ). Consequently, the stereochemically active VEMPs on xenon and nitrogen oppose one another. The geometry of  $\text{XeF}_6$  in  $\text{F}_6\text{Xe}(\text{NCCH}_3)_2 \cdot \text{CH}_3\text{CN}$  closely approximates a distorted  $\text{AX}_6\text{E}$  VSEPR arrangement having  $C_{2v}$  symmetry where the  $\text{Xe-F}$  bonds may be classified into three groups: two equatorial  $\text{Xe-F}$  bonds which are more polarized because they are located adjacent to the VEMP of Xe (1.981(2) and 1.9876(13) Å), two axial  $\text{Xe-F}$  bonds ( $2 \times 1.8936(11)$  Å), and two equatorial  $\text{Xe-F}$  bonds opposite to the Xe VEMP (1.868(2) and 1.873(2) Å). The trajectories of the  $\text{Xe}\text{-N}$  secondary bonding interactions are located close to the pseudo-mirror plane which bisects the equatorial  $\text{Xe-F}$  bonds that are adjacent to the VEMP of Xe.

Energy-minimized gas-phase geometries and vibrational frequencies were calculated for  $\text{F}_6\text{XeNCCH}_3$  and  $\text{F}_6\text{Xe}(\text{NCCH}_3)_2$ .<sup>185</sup> The Raman spectra of  $\text{F}_6\text{XeNCCH}_3$  and  $\text{F}_6\text{Xe}(\text{NCCH}_3)_2 \cdot \text{CH}_3\text{CN}$  were assigned by comparison with their calculated vibrational frequencies and intensities. In both complexes, high-frequency shifts occur for  $\nu(\text{CN})$ ,  $\nu(\text{CC})$ , and  $\delta(\text{NCC})$  in accordance with weak  $\text{Xe-N}$  bonding. The  $\nu(\text{Xe-F})$  stretching frequencies likewise occur at somewhat lower frequencies than those of  $\text{XeF}_6$ .



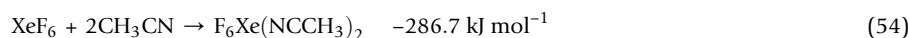
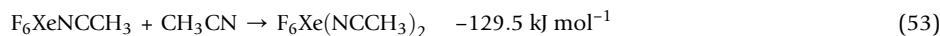
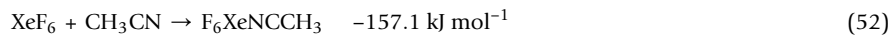
**Fig. 34** (A) The X-ray crystal structure of  $\text{F}_6\text{XeNCCH}_3$ , where ellipsoids are drawn at the 50% probability level and (B) the calculated geometry (PBE1PBE/aug-cc-pVTZ(-PP)) for  $\text{F}_6\text{XeNCCH}_3$ . Reproduced with permission from Matsumoto, K.; Haner, J.; Mercier, H. P. A.; Schrobilgen, G. J. *Angew. Chem. Int. Ed.* **2015**, *54*, 14169–14173.





**Fig. 35** (A) The X-ray crystal structure of  $F_6Xe(NCCH_3)_2 \cdot CH_3CN$ , where the thermal ellipsoids are drawn at the 50% probability level; and (B) the calculated geometry (PBE1PBE/aug-cc-pVTZ(-PP)) for  $F_6Xe(NCCH_3)_2$ . Reproduced with permission from Matsumoto, K.; Haner, J.; Mercier, H. P. A.; Schrobilgen, G. J. *Angew. Chem. Int. Ed.* **2015**, *54*, 14169–14173.

Binding energies for the Xe--N bonds in gas-phase  $F_6XeNCCH_3$  and  $F_6Xe(NCCH_3)_2$  were determined at the MP2/aug-cc-pVTZ (-PP) level of theory (Eqs. 52–54).<sup>185</sup> The energies for free  $XeF_6$  were approximated from the gas-phase optimized  $O_h$  and  $C_{3v}$  geometries, which were calculated at the CCSD(T)/CBS and CCSD(T)-F12b levels of theory because it was not possible to optimize  $XeF_6$  ( $C_{3v}$ ) at the MP2 level of theory.



NBO, QTAIM, ELF, and MEPS analyses of gas-phase  $F_6XeNCCH_3$  and  $F_6Xe(NCCH_3)_2$  were subsequently reported to further probe the nature of the Xe--N bonds and to assess and visualize the stereo-activity of the xenon VELP in coordinated  $XeF_6$ .<sup>186</sup>

The Xe atom NBO charges of gas-phase  $XeF_6$  (Xe:  $O_h$ , 3.331;  $C_{3v}$ , 3.363) are close to the average of the covalent (0) and ionic (+6) models. Accordingly, the F atom charges ( $O_h$ , -0.555;  $C_{3v}$ , -0.516 to -0.606), Xe–F bond indices ( $O_h$ , 0.538;  $C_{3v}$ , 0.492 to 0.590), and Xe valencies ( $O_h$ , 3.231;  $C_{3v}$ , 3.247) are consistent with polar-covalent Xe–F bonds. In the  $C_{3v}$  conformer of  $XeF_6$ , the three longer Xe–F bonds that define the cone occupied by the Xe VELP have more negative atom charges and lower bond indices and are therefore more ionic than those opposite to the Xe VELP.

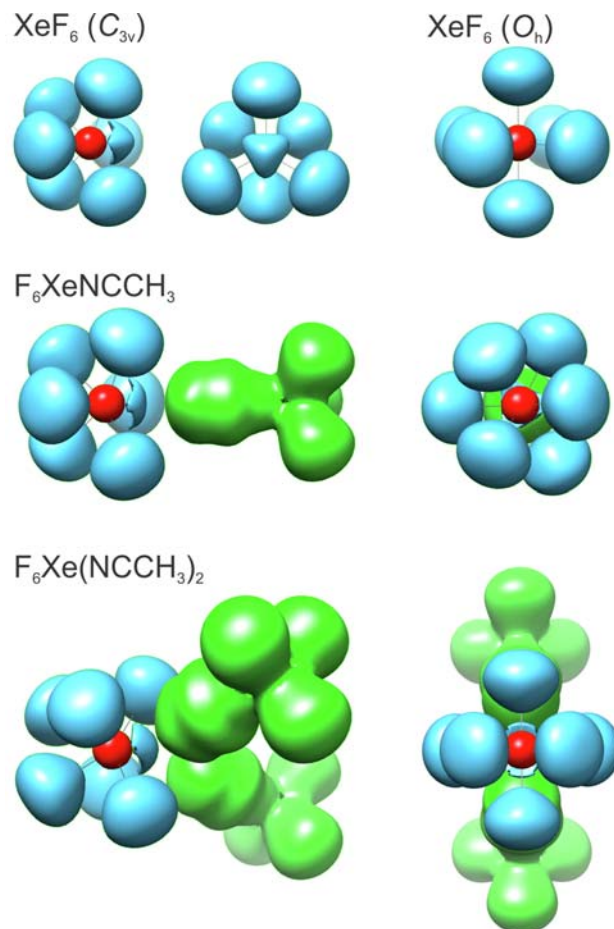
Although coordination of one  $CH_3CN$  molecule to  $XeF_6$  does not significantly affect the charges and valences of the Xe and F atoms, it does result in somewhat lower Xe–F bond indices (0.487 and 0.573) relative to those of  $XeF_6$  ( $C_{3v}$ ). Coordination of a second  $CH_3CN$  molecule further lowers the Xe–F bond indices to 0.464 for the longest equatorial bonds located in the vicinity of the Xe VELP, and 0.567 for the shortest equatorial bonds located opposite to the Xe VELP. The low Xe–N bond orders ( $F_6XeNCCH_3$ , 0.058;  $F_6Xe(NCCH_3)_2$ , 0.037)<sup>186</sup> are comparable to those of  $F_2OXeNCCH_3$  (0.033)<sup>186</sup> and are consistent with primarily electrostatic,  $\sigma$ -hole bonds.

The NBO analyses indicate that the Xe–F bonding in  $XeF_6$  ( $C_{3v}$ ) is essentially p in character for Xe. In contrast, the Xe–F bonds in  $F_6XeNCCH_3$  and  $F_6Xe(NCCH_3)_2$  have a significant degrees of d ( $F_6XeNCCH_3$ , 8–37%;  $F_6Xe(NCCH_3)_2$ , 8–38%) and f character

( $F_6XeNCCH_3$ , 1–5%;  $F_6Xe(NCCH_3)_2$ , 1–4%) relative to  $XeF_6$  ( $C_{3v}$ ), for which the d and f characters are near zero. The inclusion of d and f orbitals in the Xe–F bonding of the coordination complexes likely stabilizes the geometries of  $F_6XeNCCH_3$  and  $F_6Xe(NCCH_3)_2$ , which slightly and substantially deviate from  $XeF_6$  ( $C_{3v}$ ), respectively. The F atoms contribute approximately 91 to 92% p character and 8 to 9% s character in all Xe–F bonds. The Xe VELP of  $XeF_6$  ( $O_h$ ) has 100% s character, whereas distortions from  $O_h$  symmetry lead to significant amounts of p character in  $XeF_6$  ( $C_{3v}$ , 91% s, 9% p),  $F_6XeNCCH_3$  (94% s, 6% p), and  $F_6Xe(NCCH_3)_2$  (94% s, 6% p). A second-order perturbation analysis revealed that the sp-hybridized lone pair on the N atoms of  $CH_3CN$  in  $F_6XeNCCH_3$  and  $F_6Xe(NCCH_3)_2$  interact with the Xe atom of  $XeF_6$  through several weak  $n_N \rightarrow \sigma^*_{Xe-F}$  interactions which polarize the Xe–F bonds. The Xe VELPS of  $XeF_6$  ( $C_{3v}$ ),  $F_6XeNCCH_3$ , and  $F_6Xe(NCCH_3)_2$  are diffuse, likely as a consequence of being mixed with several molecular orbitals that are comprised of  $n_F$  and  $\sigma_{Xe-F}$  NBOs, and from their participation in several bonding interactions with  $\pi^*_F$  and  $\sigma^*_{N-C}$  orbitals that contribute small degrees of stabilization to the complexes.

The AIM properties of the Xe–F bonds in  $XeF_6$  ( $C_{3v}$ ),  $F_6XeNCCH_3$ , and  $F_6Xe(NCCH_3)_2$  are similar and consistent with well-isolated  $XeF_6$  moieties having polar-covalent Xe–F bonds. The Xe---N bond properties indicate primarily electrostatic bonding, where the AIM properties of the C–N, C–C, and C–H bonds for  $CH_3CN$  vary little upon complex formation. Inspection of the charge density contour maps ( $\nabla^2\rho$ ) and charge concentration relief maps ( $-\nabla^2\rho$ ) of  $XeF_6$ ,  $F_6XeNCCH_3$ , and  $F_6Xe(NCCH_3)_2$  reveal that although the N VELP charge densities are easily distinguished, the Xe VELP densities are considerably more diffuse and are difficult to discern. Furthermore, the charge density maps show regions of charge depletion between Xe and N, which corresponds to holes in the Xe valence shell electron densities, which expose the Xe cores. Close examination of the charge concentration relief maps along the Xe---N bond path shows subtle charge concentrations in the Xe valence region that correspond to the diffuse Xe VELP, which cannot effectively shield the Xe core from the N VELPs. It is noteworthy that no appreciable charge-density concentration is observed along the Xe---N bond path except that which arises from the Xe VELP, consistent with a description of these bonds as primarily electrostatic,  $\sigma$ -hole bonds.

Complementary ELF analyses of  $XeF_6$  ( $C_{3v}$ ),  $F_6XeNCCH_3$ , and  $F_6Xe(NCCH_3)_2$  were employed to visualize the behaviors of their Xe VELPs.<sup>186</sup> The ELF populations of the Xe and F atoms of all three molecules are consistent with semi-ionic Xe–F bonding. The most striking feature of this analysis comes from inspection of the ELF isosurface plots for  $XeF_6$  ( $C_{3v}$ ),  $F_6XeNCCH_3$ , and  $F_6Xe(NCCH_3)_2$  (Fig. 36) which reveal that the Xe VELPs are stereo-active and are perturbed by their proximities to neighboring



**Fig. 36** The ELF isosurface plots (PBE1PBE/aVTZ(-PP),  $\eta(r) = 0.50$ ) for  $XeF_6$  ( $C_{3v}$  and  $O_h$ ),  $F_6XeNCCH_3$  ( $C_{3v}$ ), and  $F_6Xe(NCCH_3)_2$  ( $C_{2v}$ ). Color code: red = xenon core basin, blue = monosynaptic basins (fluorine and Xe VELP), and green = disynaptic basins. Reproduced with permission from Haner, J.; Matsumoto, K.; Mercier, H. P. A.; Schrobilgen, G. J. *Chem. Eur. J.* **2016**, *22*, 4833–4842.

V(F) and V(N) basins which cause them to occupy smaller volumes in the coordination complexes. A prior ELF analysis of XeF<sub>6</sub> (O<sub>h</sub>) concluded that the Xe VELP resided in the Xe core,<sup>187</sup> however the present study shows that the Xe core populations are very close to the ideal noble-gas core (46 electrons), and therefore do not contain significant Xe VELP populations. Analyses of the localization reduction tree diagrams for XeF<sub>6</sub> (C<sub>3v</sub>), F<sub>6</sub>XeNCCH<sub>3</sub>, and F<sub>6</sub>Xe(NCCH<sub>3</sub>)<sub>2</sub> are consistent with well-isolated XeF<sub>6</sub> and CH<sub>3</sub>CN molecules in the coordination complexes, and the fact that complexation has little influence on the electronic structure of XeF<sub>6</sub>.

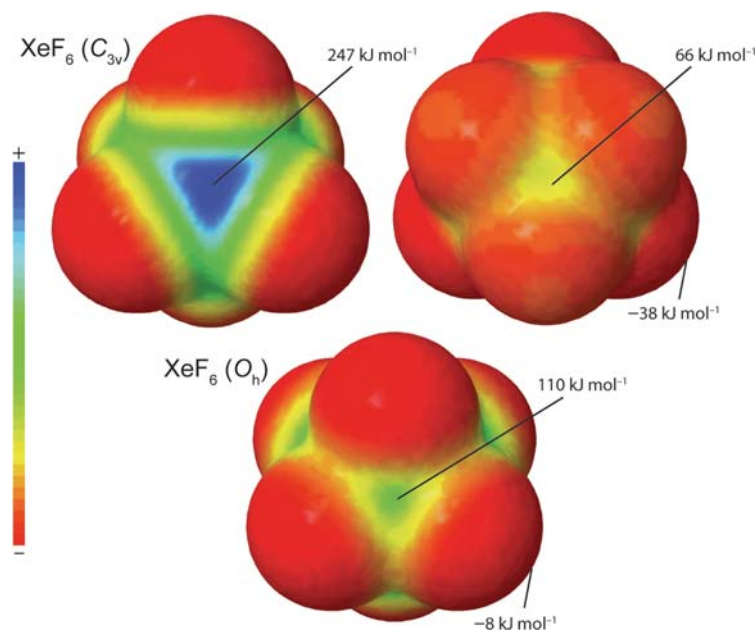
The molecular electrostatic potential surface (MEPS) of XeF<sub>6</sub> (C<sub>3v</sub>) displays significant positive electrostatic potential surfaces at the centers of the regions defined by its triangular faces (Fig. 37).<sup>186</sup> The region of most positive electrostatic potential (247 kJ mol<sup>-1</sup>) is in the open face of XeF<sub>6</sub> (C<sub>3v</sub>) which contains the stereo-active Xe VELP. Accordingly, the trajectories of the primarily electrostatic Xe--N bonds are directed towards this  $\sigma$ -hole.

#### 1.08.5.1.2 Vibrational study of XeF<sub>6</sub> and XeOF<sub>4</sub>

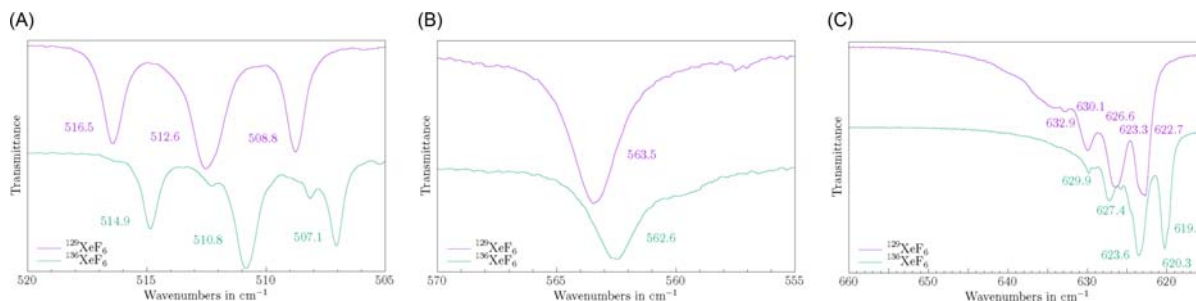
Xenon hexafluoride has been the subject of many spectroscopic and computational studies. The latter are particularly challenging, requiring a balance of relativistic, electron-correlated, and basis-set effects to accurately reproduce experimental results. Xenon hexafluoride had previously been studied in an Ar matrix,<sup>176</sup> but the spectral assignments were complicated by vibrational band broadening and band overlaps, particularly in the Xe-F stretching region. Such vibrational band broadening may arise from various interactions between XeF<sub>6</sub> and the host lattice as well as to several Xe isotopes.

In a recent study, molecular XeF<sub>6</sub> was investigated in solid neon, because neon is known to exhibit the smallest interactions with guest species; the IR spectrum of XeF<sub>6</sub>, which had been previously acquired in solid argon, was reacquired for improved resolution.<sup>188</sup> Xenon hexafluoride was prepared by thermal decomposition of Na<sub>2</sub>XeF<sub>8</sub> at 100 °C and isolated in a solid argon and neon matrices and characterized by IR spectroscopy, which revealed significant shifts of the Xe-F stretching modes to higher wavenumbers due to interactions between the isolated XeF<sub>6</sub> monomers and the noble-gas hosts. In addition, isotopically enriched samples of <sup>129</sup>XeF<sub>6</sub> and <sup>136</sup>XeF<sub>6</sub> were prepared to study line broadening effects due to isotopic line splitting, as well as isotopic frequency shifts (Fig. 38). Reaction of XeF<sub>6</sub> with trace amounts of water led to the formation of XeOF<sub>4</sub>, which was also characterized by IR spectroscopy and utilized as an internal reference, providing matrix-site and Xe-isotope splitting patterns for <sup>129</sup>XeOF<sub>4</sub> and the <sup>136</sup>XeOF<sub>4</sub> isotopologues.

For molecular XeF<sub>6</sub>, two stable structures having C<sub>3v</sub> and O<sub>h</sub> symmetry and a low-lying C<sub>3v</sub> transition state were calculated to be very close in energy (SFX2C-1e-CCSD(T)/ANO1 and PBE0-D3(BJ)/def2-QZVPP).<sup>188</sup> The O<sub>h</sub> geometry was calculated to be 186 cm<sup>-1</sup> higher than C<sub>3v</sub> with a separation barrier of only 36 cm<sup>-1</sup>. This low barrier of interconversion is consistent with the highly fluxional nature of XeF<sub>6</sub>, which rapidly interconverts between 8-fold degenerate C<sub>3v</sub> conformers by means of the O<sub>h</sub> minimum even at low temperatures.



**Fig. 37** The calculated molecular electrostatic potentials at the 0.001 e $\cdot$ a<sub>0</sub><sup>-3</sup> isosurfaces of XeF<sub>6</sub> (C<sub>3v</sub>, top) and XeF<sub>6</sub> (O<sub>h</sub>, bottom). The color scale ranges from red (-8 kJ mol<sup>-1</sup>) to blue (247 kJ mol<sup>-1</sup>). The XeF<sub>6</sub> (C<sub>3v</sub>) surfaces show the most open F(1), F(2), F(3) face orientated towards the reader (left) and the opposite, more closed F(4), F(5), F(6) face orientated towards the reader (right). The optimized geometry of XeF<sub>6</sub> (O<sub>h</sub>) and molecular electrostatic potential surfaces were calculated at the PBE1PBE/aVTZ(-PP) level of theory. Reproduced with permission from Haner, J.; Matsumoto, K.; Mercier, H. P. A.; Schrobilgen, G. J. *Chem. Eur. J.* **2016**, *22*, 4833–4842.



**Fig. 38** The matrix-isolated infrared spectra of  $\text{XeF}_6$  (3‰) in a Ne matrix at 5 K: (A) the  $\nu_6(\text{E})$ ,  $\nu_{\text{as}}(\text{Xe-F})$  stretching mode; (B) the  $\nu_2(\text{A}_1)$ ,  $\nu_{\text{s}}(\text{Xe-F})$  stretching mode; and (C) the  $\nu_1(\text{A}_1)$ ,  $\nu_{\text{s}}(\text{Xe-F})$  and  $\nu_{\text{as}}(\text{Xe-F})$  stretching modes obtained from isotopically enriched samples. Reproduced with permission from Gawrilow, M.; Beckers, H.; Riedel, S.; Cheng, L. *J. Phys. Chem. A*, **2018**, *122*, 119–129.

The observed infrared vibrational frequencies (including isotopic frequency shifts) and intensities of molecular  $\text{XeF}_6$  in the solid argon and neon matrices were well reproduced by the calculated vibrational frequencies of the  $\text{C}_{3v}$  conformer of  $\text{XeF}_6$ , whereas the strong  $t_{1u}$  band that was predicted for the  $\text{O}_h$  conformer was not observed. The absence of the  $\text{O}_h$   $\text{XeF}_6$  conformer was postulated to result from the LT of the experiment ( $\sim 5$  K) and additional stabilization provided by the host matrix, which may favor the  $\text{C}_{3v}$  conformer over the  $\text{O}_h$  conformer.

The possible side products,  $\text{XeF}_6 \cdot \text{XeOF}_4$ , two dimers of  $\text{XeF}_6$ , and the known  $\text{CH}_3\text{CN}$  adducts of  $\text{XeF}_6$ <sup>185</sup> (see Section 1.08.5.1.1) were also investigated.

### 1.08.5.2 Salts of $[\text{XeF}_5]^+$ and $[\text{Xe}_2\text{F}_{11}]^+$

The number of known  $[\text{XeF}_5]^+$  and  $[\text{Xe}_2\text{F}_{11}]^+$  salts has significantly increased in the last 10 years. As previously noted,<sup>21</sup> all the crystal structures of these salts contain  $[\text{XeF}_5]^+$  and/or  $[\text{Xe}_2\text{F}_{11}]^+$  cations that are intimately ion-paired with their respective anions by means of  $\text{Xe} \cdots \text{F} \cdots \text{M}$  secondary bonds which are significantly shorter than the sums of their Xe and F van der Waals radii.

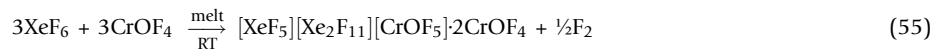
The geometric parameters of these salts are all similar to previously reported  $[\text{XeF}_5]^+$  and  $[\text{Xe}_2\text{F}_{11}]^+$  salts. The geometry of the  $[\text{XeF}_5]^+$  cation may be described in terms of a square-pyramidal  $\text{AX}_5\text{E}$  VSEPR arrangement of five bond pairs (X) and one VELP (E) around the central Xe atom (A). The Xe VELP occupies the open square face of the square pyramid and displaces the equatorial fluorine atoms towards the axial fluorine due to lone pair-bond pair repulsions between the Xe VELP domain and the  $\text{Xe}-\text{F}_{\text{eq}}$  bond-pair domains. The  $[\text{Xe}_2\text{F}_{11}]^+$  cations are comprised of two  $[\text{XeF}_5]^+$  cations that are bridged by a fluoride-ion. As observed for  $[\text{XeF}_5]^+$ , the  $\text{F}_{\text{eq}}$  ligands of  $[\text{Xe}_2\text{F}_{11}]^+$  are displaced by the Xe VELPs towards their respective  $\text{F}_{\text{ax}}$  ligands. The primarily electrostatic  $\text{Xe} \cdots \text{F}$  secondary bonds between  $[\text{XeF}_5]^+ / [\text{Xe}_2\text{F}_{11}]^+$  and neighboring fluoro- and oxyfluoro-anions and, sometimes, cocrystallized neutral molecules are directed towards regions of high positive electrostatic potential ( $\sigma$ -holes) on the Xe atoms of  $[\text{XeF}_5]^+$  and  $[\text{Xe}_2\text{F}_{11}]^+$ . These regions are located opposite to the axial  $\text{Xe}-\text{F}$  bond-pair.

#### 1.08.5.2.1 Oxyfluoro-anion salts

The syntheses of new oxyfluoro-anion salts have benefited from the high fluoro-basicity of  $\text{XeF}_6$  and its propensity to form the  $[\text{XeF}_5]^+$  and  $[\text{Xe}_2\text{F}_{11}]^+$  cations. The Xe(VI) cations provide electron-poor environments that stabilize high-oxidation state transition-metal oxyfluoro-anions such as Os(VIII) oxyfluoro-anion salts.<sup>112</sup>

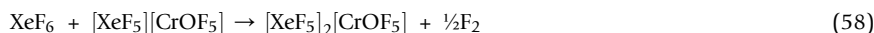
(i)  $[\text{XeF}_5][\text{Xe}_2\text{F}_{11}][\text{CrOF}_5] \cdot 2\text{CrOF}_4$ ,  $[\text{XeF}_5]_2[\text{CrF}_6] \cdot 2\text{CrOF}_4$ ,  $[\text{Xe}_2\text{F}_{11}]_2[\text{CrF}_6]$ ,  $[\text{XeF}_5]_2[\text{Cr}_2\text{O}_2\text{F}_8]$ ,  $[\text{XeF}_5]_2[\text{Cr}_2\text{O}_2\text{F}_8] \cdot 2\text{HF}$ , and  $[\text{XeF}_5]_2[\text{Cr}_2\text{O}_2\text{F}_8] \cdot 2\text{XeOF}_4$ . Until recently, studies of the chemical reactivities of Cr(IV), Cr(V), and Cr(VI) oxyfluoride species were very limited. The reactions of  $\text{CrOF}_4$  with  $\text{XeF}_6$  in melts and in the oxidatively resistant solvents aHF and  $\text{CFCl}_3$  give rise to a variety of chromium fluoro- and oxyfluoro-anions of Cr(VI), Cr(V), and Cr(V) which have  $[\text{XeF}_5]^+$  and  $[\text{Xe}_2\text{F}_{11}]^+$  as their counter ions that have been structurally characterized by LT Raman spectroscopy and/or LT SCXRD.<sup>68</sup>

Equimolar mixtures of solid  $\text{XeF}_6$  and  $\text{CrOF}_4$  liquify near room temperature to form dark purple melts that are accompanied by the vigorous evolution of  $\text{F}_2$  gas. Crystals of  $[\text{XeF}_5][\text{Xe}_2\text{F}_{11}][\text{CrOF}_5] \cdot 2\text{CrOF}_4$  were grown by slowly cooling the purple melt from 20 °C to 0 °C and were characterized by LT Raman spectroscopy and SCXRD. Upon crystallization,  $\text{CrOF}_4$  is introduced into the coordination sphere of the  $[\text{CrOF}_5]^{2-}$  anion. The net reaction leading to the formation of  $[\text{CrOF}_5]^{2-}$  is given by Eq. (55), which likely proceeds through Eqs. (56)–(60).

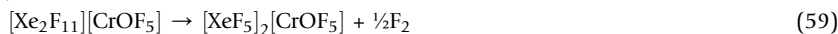


and/or



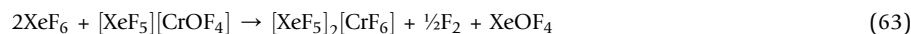
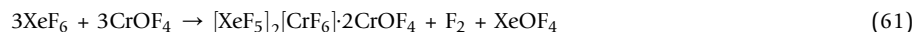


and/or

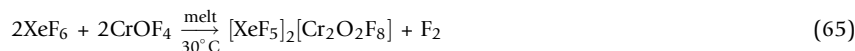
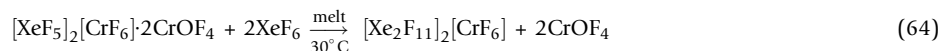


The reaction of equimolar amounts of  $\text{XeF}_6$  with  $\text{CrOF}_4$  was monitored by Raman spectroscopy as functions of time and temperature. Solid  $\text{XeF}_6$  and  $\text{CrOF}_4$  react between  $-78$  and  $0$  °C to form  $[\text{Xe}_2\text{F}_{11}][\text{CrOF}_5]$ , which was characterized by LT Raman spectroscopy. Upon warming to  $18$  °C, weak bands assigned to  $[\text{XeF}_5][\text{Xe}_2\text{F}_{11}][\text{CrOF}_5] \cdot 2\text{CrOF}_4$  began to appear, as bands due to free  $\text{CrOF}_4$  decreased in intensity. Warming to RT for up to 1 h led to gas evolution with the redox decomposition of  $[\text{Xe}_2\text{F}_{11}][\text{CrOF}_5]$  and formation of  $[\text{XeF}_5][\text{Xe}_2\text{F}_{11}][\text{CrOF}_5] \cdot 2\text{CrOF}_4$ . Crystalline  $[\text{Xe}_2\text{F}_{11}][\text{CrOF}_5]$  could not be obtained from the melts.

Reaction of 1.5 equiv.  $\text{CrOF}_4$  with  $\text{XeF}_6$  at  $60$  °C afforded dark red crystals of  $[\text{XeF}_5]_2[\text{CrF}_6] \cdot 2\text{CrOF}_4$  (Eq. 61). The proposed reaction pathway leading to this salt initially proceeds through Eq. (56) to give  $[\text{XeF}_5][\text{CrOF}_5]$ , which then decomposes with  $\text{F}_2$  evolution to yield  $[\text{XeF}_5][\text{CrOF}_4]$  (Eq. 62). The latter salt undergoes O/F metathesis with  $\text{XeF}_6$  and  $\text{F}_2$  elimination to give  $[\text{XeF}_5]_2[\text{CrF}_6]$  and  $\text{XeOF}_4$  (Eq. 63). Cocrystallized  $\text{CrOF}_4$  is introduced into the coordination sphere of the  $[\text{CrF}_6]^{2-}$  anion upon crystallization from the melt (vide infra).



When approximately four equiv. of  $\text{XeF}_6$  was allowed to react with one equiv. of  $[\text{XeF}_5]_2[\text{CrF}_6] \cdot 2\text{CrOF}_4$  in a melt at  $30$  °C, a mixture of  $[\text{Xe}_2\text{F}_{11}]_2[\text{CrF}_6]$  and  $[\text{XeF}_5]_2[\text{Cr}_2\text{O}_2\text{F}_8]$  was obtained which presumably formed according to Eqs. (64) and (65). The dinuclear  $\text{Cr(V)}$  oxyfluoro-dianion,  $[\text{Cr}_2\text{O}_2\text{F}_8]^{2-}$ , likely resulted from dimerization of transient  $[\text{CrOF}_4]^-$  anions.



Equilibrium mixtures of  $[\text{XeF}_5]_2[\text{Cr}_2\text{O}_2\text{F}_8] \cdot 2\text{HF}$  and  $[\text{XeF}_5]_2[\text{Cr}_2\text{O}_2\text{F}_8] \cdot 2\text{XeOF}_4$  form when equimolar amounts of  $\text{XeF}_6$  and HF-wetted  $\text{CrOF}_4$  react in  $\text{CFCl}_3$  solvent at room temperature to yield  $[\text{XeF}_5]_2[\text{Cr}_2\text{O}_2\text{F}_8] \cdot 2\text{HF}$  as the dominant species. Crystals of both compounds were grown from solution following dissolution of  $\text{XeF}_6$  and  $\text{CrOF}_4$  at room temperature followed by cooling to  $-78$  °C for ca. 24 h. The formation of  $[\text{XeF}_5]_2[\text{Cr}_2\text{O}_2\text{F}_8]$  presumably occurs according to Eqs. (62) and (63), where cocrystallized  $\text{XeOF}_4$  and HF are introduced into the coordination spheres of  $[\text{XeF}_5]^+$  and  $[\text{Cr}_2\text{O}_2\text{F}_8]^{2-}$  upon crystallization (Fig. 40). The salts were structurally characterized by LT SCXRD and LT Raman spectroscopy and provide the first structural characterizations of the  $[\text{Cr}^{\text{V}}\text{OF}_5]^{2-}$  and  $[\text{Cr}^{\text{V}}_2\text{O}_2\text{F}_8]^{2-}$  anions, where  $[\text{Cr}^{\text{V}}_2\text{O}_2\text{F}_8]^{2-}$  represents a new structural motif among the known oxyfluoro-anions of Group 6.

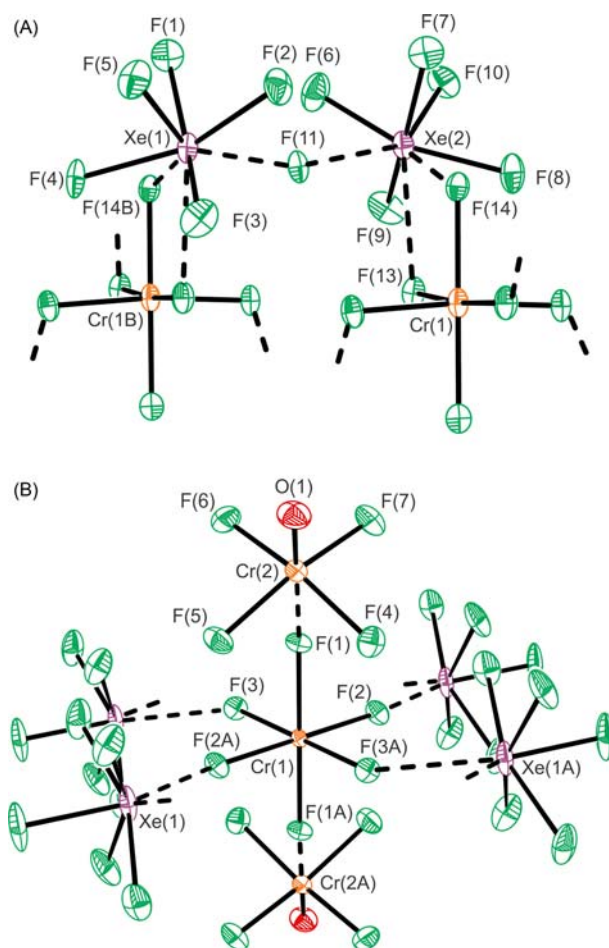
The crystal structures of  $[\text{Xe}_2\text{F}_{11}]_2[\text{CrF}_6]$ ,  $[\text{XeF}_5]_2[\text{CrF}_6] \cdot 2\text{CrOF}_4$ ,  $[\text{XeF}_5]_2[\text{Cr}_2\text{O}_2\text{F}_8]$ ,  $[\text{XeF}_5]_2[\text{Cr}_2\text{O}_2\text{F}_8] \cdot 2\text{HF}$ ,  $[\text{XeF}_5]_2[\text{Cr}_2\text{O}_2\text{F}_8] \cdot 2\text{XeOF}_4$ , and  $[\text{XeF}_5][\text{Xe}_2\text{F}_{11}][\text{CrOF}_5] \cdot 2\text{CrOF}_4$  (Figs. 39–41) contain  $[\text{XeF}_5]^+$  and/or  $[\text{Xe}_2\text{F}_{11}]^+$  cations that are strongly ion-paired with their anions through Xe---F secondary bonds that are significantly shorter than the sums of their Xe and F van der Waals radii.<sup>68</sup> Each cation and anion in  $[\text{XeF}_5]_2[\text{CrF}_6] \cdot 2\text{CrOF}_4$ ,  $[\text{Xe}_2\text{F}_{11}]_2[\text{CrF}_6]$ , and  $[\text{XeF}_5]_2[\text{Cr}_2\text{O}_2\text{F}_8]$  interacts with more than one counterion to form closely packed columns. The  $[\text{XeF}_5]_2[\text{Cr}_2\text{O}_2\text{F}_8]$  ion-pairs of  $[\text{XeF}_5]_2[\text{Cr}_2\text{O}_2\text{F}_8] \cdot 2\text{HF}$  bridge through secondary Xe---F<sub>H</sub> and H<sub>F</sub>---F<sub>Cr</sub> bonds with HF molecules to form discrete columns, whereas  $[\text{XeF}_5][\text{Xe}_2\text{F}_{11}][\text{CrOF}_5] \cdot 2\text{CrOF}_4$  and  $[\text{XeF}_5]_2[\text{Cr}_2\text{O}_2\text{F}_8] \cdot 2\text{XeOF}_4$  form well-isolated structural units.

The LT Raman spectra of  $[\text{XeF}_5][\text{Xe}_2\text{F}_{11}][\text{CrOF}_5] \cdot 2\text{CrOF}_4$  and  $[\text{XeF}_5]_2[\text{Cr}_2\text{O}_2\text{F}_8] \cdot 2\text{XeOF}_4$  were recorded on crystalline samples that were subsequently characterized by SCXRD.<sup>68</sup> Spectral assignments were made by comparison with the calculated gas-phase vibrational frequencies and intensities of the energy-minimized, gas-phase geometries of  $[\text{XeF}_5][\text{Xe}_2\text{F}_{11}][\text{CrOF}_5] \cdot 2\text{CrOF}_4$  and  $[\text{XeF}_5]_2[\text{Cr}_2\text{O}_2\text{F}_8] \cdot 2\text{XeOF}_4$  (Fig. 42) at the uPBE1PBE/aug-cc-pVDZ(Xe)-Def2SVP(F, O, Cr) level of theory. Overall, the calculated vibrational frequencies and intensities were in good agreement with experiment, and the Raman spectra were fully assigned. Vibrational assignments for cocrystallized  $\text{CrOF}_4$  and  $\text{XeOF}_4$ , and bands assigned to the  $[\text{XeF}_5]^+$  and  $[\text{Xe}_2\text{F}_{11}]^+$  cations were also aided by comparison with the vibrational spectra of  $\text{CrOF}_4$ ,  $\text{XeOF}_4 \cdot \text{XeF}_2$ , and other  $[\text{XeF}_5]^+$  and  $[\text{Xe}_2\text{F}_{11}]^+$  salts.

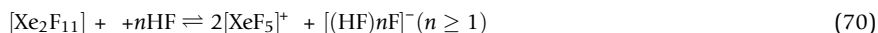
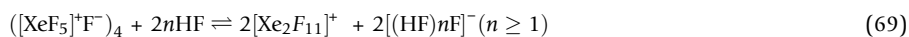
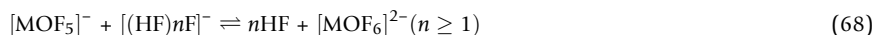
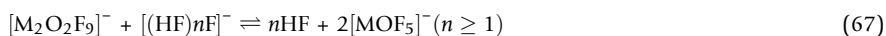
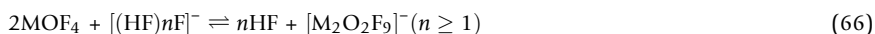
(ii)  $[\text{XeF}_5][\text{M}_2\text{O}_2\text{F}_9]$  ( $M = \text{Mo}, \text{W}$ ),  $[\text{Xe}_2\text{F}_{11}][\text{M}'\text{OF}_5]$  ( $M' = \text{Cr}, \text{Mo}, \text{W}$ ),  $[\text{XeF}_5][\text{HF}_2] \cdot \text{CrOF}_4$ , and  $[\text{XeF}_5][\text{WOF}_5] \cdot \text{XeOF}_4$ . The stabilization of Cr(VI) and Cr(V) by the  $[\text{XeF}_5]^+$  and  $[\text{Xe}_2\text{F}_{11}]^+$  cations suggest that  $[\text{MOF}_5]^-$  and  $[\text{M}_2\text{O}_2\text{F}_9]^-$  ( $M = \text{Mo}, \text{W}$ ) salts of  $[\text{XeF}_5]^+$  and  $[\text{Xe}_2\text{F}_{11}]^+$  should also form owing to the greater calculated fluoride-ion affinities of  $\text{MoOF}_4$  ( $-355 \text{ kJ mol}^{-1}$ ) and  $\text{WOF}_4$  ( $-386 \text{ kJ mol}^{-1}$ ) relative to  $\text{CrOF}_4$  ( $-285 \text{ kJ mol}^{-1}$ ).<sup>81</sup>

The  $[\text{Xe}_2\text{F}_{11}][\text{MOF}_5]$  and  $[\text{XeF}_5][\text{M}_2\text{O}_2\text{F}_9]$  salts have been obtained by varying the initial molar ratios of  $\text{XeF}_6$  and  $\text{MOF}_4$  in dilute aHF solutions in accordance with Eqs. (66)–(70).<sup>69</sup> When a stoichiometric excess of  $\text{XeF}_6$  was employed, the equilibria shifted to favor  $[\text{Xe}_2\text{F}_{11}][\text{MOF}_5]$ , and accordingly, a stoichiometric excess of  $\text{MOF}_4$  yielded  $[\text{XeF}_5][\text{M}_2\text{O}_2\text{F}_9]$ .





**Fig. 39** The X-ray crystal structures of (A)  $[\text{Xe}_2\text{F}_{11}]_2[\text{CrF}_6]$  and (B)  $[\text{XeF}_5]_2[\text{CrF}_6] \cdot 2\text{CrOF}_4$ . Thermal ellipsoids are drawn at the 50% probability level. Reproduced with permission from Goettel, J. T.; Bortolus, M. R.; Stuart, D. G.; Mercier, H. P. A.; Schrobilgen, G. J. *Chem. Eur. J.* **2019**, *25*, 15815–15829.

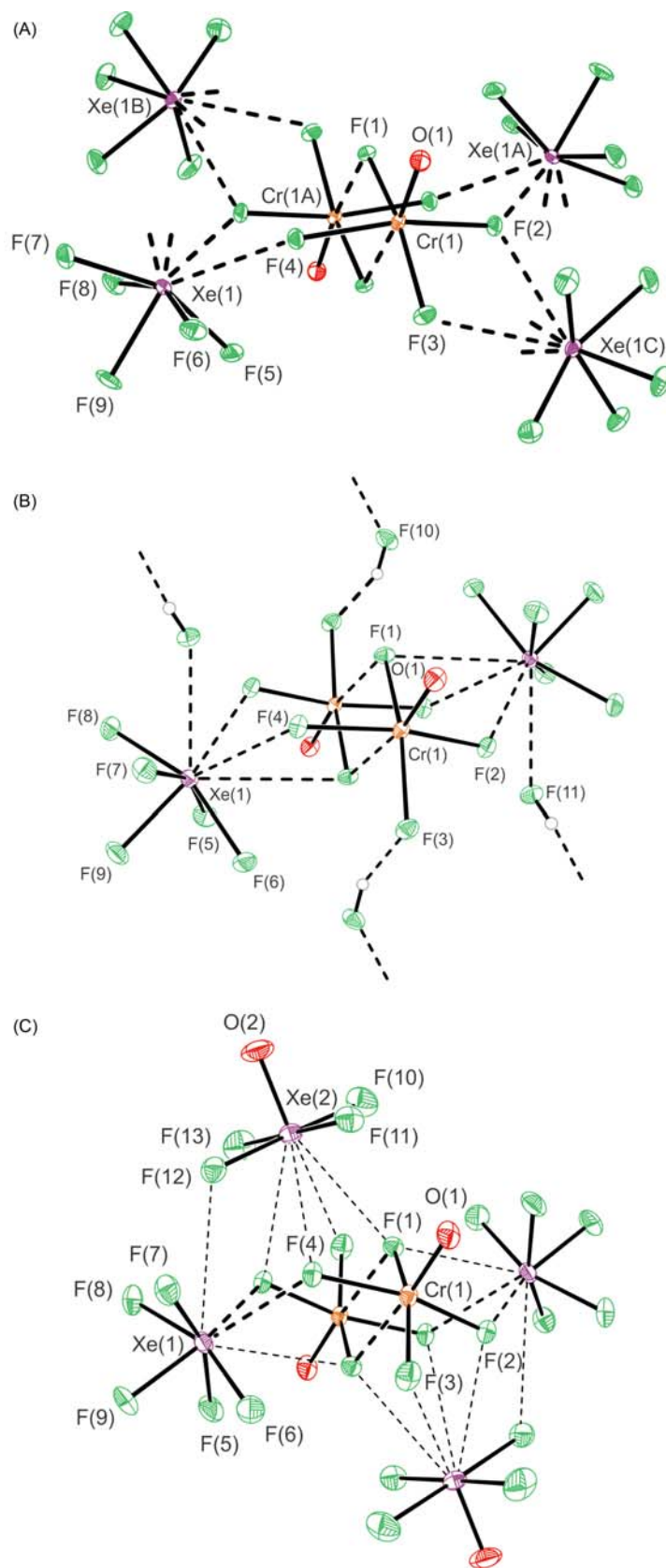


Hydrolysis of  $[\text{Xe}_2\text{F}_{11}][\text{WOF}_5]$  in aHF yielded HF,  $[\text{XeF}_5]^+$ ,  $\text{XeOF}_4$  (Eq. 71) and  $[\text{WOF}_5]^-$  which crystallized to give  $[\text{XeF}_5][\text{WOF}_5] \cdot \text{XeOF}_4$ .

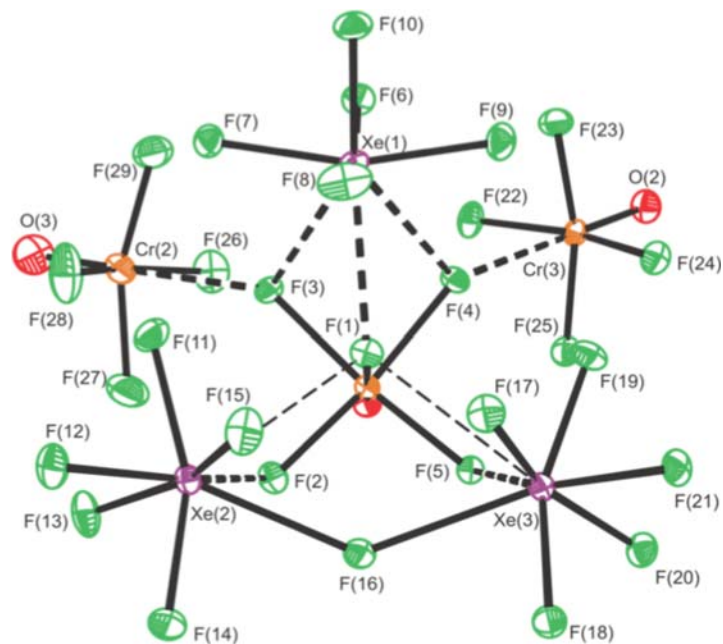


Attempts to synthesize  $[\text{XeF}_5][\text{MOF}_5]$  in  $\text{CFCl}_3$  solvent by reaction of equimolar amounts of  $\text{XeF}_6$  and  $\text{MOF}_4$  were monitored at LT as a function of temperature and time by Raman spectroscopy and were shown to yield mixtures of  $[\text{Xe}_2\text{F}_{11}][\text{MOF}_5]$  and  $[\text{XeF}_5][\text{M}_2\text{O}_2\text{F}_9]$ , which suggests that  $[\text{XeF}_5][\text{MOF}_5]$  salts may only exist as transient intermediates in the formation of  $[\text{Xe}_2\text{F}_{11}][\text{MOF}_5]$  and  $[\text{XeF}_5][\text{M}_2\text{O}_2\text{F}_9]$  under these reaction conditions.

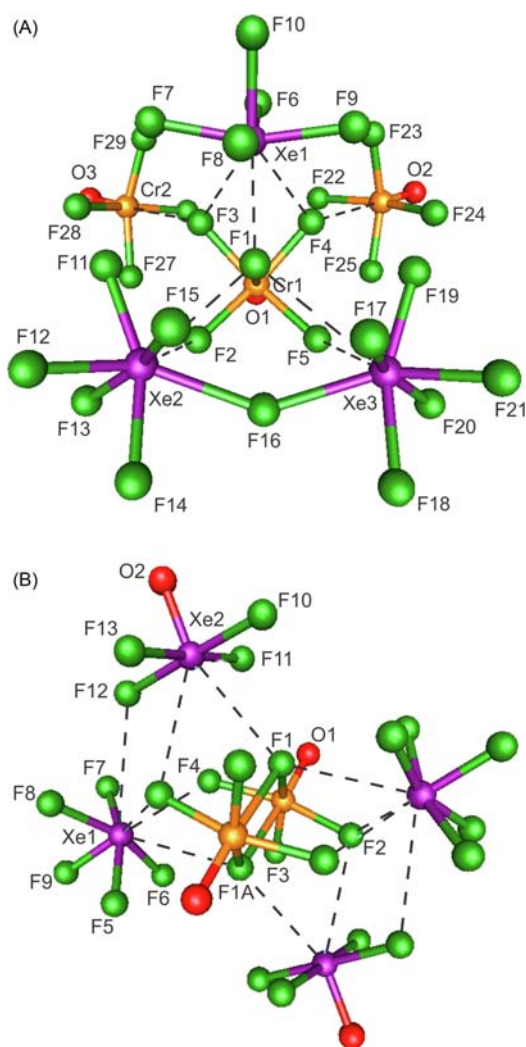
In contrast with  $\text{MoOF}_4$  and  $\text{WOF}_4$ , the reaction of  $\text{CrOF}_4$  with  $\text{XeF}_6$  in aHF failed to yield either  $[\text{CrOF}_5]^-$  or  $[\text{Cr}_2\text{O}_2\text{F}_9]^-$  salts. Instead, a separate study<sup>68</sup> showed the RT reaction of  $\text{XeF}_6$  and  $\text{CrOF}_4$  in aHF yielded the Cr(V) oxyfluoro-anion salt,  $[\text{XeF}_5]_2[\text{Cr}_2\text{O}_2\text{F}_8] \cdot 2\text{XeOF}_4$ , through a multi-step pathway which involved reductive elimination of  $\text{F}_2$  and O/F metathesis. In an effort to circumvent Cr(VI) reduction, the LT ( $-78$  to  $0^\circ\text{C}$ ) reaction of  $\text{XeF}_6$  and  $\text{CrOF}_4$  in aHF was attempted; however, only  $\alpha$ - $\text{CrOF}_4$ ,  $\beta$ - $\text{CrOF}_4$ , and  $[\text{XeF}_5][\text{HF}_2]$  were identified in the reaction mixture by X-ray crystallographic determinations of their unit cells. When a 2.21:1 molar ratio of  $\text{XeF}_6$ : $\text{CrOF}_4$  was allowed to react at  $0^\circ\text{C}$  in aHF (initial molar ratio,  $\text{XeF}_6$ : $\text{HF} \approx 1$ :100),



**Fig. 40** The X-ray crystal structures of (A)  $[\text{XeF}_5]_2[\text{Cr}_2\text{O}_2\text{F}_8]$ , (B)  $[\text{XeF}_5]_2[\text{Cr}_2\text{O}_2\text{F}_8] \cdot 2\text{HF}$ , and (C)  $[\text{XeF}_5]_2[\text{Cr}_2\text{O}_2\text{F}_8] \cdot 2\text{XeOF}_4$ . Thermal ellipsoids are drawn at the 50% probability level. Reproduced with permission from Goettel, J. T.; Bortolus, M. R.; Stuart, D. G.; Mercier, H. P. A.; Schrobilgen, G. *J. Chem. Eur. J.* **2019**, *25*, 15815–15829.



**Fig. 41** The X-ray crystal structure of  $[\text{XeF}_5][\text{Xe}_2\text{F}_{11}][\text{CrOF}_5] \cdot 2\text{CrOF}_4$ . Thermal ellipsoids are drawn at the 50% probability level. Reproduced with permission from Goettel, J. T.; Bortolus, M. R.; Stuart, D. G.; Mercier, H. P. A.; Schrobilgen, G. J. *Chem. Eur. J.* **2019**, *25*, 15815–15829.



**Fig. 42** Gas-phase geometries calculated at the uPBE1PBE/aug-ccpVDZ (Xe)-Def2-SVP (F, O, Cr) level of theory for (A)  $[\text{XeF}_5]_2[\text{Cr}_2\text{O}_2\text{F}_8] \cdot 2\text{XeOF}_4$  and (B)  $[\text{XeF}_5][\text{Xe}_2\text{F}_{11}][\text{CrOF}_5] \cdot 2\text{CrOF}_4$ . Reproduced with permission from Goettel, J. T.; Bortolus, M. R.; Stuart, D. G.; Mercier, H. P. A.; Schrobilgen, G. J. *Chem. Eur. J.* **2019**, *25*, 15815–15829.

$[\text{XeF}_5][\text{HF}_2]\cdot\text{CrOF}_4$  formed as the sole product, which was isolated from solution along with a small quantity of unreacted  $\text{XeF}_6$ . Unlike  $\text{MoOF}_4$  and  $\text{WOF}_4$ ,  $\text{CrOF}_4$  is incapable of abstracting  $\text{F}^-$  from  $[(\text{HF})_n\text{F}]^-$  at  $0^\circ\text{C}$  in aHF solution, in accordance with its lower fluoride-ion affinity.

To circumvent  $[\text{XeF}_5][\text{HF}_2]$  formation, the reaction of  $\text{XeF}_6$  and  $\text{CrOF}_4$  was carried out in the oxidatively resistant aprotic solvent,  $\text{CF}_2\text{ClCF}_2\text{Cl}$ , which resulted in fluoride-ion abstraction from  $\text{XeF}_6$  by  $\text{CrOF}_4$  to give  $[\text{Xe}_2\text{F}_{11}][\text{CrOF}_5]$  (Eq. 72).<sup>69</sup>

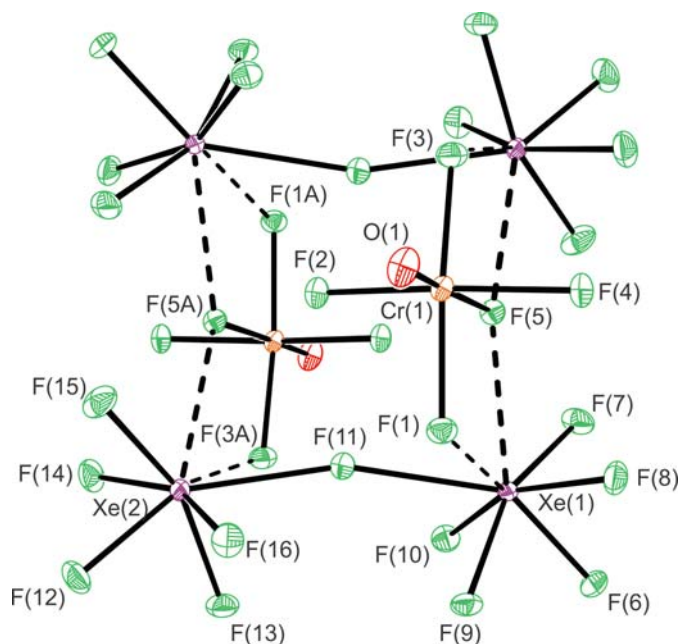


The crystal structures of  $[\text{Xe}_2\text{F}_{11}][\text{M}'\text{OF}_5]$  ( $\text{M}' = \text{Cr}, \text{Mo}, \text{W}$ ),  $[\text{XeF}_5][\text{M}_2\text{O}_2\text{F}_9]$  ( $\text{M} = \text{Mo}, \text{W}$ ),  $[\text{XeF}_5][\text{HF}_2]\cdot\text{CrOF}_4$ , and  $[\text{XeF}_5][\text{WOF}_5]\cdot\text{XeOF}_4$  consist of intimate ion-pairs in which the Lewis acidic  $[\text{XeF}_5]^+$  and  $[\text{Xe}_2\text{F}_{11}]^+$  cations interact with their respective anions by means of short Xe---F secondary bonds that are significantly shorter than the sums of the Xe and F van der Waal radii.<sup>69</sup> The crystal structures of  $[\text{Xe}_2\text{F}_{11}][\text{CrOF}_5]$  (Fig. 43),  $[\text{XeF}_5][\text{M}_2\text{O}_2\text{F}_9]$  (Fig. 44), and  $[\text{XeF}_5][\text{HF}_2]\cdot\text{CrOF}_4$  (Fig. 45) form dimeric structural units in which each cation and anion interacts with another counterion. Although the  $[\text{Xe}_2\text{F}_{11}][\text{CrOF}_5]$  and  $[\text{XeF}_5][\text{M}_2\text{O}_2\text{F}_9]$  dimers are well isolated, the dimers of  $[\text{XeF}_5][\text{HF}_2]\cdot\text{CrOF}_4$  bridge to one another through long Xe---F<sub>Cr</sub> secondary bonds to form sheets. The  $[\text{Xe}_2\text{F}_{11}][\text{MOF}_5]$  salts are isotypic and form six-membered rings which interact with one another by means of long Xe---F<sub>M</sub> secondary bonds to form columns that stack along the *a*-axes of their unit cells. Although the molecular formulae of  $[\text{Xe}_2\text{F}_{11}][\text{CrOF}_5]$  and  $[\text{Xe}_2\text{F}_{11}][\text{MOF}_5]$  are analogous, their solid-state structures are not isotypic. This is attributed to the greater fluorobasicity of  $[\text{CrOF}_5]^-$  relative to  $[\text{MOF}_5]^-$ . The crystal structure of  $[\text{XeF}_5][\text{WOF}_5]\cdot\text{XeOF}_4$  forms infinite chains which result from the formation of two short Xe---F secondary bonds between  $[\text{XeF}_5]^+$  and  $[\text{WOF}_5]^-$ , where the cocrystallized  $\text{XeOF}_4$  molecule is weakly bound to  $[\text{WOF}_5]^-$  by means of long Xe---F secondary bonds. The X-ray crystal structure of  $[\text{Xe}_2\text{F}_{11}][\text{CrOF}_5]$  is presently the only crystal structure of a  $[\text{CrOF}_5]^-$  salt.

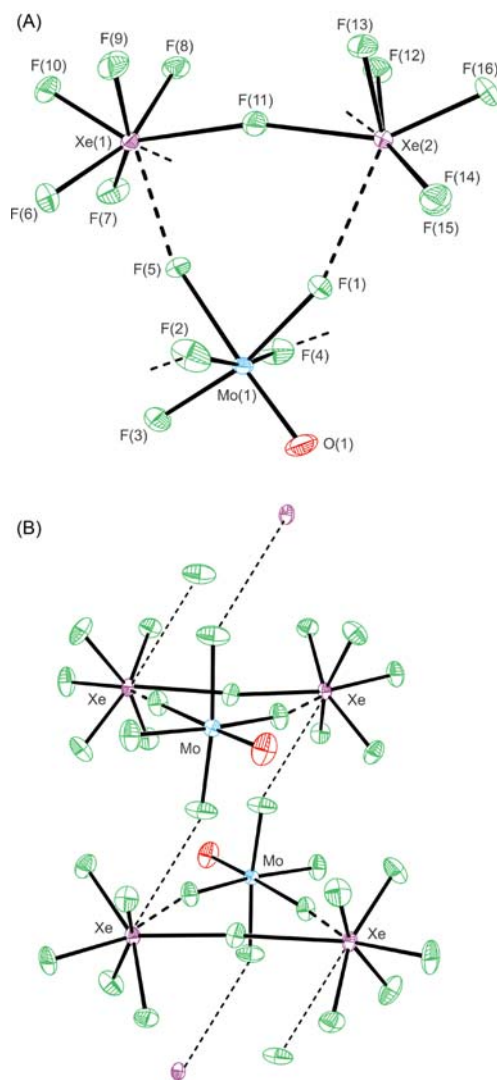
The  $[\text{XeF}_5]^+$  cations of the  $[\text{XeF}_5][\text{HF}_2]\cdot\text{CrOF}_4$  dimer bridge to each other through two  $[\text{HF}_2]^-$  anions by means of two secondary Xe---F<sub>H</sub> bonds (Fig. 46).<sup>69</sup> The geometric parameters of cocrystallized  $\text{XeOF}_4$  in  $[\text{XeF}_5][\text{WOF}_5]\cdot\text{XeOF}_4$  (Fig. 47) are similar to those of  $\text{XeOF}_4\cdot\text{XeF}_2$ <sup>189</sup> and  $[\text{XeF}_5]_2[\text{Cr}_2\text{O}_2\text{F}_8]\cdot 2\text{XeOF}_4$ .<sup>68</sup>

Spectral assignments for the LT Raman spectra of  $[\text{Xe}_2\text{F}_{11}][\text{M}'\text{OF}_5]$ ,  $[\text{XeF}_5][\text{M}_2\text{O}_2\text{F}_9]$ , and  $[\text{XeF}_5][\text{WOF}_5]\cdot\text{XeOF}_4$  were made by comparison with the calculated vibrational frequencies and mode descriptions of the energy minimized gas-phase  $[\text{M}'\text{OF}_5]^-$  and  $[\text{M}'_2\text{O}_2\text{F}_9]^-$  anions and the ion-pairs  $\{[\text{Xe}_2\text{F}_{11}][\text{CrOF}_5]\}_2$ ,  $[\text{Xe}_2\text{F}_{11}][\text{MOF}_5]$ , and  $\{[\text{XeF}_5][\text{M}_2\text{O}_2\text{F}_9]\}_2$  at the PBE1PBE/Def2-SVP level of theory (Fig. 48).<sup>69</sup> The cation Xe-F and anion M'-F stretching modes are strongly coupled, which is consistent with the degree of ion-pairing observed in their X-ray crystal structures.

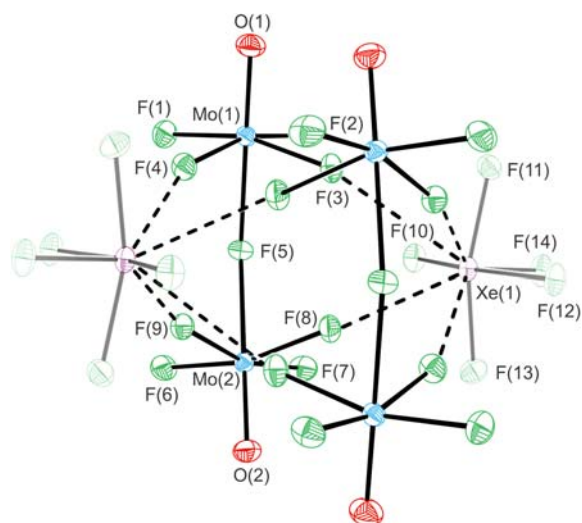
An NBO analysis was carried out for gas-phase  $\text{M}'\text{OF}_4$ ,  $[\text{M}'\text{OF}_5]^-$ ,  $[\text{M}'_2\text{O}_2\text{F}_9]^-$ ,  $\{[\text{Xe}_2\text{F}_{11}][\text{CrOF}_5]\}_2$ ,  $[\text{Xe}_2\text{F}_{11}][\text{MOF}_5]$ , and  $\{[\text{XeF}_5][\text{M}_2\text{O}_2\text{F}_9]\}_2$  to assess the bonding in these species and the effects of ion-pair formation on their bonding.<sup>69</sup> The NBO analyses are consistent with conclusions drawn from their X-ray crystal structures: (1) the M'-O bonds have significant double bond character, (2) the M'-F<sub>ax</sub> bonds have significantly more ionic character than M'-F<sub>eq</sub>, (3) the Xe---F secondary bonds in the ion-pairs are primarily electrostatic and are best described as  $\sigma$ -hole bonds. The analysis also showed that the Xe---F secondary bonds of  $\{[\text{Xe}_2\text{F}_{11}][\text{CrOF}_5]\}_2$  significantly polarize the Cr-F<sub>ax</sub> and Cr-F<sub>eq</sub> bonds of  $[\text{CrOF}_5]^-$  so that F<sub>eq</sub> is significantly less fluorobasic than F<sub>ax</sub>. Analogous behavior was not observed for the gas-phase  $[\text{Xe}_2\text{F}_{11}][\text{MOF}_5]$  ion-pairs, and may account for the dimeric structural unit of  $\{[\text{Xe}_2\text{F}_{11}][\text{CrOF}_5]\}_2$ .



**Fig. 43** The dimeric structural unit in the X-ray crystal structure of  $[\text{Xe}_2\text{F}_{11}][\text{CrOF}_5]$ , where thermal ellipsoids drawn at the 50% probability level. Reproduced with permission from Bortolus, M. R.; Mercier, H. P. A.; Schrobilgen, G. J. *Chem. Eur. J.* **2020**, *26*, 8935–8950.

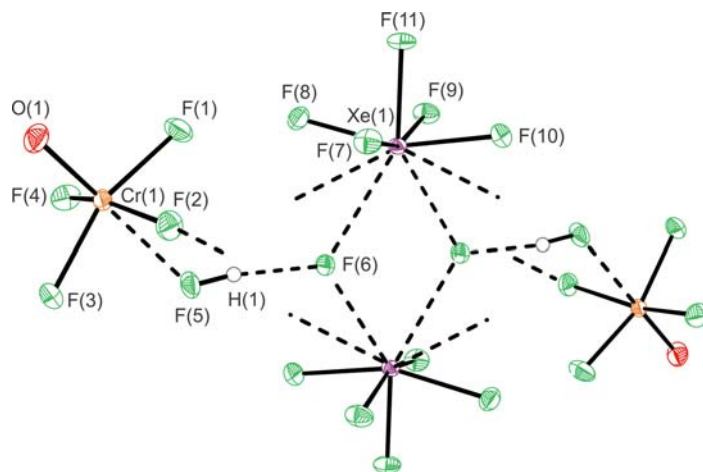


**Fig. 44** (A) The structural unit in the X-ray crystal structure of  $[\text{Xe}_2\text{F}_{11}][\text{MoOF}_5]$  and (B) a view showing the long interionic  $\text{Xe}\cdots\text{F}_{\text{eq}}$  contacts along the  $a$ -axis of the unit cell. Thermal ellipsoids are drawn at the 50% probability level. Reproduced with permission from Bortolus, M. R.; Mercier, H. P. A.; Schrobilgen, G. J. *Chem. Eur. J.* **2020**, *26*, 8935–8950.

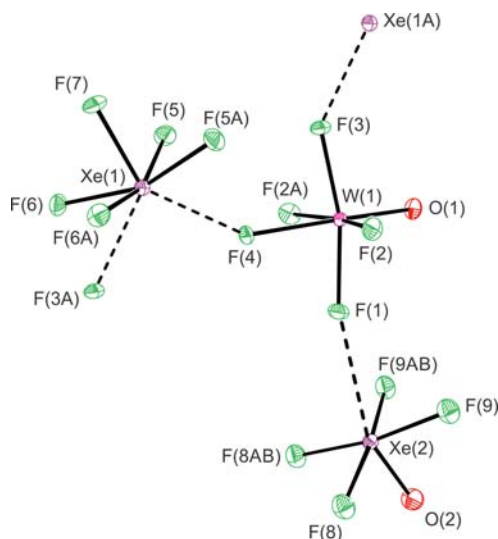


**Fig. 45** The dimeric structural unit in the X-ray crystal structure of  $[\text{XeF}_5][\text{Mo}_2\text{O}_2\text{F}_9]$ , where thermal ellipsoids are drawn at the 50% probability level. Reproduced with permission from Bortolus, M. R.; Mercier, H. P. A.; Schrobilgen, G. J. *Chem. Eur. J.* **2020**, *26*, 8935–8950.





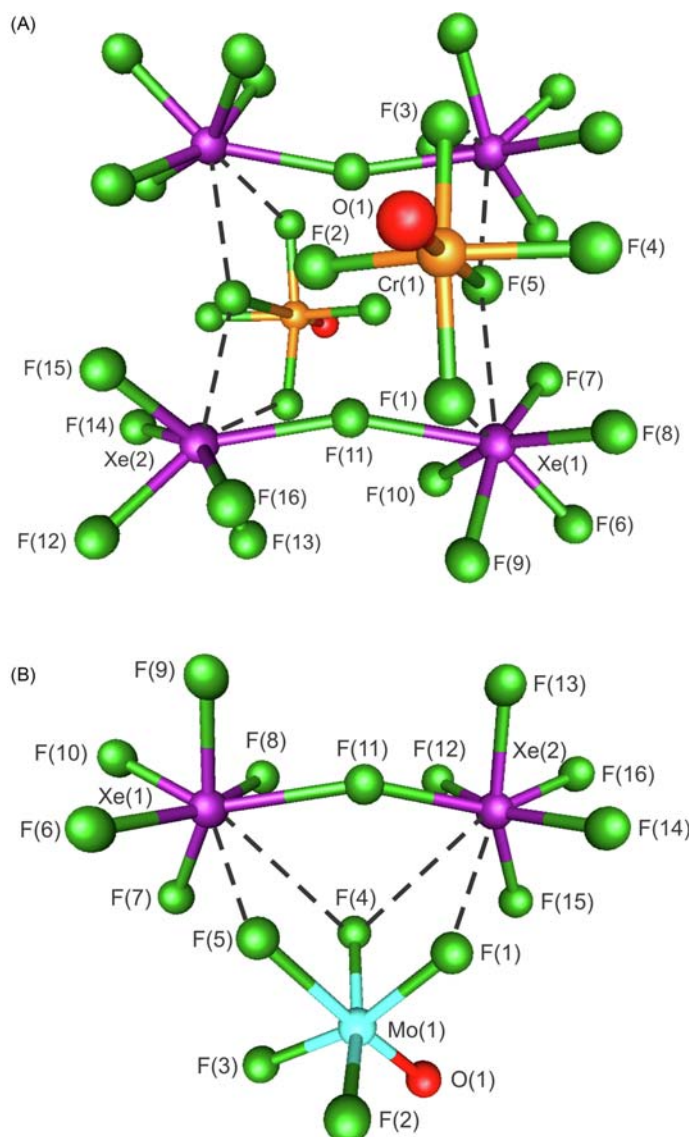
**Fig. 46** The dimeric structural unit in the X-ray crystal structure of  $[\text{XeF}_5][\text{HF}_2]\cdot\text{CrOF}_4$ , where thermal ellipsoids are drawn at the 50% probability level. Reproduced with permission from Bortolus, M. R.; Mercier, H. P. A.; Schrobilgen, G. J. *Chem. Eur. J.* **2020**, *26*, 8935–8950.



**Fig. 47** The structural unit in the X-ray crystal structure of  $[\text{XeF}_5][\text{WOF}_5]\cdot\text{XeOF}_4$ , where thermal ellipsoids are drawn at the 50% probability level. Reproduced with permission from Bortolus, M. R.; Mercier, H. P. A.; Schrobilgen, G. J. *Chem. Eur. J.* **2020**, *26*, 8935–8950.

The MEPS analyses of  $\text{M}'\text{OF}_4$  and  $[\text{M}'\text{OF}_5]^-$  support conclusions drawn from the NBO analyses and exemplify the expected periodic behavior when going from Cr to Mo and W.<sup>69</sup> The MEPS analyses show that differences among the electrostatic potential (EP) maxima/minima for  $\text{CrOF}_4$ ,  $\text{MoOF}_4$ , and  $\text{WOF}_4$  are greater between  $\text{CrOF}_4$  and  $\text{MoOF}_4/\text{WOF}_4$  than between  $\text{MoOF}_4$  and  $\text{WOF}_4$ . The EP maxima of the  $\text{M}'\text{OF}_4$  isosurfaces *trans* to the  $\text{M}'=\text{O}$  double bonds become more positive (Cr, 218; Mo, 340; W, 375  $\text{kJ mol}^{-1}$ ) upon descending Group 6, which is consistent with the calculated gas-phase FIA's of  $\text{M}'\text{OF}_4$ . The relative fluorobasicities of their F ligands are also reflected in their F atom EP minima which become more negative in going from Cr to W. A parallel trend of increasing negative EP is also observed for the O-ligand isosurfaces of  $\text{M}'\text{OF}_4$  when going from Cr to W.

The global EP minima of the  $[\text{M}'\text{OF}_5]^-$  anions (Cr,  $-567$ ; Mo,  $-512$ ; W,  $-499$   $\text{kJ mol}^{-1}$ ) lie at the intersections of their  $\text{F}_{\text{ax}}$  and  $\text{F}_{\text{eq}}$  isosurfaces and are 11 to 17 times more negative than the global EP minima of  $\text{M}'\text{OF}_4$ . The  $\text{F}_{\text{ax}}$  EP minima (Cr,  $-509$ ; Mo,  $-486$ ; W,  $-486$   $\text{kJ mol}^{-1}$ ) are significantly more negative than the  $\text{F}_{\text{eq}}$  EP minima (Cr,  $-446$ ; Mo,  $-433$ ; W,  $-431$   $\text{kJ mol}^{-1}$ ) (Fig. 49). Both the  $\text{F}_{\text{ax}}$  and  $\text{F}_{\text{eq}}$  EP minima become more positive in going from Cr to W, and reflect the relative fluorobasicities of the  $[\text{M}'\text{OF}_5]^-$  anions. These differences in EP minima likely account for structural differences among their  $[\text{Xe}_2\text{F}_{11}][\text{M}'\text{OF}_5]$  salts.



**Fig. 48** The calculated gas-phase geometries of (A) the  $\{[Xe_2F_{11}][CrOF_5]\}_2$  dimer and (B)  $[Xe_2F_{11}][MoOF_5]$  at the PBE1PBE/Def2-SVP (F, O, Cr, Xe) level of theory. Reproduced with permission from Bortolus, M. R.; Mercier, H. P. A.; Schrobilgen, G. J. *Chem. Eur. J.* **2020**, *26*, 8935–8950.

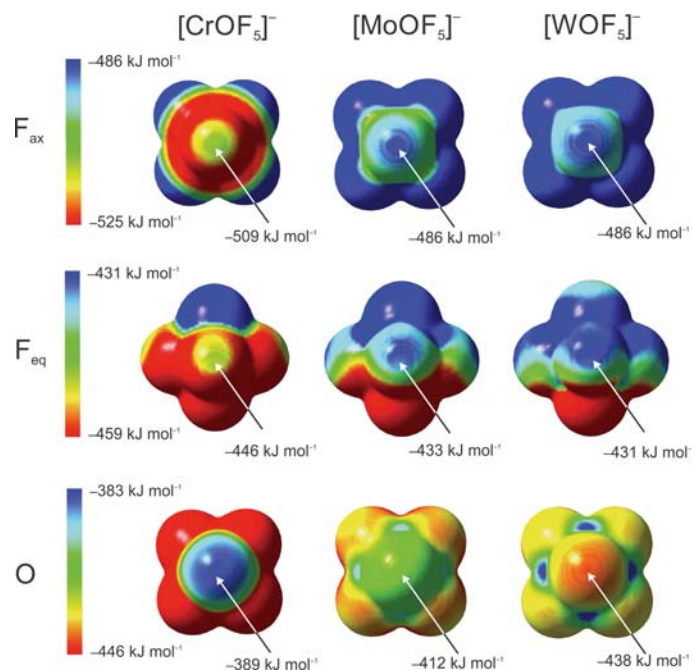
### 1.08.5.2.2 Fluoro-anion salts

Several new fluoro-anion salts of  $[XeF_5]^+$  and  $[Xe_2F_{11}]^-$  were obtained by (i) reaction of  $[XeF_5][SbF_6]$  with  $A(SbF_6)$  ( $A = NO_2, Cs, Rb$ ) or  $A'(SbF_6)_2$  ( $A' = Cu, Ni, Mg, Zn, Co, Mn, Pd, Hg$ ) in aHF at different A and A' molar ratios and (ii) reaction of  $XeF_2$  with  $MF_2$ ,  $MF_3$ , or  $MF_4$  ( $M = Ti, Mn, Sn, Pb$ ) in the presence of UV-photolyzed  $F_2$  in aHF solvent. When available, the Raman spectra were tentatively assigned by comparison with literature values of known  $[XeF_5]^+$  and  $[Xe_2F_{11}]^+$  salts.<sup>21,22</sup>

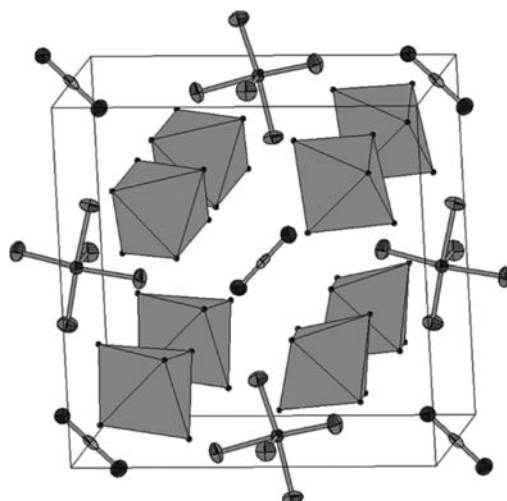
(i)  $[NO_2][XeF_5][SbF_6]$ , and  $[XeF_5][Cu(SbF_6)_3]$ . Until recently, and although numerous  $[XeF_5]^+$  and  $[Xe_2F_{11}]^+$  salts of different fluoro-anions were known,<sup>111,190,191</sup> no mixed cation salts had been reported which contained either  $[XeF_5]^+$  or  $[Xe_2F_{11}]^+$  and another cation.

The reaction of  $[XeF_5][SbF_6]$  with  $[NO_2][SbF_6]$  at RT in aHF solvent yielded the first such mixed cation salt of  $[XeF_5]^+$ ,  $[XeF_5][NO_2][SbF_6]_2$  (Eq. 73).<sup>192</sup> Similarly, the reaction of  $[XeF_5][SbF_6]$  with  $Cu[SbF_6]_2$  in aHF yielded  $[XeF_5][Cu(SbF_6)_3]$  (Eq. 74).<sup>192</sup> Pursuant to the synthesis of  $[XeF_5][Cu(SbF_6)_3]$ , other examples of mixed  $[XeF_5]^+$ /metal cation salts have also been synthesized, but  $[XeF_5][NO_2][SbF_6]_2$  remains the only example of a mixed  $[XeF_5]^+$ /non-metal cation salt.

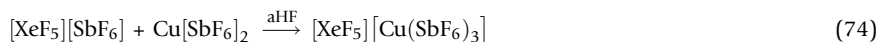




**Fig. 49** The MEPS contours calculated at the  $0.001 e a_0^{-3}$  isosurfaces for  $[M'OF_5]^-$  ( $M' = \text{Cr, Mo, W}$ ). Extrema of selected electrostatic potentials for the  $F_{\text{ax}}$ ,  $F_{\text{eq}}$ , and O atoms are indicated by arrows. The optimized geometries and MEPS were calculated at the PBE1PBE/Def2-SVP (O, F, Cr, Mo, W) level of theory. Reproduced with permission from Bortolus, M. R.; Mercier, H. P. A.; Schrobilgen, G. J. *Chem. Eur. J.* **2020**, *26*, 8935–8950.

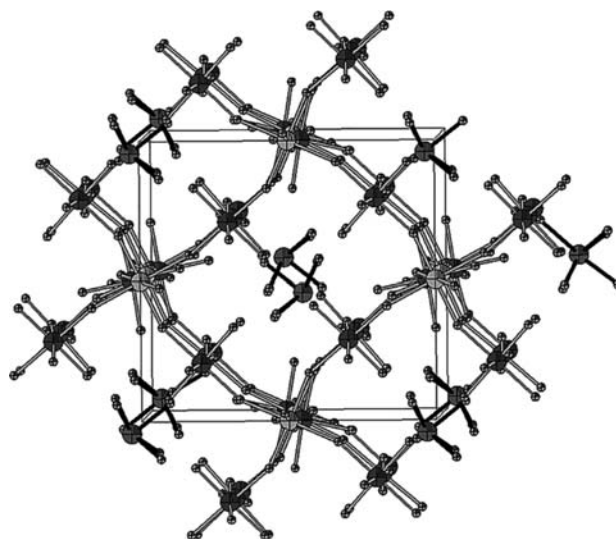


**Fig. 50** Packing diagram for the  $[\text{NO}_2]^+$  and  $[\text{XeF}_5]^+$  cations, and  $[\text{SbF}_6]^-$  anions in the X-ray crystal structure of  $[\text{NO}_2][\text{XeF}_5][\text{SbF}_6]_2$ . Thermal ellipsoids are drawn at the 50% probability level. Only one of two orientations for the disordered  $[\text{SbF}_6]^-$  anions is depicted. Reproduced with permission from Mazej, Z.; Goresnik, E. *Eur. J. Inorg. Chem.* **2015**, 1453–1456.



The crystal structure of  $[\text{XeF}_5][\text{NO}_2][\text{SbF}_6]_2$  consists of discrete  $[\text{NO}_2]^+$  and  $[\text{XeF}_5]^+$  cations and  $[\text{SbF}_6]^-$  anions (Fig. 50). Each  $[\text{XeF}_5]^+$  cation forms four symmetry equivalent Xe---F<sub>Sb</sub> secondary bonds (2.786 Å) with four different  $[\text{SbF}_6]^-$  anions. The geometric parameters of the individual ions are comparable to those observed in their respective simple salts and are not discussed further.

The crystal structure of  $[\text{XeF}_5][\text{Cu}(\text{SbF}_6)_3]$  is comprised of eight-membered rings with alternating  $\text{CuF}_6$  and  $\text{SbF}_6$  octahedra that share apices; the rings are connected to an infinite three-dimensional network (Fig. 51), where the  $[\text{XeF}_5]^+$  cations occupy cavities within these rings. Similar three-dimensional frameworks have been observed or  $\text{AM}[\text{AsF}_6]_3$  ( $A = [\text{H}_3\text{O}]^+, [\text{NH}_4]^+, [\text{O}_2]^+, [\text{NO}]^+, \text{K}^+, \text{M} = \text{Mn, Fe, Co, Ni, Zn}$ ). This arrangement leads to cavities that are occupied by  $[\text{XeF}_5]^+$  cations. Owing to strong Xe---F<sub>Sb</sub> secondary



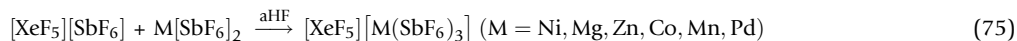
**Fig. 51** The crystal structure of  $[\text{XeF}_5][\text{Cu}(\text{SbF}_6)_3]$  showing rings of  $\text{CuF}_6$  octahedra sharing their apices with  $\text{SbF}_6$  octahedra, to give an infinite three-dimensional network. Reproduced with permission from Mazej, Z.; Goreshnik, E. *Eur. J. Inorg. Chem.* **2015**, 1453–1456.

bonds, the  $[\text{XeF}_5]^+$  cations are somewhat shifted away from the cavity centers. Each  $[\text{XeF}_5]^+$  cation forms four Xe---F secondary bonds with four different  $[\text{SbF}_6]^-$  anions.

The Raman spectra of the  $[\text{NO}_2][\text{XeF}_5][\text{SbF}_6]_2$  and  $[\text{XeF}_5][\text{Cu}(\text{SbF}_6)_3]$  salts were assigned<sup>192</sup> by comparison with literature values of the  $[\text{NO}_2]^+$ ,  $[\text{XeF}_5]^+$ , and  $[\text{SbF}_6]^-$  ions.

(ii)  $[\text{XeF}_5][\text{M}(\text{SbF}_6)_3]$  ( $M = \text{Ni, Mg, Cu, Zn, Co, Mn, Pd}$ ) and  $[\text{XeF}_5]_3[\text{Hg}(\text{HF})_2][\text{SbF}_6]_7$ . The synthesis of  $[\text{XeF}_5][\text{Cu}(\text{SbF}_6)_3]$  provided impetus to synthesize and structurally characterize other mixed  $[\text{XeF}_5][\text{M}(\text{SbF}_6)_3]$  ( $M = \text{Ni, Mg, Zn, Co, Fe, V, Cr, Mn}$ ) salts.<sup>193</sup> The primary objective of this study was to investigate the effects of increasing the sizes of six-coordinate  $M^{2+}$  cations for  $\text{Ni}^{2+} < \text{Mg}^{2+} < \text{Cu}^{2+} < \text{Zn}^{2+} < \text{V}^{2+} < \text{Cr}^{2+} < \text{Mn}^{2+}$  on the solid-state structures of  $[\text{XeF}_5][\text{M}(\text{SbF}_6)_3]$  salts. Reactions with larger cations such as  $\text{Ca}^{2+}$ ,  $\text{Sr}^{2+}$ ,  $\text{Ba}^{2+}$ ,  $\text{Ag}^{2+}$ ,  $\text{Pd}^{2+}$ ,  $\text{Cd}^{2+}$ , and  $\text{Hg}^{2+}$  were also explored. The solid-state structure of  $[\text{XeF}_5][\text{Cu}(\text{SbF}_6)_3]$ <sup>192</sup> showed 4 + 2 elongations and 2 + 4 compressions of the  $\text{CuF}_6$  octahedra, so that the secondary goal of this study was to determine whether these distortions are due to packing effects, Jahn-Teller distortions, or a mixture of both effects. Salts of  $\text{V}^{2+}$ ,  $\text{Ni}^{2+}$ ,  $\text{Zn}^{2+}$ , and  $\text{Mg}^{2+}$  were not affected by Jahn-Teller distortions, whereas cations such as  $\text{Cr}^{2+}$ , with a high-spin  $d^4$  electronic configurations, showed significant Jahn-Teller distortions. Comparisons among the solid-state structures of these salts were used to assess the factors that give rise to the distortions of the  $\text{MF}_6$  octahedra.

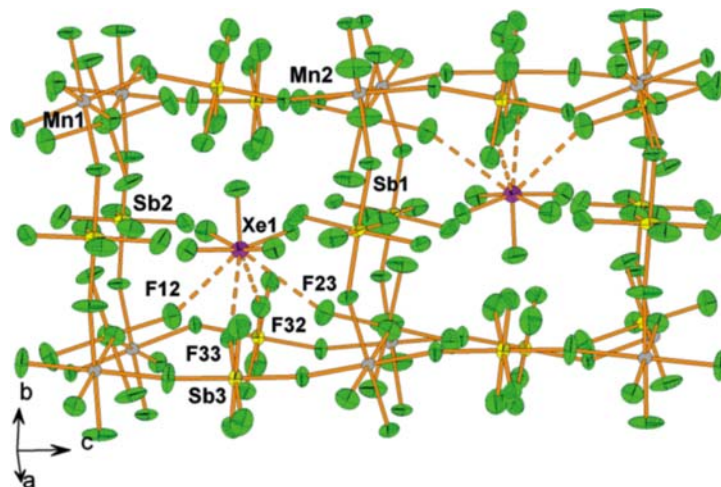
Reactions of  $[\text{XeF}_5][\text{SbF}_6]$  with  $\text{M}[\text{SbF}_6]_2$  ( $M^{2+} = \text{Ni, Mg, Zn, Co, Mn, Pd}$ ) in aHF in a 1:1 molar ratio yielded  $[\text{XeF}_5][\text{M}(\text{SbF}_6)_3]$  upon crystallization (Eq. 75).<sup>193</sup> The salts were crystallized using a method similar to that described for  $[\text{XeF}_5][\text{Cu}(\text{SbF}_6)_3]$ . Similar attempts to prepare new  $[\text{XeF}_5]^+/\text{M}^{2+}$  mixed-cation salts with  $M^{2+} = \text{Ca, Sr, Ba, Cr, Fe, Ag, Cd, and Hg}$  were only successful for Hg, which yielded  $[\text{XeF}_5]_3[\text{Hg}(\text{HF})_2][\text{SbF}_6]_7$  (Eq. 76).



The syntheses of  $[\text{XeF}_5][\text{Cr}(\text{SbF}_6)_3]$  and  $[\text{XeF}_5][\text{Fe}(\text{SbF}_6)_3]$  likely failed owing to oxidation of  $\text{Cr}^{2+}$  and  $\text{Fe}^{2+}$  to  $\text{Cr}^{3+}$  and  $\text{Fe}^{3+}$  by  $[\text{XeF}_5]^+$ . The oxidizing strengths of xenon fluorides increase in the sequence,  $\text{XeF}_2 < \text{XeF}_4 < \text{XeF}_6$ , as do their corresponding cations,  $[\text{XeF}]^+ < [\text{XeF}_3]^+ < [\text{XeF}_5]^+$  which are even more potent oxidative fluorinating agents. The standard redox potential of the  $M^{3+}/M^{2+}$  ( $M = \text{Cr, Ti, V, Fe, Mn, Cu}$ ) and  $M^{4+}/M^{2+}$  ( $M = \text{Pd, Ni}$ ) couples increase in the order  $\text{Ti} < \text{Cr} < \text{V} < \text{Fe} < \text{Mn} < \text{Pd} < \text{Co} < \text{Cu} < \text{Ni}$ . The study indicated that the redox potential of Mn [ $E^\circ(M^{3+}/M^{2+}) = -1.51 \text{ V}$ ] is the current empirical limit for  $M^{2+}$  to resist oxidation by the strongly oxidizing  $[\text{XeF}_5]^+$  cation in aHF solvent. Consequently, mixed salts with  $\text{Ti}^{2+}$  and  $\text{V}^{2+}$  are also expected to be oxidized, thus their syntheses were not attempted.

The crystal structures of  $[\text{XeF}_5][\text{M}(\text{SbF}_6)_3]$  ( $M^{2+} = \text{Mg, Co, Ni, Zn}$ ) and the LT phase,  $\alpha$ - $[\text{XeF}_5][\text{Mn}(\text{SbF}_6)_3]$  (Fig. 52), were characterized at 150 K by SCXRD and are isotopic with  $[\text{XeF}_5][\text{Cu}(\text{SbF}_6)_3]$ . The unit cell volumes increase with increasing size of  $M^{2+}$  in the order  $\text{Ni}^{2+} < \text{Mg}^{2+} < \text{Cu}^{2+} < \text{Zn}^{2+} < \text{Co}^{2+} < \text{Mn}^{2+}$ . The unit cell axes of  $[\text{XeF}_5][\text{Mg}(\text{SbF}_6)_3]$  and  $[\text{XeF}_5][\text{Zn}(\text{SbF}_6)_3]$  differ significantly from those of  $[\text{XeF}_5][\text{Cu}(\text{SbF}_6)_3]$  because their  $M^{2+}$  cations are located in nearly regular octahedral coordination environments, whereas the Cu atoms in  $[\text{XeF}_5][\text{Cu}(\text{SbF}_6)_3]$  display 4 + 2 elongated and 2 + 4 compressed coordination environments. The M–F bond lengths of  $[\text{XeF}_5][\text{M}(\text{SbF}_6)_3]$  ( $M = \text{Ni, Mg, Zn, Co, Mn}$ ) are comparable to those of other  $M^{2+}$  salts that have octahedral  $M^{2+}$  coordination environments, such as  $\text{KNi}[\text{AsF}_6]_3$  and  $\text{KM}[\text{AsF}_6]_3$  ( $M = \text{Mg, Zn, Co, Mn}$ ). In the case of the Mn salt, there is a phase transition at ca. 235 K, and for Pd at 260–296 K.





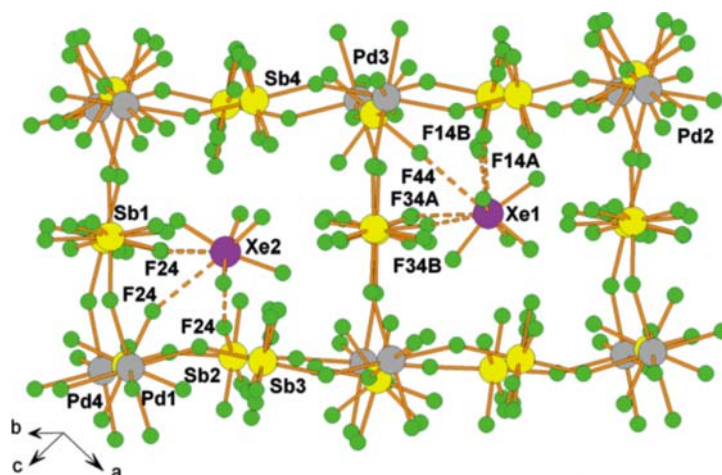
**Fig. 52** A portion of the X-ray crystal structure of  $\alpha$ -[XeF<sub>5</sub>][Mn(SbF<sub>6</sub>)<sub>3</sub>]. Only F atoms involved in secondary Xe $\cdots$ F bonds are labeled. Thermal ellipsoids are drawn at the 40% probability level. Reproduced with permission from Mazej, Z.; Goresnik, E. *Eur. J. Inorg. Chem.* **2016**, 3356–3364.

The mixed [XeF<sub>5</sub>][Pd(SbF<sub>6</sub>)<sub>3</sub>] salt adopts trigonal  $R\bar{3}$  symmetry at 298 K and monoclinic  $P2_1/c$  symmetry below 260 K (Fig. 53).<sup>193</sup> Although neither structure is isotopic with [XeF<sub>5</sub>][M(SbF<sub>6</sub>)<sub>3</sub>] ( $M^{2+} = \text{Ni, Mg, Zn, Co, Mn}$ ), the main structural motif is the same, i.e., a 3-D framework consisting of rings of MF<sub>6</sub> octahedra that share their apices with SbF<sub>6</sub> octahedra, forming cavities that accommodate the [XeF<sub>5</sub>]<sup>+</sup> cations. The [XeF<sub>5</sub>]<sup>+</sup> cations of  $\beta$ -[XeF<sub>5</sub>][Pd(SbF<sub>6</sub>)<sub>3</sub>] (296 K) are disordered, whereas they are ordered in the  $\alpha$ -phase (260 K).

The crystal structure of [XeF<sub>5</sub>]<sub>3</sub>[Hg(HF)]<sub>2</sub>[SbF<sub>6</sub>]<sub>7</sub> consists of columns of [Hg(HF)]<sup>2+</sup> cations bridged to [SbF<sub>6</sub>]<sup>-</sup> anions (Fig. 54). The charge balance is maintained by [XeF<sub>5</sub>]<sup>+</sup> cations which form secondary contacts with the F atoms of neighboring [SbF<sub>6</sub>]<sup>-</sup> anions. The Hg $\cdots$ F<sub>H</sub> secondary bonds between Hg<sup>2+</sup> and the F atoms of coordinated HF in [XeF<sub>5</sub>]<sub>3</sub>[Hg(HF)]<sub>2</sub>[SbF<sub>6</sub>]<sub>7</sub> are intermediate with respect to those of [Hg(HF)]<sub>2</sub>[AsF<sub>6</sub>]<sub>2</sub><sup>194</sup> and [Hg(HF)][PnF<sub>6</sub>] (Pn = Sb, As).<sup>194</sup> The primary and secondary coordination spheres of the [XeF<sub>5</sub>]<sup>+</sup> and [SbF<sub>6</sub>]<sup>-</sup> ions are comparable to those in other salts containing these ions and are not discussed further.

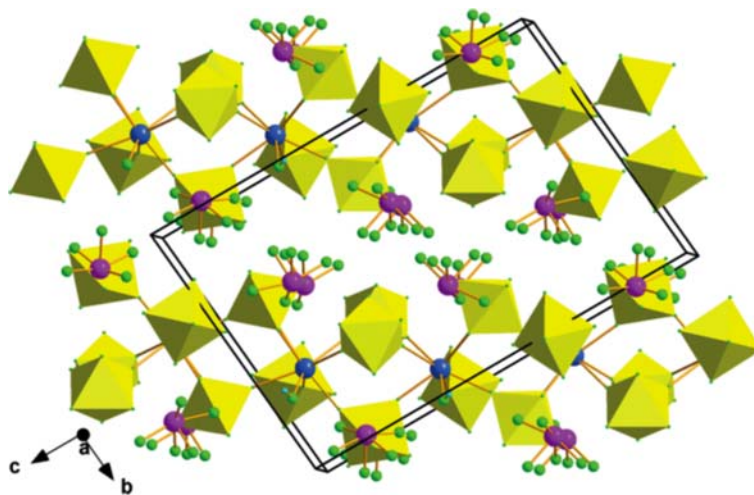
(iii)  $A[\text{XeF}_5][\text{SbF}_6]_2$  ( $A = \text{Cs, Rb}$ ) and  $\text{Cs}[\text{XeF}_5][\text{Bi}_x\text{Sb}_{1-x}\text{F}_6]_2$  ( $x = 0.37\text{--}0.39$ ). A subsequent study reported the reactions of  $A[\text{SbF}_6]$  ( $A = [\text{H}_3\text{O}]^+, \text{K, Rb, Cs}$ ; Pn = P, As, Sb, Bi),  $\text{ABF}_4$  ( $A = \text{K, Cs}$ ), and  $\text{Cs}_2\text{MnF}_6$  with [XeF<sub>5</sub>][PnF<sub>6</sub>] (Pn = As, Sb) in aHF solvent.<sup>195</sup>

Reactions of equimolar amounts of  $A[\text{SbF}_6]$  ( $A = \text{Cs, Rb}$ ) and [XeF<sub>5</sub>][SbF<sub>6</sub>] in aHF solvent yielded the isotopic salts  $A[\text{XeF}_5][\text{SbF}_6]_2$  upon crystallization (Eq. 77). No reaction was observed when the smaller [H<sub>3</sub>O]<sup>+</sup> or K<sup>+</sup> cations were used.

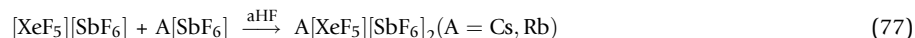


**Fig. 53** A portion of the X-ray crystal structure (260 K) of  $\alpha$ -[XeF<sub>5</sub>][Pd(SbF<sub>6</sub>)<sub>3</sub>] in which only the F atoms that are involved in secondary Xe $\cdots$ F bonds are labeled. Thermal ellipsoids are drawn at the 50% probability level. Reproduced with permission from Mazej, Z.; Goresnik, E. *Eur. J. Inorg. Chem.* **2016**, 3356–3364.

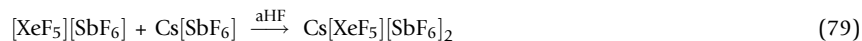




**Fig. 54** The packing diagram showing the  $[\text{Hg}(\text{HF})_2]^{2+}$  columns in the crystal structure of  $[\text{XeF}_5]_3[\text{Hg}(\text{HF})_2][\text{SbF}_6]_7$ . Reproduced with permission from Mazej, Z.; Goreschnik, E. *Eur. J. Inorg. Chem.* **2016**, 3356–3364.

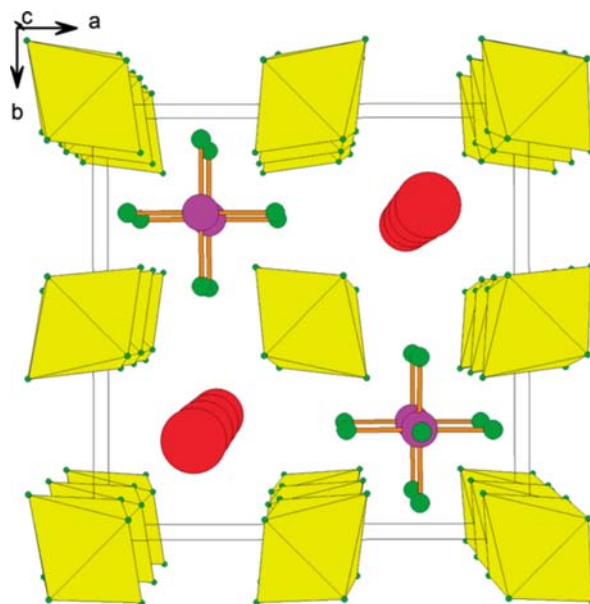


Attempts to prepare  $[\text{AsF}_6]^-$  analogues failed; however, the equimolar reaction of  $\text{Cs}[\text{BiF}_6]$  and  $[\text{XeF}_5][\text{SbF}_6]$  yielded a mixed-cation/mixed-anion salt having a formula close to  $\text{Cs}[\text{XeF}_5][\text{Bi}_x\text{Sb}_{1-x}\text{F}_6]_2$  ( $x = 0.37\text{--}0.39$ ). Reaction of  $\text{Cs}[\text{PF}_6]$  with  $[\text{XeF}_5][\text{SbF}_6]$  proceeded by displacement of the weaker Lewis acid  $\text{PF}_5$  to give  $[\text{Xe}_2\text{F}_{11}][\text{SbF}_5]$  and  $\text{Cs}[\text{SbF}_6]$  (Eq. 78), which reacted with  $[\text{XeF}_5][\text{SbF}_6]$  to give  $\text{Cs}[\text{XeF}_5][\text{SbF}_6]_2$  (Eq. 79).



Attempts to prepare mixed  $[\text{BF}_4]^-/[\text{SbF}_6]^-$  and  $[\text{MnF}_6]^{2-}/[\text{SbF}_6]^-$  salts by reaction of  $[\text{XeF}_5][\text{SbF}_6]$  with  $\text{Cs}[\text{BF}_4]$  and  $\text{Cs}_2[\text{MnF}_6]$  resulted in salt metatheses to give  $[\text{XeF}_5][\text{BF}_4]/[\text{XeF}_5]_2[\text{MnF}_6]$  and  $\text{Cs}[\text{SbF}_6]$ , respectively.

The  $\text{A}[\text{XeF}_5][\text{SbF}_6]_2$  ( $\text{A} = \text{Rb, Cs}$ ) and  $\text{Cs}[\text{XeF}_5][\text{Bi}_x\text{Sb}_{1-x}\text{F}_6]_2$  salts crystallize in two crystal modifications at low ( $\alpha$ -phase, 150 K, Fig. 55) and ambient ( $\beta$ -phase) temperatures. The crystal structures of  $\beta\text{-Rb}[\text{XeF}_5][\text{SbF}_6]_2$ ,  $\beta\text{-Cs}[\text{XeF}_5][\text{SbF}_6]_2$ , and  $\beta\text{-Cs}[\text{XeF}_5][\text{Bi}_x\text{Sb}_{1-x}\text{F}_6]_2$  ( $x = 0.37\text{--}0.39$ ) are isotypic, although the latter two structures exhibit a twofold rotational disorder of four fluorine atoms on the anions. In contrast, the three  $\alpha$ -phases are ordered. The simultaneous presence of both  $[\text{SbF}_6]^-$  and  $[\text{BiF}_6]^-$  in  $\text{Cs}[\text{XeF}_5][\text{Bi}_x\text{Sb}_{1-x}\text{F}_6]_2$  was also confirmed by Raman spectroscopy. The Raman spectra of the mixed salts  $\text{A}[\text{XeF}_5][\text{SbF}_6]_2$  ( $\text{A} = \text{Rb, Cs}$ ) and



**Fig. 55** The packing diagram showing the  $\text{Rb}^+$  and  $[\text{XeF}_5]^+$  cations and  $[\text{SbF}_6]^-$  anions in the crystal structure of  $\alpha\text{-Rb}[\text{XeF}_5][\text{SbF}_6]_2$  (150 K). Reproduced with permission from Mazej, Z.; Goreschnik, E. *Eur. J. Inorg. Chem.* **2017**, 2800–2807.

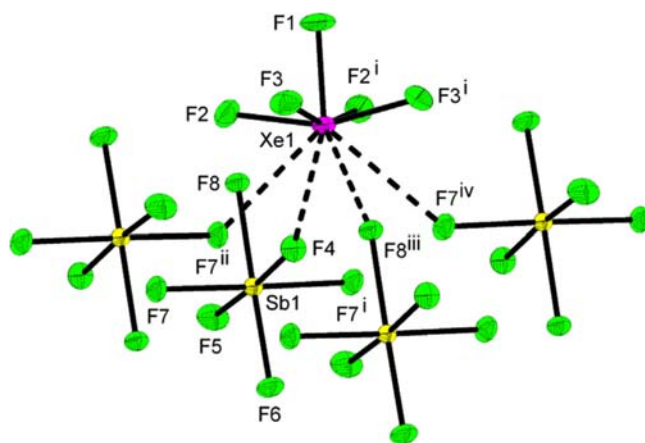
$\text{Cs}[\text{XeF}_5][\text{Bi}_x\text{Sb}_{1-x}\text{F}_6]_2$  ( $x = 0.37\text{--}0.39$ ) were obtained from samples comprised of randomly oriented single crystals.<sup>195</sup> Vibrational bands were assigned by comparison with known salts of  $[\text{XeF}_5]^+$  and  $[\text{SbF}_6]^-$ , and  $[\text{BiF}_6]^-$  in the case of  $\text{Cs}[\text{XeF}_5][\text{Bi}_x\text{Sb}_{1-x}\text{F}_6]_2$ .

(iv)  $[\text{XeF}_5][\text{SbF}_6]$ ,  $[\text{XeF}_5][\text{Sb}_2\text{F}_{11}]$ ,  $[\text{Xe}_2\text{F}_{11}][\text{SbF}_6]$ , and  $[\text{XeF}_5][\text{BF}_4]$ . Crystalline  $[\text{XeF}_5][\text{SbF}_6]$  and  $[\text{XeF}_5][\text{Sb}_2\text{F}_{11}]$  were obtained in the attempted syntheses of mixed ion salts such as  $[\text{NO}_2][\text{XeF}_5][\text{SbF}_6]_2$  by dissolution of their respective salts in aHF solvent followed by slow solvent evaporation over a period of up to two months.<sup>196</sup> Crystalline  $[\text{XeF}_5][\text{SbF}_6]$  was obtained from an equimolar mixture of  $[\text{H}_3\text{O}][\text{SbF}_6]$  and  $[\text{XeF}_5][\text{SbF}_6]$  in aHF. The  $[\text{XeF}_5][\text{Sb}_2\text{F}_{11}]$  salt was prepared by crystallization from an equimolar mixture of  $[\text{O}_2][\text{SbF}_6]$  and  $[\text{XeF}_5][\text{SbF}_6]$  in aHF. Single crystals of  $[\text{NO}_2][\text{XeF}_5][\text{SbF}_6]_2$  were also obtained when attempting to prepare  $[\text{NO}_2][\text{XeF}_5][\text{SbF}_6]_2$  by reaction of  $[\text{XeF}_5][\text{SbF}_6]$  with  $[\text{NO}_2][\text{SbF}_6]$  in aHF.<sup>196</sup>

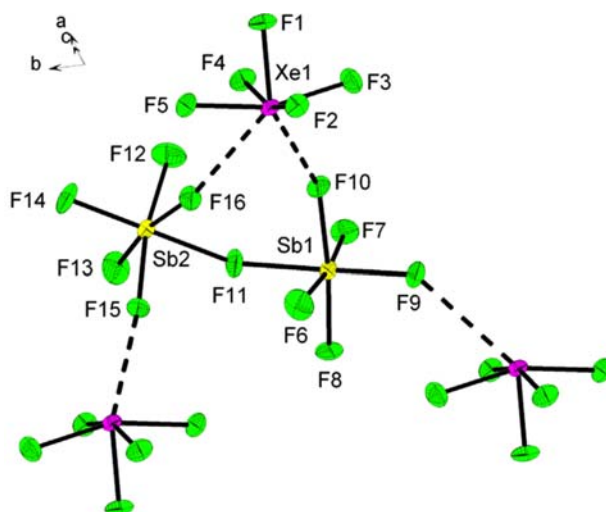
Crystalline  $[\text{Xe}_2\text{F}_{11}][\text{SbF}_6]$  was obtained by reaction of  $\text{Cs}[\text{PF}_6]$  and  $[\text{XeF}_5][\text{SbF}_6]$  in aHF at RT.<sup>195</sup> The reaction proceeded by displacement of  $\text{PF}_5$  by the strong Lewis acid,  $\text{SbF}_5$ , to give  $[\text{Xe}_2\text{F}_{11}][\text{SbF}_6]$  and  $\text{Cs}[\text{SbF}_6]$ , which reacted with the starting material  $[\text{XeF}_5][\text{SbF}_6]$  to give  $\text{Cs}[\text{XeF}_5][\text{SbF}_6]_2$ .<sup>195</sup>

Crystalline  $[\text{XeF}_5][\text{BF}_4]$  was obtained by a metathesis reaction between  $\text{Cs}[\text{BF}_4]$  and  $[\text{XeF}_5][\text{SbF}_6]$ , which led to  $[\text{XeF}_5][\text{BF}_4]$  and  $\text{Cs}[\text{SbF}_6]$ .<sup>195</sup> The latter salt reacted with the starting material  $[\text{XeF}_5][\text{SbF}_6]$  to give  $\text{Cs}[\text{XeF}_5][\text{SbF}_6]_2$ .

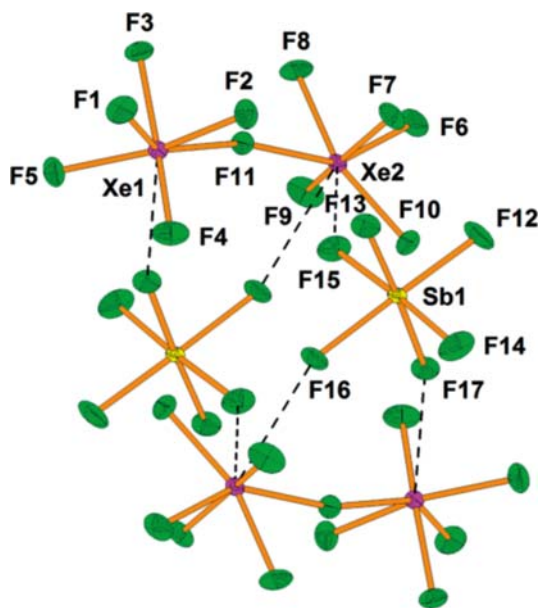
The crystal structure of  $[\text{XeF}_5][\text{SbF}_6]$  is isotypic with those of  $[\text{XeF}_5][\text{MF}_6]$  ( $M = \text{Ru}$ ,<sup>197</sup>  $\text{Pt}$ <sup>198</sup>). The geometric parameters in  $[\text{XeF}_5][\text{SbF}_6]$  are comparable to those of  $[\text{XeF}_5][\text{SbF}_6] \cdot \text{XeOF}_4$ .<sup>110</sup> The crystal structures of  $[\text{XeF}_5][\text{SbF}_6]$  (Fig. 56) and  $[\text{XeF}_5][\text{Sb}_2\text{F}_{11}]$  (Fig. 57) are comprised of strongly ion-paired cations and anions that interact by means of four relatively short Xe...F secondary bonds. Each  $[\text{XeF}_5]^+$  cation has four secondary bonds with four neighboring  $[\text{SbF}_6]^-$  and three neighboring  $[\text{Sb}_2\text{F}_{11}]^-$  anions, giving a total xenon coordination number of 9.



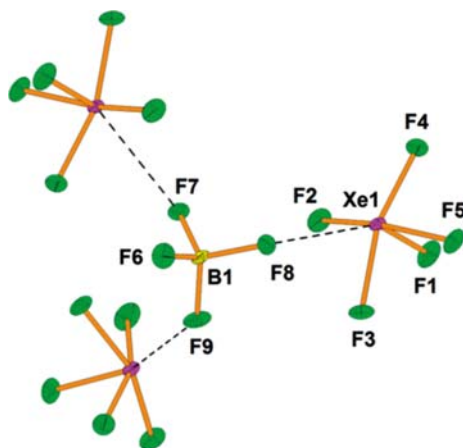
**Fig. 56** A portion of the X-ray crystal structure of the  $[\text{XeF}_5][\text{SbF}_6]$  showing the interactions between the  $[\text{XeF}_5]^+$  cation and  $[\text{SbF}_6]^-$  anions; thermal ellipsoids are drawn at the 50% probability level. Reproduced with permission from Mazej, Z.; Goreschnik, E. *J. Fluorine Chem.* **2015**, 175, 47–50.



**Fig. 57** A portion of the X-ray crystal structure of  $[\text{XeF}_5][\text{Sb}_2\text{F}_{11}]$  showing the interactions between the  $[\text{Sb}_2\text{F}_{11}]^-$  anion and three  $[\text{XeF}_5]^+$  cations; thermal ellipsoids are drawn at the 50% probability level. Reproduced with permission from Mazej, Z.; Goreschnik, E. *J. Fluorine Chem.* **2015**, 175, 47–50.



**Fig. 58** A portion of the X-ray crystal structure of  $[\text{Xe}_2\text{F}_{11}][\text{SbF}_6]$ . Thermal ellipsoids are drawn at the 50% probability level. Reproduced with permission from Mazej, Z.; Goreshnik, E. *Eur. J. Inorg. Chem.* **2017**, 2800–2807.



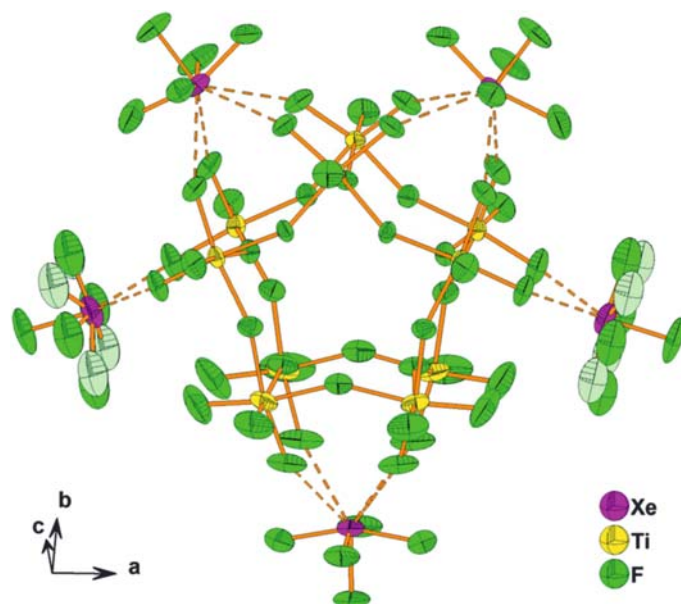
**Fig. 59** A portion of the X-ray crystal structure of  $[\text{XeF}_5][\text{BF}_4]$ . Thermal ellipsoids are drawn at the 50% probability level. Reproduced with permission from Mazej, Z.; Goreshnik, E. *Eur. J. Inorg. Chem.* **2017**, 2800–2807.

High-precision LT SCXRD structures of  $[\text{Xe}_2\text{F}_{11}][\text{SbF}_6]$  (Fig. 58) and  $[\text{XeF}_5][\text{BF}_4]$  (Fig. 59) were obtained,<sup>195</sup> which filled a gap in prior structural studies of  $[\text{XeF}_5]^+$  and  $[\text{Xe}_2\text{F}_{11}]^+$  salts. The geometry of the  $[\text{Xe}_2\text{F}_{11}]^+$  cation in  $[\text{Xe}_2\text{F}_{11}][\text{SbF}_6]$  is comparable to that in  $[\text{Xe}_2\text{F}_{11}][\text{XF}_6]$  ( $X = \text{V},^{199} \text{Au}$ )<sup>200</sup> and in the more recently characterized oxyfluoro-anion salts.<sup>68,69</sup> Each  $[\text{XeF}_5]^+$  cation of  $[\text{XeF}_5][\text{BF}_4]$  forms only three  $\text{Xe}\cdots\text{F}_\text{B}$  secondary bonds between the Xe atom and  $\text{F}_\text{B}$  atoms of  $[\text{BF}_4]^-$ .

(v)  $[\text{XeF}_5][\text{TiF}_5]$ ,  $[\text{XeF}_5]_5[\text{Ti}_{10}\text{F}_{45}]$ , and  $[\text{XeF}_5][\text{Ti}_3\text{F}_{13}]$ . The  $[\text{XeF}_5]_3[\text{Ti}_4\text{F}_{19}]$  salt had been previously synthesized by reaction of  $\text{XeF}_2$ ,  $\text{TiF}_4$ , and UV-irradiated  $\text{F}_2$  in aHF solvent.<sup>111</sup> This result provided impetus to further explore this system by varying the initial molar ratios,  $\text{XeF}_2:\text{TiF}_4$ , for the attempted syntheses of  $[\text{XeF}_5]^+$  and  $[\text{Xe}_2\text{F}_{11}]^+$  salts of new monomeric, oligomeric, and two-dimensional (chains, columns, layered structures) titanium fluoro-anions.

The RT reactions of varying amounts of  $\text{XeF}_2$  with  $\text{TiF}_4$  in the presence of UV-irradiated  $\text{F}_2$  under aHF solvent over ca. 10–20 days yielded mixtures of  $[\text{XeF}_5][\text{TiF}_5]$ ,  $[\text{XeF}_5]_5[\text{Ti}_{10}\text{F}_{45}]$ , and  $[\text{XeF}_5][\text{Ti}_3\text{F}_{13}]$ .<sup>201</sup> The crystalline salts were obtained by a previously described method.<sup>192</sup> Reaction of  $\text{XeF}_2$  with UV-irradiated elemental  $\text{F}_2$  in aHF solvent in the absence of  $\text{TiF}_4$  yielded  $\text{XeF}_4$ . Raman spectroscopy was mainly used to speculate the titanium fluoro-anion salts formed for various reaction mixtures.

Cation-anion interactions in  $[\text{XeF}_5][\text{TiF}_5]$ ,  $[\text{XeF}_5]_5[\text{Ti}_{10}\text{F}_{45}]$ , and  $[\text{XeF}_5][\text{Ti}_3\text{F}_{13}]$  occur through  $\text{Xe}\cdots\text{F}$  secondary bonds that are significantly shorter than the sums of the Xe and F van der Waals radii and are comparable to those of other  $[\text{XeF}_5]^+$  salts. The  $[\text{XeF}_5]_5[\text{Ti}_{10}\text{F}_{45}]$  salt crystallizes in two modifications at low ( $\alpha$ -phase, 150 K) and ambient ( $\beta$ -phase, 296 K) temperatures. The crystal structure of  $[\text{XeF}_5]_5[\text{Ti}_{10}\text{F}_{45}]$  provides the largest known discrete titanium fluoro-anion,  $[\text{Ti}_{10}\text{F}_{45}]^{5-}$ , which is comprised of



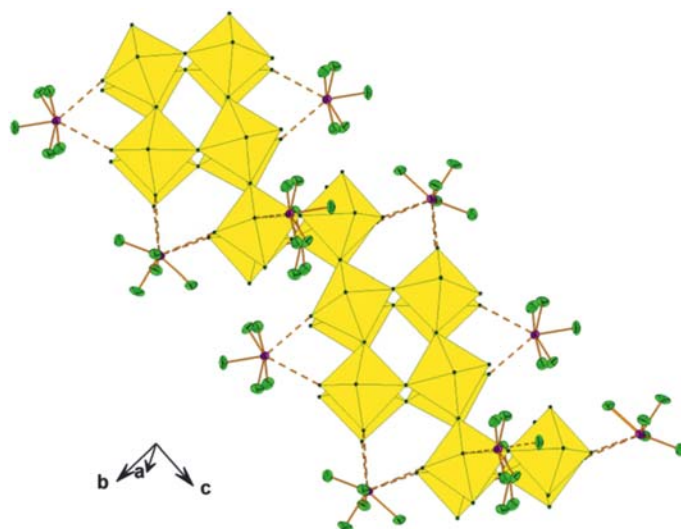
**Fig. 60** The  $[\text{XeF}_5]^+$  cations and  $[\text{Ti}_{10}\text{F}_{45}]^{5-}$  anions in the X-ray crystal structure of  $\beta$ - $[\text{XeF}_5]_5[\text{Ti}_{10}\text{F}_{45}]$ . The thermal ellipsoids are drawn at the 50% probability level. Reproduced with permission from Mazej, Z.; Goresnik, E. *New. J. Chem.* **2016**, *40*, 7320–7325.

10  $\text{TiF}_6$  octahedra that share vertices to form a double-star shaped structural unit (Fig. 60). The  $[\text{XeF}_5]^+$  cations are ordered in the  $\alpha$ -phase, whereas one of three crystallographically unique  $[\text{XeF}_5]^+$  cations is two-fold disordered in the  $\beta$ -phase.

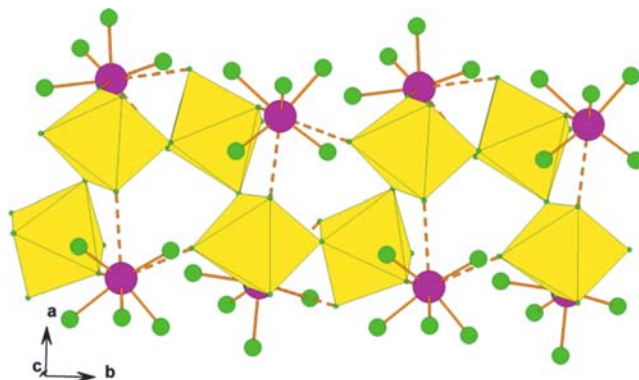
The  $[\text{Ti}_3\text{F}_{13}]^-$  anion in  $[\text{XeF}_5][\text{Ti}_3\text{F}_{13}]$  consists of tetrameric  $\text{Ti}_4\text{F}_{20}$  and octameric  $\text{Ti}_8\text{F}_{36}$  units sharing vertices that are alternately linked to  $([\text{Ti}_3\text{F}_{13}]^-)_\infty$  columns. The  $[\text{XeF}_5]^+$  cations form secondary  $\text{Xe}\cdots\text{F}$  bonds with fluorine atoms of the  $([\text{Ti}_3\text{F}_{13}]^-)_\infty$  columns (Fig. 61).

The main structural feature of  $[\text{XeF}_5][\text{TiF}_5]$  is an infinite chain of distorted  $\text{TiF}_6$  octahedra joined by *cis*-vertices (Fig. 62). Owing to unresolved twinning, the crystal structure of  $[\text{XeF}_5][\text{TiF}_5]$  is of low quality and the structural diagram only provides connectivities.

(vi)  $[\text{XeF}_5]_2[\text{MnF}_6]$ ,  $[\text{XeF}_5][\text{MnF}_5]$ , and  $[\text{XeF}_5]_4[\text{Mn}_4\text{F}_{36}]$ . Reactions of  $\text{MnF}_2$  with  $\text{XeF}_6$  yielded  $4\text{XeF}_6\cdot\text{MnF}_4$ ,  $2\text{XeF}_6\cdot\text{MnF}_4$ ,  $\text{XeF}_6\cdot\text{MnF}_4$ , and  $\text{XeF}_6\cdot 2\text{MnF}_4$ , which were characterized by elemental analysis, IR spectroscopy, and magnetic susceptibility measurements.<sup>133</sup> Although  $4\text{XeF}_6\cdot\text{MnF}_4$  and  $2\text{XeF}_6\cdot\text{MnF}_4$  were formulated as  $[\text{Xe}_2\text{F}_{11}]_2[\text{MnF}_6]$  and  $[\text{XeF}_5]_2[\text{MnF}_6]$  salts based on their vibrational spectra,<sup>202</sup> neither salt has been characterized by SCXRD.



**Fig. 61** A portion of the infinite  $([\text{Ti}_3\text{F}_{13}]^-)_\infty$  column in the X-ray crystal structure of  $[\text{XeF}_5][\text{Ti}_3\text{F}_{13}]$ . Thermal ellipsoids are drawn at the 50% probability level. Reproduced with permission from Mazej, Z.; Goresnik, E. *New. J. Chem.* **2016**, *40*, 7320–7325.



**Fig. 62** A portion of the infinite  $([\text{TiF}_5]^-)_\infty$  chain in the X-ray crystal structure of  $[\text{XeF}_5][\text{Ti}_3\text{F}_{13}]$ . Reproduced with permission from Mazej, Z.; Goreshnik, E. *New. J. Chem.* **2016**, *40*, 7320–7325.

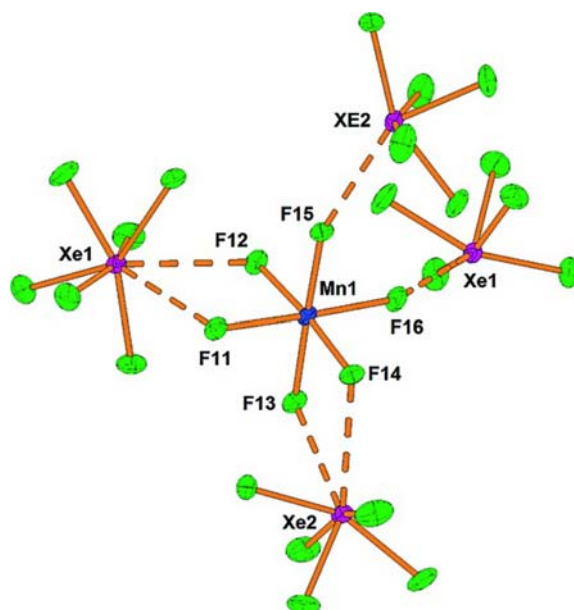
The successful syntheses of  $[\text{XeF}_5][\text{TiF}_5]$ ,  $[\text{XeF}_5]_5[\text{Ti}_{10}\text{F}_{45}]$ , and  $[\text{XeF}_5][\text{Ti}_3\text{F}_{13}]$ , prompted the reactions of  $\text{XeF}_2$  with  $\text{MnF}_3$  and UV-irradiated elemental  $\text{F}_2$  in aHF solvent which yielded  $[\text{XeF}_5]_2[\text{MnF}_6]$ ,  $[\text{XeF}_5][\text{MnF}_5]$ , and small quantities of  $[\text{XeF}_5]_4[\text{Mn}_8\text{F}_{36}]$ .<sup>203</sup> The fluoro-anion salts of Mn are extremely sensitive to irradiation in a He-Ne laser Raman laser beam (power > 1.7 mW), which initially resulted in  $[\text{XeF}_5]_2[\text{MnF}_6]$  decomposition at RT to  $[\text{XeF}_5][\text{MnF}_5]$  and then to  $\text{MnF}_3$  with increasing laser power. The Raman spectra of  $[\text{XeF}_5]_2[\text{MnF}_6]$  and  $[\text{XeF}_5][\text{MnF}_5]$  were obtained at the lowest possible laser power. Although these spectra were of low quality, they confirm the presence of  $[\text{XeF}_5]^+$  and allow assignments of Mn-F stretching frequencies.

The crystal structure of  $[\text{XeF}_5]_2[\text{MnF}_6]$  is isotypic with  $[\text{XeF}_5]_2[\text{PdF}_6]$ ,<sup>105</sup> and has an asymmetric structural unit that consists of two crystallographically unique  $[\text{XeF}_5]^+$  cations and a  $[\text{MnF}_6]^{2-}$  anion (Fig. 63).

The crystal structure of  $\text{XeF}_6 \cdot 2\text{MnF}_4$  shows that this compound is better formulated as  $[\text{XeF}_5]_4[\text{Mn}_8\text{F}_{36}]$  (Fig. 64). The discrete  $[\text{Mn}_8\text{F}_{36}]^{4-}$  anions consist of eight  $\text{MnF}_6$  octahedra, each sharing three vertices, to form a ring that differs from that of the previously known cubic  $[\text{Ti}_8\text{F}_{36}]^{4-}$  anion.<sup>204</sup> The cations and anions interact by means of Xe...F secondary bonds.

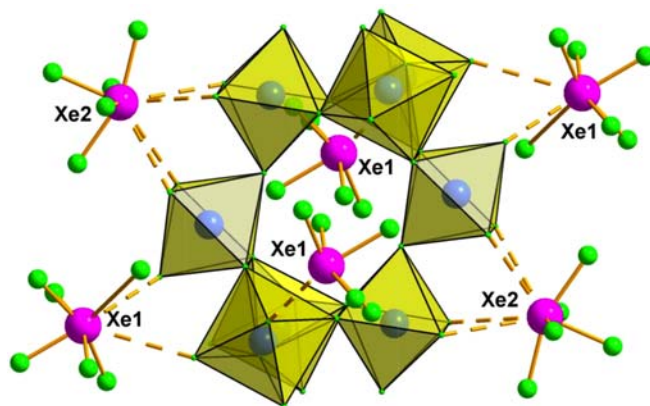
The crystal structure of  $[\text{XeF}_5][\text{MnF}_5]$  (determined from both SCXRD and synchrotron X-ray powder diffraction data) is comprised of infinite zigzag-shaped chains of distorted  $\text{MnF}_6$  octahedra that share *cis*-vertices (Fig. 65). The  $[\text{XeF}_5][\text{MnF}_5]$  salt is paramagnetic in the temperature range 296–200 K, with a Curie constant,  $C = 1.87 \text{ emu K mol}^{-1}$  ( $\mu_{\text{eff}} = 3.87 \mu_{\text{B}}$ ) and a Curie-Weiss temperature,  $\theta = -9.3 \text{ K}$ .

(vii)  $[\text{Xe}_2\text{F}_{11}]_2[\text{SnF}_6]$ ,  $[\text{Xe}_2\text{F}_{11}]_2[\text{PbF}_6]$ , and  $[\text{XeF}_5]_4[\text{Sn}_5\text{F}_{24}]$ . The xenon fluoro-stannates,  $4\text{XeF}_6 \cdot \text{SnF}_4$ ,  $2\text{XeF}_6 \cdot \text{SnF}_4$ ,  $4\text{XeF}_6 \cdot 3\text{SnF}_4$ ,  $3\text{XeF}_6 \cdot 4\text{SnF}_4$ ,  $\text{XeF}_6 \cdot 4\text{SnF}_4$ , fluoro-plumbates  $4\text{XeF}_6 \cdot \text{PbF}_4$ ,  $\text{XeF}_6 \cdot \text{PbF}_4$ ,  $3\text{XeF}_6 \cdot 4\text{PbF}_4$ ,  $\text{XeF}_6 \cdot 4\text{PbF}_4$ , fluoro-zirconate  $\text{XeF}_6 \cdot \text{ZrF}_4$ , and

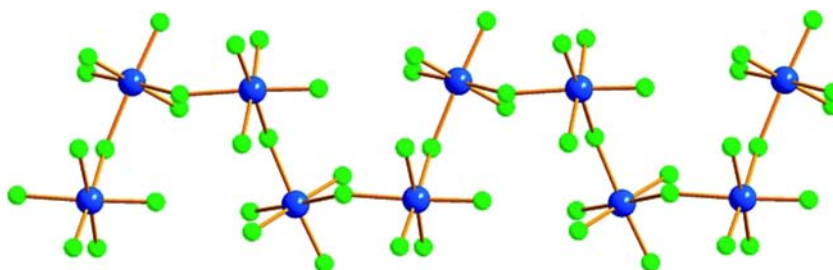


**Fig. 63** The secondary bonds (dashed lines) between the  $[\text{MnF}_6]^{2-}$  anions and  $[\text{XeF}_5]^+$  cations in the X-ray crystal structure of  $[\text{XeF}_5]_2[\text{MnF}_6]$ . Thermal ellipsoids are drawn at the 50% probability level. Reproduced with permission from Mazej, Z.; Goreshnik, E.; Jagličić, Z.; Filinchuck, Y.; Tumanov, N.; Akselrud, L. G. *Eur. J. Inorg. Chem.* **2017**, 2130–2137.





**Fig. 64** The secondary Xe...F bonds between the  $[\text{Mn}_8\text{F}_{36}]^{4-}$  anion and the  $[\text{XeF}_5]^+$  cations in the X-ray crystal structure of  $[\text{XeF}_5]_4[\text{Mn}_8\text{F}_{36}]$ . Thermal ellipsoids are drawn at the 50% probability level. Reproduced with permission from Mazej, Z.; Goreshnik, E.; Jagličić, Z.; Filinchuck, Y.; Tumanov, N.; Akselrud, L. G. *Eur. J. Inorg. Chem.* **2017**, 2130–2137.



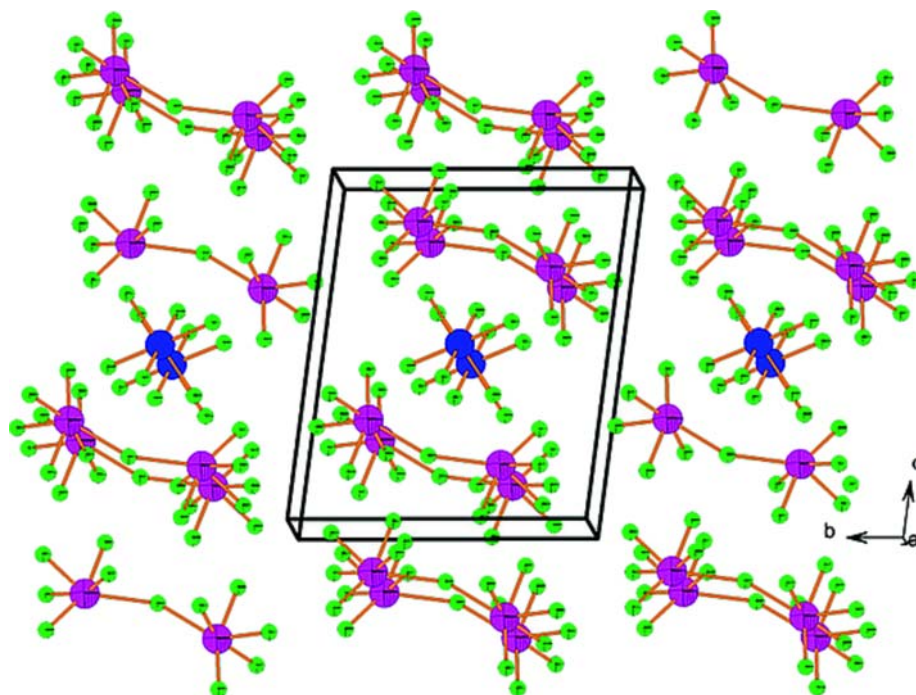
**Fig. 65** A portion of the  $([\text{MnF}_5]^-)_\infty$  infinite chain in the X-ray crystal structure of  $[\text{XeF}_5][\text{MnF}_5]$ . Reproduced with permission from Mazej, Z.; Goreshnik, E.; Jagličić, Z.; Filinchuck, Y.; Tumanov, N.; Akselrud, L. G. *Eur. J. Inorg. Chem.* **2017**, 2130–2137.

fluoro-halfnate  $\text{XeF}_6\cdot\text{HfF}_4$  had only been characterized by mass-balance measurements, chemical analysis, and, in several cases, vibrational spectroscopy.<sup>205</sup> The crystal structures of these complexes were unknown, consequently the reactions of their simple fluorides with  $\text{XeF}_2$  and UV irradiated  $\text{F}_2$  in aHF solution were explored by analogy with  $\text{TiF}_4$  and  $\text{MnF}_4$ . The solid-state structures of their oligomeric, one-dimensional, and two-dimensional anions are of particular interest for comparison with those of Ti and Mn.

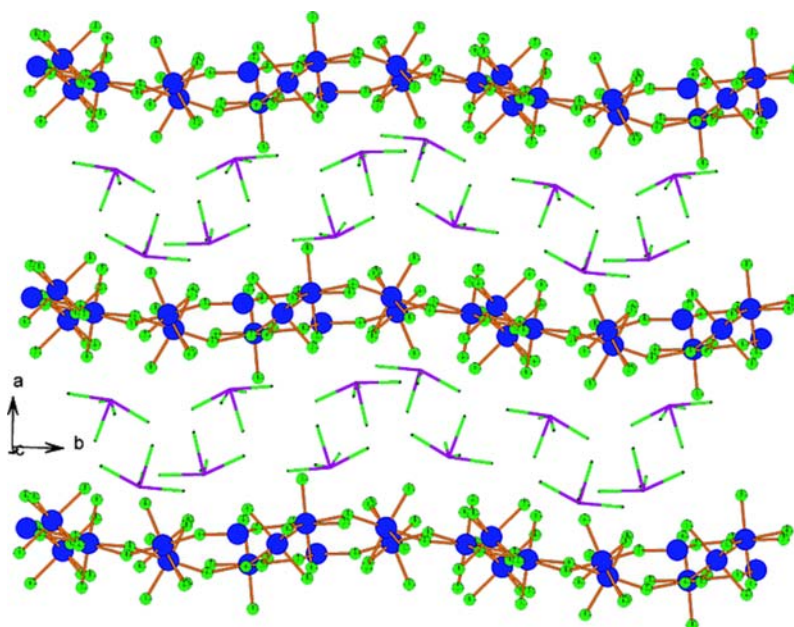
Reaction products were identified by Raman spectroscopy, which showed that only  $[\text{Xe}_2\text{F}_{11}][\text{MF}_6]$  ( $M = \text{Sn}, \text{Pb}$ ),  $4\text{XeF}_6\cdot 3\text{SnF}_4$ , and  $3\text{XeF}_6\cdot 4\text{PbF}_4$  had been synthesized.<sup>205</sup> Single crystals of  $[\text{Xe}_2\text{F}_{11}]_2[\text{SnF}_6]$ ,  $[\text{Xe}_2\text{F}_{11}]_2[\text{PbF}_6]$ , and  $[\text{XeF}_5]_4[\text{Sn}_5\text{F}_{24}]$  were obtained from saturated aHF solutions using a similar prescribed method.<sup>192</sup> Attempts to grow single-crystals of  $3\text{XeF}_6\cdot 4\text{PbF}_4$  failed owing to its insolubility in aHF solvent. Attempts to synthesize and grow single crystals of the  $[\text{XeF}_5][\text{MF}_5]$  ( $M = \text{Zr}, \text{Hf}, \text{Ni}, \text{Pd}$ ) compounds also failed. The Raman spectra of  $[\text{Xe}_2\text{F}_{11}]_2[\text{MF}_6]$  ( $M = \text{Sn}, \text{Pb}$ ) and  $[\text{XeF}_5]_4[\text{Sn}_5\text{F}_{24}]$  were obtained from randomly oriented single crystals.

The crystal structures of  $[\text{Xe}_2\text{F}_{11}]_2[\text{SnF}_6]$  and  $[\text{Xe}_2\text{F}_{11}]_2[\text{PbF}_6]$  consist of discrete  $[\text{Xe}_2\text{F}_{11}]^+$  cations and  $[\text{MF}_6]^{2-}$  anions ( $M = \text{Sn}, \text{Pb}$ ) that interact by means of fluorine bridges (Fig. 66).<sup>205</sup> The geometric parameters of  $[\text{Xe}_2\text{F}_{11}]^+$  in  $[\text{Xe}_2\text{F}_{11}]_2[\text{MF}_6]$  ( $M = \text{Sn}, \text{Pb}$ ) are comparable to those in other  $[\text{Xe}_2\text{F}_{11}]^+$  salts.

The X-ray crystal structure of  $[\text{XeF}_5]_4[\text{Sn}_5\text{F}_{24}]$  consists of two-dimensional undulating grids of  $([\text{Sn}_5\text{F}_{24}]^{4-})_\infty$  anions that alternate with a double layer of  $[\text{XeF}_5]^+$  cations that are sandwiched between them (Fig. 67).<sup>205</sup> The  $([\text{Sn}_5\text{F}_{24}]^{4-})_\infty$  layer is comprised of both six- and seven-coordinate Sn(IV) atoms which are interconnected by bridging fluorine atoms. There are three crystallographically unique Sn atoms in the crystal structure of  $[\text{XeF}_5]_4[\text{Sn}_5\text{F}_{24}]$ , where the primary coordination spheres of Sn1 and Sn3 are regular octahedra as in  $[\text{SnF}_6]^{2-}$ , and that of Sn2 is a pentagonal bipyramid. Seven-coordinate Sn(IV) was unprecedented and provides the first example of a Sn(IV) fluoro-anion having  $\text{CN}_{\text{Sn}} > 6$ . The octahedral coordination spheres of Sn1 and Sn2 result from Xe...F-Sn secondary bonding interactions, whereas the Sn2 atoms with a coordination number of seven exclusively form Sn-F-Sn bridges.



**Fig. 66** A diagram showing the packing of the  $[\text{Xe}_2\text{F}_{11}]^+$  cations and  $[\text{MF}_6]^{2-}$  anions in the X-ray crystal structures of  $[\text{Xe}_2\text{F}_{11}]_2[\text{MF}_6]$  ( $M = \text{Pb}, \text{Sn}$ ). Reproduced with permission from Mazej, Z.; Goreshnik, E. *Eur. J. Inorg. Chem.* **2019**, 1265–1272.



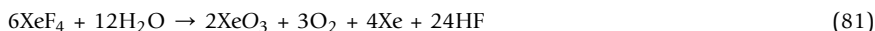
**Fig. 67** The two-dimensional  $([\text{Sn}_5\text{F}_{24}]^{4-})_\infty$  layers with alternating double layers of  $[\text{XeF}_5]^+$  cations sandwiched between them in the X-ray crystal structure of  $[\text{XeF}_5]_4[\text{Sn}_5\text{F}_{24}]$ . For clarity, only the Xe–F bonds of the  $[\text{XeF}_5]^+$  cations are shown. Reproduced with permission from Mazej, Z.; Goreshnik, E. *Eur. J. Inorg. Chem.* **2019**, 1265–1272.

### 1.08.5.3 Chemistry of $\text{XeO}_3$

Xenon trioxide was the first xenon oxide to be synthesized and structurally characterized.<sup>206–209</sup> It is a deliquescent, colorless, endothermic solid compound, that is highly sensitive to mechanical and thermal shock, detonating with the release of  $-402 \pm 8 \text{ kJ mol}^{-1}$  of energy. The kinetic and thermodynamic instabilities of  $\text{XeO}_3$  have hampered its study, particularly in the solid state. Until this study and aside from the X-ray crystal structure of solid  $\text{XeO}_3$ ,<sup>210</sup> the only crystal structures reported that contain the  $\text{XeO}_3$  moiety were those of  $\text{K}[\text{FXeO}_3]$ <sup>211</sup> and  $\text{M}_9(\text{XeO}_3\text{Cl}_2)_4\text{Cl}$ <sup>212</sup> ( $M = \text{Cs}, \text{Rb}$ ); however, the chloro-anion structures were disordered and, along with  $\text{K}[\text{FXeO}_3]$ , are of low precision.

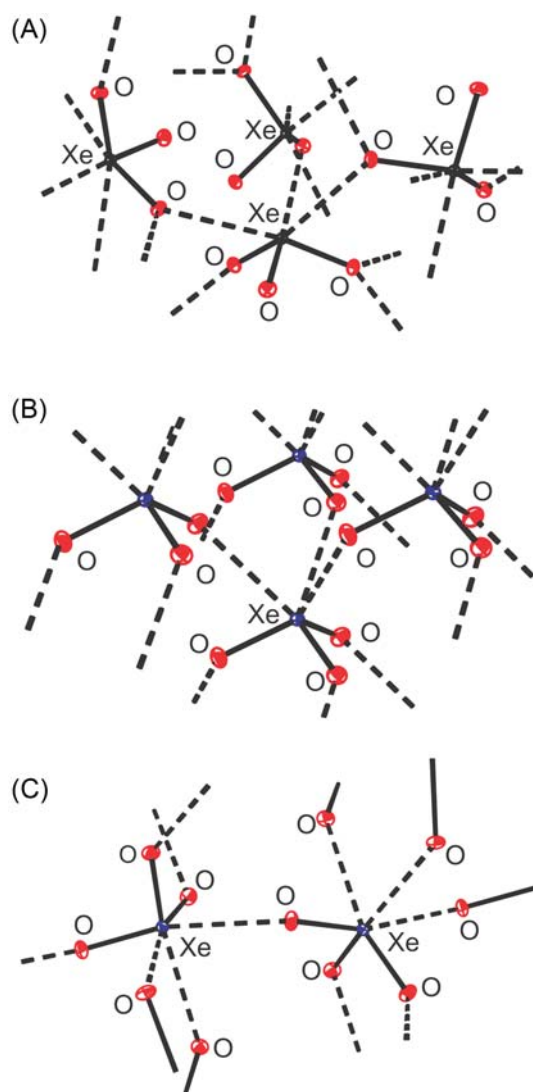
### 1.08.5.3.1 Solid-state structures of XeO<sub>3</sub>: $\alpha$ -XeO<sub>3</sub>, $\beta$ -XeO<sub>3</sub>, and $\gamma$ -XeO<sub>3</sub>

Xenon trioxide has been synthesized by the hydrolysis of XeF<sub>6</sub> or XeF<sub>4</sub> according to Eqs. (80) and (81) respectively.<sup>213</sup> The hydrolysis of XeF<sub>4</sub> proceeds by redox disproportionation through transient bright yellow to yellow-orange XeO<sub>2</sub>,<sup>214</sup> and yields a large molar excess of HF with respect to XeO<sub>3</sub> that results in only one third of the total Xe being converted to XeO<sub>3</sub>. Excess HF is removed by co-evaporation with H<sub>2</sub>O or by neutralization with MgO, however small amounts of residual MgF<sub>2</sub> that contaminate the latter solutions interfere with crystallization, so that co-evaporation of HF/H<sub>2</sub>O is preferred.



The early low-precision X-ray crystal solid-state structure of xenon trioxide, XeO<sub>3</sub>, was reinvestigated by low-temperature SCXRD and shown to exhibit polymorphism that is dependent on crystallization conditions.<sup>213</sup> The previously reported  $\alpha$ -phase (orthorhombic, *P*2<sub>1</sub>2<sub>1</sub>2<sub>1</sub>) was obtained by evaporation of aqueous 48% HF solutions of XeO<sub>3</sub>. Two new phases,  $\beta$ -XeO<sub>3</sub> (rhombohedral, *R*3) and  $\gamma$ -XeO<sub>3</sub> (rhombohedral, *R*3*c*), were also obtained by slow evaporation of aqueous solutions of XeO<sub>3</sub>, where the  $\beta$ -phase was favored with slower solvent evaporation. Crystalline  $\gamma$ -XeO<sub>3</sub> was also obtained by dissolution of XeO<sub>3</sub> in CH<sub>3</sub>CH<sub>2</sub>CN followed by slow solvent evaporation.

The extended structures of all three phases (Fig. 68) result from Xe–O---Xe secondary bridge bond interactions among XeO<sub>3</sub> molecules that arise from the amphoteric donor–acceptor nature of XeO<sub>3</sub>. The Xe atoms of the trigonal-pyramidal XeO<sub>3</sub> units in the crystal structures of  $\alpha$ -XeO<sub>3</sub>,  $\beta$ -XeO<sub>3</sub>, and  $\gamma$ -XeO<sub>3</sub> have three Xe---O secondary bonding interactions. The  $\alpha$ -phase displays the



**Fig. 68** The low-temperature X-ray crystal structures of (A)  $\alpha$ -XeO<sub>3</sub> (*P*2<sub>1</sub>2<sub>1</sub>2<sub>1</sub>), (B)  $\beta$ -XeO<sub>3</sub> (*R*3), and (C)  $\gamma$ -XeO<sub>3</sub> (*R*3*c*) showing their secondary Xe---O bonds. Thermal ellipsoids are drawn at the 50% probability level. Reproduced with permission from Goettel, J. T.; Schrobilgen, G. J. *Inorg. Chem.* **2016**, *55*, 12975–12981.

greatest degree of variation among the contact distances and has a significantly higher density than the  $\beta$ - and  $\gamma$ -phases. Variations among the primary Xe–O bond lengths [1.7558(11)–1.7801(11) Å] and the primary O–Xe–O bond angles [100.51(5)–105.09(6)°] in the  $\alpha$ -phase are greater than those of the  $\beta$ - and  $\gamma$ -phases [ $\beta$ : 1.768(4) Å, 102.9(2)° and  $\gamma$ : 1.763(2)–1.766(2) Å, 101.72(10)–102.52(11)°].<sup>213</sup> The differences likely arise from the range of O-bridged coordination modalities that occur in  $\alpha$ -XeO<sub>3</sub> where only two O atoms have contacts with Xe atoms in the  $\alpha$ -phase [Xe---O; 2.6914(11), 2.8387(12), 2.8403(11) Å], whereas in the  $\beta$ - and  $\gamma$ -phases, all three O atoms have contacts with Xe atoms [ $\beta$ : 2.754(4) Å and  $\gamma$ : 2.678(2)–2.724(2) Å]. The ambient-temperature Raman spectra of solid  $\alpha$ - and  $\gamma$ -XeO<sub>3</sub> have also been obtained and assigned for the first time. The extreme shock sensitivity of solid XeO<sub>3</sub> is largely attributable to extended  $-(\text{---O---Xe---O---Xe---})_n$  networks which occur in all three solid phases of XeO<sub>3</sub> and provide an efficient means to propagate detonation shock waves throughout their respective crystal lattices.

### 1.08.5.3.2 Xenon trioxide adducts of N- and O-donor ligands

A variety of crystalline adducts of XeO<sub>3</sub> with organic oxygen and nitrogen bases have been synthesized and characterized by LT SCXRD and Raman spectroscopy. The XeO<sub>3</sub> adducts exhibit remarkable levels of kinetic stabilization of coordinated XeO<sub>3</sub> relative to the solid phases of XeO<sub>3</sub>. Unlike the crystal structures of XeO<sub>3</sub>, the XeO<sub>3</sub> moieties are better isolated from one another in the adducts, which serves to inhibit decomposition by radical chain propagation.

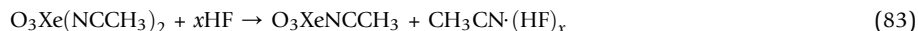
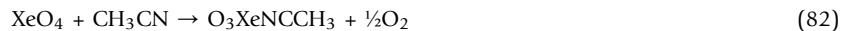
The primary Xe–O bond lengths and O–Xe–O bond angles and Xe---O secondary bonds lie within the bond length and bond angle ranges of the three solid phases of XeO<sub>3</sub>.<sup>213</sup>

The most prominent features in the Raman spectra of the XeO<sub>3</sub> adducts are the Xe–O stretching and bending modes whose assignments were derived from the four Raman-active bands observed for XeO<sub>3(aq)</sub> ( $\nu_{\text{as}}(\text{E})$ , 833;  $\nu_{\text{s}}(\text{A}_1)$ , 780;  $\delta_{\text{umb}}(\text{A}_1)$ , 344;  $\delta_{\text{as}}(\text{E})$ , 317 cm<sup>-1</sup>)<sup>215</sup> and were confirmed by QC calculations.

(i) *Xenon trioxide alkylnitrile adducts.* Xenon trioxide was shown to interact with CH<sub>3</sub>CN and CH<sub>3</sub>CH<sub>2</sub>CN to form O<sub>3</sub>XeNCCH<sub>3</sub>, O<sub>3</sub>Xe(NCCH<sub>3</sub>)<sub>2</sub>, O<sub>3</sub>XeNCCH<sub>2</sub>CH<sub>3</sub>, and O<sub>3</sub>Xe(NCCH<sub>2</sub>CH<sub>3</sub>)<sub>2</sub>.<sup>216</sup>

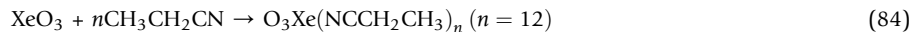
Pure XeO<sub>3</sub> was synthesized by hydrolysis of XeF<sub>6</sub> with three equivalents of water in Freon-114 followed by removal of HF and the solvent under dynamic vacuum between -78 and 0 °C, and CH<sub>3</sub>CN was carefully added to XeO<sub>3</sub> to form O<sub>3</sub>Xe(NCCH<sub>3</sub>)<sub>2</sub>. However, handling of pure XeO<sub>3</sub> without detonation proved to be difficult. A safer and more reliable method was to initially hydrolyze XeF<sub>6</sub> in CH<sub>3</sub>CN solvent at 0 °C. Slow cooling of this solution led to the growth of large block-shaped crystals of O<sub>3</sub>Xe(NCCH<sub>3</sub>)<sub>2</sub> which were structurally characterized by LT SCXRD.

The O<sub>3</sub>XeNCCH<sub>3</sub> complex was initially synthesized by reaction of XeO<sub>4</sub> with CH<sub>3</sub>CN at -40 °C (Eq. 82); as XeO<sub>4</sub> decomposed, large, colorless plates crystallized. An alternative synthesis involving the solvolysis of O<sub>3</sub>Xe(NCCH<sub>3</sub>)<sub>2</sub> in aHF also afforded O<sub>3</sub>XeNCCH<sub>3</sub> and CH<sub>3</sub>CN·(HF)<sub>x</sub> (Eq. 83).



The O<sub>3</sub>XeNCCH<sub>3</sub> complex is a thermodynamically unstable, highly shock-sensitive compound that requires very careful handling. In marked contrast, crystalline O<sub>3</sub>Xe(NCCH<sub>3</sub>)<sub>2</sub> appears to be insensitive to mechanical shock and is kinetically stable at RT, but slowly loses CH<sub>3</sub>CN in air. Crystalline samples did not detonate when struck with a hammer, but detonated on contact with cellulose. The difference in shock sensitivity is likely due to packing differences. Samples of O<sub>3</sub>Xe(NCCH<sub>3</sub>)<sub>2</sub> lost CH<sub>3</sub>CN under dynamic vacuum at -15 °C, which resulted in O<sub>3</sub>XeNCCH<sub>3</sub> formation.

Both O<sub>3</sub>XeNCCH<sub>2</sub>CH<sub>3</sub> and O<sub>3</sub>Xe(NCCH<sub>2</sub>CH<sub>3</sub>)<sub>2</sub> were synthesized by reaction of XeO<sub>3</sub> with neat CH<sub>3</sub>CH<sub>2</sub>CN (Eq. 84). By varying the concentration of XeO<sub>3</sub>, O<sub>3</sub>Xe(NCCH<sub>2</sub>CH<sub>3</sub>)<sub>2</sub> was formed at lower temperatures and lower concentrations, whereas O<sub>3</sub>XeNCCH<sub>2</sub>CH<sub>3</sub> formed at higher temperatures in more concentrated solutions.



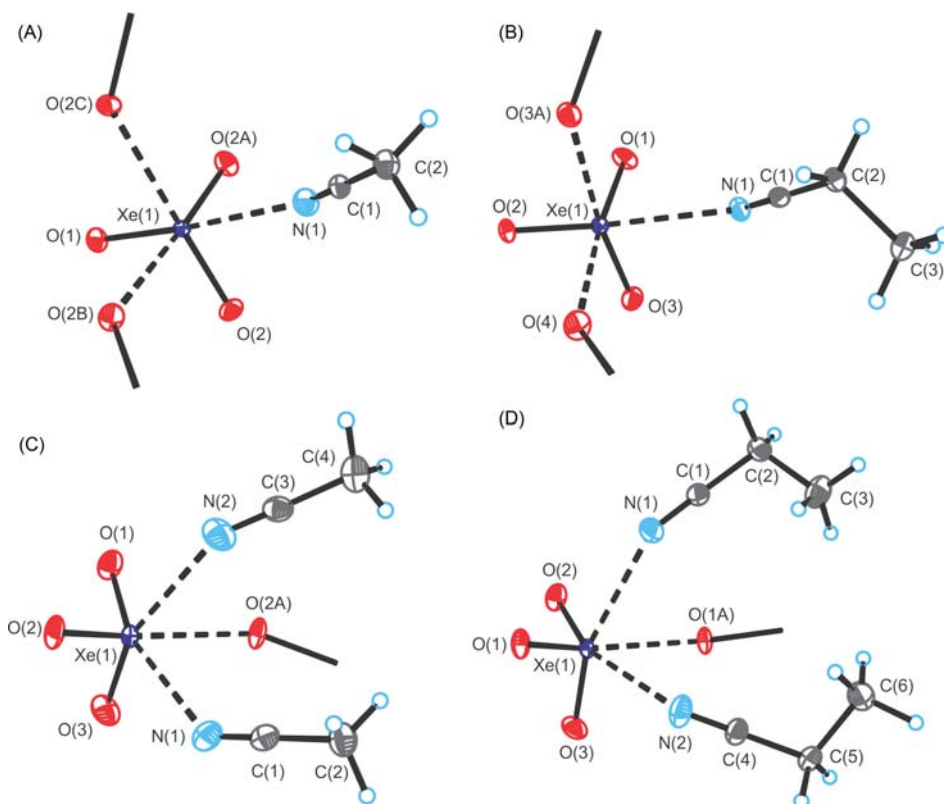
Attempts to isolate O<sub>3</sub>Xe(NCCH<sub>3</sub>)<sub>3</sub> and O<sub>3</sub>Xe(NCCH<sub>2</sub>CH<sub>3</sub>)<sub>3</sub> by use of other solvents such as SO<sub>2</sub>ClF, aHF, and Freon-114 at LT were unsuccessful.

The LT X-ray crystal structures of O<sub>3</sub>XeNCCH<sub>3</sub>, O<sub>3</sub>Xe(NCCH<sub>3</sub>)<sub>2</sub>, O<sub>3</sub>XeNCCH<sub>2</sub>CH<sub>3</sub>, and O<sub>3</sub>Xe(NCCH<sub>2</sub>CH<sub>3</sub>)<sub>2</sub> were obtained (Fig. 69) along their LT Raman spectra. The crystal structure of O<sub>3</sub>XeNCCH<sub>3</sub> consists of layers of trigonal-pyramidal XeO<sub>3</sub> molecules separated by CH<sub>3</sub>CN layers. In contrast, the crystal structure of O<sub>3</sub>Xe(NCCH<sub>3</sub>)<sub>2</sub> is comprised of infinite chains that are well isolated from one another.

The X-ray crystal structures show that the xenon atoms of XeO<sub>3</sub> are coordinated to three donor atoms, to give pseudo-octahedral Xe coordination spheres. The adduct series provides the first examples of a neutral xenon oxide bound to nitrogen bases and are among the first examples of Xe<sup>VI</sup>---N bonds. The Xe---N bond lengths (2.766(2)–2.8560(8) Å, with the shorter Xe---N bonds occurring in O<sub>3</sub>XeNCCH<sub>3</sub> and O<sub>3</sub>XeNCCH<sub>2</sub>CH<sub>3</sub>), are consistent with complex formation. Energy-minimized gas-phase geometries and vibrational frequencies were also obtained for O<sub>3</sub>Xe(NCCH<sub>3</sub>)<sub>n</sub> ( $n = 1$ –3) and O<sub>3</sub>Xe(NCCH<sub>3</sub>)<sub>n</sub>·[O<sub>3</sub>Xe(NCCH<sub>3</sub>)<sub>2</sub>]<sub>2</sub> ( $n = 1, 2$ ). NBO, QTAIM, ELF, and MEPS analyses were carried out to further probe the nature of the bonding in these compounds.

In the Raman spectra,<sup>216</sup> XeO<sub>3</sub> coordination resulted in shifts of the most intense XeO<sub>3</sub> stretching band,  $\nu_{\text{s}}(\text{A}_1)$ , to low frequencies relative to XeO<sub>3(aq)</sub>,<sup>215</sup> with larger shifts being observed for the acetonitrile complexes. A similar trend was observed for the  $\delta_{\text{as}}(\text{E})$  bending modes, whereas those of the  $\delta_{\text{umb}}(\text{A}_1)$  bending modes tend to be shifted to higher frequencies. The frequency of





**Fig. 69** The X-ray crystal structures of (A)  $\text{O}_3\text{XeNCCH}_3$ , (B)  $\text{O}_3\text{Xe}(\text{NCCH}_3)_2$ , (C)  $\text{O}_3\text{XeNCCH}_2\text{CH}_3$ , and (D)  $\text{O}_3\text{Xe}(\text{NCCH}_2\text{CH}_3)_2$ . Thermal ellipsoids are drawn at the 50% probability level. Reproduced with permission from Goettel, J. T.; Matsumoto, K.; Mercier, H. P. A.; Schrobilgen, G. J. *Angew. Chem. Int. Ed.* **2016**, *55*, 13780–13783.

the asymmetric  $\text{XeO}_3$  stretching mode,  $\nu_{\text{as}}(\text{E})$ , bracketted that of aqueous  $\text{XeO}_3$ . The C-N stretching bands exhibit complexation shifts that occur at higher frequencies than those of solid  $\text{CH}_3\text{CN}$  and  $\text{CH}_3\text{CH}_2\text{CN}$ , consistent with adduct formation.

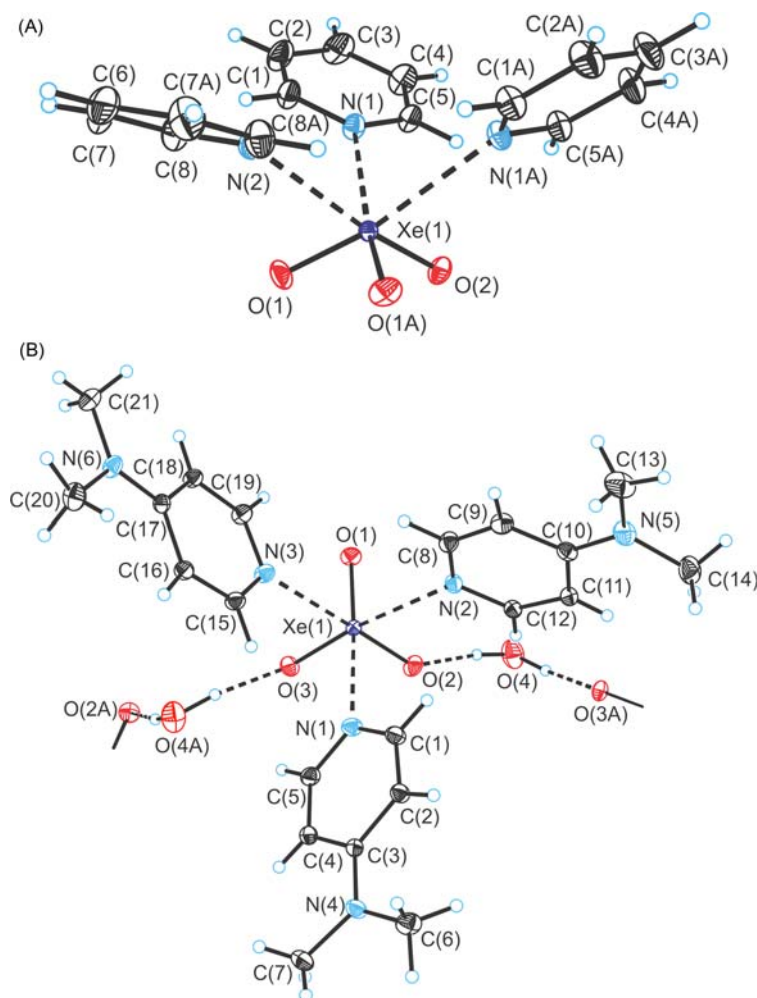
(ii) *XeO<sub>3</sub> adducts of pyridine, 4-dimethylaminopyridine, and their pyridinium salts.* Xenon trioxide forms  $\text{Xe}\cdots\text{N}$  bonded complexes with pyridine and 4-dimethylaminopyridine (4-DMAP).<sup>217</sup> The reactions of pyridine and 4-DMAP with  $\text{XeO}_3$  in rigorously dried  $\text{CH}_3\text{CN}$  and in  $\text{CH}_3\text{CN}$  that had not been dried yielded  $(\text{C}_5\text{H}_5\text{N})_3\text{XeO}_3$  and  $(4-(\text{CH}_3)_2\text{NC}_5\text{H}_5\text{N})_3\text{XeO}_3\cdot\text{H}_2\text{O}$ , respectively, whereas their reactions in HF-acidified  $\text{CH}_3\text{CN}$  yielded  $[\text{C}_5\text{H}_5\text{NH}]_4[\text{HF}_2]_2[\text{F}]_2(\text{XeO}_3)_2$  and  $[4-(\text{CH}_3)_2\text{NC}_5\text{H}_4\text{NH}][\text{HF}_2]\text{XeO}_3$ . Crystalline  $(\text{C}_5\text{H}_5\text{N})_3\text{XeO}_3$ ,  $[\text{C}_5\text{H}_5\text{NH}]_4[\text{HF}_2]_2[\text{F}]_2(\text{XeO}_3)_2$ , and  $[4-(\text{CH}_3)_2\text{NC}_5\text{H}_4\text{NH}][\text{HF}_2]\text{XeO}_3$  failed to detonate when subjected to mechanical shock; however,  $(4-(\text{CH}_3)_2\text{NC}_5\text{H}_5\text{N})_3\text{XeO}_3\cdot\text{H}_2\text{O}$  proved to be more sensitive to mechanical and thermal shock than solid  $\text{XeO}_3$ .

The neutral complexes and their pyridinium-adduct salts were structurally characterized by LT SCXRD and Raman spectroscopy. The crystal structures of  $(\text{C}_5\text{H}_5\text{N})_3\text{XeO}_3$  and  $(4-(\text{CH}_3)_2\text{NC}_5\text{H}_5\text{N})_3\text{XeO}_3\cdot\text{H}_2\text{O}$  consist of  $\text{XeO}_3$  molecules that are N-bonded to three pyridine or 4-DMAP ligands (Fig. 70). A water molecule is also H-bonded to two oxygen atoms of two adjacent  $\text{XeO}_3$  molecules in  $(4-(\text{CH}_3)_2\text{NC}_5\text{H}_5\text{N})_3\text{XeO}_3\cdot\text{H}_2\text{O}$ . The pyridinium cations of  $[\text{C}_5\text{H}_5\text{NH}]_4[\text{HF}_2]_2[\text{F}]_2(\text{XeO}_3)_2$  and  $[4-(\text{CH}_3)_2\text{NC}_5\text{H}_4\text{NH}][\text{HF}_2]\text{XeO}_3$  are H-bonded to  $\text{F}^-$  and/or  $[\text{HF}_2]^-$  ions that are, in turn, F-coordinated to  $\text{XeO}_3$  (Fig. 71). Both  $\text{F}^-$  ions of  $[\text{C}_5\text{H}_5\text{NH}]_4[\text{HF}_2]_2[\text{F}]_2(\text{XeO}_3)_2$  bridge two  $\text{XeO}_3$  molecules to form  $\text{Xe}_2\text{F}_2$ -rings. Each  $[\text{HF}_2]^-$  anion of  $[4-(\text{CH}_3)_2\text{NC}_5\text{H}_4\text{NH}][\text{HF}_2]\text{XeO}_3$  bridges two cations and to two  $\text{XeO}_3$  molecules by means of  $\text{Xe}\cdots\text{F}$  secondary bonds and  $\text{NH}\cdots\text{FH}$ -bonds. Quantum-chemical calculations for  $(\text{C}_5\text{H}_5\text{N})_3\text{XeO}_3$  and  $[\text{C}_5\text{H}_5\text{NH}]_4[\text{HF}_2]_2[\text{F}]_2(\text{XeO}_3)_2$  provided energy-minimized geometries, and calculated vibrational frequencies and intensities which were used to assign their Raman spectra. The NBO analyses showed the  $\text{Xe}\cdots\text{N}$ ,  $\text{Xe}\cdots\text{O}$ , and  $\text{Xe}\cdots\text{F}$  secondary bonds are primarily electrostatic in nature and may be described as  $\sigma$ -hole bonds.

The  $\text{XeO}_3$  stretching and bending modes are very similar to those of  $\text{O}_3\text{Xe}(\text{NCCH}_3)_n$  and  $\text{O}_3\text{Xe}(\text{NCCH}_2\text{CH}_3)_n$  ( $n = 1, 2$ ).<sup>216</sup> Bands assigned to the ring breathing modes of  $(\text{C}_5\text{H}_5\text{N})_3\text{XeO}_3$  and  $[\text{C}_5\text{H}_5\text{NH}]_4[\text{HF}_2]_2[\text{F}]_2(\text{XeO}_3)_2$  are shifted to higher frequencies relative to those of solid  $\text{C}_5\text{H}_5\text{N}$ , consistent with adduct formation. Similar behavior was observed for the  $4-(\text{CH}_3)_2\text{NC}_5\text{H}_4\text{N}$  groups of  $[4-(\text{CH}_3)_2\text{NC}_5\text{H}_4\text{N}]_3\text{XeO}_3\cdot\text{H}_2\text{O}$  and  $[4-(\text{CH}_3)_2\text{NC}_5\text{H}_4\text{NH}][\text{HF}_2]\text{XeO}_3$  where the bands associated with the ring breathing modes are shifted to higher frequencies relative to solid  $(\text{CH}_3)_2\text{NC}_5\text{H}_4\text{N}$ .

(iii) *Xenon trioxide adducts of O-donor ligands;  $[(\text{CH}_3)_2\text{CO}]_3\text{XeO}_3$ ,  $[(\text{CH}_3)_2\text{SO}]_3(\text{XeO}_3)_2$ ,  $(\text{C}_5\text{H}_5\text{NO})_3(\text{XeO}_3)_2$ , and  $[(\text{C}_6\text{H}_5)_3\text{PO}]_2\text{XeO}_3$ .* Xenon trioxide forms adducts with triphenylphosphine oxide, dimethylsulfoxide, pyridine-N-oxide, and acetone by coordination of the ligand oxygen atoms to the  $\text{Xe}^{\text{VI}}$  atom of  $\text{XeO}_3$ .<sup>218</sup> The crystalline complexes were characterized



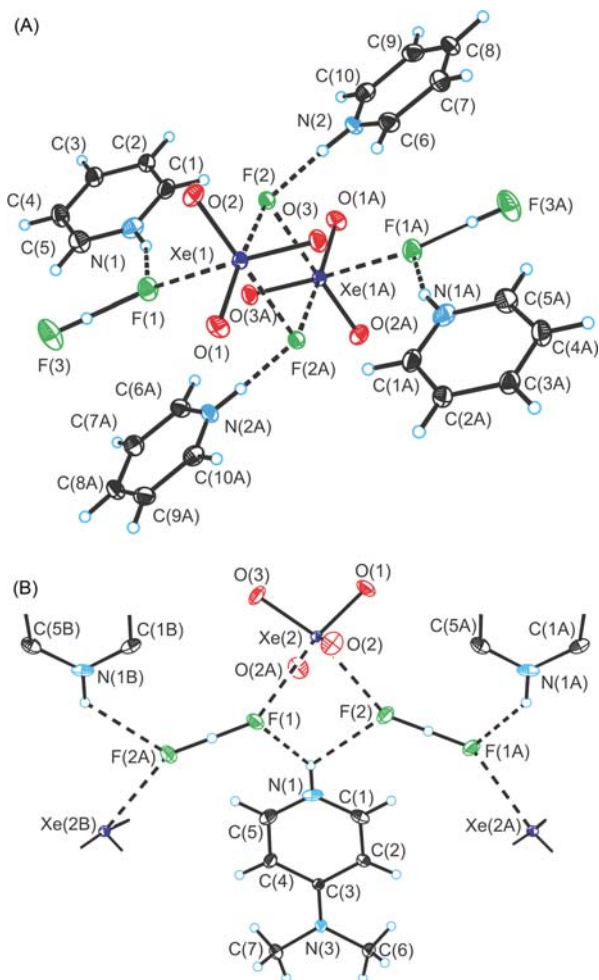


**Fig. 70** The X-ray crystal structures of (A)  $(\text{C}_5\text{H}_5\text{N})_3\text{XeO}_3$  and (B)  $4\text{-(CH}_3)_2\text{NC}_5\text{H}_5\text{N)}_3\text{XeO}_3\cdot\text{H}_2\text{O}$ . Thermal ellipsoids are drawn at the 50% probability level. Reproduced with permission from Goettel, J. T.; Mercier, H. P. A.; Schrobilgen, G. J. *J. Fluorine Chem.* **2018**, *211*, 60–69.

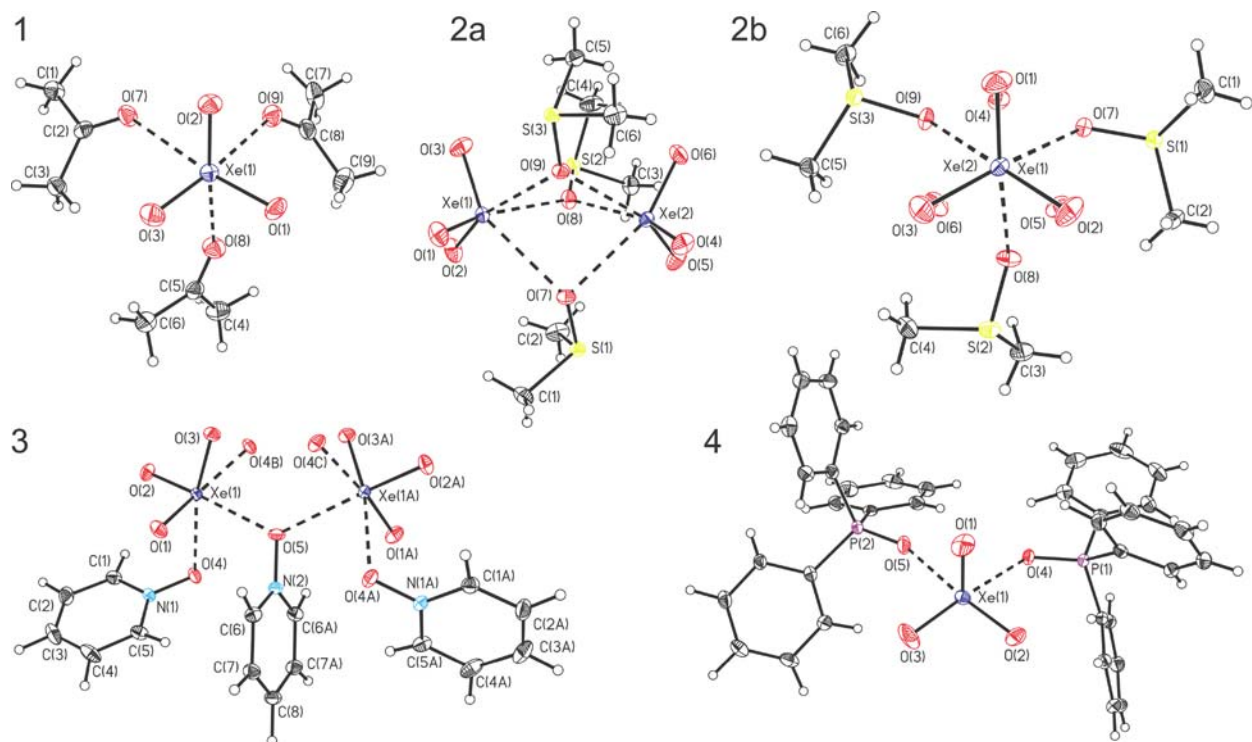
by LT, SCXRD and Raman spectroscopy. Unlike solid  $\text{XeO}_3$ , which detonates when mechanically shocked, solid  $(\text{C}_5\text{H}_5\text{NO})_3(\text{XeO}_3)_2$ ,  $[(\text{C}_6\text{H}_5)_3\text{PO}]_2\text{XeO}_3$ , and  $[(\text{CH}_3)_2\text{SO}]_3(\text{XeO}_3)_2$  are insensitive to mechanical shock. The  $[(\text{CH}_3)_2\text{SO}]_3(\text{XeO}_3)_2$  complex slowly undergoes redox decomposition over several days to  $(\text{CH}_3)_2\text{SO}_2$ , Xe, and  $\text{O}_2$ . All three complexes undergo rapid deflagration when ignited by a flame. Both  $[(\text{C}_6\text{H}_5)_3\text{PO}]_2\text{XeO}_3$  and  $(\text{C}_5\text{H}_5\text{NO})_3(\text{XeO}_3)_2$  are RT stable, whereas  $[(\text{CH}_3)_2\text{CO}]_3\text{XeO}_3$  dissociates at RT to form a stable solution of  $\text{XeO}_3$  in acetone.

The xenon coordination sphere of  $[(\text{C}_6\text{H}_5)_3\text{PO}]_2\text{XeO}_3$ , a distorted square pyramid, provides the first example of a five-coordinate  $\text{XeO}_3$  complex having only two  $\text{Xe}\cdots\text{O}$  bonds with the ligand (Fig. 72). The xenon coordination spheres of the remaining complexes are distorted octahedra comprised of three  $\text{Xe}\cdots\text{O}$  secondary bonds that are approximately *trans* to the primary  $\text{Xe}\text{--}\text{O}$  bonds of  $\text{XeO}_3$  (Fig. 72). Quantum-chemical calculations were used to assess the nature of the  $\text{Xe}\cdots\text{O}$  adduct bonds, which are described as predominantly electrostatic bonds between the nucleophilic oxygen atoms of the bases and the  $\sigma$ -holes of the electrophilic xenon atoms.

Coordination of  $\text{XeO}_3$  also resulted in a frequency shift of the  $\nu_s(\text{A}_1)$  band to lower frequency relative to that of  $\text{XeO}_3(\text{aq})$ .<sup>215</sup> The shift is significantly larger for  $[(\text{CH}_3)_2\text{SO}]_3(\text{XeO}_3)_2$  and  $(\text{C}_5\text{H}_5\text{NO})_3(\text{XeO}_3)_2$ , which correlates with the ligand protonation enthalpies of the four  $\text{XeO}_3$  adducts.<sup>219</sup> A similar trend was observed for the asymmetric  $\text{XeO}_3$  stretching mode,  $\nu_{\text{as}}(\text{E})$ . The frequencies of the  $\delta_{\text{umb}}(\text{A}_1)$  bending modes are essentially unshifted upon complexation, whereas those of the  $\delta_{\text{as}}(\text{E})$  bending modes are shifted to lower frequencies. In contrast with the C–N stretching bands, the P–O and C–O stretching bands are shifted to lower frequencies relative to those of solid  $(\text{C}_6\text{H}_5)_3\text{PO}$  and  $(\text{CH}_3)_2\text{CO}$ , consistent with complex formation. Although  $\nu(\text{S}\text{--}\text{O})$  and  $\nu(\text{N}\text{--}\text{O})$  were not observed, they are also expected to display similar low-frequency shifts relative to  $(\text{CH}_3)_2\text{SO}$  and  $\text{C}_6\text{H}_5\text{NO}$ .



**Fig. 71** The X-ray crystal structures of (A)  $[\text{C}_5\text{H}_5\text{NH}]_4[\text{HF}_2]_2[\text{F}]_2(\text{XeO}_3)_2$  and (B)  $[4\text{-(CH}_3)_2\text{NC}_5\text{H}_4\text{NH}][\text{HF}_2]\text{XeO}_3$ . Thermal ellipsoids are drawn at the 50% probability level. Reproduced with permission from Goettel, J. T.; Mercier, H. P. A.; Schrobilgen, G. J. *J. Fluorine Chem.* **2018**, *211*, 60–69.



**Fig. 72** The structural units in the crystal structures of (1)  $[(\text{CH}_3)_3\text{CO}]_3\text{XeO}_3$ ;  $[(\text{CH}_3)_2\text{SO}]_3(\text{XeO}_3)_2$  viewed (2a) perpendicular to and (2b) along the Xe...Xe axis; (3)  $(\text{C}_5\text{H}_5\text{NO})_3(\text{XeO}_3)_2$ ; and (4)  $[(\text{C}_6\text{H}_5)_3\text{PO}]_2\text{XeO}_3$ . Thermal ellipsoids are drawn at the 50% probability level. Reproduced with permission from Marczenko, K. M.; Goettel, J. T.; Mercier, H. P. A.; Schrobilgen, G. J. *Chem. Eur. J.* **2019**, *25*, 12357–12366.

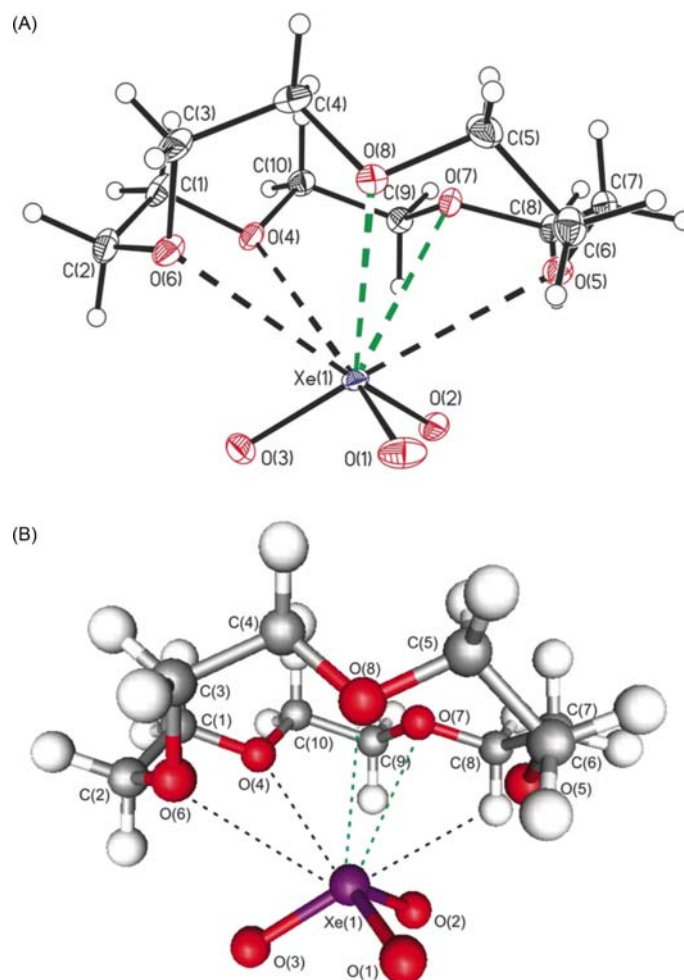
### 1.08.5.3.3 A stable crown ether complex with a noble-gas compound

Crown ethers have been known for over 50 years, but no example of a complex between a noble-gas compound and a crown ether or other polydentate ligand had been previously reported.

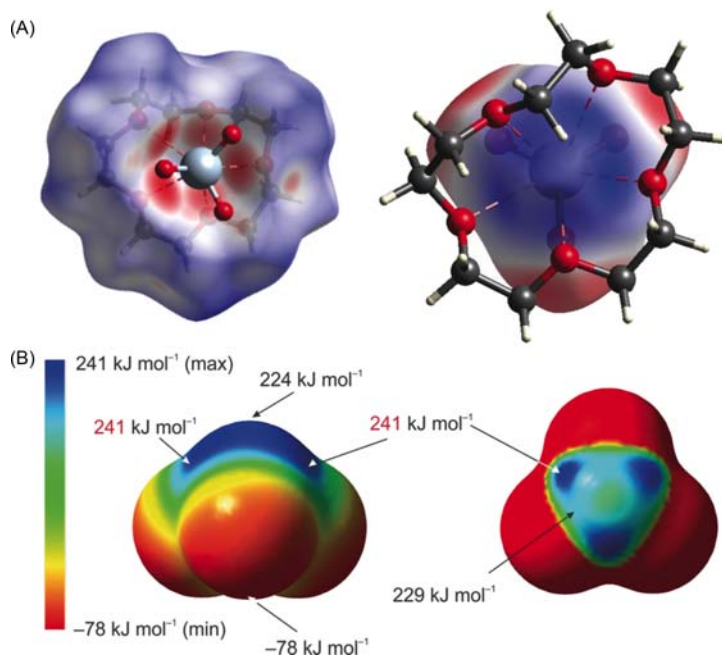
The 15-crown-5 adduct of  $\text{XeO}_3$  was synthesized at RT by reaction of 15-crown-5 with an HF-acidified aqueous solution of  $\text{XeO}_3$  or by addition of liquid 15-crown-5 to a solution of  $\text{XeO}_3$  in acetone at RT.<sup>220</sup> Remarkably, solid  $\text{XeO}_3$  quiescently dissolved in acetone without detonation. In both instances, slow evaporation of the solvent in air gave colorless, block-shaped crystals of  $(\text{CH}_2\text{CH}_2\text{O})_5\text{XeO}_3$ . In marked contrast with solid  $\text{XeO}_3$ , crystalline  $(\text{CH}_2\text{CH}_2\text{O})_5\text{XeO}_3$  failed to detonate when mechanically shocked, but underwent rapid deflagration when ignited in a flame. Raman spectra of the complex were recorded at intervals in air at 20 °C over a period of several days, confirming that the solid adduct is stable at RT and insensitive to atmospheric moisture.

The crystal structure shows that the five oxygen atoms of the crown ether are coordinated to the xenon atom of  $\text{XeO}_3$  (Fig. 73). The complex exhibits the highest xenon coordination number observed thus far for  $\text{XeO}_3$  and is presently the only example of  $\text{XeO}_3$  coordinated to a polydentate ligand. The primary Xe–O bond lengths (1.763(1)–1.767(1) Å) and O–Xe–O bond angles (99.80(5)–102.53(5)°) lie within the bond length and bond angle ranges of the three solid phases of  $\text{XeO}_3$ .<sup>213</sup> The Xe···O secondary bond lengths (2.895(1)–2.970(1) Å) are also similar to those of  $\text{XeO}_3$ , except for two very weak Xe···O bonding interactions (3.114(1), 3.124(1) Å).

The gas-phase Wiberg bond valences and indices and the empirical bond valences indicate that the Xe–O<sub>crown</sub> bonds are predominantly electrostatic and are consistent with  $\sigma$ -hole bonding. Mappings of the electrostatic potential (EP) onto the Hirshfeld surfaces of  $\text{XeO}_3$  and 15-crown-5 in  $(\text{CH}_2\text{CH}_2\text{O})_5\text{XeO}_3$  (Fig. 74) and a detailed examination of the MEPS of  $\text{XeO}_3$  and  $(\text{CH}_2\text{CH}_2\text{O})_5$  reveal regions of negative EP on the oxygen atoms of  $(\text{CH}_2\text{CH}_2\text{O})_5$  and regions of high positive EP on the xenon atom, which are also in accordance with  $\sigma$ -hole interactions.



**Fig. 73** (A) Side-on view of the structural unit in the X-ray crystal structure of  $(\text{CH}_2\text{CH}_2\text{O})_5\text{XeO}_3$  and (B) the calculated gas-phase structure of  $(\text{CH}_2\text{CH}_2\text{O})_5\text{XeO}_3$ . Thermal ellipsoids are drawn at the 50% probability level. The two longest Xe···O contacts are shown in green. Reproduced with permission from Marczenko, K. M.; Mercier, H. P. A.; Schrobilgen, G. J. *Angew. Chem. Int. Ed.* **2018**, *57*, 12448–12452.



**Fig. 74** (A) The Hirshfeld surfaces in  $(\text{CH}_2\text{CH}_2\text{O})_5\text{XeO}_3$  mapped with the  $d_{\text{norm}}$  function of 15-crown-5 (left) and the electrostatic potential surface (B88LYP/321-G) of  $\text{XeO}_3$  (right). (B) The MEPS of  $\text{XeO}_3$  at the 0.001 e·a<sub>0</sub><sup>-3</sup> isosurfaces (right; APFD/Def2-TZVPD) and the top 20% of the positive electrostatic potential range (left; 193–241 kJ mol<sup>-1</sup>). Reproduced with permission from Marzhenko, K. M.; Mercier, H. P. A.; Schrobilgen, G. J. *Angew. Chem. Int. Ed.* **2018**, *57*, 12448–12452.

A lower frequency shift, relative to  $\text{XeO}_{3(\text{aq})}$ , of the most intense  $\nu_{\text{sym}}(\text{A}_1)$  (772 cm<sup>-1</sup>) band confirms complex formation; the remaining  $\text{XeO}_3$  bands of the adduct ( $\nu_{\text{as}}(\text{E})$ : 811, 825, 853 cm<sup>-1</sup>;  $\delta_{\text{umb}}(\text{A}_1)$ : 346, 356 cm<sup>-1</sup>;  $\delta_{\text{as}}(\text{E})$ : 302, 317 cm<sup>-1</sup>) are similar to those of  $\text{XeO}_{3(\text{aq})}$ .

#### 1.08.5.3.4 Stable chloro- and bromoxenate cage anions; $[\text{X}_3(\text{XeO}_3)_3]^{3-}$ and $[\text{X}_4(\text{XeO}_3)_4]^{4-}$ (X = Cl or Br)

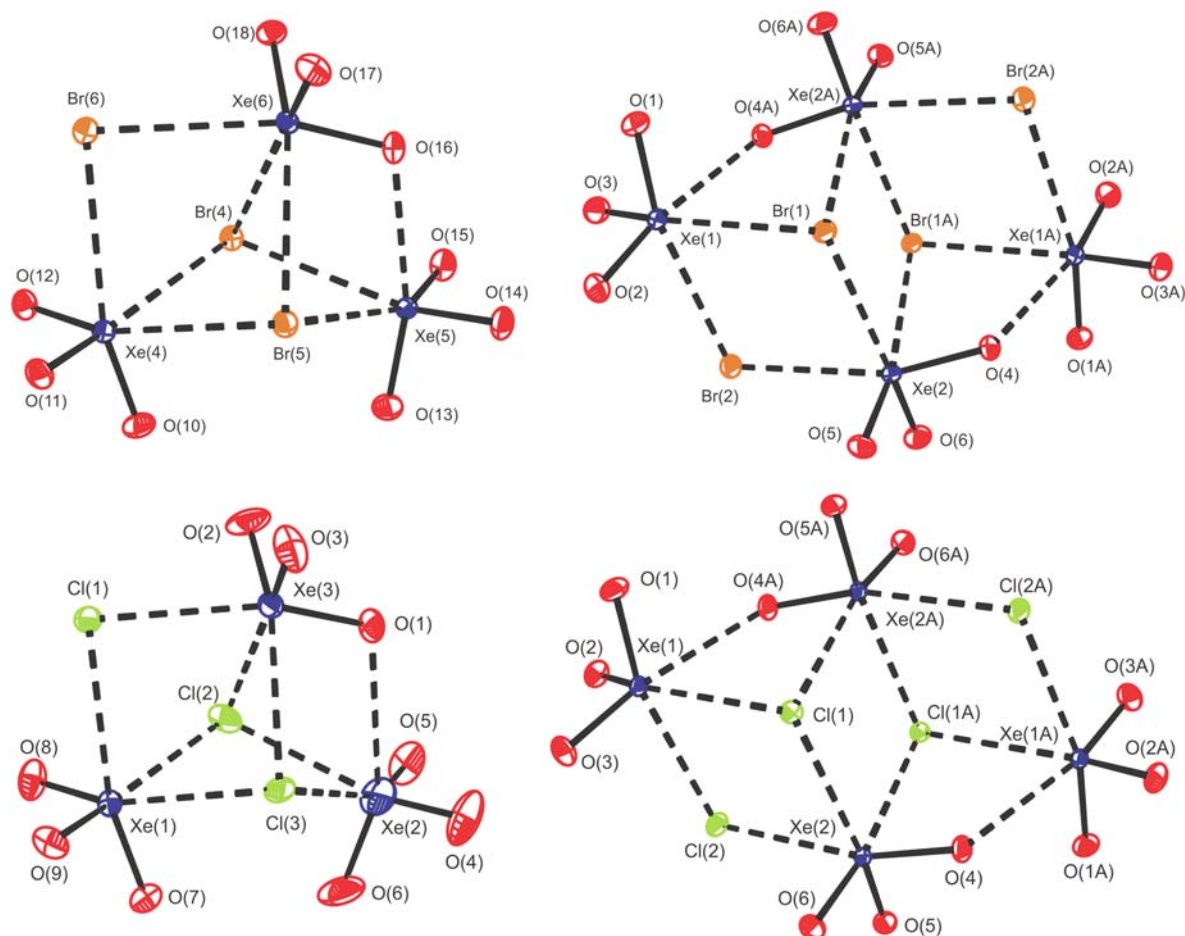
The number of isolable compounds which contain different noble-gas element bonds is limited for xenon and even more so for krypton. Examples of Xe–Cl bonds are rare,<sup>54,212,221</sup> and no Xe–Br bonded compound had been previously isolated and structurally characterized.

The reactions of  $\text{XeO}_3$  with  $[\text{N}(\text{CH}_3)_4]\text{Br}$  and  $[\text{N}(\text{C}_2\text{H}_5)_4]\text{Br}$  provided two bromoxenate salts,  $[\text{N}(\text{C}_2\text{H}_5)_4]_3[\text{Br}_3(\text{XeO}_3)_3] \cdot 2\text{CH}_3\text{CN}$  and  $[\text{N}(\text{CH}_3)_4]_4[\text{Br}_4(\text{XeO}_3)_4]$ .<sup>222</sup> Isostructural chloroxenate salts,  $[\text{N}(\text{C}_2\text{H}_5)_4]_3[\text{Cl}_3(\text{XeO}_3)_3]$  and  $[\text{N}(\text{CH}_3)_4]_4[\text{Cl}_4(\text{XeO}_3)_4]$ , were synthesized by analogy with their bromine analogues. The  $[\text{X}_3(\text{XeO}_3)_3]^{3-}$  and  $[\text{X}_4(\text{XeO}_3)_4]^{4-}$  (X = Br, Cl) anions are the only known cage anions that contain a noble-gas and the  $[\text{Br}_3(\text{XeO}_3)_3]^{3-}$  and  $[\text{Br}_4(\text{XeO}_3)_4]^{4-}$  salts are the first compounds to contain Xe---Br bonds. The bromo- and chloroxenate salts are room-temperature stable in the atmosphere and were characterized in the solid state by Raman spectroscopy and LT SCXRD (Fig. 75), and in the gas phase by quantum-chemical calculations. The Xe atoms occupy bridgehead positions in the cages and the halogen atoms occupy bridging sites, whereas the oxygen atoms occupy bridging and terminal sites. Two types of bridging halogen atoms are found in both anions:  $\mu$ -X atoms that are coordinated to two Xe atoms ( $[\text{X}_3(\text{XeO}_3)_3]^{3-}$ ; Br: 3.1047(7)–3.2649(8) Å and Cl: 2.9448(14), 3.0808(13) Å –  $[\text{X}_4(\text{XeO}_3)_4]^{4-}$ ; Br: 3.0838(3), 3.2132(3) Å and Cl: 2.9316(2), 2.9686(3) Å) and  $\mu_3$ -X atoms that are coordinated to three Xe atoms ( $[\text{X}_3(\text{XeO}_3)_3]^{3-}$ ; Br: 3.1698(7)–3.2738(7) Å and Cl: 3.070(4), 3.101(4) Å –  $[\text{X}_4(\text{XeO}_3)_4]^{4-}$ ; Br: 3.1200(2), 3.1691(2) Å and Cl: 3.0192(2), 3.0967(2) Å). The Xe---Br and Xe---Cl bonds are weakly covalent and can be viewed as  $\sigma$ -hole bonds, similar to those encountered in halogen bonding. The halogen atoms in these cases are valence electron lone pair donors, and the  $\sigma_{\text{Xe-O}}^*$  orbitals are lone pair acceptors. The Xe---O<sub>b</sub> bridge bonds ( $[\text{X}_3(\text{XeO}_3)_3]^{3-}$ ; Br: 1.788(5), 1.794(5) Å and Cl: 1.785(4) Å –  $[\text{X}_4(\text{XeO}_3)_4]^{4-}$ ; Br: 1.7988(11) Å and Cl: 1.7937(7) Å) are slightly longer than the terminal Xe–O<sub>t</sub> bonds ( $[\text{X}_3(\text{XeO}_3)_3]^{3-}$ ; Br: 1.760(6)–1.779(5) Å and Cl: 1.710(11)–1.836(11) Å –  $[\text{X}_4(\text{XeO}_3)_4]^{4-}$ ; Br: 1.7719(14)–1.7753(14) Å and Cl: 1.7714(7)–1.7766(7) Å) which are similar to those of  $\text{XeO}_3$ .<sup>213</sup> The Xe---O<sub>b</sub> distances are somewhat shorter in the Br anions than in their Cl analogues ( $[\text{X}_3(\text{XeO}_3)_3]^{3-}$ ; Br: 2.764(6), 2.861(5) Å and Cl: 2.993(5) Å –  $[\text{X}_4(\text{XeO}_3)_4]^{4-}$ ; Br: 2.7129(12) Å and Cl: 2.7721(7) Å).

The most prominent features in the RT Raman spectra of the haloxenate salts are the Xe–O stretching and bending modes whose assignments were derived from the four Raman-active bands observed for aqueous  $\text{XeO}_3$ , where the frequency shifts are similar to those observed for  $\alpha$ - $\text{XeO}_3$ <sup>213</sup> and the acetonitrile complexes.<sup>216</sup> It was not possible to observe any mode involving Br or Cl, including  $\nu(\text{Xe-Br})$  and  $\nu(\text{Xe-Cl})$ , as they are all expected to occur at low frequencies and to be coupled to  $\text{XeO}_3$  deformation modes.

Attempts to synthesize iodoxenate anions failed because iodide is more readily oxidized than chloride or bromide, and yielded  $[\text{IO}_3]^-$  instead.





**Fig. 75** X-ray crystal structures of the  $[X_3(XeO_3)_3]^{3-}$  and  $[X_4(XeO_3)_4]^{4-}$  anions in  $[N(C_2H_5)_4]_3[X_3(XeO_3)_3]$  and  $[N(CH_3)_4]_4[X_4(XeO_3)_4]$  ( $X = Br, Cl$ ). Thermal ellipsoids are drawn at the 50% probability level. Reproduced with permission from Goettel, J. T.; Haensch, V. G.; Schrobilgen, G. J. *J. Am. Chem. Soc.* **2017**, *139*, 8725–8733.

### 1.08.6 Xenon(VIII) compounds

Isolable compounds containing elements in the +8 oxidation state have only been observed for ruthenium, osmium, xenon, and iridium. Despite its hazardous nature,<sup>223</sup> the molecular structure of gas-phase  $XeO_4$  has been established by electron diffraction<sup>224</sup> and the vibrational frequencies for  $XeO_4$  have been obtained by gas-phase IR spectroscopy,<sup>225</sup> and by Raman spectroscopy in the solid-state<sup>226</sup> and in aHF solution.<sup>227</sup> The shock- and temperature-sensitive nature of  $XeO_4$  has impeded the development of  $Xe^{VIII}$  oxide chemistry, which has been limited to the syntheses and structural characterization of stable salts of the perxenate anion,  $[XeO_6]^{4-}$ ,<sup>142,228–230</sup> and of  $XeO_4$  itself.<sup>224–226</sup> The fluoride precursor for  $Xe^{VIII}$  chemistry,  $XeF_8$ , is unknown, and the only other known  $Xe^{VIII}$  compounds are  $XeO_3F_2$ , which has been characterized by matrix-isolation IR and Raman spectroscopy and in solution by  $^{19}F$  and  $^{129}Xe$  NMR spectroscopy,<sup>231</sup> and  $XeO_2F_4$ , which was characterized in the gas-phase by mass spectroscopy.<sup>232</sup> Both  $XeO_3F_2$  and  $XeO_2F_4$  are prepared by O/F metathesis of  $XeO_4$  with  $XeF_6$ .

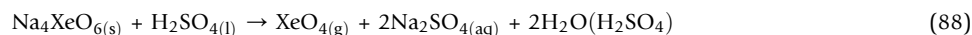
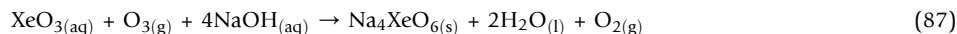
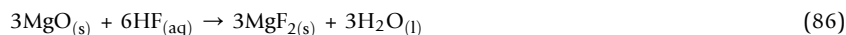
A detailed procedure for the preparation of synthetically useful amounts of  $XeO_4$  in the oxidatively resistant solvents  $SO_2ClF$ ,  $BrF_5$ , and aHF was reported in 2002,<sup>227</sup> allowing for the kinetic stabilization of  $XeO_4$  in solution and, hence, possible further development of  $Xe^{VIII}$  chemistry. In a recent study,  $XeO_4$  was characterized by matrix-isolation spectroscopy and its photolytic behavior was investigated by UV irradiation in Ne, Ar, and  $F_2$  matrices.<sup>233</sup>

#### 1.08.6.1 Infrared spectra of $XeO_4$ and $Na_4[XeO_6]$ in Ne and Ar matrices

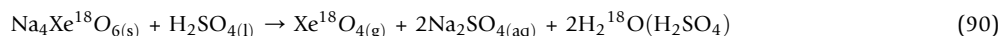
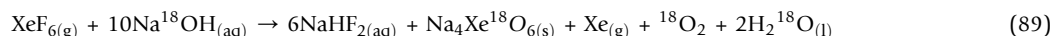
Natural abundance and  $^{18}O$  enriched  $XeO_4$  and  $Na_4XeO_6$  were prepared using modifications of previously published procedures according to Eqs. (85)–(90).



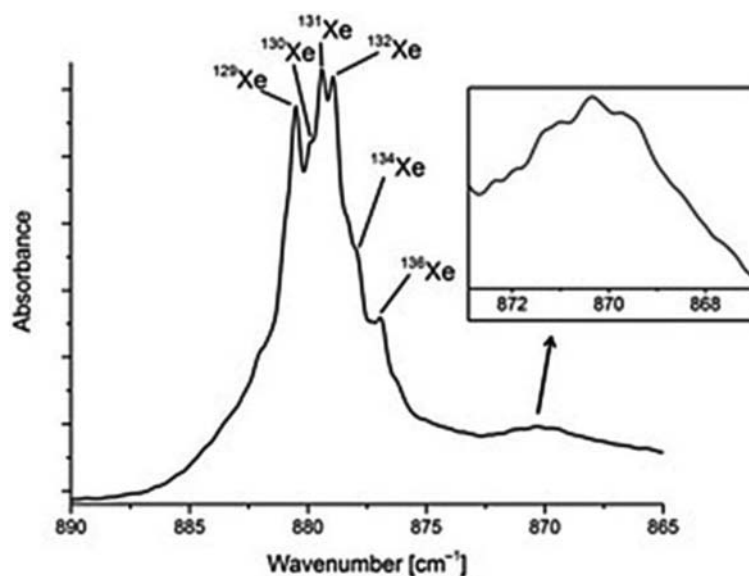




and



Matrix-isolation IR spectroscopy of  $\text{XeO}_4$  in Ne (Fig. 76) and Ar matrices afforded natural abundance xenon isotopic patterns for  $\text{XeO}_4$ , which were in good agreement with calculated harmonic frequencies at the CCSD(T)/aVTZ level of theory (Table 5). Enriched  $\text{Xe}^{18}\text{O}_4$  and mixed  $\text{Xe}^{16/18}\text{O}_4$  isotopomers were prepared and characterized by matrix-isolation IR spectroscopy to provide  $^{16/18}\text{O}$  vibrational frequency shifts for xenon tetroxide (Fig. 77). The calculated isotope shifts of  $\text{XeO}_4$  agree well with experiment. The Raman spectra of natural-abundance and  $^{18}\text{O}$ -enriched  $\text{Na}_4\text{XeO}_6$  were also obtained for comparison with the  $^{16}\text{O}/^{18}\text{O}$  isotopic shifts of  $\text{XeO}_4$  (Table 6). Although the Raman spectrum of  $\text{Na}_4\text{XeO}_6 \cdot 0.4\text{H}_2\text{O}$  has been reported, no definitive assignments of the Raman-active vibrational bands were provided, nor were the  $^{16}\text{O}/^{18}\text{O}$  isotopic shifts of  $[\text{XeO}_6]^{4-}$  reported. Overall, the magnitudes of the  $^{16}\text{O}/^{18}\text{O}$  isotopic shifts of the  $[\text{XeO}_6]^{4-}$  anion are significantly less than those of  $\text{XeO}_4$ , which are consistent with the greater double-bond character of the Xe–O bonds.

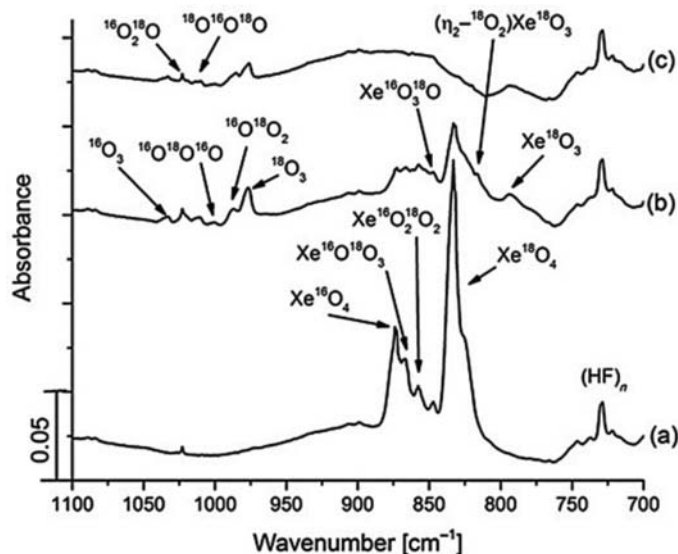


**Fig. 76** The IR spectrum of  $\text{XeO}_4$  in a Ne matrix (4 K) showing the resolved xenon isotopic pattern in the  $\nu_3(\text{T}_2)$  band. Reproduced with permission from Vent-Schmidt, T.; Goettel, J. T.; Schrobilgen, G. J.; Riedel, S. *Chem. Eur. J.* **2015**, *21*, 11244–11252.

**Table 5** Comparison of calculated and observed IR frequencies of  $\nu_3(\text{T}_2)$  for natural abundance (N.A.)  $\text{XeO}_4$  in noble-gas matrices.<sup>a</sup>

Isotopomer (% N.A.)	CCSD(T)	Ne	Ar
$^{129}\text{XeO}_4$ (26.44)	881.9	880.5	874.0
$^{130}\text{XeO}_4$ (4.08)	881.4	879.9	–
$^{131}\text{XeO}_4$ (21.18)	880.9	879.4	873.0
$^{132}\text{XeO}_4$ (26.89)	880.4	878.9	872.6
$^{134}\text{XeO}_4$ (10.44)	879.4	877.9	871.5
$^{136}\text{XeO}_4$ (8.87)	878.4	876.9	870.5

<sup>a</sup>Reproduced with permission from Ref. 233.



**Fig. 77** IR spectra of  $^{18}\text{O}$ -enriched  $\text{XeO}_4$  in an argon matrix for (a) deposition at 10 K for 45 min, (b) photolysis at 365 nm for 150 min, and (c) photolysis with an unfiltered Hg arc for 20 min. Reproduced with permission from Vent-Schmidt, T.; Goettel, J. T.; Schrobilgen, G. J.; Riedel, S. *Chem. Eur. J.* **2015**, *21*, 11244–11252.

**Table 6** Raman frequencies ( $\text{cm}^{-1}$ ) of the perxenate anions in  $\text{Na}_4\text{Xe}^{16}\text{O}_6$  and  $\text{Na}_4\text{Xe}^{18}\text{O}_6$ .<sup>a</sup>

$\text{Na}_4\text{Xe}^{16}\text{O}_6$	$\text{Na}_4\text{Xe}^{18}\text{O}_6$	$\Delta\nu(^{16}/^{18}\text{O})$	$\nu(^{16}\text{O})/\nu(^{18}\text{O})$	Assignment
653.2(100)	618.9(100)	−34.3	1.055	$\nu_1(\text{A}_{1g})$
627.9(38)	596.7(32)	−31.2	1.052	$\nu_2(\text{E}_g)$
611.1 <sup>b</sup>	579.3(3)	−31.9 <sup>b</sup>	1.055 <sup>b</sup>	$\nu_3(\text{T}_{1u})$
486.2(10)	459.6(8)	−26.6	1.058	$\nu_5(\text{T}_{2g})$

<sup>a</sup>Reproduced with permission from Ref. 233.

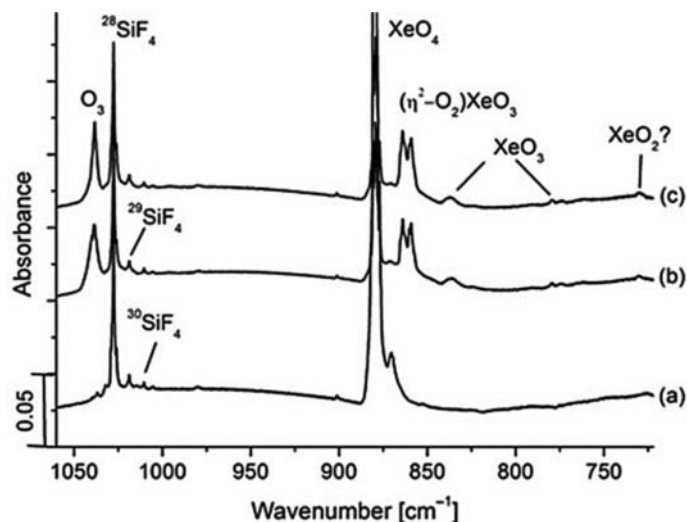
<sup>b</sup>The  $\nu(^{16}\text{O})/\nu(^{18}\text{O})$  value was estimated from the average of its values for  $\nu_1(\text{A}_{1g})$ ,  $\nu_2(\text{E}_g)$  and  $\nu_5(\text{T}_{2g})$ . The frequency for  $\nu_3(\text{T}_{1u})$  of  $\text{Na}_4\text{Xe}^{16}\text{O}_6$  was calculated from the estimated value of  $\nu(^{16}\text{O})/\nu(^{18}\text{O})$  and the experimental value of  $\nu_3(\text{T}_{1u})$  for  $\text{Na}_4\text{Xe}^{18}\text{O}_6$ .

### 1.08.6.2 Photolysis of $\text{XeO}_4$ and formation of $(\eta^2\text{-O}_2)\text{XeO}_3$ and its infrared spectra in Ne, Ar, Kr, and $\text{F}_2$ matrices

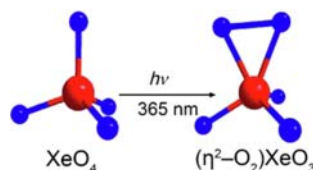
Xenon tetroxide was found to be chemically inert towards neat  $\text{F}_2$  and  $\text{F}_2$ -doped argon and neon matrices under both dark and photolytic conditions at temperatures as high as 40 K. Photodecomposition of  $\text{XeO}_4$  using a mercury arc lamp led to its decomposition without the observation of other xenon oxides or oxide fluorides. In contrast, photodecomposition at 365 nm led to the formation of  $\text{O}_3$ ,  $\text{XeO}_3$ ,  $\text{XeO}_2$ ,  $\text{SiF}_4$  (formed from the reaction of HF contaminant with the glass reactor) and a new set of bands (Fig. 78) that were assigned to a new Xe(VIII) oxide,  $(\eta^2\text{-O}_2)\text{XeO}_3$ , based on comparisons with quantum-chemical calculations (Fig. 79, Table 7).<sup>233</sup>

Photodecomposition of  $\text{Xe}^{18}\text{O}_4$  and mixed  $\text{Xe}^{16/18}\text{O}_4$  isotopomers at 365 nm led to the formation of  $^{18}\text{O}$  enriched  $(\eta^2\text{-}^{18}\text{O}_2)\text{Xe}^{18}\text{O}_3$ . The calculated isotopic shifts of  $(\eta^2\text{-}^{18}\text{O}_2)\text{Xe}^{18}\text{O}_3$  agree well with their observed shifts, which provide further support for the photolytic formation of  $(\eta^2\text{-O}_2)\text{XeO}_3$  (Table 7).

Calculations of the UV spectrum of  $\text{XeO}_4$  show that photodecomposition is induced by a  $n \rightarrow \sigma^*$  transition, but the nature of the excitation differs when different light sources are used. The main excitation for  $\text{XeO}_4$  in the 200–300 nm range is a singlet at 250 nm, whereas excitation at 365 nm results in a spin-forbidden triplet transition at 350 nm. Prior kinetic measurements showed that the reaction  $\text{XeO}_4 + h\nu \rightarrow \text{Xe} + 4\text{O}$  dominates photodecomposition when a 200–300 nm source is used, and a similar dissociation has also been calculated in this region for  $\text{XeO}_3$ . The predicted photolytic behavior of  $\text{XeO}_4$  is therefore consistent with its complete decomposition upon irradiation with a mercury arc lamp. Photolysis of  $\text{XeO}_4$  at wavelengths exceeding 300 nm also produces  $\text{XeO}_3$ , however further photodissociation is not predicted or observed. The formation of  $\text{XeO}_3$  allows for the formation of mobile  $^1\text{D}$  excited O atoms in the case of excitation at 365 nm, which may then react, on the basis of reaction enthalpies, with  $\text{XeO}_4$  to form  $(\eta^2\text{-O}_2)\text{XeO}_3$  (exothermic by  $33.6 \text{ kJ mol}^{-1}$ ). TDDFT and CC2 calculations indicate that the photogeneration of O atoms is dependent on the excitation wavelength and whether this excitation leads to a singlet or triplet state. Although the



**Fig. 78** The IR spectra of  $\text{XeO}_4$  in a neon matrix, (a)  $\text{XeO}_4$  deposition at 3.5 K for 45 min, (b) photolysis at 365 nm for 105 min, and (c) annealed to 11 K. Reproduced with permission from Vent-Schmidt, T.; Goettel, J. T.; Schrobilgen, G. J.; Riedel, S. *Chem. Eur. J.* **2015**, *21*, 11244–11252.



**Fig. 79** Optimized geometry of  $\text{XeO}_4$  and  $(\eta^2\text{-O}_2)\text{XeO}_3$ . Reproduced with permission from Vent-Schmidt, T.; Goettel, J. T.; Schrobilgen, G. J.; Riedel, S. *Chem. Eur. J.* **2015**, *21*, 11244–11252.

**Table 7** Observed frequencies ( $\text{cm}^{-1}$ ) for  $(\eta^2\text{-O}_2)\text{XeO}_3$  obtained after irradiation of  $\text{XeO}_4$  at 365 nm in various matrices.<sup>a</sup>

Ne	Ar	Kr	$F_2$	B3LYP	CCSD(T)	Assignment
864.0	856.8			836.9	878.4	$\nu_9(\eta^2\text{-}^{16}\text{O}_2)\text{Xe}^{16}\text{O}_3$
859.1						
860.4	852.4	856	858	835.9	870.8	$\nu_1(\eta^2\text{-}^{16}\text{O}_2)\text{Xe}^{16}\text{O}_3$
822.4					836.5	$\nu_9(\eta^2\text{-}^{18}\text{O}_2)\text{Xe}^{18}\text{O}_3$
818.7	817.0				827.9	$\nu_1(\eta^2\text{-}^{18}\text{O}_2)\text{Xe}^{18}\text{O}_3$

<sup>a</sup>Data from Ref. 233.

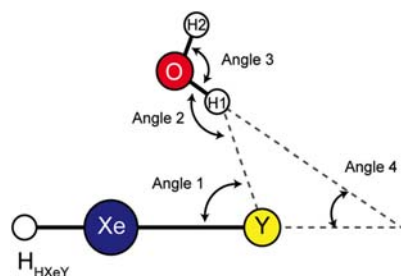
determination of the exact reaction pathway was beyond the scope of this study, there is strong evidence that the oxygen atoms that form are in the  $^1\text{D}$  state and are mobile in noble-gas matrices.

The bonding in  $(\eta^2\text{-O}_2)\text{XeO}_3$  was explored by an NBO analysis which showed that the coordinated  $\eta^2\text{-O}_2$  fragment in  $(\eta^2\text{-O}_2)\text{XeO}_3$  is covalently bound to the  $\text{XeO}_3$  fragment. Comparisons of calculated bond lengths and Mayer bond orders show that the Xe–O bonds of the  $\eta^2\text{-O}_2$  fragment of  $(\eta^2\text{-O}_2)\text{XeO}_3$  are somewhat weaker than the Xe–O bonds of  $\text{XeO}_4$ . Accordingly, the O–O bond in  $(\eta^2\text{-O}_2)\text{XeO}_3$  is somewhat weaker than that of gas-phase  $\text{O}_2$ . Analysis of the donor-acceptor contributions reveals strong hyperconjugation from all bonding Xe–O orbitals into neighboring antibonding Xe–O orbitals, which results in extensive electron delocalization and Xe–O bond stabilization through mesomeric effects.

### 1.08.7 Noble-gas molecules characterized by matrix isolation

An interesting aspect of noble-gas chemistry is the formation and study of unstable compounds that are formulated as  $\text{XNgY}$  molecules (Ng is a noble-gas atom, Y is an electronegative atom or group) that are isolated in low-temperature matrices and structurally





**Fig. 80** The structure ( $C_s$  symmetry, planar) of the  $\text{HXeY}\cdots\text{H}_2\text{O}$  complex. Reproduced with permission from Tsuge, M.; Berski, S.; Räsänen, M.; Latajka, Z.; Khriachtchev, L. *J. Chem. Phys.* **2014**, *140*, 044323.

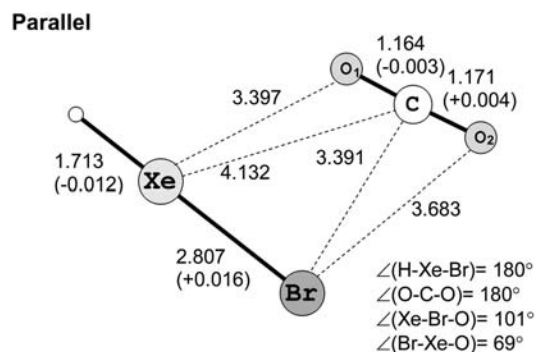
The stabilities of  $\text{HXeY}$  ( $Y = \text{Cl}, \text{Br}, \text{I}$ ) molecules make them suitable for studies that assess matrix effects, namely, correlations between bond strength and the complexation shift. Numerous matrix-isolated  $\text{HXeY}\cdots\text{X}$  complexes have been formed that provide a variety of new van der Waals complexes, i.e.,  $\text{HXeCl}\cdots\text{H}_2\text{O}$ ,<sup>241,242</sup>  $\text{HXeBr}\cdots\text{H}_2\text{O}$ ,<sup>241</sup>  $\text{HXeBr}\cdots\text{CO}_2$ ,<sup>243</sup>  $\text{HXeI}\cdots\text{H}_2\text{O}$ ,<sup>241</sup>  $\text{HXeI}\cdots\text{HCCH}$ ,<sup>244</sup>  $\text{HXeI}\cdots\text{HCl}$ ,<sup>244</sup>  $\text{HXeI}\cdots\text{HBr}$ ,<sup>245</sup>  $\text{HXeI}\cdots\text{HI}$ .<sup>245</sup> The formation of a  $\text{HNgY}\cdots\text{X}$  complex usually entails photodissociation of the  $\text{HY}\cdots\text{X}$  complex in a noble-gas matrix followed by a thermal annealing-induced reaction (Eq. 92).



For  $\text{HXeY}\cdots\text{H}_2\text{O}$  complexes ( $Y = \text{Cl}, \text{Br}, \text{and I}$ ),<sup>241</sup> the precursors are the  $\text{HY}\cdots\text{H}_2\text{O}$  complexes that are photolyzed by irradiation at 193 nm to form an H atom and  $\text{Y}\cdots\text{H}_2\text{O}$  in a Xe matrix. Annealing above 35 K mobilizes the H atoms, and the reaction  $\text{H} + \text{Xe} + (\text{Y}\cdots\text{H}_2\text{O})$  yields the corresponding  $\text{HXeY}\cdots\text{H}_2\text{O}$  complex. In all cases, the IR spectra show extensive splitting of the  $\nu(\text{Xe-H})$  stretching bands. The Xe-H stretching bands of the  $\text{HXeY}\cdots\text{H}_2\text{O}$  complexes occur at 1710.6 and 1730.3  $\text{cm}^{-1}$  (Cl), 1568.8, 1573.6, 1577.0, 1595.3, and 1605.0  $\text{cm}^{-1}$  (Br), and 1267.0, 1280.0, and 1331.6  $\text{cm}^{-1}$  (I). The monomer-to-complex shifts increase in the order  $\text{I} > \text{Br} > \text{Cl}$ , consistent with a significant increase in the complexation effect for more weakly bound molecules. Calculations show that the most stable structures for the  $\text{HXeY}\cdots\text{H}_2\text{O}$  complexes are planar with bent  $(\text{HO})\text{H}\cdots\text{Y}-\text{Xe}$  angles (Fig. 80). Using this model, the calculated H-Xe stretching frequency shifts increase from Cl to I, in accordance with experiment.

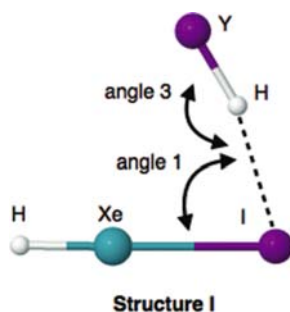
The thermal decomposition of  $\text{HXeCl}\cdots\text{H}_2\text{O}$  in a Xe matrix has also been investigated.<sup>242</sup> The identification of  $\text{HCl}\cdots\text{H}_2\text{O}$  as a decomposition product showed that the decomposition channel is a unimolecular, two-body decomposition, in agreement with theoretical predictions.

The  $\text{HXeBr}\cdots\text{CO}_2$  complex was formed by photolysis of  $\text{HBr}\cdots\text{CO}_2$  trapped in a Xe matrix followed by thermal mobilization of its H-atom.<sup>243</sup> The Xe-H stretch of  $\text{HXeBr}\cdots\text{CO}_2$  was observed at 1557  $\text{cm}^{-1}$ , 53  $\text{cm}^{-1}$  higher than that of the  $\text{HXeBr}$  monomer. The high-frequency shift of  $\text{HXeBr}\cdots\text{CO}_2$  is greater than that of  $\text{HXeBr}\cdots\text{N}_2$  where the Xe-H stretch was observed at 1515.5 and 1520  $\text{cm}^{-1}$  (shifts of 11.5 and 16  $\text{cm}^{-1}$ , respectively),<sup>238</sup> indicating that quadrupole moments play a significant role in stabilizing the Xe-H bond. Parallel and linear structures were found computationally, where the parallel structure was found to be more stable (Fig. 81). An important finding from this study is the formation of  $\text{HXeBr}$  in  $\text{CO}_2$  ice,<sup>243</sup> which is the first observation of a noble-gas hydride in a molecular solid. Deuterated  $\text{DXeBr}$  was also formed to confirm the assignment of the Xe-H stretching frequency. The



**Fig. 81** The structure of the parallel  $\text{HXeBr}\cdots\text{CO}_2$  complex (CCSD(T)/aug-cc-pVTZ-PP), bond lengths are in Å. The values in parentheses show the effect of the complex formation relative to free  $\text{HXeBr}$  and  $\text{CO}_2$  optimized at the same level of theory. Reproduced with permission from Tsuge M., Berski S., Stachowski R., Räsänen M., Latajka Z., Khriachtchev L. *J. Phys. Chem.*, **2012**, *116*, 4510–4517.





**Fig. 82** The most stable structure for the HXeI...HY complexes (Y = Br and I; MP2(full)/def2-TZVPPD and CCSD(T)/def2-TZVPPD). Reproduced with permission from Tsuge, M.; Berski, S.; Räsänen, M.; Latajka, Z.; Khriachtchev, L. *J. Chem. Phys.* **2013**, *138*, 104314.

Xe-H/D stretching frequencies of HXeBr and DXeBr in CO<sub>2</sub> matrices are 1646 and 1200 cm<sup>-1</sup>, respectively, with a  $\nu(\text{Xe-H})/\nu(\text{Xe-D})$  ratio of 1.372. The large matrix-induced shift difference between CO<sub>2</sub> and Ne matrices ( $\sim 200$  cm<sup>-1</sup>) indicates a significant degree of Xe-H bond stabilization by the CO<sub>2</sub> matrix molecules. The HXeBr molecule is stable in a CO<sub>2</sub> matrix, well above the cryogenic limit of at least 100 K, i.e., under conditions that may occur in nature.

The HXeI...HY (Y = Cl,<sup>244</sup> Br,<sup>245</sup> I)<sup>245</sup> complexes were obtained by irradiation and annealing of HI/HY/Xe matrices containing varying ratios of HI and HY. The use of different HI/HY ratios revealed concentration dependencies in the HXe and HY regions of the IR spectra, i.e., the relative amounts of HI and HY were correlated with the intensities of new bands, allowing their assignments to HXeI...HY complexes. Six new bands were assigned to HXeI...HCl bands at 1287, 1304, 1348 cm<sup>-1</sup>, which are shifted by +94, +111, and +155 cm<sup>-1</sup> from the HXeI monomer bands and bands at 2501, 2586, and 2651 cm<sup>-1</sup>, which are shifted by -337, -252, and -187 cm<sup>-1</sup> from the Q branch of monomeric HCl.<sup>244</sup> Similar complexation shifts were observed for HXeI...HBr (1281.0, 1302.7, 1349.9 and 2254.2 and 2141.5 cm<sup>-1</sup>) and HXeI...HCl (1230.4, 1268.0, 1289.2 and 2048.0 cm<sup>-1</sup>).<sup>245</sup> In all cases, the experimental complexation shifts were best reproduced using a model in which the structure is stabilized by an H...I hydrogen bond (Fig. 82). Irradiation and annealing of HI/HCCH/Xe matrices resulted in a new band at 1242 cm<sup>-1</sup> that was assigned to  $\nu(\text{Xe-H})$  of HXeI...HCCH.<sup>244</sup>

The xenon hydrides, HXeH and HXeSH, have been shown to be remarkably stable, if not the most stable xenon hydrides obtained thus far by matrix-isolation techniques.<sup>246,247</sup> Comparative studies of the photoinduced transformations of HXeH and HXeSH excited at different frequencies have been reported.<sup>248</sup> The latter hydrides and their isotopologues formed upon annealing of the X-ray irradiated samples containing H<sub>2</sub>S/HDS/D<sub>2</sub>S in solid xenon. The decompositions of HXeSH and HXeH and their isotopologues (HXeSH(D), DXeSH(D), DXeH, DXeD) were studied by irradiation in the IR and visible regions of the spectrum.<sup>248</sup>

Aside from HXeSH, HXeOBr is the only xenon hydride presently known in which Xe is bonded to a Group 16 atom.<sup>249</sup> The latter compound was formed in a Xe matrix (8.5 K) by UV irradiation (193 nm) of a HBr/N<sub>2</sub>O mixture, followed by thermal annealing. Deuteration experiments supported the vibrational assignments and molecular structure, based on the Xe-H/Xe-D stretching frequency ratio (1.374). The  $\nu(\text{Xe-H})$  stretching frequency of HXeOBr was observed at 1634 cm<sup>-1</sup>, which is 56 cm<sup>-1</sup> higher than  $\nu(\text{Xe-H})$  of HXeOH (1577.6 cm<sup>-1</sup>).<sup>250</sup> Upon deuteration of the precursor, HBr, the corresponding  $\nu(\text{Xe-D})$  band of DXeOBr was observed at 1190 cm<sup>-1</sup>. The experiments showed the thermal stability of HXeOBr is greater than that of HXeOH in Xe matrices.<sup>249</sup> Thus far, attempts to prepare HXeOCl have been unsuccessful.<sup>249</sup>

Another emerging family of hydrides are the organoxenon and organokrypton hydrides. The HXeCCH complex was originally formed in Ar,<sup>251</sup> Kr,<sup>252</sup> and Xe,<sup>253</sup> matrices by irradiation of H<sub>2</sub>C<sub>2</sub>/Ng, and has also been studied in N<sub>2</sub> (1534.8, 1529.5, 1507.1 cm<sup>-1</sup>) and Ne (1452.8 cm<sup>-1</sup>) matrices (Table 9).<sup>237</sup> The vibrational spectra of HXeCCH in different noble-gas matrices reveal a frequency shift trend for the Xe-H stretching frequencies that is similar to that of HXeBr, i.e.,  $\nu(\text{Ne}) < \nu(\text{Xe}) < \nu(\text{Kr}) < \nu(\text{Ar})$ . A subsequent paper<sup>254</sup> showed that in order to reproduce these experimental trends, a more realistic model of the matrix environments is needed.

The krypton analogue, HKrCCH, was obtained by irradiation of C<sub>2</sub>H<sub>2</sub> in a Kr matrix (7–30 K).<sup>239</sup> Its formation was accompanied by the appearance of three new bands in the IR spectrum (1242, 1250, 1257 cm<sup>-1</sup>) which were assigned to Kr-H stretches. The van der Waals HKrCCH...HCCH complex also formed in a Kr matrix at ca. 40 K presumably by attachment of mobile acetylene molecules to HKrCCH monomers formed during annealing at ca. 30 K (Fig. 83).<sup>255</sup> An analogous mechanism was previously proposed for the formation of HXeCCH...HCCH in a Xe matrix.<sup>256</sup> The complex was identified in a Kr matrix by two Kr-H stretching bands at 1316.5 and 1305 cm<sup>-1</sup>. The monomer-to-complex shift for the Kr-H stretching band (ca. +60 cm<sup>-1</sup>) is significantly greater than that previously reported for HXeCCH...HCCH in a Xe matrix (ca. +25 cm<sup>-1</sup>). The spectral shifts are well reproduced by quantum-chemical calculations using a bent conformer.

More recently, the first CO<sub>2</sub> complex of a krypton hydride, HKrCCH...CO<sub>2</sub>, was obtained by the annealing-induced reaction H + Kr + CCH...CO<sub>2</sub> in a Kr matrix, where the CCH...CO<sub>2</sub> complex was generated by UV photolysis of propiolic acid (HCCCOOH).<sup>257</sup> The H-Kr stretching frequency of HKrCCH...CO<sub>2</sub> (1316 cm<sup>-1</sup>) is shifted to higher frequency by 74 cm<sup>-1</sup> with respect to the most intense Kr-H stretching band of the HKrCCH monomer (1242 cm<sup>-1</sup>). The high-frequency shift indicates stabilization of the Kr-H bond upon complexation, which is characteristic of noble-gas hydride complexes. This spectral shift is

**Table 9** Experimental H-Xe stretching frequencies ( $\text{cm}^{-1}$ ) of HXeBr and HXeCCH isotopologues in different matrices.<sup>a,b,c</sup>

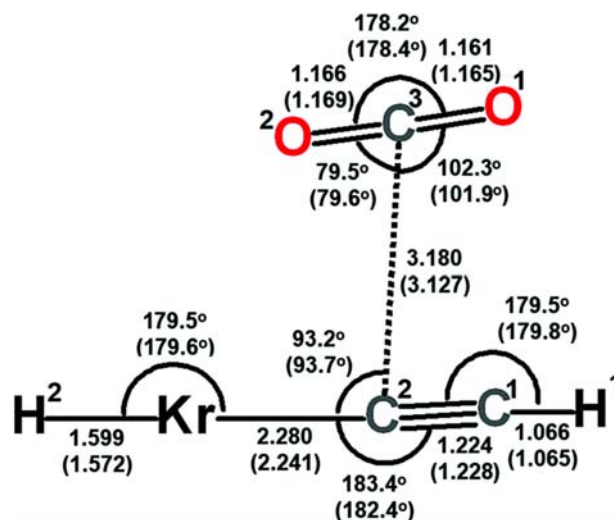
	HXeBr	DXeBr	H/D ratio <sup>c</sup>	HXeCCH <sup>d</sup>	HXe <sup>13</sup> C <sup>13</sup> CH	DXeCCD	H/D ratio <sup>c</sup>
Ne	1453	1064.1	1.365	<b>1452.8</b>	<b>1452.8</b>	<b>1053.9</b>	1.378
				1450.9	1450.9	1052.5	
				1448.8	1448.7	1051.0	
				1446.8	1446.8		
				1444.2	1444.4		
Ar	1541(+88)	...	...	<b>1531.3(+78.5)</b>	...	...	...
				1517.4			
				1482.2			
				1479.9			
Kr	1527(+74)	...	...	<b>1518.7(+65.9)</b>	...	...	...
				1505.6			
				1498.3			
Xe	1504(+51)	1100	1.367	<b>1486.4(+33.6)</b>	<b>1486.5</b>	1077.5	1.379
				1480.7	1480.9		
N <sub>2</sub>	1641	1184	1.372	1534.8	1535.0	1113.0	1.379
	<b>1625(+172)</b>			<b>1529.5(+76.7)</b>	<b>1529.8</b>	<b>1108.6</b>	
	1620			1507	1507	1093.4	
	1614						
CO <sub>2</sub>	1646(+193)	1200	1.372	...	...	...	...

<sup>a</sup>From reference 237 and references therein.<sup>b</sup>The strongest bands are indicated by bold.<sup>c</sup>The shifts,  $\nu(X)-\nu(\text{Ne})$  ( $X = \text{Ar}, \text{Kr}, \text{Xe}, \text{N}_2$ , and  $\text{CO}_2$ , were calculated for the strongest bands and shown in parentheses.<sup>d</sup>Frequency ratio  $\nu(\text{H})-\nu(\text{Xe})/\nu(\text{D})-\nu(\text{Xe})$ .**Fig. 83** The optimized structure of the HKrCCH...HCCH complex. Willmann, K.; Vent-Schmidt, T.; Räsänen, M.; Riedel, S.; Khriachtchev, L. *RSC Adv.* **2015**, *5*, 35783–35791.

significantly greater than that of HXeCCH...CO<sub>2</sub> (+6  $\text{cm}^{-1}$ ).<sup>258</sup> The spectral shifts are well reproduced by the calculations using the near-parallel conformation depicted in Fig. 84.

A new class of Ng hydrides, HKrCCCl and HXeCCCl, has been formed by UV photolysis at 193 nm followed by thermal annealing of HCCCl/Ng matrices (Ng = Kr and Xe).<sup>259</sup> The  $\nu(\text{Xe-H(D)})$  stretching frequencies of HNgCCCl (Kr: 1306, 1315  $\text{cm}^{-1}$ ; Xe: 1550, 1569  $\text{cm}^{-1}$ ) and DNgCCCl (Kr: 970, 980  $\text{cm}^{-1}$ ; Xe: 1122, 1135  $\text{cm}^{-1}$ ) are higher than those of the related H(D)NgCCH hydrides. The H/D frequency ratio for the Kr-H/D stretch of H/DKrCCCl (1.344) is less than that of H/DKrCCF (1.370),<sup>260</sup> whereas the H/D frequency ratio of the Xe-H/D stretching mode of H/DXeCCCl (1.380) is equal to that of H/DXeCCF (1.380).<sup>260</sup> The experimental assignments were also supported by following the changes in C≡C stretching frequencies from HCCCl to HNgCCCl, decreased by -35  $\text{cm}^{-1}$  (Kr) and -25  $\text{cm}^{-1}$  (Xe), respectively, upon formation of HNgCCCl. Although the  $\nu(\text{C-Cl})$  stretching frequencies were predicted to occur at ca. 800  $\text{cm}^{-1}$ , no experimental values were reported.

The cyanodiacetylene derivatives, HNgC<sub>5</sub>N (Ng = Kr, Xe), were synthesized and characterized by IR spectroscopy,<sup>261</sup> and are the largest molecules among the known noble-gas hydrides formed and identified thus far by matrix-isolation IR spectroscopy; followed by HNgC<sub>4</sub>H (Ng = Kr, Xe).<sup>262</sup> The cyanodiacetylene derivatives were synthesized by either UV laser photolysis of solid noble-gas matrices that have been doped with cyanodiacetylene (HC<sub>5</sub>N), or by passage of electrical discharges through appropriate gas mixtures, followed by the cryogenic trapping of products. Spectral assignments are based on theoretical calculations for HNgC<sub>5</sub>N and comparisons of the calculated frequencies with those of the known HNgC<sub>3</sub>N (Ng = Kr, Xe) derivatives.<sup>263</sup> The

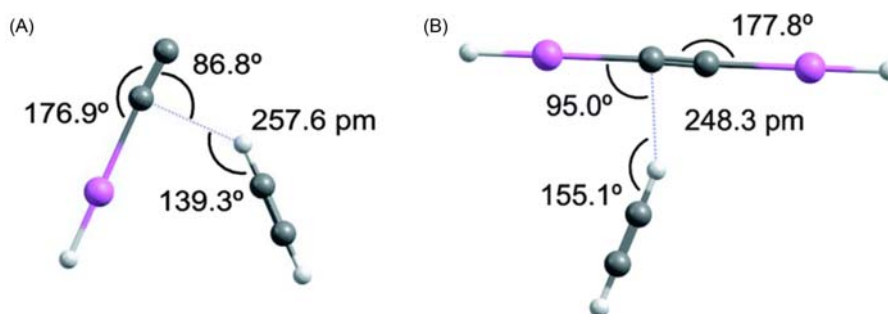


**Fig. 84** The optimized structure of HKrCCH...CO<sub>2</sub> obtained at the CCSD(T)/L2a\_3 (MP2/L2a\_3) levels of theory. The bond lengths are in Å. Ryazantsev, S. V.; Tyurin, D. A.; Nuzhdin, K. B.; Feldman, V. I.; Khriachtchev, L. *Phys. Chem. Chem. Phys.* **2019**, *21*, 3656–3661.

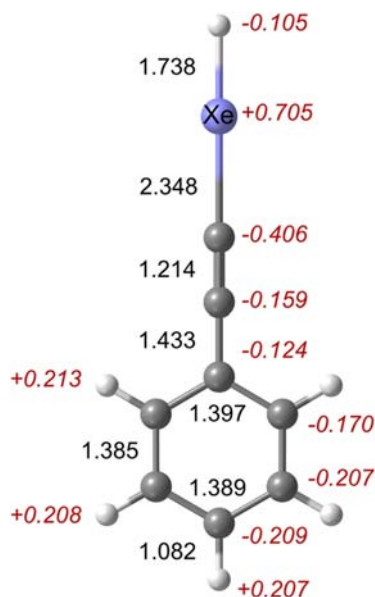
observation of the IR bands,  $\nu_1(\text{C-N})$  (Kr: 2235, 2231.5, 2237.0  $\text{cm}^{-1}$ ; Xe: 2230.5, 2228.1  $\text{cm}^{-1}$ ),  $\nu_4(\text{Ng-H})$  (Kr: 1550.0, 1548.1, 1546.7, and 1539.2  $\text{cm}^{-1}$ ; Xe: 1622  $\text{cm}^{-1}$ ) and  $\nu_7(\text{C-C})$  (Kr: 649.7  $\text{cm}^{-1}$ ; Xe: 648.9  $\text{cm}^{-1}$ ) were key to the final structural assignments; although the assignment of  $\nu_7$  was tentative. The frequencies,  $\nu_1$  and  $\nu_7$ , agree with those of the parent HC<sub>5</sub>N molecule.

The xenon hydrides, HXeCC and HXeCCXeH, are unusual because they provide the only examples of open-shell noble-gas hydride complexes and of a neutral molecule with two noble-gas atoms, respectively.<sup>252</sup> Their complexes with acetylene, HXeCC...HCCH and HXeCCXeH...HCCH, were prepared by photolysis (250 nm) and annealing (55–65 K) of HCCH/Xe matrices (Fig. 85).<sup>264</sup> The H-Xe asymmetric stretch of HXeCCXeH...HCCH has bands at 1309.9/1312.3  $\text{cm}^{-1}$  that are blue-shifted by ca 17  $\text{cm}^{-1}$  with respect to the strongest bands of HXeCCXeH monomer (1305.8, 1300.9, 1294.3  $\text{cm}^{-1}$ ). The H-Xe stretching bands of HXeCC...HCCH at 1521.6, 1512.8, and 1498.9  $\text{cm}^{-1}$  are also shifted by up to +44, +35, and +21  $\text{cm}^{-1}$  with respect to the strongest HXeCC monomer bands (1477.7, 1478.3, 1474.7  $\text{cm}^{-1}$ ). The observed blue shifts indicate H–Xe bond stabilization upon complexation, a characteristic of noble-gas hydrides, and were well reproduced by calculations using bent structures.

The compound, C<sub>6</sub>H<sub>5</sub>C≡XeH, is the first aromatic noble-gas hydride and the first halogen-free aromatic noble-gas compound (Fig. 86).<sup>265</sup> The molecule was formed by photolysis (250 nm) of matrix-isolated phenylacetylene (C<sub>6</sub>H<sub>5</sub>C≡CH) in a Xe matrix and subsequent thermal mobilization of H atoms at ca. 40 K. The hydride was identified by IR spectroscopy and deuterium substitution experiments, which aided its vibrational assignments. The bands at 1503.7, 1500.6, 1494.8, 1490.2, 1484.1, and 1479.0  $\text{cm}^{-1}$  were assigned to the Xe-H stretch of C<sub>6</sub>H<sub>5</sub>C≡XeH; the corresponding Xe-D stretching frequencies of C<sub>6</sub>D<sub>5</sub>C≡XeD occurred at 1088.6, 1083.3, 1078.2, and 1072.0  $\text{cm}^{-1}$ , giving a H/D frequency ratio of 1.381 (calculated for the most intense bands at 1503.7 and 1088.6  $\text{cm}^{-1}$ ). Bands at 636.3 and 631.7  $\text{cm}^{-1}$  were tentatively assigned to the in-plane and out-of-plane  $\delta(\text{C-Xe-H})$  bends. Bands



**Fig. 85** The most stable optimized structures of (A) HXeCC...HCCH and (B) HXeCCXeH...HCCH (CCSD/cc-pVTZ-PP). Reproduced with permission from Duarte, L.; Khriachtchev, L. *RSC Adv.* **2017**, *7*, 813–820.



**Fig. 86** The optimized structure of C<sub>6</sub>H<sub>5</sub>CCXe (M06-2X/aug-cc-pVTZ-PP). The bond lengths (Å) are in black and the NPA atomic charges are in red. Reproduced with permission from Duarte, L.; Khriachtchev, L. *Sci. Rep.* **2017**, *7*, 3130.

at 1462, 759 and 510 cm<sup>-1</sup> were confidently assigned to ring modes, i.e.,  $\nu(\text{C-C})_{\text{ring}} + \nu(\text{Xe-H})$  and  $\delta(\text{C-C-C})$ , with the deuterated analogue,  $\nu(\text{C-C})_{\text{ring}} + \nu(\text{Xe-D})$ , observed at 1057 cm<sup>-1</sup>.

### 1.08.7.2 bis-Noble-gas hydrides

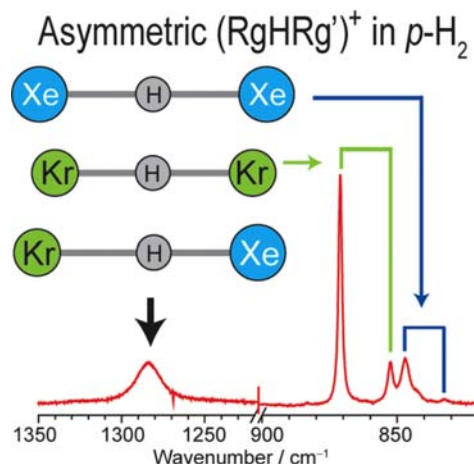
Although the *bis*-noble-gas hydrides [NgHNg]<sup>+</sup> have been previously reported,<sup>266–269</sup> a new approach has been used for their syntheses in which electron bombardment was applied during the deposition of Xe, Kr, or Xe/Kr mixtures in the matrix hosts, *p*-H<sub>2</sub>, *n*-H<sub>2</sub>, and *n*-D<sub>2</sub> at 3.2 K.<sup>270</sup> As in previous studies, characterization relied on IR spectroscopy and the observation of the anti-symmetric stretching band  $\nu_3$ , [ $\nu(\text{Ng-H}) - \nu(\text{Ng-H})$ ], and its combination band with the symmetric  $\nu_1$ , [ $\nu(\text{Ng-H}) + \nu(\text{Ng-H})$ ], stretching mode to give [ $\nu(\text{Ng-H}) + \nu(\text{Ng-H})$ ] + [ $\nu(\text{Ng-H}) - \nu(\text{Ng-H})$ ]. Bands assigned to [XeHXe]<sup>+</sup> (847.0, 972.1 cm<sup>-1</sup>) and [KrHKr]<sup>+</sup> (871.1, 974.0 cm<sup>-1</sup>) were observed in solid *p*-H<sub>2</sub> that were slightly shifted and broadened in solid *n*-H<sub>2</sub> (Xe: 844.7, 965.3 cm<sup>-1</sup>; Kr: 871.1, 974.9 cm<sup>-1</sup>). The latter frequencies are in agreement with previously reported values for [XeHXe]<sup>+</sup> and [KrHKr]<sup>+</sup> in solid Xe, Kr, and Ar,<sup>266–269</sup> and the calculated frequencies of  $\nu_3$  and  $\nu_1$  for both gas-phase species (Xe: 726, 132 cm<sup>-1</sup>; Kr: 919, 203 cm<sup>-1</sup>). Replacement of *n*-H<sub>2</sub> by *n*-D<sub>2</sub> resulted in shifts for the  $\nu_3$  lines of [XeHXe]<sup>+</sup> (602.4 cm<sup>-1</sup>) and [KrHKr]<sup>+</sup> (648.8 cm<sup>-1</sup>). The H/D isotopic ratios of [XeHXe]<sup>+</sup> (1.402) and [KrHKr]<sup>+</sup> (1.343) are also in agreement with the calculated values.

Although evidence for the mixed [KrHXe]<sup>+</sup> cation had been reported,<sup>268,269</sup> it was subsequently questioned.<sup>271</sup> A more recent study has reported the first confirmed synthesis of [KrHXe]<sup>+</sup>,<sup>270</sup> by subjecting a mixture of Xe and Kr in *p*-H<sub>2</sub> to electron bombardment during deposition. A broad band was observed at 1284 cm<sup>-1</sup> that was assigned to  $\nu_3$ , [ $\nu(\text{Kr-H}) - \nu(\text{Xe-H})$ ], of [KrHXe]<sup>+</sup> (Fig. 87); this band shifted to 1280 cm<sup>-1</sup> in solid *n*-H<sub>2</sub>. High-frequency shifts of the  $\nu_3$  band of [KrHXe]<sup>+</sup> relative to those of [XeHXe]<sup>+</sup> and [KrHKr]<sup>+</sup> were reproduced by the calculations (1279 cm<sup>-1</sup>). The corresponding band for [KrDXe]<sup>+</sup> was observed at 954 cm<sup>-1</sup> in an *n*-D<sub>2</sub> matrix that was predicted to occur at 916 cm<sup>-1</sup>.

The matrix-isolation shifts of the [XeHXe]<sup>+</sup> and [KrHKr]<sup>+</sup> bands in solid *p*-H<sub>2</sub> are less than those of [XeHXe]<sup>+</sup> in solid Xe and [KrHKr]<sup>+</sup> in solid Kr. The preparation of the mixed noble-gas cation, [KrHXe]<sup>+</sup>, demonstrates the advantages of using electron bombardment and *p*-H<sub>2</sub> as a matrix host. Failure to form the lighter H-bridged *bis*-argon cation, [ArHAr]<sup>+</sup>, is attributed to the low proton affinity of Ar (371 kJ mol<sup>-1</sup>),<sup>272</sup> which is notably less than that of H<sub>2</sub> (424 kJ mol<sup>-1</sup>).<sup>272</sup>

### 1.08.7.3 Noble-gas insertion compounds

A new class of noble-gas insertion compounds having the general formula XNgY, where X and Y are two different electronegative atoms/groups, has emerged and is represented by the halogenated series, HalNgCN (Hal = F, Cl and Br, Ng = Kr and Xe). The FXeCN, FXeNC, and FKrCN molecules were prepared by UV photolysis of FCN in Xe and Kr matrices with subsequent thermal



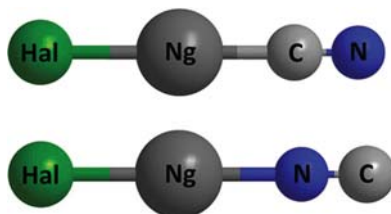
**Fig. 87** The experimental infrared spectrum of a mixture of Xe and Kr in  $p$ -H<sub>2</sub> showing the asymmetric Ng-H-Ng stretching bands of [XeHXe]<sup>+</sup>, [KrHKr]<sup>+</sup>, and [KrHXe]<sup>+</sup>. Reproduced with permission from Tsuge, M.; Kalinowski, J.; Gerber, R. B.; Lee, Y.-P. *J. Phys. Chem.* **2015**, *119*, 2651–2660.

annealing.<sup>273</sup> The FCN precursor was generated by microwave discharge of a gaseous (FCN)<sub>3</sub>/Ng mixture. The ClXeCN, ClXeNC, and BrXeCN molecules were generated by photolysis at 193 nm and thermal annealing of ClCN and BrCN in a Xe matrix (Fig. 88).<sup>274</sup>

In the case of FNgCN, three characteristic bands were assigned to  $\nu(\text{C-N})$ ,  $\nu(\text{Ng-F})$ , and  $\nu(\text{Ng-C})$ , Xe: 2159, 487, 366 cm<sup>-1</sup> and Kr: 2158, 505, 357 cm<sup>-1</sup>, respectively; whereas only two bands were observed for FXeNC (2041, 517 cm<sup>-1</sup>), where  $\nu(\text{Xe-N})$  was predicted at 355 cm<sup>-1</sup>. Only two bands were observed for ClXeCN and BrXeCN (Cl: 2145, 319 cm<sup>-1</sup>; Br: 2139, 297 cm<sup>-1</sup>), and for ClXeNC (2030, 343 cm<sup>-1</sup>). The 297 cm<sup>-1</sup> band was assigned to  $\nu(\text{Xe-C})$ , whereas the bands at 319 and 343 cm<sup>-1</sup> were assigned to the asymmetrically coupled,  $[\nu(\text{Xe-Cl}) - \nu(\text{Xe-C/Xe-N})]$ , stretches. Assignments of the Cl and Br spectra were also aided by measurement of the <sup>13</sup>C/<sup>12</sup>C isotopic shifts for the C≡N stretching modes. All frequencies and isotopic shifts were very well reproduced by calculations.

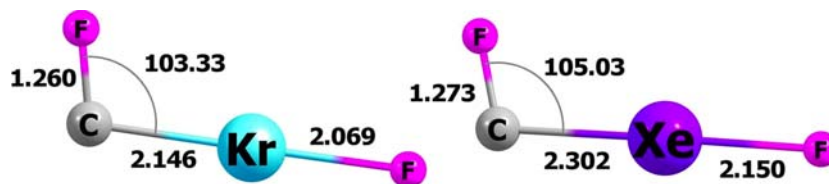
The  $\nu(\text{C-N})$  frequency increases with the electronegativity of the halogen atom in HalXeCN and HalXeNC which both exhibit strong charge transfer character, where the positive Ng atom charge increases from Kr to Xe, and the Hal atom and the CN group carry negative charges.

Following these studies, a new series of neutral noble-gas insertion compounds with halocarbenes, FNgCX (Ng = Kr, and Xe; X = F, Cl, Br, and I) were predicted by ab initio quantum-chemical calculations, and their structures (Fig. 89), stabilities, charge distributions, harmonic vibrational frequencies, and topological properties were investigated.<sup>275</sup> Unlike XNgY (Y = CN), the FNgCF molecules have planar geometries with C<sub>s</sub> symmetry in the minimum energy state, whereas their transition states are non-planar bent structures with C<sub>1</sub> symmetry. The calculated bond lengths, energetics, vibrational frequencies, and force constants suggest the Ng-F bonds are primarily ionic with small amounts of covalent character, whereas the Ng-C bonds are predominantly covalent. Furthermore, Mulliken population, NBO, and QTAIM analyses indicate that the predicted species are best described by the ionic formulation, F<sup>-</sup>[NgCX]<sup>+</sup>.



**Fig. 88** The optimized structures (MP2/aug-cc-pVTZ and B3LYP/aug-cc-pVTZ) of the HalNgCN isomers (Hal = Cl and Br; Ng = Kr and Xe). Reproduced with permission from Arppe, T.; Khriachtchev, L.; Lignell, A.; Domanskaya, A. V.; Räsänen, M. *Inorg. Chem.* **2012**, *51*, 4398–4402.





**Fig. 89** The geometries of FKrCF and FXeCF (MP2/L2a\_3; bond lengths are in Å; bond angles are in degrees). Reproduced with permission from Sosulin, I. S.; Tyurin, D. A.; Feldman, V. I. *Chem. Phys. Lett.* **2020**, 744, 137, 211.

Both FKrCF and FXeCF were formed at cryogenic temperatures by reaction of mobile F atoms and trapped CF fragments in solid Kr and Xe matrices.<sup>276</sup> The CF fragments were generated by X-ray radiolysis of CH<sub>2</sub>F<sub>2</sub> in their respective matrices. Radiolysis of CH<sub>2</sub>F<sub>2</sub>/Ar did not yield FArCF, a result supported by calculations. The  $\nu(\text{C-F})$  stretching bands were observed for FXeCF (1239.6 cm<sup>-1</sup>) and FKrCF (1300.5 cm<sup>-1</sup>) but only the  $\nu(\text{Kr-F})$  band was observed at 438.6 cm<sup>-1</sup>. The  $\nu(\text{Xe-F})$  band of FXeCF, although expected to be rather intense, was not observed and was predicted at a lower frequency (428.9 cm<sup>-1</sup>). The agreement between experimental and calculated frequencies was very good at all levels of theory.

The observation of HKrH and HXeF indicated that hydrogen atoms were also trapped in Kr and Xe matrices after annealing of the irradiated CH<sub>2</sub>F<sub>2</sub>/Xe and CH<sub>2</sub>F<sub>2</sub>/Kr samples; however there was no evidence for HKrCF or HXeCF.

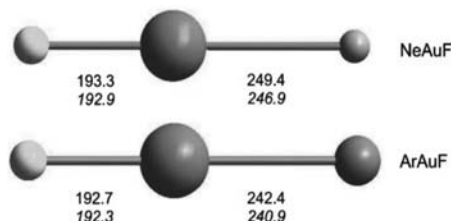
#### 1.08.7.4 Gold complexes

The noble-gas fluoride compounds, Ar–AuF,<sup>277</sup> Kr–AuF,<sup>278</sup> and Xe–AuF<sup>279</sup> have been reported, but Ne–AuF<sup>280–282</sup> has only been studied computationally.

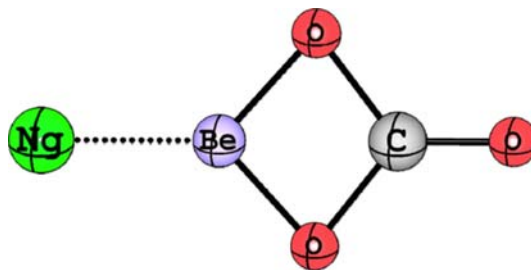
A more recent study reports the products of laser-ablated Au atoms with F<sub>2</sub> in excess Ar and Ne during co-deposition of Au atoms with a F<sub>2</sub>/Ne or F<sub>2</sub>/Ar mixture on a CsI window at 4 K.<sup>283,284</sup> Along with other gold fluoride species, such as AuF<sub>2</sub> and AuF<sub>5</sub>, the IR spectrum also showed bands that were assigned to the  $\nu(\text{Au-F})$  stretches of Ne–AuF (567.2 cm<sup>-1</sup>) and Ar–AuF (575.1 cm<sup>-1</sup>) (Fig. 90). These assignments were supported by calculations (Ne: 558.5 cm<sup>-1</sup>; Ar: 580.7 cm<sup>-1</sup>) and were also based on fluorine concentration dependencies, which confirmed that only one Ng atom was coordinated to an AuF group. This finding was also supported by calculations, which showed that only one Ng atom can strongly coordinate to AuF to form a linear molecule. The binding energy of Ar–AuF (38.5 kJ mol<sup>-1</sup>) is greater than that of Ne–AuF (8.8 kJ mol<sup>-1</sup>), with both Ar–Au and Ne–Au being less covalent.

#### 1.08.7.5 Beryllium complexes

The first Ng–Be donor-acceptor complexes Ng–BeO (Ng = Ar, Kr, Xe) were formed by use of pulsed-laser ablation matrix-isolation spectroscopy.<sup>285</sup> A considerable number of theoretical investigations of various Ng–BeY complexes ensued (e.g., Y = O,<sup>285–288</sup> S,<sup>287,289</sup> Se,<sup>287</sup> Te,<sup>287</sup> CO<sub>3</sub>,<sup>288</sup> SO<sub>4</sub>).<sup>288</sup> The studies showed that the Ng–BeY bonds are mainly charge-induced dipole interactions (donor-acceptor interactions). There are several reports of calculated frequencies for the  $\nu(\text{Ng-Be})$  and  $\delta(\text{NgBeY})$  vibrational modes that show these bands are expected to occur well below the observable frequency range for matrix-isolation IR spectroscopy, i.e., Ng–BeO (Ng = Ar, Kr, Xe):  $\nu(\text{Ng-Be})$ ; 284, 256, 241 cm<sup>-1</sup> and  $\delta(\text{NgBeO})$ ; 187, 180, 175 cm<sup>-1</sup><sup>286</sup>; Ar–BeS:  $\nu(\text{Ar-Be})$ ; 233.3 cm<sup>-1</sup> and  $\delta(\text{ArBeS})$ ; 147.1 cm<sup>-1</sup><sup>289</sup>; Ng–BeSO<sub>4</sub> (Ng = Ar, Kr, Xe):  $\nu(\text{Ng-Be})$ ; 184.13, 146.42, 132.14 cm<sup>-1</sup>.<sup>288</sup> Characterization of Ng–BeY complexes is completely reliant on the vibrational frequencies of the BeY group, where Y can be an atom or a polyatomic moiety; hence the importance of using isotopic substitution within the group in support of vibrational assignments, e.g., the first experimental evidence for Ng–BeO was supported by <sup>16</sup>O/<sup>18</sup>O isotopic labeling.<sup>285</sup>



**Fig. 90** The optimized structures of the Ne–AuF and Ar–AuF complexes (CCSD(T)/aug-cc-pVTZ and CCSD(T)/aug-cc-pVQZ). For comparison, the Au–F bond length in AuF is 1.938 Å. Reproduced with permission from Wang, X.; Andrews, L.; Willmann, K.; Brosi, F.; Riedel, S. *Chem. Eur. J.* **2013**, 19, 1397–1409.

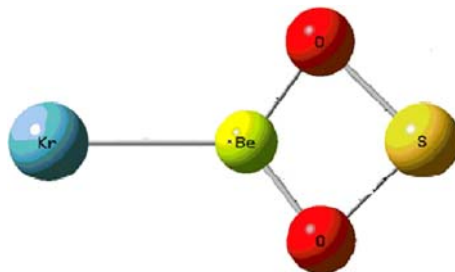


**Fig. 91** The optimized geometry (M06-2X/def2-TZVPP, MP2/cc-pVTZ and CCSD(T)/cc-pVTZ) of Ng-BeCO<sub>3</sub>. Reproduced with permission from Zhang, Q.; Chen, M.; Zhou, M.; Andrada, D. M.; Frenking, G. *J. Phys. Chem. A* **2015**, *119*, 2543–2552.

Matrix-isolation IR spectroscopy also provided evidence for Ng-BeCO<sub>3</sub> (Ng = Ne, Ar, Kr, Xe),<sup>290</sup> Ng-BeS,<sup>291</sup> and Ng-BeSO<sub>2</sub>.<sup>292</sup> The Ne-BeCO<sub>3</sub> complex (**Fig. 91**) was prepared in a Ne matrix by co-deposition of laser-evaporated beryllium atoms with CO/O<sub>2</sub> mixtures in excess Ne at 4 K.<sup>290</sup> Doping with the heavier noble-gas atoms argon, krypton, and xenon yielded the series of Ng-BeCO<sub>3</sub> (Ng = Ar, Kr, Xe) complexes. Isotopically enriched <sup>13</sup>CO, C<sup>18</sup>O and <sup>18</sup>O<sub>2</sub> were used to aid in the vibrational assignments. The authors note it is more important to reproduce isotopic frequency shifts than precise vibrational frequencies because the latter are more dependent on the level of theory. Thus, the calculated red shifts of  $\nu(\text{C-O})$ ,  $[\nu(\text{C-O}) - \nu(\text{C-O})] + [\nu(\text{Be-O}) - \nu(\text{Be-O})]$ , and  $[\nu(\text{Be-O}) + \nu(\text{Be-O})]$  modes, and the blue shifts of  $\delta(\text{CO}_3)_{\text{umb}}$ ,  $\delta(\text{OBeO})$ , and  $\delta(\text{OCO})$  modes are within 5 cm<sup>-1</sup> of the experimental values. The  $\nu(\text{Ng-Be})$  bands were not detected due to their very low intensities and frequencies: 211, 198, 162, and 146 cm<sup>-1</sup> (Ng = Ne, Ar, Kr, Xe, calculated at the CCSD(T)/cc-pVTZ level of theory). Calculations at other levels of theory gave the same trends for the Ng-Be stretching modes of Ng-BeO and Ng-BeCO<sub>3</sub> (He > Ne > Ar > Kr > Xe), which correlate with the mass of the noble-gas atom. The  $\nu(\text{Ng-Be})$  frequency of Ng-BeO for a given atom Ng is always higher than that of Ng-BeCO<sub>3</sub>. The bonding of Ng-BeCO<sub>3</sub> was compared with that of Ng-BeO. The Ng-Be bonds of Ng-BeCO<sub>3</sub> are slightly longer and weaker than those of Ng-BeO. The energy decomposition analyses for the Ng-Be bonds indicate that the attractive interactions mainly arise from the Ng → BeCO<sub>3</sub> and Ng → BeO σ-donation.

Laser-ablated beryllium atoms react with H<sub>2</sub>S to form Ng-BeS (Ng = He, Ne, Ar) in solid noble-gas matrices which were characterized by matrix-IR spectroscopy by use of D<sub>2</sub>S, H<sub>2</sub><sup>34</sup>S, and H<sub>2</sub><sup>32</sup>S + H<sub>2</sub><sup>34</sup>S mixtures.<sup>291</sup> The BeS<sub>2</sub> molecule was also identified. Evidence for Ng-BeS (Ng = He, Ne, Ar) is solely based on the observation of significant shifts of the asymmetric stretching band,  $\nu(\text{Be-S}) - \nu(\text{Ng-Be})$ , when changing matrices and upon isotopic substitution. Bands involving Ng could not be observed because they are expected to occur at very low frequencies.<sup>289</sup> Calculations reproduced frequency changes (i.e., shifts to higher or lower frequencies) that occur upon going from Ne to Xe.

The Ng-BeSO<sub>2</sub> (Ng = Ne, Ar, Kr, Xe) complexes were prepared by reaction of laser-evaporated beryllium atoms with SO<sub>2</sub> in low-temperature noble-gas matrices (**Fig. 92**).<sup>292</sup> When doped with heavier noble-gas atoms, the guest (Ar, Kr, Xe) atom displaces Ne to form more stable noble-gas complexes. Isotopically labeled S<sup>18</sup>O<sub>2</sub>, S<sup>16,18</sup>O<sub>2</sub>, S<sup>16</sup>O<sub>2</sub>, and <sup>34</sup>SO<sub>2</sub> were also used to substantiate vibrational assignments. Significant frequency shifts were observed upon changing matrices, implying that not all absorptions are attributable to isolated Be(η<sup>2</sup>-O<sub>2</sub>S), but coupling of noble-gas atoms must also be taken into account. Quantum-chemical calculations confirmed the presence of the Be(η<sup>2</sup>-O<sub>2</sub>S) group and that a single Ng atom is bound to Be by reproducing the frequency changes that occur upon going from Ne to Xe. Many of the key mode frequencies that involve the Be(η<sup>2</sup>-O<sub>2</sub>S) group decrease in the order:  $[\nu(\text{Be-O}) - \nu(\text{Be-O})] > [\nu(\text{Be-O}) + \nu(\text{Be-O})] > [\nu(\text{S-O}) + \nu(\text{S-O})] > \delta(\text{OBeO}) > [\nu(\text{S-O}) - \nu(\text{S-O})] > \delta(\text{OSO})$ . The calculated frequencies of  $\nu(\text{Ng-Be})$  stretches were not reported. Quantum-chemical calculations demonstrate that the Ng-Be bonds of Ng-BeSO<sub>2</sub> can



**Fig. 92** The optimized structure for Kr-BeSO<sub>2</sub> (B3LYP/6-311++g(3df,3pd) and BPW91/6-311++g(3df,3pd)). Reproduced with permission from Yu W., Liu X., Xu B., Xing X., Wang X. *J. Phys. Chem. A*, **2016**, *120*, 8590–9598.

be formed through a combination of electron-donation and ion-induced dipole interactions. The WBI (Wiberg bond index) values of Ng–Be bonds and LOL (localized orbital locator) profile indicate that the Ng–Be bonds exhibit gradual increases in covalent character when descending Group 18 from Ne to Xe.

### 1.08.7.6 Xenon van der Waals complexes with aromatic rings

The interaction of Xe with aromatic rings has given rise to another class of noble-gas species. These complexes are best described as van der Waals molecules owing to their weak Xe⋯ring interactions, where the calculated Xe⋯C distances are at or greater than the sum of van der Waals radii of Xe (2.16) and C (1.70) = 3.86 Å.<sup>102</sup>

The phenol⋯Xe complex<sup>293</sup> was formed by interaction of phenol molecules with xenon (1:1) in a Ne matrix. The theoretically most stable 1:1 structure is the  $\pi$ -complex, where the Xe atom is located above the aromatic ring with a small shift towards the hydroxyl oxygen atom. However, the complex exhibits no spectroscopic features in its IR spectrum, making its characterization more challenging. The formation of the phenol⋯Xe complex is mainly based on comparisons with experimental data for the phenol⋯N<sub>2</sub> complex and from xenon concentration dependencies. The formation of polyxenon complexes, phenol⋯Xe<sub>*n*</sub>, was also reported in the same study.<sup>293</sup> These findings are in accordance with a prior study which also concluded that phenol forms  $\pi$ -complexes with noble-gas atoms.<sup>294</sup>

The toluene⋯Xe and *p*-cresol⋯Xe complexes<sup>295</sup> were subsequently studied in Ne matrices. In contrast with phenol⋯Xe, both aromatic complexes have a methyl group that serves as an indicator of  $\pi$ -complex formation. The vibrational analyses were aided by use of toluene-*d*<sub>3</sub> and *p*-cresol-*d*<sub>3</sub>. The deuterated molecules have simpler spectra in their methyl stretching regions compared to the spectra of the non-deuterated complexes, leading to distinguishable spectral shifts in the toluene⋯Xe and *p*-cresol⋯Xe complexes, thus providing spectroscopic fingerprints that confirm their  $\pi$ -structures.

## 1.08.8 High-pressure noble-gas chemistry

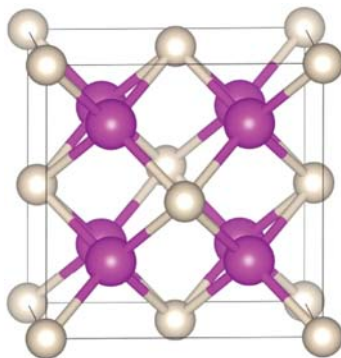
High-pressure noble-gas chemistry is a relatively new and growing field. Early calculations<sup>11,296</sup> suggested that high-pressure conditions up to hundreds of GPa allow the formation of unique compounds and bonding motifs that would otherwise be inaccessible. In addition to their intrinsic interest, high-pressure species have important implications in Nature because they are suggestive of processes that occur in the interiors of Earth, outer planets, and other celestial bodies.

A large number of such compounds have been theoretically predicted but only a few have been formed and experimentally characterized. In most instances, the syntheses are made possible by use of diamond-anvil cell (DAC) techniques,<sup>297</sup> the technology used to investigate the noble-gas chemistry at ultra-high pressures. The most common characterization methods are single-crystal synchrotron X-ray diffraction and laser Raman spectroscopy.

### 1.08.8.1 Helium compounds

A recent significant achievement in the field of high-pressure noble-gas chemistry has been the synthesis of Na<sub>2</sub>He,<sup>298</sup> the first thermodynamically stable helium compound.

The compound was formed by loading Na into a He medium in a laser-heated DAC and compressed up to 155 GPa. The crystal structure of Na<sub>2</sub>He is a fluorite-type structure that is stable at pressures > 113 GPa (Fig. 93). It was shown that the presence of He



**Fig. 93** The crystal structure of Na<sub>2</sub>He at 300 GPa is depicted as a ball-and-stick representation (pink and grey atoms represent Na and He, respectively). Reproduced with permission from Dong, X.; Oganov, A. R.; Goncharov, A. F.; Stavrou, E.; Lobanov, S.; et al. *Nat. Chem.* **2017**, *9*, 440–445.

atoms results in significant electron localization, which renders this material an insulator. The phase is an electride, with electron pairs localized in the interstices that form eight-center, two-electron bonds within empty  $\text{Na}_8$  cubes. The existence of  $\text{Na}_2\text{HeO}$  is also predicted to form at pressures above 15 GPa with a similar structure.

The formation of the  $\text{As}_4\text{O}_6 \cdot 2\text{He}$  clathrate was detected when an arsenolite ( $\text{As}_4\text{O}_6$ ) crystal, immersed in helium, was compressed between 0 and 30 GPa in a DAC.<sup>299</sup> Starting at 3 GPa, weak additional reflections appeared in the X-ray diffraction pattern, which increased in intensity with pressure, to reach 10–15% of the main reflections at 29.83 GPa. The new reflections were associated with a  $\text{As}_4\text{O}_6 \cdots \text{He}$  clathrate in which the large octahedral interstitial holes of  $\text{As}_4\text{O}_6$  are occupied by He atoms. It was shown that  $\text{As}_4\text{O}_6 \cdot 2\text{He}$  is only formed on the surface of the arsenolite crystal, and that the He permeation depth increases with pressure.

### 1.08.8.2 Neon compounds

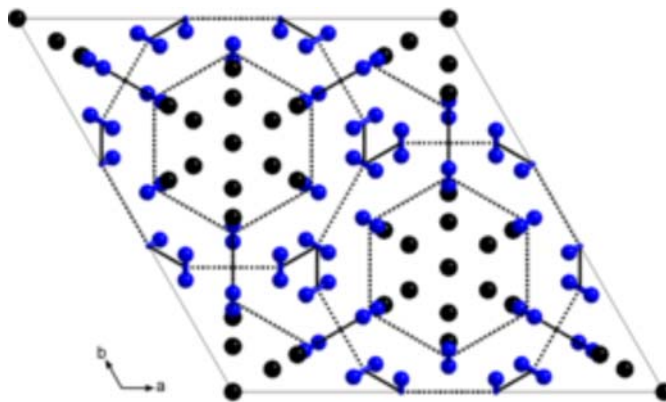
The existence of the van der Waals insertion compound,  $(\text{N}_2)_6\text{Ne}_7$ , was established while studying the binary phase diagram of  $\text{N}_2$ -Ne mixtures at 296 K in a DAC.<sup>300</sup> The compound was obtained by compressing the  $\text{N}_2$ -Ne mixture above 9.6 GPa, where it is in equilibrium in the solid phase with solid Ne and/or solid  $\text{N}_2$ . By decreasing the pressure below the two eutectic points, the final component solids melted and a pure compound was stabilized. A single crystal was grown from a small grain of  $(\text{N}_2)_6\text{Ne}_7$  at its melting point. The structure of  $(\text{N}_2)_6\text{Ne}_7$  was solved by single-crystal synchrotron X-ray diffraction (Fig. 94). The  $\text{N}_2$  molecules form the guest lattice, which hosts the Ne atoms. This insertion compound may be viewed as a clathrate with the centers of the  $\text{N}_2$  molecules forming distorted dodecahedron cages, each enclosing 14 Ne atoms. The  $(\text{N}_2)_6\text{Ne}_7$  compound is the first van der Waals clathrate that is organized by quadrupole-quadrupole interactions, one of the anisotropic components of van der Waals interactions.

### 1.08.8.3 Argon, xenon, and krypton compounds

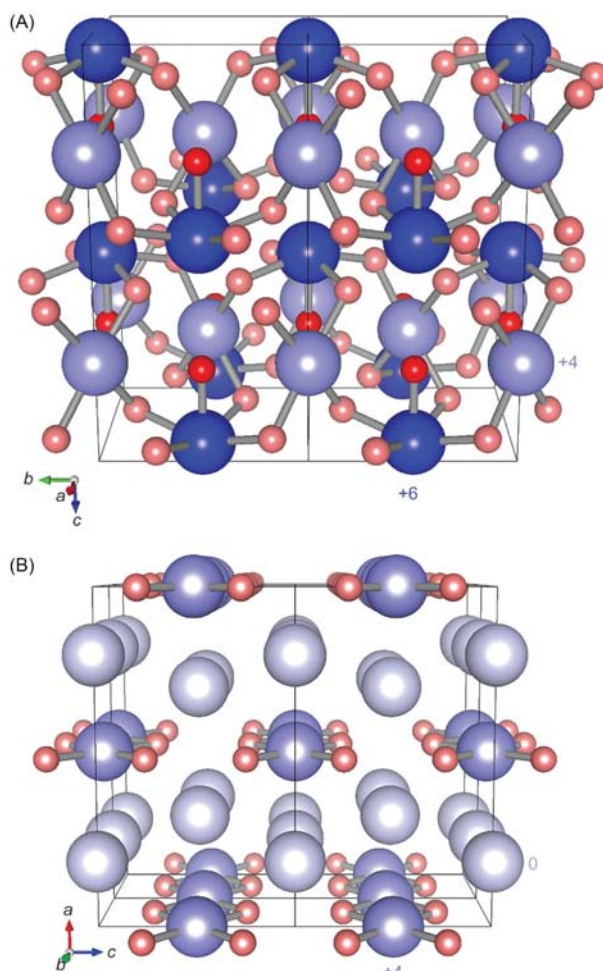
Many recent high-pressure studies have geological implications as their underlying motivation. For example, one such investigation has focused on the stabilities of Xe compounds of O, the most abundant element in the Earth's mantle, while others focus on recurring questions concerned with the composition of the Earth's core, for example, how much Ar and Xe are present in the Earth's core and what is the reactivity of Ar and Xe with major constituents of the Earth's core such as Fe and Ni?

Several xenon oxides are well characterized and have been observed at low or ordinary pressures, e.g.,  $\text{XeO}_2$ ,<sup>214</sup>  $\text{XeO}_3$ ,<sup>213</sup> and  $\text{XeO}_4$ .<sup>227</sup> Using a DAC at above 80 GPa, it was possible to directly combine xenon and oxygen to form  $\text{Xe}_2\text{O}_5$  under oxygen-rich conditions and  $\text{Xe}_3\text{O}_2$  under oxygen-poor conditions (Fig. 95).<sup>301</sup> In contrast with other known xenon oxides, the Xe atoms adopt mixed oxidation states of 0 and +4 in  $\text{Xe}_3\text{O}_2$ , and +4 and +6 in  $\text{Xe}_2\text{O}_5$ , and combine with the O atoms to form extended networks that incorporate oxygen-sharing  $\text{XeO}_4$  squares, and  $\text{Xe}_2\text{O}_5$  also incorporates oxygen-sharing  $\text{XeO}_5$  square pyramids.

Earlier calculations predicted the formation of stable Xe-Fe and Xe-Ni compounds under high-pressure.<sup>302</sup> The most stable were  $\text{XeFe}_3$  and  $\text{XeNi}_3$ , which were shown to be stable at the pressures and temperatures found in the Earth's core. The formation of  $\text{XeNi}_3$  was attained in a subsequent study.<sup>303</sup> It required a further study to confirm both predictions when high-pressure experiments were conducted in a laser-heated DAC on Xe-Fe/Ni mixtures at thermodynamic conditions representative of the Earth's core.<sup>304</sup> Using in situ synchrotron X-ray diffraction and Raman spectroscopy, both  $\text{XeNi}_3$  (~150 GPa/1500 K) and  $\text{XeFe}_3$  (~220 GPa/2000 K)



**Fig. 94** The crystal structure of  $(\text{N}_2)_6\text{Ne}_7$  where neon and nitrogen are represented by black and blue spheres, respectively, and the black dashed lines join the centers of adjacent  $\text{N}_2$  molecules. The unit cell is viewed along the  $c$ -axis ([001]). Reproduced with permission from Plisson, T.; Weck, G.; Loubeyre, P. *Phys. Rev. Lett.* **2014**, *113*, 025702.



**Fig. 95** Structures of stable xenon oxides at 83 GPa: (A)  $\text{Xe}_2\text{O}_5$  and (B)  $\text{Xe}_3\text{O}_2$ . Xenon atoms are shown in blue and oxygen atoms in red. The oxygen atoms have an oxidation state of  $-2$ , and the darker shade of red indicates an oxygen atom that bonds to one xenon atom. The oxidation states of the xenon atoms are indicated by different shades of blue. The lightest blue shade indicates an oxidation state of  $0$ , the medium shade  $+4$  and the darkest blue shade  $+6$ . The xenon atoms in  $\text{Xe}_2\text{O}_5$  and  $\text{Xe}_3\text{O}_2$  exist in two different oxidation states within each structure,  $+4$  and  $+6$  in  $\text{Xe}_2\text{O}_5$  and  $0$  and  $+4$  in  $\text{Xe}_3\text{O}_2$ . Reproduced with permission from Dewaele, A.; Worth, N.; Pickard, C. J.; Needs, R. J.; Pascarelli, S. *Nat. Chem.* **2016**, *8*, 784–790.

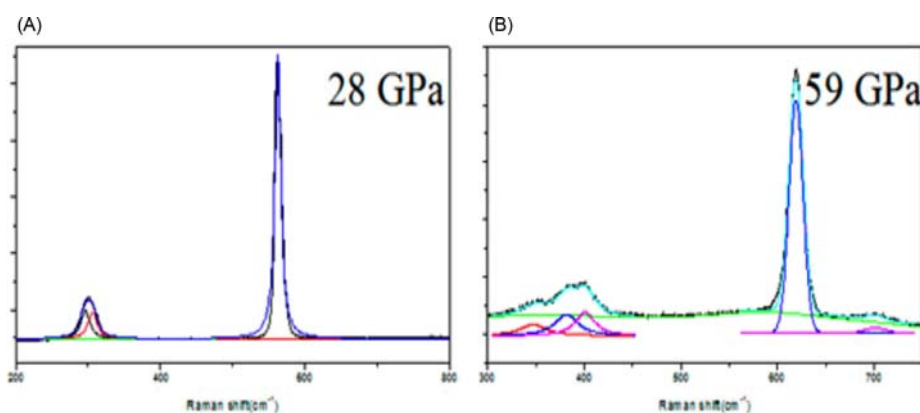
were identified. The predicted crystal structures of Xe-Fe/Ni compounds are distinct from the structures of elemental Xe, Fe, and Ni under the same thermodynamic conditions, suggesting that the formation mechanism of these compounds goes beyond simple element substitution. From a chemical point of view, it is significant that Xe can be oxidized by Fe or Ni under high pressure, as shown by the large calculated charge transfer from Xe to Fe/Ni in these compounds. A more recent development is the synthesis of ArNi above 140 GPa by laser heating ( $T > 1500$  K).<sup>305</sup> ArNi is an intermetallic Laves phase, with no bonding but significant electron transfer between Ar and Ni atoms.

The binary systems, Ng-H<sub>2</sub> (Ng = Ar, Kr, Xe) have been investigated at high pressures and shown to form the van der Waals compounds: Ar(H<sub>2</sub>)<sub>2</sub> (at 4.3 GPa<sup>306</sup> and stable to at least 358 GPa<sup>307</sup>), Kr(H<sub>2</sub>)<sub>4</sub> (at 5.3 GPa and stable to at least 50 GPa),<sup>308</sup> and Xe(H<sub>2</sub>)<sub>8</sub> (at 4.8 GPa and stable to at least 255 GPa).<sup>309</sup> Raman and/or infrared spectroscopy have shown that hydrogen is present as freely rotating molecular H<sub>2</sub> in these compounds, with no indication of H-noble-gas bonding.

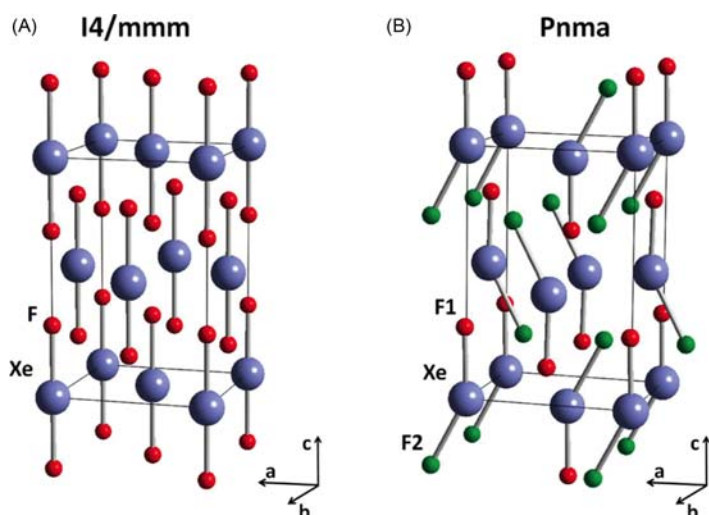
High-pressure experiments were conducted at ambient temperature on the binary Xe-N<sub>2</sub> system,<sup>310,311</sup> at pressures as high as ca. 70 GPa by use of a DAC. High-pressure, in situ synchrotron X-ray diffraction, and Raman spectroscopy were used to monitor structural transitions. A Laves phase was obtained for the van der Waals compound Xe(N<sub>2</sub>)<sub>2</sub> at pressures greater than 4.4 GPa.<sup>310</sup> Further compression results in transition to a tetragonal Xe(N<sub>2</sub>)<sub>2</sub>-II phase at 14 GPa.<sup>311</sup> The latter phase appears to be stable to at least 180 GPa even when heated above 2000 K. Raman spectroscopy indicates a significant weakening of the N≡N bond of the dinitrogen molecule above 60 GPa. Visible and mid-infrared transmission measurements suggest metallization of the compound at ca. 100 GPa.



The effects of high pressure on the crystal structure of XeF<sub>2</sub> were investigated,<sup>312</sup> which solved a long-lasting high-pressure structural controversy.<sup>313–315</sup> Systematic high-pressure DAC studies were carried out by use of Raman and UV-VIS absorption spectroscopies (up to 82 GPa) and synchrotron X-ray diffraction (up to 86 GPa). DFT calculations were also employed to support the experimental data. It was shown that the tetragonal *I4/mmm* structure of XeF<sub>2</sub> at ambient temperature remained stable up to 28 GPa, where it transformed to the orthorhombic *Immm* structure. Above 59 GPa, XeF<sub>2</sub> formed an orthorhombic *Pnma* structure. As the pressure increased, all the Raman bands shifted to higher frequencies, indicating enhanced interactions among atoms. The frequency of the symmetric stretching mode changed linearly upon compression. Additional bands appeared as the pressure increased, consistent with symmetry lowering of XeF<sub>2</sub> (Fig. 96). The *Pnma* structure features bent XeF<sub>2</sub> molecules (Fig. 97), with non-equivalent Xe–F bond lengths. It is noteworthy that the same high-pressure *Pnma* phase was expected above 105<sup>314</sup> and 110 GPa<sup>315</sup> in earlier theoretical studies. The authors associate the pressure differences with the use of non-hydrostatic conditions in their experiments.<sup>312</sup> The high-pressure X-ray diffraction results rule out the decomposition of XeF<sub>2</sub> into Xe<sub>2</sub>F and XeF<sub>4</sub> at high pressures that was predicted earlier.<sup>315</sup> The optical band gap of XeF<sub>2</sub> at 82 GPa is 1.83 eV, with an estimated metallic pressure at 152 GPa.



**Fig. 96** Several Gaussian peak fittings for the Raman spectra of XeF<sub>2</sub> at (A) 28 GPa and (B) 59 GPa. The Raman spectra of *I4/mmm*, *Immm* and *Pnma* are black, red and blue, respectively. Reproduced with permission from Wu, G.; Huang, X.; Huang, Y.; Pan, L.; Li, F.; Li, X.; Liu, M.; Liu, B.; Cui, T. *J. Phys. Chem. C* **2017**, *121*, 6264–6271.



**Fig. 97** (A) The crystal structure of the ambient-pressure polymorph of XeF<sub>2</sub> (*I4/mmm*). Blue/red spheres indicate Xe/F atoms. (B) The crystal structure of XeF<sub>2</sub> (*Pnma*) at 105 GPa. Blue spheres indicate Xe atoms, and red/green spheres indicate F1 and F2 atoms, respectively. Reproduced with permission from Kurzydłowski, D.; Zaleski-Ejgierd, P.; Grochala, W.; Hoffmann, R., *Inorg. Chem.* **2011**, *50*, 3832–3840.

### 1.08.9 Perspective and outlook

Since the discovery of noble-gas reactivity<sup>6</sup> by Neil Bartlett 60 years ago, the syntheses and structural characterizations of a diverse range of noble-gas compounds at the very edge of the Periodic Table continue to provide a fascinating and highly challenging topic in contemporary inorganic chemistry. Noble-gas chemistry continues to provide insights into thermochemistry, bonding relationships, and chemistry beyond the valence octet (hyper-valent behavior) in the context of the Periodic Table. Neil Bartlett's discovery of noble-gas reactivity resulted in an outpouring of synthetic and structural work in the field that quickly revealed the true nature of two of the Group 18 elements, xenon and krypton, and vanquished the octet dogma then prevalent in chemistry textbooks.

The present chapter summarizes only 10 years of progress in noble-gas chemistry and illustrates how noble-gas chemistry remains a vibrant research field that is rife with a surprising array of interesting new compounds, bonding modalities, rich structural chemistry, and intriguing synthetic applications. Recent and future research achievements in noble-gas chemistry promise new and exciting developments in fundamental and applied chemistry that were not dreamt of by Neil Bartlett and fellow researchers in the formative years of noble-gas chemistry. Future developments in noble-gas chemistry will continue to be intimately tied to researchers who have the technical skills, curiosity, and creativity to confront this very challenging topic and to those who have the foresight to support curiosity-driven fundamental research.

### References

- Oganessian, Y. T.; Utyonkov, V. K.; Lobanov, Y. V.; Abdullin, F. S.; Polyakov, A. N.; et al. *Phys. Rev. C* **2006**, *74*, 044602.
- Karola, P. J.; Barber, R. C.; Sherrill, B. M.; Vardaci, E.; Yamazaki, T. *Pure Appl. Chem.* **2016**, *88*, 155–160.
- Smits, O. R.; Mewes, J. M.; Jerabek, P.; Schwerdtfeger, P. *Angew. Chem. Int. Ed.* **2020**, *39*, 23636–23640.
- (a) The Periodic Table I – Historical Development and Essential Features. Michael, D., Mingos, P., Eds., In *Structure and Bonding*; Springer Nature, Berlin, Heidelberg, 2019; p 181; (b) The Periodic Table II – Catalytic, Materials, Biological and Medical Applications. Michael, D., Mingos, P., Eds., In *Vol. 182 of Structure and Bonding*, Springer Nature: Berlin, Heidelberg, 2020.
- Chemistry at the Edge of the Periodic Table: the Importance of Periodic Trends on the Discovery of the Noble Gases and the Development of Noble-Gas Chemistry. In *The Periodic Table I – Historical Development and Essential Features*; Structure and Bonding; Schrobilgen, G. J., Michael, D., Mingos, P., Eds.; Springer Nature: Berlin, Heidelberg, 2019; vol. 181; pp 157–196, (Chapter 49).
- Bartlett, N. *Proc. Chem. Soc.* **1962**, 218.
- Bartlett, N. *Mendeleev Chem. J.* **1983**, *28*, 628–636.
- Bartlett, N. *Chem. Can.* **1963**, *15*, 33–40.
- Bartlett, N. *Endeavour* **1964**, *23*, 3–7.
- Bartlett, N.; Sladky, F. O. In *Comprehensive Inorganic Chemistry*; Bailar, J. C., Emeléus, H. J., Nyholm, R., Trotman-Dickenson, A. F., Eds.; Pergamon Press LTD.: Oxford, 1973. vol. 1; pp 213–330. Chapter 6.
- Grandinetti, F., Ed.; *Noble Gas Chemistry: Structure, Bonding, and Gas-Phase Chemistry*, John Wiley & Sons, 2018.
- Hope, E. G. *Coord. Chem. Rev.* **2013**, *257*, 902–909.
- Haner, J.; Schrobilgen, G. J. *Chem. Rev.* **2015**, *115*, 1255–1295.
- Pan, S.; Jana, G.; Merino, G.; Chattaraj, P. K. *ChemistryOpen* **2019**, *8*, 173–187.
- Mazej, Z. *Molecules* **2020**, *25*, 3014.
- Nabiev, S. S.; Sokolov, V. B.; Chaivanov, B. B. *Russ. Chem. Rev.* **2014**, *83*, 1135–1180.
- Khriachtchev, L. *J. Phys. Chem. A* **2015**, *119*, 2735–2746.
- Miao, M. *Front. Chem.* **2020**, *8*, 570492.
- Saha, R.; Jana, G.; Pan, S.; Merino, G.; Chattaraj, P. K. *Molecules* **2019**, *24*, 2933.
- Gomila, R. M.; Frontera, A. *Front. Chem.* **2020**, *8*, 395.
- Brock, D. S.; Schrobilgen, G. J.; Žemva, B. In *Comprehensive Inorganic Chemistry II*; Reedijk, J., Poeppelemeier, K., Eds.; Elsevier: Oxford, 2013. vol. 1; pp 755–822.
- Tramšek, M.; Žemva, B. *Acta Chim. Slov.* **2006**, *53*, 105–116.
- Easter, C.; O'Neal, C. B. *J. Microelectromech. Syst.* **2009**, *18*, 1054–1061.
- Schrobilgen, G. J.; Firna, G.; Chirakal, R.; Garnett, E. S. *J. Chem. Soc., Chem. Commun.* **1981**, 198–199.
- Vasdev, N.; Pointner, B. E.; Chirakal, R.; Schrobilgen, G. J. *J. Am. Chem. Soc.* **2002**, *124*, 12863–12868.
- Shuiyu, L.; Pike, V. W. *J. Fluorine Chem.* **2010**, *131*, 1032–1038.
- Yamaguchi, S.; Shirasaka, T.; Tamao, K. *Organometallics* **2002**, *21*, 2555–2558.
- Yamaguchi, S.; Akiyama, S.; Tamao, K. *J. Organomet. Chem.* **2002**, *646*, 277–281.
- Klapötke, T. M.; Krumm, B.; Mayer, P.; Piotrowski, H.; Ruscitti, O. P.; Schiller, A. *Inorg. Chem.* **2002**, *41*, 1184–1193.
- Yahav, A.; Goldberg, I.; Vignalok, A. *J. Am. Chem. Soc.* **2003**, *125*, 13634–13635.
- Bernhardt, E.; Bach, C.; Bley, B.; Wartchow, R.; Westphal, U.; et al. *Inorg. Chem.* **2005**, *44*, 4189–4205.
- Yahav, A.; Goldberg, I.; Vignalok, A. *Inorg. Chem.* **2005**, *44*, 1547–1553.
- Jeon, K.-J.; Lee, Z.; Pollak, E.; Moreschini, L.; Bostwick, A.; et al. *ACS Nano* **2011**, *5*, 1042–1046.
- Patrick, T. B.; Mortezaian, R. *J. Org. Chem.* **1988**, *53*, 5153–5155.
- Halpern, D. F.; Tavcar, G.; Tramšek, M. Xenon(II) Fluoride. In *Encyclopedia of Reagents for Organic Synthesis*; 2017. <https://doi.org/10.1002/047084289X.rx001.pub2>.
- Shen, C.; Hagiwara, R.; Mallouk, T. E.; Bartlett, N. Thermodynamic Aspects of the Remarkable Oxidizing Capabilities of Fluorine–Lewis-Fluoroacid Mixtures. In *Inorganic Fluorine Chemistry, Toward the 21st Century, ACS Symposium Series 555*; Thrasher, J., Strauss, S. H., Eds., American Chemical Society: Washington, DC, 1994; pp 26–39. Chapter 2.
- Adams, R. M. *Fluorine-18 Tracer Studies of Inorganic and Organic Electrophilic Fluorine Sources* (MSc thesis), McMaster University: Hamilton, ON, Canada, 1994.

38. Breddemann, U.; Debackere, J. R.; Schrobilgen, G. J. A Room Temperature Non-Irradiative Synthesis of XeF<sub>2</sub>. In *Efficient Preparations of Fluorine Compounds*; 1st ed.; Roesky, H. W., Ed., John Wiley & Sons, Inc., 2013; pp 11–15. Chapter 4.
39. Poleschner, H.; Seppelt, K. *Angew. Chem. Int. Ed.* **2013**, *52*, 12838–12842.
40. Sato, S.; Ameta, H.; Horn, E.; Takahashi, O.; Furukawa, N. *J. Am. Chem. Soc.* **1997**, *119*, 12374–12375.
41. Finze, M.; Bernhardt, E.; Willner, H.; Lehmann, C. W.; Aubke, F. *Inorg. Chem.* **2005**, *44*, 4206–4214.
42. Connelly, N. G.; Geiger, W. E. *Chem. Rev.* **1996**, *96*, 877–910.
43. Frohn, H.-J.; Bardin, V. V. In *Recent Developments in Carbocation and Onium Ion Chemistry*, ACS Symposium Series 965; Laali, K. K., Ed., American Chemical Society: Washington, USA, 2007; pp 428–457.
44. Tyrra, W.; Naumann, D. In *Inorganic Chemistry Highlights*; Meyer, G., Naumann, D., Wesemann, L., Eds., Wiley-VCH: Weinheim, Germany, 2002; pp 297–316.
45. Frohn, H.-J.; Bardin, V. V. *Organometallics* **2001**, *20*, 4750–4762.
46. Bock, H.; Scherer, H.; Tyrra, W.; Naumann, D. *J. Fluorine Chem.* **2006**, *127*, 1440–1445.
47. Frohn, H.-J.; Theisen, M. *Angew. Chem. Int. Ed.* **2000**, *39*, 4591–4593.
48. Frohn, H.-J.; Theisen, M. *J. Fluorine Chem.* **2004**, *125*, 981–988.
49. Maggiorosa, N.; Naumann, D.; Tyrra, W. *Angew. Chem. Int. Ed.* **2000**, *39*, 4588–4591.
50. Bilir, V.; Frohn, H.-J. *Acta Chim. Slov.* **2013**, *60*, 505–512.
51. Frohn, H.-J.; Klose, A.; Schroer, T.; Henkel, G.; Buss, V.; Opitz, D.; Vahrenhorst, R. *Inorg. Chem.* **1998**, *37*, 4884–4890.
52. Koppe, K.; Frohn, H.-J.; Mercier, H. P. A.; Schrobilgen, G. J. *Inorg. Chem.* **2008**, *47*, 3205–3217.
53. Elliot, H. S. A.; Lehmann, J. F.; Mercier, H. P. A.; Jenkins, H. D. B.; Schrobilgen, G. J. *Inorg. Chem.* **2010**, *49*, 8504–8523.
54. Frohn, H.-J.; Schroer, T.; Henkel, G. *Angew. Chem. Int. Ed.* **1999**, *38*, 2554–2556.
55. Bartlett, N.; Wechsberg, M.; Sladky, F. O.; Bulliner, P. A.; Jones, G. R.; Burbank, R. D. *J. Chem. Soc. D* **1969**, 703–704.
56. Wechsberg, M.; Bulliner, P. A.; Sladky, F. O.; Mews, R.; Bartlett, N. *Inorg. Chem.* **1972**, 3063–3070.
57. Gillespie, R. J.; Netzer, A.; Schrobilgen, G. J. *Inorg. Chem.* **1974**, *13*, 1455–1459.
58. Schrobilgen, G. J.; Holloway, J. H.; Granger, P.; Brevard, C. *Inorg. Chem.* **1978**, *17*, 980–987.
59. Malischewski, M.; Seppelt, K. *Acta Crystallogr.* **2015**, *E71*, 363–365.
60. Bartlett, N.; Wechsberg, M.; Jones, G. R.; Burbank, R. D. *Inorg. Chem.* **1972**, *11*, 1124–1127.
61. Lehmann, J. F.; Mercier, H. P. A.; Schrobilgen, G. J. *Coord. Chem. Rev.* **2002**, *233–234*, 1–39. and references therein.
62. Mazej, Z.; Goreschnik, E. *Eur. J. Inorg. Chem.* **2021**, 2669–2681.
63. Bortolus, M. R.; Ellwanger, M.; Haner, J.; Schrobilgen, G. J. *J. Fluorine Chem.* **2021**, *250*, 109814.
64. Brock, D. S.; Casalis de Pury, J. J.; Mercier, H. P. A.; Schrobilgen, G. J.; Silvi, B. *J. Am. Chem. Soc.* **2010**, *132*, 3533–3542.
65. Brock, D. S.; Casalis de Pury, J. J.; Mercier, H. P. A.; Schrobilgen, G. J.; Silvi, B. *Inorg. Chem.* **2010**, *49*, 6673–6689.
66. Žemva, B.; Jesih, A.; Templeton, D. H.; Zalkin, A.; Cheetham, A. K.; Bartlett, N. *J. Am. Chem. Soc.* **1987**, *109*, 7420–7427.
67. Mercier, H. P. A.; Breddemann, U.; Brock, D. S.; Bortolus, M. R.; Schrobilgen, G. J. *Chem. Eur. J.* **2019**, *25*, 12105–12119.
68. Goettel, J. T.; Bortolus, M. R.; Stuart, D. G.; Mercier, H. P. A.; Schrobilgen, G. J. *Chem. Eur. J.* **2019**, *25*, 15815–15829.
69. Bortolus, M. R.; Mercier, H. P. A.; Schrobilgen, G. J. *Chem. Eur. J.* **2020**, *26*, 8935–8950.
70. Bortolus, M. R.; Mercier, H. P. A.; Brock, D. S.; Schrobilgen, G. J. *Chem. Eur. J.* **2022**, *28*, e2021037.
71. DeBackere, J. R.; Mercier, H. P. A.; Schrobilgen, G. J. *J. Am. Chem. Soc.* **2014**, *136*, 3888–3903.
72. Lozinšek, M.; Mercier, H. P. A.; Schrobilgen, G. J. *Angew. Chem. Int. Ed.* **2021**, *60*, 8149–8156.
73. Lozinšek, M.; Mercier, H. P. A.; Schrobilgen, G. J.; Žemva, B. *Angew. Chem. Int. Ed.* **2017**, *56*, 6251–6254.
74. DeBackere, J. R.; Schrobilgen, G. J. *Angew. Chem. Int. Ed.* **2018**, *57*, 13167–13171.
75. Lehmann, J. F.; Dixon, D. A.; Schrobilgen, G. J. *Inorg. Chem.* **2001**, *40*, 3002–3017.
76. Holloway, J. H.; Schrobilgen, G. J. *Inorg. Chem.* **1981**, *20*, 3363–3368.
77. Politzer, P.; Murray, J. S.; Clark, T.; Resnati, G. *Phys. Chem. Chem. Phys.* **2017**, *19*, 32166–32178.
78. Christe, K. O.; Wilson, W. W.; Bougon, R. A. *Inorg. Chem.* **1986**, *25*, 2163–2169.
79. Tucker, P. A.; Taylor, P. A.; Holloway, J. H.; Russell, D. R. *Acta Crystallogr.* **1975**, *B31*, 906–908.
80. Holloway, J. H.; Schrobilgen, G. J. *Inorg. Chem.* **1980**, *19*, 2632–2640.
81. Craciun, R.; Dixon, D. A., private communication.
82. Hagiwara, R.; Hollander, F.; Maines, C.; Bartlett, N. *Eur. J. Solid State Inorg. Chem.* **1991**, *28*, 855–866.
83. Matsumoto, K.; Hagiwara, R.; Ito, Y.; Tamada, O. *Solid State Sci.* **2002**, *4*, 1465–1469.
84. Tavčar, G.; Žemva, B. *Inorg. Chem.* **2013**, *52*, 4319–4323.
85. Tavčar, G.; Goreschnik, E.; Mazej, Z. *J. Fluorine Chem.* **2006**, *127*, 1368–1373.
86. Mazej, Z.; Goreschnik, E. *Inorg. Chem.* **2008**, *47*, 4209–4214.
87. Tavčar, G.; Tramšek, M. *J. Fluorine Chem.* **2015**, *174*, 14–21.
88. Lutar, K.; Bormann, H.; Mazej, Z.; Tramšek, M.; Benkič, P.; Žemva, B. *J. Fluorine Chem.* **2000**, *101*, 155–160.
89. Tramšek, M.; Benkič, P.; Turičnik, A.; Tavčar, G.; Žemva, B. *J. Fluorine Chem.* **2002**, *114*, 143–148.
90. Tramšek, M.; Lork, E.; Mews, R.; Žemva, B. *J. Solid State Chem.* **2001**, *162*, 243–249.
91. Mazej, Z. *Ph.D. thesis*, University of Ljubljana, 2000.
92. Barraclough, C. G.; Cockman, R. W.; O'Donnell, T. A. *Inorg. Chem.* **1977**, *16*, 673–677.
93. Persson, I.; D'Angelo, P.; De Panfilis, S.; Sandström, M.; Eriksson, L. *Chem. Eur. J.* **2008**, *14*, 3056–3066.
94. Mazej, Z.; Goreschnik, E.; Hironaka, K.; Katayama, Y.; Hagiwara, R. *Z. Anorg. Allg. Chem.* **2009**, *635*, 2309–2315.
95. Scheibe, B.; Karttunen, A. J.; Kraus, F. *Eur. J. Inorg. Chem.* **2021**, *4*, 405–421.
96. Nabiev, S. S.; Sokolov, V. B.; Spirin, S. N.; Chaivanov, B. B. *Russ. J. Phys. Chem. A* **2011**, *85*, 1931–1941.
97. Solov'ev, S. N.; Korunov, A. A.; Zubkov, K. G.; Minasyan, K. A. *Russ. J. Phys. Chem. A* **2012**, *86*, 320–322.
98. Tramšek, M.; Benkič, P.; Žemva, B. *Inorg. Chem.* **2004**, *43*, 699–703.
99. Tavčar, G.; Žemva, B. *Angew. Chem. Int. Ed.* **2009**, *48*, 1432–1434.
100. Schreiner, F.; Malm, J. G.; Hindman, J. C. *J. Am. Chem. Soc.* **1965**, *87*, 25–28. and references therein.
101. Bartlett, N.; Wechsberg, M. *Z. Anorg. Allg. Chem.* **1971**, *385*, 5–17.
102. Bondi, A. *J. Phys. Chem.* **1964**, *68*, 441–451.
103. Alvarez, S. *Dalton Trans.* **2013**, *42*, 8617–8636.

104. Bartlett, N.; Einstein, F.; Stewart, D. F.; Trotter, J. *J. Chem. Soc. A* **1967**, 1190–1193.
105. Leary, K.; Templeton, D. H.; Zalkin, A.; Bartlett, N. *Inorg. Chem.* **1973**, *12*, 1726–1730.
106. Bartlett, N.; DeBoer, B. G.; Hollander, F. J.; Sladky, F. O.; Templeton, D. H.; Zalkin, A. *Inorg. Chem.* **1974**, *13*, 780–785.
107. Lutar, K.; Jesih, A.; Leban, I.; Žemva, B.; Bartlett, N. *Inorg. Chem.* **1989**, *28*, 3467–3471.
108. Jesih, A.; Lutar, K.; Leban, I.; Žemva, B. *Eur. J. Solid State Inorg. Chem.* **1991**, *28*, 829–840.
109. Lutar, K.; Leban, I.; Ogrin, T.; Žemva, B. *Eur. J. Solid State Inorg. Chem.* **1992**, *29*, 713–727.
110. Pointner, B. E.; Suontamo, R. J.; Schrobilgen, G. J. *Inorg. Chem.* **2006**, *45*, 1517–1534.
111. Mazej, Z.; Goresnik, E. *Eur. J. Inorg. Chem.* **2009**, 4503–4506.
112. Hughes, M. J.; Mercier, H. P. A.; Schrobilgen, G. J. *Inorg. Chem.* **2010**, *49*, 3501–3515.
113. Fir, B. A.; Gerken, M.; Pointner, B. E.; Mercier, H. P. A.; Dixon, D. A.; Schrobilgen, G. J. *J. Fluorine Chem.* **2000**, *105*, 159–167.
114. Radan, K.; Goresnik, E.; Žemva, B. *Angew. Chem. Int. Ed.* **2014**, *53*, 13715–13719.
115. Gillespie, R. J.; Schrobilgen, G. J. *Inorg. Chem.* **1976**, *15*, 22–31.
116. Bortolus, M. R.; Mercier, H. P. A.; Nguyen, B.; Schrobilgen, G. J. *Angew. Chem. Int. Ed.* **2022**, *60*, 23678–23686.
117. Allen, L. C. *Int. J. Quantum Chem.* **1994**, *49*, 253–277.
118. Rahm, M.; Zeng, T.; Hoffmann, R. *J. Am. Chem. Soc.* **2019**, *141*, 342–351.
119. Burns, J. H. *J. Phys. Chem.* **1963**, *67*, 536.
120. Ivanova, M. V.; Mercier, H. P. A.; Schrobilgen, G. J. *J. Am. Chem. Soc.* **2015**, *137*, 13398–13413. and references therein.
121. Dunning, T. H.; Hay, P. J. *J. Chem. Phys.* **1977**, *66*, 3767–3777.
122. Yamanishi, M.; Hirao, K.; Yamashita, K. *J. Chem. Phys.* **1998**, *108*, 1514–1521.
123. Ault, B. S.; Andrews, L. *Chem. Phys. Lett.* **1976**, *43*, 350–352.
124. Gerken, M.; Moran, M. D.; Mercier, H. P. A.; Pointner, B. E.; Schrobilgen, G. J.; Hoge, B.; Christe, K. O.; Boatz, J. A. *J. Am. Chem. Soc.* **2009**, *131*, 13474–13489.
125. Ivanova, M. V.; Köchner, T.; Mercier, H. P. A.; Schrobilgen, G. J. *Inorg. Chem.* **2013**, *52*, 6806–6819.
126. Fir, B. A.; Mercier, H. P. A.; Sanders, J. C. P.; Dixon, D. A.; Schrobilgen, G. J. *J. Fluorine Chem.* **2001**, *110*, 89–107.
127. Moran, M. D.; Brock, D. S.; Mercier, H. P. A.; Schrobilgen, G. J. *J. Am. Chem. Soc.* **2010**, *132*, 13823–13839.
128. Mercier, H. P. A.; Moran, M. D.; Sanders, J. C. P.; Schrobilgen, G. J. *Inorg. Chem.* **2005**, *44*, 49–60.
129. DeBackere, J. R.; Bortolus, M. R.; Schrobilgen, G. J. *Angew. Chem. Int. Ed.* **2016**, *55*, 11917–11920.
130. Žemva, B.; Slivnik, J.; Bohinc, M. *J. Inorg. Nucl. Chem.* **1976**, *38*, 73–74.
131. Lutar, K.; Borrmann, H.; Žemva, B. *Inorg. Chem.* **1998**, *37*, 3002–3006.
132. Žemva, B.; Zupan, J.; Slivnik, J. *J. Inorg. Nucl. Chem.* **1971**, *33*, 3953–3955.
133. Bohinc, M.; Grannec, J.; Slivnik, J.; Žemva, B. *J. Inorg. Nucl. Chem.* **1976**, *38*, 75–76.
134. Bartlett, N.; Jha, N. K. In *Noble Gas Compounds*; Hyman, H. H., Ed., University of Chicago Press: Chicago, 1963; p 23.
135. Bartlett, N.; Žemva, B.; Graham, L. *J. Fluorine Chem.* **1976**, *7*, 301–320.
136. Graham, L.; Graudejus, O.; Jha, N. K.; Bartlett, N. *Coord. Chem. Rev.* **2000**, *197*, 321–334.
137. Družina, B.; Žemva, B. *J. Fluorine Chem.* **1986**, *34*, 233–239.
138. Tramšek, M.; Goresnik, E.; Tavčar, G. *Acta Chim. Slov.* **2016**, *63*, 369–375.
139. Seidel, S.; Seppelt, K. *Angew. Chem. Int. Ed.* **2000**, *39*, 2000–2002.
140. Tamadon, F.; Seidel, S.; Seppelt, K. *Acta Chim. Slov.* **2013**, *60*, 491–494.
141. Williamson, S. M.; Koch, C. W. *Science* **1963**, *139*, 1046–1047.
142. Appelman, E. H.; Malm, J. G. *J. Am. Chem. Soc.* **1964**, *86*, 2141–2148.
143. Brock, D. S.; Bilir, V.; Mercier, H. P. A.; Schrobilgen, G. J. *J. Am. Chem. Soc.* **2007**, *129*, 3598–3611.
144. Brock, D. S.; Mercier, H. P. A.; Schrobilgen, G. J. *J. Am. Chem. Soc.* **2010**, *132*, 10935–10943.
145. Gillespie, R. J.; Landa, B.; Schrobilgen, G. J. *J. Chem. Soc. D* **1971**, 1543–1544.
146. McKee, D. E.; Zalkin, A.; Bartlett, N. *Inorg. Chem.* **1973**, *12*, 1713–1717.
147. McKee, D. E.; Adams, C. J.; Bartlett, N. *Inorg. Chem.* **1973**, *12*, 1722–1725.
148. Boldrini, P.; Gillespie, R. J.; Ireland, P. R.; Schrobilgen, G. J. *Inorg. Chem.* **1974**, *13*, 1690–1694.
149. Gillespie, R. J.; Schrobilgen, G. J. *Inorg. Chem.* **1974**, *13*, 2370–2374.
150. Gillespie, R. J.; Landa, B.; Schrobilgen, G. J. *Inorg. Chem.* **1976**, *15*, 1256–1263.
151. Syvret, R. G.; Mitchell, K. M.; Sanders, J. C. P.; Schrobilgen, G. J. *Inorg. Chem.* **1992**, *31*, 3381–3385.
152. Frohn, H.-J.; Leblond, N.; Lutar, K.; Žemva, B. *Angew. Chem., Int. Ed.* **2000**, *39*, 391–393.
153. Klänning, U. K.; Appelman, E. H. *Inorg. Chem.* **1988**, *27*, 3760–3762.
154. Brock, D. S.; Mercier, H. P. A.; Schrobilgen, G. J. *J. Am. Chem. Soc.* **2013**, *135*, 5089–5104.
155. Tramšek, M.; Žemva, B. *J. Fluorine Chem.* **2006**, *127*, 1275–1284. and references therein.
156. Hoyer, S.; Emmeler, T.; Seppelt, K. *J. Fluorine Chem.* **2006**, *127*, 1415–1422.
157. Mootz, D.; Bartmann, K. *Angew. Chem., Int. Ed.* **1988**, *27*, 391–392.
158. Mootz, D.; Bartmann, K. *Z. Naturforsch., B: J. Chem. Sci.* **1991**, *46*, 1659–1663.
159. Frohn, H.-J.; Bardin, V. V. *J. Chem. Soc., Chem. Commun.* **1993**, 1072–1074.
160. Frohn, H.-J.; Bardin, V. V. *Z. Anorg. Allg. Chem.* **2003**, *629*, 2465–2469.
161. Frohn, H.-J.; Adonin, N. Y.; Bardin, V. V. *Z. Anorg. Allg. Chem.* **2003**, *629*, 2499–2508.
162. Zhdankin, V. V.; Stang, P. J.; Zefirov, N. S. *J. Chem. Soc., Chem. Commun.* **1992**, 578–579.
163. Frohn, H.-J.; Bardin, V. V. *Chem. Commun.* **2003**, 2352–2353.
164. Frohn, H.-J.; Bardin, V. V. *Eur. J. Inorg. Chem.* **2006**, 3948–3953.
165. Bock, H.; Hinz-Hübner, D.; Ruschewitz, U.; Naumann, D. *Angew. Chem., Int. Ed.* **2002**, *41*, 448–450.
166. Koppe, K.; Haner, J.; Mercier, H. P. A.; Frohn, H.-J.; Schrobilgen, G. J. *Inorg. Chem.* **2014**, *53*, 11640–11661.
167. Koppe, K.; Bilir, V.; Frohn, H.-J.; Mercier, H. P. A.; Schrobilgen, G. J. *Inorg. Chem.* **2007**, *46*, 9425–9437.
168. Gillespie, R. J.; Hargittai, I. *The VSEPR Model of Molecular Geometry*, Allyn and Bacon: Boston, MA, 1991.
169. Bartell, L. S.; Gavin, R. M., Jr.; Thompson, H. B.; Chernick, C. L. *J. Chem. Phys.* **1965**, *43*, 2547–2548.
170. Hedberg, K.; Peterson, S. H.; Ryan, R. R.; Weinstock, B. *J. Chem. Phys.* **1966**, *44*, 1726.
171. Harshbarger, W.; Bofn, R. K.; Bauer, S. H. *J. Am. Chem. Soc.* **1967**, *89*, 6466–6469.
172. Gavin, R. M., Jr.; Bartell, L. S. *J. Chem. Phys.* **1968**, *48*, 2460–2464.



173. Bartell, L. S.; Gavin, R. M., Jr. *J. Chem. Phys.* **1968**, *48*, 2466–2483.
174. Kim, H.; Claassen, H. H.; Pearson, E. *Inorg. Chem.* **1968**, *7*, 616–617.
175. Gasner, E. L.; Claassen, H. H. *Inorg. Chem.* **1967**, *6*, 1937–1938.
176. Claassen, H. H.; Goodman, G. L.; Kim, H. *J. Chem. Phys.* **1972**, *56*, 5042–5053.
177. Tse, J. S.; Bristow, D. J.; Bancroft, G. M.; Schrobilgen, G. J. *Inorg. Chem.* **1983**, *22*, 2673–2677.
178. Cutler, J. N.; Bancroft, G. M.; Bozek, J. D.; Tan, K. H.; Schrobilgen, G. J. *J. Am. Chem. Soc.* **1991**, *113*, 9125–9131.
179. Peterson, K. A.; Dixon, D. A.; Stoll, H. *J. Phys. Chem. A* **2012**, *116*, 9777–9782.
180. Seppelt, K.; Bartlett, N. *Z. Anorg. Allg. Chem.* **1977**, *436*, 122–126.
181. Peacock, R. D.; Selig, H.; Sheft, I. *Proc. Chem. Soc.* **1964**, 285.
182. Peterson, S. W.; Holloway, J. H.; Coyle, B. A.; Williams, J. M. *Science* **1971**, *173*, 1238–1239.
183. Christe, K. O.; Wilson, W. W. *Inorg. Chem.* **1982**, *21*, 4113–4117.
184. Smith, G. L.; Schrobilgen, G. J. *Inorg. Chem.* **2009**, *48*, 7714–7728. and references therein.
185. Matsumoto, K.; Haner, J.; Mercier, H. P. A.; Schrobilgen, G. J. *Angew. Chem. Int. Ed.* **2015**, *54*, 14169–14173.
186. Haner, J.; Matsumoto, K.; Mercier, H. P. A.; Schrobilgen, G. J. *Chem. Eur. J.* **2016**, *22*, 4833–4842.
187. Pilmö, J.; Robinson, E. A.; Gillespie, R. J. *Inorg. Chem.* **2006**, *45*, 6198–6204.
188. Gawrilow, M.; Beckers, H.; Riedel, S.; Cheng, L. *J. Phys. Chem. A* **2018**, *122*, 119–129.
189. Hughes, M. J.; Brock, D. S.; Mercier, H. P. A.; Schrobilgen, G. J. *J. Fluorine Chem.* **2011**, *132*, 660–668.
190. Žemva, B. *Croat. Chem. Acta* **1988**, *61*, 163–187.
191. Atwood, D. A. Noble Gases: Inorganic Chemistry. In *Encyclopedia of Inorganic Chemistry*, 2nd ed.; King, R. B., Ed. Wiley-VCH: Weinheim, Germany, 2005.
192. Mazej, Z.; Goreschnik, E. *Eur. J. Inorg. Chem.* **2015**, 1453–1456. and references therein.
193. Mazej, Z.; Goreschnik, E. *Eur. J. Inorg. Chem.* **2016**, 3356–3364.
194. Mazej, Z.; Goreschnik, E. *J. Solid State Chem.* **2015**, *228*, 53–59.
195. Mazej, Z.; Goreschnik, E. *Eur. J. Inorg. Chem.* **2017**, 2800–2807.
196. Mazej, Z.; Goreschnik, E. *J. Fluorine Chem.* **2015**, *175*, 47–50.
197. Bartlett, N.; Gennis, M.; Gibler, D. D.; Morrell, B. K.; Zalkin, A. *Inorg. Chem.* **1973**, *12*, 1717–1721.
198. Bartlett, N.; Einstein, F.; Stewart, D. F.; Trotter, J. *Chem. Commun.* **1966**, 550–552.
199. Benkič, P.; Golič, L.; Koller, J.; Žemva, B. *Acta Chim. Slov.* **1999**, *46*, 239–252.
200. Leary, K.; Zalkin, A.; Bartlett, N. *Inorg. Chem.* **1974**, *13*, 775–779.
201. Mazej, Z.; Goreschnik, E. *New. J. Chem.* **2016**, *40*, 7320–7325.
202. Jesih, A.; Žemva, B. *Vestn. Slov. Kem. Drus.* **1991**, *38*, 161–168 (in English).
203. Mazej, Z.; Goreschnik, E.; Jagličić, Z.; Filinchuk, Y.; Tumanov, N.; Akselrud, L. G. *Eur. J. Inorg. Chem.* **2017**, 2130–2137.
204. Shlyapnikov, I. M.; Goreschnik, E. A.; Mazej, Z. *Chem. Commun.* **2013**, *49*, 2703–2705.
205. Mazej, Z.; Goreschnik, E. *Eur. J. Inorg. Chem.* **2019**, 1265–1272. and references therein.
206. Gunn, R. S. In *Noble-Gas Compounds*; Hyman, H. H., Ed., University of Chicago: Chicago, IL, 1963; pp 149–151.
207. Pitzer, K. S. *Science* **1963**, *139*, 414.
208. Bartlett, N.; Rao, P. R. *Science* **1963**, *139*, 506.
209. Smith, D. F. *J. Am. Chem. Soc.* **1963**, *85*, 816–817.
210. Templeton, D. H.; Zalkin, A.; Forrester, J. D.; Williamson, S. M. *J. Am. Chem. Soc.* **1963**, *85*, 817.
211. Hodgson, D.; Ibers, J. A. *Inorg. Chem.* **1969**, *8*, 326–331.
212. Willett, R. D.; Peterson, S. W.; Coyle, B. A. *J. Am. Chem. Soc.* **1977**, *99*, 8202–8207.
213. Goettel, J. T.; Schrobilgen, G. J. *Inorg. Chem.* **2016**, *55*, 12975–12981.
214. Brock, D. S.; Schrobilgen, G. J. *J. Am. Chem. Soc.* **2011**, *133*, 6265–6269.
215. Claassen, H. H.; Knapp, G. *J. Am. Chem. Soc.* **1964**, *86*, 2341–2342.
216. Goettel, J. T.; Matsumoto, K.; Mercier, H. P. A.; Schrobilgen, G. J. *Angew. Chem. Int. Ed.* **2016**, *55*, 13780–13783.
217. Goettel, J. T.; Mercier, H. P. A.; Schrobilgen, G. J. *J. Fluorine Chem.* **2018**, *211*, 60–69.
218. Marczenko, K. M.; Goettel, J. T.; Mercier, H. P. A.; Schrobilgen, G. J. *Chem. Eur. J.* **2019**, *25*, 12357–12366.
219. Laurence, C.; Gal, J.-F. *Lewis Basicity and Affinity Scales: Data and Measurement*, Wiley: Chichester, 2010; p 5.
220. Marczenko, K. M.; Mercier, H. P. A.; Schrobilgen, G. J. *Angew. Chem. Int. Ed.* **2018**, *57*, 12448–12452.
221. Seidel, S.; Seppelt, K. *Angew. Chem., Int. Ed.* **2001**, *40*, 4225–4227.
222. Goettel, J. T.; Haensch, V. G.; Schrobilgen, G. J. *J. Am. Chem. Soc.* **2017**, *139*, 8725–8733.
223. Gunn, S. R. *J. Am. Chem. Soc.* **1965**, *87*, 2290–2291.
224. Gundersen, G.; Hedberg, K.; Huston, J. L. *J. Chem. Phys.* **1970**, *52*, 812–815.
225. Selig, H.; Claassen, H. H.; Chernick, C. L.; Malm, J. G.; Huston, J. L. *Science* **1964**, *143*, 1322–1323.
226. Huston, J. L.; Claassen, H. H. *J. Chem. Phys.* **1970**, *52*, 5646–5648.
227. Gerken, M.; Schrobilgen, G. J. *Inorg. Chem.* **2002**, *41*, 198–204.
228. Malm, J. G.; Holt, B. D.; Bane, R. W. In *Noble Gas Compounds*; Hyman, H. H., Ed., University of Chicago Press: Chicago, 1963; pp 167–173.
229. Ibers, J. A.; Hamilton, W. C.; MacKenzie, D. R. *Inorg. Chem.* **1964**, *3*, 1412–1416.
230. Zalkin, A.; Forrester, J. D.; Templeton, D. H. *Inorg. Chem.* **1964**, *3*, 1417–1421.
231. Gerken, M.; Schrobilgen, G. J. *Coord. Chem. Rev.* **2000**, *197*, 335–395.
232. Huston, J. L. *Inorg. Nucl. Chem. Lett.* **1968**, *4*, 29–30.
233. Vent-Schmidt, T.; Goettel, J. T.; Schrobilgen, G. J.; Riedel, S. *Chem. Eur. J.* **2015**, *21*, 11244–11252.
234. Khriachtchev, L.; Räsänen, M.; Gerber, R. B. *Acc. Chem. Res.* **2009**, *42*, 183–191. and references therein.
235. Zhu, C.; Niimi, K.; Taketsugu, T.; Tsuge, M.; Nakayama, A.; Khriachtchev, L. *J. Chem. Phys.* **2015**, *142*, 054305. and references therein.
236. Kalinowski, J.; Gerber, R. B.; Räsänen, M.; Lignell, A.; Khriachtchev, L. *J. Chem. Phys.* **2014**, *140*, 094303.
237. Tsuge, M.; Lignell, A.; Räsänen, M.; Khriachtchev, L. *J. Chem. Phys.* **2013**, *139*, 204303.
238. Khriachtchev, L.; Tapio, S.; Räsänen, M.; Domanskaya, A.; Lundell, J. *J. Chem. Phys.* **2010**, *133*, 084309.
239. Kameneva, S. V.; Kobzarenko, A. V.; Feldman, V. I. *Radiat. Phys. Chem.* **2015**, *110*, 17–23.
240. Pettersson, M.; Khriachtchev, L.; Lignell, A.; Räsänen, M.; Bihary, Z.; Gerber, R. B. *J. Chem. Phys.* **2002**, *116*, 2508–2515.



241. Tsuge, M.; Berski, S.; Räsänen, M.; Latajka, Z.; Khriachtchev, L. *J. Chem. Phys.* **2014**, *140*, 044323.
242. Tsuge, M.; Räsänen, M.; Khriachtchev, L. *Chem. Phys. Lett.* **2019**, *739*, 136987.
243. Tsuge, M.; Berski, S.; Stachowski, R.; Räsänen, M.; Latajka, Z.; Khriachtchev, L. *J. Phys. Chem.* **2012**, *116*, 4510–4517.
244. Zhu, C.; Tsuge, M.; Räsänen, M.; Khriachtchev, L. *J. Chem. Phys.* **2015**, *142*, 144306.
245. Tsuge, M.; Berski, S.; Räsänen, M.; Latajka, Z.; Khriachtchev, L. *J. Chem. Phys.* **2013**, *138*, 104314.
246. Pettersson, M.; Nieminen, J.; Khriachtchev, L.; Räsänen, M. *J. Chem. Phys.* **1997**, *107*, 8423.
247. Pettersson, M.; Lundell, J.; Khriachtchev, L.; Isoniemi, E.; Räsänen, M. *J. Am. Chem. Soc.* **1998**, *120*, 7979.
248. Ryazantsev, S. V.; Kobzareno, A. V.; Feldman, V. I. *J. Chem. Phys.* **2013**, *139*, 124315. and references therein.
249. Khriachtchev, L.; Lundell, J.; Tapio, S.; Domanskaya, A.; Räsänen, M.; Isokoski, K. *J. Chem. Phys.* **2011**, *134*, 124307.
250. Pettersson, M.; Khriachtchev, L.; Lundell, J.; Räsänen, M. *J. Am. Chem. Soc.* **1999**, *121*, 11904–11905.
251. Tanskanen, H.; Khriachtchev, L.; Lundell, J.; Räsänen, M. *J. Chem. Phys.* **2006**, *125*, 074501.
252. Khriachtchev, L.; Tanskanen, H.; Lundell, J.; Pettersson, M.; Kiljunen, H.; Räsänen, M. *J. Am. Chem. Soc.* **2003**, *125*, 4696–4697.
253. Tanskanen, H.; Khriachtchev, L.; Lundell, J.; Räsänen, M. *J. Chem. Phys.* **2004**, *121*, 8291–8298.
254. Niimi, K.; Taketsugu, T.; Nakayama, A. *Phys. Chem. Chem. Phys.* **2015**, *17*, 7872–7880.
255. Willmann, K.; Vent-Schmidt, T.; Räsänen, M.; Riedel, S.; Khriachtchev, L. *RSC Adv.* **2015**, *5*, 35783–35791.
256. Domanskaya, A.; Kobzareno, A. V.; Tsvion, E.; Khriachtchev, L.; Feldman, V. I.; Gerber, R. B.; Räsänen, M. *Chem. Phys. Lett.* **2009**, *481*, 83–87.
257. Ryazantsev, S. V.; Tyurin, D. A.; Nuzhdin, K. B.; Feldman, V. I.; Khriachtchev, L. *Phys. Chem. Chem. Phys.* **2019**, *21*, 3656–3661.
258. Tanskanen, H.; Johansson, S.; Lignell, A.; Khriachtchev, L.; Räsänen, M. *J. Chem. Phys.* **2007**, *127*, 154313.
259. Zhu, C.; Räsänen, M.; Khriachtchev, L. *J. Chem. Phys.* **2015**, *143*, 244319.
260. Khriachtchev, L.; Domanskaya, A.; Lundell, J.; Akimov, A.; Räsänen, M.; Misochko, E. *J. Phys. Chem. A* **2010**, *114*, 4181–4187.
261. Turowski, M.; Gronowski, M.; Guillemin, J.-C.; Kolos, R. *J. Mol. Struct.* **2012**, *1025*, 140–146.
262. Tanskanen, H.; Khriachtchev, L.; Lundell, J.; Kiljunen, H.; Räsänen, M. *J. Am. Chem. Soc.* **2003**, *125*, 16361–16366.
263. Khriachtchev, L.; Lignell, A.; Tanskanen, H.; Lundell, J.; Kiljunen, H.; Räsänen, M. *J. Phys. Chem. A* **2006**, *110*, 11876–11885.
264. Duarte, L.; Khriachtchev, L. *RSC Adv.* **2017**, *7*, 813–820.
265. Duarte, L.; Khriachtchev, L. *Sci. Rep.* **2017**, *7*, 3130.
266. Kunttu, H.; Seetula, J.; Räsänen, M.; Apkarian, V. A. *J. Chem. Phys.* **1992**, *96*, 5630–5635.
267. Kunttu, H. M.; Seetula, J. A. *Chem. Phys.* **1994**, *189*, 273–292.
268. Fridgen, T. D.; Parnis, J. M. *J. Chem. Phys.* **1998**, *109*, 2155–2161.
269. Fridgen, T. D.; Parnis, J. M. *J. Chem. Phys.* **1998**, *109*, 2162–2168.
270. Tsuge, M.; Kalinowski, J.; Gerber, R. B.; Lee, Y.-P. *J. Phys. Chem.* **2015**, *119*, 2651–2660.
271. Lundell, J.; Pettersson, M.; Räsänen, M. *Phys. Chem. Chem. Phys.* **1999**, *1*, 4151–4155.
272. Hunter, E. P. L.; Lias, S. G. *J. Phys. Chem. Ref. Data* **1998**, *27*, 413–656.
273. Zhu, C.; Räsänen, M.; Khriachtchev, L. *J. Chem. Phys.* **2015**, *143*, 074306.
274. Arppe, T.; Khriachtchev, L.; Lignell, A.; Domanskaya, A. V.; Räsänen, M. *Inorg. Chem.* **2012**, *51*, 4398–4402.
275. Chopra, P.; Ghosh, A.; Roy, B.; Ghanty, T. K. *Chem. Phys.* **2017**, *494*, 20–30.
276. Sosulin, I. S.; Tyurin, D. A.; Feldman, V. I. *Chem. Phys. Lett.* **2020**, *744*, 137211.
277. Evans, C. J.; Rubinfoff, D. S.; Gerry, M. C. L. *Phys. Chem. Chem. Phys.* **2000**, *2*, 3943–3948.
278. Thomas, J. M.; Walker, N. R.; Cooke, S. A.; Gerry, M. C. L. *J. Am. Chem. Soc.* **2004**, *126*, 1235–1246.
279. Cooke, S. A.; Gerry, M. C. L. *J. Am. Chem. Soc.* **2004**, *126*, 17000–17008.
280. Zou, W.; Liu, Y.; Boggs, J. E. *Chem. Phys. Lett.* **2009**, *482*, 207–210.
281. Evans, C. J.; Wright, T. G.; Gardner, A. M. *J. Phys. Chem. A* **2010**, *114*, 4446–4454.
282. Lai, T.-Y.; Yang, C.-Y.; Lin, H.-J.; Yang, C.-Y.; Hu, W.-P. *J. Chem. Phys.* **2011**, *134*, 244110.
283. Wang, X.; Andrews, L.; Willmann, K.; Brosi, F.; Riedel, S. *Angew. Chem. Int. Ed.* **2012**, *51*, 10628–10632.
284. Wang, X.; Andrews, L.; Willmann, K.; Brosi, F.; Riedel, S. *Chem. Eur. J.* **2013**, *19*, 1397–1409.
285. Thompson, C. A.; Andrews, L. *J. Am. Chem. Soc.* **1994**, *116*, 423–424.
286. Veldkamp, A.; Frenking, G. *Chem. Phys. Lett.* **1994**, *226*, 11–16.
287. Pan, S.; Jalife, S.; Kumar, R. M.; Subramanian, V.; Merino, G.; Chattaraj, P. K. *Chem. Phys. Chem.* **2013**, *14*, 2511–2517.
288. Saha, R.; Pan, S.; Merino, G.; Chattaraj, P. K. *J. Phys. Chem. A* **2015**, *119*, 6746–6752.
289. Borocci, S.; Bronzolino, N.; Grandinetti, F. *Chem. Phys. Lett.* **2004**, *384*, 25–29.
290. Zhang, Q.; Chen, M.; Zhou, M.; Andrada, D. M.; Frenking, G. *J. Phys. Chem. A* **2015**, *119*, 2543–2552.
291. Wang, Q.; Wang, X. *J. Phys. Chem.* **2013**, *117*, 1508–1513.
292. Yu, W.; Liu, X.; Xu, B.; Xing, X.; Wang, X. *J. Phys. Chem. A* **2016**, *120*, 8590–8598.
293. Cao, Q.; Andrijchenko, N.; Ahola, A.-E.; Domanskaya, A. V.; Räsänen, M.; Ermilov, A.; Nemukhin, A.; Khriachtchev, L. *J. Chem. Phys.* **2012**, *137*, 134305.
294. Ullrich, S.; Tarczay, G.; Müller-Dethlefs, K. *J. Phys. Chem. A* **2002**, *106*, 1496–1503.
295. Cao, Q.; Andrijchenko, N.; Ermilov, A.; Räsänen, M.; Nemukhin, A.; Khriachtchev, L. *J. Chem. Phys.* **2015**, *119*, 2587–2593.
296. Grochala, W. *Chem. Soc. Rev.* **2007**, *36*, 1632–1655.
297. Nelson, D. A., Jr.; Ruoff, A. L. *Phys. Rev. Lett.* **1979**, *42*, 383–386.
298. Dong, X.; Oganov, A. R.; Goncharov, A. F.; Stavrou, E.; Lobanov, S.; et al. *Nat. Chem.* **2017**, *9*, 440–445.
299. Guńka, P. A.; Dziubek, K. F.; Gladysiak, A.; Dranka, M.; Piechota, J.; et al. *Cryst. Growth Des.* **2015**, *15*, 3740–3745.
300. Plisson, T.; Weck, G.; Loubeyre, P. *Phys. Rev. Lett.* **2014**, *113*, 025702.
301. Dewaele, A.; Worth, N.; Pickard, C. J.; Needs, R. J.; Pascarella, S. *Nat. Chem.* **2016**, *8*, 784–790.
302. Zhu, L.; Liu, H.; Pickard, C. J.; Zou, G.; Ma, Y. *Nat. Chem.* **2014**, *6*, 644–648.
303. Dewaele, A.; Pépin, C. M.; Geneste, G.; Garbino, G. *High Press. Res.* **2017**, *37*, 137–146.
304. Stavrou, E.; Yao, Y.; Goncharov, A. F.; Lobanov, S. S.; Zaig, J. M.; et al. *Phys. Rev. Lett.* **2018**, *120*, 096001.
305. Adeleke, A. A.; Kunz, M.; Greenberg, E.; Prakapenka, V. B.; Yao, Y.; Stavrou, E. *ACS Earth Space Chem.* **2019**, *3*, 2517–2524.
306. Loubeyre, P.; LeToullec, R.; Pinceaux, J. P. *Phys. Rev. Lett.* **1994**, *72*, 1360–1363.
307. Ji, C.; Goncharov, A. F.; Shukla, V.; Jena, N. K.; Popov, D.; Li, B.; et al. *Proc. Natl. Acad. Sci. U. S. A.* **2017**, *114*, 3596–3600.
308. Kleppe, A. K.; Amboage, M.; Jephcoat, A. P. *Sci. Rep.* **2014**, *4*, 4989.
309. Somayazulu, M.; Dera, P.; Smith, J.; Hemley, R. J. *J. Chem. Phys.* **2015**, *142*, 104503.

310. Niwa, K.; Matsuzaki, F.; Hasegawa, M. *Phys. Chem. Chem. Phys.* **2016**, *19*, 59–63.
311. Howie, R. T.; Turnbull, R.; Binns, J.; Frost, M.; Dalladay-Simpson, P.; Gregoryanz, E. *Sci. Rep.* **2016**, *6*, 34896.
312. Wu, G.; Huang, X.; Huang, Y.; Pan, L.; Li, F.; et al. *J. Phys. Chem. C* **2017**, *121*, 6264–6271.
313. Kim, M.; Debessai, M.; Yoo, C.-S. *Nat. Chem.* **2010**, *2*, 784–788.
314. Kurzydłowski, D.; Zaleski-Ejgierd, P.; Grochala, W.; Hoffmann, R. *Inorg. Chem.* **2011**, *50*, 3832–3840.
315. Peng, F.; Botana, J.; Wang, Y.; Ma, Y.; Miao, M.-S. *J. Phys. Chem. Lett.* **2016**, *7*, 4562–4567.

## 1.09 Syntheses and molecular structures of cyclic selenoethers and their derivatives

Raija Ollunkaniemi and Risto S. Laitinen, Laboratory of Inorganic Chemistry, Environmental and Chemical Engineering, University of Oulu, Oulu, Finland

© 2023 Elsevier Ltd. All rights reserved.

1.09.1	Introduction	527
1.09.2	Saturated selenoethers	527
1.09.2.1	Synthesis	527
1.09.2.2	Molecular structures	529
1.09.2.3	Adducts and coordination compounds	531
1.09.2.3.1	General	531
1.09.2.3.2	Se(CH <sub>2</sub> ) <sub>4</sub> , Se <sub>2</sub> (CH <sub>2</sub> ) <sub>4</sub> , and Se <sub>3</sub> (CH <sub>2</sub> ) <sub>3</sub>	532
1.09.2.3.3	Se <sub>2</sub> (CH <sub>2</sub> ) <sub>6</sub>	534
1.09.2.3.4	Se <sub>4</sub> (CH <sub>2</sub> ) <sub>12</sub> and Se <sub>6</sub> (CH <sub>2</sub> ) <sub>18</sub>	538
1.09.2.3.5	Crown-ether analogs	540
1.09.2.4	Cyclic selenoether cations	541
1.09.3	Unsaturated selenoethers	543
1.09.3.1	Selenoethers with alkene spacers	543
1.09.3.2	Selenoethers with alkyne spacers	552
1.09.4	Summary	554
References		554

### Abstract

The preparation and structures of monocyclic selenoethers containing unbranched saturated or unsaturated hydrocarbon spacers are reviewed. The main emphasis is in the bonding and intermolecular interactions involving selenium atoms. Chalcogen bonding plays a role in the crystallization of various selenoethers and their derivatives and the solid-state lattices generally show columnar stacking of the rings. The resulting infinite cavities in the lattices are not unlike those in zeolites, and small molecules can be trapped therein.

### 1.09.1 Introduction

The advent of macrocyclic crown-ethers dates back to late 1960s.<sup>1</sup> They have shown extensive utility in many areas of natural science and have played a significant role in synthetic chemistry, biological activity, crystal engineering, and supramolecular chemistry to name a few examples. There are numerous reviews on the preparation, structure, properties, and applications of crown-ethers (see for instance Ref. 2 and references therein).

The progress in the chemistry and utility of crown-ethers has led to rapidly growing interest in the related species containing macrocycles of heavier chalcogen elements, as reflected by the large number of reviews during the current millennium that describe the developments in synthetic methods, structural characterization, and coordination chemistry of heterocyclic chalcogenoethers.<sup>3–16</sup>

The complete review of the different aspects of the chemistry of heterocyclic selenoethers is beyond the scope of this chapter, and this discussion is restricted to monocyclic selenoethers containing unbranched alkane, alkene, and alkyne spacers, and their ions, adducts, and coordination compounds. Furthermore, the intermolecular interactions of heavy chalcogen heterocycles involve chalcogen bonding in the solid state with applications in supramolecular chemistry and crystal engineering,<sup>17–22</sup>

### 1.09.2 Saturated selenoethers

#### 1.09.2.1 Synthesis

The identified and characterized heterocyclic selenoethers have been listed in **Chart 1**. Se(CH<sub>2</sub>)<sub>4</sub> (**1**) and Se(CH<sub>2</sub>)<sub>5</sub> (**2**) are the oldest known selenoethers, and their preparations have already been reported in late 1920s by Morgan and Burstall<sup>23,24</sup> requiring the use of hydrogen selenide, hydrogen gas, and metallic sodium. A more convenient preparation involved the reduction of elemental selenium with sodium hydroxymethylsulfate(IV) and the treatment of the selenide thus formed with  $\alpha\omega$ -Br(CH<sub>2</sub>)<sub>m</sub>Br ( $m = 4, 5$ ).<sup>25</sup> The

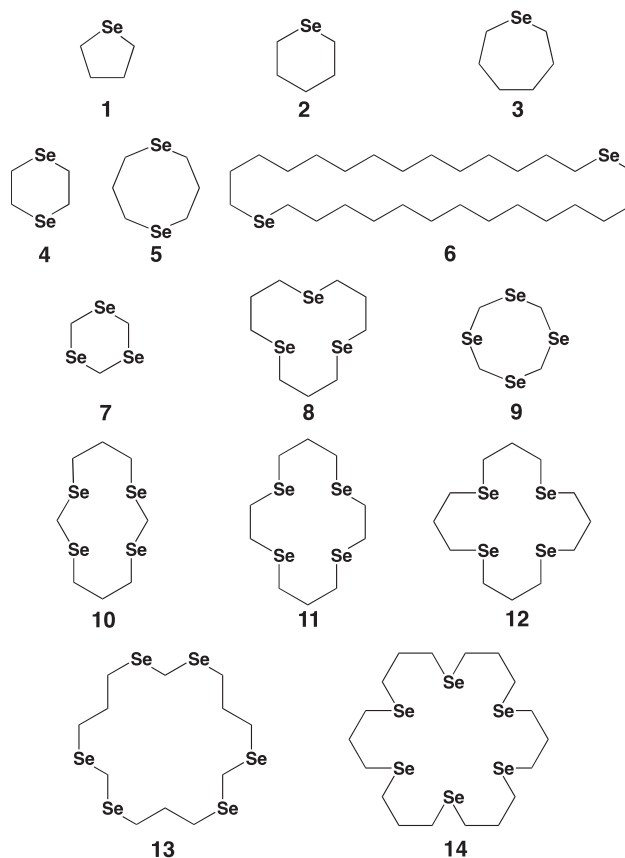


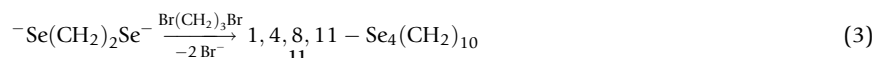
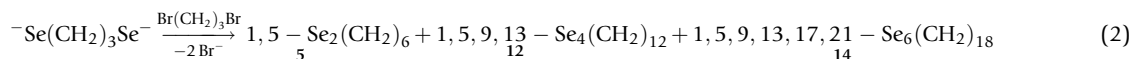
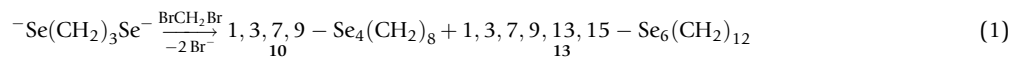
Chart 1 Saturated heterocyclic selenoethers.

related hybrid selenoethers  $1,4\text{-SeO}(\text{CH}_2)_4$  and  $1,4\text{-SeS}(\text{CH}_2)_4$  could be prepared invoking the similar methodology. The reaction of lithium selenide and 1,2-dichloroethane afforded  $1,4\text{-Se}_2(\text{CH}_2)_4$  (4).<sup>26</sup> Sodium tetrahydridoborate,<sup>27</sup> lithium triethylhydridoborate,<sup>28</sup> lithium tetrahydridoaluminate,<sup>29</sup> and hydrazine hydrate—potassium hydroxide<sup>30</sup> have also been utilized as reducing agents of elemental chalcogen. The ring size can be controlled by the number of the methylene groups ( $m$ ) in  $\alpha\omega\text{-X}(\text{CH}_2)_m\text{X}$ .

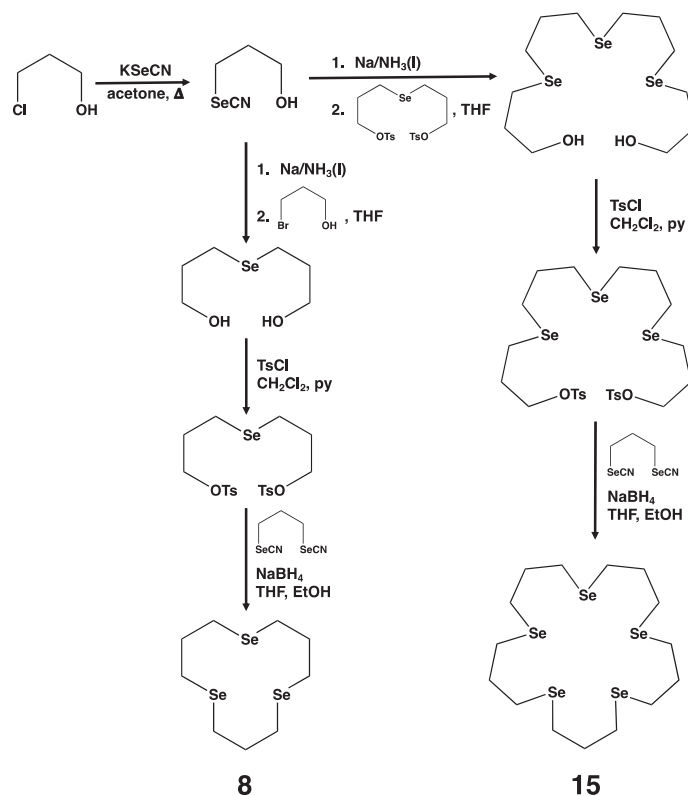
Monoselenoethers  $\text{Se}(\text{CH}_2)_4$  (1),  $\text{Se}(\text{CH}_2)_5$  (2), and  $\text{Se}(\text{CH}_2)_6$  (3) have been prepared in good yields at the NMR scale by irradiating thiohydroxamic esters of *n*-(benzylseleno)pentanoic, -hexanoic, and -heptanoic acid.<sup>31</sup>

It was recently observed that macrocyclic  $1,15\text{-Se}_2(\text{CH}_2)_{28}$  (6) is formed upon decomposition of  $[\text{PtCl}_2\{\text{Se}[(\text{CH}_2)_6(\text{CH}=\text{CH})_2]_2\}]_2$ , which was synthesized from  $\text{PtCl}_2$  and  $\text{Se}\{(\text{CH}_2)_6(\text{CH}=\text{CH})_2\}_2$ .<sup>32</sup>  $1,3,5\text{-Se}_3(\text{CH}_2)_3$  (7)<sup>33</sup> was obtained from hydrogen selenide and formaldehyde, as well as from  $\text{Na}_2\text{Se}$  and  $\text{CH}_2\text{Cl}_2$ .<sup>34</sup> The latter reaction also afforded small amounts of  $1,3,5,7\text{-Se}_4(\text{CH}_2)_4$  (9). The preparation of macrocyclic polyselenoethers  $1,5,9\text{-Se}_3(\text{CH}_2)_9$  (8) and  $1,5,9,13,17\text{-Se}_5(\text{CH}_2)_{15}$  (15) is shown in Scheme 1.<sup>35</sup>

Diselenolates  $^-\text{Se}(\text{CH}_2)_n\text{Se}^-$  ( $n = 2, 3$ ) are formed by reduction of  $\text{NCSe}(\text{CH}_2)_n\text{SeCN}$  with metallic sodium in liquid ammonia. Upon treatment with  $\alpha\omega\text{-Br}(\text{CH}_2)_m\text{Br}$  ( $m = 1\text{--}3$ ), mixtures of macrocyclic selenoethers are formed (Eqs. 1–3).<sup>36</sup> The methylene groups in the reactants serve as spacers for the selenium atoms.



The formation of a few other cyclic selenoethers has also been reported, but their identification and structural characterization are still incomplete.<sup>37–42</sup> The reported preparation of  $1,2\text{-Se}_2(\text{CH}_2)_3$  (16)<sup>39,40</sup> is particularly interesting. Its formation was verified by the following reactions: The product was reduced with  $\text{NaBH}_4$  followed by the treatment with  $\text{Br}(\text{CH}_2)_3\text{Br}$ , which resulted in the formation of  $1,5\text{-Se}_2(\text{CH}_2)_6$  (5). Two-electron oxidation of 5 by  $\text{NOPF}_6$  afforded  $[1,5\text{-Se}_2(\text{CH}_2)_6][\text{PF}_6]_2$ .<sup>43</sup> This methodology was



**Scheme 1** Preparation of 1,5,9-Se<sub>3</sub>(CH<sub>2</sub>)<sub>9</sub> (**8**) and 1,5,9,13,17-Se<sub>5</sub>(CH<sub>2</sub>)<sub>15</sub> (**15**).<sup>35</sup>

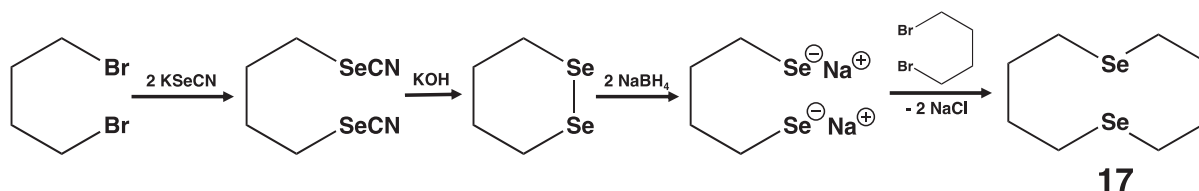
later extended to the preparation of 1,6-Se<sub>2</sub>(CH<sub>2</sub>)<sub>8</sub> (**17**) with *ca.* 3% yield (see **Scheme 2**).<sup>44</sup> The treatment of [Pt<sub>2</sub>(μ-Se)<sub>2</sub>(PPh<sub>3</sub>)<sub>4</sub>] with the large excess of Br(CH<sub>2</sub>)<sub>4</sub>Br afforded **17** with an improved yield.<sup>45</sup>

Mixed-chalcogen selenoethers 1,4-SeO(CH<sub>2</sub>)<sub>4</sub> and 1,4-SeS(CH<sub>2</sub>)<sub>4</sub> have been prepared by a suitable modification of the reagents in the methods described above.<sup>25</sup> The reduction of selenium in liquid ammonia followed by the reaction with Cl(CH<sub>2</sub>CH<sub>2</sub>)O(CH<sub>2</sub>CH<sub>2</sub>)O(CH<sub>2</sub>CH<sub>2</sub>)Cl in ethanol under conditions of high dilution afforded 1,4,10,13-tetraoxa-7,16-diselenaooctadecane Se<sub>2</sub>O<sub>4</sub>(CH<sub>2</sub>)<sub>12</sub>.<sup>46</sup> A side-product, 1,4-dioxa-7-selena-nonane was obtained as a yellow oil. The treatment of NCSe(CH<sub>2</sub>)<sub>3</sub>SeCN with NaBH<sub>4</sub> and Cl(CH<sub>2</sub>)<sub>3</sub>SH followed by the reaction with Br(CH<sub>2</sub>)<sub>3</sub>Br in the presence of Cs<sub>2</sub>(CO)<sub>3</sub> in DMF at 70 °C afforded 1,5-diselena-9,13-dithiacyclohexadecane.<sup>47</sup>

### 1.09.2.2 Molecular structures

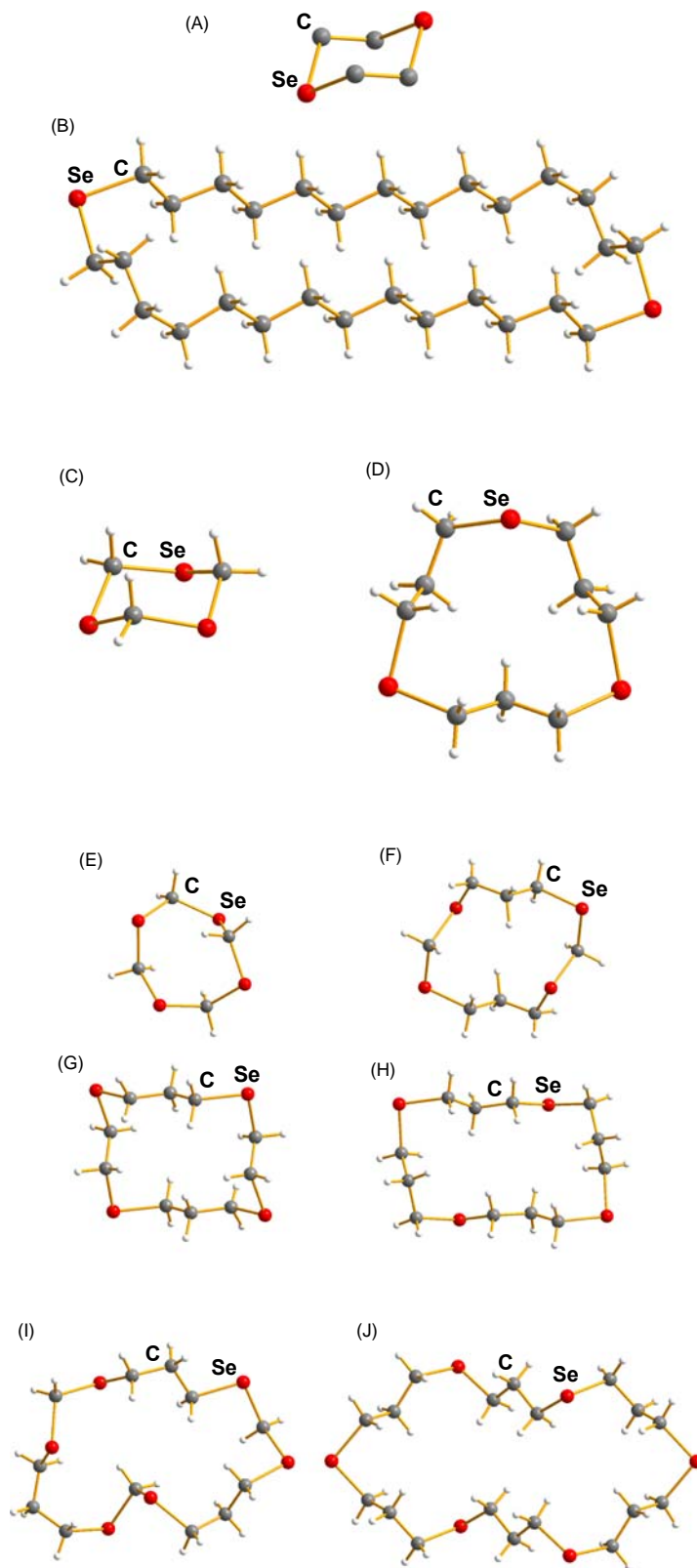
The three smallest molecules in **Chart 1**, Se(CH<sub>2</sub>)<sub>4</sub> (**1**), Se(CH<sub>2</sub>)<sub>5</sub> (**2**) and Se(CH<sub>2</sub>)<sub>6</sub> (**3**) are light-yellow liquids at room temperature. All larger molecules are crystalline solids, and the crystal structures of most of them have been determined by single-crystal X-ray diffraction techniques (see **Fig. 1**). Their bond parameters have been summarized in **Table 1** and are consistent with the values expected for single bonds.

The compounds **4** and **7** [**Fig. 1**(a) and (c)] exhibit chair conformations with the torsional angles spanning 64.69(8)–73.08(9)<sup>48</sup> and 62.06(2)–69.29(12)<sup>49</sup> respectively (the motif of the torsional angles in both molecules is + – + – + –). While the torsional angles in **6** of 62.5(3) and 64.3(3)<sup>°</sup> involving the Se–C bonds also show values, which are consistent with those of **4** and **7**, most torsional angles involving the C–C bonds are approximately 180<sup>°</sup>.<sup>32</sup> Consequently, the molecule is strongly elongated [see **Fig. 1**(b)].



**Scheme 2** Preparation of 1,6-Se<sub>2</sub>(CH<sub>2</sub>)<sub>8</sub> (**17**).<sup>44</sup>





**Fig. 1** Molecular structures of (a) 1,4- $\text{Se}_2(\text{CH}_2)_6$  (hydrogen atoms not shown),<sup>48</sup> (b) 1,15- $\text{Se}_2(\text{CH}_2)_{28}$ ,<sup>32</sup> (c) 1,3,5- $\text{Se}_3(\text{CH}_2)_3$ ,<sup>49</sup> (d) 1,5,9- $\text{Se}_3(\text{CH}_2)_9$ ,<sup>33,47</sup> (e) 1,3,5,7- $\text{Se}_4(\text{CH}_2)_4$ ,<sup>50</sup> (f) 1,3,7,9- $\text{Se}_4(\text{CH}_2)_8$ ,<sup>36</sup> (g) 1,4,8,11- $\text{Se}_4(\text{CH}_2)_{10}$ ,<sup>36</sup> (h) 1,5,9,13- $\text{Se}_4(\text{CH}_2)_{12}$ ,<sup>36</sup> (i) 1,3,7,9,13,15- $\text{Se}_6(\text{CH}_2)_{12}$ ,<sup>36,47</sup> and (j) 1,5,9,13,17,21- $\text{Se}_6(\text{CH}_2)_{18}$ .<sup>36</sup>

**Table 1** Bond parameters in saturated selenoether heterocycles.

Molecule	$r_{SeC}$ (Å)	$r_{CC}$ (Å)	$\alpha_{Se}$ (°)	$\alpha_C$ (°)	Ref.
1,4- $Se_2(CH_2)_4$ ( <b>4</b> )	1.985(5), 2.033(5)	1.498(3)	97.86(6)	109.83(7)–110.61(8)	48
1,15- $Se_2(CH_2)_{28}$ ( <b>6</b> )	1.965(4), 1.968(4)	1.513(5)–1.540(5)	98.1(2)	111.4(3)–115.0(3)	32
1,3,5- $Se_3(CH_2)_3$ ( <b>7</b> )	1.9443(9)–1.9679(13)	–	98.113(9)–101.736(6)	114.700(15)–119.017(7)	49
1,5,9- $Se_3(CH_2)_9$ ( <b>8</b> )	1.923(8)–1.963(7)	1.504(11)–1.515(12)	97.4(3)–100.6(3)	109.7(5)–116.6(5)	47
1,3,5,7- $Se_4(CH_2)_4$ ( <b>9</b> )	1.9173(10)–1.9742(10)	–	98.113(9)–101.736(6)	114.700(15)–119.017(7)	50
1,3,7,9- $Se_4(CH_2)_8$ ( <b>10</b> )	1.924(13)–1.972(11)	1.480(15)–1.535(16)	91.5(4)–100.1(5)	110.0(5)–114.5(7)	36
1,4,8,11- $Se_4(CH_2)_{10}$ ( <b>11</b> )	1.958(4)–1.963(4)	1.508(8)–1.512(7)	91.81(18), 99.79(18)	111.2(4)–114.6(3)	36
1,5,9,13- $Se_4(CH_2)_{12}$ ( <b>12</b> )	1.93(5)–1.98(2)	1.50(10)–1.53(4)	97.2(14)–100.0(14)	111(4)–114(4)	36
1,3,7,9,13,15- $Se_6(CH_2)_{12}$ ( <b>13</b> )	1.907(6)–1.972(6)	1.503(10)–1.532(8)	94.2(2)–100.4(3)	108.9(4)–118.5(3)	36
1,5,9,13,17,21- $Se_6(CH_2)_{18}$ ( <b>14</b> )	1.945(8)–1.967(11)	1.471(14)–1.536(12)	96.6(4)–99.0(4)	110.0(8)–118.0(8)	36

The distribution of the torsional angles in all heterocyclic selenoethers in Fig. 1 are shown in Fig. 2.

It can be seen that the torsional angles about the Se–C bonds are generally concentrated near to 60° with smaller distribution maxima near 90 and 180°. In a similar fashion, those involving the C–C bonds mostly show torsional angles of 180° with a smaller maximum around 60°. The signs of the torsional angles can be both positive and negative (rotation clockwise of counterclockwise, respectively). These distribution maxima can be rationalized by electron-pair interactions, as shown in Fig. 3.

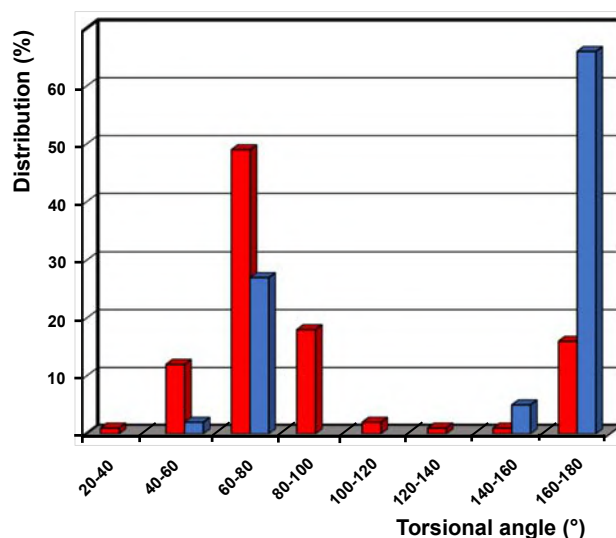
The characteristic feature in many macrocyclic chalcogenoethers is the columnar packing in the solid lattices, as shown for 4, 7, 8, 9, 10, 11, 13, and 14 in Fig. 4. All these species show several Se···Se close contacts, which have been depicted in the figure. These contacts indicate only weak interactions, since they span a range of 3.457(14)–4.402(9) Å, which are relatively close to the sum of the van der Waals radii of two selenium atoms (4.0 Å<sup>51</sup>). The nature of these secondary bonding interactions, which are currently called also chalcogen bonds, have been discussed in recent reviews.<sup>20–22</sup>

There are two notable exceptions in the packing of the known selenoethers. While 6 shows similar columnar packing as the selenoethers shown in Fig. 4. It has no selenium-selenium close contacts [see Fig. 5(a)].<sup>32</sup> The second exception is 12. While there are Se···Se close contacts of 3.457(14)–3.956(17) Å indicating similar interaction strengths as in the species in Fig. 4, the molecules do not pack in a columnar fashion in the lattice [see Fig. 5(b)].<sup>36</sup> Furthermore, one of the molecules in the asymmetric unit is disordered with the molecules assuming random distribution of two orientations.

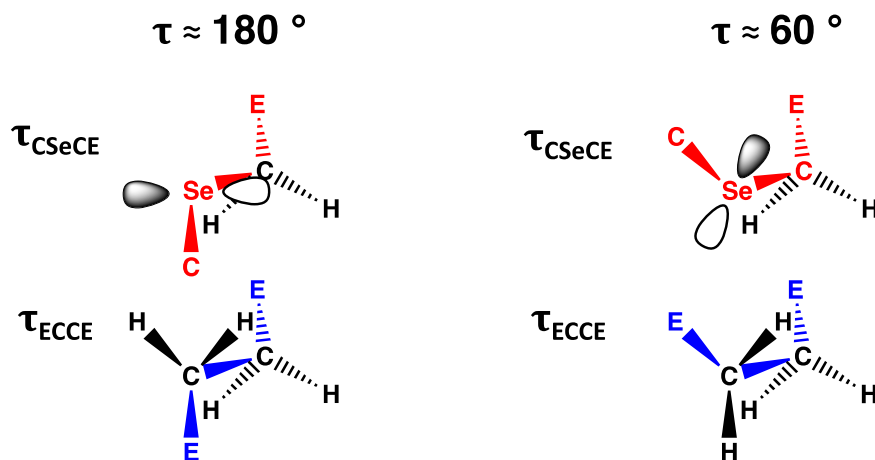
### 1.09.2.3 Adducts and coordination compounds

#### 1.09.2.3.1 General

Cyclic selenoethers form compounds with a number of Lewis acids involving both main group elements and transition metals. In case of the interaction with non-metal compounds in which the molecular identity of the acid molecule is identifiable, these compounds are referred as adducts. In case of many main group elements and transition metals, the selenoethers act as ligands



**Fig. 2** The distribution of torsional angles in heterocyclic selenoethers (see Fig. 1). The torsional angles about the C–Se bonds are indicated in red and those involving C–C bonds in blue.



**Fig. 3** The CH bonding pair and selenium lone pair interactions leading to the favorable torsional angles of 60 and 180°. E = Se or CH<sub>2</sub>. The torsional angles about the C–Se bonds are indicated in red and those involving C–C bonds in blue.

to a central atom with selenium as a donor. These entities are formally coordination compounds, though in the spirit of A. Werner's original terminology they are often called complexes, in particular in inorganic chemistry, even though it is currently well-established that the principles in bonding of these species are not more complicated than in simple inorganic and organic compounds. While International Union of Pure and Applied Chemistry (IUPAC) currently discourages the use of the term complex for coordination entities, it is often rather convenient to use. In the current treatise, the terms "coordination compound," "coordination entity," and "complex" are used interchangeably, as appropriate. It should further be emphasized that the use of the term complex does not imply that the structure of the compound is not known.

### 1.09.2.3.2 Se(CH<sub>2</sub>)<sub>4</sub>, Se<sub>2</sub>(CH<sub>2</sub>)<sub>4</sub>, and Se<sub>3</sub>(CH<sub>2</sub>)<sub>3</sub>

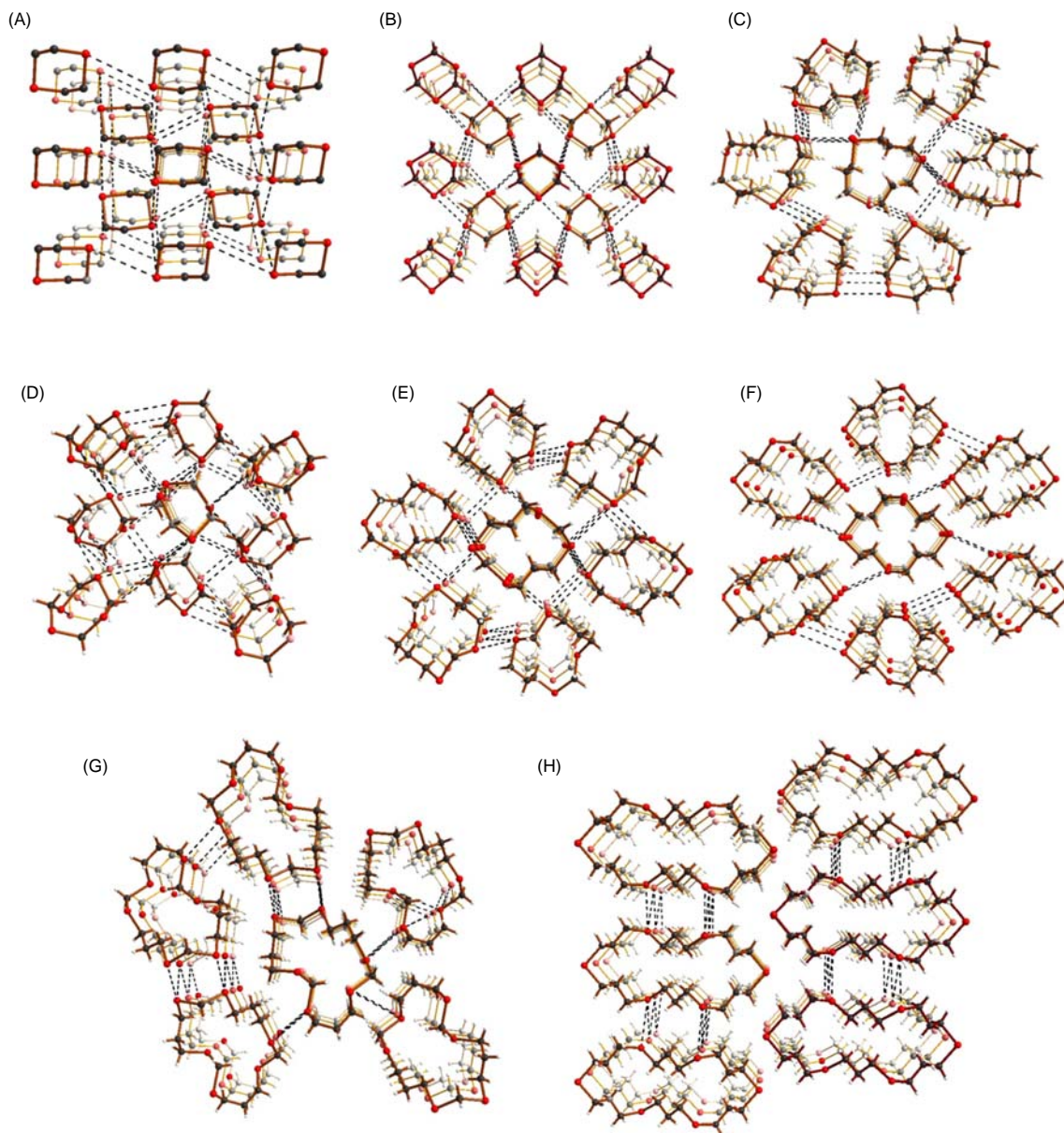
It has been reported that Se(CH<sub>2</sub>)<sub>4</sub> (**1**) forms coordination compounds with mercury halogenides HgX<sub>2</sub> (X = Cl, Br, I)<sup>52,53</sup> and adducts with elemental iodine.<sup>54</sup> It has enabled the elucidation of the molecular structure of Se(CH<sub>2</sub>)<sub>4</sub> by X-ray diffraction, which has been difficult otherwise, since **1** is liquid at room temperature. The [HgCl<sub>2</sub>{Se(CH<sub>2</sub>)<sub>4</sub>}] moieties are associated into infinite chains through weak Hg⋯Cl interactions of 3.164(2) Å [see Fig. 6(a)].<sup>52</sup> The crystal structures of [HgX<sub>2</sub>{Se(CH<sub>2</sub>)<sub>4</sub>}<sub>2</sub>] (X = Br, I) are mutually rather similar, though the packing of the molecular chains are different [Fig. 6(b) and (c)].<sup>53</sup> The bromine and iodine complexes do not show short Hg⋯X contacts, but the chains are formed through Se⋯Hg secondary bonding interactions of 3.773(3)–3.381(2) Å and 3.8195(15)–4.0312(16) Å for [HgBr<sub>2</sub>{Se(CH<sub>2</sub>)<sub>4</sub>}<sub>2</sub>] and [HgI<sub>2</sub>{Se(CH<sub>2</sub>)<sub>4</sub>}<sub>2</sub>], respectively.

The coordination of **1** to mercury involves the selenium 4p lone-pair, which is perpendicular to the plane of the two Se–C bonds. Therefore, the bond parameters of the ligand can be expected to represent those of the free ligand. The Se–C bond lengths in all three compounds span a narrow range of 1.986(12)–2.007(10) Å and the bond angles  $\alpha_{\text{Se}} = 89.6(4)$ – $90.4(3)^\circ$ , and  $\alpha_{\text{C}} = 103.4(5)$ – $122.9(15)^\circ$ .<sup>52,53</sup> While most of the bond angles in the three coordination entities are close to the expected values, [HgI<sub>2</sub>{Se(CH<sub>2</sub>)<sub>4</sub>}<sub>2</sub>] shows both the smallest and the highest values. It is suggested to be due to conformational disorder.<sup>53</sup>

The five-membered Se(CH<sub>2</sub>)<sub>4</sub> ring molecule has significant ring strain, as can be judged from the torsional angles. The tetrahydro-selenophene ring in [HgCl<sub>2</sub>{Se(CH<sub>2</sub>)<sub>4</sub>}] and the two rings in [HgX<sub>2</sub>{Se(CH<sub>2</sub>)<sub>4</sub>}<sub>2</sub>] (X = Br, I) show rather similar values of the torsional angles [ $\tau_{\text{SeC}}$  angles span a range of 7.3(7)–19.3(8)° and that of  $\tau_{\text{CC}}$  is 33.3(10)–57.5(10)°]. The motif of the torsional angles starting from the selenium atom is (+ – + – + – +).<sup>52,53</sup> By contrast, one tetrahydro-selenophene ring in [HgI<sub>2</sub>{Se(CH<sub>2</sub>)<sub>4</sub>}<sub>2</sub>] is virtually planar. This is probably also a consequence of crystallographic disorder.

The interaction between Se(CH<sub>2</sub>)<sub>4</sub> and I<sub>2</sub>, which is shown in Fig. 7(a), is one of the early examples of secondary bonding interactions,<sup>54</sup> the term of which was somewhat later coined by Alcock.<sup>58</sup> The intermolecular Se⋯I close contact is observed to be 3.633(3) Å,<sup>54</sup> which is significantly shorter than the sum of the van der Waals radii of 4.15 Å.<sup>51</sup> The interaction between selenium and iodine can be represented either by the 4p electron lone-pair orbital overlapping with the  $\sigma^*$ (I–I) orbital of I<sub>2</sub> [see Fig. 8(a)] or by the interaction of the  $\sigma$ -hole at the extension of the I–I bond with the above-mentioned 4p lone-pair of selenium [see Fig. 8(b)]. The exocyclic Se–I bond of 2.762(5) Å<sup>54</sup> is only slightly longer than the expected single bond length of 2.50 Å.<sup>51</sup> The I–I bond length of 2.914(4) Å in Se(CH<sub>2</sub>)<sub>4</sub>·I<sub>2</sub> is significantly longer than the I–I single bond length of 2.716(6) Å in I<sub>2</sub><sup>59</sup> and is the consequence of the interactions shown in Fig. 8.

1,4-Se<sub>2</sub>(CH<sub>2</sub>)<sub>4</sub>, 1,3,5-Se<sub>3</sub>(CH<sub>2</sub>)<sub>3</sub>, and the related 1,4-SeO(CH<sub>2</sub>)<sub>4</sub> also form adducts with I<sub>2</sub><sup>55–57</sup> and other iodine-containing species.<sup>60–63</sup> Their close Se⋯I contacts are shown in Fig. 7(b)–(d), and the metrical interatomic distances are presented in Table 2. They are a consequence of a combination of  $n^2(\text{Se}) \rightarrow \sigma^*(\text{I–I})$  interaction and the electrostatic attraction between the  $\sigma$ -hole and selenium lone pair (see Fig. 8). In addition, these species may also show  $\pi^*(\text{I–I}) \rightarrow \sigma^*(\text{C–Se})$  interactions. The  $n^2(\text{Se}) \rightarrow \sigma^*(\text{I–I})$  interactions should lead to the elongation of the I–I bond, whereas the  $\pi^*(\text{I–I}) \rightarrow \sigma^*(\text{C–Se})$  interactions should result in the shortening of the I–I bond. Since the Se⋯I distances are close to the sum of van der Waals radii, these effects are not expected to be large.



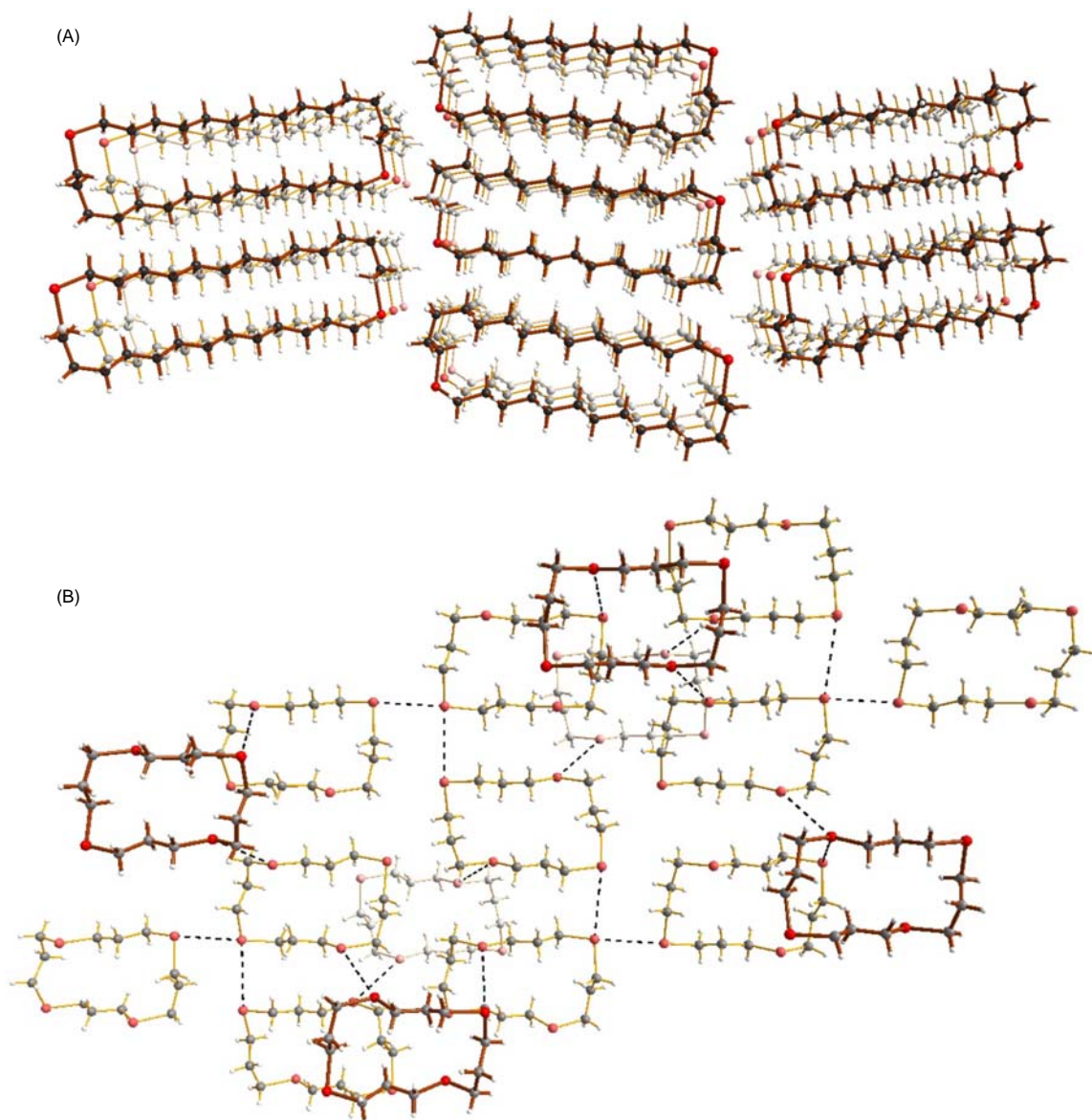
**Fig. 4** Packing of selenoethers in the solid state. (a) **4**,<sup>48</sup> (b) **7**,<sup>49</sup> (c) **8**,<sup>47</sup> (d) **9**,<sup>50</sup> (e) **10**,<sup>36</sup> (f) **11**,<sup>36</sup> (g) **13**,<sup>36</sup> and (h) **14**.<sup>36</sup> Selenium atoms are indicated in red, carbon atoms in gray, and hydrogen in white.

It can be seen from **Table 2** that like in case of  $\text{Se}(\text{CH}_2)_4 \cdot \text{I}_2$ , the Se–I bonds in  $1,4\text{-Se}_2(\text{CH}_2)_4 \cdot 2\text{I}_2$ ,  $1,3,5\text{-Se}_3(\text{CH}_2)_3 \cdot \text{I}_2$ ,  $1,4\text{-SeO}(\text{CH}_2)_4 \cdot \text{I}_2$ , and  $1,4\text{-SeO}(\text{CH}_2)_4 \cdot \text{ICl}$  are longer than the single bond but well shorter than the sum of van der Waals radii of selenium and iodine. The elongation of the I–I or the I–Cl bond is strongly dependent on the strength of the Se–I interaction and is consistent with the  $n^2(\text{Se}) \rightarrow \sigma^*(\text{I-I})$  charge transfer. This has been discussed in case of a related system involving the iodine adduct of *tert*-butyl tellurium diimide dimer.<sup>64</sup> The intermolecular Se $\cdots$ I interactions are relatively weak and do not play a significant role in the molecular parameters.

Tetrahydroselephenone reacts slowly with iodine and metallic gold in aqueous solution of ethanol to afford a small crop of light yellow crystals on the surface of the metal.<sup>65</sup> These crystals, which have been formulated as  $[\text{Au}\{\text{Se}(\text{CH}_2)_4\}_n][\text{AuI}_2]_n$  can be stored for a short while in air. The molecular structure is shown in **Fig. 9**. The bond parameters and conformation of the  $\text{Se}(\text{CH}_2)_4$  rings are similar to those found in the  $\text{I}_2$  adduct and Hg complexes.

$[\text{Ag}\{\text{Se}_3(\text{CH}_2)_3\}_2][\text{AsF}_6] \cdot \text{SO}_2$  was prepared almost quantitatively from  $1,3,5\text{-Se}_3(\text{CH}_2)_3$  and  $\text{AgAsF}_6$  at  $-196^\circ\text{C}$  in liquid  $\text{SO}_2$ .<sup>66</sup> The coordination environment around silver in the  $[\text{Ag}\{\text{Se}_3(\text{CH}_2)_3\}_2]^+$  cation is approximately an octahedron. The comparison of the structure of  $[\text{Ag}\{\text{Se}_3(\text{CH}_2)_3\}_2]^+$  with that of the  $[\text{Ag}_2(\text{Se}_{12})]^{2+}$  dication<sup>67</sup> is shown in **Fig. 10**.





**Fig. 5** The molecular packing in (a) **6**<sup>32</sup> and (b) **12**.<sup>36</sup> Selenium atoms are indicated in red, carbon in gray, and hydrogen in white.

The Ag–Se bond lengths in the  $[\text{Ag}\{\text{Se}_3(\text{CH}_2)_3\}_2]^+$  cation span the range 2.78(1)–3.05(1) Å,<sup>66</sup> while those in the  $[\text{Ag}_2(\text{Se}_{12})]^{2+}$  dication show a narrow range of 2.644(1)–2.646(1) Å.<sup>67</sup> While  $[\text{Ag}\{\text{Se}_3(\text{CH}_2)_3\}_2]^+$  is a mononuclear distorted octahedron, both silver atoms in  $[\text{Ag}_2(\text{Se}_{12})]^{2+}$  show almost a trigonal planar coordination to three selenium atoms. One Ag is coordinated to the selenium atoms 1, 5, and 9, and the other to atoms 3, 7, and 11. In addition, there is an Ag–Ag bond of 2.971(1) Å.

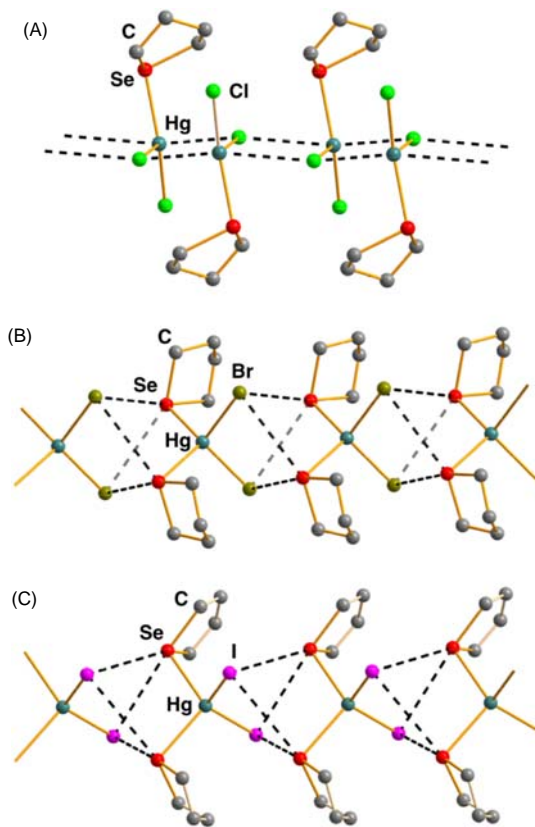
1,4-SeO(CH<sub>2</sub>)<sub>4</sub> reacts readily with transition metal dihalogenides in a suitable organic solvent. The reaction of PdBr<sub>2</sub> and 1,4-SeO(CH<sub>2</sub>)<sub>4</sub> affords *trans*-[PtBr<sub>2</sub>{1,4-SeO(CH<sub>2</sub>)<sub>4</sub>}] in which the coordination polyhedron is square-planar and the organic ligand is ligated via the selenium donor.<sup>68</sup> The Pd–Se and Pd–Br bond lengths are 2.430(2) and 2.442(2) Å, respectively, and the Br–Pd–Se bond angle is 93.3(1)°.

### 1.09.2.3.3 Se<sub>2</sub>(CH<sub>2</sub>)<sub>6</sub>

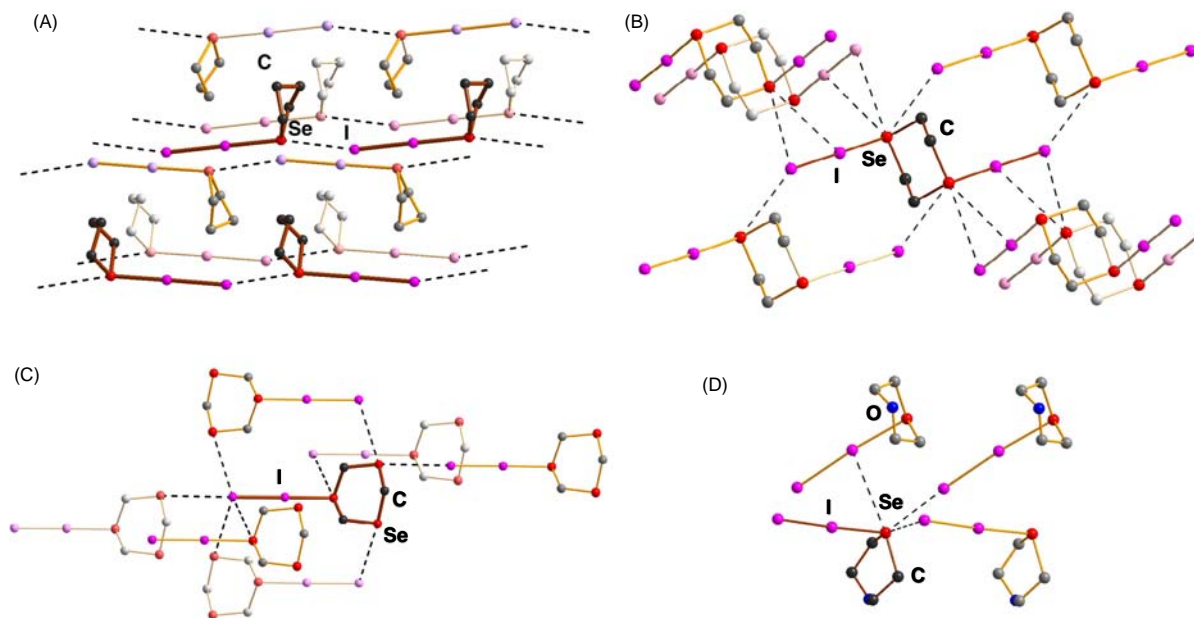
The reaction of MX<sub>3</sub> (M = As, Sb, Bi; X = Cl, Br, I) with 1,5-Se<sub>2</sub>(CH<sub>2</sub>)<sub>6</sub> (**5**) affords [MX<sub>3</sub>(**5**)]<sub>n</sub> in good yields.<sup>69–71</sup> The crystal structures of [MCl<sub>3</sub>(**5**)]<sub>n</sub> (M = As, Sb) are shown in **Fig. 11**(a) and (b)<sup>72</sup> and that of the bismuth analog in **Fig. 11**(c).<sup>71</sup>

The bond lengths and angles involving the 1,5-Se<sub>2</sub>(CH<sub>2</sub>)<sub>6</sub> (**5**) rings in [MX<sub>3</sub>(**5**)]<sub>n</sub> (M = As,<sup>72</sup> Sb,<sup>72</sup> Bi<sup>71</sup>) are relatively similar ( $r_{\text{Se-C}} = 1.954(8)$ – $2.053(9)$  Å, average 1.982 Å;  $\alpha_{\text{Se}} = 97.3(14)$ – $100.4(2)^\circ$ , average 99.6°;  $r_{\text{CC}} = 1.38(4)$ – $1.65(5)$  Å, average 1.516 Å) with largest deviations observed in [BiCl<sub>3</sub>(**5**)]<sub>n</sub>,<sup>71</sup> which also shows the least accuracy in the parameters. The





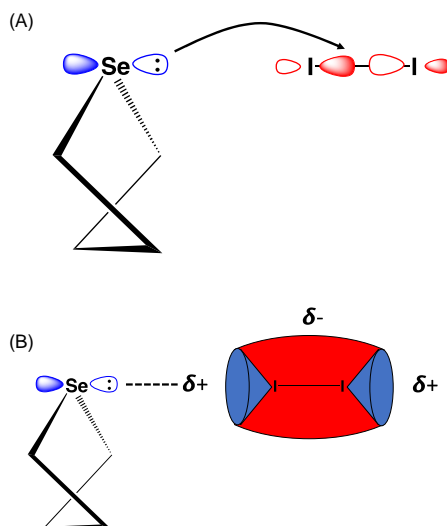
**Fig. 6** The crystal structures of (a)  $[\text{HgCl}_2(\text{Se}(\text{CH}_2)_4)]$ ,<sup>52</sup> (b)  $[\text{HgBr}_2(\text{Se}(\text{CH}_2)_4)_2]$ ,<sup>53</sup> and (c)  $[\text{HgI}_2(\text{Se}(\text{CH}_2)_4)_2]$ .<sup>53</sup>



**Fig. 7** The Se...I close contacts in (a)  $\text{Se}(\text{CH}_2)_4 \cdot \text{I}_2$ ,<sup>54</sup> (b)  $1,4\text{-Se}_2(\text{CH}_2)_4 \cdot 2\text{I}_2$ ,<sup>55</sup> (c)  $1,3,5\text{-Se}_3(\text{CH}_2)_3 \cdot \text{I}_2$ ,<sup>56</sup> and (d)  $1,4\text{-SeO}(\text{CH}_2)_4 \cdot \text{I}_2$ .<sup>57</sup>

conformations of the  $1,5\text{-Se}_2(\text{CH}_2)_6$  rings are somewhat different. In  $[\text{AsCl}_3(5)]_n$  and in  $[\text{SbCl}_3(5)]_n$ , the ligand assumes a boat-chair conformation, while in the related  $\text{BiCl}_3$  species it is in boat-boat conformation [see Fig. 11(a)–(c)].

All three  $[\text{MCl}_3(5)]_n$  coordination compounds form continuous quasi-1D assemblies. While the structures look rather similar, an unexpected irregularity between the three species has been noted.<sup>72</sup> Both arsenic and bismuth centers show a rather symmetric



**Fig. 8** (a) The  $n^2(\text{Se}) \rightarrow \sigma^*(\text{I-I})$  interaction in  $\text{Se}(\text{CH}_2)_4 \cdot \text{I}_2$ . (b) The electrostatic interaction between the  $\sigma$ -hole and selenium lone-pair.

**Table 2** Interatomic Se-I and I-I distances (Å) and angles (°) in  $\text{Se}(\text{CH}_2)_4 \cdot \text{I}_2$ ,  $1,4\text{-Se}_2(\text{CH}_2)_4 \cdot 2\text{I}_2$ ,  $1,3,5\text{-Se}_3(\text{CH}_2)_3 \cdot \text{I}_2$ ,  $1,4\text{-SeO}(\text{CH}_2)_4 \cdot \text{I}_2$ , and  $1,4\text{-SeO}(\text{CH}_2)_4 \cdot \text{ICl}$ .

Adduct	Se-I	I-X <sup>a</sup>	Se...I <sup>b</sup>	Ref.
$\text{Se}(\text{CH}_2)_4 \cdot \text{I}_2$	2.762(5)	2.914(4)	3.636(3)	54
$1,4\text{-Se}_2(\text{CH}_2)_4 \cdot 2\text{I}_2$	2.829(4)	2.870(3)	3.889(4)–4.008(3)	55
$1,3,5\text{-Se}_3(\text{CH}_2)_3 \cdot \text{I}_2$	2.734(1)	2.944(1)	3.764(1)–3.950(1)	56
$1,4\text{-SeO}(\text{CH}_2)_4 \cdot \text{I}_2$	2.755(3)	2.955(3)	3.708(3)–4.123(7)	57
$1,4\text{-SeO}(\text{CH}_2)_4 \cdot \text{ICl}$	2.630(6)	2.731(12)	3.963(5)–3.969(5)	63

<sup>a</sup>X = I or Cl.

<sup>b</sup>Only contacts, which are shorter than the sum of van der Waals radii of selenium and iodine, are shown.

octahedral coordination environments. The two terminal As–Cl bonds are 2.2734(17) and 2.2821(17) Å.<sup>72</sup> The bridging As–Cl bonds are expectedly somewhat longer [2.7451(18) and 2.7766(19) Å]. In  $[\text{BiCl}_3(5)]_n$ , the corresponding Bi–Cl bonds are 2.50(1)–2.61(1) Å and 2.77(1)–2.95(1) Å,<sup>71</sup> respectively. The respective two M–Se distances are 2.7840(7) Å (two bonds of equal lengths) and 2.977(4)–3.067(4) Å, respectively.<sup>71</sup>

By contrast, the  $[\text{SbCl}_3(5)]_n$  is rather distorted. The Sb–Cl bonds reproduce the same trend as was observed in  $[\text{AsCl}_3(5)]_n$  and  $[\text{BiCl}_3(5)]_n$  [terminal Sb–Cl bonds show the lengths of 2.438(2) and 2.499(2) Å, and the bridging Sb–Cl bonds 2.751(2) and 2.881(2)].<sup>72</sup> The Sb–Se distances, however, show a marked difference of 2.7839(13) and 3.2904(13) Å.

The explanation of this trend is not clear. It has been suggested that the differences in stereochemical directionality of the pnictogen lone pairs may play a role.<sup>72</sup> According to the VSEPR model,<sup>74</sup> the lone pair can occupy either the s orbital, in which case it is stereochemically inactive and will result in some elongation of all six bonds in the octahedral coordination, or it can occupy an orbital with p orbital contribution, in which case it will have stereochemical consequences. It has been inferred<sup>72</sup> that in  $[\text{AsCl}_3(5)]_n$ , the lone-pair is stereochemically inactive, whereas it is thought to be active in  $[\text{SbCl}_3(5)]_n$ . The distortion from octahedral geometry would be expected even greater in  $[\text{BiCl}_3(5)]_n$ , but the coordination geometry around bismuth resembles more closely that around arsenic. This has been explained to be due to relativistic effects that stabilize the 6 s electron pair of bismuth.<sup>72</sup>

The related  $[\text{GeCl}_2(5)]_n$  coordination compound was obtained by mixing the 1,4-dioxane solution of  $\text{GeCl}_2$  with the dichloromethane solution of 1,5- $\text{Se}_2(\text{CH}_2)_6$  (5).<sup>73</sup> The structure of  $[\text{GeCl}_2(5)]_n$  is shown in Fig. 11(d). The general features of the crystal structure are quite similar to those in  $[\text{MCl}_3(5)]_n$ . The Se–C and C–C bond lengths are 1.950(6)–1.951(5) and 1.509(7)–1.510(7) Å, respectively, the bond angle involving selenium as a central atom is 101.8(2)° and those involving carbon atoms 116.2(3)–119.3(3)°. The 1,5- $\text{Se}_2(\text{CH}_2)_6$  rings show a similar boat-chair conformation as those in  $[\text{AsCl}_3(5)]_n$  and  $[\text{SbCl}_3(5)]_n$ . The two symmetry-related Ge–Se bonds are 2.8465(8) Å.  $[\text{GeCl}_2(5)]_n$  also forms an infinite quasi-one dimensional assembly. The polymeric strands are linked by weak Ge...Cl interactions of 3.589(2) Å.<sup>73</sup>

The 1,5- $\text{Se}_2(\text{CH}_2)_6$  rings can also coordinate with transition metal centers. Both selenium atoms in the ring act as donors in the coordination. The known crystal structures are shown in Fig. 12.

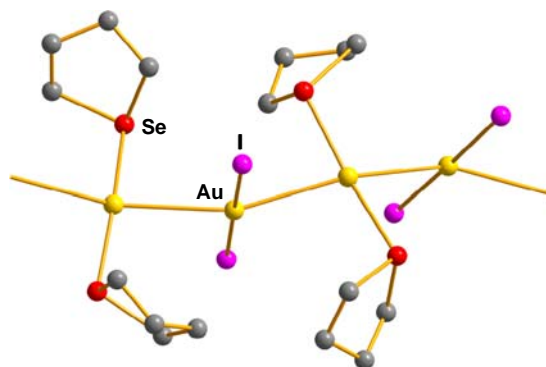


Fig. 9 Molecular structure of  $[\text{Au}\{\text{Se}(\text{CH}_2)_4\}_2]_n[\text{AuI}_2]_n$ .<sup>65</sup>

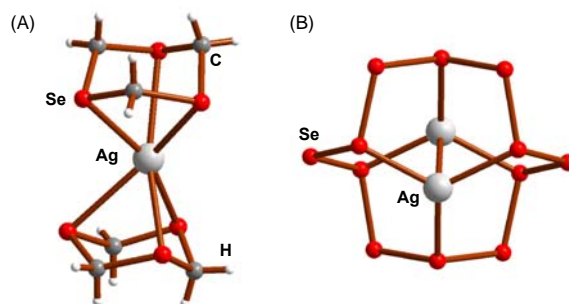


Fig. 10 The structure of (a)  $[\text{Ag}\{\text{Se}_3(\text{CH}_2)_3\}_2]^+$  cation<sup>66</sup> and (b)  $[\text{Ag}_2(\text{Se}_{12})]^{2+}$  dication.<sup>67</sup>

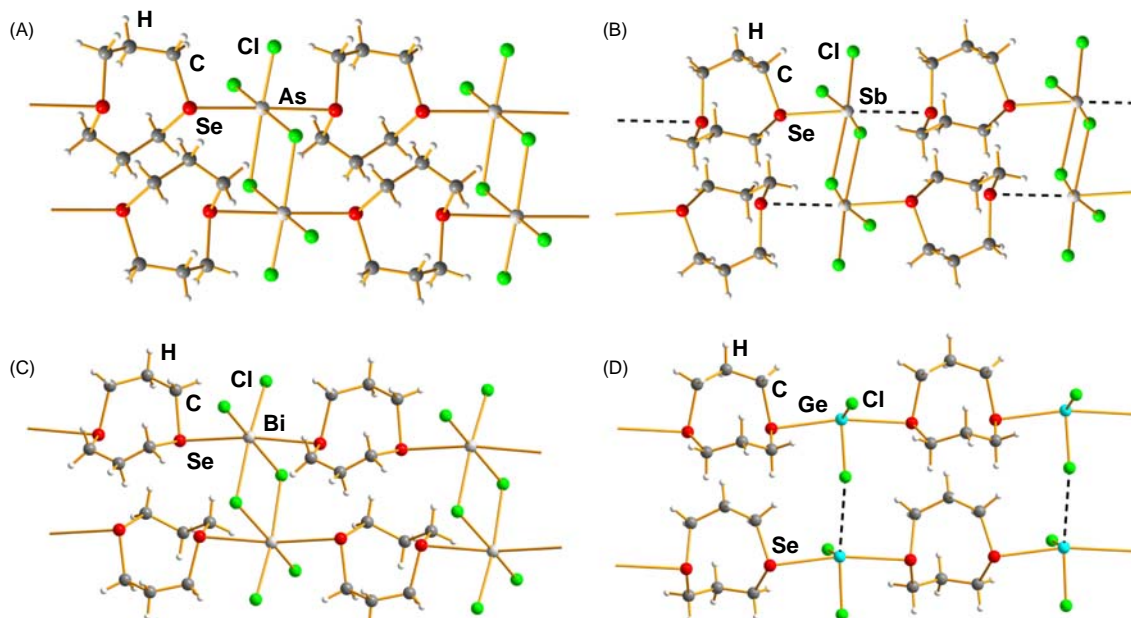
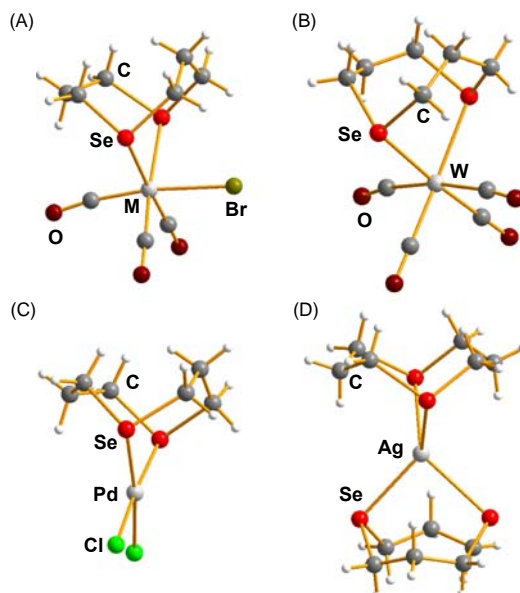


Fig. 11 The crystal structures of (a)  $[\text{AsCl}_3(\mathbf{5})]_n$ ,<sup>72</sup> (b)  $[\text{SbCl}_3(\mathbf{5})]_n$ ,<sup>72</sup> (c)  $[\text{BiCl}_3(\mathbf{5})]_n$ ,<sup>71</sup> and (d)  $[\text{GeCl}_2(\mathbf{5})]_n$ .<sup>73</sup>

$[\text{MX}(\text{CO})_3(\mathbf{5})]$  ( $\text{M} = \text{Mn}$ ,  $\text{X} = \text{Cl}$ ,  $\text{Br}$ ,  $\text{I}$ ;  $\text{M} = \text{Re}$ ,  $\text{X} = \text{Cl}$ ,  $\text{Br}$ ) were prepared in good yields by the reaction of  $[\text{M}(\text{CO})_5\text{X}]$  and 1,5- $\text{Se}_2(\text{CH}_2)_6$  by reflux in chloroform.<sup>75</sup> The products were characterized by elemental analysis, FAB mass spectrometry, and  $^1\text{H}$  NMR spectroscopy. The crystal structures were determined for  $[\text{MnBr}(\text{CO})_3(\mathbf{5})]$  and  $[\text{ReBr}(\text{CO})_3(\mathbf{5})]$  [see Fig. 12(a)].

The two coordination compounds are isomorphous and show the facial arrangement of the three carbonyl ligands. The 1,5- $\text{Se}_2(\text{CH}_2)_6$  ligand coordinates through selenium atoms and shows a similar boat-chair conformation as in  $[\text{MCl}_3(\mathbf{5})]$  ( $\text{M} = \text{As}$ ,



**Fig. 12** Molecular structure of (a)  $[\text{MBr}(\text{CO})_3(\mathbf{5})]$  ( $\text{M} = \text{Mn}, \text{Re}$ ),<sup>75</sup> (b)  $[\text{W}(\text{CO})_4(\mathbf{5})]$ ,<sup>75</sup> (c)  $[\text{PdCl}_2(\mathbf{5})]$ ,<sup>76</sup> and (d) the cation of  $[\text{Ag}(\mathbf{5})_2][\text{BF}_4]$ .<sup>77</sup>

Sb); *c.f.* Figs. 11(a) and (b) and 12(a). The bond parameters in the 1,5- $\text{Se}_2(\text{CH}_2)_6$  rings in  $[\text{MnBr}(\text{CO})_3(\mathbf{5})]$  and  $[\text{ReBr}(\text{CO})_3(\mathbf{5})]$  are 1.956(7)–1.982(6) Å and 1.97(2)–2.00(2) Å, respectively, and the respective bond angles are  $\alpha_{\text{Se}} = 97.1(3)$ – $97.5(3)^\circ$  and  $97.1(7)$ – $98.1(7)^\circ$ .<sup>75</sup> The Mn–Se and Re–Se bond lengths are 2.480(1)–2.488(1) Å and 2.607(2)–2.611(2) Å, respectively, which are quite typical.

The series of  $[\text{M}(\text{CO})_4(\mathbf{5})]$  ( $\text{M} = \text{Cr}^0, \text{Mo}^0, \text{W}^0$ ) was prepared by refluxing  $[\text{M}(\text{CO})_4(\text{nb})]$  ( $\text{M} = \text{Cr}, \text{Mo}$ ; nb = norbornadiene) or  $[\text{W}(\text{CO})_4(\text{TMPA})]$  (TMPA = *N, N, N', N'*-tetramethyl-1,3-diaminopropane) in toluene.<sup>75</sup> The products were identified by their IR, and FAB or ESI mass spectra. The assignment of the spectra and the identification of the coordination compounds were confirmed by the crystal structure determination of  $[\text{W}(\text{CO})_4(\mathbf{5})]$  [see Fig. 12(b)].

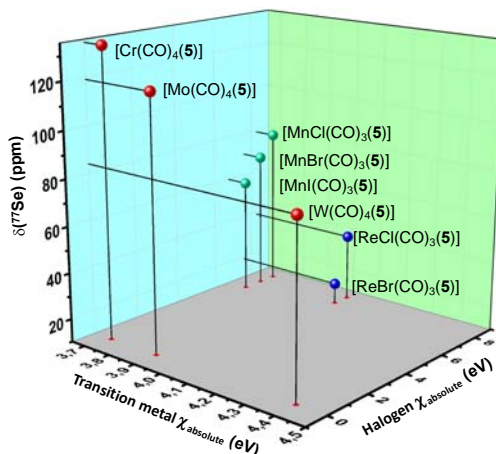
The basic structural features of the 1,5- $\text{Se}_2(\text{CH}_2)_6$  ligand are the same as in  $[\text{MBr}(\text{CO})_3(\mathbf{5})]$  ( $\text{M} = \text{Mn}, \text{Re}$ ) that are shown in Fig. 12(a). The heterocyclic ring shows the boat-chair conformation, and the bond parameters are similar in all complexes.

The trend in the  $^{77}\text{Se}$  chemical shifts is shown in Fig. 13.

#### 1.09.2.3.4 $\text{Se}_4(\text{CH}_2)_{12}$ and $\text{Se}_6(\text{CH}_2)_{18}$

Several adducts and coordination compounds with both main group halides and transition metals have been reported for 1,5,9,13- $\text{Se}_4(\text{CH}_2)_{12}$ . The molecule shows remarkable conformational flexibility in these species.

In a similar fashion to the reaction of 1,5- $\text{Se}_2(\text{CH}_2)_6$  with arsenic trihalide, the treatment of 1,5,9,13- $\text{Se}_4(\text{CH}_2)_{12}$  (12) with  $\text{AsCl}_3$  and  $\text{AsBr}_3$  affords a 1:1 adduct.<sup>69</sup> The related reaction with antimony tribromide also yields  $[\text{SbBr}_3(\mathbf{12})]$ ,<sup>78</sup> as does  $\text{BiBr}_3$ ,<sup>71</sup> though



**Fig. 13** The  $^{77}\text{Se}$  chemical shifts in  $[\text{M}(\text{CO})_4(\mathbf{5})]$  ( $\text{M} = \text{Cr}, \text{Mo}, \text{W}$ ) and  $[\text{MX}(\text{CO})_3(\mathbf{5})]$  ( $\text{M} = \text{Mn}, \text{Re}$ ;  $\text{X} = \text{Cl}, \text{Br}, \text{I}$ )<sup>75</sup> as a function of absolute electronegativity (in eV).



the latter reaction has been carried out in acetonitrile. Furthermore, the reaction of  $\text{GeCl}_2$  (dioxane),  $\text{GeBr}_2$ , and  $\text{GeI}_2$  in dichloromethane with 1,5,9,13- $\text{Se}_4(\text{CH}_2)_{12}$  leads to the formation of  $[(\text{GeX}_2)_2(\mathbf{12})]$  ( $\text{X} = \text{Cl}, \text{Br}, \text{I}$ ).<sup>73</sup> Their crystal structures have been shown in Fig. 14.

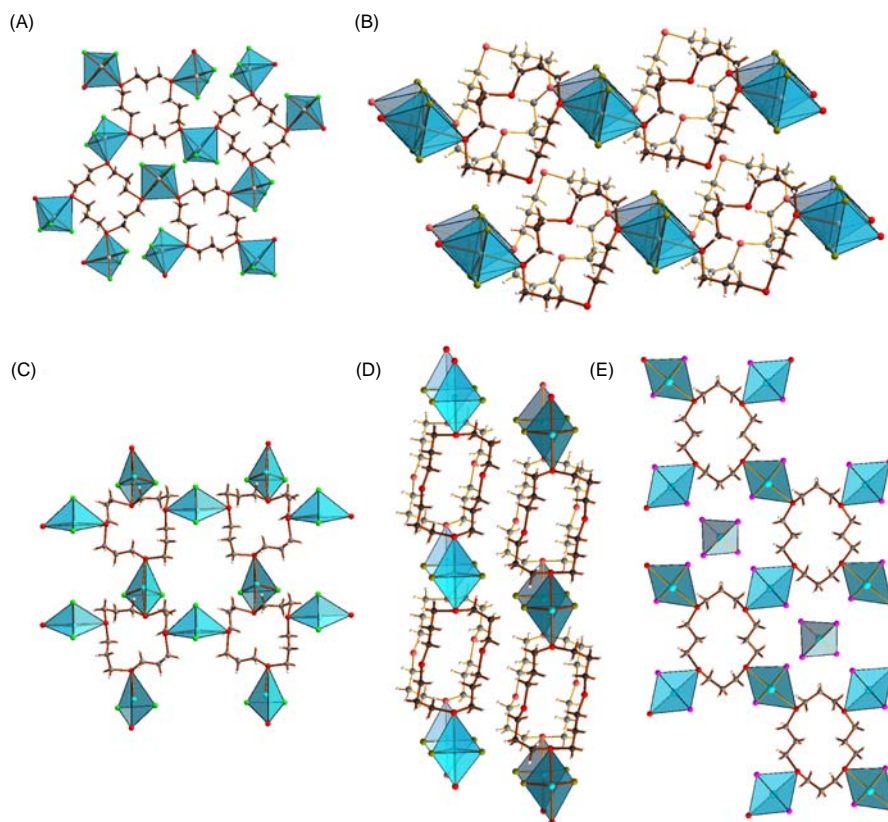
The treatment of  $\text{MCl}_3$  ( $\text{M} = \text{Ga}, \text{In}$ ) in dichloromethane affords ionic  $[\text{MCl}_2(\mathbf{12})][\text{MCl}_4]$  [see Fig. 15(a)].<sup>79</sup> The reactions were carried out in the non-coordinating solvent  $\text{CH}_2\text{Cl}_2$ , but a small amount of acetonitrile was added to improve the solubility of the starting halides.

The 1,5,9,13- $\text{Se}_4(\text{CH}_2)_{12}$  ring has also been reported to coordinate with different transition metal centers [see two examples in Fig. 15(b) and (c)]. The coordination compounds are generally prepared from appropriate halogenides  $\{[\text{Ru}(\text{DMF})_6]\text{Cl}_3$ ,<sup>80</sup>  $\text{CoX}_2$  ( $\text{X} = \text{Cl}, \text{Br}$ ),  $\text{MX}_3$  ( $\text{M} = \text{Rh}, \text{X} = \text{Cl}$ ;  $\text{M} = \text{Ir}, \text{X} = \text{Cl}, \text{Br}$ ),<sup>81</sup> and  $\text{MCl}_2$  ( $\text{M} = \text{Pd}, \text{Pt}$ )<sup>82–84</sup> and  $\text{Cu}(\text{OTf})_n$  ( $n = 1, 2$ ;  $\text{OTf} = \text{CF}_3\text{SO}_3$ , triflate)<sup>85,86</sup> and  $\text{Hg}(\text{CN})_2$ .<sup>86</sup> The reactions are carried out in a polar solvent. The crystallization of the products is generally accomplished by utilizing a suitable bulky and non-coordinating counter-anion, such as  $\text{PF}_6^-$ ,  $\text{BF}_4^-$ , and  $\text{BPh}_4^-$ .<sup>81–83</sup>

The bond parameters of the 1,5,9,13- $\text{Se}_4(\text{CH}_2)_{12}$  ring are very similar in all adducts and coordination compounds, as shown in Table 3. They are also very similar to those of the free molecules (see Table 1). As shown in Fig. 16, the torsional angles are mainly grouped near to  $60^\circ$  and  $180^\circ$  in the similar fashion as in the case of free heterocyclic selenoether molecules (c.f. Fig. 2). The differences in the torsional angles about the individual bonds lead to remarkable differences in the conformations of 1,5,9,13- $\text{Se}_4(\text{CH}_2)_{12}$  ring and consequently in the shape of the molecules.

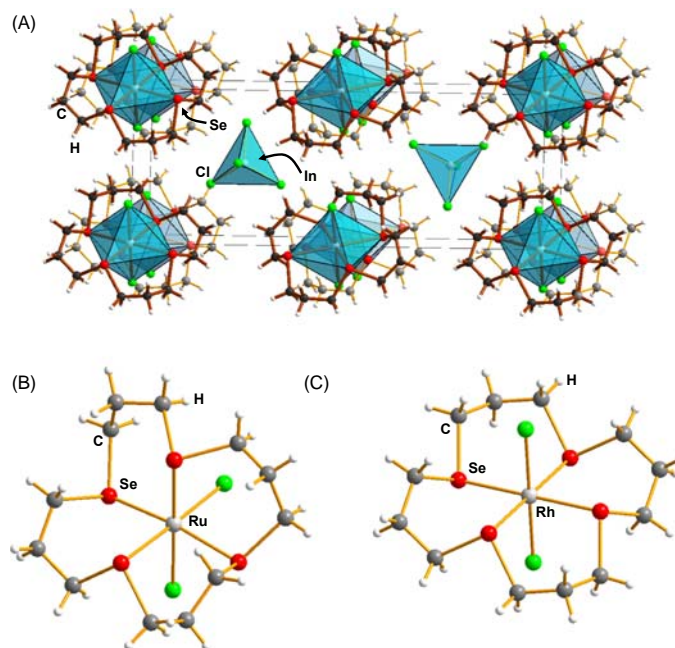
The conformational differences are specially notable in the case of the main group adducts. It can be seen in Fig. 14 that the halogenides  $\text{MX}_n$  ( $\text{M} = \text{a Group 14 or 15 element}, \text{X} = \text{Cl}, \text{Br}, \text{I}$ ) are bonded to the selenium atoms of the 1,5,9,13- $\text{Se}_4(\text{CH}_2)_{12}$  ring on the outside and the conformation and the shape of the molecule is apparently dependent on the packing effects in the solid lattice. Some of the molecules are rather symmetric, while the others show elongation. The convenient way to judge the ring geometry is to consider the distance between the selenium atoms 1 and 9 on one hand, and selenium atoms 5 and 13 on the other. This comparison has also been presented in Table 3.

The situation in the metal complexes of 1,5,9,13- $\text{Se}_4(\text{CH}_2)_{12}$  is much more restricted, as exemplified in Fig. 15. All metal centers show octahedral coordination. The ligand is tetraligated through donation from the selenium 4p lone-pair electrons. The two other ligands can be in *cis*-positions [see Fig. 15(b)] or in *trans* positions [see Fig. 15(c)]. The latter arrangement is more common and forces the four selenium atoms to be almost coplanar with the metal center and the CSeC planes are almost perpendicular to the metal-selenium bond. One of the consequences is that the distances between the selenium atoms 1,9 and 5,13 are nearly identical. Virtually all torsional angles about the C–Se bonds are close to  $180^\circ$  (see Fig. 16).



**Fig. 14** Crystal structures of (a)  $[\text{MX}_3(\mathbf{12})]$  ( $\text{M} = \text{As}, \text{X} = \text{Cl}, \text{Br}; \text{M} = \text{Sb}; \text{X} = \text{Br}$ ),<sup>69</sup> (b)  $[\text{BiCl}_3(\mathbf{12})]$ ,<sup>70</sup> (c)  $[(\text{GeCl}_2)_2(\mathbf{12})]$ ,<sup>73</sup> (d)  $[(\text{GeBr}_2)_2(\mathbf{12})]$ ,<sup>73</sup> and (e)  $[(\text{GeI}_2)_2(\mathbf{12})] \cdot (\text{GeI}_4)$ .<sup>73</sup> Selenium is indicated in red, carbon in gray, and hydrogen in white.





**Fig. 15** Examples of the molecular structures of main group and transition metals coordinated to 1,5,9,13- $\text{Se}_4(\text{CH}_2)_{12}$ . (a)  $[[\text{InCl}_2(\mathbf{12})][\text{InCl}_4]]^+$ ,<sup>79</sup> (b)  $\text{cis-}[\text{RuCl}_2(\mathbf{12})]^+$  cation,<sup>80</sup> (c)  $\text{trans-}[\text{RhCl}_2(\mathbf{12})]^+$  cation.<sup>81</sup>

**Table 3** Bond parameters in adducts and complexes of saturated selenoether heterocycles.

Complex	$r_{\text{SeC}}$ (Å)	$r_{\text{CC}}$ (Å)	$\alpha_{\text{Se}}$ (°)	$\alpha_{\text{C}}$ (°)	$d_{\text{Se}\dots\text{Se}(1)}$ (Å) <sup>a</sup>	$d_{\text{Se}\dots\text{Se}(2)}$ (Å) <sup>b</sup>	Ref.
$[\text{AsCl}_3(\mathbf{12})]$	1.94(2)–1.97(11)	1.51(18)–1.56(17)	99.0(5)–99.8(6)	108.5(7)–113.2(8)	7.7471(17)	7.796(2)	69
$[\text{AsBr}_3(\mathbf{12})]$	1.965(11)–1.974(6)	1.512(11)–1.528(10)	99.0(3)–100.4(3)	109.2(5)–114.1(5)	7.6752(12)	7.9594(10)	69
$[\text{SbBr}_3(\mathbf{12})]$	1.945(12)–1.972(9)	1.509(15)–1.535(16)	99.3(4)–99.5(4)	110.5(7)–113.9(7)	7.776(2)	7.798(2)	78
$[\text{BiBr}_3(\mathbf{12})]$	1.93(2)–1.985(18)	1.38(3)–1.58(3)	99.4(5)–99.7(8)	110.3(11)–125.7(19)	6.108(3)	6.863(3)	72
$[(\text{GeCl}_2)_2(\mathbf{12})]$	1.960(3)–1.971(3)	1.522(4)–1.523(4)	99.58(12)	108.5(19)–114(2)	5.5105(6)	5.5105(6)	73
$[(\text{GeBr}_2)_2(\mathbf{12})]$	1.960(6)	1.510(9)–1.527(10)	98.2(3)–100.0(2)	108.9(5)–114.4(6)	4.6557(16)	7.747(3)	73
$[(\text{GeI}_2)_2(\mathbf{12})]$	1.939(12)–1.98(3)	1.524(18)–1.539(14)	92.1(9)–98.7(6)	107.5(8)–124.8(18)	6.616(2)	6.616(2)	73
$[\text{GaCl}_2(\mathbf{12})][\text{GaCl}_4]$	1.960(5)–1.9675(5)	1.502(8)–1.525(7)	94.7(2)–97.3(2)	111.8(3)–117.1(4)	5.1937(9)	5.2191(10)	79
$[[\text{InCl}_2(\mathbf{12})][\text{InCl}_4]]^+$	1.950(11)–1.987(9)	1.499(17)–1.522(16)	96.5(4)–97.7(5)	111.0(8)–117.7(10)	5.4379(17)	5.4786(19)	79
$[\text{RuCl}(\text{PPh}_3)(\mathbf{12})]^+$	1.93(4)–2.04(5)	1.28(8)–1.54(5)	86.4(18)–92(2)	107(2)–130(4)	4.961(4)	4.976(4)	80
$[\text{CoBr}_2(\mathbf{12})]^+$	1.941(13)–1.978(12)	1.523(17)–1.528(17)	92.7(5)–94.0(5)	112.2(8)–116.1(10)	4.785(2)	4.805(2)	81
$[\text{RhCl}_2(\mathbf{12})]^+$	1.939(8)–1.968(8)	1.467(10)–1.5094(11)	94.6(3)–95.0(3)	111.9(5)–116.9(7)	4.912(2)	4.922(2)	81
$[\text{IrBr}_2(\mathbf{12})]^+$	1.91(3)–1.98(2)	1.44(3)–1.55(4)	95.5(11)–96.7(12)	109.8(16)–117(2)	4.929(4)	4.931(4)	81
$[\text{Pd}(\mathbf{12})]^{2+}$	1.936(12)–1.959(10)	1.452(15)–1.550(16)	93.2(4)–98.6(5)	110.8(7)–119.3(6)	4.854(15)	4.85(2)	82,83
$[\text{Pt}(\mathbf{12})]^{2+}$	1.92(3)–1.94(2)	1.46(4)–1.52(3)	94.5(10)–96.0(11)	112(2)–117.1(15)	4.834(4)	4.840(4)	84
$[\text{Cu}^{\text{II}}(\mathbf{12})]^{2+}$	1.897(4)–1.974(7)	1.555(6)–1.529(11)	93.3(3)–95.61(17)	110.5(5)–114.7(6)	4.8190(12)	4.9185(16)	85
$[\text{Cu}^{\text{I}}(\mathbf{12})]^+$	1.863(6)–1.930(6)	1.506(6)–1.532(11)	98.4(3)–103.8(4)	109.0(7)–118.6(4)	3.8366(16)	3.9819(13)	86
$[\text{Hg}(\text{CN})_2(\mathbf{12})]$	1.905(11)–1.949(13)	1.462(16)–1.553(18)	96.1(5)–96.9(5)	111.6(7)–117.1(8)	6.227(2)	8.867(2)	86

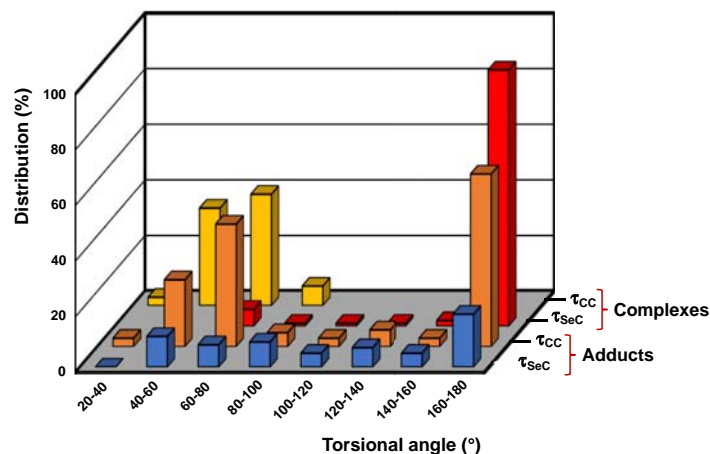
<sup>a</sup>The Se–Se distance from the selenium atoms in formal positions 1 and 9.

<sup>b</sup>The Se–Se distance from the selenium atoms in formal positions 5 and 13.

The 1,5,9,13,17,21- $\text{Se}_6(\text{CH}_2)_{18}$  (**14**) ring behaves in an analogous manner to the smaller selenoether heterocycles. The direct reaction with  $\text{AsCl}_3$  in dichloromethane generated the  $[(\text{AsCl}_3)_4(\mathbf{14})]$ ,<sup>87</sup> and the reaction with  $\text{PdCl}_2$  in acetonitrile followed by the anion change with  $\text{NaBF}_4$  afforded  $[\text{Pd}_2\text{Cl}_2(\mathbf{14})][\text{BF}_4]_2$ .<sup>82</sup> The molecular structures of both species are shown in Fig. 17.

### 1.09.2.3.5 Crown-ether analogs

1,4,10,13-tetraoxa-7,16-diselenaoctadecane  $\text{Se}_2\text{O}_4(\text{C}_2\text{H}_4)_6$  is a crown-ether analog in which two oxygen atoms have been replaced by selenium atoms.<sup>46</sup> In addition to oxygen, selenium that is a soft donor has also been shown to coordinate with alkali metals,<sup>88</sup> some alkaline earth metals,<sup>89,90</sup> and rare-earth elements.<sup>91,92</sup> The ligand encompasses the central atom in a similar fashion to



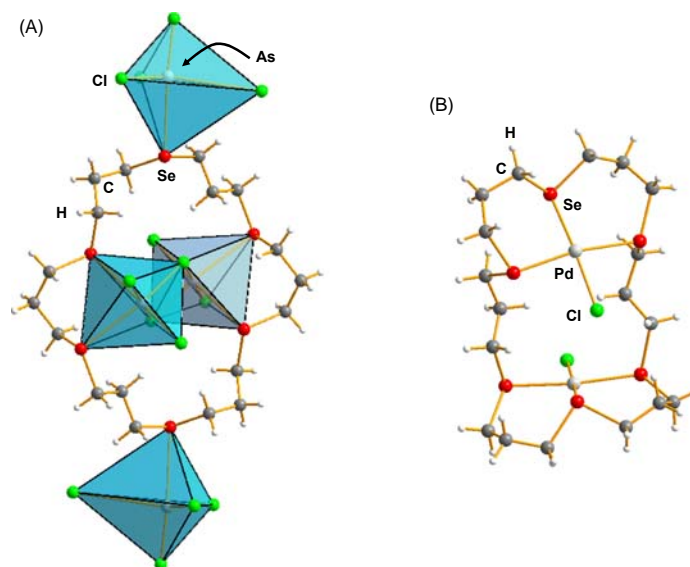
**Fig. 16** The distribution of torsional angles in the adducts and coordination compounds of **12** listed in **Table 3**.

crown-ether ligands, as exemplified by the cations in  $[\text{Na}\{\text{Se}_2\text{O}_4(\text{C}_2\text{H}_4)_6\}][\text{B}\{\text{C}_6\text{H}_3\text{Me}_2\text{-}3,5\}_4]$ ,  $[\text{Ca}\{\text{Se}_2\text{O}_4(\text{C}_2\text{H}_4)_6\}](\text{I})_2$ , and  $[\text{Sr}\{\text{Se}_2\text{O}_4(\text{C}_2\text{H}_4)_6\}(\text{OH}_2)_3](\text{I})_2$  [see **Fig. 18(a)–(c)**, respectively].

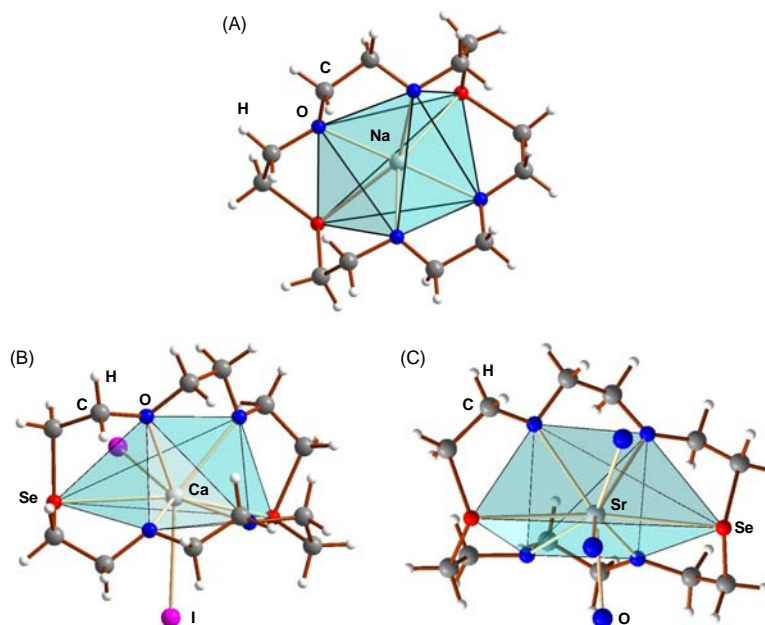
1,4,10,13-tetraoxa-7,16-diselenaoctadecane has also been shown to coordinate to a soft platinum center.<sup>46</sup> The complex was made by treating  $\text{Se}_2\text{O}_4(\text{C}_2\text{H}_4)_6$  with  $[\text{PtX}_2(\text{NCMe})_2]$  ( $\text{X} = \text{Cl}, \text{Br}$ ). Platinum expectedly coordinates via selenium atoms forming a transannular Se-Pt-Se fragment. Some antimony and lead salts have also reacted with  $\text{Se}_2\text{O}_4(\text{C}_2\text{H}_4)_6$ .<sup>93,94</sup> The antimony salt was prepared by stirring the ligand with  $\text{SbCl}_3$  in acetonitrile. The treatment of the ligand with  $\text{PbX}_2$  ( $\text{X} = \text{BF}_4^-, \text{PF}_6^-$  or  $\text{NO}_3^-$ ) affords  $[\text{Pb}(\text{L})][\text{X}]_2$  ( $\text{L} = \text{Se}_2\text{O}_4(\text{C}_2\text{H}_4)_6$ ). The Pb-O distances span a range of 2.584(5)–2.717(4), 2.543(4)–2.664(3), and 2.777(8)–2.929(8) Å, respectively.<sup>94</sup> The corresponding respective Pb-Se distances are 3.1820(14), 3.173(1), and 3.174(2) Å. The unprecedented interactions between the weakly-coordinating counter anions and lead was also observed (see **Fig. 19**). The stronger  $\text{Pb}^{2+} \cdots (\text{O}_2\text{NO})^-$  interaction compared to  $\text{Pb}^{2+} \cdots (\text{F}_2\text{BF}_2)^-$  and  $\text{Pb}^{2+} \cdots (\text{F}_2\text{PF}_2)^-$  seems to result in somewhat longer Pb-O distances between the central atom and the heterocyclic ligand, though the trend is hardly statistically significant.

#### 1.09.2.4 Cyclic selenoether cations

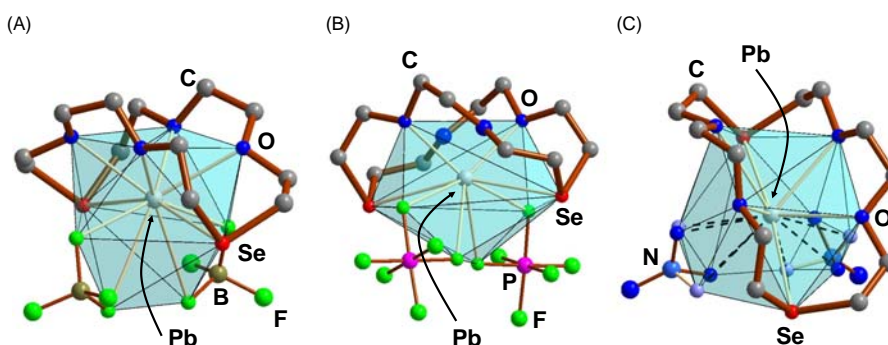
The treatment of 1,5- $\text{Se}_2(\text{CH}_2)_6$  (**5**) with two equivalents of  $\text{GaCl}_3$  in anhydrous dichloromethane followed by brief air oxidation and recrystallization at low temperature affords red crystals of  $[(5)\text{Cl}][\text{GaCl}_4] \cdot \text{CH}_2\text{Cl}_2$  and yellow crystals of  $[(5)_2][\text{GaCl}_4]_2$ .<sup>79</sup> The



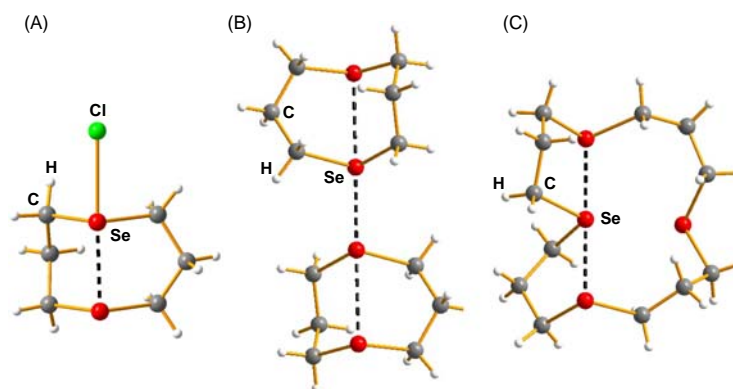
**Fig. 17** Molecular structures of (a)  $[(\text{AsCl}_3)_4(\mathbf{14})]^{87}$  and (b)  $[\text{Pd}_2\text{Cl}_2(\mathbf{14})]^{2+}$  cation.<sup>82</sup>



**Fig. 18** Molecular structures of (a)  $[\text{Na}\{\text{Se}_2\text{O}_4(\text{C}_2\text{H}_4)_6\}]^+$ ,<sup>88</sup> (b)  $[\text{Ca}\{\text{Se}_2\text{O}_4(\text{C}_2\text{H}_4)_6\}](\text{I})_2$ ,<sup>89</sup> and (c)  $[\text{Sr}\{\text{Se}_2\text{O}_4(\text{C}_2\text{H}_4)_6\}(\text{OH}_2)_3]^{2+}$ .<sup>89</sup>



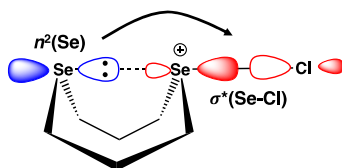
**Fig. 19**  $[\text{Pb}(\text{L})][\text{X}]_2$  [ $\text{L} = \text{Se}_2\text{O}_4(\text{C}_2\text{H}_4)_6$ ]; (a)  $\text{X} = \text{BF}_4^-$ , (b)  $\text{X} = \text{PF}_6^-$ , (c)  $\text{X} = \text{NO}_3^-$ .<sup>94</sup>



**Fig. 20** The structure of (a) the  $[(5)\text{Cl}]^+$  cation,<sup>79</sup> (b) the  $[(5)_2]^{2+}$  cation,<sup>79</sup> and (c) the  $(12)^{2+}$  cation.<sup>85</sup>

structures of the cations are shown in Fig. 20(a) and (b). The dissolution of  $[\text{Cu}(12)][\text{OTf}]_2$  ( $\text{OTf} = \text{CF}_3\text{SO}_3$ ) in the (1/1) mixture of  $\text{CH}_2\text{Cl}_2/\text{CH}_3\text{CN}$  followed by cooling, yielded yellow crystals of  $(12)[\text{OTf}]_2$ .<sup>85</sup> The structure of the cation is shown in Fig. 20(c).

The bond parameters within the ring cations show quite normal single bond values [ $r_{\text{SeC}} = 1.945(11)$ – $1.981(3)$  Å;  $\alpha_{\text{Se}} = 88.99(6)$ – $101.93(9)^\circ$ ].<sup>79,85</sup> The presence of transannular bonds in the cations are typical secondary bonding interactions



**Fig. 21** The donation of the 4p lone pair of selenium to the antibonding  $\sigma^*(\text{Se-Cl})$  orbital.

and can be rationalized by considering both the intramolecular donor-acceptor behavior and the electrostatic attraction between the  $\sigma$ -hole and the selenium lone pair. This is exemplified for the  $[\{1,5\text{-Se}_2(\text{CH}_2)_6\}\text{Cl}]^+$  cation in **Fig. 21**.

The  $\text{Se}\cdots\text{Se}$  contact of  $2.5229(4) \text{ \AA}^{79}$  is significantly shorter than the sum of the van der Waals radii of two selenium atoms ( $4.00 \text{ \AA}^{51}$ ). The  $\text{Se-Cl}$  bond distance of  $2.5346(6) \text{ \AA}^{79}$  is significantly elongated from the single bond (the sum of the covalent radii of selenium and chlorine is  $2.16 \text{ \AA}^{51}$ ) indicating the intramolecular charge transfer. A similar interactions have been observed for  $\text{ClSe}[\text{N}(\text{tBu})\text{Se}]_n\text{Cl}$  ( $n = 2-3$ )<sup>95</sup> and have resulted in the  $\text{Se}\cdots\text{Se}$  distances of  $2.891(10) \text{ \AA}$  ( $n = 2$ ) and  $3.36297(17)$ – $3.3445(9)$  ( $n = 3$ )<sup>96</sup> and a similar elongation of the bonds opposite to this interaction.

The  $[\{1,5\text{-Se}_2(\text{CH}_2)_6\}_2]^{2+}$  dication shows both *endo*- and *exocyclic* secondary bonding interactions [ $2.891(1)$  and  $2.6662(7) \text{ \AA}$ , respectively<sup>79</sup>]. The interactions are depicted in **Fig. 22**.

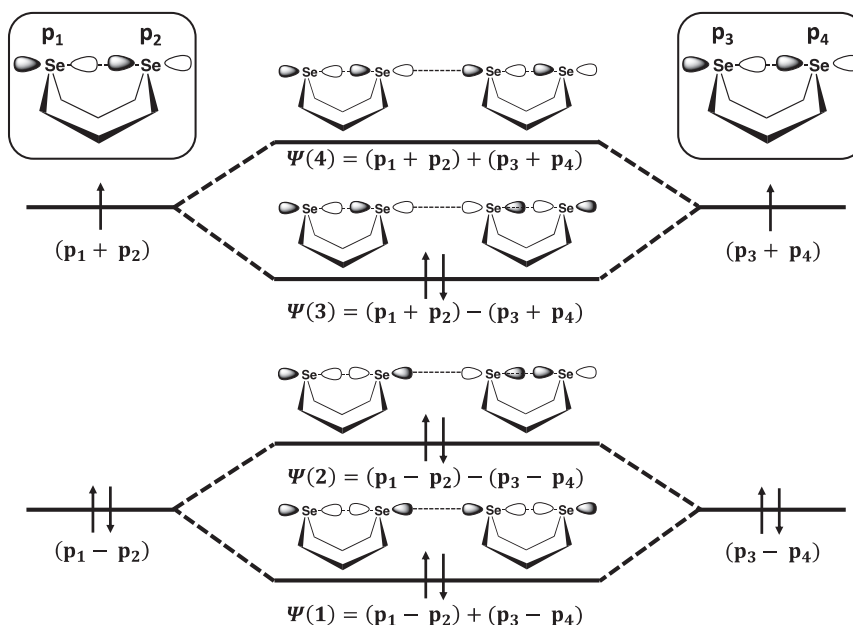
The net effect of the orbital overlap is the weakly attractive  $\text{Se}\cdots\text{Se}$  interaction and explain the observed contact distances. The transannular bonds in the  $[1,5,9,13\text{-Se}_4(\text{CH}_2)_{12}]^{2+}$  dication can be explained in the similar fashion to the  $3c\text{-}4e$  bonding involving the 4p lone-pair orbitals of selenium atoms. A related bonding arrangement is found in both cyclic  $\text{Se}_8^{2+}$  and  $\text{Te}_8^{2+}$  cations.<sup>97-99</sup>

The systematic study of the electrochemical and chemical oxidation of  $1,5\text{-E}_1\text{E}_2(\text{CH}_2)_6$  ( $\text{E}_1, \text{E}_2 = \text{S}, \text{Se}, \text{Te}$ ) showed that all chalcogenoethers may undergo reversible two-electron oxidation with inverted potentials to afford  $[1,5\text{-E}_1\text{E}_2(\text{CH}_2)_6]^{2+}$ .<sup>100</sup> On the other hand, one-electron oxidative dimerization of the starting chalcogenoethers also takes place (see **Scheme 3**). The X-ray crystal structure of  $[\text{S}\{(\text{CH}_2)_3\}_2\text{Se-}\text{Se}\{(\text{CH}_2)_3\}_2\text{S}]^{2+}$  exhibits the dimeric dication showing the *exocyclic*  $\text{Se}\cdots\text{Se}$  inter-ring interaction. It was concluded that the relative strengths of the dicationic interactions follow the three trends:  $\text{Te}\cdots\text{Te} > \text{Se}\cdots\text{Se} > \text{S}\cdots\text{S}$ ,  $\text{Se}\cdots\text{Se} > \text{Se}\cdots\text{S}$ , and  $\text{Te}\cdots\text{Te} > \text{Te}\cdots\text{S}$ .<sup>100</sup>

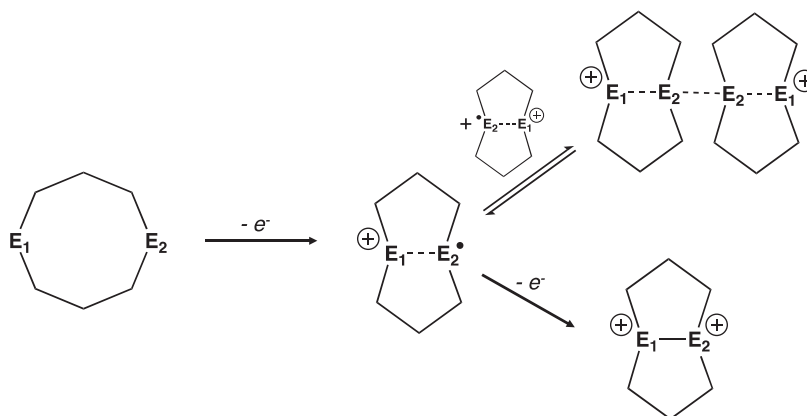
### 1.09.3 Unsaturated selenoethers

#### 1.09.3.1 Selenoethers with alkene spacers

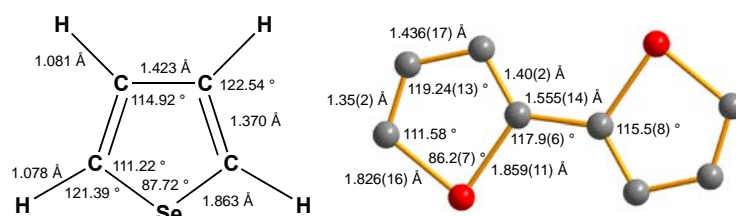
The smallest known heterocycle containing the alkene spacer is selenophene  $\text{Se}(\text{CH})_4$ , which is commercially available. It is a light-yellow liquid in room temperature. Its molecular structure has been determined by microwave spectroscopy<sup>101,102</sup> and NMR spectroscopy in liquid crystal media.<sup>103</sup> This crystal structure has been compared to the crystal structure of 2,2'-biselenophene<sup>104</sup> in **Fig. 23**.



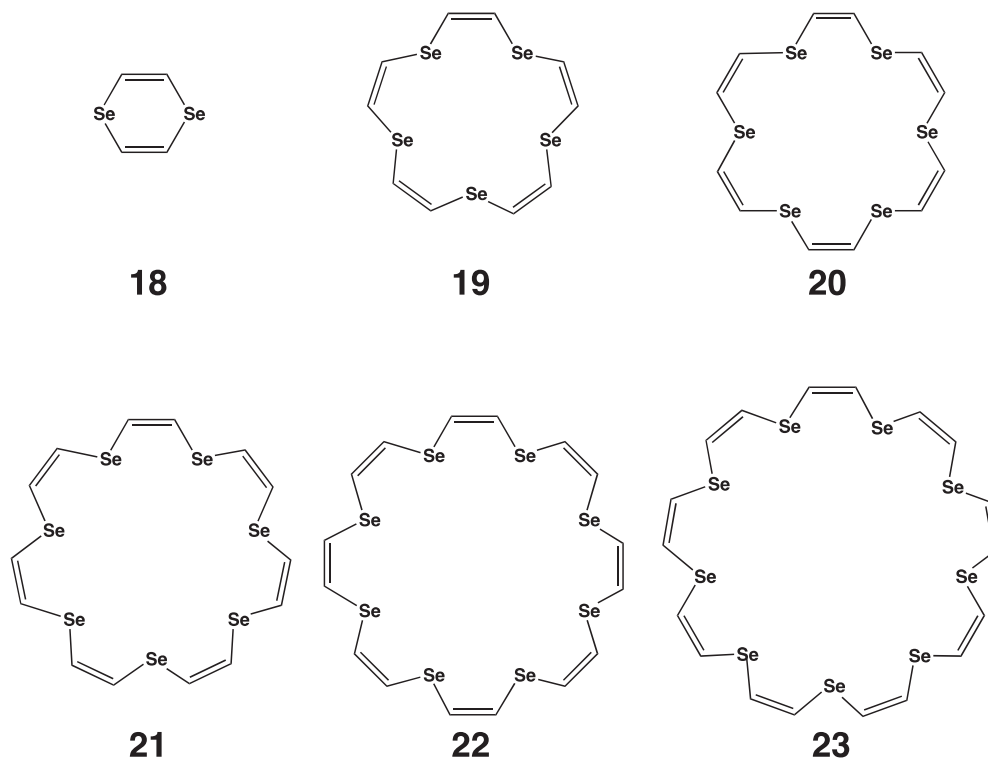
**Fig. 22** The transannular (*endo*) and inter-ring (*exo*) interactions in the  $[\{1,5\text{-Se}_2(\text{CH}_2)_6\}_2]^{2+}$  dication.



**Scheme 3** Oxidation of 1,5-E<sub>1</sub>E<sub>2</sub>(CH<sub>2</sub>)<sub>6</sub> (E<sub>1</sub> = S, Se; E<sub>2</sub> = Se).<sup>100</sup>



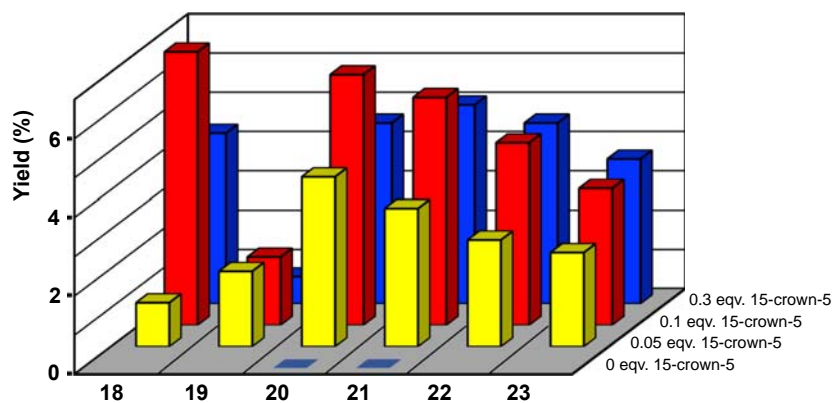
**Fig. 23** The structure of gaseous selenophene<sup>101</sup> and the crystal structure of 2,2'-biselenophene.<sup>104</sup>



**Chart 2** Se<sub>n</sub>(HC=CH)<sub>n</sub> heterocycles.

The structural parameters of the microwave determinations of gaseous selenophene<sup>101,102</sup> agree well with those extracted from the crystal structure determination of 2,2'-biselenophene.<sup>104</sup> The ab initio and DFT computations of selenophene and 2,2'-biselenophene also reproduce the experimental bond parameters.<sup>105</sup> While the computations in vacuum at most level of





**Fig. 24** The product distribution of the selenoether heterocycles  $\text{Se}_n(\text{HC}=\text{CH})_n$  (**18–23**) as determined from the reaction solution by  $^1\text{H}$  NMR spectroscopy.<sup>107</sup>

theory predict an anti-gauche conformation to lie at lowest energy, in the solid state the packing effects lead to a planar anti conformation.

The heterocyclic selenoethers containing ethylene spacers have been listed in **Chart 2**.

All heterocycles **18–23** are prepared by the equimolar reaction of sodium selenide with *cis*-dichloroethene.<sup>106,107</sup> 15-crown-5 was used as a catalyst, and it played a significant role in the product distribution, as shown in **Fig. 24**.

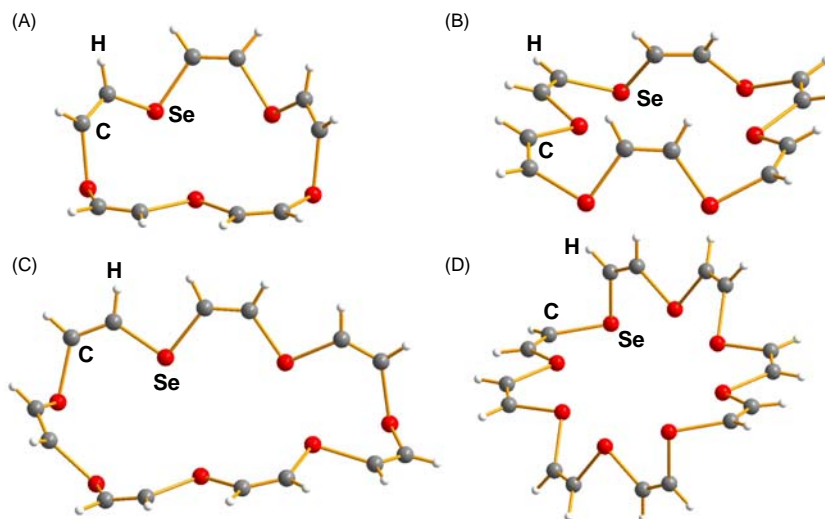
When the reaction was carried out without the catalyst, only traces of  $\text{Se}_6(\text{HC}=\text{CH})_6$  (**20**) and  $\text{Se}_7(\text{HC}=\text{CH})_7$  (**21**) were formed (see **Fig. 24**).<sup>107</sup> With the introduction of 15-crown-5, the total yield increased significantly and new heterocycles (**18**, **19**, **22**, and **23**) were observed in the reaction mixture. At the same time the total yield increased significantly. The optimum was inferred to be at the level of 0.1 eqv. of 15-crown-5.<sup>107</sup>

The molecular structures of **19–22**, which have been determined by single crystal X-ray diffraction, are shown in **Fig. 25**.

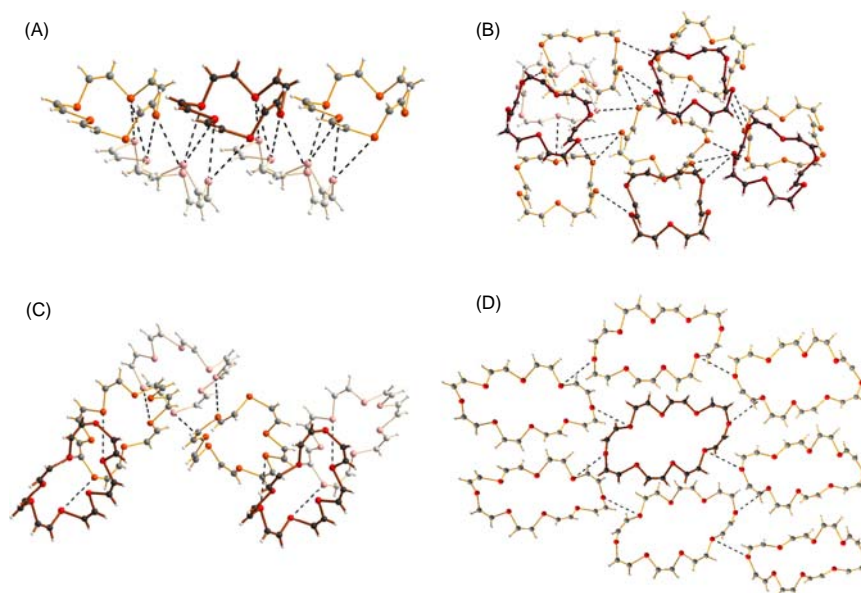
The Se–C bonds in **19–22** span a length of 1.88(2)–1.94(2) Å, the C=C bond lengths are 1.28(3)–1.33(2) Å, and the bond angles  $\alpha_{\text{Se}} = 94.6(8)$ – $102.0(8)$ ,  $\alpha_{\text{C}} = 120.6(14)$ – $128.0(16)^\circ$ .<sup>106,107</sup> All selenium atoms in each molecule are in *cis*-positions with respect to the double bonds and therefore the torsional angles about the C=C bonds are close to  $0^\circ$ . The torsional angles about the Se–C bonds show a clear distribution maximum in the range  $160$ – $180^\circ$  in a similar fashion as in the saturated selenoethers (see **Fig. 2**).

The rigid ethylene groups restrict the possibility for different conformations. It can interestingly be seen that all  $\text{Se}_n(\text{HC}=\text{CH})_n$  molecules have a shape of a flat bowl (see **Fig. 26**). They all show weak  $\text{Se}\cdots\text{Se}$  secondary bonding interactions of 3.963(3)–4.175(9) Å,<sup>106,107</sup> but contrary to the saturated selenoethers, their presence does not lead to tubular packing.

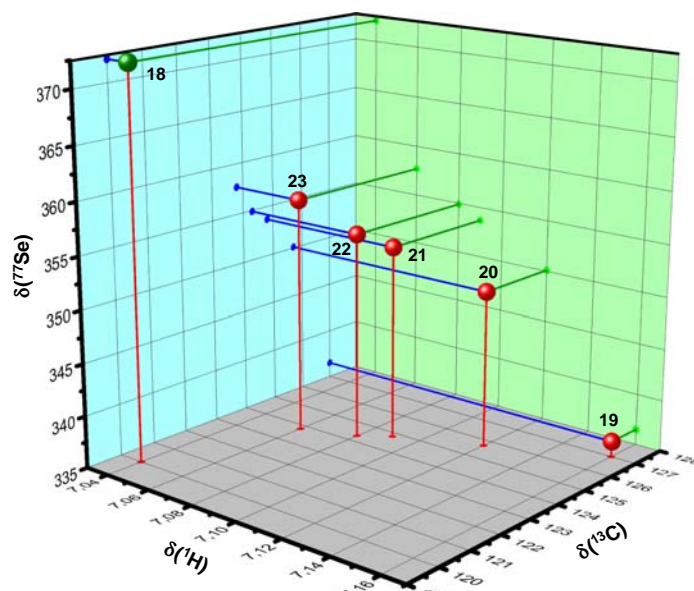
The crystal structures of  $\text{Se}_2(\text{HC}=\text{CH})_2$  (**18**) and  $\text{Se}_9(\text{HC}=\text{CH})_9$  (**23**) are not known, but these species have been identified and characterized by  $^1\text{H}$ ,  $^{13}\text{C}$ , and  $^{77}\text{Se}$  NMR spectroscopy and elemental analyses. The correlation of  $^1\text{H}$ ,  $^{13}\text{C}$ , and  $^{77}\text{Se}$  chemical shifts has been shown in **Fig. 27**. It can be seen that with the exception of the smallest member of the series,  $\text{Se}_2(\text{HC}=\text{CH})_2$  (**18**), there is



**Fig. 25** The molecular structures of (a)  $\text{Se}_5(\text{HC}=\text{CH})_5$  (**19**),<sup>106</sup> (b)  $\text{Se}_6(\text{HC}=\text{CH})_6$  (**20**),<sup>106</sup> (c)  $\text{Se}_7(\text{HC}=\text{CH})_7$  (**21**),<sup>107</sup> and (d)  $\text{Se}_8(\text{HC}=\text{CH})_8$  (**22**).<sup>107</sup>



**Fig. 26** The intermolecular Se...Se contacts in (a) **19**,<sup>106</sup> (b) **20**,<sup>106</sup> (c) **21**,<sup>107</sup> and (d) **22**.<sup>107</sup> Selenium atoms are depicted in red, carbon in gray, and hydrogen in white.

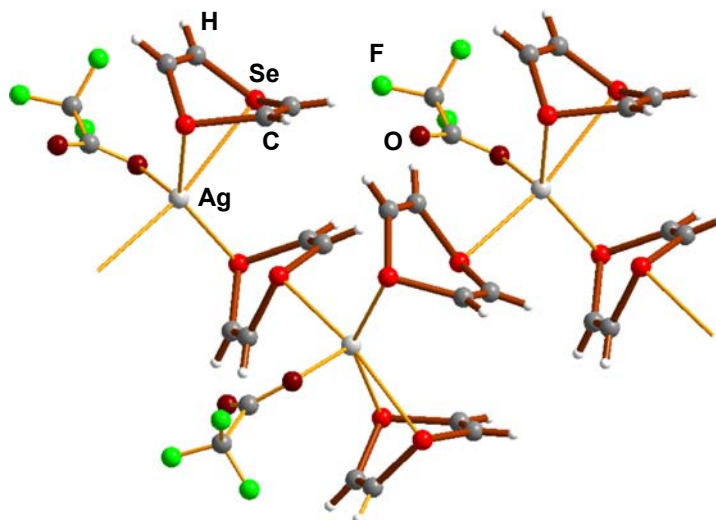


**Fig. 27** The dependence of the  $^1\text{H}$ ,  $^{13}\text{C}$ , and  $^{77}\text{Se}$  chemical shifts on the ring size of  $\text{Se}_n(\text{HC}=\text{CH})_n$ .<sup>107</sup>

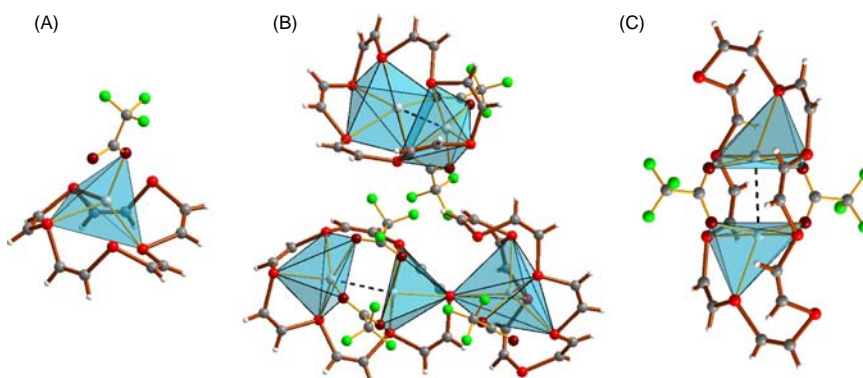
a monotonous relationship between the three chemical shifts and the ring size. The trend has been explained to be due to the increased electron density in ethylene, as the ring size grows.<sup>107</sup>

The lightest member of the series,  $\text{Se}_2(\text{HC}=\text{CH})_2$  (**18**) is a light-yellow liquid with the boiling point of 142 °C.<sup>107</sup> It was identified and characterized with a number of spectroscopic techniques and exhibited a reasonable elemental composition. The treatment of one or two equivalents of **18** with  $\text{Ag}(\text{OOC}\text{CF}_3)$  in acetone afforded crystalline products  $[\text{Ag}\{\text{Se}_2(\text{HC}=\text{CH})_2\}](\text{OOC}\text{CF}_3)$  and  $[\text{Ag}\{\text{Se}_2(\text{HC}=\text{CH})_2\}_2](\text{OOC}\text{CF}_3)$ . The crystal structure of the latter complex is shown in Fig. 28.

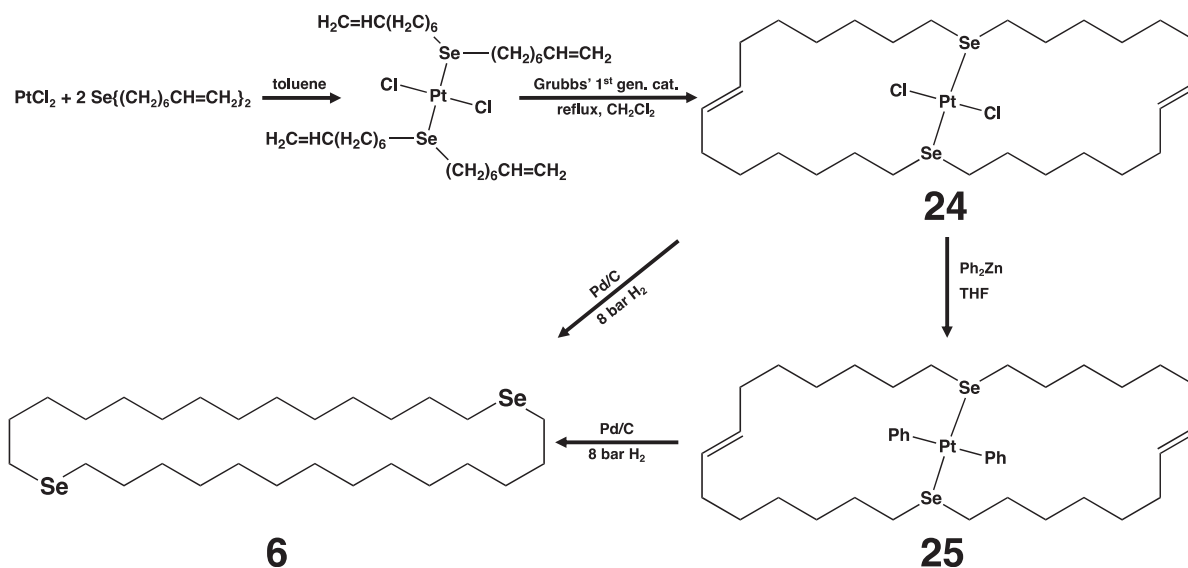
The complex  $[\text{Ag}(\text{18})_2](\text{OOC}\text{CF}_3)$  is a quasi-1D-polymeric arrangement with one  $\text{Se}_2(\text{HC}=\text{CH})_2$  ligand bridging two adjacent silver centers.<sup>107</sup> The other one is a chelating ligand. The Se–C bonds show the lengths of 1.878(11)–1.931(9) Å, the C=C bonds range 1.290(17)–1.343(16) Å, the bond angles are  $\alpha_{\text{Se}} = 96.8(4)$ – $98.8(5)^\circ$  and  $\alpha_{\text{C}} = 120.0(9)$ – $125.1(9)^\circ$ , and the torsional angles  $\tau_{\text{SeC}} = 38.6(11)$ – $44.1(11)^\circ$ . Both ligand molecules show the boat conformation with  $\tau_{\text{CC}}$  virtually  $0^\circ$  (the motif of the torsional angles from one of the selenium atoms is + – – + – –).



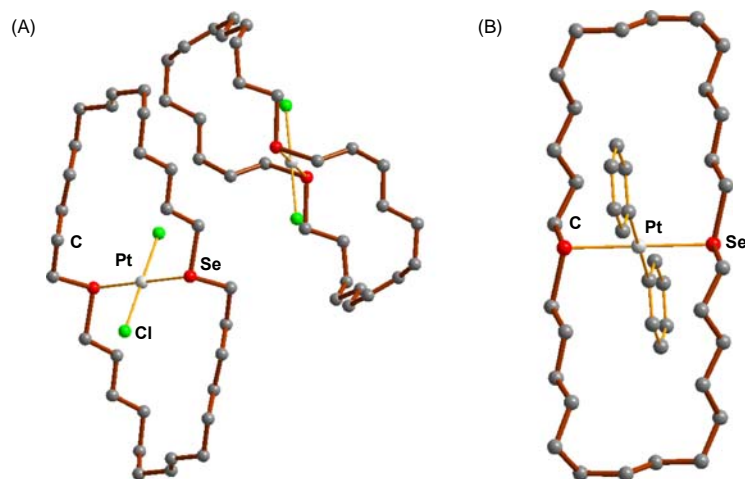
**Fig. 28** The quasi-1D structure of  $[Ag\{Se_2(HC=CH)_2\}_2](OCCF_3)$ .<sup>107</sup>



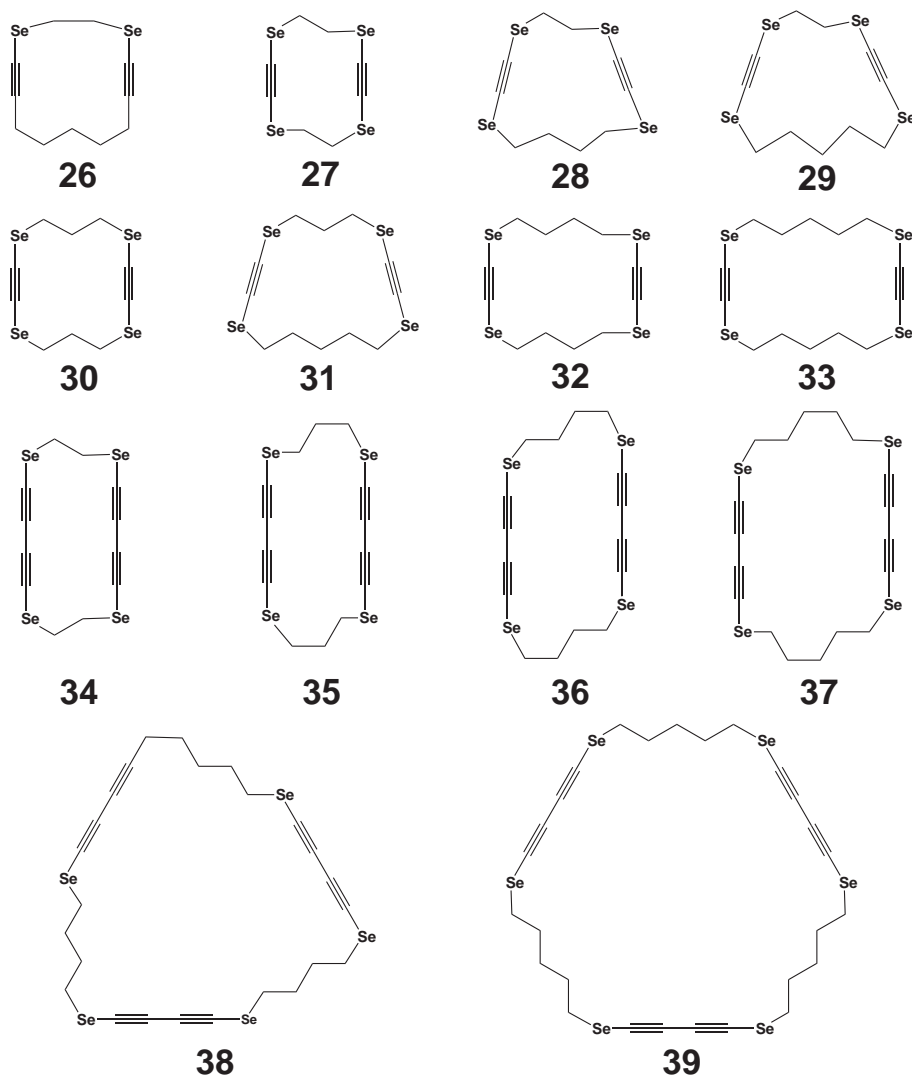
**Fig. 29** Structures of (a)  $[Ag\{Se_5(HC=CH)_5\}](OCCF_3)$ ,<sup>106</sup> (b)  $[Ag_5\{Se_6(HC=CH)_6\}_3](OCCF_3)_5$ ,<sup>106</sup> (c)  $[Ag_2\{Se_8(HC=CH)_8\}](OCCF_3)_2$ .<sup>107</sup>



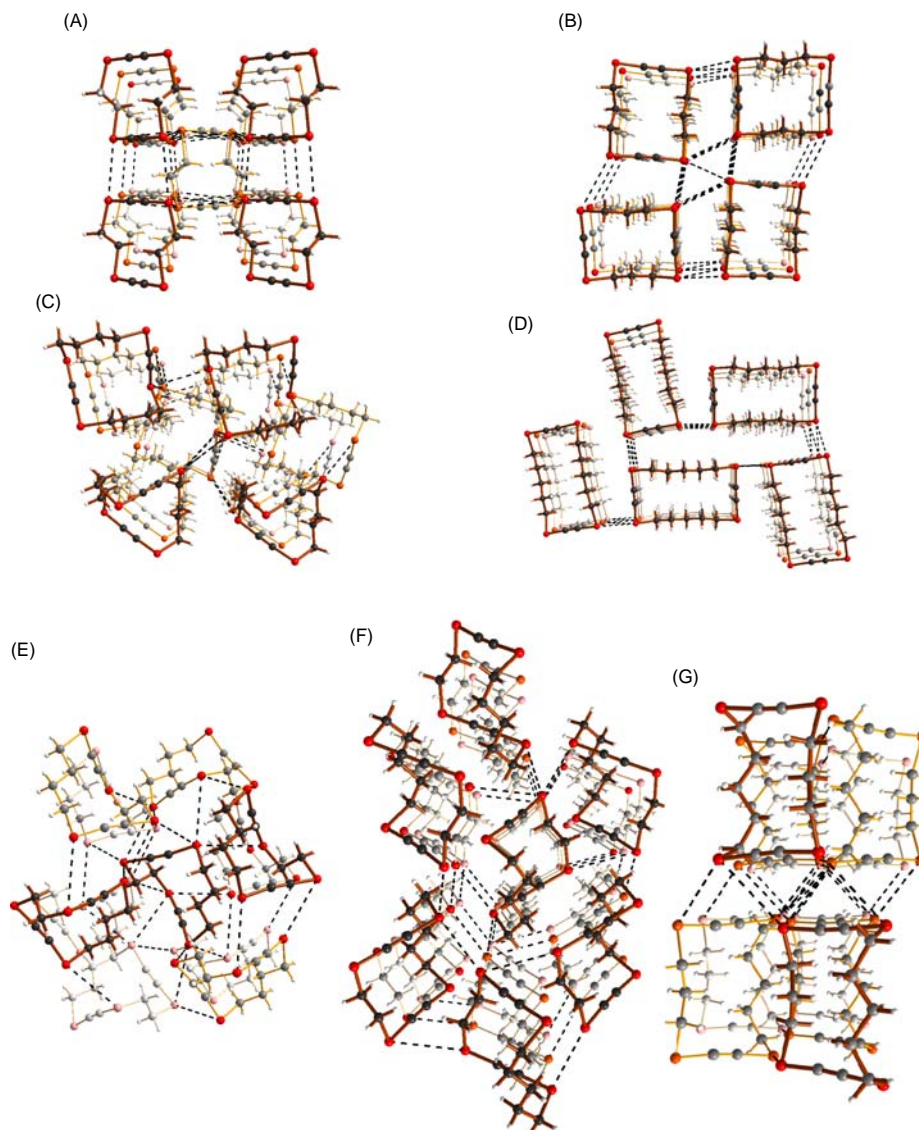
**Scheme 4** Preparation of  $[PtR_2\{Se(CH_2)_6(CH=CH)(CH_2)_6\}_2]$  ( $R = Cl$  (**24**),  $Ph$  (**25**)) as intermediates in the formation of  $1,15-Se_2(CH_2)_{28}$ .<sup>32</sup>



**Fig. 30** Crystal structures of (a)  $[PtCl_2\{Se(CH_2)_6(CH=CH)(CH_2)_6\}_2]$  (**24**), and (b)  $[PtPh_2\{Se(CH_2)_6(CH=CH)(CH_2)_6\}_2]$  (**25**).<sup>32</sup>



**Chart 3** Cyclic di-, tetra-, and hexaseleno diynes, tetraynes, and hexaynes.



**Fig. 31** The solid lattices in (a) 1,4,7,10-Se<sub>4</sub>-2,8-(C<sub>2</sub>)<sub>2</sub>(C<sub>2</sub>H<sub>4</sub>)<sub>2</sub> (**27**), (b) 1,4,8,11-Se<sub>4</sub>-2,9-(C<sub>2</sub>)<sub>2</sub>(C<sub>3</sub>H<sub>6</sub>)<sub>2</sub> (**30**), (c) 1,4,9,12-Se<sub>4</sub>-2,10-(C<sub>2</sub>)<sub>2</sub>(C<sub>4</sub>H<sub>8</sub>)<sub>2</sub> (**32**), (d) 1,4,10,13-Se<sub>4</sub>-2,11-(C<sub>2</sub>)<sub>2</sub>(C<sub>5</sub>H<sub>10</sub>)<sub>2</sub> (**33**), (e) 1,4,7,10-Se<sub>4</sub>-2,8-(C<sub>2</sub>)<sub>2</sub>(C<sub>2</sub>H<sub>4</sub>)(C<sub>4</sub>H<sub>8</sub>) (**28**), (f) 1,4,7,10-Se<sub>4</sub>-2,8-(C<sub>2</sub>)<sub>2</sub>(C<sub>2</sub>H<sub>4</sub>)(C<sub>5</sub>H<sub>10</sub>) (**29**), (g) 1,4,8,11-Se<sub>4</sub>-2,9-(C<sub>2</sub>)<sub>2</sub>(C<sub>3</sub>H<sub>6</sub>)(C<sub>5</sub>H<sub>10</sub>) (**31**).<sup>109</sup>

In spite of the rigid C=C bonds, the larger Se<sub>n</sub>(HC=CH)<sub>n</sub> rings are flexible and can engulf a metal center in a similar fashion to crown-ethers, as exemplified by [Ag<sub>m</sub>{Se<sub>n</sub>(HC=CH)<sub>n</sub>}] [OCCF<sub>3</sub>]<sub>m</sub> (see Fig. 29), which were prepared by treating the appropriate unsaturated selenoether with Ag(OCCF<sub>3</sub>) in acetone.<sup>106,107</sup> The larger rings lead to polynuclear complex entities. All bond parameters are similar to those in the free ligands ( $r_{\text{SeC}} = 1.73(3)\text{--}1.96(2)$ ,  $r_{\text{CC}} = 1.266(10)\text{--}1.38(4)$  Å,  $\alpha_{\text{Se}} = 94.0(4)\text{--}100.5(4)^\circ$  and  $\alpha_{\text{C}} = 120.3(15)\text{--}129(3)^\circ$ ).<sup>106,107</sup>

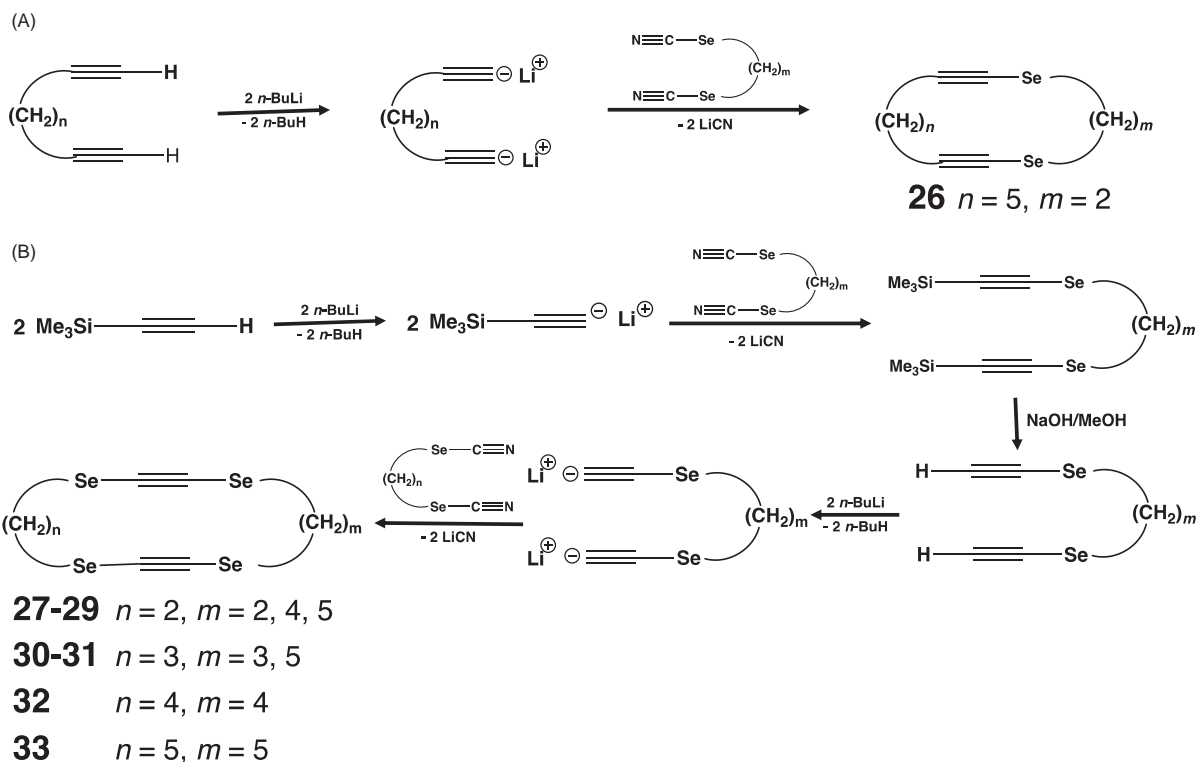
The crystalline lattice of [Ag<sub>5</sub>(**20**)<sub>3</sub>](OCCF<sub>3</sub>)<sub>5</sub>, is a solid solution of two complex entities: A dinuclear [Ag<sub>2</sub>(**20**)](OCCF<sub>3</sub>)<sub>2</sub> and a trinuclear [Ag<sub>3</sub>(**20**)<sub>2</sub>](OCCF<sub>3</sub>)<sub>3</sub>.<sup>106,107</sup> The latter complex consists of a dinuclear [Ag<sub>2</sub>(**20**)](OCCF<sub>3</sub>)<sub>2</sub> and a mononuclear [Ag(**20**)](OCCF<sub>3</sub>). The Se<sub>6</sub>(HC=CH)<sub>6</sub> ring in the dinuclear complex is a bridging ligand with one selenium atom shared by the two Ag centers. It was observed that in solution, the <sup>1</sup>H NMR spectrum exhibited only one resonance. This was inferred to indicate rapid interconversion between the [Ag<sub>3</sub>(**20**)<sub>2</sub>](OCCF<sub>3</sub>)<sub>3</sub> and [Ag(**20**)](OCCF<sub>3</sub>).<sup>107</sup>

In addition to the formation of 1,15-Se<sub>2</sub>(CH<sub>2</sub>)<sub>28</sub> (**6**), the reaction of PtCl<sub>2</sub> with two equivalents of Se{(CH<sub>2</sub>)<sub>6</sub>CH=CH<sub>2</sub>}<sub>2</sub> afforded two platinum complexes containing macrocyclic unsaturated selenoether ligands (see Scheme 4).<sup>32</sup>

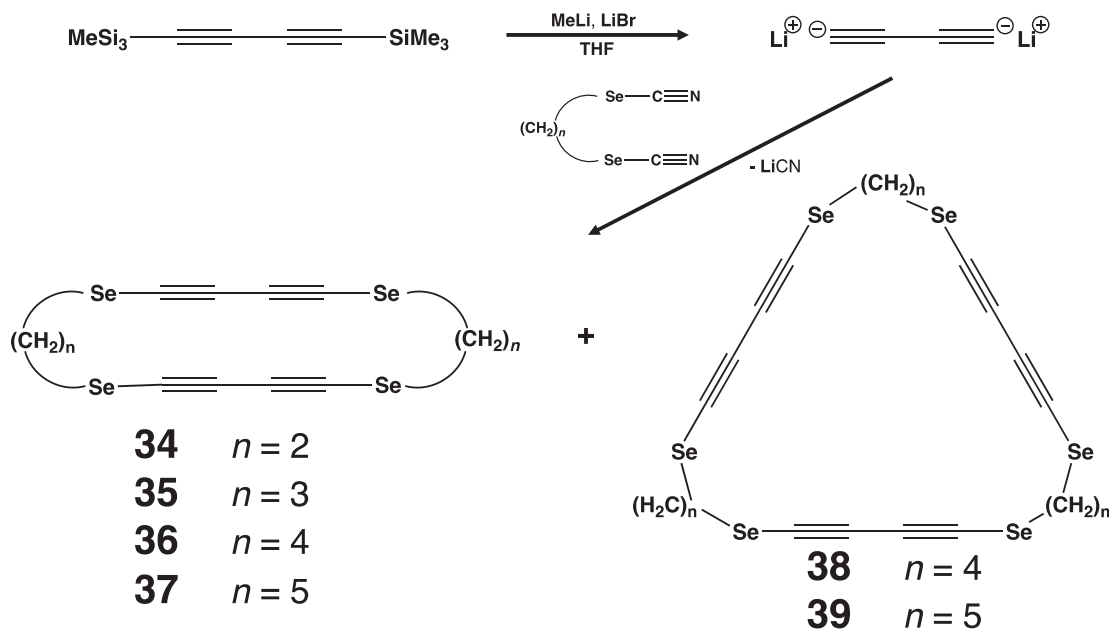
The crystal structures of **24** and **25** are shown in Fig. 30.

In the solid state, both complexes **24** and **25** show the presence of *trans*-isomers with respect to both C=C double bonds. Furthermore, the two CSeC planes are mutually in the *anti*-conformation.<sup>32</sup> The <sup>13</sup>C{<sup>1</sup>H} NMR spectra recorded in C<sub>6</sub>H<sub>5</sub>Br at





**Scheme 5** Preparation of (a) cyclic diselena diynes<sup>108</sup> and (b) tetraselena diynes.<sup>109,110</sup>



**Scheme 6** Preparation of cyclic tetraselena tetraynes and hexaselena hexaynes.<sup>111,112</sup>

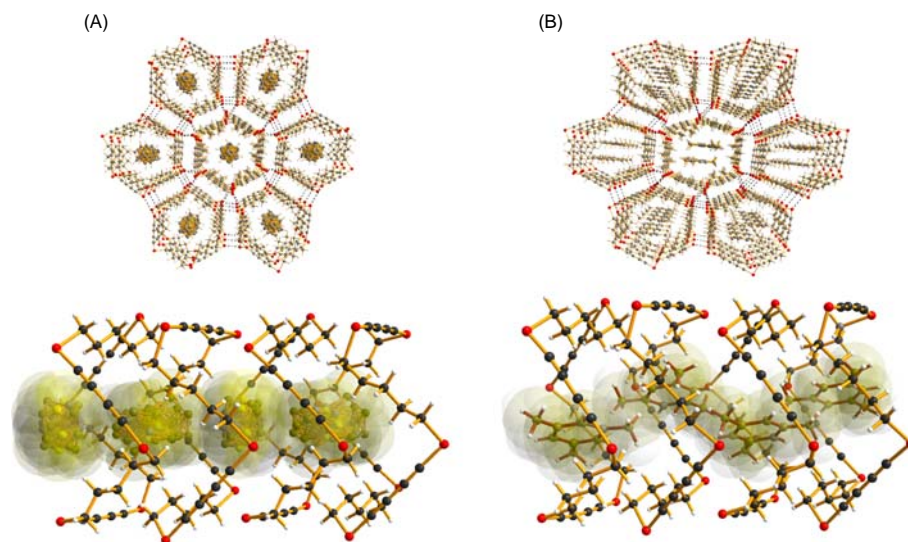
elevated temperatures indicated interconversion between the *syn*- and *anti*-isomers. The asymmetric unit in 24 [see Fig. 30(a)] contains two independent complexes. The conformations of the heterocyclic ligands differed by their *anti/gauche* sequences.

It was unexpectedly found<sup>32</sup> that the attempts to hydrogenate C=C double bonds resulted in the detachment of the macrocyclic ligand from the complex and the isolation of the free macrocycle 1,15-Se<sub>2</sub>(CH<sub>2</sub>)<sub>28</sub> (6), as shown in Scheme 4.

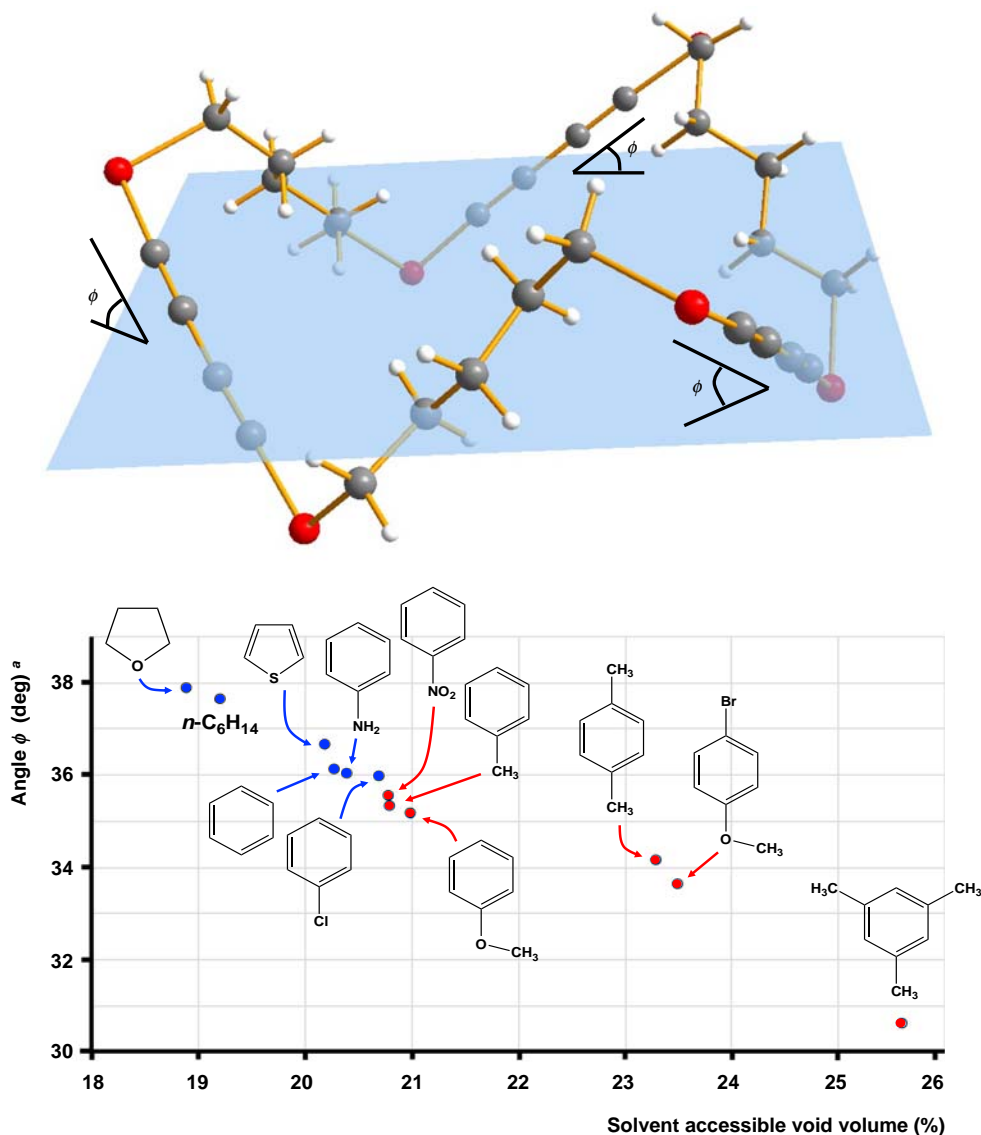
**Table 4** Bond parameters in tetra- and hexaselena di-, tetra-, and hexaynes.

Complex	$r_{SeC}$ (Å)	$r_{CC}$ (Å)	$r_{C \equiv C}$ (Å)	$\alpha_{Se}$ (°)	$\alpha_C$ (°) <sup>a</sup>	Ref.
1,4- $Se_2$ -5,12-( $C_2$ ) <sub>2</sub> ( $CH_2$ ) <sub>7</sub> ( <b>26</b> )	1.834(8)– 2.032(14)	1.337(19)– 1.47(3)	1.185(12)	92.8(7)–99.3(6)	115.3(8)– 135.0(11)	108
1,4,7,10- $Se_4$ -2,8-( $C_2$ ) <sub>2</sub> ( $C_2H_4$ ) <sub>2</sub> ( <b>27</b> )	1.836(3)– 1.977(3)	1.528(6)	1.204(5)	95.45(16)	100.6(2)	109
1,4,7,10- $Se_4$ -2,8-( $C_2$ ) <sub>2</sub> ( $C_2H_4$ )( $C_4H_8$ ) ( <b>28</b> )	1.821(6)– 1.969(5)	1.462(8)– 1.535(9)	1.200(8)– 1.204(8)	96.0(3)–101.1(3)	112.0(4)–114.9(4)	109
1,4,7,10- $Se_4$ -2,8-( $C_2$ ) <sub>2</sub> ( $C_2H_4$ )( $C_5H_{10}$ ) ( <b>29</b> )	1.830(6)– 1.984(9)	1.506(8)– 1.524(7)	1.191(7)– 1.192(8)	97.2(2)–98.4(2)	111.9(4)–114.5(4)	109
1,4,8,11- $Se_4$ -2,9-( $C_2$ ) <sub>2</sub> ( $C_3H_6$ ) <sub>2</sub> ( <b>30</b> )	1.836(3)– 1.971(3)	1.518(4)– 1.518(4)	1.196(3)	97.93(11)– 98.24(10)	110.01(19)– 112.66(16)	110
1,4,8,11- $Se_4$ -2,9-( $C_2$ ) <sub>2</sub> ( $C_3H_6$ )( $C_5H_{10}$ ) ( <b>31</b> )	1.828(9)– 1.962(9)	1.392(19)– 1.520(11)	1.206(13)	97.1(5)–98.9(4)	111.5(5)–119.7(7)	109
1,4,9,12- $Se_4$ -2,10-( $C_2$ ) <sub>2</sub> ( $C_4H_8$ ) <sub>2</sub> ( <b>32</b> )	1.815(8)– 1.977(7)	1.392(19)– 1.534(9)	1.194(10)– 1.206(13)	96.3(3)–98.9(4)	110.3(5)–119.7(7)	109
1,4,10,13- $Se_4$ -2,11-( $C_2$ ) <sub>2</sub> ( $C_5H_{10}$ ) <sub>2</sub> ( <b>33</b> )	1.821(5)– 1.961(5)	1.506(7)– 1.534(7)	1.208(7)	97.7(2)–98.6(2)	111.7(4)–114.6(4)	110
1,6,9,14- $Se_4$ -2,4,10,12-( $C_2$ ) <sub>4</sub> ( $C_2H_4$ ) <sub>2</sub> ( <b>34</b> )	1.829(9)– 1.979(10)	1.370(12)– 1.478(15)	1.184(18)– 1.201(12)	94.0(4)–95.1(4)	111.4(7)–111.6(7)	111
1,6,10,15- $Se_4$ -2,4,11,13-( $C_2$ ) <sub>4</sub> ( $C_3H_6$ ) <sub>2</sub> ( <b>35</b> )	1.830(4)– 1.977(5)	1.392(7)– 1.519(6)	1.197(7)	96.9(2)–97.9(2)	110.3(3)–112.0(4)	111
1,6,11,16- $Se_4$ -2,4,12,14-( $C_2$ ) <sub>4</sub> ( $C_4H_8$ ) <sub>2</sub> ( <b>36</b> )	1.822(7)– 1.984(8)	1.399(10)– 1.511(8)	1.178(10)	95.2(3)–96.0(3)	112.5(6)–116.0(6)	111
1,6,12,17- $Se_4$ -2,4,13,15-( $C_2$ ) <sub>4</sub> ( $C_5H_{10}$ ) <sub>2</sub> ( <b>37</b> )	1.826(3)– 1.959(3)	1.369(5)– 1.529(4)	1.198(4)	97.65(13)– 98.00(13)	111.4(2)–113.8(2)	111
1,6,11,16,21,26- $Se_6$ -2,4,12,14,22,24-( $C_2$ ) <sub>6</sub> ( $C_4H_8$ ) <sub>3</sub> ( <b>38</b> )	1.820(12)– 2.016(13)	1.333(11)– 1.587(17)	1.171(11)– 1.208(12)	94.0(3)–100.1(4)	102.6(9)–114.7(7)	111
1,6,12,17,23,28- $Se_6$ -2,4,13,15,24,26-( $C_2$ ) <sub>6</sub> ( $C_5H_{10}$ ) <sub>3</sub> ( <b>39</b> )	1.781(15)– 1.988(9)	1.335(19)– 1.570(8)	1.17(2)–1.22(2)	92.1(8)–99.2(4)	109.6(7)–122(2)	111,112

<sup>a</sup>The bond angles have only been reported for -CH<sub>2</sub>- carbon atoms.



**Fig. 32** Two examples of the guest molecules in the channels of 1,6,12,17,23,28- $Se_6$ -2,4,13,15,24,26-( $C_2$ )<sub>6</sub>( $C_5H_{10}$ )<sub>3</sub> (**39**). (a) **39** thiophene (trigonal space group  $R\bar{3}$ ), (b) **39** mesitylene (triclinic space group  $P\bar{1}$ ).<sup>111</sup> Top: view along the crystallographic  $a$  axis. Bottom: crystallographic  $a$  axis toward left. The guest molecules together with their van der Waals surfaces have been indicated in green.



**Fig. 33** The dependence of the size of the solvent accessible volume on the angle  $\phi$ , which is the angle between the medium plane of the **39** macrocycle and the virtually linear SeCCCCSe unit.<sup>111</sup> The trigonal space group  $R\bar{3}$  is indicated in blue, the triclinic space group  $P\bar{1}$  in red.

### 1.09.3.2 Selenoethers with alkyne spacers

Gleiter and co-workers have reported the syntheses, structures, and properties of a large number of selenoethers containing alkyne moieties (for a review, see Ref. 21). They can be divided into three classes depending on the nature of the spacer: diynes contain two  $\text{--C}\equiv\text{C--}$  units in the ring, tetraynes contain two conjugated  $\text{--C}\equiv\text{C--C}\equiv\text{C--}$  moieties, and hexaynes contain three  $\text{--C}\equiv\text{C--C}\equiv\text{C--}$  moieties in the ring molecule (see Chart 3).

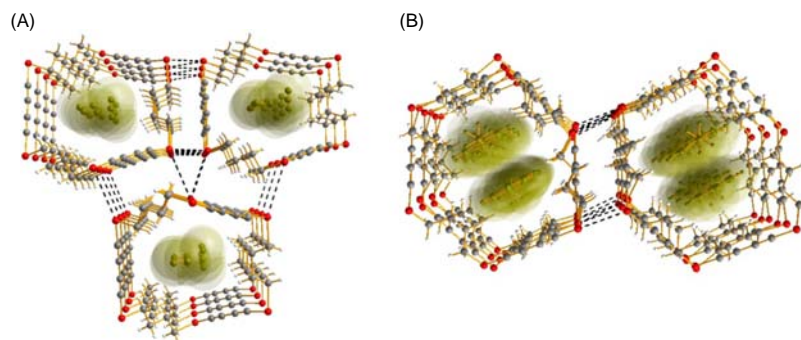
They are prepared by lithiating alkynes and treating them with selenonitriles, as shown for diynes in Scheme 5.

The related reaction scheme has been used for the preparation of tetra- and hexaseleno tetra- and hexaynes, as shown in Scheme 6.

The  $\text{Se--C}\equiv\text{C--Se}$  and  $\text{Se--C}\equiv\text{C--C}\equiv\text{C--Se}$  backbones are virtually linear. The selected bond lengths and bond angles are presented in Table 4.

Like in the case of saturated selenoethers, the di- and tetraseleno diynes **26**–**33** are linked together by weak intermolecular selenium-selenium interactions, which lead to a tendency toward tubular packing, as exemplified for tetraseleno diynes **27**–**33** in Fig. 31. However, only the lattices of **30** [Fig. 31(b)], **33** [Fig. 31(d)], and **31** [Fig. 31(g)] show clear channels throughout the lattices. The shortest intermolecular  $\text{Se}\cdots\text{Se}$  contacts in different molecules span a range of 3.5822(8)–3.9617(9) Å.<sup>109,110</sup>

Whereas 1,6,9,14- $\text{Se}_4\text{--}2,4,10,12\text{--}(\text{C}_2)_4(\text{C}_2\text{H}_4)_2$  (**34**), 1,6,10,15- $\text{Se}_4\text{--}2,4,11,13\text{--}(\text{C}_2)_4(\text{C}_3\text{H}_6)_2$  (**35**), and 1,6,12,17- $\text{Se}_4\text{--}2,4,13,15\text{--}(\text{C}_2)_4(\text{C}_5\text{H}_{10})_2$  (**37**) also show short  $\text{Se}\cdots\text{Se}$  contacts of 3.8955(15)–4.1181(16), 3.8179(8)–4.267(8), and 3.8858(5)–4.1614(4),



**Fig. 34** The host-guest arrangement of 1,6,11,16,21,26- $\text{Se}_6$ -2,4,12,14,22,24- $(\text{C}_2)_6(\text{C}_4\text{H}_8)_3$  (**38**) with (a) *n*-hexane (space group *Fdd2*) and (b) toluene (space group *P-1*).<sup>111</sup>

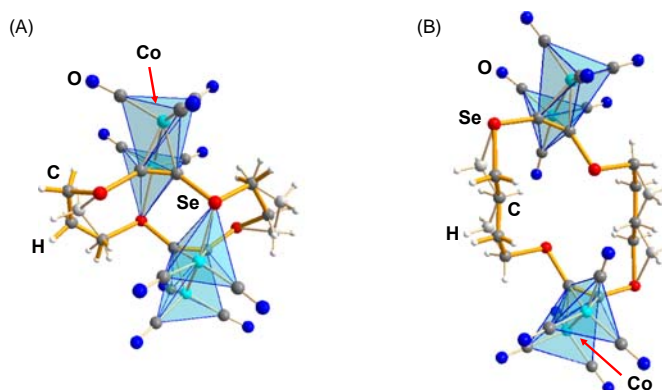
respectively, it is only **37** that exhibits columnal packing.<sup>111</sup> Interestingly, there are no  $\text{Se}\cdots\text{Se}$  interactions in the lattice of 1,6,11,16- $\text{Se}_4$ -2,4,12,14- $(\text{C}_2)_4(\text{C}_4\text{H}_8)_2$  (**36**), but the molecules are linked together through  $\text{Se}\cdots\text{H}$  hydrogen bonds.<sup>109</sup>

The channels in 1,6,12,17- $\text{Se}_4$ -2,4,13,15- $(\text{C}_2)_4(\text{C}_5\text{H}_{10})_2$  (**37**), 1,6,11,16,21,26- $\text{Se}_6$ -2,4,12,14,22,24- $(\text{C}_2)_6(\text{C}_4\text{H}_8)_3$  (**38**) and 1,6,12,17,23,28- $\text{Se}_6$ -2,4,13,15,24,26- $(\text{C}_2)_6(\text{C}_5\text{H}_{10})_3$  (**39**) are wide enough that they can accommodate guest molecules.<sup>111</sup> This is exemplified by inclusion of thiophene or mesitylene in the channels of **39** (see Fig. 32a and b, respectively).

A detailed study of the effect of twelve different guest molecules on the lattice of **39** has been summarized in Fig. 33.<sup>111</sup> The solvent accessible volume of the crystal correlates with angle  $\phi$  between the mean medium plane of the macrocycle **39** and the virtually linear  $\text{SeCCCCSe}$  units. It was shown that on the other hand this angle correlates with the  $\text{C}\equiv\text{CSeC}$  torsional angles. It was concluded that  $\text{C}\equiv\text{C}-\text{Se}-\text{C}$  unit acts as a hinge allowing the ring and thus the cavity diameter to expand, when the size of the guest molecule increases. As shown in Fig. 33, in case of the smaller guest molecules the material crystallizes in a trigonal space group *R-3* forcing the guest molecule to be disordered. While the packing of the macrocyclic ring remains unchanged, the larger guest molecules force the lowering of the symmetry to a triclinic space group *P-1*. As a consequence, the orientation of the guest is fixed and the crystal structure is ordered. The intermolecular  $\text{Se}\cdots\text{Se}$  contacts between the ring molecules in **39** are unaffected by the identity of the guest.

The effect of the guest molecules in 1,6,11,16,21,26- $\text{Se}_6$ -2,4,12,14,22,24- $(\text{C}_2)_6(\text{C}_4\text{H}_8)_3$  (**38**) is even more dramatic, as depicted in Fig. 34, in which the crystal structures of **38**·hexane and **38**·toluene have been compared. It can be seen that the guest molecule has an impact on the conformation of the host molecule.<sup>111</sup> **38**·hexane crystallizes in the orthorhombic space group *Fdd2* and shows the AAA stacking arrangement. By contrast, the **38** rings in **38**·toluene display the ABCD stacking.

The reaction of 1,4,7,10- $\text{Se}_4$ -2,8- $(\text{C}_2)_2(\text{C}_2\text{H}_6)(\text{C}_3\text{H}_6)$  (**40**) or 1,4,9,12- $\text{Se}_4$ -2,10- $(\text{C}_2)_2(\text{C}_4\text{H}_8)_2$  (**32**) with  $[\text{Co}_2(\text{CO})_{12}]$  afford complexes, in which the selenamacrocycle acts as a bridging ligand between  $\text{Co}_2\text{C}_2$  tetrahedra (see Fig. 35).<sup>113</sup> Both  $[\{\text{Co}_2(\text{CO})_5\}_2(\mathbf{40})]$  and  $[\{\text{Co}_2(\text{CO})_6\}_2(\mathbf{32})]$  are disordered with the  $\text{C}_n\text{H}_{2n}$  chains assuming two orientations. Both ligands are coordinated to cobalt via  $\eta^2$  mode from the two  $\text{C}\equiv\text{C}$  bonds in the heterocycle involving an electron pair in one of the  $\pi$ -orbitals of both triple bonds. As a consequence, the CC bond length is extended from ca. 1.2 Å (see Table 4) virtually to a double bond length of 1.350(4) and 1.339(8) Å in case of  $[\{\text{Co}_2(\text{CO})_5\}_2(\mathbf{40})]$  and  $[\{\text{Co}_2(\text{CO})_6\}_2(\mathbf{32})]$ , respectively, and the ligand is bent away from the central atom [the  $\text{CCSe}$  bond angles span a range of 134.4(2)–142.4(4)°]. Upon crystallization of  $[\{\text{Co}_2(\text{CO})_5\}_2(\mathbf{40})]$ , two moles of CO are liberated, and the vacant coordination site is filled by the formation of a transannular  $\text{Co}-\text{Se}$  bond of 2.3645(6) Å.<sup>113</sup>



**Fig. 35** Crystal structures of (a)  $[\{\text{Co}_2(\text{CO})_5\}_2(\mathbf{40})]$  and (b)  $[\{\text{Co}_2(\text{CO})_6\}_2(\mathbf{32})]$ .<sup>113</sup>

### 1.09.4 Summary

While the first reports of the preparation of heterocyclic selenoethers date back to late 1920s, it was only with the advent of modern instrumental analytical techniques and development of synthetic methodologies that more systematic information about the structures and properties of these species has been obtained. Though the total volume of research literature on cyclic selenoethers is still smaller than that of crown ethers and cyclic thioethers, selenoethers have shown a rapidly increasing number of adducts and metal complexes despite the commonly held belief that heavy chalcogenoethers are relatively weak  $\sigma$ -donors and therefore have only a weak ligating propensity (for more detailed discussion, see for instance Refs. 3, 7, 8).

This chapter was concerned with monocyclic selenoethers containing unbranched saturated or unsaturated hydrocarbon spacers. The main emphasis was in bonding and intermolecular interactions involving selenium atoms. Interestingly, the solid-state lattices generally show columnar stacking of the rings resulting in infinite cavities in the lattices, which are not unlike those in zeolites. It has been demonstrated that in some cases small molecules can be trapped in the cavities of the solid lattices. Chalcogen bonding plays a role in the crystallization of various selenoethers and their derivatives, though the main importance of these interactions is only seen in case of related telluroether analogs.

### References

- Pedersen, C. J. *J. Am. Chem. Soc.* **1967**, *89*, 7017–7036.
- Gokel, G. W.; Negin, S.; Catwell, R.; Atwood, J. L. In *Crown Ethers, Comprehensive Supramolecular Chemistry II*; Gokel, G. W., Barbour, L. J., Eds.; vol. 3; Elsevier: Amsterdam, 2017; pp 3–48.
- Singh, A. K.; Sharma, S. *Coord. Chem. Rev.* **2000**, *209*, 49–98.
- Levason, W.; Reid, G. *J. Chem. Soc. Dalton Trans.* **2001**, 2953–2960.
- Levason, W.; Reid, G. *J. Chem. Res. Synop.* **2002**, 467–472, 1001–1022.
- Levason, W.; Orchard, S. D.; Reid, G. *Coord. Chem. Rev.* **2002**, *225*, 159–199.
- Barton, A. J.; Genge, A. R. J.; Hill, N. J.; Levason, W.; Orchard, S. D.; Patel, B.; Reid, G.; Ward, A. J. *Heteroat. Chem.* **2002**, *13*, 550–560.
- Levason, W.; Reid, G. In *Comprehensive Coordination Chemistry II*; McCleverty, J. A., Meyer, T. J., Eds.; Elsevier: Amsterdam, 2004; pp 399–410.
- Segi, M. *Sci. Synth.* **2007**, *39*, 1069–1082.
- Panda, A. *Coord. Chem. Rev.* **2009**, *253*, 1056–1098.
- Levason, W.; Reid, G. In *Handbook of Chalcogen Chemistry*; Devillanova, F. A., Ed.; RSC Publishing: Cambridge, 2007; pp 81–106.
- Sommen, G. L. In *Comprehensive Heterocyclic Chemistry III*; Katritzky, A. R., Ramsden, C. A., Scriven, E. F. V., Taylor, R. J. K., Eds.; Elsevier: Amsterdam, 2008; pp 863–900.
- Levason, W.; Reid, G.; Zhang, W.-J. *Dalton Trans.* **2011**, *40*, 8491–8506.
- Jain, V. K.; Chauhan, R. S. *Coord. Chem. Rev.* **2016**, *306*, 270–301.
- Gahan, L. R. *Coord. Chem. Rev.* **2016**, *311*, 168–223.
- Moorefield, C. N.; Newcombe, G. R. *Prog. Heterocycl. Chem.* **2020**, *31*, 649–669.
- Boyle, P. D.; Godfrey, S. M. *Coord. Chem. Rev.* **2001**, *223*, 265–299.
- Cozzolino, A. F.; Elder, P. J. W.; Vargas-Baca, I. *Coord. Chem. Rev.* **2011**, *255*, 1426–1438.
- du Mont, W.-W.; Hrib, C. G. In *Handbook of Chalcogen Chemistry: New Perspectives in Sulfur, Selenium and Tellurium*; Devillanova, F. A., du Mont, W.-W., Eds., 2nd ed.; vol. 2; RSC Publishing: Cambridge, 2013; pp 273–316.
- Chivers, T.; Laitinen, R. S. *Chem. Soc. Rev.* **2015**, *44*, 1725–1739.
- Gleiter, R.; Haberhauer, G.; Werz, D. B.; Rominger, F.; Leiholder, C. *Chem. Rev.* **2018**, *118*, 2010–2041.
- Kolb, S.; Oliver, G. A.; Werz, D. B. *Angew. Chem. Int. Ed.* **2020**, *59*, 22306–22310.
- Morgan, G. T.; Burstall, F. H. *J. Chem. Soc.* **1929**, 1096–1103.
- Morgan, G. T.; Burstall, F. H. *J. Chem. Soc.* **1929**, 2197–2202.
- McCullough, J. D.; Lefohn, A. *Inorg. Chem.* **1966**, *5*, 150–151.
- Gould, E. S.; McCullough, J. D. *J. Am. Chem. Soc.* **1951**, *73*, 1105–1106.
- Klayman, D. I.; Griffin, T. S. *J. Am. Chem. Soc.* **1973**, *95*, 197–199.
- Gladysz, J. A.; Hornby, J. L.; Garbe, J. E. *J. Org. Chem.* **1978**, *43*, 1204–1208.
- Ishihara, H.; Koketsu, M.; Fukuta, Y.; Nada, F. *J. Am. Chem. Soc.* **2001**, *123*, 8408–8409.
- Levanova, E. P.; Grabel'nykh, V. A.; Elaev, A. V.; Russavskaya, N. V.; Klyba, L. V.; Albanov, A. I.; Korchevin, N. A. *Chem. Heterocycl. Compd.* **2012**, *47*, 1345–1352.
- Schiesser, C. H.; Sutej, K. *J. Chem. Soc. Chem. Commun.* **1992**, 57–59.
- Joshi, H.; Kharel, S.; Bhuvanesh, N.; Gladysz, J. A. *J. Organomet. Chem.* **2018**, *875*, 80–87.
- Mortillaro, L.; Credali, L.; Mammi, M.; Valle, G. *J. Chem. Soc.* **1965**, 807–808.
- Russo, M.; Mortillaro, L.; Credali, L.; Checchi, D. *J. Polym. Sci.* **1966**, *4*, 248–251.
- Cordova-Reyes, I.; VandenHoven, E.; Moihammed, A.; Pinto, B. M. *Can. J. Chem.* **1995**, *73*, 113–116.
- Batchelor, R. J.; Einstein, F. W. B.; Gay, I. D.; Gu, J.-H.; Johnston, B. D.; Pinto, B. M. *J. Am. Chem. Soc.* **1989**, *111*, 6582–6591. Erratum. 1990, *112*, 1297.
- Schmidt, M.; Blaettner, K.; Kochendörfer, P.; Ruz, H. *Z. Naturforsch.* **1966**, *21b*, 622–625.
- Weissflog, E. *Z. Anorg. Allg. Chem.* **1982**, *488*, 60–68.
- Morgan, G. T.; Burstall, F. H. *J. Chem. Soc.* **1930**, 1497–1502.
- Syper, L.; Mlochowski, J. *Tetrahedron* **1988**, *44*, 6119–6130.
- Russavskaya, N. V.; Levanova, E. P.; Sukhomazova, E. N.; Grabel'nykh, V. A.; Klyba, L. V.; Zhanchipova, E. R.; Albanov, A. I.; Korchevin, N. A. *Russ. J. Gen. Chem.* **2006**, *76*, 229–234.
- Papernaya, L. K.; Levanova, E. P.; Sukhomazova, E. N.; Klyba, L. V.; Zhanchipova, E. R.; Albanov, A. I.; Korchevin, N. A.; Deryagina, E. N. *Russ. J. Gen. Chem.* **2006**, *76*, 1123–1130.
- Fujihara, H.; Akaishi, R.; Erata, T.; Furukawa, N. *J. Chem. Soc. Chem. Commun.* **1989**, 1789–1790.
- Fujihara, H.; Akaishi, R.; Furukawa, N. *Tetrahedron* **1993**, *49*, 1605–1618.
- Yeo, J. S. L.; Vittal, J. J.; Hor, T. S. A. *Eur. J. Inorg. Chem.* **2003**, 277–280.
- Hesford, M. J.; Levason, W.; Matthews, M. L.; Reid, G. *Dalton Trans.* **2003**, 2852–2858.



47. Batchelor, R. J.; Einstein, F. W. B.; Gay, I. D.; Gu, J.-H.; Mehta, S.; Pinto, B. M.; Zhou, X.-M. *Inorg. Chem.* **2000**, *39*, 2558–2571.
48. Marsh, R. E.; McCullough, J. D. *J. Am. Chem. Soc.* **1951**, *73*, 1106–1109.
49. Mammì, M.; Carazzolo, G.; Valle, G.; Del Pra, A. Z. *Kristallogr.* **1968**, *127*, 401–414.
50. Valle, G.; Zanotti, G.; Mammì, M. *Acta Crystallogr., Sect. B* **1978**, *34*, 2634–2636.
51. Emsley, J. *The Elements*, 3rd. Ed.; Clarendon Press: Oxford, 1998, 292 pp.
52. Stålhandske, C.; Zintl, F. *Acta Crystallogr., Sect. C* **1986**, *C42*, 1449–1450.
53. Stålhandske, C.; Zintl, F. *Acta Crystallogr., Sect. C* **1988**, *C44*, 253–255.
54. Hope, H.; McCullough, J. D. *Acta Crystallogr.* **1964**, *17*, 712–718.
55. Chao, G. Y.; McCullough, J. D. *Acta Crystallogr.* **1961**, *14*, 940–945.
56. Arca, M.; Cristiani, F.; Devillanova, F. A.; Garau, A.; Isaia, F.; Lippolis, V.; Verani, G.; Demartin, F. *Polyhedron* **1997**, *16*, 1983–1991.
57. Maddox, H.; McCullough, J. D. *Inorg. Chem.* **1966**, *5*, 522–526.
58. Alcock, N. W. *Adv. Inorg. Chem. Radiochem.* **1972**, *15*, 1–58.
59. van Bolhuis, F.; Koster, P. B.; Migchelsen, T. *Acta Crystallogr.* **1967**, *23*, 90–91.
60. Dahl, T.; Hassel, O. *Acta Chem. Scand.* **1965**, *19*, 2000–2001.
61. Holmestad, O.; Rømming, C. *Acta Chem. Scand.* **1965**, *20*, 2601–2610.
62. Björvatten, T. *Acta Chem. Scand.* **1963**, *17*, 2292–2300.
63. Knobler, C.; McCullough, J. D. *Inorg. Chem.* **1968**, *7*, 365–369.
64. Konu, J.; Chivers, T.; Schatte, G.; Parvez, M.; Laitinen, R. S. *Inorg. Chem.* **2005**, *44*, 2973–2982.
65. Ahrland, S.; Dreisch, K.; Norén, B.; Oskarsson, Å. *Mater. Chem. Phys.* **1993**, *35*, 281–289.
66. Hofmann, H.; Jones, P. G.; Noltemeyer, M.; Peymann, E.; Pinkert, W.; Roesky, H. W.; Sheldrick, G. M. *J. Organomet. Chem.* **1983**, *249*, 97–102.
67. Köchner, T.; Trapp, N.; Engesser, T. A.; Lehner, A. J.; Röhr, C.; Riedel, S.; Knapp, C.; Scherer, H.; Krossing, I. *Angew. Chem. Int. Ed.* **2011**, *50*, 11253–11256.
68. Barnes, J. C.; Hunter, G.; Lown, M. W. *J. Chem. Soc. Dalton Trans.* **1977**, 458–460.
69. Hill, N. J.; Levason, W.; Reid, G. *Inorg. Chem.* **2002**, *41*, 2070–2076.
70. Barton, A. J.; Hill, N. J.; Levason, W.; Reid, G. *J. Chem. Soc. Dalton Trans.* **2001**, 1621–1627.
71. Barton, A. J.; Genge, A. R. J.; Levason, W.; Reid, G. *J. Chem. Soc. Dalton Trans.* **2000**, 2163–2166.
72. Hill, N. J.; Levason, W.; Patel, R.; Reid, G.; Webster, M. *Dalton Trans.* **2004**, 980–983.
73. Hector, A. L.; Levason, W.; Reid, G.; Webster, M.; Zhang, W. *Dalton Trans.* **2011**, *40*, 694–700.
74. Gillespie, R. J.; Hargittai, I. *The VSEPR Model of Molecular Geometry*, Allyn and Bacon: Boston, 1991.
75. Davies, M. K.; Durrant, M. C.; Levason, W.; Reid, G.; Richards, R. L. *J. Chem. Soc. Dalton Trans.* **1999**, 1077–1083.
76. Champness, N. R.; Levason, W.; Quirk, J. J.; Reid, G.; Frampton, C. S. *Polyhedron* **1995**, *14*, 2753–2758.
77. Booth, D. G.; Levason, W.; Quirk, J. J.; Reid, G. *J. Chem. Soc. Dalton Trans.* **1997**, 3493–3500.
78. Barton, A. J.; Hill, N. J.; Levason, W.; Patel, B.; Reid, G. *Chem. Commun.* **2001**, 95–96.
79. George, K.; Jura, M.; Levason, W.; Light, M. E.; Ollivere, L. P.; Reid, G. *Inorg. Chem.* **2012**, *51*, 2231–2240.
80. Levason, W.; Quirk, J. J.; Reid, G.; Smith, S. M. *J. Chem. Soc. Dalton Trans.* **1997**, 3719–3724.
81. Levason, W.; Quirk, J. J.; Reid, G. *J. Chem. Soc. Dalton Trans.* **1996**, 3713–3719.
82. Batchelor, R. J.; Einstein, F. W. B.; Gay, I. D.; Gu, J.; Pinto, B. M.; Zhou, X. *Inorg. Chem.* **1996**, *35*, 3667–3674.
83. Champness, N. R.; Kelly, P. F.; Levason, W.; Reid, G.; Slawin, A. M. Z.; Williams, D. J. *Inorg. Chem.* **1995**, *34*, 651–657.
84. Levason, W.; Quirk, J. J.; Reid, G. *Inorg. Chem.* **1994**, *33*, 6120–6122.
85. Batchelor, R. J.; Einstein, F. W. B.; Gay, I. D.; Gu, J.-H.; Pinto, B. M.; Zhou, X.-M. *J. Am. Chem. Soc.* **1990**, *112*, 3706–3707.
86. Batchelor, R. J.; Einstein, F. W. B.; Gay, I. D.; Gu, J.-H.; Pinto, B. M. *J. Organomet. Chem.* **1991**, *411*, 147–157.
87. Barton, A. J.; Hill, N. J.; Levason, W. *J. Am. Chem. Soc.* **2001**, *123*, 11801–11802.
88. Champion, M. J. D.; Levason, W.; Pugh, D.; Reid, G. *Dalton Trans.* **2015**, *44*, 18748–18759.
89. Farina, P.; Levason, W.; Reid, G. *Dalton Trans.* **2013**, *42*, 89–99.
90. Levason, W.; Pugh, D.; Purkis, J. M.; Reid, G. *Dalton Trans.* **2016**, *45*, 7900–7911.
91. Champion, M. J. D.; Farina, P.; Levason, W.; Reid, G. *Dalton Trans.* **2013**, *42*, 13179–13189.
92. Bartlett, P. N.; Champion, J. D.; Light, M. E.; Levason, W.; Reid, G.; Richardson, P. W. *Dalton Trans.* **2015**, *44*, 2953–2955.
93. Farina, P.; Levason, W.; Reid, G. *Polyhedron* **2013**, *55*, 102–108.
94. Farina, P.; Latter, T.; Levason, W.; Reid, G. *Dalton Trans.* **2013**, *42*, 4714–4724.
95. Maaninen, T.; Chivers, T.; Laitinen, R. S.; Wegelius, E. *Chem. Commun.* **2000**, 759–760.
96. Karhu, A. J.; Pakkanen, O. J.; Rautiainen, M. J.; Oilunkaniemi, R.; Chivers, T.; Laitinen, R. S. *Dalton Trans.* **2016**, *45*, 6210–6221.
97. Cameron, T. S.; Deeth, R. J.; Dionne, I.; Du, H.; Jenkins, H. D. B.; Krossing, I.; Passmore, J.; Roobottom, H. K. *Inorg. Chem.* **2000**, *39*, 5614–5631.
98. Collins, M. J.; Gillespie, R. J.; Sawyer, J. F. *Acta Crystallogr. Sect. C* **1988**, *44*, 405–409.
99. Beck, J.; Müller-Buschbaum, K. Z. *Anorg. Allg. Chem.* **1997**, *623*, 409–413.
100. Evans, D. H.; Gruhn, N. E.; Jin, J.; Li, B.; Lorange, E.; Okumura, N.; Macias-Ruvalcaba, N. A.; Zakai, U. I.; Zhang, S.-Z.; Block, E.; Glass, R. S. *J. Org. Chem.* **2010**, *75*, 1997–2009.
101. Brown, R. D.; Burden, F. R.; Godfrey, P. D. *J. Mol. Spectrosc.* **1968**, *25*, 415–421.
102. Pozdeev, N. M.; Akulinin, O. B.; Shapkin, A. A.; Magdesieva, N. N. *Russ. J. Struct. Chem.* **1970**, *11*, 804–809.
103. Bechtold, W.; Magruder, W.; Brock, G.; Goldstein, J. H. *Org. Magn. Reson.* **1982**, *19*, 173–175.
104. Inoue, S.; Tetsuya, J.; Nozoe, H.; Aso, Y.; Ogura, F.; Otsubo, T. *Heterocycles* **2000**, *52*, 159–170.
105. Millefiori, S.; Alparone, A. *Synth. Met.* **1998**, *95*, 217–224.
106. Shimizu, T.; Kawaguchi, M.; Tsuchiya, T.; Hirabayashi, K.; Kamigata, N. *Org. Lett.* **2003**, *5*, 1443–1445.
107. Shimizu, T.; Kawaguchi, M.; Tsuchiya, T.; Hirabayashi, K.; Kamigata, N. *J. Org. Chem.* **2005**, *70*, 5036–5044.
108. Schulte, J. H.; Werz, D. B.; Rominger, F.; Gleiter, R. *Org. Biomol. Chem.* **2003**, *1*, 2788–2794.
109. Werz, D. B.; Gleiter, R.; Rominger, F. *J. Org. Chem.* **2002**, *67*, 4290–4297.
110. Werz, D. B.; Staeb, T. H.; Benisch, C.; Rausch, B. J.; Rominger, F.; Gleiter, R. *Org. Lett.* **2002**, *4*, 339–342.
111. Werz, D. B.; Gleiter, R.; Rominger, F. *J. Org. Chem.* **2004**, *69*, 2945–2952.
112. Werz, D. B.; Gleiter, R.; Rominger, F. *J. Am. Chem. Soc.* **2002**, *124*, 10638–10639.
113. Werz, D. B.; Schulte, J. H.; Rausch, B. J.; Gleiter, R.; Rominger, F. *Eur. J. Inorg. Chem.* **2004**, 2585–2593.

## 1.10 [FeFe]-Hydrogenase mimics containing heavy p block elements

Hassan Abul-Futouh<sup>a</sup> and Wolfgang Weigand<sup>b</sup>, <sup>a</sup> Faculty of Science, Department of Chemistry, The Hashemite University, Zarqa, Jordan; and <sup>b</sup> Institut für Anorganische und Analytische Chemie, Friedrich-Schiller-Universität Jena, Jena, Germany

© 2023 Elsevier Ltd. All rights reserved.

1.10.1	Introduction	556
1.10.2	Synthetic complexes with aliphatic diselenolate linkers	557
1.10.2.1	General	557
1.10.2.2	Hexacarbonyl complexes	557
1.10.3	Synthetic complexes with aromatic diselenolate linkers	567
1.10.3.1	General	567
1.10.3.2	General aspects for the structures and syntheses of iron mimetic complexes with aromatic diselenolate linkers	567
1.10.4	Summary	570
References		570

### Abstract

This chapter demonstrates an overview of diiron complexes containing diselenato and ditellurato linkers which mimic the H cluster of [FeFe]-hydrogenase. The emphasis is on the significant role of incorporation of the selenium/tellurium atom into the synthetic H cluster. These synthetic models tolerate direct comparison with those of dithiolato model analogues for their catalytic activity to generate H<sub>2</sub> in the presence of a proton source. A seemingly logic conclusion indicates that the replacement of the two sulfur atoms with heavier chalcogens improves the electron density of the iron cores and hence increases their catalytic activity.

### 1.10.1 Introduction

Nowadays, climate change is considered one of the greatest environmental challenges, and the concern about it raises year by year by the scientific community. Therefore, the decarbonization strategy, which is defined as the method of lowering the amount of carbon, mainly CO<sub>2</sub>, is one of the aims that countries around the world have planned in the coming decades. To obtain this, it is a desideratum to replace the current fossil fuels with more eco-friendly alternative, such as green hydrogen owing to its clean cold combustion in fuel cells.<sup>1–3</sup> Consequently this triggered new developments in production of hydrogen and many researchers have reported studies on this process.<sup>4–8</sup> A high purity of hydrogen can be produced by water electrolysis, which is one of the cleanest ways as it produces only oxygen besides the hydrogen.<sup>9</sup> However, the efficient but expensive, platinum is still used as a catalyst for this method and hence restricts the widespread adoption of hydrogen economy.<sup>10</sup> Accordingly, many researchers have been done their work related to design a cheap, efficient (low overpotential and high catalytic activity) and robust catalyst to substitute platinum.

In contrast to present industrial method, great attention has been driven to enzymes called *hydrogenases*, which are known to serve as highly active catalysts for the reversible oxidation of hydrogen in nature.<sup>11–16</sup> These enzymes are categorized according to the metal composition of their active center into three major families: (i) [Fe]-hydrogenases, (ii) [FeFe]-hydrogenases and (iii) [NiFe]-hydrogenases.<sup>11–16</sup> A subclass of the latter, which is known as [NiFeSe]-enzymes incorporate a selenocysteine bounded to the Ni in place of one of the terminal cysteine residue of the typical [NiFe]-hydrogenase.<sup>17</sup> Among these different classes, [FeFe]-hydrogenase is considered to have the strongest catalytic ability for hydrogen formation, in which it can produce 9000 molecules of hydrogen per second under optimum condition.<sup>14,18</sup> Based on that, considerable attention has been paid on this type of hydrogenases as alternative biological catalysts to the commonly used platinum one. The topology of the active site of [FeFe]-hydrogenase, the so-called H-cluster, which is responsible for the catalytic process has been resolved in the late twentieth century by the groups of Peters and Fontecilla-Camps.<sup>19,20</sup> Crystallographic and spectroscopic studies have confirmed that this H-cluster contains two Fe centers which is coordinated by three carbon monoxides (CO), two cyanides (CN) and a bridging azadithiolate (ADT) ligand as shown in Fig. 1.<sup>19,21–24</sup> Furthermore, one of the two Fe centers is bound to a Fe<sub>4</sub>S<sub>4</sub> ferredoxin cluster via a cysteinyl residue. It is worth mentioning that the molecular structure of the H-cluster shows a unique feature in which one iron core is rotated with respect to the other iron unit making one CO ligand to be in bridging position between the two iron atoms (Fig. 1). This feature provides a vacant site to which hydrogenic species like a proton is proposed to bind during the catalytic process.<sup>25</sup> The significant of the NH moiety of the ADT linker is to act as an internal basic site that bind a proton as well as serves as a proton relay to the vacant site via agostic interaction.<sup>26,27</sup>

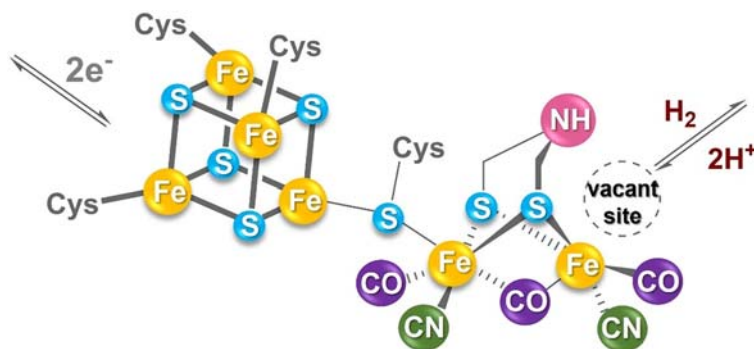


Fig. 1 Structure of the H-cluster of [FeFe]-hydrogenase.

Over the past few decades, several model complexes that mimic the natural archetype have been synthesized and their electrocatalytic activity toward hydrogen production is well reported in the literature.<sup>16</sup> The diversity of these synthetic approaches could help to understand the enzymatic mechanism of the H-cluster and give the chance to design effective and durable catalysts. Fig. 2 illustrates the major modifications of [FeFe]-hydrogenase mimicking complexes, which is focused on three aspects as follows: (i) alteration the dithiolate linker of the synthetic H-cluster mimics, (ii) the replacement of the  $\mu$ -S of diiron dithiolato models by  $\mu$ -Se or  $\mu$ -Te atoms and (iii) substitution of one or more of the CO ligands with a stronger  $\sigma$ -donor, such as phosphane or phosphite ligands.

Reviewing the literature, one can find an enormous number of publications regarding these aspects within the past 20 years. Therefore, this chapter briefly draws out some of salient features of the synthetic approaches containing the 3rd and 4th row chalcogen atoms, selenium and tellurium, as an alternative of sulfur. Additionally, this chapter depicts the distinct properties of such [FeFe]-hydrogenase mimicking complexes, relative to those of sulfur analogues.

## 1.10.2 Synthetic complexes with aliphatic diselenolate linkers

### 1.10.2.1 General

While the literature is very rich with articles concerning the diiron dithiolato complexes that mimic the butterfly [Fe<sub>2</sub>S<sub>2</sub>] subcluster of the H-cluster,<sup>30</sup> the heavier analogues, including selenium and tellurium, are sparsely known. Nowadays, much concern has been expressed in exploring the important role of selenium in the biological processes.<sup>31</sup> This is because the selenium element improves the chemical reactivity of the enzymatic reactions in comparison to that of sulfur analogues.<sup>31</sup> Therefore, we and others are giving close and thoughtful attention to model complexes having the heavier chalcogens like Se or Te as a substitute of S atom.<sup>32</sup> With this in mind, we decided to emphasize recent work in this area for the purpose of giving the reader an overview of the significant role of substituting Se or Te in lieu of S atom in [FeFe]-hydrogenase mimicking complexes.

### 1.10.2.2 Hexacarbonyl complexes

The synthesis of diiron hexacarbonyl complexes containing diselenolato, and ditelluroolato linkers can be achieved through several pathways. For example, the reaction of electrophiles such as organic halides with the in situ generated [Fe<sub>2</sub>(CO)<sub>6</sub>{ $\mu$ -(LiE)<sub>2</sub>}] (E = Se, Te), which is produced by reduction of [Fe<sub>2</sub>(CO)<sub>6</sub>{ $\mu$ -E<sub>2</sub>}] by 2 equiv. of [LiHBEt<sub>3</sub>] ("Super Hydride"), afforded the

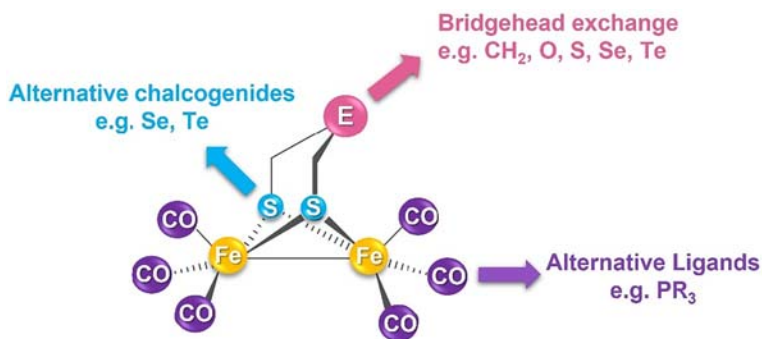
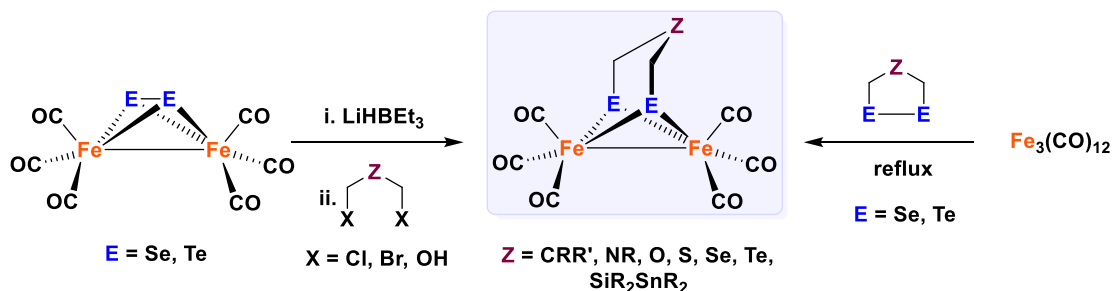


Fig. 2 Possible modifications of the synthetic approaches.<sup>28–30</sup>



**Scheme 1** Synthetic pathways of obtaining hydrogenase mimics.

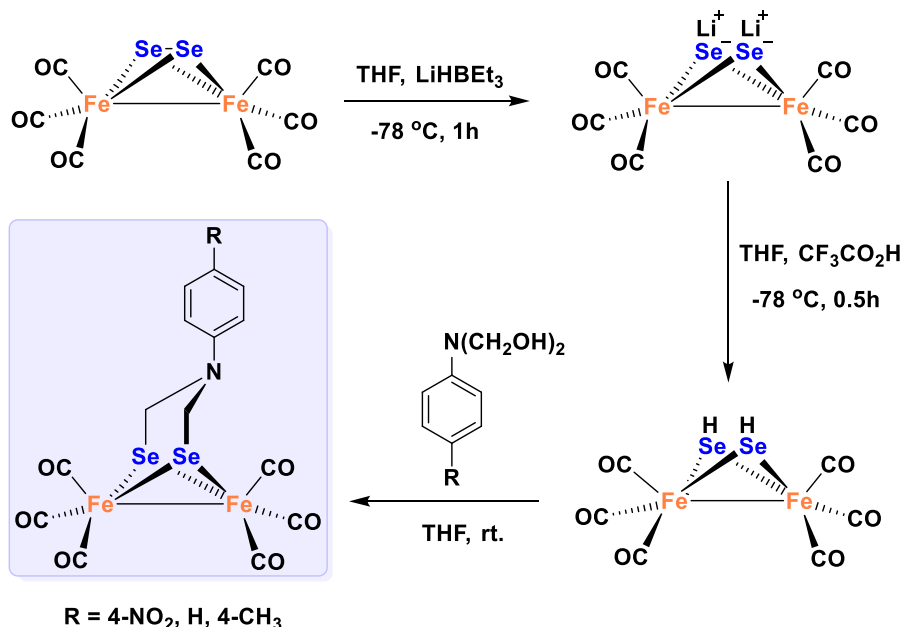
corresponding hydrogenase mimics (Scheme 1).<sup>32–35</sup> However, this method is efficient for cases in which the corresponding organo-selenium or tellurium compounds that possess diselenides or ditellurides bonds are not easily available.<sup>36</sup>

Otherwise, compounds containing diselenides or ditellurides bonds can be reacted with  $[\text{Fe}_3(\text{CO})_{12}]$  under reflux conditions to provide the analogous hydrogenase mimics in easier way and better yields as shown in Scheme 1.<sup>36</sup> Overall, the presence of heavier chalcogenolato ligands in such hydrogenase mimics enhance the electron density at the iron cores, and hence influence their reactivity as well as the redox properties.

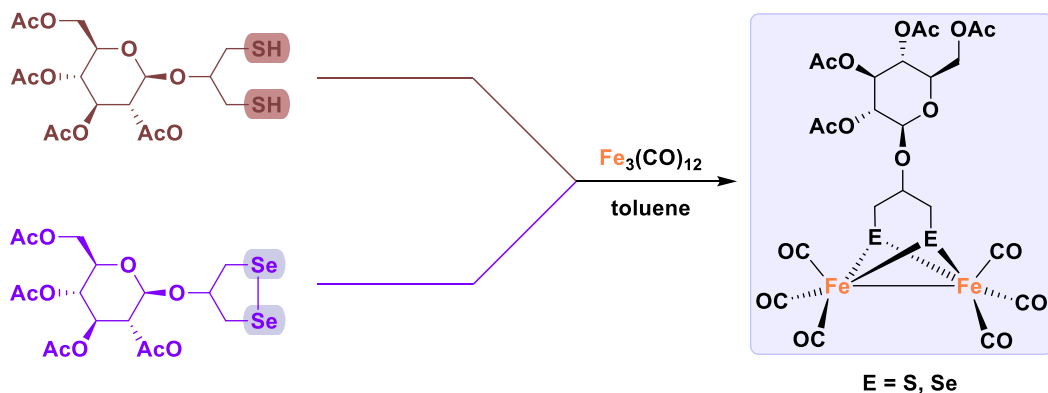
In 2008, Peng and co-workers have reported for the first time the synthesis of [FeFe]-hydrogenase H-cluster mimic mediated by N-substituted selenium-bridged with the general formula  $[\text{Fe}_2(\text{CO})_6\{\mu-(\text{SeCH}_2)_2\text{NC}_6\text{H}_4\text{R}\}]$  ( $\text{R} = 4\text{-NO}_2, \text{H}, 4\text{-CH}_3$ ) as shown in Scheme 2.<sup>37</sup>

In their study, the influence of substituting Se atoms as an alternative of S atoms on the electrochemical properties as well as the electrocatalytic activity for proton reduction was evaluated using IR spectroscopy and cyclic voltammetry. As a result, it has been found that complexes containing diselenolato linkers show a small shift (ca.  $9\text{ cm}^{-1}$ ) of their CO stretching bands to lower wavenumbers in the IR spectra compared to those of sulfur analogues. However, these complexes showed the same reduction potentials but slightly higher electrocatalytic activity for proton reduction when it is compared with those of the corresponding sulfur analogues.<sup>37</sup> During the same period, similar conclusion has been reported by Weigand and co-workers, in which they could obtain a water-soluble [FeFe]-hydrogenase mimics mediated by sugar residue with a  $[\text{Fe}_2\text{E}_2]$  ( $\text{E} = \text{S, Se}$ ) core having the general formula  $[\text{Fe}_2(\text{CO})_6\{\mu-(\text{ECH}_2)_2\text{CHR}\}]$  ( $\text{E} = \text{S, Se}$ ) ( $\text{R} = \text{tetra-}O\text{-acetyl-}\beta\text{-D-glucopyranoside}$ ) as illustrated in Scheme 3.<sup>38</sup>

It is worth mentioning that the presence of the sugar residue will enhance the solubility of such models in aqueous system, and hence water will serve as solvent and as a proton source at the same time.<sup>39</sup> The impact of substituting Se atoms as an alternative of S atoms in their hydrogenase mimics has recognized in the stability of these models in aqueous solution as well as the activity toward hydrogen formation. Overall, the complex containing diselenolato linker shows higher stability and higher activity for proton reduction to molecular hydrogen, but at considerably more negative potentials than the corresponding sulfur analogue. This can be



**Scheme 2** The synthetic procedure of  $[\text{Fe}_2(\text{CO})_6\{\mu-(\text{SeCH}_2)_2\text{NC}_6\text{H}_4\text{R}\}]$  ( $\text{R} = 4\text{-NO}_2, \text{H}, 4\text{-CH}_3$ ) complexes.



**Scheme 3** Synthetic pathways of obtaining  $[\text{Fe}_2(\text{CO})_6\{\mu\text{-(ECHR)}_2\text{CHR}\}]$  ( $\text{E}=\text{S, Se}$ ) ( $\text{R}$  = tetra-*O*-acetyl- $\beta$ -*D*-glucopyranoside).

attributed to the stronger electropositivity of Se atom compared to that of S atom, and hence increases the electron density at the iron core.<sup>38</sup>

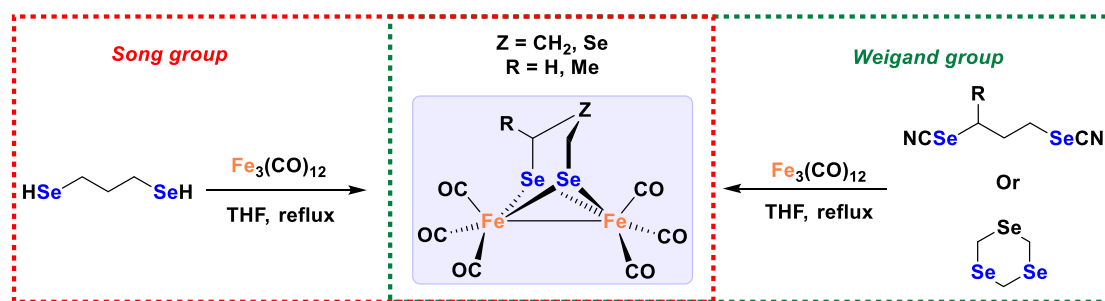
One year later, the replacement of the  $\mu$ -S of propanedithiolate-based [FeFe]-complex,  $[\text{Fe}_2(\text{CO})_6\{\mu\text{-(SCH}_2)_2\text{CH}_2\}]$ , by  $\mu$ -Se atoms has been reported for the first time by Weigand, Song and their co-workers independently as shown in **Scheme 4**.<sup>40,41</sup> In their study they could also show that the presence of Se atoms in lieu of S atoms of their synthetic approaches improves the activity toward hydrogen formation in comparison with the corresponding  $[\text{Fe}_2(\text{CO})_6\{\mu\text{-(SCH}_2)_2\text{CH}_2\}]$  complex. Moreover, Weigand group have succeeded to extend their study to obtain the analogous methyl-substituted complex from the reaction of  $[\text{Fe}_3(\text{CO})_{12}]$  with the in situ generated compound 3-methyl-1,2-diselenolane (**Scheme 4**).<sup>40</sup> This modification might improve the stability of the resulting complex.<sup>42</sup>

Within the same research work, Weigand and co-workers also succeeded in replacing the bridgehead Z in the linker  $\text{-Se-CHR-Z-CH}_2\text{-Se-}$  ( $\text{R}=\text{H}$ ;  $\text{Z}=\text{CH}_2$ ) by Se atom through the reaction of 1,3,5-triselenane with  $[\text{Fe}_3(\text{CO})_{12}]$  under reflux condition as exhibited in **Scheme 4**.<sup>40</sup> Once more, the presence of Se atom in the obtaining complexes of their research work afford higher catalytic activity for proton reduction to hydrogen under electrochemical environments. These results were supported by photoelectron ionization experiment and DFT computations, which revealed that its reorganization energy is considerably lower than that for sulfur-analogue, and hence predicts faster electron transfer which in turn causes the high activity of Se-containing complexes.<sup>40</sup>

As a continuation of these initial results on the synthetic H-cluster mimics, two new complexes of “closed” and “open” butterfly  $[\text{Fe}_2\text{Se}_2]$  cluster have been reported by Song and their co-workers.<sup>43</sup> In their study, the oxidative addition of  $[\text{Fe}_3(\text{CO})_{12}]$  with 1,3-dihydroselenopropane-2-ol compound afforded the “closed” selenium containing complex with the general formula  $[\text{Fe}_2(\text{CO})_6\{\mu\text{-(SeCH}_2)_2\text{CH(OH)}\}]$  as shown in **Scheme 5**.

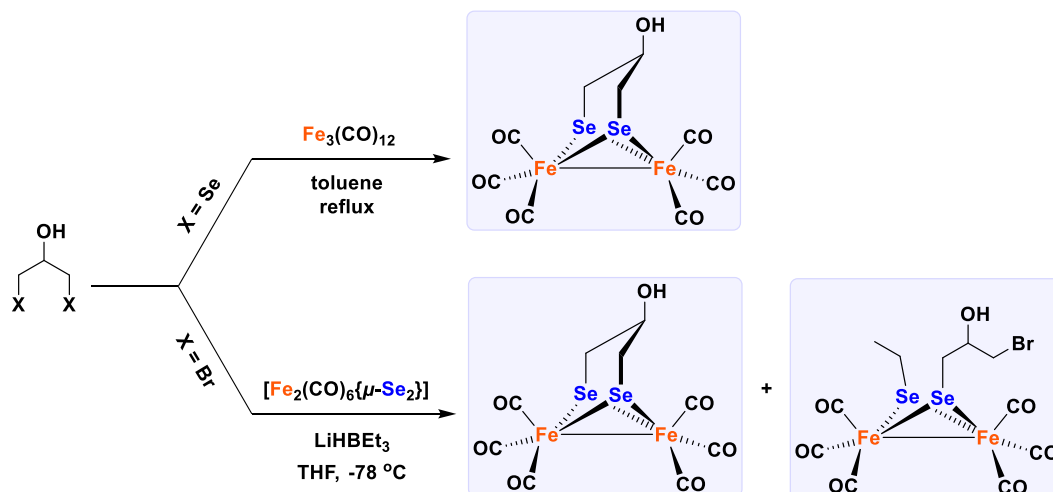
Another synthetic approach can give two types of products (the “closed” and “open” structures) with different yields through the reaction of the in situ generated  $[\text{Fe}_2(\text{CO})_6\{\mu\text{-(LiSe)}_2\}]$  with 1,3-dibromo-2-propanol in THF solution (**Scheme 5**). The yields of such type of reaction depends on the different of the molar ratio between the intermediate  $[\text{Fe}_2(\text{CO})_6\{\mu\text{-(LiSe)}_2\}]$  and 1,3-dibromo-2-propanol compound.<sup>43</sup> It is worth pointing out that the “open” system adopts three possible stereoisomers: (i) axial-*R*/equatorial-Et (*ae*), (ii) axial-Et/equatorial-*R*, and (iii) equatorial-Et/equatorial-*R* (*ee*) ( $\text{R}=\text{CH}_2\text{CH(OH)CH}_2\text{Br}$ ) as shown in **Fig. 3**. The axial-Et/axial-*R* (*aa*) isomer does not form due to the strong steric repulsions between the two substituents.<sup>44,45</sup> The cyclic voltammogram of  $[\text{Fe}_2(\text{CO})_6\{\mu\text{-(SeCH}_2)_2\text{CH(OH)}\}]$  exhibits similar behavior, but at considerably more negative potentials than the corresponding sulfur analogue.

In light of the above-mentioned results, the number of articles that focus on the synthetic mimics of the active site of [FeFe] hydrogenase containing heavier chalcogen, such as selenium or even tellurium is increased year after year. For example, the Weigand

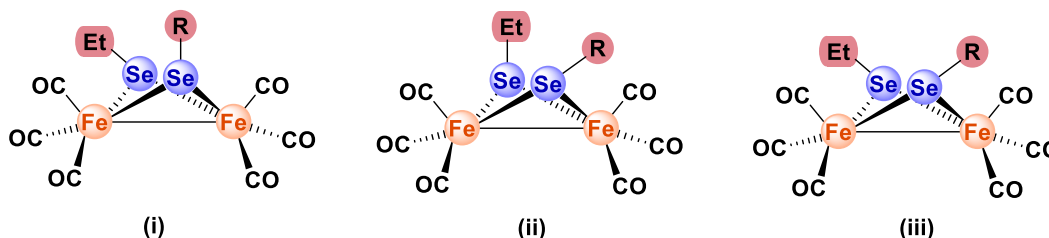


**Scheme 4** Synthetic pathways of Weigand and Song hydrogenase mimics.<sup>40,41</sup>





**Scheme 5** Synthetic pathways of obtaining the “closed” and “open” structures of the synthetic H-cluster mimics reported by Song et al.<sup>43</sup>

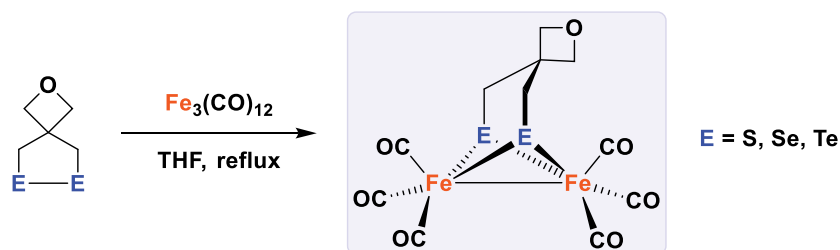


**Fig. 3** Three possible isomers of the “open” system reported by Song et al. (i) axial-R/equatorial-Et (*ae*), (ii) axial-Et/equatorial-R, and (iii) equatorial-Et/equatorial-R (*ee*) ( $R = \text{CH}_2\text{CH}(\text{OH})\text{CH}_2\text{Br}$ ).

group has extended their investigation on the influence of the heavier atoms in a series of [FeFe]-hydrogenase model complexes with the general formula  $[\text{Fe}_2(\text{CO})_6\{\mu\text{-(ECH}_2)_2\text{C}_3\text{H}_4\text{O}\}]$  ( $E = \text{S, Se, Te}$ ).<sup>46</sup> The main purpose of their study was to demonstrate the basis for the difference in reorganization energy of  $[\text{Fe}_2\text{E}_2]$  ( $E = \text{S, Se, and Te}$ ) cores. It has been found that the presence of the oxetane ring has a remarkable influence on stabilizing the cyclic diselenium and ditellurium precursor compounds, and hence gives the chance to synthesize the homologous sulfur, selenium, and tellurium series. As described in their article, the complexes  $[\text{Fe}_2(\text{CO})_6\{\mu\text{-(ECH}_2)_2\text{C}_3\text{H}_4\text{O}\}]$  ( $E = \text{S, Se, Te}$ ) can be obtained by the reaction of equimolar amounts of  $[\text{Fe}_3(\text{CO})_{12}]$  with 2-oxa-6,7-dithiaspiro[3,4]octane, 2-oxa-6,7-diselenaspiro[3,4]octane or 2-oxa-6,7-ditelluraspiro[3,4]octane, respectively, in boiling THF as exhibited in **Scheme 6**.

As a result of this investigation, the electronic effects of substitution from sulfur to selenium to tellurium are small. Moreover, the ability of these complexes to catalyze the electrochemical reduction of protons to generate dihydrogen was studied using cyclic voltammetry, and the catalytic activity is found to decrease on going from the sulfur to selenium to tellurium complexes. This observation was also supported by DFT calculations, which show the disability of their anionic species to adopt the rotated structures and to provide a vacant coordination site. However, the reason behind this performance might be explained in terms of the increase of the size of the chalcogen atoms ongoing from S to Te and consequently increases the distance between the two iron atoms.<sup>47</sup>

As a part of the Weigand group ongoing interest in studying the influence of replacing the  $\mu\text{-S}$  of the synthetic mimics of the active site of [FeFe] hydrogenase by heavier chalcogen atoms, mixed (S, Se) and (S, Te) [FeFe]-hydrogenase model complexes



**Scheme 6** Synthesis of  $[\text{Fe}_2(\text{CO})_6\{\mu\text{-(ECH}_2)_2\text{C}_3\text{H}_4\text{O}\}]$  ( $E = \text{S, Se, Te}$ ) complexes reported by Weigand and co-workers.<sup>46</sup>

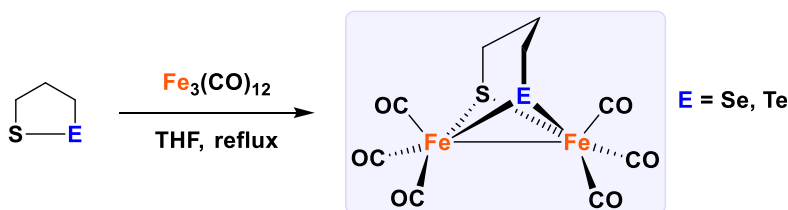
have been synthesized and characterized in order to compare them with the much-studied molecule  $[\text{Fe}_2(\text{CO})_6\{\mu\text{-(SCH}_2)_2\text{CH}_2\}]$ .<sup>48</sup> In this research work only one sulfur atom is replaced either by one selenium atom or by one tellurium atom through the reaction of 1,2-thiaselenolane or 1,2-thiatellurolane with  $[\text{Fe}_3(\text{CO})_{12}]$  as shown in **Scheme 7**.

The features of the resulting complexes were compared with the corresponding sulfur analogues. As a conclusion of this work, the presence of only single chalcogen substitutions at the diiron core is also increasing the electron richness at the metal centers and hence elongate the bond between the two iron atoms as in the case of replacing the two sulfur atoms. This assumption was supported spectroscopically by noting the red shift of the carbonyl stretching frequencies of the IR spectra as well as lower ionization energies of these complexes compared to that of  $[\text{Fe}_2(\text{CO})_6\{\mu\text{-(SCH}_2)_2\text{CH}_2\}]$ . However, there is no significant enhancement of the catalysts properties for the hydrogen generation compared to their sulfur counterparts.<sup>48</sup>

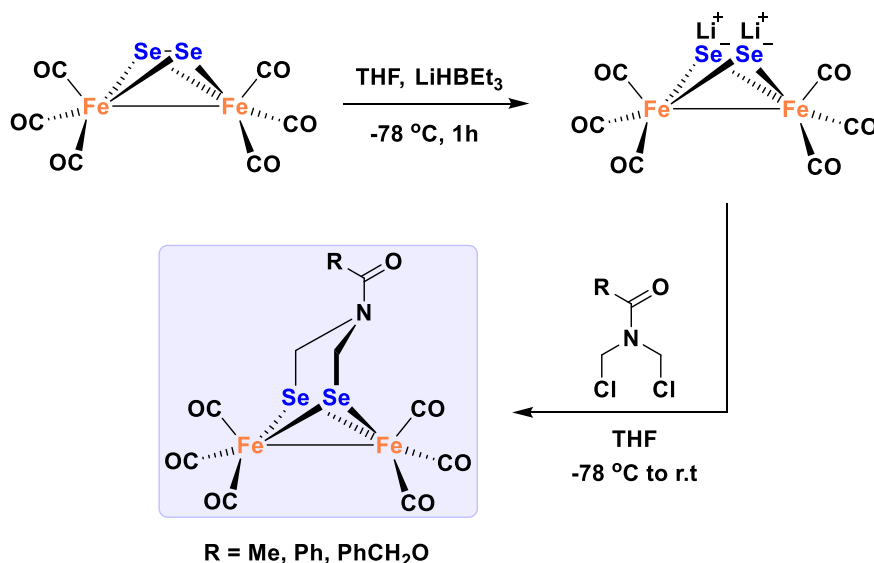
In fact, one should note that all the synthetic approaches mentioned above, which are related to the structure of the H-cluster are classified as artificial models with abiological linkers. Consequently, complexes mediated by azadithiolate (ADT) linkers can be classified as bioinspired models.<sup>49–64</sup> Along this line, the preparation of  $[\text{Fe}_2(\text{ADT})(\text{CO})_6]$ -like models was reported for the first time by Rauchfuss and co-workers in 2001.<sup>49,50,65</sup> Therefore, this triggered new developments in extending the chalcogenide exchange to the ADT models with selenium by Song and his co-workers.<sup>66</sup> Here, the dilithium salt of  $[\text{Fe}_2(\text{CO})_6\{\mu\text{-Se}_2\}]$  was generated via reaction of  $[\text{Fe}_2(\text{CO})_6\{\mu\text{-Se}_2\}]$  by 2 equiv. of  $[\text{LiHBET}_3]$  and afforded the N-functionalized models  $[\text{Fe}_2(\text{CO})_6\{\mu\text{-(SeCH}_2)_2\text{NC(O)R}\}]$  (R = Me, Ph,  $\text{PhCH}_2\text{O}$ ) upon reaction with the corresponding *N,N*-bis(chloromethyl)amide in THF from  $-78^\circ\text{C}$  to room temperature as illustrated in **Scheme 8**.

It was further reported that the parent complex  $[\text{Fe}_2(\text{CO})_6\{\mu\text{-(SeCH}_2)_2\text{NH}\}]$  can be obtained through the N-substituted complex  $[\text{Fe}_2(\text{CO})_6\{\mu\text{-(SeCH}_2)_2\text{NC(O)PhCH}_2\text{O}\}]$  as a precursor by using the N-deprotecting method.<sup>66,67</sup> The reaction of this precursor with  $\text{BF}_3 \cdot \text{OEt}_2/\text{Me}_2\text{S}$  reagent in  $\text{CH}_2\text{Cl}_2$  solution afforded  $[\text{Fe}_2(\text{CO})_6\{\mu\text{-(SeCH}_2)_2\text{NH}\}]$  complex.<sup>66</sup> Consequently, the latter can be used as a precursor to get the N-functionalized models  $[\text{Fe}_2(\text{CO})_6\{\mu\text{-(SeCH}_2)_2\text{NC(O)R}\}]$  (R = Me, Ph,  $\text{PhCH}_2\text{O}$ ) in high yields (**Scheme 9**) compared to the method involving the reaction of  $[\text{Fe}_2(\text{CO})_6\{\mu\text{-(LiSe)}_2\}]$  with the respective *N,N*-bis(chloromethyl)amide compounds as described in **Scheme 8**.<sup>66</sup>

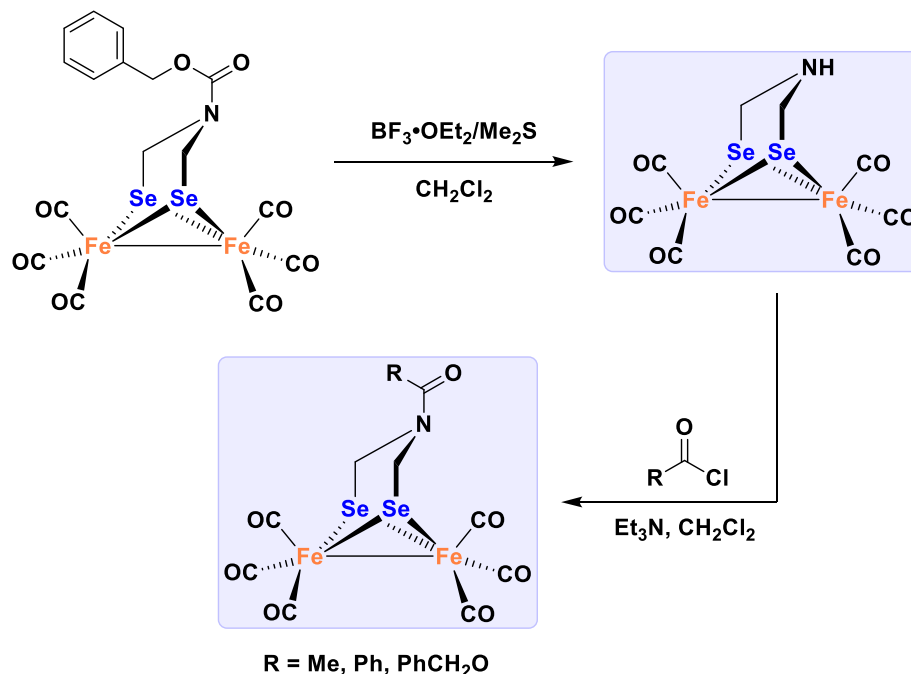
In 2013, the Liu group has investigated the bioactivity of the  $[\text{Fe}_2(\text{CO})_6\{\mu\text{-(SeCH}_2)_2\text{CH(OH)}\}]$  (SFOH) and  $[\text{Fe}_2(\text{CO})_6\{\mu\text{-(SeCH}_2)_2\text{CH(OOCCH}_3)\}]$  (SFOA) complexes as an antioxidant against radical-induced oxidation of DNA.<sup>68</sup> As a result, the aliphatic hydroxyl group in  $[\text{Fe}_2\text{Se}_2]$  cluster was the antioxidant group of SFOH in protecting DNA against 2,2'-azobis(2-amidinopropane hydrochloride) (AAPH)-induced oxidation as shown in **Scheme 10**.



**Scheme 7** Synthetic pathway of obtaining the mixed (S, Se) and (S, Te)  $[\text{FeFe}]$ -hydrogenase model complexes.<sup>48</sup>

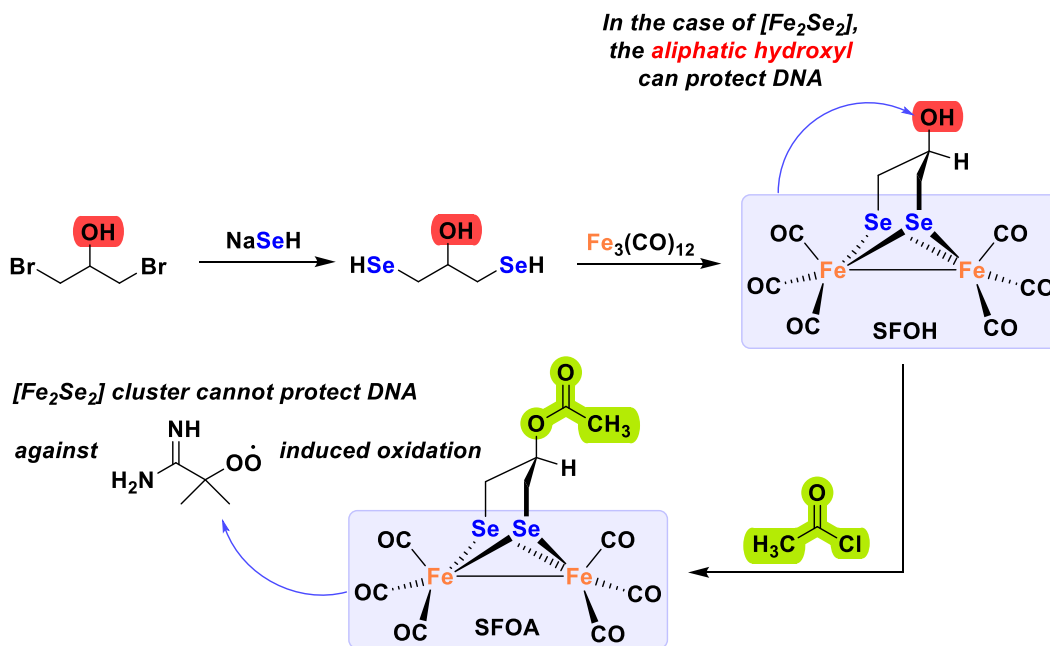


**Scheme 8** Synthetic pathway to the N-functionalized models  $[\text{Fe}_2(\text{CO})_6\{\mu\text{-(SeCH}_2)_2\text{NC(O)R}\}]$  (R = Me, Ph,  $\text{PhCH}_2\text{O}$ ) reported by Song et al.<sup>66</sup>

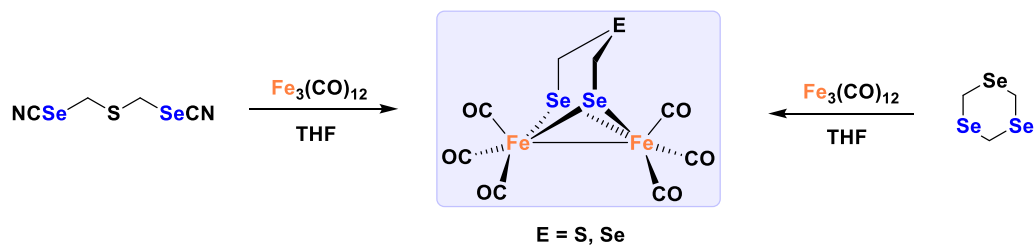


**Scheme 9** Synthetic pathways toward  $[\text{Fe}_2(\text{CO})_6\{\mu\text{-(SeCH}_2)_2\text{NH}\}]$  and  $[\text{Fe}_2(\text{CO})_6\{\mu\text{-(SeCH}_2)_2\text{NC(O)R}\}]$  ( $\text{R}=\text{Me, Ph, PhCH}_2\text{O}$ ) complexes.<sup>66</sup>

Harb et al. has also reported the incorporation of a sulfur or a selenium atom instead of  $\text{CH}_2$  at the bridgehead linker of  $[\text{Fe}_2(\text{CO})_6\{\mu\text{-(SeCH}_2)_2\text{CH}_2\}]$  complex to examine the influence of the central sulfur and selenium atoms in such complexes.<sup>40,69</sup> It is worth noting that the central sulfur/selenium atom has the same number of electrons as the actual active sites head group  $\text{NH}$ , both units are isolobal to each other. The results of this study were supported by different methods such as, gas-phase photoelectron spectroscopy, DFT calculations and cyclic voltammetry to get insight into the features of these hydrogenase mimics. The reaction of bis(selenocyanatomethyl)sulfane with  $[\text{Fe}_3(\text{CO})_{12}]$  in refluxing THF afforded the  $[\text{Fe}_2(\text{CO})_6\{\mu\text{-(SeCH}_2)_2\text{S}\}]$  complex, while the reaction of 1,3,5-triselenane with  $[\text{Fe}_3(\text{CO})_{12}]$  in boiling THF afforded the  $[\text{Fe}_2(\text{CO})_6\{\mu\text{-(SeCH}_2)_2\text{Se}\}]$  complex as shown in Scheme 11.<sup>40,69</sup>



**Scheme 10** Synthesis of  $[\text{Fe}_2(\text{CO})_6\{\mu\text{-(SeCH}_2)_2\text{CH(OH)}\}]$  (SFOH) and  $[\text{Fe}_2(\text{CO})_6\{\mu\text{-(SeCH}_2)_2\text{CH(OOCCH}_3)\}]$  (SFOA) complexes.<sup>68</sup>



**Scheme 11** Synthetic pathways of obtaining  $[\text{Fe}_2(\text{CO})_6\{\mu\text{-(SeCH}_2)_2\text{S}\}]$  and  $[\text{Fe}_2(\text{CO})_6\{\mu\text{-(SeCH}_2)_2\text{Se}\}]$  complexes reported by Harb et al.<sup>40,69</sup>

As a result, significant consequences for the physical and electrochemical properties of their synthetic approaches have been obtained based on gas-phase photoelectron spectroscopy, DFT calculations and cyclic voltammetry experiments.<sup>40,69</sup> They have found that the influence of the central sulfur or selenium atoms at the bridgehead linker of  $[\text{Fe}_2(\text{CO})_6\{\mu\text{-(SeCH}_2)_2\text{E}\}]$  ( $\text{E} = \text{S, Se}$ ) has considerable impacts on the stabilization of the cations of these complexes as indicated by the photoelectron spectra, cyclic voltammograms, and computations.<sup>40,69</sup> While the HOMO of  $[\text{Fe}_2(\text{CO})_6\{\mu\text{-(SeCH}_2)_2\text{CH}_2\}]$  complex is primarily the  $\sigma_{\text{Fe}-\text{Fe}}$  bond, the HOMO of  $[\text{Fe}_2(\text{CO})_6\{\mu\text{-(SeCH}_2)_2\text{E}\}]$  ( $\text{E} = \text{S, Se}$ ) complexes is primarily the bridgehead Sulfur/selenium lone pair with some delocalization to the bimetallic core according to the computations data. This results in structural changes of the cations compared to the neutral molecule, where one  $[\text{Fe}(\text{CO})_3]$  unit is rotated with respect to the other iron unit making one CO ligand to be in a semi-bridging position between the two iron atoms. This behavior is comparable to the structure of the active site of the natural archetype. Moreover, the positive charge of this cation is stabilized by the lone pair of the bridgehead atom that bend toward the resulting vacant site of the rotated Fe atom.<sup>69</sup>

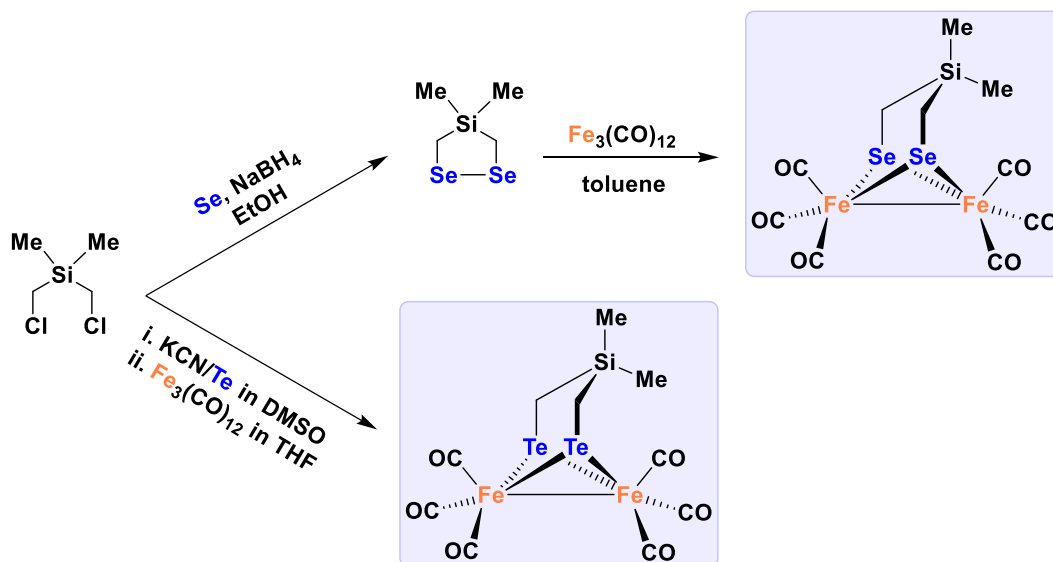
Another remarkable effect of this alteration was also detected in the redox features of the obtaining complexes. Since the first reduction event of  $[\text{Fe}_2(\text{CO})_6\{\mu\text{-(SeCH}_2)_2\text{CH}_2\}]$  is reported to be a one-electron process,<sup>40,41</sup> the reductions of  $[\text{Fe}_2(\text{CO})_6\{\mu\text{-(SeCH}_2)_2\text{E}\}]$  ( $\text{E} = \text{S, Se}$ ) occur after two-electrons processes with potential inversion. The nature of the transfer of these two-electrons is assigned to an intervening chemical process of an ECE mechanism ( $\text{E} =$  electrochemical process,  $\text{C} =$  chemical process). In this chemical process, one  $[\text{Fe}(\text{CO})_3]$  unit rotates to put one CO ligand in a bridging position, followed by cleavage of one Fe–Se bond.<sup>70</sup> Accordingly, the lone pair of the bridgehead atom is withdrawn away from the iron to minimize the electron-electron repulsions.

Along this line, Song and co-workers have also reported a comparison study between diiron oxadiselenolate (ODSe) complex and the known diiron thiodiselenolate (TDSe) complex as models for the active site of [FeFe]-hydrogenases.<sup>71</sup> Here, the synthesis of diiron-ODSe complex was reported for the first time by the oxidative addition of  $\text{HSeCH}_2\text{OCH}_2\text{SeH}$  compound with  $[\text{Fe}_3(\text{CO})_{12}]$  in boiling THF to afford the target complex with the general formula  $[\text{Fe}_2(\text{CO})_6\{\mu\text{-(SeCH}_2)_2\text{O}\}]$ . As a result, it has been found that the catalytic activity of hydrogen formation of  $[\text{Fe}_2(\text{CO})_6\{\mu\text{-(SeCH}_2)_2\text{O}\}]$  is slightly higher than that of  $[\text{Fe}_2(\text{CO})_6\{\mu\text{-(SeCH}_2)_2\text{S}\}]$ . Moreover, this study also showed that the catalytic activity of both diiron-ODSe and diiron-TDSe complexes is slightly lower than that of their sulfur analogues.

The Weigand group could provide another option to alter the bridgehead atom of  $[\text{Fe}_2(\text{CO})_6\{\mu\text{-(SCH}_2)_2\text{C}(\text{Me}_2)\}]$ <sup>72,73</sup> by silicon atom together with the replacement of the  $\mu\text{-S}$  atoms by  $\mu\text{-Se}$  or  $\mu\text{-Te}$  atoms.<sup>74</sup> In previous work, it has been reported that the presence of the central silicon atom at the bridgehead linker of  $[\text{Fe}_2(\text{CO})_6\{\mu\text{-(SCH}_2)_2\text{Si}(\text{Me}_2)\}]$  is found to have a significant influence on increasing the electron density at the  $\mu\text{-S}$ -atoms due to the repulsive interaction of the  $\sigma(\text{Si}-\text{C})$  and  $3\text{p}(\text{S})$  orbitals (filled-filled interaction).<sup>75</sup> Therefore, it is worth investigating the influence of presence the silicon atom at the bridgehead linker instead of carbon atom together with the replacement of  $\mu\text{-S}$  by heavier chalcogen, such as selenium and tellurium atoms. In this study, the reaction of bis(chloromethyl)dimethylsilane with the in situ generated sodium diselenide, which is produced from the reaction of selenium and sodium borohydride in absolute ethanol, afforded the compound 4,4-dimethyl-1,2,4-diselenasilolane (Scheme 12). Consequently, the reaction of the latter with equimolar amount of  $[\text{Fe}_3(\text{CO})_{12}]$  in boiling toluene generated the corresponding hydrogenase mimics with the general formula  $[\text{Fe}_2(\text{CO})_6\{\mu\text{-(SeCH}_2)_2\text{Si}(\text{Me}_2)\}]$  as depicted in Scheme 12.

On the other hand, the synthesis of  $[\text{Fe}_2(\text{CO})_6\{\mu\text{-(TeCH}_2)_2\text{Si}(\text{Me}_2)\}]$  complex was carried out in a different route since 4,4-dimethyl-1,2,4-diselenasilolane could not be obtained using the same method. Upon this, two mol-equivalents of the freshly prepared potassium tellurocyanate, which is obtained by heating tellurium and potassium cyanide in refluxing dimethyl sulfoxide (DMSO), were treated with bis(chloromethyl)dimethylsilane to afford the in situ generated 4,4-dimethyl-1,2,4-ditellurasilolane. The latter was then added immediately to a solution of  $[\text{Fe}_3(\text{CO})_{12}]$  in THF and heated under reflux conditions to generate  $[\text{Fe}_2(\text{CO})_6\{\mu\text{-(TeCH}_2)_2\text{Si}(\text{Me}_2)\}]$  as shown in Scheme 12.

By comparing the CO stretching vibration modes of the obtained complexes with those of the sulfur analogue  $[\text{Fe}_2(\text{CO})_6\{\mu\text{-(SCH}_2)_2\text{Si}(\text{Me}_2)\}]$ , it was found that the CO vibrations are shifted to smaller frequencies on going from S to Se to Te. This indicates that the electron density on the iron center is increased by the heavier Se- and Te-homologues. However, the cyclic voltammograms of these complexes do not show any differences in the reduction potentials suggesting similar energies for the LUMO orbitals. Furthermore, the catalytic activity of hydrogen production by using acetic acid as a source of protons decreases on going from S to Se to Te despite the increase of the electron density on the iron center. The reason behind this performance might be explained



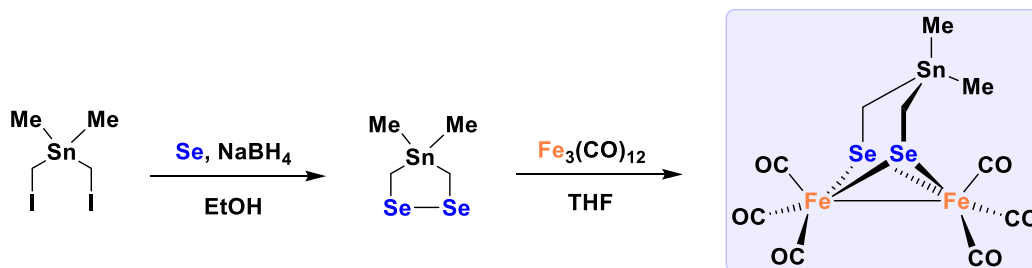
**Scheme 12** Synthetic pathways of obtaining  $[\text{Fe}_2(\text{CO})_6\{\mu\text{-(ECH}_2)_2\text{Si(Me)}_2\}]$  ( $\text{E}=\text{Se, Te}$ ) complexes.<sup>74</sup>

in terms of increasing the size of the chalcogen atoms ongoing from S to Te and consequently the distance between the two iron atoms increases, which results in the disability of these complexes to form the rotated structure and offer a vacant site for protonation as reported in the literature.<sup>46</sup>

Likewise, Abul-Futouh et al. have reported a study that concerns about the impact of substituting the central atom, E, in complexes containing  $[\mu\text{-(SCH}_2)_2\text{ER}_2]$  linkers with the series of group 14 atoms going from C to Sn on the electron richness of the  $[\text{Fe}_2\text{S}_2]$  core.<sup>76</sup> As a result, they have found that the electron density of the  $[\text{Fe}_2\text{S}_2]$  core increases upon going from C to Sn in  $[\text{Fe}_2(\text{CO})_6\{\mu\text{-(SCH}_2)_2\text{EME}_2\}]$  ( $\text{E}=\text{C, Si, Ge}$  and  $\text{Sn}$ ) complexes. This can be explained in terms of increasing orbital interaction between the  $\sigma(\text{C-E})$  bond and the sulfur lone pair p orbital and hence the sulfur character in the HOMO enhances down the series. In a comparable approach, Abul-Futouh et al. have succeeded in obtaining complex that mimics the structure of the active site of [FeFe]-hydrogenase which contains a Sn atom at the bridgehead linker with the replacement of  $\mu\text{-S}$  donor atoms by  $\mu\text{-Se}$  atoms.<sup>77</sup> The aim of this study is to investigate the protonation reactions of these mimicking complexes in the presence of strong and moderate acids, respectively. Here, the reaction of bis(iodomethyl)dimethylstannane with the in situ generated sodium diselenide, which is produced from the reaction of selenium and sodium borohydride in absolute ethanol, afforded the compound 4,4-dimethyl-1,2,4-diselenastannolane (Scheme 13). Subsequently, the reaction of the latter with equimolar amount of  $[\text{Fe}_3(\text{CO})_{12}]$  in boiling THF afforded the corresponding hydrogenase mimics with the general formula  $[\text{Fe}_2(\text{CO})_6\{\mu\text{-(SeCH}_2)_2\text{Sn(Me)}_2\}]$  as depicted in Scheme 13.

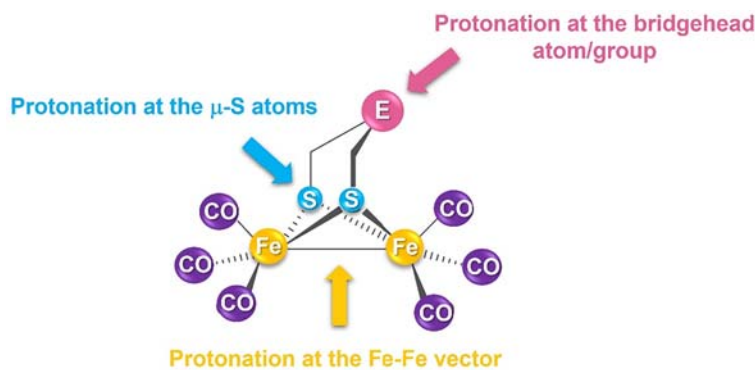
In fact, one should consider the impact of an existing internal basic site of the synthetic H-cluster mimics that could be protonated in the presence of a Brønsted acid which is a crucial step in the catalytic cycle. In general, protonation of the bimetallic hexacarbonyl complexes may occur at different positions as shown in Fig. 4, with the consideration of the strength and amount of the acid added. While protonation at the  $\mu\text{-S}$  is very difficult owing to its low basicity, protonation at the bridgehead atom/group in  $[\text{Fe}_2(\text{CO})_6\{\mu\text{-(SCH}_2)_2\text{E}\}]$  complexes is possible only when  $\text{E}=\text{NR}$  or  $\text{PhP}=\text{O}$  are treated with strong acids such as  $\text{HBF}_4 \cdot \text{Et}_2\text{O}$ ,  $\text{HOTf}$  and  $\text{HClO}_4$  as reported in the literature.<sup>52,78–82</sup>

On the other hand, protonation at the Fe–Fe core of diiron dithiolato hexacarbonyl complexes cannot be occurred by acids weaker than or similar to  $\text{HBF}_4 \cdot \text{Et}_2\text{O}$ . One exceptional case had been reported by Heinekey, Chiang and their co-workers in which they could develop a method to protonate  $[\text{Fe}_2(\text{CO})_6\{\mu\text{-(xdt)}\}][\text{B}(\text{C}_6\text{F}_5)_4]$  ( $\text{xdt} = \text{pdt}$  (propanedithiolato),  $\text{edt}$  (ethanedithiolato)



**Scheme 13** Synthetic pathways of obtaining  $[\text{Fe}_2(\text{CO})_6\{\mu\text{-(SeCH}_2)_2\text{Sn(Me)}_2\}]$  complex reported by Abul-Futouh et al.<sup>77</sup>



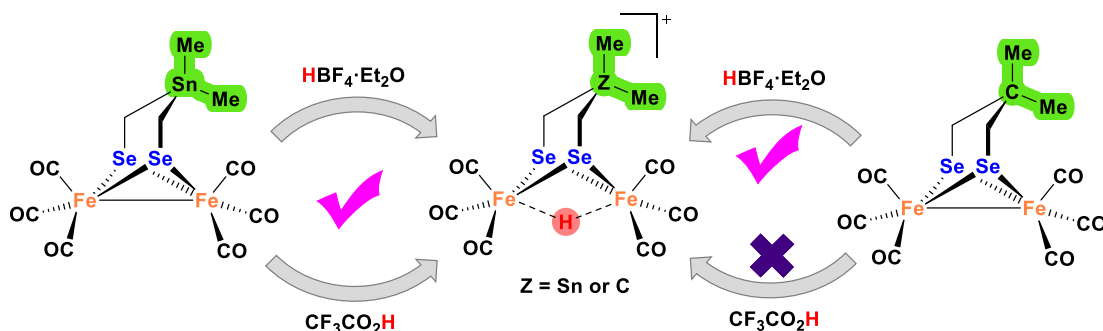


**Fig. 4** Possible protonation positions of  $[\text{Fe}_2(\text{CO})_6\{\mu\text{-(SCH}_2)_2\text{E}]\}$  complexes.

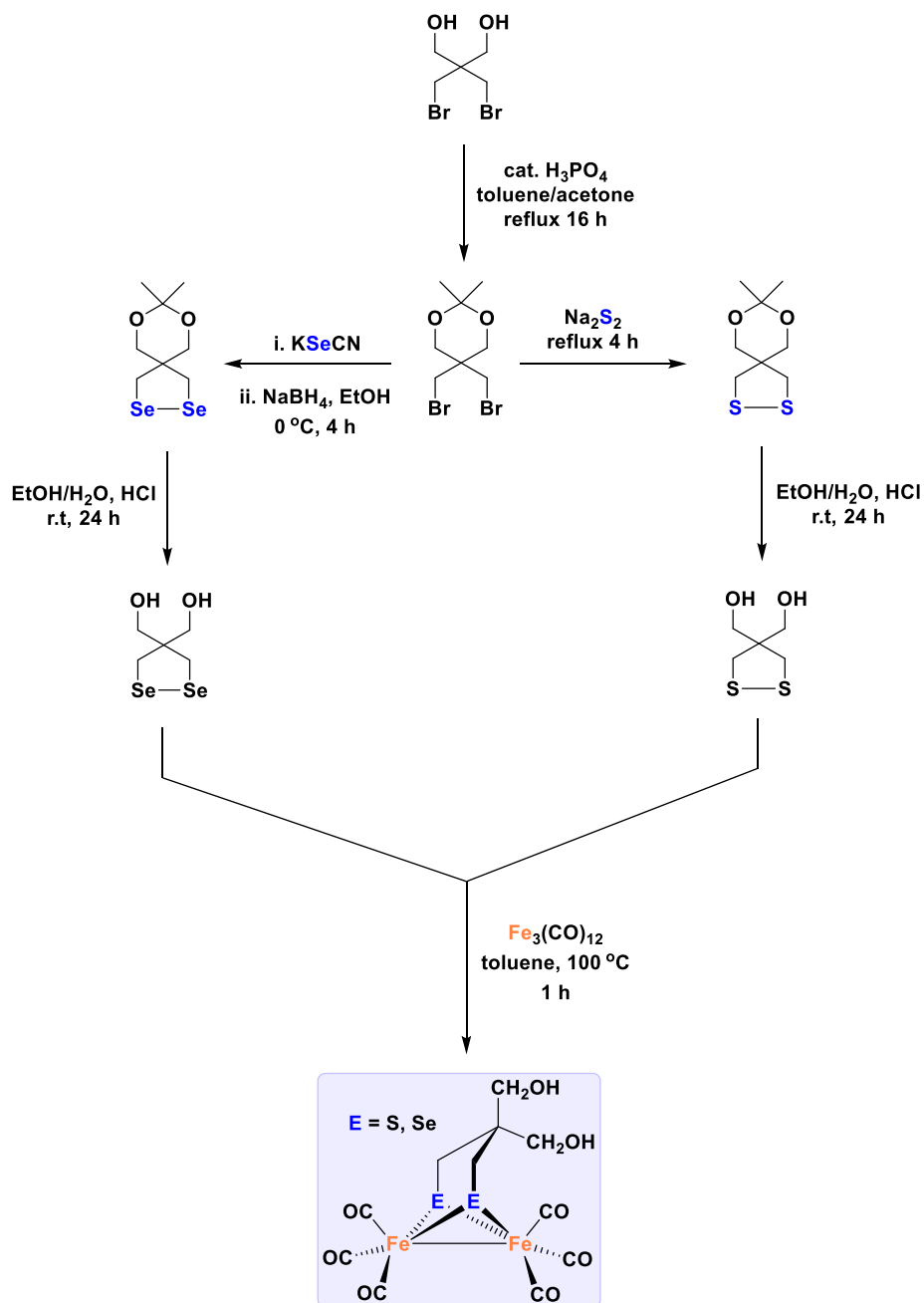
and bdt (benzenedithiolato)) model complexes at the Fe–Fe core using HCl in the presence of the very strong Lewis acid  $[\text{SiEt}_3](\text{B}(\text{C}_6\text{F}_5)_4)]$ .<sup>83–85</sup> Having this in mind, the ability of diiron diselenolato hexacarbonyl complexes toward protonation has not been previously tested before. Therefore, Abul-Futouh et al. has investigated the ability of  $[\text{Fe}_2(\text{CO})_6\{\mu\text{-(SeCH}_2)_2\text{E}(\text{Me}_2)\}]$  ( $\text{E} = \text{C, Sn}$ ) complexes toward protonation upon addition of strong and moderate acids.<sup>77</sup> This study has answered two inquiries, which are: (i) does the presence of  $\mu\text{-Se}$  atoms improves the protonation process? or (ii) does the presence of the Sn atom at the bridgehead linker together with the  $\mu\text{-Se}$  atoms enhance the electron density at the iron cores and hence facilitate the protonation process? Overall, it has been found that the presence of the Sn atom together with the  $\mu\text{-Se}$  atoms in  $[\text{Fe}_2(\text{CO})_6\{\mu\text{-(SeCH}_2)_2\text{Sn}(\text{Me}_2)\}]$  enhance the basicity of the iron cores to be protonated across the Fe–Fe core by using moderate ( $\text{CF}_3\text{CO}_2\text{H}$ ) and strong ( $\text{HBF}_4 \cdot \text{Et}_2\text{O}$ ) acids, while in the absence of the Sn atom in  $[\text{Fe}_2(\text{CO})_6\{\mu\text{-(SeCH}_2)_2\text{C}(\text{Me}_2)\}]$  protonation reactions are possible only in the case of rather strong acids as clarified in **Scheme 14**. This outcome contrasts with the corresponding sulfur analogues, which are not basic enough to form the  $\mu\text{-hydride}$  ( $\mu\text{-H}$ ) between the two iron cores by using excess  $\text{HBF}_4 \cdot \text{Et}_2\text{O}$  as described in the literature.<sup>83–85</sup>

To shed light into the influence of substituents at the bridgehead carbon of the linker in the active center of the [FeFe]-hydrogenase mimics, the Weigand group had reported synthetic models mediated by  $[\mu\text{-(ECH}_2)_2\text{C}(\text{CH}_2\text{OH})_2]$  ( $\text{E} = \text{S, Se}$ ) linkers.<sup>86</sup> This alteration provides direct comparison regarding the steric interaction between the bulky bridgehead groups and the apical CO with their analogues  $[\mu\text{-(SCH}_2)_2\text{CR}^1\text{R}^2]$  ( $\text{R}^1/\text{R}^2 = \text{Me/Me, Et/Et, Bu/Et}$ )<sup>72</sup> toward the redox features. The synthetic procedures of precursors (1,2-dithiolane-4,4-diyl)dimethanol and (1,2-diselenolane-4,4-diyl)dimethanol needed for the synthesis of the target complexes were prepared as described in **Scheme 15**.<sup>87,88</sup> Accordingly, these precursors were reacted with  $[\text{Fe}_3(\text{CO})_{12}]$  in hot toluene solution to generate the corresponding hydrogenase mimics having the general formula  $[\text{Fe}_2(\text{CO})_6\{\mu\text{-(ECH}_2)_2\text{C}(\text{CH}_2\text{OH})_2\}]$  ( $\text{E} = \text{S, Se}$ ) as presented in **Scheme 15**. Cyclic voltammetry experiment was carried out to investigate the influence of the  $\text{CH}_2\text{OH}$  moiety on the mechanism of the cathodic process and the reduction potentials of the model complexes.

The conclusion that derived from this study states that the existence of sterically demanding groups, such as  $\text{CH}_2\text{OH}$  at the bridgehead of the synthetic approaches results in the torsion angle, which is identified by the apical CO across the Fe–Fe core. Moreover, this  $\text{CH}_2\text{OH}$  moiety causes a change in the number of electrons transferred of the cathodic process as well as lowering the reduction potential values compared to that of their analogues  $[\mu\text{-(SCH}_2)_2\text{CR}^1\text{R}^2]$  ( $\text{R}^1/\text{R}^2 = \text{Me/Me, Et/Et, Bu/Et}$ ) linkers. This was explained due to the formation of the rotated structure during the cathodic process, which involves an interaction between the OH group and the iron or the sulfur atom via the formation of hydrogen bonding.<sup>86</sup> Furthermore, the replacement of sulfur by selenium in these synthetic approaches results in an elongation of the Fe–Fe bond, smaller CO wavenumbers and a higher overpotential concerning the catalytic reduction of AcOH.



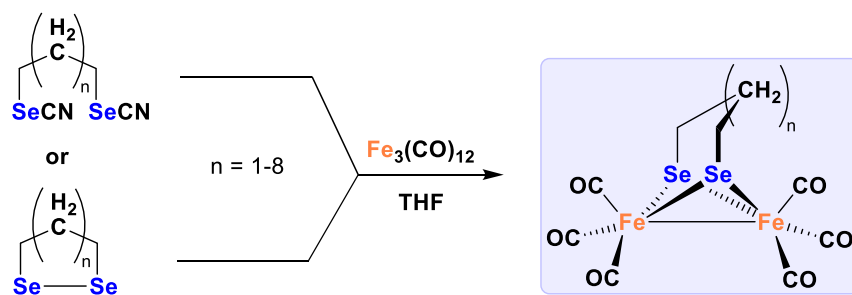
**Scheme 14** Summary scheme for the protonation processes reported by Abul-Futouh et al.<sup>77</sup>



**Scheme 15** Synthetic pathways of preparing  $[\text{Fe}_2(\text{CO})_6\{\mu\text{-(ECH}_2)_2\text{C(CH}_2\text{OH)}_2\}]$  ( $\text{E} = \text{S, Se}$ ) complexes reported by Weigand group.<sup>86</sup>

Darensbourg and co-workers have reported a study which is supported by computational studies to explore the relationship between the increased length of the bridging dithiolate linkers and the formation of the rotated structure.<sup>89</sup> Overall, it has been found that increasing the linker length causes a reduction in energy between the none-rotated and rotated structures. This can be explained due to the steric interaction between a methylene carbon and the apical CO on one of the Fe centers and hence facilitates the formation of a rotated structure. Moreover, they have found that the stability of the rotated form is enhanced through an agostic interaction between the hydrogen atom at the bridgehead methylene carbon and the vacant site that generated in the rotated structure.

Having this in mind, Harb et al. have reported a study to explore the effect of replacing the  $\mu\text{-S}$  by Se atom together with the systematic increase of the carbon atoms of the linker of [FeFe]-hydrogenase synthetic models having the general formula  $[\text{Fe}_2(\text{CO})_6\{\mu\text{-(SeCH}_2)_2(\text{CH}_2)_n\}]$  ( $n = 1\text{--}8$ ).<sup>90,91</sup> In this study, the reaction of cyclic alkane diselenide or  $\text{NCSe(CH}_2)_n\text{SeCN}$  ( $n = 2\text{--}9$ ) compounds with equimolar amount of  $[\text{Fe}_3(\text{CO})_{12}]$  in refluxing THF afforded the desired complexes as shown in Scheme 16.



**Scheme 16** Synthetic pathway of obtaining  $[\text{Fe}_2(\text{CO})_6\{\mu\text{-(SeCH}_2)_2(\text{CH}_2)_n\}]$  ( $n = 1\text{--}8$ ) complexes reported by Harb et al.<sup>90,91</sup>

As a result, it has been found that the incorporation of selenium into the butterfly core causes a decrease in the stretching vibration bands of carbonyl ligands compared to that of sulfur analogues. However, it has been noticed that increasing the length of the linker does not dramatically affect the carbonyl frequencies as indicated by the experimental observations and computations. Once more, substitution of selenium instead of sulfur in such models results in elongation of the Fe–Fe bond due to the increased size of selenium versus sulfur. Additionally, the quantum chemical calculations indicate the occurrence of structural rearrangements of the cations of these models, in which one  $[\text{Fe}(\text{CO})_3]$  unit rotates and a semibridging CO forms to assist stabilize the positive charge, especially in the case of  $[\text{Fe}_2(\text{CO})_6\{\mu\text{-(SeCH}_2)_2(\text{CH}_2)_n\}]$  ( $n = 2, 3$ ). Further stabilization of this cation has been found through an agostic interaction between the vacant site on the rotated Fe center and the  $\text{CH}_2$  moiety in the Se-to-Se linker.<sup>90,91</sup> Moreover, it has been found that the reduction potential values of these complexes decreases as the linker length increases.<sup>90,91</sup>

### 1.10.3 Synthetic complexes with aromatic diselenolate linkers

#### 1.10.3.1 General

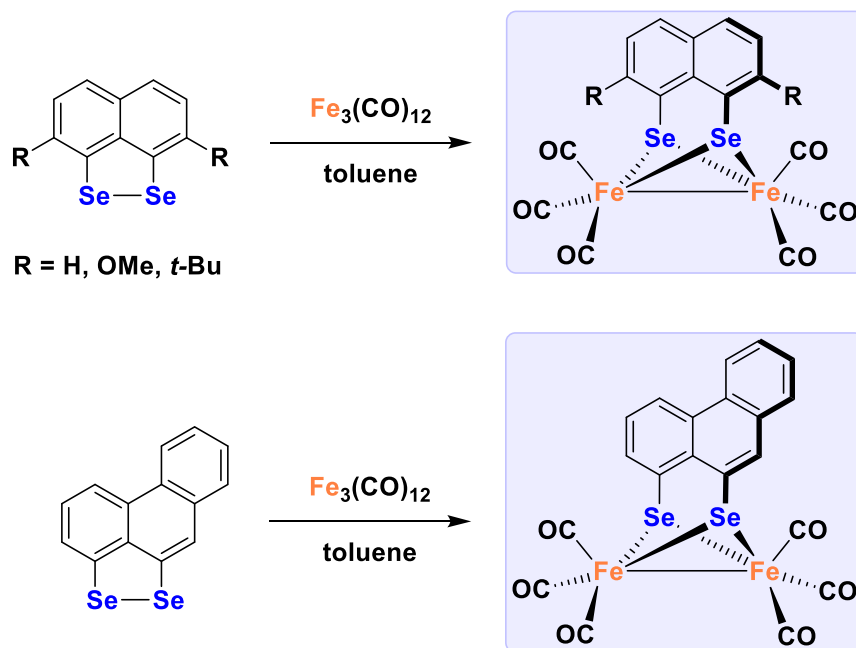
One of the major limitations of  $[\text{FeFe}]$ -hydrogenase mimicking complexes mediated by aliphatic dichalcogenate linkers mentioned above is that their cyclic voltammograms are less reversible and exhibit high negative reduction potentials.<sup>92</sup> This limitation restricts their ability to act as utilizable electrocatalysts for hydrogen formation. Interestingly, it has been found that the presence of aromatic dichalcogenate linkers in lieu of the aliphatic ones makes the diiron complexes more robust and readily reducible. Even though such type of architectural complexes did not identically resemble the structure of the H-cluster, it is still worthy to focus on this series of complexes due to several points as follows: (i) the stability of their backbone has a significant role in the improvement of the stability of the reduced species, (ii) the reversibility of their redox waves in cyclic voltammograms makes it convenient for mechanistic study of the catalytic cycle, and (iii) their reduction potentials values can be controlled through appropriate chemical adjustment of the backbone, for example the presence of electron-withdrawing substituents results in a shift of the reduction potential to less negative value.

For instance, it has been figured out that the reduction of complexes containing 1,2-benzenedithiolato ligands and its derivatives occurred via transfer of two electrons at the same applied potential owing to potential inversion of the two reduction steps,<sup>70,93,94</sup> in contrast to the propanedithiolate analogue whose primary reduction step is described to occur via an irreversible one-electron reaction.<sup>95</sup> This can be explained due to the delocalization of electrons over the phenyl ring that improves the stability of the reduced species. On the basis of these findings, the following section will introduce procedures and protocols that address recent work in this area for the purpose of giving the reader an overview of the significant role of substituting Se in lieu of S atom in  $[\text{FeFe}]$ -hydrogenase mimicking complexes mediated by aromatic linkers.

#### 1.10.3.2 General aspects for the structures and syntheses of iron mimetic complexes with aromatic diselenolate linkers

The synthetic diiron complex containing the 1,2-benzenedithiolato ligand is considered as the first example that mimics the H-cluster with an aromatic dithiolate linker. That opened a new research area to develop more sophisticated models bearing different aromatic bridging linkages, which are prepared to modulate the structures of the diiron subsite. For example, the incorporation of a naphthalene-1,8-dithiolato ligand into the synthetic models of  $[\text{FeFe}]$ -hydrogenase also enhanced the stability of the reduced species to proceed via two sequential reversible one-electron steps.<sup>96–98</sup>

In light of the above-mentioned considerations, Grainger and co-workers have investigated the influence of alteration the naphthalene skeleton of the diiron subsite by introducing electron-donating groups, such as 3,8-di-*tert*-butyl, and 2,7-dimethoxy into its backbone, incorporation of selenium instead of sulfur, and increasing the degree of conjugation in the aromatic backbone on the catalytic activity toward hydrogen formation.<sup>99</sup> Here the oxidative insertion of  $[\text{Fe}_3(\text{CO})_{12}]$  into the Se–Se bonds of naphtho[1,8-cd][1,2]diselenole, 3,8-dimethoxynaphtho[1,8-cd][1,2]diselenole, 3,8-di-*tert*-butylnaphtho[1,8-cd][1,2]diselenole, and phenanthro[1,10-cd][1,2]diselenole precursors afforded the desired complexes as shown in **Scheme 17**. Since selenium is less electronegative than sulfur, the iron centers that is coordinated to the selenium-based ligands are more electron rich and hence the  $\nu(\text{CO})$  vibration bands will be shifted to smaller wavenumbers as indicated by the IR data obtained for their synthetic approaches.



**Scheme 17** Reaction pathways of obtaining iron mimetic complexes with aromatic diselenolate linkers reported by Grainger and co-workers.<sup>99</sup>

Moreover, the electron-donating substituents at the naphthalene ring cause a bathochromic shift of the carbonyl stretching vibrations compared to that in sulfur analogues.

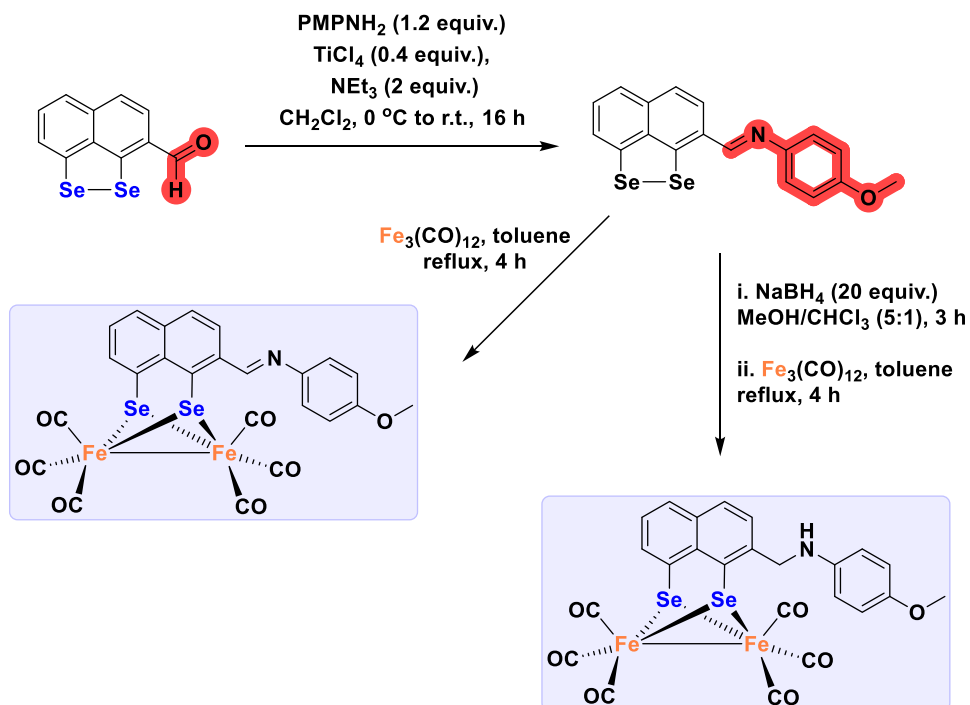
Based on the electrochemical studies, the naphthalene as well as phenanthrene-based diselenide ligands have a significant role in enhancing the stability of the reduced species compared to that of the aliphatic backbones. Moreover, another benefit of these alterations was observed for the reduction potentials of these complexes in which it is shifted to less negative potential compared to that of the corresponding aliphatic dithiolate analogues. The catalytic activity toward hydrogen production was found to be more efficient in diselenolate-based models.

One year later, the same group was successful in obtaining a synthetic H-cluster mimic mediated by *peri*-substituted naphthalene diselenides linker with imine/amine-substituent at the naphthalene ring.<sup>98</sup> It is well known that the nitrogen-containing linker can offer a basic site suitable for protonation under acidic conditions.<sup>100</sup> Therefore, the synthetic approaches obtained by Grainger group were tested to figure out if the amino and imino groups can be protonated under acidic conditions by applying cyclic voltammetry experiment.<sup>98</sup> In addition, they have extended their synthetic strategy to prepare a molecular dyad containing a tetraphenylporphyrinato zinc as a potential photosensitizer.<sup>98</sup> Here, the synthetic procedures of the precursors needed for the preparation of the desired complexes are illustrated in **Scheme 17**. These precursors were then treated with equimolar amount of  $[\text{Fe}_3(\text{CO})_{12}]$  in boiling toluene to afford the imine/amine-substituted naphthalene-based [FeFe] complexes as shown in **Scheme 18**.<sup>98</sup>

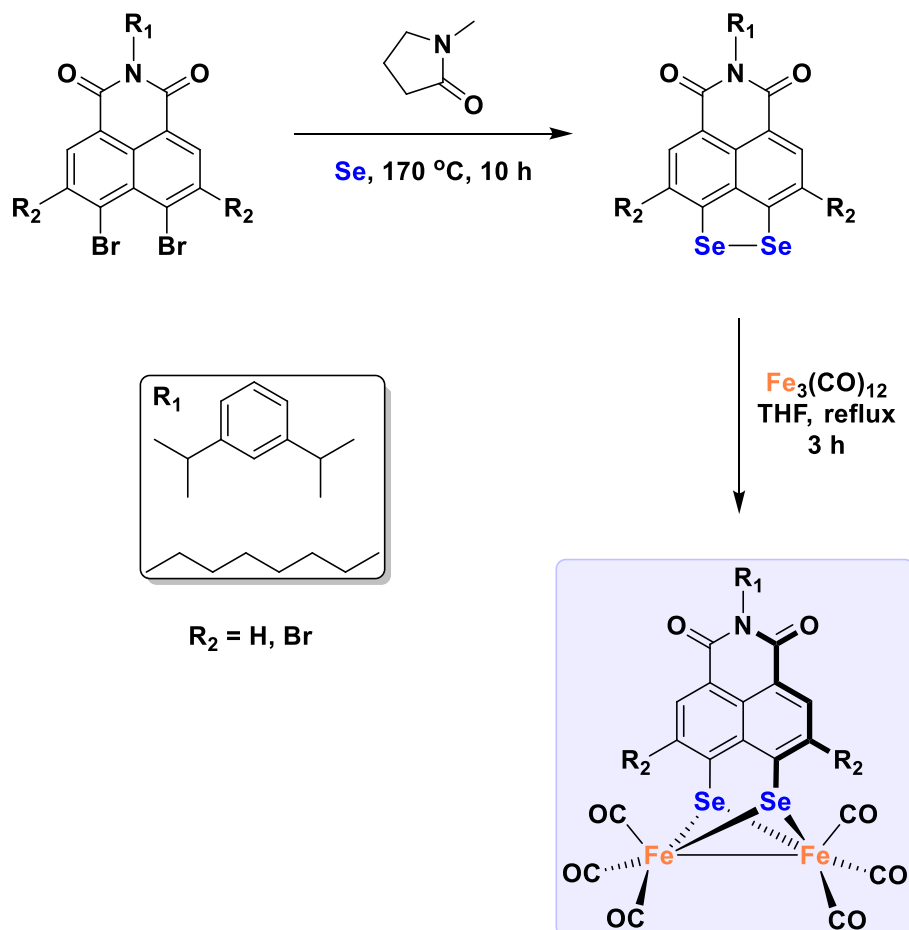
As a result of the cyclic voltammetry experiment, it has been reported that the amino and imino groups can be protonated upon addition of *p*TsOH acid. Moreover, it has been found that the diselenolate bridged [FeFe]-complexes are more efficient catalysts for proton reduction compared to these of the sulfur analogues. Unfortunately, the synthesis of the selenium-containing molecular dyad could not be obtained due to the degradation of the desired complex during the synthetic process.<sup>98</sup>

Another strategy to optimize the properties of the naphthalene skeleton is by introducing an imide group into its backbone. This modification offered additional stability to the monoanionic species as reported by Wasielewski group and others.<sup>101–103</sup> On the basis of this finding, Abul-Futouh et al. have reported the first time the preparation of naphthalene mono-imide diselenolate derivatives.<sup>104</sup> These derivatives were used as proligands for the synthesis of new models that mimics the structure of the H-cluster in an attempt to investigate their electrochemical and fluorescence properties.<sup>104</sup> Moreover, they were successful in modifying the naphthalene mono-imide diselenolate backbone by incorporation of two halogen atoms at the *ortho*-position to the two selenium atoms, and hence provides further fine-tuning of the reduction potentials of the corresponding complexes. As illustrated in **Scheme 19**, Abul-Futouh model complexes were obtained by the reaction of the naphthalene mono-imide diselenolate compounds with  $[\text{Fe}_3(\text{CO})_{12}]$  in THF under reflux conditions. Overall, it has been found that the presence of the imide functionality enhances the chemical stability of the mono- and di-reduced species as demonstrated by their voltammetric profiles. Thus, the incorporation of bromine substituents at the 2- and 7-positions of the naphthalene skeleton caused a fine-tuning of the reduction potential. In addition, the main reduction peaks were shifted to less negative value compared to that of their sulfur analogues.

The photophysical properties of the obtained complexes were examined by means of steady state absorption and emission spectroscopy. The potential of these complexes to directly transfer a photo-excited electron from the chromophore toward the [FeFe] moiety was confirmed by quantum chemical calculations.



**Scheme 18** Synthetic pathways of obtaining the imine/amine-substituted naphthalene-based [FeFe] complexes.<sup>98</sup>



**Scheme 19** Synthetic pathways of obtaining diiron complexes mediated by naphthalene mono-imide diselenolate linkers reported by Abul-Futouh et al.<sup>104</sup>



### 1.10.4 Summary

In summary, we herein shed light on the development of diiron complexes with heavier chalcogens, including selenium and tellurium instead of sulfur as the molecular mimics of the H-cluster of [FeFe]-hydrogenase. As it is shown, substitution of selenium or tellurium in lieu of sulfur atoms in [FeFe]-hydrogenase mimicking complexes results in an enhancement of the catalytic activity of these model complexes. This could be explained due to the stronger donor ability of selenium or tellurium donor atoms in comparison to sulfur and hence the electron density at the Fe–Fe core is increased. There is no doubt that there are some limitations about this conclusion owing to the disability of the anions of complexes containing heavier chalcogens to form the rotated structure. To overcome this issue, researchers made some alterations of the nature of the bridging linkers, such as increasing the length of the bridging diselenolato ligands or incorporation of aromatic ligands into the synthetic models of [FeFe]-hydrogenases. Moreover, we have also shown that the presence of  $\mu$ -Se instead of  $\mu$ -S atoms enhances the basicity of the iron cores to form the  $\mu$ -hydride between the two iron cores in the presence of a source of proton. In addition, the incorporation of aromatic linkers into the synthetic approaches has found to have a myriad of benefits such enhancement the stability of the catalytic intermediates and lowering their reduction potential to less negative values.

### References

- Nicolet, Y.; Cavazza, C.; Fontecilla-Camps, J. C. *Inorg. Biochem.* **2002**, *91*, 1–8.
- Shima, S.; Pilak, O.; Vogt, S.; Schick, M.; Stagni, M. S.; Klaucke, W. M.; Warkentin, E.; Thauer, R. K.; Ermler, U. *Science* **2008**, *321*, 572–575.
- Happe, T.; Hemschemeier, A.; Winkler, M.; Kaminski, A. *Trends Plant Sci.* **2002**, *7*, 246–250.
- Antal, M. J.; Allen, S. G.; Schulman, D.; Xu, X.; Divilio, R. J. *Ind. Eng. Chem. Res.* **2000**, *39*, 4040–4053.
- Hallenbeck, P. C.; Benemann, J. R. *Int. J. Hydrogen Energy* **2002**, *27*, 1185–1193.
- Cortright, R. D.; Davda, R. R.; Dumesic, J. A. *Nature* **2002**, *418*, 964–967.
- Huber, G. W.; Shabaker, J. W.; Dumesic, J. A. *Science* **2003**, *300*, 2075–2077.
- Adams, M. W. W.; Stiefel, E. I. *Science* **1998**, *282*, 1842–1843.
- Pilavachi, P. A.; Chatzipanagi, A. I.; Spyropoulou, A. I. *Int. J. Hydrogen Energy* **2009**, *34*, 5294–5303.
- Borup, R.; Meyers, J.; Pivovar, B.; Kim, Y. S.; Mukundan, R.; Garland, N.; Myers, D.; Wilson, M.; Garzon, F.; Wood, D.; Zelenay, P.; More, K.; Stroh, K.; Zawodzinski, T.; Boncella, J.; McGrath, J. E.; Inaba, M.; Miyatake, K.; Hori, M.; Ota, K.; Ogumi, Z.; Miyata, S.; Nishikata, A.; Siroma, Z.; Uchimoto, Y.; Yasuda, K.; Kimijima, K. I.; Iwashita, N. *Chem. Rev.* **2007**, *107*, 3904–3951.
- Das, D.; Dutta, T.; Nath, K.; Meher Kotay, S.; Das, A. K.; Veziroglu, N. T. *Curr. Sci.* **2006**, *90*, 1627–1637.
- Tard, C.; Pickett, C. *Chem. Rev.* **2009**, *109*, 2245–2274.
- Frey, M. *Chem. Bio. Chem.* **2002**, *3*, 153–160.
- Cammack, R. *Nature* **1999**, *397*, 214–215.
- Vignais, P. M.; Billoud, B. *Chem. Rev.* **2007**, *107*, 4206–4272.
- Fontecilla-Camps, J. C.; Volbeda, A.; Cavazza, C.; Nicolle, Y. *Chem. Rev.* **2007**, *107*, 4273–4303.
- Garcin, E.; Verne, X.; Hatchikian, E. C.; Volbeda, A.; Frey, M.; Fontecilla-Camps, J. C. *Structure* **1999**, *7*, 557–566.
- Hatchikian, E. C.; Forget, N.; Fernandez, V. M.; Williams, R.; Cammack, R. *Eur. J. Biochem.* **1992**, *209*, 357–365.
- Peters, J. W.; Lanzilotta, W. N.; Lemon, B. J.; Seefeldt, L. C. *Science* **1998**, *282*, 1853–1858.
- Nicolet, Y.; Piras, C.; Legrand, P.; Hatchikian, C. E.; Fontecilla-Camps, J. C. *Structure* **1999**, *7*, 13–23.
- Adamska, A.; Roy, S.; Stebel, J. F.; Simmons, T. R.; Fontecave, M.; Artero, V.; Reijerse, E.; Lubitz, W. *J. Am. Chem. Soc.* **2015**, *137*, 12744–12747.
- Adamska, A.; Silakov, A.; Lambert, C.; Rüdiger, O.; Happe, T.; Reijerse, E.; Lubitz, W. *Angew. Chem. Int. Ed.* **2012**, *124*, 11624–11629.
- Fan, H.-J.; Hall, M. B. *J. Am. Chem. Soc.* **2001**, *123*, 3828–3829.
- Nicolet, Y.; de Lacey, A. L.; Verne, X.; Fernandez, V. M.; Hatchikian, E. C.; Fontecilla-Camps, J. C. *J. Am. Chem. Soc.* **2001**, *123*, 1596–1601.
- Sommer, C.; Adamska-Venkatesh, A.; Pawlak, K.; Birrell, J. A.; Rüdiger, O.; Reijerse, E. J.; Lubitz, W. *J. Am. Chem. Soc.* **2017**, *139*, 1440–1443.
- Adamska, A.; Silakov, A.; Lambert, C.; Rüdiger, O.; Happe, T.; Reijerse, E.; Lubitz, W. *Angew. Chem. Int. Ed.* **2012**, *51*, 11458–11462.
- Lubitz, W.; Reijerse, E.; van Gestel, M. *Chem. Rev.* **2007**, *107*, 4331–4365.
- Singleton, M. L.; Bhuvanesh, N.; Reibenspies, J. H.; Darensbourg, M. Y. *Angew. Chem. Int. Ed.* **2008**, *47*, 9492–9495.
- Almazahreh, L. R.; Imhof, W.; Talarmin, J.; Schollhammer, P.; Görls, H.; El-khateeb, M.; Weigand, W. *Dalton Trans.* **2015**, *44*, 7177–7189.
- Jiang, X.; Xiao, Z.; Zhong, W.; Liu, X. *Coord. Chem. Rev.* **2021**, *429*, 213634. and references therein.
- Reich, H. J.; Hondal, R. J. *ACS Chem. Biol.* **2016**, *11*, 821–841. and references therein.
- Harb, M. K.; Apfel, U.-P.; Sakamoto, T.; El-khateeb, M.; Weigand, W. *Eur. J. Inorg. Chem.* **2011**, 986–993.
- Hieber, W.; Gruber, J. *Z. Anorg. Allg. Chem.* **1958**, *296*, 91–103.
- Seyferth, D.; Henderson, R. H. *J. Organomet. Chem.* **1981**, *204*, 333–343.
- Hieber, W.; Beck, W. *Z. Anorg. Allg. Chem.* **1960**, *305*, 265–273.
- Li, Y.; Rauchfuss, T. B. *Chem. Rev.* **2016**, *116*, 7043–7077.
- Gao, S.; Fan, J.; Sun, S.; Peng, X.; Zhao, X.; Hou, J. *Dalton Trans.* **2008**, 2128–2135.
- Apfel, U.-P.; Halpin, Y.; Gottschaldt, M.; Görls, H.; Vos, J. G.; Weigand, W. *Eur. J. Inorg. Chem.* **2008**, 5112–5118.
- Na, Y.; Wang, M.; Jin, K.; Zhang, R.; Sun, L. *J. Organomet. Chem.* **2006**, *691*, 5045–5051.
- Harb, M. K.; Niksch, T.; Windhager, J.; Görls, H.; Holze, R.; Lockett, L. T.; Okumura, N.; Evans, D. H.; Glass, R. S.; Lichtenberger, D. L.; El-khateeb, M.; Weigand, W. *Organometallics* **2009**, *28*, 1039–1048.
- Song, L.-C.; Gai, B.; Wang, H.-T.; Hu, Q.-M. *J. Inorg. Biochem.* **2009**, *103*, 805–812.
- Stanley, J. L.; Heiden, Z. M.; Rauchfuss, T. B.; Wilson, S. R. *Organometallics* **2008**, *27*, 119–125.
- Song, L.-C.; Gao, W.; Feng, C.-P.; Wang, D.-F.; Hu, Q.-M. *Organometallics* **2009**, *28*, 6121–6130.
- Shaver, A.; Fitzpatrick, P. J.; Steliou, K.; Butler, I. S. *J. Am. Chem. Soc.* **1979**, *101*, 1313–1315.
- Seyferth, D.; Henderson, R. S.; Song, L.-C. *Organometallics* **1982**, *1*, 125–133.
- Harb, M. K.; Apfel, U.-P.; Kübel, J.; Görls, H.; Felton, G. A. N.; Sakamoto, T.; Evans, D. H.; Glass, R. H.; Lichtenberger, D. L.; El-khateeb, M.; Weigand, W. *Organometallics* **2009**, *28*, 6666–6675.
- Li, P.; Wang, M.; He, C.; Li, G.; Liu, X.; Chen, C.; Akermark, B.; Sun, L. *Eur. J. Inorg. Chem.* **2005**, 2506–2513.

48. Harb, M. K.; Görls, H.; Sakamoto, T.; Felton, G. A. N.; Evans, D. H.; Glass, R. S.; Lichtenberger, D. L.; El-khateeb, M.; Weigand, W. *Eur. J. Inorg. Chem.* **2010**, *25*, 3976–3985; Harb, M. K.; Görls, H.; Sakamoto, T.; Felton, G. A. N.; Evans, D. H.; Glass, R. S.; Lichtenberger, D. L.; El-khateeb, M.; Weigand, W. *Eur. J. Inorg. Chem.* **2010**, *28*, 4561.
49. Lawrence, J. D.; Li, H. X.; Rauchfuss, T. B.; Benard, M.; Rohmer, M. M., Eds. *Angew. Chem. Int. Ed.* **2001**, *40*, 1768–1771. *Angew. Chem.* 2001, *113*, 1818–1821.
50. Lawrence, J. D.; Li, H.; Rauchfuss, T. B. *Chem. Commun.* **2001**, 1482–1483.
51. Capon, J.-F.; Ezzaher, S.; Gloaguen, F.; Pétilion, F. Y.; Schollhammer, P.; Talarmin, J.; Davin, T. J.; McGrady, J. E.; Muir, K. W. *New J. Chem.* **2007**, *31*, 2052–2064.
52. Wang, F.; Wang, M.; Liu, X.; Jin, K.; Dong, W.; Sun, L. *Dalton Trans.* **2007**, 3812–3819.
53. Cui, H.-G.; Wang, M.; Dong, W.-B.; Duan, L.-L.; Li, P.; Sun, L.-C. *Polyhedron* **2007**, *26*, 904–910.
54. Jiang, S.; Liu, J.; Sun, L. *Inorg. Chem. Commun.* **2006**, *9*, 290–292.
55. Wang, Z.; Liu, J.-H.; He, C.-J.; Jiang, S.; Åkermark, B.; Sun, L.-C. *J. Organomet. Chem.* **2007**, *692*, 5501–5507.
56. Wang, W.-G.; Wang, H.-Y.; Si, G.; Tung, C.-H.; Wu, L.-Z. *Dalton Trans.* **2009**, 2712–2720.
57. Na, Y.; Wang, M.; Pan, J.; Zhang, P.; Åkermark, B.; Sun, L. *Inorg. Chem.* **2008**, *47*, 2805–2810.
58. Wang, Z.; Liu, J.; He, C.; Jiang, S.; Åkermark, B.; Sun, L. *Inorg. Chim. Acta* **2007**, *360*, 2411–2419.
59. Si, Y.; Ma, C.; Hu, M.; Chen, H.; Chen, C.; Liu, Q. *New J. Chem.* **2007**, *31*, 1448–1454.
60. Schwartz, L.; Eilers, G.; Eriksson, L.; Gogoll, A.; Lomoth, R.; Ott, S. *Chem. Commun.* **2006**, 520–526.
61. Eilers, G.; Schwartz, L.; Stein, M.; Zampella, G.; de Gioia, L.; Ott, S.; Lomoth, R. *Chem. A Eur. J.* **2007**, *13*, 7075–7084.
62. Hou, J.; Peng, X.; Liu, J.; Gao, Y.; Zhao, X.; Gao, S.; Han, K. *Eur. J. Inorg. Chem.* **2006**, 4679–4686.
63. Ezzaher, S.; Orain, P.-Y.; Capon, J.-F.; Gloaguen, F.; Pétilion, F. Y.; Roisnel, T.; Schollhammer, P.; Talarmin, J. *Chem. Commun.* **2008**, 2547–2549.
64. Carroll, M. E.; Barton, B. E.; Rauchfuss, T. B.; Carroll, P. J. *J. Am. Chem. Soc.* **2012**, *134*, 18843–18852.
65. Kleinhaus, J. T.; Wittkamp, F.; Yadav, S.; Siegmund, D.; Apfel, U.-P. *Chem. Soc. Rev.* **2021**, 1668–1784.
66. Gao, W.; Song, L.-C.; Yin, B.-S.; Zan, H.-N.; Wang, D.-F.; Song, H.-B. *Organometallics* **2011**, *30*, 4097–4107.
67. Kertess, L.; Wittkamp, F.; Sommer, C.; Esselborn, J.; Rüdiger, O.; Reijerse, E. J.; Hofmann, E.; Lubitz, W.; Winkler, M.; Happe, T.; Apfel, U.-P. *Dalton Trans.* **2017**, *46*, 16947–16958.
68. Li, P.-Z.; Liu, Z. Q. *Med. Chem. Res.* **2013**, *22*, 2809–2814.
69. Harb, M. K.; Windhager, J.; Niksch, T.; Görls, H.; Sakamoto, T.; Smith, E. R.; Glass, R. S.; Lichtenberger, D. L.; Evans, D. H.; El-khateeb, M.; Weigand, W. *Tetrahedron* **2012**, *68*, 10592–10599.
70. Felton, G. A. N.; Vannucci, A. K.; Chen, J.; Lockett, L. T.; Okumura, N.; Petro, B. J.; Zakai, U. I.; Evans, D. H.; Glass, R. S.; Lichtenberger, D. L. *J. Am. Chem. Soc.* **2007**, *129*, 12521–12530.
71. Song, L.-C.; Gai, B.; Feng, Z.-H.; Du, Z.-Q.; Xie, Z.-J.; Sun, X.-J.; Song, H.-B. *Organometallics* **2013**, *32*, 3673–3684.
72. Singleton, M. L.; Jenkins, R. M.; Klemashevich, C. L.; Darensbourg, M. Y. *C. R. Chim.* **2008**, *11*, 861–874.
73. Crouthers, D. J.; Denny, J. A.; Bethel, R. D.; Munoz, D. G.; Darensbourg, M. Y. *Organometallics* **2014**, *33*, 4747–4755.
74. Apfel, U.-P.; Görls, H.; Felton, G. A. N.; Evans, D. H.; Glass, R. S.; Lichtenberger, D. L.; Weigand, W. *Helv. Chim. Acta* **2012**, *95*, 2168–2175.
75. Apfel, U.-P.; Troegel, D.; Halpin, Y.; Tschierlei, S.; Uhlemann, U.; Görls, H.; Schmitt, M.; Popp, J.; Dunne, P.; Venkatesan, M.; Coey, M.; Rudolph, M.; Vos, J. G.; Tacke, R.; Weigand, W. *Inorg. Chem.* **2010**, *49*, 10117–10132.
76. Abul-Futouh, H.; Almazahreh, L. R.; Sakamoto, T.; Stessman, N. Y. T.; Lichtenberger, D. L.; Glass, R. S.; Görls, H.; El-khateeb, M.; Schollhammer, P.; Mloston, G.; Weigand, W. *Chem. A Eur. J.* **2017**, *23*, 346–359.
77. Abul-Futouh, H.; El-khateeb, M.; Görls, H.; Asali, K. J.; Weigand, W. *Dalton Trans.* **2017**, *46*, 2937–2947.
78. Almazahreh, L. R.; Apfel, U.-P.; Imhof, W.; Rudolph, M.; Görls, H.; Talarmin, J.; Schollhammer, P.; El-khateeb, M.; Weigand, W. *Organometallics* **2013**, *32*, 4523–4530.
79. Gao, W.; Sun, J.; Åkermark, T.; Li, M.; Eriksson, L.; Sun, L.; Åkermark, B. *Chem. A Eur. J.* **2010**, *16*, 2537–2546.
80. Ott, S.; Kritikos, M.; Åkermark, B.; Sun, L.; Lomoth, R. L. *Angew. Chem. Int. Ed.* **2004**, *116*, 1024.
81. Lawrence, J. D.; Li, H.; Rauchfuss, T. B.; Bénard, M.; Rohmer, M.-M. *Angew. Chem. Int. Ed.* **2001**, *40*, 1768–1771.
82. Jiang, S.; Liu, J.; Shi, Y.; Wang, Z.; Åkermark, B.; Sun, L. *Dalton Trans.* **2007**, 896–902.
83. Matthews, S. L.; Heinekey, D. M. *Inorg. Chem.* **2010**, *49*, 9746–9748.
84. Liu, Y.-C.; Chu, K.-T.; Huang, Y.-L.; Hsu, C.-H.; Lee, G.-H.; Tseng, M.-C.; Chiang, M.-H. *ACS Catal.* **2016**, *6*, 2559–2576.
85. Schilter, D.; Camara, J. M.; Huynh, M. T.; Hammes-Schiffer, S.; Rauchfuss, T. B. *Chem. Rev.* **2016**, *116*, 8693–8749.
86. Trautwein, R.; Almazahreh, L. R.; Görls, H.; Weigand, W. *Z. Anorg. Allg. Chem.* **2013**, *639*, 1512–1519.
87. Gropeanu, R.; Tintas, M.; Pilon, C.; Morin, M.; Breau, L.; Turdean, R.; Grosu, I. *J. Heterocyclic Chem.* **2007**, *44*, 521–527.
88. Niksch, T.; Görls, H.; Friedrich, M.; Oilunkaniemi, R.; Laitinen, R.; Weigand, W. *Eur. J. Inorg. Chem.* **2010**, 74–94.
89. Tye, J. W.; Darensbourg, M. Y.; Hall, M. B. *Inorg. Chem.* **2006**, *45*, 1552–1559.
90. Harb, M. K.; Daraosheh, A.; Görls, H.; Smith, E. R.; Meyer, G. J.; Swenson, M. T.; Sakamoto, T.; Glass, R. S.; Lichtenberger, D. L.; Evans, D. H.; Elkhateeb, M.; Weigand, W. *Heteroatom Chem.* **2014**, *25*, 592–606.
91. Harb, M. K.; Alshurafa, H.; El-khateeb, M.; Al-Zuheiri, A.; Görls, H.; Abul-Futouh, H.; Weigand, W. *ChemistrySelect* **2018**, *3*, 8867–8873.
92. Gao, S.; Liu, Y.; Shao, Y.; Jiang, D.; Duan, Q. *Coord. Chem. Rev.* **2020**, *402*, 213081.
93. Gloaguen, F.; Morvan, D.; Capon, J.-F.; Schollhammer, P.; Talarmin, J. *J. Electroanal. Chem.* **2007**, *603*, 15–20.
94. Chen, J.; Vannucci, A. K.; Mebi, C. A.; Okumura, N.; Borowski, S. C.; Swenson, M.; Lockett, L. T.; Evans, D. H.; Glass, R. S.; Lichtenberger, D. L. *Organometallics* **2010**, *29*, 5330–5340.
95. Trautwein, R.; Almazahreh, L. R.; Görls, H.; Weigand, W. *Dalton Trans.* **2015**, *44*, 18780–18794.
96. Wright, R. J.; Lim, C.; Tilley, T. D. *Chem. A Eur. J.* **2009**, *15*, 8518–8525.
97. Qian, G.; Zhong, W.; Wei, Z.; Wang, H.; Xiao, Z.; Long, L.; Liu, X. *New J. Chem.* **2015**, *39*, 9752–9760.
98. Figliola, C.; Male, L.; Horswell, S. L.; Grainger, R. S. *Eur. J. Inorg. Chem.* **2015**, *2015*, 3146–3156.
99. Figliola, C.; Male, L.; Horton, P. N.; Pttak, M. B.; Coles, S. J.; Horswell, S. L.; Grainger, R. S. *Organometallics* **2014**, *33*, 4449–4460.
100. Tschierlei, S.; Ott, S.; Lomoth, R. *Energ. Environ. Sci.* **2011**, *4*, 2340–2352.
101. Samuel, A. P. S.; Co, D. T.; Stern, C. L.; Wasielewski, M. R. *J. Am. Chem. Soc.* **2010**, *132*, 8813–8815.
102. Li, P.; Amirjalayer, S.; Hartl, F.; Lutz, M.; Bruin, B.; Becker, R.; Woutersen, S.; Reek, J. N. H. *Inorg. Chem.* **2014**, *53*, 5373–5383.
103. Poddutoori, P.; Co, D. T.; Samuel, A. P. S.; Kim, C. H.; Vagnini, M. T.; Wasielewski, M. R. *Energ. Environ. Sci.* **2011**, *4*, 2441–2450.
104. Abul-Futouh, H.; Zagranjarski, Y.; Mueller, C.; Schulz, M.; Kupfer, S.; Görls, H.; El-khateeb, M.; Gräfe, S.; Dietzek, B.; Peneva, K.; Weigand, W. *Dalton Trans.* **2017**, *46*, 11180–11191.

## 1.11 Computational modeling and characterization of secondary bonding in compounds of late p-block elements

Ignacio Vargas-Baca, Department of Chemistry and Chemical Biology, McMaster University, Hamilton, ON, Canada

© 2023 Elsevier Ltd. All rights reserved.

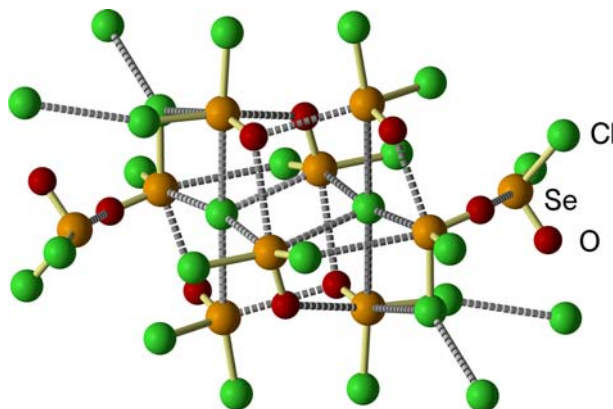
1.11.1	Introduction	572
1.11.2	Structure	573
1.11.3	Energy	573
1.11.4	Electron density analysis	576
1.11.5	Polarization and charge transfer	581
1.11.6	Multimolecular systems	582
1.11.7	Conclusion	584
References		584

### Abstract

Secondary bonding, the supramolecular interaction in which a heavy main-group element acts as an electrophilic center despite having its primary valences already satisfied, is generating strong interest in current literature. Recent studies have greatly expanded the variety of known examples and demonstrated applications of these interactions. Experimental work in this area is often supported by computational investigations with a wide variety of tools. The purpose of this article is to facilitate the interpretation of the information provided by each method and aid in the comparison and integration of results from dissimilar techniques. The discussion includes methods to model structure, evaluate and analyze interaction energies, and dissect the factors that contribute to the stabilization of these interactions.

### 1.11.1 Introduction

As X-ray diffraction became a routine tool for the characterization of inorganic compounds, it soon became apparent that many crystal structures of compounds of the heavy *p*-block elements display features that conflict with the simple but very successful Lewis Octet and Valence-Shell Electron Pair Repulsion models of bonding and structure. Frequently, the heavy atoms are found in close proximity to other atoms in electron rich centers, at distances that are intermediate between the sums of the van der Waals radii and covalent radii. In many cases a short contact of this type would subtend a nearly straight angle with another bond of the heavy atom. N. W. Alcock<sup>1</sup> proposed the term “secondary bond” to designate this feature and distinguish it from the “primary bonds” that define a molecular species (see an example in Fig. 1).



**Fig. 1** Secondary bonding interactions (SBIs) in the crystal structure of  $(\text{SeOCl}_2)_5\text{NMe}_4\text{Cl}$ .<sup>2</sup> Data from Hermodsson, Y.; Kjekshus, A.; Santesson, J.; Holmberg, P.; Eriksson, G.; Blinc, R.; Paušak, S.; Ehrenberg, L.; Dumanović, J. *Acta Chem. Scand.* **1967**, *21*, 1328–1342.  $\text{SeOCl}_2$  molecules and  $\text{Cl}^-$  anions are organized in  $[(\text{SeOCl}_2)_{10}\text{Cl}_2]^{2-}$  clusters. The longer  $\text{Se}\cdots\text{Cl}$  (2.93–3.60 Å) and  $\text{Se}\cdots\text{O}$  (2.82–3.14 Å) distances correspond to SBIs (Cf.  $\Sigma r_{\text{covSe-Cl}} = 2.15$  Å,  $\Sigma r_{\text{vdWSe-Cl}} = 3.65$  Å,  $\Sigma r_{\text{covSe-O}} = 1.89$  Å,  $\Sigma r_{\text{vdWSe-O}} = 3.42$  Å), specifically chalcogen bonds.  $\text{Cl}\cdots\text{Cl}$  halogen bonds connect neighboring clusters, which are not shown for clarity.

Interest in secondary bonding grew slowly during the late 20th century but was greatly invigorated by demonstrations of its applications (e.g., in crystal engineering) and the formal definitions of halogen (XB) and chalcogen bonds (ChB) by the IUPAC:

*"A halogen bond occurs when there is evidence of a net attractive interaction between an electrophilic region associated with a halogen atom in a molecular entity and a nucleophilic region in another, or the same, molecular entity."*<sup>3</sup>

*"(A) chalcogen bond (is a) net attractive interaction between an electrophilic region associated with a chalcogen atom in a molecular entity and a nucleophilic region in another, or the same, molecular entity."*<sup>4</sup>

Analogous names have been proposed for the cases in which the electrophilic centers belong to other p-block elements<sup>5</sup> and even covalent d-block species.<sup>6,7</sup>

A number of computational studies have been dedicated to this phenomenon. Initial research was constrained by the inherent inability of early methods to model heavy atoms with sufficient accuracy; consequently, its conclusions should be treated with great caution. Currently available methods and computational infrastructure have enabled a good understanding of the factors that stabilize this type of supramolecular interaction and current literature always includes computational investigations as part of the characterization of SBIs. Computational modeling is especially valuable to examine systems in solution or gas phase for which a structural determination might be difficult if not impossible. This overview includes commonly used methodologies with selected examples from literature. Full theoretical details of each model are beyond the scope of this chapter, but comprehensive introductions are available in Cramer's book.<sup>8</sup>

### 1.11.2 Structure

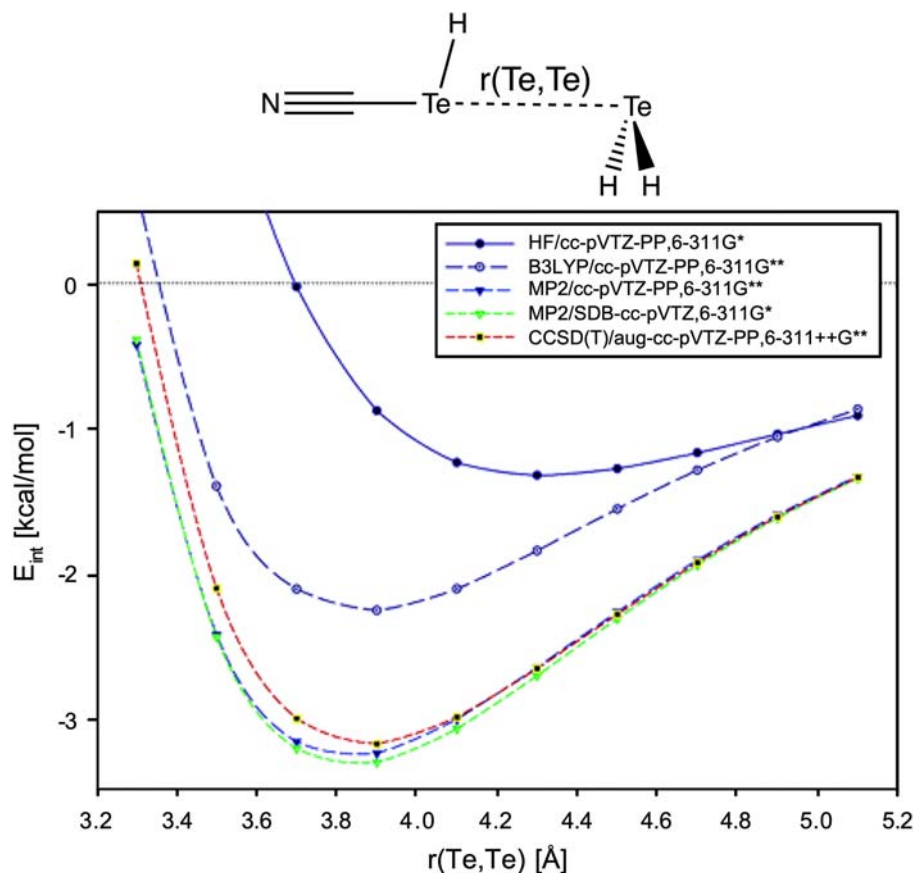
The quality of any computational model must be assessed by its ability to reproduce experimental observations. In this regard, the primary observable of SBIs in a crystal structure are the interatomic distances and angles. Accurate measurements of the electron distribution are possible, but charge density measurements are far from routine as they require high-resolution X-ray diffraction measurements at low temperature. Modern quantum mechanical methods are capable of reproducing structures with good accuracy, but deviations of ca. 0.2 Å for SBIs are not unusual. Density Functional Theory (DFT) calculations are preferred for expediency; within this family, GGA (e.g., PW91, PBE) and meta GGA (e.g., M06L) functionals are adequate. Hybrid functionals (e.g., PEB0, B3LYP) are in principle more accurate but less so than MP2 and coupled-cluster calculations. In the example in Fig. 2 (((H)(NC)Te...TeH<sub>2</sub>)<sup>9</sup> the potential energy profiles show that the HF method is unable to model distance and energy and, although the popular DFT hybrid functional B3LYP is adequate for calculation of the chalcogen bond distance, it underestimates the interaction energy. The MP2 calculations approach the coupled cluster CCSD(T) surface in this case. Further Symmetry Adapted Perturbation Theory (SAPT) calculations for this and closely related systems indicate that dispersion is a major component of the interaction energy.<sup>10</sup> However, the most accurate methods are only viable for small molecules. In any case, DFT calculations must include relativistic effects and be corrected for dispersion; Grimme's D3 scheme being the dominant approach. Such corrections are good estimates of but not the actual dispersion contributions. Periodic boundaries are necessary when modeling infinite chains and lattices (Fig. 3).

### 1.11.3 Energy

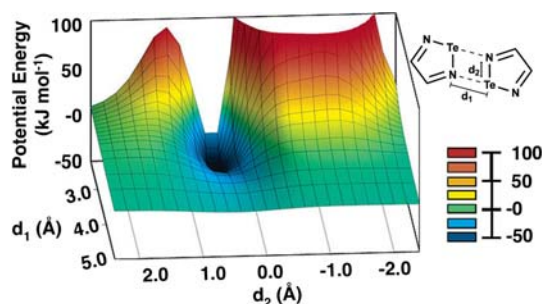
The strength of an SBI is usually gauged by the magnitude of the corresponding binding energy. This involves comparing the energies of the equilibrium structures of the individual molecules and their aggregate or "supermolecule". The immediate result of calculating these two stationary points of the system is the electronic energy. Supplemental vibrational calculations provide the corresponding enthalpy, entropy and Gibbs free energy at a given temperature. A detailed calculation would take into consideration the structural changes, however small, that the constituting molecules undergo upon association; their contribution is termed the "preparation energy". It should be noted that the calculation of the aggregate artificially decreases the energy of the system due to the basis set superposition error (BSSE), which can be estimated with a counterpoise (CP) correction. The BSSE is especially important for small molecules.

*Energy decomposition analyses (EDA)*. To facilitate interpretation, electronic interaction energies often are parsed into components that have chemical significance. Amongst the most common approaches is the Morokuma<sup>14</sup> scheme, which splits the energy into four components (Eq. 1).

$$E_{\text{interaction}} = E_{\text{electrostatic}} + E_{\text{polarization}} + E_{\text{exchange}} + E_{\text{charge transfer}} \quad (1)$$



**Fig. 2** Potential energy surface (PES) calculated for the NC-Te...Te chalcogen bond between HTeCN and H<sub>2</sub>Te with several computational methods.<sup>9</sup> Adapted for clarity with permission from Bleiholder, C.; Werz, D. B.; Köppel, H.; Gleiter, R. *J. Am. Chem. Soc.* **2006**, *128*, 2666–2674. Copyright 2006 American Chemical Society.



**Fig. 3** Potential energy surface (ADF, PW91, all electron TZP ZORA) calculated for the in-plane deformation of a dimer of 1,2,5-telluradiazole.<sup>11</sup> Adapted with permission from Cozzolino, A. F.; Vargas-Baca, I.; Mansour, S.; Mahmoudkhani, A. H. *J. Am. Chem. Soc.* **2005**, *127*, 3184–3190. Copyright 2005 American Chemical Society. The steep potential profiles show that the square ring formed by a pair of antiparallel Te...N chalcogen bonds (i.e., the now ubiquitous [Ch-N]<sub>2</sub> supramolecular synthon<sup>12,13</sup>) is a very robust structural unit.

- Electrostatic, i.e., the coulombic interaction between molecules without any mixing of their molecular orbitals.
- Polarization, resulting from the mixing of occupied and empty orbitals within each molecule in response to the total electric field.
- Exchange (Pauli or steric) repulsion, from the interaction between occupied molecular orbitals.
- Charge Transfer, from the mixing of occupied and empty molecular orbitals between molecules with the concomitant delocalization of electrons.

The Ziegler-Rauk<sup>15,16</sup> method keeps Morokuma's electrostatic and exchange components and regards their combination as the "total steric interaction" in a "transition-state" in which the system has the final equilibrium geometry, but their electronic densities



are not allowed to relax. Polarization and charge transfer are treated as a single orbital interaction contribution. A recent update to this scheme includes corrections to the energy due to dispersion.

The natural energy decomposition analysis (NEDA)<sup>17</sup> is, an alternative approach based on the Natural Bond Orbital method of orbital localization, considers four components:

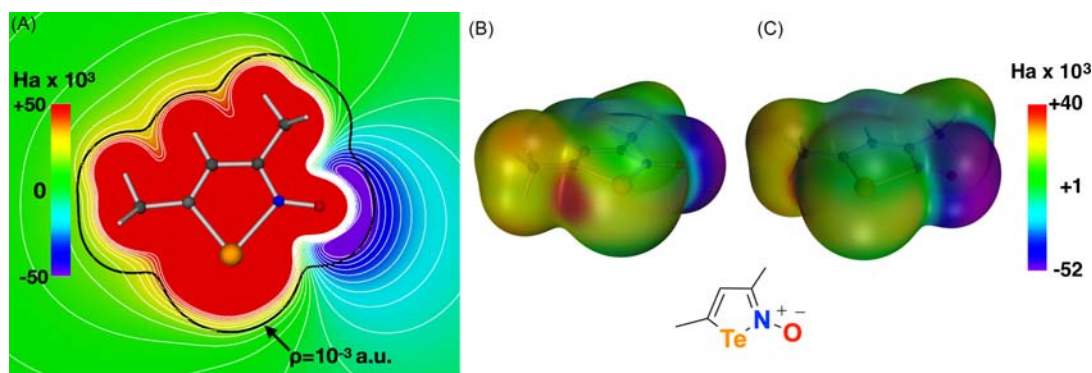
- Deformation from the cost of distortion of the wave function of the fragments in the supermolecule.
- Electrostatic from the interaction between deformed fragments.
- Charge Transfer, due to the transfer of electrons from donor to acceptor orbitals of the deformed fragments.
- The basis set superposition error.

Whatever the EDA scheme, the contributing terms are not really independent of each other. Relaxation of the electron density of the building blocks necessarily changes their internal electric multipoles and the electrostatic interaction between them; variations in the composition of the molecular orbitals does impact the exchange interaction. The components extracted from an energy decomposition analysis are thus path properties,<sup>18</sup> comparison of values only makes sense within the same EDA approach. Nevertheless, these analyses are valuable as they permit identifying traits and trends useful for chemists to understand and make use of these supramolecular interactions.

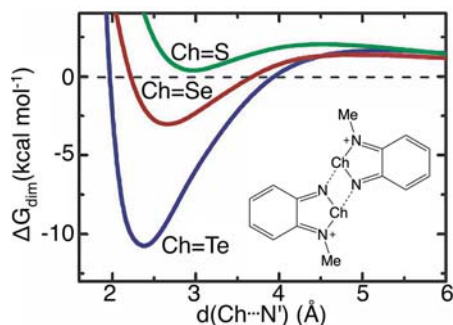
**Electrostatic potential maps.** The electrostatic contribution to an SBI originates in the sharing of electrons between atoms linked by covalent primary bonds. Localization of electron density in the internuclear region takes place at the expense of the antipodal regions of space, the depletion of electron density creates a positive potential even in the case of a homo-diatom molecules such as I<sub>2</sub>. Such electrophilic areas are usually visualized with maps of electrostatic potential on the isodensity surface of a molecule. Such surfaces are usually calculated at a 10<sup>-3</sup> a.u. of density (Fig. 4) but, in some cases, different values might be necessary to identify the electrophilic zones.

Although the term “sigma hole” is routinely used to refer to the electrophilic patch on the surface of a molecules, the maximum of potential ( $V_{\max}$ ) is coincident with the minimum of electron density ( $\rho_{\min}$ ) only when the heavy atom has one “primary bond”. In the case of  $\lambda^2$  chalcogen atoms,  $V_{\max}$  can be significantly displaced from  $\rho_{\min}$ , especially when highly electronegative groups are bonded.<sup>20</sup> The sigma holes are often invoked in literature to justify the apparent directionality of SBIs. However, steric repulsion cannot be ignored and the observed geometries result from the balance of all contributions.<sup>21</sup>

**Solvation.** In first instance quantum mechanical calculations assume that the interacting molecules are in gas phase. The effect of a condensed liquid phase can be examined with models of solvation. The solvent is in first instance modelled as a continuum that interacts electrostatically with the solute molecule inserted in a cavity. At the root of the solvation models is the electrostatic potential that arises from the charge density and dielectric constant of the medium. The properties of the medium account for the average that results from the thermal motion of solvent molecules. The details of the cavity construction and the specific properties used to model the medium define the difference between solvation methods. One of the most common approaches is the Polarized Continuum Medium (PCM or MST, after Miertus, Scrocco, and Tomasi)<sup>22</sup> method, which provides very good estimates of the free energies for chalcogen bonding between anions and an amine with benzochalcogenadiazoles.<sup>23</sup> While PCM treats the medium as a dielectric, it is more efficient to assume the opposite, as in the conductor-like screening model (COSMO). In that case, the energy is calculated assuming that the medium is a conductor, so that the charge distribution at the surface of the cavity is an image of the solute's; the energy terms are then scaled by  $(\epsilon + 1)/(\epsilon + x)$ , where  $\epsilon$  is the dielectric constant and  $x$  is an empirical factor. Solvation effects on the stability of chalcogen bonds can be dramatic. While gas-phase calculations for the dimers of *N*-methyl-benzochalcogenadiazolium cations (Fig. 5)<sup>24</sup> imply that all three dimers would be unstable, the stabilizing effect of solvation in



**Fig. 4** Electrostatic potential (AMS SCM, PBE, all-electron TZ2P ZORA) maps of an isotellurazole *N*-oxide.<sup>19</sup> (A) Contour plot in the heterocyclic plane and isodensity contour at 10<sup>-3</sup> a.u. (B) and (C) two perspectives of the map plotted on the surface of the 10<sup>-3</sup> a.u. isodensity offer. Panels b and c are adapted from Ho, P. C.; Szydłowski, P.; Sinclair, J.; Elder, P. J. W.; Kübel, J.; Gendy, C.; Lee, L. M.; Jenkins, H.; Britten, J. F.; Morim, J. R.; Vargas-Baca, I. *Nat. Commun.* **2016**, *7*, 11299 under a CC BY 4.0 license. The scales are chosen to facilitate the location of the maximum and minimum of potential.



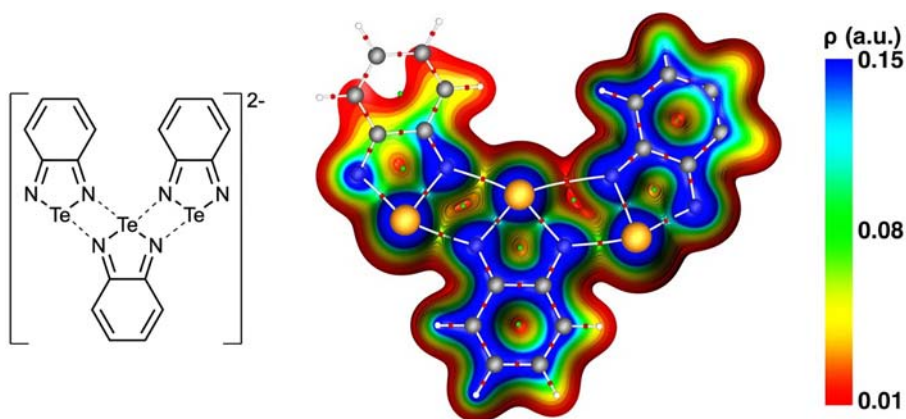
**Fig. 5** Calculated free energy profile (Gaussian, B3LYP, 6-31G(d,p) (E = S) or 6-31G(d,p)/SDB-cc-pVTZ (E = Se, Te), PCM) for the dimerization of *N*-methyl-benzochalcogenadiazolyl cations in acetonitrile solution.<sup>24</sup> Reproduced with permission from Risto, M.; Reed, R. W.; Robertson, C. M.; Oilunkaniemi, R.; Laitinen, R. S.; Oakley, R. T. *Chem. Commun.* **2008**, 3278–3280. Copyright 2008 Royal Society of Chemistry.

acetonitrile is enough to overcome electrostatic repulsion and permit dimerization by a pair of  $\text{Te}\cdots\text{N}$  chalcogen bonds. The more anodic reduction potential measured in DMSO for the tellurium congener suggests that such dimer does exist in solution.

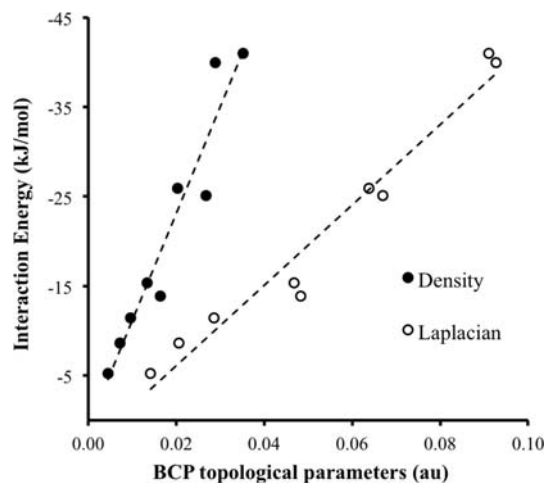
#### 1.11.4 Electron density analysis

The distribution of electrons in space is key to interpret bonding. The most common approaches in the analysis of SBIs are based on topological analysis and localization descriptors.

*Atoms in Molecules (AIM).* The topological analysis of the average spatial distribution of electron density ( $\rho(\mathbf{r})$ ) of a molecule or crystal is at the core of Bader's theory of atoms in molecules.<sup>25</sup> Here, the molecular structure is defined by the stationary points of  $\rho(\mathbf{r})$  and the gradient ( $\nabla\rho(\mathbf{r})$ ) lines that connect them. The electron density is maximum at the position of the atomic nuclei and bonds are characterized by lines of maximum density or *bond paths*. The point of minimum electron density along the path is designated as the *bond critical point* (BCP). The classification of stationary points is easily extended to ring and cage critical points (Fig. 6). The Laplacian ( $\nabla^2\rho(\mathbf{r})$ ) identifies the regions of space where the electron density is concentrated or depleted, thus providing a map that locates the electron pairs that are central to the Lewis bonding and VSEPR structural models. Secondary bonding is interpreted by AIM just like any other bond, by locating the bp and BCP. The AIM analysis is applicable not only to calculated but to experimental charge densities.<sup>27</sup> There is some correlation between the density at the ( $\rho_{\text{BCP}}$ ) (or the Laplacian) and the secondary bonding energy for homologous series of compounds (Fig. 7). However, AIM is often criticized because it can find bond paths between any close neighbors, even the hydrogen atoms in a hydrocarbon crystal. On the other hand, the space grid must be carefully chosen to find BCPs when  $\nabla\rho(\mathbf{r})$  along the SBI bp is small.



**Fig. 6** Electron density map (ADF, B3LYP-D3, all-electron TZ2P ZORA) calculated for the dianionic trimer of benzotelluradiazole.<sup>26</sup> Adapted with permission from Dmitriev, A. A.; Pushkarevsky, N.; Smolentsev, A. I.; Vargas-Baca, I.; Gritsan, N. P.; Beckmann, J.; Zibarev, A. V. *Chem. Commun.* **2020**, 56, 1113–1116. Copyright 2020 Royal Society of Chemistry. Isodensity surfaces are plotted within the range 0.01–0.15 a.u. and clipped off at the average plane of the tellurium atoms. Atom sphere models, bond paths (white rods) and critical points (red spheres for bonds and green spheres for rings) are overlaid for clarity. The asymmetry of the structure is likely related to a second-order Jahn-Teller distortion resulting from electron delocalization over the pi manifold of the trimer, and packing in the crystal. The correlation between electron density at the critical point and bond distance is apparent in the  $\text{Te}\cdots\text{N}$  chalcogen bonds.



**Fig. 7** Correlation of the calculated chalcogen-bond interaction energy (ADF, PW91, all-electron TZP ZORA) between chalcogenadiazoles and solvent molecules (benzene, dimethyl sulfoxide and pyridine) with the electron density at the bond critical point and its laplacian.<sup>28</sup> Reprinted from Cozzolino, A. F.; Elder, P. J. W.; Lee, L. M.; Vargas-Baca, I. *Can. J. Chem.* **2013**, *91*, 338–347. Energy values follow the order thiadiazole < selenadiazole < telluradiazole. The three lowest energies correspond to the interaction with benzene. Binding energies to pyridine are slightly larger than those of DMSO.

The electron localization function (ELF,  $\eta$ ) originally proposed by Becke and Edgecombe<sup>29</sup> is based on the probability density for a pair of electrons with the same spin. Savin<sup>30</sup> reformulated the definition based on the Pauli kinetic energy density of noninteracting electrons to enable its application with DFT as:

$$\eta(r) = 1/(1 + \chi_{\sigma}^2(r)) \quad (2)$$

Where:

$$\chi_{\sigma}(r) = D_{\sigma}(r)/D_{\sigma}^0(r) \quad (3)$$

$$D_{\sigma}(r) = \tau_{\sigma}(r) - 1/4 ((\nabla\rho_{\sigma}(r))^2/\rho_{\sigma}(r)) \quad (4)$$

is the fermionic contribution to the kinetic energy in the molecule;

$$D_{\sigma}^0(r) = 3/5 (6\pi^2)^{2/3} (\nabla\rho_{\sigma}(r))^{5/3} \quad (5)$$

is the fermionic contribution to the kinetic energy in the uniform electron gas with  $\rho_{\sigma}(\rho)$ ;  $\rho_{\sigma}$  is the spin density; and  $\tau_{\sigma}$  is the kinetic energy density.

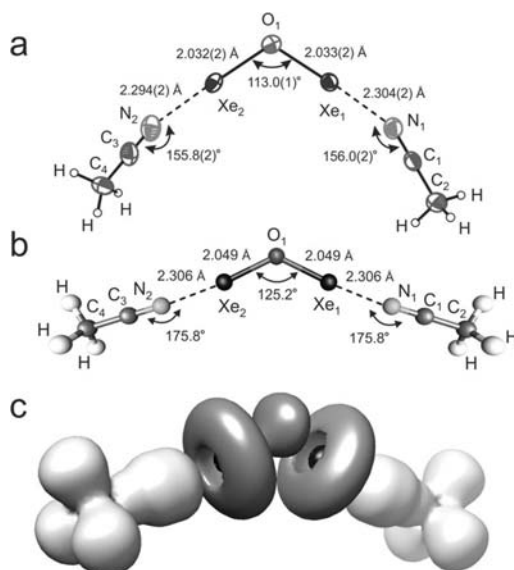
ELF measures the likelihood of finding an electron in the vicinity of a reference electron with the same spin at any point in space. It is a measurement of the extent of localization of the reference electron, and provides a method for mapping electron pair probability in space. Possible values of ELF range from zero to one. In the homogeneous electron gas, ELF takes a 0.5 value. ELF approaches the maximum in space regions occupied by bonding and lone pairs; and the minimum for regions between two electron shells.<sup>30</sup> The ELF provides an intuitive visualization of the regions of space occupied by core, bonding and lone pairs of electrons. Sigma holes (Fig. 8) and their interactions with electron pairs are also identifiable. In the Fig. 9 example, the smaller volume of the Sb basins close to Te suggests electron depletion from the pnictogen. On the basis of these features, the interaction was interpreted as a case of chalcogen bonding. However, the apparent volume decrease in the volume of the localization domain on the interacting tellurium atoms suggests a degree of backdonation into Sb.<sup>32</sup>

The Electron Localizability Indicator (ELI) is an alternative approach to ELF that is based on restricted populations. The space is divided in microcells with volumes chosen so that the integral of a calculated control property is the same in each microcell and can be compared with a calculated sampling property. ELI-D<sup>35,36</sup> is the ELI variant for electrons with the same spin. For electrons with  $\sigma$  spin, ELI-D is:

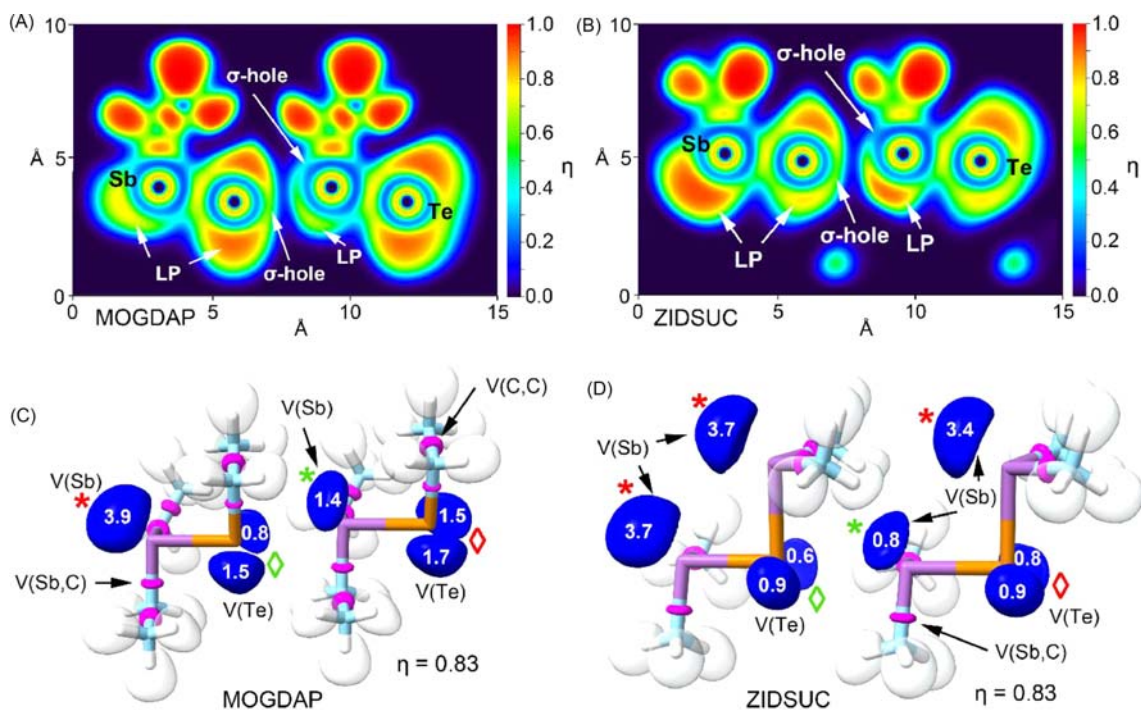
$$\gamma_D^{\sigma}(r) = r\sigma(r)V_D(r) \quad (6)$$

As with the ELF, the topological analysis of the electron pair density by ELI-D identifies core, bonding, and lone-pair basins. Integration quantifies the electron density in each basin.

Noncovalent Interaction index (NCI).<sup>37,38</sup> This approach is also based on the electron density and its reduced (dimensionless) derivatives. Here the areas of noncovalent interaction are characterized by:



**Fig. 8** Comparison of experimental (A) and calculated (B, Gaussian, B3LYP/aug-cc-pVTZ(-PP)) structures of the acetonitrile adduct of the  $\text{Xe}_2\text{O}_2^{2+}$  cation ( $[\text{AsF}_6]^-$  salt) and ELF isosurface at  $\eta(r) = 0.54$ .<sup>31</sup> Reprinted with permission from DeBackere, J. R.; Bortolus, M. R.; Schrobilgen, G. *J. Angew. Chem. Int. Ed.* **2016**, *55*, 11917–11920. Copyright 2016 John Wiley and Sons. The sigma holes are clearly visible in the Xe valence basins (dark gray).



**Fig. 9** ELF analysis of the  $\text{Te}\cdots\text{Sb}$  interactions observed in the crystal structures of two stibanyl telluranes.<sup>32</sup> Adapted with permission from Gomila, R. M.; Frontera, A. *J. Organomet. Chem.* **2021**, *954–955*, 122092. Copyright 2021 Elsevier. The compounds are identified by their CSD codes: MOGDAP ( $\text{Et}_2\text{Sb-TeEt}$ )<sup>33</sup> and ZIDSUC ( $\text{Et}_2\text{Sb-Te-SbEt}_2$ ).<sup>34</sup> Model dimers were calculated using DFT (PBE0-D3/def2-TZVP). (A) and (B) map the ELF in a plane, which permits visualizing the lone pairs of electrons (LP) and the sigma holes. In this map, the Sb LP is oriented toward the Te sigma hole. (C) and (D) displays electron localization domains as blue isosurfaces ( $\eta = 0.83$ ) with volume values ( $V(E)$ ,  $\text{\AA}^3$ ) of the valence basins of Sb and Te.



- small values of  $\rho(r)$  and is reduced gradient.

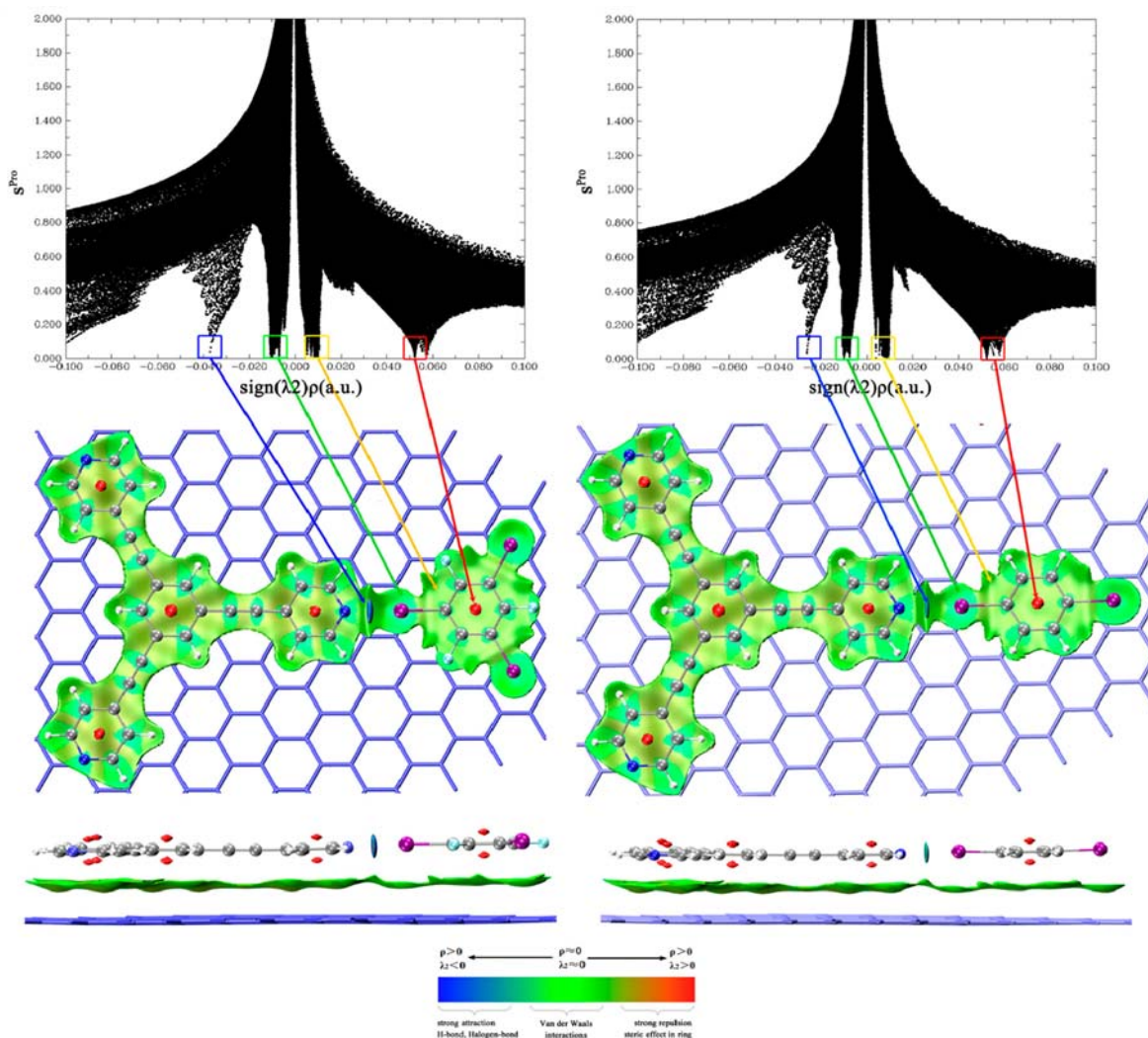
$$s = \frac{1}{2} (3 \pi^2)^{-1/3} \nabla \rho(r) \rho(r)^{-4/3} \quad (7)$$

- a curvature of  $\rho(r)$  characterized by a negative to small positive second eigenvalue of the Hessian ( $\lambda_2$ ).
- a strictly negative  $\lambda_2$  is characteristic of hydrogen bonding,
- slightly positive  $\lambda_2$  corresponds to van der Waals interactions.

Thus a mapping of  $\lambda_2$ , on the NCI surface identifies steric repulsion ( $\lambda_2 > 0$ ), van-der-Waals like ( $\lambda_2 \approx 0$ ), and attractive ( $\lambda_2 < 0$ ) interactions. For large systems, the analysis can be approximated using promolecular electron densities, i.e., the spherically-averaged densities of the constituting atoms (Fig. 10).

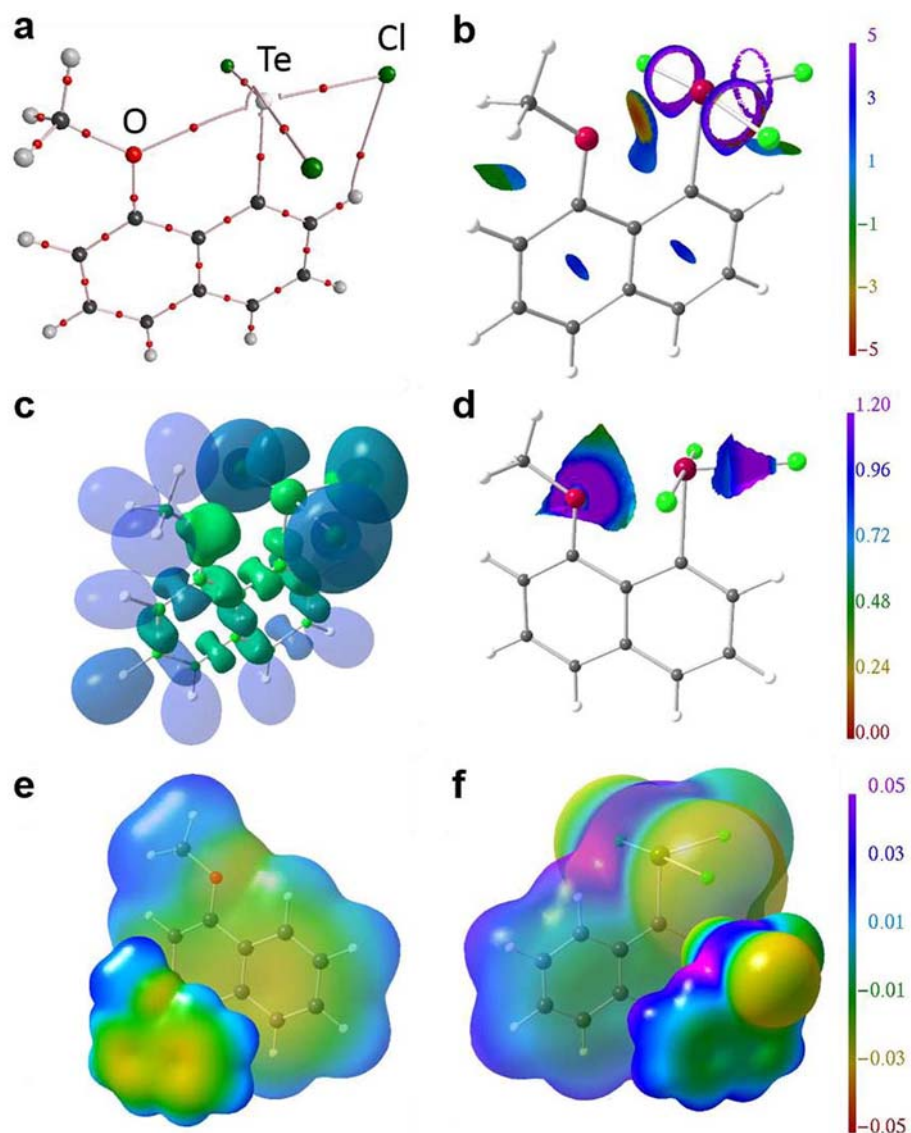
Although different, AIM, NCI, ELF and ELI-D descriptors are useful complementary tools for the description and analysis of SBIs Fig. 11.

*Hirshfeld surfaces.* This method to characterize the interaction between molecular entities in a crystal is based on the analysis of electron density. The region of space occupied by a molecule is defined as the area in which the contribution to the electron density



**Fig. 10** Scatter plots of  $s^{Pro}$  versus  $\rho^{Pro}(r)$  multiplied by  $sign(\lambda_2(r))$  and NCI isosurfaces and  $s$  for the I...N halogen bonds between pyridyl group and iodobenzenes on graphite surfaces.<sup>39</sup> Reprinted with permission from Zhang, S.; Lu, Y.; Zhang, Y.; Peng, C.; Liu, H. *J. Phys. Chem. C* **2017**, *121*, 4451–4461. Copyright 2017 American Chemical Society. The large green isosurfaces denote the  $\pi$ -stacking interaction between molecules and isosurfaces and contrast with the blue surfaces from the halogen bond and the red areas of repulsion. The points corresponding each of these interaction types are identified in the scatter plots.





**Fig. 11** Computational analysis of the Te...O intramolecular interaction in the structure of 8-methoxynaphthyltellurium trichloride.<sup>40</sup> (A) The QTAIM analysis clearly identifies a bond path and a BCP between tellurium and oxygen. (B) the NCI isosurface ( $s(r) = 0.5$ ), (C) The ELI-D isosurface ( $Y = 1.3$ ), and (D) ELI-D distribution mapped on relevant ELI-D basins. ELI-D and NCI show complementary spatial distribution suggesting a clear separation of covalent and non-covalent bonding contributions. Reprinted with permission from Wohltmann, W.; Mostaghimi, F.; Bolsinger, J.; Lork, E.; Mebs, S.; Beckmann, J. *Inorg. Chim. Acta* **2018**, 475, 73–82. Copyright 2018 Elsevier.

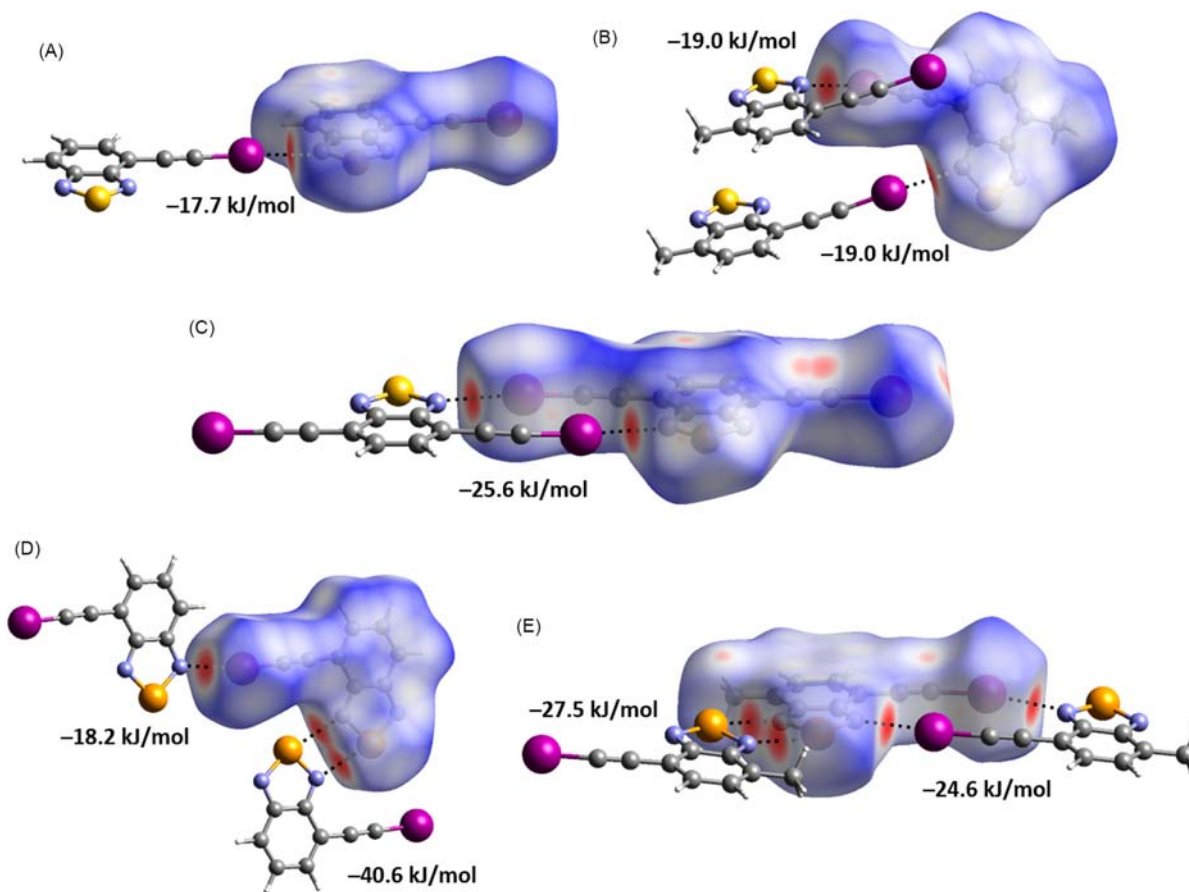
from the promolecule to the procrystal is greater than that of any other molecule, and is defined by the ratio of the densities being greater than 0.5.

$$w(r) = \rho_{\text{promolecule}} / \rho_{\text{procrystal}} \quad (8)$$

The volume occupied by a molecule is thus delimited by the isosurface of  $w(r) = 0.5$ , the Hirshfeld surface -called so because the approach to construct it follows Hirshfeld's stockholder partitioning method for atoms in a molecule.<sup>41</sup> The promolecular and procrystal densities are evaluated as the sums of the densities of the constituting atoms. For convenience, these are taken from literature data.<sup>42–45</sup> Several functions of distance and curvature can be mapped on the Hirshfeld surface, the normalized distance ( $d_{\text{norm}}$ ) being one of the most useful (Fig. 12).

$$d_{\text{norm}} = \left( \left( d_i + r_i^{\text{vdW}} \right) / r_i^{\text{vdW}} \right) + \left( \left( d_e + r_e^{\text{vdW}} \right) / r_e^{\text{vdW}} \right) \quad (9)$$

Where  $d_i$  and  $d_e$  are, respectively, the distances from any point to the nearest internal and external nuclei;  $r_i^{\text{vdW}}$  are the corresponding sums of van der Waals radii. This visual tool provides a convenient means to identify meaningful intermolecular contacts Fig. 12.



**Fig. 12** Hirshfeld surfaces of iodoethynyl-substituted benzochalcogenadiazoles.<sup>46</sup> Reprinted from Alfuth, J.; Zadykovicz, B.; Wicher, B.; Kazimierczuk, K.; Półniński, T.; Olszewska, T. *Cryst. Growth Des.* **2022**, *22*, 1299–1311 under a CC BY 4.0 license. The chalcogen is sulfur in panels A–C, and selenium in D–E. The isosurfaces are mapped with the value of  $d_{\text{norm}}$ , the color scale is adjusted to facilitate interpretation; blue regions are points beyond the van der Waals surface while the red spots correspond to contacts shorter than the sum of van der Waals radii, chalcogen and halogen bonds in this case. Selected neighboring molecules forming close contacts are shown along with the values of calculated (HF, 3-21G) interaction energies between the molecules.

### 1.11.5 Polarization and charge transfer

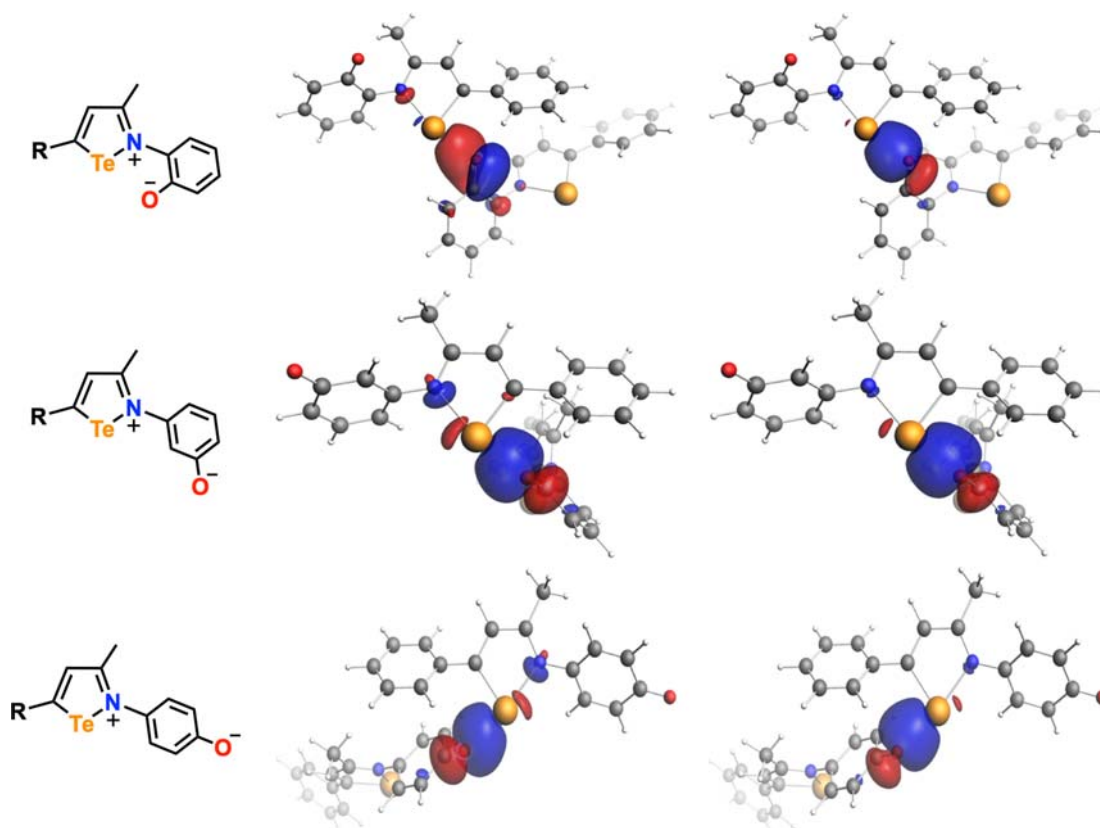
An inherent limitation of the EDA schemes in Section 1.11.3 is that the polarization term includes both the intramolecular reorganization of electron density and any intermolecular charge transfer between interacting molecules. The latter is of particular interest because it quantifies the degree of covalency of the secondary interactions, assuming that the electrons are shared between the interacting molecular fragments.

The straightforward approach to assess covalency analyses orbital mixing between molecular fragments, evaluates molecular orbital populations and charge changes in the molecular fragments, which can be graphically presented as plots of deformation densities. Comparisons are only possible between systems calculated with the same method as results depend markedly on basis set, and functional or HF level.<sup>47</sup> Charges based on electron densities, e.g., Hirshfeld, are less influenced by the basis set than population based values, e.g., Mülliken, Natural Population Analysis (NPA). Calculations for symmetrical dimers are problematic but can be approached by the Constrained Space Orbital Variation (CSOV) method.<sup>48</sup>

Alternatively, the covalency of an SBI can be gauged from localized molecular orbitals and derived bond orders. The Natural Bond Orbitals (NBO)<sup>49</sup> approach is the most common of the methods to transform a set of delocalized molecular orbitals into an equivalent set of one- and two-center functions with maximum electron density. Other approaches include the Boys-Foster method,<sup>50</sup> which minimizes the extension of the orbitals about their center of gravity. NBO yields orbital energies that can be interpreted as the covalent contribution to the SBI. NPA charges are also derived from the population analysis of NBOs (Fig. 13).

*ETS-NOCV. Natural orbitals of chemical valence* (NOCVs)<sup>52,53</sup> are derived by partitioning of the deformation density. The analysis is based on the interaction between molecular fragments, with each NOCV being an eigenvector of the deformation density matrix ( $\Delta R$ ) calculated from the combination of fragment orbitals ( $\lambda_i$ ) into the wavefunction ( $\psi_i$ ).

$$\Delta P \psi_i = v_i \psi_i, \quad \psi_i = |\lambda_1 \lambda_2 \dots \lambda_n| \quad (10)$$



**Fig. 13** Comparison of the NBO and Boys-Foster localized molecular orbitals (0.03 a.u. isosurfaces) calculated for pairs of iso-tellurazolium *N*-phenoxides linked by Te...O chalcogen bonding.<sup>51</sup> Reprinted with permission from Ho, P. C.; Tomassetti, V.; Britten, J. F.; Vargas-Baca, I. *Inorg. Chem.* **2021**, *60*, 16726–16733. Copyright 2021 American Chemical Society. While the results are comparable, the Boys-Foster method provides better localization for the dimer of the *meta* isomer.

Here the total deformation density is a sum of complementary pairs  $(\psi_{-j}, \psi_j)$  corresponding to the eigenvalues  $v_j$  and  $v_{-j} = -v_j$ .

$$\Delta\rho(r) = \sum \Delta\rho_j(r) = \sum v_j \left( -\psi_{-j}^2(r) + \psi_j^2(r) \right) \quad (11)$$

The deformation density from each of these pairs has a well-defined contribution to the Ziegler-Rauk total orbital interaction and its graphical representation usually correlates with the interaction of fragment orbitals and allows the distinction between electron donor-acceptor interactions and polarization. For instance, in Fig. 14, NOCV deformation densities arising from the donation of an oxygen lone pair into the  $\sigma^* \text{Te-N}$  orbital are characterized by the electron density increase in the space between the oxygen and tellurium atoms.

### 1.11.6 Multimolecular systems

Full quantum mechanical calculations of large systems are challenging even with DFT methods. It is therefore necessary to employ tools that simplify the modeling of structures and their evolution over time.

*Molecular mechanics* is a very approximate method that is concerned with the energy of a molecular system that results from deviation of structural parameters from their ideal values for a given combination of elements. This strain or distortion energy is evaluated with classical functions, the combination of which is the force field.

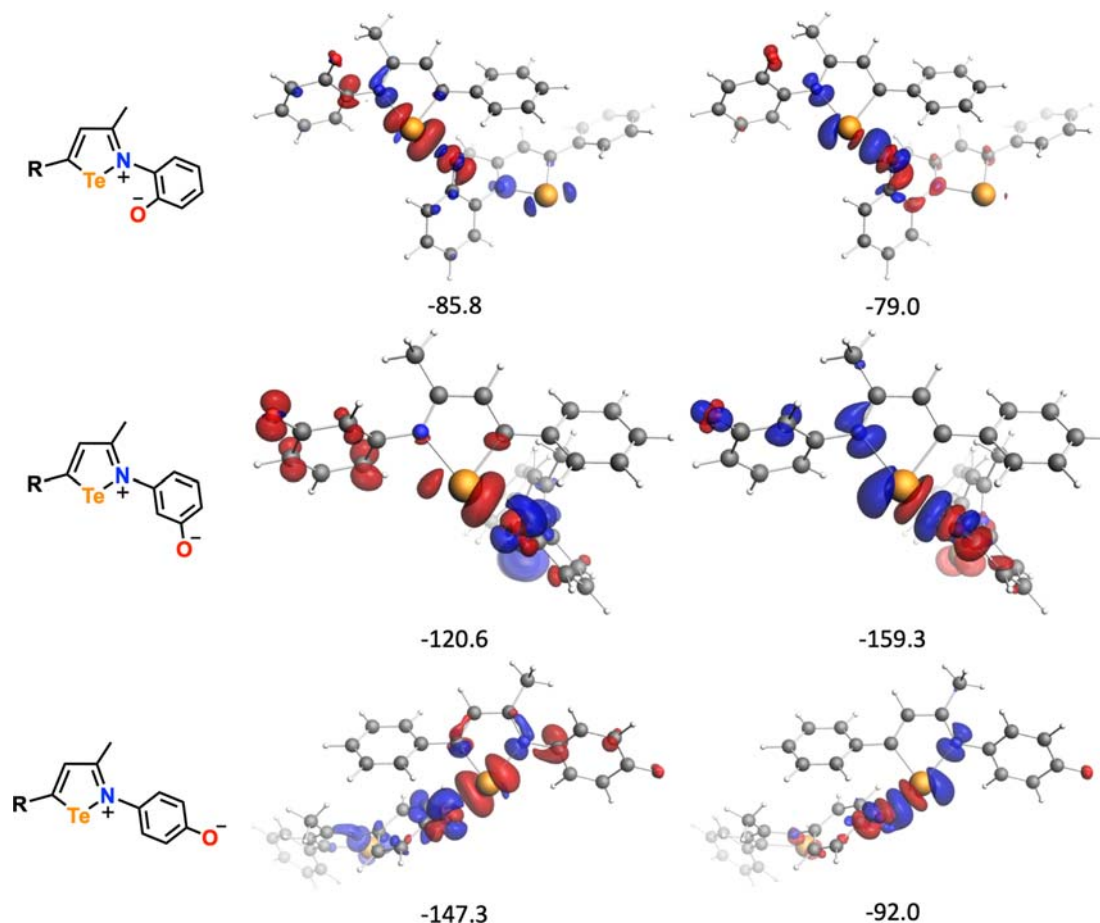
For example, in the AMBER<sup>54</sup> force field:

$$E_{\text{strain}} = E_{\text{BondStretch}} + E_{\text{AngleBending}} + E_{\text{Torsion}} + E_{\text{vanderWaals}} + E_{\text{Electrostatic}} \quad (12)$$

Where each contribution takes the form:

$$E_{\text{BondStretch}} = K_r (r - r_{\text{eq}})^2 \quad (13)$$

$$E_{\text{AngleBending}} = K_\theta (\theta - \theta_{\text{eq}})^2 \quad (14)$$



**Fig. 14** Deformation densities (0.002 a.u. isosurfaces) of the top two ETS-NOCV contributions to the orbital interaction stabilizing the Te...O chalcogen bonds in the iso-tellurazolium *N*-phenoxide dimers.<sup>51</sup> Reprinted with permission from Ho, P. C.; Tomassetti, V.; Britten, J. F.; Vargas-Baca, I. *Inorg. Chem.* **2021**, *60*, 16726–16733. Copyright 2021 American Chemical Society. Energy contributions in kJ mol<sup>-1</sup>. Blue and red identify the regions of electron concentration and depletion, respectively.

$$E_{Torsion} = \sum_n \frac{1}{2} V_i (1 + \cos(n\phi_i - \gamma_i)) \quad (15)$$

$$E_{vanderWaals} = \varepsilon_{ij} \left[ \left( \frac{r_{ij}^{eq}}{r_{ij}} \right)^{12} - 2 \left( \frac{r_{ij}^{eq}}{r_{ij}} \right)^6 \right] \quad (16)$$

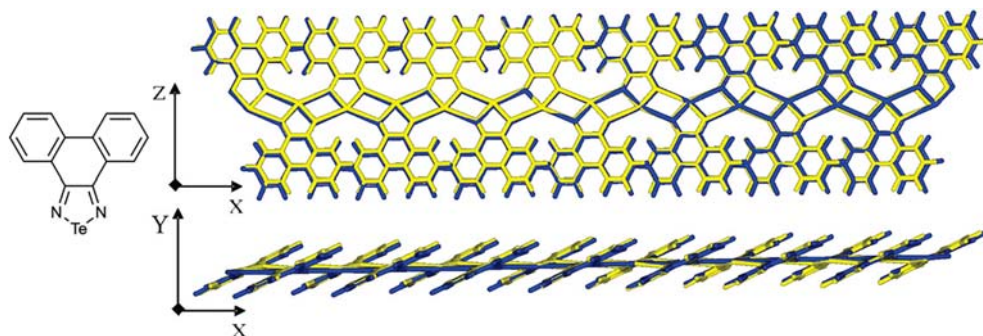
$$E_{Electrostatic} = f_{ij} q_i q_j / (4 \pi \varepsilon_0 r_{ij}) \quad (17)$$

These are gross approximations to the potential energy surface. Other force-fields seek better accuracy with more realistic functions. For example, the stretching potential could include anharmonic terms or be replaced with a Morse curve. In any case, the parameters (e.g., force constants and weighing coefficients) are obtained by fitting to experimental data sets or high-quality quantum calculations, and are specific for each element and the nature and spatial arrangement of its close neighbors in the structure. Therefore, modeling secondary bonding requires custom force fields or at least custom parameters. A properly parameterized force field is capable of accounting for molecular distortions that result from intermolecular association (Fig. 15).

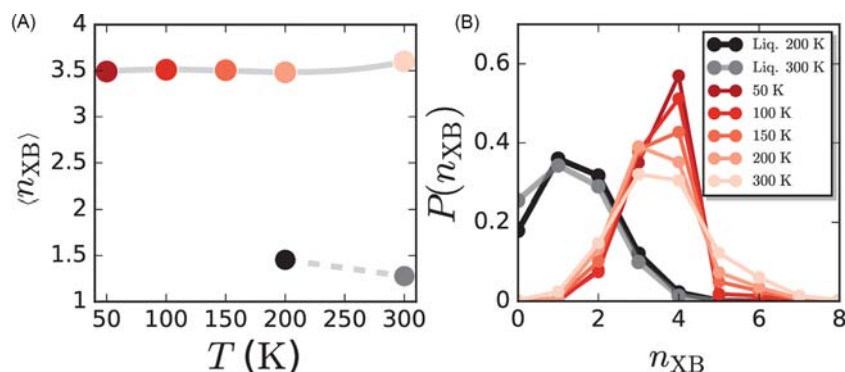
**Molecular dynamics.** Beyond the static picture from a geometry optimization, molecular dynamics models the properties of a large system (i.e., a big molecule, a crystal, or an ensemble of molecules) as it evolves in time. The key is to simulate the trajectory with a model that permits predicting the next point. Knowledge of all the position and momenta of all particles and their interaction potentials allows such prediction for a large ensemble in the absence of an external force. Secondary bonding in this case is one of the contributions to the intermolecular potential. The calculations can be carried out based on quantum methods or with force fields, with their intrinsic limitations. Although less accurate, force fields allow simulations spanning longer times.

Applications of molecular dynamics to secondary bonding are still limited, but notable investigations begin to reveal significant details of these interactions in solid and liquid phase Fig. 16.





**Fig. 15** Comparison of the experimental crystal structure of phenantrotelluradiazole (yellow) with a model minimized with the MMX force field (blue).<sup>55</sup> Adapted with permission from Cozzolino, A. F.; Vargas-Baca, I. *Cryst. Growth Des.* **2011**, *11*, 668–677. Copyright 2010 American Chemical Society. While steric repulsion would prevent formation of the supramolecular ribbon polymer from the flat molecule, torsion of the heterocycle out of the plane enables Te...N chalcogen bonding.



**Fig. 16** Ab initio molecular dynamics simulation of the formation of Cl–Cl...Cl halogen bonds in Cl<sub>2</sub>.<sup>56</sup> (A) average number of halogen bonds ( $\langle n_{XB} \rangle$ ) formed per Cl<sub>2</sub> molecule in liquid (black and gray) and solid state (red to pink). (B) Probability distribution of  $n_{XB}$ . In crystalline state, each Cl atom forms two halogen bonds, one as a donor and the other as acceptor, i.e.,  $n_{XB} = 4$  for each Cl<sub>2</sub> molecule. The simulation (CP2K-QUICKSTEP, PBE-D3, TZVP-MOLOPT-GTH, GTH-PADE) illustrates the dissociation of halogen bonds upon the increase of temperature and melting. Adapted with permission from Remsing, R. C.; Klein, M. L. *J. Phys. Chem. B* **2019**, *123*, 6266–6273. Copyright 2019. American Chemical Society.

### 1.11.7 Conclusion

A number of computational tools are now available for the identification and characterization of secondary bonding, based on interatomic distances, electron density, and energy. Methods that produce visual results are particularly useful to chemists because they can be readily interpreted in terms of well-established concepts of molecular structure. Energy decomposition analyses provide deep understanding of the factors that contribute to the stabilization of these interactions and can suggest strategies to influence their strength. Most investigations have been concerned with structure and thermodynamics, but the application of methods for the calculation of spectroscopic and macroscopic electronic properties will likely enable new applications of secondary bonding.

### References

- Alcock, N. W. *Adv. Inorg. Chem. Radiochem.* **1972**, *15*, 1–58.
- Hermansson, Y.; Kjekshus, A.; Santesson, J.; Holmberg, P.; Eriksson, G.; Blinc, R.; Paušak, S.; Ehrenberg, L.; Dumanović, J. *Acta Chem. Scand.* **1967**, *21*, 1328–1342.
- Desiraju, G. R.; Ho, P. S.; Kloo, L.; Legon, A. C.; Marquardt, R.; Metrangolo, P.; Politzer, P.; Resnati, G.; Rissanen, K. *Pure Appl. Chem.* **2013**, *85*, 1711–1713.
- Akeroy, C. B.; Bryce, D. L.; Desiraju, G. R.; Frontera, A.; Legon, A. C.; Nicotra, F.; Rissanen, K.; Scheiner, S.; Terraneo, G.; Metrangolo, P.; Resnati, G. *Pure Appl. Chem.* **2019**, *91*, 1889–1892.
- Cavallo, G.; Metrangolo, P.; Pilati, T.; Resnati, G.; Terraneo, G. *Cryst. Growth Des.* **2014**, *14*, 2697–2702.
- Daolio, A.; Pizzi, A.; Calabrese, M.; Terraneo, G.; Bordignon, S.; Frontera, A.; Resnati, G. *Angew. Chem. Int. Ed.* **2021**, *60*, 20723–20727.
- Daolio, A.; Pizzi, A.; Terraneo, G.; Frontera, A.; Resnati, G. *ChemPhysChem* **2021**, *22*, 2281–2285.
- Cramer, C. J. *Essentials of Computational Chemistry: Theories and Models*, 2nd ed.; John Wiley and Sons Ltd: Chichester, England, 2004.
- Bleilholder, C.; Werz, D. B.; Köppel, H.; Gleiter, R. *J. Am. Chem. Soc.* **2006**, *128*, 2666–2674.
- Bleilholder, C.; Gleiter, R.; Werz, D. B.; Köppel, H. *Inorg. Chem.* **2007**, *46*, 2249–2260.
- Cozzolino, A. F.; Vargas-Baca, I.; Mansour, S.; Mahmoudkhani, A. H. *J. Am. Chem. Soc.* **2005**, *127*, 3184–3190.
- Desiraju, G. R. *Angew. Chem. Int. Ed.* **1995**, *34*, 2311–2327.
- Cozzolino, A. F.; Elder, P. J. W.; Vargas-Baca, I. *Coord. Chem. Rev.* **2011**, *255*, 1426–1438.



14. Kitaura, K.; Morokuma, K. *Int. J. Quantum Chem.* **1976**, *10*, 325–340.
15. Ziegler, T.; Rauk, A. *Inorg. Chem.* **1979**, *18*, 1755–1759.
16. Ziegler, T.; Rauk, A. *Inorg. Chem.* **1979**, *18*, 1558–1565.
17. Glendening, E. D.; Streitwieser, A. *J. Chem. Phys.* **1994**, *100*, 2900–2909.
18. Andrada, D. M.; Foroutan-Nejad, C. *Phys. Chem. Chem. Phys.* **2020**, *22*, 22459–22464.
19. Ho, P. C.; Szydłowski, P.; Sinclair, J.; Elder, P. J. W.; Kübel, J.; Gendy, C.; Lee, L. M.; Jenkins, H.; Britten, J. F.; Morim, D. R.; Vargas-Baca, I. *Nat. Commun.* **2016**, *7*, 11299.
20. Politzer, P.; Murray, J. *Crystals* **2017**, *7*, 212.
21. Haberhauer, G.; Gleiter, R. *Angew. Chem. Int. Ed.* **2020**, *59*, 21236–21243.
22. Miertuš, S.; Scrocco, E.; Tomasi, J. *Chem. Phys.* **1981**, *55*, 117–129.
23. Garrett, G. E.; Gibson, G. L.; Straus, R. N.; Seferos, D. S.; Taylor, M. S. *J. Am. Chem. Soc.* **2015**, *137*, 4126–4133.
24. Risto, M.; Reed, R. W.; Robertson, C. M.; Oilunkaniemi, R.; Laitinen, R. S.; Oakley, R. T. *Chem. Commun.* **2008**, 3278–3280.
25. Bader, R. F. W. *Chem. Rev.* **1991**, *91*, 893–928.
26. Dmitriev, A. A.; Pushkarevsky, N.; Smolentsev, A. I.; Vargas-Baca, I.; Gritsan, N. P.; Beckmann, J.; Zibarev, A. V. *Chem. Commun.* **2020**, *56*, 1113–1116.
27. Koritsanszky, T. S.; Coppens, P. *Chem. Rev.* **2001**, *101*, 1583–1628.
28. Cozzolino, A. F.; Elder, P. J. W.; Lee, L. M.; Vargas-Baca, I. *Can. J. Chem.* **2013**, *91*, 338–347.
29. Becke, A. D.; Edgecombe, K. E. *J. Chem. Phys.* **1990**, *92*, 5397–5403.
30. Savin, A.; Jepsen, O.; Flad, J.; Andersen, O. K.; Preuss, H.; von Schnering, H. G. *Angew. Chem. Int. Ed.* **1992**, *31*, 187–188.
31. DeBackere, J. R.; Bortolus, M. R.; Schrobilgen, G. J. *Angew. Chem. Int. Ed.* **2016**, *55*, 11917–11920.
32. Gomila, R. M.; Frontera, A. *J. Organomet. Chem.* **2021**, *954–955*, 122092.
33. Heimann, S.; Kuczkowski, A.; Bläser, D.; Wölper, C.; Haack, R.; Jansen, G.; Schulz, S. *Eur. J. Inorg. Chem.* **2014**, *2014*, 4858–4864.
34. Heimann, S.; Schulz, S.; Bläser, D.; Wölper, C. *Eur. J. Inorg. Chem.* **2013**, *2013*, 4909–4915.
35. Kohout, M.; Wagner, F. R.; Grin, Y. *Theor. Chem. Acc.* **2008**, *119*, 413–420.
36. Wagner, F. R.; Kohout, M.; Grin, Y. *J. Phys. Chem.* **2008**, *112*, 9814–9828.
37. Johnson, E. R.; Keinan, S.; Mori-Sánchez, P.; Contreras-García, J.; Cohen, A. J.; Yang, W. *J. Am. Chem. Soc.* **2010**, *132*, 6498–6506.
38. Contreras-García, J.; Johnson, E. R.; Keinan, S.; Chaudret, R.; Piquemal, J.-P.; Beratan, D. N.; Yang, W. *J. Chem. Theory Comput.* **2011**, *7*, 625–632.
39. Zhang, S.; Lu, Y.; Zhang, Y.; Peng, C.; Liu, H. *J. Phys. Chem. C* **2017**, *121*, 4451–4461.
40. Wohltmann, W.; Mostaghimi, F.; Bolsinger, J.; Lork, E.; Mebs, S.; Beckmann, J. *Inorg. Chim. Acta* **2018**, *475*, 73–82.
41. Hirshfeld, F. L. *Theor. Chim. Acta.* **1977**, *44*, 129–138.
42. Spackman, P. R.; Turner, M. J.; McKinnon, J. J.; Wolff, S. K.; Grimwood, D. J.; Jayatilaka, D.; Spackman, M. A. *J. Appl. Cryst.* **2021**, *54*, 1006–1011.
43. Clementi, E.; Roetti, C. *Atom. Data Nucl. Data* **1974**, *14*, 177–478.
44. Koga, T.; Tatewaki, H.; Thakkar, A. J. *Phys. Rev. A* **1993**, *47*, 4510–4512.
45. Koga, T.; Kanayama, K.; Watanabe, T.; Imai, T.; Thakkar, A. J. *Theor. Chem. Acc.* **2000**, *104*, 411–413.
46. Alfuth, J.; Zadykiewicz, B.; Wicher, B.; Kazimierczuk, K.; Poloński, T.; Olszewska, T. *Cryst. Growth Des.* **2022**, *22*, 1299–1311.
47. Wiberg, K. B.; Rablen, P. R. *J. Comput. Chem.* **1993**, *14*, 1504–1518.
48. Bagus, P. S.; Hermann, K.; Bauschlicher, C. W. *J. Chem. Phys.* **1984**, *80*, 4378–4386.
49. Reed, A. E.; Curtiss, L. A.; Weinhold, F. *Chem. Rev.* **1988**, *88*, 899–926.
50. Autschbach, J.; King, H. F. *J. Chem. Phys.* **2010**, *133*, 044109.
51. Ho, P. C.; Tomassetti, V.; Britten, J. F.; Vargas-Baca, I. *Inorg. Chem.* **2021**, *60*, 16726–16733.
52. Mitoraj, M. P.; Michalak, A.; Ziegler, T. *J. Chem. Theory Comput.* **2009**, *5*, 962–975.
53. Mitoraj, M. P.; Michalak, A.; Ziegler, T. *Organometallics* **2009**, *28*, 3727–3733.
54. Cornell, W. D.; Cieplak, P.; Bayly, C. I.; Gould, I. R.; Merz, K. M.; Ferguson, D. M.; Spellmeyer, D. C.; Fox, T.; Caldwell, J. W.; Kollman, P. A. *J. Am. Chem. Soc.* **1995**, *117*, 5179–5197.
55. Cozzolino, A. F.; Vargas-Baca, I. *Cryst. Growth Des.* **2011**, *11*, 668–677.
56. Remsing, R. C.; Klein, M. L. *J. Phys. Chem. B* **2019**, *123*, 6266–6273.

## 1.12 Halogen-bonded halogen(I) ion complexes

Jas S. Ward<sup>a</sup>, Khai-Nghi Truong<sup>a</sup>, Mate Erdélyi<sup>b</sup>, and Kari Rissanen<sup>a</sup>, <sup>a</sup>Department of Chemistry, University of Jyväskylä, Jyväskylä, Finland; and <sup>b</sup>Department of Chemistry - BMC, Uppsala University, Uppsala, Sweden

© 2023 Elsevier Ltd. All rights reserved.

<b>1.12.1</b>	<b>Introduction</b>	<b>586</b>
<b>1.12.2</b>	<b>Halogen(I) complexes in the solid-state</b>	<b>588</b>
1.12.2.1	Preamble	588
1.12.2.2	Aromatic iodine(I) [L–I–L] <sup>+</sup> complexes	588
1.12.2.3	Aromatic bromine(I) [L–Br–L] <sup>+</sup> complexes	589
1.12.2.4	Alkyl iodine(I) [L–X–L] <sup>+</sup> complexes	589
1.12.2.5	Multi-halogen(I) ion structures (discrete, supramolecular, XOF)	590
1.12.2.6	Nucleophilic iodine(I) interactions (NIIs)	592
<b>1.12.3</b>	<b>Other halogen(I) ion complexes</b>	<b>593</b>
1.12.3.1	Anionic [N–I–O] <sup>–</sup> complexes	593
1.12.3.2	Anionic [O–I–O] <sup>–</sup> complexes	593
1.12.3.3	Cationic [S–X–S] <sup>+</sup> complexes	594
<b>1.12.4</b>	<b>Halogen(I) ion complexes in solution</b>	<b>595</b>
<b>1.12.5</b>	<b>Outlook</b>	<b>598</b>
<b>References</b>		<b>600</b>

### Abstract

Halogen bonding occurs between a positive region of a polarized halogen (X), most commonly with an iodine or bromine atom. The polarization, caused by an electron withdrawing group (R), induces electron deficiency onto the halogen atom, creating an electropositive region known as a  $\sigma$ -hole. This  $\sigma$ -hole then interacts with electron-rich nucleophiles (such as Lewis bases, B) forming a linear R–X $\cdots$ B halogen bond. When an electron is completely removed from a halogen, a halogen (I) ion (X<sup>+</sup>) is formed. A halogen(I) ion itself is highly reactive, but can be ‘trapped’ in between two Lewis bases creating a [L–X–L]<sup>+</sup> 3-center, 4-electron halogen bond between the halogen(I) ion and two donor atoms of the Lewis bases (typically nitrogen). Halogen(I) complexes form a special family manifesting a strong halogen bond, which demonstrate good stability in both the solution and solid-states. An overview of the current state of halogen bonding of halogen(I) ion complexes is included, as well as the many advancements made to those fields in recent years.

### 1.12.1 Introduction

Halogen bonding (XB) has become one of the most studied supramolecular interactions, as indicated by a rapid increase in the number of related publications since 2007.<sup>1–4</sup> The halogen bond has been recently defined to occur between a positive region of the electrostatic surface potential of a halogen acting as the electrophilic entity and a nucleophile.<sup>5</sup>

In a halogen bonded complex, R–X $\cdots$ Y, where X is a halogen and R–X is defined as the halogen bond donor, with Y as the halogen bond acceptor, the interatomic distance between X and Y is shorter than the sum of the Van der Waals radii of the involved X and Y atoms. Due to the X $\cdots$ Y interaction, the covalent R–X bond becomes lengthened relative to the R–X bond length in a non-interacting molecule. The halogen bond is directional, with the R–X $\cdots$ Y bond angle being typically close to 180°. The interaction has originally been described as a charge-transfer bond,<sup>6</sup> later marketed as a  $\sigma$ -hole interaction. The latter being simple and easy to visualize has driven much of the progress over the past decade, however, the  $\sigma$ -hole concept and the purely electrostatic nature of the interaction in general has lately been challenged,<sup>7–18</sup> indicating the need for further fundamental studies.

With still continuing debate about its true nature,<sup>11,19,20</sup> halogen bonding is frequently used as the non-covalent interaction to construct supramolecular complexes. Due to the similarity of the bonding geometries and directionality, its kinship with hydrogen bonding is more than evident. Halogen bonding has been successfully applied to control the self-assembly of a multitude of host-guest systems, from porous, magnetic and phosphorescent materials, liquid-crystals, ion-pair recognition, biomolecules and chemical separations.<sup>1,2</sup> Crystal engineering,<sup>1–4,21</sup> the birthplace of halogen bonding, coined the directionality, specificity, and high strength, resulting in complex structures with appealing architectures. Due to the demand of very precise design principles, hollow capsular molecular assemblies solely based on halogen bonding have only recently been prepared.<sup>22,23</sup> Due to its nature, halogen bonding is more directional than hydrogen bonding,<sup>24</sup> yet it is much more sensitive to the external forces in solution and has therefore been demonstrated mostly in the solid-state.<sup>25–28</sup>

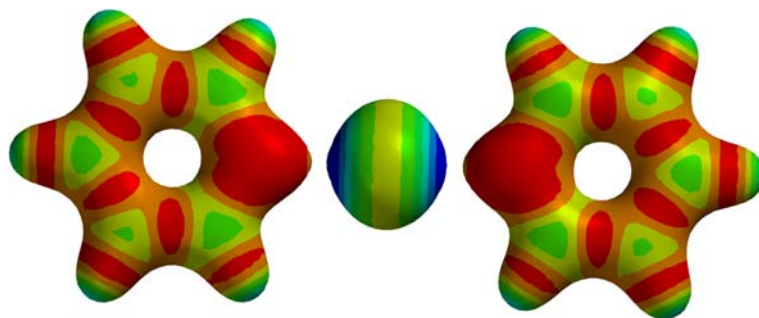
When an electron is removed from the halogen atom, it becomes a positively charged halogen(I), or halenium, ion  $X^+$  ( $X = \text{I}, \text{Br}$  or  $\text{Cl}$ ). This can be considered as an extremely polarized halogen and a strong XB donor.<sup>29</sup> However, the reactivity of the free halogen(I) ion prohibits its effective use as such. By applying suitable Lewis bases, a halogen(I) ion can be trapped into a  $[\text{L}-\text{X}-\text{L}]^+$  ( $\text{L} =$  suitable Lewis base) complex that exhibits a three-center, four-electron (3c-4e) bond.<sup>30</sup> First of these complexes, namely the *bis*(pyridine) iodine(I) complex with a  $[\text{N}-\text{I}-\text{N}]^+$  3c-4e bond, was reported in the 1960s by Hassel et al.,<sup>31</sup> Crichton et al.,<sup>32,33</sup> and Hague et al.<sup>34</sup> The three-center halogen bond of halogen(I) ions has attracted a lot of attention, especially within the halogen bonding community and has recently been reviewed.<sup>29,35</sup> Barluenga's reagent,<sup>36</sup> *bis*(pyridine)iodine(I)<sup>+</sup> tetrafluoroborate, is a mild iodine atom transfer reagent and an oxidant. It is a stable white solid that is soluble in both organic and, to a lesser extent, in aqueous solutions (it rapidly decomposes).<sup>37</sup>

Conventional halogen bonds are established through the attractive interaction of a Lewis base with the  $\sigma$ -hole of a halogen, which in turn corresponds to the anti-bonding orbital of the covalent bond of the halogen atom. This interaction is typically weak, and does not cause an extensive shortening of the interatomic distance of the atoms involved. A halogen bond is significantly strengthened by increasing the positive charge of the halogen, which is most efficiently achieved by its oxidation to halogen(I),  $X^+$ .<sup>29,35</sup> This has been observed to have a preference for simultaneous interaction with two Lewis bases, resulting in a halogen bonded halogen(I) ion, that is a halonium  $[\text{L}-\text{X}-\text{L}]^+$  complex.<sup>38</sup> Here the halogen(I) forms halogen bonds to the Lewis bases (L), though without the participation of the  $\sigma$ -hole. The valence shell of the central halogen(I) ion,  $X^+$ , has  $s^2p^4$  electron configuration and its p-orbitals are occupied in the spin paired  $p_x^2p_y^2p_z^0$  arrangement, induced by the electrostatic field of the interacting Lewis bases. The two lobes of its empty  $p_z^0$  orbital carry the charge and hence the halogen bond is in this case formed by charge transfer from the Lewis bases to this empty  $p_z$  orbital. Therewith it is a  $\pi$ -hole rather than a  $\sigma$ -hole interaction (Fig. 1). The resulting complex possesses remarkably short donor  $\cdots$  acceptor distances [ $R_{\text{XB}} = 0.65\text{--}0.69$ ,  $R_{\text{XB}}$  = the  $\text{X} \cdots \text{B}$  distance divided by the sum of the van der Waals radii of X and B] and unusual strength (typically 80–180 kJ/mol). The interaction has been shown to be partly electrostatic and partly covalent, with the extent of contribution of these being strongly dependent on the type of the halogen involved and dispersion forces having a negligible contribution.<sup>34</sup>

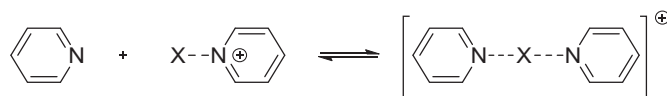
The unusual interaction strength is explained by the formation of a 3c-4e bond that involves the two electron donor Lewis bases and the electron acceptor halogen(I), and by an efficient charge transfer when aromatic Lewis bases, such as pyridine, are involved.<sup>29,35,39</sup> As a result of the charge transfer, the positive charge of the halogen(I) ion is distributed over the aromatic rings leaving only a 10–50% partial charge on the halogen(I). This efficient charge transfer and the consequent "loss of charge" on the halogen(I) makes the close packing ( $R_{\text{XB}} < 1.0$ ) of halogen(I)s embedded into *bis*(heteroaryl)halogen(I)<sup>+</sup> moieties straightforward.<sup>40</sup> It should also be noted that the coplanar geometry of the aromatic rings, observed in crystals, is a transition state in solution, whereas that with perpendicular pyridine rings corresponds to the global energy minimum.<sup>41</sup> Despite undergoing rapid association-dissociation equilibria (Fig. 2), the iodine(I) and bromine(I) complexes are stable in the solid-state for extended periods, and also in solution in the absence of nucleophiles, such as moisture, for hours or sometimes even for days.<sup>42</sup>

Chlorine(I) and fluorine(I) complexes could so far only be studied at low temperature in solution,<sup>39</sup> and their solid-state structures have not yet been reported. It should be noted that in contrast to the heavier halogens that form symmetric geometric arrangements with equally long and strong Lewis base halogen(I) bonds, fluorine shows a strong preference to the conventional asymmetric arrangement, that is  $\text{L}-\text{X} \cdots \text{L}$ .

It is important to emphasize here that the bonding situation of the halogen bond complexes of halogen(I) ions can be interpreted in various ways,<sup>35</sup> but they should not be described as classical coordination complexes of  $X^+$ , with six valence electrons, and two Lewis bases L:  $X^+ : \text{L}$ . Despite some similarities, the behavior of halogen(I) complexes toward counter-ions, excess of Lewis bases and solvents is different from that of metal complexes,<sup>43,44</sup> they may prefer different aggregation states and geometrical arrangements,<sup>45</sup> and show vastly different behavior.<sup>46</sup>



**Fig. 1** The surface electrostatic potential of the *bis*(pyridine)iodine(I)<sup>+</sup> complex. The antiparallel p-holes of iodine(I) (blue), corresponding to its empty  $p_z$  orbital, are separated by an equator of neutral charge (yellow), which corresponds to the filled  $p_x$  and  $p_y$  orbitals. Each p-hole interacts with the nonbonding electron pair of a pyridine nitrogen. The surface was computed on a 0.008 a.u. contour of the electronic density for visualization. Color ranges, in kJ/mol, are as follows: red, less than 350, yellow between 350 and 390, green between 390 and 470, light blue between 470 and 490, and blue greater than 490.<sup>35</sup>



**Fig. 2**  $[bis(\text{pyridine})\text{halogen}(\text{I})]^+$  complexes undergo rapid association-dissociation equilibria in solution, with the life-time of the complex being dependent on the electron density of the pyridine involved, and typically being  $< 5$  s.

## 1.12.2 Halogen(I) complexes in the solid-state

### 1.12.2.1 Preamble

Halogen(I) complexes (also known as halonium complexes),  $[\text{L}-\text{X}-\text{L}]^+$  ( $\text{X} = \text{Cl}, \text{Br}, \text{I}$ ), are the instances of when a halogen atom has been terminally ionized to a formally cationic state,  $\text{X}^+$ ,<sup>29,47</sup> and then by necessity stabilized by a pair of Lewis bases (L). These complexes were first reported in the 1960s,<sup>31–33</sup> and popularized by Barluenga from the 1990s onwards due to the myriad of organic transformations he demonstrated, including the electrophilic iodination of unactivated arenes, the promotion of C–C and C–X bond formation, and the selective direct iodination of peptides.<sup>48–50</sup> This utility certainly prompted renewed interest in halogen(I) complexes, though other recent advances (*vide infra*) have now also helped reinvigorate the field.

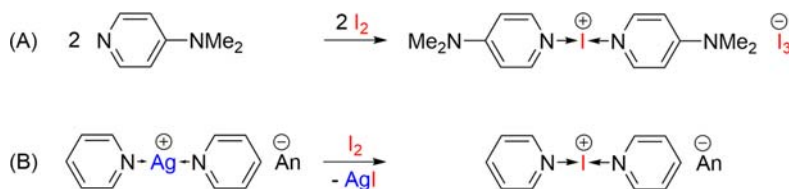
The  $[bis(\text{ligand})\text{halogen}(\text{I})]^+$  complexes can be straightforwardly prepared (Fig. 3) via cation exchange from their respective 2-coordinate silver(I) complexes, which is more reliable due to the strong driving force for the reaction from the precipitation of the  $\text{AgX}$  side product.<sup>29</sup> The direct use of elemental iodine ( $\text{I}_2$ ) in the formation of the  $[\text{L}-\text{I}-\text{L}]^+$  iodine(I) complex is restricted to only very strong Lewis bases like DMAP (Fig. 3, route A).

### 1.12.2.2 Aromatic iodine(I) $[\text{L}-\text{I}-\text{L}]^+$ complexes

The largest sub-group of  $[bis(\text{ligand})\text{halogen}(\text{I})]^+$  complexes is the  $[bis(\text{ligand})\text{iodine}(\text{I})]^+$  complexes, owing to the fact that their stability is in the order:  $[\text{L}-\text{I}-\text{L}]^+ > [\text{L}-\text{Br}-\text{L}]^+ > [\text{L}-\text{Cl}-\text{L}]^+$ . The  $[bis(\text{ligand})\text{halogen}(\text{I})]^+$  complexes are most commonly comprised of N-heterocyclic ligands (Fig. 4), with a  $[\text{N}-\text{I}-\text{N}]^+$  3e-4c bond, with derivatives of pyridine being the dominant motif. These complexes should be prepared in dry solvents (to avoid water protonating the Lewis bases) and commonly display reasonable stability as solids, with some examples such as  $[bis(\text{pyridine})\text{iodine}(\text{I})]\text{BF}_4$  (Barluenga's reagent) even being available commercially.

The stability of these iodine(I) complexes has permitted extensive solid-state examples to be reported, enabling a thorough interrogation of their structural features. All reported discrete  $[bis(\text{ligand})\text{iodine}(\text{I})]^+$  complexes have  $\text{I}^+-\text{N}$  bond lengths that lie within the narrow range of 2.23(1)–2.316(6) Å.<sup>51</sup> Steric and electronic effects only do marginally influence the solid-state  $\text{I}^+-\text{N}$  bond lengths,<sup>52</sup> though these do provide major contributions to electron distribution, bond strength and reactivity (Fig. 5). For example, if  $[bis(\text{pyridine})\text{iodine}(\text{I})]^+$  ( $\text{I}^+-\text{N} = 2.238(3)\text{--}2.268(3)$  Å;<sup>51</sup> average = 2.256 Å) is taken as a baseline for comparison, then the more Lewis basic 4-aminopyridine (4-NH<sub>2</sub>py) would be expected to form shorter and stronger I–N bonds in  $[bis(4\text{-aminopyridine})\text{iodine}(\text{I})]^+$ , which has been observed ( $\text{I}^+-\text{N} = 2.228(9)\text{--}2.269(4)$  Å;<sup>51</sup> average = 2.245 Å). Similarly, the more sterically bulky 2,4,6-trimethylpyridine (2,4,6-Me<sub>3</sub>py), which would be expected to demonstrate longer  $\text{I}^+-\text{N}$  bonds in  $[bis(2,4,6\text{-trimethylpyridine})\text{iodine}(\text{I})]^+$  due to the steric hindrance of the two *ortho*-methyl groups with the  $\text{I}^+$ , also follows the predicted trend ( $\text{I}^+-\text{N} = 2.266(3)\text{--}2.311(3)$  Å;<sup>51</sup> average = 2.288 Å).<sup>52</sup> Overall, the influence of steric and electronic effects on the  $\text{I}^+-\text{N}$  bond strengths are incomparably larger than on the  $\text{I}^+-\text{N}$  bond length, indicating that interaction strength should be carefully interpreted in terms of bond strength.<sup>52</sup>

The halogen bonding of  $[bis(\text{ligand})\text{halogen}(\text{I})]^+$  complexes also ensures that an almost perfect 2-coordinate linear geometry, with 180° N–I<sup>+</sup>–N angles, is found in all reported instances. The largest deviation of the linear geometry was reported for  $[bis(4\text{-trifluoromethylpyridine})\text{iodine}(\text{I})]^+$  with a N–I<sup>+</sup>–N angle of 175.2(2)°.<sup>52</sup> It should be noted that halonium complexes have been reported with a myriad of anions, though there have been no reports of interactions between the halonium ions and their anions,<sup>43</sup> making the identity of the anions themselves trivial (other than with respect to solubility and packing effects upon crystallization), and therefore require no further discussion herein.



**Fig. 3** The synthetic methods to prepare  $[bis(\text{ligand})\text{halogen}(\text{I})]^+$  complexes, either directly (route A) or via cation exchange from their respective silver(I) salts (route B) using pyridine as an example (An = anion).

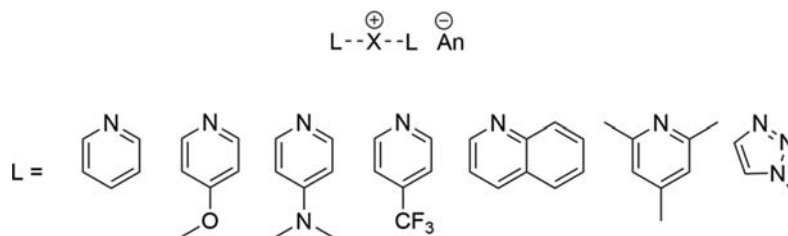


Fig. 4 Some examples of the aromatic N-heterocyclic ligands used to synthesize  $[bis(\text{ligand})\text{halogen}(\text{I})]^+$  complexes.

### 1.12.2.3 Aromatic bromine(I) $[L-\text{Br}-L]^+$ complexes

The increased reactivity/diminished stability of bromine-based halogen(I) ions (*vide supra*), also known as bromonium ions, compared to their iodine(I) analogues is immediately apparent, with far fewer examples of  $[bis(\text{ligand})\text{bromine}(\text{I})]^+$  complexes appearing in the literature. Once again, the largest sub-group of  $[bis(\text{ligand})\text{bromine}(\text{I})]^+$  complexes are those comprised of N-heterocyclic ligands such as substituted pyridines, with  $\text{Br}^+-\text{N}$  bond lengths within the range of 2.049(2)–2.144(6) Å,<sup>51</sup> and  $\text{N}-\text{Br}^+-\text{N}$  angles all lying in the range 176.2(2)–180° (that is a symmetry-enforced, exact 180°),<sup>51</sup> with one exception:  $[bis(3\text{-methylpyridine})\text{bromine}(\text{I})]^+$  with a  $\text{N}-\text{Br}^+-\text{N}$  angle of 173.89° (no esd available).<sup>55</sup> The longest  $\text{Br}^+-\text{N}$  bond length of that range was reported for  $[bis(2,4,6\text{-trimethylpyridine})\text{bromine}(\text{I})]^+$ ,<sup>54</sup> and the shortest for  $[bis(\text{pyridine})\text{bromine}(\text{I})]^+$  (the bromonium analogue of Barluenga's  $[bis(\text{pyridine})\text{iodine}(\text{I})]^+$  reagent),<sup>56</sup> which is significant because of the absence of bromine(I) complexes being reported with electron poor ligands (such as those reported for iodine(I) ions, e.g.  $[bis(4\text{-trifluoromethylpyridine})\text{iodine}(\text{I})]^+$ ),<sup>52</sup> which would be expected to produce weaker and longer  $\text{Br}^+-\text{N}$  bond lengths, again reinforcing their need for stronger Lewis bases to offset their reduced stability when compared to iodine (I) complexes. It should be noted that the actual longest  $\text{Br}^+-\text{N}$  bond length of 2.1862 Å (no esd available) was not included in this range because it is from a room temperature data collection reported in 1975,<sup>57</sup> and therefore might not be appropriate to compare to other modern, low temperature data collections.

### 1.12.2.4 Alkyl iodine(I) $[L-\text{X}-L]^+$ complexes

In comparison to the relatively common occurrence of  $[bis(\text{ligand})\text{iodine}(\text{I})]^+$  and  $[bis(\text{ligand})\text{bromine}(\text{I})]^+$  complexes comprised of N-heterocyclic ligands (e.g., substituted pyridines), halogen(I) complexes incorporating amines as the stabilizing ligands are extremely rare, such that the confirmed solid-state examples can be summarized as having one of three ligand architectures as the coordinating group: quinuclidine,<sup>58–60</sup> DABCO (1,4-diazabicyclo[2.2.2]octane),<sup>61,62</sup> or hexamethylenetetramine (Fig. 6).<sup>63,64</sup> Computational calculations have been implemented to explore the origins of the imbalance of halogen(I) ions predominantly comprised of aromatic N-heterocyclic Lewis bases, and confirmed that while the tertiary amine based  $[bis(\text{ligand})$

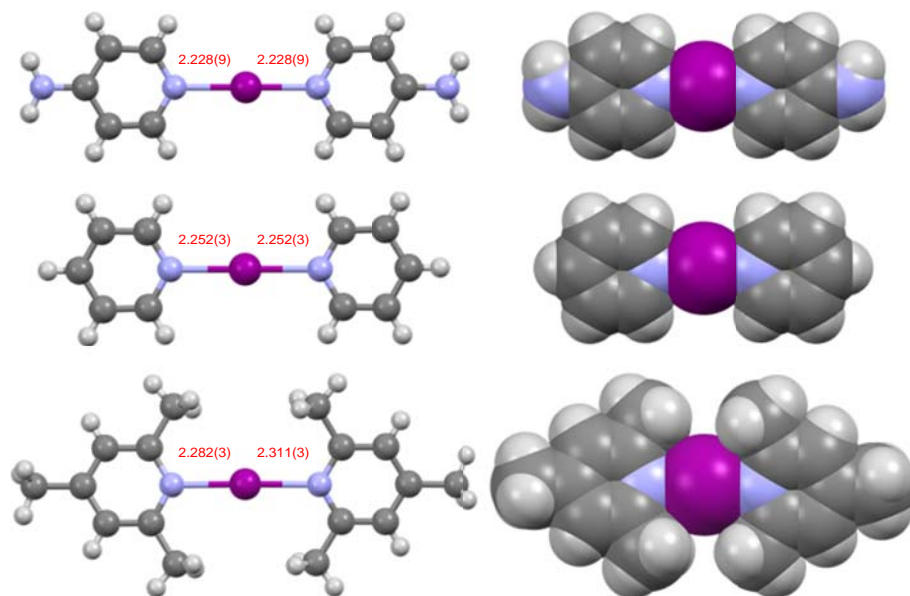
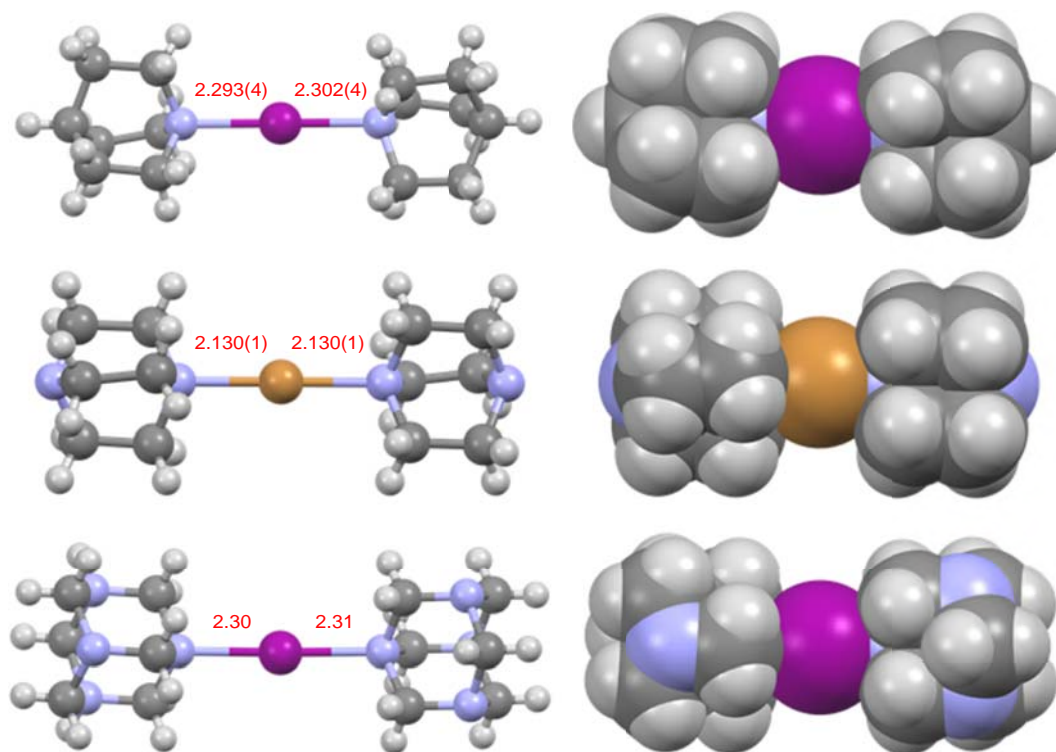


Fig. 5 A comparison of the  $\text{I}^+-\text{N}$  bond lengths of three  $[bis(\text{ligand})\text{iodine}(\text{I})]^+$  complexes representing the subtle effects caused by electronic and steric factors (left; all distances in Å), and their respective spacefill representations (right) (counter-ions omitted for clarity).<sup>43,53,54</sup>





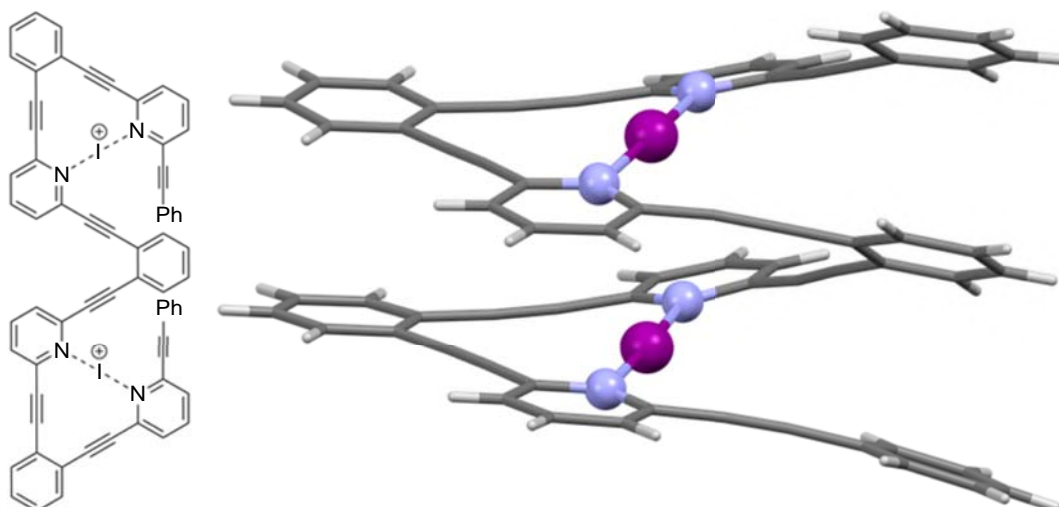
**Fig. 6** Examples of the three coordinating motifs that comprise all reported solid-state examples of  $[\text{bis}(\text{ligand})\text{halogen}(\text{I})]^+$  complexes incorporating tertiary amines (left; all distances in Å), and their respective spacefill representations (right) (counter-ions omitted for clarity). The solid-state structure of  $[\text{bis}(\text{hexamethylenetetramine})\text{iodine}(\text{I})]^+$  published in 1975 did not include hydrogen atoms, which have been included here in ideal positions (as per modern convention, though without refinement due to lack of available reflection data) to give a true representation of the steric considerations, and ESDs for the bond lengths were also not available.<sup>60,63,64</sup>

iodine(I)<sup>+</sup> complexes lack the potential favorable  $\pi$ -stabilization of their N-heterocyclic analogues, the resulting tertiary amine iodonium complexes still generally enjoy the same stability as their aromatic counterparts.<sup>60</sup> Solid-state examples of  $[\text{bis}(\text{ligand})\text{halogen}(\text{I})]^+$  complexes based on tertiary amines are few (currently < 10), with bond length ranges of 2.268–2.319 Å (no esds available) for  $\text{I}^+-\text{N}$  and 2.1202–2.1572 Å (no esds available) for  $\text{Br}^+-\text{N}$ .<sup>51</sup> These ranges overlap at the longer end of the ranges previously discussed for aromatic N-heterocyclic examples of  $[\text{bis}(\text{ligand})\text{halogen}(\text{I})]^+$  complexes (and for the alkyl  $\text{Br}^+-\text{N}$  slightly exceeds it), which is to be expected given the slightly larger steric bulk of the tertiary amines and the aforementioned lack of  $\pi$ -stabilization with the halogen(I) ions.

As a number of the reported examples of tertiary amine  $[\text{bis}(\text{ligand})\text{halogen}(\text{I})]^+$  complexes were synthesized unintentionally, a recent study sought to deliberately expand this group beyond the known *bicyclic* examples using the *monocyclic* analogue 1-ethylpiperidine (1-Etpip).<sup>60</sup> While this study revealed that formation of the desired  $[\text{bis}(\text{ligand})\text{iodine}(\text{I})]^+$  ion,  $[\text{I}(\text{1-Etpip})_2]^+$ , could be achieved, the resulting complex was incredibly reactive and decomposed within minutes. This was in stark contrast to the  $[\text{bis}(\text{ligand})\text{halogen}(\text{I})]^+$  complexes (with either iodine(I) or bromine(I) ions) that incorporated bicyclic tertiary amines, which tolerated isolation/recrystallization, permitting their analysis in solution and in the solid-state.

#### 1.12.2.5 Multi-halogen(I) ion structures (discrete, supramolecular, XOF)

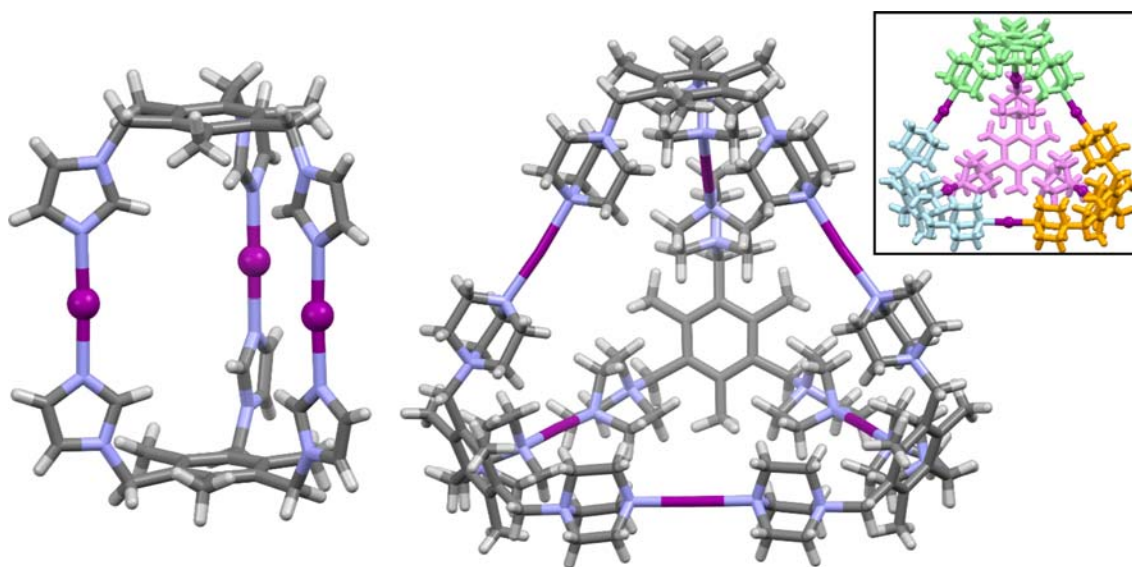
There are noteworthy instances of where the consistency of  $[\text{bis}(\text{ligand})\text{halogen}(\text{I})]^+$  ion formation with aromatic N-heterocyclic Lewis bases, via their respective silver(I) complexes, have been deftly utilized to construct advanced architectures. Such architectures can be accessed through appropriate ligand design, with an excellent example being the first example of an iodine(I) ion based helix reported in 2019 (Fig. 7).<sup>40</sup> The unique helical form has no apparent effect on the  $\text{I}^+-\text{N}$  bond lengths, with the values (2.253(4)–2.302(4) Å) being within the range observed for discrete iodine (I) complexes incorporating the parent pyridine as the stabilizing Lewis bases (*vide supra*), though the helix does induce a close proximity between the two  $\text{I}^+$  centers of 3.887(1) Å. This close proximity, which is closer than the Van der Waals radii of two iodine atoms (3.96 Å), is rarely observed in the solid-state. Given the fact that most of the positive charge in such  $[\text{bis}(\text{pyridine})\text{halogen}(\text{I})]^+$  complexes is transferred into the aromatic Lewis bases,<sup>39</sup> the iodine(I) carries only a partial charge and hence there is barely any repulsion experienced between the iodine(I) centers. In lack of electrostatic repulsion, the helix is thus stabilized by the strong 3c-4e halogen bonds along with the efficient hydrophobic packing



**Fig. 7** The solid-state structure of the first reported example of a halogen(I) ion helix, which contains two iodine(I) centers in close proximity (counter-ions omitted and ligand simplified for clarity).<sup>40</sup>

of the aromatic rings. Unsurprisingly, the electron rich  $[bis(4\text{-dimethylaminopyridine})iodine(I)]^+$  complex packs with an even shorter 3.7774(19) Å,  $I^+ \cdots I^+$  distance.<sup>65</sup>

The reliability of  $[bis(\text{ligand})halogen(I)]^+$  formation, with its high degree of (linear) directionality and reproducible bonding characteristics, makes it an ideal candidate as a self-assembling process toward supramolecular architectures,<sup>29</sup> though this has only been achieved recently. The theme of using the same coordinating ligand motifs as previously discussed, e.g., pyridine and DABCO, incorporated into appropriately rigid molecular backbones has enabled the manufacture of halogen(I)-based supramolecular cages (Fig. 8),<sup>66,67</sup> Subtle changes, such as using synthons based on either *meta*- or *para*-connected pyridyl groups has even permitted a Stang-type methodology to be implemented in the generation of different supramolecular compositions,<sup>68</sup> with solvent dependent rearrangements also being observed in such systems, and being attributed to factors such as micro-solvation and entropic considerations.<sup>69</sup> These methodologies have also been applied toward the manufacture of polymeric halogen(I) species, described as halogen-bonded organic frameworks (XOFs),<sup>70</sup> which pushes the field of study beyond the discrete complexes into the context of organic molecular frameworks, further opening up the potential of halogen(I) complexes.



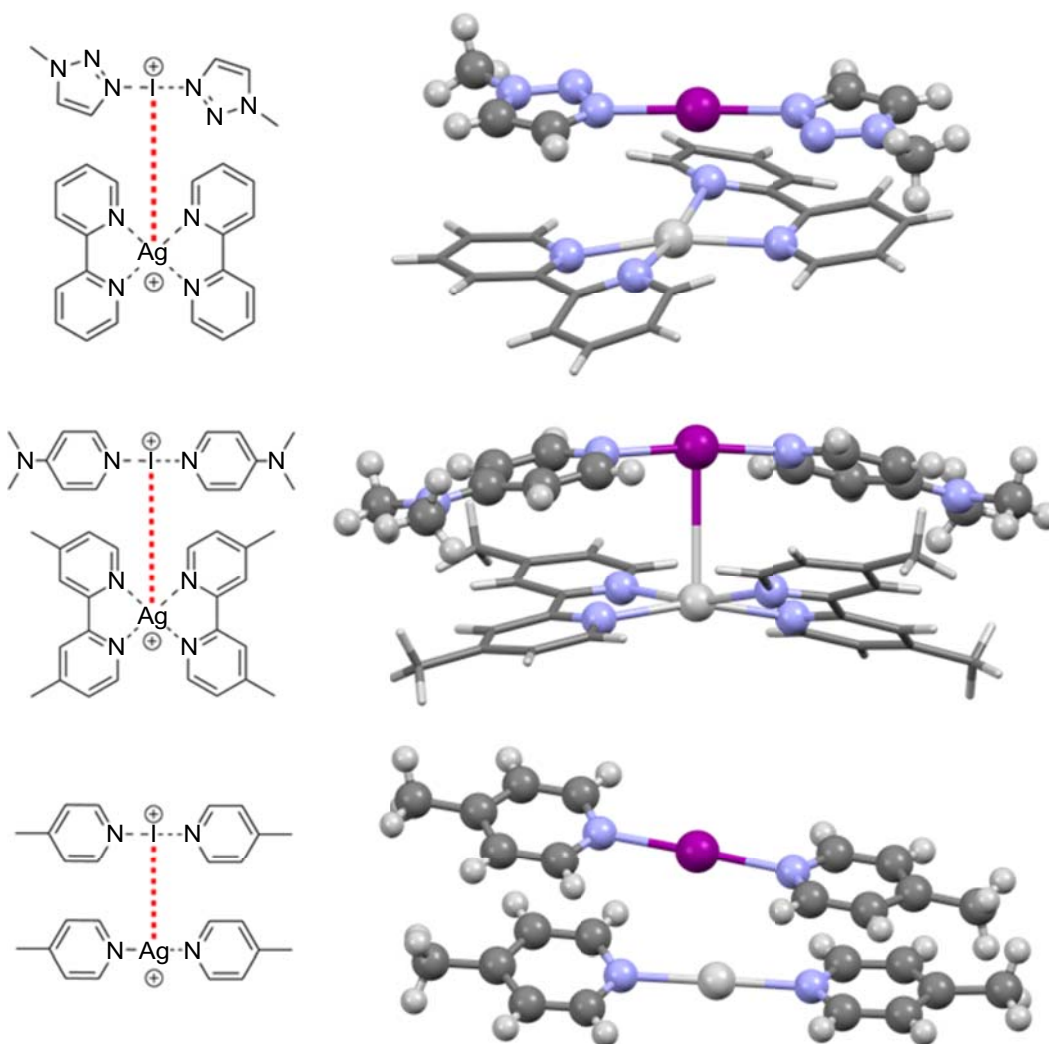
**Fig. 8** Some examples of supramolecular architectures constructed from iodine(I) ions (counter-ions omitted for clarity).<sup>66,67</sup>

## 1.12.2.6 Nucleophilic iodine(I) interactions (NIIs)

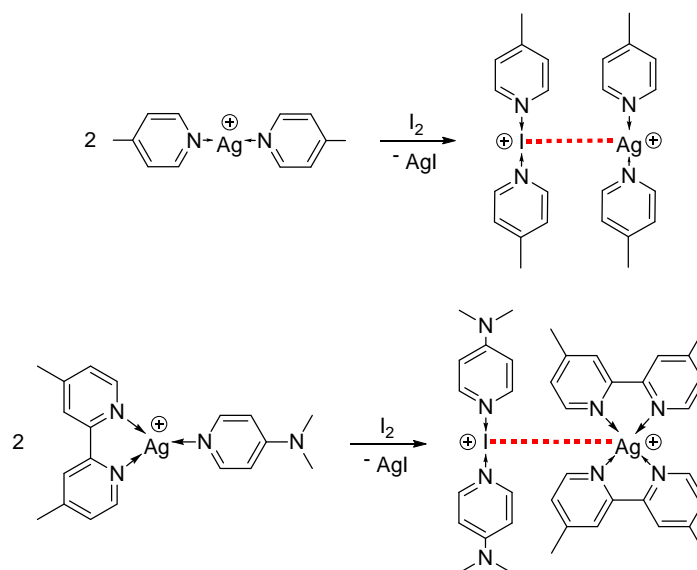
Given their 50+ years of history in the literature there are, unsurprisingly, few uses of halogen(I) complexes that does not involve them being consumed in organic transformations as reagents; this can be directly related to the inherent reactivity of halogen(I) complexes dictating, or perhaps more accurately, *limiting* their potential uses. In 2021, some examples of a new type of intermolecular  $I^+ \cdots Ag^+$  contact was observed in the solid-state,<sup>47,71,72</sup> and in one case also unambiguously proved in solution by isothermal microcalorimetry (ITC).<sup>47</sup>

The short  $I^+ \cdots Ag^+$  contact can also be described as new intermolecular interaction, now referred to as a Nucleophilic Iodonium Interaction (NII),<sup>72</sup> which involves the iodine(I) center acting as a nucleophile toward an appropriate electrophile, which in all instances reported to date has been a  $Ag^+$  metal center of a 4- or 2-coordinate complex. Defining this interaction is troublesome despite the visual similarities to  $Ag^+ \cdots Ag^+$  argentophilic interactions frequently observed in the solid-state structures of Ag-complexes. Computational calculations based on the solid-state structures manifesting short  $I^+ \cdots Ag^+$  contacts show that the iodine (I) ions are acting as nucleophiles, with no retrodonation from the silver(I) metal centers, and quite strong  $I^+ \cdots Ag^+$  interaction energies.<sup>47</sup> Due to the elusive nature of this interaction, to date only three examples have been confirmed in the solid-state by X-ray diffraction (Fig. 9), with  $I^+ \cdots Ag^+$  distances of 3.5184(7) Å,<sup>72</sup> 3.4608(3) Å,<sup>47</sup> and the current shortest of 3.4043(4) Å,<sup>71</sup> which are clearly shorter than the sum of the van der Waals radii of an iodine and a silver atom (3.70 Å).

The NII solid-state complexes can be isolated from the straightforward dissolution of compatible pairs of 2-coordinate  $[L-I-L]^+$  and  $[L-Ag-L]^+$  complexes in a 1:1 ratio despite the fast ligand exchange in solution.<sup>72</sup> Bipyridine-based 3-coordinate silver(I)  $[bpy-Ag-L]^+$  complexes (Fig. 10) can also be used to create NIIs as the resulting 4-coordinate Ag-complexes  $[bpy-Ag-bpy]^+$  are unreactive toward elemental iodine, and the  $I^+$  only permits a linear 2-coordinate geometry.<sup>47,71</sup>



**Fig. 9** The three solid-state examples of Nucleophilic Iodine(I) Interactions (NIIs, represented by dashed red lines) in chronological order (all distances in Å; counter-ions omitted for clarity; bidentate ligands simplified).<sup>47,71,72</sup>



**Fig. 10** The synthetic routes to prepare NII complexes via 2- or 3-coordinate silver(I) complexes.<sup>71,72</sup>

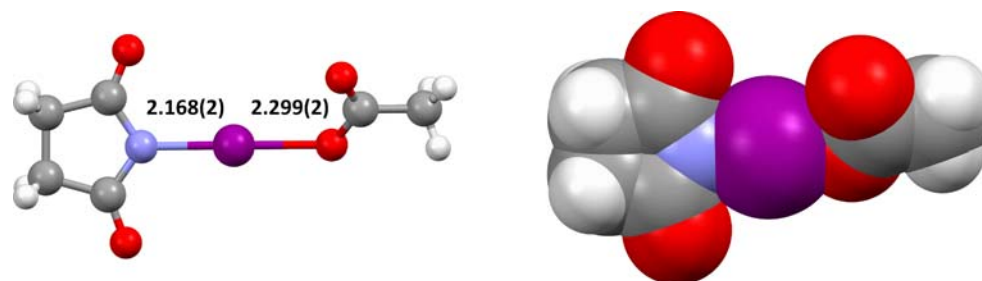
### 1.12.3 Other halogen(I) ion complexes

#### 1.12.3.1 Anionic [N–I–O]<sup>−</sup> complexes

A small number of N–I–O XB complexes have been hitherto reported in solid-state. Most of the complexes are neutral, though one structure consists of *N*-iodosuccinimide-acetate anion with tetrabutyl ammonium as the counter-cation. It should be noted that the formally neutral N–I–O compounds will be left out from this discussion. Guzmán Santiago et al.<sup>73</sup> reported the structure [Bu<sub>4</sub>N][C<sub>4</sub>H<sub>4</sub>O<sub>2</sub>N]I(OCOCH<sub>3</sub>), which was obtained from the reaction of *N*-iodosuccinimide with tetrabutylammonium acetate (Fig. 11). The N–I–O angle with *ca.* 174° and N⋯O distance with *ca.* 4.46 Å are similar to the neutral hypoiodites reported by Hartl and Hedrich,<sup>74,75,76</sup> however, the distances are reversed with N–I shorter than the I–O bond. Similar behavior has been observed for the structures of *N*-iodosaccharin monohydrate and *N*-iodosaccharin tetrahydrofuran solvate.<sup>77</sup> The solvates are more weakly bound to NISac resulting in a longer N⋯O (4.538(3), 4.584(3) Å) and I–O (2.443(4), 2.512(2) Å) distance. The N–I bond lengths are in both structures *ca.* 2.08 Å with almost linear N–I–O geometry (*ca.* 178°).

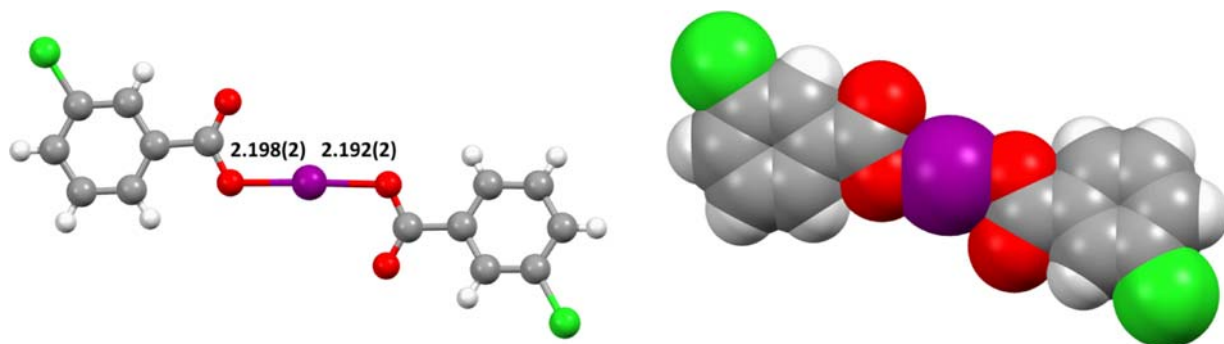
#### 1.12.3.2 Anionic [O–I–O]<sup>−</sup> complexes

Solid-state structures of the corresponding O-acceptor [O–I–O] XB complexes have been reported much later than the previously described N–I–O complexes. In 2015, Martínez and Muñoz have used [Bu<sub>4</sub>N][bis(*m*-chlorobenzoate)iodine(I)] as iodine reagent in organic synthesis (Fig. 12).<sup>78</sup> It has been synthesized from the commercially available hypervalent reagent PhI(*m*CBA)<sub>2</sub> and tetrabutylammonium iodide in chloroform. The I–O distance in the homoleptic [bis(*m*CBA)I]<sup>−</sup> core is *ca.* 2.195 Å (comparable to the neutral N–I–O hypoiodites)<sup>74,75</sup> with an O⋯O distance of 4.390(3) Å and an almost linear coordination geometry (178.24(9)°). Several other anionic dioxiodane complexes, [R–COO–I–OOC–R]<sup>−</sup>, using different benzoate derivatives were reported later by Muñoz et al.<sup>79</sup>



**Fig. 11** The solid-state structure of the first reported example of an anionic O–I–N complex (left; all distances in Å), and its respective spacefill representation (right) (second crystallographic independent O–I–N complex and counter-ions omitted for clarity).<sup>73</sup>



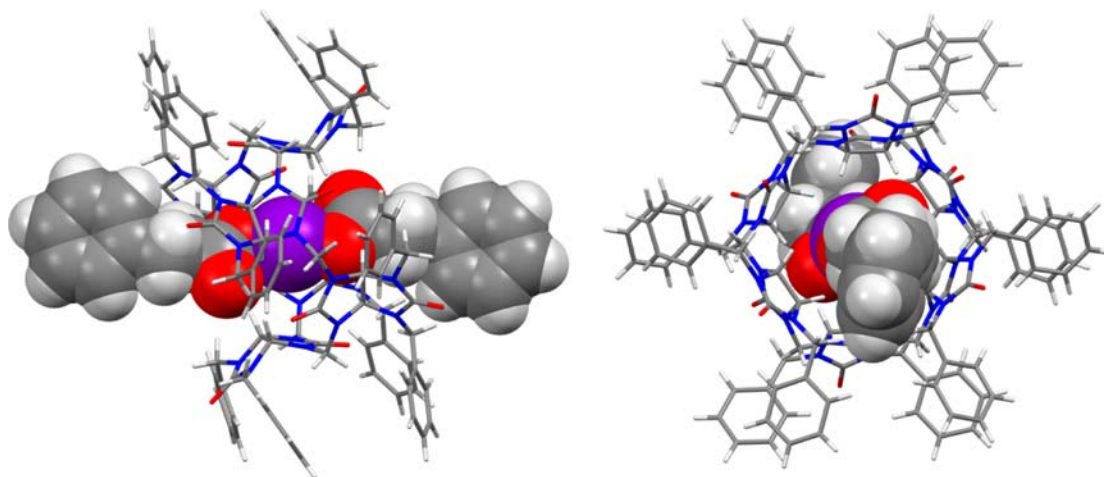


**Fig. 12** Ball-and-stick model of the anionic O–I–O complex  $[\text{Bu}_4\text{N}][\text{I}(\text{mCBA})_2]$  (left, all distances in Å) and its respective spacefill representation (right; counter-ion omitted for clarity).<sup>78</sup>

Recently, those  $[\text{bis}(\text{acyloxy})\text{iodine}(\text{I})]^-$  anions have been used for preparation of interlocked molecules with macrocyclic bambusuril anion receptors (Fig. 13).<sup>80</sup> The bond lengths and angles of the O–I–O complexes are similar to the earlier described  $[\text{Bu}_4\text{N}][\text{I}(\text{mCBA})_2]$ .

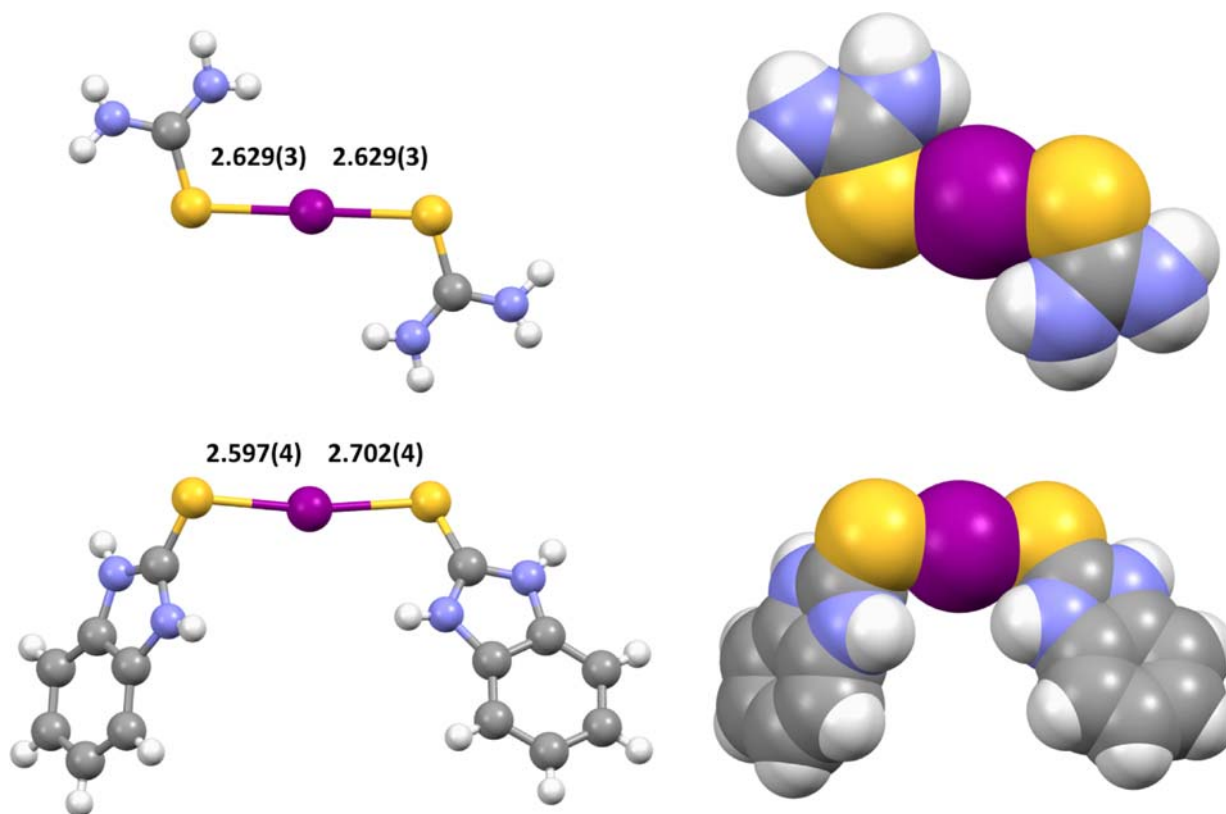
### 1.12.3.3 Cationic $[\text{S}-\text{X}-\text{S}]^+$ complexes

Lin and Hope reported the first X-ray structure of  $[\text{S}-\text{X}-\text{S}]^+$  systems.<sup>81</sup> The compound  $[\text{bis}(\text{SC}(\text{NH}_2)_2)\text{I}]^+\text{I}^-$  was formed from an equimolar reaction of thiourea and iodine in methylene chloride. The S–I bond length is 2.629(3) Å with an  $\text{S}\cdots\text{S}$  distance of 5.258(5) Å. A search in the Cambridge Structural Database (CSD) resulted in 13 more hits.<sup>82–91</sup> Using different S-containing ligands or having different counter ions (mostly polyiodides) in the structure can slightly change the coordination geometries of those  $[\text{S}-\text{X}-\text{S}]^+$  systems. The biggest deviation from  $[\text{bis}(\text{SC}(\text{NH}_2)_2)\text{I}]\text{I}$  has been found in  $[\text{bis}(\text{MBZIM})\text{I}]\text{I}_3 \cdot [\text{bis}(\text{MBZIM})\text{I}]$  (MBZIM = *N*-methylbenzothiazole-2-thione; Fig. 14, bottom).<sup>86</sup> The structure comprises two components: one molecular diiodine adduct and one ionic adduct. The structure of the neutral diiodine adduct consists of a thione ligand bonded to one of the iodine atoms through sulfur with an S–I distance of 2.670(4) Å. The I–I bond distance is 2.887(2) Å, which is elongated (compared to uncoordinated I–I: ca. 2.73 Å) owing to the formation of the S–I bond. The structure of the ionic adduct comprises two residues: one cationic complex containing the linear  $[\text{S}-\text{I}-\text{S}]^+$  linkage, and a  $\text{I}_3^-$  counter-anion. The S–I–S interactions are asymmetric with one S–I distance clearly shorter than the other one with an angle of 171.33(12)° and a  $\text{S}\cdots\text{S}$  distance of 5.283(5) Å. To the best of our knowledge, these bond distances represent the shortest and longest as well as the largest deviation from linearity among all S–X–S compounds.



**Fig. 13** Side and top view of the X-ray structure of an interlocked system (solvent molecules, counter-ions and atom sites of disorder with minor occupancies omitted for clarity).<sup>80</sup>





**Fig. 14** Comparison of two  $[S-I-S]^+$  complexes:  $\{I[SC(NH_2)_2]_2\}I$  (top),<sup>81</sup>  $\{[(MBZIM)_2]I_3\} \cdot [(MBZIM) \cdot I_2]$  (bottom),<sup>86</sup> and their respective spacefill representations (right; all distances in Å, counter-ions and non S-I-S complexes omitted for clarity).

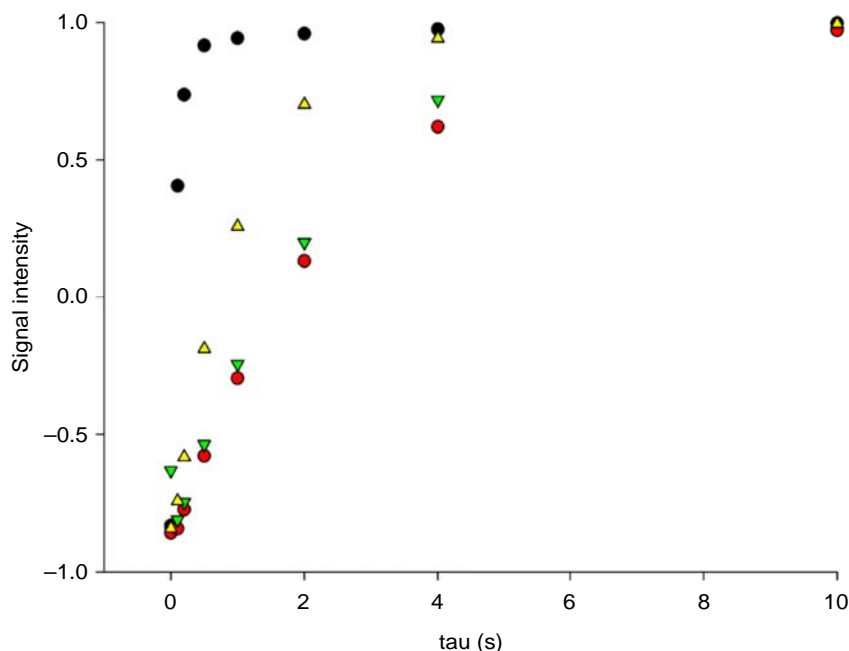
#### 1.12.4 Halogen(I) ion complexes in solution

The halogen bonds of halogen(I) ions are among the strongest known secondary interactions,<sup>29</sup> whose observation has triggered investigations toward understanding their properties. These fundamental studies began in 2010 and have primarily been carried out by solution spectroscopic techniques, and subsequently corroborated by computational calculations.<sup>41,92</sup>

The smallest halogen, fluorine(I), has been shown to prefer conventional halogen bonds,  $L^+ - F \cdots L$ , with a distinct short and strong covalent L-F bond and a second, weaker and longer,  $L \cdots F$  halogen bond.<sup>39</sup> The positive charge of the complex is located on the ligand,  $L$ , covalently bound to fluorine. This bond resembles conventional halogen bonds, and thus acts through a  $\sigma$ -hole. Fluorine-centered halogen bonds are uncommon and only form with a fluorine that is directly attached to a strongly electron withdrawing functionality, such as a pyridine nitrogen that augments its  $\sigma$ -hole. The existence of the complex has been demonstrated by diffusion NMR spectroscopy through detection of a slower diffusion rate for the *N*-fluoropyridinium ion in the presence of pyridine ( $D = 41 \times 10^{-10} \text{ m}^2/\text{s}$ ), than in its absence ( $D = 120 \times 10^{-10} \text{ m}^2/\text{s}$ ), with the rate becoming more similar to that of pyridine ( $D = 46 \times 10^{-10} \text{ m}^2/\text{s}$ ).<sup>39</sup> The complex is stable at  $-35^\circ\text{C}$  in solution, but quickly decomposes at ambient temperature.<sup>39</sup> The protonated form of this complex, *N*-fluoropyridinium pyridinium tetrafluoroborate trifluorohydroxyborate, has been marketed under the name 1-fluoropyridinium heptafluorodiborate pyridine as a fluorinating agent for synthetic chemistry. It is stabilized by protonation of the pyridine not covalently bound to fluorine, which is thereby deactivated for electrophilic fluorine(I) approach.

The corresponding  $[bis(\text{pyridine})\text{chlorine(I)}]^+$  complex was stable at  $-80^\circ\text{C}$  in a dichloromethane solution,<sup>39</sup> allowing the confirmation of its existence by relaxation studies (Fig. 15). Hence the protons close to the chlorine(I) ion were observed to relax quickly ( $T_1 = 0.08 \text{ s}$ ), much quicker than the static pyridine and  $L_1$ -triflate ( $T_1 = 1.61 \text{ s}$  and  $1.49 \text{ s}$ , respectively) or the dynamic  $[bis(\text{pyridine})\text{proton complex}]^+$  ( $T_1 = 0.90 \text{ s}$ ). As a consequence of rapid relaxation, only  $^1\text{H}$ ,  $^{13}\text{C}$  but not  $^1\text{H}$ ,  $^{15}\text{N}$  HMBC could be observed for this complex.

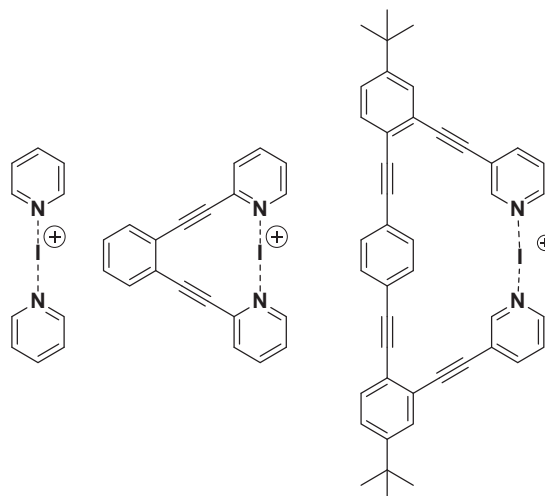
Iodine(I) and bromine(I) form 3c-4e bonds,  $[L \cdots X \cdots L]^+$ , that behave comparably to chlorine(I) complexes in solution. These complexes are stable as dichloromethane and acetonitrile solutions at ambient temperature, with the bromine(I) complexes being significantly more moisture sensitive.<sup>41,92</sup> These complexes are centrosymmetric, as shown by isotropic perturbation of equilibrium measurements using NMR,<sup>35,41,92</sup> and retain their symmetry also in the solid-state.<sup>35</sup> While they are stable in solution, they are in a dynamic equilibrium involving quick association – dissociation equilibria.<sup>92</sup> The properties of such complexes have initially been studied using monodentate ligands, though this is not recommended as the dynamic equilibrium may result in data that is easy to



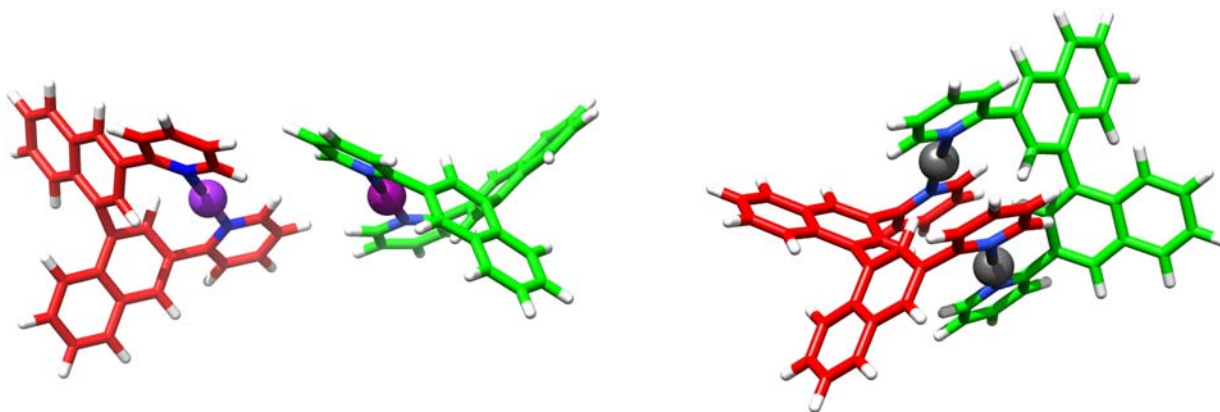
**Fig. 15** The longitudinal spin–lattice ( $T_1$ ) relaxation rate of H-2 as measured by inversion-recovery experiment at  $-80^\circ\text{C}$  in  $\text{CD}_2\text{Cl}_2$  solution and visualized by plotting signal intensity vs. time. The data points of *bis*(pyridine)chlorine(I) triflate are in black ( $T_1 = 0.08$  s), those of *bis*(pyridine)silver(I) triflate in green ( $T_1 = 1.49$  s), those of pyridine in red ( $T_1 = 1.61$  s), and those of the  $[\textit{bis}(\textit{pyridine})\textit{proton}]^+$  complex in yellow ( $T_1 = 0.90$  s).<sup>39</sup>

misinterpret. The investigation of analogous bidentate systems, such as those shown in Fig. 16 is recommended as these are entropically favored and suffer less from chemical exchange processes.<sup>29,91,93</sup>

Besides the fundamental nature of the interaction (*vide supra*), the factors influencing the symmetry of these 3-center, 4-electron bonds have been initially studied. Solvent polarity has been shown to be unable to desymmetrize the centrosymmetric complex, however, does influence counter-ion coordination that in turn is expected to, at least partly, explain the solvent dependent reactivity of  $[\textit{bis}(\textit{pyridine})\textit{halogen}(\text{I})]^+$  complexes, such as Barluenga's reagent.<sup>46</sup> Counter-ions have been shown to pack asymmetrically in the solid-state, but not have any desymmetrizing effect on the  $[\text{N}–\text{X}–\text{N}]^+$  bond itself.<sup>43</sup> An important difference of the behavior of



**Fig. 16**  $[\textit{Bis}(\textit{pyridine})\textit{iodine}]^+$  and geometrically restrained  $[\textit{1,2-bis}(\textit{pyridine-2-ylethynyl})\textit{benzene}]^+$  complexes were used as model systems for assessment of the nature and geometry on the  $[\text{N}–\text{I}–\text{N}]^+$  halogen bond. The *bis*(pyridine)-type complex (left) is involved into dynamic association-dissociation equilibrium, resulting in ligand scrambling. The 1,2-diethynylbenzene backbone of the complex in the middle is entropically favored and does not suffer from ligand scrambling. It inhibits pyridine rotation around the N–I–N axis and therefore imposes slight strain in the N–I bonds, though still allowing a geometrically optimal  $[\text{N}–\text{I}–\text{N}]^+$  distance. The flexible analogue on the right does not suffer from strain, though remains to provide the entropic advantage that prevents ligand scrambling.<sup>92,93,95</sup>



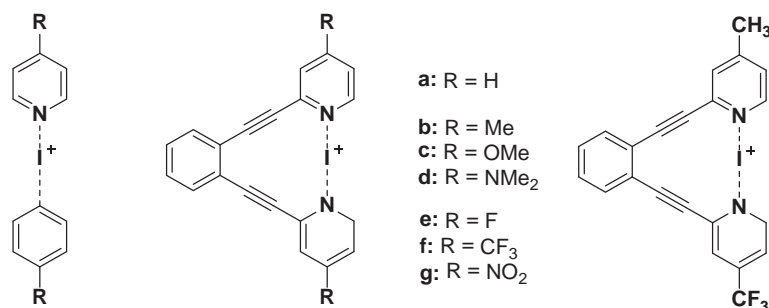
**Fig. 17** The halogen bond complex of the bidentate ligand 3,3'-di(pyridin-2-yl)-1,1'-binaphthalene (left) and the analogous coordinative bond complex of silver(I) (right) prefer different geometries in solution and in the solid-state. Diffusion NMR shows a counter-ion dependence for the structure of the silver(I) complex, whereas the geometry of the iodine(I) complex appears unaffected.<sup>45</sup>

halogen(I) to silver(I) complexes has been observed with silver(I) preferring to coordinate anions and form argentophilic interactions, which the  $[N-X-N]^+$  complexes are not capable of due to the lack of empty orbitals that could act as a Lewis acid. This difference has been further corroborated by studies of bidentate systems that allow the formation of both monomeric and dimeric complexes (Fig. 17).<sup>45</sup> Diffusion NMR studies, supported by computational calculations and X-ray crystallography, indicated that silver(I) forms dimers or polymers with the 3,3'-di(pyridin-2-yl)-1,1'-binaphthalene ligand, whereas iodine(I) prefers to form monomeric ones.

The electron density of the Lewis base has been demonstrated to not have a major influence on the geometry of the  $[N-I-N]^+$  complexes, but it does on the strength of the bonds when the electron density is increased or decreased in a symmetric way,<sup>52</sup> that is on both coordinating Lewis bases (Fig. 18). The more electron poor systems show weaker halogen bonding, and accordingly higher reactivity in halogen(I) transfer reactions.

Asymmetric variation of the electron density induces asymmetric halogen bonds as confirmed in solution by NMR spectroscopy,<sup>93</sup> and in the solid-state by X-ray crystallography.<sup>65</sup> The asymmetry of the bond is indicated by the magnitude of the coordination shifts of the nitrogen atoms involved in the bond formation (Table 1). Hence, the  $\Delta\delta^{15}N_{\text{coord}}$  of the nitrogen atoms of the asymmetric system, possessing a methyl and a trifluoromethyl substituted pyridine, are  $\sim 10$  ppm larger vs smaller when compared to the systems possessing two  $\text{CH}_3$  or two  $\text{CF}_3$  groups on their pyridine rings, respectively. This suggests that the  $\delta^{15}N$  of the nitrogen atoms of the asymmetric complex differ not only because of their different electron densities, but also due to the formation of  $N-I$  bonds of different strength and length. The  $\Delta\delta^{15}N_{\text{coord}}$ s indicate that the iodine(I) of this complex is closer to the more electron-rich nitrogen of the 4- $\text{CH}_3$  substituted pyridine ring as compared to that of the less electron-rich, 4- $\text{CF}_3$  substituted pyridine. These experimental findings were corroborated by computational calculations. A recent follow up study confirmed these observations by X-ray crystallographic analysis of analogous asymmetric bis(pyridine) complexes (Fig. 19).<sup>65</sup>

As  $[\text{bis}(\text{pyridine})\text{halogen}(\text{I})]^+$  complexes suffer from ligand scrambling, the backbone of bidentate ligands play an important role with respect to the geometry and stability of the complexes. The backbone of the  $[1,2\text{-bis}((\text{pyridine-2-ylethynyl})\text{benzene})\text{iodine}]^+$  complexes (Fig. 20) introduces some strain, slightly weakening the  $[N-X-N]^+$  halogen bond yet allowing comparable  $N-X$  bond lengths to that observed for  $[\text{bis}(\text{pyridine})\text{halogen}(\text{I})]^+$  analogues.<sup>91</sup> The nitrogen-nitrogen distance plays a pivotal



**Fig. 18** A systematic alteration of the electron density of the  $[N-I-N]^+$  halogen bond was achieved by variation of the substituents of pyridines, resulting in complexes with an increasing electron density in the order  $\text{NO}_2 < \text{CF}_3 < \text{H} < \text{F} < \text{Me} < \text{OMe} < \text{NMe}_2$ .<sup>52</sup> The symmetric alteration of the electron density did not influence the geometry, but did influence the strength of the  $[N-I-N]^+$  halogen bonds. An asymmetric Lewis base, in contrast, induces asymmetry in the  $[N-I-N]^+$  halogen bonds.<sup>94</sup>

**Table 1** The  $^{15}\text{N}$  NMR chemical shifts and coordination shifts (ppm) of the iodine(I) complexes of symmetric and asymmetric  $[\text{N}-\text{I}-\text{N}]^+$  complexes, and those of the corresponding Lewis bases (all values in ppm).<sup>93</sup>

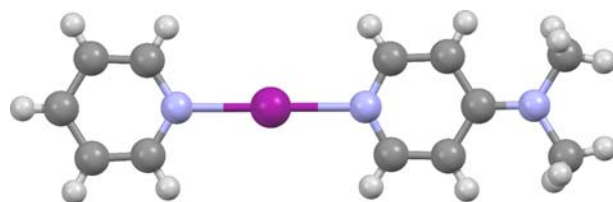
Structure	R/R'	$\delta^{15}\text{N}_{\text{compl}}$	$\delta^{15}\text{N}_{\text{lig}}$	$\Delta\delta^{15}\text{N}_{\text{coord}}$
	$\text{CH}_3/\text{CH}_3$	-170.3	-69.2	-101.1
	$\text{CH}_3$ $\text{CH}_3$	-183.1	-71.8	-111.3
	$\text{CH}_3$ $\text{CF}_3$	-145.1	-53.7	-91.4
	$\text{CF}_3/\text{CF}_3^{\text{a}}$	-156.7	-53.4	-103.3

role for the stability of such complexes and has been shown to be optimal at 4.5 Å for the  $[\text{N}-\text{I}-\text{N}]^+$  bonds, with ligands enforcing a nitrogen–nitrogen distance larger than 4.8 Å being expected to be asymmetric.<sup>94</sup> In practice, the latter turned out to be an unstable arrangement that prefers to rearrange into a dimeric species. The 3,3'-di(pyridin-2-yl)-1,1'-binaphthalene offering  $r_{\text{NN}} \sim 4.7$  Å (Fig. 17) is just on the limit to allow formation of stable  $[\text{N}-\text{I}-\text{N}]^+$  complexes.<sup>45</sup> A non-restrained *bis*(pyridine) ligand has recently been introduced (Fig. 16), which provides entropic advantages without enforcing a too short or too long nitrogen–nitrogen distance that could weaken the complex.<sup>95</sup> The similar coordination strength of iodine(I) to this ligand to that of pyridine in a *bis*(pyridine) halogen(I)<sup>+</sup> complex has been confirmed by its  $^{15}\text{N}$  NMR coordination shift (Table 2).

A photoswitchable analogue possessing an enediyne backbone has also been studied recently (Fig. 20). In contrast to a metal coordination bond, an  $[\text{N}-\text{I}-\text{N}]^+$  bond allows *cis* to *trans* photoisomerization, even if at a lower rate than the ligand itself would photoisomerize at. The *trans* enediyne complex of iodine(I) is unstable and quickly converts into a protonated complex, making the photoisomerization monodirectional.<sup>46</sup>

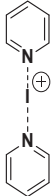
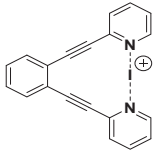
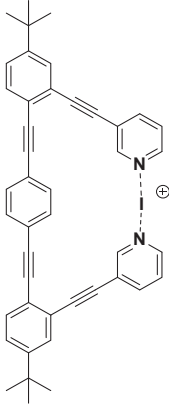
### 1.12.5 Outlook

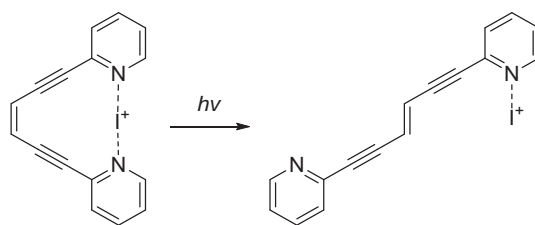
Halogen(I) ion complexes offer a versatile family of halogen-bonded complexes that still capture the attention of researchers to this day. The special feature of halogen(I) complexes is the 3c-4e  $[\text{L}-\text{X}-\text{L}]^+$  bond (X = halogen and L = Lewis base). The 3c-4e bond



**Fig. 19** The solid-state structure of an unrestrained asymmetric iodine(I)  $[\text{L}_1-\text{I}-\text{L}_2]^+$  complex (counter-ion omitted for clarity).<sup>65</sup>

**Table 2** The  $^{15}\text{N}$  Chemical shift ( $\delta^{15}\text{N}_{\text{complex}}$ ) and coordination shift ( $\Delta\delta^{15}\text{N}_{\text{coord}}$ ) of the complexes shown in Fig. 16, and of the corresponding free ligands ( $\delta^{15}\text{N}_{\text{ligand}}$ ) (all values in ppm).<sup>95</sup>

Structure	$\delta^{15}\text{N}_{\text{complex}}$	$\delta^{15}\text{N}_{\text{ligand}}$	$\Delta\delta^{15}\text{N}_{\text{coord}}$
	-175.1	-67.0	-108.1
	-163.6	-64.5	-99.1
	-173.6	-65.5	-108.1



**Fig. 20** An enediyne ligand was used to evaluate whether halogen bonding can modulate photoisomerization.<sup>46</sup>

between the halogen and the Lewis bases has two sides: it simultaneously possesses a strong halogen bond, while at the same time still being chemically reactive, such that the complexes eagerly transfer their  $X^+$  cation, thus making them useful as halogenating reagents. The most iconic halogen(I) complex,  $[\text{bis}(\text{pyridine})\text{iodine}(\text{I})]\text{BF}_4$  (Barluenga's reagent), enjoys widespread use as a mild iodination reagent and oxidant in organic syntheses. The halogen(I) complexes form a special family of reactive halogen-bonded complexes, and even to date remain scarcely studied in comparison to other non-covalent interactions. Even though asymmetric halogen(I) ion complexes have been reported in the solid-state, if unrestrained they are prone to rapid ligand exchange. Through careful ligand design, restrained asymmetric mono- or multi-halogen(I) ion complexes have already been reported, though their reactivities as reagents are yet to be explored. Interesting future targets might include halogen(I) ions that are part of optically pure complexes, which might show unprecedented enantioselectivities and reactivities when implemented in organic transformations. Even farther in the future are the halogen(I) ion rotaxanes and catenanes, ambitiously built upon already known supramolecular advancements incorporating halogen(I) ions, which could act as recyclable reagents due to the fact that the  $\text{I}^+$  binding of the Lewis bases are spatially tied together, and therefore such species cannot dissociate as readily (if at all), as observed for the discrete halogen(I) complexes that dominate the known literature at present. The slew of advancements made in recent years in the field of



halogen(I) chemistry is truly remarkable, both in their scope and impact, highlighting that more extensive expeditions should follow these previous forays and continue to reveal as-of-yet unimagined treasures.

## References

- Cavallo, G.; Metrangolo, P.; Milani, R.; Pilati, T.; Priimagi, A.; Resnati, G.; Terraneo, G. *Chem. Rev.* **2016**, *116* (4), 2478–2601.
- Gilday, L. C.; Robinson, S. W.; Barendt, T. A.; Langton, M. J.; Mullaney, B. R.; Beer, P. D. *Chem. Rev.* **2015**, *115* (15), 7118–7195.
- Kolář, M. H.; Hobza, P. *Chem. Rev.* **2016**, *116* (9), 5155–5187.
- Wang, H.; Wang, W.; Jin, W. J. *Chem. Rev.* **2016**, *116* (9), 5072–5104.
- Desiraju, G. R.; Ho, P. S.; Kloo, L.; Legon, A. C.; Marquardt, R.; Metrangolo, P.; Politzer, P.; Resnati, G.; Rissanen, K. *Pure Appl. Chem.* **2013**, *85* (8), 1711–1713.
- Turunen, L.; Hansen, L. P.; Erdélyi, M. *Chem. Rec.* **2021**, *21* (5), 1252–1257.
- Rosokha, S. V.; Neretin, I. S.; Rosokha, T. Y.; Hecht, J.; Kochi, J. K. *Heteroat. Chem.* **2006**, *17* (5), 449–459.
- Wolters, L. P.; Bickelhaupt, F. M. *ChemistryOpen* **2012**, *1* (2), 96–105.
- Thirman, J.; Engelage, E.; Huber, S. M.; Head-Gordon, M. *Phys. Chem. Chem. Phys.* **2018**, *20* (2), 905–915.
- Inscoc, B.; Rathnayake, H.; Mo, Y. *J. Phys. Chem. A* **2021**, *125* (14), 2944–2953.
- Huber, S. M.; Jimenez-Izal, E.; Ugalde, J. M.; Infante, I. *Chem. Commun.* **2012**, *48* (62), 7708–7710.
- Rosokha, S. V.; Stern, C. L.; Ritzert, J. T. *Chem. – A Eur. J.* **2013**, *19* (27), 8774–8788.
- Wang, C.; Danovich, D.; Mo, Y.; Shaik, S. *J. Chem. Theory Comput.* **2014**, *10* (9), 3726–3737.
- Wolters, L. P.; Schyman, P.; Pavan, M. J.; Jorgensen, W. L.; Bickelhaupt, F. M.; Kozuch, S. *WIREs Comput. Mol. Sci.* **2014**, *4* (6), 523–540.
- Wolters, L. P.; Smits, N. W. G.; Guerra, C. F. *Phys. Chem. Chem. Phys.* **2015**, *17* (3), 1585–1592.
- Robinson, S. W.; Mustoe, C. L.; White, N. G.; Brown, A.; Thompson, A. L.; Kennepohl, P.; Beer, P. D. *J. Am. Chem. Soc.* **2015**, *137* (1), 499–507.
- Oliveira, V.; Kraka, E.; Cremer, D. *Phys. Chem. Chem. Phys.* **2016**, *18* (48), 33031–33046.
- Oliveira, V.; Kraka, E.; Cremer, D. *Inorg. Chem.* **2017**, *56* (1), 488–502.
- Engelage, E.; Reinhard, D.; Huber, S. M. *Chem. – A Eur. J.* **2020**, *26* (17), 3843–3861.
- Huber, S. M.; Scanlon, J. D.; Jimenez-Izal, E.; Ugalde, J. M.; Infante, I. *Phys. Chem. Chem. Phys.* **2013**, *15* (25), 10350–10357.
- Rissanen, K. *CrystEngComm* **2008**, *10* (9), 1107–1113.
- Beyeh, N. K.; Pan, F.; Rissanen, K. *Angew. Chem. Int. Ed.* **2015**, *54* (25), 7303–7307.
- Dumele, O.; Trapp, N.; Diederich, F. *Angew. Chem. Int. Ed.* **2015**, *54* (42), 12339–12344.
- Arunan, E.; Desiraju, G. R.; Klein, R. A.; Sadlej, J.; Scheiner, S.; Alkorta, I.; Clary, D. C.; Crabtree, R. H.; Dannenberg, J. J.; Hobza, P.; Kjaergaard, H. G.; Legon, A. C.; Mennucci, B.; Nesbitt, D. J. *Pure Appl. Chem.* **2011**, *83* (8), 1619–1636.
- Trofi, R. W.; Mäkelä, T.; Topić, F.; Valkonen, A.; Raatikainen, K.; Rissanen, K. *European J. Org. Chem.* **2013**, *2013* (9), 1617–1637.
- Raatikainen, K.; Rissanen, K. *Chem. Sci.* **2012**, *3* (4), 1235–1239.
- Puttreddy, R.; Jurček, O.; Bhowmik, S.; Mäkelä, T.; Rissanen, K. *Chem. Commun.* **2016**, *52* (11), 2338–2341.
- Raatikainen, K.; Rissanen, K. *CrystEngComm* **2011**, *13* (23), 6972–6977.
- Turunen, L.; Erdélyi, M. *Chem. Soc. Rev.* **2020**, *49* (9), 2688–2700.
- Reiersølmoen, A. C.; Battaglia, S.; Øien-Ødegaard, S.; Gupta, A. K.; Fiksdahl, A.; Lindh, R.; Erdélyi, M. *Chem. Sci.* **2020**, *11* (30), 7979–7990.
- Hassel, O.; Hope, H. *Acta Chem. Scand.* **1961**, *15*, 407–416.
- Creighton, J. A.; Haque, I.; Wood, J. L. *Chem. Commun.* **1966**, (8), 229.
- Creighton, J. A.; Haque, I.; Wood, J. L. *Chem. Commun.* **1966**, (23), 892.
- Haque, I.; Wood, J. L. *J. Mol. Struct.* **1968**, *2* (3), 217–238.
- Hakkert, S. B.; Erdélyi, M. *J. Phys. Org. Chem.* **2015**, *28* (3), 226–233.
- Barluenga, J.; Trincado, M.; Rubio, E.; González, J. M. *Angew. Chem. Int. Ed.* **2003**, *42* (21), 2406–2409.
- Chalker, J. M.; Thompson, A. L.; Davis, B. G.; Zaware, N.; Wipf, P. *Organic Syntheses* **2010**, 288–298.
- Carlsson, A.-C. C.; Uhrborn, M.; Karim, A.; Brath, U.; Gräfenstein, J.; Erdélyi, M. *CrystEngComm* **2013**, *15* (16), 3087–3092.
- Karim, A.; Reitti, M.; Carlsson, A.-C. C.; Gräfenstein, J.; Erdélyi, M. *Chem. Sci.* **2014**, *5* (8), 3226–3233.
- Vanderkooy, A.; Gupta, A. K.; Földes, T.; Lindblad, S.; Orthaber, A.; Pápai, I.; Erdélyi, M. *Angew. Chem. Int. Ed.* **2019**, *58* (27), 9012–9016.
- Carlsson, A.-C. C.; Gräfenstein, J.; Laurila, J. L.; Bergquist, J.; Erdélyi, M. *Chem. Commun.* **2012**, *48* (10), 1458–1460.
- Carlsson, A.-C. C.; Veiga, A. X.; Erdélyi, M. *Top. Curr. Chem.* **2015**, 49–76. Springer International Publishing.
- Bedin, M.; Karim, A.; Reitti, M.; Carlsson, A.-C. C.; Topić, F.; Cetina, M.; Pan, F.; Havel, V.; Al-Ameri, F.; Sindelar, V.; Rissanen, K.; Gräfenstein, J.; Erdélyi, M. *Chem. Sci.* **2015**, *6* (7), 3746–3756.
- Lindblad, S.; Németh, F. B.; Földes, T.; Vanderkooy, A.; Pápai, I.; Erdélyi, M. *Chem. Commun.* **2020**, *56* (67), 9671–9674.
- Turunen, L.; Németh, F. B.; Decato, D. A.; Pápai, I.; Berryman, O. B.; Erdélyi, M. *Bull. Chem. Soc. Jpn.* **2021**, *94* (1), 191–196.
- Lindblad, S.; Sethio, D.; Berryman, O. B.; Erdélyi, M. *Chem. Commun.* **2021**, *57* (51), 6261–6263.
- Yu, S.; Kumar, P.; Ward, J. S.; Frontera, A.; Rissanen, K. *Chem* **2021**, *7* (4), 948–958.
- Barluenga, J.; González, J. M.; Garcia-Martin, M. A.; Campos, P. J.; Asensio, G. J. *Chem. Soc., Chem. Commun.* (14), 1016–1017.
- Ezquerro, J.; Pedregal, C.; Lamas, C.; Barluenga, J.; Pérez, M.; Garcia-Martin, M. A.; González, J. M. *J. Org. Chem.* **1996**, *61* (17), 5804–5812.
- Espuña, G.; Arsequell, G.; Valencia, G.; Barluenga, J.; Pérez, M.; González, J. M. *Chem. Commun.* (14), 1307–1308.
- Groom, C. R.; Bruno, I. J.; Lightfoot, M. P.; Ward, S. C. *Acta Crystallogr. Sect. B* **2016**, *72* (2), 171–179.
- Carlsson, A.-C. C.; Mehmeti, K.; Uhrborn, M.; Karim, A.; Bedin, M.; Puttreddy, R.; Kleinmaier, R.; Neverov, A. A.; Nekouieishahraki, B.; Gräfenstein, J.; Rissanen, K.; Erdélyi, M. *J. Am. Chem. Soc.* **2016**, *138* (31), 9853–9863.
- Kukkonen, E.; Malinen, H.; Haukka, M.; Konu, J. *Cryst. Growth Des.* **2019**, *19* (4), 2434–2445.
- Morgan, L. C. F.; Kim, Y.; Blandy, J. N.; Murray, C. A.; Christensen, K. E.; Thompson, A. L. *Chem. Commun.* **2018**, *54* (70), 9849–9852.
- Eraković, M.; Cincić, D.; Molčanov, K.; Stilić, V. *Angew. Chem. Int. Ed.* **2019**, *58* (44), 15702–15706.
- Kim, Y.; Mckinley, E. J.; Christensen, K. E.; Rees, N. H.; Thompson, A. L. *Cryst. Growth Des.* **2014**, *14* (12), 6294–6301.
- Alcock, N. W.; Robertson, G. B. *J. Chem. Soc. Dalton Trans.* **1975**, (23), 2483–2486.
- Blair, L. K.; Parris, K. D.; Hii, P.; Sen; Brock, C. P. *J. Am. Chem. Soc.* **1983**, *105* (11), 3649–3653.
- Brock, C. P.; Fu, Y.; Blair, L. K.; Chen, P.; Lovell, M. *Acta Crystallogr. Sect. C* **1988**, *44* (9), 1582–1585.
- Ward, J. S.; Frontera, A.; Rissanen, K. *Dalton Trans.* **2021**, *50* (24), 8297–8301.
- Wang, Y.-M.; Wu, J.; Hoong, C.; Rauniyar, V.; Toste, F. D. *J. Am. Chem. Soc.* **2012**, *134* (31), 12928–12931.
- Weinberger, C.; Hines, R.; Zeller, M.; Rosokha, S. V. *Chem. Commun.* **2018**, *54* (58), 8060–8063.

63. Bowmaker, G. A.; Hannan, S. F. *Aust. J. Chem.* **1971**, *24* (11), 2237–2248.
64. Pritzkow, H. *Acta Crystallogr. Sect. B* **1975**, *31* (5), 1505–1506.
65. Ward, J. S.; Fiorini, G.; Frontera, A.; Rissanen, K. *Chem. Commun.* **2020**, *56* (60), 8428–8431.
66. Turunen, L.; Warzok, U.; Puttreddy, R.; Beyeh, N. K.; Schalley, C. A.; Rissanen, K. *Angew. Chem. Int. Ed.* **2016**, *55* (45), 14033–14036.
67. Turunen, L.; Peuronen, A.; Forsblom, S.; Kalenius, E.; Lahtinen, M.; Rissanen, K. *Chem. - A Eur. J.* **2017**, *23* (48), 11714–11718.
68. Northrop, B. H.; Yang, H.-B.; Stang, P. J. *Chem. Commun.* **2008**, 5896–5908.
69. Warzok, U.; Marianski, M.; Hoffmann, W.; Turunen, L.; Rissanen, K.; Pagel, K.; Schalley, C. A. *Chem. Sci.* **2018**, *9* (44), 8343–8351.
70. Gong, G.; Lv, S.; Han, J.; Xie, F.; Li, Q.; Xia, N.; Zeng, W.; Chen, Y.; Wang, L.; Wang, J.; Chen, S. *Angew. Chem. Int. Ed.* **2021**, *60* (27), 14831–14835.
71. Ward, J. S.; Frontera, A.; Rissanen, K. *Inorg. Chem.* **2021**, *60* (7), 5383–5390.
72. Ward, J. S.; Frontera, A.; Rissanen, K. *Chem. Commun.* **2021**, *57* (41), 5094–5097.
73. Guzmán Santiago, A. J.; Brown, C. A.; Sommer, R. D.; Ison, E. A. *Dalton Trans.* **2020**, *49* (45), 16166–16174.
74. Hartl, H.; Hedrich, M. *Zeitschrift für Naturforsch. B* **1981**, *36b*, 922–928.
75. Yu, S.; Ward, J. S.; Truong, K.-N.; Rissanen, K. *Angew. Chem. Int. Ed.* **2021**, *60* (38), 20739–20743.
76. Kramer, E.; Yu, S.; Ward, J. S.; Rissanen, K. *Dalton Trans.* **2021**, *50* (42), 14990–14993.
77. Dolenc, D.; Modec, B. *New J. Chem.* **2009**, *33* (11), 2344–2349.
78. Martínez, C.; Muñoz, K. *Angew. Chem. Int. Ed.* **2015**, *54* (28), 8287–8291.
79. Muñoz, K.; García, B.; Martínez, C.; Piccinelli, A. *Chem. - A Eur. J.* **2017**, *23* (7), 1539–1545.
80. Kandrnálová, M.; Kokan, Z.; Havel, V.; Nečas, M.; Šindelář, V. *Angew. Chem. Int. Ed.* **2019**, *58* (50), 18182–18185.
81. Lin, G. H.-Y.; Hope, H. *Acta Crystallogr. Sect. B* **1972**, *28* (2), 643–646.
82. Nosco, D. L.; Heeg, M. J.; Glick, M. D.; Elder, R. C.; Deutsch, E. *J. Am. Chem. Soc.* **1980**, *102* (26), 7784–7786.
83. Demartin, F.; Deplano, P.; Devillanova, F. A.; Isaia, F.; Lippolis, V.; Verani, G. *Inorg. Chem.* **1993**, *32* (17), 3694–3699.
84. Boyle, P. D.; Christie, J.; Dyer, T.; Godfrey, S. M.; Howson, I. R.; McArthur, C.; Omar, B.; Pritchard, R. G.; Williams, G. R. *J. Chem. Soc. Dalton Trans.* **2000**, (18), 3106–3112.
85. Daga, V.; Hadjikakou, S. K.; Hadjiladis, N.; Kubicki, M.; dos Santos, J. H. Z.; Butler, I. S. *Eur. J. Inorg. Chem.* **2002**, *2002* (7), 1718–1728.
86. Corban, G. J.; Hadjikakou, S. K.; Hadjiladis, N.; Kubicki, M.; Tieckinck, E. R. T.; Butler, I. S.; Drougas, E.; Kosmas, A. M. *Inorg. Chem.* **2005**, *44* (23), 8617–8627.
87. Tamilselvi, A.; Muges, G. *Bioorg. Med. Chem. Lett.* **2010**, *20* (12), 3692–3697.
88. Chernov'yants, M. S.; Burykin, I. V.; Starikova, Z. A.; Erofeev, N. E. *J. Mol. Struct.* pp 379–382.
89. Koskinen, L.; Hirva, P.; Kalenius, E.; Jääskeläinen, S.; Rissanen, K.; Haukka, M. *CrystEngComm* **2015**, *17* (6), 1231–1236.
90. Londero, A. J. Z.; Pineda, N. R.; Matos, V.; Piquini, P. C.; Abram, U.; Lang, E. S. *J. Organomet. Chem.* **2020**, *929*, 121553.
91. Bol'shakov, O. I.; Yushina, I. D.; Stash, A. I.; Aysin, R. R.; Bartashevich, E. V.; Rakitin, O. A. *Struct. Chem.* **2020**, *31* (5), 1729–1737.
92. Carlsson, A.-C. C.; Gräfenstein, J.; Budnjo, A.; Laurila, J. L.; Bergquist, J.; Karim, A.; Kleinmaier, R.; Brath, U.; Erdélyi, M. *J. Am. Chem. Soc.* **2012**, *134* (12), 5706–5715.
93. von der Heiden, D.; Rissanen, K.; Erdélyi, M. *Chem. Commun.* **2020**, *56* (92), 14431–14434.
94. Lindblad, S.; Mehmeti, K.; Veiga, A. X.; Nekoueiashahraki, B.; Gräfenstein, J.; Erdélyi, M. *J. Am. Chem. Soc.* **2018**, *140* (41), 13503–13513.
95. Lindblad, S.; Boróka Németh, F.; Földes, T.; et al. *Chem. Eur. J.* **2021**, *27*, 13748–13756.

## 1.13 Chalcogen bonding in supramolecular structures, anion recognition, and catalysis

Simon Kolb, Gwyndaf A. Oliver, and Daniel B. Werz, Technische Universität Braunschweig, Institute of Organic Chemistry, Braunschweig, Germany

© 2023 Elsevier Ltd. All rights reserved.

<b>1.13.1</b>	<b>Introduction</b>	<b>602</b>
<b>1.13.2</b>	<b>Chalcogen bonding in the solid state</b>	<b>603</b>
1.13.2.1	Chalcogen-chalcogen interactions	603
1.13.2.1.1	Linear systems with chalcogen centers	603
1.13.2.1.2	Cyclic systems with chalcogen centers	605
1.13.2.1.3	Chalcogens in aromatic systems	610
1.13.2.1.4	Other systems	610
1.13.2.2	Chalcogen-pnictogen interactions	613
1.13.2.2.1	Chalcogenocyanates	613
1.13.2.2.2	Benzochalcogenazoles and benzochalcogenadiazoles	616
1.13.2.3	Chalcogen-halogen interactions	620
1.13.2.4	Other chalcogen interactions	621
1.13.2.4.1	Radicals	622
1.13.2.4.2	Chalcogen-oxygen interactions	623
1.13.2.4.3	Chalcogen-hydrogen interactions	625
<b>1.13.3</b>	<b>Self-assembly by chalcogen interactions</b>	<b>625</b>
1.13.3.1	Capsules	625
1.13.3.2	Polymers and materials	626
<b>1.13.4</b>	<b>Chalcogen-anion coordination</b>	<b>630</b>
1.13.4.1	Anion binding and recognition	630
1.13.4.2	Anion transport	632
1.13.4.3	Other examples of halide coordination	634
<b>1.13.5</b>	<b>Chalcogen bonding in catalysis and synthesis</b>	<b>634</b>
1.13.5.1	Synthesis and structure rigidification by intramolecular chalcogen bonding	634
1.13.5.2	Lewis base catalysis by transient chalcogen bonding interactions	634
1.13.5.3	Catalysis by intermolecular chalcogen bonding	635
1.13.5.4	Isothiourea catalysis	639
1.13.5.5	Special chalcogen interactions in catalysis	641
<b>1.13.6</b>	<b>Theoretical and computational studies</b>	<b>642</b>
1.13.6.1	Definition of interaction energy, choice of basis sets and methods	643
1.13.6.2	Model systems	644
1.13.6.2.1	Interaction energies and potential energy surfaces	644
1.13.6.2.2	Natural bond orbital (NBO) analyses	645
1.13.6.2.3	$\sigma$ -Hole bonding	646
<b>1.13.7</b>	<b>Conclusion</b>	<b>647</b>
<b>References</b>		<b>647</b>

### Abstract

Chalcogen bonding has developed to become a crucial platform for numerous types of chemistry. While solid-state chemists apply such interactions to design and engineer crystals, chalcogen contacts are used in solution to establish powerful catalytic transformations and to track anion processes. In addition to the mentioned fields, this book chapter provides an insight into the nature of this phenomenon by presenting theoretical considerations.

### 1.13.1 Introduction

The behavior of molecules in solution and especially in the solid state strongly depends on their interactions with other molecules. Most molecules are not completely uniform in their appearance, but they are polarized to some extent. Parts with electron-

withdrawing groups or electronegative elements commonly show a surplus of negative charge whereas electropositive elements show a surplus of positive charge. As long as no salts comprising of positively or negatively charged entities are formed resulting in a very strong interaction, the interaction of these parts is much weaker, but not negligible. The most important weak interaction is hydrogen bonding where positively polarized hydrogen atoms interact with negatively polarized atoms such as oxygen and nitrogen.<sup>1</sup> Water's nature, the structure of ice, the structure and elasticity of cellulose, and also numerous other biological phenomena can be traced back to this kind of bonding. In recent times other types of bonding have captured the interest of chemists. It was found that close interactions between halogen atoms, but also of halogen atoms with other electron donors, show a certain directionality and can be used for supramolecular architecture and catalytic applications.<sup>2</sup> The same holds true for the interaction of chalcogen atoms with other chalcogen atoms, but also the interaction of chalcogen atoms with other electron donors. Originally, this type of interaction was termed "chalcogen-chalcogen interactions" whereas in the recent decade the shorter, more concise term "chalcogen bonding"—in analogy to hydrogen and halogen bonding—increasingly entered the field.<sup>3</sup> Simultaneously, the term chalcogen bonding goes further and includes also other circumstances, e.g., the interactions of Lewis-acidic chalcogens with pnictogens. In a very simplified view the attraction can be understood by the interaction of filled p-orbitals of donating atoms (Lewis bases) with unoccupied  $\sigma^*$  orbitals of chalcogen-based Lewis acids resulting in a certain directionality (Fig. 1). More intensive computations have revealed that this picture is too simplistic to explain the overall interaction energies (see Section 1.13.6).

The following chapter provides an overview of chalcogen bonding in various different situations such as solid-state chemistry, supramolecular chemistry, and catalysis, and provides at the end some theoretical insights explaining the strength and directionality of this type of interaction.

## 1.13.2 Chalcogen bonding in the solid state

### 1.13.2.1 Chalcogen-chalcogen interactions

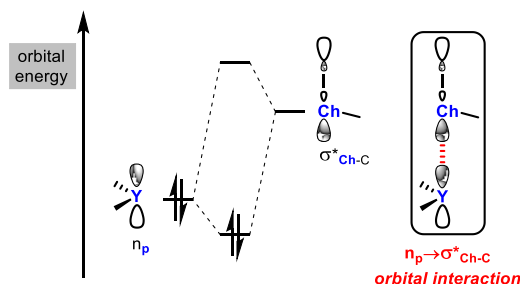
Noncovalent chalcogen-chalcogen interactions are displayed widely in sulfur, selenium, and tellurium containing compounds. Although these bonds are considerably weaker than a covalent chalcogen-chalcogen bond, they are important in the formation of many structures of organochalcogen molecules. Supramolecular assemblies containing chalcogen bonding form macrocycles, helices, columnar structures, chains, and many other types of structure. Examples of supramolecular assemblies of sulfur,<sup>4</sup> selenium,<sup>5</sup> and tellurium<sup>6</sup> compounds are given in Figs. 2 and 3. While in this section, solid-state investigations will be discussed, high level quantum chemical calculations have been applied to further understand these interactions (see Section 1.13.6).

#### 1.13.2.1.1 Linear systems with chalcogen centers

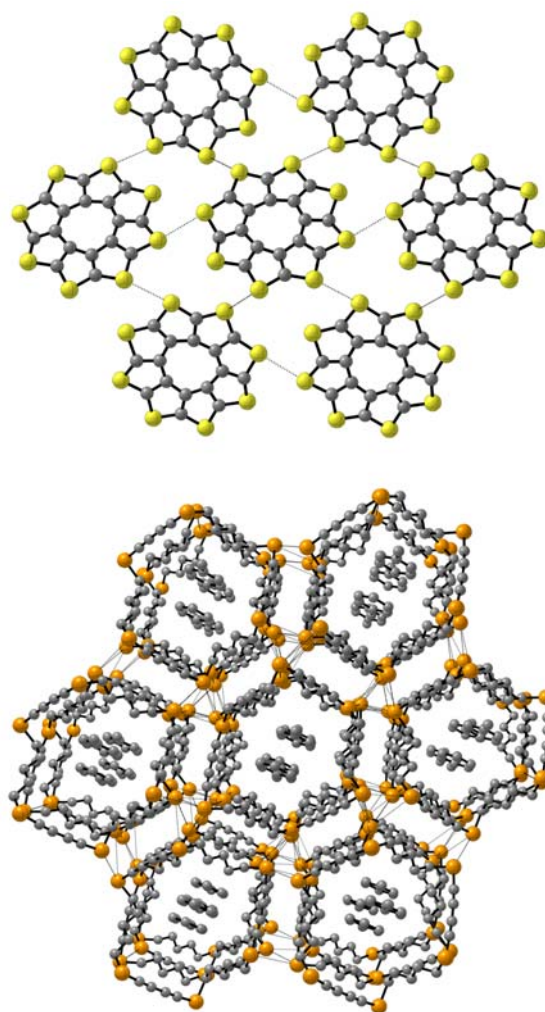
Linear systems with chalcogen centers provide a variety of structures in the solid state with the length of the carbon system, along with the chalcogen atom present having an effect upon the supramolecular systems formed. Methylchalcogen units capping the ends of carbon rods were used as model systems to study the interactions between chalcogen centers in the early 2000's and their relatively simple, although low-yielding, synthesis has allowed a variety of chain lengths to be investigated for sulfur, selenium and tellurium.<sup>6,7</sup> The sulfur-capped systems were found to be oils, however the selenium and tellurium systems were solids which could be subjected to X-ray crystallographic analysis.

Acetylene-based systems form crystals with highly complex structures and very large cells, therefore most work has been carried out on di-, tri- and tetrayne compounds. In Fig. 3, the side view (*Left*) and top view (*Right*) of the tellurium containing diyne system is shown. A triple helix is formed by the  $C_2$  symmetric diyne rods, which are connected by short  $Te \cdots Te$  interactions to neighboring helices. Inside the channels residual electron density due to the *n*-hexane molecules from recrystallization is visible.

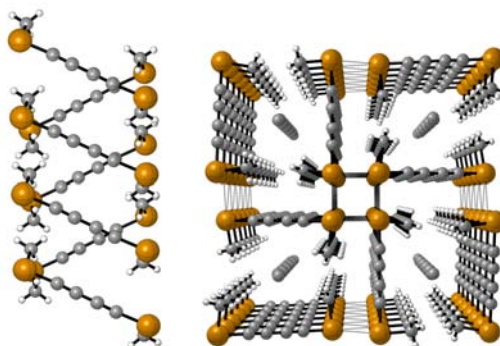
Triyne systems containing selenium were isolated as oils, however the tellurium triyne afforded crystals for analysis. The rhombohedral arrangement of the piles formed are depicted in Fig. 4 (*Top*). Elongating the rod to a tetrayne system provided solids for



**Fig. 1** Directional bonding of Lewis base (Y) with a chalcogen-based Lewis acid by  $n_p \rightarrow \sigma^*_{Ch-C}$  interaction.

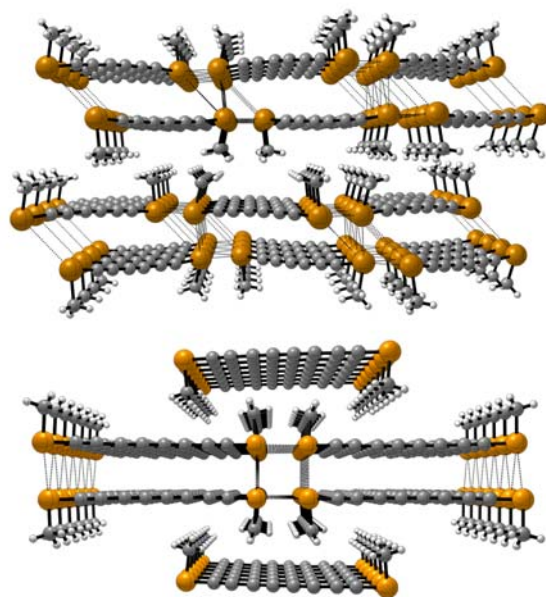


**Fig. 2** Solid-state structures of C<sub>16</sub>S<sub>8</sub> (“sulflower,” *Top*) and a hexaselenacyclohexane with toluene embedded in the channels (*Bottom*). From Chernichenko, K. Y.; Sumerin, V. V.; Shpanchenko, R. V.; Balenkova, E. S.; Nenajdenko, V. G. “Sulflower”: A New Form of Carbon Sulfide. *Angew. Chem. Int. Ed.* **2006**, *45*, 7367–7370; Werz, D. B.; Gleiter, R.; Rominger, F. Cyclic Tetra- and Hexaynes Containing 1,4-Donor-Substituted Butadiyne Units: Synthesis and Supramolecular Organization. *J. Org. Chem.* **2004**, *69*, 2945–2952.



**Fig. 3** Side view (*Left*) and top view (*Right*) of 2,7-ditellura-3,5-octadiyne (top view shows residual electron density in the channels due to disordered *n*-hexane molecules). From Werz, D. B.; Gleiter, R.; Rominger, F. Tellurium-Capped Carbon Rods: Syntheses and Electronic and Structural Properties. *Organometallics* **2003**, *22*, 843–849.





**Fig. 4** Top views of the solid-state structures of a methyltelluride capped triyne (*Top*) and a methylselenide capped tetrayne (*Bottom*). From Werz, D. B.; Gleiter, R.; Rominger, F. Tellurium-Capped Carbon Rods: Syntheses and Electronic and Structural Properties. *Organometallics* **2003**, *22*, 843–849.

both the selenium and tellurium compounds. In these examples the piles formed are arranged in rectangles (**Fig. 4, Bottom**), with both chalcogens providing very similar (but not isomorphous) structures. Space saving is observed in all these structures, as the methyl groups of one molecule fill the spaces left by methyl groups in the neighboring pile.

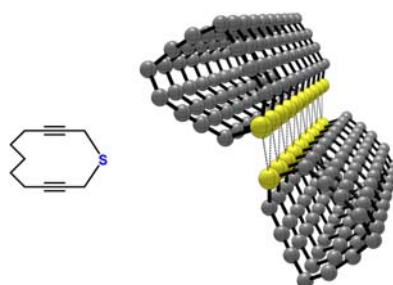
#### 1.13.2.1.2 Cyclic systems with chalcogen centers

Cyclic systems containing chalcogen centers are generally prone to self-organization which leads to columnar structures. Chalcogen-chalcogen distances in these examples are usually slightly shorter than the sum of their van der Waals radii. 1-Thiacyclododeca-3,10-diyne forms a rather flat ring, because of the alkyne units being joined at one end by a  $\text{CH}_2\text{—S—CH}_2$  bridge, and at the other with a pentamethylene bridge.<sup>8</sup> The flatness of the rings formed allows effective stacking, and the sulfur center of one ring of one stack is connected to two sulfur centers of neighboring rings in another stack by a close contact (**Fig. 5**).<sup>9</sup>

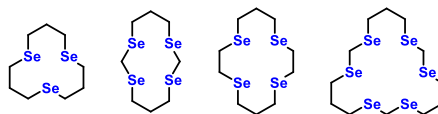
Further examples of alkane chain linked chalcogen centers forming columnar structures are the selenium coronands (**Fig. 6**). These compounds may be synthesized by a straightforward reaction of the bis-sodium salts of propene-1,3-bis(selenolate), or ethane-1,2-bis(selenolate) with  $\alpha,\omega$ -dibromoalkanes.<sup>10</sup>

Single crystal X-ray investigations into the structures of these selenium coronands showed intermolecular  $\text{Se}\cdots\text{Se}$  close-contacts linking the rings. Columnar structures with  $\text{Se}\cdots\text{Se}$  interactions between neighboring stacks were observed similarly to those found in 1-thiacyclododeca-3,10-diyne.<sup>11</sup> The arrangements in the solid state of two of these coronands are shown in **Fig. 7**.

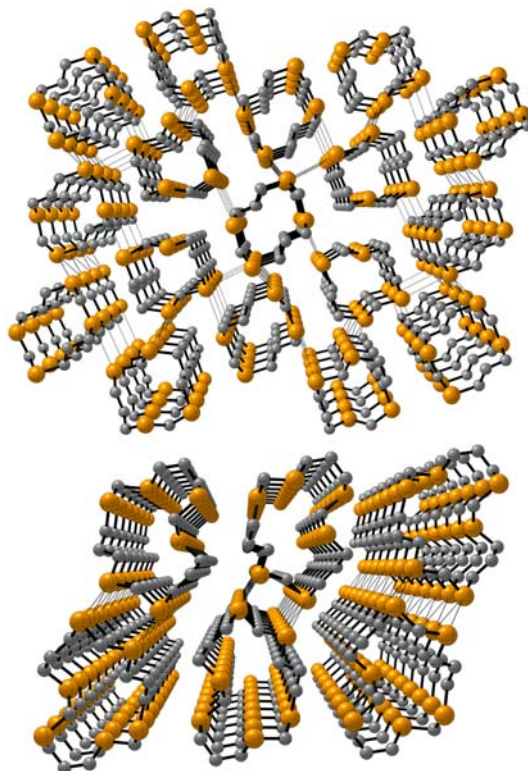
Laitinen and co-workers presented seven tellurium-containing macrocycles, in work similar to the above mentioned selenium coronands.<sup>12</sup> Having successfully synthesized and identified these seven macrocycles, they were also able to obtain X-ray crystallographic data for all of the reported compounds. Each of the structures displayed  $\text{Te}\cdots\text{Te}$  close contacts forming columnar structures,



**Fig. 5** Molecular structure of 1-thiacyclododeca-3,10-diyne and top view of the solid-state stacks formed. Hydrogen atoms are omitted for clarity. From Gleiter, R.; Classen, J.; Rausch, B. J.; Oeser, T.; Rominger, F. Interaction of cyclic thiadiynes with  $\text{CpCo}(\text{COD})$ —selectivity and reactivity. *J. Organomet. Chem.* **2002**, *641*, 3–8.



**Fig. 6** Molecular structures of various selenium coronands.



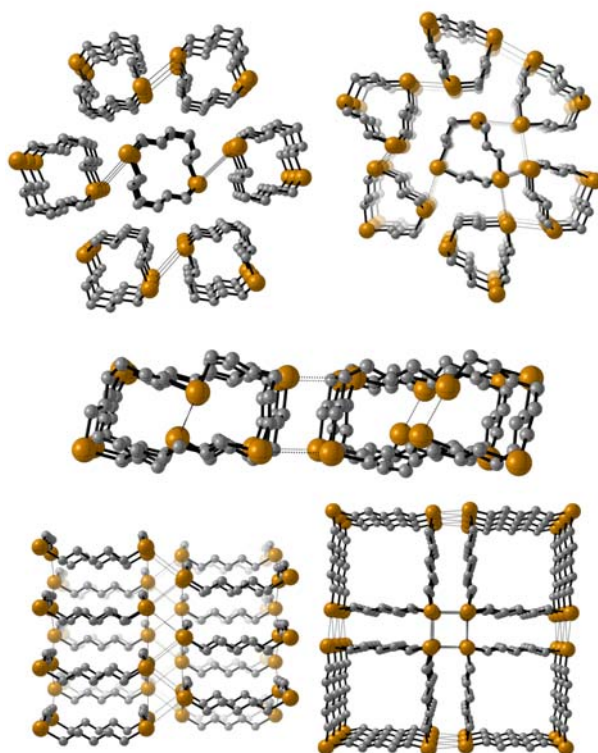
**Fig. 7** Plot of the columnar arrangements of two selenium coronands. Broken lines indicate Se...Se distances less than 4 Å. Hydrogen atoms are omitted for clarity. From Werz, D. B.; Rausch, B. J.; Gleiter, R. Self-Organization of Cyclic Selenoethers to Yield Columnar Structures. *Tetrahedron Lett.* **2002**, *43*, 5767–5769.

with interactions between neighboring columns. In 1,7,13,19- $\text{Te}_4(\text{CH}_2)_{20}$ , 1,8,15,22- $\text{Te}_4(\text{CH}_2)_{20}$ , and 1,9,17,25- $\text{Te}_4(\text{CH}_2)_{20}$ , it was observed that the coordination of each tellurium atom is expanded from two to six, with four secondary bonding interactions. A quasi-octahedral bonding sphere is therefore formed. This phenomenon was exclusive to the molecules containing four tellurium atoms (**Fig. 8**).

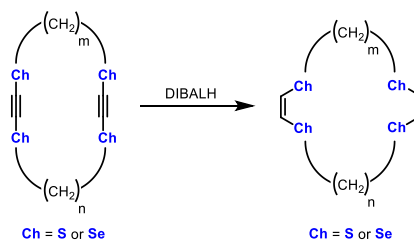
By replacing some  $\text{CH}_2$  groups with doubly or triply bonded carbon centers, the rigidity of large ring systems can be increased. In order to synthesize these molecules, one must use trimethylsilyl acetylene as a starting material, and following lithiation and reaction with  $\alpha,\omega$ -dichalcogenocynoalkanes, the  $\alpha,\omega$ -bis(trimethylsilylalkynechalcogeno)alkanes are formed. Treatment with NaOH yields the terminal diynes, and this is followed by lithiation and reaction with a further  $\alpha,\omega$ -dichalcogenocynoalkane to give the ring-closed products.<sup>13</sup> This synthesis applies to both the sulfur and selenium containing compounds.<sup>14</sup> The tetrachalcogenadiynes formed in this sequence can subsequently be reduced with diisobutylaluminium hydride (DIBALH) to the tetrachalcogenadienes (**Scheme 1**).<sup>15</sup>

Torsional angles between the two alkyne linkers in the tetrachalcogenadiynes define the conformations adopted by these ring systems. When the number of methylene bridges in the alkane chains ( $m$ ,  $n$ ) are both odd, there is usually an angle of  $0^\circ$  between the triple bonds, which results in a chair conformation being adopted. Conversely, when one or both alkane chains has an even number of methylene bridges, the angle is  $>0^\circ$ , and a twist conformation is adopted. A combination of steric and electronic factors are involved in the geometries of these rings, with the 3p (S) or 4p (Se) lone pairs interacting through the  $\pi$ -system and preferring a perpendicular position. This has been supported by B3LYP/6-31G\* calculations.<sup>13</sup>

The rectangular structure seen in the sulfur-containing (5,5) diyne system (**Fig. 9**) is rather flat, and the positions of the sulfur atoms at the four corners means they are located ideally to interact with the sulfur centers of a molecule in a neighboring column.<sup>9</sup> The diene system also shows close contact of sulfur pairs between neighboring columns. These diene systems contain



**Fig. 8** Solid-state structures of 1,8- $\text{Te}_2(\text{CH}_2)_{12}$  (Top Right), 1,5,9- $\text{Te}_3(\text{CH}_2)_9$  (Top Left), 1,8,15- $\text{Te}_3(\text{CH}_2)_{18}$  (Middle) and 1,7,13,19- $\text{Te}_4(\text{CH}_2)_{20}$  (Bottom Left: side view, Bottom Right: top view). From Rodewald, M.; Rautiainen, J. M.; Nicksch, T.; Görls, H.; Oilunkaniemi, R.; Weigand, W.; Laitinen, R. S. Chalcogen Bonding Interactions in Telluroether Heterocycles  $[\text{Te}(\text{CH}_2)_m]_n$  ( $n=1-4$ ;  $m=3-7$ ). *Chem. Eur. J.* **2020**, *26*, 13806–13818.



**Scheme 1** Reduction of cyclic tetrachalcogenadiynes to cyclic tetrachalcogenadienes.

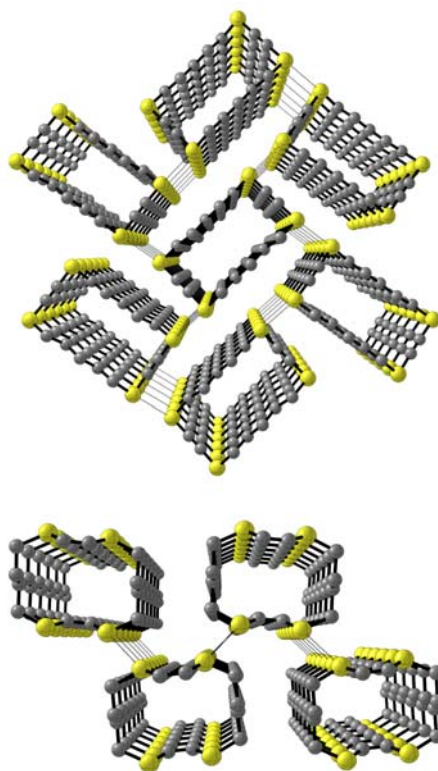
*cis*-configurations at the double bonds, and the S–CH=CH–S linkage is almost planar. Another common feature is the tendency to adopt a conformation in which the two double bonds are *anti* with respect to each other (Fig. 10).

By adding other units to the chains between the rigid triply bonded chalcogen units of these types of molecules, variations can be synthesized. [6.6]Cyclophanes were synthesized by the group of Gleiter in 2009 (*o*-, *m*-, and *p*-) and single crystals were obtained.<sup>16</sup> These rings were also found to stack upon one another. Remarkably, only one Se–C≡C–Se unit from each molecule takes part in strong intermolecular interactions, leading to cyclophanes alternating on both sides of a one-dimensional thread of  $\cdots\text{Se}-\text{C}\equiv\text{C}-\text{Se}\cdots$  chains, and weaker interactions connecting parallel strings. A variety of other linkers have also been investigated and shown to have structures containing non-covalent chalcogen close contacts (Fig. 11).<sup>17</sup>

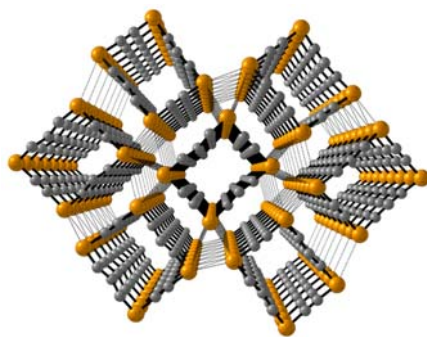
Inclusion of guest molecules in the cavities of all the above mentioned tubular structures is not possible, as the cavities were all found to be far too small. Larger spaces could however be provided by enlarging the ring structures. Three types of enlargements were envisioned and performed successfully, and their products are shown in Fig. 12.

As a side product of the synthesis of the original tetrachalcogenadiynes, the first systems (Fig. 12, Left) were successfully synthesized. In the relatively short system ( $n = 3$ ), the cavity could be measured with a tube diameter of 6 Å.<sup>18</sup> Upon extending the linker to a hexyl chain, the potential cavity collapsed to yield T-shaped molecules stacked in columns (Fig. 13). This T-shape is favored because of intertubular S $\cdots$ S interactions forming which dictate the structure.<sup>19</sup>

During the synthesis of the family of molecules shown on the right of Fig. 12, not only were the cyclic bis(diyne)s formed, but also the cyclohexynes.<sup>5</sup> In the solid state, all the tetraynes adopted a chair conformation. For larger systems ( $n = 5$ ), channel-like



**Fig. 9** Columnar structures of a sulfur-containing (5,5) diyne system (*Top*) and (6,6) diene system (*Bottom*). Hydrogen atoms are omitted for clarity. From Werz, D. B.; Staeb, T. H.; Benisch, C.; Rausch, B. J.; Rominger, F.; Gleiter, R. Self-Organization of Chalcogen-Containing Cyclic Alkynes and Alkenes to Yield Columnar Structures. *Org. Lett.* **2002**, *4*, 339–342.



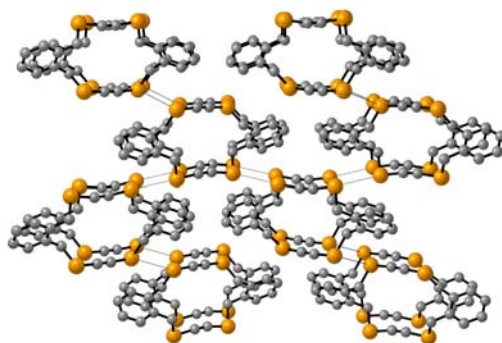
**Fig. 10** Columnar structure of a selenium-containing (3,3) diyne system. Hydrogen atoms are omitted for clarity. From Werz, D. B.; Staeb, T. H.; Benisch, C.; Rausch, B. J.; Rominger, F.; Gleiter, R. Self-organization of Chalcogen-Containing Cyclic Alkynes and Alkenes to Yield Columnar Structures. *Org. Lett.* **2002**, *4*, 339–342.

structures were obtained, and the enlarged rectangular cavities featuring chalcogen atoms on the edges are once again rather flat. The crystal structure of the sulfur system ( $n = 5$ ) is shown in Fig. 14, and is seen to contain one molecule of toluene per two cyclooctatetrayne units, which sits in the channel formed by the cyclic molecules.

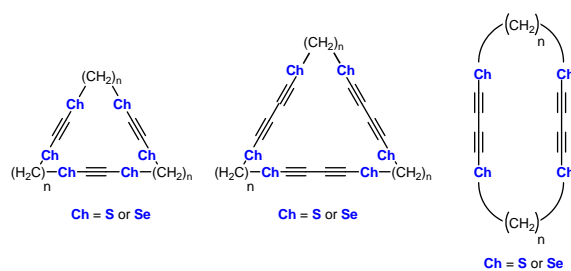
When the hexaselenacyclohexane systems were synthesized, it was noted that two modifications of the  $n = 4$  molecule are observed, depending upon the solvent used for recrystallization. By using *n*-hexane, a structure containing disordered *n*-hexane molecules in the channels of AAA stacked molecules is obtained (Fig. 15, *Top*). These stacks show only a few interactions with neighboring stacks. By recrystallizing from toluene, a different modification is found, with toluene molecules in the channels, but the stacks formed are ABAB stacks. This modification contains more interactions between neighboring stacks, with Se $\cdots$ Se interactions of considerably shorter length than the sum of the van der Waals radii.

Using the hexaselenacyclohexane with  $n = 5$ , a systematic study was carried out to inspect the solid-state behavior when guest molecules are included (aliphatic, aromatic, electron-rich and electron-poor molecules).<sup>5</sup> Results showed that while all these

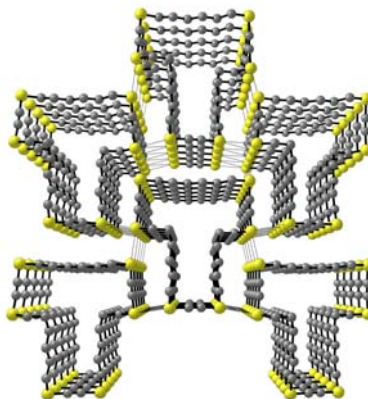




**Fig. 11** Threaded arrangement in the solid state of a [6.6]cyclophane. Hydrogen atoms are omitted for clarity. From Lari, A.; Gleiter, R.; Rominger, F. Supramolecular Organization Based on van der Waals Forces: Syntheses and Solid State Structures of Isomeric [6.6]Cyclophanes with 2,5-Diselena-hex-3-yne Bridges. *Eur. J. Org. Chem.* **2009**, 2267–2274.



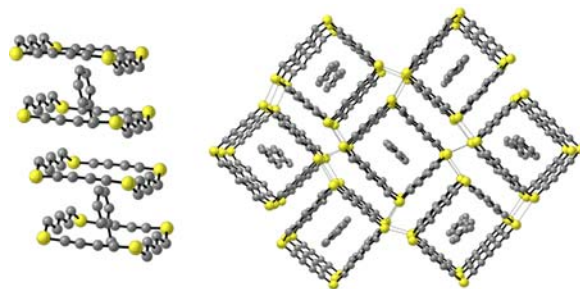
**Fig. 12** Systems with enlarged cavities.



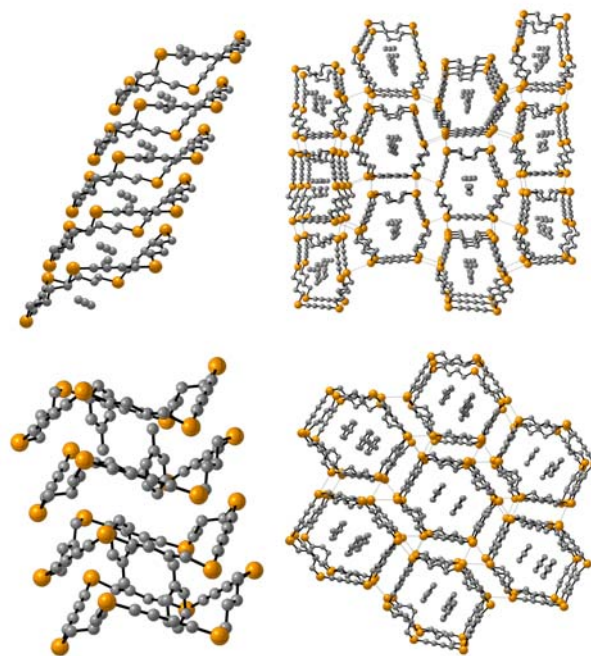
**Fig. 13** Top view of the columnar structure of a T-shaped hexathiatriyne system with hexyl chain linkers. Hydrogen atoms are omitted for clarity. From Gleiter, R.; Werz, D. B. Elastic Cycles as Flexible Hosts: How Tubes Built by Cyclic Chalcogenaalkynes Individually Host Their Guests. *Chem. Lett.* **2005**, *34*, 126–131.

structures have very similar primitive unit cells, the tubes are widened, and the larger the guest molecule, the greater the widening of the tube. Another difference is the angle between the medium plane of the macrocycle and the Se–C≡C–Se units. This angle becomes smaller with larger guest molecules, which in turn makes the diameter of the rings larger. An example of this is the comparison between the modification containing toluene and the modification containing a larger mesitylene group (Fig. 16). These findings revealed that these ring systems are in fact rather flexible, and therefore it has been suggested that such species should be known as elastic cycles.<sup>5</sup>





**Fig. 14** Columnar structures (*Left*) and side view (*Right*) of the cyclooctatetrayne system (Ch = S,  $n = 5$ ) including toluene as guest. Hydrogen atoms are omitted for clarity. From Werz, D. B.; Gleiter, R.; Rominger, F. Cyclic Tetra- and Hexaynes Containing 1,4-Donor-Substituted Butadiyne Units: Synthesis and Supramolecular Organization. *J. Org. Chem.* **2004**, *69*, 2945–2952.



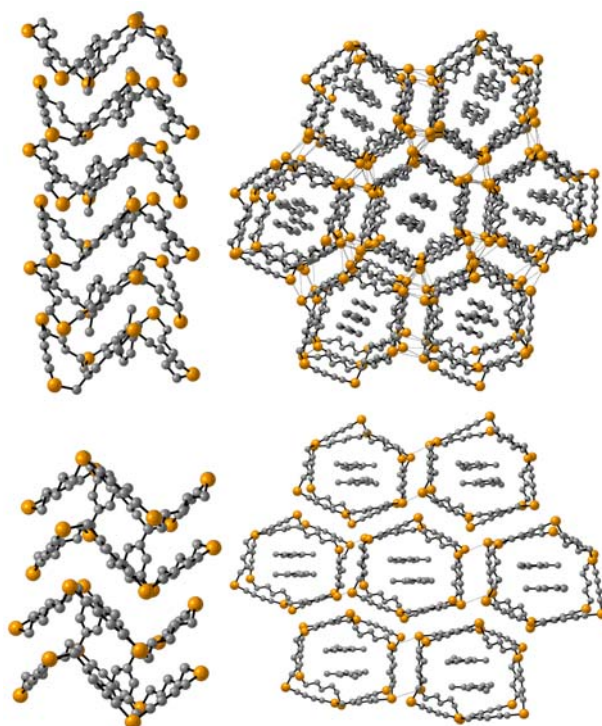
**Fig. 15** Tubular structures of two modifications of a hexaselenacyclohexane ( $n = 4$ ) top view at *right* and side view at *left*. The upper modification was obtained by recrystallization from *n*-hexane, and the lower modification from toluene. Hydrogen atoms are omitted for clarity. From Benisch, C.; Bethke, S.; Gleiter, R.; Oeser, T.; Pritzkow, H.; Rominger, F. Syntheses and Structural Properties of Cyclic Tetrathiadiynes. *Eur. J. Org. Chem.* **2000**, 2479–2488.

#### 1.13.2.1.3 Chalcogens in aromatic systems

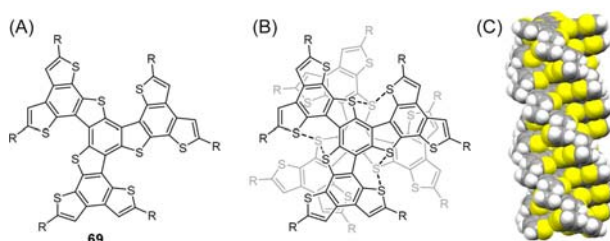
In the solid state, aromatic compounds have a tendency to form staggered structures, with the main driving force for stacking coming from  $\pi$ - $\pi$  interactions between the aromatic molecules.<sup>20</sup> It has, however, been shown that in some cases chalcogen-containing aromatic compounds can form self-organized structures through chalcogen-chalcogen interactions. One such example is the oligothiophene shown in Fig. 17.<sup>21</sup> Nine non-linearly connected units of oligothiophene come together and, according to density functional theory (DFT) calculations, the aromatic core of this molecule is not planar. Because of steric repulsion, it instead adopts a  $C_3$ -symmetric propeller shape. Upon synthesis and crystallization, it was observed that this compound self-assembles into a hexagonal columnar liquid crystalline mesophase. It was then confirmed that along the axis of the columns, a triple-helical geometry is adopted. Three intermolecular S $\cdots$ S interactions occur in a stacked dimer, as shown in Fig. 17 (*Middle*). A schematic representation of the helical columnar assembly for the core of this molecule is shown in Fig. 17 (*Right*).

#### 1.13.2.1.4 Other systems

A Cambridge Structural Database (CSD) search in 2018 by Frontera and Bauza revealed that trisulfide and triselenide compounds are also capable of chalcogen bonding interactions.<sup>22</sup> From the 123 trisulfide and 36 triselenide compounds they found, 10 trisulfides and 8 triselenides had crystal structures in which the packing is dictated by chalcogen-chalcogen interactions. Fig. 18 shows the two patterns that emerge in the solid state of these molecules, *anti*- and *syn*-conformations. In the *anti*-structures (Fig. 18, *Top*),



**Fig. 16** Side view (*Left*) and top view (*Right*) of the hexaselenacyclohexane molecule ( $n = 5$ ) including toluene (*Top*) and mesitylene (*Bottom*), showing larger cavities in the case of mesitylene. Hydrogen atoms are omitted for clarity. From Werz, D. B.; Gleiter, R.; Rominger, F. Cyclic Tetra- and Hexaynes Containing 1,4-Donor-Substituted Butadiyne Units: Synthesis and Supramolecular Organization. *J. Org. Chem.* **2004**, *69*, 2945–2952.



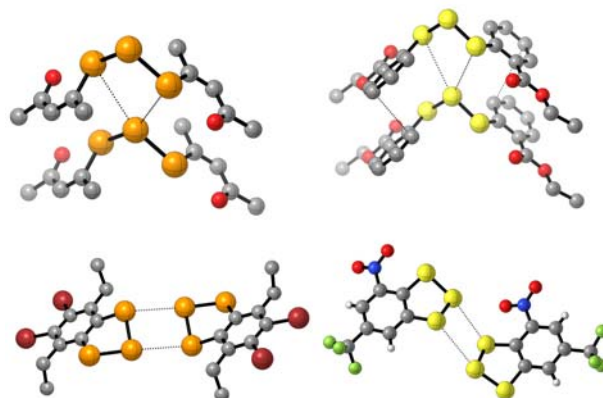
**Fig. 17** A fused oligothiophene ( $R = C_{12}H_{25}$ ); chemical structure (*Left*), schematic illustration of a stacked dimer (*Middle*) schematic illustration of the triple-helical geometry of the columnar assembly of the core structure ( $R = H$ ), formed by multiple  $S \cdots S$  contacts (*Right*). Reprinted with permission from Xiao, Q.; Sakurai, T.; Fukino, T.; Akaike, K.; Honsho, Y.; Saeki, A.; Seki, S.; Kato, K.; Takata, M.; Aida, T. Propeller-Shaped Fused Oligothiophenes: A Remarkable Effect of the Topology of Sulfur Atoms on Columnar Stacking. *J. Am. Chem. Soc.* **2013**, *135*, 18268–18271. Copyright 2013 American Chemical Society.

one-dimensional infinite columns form in an “arrow-like” interaction.<sup>23,24</sup> In the *syn*-conformation, double chalcogen bonds are observed, providing a completely different solid-state structure.<sup>25,26</sup> This structure is dominated by zig-zag dimers which self-assemble. An in-depth computational study was also completed on the four molecules we show here, to better analyze the energetic and geometric parameters of the structural patterns.

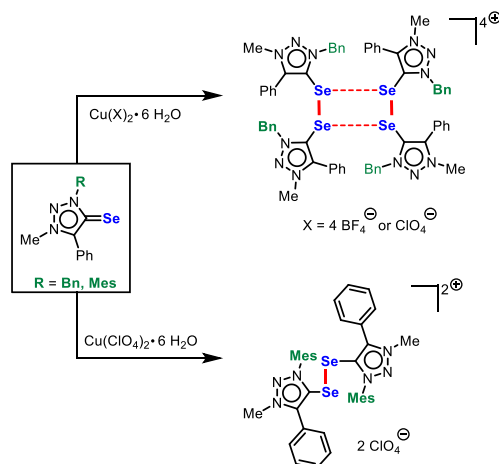
The group of Prabusankar oxidized mesoionic selones using copper(II) salts in 2020.<sup>27,28</sup> Colored products were observed, with different counterions providing different colors. Upon crystallization, the benzyl-substituted products with  $BF_4^-$  and  $ClO_4^-$  counterions form tetraselenide salts, however the mesityl substituted product forms only a diselenide salt. The synthetic routes to these products are given in **Scheme 2**.

Tetraselenide salts with  $BF_4^-$  and  $ClO_4^-$  counterions were isostructural, and can be considered as dimerized diselenides, with  $Se \cdots Se$  chalcogen bonds holding the dimer together (**Fig. 19**). A distorted square planar geometry is observed in the tetraselenide core, with a semi-*trans* orientation of the heterocyclic groups. No such chalcogen-chalcogen interactions are observed in the mesityl-substituted products.

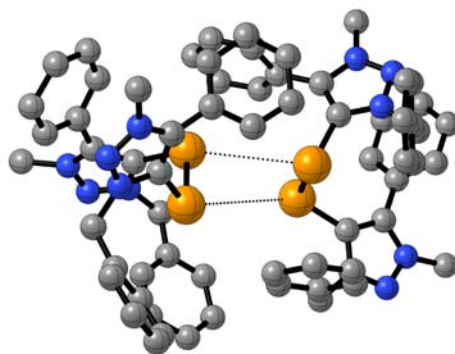
Fourmigué et al. expanded on Gleiter’s 2002 work with methyl-capped tellurodienes (**Fig. 20**) by investigating the ability of arene-expanded chalcogen-capped diynes to form co-crystals with Lewis bases utilizing chalcogen bonding interactions.<sup>29</sup> These



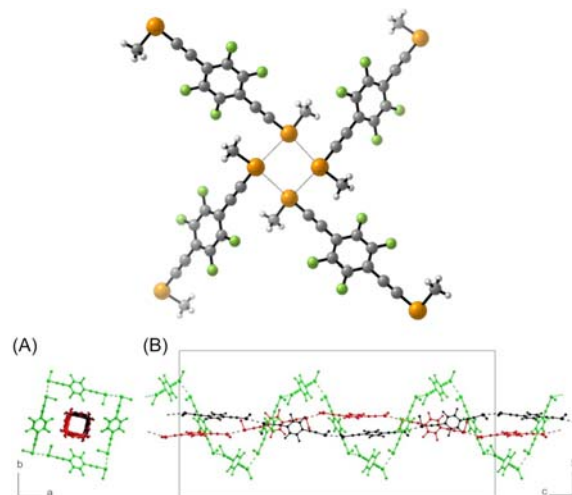
**Fig. 18** Structures of  $\text{Se}_3/\text{S}_3$  compounds (*Top*) in the *anti*-conformation, (*Bottom*) in the *syn*-conformation. Boukebbous, K.; Laifa, E. A.; Mallmann, A. de; Taoufik, M. Diethyl 2,2'-(trisulfane-1,3-diyl)dibenzoate. IUCrData 2016, 1; Arnold, A. P.; Cavell, K. J.; Edwards, A. J.; Hoskins, B. F.; Peacock, E. J. Preparation and X-Ray Crystal-Structure of 4,4'-Triselenobis(pent-3-en-2-one). *Aust. J. Chem.* **1988**, *41*, 1601; Kimura, T.; Yomogita, A.; Matsutani, T.; Suzuki, T.; Tanaka, I.; Kawai, Y.; Takaguchi, Y.; Wakahara, T.; Akasaka, T. Preparation of Phthalocyanines with Eight Benzylchalcogeno Substituents from 5,6-Dibromo-4,7-Diethylbenzo[1,2,3]trichalcogenoles. *J. Org. Chem.* **2004**, *69*, 4716–4723; Chenard, B. L.; Harlow, R. L.; Johnson, A. L.; Vladuchick, S. A. Synthesis, Structure, and Properties of Pentathiepins. *J. Am. Chem. Soc.* **1985**, *107*, 3871–3879.



**Scheme 2** Oxidation of mesoionic selones. From Vaddamanu, M.; Prabusankar, G. Chalcogen Bonding Induced Tetraselenides from Twisted Diselenides. *Eur. J. Inorg. Chem.* **2020**, 2403–2407.



**Fig. 19** The solid-state structure of a dimerized oxidized mesoionic selone.<sup>27</sup>  $\text{BF}_4^-$  or  $\text{ClO}_4^-$  counterion and hydrogen atoms are omitted for clarity. From Vaddamanu, M.; Prabusankar, G. Chalcogen Bonding Induced Tetraselenides from Twisted Diselenides. *Eur. J. Inorg. Chem.* **2020**, 2403–2407.



**Fig. 20** (Top) A tetrahedral motif formed by Se...Se interactions in a selenium-capped expanded diyne. (Bottom) Solid-state arrangement showing the helical organization of molecules (one of six helices shown in green), with two other molecules inserted inside the channels (red and black). Reproduced with permission from Dhaka, A.; Jeannin, O.; Jeon, I.-R.; Aubert, E.; Espinosa, E.; Fourmigué, M. Activating Chalcogen Bonding (ChB) in Alkylseleno/Alkyltelluroacetylenes Toward Chalcogen Bonding Directionality Control. *Angew. Chem. Int. Ed.* **2020**, *59*, 23583–23587. Copyright 2020 Wiley-VCH.

molecules were shown to form tetrahedral centers through chalcogen bonding interactions when no Lewis base was present (Fig. 20), with a helical organization of the molecules.

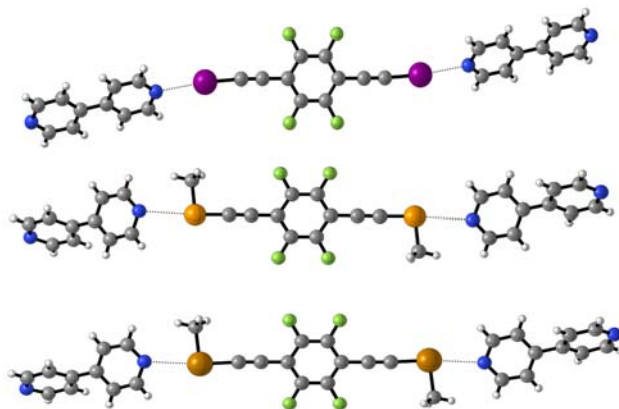
While investigating the interactions with Lewis bases, they found that the strength and directionality of chalcogen bonds formed by their selenium- and tellurium-containing molecules were comparable to those of the halogen bonds formed by the equivalent iodinated molecules (Fig. 21). This was not only true with 4,4'-bipyridine (bipy), but also with 1,4-di(pyridine-4-yl)piperazine (bipy-pip)<sup>30</sup> which has a stronger Lewis base character.

### 1.13.2.2 Chalcogen-pnictogen interactions

Chalcogen-pnictogen interactions are also widespread in solid-state structures, particularly chalcogen-nitrogen interactions. Organic chalcogenocyanates,<sup>31</sup> benzochalcogenazoles<sup>32</sup> and benzochalcogenadiazoles<sup>33</sup> have been particularly popular for studies. In all these examples, chalcogen bonding has a profound effect upon the structure in the crystal.

#### 1.13.2.2.1 Chalcogenocyanates

Thio-, seleno- and telluracyanates all display chalcogen-nitrogen interactions in the solid state. Selenocyanates are the most widely studied of these, with over 30 crystal structures available in the Cambridge Crystallographic Data Centre (CCDC),<sup>34</sup> and are therefore the main focus of this chapter. Even the simple diselenocyanate molecule shows chalcogen bonding Se...N interactions, with



**Fig. 21** Solid-state structures of 1:1 co-crystals with bipy: (Top) iodine-capped, (Middle) selenium-capped, (Bottom) tellurium-capped. From Dhaka, A.; Jeannin, O.; Jeon, I.-R.; Aubert, E.; Espinosa, E.; Fourmigué, M. Activating Chalcogen Bonding (ChB) in Alkylseleno/Alkyltelluroacetylenes Toward Chalcogen Bonding Directionality Control. *Angew. Chem. Int. Ed.* **2020**, *59*, 23583–23587.

both  $\sigma$ -holes used on both selenium atoms.<sup>35</sup> These structures showed short and highly directional interactions, and the co-crystal with  $\text{PhNMe}_3^+ \text{Br}^-$  showed short  $\text{Se}\cdots\text{N}$  and  $\text{Se}\cdots\text{Br}$  interactions with strong linearity.<sup>36</sup>

Organic selenocyanates show highly ordered crystal structures because of  $\text{Se}\cdots\text{N}$  interactions, and a great variety of interesting solid-state structures have been reported with various carbon backbones. Electron-withdrawing groups enhance the chalcogen bonding capabilities of chalcogen atoms by making the  $\sigma$ -holes more electron-poor. This explains the particularly strong chalcogen bonding interactions observed in selenocyanates, regardless of the poor electron-donating properties of the lone pair on nitrogen.

Linear  $\text{Se}\cdots\text{N}$  contacts in aromatic selenocyanates lead to the formation of chain-like patterns, with recurrent  $\cdots\text{Se}(R)-\text{CN}\cdots\text{Se}(R)-\text{CN}\cdots$  motifs. Addition of stronger electron-withdrawing substituents to the aromatic group results in a stronger chalcogen bond, because of the enhancement of the  $\sigma$ -holes on selenium. A series of these one-dimensional structures is shown in Fig. 22.<sup>37–39</sup>

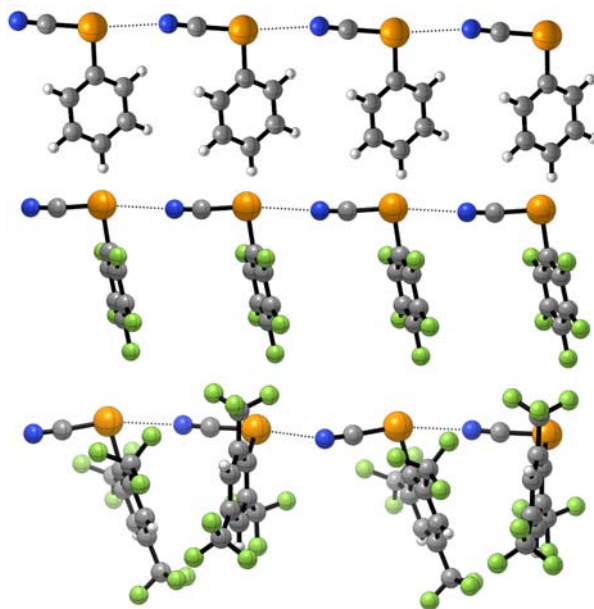
Benzylic selenocyanates display similar one-dimensional chain-like motifs and are easily synthesized from benzyl halides and potassium selenocyanate.<sup>16,40–42</sup> This simple preparation has allowed many examples to be reported and their structures characterized. Recurrent chain motifs of  $\text{Se}\cdots\text{N}$  chalcogen bonded molecules have been reported for benzylselenocyanate, as well as *ortho*-, *meta*-, and *para*-bis(selenocyanato)xylene (Fig. 23). Both selenocyanate moieties in the bis-selenocyanates take part in chalcogen bonding interactions, in the same direction for the *ortho*-substitution pattern, and in opposing directions along the chain in the *meta*- and *para*- examples.

3-Selenocyanatopyridine is a particularly interesting example, where the pyridinyl nitrogen atom engages in the chalcogen bond, rather than the nitrile nitrogen atom.<sup>43</sup> This example perfectly demonstrates that the nitrile N-atom can easily be displaced from the chalcogen bond by an atom with stronger Lewis basicity. Because of the chalcogen bond now being from the selenocyanate to the 3-position of the next molecule, the chains formed are no longer linear, and demonstrate the strong directionality of chalcogen bonding (Fig. 24).

Fourmigué and co-workers presented the structures of several tris- and tetrakis(selenocyanato)arenes in 2018.<sup>31</sup> These structures, similarly to the mono- and bis(selenocyanates), also show chain-like motifs in their solid-state structures. However, the existence of more selenocyanate groups in various orientations means that the structures often contain chalcogen bonding interactions in two dimensions, thereby linking the one-dimensional chain structures. 1,3,5-Tris(selenocyanatomethyl)benzene (Fig. 25) contains two strong  $\text{Se}\cdots\text{N}$  interactions which allow the formation of infinite chains in the *a* direction of the crystal.<sup>31</sup> These chains are connected along the *b* direction through a weaker chalcogen bond between the third selenocyanate groups of the molecules in adjacent chains.

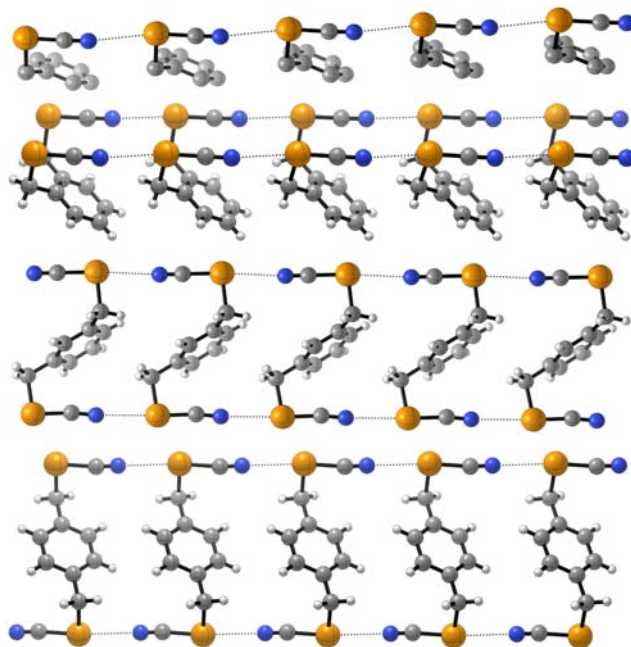
1,3,5-Tris(selenocyanatomethyl)-2,4,6-trimethylbenzene shows a more complex structure (Fig. 26).<sup>31</sup> Two  $\text{Se}\cdots\text{N}$  interactions are formed from each molecule in the [1,-1,0] direction, with a third disordered Se atom making a very short  $\text{Se}\cdots\text{Se}$  contact linking chains. This  $\text{Se}\cdots\text{Se}$  interaction between chains causes one nitrogen atom not to be engaged in a chalcogen bonding contact.

Crystallographic analysis of 1,2,4,5-tetrakis(selenocyanatomethyl)benzene showed the formation of layers (Fig. 27).<sup>31</sup> These layers are held together by strong  $\text{Se}\cdots\text{N}$  interactions involving two of the selenocyanate groups. Interconnection of the layers occurs

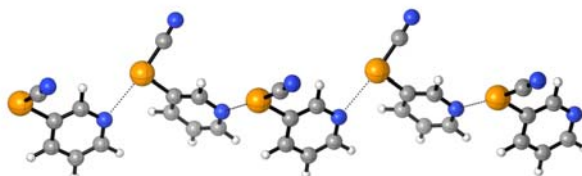


**Fig. 22** One dimensional chain structures of (Top) phenylselenocyanate, (Middle) pentafluorophenylselenocyanate, (Bottom) 2,4,6-tris(trifluoromethyl)phenylselenocyanate. From Barnes, N. A.; Godfrey, S. M.; Halton, R. T.A.; Mushtaq, I.; Parsons, S.; Pritchard, R. G.; Sadler, M. A Comparison of the Solid-State Structures of a Series of Phenylseleno-Halogen and Pseudohalogen Compounds,  $\text{PhSeX}$  ( $X=\text{Cl}, \text{CN}, \text{SCN}$ ). *Polyhedron* **2007**, 26, 1053–1060; Klapötke, T. M.; Krumm, B.; Polborn, K. Synthesis, Chemistry, and Characterization of Perfluoroaromatic Selenium Derivatives. *Eur. J. Inorg. Chem.* **1999**, 1359–1366; Klapötke, T. M.; Krumm, B.; Mayer, P.; Piotrowski, H.; Vogt, M. Z. *Anorg. Allg. Chem.* **2003**, 629, 1117–1123.

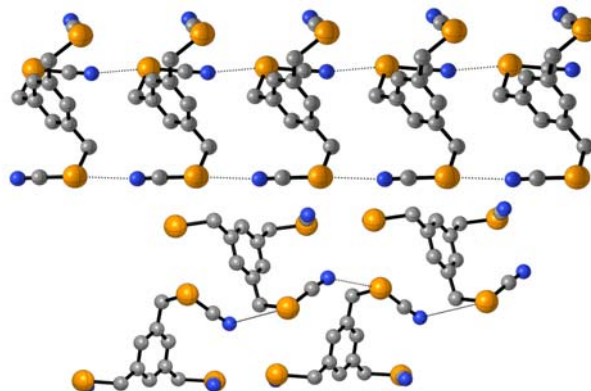




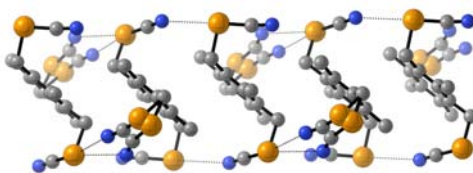
**Fig. 23** Chain-like structures of (Top) benzylselenocyanate (hydrogen atoms omitted for clarity) and the different substitution patterns of bis(selenocyanato)xylene, (Upper Middle) *ortho*-, (Lower Middle) *meta*-, (Bottom) *para*-. From Lari, A.; Gleiter, R.; Rominger, F. Supramolecular Organization Based on van der Waals Forces: Syntheses and Solid State Structures of Isomeric [6.6]Cyclophanes with 2,5-Diselenahex-3-yne Bridges. *Eur. J. Org. Chem.* **2009**, 2267–2274; Huynh, H.-T.; Jeannin, O.; Fourmigué, M. Organic Selenocyanates as Strong and Directional Chalcogen Bond Donors for Crystal Engineering. *Chem. Commun.* **2017**, 53, 8467–8469; Maartmann-Moe, K.; Sanderud, K. A.; Songstad, J.; Sillanpää, R.; Fernholt, L.; Rømming, C. The Crystal Structure of 4-Nitrobenzyl Tellurocyanate, 4-Nitrobenzyl Selenocyanate, 4-Nitrobenzyl Thiocyanate and Benzyl Selenocyanate. *Acta Chem. Scand.* **1984**, 38a, 187–200; McWhinnie, S. L. W.; Brooks, A. B.; Abrahams, I.  $\alpha\alpha'$ -Diselenocyanato-ortho-xylene. *Acta Cryst. C* **1998**, 54, 126–128.



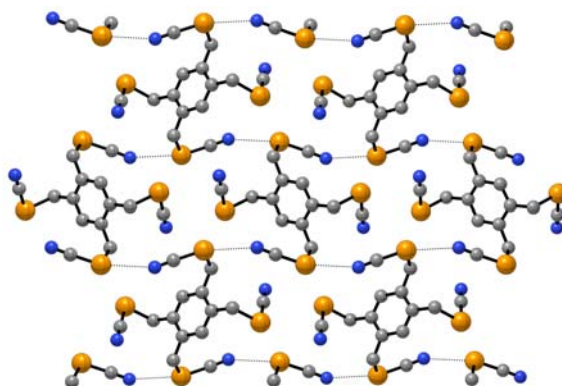
**Fig. 24** Non-linear chain-like structure of 3-selenocyanatopyridine displaying chalcogen bonds from Se to the pyridinyl nitrogen atom. From Dunne, S. J.; Summers, L. A.; Nagy-Felsobuki, E. I. von; Mackay, M. F. 3-Selenocyanatopyridine. *Acta Cryst. C* **1994**, 50, 971–974.



**Fig. 25** Structure of 1,3,5-tris(selenocyanatomethyl)benzene in the solid state. (Top) Infinite chains in the *a* direction, (Bottom) *b* direction contacts connecting the chains. Jeannin, O.; Huynh, H.-T.; Riel, A. M. S.; Fourmigué, M. Chalcogen Bonding Interactions in Organic Selenocyanates: From Cooperativity to Chelation. *New J. Chem.* **2018**, 42, 10502–10509.



**Fig. 26** Structure of 1,3,5-tris(selenocyanatomethyl)-2,4,6-trimethylbenzene showing the disordered selenocyanate groups. From Jeannin, O.; Huynh, H.-T.; Riel, A. M. S.; Fourmigué, M. Chalcogen Bonding Interactions in Organic Selenocyanates: From Cooperativity to Chelation. *New J. Chem.* **2018**, *42*, 10502–10509.



**Fig. 27** Structure of the layers of 1,2,4,5-tetrakis(selenocyanatomethyl)benzene. Jeannin, O.; Huynh, H.-T.; Riel, A. M. S.; Fourmigué, M. Chalcogen Bonding Interactions in Organic Selenocyanates: From Cooperativity to Chelation. *New J. Chem.* **2018**, *42*, 10502–10509.

through weaker chalcogen bonding interactions by the other two selenocyanate groups and further weak interactions from the selenium atoms involved in the layer formation.

Co-crystallization of these tris- and tetrakis(selenocyanates) with solvent molecules afford very different structures to those of the pure crystals.<sup>31</sup> Se $\cdots$ N interactions are still a key part of the structures, however Se $\cdots$ O interactions also play a part now. In the case of 1,3,5-tris(selenocyanatomethyl)-2,4,6-trimethylbenzene·DMF (DMF = dimethylformamide), the structure now contains three short Se $\cdots$ N interactions running parallel to each other to form infinite chains, with each molecule having a single weak Se $\cdots$ O interaction to a solvent molecule. The EtOAc co-crystal of the same molecule shows that the infinite chains previously displayed (Fig. 28) are now made up of segments of three distinct interactions. 1,2,4,5-Tetrakis(selenocyanatomethyl)benzene·(DMF)<sub>2</sub> shows only Se $\cdots$ O interactions between the selenocyanate and the carbonyl oxygen of DMF, this is possible because of the attractive chelating system that is formed by the two adjacent selenocyanate groups.

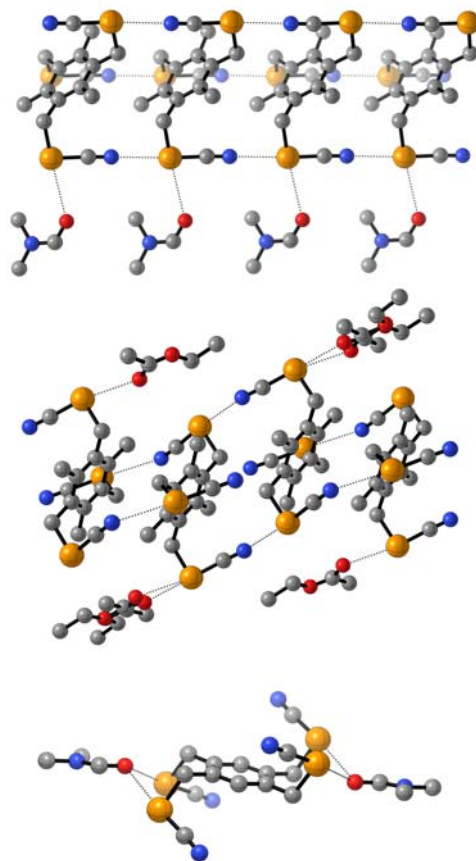
Extension of the carbon chain between the aromatic group and selenocyanate gives rise to interesting bis(selenocyanato) compounds.<sup>44</sup> In the solid-state, the *anti*-compound displays chalcogen bonding by which each molecule contains chalcogen bonds to four other molecules. One selenium atom donates two chalcogen bonds, the shorter of which is the prolongation of the Se–CN bond. The N-atom of the same selenocyanate group receives a chalcogen bond from a third molecule. The final chalcogen bond is an Se $\cdots$ Se interaction from the second selenium atom to a fourth molecule. This contrasts the far simpler chain-like structures shown in Fig. 29 for the bis(selenocyanato)-xylylenes. The *syn*-congener however displays a much simpler chain-like structure more similar to those mentioned above, although the intermolecular distances are larger, and linearity is decreased. Co-crystallization of the *anti*-congener with 4,4'-bipyridine showed a trimolecular adduct with a 2:1 stoichiometry as (*anti*)<sub>2</sub>(bipy). Two *anti*-molecules form chalcogen bonds to each nitrogen of a bipy molecule, while one selenium is in close contact to the N-atom of a nearby selenocyanate, and the other forms an Se $\cdots$ Se contact to a further selenocyanate molecule.

Intramolecular chalcogen bonds are also known in selenocyanates, as shown in Fig. 30.<sup>41,45,46</sup> These come in the form of Se $\cdots$ O and Se $\cdots$ N contacts in most cases. Similar intramolecular chalcogen bonds can be seen in some diselenide molecules with nearby amine or imine groups, and are also shown in Fig. 30.<sup>45,47</sup>

### 1.13.2.2 Benzochalcogenazoles and benzochalcogenadiazoles

1,3-Benzochalcogenazoles are relevant as bioactive compounds and molecular materials.<sup>48,49</sup> As such, their properties have been thoroughly studied. Intramolecular chalcogen bonding is often important in locking the conformation of some residues, and therefore is a key component of any bioactivity.<sup>50</sup>

Intermolecular chalcogen bonds are also often present in benzochalcogenazoles, with the azole nitrogen acting as the acceptor. Fig. 31 shows chains formed by chalcogen bonding in thio-, seleno- and telluradiazoles.<sup>51–53</sup> The ability of all three of these molecules to form similar interactions (3.21–3.36 Å chalcogen bond length, 161–174° C–Ch $\cdots$ N angle) shows the reliability of the



**Fig. 28** Solid-state structures of solvent co-crystals. (Top) 1,3,5-Tris(selenocyanatomethyl)-2,4,6-trimethylbenzene·DMF. (Middle) 1,3,5-Tris(selenocyanatomethyl)-2,4,6-trimethylbenzene·EtOAc (including disorder at EtOAc molecules). (Bottom) 1,2,4,5-Tetrakis(selenocyanatomethyl)benzene·(DMF)<sub>2</sub>. From Jeannin, O.; Huynh, H.-T.; Riel, A. M. S.; Fourmigué, M. Chalcogen Bonding Interactions in Organic Selenocyanates: From Cooperativity to Chelation. *New J. Chem.* **2018**, *42*, 10502–10509.

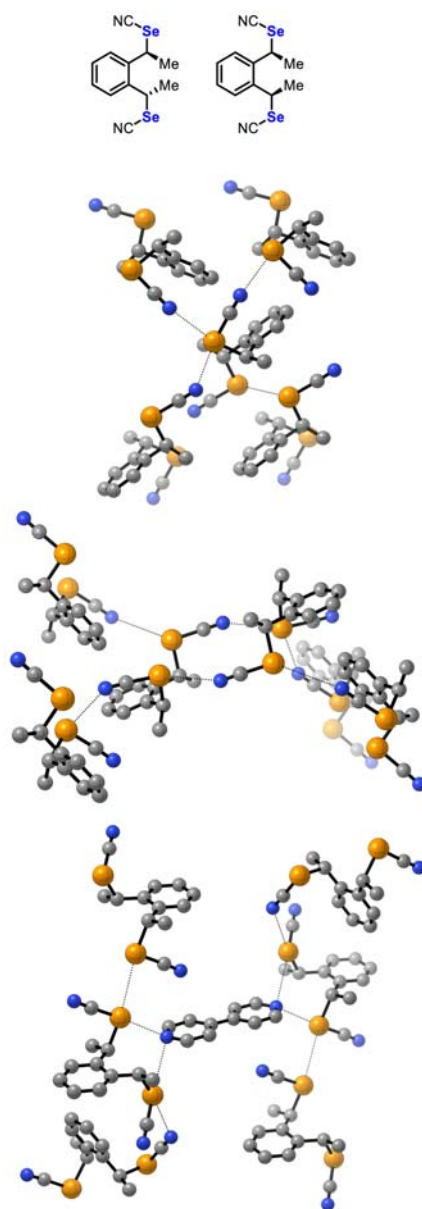
chalcogen $\cdots$ N supramolecular synthon with such small changes although both the chalcogen atom and C2 substituent are changed.

Benzochalcogenadiazoles have also been heavily investigated in recent years, with a particularly noteworthy addition to the literature made by Diederich et al. in 2019.<sup>33</sup> These molecules display, with very few exceptions, 2S-2N square interactions<sup>54,55</sup> in dimeric or polymeric systems. By exchanging the substituents on the benzochalcogenadiazole, the solid-state structure may be modified, and in some cases other interactions can be seen having an effect on the crystal packing. The availability of all four positions 4–7 on the benzo ring allows the possibility of systematic substitutions to investigate many different trends and interactions.

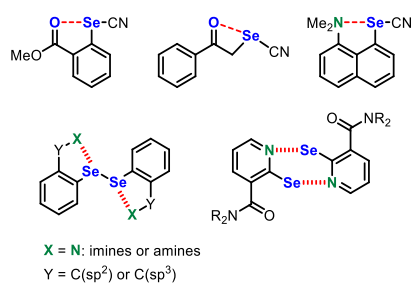
Considering firstly the unsubstituted 2,1,3-benzochalcogenadiazoles (O, S, Se, Te), only the tellurium containing compound shows highly aligned, short 2Te-2N square interactions.<sup>56</sup> In contrast to this, the S<sup>57,58</sup> and Se<sup>59</sup> containing molecules form very similar distorted squares. Cozzolino and co-workers postulated that while the steric demands of the benzo-tail were too high in the sulfur and selenium compounds, the strength of the Te $\cdots$ N interactions outweighed these sterics.<sup>60</sup> When the chalcogen atom is oxygen, square interactions do not occur, with a structure of head-tail columns preferred.<sup>57</sup>

Extensive study of substituted benzothiadiazoles<sup>58,61–64</sup> unearthed several interesting trends, most notable of which is that a large majority of these compounds display square interactions with close S $\cdots$ N contacts.<sup>33</sup> The S $\cdots$ N thiazole contacts stabilize the squares, however the broad range of substituents that continued to allow this interaction in the solid-state also indicates that these substituents have more of an effect upon dimerization than simply adjusting the polarization. Symmetrically substituted 5,6-dimethyl and 5,6-difluorobenzothiadiazole display this very clearly in their crystal structures (Fig. 32) with F $\cdots$ F interactions in the latter being a key part of the structure. These tail $\cdots$ tail interactions allow the formation of Teflon-like ribbons in the difluoro compound, and close F $\cdots$ H contacts<sup>63</sup> (not shown) afford further stabilization.

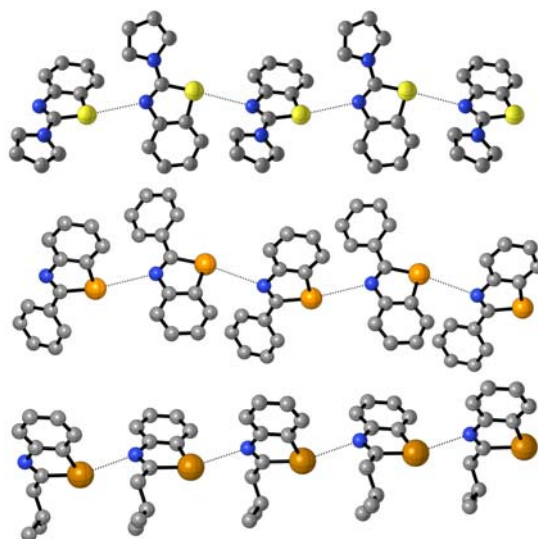
Unsymmetrically substituted benzothiadiazoles can show either an *anti*-square or *syn*-square interaction, where *anti*-square is preferred in almost all cases (Fig. 33). Somewhat surprisingly, the electron-withdrawing or -donating nature of the substituents appears to have no effect upon this orientation or in fact the chalcogen bonding in the squares.<sup>53</sup> An example of this phenomenon is shown in the cases of dimers of the 5-methyl and 5-nitro substituted compounds.<sup>61</sup> Although the electronic properties of CH<sub>3</sub> and



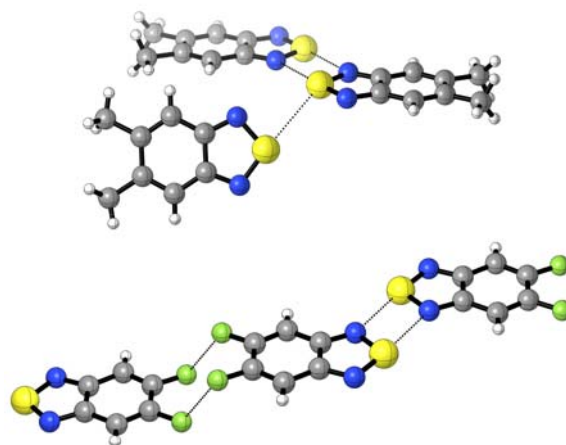
**Fig. 29** Solid-state structures of (Top) the *anti*-congener, (Middle) the *syn*-congener and (Bottom) (*anti*)<sub>2</sub>(bipy). Only the major components of disordered SeCN groups are shown. From Huynh, H-T.; Jeannin, O.; Aubert, E.; Espinosa, E.; Fourmigué, M. Chalcogen Bonding Interactions in Chelating, Chiral Bis(selenocyanates). *New J. Chem.* **2021**, *45*, 76–84.



**Fig. 30** Intramolecular chalcogen-pnictogen interactions in selenocyanates and diselenides.



**Fig. 31** Chain-like structures of (*Top*) 2-(1*H*-pyrrol-1-yl)-1,3-benzothiazole, (*Middle*) 2-phenyl-1,3-benzoselenazole, (*Bottom*) 2-isobutyl-1,3-benzotellurazole. From Kremer, A.; Fermi, A.; Biot, N.; Wouters, J.; Bonifazi, D. Supramolecular Wiring of Benzo-1,3-Chalcogenazoles Through Programmed Chalcogen Bonding Interactions. *Chem. Eur. J.* **2016**, *22*, 5665–5675; Hedidi, M.; Bentabed-Ababsa, G.; Derdour, A.; Roisnel, T.; Dorcet, V.; Chevallier, F.; Picot, L.; Thiéry, V.; Mongin, F. Synthesis of C,N'-linked Bis-Heterocycles Using a Deprotometalation-Iodination-N-Arylation Sequence and Evaluation of Their Antiproliferative Activity in Melanoma Cells. *Bioorg. Med. Chem.* **2014**, *22*, 3498–3507; Cozzolino, A. F.; Vargas-Baca, I. Parametrization of a Force Field for Te–N Secondary Bonding Interactions and Its Application in the Design of Supramolecular Structures Based on Heterocyclic Building Blocks. *Cryst. Growth Des.* **2011**, *11*, 668–677.



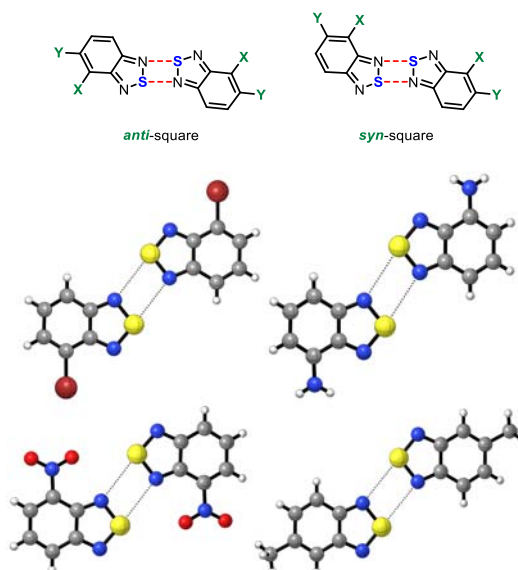
**Fig. 32** S...N square interactions in symmetric 5,6-substituted benzothiadiazoles. (*Top*) 5,6-Dimethylbenzothiadiazole, (*Bottom*) 5,6-difluorobenzothiadiazole. From Ams, M. R.; Trapp, N.; Schwab, A.; Milić, J. V.; Diederich, F. Chalcogen Bonding “2S-2N Squares” versus Competing Interactions: Exploring the Recognition Properties of Sulfur. *Chem. Eur. J.* **2019**, *25*, 323–333.

NO<sub>2</sub> substituents are profoundly different, their average chalcogen bond lengths are 3.09 Å and 3.14 Å respectively, and their average angles are all within 7° of each other.

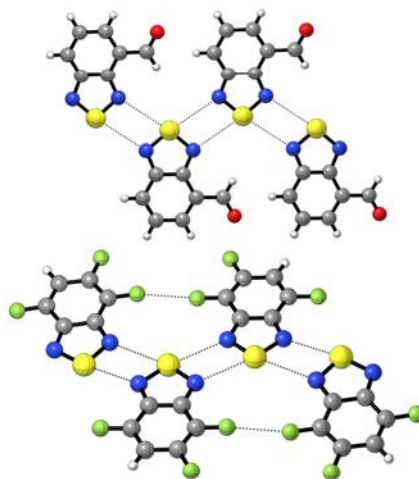
The two exceptions to this *anti*-orientation are 4-CHO- and 4,5,7-trifluorobenzothiadiazole (**Fig. 34**).<sup>62</sup> These are both rare examples of square-ribbon complexes of benzothiadiazoles, which contain square interactions repeating from the thiazole edges.<sup>65</sup> In the 4,5,7-trifluoro case there are also F...F interactions which further stabilize the structure. It has been proposed that such ribbon structures could find applications in supramolecular wiring.<sup>48,51,60</sup>

Further study of this class of molecules showed that the members bearing heavier halogens appear to display halogen bonding which outcompetes the chalcogen bonding interactions.<sup>66</sup> When this effect is exaggerated by addition of an electron-withdrawing substituent next to the heavier halogen (such as 5-fluoro-4-iodo- substitution) it is possible to completely suppress the S...N square interactions. This also holds true for 5,6-dihalogenated compounds (F, Br or F, I combinations). 4,7-Dihalogenated compounds (Br, Br and I, I), display at least two Br...Br or I...I interactions per monomer that are below the sum of the van der Waals radii, with no S...N square interactions.





**Fig. 33** *anti*-Square interactions in benzothiadiazoles. From Ams, M. R.; Trapp, N.; Schwab, A.; Milić, J. V.; Diederich, F. Chalcogen Bonding “2S-2N Squares” versus Competing Interactions: Exploring the Recognition Properties of Sulfur. *Chem. Eur. J.* **2019**, *25*, 323–333. Bashirov, D. A.; Sukhikh, T. S.; Kuratieva, N. V.; Chulanova, E. A.; Yushina, I. V.; Gritsan, N. P.; Konchenko, S. N.; Zibarev, A. V. Novel Applications of Functionalized 2,1,3-Benzothiadiazoles for Coordination Chemistry and Crystal Engineering. *RSC Adv.* **2014**, *4*, 28309.

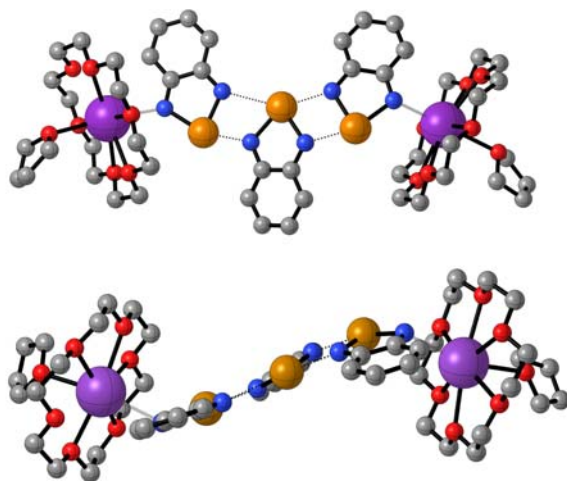


**Fig. 34** *syn*-Square interactions in 4-CHO and 4,5,7-trifluorobenzothiadiazole displaying formation of square-ribbon complexes. From Ams, M. R.; Trapp, N.; Schwab, A.; Milić, J. V.; Diederich, F. Chalcogen Bonding “2S-2N Squares” versus Competing Interactions: Exploring the Recognition Properties of Sulfur. *Chem. Eur. J.* **2019**, *25*, 323–333. Makarov, A. G.; Selikhova, N. Y.; Makarov, A. Y.; Malkov, V. S.; Bagryanskaya, I. Y.; Gatilov, Y. V.; Knyazev, A. S.; Slizhov, Y. G.; Zibarev, A. V. New Fluorinated 1,2-Diaminoarenes, Quinoxalines, 2,1,3-Arenothia(selena)diazoles and Related Compounds. *J. Fluor. Chem.* **2014**, *165*, 123–131.

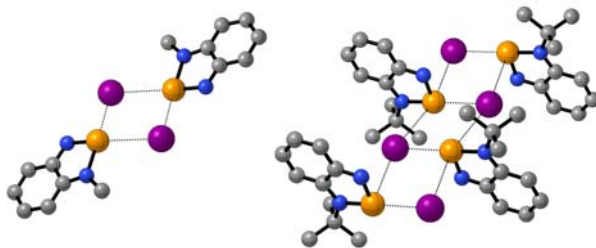
Benzotelluradiazole has been shown to form  $\text{Te}\cdots\text{N}$  squares in a rather specialized system.<sup>67</sup> A central, neutral benzotelluradiazole molecule shows chalcogen bonding to two benzotelluradiazolidyl radicals, which in turn show  $\text{N}\cdots\text{K}$  coordination (Fig. 35). This trimer is unusual in its lack of planarity, caused by the delocalization of the charge over the  $\pi$ -orbital manifold of the three benzotelluradiazoles, meaning a more symmetrical structure would distort and be easily deformed in the lattice by packing interactions.

### 1.13.2.3 Chalcogen-halogen interactions

Taylor and Vargas-Baca expanded the field of chalcogen bonding to include chalcogen-halogen interactions.<sup>33,55,60,68–72</sup> The solid-state structures of Vargas-Baca’s *N*-alkylated cationic benzo-selenodiazonium compounds crystallized with iodide or triiodide anions are dominated by the  $\text{Se}\cdots\text{I}$  chalcogen bonding interactions (see Fig. 36).<sup>55</sup> The cationic nature of these compounds was



**Fig. 35** X-ray of  $[K(18-C-6)(THF)]_2[(C_6H_4N_2Te)_3]$  in (Top) top view, (Bottom) side view. From Puskarevsky, N. A.; Smolentsev, A. I.; Dmitriev, A. A.; Vargas-Baca, I.; Gritsan, N. P.; Beckmann, J.; Zibarev, A. V. Bis(2,1,3-benzotelluradiazolidyl)2,1,3-Benzotelluradiazole: A Pair of Radical Anions Coupled by TeN Chalcogen Bonding. *Chem. Commun.* **2020**, *56*, 1113–1116.



**Fig. 36** X-ray crystal structures of the *N*-alkylated cationic benzo-selenodiazonium compounds with iodide. Hydrogen atoms are omitted for clarity. From Lee, L. M.; Corless, V. B.; Tran, M.; Jenkins, H.; Britten, J. F.; Vargas-Baca, I. Synthetic, Structural, and Computational Investigations of *N*-Alkyl Benzo-2,1,3-Selenadiazolium Iodides and Their Supramolecular Aggregates. *Dalton Trans.* **2016**, *45*, 3285–3293.

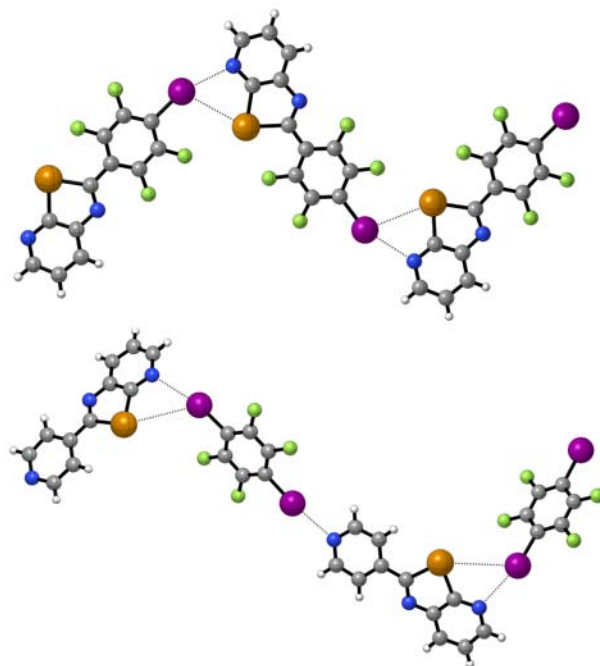
required to enhance the electron deficiency of the Se atoms, allowing efficient interactions with the electron-rich anions. In all structures, the geometry showed the influence of both Se  $\sigma$ -holes, as the anion binding occurs along elongations of both Se–N bonds. The alkyl substituent at nitrogen was found to have a significant impact upon the structure due to its steric influence. While a methyl group allowed formation of iodide-bridged dimers, the *N*-isopropyl compound formed infinite  $[SeI]_\infty$  chains.

Bonifazi et al. in 2020 published a rare example of chalcogen-halogen interactions in neutral compounds.<sup>70</sup> These chalcogen bonding examples were observed in the crystal structure alongside halogen bonding interactions forming supramolecular polymers for crystal engineering applications. While aiming to form multi-component supramolecular polymers using chalcogenazopyridine (CGP) based scaffolds, the crystal structure of one such tellurium containing scaffold displayed non-covalent  $Te \cdots I$  interactions along with  $N \cdots I$  interactions (see Fig. 37, Top). When analyzing the structures of another CGP based scaffold in a 1:1 co-crystal with 1,4-diodotetrafluorobenzene (DITFB) the same interaction was discovered forming a zig-zag shaped chain in the crystal (Fig. 37, Bottom). Co-crystals (1:2) of this CGP with DITFB showed  $Te \cdots I$  interactions once again, although a larger network was formed rather than chains. Finally, a  $Te \cdots F$  interaction was observed in a 2:1 benzochalcogenazole/DITFB co-crystal.

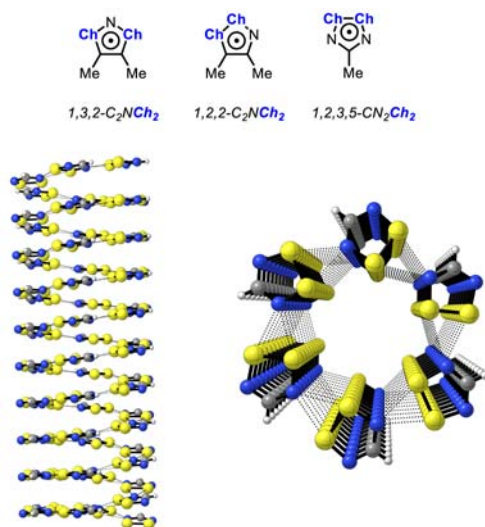
Further discussion of chalcogen bonding with halide anions can be found in Section 1.13.4.1 (Anion Binding and Recognition), as the importance of these interactions is far greater in solution for further applications.

#### 1.13.2.4 Other chalcogen interactions

Chalcogen bonding as a phenomenon also extends to several other special cases outside of chalcogen-chalcogen, -pnictogen and -halogen interactions. These include radical-radical chalcogen bonding, heavier chalcogen-oxygen interactions, and chalcogen-hydrogen interactions.



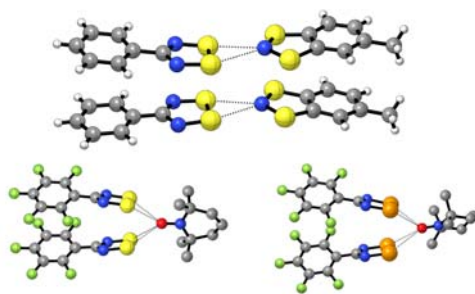
**Fig. 37** X-ray crystal structures of (Top) a crystallized CGP based scaffold and (Bottom) a 1:1 co-crystal of a CGP based scaffold with DITFB. From Biot, N.; Bonifazi, D. Concurring Chalcogen- and Halogen-Bonding Interactions in Supramolecular Polymers for Crystal Engineering Applications. *Chem. Eur. J.* **2020**, *26*, 2904–2913.



**Fig. 38** (Top) Structures of dichalcogenazolyl and dichalcogenadiazolyl radical heterocycles. (Bottom) X-ray crystal structure of the dithiadiazolyl radicals showing the spiral arrangement. Iodine atoms are located along the center but are omitted for clarity. From Beldjoudi, Y.; Nascimento, M. A.; Cho, Y. J.; Yu, H.; Aziz, H.; Tonouchi, D.; Eguchi, K.; Matsushita, M. M.; Awaga, K.; Osorio-Roman, I.; Constantinides, C. P.; Rawson, J. M. Multifunctional Dithiadiazolyl Radicals: Fluorescence, Electroluminescence, and Photoconducting Behavior in Pyren-1'-yl-dithiadiazolyl. *J. Am. Chem. Soc.* **2018**, *140*, 6260–6270.

#### 1.13.2.4.1 Radicals

Stable open-shell compounds, such as those displayed in Fig. 38, are often a key part of developing materials with wide ranging magnetic and conductive properties. Most work in this field has been carried out with sulfur and selenium containing compounds, because of the instability of the tellurium analogs. Intermolecular interactions (chalcogen bonding and particularly  $\pi$ -stacking) are somewhat favorable to electron mobility; dimerization and Peierls distortions on the other hand are detrimental to the electrical conductivity.



**Fig. 39** X-ray crystal structures of Ar-CNChChN dimers with (Top) MBDTA, Ch = S and (Bottom) TEMPO Ch = S (Left), Se (Right). From Nascimento, M. A.; Heyer, E.; Clarke, J. J.; Cowley, H. J.; Alberola, A.; Stephaniuk, N.; Rawson, J. M. On the Design of Radical-Radical Cocrystals. *Angew. Chem. Int. Ed.* **2019**, *58*, 1371–1375.

Radical chalcogen bonding interactions act in similar ways to the other forms of chalcogen bonds, in that they may also occur between two chalcogens, a chalcogen and a pnictogen, or a chalcogen and a halogen. A particularly interesting structural motif resulting from these interactions is observed in Fig. 38,<sup>73</sup> in which a nitrogen atom of the heterocycle acts as the chalcogen bond acceptor. These dithiadiazolyl radicals form a spiral column in a hexagonal phase doped with iodine (located along the center of the spiral).

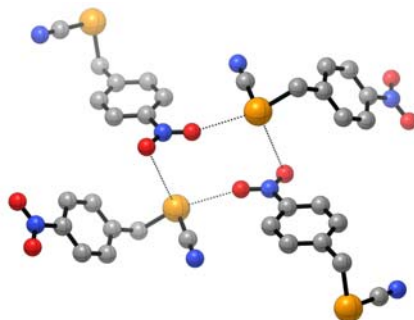
Radical chalcogen bonding interactions can also occur in non-aromatic compounds.<sup>74</sup> Ar-CNChChN structures have been shown to form radical-radical co-crystals with stable radical molecules such as (2,2,6,6-tetramethylpiperidin-1-yl)oxyl (TEMPO) and methylbenzodithiazolyl (MBDTA) (Fig. 39).<sup>75</sup> In these X-ray structures the chalcogen-pnictogen radical interactions can be seen for the MBDTA containing co-crystal, with both molecules dimerizing and forming tetramers after radical-radical chalcogen bonds form between the N-atoms of MBDTA and both sulfur atoms of the Ar-CNSSN molecules. In the case of the TEMPO containing structures, a chalcogen-oxygen interaction is observed with the O-atom of the TEMPO interacting with the four chalcogen atoms of the  $\pi$ -stacked Ar-CNChChN dimers.

#### 1.13.2.4.2 Chalcogen-oxygen interactions

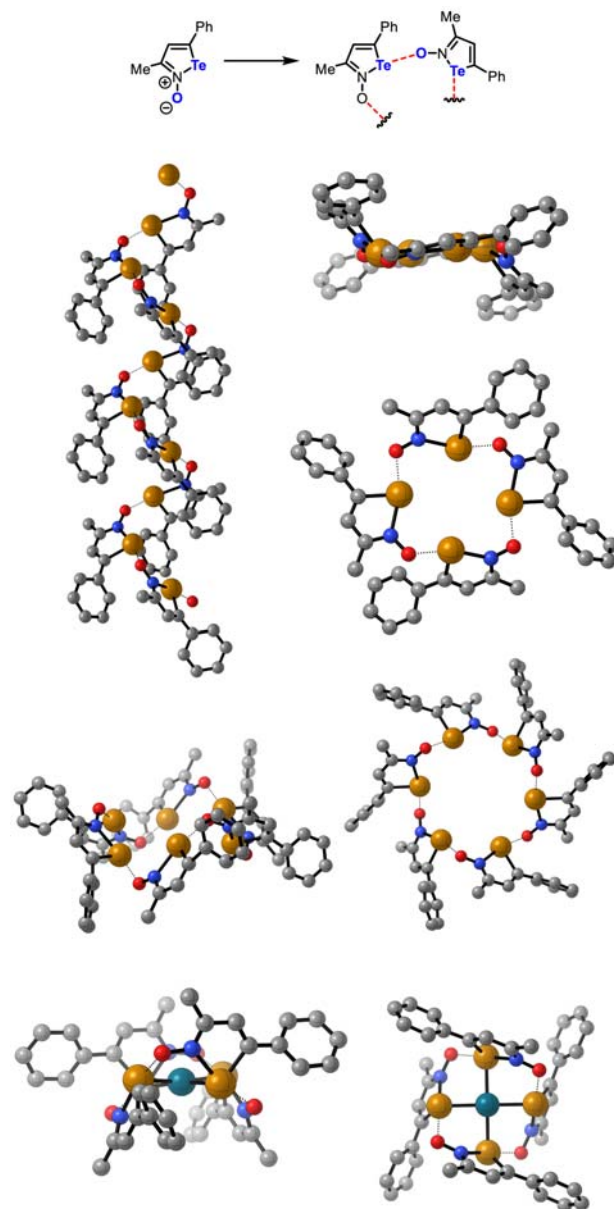
While the reader will recognize that oxygen itself is a member of the chalcogens, we consider these interactions separately as they have a distinct chalcogen bond donor and acceptor. Oxygen itself acts almost exclusively as a chalcogen bond acceptor, with only few special cases of its acting as a donor. The particular interest of these Ch $\cdots$ O interactions is largely due to the strength of interaction between selenium or tellurium and oxygen, the possibility to combine chalcogen bonding effects with other interactions which the highly electronegative oxygen atom can take part in, and the prevalence of oxygen in a great variety of interesting molecules. Their potential utility in the template-free formation of macrocycles could also have a significant impact on the ease of formation of molecules which potentially have useful properties similar to those of crown ethers, tetrapyrroles, calixarenes and cyclodextrins.

Selenium-oxygen interactions were found to occur both intra- and intermolecularly by Fourmigué et al. in 2018.<sup>31</sup> Fig. 40 shows the structures of two intramolecular examples, in which the stability of the internal chalcogen bond allows the molecules to remain planar despite steric constraints.<sup>76</sup> Se $\cdots$ O distances here are very short, and the Se–CN bond is elongated by the selective activation of one  $\sigma$ -hole site on the Se atom by the nitrile group.

4-Nitrobenzylselenocyanate shows a particularly interesting example of intermolecular Se $\cdots$ O chalcogen bonding (Fig. 40).<sup>41</sup> Tetrameric structures are observed in which the oxygen atoms of the nitrile groups are each involved in a chalcogen bond with the



**Fig. 40** X-ray crystal structure of 4-nitrobenzylselenocyanate tetramers. Hydrogen atoms are omitted for clarity. From Maartmann-Moe, K.; Sanderud, K. A.; Songstad, J.; Sillanpää, R.; Fernholt, L.; Rømming, C. The Crystal Structure of 4-Nitrobenzyl Tellurocyanate, 4-Nitrobenzyl Selenocyanate, 4-Nitrobenzyl Thiocyanate and Benzyl Selenocyanate. *Acta Chem. Scand.* **1984**, *38a*, 187–200.



**Fig. 41** X-ray crystal structures of supramolecular structures formed by association of an iso-tellurazole-*N*-oxide (*Top Left*) from benzene, (*Top Right*) from MeCN/CH<sub>2</sub>Cl<sub>2</sub> or CHCl<sub>3</sub>, (*Middle*) from THF, and (*Bottom*) with a Pd(II) salt.<sup>77</sup> Hydrogen atoms are omitted for clarity. From Ho, P. C.; Szydłowski, P.; Sinclair, J.; Elder, P. J. W.; Kübel, J.; Gendy, C.; Lee, L. M.; Jenkins, H.; Britten, J. F.; Morim, D. R.; Vargas-Baca, I. Supramolecular Macrocycles Reversibly Assembled by Te(⋯)O Chalcogen Bonding. *Nat. Commun.* **2016**, *7*, 11299.

selenium atom of another molecule, and each selenium forms two Se⋯O contacts to different molecules demonstrating that the two  $\sigma$ -holes are involved in separate chalcogen bonding interactions. Their interaction strengths here are different, the stronger interaction at 180° to the selenocyanate group provides the shortest Se⋯O distance, whereas the weaker interaction at 180° to the *para*-nitrobenzyl group gives a longer Se⋯O contact. Both of these contacts are still significantly shorter than the sum of the van der Waals radii.

Te⋯O connections have also been reported, and led to the aforementioned proposal for macrocyclic structures. Iso-tellurazole-*N*-oxides provide the basis for this work by the group of Vargas-Baca (Fig. 41).<sup>77,78</sup> Upon crystallization from various solvent systems, they obtained a variety of different supramolecular structures (Fig. 41) which highlight the versatility of these Te⋯O interactions and their potential for a wide range of macrocyclic applications. Benzene allowed access to infinite spiral chains coiling in alternating directions. Non-solvated crystals from chloroform, or layering acetonitrile over dichloromethane provided tetrameric macrocycles with two distinct Te⋯Te transannular distances, and a chair-like conformation. Crystallization from tetrahydrofuran (THF) yielded crystals with a hexameric macrocycle crystallizing around THF molecules. Packing in this case forms a hexagonal



lattice and all Te...Te distances are the same. Loss of solvent over time causes the crystals to become opaque, as the disordered THF molecules leave the macrocycle cavities. Use of dichloromethane/hexane mixtures also formed hexamers, however the solvent here occupies voids external to two crystallographically distinct macrocycles. Distortion of the macrocycles due to packing presents the interesting case of three different transannular Te...Te distances in each ring (i.e., six distinct Te...Te distances).

Addition of a transition-metal ion ( $\text{Pd}^{2+}$ ) gives rise to a complex of 1:4 stoichiometry. The crystal structure in this case shows a boat conformation of the tetrameric aggregate, with the central palladium ion exhibiting a square planar coordination geometry. Pd–Te distances are comparable to those measured for anionic tellurium ligand complexes.

An example of oxygen taking part as both donor and acceptor was demonstrated in 2020 by White et al. when they obtained experimental evidence of the interactions in an *o*-nitro-*O*-aryl oxime.<sup>79</sup> A close intramolecular O...O contact is present, and by a combination of crystal structure analysis and computation, it was possible to conclude that the interaction taking place is consistent with the charge transfer model of chalcogen bonding. Fig. 42 shows some examples of *o*-nitro-*O*-aryl compounds which display these interactions.

#### 1.13.2.4.3 Chalcogen-hydrogen interactions

As early as 1994, Tomoda and Iwaoka observed Se...H interactions in the solid-state structures of a diselenocin.<sup>80</sup> These contacts could be seen in the crystal structure of both the chair conformation and boat conformation of their molecules (Fig. 43), with exchange processes occurring in solution. At the time, these observations were tentatively described to be similar in nature to those of O...H hydrogen bonding interactions. Confirmation of the interaction was obtained by NMR studies in which the spin-spin coupling between the selenium and the nearby benzylic hydrogen was determined. Only one of the benzylic hydrogen atoms showed satellites from <sup>77</sup>Se (natural abundance 7.6%), and the peaks observed could be assigned to direct spin-spin coupling, due to the observed <sup>1</sup>J<sub>Se...H</sub> coupling constants being far larger in comparison to those of the <sup>2</sup>J<sub>Se...H</sub> coupling of selenoanisoles. The value of the coupling constant <sup>1</sup>J<sub>Se...H</sub> was observed to be greater in the boat conformation than the chair for this molecule, and using spin decoupling experiments further detailed information regarding the bonding and interactions was gathered.

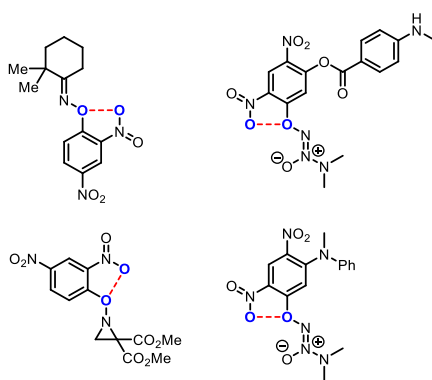
This first example of chalcogen-hydrogen interactions was later followed by an intermolecular example in 2019. Xu et al. observed that the solid-state structure of dibenzotellurophene not only shows close Te...Te contacts indicative of strong chalcogen bonding, but also Te...H interactions (Fig. 44).<sup>81</sup> The dibenzotellurophenes developed in this work were of further interest because they displayed room temperature phosphorescence leading to a great many potential applications.

### 1.13.3 Self-assembly by chalcogen interactions

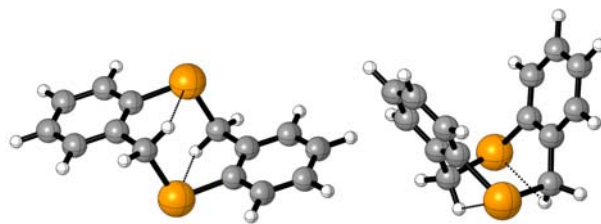
Chalcogen interactions have emerged as a powerful tool for supramolecular self-assembly. Compared to hydrogen bond acceptors the chalcogen derivatives are often superior in regards to anion binding strength and selectivity. The careful design of chalcogen containing subunits can lead to unique supramolecular architectures that are useful for nanotechnological applications.<sup>82,83</sup>

#### 1.13.3.1 Capsules

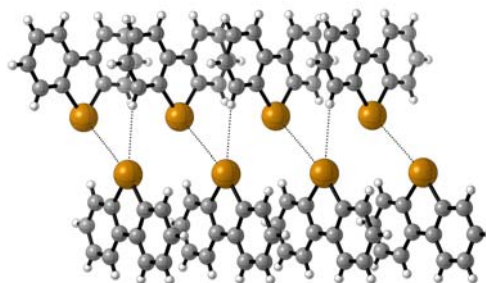
Chalcogen-bonded supramolecular capsules which result from dimerization of 2,1,3-benzochalcogenadiazoles through Ch...N square interactions were a major research area of the Diederich group (Fig. 45).<sup>33,71</sup> These molecules were later embedded into resorcin[4]arene-based cavitands, so that they appeared at the top of each half capsule. The decoration of the bottom of these half capsules with alkyl chains led to improved solubility in organic solvents and made crystallization possible. In the crystal, remarkable contrasts between the tellurium and the sulfur variants were displayed which can be explained by the difference in



**Fig. 42** Examples of White's *o*-nitro-*O*-aryl compounds which display O...O interactions. From Fellowes, T.; Harris, B. L.; White, J. M. Experimental Evidence of Chalcogen Bonding at Oxygen. *Chem. Commun.* **2020**, 56, 3313–3316.



**Fig. 43** Solid-state structure of the diselenocin showing Se...H interactions in the chair (*Left*) and boat (*Right*) conformations. From Iwaoka, M.; Tomoda, S. First Observation of a C-H...Se "Hydrogen Bond". *J. Am. Chem. Soc.* **1994**, *116*, 4463–4464.



**Fig. 44** X-ray of dibenzotellurophene showing Te...Te and Te...H interactions. From Jiang, M.; Guo, J.; Liu, B.; Tan, Q.; Xu, B. Synthesis of Tellurium-Containing  $\pi$ -Extended Aromatics with Room-Temperature Phosphorescence. *Org. Lett.* **2019**, *21*, 8328–8333.

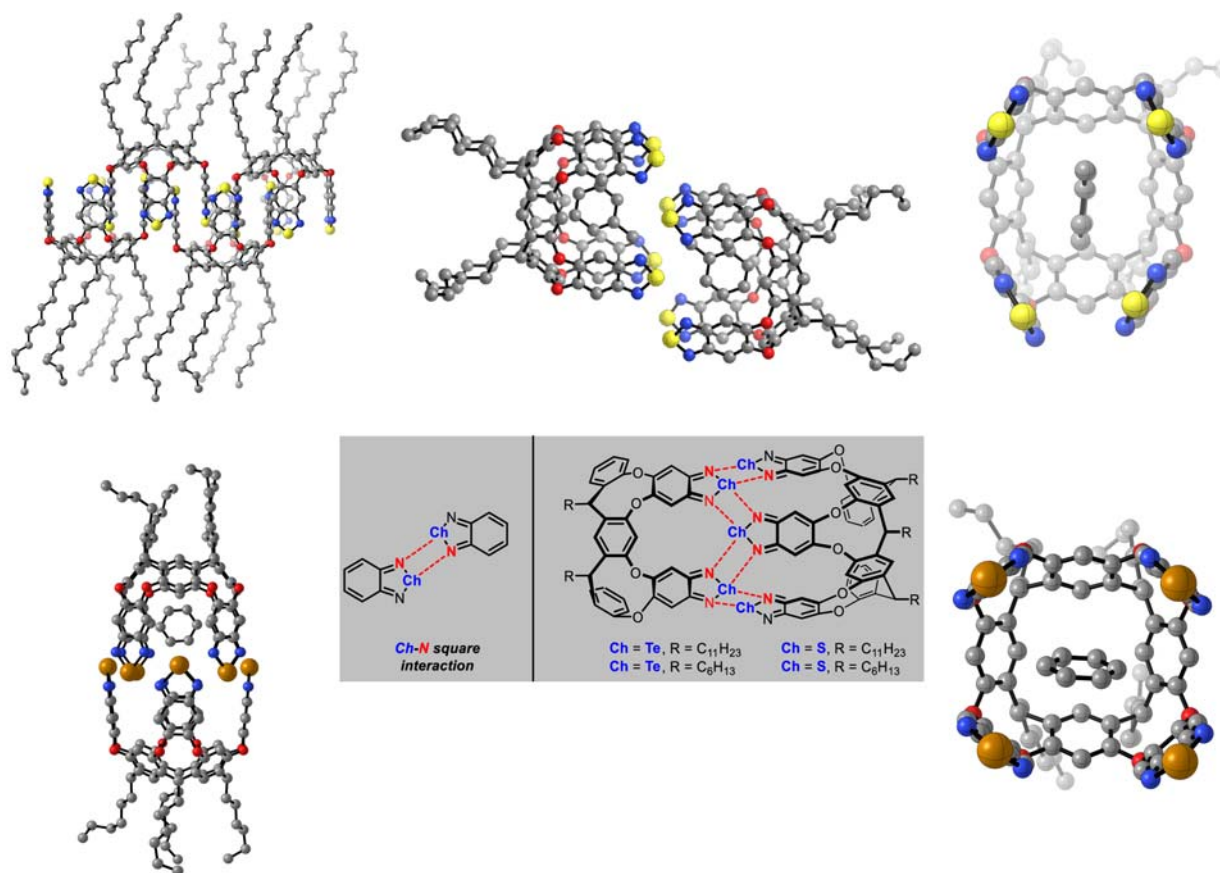
association strength between S...N and Te...N interactions. While the tellurium based capsule was assembled in a highly linear manner showing 16 close Te...N contacts in the crystal, a time-dependent transformation from a kinked to a linear species was observed in solution. The sulfur containing congener showed a kinked and shifted capsule assembly in the crystal. The thermodynamically more stable species was generally present in the solid state. Additionally, a benzene molecule was trapped deep inside every half capsule in the obtained crystal structures. The capsule formation and the transformation between species was solvent and concentration dependent. Association constants for the dimerization of cavitands were determined by electrospray ionization mass spectrometry (ESI-MS) titration.

Based on the work from the Diederich group, Yu et al. developed Se-based cavitands, which assembled water-stable containers (**Fig. 46**).<sup>72,84</sup> Chalcogen bonding in water is rarely observed, which might be explained by the competition between hydrogen and chalcogen bonding events.<sup>85</sup> Investigations on the binding properties of guests were carried out via <sup>1</sup>H NMR experiments in D<sub>2</sub>O. These studies revealed differences for hydrophobic and amphiphilic guests and showed host-guest stoichiometries of 1:1, 2:2 or 2:1 after supramolecular assembly. While small guests such as hexane isomers favored the formation of 2:2 complexes, larger guests (e.g., cyclodecane) assembled 1:1 type host-guest adducts. Guests bearing long linear chains (*n*-dodecane or amides) led to 2:1 dimeric capsular complexes that appeared to be stable for up to 2 weeks. Other interactions such as hydrophobic forces, hydrogen-bonding attractions, polarizability or magnetic anisotropy that influence the stability of these structures were further explored experimentally and by computational calculations.

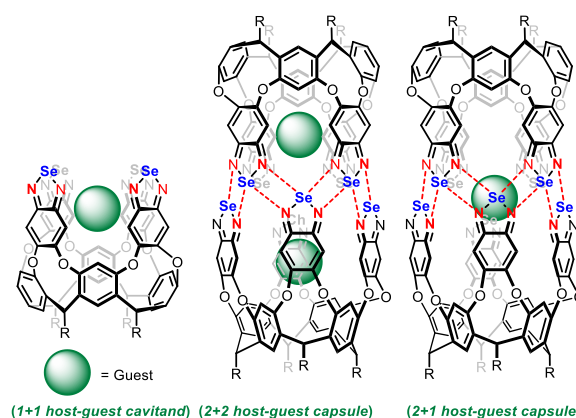
### 1.13.3.2 Polymers and materials

The Yan lab reported the first assembly of supramolecular architecture in solution by chalcogen bonding interactions in 2018.<sup>86</sup> Combining a quasi-calix[4]chalcogenadiazole as a multi-side donor with a pyridine-*N*-oxide acceptor led to the assembly of supramolecular amphiphiles in aqueous solution (**Fig. 47**). Variation of the chalcogen atoms opens access to a variety of architectures because of the difference in strength of the formed chalcogen bonds. While the self-assembly of the selenium based donors delivers nanofibers with uniform radial diameters, the tellurium analog assembles to spherical micelles. As observed by transmission electron microscopy, the micelles displayed sizes of 40 to 130 nm. Further, the membrane thickness was tested by small-angle X-ray scattering and the character of the chalcogen bonding interactions was investigated by NMR and UV-vis spectroscopy, mass spectrometry and isothermal titration calorimetry. The disassembly of the micelles was favored at low pH values or by the addition of halide anions.

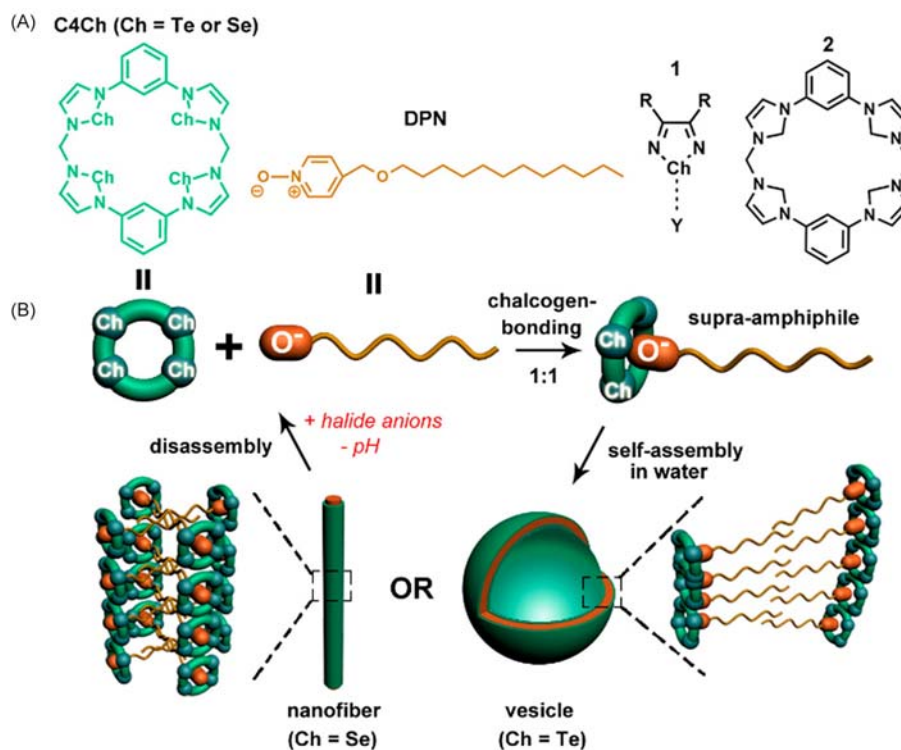
The same research group applied the previously described chalcogen bonding strategy to form supramolecular polymers. While calix[4]chalcogenadiazoles linked by a tetraethylene glycol motif were used as the monomeric chalcogen acceptors, 4,4'-decyl-bispyridine *N*-oxide acted as the double headed chalcogen bond donor (**Fig. 48**).<sup>87</sup> Mixing both monomers in aqueous media resulted in the organization of polymer arrays via end-to-end Ch...O contacts. The self-assembly of the supramolecular polymers led to the formation of hydrogel fibers which again could be disassembled by the addition of halide anions. Due to different



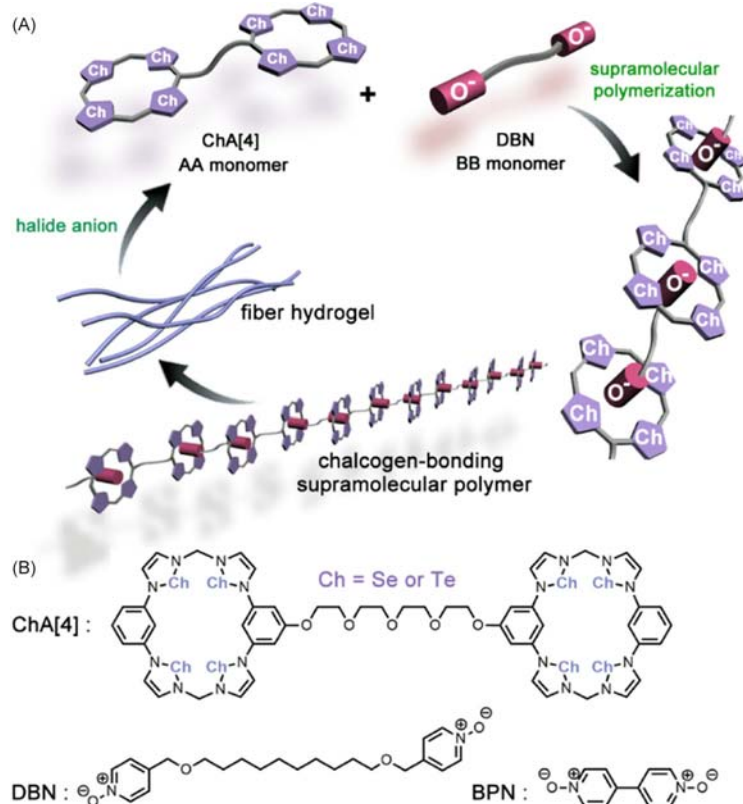
**Fig. 45** A dimeric molecular capsule formed by attractive  $S \cdots N$  or  $Te \cdots N$  interactions. (Top) Crystal structures of a capsule containing  $Ch = S$  and  $R = C_{11}H_{23}$  (Left), its shifted capsule assembly (Middle,  $R = C_6H_{13}$ ) and a half capsule inheriting benzene (top view, Right). (Bottom) Crystal structures of the linear assembly of a  $Ch = Te$  and  $R = C_6H_{13}$  containing capsule (Left) and a half capsule inheriting benzene (top view, Right). From Ams, M. R.; Trapp, N.; Schwab, A.; Milić, J. V.; Diederich, F. Chalcogen Bonding “2S-2N Squares” versus Competing Interactions: Exploring the Recognition Properties of Sulfur. *Chem. Eur. J.* **2019**, *25*, 323–333. Riwar, L.-J.; Trapp, N.; Root, K.; Zenobi, R.; Diederich, F. Supramolecular Capsules: Strong versus Weak Chalcogen Bonding. *Angew. Chem. Int. Ed.* **2018**, *57*, 17259–17264.



**Fig. 46** Host-guest cavitands and capsules bonded by chalcogen interactions. From Rahman, F.-U.; Tzeli, D.; Petsalakis, I. D.; Theodorakopoulos, G.; Ballester, P.; Rebek, J.; Yu, Y. Chalcogen Bonding and Hydrophobic Effects Force Molecules into Small Spaces. *J. Am. Chem. Soc.* **2020**, *142*, 5876–5883. Zhu, Y.-J.; Gao, Y.; Tang, M.-M.; Rebek, J.; Yu, Y. Dimeric Capsules Self-Assembled Through Halogen and Chalcogen Bonding. *Chem. Commun.* **2021**, *57*, 1543–1549.

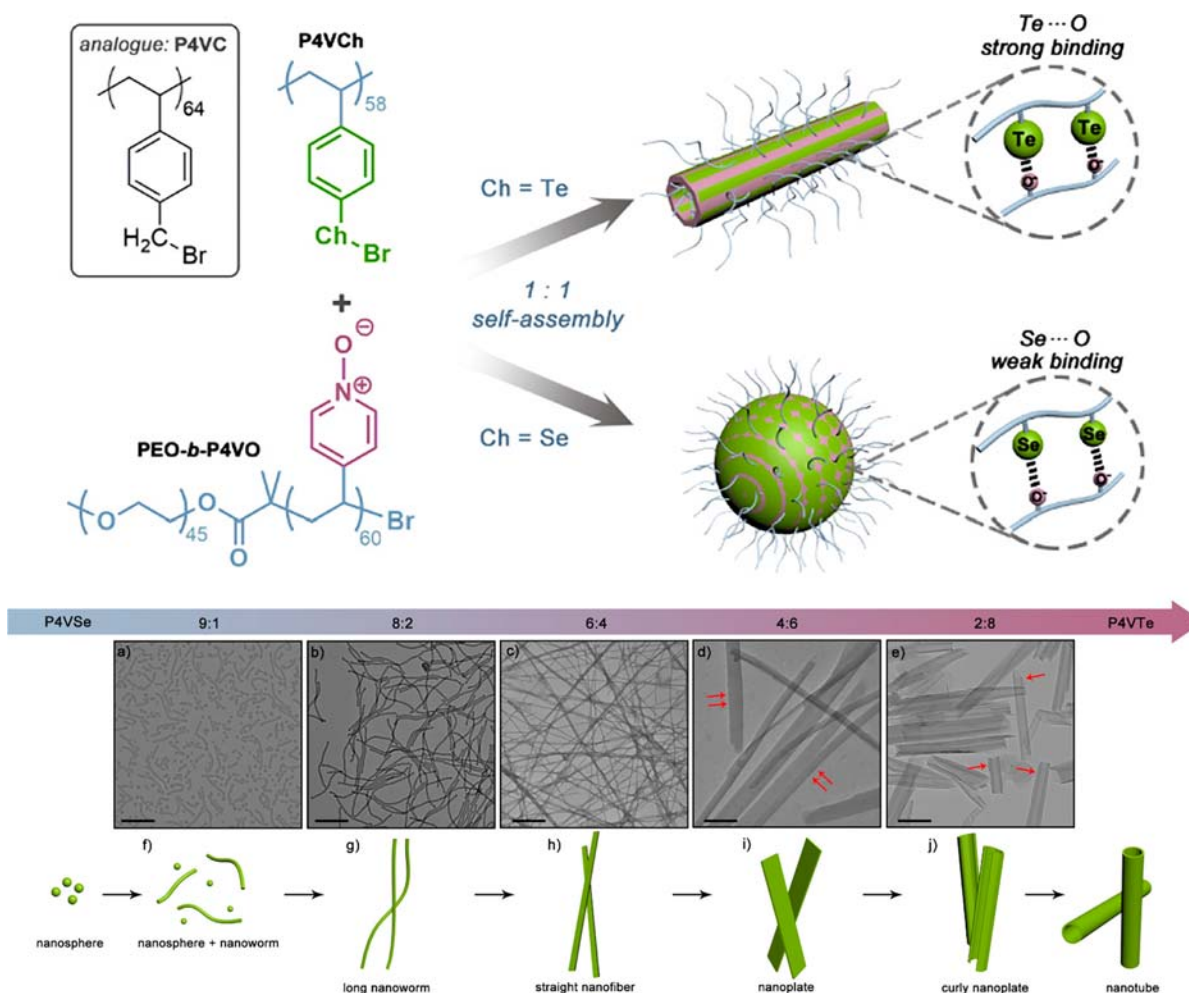


**Fig. 47** Self-assembly of supra-amphiphiles in solution via chalcogen-chalcogen contacts. Reprinted with permission from Chen, L.; Xiang, J.; Zhao, Y.; Yan, Q. Reversible Self-Assembly of Supramolecular Vesicles and Nanofibers Driven by Chalcogen Bonding Interactions. *J. Am. Chem. Soc.* **2018**, *140*, 7079–7082. Copyright 2018 American Chemical Society.



**Fig. 48** Supramolecular polymers and their assembly to hydrogel fibers in solution by chalcogen-chalcogen interactions. Reprinted with permission from Zeng, R.; Gong, Z.; Yan, Q. Chalcogen Bonding Supramolecular Polymers. *J. Org. Chem.* **2020**, *85*, 8397–8404. Copyright 2020 American Chemical Society.





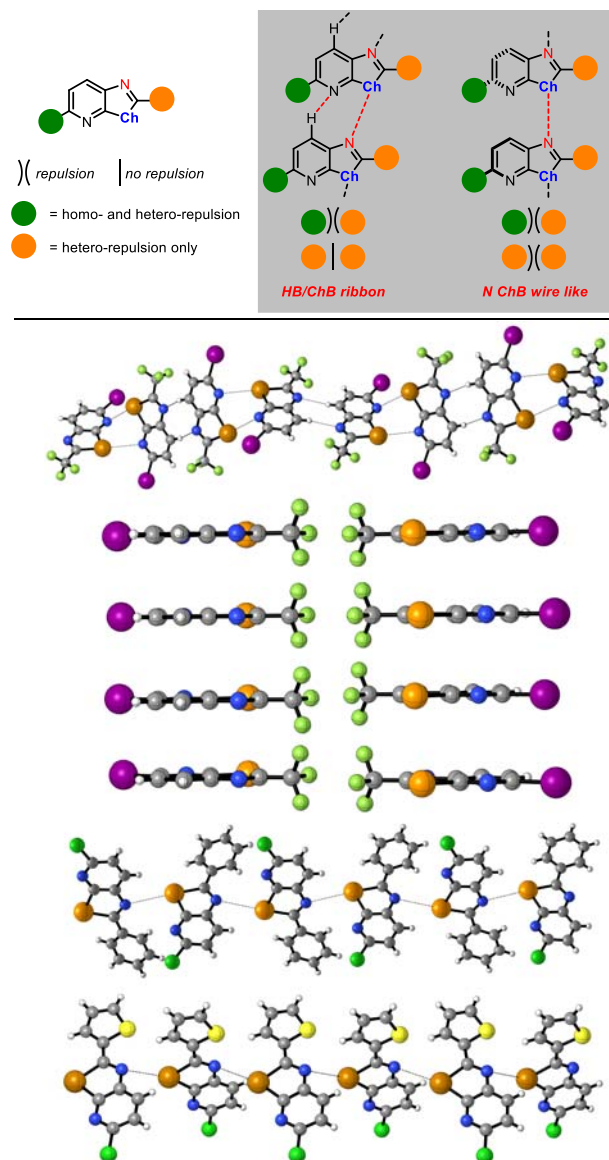
**Fig. 49** Supramolecular formation of partner polymers in solution by chalcogen bonding. (Top) Principle of the polymer formation. (Bottom) Structural outcome based on the mixing ratio of monomers. Reprinted with permission from Zeng, R.; Gong, Z.; Chen, L.; Yan, Q. Solution Self-Assembly of Chalcogen Bonding Polymer Partners. *ACS Macro Lett.* **2020**, *9*, 1102–1107. Copyright 2020 American Chemical Society.

chalcogen bond strength, the properties of the formed polymers are dependent on the chalcogen atoms in the monomeric units. Based on this study new perspectives on chalcogen bonding assisted supramolecular material engineering will become available.

In another project, Yan et al. exploited chalcogen contacts to form different classes of partner polymers (Fig. 49).<sup>87</sup> This polymerization strategy was enabled by the decoration of polymers with either bromochalco-benzene units for chalcogen bond donation or pyridine *N*-oxide sites for chalcogen bond acceptance. This substitution allows the polymers to form non-covalent donor-acceptor complexes and to assemble in a tubular (for tellurium) or spherical manner (for selenium). The resulting geometries are again a consequence of the difference in chalcogen bonding strength between Se...O and Te...O contacts. Interestingly, when selenium and tellurium containing donor polymers were mixed in this process, a variety of morphologies became accessible upon variation of the ratio of monomeric chalcogen bond donors. The morphological transition of the polymeric structures from nanospheres to nanotubes was explored via transition electron microscopy.

Bonifazi and co-workers developed a protocol for the supramolecular assembly of chalcogen-bonded nanoribbons in the crystal.<sup>88</sup> Decisive for the ribbon formation was the choice of substituents in the 2- and 5-positions of the chalcogenazolo [5,4- $\beta$ ]pyridine subunits (Fig. 50). Depending on the steric and electronic properties which lead to homo- and hetero-repulsive events different solid-state structures are obtained. Substitution by CF<sub>3</sub> in the 2-position led to the formation of desired head-to-tail hydrogen and chalcogen bonded nanoribbons when combined with Me, Cl or oxazole residues in the 5-position. While a kinked supramolecular ribbon was obtained from the 5-iodo-substituted Te–CF<sub>3</sub> congener, sterically demanding groups (e.g., phenyl or thienyl) favored a wiring organization in the solid state. Crystal design through cooperative hydrogen and chalcogen bonding events is considered to be very important for applications in sensing and optoelectronic research.





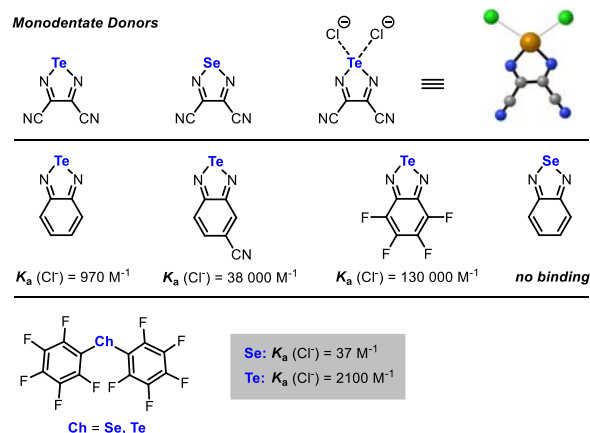
**Fig. 50** Supramolecular formation of nanoribbons in the crystal. Formations in the crystal: (Top) Kinked ribbon arrangements of \*2-I and 5-CF<sub>3</sub>-substituted tellurazopyridines and (Upper Middle) columnar orientation. Wire supramolecular arrangements of (Lower Middle) 2-Cl- and 5-phenyl-substituted tellurazopyridines and (Bottom) 2-Cl- and 5-thienyl-substituted tellurazopyridines. From Biot, N.; Romito, D.; Bonifazi, D. Substituent-Controlled Tailoring of Chalcogen-Bonded Supramolecular Nanoribbons in the Solid State. *Cryst. Growth Des.* **2021**, *21*, 536–543.

### 1.13.4 Chalcogen-anion coordination

#### 1.13.4.1 Anion binding and recognition

Chalcogen containing diazoles are well-established structures for research on anion binding in solution (Fig. 51). Investigations by the group of Zibarev on association constants of nitrile-substituted tellura- and selenadiazole by optical absorbance spectroscopy revealed higher anion affinities for heavier, less electronegative chalcogens.<sup>89</sup> While binding of thiophenolate, iodide, thiocyanate and selenocyanate anions was possible with telluradiazole, only binding of thiophenolate to selenadiazole was detected.<sup>90</sup> The results also clearly showed the solvent dependency of such interactions.

Taylor et al. published a study about the anion binding abilities of benzotelluradiazoles in 2015.<sup>68</sup> Even unsubstituted benzene systems showed association constants of 970 M<sup>-1</sup> for chloride anions when measured via absorbance spectroscopy. Attaching electron-withdrawing groups like nitriles or fluorine atoms to the benzene core enhances the affinity for anion binding drastically (38,000 M<sup>-1</sup>/130,000 M<sup>-1</sup>). When measuring the constants in THF, addition of tetrabutylammonium chloride favored a red-shift in the wavelength of maximum optical absorbance. Interestingly, benzoselenadiazoles only interacted weakly with chloride anions. These experimentally discovered trends were confirmed by additional quantum-chemical calculations in THF solvent models.



**Fig. 51** Monodentate chalcogen donors for anion binding. From Benz, S.; Poblador-Bahamonde, A. I.; Low-Ders, N.; Matile, S. *Catalysis with Pnictogen, Chalcogen, and Halogen Bonds*. *Angew. Chem. Int. Ed.* **2018**, *57*, 5408–5412.

As part of an extensive study on chalcogen, pnictogen and halogen bond catalysts the group of Matile determined the association constant of the perfluorinated structures via  $^{19}\text{F}$  NMR spectroscopy (Fig. 51).<sup>91</sup> In addition to higher catalytic activity, larger complex formation constants were observed for the tellurium containing catalyst.

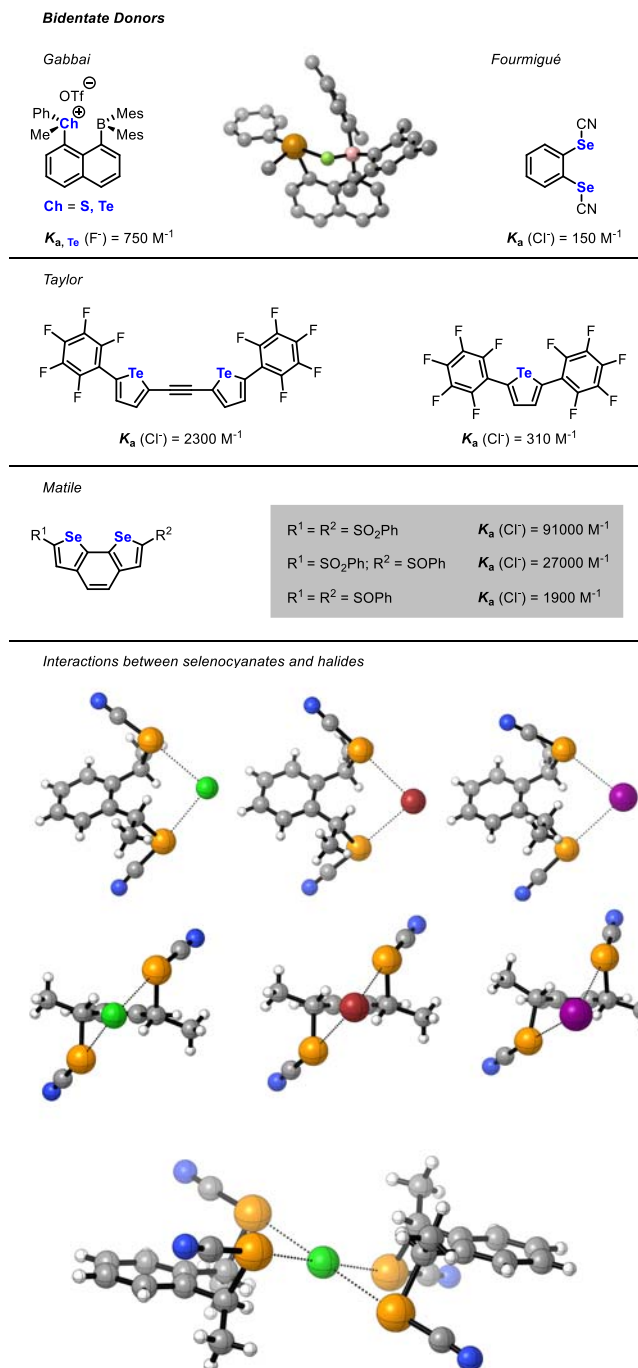
The very first example of chalcogen bonded anion recognition was reported by Gabbai et al. in 2010 by using mixed bidentate 1,8-boron-chalcogenium-naphthalenes (Fig. 52).<sup>92</sup> UV spectroscopy revealed association constants of  $750 \text{ M}^{-1}$  for fluoride anions in methanol for the more active tellurium and boron based donor. Additionally, binding to fluoride was found to be very selective, since other anions remained unbound. Further evidence for the binding event taking place was collected via  $^{19}\text{F}$  and  $^{125}\text{Te}$  NMR spectroscopy and X-ray diffraction analysis. In the crystal of the fluoride complex a directional chalcogen bond ( $d = 2.506 \text{ \AA}$ , F-Te-C<sub>ph</sub> angle  $174.0^\circ$ ) was observed. Analogous studies on the weaker sulfur containing donor showed related chalcogen bond values ( $d = 2.548 \text{ \AA}$ , F-S-C<sub>ph</sub> angle  $176.6^\circ$ ), but no Se...F bonding was detected via UV spectroscopy.

Since selenocyanates are known to interact with Lewis bases in the crystal, the group of Fourmigué tested bis(selenocyanate) for anion recognition purposes.<sup>40,93</sup> While this donor is able to build complexes with  $\text{Ph}_4\text{P}^+\text{Cl}^-$  and  $\text{Ph}_4\text{P}^+\text{Br}^-$  by a two-point interaction with the halide in the solid state, binding of chloride anions in solution is possible ( $K_a = 150 \text{ M}^{-1}$ ) as explored by NMR spectroscopic titration.

Taylor et al. designed chalcogen bond donors based on the tellurophene motif (Fig. 52).<sup>94</sup> Particularly bidentate alkynylene-linked bis(tellurophene) showed a large association constant of  $2300 \text{ M}^{-1}$  for chloride anions in THF. Monodentate donors bearing this motif showed significantly lower constants in comparison. Computational work on the alkynylene-bridged version uncovered that the chloride anion engages both tellurium atoms ( $d = 3.23 \text{ \AA}$ , F-Te-C angle  $170^\circ$ ). However, these studies made it clear that the previously described monodentate donors from the Taylor group exhibit better probabilities for anion recognition.

Searching for efficient bidentate donors, Matile and co-workers developed substituted benzodiselenazoles which additionally show catalytic activity (Fig. 52).<sup>95</sup> Spectroscopic investigations revealed superb association constants, with  $91,000 \text{ M}^{-1}$  being the highest when interacting with chloride anions in THF. As expected, lower affinities for chloride anions were obtained when less electron-withdrawing groups were installed on the donor skeleton.

Beer et al. synthesized macrocyclic chalcogen bond donors bearing two charged methylselenotriazolium groups for anion binding purposes (Fig. 53).<sup>96</sup> Investigations on the macrocycle containing a phenyl bridge showed good binding to heavier halogens, which arises most likely from favorable interactions and due to lower solvation energies compared to lighter halogens ( $K_a = 1200\text{--}1500 \text{ M}^{-1}$  in acetone  $d_6/D_2O$ ). Computational investigations shed light on the influence of the methylseleno-substituents. Macrocycles not bearing this substitution pattern showed, for instance, a higher binding affinity for bromide anions than iodide anions. Additionally, the phenyl bridged macrocycle was applied for the synthesis of a rotaxane which was also explored in regard to anion recognition properties. *N*-Methylpyridinium bridged chalcogenotriazoles were further utilized to compare the thermodynamics of anion recognition probabilities of tellurium- and selenium-based donors. For the methyltelluro-substituted derivative, association constants of up to  $650 \text{ M}^{-1}$  (in MeCN) were found for halide anions. While these constants displayed high solvent dependence, compounds without chalcogen bond donors exhibited a lower affinity for all tested anions. Studies on the entropies and enthalpies of such interactions were undertaken by the utilization of van't Hoff plots. The enthalpic term was found to primarily contribute to the interactions with anions for the tellurium species in MeCN, hence leading to the observed anion selectivity. Contrary to this, due to desolvation of the host and guest species during the binding process, the driving force of anion binding for the selenium containing molecules turned out to be entropy.

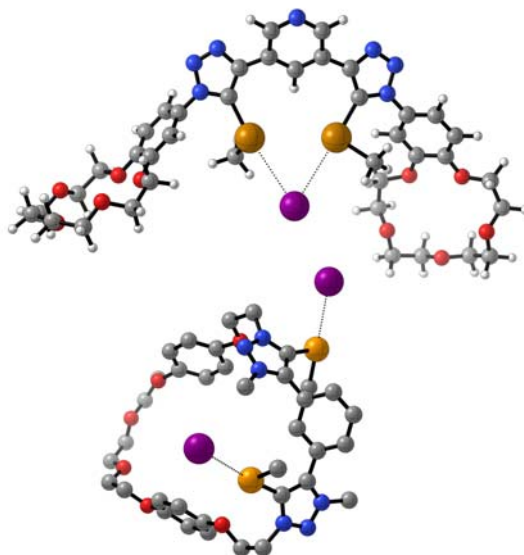
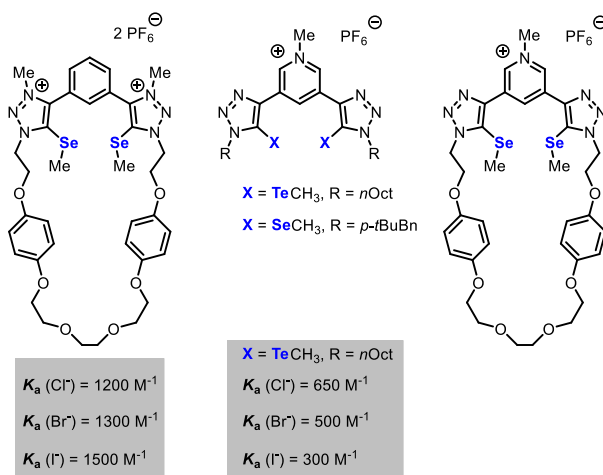


**Fig. 52** Bidentate chalcogen donors for anion binding.<sup>44</sup> Crystal structures of bidentate selenocyanates coordinating to halides (side view, front view and dimeric coordination). From Huynh, H.-T.; Jeannin, O.; Aubert, E.; Espinosa, E.; Fourmigué, M. Chalcogen Bonding Interactions in Chelating, Chiral Bis(selenocyanates). *New J. Chem.* **2021**, *45*, 76–84. Benz, S.; Macchione, M.; Verolet, Q.; Mareda, J.; Sakai, N.; Matile, S. Anion Transport with Chalcogen Bonds. *J. Am. Chem. Soc.* **2016**, *138*, 9093–9096. Garrett, G. E.; Carrera, E. I.; Seferos, D. I.; Taylor, M. S. Anion Recognition by a Bidentate Chalcogen Bond Donor. *Chem. Commun.* **2016**, *52*, 9881–9884.

### 1.13.4.2 Anion transport

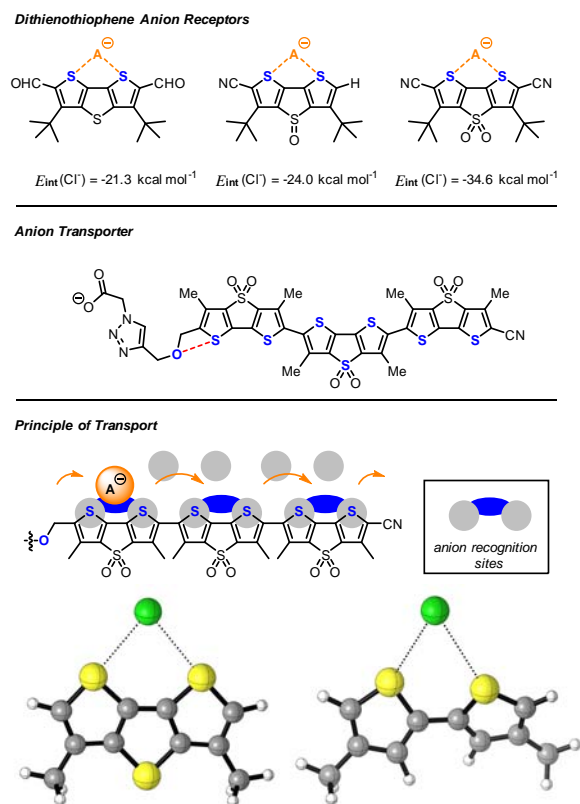
The dithienothiophene (DTT) scaffold was heavily exploited by the Matile group for functional supramolecular chemistry (Fig. 54).<sup>97</sup> Especially in terms of anion recognition and anion transport, molecules based on the DTT motif show superb properties.<sup>82</sup> Complexation of halides becomes possible due to the chelation of the anions to two sulfur atoms. The non-oxidized DTT and its oxidized relatives show interaction energies of over  $20\text{ kcal mol}^{-1}$  when engaged with chloride anions in the gas phase. These

## Charged donors



**Fig. 53** (Top) Charged chalcogen donors for anion binding. (Middle) Computational structure of an *N*-Me-pyridinium-bridged donor. (Bottom) X-ray structure of a charged macrocyclic donor bearing a phenyl bridge. From Lim, J. Y. C.; Marques, I.; Thompson, A. L.; Christensen, K. E.; Félix, V.; Beer, P. D. Chalcogen Bonding Macrocycles and [2]Rotaxanes for Anion Recognition. *J. Am. Chem. Soc.* **2017**, *139*, 3122–3133. Lim, J. Y. C.; Marques, I.; Félix, V.; Beer, P. D. Chiral Halogen and Chalcogen Bonding Receptors for Discrimination of Stereo- and Geometric Dicarboxylate Isomers in Aqueous Media. *Chem. Commun.* **2018**, *54*, 10851–10854.

energies usually increase with higher sulfur oxidation states. Additionally, the electron-withdrawing character in the  $\pi$ -system can be manipulated by substituents on the outer thiophenes (e.g., aldehydes, cyanides) which leads to stronger bonds. Extended structures of three oxidized DTT subunits with deep  $\sigma$ -holes were found to be suitable molecules for anion transport across lipid bilayers. The anion can hop from one recognition site to the next and therefore transport across such membranes is possible in a chalcogen bonding cascade. Conductance experiments supported the formation of dynamic bundles from the preferred trimer amphiphiles. Other trimeric derivatives and dimers that contained DTT units of lower sulfur oxidation states displayed no transport properties. Investigation of the  $EC_{50}$  values (effective concentration required to reach 50% of maximal activity) revealed values for the controls that are more than an order of magnitude ( $EC_{50} = 280 \text{ nM}$ ) above the values for the active species.



**Fig. 54** DTT based anion receptors and anion transport. Computational structures of DTT (*Top*) and a bithiophene motif binding to a chloride anion (*Bottom*). From Strakova, K.; Assies, L.; Goujon, A.; Piazzolla, F.; Humeniuk, H. V.; Matile, S. Dithienothiophenes at Work: Access to Mechanosensitive Fluorescent Probes, Chalcogen Bonding Catalysis, and Beyond. *Chem. Rev.* **2019**, *119*, 10977–11005.

### 1.13.4.3 Other examples of halide coordination

In addition to the described work from Sections 1.13.4.1 and 1.13.4.2 other molecular designs have been used for halide coordination. Cyclic telluroxanes were used to capture bromide or form sandwich-complexes with iodide anions (Fig. 55).<sup>98</sup> Carboranes decorated with alkylchalcogeno substituents were utilized for such purposes by Jeon et al. in 2021.<sup>99</sup>

## 1.13.5 Chalcogen bonding in catalysis and synthesis

### 1.13.5.1 Synthesis and structure rigidification by intramolecular chalcogen bonding

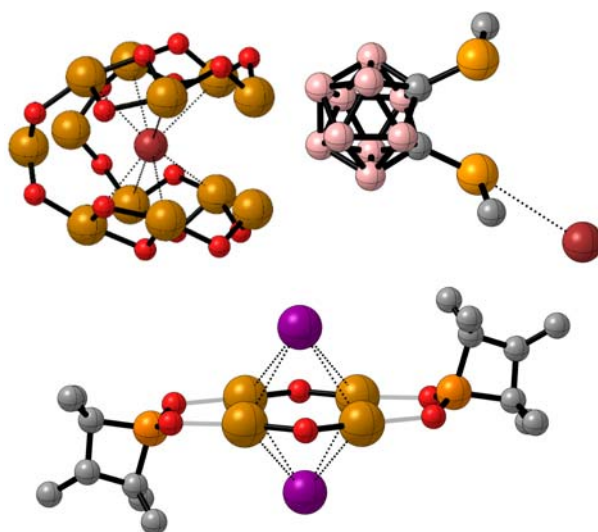
The rigidification of organochalcogen compounds is possible by the formation of five- and six-membered rings via attractive intramolecular chalcogen interactions with Lewis basic atoms. The group of Singh utilized non-covalent Se/Te $\cdots$ N bonding to rigidify Se- or Te-substituted azobenzenes (Scheme 3).<sup>100</sup>

For synthetic purposes, strategies exploiting chiral Se- and S-containing catalysts are most used. Pioneering work by Tomoda et al. covered a methoxy-selenylation of (*E*)-methylstyrenes catalyzed by a chiral diselenide (Scheme 3).<sup>101</sup> The active species is rigidified by a 1,5-Se $\cdots$ N contact that allows transfer of the chiral information and the synthesis of the *anti*-substituted products exclusively. After proving the applicability of this concept for synthesis, Wirth<sup>102</sup> (1995) and Tiecco<sup>103</sup> (2002) exploited different catalysts for the conversion of styrenes to ethers or lactones (Scheme 3). In both examples the active species are formed from chiral diselenides, which differentiate by the chalcogen atoms responsible for the fixation of the reagent (Wirth: Se $\cdots$ O, Tiecco: Se $\cdots$ S). After addition to the olefin, the selenium containing species is cleaved off oxidatively or by radicals and the desired reaction products are released enantioselectively. With an enantiomeric excess up to 88% and moderate yields (33–70%) Wirth's reagents showed better performance than Tiecco's counterparts.

### 1.13.5.2 Lewis base catalysis by transient chalcogen bonding interactions

In synthesis, chalcogen-containing compounds can act as Lewis base catalysts for the activation of other reagents via transient non-covalent chalcogen bonding.<sup>104</sup> Yeung utilized this concept for a chloroamidation of substituted olefins (Scheme 4).<sup>105</sup> The





**Fig. 55** (Top Left) A  $\text{Te}_{12}\text{O}_{16}$  telluroxane ring with trapped bromide in the crystal. (Top Right) Crystal structure of a methylseleno-substituted dodecacarborane that coordinates to a bromide anion. (Bottom) Crystal structure of a sandwich-complex between a dicationic organotelluroxane macrocycle adduct with iodide. From Chandrasekhar, V.; Thirumoorthi, R. Halide-Capped Tellurium-Containing Macrocycles. *Inorg. Chem.* **2009**, *48*, 10330–10337. Citeau, H.; Kirschbaum, K.; Conrad, O.; Giolando, D. M. A Novel Cage Organotellurate(IV) Macrocyclic Host Encapsulating a Bromide Anion Guest:  $\text{Li}(\text{THF})_4(\text{PriTe})_{12}\text{O}_{16}\text{Br}_4(\text{Li}(\text{THF})\text{Br})_4\text{Br}\cdot 2\text{THF}$ . *Chem. Commun.* **2001**, 2006–2007; Beau, M.; Lee, S.; Kim, S.; Han, W.-S.; Jeannin, O.; Fourmigué, M.; Aubert, E.; Espinosa, E.; Jeon, I.-R. Strong  $\sigma$ -Hole Activation on Icosahedral Carborane Derivatives for a Directional Halide Recognition. *Angew. Chem. Int. Ed.* **2021**, *60*, 366–370.

selenium catalyst is first employed to activate the electrophilic chlorine source (NCS) via a  $\text{Se}\cdots\text{Cl}$  interaction, which subsequently leads to the formation of a chloronium ion from the olefin *in situ*. This cationic species is again stabilized by the Lewis base catalyst before ring opening to the final products occurs.

In 2018 Zhao et al. made use of a chiral selenium organocatalyst to difunctionalize olefins with  $\text{SCF}_3$  electrophiles and various nucleophiles.<sup>106</sup> Crucial for the reaction to proceed stereoselectively is the transient  $\text{Se}\cdots\text{S}$  interaction between the catalyst and the *in situ* formed thiiranium cation. This species is additionally stabilized by  $\text{N}\cdots\text{H}$  bonding between the  $\text{NTf}_2$  anion and the organocatalyst. Especially for the enantiocontrolled functionalization of alkenes such strategies imply high potential without demand for any assisting directing group.

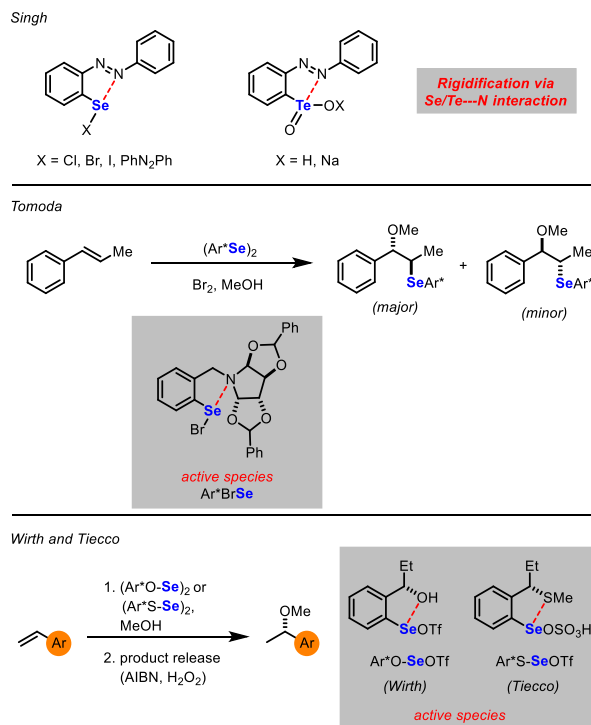
### 1.13.5.3 Catalysis by intermolecular chalcogen bonding

The utilization of Lewis acid catalysts for organic transformations via intermolecular chalcogen bonding has recently been a rapidly growing field with high potential, in contrast to its intramolecular counterpart (see Section 1.13.5.1).<sup>107</sup>

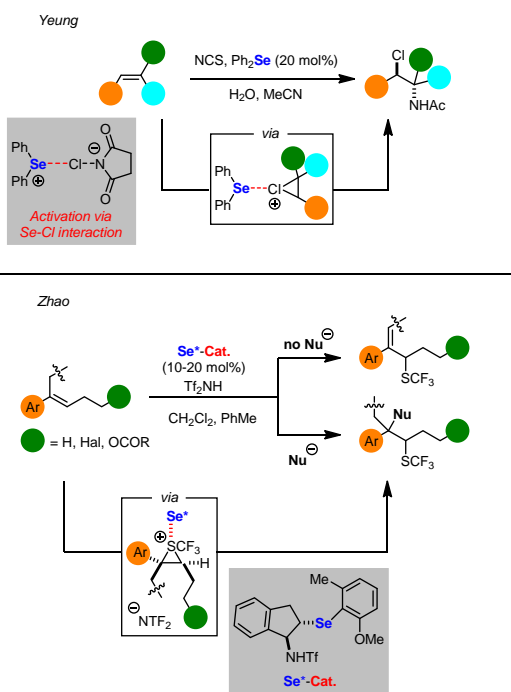
The groups of Matile and Huber applied different types of chalcogen bonding organocatalysts for similar reactions (Scheme 5). While Matile's chalcogen bonding ligands are based on the previously introduced DTT or the benzodiselenazole motif,<sup>108–110</sup> Huber's cations contain bis-(benzimidazolium) and bis-(triazolium)benzene structures.<sup>111</sup> However, all of these chalcogen bonding donors undergo intermolecular chalcogen-chalcogen interactions with Lewis basic atoms to activate molecules for organic transformations. First, catalytic systems A or D were used for the transfer hydrogenation of a quinolone (Scheme 5A).<sup>108,112</sup> The bidentate ligands form a complex with the nitrogen through two non-covalent  $\text{Ch}\cdots\text{N}$  interactions, resulting in the transfer of electron density to the chalcogen via  $\sigma$ -holes. While both catalysts facilitate the formation of the tetrahydroquinoline product in excellent yields, a significantly lower catalyst loading is required for Huber's catalyst A.

Bidentate tellurium ligands of type B were employed by the Huber group for nitro-Michael reactions between an electron-rich indole and a nitro olefin (Scheme 5B).<sup>113</sup> Efficient catalysis is exclusively processed through the bonding of the oxygen atoms of the nitro group with tellurium, whereas analogous sulfur and selenium containing catalysts have no noteworthy effect. Additionally, telluro ligand B shows a major improvement in the acceleration of the reaction upon thiourea catalysts in comparable systems.

The activation of carbon-chloride bonds to synthesize ester functionalized isochromanes was achieved by Huber and co-workers using bis-(benzimidazolium) ligands of type B (Scheme 5C).<sup>114</sup> Similar to the recently discussed nitro-Michael reaction, the tellurium based catalysts exhibited strong activity in contrast to other analogous ligands containing other chalcogens in this benchmark

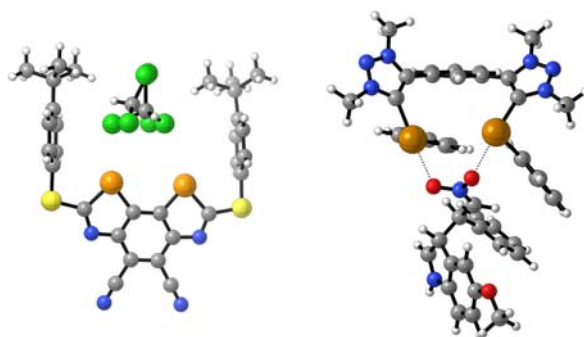
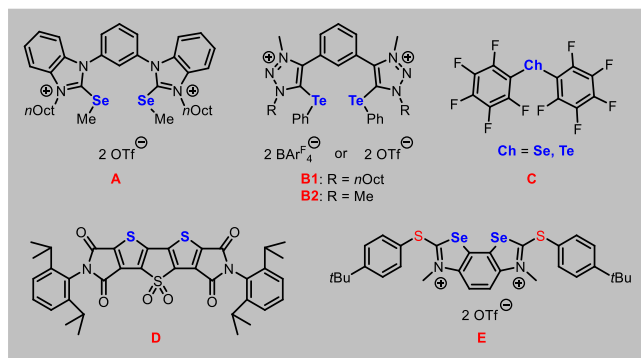
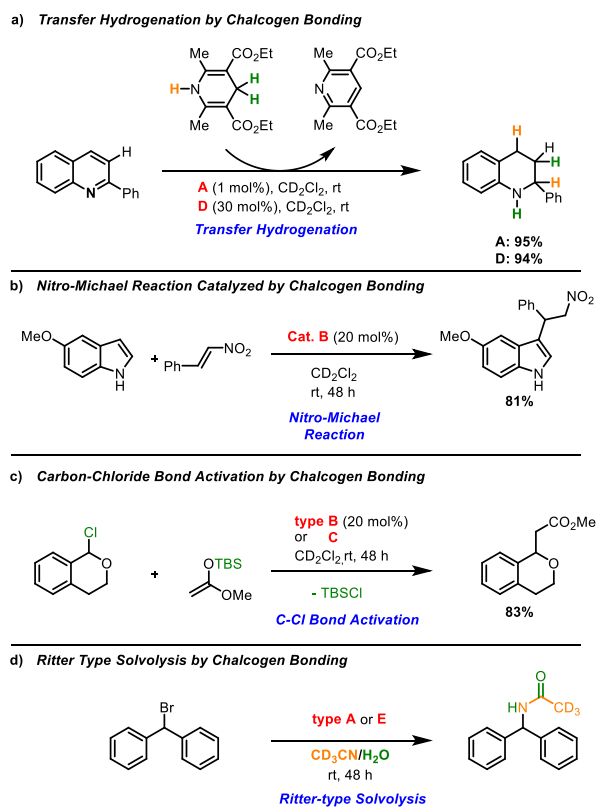


**Scheme 3** (Top) Rigidification of structures via intramolecular Ch–N bonding. (Middle) Utilization of rigidification by Ch–N bonding in synthetic transformations. (Bottom) Utilization of rigidification by Se–O and Se–S bonds in synthetic transformations.



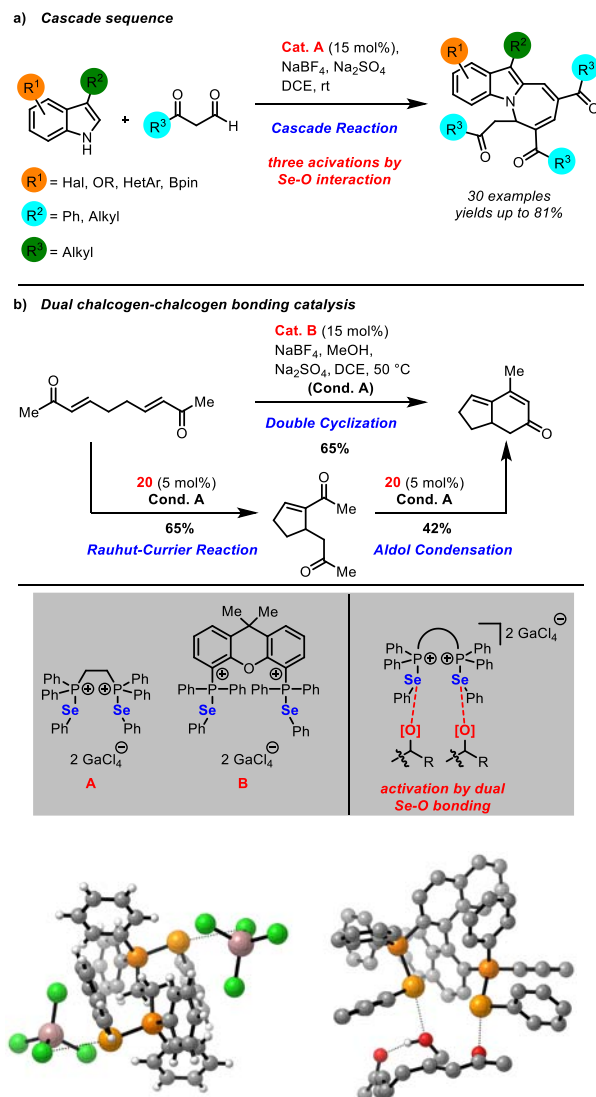
**Scheme 4** Lewis base catalysis by transient chalcogen bonding.

reaction. Additionally, *syn*-isomers of type B catalysts showed higher activity than corresponding *anti*-isomers because of bidentate binding being possible. Matile et al. reported the same reaction with perfluorinated chalcogen bonding donors as part of a general study involving pnictogen bonding catalysis.<sup>91</sup> The determined yield of 48% after 55 h was significantly worse than the yield (83%) achieved with Huber's system.



**Scheme 5** Activation of carbonyls by dual chalcogen-chalcogen bonding catalysis. Crystal structure of a type **E** catalyst with  $\text{CHCl}_3$  (Left) and computationally calculated activation mode of the bidentate tellurium ligand **B2** for the nitro-Michael reaction (Right). From Lenardão, E. J.; Feijó, J. d. O.; Thurow, S.; Perin, G.; Jacob, R. G.; Silveira, C. C. Selenonium Ionic Liquid as Efficient Catalyst for the Baylis–Hillman Reaction. *Tetrahedron Lett.* **2009**, *50*, 5215–5217. He, X.; Wang, X.; Tse, Y.-L. S.; Ke, Z.; Yeung, Y.-Y. Applications of Selenonium Cations as Lewis Acids in Organocatalytic Reactions. *Angew. Chem. Int. Ed.* **2018**, *57*, 12869–12873; Benz, S.; López-Andarias, J.; Mareda, J.; Sakai, N.; Matile, S. Catalysis with Chalcogen Bonds. *Angew. Chem. Int. Ed.* **2017**, *56*, 812–815; Benz, S.; Mareda, J.; Besnard, C.; Sakai, N.; Matile, S. Catalysis with Chalcogen Bonds: Neutral Benzodiselenazole Scaffolds with High-Precision Selenium Donors of Variable Strength. *Chem. Sci.* **2017**, *8*, 8164–8169; Benz, S.; Besnard, C.; Matile,

A benchmark reaction for testing the efficiency of cationic chalcogen bonding catalysts is the Ritter-type solvolysis (Scheme 5D). This simple reaction, which was already used by Huber and Matile to investigate their catalytic systems of type A and E, allows the formation of *N*-benzhydryl acetamide from benzhydryl bromide in wet CD<sub>3</sub>CN.<sup>110,115</sup> Crucial and rate-limiting is the formation of the carbocation resulting from elimination of the bromide by chalcogen bonding activation. Since the eliminated bromide is able to deactivate the catalyst, catalysts for this reaction are generally used in stoichiometric amounts. Hence, the tested structure acts formally as an activator of the solvolysis. Kinetic parameters such as reaction rates and the rate acceleration are further determined by a set of time-based and concentration-dependent solvolysis reactions.



**Scheme 6** Reactions catalyzed by intermolecular chalcogen-chalcogen interactions. Crystal structure of a type A catalyst with CCl<sub>4</sub> (Left) and calculated computation of the activation mode of the Rauhut-Currier reaction (Right). From Wang, W.; Zhu, H.; Liu, S.; Zhao, Z.; Zhang, L.; Hao, J.; Wang, Y. Chalcogen-Chalcogen Bonding Catalysis Enables Assembly of Discrete Molecules. *J. Am. Chem. Soc.* **2019**, *141*, 9175–9179. Wang, W.; Zhu, H.; Feng, L.; Yu, Q.; Hao, J.; Zhu, R.; Wang, Y. Dual Chalcogen-Chalcogen Bonding Catalysis. *J. Am. Chem. Soc.* **2020**, *142*, 3117–3124.

S. Chalcogen Bonding Catalysis: From Neutral to Cationic Benzodiselenazole Scaffolds. *Helv. Chim. Acta* **2018**, *101*, e1800075; Vogel, L.; Wonner, P.; Huber, S. M. Chalcogen Bonding: An Overview. *Angew. Chem. Int. Ed.* **2019**, *58*, 1880–1891; Wonner, P.; Steinke, T.; Huber, S. M. Activation of Quinolines by Cationic Chalcogen Bond Donors. *Synlett* **2019**, *30*, 1673–1678; Wonner, P.; Dreger, A.; Vogel, L.; Engelage, E.; Huber, S. M. Chalcogen Bonding Catalysis of a Nitro-Michael Reaction. *Angew. Chem. Int. Ed.* **2019**, *58*, 16923–16927; Steinke, T.; Wonner, P.; Engelage, E.; Huber, S. M. Catalytic Activation of a Carbon–Chloride Bond by Dicationic Tellurium-Based Chalcogen Bond Donors. *Synthesis* **2021**, *53*, 2043–2050; Wonner, P.; Vogel, L.; Düser, M.; Gomes, L.; Knief, F.; Mallick, B.; Werz, D. B.; Huber, S. M. Carbon-Halogen Bond Activation by Selenium-Based Chalcogen Bonding. *Angew. Chem. Int. Ed.* **2017**, *56*, 12009–12012.

Wang and co-workers rationally designed catalysts that assemble discrete molecules by intermolecular Ch $\cdots$ O interactions.<sup>116</sup> Selenium based catalyst **A** was applied for the synthesis of fused tricyclic molecules (30 examples, up to 81% yield, **Scheme 6A**) by a cascade reaction between substituted indoles and three units of  $\beta$ -ketoaldehydes. Other bidentate systems that also favor this reaction are based on bidentate phosphine ligands such as XantPhos and ([1,1'-binaphthalene]-2,2'-diyl)bis(diphenylphosphane) (BINAP) (see **B** and crystals). Through consecutive chalcogen bonding interactions the reaction intermediates are activated for the next step of the cascade. The enamine species resulting from the condensation of the indole and the  $\beta$ -ketoaldehyde, which was successfully isolated, undergoes a Michael addition with another  $\beta$ -ketoaldehyde unit. After the third and final activation by chalcogen-chalcogen bonding an aldol condensation takes place, followed by an uncatalyzed cyclization to give the final products. Work from the Wang group in 2020 dealt with the new concept of dual chalcogen-chalcogen bonding catalysis (**Scheme 6B**). Experimental and quantum chemical investigation revealed that the activation of a pair of functional groups within one molecule by bidentate ligands is possible. Catalyst **B** enabled a Rauhut-Currier reaction by the activation of a double  $\alpha,\beta$ -unsaturated ketone in 65% yield. Cyclization only occurs in the presence of catalytic amounts of methanol, while higher methanol concentrations lead to the inhibition of the catalytic system. When the cyclized product further reacted with **B**, a bicyclic ketone was accessed via an aldol condensation (42%). A one-pot process to form the final product in 65% yield was achieved under adjusted reaction conditions.

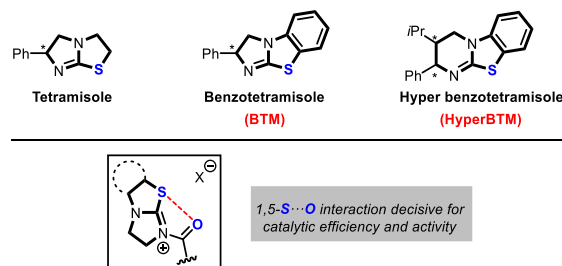
#### 1.13.5.4 Isothiourea catalysis

Nature utilizes non-covalent S $\cdots$ O contacts frequently to stabilize certain protein conformations.<sup>117</sup> These attractive interactions were also exploited in many organocatalytic transformations.<sup>118</sup> Chiral isothiourea catalysts for such purposes were first developed by Birman based on the tetramisole skeleton (**Fig. 56**).<sup>119</sup> Further development led to the bulkier and more efficient class of benzotetramisole (BTM) and HyperBTM catalysts. Decisive for the catalytic activity is a non-covalent 1,5-S $\cdots$ O interaction after initial acylation of the nucleophilic catalyst. Due to a smaller dispersion contribution, the energy gain from an S $\cdots$ O interaction is in general smaller than from equivalent contacts between heavier chalcogens. However, negatively charged oxygen atoms (e.g., enolates) show increased donor properties leading to enhanced chalcogen-chalcogen attraction.

The group of Smith showed the potential of isothiourea catalysis in a variety of stereoselective organic reactions. **Scheme 7** depicts the enantioselective Michael addition of dihydropyrazol-5-ones with  $\alpha,\beta$ -unsaturated *p*-nitrophenyl esters.<sup>120</sup> The initial acylation step of the HyperBTM catalyst **A** proceeds very easily because of the excellently stabilized *p*-nitrophenolate. The conformation of the resulting intermediate **B** is fixed by an O $\cdots$ S interaction, giving rise to facial selectivity of the  $\pi$ -system. Steric hindrance between the reacting substrate and the phenyl residues of the isothiourea catalyst cause attack of the nucleophile to occur exclusively from the front. Transition state stabilization may also occur through C-H $\cdots$ O interactions. Following protonation of enolate **C** and elimination of the catalyst, which closes the catalytic cycle, the addition product is obtained in excellent diastereomeric ratios, and even better enantiomeric ratios.

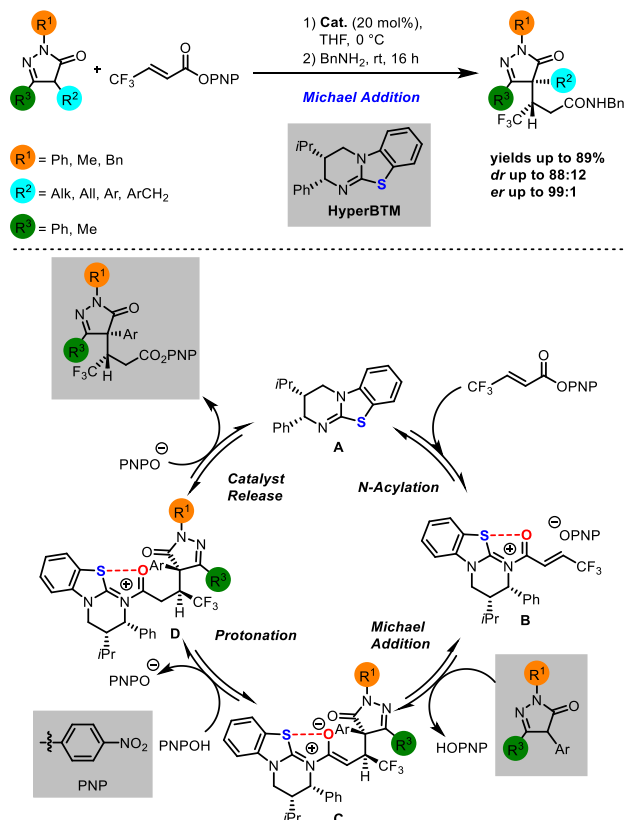
Furthermore, Smith and co-workers successfully applied isothiourea catalysis to sequentially desymmetrize biaryl phenols (**Scheme 8**).<sup>121</sup> This reaction delivers axially chiral phenols which are frequently found in nature and are valuable building blocks for catalysts and ligands. Depending on the substituent pattern of the biaryl, HyperBTM or BTM facilitated the desired reaction best, leading to a library of 14 acylated products with excellent enantiomeric ratios (*er* up to 98:2). Extensive experimental studies gave evidence for an initial enantioselective desymmetrization followed by a chiroablative kinetic resolution taking place. Additionally, computational calculations clarified the importance of the 1,5-S $\cdots$ O interaction in the key acyl intermediate (see computational model) for the atroposelective acylation and the high enantiocontrol of this strategy.

Another work by Smith features the enantioselective formation of perfluoroalkyl-substituted  $\beta$ -lactones from symmetric anhydrides and fluorine-rich ketones via isothiourea catalyzed (2 + 2) cycloaddition (**Scheme 9**).<sup>122</sup> Initial addition of HyperBTM to the anhydride leads to the acylated catalyst and acetate ion pair. Next, the (*Z*)-ammonium enolate which shows the rigidifying and stabilizing 1,5-S $\cdots$ O contact is favorably formed by basic deprotonation. This key intermediate reacts from the depicted arrangement in a concerted asynchronous (2 + 2)-cycloaddition with fluorinated ketones. Intensive computational and kinetic isotopic effect studies suggested that the concerted (2 + 2)-mechanism is favored over a potential aldol-lactonization sequence. In

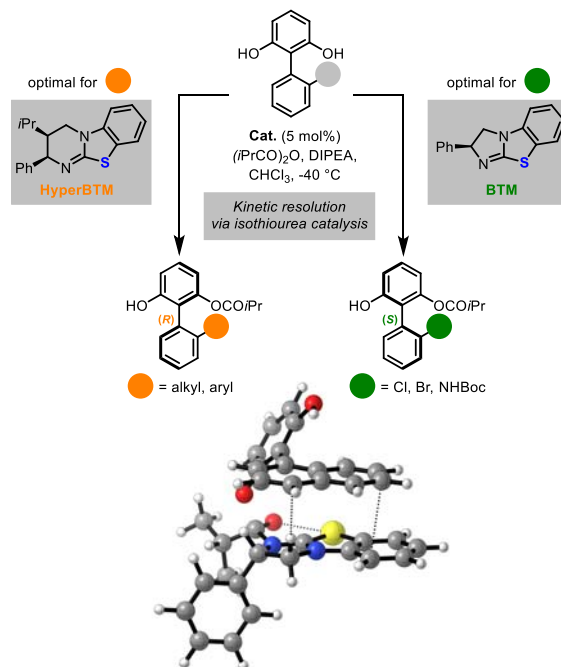


**Fig. 56** Tetramisole based isothiourea catalysts and decisive 1,5-S $\cdots$ O interaction.

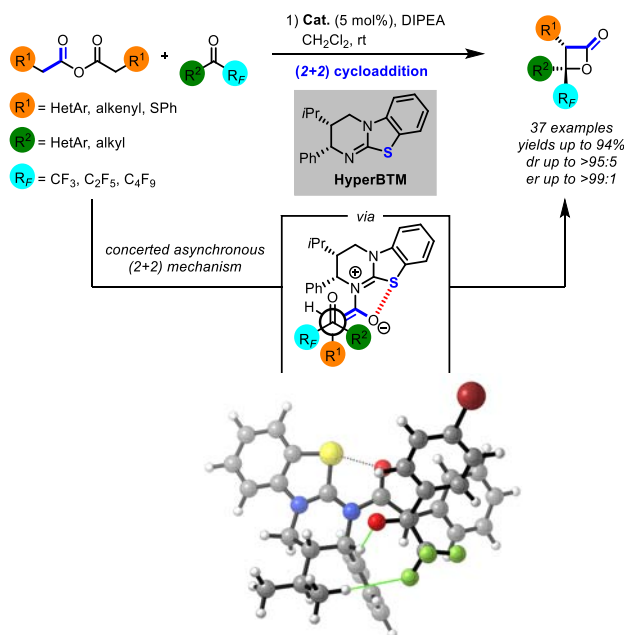




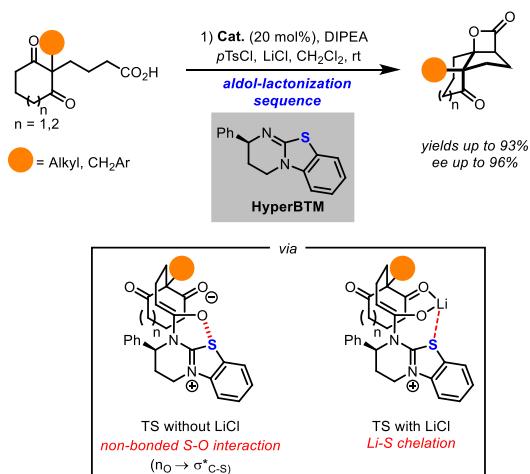
**Scheme 7** Michael addition utilizing isothiurea catalysis; the interaction shown in red is decisive in fixing the conformation.



**Scheme 8** (Top) Desymmetrization/kinetic resolution sequence of biaryl phenols using isothiurea catalysis. (Bottom) Crystal structure of the interaction between a biaryl phenol and the HyperBTM catalyst. From Munday, E. S.; Grove, M. A.; Feoktistova, T.; Brueckner, A. C.; Walden, D. M.; Young, C. M.; Slawin, A. M. Z.; Campbell, A. D.; Cheong, P. H.-Y.; Smith, A. D. Isothiurea-Catalyzed Atropselective Acylation of Biaryl Phenols via Sequential Desymmetrization/Kinetic Resolution. *Angew. Chem. Int. Ed.* **2020**, *59*, 7897–7905.



**Scheme 9** HyperBTM catalyzed (2 + 2)-cycloaddition and computed activation mode thereof. From Barrios Antúnez, D.-J.; Greenhalgh, M. D.; Brueckner, A. C.; Walden, D. M.; Elías-Rodríguez, P.; Roberts, P.; Young, B. G.; West, T. H.; Slawin, A. M. Z.; Ha-Yeon Cheong, P.; Smith, A. D. Catalytic Enantioselective Synthesis of Perfluoroalkyl-Substituted  $\beta$ -Lactones Via a Concerted Asynchronous (2 + 2) Cycloaddition: A Synthetic and Computational Study. *Chem. Sci.* **2019**, *10*, 6162–6173.



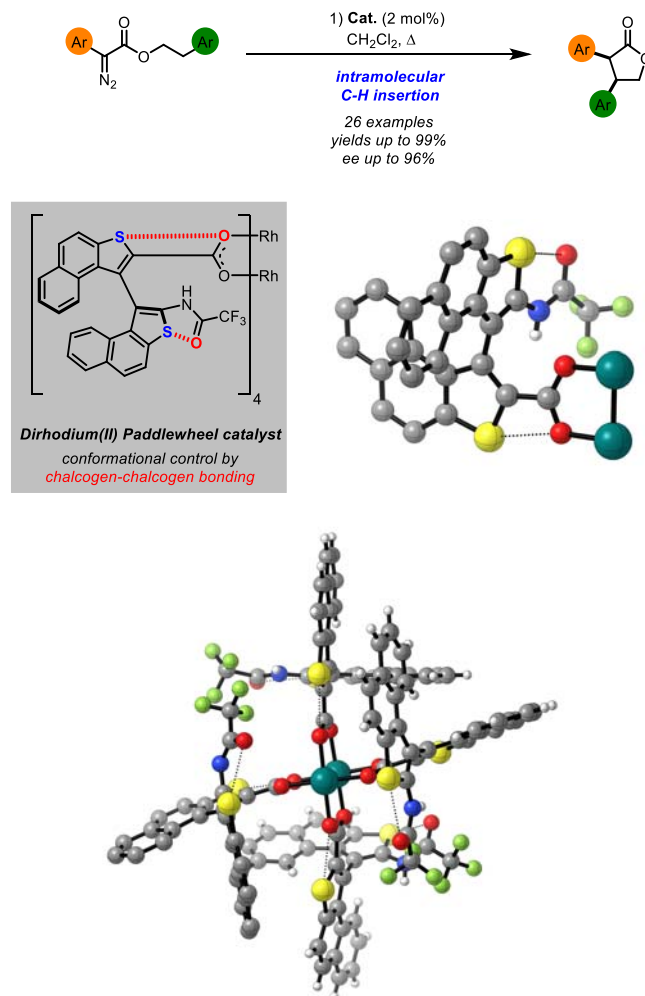
**Scheme 10** Aldol-lactonization sequence via isothiurea catalysis.

conclusion, 37 examples of  $\beta$ -lactones with excellent yields (up to 94%) and stereochemical outcomes (*dr* up to 95:5, *er* up to 99:1) were synthesized by applying this organocatalytic strategy.

Tricyclic  $\beta$ -lactones from keto acids via a HyperBTM catalyzed aldol-lactonization sequence were already accessed enantioselectively by Romo and co-workers in 2010 (Scheme 10).<sup>123</sup> The enantiocontrol of this method arises from structure rigidification by an  $n_{\text{O}} \rightarrow \sigma^*_{\text{C-S}}$  chalcogen interaction within the depicted ammonium enolate. However, if LiCl was used as an additive, chelation of the sulfur to the formed lithium enolate becomes the crucial rigidifying interaction. Under optimized, lithium-containing conditions excellent yields and high stereocontrol were achieved. Additionally, a small library of bicyclic  $\beta$ -lactones was synthesized.

### 1.13.5.5 Special chalcogen interactions in catalysis

In 2021 Furuta et al. developed a  $D_2$ -symmetric dirhodium(II) catalyst containing axially chiral paddlewheel ligands for the stereoselective synthesis of  $\gamma$ -lactones by intramolecular C–H insertion (Scheme 11).<sup>124</sup> These ligands, derived from

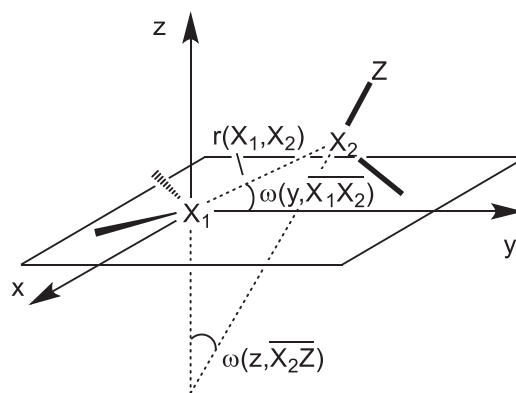


**Scheme 11** Chalcogen bonding in a dirhodium(II) paddlewheel catalyst facilitates the stereoselective formation of lactones. X-ray structures of a single ligand bound to the dirhodium center (*Right*) and of the dirhodium(II) paddlewheel catalyst (*Bottom*). From Murai, T.; Lu, W.; Kuribayashi, T.; Morisaki, K.; Ueda, Y.; Hamada, S.; Kobayashi, Y.; Sasamori, T.; Tokitoh, N.; Kawabata, T.; Furuta, T. Conformational Control in Dirhodium(II) Paddlewheel Catalysts Supported by Chalcogen Bonding Interactions for Stereoselective Intramolecular C–H Insertion Reactions. *ACS Catal.* **2021**, *11*, 568–578.

binaphthothiophene  $\delta$ -amino acid allow conformational control because of  $\text{S} \cdots \text{O}$  interactions which can be observed in the crystal. Additionally, the chiral ligands provide well-defined uniform environments around the metal centers most likely because of the chalcogen-chalcogen interactions as indicated by X-ray diffraction. Natural bond orbital analysis revealed overlap between the oxygen lone pair and the antibonding orbital of the C–S bond ( $n_{\text{O}} \rightarrow \sigma^*_{\text{C-S}}$ ), thus confirming the attractive chalcogen contacts in each ligand. Considering the excellent activity in this model reaction (26 examples, yields up to 99%, *ee* up to 96%) chalcogen bonding might become an important tool for the structural design of novel metal-based catalytic systems.

### 1.13.6 Theoretical and computational studies

Most commonly, chalcogen bonding takes place between closed shell species of zero charge; thus, no strong attractions are expected. But, as the examples presented above demonstrate, weak non-covalent interactions are also able to play a significant role in the binding between different molecules. For a description of these interactions, directional forces were suggested. The first qualitative ideas stem from the 1960s.<sup>125,126</sup> Originally, the interaction was rationalized by the overlap of a filled chalcogen p-orbital with a low-lying  $\sigma^*$ -orbital of a chalcogen-carbon bond.<sup>127</sup> However, this interpretation is based on a single-electron picture and therefore incomplete. In-depth theoretical studies in the last 25 years have demonstrated that inclusion of electron correlation is crucial for a thorough understanding of non-covalent interactions between closed shell species such as divalent chalcogen atoms.<sup>125,126,128</sup>



**Fig. 57** Definition of the three most important parameters used in Eq. (1). The distance  $r(X_1, X_2)$  and the orientation angles  $\omega(y, \overline{X_1X_2})$  and  $\omega(z, \overline{X_2Z})$ , which were used to characterize the optimized geometries of the molecules R- $X_1$ -R and R- $X_2$ -Z, are shown. Reprinted with permission from Bleiholder, C.; Werz, D. B.; Köppel, H.; Gleiter, R. Theoretical Investigations on Chalcogen-Chalcogen Interactions: What Makes These Nonbonded Interactions Bonding? *J. Am. Chem. Soc.* **2006**, *128*, 2666–2674. Copyright 2006 American Chemical Society.

### 1.13.6.1 Definition of interaction energy, choice of basis sets and methods

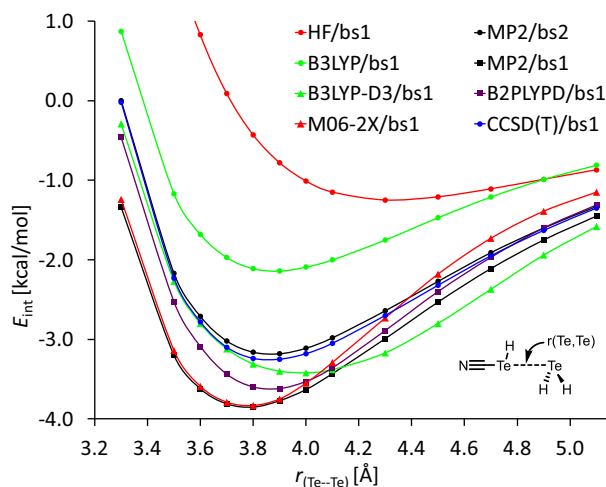
The interaction energy between two closed shell molecules A and B, denoted as  $E_{int}$ , is defined according to Eq. (1).

$$E_{int}(\vec{r}, \vec{\zeta}, Q_A, Q_B) = E_{AB}(\vec{r}, \vec{\zeta}, Q_A, Q_B) - E_A(Q_A) - E_B(Q_B) \quad (1)$$

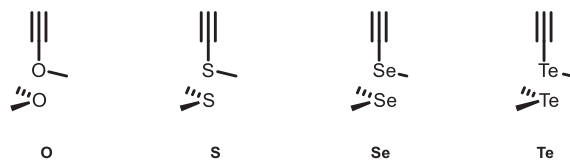
This equation calculates the interaction energy ( $E_{int}$ ) as the difference between the energy of a molecular aggregate  $E_{AB}$  and the separated monomers ( $E_A, E_B$ ), where the monomers are in the same internal coordinates  $Q_A, Q_B$  as in the molecular aggregate. The relative orientation of the monomers is described by the intermolecular vector  $\vec{r}$  and the orientational angles  $\vec{\zeta}$  (see Fig. 57).<sup>129,130</sup> For such weak interactions it is also important to correct the obtained values for basis set superposition errors; however, according to the equation, zero-point corrections are not taken into account.

Polarization- or diffuse augmented split-valence triple- $\zeta$  basis sets in combination with electron-correlation methods are required to obtain reliable results for van der Waals-type interactions.<sup>131</sup> In addition, for tellurium-containing compounds a good effective core potential (ECP) is also needed. Hence, in most cases Dunning's correlation-consistent basis sets (correlation consistent polarized valence triple- $\zeta$ , cc-pVTZ, cc-pVTZ-PP, SDB-cc-pVTZ) were chosen for such computations.

Benchmark computations of a Te–Te interaction had shown that the HF level of theory is completely insufficient for even describing the intermolecular distances—the found Te–Te distance was too long. The B3LYP method leads to quite good



**Fig. 58** Potential energy curves of  $H_2Te \cdots Te(H)CN$  as derived by different methods (bs1 = aug-cc-pVTZ for C, N, H and aug-cc-pVTZ-PP for Te; bs2 = 6-311G\* for C, N, H and SDB-cc-pVTZ for Te). Reprinted with permission from Bleiholder, C.; Werz, D. B.; Köppel, H.; Gleiter, R. Theoretical Investigations on Chalcogen-Chalcogen Interactions: What Makes These Nonbonded Interactions Bonding? *J. Am. Chem. Soc.* **2006**, *128*, 2666–2674. Copyright 2006 American Chemical Society.



**Fig. 59** Dimeric homonuclear model systems from O–Te with one alkyne unit as acceptor group in the upper part.

geometries, but is unable to recover much of the interaction energy. The B3LYP-D3, M06-2X, MP2 and B2PLYPD methods overestimate the interaction energy. However, the extent of the deviation from the coupled cluster single, double and perturbative triple (CCSD(T)) energy is small (Fig. 58). A comparison shows that the use of a smaller basis set for MP2 calculations leads to an energy curve which matches almost perfectly the CCSD(T) curve using the highest basis set (compare MP2/bs2 with CCSD(T)/bs1 in Fig. 58).

In addition, special attention needs to be paid to the flatness of a van der Waals potential energy surface. Therefore, the convergence criteria during geometry optimizations have to be set rather tightly to reach the minima as closely as possible.

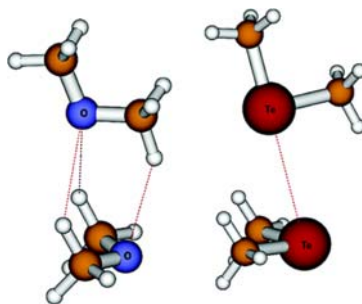
### 1.13.6.2 Model systems

#### 1.13.6.2.1 Interaction energies and potential energy surfaces

Much of the early solid-state work in chalcogen bonding has used alkyne-substituted chalcogens acting as acceptor units. Therefore, the model systems from O–Te as depicted in Fig. 59 were in the focus, where dimethylsubstituted chalcogen units act as donors. As mentioned above, the interaction of both units can be qualitatively described as a  $p\text{-}\sigma^*$  interaction. A look into the literature shows that this assumption is not always justified. Gas phase studies on the dimer of dimethylether by molecular beam Fourier transform microwave and free jet millimeter wave absorption spectroscopies<sup>132</sup> revealed a  $C_s$  symmetrical geometry with the two monomers bound by three weak  $C\text{-H}\cdots O$  hydrogen bonds as shown in Fig. 60. As a result a similar geometry as anticipated from a  $p\text{-}\sigma^*$  type interaction emerges. For comparison we show in this figure the structure of the dimer of dimethyltellurium which will be discussed later. High level *ab initio* calculations show that there is no  $C\text{-H}\cdots Te$  interaction possible for geometric reasons. The  $C_s$  symmetrical structure of the dimer of dimethyltellurium is due to a non-covalent interaction between the Te centers and can be described by a  $p\text{-}\sigma^*$  interaction of the 5p lone pair of the lower Te center with the  $\sigma^*$  orbital of the  $Te\text{-Me}$  bond.<sup>5</sup>

In Table 1 the calculated interaction energies  $E_{int, MP2}^{cc-pVTZ, ECP}$ , the equilibrium distances  $r(X_1X_2)$ , and the orientation angles,  $\omega$ , are given. As anticipated, one finds for O that the calculated bond distance between the oxygen centers (3.52 Å) is considerably longer than the van der Waals distance of two oxygen centers (2.8 Å).<sup>3,6</sup> For S to Te the value for  $r(X_1X_2)$  is smaller than the corresponding sum of the van der Waals radii of S (3.7 Å), Se (4.0 Å) and Te (4.4 Å).<sup>133</sup> The values calculated for the orientation angles  $\omega(y, \bar{X}_1\bar{X}_2)$  and  $\omega(z, \bar{X}_2\bar{Z})$  are close to those expected for a  $p\text{-}\sigma^*$  interaction. The deviation from an ideal geometric arrangement for a  $p\text{-}\sigma^*$  interaction [ $\omega(z, \bar{X}_2\bar{Z}) \approx 0^\circ$ ,  $\omega(y, \bar{X}_1\bar{X}_2) \approx 90^\circ$ ] can be ascribed to steric effects.

The interaction energies shown in Table 1 reveal an increase from O to Te. In Fig. 61 the potential energy profiles at the MP2/cc-pVTZ-ECP level of theory for O–Te are plotted. It can be seen that the energy minima increase only slightly between O, S, and Se, but considerably for Te. The trends from this discussion, documented in Fig. 61 and Table 1, are in qualitative agreement with the interaction model shown in Fig. 1. According to this qualitative model the interaction should increase with decreasing energy difference between the p donor orbital and the  $\sigma^*$  ( $X_2\text{-C}$ ) acceptor orbital.<sup>20</sup> The energy of the donor orbital increases in the series  $O \rightarrow S \rightarrow Se \rightarrow Te$  as exemplified by the first ionization energies of  $Me_2X$  ( $X = O, S, Se, Te$ ) obtained by photoelectron spectroscopy.<sup>134</sup> The energy of the acceptor  $\sigma^*$  orbital of the  $X\text{-C}\equiv\text{CH}$  bond should decrease. More recent computations also corroborate this view.<sup>135</sup>

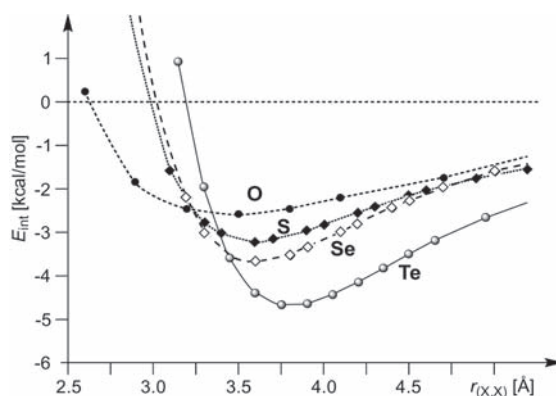


**Fig. 60** Minimum geometries of two dimethylethers (Left) and two dimethyltellurides (Right). Reprinted with permission from Bleiholder, C.; Werz, D. B.; Köppel, H.; Gleiter, R. Theoretical Investigations on Chalcogen-Chalcogen Interactions: What Makes These Nonbonded Interactions Bonding? *J. Am. Chem. Soc.* **2006**, *128*, 2666–2674. Copyright 2006 American Chemical Society.



**Table 1** Calculated interaction energies  $E_{int, MP2}^{cc-pVTZ, ECP}$  [kcal mol<sup>-1</sup>], intermolecular equilibrium distance  $r(X_1X_2)$  [Å], and the orientation angles  $\omega(y, \overline{X_1X_2})$  and  $\omega(z, \overline{X_2Z})$  [°] of O–Te.

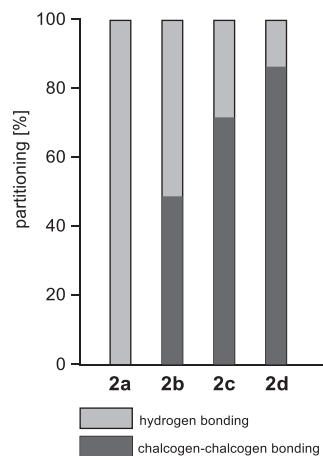
Dimer	$E_{int, MP2}^{cc-pVTZ, ECP}$ <sup>a</sup>	$r(X_1X_2)$ <sup>b</sup>	$\omega(y, \overline{X_1X_2})$ <sup>b</sup>	$\omega(z, \overline{X_2Z})$ <sup>b</sup>
O	-2.58	3.52	103.1	21.2
S	-3.23	3.63	102.0	16.8
Se	-3.66	3.63	100.0	15.3
Te	-4.64	3.76	100.5	13.7

<sup>a</sup>Corrected for basis set superposition error.<sup>b</sup>For the definition of the parameters, see Fig. 57.**Fig. 61** Interaction energies at the MP2/cc-pVTZ-ECP level of theory of the alkynyl-substituted dimers from O to Te as a function of  $r(X_1X_2)$ .**Table 2** Partition of interaction terms of model systems from O to Te as derived by an NBO second-order perturbation analysis in chalcogen-chalcogen interactions ( $E_{xx}$ ) and hydrogen bonding ( $E_{H-bond}$ ), the largest matrix element of the perturbation analysis ( $E_{max}$ ) and charge transfer (CT) from donating units Me–X<sub>1</sub>–Me to accepting units Me–X<sub>2</sub>–C≡CH is given in 10<sup>-3</sup> electrons. The energies are given in kcal mol<sup>-1</sup>.

Dimer	$E_{xx}$	$E_{H-bond}$	CT
O	0.00	2.81	+1.80
S	1.82	1.93	+5.41
Se	4.42	1.75	+14.02
Te	10.85	1.78	+37.81

### 1.13.6.2.2 Natural bond orbital (NBO) analyses

NBO analysis<sup>136</sup> provides an alternative way to characterize a non-covalent interaction in terms of the functional groups involved in a molecular aggregate. For chemists such an analysis often facilitates ease of understanding. Thus, bonding can be divided into an amount for hydrogen bonding (between C–H groups and chalcogen atoms) and chalcogen-chalcogen interactions of the two chalcogen centers. Mathematically, such NBO analyses are performed by interpreting the sums of the second-order interaction terms of the NBO program in terms of hydrogen and chalcogen-chalcogen bonding. **Table 2** shows the results of these analyses for the four model systems given above. Whereas the absolute amounts of hydrogen bonding vary only slightly (from 1.8 to 2.8 kcal mol<sup>-1</sup>), the values for the chalcogen-chalcogen bonding strongly increase from oxygen to tellurium (from 0.0 to 10.9 kcal mol<sup>-1</sup>). With the exception of the oxygen- and sulfur species the hydrogen bonds are weaker than the chalcogen-chalcogen interactions. The partitioning is depicted in **Fig. 62**. For the heavier chalcogen species (S, Se, Te) the major single intermolecular NBO interaction term



**Fig. 62** Partitioning of hydrogen bonding and chalcogen-chalcogen bonding in model systems O to Te derived from NBO analysis.

is of  $p-\sigma^*$  type. Also of note is the fact that charge transfer (CT) from the donating to the accepting unit is observed: the heavier the chalcogen involved, the greater the CT.

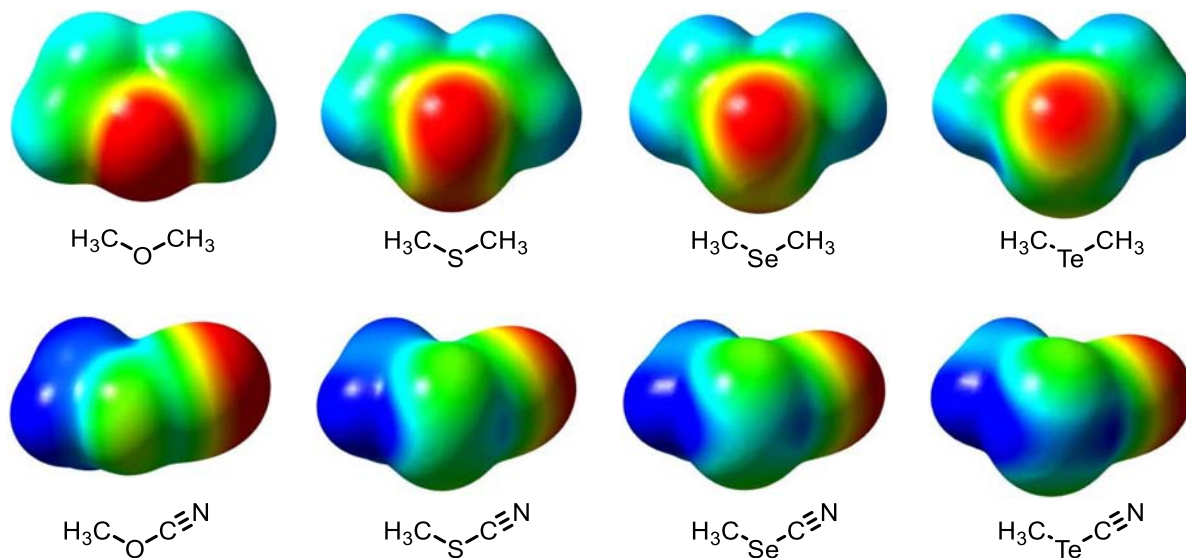
### 1.13.6.2.3 $\sigma$ -Hole bonding

Another method to explain the extent of the chalcogen bonding and especially its directionality is the concept of  $\sigma$ -hole bonding.<sup>137,138</sup> It is traced back to the electrostatic potential  $V(r)$ . In atomic units for a set of atomic nuclei and electrons, the electrostatic potential  $V(r)$  at spatial position  $r$  is given by Eq. (2).

$$V(r) = \sum_A \frac{Z_A}{|R_A - r|} - \int \frac{\rho(r_e) dr_e}{|r_e - r|} \quad (2)$$

in which  $Z_A$  is the charge on nucleus A located at position  $R_A$ , and  $\rho$  is the electron density at position  $r_e$ . The first positive term represents the electrostatic potential generated by the atomic nuclei, while the latter negative term accounts for the electrostatic potential of the electron cloud. The electrostatic potential is a physical observable; thus, it can be obtained either experimentally<sup>139</sup> or by computation.<sup>137,138</sup>

In general, to visualize potential surfaces the surface is drawn with an electron density of 0.001 au and the electrostatic potential is projected onto it.<sup>137,138</sup> In Fig. 63 the molecular electrostatic potential of  $\text{Me}_2\text{O}$ ,  $\text{Me}_2\text{S}$ ,  $\text{Me}_2\text{Se}$ ,  $\text{Me}_2\text{Te}$ ,  $\text{MeO}-\text{CN}$ ,



**Fig. 63** (Top) Calculated (B3LYP/cc-pVTZ(-PP)) molecular electrostatic potential on the 0.001 au electron density isosurface of  $\text{Me}_2\text{O}$ ,  $\text{Me}_2\text{S}$ ,  $\text{Me}_2\text{Se}$  and  $\text{Me}_2\text{Te}$ . Color scheme spanning between  $-0.03$  (red) to  $+0.03$  (blue). (Bottom) Calculated (B3LYP/cc-pVTZ(-PP)) molecular electrostatic potential on the 0.001 au electron density isosurface of  $\text{MeO}-\text{CN}$ ,  $\text{MeS}-\text{CN}$ ,  $\text{MeSe}-\text{CN}$  and  $\text{MeTe}-\text{CN}$ . Color scheme spanning between  $-0.04$  (red) to  $+0.04$  (blue).

MeS–CN, MeSe–CN and MeTe–CN are compared. In Me<sub>2</sub>O, the surface of the chalcogen atom is completely negative (Fig. 63). In the case of the heavier chalcogens S, Se, and Te, the chalcogen atoms show a positive outer region with two local maxima. These regions with positive electrostatic potential on the outer surface are located along the extensions of the X–C bonds and are named  $\sigma$ -holes.<sup>140</sup> The  $\sigma$ -holes are most pronounced for Se and Te. This trend can easily be explained by the concept of atomic orbitals. Since the hybridization becomes more difficult for higher chalcogens than for oxygen, the contribution of the higher chalcogens to the X–C bonds contain almost pure half-filled p-orbitals. This leads to a lack of electron density in the outer (uninvolved) orbital lobe. Therefore, the  $\sigma$ -holes, the regions of positive electrostatic potential, are located along the extensions of the X–C bonds.

In addition, the  $\sigma$ -holes increase when electron-withdrawing substituents are bonded to the chalcogen atoms (as depicted in Fig. 63); this effect becomes even more pronounced with decreasing electronegativity and polarizability (from S to Se to Te). The directionality of the chalcogen bonding in the simple dimeric model systems can be explained as the electrostatic attraction between a  $\sigma$ -hole of the Lewis acidic chalcogen moiety with the lone pair of the donating chalcogen atom. The resulting relative orientations of the two molecules are such that the  $\sigma$ -hole of the chalcogen atom with the higher positive outer region (Me–X<sub>2</sub>–CN) is approaching a negative region on a lateral side of the other chalcogen atom (Me<sub>2</sub>X<sub>1</sub>). This model displays the interaction of an occupied p-orbital at center X<sub>1</sub> and the empty C–X<sub>2</sub>  $\sigma^*$ -orbital (Fig. 63).

### 1.13.7 Conclusion

Interactions of Lewis acidic chalcogen moieties with Lewis bases are commonly termed nowadays as chalcogen bonding. The type of Lewis base can vary greatly: most often chalcogens, halogens or pnictogens are utilized. The term is analogous to the terms hydrogen bonding and halogen bonding. The effect is of importance for solid-state chemistry, in supramolecular chemistry, and catalysis. Many chalcogen-rich crystal structures are strongly determined by chalcogen bonding. Capsules can be held together by such attractive interactions and organocatalysts or ligands used for metal catalysis can be adjusted in their shape. Theoretical investigations have revealed that the weakest interactions are found between oxygen atoms. Commonly their strengths increase with increasing atomic number of the chalcogen in the chalcogen-based Lewis acid. The more electron-withdrawing groups are attached to the chalcogen Lewis acid, the stronger the interaction. A simplified view considers an orbital overlap between a filled p-orbital of the Lewis base with a low-lying  $\sigma^*$ -orbital of the chalcogen-based Lewis acid. Although directionality is somewhat explained by this simple model, it does not account for the overall interaction energy. More sophisticated computations have revealed that a major part of the energy gain is the result of dispersive interactions which increase with increasing size of the chalcogen. An alternative theoretical approach uses the potential energy surfaces of donor and acceptor units. In this case the attractive interaction is explained by filling electron density from the donor into the  $\sigma$ -holes of the acceptor moieties.

### References

- (a) Cannon, C. G. The Nature of Hydrogen Bonding. *Spectrochimica Acta* **1958**, *10*, 341–368; (b) Pimentel, G. C.; McClellan, A. L. Hydrogen Bonding. *Annu. Rev. Phys. Chem.* **1971**, *22*, 347–385; (c) Grabowski, S. J. *Hydrogen Bonding—New Insights*, 3rd ed., Springer: Netherlands, 2006; (d) Herschlag, D.; Pinney, M. M. Hydrogen Bonds: Simple after All? *Biochemistry* **2018**, *57*, 3338–3352.
- (a) Metrangolo, P.; Resnati, G. Halogen Bonding: A Paradigm in Supramolecular Chemistry. *Chem. Eur. J.* **2001**, *7*, 2511–2519; (b) Metrangolo, P.; Neukirch, H.; Pilati, T.; Resnati, G. Halogen Bonding Based Recognition Processes: A World Parallel to Hydrogen Bonding. *Acc. Chem. Res.* **2005**, *38*, 386–395; (c) Politzer, P.; Lane, P.; Concha, M. C.; Ma, Y.; Murray, J. S. An Overview of Halogen Bonding. *J. Mol. Model.* **2007**, *13*, 305–311; (d) Metrangolo, P.; Meyer, F.; Pilati, T.; Resnati, G.; Terraneo, G. Halogen Bonding in Supramolecular Chemistry. *Angew. Chem. Int. Ed.* **2008**, *47*, 6114–6127; (e) Erdélyi, M. Halogen Bonding in Solution. *Chem. Soc. Rev.* **2012**, *41*, 3547; (f) Scholfield, M. R.; Zanden, C. M. V.; Carter, M.; Ho, P. S. Halogen Bonding (X-Bonding): A Biological Perspective. *Protein Science* **2013**, *22*, 139–152.
- Kolb, S.; Oliver, G. A.; Werz, D. B. Chemistry Evolves, Terms Evolve, but Phenomena Do Not Evolve: From Chalcogen–Chalcogen Interactions to Chalcogen Bonding. *Angew. Chem. Int. Ed.* **2020**, *59*, 22306–22310.
- Chernichenko, K. Y.; Sumerin, V. V.; Shpanchenko, R. V.; Balenkova, E. S.; Nenajdenko, V. G. "Sulflower": a New Form of Carbon Sulfide. *Angew. Chem. Int. Ed.* **2006**, *45*, 7367–7370.
- Werz, D. B.; Gleiter, R.; Rominger, F. Cyclic Tetra- and Hexaynes Containing 1,4-Donor-Substituted Butadiyne Units: Synthesis and Supramolecular Organization. *J. Org. Chem.* **2004**, *69*, 2945–2952.
- Werz, D. B.; Gleiter, R.; Rominger, F. Tellurium-Capped Carbon Rods: Syntheses and Electronic and Structural Properties. *Organometallics* **2003**, *22*, 843–849.
- (a) Werz, D. B.; Gleiter, R. Polyalkynes Capped by Sulfur and Selenium. *J. Org. Chem.* **2003**, *68*, 9400–9405; (b) Eastmond, R.; Johnson, T. R.; Walton, D. R. M. Silylation as a Protective Method for Terminal Alkynes in Oxidative Couplings. *Tetrahedron* **1972**, *28*, 4601–4616; (c) Gleiter, R.; Werz, D. B. Alkynes between Main Group Elements: From Dumbbells Via Rods to Squares and Tubes. *Chem. Rev.* **2010**, *110*, 4447–4488; (d) Brandsma, L. Preparative Acetylenic Chemistry. In *Studies in Organic Chemistry*, 2nd ed.; Elsevier Science, 1988.
- Gleiter, R.; Classen, J.; Rausch, B. J.; Oeser, T.; Rominger, F. Interaction of Cyclic Thiadiynes with CpCo(COD)—Selectivity and Reactivity. *J. Organomet. Chem.* **2002**, *641*, 3–8.
- Werz, D. B.; Staeb, T. H.; Benisch, C.; Rausch, B. J.; Rominger, F.; Gleiter, R. Self-Organization of Chalcogen-Containing Cyclic Alkynes and Alkenes to Yield Columnar Structures. *Org. Lett.* **2002**, *4*, 339–342.
- (a) Batchelor, R. J.; Einstein, F. W. B.; Gay, I. D.; Gu, J. H.; Johnston, B. D.; Pinto, B. M. Selenium Coronands: Synthesis and Conformational Analysis. *J. Am. Chem. Soc.* **1989**, *111*, 6582–6591; (b) Batchelor, R. J.; Einstein, F. W.; Gay, I. D.; Gu, J. H.; Mehta, S.; Pinto, B. M.; Zhou, X. M. Synthesis, Characterization, and Redox Behavior of New Selenium Coronands and of Copper(I) and Copper(II) Complexes of Selenium Coronands. *Inorg. Chem.* **2000**, *39*, 2558–2571.
- Werz, D. B.; Rausch, B. J.; Gleiter, R. Self-Organization of Cyclic Selenoethers to Yield Columnar Structures. *Tetrahedron Lett.* **2002**, *43*, 5767–5769.
- Rodewald, M.; Rautiainen, J. M.; Niksch, T.; Görls, H.; Oitunkaniemi, R.; Weigand, W.; Laitinen, R. S. Chalcogen Bonding Interactions in Telluroether Heterocycles [Te(CH<sub>2</sub>)<sub>m</sub>]<sub>n</sub> (n = 1–4; m = 3–7). *Chem. Eur. J.* **2020**, *26*, 13806–13818.

13. Benisch, C.; Bethke, S.; Gleiter, R.; Oeser, T.; Pritzkow, H.; Rominger, F. Syntheses and Structural Properties of Cyclic Tetrathiadiynes. *Eur. J. Org. Chem.* **2000**, 2479–2488.
14. Werz, D. B.; Gleiter, R.; Rominger, F. Cyclic Tetraselenadiynes: Rigid Cycles with Long-Range Van der Waals Forces between Chalcogen Centers. *J. Org. Chem.* **2002**, *67*, 4290–4297.
15. Staeb, T. H.; Gleiter, R.; Rominger, F. Preparation and Structures of Cyclic Tetrathiadienes and Tetrathiaenyne. *Eur. J. Org. Chem.* **2002**, 2815–2822.
16. Lari, A.; Gleiter, R.; Rominger, F. Supramolecular Organization Based on Van der Waals Forces: Syntheses and Solid State Structures of Isomeric [6.6]Cyclophanes with 2,5-Diselenahex-3-yne Bridges. *Eur. J. Org. Chem.* **2009**, 2267–2274.
17. Werz, D. B.; Fischer, F. R.; Kornmayer, S. C.; Rominger, F.; Gleiter, R. Macrocyclic cyclophanes with two and three alpha,omega-dichalcogena-1,4-diethynylaryl units: syntheses and structural properties. *J. Org. Chem.* **2008**, *73*, 8021–8029.
18. (a) Werz, D. B.; Gleiter, R.; Rominger, F. Nanotube Formation Favored by Chalcogen-Chalcogen Interactions. *J. Am. Chem. Soc.* **2002**, *124*, 10638–10639; (b) Gleiter, R.; Werz, D. B.; Rausch, B. J. A World beyond Hydrogen Bonds? - Chalcogen-Chalcogen Interactions Yielding Tubular Structures. *Chem. Eur. J.* **2003**, *9*, 2676–2683.
19. Gleiter, R.; Werz, D. B. Elastic Cycles as Flexible Hosts: How Tubes Built by Cyclic Chalcogenaalkynes Individually Host their Guests. *Chem. Lett.* **2005**, *34*, 126–131.
20. Gleiter, R.; Haberhauer, G. *Aromaticity and Other Conjugation Effects*, Wiley-VCH: Weinheim, 2012.
21. Xiao, Q.; Sakurai, T.; Fukino, T.; Akaike, K.; Honsho, Y.; Saeki, A.; Seki, S.; Kato, K.; Takata, M.; Aida, T. Propeller-Shaped Fused Oligothiophenes: a Remarkable Effect of the Topology of Sulfur Atoms on Columnar Stacking. *J. Am. Chem. Soc.* **2013**, *135*, 18268–18271.
22. Bauzá, A.; Frontera, A. Chalcogen 'like-like' Interactions Involving Trisulphide and Triselenide Compounds: A Combined CSD and Ab Initio Study. *Molecules* **2018**, *23*, 699.
23. Boukebbous, K.; Laifa, E. A.; Mallmann, A.d.; Taoufik, M. Diethyl 2,2'-(trisulfane-1,3-diyl)dibenzoate. *IUCrData* **2016**, *1*, x161708.
24. Arnold, A. P.; Cavell, K. J.; Edwards, A. J.; Hoskins, B. F.; Peacock, E. J. Preparation and X-Ray Crystal-Structure of 4,4'-Triselenobis(Pent-3-en-2-One). *Aust. J. Chem.* **1988**, *41*, 1601–1606.
25. Kimura, T.; Yomogita, A.; Matsutani, T.; Suzuki, T.; Tanaka, I.; Kawai, Y.; Takaguchi, Y.; Wakahara, T.; Akasaka, T. Preparation of Phthalocyanines with Eight Benzyl-chalcogeno Substituents from 5,6-Dibromo-4,7-diethylbenzo[1,2,3]trichalcogenoles. *J. Org. Chem.* **2004**, *69*, 4716–4723.
26. Chenard, B. L.; Harlow, R. L.; Johnson, A. L.; Vladuchick, S. A. Synthesis, Structure, and Properties of Pentathiepins. *J. Am. Chem. Soc.* **1985**, *107*, 3871–3879.
27. Vaddamanu, M.; Prabusankar, G. Chalcogen Bonding Induced Tetraselenides from Twisted Diselenides. *Eur. J. Inorg. Chem.* **2020**, 2403–2407.
28. Vaddamanu, M.; Velappan, K.; Prabusankar, G. Highly Active Mesoionic Chalcogenone Zinc(II) Derivatives for C–S Cross-Coupling Reactions. *New J. Chem.* **2020**, *44*, 129–140.
29. Dhaka, A.; Jeannin, O.; Jeon, I.-R.; Aubert, E.; Espinosa, E.; Fourmigué, M. Activating Chalcogen Bonding (ChB) in Alkylseleno/Alkyltelluroacetylenes toward Chalcogen Bonding Directionality Control. *Angew. Chem. Int. Ed.* **2020**, *59*, 23583–23587.
30. Louërat, F.; Gros, P.; Fort, Y. Metallation Versus Heteroatom Lithium Complexation: Mono- and -Dilithiation of Dipyrildipiperazines. *Synlett* **2006**, 1379–1383.
31. Jeannin, O.; Huynh, H.-T.; Riel, A. M. S.; Fourmigué, M. Chalcogen Bonding Interactions in Organic Selenocyanates: From Cooperativity to Chelation. *New J. Chem.* **2018**, *42*, 10502–10509.
32. Scilabra, P.; Terraneo, G.; Resnati, G. The Chalcogen Bond in Crystalline Solids: A World Parallel to Halogen Bond. *Acc. Chem. Res.* **2019**, *52*, 1313–1324.
33. Ams, M. R.; Trapp, N.; Schwab, A.; Milić, J. V.; Diederich, F. Chalcogen Bonding "2S-2N Squares" Versus Competing Interactions: Exploring the Recognition Properties of Sulfur. *Chem. Eur. J.* **2019**, *25*, 323–333.
34. Fourmigué, M.; Dhaka, A. Chalcogen Bonding in Crystalline Diselenides and Selenocyanates: From Molecules of Pharmaceutical Interest to Conducting Materials. *Coord. Chem. Rev.* **2020**, *403*, 213084.
35. (a) Scilabra, P.; Murray, J. S.; Terraneo, G.; Resnati, G. Chalcogen Bonds in Crystals of Bis(o-anilinium)diselenide Salts. *Cryst. Growth Des.* **2019**, *19*, 1149–1154; (b) Burchell, C. J.; Kilian, P.; Slawin, A. M. Z.; Woollins, J. D.; Tersago, K.; van Alsenoy, C.; Blockhuys, F. E2(CN)2 (E = S, Se) and Related Compounds. *Inorg. Chem.* **2006**, *45*, 710–716.
36. Hauge, S.; Marøy, K.; Svensson, S. C. T.; Classon, B.; Samuelsson, B.; Kady, M. M.; Christensen, S. B. Reactions between Selenocyanate and Bromine. Syntheses and Crystal Structures of Phenyltrimethylammonium Salts of Dibromoselenocyanate, [C6H5(CH3)3N][SeCNBr2], and Bromodiselenocyanate, [C6H5(CH3)3N][SeCN]2. *Acta Chem. Scand.* **1992**, *46*, 1166–1169.
37. Barnes, N. A.; Godfrey, S. M.; Halton, R. T. A.; Mushtaq, I.; Parsons, S.; Pritchard, R. G.; Sadler, M. A Comparison of the Solid-State Structures of a Series of Phenylseleno-Halogen and Pseudohalogen Compounds, PhSeX (X = Cl, CN, SCN). *Polyhedron* **2007**, *26*, 1053–1060.
38. Klapötke, T. M.; Krumm, B.; Polborn, K. Synthesis, Chemistry, and Characterization of Perfluoroaromatic Selenium Derivatives. *Eur. J. Inorg. Chem.* **1999**, 1359–1366.
39. Klapötke, T. M.; Krumm, B.; Mayer, P.; Piotrowski, H.; Vogt, M. *Z. Anorg. Allg. Chem.* **2003**, *629*, 1117–1123.
40. Huynh, H.-T.; Jeannin, O.; Fourmigué, M. Organic Selenocyanates as Strong and Directional Chalcogen Bond Donors for Crystal Engineering. *Chem. Commun.* **2017**, *53*, 8467–8469.
41. Maartmann-Moe, K.; Sanderud, K. A.; Songstad, J.; Sillanpää, R.; Fernholt, L.; Rømming, C. The Crystal Structure of 4-Nitrobenzyl Tellurocyanate, 4-Nitrobenzyl Selenocyanate, 4-Nitrobenzyl Thiocyanate and Benzyl Selenocyanate. *Acta Chem. Scand.* **1984**, *38a*, 187–200.
42. McWhinnie, S. L. W.; Brooks, A. B.; Abrahams, I.  $\alpha\alpha'$ -Diselenocyanato-Ortho-Xylene. *Acta Cryst. C* **1998**, *54*, 126–128.
43. Dunne, S. J.; Summers, L. A.; Nagy-Felsobuki, E. I.v.; Mackay, M. F. 3-Selenocyanatopyridine. *Acta Cryst. C* **1994**, *50*, 971–974.
44. Huynh, H.-T.; Jeannin, O.; Aubert, E.; Espinosa, E.; Fourmigué, M. Chalcogen Bonding Interactions in Chelating, Chiral Bis(Selenocyanates). *New J. Chem.* **2021**, *45*, 76–84.
45. Jones, P. G.; Arellano, M. C. R.d. Synthesis of aryl selenides using arylmercurials. Cyclopalladation of Se(R)Ph [R = C6H3(N=NC6H4Me-4)-2,Me-5]. Crystal structures of Se2R2 and [Pd(C6H3[N=NC6H3(SePh)-2',Me-4']-2,Me-5)Cl]. *J. Chem. Soc., Dalton Trans.* **1996**, 2713–2717.
46. Rakesh, P.; Singh, H. B.; Butcher, R. J. Synthesis of Selenonium Ions: Isolation of Highly Conjugated, pH-Sensitive 4,4'-Bis(Methylimino)-1,1'-Binaphthylene-5-Diselenonium(II) Triflate. *Organometallics* **2013**, *32*, 7275–7282.
47. (a) Kaur, R.; Singh, H. B.; Patel, R. P. Synthesis, Characterisation and Reactions of Bis[2-(Dimethylaminomethyl)-Phenyl] Diselenide: Its Structure and that of [2-(Dimethylaminomethyl)Phenyl]-Selenium Bromide. *J. Chem. Soc., Dalton Trans.* **1996**, 2719; (b) Mughesh, G.; Panda, A.; Singh, H. B.; Punekar, N. S.; Butcher, R. J. Diferrocenyl Diselenides: Excellent Thiol Peroxidase-like Antioxidants. *Chem. Commun.* **1998**, 2227–2228; (c) Miyake, Y.; Nishibayashi, Y.; Uemura, S. Asymmetric Baeyer-Villiger Oxidation of Cyclic Ketones Using Chiral Organoselenium Catalysts. *Bull. Chem. Soc. Jpn.* **2002**, *75*, 2233–2237; (d) Kumar, S.; Kandasamy, K.; Singh, H. B.; Butcher, R. J. Synthesis of Organochalcogens Stabilized by Intramolecular Non-bonded Interactions of Sterically Unhindered 2-Phenyl-2-Oxazoline. *New J. Chem.* **2004**, *28*, 640; (e) Kulcsar, M.; Beleaga, A.; Silvestru, C.; Nicolescu, A.; Deleanu, C.; Todasca, C.; Silvestru, A. Solid State Structure and Solution Behaviour of Organoselenium(II) Compounds Containing 2-[E(CH2CH2)2NCH2]C6H4 Groups (E = O, NMe). *Dalton Trans.* **2007**, 2187–2196; (f) Bhabak, K. P.; Mughesh, G. Synthesis and Structure-Activity Correlation Studies of Secondary- and Tertiary-Amine-Based Glutathione Peroxidase Mimics. *Chem. Eur. J.* **2009**, *15*, 9846–9854; (g) Pöllnitz, A.; Rotar, A.; Silvestru, A.; Silvestru, C.; Kulcsar, M. Group 12 Metal Aryl Selenolates. Crystal and Molecular Structure of [2-(Et2NCH2)C6H4]2Se2 and [2-(Me2NCH2)C6H4Se]2M (M = Zn, Cd). *J. Organomet. Chem.* **2010**, *695*, 2486–2492; (h) Pöllnitz, A.; Silvestru, C.; Carpentier, J.-F.; Silvestru, A. Diorganodiselenides and Zinc(II) Organoselenolates Containing (Mino)Aryl Groups of Type 2-(RN=CH)C6H4. *Dalton Trans.* **2012**, *41*, 5060–5070; (i) Bhowmick, D.; Mughesh, G. Tertiary Amine-Based Glutathione Peroxidase Mimics: Some Insights into the Role of Steric and Electronic Effects on Antioxidant Activity. *Tetrahedron* **2012**, *68*, 10550–10560; (j) Panda, S.; Dutta, P. K.; Ramakrishna, G.; Reddy, C. M.; Zade, S. S. Azomethine Diselenides: Supramolecular Structures and Facile Formation of a Bis-Oxazoline Diselenide. *J. Organomet. Chem.* **2012**, *717*, 45–51.
48. Biot, N.; Bonifazi, D. Programming Recognition Arrays through Double Chalcogen Bonding Interactions. *Chem. Eur. J.* **2018**, *24*, 5439–5443.
49. (a) Thomas, S. P.; Veccham, S. P. K. P.; Farrugia, L. J.; Guru Row, T. N. "Conformational Simulation" of Sulfamethizole by Molecular Complexation and Insights from Charge Density Analysis: Role of Intramolecular S...O Chalcogen Bonding. *Cryst. Growth Des.* **2015**, *15*, 2110–2118; (b) Thomas, S. P.; Jayatilaka, D.; Guru Row, T. N. S...O Chalcogen Bonding in Sulfa Drugs: Insights from Multipole Charge Density and X-Ray Wavefunction of Acetazolamide. *Phys. Chem. Chem. Phys.* **2015**, *17*, 25411–25420.



50. (a) Rooth, W.; Srikrishnan, T. J. *Chem. Crystallogr.* **1999**, *29*, 1187–1192; (b) Mondal, P. K.; Rao, V.; Mittapalli, S.; Chopra, D. Exploring Solid State Diversity and Solution Characteristics in a Fluorine-Containing Drug Riluzole. *Cryst. Growth Des.* **2017**, *17*, 1938–1946.
51. Kremer, A.; Fermi, A.; Biot, N.; Wouters, J.; Bonifazi, D. Supramolecular Wiring of Benzo-1,3-Chalcogenazoles through Programmed Chalcogen Bonding Interactions. *Chem. Eur. J.* **2016**, *22*, 5665–5675.
52. Hedidi, M.; Bentabed-Ababsa, G.; Derdour, A.; Roisnel, T.; Dorcet, V.; Chevallier, F.; Picot, L.; Thiéry, V.; Mongin, F. Synthesis of C,N'-linked bis-heterocycles using a deprotometalation-iodination-N-arylation sequence and evaluation of their antiproliferative activity in melanoma cells. *Bioorg. Med. Chem.* **2014**, *22*, 3498–3507.
53. Cozzolino, A. F.; Vargas-Baca, I. Parametrization of a Force Field for Te–N Secondary Bonding Interactions and its Application in the Design of Supramolecular Structures Based on Heterocyclic Building Blocks. *Cryst. Growth Des.* **2011**, *11*, 668–677.
54. Boudebous, A.; Constable, E. C.; Housecroft, C. E.; Neuburger, M.; Schaffner, S. The Structure of 4,7-Bis(Trimethylsilyl)Ethynyl)Benzo[C][1,2,5]Thiadiazole and Identification of a Widespread S···N Structural Motif. *Aust. J. Chem.* **2008**, *61*, 755.
55. Lee, L. M.; Corless, V. B.; Tran, M.; Jenkins, H.; Britten, J. F.; Vargas-Baca, I. Synthetic, Structural, and Computational Investigations of N-Alkyl Benzo-2,1,3-Selenadiazolium Iodides and their Supramolecular Aggregates. *Dalton Trans.* **2016**, *45*, 3285–3293.
56. (a) Cozzolino, A. F.; Britten, J. F.; Vargas-Baca, I. The Effect of Steric Hindrance on the Association of Telluradiazoles through Te–N Secondary Bonding Interactions. *Cryst. Growth Des.* **2006**, *6*, 181–186; (b) Cozzolino, A. F.; Yang, Q.; Vargas-Baca, I. Engineering Second-Order Nonlinear Optical Activity by Means of a Noncentrosymmetric Distortion of the [Te–N]<sub>2</sub> Supramolecular Synthone. *Cryst. Growth Des.* **2010**, *10*, 4959–4964; (c) Cozzolino, A. F.; Whitfield, P. S.; Vargas-Baca, I. Supramolecular Chromotropism of the Crystalline Phases of 4,5,6,7-Tetrafluorobenzo-2,1,3-Telluradiazole. *J. Am. Chem. Soc.* **2010**, *132*, 17265–17270.
57. Luzzati, V. Structure cristalline de piásélenol, piázthiol et benzofurazane. *Acta Cryst.* **1951**, *4*, 193–200.
58. Suzuki, T.; Tsuji, T.; Okubo, T.; Okada, A.; Obana, Y.; Fukushima, T.; Miyashi, T.; Yamashita, Y. Preparation, Structure, and Amphoteric Redox Properties of P-Phenylenediamine-Type Dyes Fused with a Chalcogenadiazole Unit. *J. Org. Chem.* **2001**, *66*, 8954–8960.
59. Gomes, A. C.; Biswas, G.; Banerjee, A.; Duax, W. L. Structure of a Planar Organic Compound: 2,1,3-Benzoselenadiazole (Piaselenole). *Acta Cryst. C* **1989**, *45*, 73–75.
60. Cozzolino, A. F.; Vargas-Baca, I.; Mansour, S.; Mahmoudkhani, A. H. The Nature of the Supramolecular Association of 1,2,5-Chalcogenadiazoles. *J. Am. Chem. Soc.* **2005**, *127*, 3184–3190.
61. Bashirov, D. A.; Sukhikh, T. S.; Kuratieva, N. V.; Chulanova, E. A.; Yushina, I. V.; Gritsan, N. P.; Konchenko, S. N.; Zibarev, A. V. Novel Applications of Functionalized 2,1,3-Benzothiadiazoles for Coordination Chemistry and Crystal Engineering. *RSC Adv.* **2014**, *4*, 28309.
62. Makarov, A. G.; Selikhova, N. Y.; Makarov, A. Y.; Malkov, V. S.; Bagryanskaya, I. Y.; Gatilov, Y. V.; Knyazev, A. S.; Slizhov, Y. G.; Zibarev, A. V. New Fluorinated 1,2-Diaminoarenes, Quinoxalines, 2,1,3-Arenothia(Selena)Diazoles and Related Compounds. *J. Fluor. Chem.* **2014**, *165*, 123–131.
63. Taylor, R. It Isn't, It Is: The C–H···X (X = O, N, F, Cl) Interaction Really Is Significant in Crystal Packing. *Cryst. Growth Des.* **2016**, *16*, 4165–4168.
64. (a) Allen, F. H. The Cambridge Structural Database: a Quarter of a Million Crystal Structures and Rising. *Acta Cryst. B* **2002**, *58*, 380–388; (b) Groom, C. R.; Bruno, I. J.; Lightfoot, M. P.; Ward, S. C. The Cambridge Structural Database. *Acta Cryst. B* **2016**, *72*, 171–179; (c) Konstantinova, L. S.; Knyazeva, E. A.; Obruchnikova, N. V.; Gatilov, Y. V.; Zibarev, A. V.; Rakiitin, O. A. Reactions of Vicinal Nitroamines with Sulfur Monochloride—A Short and Convenient Route to Fused 1,2,5-Thiadiazoles and their N-Oxides. *Tetrahedron Lett.* **2013**, *54*, 3075–3078; (d) Mikhailovskaya, T. F.; Makarov, A. G.; Selikhova, N. Y.; Makarov, A. Y.; Pritchina, E. A.; Bagryanskaya, I. Y.; Vorontsova, E. V.; Ivanov, I. D.; Tikhova, V. D.; Gritsan, N. P.; Slizhov, Y. G.; Zibarev, A. V. Carbocyclic Functionalization of Quinoxalines, their Chalcogen Congeners 2,1,3-Benzothia/Selenadiazoles, and Related 1,2-Diaminobenzenes Based on Nucleophilic Substitution of Fluorine. *J. Fluor. Chem.* **2016**, *183*, 44–58; (e) Tomura, M.; Yamashita, Y. Crystal structure of 4,7-dibromo-2,1,3-benzothiadiazole, C<sub>6</sub>H<sub>2</sub>Br<sub>2</sub>N<sub>2</sub>S. *Z. Kristallogr. NCS* **2003**, *218*, 555–556; (f) Tomura, M.; Akhtaruzzaman, M.; Suzuki, K.; Yamashita, Y. 4,7-Diiodo-2,1,3-Benzothiadiazole and 7,7'-Diiodo-4,4'-Bi(2,1,3-Benzothiadiazole). *Acta Cryst. C* **2002**, *58*, 373.
65. Berionni, G.; Pégot, B.; Marrot, J.; Goumont, R. Supramolecular Association of 1,2,5-Chalcogenadiazoles: An Unexpected Self-Assembled Dissymmetric [Se···N]<sub>2</sub> Four-Membered Ring. *CrystEngComm* **2009**, *11*, 986–988.
66. Kusamoto, T.; Yamamoto, H. M.; Kato, R. Utilization of  $\sigma$ -Holes on Sulfur and Halogen Atoms for Supramolecular Cation···Anion Interactions in Bilayer Ni(Dmit) 2 Anion Radical Salts. *Cryst. Growth Des.* **2013**, *13*, 4533–4541.
67. Puskarevsky, N. A.; Smolentsev, A. I.; Dmitriev, A. A.; Vargas-Baca, I.; Gritsan, N. P.; Beckmann, J.; Zibarev, A. V. Bis(2,1,3-Benzotelluradiazolidyl)2,1,3-Benzotelluradiazole: a Pair of Radical Anions Coupled by TeN Chalcogen Bonding. *Chem. Commun.* **2020**, *56*, 1113–1116.
68. Garrett, G. E.; Gibson, G. L.; Straus, R. N.; Seferos, D. S.; Taylor, M. S. Chalcogen Bonding in Solution: Interactions of Benzotelluradiazoles with Anionic and Uncharged Lewis Bases. *J. Am. Chem. Soc.* **2015**, *137*, 4126–4133.
69. (a) Lim, J. Y. C.; Liew, J. Y.; Beer, P. D. Thermodynamics of Anion Binding by Chalcogen Bonding Receptors. *Chem. Eur. J.* **2018**, *24*, 14560–14566; (b) Borissov, A.; Marques, I.; Lim, J. Y. C.; Félix, V.; Smith, M. D.; Beer, P. D. Anion Recognition in Water by Charge-Neutral Halogen and Chalcogen Bonding Foldamer Receptors. *J. Am. Chem. Soc.* **2019**, *141*, 4119–4129; (c) Taylor, M. S. Anion Recognition Based on Halogen, Chalcogen, Pnictogen and Tetrel Bonding. *Coord. Chem. Rev.* **2020**, *413*, 213270.
70. Biot, N.; Bonifazi, D. Concurring Chalcogen- and Halogen-Bonding Interactions in Supramolecular Polymers for Crystal Engineering Applications. *Chem. Eur. J.* **2020**, *26*, 2904–2913.
71. Riwar, L.-J.; Trapp, N.; Root, K.; Zenobi, R.; Diederich, F. Supramolecular Capsules: Strong Versus Weak Chalcogen Bonding. *Angew. Chem. Int. Ed.* **2018**, *57*, 17259–17264.
72. Rahman, F.-U.; Tzeli, D.; Petsalakis, I. D.; Theodorakopoulos, G.; Ballester, P.; Rebek, J.; Yu, Y. Chalcogen Bonding and Hydrophobic Effects Force Molecules into Small Spaces. *J. Am. Chem. Soc.* **2020**, *142*, 5876–5883.
73. Beldjoudi, Y.; Nascimento, M. A.; Cho, Y. J.; Yu, H.; Aziz, H.; Tonouchi, D.; Eguchi, K.; Matsushita, M. M.; Awaga, K.; Osorio-Roman, I.; Constantinides, C. P.; Rawson, J. M. Multifunctional Dithiadiazolyl Radicals: Fluorescence, Electroluminescence, and Photoconducting Behavior in Pyren-1'-yl-Dithiadiazolyl. *J. Am. Chem. Soc.* **2018**, *140*, 6260–6270.
74. Galmés, B.; Adrover, J.; Terraneo, G.; Frontera, A.; Resnati, G. Radicalradical Chalcogen Bonds: CSD Analysis and DFT Calculations. *Phys. Chem. Chem. Phys.* **2020**, *22*, 12757–12765.
75. Nascimento, M. A.; Heyer, E.; Clarke, J. J.; Cowley, H. J.; Alberola, A.; Stephaniuk, N.; Rawson, J. M. On the Design of Radical-Radical Cocrystals. *Angew. Chem. Int. Ed.* **2019**, *58*, 1371–1375.
76. (a) Maartmann-Moe, K.; Nevstad, G. O.; Songstad, J.; Zingales, R.; Vikholm, I.; Urso, F.; Weidlein, J.; Zingaro, R. A. The Crystal Structure of the 2-Oxo-2-Phenylethyl Esters of Thiocyanic and Selenocyanic Acid (Phenacyl Thiocyanate and Phenacyl Selenocyanate). *Acta Chem. Scand.* **1986**, *40a*, 182–189; (b) Jones, P. G.; Wismach, C.; Mughes, G.; Du Mont, W.-W. Methyl 2-Selenocyanatobenzoate. *Acta Cryst. E* **2002**, *58*, 1298–1300.
77. Ho, P. C.; Szydłowski, P.; Sinclair, J.; Elder, P. J. W.; Kübel, J.; Gendy, C.; Lee, L. M.; Jenkins, H.; Britten, J. F.; Morim, D. R.; Vargas-Baca, I. Supramolecular Macrocycles Reversibly Assembled by Te(···)O Chalcogen Bonding. *Nat. Commun.* **2016**, *7*, 11299.
78. (a) Kübel, J.; Elder, P. J. W.; Jenkins, H. A.; Vargas-Baca, I. Structure and Formation of the First (–O–Te–N)<sub>4</sub> Ring. *Dalton Trans.* **2010**, *39*, 11126–11128; (b) Shimada, K.; Moro-oka, A.; Maruyama, A.; Fujisawa, H.; Saito, T.; Kawamura, R.; Kogawa, H.; Sakuraba, M.; Takata, Y.; Aoyagi, S.; Takikawa, Y.; Kabuto, C. Synthesis of Iso-chalcogenazole Rings by Treating  $\beta$ -(N,N-Dimethylcarbamoylchalcogenyl)alkenyl Ketones with Hydroxylamine-O-sulfonic Acid. *Bull. Chem. Soc. Jpn.* **2007**, *80*, 567–577.
79. Fellowes, T.; Harris, B. L.; White, J. M. Experimental Evidence of Chalcogen Bonding at Oxygen. *Chem. Commun.* **2020**, *56*, 3313–3316.
80. Iwaoka, M.; Tomoda, S. First Observation of a C–H···Se “Hydrogen Bond”. *J. Am. Chem. Soc.* **1994**, *116*, 4463–4464.
81. Jiang, M.; Guo, J.; Liu, B.; Tan, Q.; Xu, B. Synthesis of Tellurium-Containing  $\pi$ -Extended Aromatics with Room-Temperature Phosphorescence. *Org. Lett.* **2019**, *21*, 8328–8333.
82. Ho, P. C.; Wang, J. Z.; Meloni, F.; Vargas-Baca, I. Chalcogen Bonding in Materials Chemistry. *Coord. Chem. Rev.* **2020**, *422*, 213464.



83. Geoffrey, S. S.; Claridge, R. C. M.; Kukor, A. J.; Hopkins, W. S.; Schipper, D. J. N-Oxide S–O chalcogen bonding in conjugated materials. *Chem. Sci.* **2021**, *12*, 2304–2312.
84. Zhu, Y.-J.; Gao, Y.; Tang, M.-M.; Rebek, J.; Yu, Y. Dimeric Capsules Self-Assembled through Halogen and Chalcogen Bonding. *Chem. Commun.* **2021**, *57*, 1543–1549.
85. Spicer, R. L.; Stergiou, A. D.; Young, T. A.; Duarte, F.; Symes, M. D.; Lusby, P. J. Host-Guest-Induced Electron Transfer Triggers Radical-Cation Catalysis. *J. Am. Chem. Soc.* **2020**, *142*, 2134–2139.
86. Chen, L.; Xiang, J.; Zhao, Y.; Yan, Q. Reversible Self-Assembly of Supramolecular Vesicles and Nanofibers Driven by Chalcogen Bonding Interactions. *J. Am. Chem. Soc.* **2018**, *140*, 7079–7082.
87. (a) Zeng, R.; Gong, Z.; Yan, Q. Chalcogen Bonding Supramolecular Polymers. *J. Org. Chem.* **2020**, *85*, 8397–8404; (b) Zeng, R.; Gong, Z.; Chen, L.; Yan, Q. Solution Self-Assembly of Chalcogen Bonding Polymer Partners. *ACS Macro Lett.* **2020**, *9*, 1102–1107.
88. Biot, N.; Romito, D.; Bonifazi, D. Substituent-Controlled Tailoring of Chalcogen-Bonded Supramolecular Nanoribbons in the Solid State. *Cryst. Growth Des.* **2021**, *21*, 536–543.
89. Semenov, N. A.; Lonchakov, A. V.; Pushkarevsky, N. A.; Suturina, E. A.; Korolev, V. V.; Lork, E.; Vasiliev, V. G.; Konchenko, S. N.; Beckmann, J.; Gritsan, N. P.; Zibarev, A. V. Coordination of Halide and Chalcogenolate Anions to Heavier 1,2,5-Chalcogenadiazoles: Experiment and Theory. *Organometallics* **2014**, *33*, 4302–4314.
90. Semenov, N. A.; Gorbunov, D. E.; Shakhova, M. V.; Sahnikov, G. E.; Bagryanskaya, I. Y.; Korolev, V. V.; Beckmann, J.; Gritsan, N. P.; Zibarev, A. V. Donor-Acceptor Complexes between 1,2,5-Chalcogenadiazoles (Te, Se, S) and the Pseudohalides CN<sup>-</sup> and XCN<sup>-</sup> (X=O, S, Se, Te). *Chem. Eur. J.* **2018**, *24*, 12983–12991.
91. Benz, S.; Poblador-Bahamonde, A. I.; Low-Ders, N.; Matile, S. Catalysis with Pnictogen, Chalcogen, and Halogen Bonds. *Angew. Chem. Int. Ed.* **2018**, *57*, 5408–5412.
92. Zhao, H.; Gabbai, F. P. A Bidentate Lewis Acid with a Tellurium Ion as an Anion-Binding Site. *Nature Chem.* **2010**, *2*, 984–990.
93. Riel, A. M. S.; Huynh, H.-T.; Jeannin, O.; Berryman, O.; Fourmigué, M. Organic Selenocyanates as Halide Receptors: From Chelation to One-Dimensional Systems. *Cryst. Growth Des.* **2019**, *19*, 1418–1425.
94. Garrett, G. E.; Carrera, E. I.; Seferos, D. I.; Taylor, M. S. Anion Recognition by a Bidentate Chalcogen Bond Donor. *Chem. Commun.* **2016**, *52*, 9881–9884.
95. Benz, S.; Macchione, M.; Veroleto, Q.; Mareda, J.; Sakai, N.; Matile, S. Anion Transport with Chalcogen Bonds. *J. Am. Chem. Soc.* **2016**, *138*, 9093–9096.
96. (a) Lim, J. Y. C.; Marques, I.; Thompson, A. L.; Christensen, K. E.; Félix, V.; Beer, P. D. Chalcogen Bonding Macrocycles and [2]Rotaxanes for Anion Recognition. *J. Am. Chem. Soc.* **2017**, *139*, 3122–3133; (b) Lim, J. Y. C.; Marques, I.; Félix, V.; Beer, P. D. Chiral Halogen and Chalcogen Bonding Receptors for Discrimination of Stereo- and Geometric Dicarboxylate Isomers in Aqueous Media. *Chem. Commun.* **2018**, *54*, 10851–10854.
97. Strakova, K.; Assies, L.; Goujon, A.; Piazzolla, F.; Humeniuk, H. V.; Matile, S. Dithienothiophenes at Work: Access to Mechanosensitive Fluorescent Probes, Chalcogen Bonding Catalysis, and beyond. *Chem. Rev.* **2019**, *119*, 10977–11005.
98. (a) Chandrasekhar, V.; Thirumoorthy, R. Halide-Capped Tellurium-Containing Macrocycles. *Inorg. Chem.* **2009**, *48*, 10330–10337; (b) Citeau, H.; Kirschbaum, K.; Conrad, O.; Giolando, D. M. A novel cage organotellurate(IV) macrocyclic host encapsulating a bromide anion guest: [Li(THF)4][[PrTe]12O16Br4]Br·2THF. *Chem. Commun.* **2001**, 2006–2007.
99. Beau, M.; Lee, S.; Kim, S.; Han, W.-S.; Jeannin, O.; Fourmigué, M.; Aubert, E.; Espinosa, E.; Jeon, I.-R. Strong  $\sigma$ -Hole Activation on Icosahedral Carborane Derivatives for a Directional Halide Recognition. *Angew. Chem. Int. Ed.* **2021**, *60*, 366–370.
100. (a) Mukherjee, A. J.; Zade, S. S.; Singh, H. B.; Sunoj, R. B. Organoselenium Chemistry: Role of Intramolecular Interactions. *Chem. Rev.* **2010**, *110*, 4357–4416; (b) Srivastava, K.; Chakraborty, T.; Singh, H. B.; Butcher, R. J. Intramolecularly Coordinated Azobenzene Selenium Derivatives: Effect of Strength of the Se···N Intramolecular Interaction on Luminescence. *Dalton Trans.* **2011**, *40*, 4489–4496; (c) Selvakumar, K.; Singh, H. B.; Goel, N.; Singh, U. P. Methyl Ester Function: An Intramolecular Electrophilic Trap for the Isolation of Aryltellurenyl Hydroxide and Diorganotellurium Dihydroxide. *Organometallics* **2011**, *30*, 3892–3896.
101. (a) Iwaoka, M.; Tomoda, S. Nature of the Intramolecular se···N Nonbonded Interaction of 2-Selenobenzylamine Derivatives. An Experimental Evaluation by <sup>1</sup>H, <sup>77</sup>Se, and <sup>15</sup>N NMR Spectroscopy. *J. Am. Chem. Soc.* **1996**, *118*, 8077–8084; (b) Fujita, K.-I.; Iwaoka, M.; Tomoda, S. Synthesis of Diaryl Diselenides Having Chiral Pyrrolidine Rings with C<sub>2</sub> Symmetry. Their Application to the Asymmetric Methoxyselenenylation of Trans- $\beta$ -Methylstyrenes. *Chem. Lett.* **1994**, *23*, 923–926.
102. Wirth, T. Enantioselective Alkylation of Aldehydes Catalyzed by New Chiral Diselenides. *Tetrahedron Lett.* **1995**, *36*, 7849–7852.
103. Tiecco, M.; Testaferri, L.; Santi, C.; Tomassini, C.; Marini, F.; Bagnoli, L.; Temperini, A. Preparation of a New Chiral Non-Racemic Sulfur-Containing Diselenide and Applications in Asymmetric Synthesis. *Chem. Eur. J.* **2002**, *8*, 1118–1124.
104. Wirth, T. Organoselenium Chemistry in Stereoselective Reactions. *Angew. Chem. Int. Ed.* **2000**, *39*, 3740–3749.
105. Tay, D. W.; Tsoi, I. T.; Er, J. C.; Leung, G. Y. C.; Yeung, Y.-Y. Lewis Basic Selenium Catalyzed Chloroamidation of Olefins Using Nitriles as the Nucleophiles. *Org. Lett.* **2013**, *15*, 1310–1313.
106. Liu, X.; Liang, Y.; Ji, J.; Luo, J.; Zhao, X. Chiral Selenide-Catalyzed Enantioselective Allylic Reaction and Intermolecular Difunctionalization of Alkenes: Efficient Construction of C-SCF<sub>3</sub> Stereogenic Molecules. *J. Am. Chem. Soc.* **2018**, *140*, 4782–4786.
107. (a) Lenardão, E. J.; Feijó, J. O.; Thurow, S.; Perin, G.; Jacob, R. G.; Silveira, C. C. Selenonium ionic liquid as efficient catalyst for the Baylis–Hillman reaction. *Tetrahedron Lett.* **2009**, *50*, 5215–5217; (b) He, X.; Wang, X.; Tse, Y.-L. S.; Ke, Z.; Yeung, Y.-Y. Applications of Selenonium Cations as Lewis Acids in Organocatalytic Reactions. *Angew. Chem. Int. Ed.* **2018**, *57*, 12869–12873.
108. Benz, S.; López-Andarias, J.; Mareda, J.; Sakai, N.; Matile, S. Catalysis with Chalcogen Bonds. *Angew. Chem. Int. Ed.* **2017**, *56*, 812–815.
109. Benz, S.; Mareda, J.; Besnard, C.; Sakai, N.; Matile, S. Catalysis with Chalcogen Bonds: Neutral Benzodiselenazole Scaffolds with High-Precision Selenium Donors of Variable Strength. *Chem. Sci.* **2017**, *8*, 8164–8169.
110. Benz, S.; Besnard, C.; Matile, S. Chalcogen Bonding Catalysis: From Neutral to Cationic Benzodiselenazole Scaffolds. *Helv. Chim. Acta* **2018**, *101*, e1800075.
111. Vogel, L.; Wonner, P.; Huber, S. M. Chalcogen Bonding: An Overview. *Angew. Chem. Int. Ed.* **2019**, *58*, 1880–1891.
112. Wonner, P.; Steinke, T.; Huber, S. M. Activation of Quinolines by Cationic Chalcogen Bond Donors. *Synlett* **2019**, *30*, 1673–1678.
113. Wonner, P.; Dreger, A.; Vogel, L.; Engelage, E.; Huber, S. M. Chalcogen Bonding Catalysis of a Nitro-Michael Reaction. *Angew. Chem. Int. Ed.* **2019**, *58*, 16923–16927.
114. Steinke, T.; Wonner, P.; Engelage, E.; Huber, S. M. Catalytic Activation of a Carbon–Chloride Bond by Dicationic Tellurium-Based Chalcogen Bond Donors. *Synthesis* **2021**, *53*, 2043–2050.
115. Wonner, P.; Vogel, L.; Düser, M.; Gomes, L.; Kniep, F.; Mallick, B.; Werz, D. B.; Huber, S. M. Carbon-Halogen Bond Activation by Selenium-Based Chalcogen Bonding. *Angew. Chem. Int. Ed.* **2017**, *56*, 12009–12012.
116. (a) Wang, W.; Zhu, H.; Liu, S.; Zhao, Z.; Zhang, L.; Hao, J.; Wang, Y. Chalcogen-Chalcogen Bonding Catalysis Enables Assembly of Discrete Molecules. *J. Am. Chem. Soc.* **2019**, *141*, 9175–9179; (b) Wang, W.; Zhu, H.; Feng, L.; Yu, Q.; Hao, J.; Zhu, R.; Wang, Y. Dual Chalcogen-Chalcogen Bonding Catalysis. *J. Am. Chem. Soc.* **2020**, *142*, 3117–3124.
117. (a) Iwaoka, M.; Takemoto, S.; Okada, M.; Tomoda, S. Statistical Characterization of Nonbonded S···O Interactions in Proteins. *Chem. Lett.* **2001**, *30*, 132–133; (b) Fick, R. J.; Kroner, G. M.; Nepal, B.; Magnani, R.; Horowitz, S.; Houtz, R. L.; Scheiner, S.; Trievel, R. C. Sulfur-Oxygen Chalcogen Bonding Mediates AdoMet Recognition in the Lysine Methyltransferase SET7/9. *ACS Chem. Biol.* **2016**, *11*, 748–754.
118. (a) Bitai, J.; Westwood, M. T.; Smith, A. D.  $\alpha,\beta$ -Unsaturated acyl ammonium species as reactive intermediates in organocatalysis: an update. *Org. Biomol. Chem.* **2021**, *19*, 2366–2384; (b) McLaughlin, C.; Smith, A. D. Generation and Reactivity of C(1)-Ammonium Enolates by Using Isothiourea Catalysis. *Chem. Eur. J.* **2021**, *27*, 1533–1555.
119. (a) Birman, V. B.; Li, X. Benzotetramisole: a Remarkably Enantioselective Acyl Transfer Catalyst. *Org. Lett.* **2006**, *8*, 1351–1354; (b) Birman, V. B.; Li, X. Homobenzotetramisole: An Effective Catalyst for Kinetic Resolution of Aryl-Cycloalkanols. *Org. Lett.* **2008**, *10*, 1115–1118; (c) Yang, X.; Birman, V. B. Homobenzotetramisole-Catalyzed Kinetic Resolution of  $\alpha$ -Aryl-,  $\alpha$ -Aryloxy-, and  $\alpha$ -Arylthioalkanoic Acids. *Adv. Synth. Catal.* **2009**, *351*, 2301–2304; (d) Yang, X.; Birman, V. B. Kinetic Resolution of  $\alpha$ -Substituted Alkanoic Acids Promoted by Homobenzotetramisole. *Chem. Eur. J.* **2011**, *17*, 11296–11304.
120. Shu, C.; Liu, H.; Slawin, A. M. Z.; Carpenter-Warren, C.; Smith, A. D. Isothiourea-catalysed enantioselective Michael addition of N-heterocyclic pronucleophiles to  $\alpha,\beta$ -unsaturated aryl esters. *Chem. Sci.* **2020**, *11*, 241–247.

121. Munday, E. S.; Grove, M. A.; Feoktistova, T.; Brueckner, A. C.; Walden, D. M.; Young, C. M.; Slawin, A. M. Z.; Campbell, A. D.; Cheong, P. H.-Y.; Smith, A. D. Isothiourea-Catalyzed Atropselective Acylation of Biaryl Phenols Via Sequential Desymmetrization/Kinetic Resolution. *Angew. Chem. Int. Ed.* **2020**, *59*, 7897–7905.
122. Barrios Antúnez, D.-J.; Greenhalgh, M. D.; Brueckner, A. C.; Walden, D. M.; Elías-Rodríguez, P.; Roberts, P.; Young, B. G.; West, T. H.; Slawin, A. M. Z.; Ha-Yeon Cheong, P.; Smith, A. D. Catalytic Enantioselective Synthesis of Perfluoroalkyl-Substituted  $\beta$ -Lactones Via a Concerted Asynchronous (2 + 2) Cycloaddition: a Synthetic and Computational Study. *Chem. Sci.* **2019**, *10*, 6162–6173.
123. Leverett, C. A.; Purohit, V. C.; Romo, D. Enantioselective, Organocatalyzed, Intramolecular Aldol Lactonizations with Keto Acids Leading to Bi- and Tricyclic  $\beta$ -Lactones and Topology-Morphing Transformations. *Angew. Chem. Int. Ed.* **2010**, *49*, 9479–9483.
124. Murai, T.; Lu, W.; Kuribayashi, T.; Morisaki, K.; Ueda, Y.; Hamada, S.; Kobayashi, Y.; Sasamori, T.; Tokitoh, N.; Kawabata, T.; Furuta, T. Conformational Control in Dirhodium(II) Paddlewheel Catalysts Supported by Chalcogen bonding Interactions for Stereoselective Intramolecular C–H Insertion Reactions. *ACS Catal.* **2021**, *11*, 568–578.
125. Klinkhammer, K. W.; Pyykkö, P. Ab Initio Interpretation of the Closed-Shell Intermolecular E $\cdots$ E Attraction in Dipnicogen (H<sub>2</sub>E–EH)<sub>2</sub> and Dichalcogen (HE–EH)<sub>2</sub> Hydride Model Dimers. *Inorg. Chem.* **1995**, *34*, 4134–4138.
126. Pyykkö, P. Strong Closed-Shell Interactions in Inorganic Chemistry. *Chem. Rev.* **1997**, *97*, 597–636.
127. (a) Rosenfield, R. E.; Parthasarathy, R.; Dunitz, J. D. Directional Preferences of Nonbonded Atomic Contacts with Divalent Sulfur. 1. Electrophiles and Nucleophiles. *J. Am. Chem. Soc.* **1977**, *99*, 4860–4862; (b) Glusker, J. P. Directional Aspects of Intermolecular Interactions. *Top. Curr. Chem.* **1998**, *198*, 1–56.
128. (a) Szalewicz, K. Symmetry-Adapted Perturbation Theory of Intermolecular Forces. *WIREs Comput. Mol. Sci.* **2012**, *2*, 254–272; (b) Jansen, G. Symmetry-Adapted Perturbation Theory Based on Density Functional Theory for Noncovalent Interactions. *WIREs Comput. Mol. Sci.* **2014**, *4*, 127–144; (c) Grimme, S. In *The Chemical Bond*; Frenking, G., Shaik, S., Eds.; vol. 2; Wiley-VCH: Weinheim, 2014; pp 477–499.
129. Bleiholder, C.; Gleiter, R.; Werz, D. B.; Köppel, H. Theoretical Investigations on Heteronuclear Chalcogen-Chalcogen Interactions: On the Nature of Weak Bonds between Chalcogen Centers. *Inorg. Chem.* **2007**, *46*, 2249–2260.
130. Bleiholder, C.; Werz, D. B.; Köppel, H.; Gleiter, R. Theoretical Investigations on Chalcogen-Chalcogen Interactions: What Makes these Nonbonded Interactions Bonding? *J. Am. Chem. Soc.* **2006**, *128*, 2666–2674.
131. Del Bene, J. E.; Shavitt, I. In *Molecular Interactions. From Van der Waals to Strongly Bound Complexes*; Scheiner, S., Ed.; John Wiley & Sons: New York, 1997.
132. Tatamitani, Y.; Liu, B.; Shimada, J.; Ogata, T.; Ottaviani, P.; Maris, A.; Caminati, W.; Alonso, J. L. Weak, Improper, C–O $\cdots$ H–C Hydrogen Bonds in the Dimethyl Ether Dimer. *J. Am. Chem. Soc.* **2002**, *124*, 2739–2743.
133. Pauling, L. *The Nature of the Chemical Bond*, 3rd ed.; Cornell University Press: Ithaca, 1960.
134. (a) Cradock, S.; Whiteford, R. A. Photoelectron Spectra of the Methyl, Silyl and Germyl Derivatives of the Group VI Elements. *J. Chem. Soc., Faraday Trans. 2* **1972**, *68*, 281–288; (b) Kimma, K.; Katsumata, S.; Achiba, Y.; Yamazaki, T.; Iwata, S. *Handbook of the He(I) Photoelectron Spectra of Fundamental Organic Molecules*, Japan Scientific Society Press: Tokyo, 1981.
135. Pascoe, D. J.; Ling, K. B.; Cockroft, S. L. The Origin of Chalcogen Bonding Interactions. *J. Am. Chem. Soc.* **2017**, *139*, 15160–15167.
136. Reed, A. E.; Curtiss, L. A.; Weinhold, F. Intermolecular Interactions from a Natural Bond Orbital, Donor-Acceptor Viewpoint. *Chem. Rev.* **1988**, *88*, 899–926.
137. Murray, J. S.; Lane, P.; Clark, T.; Politzer, P.  $\sigma$ -Hole Bonding: Molecules Containing Group VI Atoms. *J. Mol. Model.* **2007**, *13*, 1033–1038.
138. Kolář, M. H.; Hobza, P. Computer Modeling of Halogen Bonds and Other  $\sigma$ -Hole Interactions. *Chem. Rev.* **2016**, *116*, 5155–5187.
139. (a) Stewart, R. F. On the Mapping of Electrostatic Properties from Bragg Diffraction Data. *Chem. Phys. Lett.* **1979**, *65*, 335–342; (b) Koritsanszky, T. S.; Coppens, P. Chemical Applications of X-Ray Charge-Density Analysis. *Chem. Rev.* **2001**, *101*, 1583–1628.
140. (a) Clark, T.; Hennemann, M.; Murray, J. S.; Politzer, P. Halogen Bonding: The  $\sigma$ -Hole. *J. Mol. Model.* **2007**, *13*, 291–296; (b) Clark, T.  $\sigma$ -Holes. *WIREs Comput. Mol. Sci.* **2013**, *3*, 13–20.

## 1.14 Supramolecular chemistry of p-block elements

D.S. Wright and H.-C. Niu, Yusuf Hamied Department of Chemistry, University of Cambridge, Cambridge, United Kingdom

© 2023 Elsevier Ltd. All rights reserved.

1.14.1	Introduction	652
1.14.2	Heteroatomic p-block hosts	653
1.14.2.1	Group 15 host-guest chemistry	653
1.14.2.2	Group 14 host-guest chemistry	657
1.14.2.3	Other systems	660
1.14.3	Homoatomic p-block hosts	661
1.14.4	Outlook	662
References		662

### Glossary

**Complementarity** The spatial and/or chemical matching of the host and guest.

**Heteroatomic** Involving two or more types of atoms.

**Homoatomic** Involving one type of atom.

**Host-Guest** A complex in which the guest molecule is coordinated by the host.

**Hydrophobic interactions** Non-polar interactions involving organic groups.

**Isoelectronic** The same number of electrons.

**Macrocyclic** A cyclic macromolecule or macromolecular portion of a molecule.

**Non-tiling** The geometric inability to form a flat surface using a particular geometric shape.

**Receptor** An alternative name for a host, but normally with a selective function for a guest.

**Reorganization energy** The energy for change in molecular arrangement upon coordination.

**Templating** The ability of a template molecule to direct the formation of a host molecule around it.

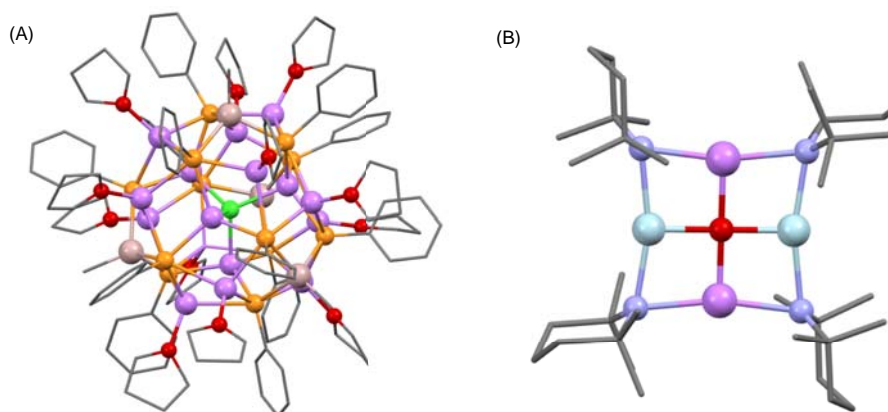
### Abstract

This review concerns development of the area of p-block element host-guest chemistry since Comprehensive Inorganic Chemistry II. The focus is largely on the most thermodynamically stable host systems.

### 1.14.1 Introduction

Host-guest complexes involve the coordination of cationic, anionic or neutral guests within discrete host molecules or supramolecular host assemblies using noncovalent (H-bonding, ionic, van der Waals or hydrophobic) interactions.<sup>1</sup> While this definition provides workable boundaries in the well-established area of organic hosts (like crown ethers, calixarenes and porphyrins), some reflection on this definition is valuable when extending this concept to host assemblies constructed from elements other than carbon. This is because many (especially ionic) inorganic hosts or host assemblies do not necessarily have an independent ("discrete") existence in the absence of the guest. This is especially the case for s-block host-guest complexes. A case in point is the series of isostructural cages [ $\{\text{MeE}(\text{PPh})_3\text{Li}_4 \cdot 3\text{thf}\}_4(\mu_4\text{-X})\}^-$  (**1**) (E = Al, Ga, In; X = Cl, Br) in which four  $[\text{MeE}(\text{PPh})_3\text{Li}_4]$  units form as tetrahedral host assembly around  $\tilde{\text{X}}$  anions (Fig. 1A).<sup>2</sup> Although there is no doubt that this and related inverse-crown arrangements of electropositive metals<sup>3</sup> like **2**<sup>4</sup> (Fig. 1B) can be described as host-guest complexes, in neither do the host frameworks ( $\{\{\text{MeE}(\text{PPh})_3\text{Li}_4 \cdot 3\text{thf}\}_4\}$  in **1** and  $[\text{Li}_2\text{Mg}_2(\text{TMP})_4]^{2+}$  (TMP = 2,2,6,6-tetramethyl piperidine) in **2**) exist as a separate, functional entities in their own right.

This article builds on the previously review of the host-guest chemistry of p-block systems published in 2013 in Comprehensive Coordination Chemistry II,<sup>5</sup> and mainly focuses on more robust molecular or supramolecular host arrangements. The periodic increase in effective nuclear charge of the p-block elements brings with it increased covalent character, with the opportunity for the design of robust host molecules which mirror those found in classical host-guest chemistry based on carbon. It can be seen, however, that many of the thermodynamic and kinetic principles that govern the inherent stability of classical organic hosts (like crowns ethers) also extend to p-block metal host systems, so that for a viable p-block host molecule to exist in its own right the bonding arrangement is most likely to consist of strong bonds, preferably non-polar ones. For this reason, p-block host systems



**Fig. 1** The host-guest complexes (A) **1** and (B) **2**. Color code: P (orange), O (red), N (blue), Mg (light blue), Li (magenta).

have continued to be dominated in the past 7 years by thermodynamically and kinetically stable arrangements of this type, pre-eminently phosphazanes (P–N) and siloxanes (Si–O), as well as some notable, ground-breaking studies of P–P bonded hosts. Once again, a common theme and motivation in these studies has been the structural relationship to organic host systems and the often-cited isoelectronic relationships between the archetypal C–C bonded arrangements and inorganic counterparts.

Whereas the historical development of p-block element based host systems has been dominated by structural curiosity, with many of the host-guest adducts being discovered more by chance than design in previous studies, perhaps the greatest advance in this area in the past decade or so has been the focus on systematic design, functionality and application. Thus, it appears that many of the cutting-edge developments in this area now aspire to the same level of complexity as is commonplace in the organic arena.

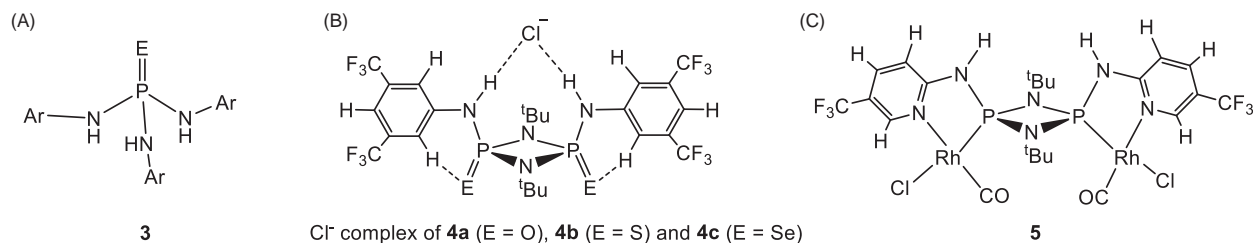
## 1.14.2 Heteroatomic p-block hosts

### 1.14.2.1 Group 15 host-guest chemistry

The past decade has seen increasing interest in the applications of Group 15 hosts in anion coordination and recognition. In the areas of P–N bonded phosph(III/V)azane chemistry this has largely involved the development of new H-bond donor host arrangements, while newly introduced receptor molecules based on the heavier Group 15 elements (Sb in particular) take advantage of the Lewis acidity of the metal centers for anion binding. The general area of inorganic receptor molecules is a developing field which has been reviewed previously.<sup>6</sup>

Anion binding and sensing using small H-bond donor organic receptor molecules is a well-established area of research.<sup>7</sup> Ureas and squaramides are some of the most common classes of organic receptors used in this field, which have been applied in anion-sensing, anion-transport and counterion-catalysis.<sup>8</sup> Small molecular p-block counterparts based on a range of functional groups have recently been introduced, including phosphoramides [ $R_2P(=O)NHR$ ], sulfonamide [ $RS(=O)_2NHR$ ], boronic acids [ $RB(OH)_2$ ], boronic acids ( $R_2BOH$ ), silanols ( $R_3SiOH$ ), phosphoric acids [ $RO_2P(=O)OH$ ], and phosphonium cations [ $(R_2N)_2P(NHR)_2^+$ ].<sup>9</sup>

Particularly interesting examples of these are small H-bond receptor molecules based on P–N bonded arrangements. Gale and coworkers have shown that phosphoric- and thiophosphoric- triamides of the type  $[(ArNH)_3P=E]$  ( $E = O, S$ ;  $Ar = 3,5-(CF_3)_2C_6H_3$ ) (**3**) are effective new receptors for the recognition and transport of anions (Fig. 2A), showing high values of stability constants for the formation of 1:2 halides and organic carboxylate complexes in MeCN. The anion transport mechanism through lipid layers was shown to be similar to that observed for thioureas and squaramides (involving an anion-anion antiport mechanism).<sup>9</sup> Goldfuss and coworkers have investigated the air-stable phosph(V)azane dimers  $[ArNH(E)P(\mu-N^tBu)]_2$  ( $E = O$ ) (**4a**),



**Fig. 2** The anion receptor molecules (A) **3**, (B) **4a–4c**, and (C) **5**.

S (**4b**), Ar = 3,5-(CF<sub>3</sub>)<sub>2</sub>C<sub>6</sub>H<sub>3</sub>) (Fig. 2A), whose bidentate H-bond donor arrangements are related to ureas and squaramides.<sup>10</sup> Phosph(V)azane **4a** binds to Cl<sup>-</sup> significantly more strongly (with log*K* = 5.43: *K* = binding constant) than the corresponding diaryl urea (log*K* = 4.25) and aryl-squaramide (log*K* = 5.13) (containing the same 3,5-(CF<sub>3</sub>)<sub>2</sub>C<sub>6</sub>H<sub>3</sub> groups). This high anion affinity makes **4a** useful in counterion-catalysis. On the basis of DFT calculations, the lower affinity of the sulfur derivative **4b** for Cl<sup>-</sup> was explained by the effect of stabilizing *ortho*-C–H...O=P interactions in the O-analog **4a** on the conformation of the dimer, making the chelating N-H “in-in” conformation (necessary for bifurcated Cl<sup>-</sup> coordination) more energetically accessible (Fig. 2B). Interestingly, the selenium derivative [ArNH(Se)P(μ-N<sup>t</sup>Bu)]<sub>2</sub> (**4c**) was recently found to have a similar binding constant to that of the oxygen derivative **4a** (log*K* = 5.74 M<sup>-1</sup>).<sup>11</sup> In contrast to **4a**, **4c** is hydrolytically stable and has been shown to be an excellent receptor for the transport of Cl<sup>-</sup> ions through lipid layers under aqueous conditions; the observed order of transport activity being **4c** > **4b** > **4a**, with **4c** having a similar activity to that of the corresponding thiourea (containing the same 3,5-(CF<sub>3</sub>)<sub>2</sub>C<sub>6</sub>H<sub>3</sub> groups).

Taking a cue from these previous studies, it was found that coordination of the P<sup>III</sup> atoms of the dimeric phosph(III)azanes of the type [(2-py')NHP(μ-N<sup>t</sup>Bu)]<sub>2</sub> (where 2-py' is a substituted or unsubstituted 2-pyridyl group) to transition metal centers can not only stabilize the P<sup>III</sup> frameworks, making the new, receptor complexes hydrolytically stable, but can also be used to “lock” the conformation of the N-H groups into the optimum “in-in” arrangement for anion binding.<sup>12</sup> Metal coordination also results in superior binding constants even compared to selenium oxidation (as in the case of **4c**, above). The best receptor of this type [(5-CF<sub>3</sub>-2-pyridyl)(Rh(CO)Cl)NHP(μ-N<sup>t</sup>Bu)]<sub>2</sub> (**5**) (Fig. 2C) exhibits 2: 1 binding behavior to Cl<sup>-</sup> ions in DMSO with a binding constant (*K*) of ca. 4900 M<sup>-1</sup>. This compares to a binding constant of ca. 520 M<sup>-1</sup> for the best selenium receptor **4c**, and is one to two orders of magnitude higher than the best squaramide and thiourea receptors under the same conditions.

Receptor **5** has similar transport activity through lipid layers under aqueous conditions to the best squaramide transporter reported, even though it has only two rather than four CF<sub>3</sub> groups in the aromatic substituents, illustrating that this metal coordination strategy can outcompete structurally related organic transporters which are commonly used in this area. DFT calculations have been used to probe the reasons for the enhanced H-bond donor properties of seleno-phosph(V)azanes (like **4c**) and metal-coordinated phosph(III)azanes (like **5**). The primary effect of oxidation or metal coordination of the P<sup>III</sup> centers is an increase in back-bonding of the *exo*-N lone pairs into the σ\* orbitals of the P–N bonds within the P<sub>2</sub>N<sub>2</sub> ring units, which results directly in increased polarization of the N–H bonds (Fig. 3). A further strategy for increasing anion binding is the use of charged phosph(V)azane receptor frameworks like [<sup>t</sup>BuNH(Se=)P(μ-N<sup>t</sup>Bu)<sub>2</sub>P(Me)HN<sup>t</sup>Bu]<sup>+</sup> (**6**), the effect of which on N–H bond polarity is similar to selenium oxidation and metal coordination, but with the additional effect of increased Coulombic attraction between the receptor and the anionic guest.<sup>13</sup>

The applications of cyclodiphosphazanes as building blocks to a range of small-molecular, macrocyclic and polymeric arrangements has been highlighted in a comprehensive recent review.<sup>14</sup> Of particular interest in this area are macrocyclic compounds in which P<sub>2</sub>N<sub>2</sub> ring units are bridged by metals<sup>15</sup> and non-metals<sup>16</sup> into cyclic arrangements. Recent examples of both types of macrocycle illustrate their ability to form host-guest complexes, involving H-bonding and hydrophobic interactions.<sup>17,18</sup> For example, the metal-bridged pentamer [{(PhC≡C)P(μ-N<sup>t</sup>Bu)}<sub>2</sub>{Rh(CO)Cl}]<sub>5</sub> (**7**), formed by the reaction of the neutral phosph(III)azane dimer [(PhC≡C)P(μ-N<sup>t</sup>Bu)]<sub>2</sub> with [Rh(CO)<sub>2</sub>Cl]<sub>2</sub>, forms an H-bonded host-guest complex with solvent MeCN molecules above and below the mean plane of the macrocycle involving the *endo*-CO O-atoms.<sup>17a</sup> The N-H bridged pentamer [{P(μ-N<sup>t</sup>Bu)}<sub>2</sub>(NH)]<sub>5</sub> (**8**) has also been shown to have a remarkable tendency for H-bonding of neutral guests within its cavity, resulting largely from the high polarity of N–H bonds due to the polarity of its P–N bonded core.<sup>18d</sup> A dramatic demonstration of this is the formation of a 1:1 host-guest complex with PhC≡CH, resulting primarily from highly unusual N–H...π(C≡C) bonding ([**8** ⊂ PhC≡CH] Fig. 4). The binding host-guest constant is around 55 M<sup>-1</sup> in hexane. It is worthwhile noting that this type of host-guest interaction has not been observed previously for less polar organic macrocycles.

The phosph(III)azane macrocycle **8** can be used to trap guests within its cavity irreversibly. Although the host-guest complex [**8** ⊂ I<sup>-</sup>] exhibits dynamic behavior in solution (involving coordination and de-coordination of I<sup>-</sup> ions), oxidation of the P<sup>III</sup> atoms of the core with sulfur, giving the host-guest complex [**9** ⊂ I<sup>-</sup>], results in the steric blocking of the H-bonding coordination site by the <sup>t</sup>Bu groups. Such is the extent of this blocking that even reaction with excess MeOTf (Tf = triflate) fails to release the I<sup>-</sup> ion (as MeI). Instead, methylation of one of the S-atoms at the periphery occurs to give the neutral species **10** (Fig. 5). The host **9** traps I<sup>-</sup> ions more effectively than any organic or metallo-organic halide receptor known (although this is kinetic rather than thermodynamic in this case).

Turning to Lewis acidic anion receptors, small, molecular boron compounds have dominated this area and have extensive applications in the important field of optical chemosensing of anions. The use of boron compounds in this area has recently been reviewed in detail.<sup>19</sup> Gabbaï and coworkers have been particularly active in the development of water-stable Lewis acidic Group

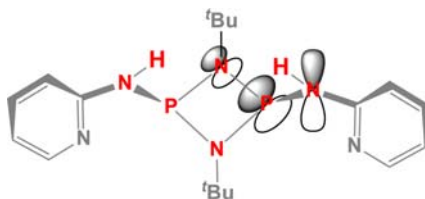
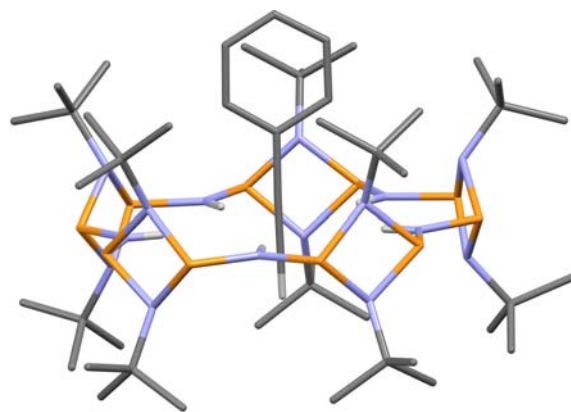
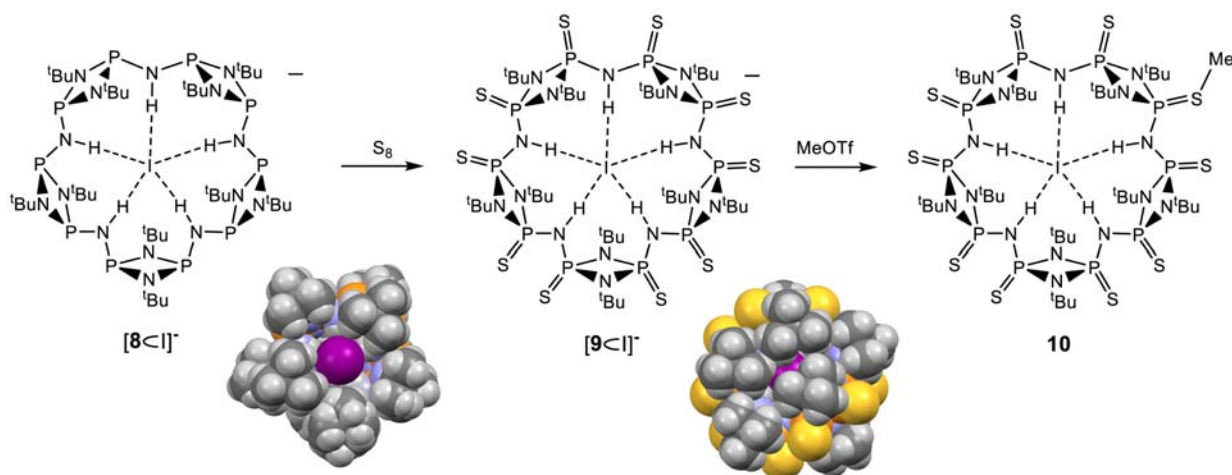


Fig. 3 Schematic of the back-bonding interaction in seleno-phosph(V)azanes (like **4c**) and metal-coordinated phosph(III)azanes (like **5**).



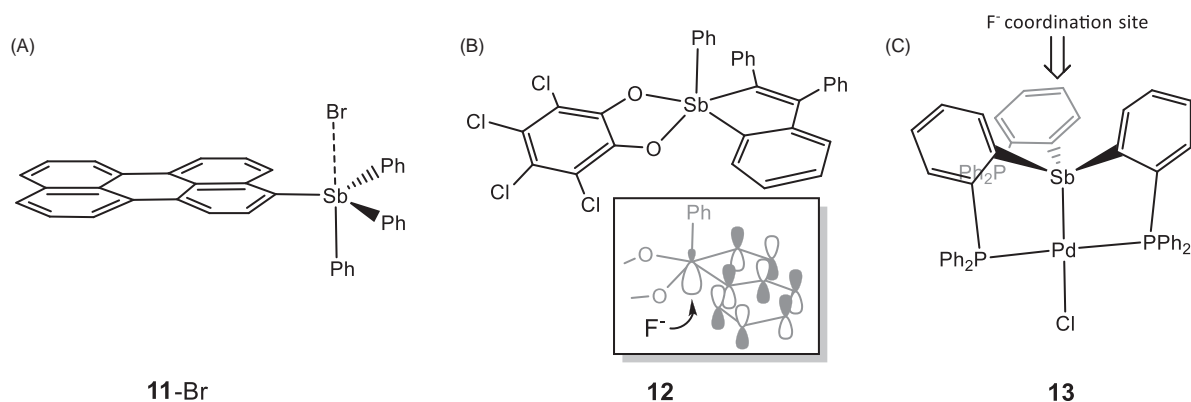


**Fig. 4** The host-guest complex  $[8 \subset \text{PhC}\equiv\text{CH}]$ . Color code: P (orange), N (blue), C (gray).



**Fig. 5** Oxidation of the phosph(III)azane framework of the host-guest complex  $[8 \subset \text{I}]^-$  to the phosph(V)azane framework of complex  $[9 \subset \text{I}]^-$ , and the result of reaction with MeOTf giving **10**. The space-filling diagrams show the blocking of the cavity by the <sup>t</sup>Bu groups.

15, Sb(III) and Sb(V), receptors for fluoride ion sensing, which are compatible with measurement of drinking or even untreated water.<sup>20</sup> Three recent examples of this type of receptor are shown in **Fig. 6**, which illustrate the principles involved in their design. The organo-Sb(V) bromide  $[\text{Ar}(\text{Br})\text{SbPh}_3]$  ( $\text{Ar} = 3\text{-perylene}$ ) (**11-Br**) exhibits weak  $\text{Sb} \cdots \text{Br}$  in the solid state (2.921 Å) and dissociates completely into the free stibonium cation  $[\text{ArSbPh}_3]^+$  and  $\text{Br}^-$  in acidic solution (**Fig. 6A**).<sup>20c</sup> Addition of  $\text{F}^-$  ions results in a blue shift of the perylene-based absorption bands and a large enhancement in fluorescence intensity in the visible region, stemming from the formation of  $[\text{Ar}(\text{F})\text{SbPh}_3]$  (**11-F**). The pre-receptor **11-Br** can be employed in the quantitative measurement of  $\text{F}^-$



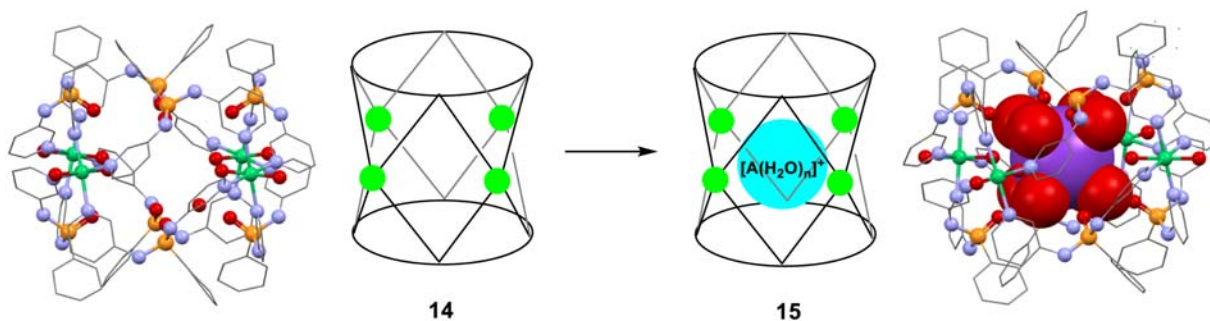
**Fig. 6** Examples of small-molecule, Lewis acidic receptors developed by Gabbai and coworkers.

concentration in drinking water by monitoring the emission band in the visible region at 423 nm. In the Sb(V) 1 $\lambda$ -stibaindole receptor **12** (Fig. 6B), the installation of an electron withdrawing chloranil group lowers the energy of the  $\sigma^*$ -orbitals of the Ph–Sb bond sufficiently to allow significant conjugation with the  $\pi^*$  system of the heterocyclic C<sub>4</sub>Sb ring unit and results in a narrow  $\pi$ - $\pi^*$  gap.<sup>20f</sup> The  $\sigma^*$ - $\pi^*$  conjugation can be turned off by the coordination of a F<sup>-</sup> anion to the pseudo-square-based pyramidal Sb(V) atom, resulting in a color change that can also be used to measure F<sup>-</sup> concentration in water quantitatively. The coordination of a F<sup>-</sup> anion to the Sb center of the cationic Pd(II)/Sb(V) receptor **13** (Fig. 6C), along the axis of the Pd–Sb bond, results in a yellow-to-orange color change.<sup>20c</sup> DFT calculations suggest that the coordination of F<sup>-</sup> results in (what can be described by a valence bond model as) a change from Sb:  $\rightarrow$  Pd to Pd:  $\rightarrow$  Sb donation. The color response of receptor **13** is apparently selective for F<sup>-</sup>, with no color change being observed for a range of other anions (including Cl<sup>-</sup> and Br<sup>-</sup>).

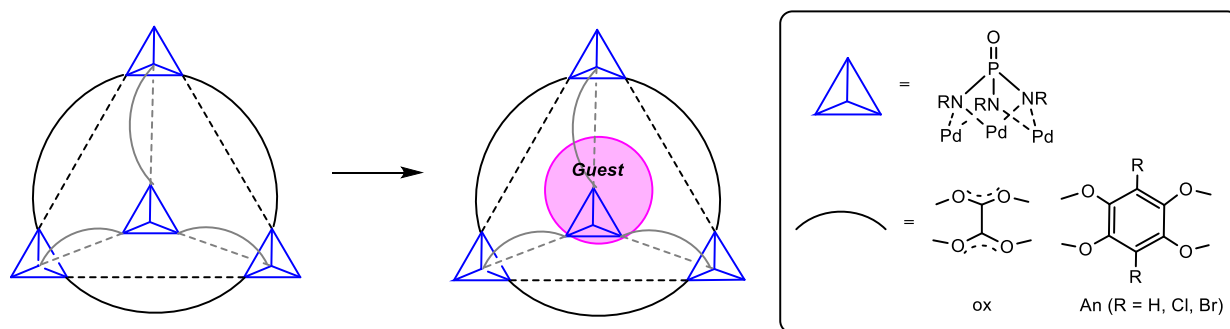
The encapsulation of neutral guests is a feature of a growing number of ‘metallo-inorganic’ host molecules involving structure-directing, small P–N bonded ligands. Boomishankar and coworkers have made some particularly exciting contributions to this emerging field of supramolecular chemistry, which mirrors the classical area of metallo-organic host chemistry (involving structure-directing organic ligands). The host cage arrangements are derived from [Ph(O=)P{NH(3-py)}<sub>2</sub>]<sup>21</sup> and [E = P(NHR)<sub>3</sub>]<sup>22</sup> (E = O, S; R = aryl or alkyl) building blocks and a range of transition metals.

Depending on the anion present, the reactions of [Ph(O=)P{NH(3-py)}<sub>2</sub>] ligand (L) with Cu<sup>II</sup>X<sub>2</sub> give polymeric arrangements (in the case of X = ClO<sub>4</sub><sup>-</sup>) or discrete molecular arrangements (in the case of NO<sub>3</sub><sup>-</sup>).<sup>21a</sup> The latter exhibit interesting host-guest chemistry, for example, the [Cu<sub>4</sub>L<sub>8</sub>]<sup>8+</sup> cation of [Cu<sub>4</sub>L<sub>8</sub>·5H<sub>2</sub>O] [NO<sub>3</sub>]<sub>8</sub> (**14a**) has a cavitated arrangement that can be viewed as a metal-ligand analog of a cucurbituril, having a contact surface volume of around 153 Å<sup>3</sup>. While this cavity is occupied by H<sub>2</sub>O molecules in the solid-state structure of the solvate of **14**, addition of KNO<sub>3</sub> in aqueous media results in the encapsulation of a distorted dodecahedral K(H<sub>2</sub>O)<sub>8</sub><sup>+</sup> cation within the void. Although similar encapsulation using NaNO<sub>3</sub> was not observed, analogous cavitated [M<sub>4</sub>L<sub>8</sub>]<sup>8+</sup> cations (**14b** and **14c**, respectively) are also produced with Ni(NO<sub>3</sub>)<sub>2</sub> and Co(NO<sub>3</sub>)<sub>2</sub>, which form the full range of host-guest [M<sub>4</sub>L<sub>8</sub> C A(H<sub>2</sub>O)<sub>n</sub>]<sup>9+</sup> complexes, **15** [A = Li (n = 5), Na (n = 5), K (n = 8), Rb (n = 9), Cs (n = 10)] (Fig. 7).<sup>21b</sup> The unprecedentedly high hydration numbers of the alkali metal cations in these species appears to be the combined result of confinement and the hydrophobic nature of the cavities. Interestingly, the ferromagnetic behavior of these host-guest complexes is dependent on the hard-soft characteristics of the alkali metal cation guests, providing the potential for tuning ferromagnetic character.

Neutral tetrahedral clusters of the type [(Pd<sub>3</sub>L<sup>1</sup>)<sub>4</sub>(X)<sub>6</sub>] [L=O=P(NR)<sub>3</sub><sup>3-</sup>, X = oxalate (ox) or anilates (An)], in which [PdL<sub>3</sub>] units form the apices, exhibit extensive host-guest chemistry. The first of these to be reported, [(Pd<sub>3</sub>L (1))<sub>4</sub>(ox)<sub>6</sub>] (L<sup>1</sup>=O=P(N<sup>1</sup>Pr)<sub>3</sub><sup>3-</sup>) (**16**), acts as a selective host for a range of neutral solvents, depending on the size of the guest with respect to the host cavity (volume 85 Å<sup>3</sup>) (Fig. 8).<sup>22b</sup> Thus, the host-guest complexes of **16** C CCl<sub>4</sub>, **16** C CHCl<sub>3</sub>, **16** C CH<sub>2</sub>Cl<sub>2</sub> and **16** C C<sub>5</sub>H<sub>10</sub> are all readily formed by the interaction of the corresponding solvents with the DMSO complex **16** C DMSO, while



**Fig. 7** Encapsulation of A(H<sub>2</sub>O)<sub>n</sub><sup>+</sup> cations by cucurbituril-like arrangement (**14**), producing **15** (illustrated by the encapsulation of a K(H<sub>2</sub>O)<sub>8</sub><sup>+</sup> guest by the Ni(II) host **14b**). Color code: P (yellow), N (blue), O (red), Ni (green), K (purple).



**Fig. 8** Formation of host-guest complexes using **16** and **17**.

larger solvents like  $C_7H_8$ ,  $C_6H_5Cl$  and  $C_6H_5F$  are too big to be encapsulated (with volumes  $> 100 \text{ \AA}^3$ ). Competitive experiments together with theoretical calculations show that **16** has greatest affinity for benzene over the small chlorinated guests and has potential in solvent separation. The size selection of hosts in this way (depending on the relative size of the host and guest) is akin to that found more commonly in related metallo-organic hosts.<sup>23</sup>

Using the longer connector anilate ligands (An) results in larger cavities in the guests  $[(Pd_3L(1))_4(An)_6]$  (**17**), with cavity volumes in the range  $230\text{--}240 \text{ \AA}^3$ .<sup>22h</sup> In contrast to **16**, these cages are now able to encapsulate toluene, *o*-, *m*- and *p*-xylene and mesitylene, depending on the portal radius of the cages (Fig. 8). Thus, with smaller, unsubstituted An ligands ( $R = H$ ) which allow greater access to the cavity, host-guest complexes of toluene, *o*-, *m*- and *p*-xylene and mesitylene are formed, for chloro-anilate ( $R = Cl$ ) only toluene, and *o*-, *m*- and *p*-xylene complexes, and for bromo-anilate ( $R = Br$ ) only the mesitylene complex. Placing chiral (*R*- and *S*-) $\alpha$ -methylbenzylamide groups within the  $O=P(NR)_3^{3-}$  anions gives the enantiopure chiral hosts  $[(Pd_3L^*)_4(ox)_6]$  (**18**) and  $[(Pd_3L^*)_4(An)_6]$  (**19**) which have been shown to be capable of enantioselective separation of racemic mixtures of chiral epoxides, lactones and ketones by crystallization of **18** and **19** in the presence of the racemic analytes.<sup>22e,g</sup>

#### 1.14.2.2 Group 14 host-guest chemistry

There has been continued development of the coordination chemistry of silicon-based macrocyclic hosts since 2013. Recent progress in this area has mainly focused on cyclic siloxanes of the type  $cyclo-[Me_2SiO]_n$ <sup>24</sup> and novel hybrid macrocycles in which the  $C_2$  units of conventional crown ethers are replaced by disilane  $Si(Me)_2Si(Me)_2$  units,<sup>25</sup> with very few recent studies concerning isoelectronic Si–N bonded macrocycles.<sup>26</sup> It has been noted that cyclic siloxanes coordinate metal ions only weakly as a result of the low Lewis basicity of the donor O-atoms compared to crown ethers. This stems from the presence of lone-pair  $p(O) \rightarrow \sigma^*(Si-C)$  hyperconjugation interactions which decrease the electron density on the O-atoms,<sup>27,28</sup> as well as from repulsion between the electrophilic Si atoms of the macrocycles and the coordinated ions.<sup>24a,27b</sup> The presence of  $SiMe_2$  connecting groups (as opposed to  $C_2$  linkers) also means that the cyclic siloxanes adopt very different conformations to the corresponding crown ethers which can result in higher reorganization energies of their macrocyclic frameworks upon metal coordination. As a result of this weak coordination ability, comparatively few metal complexes had been reported previously [containing  $Li^+$ ,<sup>28</sup>  $K^+$ ,<sup>24b,29</sup>  $Zr^{4+}$ ,<sup>30</sup> and  $Ag^+$ <sup>31</sup> coordinated by  $[Me_2SiO]_n$ ,  $n = 4, 5, 6, 7$ ] (examples of these are shown in Fig. 9).

In earlier work, the cyclic siloxane frameworks were commonly generated serendipitously by in situ reactions of organometallics with vacuum grease (via nucleophilic attack of polymeric  $[Me_2SiO]_n$ ). More recently, however, the research has focused on the coordination chemistry of the pre-formed hosts themselves. A recent report has reinvestigated the coordination of  $[Me_2SiO]_n$  with  $Ag^+$ .<sup>24a</sup> Previously, it had been shown that addition of  $AgSbF_6$  in  $SO_2$  to a mixture of  $[Me_2SiO]_n$  ( $n = 3\text{--}6$ ) gave the 6-, 7- and 8-membered siloxanes, from which  $[Ag(MeSiO)_7][SbF_6]$  (**20**) was isolated (the cation of which is shown in Fig. 9C).<sup>31</sup> These ring transformation reactions were assumed to be metal-induced and result from  $F^-$  abstraction from the  $SbF_6^-$  ion, giving a mixture of the most thermodynamically stable rings. By using the  $Ag^+$  salts of the very weakly coordinating anions  $Ag[Al(OR)_4]$  and  $Ag[FAl(OR)_3]$  ( $R = C(CF_3)_3$ ), which have significantly higher  $F^-$  affinities, these ring transformations are suppressed, allowing the exclusive isolation of complexes containing the  $[Ag(MeSiO)_6]^+$  cation directly from  $[Me_2SiO]_6$  in  $SO_2$ . Calculations reveal that  $[MeSiO]_7$  forms more stable complexes with  $Ag^+$  in the gas and solution phases than  $[MeSiO]_6$ , supporting the previous proposal of the thermodynamic selection of **20**.

In a further recent study it has been shown that the direct formation of alkaline earth metal complexes of  $[Me_2SiO]_n$  is possible, even in the presence of strongly coordinating anions.<sup>24c</sup> It was proposed previously that anion-cation interactions were unfavorable to complex formation with cyclic siloxanes (bearing in mind the weak coordination ability of cyclic-siloxanes).<sup>28</sup> In contrast to this assertion, direct coordination of  $MgI_2$  and  $CaI_2$  by  $[Me_2SiO]_n$  ( $n = 6$  and  $7$ , respectively) occurs in  $\alpha, \alpha, \alpha$ -trifluorotoluene, giving the new complexes  $[MgI_2(Me_2SiO)_6]$  (**21**) (Fig. 10) and  $[CaI_2(Me_2SiO)_7]$  (**22**). However, this complexation is extremely slow for  $SrI_2$  and only the impure complex could be obtained in low yield in this case. Addition of  $Gal_3$  to the  $SrI_2$  and  $BaI_2$  reactions of

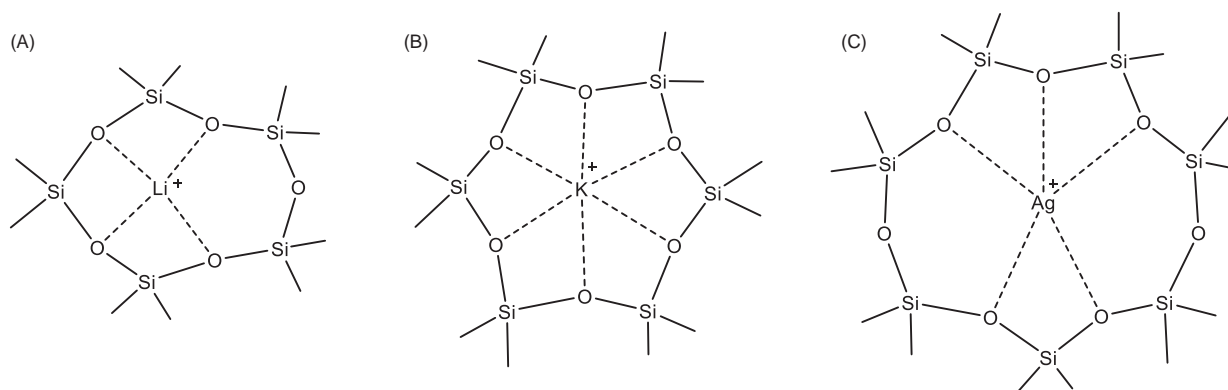
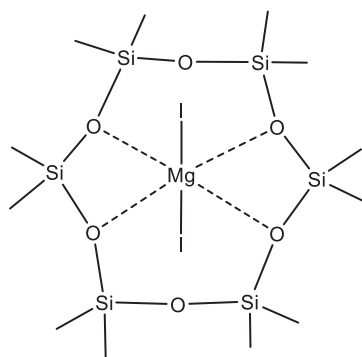


Fig. 9 Some of the structurally-characterized  $Li^+$ ,  $K^+$ ,  $Ag^+$  complexes of cyclic siloxanes,  $[Me_2SiO]_n$ .



21

Fig. 10 Structure of  $[MgI_2(Me_2SiO)_6]$  (21).

$[Me_2SiO]_7$ , however, overcomes this difficulty and results in the ion-paired complexes  $[Sr(GaI_4)_2(Me_2SiO)_7]$  (23) and  $[Ba(GaI_4)_2(Me_2SiO)_7]$  (24). Theoretical calculations have been used to probe the thermodynamics of these reactions, which indicate that the difficulty in the complexation of  $Sr^{2+}$  and  $Ba^{2+}$  with  $[Me_2SiO]_7$  is due to the decrease in the net binding energy of macrocycle to these salts going down group 2 (which cannot offset the unfavorable effect of lattice energy), making coordination endothermic. This binding energy is greater for the  $Sr(GaI_4)_2$  and  $Be(GaI_4)_2$ , so that complexation becomes favorable.

Hybrid disilane macrocycles, introduced recently by von Hähnisch and coworkers, are shown in Fig. 11. A major challenge in this area remains a fully inorganic representative  $[(SiR_2)_2O]_n$  in which all of the C-atoms of the crown arrangement are replaced by valence-isoelectronic  $SiR_2SiR_2$  groups.

As a result of the insertion of disilane units instead of the  $Si(Me_2)$  units of cyclic siloxanes, the distance between the Si atoms and the coordinated metal ion in these hybrid macrocycles is increased, resulting in far lower metal...Si repulsion, which (as noted previously) is one of the major factors responsible for the poor coordination ability of cyclic siloxanes compared to organic

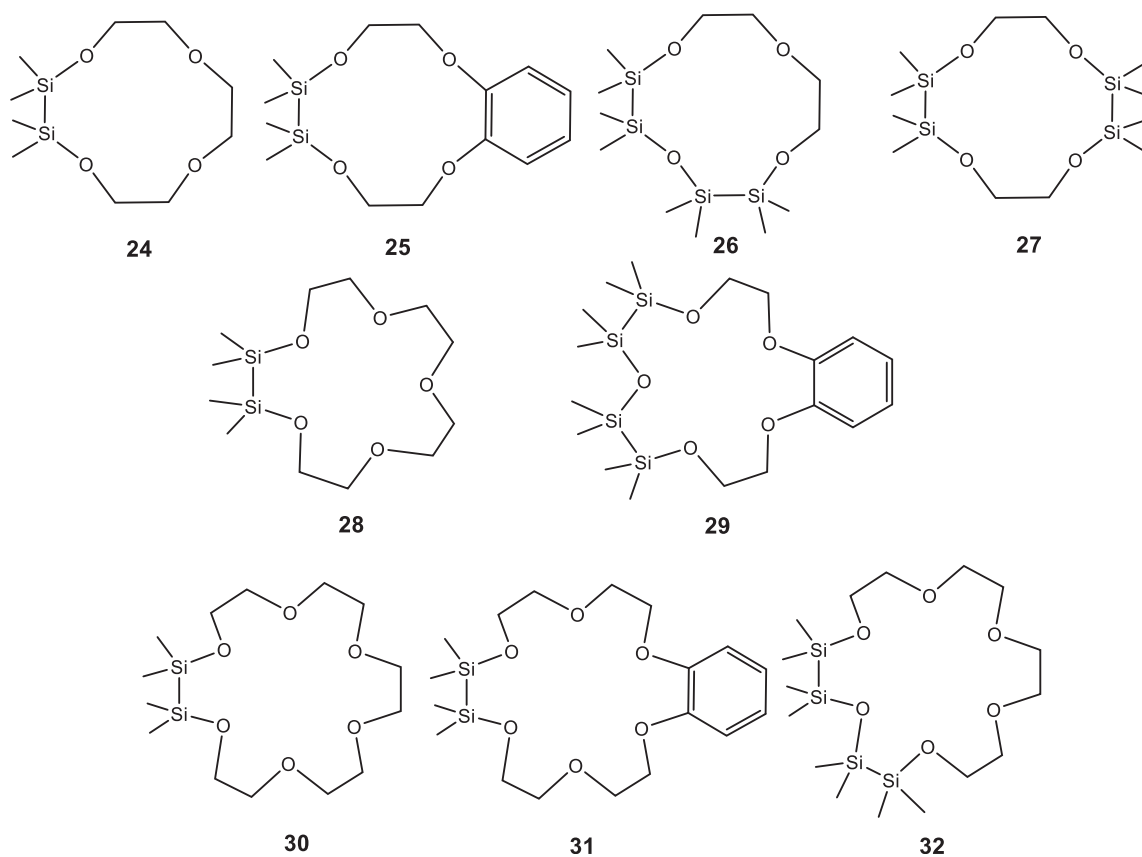


Fig. 11 New hybrid disilane macrocycles.

counterparts. Based on DFT calculations and competitive NMR experiments, it was concluded that the coordination ability of 24 and 27 towards  $\text{Li}^+$  are similar to directly analogous, fully-organic 12-crown-4.<sup>25a</sup> This is in spite of the fact that the reorganization energy of their macrocyclic frameworks (going from the free ligands to the  $\text{Li}^+$  complexes) are greater. This suggests that  $\text{p}(\text{O}) \rightarrow \sigma^*(\text{Si}-\text{C})$  hyperconjugation interactions, which reduce the Lewis basicity of cyclic siloxanes, are a less important influence in hybrid systems. The unfavorable reorganization energy is offset by greater electrostatic interactions with the  $\text{Li}^+$  cations in these complexes, which is supported by the observation of shorter O–Li bonds with the O-atoms adjacent to the Si atoms in the solid-state structures compared to the O–Li bonds made with the all-ethylene substituted O-atoms. Further studies of 26 (the constitutional isomer of 27) show that this macrocycle actually has a higher binding energy to  $\text{Li}^+$  than 12-crown-4.<sup>25b</sup> This may be partly due to the better geometric fit of  $\text{Li}^+$  into the cavity of 26 (which is slightly bigger than in 12-crown-4), but is also the result of the highly Lewis basic character of the Si–O–Si O-atom. This is mirrored in the large, up-field change in the  $^{29}\text{Si}$  NMR chemical shift of the Si atoms in this fragment upon complexation to  $\text{Li}^+$ .

Further work in this area has focused mainly on the coordination of alkali and alkaline earth metals.<sup>g,25c–e</sup> Like the parent all-carbon crown ethers, size complementarity (matching of the ion with the size of the coordination cavity) is an important factor in the formation of metal complexes of hybrid disilane crowns, with the involvement of the C–O–C, C–O–Si and Si–O–Si O-atoms varying depending on the size of the s-block ions involved. The involvement of the C–O–Si and Si–O–Si O-atoms can be readily assessed by  $^{29}\text{Si}$  NMR spectroscopy. For example, in Group 1 and 2 complexes of 29 the Si resonances of both fragments show marked up-field shifts if involved in metal coordination, which are roughly proportional to the strength of the bonding.<sup>25g</sup> The ability of the hybrid macrocycles to coordinate Group 2 metal ions in the presence of strongly coordinating anions (even for the heavier alkaline earth metals, such as in  $[(29)\text{SrI}_2]$ , Fig. 12) illustrates their greater coordination ability over cyclic siloxane macrocycles. However, the greater Lewis acidity of  $\text{Be}^{2+}$  can result in the decomposition of the hybrid frameworks, as shown by a study of the coordination of  $\text{BeCl}_2$  by 24 and 25 which results in extrusion of the  $\text{Si}_2$  units (via loss of  $\text{ClSi}_2\text{Me}_4\text{Cl}$  and  $\text{ClC}_2\text{H}_4\text{OSi}_2\text{Me}_4\text{Cl}$ ).<sup>25h</sup>

An extensive series of metal cage compounds containing cyclic and linear silsesquioxanes has been investigated. The cyclic silsesquioxanes of formula  $[\text{RSi}(\text{O})\text{O}]_n^{n-}$  are isoelectronic with cyclic siloxanes (Fig. 13, bottom) and can function as structure-directing building blocks in these systems.<sup>33</sup> The standard method of synthesis involves reaction of  $\text{RSi}(\text{OR})_3$  with alkali metal hydroxides (MOH), generating oligomeric  $[(\text{RSi}(\text{O})\text{O})_n\text{M}]$  in situ, followed by reaction with various transition metals. Systematic synthesis of cage assemblies has so far not been possible in this area, largely as a result of the high ionic character of Si–O bonds, and the resulting tendency for rearrangement of the initially formed oligomers. Ultimately, the cage formed in a particular reaction depends very much on the metal ions present as well as the presence of anionic or neutral templates. The main focus of studies so far has been in the use of these cages in the areas of catalysis and magnetism. As a general rule, more condensed cage architectures are found where smaller ( $n = 3$  and 4) cyclic silsesquioxane ligands are present,<sup>34</sup> while as the rings size increases to  $n = 5$  and beyond more open cages containing large cavities are formed.<sup>35,36</sup> The structures of a number of these cages, containing tubular cavitand-like arrangements, reveal interesting host-guest behavior. Two examples of these are shown in Fig. 13 (33, a Cu(II) host containing a DMSO guest, and 34, a Ni(II) host containing an  $\text{OH}^-$  guest). So far, however, the host-guest chemistry of this interesting family of compounds has not been investigated in its own right.

Self-assembly of supramolecular cages using p-block elements is an emerging field of study, which has been highlighted in a previous review.<sup>37</sup> An early example of this is a tetrahedral metallo-organic  $[\text{Ga}_4\text{L}_6]^{12-}$  cage (L = an organic dicatecholamide ligand) which self assembles in the presence of  $\text{R}_4\text{N}^+$  cations.<sup>38</sup> This area is a direct parallel to the far more well developed field of metal-directed self-assembly involving transition metals.<sup>23</sup> A related direction is that of transition metal directed self-assembly using p-block metal based (rather than organic) ligands, which has the ability to build heterometallic arrangements. The *tris*(3-pyridyl)-Si and -Sn ligands  $[\text{MeSi}(3\text{-py})_3]$  (35)<sup>39</sup> and  $[\text{PhSn}(3\text{-py})_3]$  (36)<sup>40</sup> are good examples of these, which are readily prepared by the reactions of the corresponding trihalides ( $\text{RECl}_3$ ) with 3-lithio-pyridyl or the turbo Grignard reagent. The host-guest chemistry of 36 is of particular interest.<sup>40</sup> In the presence of transition metal halides containing strongly coordinating anions (such as  $\text{Cl}^-$ ), polymeric structures are formed in which the pyridyl-N atoms of 36 bridge the transition metal ions. However, self-assembled host-guest complexes can result where more weakly coordinating anions are present. An example is the reaction of

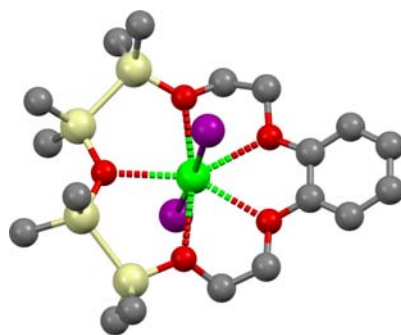
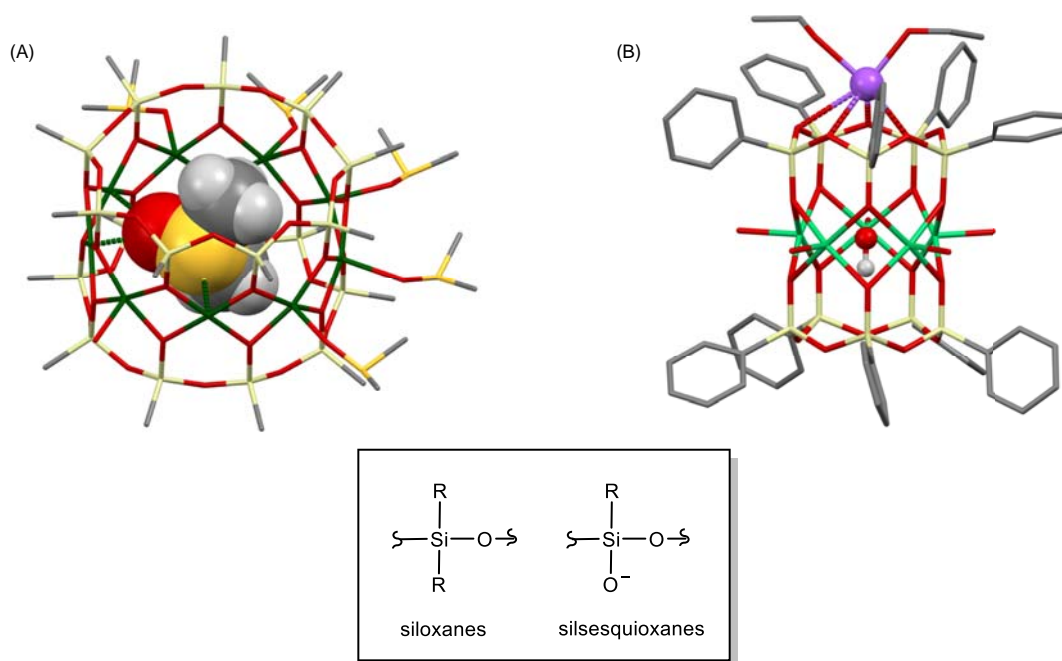


Fig. 12 X-ray structure of  $[(29)\text{SrI}_2]$ . Color code: Ca (green), Si (yellow), O (red), I (purple), C (gray).



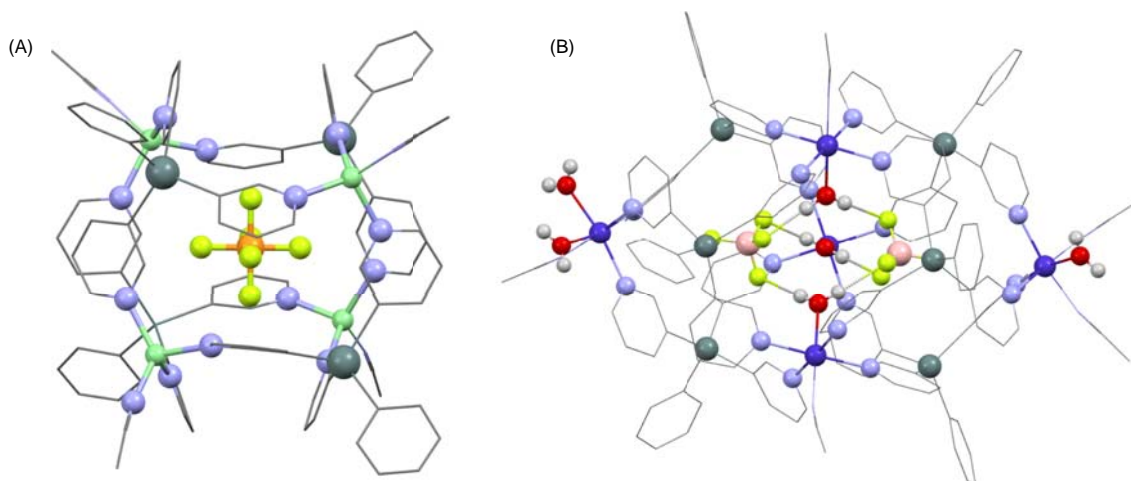


**Fig. 13** Structures of host-guest complexes of metal-silsesquioxanes, containing larger ring units. (A) **33**, (B) **34**. Color code: Cu (dark green), Ni (light green), O (red), Si (light yellow), S (yellow), C (dark gray), Na (purple).

**36** with  $\text{CuPF}_6$ , resulting in the host-guest complex **37** shown in Fig. 14A, in which a  $\text{Cu}_4\text{Sn}_4$  cubane arrangement encapsulates a  $\text{PF}_6^-$  anion (a polymeric arrangement is formed in the case of CuI under similar conditions).  $^1\text{H}/^{19}\text{F}$  DOSY NMR studies show that **37** is intact in MeCN at 228 K, but highly dynamic at room temperature. A related cage (**38**) is formed in the presence of  $\text{Co}(\text{BF}_4)_2$  (Fig. 14B), in which two  $\text{BF}_4^-$  anions are encapsulated (being H-bonded to two *endo*- $\text{H}_2\text{O}$  molecules within the cavity).

### 1.14.2.3 Other systems

A number of other new host systems have been introduced recently that are based on more exotic p block bonding arrangements. An interesting example are macrocycles based on  $\text{Te} \cdots \text{O}$  chalcogen bonding<sup>41</sup> developed by Vargas-Baca and coworkers.<sup>42</sup> Although there is still some debate concerning the nature of this type of interaction, they are thought to involve a combination of electrostatics, dispersion forces and  $n(\text{lone-pair, donor})-\sigma^*(\text{chalcogen, acceptor})$  bonding (the contribution from each component varying with the element combination involved). These interactions are therefore closely related in origin to H-bonding and can have



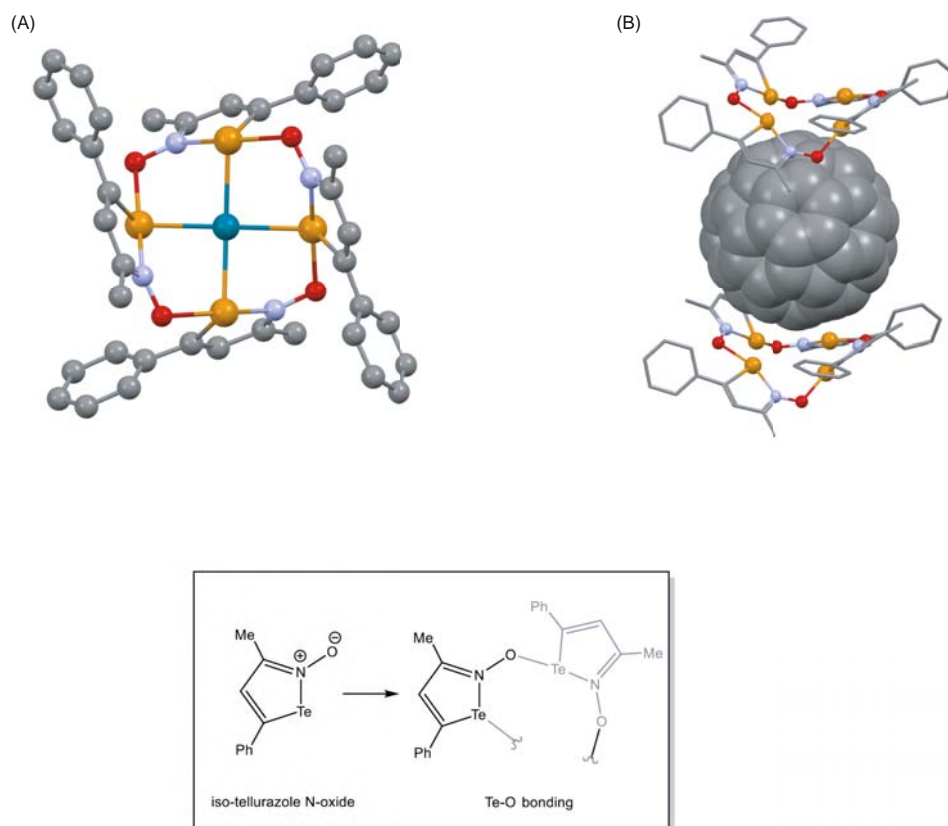
**Fig. 14** Solid-state structures of host-guest complexes (A) **37** and (B) **38**. Color code: Cu (green), Sn (gray), Co (blue), O (red), N (light blue), P (orange), B (orange), F (yellow), H (light gray).

a similar range of bond energies (up to ca.  $70 \text{ kJ mol}^{-1}$ ). Iso-tellurazole N-oxides (Fig. 15, bottom) aggregate in the solid and solution states and, depending on the solvent and the presence of metallic or non-metallic templates, can form hexameric or tetrameric macrocyclic host arrangements. Examples of host-guest complexes include metal complexes (like the  $\text{Pd}^{2+}$  complex  $39^{2+}$ , Fig. 15A) and a host-guest complex of  $\text{C}_{60}$  formed in the solid state (40, Fig. 15B). This area shows remarkable promise for future developments in supramolecular main group chemistry.

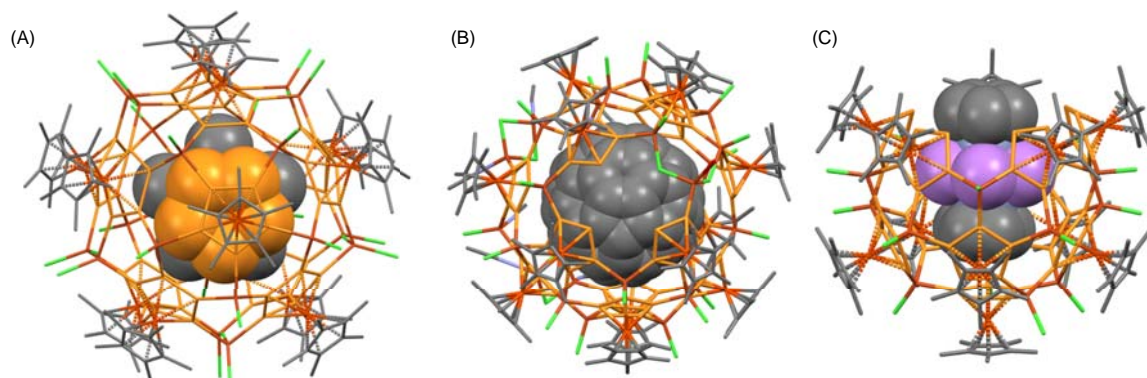
### 1.14.3 Homoatomic p-block hosts

Perhaps the most pre-eminent class of host-guest complexes involving homoatomic p-block arrangements investigated in recent years are fullerene-like assemblies based on  $[\text{Cp}^*\text{Fe}(\eta(5)\text{-P}_5)]$  ( $\text{Cp}^*$  = a penta-substituted cyclopentadienide) building blocks, formed upon coordination of the P-atom to  $\text{Cu(I)X}$  ( $X$  = halide).<sup>32,43</sup> The formation of capsule arrangements is the result of the non-tiling, pentagonal  $\text{P}_5$ -units which adopt an  $\eta^5:\eta^1:\eta^1:\eta^1:\eta^1$ -bonding mode at the surface of the cages. Among various factors, their size and topology depend on the organic substituents on the cyclopentadienide ring, the halide ion present in  $\text{CuX}$ , and on the presence of neutral or charged guest molecules, which act as templates. The first of these to be reported by Scheer and coworkers in 2003 was  $[\{\text{Cp}^*\text{Fe}(\text{P}_5)\}_{12}\{\text{CuCl}\}_{10}\{\text{Cu}_2\text{Cl}_3\}_5\{\text{Cu}(\text{CH}_3\text{CN})_2\}_5]$  ( $\text{Cp}^*$  =  $\text{Me}_5\text{C}_5$ ) (41) (Fig. 16A), having a similar structural motif to  $\text{C}_{60}$  but with an external radius three times as large.<sup>43a</sup> The largest of these capsules to be prepared so far is rugby-ball shaped  $[\{\text{Cp}^{\text{Bn}}\text{Fe}(\text{P}_5)\}_{24}\text{Cu}_{96}\text{Br}_{96}]$  ( $\text{Cp}^{\text{Bn}}$  =  $(\text{PhCH}_2)_5\text{C}_5$ ) (42), which is around 61 times the size of  $\text{C}_{60}$ . With approximate dimensions  $3.7 \times 4.6 \text{ nm}$ , 42 is verging on the size of a protein and is one of the largest molecular species known.<sup>32f</sup>

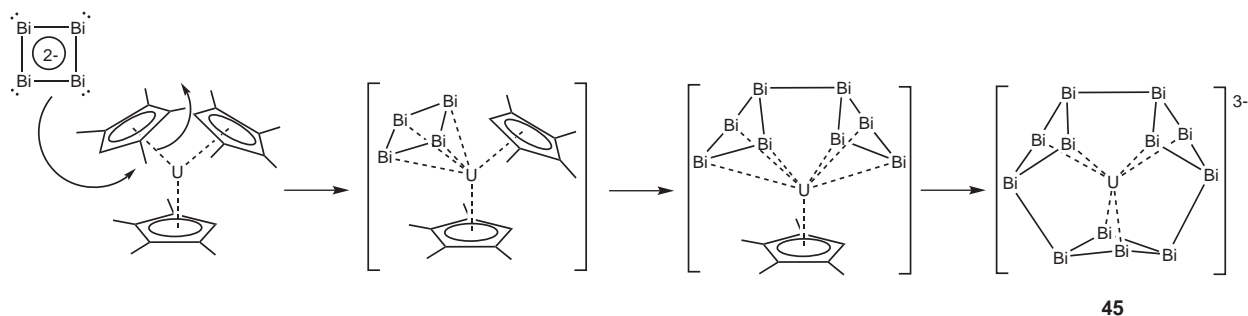
The spherical void of 41 was found to be occupied by a disordered  $[\text{Cp}^*\text{Fe}(\eta(5)\text{-P}_5)]$  molecule, which provided a first indication of the remarkable host-guest chemistry in this area. Since this starting point, a broad range of templates has been encapsulated within such arrangements, including *ortho*-carborane  $o\text{-C}_2\text{B}_{10}\text{H}_{12}$ <sup>43d</sup> and  $\text{C}_{60}$  itself (43, Fig. 16B),<sup>43c</sup> reactive main group species such as  $\text{E}_4$  ( $\text{E} = \text{P}, \text{As}$ ),<sup>32b</sup> and reactive transition metal compounds [such as  $16e \text{ CpCr}(\eta^5\text{-As}_5)$ , which has not been observed previously as a free molecule<sup>32a</sup>]. A recent innovation in this area has been the observation of bowl-shaped arrangements which resemble the truncated fullerenes  $\text{I}_h\text{-C}_{80}$ .<sup>32i</sup> Remarkably, this change in topology results from simply switching the solvent system. In earlier work it was found that the triple-decker sandwich compound  $[\text{CpFe}(\mu\text{-}\eta^5, \eta^5\text{-As}^5)\text{FeCp}]$  is encapsulated *intact* by  $[\text{Cp}^*\text{Fe}(\eta^5\text{-P}_5)]$  in the presence of  $\text{CuBr}$  in toluene/MeCN solvent, whereas under the same conditions  $\text{CuCl}$  results in the encapsulation of  $16e$



**Fig. 15** Examples of host-guest complexes formed with isotellurazole N-oxides. (A)  $39^{2+}$ , (B) 40. Color code: Pd (green), O (red), N (blue), Te (orange).



**Fig. 16** Structures of (A) **41** (the Cu-coordinated MeCN ligands have been removed for clarity), (B) **43** and (C) **44**.



**Fig. 17** Formation and structure of **45**. Color code: Bi (purple), U (blue).

CpCr( $\eta^5$ -As<sub>5</sub>). Changing the solvent to CH<sub>2</sub>Cl<sub>2</sub>/MeCN gives an open, bowl-arrangement containing [CpFe( $\mu$ - $\eta^5$ , $\eta^5$ -As<sub>5</sub>)FeCp] as the guest (**44**, Fig. 16C). The highly dynamic nature of these fullerene-like arrangements has also been explored in a detailed solution- and solid-state study.<sup>32e</sup> The manipulation of the solvent system can be used to switch the supramolecular structure in solution, which allows the selective incorporation of guests (such as ferrocene). These findings have moved this chemistry into the realms of classical supramolecular chemistry and dynamic self-assembly.

A few heterometallic Zintl compounds are also worthy of note in regard to the general concept of host-guest chemistry.<sup>44,45</sup> A particularly striking example is the [U@Bi<sub>12</sub>]<sup>3-</sup> anion (**45**), which is obtained by reaction of (GaBi<sub>3</sub>)<sup>2-</sup> with [U<sup>III</sup>(C<sub>5</sub>Me<sub>4</sub>H)<sub>3</sub>] or [U<sup>IV</sup>(C<sub>5</sub>Me<sub>4</sub>H)<sub>3</sub>Cl] in 1,2-diaminoethane (Fig. 17).<sup>44</sup> The anion **45** has a unique macrocyclic polybismuthide architecture consisting of three Bi<sub>4</sub> ring units linked together by Bi-Bi bonds. Magnetic measurements show that **45** is composed of a central U<sup>4+</sup> ion which is coordinated by a radical [Bi<sub>12</sub>]<sup>7-</sup> anion. From a mechanistic standpoint, **45** appears to be formed by a templating reaction involving the sequential coordination of  $\sigma\pi$ -aromatic [Bi<sub>4</sub>]<sup>2-</sup> anions to the U center of the organometallic uranium precursor. Bonding of these units together results in de-aromatization and folding of the Bi<sub>4</sub> rings, as observed in the solid-state structure and reproduced by quantum chemical calculations.

#### 1.14.4 Outlook

This brief survey of recent aspects of host-guest chemistry involving p-block elements shows just how varied the concept of host-guest chemistry can be in this area; covering all the aspects of macrocyclic, small receptor and self-assembly that are in the classical domains of organic and metallo-organic supramolecular chemistry, but combined with the greater functionality and more varied bonding arrangements of the p-block elements. The noticeable shift towards systematic design and assembly in this area is likely to be a continuing trend in the future, as are new-found applications of p-block host-guest chemistry. This is an area which, in all of its different forms, is coming of age.

#### References

1. Busch, D. H. *Chem. Rev.* **1993**, *93*, 847; Lehn, J.-M. *Angew. Chem. Int. Ed.* **1988**, *27*, 89.
2. Duer, M. J.; García, F.; Kowenicki, R. A.; Naseri, V.; McPartlin, M.; Stein, R.; Wright, D. S. *Angew. Chem. Int. Ed.* **2005**, *44*, 5729; Duer, M. J.; García, F.; Goodman, J. M.; Hehn, J. P.; Kowenicki, R. A.; Naseri, V.; McPartlin, M.; Stead, M. L.; Stein, R.; Wright, D. S. *Chem. A Eur. J.* **2007**, *1251*.

3. Mulvey, R. E. *Chem. Commun.* **2001**, 1049; Martínez-Martínez, A. J.; Armstrong, D. R.; Conway, B.; Fleming, B. J.; Klett, J.; Kennedy, A. R.; Mulvey, R. E.; Robertson, S. D.; O'Hara, C. T. *Chem. Sci.* **2014**, *5*, 771; Haiduc, I. *Coord. Chem. Rev.* **2017**, *338*, 1.
4. Kennedy, A. R.; Mulvey, R. E.; Rowlings, R. B. *Angew. Chem. Int. Ed.* **1998**, *37*, 3180.
5. Wright, D. S. In *Comprehensive Inorganic Chemistry II*; Chivers, T., Ed.; Elsevier, 2013; p 953.
6. Beer, P. D.; Smith, D. K. In *Prog. Inorg. Chem; Anion Binding and Recognition by Inorganic Based Receptors*; Karlin, K. D., Ed.; vol. 46; Wiley, 1997; p 1.
7. Gale, P. A.; Busschaert, N.; Haynes, C. J. E.; Karagiannidis, L. E.; Kirby, I. L. *Chem. Soc. Rev.* **2014**, *43*, 205; Wenzel, M.; Hiscock, J. R.; Gale, P. A. *Chem. Soc. Rev.* **2012**, *41*, 480; Gale, P. A.; Howe, E. N. W.; Wu, X. *Chem* **2016**, *1*, 351.
8. Wu, X.; Howe, E. N. W.; Gale, P. A. *Acc. Chem. Res.* **2018**, *51*, 1870; Amendola, V.; Bergamaschi, G.; Boiocchi, M.; Fabbrizzi, L.; Milani, M. *Chem. A Eur. J.* **2010**, *16*, 4368; Blažek Bregović, V.; Basarić, N.; Mlinarić-Majerski, K. *Coord. Chem. Rev.* **2015**, *295*, 80; Rostami, A.; Wei, C. J.; Guérin, G.; Taylor, M. S. *Angew. Chem. Int. Ed.* **2011**, *50*, 2059.
9. Pinter, T.; Jana, S.; Courtemanche, R. J. M.; Hof, F. *J. Org. Chem.* **2011**, *76*, 3733; Yu, X.; Wang, W. *Chem. Asian J.* **2008**, *3*, 516; Cranwell, P. B.; Hiscock, J. R.; Haynes, C. J. E.; Light, M. E.; Wells, N. J.; Gale, P. A. *Chem. Commun.* **2013**, *49*, 874; Uruguchi, D.; Ueki, Y.; Ooi, T. *Science* **2009**, *326*, 120; Chen, C.-H.; Gabbai, F. P. *Angew. Chem. Int. Ed.* **2018**, *57*, 521; Schafer, A. G.; Wieting, J. M.; Fisher, T. J.; Mattson, A. E. *Angew. Chem. Int. Ed.* **2013**, *125*, 11531; Martínez-Aguirre, M. A.; Yatsimirsky, A. K. *J. Org. Chem.* **2015**, *80*, 4985.
10. Klare, H.; Hanft, S.; Neudörfel, J. M.; Schlörer, N. E.; Griesbeck, A.; Goldfuss, B. *Chem. A Eur. J.* **2014**, *20*, 11847; Wolf, F. F.; Neudörfel, J.-M.; Goldfuss, B. *New J. Chem.* **2018**, *42*, 4854; Klare, H.; Neudörfel, J. M.; Goldfuss, B. *Beilstein J. Org. Chem.* **2014**, *10*, 224.
11. Plajer, A. J.; Zhu, J.; Pröhm, P.; Bond, A. D.; Keyser, U. F.; Wright, D. S. *J. Am. Chem. Soc.* **2019**, *141*, 8807.
12. Plajer, A. J.; Zhu, J.; Pröhm, P.; Ruzzuto, F. J.; Keyser, U. F.; Wright, D. S. *J. Am. Chem. Soc.* **2020**, *142*, 1029.
13. Plajer, A. J.; Lee, S.; Bond, A.; Goodman, J. M.; Wright, D. S. *Dalton Trans.* **2020**, *49*, 3403.
14. Balakrishna, M. S. *Dalton Trans.* **2016**, *45*, 12252.
15. Reddy, V. S.; Krishnamurthy, S. S.; Nethaji, M. *Dalton Trans.* **1995**, 1933; Suresh, D.; Balakrishna, M. S.; Mague, J. T. *Dalton Trans.* **2008**, 3272; Chandrasekaran, P.; Mague, J. T.; Balakrishna, M. S. *Dalton Trans.* **2009**, 5478; Chandrasekaran, P.; Mague, J. T.; Balakrishna, M. S. *Organometallics* **2005**, *24*, 3780; Chandrasekaran, P.; Mague, J. T.; Balakrishna, M. S. *Inorg. Chem.* **2005**, *44*, 7925.
16. Niu, H.-C.; Plajer, A. J.; García-Rodríguez, R.; Singh, S.; Wright, D. S. *Chem. A Eur. J.* **2018**, *24*, 3073.
17. (a) Siddiqui, M. M.; Mague, J. T.; Balakrishna, M. S. *Inorg. Chem.* **2015**, *54*, 1200; (b) Ananthnag, G. S.; Mague, J. T.; Balakrishna, M. S. *Dalton Trans.* **2015**, *44*, 3785.
18. (a) Nordheider, A.; Chivers, T.; Thirumoorthi, R.; Vargas-Baca, I.; Woollins, J. D. *Chem. Commun.* **2012**, *48*, 6346; (b) Plajer, A. J.; García-Rodríguez, R.; Benson, C. G. M.; Matthews, P. D.; Bond, A. D.; Singh, S.; Gade, L. H.; Wright, D. S. *Angew. Chem. Int. Ed.* **2017**, *56*, 9087; (c) Plajer, A. J.; Niu, H.-C.; Rizzuto, F. J.; Wright, D. S. *Dalton Trans.* **2018**, *47*, 6675; (d) Plajer, A. J.; Rizzuto, F. J.; Niu, H.-C.; Lee, S.; Goodman, J. M.; Wright, D. S. *Angew. Chem. Int. Ed.* **2019**, *58*, 10655.
19. Galbraith, E.; James, T. D. *Chem. Soc. Rev.* **2010**, *39*, 3831.
20. (a) Wade, C. R.; Gabbai, F. P. *Organometallics* **2011**, *30*, 4479; (b) Ke, I.-S.; Myahkostupov, M.; Castellano, F. N.; Gabbai, F. P. *J. Am. Chem. Soc.* **2012**, *134*, 15309; (c) Wade, C. R.; Ke, I.-S.; Gabbai, F. P. *Angew. Chem. Int. Ed.* **2012**, *51*, 478; (d) Hirai, H.; Gabbai, F. P. *Chem. Sci.* **2014**, *5*, 1886; (e) Hirai, H.; Myahkostupov, M.; Castellano, F. N.; Gabbai, F. P. *Organometallics* **2016**, *35*, 1854; (f) Christianson, A. M.; Rivard, E.; Gabbai, F. P. *Organometallics* **2017**, *36*, 2670; (g) Christianson, A. M.; Gabbai, F. P. *Organometallics* **2017**, *36*, 3013; (h) Christianson, A. M.; Gabbai, F. P. *Chem. Commun.* **2017**, *53*, 2471.
21. (a) Srivastava, A. K.; Praveenkumar, B.; Mahawar, I. K.; Divya, P.; Shalini, S.; Boomishankar, R. *Chem. Mater.* **2014**, *26*, 3811; (b) Srivastava, A. K.; Vijayakanth, T.; Divya, P.; Praveenkumar, B.; Steiner, A.; Boomishankar, R. *J. Mater. Chem. C* **2017**, *5*, 7352.
22. (a) Gupta, A. K.; Reddy, S. A. D.; Boomishankar, R. *Inorg. Chem.* **2013**, *52*, 7608; (b) Gupta, A. K.; Yadav, A.; Srivastava, A. K.; Ramya, K. R.; Paithankar, H.; Nandi, S.; Chugh, J.; Boomishankar, R. *Inorg. Chem.* **2015**, *54*, 3196; (c) Gupta, A. K.; Reddy, S. A. D.; Rajasekar, P.; Prakash, P.; Boomishankar, R. *ChemistrySelect* **2017**, *2*, 10636; (d) Yadav, A.; Gupta, A. K.; Steiner, A.; Boomishankar, R. *Chem. A Eur. J.* **2017**, *23*, 18296; (e) Rajasekar, P.; Pandey, S.; Paithankar, H.; Chugh, J.; Steiner, A.; Boomishankar, R. *Chem. Commun.* **2018**, *54*, 1873; (f) Yadav, A.; Kulkarni, P.; Praveenkumar, B.; Steiner, A.; Boomishankar, R. *Chem. A Eur. J.* **2018**, *24*, 14639; (g) Rajasekar, P.; Pandey, S.; Ferrara, J. D.; Del Campo, M.; Le Magueres, P.; Boomishankar, R. *Inorg. Chem.* **2019**, *58*, 15017; (h) Yadav, A.; Sarkar, M.; Subrahmanyam, S.; Chaudhary, A.; Hey-Hawkins, E.; Boomishankar, R. *Chem. A Eur. J.* **2020**, *26*, 4209.
23. Zarra, S.; Wood, D. M.; Roberts, D. A.; Nitschke, J. R. *Chem. Soc. Rev.* **2015**, *44*, 419.
24. (a) Cameron, T. S.; Decken, A.; Krossing, I.; Passmore, J.; Rautiainen, J. M.; Wang, X.; Zeng, X. *Inorg. Chem.* **2013**, *52*, 3113; (b) Sängler, I.; Gärtner, M.; Bolte, M.; Wagner, M.; Lerner, H.-W. *Z. Anorg. Allg. Chem.* **2018**, *644*, 925; (c) Dankert, F.; Weigend, F.; von Hänisch, C. *Inorg. Chem.* **2019**, *58*, 15417.
25. (a) Reuter, K.; Buchner, M. R.; Thiele, G.; von Hänisch, C. *Inorg. Chem.* **2016**, *55*, 4441; (b) Reuter, K.; Thiele, G.; Hafner, T.; Uhlig, F.; von Hänisch, C. *Chem. Commun.* **2016**, *52*, 13265; (c) Dankert, F.; Reuter, K.; Donsbach, C.; von Hänisch, C. *Dalton Trans.* **2017**, *46*, 8727; (d) Reuter, K.; Rudel, S. S.; Buchner, M. R.; Kraus, F.; von Hänisch, C. *Chem. A Eur. J.* **2017**, *23*, 9607; (e) Reuter, K.; Dankert, F.; Donsbach, C.; von Hänisch, C. *Inorganics* **2017**, *5*, 11; (f) Dankert, F.; Reuter, K.; Donsbach, C.; von Hänisch, C. *Inorganics* **2018**, *6*, 15; (g) Dankert, F.; von Hänisch, C. *Inorg. Chem.* **2019**, *58*, 3518; (h) Buchner, M. R.; Muller, M.; Dankert, D.; Reuter, F.; von Hänisch, C. *Dalton Trans.* **2018**, *47*, 16393.
26. Kownacka, A.; Kownacki, I.; Kubicki, M.; Marciniak, B.; Taylor, R. J. *Organomet. Chem.* **2014**, *750*, 132.
27. (a) Weinhold, F.; West, R. *Organometallics* **2011**, *30*, 5815; (b) Passmore, J.; Rautiainen, J. M. *Eur. J. Inorg. Chem.* **2012**, 6002; (c) Weinhold, F.; West, R. *J. Am. Chem. Soc.* **2013**, *135*, 5762.
28. Decken, A.; Passmore, J.; Wang, X. *Angew. Chem. Int. Ed.* **2006**, *45*, 2773.
29. Churchill, M. R.; Lake, C. H.; Chao, S.-H. L.; Beachley, O. T. *Chem. Commun.* **1993**, *1*, 1577; Eaborn, C.; Hitchcock, P. B.; Izod, K.; Smith, J. D. *Angew. Chem. Int. Ed. Engl.* **1996**, *34*, 2679.
30. Ernst, R. D.; Glöckner, A.; Arif, A. M. *Z. Kristallogr. - New Cryst. Struct.* **2007**, *222*, 333.
31. Decken, A.; LeBlanc, F. A.; Passmore, J.; Wang, X. *Eur. J. Inorg. Chem.* **2006**, 4033.
32. Most recently: (a) Schindler, A.; Heindl, C.; Balázs, G.; Gröger, C.; Virovets, A. V.; Peresyphina, E. V.; Scheer, M. *Chem. A Eur. J.* **2012**, *18*, 829 (b) Schwarzmaier, C.; Schindler, A.; Heindl, C.; Scheuermayer, S.; Peresyphina, E. V.; Virovets, A. V.; Neumeier, M.; Gschwind, R.; Scheer, M. *Angew. Chem. Int. Ed.* **2013**, *52*, 10896; (c) Peresyphina, E. V.; Heindl, C.; Schindler, A.; Bodensteiner, M.; Virovets, A. V.; Scheer, M. *Z. Krist.* **2014**, *229*, 735; (d) Dielmann, F.; Heindl, C.; Hastreiter, F.; Peresyphina, E. V.; Virovets, A. V.; Gschwind, R. M.; Scheer, M. *Angew. Chem. Int. Ed.* **2014**, *53*, 13605; (e) Dielmann, F.; Fleischmann, M.; Heindl, C.; Peresyphina, E. V.; Virovets, A. V.; Gschwind, R. M.; Scheer, M. *Chem. A Eur. J.* **2015**, *21*, 6208; (f) Heindl, C.; Peresyphina, E. V.; Virovets, A. V.; Kremer, W.; Scheer, M. *J. Am. Chem. Soc.* **2015**, *137*, 10938; (g) Heindl, C.; Peresyphina, E.; Virovets, E. V.; Bushmarinov, I. S.; Medvedev, M. G.; Krämer, B.; Dittrich, B.; Scheer, M. *Angew. Chem. Int. Ed.* **2017**, *56*, 13237; (h) Peresyphina, E.; Heindl, C.; Virovets, A.; Brake, H.; Mäd, E.; Scheer, M. *Chem. A Eur. J.* **2018**, *24*, 2503; (i) Brake, H.; Peresyphina, E.; Heindl, C.; Virovets, A. V.; Kremer, W.; Scheer, M. *Chem. Sci.* **2019**, *10*, 2940.
33. Markovic, E.; Constantopolous, K.; Matison, J. G.; Hartmann-Thompson, C. *Advances in Silicon Science*; vol. 3; Springer, 2011; p 1; Cordes, D. B.; Lickiss, P. D.; Hartmann-Thompson, C. *Advances in Silicon Science*; vol. 3; Springer, 2011; p 47.
34. For example, Anisimov, A.A.; Zhemchugov, P.V.; Milenin, S.A.; Goloveshkin, A.S.; Tsareva, U.S.; Bushmarinov, I.S.; Korlyukov, A.A.; Takazova, R.U.; Molodtsova, Yu.A.; Muzafarov, A.M.; Shchegolikhina, O.I. *J. Organomet. Chem.* **2016**, *823*, 103  
Liu, Y.-N.; Su, H.-F.; Li, Y.-W.; Liu, Q.-Y.; Jagličić, Z.; Wang, W.-G.; Tung, C.-H.; Sun, D. *Inorg. Chem.* **2019**, *58*, 4574; Bilyachenko, A. N.; Yalymov, A. I.; Korlyukov, A. A.; Long, J.; Larionova, J.; Guari, Y.; Zubavichus, Y. V.; Trigub, A. L.; Shubina, E. S.; Eremenko, I. L.; Efimov, N. N.; Levitsky, M. M. *Chem. A Eur. J.* **2015**, *21*, 18563.



35. Host-guest complexes containing  $[\text{RSi}(\text{O})_5]^{5-}$  anions: (a) Bilyachenko, A. N.; Yalymov, A. I.; Korlyukov, A. A.; Long, J.; Larionova, J.; Guari, Y.; Vologzhanina, A. V.; Es'kova, M. A.; Shubina, E. S.; Levitsky, M. M. *Dalton Trans.* **2016**, *45*, 7320  
(b) Bilyachenko, A. N.; Yalymov, A. I.; Levitsky, M. M.; Korlyukov, A. A.; Es'kova, M. A.; Long, J.; Larionova, J.; Guari, Y.; Shul'pina, L. S.; Ikonnikov, N. S.; Trigub, A. L.; Zubavichus, Y. V.; Golub, I. E.; Shubina, E. S.; Shul'pin, G. B. *Dalton Trans.* **2016**, *45*, 13663; (c) Bilyachenko, A. A.; Kulakova, A. N.; Levitsky, M. M.; Petrov, A. A.; Korlyukov, A. A.; Shul'pina, L. S.; Khrustalev, V. N.; Dorovatovskii, P. V.; Vologzhanina, A. V.; Tsareva, U. S.; Golub, I. E.; Gulyaeva, E. S.; Shubina, E. S.; Shul'pin, G. B. *Inorg. Chem.* **2017**, *56*, 4093; (d) Bilyachenko, A. N.; Yalymov, A.; Dronova, M.; Korlyukov, A. A.; Vologzhanina, A. V.; Es'kova, M. A.; Long, J.; Larionova, J.; Guari, Y.; Dorovatovskii, P. V.; Shubina, E. S.; Levitsky, M. M. *Inorg. Chem.* **2017**, *56*, 12751; (e) Bilyachenko, A. N.; Kulakova, A. N.; Shul'pina, L. S.; Levitsky, M. M.; Korlyukov, A. A.; Khrustalev, V. N.; Zubavichus, Y. V.; Dorovatovskii, P. V.; Tsareva, U. S.; Shubina, E. S.; Petrov, A. A.; Vorontsov, N. V.; Shul'pin, G. B. *J. Organomet. Chem.* **2018**, *867*, 133.
36. Host-guest complexes containing  $[\text{RSi}(\text{O})_6]^{6-}$  and  $[\text{RSi}(\text{O})_7]^{7-}$  anions: (a) Sergienko, A. V.; Korlyukov, A. A.; Arkhipov, D. E.; Novikov, V. V.; Eskova, M. A.; Zavin, B. G. *Mendeleev Commun.*, **2016**, *26*, 344  
(b) Bilyachenko, A. N.; Kulakova, A. N.; Levitsky, M. M.; Korlyukov, A. A.; Khrustalev, V. N.; Vologzhanina, A. V.; Titov, A. A.; Dorovatovskii, P. V.; Shul'pina, L. S.; Lamaty, F.; Bantreil, X.; Villemejeanne, B.; Ruiz, C.; Martinez, J.; Shubina, E. S.; Shul'pin, G. B. *ChemCatChem* **2017**, *9*, 4437. See also ref 35d.
37. Pitt, M. A.; Johnson, D. W. *Chem. Soc. Rev.* **2007**, *36*, 1441.
38. Johnson, D. W.; Raymond, K. N. *Inorg. Chem.* **2001**, *40*, 5157.
39. Deshmukh, M. S.; Yadav, A.; Pant, R. R.; Boomishankar, R. *Inorg. Chem.* **2015**, *54*, 1337; Deshmukh, M. S.; Mane, V. S.; Kumbhar, A. S.; Boomishankar, R. *Inorg. Chem.* **2017**, *56*, 13286.
40. Yang, E. S.; Plajer, A. J.; García-Romero, Á.; Bond, A. D.; Ronson, T. K.; Álvarez, C. M.; García-Rodríguez, R.; Colebatch, A. L.; Wright, D. S. *Chem. A Eur. J.* **2019**, *25*, 14003.
41. Cozzolino, A. F.; Vargas-Baca, I.; Mansour, S.; Mahmoudkhani, A. H. *J. Am. Chem. Soc.* **2005**, *127*, 3184; Cozzolino, A. F.; Elder, P. J. W.; Vargas-Baca, I. *Coord. Chem. Rev.* **2011**, *255*, 1426.
42. (a) Kübel, J.; Elder, P. J. W.; Jenkins, H. A.; Vargas-Baca, I. *Dalton Trans.* **2010**, *39*, 11126; (b) Ho, P. C.; Szydłowski, P.; Sinclair, J.; Elder, P. J. W.; Kübel, J.; Gendy, C.; Myongwon Lee, L.; Jenkins, H.; Britten, J. F.; Morim, D. R.; Vargas-Baca, I. *Nat. Commun.* **2016**, *7*, 11299; (c) Ho, P. C.; Bui, R.; Cevallos, A.; Sequeira, S.; Britten, J. F.; Vargas-Baca, I. *Dalton Trans.* **2019**, *48*, 4879; (d) Wang, J.; Ho, P. C.; Britten, J. F.; Tomassetti, V.; Vargas-Baca, I. *New J. Chem.* **2019**, *43*, 12601.
43. Before Comp. Inorganic Chem. II: (a) Bai, J.; Virovets, A. V.; Scheer, M. *Science*, **2003**, *300*, 781  
(b) Scheer, M.; Bai, J.; Johnson, B. P.; Merkle, R.; Virovets, A. V.; Anson, C. E. *Eur. J. Inorg. Chem.* **2005**, 4023; (c) Scheer, M.; Schindler, A.; Merkle, R.; Johnson, B. P.; Linseis, M.; Winter, R.; Anson, C. E.; Virovets, A. V. *J. Am. Chem. Soc.*, **2007**, *129*, 13386  
(d) Scheer, M.; Schindler, A.; Gröger, C.; Virovets, A. V.; Peresyphkina, E. V. *Angew. Chem. Int. Ed.* **2009**, *48*, 5046; (e) Welsch, S.; Gröger, C.; Sierka, M.; Scheer, M. *Angew. Chem. Int. Ed.* **2011**, *50*, 1435; (f) Scheer, M.; Schindler, A.; Bai, J.; Johnson, B. P.; Merkle, R.; Winter, R.; Virovets, A. V.; Peresyphkina, E. V.; Blatov, V. A.; Sierka, M.; Eckert, H. *Chem. A Eur. J.* **2010**, *16*, 2092.
44. Lichtenberger, N.; Wilson, R. J.; Eulenstein, A. R.; Massa, W.; Clérac, R.; Weigend, F.; Dehnen, S. *J. Am. Chem. Soc.* **2016**, *138*, 9033.
45. Weinert, B.; Müller, F.; Harms, K.; Clérac, R.; Dehnen, S. *Angew. Chem. Int. Ed.* **2014**, *53*, 11979.



## 1.15 Metallophilic interactions

Linda H. Doerrer, Cathlene Del Rosario, and Alice Fan, Department of Chemistry, Boston University, Boston, MA, United States

© 2023 Elsevier Ltd. All rights reserved.

<b>1.15.1</b>	<b>Metallophilicity</b>	<b>666</b>
1.15.1.1	History of metallophilicity	667
1.15.1.2	Nomenclature	668
1.15.1.3	Requirements for metallophilicity	668
1.15.1.4	Computational studies on metallophilicity	669
<b>1.15.2</b>	<b>Scope and organization</b>	<b>669</b>
<b>1.15.3</b>	<b>Homodinuclear <i>d</i>-block (groups 8–12) <math>M \cdots M</math> complexes with metallophilic interactions</b>	<b>669</b>
1.15.3.1	Ru $\cdots$ Ru metallophilic interactions	669
1.15.3.1.1	Intermolecular Ru $\cdots$ Ru metallophilic interactions	669
1.15.3.2	Ir $\cdots$ Ir metallophilic interactions	670
1.15.3.2.1	Intermolecular Ir $\cdots$ Ir metallophilic interactions	670
1.15.3.2.2	Intramolecular Ir $\cdots$ Ir metallophilic interactions	670
1.15.3.3	Rh $\cdots$ Rh metallophilic interactions	671
1.15.3.3.1	Intermolecular Rh $\cdots$ Rh metallophilic interactions	671
1.15.3.3.2	Intramolecular Rh $\cdots$ Rh metallophilic interactions	673
1.15.3.4	Pt $\cdots$ Pt metallophilic interactions	675
1.15.3.4.1	Intermolecular Pt $\cdots$ Pt metallophilic interactions	675
1.15.3.4.2	Intramolecular Pt $\cdots$ Pt metallophilic interactions	679
1.15.3.5	Pd $\cdots$ Pd metallophilic interactions	681
1.15.3.5.1	Intermolecular Pd $\cdots$ Pd metallophilic interactions	682
1.15.3.5.2	Intramolecular Pd $\cdots$ Pd metallophilic interactions	682
1.15.3.6	Au $\cdots$ Au metallophilic interactions	689
1.15.3.6.1	Intermolecular Au $\cdots$ Au metallophilic interactions	690
1.15.3.6.2	Intramolecular Au $\cdots$ Au metallophilic interactions	693
1.15.3.7	Ag $\cdots$ Ag metallophilic interactions	697
1.15.3.7.1	Intermolecular Ag $\cdots$ Ag metallophilic interactions	697
1.15.3.7.2	Intramolecular Ag $\cdots$ Ag metallophilic interactions	701
1.15.3.8	Cu $\cdots$ Cu interactions	704
1.15.3.8.1	Intermolecular Cu $\cdots$ Cu metallophilic interactions	705
1.15.3.8.2	Intramolecular Cu $\cdots$ Cu metallophilic interactions	706
1.15.3.9	Hg $\cdots$ Hg metallophilic interactions	709
1.15.3.9.1	Intermolecular Hg $\cdots$ Hg metallophilic interactions	709
1.15.3.9.2	Intramolecular Hg $\cdots$ Hg metallophilic interactions	709
<b>1.15.4</b>	<b>Homodinuclear <i>p</i>-block (groups 13–15) <math>M \cdots M</math> complexes with metallophilic interactions</b>	<b>711</b>
1.15.4.1	Tl $\cdots$ Tl metallophilic interactions	711
1.15.4.1.1	Intermolecular Tl $\cdots$ Tl metallophilic interactions	711
1.15.4.1.2	Intramolecular Tl $\cdots$ Tl metallophilic interactions	712
1.15.4.2	Pb $\cdots$ Pb metallophilic interactions	713
1.15.4.2.1	Intermolecular Pb $\cdots$ Pb metallophilic interactions	713
1.15.4.2.2	Intramolecular Pb $\cdots$ Pb metallophilic interactions	715
1.15.4.3	Bi $\cdots$ Bi metallophilic interactions	718
1.15.4.3.1	Intermolecular Bi $\cdots$ Bi metallophilic interactions	718
1.15.4.3.2	Intramolecular Bi $\cdots$ Bi metallophilic interactions	720
<b>1.15.5</b>	<b>Heterodinuclear <math>M^1 \cdots M^2</math> complexes with metallophilic interactions</b>	<b>721</b>
1.15.5.1	Intermolecular $M^1 \cdots M^2$ metallophilic interactions	721
1.15.5.1.1	$d^{\beta} \cdots d^{10}$ , Pt(II) $\cdots$ Ag(I)	721
1.15.5.1.2	$d^{10} \cdots d^{10}$ , Au(I) $\cdots$ Ag(I)	722
1.15.5.1.3	$d^{10} \cdots s^2$ , Au(I) $\cdots$ Tl(I)	722
1.15.5.2	Intramolecular $M^1 \cdots M^2$ metallophilic interactions	722
1.15.5.2.1	$d^{\beta} \cdots d^{\beta}$ , Rh(I) $\cdots$ Pt(II)	723
1.15.5.2.2	$d^{\beta} \cdots d^{10}$ , Ir(I) $\cdots$ Ag(I)	723
1.15.5.2.3	$d^{\beta} \cdots d^{10}$ , Pt(II) $\cdots$ Au(I)	724
1.15.5.2.4	$d^{10} \cdots s^2$ , Ag(I) $\cdots$ Bi(III)	724
1.15.5.2.5	$d^{10} \cdots s^2$ , Cu(I) $\cdots$ Pb(II)	724
<b>1.15.6</b>	<b>Synthesis</b>	<b>725</b>

<b>1.15.7</b>	<b>Spectroscopy</b>	<b>726</b>
1.15.7.1	Nuclear magnetic resonance	726
1.15.7.2	Electronic absorption and emission spectroscopy	726
1.15.7.3	Vibrational spectroscopy	727
<b>1.15.8</b>	<b>Outlook</b>	<b>728</b>
<b>References</b>		<b>728</b>

### Abstract

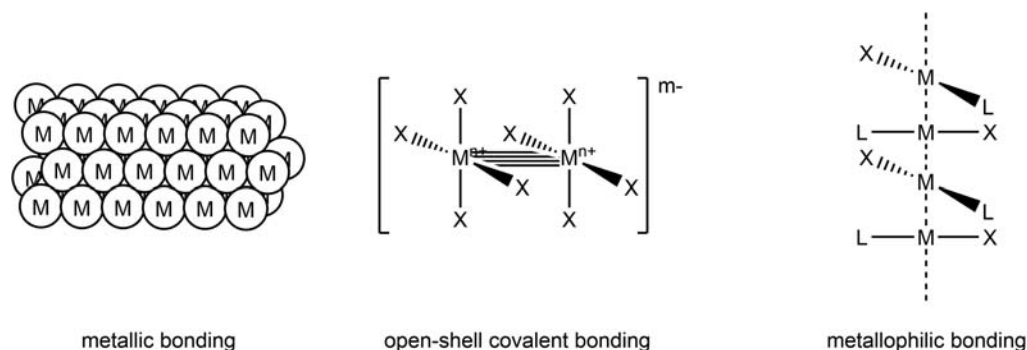
Metallophilic interactions are now a well-established phenomenon in chemistry. There are thousands of demonstrated examples from numerous different metals in homonuclear and heteronuclear combinations that are most commonly dinuclear but are also present in higher nuclearities as well. Definitive characterization originally came from SCXRD studies, which is now broadened with a wide array of solution and solid-state spectroscopic techniques, and increasingly sophisticated computational work. This Chapter gives an overview of metallophilic interactions through the literature of 2020. The examples are organized first by the participating metal centers and then by the structural motifs in which they are found. Complementary overviews of the synthetic and spectroscopic methods, as well as an introduction to the theoretical electronic structure framework, are also provided.

### 1.15.1 Metallophilicity

Metallophilic bonding is a type of bonding that is now widely observed and used to effect desired structures and properties in a plethora of compounds. This phenomenon was not predicted, but discovered via single-crystal X-ray diffraction (SCXRD) studies of Au(I) compounds. This Chapter provides a historical and structural overview of metallophilic interactions between like and different metals. It begins with a brief history of the discovery of metallophilicity, clarifies some vocabulary as currently used, and explains the steric and electronic features that characterize the phenomenon. The central portion of the chapter includes selected examples of structurally verified metallophilic interactions from all the metals in the periodic table that have been shown to participate in such bonding. The final section introduces the reader to other methods of characterizing these interactions via more selected examples. The chapter covers the literature through the end of 2020. Extensive use has been made of the Cambridge Structural Database (CSD),<sup>1</sup> and compounds in the CSD are indicated with their six-letter codes. The codes are in **bold** if the structures are shown in the Schemes, and not when not.

Bonding between metals is known in three main types: (i) metallic bonding in the zero-valent elements described by band structure theory<sup>2,3</sup> (ii) covalent bonding between oxidized metal atoms with open subshells<sup>4</sup> as exemplified by the  $d^4$  Re(III) centers in  $[\text{Re}_2\text{Cl}_8]^{2-}$ , and (iii) metallophilic bonding between metal atoms with closed (sub)shell configurations, as shown in **Scheme 1**. The metal electronic structure (formalized in oxidation state assignments) as well as the distance between neighboring atoms together determine the bonding. The third category was identified most recently<sup>5</sup> and encompasses unusual structures that can appear counterintuitive. The bonding is termed metallophilic because the metal-metal interactions do not involve traditional sharing of electrons in covalent bonds nor the sharing of delocalized electrons via a conduction band. Instead the metals possess an affinity for one another not driven by electrostatics, covalently shared electrons, or delocalized electrons among countless atoms.

These metallophilic interactions were initially discovered, and continue to be identified most easily, through SCXRD data when the distance between two metal centers is less than the sum of their van der Waals radii.<sup>6,7</sup> The metal electron configurations observed in such interactions are closed shell ones such as  $d^{10}$  (M(I) in Group 11 or M(II) in Group 12),  $s^2$  (M(I) in Group 13,



**Scheme 1**

8	9	10	11	12	13	14	15
Fe	Co	Ni	<b>Cu</b>	Zn	Ga	Ge	As
<b>Ru</b>	<b>Rh</b>	<b>Pd</b>	<b>Ag</b>	Cd	In	Sn	Sb
Os	<b>Ir</b>	<b>Pt</b>	<b>Au</b>	Hg	<b>Tl</b>	<b>Pb</b>	<b>Bi</b>
Hs	Mt	Ds	<i>Rg</i>	Cp			

Scheme 2

M(II) in Group 14, or M(III) in Group 15) or  $d^8$  (M(0) in Group 8, M(I) in Group 9, or M(II) in Group 10). The elements most often involved are shown in **Scheme 2**.

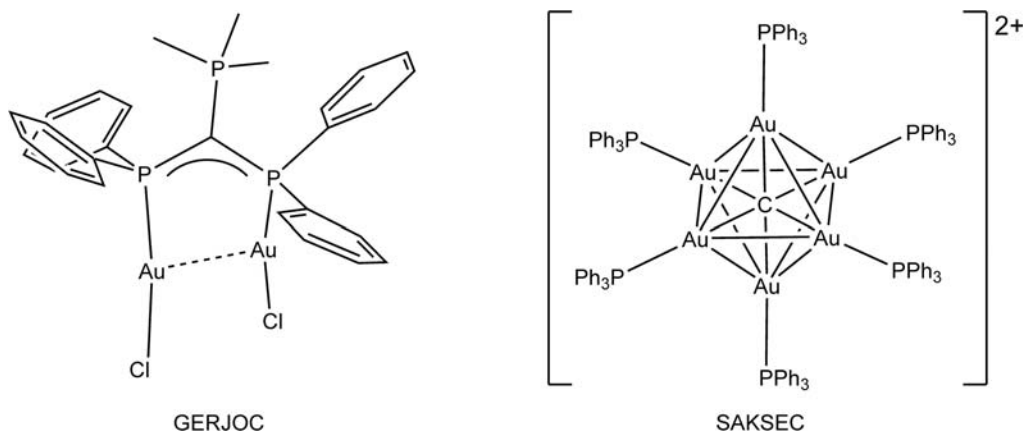
The  $d^8$  configuration can behave like a closed subshell because in  $\sim D_{4h}$  (square-planar) coordination, the  $d_{x^2-y^2}$  orbital is so much higher in energy than the other four  $d$  orbitals.

### 1.15.1.1 History of metallophilicity

Bonding between zero-valent metals is well understood and is explained by band theory which is accessed through molecular orbital or periodic potential approaches.<sup>2,3</sup> Bonding between open-shell metal atoms can result in covalent bonds of which single,<sup>8</sup> double,<sup>4</sup> triple,<sup>4</sup> quadruple,<sup>4</sup> and quintuple<sup>9,10</sup> have been experimentally demonstrated, and thoroughly described by molecular orbital theory. Hextuple bonds between two metal atoms have been computationally investigated, but not been prepared.<sup>11</sup> Molecular orbital theory also describes well the bonding in metallic clusters, which are defined as a compound with two or more metal atoms having direct and substantial metal-metal bonding.<sup>12,13</sup> None of these structures or interpretations anticipated metallophilic bonding.

In the mid-1980s, the approach of two Au(I) atoms closer than the sum of their van der Waals radii was recognized as unusual and meriting closer investigation and explanation.<sup>14</sup> Several prior publications had suggested that an unusual bonding interaction was at work, but a definitive example had yet to be prepared. Intermolecular interactions had been characterized between several different  $[\text{Au}_2(\text{LX})_2]$  units by several different authors which were shown computationally to have common electronic structures within and without the dimers. Shortly thereafter,<sup>15</sup> an Au(I)–Au(I) distance of only 3.000(1) Å was observed, as well as deviation from a linear geometry ( $170.3(1)^\circ$  and  $172.9(1)^\circ$ ) at the same two-coordinate Au atoms, and attributed to attractive interactions between two  $d^{10}$  Au(I) metal centers, in GERJOC.<sup>14</sup> Later in the same year, an investigation into the  $[\text{Ph}_3\text{PAu}]_6\text{C}]^{2+}$  cation, in SAKSEC,<sup>5</sup> two very short Au $\cdots$ Au distances of 3.090(1) and 2.974(1) Å were observed,<sup>16</sup> and the term “aurophilicity” was coined (**Scheme 3**).

Since that time, the growth in this area has been tremendous, encompassing thousands of compounds, hundreds of references, and a numerous review articles.<sup>17–22</sup> Since that time, they have been observed within hundreds of transition metal compounds that contain  $nd^8$ ,  $nd^{10}$ , or  $nd^{10}(n+1)s^2$  electronic configurations. They are observed, as will be shown in detail later in this Chapter, between neutral species, GERJOC,<sup>14</sup> ref. but also between cations, QIVCAA,<sup>23</sup> (vide infra) or between anions, XEKCOH (vide infra).<sup>24</sup> This latter phenomenon of bringing together charged moieties in opposition to coulombic forces without formation of a covalent bond is unique to metallophilic interactions.



Scheme 3

### 1.15.1.2 Nomenclature

The “metal-loving” meaning of the adjective metallophilic has considerable use outside of chemistry because the uptake of metals by cells is described with the same word. There are metallophilic macrophages,<sup>25</sup> marginal metallophilic macrophages in spleen cells,<sup>26</sup> in the thymus,<sup>27</sup> metallophilic bacteria,<sup>28</sup> and metallophilic cells.<sup>29</sup> Within chemistry, “metallophilic” has also been applied to cyclic ethers that encapsulate metal ions.<sup>30</sup> The chemical processes that result in the increased concentration of metals in the cell do not involve the phenomenon of metallophilicity as described in this chapter. Instead, broadly speaking, metal ions coordinate to non-metallic *p*-block elements from proteins or small molecules to facilitate transport into the cell.

With the terms aurophilicity and aurophilic having been coined for Au, they were quickly followed by the related terms argenophilic (Ag)<sup>31,32</sup>, cuprophilic (Cu),<sup>18,33</sup> mercuriphilic (Hg),<sup>19</sup> and thalophilic (Tl),<sup>34,35</sup> as well as the general form, metallophilic. As described in much more detail below, metallophilic interactions have been observed with other metals as well, e.g., Ir and Pb, but other more specific terms are not (yet) in common use. The well-established adjectives homobimetallic/homodimetallic and heterobimetallic/heterodimetallic are also used to describe these interactions as appropriate.

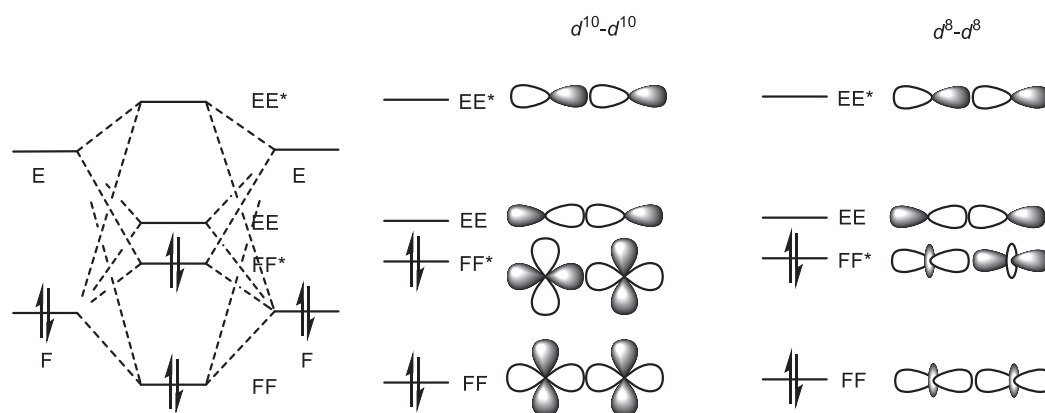
### 1.15.1.3 Requirements for metallophilicity

Metallophilic interactions have both steric and electronic requirements. Steric requirements naturally include a close approach of the two metal centers, and therefore the metal centers are coordinatively unsaturated in the absence of the metal-metal contact. If a single pairwise contact is made, the remainder of the coordination spheres can be quite full, as in the dimer of [(Ph<sub>3</sub>P)Au(3,5-pyrazolyl)] in HEMYEE.<sup>36</sup> If the coordination sphere is less full, then more contacts can be made to form rings, [Cu(mes)]<sub>5</sub> in CAK-PET<sup>37</sup> or [Cu(mes)]<sub>4</sub> in GEBQIN,<sup>38</sup> or chains of [Au(CN)<sub>2</sub>]<sup>1-</sup> anions in WETSOE.<sup>39</sup>

On the electronic side, as with all interatomic interactions that are energetically favorable, there must be a symmetry match between the orbitals that combine. Metallophilic interactions result from  $\sigma$ -type overlap between filled orbitals, shown in **Scheme 4**, on metal centers that are as close as or closer than the sum of the two van der Waals radii. To date examples with  $\pi$  or  $\delta$  overlap have not been reported. In addition to two in-phase and out-of-phase  $\sigma$  overlaps, there is often energetic mixing of other orbitals with like symmetry that provides energy stabilization to what would otherwise be a two-center, four-electron net repulsion. This mixing is also shown in **Scheme 4**.

The most common valence electronic configuration observed in metallophilic interactions is the  $d^{10}$  one, followed by  $d^8$ , and  $s^2$ . These configurations are either closed-sub-shell ones or, in the  $d^8$  case, a pseudo closed subshell, because complexes that have  $d^8$  configurations and metallophilic interactions are always square-planar ones. In this geometry, the ligand field splitting of the *d*-orbitals is such that the  $d_{x^2-y^2}$  orbital is significantly higher in energy than the other four. Those lower four orbitals when filled then make an effectively closed subshell. Paramagnetic metal centers do not, by definition, participate in metallophilic interactions. The other even-numbered electron configurations, e.g.,  $d^2$ ,  $d^4$ ,  $d^6$ , are not (yet) observed in metallophilic interactions because the electronic structures in those cases do not have filled frontier orbitals of  $\sigma$ -symmetry that are filled and have sterically accessible electron density.

As described above (and in more detail below) and shown in **Scheme 2**, metallophilic interactions are not spread evenly throughout the Periodic Table, but are clustered in the later and heavier transition metals, as well as the in heavier *p*-block metals. The characteristics of these metallic elements that promote metallophilic interactions include not only the greater radial extent of their valence orbitals, but also the relativistic effects that are present.



**Scheme 4**

### 1.15.1.4 Computational studies on metallophilicity

Significant work has also been done to establish in detail the electronic structure basis for the bonding generalizations above, as well as to quantify the strength of these interactions. Metallophilic interaction energies are on the order of hydrogen-bonding<sup>40–43</sup> and can be therefore a significant determinant of the ground state geometry. The bonding is a type of dispersion interaction<sup>40,43</sup> between the two metal centers that have the closed subshell ( $d^8$ ) or closed shell ( $s^2$  or  $d^{10}$ ) valence electron configurations. Heterometallic combinations, e.g.  $d^{10}$ - $d^8$  are common and examples are given below in [Section 1.15.5](#).

Earlier calculations at the Hartree-Fock level in  $d^{10}$  cases that included mixing of<sup>44</sup> occupied  $d_{z^2}$  and unoccupied  $s$  and/or  $p_z$  orbitals did not provide sufficient stabilization for metallophilic interactions.<sup>41,45</sup> Only when configuration interactions are also included<sup>44,46,47</sup> are the experimental structures correctly reproduced computationally. Since that time, they have been observed within hundreds of transition metal compounds that contain  $nd^8$ ,  $nd^{10}$ , or  $nd^{10}(n+1)s^2$  electronic configurations. Relativistic effects are particularly important in metallophilic interactions and accurate predictions are not obtained if the relativistic contributions are not included.<sup>40,48</sup>

## 1.15.2 Scope and organization

This Chapter covers the peer-reviewed literature through the end of 2020, with some previous reviews<sup>17–21</sup> mentioned to guide the reader. No attempt to be comprehensive has been made because the volume of examples is too great and inappropriate for this reference work. Examples have been sought via (1) structural searches of the Cambridge Structural Database<sup>1</sup> and (2) text searches of the Chemical Abstract Service. The six-letter codes from the CSD are used to identify molecules within this chapter. Some instances of metallophilic interactions may not have been recognized by authors in earlier works, and some newly-prepared compounds may not have definitive data with regard to the existence of a metallophilic interaction. Such is the nature of this fascinating and evolving phenomenon.

The central part of the Chapter, [Section 1.15.3](#), is an overview of structurally-characterized compounds with homodinuclear metallophilic interactions in the d-block that are organized by the relevant metals, and subdivided by their oxidation states and coordination numbers in the context of the MLXZ Covalent Bond Classification scheme.<sup>49,50</sup> The L-, X-, and Z-ligand types correspond to ligands that donate 2, 1, or 0 electrons to the metal center M, respectively. [Section 1.15.4](#) is organized similarly for the p-block and [Section 1.15.5](#) covers heterodinuclear complexes. [Section 1.15.6](#) describes characterization methods beyond SCXRD including spectroscopy and physical property measurements.

## 1.15.3 Homodinuclear d-block (groups 8–12) $M \cdots M$ complexes with metallophilic interactions

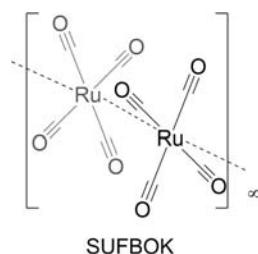
### 1.15.3.1 Ru $\cdots$ Ru metallophilic interactions

Structures with metallophilic interactions between  $d^8$  Ru(0) atoms, both inter- and intramolecular, are rare. As the van der Waals radius of Ru is 2.05 Å, only structures with Ru  $\cdots$  Ru distances less than 4.10 Å are referenced in this section.

#### 1.15.3.1.1 Intermolecular Ru $\cdots$ Ru metallophilic interactions

##### 1.15.3.1.1.1 Four-coordinate Ru(0)

In 1993,  $[\text{Ru}(\text{CO})_4]_\infty$  became the first polymeric binary metal carbonyl (CO) compound to be characterized (SUFBOK).<sup>51</sup> It is composed of chains of staggered *trans*- $D_{4h}$   $[\text{Ru}(\text{CO})_4]$  monomers with Ru(0)  $\cdots$  Ru(0) distances of 2.860 Å. At these distances between  $[\text{Ru}(\text{CO})_4]$  units, the C  $\cdots$  C interactions of the staggered vicinal carbonyls are energetically repulsive. Hypothetical rotation of the  $[\text{Ru}(\text{CO})_4]$  planes around the  $c$  axis would cause the CO ligand on different Ru centers to eclipse one another and subsequently lengthen the Ru(0)  $\cdots$  Ru(0) distances ([Scheme 5](#)).



**Scheme 5**



### 1.15.3.2 Ir···Ir metallophilic interactions

Of the few dozen  $d^8$  Ir(I) structures with intermolecular metallophilic interactions and Ir···Ir distances less than 4.00 Å, most have four-coordinate Ir(I) with two CO ligands. The other two ligands are, in order of relative frequency, a halogen and RNH<sub>2</sub> or two N-donor groups. There are a few dozen more Ir(I) structures with intramolecular (rather than intermolecular) Ir···Ir metallophilic interactions, and the majority are bridged by an anionic pyrazolyl (pyz) ligand and coordinated to the electron-withdrawing cyclo-octa-1,5-diene (COD) or one or two CO ligands.

#### 1.15.3.2.1 Intermolecular Ir···Ir metallophilic interactions

##### 1.15.3.2.1.1 Four-coordinate Ir(I)

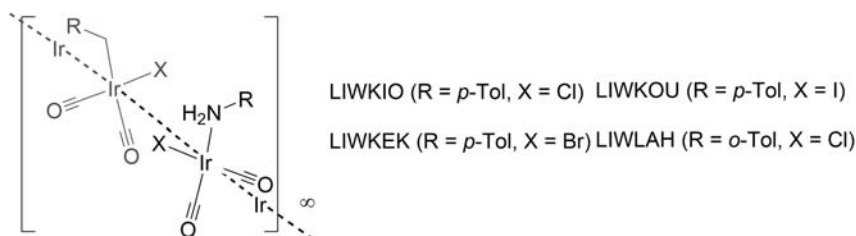
Effects of ligand size on Ir(I)···Ir(I) distances in supramolecular assembly has been observed with four-coordinate [IrL<sub>3</sub>X] structures in which X = halogen. In this family, the compounds form infinite chains of [IrL<sub>3</sub>X] centers, but the [Ir···Ir···Ir] angles are not perfectly linear because the aryl rings significantly influence the packing. For *cis*-Ir(CO)<sub>2</sub>(NH<sub>2</sub>(*p*-toluidine))X], increasing halogen size causes larger Ir(I)···Ir(I) distances: 3.334 Å when X = Cl (LIWKIO),<sup>52</sup> 3.379 Å when X = Br (LIWKEK),<sup>52</sup> 3.541 Å when X = I (LIWKOU).<sup>52</sup> Arene substitution effects are observed with methylated aniline derivatives in *cis*-Ir(CO)<sub>2</sub>(NH<sub>2</sub>R)Cl]; when R = *o*-toluidine Ir(I)···Ir(I) distance is 3.404 Å (LIWLAH),<sup>52</sup> which is longer than the 3.334 Å when R = *p*-toluidine (LIWKIO) (Scheme 6).

The steric and electronic effect of counter cations to structures with intermolecular Ir(I)···Ir(I) metallophilic interactions can be observed with a series of [IrL<sub>4</sub>]<sup>+</sup> structures with bidentate pyrazolyl-triazolyl (PyT) ligands. For the same cation with different anions, [Ir(PyT)(CO)<sub>2</sub>]A (BPh<sub>4</sub>)<sup>-</sup> has an Ir(I)···Ir(I) distance of 3.498 Å (BEKTIW), and A = (BAr<sup>F</sup><sub>4</sub>)<sup>-</sup> has an Ir(I)···Ir(I) distance of 3.306 Å (BEKTOC).<sup>53</sup> For the same anion with different cations of [Ir(N-N')(CO)<sub>2</sub>](BAr<sup>F</sup><sub>4</sub>)<sup>-</sup>, N-N' = PyT has Ir(I)···Ir(I) distances of 3.306 Å (BEKTOC), and N-N' = PyS (PyS = 4-((1*H*-pyrazol-1-yl)methyl)-1-phenyl-1*H*-1,2,3-triazole) has Ir(I)···Ir(I) distances of 3.409 Å (BEKVAQ).<sup>53</sup> Within this small group, the bulkier the substituent (R) on the triazole, the shorter the Ir(I)···Ir(I) distance, which is sterically counterintuitive, and indicates that the electron-donating character of ligands also influence these interactions (Scheme 7).

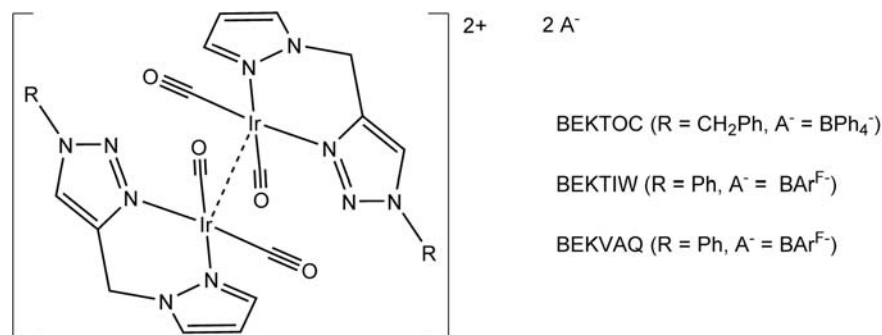
#### 1.15.3.2.2 Intramolecular Ir···Ir metallophilic interactions

##### 1.15.3.2.2.1 Two-atom bridged Ir(I)

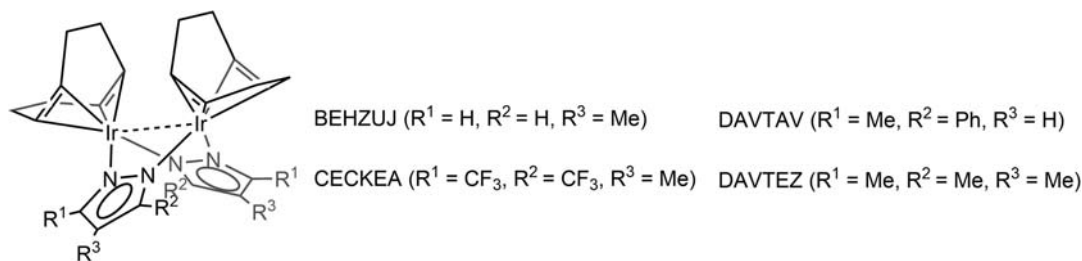
Most Ir(I) structures that exhibit intramolecular Ir(I)···Ir(I) metallophilic interactions are bridged by two pyrazolate (pyz) groups and each metal is coordinated to olefins as  $\pi$ -accepting ligands. These structures have a six-membered ring Ir-(N-N)<sub>2</sub>-Ir core with each Ir(I) coordinated to COD. The simplest of these structures is [Ir( $\mu$ -pyz)(COD)]<sub>2</sub>, which has an Ir(I)···Ir(I) distance of 3.216 Å (BEHZUJ).<sup>54</sup> Ir(I) structures with substituents in the 3, 4, or 5 positions of pyz groups show minimal effect on Ir(I)···Ir(I) distances: 3.073 Å for [Ir( $\mu$ -3,5(CF<sub>3</sub>)Pyz)(COD)]<sub>2</sub> (CECKEA),<sup>55</sup> 3.080 Å for [Ir( $\mu$ -3-Ph-5-(Me)Pyz)(COD)]<sub>2</sub> (DAVTAV), and 3.082 Å for [Ir( $\mu$ -3,4,5(Me)Pyz)(COD)]<sub>2</sub> (DAVTEZ).<sup>56</sup> (Scheme 8).



Scheme 6



Scheme 7



Scheme 8

Other pyz-bridged Ir(I) structures that exhibit intramolecular Ir(I)···Ir(I) metallophilic interactions are coordinated to at least one CO group,  $[\text{Ir}(\mu\text{-pyz})(\text{CO})_n]_2$ , again showing the need for  $\pi$ -acidic ligands in structures with low metal oxidation states. These structures also assume a boat conformation in the six-membered Ir–(N–N)<sub>2</sub>–Ir rings. For  $[\text{Ir}(\mu\text{-pyz})(\text{CO})(\text{PPh}_3)]_2$ , the Ir(I)···Ir(I) distance is 3.162 Å (BEHSEM10).<sup>54</sup> The effect of the larger PPh<sub>3</sub> groups compared to CO groups can be observed with the Ir(I)···Ir(I) distance of 3.506 Å (DATKOY)<sup>57</sup> of  $[\text{Ir}(\mu\text{-pyz})(\text{CO})_2]_2$ . As observed with  $[\text{Ir}(\mu\text{-pyz})(\text{COD})]_2$ , substituents on the 3,5 positions of pyz groups impact Ir(I)···Ir(I) distances. For  $[\text{Ir}(\mu\text{-3,5}(\text{Me})_2\text{pyz})(\text{CO})_2]_2$ , this distance is 3.245 Å (DATKUE),<sup>57</sup> and for  $[\text{Ir}(\mu\text{-3,5}(\text{CF}_3)_2\text{pyz})(\text{CO})_2]_2$ , this distance is 3.122 Å (MUZXEK)<sup>58</sup> (Scheme 9).

### 1.15.3.3 Rh···Rh metallophilic interactions

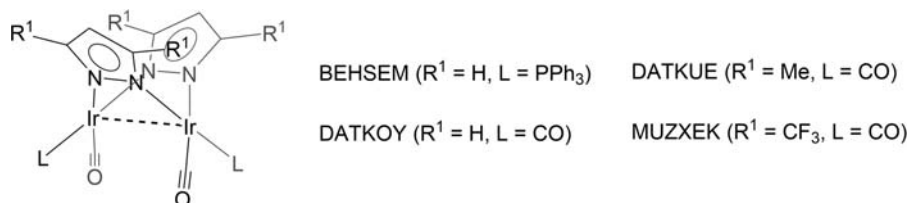
The van der Waals radius of Rh is 2.00 Å, and therefore only structures with Rh(I)···Rh(I) distances less than 4.00 Å are described in this section. As observed with both Ru and Ir, most structures contain a  $d^8$  Rh(I) with coordinated  $\pi$ -acidic CO or cyclooctadiene ligands, which are present in the metal starting material. Most Rh(I) structures with intermolecular metallophilic interactions have four-coordinate metal centers. Two of the ligands coordinated to the square-planar  $d^8$  Rh atom are commonly CO, and the other two ligands are, in order by frequency, a halogen and N-donor group, two N-donor groups, two O-donor groups, or two halogen atoms. Most Rh(I) structures with intramolecular metallophilic interactions are bridged by two atoms or three atoms, typically two pyrazolate or two carboxylate ligands.

#### 1.15.3.3.1 Intermolecular Rh···Rh metallophilic interactions

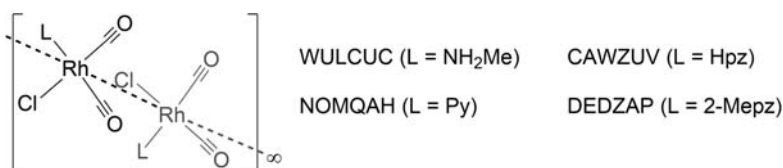
##### 1.15.3.3.1.1 Four-coordinate Rh(I)

The most common structural motif that exhibits intermolecular Rh(I)···Rh(I) metallophilic interactions is the neutral  $[\text{RhL}_3\text{X}]$  moiety. Many compounds have  $[\text{Rh}(\text{CO})_2\text{LX}]$  stoichiometries that form infinite stacks of these units, in which the  $[\text{Rh}\cdots\text{Rh}\cdots\text{Rh}]$  angles are average  $\sim 170^\circ$ , but are only perfectly linear when the (LX) group is flat as with tropolonate in  $[\text{Rh}(\text{CO})_2(\kappa_2\text{-C}_7\text{O}_2\text{H}_5)]$ , CTROPR.<sup>59</sup> For the  $[\text{Rh}(\text{CO})_2\text{LCl}]$  structures, the nature and size of the N-donor L affects the Rh(I)···Rh(I) distance: 3.393 Å when L = NH<sub>2</sub>Me (WULCUC),<sup>60</sup> 3.452 Å when L = pyz (CAWZUV),<sup>61</sup> 3.479 Å when L = py and (NOMQAH),<sup>62</sup> and 3.591 Å when L = 2-Mepyz (DEDZAP)<sup>63</sup> (Scheme 10).

Halide size also affects the intermolecular Rh(I)···Rh(I) distances, which are longer in the I<sup>−</sup> analogues compared to the Cl<sup>−</sup> ones. For  $[\text{Rh}(\text{CO})_2(\text{Hpyz})\text{X}]$ , the distance is 3.452 Å when X = Cl (CAWZUV),<sup>61</sup> compared to 3.599 Å when X = I (DEDZOD).<sup>63</sup>



Scheme 9



Scheme 10

For  $[\text{Rh}(\text{CO})_2(3\text{-Mepyz})\text{X}]$ , the distance is 3.283 Å when  $\text{X} = \text{Cl}$  (VASMIL)<sup>64</sup>; compared to 3.875 Å when  $\text{X} = \text{I}$  (DEDZIX)<sup>63</sup> (Scheme 11).

Another common Rh(I) structure that exhibits intermolecular Rh(I)··Rh(I) metallophilic interactions has two CO ligands and a neutral bidentate N, N'-donor ligand. These  $[\text{RhL}_4]^+$  structures also have a non-coordinating counteranion. Variation of the aromaticity and substituents on this N, N'-donor ligand affect the stacking of the Rh(I) cations and subsequent Rh(I)··Rh(I) distances. For a common  $[\text{Rh}(\text{CO})_2(2,2\text{-biimidazole})]^+$  cation, interactions of the bim (2,2'-biimidazole) ligand with each other, the nature and size of the counteranion (A), and interactions between the cation and the anion affect Rh(I)··Rh(I) metallophilic distances: 3.299 Å for  $\text{A} = \text{Cl}^-$  (QIVCAA),<sup>23</sup> 3.377 Å for  $\text{A} = [\text{FeCl}_4]^{2-}$  (QIVCII),<sup>23</sup> 3.366 Å for  $\text{A} = [\text{CoCl}_4]^{2-}$  (QIVCOO),<sup>23</sup> 3.238 Å for  $\text{A} = (\text{NO}_3)^-$  (RUXQAD),<sup>65</sup> 3.272 Å for  $\text{A} = (\text{BF}_4)^-$  (RUXQIL)<sup>65</sup> (Scheme 12).

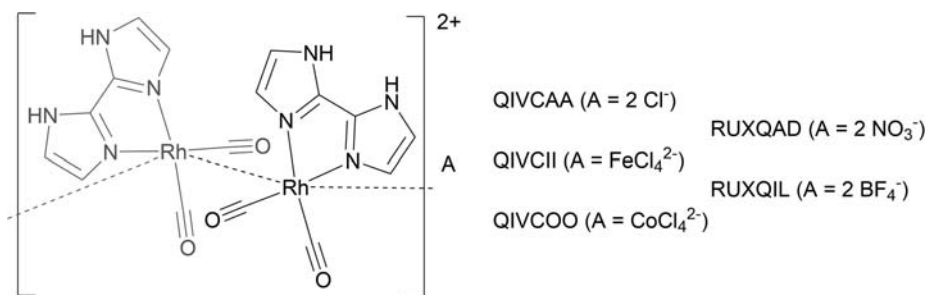
The second most common Rh(I) structure type that exhibits intermolecular Rh(I)··Rh(I) metallophilic interactions has two CO ligands coordinated to the Rh(I) atom and a bidentate O, O'-donor ligand. In the  $[\text{Rh}(\text{CO})_2(\text{R}^1, \text{R}^2\text{-}\beta\text{-diketonate})]$  family, a variety of  $\text{R}^1$  and  $\text{R}^2$  substituents on the  $\beta$ -diketonate carbonyl groups are observed in structures with Rh(I)··Rh(I) distances as follows: 3.253 Å when  $\text{R}^1$  and  $\text{R}^2 = \text{Me}$  (ACABRH02),<sup>66</sup> 3.537 Å when  $\text{R}^1 = \text{CF}_3$  and  $\text{R}^2 = \text{Ph}$  (BTFARH),<sup>67</sup> 3.308 Å when  $\text{R}^1 = \text{Ph}$  and  $\text{R}^2 = \text{Me}$  (EDOYAZ),<sup>68</sup> 3.346 Å. If bulkier groups are present on the acac backbone, dimeric interactions are seen, but the extended chain of Rh··Rh interactions are lost as when  $\text{R}^1 = \text{CF}_3$  and  $\text{R}^2 = \text{Fc}$  (KAKYUR),<sup>69</sup> 3.175 Å when  $\text{R}^1 = \text{Ph}$  and  $\text{R}^2 = \text{Et}$  (OJEWIK),<sup>70</sup> and 3.134 Å when  $\text{R}^1 = \text{COOMe}$  and  $\text{R}^2 = \text{Me}$  (WULSUT)<sup>71</sup> (Scheme 13).

A variety of salts have been prepared with  $\text{cis-}[\text{Rh}(\text{CO})_2\text{Cl}_2]^-$ , a square planar anion, that exhibits Rh(I)··Rh(I) metallophilic interactions with itself in the solid state. The nature or size of the counter cation  $\text{A}^+$  affects the particular packing arrangement between  $[\text{Rh}(\text{CO})_2\text{Cl}_2]^-$  anions as well as the intermetallic distances. For salts of the form  $\text{A}[\text{Rh}(\text{CO})_2\text{Cl}_2]$ , Rh(I)··Rh(I) distances are: 3.348 Å when  $\text{A} = [\text{C}_{60}(\text{CH}_2\text{NH}(\text{CH}_3)\text{CH}_2)]^+$  (CIYYOZ),<sup>72</sup> 3.584 Å when  $\text{A} = [(\text{H}_2\text{C}_2\text{S}_2\text{C})_2]^+$  (GABKOJ),<sup>73</sup> 3.358 Å when  $\text{A} = [\text{Rh}(4,4'\text{-Me}_2\text{-2,2'\text{-bipy}})(\text{CO}_2)]^+$  (VUHGOX),<sup>74</sup> 3.973 Å when  $\text{A} = [\text{Rh}(4,4'\text{-Me}_2\text{-2,2'\text{-bipy}})_2\text{Cl}_2]^+$  (VUHGUID).<sup>74</sup> All four species exhibit pairwise metallophilic interactions, but CIYYOZ and VUHGUID do not have chains present due to the large counter cation size (Scheme 14).

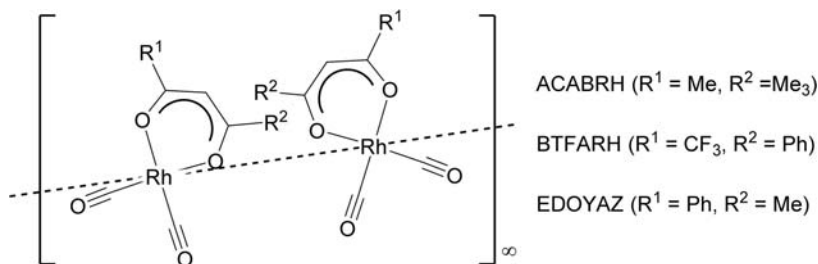
Four-coordinate Rh(I) complexes with two terminal CO ligands and one halogens can form neutral dimers with the  $[(\text{OC})_2\text{Rh}(\mu\text{-X})_2\text{Rh}(\text{CO})_2]$  stoichiometry. These  $[\text{RhL}_3\text{X}]$  centers are composed of two planar  $[\text{Rh}(\text{CO})_2]$  units linked by two bridging halides. The dihedral angle of two  $[\text{Rh}(\mu\text{-Cl})_2]$  planes is 53°, and the intermolecular Rh(I)··Rh(I) distance is 3.325 Å



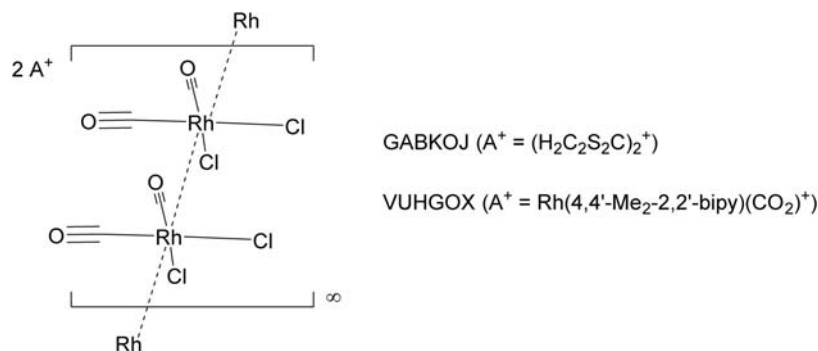
Scheme 11



Scheme 12



Scheme 13



Scheme 14

in FUZBEH.<sup>75</sup> Rhodium carbonyl iodide, [Rh(μ-I)(CO)<sub>2</sub>]<sub>2</sub>, with larger bridging halides, has a dihedral angle of 59° between the two [Rh(μ-I)]<sub>2</sub> planes and an intermolecular Rh(I)⋯Rh(I) distance of 3.633 Å (SETFUU) (Scheme 15).

### 1.15.3.3.2 Intramolecular Rh⋯Rh metallophilic interactions

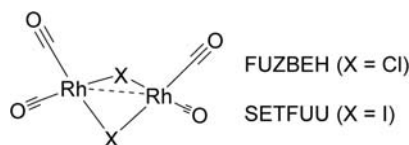
#### 1.15.3.3.2.1 Two-atom bridged Rh(I)

Not surprisingly, several of the motifs seen in Ir metallophilic chemistry are also observed with the lighter congener Rh. Neutral Rh(I) dimer structures with two pyz bridges, which are anionic LX donors, and at least one CO ligand are the most common structures with intramolecular Rh(I)⋯Rh(I) metallophilic interactions. Four-coordinate Rh(I) dimers with two bridging pyz and two CO ligands have been prepared with various R substituents on pyz. The simplest of these Rh(I) dimers has a Rh(I)⋯Rh(I) distance of 3.547 Å for [Rh(μ-pyz)(CO)<sub>2</sub>]<sub>2</sub> (TOLYAU)<sup>76</sup> and 3.259 Å for [Rh(μ-3,5-Me<sub>2</sub>pyz)(CO)<sub>2</sub>]<sub>2</sub> (CORCER).<sup>77</sup> Steric effects of the two Me groups on the bridging pyz with the CO coordinated to the same structure are proposed to cause shortening of the Rh(I)⋯Rh(I) distance. Two more related examples of [Rh(μ-3,5-R,R-*yz*)(CO)<sub>2</sub>]<sub>2</sub> have shorter intermetallic distances, where R = long-chain 4-*n*-alkyloxyphenyl substituents (C<sub>6</sub>H<sub>4</sub>OC<sub>*n*</sub>H<sub>2*n*+1</sub>); for *n* = 10, Rh(I)⋯Rh(I) distance is 3.163 Å (CAMGAZ),<sup>78</sup> for *n* = 12, Rh(I)⋯Rh(I) distance is 3.144 Å (CAMGED)<sup>78</sup> (Scheme 16).

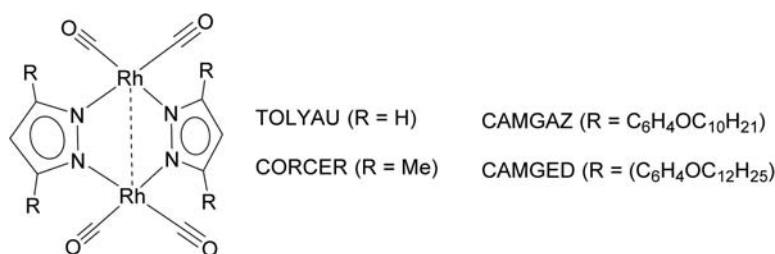
Another common feature of dimeric Rh(I) structures that exhibit metallophilic interactions, in addition to bridging pyz ligands, is coordination of each Rh(I) to one COD. For these structures, the Rh(I)⋯Rh(I) distance again decreases with increased size of substituents on the pyz bridges: 3.154 Å for [Rh(μ-3,5-Me<sub>2</sub>Pyz)(COD)<sub>2</sub>]<sub>2</sub> (CORCIV),<sup>77</sup> 3.158 Å for [Rh(μ-4-MeNH<sub>2</sub>Et-3,5-Me<sub>2</sub>Pyz)(COD)<sub>2</sub>]<sub>2</sub> (EFASAF),<sup>79</sup> 3.207 Å for [Rh(μ-3-PhPyz)(COD)<sub>2</sub>]<sub>2</sub> (WOQBEEK),<sup>80</sup> and 3.268 Å for [Rh(μ-Pyz)(COD)<sub>2</sub>]<sub>2</sub> (CECJUP)<sup>55</sup> (Scheme 17).

#### 1.15.3.3.2.2 Three-atom bridged Rh(I)

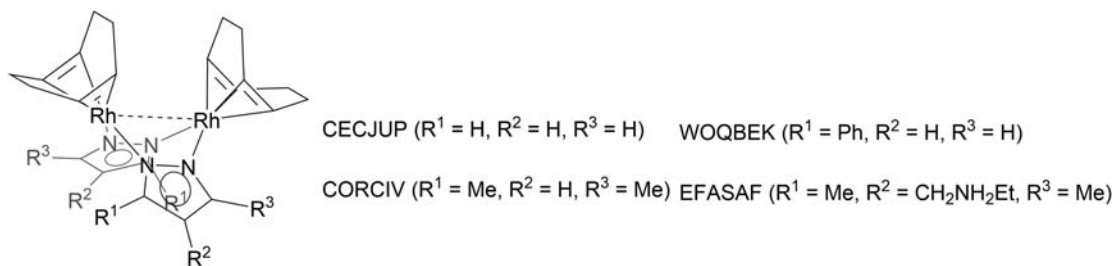
Rh(I) dimer structures with two carboxylate bridges are the second most common structures with intramolecular Rh(I)⋯Rh(I) metallophilic interactions. These structures have in common two bridging acetate (κ<sup>1</sup>,κ<sup>1</sup>-μ<sub>2</sub>-OAc) ligands and the coordination of two alkenes. For [Rh(μ-OAc)<sub>2</sub>L]<sub>2</sub>, intramolecular Rh(I)⋯Rh(I) distances are: 3.105 Å when L = norbornadiene (ACBDRH),<sup>81</sup> 3.223 Å when L = C<sub>2</sub>H<sub>4</sub> (TEFXUX),<sup>82</sup> 3.344 Å when L = COD (UQOWII)<sup>83</sup> (Scheme 18).



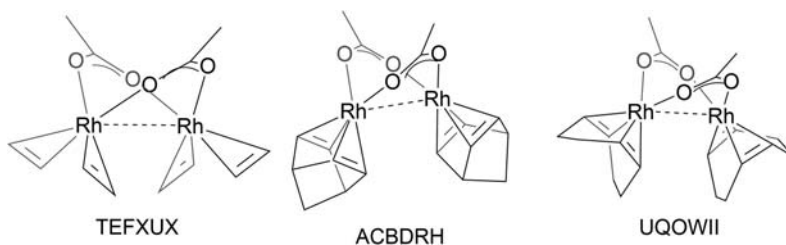
Scheme 15



Scheme 16



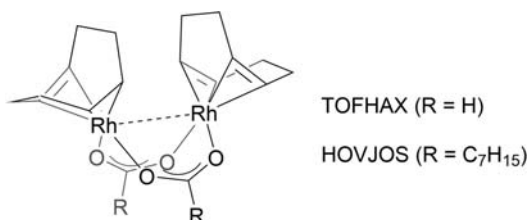
Scheme 17



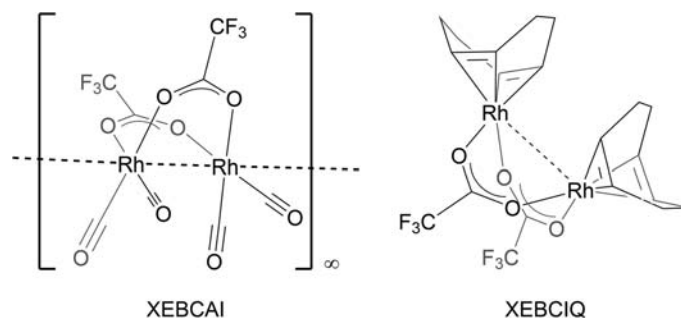
Scheme 18

For Rh(I) structures with coordinated COD, the relative size of the bridging carboxylate ligands that form the eight-membered Rh(I) dimer core affects intramolecular Rh(I)···Rh(I) distances. Like the pyrazolate groups above, the dimers with smaller bridging groups have longer measured Rh(I)···Rh(I) distances. The simplest of the bridging carboxylate groups is formate ( $\text{HC(O)O}$ ), and the structure with within  $[\text{Rh}(\mu\text{-HCOO})(\text{COD})_2]$  (**TOFHAX**) has an intramolecular Rh(I)···Rh(I) distance of 3.387 Å. This distance is longer than the Rh(I) dimer with a bridging acetate, as indicated in  $[\text{Rh}(\mu\text{-OAc})(\text{COD})_2]$  (**UQOWII**), which has a distance of 3.344 Å. An example structure with octanoate bridging carboxylate groups is  $[\text{Rh}(\mu\text{-O}_2\text{C}_8\text{H}_{15})(\text{COD})_2]$  (**HOVJOS**), which has a slightly shorter Rh(I)···Rh(I) distance of 3.339 Å (**Scheme 19**).

Another common bridging group in Rh(I) dimers is trifluoroacetate ( $\text{CF}_3\text{CO}_2$ ). The structure  $[\text{Rh}(\mu\text{-CF}_3\text{CO}_2)(\text{CO})_2]_2$  (**XEBCAI**) has particularly short intramolecular Rh(I)···Rh(I) distance of 2.984 Å. These units are typically present in a polymeric chain of dinuclear molecules aligned along the metal-metal axis, made possible by the planarity at each Rh(I) center. This polymer formation is inhibited by the bulkier COD group of  $[\text{Rh}(\mu\text{-CF}_3\text{CO}_2)(\text{COD})_2]_2$  (**XEBCIQ**),<sup>84</sup> which crystallizes in discrete units and has an intramolecular Rh(I)···Rh(I) distance of 3.464 Å (**Scheme 20**).



Scheme 19



Scheme 20



### 1.15.3.4 Pt···Pt metallophilic interactions

There are thousands of complexes that exhibit inter- and intramolecular distances between two Pt atoms consistent with metallophilic bonding in the CSD. This volume is due to the much greater air-stability of the  $d^8$  configuration in Group 10, compared to Group 11 above. As the covalent and van der Waals radii of Pt are 1.35 Å and 1.72 Å, respectively, only complexes with Pt···Pt distances between 2.70 Å and 3.44 Å are included in this discussion. Additionally, only complexes with a small number of Pt centers were analyzed, and complexes that contained traditional metallic interactions within Pt(0) clusters were particularly excluded. Within this group of four-coordinate, Pt(II) complexes, the most common PtLXZ classifications encountered are:  $[\text{PtL}_4]^{2+}$ ,  $\text{PtL}_3\text{X}^+$ ,  $\text{PtL}_2\text{X}_2$ ,  $\text{PtLX}_3$ , and  $\text{PtX}_4^{2-}$ . This section first describes complexes with Pt···Pt inter- and then intramolecular metallophilic contacts, common metal complex ligand types, then by the possible combinations of these ligand types, ordered by prevalence.

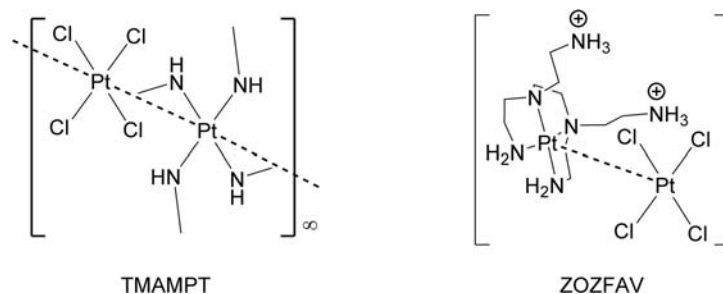
#### 1.15.3.4.1 Intermolecular Pt···Pt metallophilic interactions

As understanding of the electronic structural basis for metallophilicity increased, a renewed appreciation for chains of  $d^8$  Pt(II) species burgeoned. Review articles are available as well.<sup>85–87</sup>

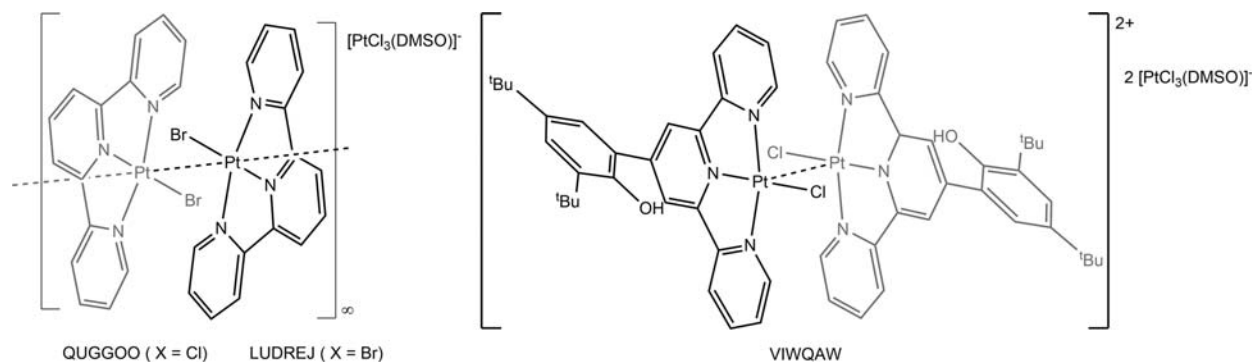
##### 1.15.3.4.1.1 Four-coordinate Pt(II)

Among compounds with pairs of Pt atoms less than 3.44 Å apart, metallophilic Pt centers are known bound to four, three, two, or one of any of the halides. Only a few salts with  $[\text{PtX}_4]^{2-}$  anions have Pt bound to four halide ligands containing  $\text{PtCl}_4^{2-}$ , and exhibit Pt···Pt intermolecular distances between 3.290 Å and 3.415 Å including JAVGUI,<sup>88</sup> TMAMPT,<sup>89,90</sup> XIMWUO,<sup>91</sup> ZOZFAV.<sup>90,92</sup> The complex TMAMPT, a derivative of the famous Magnus' green salt,  $[(\text{NH}_3)_4\text{Pt}][\text{PtCl}_4]$ , has alternating  $[\text{PtL}_4]^{2+}$  cations and  $[\text{PtCl}_4]^{2-}$  anions stacked in an infinite array. Both JAVGUI and XIMWUO have one pairwise interaction of Pt-containing cations and additional non-interacting  $[\text{PtCl}_4]^{2-}$  anions present as well. In JAVGUI the cation contains Co(III),  $[\text{Co}(\text{en})_2(\text{m}_2\text{-OH})_2\text{PtCl}_2]^+$ , and in XIMWUO a doubly protonated diaminium ligand is coordinated to  $[\text{PtCl}_2]$  via a chelating pyridine-triazole group. In ZOZFAV, a tetradentate tetramine with two pendant aminium cations forms pairs with  $[\text{PtCl}_4]^{2-}$ , but no chains are present (Scheme 21).

Complexes with the  $[\text{PtLX}_3]^{1-}$  form are limited to those with the  $[\text{PtCl}_3(\text{DMSO})]^{1-}$  anion (LUDREJ,<sup>93</sup> QUGGOO,<sup>94</sup> VIWQAW<sup>95</sup>).<sup>93–95</sup> In LUDREJ, the square-planar Pt(II)  $[\text{Pt}(\text{tpy})\text{Br}]^+$  cation stacks with itself in the solid state, and the  $[\text{PtCl}_3(\text{DMSO})]^{1-}$  anion is not involved in metallophilic interactions. The Pt···Pt interaction distances alternate in a short-long sequence (3.368 Å and 3.413 Å) reminiscent of a Peierls distortion.<sup>96</sup> The pattern is virtually identical in QUGGOO with alternating distances of 3.338 Å and 3.419 Å, with the slightly smaller short distance made possible by the smaller size of Cl.<sup>20</sup> Substitution in the *para* position on the middle pyridine of VIWQAW prevents extended chains in the crystal lattice, and the singular Pt···Pt distance within pairs of cations is 3.379 Å (Scheme 22).



Scheme 21

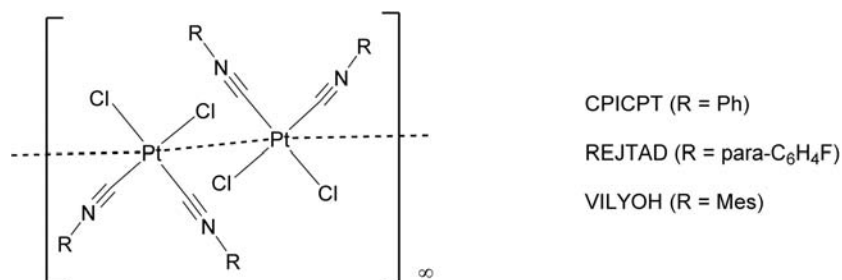


Scheme 22

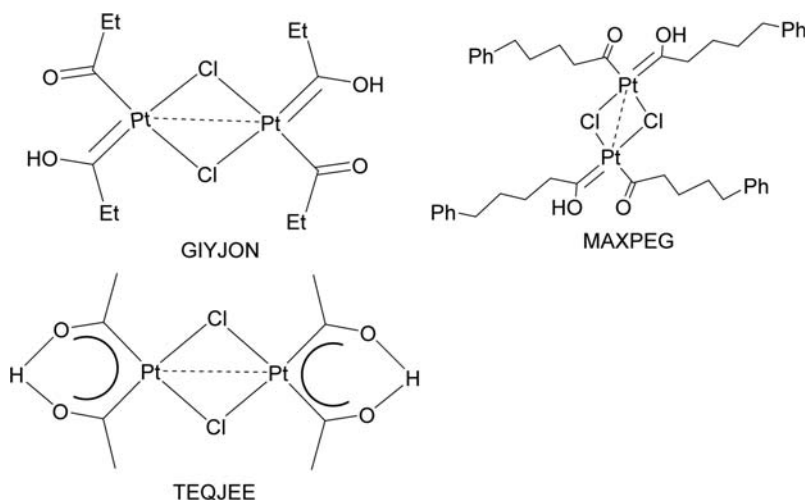
There are numerous  $[\text{PtL}_2\text{X}_2]$  complexes with monodentate L and two halide X-type ligands. The majority of the complexes have two RNC isocyanide (isonitrile) and two  $\text{Cl}^-$  ligands (CPICPT,<sup>97</sup> REJTAD,<sup>97</sup> VILYOH<sup>98</sup>). The Pt···Pt intramolecular distances are temperature dependent, which is a general phenomenon in  $d^8$ ··· $d^8$  metallophilic interactions.<sup>99</sup> In CPICPT, the distance was 3.318 Å at 300 K, and 3.246 Å at 100 K. Other complexes with two halide ligands contained Pt(II) with heavier *p*-block L donors including an unusual (*o*-BrC<sub>6</sub>H<sub>4</sub>)S(C<sub>6</sub>F<sub>5</sub>) ether (TIZQO)<sup>100</sup>, the bidentate thioether F<sub>3</sub>CSCH(CH<sub>3</sub>)CH<sub>2</sub>SCF<sub>3</sub> (FMPPT10)<sup>101</sup>, PhMeTe (JOZXOL)<sup>102</sup>, and a bridging distibine group (NEWKUW)<sup>103</sup>. The pairwise Pt···Pt distances within these structures vary widely, ranging from 3.176 Å to 3.417 Å. Pt···Pt metallophilic distances are also observed between complexes with two Pt(II) atoms bridged by two Cl atoms. The platina- $\beta$ -diketone ligands in GIYJON,<sup>104</sup> MAXPEG,<sup>105</sup> and TEQJEE<sup>106</sup> each have one carbene (L) and one carbanion (X) ligand on Pt in these unusual LX groups. The derivatives with methyl, ethyl, and pentyl-phenyl chains, respectively have Pt···Pt distances of 3.391, 3.318, and 3.351 Å (Schemes 23 and 24).

The vast majority of the approximately 90  $[\text{PtL}_3\text{X}]^+$ -containing complexes with one halide ligand have a  $[\text{Pt}(\text{tpy})\text{Cl}]^+$  unit, which is luminescent. The first  $[\text{Pt}(\text{tpy})\text{Cl}]$  structure was reported in 1993,<sup>107</sup> with a triflate counteranion. Since that time, dozens of analogues of these photophysically interesting Pt(II) complexes have been developed, including those with a single *para* substitution on the central pyridine group, with substitutions and variations on more than one pyridine of the terpyridine ligands, and numerous different counteranions. Intermolecular Pt···Pt distances from  $[\text{Pt}(\text{tpy})\text{Cl}]^+$  range from 3.269 Å to 3.434 Å with a mean distance of 3.310 Å. These flat cations often stack in a head-to-tail orientation, and flat substituents, as in OTULOF<sup>108</sup> will still support pairwise stacking, but tris-<sup>t</sup>Bu substitution of in the *para* positions<sup>109</sup> prevents metallophilic contacts. The subtle electronic factors of the tpy substitutions have minimal impact on the intermolecular Pt···Pt distances of the complexes: the shortest distance is that of 3.269 Å in  $[\text{Pt}(\text{tpy})\text{Cl}](\text{ClO}_4)$  (ZEKTEO), with no *para* substitution, and the longest distance is the pairwise distance of 3.434 Å in  $[\text{Pt}(\text{tpy}-\text{C}_6\text{H}_4-\text{CH}_3)\text{Cl}](\text{ClO}_4)$  (OTULOF)<sup>108</sup> with a *para*-tolyl group on the middle pyridine. In the middle of this distance range is a  $[\text{Pt}(\text{tpy})\text{Cl}]^+$  species with a bulky pendant polyhedral oligomeric silesquioxane moiety with a 3.347 Å Pt···Pt distance (GUSLEN).<sup>110</sup> Compared to these  $[\text{Pt}(\text{tpy})\text{Cl}]^+$  structures, the few structures with a Br<sup>-</sup> ligand<sup>111</sup> have greater distances ranging from 3.384 Å to 3.376 Å, likely due steric effects of the larger Br atom<sup>21</sup> (Scheme 25).

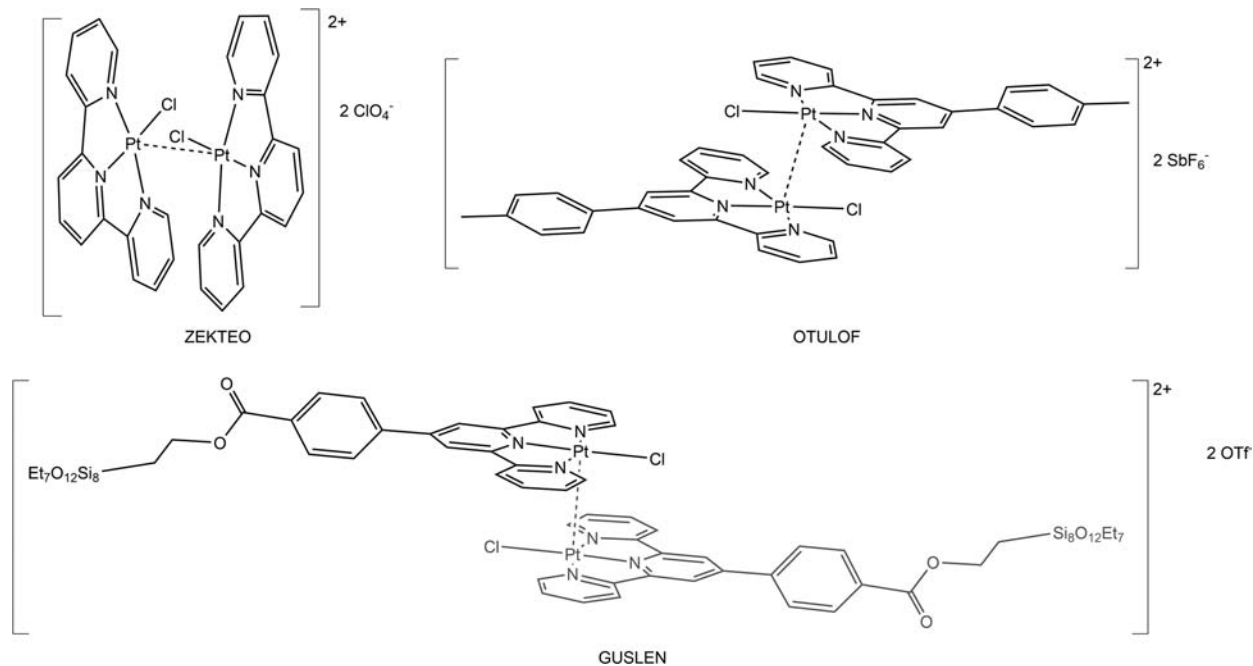
There are also  $[\text{PtL}_2\text{X}_2]$  complexes with one halide ligand and an organometallic  $[\text{L}_2\text{X}]$  ligand. The 2,6-dipyridyl-phenyl ligand is particularly well-suited for  $d^8$  chemistry. Pt(II) complexes with this ligand have intermolecular Pt···Pt distances ranging from 3.226 Å to 3.437 Å with a mean distance of 3.330 Å. This shortest distance is present in a U-shaped diplatinum molecule with an *N,N*-dimethylurea bridge, FECHIH, in which an open conformation exists with intermolecular luminescent Pt···Pt metallophilic



Scheme 23



Scheme 24

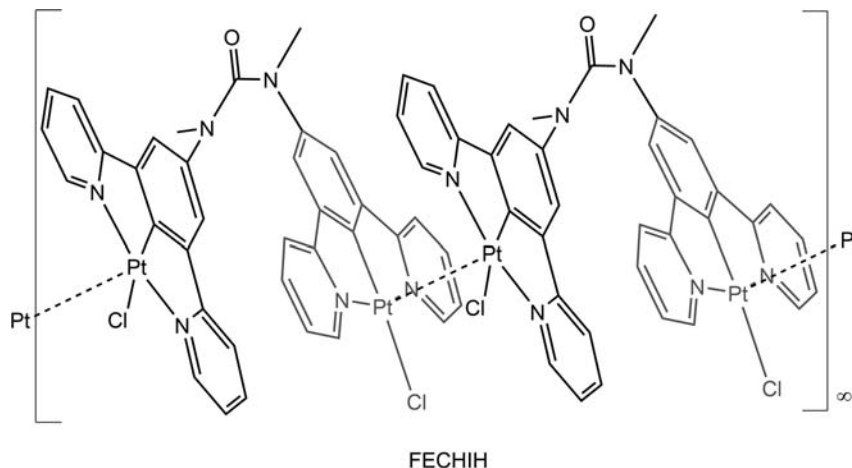


Scheme 25

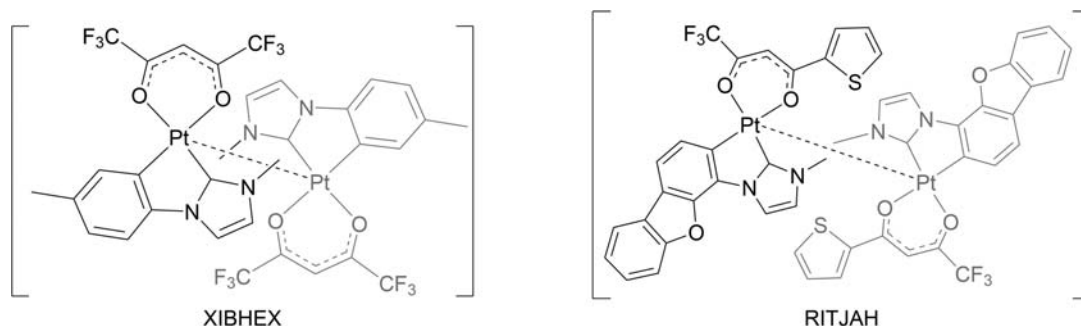
interactions on both sides of the ligand. There are therefore chains in the lattice, but only pairwise Pt $\cdots$ Pt interactions. When the ligand is in a closed conformation, there is no metallophilic interaction. With the exception of this structure, most of the PtL<sub>2</sub>X<sub>2</sub> complexes have one Pt(II) center with variable tridentate phenyl bipyridine ligands. The fascinating compound OVERUD,<sup>112</sup> [Pt(tpy-CF<sub>3</sub>)Cl], has meta CF<sub>3</sub> groups on the flanking pyridine groups and has three different polymorphs with three different colors, interconverted by grinding and/or heating. The largest intermolecular Pt $\cdots$ Pt distance of 3.437 Å is in the green form (Scheme 26).

The most prevalent structure with intermolecular Pt $\cdots$ Pt metallophilic interactions has a four-coordinate Pt(II) atom with a chelating acetylacetonate (acac or  $\beta$ -diketonate) ligand and a chelating phenyl *N*-heterocyclic carbene (NHC), both with various substituents. This combination of ligands with strong  $\sigma$ -donation to transition metals has been found to create tunable emitter materials in organic light-emitting diode applications, the earliest of which was developed in 2012.<sup>113</sup> These structures have intermolecular Pt $\cdots$ Pt distances ranging from 3.225 Å to 3.419 Å with a mean distance of 3.335 Å. The shortest distance is exhibited by the simplest form of this type of structure (XIBHEX),<sup>114</sup> while the longest is exhibited by (RITJAH)<sup>115</sup> (Scheme 27).

Diplatinum complexes with four bridging dithiocarboxylato (RC(S)S) ligands form lantern (paddlewheel) complexes and were first synthesized in 1981, and their unusual solid-state optical properties were also recognized at the time.<sup>116</sup> The major difference in composition is the thiocarboxylate R substituent, and the complexes can exhibit short intradimer Pt $\cdots$ Pt distances



Scheme 26



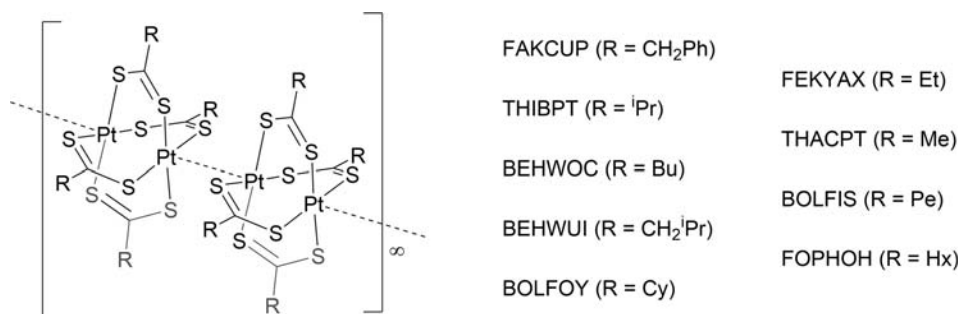
Scheme 27

around 2.7–2.8 Å, and much longer interdimer distances ranging up to 3.340 Å with a mean distance of 3.126 Å. Comparison of the substituents with the intermolecular Pt···Pt distances indicates no particular pattern, as the distance increases in order of: CH<sub>2</sub>Ph (FAKCUP),<sup>117</sup> iPr (THIBPT),<sup>116</sup> Bu (BEHWOC),<sup>118</sup> Me (THACPT01),<sup>119</sup> Pe (BOLFIS),<sup>119</sup> Hx (FOPHOH),<sup>120</sup> CH<sub>2</sub>iPr (BEHWUI),<sup>118</sup> Cy (BOLFOY),<sup>119</sup> and Et (FEKYAX)<sup>121</sup> (Scheme 28).

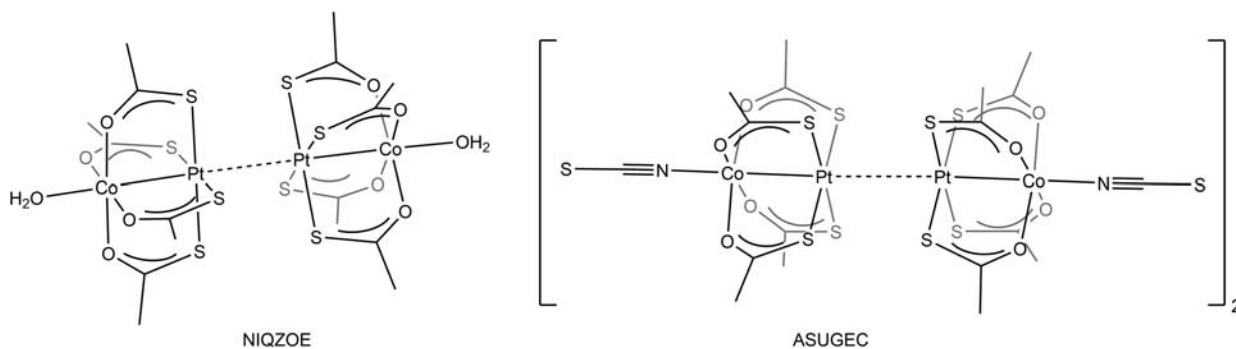
A large family of heterobimetallic lantern complexes with asymmetric monothiocarboxylate ligands has been prepared.<sup>122</sup> The complexes have the general form [PtM(S(O)CR)<sub>4</sub>(L)] in which the L ligand is bound to M, which has been most thoroughly studied for the late transition metals Mn,<sup>123</sup> Fe, Co, Ni, and Zn, and R = CH<sub>3</sub> or C<sub>6</sub>H<sub>5</sub>.<sup>124–127</sup> These complexes dimerize through unbridged metallophilic Pt···Pt contacts in the solid state only for certain L groups. Metallophilic contacts with staggered lantern configurations are known for M = Co (NIQZOE), Ni, Zn with L = H<sub>2</sub>O, one Ni example with 3-NO<sub>2</sub>-py, and with anionic terminal thiocyanate ligands has an eclipsed configuration as shown in ASUGEC (Scheme 29).

Heterobimetallic lantern complexes with traditional, symmetric carboxylate bridges containing a Pt atom bridged to a transition metal display intermolecular Pt···Pt interactions as well. In each of these structures, one Pt(II) atom is bridged to Ni (FIXCUN),<sup>128</sup> Cu (AHEQOW),<sup>129</sup> or Zn (FIXDAU)<sup>128</sup> and forms a dimeric metallophilic interaction of 3.177, 3.168, or 3.272 Å respectively with an adjacent lantern. In these [PtM[O(O)CR]<sub>4</sub>] structures a water ligand caps off each end of the dimers that are eclipsed with respect to one another<sup>128,129</sup> (Scheme 30).

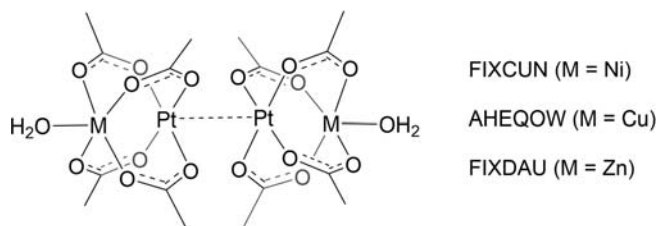
Pt(II) complexes with intermolecular metallophilic interactions are commonly seen with cyanide X and isocyanide (isonitrile) L ligands in PtL<sub>2</sub>X<sub>2</sub> classifications. The cores are rigidly planar to at least two atoms away from the Pt centers and the neutral



Scheme 28



Scheme 29



Scheme 30

compounds stack very well. The Pt···Pt distances are affected by the R substituent, variations of the *cis* and *trans* isomers of two L and two X ligands, experimental temperatures of the SCXRD analyses, and counter cations. Three complexes of *cis*-[Pt(CNR)<sub>2</sub>(CN)<sub>2</sub>] in which R is Me, <sup>i</sup>Pr, or <sup>t</sup>Bu group (TEFPOK, NUMCUU, CELJOZ)<sup>130–132</sup> have Pt···Pt distances of 3.391, 3.256, and 3.355 Å, respectively. No pattern is observed with the steric effects of the R substituents, but the [Pt(CNiPr)<sub>2</sub>(CN)<sub>2</sub>] crystal structure was taken at 173 K, compared to 298 K of the Me and <sup>t</sup>Bu analogues. As described with *cis*-[Pt(CNPh)<sub>2</sub>Cl<sub>2</sub>], CPICPT, above, the Pt···Pt distances contract slightly with significant decreases in temperature. The complex *cis*-[Pt(CNMe)<sub>2</sub>(CN)<sub>2</sub>] exhibited a Pt···Pt distance of 3.338 Å at 90 K (TEFPOK01), compared to the 3.391 Å at 298 K (Scheme 31).

The effect of *cis* and *trans* isomers on Pt···Pt distances can be observed in the SCXRD data for [Pt(CN-*p*-(C<sub>2</sub>H<sub>5</sub>)C<sub>6</sub>H<sub>5</sub>)<sub>2</sub>(CN)<sub>2</sub>] (EDUMOF, CIRPEZ),<sup>133,134</sup> both of which exhibit staggered geometries along the Pt···Pt vector and were measured at 173 K. The *cis* structure exhibits a distance of 3.125 Å, versus that in the *trans* of 3.281 Å. This slight difference can be attributed to greater repulsion between the isocyanide phenyl groups approximately perpendicular to the planar four-coordinate Pt(II) centers (Scheme 32).

Counter cation size effect on intermolecular Pt···Pt distances was observed in the fascinating crystal structures of KLn(OH<sub>2</sub>)<sub>8.75</sub>[Pt(CN)<sub>4</sub>],<sup>24</sup> where Ln = La, (XEKCOH), Pr, (XEKCEX), and Nd (XEKCIB). These isostructural compounds contain *D*<sub>4h</sub> [Pt(CN)<sub>4</sub>]<sup>2-</sup> anions *trans*-bridged by the hydrated Ln<sup>3+</sup> cations, forming planar networks layered in two-dimensional arrays organized by the Pt···Pt interactions. As expected, the Pt···Pt distance decreases in length as the atomic number and radius of the lanthanide decreases; the La, Pr, and Nd analogues have metallophilic distances of 3.291 Å, 3.285 Å, and 3.284 Å, respectively (Scheme 33).

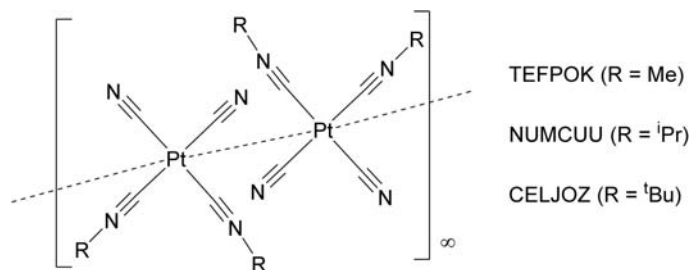
There are a small number of homoleptic complexes with four cyanide groups, with –CN in an MX<sub>4</sub><sup>2-</sup> classification (BINNIX, PAHCUW, UXOXEL),<sup>135–137</sup> and –CNMe with ML<sub>4</sub><sup>2+</sup> classification (JIQVIO).<sup>138</sup> Pt(CN)<sub>4</sub><sup>2-</sup> serves as a counteranion for bulky cations of BINNIX and PAHCUW, with Pt···Pt distances of 3.352 Å and 3.402 Å, respectively. In contrast, the cation of UXOXEL are two Cs<sup>+</sup> ions, allowing closer 3.088 Å packing of the Pt(II) centers. The Pt(CNMe)<sub>4</sub><sup>2+</sup> of JIQVIO serves as a counter cation.

### 1.15.3.4.2 Intramolecular Pt···Pt metallophilic interactions

#### 1.15.3.4.2.1 Two-atom bridged Pt(II)

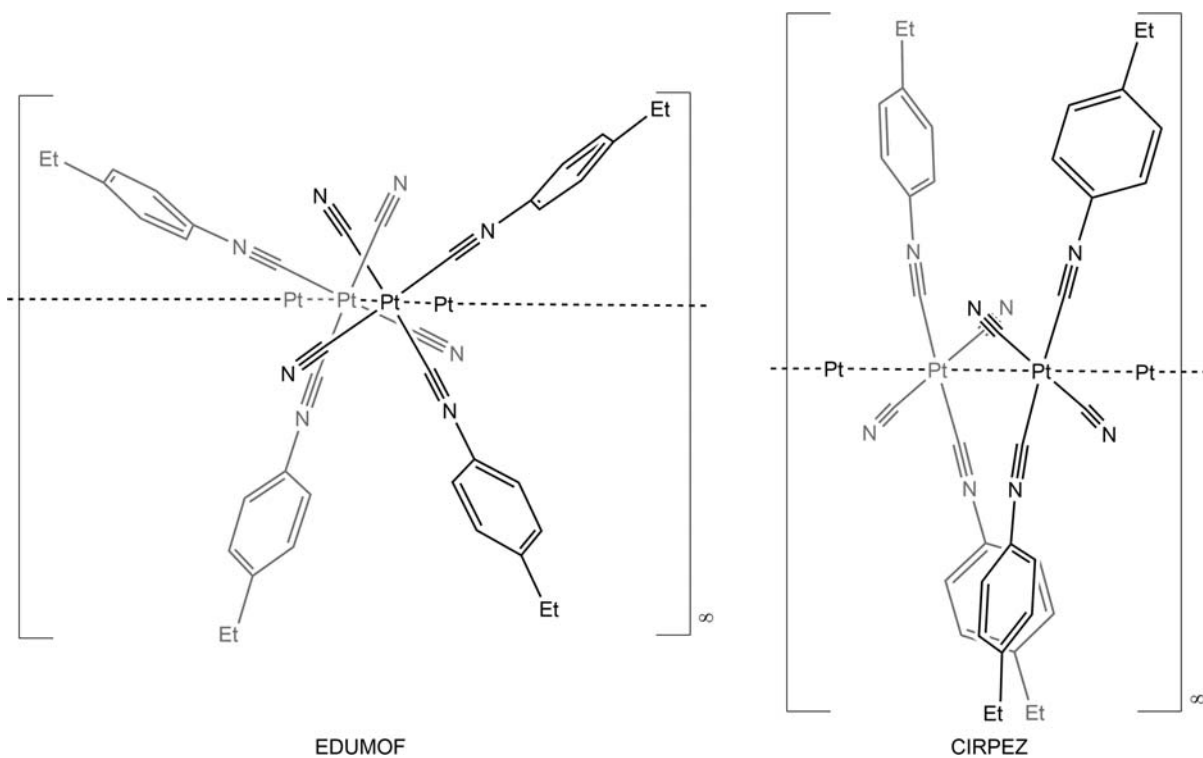
Two square-planar Pt atoms have intramolecular metallophilic interactions when supported by bridging ligands. The most common core structure with Pt···Pt distances less than 3.44 Å has a six-membered [Pt-X-X-Pt-X-X] ring with two *trans* Pt atoms and a boat conformation. The most common two-atom bridging group is –N–N–, followed by –N–O– and –N–C–. Most [Pt<sub>2</sub>] structures with such an intramolecular interaction are bridged by two pyrazole ligands, often referred to as the “wings” of the butterfly-like complexes, and the square planar Pt atoms are chelated by anionic phenylimidazole groups, as shown in FEPLUI, but neutral dipyrimidine examples are also known (ALAVAL). These structures exhibit Pt···Pt distances between 2.834 Å and 3.437 Å, depending on the pyrazole substitution. This shortest distance of 2.834 Å is attributed to a complex with a total of four <sup>t</sup>Bu groups on the two pyrazole ligands and four F on the two phenylpyridine groups that cause narrowing of the boat conformation (FEPLUI).<sup>139</sup> Conversely, the diplatinum complexes with no substituents on the bridging pyrazole like ALAVAL have Pt···Pt distances greater than 3.121 Å (Scheme 34).

One of the first diplatinum structures with a six-membered ring of boat conformation was synthesized in 1979, bridged by CN<sup>t</sup>Bu, with a Pt···Pt distance of 3.056 Å (BISIPT).<sup>140</sup> In 2012, an related diplatinacycle complex became the first example of an oxime ligand coordinated to the Pt via the O atom (QEKCEQ).<sup>141</sup> (Scheme 35)

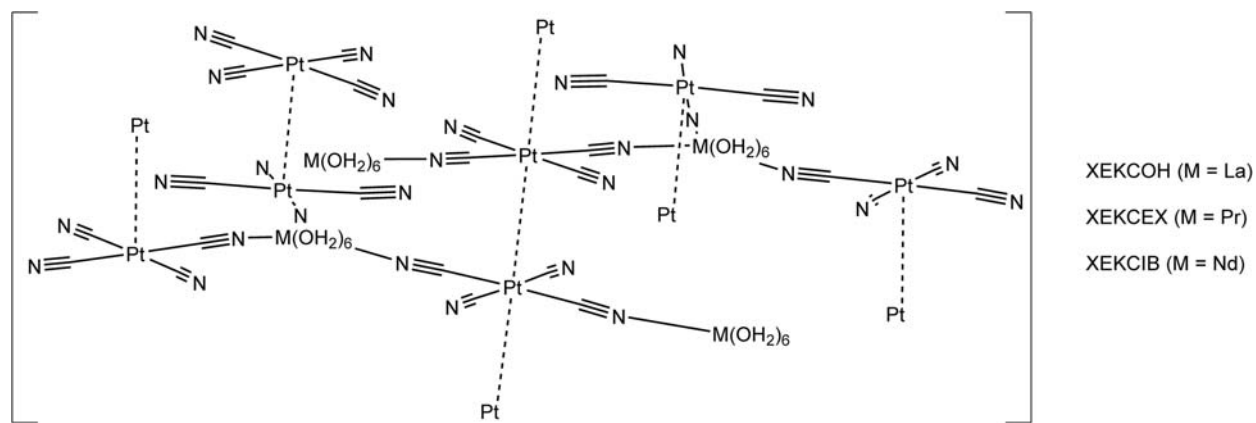


Scheme 31

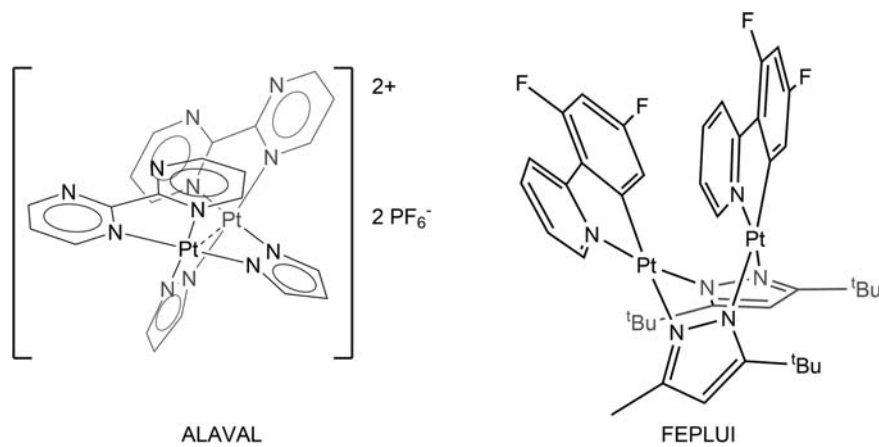




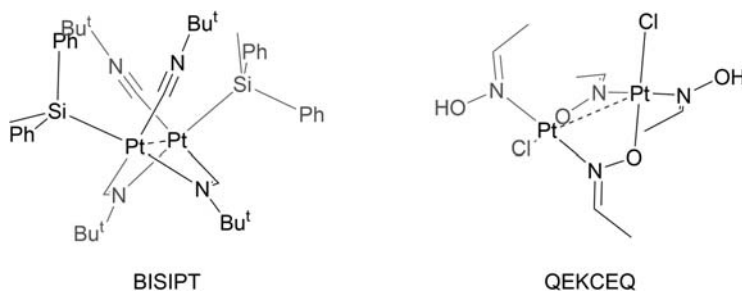
Scheme 32



Scheme 33



Scheme 34



Scheme 35

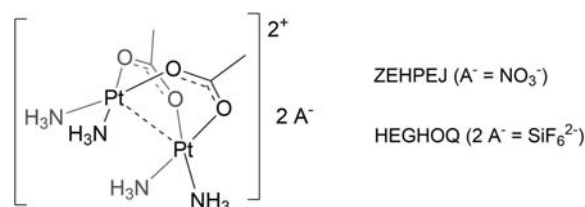
#### 1.15.3.4.2.2 Three-atom bridged Pt(II)

Diplatinum complexes with three-atom bridges have a common core of a diacetate-bridged half-lantern complex, forming an eight-membered ring in a boat conformation. Such structures were investigated as part of the interest in the mixed-valent platinum blue complexes.<sup>142</sup> The mixed-valent compounds do not have metallophilic interactions, but their reduced all-Pt(II) precursors do. The other ligands on Pt(II) are typically neutral  $\text{NH}_3$  or  $\text{NH}_2\text{R}$ , such that other non-coordinating anions are required. In an early study,<sup>143</sup> the anions  $\text{A} = \text{ClO}_4^-$ ,  $\text{NO}_3^-$ ,  $\text{BF}_4^-$ ,  $\text{PF}_6^-$ , and  $2\text{A}^- = (\text{SiF}_6)^{2-}$  were all used synthetically,  $[\text{Pt}_2(\text{NH}_3)_4(\mu\text{-OAc})_2]\text{A}_2$ , but only (HEGHOQ)<sup>143</sup> was structurally characterized at the time and the  $(\text{NO}_3)^-$  analog (ZEHPEJ),<sup>144</sup> followed later. The intramolecular  $\text{Pt} \cdots \text{Pt}$  distances are 2.971 Å and 2.921 Å, respectively, and there are also longer intermolecular  $\text{Pt} \cdots \text{Pt}$  interactions between dimers at 3.227 Å and 3.132 Å (Scheme 36).

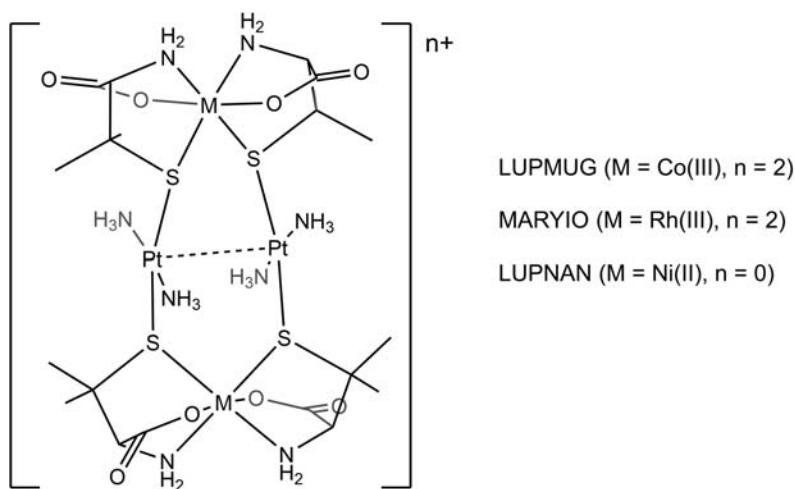
Another form of diplatinum complexes with intramolecular metallophilic interactions have three-atom bridges of  $-\text{S}-\text{M}-\text{S}-$ , M is coordinated to two polydentate ligands with amine, acetate, and thiolate donors. In the cases of Co (LUPMUG),<sup>145</sup> Rh (MARYIO),<sup>146</sup> Ni (LUPNAN),<sup>145</sup> the transition metals are octahedral but with Pd (ECAPIK)<sup>147</sup>, the Pd center is only coordinated by the N- and S-donors (Scheme 37).

#### 1.15.3.5 Pd $\cdots$ Pd metallophilic interactions

Metallophilic interactions are described for Pd(II) structures with the Pd atoms within 2.78 Å to 3.26 Å. Pd  $\cdots$  Pd metallophilic interactions, like those of Pt(II), are particularly favorable and common due to the strong ligand-field stabilization energy for



Scheme 36



Scheme 37

square-planar coordination with a  $4d^8$  electron configuration. The Pd(II) structures in this section, like those for Pt above, are separated into those that exhibit intermolecular Pd $\cdots$ Pd interactions followed by those that exhibit intramolecular Pd $\cdots$ Pd interactions. Many of the structural motifs are seen with both metals, and numerous studies compare metallophilicity in Pt compounds to that in Pd compounds.

### 1.15.3.5.1 Intermolecular Pd $\cdots$ Pd metallophilic interactions

#### 1.15.3.5.1.1 Four-coordinate Pd(II)

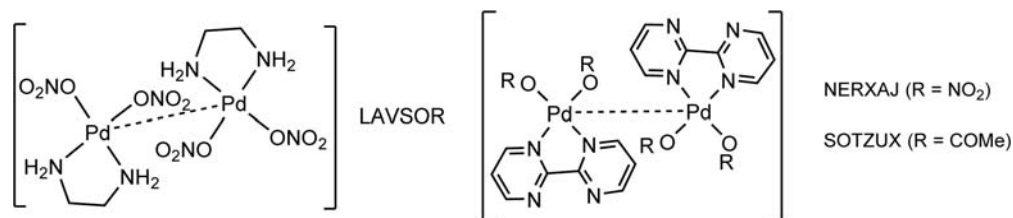
The majority of Pd(II) structures with intermolecular metallophilic interactions have [PdN<sub>2</sub>O<sub>2</sub>] coordination. The N atoms are typically part of a chelating ligand, and the O atoms are on two identical X-type ligands. One example of this type of structure is one polymorph<sup>148</sup> of [(en)Pd(ONO<sub>2</sub>)<sub>2</sub>] (en = ethylenediamine) (**LAVSOR01**), with intramolecular Pd $\cdots$ Pd distances of 3.148 Å. This compound also has hydrogen bonding connecting the monomers via the amine and nitrate ligands. Within dimers of [(bpym)Pd(NO<sub>3</sub>)<sub>2</sub>] (bpym = 2,2'-bipyrimidine) (**NERXAJ**),<sup>149</sup> the intramolecular Pd $\cdots$ Pd distance is 3.190 Å which is very similar to the acetate derivative [(bpym)Pd(OCOMe)<sub>2</sub>] (**SOTZUX**),<sup>150</sup> intramolecular Pd $\cdots$ Pd distances are measured as 3.220. In none of these three cases are there any intermolecular metallophilic interactions (**Scheme 38**).

Another common four-coordinate [PdL<sub>2</sub>X<sub>2</sub>] structure has two coordinated halogen atoms (X) and two coordinated chalcogen donor ligands (L). Most of these have two chlorides and two three-coordinate tellurium from the ether in [PdCl<sub>2</sub>(TeR<sub>2</sub>)<sub>2</sub>]. Both *cis* and *trans* geometries have been prepared in [*cis*-PdCl<sub>2</sub>(Te(pmp)(EtOH))<sub>2</sub>] (pmp = p-methoxyphenyl) (**NOSSIA**)<sup>151</sup> with intramolecular Pd $\cdots$ Pd distances of 3.171 Å, and [*trans*-PdCl<sub>2</sub>(Te(pmp)(2-(2-C<sub>3</sub>H<sub>4</sub>S)Et))<sub>2</sub>] (**PAFQOD**)<sup>152</sup> having intramolecular Pd $\cdots$ Pd distances of 3.214 Å (**Scheme 39**).

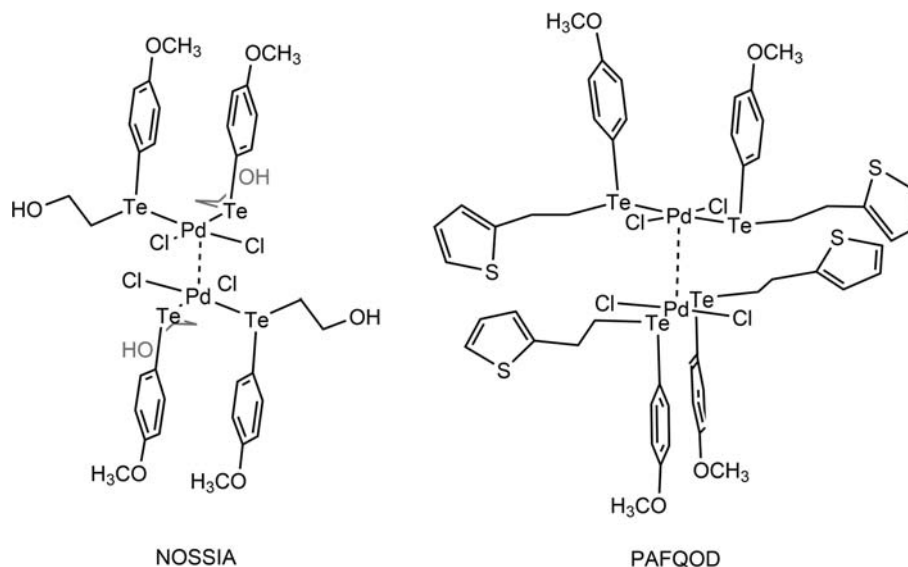
### 1.15.3.5.2 Intramolecular Pd $\cdots$ Pd metallophilic interactions

#### 1.15.3.5.2.1 One-atom bridged Pd(II)

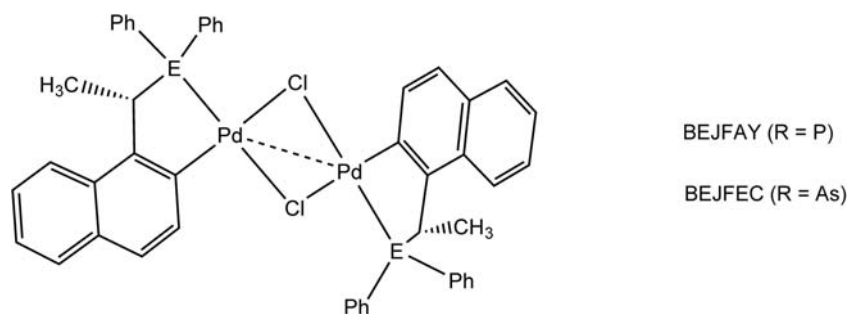
Most dimeric Pd(II) complexes that exhibit intramolecular Pd $\cdots$ Pd metallophilic interactions have two halides bridging the metal atoms, taking up two coordination sites on each Pd. Most common of these are Cl<sup>-</sup> > Br<sup>-</sup> > F<sup>-</sup> > I<sup>-</sup>. Another common feature to these one-atom bridged Pd(II) complexes is an LX chelating ligand in which the L donor is a tertiary phosphine or arsine and the X donor is C from an ortho-metalated phosphine/arsine substituent. For the structure [Pd<sub>2</sub>(μ-Cl)<sub>2</sub>(EPh<sub>2</sub>CHMe(2-naphthyl))<sub>2</sub>], when E = P (**BEJFAY**),<sup>153</sup> Pd $\cdots$ Pd distance is 2.985 Å; when E = As (**BEJFEC**)<sup>153</sup> Pd $\cdots$ Pd distance is 2.990 Å (**Scheme 40**).



**Scheme 38**



**Scheme 39**

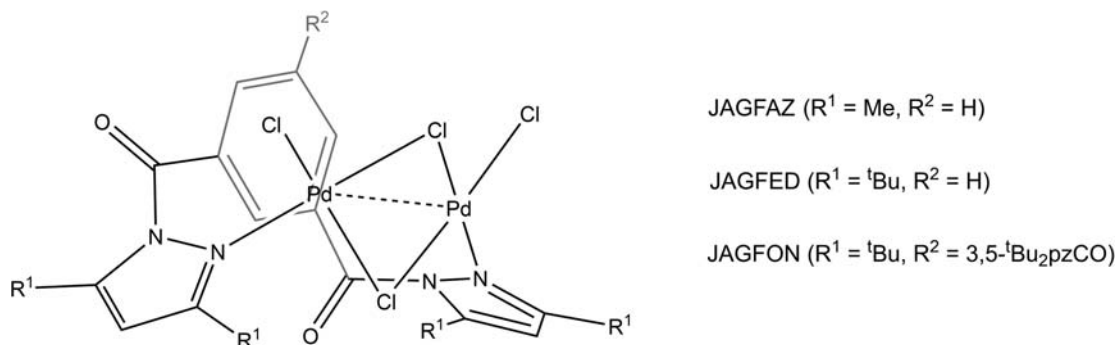


Scheme 40

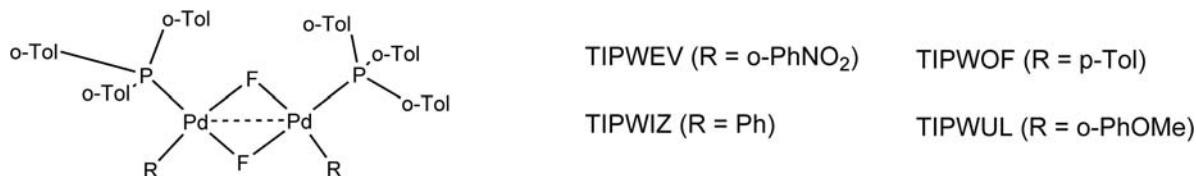
Comparison of another set of Pd(II) complexes with Pd···Pd distances based on changes with two different locations of organic substituents on the same chelating ligand to a Pd<sub>2</sub>Cl<sub>2</sub> core shows the wide range of ligands employed. In a pair of [Pd<sub>2</sub>(μ-Cl)<sub>2</sub>Cl<sub>2</sub>(3,5-R<sub>2</sub>pzCO)<sub>2</sub>-1,5-C<sub>6</sub>H<sub>4</sub>] complexes, the [PdCl(m<sub>2</sub>-Cl)<sub>2</sub>PdCl] core is bridged by a ligand with two terminal pyrazole donors connected by a phenylene group and when R = Me (JAGFED)<sup>154</sup> the Pd···Pd distance is 3.200 Å but when R = <sup>t</sup>Bu (JAGFON)<sup>154</sup> Pd···Pd distance is 3.257 Å. Interestingly, in [Pd<sub>2</sub>(μ-Cl)<sub>2</sub>Cl<sub>2</sub>(3,5-<sup>t</sup>Bu<sub>2</sub>pzCO)<sub>3</sub>-1,3,5-C<sub>6</sub>H<sub>3</sub>] (JAGFAZ),<sup>154</sup> a third pyrazole group is added to the phenyl ring, resulting in an intermediate Pd···Pd distance of 3.212 Å (Scheme 41).

The second most common bridging halide of dimeric Pd(II) complexes is F. For the structure *cis*-[Pd<sub>2</sub>(μ-F)<sub>2</sub>(P(o-Tol)<sub>3</sub>)<sub>2</sub>R<sub>2</sub>], Pd···Pd distances vary only within 0.013 Å, suggesting that the two μ-F atoms are strongly determining the metallophilic interaction. Pd···Pd distances are measured as: 3.234 Å when R = *o*-PhNO<sub>2</sub> (TIPWEV),<sup>155</sup> 3.229 Å when R = Ph (TIPWIZ),<sup>155</sup> 3.230 Å when R = *p*-Tol (TIPWOF),<sup>155</sup> 3.242 Å when R = *o*-PhMe (TIPWUL)<sup>155</sup> (Scheme 42).

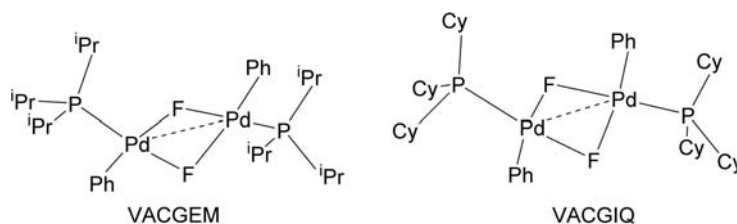
In related [Pd<sub>2</sub>(μ-F)<sub>2</sub>Ph<sub>2</sub>(PR<sub>3</sub>)<sub>2</sub>] structures with alkyl, rather than aryl, phosphines greater variation is seen. When R = <sup>i</sup>Pr (VACGEM),<sup>156</sup> the Pd···Pd distance is 3.260 Å; when R = *cy*-hexyl (VACGIQ)<sup>156</sup> the Pd···Pd distance is 3.179 Å. The structure with the <sup>i</sup>Pr substituents has a planar [Pd<sub>2</sub>F<sub>2</sub>] rhomb, whereas the structure with the cyclohexyl (*cy*) substituents has a slightly bowed, butterfly-like [Pd<sub>2</sub>F<sub>2</sub>] core (Scheme 43).



Scheme 41



Scheme 42



Scheme 43

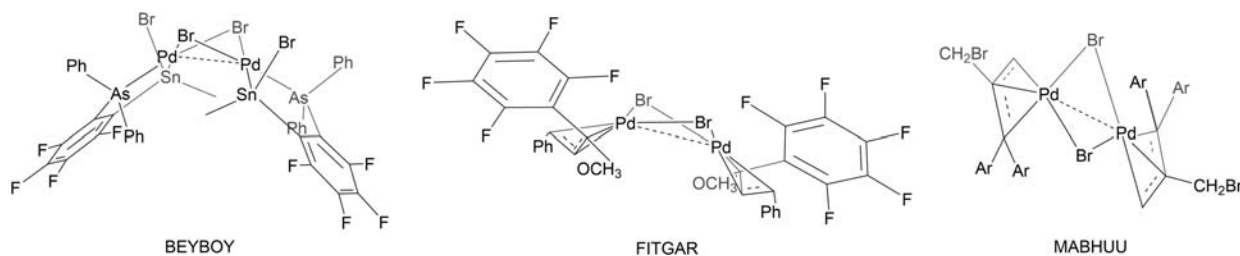
Dimeric Pd(II) complexes with bridging Br atoms and chelating ligands have butterfly-like  $[\text{Pd}_2(\mu_2\text{-Br})_2]$  cores with varying Pd···Pd distances. In  $[\text{Pd}_2(\mu\text{-Br})_2(\text{Me}(\text{BrSn})\text{C}_6\text{F}_4\text{AsPh}_2)_2]$  (**BEYBOY**),<sup>157</sup> the Sn and As atoms help form six-membered chelate rings and there is a relatively short Pd···Pd distance of 2.950 Å. The Pd(II) complex with pentafluorophenylvinyl methyl ether ligands  $[\text{Pd}_2(\mu\text{-Br})_2(\eta^3\text{-PhC}(\text{C}_6\text{F}_5)(\text{OMe}))_2]$  (**FITGAR**)<sup>158</sup> has a Pd···Pd distance of 3.061 Å. The dimeric allylpalladium(II) structure  $[\text{Pd}_2(\mu\text{-Br})_2\text{bis}(\eta^3\text{-3,3-bis(4-chlorophenyl)-2-bromomethylallyl})_2]$  (**MABHUU**)<sup>159</sup> has a Pd···Pd distance of 3.048 Å (**Scheme 44**).

Iodide bridged structures are the fewest, and these dimeric Pd(II) complexes also have varying Pd···Pd distances. Similar to those with Br, butterfly cores are observed. The structure  $[\text{Pd}_2(\mu\text{-I})_2(2\text{-}(4\text{'-}t\text{-butyloxazolin-2\text{'-yl)-3-trimethylsilylferrocen-1-yl-N})_2]$  (**BAZQUO**)<sup>160</sup> has a Pd···Pd distance of 3.232 Å. The structure  $[\text{Pd}_2(\mu\text{-I})_2\text{I}_2(\text{Me}_2\text{PCH}_2\text{PMe}_2)_2]$  (**OHOTEK**),<sup>161</sup> which was specifically synthesized to have sterically nondemanding diphosphine ligands, has a short Pd···Pd distance of 2.884 Å. Conversely, sterically demanding N-heterocyclic carbenes coordinate to the metal atoms of  $[\text{Pd}_2(\mu\text{-I})_2\text{I}_2(\text{SIBiphen})_2]$  (**SIBiphen** = *N,N'*-bis(2-biphenyl)imidazolidine) (**VEVGAF**),<sup>162</sup> which has a Pd···Pd distance of 3.223 Å (**Scheme 45**).

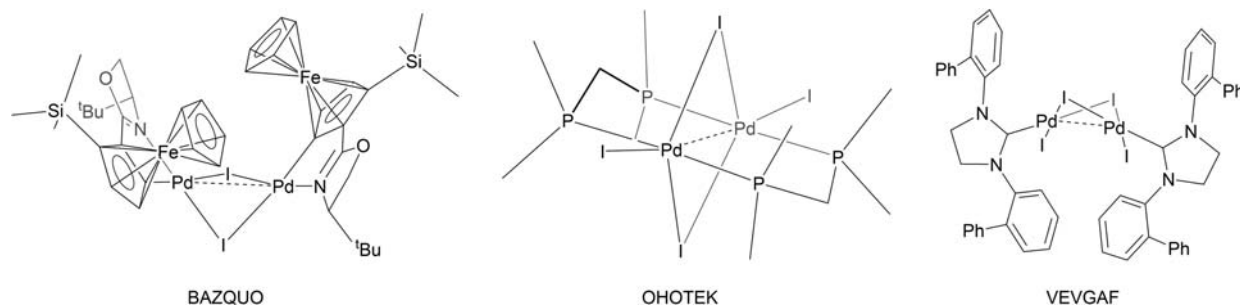
After bridging halides, thiolate-bridged complexes are the second-most prevalent one-atom separation between Pd(II) structures that exhibit intramolecular metallophilic interactions. A common structure in this category is the form  $[\text{Pd}_2(\mu\text{-SR})_2(\eta^3\text{-C}_4\text{H}_7)_2]$ , where R can be a variety of substituents. In the trio below the Pd···Pd distances are 3.205 Å when R = *p*-Tol (**EYUXUR**),<sup>163</sup> 3.131 Å when R = <sup>t</sup>Bu (**EYUYAY**),<sup>163</sup> and 3.222 Å when R = *p*-C<sub>6</sub>H<sub>4</sub>F (**UDINUQ**)<sup>164</sup> (**Scheme 46**).

Hydroxo bridges are the most common of oxygen-bridged dinuclear Pd(II) structures, and many have bidentate imine ligands, L<sub>2</sub>, requiring non-coordinating anions for charge balance. Triflate salts with the stoichiometry  $[\text{Pd}_2(\mu\text{-OH})_2\text{L}_2](\text{CF}_3\text{SO}_3)_2$ , are shown here. The Pd···Pd distance is 3.083 Å when L<sub>2</sub> = 2,2'-bipyridine (**DEGKUW**),<sup>165</sup> 2.982 Å when L<sub>2</sub> = neocuproine (**JIWWAO**),<sup>166</sup> and 3.000 Å when L<sub>2</sub> = 1,10-phenanthroline (**WIVNIZ**)<sup>165</sup> (**Scheme 47**).

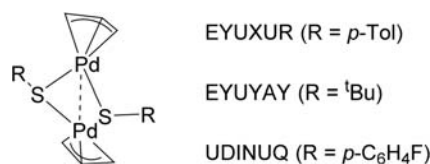
Another major category of one-atom bridges in dinuclear Pd(II) structures with diamine ligands is those with amido ligands,  $\mu_2\text{-NHR}$ . For the salt  $[\text{Pd}_2(\mu\text{-NHR})_2(\text{}^t\text{Bu}_2\text{bpy})_2](\text{BF}_4)_2$ , when R = Ph (**KIYKIN**),<sup>167</sup> the Pd···Pd distance is 3.110 Å and with R = *p*-tol (**KIYKOT**),<sup>167</sup> the Pd···Pd distance is 3.101 Å. With two monodentate terminal ligands  $[\text{Pd}_2(\mu\text{-2,6-}^i\text{Pr}_2\text{C}_6\text{H}_3\text{NH})_2\text{Cl}_2\text{py}_2]$  (**NIQXIU**),<sup>168</sup> the Pd···Pd distance is 3.118 Å. Two very similar structures are  $[\text{Pd}_2(\mu\text{-NHPh})_2(\text{PMe}_3)_2\text{L}_2]$ , when L = Ph (**POMMIN**),<sup>169</sup> with a Pd···Pd distance is 3.181 Å and with the same amide as terminal and bridging ligands, L = C<sub>6</sub>H<sub>4</sub>C(H)=NPh (**POMMOT**),<sup>169</sup> the Pd···Pd distance is 3.141 Å (**Scheme 48**).



Scheme 44

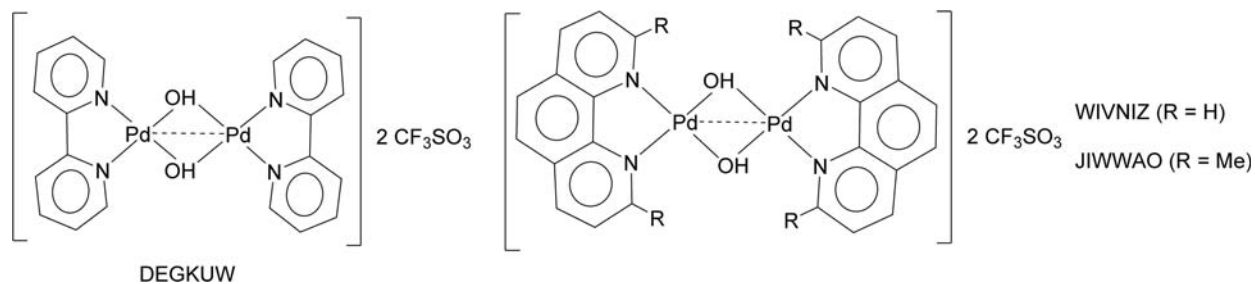


Scheme 45

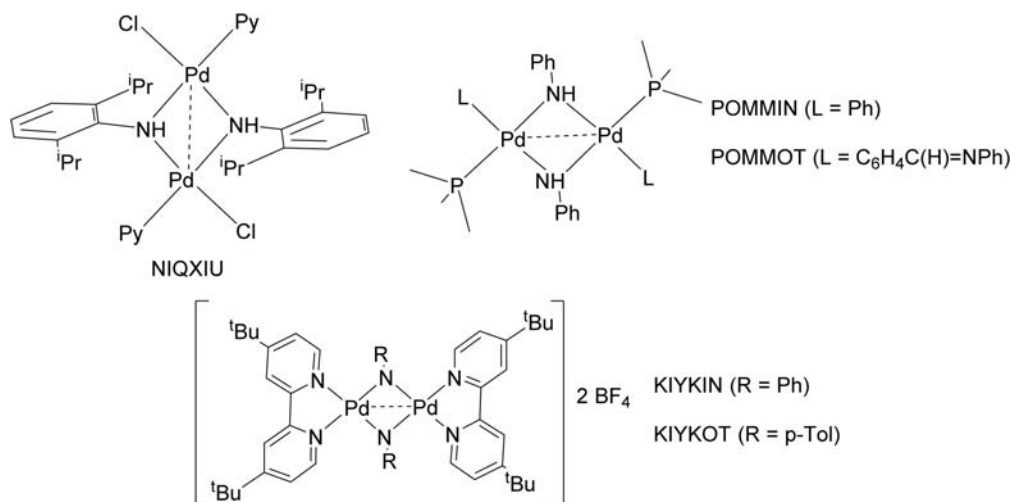


Scheme 46





Scheme 47

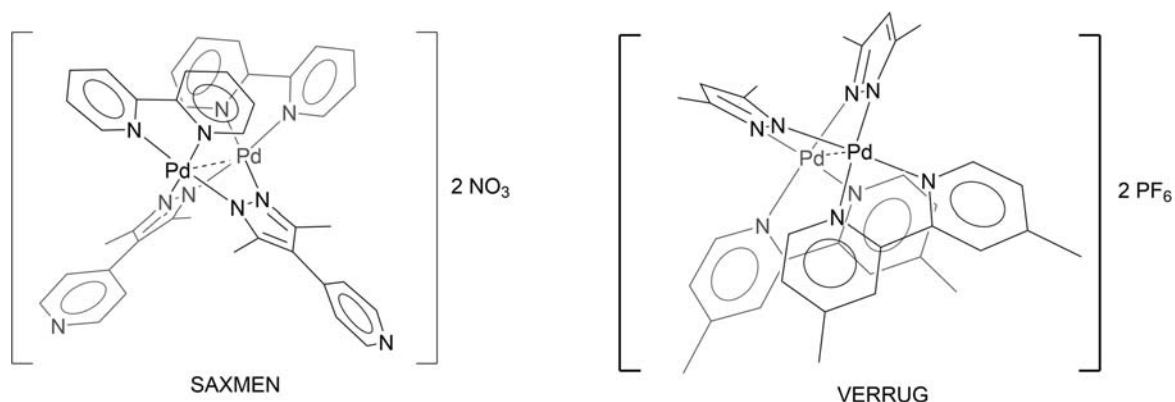


Scheme 48

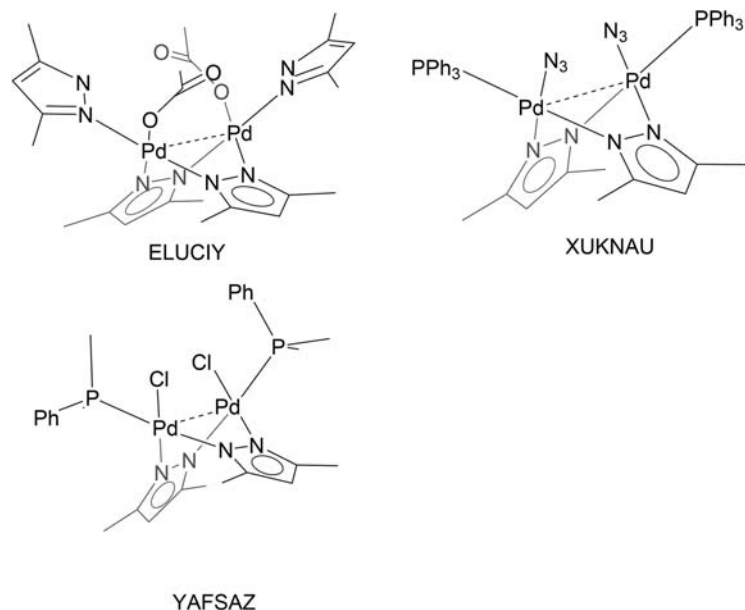
### 1.15.3.5.2.2 Two-atom bridged Pd(II)

Most dinuclear Pd(II) structures with two-atom bridges have identical coordination environments around both metal centers. The bridging ligands that connect the two Pd(II) and promote intramolecular Pd···Pd metallophilic interactions are typically coordinated to the metals by nitrogen atoms, most commonly pyrazolate (pz) derivatives. When Pd is coordinated to bpy derivatives, substituents on both ligands can intramolecular Pd···Pd distances. For [Pd<sub>2</sub>(bpy)(μ<sub>2</sub>-pz)<sub>2</sub>](NO<sub>3</sub>)<sub>2</sub> (pz = 4-(3,5-dimethyl-1*H*-pyrazol-4-yl)pyridine) (SAXMEN), the Pd···Pd distance is 3.082 Å and for [Pd<sub>2</sub>(Me<sub>2</sub>bpy)<sub>2</sub>(μ-Me<sub>2</sub>pz)<sub>2</sub>](PF<sub>6</sub>)<sub>2</sub> (Me<sub>2</sub>bpy = 4,4'-dimethyl-2,2'-bipyridine) (VERRUG),<sup>170</sup> the analogous distance is 3.149 Å (Scheme 49).

Other compounds have two Me<sub>2</sub>pz bridging Pd(II) and two monodentate terminal ligands per metal, in the form [L<sup>1</sup>L<sup>2</sup>Pd(μ-Me<sub>2</sub>pz)<sub>2</sub>PdL<sup>1</sup>L<sup>2</sup>]. For [Pd<sub>2</sub>(μ-Me<sub>2</sub>pz)<sub>2</sub>(k<sup>1</sup>-OCOME)<sub>2</sub>(Me<sub>2</sub>pz)<sub>2</sub>] (ELUCIY),<sup>171</sup> the Pd···Pd distance is 3.225 Å, for [Pd<sub>2</sub>(μ-Me<sub>2</sub>pz)<sub>2</sub>(N<sub>3</sub>)<sub>2</sub>(PPh<sub>3</sub>)<sub>2</sub>] (XUKNAU)<sup>172</sup> 3.255 Å; and 3.115 Å in [Pd<sub>2</sub>(μ-Me<sub>2</sub>pz)<sub>2</sub>Cl<sub>2</sub>(PMe<sub>2</sub>Ph)<sub>2</sub>] (YAFSAZ).<sup>173</sup> (Scheme 50)



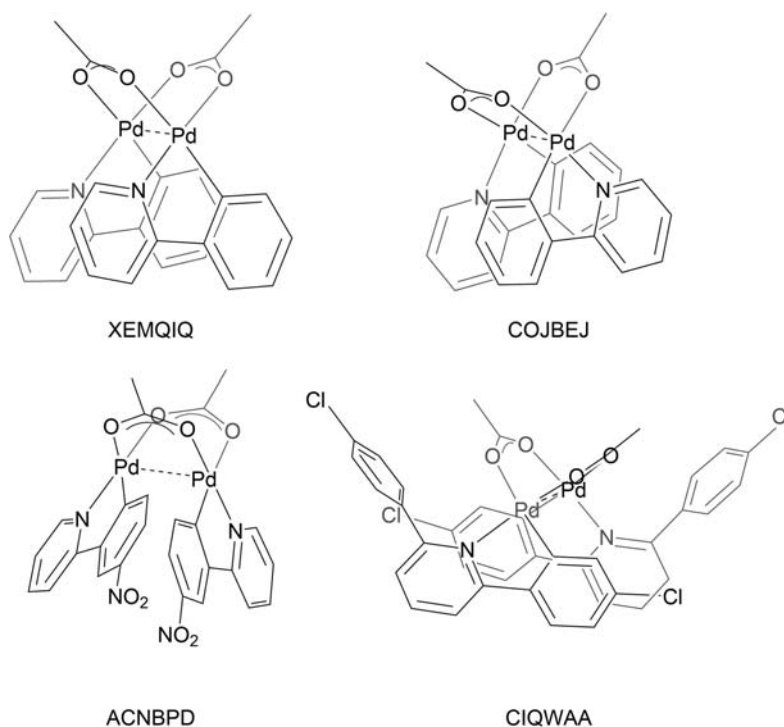
Scheme 49



Scheme 50

## 1.15.3.5.2.3 Three-atom bridged Pd(II)

The majority of three-atom-bridged Pd(II) complexes are half-lantern complexes with two  $\mu_2$ - $\kappa^2$  carboxylate ligands. The metallophilic distances in these structures are generally shorter than those described above. The other ligands are often two aryl-substituted pyridines. With this combination, the two Pd are in parallel or nearly-parallel distorted square-planar environments. The simplest of these structures is  $[\text{Pd}_2(\mu_2\text{-OAc})_2(\text{phpy})_2]$  (phpy = 2-phenylpyridine, NC donor) (**XEMQIQ01**), with a Pd···Pd distance of 2.872 Å, with the phpy ligands coordinated *cis* to one another. When crystallized with  $[\text{Hg}(\text{C}_6\text{F}_5)_2]$  (not shown) (**COJBEJ**), the phpy ligands are *trans* with respect to one another and the intramolecular Pd···Pd distance decreases to 2.839 Å. Interestingly, the intermolecular 3.106 Å distance between Pd(II) and Hg(II) of  $[\text{Pd}_2(\mu\text{-OAc})_2\text{bis}(\text{phpy})_2][\text{Hg}(\text{C}_6\text{F}_5)_2]$ , is less than the sum of the van der Waals radii of the two elements (3.4–3.7 Å), suggesting a Pd(II) → Hg(II) heterometallic metallophilic interaction. Additional substitution on the phpy ligands minimally affects the Pd···Pd metallophilic interactions, but does give rise to precise two-fold symmetry in  $[\text{Pd}_2(\mu\text{-OAc})_2(4\text{-NO}_2\text{-2-phpy})_2]$  (**ACNBPD01**)<sup>174</sup> (Pd···Pd is 2.823 Å) but is lost in  $[\text{Pd}_2(\mu\text{-OAc})_2(5\text{-Cl-2-(6-(4-ClPh)-2-phpy))}_2)]$  (**CIQWAA**),<sup>174</sup> with a Pd···Pd distance of 2.905 Å (**Scheme 51**).



Scheme 51

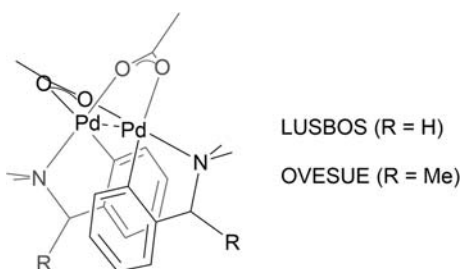
Other common ligands coordinated to doubly OAc-bridged Pd(II) dimers are chelating benzylamines. These structures have a more twisted "clamshell" conformation, and slightly longer Pd···Pd distances. For  $[\text{Pd}_2(\mu\text{-OAc})_2(\text{o-C}_6\text{H}_4\text{CHRNMMe}_2)_2]$ , when R = H (**LUSBOS**),<sup>175</sup> the Pd···Pd distance is 2.928 Å and when R = Me (**OVESUE**)<sup>176</sup> it is 2.966 Å (**Scheme 52**).

Intramolecular Pd···Pd metallophilic interactions are enforced by trifluoroacetate (TFA) groups that make similar palladacycles to those above, and with also with phenyl pyridine or benzyl amine ligands. The Pd···Pd distance below are 2.870 Å for  $[\text{Pd}_2(\mu\text{-TFA})_2\text{bis}(\text{bhq})_2]$  (bhq = benzo[*h*]quinolone) (**EBOGUA**),<sup>177</sup> 3.001 Å for  $[\text{Pd}_2(\mu\text{-TFA})_2\text{bis}(\text{o-C}_6\text{H}_4\text{CH=NPh})_2]$  (**ILEQAR**),<sup>178</sup> and 2.859 Å for  $[\text{Pd}_2(\mu\text{-TFA})_2\text{bis}(2\text{-p-tolylpyridine})_2]$  (**MAHPOC**)<sup>179</sup> (**Scheme 53**).

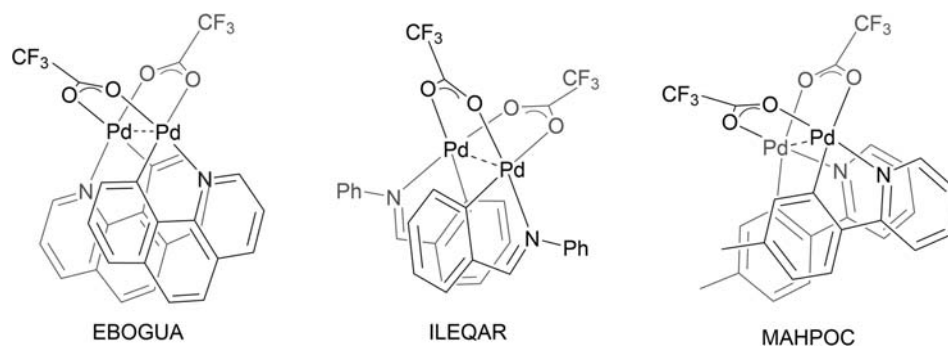
In the absence of additional ligands, four-coordinate Pd(II) and bridging OAc ligands result in the trinuclear, homoleptic  $[\text{Pd}_3(\mu\text{-OAc})_6]$  complexes. These aggregates exhibit relatively longer intramolecular Pd···Pd metallophilic interactions than binuclear  $[\text{Pd}_2(\mu\text{-OAc})_2]$ . Depending on what solvent (or a co-crystallized complex) is also within the unit cell, Pd···Pd distances vary: 3.312 Å with H<sub>2</sub>O (**AHINEM**) and 3.075 Å with  $[\text{PdCu}(\mu\text{-OAc})_4 \cdot \text{H}_2\text{O}]$  (**LAFKEK**).<sup>180</sup> Trinuclear  $[\text{Pd}_3(\mu\text{-O}_2\text{CR})_6]$  species with other carboxylates are also known structures. Depending on the R substituent, Pd···Pd distances vary: 3.191 Å for R = Et (**GEWZEN**),<sup>181</sup> 3.137 Å for R = Mes (**GEWZOX**),<sup>181</sup> 3.156 Å for Me<sup>t</sup>Bu (**VUSMII**)<sup>182</sup> (**Scheme 54**).

When acetate is replaced by pivalate as the bridging ligand in binuclear Pd(II) complexes, small structural changes are observed. With acetate in  $[\text{Pd}_2(\mu_2\text{-O}_2\text{CMe})_2\text{Ph}_2(\text{PPh}_3)_2]$  (**GECBAR**), the Pd···Pd distance is 3.079 Å; but with pivalate in  $[\text{Pd}_2(\mu_2\text{-O}_2\text{C}^t\text{Bu})_2\text{Ph}_2(\text{PPh}_3)_2]$  (**CEPVOK**), it is 3.120 Å. Furthermore, in the former, the phenyl and Ph<sub>3</sub>P ligands on each metal atom are *cis* to one another, but are *trans* in the pivalate derivative (**Scheme 55**).

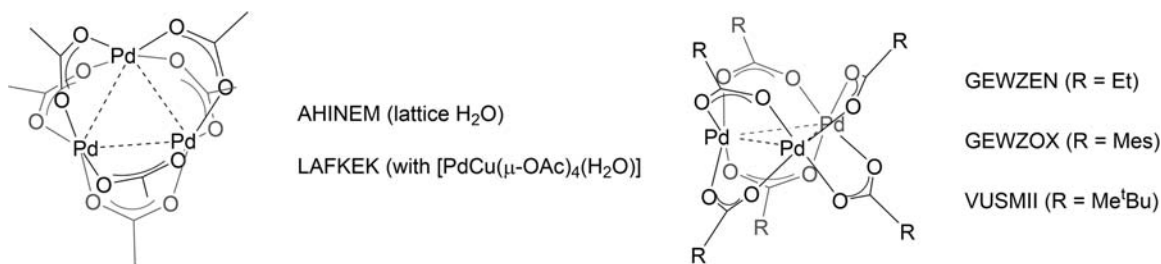
Other triatomic LX bridging ligands support Pd···Pd metallophilic interactions. In numerous complexes, Pd atoms are held together by bridging pyridyl chalcogenolate groups as in  $[\text{Pd}_2(\mu\text{-pyE})_2(\text{mesSeC}_6\text{H}_2\text{Me}_2\text{CH}_2)_2]$  (E = S or Se; mes = mesityl). When E = S (**HIGVEA**),<sup>183</sup> Pd···Pd distance is 2.929 Å; when E = Se, (**HIGVIE**)<sup>183</sup> Pd···Pd distance is 3.143 Å (**Scheme 56**).



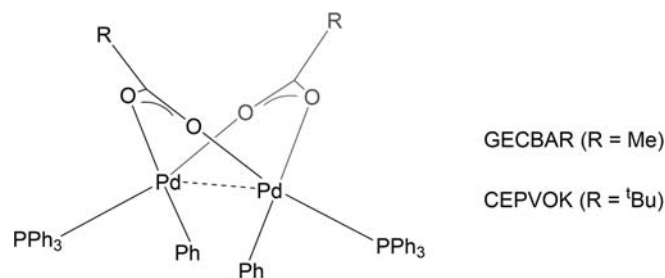
Scheme 52



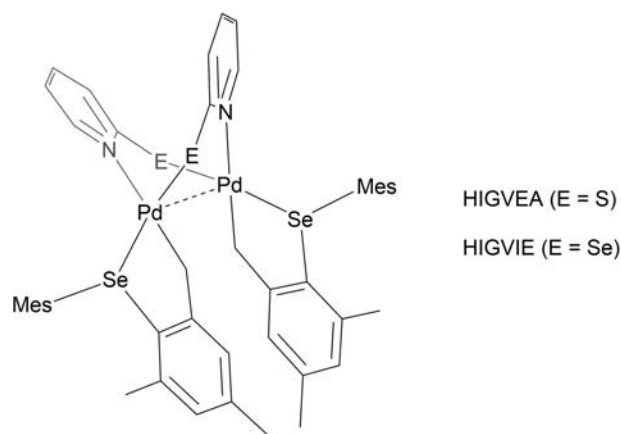
Scheme 53



Scheme 54



Scheme 55



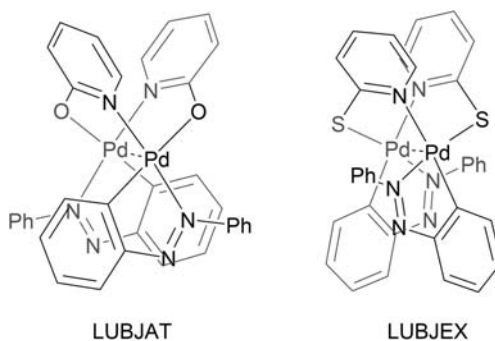
Scheme 56

In another pair of related dimeric Pd(II) complexes, changing S to O gives a relatively negligible difference in intramolecular Pd···Pd distances. For  $[\text{Pd}(\mu\text{-}2\text{-pyO})(2\text{-}(\text{phenylazo})\text{benzene})]_2$  (pyO = deprotonated hydroxypyridine) (**LUBJAT**),<sup>184</sup> the separation is 2.840 Å while in  $[\text{Pd}(\mu\text{-}2\text{-pyS})(2\text{-}(\text{phenylazo})\text{benzene})]_2$  (pyS = deprotonated mercaptopyridine) (**LUBJEX**),<sup>184</sup> that distance is 2.878 Å (**Scheme 57**).

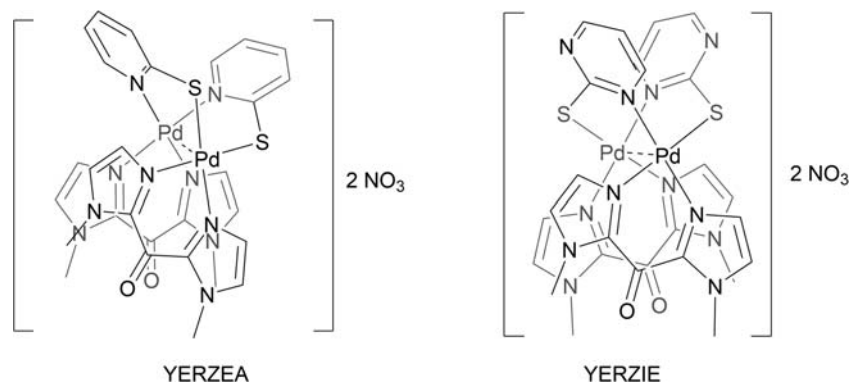
In contrast to the above, a pyridine-pyrimidine swap and subsequent conformation change have a more appreciable effect on Pd···Pd distance. A chelating bis(1-methylimidazol-2-yl)ketone (bmik) ligand is coordinated to each Pd(II) in the  $[\text{Pd}_2(\mu_2\text{-LX})_2(\text{bmik})_2]^{2+}$  anion. For  $[\text{Pd}_2(\text{bis}(\mu_2\text{-LX})_2(\text{bmik})_2)](\text{NO}_3)_2 \cdot 5 \text{H}_2\text{O}$  (pyt = pyridine-2-thiolato) (**YERZEA**), the Pd···Pd distance is 2.915 Å. For  $[\text{Pd}_2(\mu_2\text{-LX})_2(\text{bmik})_2](\text{NO}_3)_2 \cdot 5 \text{H}_2\text{O}$  (pymt = pyrimidine-2-thiolato) (**YERZIE**), the analogous distance is 2.886 Å. The bridging thiolate ligands show head-to-head orientation for the pyt analog, and head-to-tail orientation for the pymt analog, which may also affect the intramolecular distances (**Scheme 58**).

When the  $\mu_2\text{-LX}$  bridge between two Pd(II) is kept constant as mpy, but the terminal ligands are varied, intramolecular Pd···Pd distances vary slightly. For  $[\text{Pd}_2(\mu_2\text{-pyS})_2(\text{Me}_2\text{NCH}_2\text{C}_6\text{H}_4)_2]$  (**YIJPOY**),<sup>185</sup> the Pd···Pd distance is 2.976 Å; for  $[\text{Pd}_2(\mu_2\text{-pyS})_2(\text{Cl}_2(\text{P-Me}_2\text{Ph})_2)]$  (**YIKGUU**),<sup>186</sup> it is 2.922 Å and in  $[\text{Pd}_2(\mu_2\text{-pyS})_2(\text{Cl}_2(\text{PMePh}_2)_2)]$  (**YIKHAB**),<sup>186</sup> it is 2.983 Å (**Scheme 59**).

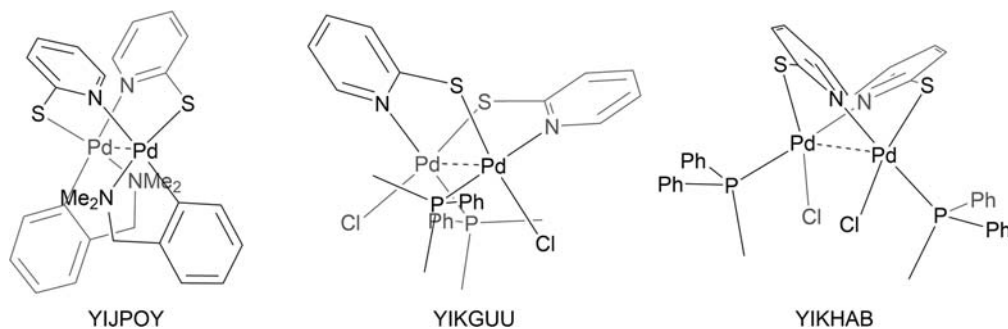
Pd(II) structures that exhibit intramolecular Pd···Pd metallophilic interactions are also commonly bridged by a NCN-connecting ligand, of which both symmetric and asymmetric examples are known. For example  $[\text{Pd}_2(\mu_2\text{-donp})_2(\text{bpy})_2]$



Scheme 57



Scheme 58

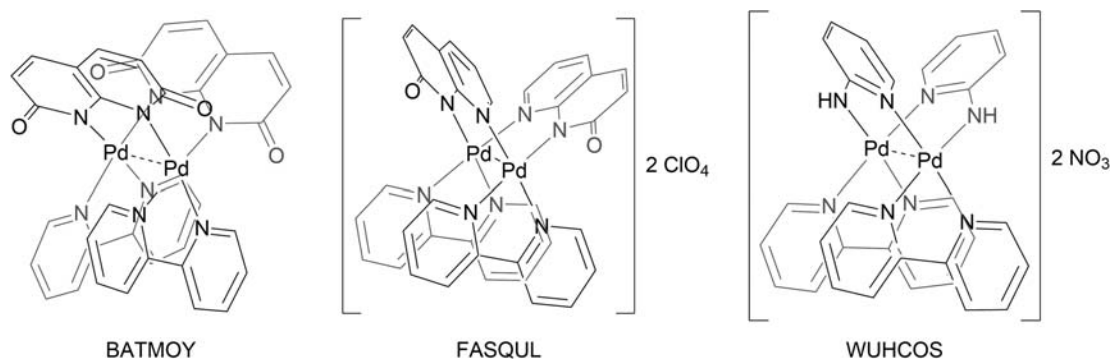


Scheme 59

(donp = 1,8-naphthyridin-2,7-dione) (BATMOY)<sup>187</sup> has a Pd···Pd distance of 2.796 Å, *cis*-[Pd<sub>2</sub>(μ<sub>2</sub>-ono)<sub>2</sub>(bpy)<sub>2</sub>]<sup>2+</sup> (onp = 1,8-naphthyridin-7-dione) (FASQUL)<sup>188</sup> has one of 2.804 Å and [Pd<sub>2</sub>(μ<sub>2</sub>-ampy)<sub>2</sub>(bpy)<sub>2</sub>]<sup>2+</sup> (ampy = 2-aminopyridine) (WUHCOS)<sup>189</sup> has a Pd···Pd distance of 2.870 Å (Scheme 60).

### 1.15.3.6 Au···Au metallophilic interactions

As previously mentioned, metallophilic interactions between closed-shell Au atoms are referred to as *aurophilic interactions*, and search of this terminology results in more references than all of other homometallic combinations, as expected. Of the Group 11 metals, aurophilic span a range of contacts between 2.72 Å and 3.32 Å. The vast majority of structures with intermolecular interactions are between two-coordinate Au(I) atoms. As done in earlier sections, for compounds with intramolecular interactions, structures are organized by the number of atoms bridging the two Au atoms, and coordination numbers at the metal center ranges from two to four. Most bridging units have three linking atoms, followed by four, five or more, then two. The majority of the intramolecular structures have Au(I) atoms, but a few Au(III) structures are also known. The highly favorable reduction potentials of Au(III) to Au(I) account for the decreased number of Au(III) d<sup>8</sup> instances.



Scheme 60



## 1.15.3.6.1 Intermolecular Au···Au metallophilic interactions

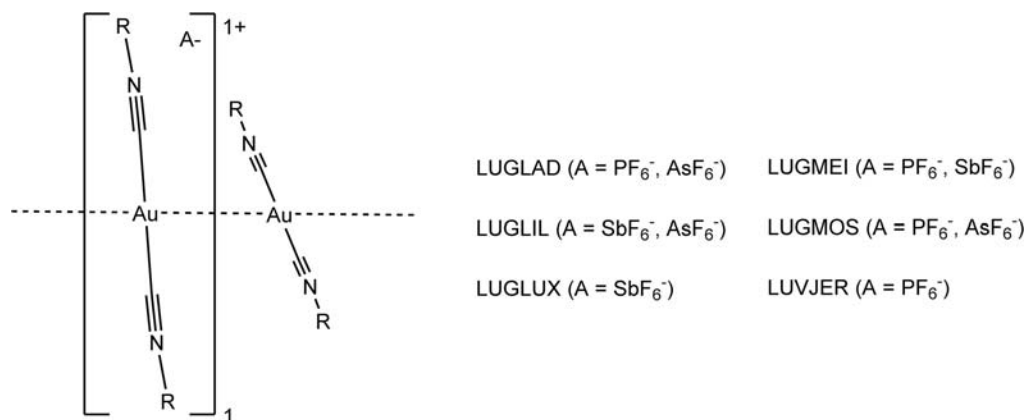
## 1.15.3.6.1.1 Two-coordinate Au(I)

Most Au(I) structures with intermolecular aurophilic interactions have Au atoms coordinated to two ligands, with  $[\text{AuL}_2]^+$ ,  $[\text{AuLX}]$ , and  $[\text{AuX}_2]^-$  motifs. The most common of the  $[\text{AuL}_2]^+$  type is Au coordinated to two isocyanide, CNR, ligands. For the dicationic  $[\text{Au}(\text{CN}(\text{cy-hexyl}))_2]_2$ , the structures crystallize into 1D slightly helical chains, depending on the anion ( $A^1$ ,  $A^2$ ). Intermolecular Au(I)···Au(I) distance varies with ratio combinations of different anions, and in order of increasing distance: 2.964 Å for  $A^1$ ,  $A^2 = 2$  ( $\text{PF}_6^-$ ) (LUVJER),<sup>190</sup> 3.030 Å for  $A^1$  and  $A^2 = 2$  ( $\text{SbF}_6^-$ ) (LUGLUX),<sup>191</sup> 3.186 Å for  $A^1 = 3$  ( $\text{PF}_6^-$ ) and  $A^2 = 1$  ( $\text{AsF}_6^-$ ) (LUGLAD),<sup>191</sup> 3.198 Å for  $A^1$  and  $A^2 = 2$  ( $\text{AsF}_6^-$ ) (MEGFIP),<sup>192</sup> 3.199 Å for  $A^1 = 1$  ( $\text{PF}_6^-$ ) and  $A^2 = 3$  ( $\text{AsF}_6^-$ ) (LUGMOS),<sup>191</sup> 3.207 Å for  $A^1 = 2$  ( $\text{PF}_6^-$ ) and  $A^2 = 2$  ( $\text{SbF}_6^-$ ) (LUGMEI),<sup>191</sup> 3.220 Å for  $A^1 = 2$  ( $\text{AsF}_6^-$ ) and  $A^2 = 2$  ( $\text{SbF}_6^-$ ) (LUGLIL).<sup>191</sup> The ratio of hexafluoro- ion present have been found to affect the luminescence of these structures (Scheme 61).

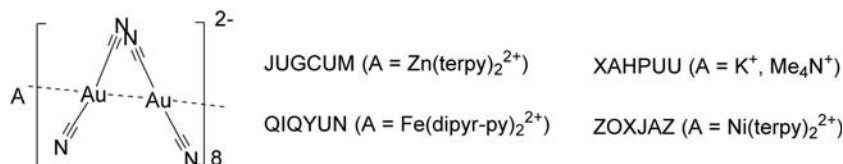
When the cyanide ligand is not bonded to an organic substituent at the N, the dicyanoaurate anion exhibits intermolecular aurophilic interactions in crystal structures with various cations. For the anionic  $[\text{AuX}_2]^-$  of  $(A^1A^2)[\text{Au}(\text{CN})_2]_2$ , Au(I)···Au(I) distances are: 3.149 Å when  $A^1$  and  $A^2 = [\text{Zn}(\text{tpy})_2]^{2+}$  (JUGCUM),<sup>193</sup> 3.216 Å when  $A^1$  and  $A^2 = [\text{Fe}(3\text{-bpp})_2]^{2+}$  (3-bpp = 2,6-di-(1*H*-pyrazol-3-yl)pyridine) (QIQYUN),<sup>194</sup> 3.102 Å when  $A^1$  and  $A^2 = [\text{Ni}(\text{tpy})_2]^{2+}$  (ZOJAZ).<sup>195</sup> Free sites around the metal centers give information of solution- and solid-state chemistry of dicyanoaurate ions (Scheme 62).

Intermolecular aurophilic interactions between  $[\text{Au}(\text{CN})_2]_\infty$  are stronger when the cation contains N–H units due hydrogen bonding between the cations and the cyano groups of the anions. Thus, Au(I)···Au(I) distances are collectively shorter for (A)  $[\text{Au}(\text{CN})_2]_2$  (A = 1° or 2° amine): 3.080 Å for A =  $(\text{C}_4\text{H}_8\text{NH}_2)^+$  (UMIYIY),<sup>196</sup> 3.087 Å for A =  $(\text{Ph}_2\text{N})\text{NH}_3^+$  (UMIYOE),<sup>196</sup> 3.097 Å for A =  $(\text{C}_5\text{H}_{10}\text{NH}_2)^+$  (UMIYUK).<sup>196</sup> This self-association of the  $[\text{Au}(\text{CN})_2]^-$  units are found to affect the luminescence of the crystals; when A =  $(n\text{-C}_3\text{H}_7)_4\text{N}^+$ , no luminescence is observed (Scheme 63).

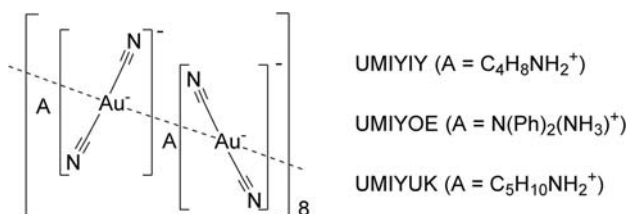
When one CN ligand is replaced with an X-type ligand, the Au atom is typically found coordinated to a phenyl, halogen, or N-donor group, in order by frequency, in an  $[\text{AuLX}]$  classification. For the structure  $[\text{Au}(\text{CNR})(\text{X})]$  (X = phenyl), Au(I)···Au(I) distances are: 3.301 Å for R = *p*-CNPh and X = *p*-Tol (EMEZAZ),<sup>197</sup> 3.243 Å for R = *p*-CF<sub>3</sub>Ph and X = *p*-Tol (EMICAG),<sup>197</sup> 3.136 Å for R and X = *p*-CF<sub>3</sub>Ph (EMICOU),<sup>197</sup> 3.309 Å for R and X = *p*-CNPh (EMIFAJ),<sup>197</sup> 3.161 Å for R and X = Ph (FINVIJ01).<sup>198</sup>



Scheme 61



Scheme 62

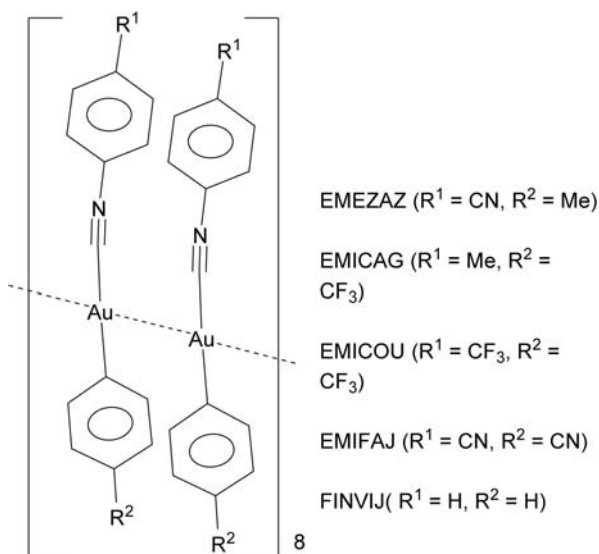


Scheme 63

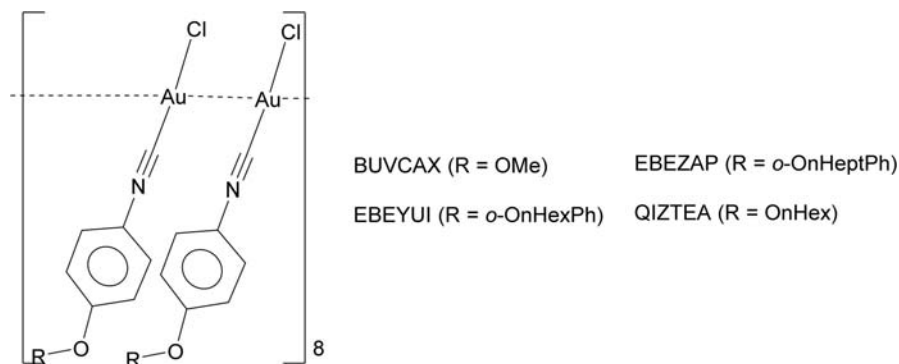
These *para*-substituted phenyl isocyanide structures have been studied for their luminescent mechanochromic properties (Scheme 64).

Steric size and proximity of a ligand coordinated to the metal affect intermolecular aurophilic interactions and can be seen with  $[\text{Au}(\text{CNR})\text{X}]_{\infty}$  where either R or X is kept constant while the other variable is changed. For the structure  $[\text{Au}(\text{CN}(\textit{p}\text{-ROPh}))\text{Cl}]$  (R = alkyl chain), Au(I)···Au(I) distances are: 3.317 Å for R = Me (BUVCAX),<sup>199</sup> 3.309 Å for R = Hp (QIZTEA).<sup>200</sup> Due to the linearity and far proximity to the Au of the extra C<sub>6</sub> hydrocarbon chain of QIXTEA, the Au(I)···Au(I) is hardly affected. For the structure type  $[\text{Au}(\text{CNBH}_2\text{NMe}_3)\text{X}]$  (X = halogen), Au(I)···Au(I) distances are: 3.191 Å for X = Cl (FIGKAI),<sup>201</sup> 3.221 Å for X = Br (FIGKEM).<sup>201</sup> Although only slightly, the larger halogen of FIGKEM imposes a weaker intermolecular Au(I)···Au(I) distance (Schemes 65 and 66).

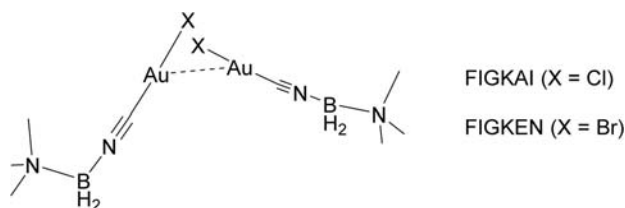
A third type of common neutral Au(I) structures that exhibit intermolecular aurophilic interactions have the structure  $[\text{AuL}(\text{CN})]$  where L = N-donor ligand. For these structures, the intermolecular Au(I)···Au(I) distances at the linear  $[\text{Au}(\text{CN})]$  motif is affected by the angle that the N-donor ligand imposes. This angle is smaller when L = C<sub>4</sub>H<sub>8</sub>NH (FIMSIF) compared to L = C<sub>5</sub>H<sub>10</sub>NH



Scheme 64



Scheme 65

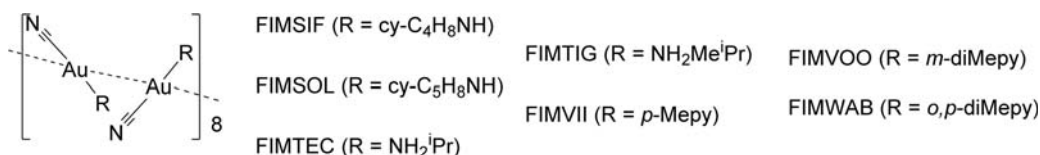


Scheme 66

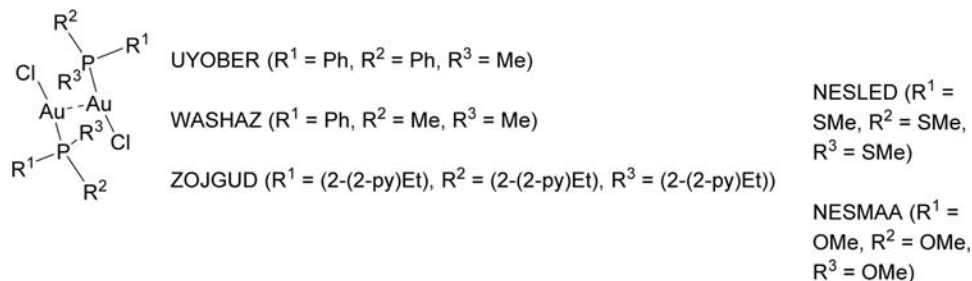
(FIMSOL), and Au(I)···Au(I) distances vary depending on the location of the proximal structure. The various distances of the linear [Au(CN)] of FIMSIF are 3.115 Å, 3.162 Å, and 3.172 Å, and the various distances of the linear [Au(CN)] of FIMSOL are 3.104 Å and 3.280 Å. N-donor ligands with linear alkyl chains of [AuL(CN)] have Au(I)···Au(I) distances: 3.317 Å for L = <sup>i</sup>PrNH<sub>2</sub> (FIMTEC), 3.060 Å for L = <sup>i</sup>PrCH<sub>2</sub>NH<sub>2</sub> (FIMTIG).<sup>202</sup> Arene substitution also plays a part, as *para*-, *ortho*-, and *meta*-locations affect the crystal packing. This can be observed with [Au(Rpy)(CN)] where R = Me. The most linear and flat variation of this structure is [Au(*p*-Mepy)(CN)] (FIMVII), which has a Au(I)···Au(I) distance of 3.161 Å. When a methyl group is added to the *ortho* position, the distance lengthens to 3.203 Å, for [Au(*o,p*-Me<sub>2</sub>py)(CN)] (FIMWAB).<sup>202</sup> For [Au(*m*-Me<sub>2</sub>py)(CN)] (FIMVOO01), Au(I)···Au(I) distance is 3.317 Å (Scheme 67).

The second most-common two-coordinate Au(I) structure is coordinated to a halogen and either a Group 5 or Group 6 donor ligand, with an [AuLX] classification. Phosphines are the most common of the L-type ligand, and substituents on the P affect the intermolecular aurophilic interaction. For the neutral structure [Au(PR<sup>1</sup>R<sup>2</sup>R<sup>3</sup>)Cl], Au(I)···Au(I) distances are: 3.080 Å for R<sup>1</sup>, R<sup>2</sup> = Ph and R<sup>3</sup> = Me (UYOBER)<sup>203</sup>; 3.262 Å for R<sup>1</sup> = Ph and R<sup>2</sup>, R<sup>3</sup> = Me (WASHAZ)<sup>204</sup>; 3.125 Å for R<sup>1</sup>, R<sup>2</sup>, R<sup>3</sup> = CH<sub>2</sub>CH<sub>2</sub>(2-py) (ZOJGUD)<sup>205</sup>; 3.164 Å for R<sup>1</sup>, R<sup>2</sup>, R<sup>3</sup> = OMe (NESMAA)<sup>206</sup>; 3.294 Å for R<sup>1</sup>, R<sup>2</sup>, R<sup>3</sup> = SMe (NESLED).<sup>206</sup> For the neutral structure [Au(PHMePh)X], Au(I)···Au(I) distances are: 3.240 Å when X = Cl (REXZAV),<sup>207</sup> 3.294 Å for X = Br (REXZEZ)<sup>207</sup> (Schemes 68 and 69).

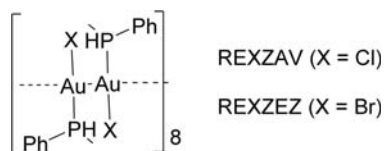
Variation of the halogen, and its effects on intermolecular aurophilic interaction can be observed with two neutral [Au(LR<sub>2</sub>)X]-type structures with L as a S-donor group. For [Au(SMe<sub>2</sub>)X], Au(I)···Au(I) distances are: 3.299 Å for X = Cl (CIBMAB),<sup>208</sup> 3.291 Å for X = Br (CIBLUU).<sup>208</sup> For [Au(S(CH<sub>2</sub>Ph)<sub>2</sub>)X], Au(I)···Au(I) distances are: 3.226 Å for X = Cl (GOJLAS),<sup>209</sup> 3.222 Å for X = Br (GIGWAU).<sup>210</sup> For both of these sets of structures, the linearity of the [SAuX] deviates in two ways; R groups are *cis* to the lone pair on the S, and repulsion of the R groups on the halogen causes the halogen to bend towards the aurophilic interaction. Thus, the more electronegative Cl is pushed more towards the intermolecular Au(I)···Au(I), lengthening the distance (Scheme 70).



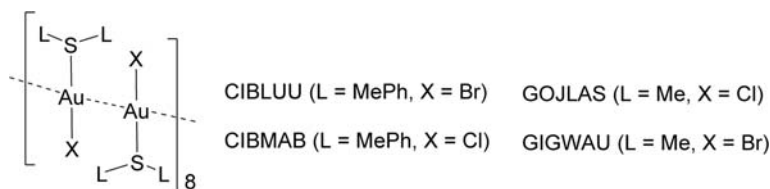
Scheme 67



Scheme 68



Scheme 69



Scheme 70

### 1.15.3.6.2 Intramolecular Au···Au metallophilic interactions

#### 1.15.3.6.2.1 Two-atom bridged Au(I)

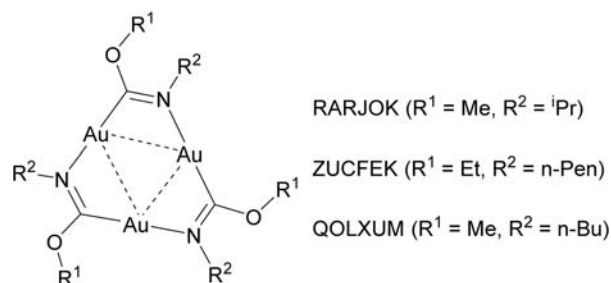
Most structures with intramolecular aurophilic interactions have these interactions between two two-coordinate Au(I) atoms. Most of these two-coordinate Au(I) have neutral [AuLX] classification. The most common structure with these parameters have three Au(I) bridged by three substituted C=N groups. The core of these structures are planar nine-membered rings, and these distances represent an average of the three present aurophilic interactions. For the structure [Au(μ-(MeOC=NR))]₃, Au(I)···Au(I) distances are: 3.295 Å (3.256 Å, 3.310 Å, 3.319 Å) for R = <sup>i</sup>Pr (RARJOK), 3.296 Å (3.292 Å, 3.297 Å, 3.300 Å) for R = <sup>n</sup>Pe (ZUCFEK), 3.301 Å (3.270 Å, 3.316 Å, 3.318 Å) for R = <sup>n</sup>Bu (QOLXUM).<sup>211</sup> Bulkiness of the bridging substituents prevent intermolecular aurophilic interactions, as intermolecular Au(I)···Au(I) distances are typically greater than 6 Å (Scheme 71).

The tetrameric form of these structures commonly form metallacycles of *D*<sub>2d</sub> symmetry. The four Au(I) maintain short intramolecular Au(I)···Au(I) contacts that attribute to the luminescence of solid and solution states of the structures. For [Au(μ-3,5-R<sup>1</sup>R<sup>2</sup>-pyz)]<sub>4</sub>, Au(I)···Au(I) distances are: 3.115 Å when R<sup>1</sup> and R<sup>2</sup> = <sup>t</sup>Bu (OKALIV),<sup>212</sup> 3.204 Å when R<sup>1</sup> = <sup>t</sup>Bu and R<sup>2</sup> = <sup>i</sup>Pr (GAFJUU)<sup>213</sup> (Scheme 72).

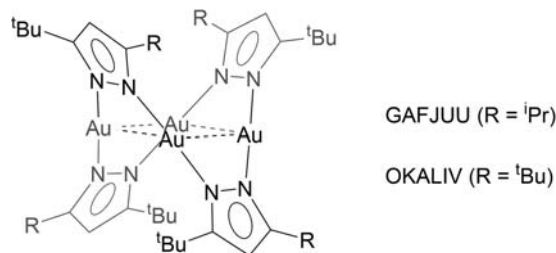
A set of examples of two-atom bridged Au(I) dimers is the structure [Au<sub>2</sub>(μ-Se<sub>2</sub>)(μ-Se<sub>*n*</sub>)](PPh<sub>4</sub>)<sub>2</sub>, composed of a ring of Au and Se atoms. These structures are interesting due to their great structural diversity, deriving from work with late-transition-metal polysulfides. For [Au<sub>2</sub>(μ-Se<sub>2</sub>)(μ-Se<sub>*n*</sub>)](PPh<sub>4</sub>)<sub>2</sub>, Au(I)···Au(I) distances are: 3.004 Å when *n* = 3 (VOFMOS), 3.132 Å when *n* = 4 (VOFNAF).<sup>214</sup> The seven-membered VOFMOS forms an envelope-shaped seven-membered ring, and the eight-membered VOFNAF forms a puckered ring (Scheme 73).

#### 1.15.3.6.2.2 Three-atom bridged Au(I) and Au(III)

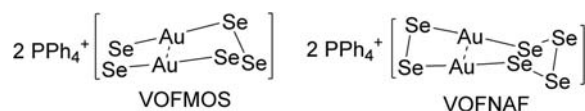
Most structures with intramolecular aurophilic interactions have three-atom bridges, and the Au is observed with two-, three-, and four-coordinate [AuL<sub>2</sub>]<sup>+</sup>, [AuLX], [AuX<sub>2</sub>]<sup>-</sup>, [AuL<sub>2</sub>X], [AuX<sub>4</sub>]. The most common of these have two [AuL<sub>2</sub>]<sup>+</sup> in a centrosymmetric cyclic dimer, with two bridging R<sub>2</sub>PCPR<sub>2</sub> phosphines and various counteranions. The eight-membered ring forms a flattened boat conformation, with the opposing methylene C atoms slightly out of this plane. For the structure [Au(μ-(Me<sub>2</sub>PCPMe<sub>2</sub>))<sub>2</sub>](A)<sub>2</sub>, Au(I)···Au(I) distance is: 3.010 Å for A = Cl<sup>-</sup> (DUKREG),<sup>215</sup> 3.019 Å for A = I<sup>-</sup> (JAFGOM),<sup>216</sup> 3.047 Å for A = (PF<sub>6</sub>)<sup>-</sup> (VOZWOW).<sup>217</sup> These intramolecular aurophilic interactions are weaker than those of the phenyl analogues, likely due to bulkiness of the eight phenyl groups. For the structure [Au(μ-(Ph<sub>2</sub>PCPPh<sub>2</sub>))<sub>2</sub>](A)<sub>2</sub>, Au(I)···Au(I) distance is: 2.931 Å for A = (BF<sub>4</sub>)<sup>-</sup> (JAMKAJ),<sup>218</sup> 2.974 Å for A = Cl<sup>-</sup> (DUMJIG),<sup>219</sup> 2.979 Å for A = (PF<sub>6</sub>)<sup>-</sup> (MUVVEE),<sup>220</sup> 2.984 Å for A = (TfO)<sup>-</sup> (INACUV)<sup>221</sup> (Scheme 74).



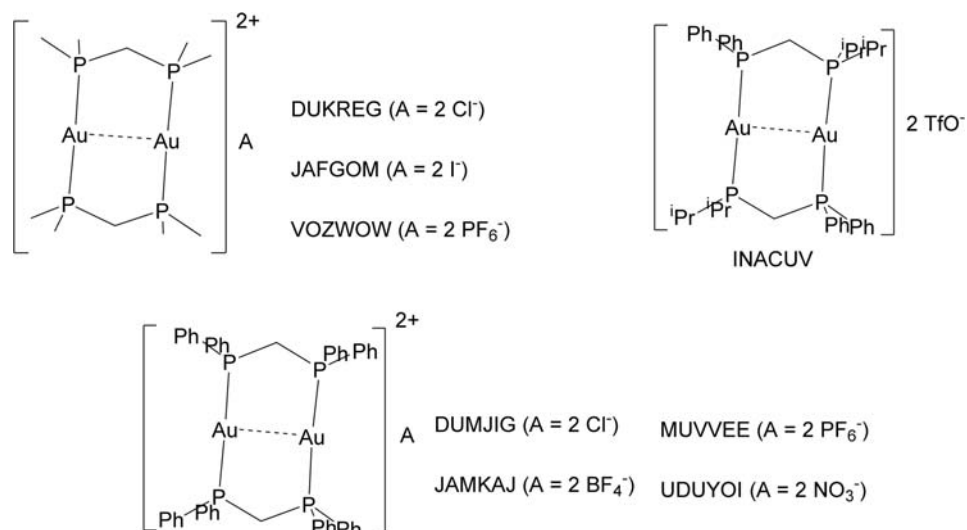
Scheme 71



Scheme 72



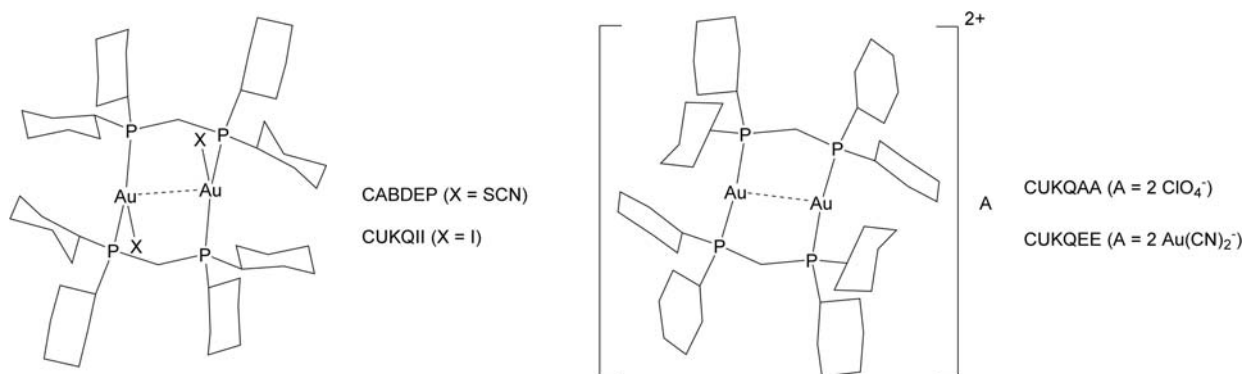
Scheme 73



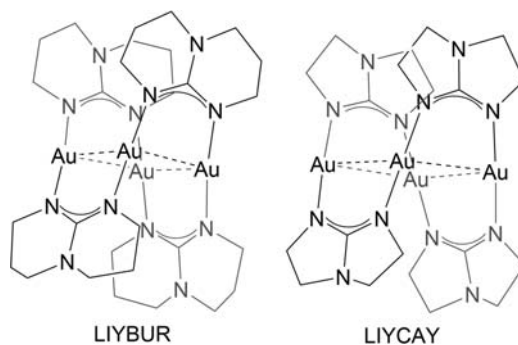
Scheme 74

This relation is observed with another set of centrosymmetric cyclic dimers that have two- and three-coordinate [AuL<sub>2</sub>]<sup>+</sup> and [AuL<sub>2</sub>X] and are bridged by bulky bis(dicyclohexylphosphino)methane groups (dcpm). For the structure [Au(μ-dcpm)<sub>2</sub>](A)<sub>2</sub>, Au(I)⋯Au(I) distance is: 2.914 Å for A = (ClO<sub>4</sub>)<sup>-</sup> (CUKQAA),<sup>222</sup> 2.988 Å for A = [Au(CN)<sub>2</sub>]<sup>-</sup> (CUKQEE).<sup>222</sup> For the structure [Au(μ-dcpm)<sub>2</sub>X<sub>2</sub>], Au(I)⋯Au(I) distance is: 2.951 Å for X = I (CUKQII),<sup>222</sup> 2.984 Å for X = SCN (CABDEP)<sup>223</sup> (Scheme 75).

There are a small number of Au(I) that have coordination to N-donor ligands. The tetranuclear structure [Au<sub>4</sub>(μ-hpp)<sub>4</sub>] (hexahydropyrimidopyrimidinate) (LIYBUR) has an average Au(I)⋯Au(I) distance of 2.921 Å (2.897 Å, 2.913 Å, 2.936 Å, and 2.939 Å). With one less CH<sub>2</sub> at each of the four bridging ligands, the tetranuclear structure [Au<sub>4</sub>(μ-tbo)<sub>4</sub>] (tbo = triazabicyclooctene) (LIYCAY) has an average Au(I)⋯Au(I) distance of 3.227 Å (3.216 Å, 3.225 Å, 3.227 Å, and 3.238 Å). Both of these structures show a bright green luminescence in solid state under UV light (Scheme 76).



Scheme 75



Scheme 76



Other centrosymmetric cyclic dimers have Au atoms coordinated to C or S bridging ligands. The structure  $[\text{Au}(\mu\text{-}(\text{C}_2\text{P}(\text{Ph}_2)))]_2$  (DEWLUM)<sup>224</sup> has an Au(I)···Au(I) distance of 2.976 Å. One example of the rare  $[\text{AuX}_2]^-$  classification is the structure  $[\text{Au}(\mu\text{-}(\text{S}_2\text{C}=\text{NCN}))]_2(\text{N}(\text{PPh}_3)_2)_2$  (ZEXGOY),<sup>225</sup> which has an Au(I)···Au(I) distance of 2.811 Å. Most of the structures with both inter- or intramolecular aurophilic interactions have been between two closed-shell  $d^{10}$  Au(I), but there are a few examples of aurophilic interactions between two  $d^8$  Au(III). For the structure  $[\text{Au}(\mu\text{-}(\text{C}_2\text{P}(\text{Ph}_2)\text{X}_2))]_2$ , Au(III)···Au(III) distances are: 3.076 Å when X = Cl (DOBMOW),<sup>226</sup> 3.091 Å when X = Br (DOBBIQ).<sup>226</sup> For these structures, the halogens are *trans* on the Au(III), but when left in a chlorinated solvent, one pair of Cl atoms of DOBMOW form *cis* conformation (Schemes 77 and 78).

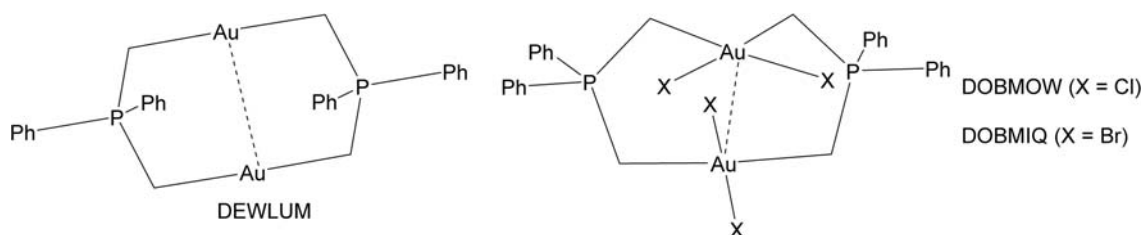
#### 1.15.3.6.2.3 Four-atom bridged Au(I)

A majority of four-atom bridged structures with intramolecular aurophilic interactions have one diphosphine bridge ( $\text{R}_2\text{P}(\text{CH}_2)_2\text{PR}_2$ ) between two  $[\text{AuLX}]$  metals. The short ethylene link between the phosphine groups allows the close approach of two metals that have the potential to facilitate metal-metal bond formation or breaking. For  $[\text{Au}_2(\mu\text{-}(\text{Ph}_2\text{P}(\text{CHR})_2\text{PPh}_2)_2\text{Cl}_2)]$ , Au(I)···Au(I) distances are: 3.049 Å for R = H (ETCLAU),<sup>227</sup> 3.191 Å for R = COOH (LAWMAY).<sup>228</sup> For the structure  $[\text{Au}_2(\mu\text{-}(\text{dcpe})\text{X}_2)]$  (dcpe = 1,2-bis(dicyclopophosphino)ethane), Au(I)···Au(I) distances are: 3.151 Å for X = Br (IQEHUJ),<sup>229</sup> 3.109 Å for X = I (IQEJAR).<sup>229</sup> These complexes have a twisted shape, and Au(I)···Au(I) distances are affected by the slightly bent inward P–Au–X angles that reflect the neighboring attractive aurophilic interactions. Interestingly, of the six structures of  $[\text{Au}_2(\mu\text{-}(\text{dppe})\text{X}_2)]$  and  $[\text{Au}_2(\mu\text{-}(\text{dcpe})\text{X}_2)]$  (dppe = 1,2-bis(diphenylphosphino)ethane; X = Cl, Br, I), only IQEJAR displays luminescence, pink upon crystallization (Scheme 79).

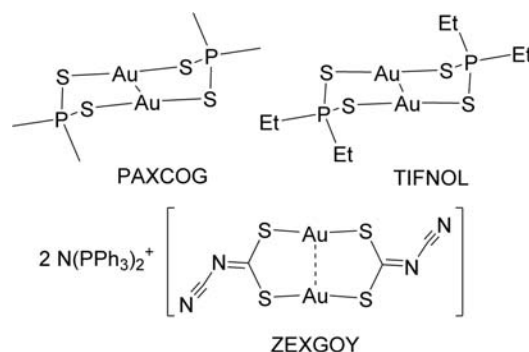
Another set of examples of four-atom bridged Au(I) dimers have  $[\text{AuL}_2]^+$  metals bridged by bipyridine (bpy) groups. Au(I)···Au(I) distance is 3.074 Å for  $[\text{Au}(\mu\text{-}(\text{biisoquinoline})(\text{PMe}_3)_2)(\text{TfO})_2]$  (DEGMIN),<sup>230</sup> and 3.075 Å for  $[\text{Au}(\mu\text{-}(\text{bipy})(\text{PPh}_3)_2)(\text{PF}_6)_2]$  (NUDMIL)<sup>231</sup> (Scheme 80).

#### 1.15.3.6.2.4 Five-atom bridged Au(I)

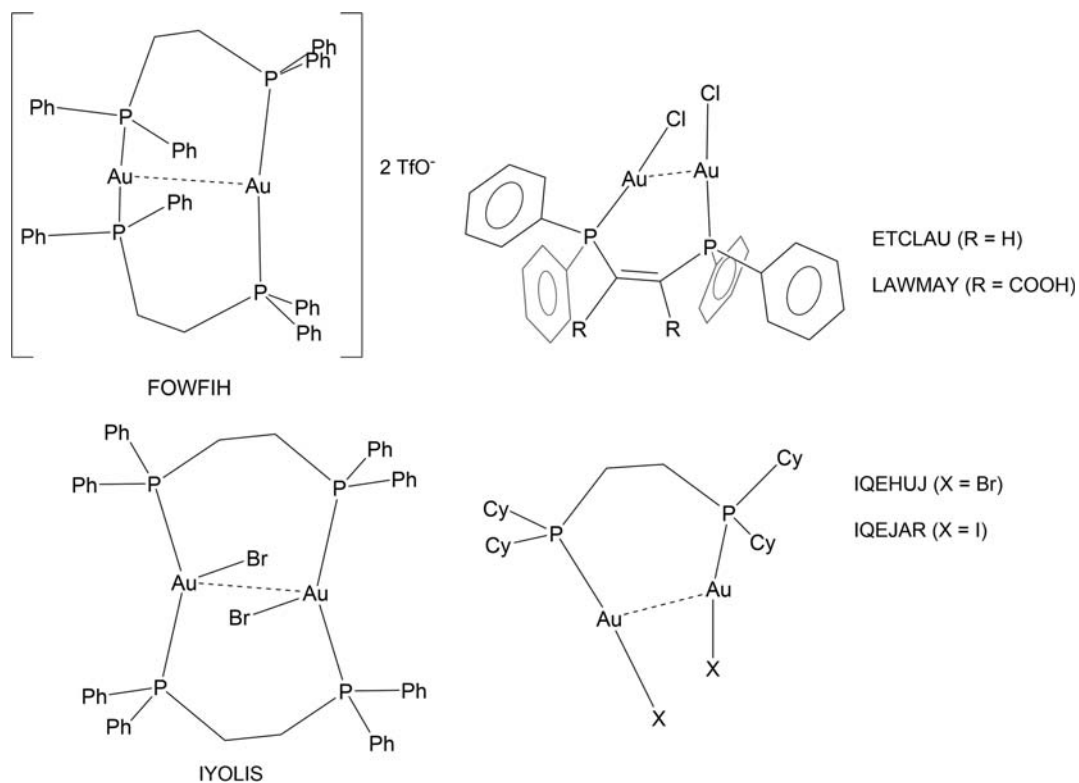
The majority of Au(I) structures with intramolecular aurophilic interactions have seven, nine, or more atoms between the two metals. Most of these structures have symmetrical bridging ligands with neutral two-coordinate  $[\text{AuLX}]$  metals. The greater number of atoms between the two Au(I), the more likely the metals are connected by two of the same ligand bridges. As observed in the following examples, dimeric Au(I) with five-atom bridges are typically connected with one bridge and coordinated to one terminal X ligand. The structure  $[\text{Au}_2(\mu\text{-}(\text{PPh}_2(\text{CH}_2)_2\text{N}(\text{R}^2, \text{R}^3, \text{R}^4, \text{R}^5, \text{R}^6\text{-Ph})\text{Cl}_2))]$  shows the effects of arene substitution on Au(I)···Au(I) distance; on the aniline group,  $\text{R}^2$  and  $\text{R}^6$  are *ortho*,  $\text{R}^3$  and  $\text{R}^5$  are *meta*, and  $\text{R}^4$  is *para*. Au(I)···Au(I) distance is: 3.072 Å when  $\text{R}^2 = \text{OH}$  and  $\text{R}^5 = \text{COOH}$  (MEDQES),<sup>232</sup> 3.121 Å when  $\text{R}^2 = \text{COOH}$  and  $\text{R}^4 = \text{OH}$  (MEDQAO),<sup>232</sup> 3.275 Å when  $\text{R}^2 = \text{COOH}$  and  $\text{R}^6 = \text{OH}$  (IPOKUT)<sup>232</sup> (Scheme 81).



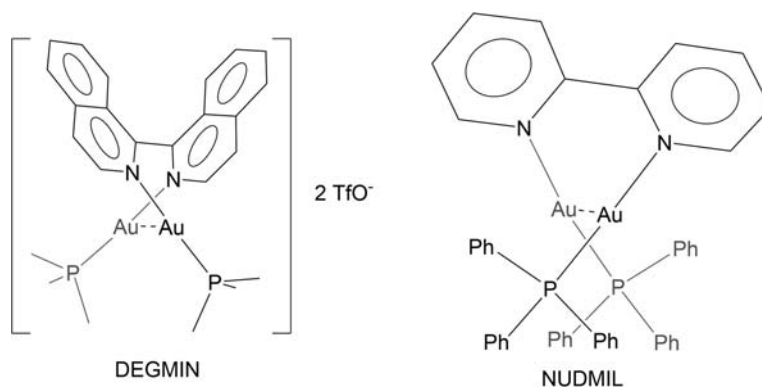
Scheme 77



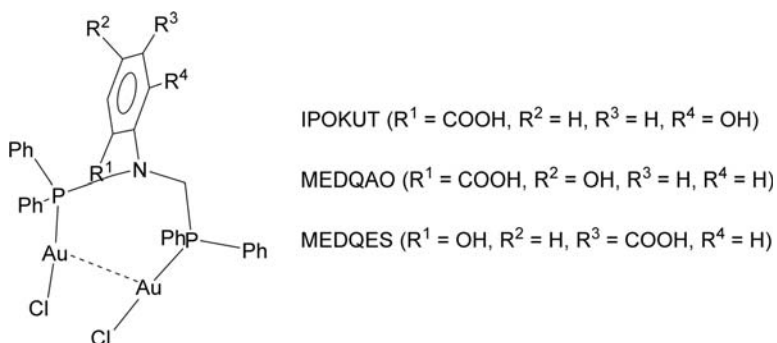
Scheme 78



Scheme 79



Scheme 80



Scheme 81

### 1.15.3.7 Ag...Ag metallophilic interactions

As previously mentioned, metallophilic interactions between closed-shell Ag atoms are referred to as *argentophilic interactions*.<sup>17,233</sup> This section is organized by inter- then intramolecular argentophilic interactions for two Ag(I) atoms within a proximity of 2.90 Å to 3.44 Å. Similar to Au, the vast majority of structures with intermolecular interactions are between two-coordinate Ag(I), and these are followed by three- and four-coordinate Ag(I). For intramolecular interactions, structures are organized by the number of atoms bridging the two Ag atoms. This section has a wider variety compared to that of Au structures, from one- to six-atom bridged. Another similarity to Au, most of the intramolecular interactions are between two Ag(I) bridged in a cyclic form by at least two of the same bridging ligands. Although organized in this section by increasing number of atoms in the bridging unit, most Ag(I)-Ag(I) bridging units are composed of three atoms, followed by one, two, six or more, four, then five.

#### 1.15.3.7.1 Intermolecular Ag...Ag metallophilic interactions

##### 1.15.3.7.1.1 Two-coordinate Ag(I)

The most common Ag(I) complexes that exhibit intermolecular metallophilic interactions contain a Ag(I) coordinated to two ligands with an  $[\text{AgL}_2]^+$  or  $[\text{AgLX}]$  classification. In order, the groups coordinated to the Ag are typically cyanide, N-donor groups, and halogens. The vast majority of two-coordinate Ag(I) structures are  $[\text{AgX}_2]^-$  anions of  $[\text{Ag}(\text{CN})_2]^-$ , which can produce 1D or 2D polymeric structures via  $\text{Ag}(\text{I}) \cdots \text{Ag}(\text{I})$  interactions or cyanido-bridges. Intermolecular  $\text{Ag}(\text{I}) \cdots \text{Ag}(\text{I})$  distances range depends on the structural and electronic properties of the counter cation,  $\text{A}[\text{Ag}(\text{CN})_2]$ . On the shorter end of this range,  $\text{Ag}(\text{I}) \cdots \text{Ag}(\text{I})$  distance is 2.985 Å for  $\text{A} = \text{TePh}_3^+$  (HUHCES),<sup>234</sup> 3.167 Å for  $\text{A} = \text{TeMe}_3^+$  (HUHBUH).<sup>234</sup> On the longer end of this range for ((*p*-R-2,3,4,5,6-H-pyr)<sub>2</sub>-1,4-Ph) $[\text{Ag}(\text{CN})_2]$ ,  $\text{Ag}(\text{I}) \cdots \text{Ag}(\text{I})$  distance is 3.294 Å for  $\text{R} = \text{CH}_3(\text{CH}_2)_2$  (AMUXUC01),<sup>235</sup> 3.324 Å for  $\text{R} = \text{CH}_3(\text{CH}_2)_{11}$  (AMUYOX)<sup>235</sup> (Scheme 82).

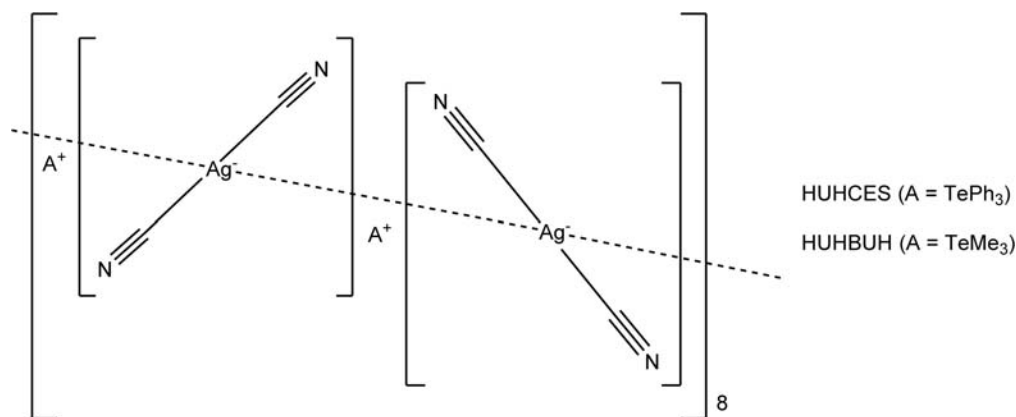
Another common N-containing group in these Ag(I) structures is pyridine (py). For the  $[\text{AgL}_2]^+$  structure  $[\text{Ag}(p\text{-R-py})_2](\text{TfO})$ , when  $\text{R} = \text{NH}_2$  (ATOLEA)<sup>236</sup>  $\text{Ag}(\text{I}) \cdots \text{Ag}(\text{I})$  distance is 3.432 Å; when  $\text{R} = \text{C}(\text{NOH})\text{py}$  (FEPBUZ)<sup>237</sup>  $\text{Ag}(\text{I}) \cdots \text{Ag}(\text{I})$  distance is 3.368 Å. The mutual core of these structures are flat, with the distal py of  $[\text{Ag}(4\text{-C}(\text{NOH})\text{py-py})_2](\text{TfO})$  at an angle to this core. With an even larger R, although at a *meta* position of the py,  $[\text{Ag}(m\text{-C}=\text{C}\text{-3,4-dialkoxyphenyl-py})_2](\text{TfO})$  (HEFFII)<sup>238</sup> has the shortest comparable  $\text{Ag}(\text{I}) \cdots \text{Ag}(\text{I})$  distance of 3.136 Å (Scheme 83).

A set of similar  $[\text{AgL}_2]^+$  structures exhibit differences in  $\text{Ag}(\text{I}) \cdots \text{Ag}(\text{I})$  distances caused by different counteranions. For the  $[\text{AgL}_2]^+$  structure  $[\text{Ag}(p\text{-3'-F-4-styrylpyridine})_2]\text{A}$ , when  $\text{A} = \text{BF}_4^-$  (GUCZAH)<sup>239</sup>  $\text{Ag}(\text{I}) \cdots \text{Ag}(\text{I})$  distance is 3.247 Å; when  $\text{A} = \text{ClO}_4^-$  (GUCZEL)<sup>239</sup>  $\text{Ag}(\text{I}) \cdots \text{Ag}(\text{I})$  distance is 3.233 Å; when  $\text{A} = \text{NO}_3^-$  (GUCZOV)<sup>239</sup>  $\text{Ag}(\text{I}) \cdots \text{Ag}(\text{I})$  distance is 3.302 Å (Scheme 84).

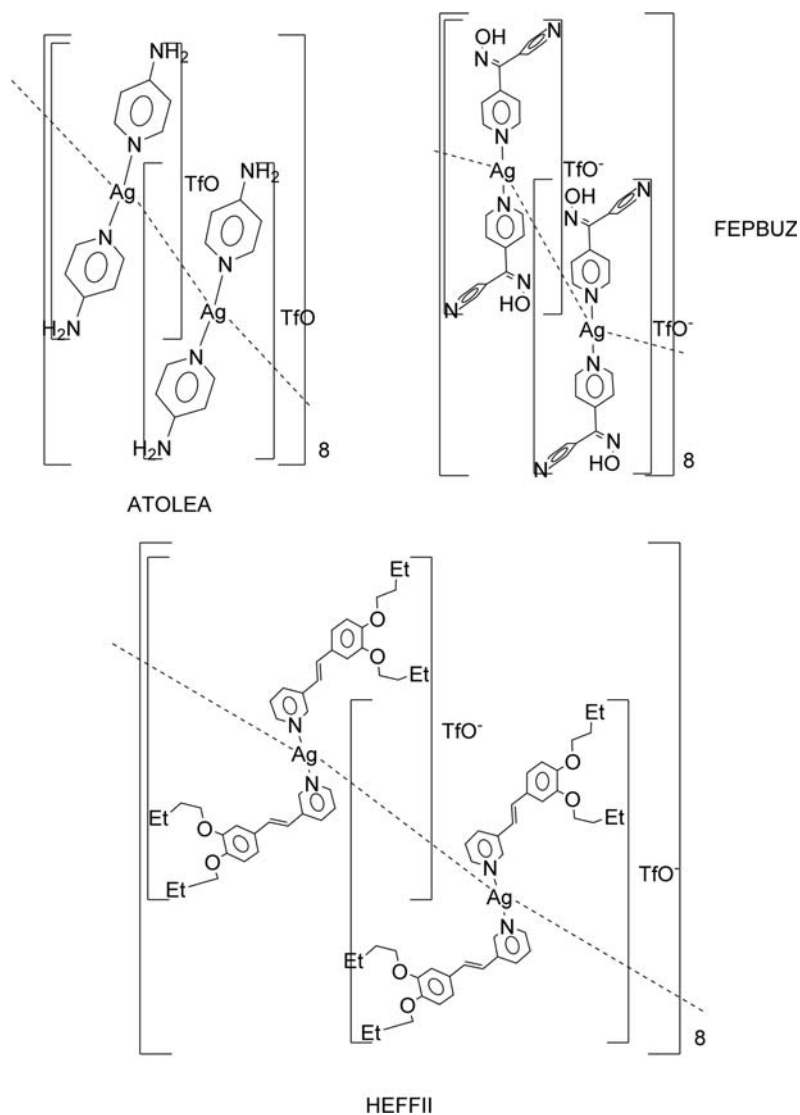
Ag(I) coordinated to two imidazole (imid) with  $[\text{AgL}_2]^+$  classification have a core that is not as flat as the py Ag(I) analogues, but exhibit similar trends. For the structure  $[\text{Ag}(\text{imid})_2]\text{A}$ , when  $\text{A} = \text{sulfosalicylate}$  (SERVIU)  $\text{Ag}(\text{I}) \cdots \text{Ag}(\text{I})$  distance is 3.180 Å; when  $\text{A} = 4\text{-benzoyl-3-methyl-1-phenyl-1H-pyrazol-5-olate}$  (SOYXAH)  $\text{Ag}(\text{I}) \cdots \text{Ag}(\text{I})$  distance is 3.202 Å (Scheme 85).

Supramolecular cyclic Ag(I) structures exhibit intermolecular interactions between flat and nearly-flat structures. The  $[\text{AgLX}]$  structures  $[(\text{Ag}(\text{mim}))_8]$  (mim = 2-methylimidazolate) (BAXLET)<sup>240</sup> and  $[(\text{Ag}(\text{pymo}))_6]$  (pymo = 2-oxopyrimidine) (NULTIX)<sup>241</sup> have intermolecular  $\text{Ag}(\text{I}) \cdots \text{Ag}(\text{I})$  distances of 2.986 Å and 2.962 Å, respectively. The  $[\text{AgL}_2]^+$  dimers  $[(\text{Ag}(\text{btp}))_2](\text{ClO}_4)_2$  (btp = (2,6-bis(*N'*-1,2,4-triazolyl)pyridine)) (PASBAN)<sup>242</sup> and  $[(\text{AgL}_2)(\text{BF}_4)_2]$  ( $\text{L} = (\text{NH}(\text{pyr})(\text{Et}))_2\text{Npyr}$ ) (SEWVUN)<sup>243</sup> have intermolecular  $\text{Ag}(\text{I}) \cdots \text{Ag}(\text{I})$  distances of 3.194 Å and 3.389 Å, respectively.

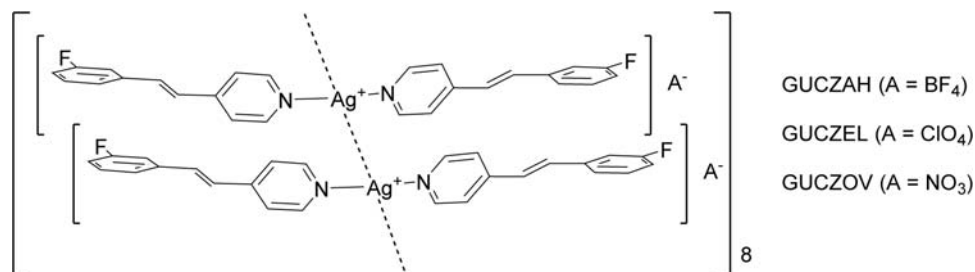
Another set of neutral  $[\text{AgLX}]$  structures exhibit variances in  $\text{Ag}(\text{I}) \cdots \text{Ag}(\text{I})$  distance caused by different halides and different R groups on an M-coordinating amine. For the dinuclear linear  $[\text{Ag}_2\text{Cl}_2\text{Et}(\text{NH}_2)_2]$  (BIQWEF)  $\text{Ag}(\text{I}) \cdots \text{Ag}(\text{I})$  distance is 3.238 Å. For the mononuclear structure  $[\text{Ag}(\text{RNH}_2)\text{X}]$ , when  $\text{R} = \text{CH}_2\text{Ph}$  and  $\text{X} = \text{Cl}$  (YUXVUI)  $\text{Ag}(\text{I}) \cdots \text{Ag}(\text{I})$  distance is 3.115 Å; when  $\text{R} = \text{CH}_2\text{Ph}$  and  $\text{X} = \text{Br}$  (YUXWAQ)  $\text{Ag}(\text{I}) \cdots \text{Ag}(\text{I})$  distance is 3.257 Å;  $\text{R} = (\text{CH}_2)_2\text{Ph}$  and  $\text{X} = \text{Cl}$  (YUXXEVE)  $\text{Ag}(\text{I}) \cdots \text{Ag}(\text{I})$  distance is 3.266 Å (Scheme 86).



Scheme 82



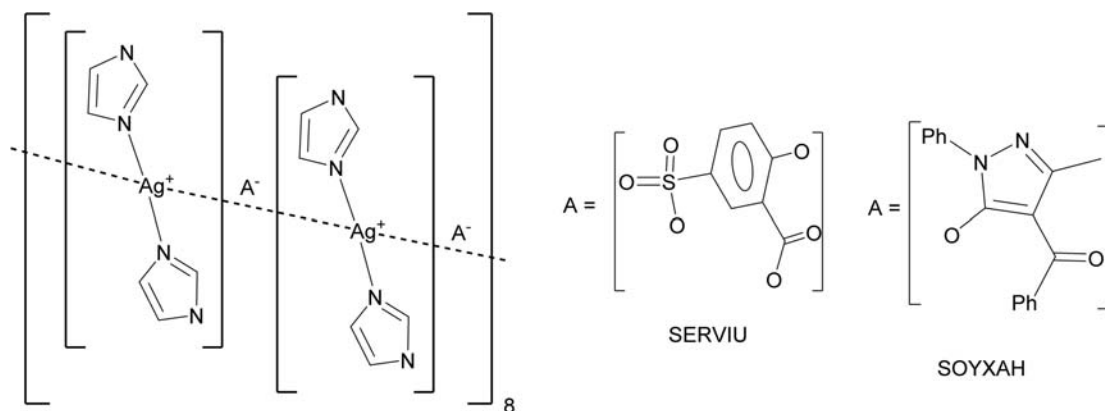
Scheme 83



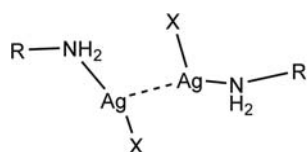
Scheme 84

#### 1.15.3.7.1.2 Three-coordinate Ag(I)

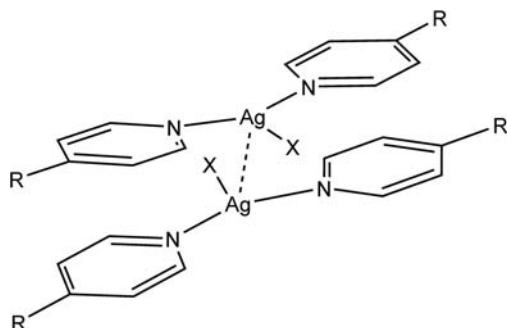
Most three-coordinate mononuclear Ag(I) structures have a neutral [AgL<sub>2</sub>X] classification and distorted T-shaped geometry. Due to the antimicrobial properties of Ag compounds and nontoxic presence of methyl pyridyl ketones in commercial consumables, there are many variations of the structure [Ag(*p*-R-py)<sub>2</sub>X], where X is an O-donor ligand. On the shorter end of the Ag(I)⋯Ag(I) range, 3.136 Å when R = CN and X = TfO (**PURYIL**),<sup>244</sup> 3.240 Å when R = MeCO and X = NO<sub>3</sub> (**BOKROL**).<sup>245</sup> On the longer end of the Ag(I)⋯Ag(I) range, 3.411 Å when R = PhN=C and X = CF<sub>3</sub>COO (**CEKCON**),<sup>246</sup> 3.358 Å when R = CN and X = C<sub>6</sub>H<sub>4</sub>COOHCOO (**EMOTUW**)<sup>247</sup> (Scheme 87).



Scheme 85

YUXVUJ (R = CH<sub>2</sub>Ph; X = Cl)YUXWAQ (R = CH<sub>2</sub>Ph; X = Br)YUXXEY (R = (CH<sub>2</sub>)<sub>2</sub>Ph; X = Cl)

Scheme 86

PURYIL (R = CN; X = SO<sub>3</sub>CF<sub>3</sub>)BOKROL (R = COMe; X = NO<sub>3</sub>)CEKCON (R = CHNPh; X = CO<sub>2</sub>CF<sub>3</sub>)EMOTUW (R = CN; X = C<sub>6</sub>H<sub>4</sub>COOHCOO)

Scheme 87

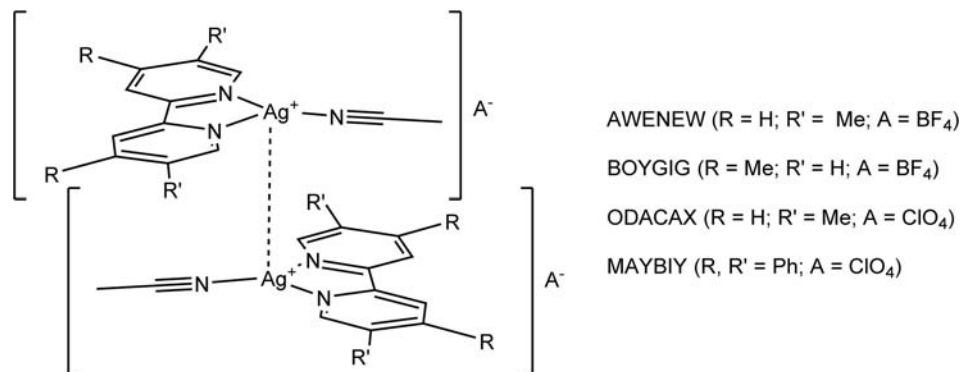
A large group of cyclic metal-organic frameworks contain a network of neutral [AgL<sub>2</sub>X], which have potential applications such as capturing or storing agents, sensors, or heterogeneous catalysis. The number of Ag atoms in these macrocycles vary, and the flatness of the overall structure affects the intermolecular argentophilic interactions. Additionally, many studies have observed the correlation of potential coordination preferences for dipyrindylmethanone (DpyM) as a bridging ligand. For the hexameric structure [Ag(3,3'-DpyM)X]<sub>6</sub>, Ag(I)⋯Ag(I) distance is: 3.225 Å when X = CF<sub>3</sub>CF<sub>2</sub>CF<sub>2</sub>COO (**FURSAN**),<sup>248</sup> 3.236 Å when X = CF<sub>3</sub>CF<sub>2</sub>COO (**FUSNIR**).<sup>248</sup> For the structure [Ag(3,4'-DpyM)(TfO)]<sub>4</sub> (**GIQNEC**),<sup>249</sup> Ag(I)⋯Ag(I) distance is 3.125 Å.

Another major category of three-coordinate Ag(I) structures has three coordinated neutral N-donor ligands, with the classification [AgL<sub>3</sub>]<sup>+</sup>. The majority of these structures are coordinated to a CNMe ligand and a chelating bpy. For the structures [Ag(R,R'-2,2'-bpy)(CNMe)]A, where R and R' are organic substituents on bpy and A is the counteranion, Ag(I)⋯Ag(I) distances are: 3.255 Å for R, R' = 5,5'-Me<sub>2</sub>, A = (BF<sub>4</sub>)<sup>-</sup> (**AWENEW**),<sup>250</sup> 3.403 Å for R, R' = 4,4'-Me<sub>2</sub>, A = (BF<sub>4</sub>)<sup>-</sup> (**BOYGIG**),<sup>250</sup> 3.412 Å for R, R' = 5,5'-Me<sub>2</sub>, A = (ClO<sub>4</sub>)<sup>-</sup> (**ODACAX**).<sup>251</sup> Considering the planarity of the structure [Ag(2,2'-biquinoline)(CNMe)](ClO<sub>4</sub>)<sup>-</sup> (**MAYBIY**),<sup>252</sup> its Ag(I)⋯Ag(I) distance of 3.271 Å indicates that added phenyl rings scarcely affect the intermolecular argentophilic interaction (**Scheme 88**).

#### 1.15.3.7.1.3 Four-coordinate Ag(I)

Four-coordinate Ag(I) make up the last category of Ag(I) structures with intermolecular argentophilic interactions, commonly classified as [AgL<sub>4</sub>]<sup>+</sup> followed by [AgL<sub>3</sub>X]. The majority of the coordinated ligands are four homoleptic N-donor or two N-donor and two O-donor. N-donor ligands are typically variations of connected py groups that allow the Ag(I) to have planar geometry, suitable for intermolecular Ag(I)⋯Ag(I) interactions: 3.223 Å for [Ag(3,6-pyr-2-pyridazine)](TfO) (**AJAZAM**),<sup>253</sup> 3.343 Å for [Ag(qtpy)](-ClO<sub>4</sub>) (qtpy = quaterpyridine) (**RASXOZ**).<sup>254</sup> Counteranion effects can be observed with supramolecular dinuclear [Ag<sub>2</sub>(1,3,4-thiadiazole-2,5-di-2-pyridyl)<sub>2</sub>]A<sub>2</sub>. Ag(I)⋯Ag(I) distances vary due to differing sizes of the counteranions: 3.302 Å when A = (BF<sub>4</sub>)<sup>-</sup>



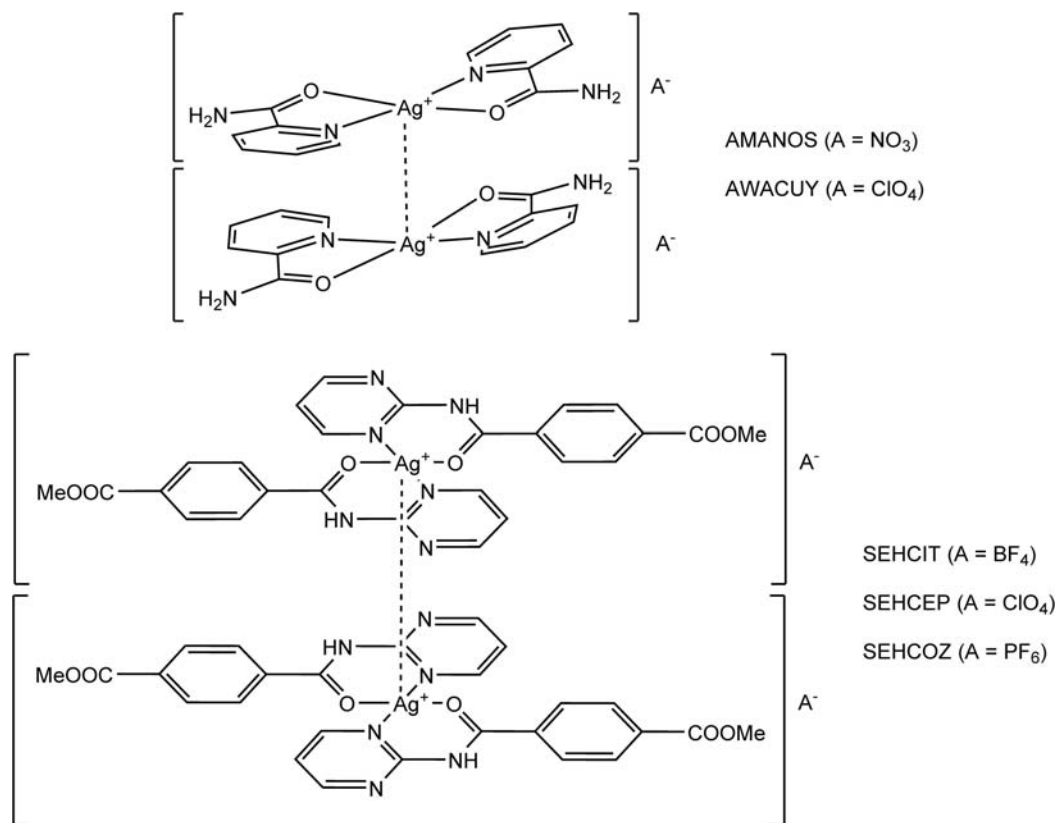


Scheme 88

(UHEYIQ),<sup>255</sup> 3.346 Å when A = (ClO<sub>4</sub>)<sup>-</sup> (UHEYOW),<sup>255</sup> 3.239 Å when A = (PF<sub>6</sub>)<sup>-</sup> (UHEYUC).<sup>255</sup> Due to the planarity of these structures, the Ag(I)···Ag(I) interactions create a 1D supramolecular chain. Conversely, when the counteranion is changed to 2 (AsF<sub>6</sub>)<sup>-</sup> or 2 (NO<sub>3</sub>)<sup>-</sup>, no Ag(I)···Ag(I) interactions are observed.

Another common [AgL<sub>4</sub>]<sup>+</sup> structure is in the form [Ag(pia)<sub>2</sub>]A (pia = picolinamide), where the central Ag(I) is chelated by the N,O-bidentate picolinamide ligands in a square planar geometry. Depending on the counteranion of [Ag(pia)<sub>2</sub>]A, Ag(I)···Ag(I) interactions are: 3.419 Å when A = (NO<sub>3</sub>)<sup>-</sup> (AMANOS),<sup>256</sup> 3.272 Å when A = (ClO<sub>4</sub>)<sup>-</sup> (AWACUY).<sup>257</sup> Hydrogen bonding between intermolecular O=C–NH<sub>2</sub> make these structures interesting for 1D, 2D, and 3D crystalline material. Another set of structures with a more complex pia ligand, [Ag(Me-4-(pyr-2-ylcarbamoyl)benzoate)]A, has Ag(I)···Ag(I) distances of: 3.119 Å when A = (BF<sub>4</sub>)<sup>-</sup> (SEHCIT),<sup>258</sup> 3.152 Å when A = (ClO<sub>4</sub>)<sup>-</sup> (SEHCEP),<sup>258</sup> 3.329 Å when A = (PF<sub>6</sub>)<sup>-</sup> (SEHCOZ).<sup>258</sup> The dimensionality of these structures are also attributed to short Ag···Ag contacts, π···π stacking interactions, and/or Ag···O interactions (Scheme 89).

The few neutral [AgL<sub>3</sub>X] structures typically have a Ag(I) coordinated with three N-donor ligands and an O-donor ligand. The structure [Ag(1,10-phenanthroline)(3,5-dicarboxy-6-methylpyridine-2-carboxylato)] has a Ag(I)···Ag(I) distance of 3.348 Å (BUBVAX). Another structure [Ag(adpa)(NO<sub>3</sub>)] (adpa = 9-anthracenylmethyl-(2-pyridinylmethyl)-2-pyridinemethanamine) (SOLYEZ)



Scheme 89

with a  $\text{Ag(I)} \cdots \text{Ag(I)}$  distance of 3.266 Å can only form pair-wise argentophilic interactions due to the anthracene group blocking one side of the planar four-coordinate  $\text{Ag(I)}$ .

### 1.15.3.7.2 Intramolecular $\text{Ag} \cdots \text{Ag}$ metallophilic interactions

#### 1.15.3.7.2.1 One-atom bridged $\text{Ag(I)}$

Most  $\text{Ag(I)}$  structures with intramolecular argentophilic interactions are doubly bridged by the same ligand. For one-atom bridged structures, the most common are halogens, followed by a Group 6 atom. The  $\text{Ag(I)}$  are typically coordinated to three or four ligands that stabilize the closed-shell metals and allow  $\text{Ag(I)} \cdots \text{Ag(I)}$  proximity between 2.90 Å and 3.44 Å. When the bridging halogens two neutral  $[\text{AgL}_3\text{X}]$  are changed, a common trend observed is the lengthening of the intramolecular  $\text{Ag(I)} \cdots \text{Ag(I)}$  as halogen size is increased. For  $[\text{Ag}(\mu\text{-X})(\text{PPh}_3)(\text{S}=\text{CNHCH}_2\text{CH}_2\text{NMe})_2]$ ,  $\text{Ag(I)} \cdots \text{Ag(I)}$  distance is: 3.402 Å when  $\text{X} = \text{Cl}$  (HIKZIM),<sup>259</sup> 3.421 Å when  $\text{X} = \text{Br}$  (HIKYOR).<sup>259</sup> For  $[\text{Ag}(\mu\text{-X})(\text{AsPh}_3)_2]$ ,  $\text{Ag(I)} \cdots \text{Ag(I)}$  distance is: 3.188 Å when  $\text{X} = \text{Br}$  (NUHRUD),<sup>260</sup> 3.222 Å when  $\text{X} = \text{I}$  (NUHROX).<sup>260</sup> (Scheme 90).

Three-coordinate  $\text{Ag(I)}$  coordinated to bridging and terminal halides form planar structures with intramolecular argentophilic interactions stronger than four-coordinate analogues. As  $[\text{AgLX}_2]^-$ , these structures are commonly found as dianions. For the structure  $((\text{PPh}_3)_2\text{CH}_2\text{CH}_2)[\text{Ag}(\mu\text{-Cl})\text{Cl}]_2$  (AZOYEV),<sup>261</sup>  $\text{Ag(I)} \cdots \text{Ag(I)}$  distance is 3.123 Å. For the structure  $((\text{PPh}_3)\text{CH}_2\text{PH})_2[\text{Ag}(\mu\text{-Br})\text{Br}]_2$  (YEMVAQ),<sup>261</sup>  $\text{Ag(I)} \cdots \text{Ag(I)}$  distance is 3.126 Å.

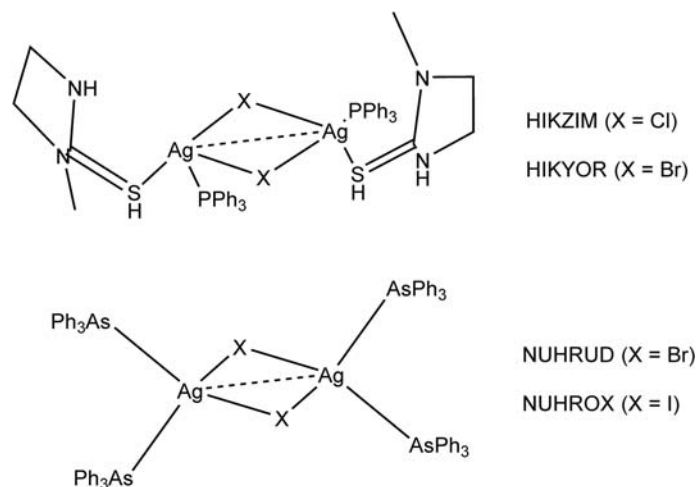
Oxidation state of the metals of symmetric binuclear structures are not always the same, and this can be seen with a few examples of  $\text{Ag(I)}$  structures with all ethylenethiourea (etu) ligands. The exocyclic S of etu is capable of coordinating to metals via  $\eta^1\text{-S}$ ,  $\mu_2\text{-S}$ ,  $\mu_3\text{-S}$ , and  $\mu_4\text{-S}$  bonding modes, and the  $\text{C}=\text{S}$  of etu can coordinate to metals in a variety of angles. Attributed to the large size of the S atom, the four-coordinate  $\text{Ag(I)}$  can have  $[\text{AgL}_4]^+$  and/or  $[\text{AgL}_3\text{X}]$  configurations. For the structure  $[\text{Ag}(\mu\text{-etu})(\text{etu})_2]_2\text{A}_n$ ,  $\text{Ag(I)} \cdots \text{Ag(I)}$  distance is: 3.307 Å when  $\text{A}_n = 2$  ( $\text{NO}_3^-$ ) (XORVOQ), 3.310 Å when  $\text{A} = (\text{NO}_3^-)$  (QUFLUZ).

Similar to the trend observed with bridging halides, dimeric  $\text{Ag(I)}$  structures with bridging Group 6 ligands have stronger intramolecular argentophilic interactions with lower-coordinated  $\text{Ag(I)}$ . The structure  $[\text{Ag}(\mu\text{-TeP}(\text{iPr})_3)(\text{N}(\text{SO}_2\text{Me})_2)_2]_2$  has a  $\text{Ag(I)} \cdots \text{Ag(I)}$  distance of 2.908 Å (CEPVAV01).<sup>262</sup> The structure  $[\text{Ag}(\mu\text{-Se}=\text{C}(\text{NMe})_2\text{CH}_2\text{CH}_2\text{Cl})_2]$  has a  $\text{Ag(I)} \cdots \text{Ag(I)}$  distance of 3.176 Å (YUQJEC).<sup>263</sup> Both of these examples of neutral structures with bridged  $[\text{AgL}_2\text{X}]$  metal centers have a planar diamond core with *trans* L ligands.

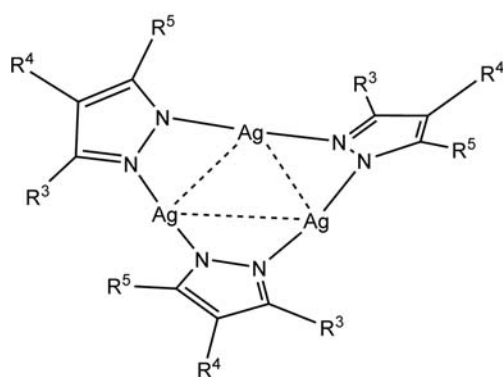
#### 1.15.3.7.2.2 Two-atom bridged $\text{Ag(I)}$

Structures with intramolecular argentophilic interactions typically have  $[\text{AgLX}]$  metals. The most-common two-atom bridging ligand is a substituted pyz, and many structures have three  $\text{Ag(I)}$  bridged by three substituted pyz in close proximity. The core of these structures are planar nine-membered rings, and referenced distances represent one of the three present argentophilic interactions. For the structure  $[\text{Ag}(\mu\text{-}(R^3, R^4, R^5\text{-pyz}))_3]$ , one of the  $\text{Ag(I)} \cdots \text{Ag(I)}$  distances are: 3.312 Å when  $R^3, R^5 = \text{Ph}$  and  $R^4 = \text{Br}$  (CENGAF),<sup>264</sup> 3.329 Å when  $R^3, R^5 = \text{Ph}$  and  $R^4 = \text{H}$  (CENGOT),<sup>264</sup> 3.342 Å when  $R^3, R^5 = \text{Ph}$  and  $R^4 = \text{Me}$  (COFQUL),<sup>265</sup> 3.408 Å when  $R^3, R^5 = \text{Ph}$  and  $R^4 = \text{Cl}$  (COFQIZ),<sup>265</sup> 3.414 Å when  $R^3, R^5 = \text{Ph}$  and  $R^4 = \text{I}$  (COFQOF),<sup>265</sup> 3.296 Å when  $R^3, R^5 = \text{iPr}$  and  $R^4 = \text{NO}_2$  (YEKRAI),<sup>266</sup> 3.382 Å when  $R^3, R^5 = \text{iPr}$  and  $R^4 = \text{Ph}$  (XOMVON).<sup>267</sup> Since these structures have fairly weak argentophilic interactions and the maximum cutoff of non-bonded  $\text{Ag(I)} \cdots \text{Ag(I)}$  distance for our CSD search was 3.44 Å, only the strongest distance was referenced (Scheme 91).

In contrast to Au, Ag also has four-coordinate  $[\text{AgL}_3\text{X}]$  and  $[\text{AgL}_2\text{X}]$  metals with two-atom bridges and intramolecular  $\text{Ag(I)} \cdots \text{Ag(I)}$  contacts. Two examples of dimeric structures with  $[\text{AgL}_3\text{X}]$  have two bridging phthalazine (phtz) groups, forming a planar five-membered complex. Despite this flatness, the other two ligands coordinated to the two  $\text{Ag(I)}$  disrupt the possibility of intermolecular



Scheme 90



CENGAF ( $R^3, R^5 = \text{Ph}; R^4 = \text{Br}$ )  
 CENGOT ( $R^3, R^5 = \text{Ph}; R^4 = \text{H}$ )  
 COFQUL ( $R^3, R^5 = \text{Ph}; R^4 = \text{Me}$ )  
 COFQIZ ( $R^3, R^5 = \text{Ph}; R^4 = \text{Cl}$ )  
 COFQOF ( $R^3, R^5 = \text{Ph}; R^4 = \text{I}$ )  
 YEKRAI ( $R^3, R^5 = {}^i\text{Pr}; R^4 = \text{NO}_2$ )  
 XOMVON ( $R^3, R^5 = {}^i\text{Pr}; R^4 = \text{Ph}$ )

Scheme 91

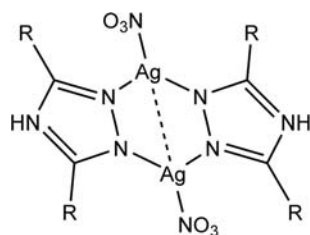
Ag(I)···Ag(I) interactions. For the structure  $[\text{Ag}(\mu\text{-phtz})\text{LX}]_2$ , Ag(I)···Ag(I) distances are: 3.386 Å when L = NCMe and X = BF<sub>4</sub> (BACSEG), 3.434 Å when L = phtz and R = NO<sub>3</sub> (VANMEC01).

Ag(I) with three-coordination  $[\text{AgL}_2\text{X}]$  are the least common two-atom bridged structures. For the structure  $[\text{Ag}(\mu\text{-}2,4\text{-R,R-}3,5\text{-trz})(\text{NO}_3)]_2$  (trz = triazole), Ag(I)···Ag(I) distance is 3.386 Å when R = <sup>i</sup>Pr (MOZTAX),<sup>268</sup> 3.437 Å when R = H (VIZBEL)<sup>269</sup> (Scheme 92).

#### 1.15.3.7.2.3 Three-atom bridged Ag(I)

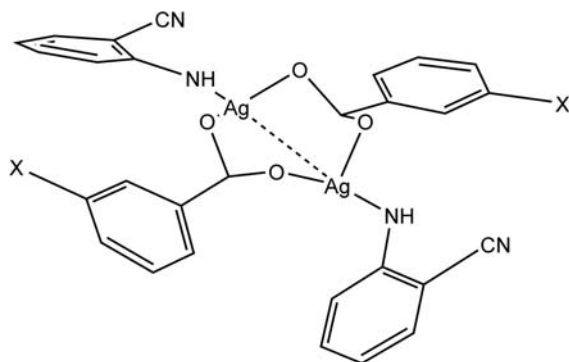
Similar to Au, most structures with intramolecular argentophilic interactions have three-atom bridges; the Ag is observed with two-, three-, and four-coordinate  $[\text{AgL}_2]^+$ ,  $[\text{AgLX}]$ ,  $[\text{AgL}_3]^+$ ,  $[\text{AgL}_2\text{X}]$ ,  $[\text{AgL}_3\text{X}]$ . Four-coordinate Ag(I) structures are the most common, and the nonbridging ligand is typically a chelating phenanthroline (phen). For the structure  $[\text{Ag}(\mu\text{-}(\text{S}_2\text{P}(\text{OR})_2)(\text{phen}))]_2$ , Ag(I)···Ag(I) distance is: 3.187 Å when R = Ph (NANFEO01), 3.231 Å when R = Me (ZONDOX), 3.248 Å when LX = Et (ZONDUD). The eight-membered rings form chair conformations, and the adjacent parallel rings of phen form 1D chains of the structures.

Structures with three-coordinate Ag(I) typically have stronger intramolecular argentophilic interactions than those with four-coordinate Ag(I). This is attributed to the planarity of the eight-membered binuclear Ag(I) ring. For the structure  $[\text{Ag}(\mu\text{-}(\text{O}_2\text{C}(3\text{-R-Ph}))(\text{abn}))]_2$  (abn = 2-aminobenzonitrile), Ag(I)···Ag(I) distance is: 2.929 Å when R = F (ZAYVUS), 2.933 Å when R = Cl (ZAYVOM).<sup>270</sup> There is only a slight difference in argentophilic strength between the two halogens, but there is significant difference when they are replaced with an electron-donating CH<sub>3</sub>− or CH<sub>3</sub>O−. The presence of the



MOZTAX (R = <sup>i</sup>Pr)  
 VIZBEL (R = H)

Scheme 92



ZAYVUS (X = F)  
 ZAYVOM (X = Cl)

Scheme 93

electron-donating group minimizes the repelling force between the Ag(I) ions, giving a shorter distance of  $\sim 2.80$  Å (Scheme 93).

Another set of examples with three-atom bridging ligands have Ag(I) in reduced  $[\text{AgL}_3]^+$  form. The structure  $[\text{Ag}(\mu\text{-NH}(\text{PPh}_2)_2)(\text{NCMe})_2[\text{Mo}((\text{SCCN})_2)_3]$  (HUKZOC),<sup>271</sup> has a Ag(I)···Ag(I) distance of 2.950 Å. The structure  $[(\text{Ag}(\mu\text{-C}(\text{PPh}_2)_2)\text{NCMe})_2(\text{ClO}_4)_2]$  (RACXAVO1)<sup>272</sup> has a Ag(I)···Ag(I) distance of 3.056 Å. Opposite of ZAYVUS and ZAYVOM, large substituents are on the all four corners of the bridging ligands.

The least-common of structures with intramolecular argentophilic interactions and three-atom bridging ligands have two-coordinate Ag(I). Typically, these ligands are resonant OCO, with a variable R substituent on the C atom. For the structure  $[\text{Ag}(\mu\text{-O}_2\text{CR})_2]$ , Ag(I)···Ag(I) distance is: 2.910 Å when R = 2,6-(OH)<sub>2</sub>Bz (KAMTUN),<sup>273</sup> 2.943 Å when R = CH<sub>2</sub>OPh<sup>F</sup> (GEVPIG).<sup>274</sup>

Similar to the three-atom-bridged  $[\text{AuL}_2]^+$  structures, there are many  $[\text{AgL}_2]^+$  in centrosymmetric cyclic dimers, with two bridging R<sub>2</sub>PCPR<sub>2</sub> phosphines and various counteranions. The eight-membered ring forms a flattened boat conformation, and opposing methylene C atoms deviate in *trans* to each other from the plane of the ring. The structure  $[\text{Ag}(\mu\text{-}(\text{Me}_2\text{PCPMe}_2))_2](\text{PF}_6)_2$  (BEPFOR) has a Ag(I)···Ag(I) distance of 3.042 Å. The structure  $[\text{Ag}(\mu\text{-}(\text{Ph}_2\text{PCPPh}_2))_2](\text{ClO}_4)_2$  (FOCJUD) has a Ag(I)···Ag(I) distance of 2.901 Å.

Coordination to S ligands are the least common for cationic three-atom-bridged  $[\text{AuL}_2]^+$  dimers. For the structure  $[\text{Ag}(\mu\text{-}1,3\text{-dithiane})_2]$ , Ag(I)···Ag(I) distance is: 2.924 Å when A = (PF<sub>6</sub>)<sup>-</sup> (WUGLUF),<sup>275</sup> 2.972 Å when A = (BF<sub>4</sub>)<sup>-</sup> (WUGMAM).<sup>275</sup>

#### 1.15.3.7.2.4 Four-atom bridged Ag(I)

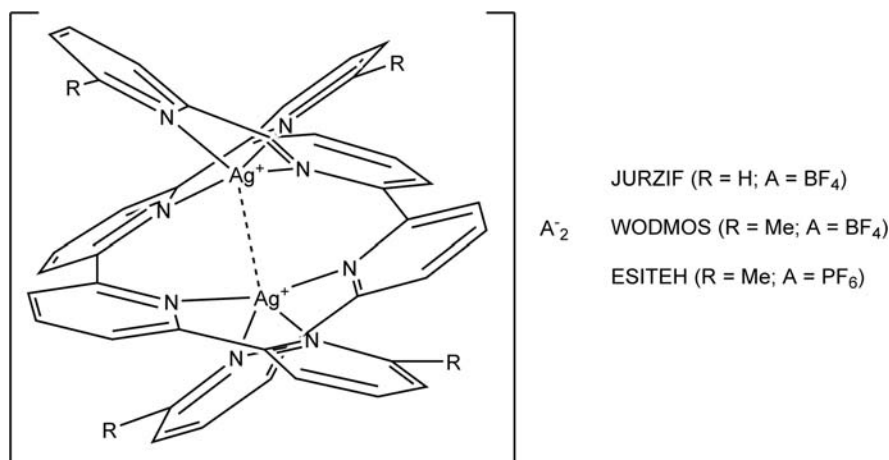
The majority of four-atom bridged structures with intramolecular argentophilic interactions are bridged at the N of pyridine (py) ligands. These structures are typically dimeric with two Ag(I) four-coordinate  $[\text{AgL}_4]^+$  metals. For the quaterpyridine (qtpy) structure  $[\text{Ag}(\mu\text{-}R,R''''\text{-qtpy})_2]A_2$ , Ag(I)···Ag(I) distance is: 3.107 Å when R, R'''' = H; A = (BF<sub>4</sub>)<sup>-</sup> (JURZIF),<sup>276</sup> 3.125 Å when R, R'''' = Me; A = (BF<sub>4</sub>)<sup>-</sup> (WODMOS),<sup>277</sup> 3.253 Å when R, R'''' = Me; A = (PF<sub>6</sub>)<sup>-</sup> (ESITEH).<sup>278</sup> Each of the metal ions adopt a pseudo-tetrahedral geometry, forming binuclear complexes with double-helical form (Scheme 94).

Other four-atom bridged Ag(I) structures have intramolecular interactions between two reduced  $[\text{AgL}_2]^+$ . Ag(I)···Ag(I) distance is 3.074 Å for  $[\text{Ag}(\mu\text{-}biisoq)]_2A_2$ , biisoq = 1,1'-biisoquinoline and A = (TfO)<sup>-</sup> (YAQRUF),<sup>279</sup> and 3.206 Å when  $[\text{Ag}(\mu\text{-}(\text{bpy}\text{-CO-crown}))_2]A_2$ , (bpy-CO-crown = dioxobipyridil-12-crown-4) and A = (NO<sub>3</sub>)<sup>-</sup> (CIRWIK).<sup>280</sup>

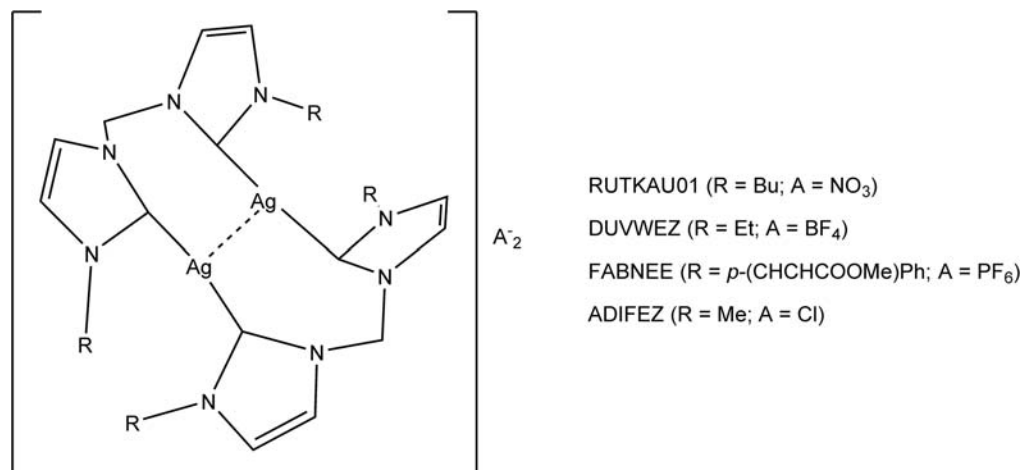
#### 1.15.3.7.2.5 Five-atom bridged Ag(I)

Similar to Au(I) structures, many Ag(I) structures with intramolecular argentophilic interactions are bridged by N-heterocyclic carbenes (NHCs). The NHCs are typically connected at opposing N by methylene or ethylene linker groups and coordinated to the interacting Ag(I) atoms by their central C. When the Ag is reduced, it has  $[\text{AgL}_2]^+$  classification and coordinated to the bridging NHCs in this way. Variations of R groups on the N and counteranion affect the strength of Ag(I)···Ag(I) interactions. For the following examples, structures with methylene linkers make up the five-atom bridging units (CNCNC). For the structure  $[\text{Ag}_2(\mu\text{-CH}_2(3,3'\text{-}R_2\text{-imid})_2)]A_2$ , Ag(I)···Ag(I) distance is: 3.231 Å when R = Bu and A = (NO<sub>3</sub>)<sup>-</sup> (RUTKAU01),<sup>281</sup> 3.246 Å when R = Et and A = (BF<sub>4</sub>)<sup>-</sup> (DUVWEZ),<sup>282</sup> 3.255 Å when R = *p*-(CH<sub>2</sub>COOMe)Ph and A = (PF<sub>6</sub>)<sup>-</sup> (FABNEE),<sup>283</sup> 3.318 Å when R = Me and A = Cl<sup>-</sup> (ADIFEZ).<sup>284</sup> (Scheme 95).

Substituents effects on bridging NHCs are easier to observe when the counteranion is the same for all structures. Due to the twisted conformation of the dimeric Ag(I) ring, sterics of the proximal R groups cause strengthening or weakening of the intramolecular Ag(I)···Ag(I) interaction. For the structure  $[\text{Ag}_2(\mu\text{-CH}_2(3\text{-}R\text{-pyz})_2)](\text{PF}_6)_{2n}$ , Ag(I)···Ag(I) distance is: 3.060 Å when R = BuN<sup>+</sup>pyr and *n* = 3 (VERJOT),<sup>285</sup> 3.226 Å when R = Me and *n* = 1 (GAGCEX),<sup>286</sup> 3.266 Å when R = Bu and *n* = 1



Scheme 94



Scheme 95

(GAGCIB).<sup>286</sup> A bulky substituent induces a greater bending angle of C–Ag–C, pushing the metals together. However, inherent conformation of the substituent could also widen the angle.

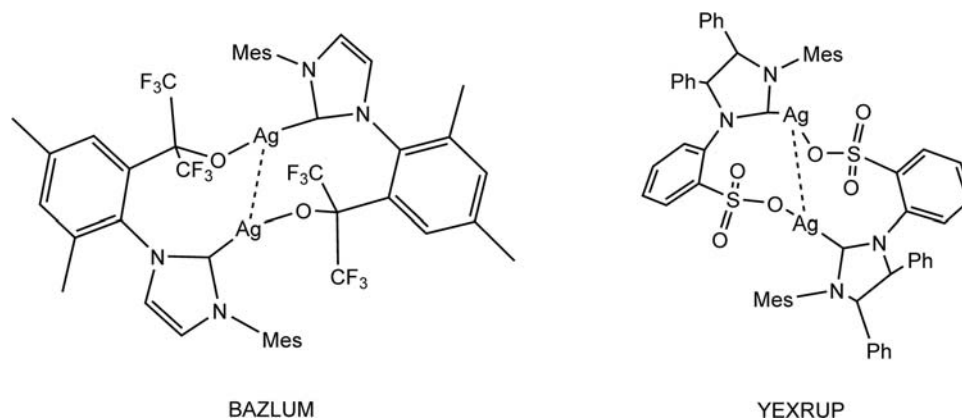
Another common form of five-bridged Ag(I)-NHCs utilizes another metal to create tetranuclear M<sup>1</sup><sub>2</sub>M<sup>2</sup><sub>2</sub> structures. In neutral or cationic form, these structures have potential for luminescence tunability. One set of examples compares neutral [AgLX] with chelated ligands on Pt(II). For the structure [Ag(μ-3,5-Me<sub>2</sub>pyz)<sub>2</sub>PtY]<sub>2</sub>, Ag(I)⋯Ag(I) distance is: 3.102 Å when Y = BHQ (MAGLOY),<sup>287</sup> 3.177 Å when Y = 2-pyrPh (MAGLEO),<sup>287</sup> 3.193 Å when Y = 2-pyr-3,5-F<sub>2</sub>Ph (MAGLIS).<sup>287</sup>

#### 1.15.3.7.2.6 Six-atom bridged Ag(I)

There are a large number of Ag(I) structures with intramolecular argentophilic interactions that are symmetrically bridged by seven, nine, and more atoms bridging the two metals. Typically, they are two-coordinate with [AgLX] classification. The following two examples are rare six-atom bridged structures with unsymmetric ligands. The structure [Ag(3-Mes(imid)-4,6-Me<sub>2</sub>Ph-2-C(CF<sub>3</sub>)<sub>2</sub>O)]<sub>2</sub> (BAZLUM)<sup>288</sup> has a Ag(I)⋯Ag(I) distance of 2.913 Å. The structure [Ag(3-Mes-4,5-Me<sub>2</sub>(imid)-Ph-2-SO<sub>2</sub>O)]<sub>2</sub> (YEXRUP)<sup>289</sup> has a Ag(I)⋯Ag(I) distance of 3.027 Å (Scheme 96).

#### 1.15.3.8 Cu⋯Cu interactions

The effects of *d*<sup>10</sup>⋯*d*<sup>10</sup> interactions in solid state compounds were recognized and reviewed in 1987,<sup>22</sup> including Cu(I)⋯Cu(I) interactions. While not part of the earliest observations termed metallophilic, cuprophilic interactions, once a topic of debate,<sup>33</sup> are now widespread in the coordination chemistry literature, and have been reviewed.<sup>18</sup> Like the heavier congeners Au and Ag, the Cu(I) *d*<sup>10</sup> ion is well-suited to metallophilic interactions due to its electronic structure. Unlike Ag and Au, Cu(I) is a quite stable oxidation state and is not so readily reduced to Cu(0). Hundreds of structures have Cu⋯Cu distances between 2.2 Å and 2.90 Å, both intra- and intermolecular. Again, as seen with Au and Ag, the lack of any directional preference due to ligand field stabilization energy, makes innumerable structural motifs possible, and is indicated in the very wide range of structures described below. As with



Scheme 96



previous sections, we have excluded cluster compounds with polynuclear species with triangular  $[\text{Cu}_3]$  or  $[\text{Cu}_2\text{M}]$  units from the structural survey.

### 1.15.3.8.1 Intermolecular $\text{Cu} \cdots \text{Cu}$ metallophilic interactions

The most clear examples of intermolecular cuprophilic interactions are unsupported ones between neutral compounds, or between ions of like charge, and particularly those that are two-coordinate. As with the  $d^{10}$  configurations in Au and Ag, there are many linear  $\text{Cu(I)}$  species, but unlike those metals, there are many more geometries as well, as will be seen later in this section.

#### 1.15.3.8.1.1 Two-coordinate $\text{Cu(I)}$

There are  $[\text{LCuX}]$  species that pair with each other with  $[\text{Cu}(\text{C}_6\text{F}_5)(\text{py})]$ , **MAKXUS**, and  $[(\text{F}_5\text{C}_6)\text{Cu}(4,4'\text{-bpy})\text{Cu}(\text{C}_6\text{F}_5)]$  units stack together through  $\text{Cu} \cdots \text{Cu}$  distances of 2.892 and 3.639 Å respectively.<sup>290</sup> The simple species  $[\text{Cu}(4\text{-NC}_6\text{H}_4\text{CO}_2)]$ , **IPINAY**, has linear  $\text{Cu(I)}$  centers linked into a quasi-1D chain via the *para* pyridyl and carboxylate groups, and whose chains stack via cuprophilic interactions at 2.778 Å<sup>291</sup> (**Scheme 97**)

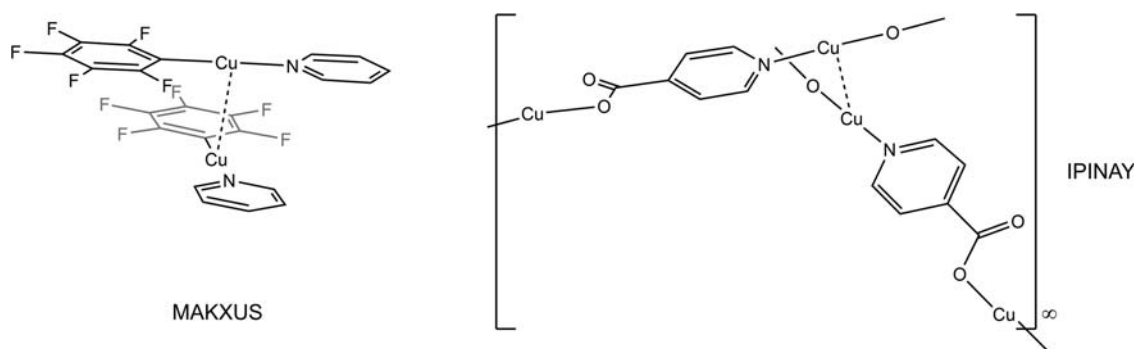
Linear  $\text{Cu(I)}$  anions with the stoichiometry  $[\text{CuX}_2]^{1-}$  in  $\text{Cs}[\text{Cu}(\text{CF}_3)_2]$  dimerize in **QOCNUU**, which was prepared to study  $\text{CF}_3$  transfers.<sup>292</sup> The  $[\text{CuCl}_2]^{1-}$  anion also dimerizes at 2.922 Å in the presence of an iminium cation, **GUWQIY**.<sup>293</sup> In both examples the linear units are in a staggered configuration with respect to one another to minimize steric repulsion (**Scheme 98**).

Examples of a  $[\text{Cu(L)}_2]^+$  without Cu in the anion are known in  $[[\text{Cu}(\text{NH}_3)_2]_2]^{2+}$ , both with  $\text{F}^-$  anions in  $[\text{Cu}(\text{NH}_3)_3]_2[\text{Cu}_2(\text{NH}_3)_4]\text{F}_4 \cdot 4\text{NH}_3$ ,<sup>294</sup> has also been characterized with a phenol-phenolate anion (not shown) in **LASYAG**.<sup>295</sup>

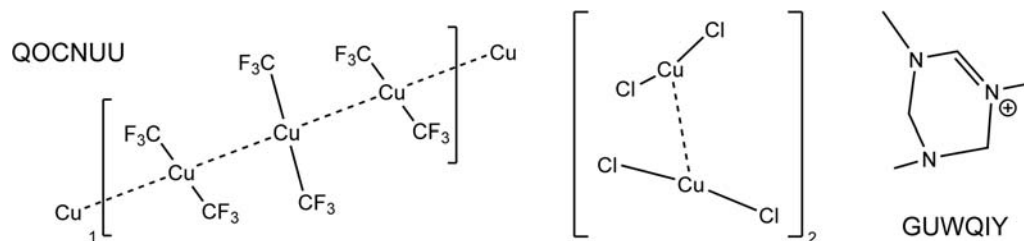
#### 1.15.3.8.1.2 Higher-coordinate $\text{Cu(I)}$

A  $[\text{Cu}(\mu_2\text{-L})(\mu_2\text{-X})_n]$  coordination polymer of  $\text{Cu(I)}$  results with bromide and thione as complementary bridging ligands and  $\text{Cu(I)} \cdots \text{Cu(I)}$  distances of 2.824 Å and 3.001 Å respectively in **TIZBOW**<sup>296</sup> (**Scheme 99**)

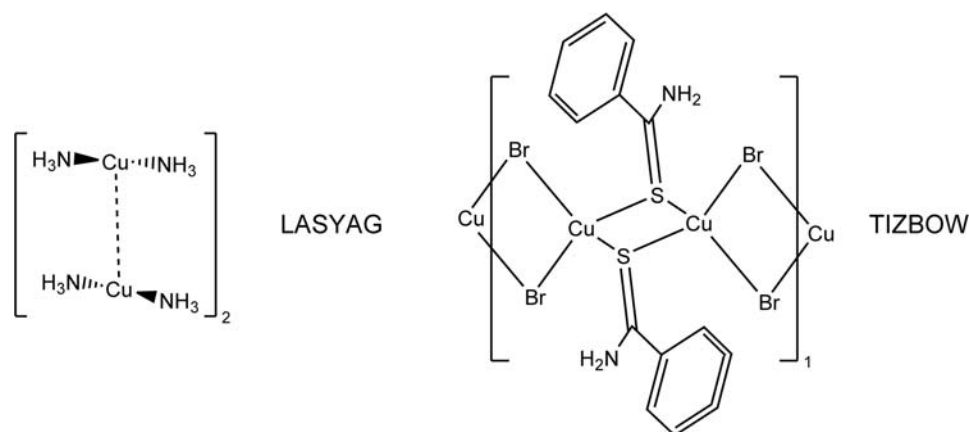
The unusual trigonal-planar  $\text{Cu(I)}$  center in  $[\text{Cu}(\text{CN})_3]^{2-}$  stacks with itself in a ladder-like chain in **CEJWOE** at a distance of 2.666 Å, as part of a mixed valent 2D assembly.<sup>297</sup> There are also unsupported cuprophilic interactions between cations and anions. Double salts of the form  $[\text{CuL}_2][\text{CuX}_2]$  are less common in Cu chemistry but a handful have been reported, such as the stacking of  $[\text{Cu}(\text{hppMe})_2][\text{CuCl}_2]$  (HppMe is an aliphatic guanidinium derivative<sup>298</sup>) and  $[(\text{CG1}')_2\text{Cu}]^+[\text{CuCl}_2]^-$ , **CIXFUN**,<sup>299</sup> in which CG1' is a cyclic guanidinium derivative. SCXRD shows the coprophilic interaction of 2.789 Å to be complemented by hydrogen bonding between Cl and NH atoms at 3.238 Å. Interestingly, the  $[(\text{CG1}')\text{CuCl}]$  monomer stacks with itself in the solid state and can interconvert via ligand exchange with the double salt in solution.<sup>299</sup> Such a salt formed an ionic liquid, **UQILAI**,<sup>300</sup> (not shown) with a dodecyl-alkylated imidazolium ligand, L, on the cation, stacking with  $[\text{CuBr}_2]^{1-}$  (**Scheme 100**).



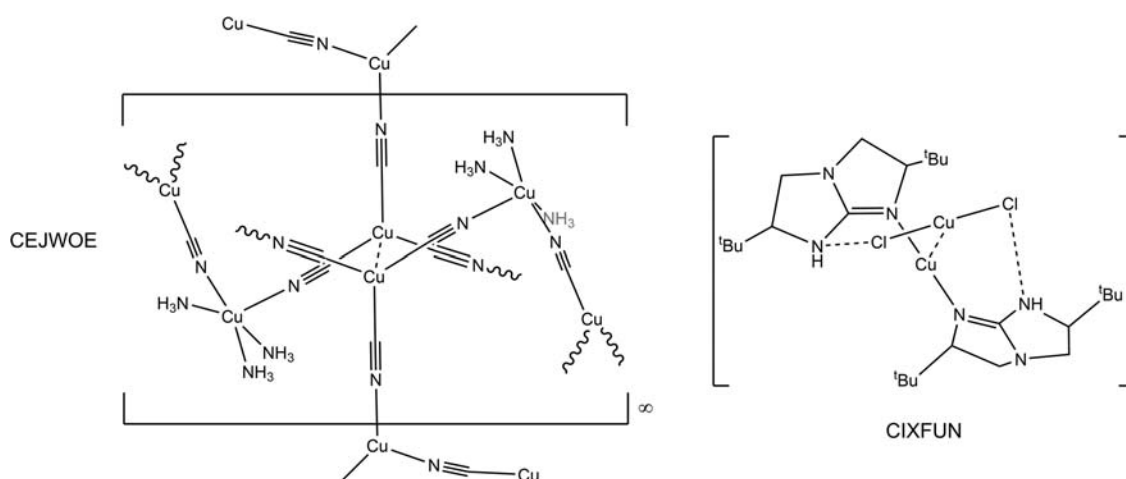
**Scheme 97**



**Scheme 98**



Scheme 99



Scheme 100

### 1.15.3.8.2 Intramolecular Cu···Cu metallophilic interactions

#### 1.15.3.8.2.1 One-atom bridged Cu(I)

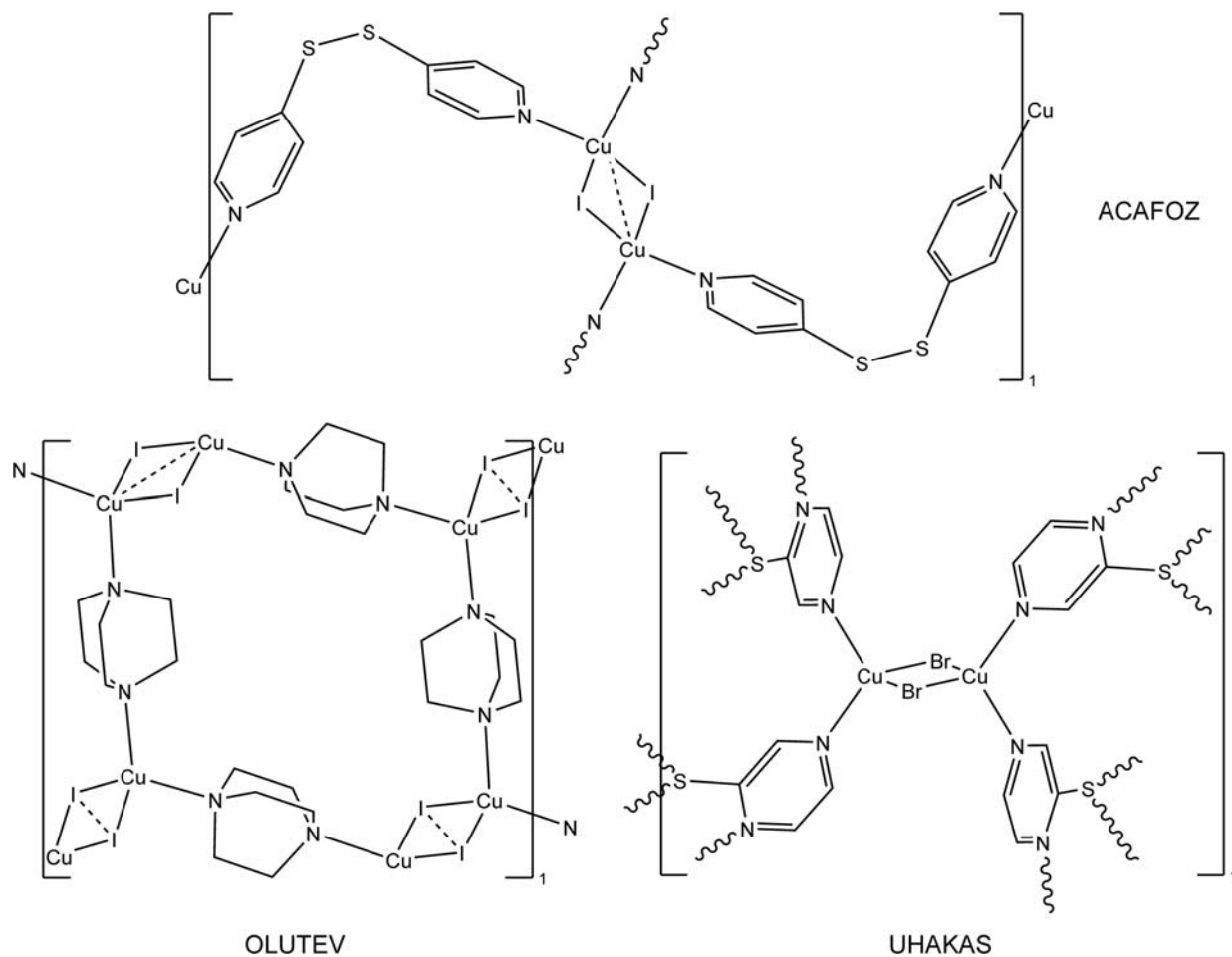
Many examples of intramolecular cuprophilic interactions have been observed due to the very wide range of ligands and coordination environments compatible with the geometrically plastic Cu(I). A very common motif in cuprophilic chemistry is a rhomb with  $[\text{Cu}(\text{I})_2(\mu_2\text{-X})_2]$  stoichiometry. Two halide ligands bridge the two Cu(I) centers between which the metallophilic interaction is present. The ligands that fill out the rest of the Cu coordination spheres are varied, but quite common is the  $[\text{L}_2\text{Cu}(\mu_2\text{-X})_2]$  motif in which each Cu center has a pseudo-tetrahedral geometry. These motifs are often a part of coordination polymers in which the L-donor ligands bridge Cu centers as shown in **ACAFOZ** (2.648 Å)<sup>301</sup> and **OLUTEV** (2.767 Å).<sup>302</sup> The most common such rhombs have the iodide-containing  $[\text{Cu}_2\text{I}_2]$  unit, though Br examples (**UHAKAS**, 2.671 Å)<sup>303</sup> are also known (**Scheme 101**).

The terminal L donors are often part of a chelate ring which can vary in size as shown in **BOYMEI**,<sup>304</sup> **BUPYUI**,<sup>305</sup> and **CBZTET**.<sup>306</sup> From left to right are visible a six-membered chelate ring with L donor phosphines and bridged telluride ligands, asymmetrically bridging acetylides that are both  $\sigma$ -donors and  $\pi$ -acceptors forming a  $[\text{Cu}_3\text{C}_3]$  ring, and the adamantane-like core in the dianionic structure  $[\text{Cu}_4(\mu_2\text{-Sph})_6]^{2-}$  that has a tetrahedron of metallophilic interactions (**Scheme 102**).

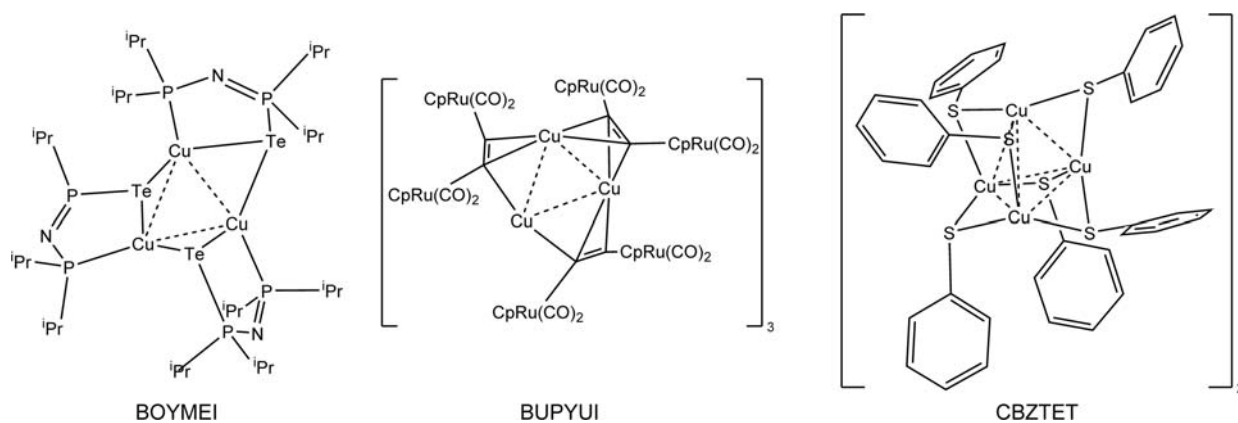
Ladders of metallophilic interactions are seen with  $[\text{LCuX}]$  units with four-coordinate Cu(I) centers alternating with  $\mu_3\text{-X}$  as seen in **FALYEW**<sup>307</sup> and **CEPFOS**.<sup>308</sup> These structures may be viewed as  $[\text{LCuX}]$  monomers that not only stack intermolecularly as described above, but are dimers that have intramolecular cuprophilic interactions and also intermolecular ones.

Another intramolecular cuprophilic motif is the  $[\text{Cu}_4(\mu_3\text{-X})_4]$  cubane (almost all with X = I) as shown in **IGITUP**<sup>309</sup> (2.657) and **NEYOG**<sup>310</sup> (2.683), and in **WUZDOL**<sup>311</sup> (2.660) which then have an L-type N donor, DABCO (1,4-diazabicyclo[2.2.2]octane) in these three cases, on each Cu that has three bridging halides also bound. When not bridged by halides a variety of other units are also observed in groups that bind to N-donors (**Scheme 103**).

Because Cu(I) can be stable with a coordination number of two, but does not exhibit a strong preference for linear coordination, a range of ring structures are common that exhibit short cuprophilic contacts within the ring. The tetramer  $[\text{Cu}_4(\text{mes})_4]$ , **NOMSAJ**,<sup>312</sup> is closely related to pentamer  $[\text{Cu}_5(\text{mes})_5]$ , **CAKPEJ**,<sup>37</sup> in which the structures show the power of metallophilic interactions

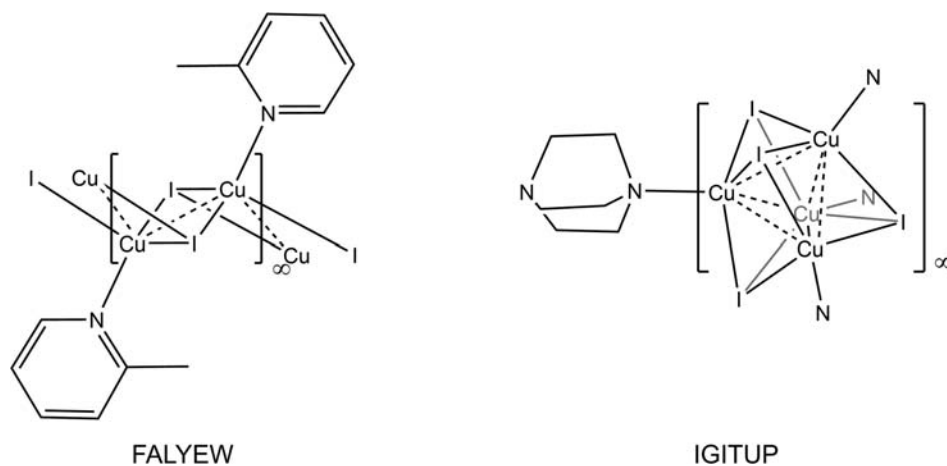


Scheme 101

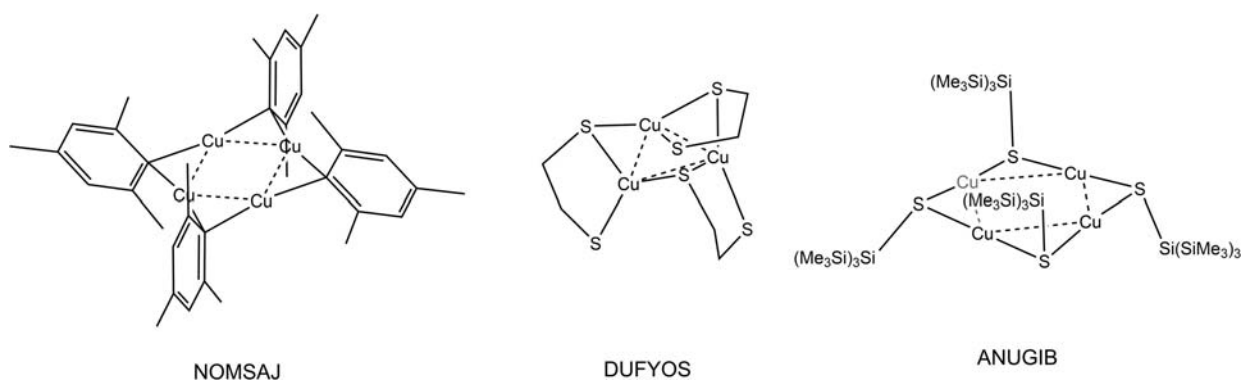


Scheme 102

to bring metal centers together. In both of these isomers, each pair of Cu centers is bridged by the negatively charged *ipso* carbon of a  $\mu_2$ -mestyl group. Six-membered rings are well known with cuprophilicity, as elsewhere in chemistry, and rings with  $[\text{Cu}_3(\mu_2\text{-X})_3]$  structures have been reported with simple anionic ligands such as terphenylthiolates in OSEMAC<sup>313</sup> or PhSe,<sup>314</sup> or more interesting ligands such as acetylene,<sup>305</sup> or the asymmetric ethane-1,2-dithiolate shown in DUFYOS<sup>315</sup> with both  $\mu_2$  and  $\kappa^1$  S donors. Furthermore, many eight-membered rings are known with  $[\text{Cu}_4(\mu_2\text{-X})_4]$  stoichiometries in which X can be a range of ligands including amides,<sup>316</sup> alkoxides,<sup>317</sup> phosphinimides,<sup>318</sup> and simple thiolates as in ANUGIB.<sup>319</sup>



Scheme 103



Scheme 104

With a different number of anions, rings with cuprophilic interactions are part of adamantane structures like KIHROI with six bridging thiolates, and cubes, as shown in CIHRIU with eight sulfides (Scheme 104).

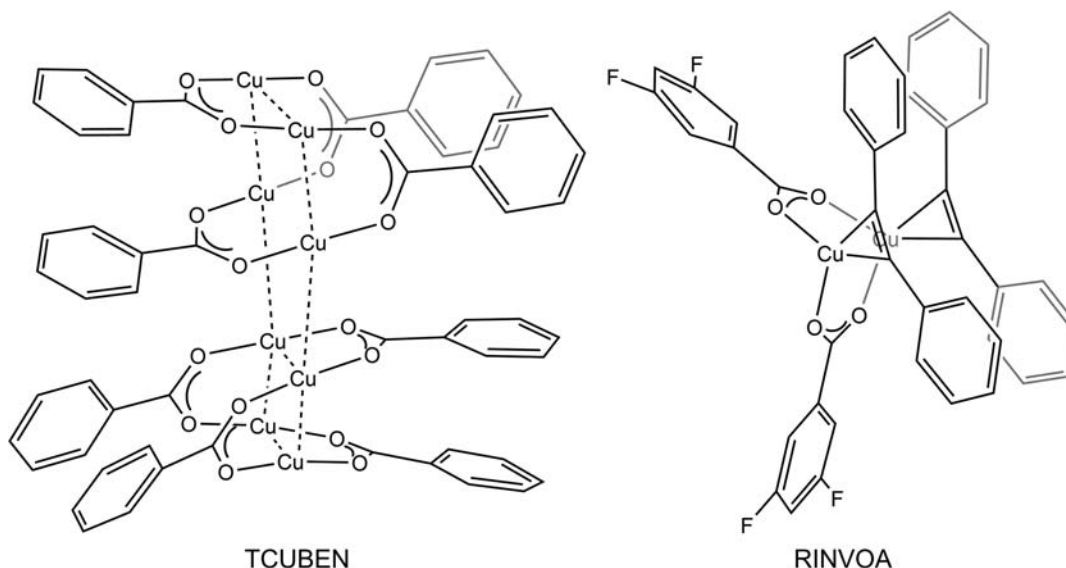
Numerous high nuclearity Cu(I) compounds have been prepared by a variety of means because the plasticity of Cu(I) coordination makes so many structures possible. The cluster  $[\text{Cu}_{15}(\text{CCTbu})_{10}(\text{O}_2\text{CCF}_3)_5]$ , UZUQIR,<sup>320</sup> exhibits strong thermochromic luminescence and can also be prepared in a related  $[\text{Cu}_{16}(\text{CCTbu})_{12}(\text{O}_2\text{CCF}_3)_4]$  stoichiometry, with distinct luminescence properties whose differences are attributed to the differences in metallophilic interactions between the two clusters.

Particularly large numbers of cuprophilic interactions are seen in a pair of Cu phosphine hydride clusters with  $[\text{Cu}_{16}\text{H}_{14}(\text{dppa})_6](\text{BF}_4)_2$  (dppa = bis(diphenylphosphino)amine) and  $[\text{Cu}_{18}\text{H}_{16}(\text{dppe})_6](\text{BF}_4)_2$  stoichiometries.<sup>321</sup>

#### 1.15.3.8.2.2 Two- or three-atom bridged Cu(I)

Cuprophilic interactions are also observed in structures with bridging groups that are diatomic or larger. Triatomic carboxylate bridges, ligands with L and X donor atoms tethered together, LX, are frequently seen because with two Cu atoms they can form five-membered rings and bring to Cu centers quite close together. Previous sections in this chapter have shown this motif with other metals such as XEBCAI (Rh<sub>2</sub>),<sup>84</sup> FIXCUN (Pt,Ni),<sup>128</sup> and COJBE<sup>322</sup> (Pd<sub>2</sub>) above. This group of structures does *not* include the legions of the paddlewheel (or lantern) Cu(II) carboxylate dimer structures,<sup>323</sup>  $[\text{Cu}_2(\text{O}_2\text{CR})_4(\text{L})_2]$ ,<sup>324,325</sup> of which  $[\text{Cu}_2(\text{OAc})_4(\text{OH}_2)_2]$  is the best known example. Because each Cu(II) center has a  $d^9$  electron configuration, the Cu···Cu interaction is not metallophilic, although the distances might seem to be in the right range. The chemistry of Cu in particular shows that the M···M distance alone is not indicative of a metallophilic interaction, because the electron configuration must also be one of the closed (sub)shell ones as described in the introduction.

When each Cu(I) center is bound only by two carboxylates, the solid state structures are often tetramers with no additional neutral ligands, e.g.  $[\text{Cu}_4(\text{O}_2\text{CR})_4]$ , as shown in TCUBEN<sup>326</sup> and is also known with trifluoroacetate<sup>327</sup> and partially fluorinated benzoates, when higher nuclearity structures are not observed.<sup>328</sup> Alternatively, when two  $\pi$ -acidic ligands are bound as in RINVOA,<sup>329</sup> each cuprophilic center is formally three-coordinate in the resulting dimer (Scheme 105).



Scheme 105

### 1.15.3.9 Hg···Hg metallophilic interactions

In the same row as Au, Hg(II)···Hg(II) contacts is often compared to the energetic contributions associated with the more widely-studied aurophilic interactions.<sup>19</sup> This section summarizes mercuriphilic interactions, within 2.55–3.69 Å.

#### 1.15.3.9.1 Intermolecular Hg···Hg metallophilic interactions

##### 1.15.3.9.1.1 Two-coordinate Hg(II)

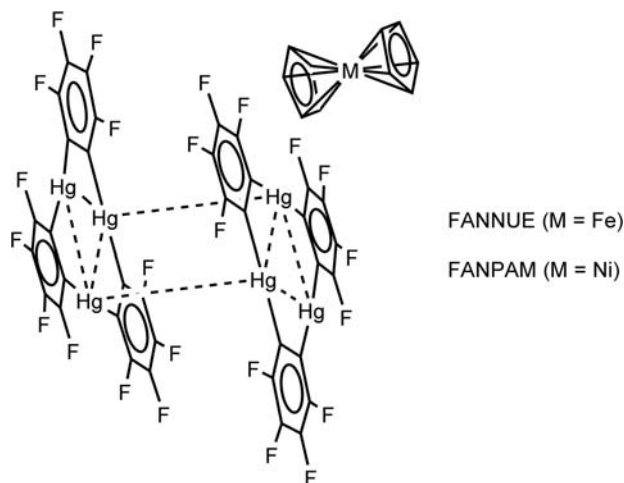
Trimeric perfluoro-*ortho*-phenylene mercury, [(*o*-C<sub>6</sub>F<sub>4</sub>Hg)<sub>3</sub>] is a highly studied polyfunctional Lewis acid with photophysical properties resulting from the mercury heavy-atom effect.<sup>330</sup> When [Cp<sub>2</sub>M] (M = Fe, Ni) is in the lattice of these structures, electrophilic double-sandwiches are formed, affecting intermolecular mercuriphilic distances. Hg(II)···Hg(II) separation of 3.4157 Å for the [Cp<sub>2</sub>Fe] adduct (FANNUE)<sup>330</sup> and 3.3996 Å for the [Cp<sub>2</sub>Ni] (FANPAM)<sup>330</sup> adduct are observed (Scheme 106).

#### 1.15.3.9.2 Intramolecular Hg···Hg metallophilic interactions

##### 1.15.3.9.2.1 One-atom bridged Hg(II)

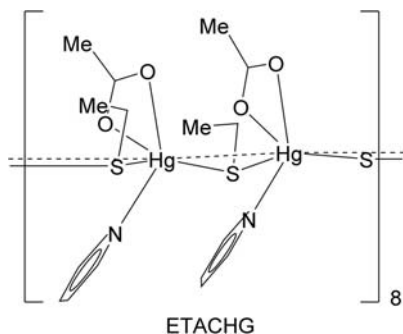
One example of an HgL<sub>3</sub>X<sub>2</sub> is (ETACHG),<sup>331</sup> composed of Hg bridged with methanethiol and crosslinked with acetate groups. The 98.4° angle of the Hg(b)-S-Hg(a) creates a 3.683 Å distance between Hg(II)···Hg(II) (Scheme 107).

Bridging Cl atoms between Hg(II) form one-dimensional chains with weak van der Waals contacts between the chains and are commonly found as counteranions in salts. The Hg–Cl bonds in the six-coordinate, elongated octahedral coordination of the



Scheme 106





Scheme 107

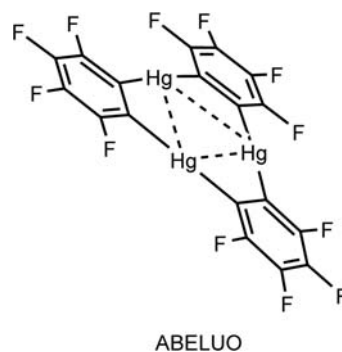
Hg(II) have bond lengths ranging from 2.312 Å to 3.120 Å, with the longest reported mercuriphilic interaction distance of 3.685 Å (CEGMOQ).<sup>332</sup>

#### 1.15.3.9.2.2 Two-atom bridged Hg(II)

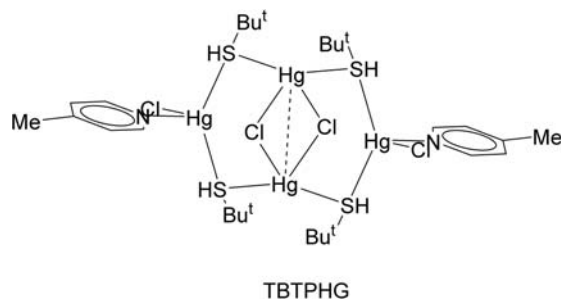
$\text{MX}_2$  classification of structures with  $\text{Hg(II)} \cdots \text{Hg(II)}$  contacts is the most common type present in literature. For the most common  $\text{MX}_2$  structures, the Hg(II) is coordinated to two sterically-demanding aromatic groups, with the most common of these groups being fluorinated aryl substituents. These structures have both inter- and intramolecular mercuriphilic interaction distances between 3.400 Å and 3.597 Å. The reaction of benzene with trimeric *o*-tetrafluorophenylene mercury forms trimeric perfluoro-*o*-phenylene mercury [ $(o\text{-C}_6\text{F}_4\text{Hg})_3$ ], which has an intramolecular distance of 3.597 Å (ABELUO).<sup>333</sup> For these stacked  $D_{3d}$  structures, Hg- $\pi$  secondary interactions are found to be the result of formation of a molecular orbital of  $A_{2u}$  symmetry and two degenerate molecular orbitals of  $e_g$  symmetry. These molecular orbitals result from  $\pi$ -electron donation of the benzene into sets of available  $6p$  orbitals of Hg (Scheme 108).

#### 1.15.3.9.2.3 Three-atom bridged Hg(II)

The TBTPHG tetrameric monomer core is both a one- and three-atom bridged complex with mercuriphilic interaction. It composed of four Hg atoms bridged by four thiol groups, with two opposing Hg bridged also by two Cl. The bulky -Hg-S- backbone creates a rigid plane of the tetramer core, and the backbone is linked to form the polymer. Due to this planarity, angles of the halide and thiol bridges give information about the  $\text{Hg(II)} \cdots \text{Hg(II)}$  distances. The  $\text{Hg(b)}\text{-Cl-Hg(b}^1\text{)}$  situates a tangential  $83.2^\circ$  angle, forming



Scheme 108



Scheme 109

one of the longest Hg(II)···Hg(II) distances of 3.648 Å. As such, the larger 102.5° angle of Hg(b)-S-Hg(a) creates a 3.852 Å distance of between the adjacent Hg, too long to be considered a mercuriphilic interaction (Scheme 109).

#### 1.15.3.9.2.4 Four-atom bridged Hg(II)

Addition of a second phenylene group between the Hg atoms of the ABELUO structure changes the symmetry from  $D_{3d}$  to  $D_3$  and contortion of the trimeric structure (BIPHHG01)<sup>334,335</sup>. Average intermolecular Hg(II)···Hg(II) separation of 3.42 Å is again observed as shorter than the intramolecular Hg(II)···Hg(II) range of 3.51–3.61 Å (Scheme 110).

E. Hupf et al. synthesized two mercuraphosphane structures of that exhibit intramolecular mercuriphilic interactions. Two diphenylphosphinoacenaphthyl ligands provide bulky bridges between an  $\text{MX}_2$  Hg(II) atom and an  $\text{ML}_2\text{X}_2$  Hg(II) atom (POZWAE)<sup>336</sup> (POZXEJ).<sup>336</sup> The  $\text{MX}_2$  Hg(II) atom is directly bound to an acenaphthyl group of the ligand, while the  $\text{ML}_2\text{X}_2$  Hg(II) atom is bound to the diphenylphosphino group. The L-type ligands of POZWAE and POZXEJ are  $\text{Cl}^-$  and  $(\text{O}_3\text{SCF}_3)^-$ , respectively. Steric hindrance of POZXEJ likely attribute to its shorter Hg(II)···Hg(II) distance of 3.0332 Å compared to 3.1401 Å of POZWAE (Scheme 111).

### 1.15.4 Homodinuclear p-block (groups 13–15) M···M complexes with metallophilic interactions

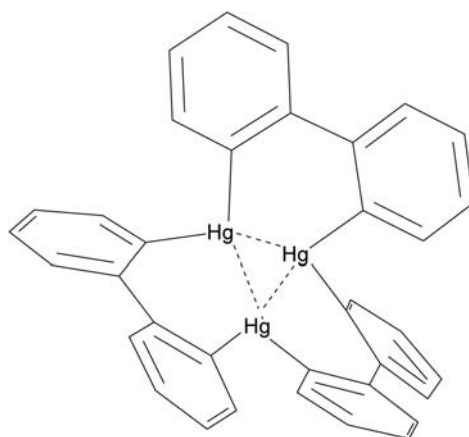
#### 1.15.4.1 Tl···Tl metallophilic interactions

Thalophilic contacts are observed within very few structures. A nonstandard coordination geometry of Tl(I) structures is partly attributed to the  $6s^2$  lone pair of electrons. As the covalent radius and van der Waals radius of Tl are 1.45 Å and 1.96 Å, respectively, only structures with Tl(I)···Tl(I) distances between 2.90 Å and 3.92 Å are discussed in this section.

##### 1.15.4.1.1 Intermolecular Tl···Tl metallophilic interactions

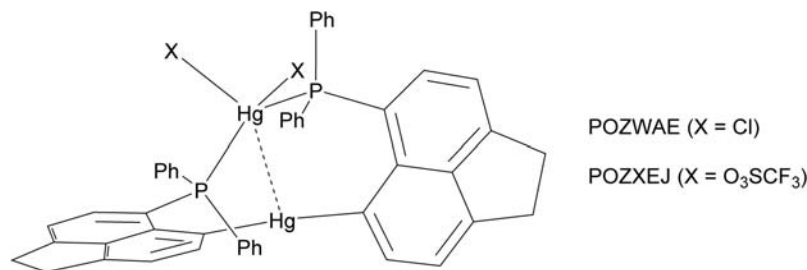
###### 1.15.4.1.1.1 Two-coordinate Tl(I)

Of the various two-coordinate Tl(I) structures, Tl(I) with ferrocenyl/pyridyl functionalized dithiocarbamate ligands are the most common. The Tl(I) dithiocarbamate core of these structures have various substituents that influence intermolecular Tl(I)···Tl(I) distance. These structures are denoted as  $[\text{Tl}(\text{L})]_\infty$ : L = (N-benzyl-N-methylpyridyl) dithiocarbamate (GOQHUR)<sup>337</sup>; L = bis(N-methylpyridyl) dithiocarbamate (GOQJED)<sup>337</sup>; L = (N-methylpiperonyl-N-methylpyridyl) dithiocarbamate (GOQJON)<sup>337</sup>;



BIPHHG01

Scheme 110



Scheme 111

L = (N-ferrocenyl-N-methylpyridyl) dithiocarbamate (GOQKAA)<sup>337</sup>; L = (N-ferrocenyl-N-methyl) dithiocarbamate (FEGHIL)<sup>338</sup>; L = (N-4-chlorobenzyl-N-3-methylpyridyl) dithiocarbamate (FEGHUX)<sup>338</sup>; L = (N-4-methylbenzyl-N-3-methylpyridyl) dithiocarbamate (FEGJAF).<sup>338</sup> Tl(I)···Tl(I) distances are 3.771 Å, 3.817 Å, 3.763 Å, 3.734 Å, 3.576 Å, 3.765 Å, 3.787 Å, respectively. The Tl(I)···Tl(I) interactions, conformational rigidity of the structures, and polymeric arrangement of the structures are found to affect luminescence in the solid state (Scheme 112).

#### 1.15.4.1.1.2 Three-coordinate Tl(I)

Three-coordinate Tl(I) structures are most commonly synthesized with tris(pyrazolyl)borate, or scorpionate, ligands. Substitution of the pyrazolyl groups, particularly in the 3-position, clearly affects the intermolecular Tl(I)···Tl(I) distances. The shortest distance of 3.639 Å (UXOFEU02),<sup>339</sup> is likely due to the opposing direction of the third mesityl group, away from the Tl(I)···Tl(I) interaction. Comparing the phenyl versus *p*-toluene substituents in ASADAZ and TAMZAI, respectively, the smaller phenyl groups allow shorter observed distance of 3.853 Å (ASADAZ)<sup>340</sup> and 3.864 Å (TAMZAI)<sup>341</sup> (Scheme 113).

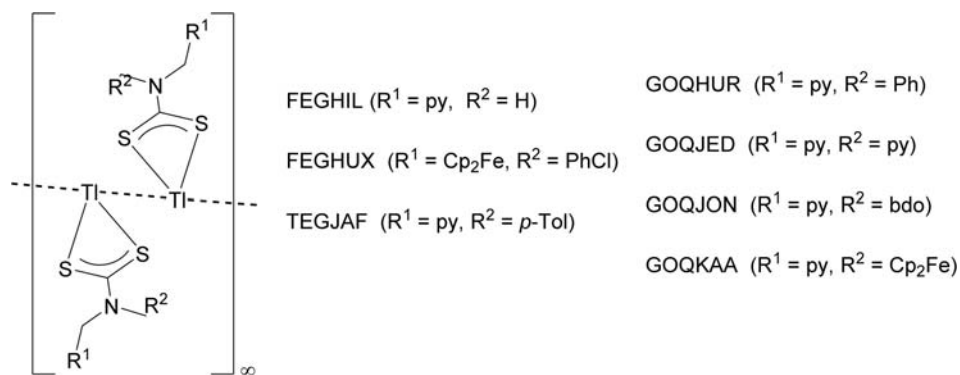
#### 1.15.4.1.1.3 Four-coordinate Tl(I)

The Tl compound WAJDIU with a 2,5-dimethyl-*N,N'*-dicyanoquinone-diimine linker forms a network of linked Tl(I) ions, with intermolecular and interplanar Tl(I)···Tl(I) distances of 3.809 Å (WAJDIU).<sup>342</sup> This structure was studied for its one-dimensional metal-like semiconducting property, which was expected to be similar to potassium and silver analogues (Scheme 114).

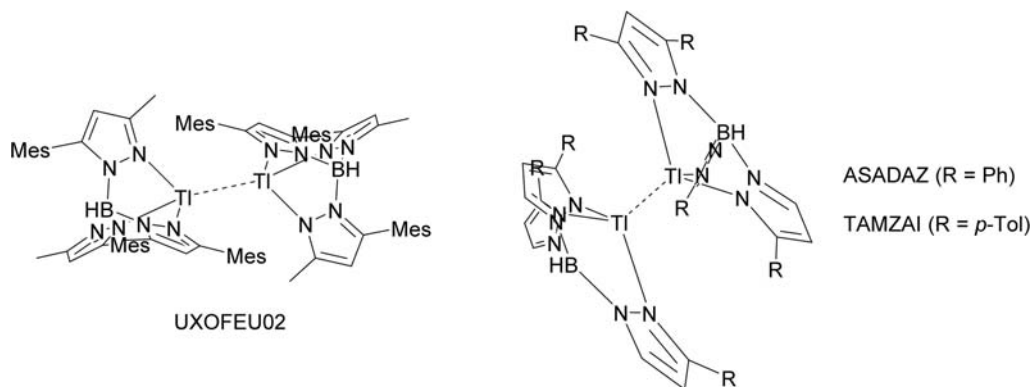
### 1.15.4.1.2 Intramolecular Tl···Tl metallophilic interactions

#### 1.15.4.1.2.1 Miscellaneous Tl(I)

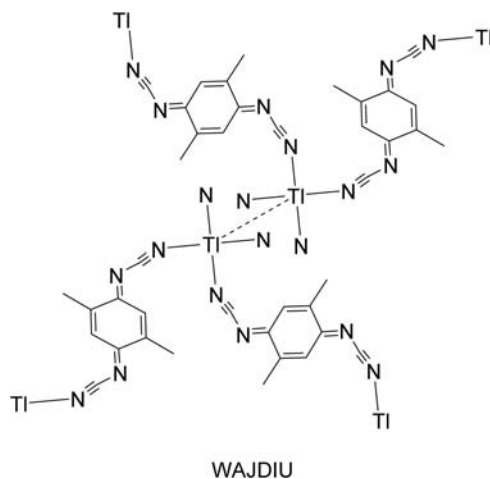
Only a few Tl(I) structures with intramolecular Tl(I)···Tl(I) metallophilic interactions have been synthesized, with distances ranging from 3.884 Å to 3.919 Å and a mean distance of 3.903 Å. The influence of thalophilic interaction on supramolecular assemblies and stability of monomers were studied with Tl(I) salicylates and anthranilates, which have a Tl(I)···Tl(I) distance of 3.906 Å in one example structure (JENVAA).<sup>343</sup> However, variations of ligand substituents for these structures caused more observable changes in the monomer aggregates (Scheme 115).



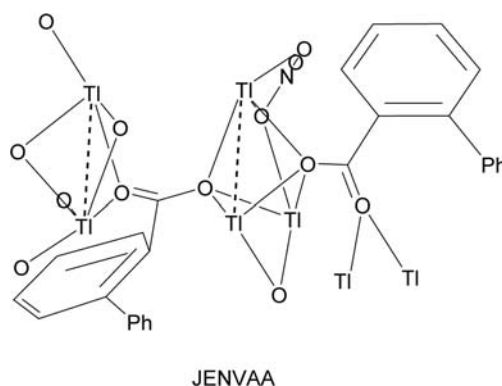
Scheme 112



Scheme 113



Scheme 114



Scheme 115

#### 1.15.4.2 Pb···Pb metallophilic interactions

Structures with Pb(II)···Pb(II) distances between 2.920 Å and 4.040 Å exhibit metallophilic interactions. These structures have Pb(II) ions, isoelectronic to Tl(I), with the  $s^2$  valence electron configuration. As a heavy  $p$ -block metal ion, Pb(II) has a large radius and flexible, hemidirected coordination environment that provides unique opportunities for geometry formation.

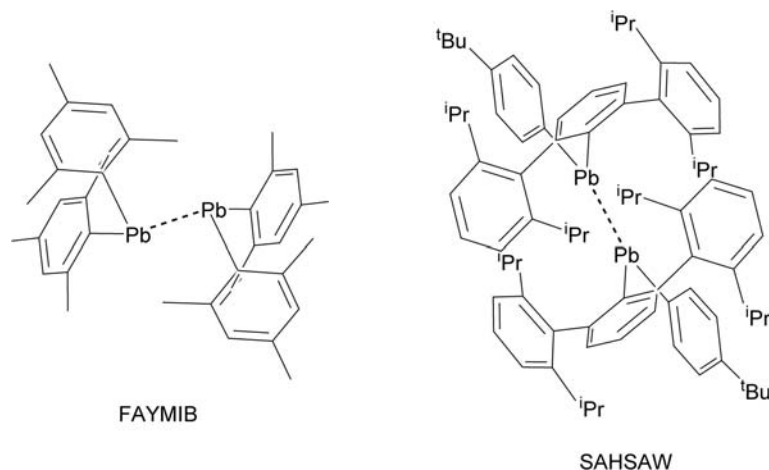
##### 1.15.4.2.1 Intermolecular Pb···Pb metallophilic interactions

###### 1.15.4.2.1.1 Two-coordinate Pb(II)

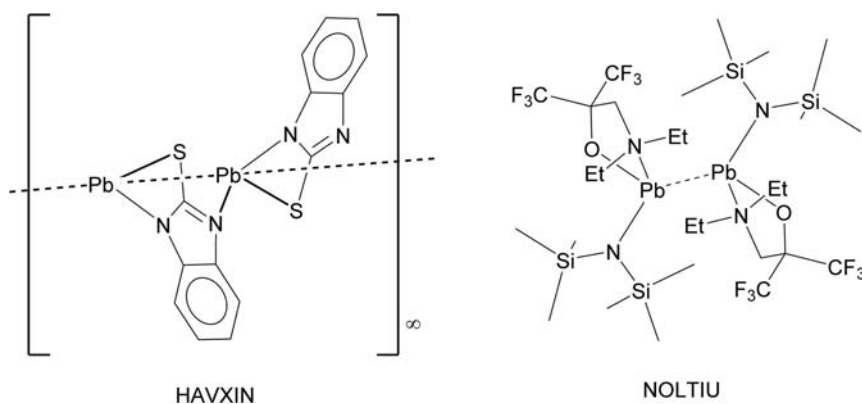
Pb(II) structures with  $PbX_2$  stoichiometries and a stereochemically active lone pair have a bent geometry and can form either diplumbenes with a  $Pb=Pb$  double bond or plumbylene dimers composed of two metallophilically bonded plumbylene monomers. The latter results from the intrinsic weakness of the donor-acceptor interaction of the valence  $6s$  orbitals of the Pb(II) atoms. One example of this structure is the bis(mesityl)plumbylene dimer with Pb(II)···Pb(II) contact of 3.355 Å (FAYMIB).<sup>344</sup> The dimer is stabilized by the weak interaction of a Br atom of a linear  $MgBr_2(THF)_4$  molecule (not shown) with a Pb atom. Close, non-bonded approach of two Pb(II) atoms of  $Pb(C_6H_4-4-tBu)Ar^iPr_2$  terphenyl monomers displays a Pb(II)···Pb(II) distance of 3.947 Å without a stabilizing Lewis acid (SAHSAW).<sup>345</sup> Crystal packing effects and steric interference of the  $p$ - $tBu$  groups on the phenyl substituents attribute to its longer Pb(II)···Pb(II) metallophilic interaction (Scheme 116).

###### 1.15.4.2.1.2 Three-coordinate Pb(II)

Three-coordinate Pb(II) structures, with  $LX_2$  donors, commonly exhibit a trigonal pyramidal geometry that allows for intermolecular metallophilic interaction, with Pb(II)···Pb(II) distances ranging from 3.771 Å to 3.990 Å with a mean distance of 3.885 Å. For example, the Pb(II) arene coordination polymer [Pb(bimS)] (HbimSH = 2-mercaptobenzimidazole) (HAVXIN).<sup>346</sup> Pb- $\pi$  interaction of the metal with opposing benzene groups exhibit a Pb(II)···Pb(II) distance of 3.937 Å. A three-coordinate heteroleptic Pb(II) amide that is also coordinated to a bidentate alkoxy amine is NOLTIU. Even without the Pb- $\pi$  interaction, the intermolecular Pb(II)···Pb(II) distances of 3.990 Å is observed, facilitated by the trigonal pyramidal geometry of the metal (Scheme 117).



Scheme 116



Scheme 117

One example of a reduced  $[\text{PbL}_2\text{X}]^+$  Pb(II) structure is that of tris(2-mercapto-1-phenylimidazolyl)hydroborato,  $[(\text{Tm}^{\text{Ph}})\text{Pb}]^+$ , which has a Pb atom bonded to three neutral S donors in **EBEXEO**.<sup>347</sup> The reduced tendency of the Pb(II) to bind to a fourth ligand, compared to the analogous  $[(\text{Tm}^{\text{Ph}})\text{Zn}(\text{NCMe})]^+$ , instead exhibits intermolecular Pb(II)⋯Pb(II) distance of 3.986 Å (**Scheme 118**).

#### 1.15.4.2.1.3 Four-coordinate Pb(II)

Four-coordinate Pb(II) structures typically have a “saw-horse” structure, with Pb(II)⋯Pb(II) distances ranging from 3.562 Å to 4.038 Å and a mean distance of 3.840 Å. Common structures are composed of Pb(II) atoms coordinated to chelating ligands such as acac (**YAGLAT**).<sup>348</sup> The tendency for Pb(II) to form also allows multiple metallophilic interactions to occur, such as the three intermolecular Pb(II)⋯Pb(II) distances of  $[\text{Pb}(\text{C}_4\text{H}_6\text{O}_3)_2]^{2-}$  that have an average separation of 3.899 Å (**ZAHHOF**)<sup>349</sup> (**Scheme 119**).

Other four-coordinate structures mix chelating groups with Group 5 and Group 6 atoms coordinated to Pb(II). Three example structures have Pb(II)⋯Pb(II) distances of 3.565 Å (**FATMEU**),<sup>350</sup> 3.610 Å (**MILLID**),<sup>351</sup> and 3.978 Å (**QEWKEL**),<sup>352</sup> varied by sizes of the chelating ligands (**Scheme 120**).

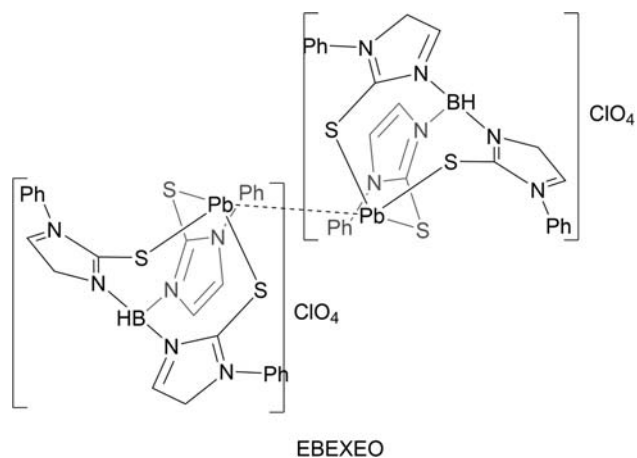
#### 1.15.4.2.1.4 Five-coordinate Pb(II)

The hemidirected coordination sphere of Pb(II) is further emphasized with five-coordinate structures. Pb(II)⋯Pb(II) distances are scarcely different from the lower-coordination Pb(II) structures, with intermolecular separation ranging from 3.632 Å to 4.024 Å with a mean distance of 3.893 Å. Coordination to bulky ligands such as terpyridine (**QASDIZ**)<sup>353</sup> and benzoate (**YICQEH**)<sup>354</sup> groups with large, extended substituents have little effect on the metallophilic interactions (**Scheme 121**).

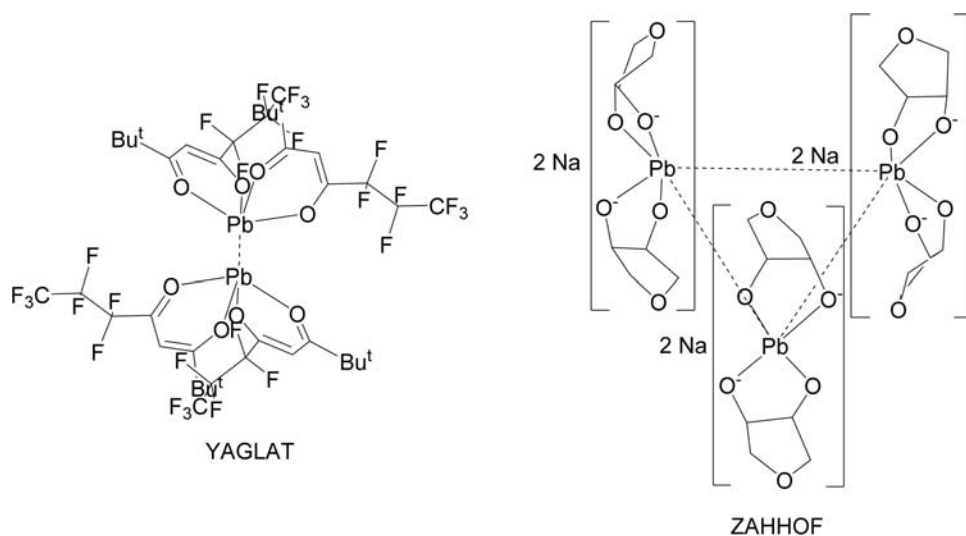
#### 1.15.4.2.1.5 Six-coordinate Pb(II)

Most six-coordinate Pb(II) structures have combinations of a bipyridine or a terpyridine ligand and two β-diketone ligands. Intermolecular Pb(II)⋯Pb(II) distances are not affected by high coordination of the metal, with separation ranging from 3.639 Å to





Scheme 118



Scheme 119

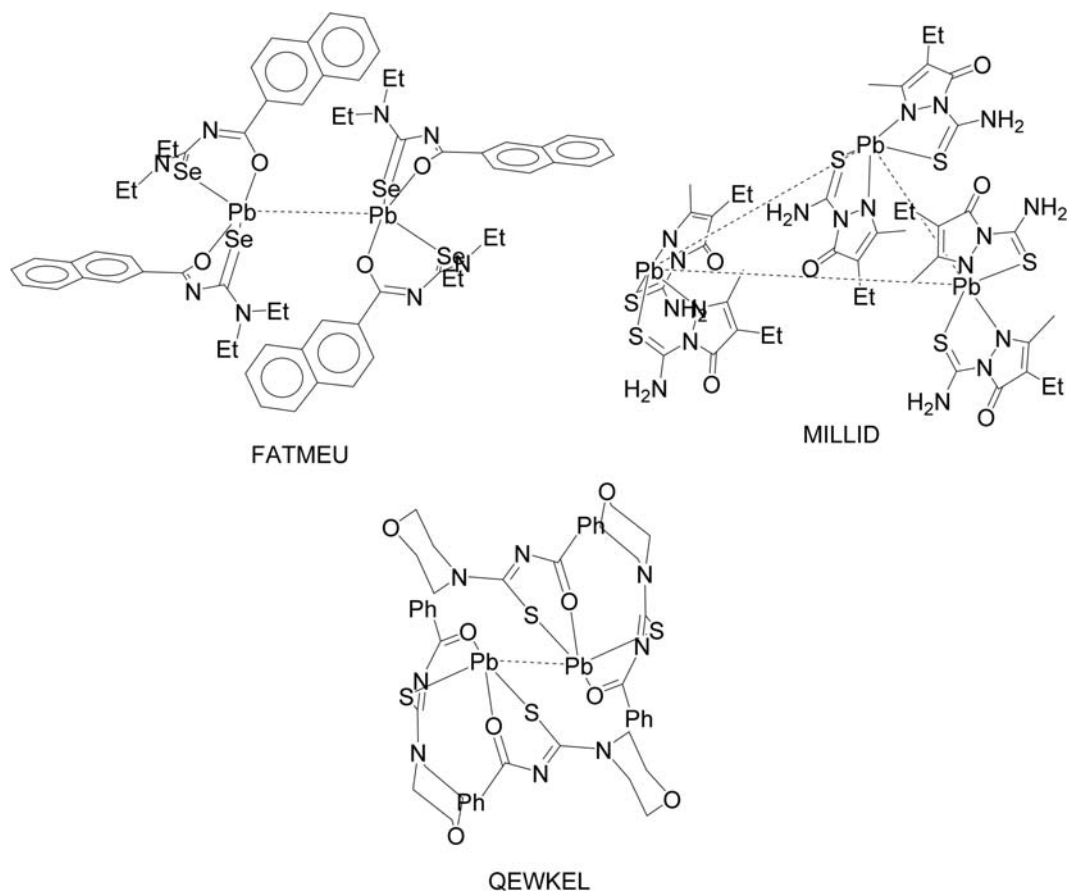
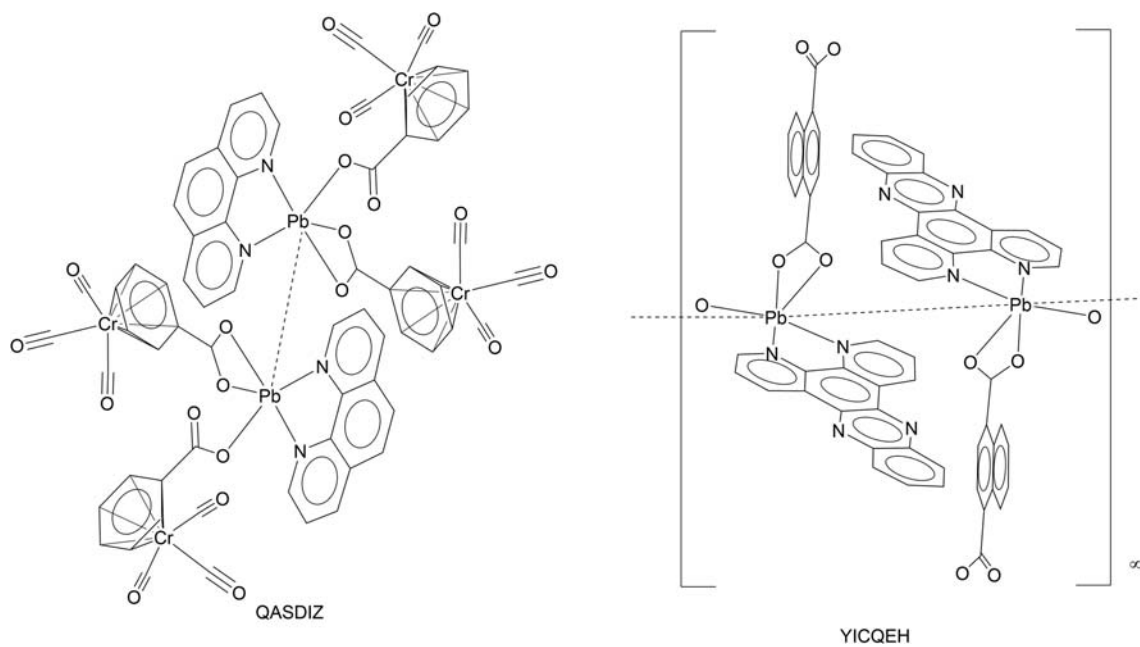
4.035 Å with a mean of 3.825 Å. Crystal packing is affected by ligand substituent position changes, seen with Pb(II) thenoyltrifluoroacetate structures with substituted 2,2'-bipyridines. Dimethyl substitution on the 4,4' positions of bipyridine exhibits a Pb(II)⋯Pb(II) distance of 3.639 Å (NUWHOD), while dimethyl substitution on the 5,5' positions of bipyridine causes a ~0.4 Å longer separation of the Pb(II) structures of 4.035 Å (NUWHUI).<sup>355</sup> However, replacing the 4,4' dimethyl groups with larger dimethoxy groups causes a shift of ~0.03 Å, with a Pb(II)⋯Pb(II) distance of 3.667 Å (NUWJAR) (Scheme 122).

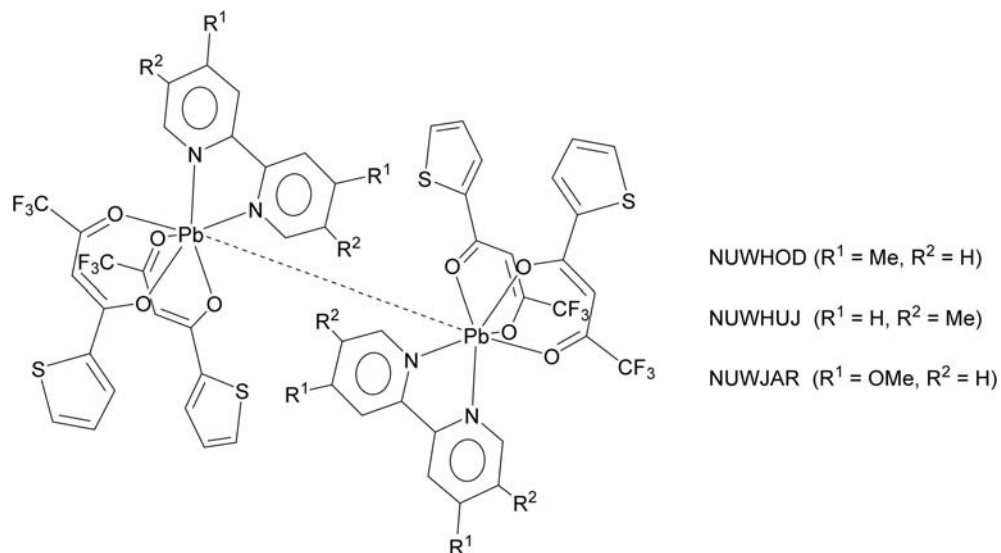
Similar observations of aromatic ring substitution affecting Pb(II)⋯Pb(II) intermolecular distance can be seen with Pb(II) structures with phenyl or naphthyl-containing fluorine β-diketones. For the Pb(II) structures with phenyl-containing fluorine β-diketones, dimethoxy substitution on the 4,4' positions of bipyridine exhibits a Pb(II)⋯Pb(II) distance of 3.856 Å (TAJKOG),<sup>356</sup> while dimethyl substitution on the 5,5' positions of bipyridine exhibits 3.980 Å separation (TAJKIA).<sup>356</sup> Further, a Pb(II)⋯Pb(II) intermolecular distance of 3.647 Å is observed with [Pb(5,5'-dm-2,2'-bpy)(tfnb)<sub>2</sub>]<sub>2</sub> (tfnb = 4,4,4-trifluoro-1-(2-naphthyl)-1,3-butanedione) (TAJKUM)<sup>356</sup> (Scheme 123).

#### 1.15.4.2.2 Intramolecular Pb⋯Pb metallophilic interactions

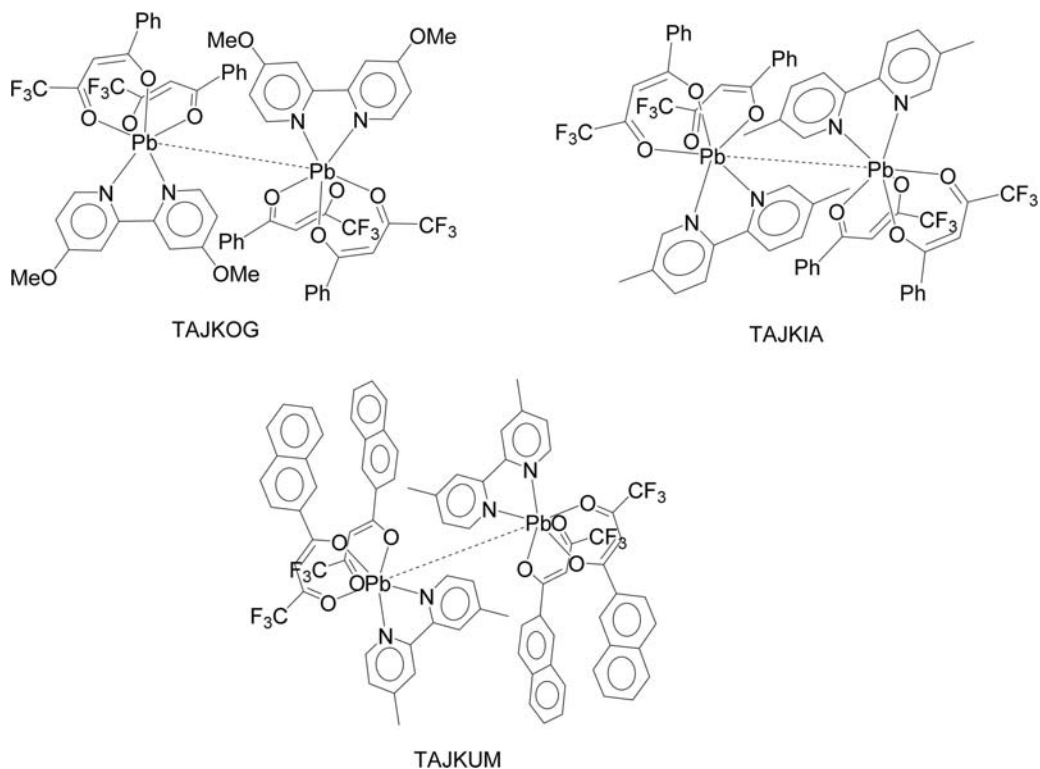
##### 1.15.4.2.2.1 Miscellaneous Pb(II)

The small number of structures that exhibit intramolecular Pb(II)⋯Pb(II) metallophilic interactions vary vastly with few common patterns. Intramolecular Pb(II)⋯Pb(II) distances range from 3.274 Å to 3.985 Å with a mean distance of 3.790 Å. Two of these structures each bridge six-coordinate Pb(II) atoms with chelating ligands, forming eight-membered rings. The Pb(II) of (2,2'-bipyridine)lead(II) saccharinate monohydrate is coordinated to two bpy N atoms, two N from saccharinate ligands, and a water molecule (BEHNUX).<sup>357</sup> The sixth coordination connects one Pb(II) center to the O of an adjacent saccharinate on the other Pb(II) atom, exhibiting an intramolecular Pb(II)⋯Pb(II) distance of 3.929 Å. The compound JEKTA has a [Pb<sub>2</sub>(O<sub>2</sub>CR)<sub>4</sub>] pseudo-

**Scheme 120****Scheme 121**



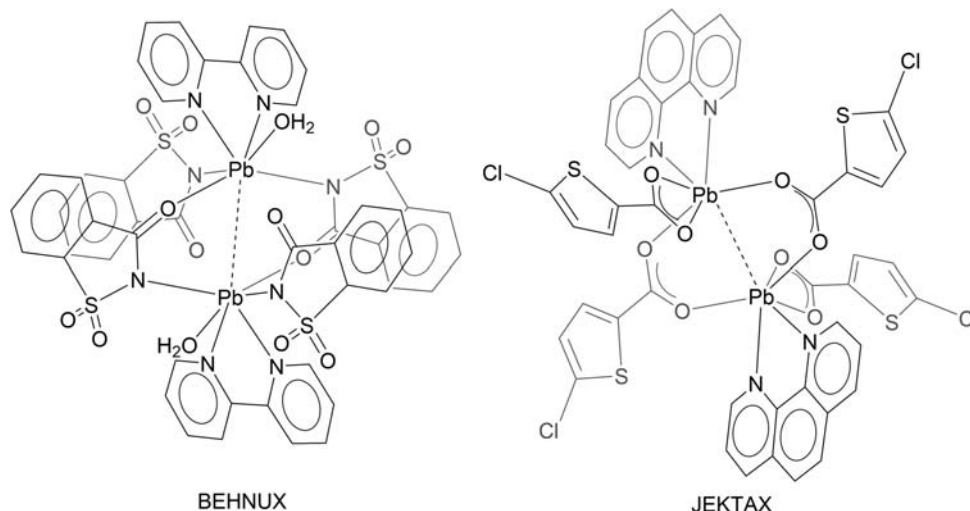
Scheme 122



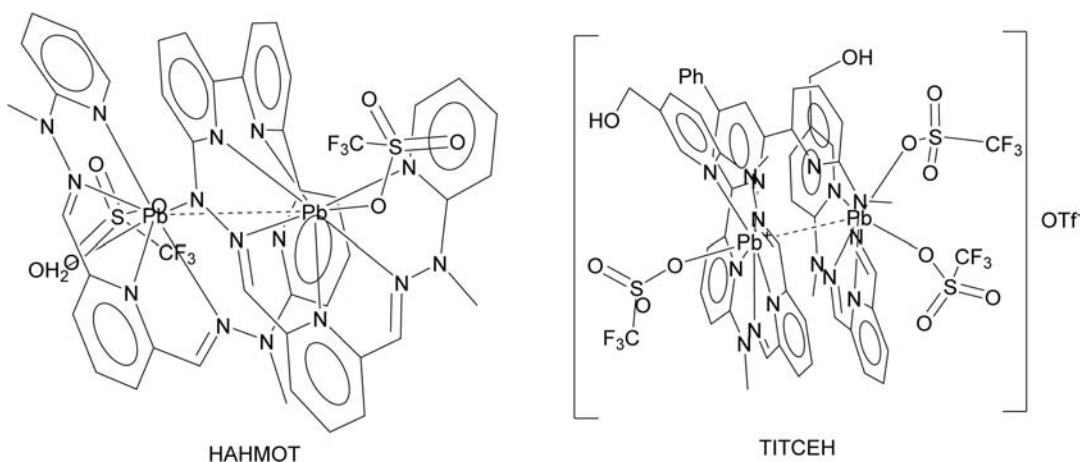
Scheme 123

paddlewheel core with a phenanthroline ligand on each Pb center. Two carboxylate groups are bridging and have a trans geometry, with the two other carboxylate groups also mutually trans, but not bridging. Crystal packing of these dimers form 1D chains along the crystallographic  $a$  axis, from the interaction of the Cl and H atoms of opposing 5-CTPC groups. The phenanthroline groups running perpendicular to this axis form  $\pi$ - $\pi$  stacking of the parallel chains, creating a 2D weave of the dimers (Scheme 124).

Intramolecular Pb(II)  $\cdots$  Pb(II) metallophilic interactions are seen in two single-stranded helicate structures. Both structures feature high-coordinate Pb(II) bonded to N of heterocyclic ligands. The discrete dinuclear structures have Pb(II)  $\cdots$  Pb(II) distances of 3.944 Å (HAHMOT)<sup>358</sup> and 3.985 Å (TITCEH)<sup>359</sup> (Scheme 125).



Scheme 124



Scheme 125

Combining both features, Pb(II) atoms in a ring within a folded structure are seen with a dinuclear lead porphyrin structure (ZARMOW).<sup>360</sup> One Pb(II) atom is four-coordinate to the N atoms of the core of a porphyrin ring and observed to be 3.727 Å away from a Pb(II) atom “hanging” above the porphyrin and bonded to two dihapto carboxylate ligands (Scheme 126).

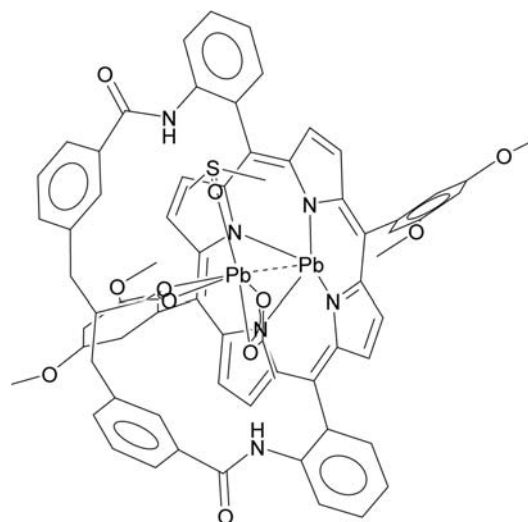
### 1.15.4.3 Bi···Bi metallophilic interactions

Similar to Tl(I) and Pb(II), structures with inter- and intramolecular Bi(III)···Bi(III) metallophilic interactions are affected by a stereochemically active  $6s^2$  lone pair of electrons at the metal. Structures with Bi(III)···Bi(III) distances between 2.964 Å and 4.140 Å are organized in this section by intermolecular Bi(III) with three-, four-, five-, or six-coordination, followed by example structures with intramolecular metallophilic interactions.

#### 1.15.4.3.1 Intermolecular Bi···Bi metallophilic interactions

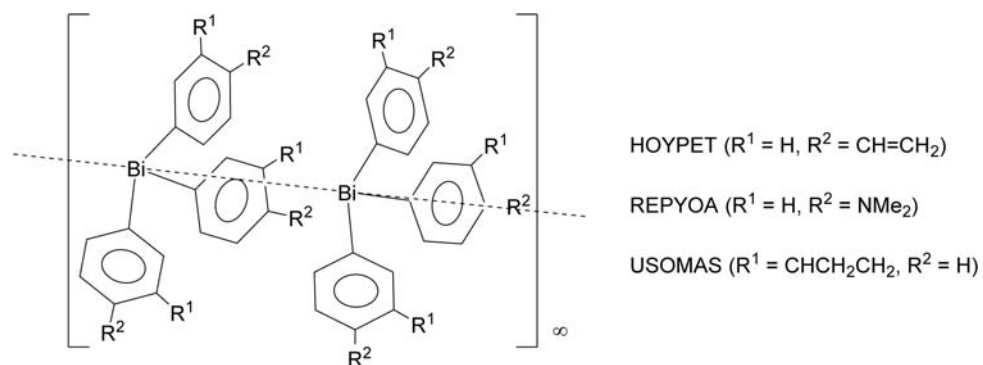
##### 1.15.4.3.1.1 Three-coordinate Bi(III)

Effects of substituent size and location on intermolecular Bi(III)···Bi(III) distances can be observed with three-coordinate Bi(III) structures. For ligands directly coordinated to the Bi atom, Bi(III)···Bi(III) separation is 3.849 Å for  $\text{NMe}_2$  groups (KOMPUX),<sup>361</sup> 3.899 Å for Me groups (HUVQOG).<sup>362</sup> For larger ligands, the general distance between Bi(III) are longer; 3.959 Å for Bi[*m*-C<sub>6</sub>H<sub>4</sub>(CHCH<sub>2</sub>CH<sub>2</sub>)]<sub>3</sub> (USOMAS),<sup>363</sup> 4.046 Å for Bi[*p*-C<sub>6</sub>H<sub>4</sub>(CH=CH<sub>2</sub>)]<sub>3</sub> (HOYPET),<sup>364</sup> 4.084 Å for Bi[*p*-C<sub>6</sub>H<sub>4</sub>(NMe<sub>2</sub>)]<sub>3</sub> (REPYOA).<sup>365</sup> Arene substitution effects on Bi(III)···Bi(III) distances can also be observed with the three latter structures (Scheme 127).



ZARMOW

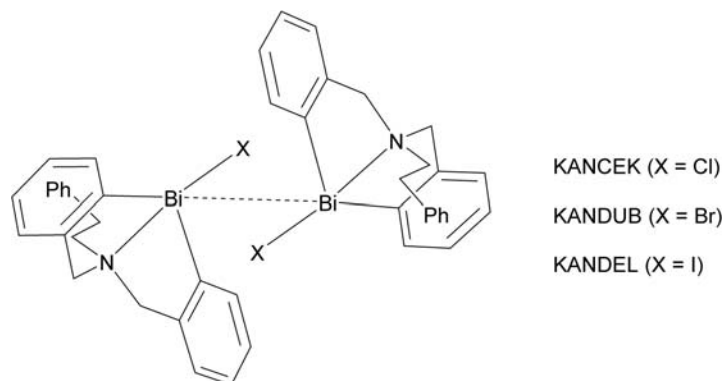
Scheme 126



Scheme 127

#### 1.15.4.3.1.2 Four-coordinate Bi(III)

Pattern between substituent size and intermolecular Bi(III)···Bi(III) distance can be easily observed with isostructural four-coordinate Bi(III) structures,  $[\text{C}_6\text{H}_5\text{CH}_2\text{N}(\text{CH}_2\text{C}_6\text{H}_4)_2]\text{BiX}$  ( $\text{X} = \text{Cl}, \text{Br}, \text{I}$ ). The Bi atoms are square-pyramidal in geometry, and the phenyl ring in the pendant arm attached to nitrogen is not involved in any intra- or inter-molecular interaction. For increasing halide size, the intermolecular Bi(III)···Bi(III) distance increases as halide radii increases; 3.974 Å when  $\text{X} = \text{Cl}$  (KANCEK),<sup>366</sup> 3.997 Å when  $\text{X} = \text{Br}$  (KANDUB),<sup>366</sup> 4.051 Å when  $\text{X} = \text{I}$  (KANDEL)<sup>366</sup> (Scheme 128).



Scheme 128



## 1.15.4.3.1.3 Five-coordinate Bi(III)

Slight changes in intermolecular Bi(III)⋯Bi(III) distance can be seen with five-coordinate Bi(III) structures. The Bi atom of PhBi(S<sub>2</sub>CR)<sub>2</sub> (R = OMe, *p*-C<sub>6</sub>H<sub>4</sub>Me, *p*-C<sub>6</sub>H<sub>4</sub>OMe) structures adopts a square pyramidal configuration with the phenyl group at the apical position. Due to this orientation, Bi(III)⋯Bi(III) distances of various R groups are within 0.020 Å: 3.995 Å for PhBi(S<sub>2</sub>COMe)<sub>2</sub> (BENXUN),<sup>367</sup> 3.999 Å for PhBi[S<sub>2</sub>C(*p*-C<sub>6</sub>H<sub>4</sub>Me)]<sub>2</sub> (HAHYEX),<sup>368</sup> 4.015 Å for PhBi[S<sub>2</sub>C(*p*-C<sub>6</sub>H<sub>4</sub>OMe)]<sub>2</sub> (ACUPIY)<sup>369</sup> (Scheme 129).

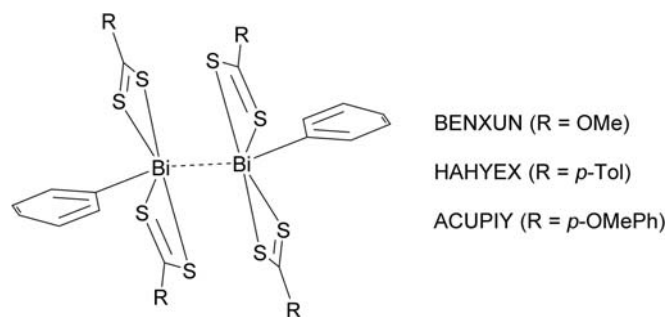
## 1.15.4.3.1.4 Six-coordinate Bi(III)

Similar to five-coordinate Bi(III) structures, most six-coordinate structures have Bi(III) bonded to chelating dithiocarbamate, Bi(S<sub>2</sub>CNR)<sub>3</sub> (R = (CH<sub>2</sub>)<sub>4</sub>, <sup>t</sup>Bu<sub>2</sub>, NEt<sub>2</sub>). Bi(III)⋯Bi(III) distances of these structures span the range of general six-coordinate Bi(III) structures: 3.651 Å for Bi[S<sub>2</sub>CNR(CH<sub>2</sub>)<sub>4</sub>]<sub>3</sub> (AXOQEJ01),<sup>370</sup> 3.831 Å for Bi[S<sub>2</sub>CN(<sup>t</sup>Bu<sub>2</sub>)]<sub>3</sub> (JISLED),<sup>370</sup> 4.135 Å for Bi[S<sub>2</sub>CN(NEt<sub>2</sub>)]<sub>3</sub> (DECBBI01).<sup>371</sup> Two additional structures with the tris(dithiocarbamate) Bi(III) core have varying R<sup>1</sup> and R<sup>2</sup> groups: 3.847 Å for Bi[S<sub>2</sub>CN(CH<sub>2</sub>CH<sub>2</sub>Ph)(C<sub>4</sub>H<sub>3</sub>O)]<sub>3</sub> (IYITIV),<sup>372</sup> 4.060 Å for Bi[S<sub>2</sub>CN(CH<sub>2</sub>C<sub>4</sub>H<sub>4</sub>NMe<sub>2</sub>)(CH<sub>2</sub>C<sub>5</sub>H<sub>4</sub>N)]<sub>3</sub> (NOTTOI)<sup>373</sup> (Scheme 130).

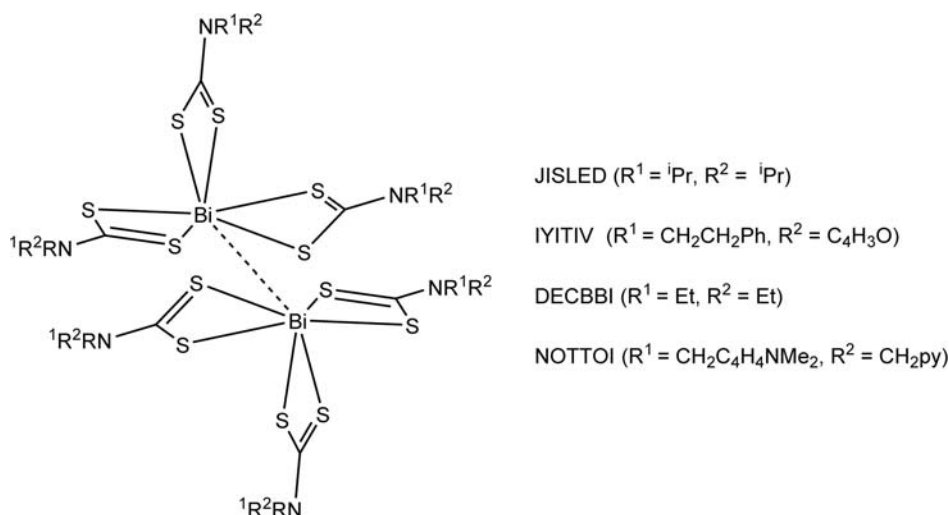
## 1.15.4.3.2 Intramolecular Bi⋯Bi metallophilic interactions

## 1.15.4.3.2.1 Miscellaneous Bi(III)

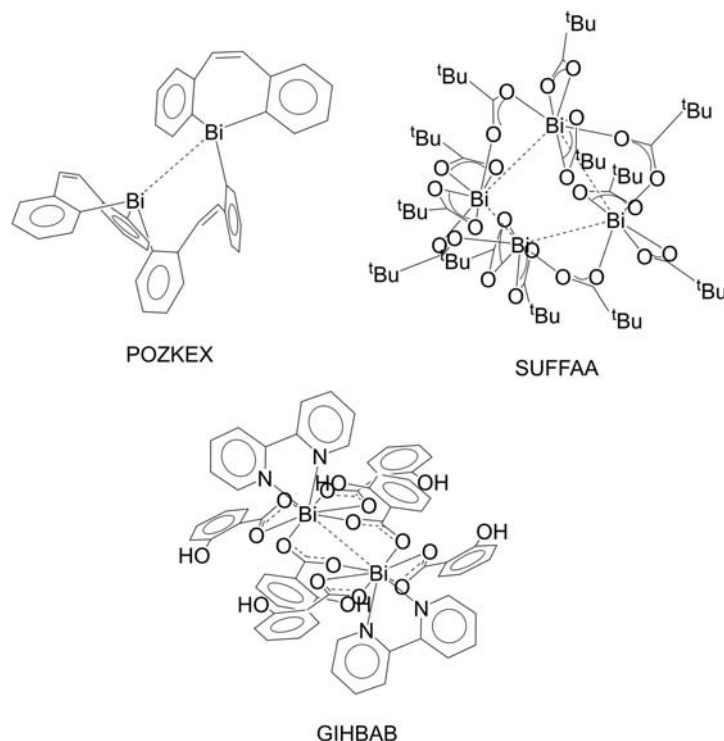
Similar to Tl and Pb, structures that exhibit intramolecular Bi(III)⋯Bi(III) metallophilic interactions vary vastly in structure with few common patterns. A dinuclear bismepine with two Bi(III) atoms coordinated to three benzyl groups in a trigonal pyramidal geometry exhibits a Bi(III)⋯Bi(III) distance of 4.098 Å (POZKEX).<sup>374</sup> Further displaying the effects of the stereochemically active lone pair of Bi(III), a tetrameric unit of [Bi(O<sub>2</sub>CCMe<sub>3</sub>)<sub>3</sub>]<sub>4</sub> with four coordinated 2,2-dimethylpropanoate exhibits average Bi(III)⋯Bi(III) distance of 4.100 Å (SUFFAA).<sup>375</sup> Additionally, the centrosymmetric dimeric structure [Bi<sub>2</sub>(C<sub>7</sub>H<sub>5</sub>O<sub>3</sub>)<sub>6</sub>(C<sub>10</sub>H<sub>8</sub>N<sub>2</sub>)<sub>2</sub>] with eight-coordinate Bi(III) exhibits a relatively short Bi(III)⋯Bi(III) distance of 3.859 Å (GIHBAB) (Scheme 131).



Scheme 129



Scheme 130



Scheme 131

### 1.15.5 Heterodinuclear $M^1 \cdots M^2$ complexes with metallophilic interactions

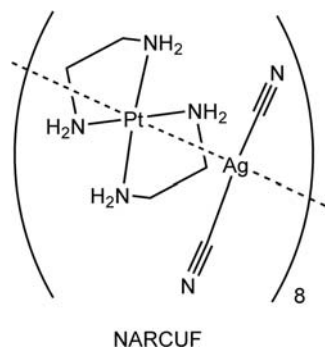
The nature of metallophilic interactions means that heterobimetallic combinations are just as feasible as homobimetallic ones, although they are fewer in number in the literature. As with homodinuclear, the electron configuration requirements for filled shell or sub-shell are the same. Therefore, there are many different pairwise combinations of  $d^8$ ,  $d^{10}$ , and  $s^2$  metal centers. Below are a handful of selected examples, chosen to illustrate the diversity of heterometallic combinations that have been observed.

#### 1.15.5.1 Intermolecular $M^1 \cdots M^2$ metallophilic interactions

One-dimensional chains of alternating metal complexes resemble insulated wires. The potentially conducting wire utilizes intermolecular or interionic metallophilic interactions and would be insulated by the coordinating ligands of the individual complexes. (The diamagnetic character that is inherent to metallophilic interactions means large HOMO-LUMO gaps in these compounds which correspond to poor semiconductor-like conductivity. If the same structural motifs can be prepared with paramagnetic centers, then higher conductivities can be achieved, but metallophilic interactions are thereby removed.) One of the most well-known examples of this type of structure is Magnus' green salt,<sup>376</sup> which is composed of an infinite chain of alternating stacks of  $[\text{Pt}(\text{NH}_3)_4]^{2+}$  and  $[\text{PtCl}_4]^{2-}$  double salts with intermolecular  $\text{Pt}(\text{II}) \cdots \text{Pt}(\text{II})$  distances of 3.25 Å. Species in which both the cation and anion are metal complexes are known as double salts. Other double salts with different metals, ligands, and intermolecular  $M \cdots M'$  contacts have been studied for their interesting physical properties such as color and conductivity.<sup>20,21</sup>

##### 1.15.5.1.1 $d^8 \cdots d^{10}$ , $\text{Pt}(\text{II}) \cdots \text{Ag}(\text{I})$

The strong ligand-field stabilization of square-planar geometries for  $d^8$  metal centers, and the ready availability of flat and chelating donors, means that many  $\text{Pt}(\text{II})$  cations are suitable for stacking in heterobimetallic combinations as they were in homobimetallic ones. Similarly, the Group 11 linear monoanions  $[\text{MX}_2]^{1-}$  make great stacking partners, so it is not surprising to find them together. One example of such a double salt is  $[\text{Pt}(\text{en})_2][\text{Ag}(\text{CN})_2]_2$  (NARCUF).<sup>377</sup> Its interionic  $\text{Pt}(\text{II}) \cdots \text{Ag}(\text{I})$  distance of 3.195 Å is much less than the sum of the van der Waals radii of the two metals (3.44 Å). Interestingly, only half of the  $[\text{Ag}(\text{CN})_2]^{1-}$  ions are part of the chain and the others, necessary for charge balance, lie outside the chain. The  $\text{Au}(\text{I})$  analog of this structure,  $[\text{Pt}(\text{en})_2][\text{Au}(\text{CN})_2]_2$ , NARCOZ,<sup>377</sup> has slightly shorter intermolecular contacts of 3.180 Å. Both form colorless crystals used in SCXRD and IR characterization (Scheme 132).



Scheme 132

### 1.15.5.1.2 $d^{10} \cdots d^{10}$ , Au(I) $\cdots$ Ag(I)

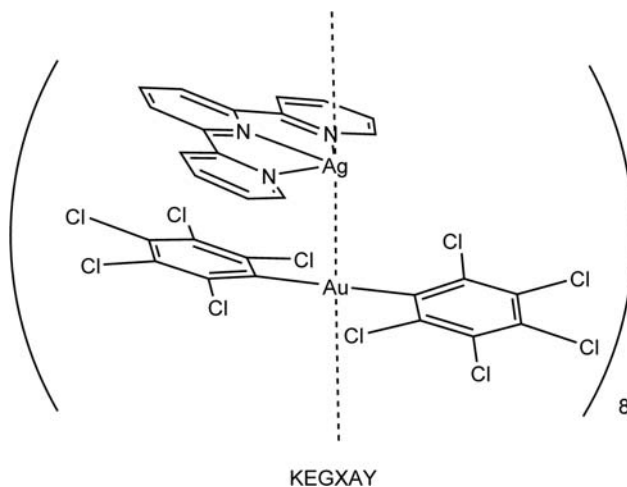
Increasingly metallophilic interactions are of interest for the luminescence which results. The heterobimetallic systems offer the greatest tunability and have therefore been heavily investigated particularly with Au. The electron-donating or -withdrawing character of coordinated ligands affects the luminescent properties of the resulting compounds, as described further below. The double-salt  $[M]^+[M]^-$  motif has been widely investigated such as the infinite one-dimensional chain is  $[Ag(tpy)][Au(C_6Cl_5)_2]$  (KEGXAY).<sup>378</sup> The distance between Ag(I)  $\cdots$  Au(I) contacts is 2.907 Å, versus the sum of the van der Waals radii of 3.38 Å. Notably the Ag center is coordinated only to the tpy ligand and the Au atom in the anion. For  $[Ag_2(\mu\text{-tpy})_2][AuX_2]$  (X =  $C_6F_5$  or  $C_6Cl_2F_3$ ), KEGWOL,<sup>378</sup> which has two bridged Au(I) monomers, the charge sequence is an atypical  $++--++--++--$  pattern (not shown), first observed in this report.<sup>378</sup> In addition to SCXRD, the structures were also characterized by  $^1H$  NMR, IR, and MALDI-TOF spectroscopies (Scheme 133).

### 1.15.5.1.3 $d^{10} \cdots s^2$ , Au(I) $\cdots$ Tl(I)

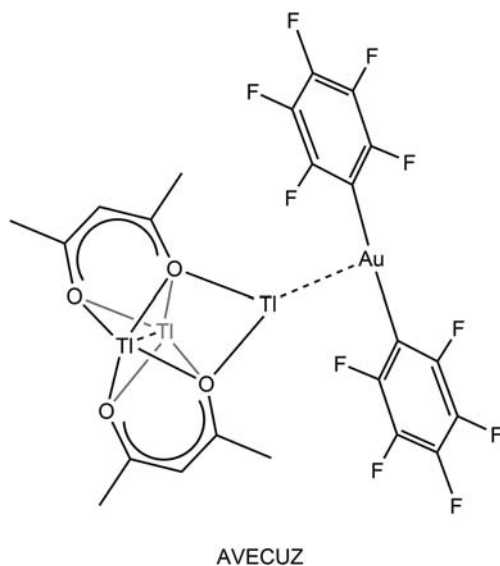
Another heavily-investigated heterobimetallic combination is that between Groups 11 and 13. One example is  $[Au(C_6F_5)_2][Tl_3(acac)_2]$  (AVECUZ),<sup>379</sup> which has a short intermolecular metallophilic interaction of 3.065 Å between Tl(I)  $\cdots$  Au(I) and a longer intramolecular metallophilic interaction of 3.669 Å between Tl(I)  $\cdots$  Tl(I) centers, both significantly less than the relevant van der Waals radii sums of 3.62 Å and 3.92 Å, respectively. Characterization methods include SCXRD and  $^1H$  and  $^{19}F$  NMR spectroscopies. The complex coordination, geometry, and flexible hard-soft character of Tl(I) adds tunability to these Group 11/13 systems. Similar to KEGXAY, time-dependent DFT (TD-DFT) was used to study the origin of the luminescence, via calculations of  $[Tl_2(acac)_2]$  without the  $[Au(C_6F_5)_2]$  unit that show that excitation of just the Tl cation in acetonitrile leads to photoemission, confirming the contribution of both inter- and intramolecular metallophilicity to the overall luminescence (Scheme 134).

### 1.15.5.2 Intramolecular $M^1 \cdots M^2$ metallophilic interactions

Numerous bridging ligands have been used to bring  $M^1$  and  $M^2$  together. One common strategy to understand the electronic structure of heterobimetallic complexes is to observe the changes as a function of asymmetric chelating ligands with hard and soft metal centers.



Scheme 133



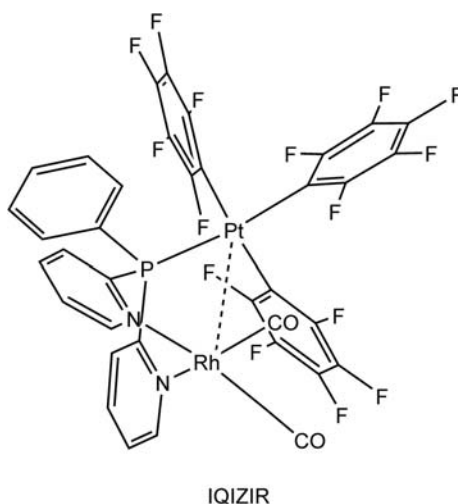
Scheme 134

### 1.15.5.2.1 $d^8 \cdots d^8$ , Rh(I) $\cdots$ Pt(II)

For example, 2-pyridylphosphine ligands, with N- and P-donor atoms, have both been heavily investigated in catalytic reactions with various metals due to some water-solubility. The compound  $[\text{Rh}(\text{CO})_2(\mu\text{-Ppy}_2\text{Ph})\text{Pt}(\text{C}_6\text{F}_5)_3]$  (py = 2-pyridyl) (**IQIZIR**)<sup>380</sup> is a heterobimetallic zwitterionic complex with intramolecular metallophilic interactions between Rh(I)  $\cdots$  Pt(II). All variations of  $\mu\text{-Ppy}_n\text{Ph}_{3-n}$  ( $n = 1, 2$ ) have P coordinated to Pt, and N coordinated to Rh. In **IQIZAR**, the Rh(I)  $\cdots$  Pt(II) distance is 3.590 Å versus the van der Waals sum of 3.72 Å. The bite angle variation as a function ligand substitution creates heterobimetallic structures with different geometries and conformations. Depending on the distribution of the P substituents, and the ring size of the resulting metallacycle, different regiochemistry is observed. Additionally, when the two CO ligands coordinated to the Rh are changed to bulkier tetrafluorobenzobarrelene or cyclooctadiene (**IQIZOX**), conformation of the structure changes so that the bite angle increases, breaking the metallophilic interaction. Although SCXRD data was not available for both compounds, the phenomenon was confirmed by extensive by  $^1\text{H}$ ,  $^{13}\text{C}$ ,  $^{19}\text{F}$ , and  $^1\text{H}\text{-}^{13}\text{C}$  HMQC NMR characterization (**Scheme 135**).

### 1.15.5.2.2 $d^8 \cdots d^{10}$ , Ir(I) $\cdots$ Ag(I)

Another approach to bring two metal together is with simple halide ligands. The biphenyl phosphines developed in the Buchwald group,  $\text{R}_2\text{Pbiph}$  ( $\text{R} = \text{}^t\text{Bu}$ ,  $\text{cycloC}_6\text{H}_{11}$ ), are sterically demanding ligands that have the potential to create enantioselective catalysts. When it was first synthesized in 2008, the heterobimetallic  $[\text{Ag}(\text{}^t\text{Bu}_2\text{Pbiph}^{\text{Me}})(\mu\text{-Cl})_2\text{Ir}(\text{COD})]$  ( $\text{biph}^{\text{Me}} = 2'\text{-methylbiphenyl}$ ; COD =  $\eta^4\text{-1,5-cyclooctadiene}$ ) (**COJMAQ**)<sup>381</sup> was the first structure with a  $\{\text{Ir}(\text{I})(\mu\text{-Cl})_2\text{Ag}(\text{I})\}$  core characterized by SCXRD. The core is sterically uncongested with Ir(I)  $\cdots$  Ag(I) distance of 3.570 Å, which is less than the sum of the van der Waals radii of



Scheme 135

the two metals (3.72 Å). The strained four-membered metallacycle is slightly bent (24.4°) at the bridging Cl atoms. In addition to SCXRD, the structure was characterized by <sup>1</sup>H, <sup>13</sup>C, and <sup>31</sup>P NMR spectroscopies and DFT. Coordination of the <sup>t</sup>Bu<sub>2</sub>Pbiph<sup>Me</sup> ligand to the Ag<sup>+</sup> was clearly observed by <sup>31</sup>P NMR spectroscopy due to coupling of the <sup>31</sup>P nucleus with the two silver isotopes <sup>107</sup>Ag and <sup>109</sup>Ag (Scheme 136).

#### 1.15.5.2.3 d<sup>8</sup>...d<sup>10</sup>, Pt(II)···Au(I)

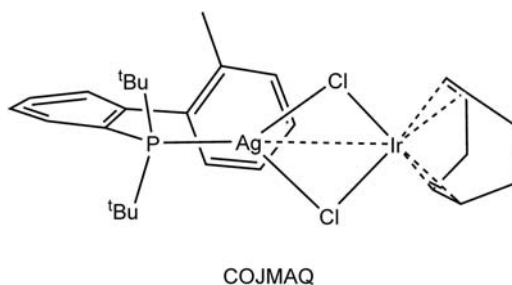
Pt(II) complexes with chelating CN ligands having imine groups are well known to have photophysical properties, which can be tuned via the CN ligand as well as inter- and intramolecular Pt(II)···M interactions. In particular, heteropolynuclear structures can have a large emissive energy difference between the HOMO and LUMO of 6p of Pt(II) ions and ns and np of monovalent Group 11 metal ions (Au(I), Ag(I), Cu(I)). For example, neutral trinuclear [PtAu<sub>2</sub>(bzq)(μ-Me<sub>2</sub>pz)<sub>3</sub>] (bzq = benzoquinolate) (MAGMAL)<sup>287</sup> has an asymmetric butterfly structure with Pt(bzq) and {Au<sub>2</sub>(Me<sub>2</sub>pz)} units bridged by two Me<sub>2</sub>pz ligands. Two intramolecular Pt(II)···Au(I) contacts of 3.3713 Å and 3.4631 Å are on the cusp of a nominal metallophilic distance (vs. 3.38 Å), but MAGMAL exhibits yellow-green luminescence at λ = 555 nm which confirms the Pt(II)···Au(I) interaction (Scheme 137).

#### 1.15.5.2.4 d<sup>10</sup>...s<sup>2</sup>, Ag(I)···Bi(III)

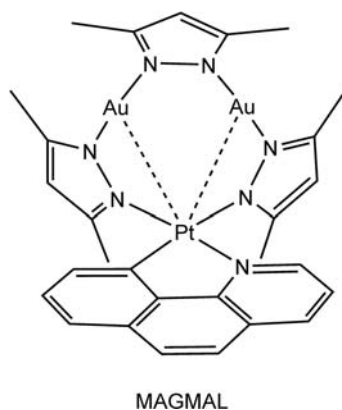
Tris-pyrazolylborates are one of the most common classes of tripodal and facially coordinating ligands, and have inspired many other ~C<sub>3v</sub> N-donor systems. They can be electronically and sterically modified by substituents on their pyrazolyl groups, and electronically and geometrically modified by replacing the bridgehead BH group with a variety of isoelectronic combinations, including a larger p-block metal. In particular, 6-methyl substitution on the three pyridyl groups and use of a Bi bridgehead creates a low-toxicity, ambiphilic ligand. Introduction of {AgA} (A = anion) in MeCN to [Bi(6-Me-2-py)<sub>3</sub>] creates a heterobimetallic salt with intramolecular metallophilic interactions between Ag(I) and Bi(III). In [Ag(NCMe){k<sup>3</sup>-(6-Me-2-pyridyl)<sub>3</sub>Bi}]A, Ag(I)···Bi(III) distances are within the metallophilic distance (3.79 Å): 3.675 Å when A = (BF<sub>4</sub>)<sup>-</sup> (VUGSIC),<sup>382</sup> 3.680 Å when A = (TfO)<sup>-</sup> (VUGSEY),<sup>382</sup> and 3.688 Å when A = (PF<sub>6</sub>)<sup>-</sup> (VUGVOL).<sup>382</sup> Studies found the introduction of electron-withdrawing 6-Br or 6-CF<sub>3</sub> in place of the 6-Me sufficiently alters the ligand properties so that thermally stable complexes do not form (Scheme 138).

#### 1.15.5.2.5 d<sup>10</sup>...s<sup>2</sup>, Cu(I)···Pb(II)

Developed in 2010, the [M(PPh<sub>3</sub>)<sub>2</sub>(μ-SCOPh)<sub>2</sub>Pb(SCOPh)] (M = Cu, Ag) complexes were the first heterobimetallic complexes containing a Group 14 metal and an S-donor ligand. The coordination geometry around the M(I) ion is distorted tetrahedral, and the Pb(II) ion is at the vertex of a trigonal pyramid due to the stereochemically active lone pair at one of its equatorial coordination sites. For M = Cu (EKIVUQ),<sup>383</sup> the intramolecular Cu(I)···Pb(II) distance is 3.377 Å, which is slightly less than 3.42 Å. This structure

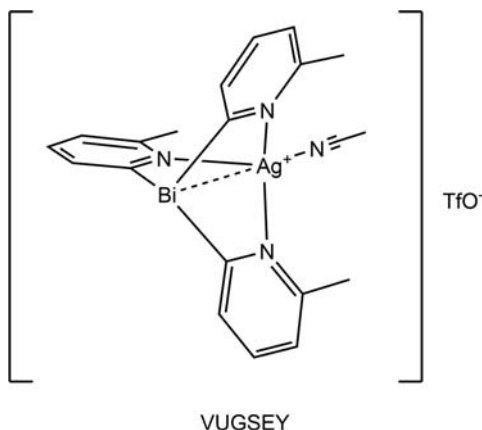


Scheme 136



Scheme 137



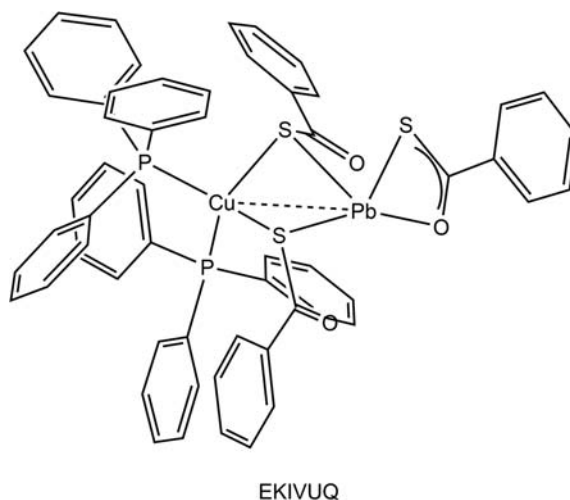


Scheme 138

was further analyzed by natural bond order (NBO) analysis using DFT calculations, finding significant intramolecular Pb···Cu interactions. Time-dependent DFT calculations were used to characterize the absorption of EKIVUQ at 375 nm due to  $n \rightarrow \pi^*$  charge transfer from the lone pairs of the Pb(II) and three S atoms to the antibonding orbital of the thiobenzoate ring. When excited at 376 nm, EKIVUQ showed a strong blue emission at 425 nm due to LLCT. Both Cu(I) and Ag(I) structures were also characterized by FTIR,  $^1\text{H}$ ,  $^{13}\text{C}$  and  $^{31}\text{P}$  NMR, CV, and TGA (Scheme 139).

### 1.15.6 Synthesis

With increased understanding of metallophilic interactions, more scientists desire to create them in discrete compounds, extended structures, and materials. The specific synthetic conditions needed are as varied as the legions of known examples. Therefore the synthetic guidelines for metallophilic interactions are those principles which lead to the desired metal oxidation state and the needed steric circumstance. Ligand substituents that favor increased electron density at each metal center are also useful. Within the metals known to form metallophilic interactions, some oxidation states are easily maintained such as Pt(II) and Pd(II), while others are more challenging. Both Au(I) and Au(III) systems readily find their way to Au(0), and Cu(I) is readily oxidized to Cu(II). Similarly, some steric conditions are easy to achieve, such as square-planar  $d^8$  complexes, or linear Au(I)  $d^{10}$  species, but the geometric plasticity in the heavier  $p$ -block elements tuning particular geometries in Tl(I), Pb(II), and Bi(III) is more subtle. The interested reader is directed to the many references contained herein, as well as the numerous existing reviews which have more details about particular molecular systems.



Scheme 139

### 1.15.7 Spectroscopy

The previous sections showed the power of single-crystal X-ray diffraction (SCXRD) to identify metallophilic interactions. SCXRD is limited, however, to appropriate crystalline samples that are not always available, and cannot characterize metallophilic interactions in solution. Other ways to observe metallophilic interactions include the use of nuclear magnetic resonance (NMR), electronic absorption and emission spectroscopy, and vibrational spectroscopy. These methods provide complementary information to solid-state, crystalline characterization and each have been used in a variety of compounds as described below. Only a few examples are given for each method, but many reviews are referenced in each section.

#### 1.15.7.1 Nuclear magnetic resonance

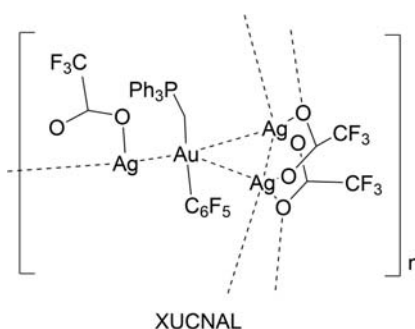
Numerous NMR-active nuclei have been used to study metallophilic interactions in solution.<sup>17,30,384,385</sup> Non-metallic nuclei from the ligands, e.g.,  $^1\text{H}$ ,  $^{13}\text{C}$ ,  $^{31}\text{P}$ , or  $^{19}\text{F}$ , can provide indirect evidence of metal-metal interactions. In one example, pulsed-gradient spin-echo (PGSE) NMR was used to show evidence of stacking of Au(I)–Ag(I) complexes in situ by relating the concentration of each species to hydrodynamic radii to degree of aggregation.<sup>384</sup> The polymeric arrangement of  $[\text{Au}(\text{C}_6\text{F}_5)(\text{CH}_2\text{PPh}_3)]$  and  $[\text{Ag}(\text{CF}_3\text{CO}_2)]$  (XUCNAL)<sup>384</sup> in a 1:3 ratio was also supported by EXAFS and SCXRD observations of metallophilic Au(I)⋯Ag(I) and Ag(I)⋯Ag(I) interactions (Scheme 140).

Direct NMR evidence of intermolecular metallophilic interactions in solution prove to be challenging to obtain due to electrostatic and dispersion interactions of other ligand and solvent molecules. Attempts to overcome this entropic dissociation include using U-shaped bridging ligands ( $\mu\text{-L}$ ) to observe intramolecular metallophilic interactions instead. Measurement of ligand exchange rate in the NMR timescale and computational analyses corroborated the presence of Au(I)⋯Au(I) contacts of homobimetallic complexes  $[(\text{Au}(\text{C}_6\text{F}_5))_2(\mu\text{-L})]$ .<sup>43</sup> Conversely, solid-state (SS) NMR is able to provide information more directly related to SCXRD information of metallophilic interactions. In one example,  $^{13}\text{C}$  and  $^{15}\text{N}$  solid-state NMR data were used to study aurophilic interactions in Au(I) and Au(III) cyanide complexes.<sup>386</sup> The cyanide ligands present in both species were discerned by homonuclear  $^{13}\text{C}$  dipolar recoupling experiments, allowing assignment to same or different materials. Additionally, the  $^{13}\text{C}$  isotropic chemical shift is found to be sensitive to alignment of the one-dimensional chains of the studied structures, giving information of aurophilic interactions.

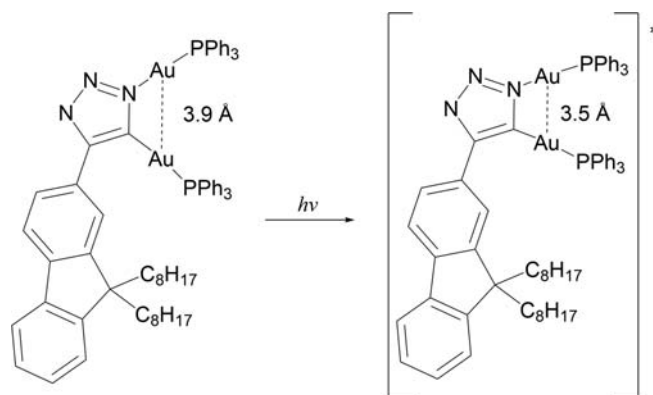
Metallic nuclei themselves are more direct reporters, and several of the most common elements in metallophilic bonding have nuclei appropriate for NMR studies, including  $^{195}\text{Pt}$ ,<sup>387–389</sup>  $^{197}\text{Au}$ ,<sup>386</sup>  $^{109}\text{Ag}$ ,<sup>390</sup>  $^{199}\text{Hg}$ ,<sup>391–394</sup> and  $^{203}\text{Tl}$ .<sup>389</sup> Nuclei of closed-shell metals with metallophilic interactions present coupling constants that differ from those of metal nuclei that are directly bonded to each other.

#### 1.15.7.2 Electronic absorption and emission spectroscopy

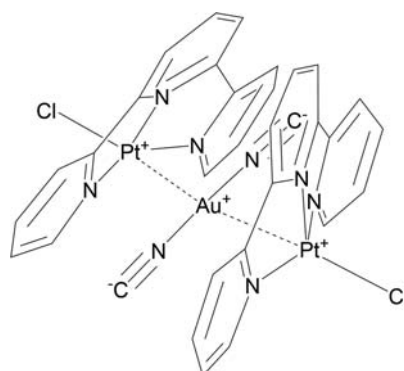
Distance between closed-shell metal centers directly determines luminescence, so when the  $\text{M}\cdots\text{M}$  distance is short, intense luminescence is observed.<sup>22,30,395–397</sup> Thus, metallophilic interactions are generally unstable in solution and unable to be directly observed. While metallophilic interactions can be classified as inter- or intramolecular, there is a further distinction of systems with intramolecular interactions being *semi-supported* or *fully-supported*; intermolecular in this case is *unsupported*.<sup>398</sup> This more detailed distinction is important for designing systems that exhibit electronic absorption or emission properties in solution.<sup>399</sup> Since the solution phase of optoelectronic materials is favorable for large-scale processing, systems with largely separated metal centers in solution and non-luminescent can be photoexcited to induce close contact of the metals. One example of this tunable property is with a semisupported Au(I)⋯Au(I) structure (below),<sup>398</sup> which contracts from 3.9 Å to 3.5 Å after photoexcitation, observed by DFT and UV-Vis measurements (Scheme 141).



Scheme 140



Scheme 141



XEMBUN

Scheme 142

### 1.15.7.3 Vibrational spectroscopy

Vibrational spectroscopies such as IR and Raman can be used to assign low energy frequencies that result from metallophilic interactions.<sup>395</sup> The ability of these vibrational tools to distinguish direct bonding from just the close proximity of atoms can also aid the presence of metallophilic interactions when the  $M \cdots M$  distance is short and challenging to observe from SCXRD, such as that with Cu–Cu contacts.<sup>400</sup> Due to the weakness of the interaction, vibrational modes corresponding to metallophilic interactions are found in the low frequency region below  $400 \text{ cm}^{-1}$ .<sup>401</sup> One method to separate lattice vibrations from metallophilic vibrations estimates the force constant  $F_{M2}$  for the metal-metal stretching vibration (in  $\text{mdyn}/\text{\AA}$ ) using the Hersbach-Laurie relationship where  $r_{M2}$  is the metal-metal separation (in  $\text{\AA}$ ).  $F_{M2}$  is then used to find the frequency  $\nu_{M2}$  (in  $\text{cm}^{-1}$ ) using the reduced mass  $\mu$  of the metal atoms.

$$r_{M2} = -0.284 \ln(F_{M2}) + 2.53$$

$$\nu_{M2} = (F_{M2})\mu^{-1}(2\pi c)^{-2}$$

Techniques employed by Raman spectroscopy can identify the optical signature of metallophilic interactions, and DFT studies to support experimental findings must account for competing interactions such as Coulomb and van der Waals ones, in addition to the strong background photoluminescence in the low-frequency region.<sup>402</sup> Angle-resolved (or polarization-dependent) Raman spectroscopy is a method that rotates the sample with respect to the incident light polarization and correlates the change in intensity of the Raman modes to characterize the anisotropic behavior of the vibrations in a crystal. The quasi-1D nanowire  $[\text{Pt}(\text{terpy})\text{Cl}][\text{Au}(\text{CN})_2]$  (XEMBUN)<sup>402</sup> composed of extended chains of a double salt, was used to study the interaction of opposite-charge ions Pt(II) and Au(I) using this technique. Of the six experimentally observed Raman-active modes, five were determined to correspond to  $A_1$  and  $B_1$  symmetries along and between chains and were analyzed to isolate the single metallophilic  $\nu_{\text{PtAu}}$  mode at  $57 \text{ cm}^{-1}$ .<sup>402</sup> (Scheme 142)

## 1.15.8 Outlook

In less than 40 years, the phenomenon of metallophilicity has gone from a structural oddity with spectroscopic consequences, to an accepted part of intermetallic interactions that can be put to use with chemical and physical applications. There is no doubt that scientists will continue to push the current manifold of known examples to different electron configurations on known metals, perhaps Ag(III)  $d^8$ , or entirely new metals, such as Os(0) in Group 10 or Rg(I) in Group 11.

## References

- Groom, C. R.; Bruno, I. J.; Lightfoot, M. P.; Ward, S. C. The Cambridge Structural Database. *Acta Crystallogr. B* **2016**, *72* (2), 171–179. <https://doi.org/10.1107/S2052520616003954>.
- Ashcroft, N. W.; Mermin, N. D. *Solid State Physics*, Holt Rinehart and Winston: New York/London, 1976.
- Kittel, C. *Kittel's Introduction to Solid State Physics*, Wiley, 2018.
- Cotton, F. A.; Murillo, C. A.; Walton, R. A. *Multiple Bonds Between Metal Atoms*, Springer Science & Business Media, 2005.
- Scherbaum, F.; Grohmann, A.; Huber, B.; Krueger, C.; Schmidbaur, H. Aurophilicity as a Consequence of Relativistic Effects: The Hexakis(Triphenylphosphineaurio)Methane Dication  $[(Ph_3PAu)_6C]^{2+}$ . *Angew. Chem. Int. Ed. Engl.* **1988**, *27* (11), 1544–1546.
- Alvarez, S. A Cartography of the Van der Waals Territories. *Dalton Trans.* **2013**, *42* (24), 8617–8636. <https://doi.org/10.1039/c3dt50599e>.
- van der Bondi, A. Waals volumes and radii. *J. Phys. Chem.* **1964**, *68* (3), 441. <https://doi.org/10.1021/j100785a001>.
- McGrady, J. E. *Introduction and General Survey of Metal-Metal Bonds*, Wiley-VCH Verlag GmbH & Co. KGaA, 2015; p 1. <https://doi.org/10.1002/9783527673353.ch1>.
- Nair, A. K.; Harisomayajula, N. V. S.; Tsai, Y.-C. The Lengths of the Metal-to-Metal Quintuple Bonds and Reactivity Thereof. *Inorg. Chim. Acta* **2015**, *424*, 51–62. <https://doi.org/10.1016/j.ica.2014.09.020>.
- Nguyen, T.; Sutton, A. D.; Brynda, M.; Fetting, J. C.; Long, G. J.; Power, P. P. Synthesis of a Stable Compound with Fivefold Bonding between Two Chromium(I) Centers. *Science* **2005**, *310* (5749), 844–847. <https://doi.org/10.1126/science.1116789>.
- Brynda, M.; Gagliardi, L.; Roos, B. O. Analysing the Chromium-Chromium Multiple Bonds Using Multiconfigurational Quantum Chemistry. *Chem. Phys. Lett.* **2009**, *471* (1–3), 1–10. <https://doi.org/10.1016/j.cplett.2009.02.006>.
- Fehlner, T.; Halet, J. F.; Saillard, J. Y. *Molecular Clusters: A Bridge to Solid-State Chemistry*, Cambridge University Press, 2007.
- Mingos, D. M. P.; Wales, D. J. *Introduction to Cluster Chemistry*, Prentice Hall, 1990.
- Schmidbaur, H.; Graf, W.; Müller, G. Weak Intramolecular Bonding Relationships: The Conformation-Determining Attractive Interaction between Gold(I) Centers. *Angew. Chem. Int. Ed. Engl.* **1988**, *27* (3), 417–419. <https://doi.org/10.1002/anie.198804171>.
- Schmidbaur, H.; Graf, W.; Mueller, G. Weak Intramolecular Binding Relationships: The Conformation Determination of Attractive Interaction between Gold(I) Centers. *Angew. Chem.* **1988**, *100* (3), 439.
- Scherbaum, F.; Grohmann, A.; Huber, B.; Krüger, C.; Schmidbaur, H. "Aurophilicity" as a Consequence of Relativistic Effects: The Hexakis(Triphenylphosphaneaurio)Methane Dication  $[(Ph_3PAu)_6C]^{2+}$ . *Angew. Chem. Int. Ed. Engl.* **1988**, *27* (11), 1544–1546. <https://doi.org/10.1002/anie.198815441>.
- Schmidbaur, H.; Schier, A. Argentophilic Interactions. *Angew. Chem. Int. Ed. Engl.* **2015**, *54* (3), 746–784.
- Harisomayajula, N. V. S.; Makovetskiy, S.; Tsai, Y.-C. Cuprophilic Interactions in and between Molecular Entities. *Chem. A Eur. J.* **2019**, *25* (38), 8936–8954. <https://doi.org/10.1002/chem.201900332>.
- Schmidbaur, H.; Schier, A. Mercurophilic Interactions. *Organometallics* **2015**, *34* (11), 2048–2066. <https://doi.org/10.1021/om501125c>.
- Doerrer, L. H. Steric and Electronic Effects in Metallophilic Double Salts. *Dalton Trans.* **2010**, *39* (15), 3543–3553. <https://doi.org/10.1039/b920389c>.
- Doerrer, L. H. Metallophilic Interactions in Double Salts: Toward 1d Metal Atom Chains. *Comments Inorg. Chem.* **2008**, *29* (3–4), 93–127. <https://doi.org/10.1080/02603590802310760>.
- Jansen, M. Homoatomic d10-d10 Interactions - Effects on Structure and Material Properties. *Angew. Chem.* **1987**, *99* (11), 1136.
- Jakonen, M.; Oresmaa, L.; Haukka, M. Solid-State Packing of the Square-Planar  $[Rh(H_2bim)(CO)_2]_2[A]$  Complexes ( $H_2bim = 2,2$ -Biimidazole;  $[A] = 2[Cl]$ ,  $2[RhCl_2(CO)_2]$ ,  $[FeCl_4]$ ,  $[CoCl_4]$ ). *Cryst. Growth Des.* **2007**, *7* (12), 2620–2626. <https://doi.org/10.1021/cg070577t>.
- Robinson, N. J.; Smith, P. A.; Grant, S.; Whitehead, K.; Crawford, C.; Assefa, Z.; Sykora, R. E. Novel Tetracyanoplatinates with the Larger  $Ln^{3+}$  ions: Synthesis, Structures, and Photoluminescence Properties of  $KLn[Pt(CN)_4]_2 \cdot 8.75H_2O$  ( $Ln = La, Pr, Nd$ ). *Inorg. Chim. Acta* **2013**, *394*, 459–465. <https://doi.org/10.1016/j.ica.2012.08.031>.
- Naito, M.; Umeda, S.; Takahashi, K.; Shultz, L. D. Macrophage Differentiation and Granulomatous Inflammation in Osteopetrotic Mice (op/op) Defective in the Production of CSF-1. *Mol. Reprod. Dev.* **1997**, *46* (1), 85–91. [https://doi.org/10.1002/\(SICI\)1098-2795\(199701\)46:1<85::AID-MRD13>3.0.CO;2-2](https://doi.org/10.1002/(SICI)1098-2795(199701)46:1<85::AID-MRD13>3.0.CO;2-2).
- Borges da Silva, H.; Fonseca, R.; Pereira, R. M.; Cassado, A. D. A.; Alvarez, J. M.; D'Império Lima, M. R. Splenic Macrophage Subsets and their Function during Blood-Borne Infections. *Front. Immunol.* **2015**, *6*. <https://doi.org/10.3389/fimmu.2015.00480>. Review.
- Miličević, N. M.; Miličević, Ž. Metallophilic Macrophages of the Rodent thymus. *Prog. Histochem. Cytochem.* **2013**, *48* (1), 1–46. <https://doi.org/10.1016/j.proghi.2012.12.001>.
- Pandey, A., Sharma, A., Eds.; *Extreme Environments: Unique Ecosystems – Amazing Microbes*, CRC Press, 2021. <https://doi.org/10.1201/9780429343452>.
- Dubreuil, R. R.; Frankel, J.; Wang, P.; Howrylak, J.; Kappil, M.; Grushko, T. A. Mutations of  $\alpha$  Spectrin and Labial Block Cuprophilic Cell Differentiation and Acid Secretion in the Middle Midgut of *Drosophila* Larvae. *Dev. Biol.* **1998**, *194* (1), 1–11. <https://doi.org/10.1006/dbio.1997.8821>.
- Mori, A.; Kubo, K.; Takeshita, H. Synthesis and Metallophilic Properties of Troponoid Thiocrown Ethers. *Coord. Chem. Rev.* **1996**, *148*, 71–96. [https://doi.org/10.1016/0010-8545\(95\)01174-9](https://doi.org/10.1016/0010-8545(95)01174-9).
- Mak, T. C. W.; Zhao, L. Multinuclear Silver Ethynide Supramolecular Synthons for the Construction of Coordination Networks. *Chem. Asian J.* **2007**, *2* (4), 456–467. <https://doi.org/10.1002/asia.200600386>.
- Guo, G.-C.; Mak, T. C. W. Novel Cyanide Coordination Models in Layer-Type Hydrated Double Salts of AgCN and AgF. *Angew. Chem. Int. Ed.* **1998**, *37* (22), 3183–3186.
- Siemeling, U.; Vorfeld, U.; Neumann, B.; Stamm, H.-G. Cuprophilicity? A Rare Example of a Ligand-Unsupported Cu-Cu Interaction. *Chem. Commun. (Camb.)* **1997**, *18*, 1723–1724. <https://doi.org/10.1039/a702793a>.
- Wiesbrock, F.; Schmidbaur, H. Complexity of Coordinative Bonding in Thallium(I) Anthranilates and Salicylates. *J. Am. Chem. Soc.* **2003**, *125* (12), 3622–3630. <https://doi.org/10.1021/ja0287783>.
- Childress, M. V.; Millar, D.; Alam, T. M.; Kreisel, K. A.; Yap, G. P. A.; Zakharov, L. N.; Golen, J. A.; Rheingold, A. L.; Doerrer, L. H. Thallophilic Interactions in Aryloxide Compounds: The  $[Tl_2(\mu_2-OAr)_4]$  Structural Motif in  $(TlOAr)_4$  and  $Tl_2Cu(OAr)_4$  Compounds. *Inorg. Chem.* **2006**, *45* (10), 3864–3877. <https://doi.org/10.1021/ic050955o>.
- Mohamed, A. A.; Grant, T.; Staples, R. J.; Fackler, J. P. Structures and Luminescence of Mononuclear and Dinuclear Base-Stabilized Gold(I) Pyrazolate Complexes. *Inorg. Chim. Acta* **2004**, *357* (6), 1761–1766. <https://doi.org/10.1016/j.ica.2003.12.006>.
- Gambarotta, S.; Floriani, C.; Chiesi-Villa, A.; Guastini, C. Ring Contraction in an Arylcopper(I) Compound Promoted by a Sulphur Donor Ligand: Penta[Mesitylcopper(I)] Forms a Tetra[Mesitylcopper(I)] Compound. *J. Chem. Soc. Chem. Commun.* **1983**, *20*, 1156–1158. <https://doi.org/10.1039/C39830001156>.

38. Eriksson, H.; Håkansson, M.; Jagner, S. Pentamethylphenylcopper(I): A Square-Planar Tetranuclear Cluster. *Inorg. Chim. Acta* **1998**, *277* (2), 233–236. [https://doi.org/10.1016/S0020-1693\(97\)06133-1](https://doi.org/10.1016/S0020-1693(97)06133-1).
39. Xu, G.-F.; Liu, Z.-Q.; Zhou, H.-B.; Guo, Y.; Liao, D.-Z. Heteropolymetallic Supramolecular Solid-State Architectures Constructed from Dicyanoaurate Ion, Phen, and 3d Metals. *Aust. J. Chem.* **2006**, *59* (9), 640–646. <https://doi.org/10.1071/CH05247>.
40. Pyykkö, P. Strong Closed-Shell Interactions in Inorganic Chemistry. *Chem. Rev.* **1997**, *97* (3), 597–636. <https://doi.org/10.1021/cr940396v>.
41. Pyykkö, P.; Runeberg, N.; Mendizabal, F. Theory of the d10-d10 Closed-Shell Attraction: 1. Dimers near Equilibrium. *Chem. A Eur. J.* **1997**, *3* (9), 1451–1457. <https://doi.org/10.1002/chem.19970030911>.
42. Pyykkö, P.; Mendizabal, F. Theory of the d10-d10 Closed-Shell Attraction: 2. Long-Distance Behavior and Nonadditive Effects in Dimers and Trimers of Type [(X-Au-L)N] (N = 2, 3; X = Cl, I, H; L = PH<sub>3</sub>, PMe<sub>3</sub>, -N≡CH). *Chem. A Eur. J.* **1997**, *3* (9), 1458–1465. <https://doi.org/10.1002/chem.19970030912>.
43. Zheng, Q.; Borsley, S.; Nichol, G. S.; Duarte, F.; Cockroft, S. L. The Energetic Significance of Metallophilic Interactions. *Angew. Chem. Int. Ed.* **2019**, *58* (36), 12617–12623. <https://doi.org/10.1002/anie.201904207>.
44. Mendizabal, F.; Pyykkö, P. Aurophilic Attraction in Binuclear Complexes with Au(I) and Au(III). A Theoretical Study. *Phys. Chem. Chem. Phys.* **2004**, *6* (5), 900–905. <https://doi.org/10.1039/B313666C>.
45. Mingos, D. M. P. Gold - A Flexible Friend in Cluster Chemistry. *J. Chem. Soc. Dalton Trans.* **1996**, *5*, 561.
46. Doll, K.; Pyykkö, P.; Stoll, H. Closed-Shell Interaction in Silver and Gold Chlorides. *J. Chem. Phys.* **1998**, *109* (6), 2339–2345. <https://doi.org/10.1063/1.476801>.
47. Crespo, O.; Laguna, A.; Fernandez, E. J.; Lopez de Luzauiaga, J. M.; Jones, P. G.; Teichert, M.; Monge, M.; Pyykkö, P.; Runeberg, N.; Schultz, M.; et al. Experimental and Theoretical Studies of the d8-d10 Interaction between Pd(II) and Au(I): Bis(Chloro(Phenylthiomethyl)Diphenylphosphine)Gold(I)-Dichloropalladium(II) and Related Systems. *Inorg. Chem.* **2000**, *39*, 4786–4792.
48. Pyykkö, P. Relativistic Effects in Structural Chemistry. *Chem. Rev.* **1988**, *88* (3), 563–594. <https://doi.org/10.1021/cr00085a006>.
49. Green, M. L. H.; Parkin, G. Application of the Covalent Bond Classification Method for the Teaching of Inorganic Chemistry. *J. Chem. Educ.* **2014**, *91* (6), 807–816. <https://doi.org/10.1021/ed400504f>.
50. Green, M. L. H. A New Approach to the Formal Classification of Covalent Compounds of the Elements. *J. Organomet. Chem.* **1995**, *500* (1), 127–148. [https://doi.org/10.1016/0022-328X\(95\)00508-N](https://doi.org/10.1016/0022-328X(95)00508-N).
51. Masciocchi, N.; Moret, M.; Cairati, P.; Ragaini, F.; Sironi, A. Solving Simple Organometallic Structures Solely from X-Ray Powder Diffraction Data: The Case of Polymer [(Ru(CO)<sub>4</sub>)]. *J. Chem. Soc. Dalton Trans.* **1993**, *3*, 471–475. <https://doi.org/10.1039/DT9300000471>.
52. Gussenhoven, E. M.; Olmstead, M. M.; Balch, A. L. Amine Involvement in the Self-Association of Planar Complexes of the Type, cis-Ir(CO)<sub>2</sub>Cl(Primary Amine). *J. Organomet. Chem.* **2019**, *883*, 17–24. <https://doi.org/10.1016/j.jorganchem.2019.01.002>.
53. Hua, C.; Vuong, K. Q.; Bhadbhade, M.; Messerle, B. A. New Rhodium(I) and Iridium(I) Complexes Containing Mixed Pyrazolyl-1,2,3-Triazolyl Ligands as Catalysts for Hydroamination. *Organometallics* **2012**, *31* (5), 1790–1800. <https://doi.org/10.1021/om201171b>.
54. Atwood, J. L.; Beveridge, K. A.; Bushnell, G. W.; Dixon, K. R.; Eadie, D. T.; Stobart, S. R.; Zaworotko, M. J. Pyrazolyl-Bridged Iridium Dimers. 4. Two-Fragment, Two-Center Oxidative Addition of Halogens and Methyl Halides to Trans-Bis(Triphenylphosphine)Dicarbonylbis(μ<sub>2</sub>-Pyrazolyl)Diiridium(I). *Inorg. Chem.* **1984**, *23* (24), 4050–4057. <https://doi.org/10.1021/ic00192a042>.
55. Beveridge, K. A.; Bushnell, G. W.; Stobart, S. R.; Atwood, J. L.; Zaworotko, M. J. Pyrazolyl-Bridged Iridium Dimers. 5. Crystal and Molecular Structures of Bis(Cycloocta-1,5-Diene)Bis(μ<sub>2</sub>-Pyrazolyl)Diiridium(I), its Dirhodium(I) Isomorph, and Two Bis(Cycloocta-1,5-Diene)Diiridium(I) Analogs Incorporating 3,5-Disubstituted μ<sub>2</sub>-Pyrazolyl Ligands. *Organometallics* **1983**, *2* (10), 1447–1451. <https://doi.org/10.1021/om50004a035>.
56. Bushnell, G. W.; Fjeldsted, D. O. K.; Stobart, S. R.; Zaworotko, M. J.; Knox, S. A. R.; MacPherson, K. A. Pyrazolyl-Bridged Iridium Dimers. 7. Synthesis and Properties of Analogs of [Ir(COD)(μ<sub>2</sub>-Pz)<sub>2</sub>] (pZH = Pyrazole), [Ir<sub>2</sub>(COD)<sub>2</sub>(μ<sub>2</sub>-Pz)(μ<sub>2</sub>-Fpz)] (fpZH = 3,5-Bis(Trifluoromethyl)Pyrazole) and [IrRh(COD)<sub>2</sub>(μ<sub>2</sub>-Pz)<sub>2</sub>]. Crystal and Molecular Structures of Bis(Cyclooctadiene)Bis(μ<sub>2</sub>-3-Phenyl-5-Methylpyrazolyl)Diiridium(I) (Disymmetric Isomer) and Bis(Cycloocta-1,5-Diene)Bis(μ<sub>2</sub>-3,4,5-Trimethylpyrazolyl)Diiridium(I). *Organometallics* **1985**, *4* (6), 1107–1114. <https://doi.org/10.1021/om00125a029>.
57. Nussbaum, S.; Rettig, S. J.; Storr, A.; Trotter, J. Iridium(I) Complexes Containing Bidentate Pyrazolylgallate Ligands. X-Ray Crystal Structures of [Me<sub>2</sub>Gap<sub>2</sub>](Ir(COD)), [Ir(μ<sub>2</sub>-Pz)(CO)<sub>2</sub>]<sub>2</sub>, and [Ir(μ<sub>2</sub>-3,5-Me<sub>2</sub>pz)(CO)<sub>2</sub>]<sub>2</sub>. *Can. J. Chem.* **1985**, *63* (3), 692–702. <https://doi.org/10.1139/v85-115> (accessed 2021/07/08).
58. Wang, Z.; Abernethy, C. D.; Cowley, A. H.; Jones, J. N.; Jones, R. A.; Macdonald, C. L. B.; Zhang, L. Synthesis and Structures of 3,5-Bis(Trifluoromethyl)Pyrazol Derivatives of rh(I), Ir(I), Pd(II) and Pt(II). *J. Organomet. Chem.* **2003**, *666* (1), 35–42. [https://doi.org/10.1016/S0022-328X\(02\)02030-2](https://doi.org/10.1016/S0022-328X(02)02030-2).
59. Steyl, G.; Kruger, G. J.; Roodt, A. Dicarbonyl(tropolonato)rhodium(I), a redetermination. *Acta Crystallogr. C* **2004**, *60* (10), m473–m475. <https://doi.org/10.1107/S0108270104019304>.
60. Jang, K.; Jung, I. G.; Nam, H. J.; Jung, D.-Y.; Son, S. U. One-Dimensional Organometallic Molecular Wires Via Assembly of rh(CO)<sub>2</sub>Cl(Amine): Chemical Control of Interchain Distances and Optical Properties. *J. Am. Chem. Soc.* **2009**, *131* (34), 12046–12047. <https://doi.org/10.1021/ja904247e>.
61. Decker, M. J.; Fjeldsted, D. O. K.; Stobart, S. R.; Zaworotko, M. J. Weak Intermolecular Bonding. A Rare Example of Molecular Stacking in a Neutral Square Planar Second-Row Transition-Metal Complex. X-Ray Crystal Structures of [rh(Cod)(cl)(dmpH)] and [rh(CO)<sub>2</sub>(cl)(pZH)] (Cod = Cyclo-Octa-1,5-Diene; dmpH = 3,5-Dimethylpyrazole; pZH = Pyrazole). *J. Chem. Soc. Chem. Commun.* **1983**, *24*, 1525–1527. <https://doi.org/10.1039/C39830001525>.
62. Heaton, T. B.; Jacob, C.; Sampanthar, T. J. Rhodium Carbonyl Complexes Containing Pyridine; Crystal Structure of an Unusual Octahedral Rhodium(I) Complex [Rh<sub>2</sub>(μ-CO)<sub>3</sub>Cl<sub>2</sub>(Py)<sub>4</sub>]. *J. Chem. Soc. Dalton Trans.* **1998**, *8*, 1403–1410. <https://doi.org/10.1039/A707435B>.
63. Adcock, R. J.; Nguyen, D. H.; Ladeira, S.; Le Berre, C.; Serp, P.; Kalck, P. Reactivity of Rhodium(I) Complexes Bearing Nitrogen-Containing Ligands toward CH<sub>3</sub>: Synthesis and Full Characterization of Neutral cis-[RhX(CO)<sub>2</sub>(L)] and Acetyl [Rh(μ-Ir)(COMe)(CO)(L)]<sub>2</sub> Complexes. *Inorg. Chem.* **2012**, *51* (16), 8670–8685. <https://doi.org/10.1021/ic2019988>.
64. Bonati, F.; Oro, L. A.; Pinillos, M. T.; Tejel, C.; Apreda, M. C.; Foces-Foces, C.; Cano, F. H. N-Substituted Imidazole Derivatives of Rhodium(I) and Iridium(I) with and without Metal-Metal Interaction. Crystal Structure of cis-(CO)<sub>2</sub>RhCl(N-Methylimidazole). *J. Organomet. Chem.* **1989**, *369* (2), 253–265. [https://doi.org/10.1016/0022-328X\(89\)88011-8](https://doi.org/10.1016/0022-328X(89)88011-8).
65. Laurila, E.; Oresmaa, L.; Niskanen, M.; Hirva, P.; Haukka, M. Metal–Metal Interactions in Stacked Mononuclear and Dinuclear Rhodium 2,2′-Biimidazole Carbonyl Complexes. *Cryst. Growth Des.* **2010**, *10* (8), 3775–3786. <https://doi.org/10.1021/cg100606f>.
66. Huq, F.; Skapski, A. C. Refinement of the Crystal Structure of Acetylacetonatodicarbonylrhodium(I). *J. Cryst. Mol. Struct.* **1974**, *4* (6), 411–418. <https://doi.org/10.1007/BF01220097>.
67. Leipoldt, J. G.; Bok, L. D. C.; Basson, S. S.; van Vollenhoven, J. S.; Gerber, T. I. A. The Crystal Structure of Benzoyl-1,1,1-Trifluoroacetatodicarbonylrhodium(I). *Inorg. Chim. Acta* **1977**, *25*, L63–L64. [https://doi.org/10.1016/S0020-1693\(00\)95646-9](https://doi.org/10.1016/S0020-1693(00)95646-9).
68. Pretorius, C.; Roodt, A. (Benzoylacetato-κ<sup>2</sup>O,O′)dicarbonylrhodium(I). *Acta Crystallogr., Sect. E: Struct. Rep.* **2012**, *68* (12), m1451–m1452. <https://doi.org/10.1107/S1600536812044893>.
69. Conradie, J.; Cameron, T. S.; Aquino, S.; Lamprecht, G. J.; Swarts, J. C. Synthetic, Electrochemical and Structural Aspects of a Series of Ferrocene-Containing Dicarbonyl β-Diketonato Rhodium(I) Complexes. *Inorg. Chim. Acta* **2005**, *358* (8), 2530–2542. <https://doi.org/10.1016/j.ica.2005.02.010>.
70. Hopmann, K. H.; Stuurman, N. F.; Muller, A.; Conradie, J. Substitution and Isomerization of Asymmetric β-Diketonato Rhodium(I) Complexes: A Crystallographic and Computational Study. *Organometallics* **2010**, *29* (11), 2446–2458. <https://doi.org/10.1021/om1000138>.
71. Pretorius, C.; Brink, A.; Roodt, A. Crystal Structure of Acetopyruvato-κ<sup>2</sup>O,O′-Dicarbonylrhodium(I), C<sub>8</sub>H<sub>7</sub>O<sub>6</sub>Rh. *Z. Krist. New Cryst. Struct.* **2014**, *229* (4), 371–372. <https://doi.org/10.1515/ncrs-2014-0195>.



72. Chancellor, C. J.; Thorn, A. A.; Beavers, C. M.; Olmstead, M. M.; Balch, A. L. Bilayer Packing of Amphiphilic Cationic Fullerenes in Crystalline Salts: Models for Self-Assembled Nanostructures. *Cryst. Growth Des.* **2008**, *8* (3), 976–980. <https://doi.org/10.1021/cg070643r>.
73. Constable, E. C.; Zhang, G.; Housecroft, C. E.; Zampese, J. A. Mix and Match: Templating Chiral Schiff Base Ligands to Suit the Needs of the Metal Ion. *Dalton Trans.* **2010**, *39* (22), 5332–5340. <https://doi.org/10.1039/C001145B>.
74. Kolari, K.; Laurila, E.; Chernysheva, M.; Hirva, P.; Haukka, M. Self-Assembly of Square Planar Rhodium Carbonyl Complexes with 4,4-Disubstituted-2,2'-Bipyridine Ligands. *Solid State Sci.* **2020**, *100*, 106103. <https://doi.org/10.1016/j.solidstatesciences.2019.106103>.
75. Walz, L.; Scheer, P. Structure of di- $\mu$ -Chloro-Bis(Dicarbonylrhodium(I)). *Acta Crystallogr. C* **1991**, *47* (3), 640–641. <https://doi.org/10.1107/S0108270190009404>.
76. Tejel, C.; Villoro, J. M.; Ciriano, M. A.; López, J. A.; Eguizábal, E.; Lahoz, F. J.; Bakhmutov, V. I.; Oro, L. A. Dynamic Behavior, Redistribution Reactions, and Intermetallic Distances of Dinuclear Bis( $\mu$ -Pyrazolato)Rhodium(I) Complexes. *Organometallics* **1996**, *15* (13), 2967–2978. <https://doi.org/10.1021/om960005y>.
77. Louie, B. M.; Rettig, S. J.; Storr, A.; Trotter, J. Rhodium(I) Complexes Containing Bidentate Pyrazolygallate Ligands. X-Ray Crystal Structures of [Me<sub>2</sub>Gapz<sub>2</sub>]Rh(COD), [Rh( $\mu$ -3,5-Me<sub>2</sub>pz)(CO)<sub>2</sub>]<sub>2</sub>, and [Rh( $\mu$ -3,5-Me<sub>2</sub>pz)(COD)]<sub>2</sub>. *Can. J. Chem.* **1984**, *62* (6), 1057–1067. <https://doi.org/10.1139/v84-175> (accessed 2021/07/08).
78. Torralba, M. C.; Cano, M.; Campo, J. A.; Heras, J. V.; Pinilla, E.; Torres, M. R. Chemistry of rh(I) Complexes Based on Mesogenic 3,5-Disubstituted Pyrazole Ligands. X-Ray Crystal Structures of 3,5-di(4-N-Butoxyphenyl)Pyrazole (Hpzbp2) and [Rh( $\mu$ -pzR<sub>2</sub>)(CO)<sub>2</sub>]<sub>2</sub> (R=C<sub>6</sub>H<sub>4</sub>OCnH<sub>2n+1</sub>, N=10, 12) Compounds. Part II. *J. Organomet. Chem.* **2002**, *654* (1), 150–161. [https://doi.org/10.1016/S0022-328X\(02\)01400-6](https://doi.org/10.1016/S0022-328X(02)01400-6).
79. Esquiús, G.; Pons, J.; Yáñez, R.; Ros, J.; Solans, X.; Font-Bardía, M. Bis[ $\mu$ -4-(Ethylammoniomethyl)-3,5-Dimethylpyrazolato- $\kappa$ 2N1:N2]Bis[( $\eta$ -4-1,5-Cyclooctadiene)Rhodium(I)] Dichloride Dichloromethane Methanol Solvate. *Acta Crystallogr. C* **2002**, *58* (2), m133–m134. <https://doi.org/10.1107/S0108270101020017>.
80. Morawitz, T.; Bao, S.; Bolte, M.; Lerner, H.-W.; Wagner, M. Rh(I)-Complexes of Ditopic Bis(Pyrazol-1-Y)Borate Ligands: Assessment of their Catalytic Activity towards Phenylacetylene Polymerization. *J. Organomet. Chem.* **2008**, *693* (26), 3878–3884. <https://doi.org/10.1016/j.jorganchem.2008.09.049>.
81. Reis, A. H.; Willi, C.; Siegel, S.; Tani, B. Molecular and Crystal Structure of Bis(Mu-Aceto)-Bis(Norbomadiene)Dirhodium(I): A Catalyst for the Isomerization of Quadricyclane to Norbornadiene. *Inorg. Chem.* **1979**, *18* (7), 1859–1863. <https://doi.org/10.1021/ci50197a029>.
82. Werner, H.; Poelsma, S.; Schneider, M. E.; Windmüller, B.; Barth, D. Synthesis and Reactivity of Bis(Ethene) Rhodium(I) and Iridium(I) Carboxylate Complexes. *Chem. Ber.* **1996**, *129* (6), 647–652. <https://doi.org/10.1002/cber.19961290609> (accessed 2021/07/08).
83. Filloux, C. M.; Rovis, T. Rh(I)-Bisphosphine-Catalyzed Asymmetric, Intermolecular Hydroheteroarylation of  $\alpha$ -Substituted Acrylate Derivatives. *J. Am. Chem. Soc.* **2015**, *137* (1), 508–517. <https://doi.org/10.1021/ja511445x>.
84. Cotton, F. A.; Dikarev, E. V.; Petrukhina, M. A. cis-Di( $\mu$ -Trifluoroacetate)Dirhodium Tetracarbonyl: Structure and Chemistry. *J. Chem. Soc.* **2000**, *23*, 4241–4243. <https://doi.org/10.1039/B006894M>.
85. Miroslaw, B. Homo- and Hetero-Oligonuclear Complexes of Platinum Group Metals (PGM) Coordinated by Imine Schiff Base Ligands. *Int. J. Mol. Sci.* **2020**, *21* (10), 3493. <https://doi.org/10.3390/ijms21103493>.
86. Aliprandi, A.; Genovese, D.; Mauro, M.; De Cola, L. Recent Advances in Phosphorescent Pt(II) Complexes Featuring Metallophilic Interactions: Properties and Applications. *Chem. Lett.* **2015**, *44* (9), 1152–1169. <https://doi.org/10.1246/cl.150592>.
87. Kobayashi, A.; Kato, M. Vapochromic Platinum(II) Complexes: Crystal Engineering toward Intelligent Sensing Devices. *Eur. J. Inorg. Chem.* **2014**, *2014* (27), 4469–4483. <https://doi.org/10.1002/ejic.201402315>.
88. Thewalt, U.; Müller, S. Cu<sup>2+</sup>-, Pd<sup>2+</sup>- und Pt<sup>2+</sup>-Komplexe Mit [(en)2Co(OH)2]<sup>+</sup>-Liganden/Cu<sup>2+</sup>-, Pd<sup>2+</sup>- and Pt<sup>2+</sup>-Complexes with [(en)2Co(OH)2]<sup>+</sup> Ligands. *Z. Naturforsch. B* **1989**, *44* (10), 1206–1210. <https://doi.org/10.1515/znB-1989-1011>.
89. Richardson, J. G.; Benjamin, H.; Moggach, S. A.; Warren, L. R.; Warren, M. R.; Allan, D. R.; Saunders, L. K.; Morrison, C. A.; Robertson, N. Probing the Structural and Electronic Response of Magnus Green Salt Compounds [Pt(NH<sub>2</sub>R<sub>4</sub>)]<sup>+</sup>[PtCl<sub>4</sub>]<sup>-</sup> (R = H, CH<sub>3</sub>) to Pressure. *Phys. Chem. Chem. Phys.* **2020**, *22* (31), 17668–17676. <https://doi.org/10.1039/D0CP03280H>.
90. Cradwick, M. E.; Hall, D.; Phillips, R. K. The Crystal Structures of Compounds Analogous to Magnus' Green Salt. *Acta Crystallogr. B* **1971**, *27* (2), 480–484. <https://doi.org/10.1107/S0567740871002401>.
91. Kitteringham, E.; Zhou, Z.; Twamley, B.; Griffith, D. M. Au(III) and Pt(II) Complexes of a Novel and Versatile 1,4-Disubstituted 1,2,3-Triazole-Based Ligand Possessing Diverse Secondary and Tertiary Coordinating Groups. *Inorg. Chem.* **2018**, *57* (19), 12282–12290. <https://doi.org/10.1021/acs.inorgchem.8b01994>.
92. Sakai, K.; Tanaka, Y.; Tsubomura, T. [N,N'-Bis(2-Aminoethyl-[Kappa]N)-N,N'-Bis(2-Ammonioethyl)Ethylendiamine-[Kappa]2N,N']Platinum(II) Bis(Tetrachloroplatinate) Trihydrate. *Acta Crystallogr. C* **1996**, *52* (3), 541–543. <https://doi.org/10.1107/S0108270195011413>.
93. Ha, K. Crystal Structure of Bromido(2,2':6',2''-Terpyridine- $\kappa$ 3N,N',N'')Platinum(II) Tribromido(Dimethyl Sulfoxide- $\kappa$ S)Platinate(II), C<sub>17</sub>H<sub>17</sub>Br<sub>4</sub>N<sub>3</sub>O<sub>2</sub>PS. *Z. Krist. New Cryst. Struct.* **2014**, *229* (2), 161–162. <https://doi.org/10.1515/ncrs-2014-0090>.
94. Cini, R.; Donati, A.; Giannettoni, R. Synthesis and Structural Characterization of Chloro(2,2':6',2''-Terpyridine)Platinum(II) Trichloro(Dimethylsulfoxide)Platinate(II). Density Functional Analysis of Model Molecules. *Inorg. Chim. Acta* **2001**, *315* (1), 73–80. [https://doi.org/10.1016/S0020-1693\(01\)00317-6](https://doi.org/10.1016/S0020-1693(01)00317-6).
95. Qin, Q.-P.; Wang, Z.-F.; Wang, S.-L.; Luo, D.-M.; Zou, B.-Q.; Yao, P.-F.; Tan, M.-X.; Liang, H. In Vitro and In Vivo Antitumor Activities of Three Novel Binuclear Platinum(II) Complexes with 4'-Substituted-2,2':6',2''-Terpyridine Ligands. *Eur. J. Med. Chem.* **2019**, *170*, 195–202. <https://doi.org/10.1016/j.ejmech.2019.03.014>.
96. He, L.; Liu, F.; Li, J.; Rignanese, G.-M.; Zhou, A. First-Principles Investigation of Monatomic Gold Wires under Tension. *Comput. Mater. Sci.* **2020**, *171*, 109226. <https://doi.org/10.1016/j.commatsci.2019.109226>.
97. Sluch, I. M.; Miranda, A. J.; Elbejirami, O.; Omary, M. A.; Slaughter, L. M. Interplay of Metallophilic Interactions,  $\pi$ - $\pi$  Stacking, and Ligand Substituent Effects in the Structures and Luminescence Properties of Neutral Pt(II) and Pd(II) Aryl Isocyanide Complexes. *Inorg. Chem.* **2012**, *51* (20), 10728–10746. <https://doi.org/10.1021/ic301104a>.
98. Kinzhalov, M. A.; Katkova, S. A.; Doronina, E. P.; Novikov, A. S.; Eliseev, I. I.; Ilchev, V. A.; Kukinov, A. A.; Starova, G. L.; Bokach, N. A. Red Photo- and Electroluminescent Half-Lantern Cyclometalated Dinuclear Platinum(II) Complex. *Z. Kristallogr. - Cryst. Mater.* **2018**, *233* (11), 795–802. <https://doi.org/10.1515/zkri-2018-2075>.
99. Connick, W. B.; Henling, L. M.; Marsh, R. E.; Gray, H. B. Emission Spectroscopic Properties of the Red Form of Dichloro(2,2'-Bipyridine)Platinum(II). Role of Intermolecular Stacking Interactions. *Inorg. Chem.* **1996**, *35* (21), 6261–6265. <https://doi.org/10.1021/ic960511f>.
100. Olivos-Suárez, A. I.; Ríos-Moreno, G.; Hernández-Ortega, S.; Toscano, R. A.; García, J. J.; Morales-Morales, D. Reactivity of Fluorinated Thioether Ligands of the Type [C<sub>6</sub>H<sub>4</sub>Br-2-(CH<sub>2</sub>SRF)] towards Transition Metal Complexes of the Group 10. *Inorg. Chim. Acta* **2007**, *360* (15), 4133–4141. <https://doi.org/10.1016/j.ica.2007.05.056>.
101. Manojlović-Muir, L.; Muir, K. W.; Solomun, T. The Crystal and Molecular Structure of cis-Dichloro[1,2-Bis(Trifluoromethylthio)Propane] Platinum(II). *Inorg. Chim. Acta* **1977**, *22*, 69–74. [https://doi.org/10.1016/S0020-1693\(00\)90901-0](https://doi.org/10.1016/S0020-1693(00)90901-0).
102. Levason, W.; Webster, M.; Mitchell, C. J. Structure of Trans-Diiodobis(Methyl Phenyl Telluride)Platinum(II). *Acta Crystallogr. C* **1992**, *48* (11), 1931–1933. <https://doi.org/10.1107/S0108270192003354>.
103. Brown, M. D.; Levason, W.; Reid, G.; Webster, M. Preparation and Coordinating Properties of {CH<sub>2</sub>(O-C<sub>6</sub>H<sub>4</sub>CH<sub>2</sub>SbMe<sub>2</sub>)<sub>2</sub>}, a Novel Wide-Angle cis-Chelating Distibine. *Dalton Trans.* **2006**, *47*, 5648–5654. <https://doi.org/10.1039/B610808C>.
104. Heinemann, F. W.; Gerisch, M.; Steinborn, D. Crystal Structure of Bis[ $\mu$ -Chloro(1-Platina-Diethyl- $\beta$ -Diketone)], [Pt<sub>2</sub>( $\mu$ -c)2{(COE)2H}2]. *Z. Krist. New Cryst. Struct.* **1997**, *212* (1), 181. <https://doi.org/10.1524/ncrs.1997.212.1.181>.
105. Steinborn, D.; Gerisch, M.; Hoffmann, T.; Bruhn, C.; Israel, G.; Müller, F. W. Crystal Structures and Spectroscopic Properties of Platina- $\beta$ -Diketones—A New Mode of Stacking in Platinum Complexes. *J. Organomet. Chem.* **2000**, *598* (2), 286–291. [https://doi.org/10.1016/S0022-328X\(99\)00726-3](https://doi.org/10.1016/S0022-328X(99)00726-3).
106. Steinborn, D.; Gerisch, M.; Merzweiler, K.; Schenzel, K.; Pelz, K.; Bögel, H.; Magull, J. Synthesis and Characterization of Platina- $\beta$ -Diketones. *Organometallics* **1996**, *15* (10), 2454–2457. <https://doi.org/10.1021/om950963k>.

107. Yip, H.-K.; Cheng, L.-K.; Cheung, K.-K.; Che, C.-M. Luminescent Platinum(II) Complexes. Electronic Spectroscopy of Platinum(II) Complexes of 2,2':6',2''-Terpyridine (Teryp) and P-Substituted Phenylterpyridines and Crystal Structure of [Pt(Teryp)Cl][CF<sub>3</sub>SO<sub>3</sub>]. *J. Chem. Soc. Dalton Trans.* **1993**, *19*, 2933–2938. <https://doi.org/10.1039/DT9930002933>.
108. Field, J. S.; Wilson, C. R.; Munro, O. Q. Non-covalent Interactions between Cations in the Crystal Structure of [Pt{4'-(P-Tolyl)Tpy}Cl]SbF<sub>6</sub>, where Tpy is 2,2':6',2''-Terpyridine, Underpin the salt's Complex Solid-State Luminescence Spectrum. *Inorg. Chim. Acta* **2011**, *374* (1), 197–204. <https://doi.org/10.1016/j.ica.2011.03.043>.
109. Baddour, F. G.; Kahn, M. I.; Golen, J. A.; Rheingold, A. L.; Doerrer, L. H. Platinum(IV)-κ<sup>3</sup>-Terpyridine Complexes: Synthesis with Spectroscopic and Structural Characterization. *Chem. Commun.* **2010**, *46* (27), 4968–4970. <https://doi.org/10.1039/C0CC00283F>.
110. Au-Yeung, H.-L.; Leung, S. Y.-L.; Tam, A. Y.-Y.; Yam, V. W.-W. Transformable Nanostructures of Platinum-Containing Organosilane Hybrids: Non-covalent Self-Assembly of Polyhedral Oligomeric Silsesquioxanes Assisted by Pt···Pt and π–π Stacking Interactions of Alkynylplatinum(II) Terpyridine Moieties. *J. Am. Chem. Soc.* **2014**, *136* (52), 17910–17913. <https://doi.org/10.1021/ja510048b>.
111. Kahn, M. I.; Golen, J. A.; Rheingold, A. L.; Doerrer, L. H. Bromido(2,2':6',2''-terpyridine)platinum(II) dibromidoaurate(II) dimethyl sulfoxide solvate. *Acta Crystallogr., Sect. E: Struct. Rep. Online* **2009**, *65* (9), m1135. Sm1135/1131–Sm1135/1139. <https://doi.org/10.1107/S1600536809033248>.
112. Nishiuchi, Y.; Takayama, A.; Suzuki, T.; Shinozaki, K. A Polymorphic Platinum(II) Complex: Yellow, Red, and Green Polymorphs and X-Ray Crystallography of [Pt(Fdpb)Cl][Hfdpb = 1,3-Bis(5-Trifluoromethyl-2-Pyridyl)Benzene]. *Eur. J. Inorg. Chem.* **2011**, *2011* (11), 1815–1823. <https://doi.org/10.1002/ejic.2011001359>.
113. Poethig, A.; Strassner, T. Triazinone-Bridged Neutral Dinuclear Gold(II)-NHC Complex. *Organometallics* **2012**, *31* (8), 3431–3434. <https://doi.org/10.1021/om3000345>.
114. Tronnier, A.; Nischan, N.; Strassner, T. C<sup>60</sup>-Cyclometalated Platinum(II) Complexes with Trifluoromethyl-Acetylacetonate Ligands – Synthesis and Electronic Effects. *J. Organomet. Chem.* **2013**, *730*, 37–43. <https://doi.org/10.1016/j.jorganchem.2012.07.046>.
115. Tronnier, A.; Nischan, N.; Metz, S.; Wagenblast, G.; Münster, I.; Strassner, T. Phosphorescent C<sup>60</sup> Cyclometalated Pt(II) Dibenzofuranyl-NHC Complexes – An Auxiliary Ligand Study. *Eur. J. Inorg. Chem.* **2014**, *2014* (1), 256–264. <https://doi.org/10.1002/ejic.201301398>.
116. Bellitto, C.; Dessy, G.; Fares, V.; Flamini, A. Two Polymorphic Forms of the Tetrakis(Dithioisobutanoato)Diplatinum(II) Complex: X-Ray Crystal Structure and Spectroscopic Evidence of Intermolecular Interactions in the Solid State. *J. Chem. Soc. Chem. Commun.* **1981**, *9*, 409–411. <https://doi.org/10.1039/C39810000409>.
117. Bellitto, C.; Bonamico, M.; Dessy, G.; Fares, V.; Flamini, A. Linear-Chain Platinum(II) Dithiocarboxylates: Crystal Structure of Tetrakis(Phenylthioacetato)Diplatinum(II). *J. Chem. Soc. Dalton Trans.* **1987**, *1*, 35–40. <https://doi.org/10.1039/DT9870000035>.
118. Pérez Paz, A.; Espinosa Leal, L. A.; Azani, M.-R.; Gujjarro, A.; Sanz Miguel, P. J.; Givaja, G.; Castillo, O.; Mas-Ballesté, R.; Zamora, F.; Rubio, A. Supramolecular Assembly of Diplatinum Species through Weak PtII···PtII Intermolecular Interactions: A Combined Experimental and Computational Study. *Chem. A Eur. J.* **2012**, *18* (43), 13787–13799. <https://doi.org/10.1002/chem.201201962>.
119. Gujjarro, A.; Castillo, O.; Calzolari, A.; Miguel, P. J. S.; Gómez-García, C. J.; di Felice, R.; Zamora, F. Electrical Conductivity in Platinum-Dimer Columns. *Inorg. Chem.* **2008**, *47* (21), 9736–9738. <https://doi.org/10.1021/ic801211m>.
120. Kawamura, T.; Ogawa, T.; Yamabe, T.; Masuda, H.; Taga, T. Structure and Oligomerization of Tetrakis(Dithioheptanoato)Diplatinum. *Inorg. Chem.* **1987**, *26* (21), 3547–3550. <https://doi.org/10.1021/ic00268a026>.
121. Givaja, G.; Castillo, O.; Mateo, E.; Gallego, A.; Gómez-García, C. J.; Calzolari, A.; di Felice, R.; Zamora, F. Electrical Behaviour of Heterobimetallic [MM'(EtCS<sub>2</sub>)<sub>4</sub>] (MM' = NiPd, NiPt, PdPt) and MM'X-Chain Polymers [PtM(EtCS<sub>2</sub>)<sub>4</sub>] (M = Ni, Pd). *Chem. A Eur. J. Dermatol.* **2012**, *18* (48), 15476–15484. <https://doi.org/10.1002/chem.201200995> (accessed 2021/05/27).
122. Beach, S. A.; Doerrer, L. H. Heterobimetallic Lantern Complexes and their Novel Structural and Magnetic Properties. *Acc. Chem. Res.* **2018**, *51* (5), 1063–1072. <https://doi.org/10.1021/acs.accounts.7b00585>.
123. Beach, S. A.; Zuckerman, L. A.; Portillo, R. I.; Shores, M. P.; Rheingold, A. L.; Doerrer, L. H. Heterobimetallic {PtMn} and {PtFe} Lantern Complexes with Exceptionally Long Metallophilic Contacts. *Inorg. Chim. Acta* **2019**, *493*, 81–90. <https://doi.org/10.1016/j.ica.2019.04.054>.
124. Baddour, F. G.; Hyre, A. S.; Guillet, J. L.; Pascual, D.; Lopez-de-Luzuriaga, J. M.; Alam, T. M.; Bacon, J. W.; Doerrer, L. H. Pt-Mg, Pt-Ca, and Pt-Zn Lantern Complexes and Metal-Only Donor-Acceptor Interactions. *Inorg. Chem.* **2017**, *56* (1), 452–469. <https://doi.org/10.1021/acs.inorgchem.6b02372>.
125. Baddour, F. G.; Fiedler, S. R.; Shores, M. P.; Golen, J. A.; Rheingold, A. L.; Doerrer, L. H. Heterobimetallic Lantern Complexes that Couple Antiferromagnetically through Noncovalent Pt···Pt Interactions. *Inorg. Chem.* **2013**, *52* (9), 4926–4933. <https://doi.org/10.1021/ic302531t>.
126. Baddour, F. G.; Fiedler, S. R.; Shores, M. P.; Bacon, J. W.; Golen, J. A.; Rheingold, A. L.; Doerrer, L. H. Pt···Pt vs. Pt···S Contacts between Pt-Containing Heterobimetallic Lantern Complexes. *Inorg. Chem.* **2013**, *52* (23), 13562–13575. <https://doi.org/10.1021/ic402075y>.
127. Dahl, E. W.; Baddour, F. G.; Fiedler, S. R.; Hoffert, W. A.; Shores, M. P.; Yee, G. T.; Djukic, J.-P.; Bacon, J. W.; Rheingold, A. L.; Doerrer, L. H. Antiferromagnetic Coupling across a Tetrametallic Unit through Noncovalent Interactions. *Chem. Sci.* **2012**, *3* (2), 602–609. <https://doi.org/10.1039/C1SC00608H>.
128. Grinberg, V. A.; Mayorova, N. A.; Pasynsky, A. A.; Shiryayev, A. A.; Vysotskii, V. V.; Stolarov, I. P.; Yakushev, I. A.; Cherkashina, N. V.; Vargaftik, M. N.; Zubavichus, Y. V.; et al. Nanosized Catalysts of Oxygen Reduction Reaction Prepared on the Base of Bimetallic Cluster Compounds. *Electrochim. Acta* **2019**, *299*, 886–893. <https://doi.org/10.1016/j.electacta.2019.01.059>.
129. Yakushev, I. A.; Stolarov, I. P.; Cherkashina, N. V.; Churakov, A. V.; Zubavichus, Y. V.; Markov, A. A.; Gekhman, A. E.; Vargaftik, M. N. Two Routes to Platinum-Based Carboxylate-Bridged Heterometallics. *Inorg. Chim. Acta* **2020**, *508*, 119631. <https://doi.org/10.1016/j.ica.2020.119631>.
130. Martellaro, P. J.; Hurst, S. K.; Larson, R.; Abbott, E. H.; Peterson, E. S. Multinuclear Nuclear Magnetic Resonance and X-Ray Crystallographic Investigation of some Mixed Ligand Alkylisocyanide Platinum(II) Complexes. *Inorg. Chim. Acta* **2005**, *358* (12), 3377–3383. <https://doi.org/10.1016/j.ica.2005.06.024>.
131. Drew, S. M.; Smith, L. I.; McGee, K. A.; Mann, K. R. A Platinum(II) Extended Linear Chain Material that Selectively Uptakes Benzene. *Chem. Mater.* **2009**, *21* (14), 3117–3124. <https://doi.org/10.1021/cm900401u>.
132. Sun, Y.; Ye, K.; Zhang, H.; Zhang, J.; Zhao, L.; Li, B.; Yang, G.; Yang, B.; Wang, Y.; Lai, S.-W.; et al. Luminescent One-Dimensional Nanoscale Materials with PtII···PtII Interactions. *Angew. Chem. Int. Ed.* **2006**, *45* (34), 5610–5613. <https://doi.org/10.1002/anie.200601588> (accessed 2021/05/27).
133. Buss, C. E.; Mann, K. R. Synthesis and Characterization of Pt(CN-P-(C<sub>2</sub>H<sub>5</sub>)C<sub>6</sub>H<sub>4</sub>)<sub>2</sub>(CN)<sub>2</sub>, a Crystalline Vapor-Luminescent Compound that Detects Vapor-Phase Aromatic Hydrocarbons. *J. Am. Chem. Soc.* **2002**, *124* (6), 1031–1039. <https://doi.org/10.1021/ja011986v>.
134. Dylla, A. G.; Janzen, D. E.; Pomije, M. K.; Mann, K. R. A Comparison of Isomers: Trans- and cis-Dicyanobis(Para-Ethylisocyanobenzene)Platinum. *Organometallics* **2007**, *26* (25), 6243–6247. <https://doi.org/10.1021/om7008167>.
135. Vavra, M.; Potočnáková, I.; Dušek, M. Low-Dimensional Compounds Containing Cyanido Groups. XXIV. Crystal Structure, Spectroscopic and Thermal Properties of Two Cu(II) Tetracyanidoplatinate Complexes with Tetradentate N-Donor Ligands. *Inorg. Chim. Acta* **2014**, *409*, 441–448. <https://doi.org/10.1016/j.ica.2013.09.016>.
136. Bencini, A.; Bianchi, A.; Dapporto, P.; Garcia-Espana, E.; Micheloni, M.; Ramirez, J. A.; Paoletti, P.; Paoletti, P. Thermodynamic and Structural Aspects of the Interaction between Macrocyclic Polyammonium Cations and Complexed Anions. *Inorg. Chem.* **1992**, *31* (10), 1902–1908. <https://doi.org/10.1021/ic00036a033>.
137. Neuhausen, C.; Pattison, P.; Schiltz, M. A New Polymorph of Dicesium Tetracyanoplatinate Monohydrate with Unusual Platinum Stacking. *CrystEngComm* **2011**, *13* (2), 430–432. <https://doi.org/10.1039/C0CE00415D>.
138. Bois, H.; Connelly, G. N.; Crossley, G. J.; Guilloit, J.-C.; Lewis, R. G.; Guy Orpen, A.; Thornton, P. Structural Studies of [Pt(CNMe)<sub>4</sub>][M(Mnt)<sub>2</sub>] [M = Pd or Pt, Mnt = [S<sub>2</sub>C<sub>2</sub>(CN)<sub>2</sub>]<sup>2-</sup>, N = 1 or 2]: Structure-Dependent Paramagnetism of Three Crystal Forms of [Pt(CNMe)<sub>4</sub>][Pt(Mnt)<sub>2</sub>]<sup>2-</sup>. *J. Chem. Soc. Dalton Trans.* **1998**, *17*, 2833–2838. <https://doi.org/10.1039/A803456G>.
139. Ma, B.; Li, J.; Djurovich, P. I.; Yousufuddin, M.; Bau, R.; Thompson, M. E. Synthetic Control of Pt···Pt Separation and Photophysics of Binuclear Platinum Complexes. *J. Am. Chem. Soc.* **2005**, *127* (1), 28–29. <https://doi.org/10.1021/ja044313w>.

140. Ciriano, M.; Green, M.; Gregson, D.; Howard, J. A. K.; Spencer, J. L.; Stone, F. G. A.; Woodward, P. Reactions of Triorganosilanes with Tris- $\mu$ -(*T*-Butyl Isocyanide)-Tris(*T*-Butyl Isocyanide)-Triangulo-Triplatinum: Crystal Structure of the Complex  $[\{Pt(CH_3NBu)(SiMePh_2)(CNBu)_2\}]_2$ . *J. Chem. Soc. Dalton Trans.* **1979**, 8, 1294–1300. <https://doi.org/10.1039/DT9790001294>.
141. Scaffidi-Domianello, Y. Y.; Legin, A. A.; Jakupec, M. A.; Roller, A.; Kukushkin, V. Y.; Galanski, M.; Keppler, B. K. Novel Oximate-Bridged Platinum(II) Di- and Trimer(S): Synthetic, Structural, and In Vitro Anticancer Activity Studies. *Inorg. Chem.* **2012**, 51 (13), 7153–7163. <https://doi.org/10.1021/ic300148e>.
142. Barton, J. K.; Szalda, D. J.; Rabinowitz, H. N.; Waszczak, J. V.; Lippard, S. J. Solid State Structure, Magnetic Susceptibility, and Single Crystal ESR Properties of cis-Diammineplatinum Alpha-Pyridone Blue. *J. Am. Chem. Soc.* **1979**, 101 (6), 1434–1441. <https://doi.org/10.1021/ja00500a012>.
143. Sakai, K.; Takeshita, M.; Tanaka, Y.; Ue, T.; Yanagisawa, M.; Kosaka, M.; Tsubomura, T.; Ato, M.; Nakano, T. A New One-Dimensional Platinum System Consisting of Carboxylate-Bridged cis-Diammineplatinum Dimers<sup>1</sup>. *J. Am. Chem. Soc.* **1998**, 120 (44), 11353–11363. <https://doi.org/10.1021/ja980055p>.
144. Wilson, J. J.; Lippard, S. J. Acetate-Bridged Platinum(II) Complexes Derived from Cisplatin. *Inorg. Chem.* **2012**, 51 (18), 9852–9864. <https://doi.org/10.1021/ic301289j>.
145. Kurioka, Y.; Kuwamura, N.; Yoshinari, N.; Igashira-Kamiyama, A.; Konno, T. A New Platinum(II) Metalloligand System with D-Penicillamine: An Excellent Stereoselectivity in the Formation of S-Bridged PtII2Coll2 and PtII2NII2 Complexes with Opposite Hydrogen-Bonding Helix Structures. *Chemistry Letters* **2015**, 44 (10), 1330–1332. <https://doi.org/10.1246/cl.150556> (Accessed 2021/05/31).
146. Chikamoto, Y.; Kawamoto, T.; Igashira-Kamiyama, A.; Konno, T. Two Stereoisomers of an S-Bridged RhIII2PtII2 Tetranuclear Complex  $[\{Pt(NH_3)_2\}_2\{Rh(Ac)_3\}_2]_{4+}$ , that Lead to a Discrete and a 1D RhIII2PtII2AgI structures by Reacting with AgI (Aet = 2-Aminoethanethiolate). *Inorg. Chem.* **2005**, 44 (5), 1601–1610. <https://doi.org/10.1021/ic048680k>.
147. Kuwamura, N.; Kurioka, Y.; Konno, T. A Platinum(II)–Palladium(II)–Nickel(II) Heterotrimetallic Coordination Polymer Showing a Cooperative Effect on Catalytic Hydrogen Evolution. *Chem. Commun.* **2017**, 53 (5), 846–849. <https://doi.org/10.1039/C6CC08789B>.
148. Morell Cerdà, M.; Costisella, B.; Lippert, B. Synthesis and X-Ray Crystal Structure Determination of a Useful PdII Starting Compound, enPd(NO<sub>3</sub>)<sub>2</sub>. *Inorg. Chim. Acta* **2006**, 359 (5), 1485–1488. <https://doi.org/10.1016/j.ica.2005.10.023>.
149. Hudgens, T.; Johnson, D.; Cordes, W.; Barclay, T.; Jeter, D. Crystal Structure of (2,2'-Bipyrimidine)-Dinitratopalladium(II) Acetone Solvate. *J. Chem. Crystallogr.* **1997**, 27 (4), 247–250. <https://doi.org/10.1007/BF02575963>.
150. Lin, B.-L.; Labinger, J. A.; Bercaw, J. E. Mechanistic Investigations of Bipyrimidine-Promoted Palladium-Catalyzed Allylic Acetoxylation of Olefins. *Can. J. Chem.* **2009**, 87 (1), 264–271. <https://doi.org/10.1139/v08-133> (accessed 2021/07/20).
151. PrabhuKumar, K. M.; Rajegowda, H. R.; Raghavendra Kumar, P.; Butcher, R. J. Synthesis, Crystal Structures and Antioxidant Studies of Pd(II) and Ru(II) Complexes of 2-(4-Methoxyphenyltelluro) Ethanol. *J. Organomet. Chem.* **2019**, 902, 120967. <https://doi.org/10.1016/j.jorganchem.2019.120967>.
152. Bali, S.; Singh, A. K.; Sharma, P.; Toscano, R. A.; Drake, J. E.; Hursthouse, M. B.; Light, M. E. 2-[2-(4-Methoxyphenyltelluro)Ethyl]Thiophene (L1) Bis[2-(2-Thienyl)Ethyl] Telluride (L2) and their Metal Complexes; Crystal Structure of Trans-Dichlorobis[2-(2-(4-Methoxyphenyltelluro)Ethyl)Thiophene-Te]Palladium(II) and [Bis[2-(2-Thienyl)Ethyl] Telluride]Dichloro(P-Cymene)Ruthenium(II). *J. Organomet. Chem.* **2004**, 689 (14), 2346–2353. <https://doi.org/10.1016/j.jorganchem.2004.04.023>.
153. Ng, J. K.-P.; Tan, G.-K.; Vittal, J. J.; Leung, P.-H. Optical Resolution and the Study of Ligand Effects on the Ortho-Metalation Reaction of Resolved ( $\pm$ )-Diphenyl[1-(1-Naphthyl) Ethyl]Phosphine and its Arsenic Analogue. *Inorg. Chem.* **2003**, 42 (23), 7674–7682. <https://doi.org/10.1021/ic0302276>.
154. Guzei, I. A.; Li, K.; Bikzhanova, G. A.; Darkwa, J.; Mapolie, S. F. Benzenedicarbonyl and Benzenetricarbonyl Linker Pyrazolyl Complexes of Palladium(II): Synthesis, X-Ray Structures and Evaluation as Ethylene Polymerisation Catalysts. *Dalton Trans.* **2003**, 4, 715–722. <https://doi.org/10.1039/B208376K>.
155. Grushin, V. V.; Marshall, W. J. Ar–F Reductive Elimination from Palladium(II) Revisited. *Organometallics* **2007**, 26 (20), 4997–5002. <https://doi.org/10.1021/om700469k>.
156. Grushin, V. V.; Marshall, W. J. Is Fluoride Bonded to Two pd Acceptors Still Basic? Three CH<sub>2</sub>Cl<sub>2</sub> Molecules Encapsulating a Pd<sub>2</sub>( $\mu$ -F)<sub>2</sub> Square and New Implications for Catalysis. *Angew. Chem. Int. Ed.* **2002**, 41 (23), 4476–4479.
157. Mirzadeh, N.; Bennett, M.; Wagler, J.; Wächter, E.; Gerke, B.; Pöttgen, R.; Bhargava, S. Dichotomy between Palladium(II)–Tin(II) and Palladium(0)–Tin(IV) in Complexes of a Sn,As-Based Chelate Ligand. *Eur. J. Inorg. Chem.* **2013**, 2013 (12), 1997–2001. <https://doi.org/10.1002/ejic.201300115> (accessed 2021/07/20).
158. Albéniz, A. C.; Espinet, P.; Manrique, R.; Pérez-Mateo, A. Aryl Palladium Carbene Complexes and Carbene–Aryl Coupling Reactions. *Chem. A Eur. J.* **2005**, 11 (5), 1565–1573. <https://doi.org/10.1002/chem.200400811> (accessed 2021/07/20).
159. Qi, M.-H.; Shao, L.-X.; Shi, M. PdCl<sub>2</sub>-Promoted Reactions of Diaryl-Substituted Methylenecyclopropanes. *Dalton Trans.* **2010**, 39 (37), 8829–8834. <https://doi.org/10.1039/C0DT00059K>.
160. Donde, Y.; Overman, L. E. High Enantioselectivity in the Rearrangement of Allylic Imidates with Ferrocenyl Oxazoline Catalysts. *J. Am. Chem. Soc.* **1999**, 121 (12), 2933–2934. <https://doi.org/10.1021/ja983263q>.
161. Pamplin, C. B.; Rettig, S. J.; Patrick, B. O.; James, B. R. Solution Behavior and Structural Diversity of Bis(Dialkylphosphino)Methane Complexes of Palladium. *Inorg. Chem.* **2003**, 42 (13), 4117–4126. <https://doi.org/10.1021/ic030048o>.
162. Fliedel, C.; Maise-François, A.; Bellemín-Lapponaz, S. Palladium(II) Complexes of a Bis-2-Aminobiphenyl N-Heterocyclic Carbene: Synthesis, Structural Studies and Catalytic Activity. *Inorg. Chim. Acta* **2007**, 360 (1), 143–148. <https://doi.org/10.1016/j.ica.2006.07.034>.
163. Weckenmann, U.; Mittler, S.; Krämer, S.; Aliganga, A. K. A.; Fischer, R. A. A Study on the Selective Organometallic Vapor Deposition of Palladium onto Self-Assembled Monolayers of 4,4'-Biphenylthiol, 4-Biphenylthiol, and 11-Mercaptoundecanol on Polycrystalline Silver. *Chem. Mater.* **2004**, 16 (4), 621–628. <https://doi.org/10.1021/cm031094p>.
164. Redón, R. O.; Cramer, R.; Bernés, S.; Morales, D.; Torrens, H. Allyl–Palladium Compounds with Fluorinated Benzenethiolate Ligands. X-Ray Crystal Structure of  $[(\eta^3-C_3H_5)_2Pd(\mu-SC_6H_4F-4)_2Pd(\eta^3-C_3H_5)]$ . *Polyhedron* **2001**, 20 (26), 3119–3125. [https://doi.org/10.1016/S0277-5387\(01\)00934-2](https://doi.org/10.1016/S0277-5387(01)00934-2).
165. Adrian, R. A.; Benson, R. E.; Daniels, L. M.; Tiekink, E. R. T.; Walmsley, J. A. Di- $\mu$ -Hydroxo-Bis-([2,2'-Bipyridine]Palladium(II)) Trifluoro-Methane-Sulfonate. *Acta Crystallogr. E* **2006**, 62 (3), m601–m603. <https://doi.org/10.1107/S1600536806005782> (accessed 2021/07/20).
166. Conley, N. R.; Labios, L. A.; Pearson, D. M.; McCrory, C. C. L.; Waymouth, R. M. Aerobic Alcohol Oxidation with Cationic Palladium Complexes: Insights into Catalyst Design and Decomposition. *Organometallics* **2007**, 26 (23), 5447–5453. <https://doi.org/10.1021/om700492n>.
167. Singh, A.; Anandhi, U.; Cinellu, M. A.; Sharp, P. R. Diimine Supported Group 10 Hydroxo, Oxo, Amido, and Imido Complexes. *Dalton Trans.* **2008**, 17, 2314–2327. <https://doi.org/10.1039/B715663D>.
168. Ragaini, F.; Cenini, S.; Demartin, F. Use of Amido Grignard Reagents in Inorganic Chemistry. Synthesis and Crystal Structure of Anti-[Pd(Cl)(Py)( $\mu$ -2,6-Pri<sub>2</sub>C<sub>6</sub>H<sub>3</sub>NH)]<sub>2</sub>. *J. Chem. Soc. Dalton Trans.* **1997**, 17, 2855–2856. <https://doi.org/10.1039/A703853D>.
169. Villanueva, L. A.; Abboud, K. A.; Boncella, J. M. Synthesis, Characterization, and Crystal Structures of Monomeric and Dimeric Palladium(II) Amide Complexes. *Organometallics* **1994**, 13 (10), 3921–3931. <https://doi.org/10.1021/om00022a031>.
170. Huang, H.-P.; Wu, Q.; Mei, G.-Q. Bis( $\mu$ -3,5-Dimethyl-Pyrazolato- $\kappa$ 2N,N')bis-([4,4'-dimethyl-2,2'-Bipyridine- $\kappa$ 2N,N')Palladium(II)] Bis-(Hexa-Fluoro-Phosphate) Acetonitrile Disolvate. *Acta Crystallogr. E* **2006**, 62 (12), m3465–m3466. <https://doi.org/10.1107/S1600536806048926> (accessed 2021/07/20).
171. Perova, E. V.; Miloserdov, F. M.; Yakovleva, M. Y.; Nefedov, S. E. Formation of Binuclear Pyrazolate-Bridged Palladium Carboxylates in the Reactions of  $[pd(Hdmpz)4](OOCR_2)$  (R = Me, But, Ph) with Heterometallic Pd-Co Acetate. *Russ. J. Inorg. Chem.* **2009**, 54 (10), 1590. <https://doi.org/10.1134/S0036023609100155>.
172. da Silva, C.; Ferreira, J. G.; Mauro, A. E.; Frem, R. C. G.; Santos, R. H. A.; da Silva, P. B.; Pavan, F. R.; Marino, L. B.; Leite, C. Q. F.; Netto, A. V. G. Synthesis and Antimicrobial Activity of New Pyrazolate-Bridged Dinuclear Complexes of the Type  $[pd(\mu-L)(N_3)(PPh_3)]_2$  (PPh<sub>3</sub>=Triphenylphosphine; L=Pyrazolates). *Inorg. Chem. Commun.* **2014**, 48, 153–155. <https://doi.org/10.1016/j.inoche.2014.09.001>.
173. Jain, V. K.; Kannan, S.; Tiekink, E. R. T. Pyrazolato-Bridged Binuclear Palladium(II) Compounds: Synthesis and Crystal Structure. *J. Chem. Soc. Dalton Trans.* **1992**, 14, 2231–2234. <https://doi.org/10.1039/DT9920002231>.



174. Selbin, J.; Abboud, K.; Watkins, S. F.; Gutierrez, M. A.; Fronczek, F. R. V. Molecular Structures of Acetate-Bridged Dimers of a 2-Arylpyridine and a 2,6-Diarylpyridine Cyclometallated by Palladium(II). *J. Organomet. Chem.* **1983**, *241* (2), 259–268. [https://doi.org/10.1016/S0022-328X\(00\)98513-9](https://doi.org/10.1016/S0022-328X(00)98513-9).
175. Milani, J.; Pridmore, N. E.; Whitwood, A. C.; Fairlamb, I. J. S.; Perutz, R. N. The Role of Fluorine Substituents in the Regioselectivity of Intramolecular C–H Bond Functionalization of Benzylamines at Palladium(II). *Organometallics* **2015**, *34* (17), 4376–4386. <https://doi.org/10.1021/acs.organomet.5b00608>.
176. Mosteiro, R.; Fernández, A.; Vázquez-García, D.; López-Torres, M.; Rodríguez-Castro, A.; Gómez-Blanco, N.; Vila, J. M.; Fernández, J. J. Cyclometallated Palladium Diphosphane Compounds Derived from the Chiral Ligand (S)-PhCH(Me)NMe<sub>2</sub>. Michael Addition Reactions to the Vinylidene Double Bond. *Eur. J. Inorg. Chem.* **2011**, *2011* (11), 1824–1832. <https://doi.org/10.1002/ejic.201000873> (accessed 2021/07/20).
177. Dudkina, Y. B.; Kholin, K. V.; Gryaznova, T. V.; Islamov, D. R.; Kataeva, O. N.; Rizvanov, I. K.; Levitskaya, A. I.; Fominykh, O. D.; Balakina, M. Y.; Sinyashin, O. G.; et al. Redox Trends in Cyclometallated Palladium(II) Complexes. *Dalton Trans.* **2017**, *46* (1), 165–177. <https://doi.org/10.1039/C6DT03786K>.
178. Bedford, R. B.; Cazin, C. S. J.; Coles, S. J.; Gelbrich, T.; Hursthouse, M. B.; Scordia, V. J. M. Phosphine and Arsenine Adducts of N-Donor Palladacycles as Catalysts in the Suzuki Coupling of Aryl Bromides. *Dalton Trans.* **2003**, *17*, 3350–3356. <https://doi.org/10.1039/B304053D>.
179. Bercaw, J. E.; Durrell, A. C.; Gray, H. B.; Green, J. C.; Hazari, N.; Labinger, J. A.; Winkler, J. R. Electronic Structures of PdII Dimers. *Inorg. Chem.* **2010**, *49* (4), 1801–1810. <https://doi.org/10.1021/ic902189g>.
180. Markov, A. A.; Klyagina, A. P.; Dolin, S. P.; Akhmadullina, N. S.; Kozitsyna, N. Y.; Cherkashina, N. V.; Nefedov, S. E.; Vargaftik, M. N.; Moiseev, I. I. On the Nature of the Chemical Bond in Heterobimetallic Palladium(II) Complexes with Divalent 3d Metals. *Russ. J. Inorg. Chem.* **2009**, *54* (6), 885–892. <https://doi.org/10.1134/S0036023609060114>.
181. Bancroft, D. P.; Cotton, F. A.; Falvello, L. R.; Schwotzer, W. Synthesis and Characterization of Trinuclear Palladium Carboxylate Complexes. *Polyhedron* **1988**, *7* (8), 615–621. [https://doi.org/10.1016/S0277-5387\(00\)80368-X](https://doi.org/10.1016/S0277-5387(00)80368-X).
182. Das, J.; Dolui, P.; Ali, W.; Biswas, J. P.; Chandrashekar, H. B.; Prakash, G.; Maiti, D. A Direct Route to Six and Seven Membered Lactones Via  $\gamma$ -C(sp<sup>3</sup>)-H Activation: A Simple Protocol to Build Molecular Complexity. *Chem. Sci.* **2020**, *11* (35), 9697–9702. <https://doi.org/10.1039/D0SC03144E>.
183. Kolay, S.; Wadawale, A.; Das, D.; Kisan, H. K.; Sunoj, R. B.; Jain, V. K. Cyclopalladation of Dimesityl Selenide: Synthesis, Reactivity, Structural Characterization, Isolation of an Intermediate Complex with C–H...Pd Intra-Molecular Interaction and Computational Studies. *Dalton Trans.* **2013**, *42* (30), 10828–10837. <https://doi.org/10.1039/C3DT50935D>.
184. Maity, S.; Roy, R.; Sinha, C.; Sheen, W.-J.; Panneerselvam, K.; Lu, T.-H. Dimeric Cyclopalladated Azobenzenes: Structural Differences between 2-Hydroxypyridine and 2-Mercaptopyridine Bridged Complexes. *J. Organomet. Chem.* **2002**, *650* (1), 202–209. [https://doi.org/10.1016/S0022-328X\(02\)01229-9](https://doi.org/10.1016/S0022-328X(02)01229-9).
185. Kolay, S.; Ghavale, N.; Wadawale, A.; Das, D.; Jain, V. K. Binuclear Orthometalated N,N-Dimethylbenzylamine Complexes of Palladium(II): Synthesis, Structures and Thermal Behavior. *Phosphorus Sulfur Silicon Relat. Elem.* **2013**, *188* (10), 1449–1461. <https://doi.org/10.1080/10426507.2012.757608>.
186. Gupta, M.; Cramer, R. E.; Ho, K.; Pettersen, C.; Mishina, S.; Belli, J.; Jensen, C. M. Trans Influence of Phosphines on Dimer-Monomer Interconversion of 2-Pyridinethiolate Complexes: Structures of [Pd(Mu.-Eta.2-pyS-N,S)Cl(L)]<sub>2</sub> (L = PMe<sub>2</sub>Ph, PMePh<sub>2</sub>) and Pd(Eta.2-pyS)Cl(PPh<sub>3</sub>). *Inorg. Chem.* **1995**, *34* (1), 60–65. <https://doi.org/10.1021/ic00105a014>.
187. Oskui, B.; Sheldrick, W. S. Di- and Tripalladium(II) and -Platinum(II) Complexes Containing 7-Amino-1,8-Naphthyridin-2-One as a Bridging Ligand – Oxidation of a [Pt<sub>3</sub>]<sup>6+</sup> Core to [Pt<sub>3</sub>]<sup>8+</sup>. *Eur. J. Inorg. Chem.* **1999**, *1999* (8), 1325–1333. [https://doi.org/10.1002/\(SICI\)1099-0682\(199908\)1999:8<1325::AID-EJIC1325>3.0.CO;2-5](https://doi.org/10.1002/(SICI)1099-0682(199908)1999:8<1325::AID-EJIC1325>3.0.CO;2-5) (accessed 2021/07/20).
188. Oskui, B.; Mintert, M.; Sheldrick, W. S. Di- and Trinuclear Pd(II) and Pt(II) Complexes Containing Bridging 2,7-Disubstituted Naphthyridines. *Inorg. Chim. Acta* **1999**, *287* (1), 72–81. [https://doi.org/10.1016/S0020-1693\(98\)00411-3](https://doi.org/10.1016/S0020-1693(98)00411-3).
189. Shen, W.-Z.; Trötscher-Kaus, G.; Lippert, B. 1H NMR Spectroscopic Identification of Binding Modes of 2,2'-Bipyridine Ligands in Complexes of Square-Planar d8 Metal Ions. *Dalton Trans.* **2009**, *39*, 8203–8214. <https://doi.org/10.1039/B904173G>.
190. White-Morris, R. L.; Olmstead, M. M.; Balch, A. L. Aurophilic Interactions in Cationic Gold Complexes with Two Isocyanide Ligands. Polymorphic Yellow and Colorless Forms of [(Cyclohexyl Isocyanide)<sub>2</sub>Au](PF<sub>6</sub>) with Distinct Luminescence. *J. Am. Chem. Soc.* **2003**, *125* (4), 1033–1040. <https://doi.org/10.1021/ja020902v>.
191. Luong, L. M. C.; Malwitz, M. A.; Moshayedi, V.; Olmstead, M. M.; Balch, A. L. Role of Anions and Mixtures of Anions on the Thermochromism, Vapochromism, and Polymorph Formation of Luminescent Crystals of a Single Cation, [(C<sub>6</sub>H<sub>11</sub>NC)<sub>2</sub>Au]<sup>+</sup>. *J. Am. Chem. Soc.* **2020**, *142* (12), 5689–5701. <https://doi.org/10.1021/jacs.9b13168>.
192. Malwitz, M. A.; Lim, S. H.; White-Morris, R. L.; Pham, D. M.; Olmstead, M. M.; Balch, A. L. Crystallization and Interconversions of Vapor-Sensitive, Luminescent Polymorphs of [(C<sub>6</sub>H<sub>11</sub>NC)<sub>2</sub>Au](AsF<sub>6</sub>) and [(C<sub>6</sub>H<sub>11</sub>NC)<sub>2</sub>Au](PF<sub>6</sub>). *J. Am. Chem. Soc.* **2012**, *134* (26), 10885–10893. <https://doi.org/10.1021/ja302025m>.
193. Priola, E.; Volpi, G.; Rabezzana, R.; Borfecchia, E.; Garino, C.; Benzi, P.; Martini, A.; Operti, L.; Diana, E. Bridging Solution and Solid-State Chemistry of Dicyanoaurate: The Case Study of Zn-Au Nucleation Units. *Inorg. Chem.* **2020**, *59* (1), 203–213. <https://doi.org/10.1021/acs.inorgchem.9b00961>.
194. Djemel, A.; Stefanczyk, O.; Marchivie, M.; Desplanches, C.; Chastanet, G.; Djemel, A.; Delimi, R.; Trzop, E.; Collet, E. Solvatomorphism-Induced 45 K Hysteresis Width in a Spin-Crossover Mononuclear Compound. *Chemistry* **2018**, *24* (55), 14760–14767.
195. White, F.; Sykora, R. E. Crystal Structure of Bis(2,2':6',2''-Terpyridine- $\kappa$ 3 N,N',N'')Nickel(II) Dicyanoaurate(II). *Acta Crystallogr., Sect. E: Struct. Rep. Online* **2014**, *70* (12), 519–521. <https://doi.org/10.1107/S1600536814024672>.
196. Stender, M.; Olmstead, M. M.; Balch, A. L.; Rios, D.; Attar, S. Cation and Hydrogen Bonding Effects on the Self-Association and Luminescence of the Dicyanoaurate Ion, [Au(CN)<sub>2</sub>]. *Dalton Trans.* **2003**, *22*, 4282–4287. <https://doi.org/10.1039/b310085e>.
197. Seki, T.; Takamatsu, Y.; Ito, H. A Screening Approach for the Discovery of Mechanochromic Gold(II) Isocyanide Complexes with Crystal-to-Crystal Phase Transitions. *J. Am. Chem. Soc.* **2016**, *138* (19), 6252–6260. <https://doi.org/10.1021/jacs.6b02409>.
198. Ito, H.; Muromoto, M.; Kurenuma, S.; Ishizaka, S.; Kitamura, N.; Sato, H.; Seki, T. Mechanical Stimulation and Solid Seeding Trigger Single-Crystal-to-Single-Crystal Molecular Domino Transformations. *Nat. Commun.* **2013**, *4* (1), 2009. <https://doi.org/10.1038/ncomms3009>.
199. Hashmi, A. S. K.; Hengst, T.; Lothschütz, C.; Rominger, F. New and Easily Accessible Nitrogen Acyclic Gold(II) Carbenes: Structure and Application in the Gold-Catalyzed Phenol Synthesis As Well as the Hydration of Alkynes. *Adv. Synth. Catal.* **2010**, *352* (8), 1315–1337. <https://doi.org/10.1002/adsc.201000126> (accessed 2021/08/16).
200. Fujisawa, K.; Okuda, Y.; Izumi, Y.; Nagamatsu, A.; Rokusha, Y.; Sadaike, Y.; Tsutsumi, O. Reversible Thermal-Mode Control of Luminescence from Liquid-Crystalline Gold(II) Complexes. *J. Mat. Chem. C* **2014**, *2* (18), 3549–3555. <https://doi.org/10.1039/C3TC31973C>.
201. Humphrey, S. M.; Mack, H.-G.; Redshaw, C.; Elsegood, M. R. J.; Young, K. J. H.; Mayer, H. A.; Kaska, W. C. Variable Solid State Aggregations in a Series of (Isocyanide)Gold(II) Halides with the Novel Trimethylamine-Isocyanoborane Adduct. *Dalton Trans.* **2005**, *3*, 439–446. <https://doi.org/10.1039/b416392c>.
202. Döring, C.; Jones, P. G. Aminkomplexe Des Goldes, Teil 7: Pseudosymmetrie Bei Aminkomplexen Des Gold(II)-Cyanids [1] / Amine Complexes of Gold, Part 7: Pseudosymmetry in Amine Complexes of Gold(II) Cyanide. *Z. Naturfor. B* **2013**, *68* (5–6), 474–492. <https://doi.org/10.5560/znb.2013-3040>.
203. Strasser, U. H.; Neumann, B.; Stammer, H.-G.; Berger, R. J. F.; Mitzel, N. W. Gilded Chalice: Tetra-Aurated Calix[4]Arenes. *Z. Naturforsch., B. J. Chem. Sci.* **2014**, *69* (11/12), 1061–1072. <https://doi.org/10.5560/znb.2014-4149>.
204. Cookson, P. D.; Tiekink, E. R. T. Chloro(Dimethylphenylphosphine)Gold(II). *Acta Crystallogr. C* **1993**, *49* (9), 1602–1603. <https://doi.org/10.1107/S0108270193002707> (accessed 2021/08/16).
205. Baranov, A. Y.; Rakhmanova, M. I.; Samsonenko, D. G.; Malysheva, S. F.; Belogorlova, N. A.; Bagryanskaya, I. Y.; Fedin, V. P.; Artem'ev, A. V. Silver(II) and Gold(II) Complexes with Tris[2-(2-Pyridyl)Ethyl]Phosphine. *Inorg. Chim. Acta* **2019**, *494*, 78–83. <https://doi.org/10.1016/j.ica.2019.05.015>.
206. Strasser, C. E.; Cronje, S.; Schmidbaur, H.; Raubenheimer, H. G. The Preparation, Properties and X-Ray Structures of Gold(II) Trithiophosphite Complexes. *J. Organomet. Chem.* **2006**, *691* (22), 4788–4796. <https://doi.org/10.1016/j.jorganchem.2006.07.034>.
207. Angermaier, K.; Sladek, A.; Schmidbaur, H. Gold(II) Complexes of Chiral Secondary Phosphines. *Z. Naturfor. B* **1996**, *51* (12), 1671–1674. <https://doi.org/10.1515/znb-1996-1201>.

208. Strähle, J.; Hiller, W.; Conzelmann, W. Notizen: Die Kristallstruktur von AuBr · S(CH<sub>2</sub>C<sub>6</sub>H<sub>5</sub>)<sub>2</sub> und AuCl · S(CH<sub>2</sub>C<sub>6</sub>H<sub>5</sub>)<sub>2</sub>/The Crystal Structure of AuBr · S(CH<sub>2</sub>C<sub>6</sub>H<sub>5</sub>)<sub>2</sub> and AuCl · S(CH<sub>2</sub>C<sub>6</sub>H<sub>5</sub>)<sub>2</sub>. *Z. Naturforsch. B* **1984**, *39* (4), 538–541. <https://doi.org/10.1515/znb-1984-0422>.
209. Jones, P. G.; Lautner, J. Chloro(Dimethyl Sulfide)Gold(I). *Acta Crystallogr. C* **1988**, *44* (12), 2089–2091. <https://doi.org/10.1107/S0108270188009151> (accessed 2021/08/16).
210. Nifontova, G. A.; Krasochkat, O. N.; Lavrent'ev, I. P.; Makitova, D. D.; Atovmyan, L. O.; Khidekel, M. L. Oxidation of Transition Metals in the Liquid Phase. 9. Direct Synthesis and X-Ray Structural Examination of Complexes [(Me<sub>2</sub>S)AuBr] and [(Me<sub>2</sub>S)AuBr<sub>3</sub>]. *Bull. Acad. Sci. USSR, Div. Chem. Sci.* **1988**, *37* (2), 369–374. <https://doi.org/10.1007/BF00957448>.
211. McDougald, R. N., Jr.; Chilukuri, B.; Jia, H.; Perez, M. R.; Rabaa, H.; Wang, X.; Nesterov, V. N.; Cundari, T. R.; Gnade, B. E.; Omary, M. A. Molecular and Electronic Structure of Cyclic Trinuclear Gold(I) Carbenate Complexes: Insights for Structure/Luminescence/Conductivity Relationships. *Inorg. Chim. Acta* **2014**, *53* (14), 7485–7499. <https://doi.org/10.1021/ic500808q>.
212. Yang, G.; Raptis, R. G. Synthesis, Structure and Properties of Tetrameric Gold(I) 3,5-di-Tert-Butyl-Pyrazolate. *Inorg. Chim. Acta* **2003**, *352*, 98–104. [https://doi.org/10.1016/S0020-1693\(03\)00150-6](https://doi.org/10.1016/S0020-1693(03)00150-6).
213. Fujisawa, K.; Ishikawa, Y.; Miyashita, Y.; Okamoto, K.-I. Pyrazolate-Bridged Group 11 Metal(I) Complexes: Substituent Effects on the Supramolecular Structures and Physicochemical Properties. *Inorg. Chim. Acta* **2010**, *363* (12), 2977–2989. <https://doi.org/10.1016/j.ica.2010.05.014>.
214. Huang, S. P.; Kanatzidis, M. G. Gold(II) Vs Gold(III): Stabilization of Two Gold(II) Polyselenide Complexes, [Au<sub>2</sub>(Se<sub>2</sub>)(Se<sub>3</sub>)<sub>2</sub>]<sup>2-</sup> and [Au<sub>2</sub>(Se<sub>2</sub>)(Se<sub>4</sub>)<sub>2</sub>]<sup>2-</sup>, by the Diselenide Unit. *Inorg. Chem.* **1991**, *30* (18), 3572–3575. <https://doi.org/10.1021/ic00018a036>.
215. Kozelka, J.; Oswald, H. R.; Dubler, E. Bis-[Mu]-[Methylenebis(Dimethylphosphine)]Digold(II) Dichloride Dihydrate and its Comparison with the Diphenylphosphine Analogue. *Acta Crystallogr. C* **1986**, *42* (8), 1007–1009. <https://doi.org/10.1107/S0108270186093691>.
216. Payne, N. C.; Puddephatt, R. J.; Ravindranath, R.; Treurnicht, I. Gold(II) Dimers. The Synthesis and Reactions of [Tert-BuC≡CAu(Dmpm—P)], and the Crystal and Molecular Structures of [Au<sub>2</sub>(μ-Dmpm)<sub>2</sub>]<sub>2</sub> · 2H<sub>2</sub>O, X = Cl, I. *Can. J. Chem.* **1988**, *66* (12), 3176–3183. <https://doi.org/10.1139/v88-491> (accessed 2021/08/16).
217. Perreault, D.; Drouin, M.; Michel, A.; Miskowski, V. M.; Schaefer, W. P.; Harvey, P. D. Silver and Gold Dimers. Crystal and Molecular Structure of Ag<sub>2</sub>(Dmpm)<sub>2</sub>Br<sub>2</sub> and [Au<sub>2</sub>(Dmpm)<sub>2</sub>](PF<sub>6</sub>)<sub>2</sub> and Relation between Metal-Metal Force Constants and Metal-Metal Separations. *Inorg. Chem.* **1992**, *31* (4), 695–702. <https://doi.org/10.1021/ic00030a031>.
218. Porter, L. C.; Khan, M. N. I.; King, C.; Fackler Jnr, J. P. Structure of the Bis[Bis(Diphenylphosphino)Methane]Digold(I) Cation in [Au<sub>2</sub>(Dppm)<sub>2</sub>](BF<sub>4</sub>)<sub>2</sub>. *Acta Crystallogr. C* **1989**, *45* (6), 947–949. <https://doi.org/10.1107/S0108270188013630> (accessed 2021/08/16).
219. Yeo, C. I.; Tan, Y. S.; Tiekink, E. R. T. Crystal Structure of Bis[μ-Bis(Diphenylphosphanyl)Methane-κ<sup>2</sup>-P:P']Digold(II) Dichloride Acetone Monosolvate Monohydrate. *Acta Crystallogr., Sect. E: Crystallogr. Commun.* **2015**, *71* (8), 937–940. <https://doi.org/10.1107/S2056989015013341>.
220. Wu, M.; Zhang, L.; Chen, Z. Bis[μ-Bis(Diphenylphosphino)Methane]Digold(II) Bis(Hexafluorophosphate) Dichloromethane Disolvate. *Acta Crystallogr. E* **2003**, *59* (2), m72–m73. <https://doi.org/10.1107/S1600536803001120>.
221. Bardaji, M.; Jones, P. G.; Laguna, A.; Villacampa, M. D.; Villaverde, N. Synthesis and Structural Characterization of Luminescent Gold(I) Derivatives with an Unsymmetric Diphosphine. *Dalton Trans.* **2003**, *23*, 4529–4536. <https://doi.org/10.1039/B309116C>.
222. Fu, W.-F.; Chan, K.-C.; Miskowski, V. M.; Che, C.-M. The Intrinsic 3[dσ\*πσ] Emission of Binuclear Gold(I) Complexes with Two Bridging Diphosphane Ligands Lies in the Near UV; Emissions in the Visible Region Are Due to Exciplexes. *Angew. Chem. Int. Ed.* **1999**, *38* (18), 2783–2785. [https://doi.org/10.1002/\(SICI\)1521-3773\(19990917\)38:18<2783::AID-ANGE2783>3.0.CO;2-I](https://doi.org/10.1002/(SICI)1521-3773(19990917)38:18<2783::AID-ANGE2783>3.0.CO;2-I) (accessed 2021/08/16).
223. Fu, W.-F.; Chan, K.-C.; Cheung, K.-K.; Che, C.-M. Substrate-Binding Reactions of the 3[dσ\*πσ] Excited State of Binuclear Gold(I) Complexes with Bridging Bis(Dicyclohexylphosphino)Methane Ligands: Emission and Time-Resolved Absorption Spectroscopic Studies. *Chem. A Eur. J.* **2001**, *7* (21), 4656–4664. [https://doi.org/10.1002/1521-3765\(20011105\)7:21<4656::AID-CHEM4656>3.0.CO;2-D](https://doi.org/10.1002/1521-3765(20011105)7:21<4656::AID-CHEM4656>3.0.CO;2-D) (accessed 2021/08/16).
224. Basil, J. D.; Murray, H. H.; Fackler, J. P.; Tocher, J.; Mazany, A. M.; Trzcinska-Bancroft, B.; Knachel, H.; Dudis, D.; Delord, T. J.; Marler, D. Experimental and Theoretical Studies of Dinuclear Gold(II) and Gold(II) Phosphorus Ylide Complexes. Oxidative Addition, Halide Exchange, and Structural Properties Including the Crystal and Molecular Structures of [Au(CH<sub>2</sub>)<sub>2</sub>PPh<sub>2</sub>]<sub>2</sub> and [Au(CH<sub>2</sub>)<sub>2</sub>PPh<sub>2</sub>]<sub>2</sub>(CH<sub>3</sub>)Br. *J. Am. Chem. Soc.* **1985**, *107* (24), 6908–6915. <https://doi.org/10.1021/ja00310a028>.
225. Assefa, Z.; Staples, R. J.; Fackler Jnr, J. P. Bis[Bis(Triphenylphosphoranylidene)Ammonium] Bis[Cyanodithiocarbimato]gold(II), [PPN]<sub>2</sub>[Au<sub>2</sub>(S<sub>2</sub>CNCN)<sub>2</sub>]. *Acta Crystallogr. C* **1995**, *51* (11), 2271–2273. <https://doi.org/10.1107/S0108270195004628> (accessed 2021/08/16).
226. Dudis, D. S.; Fackler, J. P. Geometrical Isomers of [Ph<sub>2</sub>P(CH<sub>2</sub>)<sub>2</sub>AuX<sub>2</sub>]<sub>2</sub>. Crystal and Molecular Structures of Trans,Trans-[Ph<sub>2</sub>P(CH<sub>2</sub>)<sub>2</sub>AuBr<sub>2</sub>]<sub>2</sub> and cis,trans-[Ph<sub>2</sub>P(CH<sub>2</sub>)<sub>2</sub>AuCl<sub>2</sub>]<sub>2</sub>. *Inorg. Chem.* **1985**, *24* (23), 3758–3762. <https://doi.org/10.1021/ic00217a013>.
227. Jones, P. [μ-cis-1,2-Bis(Diphenylphosphino)Ethylene-Bis(Chlorogold(II))]. *Acta Crystallogr. B* **1980**, *36* (11), 2775–2776. <https://doi.org/10.1107/S0567740880009983>.
228. Berners-Price, S. J.; Bowen, R. J.; Fernandes, M. A.; Layh, M.; Lesueur, W. J.; Mahepal, S.; Motywa, M. M.; Sue, R. E.; van Rensburg, C. E. J. Gold(II) and Silver(II) Complexes of 2,3-Bis(Diphenylphosphino)Maleic Acid: Structural Studies and Antitumour Activity. *Inorg. Chim. Acta* **2005**, *358* (14), 4237–4246. <https://doi.org/10.1016/j.ica.2005.03.056>.
229. Walters, D. T.; England, K. R.; Ghiassi, K. B.; Semma, F. Z.; Olmstead, M. M.; Balch, A. L. Steric Effects and Aurophilic Interactions in Crystals of Au<sub>2</sub>(μ-1,2-Bis(Diphenylphosphino)Ethane)<sub>2</sub> and Au<sub>2</sub>(μ-1,2-Bis(Dicyclohexylphosphino)Ethane)<sub>2</sub> (X = Cl, Br, I). *Polyhedron* **2016**, *117*, 535–541. <https://doi.org/10.1016/j.poly.2016.06.031>.
230. Bardaji, M.; Miguel-Coello, A. B.; Espinet, P. Mono- and Dinuclear Luminescent 1,1'-Biisoquinoline Gold(II) Complexes. *Inorg. Chim. Acta* **2012**, *392*, 91–98. <https://doi.org/10.1016/j.ica.2012.06.024>.
231. Luong, L. M. C.; Aristov, M. M.; Adams, A. V.; Walters, D. T.; Berry, J. F.; Olmstead, M. M.; Balch, A. L. Unsymmetrical Coordination of Bipyridine in Three-Coordinate Gold(II) Complexes. *Inorg. Chem.* **2020**, *59* (6), 4109–4117. <https://doi.org/10.1021/acs.inorgchem.0c00138>.
232. Smith, M. B.; Dale, S. H.; Coles, S. J.; Gelbrich, T.; Hursthouse, M. B.; Light, M. E. Isomeric Dinuclear Gold(II) Complexes with Highly Functionalized Tertiary Phosphines: Self-Assembly of Dimers, Rings and 1-D Polymeric Chains. *CrystEngComm* **2006**, *8* (2), 140–149. <https://doi.org/10.1039/b516023e>.
233. Jassal, A. K. Advances in Ligand-Unsupported Argentophilic Interactions in Crystal Engineering: An Emerging Platform for Supramolecular Architectures. *Inorg. Chem. Front.* **2020**, *7* (19), 3735–3764. <https://doi.org/10.1039/d0qi00447b>.
234. Klapötke, T. M.; Krumm, B.; Mayer, P.; Piotrowski, H.; Schwab, I.; Vogt, M. Synthesis and Structures of Triorganotellurium Pseudohalides. *Eur. J. Inorg. Chem.* **2002**, *2002* (10), 2701–2709. [https://doi.org/10.1002/1099-0682\(200210\)2002:10<2701::AID-EJIC2701>3.0.CO;2-G](https://doi.org/10.1002/1099-0682(200210)2002:10<2701::AID-EJIC2701>3.0.CO;2-G) (accessed 2021/08/16).
235. Dechambenoit, P.; Ferlay, S.; Kyriatsakos, N.; Hosseini, M. W. Molecular Tectonics: Control of Packing of Luminescent Networks Formed upon Combining Bisamidinium Tectons with Dicyanometallates. *CrystEngComm* **2011**, *13* (6), 1922–1930. <https://doi.org/10.1039/C0CE00607F>.
236. Zhu, H. L.; Zhang, M.; Sun, Z. Y.; Rong, N. N.; Zhang, B.; Li, Y.; Fun, H. K. Crystal Structure of di(4-Aminopyridine)Silver(II) Trifluoromethylsulfate, Ag(C<sub>5</sub>H<sub>6</sub>N<sub>2</sub>)<sub>2</sub>(CF<sub>3</sub>SO<sub>3</sub>). *Z. Kristallogr. New Cryst. Struct.* **2003**, *218* (4), 521–522. <https://doi.org/10.1524/ncrs.2003.218.4.521>.
237. Argyle, V. J.; Woods, L. M.; Roxburgh, M.; Hanton, L. R. Triflate Anion and Ligand Influences in Silver(II) Coordination Polymers of Four Isomeric Dipyrityl Ketone Oximes. *CrystEngComm* **2013**, *15* (1), 120–134. <https://doi.org/10.1039/C2CE26449H>.
238. Huck, D. M.; Nguyen, H. L.; Horton, P. N.; Hursthouse, M. B.; Guillon, D.; Donnio, B.; Bruce, D. W. Mesomorphic Silver(II) Complexes of Polycatenar 2'- and 3'-Stilbazoles. Crystal and Molecular Structure of 3,4-Dimethoxy-3'-Stilbazole and of Two Silver Triflate Complexes. *Polyhedron* **2006**, *25* (2), 307–324. <https://doi.org/10.1016/j.poly.2005.07.023>.
239. Medishetty, R.; Sahoo, S. C.; Mulijanto, C. E.; Naumov, P.; Vittal, J. J. Photosensitive Behavior of Photoreactive Crystals. *Chem. Mater.* **2015**, *27* (5), 1821–1829. <https://doi.org/10.1021/acs.chemmater.5b00021>.



240. Wang, Y.; He, C.-T.; Liu, Y.-J.; Zhao, T.-Q.; Lu, X.-M.; Zhang, W.-X.; Zhang, J.-P.; Chen, X.-M. Copper(I) and Silver(I) 2-Methylimidazolates: Extended Isomerism, Isomerization, and Host–Guest Properties. *Inorg. Chem.* **2012**, *51* (8), 4772–4778. <https://doi.org/10.1021/ic300083k>.
241. Masciocchi, N.; Corradi, E.; Moret, M.; Ardizzoia, G. A.; Maspero, A.; La Monica, G.; Sironi, A. Reversible Depolymerization of Silver Pyrimidinolate into Cyclic Hexamers. *Inorg. Chem.* **1997**, *36* (24), 5648–5650. <https://doi.org/10.1021/ic9708273>.
242. Ryu, J. Y.; Lee, J. Y.; Choi, S. H.; Hong, S. J.; Kim, C.; Kim, Y.; Kim, S.-J. Syntheses and Structures of Ag(I) Compounds Containing Btp Ligands. *Inorg. Chim. Acta* **2005**, *358* (12), 3398–3406. <https://doi.org/10.1016/j.ica.2005.04.004>.
243. Tasada, A.; Alberti, F. M.; Bauzá, A.; Barceló-Oliver, M.; García-Raso, A.; Fiol, J. J.; Molins, E.; Caubet, A.; Frontera, A. Metallomacrocycles as Anion Receptors: Combining Hydrogen Bonding and Ion Pair Based Hosts Formed from Ag(I) Salts and Flexible Bis- and Tris-Pyrimidine Ligands. *Chem. Commun.* **2013**, *49* (43), 4944–4946. <https://doi.org/10.1039/C3CC40772A>.
244. Di Nicola, C.; Effendy; Marchetti, F.; Nervi, C.; Pettinari, C.; Robinson, W. T.; Sobolev, A. N.; White, A. H. Syntheses, Structures and Spectroscopy of Uni- and Bi-Dentate Nitrogen Base Complexes of Silver(I) Trifluoromethanesulfonate. *Dalton Trans.* **2010**, *39* (3), 908–922. <https://doi.org/10.1039/B913173F>.
245. Yurdakul, Ş.; Temel, E.; Büyükgüngör, O. Crystal Structure, Spectroscopic Characterization, Thermal Properties and Theoretical Investigations on [Ag(Methyl 4-Pyridyl Ketone)<sub>2</sub>NO<sub>3</sub>]. *J. Mol. Struct.* **2019**, *1191*, 301–313. <https://doi.org/10.1016/j.molstruc.2019.04.071>.
246. Njogu, E. M.; Omondi, B.; Nyamori, V. O. Coordination Polymers and Discrete Complexes of Ag(I)-N-(Pyridylmethylene)Anilines: Synthesis, Crystal Structures and Photophysical Properties. *J. Coord. Chem.* **2017**, *70* (16), 2796–2814. <https://doi.org/10.1080/00958972.2017.1370088>.
247. Sun, D.; Wei, Z.-H.; Wang, C.-F.; Zhang, N.; Huang, R.-B.; Zheng, L.-S. pH-Dependent Ag(I) Coordination Architectures Constructed from 4-Cyanopyridine and Phthalic Acid: From Discrete Structure to 2D Sheet. *CrystEngComm* **2011**, *13* (5), 1591–1601. <https://doi.org/10.1039/C0CE00539H>.
248. Chen, X.-D.; Wan, C.-Q.; Sung, H. H. Y.; Williams, I. D.; Mak, T. C. W. Control of Channel Size for Selective Guest Inclusion with Inlaid Anionic Building Blocks in a Porous Cationic Metal–Organic Host Framework. *Chem. A Eur. J.* **2009**, *15* (26), 6518–6528. <https://doi.org/10.1002/chem.200900010>.
249. Rixhon, M.; McMorran, D. A.; Garden, A. L.; Barton, L. R. Orientation of AgI Ions in Coordination Architectures through Ligand Conformation and Anion Binding: From Polymeric Chains to Discrete Squares. *Eur. J. Inorg. Chem.* **2018**, *2018* (38), 4278–4285. <https://doi.org/10.1002/ejic.201800746> (accessed 2021/08/16).
250. Hung-Low, F.; Renz, A.; Klausmeyer, K. K. X-Ray Crystal Structures of Silver Based Molecules Containing 5,5'-Dimethyl-2,2'-Bipyridine and 2,2'-Bipyridine. *J. Chem. Crystallogr.* **2011**, *41* (8), 1174–1179. <https://doi.org/10.1007/s10870-011-0066-y>.
251. Zhu, H.-L.; Chen, Q.; Peng, W.-L.; Qi, S.-J.; Xu, A.-L.; Chen, X.-M. Syntheses, Crystal Structures and Cytotoxicities of Silver (I) Complexes of 2,2'-Bipyridines and 1,10-Phenanthroline. *Chinese J. Chem.* **2001**, *19* (3), 263–267. <https://doi.org/10.1002/cjoc.20010190310> (accessed 2021/08/16).
252. Bowmaker, G. A.; Effendy; Marfua, S.; Skelton, B. W.; White, A. H. Syntheses, Structures and Vibrational Spectroscopy of some 1:1 and 1:2 Adducts of Silver(I) Oxyanion Salts with 2,2'-Bis(Pyridine) Chelates. *Inorg. Chim. Acta* **2005**, *358* (14), 4371–4388. <https://doi.org/10.1016/j.ica.2005.04.001>.
253. Constable, E. C.; Housecroft, C. E.; Kariuki, B. M.; Neuburger, M.; Smith, C. B. Structural Diversity in Silver(<Emph Type = "6" > |</Emph>) Complexes of 3,6-Di(2-Pyridyl) Pyridazines. *Aust. J. Chem.* **2003**, *56* (7), 653–655.
254. Belli Dell'Amico, D.; Calderazzo, F.; Curiardi, M.; Labella, L.; Marchetti, F. A Planar Silver Complex of 2,2':6',2'':6'',2'''-Quaterpyridine. *Inorg. Chem. Commun.* **2005**, *8* (8), 673–675. <https://doi.org/10.1016/j.inoche.2005.04.016>.
255. Niu, C.-Y.; Wu, B.-L.; Zheng, X.-F.; Wan, X.-S.; Zhang, H.-Y.; Niu, Y.-Y.; Meng, L.-Y. Counteranion's Effects on the Structures of Supramolecular Silver Coordination Compounds of One Asymmetric and One Biting Organic Ligands. *CrystEngComm* **2009**, *11* (7), 1373–1382. <https://doi.org/10.1039/B818745B>.
256. Đaković, M.; Benko, M.; Popović, Z. Supramolecular Architecture Via Self-Complementary Amide Hydrogen Bonding in [Ag(Pia)<sub>2</sub>](NO<sub>3</sub>)·H<sub>2</sub>O: Synthesis, Thermal and Structural Studies. *J. Chem. Crystallogr.* **2011**, *41* (3), 343–348. <https://doi.org/10.1007/s10870-010-9885-5>.
257. Joardar, S.; Roy, S.; Samanta, S.; Kumar Dutta, A. Structure, Luminescence and Antimicrobial Properties of Mononuclear Silver(I) Complexes of Pyridine 2-Carboxamide. *J. Chem. Sci. (Berlin, Ger.)* **2015**, *127* (10), 1819–1826. <https://doi.org/10.1007/s12039-015-0947-2>.
258. Hsiao, H.-L.; Wu, C.-J.; Hsu, W.; Yeh, C.-W.; Xie, M.-Y.; Huang, W.-J.; Chen, J.-D. Diverse Ag(I) Complexes Constructed from Asymmetric Pyridyl and Pyrimidyl Amide Ligands: Roles of Ag–Ag and π–π Interactions. *CrystEngComm* **2012**, *14* (23), 8143–8152. <https://doi.org/10.1039/C2CE25995H>.
259. Lobana, T. S.; Sultana, R.; Butcher, R. J.; Jasinski, J. P.; Golen, J. A.; Castineiras, A.; Pröpper, K.; Fernandez, F. J.; Vega, M. C. Heterocyclic-2-thione Derivatives of Silver(I): Synthesis, Spectroscopy and Structures of Mono- and di-Nuclear Silver(I) Halide Complexes. *J. Organomet. Chem.* **2013**, *745–746*, 460–469. <https://doi.org/10.1016/j.jorganchem.2013.08.020>.
260. Bowmaker, G. A.; Effendy; Kildea, J. D.; Silva, E. N. D.; White, A. H. Lewis-Base Adducts of Group 11 Metal(I) Compounds. LXXI Synthesis, Spectroscopy and Structural Systematics of some 1: 2 Binuclear Adducts of Silver(I) Compounds with Triphenylarsine, &#91;(Ph<sub>3</sub>As)<sub>2</sub>Ag(&micro;-X)<sub>2</sub>Ag(AsPh<sub>3</sub>)<sub>2</sub>; Cl, Br, I, SCN. *Aust. J. Chem.* **1997**, *50* (6), 627–640.
261. Sharutin, V. V.; Sharutina, O. K.; Senchurin, V. S.; Neudachina, A. N. Silver Complexes [Ph<sub>3</sub>PCH<sub>2</sub>CH<sub>2</sub>PPh<sub>3</sub>]<sup>2+</sup>[Ag<sub>2</sub>Cl<sub>4</sub>]<sup>2-</sup>, [Ph<sub>3</sub>PCH<sub>2</sub>OCH<sub>3</sub>]<sup>2+</sup>[Ag<sub>2</sub>Cl<sub>4</sub>]<sup>2-</sup>, [Ph<sub>3</sub>P(-Am)]<sup>2+</sup>[Ag<sub>2</sub>Br<sub>4</sub>]<sup>2-</sup>, [Ph<sub>3</sub>PC<sub>6</sub>H<sub>11</sub>Cyclo]<sup>2+</sup>[Ag<sub>2</sub>Br<sub>4</sub>]<sup>2-</sup>, [Ph<sub>3</sub>PCH<sub>2</sub>Ph]<sup>2+</sup>[Ag<sub>2</sub>Br<sub>4</sub>]<sup>2-</sup>, and [Ph<sub>3</sub>PCH=CH<sub>2</sub>]<sup>2+</sup>[Ag<sub>2</sub>Br<sub>3</sub>]<sup>3-</sup>, [Me<sub>4</sub>P]<sup>N+</sup>[Ag<sub>2</sub>Br<sub>3</sub>]<sup>N-</sup>: Synthesis and Structure. *Russ. J. Inorg. Chem.* **2016**, *61* (4), 451–460. <https://doi.org/10.1134/S0036023616040173>.
262. Daniliuc, C.; Druckenbrodt, C.; Hrib, C. G.; Ruthe, F.; Blaschette, A.; Jones, P. G.; du Mont, W.-W. The First Trialkylphosphane Telluride Complexes of Ag(I): Molecular, Ionic and Supramolecular Structural Alternatives. *Chem. Commun.* **2007**, *20*, 2060–2062. <https://doi.org/10.1039/B700917H>.
263. Saab, M.; Nelson, D. J.; Tzouras, N. V.; Bayrakdar, A. C. A.; Nolan, S. P.; Nahra, F.; Van Hecke, K. Straightforward Access to Chalcogenoureas Derived from N-Heterocyclic Carbenes and their Coordination Chemistry. *Dalton Trans.* **2020**, *49* (34), 12068–12081. <https://doi.org/10.1039/D0DT02558E>.
264. Yang, G.; Baran, P.; Martinez, A. R.; Raptis, R. G. Substituent Effects on the Supramolecular Aggregation of AgI-Pyrazolato Trimers. *Cryst. Growth Des.* **2013**, *13* (1), 264–269. <https://doi.org/10.1021/cg301411j>.
265. Chen, J.-H.; Liu, Y.-M.; Zhang, J.-X.; Zhu, Y.-Y.; Tang, M.-S.; Ng, S. W.; Yang, G. Halogen-Involving Weak Interactions Manifested in the Crystal Structures of Silver(I) or Gold(I) 4-Halogenated-3,5-Diphenylpyrazolato Trimers. *CrystEngComm* **2014**, *16* (23), 4987–4998. <https://doi.org/10.1039/C4CE00029C>.
266. Dias, H. V. R.; Diyabalanage, H. V. K. Trimeric Silver(I) Pyrazolates with Isopropyl, Bromo, and Nitro Substituents: Synthesis and Characterization of {[3,5-(i-pr)2,4-(Br)Pz]ag<sub>3</sub>}, {[3,5-(i-pr)2,4-(NO<sub>2</sub>)Pz]ag<sub>3</sub>}. *Polyhedron* **2006**, *25* (7), 1655–1661. <https://doi.org/10.1016/j.poly.2005.11.017>.
267. Saotome, M.; Shimizu, D.; Itagaki, A.; Young, D. J.; Fujisawa, K. Structures and Photoluminescence of Silver(I) and Gold(I) Cyclic Trinuclear Complexes with Aryl Substituted Pyrazolates. *Chemistry Letters* **2019**, *48* (6), 533–536. <https://doi.org/10.1246/cl.190145> (accessed 2021/08/16).
268. Wang, Z.-Y.; Wang, Y.-L.; Yang, G.; Ng, S. W. Bis[μ<sub>2</sub>-3,5-diisopropyl-4H-1,2,4-triazole-[kappa]2N1:N2]bis[nitrate-[kappa]O]silver(I)]. *Acta Crystallogr. E* **2009**, *65* (8), m974. <https://doi.org/10.1107/S1600536809028384>.
269. Schmidbaur, H.; Mair, A.; Müller, G.; Lachmann, J.; Gamper, S. Silver Nitrate Complexes of Nitrogen-Containing Heterocycles. *Z. Naturforsch. B* **1991**, *46* (7), 912–918. <https://doi.org/10.1515/znb-1991-0710>.
270. Sun, D.; Liu, F.-J.; Hao, H.-J.; Li, Y.-H.; Huang, R.-B.; Zheng, L.-S. Six Low-Dimensional Silver(I) Coordination Complexes Derived from 2-Aminobenzonitrile and Carboxylates. *Inorg. Chim. Acta* **2012**, *387*, 271–276. <https://doi.org/10.1016/j.ica.2012.01.027>.
271. Xu, H.-W.; Chen, Z.-N.; Wu, J.-G. Bis[μ<sub>2</sub>-Bis(Diphenylphosphino)Amine-[Kappa]P:P']Bis[Acetonitrile]silver(I) Tris(cis-1,2-Dicyanoethylene-1,2-Dithiolate)Molybdate(IV). *Acta Crystallogr. E* **2002**, *58* (11), m631–m633. <https://doi.org/10.1107/S1600536802018408>.
272. Effendy; Di Nicola, C.; Nitiatmodjo, M.; Pettinari, C.; Skelton, B. W.; White, A. H. Syntheses, Spectroscopic and Structural Characterization of some (Solvated) Binuclear Adducts of the Form Ag(Oxyanion)Dpem(S) (1:1(X))<sub>2</sub> (Oxyanion = ClO<sub>4</sub>, F<sub>3</sub>CCO<sub>2</sub>, F<sub>3</sub>CSO<sub>3</sub>; Dpem = Ph<sub>2</sub>E(CH<sub>2</sub>)EPh<sub>2</sub> (E = P, As)). *Inorg. Chim. Acta* **2005**, *358* (3), 735–747. <https://doi.org/10.1016/j.ica.2004.07.032>.
273. Smith, G.; Kennard, C. H. L.; Mak, T. C. W. The Crystal Structure of Silver(I) 2-Hydroxybenzoate and Silver(I) 2,6-Dihydroxybenzoate. *Z. Kristallogr. Cryst. Mater.* **1988**, *184* (1–4), 275–280. <https://doi.org/10.1524/zkri.1988.184.14.275>.

274. Mak, T. C. W.; Yip, W. H.; Kennard, C. H. L.; Smith, G.; O'Reilly, E. J. Univalent Metal Complexes of (Perfluorophenoxy)Acetic Acid. The Crystal Structures of (2,3,4,5,6-Pentafluorophenoxy)Acetic Acid, Bis- $\beta$ -[2,3,4,5,6-Pentafluorophenoxy]Acetato-*O*,*O'*-Bisilver(I) and  $\langle I \rangle$  *Catena*  $\langle I \rangle$  -Bis- $\beta$ -[2,3,4,5,6-Pentafluorophenoxy]Acetato-*O*-Bismercury(I). *Aust. J. Chem.* **1988**, *41* (5), 683–691.
275. Brammer, L.; Rodger, C. S.; Blake, A. J.; Brooks, N. R.; Champness, N. R.; Cunningham, J. W.; Hubberstey, P.; Teat, S. J.; Wilson, C.; Schröder, M. Bridging Mode Flexibility of 1,3-Dithiacyclohexane in Silver(I) *Co*-Ordination Polymers. *J. Chem. Soc. Dalton Trans.* **2002**, *22*, 4134–4142. <https://doi.org/10.1039/B205278B>.
276. Constable, E. C.; Hannon, M. J.; Martin, A.; Raitby, P. R.; Tocher, D. A. Self-Assembly of Double-Helical Complexes of 2,2':6',2'':6'',2''':6'''-Quaterpyridine (Qtqp); the x-Ray Crystal Structures of [Cu<sub>2</sub>(Qtqp)<sub>2</sub>][PF<sub>6</sub>]<sub>2</sub> and [Ag<sub>2</sub>(Qtqp)<sub>2</sub>][BF<sub>4</sub>]<sub>2</sub>. *Polyhedron* **1992**, *11* (22), 2967–2971. [https://doi.org/10.1016/S0277-5387\(00\)83604-9](https://doi.org/10.1016/S0277-5387(00)83604-9).
277. Stefankiewicz, A. R.; Waleśa, M.; Jankowski, P.; Ciesielski, A.; Patroniak, V.; Kubicki, M.; Hnatejko, Z.; Harrowfield, J. M.; Lehn, J.-M. Quaterpyridine Ligands Forming Helical Complexes of Mono- and Dinuclear (Helicite) Forms. *Eur. J. Inorg. Chem.* **2008**, *2008* (18), 2910–2920. <https://doi.org/10.1002/ejic.200800172> (accessed 2021/08/16).
278. Adamski, A.; Fik, M. A.; Kubicki, M.; Hnatejko, Z.; Gurda, D.; Fedoruk-Wyszomirska, A.; Wyszko, E.; Kruszka, D.; Dutkiewicz, Z.; Patroniak, V. Full Characterization and Cytotoxic Activity of New Silver(I) and Copper(I) Helicates with Quaterpyridine. *New J. Chem.* **2016**, *40* (9), 7943–7957. <https://doi.org/10.1039/C5NJ03601A>.
279. Bardaji, M.; Miguel-Coello, A. B.; Espinet, P. Predominance of Bridging Coordination in Luminescent 1,1'-Biisoquinoline Silver(I) Derivatives. *Inorg. Chim. Acta* **2012**, *386*, 93–101. <https://doi.org/10.1016/j.ica.2012.01.059>.
280. Starova, G. L.; Denisova, A. S.; Dem'yanchuk, E. M. Structures of Dioxopyridyl-12-Crown-4 and its Complexes with Silver (I) and Copper (II) Cations. *J. Mol. Struct.* **2008**, *873* (1), 117–120. <https://doi.org/10.1016/j.molstruc.2007.03.010>.
281. Cebollada, A.; Velle, A.; Iglesias, M.; Fullmer, L. B.; Goberna-Ferron, S.; Nyman, M.; Sanz Miguel, P. J. Direct X-Ray Scattering Evidence for Metal-Metal Interactions in Solution at the Molecular Level. *Angew. Chem. Int. Ed.* **2015**, *54* (43), 12762–12766. <https://doi.org/10.1002/anie.201505736>.
282. Li, Z.; Mackie, E. R. R.; Ramkisson, P.; Mather, J. C.; Wiratpruk, N.; Soares da Costa, T. P.; Barnard, P. J. Synthesis, Conformational Analysis and Antibacterial Activity of au(I)-ag(I) and au(I)-hg(II) Heterobimetallic N-Heterocyclic Carbene Complexes. *Dalton Trans.* **2020**, *49* (36), 12820–12834. <https://doi.org/10.1039/D0DT02225J>.
283. Yan, T.; Sun, L.-Y.; Deng, Y.-X.; Han, Y.-F.; Jin, G.-X. Facile Synthesis of Size-Tunable Functional Polyimidazolium Macrocycles through a Photochemical Closing Strategy. *Chem. A Eur. J.* **2015**, *21* (49), 17610–17613. <https://doi.org/10.1002/chem.201503709> (accessed 2021/08/16).
284. Wang, D.-Q. Bis[ $\mu$ ]-3,3'-dimethyl-3,3'-methylenebis(2,3-dihydro-1H-imidazole)]disilver(I)(Ag-Ag) dichloride hemihydrate. *Acta Crystallogr. E* **2006**, *62* (7), m1565–m1566. <https://doi.org/10.1107/S1600536806022136>.
285. Lee, C.-S.; Lai, Y.-B.; Lin, W.-J.; Zhuang, R. R.; Hwang, W.-S. Pd(II) Complexes with Mono- and Bis-Chelate Carbene Ligands Tagged with Pyridinium Cation: Synthesis, Structures, and their Catalytic Activities toward Heck Reaction. *J. Organomet. Chem.* **2013**, *724*, 235–243. <https://doi.org/10.1016/j.jorganchem.2012.11.015>.
286. Quezada, C. A.; Garrison, J. C.; Panzner, M. J.; Tessier, C. A.; Youngs, W. J. The Potential Use of Rhodium N-Heterocyclic Carbene Complexes as Radiopharmaceuticals: The Transfer of a Carbene from ag(I) to RhCl<sub>3</sub>·3H<sub>2</sub>O. *Organometallics* **2004**, *23* (21), 4846–4848. <https://doi.org/10.1021/om049697d>.
287. Nishihara, K.; Ueda, M.; Higashitani, A.; Nakao, Y.; Arikawa, Y.; Horiuchi, S.; Sakuda, E.; Umakoshi, K. Different Structural Preference of ag(I) and au(I) in Neutral and Cationic Luminescent Heteropolynuclear Platinum(II) Complexes: Z (U)-Shaped Pt<sub>2</sub>M<sub>2</sub> Type Vs. Trinuclear PtM<sub>2</sub> Type. *Dalton Trans.* **2016**, *45* (12), 4978–4982. <https://doi.org/10.1039/C6DT00320F>.
288. Topchii, M. A.; Zotova, M. A.; Masoud, S. M.; Mailyan, A. K.; Ananyev, I. V.; Nefedov, S. E.; Asachenko, A. F.; Osipov, S. N. Fluorinated Unsymmetrical N,N'-Diaryl Imidazolium Salts—New Functionalized NHC-Ligand Precursors. *Chem. A Eur. J.* **2017**, *23* (27), 6663–6674. <https://doi.org/10.1002/chem.201700624> (accessed 2021/08/16).
289. Brown, M. K.; May, T. L.; Baxter, C. A.; Hoveyda, A. H. All-Carbon Quaternary Stereogenic Centers by Enantioselective Cu-Catalyzed Conjugate Additions Promoted by a Chiral N-Heterocyclic Carbene. *Angew. Chem. Int. Ed.* **2007**, *46* (7), 1097–1100. <https://doi.org/10.1002/anie.200604511> (accessed 2021/08/16).
290. Sundararaman, A.; Zakharov, L. N.; Rheingold, A. L.; Jaekle, F. Cuprophilic and  $\pi$ -Stacking Interactions in the Formation of Supramolecular Stacks from Dicoordinate Organocopper Complexes. *Chem. Commun.* **2005**, *13*, 1708–1710. <https://doi.org/10.1039/B417532H>.
291. Zhou, J.; Tan, X.; Hu, F.; Zou, H.-H.; Almeida Paz, F. A.; Fu, L.; Zhao, R. A 3-D Net Based on Weak Metallophilic (Cu–Cu) Interactions. *Dalton Trans.* **2016**, *45* (28), 11292–11296. <https://doi.org/10.1039/C6DT00883F>.
292. Martínez de Salinas, S.; Mudarra, Á. L.; Odena, C.; Martínez Belmonte, M.; Benet-Buchholz, J.; Maseras, F.; Pérez-Temprano, M. H. Exploring the Role of Coinage Metalates in Trifluoromethylation: A Combined Experimental and Theoretical Study. *Chem. A Eur. J.* **2019**, *25* (40), 9390–9394. <https://doi.org/10.1002/chem.201900496>.
293. Kohn, R. D.; Seifert, G.; Pan, Z.; Mahon, M. F.; Kociok-Kohn, G. Reactions of Triazacyclohexanes with CuCl<sub>2</sub>: Surprising Formation of a Dimer between Two [CuCl<sub>2</sub>]<sup>-</sup> Ions with an Unsupported Cuprophilic Attraction. *Angew. Chem. Int. Ed.* **2003**, *42* (7), 793–796. <https://doi.org/10.1002/anie.200390210>.
294. Woidy, P.; Karttunen, A. J.; Widenmeyer, M.; Niewa, R.; Kraus, F. On Copper(I) Fluorides, the Cuprophilic Interaction, the Preparation of Copper Nitride at Room Temperature, and the Formation Mechanism at Elevated Temperatures. *Chem. A Eur. J.* **2015**, *21* (8), 3290–3303. <https://doi.org/10.1002/chem.201406136>.
295. Zheng, S.-L.; Messerschmidt, M.; Coppens, P. An Unstable Ligand-Unsupported CuI Dimer Stabilized in a Supramolecular Framework. *Angew. Chem. Int. Ed.* **2005**, *44* (29), 4614–4617. <https://doi.org/10.1002/anie.200501154>.
296. Troyano, J.; Zapata, E.; Perles, J.; Amo-Ochoa, P.; Fernández-Moreira, V.; Martínez, J. I.; Zamora, F.; Delgado, S. Multifunctional Copper(I) Coordination Polymers with Aromatic Mono- and Ditopic Thioamides. *Inorg. Chem.* **2019**, *58* (5), 3290–3301. <https://doi.org/10.1021/acs.inorgchem.8b03364>.
297. Song, Y.; Xu, Y.; Wang, T.-W.; Wang, Z.-X.; You, X.-Z. Synthesis, Structure and Magnetic Properties of a 2D Cyano-Bridged Mixed-Valence CuI/Cu<sub>2</sub>I Assembly Containing Ladder-like Chain. *J. Mol. Struct.* **2006**, *788* (1), 206–210. <https://doi.org/10.1016/j.molstruc.2005.12.001>.
298. Oakley, S. H.; Coles, M. P.; Hitchcock, P. B. Structural Consequences of the Prohibition of Hydrogen Bonding in Copper–Guanidine Systems. *Inorg. Chem.* **2004**, *43* (16), 5168–5172. <https://doi.org/10.1021/ic0495970>.
299. Ge, Y.; Cui, X.-Y.; Tan, S. M.; Jiang, H.; Ren, J.; Lee, N.; Lee, R.; Tan, C.-H. Guanidine–Copper Complex Catalyzed Allylic Borylation for the Enantioconvergent Synthesis of Tertiary Cyclic Allylboronates. *Angew. Chem. Int. Ed.* **2019**, *58* (8), 2382–2386. <https://doi.org/10.1002/anie.201813490>.
300. Stricker, M.; Linder, T.; Oelkers, B.; Sundermeyer, J. Cu(I)/(II) Based Catalytic Ionic Liquids, their Metallo-Laminate Solid State Structures and Catalytic Activities in Oxidative Methanol Carbonylation. *Green Chem.* **2010**, *12* (9), 1589–1598. <https://doi.org/10.1039/C003948A>.
301. Blake, A. J.; Brooks, N. R.; Champness, N. R.; Crew, M.; Deveson, A.; Fenske, D.; Gregory, D. H.; Hanton, L. R.; Hubberstey, P.; Schröder, M. Topological Isomerism in Coordination Polymers. *Chem. Commun.* **2001**, *16*, 1432–1433. <https://doi.org/10.1039/B103612M>.
302. Braga, D.; Grepioni, F.; Maini, L.; Mazzeo, P. P.; Ventura, B. Solid-State Reactivity of Copper(I) Iodide: Luminescent 2D-Coordination Polymers of CuI with Saturated Bidentate Nitrogen Bases. *New J. Chem.* **2011**, *35* (2), 339–344. <https://doi.org/10.1039/C0NJ00547A>.
303. Liang, X.-Q.; Gupta, R. K.; Li, Y.-W.; Ma, H.-Y.; Gao, L.-N.; Tung, C.-H.; Sun, D. Structural Diversity of Copper(I) Cluster-Based Coordination Polymers with Pyrazine-2-Thiol Ligand. *Inorg. Chem.* **2020**, *59* (5), 2680–2688. <https://doi.org/10.1021/acs.inorgchem.9b02919>.
304. Ritch, J. S.; Chivers, T. Group 11 Complexes of the P<sub>3</sub>Te-Centered Ligand [TeP<sub>3</sub>Pr<sub>2</sub>NiPr<sub>2</sub>]<sup>-</sup>: Synthesis, Structures, and Insertion Reactions of the Copper(I) Complex with Chalcogens. *Inorg. Chem.* **2009**, *48* (8), 3857–3865. <https://doi.org/10.1021/ic802428b>.
305. Fuller, R. O.; Griffith, C. S.; Koutsantonis, G. A.; Skelton, B. W.; White, A. H. Anion-Directed Solid-State Structures of Copper(I) and Silver(I) Adducts of Ruthenium Ethyne-1,2-Diyl Compounds. *Organometallics* **2015**, *34* (11), 2632–2646. <https://doi.org/10.1021/om501270u>.
306. Dance, I. G.; Bowmaker, G. A.; Clark, G. R.; Seadon, J. K. The Formation and Crystal and Molecular Structures of Hexa( $\mu$ -Organothiolato)Tetracuprate(I) Cage Dianions: Bis-(Tetramethylammonium)Hexa( $\mu$ -Methanethiolato)Tetracuprate(I) and Two Polymorphs of Bis(Tetramethylammonium)Hexa( $\mu$ -Benzenethiolato)-Tetracuprate(I). *Polyhedron* **1983**, *2* (10), 1031–1043. [https://doi.org/10.1016/S0277-5387\(00\)81450-3](https://doi.org/10.1016/S0277-5387(00)81450-3).
307. Rath, N. P.; Maxwell, J. L.; Holt, E. M. Fluorescent Copper(I) Complexes: An X-Ray Diffraction Study of Complexes of Copper(I) Iodide and Pyridine Derivatives of Rhombic, [Cu<sub>2</sub>I<sub>2</sub>(3Me-Py)<sub>4</sub>], and Polymeric Structure, [(CuI(2me-Py))<sub>n</sub>] and [(CuI(2,4Me<sub>2</sub>-Py))<sub>n</sub>]. *J. Chem. Soc. Dalton Trans.* **1986**, *11*, 2449–2453. <https://doi.org/10.1039/DT9860002449>.

308. Janiak, C.; Uehlin, L.; Wu, H.-P.; Klüfers, P.; Piotrowski, H.; Scharmann, G. T. Co-Ordination Engineering: When Can One Speak of an "Understanding"? Case Study of the Multidentate Ligand 2,2'-Dimethyl-4,4'-Bipyrimidine†. *J. Chem. Soc. Dalton Trans.* **1999**, 17, 3121–3131 <https://doi.org/10.1039/A904829D>.
309. Kang, Y.; Fang, W.-H.; Zhang, L.; Zhang, J. A Structure-Directing Method to Prepare Semiconductive Zeolitic Cluster–Organic Frameworks with Cu<sub>3</sub>I<sub>4</sub> Building Units. *Chem. Commun.* **2015**, 51 (43), 8994–8997. <https://doi.org/10.1039/C5CC02598B>.
310. Bi, M.; Li, G.; Zou, Y.; Shi, Z.; Feng, S. Zeolite-Like Copper Iodide Framework with New 66 Topology. *Inorg. Chem.* **2007**, 46 (3), 604–606. <https://doi.org/10.1021/ic061163c>.
311. Zhang, Y.; Wu, T.; Liu, R.; Dou, T.; Bu, X.; Feng, P. Three-Dimensional Photoluminescent Frameworks Constructed from Size-Tunable CuI Clusters. *Cryst. Growth Des.* **2010**, 10 (5), 2047–2049. <https://doi.org/10.1021/cg1001978>.
312. Eriksson, H.; Håkansson, M. Mesitylcopper: Tetrameric and Pentameric. *Organometallics* **1997**, 16 (20), 4243–4244. <https://doi.org/10.1021/om970462u>.
313. Rungthanaphatsophon, P.; Barnes, C. L.; Walensky, J. R. Copper(I) Clusters with Bulky Dithiocarboxylate, Thiolate, and Selenolate Ligands. *Dalton Trans.* **2016**, 45 (36), 14265–14276. <https://doi.org/10.1039/C6DT02709A>.
314. Bettenhausen, M.; Eichhöfer, A.; Fenske, D.; Semmelmann, M. Synthese und Strukturen neuer selenido- und selenolatoverbrückter Kupfercluster: [Cu<sub>38</sub>Se<sub>13</sub>(SePh)<sub>12</sub>(dppb)<sub>6</sub>] (1), [Cu<sub>36</sub>Se<sub>5</sub>(SePh)<sub>18</sub>(dppp)<sub>2</sub>] (2), [Cu<sub>36</sub>Se<sub>5</sub>(SePh)<sub>26</sub>(dppa)<sub>4</sub>] (3), [Cu<sub>58</sub>Se<sub>16</sub>(SePh)<sub>24</sub>(dppa)<sub>6</sub>] (4) und [Cu<sub>3</sub>(SeMes)<sub>3</sub>(dppm)] (5). *Z. Anorg. Allg. Chem.* **1999**, 625 (4), 593–601. [https://doi.org/10.1002/\(SICI\)1521-3749\(199904\)625:4<593::AID-ZAAC593>3.0.CO;2-J](https://doi.org/10.1002/(SICI)1521-3749(199904)625:4<593::AID-ZAAC593>3.0.CO;2-J).
315. Rao, C. P.; Dorfman, J. R.; Holm, R. H. Synthesis and Structural Systematics of Ethane-1,2-Dithiolato Complexes. *Inorg. Chem.* **1986**, 25 (4), 428–439. <https://doi.org/10.1021/ic00224a011>.
316. Hope, H.; Power, P. P. X-Ray Crystal Structure of a Late-Transition-Metal Dialkylamide, [(CuNET<sub>2</sub>)<sub>4</sub>]. *Inorg. Chem.* **1984**, 23 (7), 936–937. <https://doi.org/10.1021/ic00175a027>.
317. Lopes, C.; Håkansson, M.; Jagner, S. Carbonylation of a Tetrameric Aryloxocopper(I) Cluster. *Inorg. Chem.* **1997**, 36 (15), 3232–3236. <https://doi.org/10.1021/ic961287x>.
318. Robinson, T. P.; Price, R. D.; Davidson, M. G.; Fox, M. A.; Johnson, A. L. Why Are the {Cu<sub>4</sub>N<sub>4</sub>} Rings in Copper(I) Phosphinimide Clusters [Cu<sub>μ</sub>-NPR<sub>3</sub>]<sub>4</sub> (R = NMe<sub>3</sub> or Ph) Planar? *Dalton Trans.* **2015**, 44 (12), 5611–5619 <https://doi.org/10.1039/C5DT00255A>.
319. Kotsch, M.; Gienger, C.; Schrenk, C.; Schnepf, A. The Sterically Demanding Thiosilyl Group SSi(SiMe<sub>3</sub>)<sub>3</sub> as a Ligand in Transition Metal Chemistry. *Z. Anorg. Allg. Chem.* **2016**, 642 (9–10), 670–675. <https://doi.org/10.1002/zaac.201600137>.
320. Zhuo, H.-Y.; Su, H.-F.; Cao, Z.-Z.; Liu, W.; Wang, S.-A.; Feng, L.; Zhuang, G.-L.; Lin, S.-C.; Kurmoo, M.; Tung, C.-H.; et al. High-Nuclear Organometallic Copper(I)–Alkynide Clusters: Thermochromic Near-Infrared Luminescence and Solution Stability. *Chem. A Eur. J.* **2016**, 22 (49), 17619–17626. <https://doi.org/10.1002/chem.201603797>.
321. Li, J.; Ma, H. Z.; Reid, G. E.; Edwards, A. J.; Hong, Y.; White, J. M.; Mulder, R. J.; O'Hair, R. A. J. Synthesis and X-Ray Crystallographic Characterization of Frustum-Shaped Ligated [Cu<sub>18</sub>H<sub>16</sub>(DPPe)<sub>6</sub>]<sup>2+</sup> and [Cu<sub>16</sub>H<sub>14</sub>(DPPA)<sub>6</sub>]<sup>2+</sup> Nanoclusters and Studies on their H<sub>2</sub> Evolution Reactions. *Chem. A Eur. J.* **2018**, 24 (9), 2070–2074. <https://doi.org/10.1002/chem.201705448>.
322. Kim, M.; Taylor, T. J.; Gabbai, F. P. Hg(II)–Pd(II) Metallophilic Interactions. *J. Am. Chem. Soc.* **2008**, 130 (20), 6332–6333. <https://doi.org/10.1021/ja801626c>.
323. Reger, D. L.; Debreczeni, A.; Smith, M. D.; Jezierska, J.; Ozarowski, A. Copper(II) Carboxylate Dimers Prepared from Ligands Designed to Form a Robust π–π Stacking Synthon: Supramolecular Structures and Molecular Properties. *Inorg. Chem.* **2012**, 51 (2), 1068–1083. <https://doi.org/10.1021/ic202198k>.
324. Ohba, S.; Kato, M.; Tokii, T.; Muto, Y.; Steward, O. W. Magneto-Structural Correlations in Dimeric Copper(II) Carboxylates. *Mol. Cryst. Liq. Cryst. Sci. Technol., Sect. A* **1993**, 233, 335. <https://doi.org/10.1080/10587259308054975>.
325. Doedens, R. J. Structure and Metal–Metal Interactions in Copper(II) Carboxylate Complexes. *Prog. Inorg. Chem.* **1976**, 21, 209.
326. Drew, M. G. B.; Edwards, D. A.; Richards, R. Crystal and Molecular Structure of Tetrakis[Copper(II) Benzoate]. *J. Chem. Soc. Dalton Trans.* **1977**, 3, 299–303. <https://doi.org/10.1039/DT9770000299>.
327. Cotton, F. A.; Dikarev, E. V.; Petrukhina, M. A. Syntheses and Crystal Structures of "Unligated" Copper(I) and Copper(II) Trifluoroacetates. *Inorg. Chem.* **2000**, 39 (26), 6072–6079. <https://doi.org/10.1021/ic000663h>.
328. Sevryugina, Y.; Petrukhina, M. A. Breaking Infinite CuI Carboxylate Helix Held by Cuprophilicity into Discrete Cun Fragments (N = 6, 4, 2). *Eur. J. Inorg. Chem.* **2008**, 2008 (2), 219–229. <https://doi.org/10.1002/ejic.200701035>.
329. Sevryugina, Y.; Rogachev, A. Y.; Petrukhina, M. A. The First Hexanuclear Copper(II) Carboxylate: X-Ray Crystal Structure and Reactivity in Solution and Gas-Phase Reactions. *Inorg. Chem.* **2007**, 46 (19), 7870–7879. <https://doi.org/10.1021/ic7005327>.
330. Haneline, M. R.; Gabbai, F. P. Electrophilic Double-Sandwiches Formed by Interaction of [Cp<sub>2</sub>Fe] and [Cp<sub>2</sub>Ni] with the Tridentate Lewis Acid [(O-C6F<sub>4</sub>Hg)<sub>3</sub>]. *Angew. Chem. Int. Ed.* **2004**, 43 (41), 5471–5474. <https://doi.org/10.1002/anie.200461152> (accessed 2021/05/11).
331. Canty, A. J.; Raston, C. L.; White, A. H. Structural Studies of RSHg<sup>>II</sup></sup> Complexes Containing (-hg-SR)<sub>>N</sub></sup> Rings and Chains. *Aust. J. Chem.* **1979**, 32 (2), 311–320.
332. Salah, A. B. Crystal Structure Determination of the Complexes of Trimethylammonium Chloride and Mercury(II) Chloride: (CH<sub>3</sub>)<sub>3</sub>NH<sub>2</sub>HgCl<sub>3</sub>, ((CH<sub>3</sub>)<sub>3</sub>NH)<sub>2</sub>HgCl<sub>4</sub>, and (CH<sub>3</sub>)<sub>3</sub>NH<sub>2</sub>Hg<sub>2</sub>Cl<sub>5</sub>. *Z. Kristallogr. Cryst. Mater.* **1983**, 164 (3–4), 259–272. <https://doi.org/10.1524/zkri.1983.164.3-4.259>.
333. Tsunoda, M.; Gabbai, F. P. μ<sub>6</sub>-η<sup>2</sup>:η<sup>2</sup>:η<sup>2</sup>:η<sup>2</sup>:η<sup>2</sup>:η<sup>2</sup> As a New Bonding Mode for Benzene. *J. Am. Chem. Soc.* **2000**, 122 (34), 8335–8336. <https://doi.org/10.1021/ja0016598>.
334. Stender, K.; Hinrichs, W.; Kopf, J.; Klar, G. 2,2'-Biphenylene Mercury (C<sub>12</sub>H<sub>8</sub>Hg)<sub>3</sub>. *Acta Crystallogr. C* **1981**, 10, 613–621.
335. Brown, D. S.; Al-Jabar, N. A. A.; Bowen-Jones, J.; Massey, A. G. Structure of an Orthorhombic Form of 2,2'-Biphenylenemercury. *Acta Crystallogr. C* **1986**, 42 (4), 425–427. <https://doi.org/10.1107/S0108270186095926>.
336. Hupf, E.; Lork, E.; Mebs, S.; Beckmann, J. 6-Diphenylphosphinoacene-5-Yl-Mercurials as Ligands for d<sup>10</sup> Metals. Observation of Closed-Shell Interactions of the Type Hg(II)···M; M = Hg(II), Ag(I), Au(I). *Inorg. Chem.* **2015**, 54 (4), 1847–1859. <https://doi.org/10.1021/ic502728v>.
337. Kumar, V.; Singh, V.; Gupta, A. N.; Drew, M. G. B.; Singh, N. Intermolecular TI···H-C Anagostic Interactions in Luminescent Pyridyl Functionalized Thallium(II) Dithiocarbamates. *Dalton Trans.* **2015**, 44 (4), 1716–1723.
338. Manar, K. K.; Rajput, G.; Yadav, M. K.; Yadav, C. L.; Kumari, K.; Drew, M. G. B.; Singh, N. Potential Impact of Substituents on the Crystal Structures and Properties of TI(II) Ferrocenyl/Picolyl-Functionalized Dithiocarbamates; TI–H–CANagostic Interactions. *ChemistrySelect* **2016**, 1 (18), 5733–5742. <https://doi.org/10.1002/slct.201601280> (accessed 2021/07/06).
339. Fujisawa, K.; Shimizu, M.; Szilagy, R. K. Comparison of Thallium(I) Complexes with Mesityl-Substituted Tris(Pyrazolyl)Hydroborate Ligands, [TI{HB(3-Ms-5-Mepz)<sub>3</sub>}] and [TI{HB(3-Ms-5-Mepz)<sub>2</sub>(3-Me-5-Mspz)}]. *Acta Crystallogr. C* **2016**, 72 (11), 786–790. <https://doi.org/10.1107/S2053229615023797>.
340. Ciunik, Z.; Ruman, T.; Lukaszewicz, M.; Wolowiec, S. Complexes of Heteroscorpionate Trispyrazolylborate Ligands. Part XI. Weak CH/π Interactions in Crystals of Hydrotris(3-Phenylpyrazolyl)boratothallium(II) and Hydrobis(5-Methyl-3-Phenylpyrazolyl)(3,5-Dimethylpyrazol-yl)boratothallium(II) Studied by X-Ray Crystallography. *J. Mol. Struct.* **2004**, 690 (1), 175–180. <https://doi.org/10.1016/j.molstruc.2003.12.002>.
341. Ferguson, G.; Jennings, M. C.; Lalor, F. J.; Shanahan, C. Structure of Hydridotris[3-(P-Tolyl)Pyrazolyl]boratothallium(II). *Acta Crystallogr. C* **1991**, 47 (10), 2079–2082. <https://doi.org/10.1107/S0108270191005115> (accessed 2021/07/06).
342. Hünig, S.; Meixner, H.; Metzenthin, T.; Langohr, U.; von Schütz, J. U.; Wolf, H.-C.; Tillmanns, E. A Conducting Thallium Salt of 2,5-Dimethyl-N, N'-Dicyanoquinone-Diimine, [2,5-DMe-DCNQI]<sub>2</sub>TI: Comparison with Other Related Radical Anion Salts. *Adv. Mater.* **1990**, 2 (8), 361–363. <https://doi.org/10.1002/adma.19900020805> (accessed 2021/07/06).
343. Askarinejad, A.; Morsali, A. TI<sub>2</sub>D Coordination Polymer Involving Close TI···π (Aromatic) Contacts, [TI<sub>3</sub>(μ-BPC)<sub>2</sub>(μ-N<sub>3</sub>)<sub>2</sub>]. *J. Organomet. Chem.* **2006**, 691 (17), 3563–3566. <https://doi.org/10.1016/j.jorganchem.2006.05.005>.



344. Stürmann, M.; Saak, W.; Weidenbruch, M.; Klinkhammer, K. W. A Heteroleptic Diplumbene and a Magnesium Dibromide Stabilized Plumbylene Dimer. *Eur. J. Inorg. Chem.* **1999**, *1999* (4), 579–582. [https://doi.org/10.1002/\(SICI\)1099-0682\(199904\)1999:4<579::AID-EJIC579>3.0.CO;2-E](https://doi.org/10.1002/(SICI)1099-0682(199904)1999:4<579::AID-EJIC579>3.0.CO;2-E) (accessed 2021/07/06).
345. Hino, S.; Olmstead, M.; Phillips, A. D.; Wright, R. J.; Power, P. P. Terphenyl Ligand Stabilized Lead(II) Derivatives: Steric Effects and Lead–Lead Bonding in Diplumbenes. *Inorg. Chem.* **2004**, *43* (23), 7346–7352. <https://doi.org/10.1021/ic049174y>.
346. Cheng, J.-K.; Zhang, X.; Zhang, M.-J.; Yao, Y.-G. An Exceptionally Stable pb(II) Arene Compound. *Inorg. Chem. Commun.* **2012**, *17*, 88–90. <https://doi.org/10.1016/j.inoche.2011.12.021>.
347. Bridgewater, B. M.; Parkin, G. Lead Poisoning and the Inactivation of 5-Aminolevulinic Dehydratase as Modeled by the Tris(2-Mercapto-1-Phenylimidazolyl)Hydroborato Lead Complex,  $[\text{TMPh}]\text{pb}[\text{ClO}_4]$ . *J. Am. Chem. Soc.* **2000**, *122* (29), 7140–7141. <https://doi.org/10.1021/ja001530y>.
348. Khan, L. A.; Malik, M. A.; Motevalli, M.; O'Brien, P. The X-Ray Structure of Bis-2,2-Dimethyl-6,6,7,7,8,8,8-Heptafluorooctane-3,5-Dionatolead(II): An Eight-Coordinate Dimer with Bridging Fluorine Atoms. *J. Chem. Soc. Chem. Commun.* **1992**, *17*, 1257–1259. <https://doi.org/10.1039/C39920001257>.
349. Klüfers, P.; Mayer, P.; Schuhmacher, J. Polyol-Metall-Komplexe. XIII [1].  $\text{Na}_2[\text{Be}(\text{C}_4\text{H}_6\text{O}_3)_2] \cdot 5\text{H}_2\text{O}$  und  $\text{Na}_2[\text{Pb}(\text{C}_4\text{H}_6\text{O}_3)_2] \cdot 3\text{H}_2\text{O}$  – Zwei Homoleptische Bis-Polyolato-Metallate Mit Beryllium Und Mit Blei. *Z. Anorg. Allg. Chem.* **1995**, *621* (8), 1373–1379. <https://doi.org/10.1002/zaac.19956210816> (accessed 2021/07/06).
350. Akhtar, J.; Akhtar, M.; Malik, M. A.; O'Brien, P.; Raftery, J. A Single-Source Precursor Route to Unusual PbSe Nanostructures by a Solution–Liquid–Solid Method. *J. Am. Chem. Soc.* **2012**, *134* (6), 2485–2487. <https://doi.org/10.1021/ja209831n>.
351. Casas, J. S.; Castellano, E. U.; Elena, J.; García-Tasende, M. S.; Sánchez, A.; Sordo, J.; Touceda, Á.; Rodríguez, S. V. New Lead(II) Complexes with N,S-Ligands, Including a Lead Pyrazolonate with Unusual Packing Flexibility. *Polyhedron* **2007**, *26* (15), 4228–4238. <https://doi.org/10.1016/j.poly.2007.05.016>.
352. Ketchemen, K. I. Y.; Mlowe, S.; Nyamen, L. D.; Aboud, A. A.; Akerman, M. P.; Ndifon, P. T.; O'Brien, P.; Revaprasadu, N. Heterocyclic Lead(II) Thioureto Complexes as Single-Source Precursors for the Aerosol Assisted Chemical Vapour Deposition of PbS Thin Films. *Inorg. Chim. Acta* **2018**, *479*, 42–48. <https://doi.org/10.1016/j.ica.2018.04.023>.
353. Murugesapandian, B.; Roeskys, P. W. Synthesis and Structure of Lead(II) Complexes of  $(\eta^6\text{-Benzenecarboxylato})\text{Tricarbonylchromium}$ . *Eur. J. Inorg. Chem.* **2012**, *2012* (2), 292–297. <https://doi.org/10.1002/ejic.201100948> (accessed 2021/07/06).
354. Yang, J.; Li, G.-D.; Cao, J.-J.; Yue, Q.; Li, G.-H.; Chen, J.-S. Structural Variation from 1D to 3D: Effects of Ligands and Solvents on the Construction of Lead(II)–Organic Coordination Polymers. *Chem. A Eur. J.* **2007**, *13* (11), 3248–3261. <https://doi.org/10.1002/chem.200600730> (accessed 2021/07/06).
355. Thomas, J.; Agarwal, M.; Ramanam, A.; Chernova, N.; Whittingham, M. S. Copper Pyrazole Directed Crystallization of Decavanadates: Synthesis and Characterization of  $[\text{Cu}(\text{Pz})_4][\text{Cu}(\text{Pz})_3]2\text{V}10028$  and  $(\text{Hpz})_2[\text{Cu}(\text{Pz})_4]2\text{V}10028 \cdot 2\text{H}_2\text{O}$ . *CrystEngComm* **2009**, *11* (4), 625–631. <https://doi.org/10.1039/B815840A>.
356. Marandi, F.; Rutvand, R.; Rafiee, M.; Goh, J. H.; Fun, H.-K. Synthesis, Properties and Crystal Structures of New Binuclear Lead(II) Complexes Based on Phenyl, Naphthyl-Containing Fluorine  $\beta$ -Diketones and Substituted 2,2'-Bipyridines. *Inorg. Chim. Acta* **2010**, *363* (14), 4000–4007. <https://doi.org/10.1016/j.ica.2010.07.075>.
357. Jovanovski, G.; Hergold-Brundić, A.; Grupče, O.; Matković-Calogović, D. Structure of  $(2,2'\text{-Bipyridine})\text{Lead(II) Saccharinate Monohydrate}$ . *J. Chem. Crystallogr.* **1999**, *29* (2), 233–237. <https://doi.org/10.1023/A:1009538614895>.
358. Stadler, A.-M.; Kyritsakas, N.; Lehn, J.-M. Reversible Folding/Unfolding of Linear Molecular Strands into Helical Channel-like Complexes upon Proton-Modulated Binding and Release of Metal Ions. *Chem. Commun.* **2004**, *18*, 2024–2025. <https://doi.org/10.1039/B407168A>.
359. Lobo, M. J.; Moratti, S. C.; Hanton, L. R. A Design Strategy for Single-Stranded Helicates Using Pyridine-Hydrazone Ligands and PbII. *Chem. Asian J.* **2019**, *14* (8), 1184–1193. <https://doi.org/10.1002/asia.201801784> (accessed 2021/07/06).
360. Le Gac, S.; Najjari, B.; Fusaro, L.; Roisnel, T.; Dorcet, V.; Lühmer, M.; Furet, E.; Halet, J.-F.; Boitrel, B. Translocation-Coupled Transmetalation at the Origin of a Dinuclear Lead Porphyrin Complex: Implication of a Hanging-atop Coordination Mode. *Chem. Commun.* **2012**, *48* (31), 3724–3726. <https://doi.org/10.1039/C2CC00067A>.
361. Clegg, W.; Compton, N. A.; Errington, R. J.; Fisher, G. A.; Green, M. E.; Hockless, D. C. R.; Norman, N. C. X-Ray Crystal Structure of Bismuth Dimethylamide. *Inorg. Chem.* **1991**, *30* (24), 4680–4682. <https://doi.org/10.1021/c00024a046>.
362. Schulz, S.; Kuczkowski, A.; Bläser, D.; Wölper, C.; Jansen, G.; Haack, R. Solid-State Structures of Trialkylbismuthines  $\text{BiR}_3$  (R = Me, i-Pr). *Organometallics* **2013**, *32* (19), 5445–5450. <https://doi.org/10.1021/om400730r>.
363. Hébert, M.; Petiot, P.; Benoit, E.; Dansereau, J.; Ahmad, T.; Le Roch, A.; Ottenwälder, X.; Gagnon, A. Synthesis of Highly Functionalized Triaryl bismuthines by Functional Group Manipulation and Use in Palladium- and Copper-Catalyzed Arylation Reactions. *J. Org. Chem.* **2016**, *81* (13), 5401–5416. <https://doi.org/10.1021/acs.joc.6b00767>.
364. Preda, A.-M.; Krasowska, M.; Wrobel, L.; Kitschke, P.; Andrews, P. C.; MacLellan, J. G.; Mertens, L.; Korb, M.; Rüffer, T.; Lang, H.; et al. Evaluation of Dispersion Type Metal  $\cdots\pi$  arene Interaction in Arylbismuth Compounds – An Experimental and Theoretical Study. *Beilstein J. Org. Chem.* **2018**, *14*, 2125–2145. <https://doi.org/10.3762/bjoc.14.187>.
365. Hassan, A.; Breeze, S. R.; Courtenay, S.; Deslippe, C.; Wang, S. Organobismuth(III) and Organobismuth(V) Complexes Containing Pyridyl and Amino Functional Groups. Syntheses and Characterizations of  $\text{BiIIIAR}_3$  (Ar = P-C6H4(NMe<sub>2</sub>), P-C6H4CH<sub>2</sub>(NPr<sub>2</sub>), P-C6H4[CH<sub>2</sub>N(2-Py)<sub>2</sub>]),  $\text{BiVAr}_3\text{L}_2$ ,  $[\text{BiVAr}_3\text{Cl}]_2\text{O}$ ,  $[\text{BiVAr}_4][\text{PF}_6]$ , and  $[\text{BiVAr}_4]_2[\text{Ag}_2\text{Cl}_4]$  (Ar = P-C6H4(NMe<sub>2</sub>) or P-C6H4[CH<sub>2</sub>N(2-Py)<sub>2</sub>], L = Cl, CH<sub>3</sub>CO<sub>2</sub>-, CF<sub>3</sub>CO<sub>2</sub>-). *Organometallics* **1996**, *15* (26), 5613–5621. <https://doi.org/10.1021/om960641w>.
366. Toma, A. M.; Pop, A.; Silvestru, A.; Rüffer, T.; Lang, H.; Mehring, M. Bismuth  $\cdots\pi$  arene Versus Bismuth  $\cdots\pi$  Halide Coordination in Heterocyclic Diorganobismuth(III) Compounds with Transannular N  $\rightarrow$  Bi Interaction. *Dalton Trans.* **2017**, *46* (12), 3953–3962. <https://doi.org/10.1039/C7DT00188F>.
367. Burschka, C. H. Die Kristallstruktur von P-Tolybis(Diethylthiocarbamato)-Thallium(III) Und Phenylbis(Methylxanthogenato)Bismut(III). *Z. Anorg. Allg. Chem.* **1982**, *485* (1), 217–224. <https://doi.org/10.1002/zaac.19824850121> (accessed 2021/07/06).
368. Chaudhari, K. R.; Yadav, N.; Wadawale, A.; Jain, V. K.; Bohra, R. Monoorganobismuth(III) Dithiocarbonylates: Synthesis, Structures and their Utility as Molecular Precursors for the Preparation of  $\text{Bi}_2\text{S}_3$  Films and Nanocrystals. *Inorg. Chim. Acta* **2010**, *363* (2), 375–380. <https://doi.org/10.1016/j.ica.2009.11.002>.
369. Kimura, M.; Iwata, A.; Itoh, M.; Yamada, K.; Kimura, T.; Sugiura, N.; Ishida, M.; Kato, S. Synthesis, Structures, and some Reactions of  $[\text{Thio}(\text{acyl})\text{Thio}]$ - and  $[\text{Acylseleno}(\text{acyl})\text{Thio}]$ -Antimony and -Bismuth Derivatives  $(\text{RCSS})_x\text{MR}_3\text{Rm}_{3-x}$  and  $(\text{RCOSe})_x\text{MR}_3\text{Rm}_{3-x}$  with M = Sb, Bi and x = 1–3. *Helv. Chim. Acta* **2006**, *89* (4), 747–783. <https://doi.org/10.1002/hlca.200690070> (accessed 2021/07/06).
370. Lai, C. S.; Tiekink, E. R. T. Prevalence of Intermolecular Bi  $\cdots$  S Interactions in Bismuth Dithiocarbamate Compounds:  $\text{Bi}(\text{S}_2\text{CNR}_2)_3$ . *Z. Kristallogr.* **2007**, *222* (10), 532–538. <https://doi.org/10.1524/zkri.2007.222.10.532>.
371. Raston, C. L.; White, A. H. Crystal Structures of Tris(Diethylthiocarbamato)-Antimony(III) and -Bismuth(III). *J. Chem. Soc. Dalton Trans.* **1976**, *9*, 791–794. <https://doi.org/10.1039/DT9760000791>.
372. Tamilvanan, S.; Gurumoorthy, G.; Thirumaran, S.; Ciattini, S. Bismuth(III) Furfuryl Based Dithiocarbamates: Synthesis, Structures, Biological Activities and their Utility for the Preparation of  $\text{Bi}_2\text{S}_3$  and  $\text{Bi}_2\text{O}_3$  Nanoparticles. *Polyhedron* **2017**, *123*, 111–121. <https://doi.org/10.1016/j.poly.2016.10.026>.
373. Anamika; Singh, R.; Manar, K. K.; Yadav, C. L.; Kumar, A.; Singh, R. K.; Drew, M. G. B.; Singh, N. Impact of Substituents on the Crystal Structures and Anti-Leishmanial Activity of New Homoleptic Bi(III) Dithiocarbamates. *New J. Chem.* **2019**, *43* (43), 16921–16931. <https://doi.org/10.1039/C9NJ04477A>.
374. Ramler, J.; Hofmann, K.; Lichtenberg, C. Neutral and Cationic Bismuth Compounds: Structure, Heteroaromaticity, and Lewis Acidity of Bismepines. *Inorg. Chem.* **2020**, *59* (6), 3367–3376. <https://doi.org/10.1021/acs.inorgchem.9b03189>.
375. Troyanov, S. I.; Pisarevsky, A. P. Crystal and Molecular Structure of Bismuth 2,2-Dimethylpropanoate. *J. Chem. Soc. Chem. Commun.* **1993**, *3*, 335–336. <https://doi.org/10.1039/C39930000335>.
376. Caseri, W. Derivatives of Magnus' Green Salt; from Intractable Materials to Solution-Processed Transistors. *Platinum Met. Rev.* **2004**, *48* (3), 91–100. <https://doi.org/10.1595/147106704x1504>.
377. Stork, J. R.; Rios, D.; Pham, D.; Bicocca, V.; Olmstead, M. M.; Balch, A. L. Metal–Metal Interactions in Platinum(II)/Gold(I) or Platinum(II)/Silver(I) Salts Containing Planar Cations and Linear Anions. *Inorg. Chem.* **2005**, *44* (10), 3466–3472. <https://doi.org/10.1021/ic048333a>.

378. Gil-Moles, M.; Gimeno, M. C.; Lopez-de-Luzuriaga, J. M.; Monge, M.; Olmos, M. E.; Pascual, D. Tailor-Made Luminescent Polymers through Unusual Metallophilic Interaction Arrays Au...Au...Ag...Ag. *Inorg. Chem.* **2017**, *56* (15), 9281–9290. <https://doi.org/10.1021/acs.inorgchem.7b01342>.
379. Fernández, E. J.; Laguna, A.; López-de-Luzuriaga, J. M.; Monge, M.; Montiel, M.; Olmos, M. E.; Pérez, J. Thallium(I) Acetylacetonate as Building Blocks of Luminescent Supramolecular Architectures. *Organometallics* **2004**, *23* (4), 774–782. <https://doi.org/10.1021/om034167n>.
380. Casares, J. A.; Espinet, P.; Martín-Alvarez, J. M.; Santos, V. Anionic Platinum Complexes with 2-Pyridylphosphines as Ligands for Rhodium: Synthesis of Zwitterionic Pt – Rh Organometallic Compounds. *Inorg. Chem.* **2004**, *43* (1), 189–197. <https://doi.org/10.1021/ic034863f>.
381. Dahlenburg, L.; Menzel, R.; Puchta, R.; Heinemann, F. W. Experimental and Computational Studies of Two New Mono- and Dinuclear Iridium Complexes Containing a Buchwald Biphenyl Phosphine Ligand. *Inorg. Chim. Acta* **2008**, *361* (9), 2623–2630. <https://doi.org/10.1016/j.ica.2007.11.006>.
382. García-Romero, Á.; Plajer, A. J.; Miguel, D.; Wright, D. S.; Bond, A. D.; Álvarez, C. M.; García-Rodríguez, R. Tris(2-Pyridyl) Bismuthines: Coordination Chemistry, Reactivity, and Anion-Triggered Pyridyl Coupling. *Inorg. Chem.* **2020**, *59* (10), 7103–7116. <https://doi.org/10.1021/acs.inorgchem.0c00579>.
383. Chaturvedi, J.; Bhattacharya, S.; Prasad, R. Novel Heterobimetallic Thiocarboxylato Complexes: Synthesis, Characterization and Application as Single Source Precursor for Ternary Chalcogenides. *Dalton Trans.* **2010**, *39* (37), 8725–8732. <https://doi.org/10.1039/C0DT00210K>.
384. Fernandez, E. J.; Hardacre, C.; Laguna, A.; Lagunas, M. C.; Lopez-de-Luzuriaga, J. M.; Monge, M.; Montiel, M.; Olmos, M. E.; Puelles, R. C.; Sanchez-Forcada, E. Multiple Evidence for Gold(I) – Silver(I) Interactions in Solution. *Chem. A Eur. J.* **2009**, *15* (25), 6222–6233. <https://doi.org/10.1002/chem.200900167>.
385. Olaru, M.; Koegel, J. F.; Aoki, R.; Sakamoto, R.; Nishihara, H.; Lork, E.; Mebs, S.; Vogt, M.; Beckmann, J. Tri- and Tetranuclear Metal-String Complexes with Metallophilic d10-d10 Interactions. *Chem. A Eur. J.* **2020**, *26* (1), 275–284. <https://doi.org/10.1002/chem.201904106>.
386. Harris, K. J.; Wasylishen, R. E. A <sup>13</sup>C and <sup>15</sup>N Solid-State NMR Study of Structural Disorder and Aurophilic Bonding in Aul and Aull Cyanide Complexes. *Inorg. Chem.* **2009**, *48* (5), 2316–2332. <https://doi.org/10.1021/ic8022198>.
387. Phillips, V.; Baddour, F. G.; Lasanta, T.; Lopez-de-Luzuriaga, J. M.; Bacon, J. W.; Golen, J. A.; Rheingold, A. L.; Doerrer, L. H. Metal-Metal Stacking Patterns between and with [Pt(Tpy)X] + Cations. *Inorg. Chim. Acta* **2010**, *364* (1), 195–204. <https://doi.org/10.1016/j.ica.2010.07.038>.
388. Fornies, J.; Garcia, A.; Lalinde, E.; Moreno, M. T. Luminescent One- and Two-Dimensional Extended Structures and a Loosely Associated Dimer Based on Platinum(II)-Thallium(I) Backbones. *Inorg. Chem.* **2008**, *47* (9), 3651–3660. <https://doi.org/10.1021/ic702180c>.
389. Catalano, V. J.; Bennett, B. L.; Yson, R. L.; Noll, B. C. Synthesis and Characterization of Pd(0) and Pt(0) Metallocryptands Encapsulating TI + Ion. *J. Am. Chem. Soc.* **2000**, *122* (41), 10056–10062. <https://doi.org/10.1021/ja001672s>.
390. Schaefer, S.; Gamer, M. T.; Lebedkin, S.; Weigend, F.; Kappes, M. M.; Roesky, P. W. Bis(6-Methylene-2,2'-Bipyridine)Phenylphosphine—a Flexible Ligand for the Construction of Trinuclear Coinage-Metal Complexes. *Chem. A Eur. J.* **2017**, *23* (50), 12198–12209. <https://doi.org/10.1002/chem.201701091>.
391. Raju, S.; Singh, H. B.; Butcher, R. J. Metallophilic Interactions: Observations of the Shortest Metallophilic Interactions between Closed Shell (d10...d10, d10...d8, d8...d8) Metal Ions [M...M' M = hg(II) and pd(II) and M' = cu(I), ag(I), au(I), and pd(II)]. *Dalton Trans.* **2020**, *49* (26), 9099–9117. <https://doi.org/10.1039/d0dt01008a>.
392. Patel, U.; Sharma, S.; Singh, H. B.; Dey, S.; Jain, V. K.; Wolmershaeuser, G.; Butcher, R. J. Intermetallic Bonds in Metallophilic Mercuroazametallamacrocycles of Synthetic Design. *Organometallics* **2010**, *29* (19), 4265–4275. <https://doi.org/10.1021/om100297v>.
393. Chen, K.-T.; Yang, F.-A.; Chen, J.-H.; Wang, S.-S.; Tung, J.-Y. A Novel Bismercuro(II) Complex of Bidentate N21,N22-Bridged Porphyrin: [(Benzamido-κN)Phenylmercury-κHg-N21,N22]-Meso-Tetraphenylporphyrinato-N23,N24)Phenylmercury(II) Toluene Solvate. *Polyhedron* **2008**, *27* (9–10), 2216–2220. <https://doi.org/10.1016/j.poly.2008.03.029>.
394. Hsieh, H.-Y.; Cheng, C.-W.; Yang, F.-A.; Chen, J.-H.; Tung, J.-Y.; Wang, S.-S.; Hwang, L.-P. The Structures of (Phenylato)(N-2-Thiophenecarboxamido-Meso-Tetraphenylporphyrinato)Mercury(II) and Bisphenylmercury(II) Complex of 21-(4-Tert-Butyl-Benzenesulfonamido)-5,10,15,20-Tetraphenylporphyrin. *Polyhedron* **2007**, *26* (17), 4915–4922. <https://doi.org/10.1016/j.poly.2007.06.019>.
395. Che, C.-M.; Lai, S.-W. Structural and Spectroscopic Evidence for Weak Metal-Metal Interactions and Metal-Substrate Exciplex Formations in d10 Metal Complexes. *Coord. Chem. Rev.* **2005**, *249* (13–14), 1296–1309. <https://doi.org/10.1016/j.ccr.2004.11.026>.
396. Seifert, T. P.; Naina, V. R.; Feuerstein, T. J.; Knoefel, N. D.; Roesky, P. W. Molecular Gold Strings: Aurophilicity, Luminescence and Structure-Property Correlations. *Nanoscale* **2020**, *12* (39), 20065–20088. <https://doi.org/10.1039/d0nr04748a>.
397. Rodríguez, L.; Lima, J. C. Luminescent Alkynyl Gold(I) Complexes: Structures, Properties and Applications. *Global J. Inorg. Chem.* **2011**, *2* (1), 39–76.
398. Zeman, C. J.; Shen, Y.-H.; Heller, J. K.; Abboud, K. A.; Schanze, K. S.; Veige, A. S. Excited-State Turn-on of Aurophilicity and Tunability of Relativistic Effects in a Series of Digold Triazolates Synthesized via iClick. *J. Am. Chem. Soc.* **2020**, *142* (18), 8331–8341. <https://doi.org/10.1021/jacs.0c01624>.
399. Yam, V. W.-W.; Cheng, E. C.-C. Highlights on the Recent Advances in Gold Chemistry—a Photophysical Perspective. *Chem. Soc. Rev.* **2008**, *37* (9), 1806–1813. <https://doi.org/10.1039/b708615f>.
400. Harisomayajula, N. V. S.; Wu, B.-H.; Lu, D.-Y.; Kuo, T.-S.; Chen, I. C.; Tsai, Y.-C. Ligand-Unsupported Cuprophilicity in the Preparation of Dodecacopper(II) Complexes and Raman Studies. *Angew. Chem. Int. Ed.* **2018**, *57* (31), 9925–9929. <https://doi.org/10.1002/anie.201801955>.
401. Puszynska-Tuszkano, M.; Staszak, Z.; Misiaszek, T.; Klepka, M. T.; Wolska, A.; Drzewiecka-Antonik, A.; Falynowicz, H.; Cieslak-Golonka, M. Metallophilic Interactions in Polynuclear ag(I) Complex with 1-Methylhydantoin Studied by X-Ray Absorption, Electronic and Vibrational Spectroscopies. *Chem. Phys. Lett.* **2014**, *597*, 94–98. <https://doi.org/10.1016/j.cplett.2014.02.025>.
402. Trerayapiwat, K. J.; Kitadai, H.; Pazmany, V.; Lagueux, S. P.; Skipper, H. E.; Doerrer, L. H.; Ling, X.; Sharifzadeh, S. Vibrational Signature of Metallophilic Interactions in [Pt(Terpy)Cl][Au(CN)2]. *J. Phys. Chem. C* **2021**, *125* (40), 22188–22194. <https://doi.org/10.1021/acs.jpcc.1c04596>.



## 1.16 Molecular boron clusters

Igor B. Sivaev, A.N. Nesmeyanov Institute of Organoelement Compounds, Russian Academy of Sciences, Moscow, Russia

© 2023 Elsevier Ltd. All rights reserved.

<b>1.16.1</b>	<b>Introduction</b>	<b>740</b>
<b>1.16.2</b>	<b><i>closo</i>-Borate anions and their derivatives</b>	<b>741</b>
1.16.2.1	<i>closo</i> -Dodecaborate anion $[B_{12}H_{12}]^{2-}$	741
1.16.2.1.1	General aspects	741
1.16.2.1.2	Halogen derivatives	743
1.16.2.1.3	Derivatives with B–O bond	745
1.16.2.1.4	Derivatives with B–S bond	747
1.16.2.1.5	Derivatives with B–Se bond	748
1.16.2.1.6	Derivatives with B–N bonds	748
1.16.2.1.7	Derivatives with B–P bonds	754
1.16.2.1.8	Derivatives with B–C bonds	754
1.16.2.1.9	Oxidation reactions	754
1.16.2.2	<i>closo</i> -Undecaborate anion $[B_{11}H_{11}]^{2-}$	755
1.16.2.3	<i>closo</i> -Decaborate anion $[B_{10}H_{10}]^{2-}$	755
1.16.2.3.1	General aspects	755
1.16.2.3.2	Halogen derivatives	756
1.16.2.3.3	Derivatives with B–O bond	757
1.16.2.3.4	Derivatives with B–S bond	758
1.16.2.3.5	Derivatives with B–N bond	759
1.16.2.3.6	Derivatives with B–P bonds	761
1.16.2.3.7	Derivatives with B–C bonds	761
1.16.2.3.8	Oxidation reactions	762
1.16.2.4	<i>closo</i> -Nonaborate anion $[B_9H_9]^{2-}$	762
1.16.2.5	<i>closo</i> -Octaborate anion $[B_8H_8]^{2-}$	762
1.16.2.6	<i>closo</i> -Heptaborate anion $[B_7H_7]^{2-}$	763
1.16.2.7	<i>closo</i> -Hexaborate anion $[B_6H_6]^{2-}$	763
<b>1.16.3</b>	<b>Polyhedral boranes with an open structure (<i>nido</i>- and <i>arachno</i>-boranes)</b>	<b>763</b>
1.16.3.1	Tetradecahydro- <i>nido</i> -undecaborate anion $[B_{11}H_{14}]^-$	764
1.16.3.2	Decaborane(14) $[B_{10}H_{14}]$	764
1.16.3.3	Tetradecahydro- <i>arachno</i> -nonaborate anion $[B_9H_{14}]^-$	765
<b>1.16.4</b>	<b><i>conjuncto</i>-Boranes</b>	<b>766</b>
1.16.4.1	<i>nido</i> , <i>nido</i> -Octadecaborane(22)	766
1.16.4.2	Octadecahydro- <i>closo</i> , <i>closo</i> -heneicosaborate anion $[B_{21}H_{18}]^-$	768
<b>References</b>		<b>768</b>

### Abstract

This chapter describes recent progress in the chemistry of molecular boron clusters. The greatest attention is paid to the intensively developing chemistry of *closo*-decaborate  $[B_{10}H_{10}]^{2-}$  and *closo*-dodecaborate  $[B_{12}H_{12}]^{2-}$  anions. Of the compounds with an open *nido*- and *arachno*-structures, the latest achievements in the chemistry of decaborane  $[B_{10}H_{14}]$  and macropolyhedral borane *anti*- $[B_{18}H_{22}]$  attract the most attention.

### 1.16.1 Introduction

The synthesis of polyhedral boranes, carboranes and metallaboranes was one of the major highlights in the development of inorganic chemistry over the last century.<sup>1</sup> However, while the chemistry of carboranes, metallacarboranes and metallaboranes has been the subject of numerous reviews including a series of chapters in *Comprehensive Organometallic Chemistry I-III*,<sup>2–11</sup> as well as special monographs,<sup>12–14</sup> the chemistry of polyhedral boranes as a whole has been last reviewed for more than forty years ago<sup>15,16</sup> and had never before been the subject of special consideration in *Comprehensive Inorganic Chemistry*. This edition mainly deals with studies on polyhedral boranes published after 2000 or since the publication of the latest exhaustive reviews on specific topics in this area (if any).

Since polyhedral boranes are characterized by a large variety of structural types and, consequently, a large variability in reactivity, it will be convenient to consider their chemical properties depending on their structure. In general, polyhedral boranes can be divided into two large groups according to the type of structure. The first group consists of compounds with a closed polyhedral structure or *closo*-boranes  $[\text{B}_n\text{H}_n]^{2-}$  and their derivatives. The second group includes compounds formed as a result of the formal removal of one or two boron vertices from *closo*-boranes, the so-called *nido*- and *arachno*-boranes, respectively. In addition, the joining together of two or more boron polyhedra of the above types through the B–B bond or their fusion together with the formation of a common boron vertex, edge, or face leads to the corresponding *conjuncto*-boranes.

### 1.16.2 *closo*-Borate anions and their derivatives

The family of *closo*-polyhedral borane anions constitutes a homologous series of rather stable polyhedral anions  $[\text{B}_n\text{H}_n]^{2-}$  ( $n = 6-12$ ). They have the structure of regular deltahedra, at the vertices of which there are boron atoms, each of which is bonded to an *exo*-polyhedral hydrogen atom (Fig. 1). The stability of the *closo*-polyhedral structure is achieved due to the delocalized system of  $2n + 2$  electrons, as a result of which these systems are usually considered as three-dimensional aromatics.<sup>17,18</sup>

However, due to the different availability of the *closo*-borane clusters, caused by the complicated and laborious synthesis of some of them, and the reduced stability of some others, their chemistry has been studied to a very different extent. Therefore, it is quite logical to start consideration of their chemistry with the most stable and most studied of them—*closo*-dodecaborate anion  $[\text{B}_{12}\text{H}_{12}]^{2-}$ .

#### 1.16.2.1 *closo*-Dodecaborate anion $[\text{B}_{12}\text{H}_{12}]^{2-}$

##### 1.16.2.1.1 General aspects

The dodecahydro-*closo*-dodecaborate anion was one of the first molecules to be predicted by quantum chemistry before they were synthesized. The existence of stable icosahedral borane in the form of the dianion  $[\text{B}_{12}\text{H}_{12}]^{2-}$  was predicted in 1955 by Longuet-Higgins and Roberts on the basis of MO LCAO calculations<sup>19</sup> and experimentally verified in 1960 by Hawthorne and Pitochelli when the *closo*-dodecaborate anion was prepared for the first time as a side-product of the reaction of 2-iodododecaborane with triethylamine in refluxing benzene.<sup>20</sup> The first 40 years of the chemistry of the *closo*-dodecaborate anion were reviewed in an exhaustive review by Sivaev et al.<sup>21</sup> Unfortunately, the recent review by Zhang et al.<sup>22</sup> deals mainly with the various uses of the *closo*-dodecaborate anion and its derivatives, and only to a small extent with the development of its chemistry. Therefore, we considered it necessary to present here the main directions in the development of the chemistry of the *closo*-dodecaborate anion over the past 20 years, relying (if necessary) on the earlier published exhaustive review<sup>21</sup> (Fig. 2).

In the initial period of the development of the chemistry of the *closo*-dodecaborate anion, various methods for its synthesis were developed, which were generalized in the reviews.<sup>21,22</sup> The most suitable method for the synthesis of *closo*-dodecaborate anion for laboratory purposes is based on the oxidation of sodium tetrahydroborate  $\text{NaBH}_4$  with  $\text{I}_2$  in diglyme at 100 °C to  $\text{Na}[\text{B}_3\text{H}_8]$  followed by its pyrolysis in boiling diglyme.<sup>23,24</sup> In addition, some other convenient methods have been proposed for the synthesis of anhydrous alkali metal salts  $\text{M}[\text{B}_3\text{H}_8]$  ( $\text{M} = \text{Na}, \text{K}, \text{Cs}, \text{Rb}$ ) followed by their pyrolysis to the corresponding *closo*-dodecaborates.<sup>25–28</sup> For the pilot production of the *closo*-dodecaborate anion, the preferred synthesis method is based on the solid-state pyrolysis of potassium tetrafluoroborate  $\text{KBF}_4$  and calcium hydride  $\text{CaH}_2$ .<sup>29</sup> At the same time, the solid-state reactions of dodecaborane with alkali and alkaline earth tetrahydroborates<sup>30–33</sup> were used to obtain anhydrous and solvent-free salts of the *closo*-dodecaborate

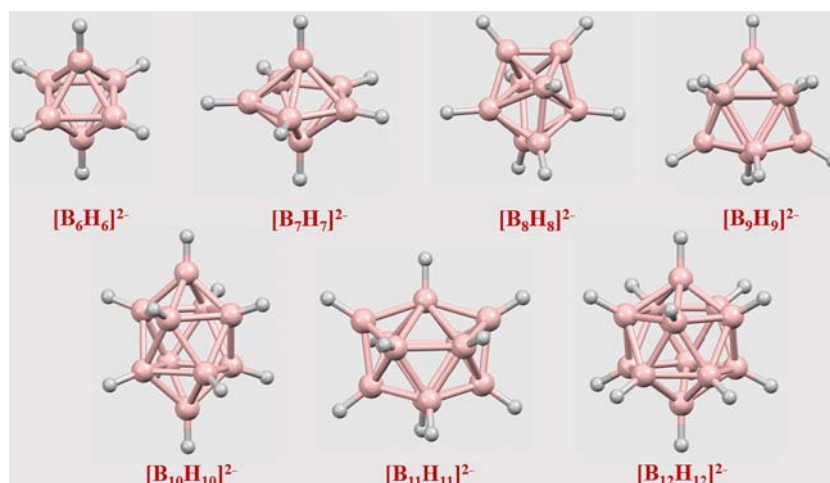
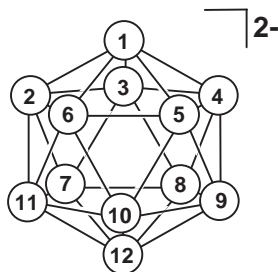


Fig. 1 Generalized structures of *closo*-polyhedral borane anions  $[\text{B}_n\text{H}_n]^{2-}$  ( $n = 6-12$ ).



**Fig. 2** Idealized structure and numbering of atoms in the *closo*-dodecaborate anion  $[B_{12}H_{12}]^{2-}$ .

anion  $M_2[B_{12}H_{12}]$  ( $M = Li, Na, K$ ) and  $M[B_{12}H_{12}]$  ( $M = Mg, Ca$ ), which are of great interest as solid state electrolytes.<sup>34,35</sup> Alternatively, anhydrous  $Mg[B_{12}H_{12}]$  was prepared by heating  $Mg[BH_4]_2$  in a  $B_2H_6$  atmosphere.<sup>36</sup> It was also found that the *closo*-dodecaborate anion is formed by thermal dehydrogenation of various simple and complex tetrahydroborates,<sup>37–40</sup> which are represent a class of promising materials for hydrogen storage applications.<sup>41–43</sup> On the other side, heating the stoichiometric mixtures of  $M_2[B_{12}H_{12}]$  and  $MH$  ( $M = Li, Na, K$ ) at 500 °C and 100 MPa  $H_2$  results in the corresponding metal borohydrides  $MBH_4$  in almost quantitative yield.<sup>44</sup>

The increased interest in the use of salts of polyhedral boron hydrides as solid electrolytes stimulated the synthesis and study of the physical properties and crystal structure of anhydrous *closo*-dodecaborates of alkali and alkaline earth metals and ammonium, as well as their crystalline hydrates.<sup>45–77</sup> In addition to crystalline hydrates, a number of alkali metal and calcium ammoniates containing the *closo*-dodecaborate anion were synthesized and characterized by X-ray diffraction.<sup>78–80</sup> The mixed sodium amide-*closo*-dodecaborate  $Na_3NH_2[B_{12}H_{12}]$  was prepared and its high performance as solid electrolyte for all-solid-state Na-ion batteries was demonstrated.<sup>81</sup> Another type of mixed salts is the alkali metal tetrahydroborate-*closo*-dodecaborates  $M_3[BH_4][B_{12}H_{12}]$ , some of which also have good potential as solid electrolytes.<sup>82–85</sup> Also, in the development of earlier research,<sup>21</sup> the mixed iodide-*closo*-dodecaborates of alkali metals and ammonium  $M_3[B_{12}H_{12}]$  ( $M = K, Rb, Cs, NH_4$ ) have been studied in detail.<sup>55</sup> Synthesis and properties of some other mixed salts of the *closo*-dodecaborate anion were discussed earlier.<sup>21</sup> Solvated lithium and magnesium *closo*-dodecaborates with THF and MeCN,<sup>86</sup> and MeOH and EtOH,<sup>61,87</sup> respectively, were synthesized and characterized by X-ray diffraction.

In addition, the preparation and crystal structure of simple salts and crystalline hydrates of *closo*-dodecaborates of some other non-transition metals, including  $[In(H_2O)_6]_2[B_{12}H_{12}]_3 \cdot 15H_2O$ ,<sup>88</sup>  $Tl_2[B_{12}H_{12}]$ ,<sup>89–91</sup>  $\{Sn(H_2O)_3[B_{12}H_{12}]\} \cdot 4H_2O$ ,<sup>92</sup>  $\{Pb(H_2O)_3[B_{12}H_{12}]\} \cdot 3H_2O$ ,<sup>90</sup> and  $[Bi_6O_4(OH)_4][B_{12}H_{12}]_3 \cdot 10H_2O$ <sup>93</sup> were described. In the structures of all these salts, except for the first one, the M-H-B interactions between the metal atom and the *closo*-dodecaborate anion are observed. The thermal dehydration of  $[Bi_6O_4(OH)_4][B_{12}H_{12}]_3 \cdot 10H_2O$  or the reaction of the aqueous solution of the  $(H_3O)_2[B_{12}H_{12}]$  acid with bismuth(III) oxide carbonate  $Bi_2O_2(CO_3)$  at about 40 °C lead to the B-H activation reaction with the formation of the neutral  $[BiB_{12}H_{11}]$  molecule which was characterized by single crystal X-ray diffraction in the form of crystalline hydrates and solvate with methanol.<sup>94</sup>

A series of anhydrous transition metal *closo*-dodecaborates  $M[B_{12}H_{12}]$  ( $M = Mn, Fe, Co, Ni$ ) was prepared by heating of their crystalline hydrates or solvates with alcohols.<sup>62,87,95</sup> Anhydrous *closo*-dodecaborates of copper  $Cu_2[B_{12}H_{12}]$ <sup>62</sup> and silver  $Ag_2[B_{12}H_{12}]$ ,<sup>96,97</sup> on the contrary, are formed directly from reaction solutions (mixtures). In the solid state, they form 3D polymeric structures due to M-H-B interactions between the metal atom and the anion. Copper and silver are also capable to form double salts with the *closo*-dodecaborate anion  $(Cat)\{M[B_{12}H_{12}]\}$  ( $M = Cu, Ag; Cat^+ = Cs^+, R_3NH^+$  and  $R_4N^+$  ( $R = Me, Et, Pr, Bu$ ),  $Ph_4P^+$ ,  $Ph_4As^+$ , etc.).<sup>96,98–100</sup>

The *closo*-dodecaborate anion is a rather weakly coordinating ligand that can only be coordinated by metals which are the soft Pearson acids, such as  $Cu^+$ ,  $Ag^+$ , and  $Cd^{2+}$ .<sup>101–112</sup> In the absence of strong ligands, other transition metals usually form crystalline hydrates or solvates with the *closo*-dodecaborate anion.<sup>113</sup> Various aspects of the coordination chemistry of the *closo*-dodecaborate anion are considered in several recent reviews.<sup>101,114–116</sup> The coordination chemistry of substituted derivatives of the *closo*-dodecaborate anion will be discussed below in the relevant sections.

A significant part of the research interest in simple and complex salts of the *closo*-dodecaborate anion is due to the ability of polyhedral boron hydrides to enhance burning rates of traditional rocket propellants.<sup>117,118</sup> In addition to studying the effect of simple salts of the *closo*-dodecaborate anion, such as  $K_2[B_{12}H_{12}]$  and  $(Et_4N)_2[B_{12}H_{12}]$ ,<sup>119–124</sup> on the combustion of traditional fuels, a number of salts with various nitrogen-rich cations including hydrazinium,<sup>125,126</sup> guanidinium,<sup>125,127–129</sup> imidazolium,<sup>130–132</sup> triazolium,<sup>125,131,133,134</sup> tetrazolium<sup>125,129,134,135</sup> and some others<sup>126,136–144</sup> were synthesized and their thermal stability and energetic properties were studied.

Of interest is the question of the hydrophilic-hydrophobic nature of the *closo*-dodecaborate anion. It is shown that despite high water solubility,  $Na_2[B_{12}H_{12}]$  in aqueous solutions has a pronounced tendency to aggregation due to the hydrophobic nature of the BH vertices.<sup>145</sup> The *closo*-dodecaborate anion is able to form an inclusion complex with  $\gamma$ -cyclodextrin demonstrating rather strong binding to the hydrophobic interior of the last one,<sup>146</sup> as well as the exclusion complexes with cucurbit[ $n$ ]urils ( $n = 6–8$ ) due to interactions with their hydrophobic exterior.<sup>147,148</sup> Thus, it demonstrates very strong chaotropic behavior beyond the scale of the Hofmeister series and considered a “superchaotrope”.<sup>149</sup>

### 1.16.2.1.2 Halogen derivatives

Halogenation was one of the first reactions of the *closo*-dodecaborate anion to be studied<sup>150</sup> and has since been the subject of much research.<sup>21</sup> In accordance with the three-dimensional aromatic nature of the  $[B_{12}H_{12}]^{2-}$  anion, its halogenation proceeds predominantly by the mechanism of aromatic electrophilic substitution. The monoiodo derivative  $[B_{12}H_{11}I]^{2-}$  can be prepared by the reaction of *closo*-dodecaborate with 1 equiv. of iodine at 0 °C in aqueous methanol.<sup>150</sup> For the synthesis of other monohalogen derivatives of the *closo*-dodecaborate anion  $[B_{12}H_{11}X]^{2-}$  ( $X = Cl, Br, I$ ), a method was previously proposed based on its reactions with the corresponding dihalomethanes in the presence of trifluoroacetic acid.<sup>151</sup> The synthesis of monohalogen derivatives  $[B_{12}H_{11}X]^{2-}$  ( $X = Cl, Br, I$ ) by the reaction of the *closo*-dodecaborate anion with the corresponding *N*-halosuccinimides in acetonitrile has recently been described.<sup>152</sup>

Previously, the synthesis of the perfluorinated *closo*-dodecaborate anion  $[B_{12}F_{12}]^{2-}$  by the reaction of the parent *closo*-dodecaborate with fluorine in anhydrous hydrogen fluoride was described.<sup>153–155</sup> It is also worth noting here the formation of *conjuncto*-borane  $[B_{24}F_{22}]^{4-}$  in which two boron icosahedra are linked by a B–B bond as a by-product of the fluorination of the *closo*-dodecaborate anion.<sup>156</sup> More recently, a more convenient method for the synthesis of  $[B_{12}F_{12}]^{2-}$  was proposed by the reaction of the parent *closo*-dodecaborate anion with fluorine gas in wet acetonitrile.<sup>157</sup> The perchlorinated *closo*-dodecaborate anion  $[B_{12}Cl_{12}]^{2-}$  can be obtained by the chlorination of the parent *closo*-dodecaborate with gaseous  $Cl_2$  in aqueous solution<sup>24,158</sup> or, in more convenient way, by the reaction with  $SO_2Cl_2$  in refluxing acetonitrile.<sup>159</sup> The perbrominated *closo*-dodecaborate anion  $[B_{12}Br_{12}]^{2-}$  can be obtained by the bromination of the parent *closo*-dodecaborate with excess of bromine in refluxing aqueous methanol.<sup>158</sup> Synthesis of the periodinated *closo*-dodecaborate anion  $[B_{12}I_{12}]^{2-}$  by the reaction of the parent *closo*-dodecaborate with iodine monochloride or a mixture of iodine and iodine monochloride in refluxing halogen alkanes was earlier described.<sup>150,158</sup> More recently, synthesis of  $[B_{12}I_{12}]^{2-}$  via microwave-assisted iodination of the parent *closo*-dodecaborate with iodine in acetic acid at 230 °C was reported.<sup>160</sup>

The perhalogenated derivatives of the *closo*-dodecaborate anion together with halogenated derivatives of carba-*closo*-dodecaborate anion constitute an important class of weakly coordinating anions.<sup>161,162</sup> This caused great interest in the study of the crystal structure of salts and complexes with perhalogenated *closo*-dodecaborate anions, mainly their perfluoro- and perchloro-derivatives. Crystal structures of the hydrated perfluorated *closo*-dodecaborate acid  $(H_3O)_2[B_{12}F_{12}] \cdot 6H_2O$ ,<sup>163</sup> numerous alkali metal salts, their crystalline hydrates and solvates,<sup>164–172</sup> as well as alkaline earth metal crystalline hydrates<sup>173</sup> have been determined. The crystal structures of a series of perchloro-, perbromo- and periodo-*closo*-dodecaborates of alkali metal  $M_2[B_{12}X_{12}]$  ( $X = Cl, Br, I$ ) and their crystalline hydrates and solvates have also been determined.<sup>158,165,174–178</sup> Lithium perfluoro-*closo*-dodecaborate  $Li_2[B_{12}F_{12}]$  has been considered as a potential electrolyte for lithium batteries.<sup>179–181</sup>

The cocrystallization of the trimethylammonium salts  $(Me_3NH)_2[B_{12}X_{12}]$  ( $X = Cl, Br, I$ ) with 1 equiv. of trimethylammonium chloride or bromide  $(Me_3NH)Y$  ( $Y = Cl, Br$ ) produces double salts  $[(Me_3NH)_3Y][B_{12}X_{12}]$ , which consist of the weakly coordinating perhalogenated *closo*-dodecaborate anions  $[B_{12}X_{12}]^{2-}$  and weakly bound discrete pyramidal  $[(Me_3NH)_3Y]^{2+}$  cations. The addition of 2 equiv. of  $(Me_3NH)Y$  to  $(Me_3NH)_2[B_{12}Cl_{12}]$  leads to  $[(Me_3NH)_2Y]_2[B_{12}Cl_{12}]$ , containing the bent  $[(Me_3NH)_2Y]^+$  cations.<sup>182</sup> Of the salts of the perhalogenated *closo*-dodecaborates with other organic cations, tritylium salts  $(Ph_3C)_2[B_{12}X_{12}]$  ( $X = F, Cl, Br$ ),<sup>24,155,183,184</sup> as well as perfluoro- and perchloro-*closo*-dodecaborate salts with various nitrogen-rich cations (imidazolium,<sup>133,185–187</sup> triazolium,<sup>185</sup> and some others<sup>185,187</sup>) are of the greatest interest.

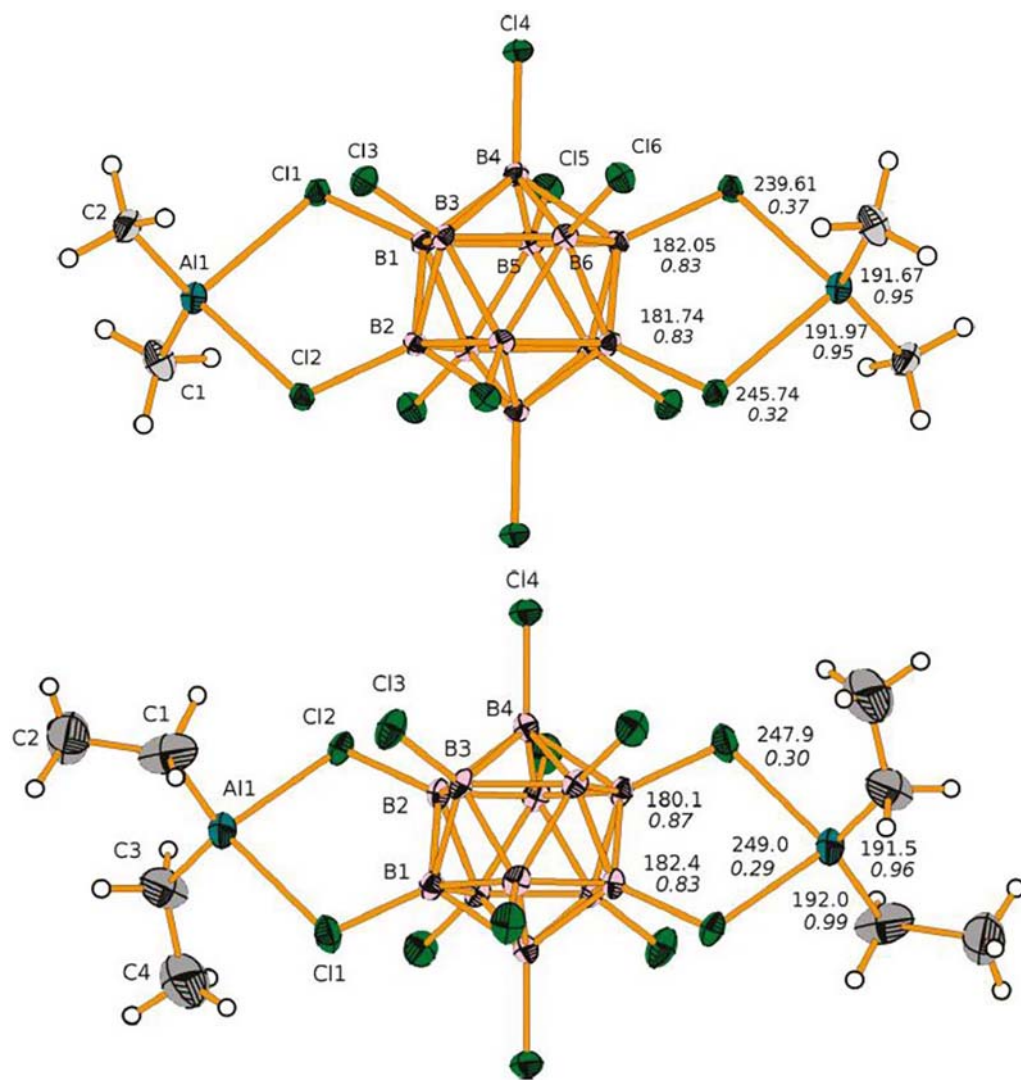
The coordination chemistry of perhalogenated *closo*-dodecaborates  $[B_{12}X_{12}]^{2-}$  has been studied much less than the coordination chemistry of the parent *closo*-dodecaborate anion  $[B_{12}H_{12}]^{2-}$ . The perhalogenated *closo*-dodecaborates have even less donor properties than the parent *closo*-dodecaborate and normally act as outer-sphere counterions. This is clearly manifested in crystalline hydrates  $[M(H_2O)_6][B_{12}X_{12}]$  ( $X = F, M = Co, Ni, Zn; X = Cl, M = Ni$ )<sup>173,188</sup> and solvates  $[M(MeCN)_6][B_{12}X_{12}]$  ( $M = Fe, X = Cl; M = Zn, X = I$ ),<sup>189,190</sup> as well as in a number of complexes of copper,<sup>191–193</sup> silver,<sup>171,192,194,195</sup> gold,<sup>192</sup> platinum,<sup>196,197</sup> palladium,<sup>198,199</sup> and zinc<sup>190</sup> where they are located in the outer sphere of the metal, however, they can have a significant effect on the formation of the inner sphere due to their large size. At the same time, in solvent-free silver dodecachloro-*closo*-dodecaborate  $Ag_2[B_{12}Cl_{12}]$ ,<sup>200</sup> as well as some silver complexes with weak ligands and the dodecafluoro-*closo*-dodecaborate anion,<sup>171,194</sup> the perhalogenated *closo*-dodecaborate anions enter inner sphere of silver.

One of the most impressive examples of the use of the perhalogenated *closo*-dodecaborates as weakly coordinating anions is the isolation of highly reactive dimethyl- and diethylaluminum cations as the dodecachloro-*closo*-dodecaborate salts  $\{(R_2Al)_2[B_{12}Cl_{12}]\}$  ( $R = Me, Et$ ) (Fig. 3) that form by the reaction of  $(Ph_3C)_2[B_{12}Cl_{12}]$  with the corresponding trialkylaluminum compounds  $R_3Al$  in *ortho*-difluorobenzene. In the solid state, the  $[R_2Al]^+$  cations are bidentate coordinated through chlorine atoms to opposite edges of the dodecachloro-*closo*-dodecaborate anion.<sup>201</sup>

Another example is the trialkylsilylium salts of the perhalogenated *closo*-dodecaborate anions  $\{(R_3Si)_2[B_{12}X_{12}]\}$  ( $X = F, R = Et; X = Cl, R = Me, Et, i-Pr; X = Br, R = Et$ ), which were prepared by the reactions of the corresponding tritylium salts  $(Ph_3C)_2[B_{12}X_{12}]$  with triethylsilane.<sup>183,202,203</sup> In the solid state the  $[Et_3Si]^+$  cations are coordinated to antipodal positions of the icosahedral anions (Fig. 4).

The salt with free tris(pentamethylphenyl)silylium cation  $((C_6Me_5)_3Si)_2[B_{12}Cl_{12}]$  was prepared by the reaction of the tritylium salt  $(Ph_3C)_2[B_{12}X_{12}]$  with the corresponding silane.<sup>184</sup> Another example of salt with “free” transition metal-stabilized silylium cation  $[(C_5H_5)Fe(C_5H_4Si(t-Bu)Me)]_2[B_{12}Cl_{12}]$  was synthesized using the same approach from the corresponding ferrocenylsilane.<sup>204</sup>

Finally, the salt with methyl carbocation  $\{(Me)_2[B_{12}Cl_{12}]\}$  was prepared by the reaction of  $Li_2[B_{12}Cl_{12}]$  with  $MeF$  and  $AsF_5$  in liquid sulfur dioxide. In the solid state, the methyl cations are coordinated to antipodal chlorine atoms of the anion (Fig. 5).



**Fig. 3** X-ray structures of  $\{(Me_2Al)_2[B_{12}Cl_{12}]\}$  (top) and  $\{(Et_2Al)_2[B_{12}Cl_{12}]\}$  (bottom). Reprinted with permission from Kessler, M.; Knapp, C.; Zogaj, A. *Organometallics* **2011**, *30*, 3786–3792. Copyright (2011) the American Chemical Society.

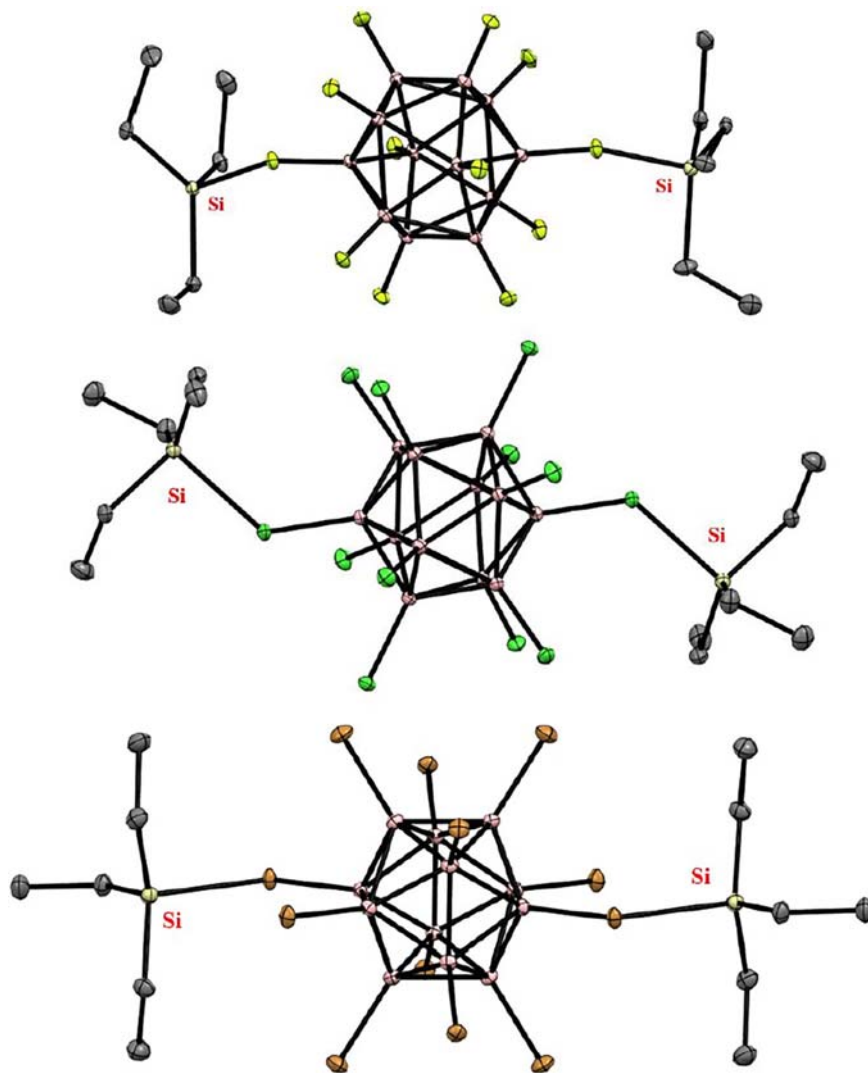
Dimethyl dodecachloro-*closo*-dodecaborate is a very strong methylating reagent that is able to convert benzene to toluene and to methylate dimethyl sulfide giving  $(Me_3S)_2[B_{12}Cl_{12}]$ .<sup>205</sup>

Based on a comparison of the  $\nu(N-H)$  stretching frequencies of the trioctylammonium salts of the perhalogenated *closo*-dodecaborates  $(Oct_3NH)_2[B_{12}X_{12}]$  ( $X = F, Cl, Br, I$ ), it was found that the basicity of the anions decreased in the series  $[B_{12}I_{12}]^{2-} > [B_{12}Br_{12}]^{2-} > [B_{12}Cl_{12}]^{2-} > [B_{12}F_{12}]^{2-}$ , i.e., the perfluorinated *closo*-dodecaborate is the least coordinating anion.<sup>178</sup>

Perfluoro-, perchloro- and perbromo-*closo*-dodecaborates were found to undergo reversible one-electron chemical oxidation with  $AsF_5$  in liquid  $SO_2$  leading to the *hypercloso*- $[B_{12}X_{12}]^{\bullet-}$  ( $X = F, Cl, Br$ ) radical anions.<sup>206–208</sup> The second one-electron oxidation results in the corresponding neutral *hypercloso*- $[B_{12}X_{12}]$  species.<sup>208</sup> The electrochemical stability of the perhalogenated *closo*-dodecaborates was found to be increased in the series  $[B_{12}F_{12}]^{2-} < [B_{12}Cl_{12}]^{2-} < [B_{12}Br_{12}]^{2-}$ ,<sup>207,208</sup> while the oxidation of the periodinated *closo*-dodecaborate  $[B_{12}I_{12}]^{2-}$  proceeds in a different way. This last fact can probably be explained by the different nature of the HOMO of this molecule.<sup>208,209</sup> Crystal molecular structures of  $[Cp_2Co]^+[B_{12}F_{12}]^{\bullet-}$ ,<sup>207</sup>  $[B_{12}Cl_{12}]$ ,<sup>207,208</sup> and  $[Na(SO_2)_6]^+[B_{12}Br_{12}]^{\bullet-}$ <sup>208</sup> were determined by single crystal X-ray diffraction. The oxidation results in an elongation of the B–B bonds with a simultaneous shortening of the B–X bonds.

The reaction of the *closo*-dodecaborate anion with arylidonium diacetates  $ArI(OAc)_2$  ( $Ar = C_6H_5, C_6H_4-4-OMe$ ) in aqueous acetic acid at  $0^\circ C$  leads to the corresponding zwitterionic arylidonium derivatives  $[B_{12}H_{11}IAr]^{-}$ ,<sup>210,211</sup> whereas the reaction in aqueous trifluoroacetic acid at  $70^\circ C$  results in a mixture of neutral 1,7- and 1,12-di(aryliodonium) derivatives.<sup>210,212</sup> The same approach can be used to introduce an arylidonium group into some derivatives of *closo*-dodecaborate anion.<sup>210,212</sup> The arylidonium group can be substituted with various nucleophiles, such as pyridines, hydroxylamine or *N,N*-dimethylthioformamide.<sup>210–213</sup>

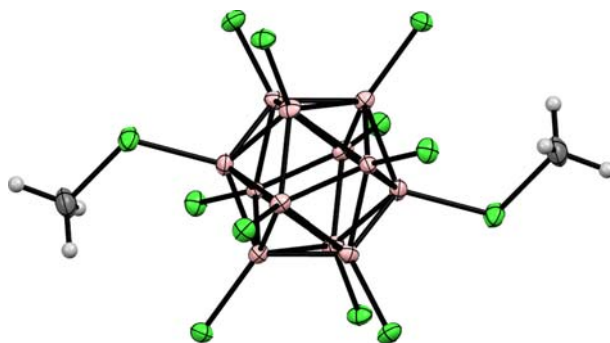




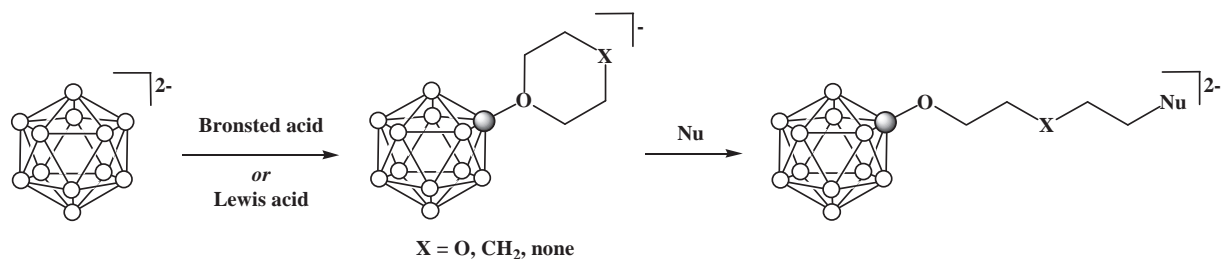
**Fig. 4** Single crystal X-ray structures of  $\{(\text{Et}_3\text{Si})_2[\text{B}_{12}\text{F}_{12}]\}$  (top),  $\{(\text{Et}_3\text{Si})_2[\text{B}_{12}\text{Cl}_{12}]\}$  (middle), and  $\{(\text{Et}_3\text{Si})_2[\text{B}_{12}\text{Br}_{12}]\}$  (bottom). Hydrogen atoms of organic substituents are removed for clarity.

#### 1.16.2.1.3 Derivatives with B–O bond

In 2000, an effective method was proposed for the functionalization of the  $[\text{B}_{12}\text{H}_{12}]^{2-}$  anion through the formation of its cyclic oxonium derivatives by reactions with cyclic esters in the presence of Lewis or Bronsted acids, followed by the ring opening by various nucleophiles (Scheme 1).<sup>214</sup> The reaction proceeds by electrophile-induced nucleophilic substitution (EINS) mechanism



**Fig. 5** Single crystal X-ray structure of  $\{(\text{Me})_2[\text{B}_{12}\text{Cl}_{12}]\}$ .



Scheme 1

which involves a primary attack of an electrophilic agent, leading to the elimination of the hydride hydrogen atom to form a quasi-borinane center on the boron atom, which is then attacked by the most abundant nucleophilic species. The reaction can also be initiated by strong Lewis acid, which abstracts a hydride from the boron atom, resulting in the formation of the quasi-borinane center. Subsequently, this approach was used to prepare a number of functional derivatives of other polyhedral boron hydrides, including the *closo*-decaborate anion (See Section 1.16.2.3.3), *nido*-carborane,<sup>215</sup> and metallacarboranes.<sup>216</sup> Later, convenient methods for the synthesis of oxonium derivatives of the *closo*-dodecaborate anion have been developed<sup>152,217,218</sup> and a series of various practically important functional derivatives have been synthesized.<sup>217,219–224</sup> This approach proved to be very convenient and effective for attaching the *closo*-dodecaborate moiety to various biomolecules, including amino acids,<sup>221,225</sup> sugars,<sup>226,227</sup> nucleosides,<sup>223,228–233</sup> porphyrins and phthalocyanines,<sup>234–238</sup> cholesterol,<sup>239,240</sup> coumarins,<sup>218,241,242</sup> and others<sup>243–256</sup> of interest for use in BNCT, as well as for preparation of boronated polymers<sup>257</sup> and nanoparticles.<sup>258,259</sup> Cyclic oxonium derivatives containing other substituents in the *closo*-dodecaborate cage also were synthesized and their ring-opening reactions were studied.<sup>260–262</sup> The advantages of this approach are a reasonable length of the spacer between the boron cage and the biologically active part of the molecule and the ability to regulate its hydrophilic-lipophilic properties by choosing a suitable cyclic ether. Recently, a convenient method for shortening the side chain formed during the opening of the dioxane ring with cyanide ion was proposed, and a series of functional derivatives  $[B_{12}H_{11}OCH_2CH_2X]^{2-}$  ( $X = OH, Br, I, OMs, N_3$ ) were obtained and applied for the synthesis of boron-containing nucleosides.<sup>263</sup>

To date, many methods have been developed for the synthesis of the hydroxy derivative of the *closo*-dodecaborate anion  $[B_{12}H_{11}OH]^{2-}$ , which were discussed in detail in the previous review.<sup>21</sup> Several examples of the alkylation of the hydroxy derivative have also been described earlier.<sup>147,264,265</sup> The reactions of  $[B_{12}H_{11}OH]^{2-}$  with *o*-, *m*- and *p*-nitrophenethyl bromides<sup>266</sup> as well as with propargyl bromide<sup>267</sup> in DMF in the presence of KOH at room temperature result in the corresponding alkoxy derivatives  $[B_{12}H_{11}OR]^{2-}$  ( $R = CH_2CH_2C_6H_4-2-NO_2, CH_2CH_2C_6H_4-3-NO_2, CH_2CH_2C_6H_4-4-NO_2, CH_2C\equiv CH$ ). The latter reacts with various functionalized azides containing aryl, carboranyl and lipid groups to form the corresponding triazoles.<sup>267</sup> The boron-containing esters of *meso*-tetra(4-carboxyphenyl)porphyrin<sup>268</sup> and protoporphyrin IX<sup>269</sup> and were prepared by acylation of the hydroxy derivative of the *closo*-dodecaborate anion.

The perchlorinated hydroxy derivative  $[B_{12}Cl_{11}OH]^{2-}$  was obtained bubbling chlorine gas through an aqueous solution of  $[B_{12}H_{11}OH]^{2-}$ .<sup>270</sup> Alternatively, the perchlorinated hydroxy derivative can be prepared by the reaction of the parent hydroxy derivative with  $SO_2Cl_2$  in refluxing acetonitrile.<sup>271</sup> Alkylation of  $[B_{12}Cl_{11}OH]^{2-}$  with alkyl bromides in DMSO in the presence of KOH leads to the corresponding alkoxy derivatives  $[B_{12}Cl_{11}OR]^{2-}$  ( $R = C_3H_7, C_8H_{17}, C_{12}H_{25}$ ).<sup>270</sup> The reaction of  $[B_{12}Cl_{11}OH]^{2-}$  with tosyl chloride in pyridine results in  $[B_{12}Cl_{11}OS(O)_2-p-Tol]^{2-}$ , while the reaction with triflic anhydride gives  $[B_{12}Cl_{11}OS(O)CF_3]^{2-}$ .<sup>271</sup> The perbrominated hydroxy derivative  $[B_{12}Br_{11}OH]^{2-}$  was obtained by heating  $[B_{12}H_{11}OH]^{2-}$  with bromine in aqueous methanol.<sup>270</sup> Alkylation of  $[B_{12}Br_{11}OH]^{2-}$  with alkyl bromides in DMSO in the presence of KOH leads to the corresponding alkoxy derivatives  $[B_{12}Br_{11}OR]^{2-}$  ( $R = C_3H_7, C_8H_{17}, C_{12}H_{25}$ ).<sup>270</sup>

The perhydroxy derivative of the *closo*-dodecaborate anion  $[B_{12}(OH)_{12}]^{2-}$  was prepared by refluxing the parent *closo*-dodecaborate with 30% hydrogen peroxide at 105 °C–110 °C.<sup>272,273</sup> Later, an improved method for the synthesis of the perhydroxy derivative was developed.<sup>274</sup> Alternatively, the perhydroxy derivative can be obtained by heating  $Cs_2[B_{12}H_{12}]$  in fuming sulfuric acid at 195 °C in the presence of catalytic amount of  $PdCl_2$  followed by acid hydrolysis of the resulting  $(H_3O)_2[B_{12}(OSO_3H)_{12}]$ .<sup>275</sup> The solid-state structures of the alkali metal salts  $M_2[B_{12}(OH)_{12}]$  and their crystalline hydrates were determined by X-ray diffraction.<sup>272,273,276</sup> Surprisingly, the reaction of  $Cs_2[B_{12}H_{12}]$  with 30% hydrogen peroxide at 65 °C resulted in the *hypercloso*- $[B_{12}(OH)_{12}]^{\cdot-}$  radical anion, which was isolated and characterized as the cesium salt  $Cs[B_{12}(OH)_{12}]^{\cdot-}$ .<sup>277</sup>

It has earlier been demonstrated that alkylation of  $[B_{12}(OH)_{12}]^{2-}$  with benzyl bromide leads to the dodeca(benzyloxy) derivative of the *closo*-dodecaborate anion  $[B_{12}(OBn)_{12}]^{2-}$ .<sup>278</sup> Later, synthesis of a series of substituted alkoxy, allyloxy, and benzyloxy derivatives  $[B_{12}(OR)_{12}]^{2-}$  was described.<sup>279–281</sup> The peralkoxy derivatives undergo two reversible sequential chemical or electrochemical oxidations giving the *hypercloso*- $[B_{12}(OR)_{12}]^{\cdot-}$  radical anions and the neutral *hypercloso*- $[B_{12}(OR)_{12}]$  species.<sup>278–280,282–284</sup>

It has been established that the redox potentials depend on the electronic effects of the R substituents, and the electron-donating substituents facilitate the oxidation process.<sup>282,283</sup> The crystal molecular structures of  $Cs(PPN)[B_{12}(OCH_2C_6H_5)_{12}]$ ,<sup>278</sup>  $(PPN)[B_{12}(OCH_2C_6H_5)_{12}]$ ,<sup>278</sup>  $(Bu_4N)[B_{12}(OCH_2C_6H_3-3,5-(CF_3)_2)_{12}]$ ,<sup>280</sup>  $[B_{12}(OEt)_{12}]$ ,<sup>280</sup>  $[B_{12}(OCH_2R)_{12}]$  ( $R = C_6H_5$ ,<sup>278,280</sup>  $C_6H_4-p-I$ ,<sup>285</sup>  $C_6H_4-p-Br$ ,<sup>279</sup>  $C_6H_4-p-Cl$ ,<sup>279</sup>  $C_6H_4-p-F$ ,<sup>279</sup>  $C_6H_4-p-CF_3$ ,<sup>282</sup>  $C_6H_3-3,5-(CF_3)_2$ ,<sup>284</sup>  $C_6H_4-p-C_6F_5$ ,<sup>281</sup>  $C_6F_5$ <sup>281</sup>) were determined by single crystal X-ray diffraction. As in the case of the perhalogenated derivatives of the *closo*-dodecaborate anion, the

oxidation leads to an elongation of the B–B bonds with a simultaneous shortening of the B–O bonds. The size of the clusomers obtained in this way, depending on the type of substituent in the benzyl group, is 1.9–2.7 nm, which is much larger than the size of fullerenes (0.7 nm for C<sub>60</sub>),<sup>281,284</sup> however it can be significantly increased through the gold-mediated substitution iodine atoms in [B<sub>12</sub>(OCH<sub>2</sub>C<sub>6</sub>H<sub>4</sub>-*p*-I)<sub>12</sub>]<sup>2-</sup> by thiols<sup>285</sup> or the nucleophilic substitution of the *p*-fluorine atoms in the end C<sub>6</sub>F<sub>5</sub> groups of [B<sub>12</sub>(OCH<sub>2</sub>C<sub>6</sub>F<sub>5</sub>)<sub>12</sub>]<sup>2-</sup> and [B<sub>12</sub>(OCH<sub>2</sub>C<sub>6</sub>H<sub>4</sub>-*p*-C<sub>6</sub>F<sub>5</sub>)<sub>12</sub>]<sup>2-</sup> with various thiolates.<sup>284</sup>

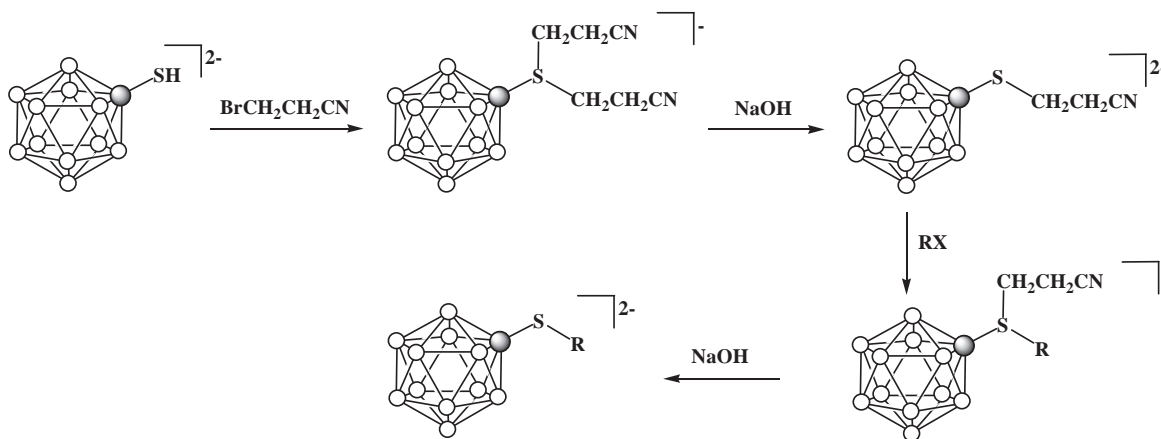
It was earlier reported that acylation of [B<sub>12</sub>(OH)<sub>12</sub>]<sup>2-</sup> with acetic anhydride or benzoyl chloride results in the corresponding dodeca(acetate) [B<sub>12</sub>(OAc)<sub>12</sub>]<sup>2-</sup> and dodeca(benzoate) [B<sub>12</sub>(OBz)<sub>12</sub>]<sup>2-</sup> derivatives.<sup>286</sup> Later, synthesis of a series of various acyloxy derivatives [B<sub>12</sub>(OC(O)R)<sub>12</sub>]<sup>2-</sup> (R = alkyl, aryl) was described.<sup>287</sup> The acylation of [B<sub>12</sub>(OH)<sub>12</sub>]<sup>2-</sup> with chloroacetic or bromoacetic anhydride results in the dodeca(chloro/bromoacetate) derivatives [B<sub>12</sub>(OC(O)CH<sub>2</sub>X)<sub>12</sub>]<sup>2-</sup> (X = Cl, Br), which upon treatment with NaN<sub>3</sub> converts into the corresponding azide [B<sub>12</sub>(OC(O)CH<sub>2</sub>N<sub>3</sub>)<sub>12</sub>]<sup>2-</sup>, which in turn can be used to obtain the triazole derivatives containing various functional groups.<sup>288–291</sup> A series of dodeca(carbonate) derivatives [B<sub>12</sub>(OC(O)OAr)<sub>12</sub>]<sup>2-</sup> were prepared by the reaction of [B<sub>12</sub>(OH)<sub>12</sub>]<sup>2-</sup> with various aryl chloroformates. The reactions of these carbonates with primary amines lead to the corresponding carbamates [B<sub>12</sub>(OC(O)NHR)<sub>12</sub>]<sup>2-</sup>, including those containing various functional groups (–C≡CH, –N<sub>3</sub>, –NHBOc, etc.).<sup>292</sup> Several methods for the synthesis of vertex-differentiated derivatives of the *closo*-dodecaborate anion via monoalkylation of [B<sub>12</sub>(OH)<sub>12</sub>]<sup>2-</sup> followed by acylation of the resulting [B<sub>12</sub>(OR)(OH)<sub>11</sub>]<sup>2-</sup> with chloroacetic anhydride or *p*-nitrophenyl chloroformate and corresponding transformations were developed.<sup>293–295</sup> The chemistry of the dodeca(hydroxy)-*closo*-dodecaborate anion [B<sub>12</sub>(OH)<sub>12</sub>]<sup>2-</sup> and its derivatives was discussed in detail in several mini-reviews.<sup>296,297</sup>

#### 1.16.2.1.4 Derivatives with B–S bond

The widespread development of the chemistry of derivatives of the *closo*-dodecaborate anion with a boron-sulfur bond is largely due to the fact that sodium mercapto-*closo*-dodecaborate has found clinical use in boron neutron capture therapy for cancer. To date, several methods have been developed for the synthesis of the mercapto derivative of the *closo*-dodecaborate anion [B<sub>12</sub>H<sub>11</sub>SH]<sup>2-</sup>, which, like its general chemistry, were discussed in detail in the previous review.<sup>21</sup> The syntheses of numerous alkylthio derivatives of the *closo*-dodecaborate anion [B<sub>12</sub>H<sub>11</sub>SR]<sup>2-</sup> via the alkylation of the mercapto derivative [B<sub>12</sub>H<sub>11</sub>SH]<sup>2-</sup> have been earlier described.<sup>21</sup> To avoid the formation of dialkylsulfonium derivatives [B<sub>12</sub>H<sub>11</sub>SR<sub>2</sub>]<sup>-</sup>, an approach based on the use of an easily removable cyanoethyl group (Scheme 2) was developed.<sup>298</sup> More recently this approach was used for the synthesis of some important simple functional derivatives of the *closo*-dodecaborate anion,<sup>299,300</sup> as well as boron-containing amino acids,<sup>301–303</sup> peptides,<sup>304,305</sup> sugars,<sup>306</sup> lipids,<sup>307–311</sup> porphyrins,<sup>312</sup> and other biologically active compounds.<sup>242,313–315</sup>

A series of dialkylsulfonium derivatives [B<sub>12</sub>H<sub>11</sub>SR<sub>2</sub>]<sup>-</sup> was prepared by direct alkylation of the mercapto derivative of the *closo*-dodecaborate anion with aryethyl bromides,<sup>266</sup> propargyl bromide<sup>299</sup> and ω-bromoalkyl carboxylic acids.<sup>300</sup> Alkylation of [B<sub>12</sub>H<sub>11</sub>SH]<sup>2-</sup> with bifunctional alkylating agents such as 1,5-dibromopentane, bis(2-chloroethyl)amine or C<sub>5</sub>H<sub>11</sub>CH(CH<sub>2</sub>CH<sub>2</sub>Br)<sub>2</sub> leads to the cyclic sulfonium derivatives [B<sub>12</sub>H<sub>11</sub>S(CH<sub>2</sub>)<sub>5</sub>]<sup>-</sup>,<sup>298</sup> [B<sub>12</sub>H<sub>11</sub>S(CH<sub>2</sub>CH<sub>2</sub>)<sub>2</sub>NH]<sup>-</sup>,<sup>316</sup> and [B<sub>12</sub>H<sub>11</sub>S(CH<sub>2</sub>CH<sub>2</sub>)<sub>2</sub>CHC<sub>5</sub>H<sub>11</sub>]<sup>-</sup>.<sup>212</sup> Treatment of the di(phenethyl)sulfonium derivatives with (Me<sub>4</sub>N)OH results in styrene elimination with the formation of the corresponding alkylthio derivatives [B<sub>12</sub>H<sub>11</sub>SCH<sub>2</sub>CH<sub>2</sub>C<sub>6</sub>H<sub>4</sub>X]<sup>2-</sup>.<sup>266</sup> The reactions of [B<sub>12</sub>H<sub>11</sub>S(CH<sub>2</sub>CH<sub>2</sub>COOH)<sub>2</sub>]<sup>-</sup> with alcohols in the presence of *N,N'*-dicyclohexylcarbodiimide (DCC) and 4-dimethylaminopyridine (DMAP) proceed with the loss of one alkyl group leading to esters [B<sub>12</sub>H<sub>11</sub>SCH<sub>2</sub>CH<sub>2</sub>COOR]<sup>2-</sup>.<sup>300</sup> The reactions of [B<sub>12</sub>H<sub>11</sub>S((CH<sub>2</sub>)<sub>n</sub>COOH)<sub>2</sub>]<sup>-</sup> (*n* = 1–3) with propargyl amine also proceed with the loss of one alkyl group resulting in the corresponding amides [B<sub>12</sub>H<sub>11</sub>S(CH<sub>2</sub>)<sub>n</sub>CONHCH<sub>2</sub>C≡CH]<sup>2-</sup>, which, in turn, react with various organic azides to form the corresponding triazoles.<sup>300</sup>

A series of boronated thioesters of protoporphyrin IX<sup>269</sup> and *meso*-tetra(4-carboxyphenyl)porphyrin<sup>268</sup> were prepared by acylation of the mercapto derivative of the *closo*-dodecaborate anion.



Scheme 2

The alkylthio derivatives also can be prepared via the Michael addition of the mercapto derivative  $[B_{12}H_{11}SH]^{2-}$  to an  $\alpha,\beta$ -unsaturated carbonyl compounds. The reaction of  $[B_{12}H_{11}SH]^{2-}$  with methyl acrylate in alkaline solution in one step leads to the corresponding boronated propionic acid  $[B_{12}H_{11}SCH_2CH_2COOH]^{2-}$ .<sup>317</sup> Addition of the mercapto derivative to the double bond of the maleimide group was used earlier to obtain boron-containing streptavidin.<sup>318</sup> Subsequently this approach was successfully used for the synthesis of other boronated peptides,<sup>319–323</sup> dendrimers<sup>324</sup> and water-soluble BODIPY dyes.<sup>325</sup>

Another approach to boron-containing polypeptides has been developed based on the reaction of  $[B_{12}H_{11}SH]^{2-}$  with activated terminal cysteines via the formation of a disulfide bond.<sup>326</sup>

The mercapto derivative of *closo*-dodecaborate anion  $[B_{12}H_{11}SH]^{2-}$  can be arylated with electron-deficient chloroaromatics and alkylsulfonyl heteroaromatics. The reaction of  $[B_{12}H_{11}SH]^{2-}$  with 4-chloro-7-nitrobenzo[*c*][1,2,5]oxadiazole in acetonitrile in the presence of  $K_2CO_3$  leads to the corresponding arylsulfide derivative,<sup>316</sup> while the reactions with 3-alkylsulfonyl-5-phenyl-, 5-(4'-bromophenyl)- and 5-methylamino-6-methylcarboxamido-1,2,4-triazines in acetonitrile in the presence of lutidine result in the corresponding boronated 1,2,4-triazines.<sup>327,328</sup> Surprisingly, that the similar reaction with 3-ethylsulfonyl-5,7-dimethyl-5,6,7,8-tetrahydropyrimido-[4,5-*e*][1,2,4]-triazine-6,8-dione results in the thiosulfinate derivative  $[B_{12}H_{11}SS(O)Et]^{2-}$ .<sup>327</sup>

1. The reactions of demethylation and realkylation of dimethylsulfonium derivatives of the *closo*-dodecaborate anion  $[B_{12}H_{11}SMe_2]^-$ ,  $[1,2-B_{12}H_{10}(SMe_2)_2]$ ,  $[1,7-B_{12}H_{10}(SMe_2)_2]$  and  $[1,12-B_{12}H_{10}(SMe_2)_2]$  were considered in detail in the earlier review.<sup>21</sup> Later, the substitution in 1,7- and 1,12-bis(dimethylsulfonium) derivatives of the *closo*-dodecaborate anion  $[1,7-B_{12}H_{10}(SMe_2)_2]$  and  $[1,12-B_{12}H_{10}(SMe_2)_2]$  was studied. The reaction of  $[1,7-B_{12}H_{10}(SMe_2)_2]$  with *N*-chlorosuccinimide in refluxing acetonitrile results in the monochloro derivative  $[1,7-B_{12}H_9(SMe_2)_2-9-Cl]$ , while the dichloro derivative  $[1,7-B_{12}H_8(SMe_2)_2-9,10-Cl_2]$  was isolated from the reaction of  $[1,7-B_{12}H_{10}(SMe_2)_2]$  with  $MeSO_2Cl$  in dichloromethane in the presence of  $AlCl_3$ . The bromination of  $[1,7-B_{12}H_{10}(SMe_2)_2]$  with  $Br_2$  in dichloromethane at room temperature leads to the monobromide  $[1,7-B_{12}H_9(SMe_2)_2-9-Br]$  or the dibromide  $[1,7-B_{12}H_8(SMe_2)_2-9,10-Br_2]$  depending on the reagent ratio. The reaction of  $[1,7-B_{12}H_{10}(SMe_2)_2]$  with  $ICl$  in refluxing dichloromethane results in the monoiodo  $[1,7-B_{12}H_9(SMe_2)_2-9-I]$  or the diiodo  $[1,7-B_{12}H_8(SMe_2)_2-9,10-I_2]$  derivatives depending on the reagent ratio. The same results were obtained using  $I_2$  in dichloromethane in the presence of  $AlCl_3$ . The cross-coupling of  $[1,7-B_{12}H_9(SMe_2)_2-9-I]$  and  $[1,7-B_{12}H_8(SMe_2)_2-9,10-I_2]$  with Grignard reagents in the presence of 5 mol%  $[(Ph_3P)_2PdCl_2]$  in THF result in the corresponding alkyl/aryl derivatives  $[1,7-B_{12}H_9(SMe_2)_2-9-R]$  and  $[1,7-B_{12}H_8(SMe_2)_2-9,10-R_2]$  ( $R = Me, Bn, Ph$ ). Reactions of  $[1,7-B_{12}H_{10}(SMe_2)_2]$  with 2,4-( $NO_2$ )<sub>2</sub>C<sub>6</sub>H<sub>3</sub>SCl and  $PhSeBr$  in refluxing acetonitrile led to  $[1,7-B_{12}H_9(SMe_2)_2-9-SC_6H_3-2',4'-(NO_2)_2]$  and  $[1,7-B_{12}H_8(SMe_2)_2-9,10-(SPh)_2]$ , respectively.<sup>329</sup> Reaction of  $[1,7-B_{12}H_{10}(SMe_2)_2]$  with DMSO upon heating in acidic solution produces  $[1,7,9-B_{12}H_9(SMe_2)_3]^+$ , which loses the methyl cation on aqueous work-up resulting in  $[1,7-B_{12}H_9(SMe_2)_2-9-SMe]$ . It is noteworthy that the substitution occurs at the boron atoms most distant from the atoms bearing strong electron-acceptor substituents.<sup>330</sup> The reaction of  $[1,12-B_{12}H_{10}(SMe_2)_2]$  with  $Me_2S \cdot Br_2$  in dichloromethane results in the monobromo derivative  $[1,12-B_{12}H_9(SMe_2)_2-2-Br]$ , whereas the monoiodo derivative  $[1,12-B_{12}H_9(SMe_2)_2-2-I]$  was prepared by the treatment of  $[1,12-B_{12}H_{10}(SMe_2)_2]$  with  $ICl$  in refluxing acetonitrile. The cross-coupling of  $[1,12-B_{12}H_9(SMe_2)_2-2-I]$  with Grignard reagents in the presence of 5 mol%  $[(Ph_3P)_2PdCl_2]$  in THF gives  $[1,12-B_{12}H_9(SMe_2)_2-2-R]$  ( $R = Me, Bn, Ph$ ).<sup>329</sup>

The reaction of the *closo*-dodecaborate anion  $[B_{12}H_{12}]^{2-}$  with thiocyanogen  $(SCN)_2$  results in mono- and disubstituted thiocyanate derivatives  $[B_{12}H_{11}SCN]^{2-}$  and  $[1,7-B_{12}H_{10}(SCN)_2]^{2-}$ , depending on the reagent ratio.<sup>331–333</sup> The disubstituted derivatives  $[1,7-B_{12}H_{10}(SCN)_2]^{2-}$  and  $[1,7-B_{12}H_{10}(SCN)_2]^{2-}$  were prepared by the reaction of the  $[B_{12}H_{12}]^{2-}$  with the thiocyanate ion under chemical oxidation conditions.<sup>334</sup>

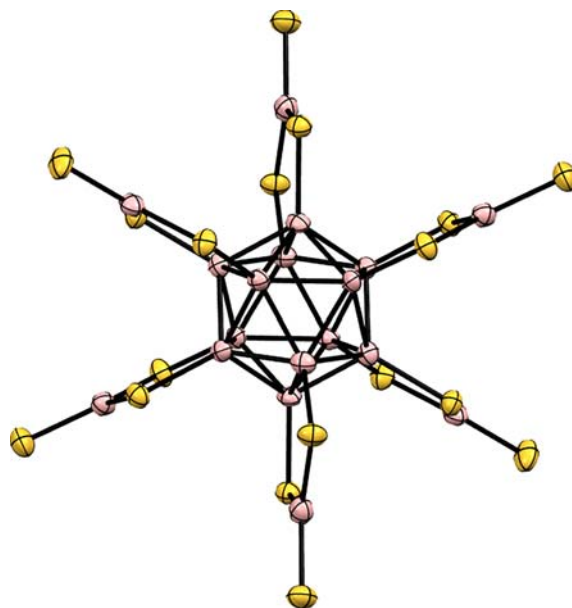
Alkali metal salts with the hexathioborato-*closo*-dodecaborate anion  $M_8[B_{12}(BS_3)_6]$  ( $M = Rb, Cs$ ) have been prepared by a direct high-temperature solid-state synthesis from the corresponding metal selenides, amorphous boron, and selenium. The  $BS_3$  thioborate groups act as bifunctional substituents decorating the boron icosahedron to form the persubstituted *closo*-dodecaborate anion (Fig. 6).<sup>335</sup> The S-persubstituted *closo*-dodecaborate clusters were found also in the structures of 3-D inorganic polymers  $\{(K_3I)[GaB_{12}(GaS_4)_3]\}_n$ ,<sup>336</sup>  $\{(K_3I)[MB_{12}(GaS_4)_3]\}_n$  ( $M = Sm, Gd$ ),<sup>337,338</sup>  $\{(M_3X)[InB_{12}(InS_4)_3]\}_n$  ( $M = K, X = Cl, Br, I; M = Rb, X = I; M = Cs, X = I$ ),<sup>336,338</sup>  $\{KEu_2In_3B_{12}S_{13}\}_n$ ,<sup>339</sup> and  $\{KNa_{0.78}Eu_{0.27}In_{3.80}B_{12}S_{12}\}_n$ .<sup>340</sup>

### 1.16.2.1.5 Derivatives with B–Se bond

A series of salts with the hexaselenoborato-*closo*-dodecaborate anion  $M_8[B_{12}(BSe_3)_6]$  ( $M = Na, K, Rb, Cs, Tl$ ) and  $M_4Hg_2[B_{12}(BSe_3)_6]$  ( $M = Rb, Cs$ ) has been obtained by a direct high-temperature solid-state synthesis from the corresponding metal selenides, amorphous boron, and selenium.<sup>341–345</sup> The structure of the  $[B_{12}(BSe_3)_6]^{8-}$  anion is like the structure of the  $[B_{12}(BS_3)_6]^{8-}$  anion (see above). The closely related structural type was found in the 1D- and 3D-polymers  $\{Na_6[B_{18}Se_{17}]\}_n$  and  $\{Na_2[B_{18}Se_{16}]\}_n$ , respectively, formed under similar conditions under sodium selenide deficiency.<sup>346,347</sup> The Se-persubstituted *closo*-dodecaborate clusters were found also in the structures of 3-D inorganic polymers  $\{(M_3X)[InB_{12}(InS_4)_3]\}_n$  ( $M = K, X = Cl, Br, I; M = Rb, X = I; M = Cs, X = Cl, I$ ),<sup>338,348</sup>  $\{CrSi_3B_{12}Se_{12}(B_2Se_3)_{1.33}\}_n$ ,<sup>349</sup>  $\{Sn_4B_{12}Se_{12}(Se_{3.80})\}_n$ <sup>350</sup> and  $\{Sn_{3.92}B_{12}Se_{12}(Se_{0.61})\}_n$ .<sup>350</sup>

### 1.16.2.1.6 Derivatives with B–N bonds

Due to the diversity of nitrogen chemistry, the chemistry of derivatives of the *closo*-dodecaborate anion with a boron-nitrogen bond is represented by a wide variety of derivatives.<sup>21</sup> One of the most important derivatives of the *closo*-dodecaborate anion is its amino



**Fig. 6** Structure of the hexathiaborato-*closo*-dodecaborate anion  $[B_{12}(BS_3)_6]^{8-}$ .

derivative, which, due to the strong electron-donating nature of the boron cluster,<sup>351,352</sup> exists as the protonated ammonium derivative  $[B_{12}H_{11}NH_3]^+$ . The synthesis of the ammonium derivative of the *closo*-dodecaborate anion by the reaction of the parent *closo*-dodecaborate with hydroxylamine-*O*-sulfonic acid was described previously.<sup>353,354</sup> Recently, an alternative method for the synthesis of the ammonium derivative was proposed through the hydrolysis of the nitrilium derivative of the *closo*-dodecaborate anion  $[B_{12}H_{11}N\equiv CMe]^{-213}$  which formed by the EINS reaction of the parent *closo*-dodecaborate with acetonitrile in the presence of trifluoroacetic acid.<sup>213,355–357</sup> Due to the interest in using *closo*-dodecaborate anion derivatives as components of hypergolic fuels,<sup>117,118</sup> a series of the imidazolium salts of its ammonium derivative  $(R\text{-mim})[B_{12}H_{11}NH_3]$  ( $R = \text{Me, Et, Pr, CH}_2\text{CH}=\text{CH}_2, \text{CH}_2\text{C}\equiv\text{CH, CH}_2\text{C}\equiv\text{N}$ ) were prepared.<sup>358</sup>

The amino derivative of the *closo*-dodecaborate anion  $[B_{12}H_{11}NH_2]^{2-}$  can act as a good ligand in complexes with various transition metals. The reaction of  $\text{Na}_2[B_{12}H_{11}NH_2]$  with  $[(\text{Ph}_3\text{P})\text{AuCl}]$  in THF in the presence of 18-crown-6 results in  $[\text{Na}(18\text{-crown-6})]\{(\text{Ph}_3\text{P})\text{Au}[B_{12}H_{11}NH_2\text{-}\kappa^1\text{-N}]\}$ . The reaction with  $[(\text{THF})_2\text{NiBr}_2]$  gives the square planar nickel complex  $\{\text{Na}_6(\text{THF})_{16}(\text{Ni}[B_{12}H_{11}NH_2\text{-}\kappa^1\text{-N}]_4)\}$ . The reaction of  $\text{Na}_2[B_{12}H_{11}NH_2]$  with  $[(\text{Ph}_3\text{P})_3\text{RhCl}]$  in THF leads to the square planar rhodium complex  $(\text{Ph}_3\text{PMe})\{(\text{Ph}_3\text{P})_2\text{Rh}[B_{12}H_{11}NH_2\text{-}\kappa^2\text{-N,H}]\}$  where the amino derivative acts as bidentate ligand (Fig. 7).<sup>359</sup>

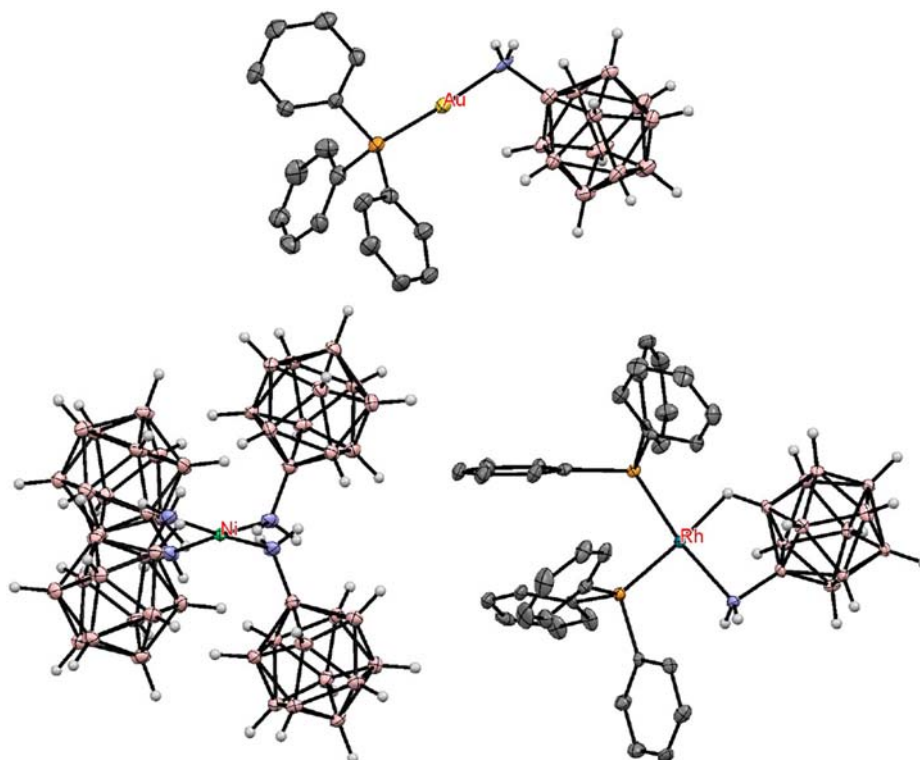
The reaction of  $\text{Na}_2[B_{12}H_{11}NH_2]$  with  $[(\text{Ph}_3\text{P})_3\text{RuCl}_2]$  in THF results in the octahedral anionic ruthenium complex  $(\text{Bu}_3\text{NMe})[(\text{Ph}_3\text{P})_2\text{RuCl}\{B_{12}H_{11}NH_2\text{-}\kappa^3\text{-N,H,H}\}]$  where the amino derivative acts as a bidentate ligand. The neutral ruthenium complex  $[(\text{Ph}_3\text{P})_2(\text{CO})\text{Ru}\{B_{12}H_{11}NH_2\text{-}\kappa^3\text{-N,H,H}\}]$  was obtained by bubbling CO through a solution of  $(\text{Bu}_3\text{NMe})[(\text{Ph}_3\text{P})_2\text{RuCl}\{B_{12}H_{11}NH_2\text{-}\kappa^3\text{-N,H,H}\}]$  in THF (Fig. 8). Another ruthenium complex  $(\text{Bu}_4\text{N})[(\text{dppb})\text{RuCl}\{B_{12}H_{11}NH_2\text{-}\kappa^3\text{-N,H,H}\}]$  was prepared in a similar way using  $[(\text{Ph}_3\text{P})(\text{dppb})\text{RuCl}_2]$ .<sup>360</sup>

A series of the trialkylammonium derivatives  $[B_{12}H_{11}NR_3]^-$  ( $R = \text{Me, Et, Pr, Bu, } n\text{-C}_5\text{H}_{11}, i\text{-C}_5\text{H}_{11}, \text{C}_6\text{H}_{13}, \text{C}_{12}\text{H}_{15}, \text{CH}_2\text{C}\equiv\text{CH}, (\text{CH}_2)_3\text{CH}=\text{CH}_2, (\text{CH}_2)_3\text{Ph}$ ) was prepared by alkylation of  $[B_{12}H_{11}NH_3]^-$  with the corresponding alkyl bromides in acetonitrile or DMF in the presence of KOH.<sup>267,361–364</sup> The dialkylammonium derivatives  $[B_{12}H_{11}NHR_2]^-$  ( $R = i\text{-Pr, Bn, CMe}_2\text{C}\equiv\text{CH}, (\text{CH}_2)_2\text{C}_6\text{H}_4\text{NO}_2, (\text{CH}_2)_3\text{C}\equiv\text{CH}$ ) were obtained using more sterically hindered alkyl bromides or less active alkyl chlorides.<sup>266,267,362</sup> The methylammonium derivative  $[B_{12}H_{11}NH_2\text{Me}]^-$  was prepared by the reaction of the parent *closo*-dodecaborate with *N*-methylhydroxylamine-*O*-sulfonic acid.<sup>363</sup> A series of the nitrophenethylammonium derivatives  $[B_{12}H_{11}NH_2\text{CH}_2\text{CH}_2\text{C}_6\text{H}_4\text{-}x\text{-NO}_2]^-$  ( $x = o, m, p$ ) was obtained via treatment of the corresponding di(nitrophenethyl)ammonium derivatives with  $(\text{Me}_4\text{N})\text{OH}$  in methanol.<sup>266</sup> A series of the benzylammonium derivatives  $[B_{12}H_{11}NH_2\text{CH}_2\text{Ar}]^-$  ( $\text{Ar} = \text{C}_6\text{H}_4\text{-}2\text{-OMe, C}_6\text{H}_3\text{-}3,4\text{-O}_2\text{CH}_2, \text{C}_6\text{H}_4\text{-}4\text{-NHCOMe, C}_6\text{H}_4\text{-}4\text{-CN}$ ) was prepared by the reduction of the corresponding imines  $[B_{12}H_{11}NH=\text{CHAr}]^-$  (see below) with  $\text{NaBH}_4$ .<sup>365</sup> The heterosubstituted trialkylammonium derivatives  $[B_{12}H_{11}NR_2R']^-$  ( $R' = \text{Me, R} = \text{Et, C}_{12}\text{H}_{25}; R' = \text{Bn, R} = \text{Et}$ ) were obtained by alkylation of the methyl- and benzylammonium derivatives.<sup>362</sup>

The reactions of the *closo*-dodecaborate anion with chlorinated iminium salts (Vilsmeier reagents) lead to mixtures of mono- and disubstituted alkyl/arylammonium derivatives  $[B_{12}H_{11}NRR'R'']^-$  and  $[1,7\text{-}B_{12}H_{10}(\text{NRR}'R'')]_2$  ( $R = R' = \text{Me, R}'' = \text{CH}_2\text{Cl}; R = \text{Me, R}' = \text{Ph, R}'' = \text{CH}_2\text{Cl}; R = R' = (\text{CH}_2\text{CH}_2)_2\text{O, R}'' = \text{CH}_2\text{Cl}; R = R' = \text{Me, R}'' = \text{CHCl}_2$ ).<sup>366</sup>

The Pd-catalyzed reactions of the iodo derivative of the *closo*-dodecaborate anion  $[B_{12}H_{11}I]^{2-}$  with anilines produce the corresponding arylamino derivatives  $[B_{12}H_{11}NH\text{Ar}]^{2-}$  in good yields (Scheme 3), while the reaction with 1-aminonaphthalene under the same conditions results in the corresponding amine only in moderate yield.<sup>367</sup> The arylamino derivative  $[B_{12}H_{11}NHC_6H_3\text{-}$



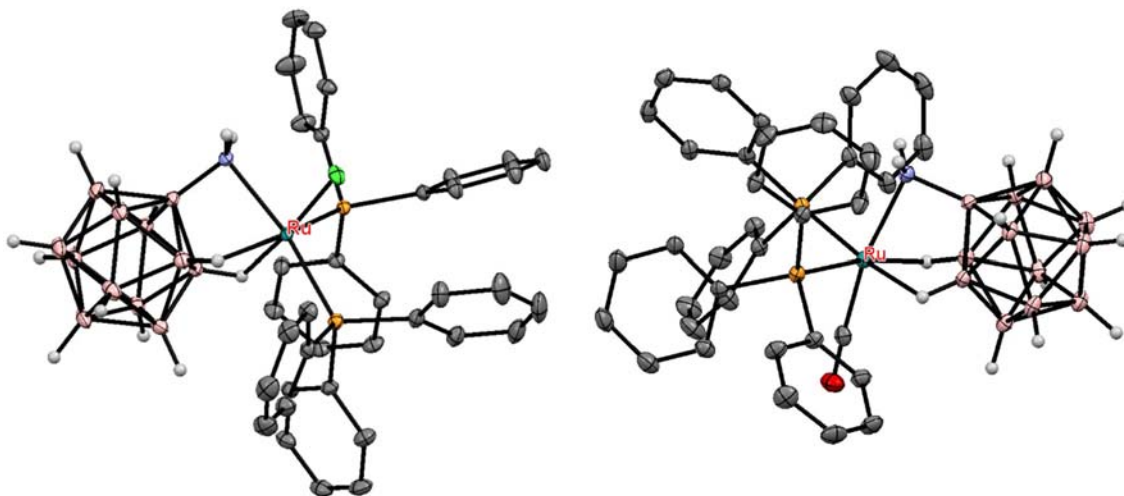


**Fig. 7** Crystal molecular structures of anionic complexes  $\{(\text{Ph}_3\text{P})\text{Au}[\text{B}_{12}\text{H}_{11}\text{NH}_2\text{-}\kappa^1\text{-M}]\}^-$  (top),  $\{\text{Ni}[\text{B}_{12}\text{H}_{11}\text{NH}_2\text{-}\kappa^1\text{-M}]_4\}^{6-}$  (bottom left) and  $\{(\text{Ph}_3\text{P})_2\text{Rh}[\text{B}_{12}\text{H}_{11}\text{NH}_2\text{-}\kappa^2\text{-N,H}]\}^-$  (bottom right). Hydrogen atoms of organic substituents and ligands are removed for clarity.

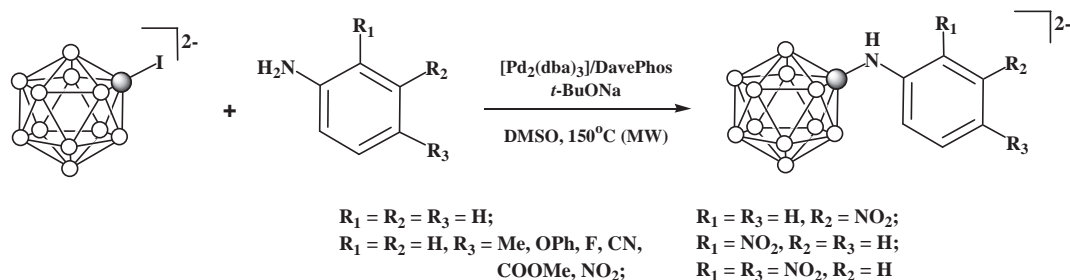
$2,4\text{-}(\text{NO}_2)_2\}^{2-}$  can be also prepared by the reaction of  $[\text{B}_{12}\text{H}_{11}\text{NH}_3]^-$  with 1-chloro-2,4-dinitrobenzene in ethanol in the presence of EtONa.<sup>368</sup>

The phenyldimethylammonium derivative  $(\text{Bu}_4\text{N})[\text{B}_{12}\text{H}_{11}\text{NMe}_2\text{Ph}]$  was obtained by heating  $(\text{Bu}_4\text{N})_2[\text{B}_{12}\text{H}_{12}]$  in *N,N*-dimethylaniline at 200 °C. Interestingly, that the similar reaction with 4-dimethylamino pyridine leads to the *para*-dimethylaminopyridinium derivative  $[\text{B}_{12}\text{H}_{11}\text{NC}_5\text{H}_4\text{-4-NMe}_2]^-$ .<sup>368</sup> The pyridinium derivative  $[\text{B}_{12}\text{H}_{11}\text{NC}_5\text{H}_5]^-$  was prepared by the reaction of the *para*-methoxyphenyliodonium derivative  $[\text{B}_{12}\text{H}_{11}\text{IC}_6\text{H}_4\text{-4-OMe}]^-$  with pyridine.<sup>211</sup> The 1,7- and 1,12-dipyridinium derivatives 1,7- and 1,12- $[\text{B}_{12}\text{H}_{10}(\text{NC}_5\text{H}_4\text{-4-OR})_2]$  ( $\text{R} = \text{C}_7\text{H}_{15}, \text{C}_9\text{H}_{19}, \text{C}_{11}\text{H}_{23}$ ) were synthesized in a similar way.<sup>212</sup>

A series of *N*-azole derivatives of the *closo*-dodecaborate anion were prepared in high yields by the Pd-catalyzed reactions of  $[\text{B}_{12}\text{H}_{11}\text{I}]^{2-}$  with carbazole, pyrrole, indole, pyrazole, and imidazole (Scheme 4).<sup>367</sup>



**Fig. 8** Crystal molecular structures of  $\{(\text{Ph}_3\text{P})_2\text{RuCl}[\text{B}_{12}\text{H}_{11}\text{NH}_2\text{-}\kappa^3\text{-N,H,H}]\}^-$  (left) and  $\{(\text{Ph}_3\text{P})_2(\text{CO})\text{Ru}[\text{B}_{12}\text{H}_{11}\text{NH}_2\text{-}\kappa^3\text{-N,H,H}]\}^-$  (right). Hydrogen atoms of organic substituents and ligands are removed for clarity.



Scheme 3

Acylation of  $[B_{12}H_{11}NH_2]^{2-}$  with aryl chlorides  $ArCOCl$  leads to amides  $[B_{12}H_{11}NHC(O)Ar]^{2-}$  ( $C_6H_5$ ,  $C_6H_4-4-F$ ,  $C_6H_4-4-I$ ,  $C_6H_4-4-OMe$ ), which can be reversibly protonated with the formation of the corresponding iminols  $[B_{12}H_{11}NH=C(OH)Ar]^-$ . In the case of the picolinic acid amide, protonation takes place at the pyridine ring resulting in  $[B_{12}H_{11}NHC(O)-2-C_5H_4NH]^-$ .<sup>369,370</sup> The latter was also obtained by the Pd-catalyzed reaction of  $[B_{12}H_{11}]^{2-}$  with picolinamide.<sup>367</sup> The aliphatic iminols  $[B_{12}H_{11}NH=C(OH)R]^-$  ( $R = Me, Et$ ) were obtained by hydrolysis of the corresponding nitrilium derivatives of the *closo*-dodecaborate anion  $[B_{12}H_{11}N\equiv CR]^-$ ,<sup>357</sup> while  $[B_{12}H_{11}NH=C(OH)Pr]^-$  was prepared by the Pd-catalyzed reaction of  $[B_{12}H_{11}]^{2-}$  with butyramide.<sup>367</sup> The secondary amide derivatives  $[B_{12}H_{11}NMe=C(OH)R]^-$  ( $R = Me, Ph$ ) were prepared in the similar way.<sup>367</sup> Boronated amides of *meso*-tetra(4-carboxyphenyl)porphyrin<sup>268</sup> and protoporphyrin IX<sup>269</sup> were prepared by acylation of the amino derivative of the *closo*-dodecaborate anion.

The reaction of  $[B_{12}H_{11}NH_2]^{2-}$  with *p*-nitrophenyl(diphenylphosphoryl)acetate leads to the amide  $[B_{12}H_{11}NH_2C(O)CH_2P(O)Ph_2]^-$ , whereas the reaction with chlorodiphenylphosphine gives diphenylphosphinamide  $[B_{12}H_{11}NH(P(O)Ph_2)_2]^-$ .<sup>260</sup> The Pd-catalyzed reactions of the iodo derivative of the *closo*-dodecaborate anion  $[B_{12}H_{11}I]^{2-}$  with *p*-tolyl sulfonamide and sulfamide result in  $[B_{12}H_{11}NH_2SO_2-p-Tol]^-$  and  $[B_{12}H_{11}NH_2SO_2NH_2]^-$ , respectively.<sup>367</sup>

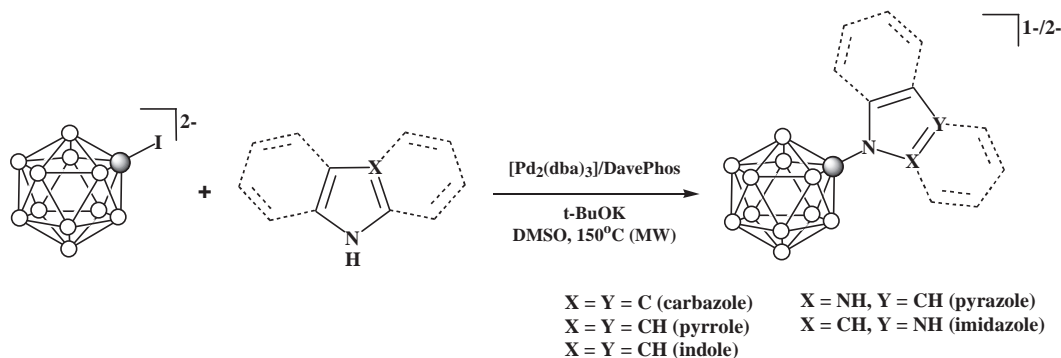
The reactions of  $[B_{12}H_{11}NH_2]^{2-}$  with aryl isocyanates  $ArNCO$  lead to boron-containing aryl ureas  $[B_{12}H_{11}NHC(O)NHAr]^{2-}$  ( $Ar = C_6H_5$ ,  $C_6H_4-4-Cl$ ).<sup>370</sup> The parent urea derivative  $[B_{12}H_{11}NH_2C(O)NH_2]^-$  was prepared by the Pd-catalyzed reaction of  $[B_{12}H_{11}I]^{2-}$  with urea.<sup>367</sup> The reaction of  $[B_{12}H_{11}NH_2]^{2-}$  with dimethylcarbamoyl chloride  $Me_2NCOCl$  in DMF leads to the urea  $[B_{12}H_{11}NHC(O)NMe_2]^{2-}$ ,<sup>371</sup> which, when heated in water, gives the isocyanate derivative of the *closo*-dodecaborate anion  $[B_{12}H_{11}NCO]^{2-}$ .<sup>370</sup>

The combination of *N,N*-dimethyl- or *N,N*-diethylformamide with 2,4,6-trimethylbenzoyl chloride produces the chlorinated iminium salt, which upon attack by  $[B_{12}H_{11}NH_2]^{2-}$  gives *N*-amidine  $[B_{12}H_{11}NH=CHNR_2]^-$  ( $R = Me, Et$ ).<sup>370</sup> The *N*-amidines  $[B_{12}H_{11}NH=C(Ar)NHR]^-$  can be prepared by activation of the arylamides  $[B_{12}H_{11}NHC(O)Ar]^{2-}$  by pentafluorobenzoyl chloride followed by the treatment with amines  $RNH_2$ .<sup>370</sup> A more convenient way to obtain the *N*-amidines  $[B_{12}H_{11}NH=C(Me)NRR']^-$  ( $R = H, R' = H, Me, i-Pr, n-Bu, Cy, Ph, CH_2CH_2OH$ ;  $R = R' = Me, Et$ ;  $RR' = (CH_2CH_2)_2O$ ) is the nucleophilic addition of ammonia or the corresponding amines to the activated  $-C\equiv N^+$ -triple bond of the acetonitrilium derivative of the *closo*-dodecaborate anion  $[B_{12}H_{11}N\equiv CMe]^-$  (Scheme 5).<sup>356,357</sup> This approach can be also used for synthesis of boronated aminoacids and peptides.<sup>372</sup>

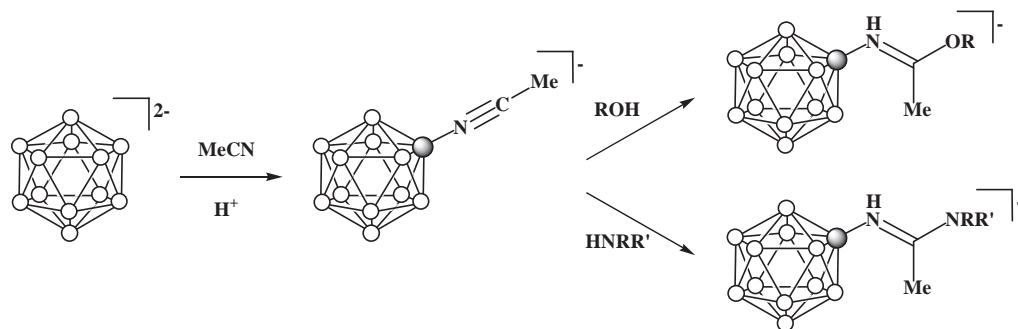
The nucleophilic addition of alcohols to the activated  $-C\equiv N^+$ -triple bond of the acetonitrilium derivative  $[B_{12}H_{11}N\equiv CMe]^-$  results in the corresponding imidates  $[B_{12}H_{11}NH=C(Me)OR]^-$  ( $R = Me, Et, i-Pr$ ) (Scheme 5).<sup>357</sup>

The reactions of the amino derivative of the *closo*-dodecaborate anion  $[B_{12}H_{11}NH_2]^{2-}$  with carbodiimides  $RN=C=NR'$  ( $R = Et, R' = (CH_2)_3NMe_2$ ;  $R = R' = (CH_2)_3NMe_2$ ;  $R = R' = cycloC_6H_{11}$ ) lead to the corresponding guanidinium derivatives  $[B_{12}H_{11}NHC(=NHR)NHR']^-$ .<sup>369</sup>

The reactions of the amino derivative of the *closo*-dodecaborate anion with aromatic and vinyl aldehydes lead to the formation of imines  $[B_{12}H_{11}NH=CHR]^-$  ( $R = C_6H_5, C_6H_4-2-OMe, C_6H_4-4-OMe, C_6H_4-4-SMe, C_6H_4-4-NMe_2, C_6H_4-4-NHCOMe, C_6H_4-4-CN,$



Scheme 4



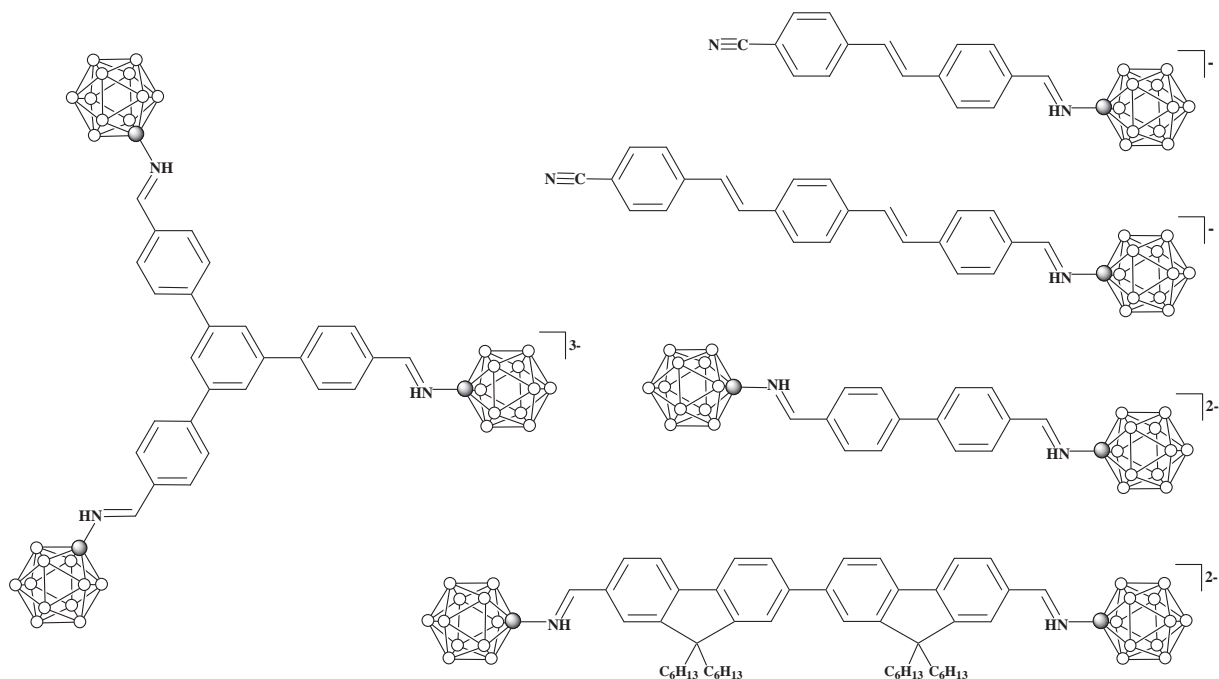
Scheme 5

C<sub>6</sub>H<sub>4</sub>-4-Br, C<sub>6</sub>H<sub>4</sub>-4-Cl, C<sub>6</sub>H<sub>3</sub>-3,4-O<sub>2</sub>CH<sub>2</sub>, 1-C<sub>10</sub>H<sub>7</sub>, 2-C<sub>10</sub>H<sub>7</sub>, CH=CHMe, CH=CHPh).<sup>365</sup> This approach was used to synthesize of a series of  $\pi$ -conjugated systems incorporating *closo*-dodecaborate clusters (Scheme 6).<sup>373–375</sup>

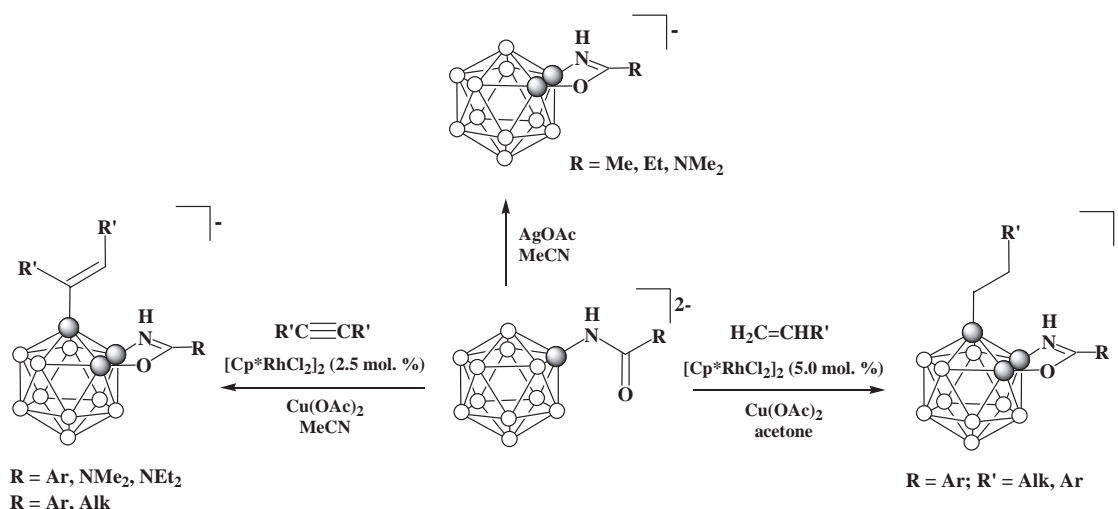
The treatment of amides [B<sub>12</sub>H<sub>11</sub>NHC(O)R]<sup>2-</sup> or [B<sub>12</sub>H<sub>11</sub>NHC(O)NMe<sub>2</sub>]<sup>2-</sup> with AgOAc in acetonitrile leads to the closure of the five-membered BNCOB diboraoxazole ring with the formation of [1,2- $\mu$ -NH=C(R)O-B<sub>12</sub>H<sub>10</sub>]<sup>-</sup> (R = Me, Et, NMe<sub>2</sub>) (Scheme 7).<sup>357,371</sup>

The reaction of the *closo*-dodecaborate based amides [B<sub>12</sub>H<sub>11</sub>NHC(O)Ar]<sup>2-</sup> or ureas [B<sub>12</sub>H<sub>11</sub>NHC(O)NR<sub>2</sub>]<sup>2-</sup> with diaryl- or dialkylacetylenes in the presence of Cu(OAc)<sub>2</sub> and catalytic amount of [Cp\*RhCl<sub>2</sub>]<sub>2</sub> in acetonitrile leads to B-H activation of the boron cage with the insertion of an olefin, as well as to the closure of the five-membered BNCOB diboraoxazole ring, giving [1,2- $\mu$ -NH=C(R)O-B<sub>12</sub>H<sub>9</sub>-3-C(R')=CH(R')]<sup>-</sup> (Scheme 7).<sup>371,376</sup> In a similar way, the reactions of the *closo*-dodecaborate based amides [B<sub>12</sub>H<sub>11</sub>NHC(O)Ar]<sup>2-</sup> with terminal olefines R-CH=CH<sub>2</sub> in acetone in the presence of catalytic amount of [Cp\*RhCl<sub>2</sub>]<sub>2</sub> and Cu(OAc)<sub>2</sub> result in the insertion of an alkane and the closure of the five-membered BNCOB diboraoxazole ring, leading to [1,2- $\mu$ -NH=C(Ar)O-B<sub>12</sub>H<sub>9</sub>-3-CH<sub>2</sub>CH<sub>2</sub>R]<sup>-</sup> (Scheme 7).<sup>376</sup> The reactions proceed through the formation of the rhodium complex [Cp\*Rh(B<sub>12</sub>H<sub>11</sub>NHC(O)R- $\kappa^3$ -O,H,H)], in which the metal atom is coordinated by two BH groups of the *closo*-dodecaborate anion (Fig. 9).<sup>371,376</sup>

The perfluorinated ammonium derivative [B<sub>12</sub>F<sub>11</sub>NH<sub>3</sub>]<sup>-</sup> was prepared by the reaction of [B<sub>12</sub>H<sub>11</sub>NH<sub>3</sub>]<sup>-</sup> with gaseous fluorine in liquid hydrogen fluoride<sup>377</sup> or acetonitrile.<sup>169</sup> Alkylation of [B<sub>12</sub>F<sub>11</sub>NH<sub>3</sub>]<sup>-</sup> with Me<sub>2</sub>SO<sub>4</sub> or C<sub>12</sub>H<sub>25</sub>Br in aqueous KOH result in the corresponding perfluorinated trialkylammonium derivatives [B<sub>12</sub>F<sub>11</sub>NR<sub>3</sub>]<sup>-</sup> (R = CH<sub>3</sub>, C<sub>12</sub>H<sub>25</sub>).<sup>377</sup> The perchlorinated ammonium derivative [B<sub>12</sub>Cl<sub>11</sub>NH<sub>3</sub>]<sup>-</sup> was prepared by heating [B<sub>12</sub>H<sub>11</sub>NH<sub>3</sub>]<sup>-</sup> in SbCl<sub>5</sub> at 190 °C<sup>378</sup> or by the reaction of [B<sub>12</sub>H<sub>11</sub>NH<sub>3</sub>]<sup>-</sup> with gaseous chlorine in aqueous solution at 300 °C.<sup>379</sup> Alternatively, the perchlorinated ammonium derivative can be prepared by the



Scheme 6

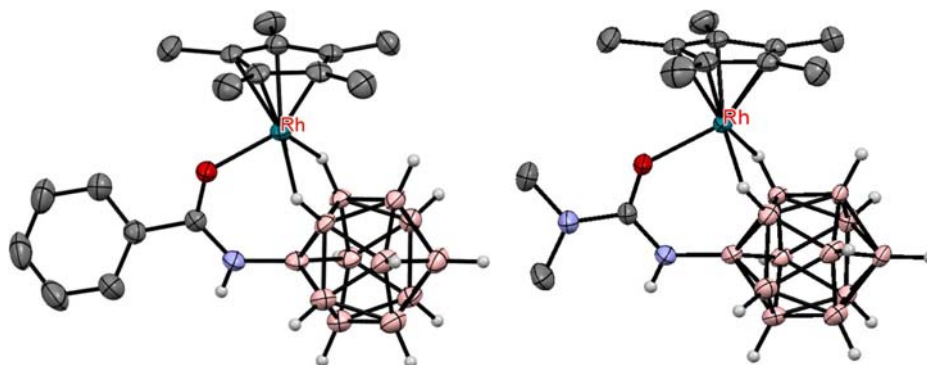


Scheme 7

reaction of the parent ammonium derivative with  $\text{SO}_2\text{Cl}_2$  in refluxing acetonitrile.<sup>271,380</sup> Methylation of  $[\text{B}_{12}\text{Cl}_{11}\text{NH}_3]^-$  with  $\text{MeI}$  or  $\text{Me}_2\text{SO}_4$  in alkaline aqueous solution results in the trimethylammonium derivative  $[\text{B}_{12}\text{Cl}_{11}\text{NMe}_3]^-$ .<sup>271,378,380</sup> Surprisingly, the alkylation of  $[\text{B}_{12}\text{Cl}_{11}\text{NH}_3]^-$  with butyl iodide in acetonitrile in the presence of  $\text{KOH}$  alkaline aqueous solution results in the mono-alkylamino derivative  $[\text{B}_{12}\text{Cl}_{11}\text{NH}_2\text{Bu}]^-$ , which on the treatment with  $\text{MeI}$  gives  $[\text{B}_{12}\text{Cl}_{11}\text{NHBuMe}]^-$ .<sup>363</sup> The hexachlorinated tripropylammonium *closo*-dodecaborate  $[\text{B}_{12}\text{H}_5\text{Cl}_6\text{NPr}_3]^-$  was prepared by the chlorination of  $[\text{B}_{12}\text{H}_{11}\text{NPr}_3]^-$  with  $\text{Cl}_2$ <sup>363</sup> or  $\text{SOCl}_2$ <sup>380</sup> in acetonitrile. The last approach was used for synthesis of  $[\text{B}_{12}\text{H}_5\text{Cl}_6\text{NBu}_3]^-$  and  $[\text{B}_{12}\text{H}_5\text{Cl}_6\text{NHex}_3]^-$ .<sup>364</sup> The perbrominated ammonium derivative  $[\text{B}_{12}\text{Br}_{11}\text{NH}_3]^-$  was prepared by the reaction of  $[\text{B}_{12}\text{H}_{11}\text{NH}_3]^-$  with bromine in aqueous solution at  $300^\circ\text{C}$ .<sup>379</sup> The reaction of  $[\text{B}_{12}\text{Br}_{11}\text{NH}_3]^-$  with epibromohydrin in THF in the presence of  $\text{NaH}$  leads to the corresponding alkylammonium derivative  $[\text{B}_{12}\text{Br}_{11}\text{NH}_2\text{CH}_2\text{CH}(\text{Me})\text{OH}]^-$ , while the reaction with ethylene oxide unexpectedly results in the hydroxylammonium derivative  $[\text{B}_{12}\text{Br}_{11}\text{NH}_2\text{OH}]^-$ .<sup>379</sup> The similar hydroxylammonium derivative  $[\text{B}_{12}\text{H}_{11}\text{NH}_2\text{OH}]^-$  was obtained by the reaction of  $[\text{B}_{12}\text{H}_{11}\text{NH}_3]^-$  with *t*-BuOOH.<sup>213</sup> The hexabrominated trialkylammonium *closo*-dodecaborates  $[\text{B}_{12}\text{H}_5\text{Br}_6\text{NR}_3]^-$  ( $R = \text{C}_2\text{H}_5, \text{C}_3\text{H}_7, \text{C}_4\text{H}_9, \text{C}_5\text{H}_{11}$ ) were prepared by the treatment of  $[\text{B}_{12}\text{H}_{11}\text{NR}_3]^-$  with *N*-bromo succinimide in acetonitrile.<sup>363</sup> The periodinated ammonium derivative  $[\text{B}_{12}\text{I}_{11}\text{NH}_3]^-$  was prepared by the reaction of  $[\text{B}_{12}\text{H}_{11}\text{NH}_3]^-$  with  $\text{ICl}$  in 1,2-dichloroethane at  $300^\circ\text{C}$ .<sup>379</sup> Like the perhalogenated salts of the *closo*-dodecaborate and *carba-closo*-dodecaborate anions, the  $[\text{B}_{12}\text{Cl}_{11}\text{NMe}_3]^-$  anion can be considered as a weakly coordinating anion.<sup>378,380–382</sup>

The perchlorinated ammonium derivative  $[\text{B}_{12}\text{Cl}_{11}\text{NMe}_3]^-$  undergoes one-electron reversible oxidation with  $\text{AsF}_5$  in liquid  $\text{SO}_2$  leading to the formation of the *hypercloso*- $[\text{B}_{12}\text{Cl}_{11}\text{NMe}_3]^-$  radical anion, which is a strong oxidizing agent capable of oxidizing hexabromobenzene to the corresponding cation and elemental iodine to the  $[\text{I}_5]^+$  cation.<sup>383</sup> The oxidation of  $[\text{B}_{12}\text{X}_{11}\text{NH}_3]^-$  ( $X = \text{F, Cl, Br, I}$ ) with hydrogen peroxide in an alkaline solution results in the corresponding perhalogenated nitro *closo*-dodecaborates  $[\text{B}_{12}\text{X}_{11}\text{NO}_2]^{2-}$ .<sup>384</sup>

Heating the ammonium derivative  $[\text{B}_{12}\text{H}_{11}\text{NH}_3]^-$  in 30% hydrogen peroxide leads to  $[\text{B}_{12}(\text{OH})_{11}\text{NH}_3]^-$ , which, when treated with  $\text{H}_2\text{O}_2$  in an alkaline solution, gives the corresponding nitro derivative  $[\text{B}_{12}(\text{OH})_{11}\text{NO}_2]^{2-}$ . The latter compound is a useful



**Fig. 9** Crystal molecular structures of  $[\text{Cp}^*\text{Rh}(\text{B}_{12}\text{H}_{11}\text{NHC}(\text{O})\text{Ph}-\kappa^3\text{-O,H,H})]$  (left) and  $[\text{Cp}^*\text{Rh}(\text{B}_{12}\text{H}_{11}\text{NHC}(\text{O})\text{NMe}_2-\kappa^3\text{-O,H,H})]$  (right). Hydrogen atoms of organic substituents and ligands are removed for clarity.

synthon for the synthesis of vertex-differentiated derivatives of the *closo*-dodecaborate anion by acylation of  $[\text{B}_{12}(\text{OH})_{11}\text{NO}_2]^{2-}$ , followed by the reduction of the nitro group to the amine one and its acylation to form  $[\text{B}_{12}(\text{OC}(\text{O})\text{R})_{11}\text{NHC}(\text{O})\text{R}']^{2-}$ .<sup>385</sup>

A complete set of disubstituted ammonium derivatives of the *closo*-dodecaborate anion 1,2-, 1,7- and 1,12- $\text{B}_{12}\text{H}_{10}(\text{NH}_3)_2$  and their perfluorinated analogues 1,2-, 1,7- and 1,12- $\text{B}_{12}\text{F}_{10}(\text{NH}_3)_2$  was obtained by the reaction in of the parent *closo*-dodecaborate  $[\text{B}_{12}\text{H}_{12}]^{2-}$  with hydroxylamine-*O*-sulfonic acid followed by fluorination with  $\text{F}_2$  in acetonitrile. The isomers were separated by column chromatography and characterized by multi-nuclear NMR and single crystal X-ray diffraction.<sup>386</sup>

#### 1.16.2.1.7 Derivatives with B–P bonds

The triphenylphosphonium derivative of the *closo*-dodecaborate anion  $[\text{B}_{12}\text{H}_{11}\text{PPh}_3]^-$  was prepared by the reaction of the iodo derivative  $[\text{B}_{12}\text{H}_{11}\text{I}]^{2-}$  with  $[(\text{Ph}_3\text{P})_4\text{Pd}]$  in THF in the presence of  $\text{Na}_2\text{CO}_3$ .<sup>387</sup> The reaction of the parent *closo*-dodecaborate  $[\text{B}_{12}\text{H}_{12}]^{2-}$  with  $[(\text{PhMe}_2\text{P})_2\text{PdCl}_2]$  in THF in the presence of  $\text{NaBH}_4$  lead to a mixture of  $[\text{B}_{12}\text{H}_{11}\text{PMe}_2\text{Ph}]^-$ , 1,7- and 1,12- $\text{B}_{12}\text{H}_{10}(\text{PMe}_2\text{Ph})_2$ .<sup>388,389</sup> A series of phosphonium derivatives  $[\text{B}_{12}\text{H}_{11}\text{PPh}_x\text{R}_y]^-$  ( $\text{R} = \text{Me}$ ,  $x = 2$ ,  $y = 1$ ;  $\text{R} = \text{Me}$ ,  $x = 1$ ,  $y = 2$ ;  $\text{R} = \text{Et}$ ,  $x = 2$ ,  $y = 1$ ) was obtained by microwave heating of the corresponding alkyltriphenyl- and dialkyldiphenylphosphonium salts of the *closo*-dodecaborate anion in acetonitrile at 180 °C.<sup>390</sup>

#### 1.16.2.1.8 Derivatives with B–C bonds

The preparation and transformation of carbonyl derivatives of the *closo*-dodecaborate anion were discussed in detail in the early review.<sup>21</sup> Later, a series of boronated esters  $[\text{B}_{12}\text{H}_{11}\text{COOR}]^{2-}$  ( $\text{R} = \text{Me}$ , *i*-Pr, *t*-Bu) and amides  $[\text{B}_{12}\text{H}_{11}\text{CONR}'\text{R}'' ]^{2-}$  ( $\text{R}' = \text{H}$ ,  $\text{R}'' = \text{Bu}$ ;  $\text{R}' = \text{R}'' = \text{Bu}$ ) were obtained by reactions of the carbonyl derivative  $[\text{B}_{12}\text{H}_{11}\text{CO}]^-$  with alcohols and amines, respectively.<sup>391</sup>

The possibility of synthesis of alkyl and aryl derivatives of the *closo*-dodecaborate anion  $[\text{B}_{12}\text{H}_{11}\text{R}]^{2-}$  ( $\text{R} = \text{CH}_3$ ,  $\text{C}_{18}\text{H}_{37}$ ,  $\text{C}_6\text{H}_5$ ) via the Pd-catalyzed cross coupling reactions of its iodo derivative  $[\text{B}_{12}\text{H}_{11}\text{I}]^{2-}$  with the corresponding Grignard reagents was earlier demonstrated.<sup>392</sup> The synthesis of the methyl derivative  $[\text{B}_{12}\text{H}_{11}\text{Me}]^{2-}$  by the reaction of  $[\text{B}_{12}\text{H}_{11}\text{I}]^{2-}$  with refluxing  $\text{AlMe}_3$  was described.<sup>393</sup> Later, the ethynyl derivative  $[\text{B}_{12}\text{H}_{11}\text{C}\equiv\text{CH}]^{2-}$  was prepared by the microwave-assisted cross-coupling reaction of the iodo derivative  $[\text{B}_{12}\text{H}_{11}\text{I}]^{2-}$  with  $\text{Me}_3\text{SiC}\equiv\text{CMgBr}$  in the presence of catalytic amount of  $[(\text{Ph}_3\text{P})_2\text{PdCl}_2]$  followed by removal of the  $\text{Me}_3\text{Si}$  protecting group by alkaline hydrolysis.<sup>394</sup> The ferrocenylethynyl derivative of the *closo*-dodecaborate anion  $[(\text{B}_{12}\text{H}_{11}\text{C}\equiv\text{CC}_5\text{H}_4)\text{Fe}(\text{C}_5\text{H}_5)]^{2-}$  was synthesized in a similar way.<sup>395</sup>

The permethylated derivative  $[\text{B}_{12}\text{Me}_{12}]^{2-}$  was prepared by heating the parent *closo*-dodecaborate anion with trimethylaluminum and methyl iodide.<sup>393</sup> The permethylated derivative can be oxidized with cerium(IV) ammonium nitrate to give the air stable anion radical  $[\text{B}_{12}\text{Me}_{12}]^{\bullet-}$ , which can be reversibly reduced with sodium tetrahydroborate.<sup>396</sup> The structures of  $(\text{Py}_2\text{CH}_2)[\text{B}_{12}\text{Me}_{12}]^{393}$  and  $(\text{PPN})[\text{B}_{12}\text{Me}_{12}]^{396}$  were determined by single crystal X-ray diffraction.

The halogen atoms in  $[\text{B}_{12}\text{X}_{12}]^{2-}$  ( $\text{X} = \text{Cl}$ ,  $\text{Br}$ ,  $\text{I}$ ) under UV-irradiation in the presence of cyanide can be replaced by the cyano groups.<sup>397,398</sup> The percyano derivative  $[\text{B}_{12}(\text{CN})_{12}]^{2-}$  was also prepared by the microwave-assisted reaction of the periodo derivative  $[\text{B}_{12}\text{I}_{12}]^{2-}$  with  $\text{CuCN}$  in the presence of catalytic amount of  $\text{PdCl}_2$ .<sup>399</sup> Due to the strong electron-donating effect of the *closo*-dodecaborate cage, the cyano groups in  $[\text{B}_{12}(\text{CN})_{12}]^{2-}$  can act as donors in complexes with transition metal atoms (Fig. 10).<sup>399</sup>

#### 1.16.2.1.9 Oxidation reactions

The electrochemical oxidation of the *closo*-dodecaborate anion in acetonitrile at +1.5 V vs. SCE results in the formation of the dimeric anion  $[\text{B}_{24}\text{H}_{23}]^{3-}$  in which two boron icosahedra are linked by a B–H–B bridge (Fig. 11).<sup>400,401</sup>

The formation of the  $[\text{B}_{24}\text{H}_{23}]^{3-}$  anion was also observed in the thermolysis of the hydrated acid  $(\text{H}_3\text{O})_2[\text{B}_{12}\text{H}_{12}] \cdot n\text{H}_2\text{O}$ <sup>402</sup> and in the oxidation of a concentrated aqueous solution of  $(\text{H}_3\text{O})_2[\text{B}_{12}\text{H}_{12}]$  with oxalic acid.<sup>403</sup> The formation of the trimeric

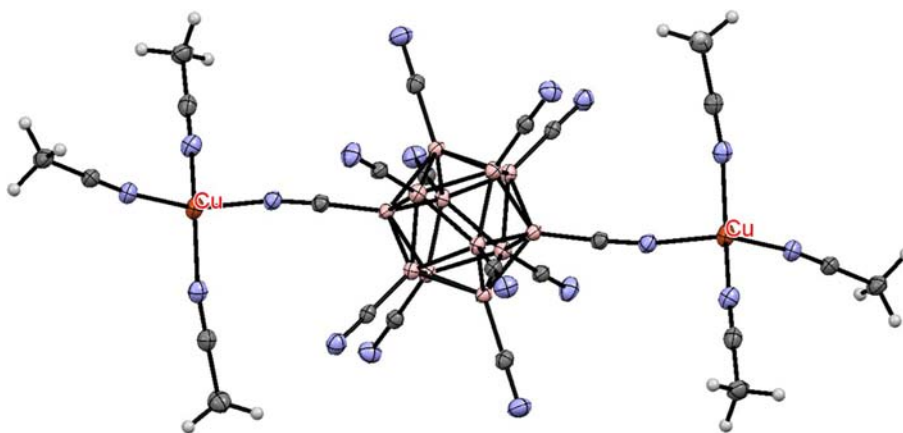
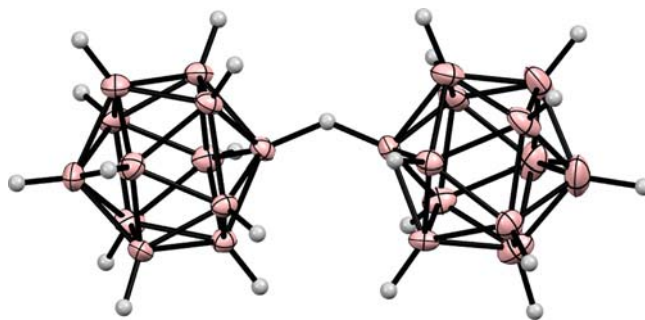


Fig. 10 Crystal molecular structure of  $[\text{1,12-(MeCN)}_3\text{Cu}]_2[\mu\text{-B}_{12}(\text{CN})_{12}]$ .





**Fig. 11** Crystal molecular structure of the  $[B_{24}H_{23}]^{3-}$  anion.

$[B_{36}H_{34}]^{4-}$  and tetrameric  $[B_{48}H_{45}]^{5-}$  anions was reported as well.<sup>402,403</sup> Complex  $[Au_9(PPh_3)_8][B_{24}H_{23}]$  was prepared by the reaction of  $Ag_2[B_{12}H_{12}]$  with  $[(Ph_3P)AuCl]$  in acetonitrile-benzene solution.<sup>404,405</sup>

The controlled oxidation of the *closo*-dodecaborate anion with sulfuric acid or hydrogen peroxide leads to the formation of hydroxy derivatives with various substitution degree up to the perhydroxy derivative  $[B_{12}(OH)_{12}]^{2-}$  (See Section 1.16.2.1.1).<sup>272–274,406</sup> It was reported that in the presence of platinum or rhodium metals the *closo*-dodecaborate anion is easily hydrolyzed to boric acid.<sup>407,408</sup> It is assumed that the process proceeds through the formation of the 1-oxa-*nido*-dodecaborate anion  $[OB_{11}H_{12}]^-$ , which was isolated on the oxidation of  $K_2[B_{12}H_{12}]$  with  $K_2S_2O_8$  in the presence of  $AgNO_3$  in an acidic aqueous solution.<sup>409</sup>

### 1.16.2.2 *closo*-Undecaborate anion $[B_{11}H_{11}]^{2-}$

Despite the fact that the *closo*-undecaborate anion  $[B_{11}H_{11}]^{2-}$  was first synthesized in the mid-1960s<sup>410</sup> and is quite accessible, its chemistry has been little studied compared to the *closo*-decaborate and *closo*-dodecaborate anions. This is largely due to the higher reactivity of the *closo*-undecaborate anion, which results from its structure, an octadecahedron with one of the vertices occupied by a hexacoordinated (with respect to boron) boron atom. This leads to a weakening of part of the boron–boron bonds in which this atom participates, and the  $[B_{11}H_{11}]^{2-}$  anion is often regarded as quasi-*closo*-polyhedral anion. As a result, the *closo*-undecaborate anion can be easily opened to the *nido*-undecaborate anion, which can exist in the form of several protonated forms, the most stable of which is the tetradecahydro-*nido*-undecaborate anion  $[B_{11}H_{14}]^-$ . All this complicates and often leads to the unpredictability of their chemical behavior. The current state of the chemistry of the *closo*-undecaborate anion  $[B_{11}H_{11}]^{2-}$  has recently been reviewed.<sup>411</sup>

### 1.16.2.3 *closo*-Decaborate anion $[B_{10}H_{10}]^{2-}$

#### 1.16.2.3.1 General aspects

The decahydro-*closo*-decaborate anion  $[B_{10}H_{10}]^{2-}$ , which was synthesized for the first time in 1959,<sup>412</sup> was the first member of the *closo*-polyhedral boron hydride  $[B_nH_n]^{2-}$  family to be discovered. In general, the chemistry of the *closo*-decaborate anion is comparable in terms of its knowledge with the chemistry of the *closo*-dodecaborate anion  $[B_{12}H_{12}]^{2-}$ . The first 50 years of the chemistry of the *closo*-decaborate anion were reviewed by Sivaev et al.,<sup>413</sup> Zhizhin et al.<sup>414</sup> and Nie et al.<sup>415</sup> Selected aspects of the current state of research in this field are discussed in the recent minireview by Naoufal et al.<sup>416</sup> Nevertheless, we considered it necessary to present here the main directions in the development of the chemistry of the *closo*-dodecaborate anion over the past 10 years, relying (if necessary) on the earlier published exhaustive review.<sup>413</sup>

There are two general approaches to the synthesis of the decahydro-*closo*decaborate anion. The first one is based on a closure of the *nido*-decaborane skeleton. The preparative syntheses include reaction of decaborane with triethylamine in refluxing benzene giving triethylammonium *closo*-decaborate  $(Et_3NH)_2[B_{10}H_{10}]$  in 92% yield.<sup>417</sup> The usefulness of this method is severely limited due to the toxicity of decaborane and its high cost. Alternative approach is based on controlled solid state pyrolysis of easily available tetraethylammonium tetrahydroborate resulting in tetraethylammonium *closo*-decaborate  $(Et_4N)_2[B_{10}H_{10}]$  in moderate yields.<sup>413</sup>

The increased interest in the use of salts of polyhedral boron hydrides as solid electrolytes stimulated the synthesis and study of the physical properties and crystal structure of anhydrous *closo*-decaborates of alkali and alkaline earth metals and ammonium, as well as their crystalline hydrates and ammoniates.<sup>58,75,76,79,418–430</sup>

In addition, the preparation and crystal structure of simple salts and crystalline hydrates of *closo*-dodecaborates of some other non-transition metals such as  $Tl_2[B_{10}H_{10}]$ ,<sup>91,431</sup>  $(Sn(H_2O)_3)[B_{10}H_{10}] \cdot 3H_2O$ ,<sup>92</sup>  $[Pb(H_2O)_3]_2[Pb[B_{10}H_{10}]_3 \cdot 5.5H_2O]$ ,<sup>432</sup> and  $[Pb(H_2O)_3][Pb[B_{10}H_{10}]_2 \cdot 1.5H_2O]$ <sup>432</sup> were described. In the structures of all these salts, M–H–B interactions between the metal atom and the *closo*-decaborate anion are observed.

Anhydrous *closo*-dodecaborates of copper  $Cu_2[B_{10}H_{10}]$ <sup>431,433,434</sup> and silver  $Ag_2[B_{10}H_{10}]$ <sup>435</sup> were found to form 3D polymeric structures due to M–H–B interactions between the metal atom and the *closo*-decaborate anion. Copper and silver are also capable

to form double *closo*-decaborate salts (Cat) $\{M[B_{10}H_{10}]\}$  ( $M = Cu, Ag$ ;  $Cat^+ = Cs^+, R_2NH_2^+, R_3NH^+, \text{ and } R_4N^+$  ( $R = Me, Et, Pr, Bu$ ),  $Ph_4P^+, Ph_4As^+$ , etc.).<sup>98,435–440</sup>

Compared to the *closo*-dodecaborate anion,  $[B_{10}H_{10}]^{2-}$  is a stronger Pearson base and can be coordinated by metals that are soft and medium Pearson acids, such as  $Cu^+, Ag^+, Pb^{2+}, Cd^{2+}$  and  $Zn^{2+}$ .<sup>101,441–446</sup> In the absence of strong ligands, other transition metals usually form crystalline hydrates<sup>429,447</sup> or solvates with the *closo*-decaborate anion.<sup>113</sup> Various aspects of the coordination chemistry of the *closo*-decaborate anion are considered in several recent reviews.<sup>101,114–116,448</sup> The coordination chemistry of substituted derivatives of the *closo*-decaborate anion will be discussed below in the relevant sections.

A significant part of the research interest in simple and complex salts of the *closo*-dodecaborate anion is due to the ability of polyhedral boron hydrides to enhance burning rates of traditional rocket propellants.<sup>117,118</sup> In addition to studying the effect of simple salts of the *closo*-dodecaborate anion, such as  $K_2[B_{10}H_{10}]$  and  $(Et_4N)_2[B_{10}H_{10}]$ ,<sup>119,449–452</sup> on the combustion of traditional fuels, a number of salts with various nitrogen-rich cations including guanidinium,<sup>127</sup> imidazolium,<sup>132</sup> triazolium,<sup>453</sup> and other<sup>142,143,454–459</sup> were synthesized.

Unlike the *closo*-dodecaborate anion, which has an icosahedral structure, the  $[B_{10}H_{10}]^{2-}$  anion has a bicapped antiprism structure (Fig. 12). This results in a large difference in the electron density on the apical (B(1) and B(10)) and equatorial (B(2)–B(9)) vertices, which leads to the use of different types of reaction for their functionalization.

The *closo*-decaborate anion is much less hydrophobic than the *closo*-dodecaborate anion<sup>145</sup> and is strongly hydrated in aqueous solutions. It is assumed that water molecules are hydrogen bonded predominantly to the apical vertices of the  $[B_{10}H_{10}]^{2-}$  anion.<sup>460</sup> Under acidic conditions there is rapid proton exchange between the *closo*-decaborate anion and water. Using catalytic amount of DCl in  $D_2O$  it was found that the H-D exchange at the apical vertices of the  $[B_{10}H_{10}]^{2-}$  anion proceeds five times faster than at the equatorial vertices and 330-fold faster than in  $[B_{12}H_{12}]^{2-}$ .<sup>461</sup> The selectively deuterated *closo*-decaborate anion  $[1,10-B_{10}H_8D_2]^{2-}$  can be prepared by the reaction of  $[B_{10}H_{10}]^{2-}$  with methanol- $d_4$  at room temperature.<sup>462</sup>

Similarly to the *closo*-dodecaborate anion, in aqueous solution the acid form of the *closo*-decaborate anion exhibits properties of strong acid comparable to sulfuric acid and can be isolated in the solid state as  $(H_3O)_2[B_{10}H_{10}] \cdot 2H_2O$ .<sup>461</sup> In aprotic organic solvents the *closo*-decaborate anion reacts with strong acids with formation of the protonated form  $[B_{10}H_{11}]^-$ . The single crystal X-ray diffraction study of  $(Ph_3PBn)[B_{10}H_{11}]$  revealed that the “extra” hydrogen atom H(\*) asymmetrically caps a polar face of the  $B_{10}$ -cluster (Fig. 13). In solution, the migration of the “extra” hydrogen atom H(\*) over the neighboring polar faces is complicated by the exchange process between the H(1) and H(\*) atoms. The fluxional behavior of H(1) and H(\*) can be stopped at low temperatures ( $-90^\circ C$ ).<sup>463</sup>

The results obtained indicate that electrophilic substitution reactions in the *closo*-decaborate anion should lead to mixtures of apically and equatorially substituted products, while reactions proceeding according to the mechanism of electrophilically induced nucleophilic substitution will proceed with the formation of exclusively equatorially substituted products.

### 1.16.2.3.2 Halogen derivatives

The halogenation reactions of the *closo*-decaborate anion were discussed in detail in the previous review.<sup>413</sup> Briefly, the halogenation of  $[B_{10}H_{10}]^{2-}$  with the halogens  $X_2$  under ambient conditions results in mixtures of derivatives with various substitution degrees  $[B_{10}H_{10-n}X_n]^{2-}$  ( $X = Cl, Br, n = 1–6$ ;  $X = I, n = 1–4$ ).<sup>150,464–467</sup> The separation of the mixture of iodo derivatives  $[B_{10}H_{10-n}I_n]^{2-}$  by electrophoresis revealed that the initial attack of iodine leads to an almost statistical distribution of 1- and 2-iodo derivatives.<sup>465</sup> The equatorially substituted halogen derivatives  $[2-B_{10}H_9X]^{2-}$  ( $X = Cl, Br$ ) were prepared by the reactions of the parent *closo*-decaborate with trityl chloride, 1-adamantyl bromide or *tert*-butyl bromide in the corresponding 1,2-dihalogenethanes under reflux conditions, proceeding by the EINS mechanism.<sup>468</sup> The 2-chloro derivative  $[2-B_{10}H_9Cl]^{2-}$  can be also prepared by the reaction of the parent *closo*-decaborate with 1,2-dichloroethane in the presence of hydrogen halides at  $40^\circ C$ , while the reaction at  $60^\circ C$  gives mainly 2,7-dichloro derivative  $[2,7-B_{10}H_8Cl_2]^{2-}$ .<sup>469</sup> The convenient method for the synthesis of the apically substituted iodo derivatives of the *closo*-decaborate anion has been proposed. The reaction of  $[B_{10}H_{10}]^{2-}$  with phenyliodonium diacetate  $PhI(OAc)_2$  in aqueous acetic acid at  $0^\circ C$  leads to the mono- and di(phenyliodonium) derivatives  $[1-B_{10}H_9I]^-$  and  $[1,10-B_{10}H_8(I)Ph]^{2-}$  depending on the reagent ratio.<sup>210</sup> The same approach can be applied to some substituted derivatives of the *closo*-decaborate anion.<sup>210,470</sup> The treatment of the phenyliodonium derivatives with *n*-BuLi in THF at  $0^\circ C$  results in  $[1-B_{10}H_9]^{2-}$  and  $[1,10-B_{10}H_8I]^{2-}$ , respectively.<sup>471</sup>

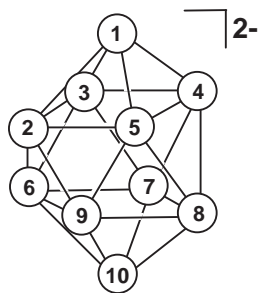
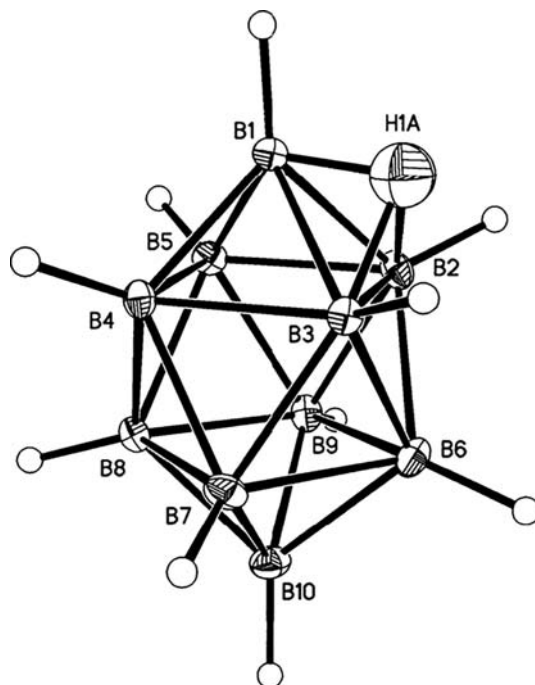


Fig. 12 Idealized structure and numbering of atoms in the *closo*-decaborate anion  $[B_{10}H_{10}]^{2-}$ .



**Fig. 13** Structure of the  $[B_{10}H_{11}]^{2-}$  anion at 150 K. Reprinted with permission from Shore, S. G.; Hamilton, E. J. M.; Bridges, A. N.; Bausch, J.; Krause-Bauer, J. A.; Dou, D.; Liu, J.; Liu, S.; Du, B.; Hall, H.; Meyers, E. A.; Vermillion, K. E. *Inorg. Chem.* **2003**, *42*, 1175–1186. Copyright (2004) the American Chemical Society.

The perhalogenated derivatives of the *closo*-decaborate anion  $[B_{10}X_{10}]^{2-}$  ( $X = Cl, Br, I$ ) were synthesized by high-temperature reactions of the parent *closo*-decaborate with  $Cl_2$ ,  $Br_2$  and  $I_2$ , respectively, in aqueous solution.<sup>150,379,472</sup> Alternatively, the perbromo derivative  $[B_{10}Br_{10}]^{2-}$  can be obtained by the reaction of  $[B_{10}H_{10}]^{2-}$  with excess of bromine in refluxing ethanol,<sup>150,473</sup> whereas the period derivative  $[B_{10}I_{10}]^{2-}$  can be obtained via microwave-assisted iodination of the parent *closo*-decaborate with  $I_2$  in acetic acid at 220 °C.<sup>160</sup> It was found that the perchlorinated *closo*-decaborate anion  $[B_{10}Cl_{10}]^{2-}$  is formed by chlorination of the *closo*-undecaborate anion  $[B_{11}H_{11}]^{2-}$  with *N*-chlorosuccinimide or molecular chlorine in dichloromethane, which opens the way to its synthesis bypassing the parent *closo*-decaborate.<sup>474</sup> The synthesis and structure of various simple and complex salts have recently been reviewed.<sup>475</sup>

The perchloro and perbromo derivatives of the *closo*-decaborate anion  $[B_{10}X_{10}]^{2-}$  ( $X = Cl, Br$ ) undergo reversible electrochemical oxidation in acetonitrile to form the corresponding violet or black radical anions *hypercloso*- $[B_{10}X_{10}]^{\bullet-}$ .<sup>473,476</sup> The *hypercloso*- $[B_{10}Cl_{10}]^{\bullet-}$  radical anion can be obtained also by the chemical oxidation of  $[B_{10}Cl_{10}]^{2-}$  with  $Tl^{3+}$  in acetonitrile<sup>473</sup> or by their treatment with  $SO_2Cl_2$  in dichloromethane.<sup>476</sup> Lithium perchloro-*closo*-decaborate  $Li_2[B_{10}Cl_{10}]$  has been proposed as a component of electrolytes for lithium cells.<sup>472,477–479</sup> Recently, lithium periodo-*closo*-decaborate  $Li_2[B_{10}I_{10}]$  has demonstrated good potential for high-temperature solid-state battery applications.<sup>480</sup>

### 1.16.2.3.3 Derivatives with B–O bond

Similarly to the *closo*-dodecaborate anion  $[B_{12}H_{12}]^{2-}$ , the cyclic oxonium derivatives of the *closo*-decaborate anion  $[2-B_{10}H_9O(CH_2)_4]^-$ ,  $[2-B_{10}H_9O(CH_2)_5]^-$  and  $[2-B_{10}H_9O(CH_2CH_2)_2O]^-$  were prepared by the reaction the parent *closo*-decaborate with the corresponding cyclic ethers in the presence of Bronsted ( $HCl$ ,  $CF_3COOH$ ,  $CF_3SO_3H$ )<sup>481–483</sup> or Lewis acids ( $BF_3 \cdot OEt_2$ ,  $Ph_3CCl$ , 1-AdBr, *t*-BuBr, etc.).<sup>468,484,485</sup> Synthesis of disubstituted oxonium derivatives  $[2,7(8)-B_{10}H_8L_2]$  ( $L = O(CH_2)_4$ ,  $O(CH_2)_5$  and  $O(CH_2CH_2)_2O$ ) was also reported.<sup>468,485</sup>

The ring-opening of the oxonium derivatives with azide<sup>486</sup> and cyanide<sup>487</sup> anions has been described. The carboxylic acid  $[2-B_{10}H_9O(CH_2)_4COOH]^{2-}$  was obtained by alkaline hydrolysis of the corresponding nitrile.<sup>487</sup> The azido derivative  $[2-B_{10}H_9O(CH_2)_4N_3]^{2-}$  was used for the synthesis of boron-containing 1,2,3-triazoles through Cu-catalyzed [3 + 2] azide-alkyne cycloaddition reactions.<sup>488</sup> The amino derivatives  $[2-B_{10}H_9(OCH_2CH_2)_2NH_3]^-$  and  $[2-B_{10}H_9O(CH_2)_4NH_3]^-$  were prepared by the ring-opening of the corresponding oxonium derivatives with potassium phthalimide in DMF followed by deprotection with hydrazine hydrate.<sup>488</sup> Alternatively,  $[2-B_{10}H_9(OCH_2CH_2)_2NH_3]^-$  was obtained by the reaction of the 1,4-dioxane derivative of the *closo*-decaborate with ammonia in refluxing ethanol.<sup>489</sup> The ring-opening of the 1,4-dioxane derivative with various amines was also described.<sup>486,489,490</sup>

A series of boron containing carboxylic acids  $[2-B_{10}H_9(OCH_2CH_2)_2OC_6H_4-x-COOH]^-$  and  $[2-B_{10}H_9O(CH_2)_4OC_6H_4-x-COOH]^-$  ( $x = m$  and  $p$ ) were prepared by ring-opening of the corresponding oxonium derivatives with methyl esters of

hydroxybenzoic acids in acetonitrile in the presence of  $K_2CO_3$ , followed by acidic hydrolysis of the ester formed.<sup>487</sup> The use of unprotected hydroxybenzoic acids leads to the products of the simultaneous ring opening with hydroxy and carboxy groups.<sup>487</sup> The reactions of the cyclic oxonium derivatives with aminoacids (glycine, cysteine, serine, *p*-aminobenzoic acid) result in the corresponding products of ring-opening with carboxy group.<sup>491</sup> The boronated tyrosine derivatives  $[2-B_{10}H_9(OCH_2CH_2)_2OC_6H_4-p-CH_2CH(NH_3)COOH]^-$  and  $[2-B_{10}H_9O(CH_2)_4OC_6H_4-p-CH_2CH(NH_3)COOH]^-$  were prepared by the ring-opening of the corresponding cyclic oxonium derivatives with ethyl *N*-trifluoroacetyl-tyrosinate in the presence of  $K_2CO_3$ , followed by acid hydrolysis of protecting groups.<sup>225</sup> The ring-opening reactions of the 1,4-dioxane derivative of the *closo*-dodecaborate anion by various nucleophiles derived from organic *CH*-acids (acetylenes, diethyl malonate, ethyl acetoacetate, triethyl orthoformate, acetylacetone, malonitrile) were described.<sup>492</sup>

Acyclic oxonium derivatives  $(Bu_4N)[2-B_{10}H_9OR_2]$  ( $R = Et, i-Pr, Bu$ ) were prepared by heating the protonated *closo*-decaborate anion  $(Bu_4N)[B_{10}H_{11}]^-$  in mixtures of the corresponding ethers and dichloromethane at 80 °C. The treatment of this oxonium derivatives with hydrazine hydrate leads to the corresponding alkoxy derivatives  $[2-B_{10}H_9OR]^{2-}$ .<sup>493</sup>

Various methods for the preparation of hydroxy derivatives of the *closo*-decaborate anion  $[1-B_{10}H_9OH]^{2-}$  and  $[2-B_{10}H_9OH]^{2-}$  as well as their alkylation reactions were considered in detail in the previous review.<sup>413</sup>

Reaction of the *closo*-decaborate  $[B_{10}H_{10}]^{2-}$  with refluxing formic acid results in the mono- and di(formyloxy) derivatives  $[2-B_{10}H_9OC(O)H]^{2-}$  and  $[2,7(8)-B_{10}H_8(OC(O)H)_2]^{2-}$ .<sup>494</sup> The formyloxy derivative  $[Co(phen)_3][2-B_{10}H_9OC(O)H]$  was also obtained from the reaction of  $(Et_3NH)_2[B_{10}H_{10}]^{2-}$  with  $CoCl_2$  in *N,N*-dimethylformamide in the presence of 1,10-phenanthroline.<sup>495</sup> The dimethylformamide derivative  $[2-B_{10}H_9OCHNMe_2]^-$  was prepared by heating the parent *closo*-decaborate with DMF in the presence of trifluoroacetic acid.<sup>495</sup> Heating the parent *closo*-decaborate in acetic acid at 70 °C results in the formation of the acetoxy derivative  $[2-B_{10}H_9OAc]^{2-}$ ,<sup>495</sup> while the reaction at 120 °C leads to a mixture of  $[2,7(8)-B_{10}H_8(OAc)_2]^{2-}$  and  $[2,6(9)-\mu-MeCO_2-B_{10}H_8]^-$ .<sup>494,496,497</sup> It was found that  $[2,6(9)-\mu-MeCO_2-B_{10}H_8]^-$  is formed by heating the acetoxy derivative  $[2-B_{10}H_9OAc]^{2-}$  in boiling 1,4-dioxane.<sup>498</sup>  $(Ph_4P)[2,6(9)-\mu-MeCO_2-B_{10}H_8]$  was also obtained by the reaction of  $(Ph_4P)_2[B_{10}H_{10}]^{2-}$  with  $Pb(NO_3)_2$  in acetic acid.<sup>499</sup>

The hydroxy derivatives  $[2-B_{10}H_9OH]^{2-}$  and  $[2,7(8)-B_{10}H_8(OH)_2]^{2-}$  were obtained by treating the corresponding acetoxy derivatives with hydrazine hydrate,<sup>496</sup> whereas  $[2,7(8)-B_{10}H_8(OH)(OAc)]^{2-}$  was obtained by alkaline hydrolysis of  $[2,7(8)-B_{10}H_8(OAc)_2]^{2-}$  in aqueous ethanol.<sup>494</sup> In a similar way,  $[2,6(9)-B_{10}H_8(OH)(OAc)]^{2-}$  was prepared by alkaline hydrolysis of  $[2,6(9)-\mu-MeCO_2B_{10}H_8]^-$  in aqueous ethanol.<sup>494</sup> The lead complex  $\{(bipy)_2Pb[2,6(9)-B_{10}H_8(OH)(OAc)]\}$  was obtained from the reaction of  $(Ph_4P)[2,6(9)-\mu-MeCO_2B_{10}H_8]^-$  with  $Pb(NO_3)_2$  and 2,2'-bipyridine (bipy) in acetonitrile.<sup>494</sup> Alkylation of  $[2-B_{10}H_9OH]^{2-}$  and  $[2,7(8)-B_{10}H_8(OH)_2]^{2-}$  with dihalosilanes  $R_2SiCl_2$  ( $R = Me, t-Bu, Ph$ ) was described.<sup>500</sup>

The apically substituted dimethylformamide derivative  $[1,10-B_{10}H_8(OCHNMe_2)_2]$  was prepared by heating  $[1,10-B_{10}H_8(IPh)_2]$  in *N,N'*-dimethylformamide at 90 °C. The treatment of  $[1,10-B_{10}H_8(OCHNMe_2)_2]$  with  $(Bu_4N)OH$  in refluxing acetonitrile results in the formation of the diformate  $(Bu_4N)_2[1,10-B_{10}H_8(OC(O)H)_2]$ , which in turn is hydrolyzed with HCl in methanol giving the 1,10-dihydroxy derivative  $(Bu_4N)_2[1,10-B_{10}H_8(OH)_2]$ . In a similar way, the heating  $[1,10-B_{10}H_8(IPh)_2]$  in *N,N'*-dimethylacetamide at 100 °C produces  $[1,10-B_{10}H_8(OC(Me)NMe_2)_2]$  which on the treatment with  $[Bu_4N]OH$  in acetonitrile gives the diacetate  $(Bu_4N)_2[1,10-B_{10}H_8(OAc)_2]$ . The acylation of the 1,10-dihydroxy derivative with benzoyl chloride in THF in the presence of NaH leads to the corresponding diester  $(Bu_4N)_2[1,10-B_{10}H_8(OC(O)Ph)_2]$ .<sup>501</sup> The reaction of  $[1,10-B_{10}H_8(IPh)_2]$  with 1 equiv.  $(Et_4N)OAc$  in acetonitrile at 60 °C leads to  $(Et_4N)[1,10-B_{10}H_8(IPh)(OAc)]$ ,<sup>210</sup> which reacts with pyridine at 90 °C giving  $(Et_4N)[1,10-B_{10}H_8(Py)(OAc)]$ .<sup>470</sup>  $(Me_4N)[1,10-B_{10}H_8(Py)(OEt)]$  was obtained by heating of  $[1,10-B_{10}H_8(Py)(IPh)]$  in ethanol at 110 °C.<sup>470</sup>

#### 1.16.2.3.4 Derivatives with B–S bond

The 1-mercapto derivative of the *closo*-decaborate anion  $[1-B_{10}H_9SH]^{2-}$  was prepared by the reaction of the diazonium derivative  $[1-B_{10}H_9N_2]^-$  with *N,N'*-dimethylthioformamide followed by alkaline hydrolysis of the formed *S*-thioamide intermediate.<sup>502</sup> The 2-mercapto derivative  $[2-B_{10}H_9SH]^{2-}$  was prepared by the reaction of the parent *closo*-decaborate with *N,N,N',N'*-tetramethylthiourea in the presence of hydrochloric acid followed by alkaline hydrolysis of the corresponding *S*-thiourea.<sup>502</sup> Later, the synthesis of the 2-dimercapto derivative was described by the reaction of the protonated *closo*-dodecaborate  $[B_{10}H_{11}]^-$  with *N,N'*-dimethylthioformamide or *N,N,N',N'*-tetramethyl- and *N,N'*-diphenylthioureas followed by the treatment of the corresponding *S*-thioamide and *S*-thioureas with hydrazine in refluxing ethanol.<sup>503,504</sup> The reaction of  $[B_{10}H_{11}]^-$  with *N,N'*-ethylenethiourea unexpectedly leads directly to the mercapto derivative  $[2-B_{10}H_9SH]^{2-}$ .<sup>504</sup>

Methylation of the mercapto derivatives  $[1-B_{10}H_9SH]^{2-}$  and  $[2-B_{10}H_9SH]^{2-}$  with trimethylsulfonium iodide results in the corresponding dimethylsulfonium derivatives  $[1-B_{10}H_9SMe_2]^-$  and  $[2-B_{10}H_9SMe_2]^{2-}$ .<sup>502</sup> Syntheses of dimethylsulfonium derivatives of the *closo*-decaborate anion by the reaction of the parent anion with dimethylsulfoxide in acidic media were considered in detail in the previous review.<sup>413</sup> Alkylation of the mercapto derivative  $[2-B_{10}H_9SH]^{2-}$  with various alkyl halides in acetonitrile or *N,N'*-dimethylformamide in the presence of  $K_2CO_3$  at 80 °C–90 °C results in the corresponding dialkylsulfonium derivatives  $[2-B_{10}H_9SR_2]^-$  ( $R = C_3H_7, i-C_3H_7, C_4H_9, C_8H_{17}, C_{12}H_{25}, C_{18}H_{37}, CH_2CH=CH_2, CH_2C_6H_5$ ).<sup>503,505,506</sup> This approach was used for synthesis of dialkylsulfonium derivatives bearing various functional groups  $[2-B_{10}H_9SR_2]^-$  ( $R = CH_2COOEt, CH_2CONH_2, (CH_2)_nN(CO)_2C_6H_4$  ( $n = 1-3$ )).<sup>505,507</sup> Removal of the phthalimide protecting group with hydrazine in ethanol gives the corresponding amines  $[2-B_{10}H_9S((CH_2)_nNH_2)_2]^-$  ( $n = 1-3$ ).<sup>507</sup> The cyclic sulfonium derivatives  $[2-B_{10}H_9S(CH_2)_4]^-$  and  $[2-B_{10}H_9S(CH_2CH_2)_2O]^-$  were prepared by the alkylation of  $[2-B_{10}H_9SH]^{2-}$  with 1,4-dibromobutane and 2-chloroethyl ether,

respectively, in DMF in the presence of  $\text{Cs}_2\text{CO}_3$  at  $80^\circ\text{C}$  or, alternatively, by the direct reaction of the *closo*-decaborate anion with tetrahydrothiophene and 1,4-thioxane in the presence of  $\text{AlCl}_3$ .<sup>485,508</sup> The reaction of  $[\text{2-B}_{10}\text{H}_9\text{SH}]^{2-}$  with 1,2-dibromoethane results in the formation of the 1,4-dithiane derivative  $[\mu\text{-S}(\text{CH}_2\text{CH}_2)_2\text{S}(\text{2-B}_{10}\text{H}_9)_2]^{2-}$ .<sup>509</sup> The alkylthio derivatives  $[\text{2-B}_{10}\text{H}_9\text{SR}]^{2-}$  ( $\text{R} = i\text{-Pr}, \text{CH}_2\text{N}(\text{CO})_2\text{C}_6\text{H}_4$ ) were obtained by alkylation of  $[\text{2-B}_{10}\text{H}_9\text{SH}]^{2-}$  with sterically hindered alkyl halides under milder conditions (DMF,  $40^\circ\text{C}$ ).<sup>503,507</sup>

The chlorination of the dialkylsulfonium derivatives of the *closo*-dodecaborate anion  $[\text{2-B}_{10}\text{H}_9\text{SR}_2]^-$  with  $\text{SO}_2\text{Cl}_2$  in acetonitrile leads to the corresponding perchloro derivatives  $[\text{2-B}_{10}\text{Cl}_9\text{SR}_2]^-$  ( $\text{R} = \text{C}_3\text{H}_7, i\text{-C}_3\text{H}_7, \text{C}_4\text{H}_9, \text{C}_8\text{H}_{17}, \text{C}_{12}\text{H}_{25}, \text{C}_{18}\text{H}_{37}, \text{CH}_2\text{C}_6\text{H}_5, (\text{CH}_2)_n\text{N}(\text{CO})_2\text{C}_6\text{H}_4$  ( $n = 1-3$ );  $\text{R}_2 = (\text{CH}_2)_4, (\text{CH}_2\text{CH}_2)_2\text{O}$ ).<sup>507,508,510</sup> The perbromo derivatives  $[\text{2-B}_{10}\text{Br}_9\text{SR}_2]^-$  ( $\text{R} = (\text{CH}_2)_n\text{N}(\text{CO})_2\text{C}_6\text{H}_4$  ( $n = 1-3$ );  $\text{R}_2 = (\text{CH}_2)_4, (\text{CH}_2\text{CH}_2)_2\text{O}$ ) were prepared by bromination of the corresponding dialkylsulfonium derivatives  $[\text{2-B}_{10}\text{H}_9\text{SR}_2]^-$  with bromine in acetonitrile.<sup>508,511</sup> The brominated amines  $[\text{2-B}_{10}\text{Br}_9\text{S}((\text{CH}_2)_n\text{NH}_2)_2]^-$  ( $n = 1-3$ ) were obtained by the treatment of the corresponding phthalimide derivatives with methylamine in refluxing ethanol.<sup>511</sup>

The reaction of the *closo*-decaborate anion with  $(\text{SCN})_2$  in dichloromethane leads to a mixture of thiocyanato derivatives  $[\text{1-B}_{10}\text{H}_9\text{SCN}]^{2-}$ ,  $[\text{2-B}_{10}\text{H}_9\text{SCN}]^{2-}$  and  $[\text{1,10-B}_{10}\text{H}_8(\text{SCN})_2]^{2-}$  that can be separated by ion-exchange chromatography.<sup>331</sup> The bifunctional apically substituted thiocyanate derivative  $[\text{1,10-B}_{10}\text{H}_8(\text{Py})(\text{SCN})]^-$  was prepared by the reaction of  $[\text{1,10-B}_{10}\text{H}_8(\text{IPh})_2]$  with 1 equiv. of triethylammonium thiocyanate in acetonitrile followed by heating the formed  $[\text{1,10-B}_{10}\text{H}_8(\text{IPh})(\text{SCN})]^-$  in pyridine or, alternatively, by the reaction of  $[\text{1,10-B}_{10}\text{H}_8(\text{Py})(\text{IPh})]$  with thiocyanate in refluxing acetonitrile.<sup>470</sup>

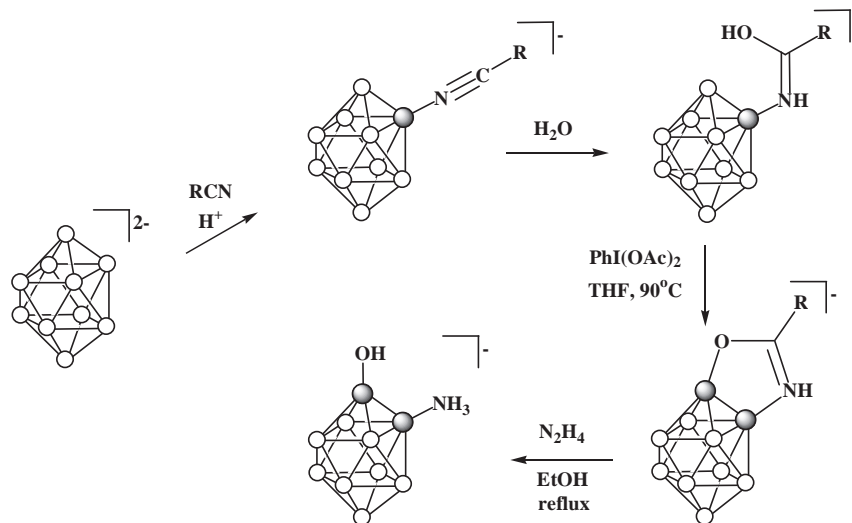
### 1.16.2.3.5 Derivatives with B–N bond

The chemistry of derivatives of the *closo*-decaborate anion with a boron-nitrogen bond is very diverse and has been actively developed since the early 1960s. The main results of its development over 50 years are summarized in the previous exhaustive review<sup>413</sup>; here we mainly consider new directions in its development, with references, where necessary, to earlier work.

The nitrilium derivatives of the *closo*-decaborate anion  $[\text{2-B}_{10}\text{H}_9\text{N}\equiv\text{CR}]^-$  ( $\text{R} = \text{Me}, \text{Et}, \text{Pr}, t\text{-Bu}, \text{Ad}, (\text{CH}_2)_n\text{CN}$  ( $n = 2-4$ ), Ph, Naph), formed by the reaction of the  $[\text{B}_{10}\text{H}_{10}]^{2-}$  anion with nitriles in the presence of strong acids,<sup>355,512-516</sup> can be used as precursors for the synthesis of various functional derivatives through the addition of nucleophiles to the activated triple bond. The addition of water to the activated triple bond proceeds smoothly resulting in the boronated iminols  $[\text{2-B}_{10}\text{H}_9\text{NH}=\text{C}(\text{OH})\text{R}]^-$  (Scheme 8).<sup>514,517,518</sup> The latter species are also formed when trying to chromatographic purification of the nitrilium derivatives.<sup>519</sup> The reactions of the iminols  $[\text{2-B}_{10}\text{H}_9\text{NH}=\text{C}(\text{OH})\text{R}]^-$  with  $\text{PhI}(\text{OAc})_2$  in THF at  $90^\circ\text{C}$  lead to closure of the five-membered cycle, with formation of diboraoxazoles  $[\text{2,1-}\mu\text{-NH}=\text{C}(\text{R})\text{O-B}_{10}\text{H}_8]^-$  ( $\text{R} = \text{Me}, \text{Et}, \text{Pr}, i\text{-Pr}, t\text{-Bu}, \text{Ph}, \text{C}_6\text{H}_4\text{-4-Cl}$ ).<sup>518</sup> The treatment of the diboraoxazoles with hydrazine hydride in refluxing ethanol results in  $[\text{1-OH-2-NH}_3\text{-B}_{10}\text{H}_8]^-$  (Scheme 8).<sup>518</sup>

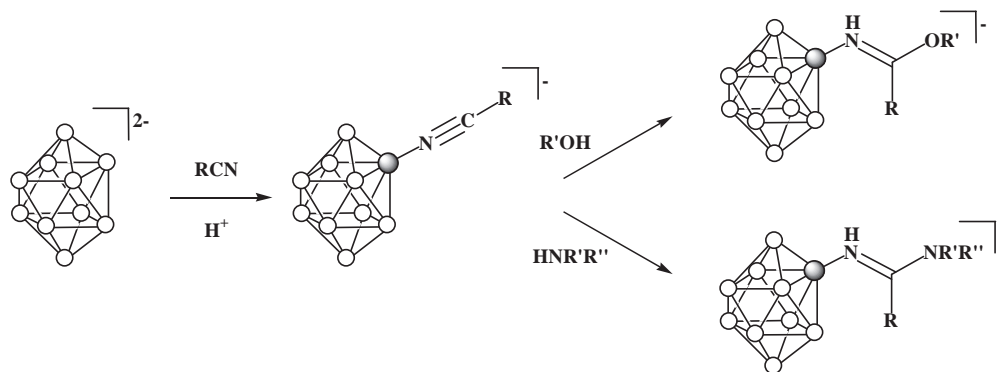
The addition of alcohols  $\text{R}'\text{OH}$  to the nitrilium derivatives  $[\text{2-B}_{10}\text{H}_9\text{N}\equiv\text{CR}]^-$  leads to the imidates  $[\text{2-B}_{10}\text{H}_9\text{NH}=\text{C}(\text{OR}')\text{R}]^-$ <sup>520,521</sup> (Scheme 9). One of the most studied reactions is the addition of amines to the activated triple bond of the nitrilium derivatives of the *closo*-decaborate anion leading to the formation of the boronated amidines  $[\text{2-B}_{10}\text{H}_9\text{NH}=\text{C}(\text{NR}'\text{R}'')\text{R}]^-$ . The reaction is applicable to both primary<sup>516,522</sup> and secondary<sup>523,524</sup> amines (Scheme 9). This approach was used for synthesis of boron-containing amino acids<sup>525-528</sup> and porphyrins.<sup>529-531</sup>

The nitrilium derivatives of the *closo*-decaborate anion also react with other nucleophiles, such as hydrazines and hydrazones,<sup>532</sup> oximes,<sup>533-535</sup> as well various carbanions derived from azomethyne ylides,<sup>536</sup> malononitrile,<sup>537</sup> benzoylacetonitrile<sup>537</sup> and ethyl benzoylacetate.<sup>537</sup> The nitrilium derivatives of the *closo*-decaborate anion, like organic nitrilium salts, are able to participate in 1,3-dipolar cycloaddition reactions. The reactions of  $[\text{2-B}_{10}\text{H}_9\text{N}\equiv\text{CR}]^-$  with sodium azide result in the corresponding boronated



Scheme 8





Scheme 9

tetrazoles  $[2-B_{10}H_9N_5C-5'-R]^{2-}$ ,<sup>538</sup> whereas the reactions with nitrones  $ArCH=N^+(Me)O^-$  lead to the corresponding boronated 2,3-dihydro-1,2,4-oxadiazoles  $[2-B_{10}H_9\{N=CRON(Me)CHAr\}]^-$ .<sup>539,540</sup>

The isocyanate derivative of the *closo*-decaborate anion  $[2-B_{10}H_9NCO]^{2-}$  was prepared by the reaction of the carbonyl derivative  $[2-B_{10}H_9CO]^-$  with sodium azide.<sup>541</sup> The reactions of the isocyanate derivative with 4-aminobenzylamine and 4-aminophenethylamine in DMF in the presence of triethylamine leads to the corresponding ureas  $[2-B_{10}H_9NHC(O)NH(CH_2)_nC_6H_4-p-NH_2]^{2-}$  ( $n = 1, 2$ ), which on treatment with thiocarbonyl diimidazole give the corresponding thiocyanates  $[2-B_{10}H_9NHC(O)NH(CH_2)_nC_6H_4-p-NCS]^{2-}$ .<sup>542,543</sup>

Reduction of the nitrilium derivatives of the *closo*-decaborate anion  $[2-B_{10}H_9N\equiv CR]^-$  with  $LiAlH_4$  in THF results in the alkylammonium derivatives  $[2-B_{10}H_9NH_2CH_2R]^-$ .<sup>515</sup> Treatment of the nitrilium derivative  $[2-B_{10}H_9N\equiv CMe]^-$  with hydrazine hydrate in refluxing ethanol results in the ammonium derivative  $[2-B_{10}H_9NH_3]^-$ .<sup>544</sup> The perhalogenated ammonium derivatives  $[2-B_{10}X_9NH_3]^-$  ( $X = Cl, Br, I$ ) were prepared by the reaction of the parent *closo*-decaborate with the corresponding halogens in 1,2-dichloroethane at 80 °C.<sup>544</sup> The trimethylammonium derivatives  $[2-B_{10}X_9NMe_3]^-$  ( $X = Cl, Br, I$ ) were prepared by the reaction of the corresponding ammonium derivatives with methyl iodide in acetonitrile in the presence of  $K_2CO_3$  at room temperature.<sup>544</sup> The reactions with benzyl bromide under the same conditions produce the benzylammonium perbromo and periodo  $[2-B_{10}X_9NH_2Bn]^-$  ( $X = Br, I$ ) and dibenzylammonium perchloro  $[2-B_{10}Cl_9NHBn_2]^-$  derivatives, whereas the synthesis of the dibenzylammonium perbromo and periodo derivatives  $[2-B_{10}X_9NHBn_2]^-$  ( $X = Br, I$ ) requires heating at 80 and 100 °C, respectively.<sup>544</sup> The alkylation of the perhalogenated ammonium derivatives  $[2-B_{10}X_9NH_3]^-$  with epibromohydrin in acetonitrile in the presence of  $K_2CO_3$  leads to the corresponding boronated oxypropanes  $[2-B_{10}X_9NH_2CH_2CH_2CH_2O]^-$  ( $X = Cl, Br, I$ ) which react with amines and phenolates giving the corresponding derivatives  $[2-B_{10}X_9NH_2CH_2CH(OH)CH_2X]^-$  ( $X = NHBu, NHBn, NEt_2, OC_6H_4-2-OMe$ ).<sup>545</sup>

Several pyridinium derivatives of the *closo*-decaborate anion have been obtained in the course of transition metal-initiated substitution reactions. The pyridinium-substituted derivatives  $\{(MeCN)_2Cu[2-B_{10}H_9-2',2''-Bipy-\kappa^2-N,H]\}$  (Fig. 14) and  $[(HNPY_2)Cu(MeCN)_2][2-B_{10}H_9NC_5H_4-2'-NH-2''-C_5H_4N]$  were obtained by reactions of  $Cu_2[B_{10}H_{10}]$  with 2,2'-bipyridine and 2,2'-bi(pyridyl)amine in acetonitrile.<sup>546</sup> The 1,2-disubstituted phenanthroline derivative  $[1,2-\mu-N_2C_{12}H_8-B_{10}H_8]$  (Fig. 14) was prepared by the  $CoCl_2$ -mediated reaction of the parent *closo*-decaborate with 1,10-phenanthroline in acetonitrile or *N,N'*-dimethylformamide.<sup>499,547</sup>

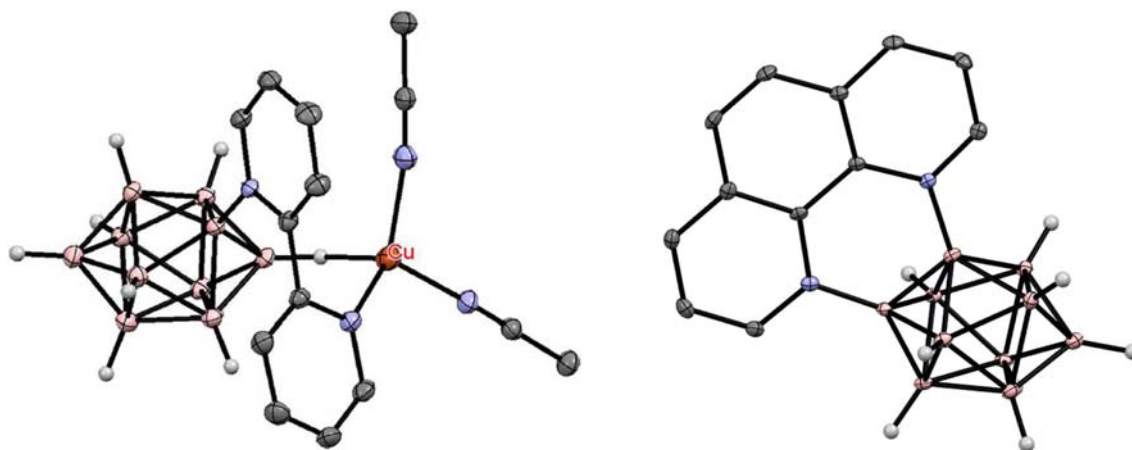


Fig. 14 Crystal molecular structures of  $\{(MeCN)_2Cu[2-B_{10}H_9-2',2''-Bipy-\kappa^2-N,H]\}$  (left) and  $[1,2-\mu-N_2C_{12}H_8-B_{10}H_8]$  (right). Hydrogen atoms of organic substituents and ligands are removed for clarity.

The apically substituted pyridinium derivatives  $[1\text{-B}_{10}\text{H}_9\text{Py}]^+$  and  $[1,10\text{-B}_{10}\text{H}_8(\text{Py})_2]^+$  were prepared by heating the corresponding phenyliodonium derivatives  $[1\text{-B}_{10}\text{H}_9\text{IPh}]^+$  and  $[1,10\text{-B}_{10}\text{H}_8(\text{IPh})_2]^+$  in pyridine at  $80^\circ\text{C}$ .<sup>471</sup> It should be noted that the synthesis of  $[1\text{-B}_{10}\text{H}_9\text{Py}]^+$  by the reaction of the diazonium derivative  $[1\text{-B}_{10}\text{H}_9\text{N}_2]^+$  with pyridine has been reported earlier.<sup>548,549</sup> In a similar way, a series of the *para*-substituted pyridinium derivatives  $[1\text{-B}_{10}\text{H}_9\text{NC}_5\text{H}_4\text{-}p\text{-X}]^+$  ( $X = \text{Me}, \text{OMe}, \text{CN}, \text{COOEt}$ )<sup>471</sup> and  $[1,10\text{-B}_{10}\text{H}_8(\text{NC}_5\text{H}_4\text{-}p\text{-OR})_2]^+$  ( $R = \text{C}_8\text{H}_{17}, \text{C}_{10}\text{H}_{21}, \text{C}_{12}\text{H}_{25}, \text{C}_{14}\text{H}_{29}, \text{C}_{16}\text{H}_{33}, \text{C}_{18}\text{H}_{37}$ )<sup>550</sup> were prepared by heating the phenyliodonium derivatives with the corresponding *para*-substituted pyridines. The cyclic dialkylammonium derivative  $[1\text{-B}_{10}\text{H}_9\text{NH}(\text{CH}_2\text{CH}_2)_2\text{O}]^+$  was prepared by heating  $[1\text{-B}_{10}\text{H}_9\text{IPh}]^+$  in morpholine. Its reaction with  $\text{PhI}(\text{OAc})_2$  in acetic acid followed by heating formed  $[1,10\text{-B}_{10}\text{H}_8(\text{IPh})(\text{NH}(\text{CH}_2\text{CH}_2)_2\text{O})]^+$  in pyridine leads to the zwitterionic bifunctional derivative  $[1,10\text{-B}_{10}\text{H}_8(\text{Py})(\text{NH}(\text{CH}_2\text{CH}_2)_2\text{O})]^+$ .<sup>471</sup>

A series of apically substituted amines  $[1\text{-B}_{10}\text{H}_9\text{NHR}'^+]$  ( $R = \text{H}, R' = \text{Bn}, \text{Ph}; R = \text{Me}, R' = \text{Ph}; R = R' = \text{Bn}, \text{Ph}$ ) and  $[1\text{-B}_{10}\text{H}_9\text{NH}_2(\text{CH}_2)_n\text{NH}_2]^+$  ( $n = 2\text{--}4, 6, 9$ ) were prepared by heating the diazonium derivative  $[1\text{-B}_{10}\text{H}_9\text{N}_2]^+$  in the corresponding amines at  $120^\circ\text{C}$ .<sup>549,551</sup> Some of them were used for the subsequent modification and preparation of boron-containing silica nanoparticles.<sup>552,553</sup> The apically substituted azido derivative  $[1\text{-B}_{10}\text{H}_9\text{N}_3]^{2+}$  was prepared by the reaction of  $[1\text{-B}_{10}\text{H}_9\text{IPh}]^+$  with tetra-butylammonium azide in acetonitrile at  $55^\circ\text{C}$ .<sup>470</sup>

The apically substituted nitro derivatives of the *closo*-decaborate anion  $[1\text{-B}_{10}\text{H}_9\text{NO}_2]^{2-}$  and  $[1,10\text{-B}_{10}\text{H}_8(\text{NO}_2)_2]^{2-}$  were earlier synthesized by the reaction of the parent *closo*-decaborate with  $\text{NO}_2$  in acetonitrile.<sup>554,555</sup> Later, these compounds were prepared by UV irradiation of solutions of *closo*-decaborate in nitroalkanes  $\text{RNO}_2$  ( $R = \text{Et}, \text{Pr}, i\text{-Pr}, t\text{-Bu}$ ) at 450 and 350 nm, respectively.<sup>556</sup>

### 1.16.2.3.6 Derivatives with B–P bonds

Similarly to the *closo*-dodecaborate anion, phosphonium derivatives of the *closo*-decaborate anion can be obtained via Pd-mediated *BH*-activation methods. The reaction of lithium *closo*-decaborate  $\text{Li}_2[\text{B}_{10}\text{H}_{10}]$  with  $[(\text{PhMe}_2\text{P})_2\text{PdCl}_2]$  in dichloromethane at room temperature followed by treatment with  $\text{NaBH}_4$  in refluxing benzene leads to a mixture of isomeric bis(phosphonium) derivatives  $[1,6\text{-B}_{10}\text{H}_8(\text{PMe}_2\text{Ph})_2]^+$ ,  $[1,10\text{-B}_{10}\text{H}_8(\text{PMe}_2\text{Ph})_2]^+$  and  $[2,7\text{-B}_{10}\text{H}_8(\text{PMe}_2\text{Ph})_2]^+$ .<sup>388</sup> Bis(phosphonium) *closo*-decaborate derivatives  $[1,6\text{-B}_{10}\text{H}_8(\text{PPh}_3)_2]^+$  and  $[2,4\text{-B}_{10}\text{H}_8(\text{PPh}_3)_2]^+$  were obtained by the reaction of tetraethylammonium *closo*-decaborate  $(\text{Et}_4\text{N})_2[\text{B}_{10}\text{H}_{10}]$  with  $[(\text{Ph}_3\text{P})_2\text{PdCl}_2]$  in ethanol at room temperature.<sup>557,558</sup>

The reaction of the 1-diazonium derivative of the *closo*-decaborate anion  $[1\text{-B}_{10}\text{H}_9\text{N}_2]^+$  with  $\text{Ph}_2\text{PH}$  in the presence of catalytic amounts of  $[(\text{Ph}_3\text{P})_2\text{PdCl}_2]$  and  $\text{CuI}$  at  $150^\circ\text{C}$  results in the formation of the corresponding phosphonium derivative  $[1\text{-B}_{10}\text{H}_9\text{PPh}_2\text{H}]^+$ , which is easily oxidized to  $[1\text{-B}_{10}\text{H}_9\text{PPh}_2\text{OH}]^+$ , and stable isomeric bis(phosphonium) derivatives  $[1,6\text{-B}_{10}\text{H}_8(\text{PPh}_2\text{H})_2]^+$  and  $[1,10\text{-B}_{10}\text{H}_8(\text{PPh}_2\text{H})_2]^+$ .<sup>559</sup>

### 1.16.2.3.7 Derivatives with B–C bonds

The cross-coupling reaction of  $[1\text{-B}_{10}\text{H}_9\text{I}]^{2-}$  with  $\text{MeO-}p\text{-C}_6\text{H}_4\text{MgBr}$  in the presence of 1 mol% PEPPSI-IPr in refluxing THF leads to the corresponding apically substituted aryl derivative  $[1\text{-B}_{10}\text{H}_9\text{C}_6\text{H}_4\text{-}p\text{-OMe}]^{2-}$ .<sup>471</sup> The apically substituted cyano derivatives  $[1\text{-B}_{10}\text{H}_9\text{CN}]^{2-}$  and  $[1,10\text{-B}_{10}\text{H}_8(\text{CN})_2]^{2-}$  were prepared by the reactions of the corresponding phenyliodonium derivatives  $[1\text{-B}_{10}\text{H}_9\text{IPh}]^+$  and  $[1,10\text{-B}_{10}\text{H}_8(\text{IPh})_2]^+$  with cyanide ion in acetonitrile.<sup>470,501</sup> Due to the electron-donating effect of the *closo*-decaborate cage, the cyano groups in  $[1,10\text{-B}_{10}\text{H}_8(\text{CN})_2]^{2-}$  can act as donors in complexes with transition metal atoms (Fig. 15).<sup>560</sup>

The early period of preparation and transformation of carbonyl derivatives of the *closo*-decaborate anion were discussed in detail in the previous review.<sup>413</sup> Recently, it was shown that the 1,10-dicarboxylic acid  $[1,10\text{-B}_{10}\text{H}_8(\text{COOH})_2]^{2-}$  can be synthesized via the *N*-methylation of the 1,10-dicyano derivative  $[1,10\text{-B}_{10}\text{H}_8(\text{CN})_2]^{2-}$  with methyl triflate followed by stepwise alkaline hydrolysis of the resulting zwitterionic nitrilium derivative  $[1,10\text{-B}_{10}\text{H}_8(\text{C}\equiv\text{NMe})_2]$ . In strongly acidic media the 1,10-dicarboxylic acid transforms into the 1,10-dicarbonyl derivative  $[1,10\text{-B}_{10}\text{H}_8(\text{CO})_2]$ , which readily react with ethoxide to give the corresponding diester  $[1,10\text{-B}_{10}\text{H}_8(\text{COOEt})_2]^{2-}$  and with ethylenediamine or *N,N'*-dimethyl ethylenediamine to give the corresponding diamides  $[1,10\text{-B}_{10}\text{H}_8(\text{CONRCH}_2\text{CH}_2\text{NH}_2)_2]$  ( $R = \text{H}, \text{Me}$ ). Treatment of the diamides with trimethylsilyl polyphosphate leads to the bifunctional carbonyl-imidazolium derivatives  $[1,10\text{-B}_{10}\text{H}_8(\text{CO})(\text{C}(\text{NRCH}_2)_2)]$ , which can be easily converted to the corresponding acids and

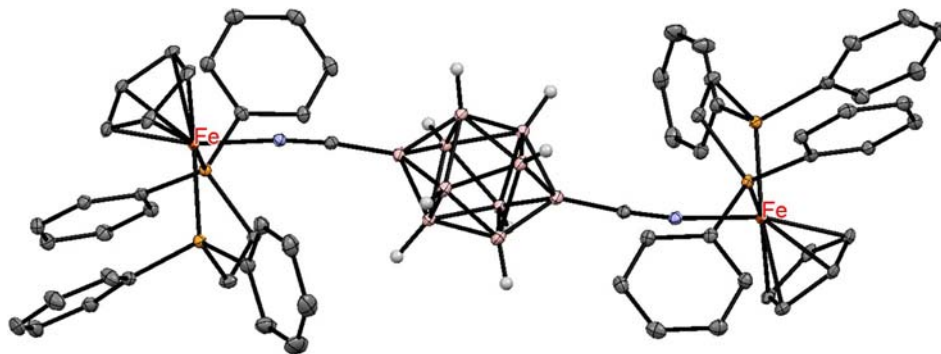


Fig. 15 Crystal molecular structure of  $\{1,10\text{-}(\text{Cp}(\text{dppe})\text{Fe})_2\}[\mu\text{-}1,10\text{-B}_{10}\text{H}_8(\text{CN})_2]$ . Hydrogen atoms of organic ligands are removed for clarity.

esters.<sup>561</sup> The reaction of the nitrilium derivative with methylamine results in the corresponding amidine [1,10-B<sub>10</sub>H<sub>8</sub>(C(NHMe)<sub>2</sub>)<sub>2</sub>].<sup>561</sup>

The reactions of the equatorially substituted carbonyl derivative of the *closo*-decaborate anion [2-B<sub>10</sub>H<sub>9</sub>CO]<sup>-</sup> with some biologically active alcohols<sup>562</sup> and amines<sup>542</sup> were reported. More recently, a series of the *closo*-decaborate derived esters [2-B<sub>10</sub>H<sub>9</sub>C(O)OR]<sup>2-</sup> (R = Me, Et, Pr, *i*-Pr, Bu, *t*-Bu) was prepared by the reaction of the carbonyl derivative [2-B<sub>10</sub>H<sub>9</sub>CO]<sup>-</sup> with the corresponding alcohols.<sup>563</sup> In a similar way, amides [2-B<sub>10</sub>H<sub>9</sub>CONRR']<sup>2-</sup> (R' = H, R' = NH<sub>2</sub>, Bu, CH<sub>2</sub>COOH, CH<sub>2</sub>COOMe, CH<sub>2</sub>CH<sub>2</sub>CH<sub>2</sub>Si(OEt)<sub>3</sub>, (CH<sub>2</sub>CH<sub>2</sub>NH)<sub>2</sub>CH<sub>2</sub>CH<sub>2</sub>NH<sub>2</sub>, CH<sub>2</sub>CH<sub>2</sub>N(Me)CH<sub>2</sub>CH<sub>2</sub>NH<sub>2</sub>, CH<sub>2</sub>CH<sub>2</sub>CH<sub>2</sub>(OCH<sub>2</sub>CH<sub>2</sub>)<sub>3</sub>CH<sub>2</sub>NH<sub>2</sub>; R' = R'' = Bu) were obtained by the reaction of [2-B<sub>10</sub>H<sub>9</sub>CO]<sup>-</sup> with amines.<sup>549,564,565</sup>

The reduction of the carbonyl derivative [2-B<sub>10</sub>H<sub>9</sub>CO]<sup>-</sup> with LiBH<sub>4</sub> in refluxing acetonitrile gives the corresponding alcohol [2-B<sub>10</sub>H<sub>9</sub>CH<sub>2</sub>OH]<sup>2-</sup>.<sup>564</sup>

A series of the *closo*-decaborate derived ketones [2-B<sub>10</sub>H<sub>9</sub>C(O)R]<sup>2-</sup> (R = C<sub>6</sub>H<sub>5</sub>, C<sub>6</sub>H<sub>4</sub>-*p*-OMe, C<sub>6</sub>H<sub>4</sub>-*p*-COOH) was prepared by the reaction of the parent *closo*-decaborate [B<sub>10</sub>H<sub>10</sub>]<sup>2-</sup> with the corresponding acyl chlorides in acetonitrile.<sup>564</sup>

### 1.16.2.3.8 Oxidation reactions

The *closo*-decaborate anion is less stable to oxidation than the *closo*-dodecaborate anion and undergoes electrochemical oxidation at 0.9 V vs. SCE in acetonitrile to *conjuncto*-borane [*trans*-B<sub>20</sub>H<sub>18</sub>]<sup>2-</sup>, in which two B<sub>10</sub> moieties are linked together by a pair of unique B–B–B bonds (Fig. 16). The chemistry of [B<sub>20</sub>H<sub>18</sub>]<sup>2-</sup> was reviewed by Hawthorne<sup>566</sup> and Avdeeva.<sup>567</sup>

In the presence of platinum, palladium or rhodium metals the *closo*-dodecaborate anion in aqueous solutions is easily oxidized to boric acid.<sup>407,408,568</sup>

### 1.16.2.4 *closo*-Nonaborate anion [B<sub>9</sub>H<sub>9</sub>]<sup>2-</sup>

The *closo*-nonaborate anion [B<sub>9</sub>H<sub>9</sub>]<sup>2-</sup> can be obtained as the cesium or rubidium salt by solid-state pyrolysis of Cs[B<sub>3</sub>H<sub>8</sub>] or Rb[B<sub>3</sub>H<sub>8</sub>] at 230 °C. The yield of the target product is 20–25%, by-products are the *closo*-decaborate and *closo*-dodecaborate anions.<sup>410</sup> The [B<sub>9</sub>H<sub>9</sub>]<sup>2-</sup> anion belongs to the group of poorly accessible polyhedral borohydrides and, therefore, its chemistry has been little studied and only a limited number of its derivatives are known, including mono-<sup>569</sup> and perhalogen,<sup>570</sup> ammonium,<sup>571</sup> sulfonium,<sup>572</sup> and nitro<sup>573</sup> derivatives. The chemistry of the *closo*-nanoborate anion was reviewed several years ago.<sup>574</sup> More recent work concerns protonation of [B<sub>9</sub>H<sub>9</sub>]<sup>2-</sup> with HCl in dichloromethane, that results in the cage opening with formation of 4,8-dichloro-*arachno*-nonaborate [4,8-B<sub>9</sub>H<sub>12</sub>Cl<sub>2</sub>]<sup>-</sup>, which reacts with liquid ammonia with the loss of the chlorine atoms and the cage-reclosing giving back the *closo*-nonaborate anion [B<sub>9</sub>H<sub>9</sub>]<sup>2-</sup>.<sup>575</sup> The reaction with acetic acid in dichloromethane resulted in the complete cage destruction giving [B<sub>2</sub>O(OAc)<sub>5</sub>]<sup>-</sup>.<sup>575</sup>

### 1.16.2.5 *closo*-Octaborate anion [B<sub>8</sub>H<sub>8</sub>]<sup>2-</sup>

The *closo*-octaborate anion [B<sub>8</sub>H<sub>8</sub>]<sup>2-</sup> is formed in ~30% yield on the air oxidation of the *closo*-nonaborate anion [B<sub>9</sub>H<sub>9</sub>]<sup>2-</sup> in 1,2-dimethoxyethane under basic conditions.<sup>576</sup> Due to the very low availability, the chemistry of the *closo*-octaborate anion remains practically unexplored. Later, it was found that protonation of [B<sub>8</sub>H<sub>8</sub>]<sup>2-</sup> with HCl in an aqueous solution or with Et<sub>3</sub>N·HCl in acetonitrile leads to the protonated form [B<sub>8</sub>H<sub>9</sub>]<sup>-</sup>. The crystal structures of (Bu<sub>4</sub>N)[B<sub>8</sub>H<sub>9</sub>] and (Ph<sub>4</sub>P)[B<sub>8</sub>H<sub>9</sub>] were determined by single crystal X-ray diffraction.<sup>577</sup>

The perchlorinated *hypercloso*-[B<sub>8</sub>Cl<sub>8</sub>] was obtained by thermal decomposition of B<sub>2</sub>Cl<sub>4</sub>.<sup>578,579</sup> The reduction of [B<sub>8</sub>Cl<sub>8</sub>] with 1 equiv. of iodide in dichloromethane or chloroform leads to the corresponding radical anion *hypercloso*-[B<sub>8</sub>Cl<sub>8</sub>]<sup>•-</sup>, while the reduction

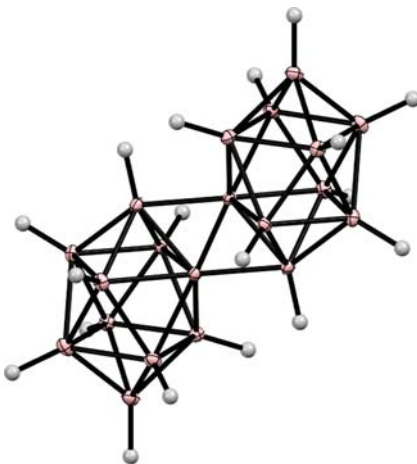


Fig. 16 Crystal molecular structure of the [*trans*-B<sub>20</sub>H<sub>18</sub>]<sup>2-</sup> anion.

with 2 equiv. of iodide results in *closo*-[B<sub>8</sub>Cl<sub>8</sub>]<sup>2-</sup>.<sup>579</sup> The crystal structures of (Ph<sub>4</sub>P)<sub>2</sub>[B<sub>8</sub>Cl<sub>8</sub>] was determined by single crystal X-ray diffraction.<sup>579</sup> The perchlorinated *closo*-octaborate anion [B<sub>8</sub>Cl<sub>8</sub>]<sup>2-</sup> has the dodecahedral *D*<sub>2d</sub> structure close to found earlier for the parent *closo*-octaborate in the structure of [Zn(NH<sub>3</sub>)<sub>4</sub>][B<sub>8</sub>H<sub>8</sub>].<sup>580</sup>

#### 1.16.2.6 *closo*-Heptaborate anion [B<sub>7</sub>H<sub>7</sub>]<sup>2-</sup>

The *closo*-heptaborate anion [B<sub>7</sub>H<sub>7</sub>]<sup>2-</sup> was in the first time prepared in less than 1% yield by air oxidation of the *closo*-octaborate anion [B<sub>8</sub>H<sub>8</sub>]<sup>2-</sup>.<sup>575</sup> and is the least studied of the series of polyhedral borane anions [B<sub>*n*</sub>H<sub>*n*</sub>]<sup>2-</sup> (*n* = 6–12).

Later, the convenient synthesis of the [B<sub>7</sub>H<sub>7</sub>]<sup>2-</sup> anion by direct oxidation of the *closo*-nonaborate anion [B<sub>9</sub>H<sub>9</sub>]<sup>2-</sup> with oxygen in a mixture of 1,2-dimethoxyethane and dichloromethane was described.<sup>581</sup> The protonation of [B<sub>7</sub>H<sub>7</sub>]<sup>2-</sup> with Et<sub>3</sub>N·HCl in acetonitrile leads to the protonated form [B<sub>7</sub>H<sub>8</sub>]<sup>-</sup>. The crystal structures of (Bu<sub>4</sub>N)<sub>2</sub>[B<sub>7</sub>H<sub>7</sub>], (Ph<sub>4</sub>P)<sub>2</sub>[B<sub>7</sub>H<sub>7</sub>] and (PNP)<sub>2</sub>[B<sub>7</sub>H<sub>7</sub>] and the protonated form (Bu<sub>4</sub>N)[B<sub>7</sub>H<sub>8</sub>] and (Ph<sub>4</sub>P)[B<sub>7</sub>H<sub>8</sub>] were determined by single crystal X-ray diffraction.<sup>581</sup>

The perbrominated *closo*-heptaborane anion [B<sub>7</sub>Br<sub>7</sub>]<sup>2-</sup> was prepared by reaction of *conjuncto*-[B<sub>6</sub>H<sub>6</sub>-B<sub>6</sub>H<sub>6</sub>]<sup>2-</sup> with excess of bromine in alkaline solution. The crystal structure of ((C<sub>5</sub>H<sub>5</sub>N)<sub>2</sub>CH<sub>2</sub>)[B<sub>7</sub>Br<sub>7</sub>] was determined by single crystal X-ray diffraction.<sup>582</sup>

#### 1.16.2.7 *closo*-Hexaborate anion [B<sub>6</sub>H<sub>6</sub>]<sup>2-</sup>

The *closo*-hexaborate anion [B<sub>6</sub>H<sub>6</sub>]<sup>2-</sup> can be synthesized in 20–25% yield by pyrolysis of Na[B<sub>3</sub>H<sub>3</sub>] in refluxing diglyme.<sup>583</sup> Due to its relative availability, the chemistry of the *closo*-hexaborate anion is much better studied than that of other lower *closo*-polyhedral anions [B<sub>*n*</sub>H<sub>*n*</sub>]<sup>2-</sup>, but it is significantly inferior to the chemistry of the *closo*-dodecaborate and *closo*-decaborate anions. A distinctive feature of the *closo*-hexaborate anion [B<sub>6</sub>H<sub>6</sub>]<sup>2-</sup>, due to the presence of an increased electron density on the faces of the B<sub>6</sub> octahedron, is the ease of its protonation to [B<sub>6</sub>H<sub>7</sub>]<sup>-</sup>, which occurs in an aqueous solution at pH 7.00.<sup>584</sup> This causes its high reactivity in reactions proceeding by the mechanism of aromatic electrophilic substitution, such as halogenation and alkylation, while reactions proceeding by the mechanism of electrophilically induced nucleophilic substitution are not typical for it. An early stage in the development of the chemistry of the *closo*-hexaborate anion [B<sub>6</sub>H<sub>6</sub>]<sup>2-</sup> and its protonated form [B<sub>6</sub>H<sub>7</sub>]<sup>-</sup> was described in an excellent review by Preetz and Peters.<sup>585</sup> More recent work in particular includes the synthesis and study of various simple and complex salts with the [B<sub>6</sub>H<sub>6</sub>]<sup>2-</sup> and [B<sub>6</sub>H<sub>7</sub>]<sup>-</sup> anions.<sup>132,586–590</sup>

Besides, the synthesis of perbenzylated derivatives (Bu<sub>4</sub>N)[B<sub>6</sub>R<sub>6</sub>H] (R = CH<sub>2</sub>C<sub>6</sub>H<sub>5</sub>, CH<sub>2</sub>C<sub>6</sub>H<sub>4</sub>-4-Br) by the reaction of (Bu<sub>4</sub>N)[B<sub>6</sub>H<sub>7</sub>] with an excess of the corresponding benzyl bromide in the presence of Et<sub>3</sub>N in toluene at 140 °C<sup>591</sup> or K<sub>3</sub>PO<sub>4</sub> in acetonitrile at 120 °C<sup>592</sup> was reported.

The reaction of (Ph<sub>3</sub>PMe)<sub>2</sub>[B<sub>6</sub>H<sub>6</sub>] with Ph<sub>2</sub>PCl in THF at –30 °C leads to phosphine [B<sub>6</sub>H<sub>6</sub>PPh<sub>2</sub>]<sup>-</sup>, which is easily alkylated with allyl bromide or methyl iodide giving the corresponding phosphonium salts [B<sub>6</sub>H<sub>6</sub>PPh<sub>2</sub>R] (R = allyl, methyl).<sup>592</sup> The iodination of [B<sub>6</sub>H<sub>6</sub>PPh<sub>2</sub>Me] with I<sub>2</sub> in acetonitrile in the presence of KI and K<sub>3</sub>PO<sub>4</sub> leads to the pentaiodo derivative Na[B<sub>6</sub>I<sub>5</sub>PPh<sub>2</sub>Me].<sup>592</sup> The reaction of (Ph<sub>3</sub>PMe)<sub>2</sub>[B<sub>6</sub>H<sub>6</sub>] with PhSeCl in THF leads to [B<sub>6</sub>H<sub>6</sub>SePh]<sup>-</sup>, which upon treatment with methyl iodide gives the protonated selenonium salt [B<sub>6</sub>H<sub>6</sub>SePhMe].<sup>592</sup>

Reactions of 1,3-dichloro-1,2,3-tris(dimethylamino)triborane(5) with lithium in tetrahydrofuran or sodium/potassium alloy in pentane at room temperature result in the formation of the corresponding *closo*-hexa(trimethylamino)hexaborates M<sub>2</sub>[B<sub>6</sub>(NMe<sub>2</sub>)<sub>6</sub>] (M = Li, K). The related *closo*-hexa(triethylamino)hexaborate [B<sub>6</sub>(NEt<sub>2</sub>)<sub>6</sub>]<sup>2-</sup> was prepared by the reaction of diethylaminodibromoborane Et<sub>2</sub>NBBR<sub>2</sub> with sodium/potassium alloy in refluxing hexane. Mild oxidation of the *closo*-hexa(trialkylamino)hexaborates with 1,2-dibromoethane in tetrahydrofuran at room temperature leads to the corresponding *hypercloso*-hexa(dialkylamino)hexaboranes [B<sub>6</sub>(NR<sub>2</sub>)<sub>6</sub>],<sup>593</sup> which, upon heating to 200 °C, transform into the known hexakis(dialkylamino)cyclohexaboranes.<sup>594,595</sup>

The reaction of (Bu<sub>4</sub>N)<sub>2</sub>[B<sub>6</sub>H<sub>6</sub>] with 1,8-diazabicyclo[5.4.0]undec-7-ene (DBU) in chloroform under reflux conditions results in the insertion of a carbene unit into the *closo*-hexaborate cage to form a mixture of *B*-substituted 2-carba-*closo*-heptaborane derivatives (Ph<sub>4</sub>P)[3-Cl-2-CB<sub>6</sub>H<sub>6</sub>] and [3-DBU-2-CB<sub>6</sub>H<sub>6</sub>].<sup>596</sup>

The oxidation of the perbenzylated derivatives [B<sub>6</sub>(CH<sub>2</sub>Ar)<sub>6</sub>H]<sup>-</sup> with tetracyano-quinodimethane (TCNQ) in THF at 0 °C results in complete destruction of the *closo*-hexaborate cluster; upon oxidation in the presence of pinacol, the pinacolates of the corresponding benzyl boronic acids, ArCH<sub>2</sub>Bpin, were obtained. The oxidation of monoalkylated derivatives [B<sub>6</sub>H<sub>6</sub>R]<sup>-</sup> proceeds in a similar way.<sup>592</sup>

### 1.16.3 Polyhedral boranes with an open structure (*nido*- and *arachno*-boranes)

After extensive development in the 1950s and 1960s, the chemistry of open-structured polyhedral boranes has attracted much less interest in recent years compared to the chemistry of polyhedral carboranes and *closo*-polyhedral boron hydride anions [B<sub>*n*</sub>H<sub>*n*</sub>]<sup>2-</sup>. At the same time, most of the recent works in this field are not related to the fundamental study of their chemistry, but to various promising areas of application of their derivatives.

### 1.16.3.1 Tetradecahydro-*nido*-undecaborate anion $[B_{11}H_{14}]^-$

Synthesis of the tetradecahydro-*nido*-undecaborate anion  $[B_{11}H_{14}]^-$  from decaborane(14) by the reaction with lithium or sodium tetrahydroborates in boiling ether solvents (1,2-dimethoxyethane, 1,4-dioxane) was described in early 1960s.<sup>597</sup> Later, in the absence of industrial-scale production of decaborane(14), another convenient approach to synthesis of the anion was developed. It is based on the reaction of sodium tetrahydroborate  $NaBH_4$  with boron trifluoride etherate in diglyme at 105 °C giving the target product in 63% as the tetraethylammonium salt.<sup>598</sup> The reaction proceeds through the formation of the  $[B_3H_8]^-$  anion; therefore, when using  $(Et_4N)[B_3H_8]$  as the starting compound, the same result was obtained. Instead of  $F_3B \cdot OEt_2$ , some other Lewis acids, such as  $BCl_3$ ,  $SiCl_4$ , and alkyl halides, can be used in the reaction with  $NaBH_4$ .<sup>598</sup> The current state of the chemistry of the  $[B_{11}H_{14}]^-$  anion has recently been reviewed.<sup>411</sup>

### 1.16.3.2 Decaborane(14) $[B_{10}H_{14}]$

The intensive development of the chemistry of decaborane took place mainly in the 1950s and early 1960s, when the main types of its transformations were discovered and described. These early studies were reviewed in the 1960s by Hawthorne<sup>599</sup> and Zakharkin et al.<sup>600</sup> This area has also been partially covered in *Boron Hydride Chemistry*<sup>601</sup> and *Comprehensive Inorganic Chemistry I*.<sup>602</sup> Recent studies in the field of the decaborane chemistry mainly deepen and expand the previously described findings using modern instrumental methods. Therefore, here we do not consider the chemistry of decaborane as a whole, but focus on recent work in this area, both completely new and continuing earlier work.

The laboratory method for the synthesis of decaborane (Fig. 17) is based on a mild oxidation of the tetradecahydro-*nido*-undecaborate anion  $[B_{11}H_{14}]^-$ .<sup>598</sup> Potassium permanganate, sodium bichromate or hydrogen peroxide can be used as the oxidants. Later it was shown that various aldehydes and ketones, in particular acetone, can be used as the oxidizing agents.<sup>603</sup>

Decaborane-14 is known to have acidic character and can be deprotonated with strong bases, such as proton sponge (PS) to give the tridecahydro-*nido*-decaborate  $[B_{10}H_{13}]^-$  anion. The structure of  $(HPS)[B_{10}H_{13}]$  was determined by single crystal X-ray diffraction.<sup>604</sup> The  $(Et_3NH)[B_{10}H_{13}]$  and  $(Et_4N)[B_{10}H_{13}]$  salts obtained by deprotonation of decaborane with  $Et_3N$  and  $(Et_4N)OH$ , respectively, have been found to trigger hypergolic reactivity of some polar aprotic organic solvents, such as tetrahydrofuran and ethyl acetate.<sup>605</sup>

Some electrophilic substitution reactions were investigated. The reaction of decaborane with  $ICl$  in the presence of  $AlCl_3$  in dichloromethane under reflux conditions results in a mixture of 1- and 2-iodo derivatives  $[1-I-B_{10}H_{13}]$  and  $[2-I-B_{10}H_{13}]$ , which were separated by fraction crystallization.<sup>606</sup> Methylation of decaborane with neat methyl iodide in the presence of  $AlCl_3$  at room temperature results in the tetramethylated derivative  $[1,2,3,4-Me_4-B_{10}H_{10}]$ , whereas the reaction at 120 °C leads to the octa-substituted product  $[1-I-2,3,4,5,6,7,8-Me_7-B_{10}H_6]$ . The similar octasubstituted derivative  $[1-TfO-2,3,4,5,6,7,8-Me_7-B_{10}H_6]$  was obtained by the reaction of decaborane with  $TfOMe$  in the presence of catalytic amount of triflic acid at 120 °C.<sup>607</sup>

It is well known that decaborane easily reacts with various Lewis bases (L) to form the corresponding 6,9-disubstituted derivatives *arachno*- $[B_{10}H_{12}L_2]$ .<sup>599</sup> The reactions of decaborane with imidazole and *N*-alkyl imidazoles produce the corresponding imidazolium derivatives *arachno*- $[6,9-B_{10}H_{12}L_2]$  (L = HIm, Melm, EtIm, BuIm) which induce hypergolicity of kerosene when present as undissolved solids.<sup>608</sup>

Reactions of nucleophilic addition of methanol and primarily and secondary amines to the highly activated  $-N^+ \equiv CR$  triple bond of 6,9-bis(acetonitrilium) derivative *arachno*- $[6,9-B_{10}H_{12}(N \equiv CMe)_2]$  were reinvestigated and the corresponding imidate *arachno*- $[6,9-B_{10}H_{12}(N = C(Me)OMe)_2]$  and a series of amidines *arachno*- $[6,9-B_{10}H_{12}(N = C(Me)NRR')_2]$  (R = H, R' = *n*-Pr, *n*-Bu, Ph; R = R' = *i*-Pr, *n*-Bu) were synthesized.<sup>609</sup>

A series of 6- and 5-substituted derivatives of decaborane were synthesized via the cage-opening reactions of the *closo*-decaborate anion. The reactions of *closo*- $[B_{10}H_{10}]^{2-}$  with ionic-liquid-based superacidic hydrogen halides proceed with the boron cage opening and formation of the 6-halogen derivatives of *nido*-decaborane *nido*- $[6-X-B_{10}H_{13}]$  (X = Cl, Br, I). The 6-halogen derivatives *nido*- $[6-X-B_{10}H_{13}]$  (X = F, Cl) can be synthesized by the reactions of *closo*- $[B_{10}H_{10}]^{2-}$  with triflic acid in the presence of 1-fluoropentane and dichloromethane, respectively.<sup>610</sup> The 6-halogen derivatives isomerize to the corresponding 5-halogen derivatives  $[5-X-B_{10}H_{13}]$  (X = Cl, Br, I) in the presence of catalytic amount of triethylamine in toluene at 60 °C.<sup>611</sup> It is assumed that the isomerization occurs through transformation of  $[6-X-B_{10}H_{13}]$  into the  $[6-X-B_{10}H_{13}]^-$  anions followed by their isomerization. The iodo derivative  $[6-I-B_{10}H_{13}]$  was found to undergo photochemical isomerization to  $[5-I-B_{10}H_{13}]$  under UV-irradiation in solution.<sup>611</sup>

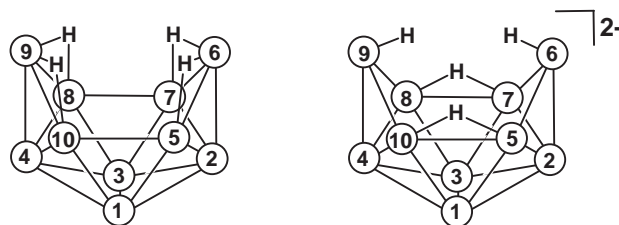


Fig. 17 Idealized structures and numbering of atoms in *nido*-decaborane  $[B_{10}H_{14}]$  (left) and *arachno*-decaborane  $[B_{10}H_{14}]^{2-}$  (right).



The reactions of halogen derivatives [5-X-B<sub>10</sub>H<sub>13</sub>] and [6-X-B<sub>10</sub>H<sub>13</sub>] (X = Cl, Br, I) with alcohols ROH in the presence of NaHCO<sub>3</sub> in dichloromethane lead to alkoxy derivatives [6-RO-B<sub>10</sub>H<sub>13</sub>] and [5-RO-B<sub>10</sub>H<sub>13</sub>] (R = Me, *t*-Bu, *c*Hx, CH<sub>2</sub>CH<sub>2</sub>SH, CH<sub>2</sub>CH<sub>2</sub>I, CH<sub>2</sub>CH<sub>2</sub>OCH<sub>2</sub>CH<sub>2</sub>Cl, (CH<sub>2</sub>)<sub>3</sub>C≡CH, CH(CH<sub>2</sub>CH=CH<sub>2</sub>)<sub>2</sub>), containing substituents in neighboring positions with respect to the original halogen derivatives. The reaction rate decreases in the halogen series I > Br > Cl.<sup>612</sup>

The 6-triflate derivative of *nido*-decaborane *nido*-[6-TfO-B<sub>10</sub>H<sub>13</sub>] was prepared by the reaction of *closo*-[B<sub>10</sub>H<sub>10</sub>]<sup>2-</sup> with neat triflic acid at ambient temperature.<sup>613,614</sup> In contrast, the reaction of *closo*-[B<sub>10</sub>H<sub>10</sub>]<sup>2-</sup> with triflic acid in 1-butyl-3-methylimidazolium triflate at 60 °C results in the 5-triflate derivative *nido*-[5-TfO-B<sub>10</sub>H<sub>13</sub>].<sup>615</sup> It was found that the reaction proceeds through formation of the 6-triflate derivative, which on heating isomerises into the 5-triflate derivative.<sup>615</sup> In the presence of catalytic amount of triethylamine, the isomerization of [6-TfO-B<sub>10</sub>H<sub>13</sub>] to [5-TfO-B<sub>10</sub>H<sub>13</sub>] proceeds even at room temperature. In a similar way, the reaction of *closo*-[B<sub>10</sub>H<sub>10</sub>]<sup>2-</sup> with sulfuric acid produces the 6-hydroxy derivative *nido*-[6-HO-B<sub>10</sub>H<sub>13</sub>].<sup>616</sup> The reactions of [5-TfO-B<sub>10</sub>H<sub>13</sub>] with methanol and 4-methoxyphenol in 1,2-dichloroethane at 70 °C result in the corresponding ethers [6-RO-B<sub>10</sub>H<sub>13</sub>] (R = Me, C<sub>6</sub>H<sub>4</sub>-4-OMe).<sup>615</sup>

The reaction of *nido*-[5-TfO-B<sub>10</sub>H<sub>13</sub>] with dimethylsulfide in toluene results in *arachno*-[5-TfO-6,9-B<sub>10</sub>H<sub>11</sub>(SMe<sub>2</sub>)<sub>2</sub>], while the similar reaction of *nido*-[6-TfO-B<sub>10</sub>H<sub>13</sub>] proceeds with substitution of the triflate group giving *arachno*-[6,9-B<sub>10</sub>H<sub>12</sub>(SMe<sub>2</sub>)<sub>2</sub>].<sup>615</sup>

The 6-acetoxy derivative *arachno*-[6-AcO-B<sub>10</sub>H<sub>13</sub>]<sup>2-</sup> was obtained by the reaction of decaborane with 1-ethyl-3-methylimidazolium acetate.<sup>617</sup>

The reactions of *closo*-[B<sub>10</sub>H<sub>10</sub>]<sup>2-</sup> with triflic acid in the presence of aromatic hydrocarbons sulfuric acid produce the corresponding 6-aryl derivatives *nido*-[6-Ar-B<sub>10</sub>H<sub>13</sub>]. The reactions with benzene and mesitylene give single products, whereas the reactions with monosubstituted aromatics (C<sub>6</sub>H<sub>5</sub>X, X = Cl, CH<sub>3</sub>, CF<sub>3</sub>) lead to mixtures of *ortho*-, *meta*-, and *para*-substituted isomers.<sup>613,614</sup> The similar reaction in cyclohexane gives in low yield the corresponding 6-alkyl derivative *nido*-[6-CHx-B<sub>10</sub>H<sub>13</sub>].<sup>613,614</sup>

The 6-alkyl- and 6-aryl derivatives of *nido*-decaborane *nido*-[6-R-B<sub>10</sub>H<sub>13</sub>] (R = Me, *n*-Bu, *t*-Bu, Ph) can be prepared by the reaction of the [B<sub>10</sub>H<sub>13</sub>]<sup>-</sup> anion with the corresponding organolithium derivatives followed by acidic workup.<sup>612</sup> Alternatively, the 6-alkyl derivatives *nido*-[6-R-B<sub>10</sub>H<sub>13</sub>] (R = *n*-Pr, *n*-Hex, *n*-Oct, Sia, Thx) can be obtained by the reaction of *arachno*-[6,9-(Me<sub>2</sub>S)<sub>2</sub>-B<sub>10</sub>H<sub>12</sub>] with the corresponding terminal alkenes followed by the treatment with Li[HBEt<sub>3</sub>] and acidic workup.<sup>618</sup>

The reactions of decaborane with various terminal alkenes in biphasic ionic-liquid/toluene mixtures lead to the corresponding 6-alkyldecaboranes *nido*-[6-R-B<sub>10</sub>H<sub>13</sub>] (R = C<sub>6</sub>H<sub>13</sub>, C<sub>8</sub>H<sub>17</sub>, CH(*i*-Pr)CH<sub>2</sub>CHMe<sub>2</sub>, (CH<sub>2</sub>)<sub>2</sub>C<sub>6</sub>H<sub>5</sub>, (CH<sub>2</sub>)<sub>3</sub>C<sub>6</sub>H<sub>5</sub>, (CH<sub>2</sub>)<sub>6</sub>Br, (CH<sub>2</sub>)<sub>6</sub>CH=CH<sub>2</sub>, (CH<sub>2</sub>)<sub>3</sub>OC<sub>3</sub>H<sub>7</sub>, (CH<sub>2</sub>)<sub>3</sub>SiMe<sub>3</sub>, (CH<sub>2</sub>)<sub>4</sub>COMe, (CH<sub>2</sub>)<sub>6</sub>OAc, (CH<sub>2</sub>)<sub>3</sub>OBn, (CH<sub>2</sub>)<sub>3</sub>OH, (CH<sub>2</sub>)<sub>3</sub>Bpin). The reaction mechanism includes the ionic-liquid-promoted formation of the [B<sub>10</sub>H<sub>13</sub>]<sup>-</sup> anion, its addition to the alkene to form [6-R-B<sub>10</sub>H<sub>12</sub>]<sup>-</sup> anion, and finally, protonation of the last one to form final product [6-R-B<sub>10</sub>H<sub>13</sub>].<sup>619</sup>

The reactions of decaborane with terminal alkenes in the presence of catalytic amounts of PtBr<sub>2</sub> or H<sub>2</sub>PtCl<sub>6</sub> lead to the 6,9-dialkyl derivatives *nido*-[6,9-R<sub>2</sub>-B<sub>10</sub>H<sub>12</sub>] (R = C<sub>2</sub>H<sub>5</sub>, C<sub>3</sub>H<sub>7</sub>, C<sub>4</sub>H<sub>9</sub>, C<sub>5</sub>H<sub>11</sub>).<sup>620</sup> The reactions of [5-TfO-B<sub>10</sub>H<sub>13</sub>] and [5-I-B<sub>10</sub>H<sub>13</sub>] with 1-pentene in the presence of catalytic amount of PtBr<sub>2</sub> at 55 °C lead to the corresponding 6,9-dialkyl derivatives [6,9-(C<sub>5</sub>H<sub>11</sub>)<sub>2</sub>-5-TfO-B<sub>10</sub>H<sub>11</sub>].<sup>615</sup>

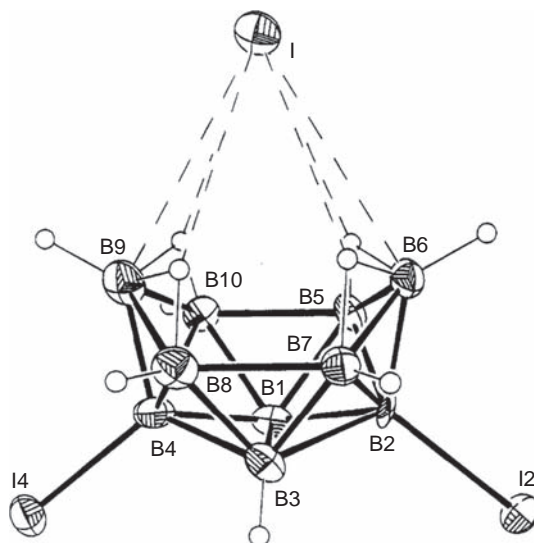
The reactions of decaborane with terminal alkynes in the presence of [Cp\*IrCl<sub>2</sub>]<sub>2</sub> in toluene lead to the corresponding 6,9-di(β-alkenyl) derivatives of decaborane [6,9-(*E*)-RCH=CH)<sub>2</sub>-B<sub>10</sub>H<sub>12</sub>] (R = H, C<sub>6</sub>H<sub>13</sub>, C<sub>6</sub>H<sub>5</sub>, (CH<sub>2</sub>)<sub>2</sub>Br, (CH<sub>2</sub>)<sub>3</sub>Cl, SiMe<sub>3</sub>), while the reactions in the presence of [(*p*-cymene)RuI<sub>2</sub>]<sub>2</sub> result in the 6,9-di(α-alkenyl) derivatives [6,9-(R(H<sub>2</sub>C=)C)<sub>2</sub>-B<sub>10</sub>H<sub>12</sub>] (R = C<sub>6</sub>H<sub>13</sub>, CH<sub>2</sub>-*c*-C<sub>6</sub>H<sub>11</sub>, (CH<sub>2</sub>)<sub>2</sub>Br, (CH<sub>2</sub>)<sub>3</sub>Cl).<sup>621,622</sup> In a similar way, the reactions of 6-alkyldecaboranes [6-R-B<sub>10</sub>H<sub>13</sub>] with terminal alkynes in the presence of [Cp\*IrCl<sub>2</sub>]<sub>2</sub> give asymmetrically substituted 6-alkyl-9-alkenyl-derivatives [6-R-9-(*E*)-R'CH=CH)<sub>2</sub>-B<sub>10</sub>H<sub>12</sub>] (R = (CH<sub>2</sub>)<sub>3</sub>SiMe<sub>3</sub>, R' = H, C<sub>6</sub>H<sub>5</sub>, C<sub>6</sub>H<sub>4</sub>-*m*-CH≡CH; CH<sub>2</sub>CH=CH<sub>2</sub>; R = C<sub>5</sub>H<sub>11</sub>, R' = H). The alkenyl-decaboranes were easily converted to other useful derivatives, including coupled-cage and functionally substituted compounds, via Ir-catalyzed hydroborations and Ru-catalyzed homo- and cross-olefin metathesis reactions.<sup>621,622</sup>

Decaborane [B<sub>10</sub>H<sub>14</sub>] and its 2,4-diiodo derivative [2,4-I<sub>2</sub>-B<sub>10</sub>H<sub>12</sub>] were found to form stable complexes with iodide anion. The structure of (Ph<sub>3</sub>PMe)<sub>2</sub>{I[2,4-I<sub>2</sub>-B<sub>10</sub>H<sub>12</sub>]} was determined by single crystal X-ray diffraction (Fig. 18).<sup>623</sup> The complex stability is explained by noncovalent charge transfer interactions between the iodide and the decaborane basket.<sup>624</sup> The binding energy for the {I[B<sub>10</sub>H<sub>14</sub>]}<sup>-</sup> complex was calculated to be 19.84 kcal/mol.<sup>625</sup>

### 1.16.3.3 Tetradecahydro-*arachno*-nonaborate anion [B<sub>9</sub>H<sub>14</sub>]<sup>-</sup>

The tetradecahydro-*arachno*-nonaborate anion [B<sub>9</sub>H<sub>14</sub>]<sup>-</sup> (Fig. 19) is a product of decaborane-14 degradation in aqueous basic media, which ensures its easy availability. Therefore, its chemistry has largely developed in parallel with the chemistry of decaborane, but is much less developed.

A series of derivatives of tetradecahydro-*arachno*-nonaborate anion with Lewis acid [4-L-B<sub>9</sub>H<sub>13</sub>] was prepared using different approaches. The reaction of *closo*-[B<sub>10</sub>H<sub>10</sub>]<sup>2-</sup> with nitriles in the presence of sulfuric or triflic acid results in nitrilium derivatives [4-RC≡N-B<sub>9</sub>H<sub>13</sub>] (R = Me, CHPh<sub>2</sub>).<sup>626</sup> The pyridinium derivative [4-Py-B<sub>9</sub>H<sub>13</sub>] was prepared by the substitution of SMe<sub>2</sub> in [4-Me<sub>2</sub>S-B<sub>9</sub>H<sub>13</sub>].<sup>627</sup> The benzylammonium derivative [4-PhCH<sub>2</sub>NH<sub>2</sub>-B<sub>9</sub>H<sub>13</sub>] was isolated from the reaction of [B<sub>9</sub>H<sub>14</sub>]<sup>-</sup> with *trans*-[PtCl<sub>2</sub>(NPh)<sub>2</sub>] in methanol.<sup>627</sup> Phosphonium derivative [4-(HC≡C)<sub>3</sub>P-B<sub>9</sub>H<sub>13</sub>] was synthesized by the reaction of [B<sub>9</sub>H<sub>14</sub>]<sup>-</sup> with the phosphine in diethyl ether in the presence of HCl.<sup>627</sup> The reactions of [4-Me<sub>2</sub>S-B<sub>9</sub>H<sub>13</sub>] with *sec*-butylamine or 4-phenylpyridine in benzene were found to mixtures of the corresponding [4-L-B<sub>9</sub>H<sub>13</sub>] and [5-L-B<sub>9</sub>H<sub>13</sub>] isomers.<sup>628</sup>



**Fig. 18** Structure of the  $[I(2,4-I_2-B_{10}H_{12})]^-$  complex. Reprinted with permission from Wermer, J. R.; Hollander, O.; Huffman, J. C.; Krause Bauer, J. A.; Dou, D.; Hsu, L.-Y.; Leussing, D. L.; Shore, S. G. *Inorg. Chem.* **1995**, *34*, 3065–3071. Copyright (1995) the American Chemical Society.

The protonation of  $[B_9H_9]^{2-}$  with HCl in dichloromethane leads to the 4,8-dichloro derivative  $[4,8-Cl_2-B_9H_{12}]^-$ .<sup>575</sup> The reaction of  $[B_9H_{14}]^-$  with  $BCl_3$  produces the 8-chloro derivative  $[8-Cl-B_9H_{13}]^-$  with some amount of the 6,7,8-trichloro derivative  $[6,7,8-Cl_3-B_9H_{11}]^-$ .<sup>629</sup> The 4,8-dibromo derivative  $[4,8-Br_2-B_9H_{12}]^-$  was prepared by the reaction of *nido*- $[B_9H_{12}]^-$  with  $HgBr_2$  in dichloromethane.<sup>627</sup>

Due to the possibility of using them as hypergolic additives to fuels, salts of the  $[B_9H_{14}]^-$  anion with nitrogen-containing cations have recently attracted interest.<sup>605,630</sup>

#### 1.16.4 conjuncto-Boranes

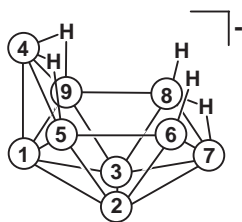
Among *conjuncto*-boranes, *nido,nido*-octadecaborane(22) *anti*- $[B_{18}H_{22}]$  and octadecahydro-*closo,closo*-heneicosaborate anion  $[B_{21}H_{18}]^-$  have recently attracted the greatest interest.

##### 1.16.4.1 *nido,nido*-Octadecaborane(22)

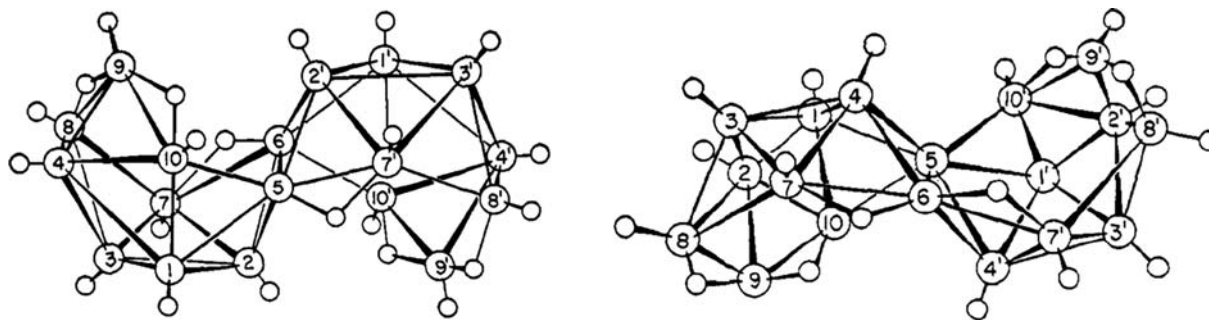
Octadecaborane(22) in the form of a mixture of *syn*- and *anti*-isomers (Fig. 20) is formed on the hydrolysis of  $(H_3O)_2[trans-B_{20}H_{18}] \cdot nH_2O$  and can be separated by fractional crystallization.<sup>631</sup> The photophysics of the both isomers have been studied by UV-vis spectroscopic techniques and quantum chemical calculations. In air-saturated hexane solution, *anti*- $[B_{18}H_{22}]$  shows fluorescence with a high quantum yield,  $\Phi_F = 0.97$ , and singlet oxygen  $O_2(^1\Delta_g)$  production ( $\Phi_\Delta \sim 0.008$ ). Conversely, isomer *syn*- $[B_{18}H_{22}]$  shows no measurable fluorescence, instead displaying much faster, picosecond nonradiative decay of excited singlet states.<sup>632</sup> Due to this, *anti*- $[B_{18}H_{22}]$  can be considered as a potential blue laser material.

The photophysical properties of *anti*- $[B_{18}H_{22}]$  can be tuned by partial substitution of hydrogen atoms with various functional groups. Because of this, combined with its high stability,<sup>633–635</sup> *anti*- $[B_{18}H_{22}]$  is attracting increasing research interest, while the *syn*- $[B_{18}H_{22}]$  isomer has received much less attention.<sup>636,637</sup>

The bromination of *anti*- $[B_{18}H_{22}]$  with bromine in the presence of  $AlCl_3$  leads to the 4-bromo or 4,4'-dibromo derivatives *anti*- $[4-Br-B_{18}H_{21}]$  or *anti*- $[4,4'-Br_2-B_{18}H_{20}]$  depending on the reagent ratio.<sup>638,639</sup> The reaction of *anti*- $[B_{18}H_{22}]$  with iodine in ethanol leads to the 4-iodo derivative *anti*- $[7-I-B_{18}H_{21}]$ , while the reaction with  $I_2$  or  $ICl$  in the presence of  $AlCl_3$  in dichloromethane results



**Fig. 19** Idealized structure and numbering of atoms in *arachno*-decaborane  $[B_9H_{14}]^-$ .



**Fig. 20** Structures and numbering of atoms in *syn*- (left) and *anti*- (right) isomers of  $[B_{18}H_{22}]$ . Reprinted with permission from Olsen, F. P.; Vasavada, R. C.; Hawthorne, M. F. *J. Am. Chem. Soc.* **1968**, *90*, 3946–3951. Copyright (1968) the American Chemical Society.

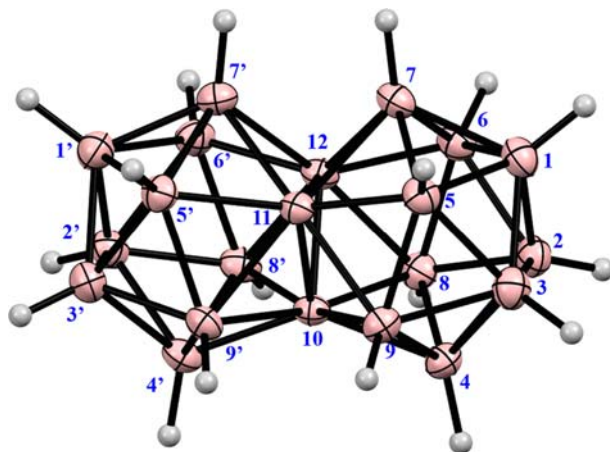
in the 4,4'-diiodo derivative *anti*-[4,4'-I<sub>2</sub>-B<sub>18</sub>H<sub>20</sub>].<sup>640</sup> The reaction of *anti*-[B<sub>18</sub>H<sub>22</sub>] with elemental sulfur in the presence of AlCl<sub>3</sub> at 125 °C leads to the 4,4'-dimercapto derivative *anti*-[4,4'-(HS)<sub>2</sub>-B<sub>18</sub>H<sub>20</sub>].<sup>641</sup>

The iodine atom in *anti*-[7-I-B<sub>18</sub>H<sub>21</sub>] can be substituted by various nucleophiles: the reaction with trifluoroacetamide in toluene in the presence of K<sub>3</sub>PO<sub>4</sub> gives the corresponding *N*-boronated amide *anti*-[7-CF<sub>3</sub>CONH-B<sub>18</sub>H<sub>21</sub>]; the reactions with *t*-BuOK, 4-FC<sub>6</sub>H<sub>4</sub>OK and 1-AdSK in toluene or tetrahydrofuran lead to the corresponding (thio)ethers *anti*-[7-RX-B<sub>18</sub>H<sub>21</sub>]. The reaction with potassium 2,6-dimethylthiophenolate in toluene results the corresponding thioether *anti*-[7-(2',6'-Me<sub>2</sub>C<sub>6</sub>H<sub>3</sub>S)-B<sub>18</sub>H<sub>21</sub>], while the reaction in tetrahydrofuran produces *anti*-[7-(2',6'-Me<sub>2</sub>C<sub>6</sub>H<sub>3</sub>S(CH<sub>2</sub>)<sub>4</sub>O)-B<sub>18</sub>H<sub>21</sub>].<sup>642</sup> The Pd-catalyzed reactions of *anti*-[7-I-B<sub>18</sub>H<sub>21</sub>] with CF<sub>3</sub>CONH<sub>2</sub>, *t*-BuOK and 2,6-Me<sub>2</sub>C<sub>6</sub>H<sub>3</sub>OK in the presence of catalytic amounts of RuPhos Pd G4 and RuPhos in 1,4-dioxane lead to the corresponding derivatives with B–N and B–O bonds *anti*-[7-X-B<sub>18</sub>H<sub>21</sub>].<sup>642</sup>

The reaction of *anti*-[B<sub>18</sub>H<sub>22</sub>] with neat methyl iodide in the presence of AlCl<sub>3</sub> at room temperature results in the 3,3',4,4'-tetramethyl derivative *anti*-[3,3',4,4'-Me<sub>4</sub>-B<sub>18</sub>H<sub>18</sub>], whereas the similar reaction with ethyl iodide gives the corresponding tetraethylated derivative *anti*-[3,3',4,4'-Et<sub>4</sub>-B<sub>18</sub>H<sub>18</sub>].<sup>643</sup> The dodecamethylated derivative *anti*-[2,2'-Cl<sub>2</sub>-1,1',3,3',4,4',7,7',8,8',10,10'-Me<sub>12</sub>-B<sub>18</sub>H<sub>8</sub>] was obtained by the reaction of *anti*-[B<sub>18</sub>H<sub>22</sub>] with methyl iodide in the presence of AlCl<sub>3</sub> in dichloromethane at 55 °C.<sup>644</sup>

Surprisingly, the reaction of *anti*-[B<sub>18</sub>H<sub>22</sub>] with pyridine in refluxing chloroform or benzene results in a twofold substitution in one of the B<sub>10</sub>-baskets to form *nido-arachno*-[6',9'-Py<sub>2</sub>-B<sub>18</sub>H<sub>20</sub>] together with some amount of *nido-nido*-[8'-Py-B<sub>18</sub>H<sub>21</sub>] and [3',8'-Py<sub>2</sub>-B<sub>16</sub>H<sub>18</sub>] as the main degradation product. In contrast to the thermochromic fluorescence of *nido-arachno*-[6',9'-Py<sub>2</sub>-B<sub>18</sub>H<sub>20</sub>] (from 620 nm brick red at room temperature to 585 nm yellow at 8 K), *nido-nido*-[8'-Py-B<sub>18</sub>H<sub>21</sub>] exhibit no luminescence.<sup>645,646</sup> The 6',9'-disubstituted derivatives with 4-picoline,<sup>646</sup> isoquinoline<sup>647</sup> and 5-hydroxyisoquinoline<sup>648</sup> were prepared in a similar way.

The reaction of *anti*-[B<sub>18</sub>H<sub>22</sub>] with methyl isonitrile MeNC in benzene leads to *anti*-[7-{(MeNH)C<sub>3</sub>N<sub>2</sub>HMe<sub>2</sub>}-B<sub>18</sub>H<sub>20</sub>] in which a reductive trimerization of MeNC gives an unusual imidazole-based carbene, {(MeNH)C<sub>3</sub>N<sub>2</sub>HMe<sub>2</sub>}, that is stabilized by coordination to the macropolyhedral boron cluster.<sup>649</sup> The reaction with *tert*-butyl isonitrile in 1,2-dichloroethane results in *anti*-[7-{(*t*-BuNHCH){*t*-BuNHC(CN)}CH<sub>2</sub>}-B<sub>18</sub>H<sub>20</sub>] in which a reductive oligomerization of *t*-BuNC has given the complex polynitrogen base {(*t*-BuNHCH){*t*-BuNHC(CN)}CH<sub>2</sub>:}, formally as a zwitterionic carbene attached to the macropolyhedral boron cluster.<sup>650</sup>



**Fig. 21** Idealized structure and numbering of atoms in the *closo-closo*-[B<sub>21</sub>H<sub>18</sub>]<sup>-</sup> anion.

#### 1.16.4.2 Octadecahydro-*closo,closo*-heneicosaborate anion $[B_{21}H_{18}]^-$

The protonation of  $trans-[B_{20}H_{18}]^{2-}$  in anhydrous hydrogen fluoride leads to the face-shared *closo-nido*- $[B_{20}H_{19}]^{-651}$  deprotonation of which gives *closo-nido*- $[B_{20}H_{19}]^{2-}$ . The reaction of  $trans-[B_{20}H_{18}]^{2-}$  with  $BF_3 \cdot OEt_2$  in 1,4-dioxane is an alternative route to the synthesis of *closo-nido*- $[B_{20}H_{19}]^{2-652}$  which on the treatment with triethylamine-borane  $Et_3N \cdot BH_3$  at 150 °C forms the face-shared *closo-closo*- $[B_{21}H_{18}]^-$  (Fig. 21).<sup>651</sup>

The reaction of *closo-closo*- $[B_{21}H_{18}]^-$  with anhydrous hydrogen fluoride at 100 °C produces, depending on the reaction time, a series of the fluoro derivatives  $[7-F-B_{21}H_{17}]^-$ ,  $[7,8-F_2-B_{21}H_{16}]^-$ ,  $[7,8'-F_2-B_{21}H_{16}]^-$ ,  $[7,8,9-F_3-B_{21}H_{15}]^-$ , and  $[7,8,9'-F_3-B_{21}H_{15}]^{-653}$

The complexation of *closo-closo*- $[B_{21}H_{18}]^-$  with cyclodextrins revealed its very low free energy of dehydration, thus qualifying it as an impressive new example of superchaotropic anions.<sup>654</sup>

## References

- McCleverty, J. A. *Annu. Rep. Prog. Chem., Sect. A: Inorg. Chem.* **2004**, *100*, 3–13.
- Onak, T. *Comprehensive Organometallic Chemistry*, vol. 1; Pergamon Press, 1982; pp 411–456.
- Grimes, R. N. *Comprehensive Organometallic Chemistry*, vol. 1; Pergamon Press, 1982; pp 459–542.
- Onak, T. *Comprehensive Organometallic Chemistry II*, vol. 1; Elsevier: Amsterdam, 1995; pp 217–255.
- Todd, L. E. *Comprehensive Organometallic Chemistry II*, vol. 1; Elsevier: Amsterdam, 1995; pp 257–273.
- Barton, L.; Srivastava, D. K. *Comprehensive Organometallic Chemistry II*, vol. 1; Elsevier: Amsterdam, 1995; pp 275–372.
- Grimes, R. N. T. *Comprehensive Organometallic Chemistry II*, vol. 1; Elsevier: Amsterdam, 1995; pp 373–430.
- Fox, M. A. *Comprehensive Organometallic Chemistry III*, vol. 3; Elsevier: Amsterdam, 2007; pp 49–112.
- Wesemann, L. *Comprehensive Organometallic Chemistry III*, vol. 3; Elsevier: Amsterdam, 2007; pp 113–131.
- Weller, A. S. *Comprehensive Organometallic Chemistry III*, vol. 3; Elsevier: Amsterdam, 2007; pp 133–174.
- Hosmane, N. S.; Maguire, J. A. *Comprehensive Organometallic Chemistry III*, vol. 3; Elsevier: Amsterdam, 2007; pp 175–264.
- Grimes, R. N., Ed.; *Metal Interactions with Boron Clusters*, Springer Science: New York, 1982.
- Grimes, R. N. *Carboranes*, 2nd ed.; Academic Press: London, 2011.
- Grimes, R. N. *Carboranes*, 3rd ed.; Academic Press: London, 2016.
- Muetterties, E. L.; Knoth, W. H. *Polyhedral Boranes*, Marcel Dekker: New York, 1968.
- Muetterties, E. L., Ed.; *Boron Hydride Chemistry*, Academic Press: New York, 1975.
- King, R. B. *Chem. Rev.* **2001**, *101*, 1119–1152.
- Chen, Z.; King, R. B. *Chem. Rev.* **2005**, *105*, 3613–3642.
- Longuet-Higgins, H. C.; de Roberts, M. V. *Proc. R. Soc. Lond. A* **1955**, *230*, 110–119.
- Hawthorne, M. F.; Pitochelli, A. R. *J. Am. Chem. Soc.* **1960**, *82*, 3228–3229.
- Sivaev, I. B.; Bregadze, V. I.; Sjöberg, S. *Collect. Czech. Chem. Commun.* **2002**, *67*, 679–727.
- Zhao, X.; Yang, Z.; Chen, H.; Wang, Z.; Zhou, X.; Zhang, H. *Coord. Chem. Rev.* **2021**, *444*, 214042.
- Wang, F.; Wang, Y.; Wang, X. *Chin. J. Appl. Chem.* **1998**, *15* (5), 111–112.
- Geis, V.; Gutsche, K.; Knapp, C.; Scherer, H.; Uzun, R. *Dalton Trans.* **2009**, 2687–2694.
- Chen, W.; Wu, G.; He, T.; Li, Z.; Guo, Z.; Liu, H.; Huang, Z.; Chen, P. *Int. J. Hydrogen Energy* **2016**, *41*, 15471–15476.
- Moury, R.; Gigante, A.; Hagemann, H. *Int. J. Hydrogen Energy* **2017**, *42*, 22417–22421.
- Chen, X.; Liu, X.-R.; Wang, X.; Chen, X.-M.; Jing, Y.; Wei, D. *Dalton Trans.* **2021**, *50*, 13676–13679.
- Chen, X.-M.; Jing, Y.; Kang, J.-X.; Wang, Y.; Guo, Y.; Chen, X. *Inorg. Chem.* **2021**, *60*, 18466–18472.
- Saldin, V. I.; Sukhovei, V. V.; Ignat'eva, L. N.; Savchenko, N. N.; Slobodyuk, A. B.; Kavun, V. Y. *Khim. Tekhnol.* **2019**, *20*, 615–619.
- He, K.; Li, H.-W.; Hwang, S. J.; Akiba, E. *J. Phys. Chem. C* **2014**, *118*, 6084–6089.
- He, L.; Li, H.-W.; Nakajima, H.; Tumanov, N.; Filinchuk, Y.; Hwang, S.-J.; Sharma, M.; Hagemann, H.; Akiba, E. *Chem. Mater.* **2015**, *27*, 5483–5486.
- He, L.; Shao, H.; Felderhoff, M.; Li, H.-W.; Li, X.; Zhu, Q.; Zhang, D.; Wu, D.; Fu, Y.; Deng, Y.; Lu, Z. *Inorg. Chim. Acta* **2017**, *464*, 147–151.
- He, L.; Li, H.-W.; Tumanov, N.; Filinchuk, Y.; Akiba, E. *Dalton Trans.* **2015**, *44*, 15882–15887.
- Duchêne, L.; Remhof, A.; Hagemann, H.; Battagli, C. *Energy Storage Mater.* **2020**, *25*, 782–794.
- Brighi, M.; Murgia, F.; Černý, R. *Cell Rep. Phys. Sci.* **2020**, *1*, 100217.
- Remhof, A.; Yan, Y.; Rentsch, D.; Borgschulte, A.; Jensen, C. M.; Züttel, A. *J. Mater. Chem. A* **2014**, *2*, 7244–7249.
- Hwang, S.-J.; Bowman, R. C.; Reiter, J. W.; Rijssenbeek, J.; Soloveichik, G. L.; Zhao, J.-C.; Kabbour, H.; Ahn, C. C. *J. Phys. Chem. C* **2008**, *112*, 3164–3169.
- Garroni, S.; Milanese, C.; Pottmaier, D.; Mulas, G.; Nolis, P.; Girella, A.; Caputo, R.; Olid, D.; Teixdor, F.; Baricco, M.; Marini, A.; Suriñach, S.; Baro, D. *J. Phys. Chem. C* **2011**, *115*, 16664–16671.
- Yan, Y.; Li, H.-W.; Maekawa, H.; Aoki, M.; Noritake, T.; Matsumoto, M.; Miwa, K.; Towata, S.; Orimo, S. *Mater. Trans.* **2011**, *52*, 1443–1446.
- Yan, Y.; Remhof, A.; Hwang, S.-J.; Li, H.-W.; Mauron, P.; Orimo, S.; Züttel, A. *Phys. Chem. Chem. Phys.* **2012**, *14*, 6514–6519.
- Orimo, S.; Nakamori, Y.; Eliseo, J. R.; Züttel, A.; Jensen, C. M. *Chem. Rev.* **2007**, *107*, 4111–4132.
- Li, H.-W.; Yan, Y.; Orimo, S.; Züttel, A.; Jensen, C. M. *Energies* **2011**, *4*, 185–214.
- Puszkiet, J.; Garroni, S.; Milanese, C.; Gennari, F.; Klassen, T.; Dornheim, M.; Pistidda, C. *Inorganics* **2017**, *5*, 74.
- Her, J.-H.; Zhou, W.; Stavila, V.; Brown, C. M.; Udovic, T. J. *J. Phys. Chem. C* **2009**, *113*, 11187–11189.
- Verdal, N.; Her, J.-H.; Stavila, V.; Soloninin, A. V.; Babanova, O. A.; Skripov, A. V.; Udovic, T. J.; Rush, J. J. *J. Solid State Chem.* **2014**, *212*, 81–91.
- White, J. L.; Newhouse, R. J.; Zhang, J. Z.; Udovic, T. J.; Stavila, V. *J. Phys. Chem. C* **2016**, *120*, 25725–25731.
- Tiritiris, I.; Schleid, T. Z. *Anorg. Allg. Chem.* **2002**, *628*, 1411–1418.
- Yousufuddin, M.; Her, J.-H.; Zhou, W.; Jalilati, S. S.; Udovic, T. J. *Inorg. Chim. Acta* **2009**, *362*, 3155–3158.
- Her, J.-H.; Yousufuddin, M.; Zhou, W.; Jalilati, S. S.; Kulleck, J. G.; Zan, J. A.; Hwang, S.-J.; Bowman, R. C.; Udovic, T. J. *Inorg. Chem.* **2008**, *47*, 9757–9759.
- Sadikun, Y.; Schouwink, P.; Brighi, M.; Łodziana, Z.; Černý, R. *Inorg. Chem.* **2017**, *56*, 5006–5016.
- Moury, R.; Łodziana, Z.; Remhof, A.; Duchêne, L.; Roedern, E.; Gigante, A.; Hagemann, H. *Acta Crystallogr. B* **2019**, *75*, 406–413.
- Solntsev, K. A.; Kuznetsov, N. T.; Ponomarev, V. I. *Dokl. Chem.* **1976**, *228*, 391.
- Ponomarev, V. I.; Lyubeznova, T. Y.; Solntsev, K. A.; Kuznetsov, N. T. *Koord. Khim.* **1991**, *17*, 21.
- Wunderlich, J. A.; Lipscomb, W. N. *J. Am. Chem. Soc.* **1960**, *82*, 4427–4428.
- Tiritiris, I.; Schleid, T. Z. *Anorg. Allg. Chem.* **2003**, *629*, 1390–1402.



56. Uspenskaya, S. I.; Solntsev, K. A.; Kuznetsov, N. T. *J. Struct. Chem.* **1975**, *16*, 450–451.
57. Tiritiris, I.; Schleid, T.; Müller, K.; Preetz, W. *Z. Anorg. Allg. Chem.* **2000**, *626*, 323–325.
58. Moury, R.; Łodziana, Z.; Remhof, A.; Duchêne, E.; Gigante, A.; Hagemann, H. *Inorg. Chem.* **2022**, *61*, 5224–5233.
59. Tang, W. S.; Udovic, T. J.; Stavila, V. *J. Alloys Compd.* **2015**, *645*, S200–S204.
60. Tiritiris, I.; Schleid, T. *Z. Anorg. Allg. Chem.* **2004**, *630*, 541–546.
61. Chen, X.; Liu, Y.-H.; Alexander, A.-M.; Gallucci, J. C.; Hwang, S.-J.; Lingam, K. H.; Huang, Z.; Wang, C.; Li, H.; Zhao, Q.; Ozkan, U. S.; Shore, S. G.; Zhao, J.-C. *Chem. A Eur. J.* **2014**, *20*, 7325–7333.
62. Didelot, E.; Sadikina, Y.; Łodziana, Z.; Černý, R. *Solid State Sci.* **2019**, *90*, 86–94.
63. Solntsev, K. I.; Kuznetsov, N. T.; Ponomarev, V. I. *Izv. Akad. Nauk SSSR Ser. Neorg. Mater.* **1976**, *12*, 1044–1048.
64. Tiritiris, I.; Schleid, T. *Z. Anorg. Allg. Chem.* **2001**, *627*, 1836–1845.
65. Solntsev, K. I.; Kuznetsov, N. T.; Rannev, N. V.; Zavodnik, V. E. *Dokl. Akad. Nauk SSSR* **1977**, *232*, 1366.
66. Zimmermann, L. W.; Schleid, T. *Z. Anorg. Allg. Chem.* **2012**, *638*, 1599.
67. Solntsev, K. I.; Kuznetsov, N. T.; Rannev, N. V. *Dokl. Akad. Nauk SSSR* **1975**, *221*, 1378.
68. Tiritiris, I.; Schleid, T.; Müller, K. *Appl. Magn. Reson.* **2007**, *32*, 459–481.
69. Skripov, A. V.; Babanova, O. A.; Soloninin, A. V.; Stavila, V.; Verdal, N.; Udovic, T. J.; Rush, J. J. *J. Phys. Chem. C* **2013**, *117*, 25961–25968.
70. Pitt, M. P.; Paskevicius, M.; Brown, D. H.; Sheppard, D. A.; Buckley, C. E. *J. Am. Chem. Soc.* **2013**, *135*, 6930–6941.
71. Udovic, T. J.; Matsuo, M.; Umemoto, A.; Verdal, N.; Stavila, V.; Skripov, A. V.; Rush, J. J.; Takamura, H.; Orimo, S. *Chem. Commun.* **2014**, *50*, 3750–3752.
72. Verdal, N.; Udovic, T. J.; Stavila, V.; Tang, W. S.; Rush, J. J.; Skripov, A. V. *J. Phys. Chem. C* **2014**, *118*, 17483–17489.
73. Teprovich, J. A.; Colón-Mercado, H.; Washington, A. K., II; Ward, P. A.; Greenway, S.; Missimer, D. M.; Hartman, H.; Velten, J.; Christian, J. H.; Zidan, R. *J. Mater. Chem. A* **2015**, *3*, 22853–22859.
74. He, L.; Li, H.-W.; Akiba, E. *Energies* **2015**, *8*, 12429–12438.
75. Grønderstev, J. B.; Lee, Y.-S.; Paskevicius, M.; Møller, K. T.; Yan, Y.; Cho, Y. W.; Jensen, T. R. *Inorg. Chem.* **2020**, *59*, 11449–11458.
76. Gradišek, A.; Krmel, M.; Paskevicius, M.; Hansen, B. R. S.; Jensen, T. R.; Dolinšek, J. *J. Phys. Chem. C* **2018**, *122*, 17073–17079.
77. Skripov, A. V.; Skoryunov, R. V.; Soloninin, A. V.; Babanova, O. A.; Stavila, V.; Udovic, T. J. *J. Phys. Chem. C* **2018**, *122*, 3256–3262.
78. Huang, Z.; Gallucci, J.; Chen, X.; Yisgedu, T.; Lingam, H. K.; Shore, S. G.; Zhao, J.-C. *J. Mater. Chem.* **2010**, *20*, 2743–2745.
79. Kraus, F.; Panda, M.; Müller, T.; Albert, B. *Inorg. Chem.* **2013**, *52*, 4692–4699.
80. Hansen, B. R. S.; Tumanov, N.; Santoru, A.; Pistidda, C.; Bednarcik, J.; Klassen, T.; Dornheim, M.; Filinchuk, Y.; Jensen, T. R. *Dalton Trans.* **2017**, *46*, 7770–7781.
81. He, L.; Lin, H.; Li, H.-F.; Filinchuk, Y.; Zhang, J.; Liu, Y.; Yang, M.; Hou, Y.; Deng, Y.; Li, H.-W.; Shao, H.; Wang, L.; Lu, Z. *J. Power Sources* **2018**, *396*, 574–579.
82. Kanaeva, O. A.; Kuznetsov, N. T.; Solntsev, K. A. *Russ. J. Inorg. Chem.* **1990**, *35*, 1421–1423.
83. Sadikina, Y.; Brighi, M.; Schouwink, P.; Černý, R. *Adv. Energy Mater.* **2015**, *5*, 1501016.
84. Sadikina, Y.; Skoryunov, R. V.; Babanova, O. A.; Soloninin, A. V.; Łodziana, Z.; Brighi, M.; Skripov, A. V.; Černý, R. *J. Phys. Chem. C* **2017**, *121*, 5503–5514.
85. Schouwink, P.; Sadikina, Y.; van Beek, W.; Černý, R. *Int. J. Hydrogen Energy* **2015**, *40*, 10902–10907.
86. Møller, K. T.; Paskevicius, M.; Andreasen, J. G.; Lee, J.; Chen-Tan, N.; Overgaard, J.; Payandeh, S. H.; Silvester, D. S.; Buckley, C. E.; Jensen, T. R. *Chem. Commun.* **2019**, *55*, 3410–3413.
87. Didelot, E.; Łodziana, Z.; Murgia, F.; Černý, R. *Crystals* **2019**, *9*, 372.
88. Van, N.-D.; Kleeberg, F. M.; Schleid, T. *Z. Anorg. Allg. Chem.* **2015**, *641*, 2484–2489.
89. Kunkely, H.; Vogler, A. *Inorg. Chim. Acta* **2007**, *360*, 679–680.
90. Tiritiris, I.; Van, N.-D.; Schleid, T. *Z. Anorg. Allg. Chem.* **2011**, *637*, 682–688.
91. Bareiß, K. U.; Kleeberg, F. M.; Ensling, D.; Jüstel, T.; Schleid, T. *Z. Naturforsch. B* **2022**, *77*, 179–187.
92. Kleeberg, F. M.; Zimmermann, L. W.; Schleid, T. *J. Clust. Sci.* **2022**, *33*. <https://doi.org/10.1007/s10876-021-02166-6>.
93. Zimmermann, L. W.; Schleid, T. *Z. Anorg. Allg. Chem.* **2011**, *637*, 1903–1908.
94. Zimmermann, L. W.; Van, N.-D.; Gudat, D.; Schleid, T. *Angew. Chem. Int. Ed.* **2016**, *55*, 1909–1911.
95. Sadikina, Y.; Didelot, E.; Łodziana, Z.; Černý, R. *Dalton Trans.* **2018**, *47*, 5843–5849.
96. Drozdova, V. V.; Malinina, E. A.; Belousova, O. N.; Polyakova, I. N.; Kuznetsov, N. T. *Russ. J. Inorg. Chem.* **2008**, *53*, 1024–1033.
97. Paskevicius, M.; Hansen, B. R. S.; Jørgensen, M.; Richter, B.; Jensen, T. R. *Nat. Commun.* **2017**, *8*, 15136.
98. Zhang, L.; Hu, P.; Zhang, G. *J. Wuhan Univ. (Nat. Sci. Ed.)* **1989**, *(2)*, 67–70.
99. Volkov, O.; Hu, C.; Paetzold, P. *Z. Anorg. Allg. Chem.* **2005**, *631*, 1107–1112.
100. Malinina, E. A.; Drozdova, V. V.; Mustyatsa, V. N.; Goeva, L. V.; Polyakova, I. N.; Votina, N. A.; Zhizhin, K. Y.; Kuznetsov, N. T. *Russ. J. Inorg. Chem.* **2006**, *51*, 1723–1727.
101. Avdeeva, V. V.; Malinina, E. A.; Sivaev, I. B.; Bregadze, V. I.; Kuznetsov, N. T. *Crystals* **2016**, *6*, 60.
102. Kochneva, I. K.; Avdeeva, V. V.; Polyakova, I. N.; Malinina, E. A. *Polyhedron* **2016**, *109*, 19–25.
103. Malinina, E. A.; Korolenko, S. E.; Kubasov, A. S.; Goeva, L. V.; Avdeeva, V. V.; Kuznetsov, N. T. *Polyhedron* **2020**, *184*, 11456.
104. Zhang, Y.; Yang, L.; Wang, L.; Duttwyler, S.; Xing, H. *Angew. Chem. Int. Ed.* **2019**, *58*, 8145–8150.
105. Zhang, Y.; Wang, L.; Hu, J.; Duttwyler, S.; Cui, X.; Xing, H. *CrystEngComm* **2020**, *22*, 2649–2655.
106. Zhang, Y.; Hu, J.; Krishna, R.; Wang, L.; Yang, L.; Cui, X.; Duttwyler, S.; Xing, H. *Angew. Chem. Int. Ed.* **2020**, *59*, 17664–17669.
107. Wang, L.; Sun, W.; Zhang, Y.; Xu, N.; Krishna, R.; Hu, J.; Jiang, Y.; He, Y.; Xing, H. *Angew. Chem. Int. Ed.* **2021**, *60*, 22865–22870.
108. Wang, L.; Sun, W.; Duttwyler, S.; Zhang, Y. *J. Solid State Chem.* **2021**, *299*, 122167.
109. Sun, W.; Hu, J.; Duttwyler, S.; Wang, L.; Krishna, R.; Zhang, Y. *Sep. Purif. Technol.* **2022**, *283*, 120220.
110. Sun, W.-Q.; Hu, J.-B.; Jiang, Y.-J.; Xu, N.; Wang, L.-Y.; Li, J.-H.; Hu, Y.-Q.; Duttwyler, S.; Zhang, Y.-B. *Chem. Eng. J.* **2022**, *439*, 135745.
111. Korolenko, S. E.; Kubasov, A. S.; Goeva, L. V.; Avdeeva, V. V.; Malinina, E. A.; Kuznetsov, N. T. *Inorg. Chim. Acta* **2021**, *527*, 120587.
112. Korolenko, S. E.; Kubasov, A. S.; Khan, N. A.; Goeva, L. V.; Burlov, A. S.; Divaeva, L. N.; Malinina, E. A.; Avdeeva, V. V.; Zhizhin, K. Y.; Kuznetsov, N. T. *J. Clust. Chem.* **2022**, *33*. <https://doi.org/10.1007/s10876-022-02263-0>.
113. Avdeeva, V. V.; Korolenko, S. E.; Malinina, E. A.; Kuznetsov, N. T. *Russ. J. Gen. Chem.* **2022**, *92*, 393–417.
114. Avdeeva, V. V.; Malinina, E. A.; Zhizhin, K. Y.; Kuznetsov, N. T. *Russ. J. Inorg. Chem.* **2020**, *65*, 514–534.
115. Korolenko, S. E.; Avdeeva, V. V.; Malinina, E. A.; Kuznetsov, N. T. *Russ. J. Inorg. Chem.* **2021**, *66*, 1350–1373.
116. Avdeeva, V. V.; Malinina, E. A.; Kuznetsov, N. T. *Coord. Chem. Rev.* **2022**, *469*, 214636.
117. Sivaev, I. B. *Chem. Heterocycl. Comp.* **2017**, *53*, 638–658.
118. Shan, Z.-X.; Sheng, L.-L.; Yang, R.-J. *Chin. J. Explos. Propellants* **2017**, *40* (3), 1–16.
119. Schroeder, M. A. *J. Propuls. Power* **1998**, *14*, 981–990.
120. Schroeder, M. A.; Fifer, R. A.; Kaste, P. J.; Liebman, S. A. *J. Propuls. Power* **2001**, *17*, 441–448.
121. Chen, F.-T.; Tan, H.-M.; Luo, Y.-J.; Duo, Y.-Q.; Chou, W.-L.; Liu, Z.-Q.; Luo, S.-G. *Chin. J. Explos. Propellants* **2000**, *23* (3), 19–21.
122. Pang, W.-Q.; Xue, Y.-N.; Fan, X.-Z.; Xu, H.-X.; Shi, X.-B.; Li, Y.; Li, Y.-H.; Wang, X.-F. *Chin. J. Energy Mater.* **2012**, *20*, 280–285.
123. Pan, X.-X.; Huang, X.-F.; Li, S.-J.; Yang, Y.-J.; Zhang, J.-K.; Jiang, Y.-K.; Shen, J.-F.; Guo, Y.-H. *Chin. J. Explos. Propellants* **2019**, *42*, 614–620.
124. Jiang, F.; Niu, Y.-L.; Bu, Y.-F.; Sun, P.-P.; Wang, X.-F.; Nan, H.; Wang, Q. *Chin. J. Energy Mater.* **2021**, *29*, 937–947.



125. Rao, M. H.; Muralidharan, K. *Polyhedron* **2016**, *115*, 105–110.
126. Derdziuk, J.; Malinowski, P. J.; Jaroń, T. *Int. J. Hydrogen Energy* **2019**, *44*, 27030–27038.
127. Malinina, E. A.; Mustyatsa, V. N.; Goeva, L. V.; Kuznetsov, N. T. *Russ. J. Coord. Chem.* **2001**, *27*, 373–376.
128. Polyakova, I. N.; Malinina, E. A.; Drozdova, V. V.; Kuznetsov, N. T. *Cryst. Rep.* **2009**, *54*, 831–839.
129. Sharon, P.; Afri, M.; Mittin, S.; Gottlieb, L.; Schmerling, B.; Grinstein, D.; Welner, S.; Frimer, A. A. *Polyhedron* **2019**, *157*, 71–89.
130. Rao, M. H.; Muralidharan, K. *Dalton Trans.* **2013**, *42*, 8854–8860.
131. Shackelford, S. A.; Belletire, J. L.; Boat, J. A.; Schneider, S.; Wheaton, A. K.; Wight, B. A.; Hudgens, L. M.; Ammon, H. L.; Strauss, S. H. *Org. Lett.* **2009**, *11*, 2623–2626.
132. Jiao, N.; Zhang, Y.; Liu, L.; Shreeve, J. M.; Zhang, S. *J. Mater. Chem. A* **2017**, *5*, 13341–13346.
133. Shackelford, S. A.; Belletire, J. L.; Boat, J. A.; Schneider, S.; Wheaton, A. K.; Wight, B. A.; Ammon, H. L.; Peryshkov, D. V.; Strauss, S. H. *Org. Lett.* **2010**, *12*, 2714–2717.
134. Belletire, J. L.; Schneider, S.; Wight, B. A.; Strauss, S. L.; Shackelford, S. A. *Synth. Commun.* **2011**, *42*, 155–169.
135. Sheng, L.; Shan, Z.; Guo, X.; Yang, R. *Chin. J. Org. Chem.* **2018**, *38*, 2093–2100.
136. Saldin, V. I.; Savchenko, N. N.; Ignat'eva, L. N.; Mashtalyar, D. V. *Vestn. Far-East. Branch. Russ. Acad. Sci.* **2018**, *5*, 63–72.
137. Saldin, V. I.; Sukhovey, V. V. *Vestn. Far-East. Branch. Russ. Acad. Sci.* **2020**, *6*, 56–60.
138. Saldin, V. I.; Karpenko, M. A.; Ignateva, L. N.; Nikolenko, Y. M.; Buznik, V. M.; Mikhailov, Y. M. *Russ. J. Inorg. Chem.* **2009**, *54*, 13–16.
139. Nedel'ko, V. V.; Mikhailov, Y. M.; Chukanov, N. V.; Saldin, V. I.; Ganina, L. V.; Buznik, V. M. *Russ. J. Phys. Chem. B* **2011**, *5*, 26–32.
140. Saldin, V. I.; Buznik, V. M.; Mikhailov, Y. M.; Ganina, L. V. *Russ. J. Phys. Chem. A* **2018**, *92*, 653–655.
141. Skachkova, V. K.; Goeva, L. V.; Grachev, A. V.; Avdeeva, V. V.; Malinina, E. A.; Shaulov, A. Y.; Berlin, A. A.; Kuznetsov, N. T. *Russ. J. Inorg. Chem.* **2017**, *62*, 84–89.
142. Mebs, S.; Kalonowski, R.; Grabowsky, S.; Förster, D.; Kickbusch, R.; Justus, E.; Morgenroth, W.; Paulmann, C.; Luger, P.; Gabel, D.; Lentz, D. *Inorg. Chem.* **2011**, *50*, 90–103.
143. Mebs, S.; Kalonowski, R.; Grabowsky, S.; Förster, D.; Kickbusch, R.; Justus, E.; Morgenroth, W.; Paulmann, C.; Luger, P.; Gabel, D.; Lentz, D. *J. Phys. Chem. A* **2011**, *115*, 1385–1395.
144. Zhao, X.; Zhang, F.; Chen, H.; Sheng, R.; Baryshnikov, G. V.; Ågren, H.; Zhou, X.; Zhang, H. *Chem. Eng. J.* **2020**, *385*, 123827.
145. Đordović, V.; Tošner, Z.; Uchman, M.; Zhigunov, A.; Reza, M.; Ruokolainen, J.; Pramanik, G.; Cigler, P.; Kaliková, K.; Gradzielski, M.; Matějček, P. *Langmuir* **2016**, *32*, 6713–6722.
146. Assaf, K. I.; Ural, M. S.; Pan, F.; Georgiev, T.; Simova, S.; Rissanen, K.; Gabel, D.; Nau, W. M. *Angew. Chem. Int. Ed.* **2015**, *54*, 6852–6856.
147. Wang, W.; Wang, X.; Cao, J.; Liu, J.; Qi, B.; Zhou, X.; Zhang, S.; Gabel, G.; Nau, W. M.; Assaf, K. I.; Zhang, H. *Chem. Commun.* **2018**, *54*, 2098–20101.
148. Wang, W.; Qi, B.; Yu, X.; Li, W.-Z.; Yang, Z.; Zhang, H.; Liu, S.; Liu, Y.; Wang, X.-Q. *Adv. Funct. Mater.* **2020**, *30*, 2004452.
149. Assaf, K. I.; Nau, W. M. *Angew. Chem. Int. Ed.* **2018**, *57*, 13968–13981.
150. Knoth, W. H.; Miller, H. C.; Sauer, J. C.; Balthis, J. H.; Chia, Y. T.; Muetterties, E. L. *Inorg. Chem.* **1964**, *3*, 159–167.
151. Haackel, O.; Preetz, W. *Z. Anorg. Allg. Chem.* **1995**, *621*, 1454–1458.
152. Al-Jourhawi, M.; Cendoya, P.; Shmalko, A.; Marei, T.; Gabel, D. *J. Organomet. Chem.* **2021**, *949*, 121967.
153. Solntsev, K. A.; Mebel, A. M.; Votínova, N. A.; Kuznetsov, N. T.; Charkin, O. P. *Russ. J. Coord. Chem.* **1992**, *18*, 296–320.
154. Solntsev, K. A.; Ivanov, S. V.; Sakharov, S. G.; Katser, S. B.; Chernayavskii, A. S.; Votínova, N. A.; Klyuchishche, E. A.; Kuznetsov, N. T. *Russ. J. Coord. Chem.* **1997**, *23*, 369–376.
155. Ivanov, S. V.; Miller, S. M.; Anderson, O. P.; Solntsev, K. A.; Strauss, S. H. *Inorg. Chem.* **2003**, *125*, 4694–4695.
156. Kobayashi, Y.; Ivanov, S. V.; Popov, A. A.; Miller, S. M.; Anderson, O. P.; Solntsev, K. A.; Strauss, S. H. *Heteroatom Chem.* **2006**, *17*, 181–187.
157. Peryshkov, D. V.; Popov, A. A.; Strauss, S. H. *J. Am. Chem. Soc.* **2009**, *131*, 18393–18403.
158. Tiritiris, I.; Schleid, T. *Z. Anorg. Allg. Chem.* **2004**, *630*, 1555–1563.
159. Gu, W.; Ozerov, O. V. *Inorg. Chem.* **2011**, *50*, 2726–2728.
160. Juhasz, M. A.; Matheson, G. R.; Chang, P. S.; Rosenbaum, A. J.; Juers, D. H. *Synth. React. Inorg., Met.-Org., Nano-Met. Chem.* **2016**, *46*, 583–588.
161. Knapp, C. *Comprehensive Inorganic Chemistry II*; vol. 1; Elsevier: Amsterdam, 2013; pp 651–679.
162. Sivaev, I. B.; Bregadze, V. I. In *Handbook of Boron Science with Applications in Organometallics, Catalysis, Materials and Medicine. Vol. 1. Boron in Organometallic Chemistry*; Hosmane, N. S., Eagling, R., Eds., World Scientific: London, 2019; pp 147–203.
163. Bukovsky, E. V.; Fiedler, S. R.; Peryshkov, D. V.; Popov, A. P.; Strauss, S. H. *Eur. J. Inorg. Chem.* **2012**, 208–212.
164. Peryshkov, D. V.; Bukovsky, E. V.; Lacroix, M. R.; Wu, H.; Zhou, W.; Jones, W. M.; Lozinšek, M.; Folsom, T. C.; Heytiger, D. L.; Udovic, T. J.; Strauss, S. H. *Inorg. Chem.* **2017**, *56*, 12023–12041.
165. Bukovsky, E. V.; Peryshkov, D. V.; Wu, H.; Zhou, W.; Tang, W. S.; Jones, W. M.; Stavila, V.; Udovic, T. J.; Strauss, S. H. *Inorg. Chem.* **2017**, *56*, 4369–4379.
166. Peryshkov, D. V.; Strauss, S. H. *J. Fluor. Chem.* **2010**, *131*, 1252–1256.
167. Peryshkov, D. V.; Bukovsky, E. V.; Folsom, T. C.; Strauss, S. H. *Polyhedron* **2013**, *58*, 197–205.
168. Peryshkov, D. V.; Popov, A. A.; Strauss, S. H. *J. Am. Chem. Soc.* **2010**, *132*, 13902–13913.
169. Bukovsky, E. V.; Pluntze, A. M.; Strauss, S. H. *J. Fluor. Chem.* **2017**, *203*, 90–98.
170. Peryshkov, D. V.; Friedemann, R.; Goreschnik, E.; Mazej, Z.; Seppelt, K.; Strauss, S. H. *J. Fluor. Chem.* **2013**, *145*, 118–127.
171. Malischewski, M.; Peryshkov, D. V.; Bukovsky, E. V.; Seppelt, K.; Strauss, S. H. *Inorg. Chem.* **2016**, *55*, 12254–12262.
172. Hollow, S. E.; Johnstone, T. C. *Chem. Commun.* **2022**, *58*, 2375–2378.
173. Lacroix, M. R.; Bukovsky, E. V.; Lozinšek, M.; Folsom, T. C.; Newell, B. S.; Liu, Y.; Peryshkov, D. V.; Strauss, S. H. *Inorg. Chem.* **2018**, *57*, 14983–15000.
174. Hansen, B. R. S.; Paskевичius, M.; Jørgensen, M.; Jensen, T. R. *Chem. Mater.* **2017**, *29*, 3423–3430.
175. Tiritiris, I.; Bareiß, K. U.; Schleid, T. *Z. Naturforsch. B* **2020**, *75*, 777–790.
176. Kravchenko, E. A.; Gippius, A. A.; Tkachev, A. V.; Golubev, A. V.; Kubasov, A. S.; Bykov, A. Y.; Zhizhin, K. Y.; Kuznetsov, N. T. *J. Solid State Chem.* **2022**, *311*, 123143.
177. Tiritiris, I.; Schleid, T. *Z. Anorg. Allg. Chem.* **2001**, *627*, 2568–2570.
178. Derendorf, J.; Keßler, M.; Knapp, C.; Rühle, M.; Schulz, C. *Dalton Trans.* **2010**, *39*, 8671–8678.
179. Arai, J.; Matsuo, A.; Fujisaki, T.; Ozawa, K. *J. Power Sources* **2009**, *193*, 851–854.
180. Chen, Z.; Liu, J.; Jansen, A. N.; Kumar, G. G.; Casteel, B.; Amine, K. *Electrochem. Solid State Lett.* **2010**, *13*, A39–A42.
181. Kumar, G. G.; Bailey, W. H., III; Peterson, B. K.; Casteel, W. J. *J. Electrochem. Soc.* **2011**, *158*, A146–A153.
182. Bolli, C.; Derendorf, J.; Jenne, C.; Keßler, M. *Eur. J. Inorg. Chem.* **2017**, 4552–4558.
183. Avelar, A.; Tham, F. S.; Reed, C. A. *Angew. Chem. Int. Ed.* **2009**, *48*, 3491–3493.
184. Schäfer, A.; Reißmann, M.; Jung, S.; Schäfer, A.; Saak, W.; Brendler, E.; Müller, T. *Organometallics* **2013**, *32*, 4713–4722.
185. Belletire, J. L.; Schneider, S.; Shackelford, S. A.; Peryshkov, D. V.; Strauss, S. H. *J. Fluor. Chem.* **2011**, *132*, 925–936.
186. Neiuwenhuyzen, M.; Seddon, K. R.; Teixidor, F.; Puga, A. V.; Viñas, C. *Inorg. Chem.* **2009**, *48*, 889–901.
187. Zhou, N.; Zhao, G.; Dong, K.; Sun, J.; Shao, H. *RSC Adv.* **2012**, *2*, 9830–9838.
188. Kleeberg, F. M.; Dinnebier, R. E.; Schleid, T. *Inorg. Chim. Acta* **2017**, *467*, 147–154.
189. Musgrave, R. A.; Hales, R. L. N.; Schäfer, A.; Russell, A. D.; Gates, P. J.; Manners, I. *Dalton Trans.* **2018**, *47*, 2759–2768.
190. Groutchik, K.; Jaiswal, K.; Dobrovetsky, R. *Org. Biomol. Chem.* **2021**, *19*, 5544–5550.

191. Chinnam, A. K.; Petrutik, N.; Wang, K.; Shlomovich, A.; Shamis, O.; Tov, D. S.; Siceska, M.; Yan, Q.-L.; Dobrovetsky, R.; Gozin, M. *J. Mater. Chem. A* **2018**, *6*, 19989–19997.
192. Exner, R. M.; Jenne, C.; Wegener, B. *Z. Anorg. Allg. Chem.* **2021**, *647*, 500–506.
193. Wang, L.; Jiang, T.; Duttwyler, S.; Zhang, Y. *CrystEngComm* **2021**, *23*, 282–291.
194. Peryshkov, D. V.; Strauss, S. H. *Inorg. Chem.* **2017**, *56*, 4072–4083.
195. Lauk, S.; Zimmer, M.; Morgenstern, B.; Huch, V.; Müller, C.; Sitzmann, H.; Schäfer, A. *Organometallics* **2021**, *40*, 618–626.
196. Friedemann, R.; Seppelt, K. *Eur. J. Inorg. Chem.* **2013**, 1197–1206.
197. Arnold, N.; Braunschweig, H.; Brenner, P.; Jimenez-Halla, J. O. C.; Kupfer, T.; Radacki, K. *Organometallics* **2012**, *31*, 1897–1907.
198. Lin, Q.; Gao, L.; Kauffmann, B.; Zhang, J.; Ma, C.; Luo, D.; Gan, Q. *Chem. Commun.* **2018**, *54*, 13447–13450.
199. Li, R.-J.; Han, M.; Tessarolo, J.; Holstein, J. J.; Lübber, J.; Dittlich, B.; Volkmann, C.; Finze, M.; Jenne, C.; Clever, G. H. *ChemPhotoChem* **2019**, *3*, 378–383.
200. Tiritiris, I.; Schleid, T. *Z. Anorg. Allg. Chem.* **2003**, *629*, 581–583.
201. Kessler, M.; Knapp, C.; Zogaj, A. *Organometallics* **2011**, *30*, 3786–3792.
202. Malischewski, M.; Bukovsky, E. V.; Strauss, S. H.; Seppelt, K. *J. Fluor. Chem.* **2018**, *212*, 107–111.
203. Kessler, M.; Knapp, C.; Sagawe, V.; Scherer, H.; Uzun, R. *Inorg. Chem.* **2010**, *49*, 5223–5230.
204. Müther, K.; Fröhlich, R.; Mück-Lichtenfeld, C.; Grimme, S.; Oestreich, M. *J. Am. Chem. Soc.* **2011**, *133*, 12442–12444.
205. Bolli, C.; Derendorf, J.; Keßler, M.; Knapp, C.; Scherer, H.; Schulz, C.; Warneke, J. *Angew. Chem. Int. Ed.* **2010**, *49*, 3536–3538.
206. Malischewski, M.; Bukovsky, E. V.; Strauss, S. H.; Seppelt, K. *Inorg. Chem.* **2015**, *54*, 11563–11566.
207. Boere, R. T.; Kacprzak, S.; Keßler, M.; Knapp, C.; Riebau, R.; Riedel, S.; Roemmele, T. L.; Rühle, M.; Scherer, H.; Weber, S. *Angew. Chem. Int. Ed.* **2011**, *50*, 549–552.
208. Boere, R. T.; Derendorf, J.; Jenne, C.; Kacprzak, S.; Keßler, M.; Riebau, R.; Riedel, S.; Roemmele, T. L.; Rühle, M.; Scherer, H.; Vent-Schmidt, T.; Warneke, J.; Weber, S. *Chem. A Eur. J.* **2014**, *20*, 4447–4459.
209. Warneke, J.; Hou, G.-L.; Apra, E.; Jenne, C.; Yang, Z.; Qin, Z.; Kowalski, K.; Wang, X.-B.; Xantheas, S. S. *J. Am. Chem. Soc.* **2017**, *139*, 14749–14756.
210. Kaszynski, P.; Ringstrand, B. *Angew. Chem. Int. Ed.* **2015**, *54*, 6576–6581.
211. Tokarz, P.; Kaszynski, P.; Domagala, S.; Wozniak, K. *J. Organomet. Chem.* **2015**, *798*, 70–79.
212. Ali, M. O.; Lasseter, J. C.; Zurawinski, R.; Pietrzak, A.; Pecyna, J.; Wojciechowski, J.; Friedli, A. C.; Pocięcha, D.; Kaszynski, P. *Chem. A Eur. J.* **2019**, *25*, 2616–2630.
213. Nelyubin, A. V.; Selivanov, N. A.; Bykov, A. Y.; Klyukin, I. N.; Novikov, A. S.; Zhdanov, A. P.; Zhizhin, K. Y.; Kuznetsov, N. T. *Russ. J. Inorg. Chem.* **2020**, *65*, 795–799.
214. Sivaev, I. B.; Semioshkin, A. A.; Breilochs, B.; Sjöberg, S.; Bregadze, V. I. *Polyhedron* **2000**, *19*, 627–632.
215. Stogniy, M. Y.; Sivaev, I. B. *Reactions* **2022**, *3*, 172–191.
216. Druzina, A. A.; Shmalko, A. V.; Sivaev, I. B.; Bregadze, V. I. *Russ. Chem. Rev.* **2021**, *90*, 785–830.
217. Sivaev, I. B.; Kulikova, N. Y.; Nizhnik, E. A.; Vichuzhanin, M. V.; Starikova, Z. A.; Semioshkin, A. A.; Bregadze, V. I. *J. Organomet. Chem.* **2008**, *693*, 519–525.
218. Serdyukov, A.; Kosenko, I.; Druzina, A.; Grin, M.; Mironov, A. F.; Bregadze, V. I.; Laskova, J. *J. Organomet. Chem.* **2021**, *946–947*, 121905.
219. Orlova, A. V.; Kondakov, N. N.; Kimel, B. G.; Kononov, L. O.; Kononova, E. G.; Sivaev, I. B.; Bregadze, V. I. *Appl. Organomet. Chem.* **2007**, *21*, 98–100.
220. Semioshkin, A. A.; Osipov, S. N.; Grebenyuk, J. N.; Nizhnik, E. A.; Godovikov, I. A.; Shchetnikov, G. T.; Bregadze, V. I. *Collect. Czech. Chem. Commun.* **2007**, *72*, 1717–1724.
221. Semioshkin, A.; Nizhnik, E.; Godovikov, I.; Starikova, Z.; Bregadze, V. I. *J. Organomet. Chem.* **2007**, *692*, 4020–4028.
222. Nakamura, H.; Kikuchi, S.; Kawai, K.; Ishii, S.; Sato, S. *Pure Appl. Chem.* **2018**, *90*, 745–753.
223. Semioshkin, A.; Laskova, J.; Ilinova, A.; Bregadze, V.; Lesnikowski, Z. J. *J. Organomet. Chem.* **2011**, *696*, 539–543.
224. Semioshkin, A. A.; Las'kova, Y. N.; Zhidkova, O. B.; Bregadze, V. I. *Russ. Chem. Bull.* **2008**, *57*, 1996–1998.
225. Prikaznov, A. V.; Las'kova, Y. N.; Semioshkin, A. A.; Sivaev, I. B.; Kisin, A. V.; Bregadze, V. I. *Russ. Chem. Bull.* **2011**, *60*, 2550–2554.
226. Kondakov, N. N.; Orlova, A. V.; Zinin, A. I.; Kimel, B. G.; Kononov, L. O.; Sivaev, I. B.; Bregadze, V. I. *Russ. Chem. Bull.* **2005**, *54*, 1352–1353.
227. Tsurubuchi, T.; Shirakawa, M.; Kurosawa, W.; Matsumoto, K.; Ubagai, R.; Umishio, H.; Suga, Y.; Yamazaki, J.; Arakawa, A.; Maruyama, Y.; Seki, T.; Shibui, Y.; Yoshida, F.; Zaboronok, A.; Suzuki, M.; Sakurai, Y.; Tanaka, H.; Nakai, K.; Ishikawa, E.; Matsumura, A. *Cell* **2020**, *9*, 1277.
228. Semioshkin, A.; Laskova, J.; Wojtczak, B.; Andrysiak, A.; Godovikov, I.; Bregadze, V.; Lesnikowski, Z. J. *J. Organomet. Chem.* **2009**, *694*, 1375–1379.
229. Semioshkin, A.; Bregadze, V.; Godovikov, I.; Ilinova, A.; Lesnikowski, Z. J.; Lobanova, I. *J. Organomet. Chem.* **2011**, *696*, 3750–3755.
230. Semioshkin, A.; Ilinova, A.; Lobanova, I.; Bregadze, V.; Paradowska, E.; Studzińska, M.; Jablonska, A.; Lesnikowski, Z. J. *Tetrahedron* **2013**, *69*, 8034–8041.
231. Ilinova, A. A.; Bregadze, V. I.; Bogomazova, A. N.; Lobanova, I. A.; Mironov, A. F.; Semioshkin, A. A. *Russ. Chem. Bull.* **2013**, *62*, 1115–1119.
232. Laskova, J.; Kozlova, A.; Bialek-Pietras, M.; Studzińska, M.; Paradowska, E.; Bregadze, V.; Lesnikowski, Z. J.; Semioshkin, A. *J. Organomet. Chem.* **2016**, *807*, 29–35.
233. Novopashina, D. S.; Vorobyeva, M. A.; Lomzov, A. A.; Silnikov, V. N.; Venyaminova, A. G. *Int. J. Mol. Sci.* **2021**, *22*, 182.
234. Grin, M. A.; Semioshkin, A. A.; Titeev, R. A.; Nizhnik, E. A.; Grebenyuk, J. N.; Mironov, A. F.; Bregadze, V. I. *Mendeleeev Commun.* **2007**, *17*, 14–15.
235. Bregadze, V. I.; Semioshkin, A. A.; Las'kova, J. N.; Berzina, M. Y.; Lobanova, I. A.; Sivaev, I. B.; Grin, M. A.; Titeev, R. A.; Brittal, D. I.; Ulybina, O. V.; Chestnova, A. V.; Ignatova, A. A.; Feofanov, A. V.; Mironov, A. F. *Appl. Organomet. Chem.* **2009**, *23*, 370–374.
236. Efremenko, A. V.; Ignatova, A. A.; Borsheva, A. A.; Grin, M. A.; Bregadze, V. I.; Sivaev, I. B.; Mironov, A. F.; Feofanov, A. V. *Photochem. Photobiol. Sci.* **2012**, *11*, 645–652.
237. Semioshkin, A.; Tsaryova, O.; Zhidkova, O.; Bregadze, V.; Wöhrle, D. J. *Porphyrins Phthalocyanines* **2006**, *10*, 1293–1300.
238. Birsöz, B.; Efremenko, A. V.; Ignatova, A. A.; Gül, A.; Feofanov, A. V.; Sivaev, I. B.; Bregadze, V. I. *Biochem. Biophys. J. Neutron Ther. Cancer Treat.* **2013**, *1*, 8–14.
239. Bregadze, V. I.; Sivaev, I. B.; Dubey, R. D.; Semioshkin, A.; Shmal'ko, A. V.; Kosenko, I. D.; Lebedeva, K. V.; Mandal, S.; Sreejith, P.; Sarkar, A.; Shen, Z.; Wu, A.; Hosmane, N. S. *Chem. A Eur. J.* **2020**, *26*, 13832–13841.
240. Druzina, A. A.; Zhidkova, O. B.; Kosenko, I. D. *Russ. Chem. Bull.* **2020**, *69*, 1080–1084.
241. Kosenko, I.; Laskova, J.; Kozlova, A.; Semioshkin, A.; Bregadze, V. I. *J. Organomet. Chem.* **2020**, *921*, 121370.
242. Justus, E.; Iztelevuova, D. T.; Kasantsev, A. V.; Axartov, M. M.; Lork, E.; Gabel, D. *Collect. Czech. Chem. Commun.* **2007**, *72*, 1740–1754.
243. Schaffran, T.; Lissel, F.; Samatanga, B.; Karlsson, G.; Burghardt, A.; Edwards, K.; Winterhalter, M.; Peschka-Süss, R.; Schubert, R.; Gabel, D. *J. Organomet. Chem.* **2009**, *694*, 1708–1712.
244. Schaffran, T.; Burghardt, A.; Barnert, S.; Peschka-Süss, R.; Schubert, R.; Winterhalter, M.; Gabel, D. *Bioconjug. Chem.* **2009**, *20*, 2190–2198.
245. Semioshkin, A.; Laskova, J.; Zhidkova, O.; Godovikov, I.; Starikova, Z.; Bregadze, V.; Gabel, D. *J. Organomet. Chem.* **2010**, *695*, 370–374.
246. Kikuchi, S.; Kanoh, K.; Sato, S.; Sakurai, Y.; Suzuki, M.; Nakamura, H. *J. Control. Release* **2016**, *237*, 160–167.
247. Couto, M.; Mastandrea, I.; Cabrera, P.; Cabral, P.; Teixidor, F.; Cerecetto, H.; Viñas, C. *Chem. A Eur. J.* **2017**, *23*, 9233–9238.
248. Sato, S.; Ishii, S.; Nakamura, H. *Eur. J. Inorg. Chem.* **2017**, *4406*–4410.
249. Ishii, S.; Nakamura, H. *J. Organomet. Chem.* **2018**, *865*, 178–182.
250. Nakagawa, F.; Kawashima, H.; Morita, T.; Nakamura, H. *Cell* **2020**, *9*, 1615.
251. Corona-López, M. M.; Muñoz-Flores, B. M.; Chaari, M.; Nuñez, R.; Jiménez-Pérez, V. M. *Eur. J. Inorg. Chem.* **2021**, 2047–2054.
252. Laskova, J.; Kosenko, I.; Serdyukov, A.; Sivaev, I.; Bregadze, V. I. *J. Organomet. Chem.* **2022**, *959*, 122186.
253. Druzina, A. A.; Grammatikova, N. E.; Zhidkova, O. B.; Nekrasova, N. A.; Dudarova, N. V.; Kosenko, I. D.; Grin, M. A.; Bregadze, V. I. *Molecules* **2022**, *27*, 2920.
254. Nishimura, K.; Harrison, S.; Kawai, K.; Morita, T.; Miura, K.; Okada, S.; Nakamura, H. *Bioorg. Med. Chem. Lett.* **2022**, *72*, 128869.
255. Goszczyński, T. M.; Kowalski, K.; Lesnikowski, Z. J.; Boratyński, J. *J. Biochim. Biophys. Acta* **1850**, *2015*, 411–418.
256. Fink, K.; Kobak, K.; Kasztura, M.; Boratyński, J.; Goszczyński, T. M. *Bioconjug. Chem.* **2018**, *29*, 3509–3515.

257. Lozinskaya, E. I.; Cotessat, M.; Shmalko, A. V.; Ponkratov, D. O.; Gumileva, L. V.; Sivaev, I. B.; Shaplov, A. S. *Polym. Int.* **2019**, *68*, 1570–1579.
258. Zhao, X.; Yang, Z.; Kuklin, A. V.; Baryshnikov, G. V.; Ågren, H.; Zhou, X.; Zhang, H. *ACS Appl. Mater. Interfaces* **2020**, *12*, 42821–42831.
259. Popova, T. V.; Pyshnaya, I. A.; Zakharova, O. D.; Akulov, A. E.; Shevelev, O. B.; Poletaeva, J.; Zavjalov, E. L.; Silnikov, V. N.; Ryabchikova, E. I.; Godovikova, T. S. *Biomedicine* **2021**, *9*, 74.
260. Bernard, R.; Cornu, D.; Grüner, B.; Dozol, J.-F.; Miele, P.; Bonnetot, B. *J. Organomet. Chem.* **2002**, *657*, 83–90.
261. Semioshkin, A.; Bregadze, V.; Godovikov, I.; Ilinova, A.; Laskova, J.; Starikova, Z. *J. Organomet. Chem.* **2011**, *696*, 2760–2762.
262. Ilinova, A. A.; Bregadze, V. I.; Laskova, Y. N.; Semioshkin, A. A.; Mironov, A. F. *Russ. Chem. Bull.* **2012**, *61*, 1663–1666.
263. Laskova, J.; Kozlova, A.; Ananyev, I.; Bregadze, V.; Semioshkin, A. *J. Organomet. Chem.* **2017**, *834*, 64–72.
264. Peymann, T.; Lork, E.; Gabel, D. *Inorg. Chem.* **1996**, *35*, 1355–1360.
265. Sivaev, I. B.; Sjöberg, S.; Bregadze, V. I.; Gabel, D. *Tetrahedron Lett.* **1999**, *40*, 3451–3454.
266. Genady, A. R.; Nakamura, H. *Org. Biomol. Chem.* **2010**, *8*, 4427–4435.
267. El-Zaria, M. E.; Genady, A. R.; Nakamura, H. *New J. Chem.* **2010**, *34*, 1612–1622.
268. Koo, M.-S.; Ozawa, T.; Santos, R. A.; Lamborn Bollen, A. W.; Deen, D. F.; Kahl, S. B. *J. Med. Chem.* **2007**, *50*, 820–827.
269. El-Zaria, M. E.; Ban, H. S.; Nakamura, H. *Chem. A Eur. J.* **2010**, *16*, 1543–1552.
270. Jenne, C.; Kirsch, C. *Dalton Trans.* **2015**, *44*, 13119–13124.
271. Zhang, Y.; Liu, J.; Duttwyler, S. *Eur. J. Inorg. Chem.* **2015**, 5158–5162.
272. Peymann, T.; Herzog, A.; Knobler, C. B.; Hawthorne, M. F. *Angew. Chem. Int. Ed.* **1999**, *38*, 1062–1064.
273. Peymann, T.; Knobler, C. B.; Khan, S. I.; Hawthorne, M. F. *J. Am. Chem. Soc.* **2001**, *123*, 2182–2185.
274. Bayer, M. J.; Hawthorne, M. F. *Inorg. Chem.* **2004**, *43*, 2018–2020.
275. Bondarev, O.; Hawthorne, M. F. *Chem. Commun.* **2011**, *47*, 6978–6980.
276. Jørgensen, M.; Jensen, S. R. H.; Humphries, T. D.; Rowles, M. R.; Sofianos, M. V.; Buckley, C. E.; Jensen, T. R.; Paskevicius, M. *J. Phys. Chem. C* **2020**, *124*, 11340–11349.
277. Van, N.; Tiritiris, I.; Winter, R. F.; Sarkar, B.; Singh, P.; Duboc, C.; Muñoz-Castro, A.; Arratia-Perez, R.; Kaim, W.; Schleid, T. *Chem. A Eur. J.* **2010**, *16*, 11242–11245.
278. Peymann, T.; Knobler, C. B.; Khan, S. I.; Hawthorne, M. F. *Angew. Chem. Int. Ed.* **2001**, *40*, 1664–1667.
279. Farha, O. K.; Julius, R. L.; Lee, M. W.; Huertas, R. E.; Knobler, C. B.; Hawthorne, M. F. *J. Am. Chem. Soc.* **2005**, *127*, 18243–18251.
280. Goswami, L. N.; Everett, T. A.; Khan, A. A.; Hawthorne, M. F. *Eur. J. Inorg. Chem.* **2020**, 377–381.
281. Qian, E. A.; Wixtrom, A. I.; Axtell, J. C.; Saebi, A.; Jung, D.; Rehak, P.; Han, Y.; Mouly, E. H.; Mosallaei, D.; Chow, S.; Messina, M. S.; Wang, J. Y.; Royappa, A. T.; Rheingold, A. L.; Maynard, H. D.; Král, P.; Spokoyny, A. M. *Nat. Chem.* **2017**, *9*, 333–340.
282. Wixtrom, A. I.; Shao, Y.; Jung, D.; Machan, C. W.; Kevork, S. N.; Qian, E. A.; Axtell, J. C.; Khan, S. I.; Kubiak, C. P.; Spokoyny, A. M. *Inorg. Chem. Front.* **2016**, *3*, 711–717.
283. Lee, M. W.; Farha, O. K.; Hawthorne, M. F.; Hansch, C. H. *Angew. Chem. Int. Ed.* **2007**, *46*, 3018–3022.
284. Aubry, T. J.; Axtell, J. C.; Basile, V. M.; Winchell, K. J.; Lindemuth, J. R.; Porter, T. M.; Liu, J.-Y.; Alexandrova, A. N.; Kubiak, C. P.; Tolbert, S. H.; Spokoyny, A. M.; Schwartz, B. J. *Adv. Mater.* **2019**, *31*, 1805647.
285. Stauber, J. M.; Qian, F. A.; Han, Y.; Rheingold, A. L.; Král, P.; Fujita, D.; Spokoyny, A. M. *J. Am. Chem. Soc.* **2020**, *142*, 327–334.
286. Maderna, A.; Knobler, C. B.; Hawthorne, M. F. *Angew. Chem. Int. Ed.* **2001**, *40*, 1661–1664.
287. Li, T.; Jalisatgi, S. S.; Bayer, M. J.; Maderna, A.; Khan, S. I.; Hawthorne, M. F. *J. Am. Chem. Soc.* **2005**, *127*, 17832–17841.
288. Goswami, L. N.; Chakravarty, S.; Lee, M. W.; Jalisatgi, S. S.; Hawthorne, M. F. *Angew. Chem. Int. Ed.* **2011**, *50*, 4689–4691.
289. Goswami, L. N.; Ma, L.; Chakravarty, S.; Cai, Q.; Jalisatgi, S. S.; Hawthorne, M. F. *Inorg. Chem.* **2013**, *52*, 1694–1700.
290. Goswami, L. N.; Ma, L.; Kueffer, P. J.; Jalisatgi, S. S.; Hawthorne, M. F. *Molecules* **2013**, *18*, 9034–9048.
291. Chakravarty, S.; Sarma, S. J.; Goswami, L. N.; Cai, Q.-Y.; Shapiro, E. M.; Hawthorne, M. F.; Ma, L. *Chem. Commun.* **2019**, *55*, 12348–12351.
292. Jalisatgi, S. S.; Kulkarni, V. S.; Tang, B.; Houston, Z. H.; Lee, M. W.; Hawthorne, M. F. *J. Am. Chem. Soc.* **2011**, *133*, 12382–12385.
293. Goswami, L. N.; Ma, L.; Cai, Q.; Sarma, S. J.; Jalisatgi, S. S.; Hawthorne, M. F. *Inorg. Chem.* **2013**, *52*, 1701–1709.
294. Goswami, L. N.; Houston, Z. H.; Sarma, S. J.; Li, H.; Jalisatgi, S. S.; Hawthorne, M. F. *J. Org. Chem.* **2012**, *77*, 11333–11338.
295. Sarma, S. J.; Khan, A. A.; Goswami, L. N.; Jalisatgi, S. S.; Hawthorne, M. F. *Chem. A Eur. J.* **2016**, *22*, 12715–12723.
296. Safronov, A. V.; Jalisatgi, S. S.; Hawthorne, M. F. *Eur. J. Inorg. Chem.* **2017**, 4378–4392.
297. Axtell, J. C.; Saleh, L. M. A.; Qian, E. A.; Wixtrom, A. I.; Spokoyny, A. M. *Inorg. Chem.* **2018**, *57*, 2333–2350.
298. Gabel, D.; Moller, D.; Harfst, S.; Roesler, J.; Ketz, H. *Inorg. Chem.* **1993**, *32*, 2276–2278.
299. El-Zaria, M.; Nakamura, H. *Inorg. Chem.* **2009**, *48*, 11896–11902.
300. Genady, A. R.; Ioppolo, J. A.; Azaam, M. M.; El-Zaria, M. E. *Eur. J. Med. Chem.* **2015**, *93*, 574–583.
301. Kusaka, S.; Hattori, Y.; Uehara, K.; Asano, T.; Tanimori, S.; Kirihata, M. *Appl. Radiat. Isot.* **2011**, *69*, 1768–1770.
302. Hattori, Y.; Kusaka, S.; Mukumoto, M.; Uehara, K.; Asano, T.; Suzuki, M.; Masunaga, S.; Ono, K.; Tanimori, S.; Kirihata, M. *J. Med. Chem.* **2012**, *55*, 6980–6984.
303. Hattori, Y.; Kusaka, S.; Mukumoto, M.; Ishimura, M.; Ohta, Y.; Takenaka, H.; Uehara, K.; Asano, T.; Suzuki, M.; Masunaga, S.; Ono, K.; Tanimori, S.; Kirihata, M. *Amino Acids* **2014**, *46*, 2715–2720.
304. Isono, A.; Tsuji, M.; Sanada, Y.; Matsushita, A.; Masunaga, S.; Hirayama, T.; Nagasawa, H. *ChemMedChem* **2019**, *14*, 823–832.
305. Hirase, S.; Aoki, A.; Hattori, Y.; Morimoto, K.; Noguchi, K.; Fujii, I.; Takatani-Nakase, T.; Futaki, S.; Kirihata, M.; Nakase, I. *Mol. Pharm.* **2022**, *19*, 1135–1145.
306. Lechtenberg, B.; Gabel, D. *J. Organomet. Chem.* **2005**, *690*, 2780–2782.
307. Nakamura, H.; Ueno, M.; Lee, J.-D.; Ban, H. S.; Justus, E.; Fan, P.; Gabel, D. *Tetrahedron Lett.* **2007**, *48*, 3151–3154.
308. Lee, J.-D.; Ueno, M.; Miyajima, Y.; Nakamura, H. *Org. Lett.* **2007**, *9*, 323–326.
309. Nakamura, H.; Lee, J.-D.; Ueno, M.; Miyajima, Y.; Ban, H. S. *Nanobiotechnol* **2007**, *3*, 135–145.
310. Justus, E.; Awad, A.; Hohnholt, M.; Schaffran, T.; Edwards, K.; Karlsson, G.; Damian, L.; Gabel, D. *Bioconjug. Chem.* **2007**, *18*, 1287–1293.
311. Nakamura, H.; Ueda, N.; Ban, H. S.; Ueno, M.; Tachikawa, S. *Org. Biomol. Chem.* **2012**, *10*, 1374–1380.
312. Asano, R.; Nagami, A.; Fukumoto, Y.; Miura, K.; Yazama, F.; Ito, H.; Sakata, I.; Tai, A. *J. Photochem. Photobiol. B* **2014**, *140*, 140–149.
313. Takeuchi, K.; Hattori, Y.; Kawabata, S.; Futamura, G.; Hiramatsu, R.; Wanibuchi, M.; Tanaka, H.; Masunaga, S.; Ono, K.; Miyatake, S.; Kirihata, M. *Cell* **2020**, *9*, 1551.
314. Mochizuki, M.; Sato, S.; Asatyas, S.; Lesnikowski, Z. J.; Hayashi, T.; Nakamura, H. *RSC Adv.* **2019**, *9*, 23973–23978.
315. Hattori, Y.; Ishimura, M.; Ohta, Y.; Takenaka, H.; Kawabata, S.; Kirihata, M. *ACS Med. Chem. Lett.* **2022**, *13*, 50–54.
316. Assaf, K. I.; Suckova, O.; Al Danaf, N.; von Glasenapp, V.; Gabel, D.; Nau, W. M. *Org. Lett.* **2016**, *18*, 932–935.
317. Nakase, I.; Katayama, M.; Hattori, Y.; Ishimura, M.; Inaura, S.; Fujiwara, D.; Takatani-Nakase, T.; Fujii, I.; Futaki, S.; Kirihata, M. *Chem. Commun.* **2019**, *55*, 13955–13968.
318. Sano, T. *Bioconjug. Chem.* **1999**, *10*, 905–911.
319. Mier, W.; Gabel, D.; Haberkorn, U.; Eisenhut, M. *Z. Anorg. Allg. Chem.* **2004**, *630*, 1258–1262.
320. Kimura, S.; Masunaga, S.; Harada, T.; Kawamura, Y.; Ueda, S.; Okuda, K.; Nagasawa, H. *Bioorg. Med. Chem.* **2011**, *19*, 1721–1728.
321. Iguchi, Y.; Michiue, H.; Kitamatsu, M.; Hayashi, Y.; Takenaka, F.; Nishiki, T.; Matsui, H. *Biomaterials* **2015**, *56*, 10–17.
322. Fujimura, A.; Yasui, S.; Igawa, K.; Ueda, A.; Watanabe, K.; Hanafusa, T.; Ichikawa, Y.; Yoshihashi, S.; Tsuchida, K.; Kamiya, A.; Furuya, S. *Cell* **2020**, *9*, 2149.
323. Kitamatsu, M.; Nakamura-Tachibana, A.; Ishikawa, Y.; Michiue, H. *Processes* **2021**, *9*, 167.
324. Yamagami, M.; Tajima, T.; Ishimoto, K.; Miyake, H.; Michiue, H.; Takaguchi, Y. *Heteroat. Chem.* **2018**, *29*, e21467.



325. Kalot, G.; Godard, A.; Busser, B.; Pliquet, J.; Broekgaarden, M.; Motto-Ros, V.; Wegner, K. D.; Resch-Genger, U.; Köster, U.; Denat, F.; Coll, J.-L.; Bodio, E.; Goze, C.; Sancey, L. *Cell* **1953**, *2020*, 9.
326. Michiue, H.; Sakurai, Y.; Kondo, N.; Kitamatsu, M.; Bin, F.; Nakajima, K.; Hirota, Y.; Kawabata, S.; Nishiki, T.; Ohmori, I.; Tomizawa, K.; Miyatake, S.; Ono, K.; Matsui, H. *Biomaterials* **2014**, *35*, 3396–2405.
327. Azev, Y.; Lork, E.; Duelcks, T.; Gabel, D. *Mendeleev Commun.* **2003**, *13*, 262–264.
328. Azev, Y.; Lork, E.; Duelcks, T.; Gabel, D. *Tetrahedron Lett.* **2004**, *45*, 3249–3252.
329. Kultyshev, R. G.; Hoitung, S. L.; Leung, H. T.; Liu, J.; Shore, S. G. *Inorg. Chem.* **2003**, *42*, 3199–3207.
330. Shore, S. G.; Hamilton, E. J. M.; Kultyshev, R. G.; Leung, H. T.; Yisgedu, T. *Pure Appl. Chem.* **2006**, *78*, 1341–1347.
331. Srebny, H.-G.; Preetz, W. *Z. Anorg. Allg. Chem.* **1984**, *513*, 7–14.
332. Sivaev, I. B.; Katsner, S. B.; Solntsev, K. A.; Kuznetsov, N. T. *Russ. J. Inorg. Chem.* **1995**, *40*, 779.
333. Lepšik, M.; Srnc, M.; Plešek, J.; Budešinsky, M.; Klepetařova, B.; Hnyk, D.; Grüner, B.; Rulišek, L. *Inorg. Chem.* **2010**, *49*, 5040–5048.
334. Morris, J. H.; Brattsev, V. A.; Gaines, D. F. In *Advances in Boron Chemistry*; Siebert, W., Ed., Royal Chem. Soc: Cambridge, 1997; p 434.
335. Kuchinke, J.; Hammerschmidt, A.; Krebs, B. *Solid State Sci.* **2003**, *5*, 189–196.
336. Sun, Z.-D.; Chi, Y.; Xue, H.-G.; Guo, S.-P. *Inorg. Chem. Front.* **2017**, *4*, 1841–1847.
337. Guo, S.-P.; Guo, G.-C.; Wang, M.-S.; Zou, J.-P.; Zeng, H.-Y.; Cai, L. Z.; Huang, J.-S. *Chem. Commun.* **2009**, 4366–4368.
338. Han, S.-S.; Yao, W.-D.; Yu, S.-X.; Sun, Y.; Gong, A.; Guo, S.-P. *Inorg. Chem.* **2021**, *60*, 3375–3383.
339. Han, S.-S.; Xu, Q.-T.; Liu, W.; Guo, S.-P. *Dalton Trans.* **2022**, *51*, 4619–4622.
340. Han, S.-S.; Yu, S.-X.; Liu, W.; Guo, S.-P. *Inorg. Chem. Front.* **2022**, *9*, 2462–2469.
341. Küper, J.; Conrad, O.; Krebs, B. *Angew. Chem. Int. Ed.* **1997**, *36*, 1903–1904.
342. Lindemann, A.; Kuchinke, J.; Krebs, B. *Z. Anorg. Allg. Chem.* **1999**, *625*, 1165–1171.
343. Döch, M.; Lindemann, A.; Hammerschmidt, A.; Krebs, B. *Acta Cryst. A* **2002**, *58*, C315.
344. Hammerschmidt, A.; Lindemann, A.; Döch, M.; Krebs, B. *Z. Anorg. Allg. Chem.* **2003**, *629*, 1249–1255.
345. Hammerschmidt, A.; Döch, M.; Pütz, S.; Krebs, B. *Z. Anorg. Allg. Chem.* **2004**, *630*, 2299–2303.
346. Hammerschmidt, A.; Lindemann, A.; Köster, C.; Krebs, B. *Z. Anorg. Allg. Chem.* **2001**, *627*, 2121–2126.
347. Hammerschmidt, A.; Döch, M.; Pütz, S.; Krebs, B. *Z. Anorg. Allg. Chem.* **2005**, *631*, 1125–1128.
348. Guo, S.-P.; Chi, Y.; Liu, B.-W.; Guo, G.-C. *Dalton Trans.* **2016**, *45*, 10459–10465.
349. Sugimori, M.; Fukuoka, H.; Imoto, H.; Saito, T. *J. Organomet. Chem.* **2000**, *611*, 547–550.
350. Chica, D. G.; Spanopoulos, I.; Hao, S.; Wolverton, C.; Kanatzidis, M. G. *Chem. Mater.* **2021**, *33*, 1723–1730.
351. Sivaev, I. B.; Prikaznov, A. V.; Anufriev, S. A. *J. Organomet. Chem.* **2013**, *747*, 254–256.
352. Sivaev, I. B. *Russ. J. Inorg. Chem.* **2020**, *65*, 1854–1861.
353. Hertler, W. R.; Raasch, M. S. *J. Am. Chem. Soc.* **1964**, *86*, 3661–3668.
354. Grüner, B.; Bonnetot, B.; Mongeot, H. *Collect. Czech. Chem. Commun.* **1997**, *62*, 1185–1204.
355. Nelyubin, A. V.; Klyukin, I. N.; Zhdanov, A. P.; Grigor'ev, M. S.; Zhizhin, K. Y.; Kuznetsov, N. T. *Russ. J. Inorg. Chem.* **2021**, *66*, 139–145.
356. Nelyubin, A. V.; Selivanov, N. A.; Bykov, A. Y.; Klyukin, I. N.; Novikov, A. S.; Zhdanov, A. P.; Karpechenko, N. Y.; Grigor'ev, M. S.; Zhizhin, K. Y.; Kuznetsov, N. T. *Int. J. Mol. Sci.* **2021**, *22*, 13391.
357. Laskova, J.; Ananiy, I.; Kosenko, I.; Serdyukov, A.; Stogniy, M.; Sivaev, I.; Grin, M.; Semioshkin, A.; Bregadze, V. I. *Dalton Trans.* **2022**, *51*, 3051–3059.
358. Li, H.; Zhang, Y.; Liu, L.; Jiao, N.; Meng, X.; Zhang, S. *New J. Chem.* **2018**, *42*, 3568–3573.
359. Kirchmann, M.; Wesemann, L. *Dalton Trans.* **2008**, 2144–2148.
360. Kirchmann, M.; Wesemann, L. *Dalton Trans.* **2008**, 444–446.
361. Justus, E.; Rischka, K.; Wishart, J. F.; Werner, K.; Gabel, D. *Chem. A Eur. J.* **2008**, *14*, 1918–1923.
362. Justus, E.; Vöge, A.; Gabel, D. *Eur. J. Inorg. Chem.* **2008**, 5245–5250.
363. Bertocco, P.; Derendorf, J.; Jenne, C.; Kirsch, C. *Inorg. Chem.* **2017**, *56*, 3459–3466.
364. Wehmschulte, R. J.; Bayliss, B.; Reed, S.; Wesenberg, C.; Morgante, P.; Peverati, R.; Neal, S.; Chouinard, C. D.; Tolosa, D.; Powell, D. R. *Inorg. Chem.* **2022**, *61*, 7032–7042.
365. Sivaev, I. B.; Bruskin, A. B.; Nesterov, V. V.; Antipin, M. Y.; Bregadze, V. I.; Sjöberg, S. *Inorg. Chem.* **1999**, *38*, 5887–5893.
366. Drozdova, V. V.; Lisovskii, M. V.; Polyakova, I. N.; Zhizhin, K. Y.; Kuznetsov, N. T. *Russ. J. Inorg. Chem.* **2006**, *51*, 1716–1722.
367. Al-Joumhawy, M. K.; Marei, T.; Shmalko, A.; Cendoya, P.; La Borde, J.; Gabel, D. *Chem. Commun.* **2021**, *57*, 10007–10010.
368. Vöge, A.; Lork, E.; Sesalan, B. S.; Gabel, D. *J. Organomet. Chem.* **2009**, *694*, 1698–1703.
369. Hoffmann, S.; Justus, E.; Ratajski, M.; Lork, E.; Gabel, D. *J. Organomet. Chem.* **2005**, *690*, 2757–2760.
370. Zhang, Y.; Sun, Y.; Wang, T.; Liu, J.; Spingler, B.; Duttwyler, S. *Molecules* **2018**, *23*, 3137.
371. Zhang, Y.; Sun, Y.; Lin, F.; Liu, J.; Duttwyler, S. *Angew. Chem. Int. Ed.* **2016**, *55*, 15609–15614.
372. Nelyubin, A. V.; Selivanov, N. A.; Klyukin, I. N.; Bykov, A. Y.; Zhdanov, A. P.; Zhizhin, K. Y.; Kuznetsov, N. T. *Russ. J. Inorg. Chem.* **2021**, *66*, 1390–1395.
373. Bernard, R.; Cornu, D.; Baldeck, P. L.; Časlavský, J.; Letoffe, J.-M.; Scharff, J.-P.; Miele, P. *Dalton Trans.* **2005**, 3065–3071.
374. Bernard, R.; Cornu, D.; Scharff, J.-P.; Chiriac, R.; Miele, P.; Baldeck, P. L.; Časlavský, J. *Inorg. Chem.* **2006**, *45*, 8743–8748.
375. Bernard, R.; Barsou, C.; Baldeck, P. L.; Andraud, C.; Cornu, D.; Scharff, J.-P.; Miele, P. *Chem. Commun.* **2008**, 3762–3764.
376. Zhang, Y.; Wang, T.; Wang, L.; Sun, Y.; Lin, F.; Liu, J.; Duttwyler, S. *Chem. A Eur. J.* **2018**, *24*, 15812–15817.
377. Ivanov, S. V.; Davis, J. A.; Miller, S. M.; Anderson, O. P.; Strauss, S. H. *Inorg. Chem.* **2003**, *42*, 4489–4491.
378. Bolli, C.; Derendorf, J.; Jenne, C.; Scherer, H.; Sindlinger, C. P.; Wegener, B. *Chem. A Eur. J.* **2014**, *20*, 13783–13792.
379. Holub, J.; El Anwar, S.; Jelinek, T.; Fojt, L.; Ruzickova, Z.; Šolinova, V.; Kašička, V.; Gabel, D.; Grüner, B. *Eur. J. Inorg. Chem.* **2017**, 4499–4509.
380. Saleh, M.; Powell, D. R.; Wehmschulte, R. *J. Inorg. Chem.* **2016**, *55*, 10617–10627.
381. Jenne, C.; Wegener, B. *Z. Anorg. Allg. Chem.* **2018**, *644*, 1123–1132.
382. Jenne, C.; van Lessen, V. *Acta Cryst. E* **2019**, *75*, 607–610.
383. Bertocco, P.; Bolli, C.; Derendorf, J.; Jenne, C.; Klein, A.; Stirnat, K. *Chem. A Eur. J.* **2016**, *22*, 16032–16036.
384. Asmis, K. R.; Beele, B. B.; Jenne, C.; Kawa, S.; Knorke, H.; Nierstenhöfer, M. C.; Wang, X.-B.; Warneke, Z.; Yuan, Q. *Chem. A Eur. J.* **2020**, *26*, 14594–14601.
385. Bondarev, O.; Khan, A. A.; Tu, X.; Sevryugina, Y. V.; Jalisatgi, S. S.; Hawthorne, M. F. *J. Am. Chem. Soc.* **2013**, *135*, 13204–13211.
386. Plunze, A. M.; Bukovsky, E. V.; Lacroix, M. R.; Newell, B. S.; Rithner, C. D.; Strauss, S. H. *J. Fluor. Chem.* **2018**, *209*, 33–42.
387. Bernard, R.; Cornu, D.; Luneau, D.; Naoufal, D.; Scharff, J.-P.; Miele, P. *J. Organomet. Chem.* **2005**, *690*, 2745–2749.
388. Jasper, S. A.; Jones, R. B.; Mattern, J.; Huffman, J. C.; Todd, L. J. *Inorg. Chem.* **1994**, *33*, 5620–5624.
389. Jasper, S. A.; Mattern, J.; Huffman, J. C.; Todd, L. J. *Polyhedron* **2007**, *26*, 3793–3798.
390. Dopke, J. A.; Lincoln, Z. S.; Blazejewski, J.; Staples, R. J.; Lee, M. E. *Inorg. Chim. Acta* **2018**, *473*, 263–267.
391. Klyukin, I. N.; Selivanov, N. A.; Bykov, A. Y.; Zhdanov, A. P.; Zhizhin, K. Y.; Kuznetsov, N. T. *Russ. J. Inorg. Chem.* **2020**, *65*, 1637–1641.
392. Peymann, T.; Knobler, C. B.; Hawthorne, M. F. *Inorg. Chem.* **1998**, *37*, 1544–1548.
393. Peymann, T.; Knobler, C. B.; Hawthorne, M. F. *J. Am. Chem. Soc.* **1999**, *121*, 5601–5602.

394. Himmelspach, A.; Finze, M.; Vöge, A.; Gabel, D. Z. *Anorg. Allg. Chem.* **2012**, *638*, 512–519.
395. Schäfer, M.; Krummenacher, I.; Braunschweig, H.; Finze, M. Z. *Anorg. Allg. Chem.* **2015**, *641*, 660–668.
396. Peymann, T.; Knobler, C. B.; Khan, S. I.; Hawthorne, M. F. *Inorg. Chem.* **2001**, *40*, 1291–1294.
397. Trofimenko, S. *J. Am. Chem. Soc.* **1966**, *88*, 1899–1904.
398. Mayer, M.; Rohdenburg, M.; van Lessen, V.; Nierstenhöfer, M. C.; Aprà, E.; Grabowsky, S.; Asmis, K. R.; Jenne, C.; Warneke, J. *Chem. Commun.* **2020**, *56*, 4591–4594.
399. Kamin, A. A.; Juhasz, M. A. *Inorg. Chem.* **2020**, *59*, 189–192.
400. Wiersma, R. J.; Middaugh, R. L. *Inorg. Chem.* **1969**, *8*, 2074–2079.
401. Volkov, O.; Hu, C.; Kölle, U.; Paetzold, P. Z. *Anorg. Allg. Chem.* **2005**, *631*, 1909–1911.
402. Paetzold, P.; Bettinger, H. F.; Volkov, O. Z. *Anorg. Allg. Chem.* **2007**, *633*, 846–850.
403. Bechtold, R.; Kaszmarczyk, A. *J. Am. Chem. Soc.* **1974**, *96*, 5953–5954.
404. Malinina, E. A.; Drozdova, V. V.; Bykov, A. Y.; Belousova, O. N.; Polyakova, I. N.; Zhizhin, K. Y.; Kuznetsov, N. T. *Dokl. Chem.* **2007**, *414*, 137–139.
405. Avdeeva, V. V.; Malinina, E. A.; Belousova, O. N.; Goeva, L. V.; Polyakova, I. N.; Kuznetsov, N. T. *Russ. J. Inorg. Chem.* **2011**, *56*, 524–529.
406. Peymann, T.; Knobler, C. B.; Hawthorne, M. F. *Inorg. Chem.* **2000**, *39*, 1163–1170.
407. Chulkov, A. S.; Bondarev, Y. M.; Ippolitov, E. G.; Solntsev, K. A.; Kuznetsov, N. T. *Russ. J. Inorg. Chem.* **1993**, *38*, 416–418.
408. Safronov, A. V.; Jalilgatji, S. S.; Lee, H. B.; Hawthorne, M. F. *Int. J. Hydrogen Energy* **2011**, *36*, 234–239.
409. Volkov, O.; Paetzold, P.; Hu, C. Z. *Anorg. Allg. Chem.* **2006**, *632*, 945–948.
410. Klanberg, F.; Muetterties, E. L. *Inorg. Chem.* **1966**, *5*, 1955–1960.
411. Sivaev, I. B. *Russ. J. Inorg. Chem.* **2019**, *64*, 955–976.
412. Hawthorne, M. F.; Pitochelli, A. R. *J. Am. Chem. Soc.* **1959**, *81*, 5519.
413. Sivaev, I. B.; Prikaznov, A. V.; Naoufal, D. *Collect. Czech. Chem. Commun.* **2010**, *75*, 1149–1199.
414. Zhizhin, K. Y.; Zhdanov, A. P.; Kuznetsov, N. T. *Russ. J. Inorg. Chem.* **2010**, *55*, 2089–2127.
415. Nie, Y.; Chen, H.; Miao, J.; Sun, G.; Dou, J. *Chin. J. Org. Chem.* **2009**, *29*, 822–834.
416. Mahfouz, N.; Abi Ghaida, F.; El Hajji, Z.; Diab, M.; Floquet, S.; Mehdi, A.; Naoufal, D. *Chem. Select* **2022**, *7*, e20220077.
417. Hawthorne, M. F.; Pilling, R. L. *Inorg. Synth.* **1967**, *9*, 16–19.
418. Wu, H.; Tang, W. S.; Stavila, V.; Zhou, W.; Rush, J. J.; Udovic, T. J. *J. Phys. Chem. C* **2015**, *119*, 6481–6487.
419. Hofmann, K.; Albert, B. Z. *Kristallogr.* **2005**, *220*, 142–146.
420. Udovic, T. J.; Matsuo, M.; Tang, W. S.; Wu, H.; Stavila, V.; Soloninin, A. V.; Skoryunov, R. V.; Babanova, O. A.; Skripov, A. V.; Rush, J. J.; Unemoto, A.; Takamura, H.; Orimo, S. *Adv. Mater.* **2014**, *26*, 7622–7626.
421. Wu, H.; Tang, W. S.; Zhou, W.; Stavila, V.; Rushab, J. J.; Udovic, T. J. *CrystEngComm* **2015**, *17*, 3533–3540.
422. Dimitrievska, M.; Stavila, V.; Soloninin, A. V.; Skoryunov, R. V.; Babanova, O. A.; Wu, H.; Zhou, W.; Tang, W. S.; Faraone, A.; Tarver, J. D.; Trump, B. A.; Skripov, A. V.; Udovic, T. J. *J. Phys. Chem. C* **2018**, *122*, 15198–15207.
423. Hofmann, K.; Albert, B. Z. *Kristallogr. Suppl.* **2001**, *18*, 88.
424. Yisgedu, T. B.; Huang, Z.; Chen, X.; Lingam, H. K.; King, G.; Highley, A.; Maharrey, S.; Woodward, P. M.; Behrens, R.; Shore, S. G.; Zhao, J.-C. *Int. J. Hydrogen Energy* **2012**, *37*, 4267–4273.
425. Yisgedu, T. B.; Chen, X.; Lingam, H. K.; Huang, Z.; Meyers, E. A.; Shore, S. G.; Zhao, J.-C. *Acta Crystallogr. C* **2010**, *66*, m1–m3.
426. Yisgedu, T. B.; Chen, X.; Lingam, H. K.; Huang, Z.; Highley, A.; Maharrey, S.; Behrens, R.; Shore, S. G.; Zhao, J.-C. *J. Phys. Chem. C* **2011**, *115*, 11793–11802.
427. Kraus, F.; Albert, B. Z. *Anorg. Allg. Chem.* **2005**, *631*, 152–154.
428. Jørgensen, M.; Zhou, W.; Wu, H.; Udovic, T. J.; Paskевичius, M.; Černý, R.; Jensen, T. R. *Inorg. Chem.* **2021**, *60*, 10943–10957.
429. Jørgensen, M.; Lee, Y.-S.; Paskевичius, M.; Hansen, B. R. S.; Jensen, T. R. *J. Solid State Chem.* **2021**, *298*, 122133.
430. Jørgensen, M.; Hansen, B. R. S.; Lee, Y.-S.; Cho, Y. W.; Jensen, T. R. *J. Phys. Chem. C* **2019**, *123*, 20160–20166.
431. Avdeeva, V. V.; Kubasov, A. S.; Korolenko, S. E.; Goeva, L. V.; Malinina, E. A.; Kuznetsov, N. T. *Russ. J. Inorg. Chem.* **2022**, *67*, 628–635.
432. Zimmermann, L. W.; Kleeberg, F. M.; Schleid, T. Z. *Anorg. Allg. Chem.* **2017**, *643*, 365–372.
433. Dobrott, R. D.; Lipscomb, W. N. *J. Chem. Phys.* **1962**, *37*, 1779–1784.
434. Paxton, T. E.; Hawthorne, M. F.; Brown, L. D.; Lipscomb, W. N. *Inorg. Chem.* **1974**, *13*, 2772–2774.
435. Malinina, E. A.; Zhizhin, K. Y.; Polyakova, I. N.; Lisovskii, M. V.; Kuznetsov, N. T. *Russ. J. Inorg. Chem.* **2002**, *47*, 1158–1167.
436. Malinina, E. A.; Goeva, L. V.; Solntsev, K. A.; Kuznetsov, N. T. *Zh. Neorg. Khim.* **1993**, *38*, 38.
437. Malinina, E. A.; Zhizhin, K. Y.; Goeva, L. V.; Polyakova, I. N.; Kuznetsov, N. T. *Dokl. Chem.* **2001**, *378*, 139–142.
438. Polyakova, I. N.; Malinina, E. A.; Kuznetsov, N. T. *Cryst. Rep.* **2003**, *48*, 84–91.
439. Malinina, E. A.; Drozdova, V. V.; Polyakova, I. N.; Kuznetsov, N. T. *Russ. J. Inorg. Chem.* **2008**, *53*, 197–201.
440. Vologzhanina, A. V.; Avdeeva, V. V.; Malinina, E. A.; Kuznetsov, N. T. Z. *Kristallogr.* **2013**, *228*, 565–569.
441. Malinina, E. A.; Solntsev, K. A.; Butman, L. A.; Kuznetsov, N. T. *Russ. J. Coord. Chem.* **1989**, *15*, 1039–1043.
442. Avdeeva, V. V.; Buzanov, G. A.; Goeva, L. V.; Gerasimenko, A. V.; Malinina, E. A.; Kuznetsov, N. T. *Inorg. Chim. Acta* **2019**, *493*, 38–42.
443. Avdeeva, V. V.; Malinina, E. A.; Churakov, A. V.; Polyakova, I. N.; Kuznetsov, N. T. *Polyhedron* **2019**, *169*, 144–150.
444. Korolenko, S. E.; Kubasov, A. S.; Goeva, L. V.; Avdeeva, V. V.; Malinina, E. A.; Kuznetsov, N. T. *Inorg. Chim. Acta* **2021**, *520*, 120315.
445. Korolenko, S. E.; Malinina, E. A.; Avdeeva, V. V.; Churakov, A. V.; Nefedov, S. E.; Kubasov, S. E.; Burlov, A. S.; Divaeva, L. N.; Zhizhin, K. Y.; Kuznetsov, N. T. *Polyhedron* **2021**, *194*, 114902.
446. Korolenko, S. E.; Zhuravlev, K. P.; Tsaryuk, V. I.; Kubasov, A. S.; Avdeeva, V. V.; Malinina, E. A.; Burlov, A. S.; Divaeva, L. N.; Zhizhin, K. Y.; Kuznetsov, N. T. *JOL* **2021**, *237*, 118156.
447. Zimmermann, L. W.; Schleid, T. Z. *Kristallogr.* **2013**, *228*, 558–564.
448. Avdeeva, V. V.; Malinina, E. A.; Kuznetsov, N. T. *Polyhedron* **2016**, *105*, 205–221.
449. Pang, W.; Fan, X.; Xue, Y.; Xu, H.; Zhang, W.; Zhang, X.; Li, Y.; Shi, X. *Propellants, Explos., Pyrotech.* **2013**, *38*, 278–285.
450. Xue, Y.; Li, J.; Hao, Z.; Wan, H.; Zhao, H.; Li, C.; Du, Y.; Lu, J.; Yu, Q.; Lü, J. *Chem. J. Chin. Univ.* **2015**, *36*, 375–380.
451. Pang, W.-Q.; Zhao, F.-Q.; Xue, Y.-N.; Xu, H.-X.; Fan, X.-Z.; Xie, W.-X.; Zhang, W.; Lv, J.; Deluca, L. T. *Cent. Eur. J. Energetic Mater.* **2015**, *12*, 537–552.
452. Pang, W.-Q.; DeLuca, L. T.; Fan, X.-Z.; Glotov, O. G.; Wang, K.; Qin, Z.; Zhao, F.-Q. *Combust. Flame* **2020**, *220*, 157–167.
453. Xue, Y.-N.; Wang, W.-Q.; Li, J.-Y.; Lu, J.-Y.; Lu, J. *Chin. J. Energy Mater.* **2016**, *24*, 274–278.
454. Wang, W.; Xue, Y.; Mei, S.; Li, Y.; Wan, H.; Zhang, Q.; Yu, Q. *Chin. J. Energy Mater.* **2014**, *22*, 428–429.
455. Fuller, D. J.; Kepert, D. L.; Skelton, B. W.; White, A. H. *Aust. J. Chem.* **1987**, *40*, 2097–2105.
456. Chantler, C. T.; Maslen, E. N. *Acta Crystallogr. B* **1989**, *45*, 290–297.
457. Orlova, A. M.; Mustyatsa, V. N.; Goeva, L. V.; Katsner, S. B.; Solntsev, K. A.; Kuznetsov, N. T. *Russ. J. Inorg. Chem.* **1856**, *1996*, 41.
458. Zhao, D.; Shan, Z.; Song, J.; Zhang, G. *Chem. J. Chin. Univ.* **1983**, *4*, 93–96.
459. Virovets, A. V.; Vakulenko, N. N.; Volkov, V. V.; Podberezskaya, N. V. *J. Struct. Chem.* **1994**, *35*, 339–344.
460. Wen, W.-Y.; Chen, C.-M. L. *J. Chem. Eng. Data* **1975**, *20*, 384–387.
461. Muetterties, E. L.; Balthis, J. H.; Chia, Y. T.; Knoth, W. H.; Miller, H. C. *Inorg. Chem.* **1964**, *3*, 444–451.



462. Sivaev, I. B.; Petrovskii, P. V.; Filin, A. M.; Shubina, E. S.; Bregadze, V. I. *Russ. Chem. Bull.* **2001**, *50*, 1115–1116.
463. Shore, S. G.; Hamilton, E. J. M.; Bridges, A. N.; Bausch, J.; Krause-Bauer, J. A.; Dou, D.; Liu, J.; Liu, S.; Du, B.; Hall, H.; Meyers, E. A.; Vermillion, K. E. *Inorg. Chem.* **2003**, *42*, 1175–1186.
464. Bührens, K.-G.; Preetz, W. *Angew. Chem. Int. Ed. Engl.* **1977**, *16*, 173–174.
465. Bührens, K.-G.; Preetz, W. *Angew. Chem. Int. Ed. Engl.* **1977**, *16*, 398–399.
466. Preetz, W.; Srebny, H.-G.; Marsmann, H. C. Z. *Naturforsch. B* **1984**, *39*, 6–13.
467. Preetz, W.; Nachtigal, C. Z. *Anorg. Allg. Chem.* **1995**, *621*, 1632–1636.
468. Retivov, V. M.; Matveev, E. Y.; Lisovskii, M. V.; Razgonyaeva, G. A.; Ochertyanova, L. I.; Zhizhin, K. Y.; Kuznetsov, N. T. *Russ. Chem. Bull.* **2010**, *59*, 550–555.
469. Drozdova, V. V.; Zhizhin, K. Y.; Malinina, E. A.; Polyakova, I. N.; Kuznetsov, N. T. *Russ. J. Inorg. Chem.* **2007**, *52*, 996–1001.
470. Kapuscinski, S.; Abdulmojeed, M. B.; Schafer, T. E.; Pietrzak, A.; Heitsoi, O.; Friedli, A. C.; Kaszynski, P. *Inorg. Chem. Front.* **2021**, *8*, 1066–1082.
471. Rzeszotarska, E.; Novozhilova, I.; Kaszynski, P. *Inorg. Chem.* **2017**, *56*, 14351–14356.
472. Johnson, J. W.; Brody, J. F. J. *Electrochem. Soc.* **1982**, *129*, 2213–2219.
473. Einholz, W.; Vaas, K.; Wieloch, C.; Speiser, B.; Wizemann, T.; Ströbele, M.; Meyer, H.-J. Z. *Anorg. Allg. Chem.* **2002**, *628*, 258–268.
474. Warneke, J.; Konieczka, S. Z.; Hou, G.-L.; Apra, E.; Kerpen, C.; Keppler, F.; Schäfer, T. C.; Deckert, M.; Yang, Z.; Bylaska, E. J.; Johnson, G. E.; Laskin, J.; Xantheas, S. S.; Wang, X.-B.; Finze, M. *Phys. Chem. Chem. Phys.* **2019**, *11*, 5903–5915.
475. Avdeeva, V. V.; Malinina, E. A.; Zhizhin, K. Y.; Kuznetsov, N. T. *Russ. J. Coord. Chem.* **2021**, *47*, 519–545.
476. Bowden, W. J. *Electrochem. Soc.* **1982**, *129*, 1249–1252.
477. Dey, A. N.; Miller, J. J. *Electrochem. Soc.* **1979**, *126*, 1445–1451.
478. Johnson, J. W.; Whittingham, M. S. J. *Electrochem. Soc.* **1980**, *127*, 1653–1654.
479. Johnson, J. W.; Thompson, A. H. J. *Electrochem. Soc.* **1981**, *128*, 932–933.
480. Li, S.; Qiu, P.; Kang, J.; Ma, Y.; Zhang, Y.; Yan, Y.; Jensen, T. R.; Guo, Y.; Zhang, J.; Chen, X. *ACS Appl. Mater. Interfaces* **2021**, *13*, 17554–17564.
481. Zhizhin, K. Y.; Mustyatsa, V. N.; Malinina, E. A.; Votina, N. A.; Matveev, E. Y.; Goeva, L. V.; Polyakova, I. N.; Kuznetsov, N. T. *Russ. J. Inorg. Chem.* **2004**, *49*, 180.
482. Akimov, S. S.; Matveev, E. Y.; Razgonyaeva, G. A.; Ochertyanova, L. I.; Votina, N. A.; Zhizhin, K. Y.; Kuznetsov, N. T. *Russ. Chem. Bull.* **2010**, *59*, 371–373.
483. Klyukin, I. N.; Kubasov, A. S.; Limarev, I. P.; Zhdanov, A. P.; Matveev, E. Y.; Polyakova, I. N.; Zhizhin, K. Y.; Kuznetsov, N. T. *Polyhedron* **2015**, *101*, 215–222.
484. Bernard, R.; Cornu, D.; Perrin, M.; Scharff, J.-P.; Miele, P. J. *Organomet. Chem.* **2004**, *689*, 2581–2585.
485. Matveev, E. Y.; Kubasov, A. S.; Razgonyaeva, G. A.; Polyakova, I. N.; Zhizhin, K. Y.; Kuznetsov, N. T. *Russ. J. Inorg. Chem.* **2015**, *60*, 776–785.
486. Matveev, E. Y.; Retivov, V. M.; Razgonyaeva, G. A.; Zhizhin, K. Y.; Kuznetsov, N. T. *Russ. J. Inorg. Chem.* **2011**, *56*, 1549–1554.
487. Prikaznov, A. V.; Shmal'ko, A. V.; Sivaev, I. B.; Petrovskii, P. V.; Bragin, V. I.; Kisin, A. V.; Bregadze, V. I. *Polyhedron* **2011**, *30*, 1494–1501.
488. El Anwar, S.; Laila, Z.; Ramsabhadra, R.; Tlais, S.; Safa, A.; Dudley, G.; Naoufal, D. J. *Organomet. Chem.* **2018**, *865*, 89–94.
489. Kubasov, A. S.; Matveev, E. Y.; Retivov, V. M.; Akimov, S. S.; Razgonyaeva, G. A.; Polyakova, I. N.; Votina, N. A.; Zhizhin, K. Y.; Kuznetsov, N. T. *Russ. Chem. Bull.* **2014**, *63*, 187–193.
490. Matveev, E. Y.; Limarev, I. P.; Nichugovskii, A. I.; Bykov, A. Y.; Zhizhin, K. Y.; Kuznetsov, N. T. *Russ. J. Inorg. Chem.* **2019**, *64*, 977–983.
491. Matveev, E. Y.; Akimov, S. S.; Kubasov, A. S.; Retivov, V. M.; Zhizhin, K. Y.; Kuznetsov, N. T. *Russ. J. Inorg. Chem.* **2019**, *64*, 1513–1521.
492. Matveev, E. Y.; Akimov, S. S.; Kubasov, A. S.; Nichugovskii, A. I.; Nartov, A. S.; Retivov, V. M.; Zhizhin, K. Y.; Kuznetsov, N. T. *Russ. J. Inorg. Chem.* **2017**, *62*, 808–813.
493. Klyukin, I. N.; Voinova, V. V.; Selivanov, N. A.; Zhdanov, A. P.; Zhizhin, K. Y.; Kuznetsov, N. T. *Russ. J. Inorg. Chem.* **2018**, *63*, 1546–1551.
494. Avdeeva, V. V.; Polyakova, I. N.; Goeva, L. V.; Malinina, E. A.; Kuznetsov, N. T. *Russ. J. Inorg. Chem.* **2014**, *59*, 1247–1258.
495. Avdeeva, V. V.; Polyakova, I. N.; Churakov, A. V.; Vologzhanina, A. V.; Malinina, E. A.; Zhizhin, K. Y.; Kuznetsov, N. T. *Polyhedron* **2019**, *162*, 65–70.
496. Klyukin, I. N.; Zhdanov, A. P.; Razgonyaeva, G. A.; Zhizhin, K. Y.; Kuznetsov, N. T. *Russ. J. Inorg. Chem.* **2013**, *58*, 1395–1399.
497. Klyukin, I. N.; Zhdanov, A. P.; Bykov, A. Y.; Razgonyaeva, G. A.; Grigor'ev, M. S.; Zhizhin, K. Y.; Kuznetsov, N. T. *Russ. J. Inorg. Chem.* **2017**, *62*, 1479–1482.
498. Klyukin, I. N.; Zhdanov, A. P.; Matveev, E. Y.; Razgonyaeva, G. A.; Grigor'ev, M. S.; Zhizhin, K. Y.; Kuznetsov, N. T. *Inorg. Chem. Commun.* **2014**, *50*, 28–30.
499. Sazonova, E. F.; Avdeeva, V. V.; Polyakova, I. N.; Vologzhanina, A. V.; Goeva, L. V.; Malinina, E. A.; Kuznetsov, N. T. *Dokl. Chem.* **2013**, *452*, 240–244.
500. Klyukin, I. N.; Zhdanov, A. P.; Bykov, A. Y.; Retivov, V. M.; Zhizhin, K. Y.; Kuznetsov, N. T. *Russ. J. Inorg. Chem.* **2018**, *63*, 213–218.
501. Jacob, L.; Rzeszotarska, E.; Pietrzak, A.; Young, V. G.; Kaszynski, P. *Eur. J. Inorg. Chem.* **2020**, 3083–3093.
502. Komura, M.; Nakai, H.; Shiro, M. *J. Chem. Soc. Dalton Trans.* **1987**, 1953–1956.
503. Kubasov, A. S.; Turishev, E. S.; Polyakova, I. N.; Matveev, E. Y.; Zhizhin, K. Y.; Kuznetsov, N. T. *J. Organomet. Chem.* **2017**, *828*, 106–115.
504. Kubasov, A. S.; Matveev, E. Y.; Polyakova, I. N.; Razgonyaeva, G. A.; Zhizhin, K. Y.; Kuznetsov, N. T. *Russ. J. Inorg. Chem.* **2015**, *60*, 198–202.
505. Kubasov, A. S.; Turishev, E. S.; Kopytin, A. V.; Shpigun, L. K.; Zhizhin, K. Y.; Kuznetsov, N. T. *Inorg. Chim. Acta* **2021**, *514*, 119992.
506. Kopytin, A. V.; Kubasov, A. S.; Zhizhin, K. Y.; German, K. E.; Shpigun, L. K.; Kuznetsov, N. T. *Dokl. Chem.* **2020**, *491*, 57–60.
507. Kubasov, A. S.; Turishev, E. S.; Golubev, A. V.; Bykov, A. Y.; Zhizhin, K. Y.; Kuznetsov, N. T. *Inorg. Chim. Acta* **2020**, *507*, 119589.
508. Kubasov, A. S.; Golubev, A. V.; Bykov, A. Y.; Matveev, E. Y.; Zhizhin, K. Y.; Kuznetsov, N. T. *J. Mol. Struct.* **2021**, *1241*, 130591.
509. Kubasov, A. S.; Matveev, E. Y.; Turyshev, E. S.; Polyakova, I. N.; Bykov, A. Y.; Kopytin, A. V.; Zhizhin, K. Y.; Kuznetsov, N. T. *Dokl. Chem.* **2018**, *483*, 263–265.
510. Golubev, A. V.; Kubasov, A. S.; Bykov, A. Y.; Zhizhin, K. Y.; Kravchenko, E. A.; Gippius, A. A.; Zhurenko, S. V.; Semenova, V. A.; Korlyukov, A. A.; Kuznetsov, N. T. *Inorg. Chem.* **2021**, *60*, 8592–8604.
511. Golubev, A. V.; Kubasov, A. S.; Turyshev, E. S.; Bykov, A. Y.; Zhizhin, K. Y.; Kuznetsov, N. T. *Russ. J. Inorg. Chem.* **2020**, *65*, 1333–1342.
512. Dou, D.; Mavunkal, I. J.; Krause Bauer, J. A.; Knobler, C. B.; Hawthorne, M. F.; Shore, S. G. *Inorg. Chem.* **1994**, *33*, 6432–6434.
513. Zhizhin, K. Y.; Mustyatsa, V. N.; Matveev, E. Y.; Drozdova, V. V.; Votina, N. A.; Polyakova, I. N.; Kuznetsov, N. T. *Russ. J. Inorg. Chem.* **2003**, *48*, 671–675.
514. Zhdanov, A. P.; Bykov, A. Y.; Kubasov, A. S.; Polyakova, I. N.; Razgonyaeva, G. A.; Zhizhin, K. Y.; Kuznetsov, N. T. *Russ. J. Inorg. Chem.* **2017**, *62*, 468–475.
515. Zhdanov, A. P.; Voinova, V. V.; Klyukin, I. N.; Kubasov, A. S.; Zhizhin, K. Y.; Kuznetsov, N. T. *J. Cluster Sci.* **2019**, *30*, 1327–1333.
516. Losytskiy, M. Y.; Kovalska, V. B.; Varzatskii, O. A.; Kuperman, M. V.; Potocki, S.; Gumienna-Kontecka, E.; Zhdanov, A. P.; Yarmoluk, S. M.; Voloshin, Y. Z.; Zhizhin, K. Y.; Kuznetsov, N. T.; Elskaya, A. V. *JOL* **2016**, *169*, 51–60.
517. Sivaev, I. B.; Votina, N. A.; Bragin, V. I.; Starikova, Z. A.; Goeva, L. V.; Bregadze, V. I.; Sjöberg, S. J. *Organomet. Chem.* **2002**, *657*, 163–170.
518. Voinova, V. V.; Selivanov, N. A.; Plyushchenko, I. V.; Vokuev, M. F.; Bykov, A. Y.; Klyukin, I. N.; Novikov, A. S.; Zhdanov, A. P.; Grigor'ev, M. S.; Rodin, I. A.; Zhizhin, K. Y.; Kuznetsov, N. T. *Molecules* **2021**, *26*, 248.
519. Laila, Z.; Yazbeck, O.; Abi Ghaida, F.; Diab, M.; El Anwar, S.; Srour, M.; Mehdi, A.; Naoufal, D. J. *Organomet. Chem.* **2020**, *910*, 121132.
520. Zhdanov, A. P.; Lisovsky, M. V.; Goeva, L. V.; Razgonyaeva, G. A.; Polyakova, I. N.; Zhizhin, K. Y.; Kuznetsov, N. T. *Russ. Chem. Bull.* **2009**, *58*, 1694–1700.
521. Zhdanov, A. P.; Klyukin, I. N.; Bykov, A. Y.; Grigor'ev, M. S.; Zhizhin, K. Y.; Kuznetsov, N. T. *Polyhedron* **2017**, *123*, 176–183.
522. Zhdanov, A. P.; Polyakova, I. N.; Razgonyaeva, G. A.; Zhizhin, K. Y.; Kuznetsov, N. T. *Russ. J. Inorg. Chem.* **2011**, *56*, 847–855.
523. Getman, T. D.; Luck, R. L.; Cienkus, C. *Acta Cryst. E* **2011**, *67*, o1682–o1683.
524. Zhdanov, A. P.; Nelyubin, A. V.; Klyukin, I. N.; Selivanov, N. A.; Bortnikov, E. O.; Grigor'ev, M. S.; Zhizhin, K. Y.; Kuznetsov, N. T. *Russ. J. Inorg. Chem.* **2019**, *64*, 841–846.
525. Nelyubin, A. V.; Klyukin, I. N.; Zhdanov, A. P.; Grigor'ev, M. S.; Zhizhin, K. Y.; Kuznetsov, N. T. *Russ. J. Inorg. Chem.* **2019**, *64*, 1499–1506.
526. Nelyubin, A. V.; Klyukin, I. N.; Novikov, A. S.; Zhdanov, A. P.; Grigor'ev, M. S.; Zhizhin, K. Y.; Kuznetsov, N. T. *Mendeleev Commun.* **2021**, *31*, 201–203.
527. Nelyubin, A. V.; Klyukin, I. N.; Zhdanov, A. P.; Zhizhin, K. Y.; Kuznetsov, N. T. *Russ. J. Inorg. Chem.* **2019**, *64*, 1750–1752.
528. Voinova, V. V.; Klyukin, I. N.; Zhdanov, A. P.; Grigor'ev, M. S.; Zhizhin, K. Y.; Kuznetsov, N. T. *Russ. J. Inorg. Chem.* **2020**, *65*, 839–845.

529. Zhdanova, K. A.; Zhdanov, A. V.; Ezhov, N. A.; Bragina, N. A.; Zhizhin, K. Y.; Ushakova, I. P.; Mironov, A. F.; Kuznetsov, N. T. *Russ. Chem. Bull.* **2014**, *63*, 194–200.
530. Zhdanova, K. A.; Zhdanov, A. P.; Ezhov, A. V.; Fakhrutdinov, A. N.; Bragina, N. A.; Zhizhin, K. Y.; Kuznetsov, N. T.; Mironov, A. F. *Macrocyclics* **2014**, *7*, 394–400.
531. Ezhov, A. V.; Vyal'ba, F. Y.; Klyukin, I. N.; Zhdanova, K. A.; Bragina, N. A.; Zhdanov, A. P.; Zhizhin, K. Y.; Mironov, A. F.; Kuznetsov, N. T. *Macrocyclics* **2017**, *10*, 505–509.
532. Burianova, V. K.; Bolotin, D. S.; Mikhredov, A. S.; Novikov, A. S.; Mokolokolo, P. P.; Roodt, A.; Boyarskiy, V. P.; Dar'in, D.; Krasavin, M.; Suslonov, V. V.; Zhdanov, A. P.; Zhizhin, K. Y.; Kuznetsov, N. T. *New J. Chem.* **2018**, *42*, 8693–8703.
533. Bolotin, D. S.; Burianova, V. K.; Novikov, A. S.; Demakova, M. Y.; Pretorius, C.; Mokolokolo, P. P.; Roodt, A.; Bokach, N. A.; Suslonov, V. V.; Zhdanov, A. P.; Zhizhin, K. Y.; Kuznetsov, N. T.; Kukushkin, V. Y. *Organometallics* **2016**, *35*, 3612–3623.
534. Bolotin, D. S.; Demakova, M. Y.; Daines, E. A.; Avdontseva, M. S.; Zhdanov, A. P.; Zhizhin, K. Y.; Kuznetsov, N. T. *Russ. J. Gen. Chem.* **2017**, *87*, 37–43.
535. Burianova, V. K.; Mikhredov, A. S.; Bolotin, D. S.; Novikov, A. S.; Mokolokolo, P. P.; Roodt, A.; Boyarskiy, V. P.; Suslonov, V. V.; Zhdanov, A. P.; Zhizhin, K. Y.; Kuznetsov, N. T. *J. Organomet. Chem.* **2018**, *870*, 97–103.
536. Mindich, A. L.; Bokach, N. A.; Kuznetsov, M. L.; Haukka, M.; Zhdanov, A. P.; Zhizhin, K. Y.; Miltsov, S. A.; Kuznetsov, N. T.; Kukushkin, V. Y. *ChemPlusChem* **2012**, *77*, 1075–1086.
537. Daines, E. A.; Bolotin, D. S.; Bokach, N. A.; Gurzhiy, V. V.; Zhdanov, A. P.; Zhizhin, K. Y.; Kuznetsov, N. T. *Inorg. Chim. Acta* **2018**, *471*, 372–376.
538. Mindich, A. L.; Bokach, N. A.; Kuznetsov, M. L.; Starova, G. L.; Zhdanov, A. P.; Zhizhin, K. Y.; Miltsov, S. A.; Kuznetsov, N. T.; Kukushkin, V. Y. *Organometallics* **2013**, *32*, 6576–6586.
539. Mindich, A. L.; Bokach, N. A.; Dolgushin, F. M.; Haukka, M.; Lisitsyn, L. A.; Zhdanov, A. P.; Zhizhin, K. Y.; Miltsov, S. A.; Kuznetsov, N. T.; Kukushkin, V. Y. *Organometallics* **2012**, *31*, 1716–1724.
540. Mindich, A. L.; Pavlishchuk, A. V.; Bokach, N. A.; Starova, G. L.; Zhizhin, K. Y. *Acta Cryst. E* **2012**, *68*, o3284–o3285.
541. Shelly, K.; Knobler, C. B.; Hawthorne, M. F. *Inorg. Chem.* **1992**, *31*, 2889–2892.
542. Wilbur, D. S.; Chyan, M.-K.; Hamlin, D. K.; Vessella, R. L.; Wedge, T. J.; Hawthorne, M. F. *Bioconjug. Chem.* **2007**, *18*, 1226–1240.
543. Wilbur, D. S.; Chyan, M.-K.; Nakamae, H.; Chen, Y.; Hamlin, D. K.; Santos, E. B.; Kornblit, B. T.; Sandmaier, B. M. *Bioconjug. Chem.* **2012**, *23*, 409–420.
544. El Anwar, S.; Holub, J.; Tok, O.; Jelinek, T.; Ružičkova, Z.; Fojt, L.; Šolínova, V.; Kašička, V.; Grüner, B. *J. Organomet. Chem.* **2018**, *865*, 189–199.
545. El Anwar, S.; Assaf, K.; Begaj, B.; Samsonov, M. A.; Ružičkova, Z.; Holub, J.; Bavol, D.; Nau, W. M.; Gabel, D.; Grüner, B. *Chem. Commun.* **2019**, *55*, 13669–13672.
546. Dziova, A. E.; Avdeeva, V. V.; Polyakova, I. N.; Belousova, O. N.; Malinina, E. A.; Kuznetsov, N. T. *Dokl. Chem.* **2011**, *440*, 253–256.
547. Avdeeva, V. V.; Vologzhanina, A. V.; Goeva, L. V.; Malinina, E. A.; Kuznetsov, N. T. *Inorg. Chim. Acta* **2015**, *428*, 154–162.
548. Leyden, R. N.; Hawthorne, M. F. *Inorg. Chem.* **1975**, *14*, 2444–2446.
549. Naoufal, D.; Grüner, B.; Bonnetot, B.; Mongeot, H. *Polyhedron* **1999**, *18*, 931–939.
550. Ali, M. O.; Pocięcha, D.; Wojciechowski, J.; Novozhilova, I.; Friedli, A. C.; Kaszyński, P. *J. Organomet. Chem.* **2018**, *865*, 226–233.
551. Naoufal, D.; Assi, Z.; Abdelhai, E.; Ibrahim, G.; Yazbeck, O.; Hachem, A.; Abdallah, H.; El Masri, M. *Inorg. Chim. Acta* **2012**, *383*, 33–37.
552. Abi-Ghaida, F.; Laila, Z.; Ibrahim, G.; Naoufal, D.; Mehdi, A. *Dalton Trans.* **2014**, *43*, 13087–13095.
553. Abi-Ghaida, F.; Clement, S.; Safa, A.; Naoufal, D.; Mehdi, A. *Nanomater.* **2015**, 608432.
554. Nachtigal, C.; Preetz, W. *Z. Anorg. Allg. Chem.* **1996**, *622*, 2057–2060.
555. Nachtigal, C.; Preetz, W. *Z. Anorg. Allg. Chem.* **1997**, *623*, 683–686.
556. Kubasov, A. S.; Matveev, E. Y.; Turyshv, E. S.; Polyakova, I. N.; Zhizhin, K. Y.; Kuznetsov, N. T. *Dokl. Chem.* **2017**, *477*, 257–260.
557. Yao, H.-J.; Hu, C.-H.; Dou, J.-M.; Sun, J.; Wei, J.-D.; Huang, Z.-E.; Jin, R.-S.; Zheng, P.-J. *Acta Crystallogr. C* **1998**, *54*, IUC9800008.
558. Yao, H.-J.; Hu, C.-H.; Dou, J.-M.; Jin, R.-S.; Zheng, P.-J. *Acta Crystallogr. C* **1999**, *55*, IUC9900033.
559. Naoufal, D.; Bonnetot, B.; Mongeot, H.; Grüner, B. *Collect. Czech. Chem. Commun.* **1999**, *64*, 856–864.
560. Guschlbauer, J.; Shaughnessy, K. H.; Pietrzak, A.; Chung, M.-C.; Sponsler, M. B.; Kaszyński, P. *Organometallics* **2021**, *40*, 2504–2515.
561. Kupašćinski, S.; Hietsoi, O.; Pietrzak, A.; Friedli, A. C.; Kaszyński, P. *Chem. Commun.* **2022**, 58, 851–854.
562. Lisovskii, M. V.; Plyavnik, N. V.; Serebrennikova, G. A.; Zhizhin, K. Y.; Malinina, E. A.; Kuznetsov, N. T. *Russ. J. Inorg. Chem.* **2005**, *50*, 20.
563. Klyukin, I. N.; Selivanov, N. A.; Bykov, A. Y.; Zhdanov, A. P.; Zhizhin, K. Y.; Kuznetsov, N. T. *Russ. J. Inorg. Chem.* **2020**, *65*, 1547–1551.
564. Wilbur, D. S.; Chyan, M.-K.; Hamlin, D. K.; Perry, M. A. *Nucl. Med. Biol.* **2010**, *37*, 167–178.
565. Klyukin, I. N.; Selivanov, N. A.; Bykov, A. Y.; Zhdanov, A. P.; Zhizhin, K. Y.; Kuznetsov, N. T. *Russ. J. Inorg. Chem.* **2019**, *64*, 1405–1409.
566. Hawthorne, M. F.; Shelly, K.; Li, F. *Chem. Commun.* **2002**, 547–554.
567. Avdeeva, V. V.; Malinina, E. A.; Zhizhin, K. Y.; Bernhardt, E.; Kuznetsov, N. T. *J. Struct. Chem.* **2019**, *60*, 692–712.
568. Chulkov, A. S.; Bondarev, Y. M.; Ippolitov, E. G.; Solntsev, K. A.; Kuznetsov, N. T. *Zh. Neorg. Khim.* **1993**, *38*, 445–448.
569. Siegburg, K.; Preetz, W. *Inorg. Chem.* **2000**, *39*, 3280–3282.
570. Wong, E. H.; Gatter, M. G.; Kabbani, R. M. *Inorg. Chem.* **1980**, *19*, 451–455.
571. Wong, E. H.; Gatter, M. G.; Kabbani, R. M. *Inorg. Chem.* **1982**, *21*, 4022–4026.
572. Wong, E. H.; Gatter, M. G. *Inorg. Chim. Acta* **1982**, *61*, 95–98.
573. Siegburg, K.; Preetz, W. *Z. Naturforsch. B* **2000**, *55*, 479–483.
574. Bykov, A. Y.; Zhdanov, A. P.; Zhizhin, K. Y.; Kuznetsov, N. T. *Russ. J. Inorg. Chem.* **2016**, *61*, 1629–1648.
575. Schlüter, F.; Bernhardt, E.; Zhizhin, K. *New J. Chem.* **2018**, *42*, 2553–2556.
576. Klanberg, F.; Eaton, D. R.; Guggenberger, L. J.; Muetterties, E. L. *Inorg. Chem.* **1966**, *6*, 1271–1281.
577. Schlüter, F.; Bernhardt, E. *Inorg. Chem.* **2012**, *51*, 511–517.
578. Emery, S. L.; Morrison, J. A. *J. Am. Chem. Soc.* **1982**, *104*, 6790–6791.
579. Einholz, W.; Hofmann, M.; Schäfer, R.; Wieloch, C.; Keller, W.; Ströbele, M.; Meyer, H.-J. *Eur. J. Inorg. Chem.* **2021**, 5037–5044.
580. Guggenberger, L. J. *Inorg. Chem.* **1969**, *8*, 2771–2774.
581. Schlüter, F.; Bernhardt, E. *Inorg. Chem.* **2011**, *50*, 2580–2589.
582. Franken, A.; Thomsen, H.; Preetz, W. *Z. Naturforsch. B* **1996**, *51*, 744–746.
583. Kabbani, R. F. *Polyhedron* **1996**, *15*, 1951–1955.
584. Preetz, W.; Heinrich, A.; Thesing, J. *Z. Naturforsch. B* **1988**, *43*, 1319–1326.
585. Preetz, W.; Peters, G. *Eur. J. Inorg. Chem.* **1999**, 1831–1846.
586. Mebs, S.; Henn, J.; Luger, P.; Lentz, D. *Z. Anorg. Allg. Chem.* **2013**, *639*, 2057–2064.
587. Panda, M.; Hofmann, K.; Prosenc, M. H.; Albert, B. *Dalton Trans.* **2008**, 3956–3958.
588. Förster, D.; Scheins, S.; Luger, P.; Lentz, D.; Preetz, W. *Eur. J. Inorg. Chem.* **2007**, 3169–3172.
589. Hofmann, K.; Prosenc, M. H.; Albert, B. *Chem. Commun.* **2007**, 3097–3099.
590. Polyanskaya, T. M.; Drozdova, M. K.; Volkov, V. V.; Myakishev, K. G. *J. Struct. Chem.* **2009**, *50*, 368–372.
591. Axtell, J. C.; Kirilkovali, K. O.; Jung, D.; Dziedzic, R. M.; Rheingold, A. L.; Spokoyne, A. M. *Organometallics* **2017**, *36*, 1204–1210.
592. Mu, X.; Axtell, J. C.; Bernier, N. A.; Kirilkovali, K. O.; Jung, D.; Umanson, A.; Qian, K.; Chen, X.; Bay, K. L.; Kirolos, M.; Rheingold, A. L.; Houk, K. N.; Spokoyne, A. M. *Chem* **2019**, *5*, 2461–2469.
593. Mesbah, W.; Soleimani, M.; Kianfar, E.; Geiseler, G.; Massa, W.; Hofmann, M.; Berndt, A. *Eur. J. Inorg. Chem.* **2009**, 5577–5582.

594. Nöth, H.; Pommerening, H. *Angew. Chem. Int. Ed.* **1980**, *19*, 482–483.
595. Baudler, M.; Rockstein, K.; Oehlert, W. *Chem. Ber.* **1991**, *124*, 1149–1152.
596. Schlüter, F.; Bernhardt, E. *Z. Anorg. Allg. Chem.* **2010**, *636*, 2462–2466.
597. Aftandilian, V. D.; Miller, H. C.; Parshall, G. W.; Muetterties, E. L. *Inorg. Chem.* **1962**, *1*, 734–737.
598. Dunks, G. B.; Barker, K.; Hedaya, E.; Hefner, C.; Palmer-Ordóñez, K.; Remec, P. *Inorg. Chem.* **1981**, *20*, 1692–1697.
599. Hawthorne, M. F. *Adv. Inorg. Chem. Radiochem.*; vol. 5; Academic Press: N.Y., 1963; pp 307–347.
600. Stanko, V. I.; Chapovskii, Y. A.; Brattsev, V. A.; Zakharkin, L. I. *Russ. Chem. Rev.* **1965**, *34*, 424–439.
601. Shore, S. G. In *Boron Hydride Chemistry*; Muetterties, E., Ed., Academic Press: N.Y., 1975; pp 79–174.
602. Greenwood, N. N. *Comprehensive Inorganic Chemistry*, vol. 1; Pergamon Press: Oxford, 1973; pp 818–837.
603. Belov, P. P.; Storozenko, P. A.; Voloshina, N. S.; Kuznetsova, M. G. *Russ. J. Appl. Chem.* **2017**, *90*, 1804–1809.
604. Pérez, S.; Sanz Miguel, P. J.; Macías, R. *Dalton Trans.* **2018**, *47*, 5850–5859.
605. McCrary, P. D.; Barber, P. S.; Kelley, S. P.; Rogers, R. D. *Inorg. Chem.* **2014**, *53*, 4770–4776.
606. Safronov, A. V.; Sevryugina, Y. V.; Jalisatgi, S. S.; Kennedy, R. D.; Barnes, C. L.; Hawthorne, M. F. *Inorg. Chem.* **2012**, *51*, 2629–2637.
607. Holub, J.; Růžicka, A.; Růžickova, Z.; Fanfrlík, J.; Hnyk, D.; Štíbr, B. *Inorg. Chem.* **2020**, *59*, 10540–10547.
608. Rachiero, G. P.; Titi, H. M.; Rogers, R. D. *Chem. Commun.* **2017**, *53*, 7736–7739.
609. Froehner, G.; Challis, K.; Gagnon, K.; Getman, T. D.; Luck, R. L. *Synth. React. Inorg. Met.-Org. Chem.* **2006**, *36*, 777–785.
610. Ewing, W. C.; Carroll, P. J.; Sneddon, L. G. *Inorg. Chem.* **2008**, *47*, 8580–8582.
611. Ewing, W. C.; Carroll, P. J.; Sneddon, L. G. *Inorg. Chem.* **2010**, *49*, 1983–1994.
612. Ewing, W. C.; Carroll, P. J.; Sneddon, L. G. *Inorg. Chem.* **2011**, *50*, 4054–4064.
613. Hawthorne, M. F.; Mavunkal, I. J.; Knobler, C. B. *J. Am. Chem. Soc.* **1992**, *114*, 4427–4429.
614. Bondarev, O.; Sevryugina, Y. V.; Jalisatgi, S. S.; Hawthorne, M. F. *Inorg. Chem.* **2012**, *51*, 9935–9942.
615. Berkeley, E. R.; Ewing, W. C.; Carroll, P. J.; Sneddon, L. G. *Inorg. Chem.* **2014**, *53*, 5348–5358.
616. Naoufal, D.; Kodeih, M.; Cornu, D.; Miele, P. *J. Organomet. Chem.* **2005**, *690*, 2787–2789.
617. Kelley, S. P.; Rachiero, G. P.; Titi, H. M.; Rogers, R. D. *ACS Omega* **2018**, *3*, 8491–8496.
618. Gaines, D. F.; Bridges, A. N. *Organometallics* **1993**, *12*, 2015–2016.
619. Kusari, U.; Carroll, P. J.; Sneddon, L. G. *Inorg. Chem.* **2008**, *47*, 9203–9215.
620. Mazighi, K.; Carroll, P. J.; Sneddon, L. G. *Inorg. Chem.* **1993**, *32*, 1963–1969.
621. Chatterjee, S.; Carroll, P. J.; Sneddon, L. G. *Inorg. Chem.* **2010**, *49*, 3095–3097.
622. Chatterjee, S.; Carroll, P. J.; Sneddon, L. G. *Inorg. Chem.* **2013**, *52*, 9119–9130.
623. Wermer, J. R.; Hollander, O.; Huffman, J. C.; Krause Bauer, J. A.; Dou, D.; Hsu, L.-Y.; Leussing, D. L.; Shore, S. G. *Inorg. Chem.* **1995**, *34*, 3065–3071.
624. Muhammad, S.; Minami, T.; Fukui, H.; Yoneda, K.; Kishi, R.; Shigeta, Y.; Nakano, M. *J. Phys. Chem. A* **2012**, *116*, 1417–1424.
625. Sioutis, I.; Pitzer, R. M. *J. Phys. Chem. A* **2006**, *110*, 12528–12534.
626. Naoufal, D.; Grüner, B.; Bonnetot, B.; Mongeot, H. *Main Group Met. Chem.* **1999**, *22*, 127–129.
627. Bould, J.; Greatrex, R.; Kennedy, J. D.; Ormsby, D. L.; Londesborough, M. G. S.; Callaghan, K. L. F.; Thornton-Pett, M.; Spalding, T. R.; Teat, S. J.; Clegg, W.; Fang, H.; Rath, N. P.; Barton, L. *J. Am. Chem. Soc.* **2002**, *124*, 7429–7439.
628. Callaghan, K. L. F.; Dorfler, U.; McGrath, T. D.; Thornton-Pett, M.; Kennedy, J. D. *J. Organomet. Chem.* **1998**, *550*, 441–444.
629. Hamilton, E. J. M.; Liu, J.; Meyers, E. A. *Polyhedron* **2006**, *25*, 1901–1908.
630. Kelley, S. P.; McCrary, P. D.; Flores, L.; Garner, E. B., III; Dixon, D. A.; Rogers, R. D. *ChemPlusChem* **2016**, *81*, 922–925.
631. Olsen, F. P.; Vasavada, R. C.; Hawthorne, M. F. *J. Am. Chem. Soc.* **1968**, *90*, 3946–3951.
632. Londesborough, M. G. S.; Hnyk, D.; Bould, J.; Serrano-Andres, L.; Sauri, V.; Oliva, J. M.; Kubat, P.; Polivka, T.; Lang, K. *Inorg. Chem.* **2012**, *51*, 1471–1479.
633. Cerdan, L.; Frances-Monerris, A.; Roca-Sanjuan, D.; Bould, J.; Dolandky, J.; Fuciman, M.; Londesborough, M. G. S. *J. Mater. Chem. C* **2020**, *8*, 12806–12818.
634. Tan, C.; Zhang, B.; Chen, J.; Zhang, L.; Huang, X.; Meng, H. *Russ. J. Inorg. Chem.* **2019**, *64*, 1359–1364.
635. Ševčík, J.; Urbanek, P.; Hanulíková, B.; Čapková, T.; Urbanek, M.; Antoš, J.; Londesborough, M. G. S.; Bould, J.; Ghasemi, B.; Petřkovský, L.; Kuřitka, I. *Materials* **2021**, *14*, 589.
636. Jelinek, T.; Grüner, B.; Cisařova, I.; Štíbr, B.; Kennedy, J. D. *Inorg. Chem. Commun.* **2007**, *10*, 125–128.
637. Bould, J.; Londesborough, M. G. S.; Litecka, M.; Macías, R.; Shea, S. L.; McGrath, T. D.; Clegg, W.; Kennedy, J. D. *Inorg. Chem.* **2022**, *61*, 1899–1917.
638. Anderson, K. P.; Waddington, M. A.; Balaich, G. J.; Stauber, J. M.; Bernier, N. A.; Caram, J. R.; Djurovich, P. I.; Spokoyny, A. M. *Dalton Trans.* **2020**, *49*, 16245–16251.
639. Anderson, K. P.; Hua, A. S.; Plumley, J. B.; Ready, A. D.; Rheingold, A. L.; Peng, T. L.; Djurovich, I.; Kerestes, C.; Snyder, N. A.; Andrews, A.; Caram, J. R.; Spokoyny, A. M. *Dalton Trans.* **2022**, *51*, 9223–9228.
640. Londesborough, M. G. S.; Dolansky, J.; Bould, J.; Braborec, J.; Kiracki, K.; Lang, K.; Cisařova, I.; Kubat, P.; Roca-Sanjuan, D.; Frances-Monerris, A.; Slušna, L.; Noskovičová, E.; Lorenz, D. *Inorg. Chem.* **2019**, *58*, 10248–10259.
641. Sauri, V.; Oliva, J. M.; Hnyk, D.; Bould, J.; Braborec, J.; Merchan, M.; Kubat, P.; Cisařova, I.; Lang, K.; Londesborough, M. G. S. *Inorg. Chem.* **2013**, *52*, 9266–9274.
642. Anderson, K. P.; Djurovich, P. I.; Rubio, V. P.; Liang, A.; Spokoyny, A. M. n.d. DOI: [10.26434/chemrxiv-2022-c52jp](https://doi.org/10.26434/chemrxiv-2022-c52jp)
643. Bould, J.; Lang, K.; Kiracki, K.; Cerdan, L.; Roca-Sanjuan, D.; Frances-Monerris, A.; Clegg, W.; Waddell, P. G.; Fuciman, M.; Polivka, T.; Londesborough, M. G. S. *Inorg. Chem.* **2020**, *59*, 17058–17070.
644. Londesborough, M. G. S.; Lang, K.; Clegg, W.; Waddell, P. G.; Bould, J. *Inorg. Chem.* **2020**, *59*, 2651–2654.
645. Londesborough, M. G. S.; Dolansky, J.; Cerdan, L.; Lang, K.; Jelinek, T.; Oliva, J. M.; Hnyk, D.; Roca-Sanjuan, D.; Frances-Monerris, A.; Martiničik, J.; Nikl, M.; Kennedy, J. D. *Adv. Optical Mater.* **2017**, *5*, 1600694.
646. Londesborough, M. G. S.; Dolansky, J.; Jelinek, T.; Kennedy, J. D.; Cisařova, I.; Kennedy, R. D.; Roca-Sanjuan, D.; Frances-Monerris, A.; Lang, K.; Clegg, W. *Dalton Trans.* **2018**, *47*, 1709–1725.
647. Chen, J.; Xiong, L.; Zhang, L.; Huang, X.; Meng, H.; Tan, C. *Chem. Phys. Lett.* **2020**, *747*, 137328.
648. Xiong, L.; Zheng, Y.; Wang, H.; Yan, J.; Huang, X.; Meng, H.; Tan, C. *Methods Appl. Fluoresc.* **2022**, *10*, 035004.
649. Jelinek, T.; Kennedy, J. D.; Štíbr, B.; Thornton-Pett, M. *J. Chem. Soc. Chem. Commun.* **1994**, 1999–2000.
650. Jelinek, T.; Kilner, C. A.; Štíbr, B.; Thornton-Pett, M.; Kennedy, J. D. *Inorg. Chem. Commun.* **2005**, *8*, 491–494.
651. Bernhardt, E.; Brauer, D. J.; Finze, M.; Willner, H. *Angew. Chem. Int. Ed.* **2007**, *46*, 2927–2930.
652. Eyrilmez, S. M.; Bernhardt, E.; Davalos, J. Z.; Lepšik, M.; Hobza, P.; Assaf, K. I.; Nau, W. M.; Holub, J.; Oliva-Enrich, J. M.; Fanfrlík, J.; Hnyk, D. *Phys. Chem. Chem. Phys.* **2017**, *19*, 11748–11752.
653. Schlüter, F.; Bernhardt, E. *Z. Anorg. Allg. Chem.* **2012**, *638*, 594–601.
654. Assaf, K. I.; Holub, J.; Bernhardt, E.; Oliva-Enrich, J. M.; Fernández Pérez, M. I.; Canle, M.; Santaballa, J. A.; Fanfrlík, J.; Hnyk, D.; Nau, W. M. *ChemPhysChem* **2020**, *21*, 971–976.

## 1.17 Chain, ring, and cluster compounds of heavy group 13 elements (Al, Ga, In, Tl)

Gerald Linti and Michael Gast, Ruprecht-Karls-Universität Heidelberg, Anorganisch-Chemisches Institut, Heidelberg, Germany

© 2023 Elsevier Ltd. All rights reserved.

<b>1.17.1</b>	<b>Introduction</b>	<b>779</b>
<b>1.17.2</b>	<b>Chain and Ring Compounds with Direct E-E-Single Bonds</b>	<b>779</b>
1.17.2.1	Synthesis and structures of compounds with solitary E <sub>2</sub> -units	779
1.17.2.1.1	Triel Dihalides	780
1.17.2.1.2	E <sub>2</sub> R <sub>4</sub> Compounds	780
1.17.2.1.3	Lewis Acidity – Higher Coordination Numbers	786
1.17.2.1.4	Heteroleptic Compounds	788
1.17.2.2	Synthesis and structure of compounds with E <sub>3</sub> -units	794
1.17.2.3	Synthesis and structure of compounds with higher E <sub>n</sub> -units	799
1.17.2.3.1	Subhalides	799
1.17.2.3.2	Nonhalide derivatives	800
1.17.2.4	Synthesis and structure of compounds with E-E' bonds	806
<b>1.17.3</b>	<b>Polyhedral Cluster Compounds</b>	<b>807</b>
1.17.3.1	Tetrahedral E <sub>4</sub> R <sub>4</sub> cluster compounds and derivatives	808
1.17.3.1.1	Synthesis and structures	808
1.17.3.1.2	Bonding	810
1.17.3.1.3	Reactivity	812
1.17.3.2	Higher [E <sub>n</sub> R <sub>n</sub> ] <sup>x-</sup> cluster compounds	814
1.17.3.3	Aromaticity of [E <sub>n</sub> R <sub>n</sub> ] <sup>x-</sup> cluster compounds	817
<b>1.17.4</b>	<b>Element-Rich Cluster Compounds</b>	<b>821</b>
1.17.4.1	Introduction	821
1.17.4.2	Aluminum cluster compounds	822
1.17.4.3	Gallium cluster compounds	824
1.17.4.3.1	Ga <sub>8</sub> , Ga <sub>9</sub> and Ga <sub>10</sub> clusters	824
1.17.4.3.2	Ga <sub>11</sub> and Ga <sub>13</sub> clusters	828
1.17.4.3.3	Ga <sub>16</sub> , Ga <sub>18</sub> and Ga <sub>19</sub> clusters	828
1.17.4.3.4	Ga <sub>22</sub> clusters	829
1.17.4.3.5	Ga <sub>23</sub> and higher clusters	831
1.17.4.4	Indium and thallium cluster compounds	833
<b>1.17.5</b>	<b>Outlook</b>	<b>835</b>
<b>References</b>		<b>836</b>

### Abbreviations

Aryl<sup>1</sup> 2,6-Trip<sub>2</sub>C<sub>6</sub>H<sub>3</sub>

Aryl<sup>2</sup> 2,6-Mes<sub>2</sub>C<sub>6</sub>H<sub>3</sub>

bipy 2,2'-Bipyridine

CAAC Cyclic (alkyl)(amino)carbene

Cp Cyclopentadienyl

Cp\* 1,2,3,4,5-Pentamethylcyclopentadienyl

Cp<sup>tBu</sup> 1,2,4-Tri-*tert*-butylcyclopentadienyl

dep 2,6-Et<sub>2</sub>C<sub>6</sub>H<sub>3</sub>

dipp 2,6-<sup>i</sup>Pr<sub>2</sub>C<sub>6</sub>H<sub>3</sub>

DMAP 4-Me<sub>2</sub>N-C<sub>5</sub>H<sub>4</sub>N

do Donor

<sup>F</sup>Mes 2,4,6-(CF<sub>3</sub>)<sub>3</sub>C<sub>6</sub>H<sub>2</sub>

Mes 2,4,6-Me<sub>3</sub>C<sub>6</sub>H<sub>2</sub>

phen 1,10-Phenanthroline

<sup>R</sup>nacnac [NR<sub>2</sub>CR']<sub>2</sub>CH

<sup>R</sup>tpz Trispyrazolylborate  $[\text{HB}(\text{C}_3\text{N}_2\text{HR}_2)_3]^-$   
 sep Skeletal electron pairs  
<sup>s</sup>Mes 2,4,6-<sup>t</sup>Bu<sub>3</sub>C<sub>6</sub>H<sub>2</sub>  
 tmeda *N,N,N',N'*-Tetramethylethane-1,2-diamine  
 tmp 2,2,6,6-Tetramethylpiperidino  
 trip 2,4,6-<sup>t</sup>Pr<sub>3</sub>C<sub>6</sub>H<sub>2</sub>  
 xyl 3,5-Me<sub>2</sub>C<sub>6</sub>H<sub>3</sub>

## Abstract

The ring and cluster chemistry of the heavier group 13 elements aluminum, gallium, indium and thallium developed fruitfully during the last three decades. The formation of bonds between the atoms of those elements, the so called triels, in molecules allowed for the build-up of electron precise chains and rings. Electron poor compounds are cluster with a fascinating variety of structures ranging from polyhedral ones to element-rich clusters, where sections of element structures are packed in a shell of substituents. The synthetic principles, structural patterns and developing properties are described.

### 1.17.1 Introduction

Chain, ring and cluster compounds of the triel elements (E) aluminum, gallium, indium and thallium incorporating bonds between the metal atoms are described in this chapter. By joining these bonds oxidation states lower than +III are adopted. The story of metal-metal bonded compounds in group 13 started mainly about 30 years ago with the pioneering work on ditriellanes E<sub>2</sub>R<sub>4</sub> by Uhl.<sup>1,2</sup> In the following years a variety of low oxidation state compounds of these elements were prepared and characterized, including chains, rings and polyhedral clusters. A series of triel rich clusters with unprecedented and fascinating structures resembling sections of triel element structures show interesting properties. Very large cluster with up to 84 triel atoms were obtained.<sup>3</sup> For those clusters Schnöckel created the nomenclature "metalloid" clusters.<sup>4-7</sup> This rapidly developing and fruitful chapter in chemistry has been reviewed several times since then.<sup>3,4,7-17</sup> Most of these reports focused on aspects of one class of compounds and describe these aspects in detail. Here the development of oligotriels starting from binuclear to higher species will be reviewed with special focus on progresses during the past two decades.

The metal-metal interactions in electron precise oligomers E<sub>m</sub>R<sub>n</sub> ( $n > m$ ) are described as 2c2e bonds. Electron deficient species  $[\text{E}_m\text{R}_n]^x$  ( $n \leq m$ ,  $x = 0, -1, -2$ ) form clustered structures with multi center bonds. For cluster compounds electron counting rules, for example the Wade-Williams-Rudolph-Mingos rules, can be applied.<sup>18-24</sup>

The 2c2e bond between heavier triel atoms is a very soft one, meaning the bond length is largely influenced by substituents. For example, a typical gallium-gallium single bond can adopt values between 235 and 256 pm in length. It has been demonstrated that changes in bond length have little influence on the bonding energy. The difference is only a few kJ mol<sup>-1</sup> if the bond length changes by  $\pm 10$  pm.<sup>25,26</sup> Formation of multiple bonds between group 13 elements is a special and intensively discussed topic, which will be not further discussed in this chapter.

Such oligotriel compounds can be either molecular compounds or parts of solid-state structures. Here we will confine to molecular oligotriel compounds. For the interesting field of solid-state structures with Zintl-type ions of triels is not treated here.

### 1.17.2 Chain and Ring Compounds with Direct E-E-Single Bonds

Triple coordinated compounds of group 13 elements are, due to the electron sextet, strong Lewis acids, commonly. The same is valid if one or more of the substituents are triel elements. This allows for the design of multiple Lewis acidic compounds, on the one hand. On the other hand, these compounds tend to get stabilized either by adduct formation or cage formation. In order to prevent the latter, meaning to form chains or rings with triel centers, it is necessary to fill the electron sextet of the triel atoms or prevent by appropriate substituents formation of multi center bonded cluster structures. Bearing this in mind, a number of electron precise compounds could be examined, which will be discussed according to their number of triel atoms, involved.

#### 1.17.2.1 Synthesis and structures of compounds with solitary E<sub>2</sub>-units

Compounds with metal-metal bonds attract special interest, because normally speaking of metals delocalized bonding in the solid is the first thought to come up. Isolation of compounds with direct metal-metal bond of d-metals in the 1950s initiated a fruitful chemistry.<sup>27,28</sup>



In gas phase  $E_2$  molecules have been studied with weak E-E bonds [ $D_{298}^0$  in  $\text{kJ mol}^{-1}$ : E = Al  $133 \pm 5.8$ , Ga  $114.5 \pm 4.9$ , In  $78.1 \pm 5.7$ , Tl 59].<sup>29–37</sup> The binary compounds  $E_2H_4$ , as the most simple compounds, are only stable under matrix-isolation condition for E = Al, Ga, In, Tl.<sup>38–40</sup> The E-E bonded structure  $H_2E-EH_2$  was shown to be the minimum structure only for boron, by quantum chemical calculations.<sup>14,41–46</sup> The heavier congeners show a minimum on the hypersurface corresponding to a dimer  $E(\mu_2-H_3)EH$ . This is also formulated as  $E^+ [EH_4]^-$ . That means, triel(II) compounds with E-E bonds tend to disproportionate into triel(I) and triel(III) compounds. Here, for a successful preparative access to ditriellanes(4)  $R_2E-ER_2$  the influence of the substituents R, their bulkiness and electronic properties, will be very important. For the control of E-E bond formation and avoiding of charge separation, influences of solvents are also effective.<sup>14,47–49</sup>

One can conclude that electron-withdrawing groups R will increase partial positive charges on the triel centers and thus will weaken E-E bonds. By contrast, ligation of additional groups will enforce E-E bonds. Steric demanding substituents will favor E-E bonded systems against bridging ones of type  $E(\mu_2-R_3)ER$ . This is the case for donor (do) adducts of triel dihalides  $X_2(do)E-EX_2(do)$  or bulky substituted ditriellanes(4)  $R_2E-ER_2$ .

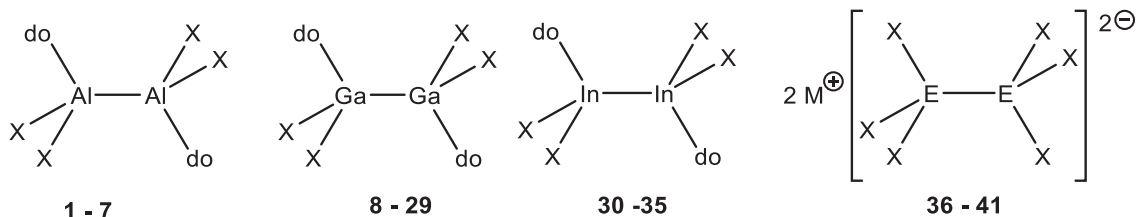
Data for those compounds indicate weak E-E bonds, which are estimated to be 69–258  $\text{kJ mol}^{-1}$  for the ditriel tetrahalides  $E_2X_4$ . The bond strength decreases from aluminum to thallium and is much lower than for boron compounds (389–454  $\text{kJ mol}^{-1}$ ).<sup>50</sup> Keeping this in mind, now ditriellanes will be discussed.

### 1.17.2.1.1 Triel Dihalides

Compounds with direct E-E bonds of type  $R_nE_2$  ( $n = 2, 3, 4, 5, 6$ , E = Al, Ga, In, Tl) were synthesized by various methods. While for E = Ga and In the element(II)halides  $X_4E_2 \cdot 2do$  (X = Cl, Br, I) (Tables 1–3 give an overview on available compounds prepared during the past 30 years) are easily prepared from subhalides with appropriate donors, corresponding  $Al_2X_4 \cdot 2do$  compounds were only accessible via metastable aluminum(I) halide solutions, which are obtained from AlX vapors by condensation with solvents.<sup>12,77–79</sup> For thallium no such derivatives are known. A rare example is a  $Tl_2^{4+}$  as structural motif in a phase  $Tl_{0.8}Sn_{0.6}Mo_7O_{11}$ .<sup>80</sup>

$EX_2$  compounds are diamagnetic and were postulated to have  $X_2E-EX_2$  molecules with E-E single bonds.<sup>81</sup> Crystallographic and spectroscopic data proved ionic structures of type  $E^+[EX_4]^-$  (E = Ga, In; X = Cl, Br, I).<sup>82–89</sup> Molecular diboron tetrahalides  $B_2X_4$  exist, for aluminum no compounds of stoichiometry  $AlX_2$  are known.<sup>90</sup> The  $E[EX_4]$  salts with  $E^{+I}$  and  $E^{+III}$  ions compropionate under influence of donors.

Especially for gallium, a large variety of derivatives  $Ga_2X_4 \cdot 2do$  has been characterized with donors like ethers, amines, phosphanes, halides and others. Common to all is a Ga–Ga bond of 239 to 247 pm, depending on the size of the donor and the electronegativity of X. A special derivative is  $(Et_3NH^+)_2[(^cHexPGa_2I_4)_2]^{2-68}$  where two  $Ga_2I_4$  units are linked by two phosphide groups forming a six membered ring. For halides as donor groups several anionic derivatives  $E_2X_6^{2-}$  have been obtained. Examples like  $[Ga(dmf)_6]_2[Ga_2Br_6]^{2-57}$  and  $(Me_4N_2CH)_2(Ga_2I_6)^{91}$  are summarized in Table 4.



### 1.17.2.1.2 $E_2R_4$ Compounds

#### • Synthetic Pathways

$E_2X_4(do)_2$  compounds are valuable starting materials for the synthesis of derivatives  $E_2R_4$  via substitution reactions. Uhl succeeded in 1989 in the synthesis of a series of  $E_2[(CH(SiMe_3)_2]_4$  compounds with E = Ga (46), In (55).<sup>1,2</sup> This method (Eq. 1) was also

**Table 1**  $X_4Al_2 \cdot 2do$  compounds.

	X	do	$d_{Al-Al}/pm$	
<b>1</b>	Cl	N Me <sub>2</sub> (SiMe <sub>3</sub> )	257.3	51
<b>2</b>	Br	N Me <sub>2</sub> (SiMe <sub>3</sub> )	256.4	51
<b>3</b>	Br	NEt <sub>3</sub>	257.1	52
<b>4</b>	Br	O(Me)Ph	252.7	53
<b>5</b>	I	Et <sub>2</sub> O	252	51
<b>6</b>	I	thf	252	54
<b>7</b>	I	PEt <sub>3</sub>	254.6	51

**Table 2** X<sub>4</sub>Ga<sub>2</sub>·2do compounds.

	<i>X</i>	<i>do</i>	<i>d</i> <sub>Ga-Ga</sub> /pm	
<b>8a</b>	Cl	Dioxane	240.6	55
<b>8b</b>	Cl	Dioxane (polymer)	238.3	56
<b>9a</b>	Cl	NEt <sub>3</sub>	244.7	57
<b>9b</b>	Cl	NMe <sub>3</sub>	242.1	58
<b>10</b>	Cl	OP(NMe <sub>2</sub> ) <sub>3</sub>	239.2	59
<b>11a</b>	Cl	NC <sub>5</sub> H <sub>4</sub> (4-Me)	241.4	60
<b>11b</b>	Cl	NC <sub>5</sub> H <sub>3</sub> (3,5-Me <sub>2</sub> )	240.0	61
<b>12a</b>	Cl	C[N(Mes)CH] <sub>2</sub>	242.4	62
<b>12b</b>	Cl	C[N(dipp)CH] <sub>2</sub>	242.7	63
<b>12c</b>	Cl	C[N(2,6-Diethylphenyl)CH] <sub>2</sub>	244.8	63
<b>12d</b>	Cl	<sup>cy</sup> CAAC	246.2	63
<b>12e</b>	Cl	<sup>Me</sup> CAAC	244.1	63
<b>13</b>	Cl	PEt <sub>3</sub>	242.7	64
<b>14</b>	Br	NEt <sub>3</sub>	245.3	57
<b>15</b>	Br	Thf	241.2	57
<b>16</b>	Br	NHEt <sub>2</sub>	243.5	57
<b>17</b>	Br	NC <sub>5</sub> H <sub>4</sub> (4- <sup>t</sup> Bu)	241.9	57
<b>18a</b>	Br	PEt <sub>3</sub>	242.7	64
<b>18b</b>	Br	PH( <sup>c</sup> Hex) <sub>2</sub>	243.5	65
<b>18c</b>	Br	<sup>cy</sup> CAAC	246.5	63
<b>19</b>	I	NH <sub>2</sub> ( <sup>c</sup> Hex)	242.9	66
<b>20</b>	I	NH <sub>2</sub> ( <sup>t</sup> Bu)	242.4	66
<b>21</b>	I	NH( <sup>c</sup> Hex) <sub>2</sub>	246.5	66
<b>22</b>	I	NEt <sub>3</sub>	249.8	67
<b>23</b>	I	(P <sup>c</sup> Hex) <sub>2</sub> <sup>-</sup>	245.0	68
<b>24</b>	I	PH( <sup>c</sup> Hex) <sub>2</sub>	243.7	66
<b>25</b>	I	PH( <sup>t</sup> Bu) <sub>2</sub>	244.5	66
<b>26</b>	I	PEt <sub>3</sub>	243.6	69
<b>27</b>	I	PPh <sub>3</sub>	244.4	69
<b>28</b>	I	AsEt <sub>3</sub>	242.8	70
<b>29a</b>	I	I, C[N(dipp)CH] <sub>2</sub> <sup>a</sup>	247.4	66
<b>29b</b>	I	<sup>cy</sup> CAAC	248.1	63

<sup>a</sup>Cation: [HC[N(dipp)CH]<sub>2</sub>]<sup>+</sup>.**Table 3** X<sub>4</sub>In<sub>2</sub>·2do compounds.

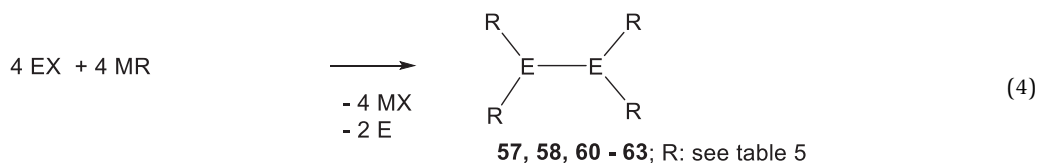
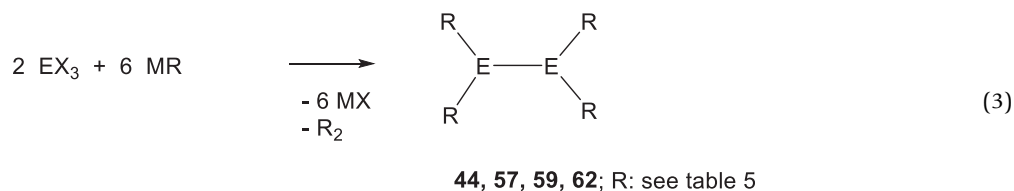
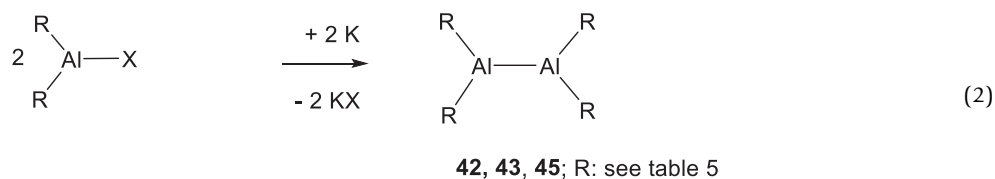
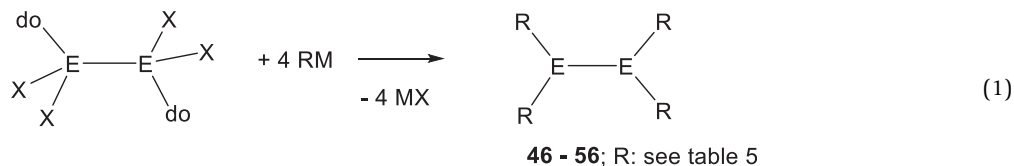
	<i>X</i>	<i>do</i>	<i>d</i> <sub>In-In</sub> /pm	
<b>30a</b>	Cl	thf	271.5	71
<b>30b</b>	2Cl, 2Br	thf	272.2	72
<b>31</b>	Br	C[N(Mes)CH] <sub>2</sub>	274.4	73
<b>32</b>	Br	tmeda	276.1	74
<b>33</b>	3Br, I	tmeda	277.5	75
<b>34</b>	I	P <sup>o</sup> Pr <sub>3</sub>	274.5	76
<b>35</b>	I	tmeda	279.2	73

useful for other derivatives with various types of substituent R (Table 5). Nevertheless, disproportionation of the triel compounds in oxidation state +II into element(III) compounds and compounds with triel atoms in oxidation states <+II are possible alternative reaction paths in these reactions. One example is the preparation of **51** from Ga<sub>2</sub>Cl<sub>4</sub>·2dioxane and [LiN(SiMe<sub>3</sub>)CH<sub>2</sub>]<sub>2</sub>CMe<sub>2</sub>, where formation of elemental gallium and Li(thf) Ga[{N(SiMe<sub>3</sub>)CH<sub>2</sub>]<sub>2</sub>CMe<sub>2</sub>]<sub>2</sub> is observed as side reaction.<sup>104</sup>

The corresponding Al compound Al<sub>2</sub>[(CH(SiMe<sub>3</sub>)<sub>2</sub>]<sub>4</sub> **42** was prepared by reduction of the corresponding diorganoaluminum dihalide with potassium (Eq. 2).<sup>115</sup> In an earlier report <sup>t</sup>Bu<sub>2</sub>Al-Al<sup>t</sup>Bu<sub>2</sub> was obtained in solution, only.<sup>116</sup>

**Table 4** Survey of compounds containing  $E_2X_6^-$  units.

	<i>E</i>	<i>X</i>	<i>M</i> <sup>+</sup>	<i>d</i> <sub>E-E</sub> /pm	
<b>36</b>	Ga	Cl	[PPh <sub>3</sub> ] <sup>+</sup>	240.4, 240.7	92
<b>37</b>	Ga	Br	[PPh <sub>3</sub> ] <sup>+</sup>	241.0	92
<b>38</b>	Ga	Br	[Ga(dm <sub>f</sub> ) <sub>6</sub> ] <sup>3+</sup>	242.0	57
<b>39</b>	Ga	I	[PPh <sub>3</sub> ] <sup>+</sup>	241.4	92
<b>40</b>	Ga	I	[CH(NMe <sub>2</sub> ) <sub>2</sub> ] <sup>+</sup>	242.3	91
<b>41</b>	In	Cl	[PPh <sub>4</sub> ] <sup>+</sup>	272.7	93



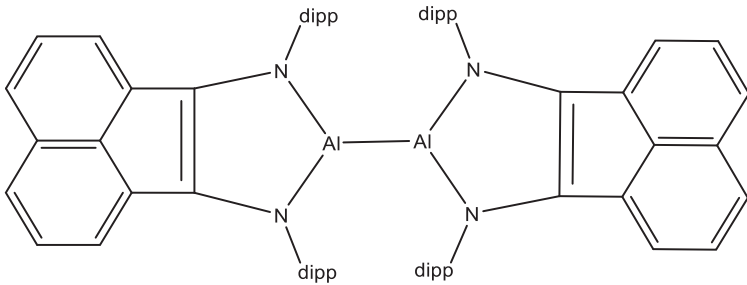
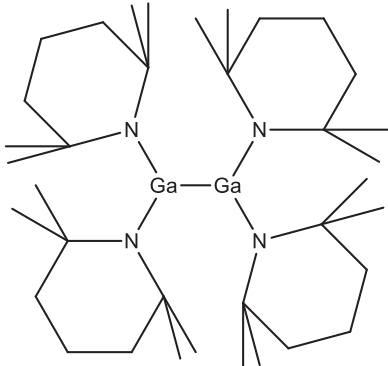
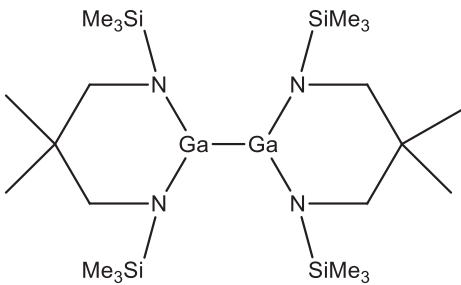
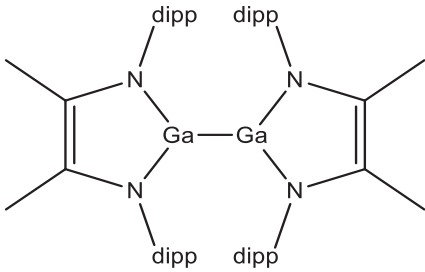
Alternative routes are the reactions of trihalides with reducing alkali metal silanides (Eq. 3) or redox disproportionation of EX (X = halide, N(SiMe<sub>3</sub>)<sub>2</sub>, Cp\*) with MR reagents (Eq. 4). By these routes several ditrirelanes with various substituents were accessible (Table 5).

#### • Structural Features

Most of these compounds exhibit monomeric E<sub>2</sub>R<sub>4</sub> molecules with planar three coordinate triel atoms. The ER<sub>2</sub> units can be oriented coplanar or twisted, with torsions angles between 0° and 90°. The ideal staggered conformation is adopted for the silyl substituted derivatives. The alkyl substituted ones have nearly planar C<sub>2</sub>E-EC<sub>2</sub> arrangements. This was explained with hyperconjugative interactions between the empty p-orbital at the triel atoms and the filled σ-orbitals of the α-C-Si bonds. Alternatively, or in addition, the ideal packing of the planar molecules in the crystal and subsequent ideal orientation of the R groups for the hyperconjugative interaction was used as explanation. In solution no rotational barriers were detected by low temperature NMR experiments.<sup>1,2,94</sup> The tetraaryl derivatives have conformations with torsion angles of approximately 45°.

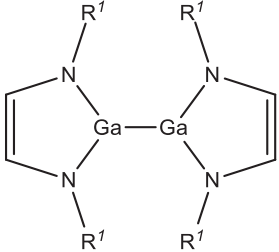
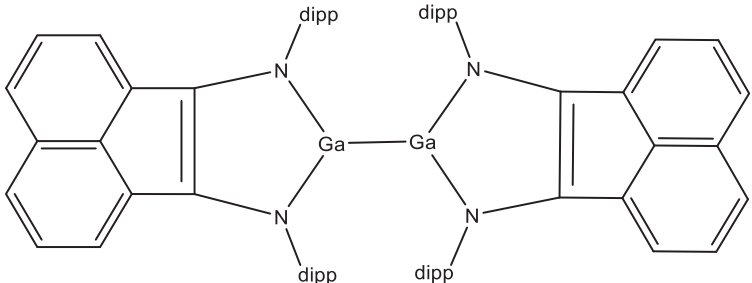
The E-E bond seems to be the chromophore of ditrirelanes, the absorption maxima of which are influenced by the substituents. While the alkyl derivatives are yellow (Al) to orange (In), the silyl substituted ones are described as dark green to red. Bathochromic shifts in UV/Vis spectra are observed with increasing ordinal number and increasing torsion angles.

**Table 5** Monomer ditrirelanes  $E_2R_4$  with three-coordinate triel atoms.

		$d_{E-E}/pm$	References
42	$[(Me_3Si)_2CH]_2Al-Al[CH(SiMe_3)_2]_2$	266.0	94
43	$Trip_2Al-AlTrip_2$	264.7	95
44	$(^tBu_3Si)_2Al-Al(Si^tBu_3)_2$	275.1	96,97
45		252.2	98
46	$[(Me_3Si)_2CH]_2Ga-Ga[CH(SiMe_3)_2]_2$	254.1	2
47	$Trip_2Ga-GaTrip_2$	251.5	99
48a	$[(Me_3Si)_3Si]_2Ga-Ga[Si(SiMe_3)_3]_2$	259.9	100
48b	$[Ph_2^tBuSi]_2Ga-Ga[SiPh_2^tBu]_2$	245.6	101
49	$(^fMes)_2Ga-Ga(^fMes)_2$	247.9	102,103
50		252.5	25
51		238.5	104:0030
52		236.3	105

(Continued)

Table 5 Monomer ditrirelanes E<sub>2</sub>R<sub>4</sub> with three-coordinate triel atoms.—cont'd

		<i>d</i> <sub>E-E</sub> /pm	References
53	 $R^1 = {}^t\text{Bu, dipp, 2,6-Et}_2\text{C}_6\text{H}_3$	233.1, 234.8, 235.9	106–108
54		236.0	106
55	$[(\text{Me}_3\text{Si})_2\text{CH}]_2\text{In-In}[\text{CH}(\text{SiMe}_3)_2]_2$	282.8	1
56	$\text{Trip}_2\text{In-InTrip}_2$	277.5	109
57	$({}^t\text{Bu}_3\text{Si})_2\text{In-In}(\text{Si}^i\text{Bu}_3)_2$	292.8	96,110
58	$({}^t\text{Bu}_2\text{PhSi})_2\text{In-In}(\text{Si}^i\text{Bu}_2\text{Ph})_2$	293.8	96
59	$[(\text{Me}_3\text{Si})_3\text{Si}]_2\text{In-In}[\text{Si}(\text{SiMe}_3)_3]_2$	286.8	111
60	$({}^t\text{Mes})_2\text{In-In}({}^t\text{Mes})_2$	274.4	102
61	$[(\text{Me}_3\text{Si})_3\text{Si}]_2\text{Tl-Tl}[\text{Si}(\text{SiMe}_3)_3]_2$	291.5	112
62	$({}^t\text{Bu}_3\text{Si})_2\text{Tl-Tl}(\text{Si}^i\text{Bu}_3)_2$	288.1	96
63	$({}^t\text{Bu}_2\text{PhSi})_2\text{Tl-Tl}(\text{Si}^i\text{Bu}_2\text{Ph})_2$	296.2	96,110,113

The largest number of these compounds was prepared with E = Ga. Here the Ga–Ga bond varies from 234 to 260 pm with the steric demand of the substituents. The longest bond was observed for the bulky silyl derivative  $[(\text{Me}_3\text{Si})_3\text{Si}]_2\text{Ga-Ga}[\text{Si}(\text{SiMe}_3)_3]_2$  **48a**. The digallane **48b** with  $\text{SiPh}_2{}^t\text{Bu}$ -substituents shows a remarkable shorter Ga–Ga bond. This might be due to dispersion interactions between the substituents, similar to the effects in multiple bonded systems.<sup>117</sup>

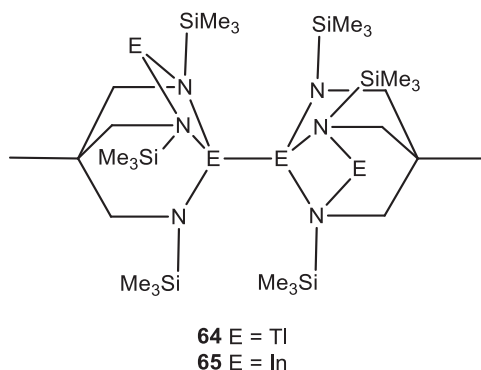
This dependence of the substituents is also demonstrated with tetra(amino)digallanes. In  $\text{tmp}_4\text{Ga}_2$  **50** the molecule parts are twisted by 31° and the Ga–Ga bond lengths is 252.5(1) pm. The less steric demanding diamine residue  $\text{Me}_2\text{C}[\text{CH}_2\text{N}(\text{SiMe}_3)]_2$  leads to an orthogonal orientation of the GaN<sub>2</sub> planes in **51** and a short Ga–Ga bond of 238.5(1) pm. With diazabutadienediide substituents  $[\text{CHN}(\text{R})]_2$  (R = <sup>t</sup>Bu, 2,6-<sup>i</sup>Pr<sub>2</sub>C<sub>6</sub>H<sub>3</sub>, 2,6-Et<sub>2</sub>C<sub>6</sub>H<sub>3</sub>) similar short Ga–Ga bonds are observed in **52–54**. Dialanes have longer E–E bonds than digallanes, because of the smaller covalent radius of gallium.

Especially, compounds of types **45** and **54** show interesting chemistry, due to their redox-active substituents.<sup>98,106,118–121</sup>

#### ● Thallium-Thallium Interactions

For thallium  $[(\text{Me}_3\text{Si})_3\text{Si}]_2\text{Tl-Tl}[\text{Si}(\text{SiMe}_3)_3]_2$  **61**, prepared by the reaction of  $\text{RbSi}(\text{SiMe}_3)_3$  and  $\text{TlN}(\text{SiMe}_3)_2$ , is a rare example with a thallium-thallium bond.<sup>112</sup> Thallium-thallium interactions are also present in a thallium tripod complex **64**.<sup>122</sup> Here, additional thallium(I) cations atoms coordinate to the tripod ligand. The thallium-thallium bond ( $d_{\text{Tl-Tl}} = 273.4$  pm) is even shorter than in the indium analog **65**.<sup>122</sup> A series of thallium(I) complexes with tripod ligands<sup>122–126</sup> and diamido ligands<sup>127,128</sup> show  $\text{Tl}\cdots\text{Tl}$  contacts, too.<sup>129,130</sup> Such interactions between closed shell  $s^2$ -thallium(I) cations are also observed in other classes of compounds and usually are weak (370 → 400 pm).<sup>129,131–135</sup>  $\text{Tl}_2[(\text{RN})_2\text{BPh}]$  (R = <sup>i</sup>Pr, <sup>t</sup>Bu) aggregates to chains, where dithallium units interact with a thallium ion of the next unit, leading to infinite chains of edge-sharing triangles ( $d_{\text{Tl-Tl}} = 295.0$  and 300.4 pm).<sup>136</sup>



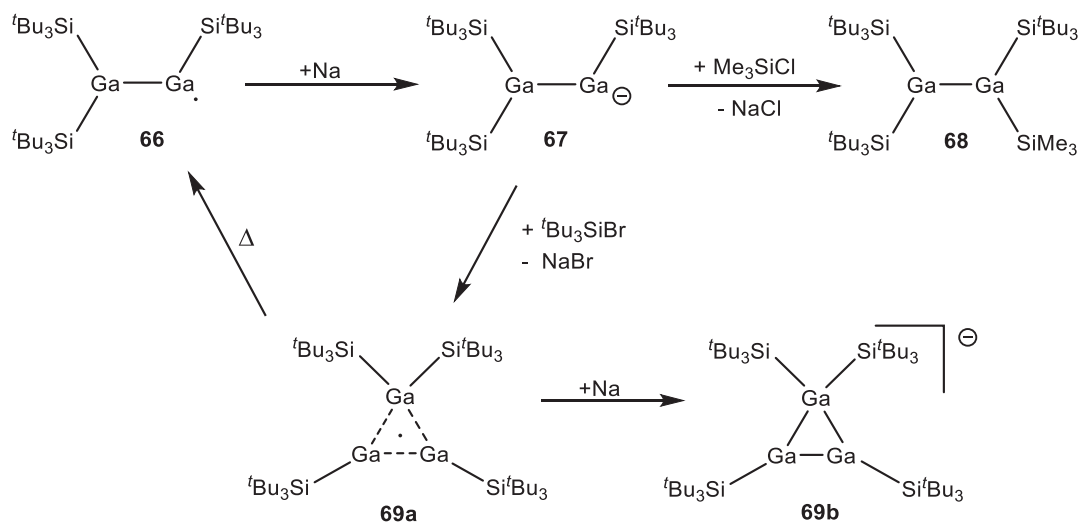


#### • Bulky Silanide Derivatives

Using the bulky silanide  ${}^t\text{Bu}_3\text{SiNa}$ , the corresponding tetrasilylditrialane, indane and thallane are accessible. For aluminum and gallium, the trihalides are reduced during the reaction (Eq. 3) and the indium and thallium derivatives are accessible via the mono-halides, respectively (Eq. 4). Only for gallium, the smallest atoms in this row Al – Tl, the tetrasilyldigallane ( ${}^t\text{Bu}_3\text{Si}$ ) $_4\text{Ga}_2$  was not stable under the reaction conditions, but lost one equivalent of  ${}^t\text{Bu}_3\text{Si}$  to afford the radical  $[({}^t\text{Bu}_3\text{Si})_3\text{Ga}_2]\bullet$  **66** ( $d_{\text{Ga-Ga}} = 242.3$  pm).<sup>137</sup> Reduction of this radical afforded  $[({}^t\text{Bu}_3\text{Si})_3\text{Ga}_2]^- (\text{Na}(\text{thf})_3)^+$  **67** ( $d_{\text{Ga-Ga}} = 237.9$  pm),<sup>137</sup> which can be used for nucleophilic substitution reactions, i.e. with trimethylchlorosilane to **68**, or can be oxidized with  ${}^t\text{Bu}_3\text{SiBr}$  to a cyclotrigallane **69a**, which then can be reduced to **69b** (Scheme 1). **66** decomposes on heating to 373 K within 10 h via the dialanylradical  $[({}^t\text{Bu}_3\text{Si})_3\text{Al}_2]\bullet$ , an analog to **66**, to  $({}^t\text{Bu}_3\text{Si})_4\text{Al}_3$ , which itself is an analog to **69a**. The gallium ring compound was not formed on heating of  $[({}^t\text{Bu}_3\text{Si})_3\text{Ga}_2]\bullet$ . The three-membered ring compounds of aluminum and gallium transform to give cluster compounds  $({}^t\text{Bu}_3\text{Si})_4\text{E}_4$  (E = Al, Ga) and others on heating. Similar,  $({}^t\text{Bu}_3\text{Si})_4\text{In}_2$  decomposes to a higher indium cluster (vide infra), which might also be the case for the thallium homolog. But here only an undefined black precipitate was obtained.

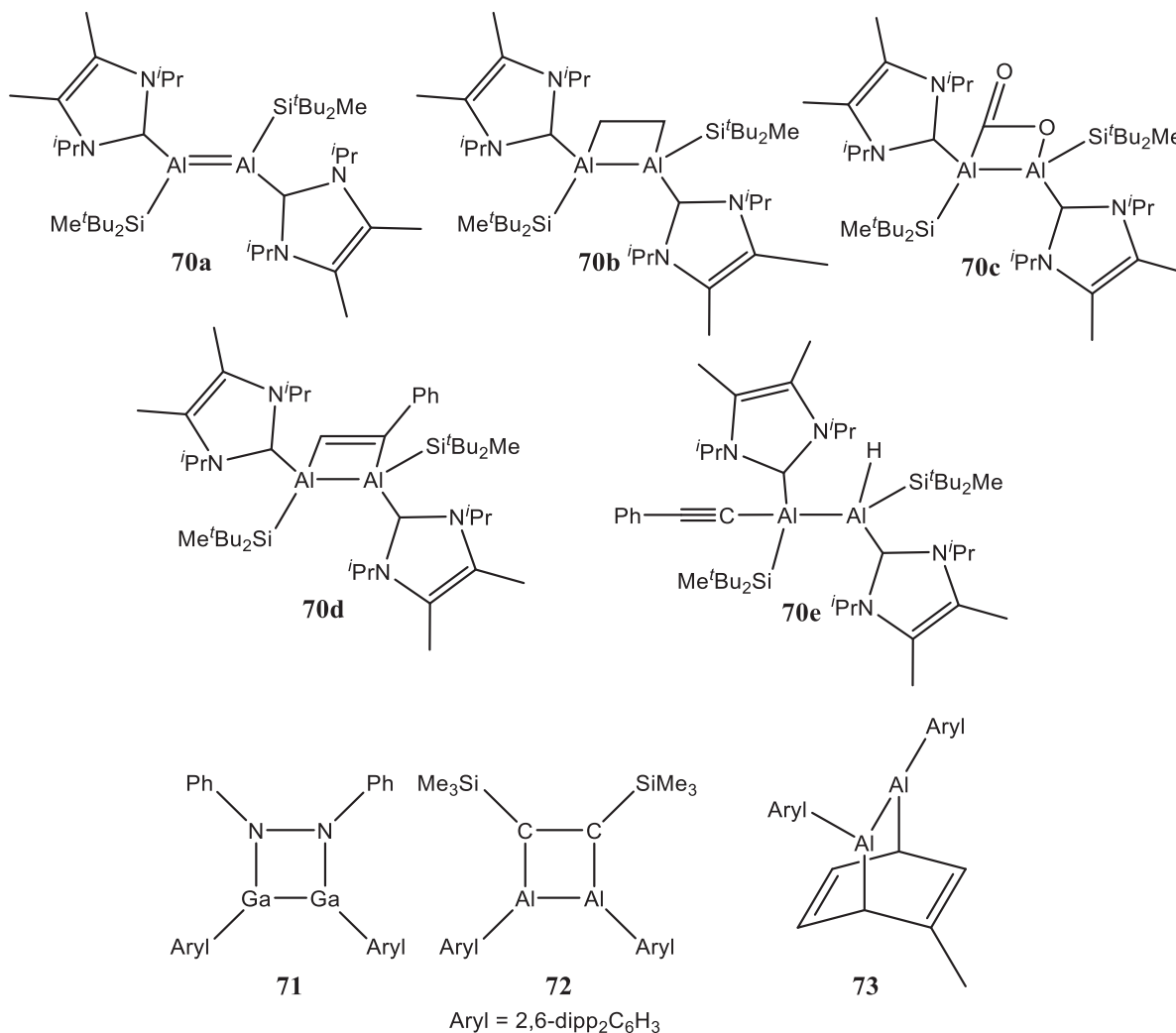
#### • Cycloaddition Products of Ditrienes

The NHC stabilized dialumene  $[\text{AlSi}({}^t\text{Bu}_2\text{Me})\text{C}\{\text{N}({}^i\text{Pr})\text{C}(\text{Me})_2\}_2]_2$  **70a** contains a Al-Al double bond and has been used for various cycloadditions.<sup>138,139</sup> Thus, **70a** reacted with ethene and carbon dioxide forming the products **70b** and **70c**, respectively. Reaction with phenylacetylene yielded cycloaddition product **70d** and insertion product **70e** in an equimolar ratio.



**Scheme 1** Reactivity of supersilylsubstituted oligogallanes.

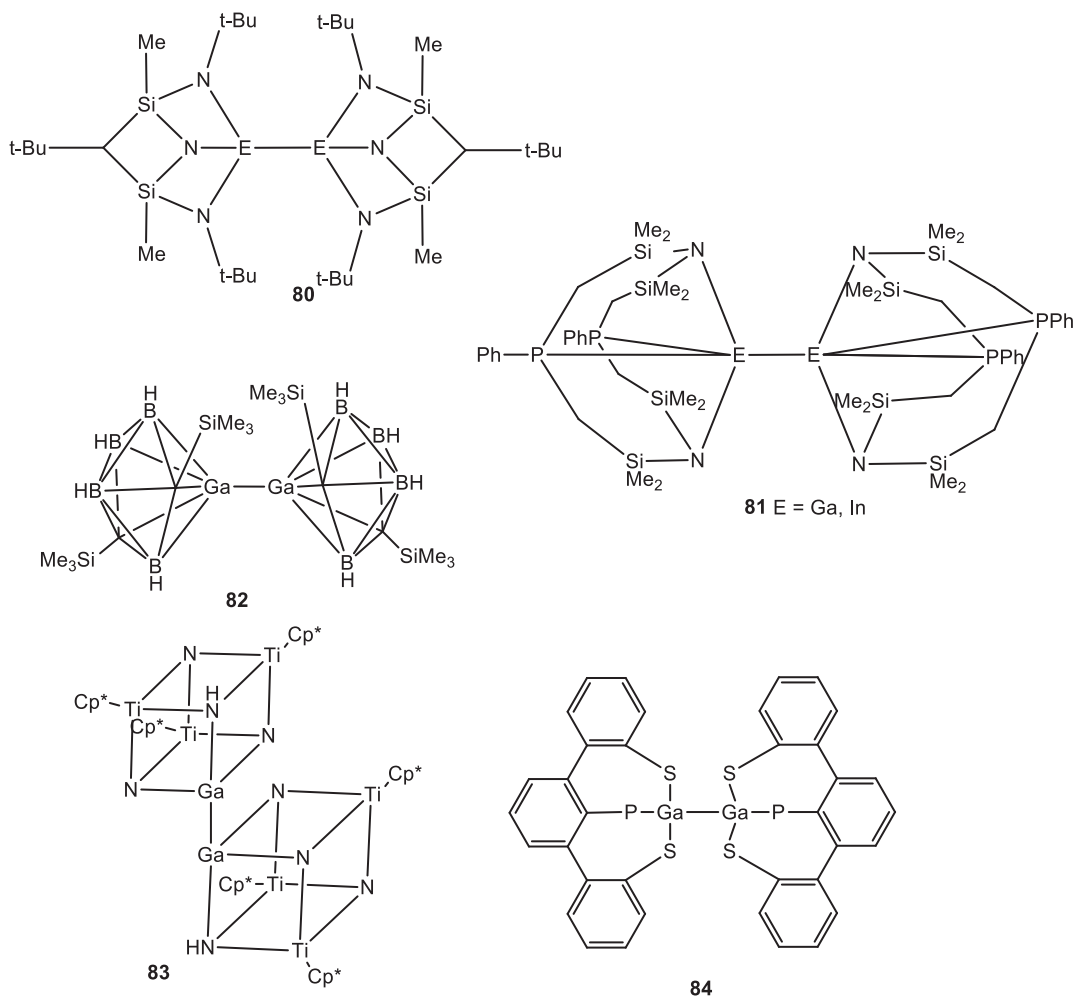
A special derivative is the cycloaddition product  $\text{ArylGa}(\text{NPh})_2\text{GaAryl}$  **71** (Aryl = 2,6-dipp<sub>2</sub>C<sub>6</sub>H<sub>3</sub>) of corresponding digallene and diazene. **71** contains a Ga<sub>2</sub>N<sub>2</sub>-ring with a Ga<sub>2</sub>-unit.<sup>140</sup> The corresponding Aryl<sub>2</sub>Al<sub>2</sub>-unit is part of an Al<sub>2</sub>C<sub>2</sub>-ring of ArylAl[C(SiMe<sub>3</sub>)<sub>2</sub>]<sub>2</sub>AlAryl **72**<sup>141</sup> and is present in (ArylAl)<sub>2</sub>(C<sub>6</sub>H<sub>5</sub>Me) **73**, the cycloaddition product of toluene and Aryl<sub>2</sub>Al<sub>2</sub>.<sup>142</sup> The latter is only one representative of a class of ditrielenes REER<sup>143</sup> (E = Al,<sup>142</sup> Ga,<sup>144,145</sup> In,<sup>146</sup> Tl<sup>147–149</sup>), which have been prepared during the last decades. They potentially can be looked upon as doubly bonded systems. Nevertheless, their long EE bonds indicate otherwise. On reduction dianionic species [REER]<sup>2-</sup> are obtained, for which the bonding situation was discussed controversially. A triple bond as well as a single bond is an extreme description for these compounds.<sup>145,150–152</sup> One-electron reduction of ditrielenes **42**, **43**, **44** and **47** gave the radical ions [R<sub>4</sub>E<sub>2</sub>]<sup>•-</sup> with a bond order of 1.5, meaning the additional electron is located in the empty p-orbitals of the E<sub>2</sub>-unit.<sup>95,99,153–157</sup>



### 1.17.2.1.3 Lewis Acidity – Higher Coordination Numbers

Chalcogenide substituents were scarcely used in this kind of chemistry. The *tert*-butoxy substituted digallane **74** forms a dimer with two parallel Ga–Ga bonds, which are linked via *tert*-butoxy bridges.<sup>104</sup> The isostructural aluminum alkoxide was prepared from AlBr solutions. The formation of these dimers shows the triel atoms in ditrielenes(4) still to be Lewis acidic.<sup>158</sup>





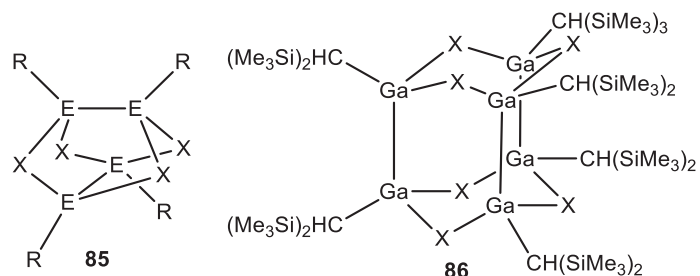
The dialane(6)  $[{}^i\text{Bu}_3\text{Al}-\text{Al}{}^i\text{Bu}_3]^{2-}$  was obtained by reduction of  ${}^i\text{Bu}_3\text{Al}$  with potassium.<sup>171</sup> Even more easily is the adduct formation with diindanes, which is due to the larger radius of indium atoms compared to the lighter homologs.

#### 1.17.2.1.4 Heteroleptic Compounds

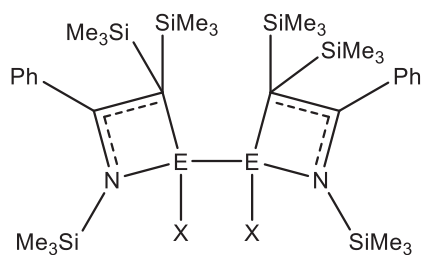
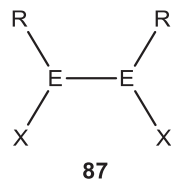
The gallium and indium compounds of type (REX)<sub>4</sub> **85a-h** (Table 6) adopt a D<sub>2d</sub>-symmetric structure, where two E<sub>2</sub>-units are linked via four halide bridges. The cage formed resembles the Realgar-structure (As<sub>4</sub>S<sub>4</sub>). With the smaller (Me<sub>3</sub>Si)<sub>2</sub>CH-substituent a trimeric fluoride derivative **86a** and the hydroxide **86b** were obtained by treatment of digallane **46** with HF or H<sub>2</sub>O, respectively. In these compounds three Ga–Ga bonds are in parallel arrangement.<sup>176</sup>

**Table 6** (REX)<sub>4</sub> compounds of type **85**.

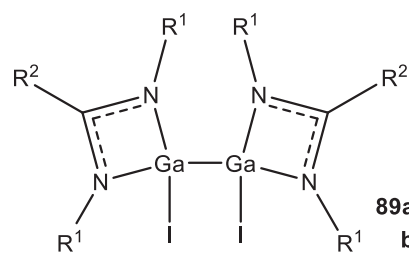
<b>85</b>	<i>E</i>	<i>R</i>	<i>X</i>	References
<b>a</b>	Ga	Si(SiMe <sub>3</sub> ) <sub>3</sub>	Cl	100
<b>b</b>	Ga	Si(SiMe <sub>3</sub> ) <sub>3</sub>	Br	172
<b>c</b>	Ga	Si <sup><i>i</i></sup> Bu <sub>3</sub>	Cl	173
<b>d</b>	In	C(SiMe <sub>3</sub> ) <sub>3</sub>	Cl	174
<b>e</b>	In	C(SiMe <sub>3</sub> ) <sub>3</sub>	Br	174
<b>f</b>	In	2,6-Mes <sub>2</sub> C <sub>6</sub> H <sub>3</sub>	Cl	175
<b>g</b>	In	2,6-Mes <sub>2</sub> C <sub>6</sub> H <sub>3</sub>	Cl <sub>0.5</sub> I <sub>0.5</sub>	175
<b>h</b>	In	2,6-Mes <sub>2</sub> C <sub>6</sub> H <sub>3</sub>	I	175



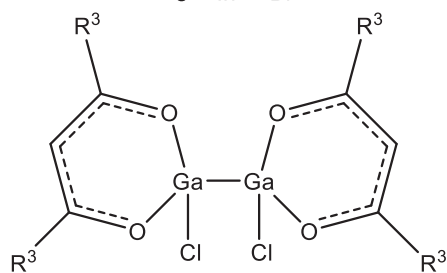
a: X = F  
b: X = OH



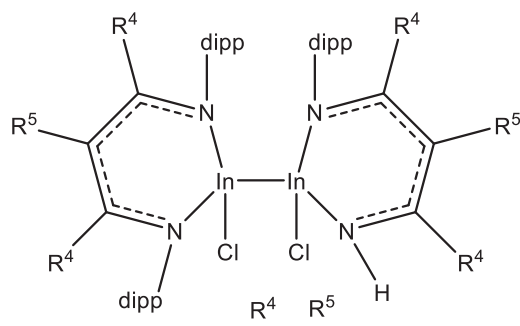
88a Al Cl  
b Ga Cl  
c In Br



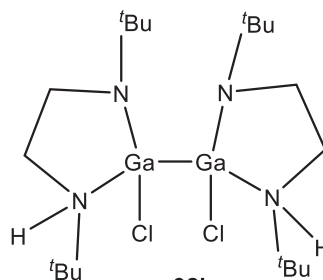
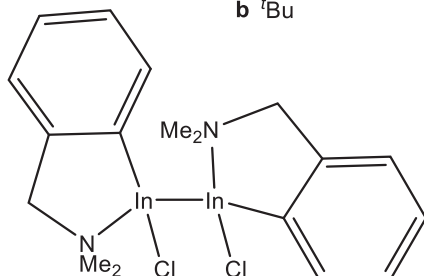
	R <sup>1</sup>	R <sup>2</sup>
<b>a</b>	dipp	H
<b>b</b>	dipp	<sup>t</sup> Bu
<b>c</b>	dipp	Me
<b>d</b>	<sup>i</sup> Pr	<sup>i</sup> Pr <sub>2</sub> N



90a Me  
b <sup>t</sup>Bu



91a H Ph  
b Me H





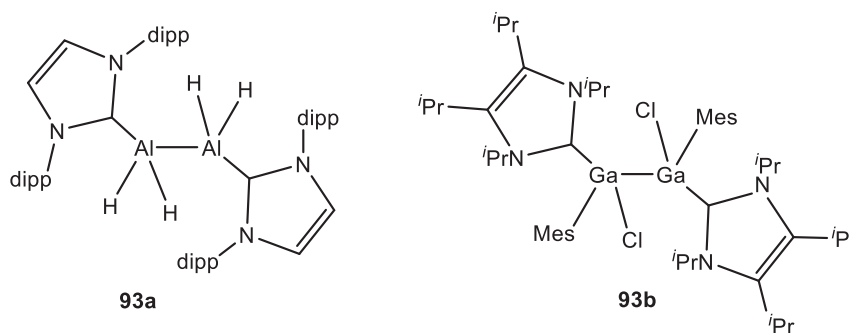
**Table 7** Monomeric  $R_2E_2X_2$  compounds.

<b>87</b>	<i>E</i>	<i>R</i>	<i>X</i>	References
<b>a</b>	Al	dipp	I	142
<b>b</b>	Ga	C(SiMe <sub>3</sub> ) <sub>3</sub>	Br	177
<b>c</b>	Ga	C(SiMe <sub>3</sub> ) <sub>3</sub>	I	178
<b>d</b>	Ga	2,4,6- <sup>t</sup> Bu <sub>3</sub> C <sub>6</sub> H <sub>2</sub>	Cl	179
<b>e</b>	Ga	2,6-dipp <sub>2</sub> C <sub>6</sub> H <sub>3</sub>	I	144
<b>f</b>	Ga	2,6-trip <sub>2</sub> C <sub>6</sub> H <sub>3</sub>	I	145

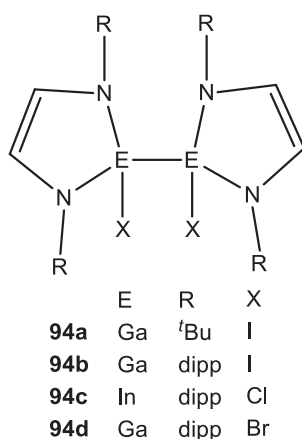
With more bulky substituents monomeric derivatives  $R_2E_2X_2$  **87a** - **f** (Table 7) with three coordinate triel atoms were synthesized.

With bidentate substituents a series of heteroleptic ditrirelanes **88**–**92**<sup>180–188</sup> with tetracoordinate galliumatoms could be obtained.

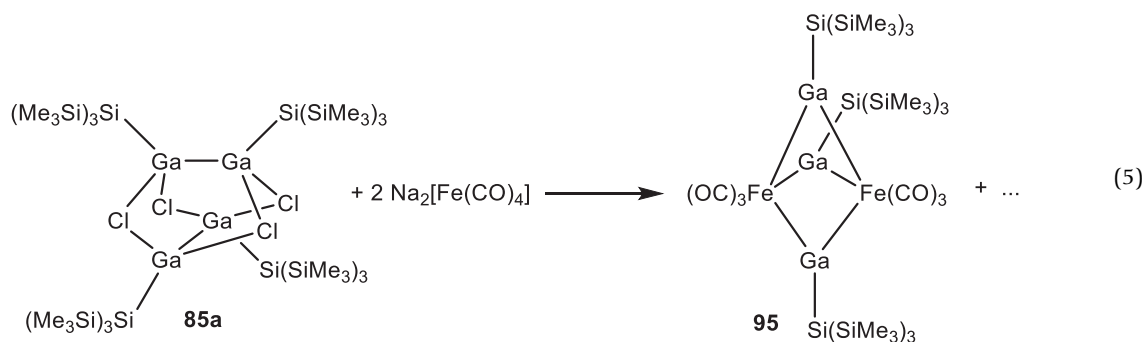
Ditrirelanes with carbenes as stabilizing donors is also a growing field. Compounds like the previously mentioned triel dihalides **12a**–**e**, **18c**, **29b** and cycloaddition products **70b**–**e** but also the heteroleptic compounds **93a**–**b**<sup>189,190</sup> have been reported.



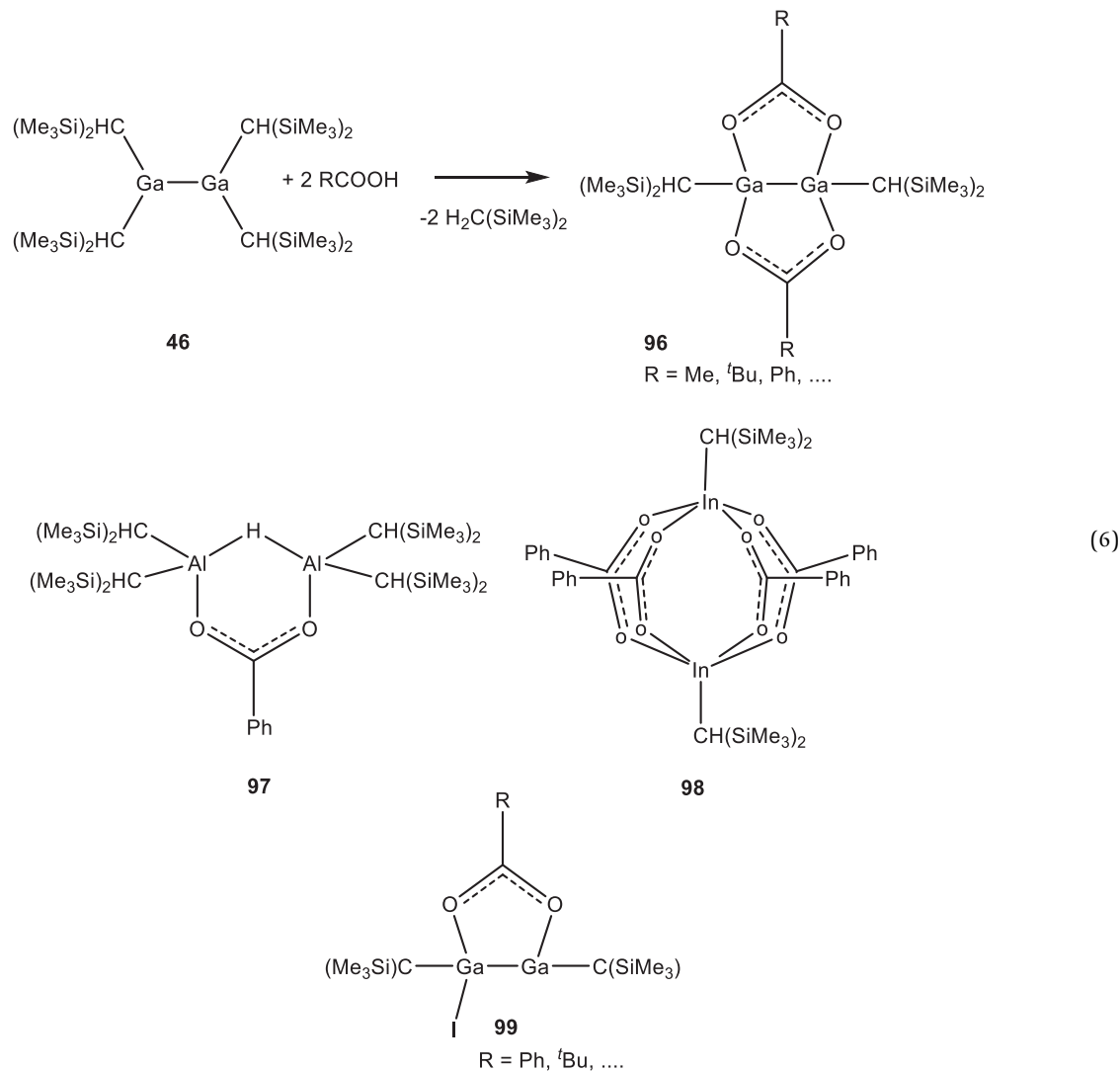
Biradical ditrirelanes **94a**–**c** are products of reactions of “GaI”<sup>191</sup> or InCl with diazabutadienes,<sup>192–194</sup> while **94d** was isolated from an obscure reaction.<sup>193</sup>



These types of functional digallanes  $[R_2E_2X_2]_n$  ( $n = 1, 2, 3$ ) normally do not undergo simple substitution reactions, which might offer a broad potential to synthesis of heterocyclic compounds with Ga-Ga-units. Mostly redox disproportionation or reduction by the nucleophile was observed. For example, **85a** reacts with Collman’s reagent to give a gallium-iron cluster **95**. Here, GaSi(SiMe<sub>3</sub>)<sub>3</sub> groups substitute for bridging CO-ligands in Fe<sub>2</sub>(CO)<sub>9</sub> (Eq. 5).<sup>195</sup> Similarly, other ER groups are versatile ligands (for reviews see for example<sup>11,12,196–199</sup>).

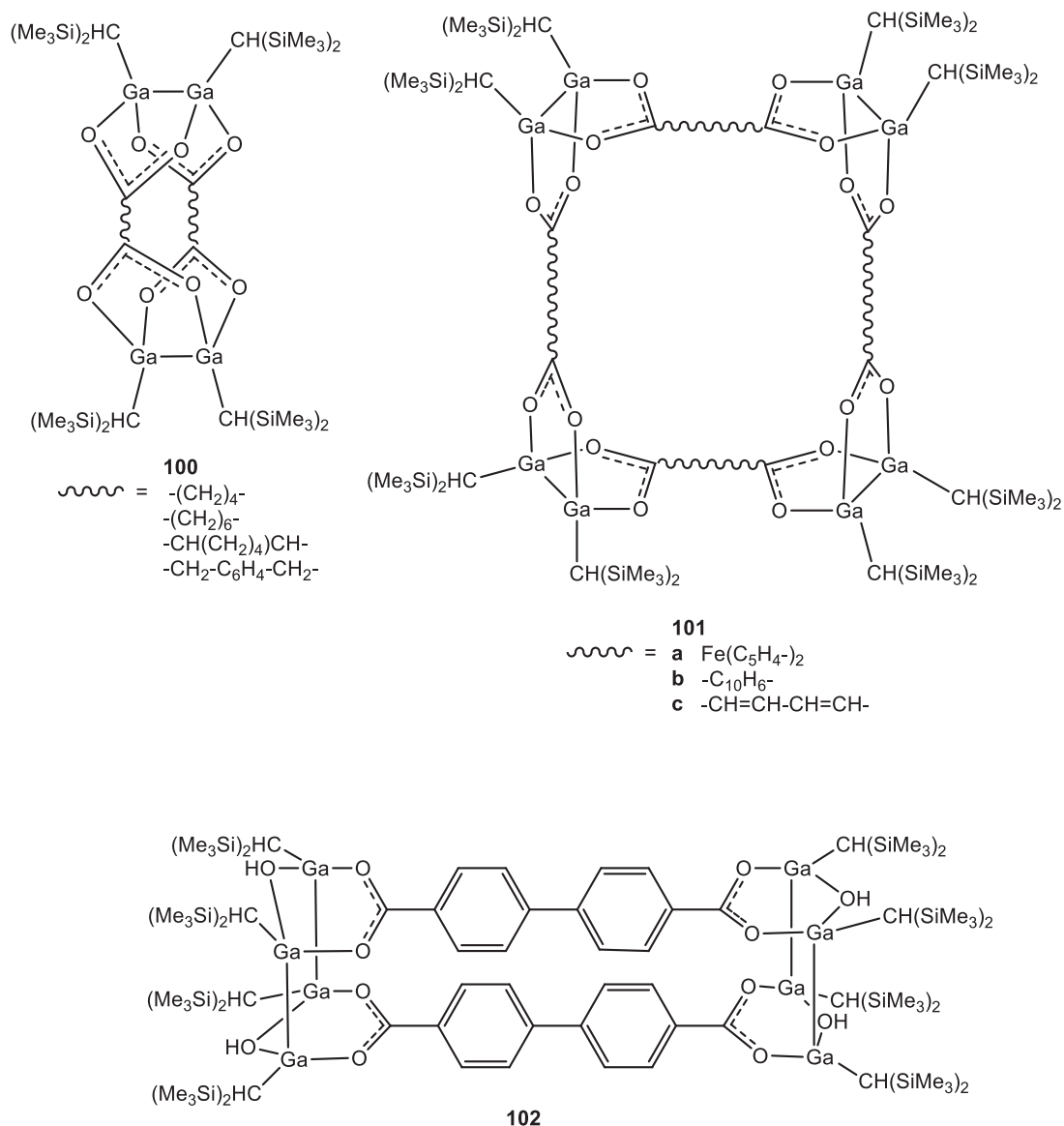


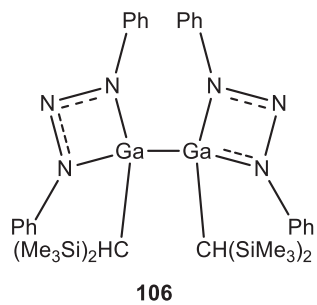
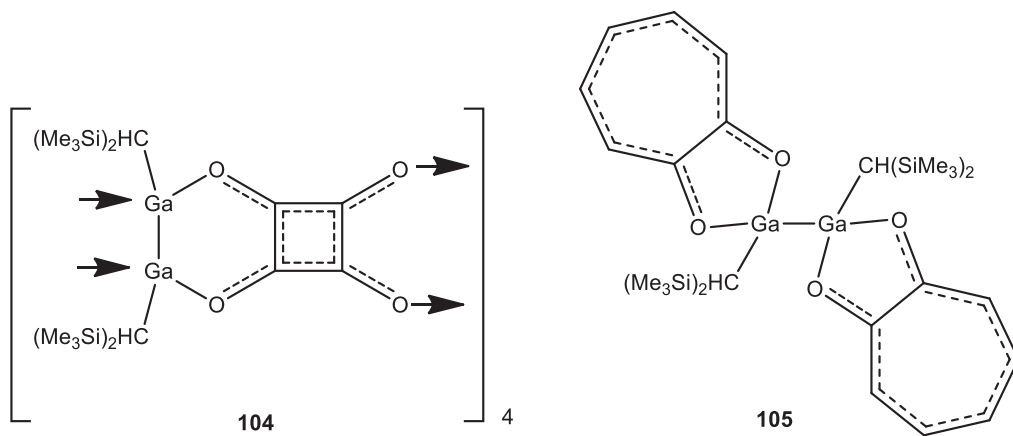
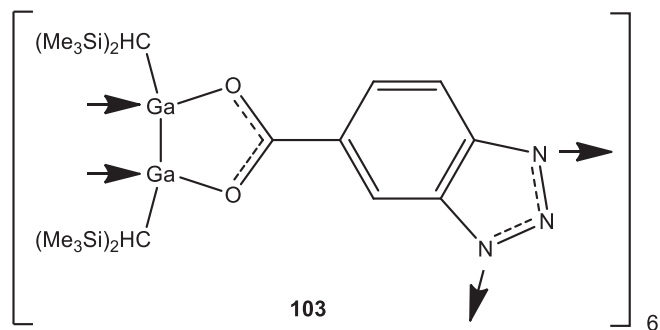
On the other hand, by reaction of  $[(\text{Me}_3\text{Si})_2\text{CH}]_2\text{Ga}-\text{Ga}[\text{CH}(\text{SiMe}_3)_2]_2$  **46** with Brønsted acids of various types a large variety of heteroleptic digallanes are accessible.<sup>200</sup> The huge number of compounds, available, cannot be fully discussed here. The principle is shown in the reaction of **46** with a carboxylic acid to form **96** (Eq. 6). Here two alkyl ligands are protonated off and the carboxylate groups are bridging the intact  $\text{Ga}_2$ -unit. For the homologous aluminum and indium compounds the protolysis reactions proceed in a different way, to produce **97** and **98**, where the E-E bond is cleaved.<sup>201</sup> Corresponding indium(II) carboxylates were prepared from **85d** by reaction with silver or lithium carboxylates.<sup>202,203</sup> Reaction of  $[(\text{Me}_3\text{Si})_3\text{CGal}]_2$  **87c** with lithium carboxylates gave unsymmetrical substituted derivatives **99**.<sup>204</sup>

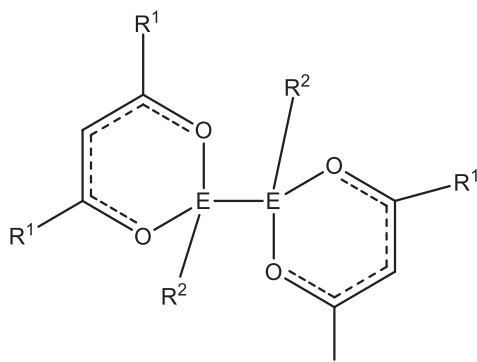
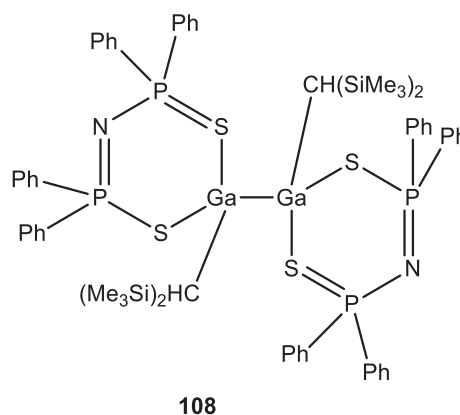
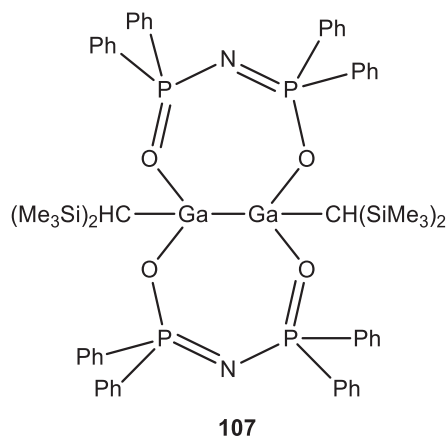


The stability of the  $\text{Ga}_2$ -unit was used to arrange up to six  $\text{Ga}_2$ -bonds in supramolecular aggregates using dicarboxylic acids. Flexible spacers allow dimeric species **100**.<sup>205</sup> 1,4-butane, 1,6-hexane-, 1,6-cyclohexane- and 1,4-dimethylbenzenedicarboxylic acid have been used as flexible spacers. Rigid spacers like, ferrocenedicarboxylic acid, naphthalenedicarboxylic acid or muconic acid, allow higher nuclear derivatives **101a**,<sup>206</sup> **101b**,<sup>207</sup> **101c**.<sup>208</sup> Here, carboxylates can either bridge a  $\text{Ga}_2$ -unit (for example **101**) or link two  $\text{Ga}_2$ -bonds (for example: **102**). With benzotriazol-5-carboxylic acid six  $\text{Ga}_2[\text{CH}(\text{SiMe}_3)_2]$  units get linked to form cage **103**.<sup>209</sup> Hereby cavities of up to 1.5 nm diameter are formed, which can contain solvent molecules. Squaric acid reacts similarly to form a tetramer aggregate **104**,<sup>208</sup> whilst tropolone reacts with **46** to give the monomeric digallane **105**.<sup>210</sup>

Those heteroleptic digallanes are valid starting materials, themselves. Thus, reaction of  $[(\text{Me}_3\text{Si})_2\text{CH}]_2\text{Ga}_2(\text{O}_2\text{CMe})_2$  **96** with lithiumdiphenyltriazenide afforded the triazenido substituted digallane **106**,<sup>211</sup> which is built analogous to amidinato substituted digallanes with the triazenido ligand bonded in terminal positions, not in a bridging one like the carboxylate. This was explained with the larger flexibility of the NNN angle compared to the  $\text{OC}(\text{Me})\text{O}$  angle.







<b>109</b>	E	R <sup>1</sup>	R <sup>2</sup>	R <sup>1</sup>
<b>a</b>	Ga	Ph	CH(SiMe <sub>3</sub> ) <sub>2</sub>	
<b>b</b>	Ga	<sup>t</sup> Bu	CH(SiMe <sub>3</sub> ) <sub>2</sub>	
<b>c</b>	Ga	Me	C(SiMe <sub>3</sub> ) <sub>3</sub>	
<b>d</b>	In	Me	C(SiMe <sub>3</sub> ) <sub>3</sub>	
<b>e</b>	In	<sup>t</sup> Bu	C(SiMe <sub>3</sub> ) <sub>3</sub>	
<b>f</b>	In	Ph	C(SiMe <sub>3</sub> ) <sub>3</sub>	

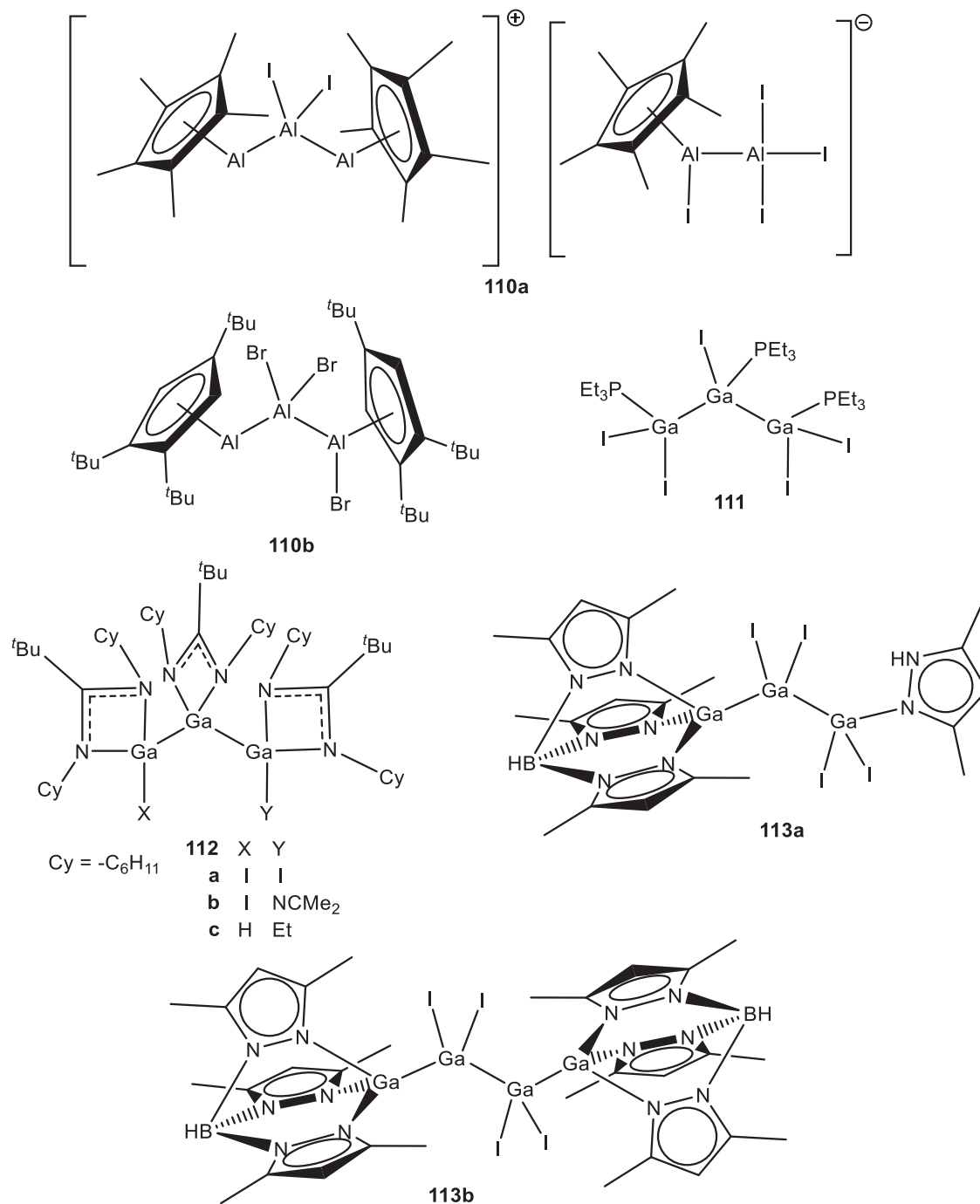
In addition, other types of protonic acids have been applied for reactions in analogy to Eq. (6). Imido-tetraphenylphosphinic acid and imido-tetraphenylthiodiphosphinic acid form the digallanes **107** and **108**, with different coordination mode of oxygen and thioligands.<sup>212</sup>

Similarly, acetylacetonato derivatives of digallanes **109** are either prepared by reaction of the neutral acetylacetonates<sup>213,214</sup> or by reaction of the lithium acetylacetonates with digallium subhalides.<sup>203,215</sup> For indium, only the route via diindium subhalides is successful.<sup>204,215</sup>

### 1.17.2.2 Synthesis and structure of compounds with E<sub>3</sub>-units

For E<sub>3</sub>-compounds chain and ring compounds are possible. An Al<sub>3</sub>-unit is present in the salt [Cp\*<sub>2</sub>Al<sub>3</sub>I<sub>2</sub>]<sup>+</sup>[Cp\*Al<sub>2</sub>I<sub>4</sub>]<sup>-</sup> **110a**,<sup>216</sup> obtained from the reaction of [Cp\*Al]<sub>4</sub> with aluminum triiodide. The structure of neutral Cp<sup>*t*Bu</sup><sub>2</sub>Al<sub>3</sub>Br<sub>3</sub> **110b** (Cp<sup>*t*Bu</sup> = 1,2,4-tri-*tert*-butylcyclopentadienyl) is derived from **110a** by bonding of an additional halide.<sup>217</sup>





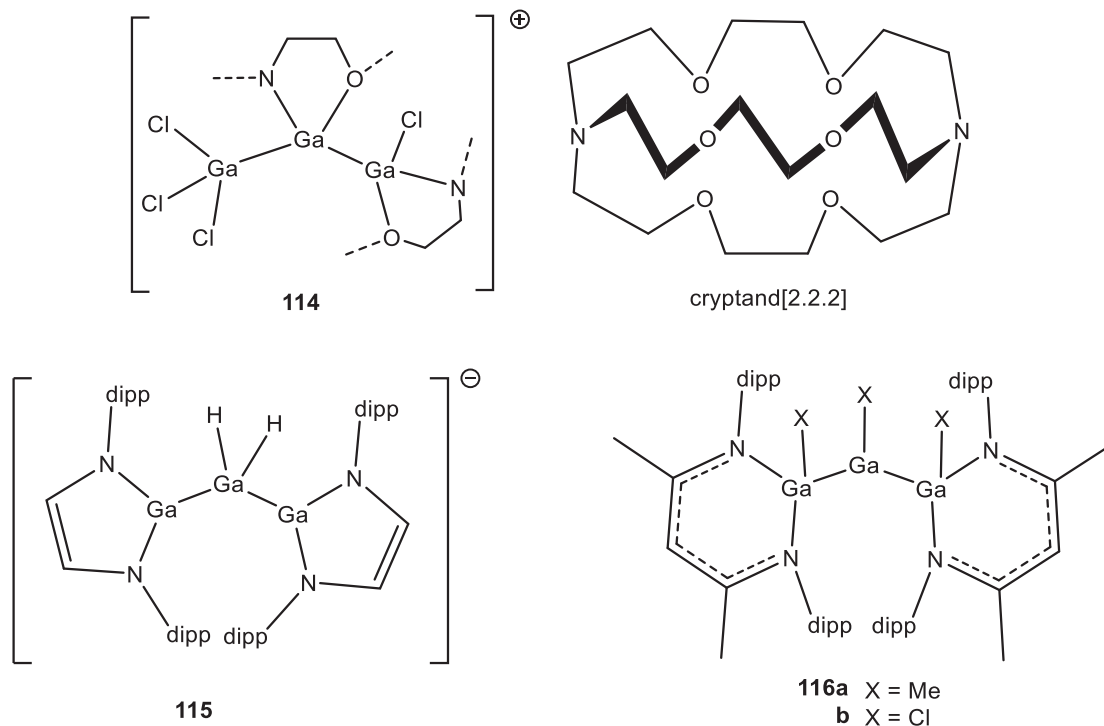
The largest variety of E<sub>3</sub>-compounds is known for the element gallium. Two types of open-chain trigallanes with bent, as well as linear, Ga<sub>3</sub>-cores were realized. Ga<sub>3</sub>I<sub>5</sub>·3PEt<sub>3</sub> **111**<sup>69</sup> is a sole example of a Ga<sub>3</sub> subhalide. With amidinato groups several trigallanes of type (amidinato)<sub>3</sub>Ga<sub>3</sub>I<sub>2</sub> **112a**, **112b** could be prepared, including a subvalent hydride **112c**. The latter was obtained by the reaction of **112a** with Na[BET<sub>3</sub>H].<sup>183</sup> The reaction of **112a** with elemental iodine in toluene at room temperature occurs immediately. It yields the gallium(III) compound (amidinato)Ga<sub>2</sub>. That allows a redox titration with an iodine standard solution in toluene.

The consumption of iodine solution corresponds with a four electron reaction. This matches with the presence of two gallium(II) and one gallium(I) in **112a**.

**112a** cocrystallizes with solvents like n-hexane, toluene and thf. This change of crystal solvent has influence on the structure of **112a**. The torsion angle I-Ga...Ga-I in solvent free and hydrocarbon containing crystals is approximately 125–126°, for the thf solvate it changes to 88°. There is no close contact between the solvent molecules and the trigallane. A possible explanation is the change in the dipoles on the twist from 5.2 to 8.3 Debye, which is counteracted by the polar solvent.

The Ga–Ga bond lengths of trigallanes **112a – c** are in the range of 241–246 pm. This is in line with the bond lengths observed for comparably substituted digallanes.

Upon reaction of “GaI” with potassium tris(3,5-dimethylpyrazolyl)hydroborate  $K[{}^{\text{Me}}\text{tpz}]$  the trigallane **113a** as well as the tetragallane **113b** can be obtained.<sup>218</sup> The bond distances are similar to **112a – c** ( $d_{\text{Ga-Ga}} = 241.9\text{--}243.1$  pm). **113a, b** may be viewed as double adducts of  $\text{Ga}_2\text{I}_4$  with  $\text{Ga}[{}^{\text{Me}}\text{tpz}]$  and 3,5-dimethylpyrazol, respectively.

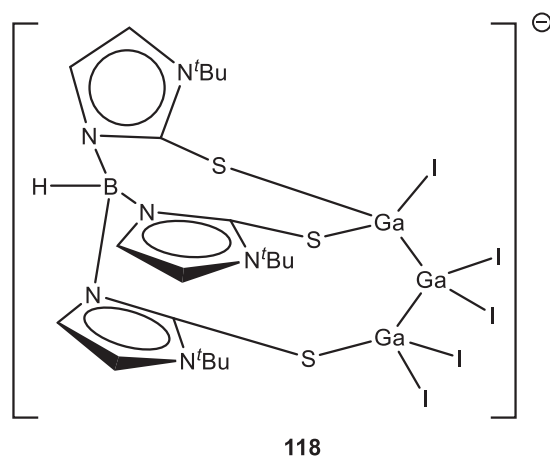
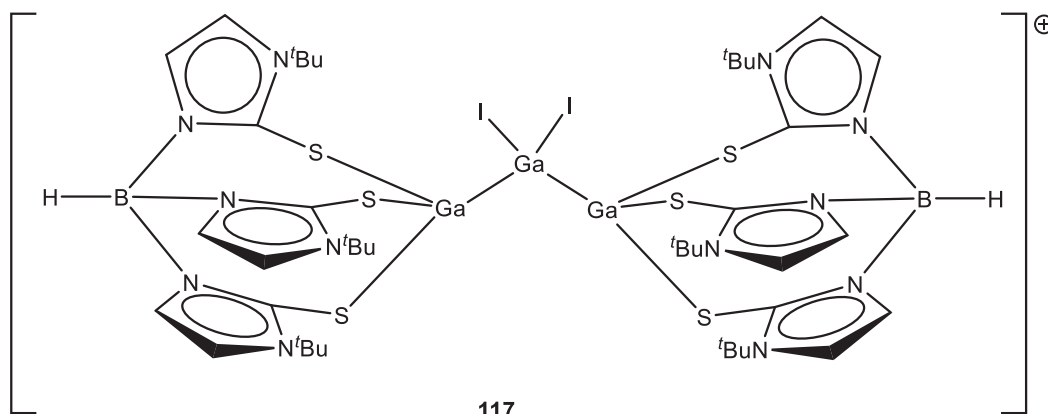


By addition of cryptand[2.2.2] to  $\text{Ga}_2\text{Cl}_4 \cdot 2\text{thf}$  the cation  $[\text{Ga}_3\text{Cl}_4(\text{cryptand-222})]^+$  **114** is obtained.<sup>219</sup> Within the structure only the  $[\text{Ga}_2\text{Cl}]^+$  moiety is captured by the cryptand, while the  $\text{GaCl}_3$  residue is located outside the cavity.

Reaction of the anionic gallium heterocycle  $[\text{Ga}\{\text{N}(\text{dipp})\text{CH}\}_2]^-$ <sup>194,220</sup> with donor stabilized gallane  $[\text{GaH}_3 \cdot \text{donor}]$  (donor = quinuclidine) affords the anionic trigallanate  $[[\text{CHN}(\text{dipp})]_2\text{Ga-GaH}_2\text{-Ga}\{\text{N}(\text{dipp})\text{CH}\}_2]^-$  **115**. This is described as donor acceptor adduct of the anionic  $[\text{Ga}\{\text{N}(\text{dipp})\text{CH}\}_2]^-$  rings to a  $\text{GaH}_2^+$  cation.<sup>221</sup>

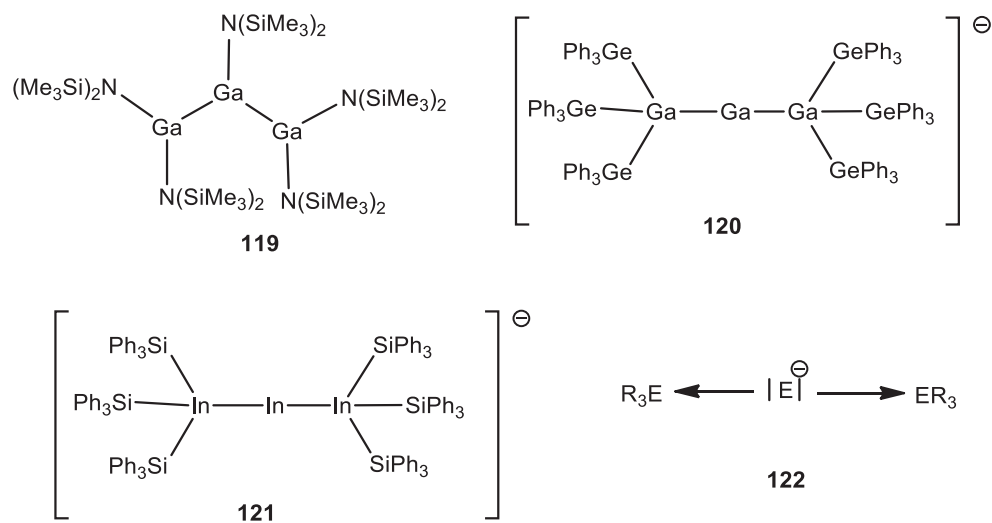
Oxidative addition reactions of  $\text{GaX}_3$  ( $X = \text{Cl, Me}$ ) to the gallium(I)bisketoimidate  $\text{Ga}(\text{nacnac})$ <sup>220</sup> produced the trigallanes  $(\text{nacnac})\text{Ga}(X)\text{Ga}(X)\text{Ga}(X)(\text{nacnac})$  **116a, b**.<sup>222</sup>

With a tris(imidazolinato)borate ligand (L) the ionic  $\text{Ga}_3$ -compounds  $[\text{L}_2\text{Ga}_3\text{I}_2]^+$  **117** ( $d_{\text{Ga-Ga}} = 245.86(5)$  pm) and  $[\text{LGa}_3\text{I}_5]^-$  **118** ( $d_{\text{Ga-Ga}} = 240.6(3)$  and  $241.2(2)$  pm) as well as the corresponding digallanes  $[\text{L}_2\text{Ga}_2]^{2+}$  ( $d_{\text{Ga-Ga}} = 241.2(3)$  pm) and  $\text{LGaGaX}_3$  ( $X = \text{Cl, I}$ ) ( $d_{\text{Ga-Ga}} = 241.4(4)$  pm) are accessible via reaction of the potassium or thallium derivative of the ligand and “GaI.”<sup>223</sup> The Ga–Ga bonds are in the typical range known from other oligogallanes.

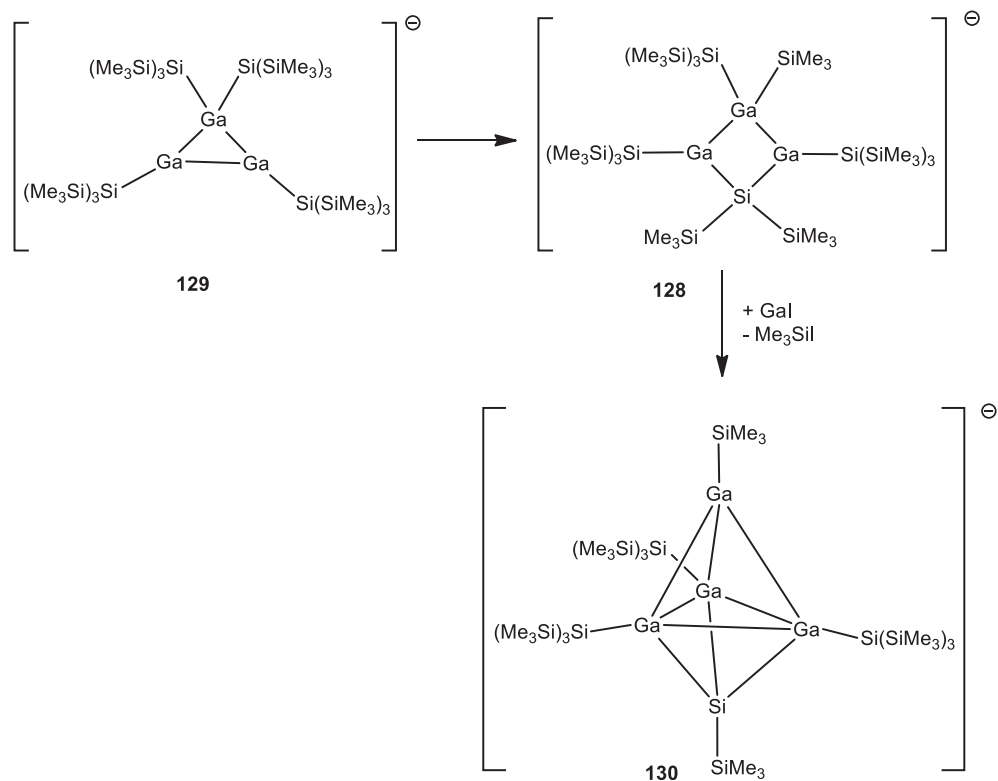


Starting from “Gal” or GaBr-solutions a  $\text{Ga}_3\text{R}_5$  derivative **119** ( $\text{R} = \text{N}(\text{SiMe}_3)_2$ ) with three coordinate gallium atoms in an angled chain can be prepared. The Ga–Ga bonds ( $d_{\text{Ga-Ga}} = 252.8 \text{ pm}$ ) are relatively long, comparable to those in digallanes with bulky substituents.<sup>224,225</sup>

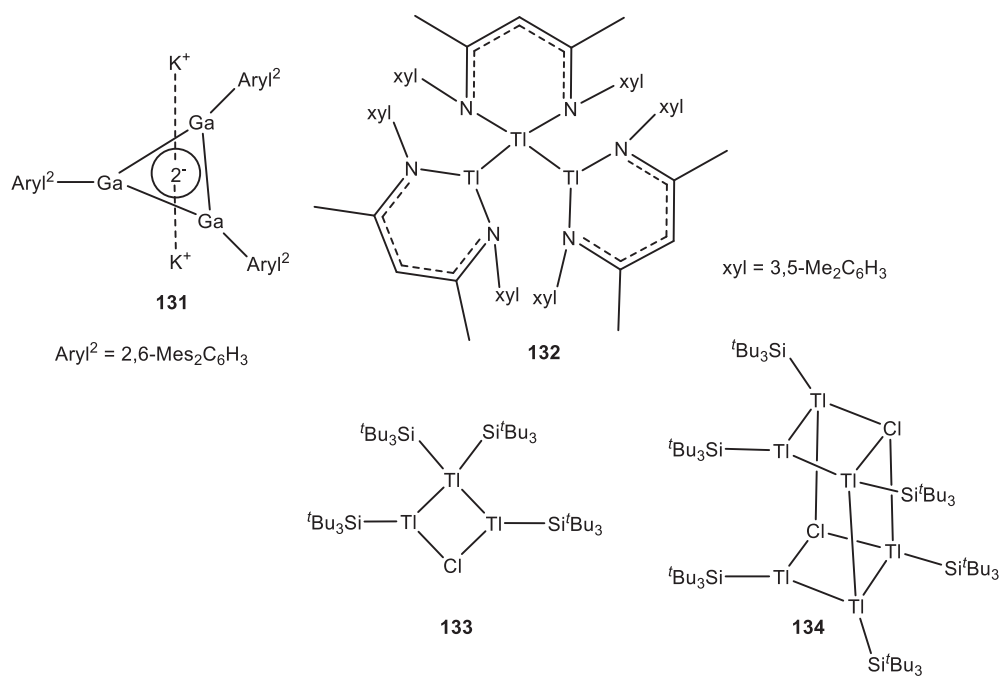
A formal  $\text{R}^-$ -adduct of a  $\text{Ga}_3\text{R}_5$  derivative is  $[\text{Ga}_3\text{R}_6]^-$  **120** ( $\text{R} = \text{GePh}_3$ ). This trigallanate, as well as the indium analog  $[\text{In}_3(\text{SiPh}_3)_6]^-$  **121**, is isolated as alkali metal salt. The cations are coordinated by thf molecules and are separated from the anions in the crystal. **120** and **121** have linear  $\text{E}_3$ -units. These are described as double Lewis-base adducts of  $\text{E}^-$  to two  $\text{ER}_3$  groups according to **122**.







**Scheme 3** Formation of gallium-silicon ring compounds **128–130**.



### 1.17.2.3 Synthesis and structure of compounds with higher E<sub>n</sub>-units

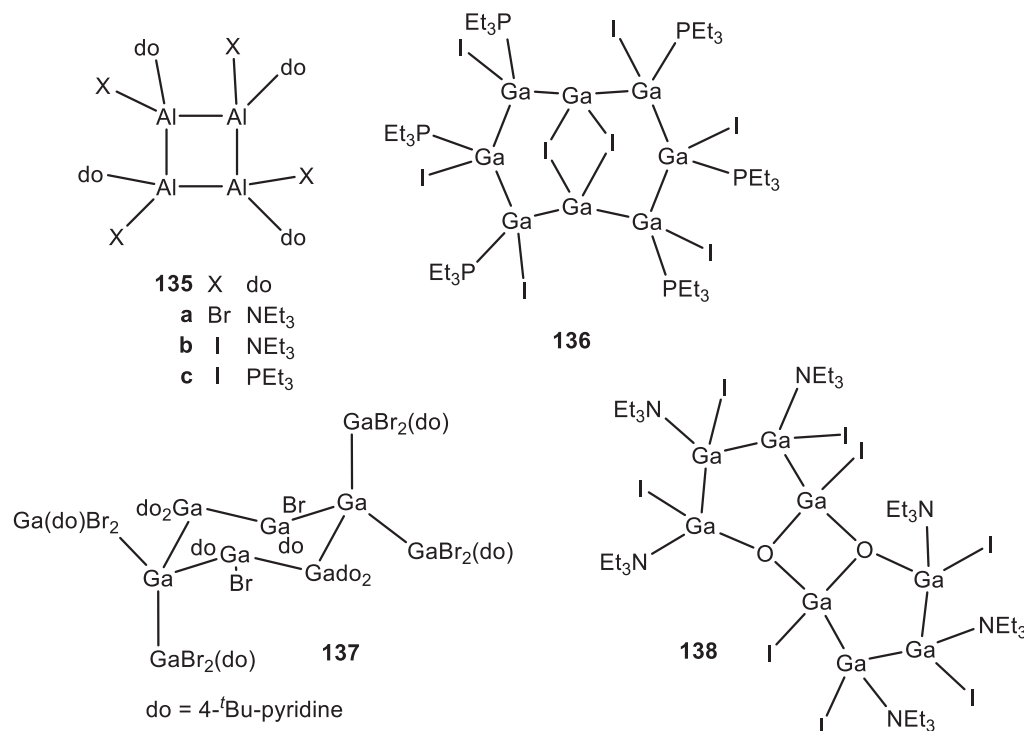
#### 1.17.2.3.1 Subhalides

Treatment of metastable solutions of Al(I) and Ga(I) halides with appropriate donor ligands afforded cyclic compounds of oligomer E(I)halide donor complexes. For E = Al planar four-membered ring compounds [AlX·do]<sub>4</sub> **135a–c** (X = Br, do = NEt<sub>3</sub><sup>240</sup>;



$X = I$ ,  $do = NEt_3$ <sup>241</sup>;  $X = I$ ,  $do = PEt_3$ <sup>242,243</sup>) are obtained. From these solutions even higher subvalent aluminum halides like  $Al_{12}[AlX_2 \cdot do]do_2$  ( $do = thf$ ,  $X = Cl, Br$ )<sup>244,245</sup> were isolated, which contain icosahedral  $Al_{12}$ -cores, which can be described as *closo*-cluster compounds according to the Wade rules.

$Al_5Br_7(thf)_5$ <sup>54</sup> is an ionic compound composed of  $[Al\{AlBr(thf)_2\}_2\{AlBr_2(thf)\}_2]^+$  cations and  $[Al\{AlBr_2(thf)\}_4]^-$  anions.



Octamer and decamer gallium(I)halides **136**<sup>67</sup> and **137**<sup>246</sup> were obtained by addition of the corresponding donors to  $GaX$ -Solutions ( $X = Br, I$ ). The core of **136** is a planar eight membered ring, where six gallium atoms bear an iodine atom and a phosphane ligand. The remaining two gallium atoms are bridged by two iodine atoms.

**137** exhibits a six membered gallium ring in a flat chair conformation, where the two gallium atoms  $Ga(1)$  and  $Ga(4)$  are connected to two terminal  $GaBr_2(4\text{-}^t\text{Bu-pyridine})$  groups. From  $GaI$ -solutions with triethylamine a partial oxidized product **138** was crystallized, which is built from two five-membered  $Ga_4O$  rings which are dimerized by two  $GaO$ -contacts.<sup>247</sup>

Starting from these  $GaX$ -solutions or alternatively sonochemically prepared " $GaI$ " several chain and ring compounds with four or more gallium atoms have been prepared. Very common are  $Ga_5$ -derivates, which contain tetrahedral  $GaGa_4$ -cores **139**.<sup>54,248-251</sup> The terminal gallium atoms are either part of  $GaX(do)_2$  or  $GaX_2(do)$  groups. Thus, a central  $Ga^0$  atom is surrounded by  $Ga^I$  and  $Ga^{II}$  centers. Homologous  $InIn_4$  derivates are also known. Those are the ammonium salts  $[In[InX_2(do)]_4]^- Hdo^+$  (**140a**:  $X = Cl$ ,<sup>74</sup> **140b**:  $X = Br$ ,<sup>252</sup>  $do = N(CH_2CH_2)_3CH$ ).

### 1.17.2.3.2 Nonhalide derivatives

Such a  $GaGa_4$  core of type **139** is also present in the salt like compound  $[Ga_6Cp^*_2(triflate)_6 \cdot 2\text{toluene}]$  **141a** (triflate =  $CF_3SO_3$ ). Here the cation is a  $Ga^+$  ion coordinated by two toluene molecules and the anion can be described as (triflate)<sub>3</sub> $Ga-Ga-Ga$ (triflate)<sub>3</sub> chain, where two  $GaCp^*$  groups coordinate to the central gallium atoms. **141a** is obtained from protolysis of  $GaCp^*$  with trifluoromethanesulfonic acid together with **141b** and several gallium(III)products.<sup>253</sup> **141b** is a tetragallane, which can be described as a double  $GaCp^*$  adduct of the digallane  $Ga_2(triflate)_4$ . Consequently, here the sequence  $Ga^I-Ga^{II}-Ga^I-Ga^I$  makes **141b** an analog to  $Ga_2Cl_4 \cdot 2\text{dioxane}$ , where the gallium(I)compound  $GaCp^*$  adopts the role of the donor molecule. Previously mentioned **113b** is a compound with similar structure as **141b**. In both structures two units  $GaR$  ( $R = ^{Me}tpz, Cp^*$ ) act as donor for  $Ga_2X_4$  ( $X = I, triflate$ ). Preparing galliumsubtriflates by oxidation of gallium with silvertriflate under ultrasonic conditions results in oligogallates  $[Ga(C_6H_5Me)]_2[Ga_2triflate_6]$ ,<sup>254</sup>  $[Ga(C_6H_5Me)(C_6Me_6)]_2[Ga_2triflate_6]$ <sup>255</sup> and  $[Ga][Ga(C_6H_5Me)]_2[Ga_3triflate_8]$ .

A tetragallane with an inverse  $Ga^{II}-Ga^I-Ga^I-Ga^{II}$  arrangement is present in the galliumamidinate **142a**.<sup>256</sup> With more steric demanding amidinates only digallanes and trigallanes were accessible. The  $Ga-Ga$  bonds ( $d_{Ca-Ga} = 245.3(1)$  and  $245.5(1)$  pm) are slightly longer than in amidinato substituted trigalliumiodides **112** and digalliumiodides **89**. This is in line with Bent's rule and the substitution pattern of the neighboring gallium atoms.

$R'_3Ga_4I_3$  **142b** ( $R' = Ph_2P[NMes]_2$ ) is obtained from " $GaI$ " and  $LiR'$ .<sup>257</sup> The  $Ga$  core of **142b** has the shape of a distorted trigonal pyramid with one short ( $d_{Ca-Ga} = 245.1(1)$  pm) and two slightly longer  $Ga-Ga$  bonds ( $d_{Ca-Ga} = 247.1(1)$ pm). The atoms

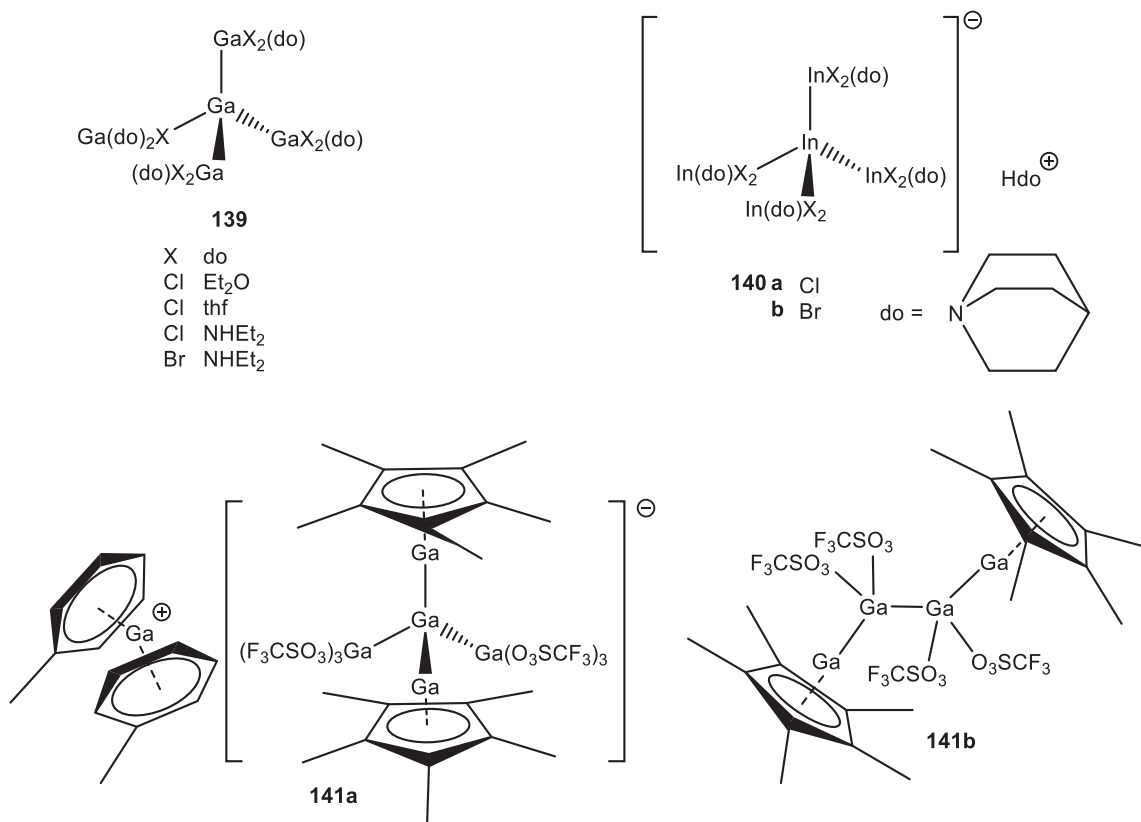
forming the base of the pyramid are bonded to one R' substituent, each, one of these and the apical gallium atom bear an iodine atom. Two gallium atoms are bridged by the third iodine atom.  $R''_3Ga_5I_4$  **142c** ( $R'' = (tBu)^{Mes}nacnac$ ) with its branched  $Ga_5$  chain is obtained by reaction of "GaI" with  $Li[R'']$ .<sup>258</sup> The chain is twice bridged by iodine atoms, forming a planar  $Ga_3I$  heterocycle. This results in an average Ga oxidation state of 1.4.

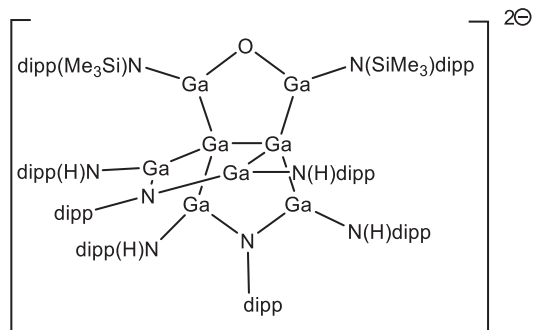
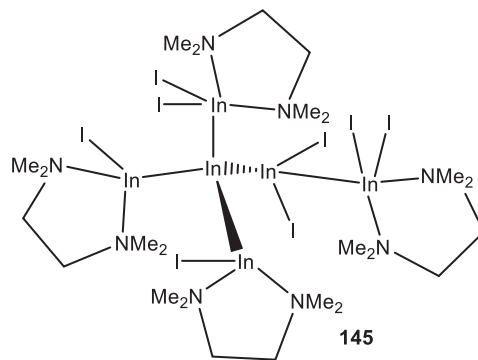
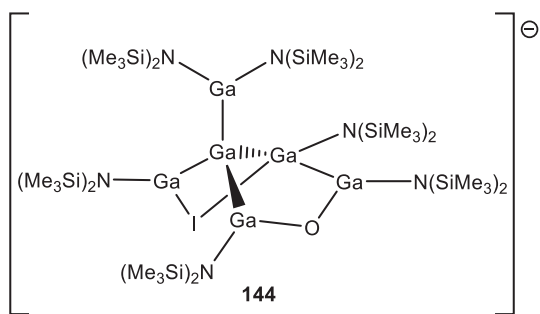
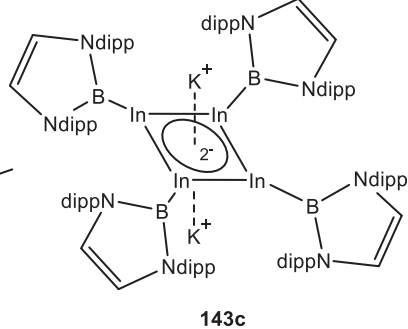
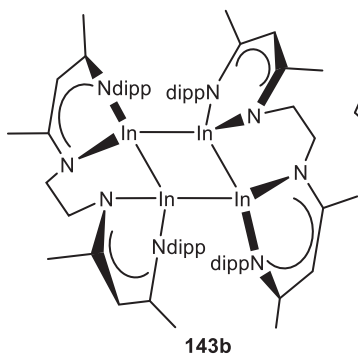
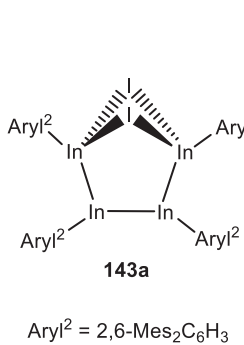
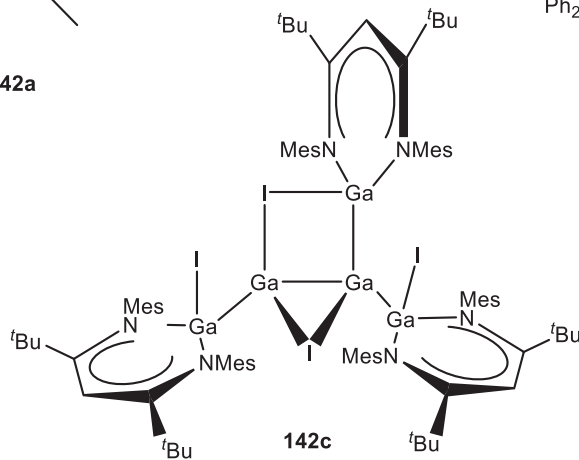
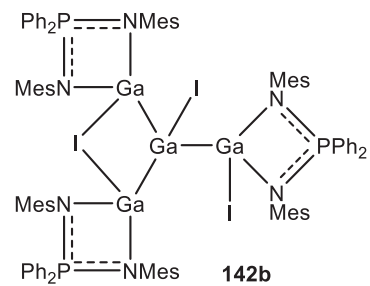
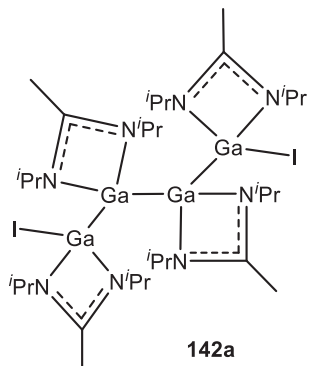
In  $Aryl_4^2In_4I_2$  **143a** ( $Aryl^2 = 2,6-Mes_2C_6H_3$ ) a  $E_n$ -chain is closed to a heterocycle by donor-acceptor interactions, like in **126a-c**. This results in an  $In^{II}-In^I-In^I-In^{II}$  arrangement similar to **142a**. **143b** consists of a planar  $In_4$ -ring with two ethylene-bridged bis- $dipp$  nacnac substituents, bound to each two In Atoms.<sup>259</sup> Here the  $In_4$ -ring is neutral.  $K_2In_4[B\{N(dipp)CH\}_2]_4$  **143c** has also a planar  $In_4$ -ring core, but with a double negative charge. Two potassium ions are coordinated 327.4 pm above and below the center of the In-ring.<sup>260</sup>

The hexagallanate **144**<sup>261</sup> is based on a tetrahedral  $GaGa_4$ -core. Here a tetrahedral  $GaGa_3(Ga_2)$  core is present, where the central gallium atom is bonded to three single gallium atoms and one digallium unit. One of the single gallium atoms bears two amide groups, the others are linked to an additional iodine or oxo group, respectively. The gallium atoms of the  $Ga_2$  unit are bonded to one amide group, each. The iodine atom and the oxygen atom are in bridging positions thus forming a  $Ga_5OI$  cage. **144** forms during the reaction of "GaI" with  $LiN(SiMe_3)_2$  in low yields instead of an anticipated gallium(I)amide.

An analogous  $In_6$ -core is present in  $[In_6I_8(tmeda)_4]$  **145** ( $tmeda = tetramethylethylenediamine$ ).<sup>73</sup> Two  $In(tmeda)I$ , one  $In(tmeda)I_2$  and an  $InI_2-InI_2(tmeda)$  groups are attached to the central indium atom. Thus, tetra- and penta-coordinate indium atoms are part of this molecule.

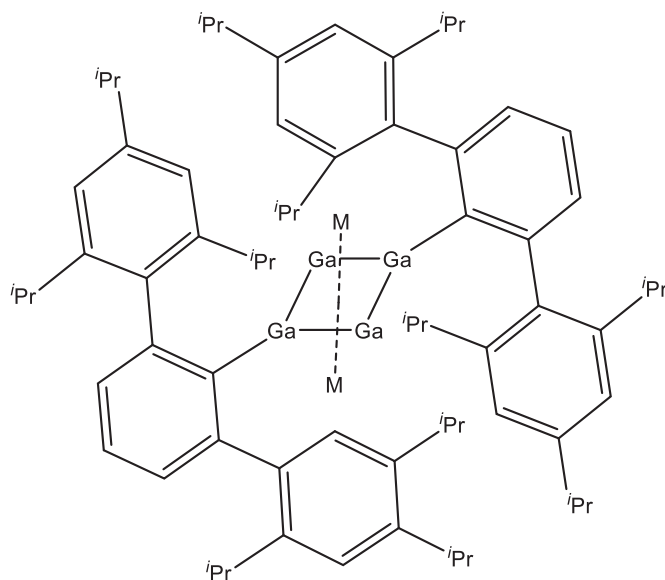
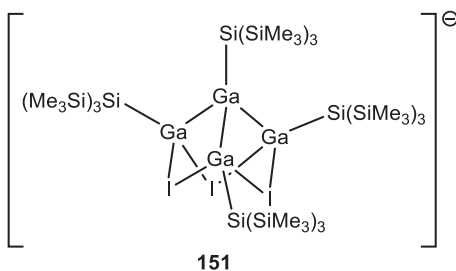
A structural related anion  $[Ga_8O\{N(SiMe_3)dipp\}_2\{Ndipp\}_2\{N(H)dipp\}_4]^{2-}$  **146**<sup>251</sup> is obtained as lithium salt from the reaction of  $LiN(SiMe_3)dipp$  with GaCl solutions at ambient temperature, that means in a temperature region, where gallium(I)chloride solutions are mostly disproportionated into gallium and halides of higher oxidation states. Here two  $GaGa_4$  units are joined via a common gallium atom. Two imide groups  $dippN$  and one oxo atom close three  $Ga_4X$  rings, which are arranged in a 3,3,3-propellane type structure.



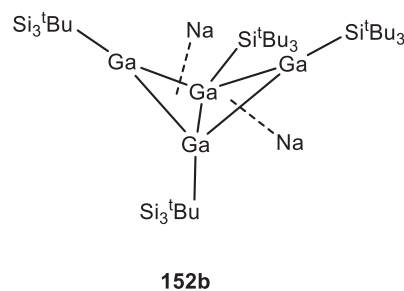


Compounds with a branched  $\text{Ga}_4$  chain were obtained starting from  $\text{Ga}_2\text{trip}_4$  [ $d_{\text{Ga-Ga}} = 251.5 \text{ pm}$ ].<sup>262</sup> While careful reduction with lithium metal (**Scheme 4**) produced the radical anion  $[\text{trip}_4\text{Ga}_2]^\bullet^-$  **147** [ $d_{\text{Ga-Ga}} = 234.3 \text{ pm}$ ], reduction with an excess of sodium in trimethylamine led to the formation of dianionic  $[(\text{trip}_2\text{Ga})_3\text{Ga}]^{2-}$  **148**, with a planar  $\text{GaGa}_3$  core. The short gallium-gallium distances [ $d_{\text{Ga-Ga}} = 238.9 \text{ pm}$ ] are in accordance with two delocalized  $\pi$  electrons in the gallium core. The neutral  $\text{GaGa}_3$  compound **149** was obtained by oxidation of **148** with dry oxygen. The gallium-gallium bonds are elongated upon this oxidation [ $d_{\text{Ga-Ga}} = 246.5\text{--}248.1 \text{ pm}$ ]. The indium analog  $(\text{trip}_2\text{In})_3\text{In}$  **150** has also been prepared.<sup>109</sup>

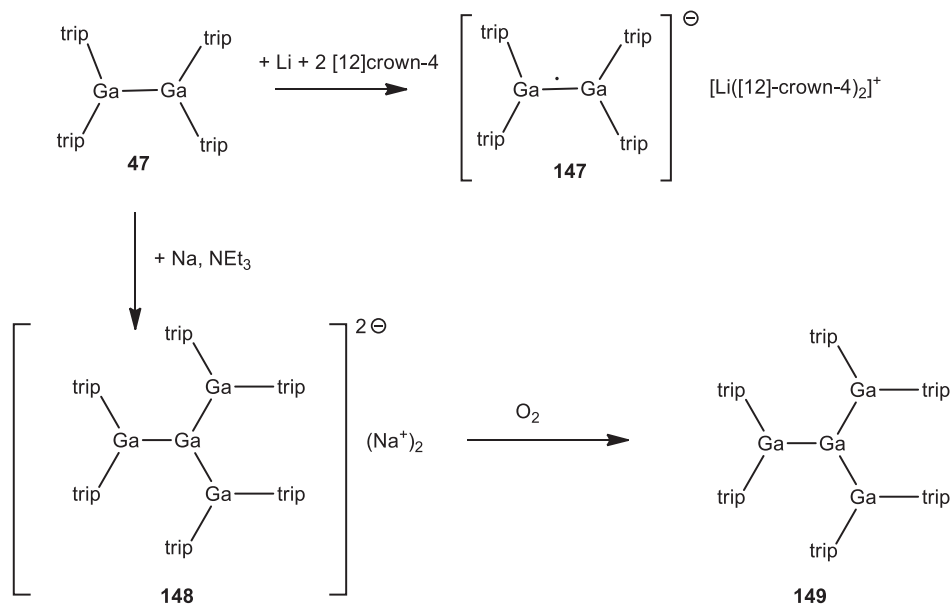
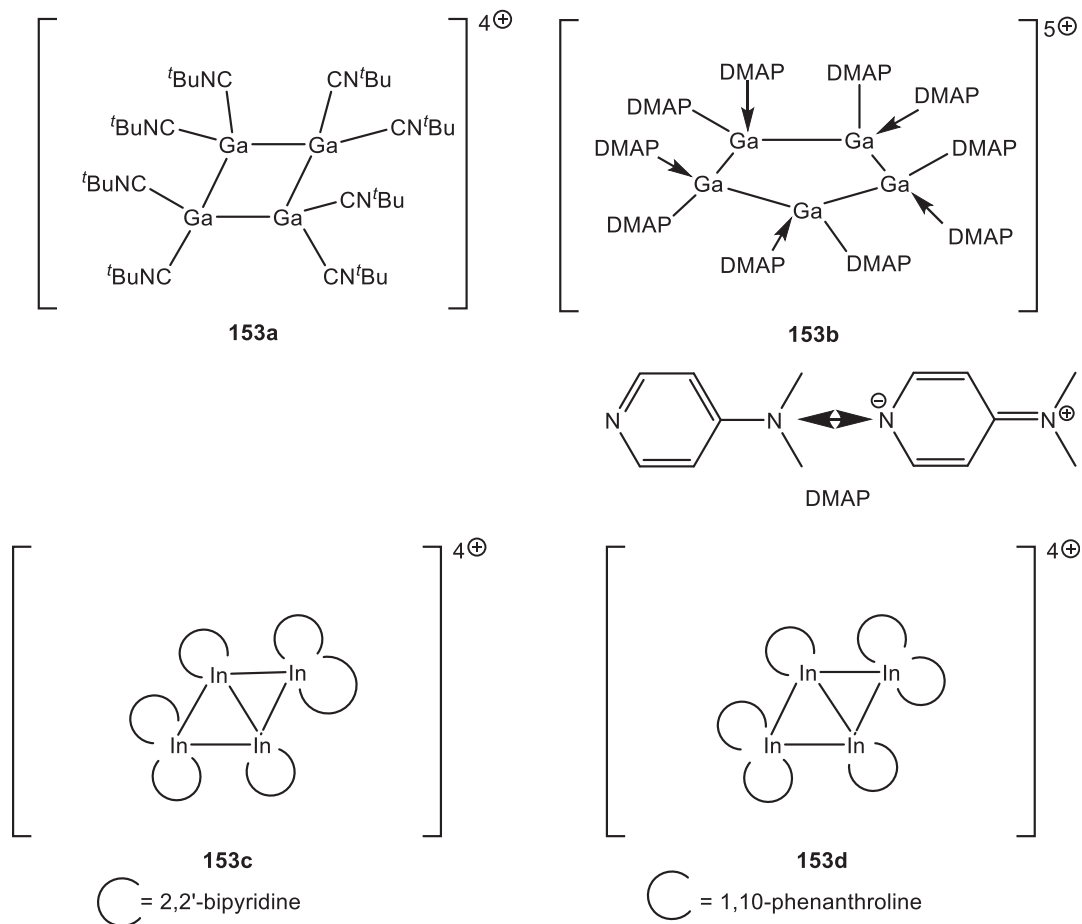
The monoanionic compound **151** of type  $[\text{RGa}(\text{GaR}_2)_3]^-$  has a pseudotetrahedral  $\text{Ga}_4$  core, where the edges of the  $\text{Ga}_3$  base are bridged by iodine atoms.<sup>263</sup> The resulting cage is described as a cube with a missing corner. The long Ga-Ga-distances [ $d_{\text{Ga-Ga}} = 253.5 \text{ pm}$ ] are in line with the bulky silyl groups at the gallium atoms.



**152a** M = Na, K



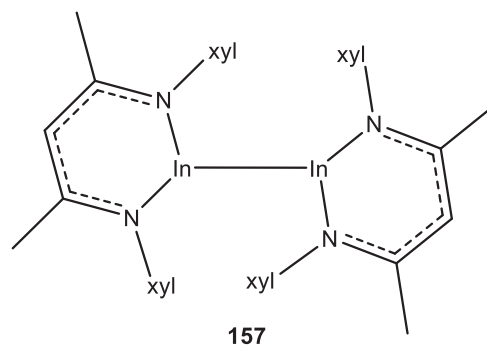
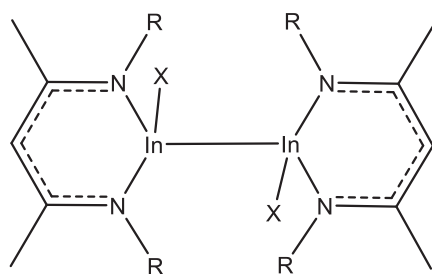
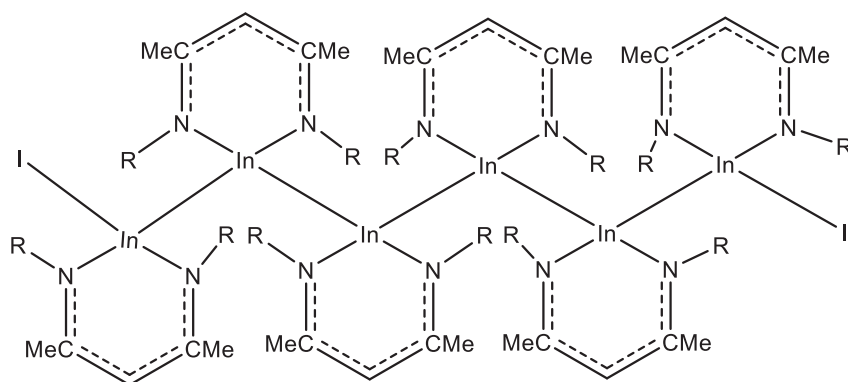
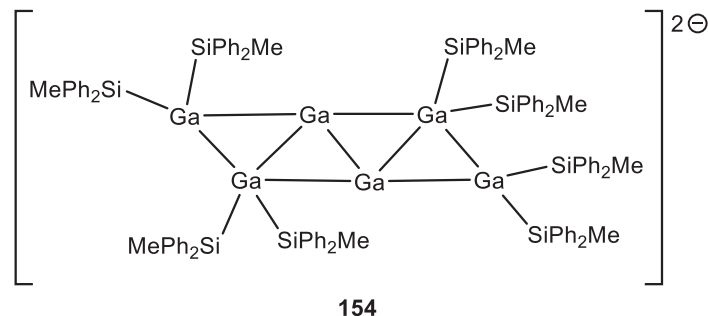
Cyclic gallium compounds are known as anionic and cationic derivatives. In  $\text{M}_2[\text{Ga}_4\text{Aryl}^1_2]$  **152a** ( $\text{Aryl}^1 = 2,6\text{-trip}_2\text{C}_6\text{H}_3$ ,  $\text{M} = \text{Na}, \text{K}$ )<sup>145,264</sup> and  $\text{Na}_2[\text{Ga}_4(\text{Si}^t\text{Bu}_3)_4]$  **152b**<sup>173</sup> anionic rings are coordinated to alkali metal ions. **152a** is obtained by reduction of  $\text{Aryl}^1\text{-GaCl}_2$  with the alkali metals and shows planar, metalloaromatic  $\text{Ga}_4$  rings with formally two  $\pi$  electrons. The metal ions coordinate to the gallium- $\pi$ -system and the  $\pi$ -system of the trip-rings. **152b** is prepared by reduction of the gallatetrahydane  $\text{Ga}_4(\text{Si}^t\text{Bu}_3)_4$  with sodium. It has a butterfly-type  $\text{Ga}_4$ -core with a delocalized  $2\pi$  system.

Scheme 4 Redox chemistry with  $\text{Ga}_2\text{trip}_4$  47

The second kind is represented by cationic rings  $[\text{Ga}_4(\text{CN}^t\text{Bu})_8]^{4+}$  153a<sup>265</sup> and  $[\text{Ga}_5(\text{DMAP})_{10}]^{5+}$  153b (DMAP = 4-Me<sub>2</sub>N-C<sub>5</sub>H<sub>4</sub>N) with the weakly coordinating counterion  $[\text{Al}\{\text{OC}(\text{CF}_3)_3\}_4]^-$ .<sup>266</sup> 153a and 153b can be prepared through reaction of  $[\text{Ga}(\text{PhF})_2][\text{Al}\{\text{OC}(\text{CF}_3)_3\}_4]$  with the respective neutral donor. Both Ga-cores are essentially planar with typical Ga–Ga bond distances (153a  $d_{\text{Ga-Ga}} = 246.1\text{--}246.6$  pm, 153b  $d_{\text{Ga-Ga}} = 248.8\text{--}250.1$  pm).



$[\text{In}_4\text{bipy}_6]^{4+}$  **153c** and  $[\text{In}_4\text{phen}_6]^{4+}$  **153d** (bipy = 2,2'-bipyridine, phen = 1,10-phenanthroline)<sup>231</sup> are expanded cyclic cations of the previously mentioned three-membered rings **127a,b**. **153c** and **153d** are obtained, similar to **153a** and **153b**, by reaction of  $[\text{In}(\text{PhF})_2][\text{Al}\{\text{OC}(\text{CF}_3)_3\}_4]$  and the respective ligands.

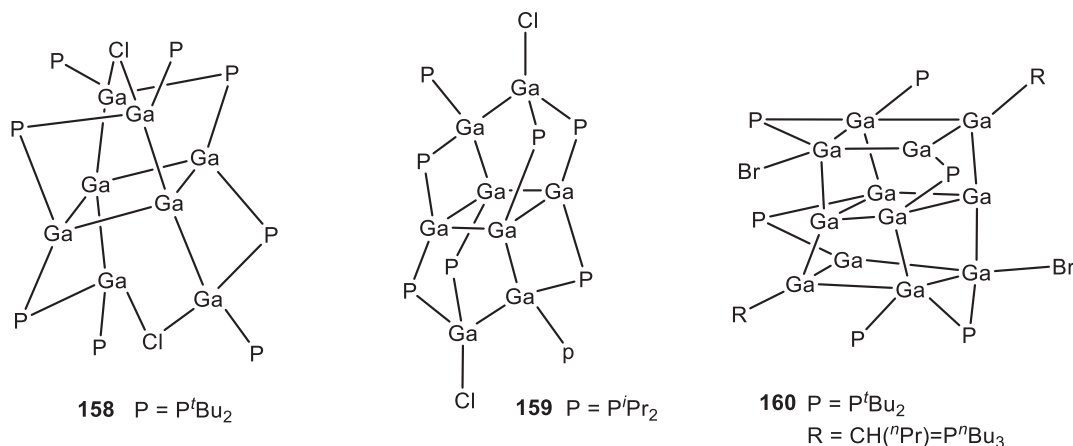


$[\text{Ga}_6(\text{SiPh}_2\text{Me})_8]^{2-}$  **154**, isolated as lithium salt, shows an unusual planar arrangement of six gallium atoms.<sup>267</sup> Formally it is derived by dimerization of two equivalents of a compound of type **122** with loss of four substituents. The delocalized bonding in **154** brings this compound at the border with cluster compounds, discussed later.

An unique example of a linear six-membered chain compound of triel elements is  $\text{In}_6\text{I}_2(\text{xyl}\text{nacnac})_6$  **155** ( $\text{xyl}\text{nacnac} = [\text{N}(3,5\text{-dimethylphenyl})\text{C}(\text{Me})_2\text{CH}]_2$ ;  $d_{\text{In-In}} = 282.2\text{--}285.4$  pm).<sup>268</sup> **155** is obtained from indium(I) iodide and the potassium salt of  $\text{xyl}\text{nacnac}$ . The bond lengths are similar to those in  $\text{nacnac}$  substituted diindium halides  $[\text{dipp}\text{nacnac}\text{InCl}]_2$  **156a** [ $d_{\text{In-In}} = 282.4$  pm]<sup>188</sup> and  $[\text{Ph}\text{nacnac}\text{InCl}]_2$  **156b** [ $d_{\text{In-In}} = 275.7$  pm].<sup>187</sup>  $[(\text{xyl}\text{nacnac})\text{In}]_2$  **157** as an example of a dimeric indium(I) derivative has a longer indium-indium bond [ $d_{\text{In-In}} = 334.0$  pm], despite the fact that a double bond may be formulated here.<sup>269</sup>

Reaction of  $\text{GaX}$ -solutions<sup>270</sup> with alkali metal phosphanides yield oligomeric gallium phosphanides  $\text{Ga}_8(\text{P}^t\text{Bu}_2)_8\text{Cl}_2$  **158**,<sup>251</sup>  $\text{Ga}_8(\text{P}^i\text{Pr}_2)_8\text{Cl}_2$  **159**<sup>251</sup> and  $\text{Ga}_{12}(\text{P}^t\text{Bu}_2)_6(\text{H}^n\text{Pr}(\text{H})\text{C}=\text{P}^n\text{Bu}_3)_2\text{Br}_2$  **160**<sup>271</sup> as well as in higher cluster compounds.<sup>272</sup> **158** and **159** are octagallium derivatives with complicated oligocyclic structures. The central  $\text{Ga}_8$ -core of **158** is described as two distorted edge-sharing  $\text{GaGa}_4$  tetrahedra, where the terminal gallium atoms are bridged by phosphanido groups. The diisopropylphosphanido derivative **159** has an oligocyclic structure with attached  $\text{Ga}_2$  units. The unusual  $\text{Ga}_{12}$  compound **160** forms by reaction of metastable  $\text{GaI}$  solutions<sup>270</sup> with  $\text{LiP}^t\text{Bu}_2$  and  $\text{H}^n\text{Pr}(\text{H})\text{C}=\text{P}^n\text{Bu}_3$ . It has a cluster core consisting of three nearly planar  $\text{Ga}_4$  rings. A related  $\text{In}_9$

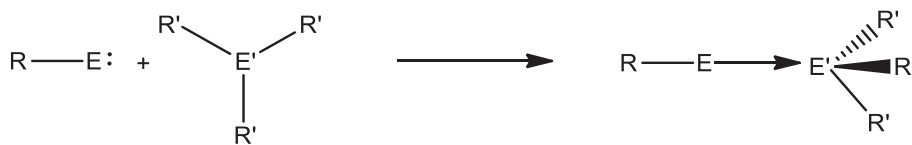
compound  $[\text{In}_3(\text{In}_2)_3(\text{PhP})_4(\text{Ph}_2\text{P})_3\text{Cl}_7(\text{PEt}_3)_3]$  featuring  $(\text{In}^{+II})_2$  units as well as  $\text{In}^{+III}$  units was prepared starting from indium trichloride and silylated phenylphosphanes. Redox reactions are responsible for indium-indium bond formation, here.<sup>273</sup>



#### 1.17.2.4 Synthesis and structure of compounds with E-E' bonds

The availability of Lewis basic triel(I) derivatives  $\text{ECp}^*$ ,<sup>274,275</sup>  $\text{E}(\text{nacnac})$ ,<sup>220</sup>  $[\text{E}[\text{N}(\text{dipp})\text{CH}]_2]^{-}$ <sup>192,194,276,277</sup> and  $\text{EL}$  ( $\text{L} =$  substituted pyrazolylborato)<sup>278</sup> offers the possibility for the preparation of mixed E-E' compounds.<sup>279</sup> We have already discussed donor-acceptor compounds of  $\text{AlCp}^*$  and  $\text{GaCp}^*$  for structures **110a** and **141b**, involving  $\text{E}^{+I}$  and  $\text{E}^{+II}$  centers. The combination  $\text{E}^{+I}$  and  $\text{E}^{+III}$  is realized in  ${}^t\text{Bu}\text{tpzGa-GaI}_3$ ,  ${}^t\text{Bu}\text{tpzIn-InI}_3$  ( ${}^t\text{Bu}\text{tpz} =$  tris-(3,5-ditertbutylpyrazolyl)hydroborate)<sup>278,280-283</sup> and  $\text{XIn}[[18]\text{-crown-6}]\text{-InX}_3$  **161** [ $d_{\text{In-In}} = 268.2$  ( $\text{X} = \text{Cl}$ ),  $270.7$  ( $\text{X} = \text{Br}$ ),  $272.5$  ( $\text{X} = \text{I}$ )].<sup>284,285</sup> **161** is obtained from  $\text{InCp}^*$  by protolysis with triflic acid and subsequent reaction with indium trihalides. The trend in bond lengths is as expected from Lewis acidities of  $\text{InX}_3$  and the steric demand of the halides.

$\text{ECp}^*$  compounds form a variety of complexes with transition metal fragments<sup>196,286-291</sup> and main group Lewis acids. With the latter often redox reactions occur (see for example **110a**), but with appropriately substituted acids  $\text{E}^{+I}\text{-E}'^{+III}$  complexes are obtained (Scheme 5, Table 8).<sup>250,293,296</sup> Two examples are **162**<sup>294</sup> and **163**,<sup>296</sup> prepared from the triel(I) compound. **164** is product of the reaction of  $\text{Cp}^*\text{Li}$  with "GaI" and can be reduced with alkali metals to  $\text{Cp}^*\text{Ga}$ .<sup>288</sup> The bond lengths of a E-E' pair seem to be dependent of the Lewis acidity of the  $\text{E}'\text{R}'_3$  part.

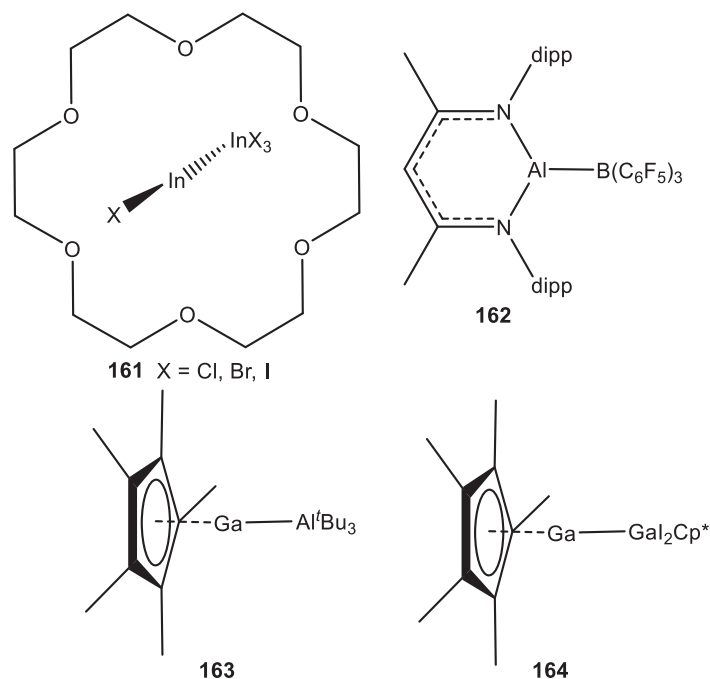


R, R': see table 8

**Scheme 5** Principle of the formation of  $\text{RE}^{+I}\text{-E}'\text{R}'_3$  complexes

**Table 8** Overview of  $\text{RE}^{+I}\text{-E}'\text{R}'_3$  complexes.

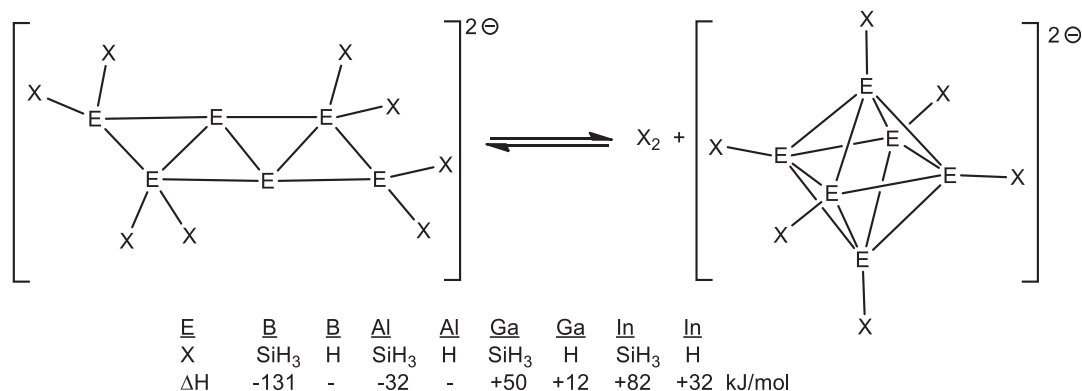
$d_{\text{E-E}'} [\text{pm}]$	$\text{AlCp}^*$	$\text{GaCp}^*$	$\text{InCp}^*$	$\text{Al}^{\text{dipp}}\text{nacnac}$
$\text{B}(\text{C}_6\text{F}_5)_3$	216.9 <sup>292</sup>	216.0 <sup>250,293</sup>		218.3 <sup>294</sup>
$\text{Al}(\text{C}_6\text{F}_5)_3$	259.1 <sup>295</sup>			
$\text{Al}^t\text{Bu}_3$	268.9 <sup>296</sup>	262.9 <sup>296</sup>	284.3 <sup>296</sup>	
$\text{Ga}^t\text{Bu}_3$	262.0 <sup>279,296</sup>		284.5 <sup>296</sup>	
$\text{GaCl}_2\text{Cp}^*$		242.5 <sup>296</sup>		
$\text{GaI}_2\text{Cp}^*$		243.7 <sup>296</sup>		



### 1.17.3 Polyhedral Cluster Compounds

With few exceptions all ring and chain compounds described so far in this chapter, are electron precise, meaning a description with  $2c2e$  bonds is valid. 154, of type  $[R_8Ga_6]^{2-}$  is an electron deficient molecule. While only ten electrons are available for Ga–Ga bonds, nine such contacts are present. A bonding description of 154 needs to make use of multicenter bonds. DFT calculations have been made for 154 and its other triel homologs  $[E_6X_8]^{2-}$  in order to examine a possible transfer into a polyhedral, here octahedral *closo*-cluster ion  $[E_6X_6]^{2-}$  by loss of  $X_2$  (Scheme 6).<sup>267,297</sup> For the lighter homologs boron and aluminum the polyhedral cluster is preferred, while for gallium and indium the equilibrium should be on the side of 154. The calculations were made for  $SiH_3$  and H as substituents, and it was observed, that the type of substituents is of large influence. This will be demonstrated by the polyhedral clusters of these elements in this section.

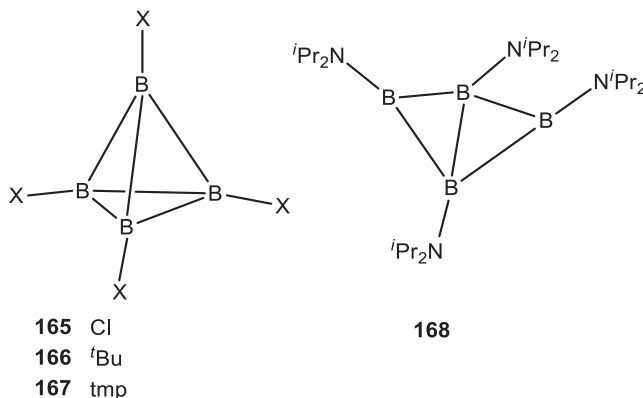
Looking at  $Al_4X_4 \cdot 4do$ , for example, removal of the donor molecules would leave an  $Al_4X_4$  ring with electron sextets at the aluminum atoms. Here formation of a tetrahedral cluster  $Al_4X_4$  would allow fulfilling the octet rule by multicenter bonds. We will discuss here polyhedral cluster compounds of the triel elements. The synthetic methods to prepare those and their structures will be described. For a discussion of the bonding in clusters we will examine how electron bookkeeping according to the Wade-Williams-Rudolph rules,<sup>18–20,298</sup> is applicable.



**Scheme 6** Possible formation of a polyhedral cluster from  $[E_6X_8]^{2-}$ .

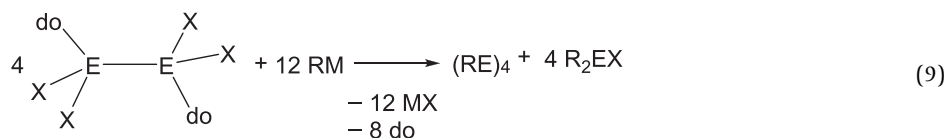
1.17.3.1 Tetrahedral E<sub>4</sub>R<sub>4</sub> cluster compounds and derivatives

The most common cluster compounds for the triels aluminum to thallium are tetrahedral E<sub>4</sub>R<sub>4</sub> clusters. These are known for all triels. The chemistry of these clusters has been reviewed extensively.<sup>4,7,12,47,143,147,270,299–307</sup> For boron the subhalide B<sub>4</sub>Cl<sub>4</sub> (165) as well as B<sub>4</sub><sup>t</sup>Bu<sub>4</sub> (166) possess a tetrahedral core. In case of boron B<sub>4</sub>R<sub>4</sub> compounds also can adopt ring structures. For amino-substituted derivatives BN-π-bonding is an alternative for the boron atoms to achieve an electron octet. 167 with the bulky tetramethylpiperidino groups is tetrahedral, while 168 with R = N<sup>i</sup>Pr<sub>2</sub> has a butterfly type ring structure.<sup>308</sup>



## 1.17.3.1.1 Synthesis and structures

The heavier congeners are prepared by reduction of REX<sub>2</sub> (Eq. 7), substitution reactions at triel(I) compounds (X = halide, triflate, amide, Cp\*) (Eq. 8) or disproportionation reactions of E<sub>2</sub>X<sub>4</sub>·2do upon substitution (Eq. 9).



For aluminum, (AlCp\*)<sub>4</sub> 169 and several derivatives (Table 9) have been prepared by routes according to Eqs. (7), (8). All of these crystallographic characterized derivatives are stabilized by bulky substituents. [Al(CH<sub>2</sub><sup>t</sup>Bu)]<sub>4</sub> was reported only in solution, and was found to be tetramer by molecular weight determinations.<sup>315</sup> Al<sub>4</sub>[N(SiMe<sub>3</sub>)dipp]<sub>4</sub> 174, the only tetrameric aluminum(I) amide, is prepared in a reaction according to Eq. (7).<sup>313</sup> Al<sub>4</sub>Cp<sub>3</sub><sup>\*</sup>[N(SiMe<sub>3</sub>)<sub>2</sub>] 175, prepared from 169 and LiN(SiMe<sub>3</sub>)<sub>2</sub>,<sup>314</sup> is an unique example of a heteroleptic cluster. The Al-Al distances in these tetrahedranes cover a wide range from 259.2 to 277.8 pm. The longest bonds are observed for Cp\* and other carbon based substituents, the shortest for silyl groups as substituents.

**Table 9** Survey on compounds Al<sub>4</sub>R<sub>4</sub>.

		<i>d</i> <sub>Al-Al</sub> [pm] (mean)	References
<b>169</b>	Al <sub>4</sub> Cp* <sub>4</sub>	277.0	274,309
<b>170</b>	Al <sub>4</sub> (C <sub>5</sub> Me <sub>4</sub> H) <sub>4</sub>	271.4	309
<b>171</b>	Al <sub>4</sub> [C(SiMe <sub>3</sub> ) <sub>3</sub> ] <sub>4</sub>	274.0	310
<b>172</b>	Al <sub>4</sub> (Si <sup>t</sup> Bu <sub>3</sub> ) <sub>4</sub>	260.6	311
<b>173</b>	Al <sub>4</sub> [Si(SiMe <sub>3</sub> ) <sub>3</sub> ] <sub>4</sub>	260.2	312
<b>174</b>	Al <sub>4</sub> [N(SiMe <sub>3</sub> )dipp] <sub>4</sub>	261.8	313
<b>175</b>	Al <sub>4</sub> Cp* <sub>3</sub> [N(SiMe <sub>3</sub> ) <sub>2</sub> ]	263.2–276.2	314

Intriguingly, in 175 long Al–Al distances between the Cp\* substituted atoms and short distances between the amido substituted ones are observed.

Most of these tetramers dissociate in solution. The degree of monomerization is correlated with the strength of the Al–Al interactions in the cluster. Thus, those with short Al–Al bonds, meaning the silyl substituted ones, show no tendency to dissociation. Al<sub>4</sub>Cp\*<sub>4</sub>, on the other hand, is monomeric in solution. This was also confirmed by <sup>27</sup>Al NMR spectroscopy, where tetramers show chemical shifts of  $\delta = -62$  to  $-111$  ppm and monomer AlR compounds exhibit  $\delta = -150$  to  $-168$  ppm.<sup>96,316</sup> Obviously short Al–Al distances in tetramers are related to stronger bonding in the cluster. This difference in stability of the tetramers depending on the type of substituents was also confirmed by quantum chemical calculations (see below). In addition, the color of these clusters is dependent on the type of substituents and thus of the Al–Al distances. 169 is yellow, 171 orange and 172 violet.

For gallium(I) compounds of type R<sub>4</sub>Ga<sub>4</sub> originally the disproportionation reaction of Ga<sub>2</sub>Cl<sub>4</sub>·2dioxane according to Eq. (9) was applied. This was successful with various substituents R. More economically these clusters are prepared by reduction of gallium(III) derivatives, either by alkali metals or by using the nucleophile MR (M = Li, Na) itself as reducing agent (Eq. 10). This was the case for R = Si<sup>t</sup>Bu<sub>3</sub>. An alternative (Eq. 8) is the use of formal gallium(I) halides, either sonochemically prepared “GaI”<sup>191</sup> or meta-stable GaX solutions obtained by high-temperature routes.<sup>270</sup>

With more bulky substituents monovalent gallium(I) species are realized. Thus the amide GaN(SiMe<sub>3</sub>)Aryl<sup>2</sup> **183** (Aryl<sup>2</sup> = 2,6-Me<sub>2</sub>C<sub>6</sub>H<sub>3</sub>) is a monomer even in solid state, while other gallium(I) compounds, which are monomeric in gas phase or solution, associate in the solid state.<sup>140</sup>

An overview on tetrahedral gallium species is given in Table 10.

Indium derivatives In<sub>4</sub>R<sub>4</sub> **184–186** (Table 11) are prepared via indium(I) compounds InI or InCp\* (Eq. 8). The use of indium(I) halides was not successful for silylsubstituted tetrahedranes, because disproportionation to indium and indium(III) derivatives R<sub>2</sub>InX<sub>2</sub>Li(thf)<sub>2</sub> was observed.

For thallium the C(SiMe<sub>3</sub>)<sub>3</sub> substituted tetrahedrane **187** has a severely distorted core. The compound is very sensitive to temperature and light. The tripod ligand substituted Tl<sub>5</sub> compound **188** contains a severely distorted tetrahedron of thallium atoms ( $d_{\text{Tl-Tl}} = 340.9\text{--}380.0$  pm). An additional thallium atom is attached in a terminal position ( $d_{\text{Tl-Tl}} = 340.3$  pm).<sup>122</sup>

For aluminum the tetramer Al<sub>4</sub>Cp\*<sub>4</sub> is a prominent example of a tetrahedral cluster compound. For the heavier congeners, i.e., gallium, indium and thallium, no such tetramer cyclopentadienyl derivatives are known. There are either monomer Cp<sup>x</sup>E compounds (Cp<sup>x</sup> = Cp\*, C<sub>5</sub>H<sub>2</sub>(SiMe<sub>3</sub>)<sub>3</sub>, C<sub>5</sub>H<sub>4</sub><sup>t</sup>Bu, C<sub>5</sub>(CH<sub>2</sub>Ph)<sub>5</sub>, C<sub>5</sub>Me<sub>4</sub>Ph, 1,2,4-P<sub>3</sub>C<sub>2</sub><sup>t</sup>Bu<sub>2</sub>, PC<sub>4</sub>H<sub>2</sub>-2,4-<sup>t</sup>Bu<sub>2</sub>)<sup>326–329</sup> in solution or gas phase, while in the solid state most of them are loosely aggregated. Cp\*Ga and Cp\*In form hexamers with very long E–E distances. Those for gallium ( $d_{\text{Ga-Ga}} = 412.2$  pm)<sup>275,326,330,331</sup> are even longer than those for indium ( $d_{\text{In-In}} = 395$  pm).<sup>332,333</sup> These hexamers are not regarded as E–E bonded systems, but are held together by CH···CH van der Waals interactions.

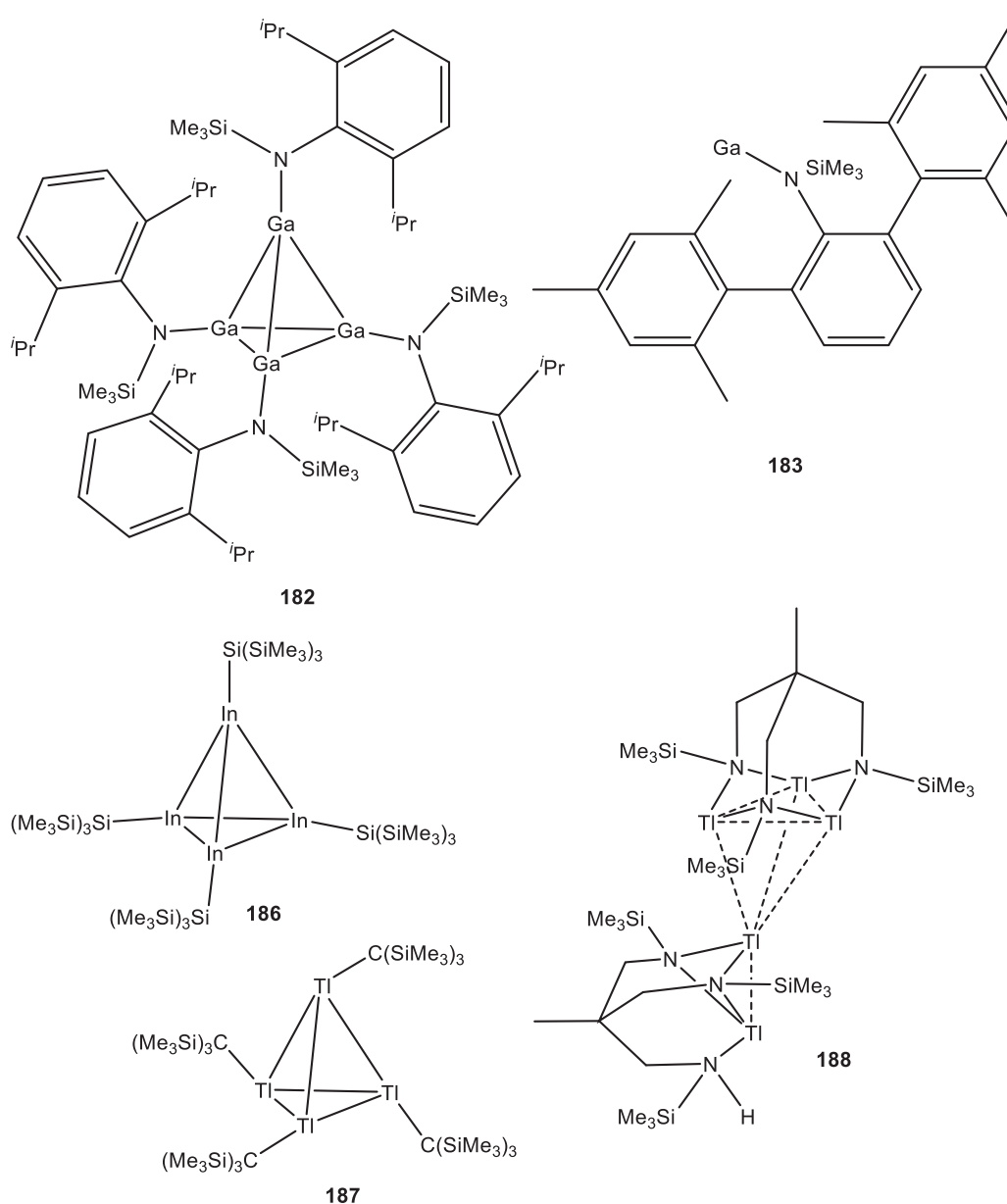
**Table 10** Overview on tetrahedral gallium species Ga<sub>4</sub>R<sub>4</sub>.

		$d_{\text{Ga-Ga}}$ [pm] (mean)	Method	References
<b>176</b>	Ga <sub>4</sub> [C(SiMe <sub>3</sub> ) <sub>3</sub> ] <sub>4</sub>	268.8	Eqs. (7–9)	317
<b>177</b>	Ga <sub>4</sub> [C(SiMe <sub>2</sub> Et) <sub>3</sub> ] <sub>4</sub>	271.1	Eq. (7)	318
<b>178</b>	Ga <sub>4</sub> [Si(SiMe <sub>3</sub> ) <sub>3</sub> ] <sub>4</sub>	258.2	Eqs. (8, 9)	319
<b>179</b>	Ga <sub>4</sub> [Ge(SiMe <sub>3</sub> ) <sub>3</sub> ] <sub>4</sub>	258.7	Eq. (9)	320
<b>180</b>	Ga <sub>4</sub> (Si <sup>t</sup> Bu <sub>3</sub> ) <sub>4</sub>	257.2	Eq. (10)	321
<b>181</b>	Ga <sub>4</sub> tmp <sub>4</sub>	258.6(1)–268.5(1)	Eq. (9)	261
<b>182</b>	Ga <sub>4</sub> [N(SiMe <sub>3</sub> )dipp] <sub>4</sub>	258.4(1)–264.2(1)	Eq. (9)	261

**Table 11** Overview on tetrameric species In<sub>4</sub>R<sub>4</sub> and Tl<sub>4</sub>R<sub>4</sub>.

		$d_{\text{E-E}}$ [pm] (mean)	Method	References
<b>184</b>	In <sub>4</sub> [C(SiMe <sub>3</sub> ) <sub>3</sub> ] <sub>4</sub>	300.2	Eq. (8)	322
<b>185a</b>	In <sub>4</sub> [C(SiMe <sub>2</sub> Et) <sub>3</sub> ] <sub>4</sub>	300.4	Eq. (8)	323
<b>185b</b>	In <sub>4</sub> [C(SiMe <sub>2</sub> Pr) <sub>3</sub> ] <sub>4</sub>	315.2	Eq. (8)	323
<b>186</b>	In <sub>4</sub> [Si(SiMe <sub>3</sub> ) <sub>3</sub> ] <sub>4</sub>	289.3	Eq. (8)	324
<b>187</b>	Tl <sub>4</sub> [C(SiMe <sub>3</sub> ) <sub>3</sub> ] <sub>4</sub>	332–364	Eq. (8)	325





### 1.17.3.1.2 Bonding

Comparing tetrahedral clusters in the row boron to thallium there are remarkable differences. The E-E distances increase from boron to aluminum and gallium to thallium. The Ga–Ga distances are shorter than the Al–Al ones. This is in line with the smaller covalent radius of gallium atoms compared to aluminum.

$\text{Ga}_4[\text{C}(\text{SiMe}_3)_3]_4$  **176** and  $\text{Ga}_4[\text{Si}(\text{SiMe}_3)_3]_4$  **178** are, on the first glance, two very similar compounds, but already the color is different, it changes from red (**176**) to violet (**178**). The Ga–Ga distances of the silyl substituted compound are shorter by approximately 10 pm. Comparable differences are observed for the Al and In derivatives, respectively. This hints to a stronger bonding in the silyl substituted cluster molecules compared to alkyl substituted ones. This is obvious in the behavior in solution and gas phase. **176** monomerizes in solution and in gas phase the structure of the monomer could be determined by electron diffraction.<sup>334</sup> The Ga–C distance in the monomer is drastically longer than in **176**. **178** remains tetrameric under these conditions.

Looking at the bonding of these tetrahedral clusters, four skeletal electron pairs (sep) are counted, which makes them different from carboratetrahedranes or  $\text{P}_4$  with six sep, for example. In the latter, six  $2c2e$  bonds can be assumed, for triel clusters four  $3c2e$  bonds on the four faces of the tetrahedron. Building the clusters from monomers ER, with a lone pair of electrons and two vacant p-type orbitals, linear combination gives the cluster orbitals (Fig. 1).

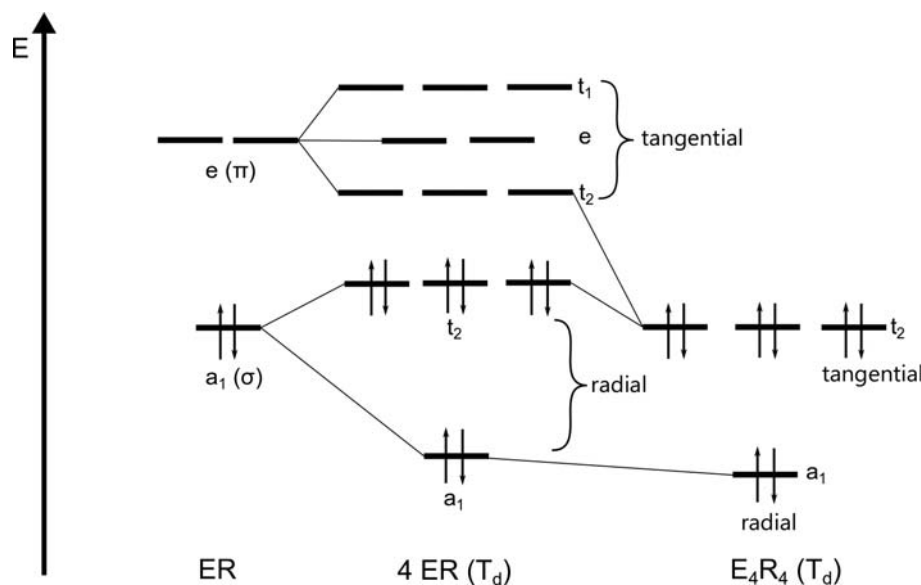


Fig. 1 Qualitative MO scheme for triel clusters  $E_4R_4$  in  $T_d$  symmetry.

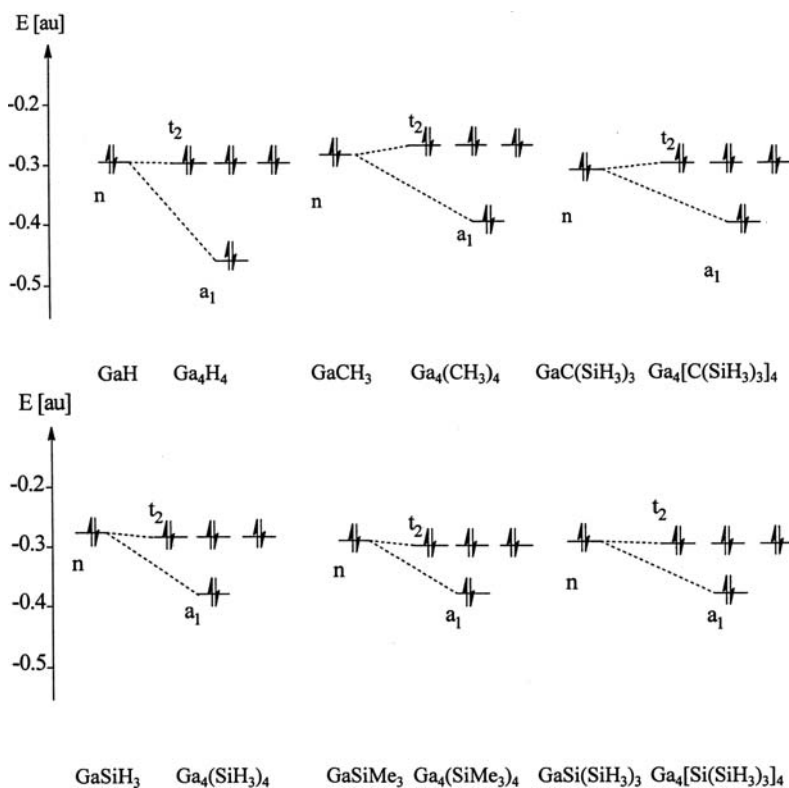
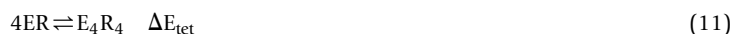


Fig. 2 Change of the HOMO energies with R for triel clusters  $E_4R_4$  in  $T_d$  symmetry.<sup>335</sup>

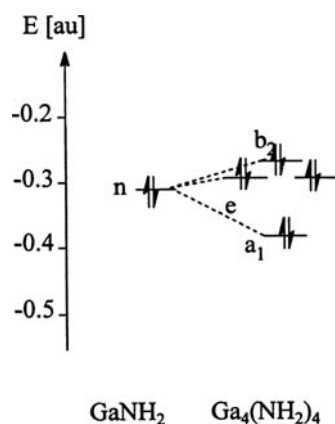
The energy of the triply degenerate HOMO is largely influenced by the type of R for a given triel E (Fig. 2). Silyl groups lead to stabilization of the HOMO compared to alkyl substituents. Consequently, large differences in tetramerization energies  $\Delta E_{tet}$  are observed (Table 12, Eq. 11) This is reflected in the experimental findings on dissociation of the clusters.



For amido substituted tetrahedranes a modified picture is valid.<sup>261</sup> Due to the lower symmetry of the substituents, the HOMO is now a non-degenerate one, which is energetically near the doubly degenerate HOMO-1 (Fig. 3). This also explains the less regular

**Table 12** Tetramerization energies of  $E_4R_4$  calculated acc. to Eq. (11).

	$\Delta E_{tet}/\text{kJ mol}^{-1}$	Method	References
$B_4H_4$	-1153	MP2	336,337
$Al_4H_4$	-571	MP2	336,337
$Ga_4H_4$	-556	MP2	319
$In_4H_4$	-337	MP2	323
$Ga_4H_4$	-424	DFT (RI; BP86; def-SV(P))	338
$Ga_4[C(SiMe_3)_3]_4$	-197	DFT (RI; BP86; def-SV(P))	338
$Ga_4[Si(SiMe_3)_3]_4$	-419	DFT (RI; BP86; def-SV(P))	338
$Ga_4[Si(CMe_3)_3]_4$	-499	DFT (RI; BP86; def-SV(P))	338
$Ga_4[Ge(SiMe_3)_3]_4$	-365	DFT (RI; BP86; def-SV(P))	338
$Ga_4[NH_2]_4$	-56	DFT (RI; BP86; def-SV(P))	261
$Ga_4[NMe_2]_4$	-50	DFT (RI; BP86; def-SV(P))	261
$Ga_4[N(SiMe_3)dipp]_4$	-150	DFT (RI; BP86; def-SV(P))	261
$Ga_4[tmp]_4$	-173	DFT (RI; BP86; def-SV(P))	261

**Fig. 3** Qualitative MO scheme for triel clusters  $E_4(NR_2)_4$  in  $D_{2d}$  symmetry.

structures of the tetramers and might be viewed as a tendency to open up the cage to a butterfly type structure as is observed for  $B_4(N^iPr_2)_4$ .<sup>308</sup>

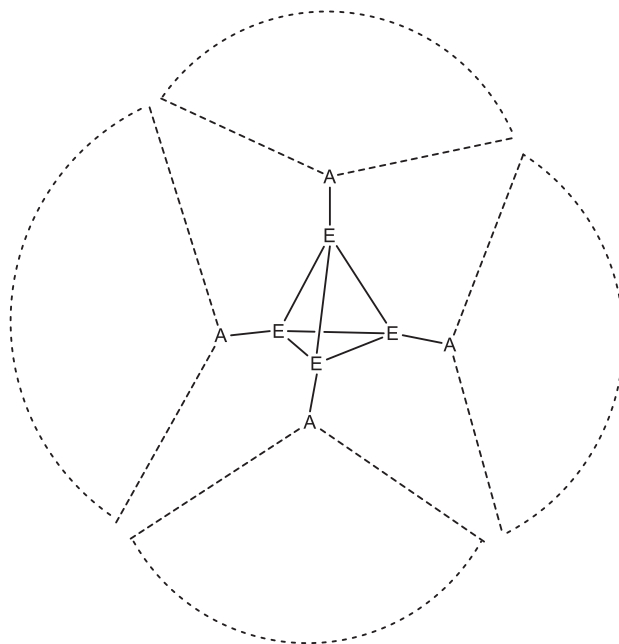
The E-X bonds shorten upon cluster formation from the monomers to tetramers, which is against the normal trend for bond lengths and coordination numbers. The lone-pair orbital of the monomers has a high s-character and is regarded as slightly antibonding regarding the E-X bond. On cluster formation it gets involved in cluster bonding and loses its antibonding character.<sup>261</sup>

In addition to these electronic arguments, simple steric ones are applicable. Thus, in **176** and **178** the four monomers  $(Me_3Si)_3AGa$  ( $A = C, Si$ ) form a cavity of a given size, determined by the size of the substituents (**Fig. 4**). The gallium atoms attached come nearer together if the Ga-A bonds are longer. Here, the gallium-carbon and gallium-silicon are approx. 30 pm different in lengths.

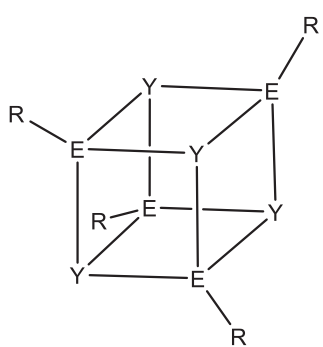
### 1.17.3.1.3 Reactivity

The cluster compounds of type  $E_4R_4$  have proved to be valuable starting materials for transition metal complexes, where ER groups are terminal or bridging ligands. Oxidation of tetrahedral clusters with chalcogens gives heterocubanes  $(REY)_4$  **189a**<sup>157,173,322,339-344</sup> or hexagonal prismatic cages  $(REY)_6$  **189b**,<sup>344-348</sup> where all E-E bonds are broken. Careful oxidation of **184** with a thiirane afforded a partially oxidized product  $R_4In_4S$  **190**.<sup>349</sup> The  $Ga_4$  core was retained in partial oxidation with halogens. For examples see **Section 1.17.2.3**.

$E_4$  cores are also present in  $[(ER)_3(ESiMe_3)Si(SiMe_3)]^-$  **191a** ( $E = Al$ )<sup>350</sup> and **191b** ( $E = Ga, R = Si(SiMe_3)_3$ )<sup>233</sup> with trigonal bipyramidal  $E_4Si$  cores. Six sep make them *closo*-clusters according to the Wade rules. An alternative description as heterobicyclopentanes is not in agreement with delocalized bonding confirmed by quantum chemical calculations. These show extensive 3c2e bonds on the  $E_3$ -faces of the cage and significant bonding interactions between the equatorial triel atoms. These clusters are obtained from ALX solutions or "Gal" with  $Li(thf)_3Si(SiMe_3)_3$ .



**Fig. 4** Schematic representation of the steric requirements for  $\text{Ga}_4$ -clusters.

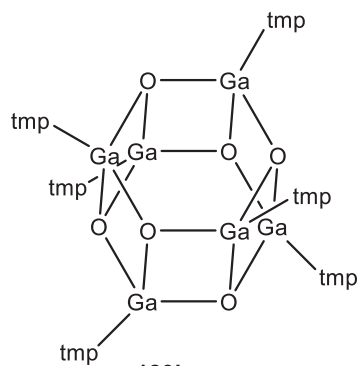


**189a**

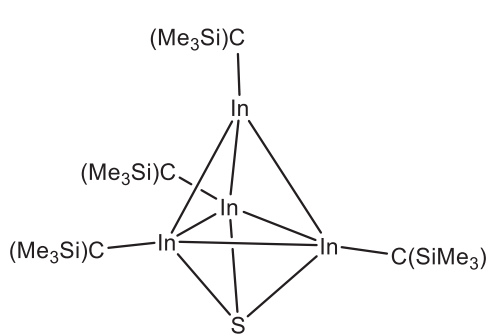
$E = \text{Al, Ga, In}$

$Y = \text{O, S, Se, Te}$

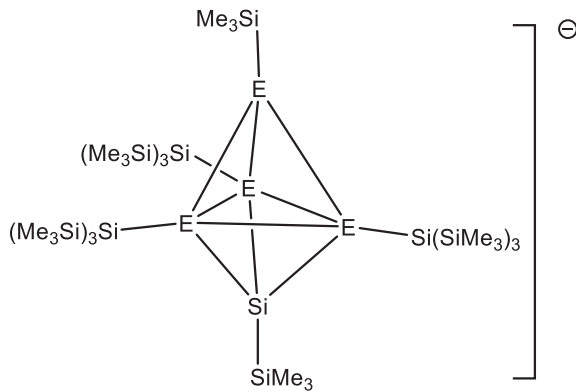
$R = \text{C}(\text{SiMe}_3)_3, \text{Si}(\text{SiMe}_3)_3,$   
 $\text{Si}^t\text{Bu}_3, \text{tmp}, \dots$



**189b**



**190**



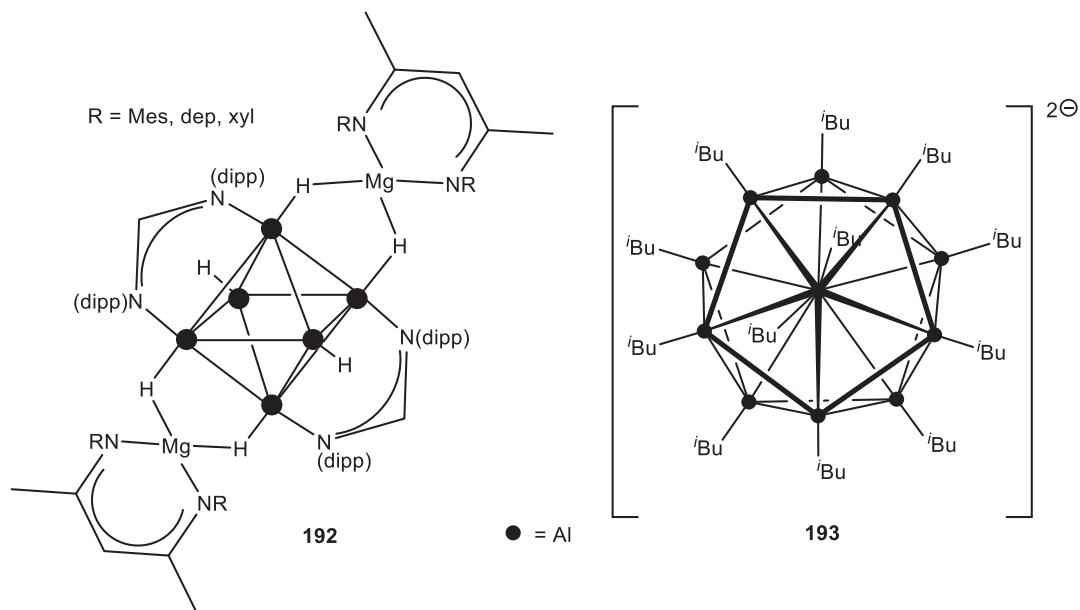
**191a**  $E = \text{Al}$

**191b**  $E = \text{Ga}$

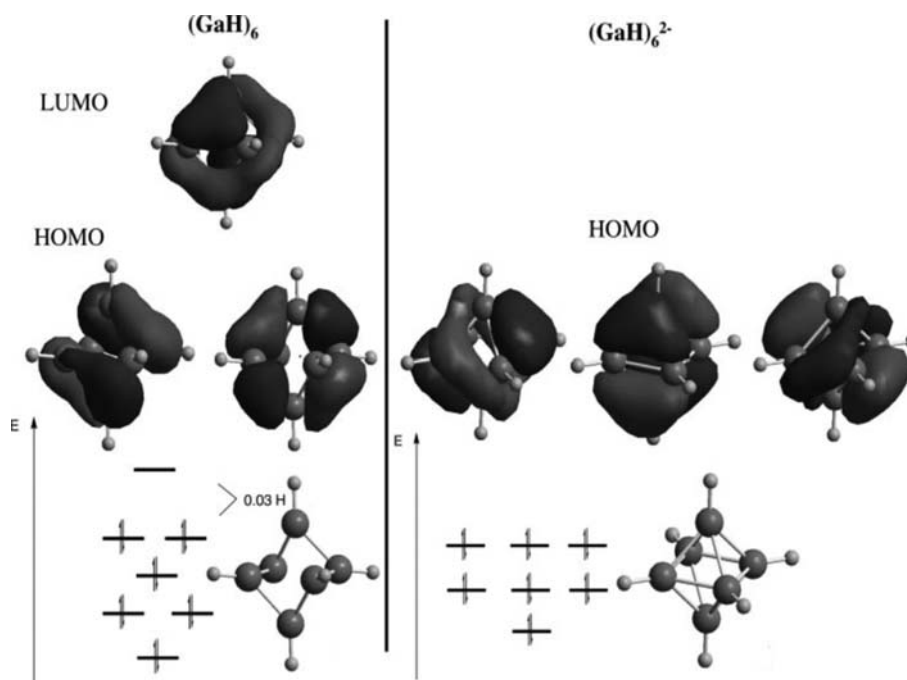
1.17.3.2 Higher  $[E_nR_n]^{x-}$  cluster compounds

Only two hexaaluminum clusters are described so far. The  $[Al_6^iBu_6]^{•-}$  radical ion is characterized on basis of its EPR spectrum, which exhibits the expected 31 lines by hyperfine coupling with six equivalent  $^{27}Al$  nuclei.<sup>351</sup> The second is the neutral  $Al_6$  cluster  $[(^Rnacnac)Mg]_2Al_6H_6\{N(dipp)\}_2CH_2$  192 (R = Mes, dep, xyl),<sup>352</sup> obtained by reaction of  $[AlH_2\{N(dipp)\}_2CH]_2$  and  $[(^Rnacnac)Mg]_2$ . This octahedral hexaalane is stabilized by the surrounding  $(^Rnacnac)Mg^+$  cations and  $[\{N(dipp)\}_2CH]^-$  anions.

The icosahedral cluster  $[Al_{12}^iBu_{12}]^{2-}$  193<sup>353</sup> was obtained and structurally characterized  $[d_{Al-Al} = 267.9-269.6 \text{ pm}]$  already in the beginning of investigations on aluminum and gallium cluster compounds. It fulfills the Wade rules for a *closo*-cluster and is a homolog to the *closo*-boranate  $[B_{12}H_{12}]^{2-}$ .



For gallium the hexagallanate  $[Ga_6(Si^iBuPh_2)_6]^{2-}$  194a features a nearly perfect octahedral cluster core, as is expected for a *closo*-cluster.<sup>101</sup> The gallium-gallium distances are in line with a regular octahedron ( $d_{Ga-Ga} = 255.0-256.1 \text{ pm}$ ). Whereas  $[Ga_6(SiPh_2Me)_4(CH_2Ph)_2]^{2-}$  194b,<sup>354</sup> due to its heteroleptic substitution, has a slightly distorted octahedral cluster core. The gallium-gallium distances vary on a larger range from 252.7 to 263.9 pm.

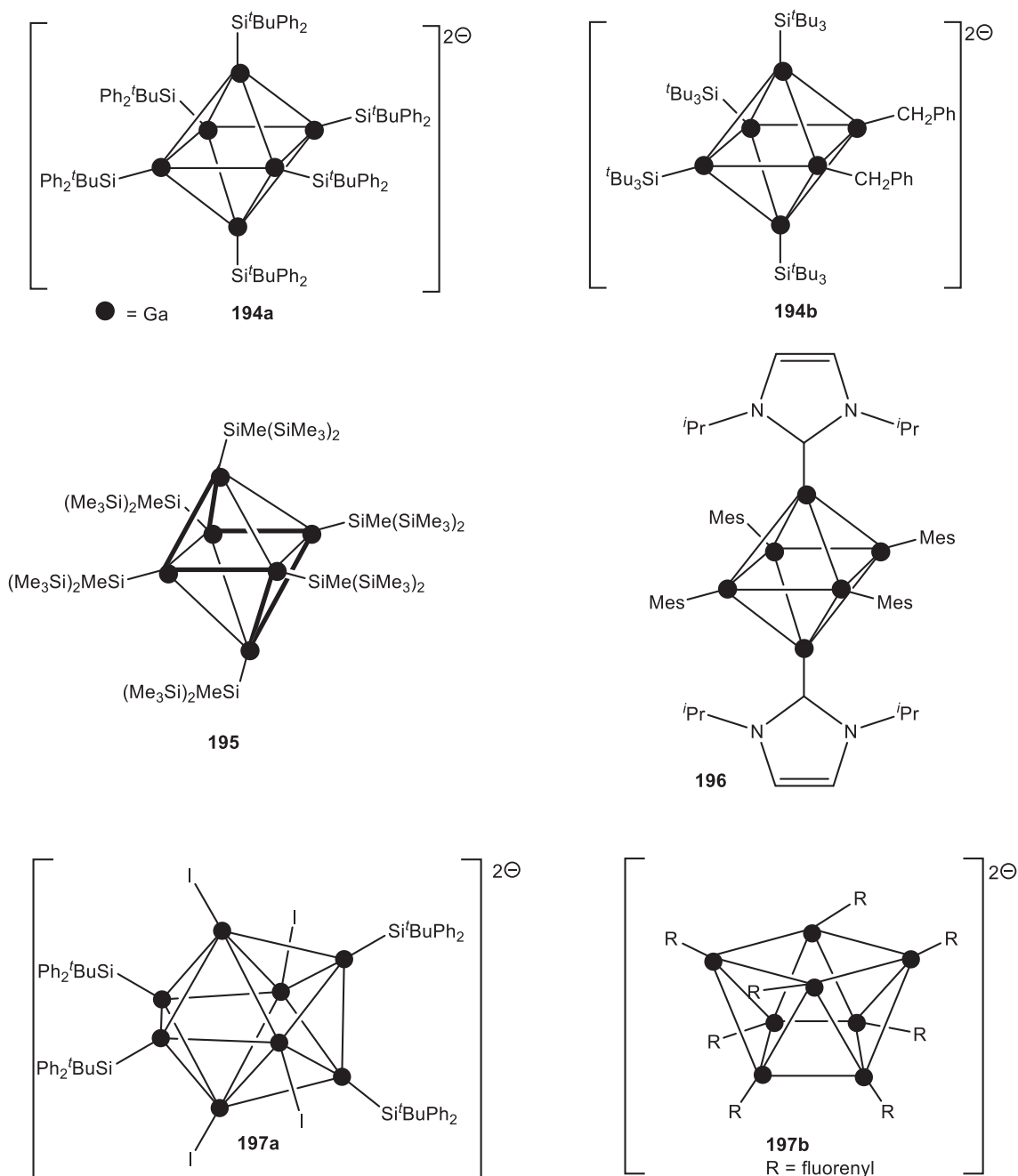


**Fig. 5** Schematic representation of the MO-scheme for distortion of  $[Ga_6H_6]^{n-}$  ( $n = 0, 2$ ). Linti, G.; Coban, S.; Dutta, D. Das Hexagallan  $Ga_6[SiMe(SiMe_3)_2]_6$  und das *closo*-Hexagallanat  $[Ga_6(Si(CMe_3)_3)_4(CH_2C_6H_5)_2]^{2-}$  - der Übergang zu einem ungewöhnlichen *precloso*-Cluster. *Z. Allg. Anorg. Chem.* **2004**, *630*, 319. Copyright Wiley-VCH Verlag GmbH & Co. KGaA. Reproduced with permission.



The neutral  $\text{Ga}_6(\text{Si}(\text{SiMe}_3)_2\text{Me})_6$  **195**<sup>354</sup> has only six sep and is regarded as *hypercloso*-cluster. As it becomes obvious from the MO scheme for octahedral clusters (Fig. 5), with only 12 cluster electrons a distorted structure is expected. This is realized for **195** as distorted octahedron with six long (296 pm) and six short (251 pm) bonds. The triple degenerate HOMO in the *closo*-cluster  $[\text{Ga}_6\text{H}_6]^{2-}$  is completely occupied. On oxidation to  $\text{Ga}_6\text{H}_6$  now only four electrons are in these orbitals, which gives rise to a Jahn-Teller distortion to a structure with only a double degenerate HOMO. An alternative distortion would be the transition to a capped trigonal bipyramid, as observed for transition metal clusters  $\text{Os}_6(\text{CO})_{18}$ <sup>28</sup> or predicted by DFT calculations for non-existent  $\text{B}_6\text{H}_6$ .<sup>355</sup> DFT calculations on  $\text{Ga}_6\text{H}_6$  show the capped trigonal bipyramidal structure to be more stable by only  $5 \text{ kJ mol}^{-1}$  than the observed distorted octahedral structure for **195**. Here, the influence of the steric demanding substituents seems to be important.

A remarkable approach to gallium cluster was given for  $\text{R}_4\text{Ga}_6(\text{L})_2$  **196**.<sup>189,356</sup> The neutral cluster was obtained by reduction of the complex  $[\text{GaCl}_2(\text{Mes})\text{L}]$  ( $\text{L}=\text{C}[\text{N}(\text{iPr})\text{CH}]_2$ ) with potassium in toluene. The six gallium atoms adopt a slightly distorted octahedral structure ( $d_{\text{Ga-Ga}} = 251.1$  to  $259.1 \text{ pm}$ ). Four RGa groups and two LGa units provide seven sep for this *closo*-cluster. This approach of reducing NHC stabilized compounds was applied for successful preparation of compounds containing  $\text{B}_2$ ,  $\text{Si}_2$  and P–P bonded units.<sup>357–360</sup>

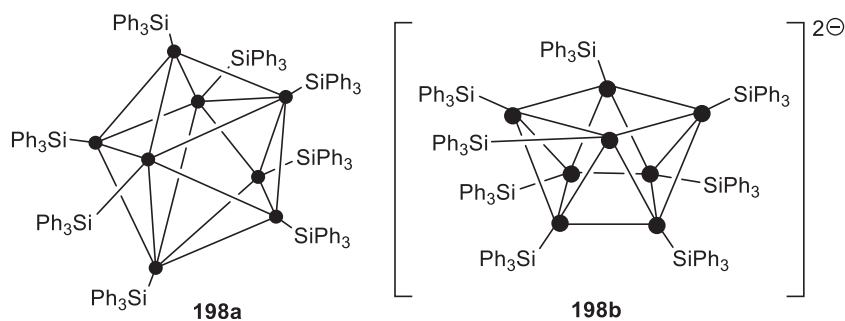
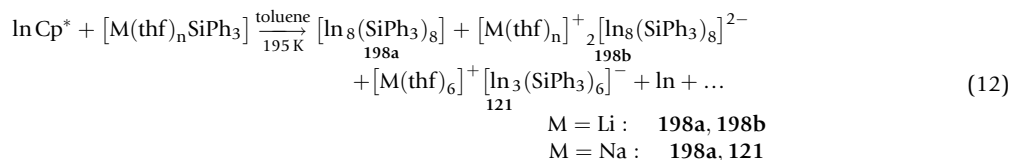


Such discrepancies between expected structures from application of the Wade rules and realized ones in triel chemistry are quite common. The *closo*-cluster ion  $[\text{Ga}_8\text{I}_4(\text{Si}^t\text{BuPh}_2)_4]^{2-}$  **197a**<sup>101</sup> adopts a snub disphenoid structure,<sup>361</sup> as expected and also found for the octaboranate  $[\text{B}_8\text{H}_8]^{2-}$ .<sup>362</sup> Even  $\text{B}_8\text{Cl}_8$  with only eight skeletal electron pairs has a disphenoidal structure.<sup>363,364</sup> On the other hand  $[\text{Ga}_8(\text{fluorenyl})_8]^{2-}$  **197b**<sup>365</sup> adopts a square antiprismatic structure and not the expected disphenoidal one.

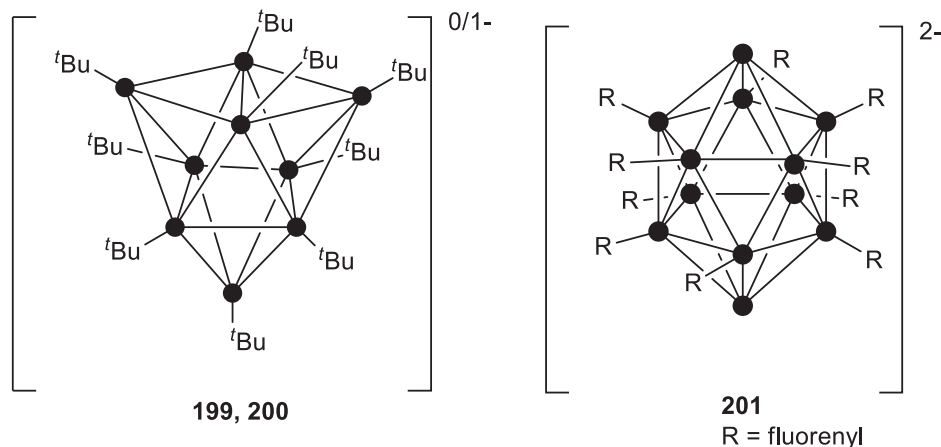
RI-DFT-calculations (BP86-functional, def2-TZVP) of different  $[\text{Ga}_8\text{R}_8]^{2-}$  species ( $\text{R} = \text{H}, \text{I}, \text{CH}_3, \text{SiH}_3$ ) show, that square antiprismatic seems to be the regular structure for  $[\text{Ga}_8\text{R}_8]^{2-}$  cluster with H, I and  $\text{CH}_3$  substituents. For  $\text{SiH}_3$  substituents (as well as for  $[\text{Ga}_8\text{I}_4(\text{SiH}_3)_4]^{2-}$ ) a snub disphenoid is preferred. This behavior can mostly be derived through stabilizing hyperconjugative interactions between the Ga–Si bonds and the cluster core in silyl-substituted clusters. Energy differences between the isomers of these  $[\text{Ga}_8\text{R}_8]^{2-}$  species are in the range from 5.8 to 10.4  $\text{kJ mol}^{-1}$ .<sup>101</sup> On this basis, square antiprismatic and snub disphenoidal structures should be regarded as possible regular structures for  $[\text{Ga}_8\text{R}_8]^{2-}$ .

The octaindium clusters  $[\text{In}_8(\text{SiPh}_3)_8]$  **198a** and  $[\text{In}_8(\text{SiPh}_3)_8]^{2-}$  **198b** are obtained from  $\text{InCp}^*$  by reaction with  $\text{MSiPh}_3$  ( $\text{M} = \text{Li}(\text{thf})_3, \text{Na}(\text{thf})_n$ ) (Eq. 12). **198a** has a snub disphenoidal  $\text{In}_8$  core, which shows a transition to distorted square antiprismatic (**198b**) upon two electron reduction.<sup>297</sup> RI-DFT calculations (BP86-functional, def-SV(P)-base) for  $[\text{In}_8\text{H}_8]^{0/2-}$  show the square antiprismatic structure to be more favorable for anionic clusters of indium (compare for gallium) and the disphenoidal for neutral ones.

Each of the indium atoms in **198a** is bonded to a triphenylsilyl group with indium–silicon distances of 260 pm on an average [ $d_{\text{In-Si}} = 257.0(5)\text{--}262.2(5)$  pm]. This is shorter than those in clusters with the more bulky tris(*tert*-butyl)silyl groups as substituents [ $d_{\text{In-Si}} = 265$  pm (**239**), 268 pm (**206**)]. The indium–indium distances in the cluster vary between 285.5 and 328.2 pm. The deviation of ideal  $D_{2d}$  symmetry is significant. This spreading is comparable to that in other indium clusters (*vide infra*). For the tetrahedral cluster **186** indium–indium distances of 290 pm are observed. On reduction to **198b** a shrinking of the indium–indium distances is observed.



A nonagallane cluster  $[\text{Ga}_9^t\text{Bu}_9]$  **199** was obtained as dark green crystals as by product of the large scale preparation of  $\text{Ga}^t\text{Bu}_3$ .<sup>305,323</sup> The gallium atoms are at the corners of a tricapped trigonal prism. Here, short Ga–Ga distances ( $d_{\text{Ga-Ga}} = 259$  pm) are observed for the capping gallium atoms, and longer ones (up to  $d_{\text{Ga-Ga}} = 299$  pm) parallel to the threefold axis of the cluster. This makes the structure near a monocapped square antiprism, which is the expected structure for a  $E_9$  cluster with nine sep. A reversible one electron reduction of **199** was demonstrated by cyclovoltammetric studies ( $E^0 = -1.74$  V against  $[\text{FeCp}_2]^{0/+1}$ ). On a preparative scale **199** was reduced to **200** by  $\text{CoCp}^*_2$ . The radical anion **200** has a very similar structure to the neutral compound **199**, only the Ga–Ga distances parallel the threefold axis shrink by 17 pm.

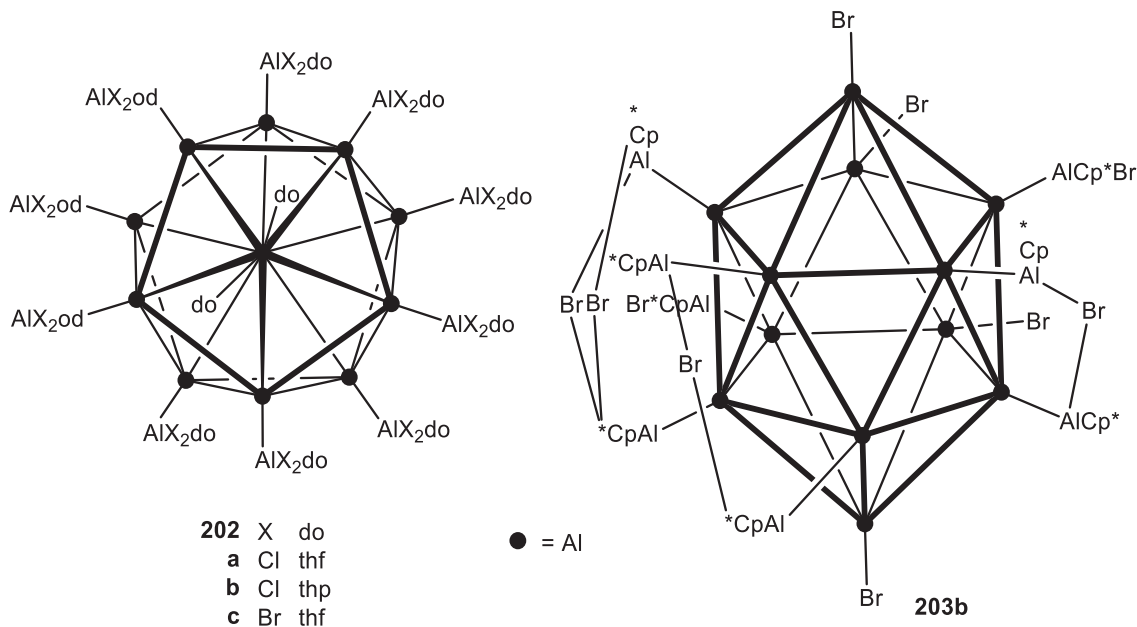


Icosahedral clusters of type  $[E_{12}R_{12}]^{2-}$  are only realized for aluminum with 193. The cluster was obtained in small amounts by reduction of  ${}^t\text{BuAlCl}_2$  with potassium. Related is  $[\text{Ga}_{12}(\text{fluorenyl})_{10}]^{2-}$  201, with an icosahedral cluster core.<sup>366</sup> The formal oxidation of this cluster to a  $[\text{Ga}_{12}\text{R}_{12}]^{2-}$  cluster is hindered by the unfavorable energy of the HOMO as quantum chemical calculations indicate.

In Section 1.17.2.3 electron precise aluminum subhalides of type  $\text{Al}_4\text{X}_4 \cdot 4\text{do}$  are described as crystallized products from metastable aluminum monohalide solutions. Under varied conditions (type of donor, concentration) higher subhalides of type  $\text{Al}_{22}\text{X}_{20} \cdot 12\text{do}$  (do = thf, thp = tetrahydropyrane) 202a-c are obtained.<sup>244,245</sup> Compounds of type 202 show icosahedral  $\text{Al}_{12}$  cores, where ten aluminum atoms are bearing  $\text{AlX}_2(\text{do})$  substituents. The apical aluminum atoms are ligated by one donor molecule, each. Thus, the *closo*- $\text{Al}_{12}$  core has 13 sep,  $10 \times 2$  electrons from 10  $\text{Al}[\text{AlX}_2(\text{do})]$  groups and  $2 \times 3$  electrons from the two  $\text{Al}(\text{do})$  fragments.

An icosahedral  $\text{Al}_{12}$  core is also present in  $\text{Al}_{20}\text{Cp}^*_8\text{X}_{10}$  ( $\text{X} = \text{Cl}, \text{Br}$ ) 203a, b.<sup>52</sup> Here, six aluminum atoms of the icosahedral core are bonded to  $\text{AlCp}^*(\text{X})$  substituents, two to  $\text{AlCp}^*$  groups. These aluminum atoms are joined by bridging halides, in addition. The remaining four cluster aluminum atoms are part of  $\text{AlBr}$  groups. Thus, electron bookkeeping for the  $\text{Al}_{12}$  cluster core makes  $4 \times 2$  ( $\text{AlBr}$ ) +  $2 \times 3$  ( $\text{AlAlCp}^*$ ) +  $6 \times 2$  ( $\text{AlAlCp}^*\text{X}$ ) = 26 electrons, as necessary for an icosahedral *closo*-polyhedron.

Several related  $\text{Ga}_{22}$  clusters with icosahedral cores are known, which will be described in Section 1.17.4.3.



### 1.17.3.3 Aromaticity of $[E_nR_n]^{x-}$ cluster compounds

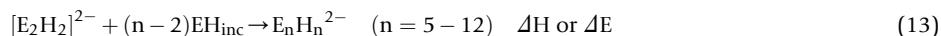
Various concepts have been introduced to explain structures and stoichiometry of main group cluster compounds. Most commonly known are the Wade-William-Rudolph-Mingos rules. Wade<sup>18–21,298,367</sup> For higher, conjugated clusters they were modified by Jemmis.<sup>368,369</sup> Element-rich clusters  $[E_nR_m]^{x-}$ , especially of heavier elements of group 13, were classified as metalloids (see Section 1.17.4.1).<sup>13,302</sup>

Cluster compounds like the polyhedral boranates  $[\text{B}_n\text{H}_n]^{2-}$  have been discussed as three-dimensional aromatic systems.<sup>370–372</sup> A diatropic ring current is the most typical property of an aromatic molecule.<sup>373</sup> For endohedral fullerenes it was proved, that chemical shifts for atoms in endohedral and exohedral positions behave comparable to shifts of atoms in and out of the ring plane of an aromatic hydrocarbon, respectively.<sup>374</sup> Quantification of aromaticity by the calculated magnetic shielding constants at selected regions of a molecule, where no atoms reside, was suggested. The resulting nuclear independent shifts (NICS) are negative (diatropic) for aromatic molecules, positive (paratropic) for anti-aromatic ones and approximately zero for non-aromatic molecules.<sup>373</sup>

The skeletal number of electrons as well as the substituents of boron cluster compounds influence the NICS values in the center of clusters.<sup>375</sup>  $\text{B}_8\text{Cl}_8$ <sup>363</sup> and  $\text{B}_9\text{Cl}_9$ <sup>376</sup> are well-known compounds, but it was not possible to prepare  $\text{B}_8\text{H}_8$  and  $\text{B}_9\text{H}_9$ .  $\text{B}_9\text{F}_9$  as well as  $[\text{B}_8\text{H}_8]^{2-}$  and  $[\text{B}_9\text{H}_9]^{2-}$  are aromatic according to NICS values in the cluster center.<sup>377</sup> Only the last one is a *closo*-cluster compound by the Wade-rules.  $\text{B}_9\text{H}_9$ , in contrast, is paratropic, that means anti-aromatic. Similarly,  $\text{B}_4\text{F}_4$  is classified as aromatic, non-existent  $\text{B}_4\text{H}_4$  as anti-aromatic.<sup>378</sup> Various criteria of aromaticity are fulfilled for the icosahedral *closo*-boranate  $[\text{B}_{12}\text{H}_{12}]^{2-}$ . For which the NICS value is diatropic.<sup>379–381</sup> The isoelectronic  $\text{Si}_{12}^{2-}$  and  $\text{Ge}_{12}^{2-}$  follow the Wade rules. Nevertheless, paratropic NICS values are obtained for these Zintl ions. This was explained by the different influence of hydrogen atoms and lone pairs on the cluster molecule orbitals. Naked cluster ions of heavier group 13 elements of type  $\text{E}_4^{2-}$  and  $[\text{E}_2\text{X}_2]^{n-}$  [ $\text{E} = \text{Al}, \text{Ga}, \text{In}; \text{X} = \text{Na}, \text{Si}, \text{Ge}$ ], with planar rings

have been characterized as aromatic compounds.<sup>382–393</sup> A  $2\pi$ -metalloaromatic ring is present in  $\text{Na}_2[\text{Ga}_3^{\text{s}}\text{Mes}_3]$  [ $^{\text{s}}\text{Mes} = 2,4,6\text{-}^{\text{t}}\text{Bu}_3\text{C}_6\text{H}_2$ ].<sup>394</sup> For example, a NICS value of  $-45$  ppm has been calculated for the model compound  $[\text{Ga}_3\text{H}_3]^{2-}$ .<sup>152,370</sup>

A detailed study on aromaticity of *closo*-boranates  $[\text{B}_n\text{H}_n]^{2-}$  ( $n = 5\text{--}12$ ) by Schleyer et al.<sup>380</sup> uses geometrical and energetic criteria as well as NICS values. As energetic criterion a reaction (Eq. 13) describing the formation of *closo*-clusters  $[\text{E}_n\text{H}_n]^{2-}$  ( $n = 5\text{--}9$ ; E = B, Al, Ga, In) from an ethyne analog  $[\text{E}_2\text{H}_2]^{2-}$  and an appropriate number of incremental EH units, is used. The formation energy increases with growing cluster size, therefore  $\Delta\text{H}/n$  as averaged bonding energy of each EH vertex is used as criterion. Plotting  $\Delta\text{H}/n$  against  $n$ , Schleyer observed local minima for clusters with highest symmetry  $[\text{B}_6\text{H}_6]^{2-}$  und  $[\text{B}_{12}\text{H}_{12}]^{2-}$ , meaning all other cluster sizes are less stabilized.



A classical criterion for aromaticity is equalization of bond lengths, for which the deviation  $\Delta\text{R}$  is a measure. The deviation in bond lengths with cluster size is not really dependent on E. Nearly ideal octahedral structures with a  $\Delta\text{R}$  near zero are calculated for  $[\text{E}_6\text{H}_6]^{2-}$ . For  $[\text{E}_8\text{H}_8]^{2-}$  the deviation is largest for all elements. Overall, in the periodic column from boron to indium the deviation  $\Delta\text{R}$  increases.

Polyhedral cluster ions  $[\text{E}_n\text{H}_n]^{2-}$  (E=B, Al, Ga, In;  $n = 5\text{--}9$ ) were investigated by the means described above.<sup>380,395,396</sup> The results are summarized in Table 13. Inspecting the change of the values  $\Delta\text{E}/n$  against the number of cluster atoms  $n$  (Fig. 6) reveals a special stabilization of octahedral clusters for boron and aluminum. Octanuclear gallium and indium clusters prefer a square antiprismatic structure slightly over a snub disphenoidal. But this is very dependent of the substituents. This has been demonstrated by 197a, b and 198a, b and previously discussed DFT-calculations. In case of aluminum and gallium the curves between values for  $[\text{E}_6\text{H}_6]^{2-}$  to  $[\text{E}_8\text{H}_8]^{2-}$  are flat, meaning in this region cluster size is not determined electronically but might be influenced by the steric demand of the substituents.

The discussion of aromaticity of  $[\text{E}_n\text{H}_n]^{2-}$  molecules (Fig. 7, Table 13 and 14) on basis of NICS values is confined here to those in the cluster centers. Because the NICS values directly on triangular cluster faces usually are negative, it is important to take into account their change on a trajectory to the cluster center. Problem is shown for  $[\text{B}_5\text{H}_5]^{2-}$ . Of  $[\text{E}_5\text{H}_5]^{2-}$  cluster ions a largely negative value classifies only the pentaboranate as aromatic system. For all other group 13 elements trigonal-bipyramidal cluster should be classified as non-aromatic. NICS values 1 Å above a  $\text{B}_3$ -face in  $[\text{B}_5\text{H}_5]^{2-}$  are  $-16.7$  ppm. The center of a face is only 0.57 Å off the center, and the cluster center itself is part of a three-membered ring with a distance of only 0.53 Å from edge to center. This means the influence of the electron densities on edges and faces sums up to a highly negative NICS value in the center. As a consequence, Aihara classified  $[\text{B}_5\text{H}_5]^{2-}$  as non-aromatic.<sup>372</sup>

A fusion of two tetrahedra via a common face is not allowed for boron.<sup>397</sup> Similarly, in  $[\text{Al}_5\text{H}_5]^{2-}$  the influence of the electron density on the faces, which are only 0.86 Å distant of the center, sums up to a negative NICS in the cluster. Thus, based on

**Table 13** Results for *closo*-cluster  $[\text{E}_n\text{H}_n]^{2-}$  (E = B, Al, Ga, In;  $n = 5\text{--}9$ ).

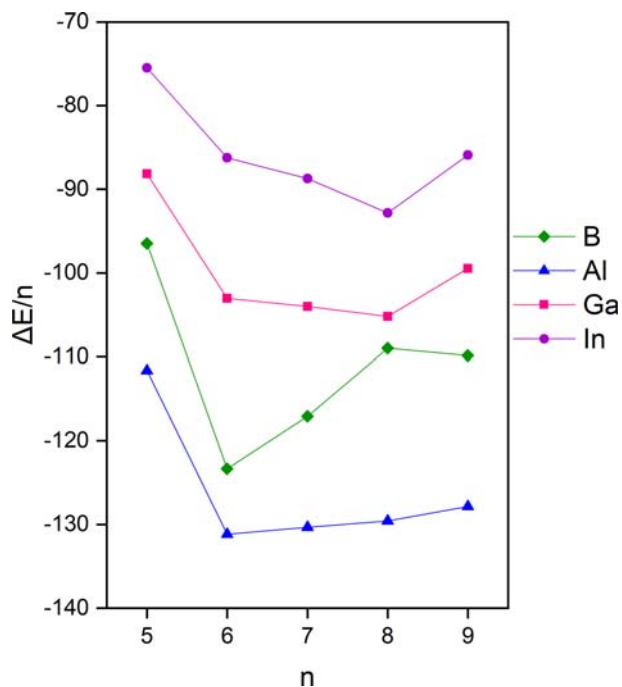
	$\Delta\text{E}/n^a$	$\Delta\text{R}^b$	NICS <sup>c</sup>	NICS <sup>d</sup>
$[\text{B}_5\text{H}_5]^{2-}$	-96.47	0.139	-24.8	
$[\text{B}_6\text{H}_6]^{2-}$	-123.35	0.002	-29.9	
$[\text{B}_7\text{H}_7]^{2-}$	-117.07	0.168	-23.4	
$[\text{B}_8\text{H}_8]^{2-}$	-109.00	0.281	-20.0	
$[\text{B}_9\text{H}_9]^{2-}$	-109.87	0.260	-22.9	
$[\text{Al}_5\text{H}_5]^{2-}$	-111.62	0.301	-7.7	
$[\text{Al}_6\text{H}_6]^{2-}$	-131.17	0.004	-24.3	
$[\text{Al}_7\text{H}_7]^{2-}$	-130.32	0.299	-22.1	
$[\text{Al}_8\text{H}_8]^{2-}$	-129.58	0.302	-18.3	
$[\text{Al}_9\text{H}_9]^{2-}$	-127.85	0.290	-14.2	
$[\text{Ga}_5\text{H}_5]^{2-}$	-88.17	0.393	0.7	-1.7
$[\text{Ga}_6\text{H}_6]^{2-}$	-103.06	0.021	-24.3	-22.5
$[\text{Ga}_7\text{H}_7]^{2-}$	-104.03	0.424	-22.1	-20.5
$[\text{Ga}_8\text{H}_8]^{2-}$	-105.19	0.618	-16.8	-16.1
$[\text{Ga}_9\text{H}_9]^{2-}$	-99.49	0.311	-12.1	-13.0
$[\text{In}_5\text{H}_5]^{2-}$	-75.51	0.531		9.7
$[\text{In}_6\text{H}_6]^{2-}$	-86.26	0.147		-15.4
$[\text{In}_7\text{H}_7]^{2-}$	-88.72	0.683		-13.0
$[\text{In}_8\text{H}_8]^{2-}$	-92.83	0.774		-17.5
$[\text{In}_9\text{H}_9]^{2-}$	-85.93	0.309		-7.6

<sup>a</sup>Averaged electronic energy per EH unit energy ( $\Delta\text{E}/n$ ,  $\text{kJ mol}^{-1}$ ) according to Eq. (13).

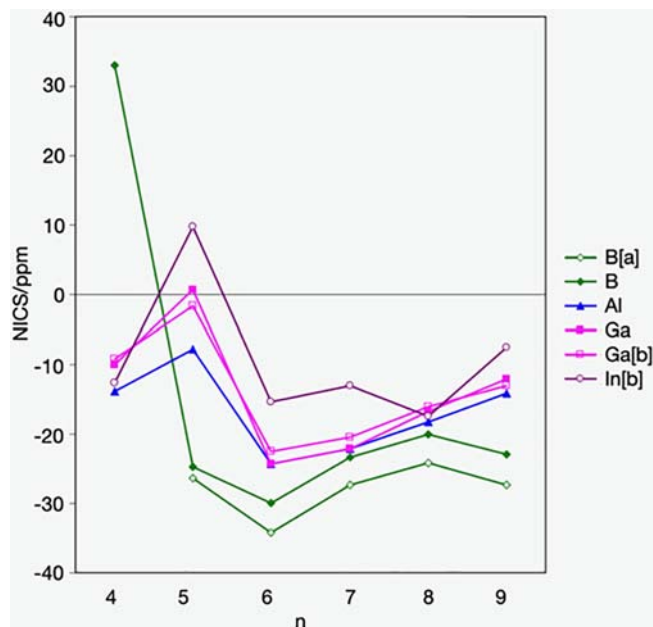
<sup>b</sup>Deviation of Bond lengths ( $\Delta\text{R}$ , Å).

<sup>c</sup>Nucleus-Independent Chemical Shifts (NICS, ppm), Functional: B3LYP, Base set: 6-311G\*\*.

<sup>d</sup>Nucleus-Independent Chemical Shifts (NICS, ppm), Functional B3LYP, Base set LANL2DZ with Huzinaga polarization.



**Fig. 6** Averaged relative energy per EH unit  $\Delta E/n$  against number of cluster atoms  $n$  in  $[E_nH_n]^{2-}$ . Linti, G.; Bühler, M.; Monakhov, K.; Zessin, T in: Comba, P. (ed.), *Modeling of Molecular Properties*, 2011, p. 455; Copyright Wiley-VCH Verlag GmbH & Co. KGaA. Reproduced with permission.



**Fig. 7** NICS values in cluster center of  $E_4H_4$  and *closo*-clusters  $[E_nH_n]^{2-}$  ( $E = B, Al, Ga, In; n = 5-9$ ) (B3LYP-functional, 6-311G\*\* base for B, Al, Ga; [a] NICS values from lit.<sup>380</sup> for *closo*-boranates  $[B_nH_n]^{2-}$  ( $n = 5-9$ ); [b] LANL2DZ base with Huzinaga polarization for Ga, In). Linti, G.; Bühler, M.; Monakhov, K.; Zessin, T. in: Comba, P. (Ed.), *Modeling of Molecular Properties*, p. 455, 2011; Copyright Wiley-VCH Verlag GmbH & Co. KGaA. Reproduced with permission.

geometrical, energetic and magnetic criteria *closo*-cluster compounds  $[E_5H_5]^{2-}$  ( $E = B, Al, Ga, In$ ) are non-aromatic. This is a possible explanation for the absence of this type of cluster. Only derivatives<sup>349,373,398,399</sup> like, for example, carbaboranes and a silagallanate  $130^{233}$  are known.

All higher clusters have negative NICS values for all elements examined. For octahedral boron, aluminum and gallium clusters the NICS values are most negative, for indium the octanuclear cluster is the extreme.





## 1.17.4 Element-Rich Cluster Compounds

### 1.17.4.1 Introduction

Reactions of triel subhalides, i.e.  $\text{Ga}_2\text{X}_4 \cdot 2\text{dioxane}$ , “GaI,” metastable EX solutions ( $E = \text{Al, Ga}$ ),  $\text{InX}$  often proceed with redox disproportionation. Thus, compounds with triel atoms in oxidation state +III and elemental triels  $E^0$  result. But the latter is not a necessity. It was observed that  $E^0$  can be incorporated in ER cluster frameworks to produce element rich clusters  $[\text{E}_m\text{R}_n]^{x-}$  ( $m > n$ ;  $x = 0, -1, \dots$ ). For those clusters, where naked triel atoms are bonded only to other triel atoms, the term metalloid was created.<sup>4–7</sup> More specifically metalloid means here, that the triel cores of the clusters resemble sections of structural features of the elements. But this is not necessarily the case for all element rich clusters, described in this section. For example, clusters of type  $[\text{Ga}_9\text{R}_6]^-$  and  $\text{Ga}_{10}\text{R}_6$  are element rich but their structure can be described on basis of polyhedral descriptions, while a  $\text{Al}_7\text{R}_6$  built from two fused tetrahedral was discussed as section of a close packed structure. This also shows that a definition of metalloid is not sharp and cannot generally be related to special bonding situations. We will use the term element rich as the more general one, and will confine metalloid to those clusters, where element structure relationships are obvious.

Mixed oxidation states are assigned to the building metal atoms in these cluster types. They average to values  $0 < X < 1$ . This makes them different from polyhedral clusters  $[\text{E}_n\text{R}_m]^{x-}$  ( $m \geq n$ ), where the Wade rules are valid and can be used for structure elucidation by electron bookkeeping.

For element rich or metalloid clusters, they often fail, or the counting has to be modified. Special types of cluster compounds are naked metal clusters, prepared and observed in gasphase. For example, mass spectrometry revealed special stability of sodium clusters of defined size. The so called Jellium model was used to explain stability islands of clusters with 8, 20, 40, 58 and 70 electrons.<sup>400–402</sup> We will not discuss such pure metal clusters here, but for some metalloid clusters this model was successfully applied.

Most of the clusters described in this section are nanoscaled cluster molecules and some of them have fascinating properties. Beginning from  $\text{Ga}_{26}$  clusters the crystals are metallic lustrous and for a  $\text{Ga}_{84}$  cluster crystals are superconducting at low temperatures. Nevertheless, the complicated synthesis and in many cases the sensitivity against air and moisture give them drawbacks compared to noble metal clusters and salt like clusters, which are sections of semiconductor material frameworks.

Preparation of these element-rich clusters starts from subhalides of the triels, normally. Monohalides are prepared by a combination of high temperature and cryo techniques. Aluminum or gallium are reacted with gaseous hydrogen halides  $\text{HX}$  ( $X = \text{Cl, Br, I}$ ) at 1100–1300 K in vacuo ( $10^{-1}$  mbar).<sup>7,12,77–79,270,403</sup> The resulting diatomic monohalides are trapped at low temperatures (100K) together with appropriate solvents, for example a toluene/thf mixture. This is done in a condensation apparatus, described elsewhere.<sup>7,12,78,79,270,403,404</sup> On warming up, metastable solutions of the monohalides are obtained, which can be stored at 195 K for months.

For gallium sonochemically initiated reaction with iodine (1:1 ratio) in toluene leads to “GaI,”<sup>191</sup> a greenish, amorphous substance, which reacts in many reactions as expected from a monohalide. Raman investigations revealed  $\text{Ga}_4\text{I}_6$  as one of the possible components (Fig. 8).<sup>405</sup> Further  $^{69/71}\text{Ga}$  solid-state NMR and  $^{127}\text{I}$  NQR experiments reveal additional insight of the composition of “GaI.” For which, the best representation would be  $[\text{Ga}^0]_2[\text{Ga}^+][\text{GaI}_4]^-$ .<sup>406</sup>

The behavior of “GaI” against donor solvents like thf is different to metastable GaI solutions, obtained via the high temperature route. It does not dissolve, but disproportionation occurs into gallium metal and gallium triiodide. With some donor molecules

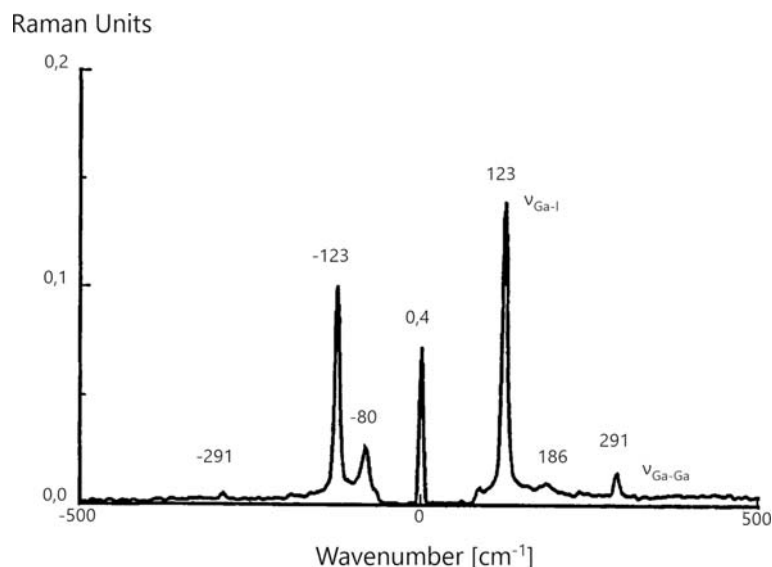


Fig. 8 FT-Raman spectrum of “GaI” showing characteristic bands for  $\text{Ga}_4\text{I}_6$ .<sup>405</sup>

intermediate oxidation states were trapped (for example: 26, 111). Alternatively "GaOSO<sub>2</sub>CF<sub>3</sub>," prepared from GaCp\* or GaCp and HOSO<sub>2</sub>CF<sub>3</sub>, was used in cluster synthesis.<sup>253</sup>

Indium halides often show disproportionation as preferred reaction pathway on attempted substitution reactions. Better results are obtained by use of InCp\* and reacting it with nucleophiles MR under elimination of MCp\* (M = Li, Na, K).

The chemistry of metalloidal aluminum and gallium clusters was reviewed several times (see for example<sup>9,10,12,302</sup>). Therefore, here a brief overview on structural variety and relationships between cluster types will be given, rather than a complete treatment on all details of synthesis and structures. Due to significant differences a separate description by the elements will be applied.

#### 1.17.4.2 Aluminum cluster compounds

Cluster sizes range from Al<sub>7</sub> to Al<sub>77</sub> (Fig. 9). [Al<sub>7</sub>R<sub>6</sub>]<sup>−</sup> 204 (R = N(SiMe<sub>3</sub>)<sub>2</sub>) consists of two corner sharing aluminum tetrahedral, with staggered orientation of the two Al<sub>3</sub>R<sub>3</sub> rings.<sup>6</sup> The Al–Al distances are about 260 pm in the Al<sub>3</sub>R<sub>3</sub> rings and up to 20 pm longer for the other distances. Therefore, an ionic description consisting of two metalloaromatic [Al<sub>3</sub>R<sub>3</sub>]<sup>2−</sup> rings coordinating a central cation Al<sup>3+</sup> was suggested, but is not consistent with results of DFT calculations, which predict no significant charge differences on the aluminum atoms. The Al<sub>7</sub> core of 204 is viewed upon as a section of a close packed aluminum structure, where six neighbors of the central aluminum atom are missing.

[Al<sub>12</sub>R<sub>8</sub>]<sup>−</sup> 205 [R = N(SiMe<sub>3</sub>)<sub>2</sub>] represents a larger section of the close packing of elemental aluminum.<sup>407</sup> Topologically, it can be described as reduced dimer of two distorted octahedral Al<sub>6</sub>R<sub>4</sub> fragments, where dimerization occurs through linkage of octahedral faces. This results in a cluster core of three penetrating octahedral and allows description as *conjuncto*-alane.

A similar structure is observed for In<sub>12</sub>(Si<sup>t</sup>Bu<sub>3</sub>)<sub>8</sub> 206, obtained by thermolysis of In<sub>2</sub>(Si<sup>t</sup>Bu<sub>3</sub>)<sub>4</sub>.<sup>408</sup> The *conjuncto*-cluster description is also in accordance with a postulated pathway of formation, starting from In<sub>2</sub>(Si<sup>t</sup>Bu<sub>3</sub>)<sub>4</sub>, which might proceed via In<sub>6</sub>(Si<sup>t</sup>Bu<sub>3</sub>)<sub>4</sub> with elimination of (Si<sup>t</sup>Bu<sub>3</sub>)<sub>2</sub>.

For the aluminum cluster the formation is thought to be a growth process initiated by disproportionation and the clusters are intermediates on the way to the metal. But both ideas need not to be exclusive. Thus, description of 205 and 206 as metalloidal clusters and as *conjuncto*-clusters, in analogy to *conjuncto*-boranes, is possible. The application and limits of electron counting rules will be discussed later in this chapter.

An even larger cluster, [Al<sub>14</sub>R<sub>6</sub>I<sub>6</sub>]<sup>2−</sup> 207 [R = N(SiMe<sub>3</sub>)<sub>2</sub>], has a skeleton of two staggered aluminum centered Al<sub>6</sub>-rings, where the ring aluminum atoms are bonded to iodine or N(SiMe<sub>3</sub>)<sub>2</sub> groups. The naked aluminum atoms are slightly above the planes of the rings. Thus, a flattened Al<sub>14</sub> polyhedron, a bicapped hexagonal antiprism, results. 207, by common counting rules, has eight skeletal electron pairs, which are necessary for a *closo*-cluster. A 14-vertex polyhedron, as bicapped hexagonal antiprism is observed for metallacarboranes, for example.<sup>409</sup> The flattening observed for 207 might be reasonable by partial participation of the aluminum lone pairs and formation of a bonding interaction between the apical aluminum atoms. Such a flattening was also discussed for certain indium and gallium clusters.<sup>410,411</sup> Thus, In<sub>11</sub><sup>7−</sup>, present in a Zintl phase, has three flattened vertices, which allows for 12 skeletal electron pairs, required for a *closo*-cluster. In line with this description are the results of quantum chemical calculations, which show a regular Al<sub>14</sub> polyhedron as energetically unfavorable.

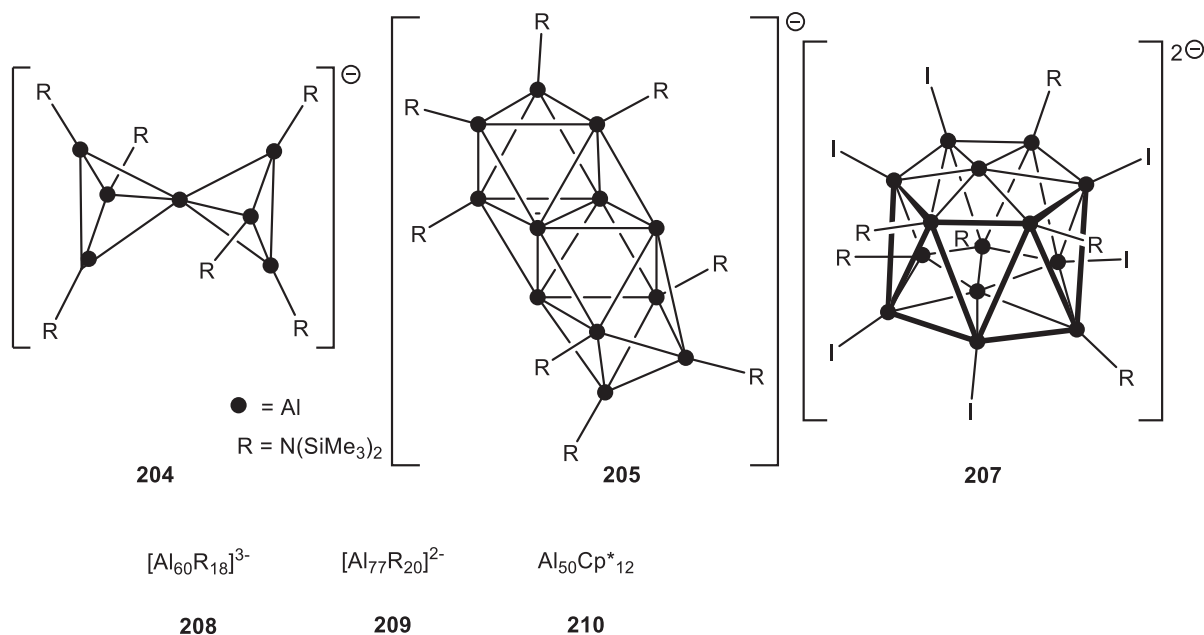
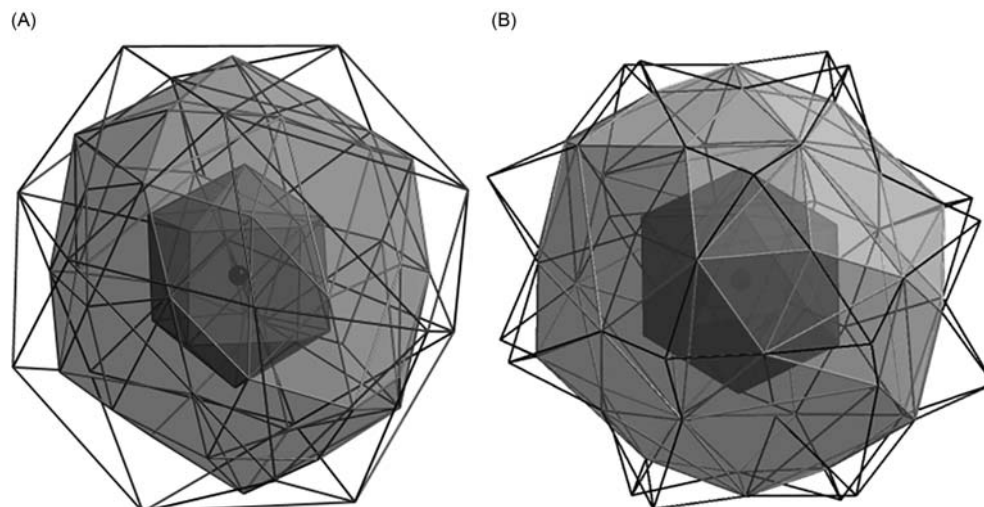


Fig. 9 Overview on element-rich aluminum cluster types.



**Fig. 10** Cluster cores of (A) **208** and (B) **209**. Dark grey: central  $\text{Al}@\text{Al}_{12}$  core; light grey: shell of 38 and 44 naked Al atoms, respectively; lines: Al  $[\text{N}(\text{SiMe}_3)_2]$  shell. Linti, G.; Schnöckel, H.; Uhl, W.; Wiberg, N. In *Molecular Clusters of the Main Group Elements*; Driess, M., Nöth, H., Eds., 2004, p 126–168. Wiley-VCH: Weinheim, 2004, Copyright Wiley-VCH Verlag GmbH & Co. KGaA. Reproduced with permission.

On the other hand, **207** is described as a typical metalloid cluster, because the core structure of two centered  $\text{Al}_6$  rings can be transformed by rotation and a translational shift into a section of the structure of metallic aluminum.

With  $\text{R} = \text{N}(\text{SiMe}_3)_2$  as substituent the largest aluminum clusters have been obtained (**Fig. 10**). Cores of 69 (**208**) and 77 (**209**) aluminum atoms are surrounded by 18 or 20 R-groups, respectively.<sup>412,413</sup> Both clusters are built up in shells, where a central aluminum atom is surrounded by 12 atoms, as inner building unit. These  $\text{Al}@\text{Al}_{12}$  ( $\text{Al}_{13}$ ) cores are center of two more shells of aluminum atoms, 38 atom and 18 atom shells in **208** and a 44 atom and outer 20 atom shell in **209**. The aluminum atoms of the outer shells are bonded to terminal R groups, each. According to this, the aluminum-aluminum distances decrease from the inner ( $d_{\text{Al-Al}} = 278$  pm on an average) to the outer shells ( $d_{\text{Al-Al}} = 268$  pm on an average), indicating transition from a metal-type bond to more localized bonding modes between the aluminum atoms. The distances of the central Al atom to the surrounding 12 Al atoms are nearly identical to those in the shell. The  $\text{Al}_{13}$  cores are different for **208** and **209**. The  $\text{Al}_{69}$  cluster has a distorted decahedral core,<sup>414</sup> based upon a  $\text{D}_{5h}$  symmetric structure, whereas in the  $\text{Al}_{77}$  cluster the  $\text{Al}_{13}$  core is nearly icosahedral.

These huge main group clusters often are compared to noble metal clusters compounds like  $\text{Au}_{55}(\text{PPh}_3)_{12}\text{Cl}_6$ <sup>415</sup> or  $\text{Pd}_{145}(\text{CO})_{60}(\text{PR}_3)_{30}$ .<sup>416</sup> For the gold cluster a central  $\text{Au}_{13}$  core with either an icosahedral or cuboctahedral structure was postulated. No crystal structure is available, up to now. 37 naked gold atoms are present. In the larger, structurally characterized  $\text{Au}_{102}$  cluster 39 naked gold atoms form the cluster core.<sup>417</sup> The  $\text{Pd}_{145}$  cluster has an filled icosahedral  $\text{Pd}@\text{Pd}_{12}$  core, where the distances of the central palladium atom to the shell are shorter than those in the shell. Obviously, the structures of the cores of these clusters ( $\text{Al}_{69}$ ,  $\text{Al}_{77}$ ,  $\text{Pd}_{145}$ ) deviate from those of the bulk metals. On the one hand the distances between the metal atoms are different and on the other hand the normal cuboctahedral environment of atoms in a close cubic packing is not exactly realized in the clusters. Nevertheless, the term metalloid is useful in this case of cluster compounds, making clear, that small metal particles are embedded in a shell of ligands. The type of ligands has obviously influence on details of the structures like inter atom distances.

The central  $\text{M}_{13}$  cores of these clusters resemble a naked  $\text{Al}_{13}$  cluster ion, prepared in a mass spectrometer. Its chemistry has been studied in gas phase.<sup>417–422</sup> Especially its reactions with HI and  $\text{I}_2$  gave rise to name this  $\text{Al}_{13}$  cluster ion as superhalide, which should not be confused with the classic pseudo halides. This  $\text{Al}_{13}$  ion has an icosahedral structure, according to quantum chemical calculations. Electron counting results in 40 electrons for this cluster, which is in accordance with the Jellium model (see above).

Isolation of **210** demonstrates that stabilization of large aluminum clusters is not confined to hexamethylsilazano substituents. This  $\text{Al}_{50}\text{Cp}^*_{12}$  cluster<sup>403,423</sup> is built around a central square antiprismatic  $\text{Al}_8$  unit ( $d_{\text{Al-Al}} = 266$  pm). This resembles structures found for  $[\text{Ga}_8\text{fluorenyl}_8]^{2-}$  **197b** and  $[\text{In}_8(\text{SiPh}_3)_8]^{2-}$  **198b**. This core is surrounded by a shell of 30 aluminum atoms ( $d_{\text{Al-Al}} = 281$  pm), which are arranged in an icosidodecahedron with 12 pentagonal and 20 trigonal faces. The pentagonal faces are capped by 12  $\text{AlCp}^*$  groups, where the 12 aluminum atoms are arranged icosahedrally ( $d_{\text{Al-Al}} = 570$  pm). The 60 methyl groups of the  $\text{Cp}^*$  rings are arranged in a five-fold symmetric manner, with distances between the methyl groups governed by van der Waals contacts between them. An intriguing idea is, that these 12  $\text{AlCp}^*$  groups form a sort of bag with a defined volume, where the remaining 38 aluminum atoms are filled in.

Model calculations on DFT level suggest a stabilization of approximately  $11,000 \text{ kJ mol}^{-1}$  for a reaction of 38 aluminum atoms in gas phase with 12  $\text{AlCp}^*$  groups. This cluster **210** with its shell of 60 carbon atoms and 60 methyl groups has a volume five times larger than  $\text{C}_{60}$  fullerene.

A further explanation for the stability of this cluster can be made with the so-called superatom complex model for ligand protected metal clusters.<sup>424–426</sup> Within this model the  $\text{Al}_{50}$  cluster core of **210** is viewed as gigantic atom (“superatom”) separated from

its exterior ligands. With three valence electrons for each Al atom minus 12 electrons for bonding the Cp\* ligands this sums up to 138 free s and p electrons for this superatom. These electrons fill shells of increasing angular momentum of a spherical system in following order:

$$1S^2 1P^6 1D^{10} 2S^2 1F^{14} 2P^6 1G^{18} 2D^{10} 1H^{22} 3S^2 2F^{14} 3P^6 1I^{26}$$

138 electrons are therefore a *magic* number, filling all shells up to  $1I^{26}$  ( $L = 6$ ) as set of highest occupied orbitals.

Three aluminum clusters are described, having not aluminum but a silicon atom as central atom. These clusters 211–213 are obtained from metastable AlX solutions and  $\text{SiCp}^*_2$  or  $\text{SiCl}_4/\text{AlCp}^*$  for 211<sup>427</sup> and  $\text{LiN}(\text{dipp})\text{SiMe}_3$  for 212<sup>428</sup> and 213.<sup>429</sup> As silicon source for the latter, decomposition of the amide  $\text{LiN}(\text{dipp})\text{SiMe}_3$  was claimed. For the  $\text{SiAl}_{14}\text{R}_6$  compounds 211 and 212 the structure is described as a body centered  $\text{Si@Al}_8$  cube, where six AlR groups are capping the faces of the cube.  $\text{SiAl}_5\text{R}_{12}$  has a shell structure consisting of a central  $\text{Si@Al}_{44}$  core capped by 12 AlR groups. The problems of assigning the correct stoichiometry by X-ray crystal structure analysis for those compounds is apparent from FT mass spectrometric analysis using MALDI of 211. These investigations show  $\text{Si}_2\text{Al}_{13}\text{Cp}_6\text{Cl}$  as additional cluster, present to approximately one third in the crystals of 211.

### 1.17.4.3 Gallium cluster compounds

For gallium an even larger variety of element rich or metalloid clusters is known than for aluminum (Fig. 11). We will see that similar principles of understanding the structures, either deriving the cluster structures from polyhedral assemblies or describing them as metalloid, are useful. Gallium seems to be special in providing several element modifications with a diversity of structural motifs. These range from digallium units in  $\alpha$ -gallium over icosahedral substructures in  $\delta$ -gallium to nearly close-packed structures in high pressure modifications gallium-III and -IV.<sup>302,430</sup> We will discuss the clusters in order of increasing numbers of gallium atoms.

#### 1.17.4.3.1 $\text{Ga}_8$ , $\text{Ga}_9$ and $\text{Ga}_{10}$ clusters

$\text{Ga}_8\text{R}_6$  is the general formula for element rich octagallium clusters. 214 ( $\text{R} = \text{C}(\text{SiMe}_3)_3$ ) is obtained from metastable GaBr solutions and  $\text{LiC}(\text{SiMe}_3)_3$ . Molecules of 214 consist of two  $\text{R}_3\text{Ga}_4$  tetrahedra linked by a gallium-gallium bond ( $d_{\text{Ga-Ga}} = 261.4$  pm).<sup>431</sup> Similarly, as for  $\text{Al}_7\text{R}_6$ , an ionic complex involving aromatic  $[\text{Ga}_3\text{R}_3]^{2-}$  rings and a  $\text{Ga}_2^{4+}$  cation might be discussed. But, two tetrahedra with four skeletal electron pairs, each (see Section 1.17.3.1), with MOs of types  $a_{1g}$  and  $t_{2u}$  seem more reasonable. The other Ga–Ga distances are in the range of 260.5–264.8 pm. This is shorter than in 176 ( $d_{\text{Ga-Ga}} = 268.8$  pm). This can be explained by less steric strain in substituting one  $\text{C}(\text{SiMe}_3)_3$  group in 176 for a  $\text{Ga}_4[\text{C}(\text{SiMe}_3)_3]_3$  residue. With this structural change the color varies from red for 176 to black for 214. This shift is in line with a change in the energetic level of HOMO and LUMO, which is sensitive to the electronegativity of the substituents and the Ga–Ga distances (Section 1.17.3.1). It was also discussed, that this is a hint for a metalloid character of 214. Here, the  $\text{Ga}_2$  unit in the center is a section of  $\alpha$ -gallium, where each of the gallium atoms is bonded to other gallium atoms only. Thus, 214 with all gallium atoms in formal oxidation state +I differs from digallanes  $\text{R}_4\text{Ga}_2$ , where three- or four-coordinate gallium(II) atoms are connected to heteroatoms. The situation that gallium atoms of a digallane are part of a cluster is also realized in the carborane substituted digallane 82. Here, an extremely short gallium-gallium bond is observed; a fact which can be explained by steric arguments. In addition, model calculations on analogs to 214 with less bulky substituents indicated short gallium-gallium bonds.<sup>431</sup> Thus, 214 can be regarded as molecule of fundamental interest, because it includes a pure metal-metal bond, free of influences of directly bonded substituents.

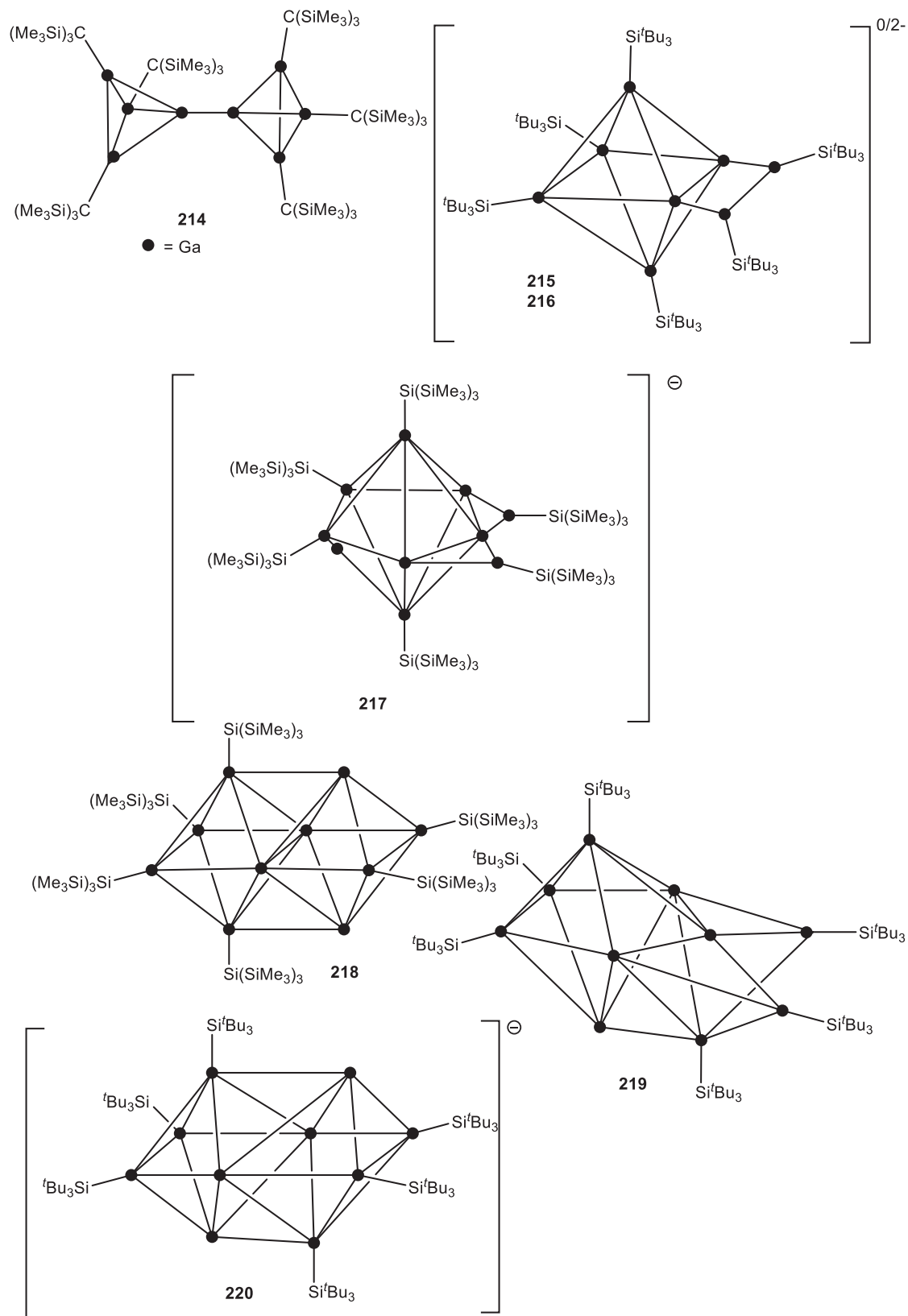
An isomer 215 ( $\text{R} = \text{Si}^t\text{Bu}_3$ ) is obtained by thermolysis of the cyclic trigallane  $[\text{R}_4\text{Ga}_3]\bullet$  in heptane together with  $[\text{Ga}_2\text{R}_3]\bullet$  and  $\text{Ga}_4\text{R}_4$ .<sup>432</sup> The structure of 215 is completely different from 214 and the octagallium cluster 197b. It has a distorted octahedral  $\text{R}_4\text{Ga}_6$  core with an  $\text{RGa-GaR}$  unit attached to two neighboring gallium atoms.

Therefore, looking upon the  $\text{RGa-GaR}$  substituent as a two-electron donating one, cluster 215 has six skeletal electron pairs. This means 215 is a *preclso*-cluster for which a face capped trigonal bipyramid is expected. Here an alternative distortion of the octahedron into a trigonal bipyramid with one edge bridged by an  $\text{RGa}$  unit is realized. The gallium-gallium distances along the edges cover a range from 251.9 to 292.5 pm. The distances of the  $\text{RGa-GaR}$  unit to the cluster core atoms are relatively short (240.6, 244.6 pm). The  $\text{RGa-GaR}$  bond length ( $d_{\text{Ga-Ga}} = 251.9$  pm) is in the typical range for silyl substituted digallanes. 215 can easily be reduced to the dianionic cluster  $[\text{R}_6\text{Ga}_8]^{2-}$  216, where the arrangement of the gallium atoms is nearly the same as in 215, with the octahedron being more regular ( $d_{\text{Ga-Ga}} = 255.1$ – $268.5.9$  pm). The bonds of the  $\text{RGa-GaR}$  substituent get longer on reduction ( $d_{\text{Ga-Ga}} = 245.3, 246.6, 253.5$  pm, respectively). This is in line with 216 having seven skeletal electron pairs, as required for a *clso*-cluster. A similar relation between an octahedral *clso*- and a distorted octahedral *preclso*-cluster is known for 194a and 195. The sodium atoms are attached to the dianionic cluster core bridging two gallium-gallium edges neighboring the  $\text{RGa-GaR}$  unit ( $d_{\text{Ga-Na}} = 300$  pm). This indicates, similar to the metalloaromatic rings 131, that the sodium atoms might be regarded as part of the cluster.

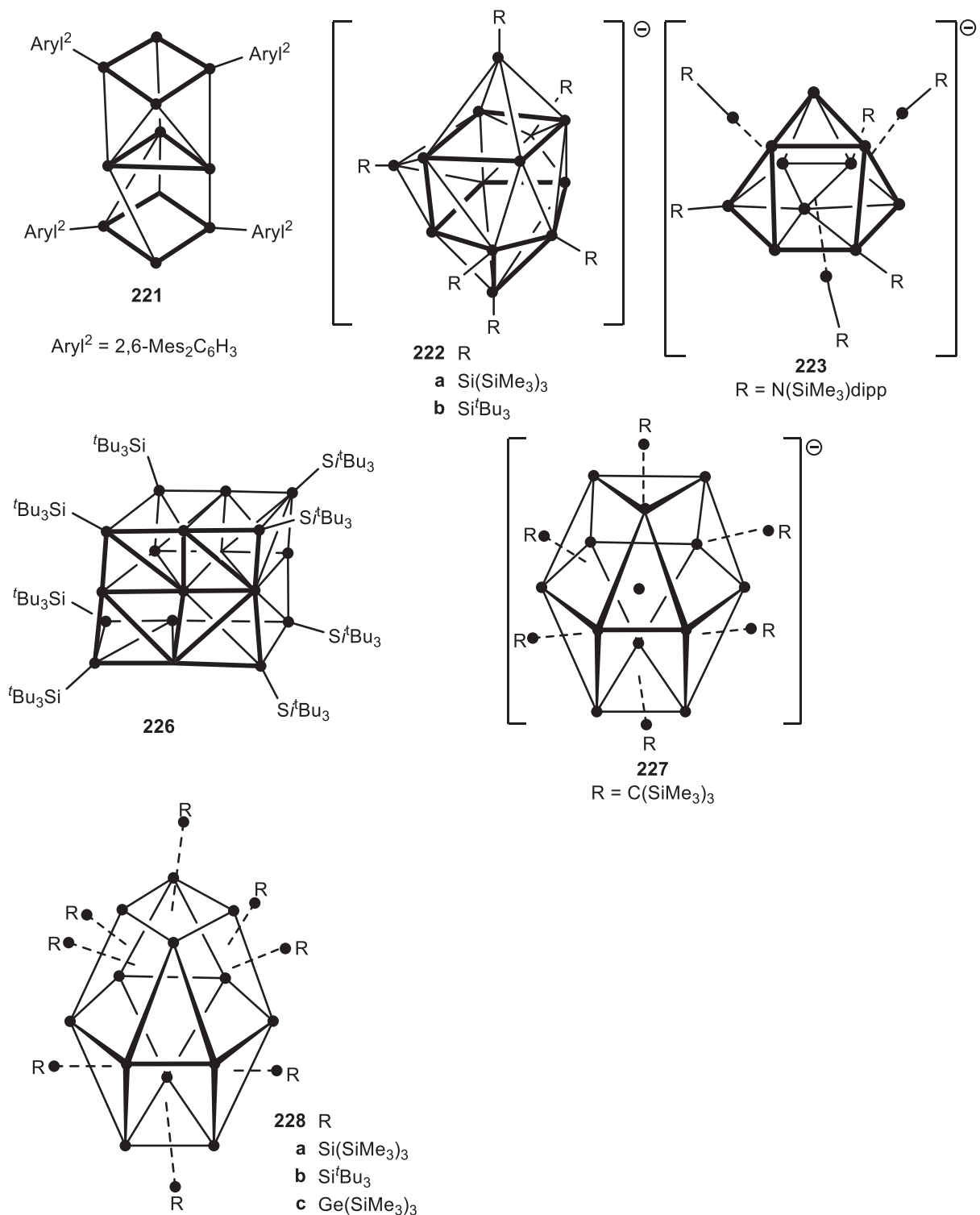
One might ask at this point, whether those element rich cluster compounds are metalloid. 215 as well as 216 show a planar  $\text{Ga}_6\text{R}_4$  arrangement as feature of their cluster cores, where two GaR residues are attached from top and bottom. Thus some resemblance to  $[\text{Ga}_6\text{R}_8]^{2-}$  154 exists, whose core can be related to gallium atom sheets in  $\beta$ -gallium.<sup>267</sup>

Later on, we will see that an  $\text{In}_8\text{R}_6$  cluster adopts a totally different structure.<sup>433</sup>





**Fig. 11** Overview on types of element rich gallium clusters (Ga<sub>8</sub> to Ga<sub>22</sub>).



**Fig. 11** (continued).

Using "GaI" as source for gallium in low oxidation state several gallium rich cluster compounds can be obtained. Due to the insolubility of "GaI" variation of reaction conditions cannot be done by changing the concentration of the gallium source. But a possible tool is to change the ratio of gallium to iodine in preparation of "GaI," which in principle can be from 2:1 to 1:3, meaning formally "Ga<sub>2</sub>I" and GaI<sub>3</sub> as products. For cluster synthesis reaction mixtures 2:1 up to 1:1.5 are useful. These gallium subiodides are then treated in a heterogeneous reaction in toluene with a slight excess of the metallated substituent MR (M = Li, Na, K).

One of the products is  $[\text{Li}(\text{thf})_4]^+[\text{Ga}_9\text{R}_6]^-$  ( $\text{R} = \text{Si}(\text{SiMe}_3)_3$ ) **217**.<sup>263</sup> A pentagonal bipyramid with two RGa groups in apical and two RGa groups and three naked gallium atoms in equatorial positions make up the cluster core ( $d_{\text{Ga-Ga}} = 242.5$  and  $289.8$  pm). The two gallium-gallium bonds of the  $\text{Ga}_3$  unit of naked gallium atoms are bridged by RGa groups ( $d_{\text{Ga-Ga}} = 234.4$  and  $237.7$  pm). Considering these bridging RGa groups as two-electron substituents, meaning the cluster is built up from four RGa and a  $(\text{RGa})_2\text{Ga}_3$  unit, delivering two and seven electrons, each, leaves a  $\text{Ga}_7$  cluster with eight skeletal electron pairs, classifying it as *closo*-cluster. Alternatively, if all nine gallium atoms are considered as cluster atoms, these eight skeletal electron pairs for a nine-vertex cluster stand for a bicapped pentagonal bipyramid. The capping in this case is restricted to bridging two edges. This might be due to steric requirements of the bulky silyl groups. This distinction seems to be a semantic one, leading to the same result, which is on the basis of a MO description of the cluster eight bonding molecular orbitals for the cluster core.

**217** is structurally closely related to the octagallium clusters **215** and **216**. Formally, regardless the different substituents, addition of a  $\text{Ga}^+$  cation to the RGa-GaR bridge in **216** widens up the  $\text{Ga}_6$  plane to a  $\text{Ga}_7$  plane (Scheme 7).

Further incorporation of a  $\text{Ga}^+$  cation into **217** produces the decagallium clusters **218** and **219**.<sup>340</sup> Attack of the gallium cation at the central atom of the naked  $\text{Ga}_3$  unit leads to cluster **218**. Here the gallium atom marked  $\text{Ga}^*$  moves out of the original  $\text{Ga}_7$  plane. If the gallium cation attacks via a  $\text{Ga}_3\text{R}_3$  face of **217** one of the original RGa groups moves toward the  $\text{Ga}^*$  atoms forming cluster **219**.

**218** is built from two fused octahedra, meaning a  $\text{R}_4\text{Ga}_6$  and a  $\text{R}_2\text{Ga}_6$  cluster fragment fuse via a common edge ( $d_{\text{Ga-Ga}} = 298.3$  pm), which is the longest of all neighboring gallium atoms in this cluster. On the other hand, the tops of the octahedra have short distances ( $d_{\text{RGa-Ga}} = 254$  pm). The other gallium-gallium bond lengths in **218** range from 258 to 279 pm. This is in the same range as observed in gallium modifications.

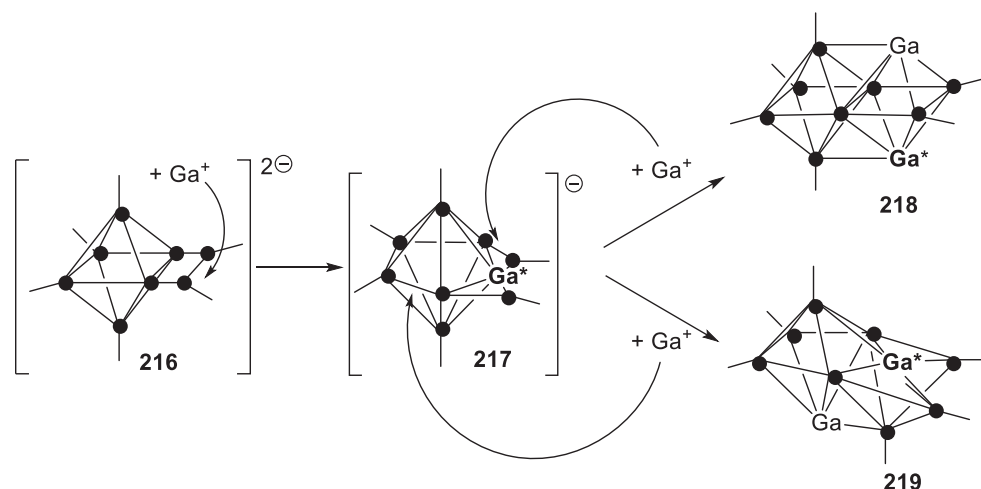
As indicated, only six gallium atoms bear  $\text{Si}(\text{SiMe}_3)_3$  groups, four of them in the  $\text{Ga}_6$  base plane of the cluster. One of the octahedra carries four bulky substituents and the other one only two. The gallium-silicon bond lengths are influenced by this imbalance of crowding in the molecule. Longer gallium-silicon bonds ( $d_{\text{Ga-Si}} = 244.3$ – $246.8$  pm) are found in the sterically more strained part of the molecule, than in the other ( $d_{\text{Ga-Si}} = 240.5$  pm). Also, the average gallium-gallium distances in the  $\text{Ga}_6\text{R}_4$  part of the molecule are 4.6 pm longer than in the  $\text{Ga}_6\text{R}_2$  part. At first glance, the seemingly unfavorable distribution of the substituents in **218** is surprising, but in line with a proposed formation (Scheme 7).

**219**, which is obtained co-crystallized with the tetragallane **180**, has a more unusual structure. The core of **219** is a flat pentagonal bipyramid of gallium atoms. Three RGa groups ( $\text{R} = \text{Si}^t\text{Bu}_3$ ) form one of the trigonal faces, the other four core atoms are naked gallium atoms.

The equatorial plane has three rather short ( $d_{\text{Ga-Ga}} = 253.1$ – $256.9$  pm) and two long Ga–Ga distances ( $d_{\text{Ga-Ga}} = 284.0$ ,  $306.0$  pm), which are bridged by gallium atoms ( $d_{\text{Ga-Ga}} = 244.1$ – $253.3$  pm). One of the bridging gallium atoms is part of a RGa group, the other of a RGa-GaR unit ( $d_{\text{Ga-Ga}} = 246.6$  pm). This broad distribution of Ga–Ga distances is typical for gallium rich cluster compounds. The Ga–Si distances also vary over a broad range. The gallium-silicon bonds ( $d_{\text{Ga-Si}} = 240.9$ – $245.5$  pm) to the bridging gallium atoms are shorter than the gallium-silicon bonds of the bipyramidal core atoms ( $d_{\text{Ga-Si}} = 246.9$ – $250.2$  pm), but comparable to those in **218**.

Alternatively, **219** is described as fused cluster of a  $\text{Ga}_8$  and a  $\text{Ga}_4$  polyhedron, sharing a  $\text{Ga}_3\text{R}$  face. DFT calculations, which indicate a large three-center bonding contribution for the Ga–Ga(R)–Ga bridge, support a description of the cluster as a bridged pentagonal bipyramid.

The bipyramid is quite flat, as noted. The Ga–Ga distance ( $d_{\text{Ga-Ga}} = 295.3$  pm) between the apical atoms, an RGa and a naked gallium atom, is similar to the lengths of edges in this cluster. For comparison, the assumed parent cluster of type **217** has a height of



Scheme 7 Cluster relations of **216**–**219**.

344 pm. This hints to an additional interaction between the apical gallium atoms, which is consistent with the results of DFT calculations.

This brings us to the point, where we have to discuss electron counting for clusters **218** and **219**.

If **218** is looked upon as *conjuncto*-cluster of two octahedra the Jemmis rules,<sup>368,369,434</sup> developed for *conjuncto*-boranes on basis of the Wade rules, might be applicable.<sup>378,435</sup> Here, for a *conjuncto*-cluster of  $m$  fused polyhedral ( $2n + 2m$ ) skeletal electrons ( $n$ : number of cluster atoms,  $m$ : number of polyhedral) are necessary. Therefore, **218** would need 24 electrons to fill the bonding cluster molecular orbitals. Six RGa groups mean 12 electrons and so the four naked gallium atoms have to contribute three electrons, each. This is not unambiguous, because quantum chemical calculations for **218** suggest lone pairs at the apical, naked gallium atoms.<sup>340</sup>

For **219** the short distance between the apical gallium atoms through the cluster make it plausible, that the bare vertex atom contributes not only one, but three electrons and four orbitals to the cluster bonding. This should also be the case for two of the other naked gallium. That makes 11 skeletal electron pairs for **219**, as required for a fused polyhedron of a Ga<sub>8</sub> (nine sep) and a Ga<sub>4</sub> (four sep) polyhedron.

The structures and electron count in bare indium clusters in Zintl phases have been discussed similarly. The flattening of vertices is deduced as a result of the contribution of four orbitals to cluster bonding by some of the vertex atoms.<sup>436,437</sup> Thus, In<sub>11</sub><sup>7-</sup>, has three flattened vertices, which results in 12 skeletal electron pairs, required for a *closo*-E<sub>11</sub>-cluster, if some indium atoms contribute more than one electron to cluster bonding.<sup>410</sup>

Obviously, counting rules only roughly give explanations for the structure of these hypoelectronic clusters but are near their limits. Therefore, a forecast of structures on this basis is not possible at all.

A third Ga<sub>10</sub> cluster is [Ga<sub>10</sub>R<sub>6</sub>]<sup>-</sup> (R = Si<sup>t</sup>Bu<sub>3</sub>) **220**, isolated as black crystals together with a Ga<sub>13</sub> cluster **222b**. Counterion is [Na(thf)<sub>6</sub>]<sup>+</sup>. The six GaR groups are distributed more regularly over the cluster and form a trigonal prism, elongated along the C<sub>3</sub> axis. A four-membered ring of naked gallium atoms is embedded between the two Ga<sub>3</sub>R<sub>3</sub> rings. As a consequence of the C<sub>3</sub>/C<sub>4</sub> symmetry mismatch of the cluster building units, the four-membered ring is disordered over three equivalent positions. The range of gallium-gallium distances is similar to that in **218** ( $d_{\text{Ga-Ga}} = 245.3$  to 288.0 pm). This arrangement of three-membered rings and embedded triel fragments is also realized in **204** and **214**, which are prototypes of metalloid clusters.

Another view on the structure of **220** emphasizes the similarity to **218**. Here, shortening of the bridging edge and elongation of the distance of the tops of the fused octahedrons brings the structures together.

DFT calculations on isomers of Ga<sub>10</sub>(SiMe<sub>3</sub>)<sub>6</sub> revealed a structure analog to **218** as more stable by 56.6 kJ mol<sup>-1</sup> than a **219** based, one. On reduction both isomers undergo a structural change to that of type **220**.

#### 1.17.4.3.2 Ga<sub>11</sub> and Ga<sub>13</sub> clusters

Ga<sub>11</sub>Aryl<sub>2</sub><sup>4</sup> **221** with bulky aryl substituents consists of two Ga<sub>4</sub>R<sub>2</sub> rings interconnected by a Ga<sub>3</sub> unit.<sup>145</sup> The paramagnetic cluster was obtained from "Gal" and LiAryl<sup>2</sup> (Aryl<sup>2</sup> = 2,6-Mes<sub>2</sub>C<sub>6</sub>H<sub>3</sub>). The EPR spectrum of **221** confirmed a radical with one unpaired electron. The gallium-gallium distances in the four-membered ring part (255 pm) are shorter than in the Ga<sub>3</sub> unit (266 pm). It has to be noted, that [Ga<sub>4</sub>R<sub>2</sub>]<sup>2-</sup> and [Ga<sub>3</sub>R<sub>3</sub>]<sup>2-</sup> rings have been isolated and characterized as metalloaromatic with contacts to alkalimetal ions.<sup>145,234</sup> It might be considered, whether in **220** or **221** that the central Ga<sub>4</sub> or Ga<sub>3</sub> rings take the role of the cations. On the other hand, the structure of this Ga<sub>11</sub> cluster core has some resemblance to that of the metalloid cluster **205**.<sup>407</sup>

The Ga<sub>12</sub> cluster **160**, already mentioned, can be described by three nearly planar four-membered rings of gallium atoms, where eight of the 10 substituents (2 Br, 6 P<sup>t</sup>Bu<sub>2</sub>, 2 ylid ligands) are bonded to the outer rings. The connection to the central ring is made by gallium-gallium interactions and phosphide bridges. The Ga<sub>12</sub> core has some resemblance of the Ga<sub>11</sub> core of **221**.

The [Ga<sub>13</sub>R<sub>6</sub>]<sup>-</sup> cluster ions are obtained as alkali metal salts from "Gal" and MR (222a: M = Li, R = Si(SiMe<sub>3</sub>)<sub>3</sub>;<sup>438</sup> **222b**: M = Na, R = Si<sup>t</sup>Bu<sub>3</sub><sup>340</sup>). Here a pseudo cuboid core is present, where seven naked gallium atoms are at the corners of a cube, and the eighth corner is occupied by a Ga<sub>3</sub>R<sub>3</sub> ring. The three complete square faces of the cube are capped by RGa units. The structure has some features of that of the silicon centered Si@Al<sub>14</sub> clusters.

Another type of a [Ga<sub>13</sub>R<sub>6</sub>]<sup>-</sup> cluster **223** is obtained with an amido substituent (R = N(SiMe<sub>3</sub>)dipp).<sup>439</sup> The framework of **223** is comprised of two stapled R<sub>3</sub>Ga<sub>6</sub> rings, one of which is gallium centered. This means nine of these atoms form a part of a cuboctahedron, where one of the Ga<sub>3</sub> units is missing. The remaining three GaR groups cap the Ga<sub>4</sub> faces of the cuboctahedral core. This structural feature makes the metalloid character of **223** more obvious, than it is for the isomers **222**.

#### 1.17.4.3.3 Ga<sub>16</sub>, Ga<sub>18</sub> and Ga<sub>19</sub> clusters

In Ga<sub>16</sub>(P<sup>t</sup>Bu<sub>2</sub>)<sub>10</sub> **224** a totally different structural motif is present. In the clusters discussed, so far, often planar four-membered Ga<sub>4</sub> rings occurred. Here, in **224** a tetrahedral Ga<sub>4</sub> core is at the center of the structure, around which a Ga<sub>12</sub>(P<sup>t</sup>Bu<sub>2</sub>)<sub>10</sub> framework of phosphido bridged gallium atoms is built.<sup>440</sup> This framework can be described as based on an adamantoid Ga<sub>4</sub>P<sub>10</sub> cage.

[Ga<sub>18</sub>(P<sup>t</sup>Bu<sub>2</sub>)<sub>10</sub>]<sup>3-</sup> **225**<sup>272</sup> and the silyl substituted cluster [Ga<sub>18</sub>(Si<sup>t</sup>Bu<sub>3</sub>)<sub>8</sub>] **226**<sup>441</sup> are obtained from metastable GaBr solutions and LiP<sup>t</sup>Bu<sub>2</sub> or NaSi<sup>t</sup>Bu<sub>3</sub>, respectively. The structure of the metalloid core of **225** is compared to that of the high pressure gallium modification Ga-II, where the gallium atoms have coordination number 10 on an average.<sup>15,442</sup>

**226** has a core of three stapled Ga<sub>6</sub> layers, which resemble the Ga<sub>6</sub> core of **154**, each. Thus, the structure can be described a section of β-gallium.

[Ga<sub>19</sub>{C(SiMe<sub>3</sub>)<sub>3</sub>}]<sup>-</sup> **227** is a metalloid cluster with a central gallium atom surrounded by 12 other gallium atoms in a distorted cuboctahedral manner.<sup>5</sup> This typical structural feature of a cubic close packed metal is here packed into a shell of six GaC(SiMe<sub>3</sub>)<sub>3</sub> groups, which cap rectangular faces.

227 is prepared via metastable GaX solutions. The cluster is unique, because in contrast to most other gallium rich clusters it is soluble in organic solvents. Therefore, a  $^{71}\text{Ga}$  NMR spectrum could be measured. The shift for the central atom ( $\delta = -134$  ppm) is different from those calculated for naked gallium metal clusters and hints to a different electronic situation.<sup>443,444</sup> 227 is also special, because in mass spectrometric experiment (ESI, laser desorption/ionization) not only the molecule ion of this metalloid cluster can be detected, but collision induced the six GaR groups can degraded stepwise, resulting in a  $\text{Ga}_{13}^-$  ion.

This fragmentation by sequentially removing RGa units is confirming the point of view, that these carbenoid units are a protecting shell for the central  $\text{Ga}_{13}^-$  core. This is comparable to CO ligands shielding a metal cluster core in transition metal clusters. The analogy of GaR and CO is also discussed for [M]-GaR complexes.

This  $\text{Ga}_{13}^-$ -cluster ion was calculated to be very stable and the corresponding neutral  $\text{Ga}_{13}$  cluster has a very high electron affinity of 3.35 eV. This is similar to that of a fluorine atom and gives the terminology superhalide, which has been brought up for the  $\text{Al}_{13}^-$  cluster ion, some justification. It was noted that these results stand for the electron deficiency of metalloid clusters of aluminum and gallium and make them different from  $\text{Ga}_n$ -Zintl ions, which are of polyhedral type.<sup>445-448</sup>

#### 1.17.4.3.4 $\text{Ga}_{22}$ clusters

For  $\text{Ga}_8$ ,  $\text{Ga}_{10}$  and  $\text{Ga}_{13}$  clusters structural isomers for the cluster cores are observed. The same is true for  $\text{Ga}_{22}$  clusters 228–231.  $\text{Ga}_{22}\text{R}_8$  228a-c (R =  $\text{Si}(\text{SiMe}_3)_3$  a,<sup>172</sup>  $\text{Ge}(\text{SiMe}_3)_3$  b,<sup>320</sup>  $\text{Si}^t\text{Bu}_3$  c<sup>441</sup>) are prepared by reaction of metastable GaBr solutions (a, c) or "GaI" (b) with the metallated substituent R. All of the three clusters are isostructural (Fig. 12).  $\text{Ga}@_{13}$  cores ( $d_{\text{Ga-Ga}} = 287$  pm) are surrounded by eight GaR units, capping  $\text{Ga}_4$  faces ( $d_{\text{Ga-Ga}} = 267$  pm). The eight GaR units are at the corners of an Archimedes' antiprism with distances of approx. 500 pm between the gallium atoms. The  $\text{Ga}@_{13}$  core is a gallium centered, widened cuboctahedron, meaning one of the triangular faces is enlarged to a  $\text{Ga}_4$  ring. Thus a 4–6–3 polyhedron, with layers of  $\text{Ga}_4$ ,  $\text{Ga}_6$  and  $\text{Ga}_3$  rings is formed. Thus, somehow a metal packing is evident in this cluster core. Electron counting results in  $22 \times 3 - 8 \times 1 = 58$  electrons for these clusters, which is in accordance with the Jellium model.

Applying the classic counting scheme of the Wade rules the cluster is separated into a  $\text{Ga}_{14}$  core and eight GaR groups, which deliver 16 electrons for cluster bonding. Adding the 14 gallium atoms, counted as contributing one electron each, a total of 15 skeletal electron pairs results for the  $\text{Ga}_{14}$  core, making it a specially filled  $\text{Ga}_{13}$ -*closo*-polyhedron. This filled polyhedron might be due to the size of the cavity defined by the eight RGa residues.

Cluster 226 is regarded as section of  $\beta$ -gallium in metalloid terms. Similar, the  $\text{Ga}_{22}^-$  clusters 228 can be looked upon derived from gallium-III, with an additional atom in the coordination sphere of the central gallium atom (Fig. 13).

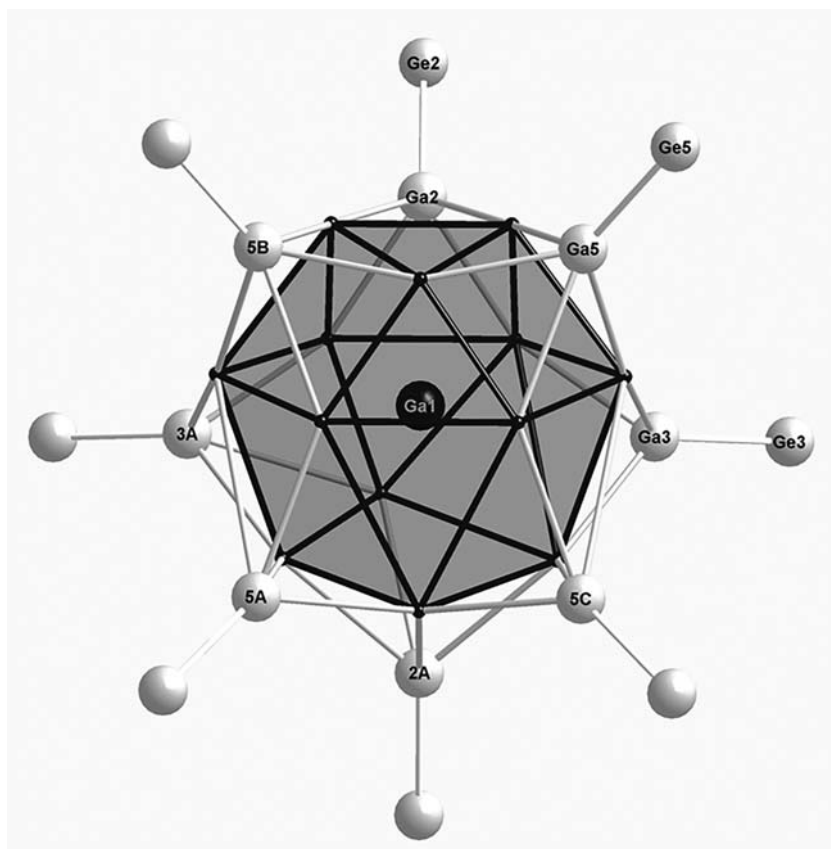
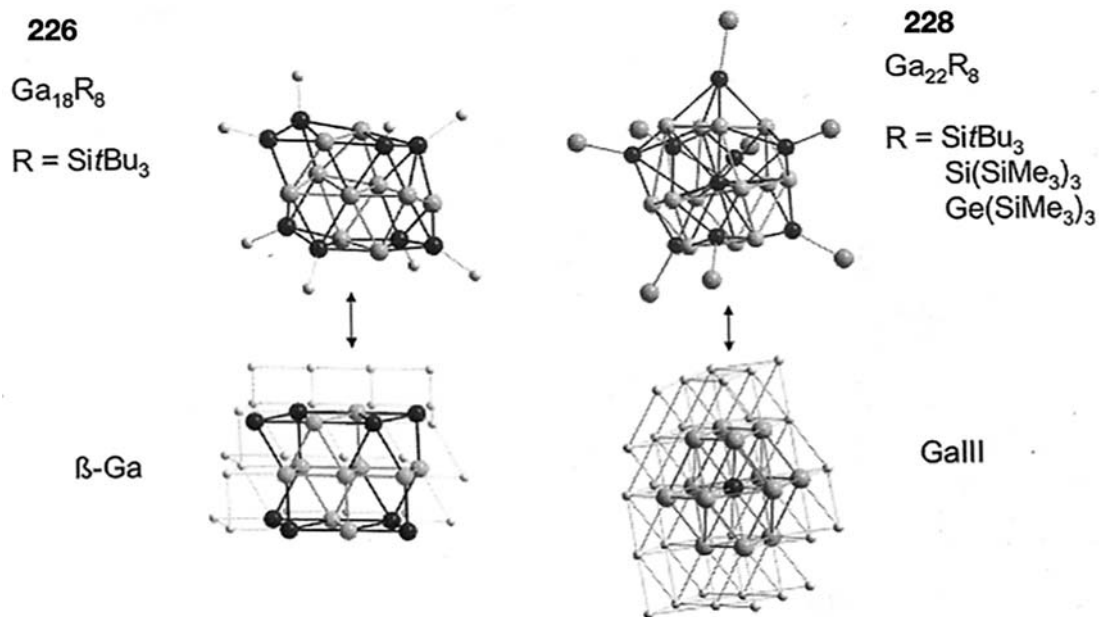
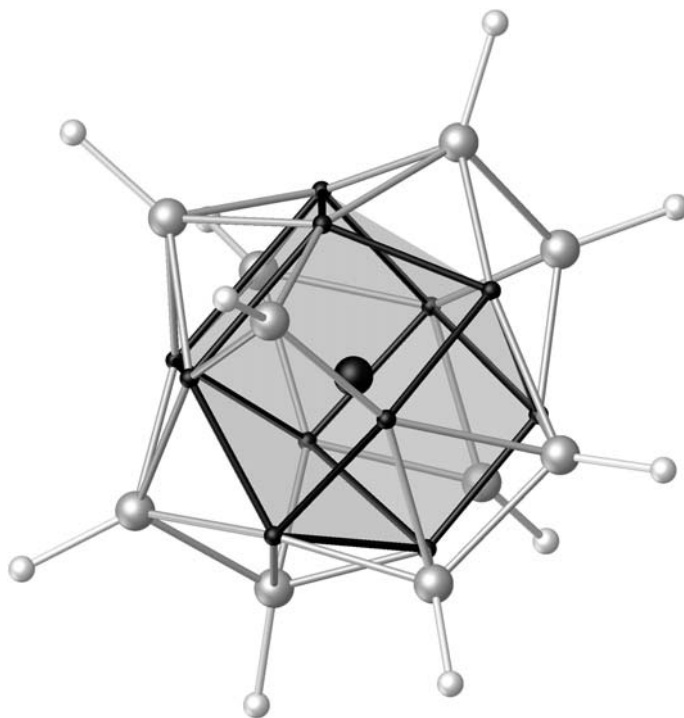


Fig. 12 View of  $\text{Ga}_{22}[\text{Ge}(\text{SiMe}_3)_3]_8$  228b (SiMe<sub>3</sub> groups omitted for clarity).





**Fig. 13** Relationships of clusters **226** and **228** to gallium modifications.<sup>302</sup> Linti, G.; Schnöckel, H.; Uhl, W.; Wiberg, N. In *Molecular Clusters of the Main Group Elements*; Driess, M., Nöth, H., Eds., 2004, p. 126–168. Wiley-VCH: Weinheim, 2004, Copyright Wiley-VCH Verlag GmbH & Co. KGaA. Reproduced with permission.



**Fig. 14** View of  $[\text{Ga}_{22}[\text{N}(\text{SiMe}_3)_2]_{10}]^{2-}$  anion **229** ( $\text{SiMe}_3$  groups omitted for clarity; Ga atoms: grey and black shade; N atoms: white).<sup>302</sup>

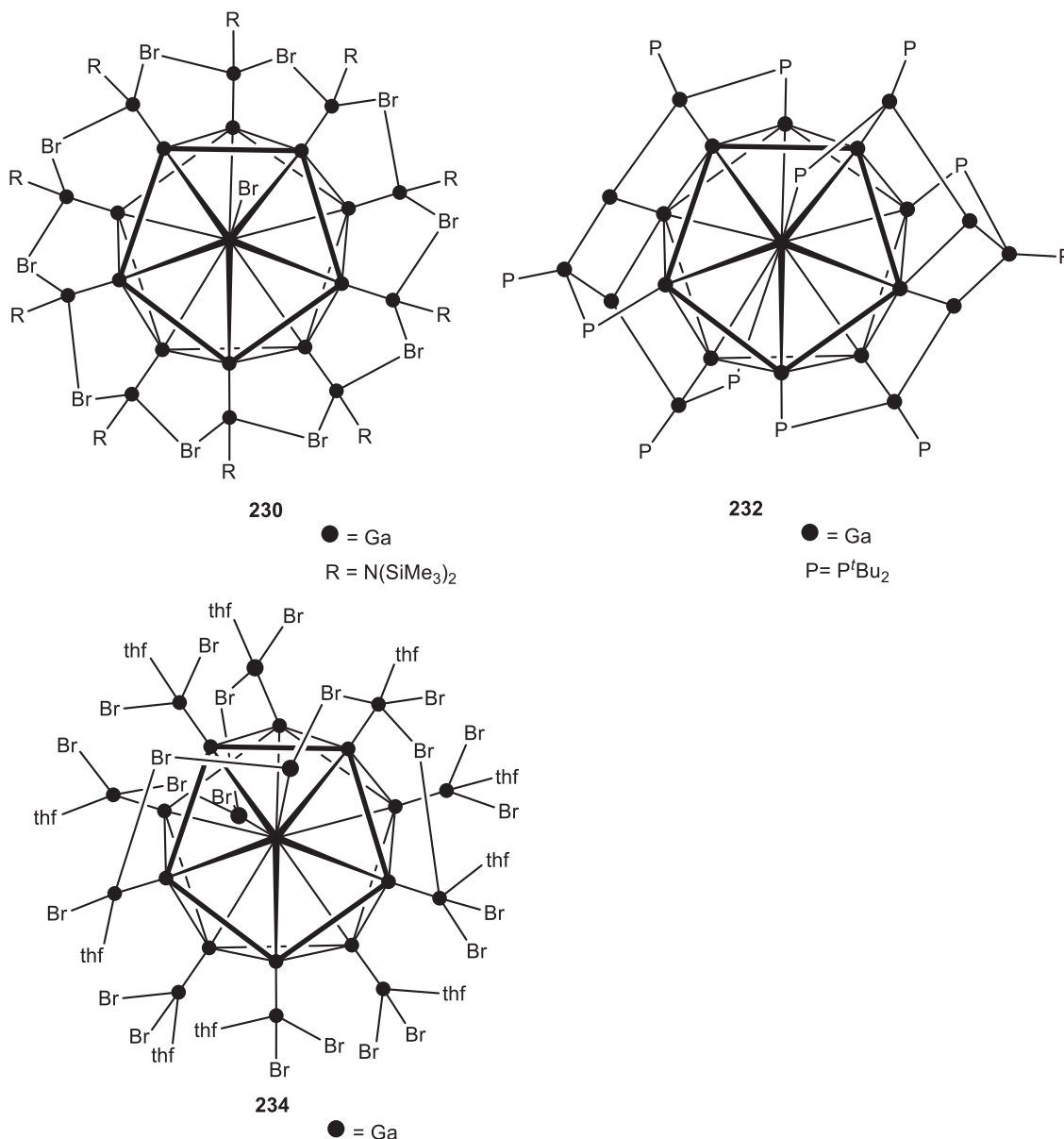
The anionic cluster  $\text{Ga}_{22}[\text{N}(\text{SiMe}_3)_2]_{10}^{2-}$  **229** (Fig. 14) has two more substituents, which are attached to gallium atoms of the naked gallium shell.<sup>449</sup> Thus, only a  $\text{Ga}@\text{Ga}_{11}$  core, with irregular structure results, which is capped by 10  $\text{RGa}$  groups.

The clusters  $[\text{Ga}_{22}\text{R}_{10}\text{Br}_{11}]^{3-}$  **230** and  $[\text{Ga}_{22}\text{R}_{10}\text{Br}_{12}]^{2-}$  **231** ( $\text{R} = \text{N}(\text{SiMe}_3)_2$ ), with a higher ratio gallium: substituents, have empty icosahedral gallium cores.<sup>450</sup> The remaining 10 gallium atoms are attached to the icosahedron with covalent  $2c2e$  bonds ( $d_{\text{Ga-Ga}} = 240$  pm), such, that the fivefold symmetry of the icosahedron is retained. One of the free apical gallium atoms of **230** is bearing a bromine atom. In **231** two  $\text{GaBr}$  groups are present. Thus, **231** is a regular icosahedral *closo*- $[\text{E}_{12}\text{X}_{12}]^{2-}$  cluster, with 10  $\text{Ga}(\text{R})\text{Br}$  and two Br substituents. An electron count for **230** reveals it also as a cluster with 13 skeletal electron pairs, if the naked

apical gallium atom retains its lone pair and contributes one electron and three orbitals to cluster bonding. The  $Al_{22}X_{20}$  clusters **202** have related structures.

$Ga_{22}(P^tBu_2)_{12}$  **232** also has an icosahedral core.<sup>451</sup> The other 10 gallium atoms form  $Ga_5$  chains wrapped around the core and attached to it via three phosphide-bridges and two gallium-gallium bonds.

These icosahedra-based structures are metalloids with regard to  $\delta$ -gallium. This modification is a network of fused, filled gallium icosahedra. The  $Ga_{12}$  core together with the two  $Ga_5$  chains represent one of these element icosahedra with parts of the next ones.



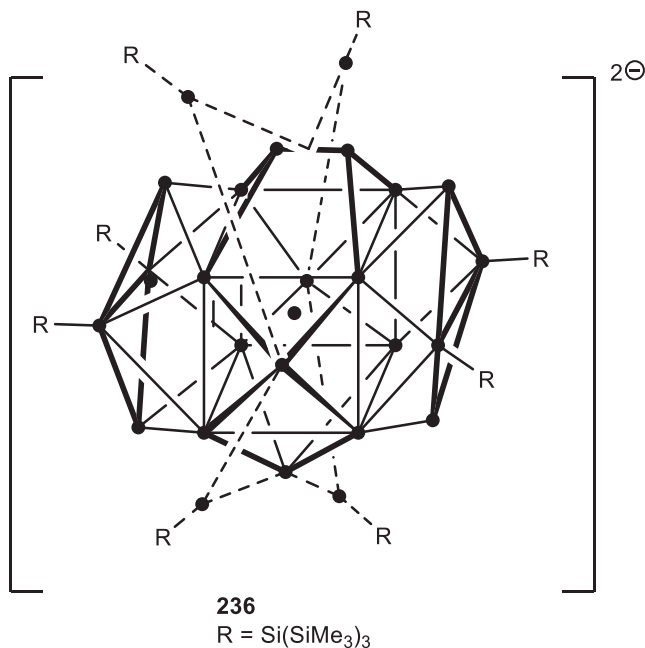
#### 1.17.4.3.5 $Ga_{23}$ and higher clusters

$Ga_{23}R_{11}$  **233** (R = N(SiMe<sub>3</sub>)<sub>2</sub>) has a body-centered core of 12 naked gallium atoms.<sup>452</sup> This is capped by 11 GaR groups. The structure is related to that of dianionic **229**. In both clusters the central gallium atom is surrounded by 11 naked gallium atoms. The shell of GaR groups in **233** contains one group more, but the number of cluster electrons of dianionic **229** and neutral **233** is the same. This might mean, the number of electrons is more important for the central cluster core than the number of shell atoms.

The gallium subhalides ( $Ga_{24}Br_{22}(thf)_{10}$ ) **234**<sup>453</sup> and ( $Ga_{24}Br_{18}Se_2(thf)_{10}$ ) **235**<sup>454</sup> are obtained from GaBr solutions with low thf content upon slow warming up to room temperature. In the case of **235** Se(SiMe<sub>3</sub>)<sub>2</sub> was added. The clusters are of the same type as **230**, meaning they have a central, non-filled icosahedron of gallium atoms. The gallium-gallium distances indicate a slight distortion ( $d_{Ga-Ga} = 255-267$  pm). Attached to the polyhedral atoms are terminal  $GaBr_x$  units ( $x = 1, 2$ ), two gallium dibromide and 10 gallium monobromide groups, which are interconnected by bromine bridges. Due to coordinated thf molecules the exopolyhedral gallium atoms are coordinated distorted tetrahedrally. Those  $2c_2e$  gallium-gallium bonds are significantly shorter ( $d_{Ga-Ga} = 240$  pm) than

the bonds in the icosahedron, as expected. In 235 four bridging bromine atoms are substituted for two selenium atoms, which are threefold capping three gallium atoms, which remain tetra coordinated. The cluster structure is not changed very much by this. A special feature is the packing of 235 in the crystal. Here,  $\text{Se}\cdots\text{Se}$  contacts (409 pm) arrange the clusters in chains. The  $\text{Se}\cdots\text{Se}$  contacts are longer than in GaSe (385 pm), but lead to a closer contact between clusters for 235 than it is in crystals of 234. Thus, a chain of  $\text{Ga}_{24}$ -“superatoms” is formed, used as model for photovoltaic properties of GaSe or selenium itself.

The largest gallium clusters prepared so far, are  $[\text{Ga}_{26}\{\text{Si}(\text{SiMe}_3)_3\}_8]^{2-}$  236,<sup>455</sup>  $[\text{Ga}_{51}(\text{P}^t\text{Bu}_2)_{14}\text{Br}_6]^{3-}$  237<sup>456</sup> and  $[\text{Ga}_{84}\{\text{N}(\text{SiMe}_3)_2\}_{20}]^{x-}$  ( $x = 3, 4$ ) 238.<sup>3,16</sup> 236 is obtained via “GaI,” the others only via metastable GaX solutions.



In 236 a central gallium atom is surrounded by eight gallium atoms, which are at the corners of a distorted cube.<sup>455</sup> Two opposite faces are capped by butterfly-shaped  $\text{Ga}_4\text{R}_2$  rings. Three single gallium atoms and a  $\text{Ga}_2$  dumbbell cap the other faces. Bridging between these five naked gallium atoms are four  $\text{GaR}$  groups. Ignoring the  $\text{Ga}_4\text{R}_2$  and  $\text{GaR}$  groups the  $\text{Ga}_{14}$  core has a central gallium atom with coordination number  $8 + 3 + 2 = 13$ , which was also found in other clusters. Taking the dumbbell as one coordinating neighbor the coordination number ( $8 + 4$ ) resembles the environment in the high-pressure modification Ga-III (Fig. 15).

Electron counting rules after Wade or Jemmis have been applied for element rich clusters. For  $\text{Ga}_{10}\text{R}_6$  and  $\text{Ga}_{22}\text{R}_8$  the counting of bare gallium atoms as one or three electron donating cluster atoms was ambiguous. For 236 a multiple capped polyhedron is expected.

At this point an alternative way of interpreting cluster structures shall be introduced. Schleyer suggested for a special class of boranes, so called “sea urchin” boranes that stable clusters with triangular, rectangular and pentagonal faces, capped on all faces larger than triangular by ER fragments, need special electron counts. He postulated a  $6m + 2n$  counting rule to fit the number of cluster valence electrons less the pairs for bonding of R groups. Here,  $m$  is the number of capped faces and  $n$  the number of triangles.<sup>457</sup>

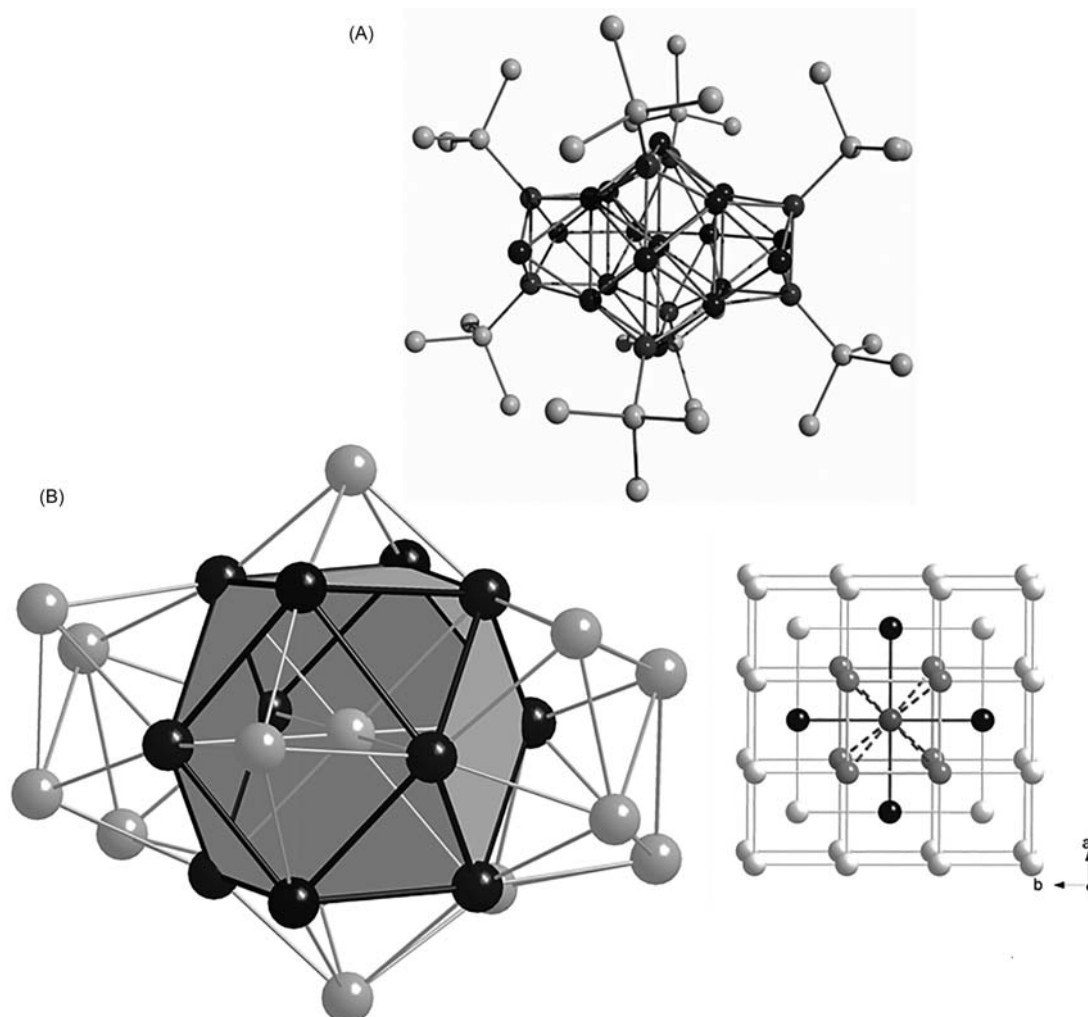
For 236 with 88 cluster valence electrons this rule was applied recently.<sup>458</sup> The centered 13 vertex polyhedron has eight triangles, four rectangles and two pentagons. Two rectangles and the pentagons are capped. The other rectangles are not isolated but fused to fragments of bicapped trigonal prisms. That means two triangles and two rectangles have to be added. The third rectangle is out of count, because it is needed for fusion. Thus, we calculate  $2 \times 8$  for triangles,  $6 \times 4$  for capped faces,  $16 \times 2$  for complex caps and  $2 \times 8$  for R groups, which totals to 88 cluster valence electrons. Whether this approach, which is not really straightforward, has generality has to be proved in future. At least, the structure of 227 has also been rationalized using this approach.<sup>458</sup>

$[\text{Ga}_{51}(\text{P}^t\text{Bu}_2)_{14}\text{Br}_6]^{3-}$  237 has a metalloid structure of a filled cuboctahedron surrounded by 38 gallium atoms, which make bonds to gallium, phosphorus or bromine.

$[\text{Ga}_{84}\{\text{N}(\text{SiMe}_3)_2\}_{20}]^{4-}$  238<sup>3</sup> is the largest main group cluster prepared and structurally characterized up to now. A  $\text{Ga}_{84}^{3-}$  cluster with the same cluster structure was obtained also.<sup>16</sup>

In 238 (Fig. 16) a central  $\text{Ga}_2$ -unit ( $d_{\text{Ga-Ga}} = 234$  pm) is surrounded by 62 naked gallium atoms, to which 20  $\text{GaR}$  groups are attached. The short bond length of the  $\text{Ga}_2$  dumbbell is comparable to that in a molecule with a formal gallium-gallium triple bond.<sup>151</sup> The 62 naked gallium atoms can be subdivided into two shells. An inner  $\text{Ga}_{32}$  shell with the shape of a football with icosahedral caps is surrounded by a belt of 30 gallium atoms.

Crystals of 238 show a metallic cluster, which was also observed for  $\text{Ga}_{26}$  cluster crystals of 236. In addition, electric conductivity and even superconduction (7 K) was observed for 238. This was explained with the packing of the cluster molecules which are aligned in chains, where the naked tops of the  $\text{Ga}_{32}$  shell are oriented to one another.<sup>459–462</sup>



**Fig. 15** (A) View of the cluster ion  $[\text{Ga}_{26}\{\text{Si}(\text{SiMe}_3)_3\}_8]^{2-}$  **236** (methyl groups omitted) and (B) relation of the cluster core to the galliummodification III.

#### 1.17.4.4 Indium and thallium cluster compounds

Several tetrahedral cluster compounds  $\text{In}_4\text{R}_4$  **184**–**185**<sup>305,322,323</sup> were prepared from reaction of lithium organyls with indium(I) halides. Silyl substituted  $\text{In}_4[\text{Si}(\text{SiMe}_3)_3]_4$  **186**<sup>324</sup> was accessible via elimination of  $\text{LiCp}^+$  from  $\text{InCp}^*$ <sup>333</sup> with  $\text{Li}(\text{thf})_3\text{Si}(\text{SiMe}_3)_3$ .  $\text{NaSi}^t\text{Bu}_3$  ( $\text{NaR}^*$ ) reacted with  $\text{InCp}^*$  to produce indium rich cluster compounds  $\text{In}_8\text{R}^*_6$  **239**<sup>433</sup> and  $\text{In}_{12}\text{R}^*_8$  **206**,<sup>408</sup> demonstrating the stronger reducing abilities of this silanide. With  $\text{M}(\text{thf})_3\text{SiPh}_3$  ( $\text{M} = \text{Li}, \text{Na}$ ) two polyhedral octaindane cluster compounds **198a** and **198b** were obtained.<sup>297</sup>

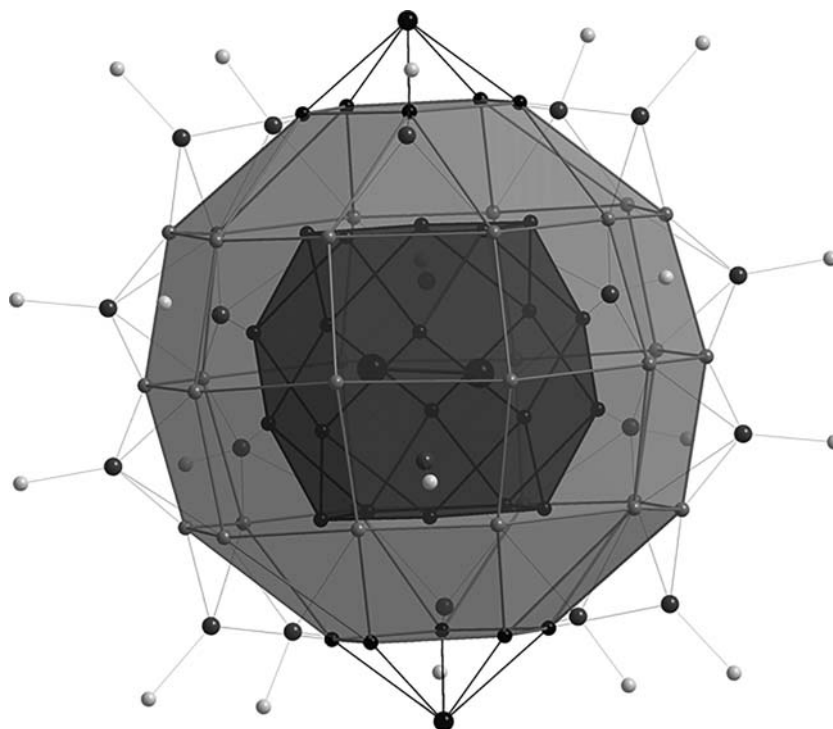
**239** has a cube of eight indium atoms lengthened along one space diagonal, where the two opposite indium atoms are ligand free. Electron counting gives seven skeletal electron pairs, allowing to categorize **239** as a *hypoprecloso*-cluster. Thus, it is described as a two-capped  $\text{In}_6\text{R}^*_4$  octahedron with two naked indium atoms at opposite vertices.

In **206** the 12 indium atoms form a section from a distorted close packing, which is similar to that in  $[\text{Al}_{12}\{\text{N}(\text{SiMe}_3)_2\}_6]^-$  **205**.<sup>407</sup>

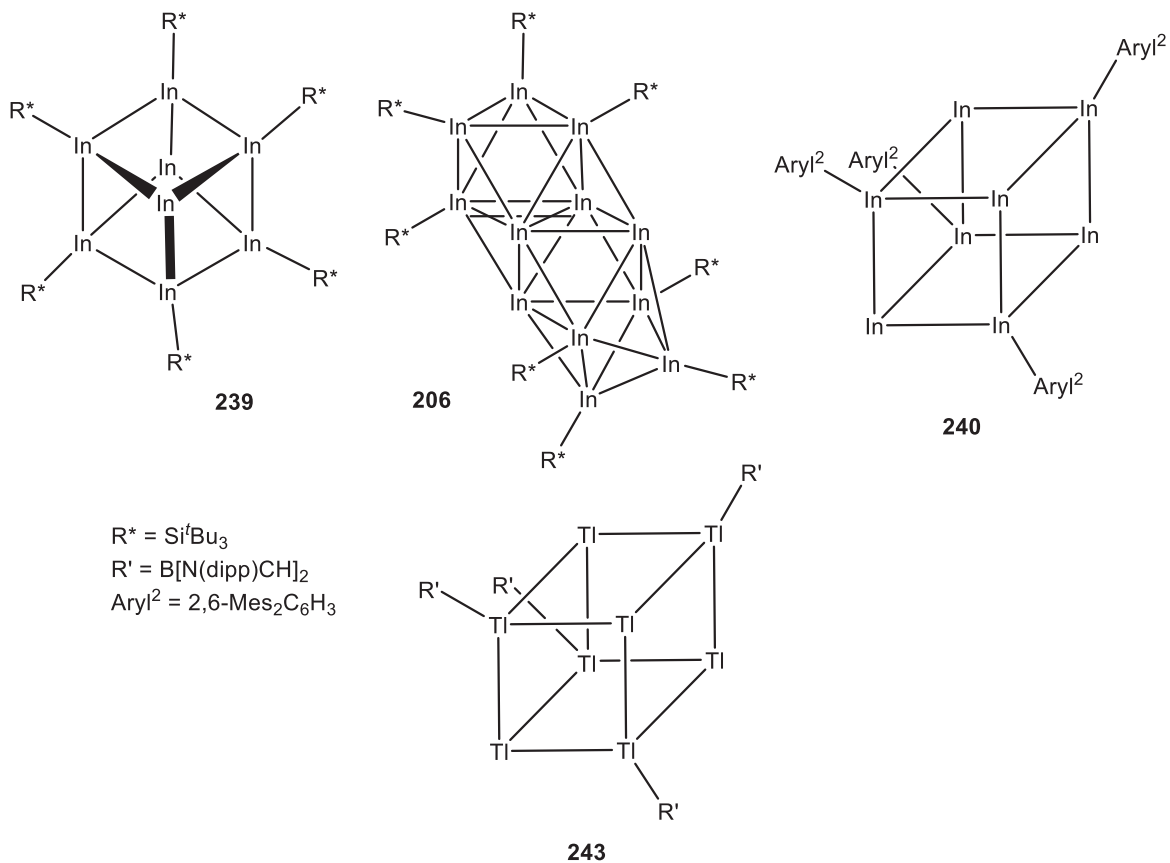
$\text{In}_8\text{Aryl}_4^2$  **240** ( $\text{Aryl}^2 = 2,6\text{-Mes}_2\text{C}_6\text{H}_3$ )<sup>463</sup> was prepared from  $\text{InCl}$  and  $\text{LiMes}$ . The core is a distorted cubic array of indium atoms. Where only the four indium atoms, located at the corners of a tetrahedron are part of  $\text{In Aryl}^2$  groups. Thus, the well-known  $\text{E}_4\text{R}_2$  fragments are present again.

The metalloindium cluster  $\text{In}_{19}[\text{B}\{\text{N}(\text{dipp})\text{CH}\}_2]$  **241** (Fig. 17, left) is obtained through disproportionation of  $[(\text{MeCCH}_2)_2][\text{In}\{\text{B}\{\text{N}(\text{dipp})\text{CH}\}_2}]$ .<sup>464</sup> The cluster has a three-layered structure with one indium at its center. The second layer consists of 12 indium atoms surrounding the center in form of a cuboctahedron. The  $\text{In}_{13}$  array thus represents a CCP phase model. The outer layer consists of six  $\text{InR}$  groups, capping the square faces.

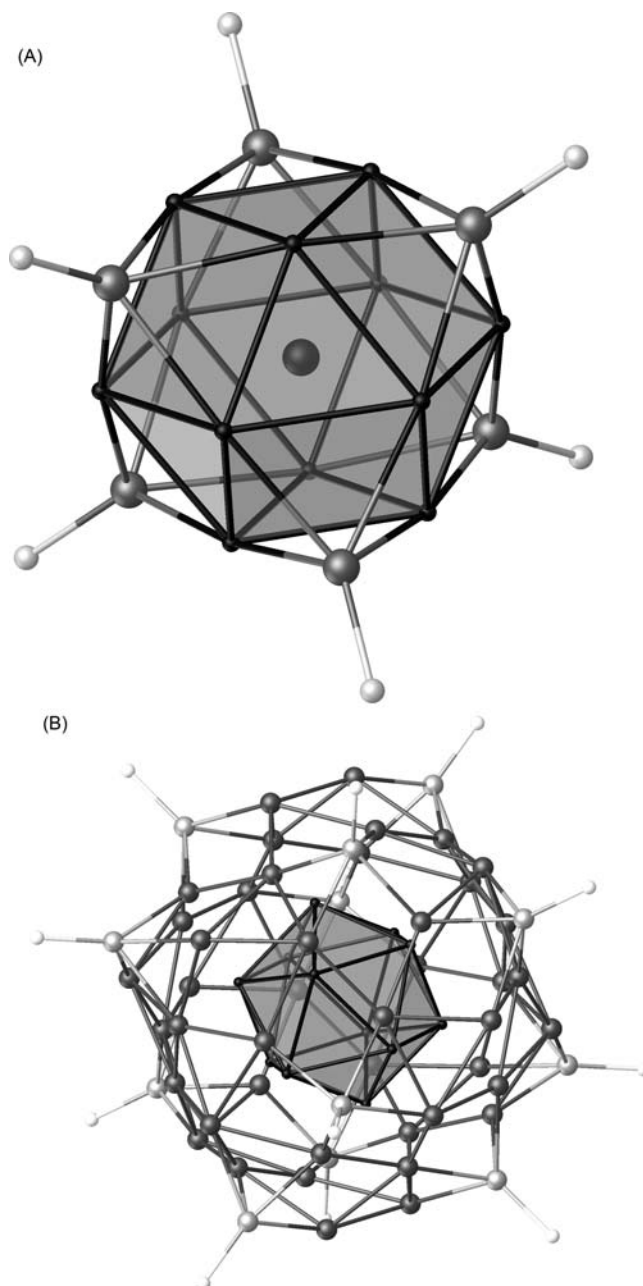
$\text{In}_{68}[\text{B}\{\text{N}(\text{dipp})\text{CH}\}_2]_{12}$  **242** is up till now the largest reported indium cluster.<sup>260</sup> **242** (Fig. 17, right) has an  $\text{In}_{12}$  core aligned as nearly perfect icosahedron ( $d_{\text{In-In}} = 310.0(1)\text{--}314.5(2)$  pm). The icosahedral core is surrounded by a shell of 44 indium atoms. This outer shell is irregularly capped by 12  $[\text{In}\{\text{B}\{\text{N}(\text{dipp})\text{CH}\}_2}]$  units.



**Fig. 16** View of the  $\text{Ga}_{34}$  cluster ion **238** showing the layered structure (Ga atoms: dark to middle grey; N atoms of R groups: light grey). The football/belt description is rationalized by viewing the three middle layers of the middle grey shaded shell as belt and the remaining gallium atoms, which are not GaR units as capped football.<sup>302</sup> Linti, G.; Schnöckel, H.; Uhl, W.; Wiberg, N. In *Molecular Clusters of the Main Group Elements*; Driess, M., Nöth, H., Eds., 2004, p 126–168. Wiley-VCH: Weinheim, 2004, Copyright Wiley-VCH Verlag GmbH & Co. KGaA. Reproduced with permission.







**Fig. 17** View of the In<sub>9</sub> cluster **241** (left) and the In<sub>68</sub> cluster ion **242** (right) with their three-layered structure (In atoms: black to grey; B atoms of R groups: white).

Regarding thallium only one element rich cluster is known. Tl<sub>8</sub>[B{N(dipp)CH}<sub>2</sub>]<sub>2</sub> **243** was prepared from Tl[N(SiMe<sub>3</sub>)<sub>2</sub>] and (thf)<sub>2</sub>Li[B{N(dipp)CH}<sub>2</sub>]<sub>2</sub>.<sup>465</sup> **243** is structured analogously to **240** with a distorted cubic array of thallium atoms. The four substituted thallium atoms are found in vertices of a tetrahedron.

### 1.17.5 Outlook

The chemistry of element-rich and polyhedral clusters of the heavier triel elements has been established during the past three decades. Several synthetic pathways are available now, but none, which allows for a planned synthesis of a specific new cluster. The complex structures stress classic bonding concepts. For smaller clusters concepts developed for boron cluster compounds are applicable. Therefore, this chapter focused on rationalizing structures by topology and attempted application of well-known electron counting rules. The higher clusters are too complex to be feasible by a simple rule. Gallium as an element adopts various

allotropic modifications, which are stable at different temperature ranges and pressure. It seems that the high pressure necessary for some modifications can be modeled by a shell of substituents. Their steric demand and electronic properties influence cluster cores, but a real understanding of the effects is far from complete. Aluminum, which has a typical metal lattice, has modified structures in the nanoscale cluster cores. With indium, which has the higher stability of oxidation state one, compared to aluminum and gallium, only a few element-rich clusters could be obtained.

A topic of special interest continues to be the formation of bonds between triel atoms in low oxidation state, where the range is from 2c2e bonds to multiple bonds and multicenter bonds. The properties of these metal-metal bonded systems including the nanoscale clusters, being described as intermediate between dissolved metals and bulk material, have begun to be investigated and offer interesting perspectives.

## References

- Uhl, W.; Layh, M.; Hiller, W. *J. Organomet. Chem.* **1989**, *368*, 139–154.
- Uhl, W.; Layh, M.; Hildenbrand, T. *J. Org. Chem.* **1989**, *364* (3), 289–300.
- Schnepf, A.; Schnöckel, H. *Angew. Chem. Int. Ed.* **2001**, *40* (4), 711–715.
- Schnöckel, H.; Schnepf, A. *Angew. Chem. Int. Ed.* **2002**, *41*, 3532–3552.
- Schnepf, A.; Stoesser, G.; Schnöckel, H. *J. Am. Chem. Soc.* **2000**, *122*, 9178.
- Purath, A.; Köppe, R.; Schnöckel, H. G. *Angew. Chem. Int. Ed.* **1999**, *38*, 2926.
- Schnöckel, H.; Schnepf, A. *Adv. Organomet. Chem.* **2001**, *47*, 235–281.
- Driess, M.; Nöth, H. *Molecular Clusters of the Main Group Elements*, Wiley-VCH: Weinheim, New York, 2004.
- Schnöckel, H. *Dalton Trans.* **2008**, (33), 4344.
- Schnöckel, H. *Chem. Rev.* **2010**, *110* (7), 4125–4163.
- Baker, R. J.; Jones, C. *Coord. Chem. Rev.* **2005**, *249* (17–18), 1857–1869.
- Linti, G.; Schnöckel, H. *Coord. Chem. Rev.* **2000**, *206–207*, 285–319.
- Schnöckel, H. *J. Chem. Soc., Dalton Trans.* **2005**, *19*, 3131–3136.
- Pardoe, J. A. J.; Downs, A. J. *Chem. Rev.* **2007**, *107* (1), 2–45.
- Schnöckel, H.; Schnepf, A. *ACS Symp. Ser.* **2002**, *822*, 154.
- Schnepf, A.; Jee, B.; Schnöckel, H. *Inorg. Chem.* **2003**, *42*, 7731–7733.
- Köppe, R.; Schnöckel, H. *Angew. Chem. Int. Ed.* **2004**, *43*, 2170.
- Wade, K. *Adv. Inorg. Chem. Radiochem.* **1976**, *18*, 1.
- Williams, R. E. *Adv. Inorg. Chem. Radiochem.* **1976**, *18*, 67.
- Rudolph, R. W. *Acc. Chem. Res.* **1976**, *9*, 446.
- Mingos, D. M. P. *Nature* **1972**, *336*, 99.
- Burgert, R.; Stokes, S. T.; Bowen, K. H.; Schnöckel, H. *J. Am. Chem. Soc.* **2006**, *128*, 7904.
- Burgert, R.; Schnöckel, H.; Grubisic, A.; Li, X.; Stokes, S. T.; Bowen, K. H.; Ganteför, G. F.; Kiran, B.; Jena, P. *Science* **2008**, *319*, 438.
- Burgert, R.; Schnöckel, H. *Chem. Comm.* **2008**, 2075.
- Linti, G.; Frey, R.; Schmidt, M. *Z. Naturforsch. Teil B* **1994**, *49b*, 958–962.
- Downs, A. J.; Himmel, H.-J. New light on the Chemistry of group 13 metals. In *The Group 13 Metals Aluminium, Gallium, Indium and Thallium*; Aldridge, S., Downs, A. J., Eds., John Wiley: New York, 2011; p 1.
- Wilson, F. C.; Schoemaker, D. P. *Naturwissenschaften* **1956**, *43*, 57.
- Elschenbroich, C. H. *Organometallchemie*, 4th ed.; Teubner: Stuttgart, 2003.
- Lide, D. R. *Handbook of Chemistry and Physics*, 90th ed.; CRC Press: Boca Raton, 2009–2010.
- Himmel, H.-J.; Manceron, L.; Downs, A. J.; Pullumbi, P. *Angew. Chem. Int. Ed.* **2002**, *41*, 796.
- Himmel, H.-J.; Manceron, L.; Downs, A. J.; Pullumbi, P. *J. Am. Chem. Soc.* **2002**, *124*, 4448.
- Huber, K. P.; Herzberg, G. *Molecular Spectra and Molecular Structure IV, Constants of Diatomic Molecules*, Van Nostrand, Reinhold: New York, 1979.
- Fu, Z.; Lemire, G. W.; Bishea, G. A.; Morse, M. D. *J. Chem. Phys.* **1990**, *93*, 8420.
- Balducci, G.; Gigli, G.; Meloni, G. *J. Chem. Phys.* **1998**, *109*, 4384.
- Fang, L.; Davis, B. L.; Lu, H.; Lombardi, J. R. *Spectrochim. Acta Part A* **2001**, *57*, 2809.
- Himmel, H.-J.; Gaertner, B. *Chem. Eur. J.* **2004**, *10*, 5936.
- Martenssen, W. Landolt-Börnstein: Numerical Data and Functional Relationships in Science and Technology. *Continuation of: Landolt-Börnstein: Zahlenwerte und Funktionen aus Physik, Chemie, Astronomie, Geophysik und Technik*, 6th ed.; Springer: Heidelberg, 1974 (Vol. 1982, 1983, 1992, 1995; II/6, II/14a, II/14b, II/19a, II/19d-1).
- Andrews, L.; Wang, X. *Angew. Chem. Int. Ed.* **2004**, *43*, 1706.
- Wang, X.; Andrews, L. *J. Phys. Chem. A* **2004**, *108*, 4440.
- Wang, X.; Wolfe, B.; Andrews, L. *J. Phys. Chem. A* **2004**, *108*, 5169.
- Aldridge, S.; Downs, A. *J. Chem. Rev.* **2001**, *101*, 3305.
- Lammertsma, K.; Güner, O. F.; Drewes, R. M.; Reed, A. E.; Schleyer, P. V. R. *Inorg. Chem.* **1989**, *28*, 313.
- Lammertsma, K.; Leszczynski, J. *J. Phys. Chem.* **1990**, *94*, 5543.
- Lammertsma, K.; Ohwada, T. *J. Am. Chem. Soc.* **1996**, *118*, 7247.
- Himmel, H.-J.; Schnöckel, H. *Chem. Eur. J.* **2002**, *8*, 2397.
- Morrison, J. A. *Chem. Rev.* **1991**, *91*, 35.
- Downs, A. J. *Chemistry of Aluminium, Gallium, Indium and Thallium*, Blackie Academic Press, 1993.
- Tuck, D. G. *Polyhedron* **1990**, *9*, 337.
- Tuck, D. G. *Coord. Chem. Rev.* **1992**, *112*, 215.
- Szabó, A.; Kovács, A.; Frenking, G. *Z. Anorg. Allg. Chem.* **2005**, *631*, 1803.
- Ecker, A.; Baum, E.; Friesen, M. A.; Junker, M. A.; Üffing, C.; Köppe, R.; Schnöckel, H. *Z. Anorg. Allg. Chem.* **1998**, *624* (3), 513–516.
- Vollet, J.; Burgert, R.; Schnöckel, H. *Angew. Chem. Int. Ed.* **2005**, *44* (42), 6956–6960.
- Mocker, M.; Robl, C.; Schnöckel, H. *Angew. Chem. Int. Ed. Engl.* **1994**, *33* (8), 862–863.
- Klemp, C.; Stößer, G.; Krossing, I.; Schnöckel, H. *Angew. Chem. Int. Ed.* **2000**, *39* (20), 3691–3694.
- Beamish, J. C.; Small, R. L. H.; Worrall, I. J. *Inorg. Chem.* **1979**, *18*, 220–223.

56. Wei, P.; Li, X.-W.; Robinson, G. H. *Chem. Commun.* **1999**, 1287.
57. Duan, T.; Schnöckel, H. Z. *Anorg. Allg. Chem.* **2004**, 630 (15), 2622–2626.
58. Pashkov, A. Y.; Belsky, V. K.; Butychev, M.; Zvukova, T. M. *Russ. Chem. Bull.* **1996**, 45 (8), 1973–1976.
59. Rickard, C. E. F.; Taylor, M. J.; Kilner, M. *Acta Cryst. Section C* **1999**, 55 (8), 1215–1216.
60. Gordon, E. M.; Hepp, A. F.; Duraj, S. A.; Habash, T. S.; Fanwick, P. E.; Schupp, J. D.; Eckles, W. E.; Long, S. *Inorg. Chim. Acta* **1997**, 257 (2), 247–251.
61. Nogai, S. D.; Schmidbaur, H. *Organometallics* **2004**, 23 (24), 5877–5880.
62. Ball, G. E.; Cole, M. L.; McKay, A. I. *Dalton Trans.* **2012**, 41 (3), 946–952.
63. Schuster, J. K.; Muessig, J. H.; Dewhurst, R. D.; Braunschweig, H. *Chem. Eur. J.* **2018**, 24 (38), 9692–9697.
64. Nogai, S.; Schmidbaur, H. *Inorg. Chem.* **2002**, 41 (18), 4770–4774.
65. Mayo, D. H.; Peng, Y.; Zavalij, P.; Bowen, K. H.; Eichhorn, B. W. *Acta Cryst. Section E* **2012**, 68 (10), m1245.
66. Baker, R. J.; Bettentrup, H.; Jones, C. *Eur. J. Inorg. Chem.* **2003**, 2003 (13), 2446–2451.
67. Doriat, C. U.; Friesen, M.; Baum, E.; Ecker, A.; Schnöckel, H. *Angew. Chem. Int. Ed. Engl.* **1997**, 36 (18), 1969–1971.
68. Baker, R. J.; Bettentrup, H.; Jones, C. *Inorg. Chem. Commun.* **2004**, 7 (12), 1289–1291.
69. Schnepf, A.; Doriat, C. *Chem. Comm.* **1997**, (21), 2111–2112.
70. Beagley, B.; Godfrey, S. M.; Kelly, K. J.; Kungwankunakorn, S.; McAuliffe, C. A.; Pritchard, R. G. *Chem. Comm.* **1996**, (18), 2179–2180.
71. Gabbai, F. P.; Schier, A.; Riede, J.; Schmidbaur, H. *Inorg. Chem.* **1995**, 34 (15), 3855–3856.
72. Hirayama, L. C.; Haddad, T. D.; Oliver, A. G.; Singaram, B. *J. Org. Chem.* **2012**, 77 (9), 4342–4353.
73. Green, S. P.; Jones, C.; Stasch, A. *Angew. Chem. Int. Ed.* **2007**, 46 (45), 8618–8621.
74. Green, S. P.; Jones, C.; Stasch, A. *Chem. Comm.* **2008**, (47), 6285–6287.
75. Khan, M. A.; Peppe, C.; Tuck, D. G. *Can. J. Chem.* **1984**, 62 (3), 601–605.
76. Godfrey, S. M.; Kelly, K. J.; Kramkowski, P.; McAuliffe, C. A.; Pritchard, R. G. *Chem. Comm.* **1997**, 11, 1001–1002.
77. Tacke, M.; Schnöckel, H. *Inorg. Chem.* **1989**, 28, 2895.
78. Schnöckel, H.; Klemp, C. In *Inorganic Chemistry Highlights*; Meyer, G., Naumann, D., Wesemann, L., Eds., Wiley-VCH: Weinheim, 2002; p 245.
79. Schnöckel, H.; Köppe, R. In *Silicon Chemistry*; Jutzi, P., Schubert, U., Eds., Wiley-VCH: Weinheim, 2003; p 20.
80. Dronskowski, R.; Simon, A. *Angew. Chem. Int. Ed.* **1989**, 28 (6), 758–760.
81. Klemm, W.; Tilk, W. Z. *Anorg. Allg. Chem.* **1932**, 207, 175.
82. Garton, G.; Powell, H. M. *J. Inorg. Nucl. Chem.* **1957**, 4, 84.
83. Corbett, J. D.; Hershafit, A. *J. Am. Chem. Soc.* **1958**, 80, 1530.
84. McMullan, R. K.; Corbett, J. D. *J. Am. Chem. Soc.* **1958**, 80, 4761.
85. Woodward, L. A.; Greenwood, N. N.; Hall, J. R.; Worrall, I. J. *J. Chem. Soc.* **1958**, 1505.
86. Clark, R. J.; Griswold, W.; Kleinberg, J. *J. Am. Chem. Soc.* **1958**, 80, 4764.
87. Schmidbaur, H.; Nowak, R.; Bublak, W. Z. *Naturforsch.* **1987**, 42b, 553.
88. Höhle, W.; Simon, A.; Gerlach, G. Z. *Naturforsch.* **1987**, 42b, 546.
89. Khan, M. A.; Tuck, D. G. *Inorg. Chim. Acta* **1985**, 97, 73.
90. Massey, A. G. *Adv. Inorg. Chem.* **1983**, 26, 1–54.
91. Tian, X.; Pape, T.; Mitzel, N. W. Z. *Naturforsch., B: Chem. Sci.* **2004**, 59, 1524–1531.
92. Khan, M. A.; Tuck, D. G.; Taylor, M. J.; Rogers, D. A. *J. Chem. Cryst.* **1986**, 16 (6), 895–905.
93. Bubenheim, W.; Frenzen, G.; Müller, U. *Acta Cryst. Section C* **1995**, C51 (6), 1120–1124.
94. Uhl, W. Z. *Naturforsch.* **1988**, 43b, 1113.
95. Wehmschulte, R. J.; Ruhlandt-Senge, K.; Olmstead, M. M.; Hope, H.; Sturgeon, B. E.; Power, P. P. *Inorg. Chem.* **1993**, 32, 2983–2984.
96. Wiberg, N.; Blank, T.; Amelunxen, K.; Nöth, H.; Schnöckel, H.; Baum, E.; Purath, A.; Fenske, D. *Eur. J. Inorg. Chem.* **2002**, 2002 (2), 341–350.
97. Wiberg, N.; Amelunxen, K.; Blank, T.; Nöth, H.; Knizek, J. *Organometallics* **1998**, 17, 5431.
98. Fedushkin, I. L.; Moskalev, M. V.; Lukoyanov, A. N.; Tishkina, A. N.; Baranov, E. V.; Abakumov, G. A. *Chem. Eur. J.* **2012**, 18 (36), 11264–11276.
99. He, X.; Bartlett, R. A.; Olmstead, M. M.; Ruhlandt-Senge, K.; Sturgeon, B. E.; Power, P. P. *Angew. Chem. Int. Ed. Engl.* **1993**, 32, 717–718.
100. Linti, G.; Köstler, W. *Angew. Chem.* **1996**, 593–595.
101. Gast, M.; Ejlli, B.; Wadepohl, H.; Linti, G. *Eur. J. Inorg. Chem.* **2019**, 2019 (25), 2964–2971.
102. Schluter, R. D.; Cowley, A. H.; Atwood, D. A.; Jones, R. A.; Bond, M. R.; Carrano, C. J. *J. Am. Chem. Soc.* **1993**, 115 (5), 2070–2071.
103. Saxena, A. K.; Zhang, H.; Maguire, J. A.; Hosmane, N. S.; Cowley, A. H. *Angew. Chem. Int. Ed. Engl.* **1995**, 34 (3), 332–334.
104. Linti, G.; Köstler, W.; Rodig, A. Z. *Anorg. Allg. Chem.* **2002**, 628, 1319–1326.
105. Baker, R. J.; Jones, C.; Mills, D. P.; Pierce, G. A.; Waugh, M. *Inorg. Chim. Acta* **2008**, 361 (2), 427–435.
106. Fedushkin, I. L.; Lukoyanov, A. N.; Ketkov, S. Y.; Hummert, M.; Schumann, H. *Chem. Eur. J.* **2007**, 13 (25), 7050–7056.
107. Brown, D. S.; Decken, A.; Cowley, A. H. *J. Am. Chem. Soc.* **1995**, 117, 5421–5422.
108. Pott, T.; Jutzi, P.; Schoeller, W. W.; Stammer, A.; Stammer, H.-G. *Organometallics* **2001**, 20 (25), 5492–5494.
109. Power, P. P.; Brothers, P. J.; Hübler, K.; Hübler, U.; Noll, B. C.; Olmstead, M. M. *Angew. Chem. Int. Ed. Engl.* **1996**, 35 (20), 2355–2357.
110. Wiberg, N.; Amelunxen, K.; Nöth, H.; Schmidt, M.; Schwenk, H. *Angew. Chem. Int. Ed. Engl.* **1996**, 35 (1), 65–67.
111. Wochele, R.; Schwarz, W.; Klinkhammer, K. W.; Locke, K.; Weidlein, J. Z. *Anorg. Allg. Chem.* **2000**, 626 (9), 1963–1973.
112. Henkel, S.; Klinkhammer, K. W.; Schwarz, W. *Angew. Chem. Int. Ed. Engl.* **1994**, 33 (6), 681–683.
113. Wiberg, N.; Amelunxen, K.; Blank, T.; Lerner, H.-W.; Polborn, K.; Nöth, H.; Littger, R.; Rackl, M.; Schmidt-Amelunxen, M.; Schwenk-Kircher, H.; Warchold, M. Z. *Naturforsch.* **2001**, 56b, 634–651.
114. Aihara, J.-I. *Inorg. Chem.* **2001**, 40 (19), 5042–5044.
115. Baker, R. J.; Jones, C.; Kloth, M.; Platts, J. A. *Organometallics* **2004**, 23 (21), 4811–4813.
116. Hoberg, H.; Krause, S. *Angew. Chem. Int. Ed. Engl.* **1976**, 15, 694.
117. Power, P. P. *Organometallics* **2020**, 39 (23), 4127–4138.
118. Fedushkin, I. L.; Dodonov, V. A.; Skatova, A. A.; Sokolov, V. G.; Piskunov, A. V.; Fukin, G. K. *Chem. Eur. J.* **2018**, 24 (8), 1877–1889.
119. Sokolov, V. G.; Koptseva, T. S.; Moskalev, M. V.; Bazyakina, N. L.; Piskunov, A. V.; Cherkasov, A. V.; Fedushkin, I. L. *Inorg. Chem.* **2017**, 56 (21), 13401–13410.
120. Fedushkin, I. L.; Lukoyanov, A. N.; Tishkina, A. N.; Maslov, M. O.; Ketkov, S. Y.; Hummert, M. *Organometallics* **2011**, 30 (13), 3628–3636.
121. Fedushkin, I. L.; Nikipelov, A. S.; Lyssenko, K. A. *J. Am. Chem. Soc.* **2010**, 132, 7874–7875.
122. Hellmann, K. W.; Gade, L. H.; Steiner, A.; Stalke, D.; Möller, F. *Angew. Chem. Int. Ed. Engl.* **1997**, 36 (1–2), 160–163.
123. Veith, M.; Spaniol, A.; Pöhlmann, J.; Gross, F.; Huch, V. *Chem. Ber.* **1993**, 126, 2625.
124. Hellmann, K. W.; Gade, L. H.; Scown, I. J.; McPartlin, M. *Chem. Commun.* **1996**, 2515.
125. Hellmann, K. W.; Gade, L. H.; Fleischer, R.; Kottke, T. *Chem. Eur. J.* **1997**, 3, 1801.
126. Galka, C. H.; Gade, L. H. *Inorg. Chem.* **1999**, 38, 1038.
127. Hellmann, K. W.; Gade, L. H.; Fleischer, R.; Stalke, D. *Chem. Commun.* **1997**, 527.

128. Hellmann, K. W.; Bergner, A.; Gade, L. H.; Scowen, I. J.; McPartlin, M. *J. Organomet. Chem.* **1999**, *573*, 156–164.
129. Dias, H. V. R. In *Comprehensive Coordination Chemistry II*; Abel, E. W., Stone, F. G. A., Wilkinson, G., Eds.; vol. 2; Pergamon Press: Oxford, 1995; p 383.
130. Gade, L. H. *Dalton Trans.* **2003**, 267.
131. Reedijk, J.; Roelofsens, G.; Siedle, A. R.; Spek, A. L. *Inorg. Chem.* **1979**, *18*, 1947.
132. Beck, J.; Strähle, J. Z. *Z. Naturforsch. B: Anorg. Chem. Org. Chem.* **1986**, *41B*, 1381.
133. Lee, H. S.; Hauber, S.-O.; Vindus, D.; Niemeyer, M. *Inorg. Chem.* **2008**, *47*, 4401.
134. Dias, H. V. R.; Singh, S.; Cundari, T. R. *Angew. Chem. Int. Ed.* **2005**, *44*, 4907.
135. Johnson, M. T.; Campana, C. F.; Foxman, B. M.; Desmarais, W.; Vela, M. J.; Miller, J. S. *Chem. Eur. J.* **2000**, *6*, 1805.
136. Manke, D. R.; Nocera, D. G. *Polyhedron* **2006**, *25*, 493.
137. Wiberg, N.; Blank, T.; Amelunxen, K.; Nöth, H.; Knizek, J.; Habereeder, T.; Kaim, W.; Wanner, M. *Eur. J. Inorg. Chem.* **2001**, 1719–1727.
138. Bag, P.; Porzelt, A.; Altmann, P. J.; Inoue, S. *J. Am. Chem. Soc.* **2017**, *139* (41), 14384–14387.
139. Weetman, C.; Bag, P.; Szilvási, T.; Jandl, C.; Inoue, S. *Angew. Chem. Int. Ed.* **2019**, *58* (32), 10961–10965.
140. Wright, R. J.; Brynda, M.; Fettingner, J. C.; Betzer, A. R.; Power, P. P. *J. Am. Chem. Soc.* **2006**, *128* (38), 12498–12509.
141. Cui, C.; Li, X.; Wang, C.; Zhang, J.; Cheng, J.; Zhu, X. *Angew. Chem. Int. Ed.* **2006**, *45* (14), 2245–2247.
142. Wright, R. J.; Phillips, A. D.; Power, P. P. *J. Am. Chem. Soc.* **2003**, *125* (36), 10784–10785.
143. Power, P. Multiple Bonding Between Heavier Group 13 Elements. In *Group 13 Chemistry I*; Roesky, H., Atwood, D., Eds.; vol. 103; Springer Berlin/Heidelberg, 2002; pp 57–84.
144. Hardman, N. J.; Wright, R. J.; Phillips, A. D.; Power, P. P. *Angew. Chem.* **2002**, *114*, 2966–2968.
145. Hardman, N. J.; Wright, R. J.; Phillips, A. D.; Power, P. P. *J. Am. Chem. Soc.* **2003**, *125*, 2667–2679.
146. Wright, R. J.; Phillips, A. D.; Hardman, N. J.; Power, P. P. *J. Am. Chem. Soc.* **2002**, *124* (29), 8538–8539.
147. Schulz, S. In *Comprehensive Organometallic Chemistry III*; Mingos, D. M. P., Crabtree, R. H., Eds.; vol. 3; Elsevier: Oxford, UK, 2007; pp 287–342.
148. Wright, R. J.; Phillips, A. D.; Hino, S.; Power, P. P. *J. Am. Chem. Soc.* **2005**, *127*, 4794.
149. Niemeyer, M.; Power, P. P. *Angew. Chem. Int. Ed.* **1998**, *37* (9), 1277–1279.
150. Wright, R. J.; Brynda, M.; Power, P. P. *Angew. Chem. Int. Ed.* **2006**, *45* (36), 5953–5956.
151. Su, J.; Li, X.-W.; Crittendon, R. C.; Robinson, G. H. *J. Am. Chem. Soc.* **1997**, *119* (23), 5471–5472.
152. Wang, Y.; Robinson, G. H. *Organometallics* **2007**, *26*, 2–11.
153. Uhl, W.; Vester, A.; Hiller, W. *J. Organomet. Chem.* **1993**, *443*, 9–17.
154. Pluta, C.; Pörschke, K.-R.; Krüger, C.; Hildenbrand, K. *Angew. Chem. Int. Ed. Engl.* **1993**, *32*, 388.
155. Uhl, W.; Vester, A.; Fenske, D.; Baum, G. *J. Organomet. Chem.* **1994**, *464*, 23.
156. Uhl, W.; Gerdinger, R.; Vester, A. *J. Organomet. Chem.* **1996**, *513*, 163.
157. Uhl, W.; Graupner, R.; Layh, M.; Schütz, U. *J. Organomet. Chem.* **1995**, 493.
158. Henke, P.; Pankewitz, T.; Klöpfer, W.; Breher, F.; Schnöckel, H. *Angew. Chem.* **2009**, *121* (43), 8285–8290.
159. Uhl, W.; Vester, A. *Chem. Ber.* **1993**, *126* (4), 941–945.
160. Uhl, W.; Schütz, U.; Pohl, S.; Saak, W. *Z. Naturforsch.* **1994**, *49b*, 637.
161. Uhl, W.; Schütz, U.; Vester, A.; Karsch, H. H. *Chem. Ber.* **1993**, *126* (12), 2637–2641.
162. Uhl, W.; Spies, T. *Z. Anorg. Allg. Chem.* **2000**, *626* (5), 1059–1064.
163. Linti, G.; Rodig, A.; Köstler, W. *Z. Anorg. Allg. Chem.* **2001**, *627* (7), 1465–1476.
164. Veith, M.; Goffing, F.; Becker, S.; Huch, V. *J. Org. Chem.* **1991**, *406* (1–2), 105–118.
165. Grocholl, L.; Schranz, I.; Stahl, L.; Staples, R. *J. Inorg. Chem.* **1998**, *37* (10), 2496–2499.
166. Chen, Y.; Araki, Y.; Hanack, M.; Fujitsuka, M.; Ito, O. *Eur. J. Inorg. Chem.* **2005**, *2005* (22), 4655–4658.
167. Bertagnolli, H.; Blau, W. J.; Chen, Y.; Dini, D.; Feth, M. P.; O'Flaherty, S. M.; Hanack, M.; Krishnan, V. *J. Mat. Chem.* **2005**, *15* (6), 683–689.
168. Chen, Y.; Barthel, M.; Seiler, M.; Subramanian, L. R.; Bertagnolli, H.; Hanack, M. *Angew. Chem. Int. Ed.* **2002**, *41* (17), 3239–3242.
169. Garcia-Castro, M.; Martín, A.; Mena, M.; Yélamos, C. *Chem. Eur. J.* **2009**, *15* (29), 7180–7191.
170. Valean, A.-M.; Gomez-Ruiz, S.; Lonneck, P.; Silaghi-Dumitrescu, I.; Silaghi-Dumitrescu, L.; Hey-Hawkins, E. *New J. Chem.* **2009**, *33* (8), 1771–1779.
171. Hoberg, H.; Krause, S. *Angew. Chem. Int. Ed. Engl.* **1978**, *17* (12), 949–950.
172. Schnepf, A.; Weckert, E.; Linti, G.; Schnöckel, H. *Angew. Chem.* **1999**, *111*, 3578–3581.
173. Wiberg, N.; Blank, T.; Westerhausen, M.; Schneiderbauer, S.; Schnöckel, H.; Krossing, I.; Schnepf, A. *Eur. J. Inorg. Chem.* **2002**, *2002* (2), 351–356.
174. Uhl, W.; Melle, S. *Chem. Eur. J.* **2001**, *7* (19), 4216–4221.
175. Serrano, O.; Fettingner, J. C.; Power, P. P. *Polyhedron* **2013**, *58*, 144–150.
176. Uhl, W.; Voss, M.; Luftmann, H. *Chem. Commun.* **2009**, (44), 6854–6856.
177. Uhl, W.; El-Hamdan, A.; Geiseler, G.; Harms, K. *Z. Anorg. Allg. Chem.* **2004**, *630* (6), 821–828.
178. Uhl, W.; El-Hamdan, A.; Prött, M.; Spühler, P.; Frenking, G. *J. Chem. Soc., Dalton Trans.* **2003**, 1360–1364.
179. Cowley, A. H.; Decken, A.; Olazábal, C. A. *J. Org. Chem.* **1996**, *524* (1–2), 271–273.
180. Klimek, K. S.; Cui, C.; Roesky, H. W.; Noltemeyer, M.; Schmidt, H.-G. *Organometallics* **2000**, *19* (16), 3085–3090.
181. Beachley, O. T.; Gardinier, J. R.; Churchill, M. R. *Organometallics* **2000**, *19* (22), 4544–4549.
182. Jones, C.; Junk, P. C.; Kloth, M.; Proctor, K. M.; Stasch, A. *Polyhedron* **2006**, *25*, 1592–1600.
183. Linti, G.; Zessin, T. *Dalton Trans.* **2011**, *40* (20), 5591–5598.
184. Rudolf, D.; Kaifer, E.; Himmel, H.-J. *Eur. J. Inorg. Chem.* **2010**, *2010* (31), 4952–4961.
185. Lomell, V.; McBurnett, B. G.; Cowley, A. H. *J. Org. Chem.* **1998**, *562* (1), 123–125.
186. Schmidt, E. S.; Schier, A.; Mitzel, N. W.; Schmidbaur, H. *Z. Naturforsch.* **2001**, *56b*, 458.
187. Cheng, Y.; Doyle, D. J.; Hitchcock, P. B.; Lappert, M. F. *Dalton Trans.* **2006**, (37), 4449–4460.
188. Stender, M.; Power, P. P. *Polyhedron* **2002**, *21* (5–6), 525–529.
189. Quillian, B.; Wei, P.; Wannere, C. S.; Schleyer, P. v. R.; Robinson, G. H. *J. Am. Chem. Soc.* **2009**, *131* (9), 3168–3169.
190. Bonyhady, S. J.; Collis, D.; Frenking, G.; Holzmann, N.; Jones, C.; Stasch, A. *Nat. Chem.* **2010**, *2* (10), 865–869.
191. Green, M. L. H.; Mountford, P.; Smout, G. J.; Speel, S. R. *Polyhedron* **1990**, *9* (22), 2763–2765.
192. Baker, R. J.; Farley, R. D.; Jones, C.; Kloth, M.; Murphy, D. M. *Chem. Comm.* **2002**, (11), 1196–1197.
193. Baker, R. J.; Farley, R. D.; Jones, C.; Mills, D. P.; Kloth, M.; Murphy, D. M. *Chem. Eur. J.* **2005**, *11* (10), 2972–2982.
194. Jones, C.; Baker, R. J.; Farley, R. D.; Kloth, M.; Murphy, D. M. *Dalton Trans.* **2002**, 3844–3850.
195. Linti, G.; Köstler, W. *Chem. Eur. J.* **1998**, *4*, 942–949.
196. Fischer, R. A.; Weiß, J. *Angew. Chem.* **1999**, *113*, 589–591.
197. Gemel, C.; Steinke, T.; Cokoja, M.; Kamptner, A.; Fischer, R. A. *Eur. J. Inorg. Chem.* **2004**, 4161–4176.
198. Vidovic, D.; Aldridge, S. *Chem. Sci.* **2011**, *2* (4), 601.
199. Whitmire, K. H. In *Comprehensive Organometallic Chemistry III*; Mingos, D. M. P., Crabtree, R. H., Eds.; vol. 3; Elsevier: Oxford, 2007; pp 343–407.



200. Uhl, W. *Chem. Soc. Rev.* **2000**, 29 (4), 259–265.
201. Uhl, W.; Graupner, R.; Pohl, S.; Saak, W.; Hiller, W.; Neumayer, M. *Z. Anorg. Allg. Chem.* **1997**, 623, 883–891.
202. Uhl, W.; El-Hamdan, A. *Eur. J. Inorg. Chem.* **2004**, 2004 (5), 969–972.
203. Uhl, W.; Lawerenz, A.; Zemke, S. *Z. Anorg. Allg. Chem.* **2007**, 633 (7), 979–985.
204. Uhl, W.; El-Hamdan, A.; Schindler, K. P. *Eur. J. Inorg. Chem.* **2006**, (9), 1817–1823.
205. Uhl, W.; Spies, T.; Saak, W. *Eur. J. Inorg. Chem.* **1998**, 11, 1661–1665.
206. Uhl, W.; Spies, T.; Haase, D.; Winter, R.; Kaim, W. *Organometallics* **2000**, 19 (6), 1128–1131.
207. Uhl, W.; Fick, A.-C.; Spies, T.; Geiseler, G.; Harms, K. *Organometallics* **2003**, 23 (1), 72–75.
208. Uhl, W.; Cuyppers, L.; Prott, M.; Harms, K. *Polyhedron* **2002**, 21 (5–6), 511–518.
209. Uhl, W.; Voß, M.; Layh, M.; Rogel, F. *Dalton Trans.* **2010**, 39 (13), 3160–3162.
210. Uhl, W.; Prött, M.; Geiseler, G.; Harms, K. *Z. Naturforsch.* **2002**, 57b (2), 141–144.
211. Uhl, W.; Spies, T.; Koch, R. *J. Chem. Soc., Dalton Trans.* **1999**, 14, 2385–2391.
212. Uhl, W.; Spies, T.; Saak, W. *Z. Anorg. Allg. Chem.* **1999**, 625 (12), 2095–2102.
213. Uhl, W.; Graupner, R.; Hahn, I.; Spies, T.; Frank, W. *Eur. J. Inorg. Chem.* **1998**, (3), 355–360.
214. Uhl, W.; Cuyppers, L.; Schuler, K.; Spies, T.; Strohmman, C.; Lehmen, K. *Z. Anorg. Allg. Chem.* **2000**, 626 (7), 1526–1534.
215. Uhl, W.; El-Hamdan, A.; Lawerenz, A. *Eur. J. Inorg. Chem.* **2005**, (6), 1056–1062.
216. Üffing, C.; Baum, E.; Köppe, R.; Schnöckel, H. *Angew. Chem. Int. Ed.* **1998**, 37 (17), 2397–2400.
217. Hofmann, A.; Tröster, T.; Kupfer, T.; Braunschweig, H. *Chem. Science* **2019**, 10 (11), 3421–3428.
218. Yurkerwicz, K.; Parkin, G. *J. Cluster Sci.* **2010**, 21 (3), 225–234.
219. Bourque, J. L.; Boyle, P. D.; Baines, K. M. *Chem. Eur. J.* **2015**, 21 (27), 9790–9796.
220. Hardman, N. J.; Eichler, B. E.; Power, P. P. *J. Chem. Soc., Chem. Commun.* **2000**, 1991–1992.
221. Baker, R. J.; Jones, C.; Kloth, M.; Platts, J. A. *Angew. Chem. Int. Ed.* **2003**, 42 (23), 2660–2663.
222. Kempster, A.; Gemel, C.; Fischer, R. A. *Inorg. Chem.* **2008**, 47 (16), 7279–7285.
223. Yurkerwicz, K.; Buccella, D.; Melnick, J. G.; Parkin, G. *Chem. Sci.* **2010**, 1 (2), 210–214.
224. Sandholzer, N.; Linti, G., *Unpublished Results* 1999.
225. Linti, G.; Schnöckel, H., *Unpublished Results*, n.d.
226. Henke, P.; Huber, M.; Steiner, J.; Bowen, K.; Eichhorn, B.; Schnöckel, H. *J. Am. Chem. Soc.* **2009**, 131 (15), 5698–5704.
227. Li, X.-W.; Wei, P.; Beck, B. C.; Xie, Y.; Schaefer, H. F., III; Su, J.; Robinson, G. H. *Chem. Commun.* **2000**, 6, 453–454.
228. Uhl, W.; Melle, S.; Geiseler, G.; Harms, K. *Organometallics* **2001**, 20 (15), 3355–3357.
229. Uhl, W.; Schmück, F.; Geiseler, G. *Z. Anorg. Allg. Chem.* **2002**, 628 (9–10), 1963–1966.
230. Vasko, P.; Mansikkamäki, A.; Fettingner, J. C.; Tuononen, H. M.; Power, P. P. *Polyhedron* **2016**, 103, 164–171.
231. Lichtenhaler, M. R.; Stahl, F.; Kratzert, D.; Heidinger, L.; Schleicher, E.; Hamann, J.; Himmel, D.; Weber, S.; Krossing, I. *Nat. Commun.* **2015**, 6, 8288.
232. Linti, G.; Köstler, W.; Rodig, A. *Eur. J. Inorg. Chem.* **1998**, 745–749.
233. Linti, G.; Köstler, W.; Piotrowski, H.; Rodig, A. *Angew. Chem.* **1998**, 110, 2331–2333.
234. Li, X.-W.; Xie, Y.; Schreiner, P. R.; Gripper, K. D.; Crittendon, R. C.; Campana, C. F.; Schaefer, H. F.; Robinson, G. H. *Organometallics* **1996**, 15, 3798.
235. Hill, M. S.; Pongtavornpinyo, R.; Hitchcock, P. B. *Chem. Commun.* **2006**, (35), 3720–3722.
236. Wiberg, N.; Blank, T.; Lerner, H.-W.; Fenske, D.; Linti, G. *Angew. Chem.* **2001**, 113, 1275–1278.
237. Hill, M. S.; Hitchcock, P. B.; Pongtavornpinyo, R. *Dalton Trans.* **2005**, 273.
238. Holland, P. L.; Cundari, T. R.; Perez, L. L.; Eckert, N. A.; Lachicotte, R. J. *J. Am. Chem. Soc.* **2002**, 124, 14416.
239. Cheng, Y.; Hitchcock, P. B.; Lappert, M. F.; Zhou, M. *Chem. Commun.* **2005**, 752.
240. Mocker, M.; Robl, C.; Schnöckel, H. *Angew. Chem. Int. Ed. Engl.* **1994**, 33 (17), 1754–1755.
241. Ecker, A.; Schnöckel, H. *Z. Anorg. Allg. Chem.* **1996**, 622 (1), 149–152.
242. Ecker, A.; Schnöckel, H. *Z. Anorg. Allg. Chem.* **1998**, 624 (5), 813–816.
243. Ecker, A.; Köppe, R.; Üffing, C.; Schnöckel, H. *Z. Anorg. Allg. Chem.* **1998**, 624 (5), 817–822.
244. Klemp, C.; Köppe, R.; Weckert, E.; Schnöckel, H. *Angew. Chem., Int. Ed.* **1999**, 38, 1740.
245. Klemp, C.; Bruns, M.; Gauss, J.; Häussermann, U.; Stösser, G.; van Wüllen, L.; Jansen, M.; Schnöckel, H. *J. Am. Chem. Soc.* **2001**, 123 (37), 9099–9106.
246. Duan, T.; Stöber, G.; Schnöckel, H. *Angew. Chem. Int. Ed.* **2005**, 44 (19), 2973–2975.
247. Duan, T.; Henke, P.; Stöber, G.; Zhang, Q.-F.; Schnöckel, H. *J. Am. Chem. Soc.* **2010**, 132, 1323–1327.
248. Duan, T.; Stöber, G.; Schnöckel, H. *Z. Anorg. Allg. Chem.* **2005**, 631, 1129–1133.
249. Loos, D.; Schnöckel, H.; Fenske, D. *Angew. Chem. Int. Ed. Engl.* **1993**, 32, 1059.
250. Hardman, N. J.; Power, P. P.; Gordon, J. D.; Macdonald, C. L. B.; Cowley, A. H. *Chem. Commun.* **2001**, (18), 1866–1867.
251. Hartig, J.; Steiner, J.; Stöber, A.; Schnöckel, H. *Chem. Eur. J.* **2007**, 13 (16), 4475–4482.
252. Cole, M. L.; Jones, C.; Kloth, M. *Inorg. Chem.* **2005**, 44 (14), 4909–4911.
253. Linti, G.; Seifert, A. *Z. Anorg. Allg. Chem.* **2008**, 634 (8), 1312–1320.
254. Scheid, D. *Untersuchungen zu Trifluormethansulfonat- und Kronenetherkomplexen von Gallium(I)*. Dissertation, Universität Heidelberg, 2012.
255. Boronski, J. T.; Stevens, M. P.; van Ijzendoorn, B.; Whitwood, A. C.; Slattery, J. M. *Angew. Chem. Int. Ed. Engl.* **2021**, 60 (3), 1567–1572.
256. Zessin, T.; Anton, J.; Linti, G. *Z. Anorg. Allg. Chem.* **2013**, 639 (12–13), 2224–2232.
257. Hawley, A. L.; Ohlin, C. A.; Fohlmeister, L.; Stasch, A. *Chem. Eur. J.* **2017**, 23 (2), 447–455.
258. Dange, D.; Choong, S. L.; Schenk, C.; Stasch, A.; Jones, C. *Dalton Trans.* **2012**, 41 (31), 9304–9315.
259. Desat, M. E.; Gärtner, S.; Kretschmer, R. *Chem. Commun.* **2017**, 53 (9), 1510–1513.
260. Protchenko, A. V.; Urbano, J.; Abdalla, J. A. B.; Campos, J.; Vidovic, D.; Schwarz, A. D.; Blake, M. P.; Mountford, P.; Jones, C.; Aldridge, S. *Angew. Chem. Int. Ed.* **2017**, 56 (47), 15098–15102.
261. Seifert, A.; Linti, G. *Eur. J. Inorg. Chem.* **2007**, 5080–5086.
262. Wehmschulte, R. J.; Power, P. P. *Angew. Chem.* **1998**, 110, 3344.
263. Linti, G.; Köstler, W. *Angew. Chem.* **1997**, 109, 2758–2760.
264. Twamley, B.; Power, P. P. *Angew. Chem. Int. Ed.* **2000**, 39 (19), 3500–3503.
265. Gloatz, K.; Kratzert, D.; Himmel, D.; Kastro, A.; Yassine, Z.; Findeisen, T.; Krossing, I. *Angew. Chem. Int. Ed.* **2018**, 57 (43), 14203–14206.
266. Gloatz, K.; Himmel, D.; Kratzert, D.; Butschke, B.; Scherer, H.; Krossing, I. *Angew. Chem. Int. Ed.* **2019**, 58 (40), 14162–14166.
267. Donchev, A.; Schnepf, A.; Baum, E.; Stöber, G.; Schnöckel, H. *Z. Anorg. Allg. Chem.* **2002**, 628 (1), 157–161.
268. Hill, M. S.; Hitchcock, P. B.; Pongtavornpinyo, R. *Science* **2006**, 311 (5769), 1904–1907.
269. Hill, M. S.; Hitchcock, P. B.; Pongtavornpinyo, R. *Dalton Trans.* **2007**, (7), 731–733.
270. Dohmeier, C.; Loos, D.; Schnöckel, H. *Angew. Chem. Int. Ed. Engl.* **1996**, 35, 129–149.
271. Steiner, J.; Stöber, G.; Schnöckel, H. *Z. Anorg. Allg. Chem.* **2004**, 630 (12), 1879–1882.



272. Steiner, J.; Schnöckel, H. *Chem. Eur. J.* **2006**, *12* (21), 5429–5433.
273. von Hänisch, C.; Fenske, D.; Kattanek, M.; Ahlrichs, R. *Angew. Chem. Int. Ed.* **1999**, *38* (18), 2736–2738.
274. Dohmeier, C.; Robl, C.; Tacke, M.; Schnöckel, H. *Angew. Chem. Int. Ed. Engl.* **1991**, *30* (5), 564–565.
275. Loos, D.; Baum, E.; Ecker, A.; Schnöckel, H.; Downs, A. J. *Angew. Chem.* **1997**, *109*, 894.
276. Schmidt, E. S.; Jokisch, A.; Schmidbaur, H. *J. Am. Chem. Soc.* **1999**, *121*, 9758.
277. Schmidbaur, H.; Schmidt, E. S.; Schier, A. *Dalton Trans.* **2001**, 505–507.
278. Kuchta, M. C.; Bonanno, J. B.; Parkin, G. *J. Am. Chem. Soc.* **1996**, *118*, 10914–10915.
279. Cowley, A. H. *Chem. Comm.* **2004**, (21), 2369–2375.
280. Dias, H. V. R.; Jin, W. *Inorg. Chem.* **2000**, *39* (4), 815–819.
281. Frazer, A.; Hodge, P.; Piggott, B. *Chem. Comm.* **1996**, (15), 1727–1728.
282. Green, C.; Suter, L. *J. Chem. Soc., Dalton Trans.* **1999**, (22), 4087–4092.
283. Reger, D. L. *Coord. Chem. Rev.* **1996**, *147*, 571–595.
284. Andrews, C. G.; Macdonald, C. L. B. *Angew. Chem.* **2005**, *117*, 7619–7622.
285. Cooper, B. F. T.; Macdonald, C. L. B. Mixed or intermediate valence group 13 metal compounds. In *The Group 13 Metals Aluminium, Gallium, Indium and Thallium - Chemical Patterns and Peculiarities*; Aldridge, S., Downs, A. J., Eds., John Wiley and Sons Ltd.: New York, 2011; pp 342–401.
286. Macdonald, C. B.; Cowley, A. H. *J. Am. Chem. Soc.* **1999**, *121*, 12113–12126.
287. Jutzi, P.; Neumann, B.; Reumann, G.; Schebaum, L. O.; Stämmler, H.-G. *Organometallics* **1999**, *18*, 2550–2552.
288. Jutzi, P.; Neumann, B.; Reumann, G.; Stämmler, H.-G. *Organometallics* **1998**, *17*, 1305–1314.
289. Weiß, J.; Stetzkamp, D.; Nuber, B.; Fischer, R. A.; Boehme, C.; Frenking, G. *Angew. Chem.* **1997**, *109*, 95–97.
290. Yu, Q.; Purath, A.; Donchev, A.; Schnöckel, H. *J. Organomet. Chem.* **1999**, *584*, 94–97.
291. Weiss, D.; Steinke, T.; Winter, M.; Fischer, R. A.; Fröhlich, N.; Uddin, J.; Frenking, G. *Organometallics* **2000**, *19* (22), 4583–4588.
292. Gorden, J. D.; Voigt, A.; Macdonald, C. L. B.; Silverman, J. S.; Cowley, A. H. *J. Am. Chem. Soc.* **2000**, *122* (5), 950–951.
293. Jutzi, P.; Neumann, B.; Reumann, G.; Schebaum, L. O.; Stämmler, H. G. *Organometallics* **2001**, *20*, 2854–2858.
294. Yang, Z.; Ma, X.; Oswald, R. B.; Roesky, H. W.; Zhu, H.; Schulzke, C.; Starke, K.; Baldus, M.; Schmidt, H.-G.; Noltemeyer, M. *Angew. Chem.* **2005**, *117*, 7234–7236.
295. Gorden, J. D.; Macdonald, C. L. B.; Cowley, A. H. *Chem. Comm.* **2001**, (1), 75–76.
296. Schulz, S.; Kuczkowski, A.; Schuchmann, D.; Flörke, U.; Nieger, M. *Organometallics* **2006**, *25* (22), 5487–5491.
297. Linti, G.; Monakhov, K.; Bühler, M.; Zessin, T. *Dalton Trans.* **2009**, *38*, 8071–8078.
298. Wade, K. *Chem. Commun.* **1971**, 792–793.
299. Uhl, W. *Naturwissenschaften* **2004**, *91* (7), 305–319.
300. Uhl, W. *Adv. Organomet. Chem.* **2004**, *51*, 53–108.
301. Baker, R. J.; Jones, C. *J. Chem. Soc., Dalton Trans.* **2005**, 1341–1348.
302. Linti, G.; Schnöckel, H.; Uhl, W.; Wiberg, N. Clusters of the heavier group 13 elements. In *Molecular Clusters of the Main Group Elements*; Driess, M., Nöth, H., Eds., Weinheim: Wiley-VCH, 2004; pp 126–168.
303. Uhl, W. *Phosphorus, Sulfur Silicon Relat. Elem.* **2004**, *179* (4–5), 743–748.
304. Rivard, E.; Power, P. P. *Inorg. Chem.* **2007**, *46* (24), 10047–10064.
305. Uhl, W. *Rev. Inorg. Chem.* **1998**, *18* (4), 239–282.
306. Power, P. P. *J. Chem. Soc., Dalton Trans.* **1998**, (18), 2939–2951.
307. Power, P. P. *Chem. Rev.* **1999**, *99* (12), 3463–3504.
308. Maier, C.-F.; Pritzkow, H.; Siebert, W. *Angew. Chem.* **1999**, *111*, 1772.
309. Huber, M.; Schnöckel, H. *Inorg. Chim. Acta* **2008**, *361* (2), 457–461.
310. Schnitter, C.; Roesky, H. W.; Röpken, C.; Herbst-Irmer, R.; Schmidt, H.-G.; Noltemeyer, M. *Angew. Chem. Int. Ed.* **1998**, *37* (13–14), 1952–1955.
311. Purath, A.; Dohmeier, C.; Ecker, A.; Schnöckel, H.; Amelunxen, K.; Passler, T.; Wiberg, N. *Organometallics* **1998**, *17* (9), 1894–1896.
312. Purath, A.; Schnöckel, H. *J. Org. Chem.* **1999**, *579* (1–2), 373–375.
313. Schiefer, M.; Reddy, N. D.; Roesky, H. W.; Vidovic, D. *Organometallics* **2003**, *22* (18), 3637–3638.
314. Sitzmann, H.; Lappert, M. F.; Dohmeier, C.; Üffing, C.; Schnöckel, H. *J. Org. Chem.* **1998**, *561* (1–2), 203–208.
315. Schram, E. P.; Sudha, N. *Inorg. Chim. Acta* **1991**, *183* (2), 213–216.
316. Gauss, J.; Schneider, U.; Ahlrichs, R.; Dohmeier, C.; Schnöckel, H. *J. Am. Chem. Soc.* **1993**, *115* (6), 2402–2408.
317. Uhl, W.; Hiller, W.; Layh, M.; Schwarz, W. *Angew. Chem. Int. Ed. Engl.* **1992**, *31* (10), 1364–1366.
318. Uhl, W.; Jantschak, A. *J. Organomet. Chem.* **1998**, *555*, 263.
319. Linti, G. *J. Organomet. Chem.* **1996**, *520*, 107–113.
320. Linti, G.; Rodig, A. *J. Chem. Soc., Chem. Commun.* **2000**, 127–128.
321. Wiberg, N.; Amelunxen, K.; Lerner, H. W.; Nöth, H.; Ponikvar, W.; Schwenk, H. *J. Organomet. Chem.* **1999**, *574*, 246.
322. Schluter, R. D.; Cowley, A. H.; Atwood, D. A.; Jones, R. A. *J. Coord. Chem.* **1993**, *30*, 25–28.
323. Uhl, W.; Jantschak, A.; Saak, W.; Kaupp, M.; Wartchow, R. *Organometallics* **1998**, *17* (23), 5009–5017.
324. Bühler, M.; Linti, G. *Z. Anorg. Allg. Chem.* **2006**, *2453*–2460.
325. Uhl, W.; Keimling, S. U.; Klinkhammer, K. W.; Schwarz, W. *Angew. Chem. Int. Ed. Engl.* **1997**, *36* (1–2), 64–65.
326. Loos, D.; Schnöckel, H. *J. Organomet. Chem.* **1993**, *463*, 37–40.
327. Buchin, B.; Gemel, C.; Cadenbach, T.; Fischer, R. A. *Inorg. Chem.* **2006**, *45*, 1789–1794.
328. Francis, M. D.; Hitchcock, P. B.; Nixon, J. F.; Schnöckel, H.; Steiner, J. *J. Org. Chem.* **2002**, *646* (1–2), 191–195.
329. Chojnacki, J.; Baum, E.; Krossing, I.; Carmichael, D.; Mathey, F.; Schnöckel, H. *Z. Anorg. Allg. Chem.* **2001**, *627* (6), 1209–1212.
330. Jutzi, P.; Schebaum, L. O. *J. Organomet. Chem.* **2002**, *654*, 176–179.
331. Haaland, A.; Martinsen, K.-G.; Volden, H. V.; Loos, D.; Schnöckel, H. *Acta Chem. Scand.* **1994**, *48*, 172–174.
332. Beachley, O. T., Jr.; Churchill, M. R.; Fettinger, J. C.; Pazik, J. C.; Victoriano, L. *J. Am. Chem. Soc.* **1986**, *108* (15), 4666–4668.
333. Beachley, O. T., Jr.; Blom, R.; Churchill, M. R.; Faegri, J.; Fettinger, J. C.; Pazik, J. C.; Victoriano, L. *Organometallics* **1989**, *8*, 346–356.
334. Haaland, A.; Martinsen, K.-G.; Volden, H. V.; Kaim, W.; Waldhoer, E.; Uhl, W.; Schuetz, U. *Organometallics* **1996**, *15* (4), 1146–1150.
335. Linti, G. *Zur Chemie der Amino- und Silylverbindungen des Galliums*. Habilitationsschrift, Universität Karlsruhe, 1995.
336. Ahlrichs, R.; Ehrig, M.; Horn, H. *Chem. Phys. Lett.* **1991**, *183*, 227.
337. Schneider, U.; Ahlrichs, R.; Horn, H.; Schäfer, A. *Angew. Chem. Int. Ed. Engl.* **1992**, *31*, 353.
338. Linti, G., *Unpublished Results*, n.d.
339. Schulz, S.; Roesky, H. W.; Koch, H. J.; Sheldrick, G. M.; Stalke, D.; Kuhn, A. *Angew. Chem. Int. Ed. Engl.* **1993**, *32*, 1107.
340. Linti, G.; Köstler, W.; Kehrwald, M.; Rodig, A.; Blank, T.; Wiberg, N. *Organometallics* **2001**, *20*, 860–867.
341. Uhl, W.; Benter, M.; Saak, W.; Jones, P. G. *Z. Anorg. Allg. Chem.* **1998**, *624* (10), 1622–1628.
342. Linti, G.; Bühler, M.; Urban, H. *Z. Anorg. Allg. Chem.* **1998**, *624*, 517–520.

343. Uhl, W.; Graupner, R.; Pohlmann, M.; Pohl, S.; Saak, W. *Chem. Ber.* **1996**, *129*, 143.
344. Uhl, W.; Pohlmann, M. *Chem. Commun.* **1998**, 451.
345. Seifert, A. *Niedervalente Galliumverbindungen und deren Reaktionen*. Dissertation, Universität Heidelberg, 2008.
346. Mason, M. R.; Smith, J. M.; Bott, S. G.; Barron, A. B. *J. Am. Chem. Soc.* **1993**, *115*, 4971–4984.
347. Storre, J.; Klemp, A.; Roesky, H. W.; Fleischer, R.; Stalke, D. *Organometallics* **1997**, *16*, 3074–3076.
348. Harlan, C. J.; Bott, S. G.; Barron, A. R. *J. Am. Chem. Soc.* **1995**, *117*, 6465–6474.
349. Uhl, W.; Graupner, R.; Hiller, W.; Neumayer, M. *Angew. Chem.* **1997**, *109*, 62–64.
350. Vollet, J.; Stösser, G.; Schnöckel, H. *Inorg. Chim. Acta* **2007**, *360* (4), 1298–1304.
351. Dohmeier, C.; Mocker, M.; Schnöckel, H.; Löt, A.; Schneider, U.; Ahlrichs, R. *Angew. Chem. Int. Ed. Engl.* **1993**, *32*, 1428–1430.
352. Bonyhady, S. J.; Collis, D.; Holzmann, N.; Edwards, A. J.; Piltz, R. O.; Frenking, G.; Stasch, A.; Jones, C. *Nat. Commun.* **2018**, *9* (1), 3079.
353. Hiller, W.; Klinkhammer, K.-W.; Uhl, W.; Wagner, J. *Angew. Chem.* **1991**, *103*, 103.
354. Linti, G.; Çoban, S.; Dutta, D. *Z. Anorg. Allg. Chem.* **2004**, *630*, 319–323.
355. McKee, M. L.; Wang, Z.-X.; Schleyer, P. V. *J. Am. Chem. Soc.* **2000**, *122*, 4781–4793.
356. Wolf, R.; Uhl, W. *Angew. Chem. Int. Ed.* **2009**, *48* (37), 6774–6776.
357. Wang, Y.; Xie, Y.; Wei, P.; King, R. B.; Schaefer, H. F.; von R. Schleyer, P.; Robinson, G. H. *Science* **2008**, *321* (5892), 1069–1071.
358. Wang, Y.; Xie, Y.; Wei, P.; King, R. B.; Schaefer, I. I. H. F.; Schleyer, P. V. R.; Robinson, G. H. *J. Am. Chem. Soc.* **2008**, *130* (45), 14970–14971.
359. Wang, Y.; Quillian, B.; Wei, P.; Xie, Y.; Wannere, C. S.; King, R. B.; Schaefer, H. F.; Schleyer, P. V. R.; Robinson, G. H. *J. Am. Chem. Soc.* **2008**, *130* (11), 3298–3299.
360. David, S. *Angew. Chem.* **2008**, *120* (11), 2021–2023.
361. Johnson, N. W. *Can. J. Math.* **1966**, *18*, 169–200.
362. Guggenberger, L. J. *Inorg. Chem.* **1969**, *8*, 2771.
363. Jacobson, R. A.; Lipscomb, W. N. *J. Chem. Phys.* **1959**, *31*, 605.
364. Pawley, G. S. *Acta Cryst.* **1966**, *20*, 631.
365. Schnepf, A.; Stöber, G.; Schnöckel, H. *Z. Anorg. Allg. Chem.* **2000**, *626*, 1676.
366. Schnepf, A.; Stöber, G.; Köppe, R.; Schnöckel, H. *Angew. Chem. Int. Ed. Engl.* **2000**, *39*, 1637.
367. Mingos, D. M. P. *Acc. Chem. Res.* **1984**, *17*, 311–319.
368. Baslarkrishnarajan, M. M.; Jemmis, E. D. *J. Am. Chem. Soc.* **2000**, *122*, 4516.
369. Jemmis, E. D.; Baslarkrishnarajan, M. M.; Pancharatna, P. D. *J. Am. Chem. Soc.* **2001**, *123*, 4313–4323.
370. Chen, Z.; Wannere, C. S.; Corminboeuf, C.; Puchta, R.; Schleyer, P. V. R. *Chem. Rev.* **2005**, *105*, 3842–3888.
371. Neuss, J. *Aromatizität, Geschichte und mathematische Analyse eines fundamentalen chemischen Begriffs*, Hyle Publications: Karlsruhe, 2002.
372. Aihara, J. *J. Am. Chem. Soc.* **1978**, *100*, 3339.
373. Schleyer, P. V. R.; Maerker, C.; Dransfeld, A.; Jiao, H.; Hommes, N. J. R. v. E. *J. Am. Chem. Soc.* **1996**, *118*, 6317–6318.
374. Saunders, M.; Jimenez-Vazquez, H. A.; Cross, R. J.; Mroczkowski, S.; Freedberg, D. I.; Anet, F. A. L. *Nature* **1994**, *367*, 256.
375. McKee, M. J. *Inorg. Chem.* **2002**, *41*, 1299.
376. Hönle, W.; Grin, Y.; Burckhardt, A.; Wedig, U.; von Schnerig, H. G.; Kallner, R.; Binder, H. *J. Solid State Chem.* **1997**, *133*, 59.
377. Corminboeuf, C.; Wodrich, M. D.; King, R. B.; von Ragué Schleyer, P. *Dalton Trans.* **2008**, (13), 1745–1751.
378. King, R. B.; Schleyer, P. V. R. Theory and concepts in Main-group cluster Chemistry. In *Molecular Clusters of the Main Group Elements*; Driess, M., Nöth, H., Eds., Wiley-VCH: Weinheim, New York, 2004; pp 1–33.
379. Schleyer, P. V. R.; Subramanian, G.; Jiao, J.; Najafian, K.; Hofmann, M. In *Advances in Boron Chemistry*; Siebert, W., Ed., Royal Society of Chemistry: Cambridge, 1997; pp 3–14.
380. Schleyer, P. V. R.; Najafian, K. In *The Borane, Carborane and Carbocation Continuum*; Casanova, J., Ed., John Wiley & Sons: New York, 1998; pp 169–190.
381. Schleyer, P. V. R.; Najafian, K. *Inorg. Chem.* **1998**, *37* (14), 3454–3470.
382. Chi, X. X.; Li, X. H.; Chen, X. J.; Yuan, Z. S. *J. Mol. Struct. Theochem.* **2004**, *677* (1), 21–27.
383. Chi, X. X.; Chen, X. J.; Yuan, Z. S. *J. Mol. Struct. Theochem.* **2005**, *732* (1), 149–153.
384. Feixas, F.; Jiménez-Halla, J. O. C.; Matito, E.; Poater, J.; Solà, M. *J. Chem. Theory Comput.* **2010**, *6* (4), 1118–1130.
385. Gortov, M.; Kloo, L. *Coord. Chem. Rev.* **2008**, *252* (15), 1564–1576.
386. Jusélius, J.; Straka, M.; Sundholm, D. *J. Phys. Chem. A* **2001**, *105* (43), 9939–9944.
387. Kuznetsov, A. E.; Boldyrev, A. I.; Li, X.; Wang, L. S. *J. Am. Chem. Soc.* **2001**, *123* (36), 8825–8831.
388. Kuznetsov, A. E.; Boldyrev, A. I. *Struct. Chem.* **2002**, *13*, 141–148.
389. Melko, J. J.; Ong, S. V.; Gupta, U.; Reveles, J. U.; D'Emidio, J.; Khanna, S. N.; Castleman, A. W. *Chem. Phys. Lett.* **2010**, *500* (4–6), 196–201.
390. Nigam, S.; Majumder, C.; Kulshreshtha, S. K. *J. Chem. Sci.* **2006**, *118* (6), 575–578.
391. Nigam, S.; Majumder, C.; Kulshreshtha, S. K. *J. Mol. Struct. Theochem.* **2005**, *755* (1–3), 187–194.
392. Zhai, H. J.; Kiran, B.; Li, J.; Wang, L. S. *Nat. Mater.* **2003**, *2* (12), 827–833.
393. Seal, P. *J. Mol. Struct. Theochem.* **2009**, *893* (1–3), 31–36.
394. Li, X.-W.; Pennington, W. T.; Robinson, G. H. *J. Am. Chem. Soc.* **1995**, *117*, 7578.
395. Bühler, M. *Synthese silylsubstituierter Indiumcluster und quantenchemische Berechnungen von Clusterverbindungen von Elementen der dritten Hauptgruppe*. Dissertation, Heidelberg University, 2007.
396. Linti, G.; Bühler, M.; Monakhov, K.; Zessin, T. Cages and clusters of indium – Spherical aromaticity?. In *Molecular Modeling*; Comba, P., Ed., Wiley-VCH: Weinheim, 2011.
397. King, R. B. *Inorg. Chim. Acta* **1981**, *49*, 237.
398. von Hänisch, C. K. F.; Üffing, C.; Junker, M. A.; Ecker, A.; Kneisel, B. O.; Schnöckel, H. *Angew. Chem.* **1996**, *108*, 3003–3005.
399. Antipin, M.; Boese, R.; Bläser, D.; Maulitz, A. *J. Am. Chem. Soc.* **1997**, *119*, 326–333.
400. Brack, M. *Rev. Mod. Phys.* **1993**, *65*, 677.
401. Martin, T. *Phys. Rep.* **1996**, *273*, 199.
402. Heer, W. A. D. *Rev. Mod. Phys.* **1993**, *65*, 611.
403. Huber, M.; Henke, P.; Schnöckel, H. *Chem. Eur. J.* **2009**, *15* (45), 12180–12183.
404. Schnöckel, H.; Schnepf, A.; Aldridge, S. Aluminium and gallium clusters: Metalloid clusters and their relationship to the bulk phases, to naked clusters and to Nanoscaled materials. In *The Group 13 Metals Aluminium, Gallium, Indium and Thallium - Chemical Patterns and Peculiarities*; Downs, A. J., Ed., John Wiley & Sons: New York, 2011; pp 402–487.
405. Çoban, S.; Linti, G., *Unpublished Results* 1999.
406. Widdifield, C. M.; Jurca, T.; Richeson, D. S.; Bryce, D. L. *Polyhedron* **2012**, *35* (1), 96–100.
407. Purath, A.; Köppe, R.; Schnöckel, H. *J. Chem. Soc., Chem. Commun.* **1999**, 1933.
408. Wiberg, N.; Blank, T.; Nöth, H.; Ponikvar, W. *Angew. Chem.* **1999**, *111*, 887.
409. Maxwell, W. M.; Weiss, R.; Sinn, E.; Grimes, R. N. *J. Am. Chem. Soc.* **1977**, *99* (12), 4016–4029.
410. Sevov, S. C.; Corbett, J. D. *Inorg. Chem.* **1991**, *30*, 4875–4877.

411. Linti, G.; Seifert, A. *Dalton Trans.* **2008**, (28), 3688–3693.
412. Ecker, A.; Weckert, E.; Schnöckel, H. *Nature* **1997**, *387*, 379.
413. Köhnlein, H.; Purath, A.; Klemp, C.; Baum, E.; Krossing, I.; Stösser, G.; Schnöckel, H. *Inorg. Chem.* **2001**, *40*, 4830–4838.
414. Bazhin, I.; Leshcheva, O.; Nikiforov, I. *Phys. Solid State* **2006**, *48* (4), 774–779.
415. Schmid, G.; Alexander, B. D.; Barthelmes, J.; Mueting, A. M.; Pignolet, L. H. *Inorg. Synth.* **1990**, 214–218.
416. Tran, N. T.; Powell, D. R.; Dahl, L. F. *Angew. Chem.* **2000**, *112* (22), 4287–4291.
417. Jadzinsky, P. D.; Calero, G.; Ackerson, C. J.; Bushnell, D. A.; Kornberg, R. D. *Science* **2007**, *318* (5849), 430–433.
418. Jarrod, M. F.; Bower, J. E.; Kraus, J. S. *J. Chem. Phys.* **1987**, *86*, 3876.
419. Jarrod, M. F.; Bower, J. E. *J. Am. Chem. Soc.* **1988**, *110*, 6706.
420. Leuchtner, R. E.; Harms, A. C.; Castleman, A. W. *J. Chem. Phys.* **1991**, *94*, 1093.
421. Kaya, K.; Fuke, K.; Nonose, S.; Kikuchi, N. *Z. Phys. D: At., Mol. Clusters* **1989**, *12*, 571.
422. Bergeron, D. E.; Roach, P. J.; Castleman, A. W.; Jones, N.; Khanna, S. N. *Science* **2005**, *307*, 231.
423. Vollet, J.; Hartig, J. R.; Schnöckel, H. *Angew. Chem.* **2004**, *116* (24), 3248–3252.
424. Clayborne, P. A.; Lopez-Acevedo, O.; Whetten, R. L.; Grönbeck, H.; Häkkinen, H. *J. Chem. Phys.* **2011**, *135* (9), 094701.
425. Clayborne, P. A.; Lopez-Acevedo, O.; Whetten, R. L.; Grönbeck, H.; Häkkinen, H. *Eur. J. Inorg. Chem.* **2011**, *2011* (17), 2649–2652.
426. Walter, M.; Akola, J.; Lopez-Acevedo, O.; Jadzinsky, P. D.; Calero, G.; Ackerson, C. J.; Whetten, R. L.; Grönbeck, H.; Häkkinen, H. *PNAS* **2008**, *105* (27), 9157–9162.
427. Purath, A.; Dohmeier, C.; Ecker, A.; Köppe, R.; Krautscheid, H.; Schnöckel, H. G.; Ahlrichs, R.; Stoermer, C.; Friedrich, J.; Jutzi, P. *J. Am. Chem. Soc.* **2000**, *122*, 6955–6959.
428. Huber, M.; Hartig, J.; Koch, K.; Schnöckel, H. *Z. Anorg. Allg. Chem.* **2009**, *635*, 423.
429. Huber, M.; Schnepf, A.; Anson, C. E.; Schnöckel, H. *Angew. Chem. Int. Ed.* **2008**, *47*, 8201.
430. Schnepf, A.; Schnöckel, H. *Angew. Chem. Int. Ed.* **2002**, *41*, 3533.
431. Schnepf, A.; Köppe, R.; Schnöckel, H. *Angew. Chem.* **2001**, *113*, 1287.
432. Wiberg, N.; Blank, T.; Nöth, H.; Suter, M.; Warchold, M. *Eur. J. Inorg. Chem.* **2002**, *4*, 929.
433. Wiberg, N.; Blank, T.; Purath, A.; Stoesser, G.; Schnöckel, H. *Angew. Chem.* **1999**, *111*, 2745.
434. Jemmis, E. D.; Baslarkrishnarajan, M. M.; Pancharatna, P. D. *J. Am. Chem. Soc.* **2000**, *123*, 4313.
435. King, R. B. *J. Organomet. Chem.* **2002**, *646*, 146–152.
436. King, R. B. *Inorg. Chim. Acta* **1996**, *252*, 115–121.
437. Wang, Z. X.; Schleyer, P. V. R. *Angew. Chem.* **2002**, *114*, 4256–4259.
438. J. Steiner, E. B., G. Linti, H. Schnöckel, *Unpublished Results Structural Data: CCDC180407*, n.d.
439. A. Stöber, H. Schnöckel, J. Steiner, C. Anson, *Unpublished Results*, n.d.
440. Steiner, J.; Stöber, G.; Schnöckel, H. *Angew. Chem. Int. Ed.* **2003**, *42* (17), 1971–1974.
441. Donchev, A.; Schnepf, A.; Stöber, G.; Baum, E.; Schnöckel, H.; Blank, T.; Wiberg, N. *Chem. Eur. J.* **2001**, *7* (15), 3348–3353.
442. Degtyareva, O.; McMahon, M. I.; Allan, D. R.; Nelmes, R. J. *Phys. Rev. Lett.* **2004**, *93* (20), 205502.
443. Weiß, K.; Schnöckel, H. *Z. Anorg. Allg. Chem.* **2003**, *629* (7–8), 1175–1183.
444. Weiß, K.; Schnöckel, H. *Anal. Bioanal. Chem.* **2003**, *377* (7), 1098–1101.
445. Corbett, J. D. Diverse naked clusters of the heavy Main-group elements. Electronic regularities and analogies. In *Structural and Electronic Paradigms*; Mingos, D. M. P., Ed.; *Cluster Chemistry*, Springer Berlin Heidelberg: Berlin, Heidelberg, 1997; pp 157–193.
446. Corbett, J. D. *Angew. Chem. Int. Ed.* **2000**, *39*, 670.
447. Corbett, J. D. *Inorg. Chem.* **2000**, *39*, 5178.
448. Ponou, S.; Fässler, T. F.; Tobias, G.; Canadell, E.; Cho, A.; Sevov, S. C. *Chem. Eur. J.* **2004**, *10*, 3615–3621.
449. Schnepf, A.; Stöber, G.; Schnöckel, H. *Angew. Chem.* **2002**, *114*, 1959–1962.
450. Schnepf, A.; Köppe, R.; Weckert, W.; Schnöckel, H. *Chem. Eur. J.* **2004**, *10*, 1977–1981.
451. Steiner, J.; Stöber, G.; Schnöckel, H. *Angew. Chem.* **2004**, *116*, 6712–6715.
452. Hartig, J.; Stöber, A.; Hauser, P.; Schnöckel, H. *Angew. Chem.* **2007**, *119*, 1689–1691.
453. Duan, T.; Baum, E.; Burgert, R.; Schnöckel, H. *Angew. Chem.* **2004**, *116*, 3252–3255.
454. Hartig, J.; Klöwer, F.; Rinck, J.; Unterreiner, A.-N.; Schnöckel, H. *Angew. Chem.* **2007**, *119* (34), 6669–6672.
455. Linti, G.; Rodig, A. *Angew. Chem.* **2000**, *112*, 3076.
456. Steiner, J.; Stöber, G.; Schnöckel, H. *Angew. Chem.* **2004**, *116*, 306–309.
457. Wang, Z.-X.; Schleyer, P. V. R. *J. Am. Chem. Soc.* **2003**, *125*, 10484.
458. Fehner, T.; Halet, J.-F.; Saillard, J.-Y. *Molecular Clusters*, Cambridge University Press: Cambridge, 2007.
459. Hartig, J.; Schnepf, A.; Jongh, L. H.d.; Bono, D.; Schnöckel, H. *Z. Anorg. Allg. Chem.* **2007**, *633*, 63–76.
460. Bakharev, O. N.; Bono, D.; Brom, H. B.; Schnepf, A.; Schnöckel, H.; Jongh, L. J.d. *Phys. Rev. Lett.* **2006**, *96*, 117002–1.
461. Bono, D.; Bakharev, O. N.; Schnepf, A.; Hartig, J.; Schnöckel, H.; Jongh, L. J.d. *Z. Anorg. Allg. Chem.* **2007**, *633*, 2173–2177.
462. Bono, D.; Schnepf, A.; Hartig, J.; Schnöckel, H.; Nieuwenhuys, G. J.; Amato, A.; Jongh, L. J.d. *Phys. Rev. Lett.* **2006**, *97*, 077601–077605.
463. Eichler, B. E.; Hardman, N. J.; Power, P. P. *Angew. Chem.* **2000**, *112*, 391.
464. Protchenko, A. V.; Dange, D.; Blake, M. P.; Schwarz, A. D.; Jones, C.; Mountford, P.; Aldridge, S. *J. Am. Chem. Soc.* **2014**, *136* (31), 10902–10905.
465. Protchenko, A. V.; Dange, D.; Harmer, J. R.; Tang, C. Y.; Schwarz, A. D.; Kelly, M. J.; Phillips, N.; Tirfain, R.; Birjumar, K. H.; Jones, C.; Kaltsayannis, N.; Mountford, P.; Aldridge, S. *Nat. Chem.* **2014**, *6* (4), 315–319.

## 1.18 Aromatic compounds bearing heavy group 14 atoms in their molecular frameworks

Masaichi Saito, Department of Chemistry, Graduate School of Science and Engineering, Saitama University, Saitama, Saitama, Japan

© 2023 Elsevier Ltd. All rights reserved.

<b>1.18.1</b>	<b>Introduction</b>	<b>844</b>
<b>1.18.2</b>	<b>Aromatic heavy group 14 atom frameworks</b>	<b>844</b>
1.18.2.1	Pioneering works	844
1.18.2.2	Cyclopentadienyl analogs	844
1.18.2.2.1	Group 14 metallole anion equivalents	844
1.18.2.2.2	Group 14 metallolide dianion equivalents	846
1.18.2.2.3	Benzannulated Group 14 metallolide dianion equivalents	850
<b>1.18.2.3</b>	<b>Benzene and polycyclic aromatic hydrocarbon analogs</b>	<b>851</b>
1.18.2.3.1	Silicon analogs of benzene and related polycyclic aromatic hydrocarbons containing one silicon atom	851
1.18.2.3.2	Germanium analogs of benzene and related polycyclic aromatic hydrocarbons containing one germanium atom	852
1.18.2.3.3	Tin analogs of benzene and related polycyclic aromatic hydrocarbons containing one tin atom	855
1.18.2.3.4	Heavy analogs of phenyl anions	856
1.18.2.3.5	Benzene and polycyclic aromatic hydrocarbon analogs containing more than two heavy group 14 atoms	856
1.18.2.4	Cyclopropenyl cation analogs	858
1.18.2.5	Cyclobutadiene dianion and dication analogs	859
<b>1.18.3</b>	<b>Conclusion and outlook</b>	<b>860</b>
<b>References</b>		<b>860</b>

### Nomenclature

Acr 9-Acrydinyl

Ad 1-Adamantyl

ASE Aromatic stabilization energy

Cp/Cp<sup>-</sup> Cyclopentadienyl

HMDS Hexamethyldisilazide

HOMO Highest occupied molecular orbital

LDA Lithium diisopropylamide

LUMO Lowest unoccupied molecular orbital

NICS Nucleus-independent chemical shift

NMR Nuclear magnetic resonance

Cp\* 1,2,3,4,5-Pentamethylcyclopentadienyl

Mes 2,4,6-Trimethylphenyl

Mes\* 2,4,6-Tri-*t*-butylphenyl

Tbt 2,4,6-Tris[bis(trimethylsilyl)methyl]phenyl

TSFPB Tetrakis[4-(*t*-butyldimethylsilyl)-2,3,5,6-tetrafluorophenyl]borate

TTFPB Tetrakis(2,3,5,6-tetrafluorophenyl)borate

12-crown-4 1,4,7,10-Tetraoxacyclododecane

18-crown-6 1,4,7,10,13,16-Hexaoxacyclooctadecane

Tbb 5-(*t*-Butyl)-1,3-bis[bis(trimethylsilyl)methyl]phenyl

Bbt 2,6-Bis[bis(trimethylsilyl)methyl]-4-[tris(trimethylsilyl)methyl]phenyl

crypt-222 [2.2.2]Cryptand, 4,7,13,16,21,24-Hexaoxa-1,10-diazabicyclo[8.8.8]hexacosane

### Abstract

The synthesis of aromatic compounds bearing heavy group 14 atoms (Si, Ge, Sn and Pb) in carbon frameworks is summarized. In most cases, the replacement of skeletal carbon atoms of aromatic compounds by heavy group 14 atoms does

not collapse the original aromaticity, even though some cases reveal that coordination to metals are of crucial importance to retain aromaticity. Some characteristics different from those of the conventional aromatic compounds are also found. The carbon-based aromatic world is now expanded to the systems containing lead and it would inspire new theory, materials, and catalytic chemistry.

### 1.18.1 Introduction

Since the discovery of benzene by Faraday in 1825<sup>1</sup> and its structure was first proposed by Kekulé in 1865,<sup>2,3</sup> the concept of aromaticity to understand the unique properties of benzene has long received considerable fundamental interest and remains discussed.<sup>4</sup> One of the most important arguments in the history of aromaticity is what is aromaticity.<sup>5–8</sup> The difficulty in this question is caused by the fact that aromaticity is not a physical quantity but a nature. However, we traditionally conclude that a molecule is aromatic when it possesses the following characteristics similar to those of benzene: 1) planarity with cyclic delocalized ( $4n + 2$ )  $\pi$ -electrons (Hückel rule),<sup>9,10</sup> 2) bond equalization (structural criterion), 3) induced diatropic ring current under an external magnetic field (magnetic criterion), and 4) thermal stability compared to that of acyclic isomers (energetic criterion). No single property cannot justify aromaticity of a compound. The aromaticity of benzene and its related compounds arises from delocalization of  $\pi$ -electrons, therefore it should be called  $\pi$ -aromaticity. Nowadays, new types of aromaticity such as homoaromaticity,<sup>11</sup>  $\sigma$ -aromaticity,<sup>12</sup> excited-state aromaticity<sup>13,14</sup> and Möbius aromaticity<sup>15,16</sup> have also received considerable attention; however, this review concentrates on  $\pi$ -aromaticity.

In parallel with the intensively investigated aromaticity in carbon chemistry, the field of main group chemistry witnessed the break of double-bond rule that had long been believed in.<sup>17</sup> The compounds with a Si=Si<sup>18</sup> and a P=P<sup>19</sup> bonds are of considerable historical importance as the first examples of stable compounds bearing double bonds between the third-row elements. After the ground-breaking results, main group chemists focused on the synthesis of compounds between different combinations of atoms. Until the late 1990s, stable double-bonded compounds with a lot of combinations were isolated,<sup>20–22</sup> and even a compound bearing the heaviest double bond, Bi=Bi,<sup>23</sup> was conquered. The replacement of carbon atoms in C=C and C-heteroatom double bonds by heavy group 14 atoms was particularly intensively investigated.<sup>24</sup>

In the course of the studies on the replacement of a carbon atoms by heavy group 14 atom, the next targeted class of compounds was an aromatic compound, thus, one of the skeletal carbon atoms of aromatic compounds such as benzene and cyclopentadienyl anion ( $\text{Cp}^-$ ) was replaced by a heavy group 14 atom. This review focuses on the synthesis of such ring compounds with Hückel  $\pi$ -aromaticity incorporated by heavy group 14 atoms into carbon skeletons.

## 1.18.2 Aromatic heavy group 14 atom frameworks

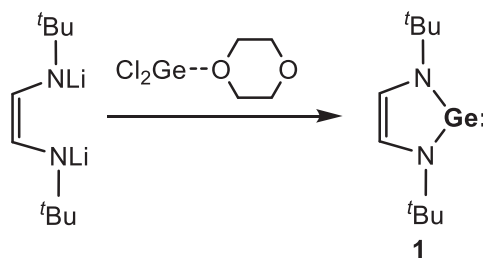
### 1.18.2.1 Pioneering works

The pioneering work is the synthesis of 1,3-bis(*tert*-butyl)-1,3-diaza-2(*2H*)-germolylidene **1** by Hermann in 1992 (Scheme 1),<sup>25</sup> inspired by the synthesis of a stable, crystalline *N*-heterocyclic carbene by Arduengo in 1991.<sup>26</sup> In Hermann's paper, aromaticity of **1** was not discussed; however, compound **1** was reported to be more stable than the corresponding saturated germylene, suggesting that electronic delocalization should stabilize **1**. The following theoretical investigations also suggested the electronic delocalization in **1**.<sup>27,28</sup> The *N*-heterocyclic framework was also utilized to stabilize the silicon analog **2**, reported by Denk and West (Scheme 2).<sup>29</sup> In the paper, they suggested  $6\pi$  aromatic delocalization of **2**, and finally aromaticity of **1** and **2** was established by their NICS calculations,<sup>30</sup> which is now widely used as an effective probe for aromaticity.<sup>31</sup> From the experimental side, the Raman spectroscopy was applied to elucidate aromaticity of **1** and **2** (Scheme 3).<sup>32,33</sup> The Raman signals assignable to the stretching vibration of C=C in compounds **1** and **2** shift to longer wavelength, compared with those of the reference compounds whose the group 14 centers are tetravalent thus without aromatic delocalization.

### 1.18.2.2 Cyclopentadienyl analogs

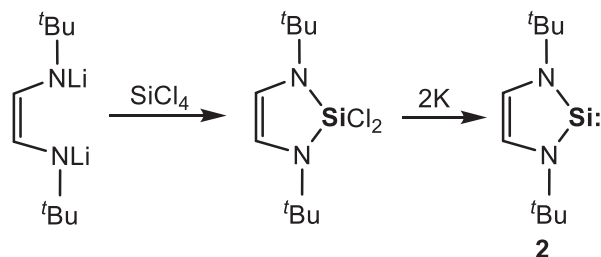
#### 1.18.2.2.1 Group 14 metallole anion equivalents<sup>34</sup>

Theoretical predictions reveal that the heavy group 14 analogs of  $\text{Cp}^-$ , a silole, a germole, a stannole and a plumbole anion, possess pyramidalized structures at the group 14 atoms and hence to be non-aromatic, in contrast to the planar structure of

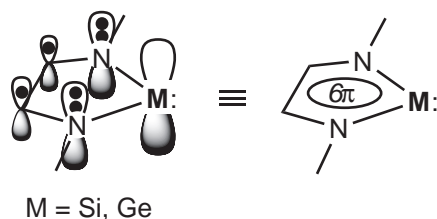


Scheme 1 Synthesis of **1**.





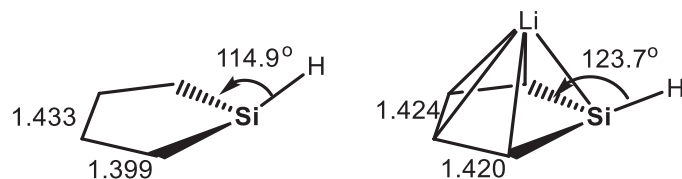
**Scheme 2** Synthesis of **2**.



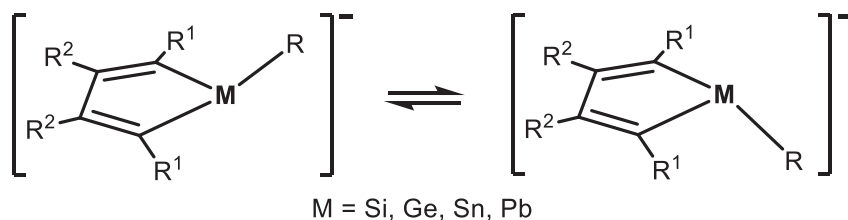
**Scheme 3** Origin of the aromaticity of *N*-heterocyclic metallylenes, 1,3-bis(*tert*-butyl)-1,3-diaza-2(*2H*)-metalloylidene.

aromatic  $\text{Cp}^-$ .<sup>35,36</sup> On the other hand,  $\eta^5$ -coordination of a metallole anion to a lithium atom is calculated to make the metal center more flattened to increase aromaticity of a molecule (Fig. 1).<sup>35,36</sup> Indeed, the X-ray diffraction analysis of alkaline metal salts of group 14 metallole anions reveal that the group 14 centers have pyramidalized geometries, indicating their non-aromatic characters.<sup>37–40</sup> The inversion barrier was experimentally estimated to be less than 8.4 kcal/mol by NMR analysis (Schemes 4).<sup>38</sup> In contrast, lithium silolides and -germolides, regarded as contact ion pairs between alkaline metals and metallole anions, possess delocalized aromatic structures (Schemes 5 and 6),<sup>41–43</sup> as was predicted in the theoretical calculations.

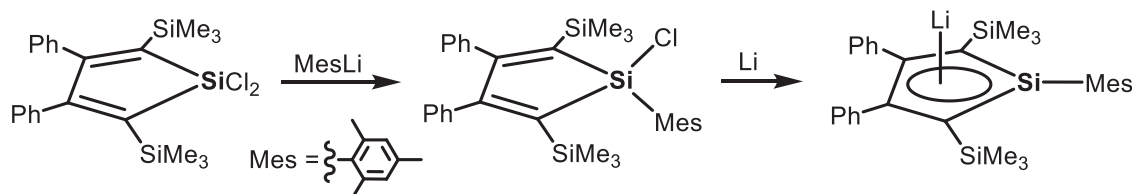
Heavy congeners of cyclopentadienyllithium ( $\text{CpLi}$ ) containing more than two heavy group atoms have also been reported. Reduction of 1,2-disila-3-germacyclopenta-2,4-diene **3** by potassium graphite afforded a potassium 1,2-disila-3-germacyclopenta-2,4-dienide, which reacted with lithium bromide to afford lithium 1,2-disila-3-germacyclopenta-2,4-dienide **4** (Scheme 7).<sup>44</sup> The structure of the five-membered ring is almost planar, and the  $^7\text{Li}$  NMR signal was observed in a high-field region, indicating its aromatic nature. A similar synthetic route was applied for the synthesis of lithium 1,2,3-trisilacyclopentadienide **5**.<sup>45</sup> The planarity of the five-membered ring and the  $^7\text{Li}$  NMR signal in a high-field region support its aromatic nature. The contact-ion-pair structure is of crucial importance to retain its aromatic nature, and addition of 12-crown-4 results in the collapse of the aromatic structure to provide isomeric trisilenide **6** through 1,2-silyl migration (Scheme 8).



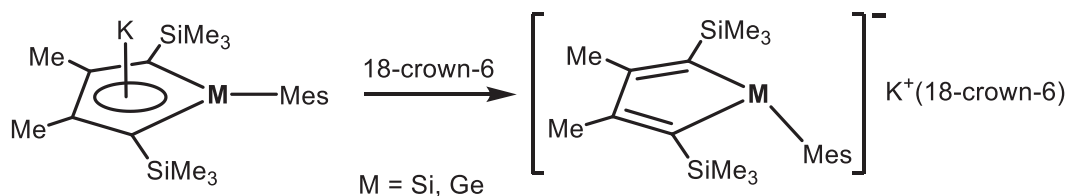
**Fig. 1** Comparison of calculated structures of the parent silolide anion (left) and lithium silolide (right) (RMP2(fc)/6-31G\*\* level, bond lengths in Å).



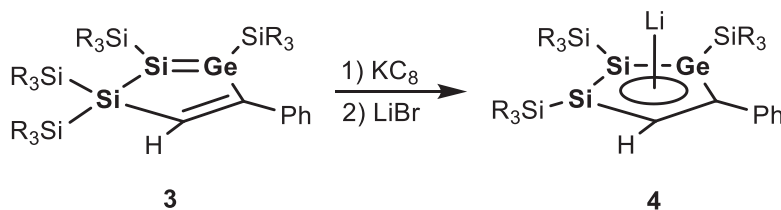
**Scheme 4** Inversion at a group 14 center of a non-aromatic metallole anion.



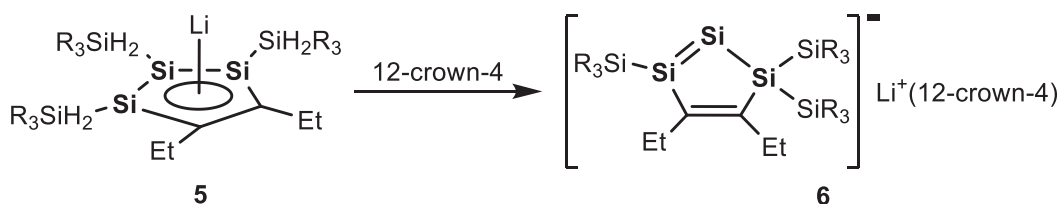
**Scheme 5** Synthesis of an aromatic lithium silolide



**Scheme 6** Aromatic and non-aromatic switch of metallolide anions.



**Scheme 7** Synthesis of a heavy CpLi containing three silicon atoms.

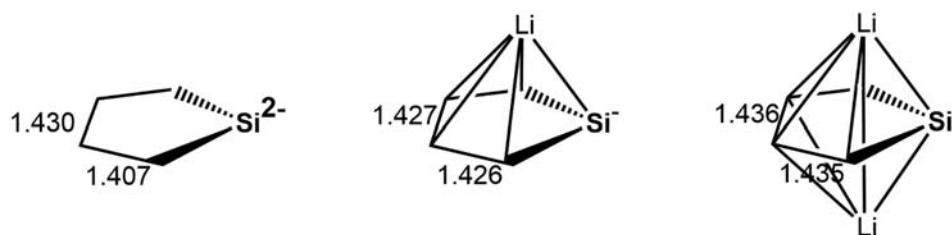


**Scheme 8** Importance of an  $\eta^5$ -coordination of a lithium atom to maintain the aromatic structure.

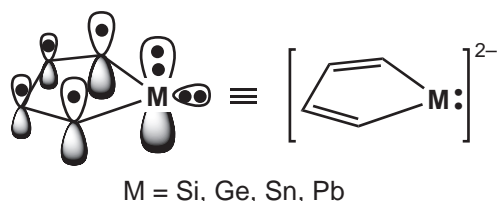
#### 1.18.2.2.2 Group 14 metallolide dianion equivalents<sup>34,46,47</sup>

The pyramidalization at group 14 centers of the metallolide anions does not take place in the metallolide dianions. Theoretical investigation reveals that the free metallolide dianions should be aromatic with small C–C bond alternation, and the  $\eta^5$ -coordinating lithium metallolide and the  $\eta^5, \eta^5$ -coordinating dilithium metallolide dianions should be more aromatic, based on the structural (C–C bond alternation), magnetic (NICS) and energetic criteria (Fig. 2). The metallolide dianions can be regarded as dianions of metal-lacyclopentadienylidene, where the diene frameworks contain  $6\pi$  electrons and the metal centers adopt divalent states (Fig. 3).<sup>48</sup>

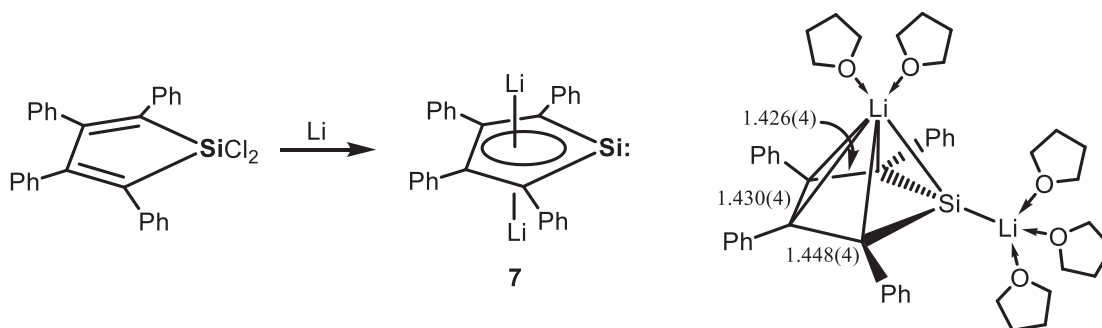
The first structural characterization of this series is dilithium silole 7 reported in 1995 (Scheme 9),<sup>49</sup> after its generation in solution had been reported a year ago.<sup>48</sup> The molecular structure is not an  $\eta^5, \eta^5$ -coordinating structure but an  $\eta^1, \eta^5$ -coordinating structure, which is calculated to be less stable than the former. The C–C bond distances in the silole ring are almost equal,



**Fig. 2** Structural changes from the parent silole to dilithium silole (B3LYP/6-31+G(d) for C and H; LanL2DZdp for Si). A similar tendency is found in the parent germole, stannole and plumbole series.



**Fig. 3** The structure of metallolediide ion.

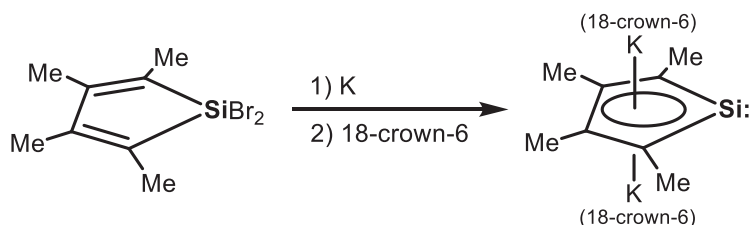


**Scheme 9** Synthesis of dilithium silole diide **7** and its X-ray structure with selected bond distances (Å).

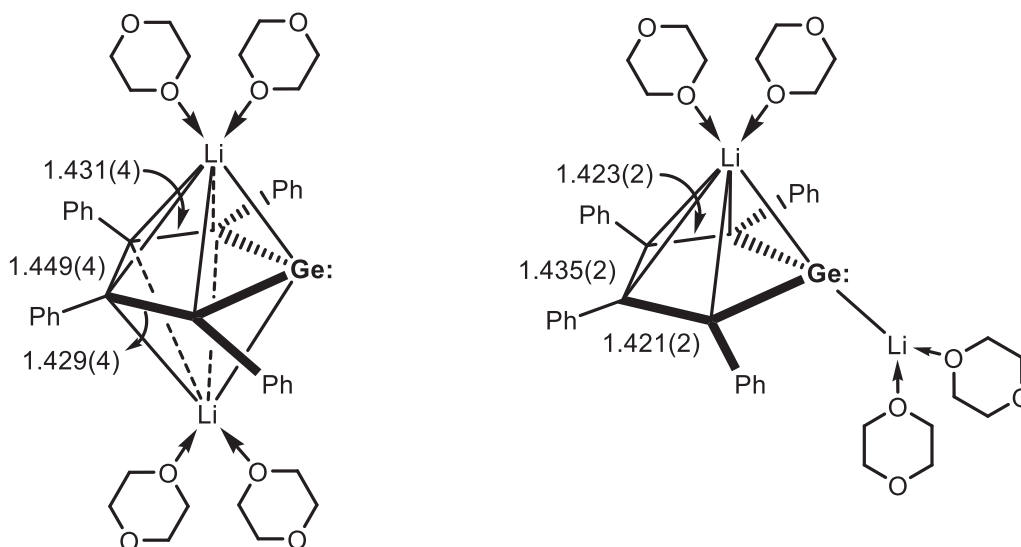
suggesting aromaticity of the compound based on the structural criterion. Dipotassium tetraalkylsilole diides are also X-ray characterized; however, their molecular structures adopt  $\eta^5, \eta^5$ -coordinating structures, and each of the potassium atoms are coordinated by a crown ether (**Scheme 10**).<sup>38,50</sup> The five-membered rings possess no C–C bond alternation, suggesting their aromatic nature. The synthesis of dilithium germolediides have also been achieved.<sup>51</sup> Dilithium tetraphenylgermolediide **8** possesses an  $\eta^5, \eta^5$ -coordinating as well as  $\eta^1, \eta^5$ -coordinating structures in the solid state (**Fig. 4**), and the former is calculated to be more unstable, as is observed in dilithium tetraphenylsilole diide **7**. The aromatic stabilization energy is estimated to be 13 kcal/mol in the calculations of the parent model compounds. In contrast, dipotassium tetramethylgermolediide **9** has an  $\eta^5, \eta^5$ -coordinating, dimeric structure in the solid state (**Scheme 11**).<sup>38</sup>

After about 10 years, the aromatic world was extended to a tin-bearing system. The generation of dilithium tetraphenylstannolediide **11** was first evidenced by NMR analysis and trapping experiments,<sup>52</sup> and its X-ray characterization was reported in 2005 (**Scheme 12**).<sup>53</sup> The five-membered ring, coordinating two lithium atoms in  $\eta^5, \eta^5$ -fashions, is almost planar with no C–C bond alternation, indicating considerable electronic delocalization. The <sup>7</sup>Li NMR signal is observed at –4.36 ppm in a region higher than those of normal organolithium compounds (–2 to 2 ppm) due to a shielding effect of the aromatic ring current on the stanole ring, and the NICS(1) of the free stanolelediide dianion<sup>54</sup> is calculated to be –6 ppm. Based on all of the data, the aromatic nature of dilithium stanolelediide **11** is established. Dilithium tetraethylstannolediide **12** was also synthesized and its aromatic nature is elucidated (**Scheme 12**).<sup>55</sup>

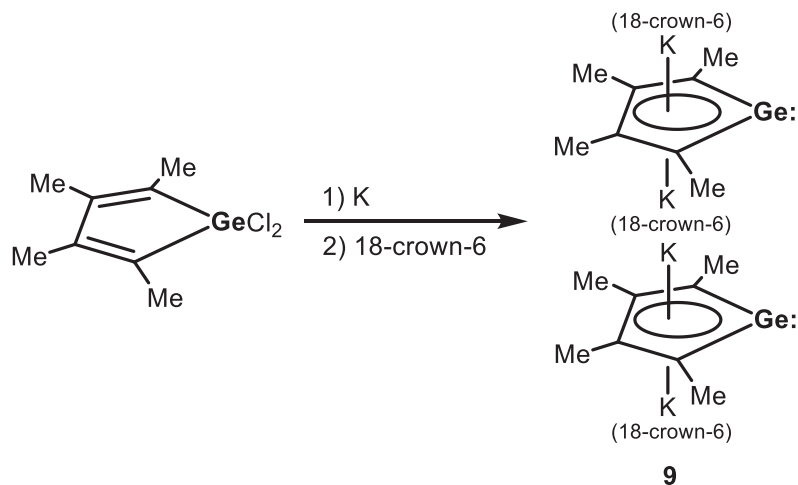
As an ultimate goal, the heaviest dilithium metallolediide, dilithium plumbolediide **13** was conquered in 2010 (**Scheme 13**).<sup>39</sup> The characterized molecular structure exhibits a lithium salt of a lithiumplumbolediide anion, where one of the two lithium atoms is coordinated by the plumbole ring in an  $\eta^5$ -fashion and the other one is coordinated by three dimethoxyethane (DME) molecules that are used in recrystallization. The plumbolide ring is almost planar with no C–C bond alternation, indicating considerable electronic delocalization. The NICS(1) of the free plumbolediide dianion is calculated to be –6.3 ppm, and accordingly, it is concluded that dilithium plumbolediide possesses aromatic nature and 2p(C) and 6p(Pb) orbitals can be sufficiently overlapped to produce aromatic delocalization. An important structural characteristic is found on the structure of dilithium plumbolediide **13**. The Pb–C bond distances are 2.242(4) and 2.265(5) Å, which are longer than those of the precursor (2.202(4) and 2.211(4) Å) with no



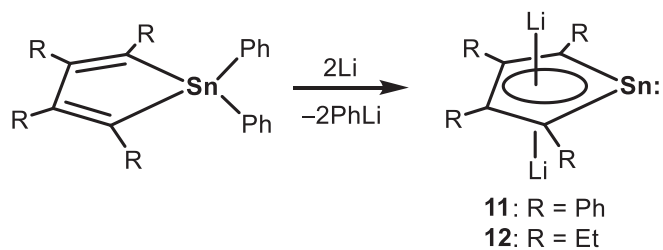
**Scheme 10** Synthesis of dipotassium tetramethylsilole diide



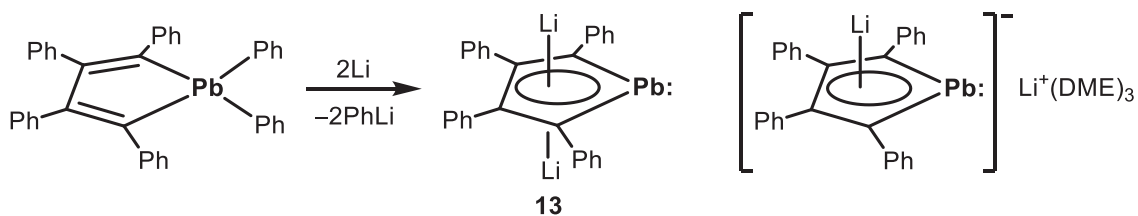
**Fig. 4** Molecular structures of dilithium tetraphenylgermoleidiide **8** and selected C–C bond distances (Å).



**Scheme 11** Synthesis of dipotassium tetramethylgermoleidiide **9** and its dimeric structure.



**Scheme 12** Synthesis of dilithium stannolides(2-) **11** and **12**.



**Scheme 13** Synthesis of dilithium plumbolediide **13** and its X-ray characterized structure [a lithium salt of a lithium plumbolide].

aromaticity.<sup>56</sup> Aromatization generally results in the shortening of the original single bonds and elongation of the original double bonds. To understand the tendency that appears to be a contradiction, theoretical consideration was reported.<sup>59</sup> The geometric optimization of the model compounds,  $C_4H_6M$ ,  $C_4H_4M$ , and  $C_4H_4M^{2-}$  ( $M = Si, Ge, Sn, Pb$ ) was performed at the B3LYP level of theory with the LanL2DZ basis set (Fig. 5). In the change from  $C_4H_6M$  to  $C_4H_4M$ , which has a divalent group 14 atom, the  $M-C(\alpha)$  bond lengthens because of an increase in  $p$ -character of the  $M-C(\alpha)$  bond caused by a lone pair on the divalent atom having more  $s$ -character than the  $M-H$  bonds of  $C_4H_6M$ . On the other hand, in the change from  $C_4H_4M$  to  $C_4H_4M^{2-}$ , the  $M-C(\alpha)$  bond shortens because of aromatic delocalization of the negative charges. The aromatic delocalization can be reasonably explained in terms of delocalization of negative charges on the group 14 atom into the LUMO of the butadiene moiety. The degree of the shortening found in  $C_4H_4Pb^{2-}$  is smaller than that found in  $C_4H_4Si^{2-}$  because of the overlapping of  $2p(C)$  and  $6p(Pb)$  orbitals is smaller than that of  $2p(C)$  and  $3p(Si)$  orbitals. Based on the discussion, it is concluded that the group 14 metallolediide dianions are regarded as dianions of metallacyclopentadienylenes (Fig. 3).

As the group 14 metallolediide dianions are regarded as dianions of metallacyclopentadienylenes, reduction of a metallacyclopentadienyliene is of considerable interest as a method for the synthesis of a metallolediide dianion. Indeed, reduction of THF-stabilized plumbacyclopentadienyliene **14**<sup>57,58</sup> by lithium afforded dilithium plumbolediide **15**<sup>59</sup> (Scheme 14). On the other hand, two-electron oxidation of **15** reproduced **14**.

The electronic perturbation by substituents on the  $\alpha$ -carbon atoms of dilithium metallolediide is investigated (Fig. 6).<sup>60,61</sup> As the negative charges on the group 14 atoms are delocalized into the LUMO of the butadiene moiety, effects of substituents of the  $\alpha$ -carbon atoms on electronic states of LUMO of the butadiene should be of considerable interest. Introduction of a silyl group into an  $\alpha$ -carbon atom decreases the LUMO energy level, resulting in the increase in interactions between the negative charges on the group 14 atom and LUMO of the butadiene and the decrease in HOMO energy level of the metallolediide dianion. Consequently, the negative charges on a group 14 atom of a silyl-substituted metallolediide dianion can be delocalized more than those of a methyl-substituted one, resulting in more metallylene (more positive) character of the group 14 atoms, which is supported by Mössbauer spectroscopic analysis of dilithium stannolelediide.<sup>60</sup>

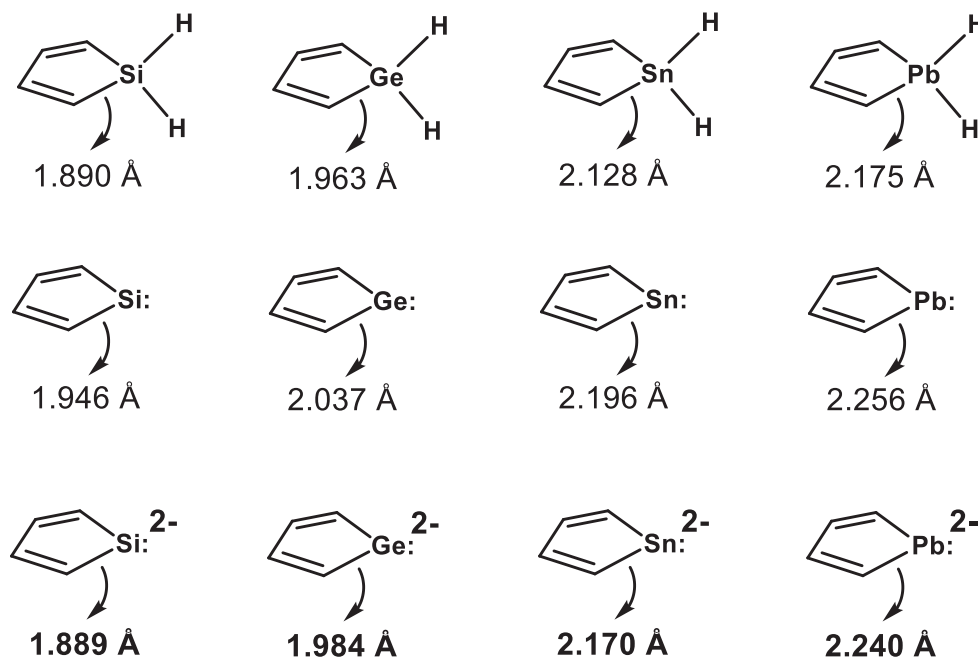
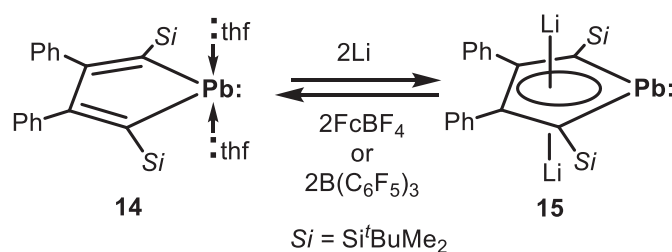
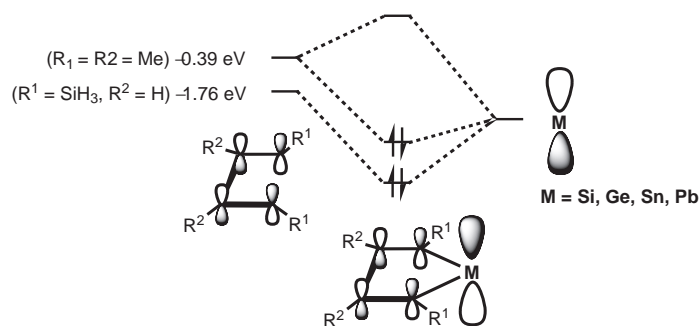


Fig. 5 Structural changes in group 14 metallacycles dependent on the electronic states of the group 14 atoms.



Scheme 14 Two-electron reversible redox behavior between plumbacyclopentadienyliene **14** and dilithium plumbolediide **15**.



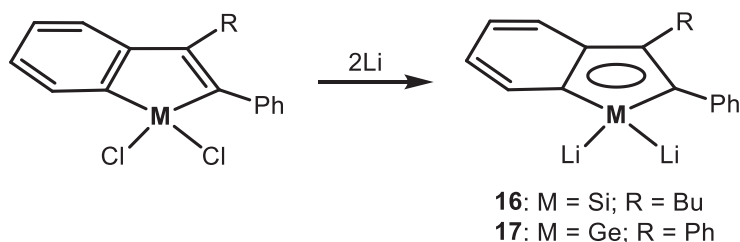


**Fig. 6** Effects of silyl substituents on the electronic structures of metallolediide dianions.

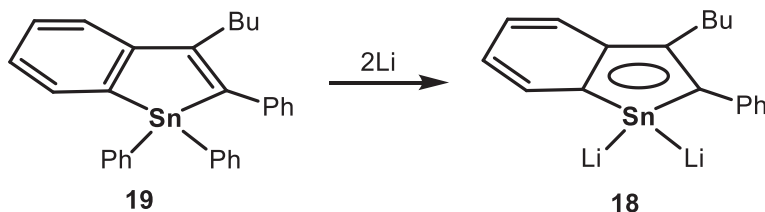
### 1.18.2.2.3 Benzannulated Group 14 metallolide dianion equivalents

Effects of benzannulation on the aromaticity of metallolide anions are also of interest because the acidity of cyclopentadiene ( $\text{pK}_a = 16$ ) is attenuated in the fused ring analog fluorene ( $\text{pK}_a = 23$ ) as a result of the reduced  $\pi$ -delocalization in the conjugate base of the annulated system.<sup>62</sup> Dilithium 1(*H*)-1-silaindenate **16** and -germaindenate **17** were synthesized and characterized by X-ray diffraction analysis (Scheme 15).<sup>63,64</sup> The C–C distances in each of the five-membered rings (1.428 to 1.455 Å and 1.438 to 1.443 Å for **16** and **17**, respectively) are almost the same, indicating aromatic nature of the five-membered rings. In contrast, the C–C distances in the six-membered ring slightly alter (1.349 to 1.455 Å and 1.350 to 1.443 Å for **16** and **17**, respectively), indicating some character of cyclohexadiene. Dilithium 1(*H*)-1-stannaindenate **18** was also synthesized by the reaction of 1,1-diphenylstannaindene **19** with lithium (Scheme 16).<sup>65</sup> Although the X-ray characterization of **18** has never been reported, an upfield resonance of  $-5.8$  ppm in the  $^7\text{Li}$  NMR indicates aromatic nature of **18**. The NICS(1) value of each of the five-membered rings is calculated to be more largely negative than that of each of the six-membered rings, indicating large aromatic characters of the metallolediide moieties (Fig. 7).<sup>65</sup>

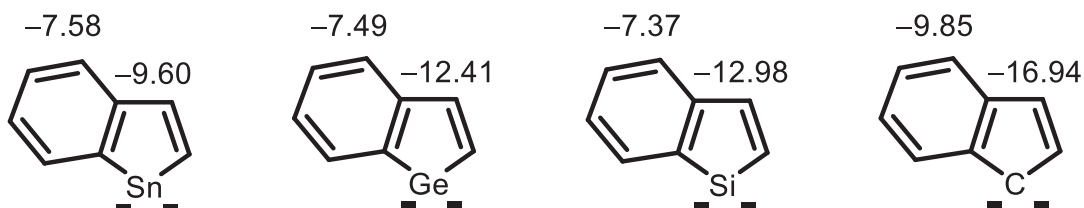
More benzannulated systems, sila- and germafluorene dianion equivalents were synthesized and characterized by X-ray diffraction analysis (Scheme 17).<sup>66,67</sup> The X-ray analysis and theoretical calculations again indicate that the aromaticity of the five-



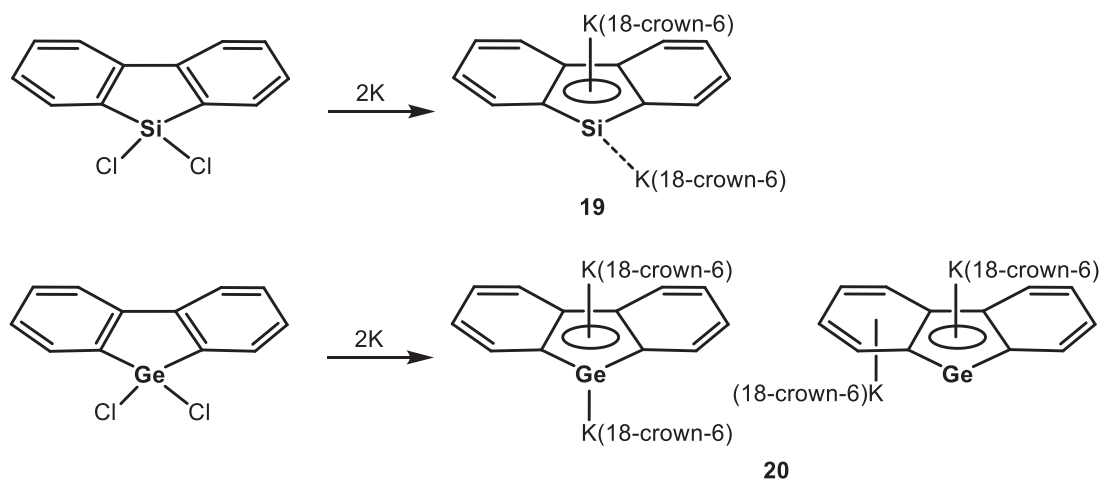
**Scheme 15** Synthesis of dilithium 1(*H*)-1-silaindenate **16** and -germaindenate **17**.



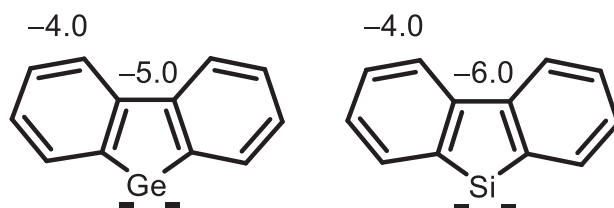
**Scheme 16** Synthesis of dilithium 1(*H*)-1-stannaindenate **18**.



**Fig. 7** NICS(1) values of metallolediide and indenate dianions calculated at B3LYP level using Huzinaga's (433,321/43321/421) (DZP) basis set and a polarization d-function ( $\zeta = 0.183$ ) for Sn and 6-31G(d) for C, H, and Li.



**Scheme 17** Synthesis of dipotassium sila- and germafluorenates **19** and **20**.



**Fig. 8** NICS(2) values of sila- and germafluorene dianions calculated at B3LYP/6-31 + G(d).

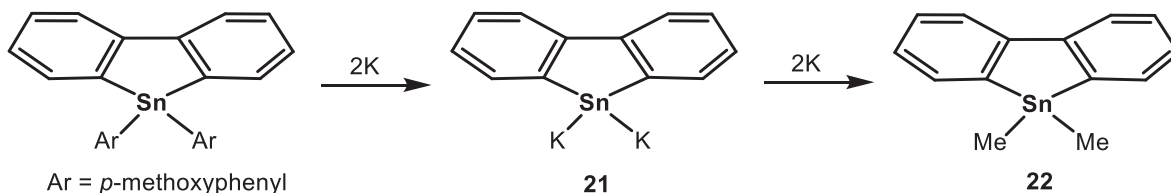
membered rings and some hexadiene character is found in the six-membered rings (Fig. 8). The generation of dipotassium stannafluorene **21** was also evidenced by a trapping experiment with iodomethane to give compound **22** (Scheme 18).<sup>68</sup> The NICS calculations of a stannafluorene dianion exhibit a tendency similar to those found in sila- and germafluorenyl dianions and the NICS(1) value of the five-membered ring ( $-8.6$  ppm) is more negatively larger than that of the six-membered ring ( $-7.8$  ppm).

### 1.18.2.3 Benzene and polycyclic aromatic hydrocarbon analogs<sup>69,70</sup>

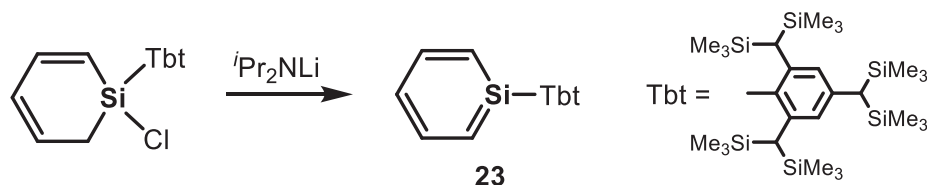
#### 1.18.2.3.1 Silicon analogs of benzene and related polycyclic aromatic hydrocarbons containing one silicon atom

##### 1.18.2.3.1.1 Synthesis

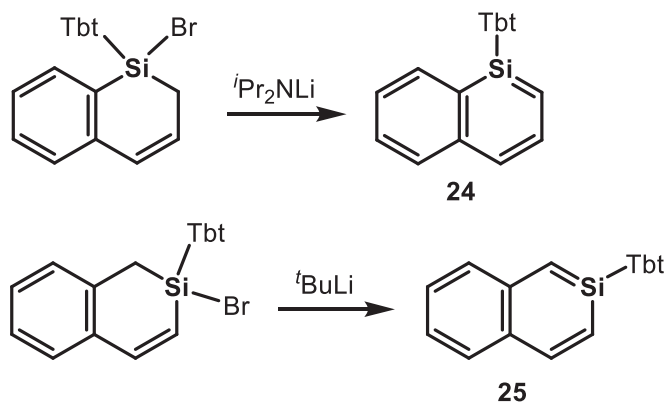
The isolation of a stable silabenzene under ambient conditions has been achieved by introducing a sterically congested substituent onto the silicon atom that can suppress its dimerization reaction. The generation of silabenzene **23** bearing a Tbt group on the silicon atom, stable in solution at room temperature in the absence of atmospheric oxygen was first reported in 2000,<sup>71</sup> and its X-ray characterization was subsequently published in the same year (Scheme 19).<sup>72</sup> Silicon-incorporating naphthalenes, 1-sila-<sup>73</sup> **24** and 2-sila-naphthalenes **25**<sup>74,75</sup> have



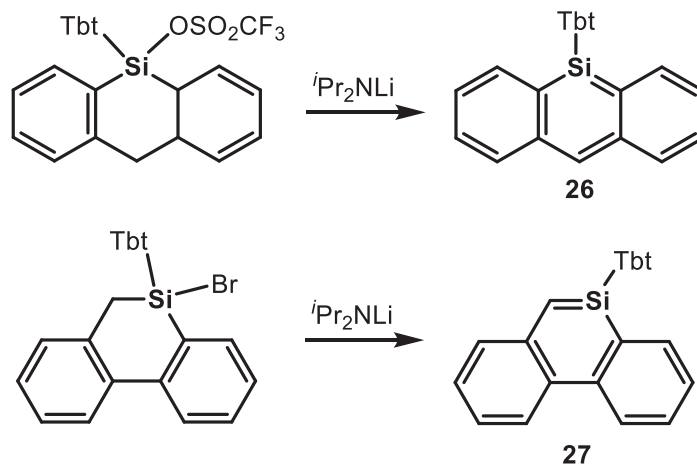
**Scheme 18** Generation of dipotassium stannafluorene **21** and its trapping reaction.



**Scheme 19** Synthesis of silabenzene **23**.



**Scheme 20** Synthesis of 1-sila- **24** and 2-sila-naphthalenes **25**.



**Scheme 21** Synthesis of 9-silaanthracene **26** and 9-silaphenanthrene **27**.

also been synthesized similarly by taking advantage of the Tbt group (Scheme 20). Further annelated systems, 9-silaanthracene **26**<sup>76</sup> and 9-silaphenanthrene **27**<sup>77</sup> have also been published (Scheme 21).

#### 1.18.2.3.1.2 Structures and aromaticity

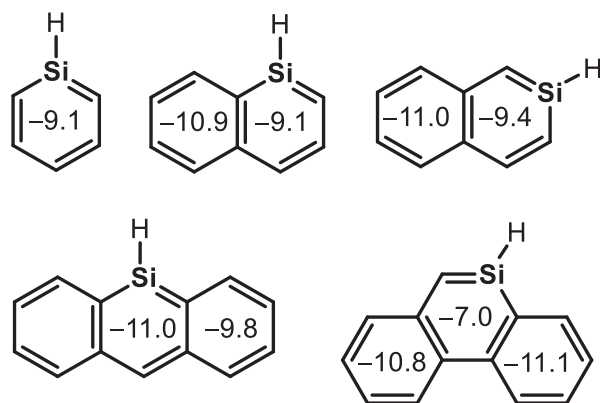
The two Si–C bond distances of **23** are almost equal (1.765(4) and 1.770(4) Å), which are in the range between those of Si–C double and single bonds (1.70 and 1.89 Å, respectively),<sup>78,79</sup> and the C–C bond distances (1.381(6)~1.399(6) Å) are almost equal and similar to those of benzene (1.39 Å). These structural features suggest aromatic nature of **23**. The <sup>1</sup>H NMR signals assignable to protons on the silabenzene ring in **23** were observed at 6.8 to 8.1 ppm, which in a region typical to the resonances of the aromatic protons. The observed <sup>1</sup>J(Si–C) of 83 Hz in **23** is much larger than those of the Si–C single bonds (about 50 Hz), indicating some double bond character of the Si–C bond. The structural and spectral characteristics similar to those of **23** were also found in compounds **24**–**27**.

Theoretical consideration also supports aromaticity of compounds **23**–**27**. The NICS(1) values of the parent compounds for **23**–**27** shown in Fig. 9 are negatively large and comparable to that of benzene (–11.1 ppm calculated at the same level of theory), indicating their aromatic nature, and it can be concluded that compounds **23**–**27** are sila-aromatic compounds from the magnetic criterion. The aromatic stabilization energy (ASE) has also been estimated. The ASE values of the parent model compounds for **23**–**25** are comparable to those of the carbon versions, and therefore their aromatic nature is established from the energetic criterion (Scheme 22).

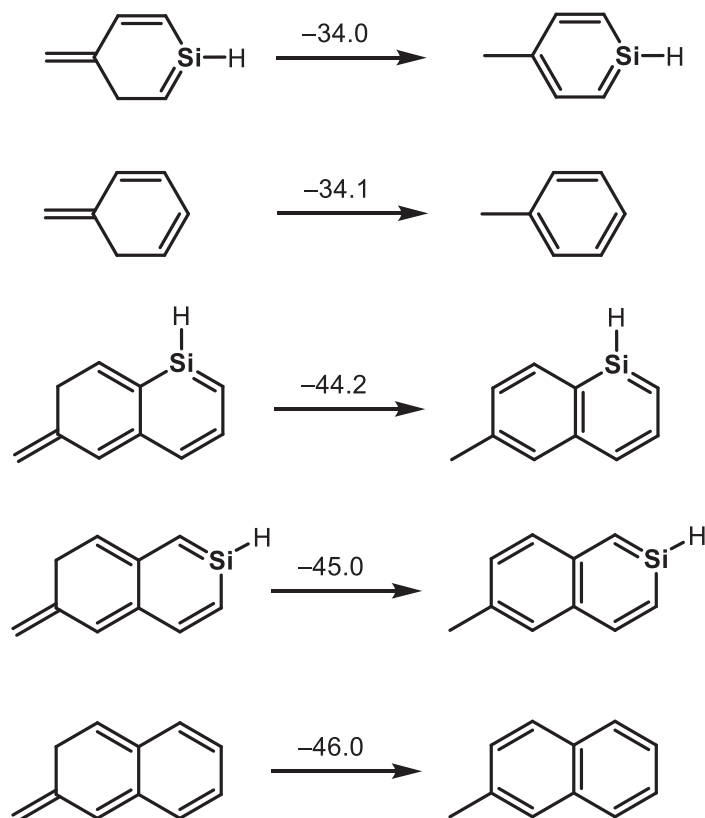
#### 1.18.2.3.2 Germanium analogs of benzene and related polycyclic aromatic hydrocarbons containing one germanium atom

##### 1.18.2.3.2.1 Synthesis

A series of germanium-bearing aromatic benzenoid compounds **28**–**31** has been synthesized by methods similar to those for the silicon versions (Fig. 10).<sup>80–83</sup> For example, germabenzene **28** was synthesized through HCl elimination reaction by LDA (Scheme 23). All these compounds are sterically protected by a Tbt or Bbt groups and X-ray characterized as thermally stable compounds at room temperature in the solid state. More recently, another synthetic route for a germabenzene has been published (Scheme 24).<sup>84</sup>



**Fig. 9** NICS(1) values of the parent compounds for **23–27** calculated at B3LYP/6-311G(d).<sup>69,77</sup>

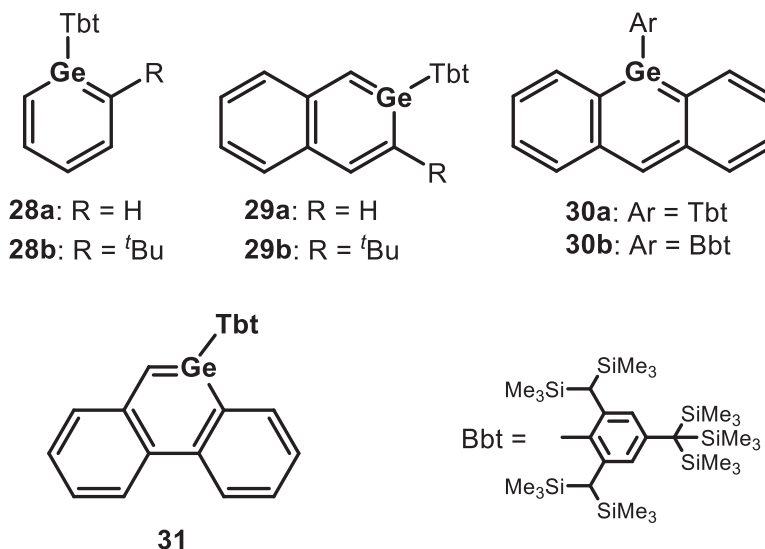


**Scheme 22** Aromatic stabilization energies (kcal/mol) of the parent compounds for **23–25** and their carbon versions calculated at B3LYP/6-311+G(d,p).<sup>75</sup>

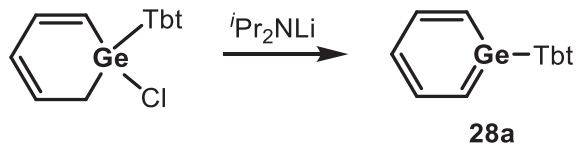
Treatment of dichlorogermene **32** with a base afforded chlorogermabenzene **33**, which was not isolated but characterized as a thermally stable compound. Compound **33** reacted with ArLi to provide Ar-substituted germabenzenes **34**.

#### 1.18.2.3.2.2 Structures and aromaticity

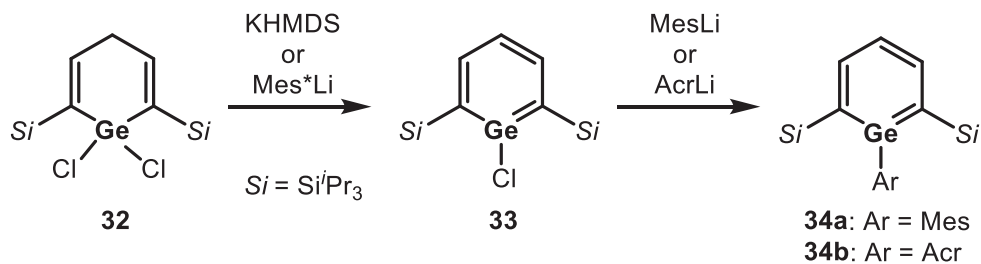
The structural characteristics of thus characterized germabenzenes and their related compounds **28–34** are similar to those of the silicon versions and benzene itself. All the ring systems show high planarity with negligible C–C bond alternation in the six-membered rings, and the spectral characteristics are also reasonably interpreted as aromatic compounds. The NICS calculations also exhibit a similar tendency and indicate that aromaticity retains in the Ge-bearing compounds (**Fig. 11**). The estimated ASE of the parent germabenzene also supports its aromatic nature (**Scheme 25**).



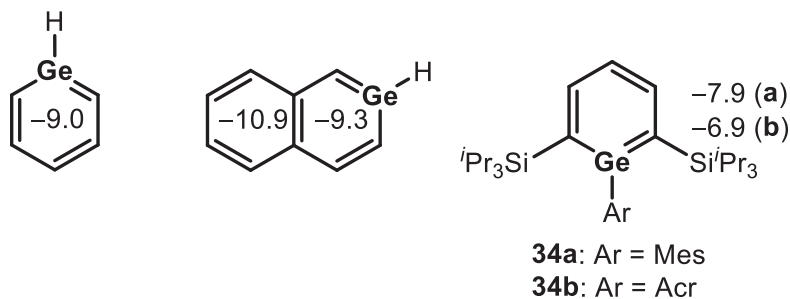
**Fig. 10** Germanium-bearing aromatic benzenoid compounds **28–31**.



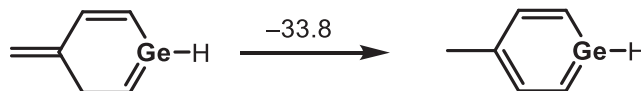
**Scheme 23** Synthesis of germabenzene **28a**.



**Scheme 24** Synthesis of germabenzenes **34** by transformation of chlorogermabenzene **33**.



**Fig. 11** NICS(1) values of the parent compounds calculated at B3LYP/6-311G(d) (B3LYP/6-311+G(2d,p) for **34**).

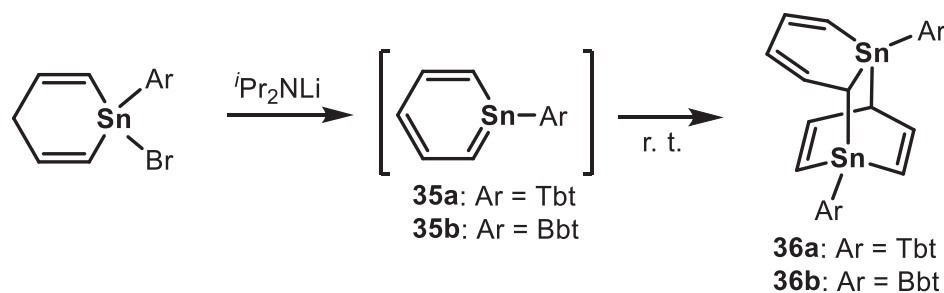


**Scheme 25** Estimated ASE of the parent germabenzene.

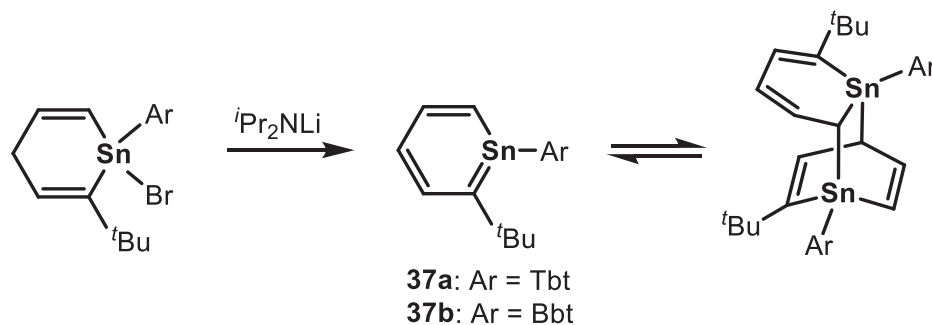


### 1.18.2.3.3 Tin analogs of benzene and related polycyclic aromatic hydrocarbons containing one tin atom

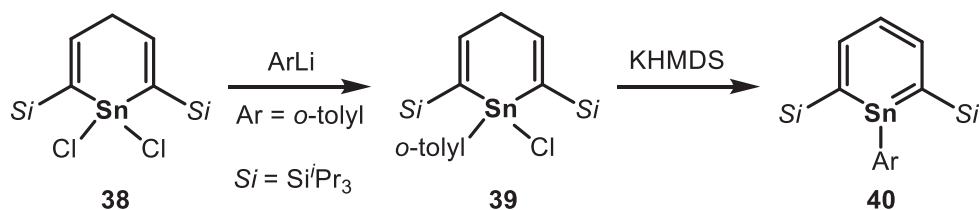
Although sila- and germabenzenes have been isolated as thermally stable compounds and characterized by X-ray diffraction analysis, stannabenzene is more difficult to conquer. The steric congestion by a Tbt and a Bbt groups that can stabilize sila and germa-benzenes is not sufficient to stabilize stannabenzenes **35**, which readily undergo [4 + 2]-dimerization to afford **36** even at room temperature (Scheme 26).<sup>85</sup> Introduction of a *t*-butyl group at the 2-position can make stannabenzenes **37** more stable (Scheme 27).<sup>86</sup> Stannabenzenes **37** exist in monomer-dimer equilibrium in solution and monomeric forms of **37** can be detected by spectroscopic measurement. Introduction of bulky substituents on the 2,6-positions enables to isolate a stannabenzene stable at room temperature in the solid state (Scheme 28). Treatment of stannacyclohexadiene **38** bearing two isopropylsilyl groups on the 2,6-positions with *o*-tolyllithium afford *o*-tolyl-bearing chlorostannane **39**, which underwent HCl elimination reaction by KHMDS to afford stannabenzene **40**.<sup>87</sup> The C–C bond distances in the planar six-membered ring are almost equal, indicating aromatic nature (structural criterion), and the NICS(1) value is calculated to be –6.3 ppm, sufficiently negatively large as an aromatic compound (magnetic criterion). Stannanaphthalene **41** has also been isolated and characterized by X-ray diffraction analysis (Scheme 29).<sup>88</sup> The synthesis of 9-stannaphenanthrene **42** has also been investigated; however, it readily undergoes dimerization to afford [2 + 2] dimer **43** (Scheme 30).<sup>89</sup>



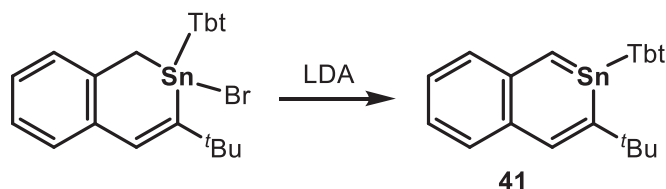
**Scheme 26** Generation of stannabenzenes **35** and their dimerization reactions.



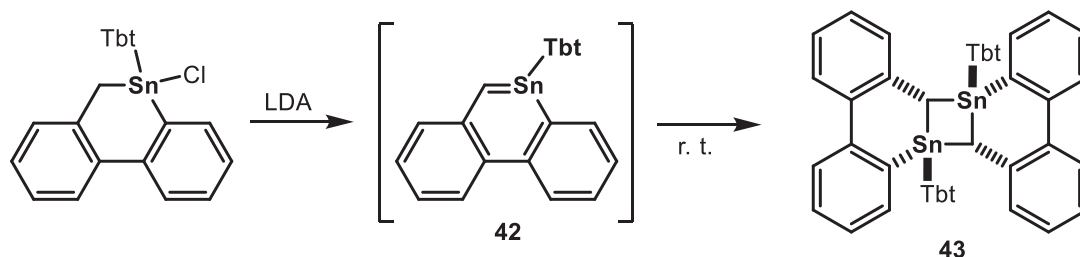
**Scheme 27** Monomer-dimer equilibrium of stannabenzenes **37**.



**Scheme 28** Synthesis of stannabenzene **40** stable in the solid state.



**Scheme 29** Synthesis of 2-stannaphthalene **41**.



**Scheme 30** Generation of 9-stannaphenanthrene **42**.

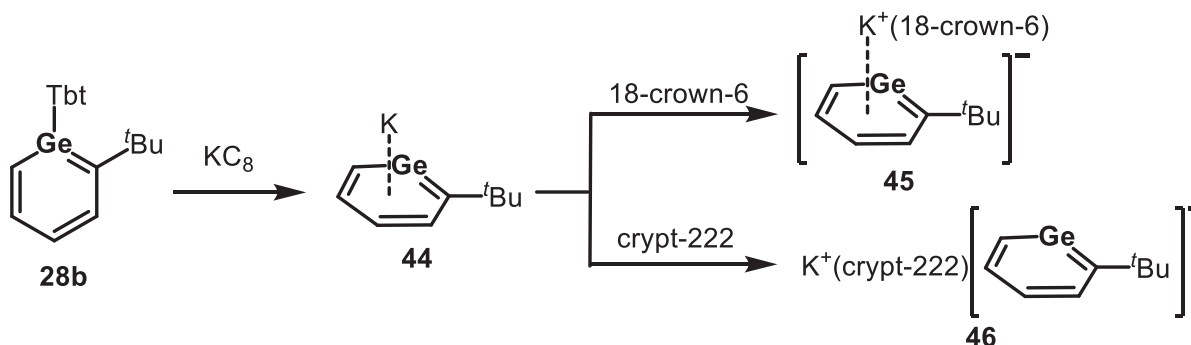
#### 1.18.2.3.4 Heavy analogs of phenyl anions

It is noted that reduction of germabenzene **28b** by potassium graphite afforded germabenzylpotassium **44**, a germanium analog of a phenyl anion, resulting from unexpected reductive cleavage of a Ge–C(Tbt) bond (**Scheme 31**).<sup>90</sup> The X-ray diffraction analysis reveals that no remarkable C–C bond alternation is found in all of the structures of **44**–**46**, indicating their aromatic nature (structural criterion). The NICS(1) value of the free germabenzyl anion (av.  $-8.0$  ppm) also supports its aromaticity (magnetic criterion). However, theoretical calculations of the parent germabenzene anion in comparison with the benzenide anion reveals canonical resonance structure of germylene **47B** cannot be excluded (**Fig. 12**).

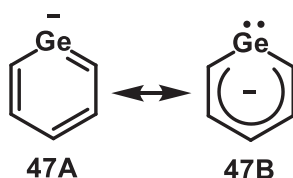
More surprisingly, potassium stannabenzene **48** was successfully synthesized by the reduction of a monomer-dimer equilibrium mixture with potassium graphite and characterized by X-ray diffraction analysis (**Scheme 32**). As reaction of **48** with chlorotrimethylsilane afforded dimer **49** of stannabenzene intermediate **50**, it is noted that electronic repulsion in **48** can suppress its dimerization. The  $^{119}\text{Sn}$  NMR signals of **48** was observed at 702 ppm, which is in a region much more low-field than those of stannabenzene **37** (271 and 276 ppm),<sup>86</sup> suggesting its stannylene character. However, the NICS(1) of the stannabenzene anion is calculated to be  $-7.3$  ppm, indicating its aromatic nature, and therefore resonance between the aromatic and stannylene structures is also of importance as in the case of the Ge analog (**Fig. 13**).

#### 1.18.2.3.5 Benzene and polycyclic aromatic hydrocarbon analogs containing more than two heavy group 14 atoms

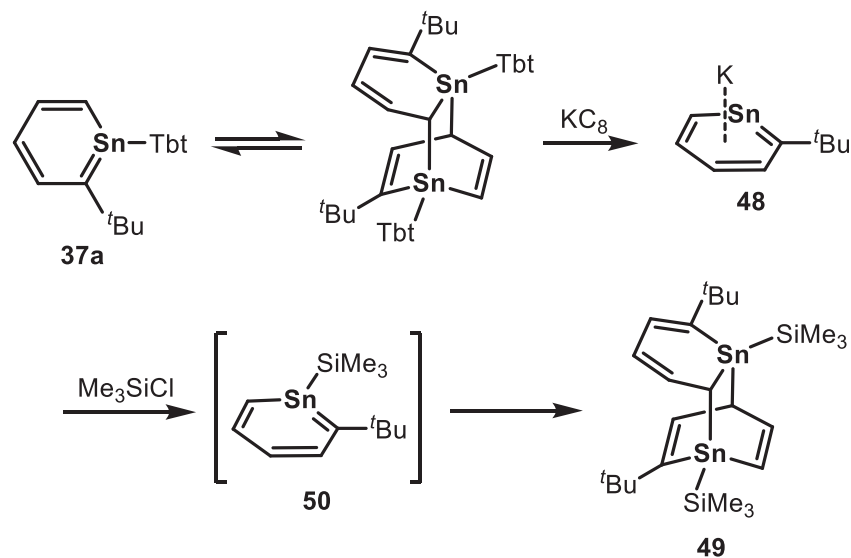
1,2-Disilabenzene and 1,2-digermapbenzen have been synthesized by the reactions of triple-bonded compounds, disilynes and digermynes. Disilyne **52**<sup>91</sup> reacted with phenylacetylene to afford a mixture of two regioisomers of 1,2-digermapbenzenes **53** and **54** in the ratio of 2:3 (**Scheme 33**).<sup>92</sup> Single crystals of **53** were obtained and its X-ray characterization was performed. The Si–Si distance of 2.2018(18) Å is intermediate between the Si–Si single and double-bond distances, and the Si–C distances (1.804(4) and 1.799(5) Å) is intermediate between the Si–C single and double-bond distances. The three C–C distances are 1.389(6), 1.386(6) and 1.452(6) Å, which are intermediate between those of C–C single and double-bond distances (1.54 and 1.34 Å, respectively). These structural characteristics suggest some aromatic nature of **53**. The NICS(1) values of model compounds **53'** and **54'** are calculated to be  $-8.0$  and  $-8.1$ , respectively, supporting aromatic nature of 1,2-digermapbenzenes **53** and **54** (**Fig. 14**).



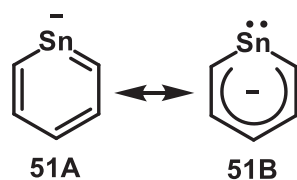
**Scheme 31** Synthesis of potassium germabenzene **44**.



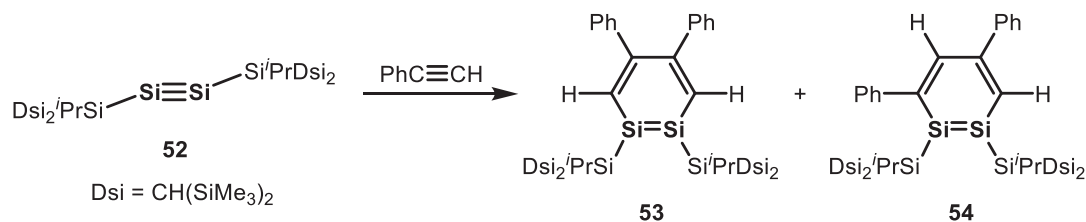
**Fig. 12** Canonical resonance structures in the parent germabenzene anion.



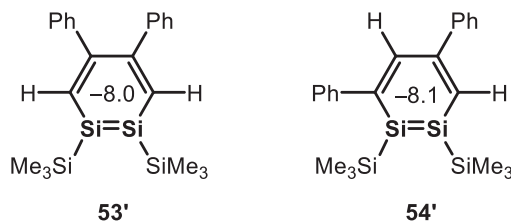
**Scheme 32** Synthesis of stannabenzylpotassium **48** and its reactivity.



**Fig. 13** Canonical resonance structures in the parent stannabenzene anion.



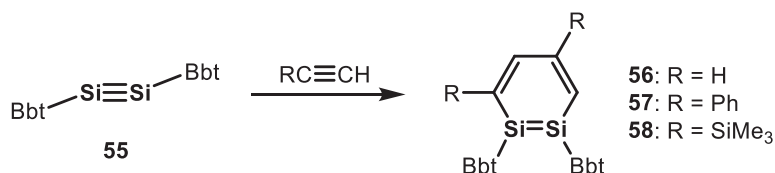
**Scheme 33** Reaction of disilyne **52** to afford 1,2-disilabenzenes **53** and **54**.



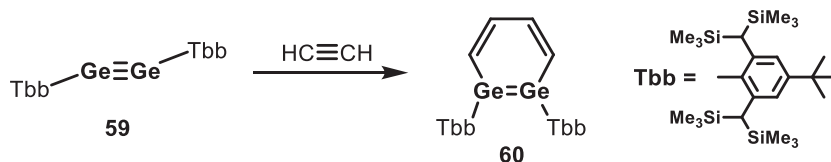
**Fig. 14** NICS(1) values of model compounds **53'** and **54'**.

Reactions of diaryldisilyne **55**<sup>93</sup> with alkynes have also been reported, and the obtained 1,2-disilabenzenes **56**–**58** have been characterized (**Scheme 34**).<sup>94</sup>

The formation of 1,2-digermabenzene **60** has been accomplished by the reaction of digermynes **59** with acetylene (**Scheme 35**).<sup>95,96</sup> The digermabenzene ring of **60** is not planar, in sharp contrast to planar 1,2-disilabenzenes; however, the NICS(1) values of **60** are calculated to be  $-6.8$  and  $-7.2$  ppm, and the aromatic stabilization energy of the parent 1,2-digermabenzene estimated by the hydrogenation reaction is calculated to be about 13 kcal/mol, and accordingly, the aromaticity of **60** is comparable to those of 1,2-disilabenzenes.



**Scheme 34** Reaction of diaryldisilyne **55** to afford 1,2-disilabenzenes **56–58**.



**Scheme 35** Formation of 1,2-digermylene **60** from digermylyne **59**.

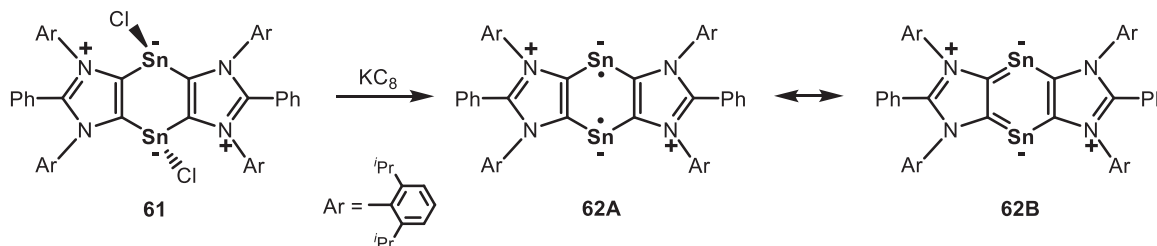
A 1,4-distannabenzene with unique electronic characteristics has been published. Reduction of bis(chlorostannylene) **61** with potassium graphite afforded compound **62** (**Scheme 36**).<sup>97</sup> The NMR signals of **62** are broadening due to contribution of its triplet state detected by EPR spectroscopy. However, the NICS(1) value of **62** is calculated to be  $-10.2$  ppm, indicating its aromatic nature (resonance form of **62B**).

### 1.18.2.4 Cyclopropenyl cation analogs

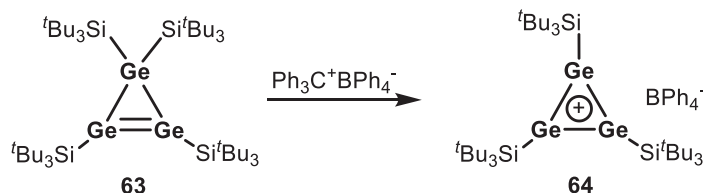
The synthesis of heavy analogs of aromatic cyclopropenyl cation<sup>98</sup> have been investigated. The first example of this series is cyclotrigermenium cation **64** prepared by the reaction of cyclotrigermene **63**<sup>99</sup> with trityl tetraphenylborate (**Scheme 37**).<sup>100</sup> The X-ray diffraction analysis reveals that the three Ge–Ge bond distances (2.321(4) to 2.333(4) Å) are almost equal and intermediate between the Ge–Ge double bond (2.239(4) Å) and the Ge–Ge single bond (2.522(4) Å) of precursor **63**. Each of the sum of the bond angles around the three germanium atoms is almost 360°, and the distance between the Ge and B atoms ranges from 6.941(3) to 9.695(3) Å. These structural characteristics indicate that cyclotrigermenium cation **64** is a  $2\pi$ -aromatic and a free germenyl cation.

A similar synthetic strategy has been applied for the synthesis of a silicon version. Treatment of cyclotrisilene **65** with  $\text{Ph}_3\text{C}^+\text{B}(\text{TSFPB})_4^-$  afforded cyclotrisilenylium cation **66** (**Scheme 38**).<sup>101</sup> The X-ray diffraction analysis reveals that the three Si–Si bond distances (av 2.217(3) Å) are intermediate between the Si–Si double bond (2.1612(8) Å) and the Si–Si single bond (2.3694(8) and 2.3762(8) Å) in precursor cyclotrisilene **65**. The NICS(1) value of the model compound,  $(\text{H}_3\text{Si})_3\text{Si}_3^+$  for **66**, is calculated to be  $-12.8$  ppm. These characteristics indicate aromatic nature of **66**.

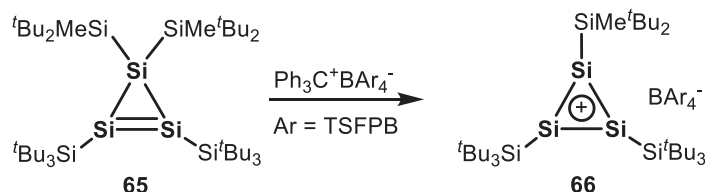
Disilacyclopropenyl cation **67** has also been synthesized by the reaction of disilacyclopropene **68** with  $\text{Ph}_3\text{C}^+\text{B}(\text{TSFPB})_4^-$  (**Scheme 39**).<sup>102</sup> The NICS(1) value of the model compound **69** is calculated to be  $-13.5$  ppm, and the calculated bond orders



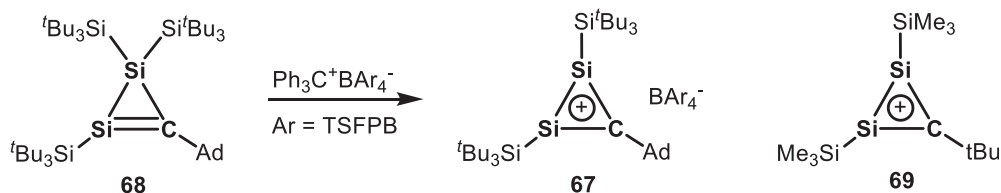
**Scheme 36** Synthesis of 1,4-distannabenzene **62** and its resonance structures.



**Scheme 37** Synthesis of a germanium analog of cyclopropenyl cation.



**Scheme 38** Synthesis of a silicon analog of cyclopropenyl cation.



**Scheme 39** Synthesis of disilacyclopropenyl cation **67** and its model compound **69**.

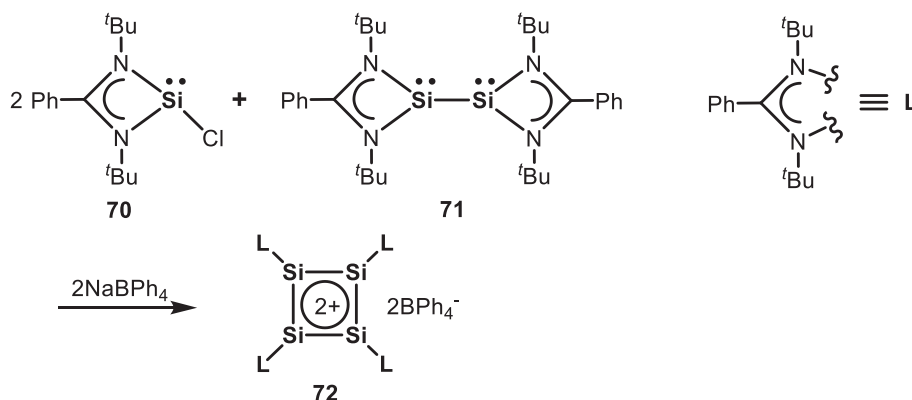
of two Si–C and an Si–Si bonds in **69** are 1.23 and 1.19, respectively. These characteristics indicate that disilacyclopropenyl cation **67** possesses a  $2\pi$ -aromatic system.

#### 1.18.2.5 Cyclobutadiene dianion and dication analogs

Cyclobutadiene dianion appears to be considered  $6\pi$ -aromatic; however, it is not simple. Early calculations predicted a butterfly-like cyclobutadiene dianion bearing an allylic delocalized anion and a localized anion.<sup>103</sup> Another model of a trapezoid structure bearing a 1,2-localized dianion and a C=C moiety was later proposed.<sup>104</sup> More recent calculations suggested that planar aromatic structure of cyclobutadiene dianion should be stabilized by two Li complexation.<sup>105</sup> Indeed, a square-planar aromatic dilithium cyclobutadienide has been reported.<sup>106</sup>

Inspired by the preceding studies, the synthesis of a dipotassium salt of tetrasilabutadienide dianion and a dipotassium salt of 1,2-disila-3,4-digermacyclobutadienide dianion has been accomplished; however, their non-planar structures and the NICS(1) calculations reveal that they are non-aromatic,<sup>107</sup> even though coordination to a transition metal enhances aromatic nature of the heavy cyclobutadiene moiety.<sup>108–110</sup>

On the other hand, a tetrasilacyclobutadiene dication is  $2\pi$ -aromatic. Reaction of donor-stabilized chlorosilylene **70**<sup>111</sup> with bis(silylene) **71**<sup>112</sup> in the presence of NaBPh<sub>4</sub> afforded tetrasilacyclobutadiene dication salt **72** (**Scheme 40**).<sup>113</sup> The four-membered ring adopts a slightly puckered square-planar geometry with a folding angle of 14°, and the sum of the internal angles is 358.3°, which only slightly deviates from the perfect planarity (360°). The Si–Si bond distances in the four-membered ring are almost equal (2.2550(6) to 2.2718(7) Å) and intermediate between those of Si–Si single (ca. 2.35 Å)<sup>114</sup> and double bonds (2.12–2.25 Å),<sup>20</sup> suggesting electronic delocalization in the four-membered ring. The NICS(1) value of a model compound that has methyl groups instead of *t*-butyl groups in **72** is calculated to be –12.7 ppm, and therefore it is concluded that tetrasilacyclobutadiene dication **72** is  $2\pi$ -aromatic.



**Scheme 40** Synthesis of tetrasilacyclobutadiene dication **72**.



### 1.18.3 Conclusion and outlook

The replacement of skeletal carbon atoms in aromatic compounds by heavy group 14 atoms (Si, Ge, Sn and Pb) has been investigated, and in most cases, aromaticity is retained, as evidenced by structural, magnetic and energetic criteria, even though coordination to metals plays an important role in retaining aromaticity in some cases. The concept of  $\pi$ -aromaticity is now expanded to lead-bearing aromatic compounds; however, characteristics derived from the introduction of heavy atoms are also found to some extent. The aromatic compounds containing heavy atoms different from group 14 atoms have also been reported, even though this review does not cover this area.<sup>115</sup> Such new knowledge has changed and will change some chapters of synthetic, structural and theoretical chemistry, and will inspire new materials and catalytic chemistry.

### References

- Faraday, M.; XX. On New Compounds of Carbon and Hydrogen, and on Certain Other Products Obtained during the Decomposition of Oil by Heat. *Phil. Trans. R. Soc. Lond.* **1825**, *115*, 440–466.
- Kekulé, A. Sur la constitution des substances aromatiques. *Bull. Soc. Chim. Fr.* **1865**, *3*, 98–110.
- Kekulé, A. Ueber einige Condensationsproducte des Aldehyds. *Justus Liebigs Ann. Chem.* **1872**, *162*, 77–124.
- Aromaticity is featured in review journals. Examples, see: Schleyer, P. v. R. *Chem. Rev.* **2001**, *101*, 1115 (editorial).
- Stanger, A. What Is... Aromaticity: A Critique of the Concept of Aromaticity—Can it Really Be Defined? *Chem. Commun.* **2009**, 1939–1947.
- Cyranowski, M. K.; Krygowski, T. M.; Katritzky, A. R.; Schleyer, P. v. R. To What Extent Can Aromaticity Be Defined Uniquely? *J. Org. Chem.* **2002**, *67*, 1333–1338.
- Schleyer, P. v. R.; Jiao, H. What Is Aromaticity? *Pure Appl. Chem.* **1996**, *68*, 209–218.
- Solà, M. Why Aromaticity Is a Suspicious Concept? Why? *Front. Chem.* **2017**. <https://doi.org/10.3389/fchem.2017.00022> (4 pages).
- Hückel, E. Quantentheoretische Beiträge zum Benzolproblem. *Z. Physik* **1931**, *70*, 204–286.
- Hückel, E. Quantentheoretische Beiträge zum Benzolproblem. *Z. Physik* **1931**, *72*, 310–337.
- Williams, R. V. Homoaromaticity. *Chem. Rev.* **2001**, *101*, 1185–1204.
- Popov, I. A.; Starikova, A. A.; Steglenko, D. V.; Boldyrev, A. I. Usefulness of the  $\sigma$ -Aromaticity and  $\sigma$ -Antiaromaticity Concepts for Clusters and Solid-State Compounds. *Chem. Eur. J.* **2018**, *24*, 292–305.
- Ottosson, H. Exciting Excited-State Aromaticity. *Nature Chem.* **2012**, *4*, 969–971.
- Baird, N. C. Quantum organic photochemistry. II. Resonance and aromaticity in the lowest  $3\pi\pi^*$  state of cyclic hydrocarbons. *J. Am. Chem. Soc.* **1972**, *94*, 4941–4948.
- Ajami, D.; Oeckler, O.; Simon, A.; Herges, R. Synthesis of a Möbius Aromatic Hydrocarbon. *Nature* **2003**, *426*, 819–821.
- Stepień, M.; Latos-Grażyński, L.; Sprutta, N.; Chwalisz, P.; Szterenber, L. Expanded Porphyrin with a Split Personality: A Hückel–Möbius Aromaticity Switch. *Angew. Chem., Int. Ed.* **2007**, *46*, 7869–7873.
- Jutzi, P. New Element-Carbon (p-p) $\pi$  Bonds. *Angew. Chem., Int. Ed. Engl.* **1975**, *14*, 232–245.
- West, R.; Fink, M. J.; Michl, J. Tetramesityldisilene, a Stable Compound Containing a Silicon-Silicon Double Bond. *Science* **1981**, *214*, 1343–1344.
- Yoshifuji, M.; Shima, I.; Inamoto, N.; Hirotsu, K.; Higuchi, T. Synthesis and Structure of Bis(2,4,6-Tri-Tert-Butylphenyl)Diphosphene: Isolation of a True Phosphobenzene. *J. Am. Chem. Soc.* **1981**, *103*, 4587–4589.
- Power, P.  $\pi$ -Bonding and the Lone Pair Effect in Multiple Bonds between Heavier Main Group Elements. *Chem. Rev.* **1999**, *99*, 3463–3504.
- Driess, M.; Grützmacher, H. Main Group Element Analogues of Carbenes, Olefins, and Small Rings. *Angew. Chem., Int. Ed.* **1996**, *35*, 828–856.
- Power, P. Homonuclear Multiple Bonding in Heavier Main Group Elements. *J. Chem. Soc., Dalton Trans.* **1998**, 2939–2951.
- Tokito, N.; Arai, Y.; Okazaki, R.; Nagase, S. Synthesis and Characterization of a Stable Dibismuthene: Evidence for a Bi-Bi Double Bond. *Science* **1997**, *277*, 78–80.
- Raabe, G.; Michl, J. Multiple Bonding to Silicon. *Chem. Rev.* **1985**, *85*, 419–509.
- Herrmann, W. A.; Denk, M.; Behm, J.; Scherer, W.; Klingan, F.-R.; Bock, H.; Solouki, B.; Wagner, M. Stable Cyclic Germanediyls (“Cyclogermynes”): Synthesis, Structure, Metal Complexes, and Thermolyses. *Angew. Chem., Int. Ed. Engl.* **1992**, *31*, 1485–1488.
- Arduengo, A. J.; Harlow, R. L.; Kline, M. A Stable Crystalline Carbene. *J. Am. Chem. Soc.* **1991**, *113*, 361–363.
- Heinemann, C.; Herrmann, W. A.; Thiel, W. Theoretical Study of Stable Silylenes and Germynes. *J. Organomet. Chem.* **1994**, *475*, 73–84.
- Boehme, C.; Frenking, G. Electronic Structure of Stable Carbenes, Silylenes, and Germynes. *J. Am. Chem. Soc.* **1996**, *118*, 2039–2046.
- Denk, M.; Lennon, R.; Hayashi, R.; West, R.; Belyakov, A. V.; Verne, H. P.; Haaland, A.; Wagner, M.; Metzler, N. Synthesis and Structure of a Stable Silylene. *J. Am. Chem. Soc.* **1994**, *116*, 2691–2692.
- Boehme, C.; Frenking, G. N-Heterocyclic Carbene, Silylene, and Germylene Complexes of MCl (M = Cu, Ag, Au). A Theoretical Study. *Organometallics* **1998**, *17*, 5801–5809.
- Chen, Z.; Wannere, C. S.; Corminboeuf, C.; Puchta, R.; Schleyer, P. v. R. Nucleus-Independent Chemical Shifts (NICS) as an Aromaticity Criterion. *Chem. Rev.* **2005**, *105*, 3842–3888.
- Leites, L. A.; Bukalov, S. S.; Zabala, A. V.; Garbuzova, I. A.; Moser, D. F.; West, R. The Raman Spectrum and Aromatic Stabilization in a Cyclic Germylene. *J. Am. Chem. Soc.* **2004**, *126*, 4114–4115.
- Leites, L. A.; Bukalov, S. S.; Denk, M.; West, R.; Haaf, M. Raman Evidence of Aromaticity of the Thermally Stable Silylene (tBuNCHNtBu)Si. *J. Mol. Struct.* **2000**, *550-551*, 329–335.
- Saito, M.; Yoshioka, M. The Anions and Dianions of Group 14 Metalloles. *Coord. Chem. Rev.* **2005**, *249*, 765–780.
- Goldfuss, B.; Schleyer, P. v. R. Aromaticity in Group 14 Metalloles: Structural, Energetic, and Magnetic Criteria. *Organometallics* **1997**, *16*, 1543–1552.
- Goldfuss, B.; Schleyer, P. v. R. The Silolyl Anion C<sub>4</sub>H<sub>4</sub>SiH<sup>-</sup> Is Aromatic and the Lithium Silolide C<sub>4</sub>H<sub>4</sub>SiHLi Even More So. *Organometallics* **1995**, *14*, 1553–1555.
- Freeman, W. P.; Tilley, T. D.; Arnold, F. P.; Rheingold, A. L.; Gantzel, P. K. Synthesis and Structure of a Free Germacyclopentadienide Ion: [Li([12]crown-4)]<sub>2</sub>[C<sub>4</sub>Me<sub>4</sub>Ge-Si(SiMe<sub>3</sub>)<sub>3</sub>]. *Angew. Chem., Int. Ed. Engl.* **1995**, *34*, 1887–1890.
- Freeman, W. P.; Tilley, T. D.; Liable-Sands, L. M.; Rheingold, A. L. Synthesis and Study of Cyclic  $\pi$ -Systems Containing Silicon and Germanium. The Question of Aromaticity in Cyclopentadienyl Analogues. *J. Am. Chem. Soc.* **1996**, *118*, 10457–10468.
- Saito, M.; Sakaguchi, M.; Tajima, T.; Ishimura, K.; Nagase, S.; Hada, M. Dilitioplumbole: A Lead-Bearing Aromatic Cyclopentadienyl Analog. *Science* **2010**, *328*, 339–342.
- Saito, M.; Kuwabara, T.; Ishimura, K.; Nagase, S. Synthesis and Structures of Lithium Salts of Stannole Anions. *Bull. Chem. Soc. Jpn.* **2010**, *83*, 825–827.
- Fekete, C.; Kovács, I.; Nyulászi, L.; Holczbauer, T. Planar Lithium Silolide: Aromaticity, with Significant Contribution of Non-classical Resonance Structures. *Chem. Commun.* **2017**, *53*, 11064–11067.
- Reinhold, C. R. W.; Schmidtmann, M.; Tumanskii, B.; Müller, T. Radicals and Anions of Siloles and Germoles. *Chem. Eur. J.* **2021**, *27*, 12063–12068.
- Dong, Z.; Schmidtmann, M.; Müller, T. Potassium Salts of 2,5-Bis(trimethylsilyl)-Germolide: Switching between Aromatic and Non-Aromatic States. *Chem. Eur. J.* **2019**, *25*, 10858–10865.

44. Lee, V. Y.; Kato, R.; Ichinohe, M.; Sekiguchi, A. The Heavy Analogue of CpLi: Lithium 1,2-Disila-3-Germacyclopentadienide, a 6 $\pi$ -Electron Aromatic System. *J. Am. Chem. Soc.* **2005**, *127*, 13142–13143.
45. Yasuda, H.; Lee, V. Y.; Sekiguchi, A. Si<sub>3</sub>C<sub>2</sub>-Rings: From a Nonconjugated Trisilacyclopentadiene to an Aromatic Trisilacyclopentadienide and Cyclic Disilenide. *J. Am. Chem. Soc.* **2009**, *131*, 6352–6353.
46. Wei, J.; Zhang, W.-X.; Xi, Z. The Aromatic Dianion Metalloles. *Chem. Sci.* **2018**, *9*, 560–568.
47. Saito, M. Challenge to Expand the Concept of Aromaticity to Tin- and Lead-Containing Carbocyclic Compounds: Synthesis, Structures and Reactions of Dilithiostannoles and Dilithioplumboles. *Coord. Chem. Rev.* **2012**, *256*, 627–636.
48. Hong, J.-H.; Boudjouk, P.; Castellino, S. Synthesis and Characterization of Two Aromatic Silicon-Containing Dianions: The 2,3,4,5-Tetraphenylsilole Dianion and the 1,1'-Disila-2,2',3,3',4,4',5,5'-Octaphenylfulvalene Dianion. *Organometallics* **1994**, *13*, 3387–3389.
49. West, R.; Sohn, H.; Bankwitz, U.; Calabrese, J.; Apeloig, Y.; Mueller, T. Dilithium Derivative of Tetraphenylsilole: An eta-1-eta-5 Dilithium Structure. *J. Am. Chem. Soc.* **1995**, *117*, 11608–11609.
50. Freeman, W. P.; Tilley, T. D.; Yap, G. P. A.; Rheingold, A. L. Silolyl Anions and Silole Dianions: Structure of [K([18]crown-6)+][C<sub>4</sub>Me<sub>4</sub>Si<sub>2</sub>-]. *Angew. Chem., Int. Ed. Engl.* **1996**, *35*, 882–884.
51. West, R.; Sohn, H.; Powell, D. R.; Müller, T.; Apeloig, Y. The Dianion of Tetraphenylgermole Is Aromatic. *Angew. Chem., Int. Ed. Engl.* **1996**, *35*, 1002–1004.
52. Saito, M.; Haga, R.; Yoshioka, M. Formation of the First Monoanion and Dianion of Stannole. *Chem. Commun.* **2002**, 1002–1003.
53. Saito, M.; Haga, R.; Yoshioka, M.; Ishimura, K.; Nagase, S. The Aromaticity of the Stannole Dianion. *Angew. Chem., Int. Ed.* **2005**, *44*, 6553–6556.
54. To exclude effects of coordinated lithium atoms, the NICS calculations should be performed in the free form.
55. Saito, M.; Kuwabara, T.; Kambayashi, C.; Yoshioka, M.; Ishimura, K.; Nagase, S. Synthesis, Structure, and Reaction of Tetraethyldilithiostannole. *Chem. Lett.* **2010**, *39*, 700–701.
56. Saito, M.; Sakaguchi, M.; Tajima, T.; Ishimura, K.; Nagase, S. Synthesis, Structures, and Properties of Plumboles. *Phosphorus, Sulfur, Silicon Relat. Elem.* **2010**, *185*, 1068–1076.
57. Saito, M.; Akiba, T.; Kaneko, M.; Kawamura, T.; Abe, M.; Hada, M.; Minoura, M. Synthesis, Structure, and Reactivity of Lewis Base Stabilized Plumbacyclopentadienylenes. *Chem. Eur. J.* **2013**, *19*, 16946–16953.
58. Kawamura, T.; Abe, M.; Saito, M.; Hada, M. Quantum-Chemical Analyses of Aromaticity, UV Spectra, and NMR Chemical Shifts in Plumbacyclopentadienylenes Stabilized by Lewis Bases. *J. Comput. Chem.* **2014**, *35*, 847–853.
59. Saito, M.; Nakada, M.; Kuwabara, T.; Minoura, M. A Reversible Two-electron Redox System Involving a Divalent Lead Species. *Chem. Commun.* **2015**, *51*, 4674–4676.
60. Kuwabara, T.; Guo, J.-D.; Nagase, S.; Minoura, M.; Herber, R. H.; Saito, M. Enhancement of Stannylene Character in Stannole Dianion Equivalents Evidenced by NMR and Mössbauer Spectroscopy and Theoretical Studies of Newly Synthesized Silyl-Substituted Dilithiostannoles. *Organometallics* **2014**, *33*, 2910–2913.
61. Dong, Z.; Reinhold, C. R. W.; Schmidtman, M.; Müller, T. Trialkylsilyl-Substituted Silole and Germole Dianions. *Organometallics* **2018**, *37*, 4736–4743.
62. March, J. *Advanced Organic Chemistry, 4th ed.* **1992**. John Wiley & Sons: New York, 1992.
63. Choi, S.-B.; Boudjouk, P.; Wei, P. Aromatic Benzannulated Silole Dianions. The Dilithio and Disodio Salts of a Silaindenyl Dianion. *J. Am. Chem. Soc.* **1998**, *120*, 5814–5815.
64. Choi, S.-B.; Boudjouk, P.; Qin, K. Aromatic Benzannulated Germole Dianions. The Dilithio and Disodio Salts of a Germaindenyl Dianion. *Organometallics* **2000**, *19*, 1806–1809.
65. Saito, M.; Shimosawa, M.; Yoshioka, M.; Ishimura, K.; Nagase, S. Synthesis of Stannaindenyl Anions and a Dianion. *Organometallics* **2006**, *25*, 2967–2971.
66. Liu, Y.; Stringfellow, T. C.; Ballweg, D.; Guzei, I. A.; West, R. Structure and Chemistry of 1-Silafluorenyl Dianion, its Derivatives, and an Organosilicon Diradical Dianion. *J. Am. Chem. Soc.* **2002**, *124*, 49–57.
67. Liu, Y.; Ballweg, D.; Müller, T.; Guzei, I. A.; Clark, R. W.; West, R. Chemistry of the Aromatic 9-Germafluorenyl Dianion and some Related Silicon and Carbon Species. *J. Am. Chem. Soc.* **2002**, *124*, 12174–12181.
68. Saito, M.; Shimosawa, M.; Yoshioka, M.; Ishimura, K.; Nagase, S. Synthesis and Characterization of Dimetallostannofluorenes. *Chem. Lett.* **2006**, *35*, 940–941.
69. Tokitoh, N. New Progress in the Chemistry of Stable Metallaaromatic Compounds of Heavier Group 14 Elements. *Acc. Chem. Res.* **2004**, *37*, 86–94.
70. Norihiro, T. Synthesis of Aromatic Species Containing a Heavier Group 14 Element by Taking Advantage of Kinetic Stabilization. *Bull. Chem. Soc. Jpn.* **2004**, *77*, 429–441.
71. Wakita, K.; Tokitoh, N.; Okazaki, R.; Nagase, S. Synthesis and Properties of an Overcrowded Silabenzene Stable at Ambient Temperature. *Angew. Chem., Int. Ed.* **2000**, *39*, 634–636.
72. Wakita, K.; Tokitoh, N.; Okazaki, R.; Takagi, N.; Nagase, S. Crystal Structure of a Stable Silabenzene and its Photochemical Valence Isomerization into the Corresponding Silabenzvalene. *J. Am. Chem. Soc.* **2000**, *122*, 5648–5649.
73. Takeda, N.; Shinohara, A.; Tokitoh, N. Synthesis and Properties of the First 1-Silanaphthalene. *Organometallics* **2002**, *21*, 4024–4026.
74. Tokitoh, N.; Wakita, K.; Okazaki, R.; Nagase, S.; von Ragué Schleyer, P.; Jiao, H. A Stable Neutral Silaaromatic Compound, 2-{2,4,6-Tris[Bis(trimethylsilyl)methyl]phenyl}-2-Silanaphthalene. *J. Am. Chem. Soc.* **1997**, *119*, 6951–6952.
75. Wakita, K.; Tokitoh, N.; Okazaki, R.; Nagase, S.; Schleyer, P. v. R.; Jiao, H. Synthesis of Stable 2-Silanaphthalenes and their Aromaticity. *J. Am. Chem. Soc.* **1999**, *121*, 11336–11344.
76. Takeda, N.; Shinohara, A.; Tokitoh, N. The First Stable 9-Silaanthracene. *Organometallics* **2002**, *21*, 256–258.
77. Tokitoh, N.; Shinohara, A.; Matsumoto, T.; Sasamori, T.; Takeda, N.; Furukawa, Y. Synthesis and Properties of a Kinetically Stabilized 9-Silaphenanthrene. *Organometallics* **2007**, *26*, 4048–4053.
78. Wiberg, N.; Wagner, G.; Müller, G. Isolation and Structure of a Stable Molecule Containing a Silicon-Carbon Double Bond. *Angew. Chem., Int. Ed. Engl.* **1985**, *24*, 229–230.
79. Gutowsky, H. S.; Chen, J.; Hajduk, P. J.; Keen, J. D.; Chuang, C.; Emilsson, T. The Silicon-Carbon Double Bond: Theory Takes a Round. *J. Am. Chem. Soc.* **1991**, *113*, 4747–4751.
80. Nakata, N.; Takeda, N.; Tokitoh, N. Synthesis and Structure of a Kinetically Stabilized 2-Germanaphthalene: The First Stable Neutral Germaaromatic Compound. *Organometallics* **2001**, *20*, 5507–5509.
81. Nakata, N.; Takeda, N.; Tokitoh, N. Synthesis and Properties of the First Stable Neutral Germaaromatic Compound, 2-{2,4,6-Tris-[Bis(trimethylsilyl)methyl]phenyl}-2-Germanaphthalene. *Organometallics* **2003**, *22*, 481–489.
82. Nakata, N.; Takeda, N.; Tokitoh, N. Synthesis and Properties of the First Stable Germabenzene. *J. Am. Chem. Soc.* **2002**, *124*, 6914–6920.
83. Sasamori, T.; Inamura, K.; Hoshino, W.; Nakata, N.; Mizuhata, Y.; Watanabe, Y.; Furukawa, Y.; Tokitoh, N. Synthesis and Characterization of Two Isomers of 14 $\pi$ -Electron Germaaromatics: Kinetically Stabilized 9-Germaanthracene and 9-Germaphenanthrene. *Organometallics* **2006**, *25*, 3533–3536.
84. Kaiya, C.; Suzuki, K.; Yamashita, M. Chlorine-Substituted Germabenzene: Generation and Application as a Precursor for Aryl-Substituted Germabenzenes. *Organometallics* **2019**, *38*, 610–613.
85. Mizuhata, Y.; Noda, N.; Tokitoh, N. Generation of Stannabenzenes and their Properties. *Organometallics* **2010**, *29*, 4781–4784.
86. Mizuhata, Y.; Fujimori, S.; Noda, N.; Kanesato, S.; Tokitoh, N. Generation of Stannabenzenes and their Monomer–Dimer Equilibration. *Dalton Trans.* **2018**, *47*, 14436–14444.
87. Kaiya, C.; Suzuki, K.; Yamashita, M. A Monomeric Stannabenzene: Synthesis, Structure, and Electronic Properties. *Angew. Chem., Int. Ed.* **2019**, *58*, 7749–7752.
88. Mizuhata, Y.; Sasamori, T.; Takeda, N.; Tokitoh, N. A Stable Neutral Stannaaromatic Compound: Synthesis, Structure and Complexation of a Kinetically Stabilized 2-Stannaphthalene. *J. Am. Chem. Soc.* **2006**, *128*, 1050–1051.
89. Yoshiyuki, M.; Nobuhiro, T.; Takahiro, S.; Norihiro, T. Generation of 9-Stannaphenanthrene and Its Reactivities. *Chem. Lett.* **2005**, *34*, 1088–1089.
90. Mizuhata, Y.; Fujimori, S.; Sasamori, T.; Tokitoh, N. Germabenzenylpotassium: A Germanium Analogue of a Phenyl Anion. *Angew. Chem., Int. Ed.* **2017**, *56*, 4588–4592.

91. Sekiguchi, A.; Kinjo, R.; Ichinohe, M. A Stable Compound Containing a Silicon-Silicon Triple Bond. *Science* **2004**, *305*, 1755–1757.
92. Kinjo, R.; Ichinohe, M.; Sekiguchi, A.; Takagi, N.; Sumimoto, M.; Nagase, S. Reactivity of a Disilyne  $\text{RSi} \equiv \text{SiR}$  ( $\text{R} = \text{Si}(\text{Pr})[\text{CH}(\text{SiMe}_3)_2]$ ) toward  $\pi$ -Bonds: Stereospecific Addition and a New Route to an Isolable 1,2-Disilabenzene. *J. Am. Chem. Soc.* **2007**, *129*, 7766–7767.
93. Sasamori, T.; Hironaka, K.; Sugiyama, Y.; Takagi, N.; Nagase, S.; Hosoi, Y.; Furukawa, Y.; Tokitoh, N. Synthesis and Reactions of a Stable 1,2-Diaryl-1,2-Dibromodisilene: A Precursor for Substituted Disilenes and a 1,2-Diaryldisilyne. *J. Am. Chem. Soc.* **2008**, *130*, 13856–13857.
94. Han, J. S.; Sasamori, T.; Mizuhata, Y.; Tokitoh, N. Reactivity of an Aryl-Substituted Silicon-Silicon Triple Bond: 1,2-Disilabenzene from the Reactions of a 1,2-Diaryldisilyne with Alkynes. *Dalton Trans.* **2010**, *39*, 9238–9240.
95. Sasamori, T.; Sugahara, T.; Agou, T.; Guo, J.-D.; Nagase, S.; Streubel, R.; Tokitoh, N. Synthesis and Characterization of a 1,2-Digermabenzene. *Organometallics* **2015**, *34*, 2106–2109.
96. Sugahara, T.; Guo, J.-D.; Sasamori, T.; Karatsu, Y.; Furukawa, Y.; Ferao, A. E.; Nagase, S.; Tokitoh, N. Reaction of a Stable Digermene with Acetylenes: Synthesis of a 1,2-Digermabenzene and a 1,4-Digermabarrelene. *Bull. Chem. Soc. Jpn.* **2016**, *89*, 1375–1384.
97. Sharma, M. K.; Rottschäfer, D.; Glodde, T.; Neumann, B.; Stammler, H.-G.; Ghadwal, R. S. An Open-Shell Singlet S<sub>n</sub> Diradical and H<sub>2</sub> Splitting. *Angew. Chem., Int. Ed.* **2021**, *60*, 6414–6418.
98. Breslow, R.; Groves, J. T.; Ryan, G. Cyclopropenyl Cation. *J. Am. Chem. Soc.* **1967**, *89*, 5048.
99. Sekiguchi, A.; Yamazaki, H.; Kabuto, C.; Sakurai, H.; Nagase, S. Cyclotrigermenes: A New Unsaturated Ring System. *J. Am. Chem. Soc.* **1995**, *117*, 8025–8026.
100. Sekiguchi, A.; Tsukamoto, M.; Ichinohe, M. A Free Cyclotrigermene Cation with a 2 $\pi$ -Electron System. *Science* **1997**, *275*, 60–61.
101. Ichinohe, M.; Igarashi, M.; Sanuki, K.; Sekiguchi, A. Cyclotrisilylium Ion: The Persilaaromatic Compound. *J. Am. Chem. Soc.* **2005**, *127*, 9978–9979.
102. Igarashi, M.; Ichinohe, M.; Sekiguchi, A. Air-Stable Disilacyclopentene with a SiC Bond and its Conversion to Disilacyclopentenylium Ion: Silicon – Carbon Hybrid 2 $\pi$ -Electron Systems. *J. Am. Chem. Soc.* **2007**, *129*, 12660–12661.
103. Hess, B. A.; Ewig, C. S.; Schaad, L. J. An Ab Initio Study of the Cyclobutadiene Dianion and Dication. *J. Org. Chem.* **1985**, *50*, 5869–5871.
104. Van Zandwijk, G.; Janssen, R. A. J.; Buck, H. M. 6 $\pi$ . Aromaticity in Four-Membered Rings. *J. Am. Chem. Soc.* **1990**, *112*, 4155–4164.
105. Balci, M.; McKee, M. L.; Schleyer, P. v. R. Theoretical Study of Tetramethyl- and Tetra-Tert-Butyl-Substituted Cyclobutadiene and Tetrahedrane. *J. Phys. Chem. A* **2000**, *104*, 1246–1255.
106. Sekiguchi, A.; Matsuo, T.; Watanabe, H. Synthesis and Characterization of a Cyclobutadiene Dianion Dilithium Salt: Evidence for Aromaticity. *J. Am. Chem. Soc.* **2000**, *122*, 5652–5653.
107. Lee, V. Y.; Takanashi, K.; Matsuno, T.; Ichinohe, M.; Sekiguchi, A. Cyclobutadiene Dianions Consisting of Heavier Group 14 Elements: Synthesis and Characterization. *J. Am. Chem. Soc.* **2004**, *126*, 4758–4759.
108. Lee, V. Y.; Ito, Y.; Yasuda, H.; Takanashi, K.; Sekiguchi, A. From Tetragermacyclobutene to Tetragermacyclobutadiene Dianion to Tetragermacyclobutadiene Transition Metal Complexes. *J. Am. Chem. Soc.* **2011**, *133*, 5103–5108.
109. Takanashi, K.; Lee, V. Y.; Sekiguchi, A. Tetrasilacyclobutadiene and Cyclobutadiene Tricarbonylruthenium Complexes:  $[\eta^4\text{-}(\text{tBu}_2\text{MeSi})_4\text{Si}_4]\text{Ru}(\text{CO})_3$  and  $[\eta^4\text{-}(\text{Me}_3\text{Si})_4\text{C}_4]\text{Ru}(\text{CO})_3$ . *Organometallics* **2009**, *28*, 1248–1251.
110. Lee, V. Y.; Takanashi, K.; Sekiguchi, A. A Two-and-a-Half-Layer Sandwich: Potassium Salt of Anionic ( $\eta^4$ -Tetrasilacyclobutadiene)( $\eta^5$ -Cyclopentadienyl)Ruthenium. *Dalton Trans.* **2010**, *39*, 9229–9231.
111. So, C.-W.; Roesky, H. W.; Magull, J.; Oswald, R. B. Synthesis and Characterization of  $[\text{PhC}(\text{tBu})_2\text{SiCl}]\text{SiCl}$ : A Stable Monomeric Chlorosilylene. *Angew. Chem., Int. Ed.* **2006**, *45*, 3948–3950.
112. Sen, S. S.; Jana, A.; Roesky, H. W.; Schulzke, C. A Remarkable Base-Stabilized Bis(Silylene) with a Silicon(II)–Silicon(II) Bond. *Angew. Chem., Int. Ed.* **2009**, *48*, 8536–8538.
113. Sun, X.; Simler, T.; Yadav, R.; Köppe, R.; Roesky, P. W. A Stable Aromatic Tetrasilacyclobutadiene Dication. *J. Am. Chem. Soc.* **2019**, *141*, 14987–14990.
114. Yokelson, H. B.; Millevolte, A. J.; Gillette, G. R.; West, R. Disilaoxiranes: Synthesis and Crystal Structure. *J. Am. Chem. Soc.* **1987**, *109*, 6865–6866.
115. Ota, K.; Kinjo, R. Heavier Element-Containing Aromatics of  $[4n+2]$ -Electron Systems. *Chem. Soc. Rev.* **2021**, *50*, 10594–10673.

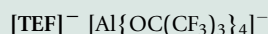
## 1.19 Chain, ring, and cluster compounds of group 15 elements (P, As, Sb, Bi)

Martyn P. Coles, School of Chemical and Physical Sciences, Victoria University of Wellington, Wellington, New Zealand

© 2023 Elsevier Ltd. All rights reserved.

<b>1.19.1</b>	<b>Introduction</b>	<b>864</b>
<b>1.19.2</b>	<b>Dipnictogens</b>	<b>866</b>
1.19.2.1	Non-supported, non-cyclic dipnictogens ( $R_2E-ER_2$ , $R_2 = \text{non-cyclic}$ )	866
1.19.2.2	Non-supported, cyclic dipnictogens ( $R_2E-ER_2$ , $R_2 = \text{cyclic}$ )	868
1.19.2.3	Supported, heterocyclic dipnictogens	869
1.19.2.4	Supported, metalated dipnictogens	870
<b>1.19.3</b>	<b>Non-cyclic <i>catena</i>-pnictogens</b>	<b>871</b>
1.19.3.1	Linear, non-metalated <i>catena</i> -pnictogens	872
1.19.3.2	Linear, metalated <i>catena</i> -pnictogens	873
1.19.3.3	Branched, metalated <i>catena</i> -pnictogens	874
<b>1.19.4</b>	<b>Monocyclic <i>catena</i>-pnictogens</b>	<b>875</b>
1.19.4.1	Monocyclic, non-metalated <i>catena</i> -pnictogens: $(E)_n = 3-6$	875
1.19.4.1.1	Cyclo- $(E)_3$ units	875
1.19.4.1.2	Cyclo- $(E)_4$ units	876
1.19.4.1.3	Cyclo- $(E)_5$ units	879
1.19.4.1.4	Cyclo- $(E)_6$ units	880
1.19.4.2	Monocyclic, metalated <i>catena</i> -pnictogens: $(E)_n = 3-6$	880
1.19.4.2.1	Metalated cyclo- $(E)_3$ units	880
1.19.4.2.2	Metalated cyclo- $(E)_4$ units	882
1.19.4.2.3	Metalated cyclo- $(E)_5$ units	883
1.19.4.2.4	Metalated cyclo- $(E)_6$ units	884
1.19.4.3	Monocyclic heterocycles containing <i>catena</i> -pnictogen groups	885
<b>1.19.5</b>	<b>Polycyclic <i>catena</i>-pnictogens</b>	<b>886</b>
1.19.5.1	Coordination chemistry of $P_4$ and $As_4$ tetrahedra	887
1.19.5.2	Synthesis of polycyclic <i>catena</i> -pnictogens from $P_4$ and $As_4$ tetrahedra	888
1.19.5.2.1	Activation of $P_4$ and $As_4$ with main-group ( <i>s</i> - and <i>p</i> -block) reagents	888
1.19.5.2.2	Activation of $P_4$ and $As_4$ with transition-metal ( <i>d</i> -block) reagents	891
1.19.5.2.3	Activation of $P_4$ and $As_4$ with lanthanide and actinide ( <i>f</i> -block) reagents	894
1.19.5.3	Synthesis of polycyclic <i>catena</i> -pnictogens from other sources	895
1.19.5.4	The chemistry of non-metalated polycyclic <i>catena</i> -pnictogens	896
1.19.5.5	The chemistry of metalated polycyclic <i>catena</i> -pnictogens	897
<b>1.19.6</b>	<b>Miscellaneous reactions forming <i>catena</i>-polypnictogens</b>	<b>898</b>
<b>1.19.7</b>	<b>Conclusions</b>	<b>898</b>
<b>References</b>		<b>899</b>

### Nomenclature



18-c-6 18-Crown-6 (1,4,7,10,13,16-hexaoxacyclooctadecane)

2.2.2-crypt [2.2.2]cryptand (4,7,13,16,21,24-hexaoxa1,10-diazabicyclo[8.8.8]hexacosane)

aceNaph 5,6-Acenaphthalendiyl

Ar Aryl (*generic*—see also Fig. 2)

E Pnictogen atom (P, As, Sb or Bi)

Fc 1,1-Ferrocenediyl

Ln Lanthanide element (*generic*)

Naph 1,8-Naphthalendiyl

NHC *N*-heterocyclic carbene (*generic*—see also Fig. 1)

$R_1BDI^{R_2} [HC(C\{R_1\}N\{R_2\})_2]^-$  ( $\beta$ -diketiminato)

$R^BBIAN$  1,2-(RN)<sub>2</sub>acenaphthene

## Abstract

This chapter describes the synthesis and reactivity of *catena*-pnictogen compounds containing (one or more) E–E single bonds (E = P, As, Sb, Bi). It is divided into sections describing linear (E)<sub>n</sub> chains (including dipnictogen compounds where *n* = 2), monocyclic (E)<sub>n</sub> ring systems and polycyclic (E)<sub>n</sub> clusters. The ring systems have been organized according to the size of the ring (*n* = 3–6) and whether or not it is associated with a metal fragment (metalated). The section on polycyclic cluster systems begins with a summary of *catena*-compounds derived from intact or ring-opened P<sub>4</sub> and As<sub>4</sub> starting materials, divided according to the nature of the activating agent (*s*- and *p*-block, *d*-block or *f*-block reagents). The concluding sections of the chapter describe the chemistry of polycyclic (E)<sub>n</sub> clusters derived from other sources.

### 1.19.1 Introduction

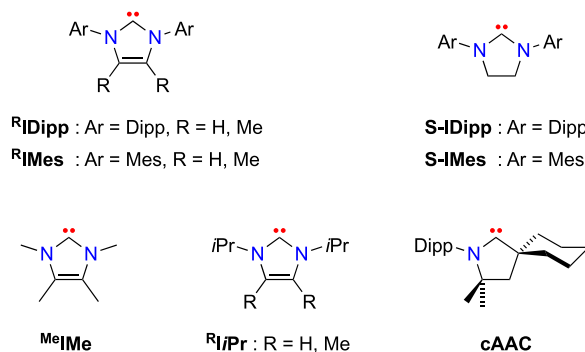
This chapter provides an overview of the chemistry of catenated compounds of the group 15 elements phosphorus (P), arsenic (As), antimony (Sb) and bismuth (Bi), covering material presented in the literature since 2013. This collection of the chemistry of the group 15 elements differs from previous volumes of this *Comprehensive Inorganic Chemistry* in which phosphorus was included in a separate chapter and serves to highlight the many similarities between the chemistry of these four members of the group. For the purposes of this review, these elements are collectively referred to as the pnictogens, excluding nitrogen as the lightest member of the group.

The ability of the pnictogens to form catenated compounds through the formation of E–E single bonds dates back to the earliest chemistry associated with these elements, with for example a major component of ‘Cadet’s fuming liquid’ (cacodyl) synthesized in 1757 being later identified as tetramethyldiarsane.<sup>1</sup> Although less stable than corresponding C–C bonds, known to form an extensive array of ring and chain structures (dealt with in the separate discipline of organic chemistry), E–E bonds (where E represents a generic pnictogen P, As, Sb, Bi) are nevertheless established in the inorganic literature with examples of linear chains, monocyclic rings and three-dimensional polycyclic (cluster) compounds known for all elements. The relative number of these examples, where P–P > As–As > Sb–Sb > Bi–Bi, likely reflects a decrease in the E–E bond strength as the group is descended.

The catenated compounds surveyed in this chapter predominantly involve three-coordinate group 15 atoms linked by one or more pnictogen–pnictogen single bonds, E–E. This typically corresponds to the elements in low-oxidation states, with the focus of this article on (R<sub>2</sub>E)<sub>n</sub> species containing formally E(II) centers. This precludes discussion of (RE)<sub>n</sub> species that contain multiple bond between the pnictogen atoms, and [E<sub>n</sub>]<sup>x-</sup> anions (Zintl ions) that are considered elsewhere in this volume. The remaining valencies on the pnictogen atom not involved in E–E bonding incorporate supporting ligands that restrict the catenation to generate molecular species. Synthetic chemists have a vast toolbox of such ligands and they have been utilized in this area, which is not restricted to purely inorganic systems, but includes extensive work involving metal coordination compounds. This chapter makes reference to an array of such ligands, many of which have been summarized in this introduction and are collected in the following categories.

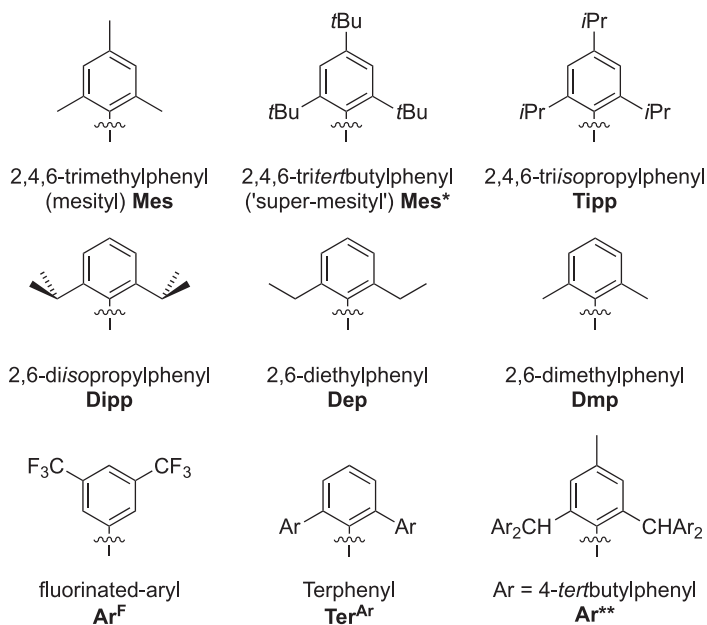
The application of neutral *N*-heterocyclic carbenes (NHCs) as ligands is established in inorganic chemistry and the ability to tune the steric and electronic properties has given access to a family of these compounds (Fig. 1). The majority of examples are based on the imidazole skeleton and involve five-membered rings in which the divalent carbon is supported by two nitrogen functional groups. Examples of saturated and unsaturated systems have been developed with different substitution patterns at the non-carbene carbon atoms. A less widely applied but equally relevant system is the cyclic alkyl(amino) carbenes (cAACs).

The use of mono-anionic aryl substituents as supporting ligands in catenated pnictogen chemistry dates back to the earliest known examples of such compounds. More recent developments that extend this class of ligand to include extremely bulky examples have facilitated the isolation of highly reactive species that would otherwise confound synthetic chemists (Fig. 2). The majority of examples rely on the presence of substituents at the 2,6-positions to provide steric protection at the pnictogen atom to which they



**Fig. 1** Classification of *N*-heterocyclic carbenes (NHCs) and cyclic alkyl(amino) carbenes (cAACs) in this chapter.

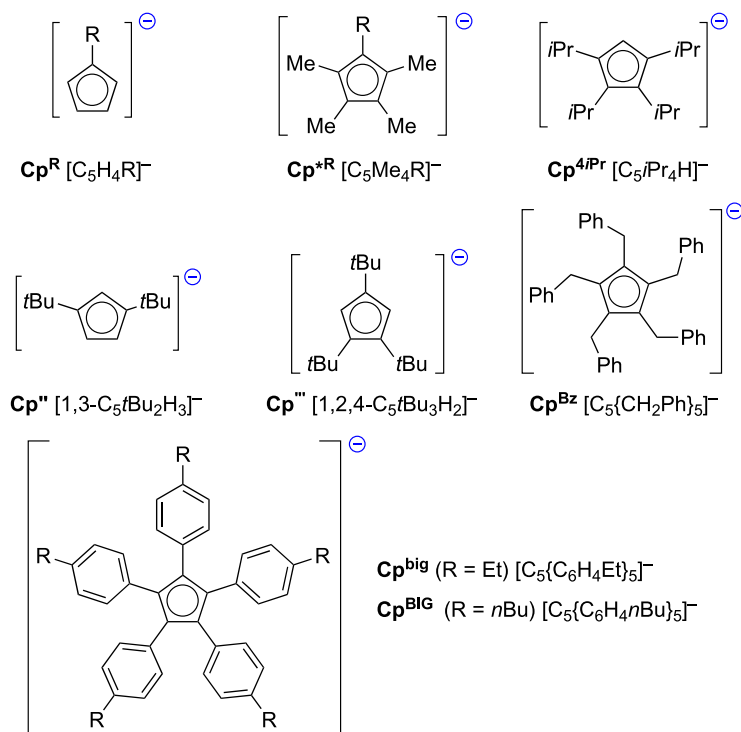




**Fig. 2** Classification of aryl derivatives in this chapter.

are bonded, thereby offering a degree of control over the extent of catenation or the direction of the reactivity. However, the incorporation of fluorinated substituents has also been employed to influence the electronic properties of these ligands.

Finally, given the prominent role that metal complexes have played in both the synthesis and stabilization of compounds containing *catena*-pnictogen groups, a range of substituted cyclopentadienyl groups that have been used in this context is summarized below (**Fig. 3**). These predominantly remain  $\eta^5$ -bound to their respective metal centers, but through variation in their substitution pattern around the  $C_5$ -ring allow specific steric profiles to be established.



**Fig. 3** Classification of cyclopentadienyl-anion derivatives in this chapter.

The work collected in this chapter is largely based on structural studies performed on compounds and metal complexes containing  $(E)_n$  units. This is a reflection of the progress that has been made with X-ray crystallography as an analytical tool, where the time taken from data collection to a fully refined structure may take a matter of minutes to hours for routine crystals, compared with days to weeks of data-collection and analysis required in the not too distant past. The accurate determination of the three-dimensional atomic arrangement in these often highly reactive compounds has enabled the chemistry of these systems to be understood to an extent previously not possible (or at least substantially more challenging) using conventional spectroscopic techniques. One must, however, exercise caution when relying solely on crystal structure data, and a recognition of the limitations of the technique to the solid state (condensed) phase must be appreciated. Neither does the structural data lend accurate information concerning the mechanistic processes leading to the formation of the final products. Thankfully, progress in computational techniques for the analysis of reaction pathways in silico has kept abreast of these experimental developments, thereby complementing the analytical techniques available to the inorganic chemist and allowing more in depth studies of molecular systems to be conducted.

### 1.19.2 Dipnictogens

The first part of this chapter describes the simplest class of *catena*-pnictogens, in which the  $(E)_n$  unit is restricted to  $n = 2$ , with a single bond between pnictogen atoms to form a dipnictogen E–E unit. It has focused on compounds in which the  $(E)_2$  group represents a major component of interest in the compound, thereby precluding examples in which phosphanes, arsanes and stibanes have been used in their capacity as a supporting ligand at another pnictogen center that does not participate in the chemical reactivity. For convenience, the work has been divided into four sections according to the environment around the dipnictogen group (Fig. 4).

Section 1.19.2.1 describes examples of dipnictogen compounds consisting of two pnictogen atoms bonded together, with a non-cyclic ligand set completing the coordination sphere of each E-atom (Fig. 4A). This includes examples in which one or more *N*-heterocyclic carbene (NHC) ligand have been used in this context in addition to traditional anionic ligands. Section 1.19.2.2 continues this theme to encompass examples in which the pnictogen atoms are supported by a bidentate ligand set (Fig. 4B), which generate an *exo*-cyclic  $(E)_2$  unit.

Section 1.19.2.3 describes examples of compounds in which the dipnictogen unit is included as a component of a heterocyclic group. This can occur in a number of different ways (Fig. 4C), including a series specifically designed to examine the nature of the donor-acceptor interactions between different pnictogen atoms. The final Section 1.19.2.4 brings together examples of compounds in which the dipnictogen component forms part of a metal containing cluster. Different bimetallic cases are included (Fig. 4D) that involve either a single dipnictogen group  $\eta^2$ -bonded to two metals in a tetrahedral  $M_2E_2$  cluster, or two distinct dipnictogens units that each engage in a  $\mu, \eta^{2:2}$ -bridging mode between the two atoms.

#### 1.19.2.1 Non-supported, non-cyclic dipnictogens ( $R_2E-ER_2$ , $R_2 = \text{non-cyclic}$ )

The observation that distibanes ( $R_2Sb-SbR_2$ ) and dibismuthanes ( $R_2Bi-BiR_2$ ) containing small alkyl substituents (e.g. Me, Et) possess the unusual characteristic of changing color as their temperature is altered has been noted since the earliest days of

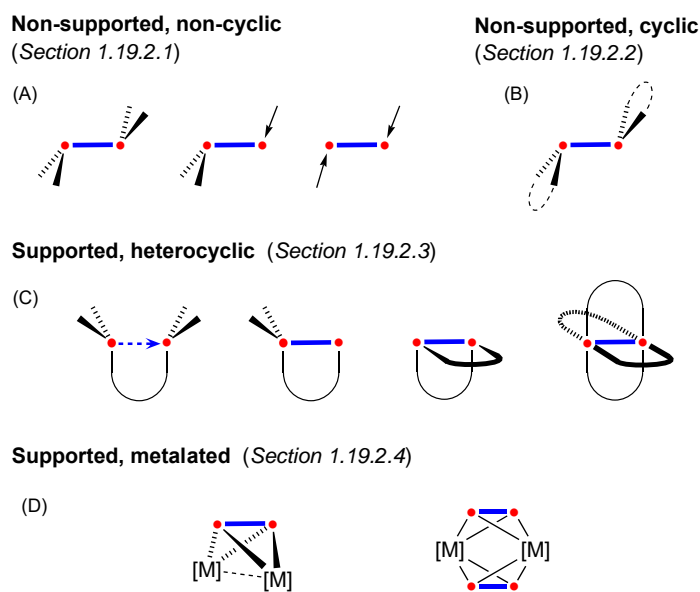


Fig. 4 Schematic representations of dipnictogen units included in Section 1.19.2.

organometallic chemistry. For example, tetramethyl dibismuthane  $\text{Me}_2\text{Bi}-\text{BiMe}_2$  is orange in the liquid state, but crystallizes as a purple solid.<sup>2</sup> For many years this thermochromic behavior was attributed to the formation of intermolecular interactions in the condensed (lower temperature) phase, generating chains of  $\cdots\text{E}-\text{E}\cdots\text{E}-\text{E}\cdots\text{E}-\text{E}\cdots$  atoms. However, a detailed investigation of the distibane  $\text{Et}_2\text{Sb}-\text{SbEt}_2$  and the structural characterization of both the yellow phase (present at  $-80^\circ\text{C}$ ) and red phase (present at  $-100^\circ\text{C}$ ) concluded that the structures were essentially identical, and that disruption of the chain structure at higher temperatures was not the cause of the thermochromism.<sup>3</sup> Indeed, no firm conclusions to explain the thermochromism were reached during this study, and the phenomenon retains its mystery. Nevertheless, the accessibility of the antimony centers in such dialkyl-distibanes has been exploited in their application as bridging ligands in coordination chemistry. This was demonstrated by the reaction of  $\text{R}_2\text{Sb}-\text{SbR}_2$  ( $\text{R} = \text{Me}, \text{Et}$ ) with *cis*- $\text{Mo}(\text{pip})_2(\text{CO})_4$  (*pip* = piperidine).<sup>4</sup> The products contain an  $\text{Sb}_4\text{Mo}_2$  core in which the Sb-atoms are *cis* at the metal centers, generating a metallacycle that is present in a chair conformation in the solid state.

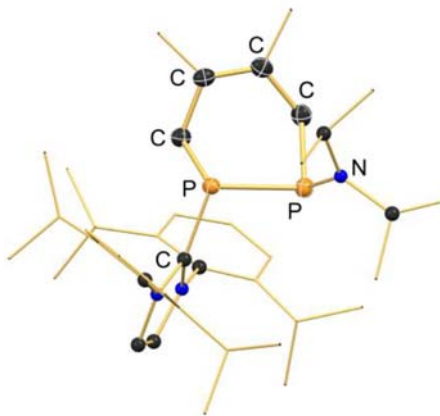
*N*-heterocyclic carbenes have been instrumental in stabilizing low-valent pnictogen complexes, including recent breakthroughs that have allowed the isolation of diatomic molecular species in which group 15 element is formally zero-valent. This has been previously documented for  $\text{P}_2$ ,<sup>5</sup> and  $\text{As}_2$ ,<sup>6</sup> but had not been extended to the heavier congeners Sb or Bi. In 2014, researchers showed that a cyclic alkyl(amino) carbene (cAAC) adduct of  $\text{SbCl}_3$  was able to support the sequential reduction of the antimony(III) center to afford the series of Sb(II), Sb(I) and Sb(0) species.<sup>7</sup> The triply reduced product, containing formally Sb(0) centers, was isolated as the dimer  $(\text{cAAC})\text{Sb}-\text{Sb}(\text{cAAC})$  with an Sb–Sb bond length of 2.8125(10) Å comparable to the typical value found in distibanes,  $\text{R}_2\text{Sb}-\text{SbR}_2$ .

The saturated *N*-heterocyclic phosphinidene  $(\text{S-IMes})\text{P}-\text{H}$  can be deprotonated with benzylpotassium to afford the salt  $\text{K}[(\text{S-IMes})\text{P}]$ .<sup>8</sup> This anion was reacted with  $t\text{Bu}_2\text{EX}$  ( $\text{E} = \text{P}, \text{As}, \text{Sb}; \text{X} = \text{Cl}; \text{E} = \text{Bi}; \text{X} = \text{Br}$ ) to produce compounds containing the full series of P–E bonds in the products,  $(\text{S-IMes})\text{P}-\text{E}(t\text{Bu})_2$ .<sup>9</sup> Structural characterization indicated that these are best described as containing a C=P double bond between the carbene and the phosphorus atoms, with the P–Sb and P–Bi derivatives representing rare examples of phosphorus bonding to these elements.

A non-symmetrical bis-carbene stabilized diphosphorus species was obtained from the reaction of the carbene-phosphinidene adduct  $(^{\text{H}}\text{IDipp})\text{P}-\text{SiMe}_3$  with  $(^{\text{H}}\text{IMes})\text{PCL}_3$ .<sup>10</sup> The intermediate chloro species  $[(^{\text{H}}\text{IDipp})\text{P}-\text{P}(\text{Cl})(^{\text{H}}\text{IMes})]\text{Cl}$  was reacted with potassium graphite ( $\text{KC}_8$ ) to afford the neutral product  $(^{\text{H}}\text{IDipp})\text{P}-\text{P}(^{\text{H}}\text{IMes})$ . Parallel work examining the reaction of  $(^{\text{H}}\text{IDipp})\text{P}-\text{SiMe}_3$  with  $(^{\text{H}}\text{IMes})\text{AsCl}_3$  led to the isolation of a carbene stabilized arsenic monophosphide  $[\text{AsP}]$  unit, its radical cation  $[\text{AsP}]^{\cdot+}$ , and the corresponding dication  $[\text{AsP}]^{2+}$ .<sup>11</sup>

In a separate study it was shown that reaction of the parent phosphinidene  $(^{\text{H}}\text{IDipp})\text{P}-\text{H}$  with  $\text{R}_2\text{PCL}_2$  ( $\text{R} = \text{Ph}, \text{NiPr}_2, \text{NMe}_2$ ) in the presence of base afforded the chlorodiphosphanes,  $(^{\text{H}}\text{IDipp})\text{P}-\text{P}(\text{R})\text{Cl}$ .<sup>12</sup> These compounds were reacted with 2 equivalents of  $\text{GaCl}_3$  to generate the dimers  $\{[(^{\text{H}}\text{IDipp})\text{P}-\text{P}(\text{R})]_2\}^{2+}$  containing a cationic tetrasubstituted all- $\sigma^3$  cyclooctaphosphane. When a single equivalent of  $\text{GaCl}_3$  was used, the monomeric cation  $[(^{\text{H}}\text{IDipp})\text{P}=\text{P}(\text{NiPr}_2)]^+$  was isolated, with the presence of a P=P double bond confirmed from the [4 + 2] Diels-alder cycloaddition with 2,3-dimethylbuta-1,3-diene to afford the cationic 1,2-diphosphanes (Fig. 5).

Modification of the  $^{\text{R}}\text{IDipp}$  carbene by substituting one of the R-groups with the electron-deficient borane  $\text{B}(\text{C}_6\text{F}_5)_3$  generates a so called ‘weakly-coordinating anionic *N*-heterocyclic carbene’ (WCA-NHC).<sup>13</sup> These compounds were used to form the pnictogen dihalides  $(\text{WCA-NHC})\text{ECl}_2$ , which were in turn reacted with  $(^{\text{H}}\text{IDipp})\text{P}-\text{SiMe}_3$  to form the chloro species  $(\text{WCA-NHC})\text{E}(\text{Cl})-\text{P}(^{\text{H}}\text{IDipp})$  containing E–P bonds.<sup>14</sup> Chloride abstraction from these compounds using  $\text{GaCl}_3$  afforded the cationic *trans*-bent dipnictenes  $[(\text{WCA-NHC})\text{E}=\text{P}(^{\text{H}}\text{IDipp})][\text{GaCl}_4]^-$  and one electron reduction with 0.5 equivalents of 1,4-bis(trimethylsilyl)-1,4-dihydropyrazine generated the neutral  $[\text{P}_2]^{\cdot}$  and  $[\text{AsP}]^{\cdot}$  radical species.



**Fig. 5** Structure of a cationic 1,2-diphosphanes derived from cycloaddition of 2,3-dimethylbuta-1,3-diene to  $[(^{\text{H}}\text{IDipp})\text{P}=\text{P}(\text{NiPr}_2)]^+$  ( $[\text{GaCl}_4]^-$  anion omitted).

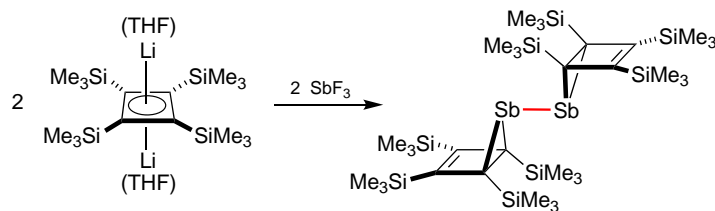
1.19.2.2 Non-supported, cyclic dipnictogens ( $R_2E-ER_2$ ,  $R_2 = \text{cyclic}$ )

The bis(silylamino)naphthyl backbone,  $[\text{Naph}\{\text{NSiR}_3\}_2]^{2-}$  is a known ancillary ligand that supports Sb(III)<sup>15</sup> and Bi(III)<sup>16</sup> centers. This stable scaffold was used to isolate the bismuthanylstibane  $(\text{Naph}\{\text{NSiEt}_3\}_2)\text{Sb}-\text{Bi}(\{\text{Me}_3\text{SiN}\}_2\text{Naph})$ , which contains a rare example of a Sb–Bi bond (Fig. 6).<sup>17</sup> The thermally stable product was obtained in a one-pot, high yielding reaction from an amine elimination reaction between  $\text{Sb}(\text{Naph}\{\text{NSiR}_3\}_2)(\text{H})$  and  $\text{Bi}(\text{Naph}\{\text{NSiR}'_3\}_2)(\text{NMe}_2)$  ( $R = \text{Et}$ ,  $i\text{Pr}$ ;  $R' = \text{Me}$ ,  $\text{Et}$ ). DFT calculations indicated that stabilization of the otherwise labile Sb–Bi bond was promoted by the silylnaphthyl ligands through a combination of inductive and dispersion donor effects. Although unreactive toward a variety of substrates (azobenzene, phenylacetylene, or pyridine *N*-oxide), it was shown that the Sb–Bi bond cleanly inserted sulfur to afford the 'Sb–S–Bi' unit, with the expected bent geometry at sulfur.

Monoanionic pincer ligands with an *N,C,N'*-bonding motif consisting of a central C-bonded aryl group with peripheral neutral imine donors in the 2- and 6-positions were employed to stabilize stibinidenes containing the Sb(I) center.<sup>18</sup> As part of this study, it was noted that the reaction of Sb(III) precursors,  $\{\text{C}_6\text{H}_3\text{-2,6-(CH=NR)}_2\}\text{SbCl}_2$  ( $R = \text{Ph}$ , *t*Bu, Dipp) with  $\text{K}[\text{B}(\text{sBu})_3\text{H}]$  proceeded with a reduction of the imine functionality in preference to the antimony center. This was utilized in the system that contained the related bidentate *C,N*-ligand scaffold,  $\{\text{C}_6\text{H}_2\text{-2-(CH=NDipp)-4,6-(tBu)}_2\}\text{SbCl}_2$ , producing the *bis*(2-*Dipp*)-1*H*-2,1-benzazastibole) in which both the ligand and Sb were reduced.

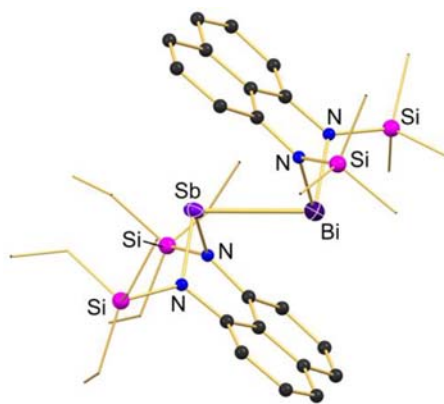
The application of chelating oligosilanyl ligands  $[(\text{R}^{\text{Si}})_2]^{2-}$  in antimony chemistry led to the formation of either the Sb(III) stibanes  $(\text{R}^{\text{Si}})_2\text{SbX}$  ( $X = \text{Cl}$ ,  $\text{Br}$ ), or the Sb(II) distibanes  $(\text{R}^{\text{Si}})_2\text{Sb}-\text{Sb}(\text{R}^{\text{Si}})_2$  during salt-metathesis reactions using the magnesium reagents  $\text{Mg}[(\text{Me}_2\text{Si})_n\{\text{Si}(\text{SiMe}_3)_2\}_2]$  and  $\text{SbCl}_3$ .<sup>19</sup> When  $n = 2$  the stibane  $[(\text{Me}_2\text{Si})_2\{\text{Si}(\text{SiMe}_3)_2\}_2]\text{SbBr}$  was isolated (where the bromide ligand resulted from a halogen exchange process), whereas when  $n = 1$  an unanticipated reduction of the antimony occurs to form the distibane  $[(\text{Me}_2\text{Si}\{\text{Si}(\text{SiMe}_3)_2\}_2)\text{Sb}]_2$ . The corresponding Sb(II) compound for the five-membered  $\text{Si}_4\text{Sb}$  derivative ( $n = 2$ ) was accessed from the reduction of the bromide with  $\text{KC}_8$ .

A relatively unusual ligand framework that has been used to support a distibane derivative was reported by researchers studying the stabilization of highly strained organic molecules.<sup>20</sup> Bicyclo[2.1.0]pentene (commonly known as 'houseene'), which is a valence isomer of cyclopentadiene, is the smallest unsaturated polycyclic hydrocarbon that has been isolated. The corresponding bis(stibahousene) was isolated directly from the reaction of  $\text{SbF}_3$  with the lithium salt of the cyclobutadiene dianion,



**Scheme 1** Synthesis of bis(stibahousene).

$[\text{Li}(\text{THF})]_2[\text{C}_4\{\text{SiMe}_3\}_4]$  (Scheme 1). <sup>1</sup>H, <sup>13</sup>C and <sup>29</sup>Si NMR spectroscopy showed only a single set of resonances for the ligand in solution, interpreted as a rapid migration of one stibahousene fragment around the other. In addition, DFT calculations confirmed that this isomer was more stable than the corresponding bis(stibapyramidane) in which the  $\text{C}_4$ -group binds as in an  $\eta^4$ -coordination mode to a central 'Sb–Sb' group.

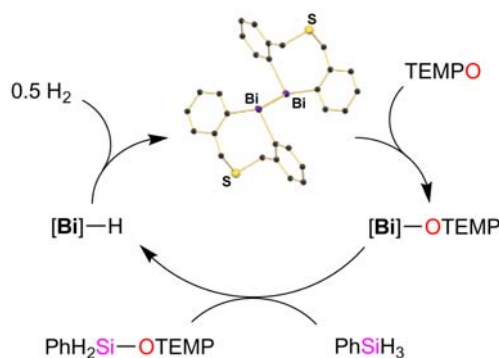


**Fig. 6** Structure of the bismuthanylstibane  $(\text{Naph}\{\text{NSiEt}_3\}_2)\text{Sb}-\text{Bi}(\{\text{NSiMe}_3\}_2\text{Naph})$ .

Increasing the steric bulk of the nitrogen substituents in the distibanes  $(\text{NON}^{\text{R}})\text{Sb}-\text{Sb}(\text{NON}^{\text{R}})$  ( $\text{NON}^{\text{R}} = [\text{O}(\text{SiMe}_2\text{NR})_2]^{2-}$ ;  $\text{R} = t\text{Bu}, \text{Ph}, \text{Dmp}$ ) resulted in the expected increase in the Sb–Sb bond length, with the longest distance of 3.0977(5) Å observed when  $\text{R} = \text{Dmp}$ .<sup>21</sup> It was noted during this study that the Dmp complex was red (in contrast with the pale yellow colors of the other derivatives) and that it reacted with  $\text{P}_4$  to generate the bicyclo[1.1.0]tetraphosphabutane dianion. This reactivity had previously been noted when the bismuth(II) species  $[\text{Bi}(\text{NON}^{\text{Dipp}})]^-$  reacted with  $\text{P}_4$ ,<sup>22</sup> and suggested homolysis of the Sb–Sb bond in solution to generate transient Sb(II) radicals. Such an equilibrium between dipnictogens and their corresponding E(II) radicals had previously been described for distibanes and dibismuthanes supported by the  $C, C'$ -chelating dialkyl ligand,  $[\{\text{CH}_2\text{C}(\text{SiMe}_3)_2\}_2]^{2-}$ .<sup>23</sup> In this system, the crystal structures show that the E–E single bonds ( $\text{E} = \text{Sb}, 3.0297(4) \text{ \AA}$ ;  $\text{E} = \text{Bi}, 3.1821(3) \text{ \AA}$ ). Evidence that these compounds dissociate in solution to form persistent  $[\text{R}_2\text{E}]^\cdot$  radicals came from NMR and UV/vis spectroscopy, with a very broad and weak signal in the EPR for  $[\text{R}_2\text{Sb}]^\cdot$ ; no observable EPR signal was detected for the corresponding bismuthinyl radical  $[\text{R}_2\text{Bi}]^\cdot$ .

The spontaneous reduction of trivalent bismuth to produce Bi(II) species was noted for the phosphanide complex  $\text{Bi}(\text{NON}^{\text{tBu}})(\text{PPh}_2)$ . Under ambient conditions, the Bi–P bond decomposed homolytically to afford the dibismuthane,  $(\text{NON}^{\text{tBu}})\text{Bi}-\text{Bi}(\text{NON}^{\text{tBu}})$  and  $\text{Ph}_2\text{P}-\text{PPh}_2$ .<sup>22</sup> A similar homolytic E–C bond cleavage was noted for the three-coordinate arsanes and stibanes  $\text{E}\{\text{M}(\text{M}_e\text{BDI}^{\text{Dipp}})\text{Cl}\}\text{Ph}(\eta^1\text{-Cp}^*)$  ( $\text{E} = \text{As}, \text{M} = \text{Ga}$ ;  $\text{E} = \text{Sb}, \text{M} = \text{Al}, \text{Ga}, \text{In}$ ).<sup>24</sup> Heating the compounds, which contain pnictogen atoms bonded directly to a trivalent group 13 metal, eliminated  $[\text{Cp}^*]^\cdot$  radicals from the pnictogen, implied by the formation of  $\text{Cp}^*_2$ . The resulting divalent  $[\text{E}\{\text{M}(\text{M}_e\text{BDI}^{\text{Dipp}})\text{Cl}\}\text{Ph}]^\cdot$  radicals reductively couple to afford the dipnictanes as  $(\mu_2, \eta^{1:1}\text{-PhE}-\text{EPh})$  ligands.

Toward the application of pnictogen atoms in catalysis, a dibismuthane supported by a chelating sulfide-linked biaryl ligand was identified as a component in the catalytic dehydrocoupling of  $\text{PhSiH}_3$  and (2,2,6,6-tetramethylpiperidin-1-yl)-oxyl (TEMPO, Scheme 2).<sup>25</sup> Although previous work had exploited bismuth radicals in a thermally activated process,<sup>26</sup> this represented the first example in which a photochemical approach has been applied to this area.



**Scheme 2** Catalytic dehydrocoupling initiated by a dibismuthane.  $[\text{Bi}] = [(\text{Si}(\text{CH}_2\text{C}_6\text{H}_4)_2)\text{Bi}]$ .

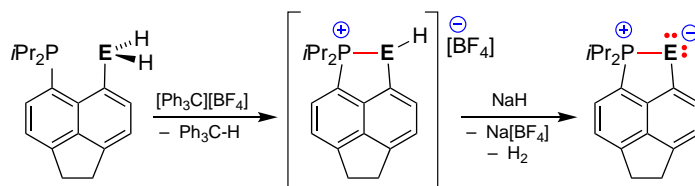
### 1.19.2.3 Supported, heterocyclic dipnictogens

In the context of this section, the donor-acceptor properties of phosphanes and a range of pnictogen groups have been examined using the *peri*-substituted acenaphthene framework.<sup>27</sup> The diphenylphosphino acenaphthyl element dichlorides, 6- $\text{Ph}_2\text{P}(\text{ace-Naph})\text{-5-ECl}_2$  ( $\text{E} = \text{P}, \text{As}, \text{Sb}, \text{Bi}$ ) form two distinct structural variants in the solid state that have notably different P–E bond lengths, depending on the environment at the E-atom. For example, the 5- $\text{AsCl}_2$  derivative has a T-shaped geometry at the pnictogen atom with a near linear Cl–As–Cl angle ( $173.75(8)^\circ$ ), whereas the 5- $\text{SbCl}_2$  analogue has an acute Cl–Sb–Cl angle ( $87.58(3)^\circ$ ) and a longer P–Sb distance. A detailed synthetic, structural and computational study focusing specifically on the P–Bi interactions has also been conducted.<sup>28</sup> As part of this study the  $^{31}\text{P}$  chemical shifts of the series 6- $i\text{Pr}_2\text{P}(\text{aceNaph})\text{-5-EPhCl}$  were examined, and it was concluded that  $\delta_{\text{P}}$  is proportional to the amount of electron density donated to the acceptor for the lighter congeners ( $\text{E} = \text{P}, \text{As}, \text{Sb}$ ), but that this trend was disturbed for the case of bismuth, likely due to relativistic effects.

Hydride extraction from the related 6- $i\text{Pr}_2\text{P}(\text{aceNaph})\text{-5-EH}_2$  ( $\text{E} = \text{P}, \text{As}$ ) compounds was achieved with  $[\text{Ph}_3\text{C}][\text{BF}_4]$ , to afford  $[6\text{-}i\text{Pr}_2\text{P}(\text{aceNaph})\text{-5-EH}][\text{BF}_4]$ .<sup>29</sup> Reaction of these salts with  $\text{NaH}$  abstracted a second hydride to give the neutral 6- $i\text{Pr}_2\text{P}(\text{aceNaph})\text{-5-E}$  arsanylidene- and phosphanylidene- $\sigma^4$ -phosphoranes (Scheme 3). Such phosphanylidene-phosphorane compounds ( $\text{E} = \text{P}$ ) may be considered as masked phosphinidenes 'RP', and it was shown that they form coordination complexes with a range of electrophilic transition-metal fragments  $\text{AuCl}$ ,  $\text{Mo}(\text{CO})_4$ ,  $\text{PtCl}_2$  and  $\text{Cp}^*\text{RhCl}_2$ .<sup>30</sup>

It was noted that under thermal conditions, P–P and P–As bond formation with 6- $i\text{Pr}_2\text{P}(\text{aceNaph})\text{-5-AsRH}$  proceeded in a dealkative pathway.<sup>31</sup> The reactions were clean with 100% diastereoselectivity, and the addition of small amounts of azobis(isobutyronitrile) dramatically increased the rate, suggesting a radical mechanism in operation. A related study of the thermal stability of 6- $i\text{Pr}_2\text{P}(\text{aceNaph})\text{-5-AsH}_2$  showed a dehydrocoupling reaction to form an arsanylidene-phosphorane.<sup>32</sup> In this instance,





**Scheme 3** Synthesis of arsanilidene- and phosphanylidene- $\sigma^4$ -phosporanes (E = P, As).

structural characterization assigned the As–P bond length as being consistent with a single bond that has ‘mild double bond character’. Exposure to limited quantities of air caused cleavage of the P–As bond and oxidation of the phosphorus centers, with subsequent oligomerization of the resulting arsinidene groups to form the cyclic-trimer and -tetramer,  $[6-\{iPr_2P=O\}-(aceNaph)-5-As]_n$  ( $n = 3$  and  $4$ ).

Work in this area has also examined phosphane–stiborane interactions in which the antimony is present in the +5 oxidation state.<sup>33</sup> X-ray crystallographic studies of  $6-iPr_2P-(aceNaph)-5-SbCl_nPh_{4-n}$  complexes represented the first examples of the  $\sigma^4P \rightarrow \sigma^6Sb$  interaction to be structurally characterized. This was also observed in the same year by a different group for the *P*-phenyl substituted derivative,  $6-Ph_2P-(aceNaph)-5-SbCl_4$ .<sup>34</sup>

The bis-substituted 1,8-naphthalendiyl framework (Naph) has also been used to support dipnictogen groups. The extended solid-state structures of the distibane,  $(Naph)_2Sb_2$ ,<sup>35</sup> and diarsane  $(Naph)_2As_2$ <sup>36</sup> were examined by quantum chemical methods, which identified that dispersion forces were the most important in stabilizing the complexes, followed by electrostatic  $E \cdots \pi$  (arene) interactions of neighboring molecules. The donor capabilities of both compounds were assessed through their reaction with  $Cr(CO)_5(coe)$  ( $coe = Z$ -cyclooctene).<sup>36</sup> When  $E = As$ , both the mono- and bis-adducts were isolated, whereas only the bis-adduct was reported for  $E = Sb$ .

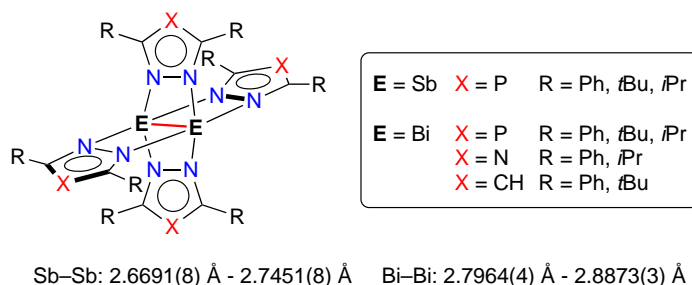
Siloxane substituted oligoarsanes have been used as ligands at group 2 metals.<sup>37</sup> Reaction of 1,1-dichloro-1,1,3,3-tetraisopropylsiloxane,  $O(Si(iPr)_2Cl)_2$  with  $Li(dme)AsH_2$  afforded  $O(Si(iPr)_2AsH_2)_2$  in addition to a small amount of the 5-membered diarsanyl siloxane ring,  $O(Si(iPr)_2AsH)_2$ . When mixtures of these compounds were reacted with  $M\{N(SiMe_3)_2\}_2(THF)_2$  ( $M = Sr$  and  $Ba$ ), metalation of the ring took place to afford dimeric  $[M\{\mu, \eta^{2,2}-(O\{Si(iPr)_2AsH\}_2)\}(dme)_2]_2$  in which each arsenic atom in the ring bonds to two metals. Treatment of these compounds with additional  $O(Si(iPr)_2Cl)_2$  eliminated  $MCl_2$  and gave the edge-linked bicyclic compound,  $As_2\{Si(iPr)_2O\}_2$ .

The spontaneous one electron reduction of trivalent bismuth and antimony compounds to give unstable  $E(II)$  radicals that dimerize to form the dipnictonide paddlewheel compounds has been noted for a series of five-membered *N*-heterocyclic ligand systems (Fig. 7). 1,2,4-diazaphospholide ligands (3,5- $R_2dp$ :  $R = Ph, tBu, iPr$ ;  $E = Bi,^{38} Sb^{39}$ ), pyrazolato ligands (3,5- $R_2pz$ :  $R = Ph, tBu$ ;  $E = Bi^{40}$ ) and 1,2,4-triazolato ligands (3,5- $R_2tz$ ,  $R = Ph, iPr$ ;  $E = Bi^{41}$ ) are eliminated from the postulated homoleptic  $E(III)$  compounds as the neutral radical species, which have been trapped using 5,5-dimethyl-1-pyrroline-*N*-oxide (DMPO) for the  $[3,5-R_2pz]^\bullet$  and  $[3,5-R_2tz]^\bullet$  radicals. The resultant compounds form a paddlewheel arrangement of bidentate heterocycles around the E–E core, which were shown by crystallography to contain very short Bi–Bi and Sb–Sb bonds.

In the reverse (oxidation) direction, it was shown that the dibismuthane  $[(Ttt^R)_2Bi]_2$  ( $Ttt^R = 1-R-5$ -thiotetrazolyl;  $R = Me, Ph$ ) oxidizes in air to form the Bi(III) complex,  $Bi(Ttt^R)_3$ .<sup>42</sup> During this process the ligands change their coordination mode from bridging across the Bi–Bi unit with one of the nitrogen atoms of the  $N_4C$  heterocycle bonds to one bismuth and the sulfur bonds to the second bismuth, to form a chelating *N,S*-mode at a single bismuth center.

#### 1.19.2.4 Supported, metalated dipnictogens

The bimetallic  $\{CpM(CO)_2\}_2(\mu, \eta^{2,2}-E_2)$  ( $M = Cr, Mo, W$ ) clusters are robust units containing dipnictogen groups that have been the subject of several studies in recent years (Fig. 4D). The pnictogen atoms both bond to each of the group 6 metal ions to form a tetrahedral  $M_2E_2$  core, and research has exploited the availability of the pnictogen lone pair to engage in further reactivity with



**Fig. 7** Paddlewheel distibanes and dibismuthanes with short E–E bonds.

a range of electron-deficient substrates. For example, the planar Lewis acid (perfluoro-*ortho*-phenylene)mercury<sup>43</sup> has been reacted with the full series of  $\{\text{CpMo}(\text{CO})_2\}_2(\mu, \eta^{2:2}\text{-E}_2)$  ( $\text{E} = \text{P}, \text{As}, \text{Sb}, \text{Bi}$ ) clusters to form supramolecular adducts that differ in the number and extent of  $\text{E} \cdots \text{Hg}$  interactions.<sup>44</sup> Structural analysis was used to determine the extent of  $\text{E} \cdots \text{Hg}$  bonding, noting that  $\{\text{CpMo}(\text{CO})_2\}_2(\mu, \eta^{2:2}\text{-E}_2)$  interacts with all three mercury atoms via a single pnictogen atom for  $\text{E} = \text{P}$  or  $\text{As}$ , whereas the larger congeners are involved in multiple  $\text{E} \cdots \text{Hg}$  contacts. The  $\text{CpMo}(\text{CO})_2(\eta^3\text{-P}_3)$  tetrahedrane compound was also investigated as part of this study.

Exploring the concept of crystal engineering, it was shown that  $\{\text{CpMo}(\text{CO})_2\}_2(\mu, \eta^{2:2}\text{-P}_2)$  formed supramolecular structures containing  $\text{P} \cdots \text{Ag}$  interactions when reacted with sources of  $\text{Ag}^+$  ions,<sup>45,46</sup> the arsenic analogue exhibited analogous behavior.<sup>47</sup> This was developed further when three component mixtures were crystallized in the presence of *N*-donor ligands.<sup>48–52</sup> Both the phosphorus and arsenic analogues have also been used to link  $\text{Cu}(\text{I})$  units together in a series of coordination compounds,<sup>53–56</sup> and they been coordinated to a pre-constructed linear  $\text{Cu}(\text{I})$  fragment.<sup>57</sup> This area of research has been further extended to include the supramolecular chemistry of the chromium and tungsten species,  $\{\text{CpM}(\text{CO})_2\}_2(\mu, \eta^{2:2}\text{-P}_2)$  ( $\text{M} = \text{Cr},$ <sup>58</sup>  $\text{W}$ <sup>59</sup>). Furthermore, the heterodiatom dipnictogen systems,  $\{\text{CpMo}(\text{CO})_2\}_2(\mu, \eta^{2:2}\text{-PE})$  ( $\text{E} = \text{As}, \text{Sb}$ ) form supramolecular systems with  $\text{Cu}(\text{I})$  salts.<sup>60</sup>

An alternative class of bimetallic compound containing dipnictogen units contains two  $\text{E}_2$ -units that span the metal centers with  $\eta^2$ -interactions (Fig. 4D). The bimetallic cobalt complex  $(\text{Cp}^{\text{III}}\text{Co})_2(\mu, \eta^{2:2}\text{-As}_2)_2$  was reacted with a series of divalent samarium compounds  $\text{Cp}^*{}_2\text{Sm}$ ,  $\text{Cp}^*{}_2\text{Sm}(\text{THF})_2$  and  $\text{Cp}^{*\text{nPr}}{}_2\text{Sm}$  to afford  $\{\text{Cp}^{\text{III}}\text{Co}\}_2\text{As}_4\{\text{Sm}(\eta^5\text{-Cp}^*\text{R})_2\}$  ( $\text{R} = \text{Me}, \text{nPr}$ ).<sup>61</sup> The core of these mixed d/f metal complexes contain an acyclic  $[\text{As}_4]^{4-}$  chain generated from a one electron reduction by samarium, which bonds to the cobalt centers to generate a  $\text{Co}_2\text{As}_4$  trigonal prismatic arrangement (Fig. 8) The redox chemistry of  $(\text{Cp}^{\text{III}}\text{Co})_2(\mu, \eta^{2:2}\text{-E}_2)_2$  ( $\text{E} = \text{P}, \text{As}$ ) compounds was also investigated using a combination of cyclic voltammetry, computational modelling and preparative scale chemical synthesis.<sup>62</sup> It was shown that complexes can be oxidized and reduced twice, with both processes leading to  $\text{E}-\text{E}$  bond formation. For example, addition of one equivalent of silver(I) salts gives one electron oxidation to generate the triple decker  $[(\text{Cp}^{\text{III}}\text{Co})_2(\mu_2, \eta^{4:4}\text{-E}_4)][\text{A}]$  compounds ( $[\text{A}] =$  weakly coordinating anion,  $[\text{BF}_4]^-$  or  $[\text{Al}(\text{F})\{\text{OC}_6\text{F}_{10}(\text{C}_6\text{F}_5)_3\}_3]^-$ ) with a central (cyclobutadiene-like)  $[\text{E}_4]^{3-}$  platform containing two short and two long  $\text{E}-\text{E}$  bonds. Using two equivalents of  $\text{Ag}[\text{TEF}]$  afforded the corresponding dication,  $[(\text{Cp}^{\text{III}}\text{Co})_2(\mu_2, \eta^{4:4}\text{-E}_4)]^{2+}$  with *cyclo*- $[\text{E}_4]^{2-}$  middle decks containing four equivalent  $\text{E}-\text{E}$  bonds. In the other redox direction, chemical reduction was achieved with one equivalent of  $\text{KC}_8$  to afford the  $[(\text{Cp}^{\text{III}}\text{Co})_2(\mu_2, \eta^{4:4}\text{-E}_4)]^-$  anion. Different ratios of  $\text{KC}_8$  or the use of excess of potassium metal afforded the prismatic ' $\text{P}_4\text{Co}_2$ ' structure ( $\text{E} = \text{P}$ ), or the bridging, allylic  $\text{As}_3$ -ligand ( $\text{E} = \text{As}$ ).

### 1.19.3 Non-cyclic *catena*-pnictogens

This section describes compounds containing catenated pnictogen groups that exist with single  $\text{E}-\text{E}$  bonds between more than two pnictogen atoms. It includes linear and branched examples (Fig. 9) but precludes cyclic systems that are covered in Sections 1.19.4 and 1.19.5 of this Chapter.

Section 1.19.3.1 describes a collection of compounds in which the *catena*-pnictogen unit consists of one or more contiguous chains of  $(\text{E})_n$  atoms ( $n > 2$ ), where the pnictogen components are not included in the coordination sphere of a metal (Fig. 9A). Recent work in this area has described examples of chains consisting of fully saturated  $\text{E}-\text{E}$  bonds, as well as those in which higher bond orders are also present between the pnictogen atoms. Examples of cationic, anionic and radical species have been included, with brief descriptions of syntheses, structures and where appropriate, reactivity.

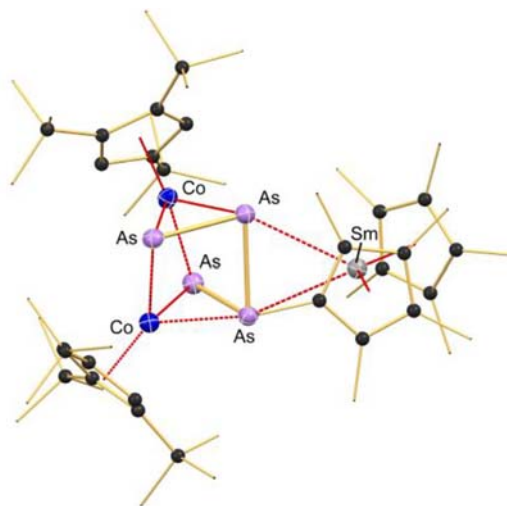
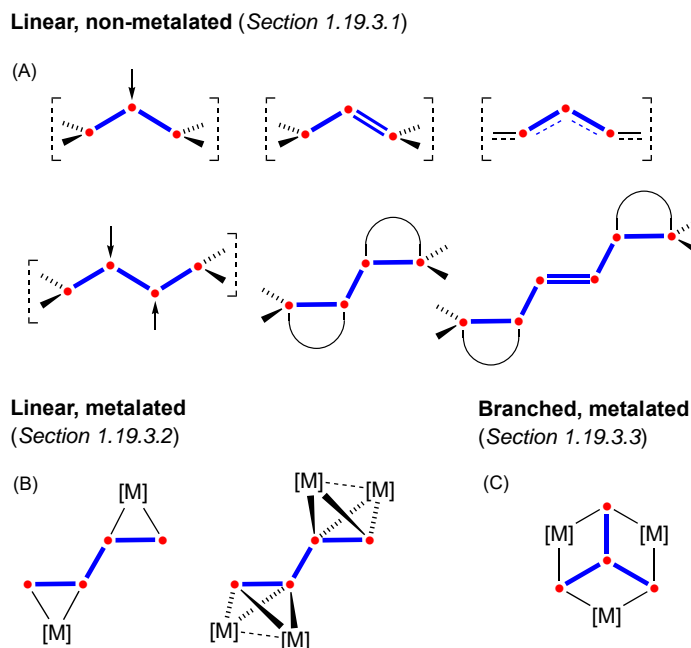


Fig. 8 Molecular structure of  $\{\text{Cp}^{\text{III}}\text{Co}\}_2\text{As}_4\{\text{Sm}(\eta^5\text{-Cp}^*)_2\}$  showing the trigonal prismatic arrangement of the  $\text{As}_4\text{Co}_2$  core.



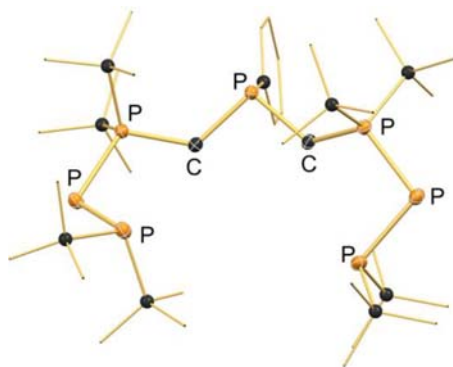
**Fig. 9** Schematic representation of *catena*-pnictogen units included in Section 1.19.3.

Section 1.19.3.2 includes examples of linear  $(E)_n$  groups in which the *catena*-pnictogen chains are coordinated to one or more metal fragments (Fig. 9B). Examples of synthetic routes that attach a pre-formed *catena*-pnictogen group to a suitable metal fragment are presented, in addition to examples that construct the *catena*-pnictogen chain from  $(E)_n$  units that are already present as ligand at a metal center. The final Section 1.19.3.3 contains an example of a *catena*-pnictogen compound, in which the  $(E)_n$  unit is non-linear and is involved in bonding to metal fragments (Fig. 9C).

### 1.19.3.1 Linear, non-metalated *catena*-pnictogens

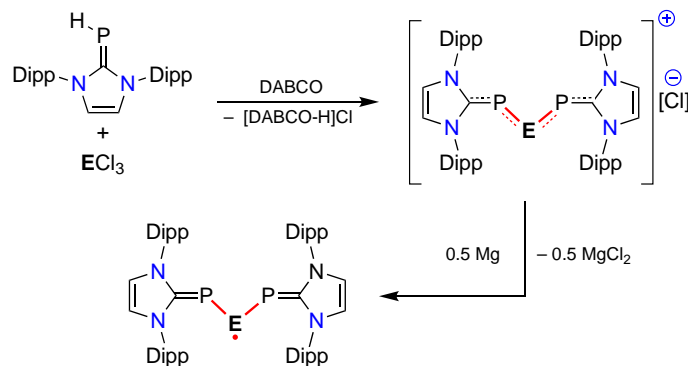
Oligomerization of *tert*-butyl substituted phosphalkyne ( $t\text{BuC}\equiv\text{P}$ ) was initiated by a series of different NHCs to give a range of *catena*-phosphorus containing products.<sup>63</sup> When  $^{\text{H}}\text{IDipp}$  was reacted with three equivalents of the phosphalkyne, the di-1,2-dihydro-1,2-diphosphete-substituted diphosphene was formed, containing a  $\text{P}_6$ -chain in a zig-zag conformation. Changing the nitrogen substituents of the NHC to  $^{\text{H}}\text{IMes}$  gave a 1,2,4-triphosphole ring containing compound, whilst reaction with the saturated carbene S-IDipp generated a 1,2,3-triphosphetene.

Cationic polyphosphanes have been derived from P–P condensation and P–N/P–P metathesis reactions.<sup>64</sup> Amongst the products reported was the  $\text{P}_4$ -chain in the salt  $[\text{Ph}_2\text{P}-\text{P}(\text{MeIME})-\text{P}(\text{MeIME})-\text{PPh}_2][\text{OTf}]_2$ , accessed from the reaction of  $[\text{P}(\text{MeIME})(\text{Me-pyr})_2][\text{OTf}]$  ( $\text{Me-pyr} = 3,5\text{-dimethylpyrazol-1-yl}$ ) with  $\text{Ph}_2\text{P}-\text{PPh}_2$ . In a separate study, the 2:1 reactions of  $t\text{Bu}_2\text{P}-\text{P}=\text{P}(t\text{Bu})_2\text{CH}_2\text{Li}$  with the dichlorophosphanes  $\text{RPhCl}_2$  ( $\text{R} = \text{Ph}, \text{Me}, \text{NEt}_2$ ) produced the phosphanylphosphinidene-phosphoranes,  $\{t\text{Bu}_2\text{P}-\text{P}=\text{P}(t\text{Bu})_2\text{CH}_2\}_2\text{PR}$ , considered by the authors as a ‘P7-chain’ (Fig. 10).<sup>65</sup> It was noted during these studies that the P7-chains decompose in solution over a few days to give the P5- and P3-chains.



**Fig. 10** An example of a ‘P7-chain’ ( $\text{R} = \text{Ph}$ ) formed from the condensation of  $t\text{Bu}_2\text{P}-\text{P}=\text{P}(t\text{Bu})_2\text{CH}_2\text{Li}$  with  $\text{PhPhCl}_2$ .

The phosphoethynolate anion  $[\text{O}-\text{C}\equiv\text{P}]^-$  (the phosphorus analogue of the cyanate ion,  $[\text{O}-\text{C}\equiv\text{N}]^-$ ) was first isolated in 1992 from the reaction of dimethylcarbonate with lithium bis(trimethylsilyl)phosphide.<sup>66</sup> This work was reinvigorated about 20 years later with the isolation of the sodium salt  $\text{Na}[\text{OCP}]$ ,<sup>67</sup> which has been used as a 'P' transfer reagent in several areas of synthetic chemistry. For example, the reaction of  $\text{Na}[\text{OCP}]$  with the imidazolium salt  $[(^{\text{H}}\text{IDipp})\text{H}]\text{Cl}$  afforded the phosphinidene carbene adduct,  $(^{\text{H}}\text{IDipp})=\text{PH}$ .<sup>68</sup> Reaction of this phosphinidene with 0.5 equivalents of  $\text{ECl}_3$  ( $\text{E} = \text{P}, \text{As}$ ) in the presence of 1,4-diazabicyclo[2.2.2]octane (DABCO) afforded  $[\{(^{\text{H}}\text{IDipp})=\text{P}\}_2(\mu\text{-E})][\text{Cl}]$  salts containing bent  $\text{P}-\text{E}-\text{P}$  groups. Crystallographic analysis showed that the carbon-phosphorus distances were significantly longer compared with the double bond in  $(^{\text{H}}\text{IDipp})=\text{PH}$ , and the  $\text{P}-\text{E}$  bonds were shorter than single bonds, indicating delocalization across the  $\text{C}-\text{P}-\text{E}-\text{P}-\text{C}$  group (Scheme 4). These salts were reduced with magnesium to form their neutral radical species,  $[\{(^{\text{H}}\text{IDipp})=\text{P}\}_2(\mu\text{-E})]^\bullet$ .



**Scheme 4** Synthesis and reduction of  $[\{(^{\text{H}}\text{IDipp})=\text{P}\}_2(\mu\text{-E})][\text{Cl}]$  salts ( $\text{E} = \text{P}, \text{As}$ ).

The reaction of the diarylphosphanide  $[\text{Na}(\text{THF})_{1.5}][\text{P}(\text{Dipp})_2]$  with 0.5 equivalents of  $\text{AsCl}_3$  afforded  $\{(\text{Dipp})_2\text{P}\}_2\text{AsCl}$ , which co-crystallized with  $(\text{Dipp})_2\text{P}-\text{P}(\text{Dipp})_2$ .<sup>69</sup> Separation of the diphosphane side-product afforded the diphosphanidochloroarsane as a yellow powder, which was reacted with  $\text{Li}[\text{TEF}]$  to afford the acyclic arsenium cation  $\{(\text{Dipp})_2\text{P}\}_2\text{As}^+$  as the  $[\text{TEF}]^-$  salt. Attempts to synthesize the corresponding diphosphaphosphenium cation were unsuccessful, instead forming the cyclic diphosphinophonium salt,  $[\text{cyclo-}\{(\text{Mes})\text{P}\}_2\text{P}(\text{Mes})_2][\text{B}(\text{Ar}_\text{F})_4]$ .

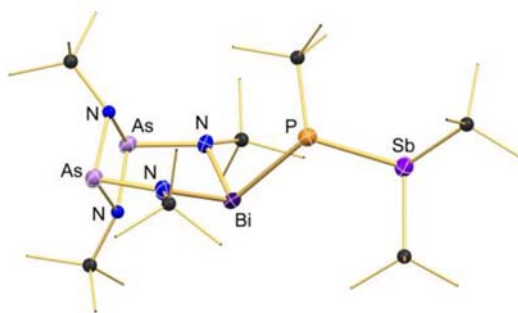
The cyclo-arsenido and -stibano phosphanides,  $[t\text{Bu}_2\text{EP}(\text{Li}\{\text{OEt}_2\})t\text{Bu}]_2$  ( $\text{E} = \text{As}, \text{Sb}$ ) containing  $\text{Li}_2\text{P}_2$ -rings with *exo*-cyclic  $\text{EtBu}_2$  groups, were reacted with  $t\text{Bu}_2\text{E}'\text{Cl}$  compounds ( $\text{E}' = \text{As}, \text{Sb}, \text{Bi}$ ) to afford the ternary compounds  $t\text{Bu}_2\text{E}(\text{PtBu})\text{E}'t\text{Bu}_2$ . Examples containing  $\text{E}-\text{P}-\text{E}'$  chains were reported for the combinations of  $\text{As}-\text{P}-\text{As}$ ,  $\text{As}-\text{P}-\text{Sb}$ ,  $\text{Sb}-\text{P}-\text{Sb}$ <sup>70</sup> and  $\text{Sb}-\text{P}-\text{Bi}$  pnictogens.<sup>71</sup>

The reaction of tris(dimethylamino)arsane,  $\text{As}(\text{NMe}_2)_3$  with two equivalents of  $\text{Mes}^*\text{PHLi}$  afforded the 1,3-diphosphaarsa-2-allyl anion,  $[(\text{Mes}^*\text{P})_2\text{As}]^-$ , an isoelectronic analogue of the allyl anion.<sup>72</sup> NMR spectroscopy showed that an equilibrium exists between the *E,E*- and *E,Z*-isomers, which depended on the extent of lithium-ion pairing. Deprotonation of the related amidarsanylphosphinidene,  $\text{Mes}^*\text{N}(\text{H})\text{As}=\text{PMes}^*$ , afforded the related group 15 allyl-analogue,  $[\text{Mes}^*\text{N}-\text{P}-\text{AsMes}^*]^-$ .<sup>73</sup> Although it was not possible to isolate the anion, quenching it in situ with  $\text{SbCl}_3$  generated the neutral compound  $\text{Mes}^*\text{N}(\text{SbCl}_2)\text{AsPMes}^*$  which contains four adjacent pnictogen atoms.<sup>§</sup> This approach was extended to the reaction between the tricyclic  $(t\text{BuNAs})_2(t\text{BuN})_2[\text{ECl}]$  ( $\text{E} = \text{As}, \text{Sb}, \text{Bi}$ ) and  $[t\text{Bu}_2\text{SbP}(\text{Li}\{\text{OEt}_2\})t\text{Bu}]_2$ , which afforded a product that formally contains a contiguous chain of five-pnictogen atoms<sup>§</sup> (e.g. Fig. 11).<sup>74</sup> (§ the authors of these studies included nitrogen in this count).

A rare example of a *catena*- $\text{Bi}_4$  chain was isolated from the reaction of bis(diisopropylphosphino)amine with  $\text{BiCl}_3$ .<sup>75</sup> The product contains bridging diphosphane ligands that span the two bismuth atoms in each of the terminal  $\text{Bi}-\text{BiCl}_2$  units, with a unsupported  $\text{Bi}-\text{Bi}$  bond at the center of the chain. Structural analysis showed that the  $\text{Bi}-\text{Bi}$  bond lengths do not differ significantly along the  $\text{Bi}_4$ -chain and are consistent with  $\text{Bi}-\text{Bi}$  single bonds. Extended  $(\text{Bi})_n$  chains were noted in the ammonia solvated potassium bismuthide,  $\text{KBi}\cdot\text{NH}_3$ .<sup>76</sup> The solid-state structure was shown to consist of a flat zig-zag polymeric chain with two-connected bismuth atoms, and the compound exhibits metallic properties. This is structurally and physically distinct from the non-solvated form  $\text{KBi}$ , which consists of a helical chain of  $\text{Bi}$ -atoms and is semi-conducting.<sup>77</sup>

### 1.19.3.2 Linear, metalated *catena*-pnictogens

The lithiated diphosphanylphosphide,  $\text{R}_2\text{P}-\text{P}(\text{Li})-\text{PR}'_2$  ( $\text{R} = t\text{Bu}, i\text{Pr}$ ;  $\text{R}' = \text{NEt}_2, i\text{Pr}$ ) was reacted with group 6 metal bis-imido complexes  $\text{M}(\text{NDipp})_2\text{Cl}_2(\text{dme})$  ( $\text{M} = \text{Mo}, \text{W}$ ) to afford  $\text{M}(\text{NDipp})_2\text{Cl}(\text{1,2-}\eta^2\text{-R}_2\text{P}-\text{P}-\text{PR}'_2)$  species.<sup>78</sup> Reaction of these  $\text{P}_3$ -containing products with  $\text{Ph}_2\text{PLi}$  proceeded with elimination of diphosphanes ( $\text{R}'_2\text{P}-\text{PPh}_2$ ) to give the phosphanylphosphinidene complexes,  $\text{Li}[\text{M}(\text{NDipp})_2\text{Cl}(\eta^2\text{-P}-\text{PR}_2)]$ . This reactivity was essentially reversed when  $[\text{Li}(\text{dme})_3][\text{W}(\text{NDipp})_2\text{Cl}(\eta^2\text{-P}-\text{PtBu}_2)]$  was reacted with  $\text{Ph}_2\text{PBr}$  to generate the  $1,2\text{-}\eta^2\text{-Ph}_2\text{P}-\text{P}-\text{PtBu}_2$  ligand directly at the tungsten center.<sup>79</sup> It was demonstrated that



**Fig. 11** Molecular structure of a compound containing a chain of the five different pnictogen atoms, As–N–Bi–P–Sb.

this process can be exploited to generate longer *catena*-polyphosphorus ligands by using the dichlorophosphane  $\text{PhPCl}_2$  to link two metal units together, forming the  $\{t\text{Bu}_2\text{P}-\text{P}\}_2\text{PPh}$  bridging ligand. Related chemistry afforded the phosphanylphosphinidene ligand in  $\{\text{Cp}^*\text{M}(\text{CO})_3\}_2(\eta^2\text{-P}-\text{PtBu}_2)_2$  from coupling two ' $t\text{Bu}_2\text{P}-\text{P}'$  units at molybdenum and tungsten centers.<sup>80</sup>

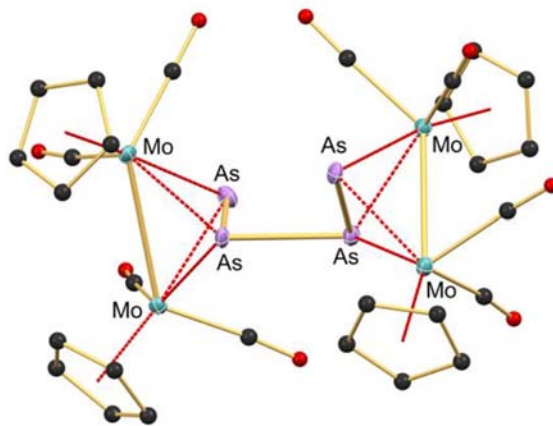
**Section 1.19.2.4** includes a description of the coordination chemistry of the organomolybdenum dipnictogen compounds  $\{\text{CpMo}(\text{CO})_2\}_2(\mu, \eta^{2:2}\text{-E}_2)$ , in which this intact unit is used as a building block for the synthesis of supramolecular structures. However, when the bimetallic compounds ( $\text{E} = \text{P}, \text{As}, \text{Sb}, \text{Bi}$ ) are exposed to the strong one electron oxidant  $[\text{C}_{12}\text{H}_8\text{S}_2][\text{TEF}]$  ( $[\text{C}_{12}\text{H}_8\text{S}_2]^+ =$  thianthrenium, the cation of 9,10-dithiaanthracene) a new E–E bond is formed and two units are joined together to form a dicationic  $[\text{E}_4]^{2+}$  chain. This was demonstrated for the full range of pnictogens P, As, Sb and Bi in the compounds  $\{\{\text{CpMo}(\text{CO})_2\}_4(\mu_4, \eta^{2:2:2:2}\text{-E}_4)\}^{2+}$ .<sup>81</sup> X-ray diffraction shows that the structure of the chains is not uniform across this series. The lighter congeners P and As form zigzag chains with a gauche conformation (**Fig. 12**), whereas the heavier  $[\text{Sb}_4]^{2+}$  and  $[\text{Bi}_4]^{2+}$  chains contain secondary  $\text{E}\cdots\text{E}$  contacts that generate heavily distorted bicyclo[1.1.0]butane (butterfly-like) structures.

The reduction of  $\{\text{Cp}^*\text{Co}\}_2(\mu_2, \eta^{2:2}\text{-P}_2)_2$  by  $\text{Cp}^*\text{Sm}(\text{THF})_2$  proceeded with coupling of the two  $\text{P}_2$ -units to form a  $\text{P}_4$ -chain within a trimetallic  $\text{Co}_2\text{Sm}$  cluster.<sup>82</sup> Computational analysis of the mechanism determined that, rather than a direct reduction of the phosphorus atoms the reaction involves the initial localization of spin density on cobalt. A subsequent transfer of positive charge from Co to Sm lead to aggregation of the two  $[\text{P}_2]^{2-}$  units with a weak  $\pi^*-\pi^*$  interaction and rearrangement to form the  $[\text{P}_4]^{4-}$  chain.

The stepwise formation of a 1,3-butadiene analogue containing only phosphorus and arsenic atoms has been reported (**Scheme 5**).<sup>83</sup> The tungsten arsinidene complex  $(\eta^1\text{-Cp}^*)\text{As}\{\text{W}(\text{CO})_5\}_2$  reacted with di-*t*-butylcarboimidophosphene  $t\text{BuN}=\text{C}=\text{PtBu}$ , to afford the arsaphosphene compound  $\{\text{W}(\text{CO})_5\}(\eta^2\text{-Cp}^*\text{As}=\text{PtBu})\{\text{W}(\text{CO})_5\}$ . This compound was reacted with a second equivalent of the carboimidophosphene to afford the  $\{\text{W}(\text{CO})_5\}(\eta^2\text{-}\{\text{Cp}^*(t\text{Bu})\text{P}\}\text{As}=\text{PtBu})\{\text{W}(\text{CO})_5\}$ , whereas at room temperature, a radical process occurred leading to formation of  $\{t\text{BuP}=\text{As}-\text{As}=\text{PtBu}\}\{\text{W}(\text{CO})_5\}_4$  containing two  $\text{As}=\text{P}$  double bonds linked by an As–As single bond. The related 2,3-diphospha-1,3-butadiene and 2,3-diarsa-1,3-butadiene ligands,  $\text{H}_2\text{C}=\text{E}-\text{E}=\text{CH}_2$  were stabilized by four  $\text{W}(\text{CO})_5$  groups, two of which coordinate  $\eta^1$ -to the pnictogenide atoms and the remaining two present with side-on  $\pi$ -interactions with each unsaturated ' $\text{C}=\text{E}'$  group.<sup>84</sup>

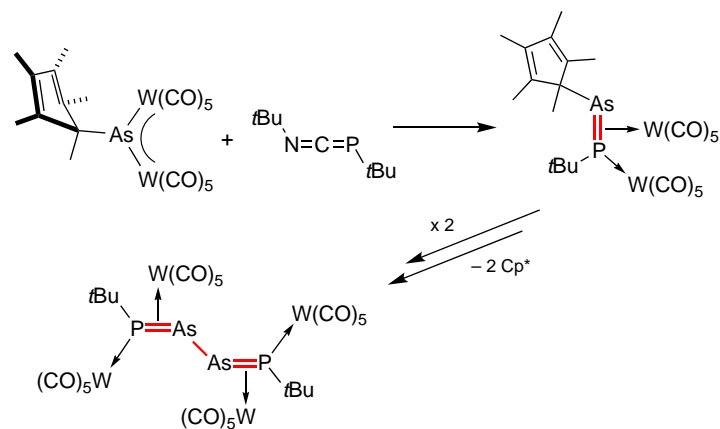
### 1.19.3.3 Branched, metalated *catena*-pnictogens

A novel approach for the application of antimony-based ligands in the development of single molecule magnets led to the discovery of a hydrostibination reaction and the isolation of  $\text{Sb}_4\text{Ln}_3$  polymetallic clusters.<sup>85</sup> The reaction of in situ generated  $\text{Cp}^{\text{Me}_2}\text{Ln}(n\text{Bu})$



**Fig. 12** Gauche conformation of  $[\text{As}_4]^{2+}$  in dicationic  $[\{\text{CpMo}(\text{CO})_2\}_4(\mu_4, \eta^{2:2:2:2}\text{-As}_4)]^{2+}$  ( $[\text{TEF}]^-$  anions omitted).





**Scheme 5** Stepwise formation of 1,3-butadiene analogue incorporating P and As.

(Ln = Y, Dy) with four equivalents of  $\text{Sb}(\text{Mes})_2\text{H}$  generated  $(\eta^5\text{-Cp}^{\text{Me}}_2\text{Ln})_3\{\mu\text{-(SbMes)}_3\text{Sb}\}$ , containing a cyclic  $\text{Sb}_3\text{Ln}_3$  ring in a chair configuration that is capped by an Sb-atom that links the three 'Sb(Mes)' units (**Fig. 13**). The zero-field anisotropy barrier of the dysprosium derivative ( $U_{\text{eff}} = 270 \text{ cm}^{-1}$ ) was amongst the highest reported, and work is ongoing to extend this to bismuth, where the larger radius of the pnictogen is predicted to give higher values of  $U_{\text{eff}}$ .

### 1.19.4 Monocyclic *catena*-pnictogens

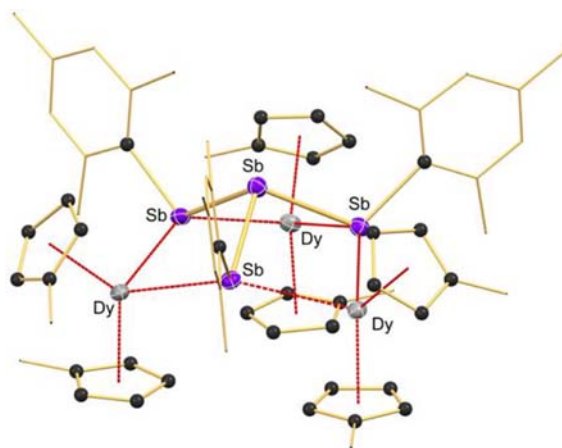
This section collates developments in the synthesis and reactivity of *catena*-pnictogen in which the pnictogen atoms form, or are part of, a monocyclic system. **Sections 1.19.4.1 and 1.19.4.2** contain work on systems in which the cyclic component is comprised of only pnictogen atoms, whilst **Section 1.19.4.3** describes systems in which the *catena*-pnictogen unit is part of a larger heterocycle. For convenience, **Sections 1.19.4.1 and 1.19.4.2** have been further divided into parts that are associated with the synthesis and reactivity of cyclic systems comprised of different ring-sizes, ranging from *cyclo*-(E)<sub>3</sub> to *cyclo*-(E)<sub>6</sub> groups.

#### 1.19.4.1 Monocyclic, non-metalated *catena*-pnictogens: (E)<sub>n</sub> = 3–6

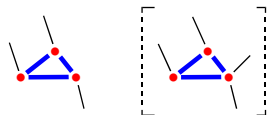
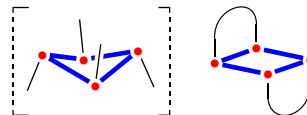
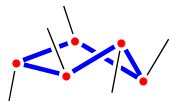
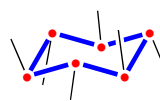
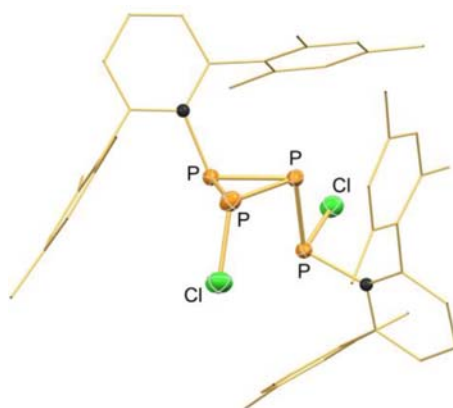
This Section collects together chemistry of pnictogen compounds with *cyclo*-(E)<sub>n</sub> groups that can be summarized according to (**Fig. 14**).

##### 1.19.4.1.1 *Cyclo*-(E)<sub>3</sub> units

The reaction of  $\text{Ter}^{\text{Mes}}\text{PH}_2$  ( $\text{Ter}^{\text{Mes}} = 2,6\text{-Mes}_2\text{C}_6\text{H}_3$ ) with excess of  $\text{PCl}_3$  (in the presence of  $\text{NEt}_3$ ) afforded the cyclotriphosphane  $(\text{Ter}^{\text{Mes}}\text{P})(\text{Cl})\text{P}\{\text{P}(\text{Cl})\text{Ter}^{\text{Mes}}\}$ , containing an *exo*-cyclic chlorophosphanyl substituent (**Fig. 15**).<sup>86</sup> This compound slowly isomerized on heating ( $75^\circ\text{C}$ , 4 weeks) to afford the dichloro-cyclotetraphosphane  $[\text{ClP}(\mu\text{-PTer}^{\text{Mes}})]_2$ . Related homoleptic triaryl



**Fig. 13** The molecular structure of  $(\eta^5\text{-Cp}^{\text{Me}}_2\text{Ln})_3\{\mu\text{-(SbMes)}_3\text{Sb}\}$ , containing a branched *catena*-pnictogen group.

**Monocyclic (non-metalated)** (Section 1.19.4.1)(A)  $n = 3$  (Section 1.19.4.1.1)(B)  $n = 4$  (Section 1.19.4.1.2)(C)  $n = 5$  (Section 1.19.4.1.3)(D)  $n = 6$  (Section 1.19.4.1.4)**Fig. 14** Schematic representation of non-metalated, monocyclic pnictogen units included in Section 1.19.4.1.**Fig. 15** Molecular structure of  $(\text{Ter}^{\text{Mes}}\text{P})(\text{PCl})\text{P}(\text{P}(\text{Cl})\text{Ter}^{\text{Mes}})$ .

cyclotriphosphanes  $\text{cyclo-}[\text{ArP}]_3$  (Ar = Dipp, Tipp, Mes) were synthesized using a mixture of zinc powder and  $\text{PMe}_3$  to reduce the  $\text{ArPCL}_2$  precursors.<sup>87</sup> The reaction of these  $\text{P}_3$ -ring compounds with  $\text{Cp}_2\text{Ti}(\eta^2\text{-C}_2\{\text{SiMe}_3\}_2)$ , used as a source of the reactive 14 electron ' $\text{Cp}_2\text{Ti}$ ' fragment formed by the facile release of  $\text{Me}_3\text{Si-C}\equiv\text{C-SiMe}_3$  from the titanium center, afforded the coordinated diphosphene compounds,  $\text{Cp}_2\text{Ti}(\eta^2\text{-P}_2\text{Ar}_2)$ . The corresponding cyclotriarsanes  $[\text{ArAs}]_3$  (Ar = Dipp, Tipp) were generated using an analogous synthetic procedure.<sup>88</sup> Both derivatives crystallized with the expected *cis,trans,trans*-configuration, and exhibited the same reactivity with  $\text{Cp}_2\text{Ti}(\eta^2\text{-C}_2\{\text{SiMe}_3\}_2)$ , to afford the corresponding diarsene compounds,  $\text{Cp}_2\text{Ti}(\eta^2\text{-As}_2\text{Ar}_2)$ .

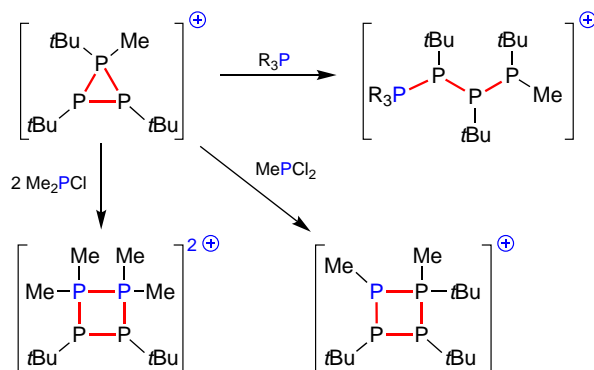
A study examining the reactivity of the alkyl-substituted cyclotriphosphane  $[\text{tBuP}]_3$  noted that the addition of a range of nitriles afforded the corresponding 1-aza-2,3,4-triphospholenes in a high yielding, one-pot reaction considered as an 'inorganic click-reaction'.<sup>89</sup> The HOMO of the electron-rich, five-membered  $\text{P}_3\text{CN}$ -heterocyclic product was calculated, and showed prominent lobes at all pnictogen atoms, indicating the potential for a rich coordination chemistry.

Addition of the  $[\text{Ph}_2\text{P}]^+$  unit (generated in situ from mixtures of  $\text{Ph}_2\text{PCL}/\text{GaCl}_3$  or  $\text{Ph}_2\text{PCL}/\text{Me}_3\text{SiOTf}$ ) to the cyclophosphanes  $[\text{tBuP}]_3$  and  $[\text{tBuP}]_4$ , gave a ring-expansion to the  $[\{\text{tBuP}\}_n\text{PPh}_2]^+$  ( $n = 3, 4$  respectively).<sup>90</sup> Analysis of the  $[\{\text{tBuP}\}_3\text{PPh}_2]^+$  cation by  $^{31}\text{P}$  NMR spectroscopy indicated an  $\text{AM}_2\text{X}$  spin system for the  $\text{P}_4$ -ring, consistent with the  $[\text{Ph}_2\text{P}]^+$  group being located between two P-atoms with the *tBu* groups in a *cis*-arrangement; this conformation was subsequently confirmed by X-ray crystallography.

The reactivity of the cyclodiphosphinophosphonium cation  $\text{cyclo-}[\{\text{tBuP}\}_2(\text{PtBuMe})]^+$  toward Lewis bases was explored (Scheme 6), with formation of new  $\text{P}_3$ - (not shown) and  $\text{P}_4$ -open chain and  $\text{cyclo-}(\text{P})_4$  catena-phosphorous scaffolds noted.<sup>91</sup> Ring-expansion to give  $\text{cyclo-}[\{\text{tBuP}\}_2(\text{PtBuMe})(\text{PMe})]^+$  was observed when the cation was reacted with one equivalent of  $\text{MePCL}_2$ ; the analogous reaction with two equivalents of  $\text{Me}_2\text{PCL}$  gave  $\text{cyclo-}[\{\text{tBuP}\}_2(\text{PMe}_2)_2]^{2+}$ . In contrast, ring-opening occurred when exposed to  $\text{PMe}_3$  or *dmap* (*dmap* = 4-dimethylaminopyridine), giving  $[\text{Me}_3\text{P}(\text{PtBu})_2\text{-PtBuMe}]^+$  and  $[(\text{dmap})\text{-}(\text{PtBu})_2\text{-PtBuMe}]^+$  chains, respectively.

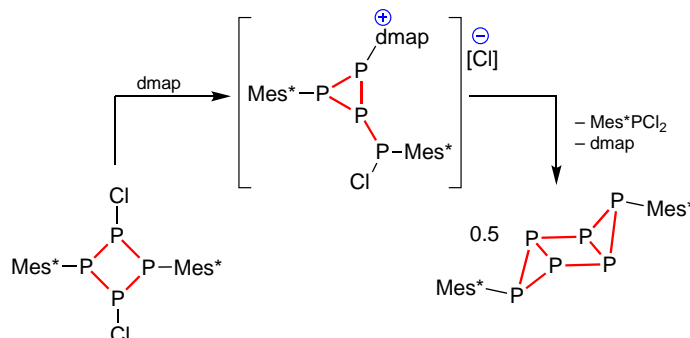
**1.19.4.1.2 Cyclo-(E)<sub>4</sub> units**

The NHC  $^{\text{H}}\text{LiPr}$ , with relatively small nitrogen substituents compared with the more widely applied  $^{\text{R}}\text{IDipp}$  and  $^{\text{R}}\text{IMes}$  derivatives, has been used to promote dehydrogenative coupling of primary phosphanes to afford the cyclic species  $[\text{ArP}]_n$  (Ar = Ph, *p*-tol;  $n = 4, 5, 6$ ).<sup>92</sup> The NHC-phosphinidene adduct  $(^{\text{H}}\text{LiPr})=\text{PAr}$  was identified as a key intermediate species in this reaction pathway. An



**Scheme 6** Reactivity of  $\text{cyclo}[\text{tBuP}]_2(\text{PtBuMe}]^+$  toward Lewis basic phosphanes.

analogous reaction to that employed for the synthesis of  $\text{TerP}_3(\text{Cl})\text{P}(\text{Cl})\text{Ter}$  using  $\text{Mes}^*\text{PH}_2$  formed the cyclotetraphosphane  $[\text{ClP}(\mu\text{-PMes}^*)]_2$  directly as the main product.<sup>86</sup> This compound has been coordinated to  $\text{Ag}^+$  cations at low temperature to afford the dimer  $[\text{Ag}_2\{\text{ClP}(\mu\text{-PMes}^*)\}_2]^{2+}$  as the  $[\text{TEF}]^-$  salt,<sup>93</sup> which upon warming to  $0^\circ\text{C}$  eliminated  $\text{AgCl}$  to give the cation  $[\text{Mes}^*(\text{P}_4)(\text{Cl})\text{Mes}^*]^+$  incorporating a positively charged phosphorus in the bicyclic  $\text{P}_4$ -scaffold. A more direct route to this  $\text{P}_4$ -cationic species was reported from the reaction of the neutral tetraphosphane  $[\text{ClP}(\mu\text{-PMes}^*)]_2$  with  $\text{GaCl}_3$ , which afforded the corresponding bicyclo[1.1.0]tetraphosphabutane-2-ium salt,  $[\text{Mes}^*(\text{P}_4)(\text{Cl})\text{Mes}^*][\text{GaCl}_4]^-$ .<sup>94</sup> In further work,  $[\text{ClP}(\mu\text{-PMes}^*)]_2$  was reacted with *dmap* to afford the tricyclic [3.1.0.0<sup>2,4</sup>]-hexaphosphane,  $\text{Mes}^*(\text{P}_6)\text{Mes}^*$ , in which the two  $\text{P}_3$ -triangular units project above and below the central cyclo $\text{P}_4$  ring (Scheme 7).<sup>95</sup> The high symmetry of this species in solution led to an unusual AA'BB'B''B''' spin system observed in the  $^{31}\text{P}$  NMR spectrum, consistent with the solid-state structure.



**Scheme 7** Synthesis of the tricyclic [3.1.0.0<sup>2,4</sup>]-hexaphosphane,  $\text{Mes}^*(\text{P}_6)\text{Mes}^*$ .

Related studies describing the chemistry of mixed  $\text{P}_3\text{N}$ - and  $\text{P}_2\text{N}_2$ -ring containing analogues have been reported.<sup>96,97</sup> The complete series of 1,3-dichloro-1,3-dipnicta-2,4-diphosphanes,  $[\text{ClE}(\mu\text{-PTer}^{\text{Mes}})]_2$  ( $\text{E} = \text{P, As, Sb, Bi}$ ;  $\text{Ter}^{\text{Mes}} = 2,6\text{-Mes}_2\text{C}_6\text{H}_3$ ) have been isolated, showing puckered four membered rings with the  $\text{E-Cl}$  bonds present in the *cis* (*exo,exo*) isomer for  $\text{E} = \text{P}$ , and the *trans* (*exo,endo*) isomer for  $\text{E} = \text{As, Sb, Bi}$ .<sup>98</sup> The monocyclic  $[\text{As}(\mu\text{-PTer}^{\text{Mes}})]_2$  ring with a bicyclo[1.1.0]butane core containing a transannular  $\text{As-As}$  bond was also isolated during this work.

During a study of the chemistry of the tetra-cyclic 3a,6a-diaza-1,4-diphosphapentalene it was noted that a diethyl ether solution slowly changed color from orange to yellow, with concomitant formation of a crystalline precipitate. Analysis of the solid product showed it to be the 1,2,3-diazaphosphole-substituted cyclotetraphosphane.<sup>99</sup> Further study showed that this oligomerization is promoted when the  $\text{P-N}$  bond is lengthened by adding weak Lewis acids and bases.

A phosphorus analogue of *para*-quinodimethane, with a planar  $\text{P}_4$ -ring and *trans*-apical vinylidene ligands, was synthesized from the  $\text{KC}_8$  reduction of  $(^{\text{H}}\text{IDipp})\text{-C}\{\text{P-Cl}_2\}_2$  (Fig. 16).<sup>100</sup> Photoinduced ring contraction was observed when the compound was exposed to UV light, with evidence for the elimination of ' $\text{P}_2$ ' presented from a trapping reaction of this reactive species with 1,3-cyclohexadiene.

A series of di-spirocyclic tetrakis(amino)  $\lambda^3, \lambda^5$ -tetraphosphetes  $[\text{R}_2\text{Si}(\text{NR}')(\text{NR}'')\text{P}_2]_2$  ( $\text{R} = \text{Me/Ph}$ ,  $\text{R}' = \text{tBu}$ , *tert*-pentyl) were prepared by photolysis of the respective bis(trimethylsilyl)phosphanyl diazaphosphasiletidines.<sup>101</sup> Detailed computational analysis of the  $\text{P}_4$ -rings, previously referred to as 'tetraphosphacyclobutadienes', revealed a more complex bonding situation in which the lone-pair density of the  $\sigma^2\text{-P}$  atom is divided into *exo*- and *endo*-cyclic parts.

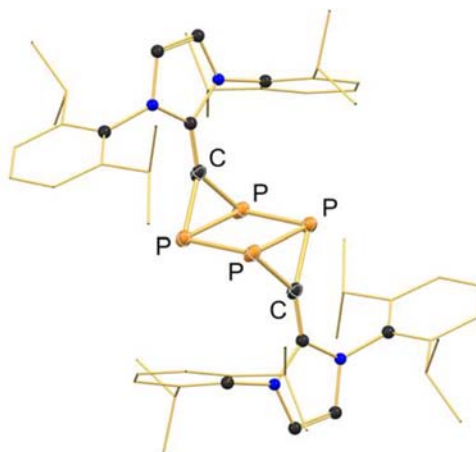


Fig. 16 Molecular structure of the para-quinodimethane analogue,  $(t\text{Dipp})\text{Cl}_2(\text{cyclo-P}_4)$ .

The reaction of  $\text{RP}(\text{Me}^e\text{pyr})_2$  ( $\text{R} = \text{Py}$ ,  $\text{Btz} = \text{benzo}[d]\text{thiazole}$ ), with  $\text{R}'_2\text{PH}$  ( $\text{R}' = \text{Cy}$ ,  $t\text{Bu}$ ) afforded the triphosphanes  $\text{R}'_2\text{PP}(\text{R})\text{PR}'_2$ .<sup>102</sup> These compounds were examined as ligands in coordination chemistry, showing different coordination modes at  $\text{Cu}^+$ ,  $\text{Ag}^+$  and  $\text{Au}^+$  centers. During this study, the formation of cyclopentaphosphanes  $[\text{RP}]_5$  ( $\text{R} = \text{Py}$ ,  $\text{Btz}$ ) was noted, which can only occur through a selective scrambling reaction. Analogous reactions of  $\text{RP}(\text{Me}^e\text{pyr})_2$  ( $\text{R} = \text{Ph}$ ,  $\text{Py}$ ) with  $t\text{BuPH}_2$  at  $-30^\circ\text{C}$  afforded the  $\text{C}_{2v}$ -symmetric tetraphosphetane rings  $[\text{RP}-t\text{Bu}]_4$  as the exclusive products.<sup>103</sup> The compounds adopt analogous conformations to their homo-substituted counterparts  $[\text{PhP}]_4$ <sup>104</sup> and  $[\text{CyP}]_4$ ,<sup>105</sup> with all *trans*-arrangement of substituents around a folded  $\text{cyclo-P}_4$  rings. Addition of  $\text{MeOTf}$  to the  $\text{Py}$ -derivative results in methylation at the pyridine substituents to give the dicationic  $[\{(\text{Me-Py})\text{P}-t\text{Bu}\}_2]^{2+}$  along with the trication  $[\{(\text{Me-Py})\text{P}\}_2\{\text{PMe}t\text{Bu}\}\{t\text{Bu}\}]^{3+}$  in which one of the 'tBu' groups has also been methylated. The  $\text{Py}$ -derivative was also shown to chelate to  $\text{Cu}^+$ ,  $\text{Ag}^+$  and  $\text{Au}^+$  centers via  $\text{P},\text{N}$ -interactions.

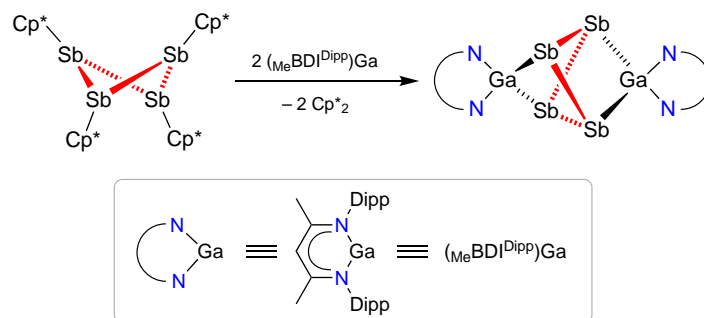
Treatment of the neutral cyclo-tetraphosphane  $[(i\text{Pr}_2\text{N})\text{P}]_4$  with a mixture of  $[\text{NO}][\text{SbF}_6]$  and  $\text{Li}[\text{TEF}]$  gave the intensely purple radical cation salt,  $[\{(i\text{Pr}_2\text{N})\text{P}\}_4][\text{TEF}]$ .<sup>106</sup> X-ray crystallography showed a slight elongation of the  $\text{P}-\text{P}$  bond lengths in the cation compared with the neutral  $\text{cyclo-P}_4$  precursor, prompting a computational analysis of the electronic structure. The results of a DFT study and EPR measurements show that the spin density for  $[\{(i\text{Pr}_2\text{N})\text{P}\}_4]^+$  lies mainly on the *exo*-cyclic nitrogen atoms.

Ring systems in which a formal charge is associated with the  $\text{E}_4$ -ring have also been the subject of investigations. The sodium salt of the tetramesityltetraphosphanide  $[\text{Mes}_4\text{P}_4]^{2-}$  is ring-opened by the organotin reagent  $n\text{Bu}_3\text{SnCl}$  to afford the open chain phosphane, 1,2,3,4-tetramesityl-1,4-bis(*n*-butyltin)tetraphosphane.<sup>107</sup> When the anion is reacted with five equivalents of cyclohexylisocyanide, a three component mixture of *cyclo*- $\{\text{P}_4\text{Mes}_4\text{C}(\text{NCy})\}$  (containing a five-membered  $\text{P}_4\text{C}$ -ring), 1,3,5-triphospha-1,4-pentadiene and a trace amount of the dimeric iminomethylidene phosphane is formed.<sup>108</sup> Adding catalytic amounts of  $\text{AgBF}_4$  afforded *cyclo*- $\{\text{P}_4\text{Mes}_4\text{C}(\text{NCy})\}$  as the major product. It was shown that this species can be protonated at the *exo*-cyclic nitrogen atom to afford the  $[\text{cyclo}\{-\text{P}_4\text{Mes}_4\text{C}(\text{NHCy})\}]^+$  cation.<sup>109</sup>

The tetracationic, cyclotetraphosphane  $[\{(\text{Me}^e i\text{Pr})_4\text{P}_4\}]^{4+}$  is isolated as the triflate salt from the reduction of the corresponding  $[\{(\text{Me}^e i\text{Pr})\text{P}\}_4\text{Cl}_2]^+$  with 1,4-bis(trimethylsilyl)-1,4-dihydropyrazine.<sup>110</sup> Further reduction gave the nortricyclane  $\text{P}_7$ -cluster species  $[\{(\text{Me}^e i\text{Pr})_3\text{P}_7\}][\text{OTf}]_3$ . Reaction of this species with the low oxidation-state transition-metal complexes  $\text{Fe}_2(\text{CO})_9$  and  $\text{M}(\text{PPh}_3)_4$  ( $\text{M} = \text{Pd}$ ,  $\text{Pt}$ ) gave  $[2 + 2]$ -fragmentation leading to dicationic  $\eta^2$ -diphosphene complexes. In contrast, reaction with  $\text{AuCl}(\text{tth})$  ( $\text{tth} = \text{tetrahydrothiophene}$ ) gave a 5-membered ' $\text{P}_4\text{Au}$ ' ring species.

This area of chemistry also extends to include cyclic species incorporating antimony. Reaction of the cyclotetrestibane  $[\text{Cp}^*\text{Sb}]_4$ <sup>111</sup> with the magnesium(I) guanidinate reagent  $[\text{Mg}(i\text{Pr}_2\text{N}\{\text{NDipp}\})]_2$ <sup>112</sup> afforded  $\{\text{Mg}(i\text{Pr}_2\text{N}\{\text{NDipp}\})\}_4(\mu_4, \eta^{1:2:2:2}-\text{Sb}_4)$ , in which the antimony atoms are present in the  $[1,2]$ -edge-missing tetrahedral arrangement (Scheme 13).<sup>113</sup> When the reduction was carried out with the gallium(I) reagent  $\text{Ga}(\text{MeBDI}^{\text{Dipp}})$ , the product was identified as  $\{\text{Ga}(\text{MeBDI}^{\text{Dipp}})\}_2(\mu, \eta^{2:2}-\text{Sb}_4)$  containing a  $[1,4]$ -edge missing tetrahedral arrangement of the  $\text{Sb}_4$  core (Scheme 8).

The tetracation,  $[\text{Sb}_4(\text{PMe}_3)_4]^{4+}$  was isolated from the reaction of  $\text{SbF}_3$  with trimethylsilyl triflate, followed by the addition of  $\text{PMe}_3$ .<sup>114</sup> The antimony atoms form a folded square arrangement with four *exo*-cyclic  $\text{Sb}-\text{PMe}_3$  bonds. Further  $\text{Sb}\cdots\text{O}$  stabilizing interactions with the triflate anions were noted in the solid state. Calculations indicate that although this unit can be considered as an ' $[\text{Sb}_4]^{4+}$  cation' with four phosphane ligands, a more accurate description is the neutral cyclotetrestibino group with *exo*-cyclic phosphonium groups. The chemistry of these  $[\text{Sb}_4(\text{PR}_3)_4]^{4+}$  ( $\text{R} = \text{Me}$ ,  $\text{Et}$ ) species was studied in detail,<sup>115</sup> with the reductive elimination of *catena*  $\text{P}_2$ - and  $\text{P}_3$ -cations and formation of  $\text{Sb}(0)$  dominating the reactivity. This reductive catenation process was utilized in the formation of related  $\text{Sb}/\text{P}$  cations. The reaction of  $\text{SbF}(\text{OTf})_2$  with two equivalents of  $\text{PPh}_3$  gave the bis(phosphino) antimony compound,  $\text{SbF}(\text{OTf})_2(\text{PPh}_3)$  with a linear  $\text{P}-\text{Sb}-\text{P}$  chain.<sup>116</sup> This compound spontaneously eliminated the fluorophosphonium salt  $[\text{Ph}_3\text{PF}][\text{OTf}]$  to form the  $[\text{Sb}_6(\text{PPh}_3)_4]^{4+}$  cation containing the bicyclo[3.1.0]hexastibine cluster. The proposed mechanism involves formation of intermediate  $[\text{Sb}(\text{PPh}_3)]^+$  units that catenate to form  $[\text{Sb}_6(\text{PPh}_3)_6]^{6+}$ , followed by elimination of  $[\text{Ph}_3\text{P}-\text{PPh}_3]^{2+}$ .



**Scheme 8** Reduction of  $[\text{Cp}^*\text{Sb}]_4$  with  $(\text{MeBDI}^{\text{Dipp}})\text{Ga}$ .

Examples of *cyclo*-(E)<sub>4</sub> systems comprised of mixed As/P units have been described. A head-to-tail dimeric cyclic-arsaphosphene was produced when a catalytic amount of  $\text{B}(\text{C}_6\text{F}_5)_3$  was added to the (arsino)phosphaketene,  $\text{As}\{(\text{CH}_2\text{NDipp})_2\}(\text{PCO})$ .<sup>117</sup> The product contains a central  $\text{As}_2\text{P}_2$  ring that formed from the formal  $[2 + 2]$  cycloaddition of the monomeric *cis*-arsaphosphene (Fig. 17). A thermal isomerization occurred when this compound was heated to 110 °C, which generated the corresponding head-to-head dimer. This study also described the decarbonylation of the (arsino)phosphaketene at 60 °C to afford the dimer of an arsino-phosphinidene,  $\text{As}\{(\text{CH}_2\text{NDipp})_2\}(\text{P})$ .

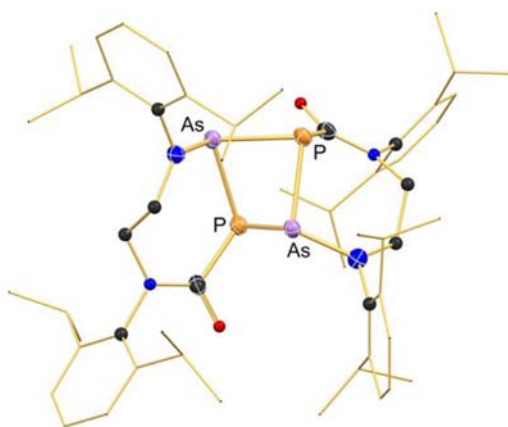
The reaction of  $(i\text{Pr}_2\text{N})_2\text{ECl}$  (E = As, P) with  $\text{Na}[\text{OCP}]$  generated transient diphospha- and arsaphospha-acrylamides  $i\text{Pr}_2\text{N}-\text{E}=\text{P}-\text{C}(\text{O})\text{NiPr}_2$ .<sup>118</sup> The unstable species undergo rapid dimerization to afford four-membered  $\text{E}_2\text{P}_2$ -rings. In the presence of excess  $\text{Na}[\text{OCP}]$ , the carboxytriphosphido anions  $[(i\text{Pr}_2\text{N})\text{EP}_2\text{CO}(\text{CONiPr}_2)]^-$  were formed from the  $[2 + 2]$  cycloaddition of  $[\text{OCP}]^-$  with an intermediate  $i\text{Pr}_2\text{NP}=\text{PCONiPr}_2$ .

The bulky  $\text{Ar}^{**}$  group ( $\text{Ar}^{**} = 2,6\text{-}\{(4\text{-}t\text{BuC}_6\text{H}_4)_2\text{CH}\}_2\text{-}4\text{-Me-C}_6\text{H}_2$ ) was used in an attempt to stabilize  $\{(\text{CH}_2\text{NAr}^{**})_2\}(\text{P}(\text{AsCO}))$  generated from the reaction of the chlorodiazaphospholidine  $\{(\text{CH}_2\text{NAr}^{**})_2\}\text{P}-\text{Cl}$  with  $\text{Na}[\text{AsCO}]$ .<sup>119</sup> Despite the presence of these sterically demanding groups, the phosphino arsaketene readily loses CO under ambient conditions to generate the transient phosphinoarsinidene,  $\text{P}\{(\text{CH}_2\text{NAr}^{**})_2\}(\text{As})$ , which reacts via a cycloaddition with excess  $[\text{AsCO}]^-$  to afford  $\text{Na}[\text{P}\{(\text{CH}_2\text{NAr}^{**})_2\}_2(\mu, \eta^{2-1}\text{-As}_3)]$ ,  $[\text{Na}(18\text{-c-}6)]\{\text{P}\{(\text{CH}_2\text{NAr}^{**})_2\}(\text{As}_2\text{C}=\text{O})\}$  or  $[\text{P}\{(\text{CH}_2\text{NAr}^{**})_2\}_2(\mu, \eta^{1:1}\text{-As}_4)]$ .

The corresponding reactions with the phosphaketene  $\{(\text{CH}_2\text{NAr}^{**})_2\}\text{P}(\text{PCO})$  afforded the isolable (phosphino)phosphinidene  $\{(\text{CH}_2\text{NAr}^{**})_2\}\text{P}(\text{P})$  (Scheme 9).<sup>120</sup> When sterically less demanding Dipp-substituents were used at the nitrogen positions, the transient analogue  $\{(\text{CH}_2\text{NDipp})_2\}\text{P}(\text{P})$  was formed, which dimerizes under ambient conditions to form  $\{(\text{CH}_2\text{NDipp})_2\}\text{P}-\text{P}=\text{P}-\text{P}\{(\text{CH}_2\text{NDipp})_2\}$ . Interestingly, the electronic ground state calculations of  $\{(\text{CH}_2\text{NAr}^{**})_2\}\text{P}(\text{P})$  suggest P–P multiple bond character with a negative charge at the terminal phosphorus, whereas the observed reactivity with CO, singlet carbenes and phosphanes indicates electrophilic behaviour.<sup>121</sup>

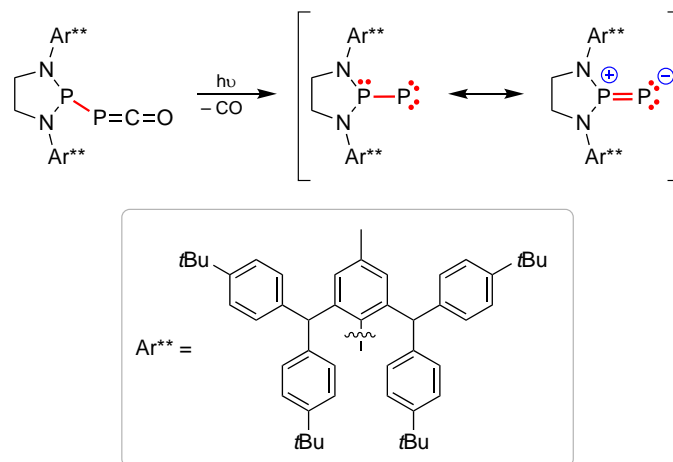
#### 1.19.4.1.3 *Cyclo*-(E)<sub>5</sub> units

Group 6 metal carbonyls  $\text{M}(\text{CO})_6$  (M = Cr, Mo, W) react with *cyclo*-[PhP]<sub>5</sub> to afford adducts in which the metal fragment coordinates to an intact cyclopentaphosphane ring.<sup>122</sup> The substitution pattern around the  $\text{P}_5$ -ring depends on the group 6 metal and the carbonyl-containing starting material. For example, mono-substitution with a mono-dentate  $\text{P}_5$ -ring was observed in the chromium complex  $\{(\text{CO})_5\text{Cr}\}\{\text{cyclo}-(\text{P}_5\text{Ph}_5)\text{-}\kappa\text{P}^1\}$ , whereas a bidentate bonding mode was observed in  $\{(\text{CO})_4\text{M}\}\{\text{cyclo}-(\text{P}_5\text{Ph}_5)\text{-}\kappa\text{P}^1, \text{P}^3\}$  (M = Cr, Mo and W). In the latter compound with M = W, both *endo*- and *exo*-isomers were observed. An unusual oxidative



**Fig. 17** Molecular structure of the head-to-tail dimer of a *cis*-arsaphosphene.





**Scheme 9** Synthesis of an isolable (phosphino)phosphinidene.

addition/acetonitrile insertion was observed when  $M(\text{CO})_4\{\text{cyclo}-(\text{P}_5\text{Ph}_5)-\kappa\text{P}^1, \text{P}^3\}$  was reacted with an additional equivalent of  $M(\text{CO})_4(\text{L})_x$  ( $M = \text{Cr}, \text{W}, \text{L} = \text{MeCN}, x = 2$ ;  $M = \text{Mo}, \text{L} = 2,5\text{-norbornadiene}, x = 1$ ) under forcing conditions ( $120^\circ\text{C}$ , toluene).<sup>123</sup> The products contain the  $[\{\text{PhP}\}_4\text{CMe}=\text{N}-\text{PPh}]^{2-}$  ligand, which crystallizes with an all *trans*-arrangement of phenyl groups.

#### 1.19.4.1.4 *Cyclo-(E)<sub>6</sub>* units

The reduction of sodium arsonoacetate,  $\text{Na}_3[\text{As}(\text{CH}_2\text{COO})(\text{O})_3]$  with an aqueous mixture of conc.  $\text{H}_2\text{SO}_4$  and  $\text{H}_3\text{PO}_2$  afforded orange crystals of arsenoacetic acid,  $[\text{As}(\text{CH}_2\text{COOH})]_n$ .<sup>124</sup> X-ray diffraction showed a cyclic hexamer formed in the solid state with a puckered  $\text{As}_6$ -ring with alternating 'up' and 'down' positions for the organic groups in an idealized  $\text{C}_{3v}$  structure (Fig. 18).

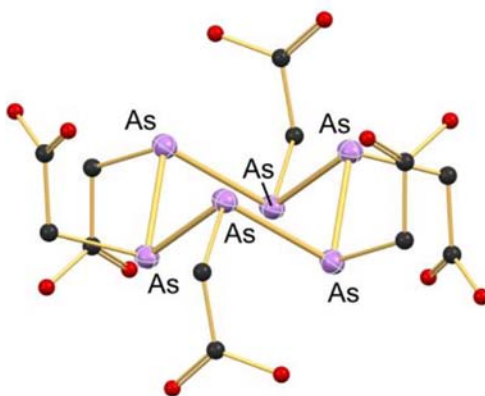
#### 1.19.4.2 Monocyclic, metalated *catena*-pnictogens: $(\text{E})_n = 3-6$

This section collects together the chemistry of pnictogen compounds with *cyclo*-( $\text{E})_n$  groups that are incorporated into the coordination sphere of one or more metal fragments, and can be summarized according to (Fig. 19).

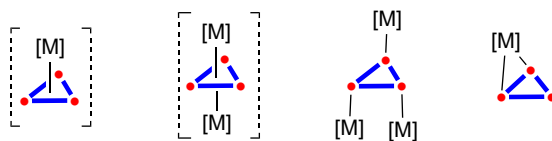
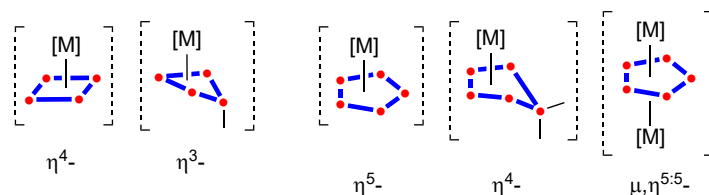
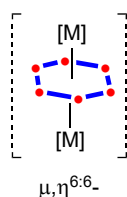
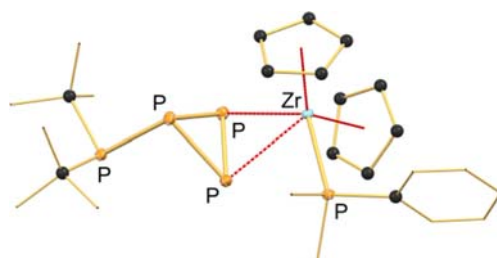
##### 1.19.4.2.1 Metalated *cyclo*-( $\text{E})_3$ units

Zirconium and hafnium metallocene complexes  $\text{Cp}_2\text{MCl}_2$  ( $M = \text{Zr}, \text{Hf}$ ) react with  $\text{Li}[\text{R}_2\text{P}-\text{P}(\text{SiMe}_3)]$  ( $R = t\text{Bu}, i\text{Pr}, i\text{Pr}_2\text{N}$ ) to form polyphosphorus ligands at the metal center, which the authors consider as intermediates in the formation of the bicyclo[1.1.0]tetraphosphabutane skeleton.<sup>125</sup> Structurally characterized examples from this study include compounds incorporating the *cyclo*-( $\text{P})_3$  derivatives (Fig. 20), as well as the bimetallic  $\text{P}_6$ -chain containing compound.

The reducing power of divalent lanthanide complexes has been exploited in this area of research, providing access to metalated products not otherwise available when using more conventional reducing agents. In this context, the reaction of  $\text{Cp}^*\text{Mo}(\text{CO})_2(\eta^3\text{-P}_3)$  with  $\text{Cp}^*\text{Ln}(\text{THF})_2$  ( $\text{Ln} = \text{Sm}, \text{Yb}$ ) afforded the isostructural products  $(\text{Cp}^*\text{Ln})_2(\text{P}_6)\{\text{Cp}^*\text{Mo}(\text{CO})_2\}_2$ , in which a one electron reduction took place at the  $\text{P}_3$ -ligand to form a  $\text{P}_6$ -unit that consisted of two  $\text{P}_3$ -triangles linked by a newly formed P–P single



**Fig. 18** Molecular structure of the arsenoacetic acid cyclic hexamer.

**Monocyclic (metalated)** (Section 1.19.4.2)(A)  $n = 3$  (Section 1.19.4.2.1)(B)  $n = 4$  (Section 1.19.4.2.2)(C)  $n = 5$  (Section 1.19.4.2.3)(D)  $n = 5$  (Section 1.19.4.2.4)**Fig. 19** Schematic representation of metalated, monocyclic pnictogen units included in Section 1.19.4.2.**Fig. 20** An example of a zirconocene derivatives containing a P<sub>3</sub>-ring systems formed from the reaction of Cp<sub>2</sub>ZrCl<sub>2</sub> and Li[*t*Bu<sub>2</sub>P–P(SiMe<sub>3</sub>)].

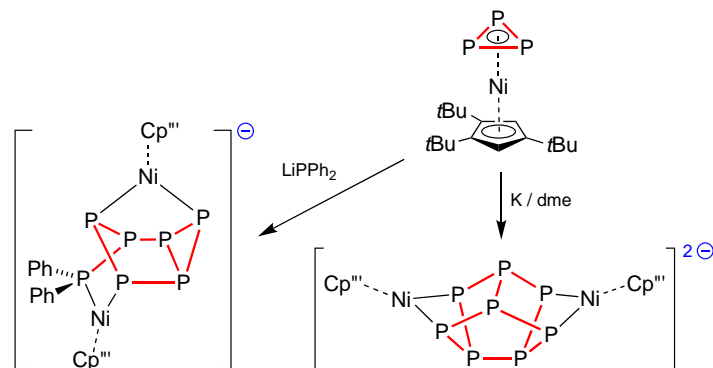
bond.<sup>126</sup> This compound represented the first example of a 4d/4f polyphosphide and highlighted the tendency for the Ln(III) product to be retained in the bimetallic products.

The sandwich compound Cp<sup>'''</sup>Ni(η<sup>3</sup>-P<sub>3</sub>) was reacted with main group nucleophiles and reducing agents to generate a series of metalated P-cluster compounds.<sup>127</sup> Reaction with potassium metal generated the P<sub>8</sub> 'realgar-like' core within the anion [(Cp<sup>'''</sup>Ni)<sub>2</sub>(μ,η<sup>2:2</sup>-P<sub>8</sub>)]<sup>2-</sup> (Scheme 10), whilst treatment with NaNH<sub>2</sub> gave the triple decker anion [(Cp<sup>'''</sup>Ni)<sub>2</sub>(μ,η<sup>3:3</sup>-P<sub>3</sub>)]<sup>-</sup>, which was oxidized to the neutral species using AgOTf. In contrast, reaction with LiPPh<sub>2</sub> gave [(Cp<sup>'''</sup>Ni)<sub>2</sub>(μ,η<sup>2:2</sup>-P<sub>6</sub>PPh<sub>2</sub>)]<sup>-</sup> containing a bicyclic P<sub>7</sub> fragment capped by two Cp<sup>'''</sup>Ni groups. Finally in this study, the reaction with LiNMe<sub>2</sub> proceeded by nucleophilic attack at the P<sub>3</sub>-ring to give [Cp<sup>'''</sup>Ni(η<sup>2</sup>-P<sub>3</sub>NMe<sub>3</sub>)]<sup>-</sup>.

The reaction of Cp<sup>'''</sup>Ni(η<sup>3</sup>-P<sub>3</sub>) with {Cp<sup>'''</sup>Co}<sub>2</sub>(μ,η<sup>4:4</sup>-C<sub>7</sub>H<sub>8</sub>) afforded the heterobimetallic complex {Cp<sup>'''</sup>Ni}{Cp<sup>'''</sup>Co}(μ,η<sup>3:3</sup>-P<sub>3</sub>).<sup>128</sup> It was shown that central P<sub>3</sub>-deck of the complex was able to accommodate an additional metal in the heterotrimetallic complex, {Cp<sup>'''</sup>Ni}{Cp<sup>'''</sup>Co}(μ<sub>3</sub>,η<sup>3:2:1</sup>-P<sub>3</sub>){W(CO)<sub>5</sub>}.

Reaction of the niobium anion [Nb(ODipp)<sub>3</sub>(η<sup>3</sup>-P<sub>3</sub>)]<sup>-</sup> with the phosphinidene complex Cp\*P{W(CO)<sub>5</sub>} resulted in a ring-expansion to afford the [{W(CO)<sub>5</sub>]<sub>2</sub>(μ<sub>3</sub>,η<sup>3:1:1</sup>-P<sub>4</sub>Cp\*)Nb(ODipp)<sub>3</sub>]<sup>-</sup> anion.<sup>129</sup> The *cyclo*-(P)<sub>4</sub> ring retained a planar η<sup>3</sup>-interaction with the niobium center, with the W(CO)<sub>5</sub> group bound to one of the three phosphorus atoms. The remaining phosphorus atom of the P<sub>4</sub>-unit was located above the P<sub>3</sub>-plane, η<sup>1</sup>-bonded to a Cp\* ligand and a second W(CO)<sub>5</sub> group.

Although less common than the P<sub>3</sub>-systems, examples of *cyclo*-(E)<sub>3</sub> units in the coordination spheres of metals also exist for arsenic and antimony. As part of a study aimed toward understanding the mechanism of Sb=Sb and Ga=Sb multiple bond formation, the gallium(I) reagent Ga(Me<sub>2</sub>BDI<sup>Dipp</sup>) was reacted with SbCl<sub>3</sub>, leading to formation of the cyclotristibane, {Ga(Me<sub>2</sub>BDI<sup>Dipp</sup>)



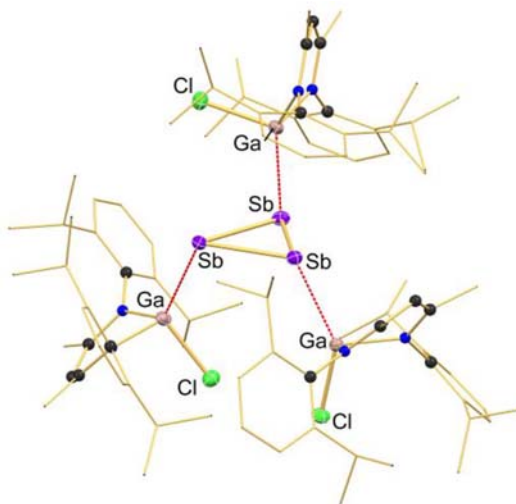
**Scheme 10** Synthesis of  $[(\text{Cp}''\text{Ni})_2(\mu, \eta^{2:2}\text{-P}_8)]^{2-}$  and  $[(\text{Cp}''\text{Ni})_2(\mu, \eta^{2:2}\text{-P}_6\text{PPh}_2)]^{-}$  from reduction of  $\text{Cp}''\text{Ni}(\eta^3\text{-P}_3)$  ( $[\text{K}_2(18\text{-c-6})(\text{dme})]^{2+}$  and  $\text{Li}^+$  cations omitted).

$\text{Cl}\}_3(\text{Sb}_3)$  (Fig. 21).<sup>130</sup> This product likely formed from the trimerization of ‘ $\text{Ga}(\text{MeBDI}^{\text{Dipp}})\text{Cl}\}\text{Sb}$ ’ units that are generated upon loss of  $\text{Ga}(\text{MeBDI}^{\text{Dipp}})\text{Cl}_2$  from the initially formed  $\{\text{Ga}(\text{MeBDI}^{\text{Dipp}})\text{Cl}\}_2\text{SbCl}$  intermediate. Studies toward the analogous gallaarsene containing the  $\text{Ga}=\text{As}$  double bond from the reaction of  $\text{Cp}^*\text{AsCl}_2$  with  $\text{Ga}(\text{MeBDI}^{\text{Dipp}})$  afforded a small but reproducible amount of  $\{\eta^1\text{-Cp}^*\text{Ga}(\text{MeBDI}^{\text{Dipp}})\}\{\eta^2\text{-Ga}(\text{MeBDI}^{\text{Dipp}})\}\{\mu\text{-As}_3\}$ .<sup>131</sup> The  $\eta^{2:1}$ -coordination of the  $\text{As}_3$ -ring had not been previously observed.

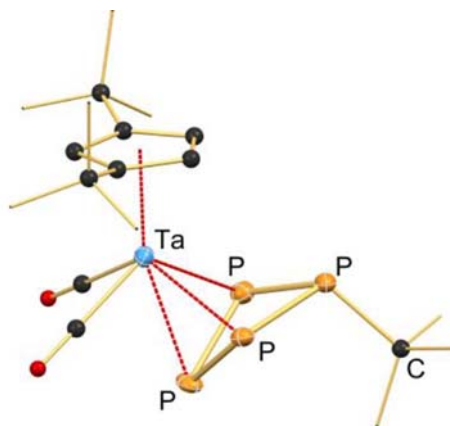
#### 1.19.4.2.2 Metalated *cyclo*-(E)<sub>4</sub> units

The tantalum compound  $\text{Cp}''\text{Ta}(\text{CO})_2(\eta^4\text{-P}_4)$  consists of a bent metallocene type structure defined by the planar  $\text{Cp}''$  and  $\text{P}_4$  ligands. It was shown that reaction with  $t\text{BuLi}$  alkylated the phosphorus ring to afford the salt  $[\text{Li}(\text{THF})_4][\text{Cp}''\text{Ta}(\text{CO})_2(\eta^3\text{-P}_4t\text{Bu})]$  (Fig. 22).<sup>132</sup> A similar *cyclo*-(P)<sub>4</sub> unit consisting of the  $[\eta^3\text{-P}_3\{\text{P}(\text{O})\text{H}\}]$  ligand was generated when  $\text{Cp}''\text{Ta}(\text{CO})_2(\eta^4\text{-P}_4)$  was reacted with IDipp in the presence of  $\text{H}_2\text{O}$ . In the absence of  $\text{H}_2\text{O}$ , an abstraction of one of the P-atoms from the  $\text{P}_4$ -ring was observed to afford the salt  $[(\text{IDipp})_2\text{P}][\text{Cp}''\text{Ta}(\text{CO})_2(\eta^3\text{-P}_3)]$  with a cyclic  $\text{P}_3$ -ring.<sup>133</sup>

In a similar study, the *cyclo*-(P)<sub>4</sub> ligand in the cobalt complex  $\text{Cp}''\text{Co}(\eta^4\text{-P}_4)$  was examined for its reactivity toward reduction and main group nucleophiles.<sup>134</sup> Chemical reduction was achieved using  $\text{K}[\text{CpFe}(\text{CO})_2]$  to afford the dinuclear dianion  $[\{\text{Cp}''\text{Co}\}_2(\mu, \eta^{3:3}\text{-P}_8)]^{2-}$  with an ‘open realgar-like’  $\text{P}_8$ -cage that interacts with the metal fragments via a double  $\eta^3$ -coordination. In contrast, reaction of  $\text{Cp}''\text{Co}(\eta^4\text{-P}_4)$  with  $t\text{BuLi}$  or  $\text{LiCH}_2\text{SiMe}_3$  gave the metastable alkylated species  $[\text{Cp}''\text{Co}(\eta^3\text{-P}_4\text{R})]^{-}$  ( $\text{R} = t\text{Bu}, \text{CH}_2\text{SiMe}_3$ ), which reacted with a second equivalent of the cobalt starting material to give the  $[\{\text{Cp}''\text{Co}\}_2(\mu, \eta^{3:3}\text{-P}_8\text{R})]^{-}$  anions. Using the ring expansion developed for the niobium anions with  $\eta^3\text{-P}_3$  ligands (see Section 1.19.4.2.1),  $\text{Cp}^*\text{E}\{\text{W}(\text{CO})_5\}$  ( $\text{E} = \text{P}, \text{As}$ ) was reacted with  $\text{Cp}''\text{Co}(\eta^4\text{-P}_4)$  to give  $\text{Cp}''\text{Co}(\mu_3, \eta^{4:1:1}\text{-P}_5\text{Cp}^*)\{\text{W}(\text{CO})_5\}_2$  and three isomeric forms of  $\text{Cp}''\text{Co}(\mu_3, \eta^{4:1:1}\text{-AsP}_4\text{Cp}^*)\{\text{W}(\text{CO})_5\}_2$ .<sup>129</sup>



**Fig. 21** Molecular structure of  $\{\text{Ga}(\text{MeBDI}^{\text{Dipp}})\text{Cl}\}_3(\text{Sb}_3)$ .



**Fig. 22** Molecular structure of the anion  $[\text{Cp}''\text{Ta}(\text{CO})_2(\eta^3\text{-P}_4\text{tBu})]^-$  obtained from the alkylation of the  $\text{P}_4$ -ring of  $\text{Cp}''\text{Ta}(\text{CO})_2(\eta^4\text{-P}_4)$  ( $[\text{Li}(2.2.2\text{-crypt})]^+$  cation omitted).

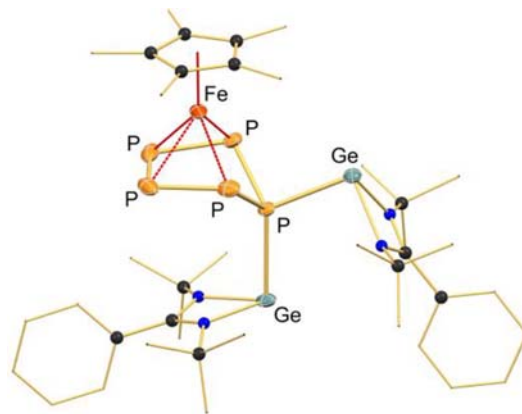
#### 1.19.4.2.3 Metalated *cyclo-(E)<sub>5</sub>* units

This area of research remains largely dominated by the chemistry of the pentaphosphaferrocene molecules  $\text{CpFe}(\eta^5\text{-P}_5)$  and  $\text{Cp}^*\text{Fe}(\eta^5\text{-P}_5)$ , with some recent advances extending this to compare and contrast with that of the heavier analogues incorporating the  $\eta^5\text{-As}_5$  ligand. A fundamental study comparing the redox chemistry of ferrocene and pentaphosphaferrocene  $\text{CpFe}(\eta^5\text{-P}_5)$ , concluded that  $\text{Cp}_2\text{Fe}$  features mainly iron-based redox chemistry, whereas the  $\text{P}_5$ -ring is involved during redox processes for the phosphorus containing derivative.<sup>135</sup> This is manifest in a tilting of the  $\text{P}_5$ -ligand facilitating dimerization to give  $\text{P}_{10}$  complexes of iron.

The reactivity of  $\text{Cp}^*\text{Fe}(\eta^5\text{-P}_5)$  toward a range of NHCs ( $^{\text{Me}}\text{Ime}$ ,  $^{\text{H}}\text{Imes}$  and  $^{\text{H}}\text{IDipp}$ ) was investigated, affording the neutral complexes  $\text{Cp}^*\text{Fe}(\eta^4\text{-P}_5\{\text{NHC}\})$  in which the  $\text{P}_5$ -ring loses its planarity and adopts an envelope conformation.<sup>133</sup> Analogous results were observed when the iron complex was reacted with sources of main group element nucleophiles ( $\text{LiCH}_2\text{SiMe}_3$ ,  $\text{LiNMe}_2$ ).<sup>136</sup> When  $\text{NaNH}_2$  was used however, the trianionic complex  $[\{\text{Cp}^*\text{Fe}(\eta^4\text{-P}_5)\}_2\text{N}]^{3-}$  was formed whereas  $\text{LiPH}_2$  yielded a mixture of  $[\text{Cp}^*\text{Fe}(\eta^4\text{-P}_5\text{PH}_2)]^-$  (main) and  $[\{\text{Cp}^*\text{Fe}(\eta^4\text{-P}_5)\}_2\text{PH}]^{2-}$  (minor).

The iodination of the pentaphosphaferrocene derivative  $\text{Cp}^*\text{Fe}(\eta^5\text{-P}_5)$ , and its ruthenium analogue  $\text{Cp}^*\text{Ru}(\eta^5\text{-P}_5)$  proceeded in a one-pot procedure to afford the all *cis*-tripodal triphosphino-cyclotriphosphane ligand, *cyclo*- $\{\text{P}(\text{P}t_2)\}_3$ .<sup>137</sup> The core of the resulting molecule contains an  $\text{MP}_6$ -unit that resembles the nortricyclane structure observed in the  $[\text{P}_7]^{3-}$  anion.  $\text{Cp}^*\text{Fe}(\eta^5\text{-P}_5)$  was also used as a synthon for the formation of the heterobimetallic  $\{\text{Cp}^*\text{Fe}\}\{\text{Cp}^{\text{III}}\text{Co}\}(\mu, \eta^{5:4}\text{-P}_5)$ , which when reacted with  $\text{W}(\text{CO})_5(\text{THF})$  afforded the mono- and bis-tungsten adducts.<sup>128</sup>

In *p*-block chemistry,  $\text{Cp}^*\text{Fe}(\eta^5\text{-P}_5)$  was used as a polyphosphorus source to generate silicon and germanium phosphide species. The reaction with silylene  $(\text{PhC}\{\text{NtBu}\}_2)\text{SiCl}$  leads to formation of  $\text{Cp}^*\text{Fe}(\eta^4\text{-P}_4\text{Si}(\text{PhC}\{\text{NtBu}\}_2))$ , in which the silicon has inserted into a  $\text{P-P}$  bond.<sup>138</sup> No reaction was observed when the corresponding germylene  $(\text{PhC}\{\text{NtBu}\}_2)\text{GeCl}$  was used. However the digermylene  $[(\text{PhC}\{\text{NtBu}\}_2)\text{Ge}]_2$ , containing formally  $\text{Ge}(\text{I})$  centers reacted to afford  $\text{Cp}^*\text{Fe}(\eta^4\text{-P}_5)\{\text{Ge}(\text{PhC}\{\text{NtBu}\}_2)\}_2$  (Fig. 23).<sup>139</sup> In related chemistry, the  $\text{Al}(\text{I})$  species  $\text{Al}(\text{MeBDI}^{\text{Dipp}})$  inserts into a  $\text{P-P}$  bond of  $\text{Cp}^*\text{Fe}(\eta^5\text{-P}_5)$  to afford the



**Fig. 23** Molecular structures of the product of  $\text{Cp}^*\text{Fe}(\eta^5\text{-P}_5)$  with a source of  $\text{Ge}(\text{I})$ — $[(\text{PhC}\{\text{NtBu}\}_2)\text{Ge}]_2$ .

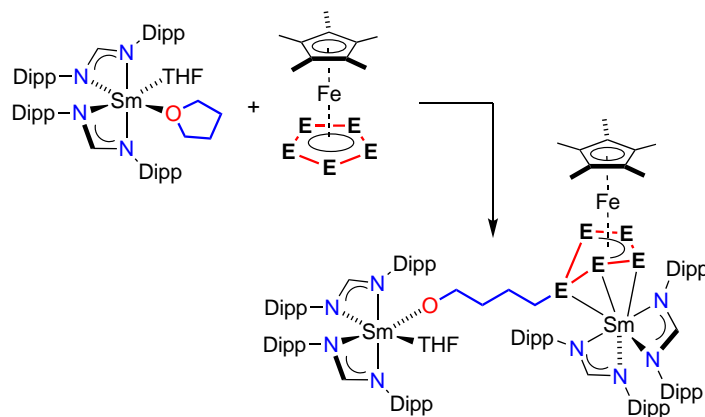
triple-decker  $\{\text{Al}(\text{MeBDI}^{\text{Dipp}})\}(\mu, \eta^{3:4}\text{-P}_5)(\text{FeCp}^*)$ , with an envelope-shaped  $\text{P}_5$ -deck.<sup>140</sup> The reaction with  $[\text{Cp}^*\text{Al}]_4$  however results in a six-fold reduction of the  $\text{P}_5$ -ring by three equivalents of 'Cp\*Al' to give  $(\mu_3\text{-P})(\text{Cp}^*\text{Al})_2\{\text{P}_4(\text{AlCp}^*)\}(\text{FeCp}^*)$ .

The chemistry of the corresponding iron-arsenic compound,  $\text{Cp}^*\text{Fe}(\eta^5\text{-As}_5)$  is often very distinct when compared with the phosphorus analogue. For example, the reaction of  $\text{Cp}^*\text{Fe}(\eta^5\text{-As}_5)$  with  $\text{I}_2$  afforded the triple-decker  $[(\text{Cp}^*\text{Fe})_2(\mu, \eta^{5:5}\text{-As}_5)]^{2+}$  cation as the  $[\text{As}_6\text{I}_8]^{2-}$  salt, in addition to the arsenic-iodide anions  $[\text{As}_6\text{I}_8]^{2-}$  and  $[\text{As}_4\text{I}_4]^{2-}$  anions which formed as the  $[\text{Fe}(\text{CN})_6]^{2+}$  salts.<sup>137</sup> Using the Ru complex in an attempt to prevent cleavage of the arsenic ligand during the reaction was successful, but again formed a mixture of species from which  $[(\text{Cp}^*\text{Ru})_2(\mu, \eta^{5:5}\text{-As}_5)][\text{As}_6\text{I}_8]_{0.5}$ ,  $(\text{Cp}^*\text{Ru})_2(\mu, \eta^{4:4}\text{-As}_4\text{I}_4)$  and  $(\text{Cp}^*\text{Ru})_2(\text{As}_8\text{I}_6)$  were separated and characterized. Crystallographic analysis of the latter complex showed that it contains bridging  $\{\text{AsI}_2\}$  and  $\{\text{As}_7\text{I}_4\}$  ligands.

Reacting  $\text{Cp}^*\text{Fe}(\eta^5\text{-As}_5)$  with the triple decker complex  $\{\text{Cp}^*\text{Co}\}_2(\mu, \eta^{4:4}\text{-C}_7\text{H}_8)$  formed the metastable  $(\text{Cp}^*\text{Fe})(\text{Cp}^*\text{Co})(\mu, \eta^{5:4}\text{-As}_5)$ .<sup>141</sup> This compound was found to decompose in MeCN to form mixtures of  $(\text{Cp}^*\text{Fe})(\text{Cp}^*\text{Co})(\mu, \eta^{3:3}\text{-As}_3)$  and  $(\text{Cp}^*\text{Fe})_2(\text{Cp}^*\text{Co})(\mu_4, \eta^{4:4:4:3}\text{-As}_{11})$ , the latter structure containing the  $\text{As}_{11}$ -unit as a *cyclo*-(As)<sub>5</sub> group in an envelope conformation joined to a *cyclo*-(As)<sub>6</sub> group in a chair conformation. Further fragmentation was observed under thermolysis conditions, affording  $(\text{Cp}^*\text{Fe})_2(\text{Cp}^*\text{Fe})(\mu_3, \eta^{2:2:2}\text{-As}_3)_2$  as the major product.

When divalent samarocenes  $\text{Cp}^*\text{R}_2\text{Sm}(\text{THF})_2$  (R = Me, *n*Pr) were reacted with  $\text{Cp}^*\text{Fe}(\eta^5\text{-P}_5)$ , a reductive dimerization was observed.<sup>142</sup> The  $\{\text{Cp}^*\text{Fe}\}_2\text{P}_{10}\{\text{Sm}(\eta^5\text{-C}_5\text{Me}_4\text{R}_2)\}_2$  (R = Me, *n*Pr) products contain a central  $\text{P}_{10}$  unit consisting of two  $\text{P}_5$ -rings in an envelope conformation formed by a P–P bond between the non-planar P-atom. This reductive coupling of two  $\text{P}_n$ -groups mirrors that described above during the synthesis of  $(\text{Cp}^*_2\text{Ln})_2(\text{P}_6)\{\text{Cp}^*\text{Mo}(\text{CO})_2\}_2$  (see Section 1.19.4.2.1).

Reduction of the  $\text{Cp}^*\text{Fe}(\eta^5\text{-E}_5)$  (E = P, As) with the Sm(II) formamidinate compound  $\text{Sm}(\text{HC}\{\text{NDipp}\}_2)_2(\text{THF})_2$  provoked ring-opening of the THF solvent and formation of  $(\text{HC}\{\text{NDipp}\}_2)_2\text{Sm}(\text{Cp}^*\text{Fe})(\text{E}_5)\{(\text{CH}_2)_4\text{O}\}\text{Sm}(\text{HC}\{\text{NDipp}\}_2)_2(\text{THF})$ .<sup>143</sup> Reduction of the  $[\text{E}_5]^-$  anion causes one of the pnictogen atoms to move out of the plane of the remaining four E-atoms to generate an 'envelope' conformation, in which the non-planar E-atom bonds to the methylene group of the ring-opened THF (Scheme 11).



**Scheme 11** Ring opening of THF during the reduction of  $\text{Cp}^*\text{Fe}(\eta^5\text{-E}_5)$  (E = P, As) by Sm(II) reagent,  $\text{Sm}(\text{HC}\{\text{NDipp}\}_2)_2(\text{THF})_2$ .

The analogous reaction with  $\text{Cp}^*\text{Sm}(\text{THF})_2$  led to formation of  $\{\text{Cp}^*\text{Sm}\}\{\text{Cp}^*\text{Fe}\}(\mu, \eta^{4:4}\text{-As}_4)$  and  $\{\text{Cp}^*\text{Sm}\}_2\{\text{Cp}^*\text{Fe}\}(\mu_3, \eta^{3:3:4}\text{-As}_7)$ .<sup>144</sup> The  $[\text{As}_7]^{3-}$  cage in the latter complex has a norbornadiene-like structure, with two short As–As bonds.

The complexity associated with the chemistry of  $\text{Cp}^*\text{Fe}(\eta^5\text{-As}_5)$  is further illustrated by its reaction with KH in dme, which afforded a complex mixture of iron stabilized polyarsenide anions. Compounds that were characterized included the triple decker  $[(\text{Cp}^*\text{Fe}(\mu, \eta^{2:2}\text{-As}_2))_2]^-$ ,  $[(\text{Cp}^*\text{Fe})_2(\mu, \eta^{4:4}\text{-As}_{10})]^{2-}$ ,  $[(\text{Cp}^*\text{Fe})_2(\mu, \eta^{2:2:2:2}\text{-As}_{14})]^{2-}$  and  $[(\text{Cp}^*\text{Fe})_4(\mu_4, \eta^{4:3:3:2:2:1:1}\text{-As}_{18})]^{2-}$  (Fig. 24).<sup>145</sup>

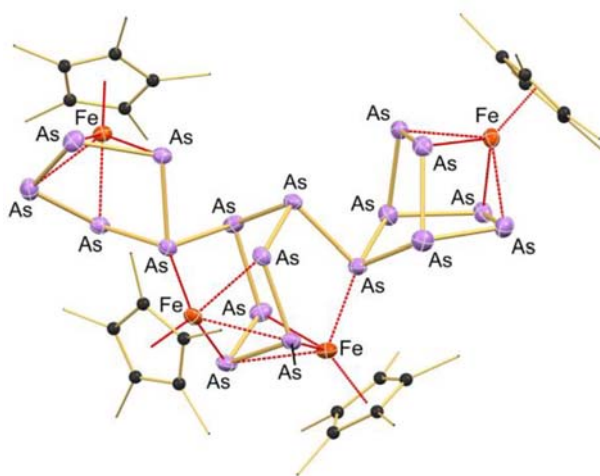
The  $[\text{Cp}^*\text{Fe}(\eta^4\text{-P}_5\text{R})]^-$  (R =  $\text{CH}_2\text{SiMe}_3$ ,  $\text{NMe}_2$ ) anions that contain a mono-substituted  $\text{P}_5$ -ring react with dimeric  $[\text{Cp}^*\text{M}(\mu\text{-X})]_2$  (M = Cr, Fe, Co, Ni; X = Cl, Br) compounds to afford triple decker compounds with a bent *cyclo*-(P)<sub>5</sub> middle ring.<sup>146</sup> Whilst the  $\eta^4$ -coordination of the  $\text{P}_5$ -ring is maintained at iron, interaction with the other transition-metal varies from  $\eta^3$ - (for Co, Ni) to  $\eta^5$ - (for Cr).

Finally it was noted that the heterobimetallic complex  $[\text{K}(\text{dme})_2][(\text{Mes}^*\text{BIAN})\text{Co}(\mu, \eta^{4:2}\text{-P}_4)\text{Ga}(\text{MeBDI}^{\text{Dipp}})]$  ( $\text{Mes}^*\text{BIAN}$  = 1,2-(Mes-N)<sub>2</sub>acenaphthene) reacted with  $\text{R}_2\text{PCl}$  (R = *i*Pr, *t*Bu, Cy) with elimination of  $\text{Ga}(\text{MeBDI}^{\text{Dipp}})$  to afford  $(\text{Mes}^*\text{BIAN})\text{Co}(\text{P}_5\text{R}_2)$  containing an 1,1-dialkylated  $\text{P}_5$ -ring present in an envelope conformation that is  $\eta^4$ -bonded to the cobalt.<sup>147</sup> The intermediate  $(\text{Mes}^*\text{BIAN})\text{Co}(\mu, \eta^{4:2}\text{-P}_5\text{R}_2)\text{Ga}(\text{MeBDI}^{\text{Dipp}})$  was identified by <sup>31</sup>P NMR spectroscopy and single crystal X-ray diffraction.

#### 1.19.4.2.4 Metalated *cyclo*-(E)<sub>6</sub> units

In contrast to the reaction of  $\text{Cp}^*\text{Fe}(\eta^5\text{-P}_5)$  that formed the  $(\eta^4\text{-P}_5\{\text{Me}^*\text{Ime}\})$  ligand at iron (see Section 1.19.4.2.3), a carbene induced ring contraction of the polypnictonide ligand was observed when  $\text{Me}^*\text{Ime}$  was reacted with  $\{\text{Cp}^*\text{Mo}\}_2(\mu, \eta^{6:6}\text{-E}_6)$  (E = P, As) and  $\text{Cp}^*\text{Co}(\eta^4\text{-P}_4)$ .<sup>148</sup> The products contain the anions  $[(\text{Cp}^*\text{Mo})_2(\mu, \eta^{5:5}\text{-E}_5)]^-$  and  $[\text{Cp}^*\text{Co}(\eta^3\text{-P}_3)]^-$ , respectively,



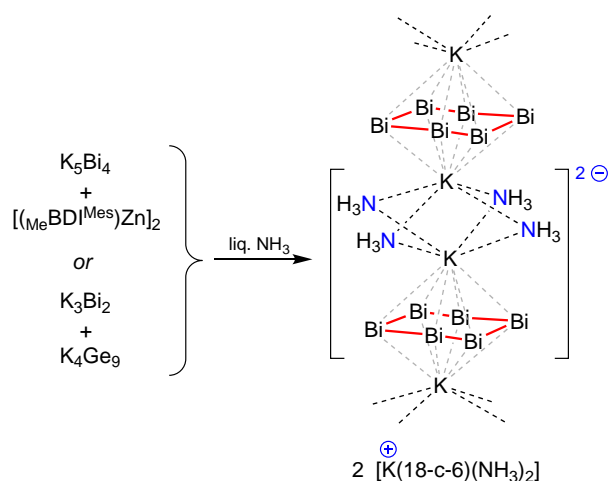


**Fig. 24** Molecular structure of the dianion  $[(\text{Cp}^*\text{Fe})_4(\mu_4, \eta^{4:3:3:2:2:1:1}\text{-As}_{18})]^{2-}$ .

charge balanced by the corresponding  $[(^{\text{Me}}\text{IME})_2\text{E}]^+$  cation. When the reaction was repeated using  $\{\text{Cp}^*\text{V}\}_2(\mu, \eta^{6:6}\text{-P}_6)$ , a mixture of the expected salt  $[(^{\text{Me}}\text{IME})_2\text{P}][\{\text{Cp}^*\text{V}\}_2(\mu, \eta^{5:5}\text{-P}_5)]$  was generated, in addition to  $[(^{\text{Me}}\text{IME})_2\text{P}][\{\text{Cp}^*\text{V}\}_2(\mu, \eta^{6:6}\text{-P}_6)]$  and  $\{\text{Cp}^*\text{V}\}_2(\mu, \eta^{3:3}\text{-P}_3)(\mu\text{-P}^{\text{Me}}\text{IME})$ .

The reaction of  $\{\text{Cp}^*\text{Mo}\}_2(\mu, \eta^{6:6}\text{-P}_6)$  with  $\text{CuX}$  ( $\text{X} = \text{Br}, \text{I}$ ) leads to self-assembly to give 2-D networks of  $[(\{\text{Cp}^*\text{Mo}\}_2\text{P}_6)(\text{CuBr})_4]_n$  and  $[(\{\text{Cp}^*\text{Mo}\}_2\text{P}_6)(\text{CuI})_2]_n$ .<sup>149</sup> When the reaction was repeated with 'naked' cations  $\text{Cu}^+$ ,  $\text{Ag}^+$  and  $\text{Tl}^+$  (introduced as the  $[\text{TEF}]^-$  salts) in  $\text{CH}_2\text{Cl}_2$ , a single electron oxidation gave the corresponding triple decker cations in which the middle phosphorus deck adopted a *bis*-allylic distorted  $\text{cycloP}_6$  ring structure.<sup>150</sup> Changing the solvent to toluene avoided oxidation and afforded compounds with the  $\{\text{Cp}^*\text{Mo}\}_2(\mu, \eta^{6:6}\text{-P}_6)$  coordinated to the metal cation via a side-on interaction with the  $\text{P}_6$ -ring.

Although once again less well represented than the lighter P and As pnictogens, it is worthy to note that the anionic  $[\text{Bi}_6]^{4-}$  ring was obtained from reduction of  $\text{K}_5\text{Bi}_4$  with  $[\text{Zn}(\text{MeBDI}^{\text{Mes}})]_2$  or a mixture of  $\text{K}_3\text{Bi}_2$  and  $\text{K}_4\text{Ge}_9$  in liquid ammonia.<sup>76</sup> The rings adopts a 'strongly flattened' chair conformation with potassium cations above and below in an 'inverse-sandwich' type structure (Scheme 12).

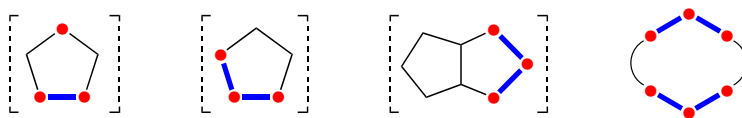


**Scheme 12** Synthesis of  $[\text{K}(18\text{-c-6})(\text{NH}_3)_2]_2[\text{K}_2(\text{Bi}_6)(\text{NH}_3)_4]$  showing 1-D chain.

### 1.19.4.3 Monocyclic heterocycles containing catena-pnictogen groups

This section contains reference to the chemistry of compounds in which the *catena*-pnictogen unit is a component of a larger heterocyclic system, and can be summarized according to (Fig. 25). Examples are limited to  $(\text{E})_n$  units where  $n = 2$  or 3, and include mono- and bicyclic systems.

Phosphohyl anions, analogues of the cyclopentadienyl anion in which one or more methine groups are placed by phosphorus,  $[\{\text{CH}\}_n\{\text{P}\}_{5-n}]^-$ , have been studied in depth for  $n = 1, 3$  and 5. However, the corresponding arsoyl anions are less common. The



**Fig. 25** Schematic representation of monocyclic heterocycles containing *catena*-pnictogen atoms included in **Section 1.19.4.3**.

first 1,2,4-triarsolyl and tetraarsolyl anions can now be added to this family of compounds, isolated as (a mixture of) the cesium salts from the one-pot reaction of  $\text{TippC(O)Cl}$  and  $\text{As}(\text{SiMe}_3)_3$  with  $\text{CsF}$  in refluxing dioxane.<sup>151</sup> The corresponding phospholyl anions were produced when  $\text{P}(\text{SiMe}_3)_3$  was used.

A versatile route to a series of 1,2,3-tripnictolide anions  $[\text{E}_3\text{C}_2\text{RR}']^-$  ( $\text{E} = \text{As}, \text{P}; \text{R/R}' = \text{H}, \text{Ph}$ ) was demonstrated from the reaction of the corresponding  $[\text{E}_7]^{3-}$  or  $[\text{HE}_7]^{2-}$  clusters with alkynes  $\text{RC}\equiv\text{CR}'$  ( $\text{R} = \text{R}' = \text{H}; \text{R} = \text{H}, \text{R}' = \text{Ph}; \text{R} = \text{R}' = \text{Ph}$ ).<sup>152</sup> The compounds were isolated directly as the potassium salts, which were reacted with  $\text{Mo}(\text{CO})_3(\text{L})_3$  ( $\text{L} = \text{CO}, \text{MeCN}$ ) to demonstrate  $\eta^5$ -coordination to the molybdenum in the anions  $[\text{Mo}(\eta^5\text{-E}_3\text{C}_2\text{R}_2)(\text{CO})_3]^-$ .

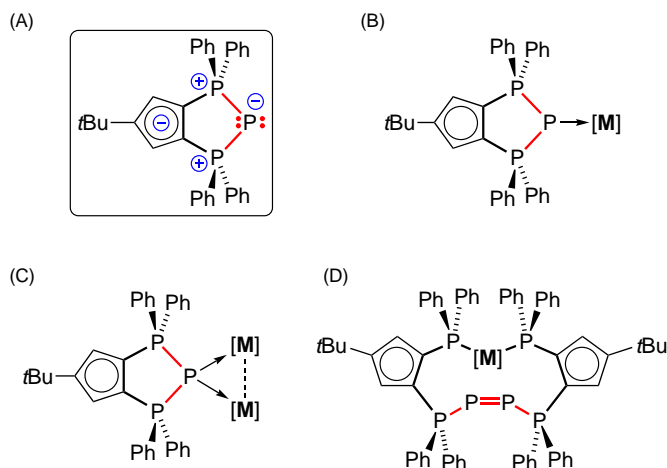
The coordination chemistry of the triphosphenium zwitterion  $t\text{Bu}(\text{C}_5\text{H}_2)(\text{Ph}_2\text{P})_2\text{P}$  (**Fig. 26A**), comprised of a 2,3,4-triphosphabicyclo[3.3.0]octane skeleton, has been explored. When reacted with metal carbonyl fragments the compounds adopts either a monodentate coordination through the P(I) center (**Fig. 26B**,  $[\text{M}] = \text{Cr}(\text{CO})_5, \text{Mo}(\text{CO})_5, \text{W}(\text{CO})_5, \text{Fe}(\text{CO})_4$ ), or bridges between two metals (**Fig. 26C**,  $[\text{M}]_2 = \text{Mn}_2(\text{CO})_8, \text{Co}_2(\text{CO})_6$ ).<sup>153</sup> However, reaction with the metal(0) complexes  $\text{Ni}(\text{cod})_2$  ( $\text{cod} = 1,5\text{-cyclooctadiene}$ ) or  $\text{Pd}_2(\text{dba})_3$  ( $\text{dba} = \text{dibenzylideneacetone}$ ) proceeded with insertion of the metal into one of the P– $\text{PR}_3$  bonds of two ligands, with a dimerization of the P(I) atoms to form a diphosphoniodiphosphene fragment that coordinates with an  $\eta^2$ -mode to the metal (**Fig. 26D**).<sup>154</sup>

A phosphorus rich heterocyclic ring has been prepared from the reaction of the triphosphenium bromide P(I) precursor  $[(\text{dppe})\text{P}]\text{Br}$  ( $\text{dppe} = \text{diphenylphosphinoethane}$ ) with  $\text{Li}[\text{N}(\text{PPh}_2)_2]$ .<sup>155</sup> The resulting  $[(\{\text{Ph}_2\text{P}\}_2\text{P})\text{N}]_2$  compound contains a *cyclo*-( $\text{P}_6\text{N}_2$ ) ring that was used to coordinate  $\text{MBr}$  ( $\text{M} = \text{Ag}, \text{Cu}$ ) metal fragments through the P(I) centers. In contrast, when  $[(\text{dppe})\text{P}]\text{Br}$  was reacted with  $\text{Li}[\text{N}(\text{PiPr}_2)_2]$  the product consisted of two five-membered  $\text{P}_4\text{N}$ -rings linked by a P–P bond.

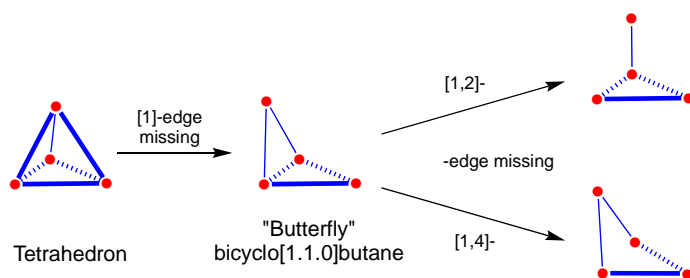
### 1.19.5 Polycyclic *catena*-pnictogens

In recognition of the prominent role that white phosphorus ( $\text{P}_4$ )<sup>156–158</sup> and yellow arsenic ( $\text{As}_4$ )<sup>159</sup> have contributed to the area of polycyclic *catena*-pnictogen compounds, the first two sections in this part of the chapter are dedicated to chemistry associated with these allotropes. **Section 1.19.5.1** summarizes developments in the chemistry of  $\text{P}_4$  and  $\text{As}_4$  in which the tetrahedral arrangement of pnictogen atoms is retained in the product. It includes examples of systems that have been used to encapsulate  $\text{E}_4$ -units, as well as complexes in which a metal fragment is coordinated to the  $\text{E}_4$  group without causing any E–E bond disruption.

**Section 1.19.5.2** collates the extensive work that has utilized the  $\text{P}_4$  and  $\text{As}_4$  tetrahedra as starting materials for the synthesis of *catena*-polyphosphorus and -polyarsenic compounds. The material has been further organized into areas describing the reactivity of with main-group (*s*- and *p*-block), transition-metal (*d*-block) and lanthanide/actinide (*f*-block) reagents with  $\text{P}_4$  and  $\text{As}_4$ . Many of the complexes isolated from these reactions retain a polycyclic  $\text{E}_4$ -arrangement of the pnictogen atoms, which are generated from the



**Fig. 26** Coordination chemistry of a triphosphenium zwitterion ( $[\text{M}] = \text{Cr}(\text{CO})_5, \text{Mo}(\text{CO})_5, \text{W}(\text{CO})_5, \text{Fe}(\text{CO})_4$ ;  $[\text{M}]_2 = \text{Mn}_2(\text{CO})_8, \text{Co}_2(\text{CO})_6$ ).



**Scheme 13** Relationship between the tetrahedron, bicyclo[1.1.0]butane, and [1,2]- and [1,4]-edge missing tetrahedra for  $E_4$  structures.

sequential cleavage of E–E bonds from the original tetrahedral cluster (**Scheme 13**). Thus breaking a single E–E bond generates the bicyclo[1.1.0]butane core, commonly referred to as a ‘butterfly’ arrangement of atoms. Breaking a second E–E bond can occur in two ways to generate [1,2]- and [1,4]-edge missing tetrahedra and examples of each type of structure are presented herein.

The remaining sections cover the synthesis (**Section 1.19.5.3**) and chemistry of non-metalated (**Section 1.19.5.4**) and metalated (**Section 1.19.5.5**) polycyclic pnictogen clusters.

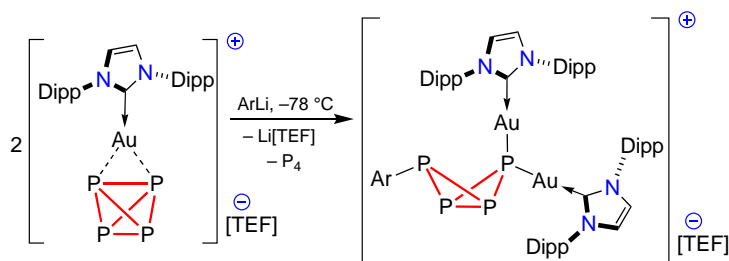
### 1.19.5.1 Coordination chemistry of $P_4$ and $As_4$ tetrahedra

Building on the seminal report that described the encapsulation of  $P_4$  in a self-assembled tetrahedral capsule that was first reported in 2009,<sup>160</sup> several new organic cages have been used to capture and stabilize the  $P_4$  unit. This has also been extended to the highly reactive  $As_4$  molecule. For example, anion coordination based tetrahedral cages that combine oligo-bis(urea) ligands and phosphate anions were used to incorporate both molecules.<sup>161</sup> Computational analysis indicated that in addition to the presence of a tetrahedral cavity, the presence of multiple aromatic groups enabled  $\sigma$ - $\pi$  and (lone-pair)- $\pi$  enhanced stabilization. A related study described a purely organic cage prepared from the condensation of a triamino linker with a triformyl precursor that was able to accommodate  $P_4$ .<sup>162</sup> This system differed from the previous example that can manipulate uptake and release of the  $E_4$  tetrahedra through acid-base modulation, as the presence of only covalent linkages in the latter cage produces a stable system that is not prone to lability or exchange processes.

The  $P_4$  and  $As_4$  units have also been incorporated into tetrahedral voids within the crystal structure of a copper/iron system. The reaction of  $CuCl$  with  $Cp^*Fe(\eta^5-P_5)$  in the presence of  $P_4$  or  $As_4$  afforded the isostructural compounds  $[Cu_2Cl_2\{Cp^*Fe(\eta^5-P_5)\}_2] \cdot (E_4)_x$  ( $E = P, x = 1$ ;  $E = As, x = 0.75$ ).<sup>163</sup> The resulting crystals are light and air stable for days, and furthermore this study represented the first structural determination of the  $As_4$  tetrahedron by single-crystal X-ray diffraction.

In addition to encapsulation within the voids of a crystalline material, the  $P_4$  tetrahedron has also been used as a ligand in the coordination sphere of transition-metal groups. It was shown that the coordination of  $P_4$  to iron centers in  $[CpFe(CO)(L)(\eta^1-P_4)][TEF]$  ( $L = CO, PPh_3$ ) decreased the average P–P bond length and blue-shifted the  $P_4$  breathing mode in the Raman spectrum.<sup>164</sup> This was interpreted as a shift toward a more ‘phosphonium-like’ situation upon coordination to the electron-poor metal centers.

NHC adducts  $MCl(\text{H}^1\text{Dipp})$  ( $M = Cu, Au$ ) react with  $P_4$  in the presence of  $Li[TEF]$ , which acts as a chloride scavenger, to give  $[M(\text{H}^1\text{Dipp})(\eta^2-P_4)][TEF]$ .<sup>165</sup> The crystal structure revealed distorted trigonal planar metal coordination environments and essentially equivalent M–P bond distances. Addition of  $LiAr$  ( $Ar = Dmp, Mes$ ) to the gold derivative gave the bimetallic compounds,  $\{Au(\text{H}^1\text{Dipp})\}_2(Ar)(\mu, \eta^{1:1:1}-P_4)[TEF]$ , in which two gold fragments were coordinated to the same P-atom (**Scheme 14**). Gold and copper phosphane/NHC compounds were also used in this context, showing analogous  $\eta^2-P_4$  coordination at the metal.<sup>166</sup>



**Scheme 14** Synthesis of  $[\{Au(\text{H}^1\text{Dipp})\}_2(Ar)(\mu, \eta^{1:1:1}-P_4)][TEF]$  ( $Ar = Dmp, Mes$ ).

Coordination chemistry with the manganese compound  $Cp^{\text{BIG}}Mn(CO)_2(THF)$  proceeded to give either the 1:1 adduct  $Cp^{\text{BIG}}Mn(CO)_2(\eta^1-P_4)$  or the bimetallic compound  $\{Cp^{\text{BIG}}Mn(CO)_2\}_2(\mu, \eta^{1:1}-P_4)$ .<sup>167</sup> NMR analysis confirmed that both species were fluxional in solution, attributed to a ‘tumbling’ of the coordinated  $P_4$  ligand. In a separate study, the ruthenium salt

$[\text{Ru}(\text{MeIme})_4(\text{H})(\eta^1\text{-P}_4)][\text{BAR}_4^{\text{F}}]$  was prepared as part of an experiment examining the  $^1\text{H}$  NMR chemical shift of the hydride ligand by density functional theory.<sup>168</sup> The results showed a good correlation between the computational and experimental data when a scalar relativistic correction was included, with an even greater improvement in the quantitative agreement when spin-orbit effects were included in the model.

It has been shown that two  $\text{As}_4$ -tetrahedra will coordinate with a previously unknown side-on mode in the homoleptic silver complex  $[\text{Ag}(\eta^2\text{-As}_4)_2][\text{TEF}]$ .<sup>169</sup> The reaction of this salt with  $\text{AuCl}(\text{PPh}_3)$  transferred an intact  $\text{As}_4$  unit to the gold center to form the heteroleptic gold salt,  $[\text{Au}(\eta^2\text{-As}_4)(\text{PPh}_3)][\text{TEF}]$ . Alternatively, an end-on coordination of the  $\text{As}_4$  group was observed when  $[\text{Ag}(\eta^2\text{-As}_4)_2][\text{TEF}]$  was reacted with  $\text{Cp}^*\text{Ru}(\text{dppe})\text{Cl}$ , giving the  $[\text{Cp}^*\text{Ru}(\text{dppe})(\eta^1\text{-As}_4)][\text{TEF}]$  salt (Fig. 27).<sup>170</sup> Reaction of this complex with  $[\text{CpRu}(\text{PPh}_3)_2][\text{TEF}]$  as a source of cationic ruthenium cleaved one of the As–As bonds to give  $\{[\text{Cp}^*\text{Ru}(\text{dppe})](\mu, \eta^{1:3}\text{-As}_4)\}[\text{CpRu}(\text{PPh}_3)_2][\text{TEF}]_2$ .

Related work showed that a Cu(I) fragment supported by a BDI-ligand was also able coordinate to  $\text{E}_4$ -tetrahedra in the bimetallic complexes  $\{\text{Cu}(\text{MeBDI}^{\text{Dipp}})\}_2(\mu, \eta^{2:2}\text{-E}_4)$  ( $\text{E} = \text{P}, \text{As}$ ), in which the two metals span opposite edges of the tetrahedron.<sup>171</sup> Low temperature work-up of the exchange reaction between  $\{\text{Cu}(\text{MeBDI}^{\text{Dipp}})\}_2(\mu, \eta^{2:2}\text{-P}_4)$  with additional  $\text{P}_4$  allowed the monometallic compound  $\{\text{Cu}(\text{MeBDI}^{\text{Dipp}})\}(\eta^2\text{-P}_4)$  to be isolated in which the ligand retains an  $\eta^2$ -bonding mode.

An investigation of the influence of the phosphane ligand on the reactivity of  $[\text{CpRu}(\text{PR}_3)_2]^+$  cations with  $\text{P}_4$  showed differing behavior between the  $\text{PPh}_3$  and the (less sterically demanding and more basic)  $\text{PMe}_3$  derivatives. The  $\text{PPh}_3$  derivative was known to form the mono-metallic cationic adduct,  $[\text{CpRu}(\text{PPh}_3)_4(\text{P}_4)]^+$ ,<sup>172</sup> whilst the  $\text{PMe}_3$  complex gave the bimetallic dication  $\{[\text{CpRu}(\text{PMe}_3)_2]_2(\mu, \eta^{1:1}\text{-P}_4)\}^{2+}$ .<sup>173</sup>

### 1.19.5.2 Synthesis of polycyclic *catena*-pnictogens from $\text{P}_4$ and $\text{As}_4$ tetrahedra

#### 1.19.5.2.1 Activation of $\text{P}_4$ and $\text{As}_4$ with main-group (s- and p-block) reagents

A series of electrophilic ‘carbonyl-decorated carbenes’ (CDCs) were investigated for the functionalization of  $\text{P}_4$  (Fig. 28).<sup>174</sup> Three equivalents of the symmetric carbene  $\text{CDC}^1$  cleaved three of the P–P bonds to give  $\text{P}\{\text{P}=\text{CDC}^1\}_3$  whilst the non-symmetric analogue  $\text{CDC}^2$  gave a  $\text{P}_8$ -species consisting of a [1,4]-edge missing tetrahedron of  $\text{P}_4$  decorated at each P-atom with ‘ $\text{P}=\text{CDC}^2$ ’ groups. When  $\text{P}_4$  was present in excess,  $\text{CDC}^1$  reacted to give the tetracarbene  $\text{P}_8$ -cluster consisting of a central  $\text{P}_4$ -ring with four  $\{\text{P}=\text{CDC}^1\}$  groups bonded to the P-atoms.<sup>175</sup> In contrast, the seven-membered  $\text{CDC}^3$  inserted the carbene C-atom into one of the P–P bonds, a mode reminiscent of the insertion of main group and transition-metals (see Section 1.19.5.2.2).

The stoichiometric reaction between chlorophosphanes  $\text{R}_2\text{PCL}$  ( $\text{R} = \text{Cy}, i\text{Pr}, \text{Et}, \text{Me}, \text{Ph}, \text{C}_6\text{F}_5, \text{Mes}, \text{Dipp}$ ),  $\text{GaCl}_3$  and  $\text{P}_4$  afforded a series of cationic  $[\text{R}_2\text{P}_5]^+$  cages.<sup>176</sup> The subsequent reaction with elemental sulfur or selenium was investigated, leading to the formation of  $[\text{R}_2\text{P}_5(\text{S/Se})_2]^+$  cations with a nortricyclane ‘ $\text{P}_5(\text{S/Se})_2$ ’-core.

Functionalization of  $\text{P}_4$  was achieved with aryllithium reagents when 1:1:1 mixtures of  $\text{P}_4$ ,  $\text{LiAr}$  ( $\text{Ar} = \text{Mes}^*, \text{Ter}^{\text{Mes}}$ ) and  $\text{BAR}_3$  ( $\text{Ar} = \text{Ph}, \text{C}_6\text{F}_5$ )<sup>178</sup> were combined. The products consisted of the lithium salt of the bicyclo[1.1.0]tetraphosphabutane anion, which was stabilized at phosphorus by the Lewis acidic borane. Alkylation at the nucleophilic P-site was achieved using  $[\text{Ph}_3\text{C}][\text{PF}_6]$  or  $\text{MeI}$ , leading to the formation of non-symmetric derivatives. The triphenylborane adduct  $\text{Li}[\text{Mes}^*(\text{P}_4)\text{-BPh}_3]$  reacted with an imidazolium salt or phenylisocyanate via a ‘P1-extrusion’ to generate the transient triphosphirane  $\text{Mes}^*\text{P}_3$ , which was isolated as the dimer or the Diels–Alder adduct with 1,3-cyclohexadiene.<sup>179</sup>

A related study showed that 1,4-dilithio-1,3-butadienes react with  $\text{P}_4$  to afford phospholyl lithium in a highly efficient one-pot procedure.<sup>180</sup> The residual ‘ $\text{LiP}_3$ ’ unit was found to aggregate to give a series of  $[\text{P}_7]^{3-}$ ,  $[\text{P}_{14}]^{4-}$ ,  $[\text{P}_{16}]^{2-}$  and  $[\text{P}_{26}]^{4-}$  clusters.<sup>181</sup>

Silanide anions  $[\text{SiR}_3]^-$  have also been applied in this area. The reaction of  $\text{P}_4$  with one equivalent of  $\text{Li}[\text{Si}t\text{Bu}_3]$  afforded a number of different products including the bicyclo[1.1.0]tetraphosphabutane  $\text{P}_4(\text{Si}t\text{Bu}_3)_2$ , the heptaphosphanortricyclane  $\text{P}_7(\text{Si}t\text{Bu}_3)_3$ , the tetraphosphides  $\text{Li}_3[\text{P}(\text{PSi}t\text{Bu}_3)_3]$ , and the pentaphosphacyclopentadienide  $\text{Li}[\text{P}_5]$ .<sup>182</sup> As part of the same study it was shown that the reaction of the siloxide  $\text{Li}[\text{OSi}t\text{Bu}_3]$  generated  $\text{Li}[\text{P}_7(\text{Si}t\text{Bu}_3)_2]$ . This salt crystallized as a cluster consisting

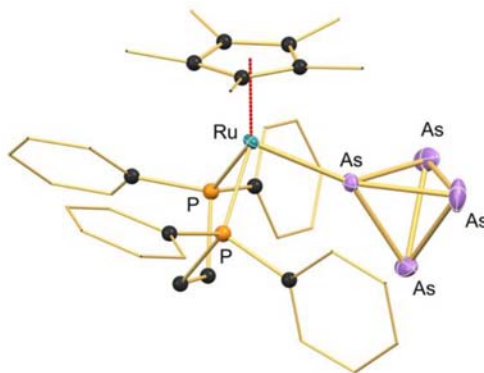
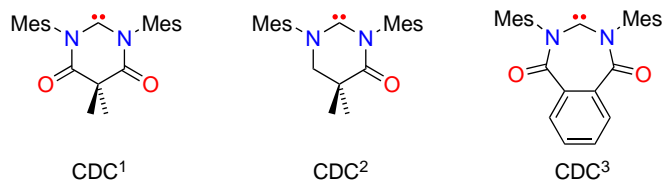


Fig. 27 Molecular structure of  $[\text{Cp}^*\text{Ru}(\text{dppe})(\eta^1\text{-As}_4)]^+$  ([TEF] anion omitted).



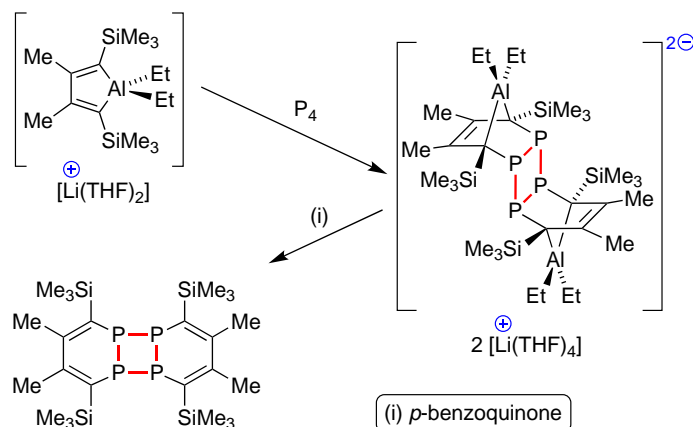
**Fig. 28** Carbonyl-decorated carbenes (CDCs) used to activate  $P_4$ .

of three crystallographically distinct and configurationally identical (chiral) lithium heptaphosphanotricyclanide units, a silanolate  $Li[OSi(t)Bu_3]$  with a benzene solvate.

The dimeric cyclodiphosphazane  $[DmpNPCl]_2$  was reacted with two equivalents of  $GaCl_3$  to afford a mixture of the cationic species  $[(DmpN)_2P_2Cl]^+$  and  $[(DmpN)_3P_3Cl_2]^+$ .<sup>183</sup> Each of these cations reacts with  $P_4$  via insertion of the charged P-atom into a P–P bond of the cluster to generate a new  $P_5$ -cluster fused to the  $PN_2$  or  $P_2N_3$ -ring.

The organomagnesium reagent  $Mg(MeBDI^{Dipp})(nBu)$  was reacted with  $P_4$  in a 2:1 ratio to afford  $\{Mg(MeBDI^{Dipp})\}_2(\mu, \eta^{2:2}-P_4(nBu)_2)$ , in which the alkyl groups are present on adjacent P-atoms in a non-planar  $P_4$ -ring.<sup>184</sup> Further reaction incorporated a second equivalent of  $P_4$  to give the  $[P_8(nBu)_2]^{2-}$  ligand. Reactions of the magnesium hydride  $[Mg(MeBDI^{Dipp})H]_2$  or the *N*-mesityl analogue  $Mg(MeBDI^{Mes})(nBu)$  with  $P_4$  were less discriminating, affording a mixture of products including structurally characterized primary phosphide  $[Mg(MeBDI^{Dipp})(PH_2)]_3$  and the  $[P_7]^{3-}$  Zintl ion complex,  $\{Mg(MeBDI^{Mes})\}_3(\mu_3, \eta^{2:2:2}-P_7)$ .

The aluminacyclopentadienes  $[Li(THF)_2][Al(C_4R_2\{SiMe_3\}_2)Et_2]$  ( $R = Me, \{CH_2\}_4$ ) react with  $P_4$  to give cyclotetraphosphanes containing an *anti*-arrangement of two 5,6-diphospha-7-aluminanorbornene groups (**Scheme 15**).<sup>185</sup> These products result from



**Scheme 15** 1,1-*P*-insertion/Diels-Alder/isomerization cascade process involving the reaction of aluminacyclopentadienes with  $P_4$ .

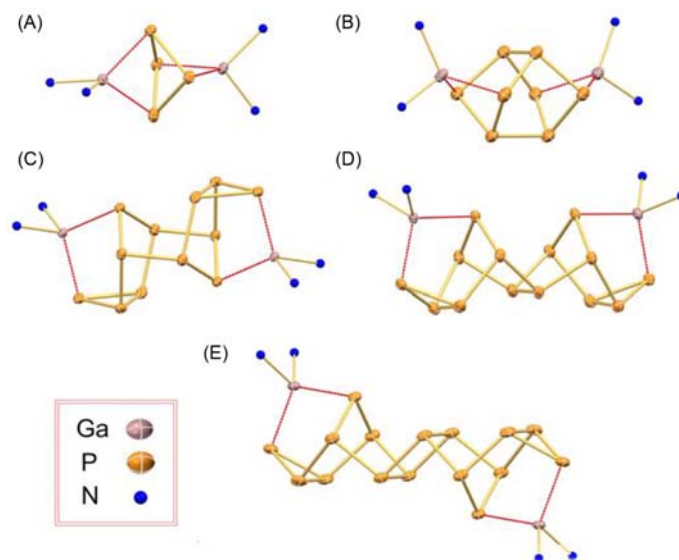
‘an unexpected 1,1-*P*-insertion/Diels-Alder/isomerization cascade process’. Furthermore, it was demonstrated that the phosphorus component can be removed from the metal as the neutral  $[(C_4R_2\{SiMe_3\}_2)P_2]_2$  compound on addition of *p*-benzoquinone.

The reaction of  $Ga(MeBDI^{Dipp})$  with  $P_4$  was first reported in 2010,<sup>186</sup> with the product identified as  $\{Ga(MeBDI^{Dipp})\}(\eta^{1:1}-P_4)$  resulting from the insertion of the gallium into one of the P–P bonds. However, a more detailed investigation that explored different reaction conditions showed a range of products are formed (**Fig. 29**), including the di-inserted  $\{Ga(MeBDI^{Dipp})\}_2(\mu, \eta^{2:2}-P_4)$  (**Fig. 29A**) and the larger polyphosphorus compounds  $\{Ga(MeBDI^{Dipp})\}_2(P_6)$ ,  $\{Ga(MeBDI^{Dipp})\}_2(P_8)$  (**Fig. 29B**),  $\{Ga(MeBDI^{Dipp})\}_2(P_{12})$  (**Fig. 29C**),  $\{Ga(MeBDI^{Dipp})\}_2(P_{14})$  (**Fig. 29D**) and  $\{Ga(MeBDI^{Dipp})\}_2(P_{16})$  (**Fig. 29E**).<sup>187</sup> The selective derivatization of the  $P_6$ -cage complex with Brønsted acids,  $MeOTf$ ,  $Ph_2ECl$  ( $E = P, As$ ) and  $Na[OCp]$  was also investigated, leading to the formation of a range of functionalized hexa- and heptaphosphanes.

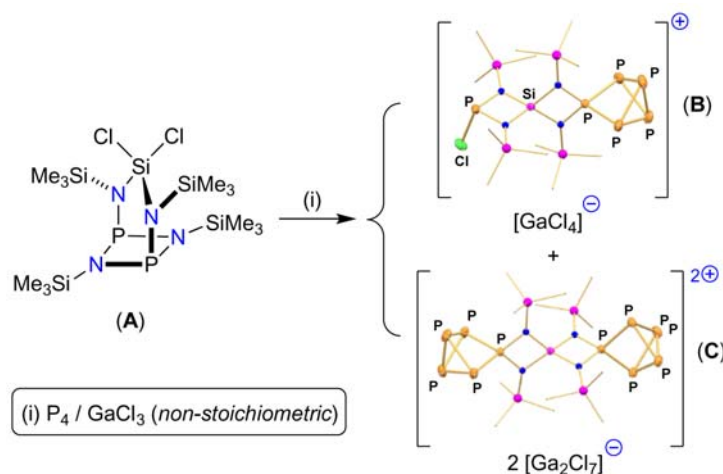
A bicyclic N–P–Si heterocycle, containing an  $[NP]_2$ -ring bridged at each phosphorus by the *N,N'*-bound ‘ $Cl_2Si\{Me_3SiN\}_2$ ’ unit (**A**), reacts with  $GaCl_3$  and  $P_4$  to afford products in which the phosphorus atoms from the four-membered ring have inserted into one of the P–P bonds of  $P_4$  (**Scheme 16**).<sup>188</sup> The reactions were performed with a 1:1 and 1:2 ratio of  $P_4$ , yielding  $[ClP(NSiMe_3)_2Si(NSiMe_3)_2P_5]^+$  (**B**) and  $[P_5(NSiMe_3)_2Si(NSiMe_3)_2P_5]^{2+}$  (**C**), respectively.

The two-coordinate acyclic iminosiloxysilylene ( $\{IDipp\}=\text{N}\}Si(OSi(t)Bu_3)$  oxidizes  $P_4$  to give the four-coordinate silicon compounds with an  $\eta^2-P_4$  ligand generated by insertion of Si into a P–P bond.<sup>189</sup> The germylene  $Ge(Ter^{Mes})_2$  gives an analogous product that was shown to be a reversible process that reverts to the starting materials on exposure to UV light.<sup>190</sup> The  $P_4$ -activated product was however trapped as an adduct at  $M(CO)_5$  ( $M = Cr, Mo, W$ ) and  $AuCl$  fragments.<sup>191</sup> Similar reactions between the vinyl silylsilylene  $(^MeIDipp)Si\{Si(SiMe_3)_3\}$  and  $P_4$  afforded a new bonding mode for the [1,2]-edge missing tetrahedral  $P_4$ -group that





**Fig. 29** Core structures of the products of the reaction of  $\text{Ga}(\text{MeBDI}^{\text{Dipp}})$  with  $\text{P}_4$ . (A)  $\{\text{Ga}(\text{MeBDI}^{\text{Dipp}})\}_2(\text{P}_4)$ ; (B)  $\{\text{Ga}(\text{MeBDI}^{\text{Dipp}})\}_2(\text{P}_8)$ ; (C)  $\{\text{Ga}(\text{MeBDI}^{\text{Dipp}})\}_2(\text{P}_{12})$ ; (D)  $\{\text{Ga}(\text{MeBDI}^{\text{Dipp}})\}_2(\text{P}_{14})$ ; (E)  $\{\text{Ga}(\text{MeBDI}^{\text{Dipp}})\}_2(\text{P}_{16})$ .

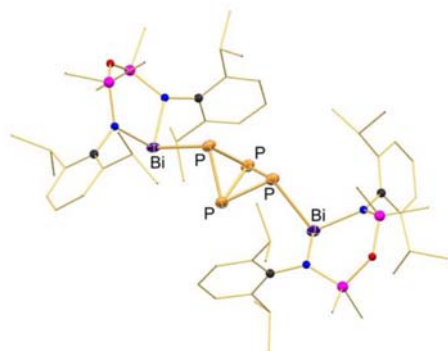


**Scheme 16** Reaction of a bicyclic N–P–Si heterocycle (A) with mixtures of  $\text{P}_4/\text{GaCl}_3$  affording cationic (B) and dicationic (C) products from the insertion of phosphorus into a P–P bond of  $\text{P}_4$ .

binds with a P–P side-on and terminal Si–P bond as a result of 1,2-migration of the hypersilyl ligand.<sup>192</sup> In contrast, the reaction of the amidinate supported silylene  $(\text{PhC}\{\text{N}t\text{Bu}\}_2)\text{Si}-\text{N}\{\text{SiMe}_3\}_2$  with  $\text{As}_4$  gave an unprecedented  $\text{As}_{10}$ -cage structure consisting of an  $\text{As}_7$ -nortricyclane core with three-coordinated arsasilene groups.<sup>193</sup> The same study reported the reaction of the disilene  $[(\{\text{Me}_3\text{Si}\}_2\text{N})(\eta^1\text{-Cp}^*)\text{Si}]_2$  with  $\text{As}_4$  which gave low yields of the bicyclo[1.1.0]-1,3-diarsa-2,4-disila butane,  $[(\{\text{Me}_3\text{Si}\}_2\text{N})(\eta^1\text{-Cp}^*)\text{SiAs}]_2$ .

The organic-substituted bicyclo[1.1.0]tetraarsabutane compound  $(\text{Cp}^{\text{big}})_2\text{As}_4$  was formed when a solution of  $[\text{Cp}^{\text{big}}]\bullet$  radicals was reacted with  $\text{As}_4$ .<sup>194</sup> The fold angle in the  $\text{As}_4$ -core ( $97.574(13)^\circ$ ) is greater than the corresponding angle in  $\{\text{Cp}^{\text{big}}\text{Fe}(\text{CO})_2\}$  ( $96.10(7)^\circ$ )  $\{\text{Cp}^{\text{BIG}}\text{Fe}(\text{CO})_2\}$  ( $89.033(13)^\circ$ ) and  $\{\text{Cp}^*\text{Cr}(\text{CO})_3\}$  ( $90.50(3)^\circ$ – $92.39(3)^\circ$ ) derivatives, consistent with the high steric demand of the  $\eta^1\text{-Cp}^{\text{big}}$  ligand. This work followed an earlier study describing the reaction of  $\text{NaCp}^{\text{R}}$  ( $\text{Cp}^{\text{R}} = \text{Cp}^{\text{BIG}}, \text{Cp}^{\text{big}}, \text{Cp}^*$  and  $\text{Cp}^{4\text{IPr}}$ ) with  $\text{P}_4$  (performed in the presence of  $\text{CuBr}$  or  $\text{FeBr}_3$  to generate the  $[\text{Cp}^{\text{R}}]\bullet$  radicals), which gave the corresponding  $(\text{Cp}^{\text{R}})_2\text{P}_4$  bicyclo[1.1.0]tetraphosphabutane compounds.<sup>195</sup>

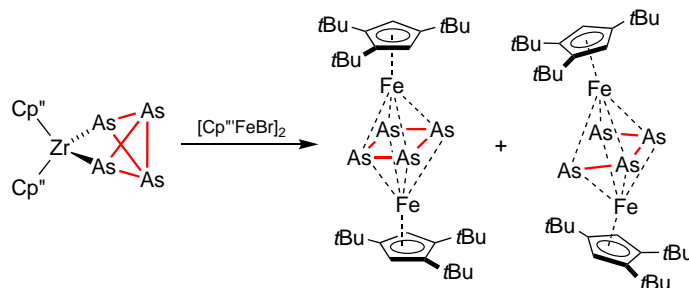
Finally, it was reported that an isolable bismuth(II) radical<sup>196</sup> promoted the homoleptic cleavage of a P–P bond to afford the substituted bicyclo[1.1.0]tetraphosphabutane core with Bi–P bonds to the wing-tip phosphorus atoms (Fig. 30).<sup>22</sup> NMR spectroscopy performed on a sample of the isolated crystals confirmed a mixture of the product and starting materials was present in solution, indicating a reversible process, confirmed with variable temperature studies.



**Fig. 30** Molecular structure of  $\{\text{Bi}(\text{NON}^{\text{Dipp}})\}_2(\mu, \eta^{1:1}\text{-P}_4)$ .

#### 1.19.5.2.2 Activation of $\text{P}_4$ and $\text{As}_4$ with transition-metal (d-block) reagents

An improved synthesis of  $\text{Cp}''_2\text{Zr}(\eta^{1:1}\text{-P}_4)$  was developed by heating solutions of  $\text{Cp}''_2\text{Zr}(\text{CO})_2$  with  $\text{P}_4$  in xylene.<sup>197</sup> The capacity of the compound to behave as a phosphorus-centered Lewis base toward various transition-metal fragments ( $\text{W}(\text{CO})_5$ ,  $\text{CpMn}(\text{CO})_2$ ,  $\text{Fe}(\text{CO})_4$ ) and main group Lewis acids  $\text{AlR}_3$  ( $\text{R} = \text{Me}, \text{Et}$ ) was probed, resulting in polymetallic complexes with P–M bonds formed to phosphorus atoms from each of the two inequivalent positions of the  $\text{P}_4$  ligand in various combinations. Analogous reactions with  $\text{As}_4$  afforded  $\text{Cp}''_2\text{Zr}(\eta^{1:1}\text{-As}_4)$  in good yield.<sup>198</sup> This compound served as a transfer reagent for the ‘ $\text{As}_4$ ’ group, demonstrated by reactivity with  $[\text{Cp}''' \text{Fe}(\mu\text{-Br})]_2$  to afford a mixture of  $(\text{Cp}''' \text{Fe})_2(\mu, \eta^{4:4}\text{-As}_4)$  (with a non-cyclic  $\text{As}_4$ -unit between the two iron centers) and  $(\text{Cp}''' \text{Fe})_2\{\mu, \eta^{4:4}\text{-cyclo}(\text{As})_4\}$  (Scheme 17). The reaction with  $[\text{Cp}^{\text{Bz}} \text{Fe}(\mu\text{-Br})]_2$  gave exclusively  $(\text{Cp}^{\text{Bz}} \text{Fe})_2(\mu, \eta^{4:4}\text{-As}_4)$ .

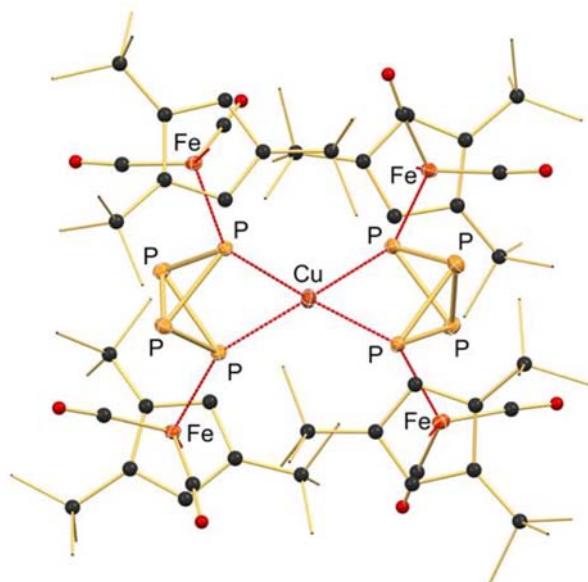


**Scheme 17** Transfer of an ‘ $\text{As}_4$ -group’ from Zr to Fe and synthesis of  $(\text{Cp}''' \text{Fe})_2(\mu, \eta^{4:4}\text{-As}_4)$  and  $(\text{Cp}''' \text{Fe})_2\{\mu, \eta^{4:4}\text{-cyclo}(\text{As})_4\}$ .

Bulky Lewis acids (LA) ( $\text{LA} = \text{BPh}_3, \text{B}(\text{C}_6\text{F}_5)_3$ ) were used to trap the products of  $\text{P}_4$  activation by  $[\text{Cp}^* \text{Fe}(\text{CO})_2]^-$ , affording the anionic  $[\text{Cp}^* \text{Fe}(\text{CO})_2(\eta^{1:1}\text{-P}_4 \cdot \text{LA})]^-$  adducts in which the bicyclo[1.1.0]tetraphosphabutane framework is supported by the iron and boron groups at the wing-tip positions.<sup>199</sup> The nucleophilic phosphorus was protonated using  $[\text{Me}_3\text{NH}][\text{BF}_4]$  to generate the neutral  $\text{Cp}^* \text{Fe}(\text{CO})_2(\eta^{1:1}\text{-P}_4\text{H})$  compounds that exist as *exo,endo*- and *exo,exo*-isomers.

Synthesis of iron and chromium substituted phosphorus and arsenic species,  $\{\text{Cp}''' \text{Fe}(\text{CO})_2\}_2(\mu, \eta^{1:1}\text{-E}_4)$  and  $\{\text{Cp}^* \text{Cr}(\text{CO})_2\}_2(\mu, \eta^{1:1}\text{-E}_4)$  ( $\text{E} = \text{As}, \text{P}$ ) with the bicyclo[1.1.0]butane arrangement of pnictogen atoms was achieved from the reaction of  $\text{P}_4$  and  $\text{As}_4$  with M–M bonded dimers,  $[\text{Cp}''' \text{Fe}(\text{CO})_2]_2$  and  $[\text{Cp}^* \text{Cr}(\text{CO})_3]_2$ .<sup>200</sup> Photolysis of the Fe/As complex resulted in loss of CO and formation of  $\{\text{Cp}''' \text{Fe}(\text{CO})_2\}\{\text{Cp}''' \text{Fe}(\text{CO})\}(\mu, \eta^{1:2}\text{-As}_4)$  and  $\{\text{Cp}''' \text{Fe}(\text{CO})_2\}_2\{\mu, \eta^{1:1:2:2}\text{-As}_8\}$ , the latter containing a  $[\text{As}_8]^{4-}$  cuneane core with terminal ‘ $\text{Cp}''' \text{Fe}(\text{CO})_2$ ’ groups and bridging ‘ $\text{Cp}''' \text{Fe}(\text{CO})$ ’ groups. The Cr/As analogue gave the related  $\{\text{Cp}^* \text{Cr}(\text{CO})_3\}_4(\mu, \eta^{1:1:1:1}\text{-As}_8)$  when left under ambient conditions in solution. The  $\{\text{Cp}''' \text{Fe}(\text{CO})_2\}_2(\mu, \eta^{1:1}\text{-E}_4)$  compounds have been examined as chelating ligands in coordination chemistry.<sup>201</sup> Both mono- ( $\text{E} = \text{P}$ ) and bis- ( $\text{E} = \text{P}, \text{As}$ ) adducts were formed when reacted with  $[\text{Cu}(\text{MeCN})_4][\text{BF}_4]$ , showing the expected coordination at copper via the ‘wing-tip’ pnictogen atoms (Fig. 31). Reactivity of the phosphorus analogue with other transition-metal fragments has allowed further elaboration of the intact  $\mu, \eta^{1:1}\text{-P}_4$  ligand in the compounds  $\{\text{Cp}''' \text{Fe}(\text{CO})_2\}_2(\mu, \eta^{1:1:1:1}\text{-P}_4)\{\text{Au}(\text{PPh}_3)\}$ ,  $\{\text{Cp}''' \text{Fe}(\text{CO})_2\}_2(\mu, \eta^{1:1:1:1}\text{-P}_4)\{\text{M}(\text{CO})_4\}$  ( $\text{M} = \text{Cr}, \text{Mo}, \text{W}$ ) and the spiro complex  $[(\{\text{Cp}''' \text{Fe}(\text{CO})_2\}_2\mu, \eta^{1:1:1:1}\text{-P}_4)_2\text{Ag}][\text{PF}_6]$ .<sup>202</sup> On the other hand, reaction with  $\text{Co}_2(\text{CO})_8$  and  $\text{Fe}_2(\text{CO})_9$  caused a rearrangement of the  $\text{P}_4$ -group to give a folded *cyclo*-( $\text{P}_4$ ) in  $\{\text{Cp}''' \text{Fe}(\text{CO})_2\}_2\{\text{Co}(\text{CO})_3\}_2(\mu, \eta^{2:2:1:1}\text{-P}_4)$  and a tetraphosphole structure in  $\{\text{Cp}''' \text{Fe}(\text{CO})_2\}_2(\mu, \eta^{1:1:1:3}\text{-P}_4\text{CO})\{\text{Fe}(\text{CO})_4\}\{\text{Fe}(\text{CO})_3\}$ .

For reactions in which the low-valent iron is generated in situ, it was noted that nature of the reducing agent can lead to the formation of different activation products when exposed to  $\text{P}_4$ . For example, the reduction of  $[\text{Cp}^{\text{BIG}} \text{Fe}(\mu\text{-Br})]_2$  with potassium naphthalenide followed by the addition of  $\text{P}_4/18\text{-crown-6}$  afforded  $[\text{K}(18\text{-c-6})][\text{Cp}^{\text{BIG}} \text{Fe}(\eta^4\text{-P}_4)]$  as a ‘pseudo-triple decker’ complex with a *cyclo*-( $\text{P}_4$ ) ligand bridging the Fe and K centers.<sup>203</sup> When sodium amalgam was used in the presence of  $\text{P}_4$  the *bis*-iron complex

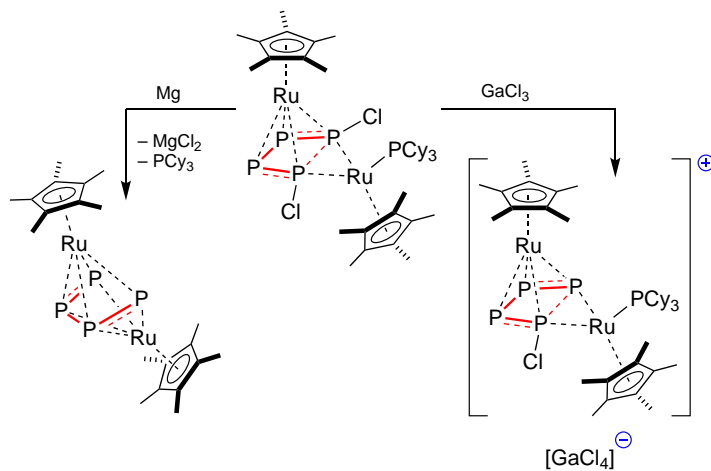


**Fig. 31** Molecular structure of  $[(\text{Cp}^{\text{'''}}\text{Fe}(\text{CO})_2)_2(\mu_3, \eta^{1:1}\text{-P}_4)_2\text{Cu}]^+$  ( $[\text{BF}_4]^-$  anion omitted).

$[\text{Na}_2(\text{THF})_5][\{\text{Cp}^{\text{BIG}}\text{Fe}\}_2(\mu, \eta^{4:4}\text{-P}_4)]$  resulted. The analogous neutral  $\{\text{Cp}^{\text{BIG}}\text{Fe}(\text{CO})_2\}_2(\mu, \eta^{1:1}\text{-E}_4)$  ( $\text{E} = \text{P}, \text{As}$ ) species were formed when the isolated low-valent complex  $[\text{Cp}^{\text{BIG}}\text{Fe}(\text{CO})_2]_2$  was reacted directly with  $\text{P}_4$  or  $\text{As}_4$ .<sup>204</sup> Reactivity studies of these two complexes showed different reaction pathways under thermolysis and photolysis conditions.<sup>205</sup> For example, exposing the compounds to UV light resulted in complete decarbonylation of the iron centers to afford the triple decker  $\{\text{Cp}^{\text{BIG}}\text{Fe}\}_2(\mu, \eta^{4:4}\text{-E}_4)$  compounds that contain either the *cis*-tetraphosphabutadiene ligand ( $\text{E} = \text{P}$ ) or a *cyclo*- $(\text{As})_4$  ligand ( $\text{E} = \text{As}$ ); the phosphorus reaction also afforded a small amount of bimetallic  $\{\text{Cp}^{\text{BIG}}\text{Fe}\}\{\text{Cp}^{\text{BIG}}\text{Fe}(\text{CO})_2\}(\mu, \eta^{4:1}\text{-P}_4)$ . In contrast, heating the arsenic analogue (in the presence of excess  $\text{As}_4$ ) gave a mixture of the arsenic rich iron compounds,  $\text{Cp}^{\text{BIG}}\text{Fe}(\eta^5\text{-As}_5)$ , the same  $\{\text{Cp}^{\text{BIG}}\text{Fe}\}_2(\mu, \eta^{4:4}\text{-As}_4)$  derivative that was also isolated from the photolysis experiment, and  $\{\text{Cp}^{\text{BIG}}\text{Fe}\}_3(\mu_3, \eta^{4:4:4}\text{-As}_6)$  containing a trigonal prismatic core of As-atoms triply capped by  $\text{FeCp}^{\text{BIG}}$  units.

The products of the reaction of low-valent iron complexes  $\text{Fe}(\text{R}_1\text{BDI}^{\text{R}2}) \cdot (\text{toluene})$  ( $\text{R}_1 = \text{Me}, \text{R}_2 = \text{Dmp}; \text{R}_1 = \text{H}, \text{R}_2 = \text{Dmp}; \text{R}_1 = \text{Me}, \text{R}_2 = \text{Dipp}$ ) with  $\text{P}_4$  were shown to be dependent on the  $\text{R}_1$  and  $\text{R}_2$  substitution of the  $\beta$ -diketiminato ligand.<sup>206</sup> When flanking Dmp groups are present reactions proceed to afford the tetrametallic  $\{\text{Fe}(\text{R}_1\text{BDI}^{\text{Dmp}})\}_4(\mu_4, \eta^{2:2:2:2}\text{-P}_8)$  with a realgar-type  $\text{P}_8$ -cluster, irrespective of the backbone substituent,  $\text{R}_1$ . When the bulkier  $\text{MeBDI}^{\text{Dipp}}$ -ligand is employed, the bimetallic compound  $\{\text{Fe}(\text{MeBDI}^{\text{Dipp}})\}_2(\mu, \eta^{4:4}\text{-P}_4)$  formed with a *cyclo*- $[\text{P}_4]^{2-}$  ligand, whereas  $\text{Fe}(\text{HBDI}^{\text{Dipp}})(\eta^6\text{-toluene})$  cleaved the  $\text{P}_4$  tetrahedron into two  $\text{P}_2$  units under mild conditions to afford the bimetallic compound  $\{\text{HBDI}^{\text{Dipp}}\text{Fe}\}_2(\mu_2, \eta^{2:2}\text{-P}_2)_2$ .<sup>207</sup>

The rhenium(II) complex  $\text{CpRe}(\text{MeBDI}^{\text{Dipp}})$  reacts with  $\text{P}_4$  to give the Re(V) product  $\text{CpRe}(\text{MeBDI}^{\text{Dipp}})(\eta^3\text{-P}_3)$  with a *cyclo* $\text{P}_3$  ligand.<sup>208</sup> This complex was oxidized further with  $\text{AgOTf}$  to give the Re(VI) salt,  $[\text{CpRe}(\text{MeBDI}^{\text{Dipp}})(\eta^3\text{-P}_3)][\text{OTf}]$ .

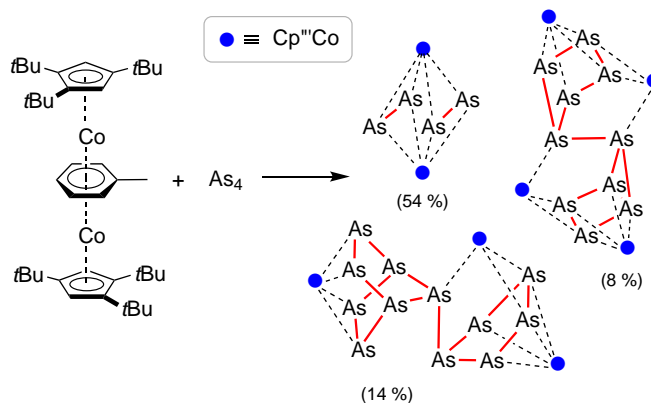


**Scheme 18** Sequential removal of chloride from  $[\text{Cp}^*\text{Ru}(\text{PCy}_3)]\{\text{Cp}^*\text{Ru}\}(\mu, \eta^{2:4}\text{-P}_4\text{Cl}_2)$ .

Work with ruthenium compounds showed the two equivalents of the sixteen electron complex  $\text{Cp}^*\text{RuX}(\text{PCy}_3)$  ( $X = \text{Cl}, \text{Br}$ ) react with  $\text{P}_4$  to generate the bimetallic complex  $\{\text{Cp}^*\text{Ru}(\text{PCy}_3)\}\{\text{Cp}^*\text{Ru}\}(\mu, \eta^{2:4}\text{-P}_4\text{X}_2)$ , in which the planar  $\text{P}_4\text{X}_2$  ligand is best described as a tetraphosphabutadiene,  $\text{X}-\text{P}=\text{P}-\text{P}=\text{P}-\text{X}$ .<sup>209</sup> In further reactivity, the halogen atom was sequentially removed from the phosphorus ligand using either  $\text{GaCl}_3$  (remove one halide) or  $\text{Mg}$  (remove two halides) (Scheme 18). The study also described the reaction with  $n\text{BuLi}$  that alkylated the  $\text{P}_4$  group to generate the  $[\{\text{Cp}^*\text{Ru}\}(\mu_3, \eta^{2:4}\text{-P}_4\{\text{nBu}\}_2)\{\text{RuCp}^*\}]_2$  dimeric cluster.

Low-valent cobalt compounds have also been investigated as reagent for the activation of  $\text{E}_4$  ( $\text{E} = \text{P}, \text{As}$ ). The formally zero-valent cobalt complex,  $\text{K}_2[\{\text{Co}(\text{Me}_6\text{BDI}^{\text{Dipp}})\}_2(\mu, \eta^{1:1}\text{-N}_2)]$  was reacted with  $\text{P}_4$  to give a mixture of the P-containing anions  $[\text{K}(\text{THF})_6][\{\text{Co}(\text{Me}_6\text{BDI}^{\text{Dipp}})\}_2(\mu, \eta^{4:4}\text{-P}_4)]$  and  $[\text{K}(\text{THF})_6][\{\text{Co}(\text{Me}_6\text{BDI}^{\text{Dipp}})\}_2(\mu, \eta^{3:3}\text{-P}_3)]$  containing the *cyclo*-( $\text{P}$ )<sub>4</sub> and *cyclo*-( $\text{P}$ )<sub>3</sub> groups, respectively.<sup>210</sup> When  $\text{Co}(\text{RBDI}^{\text{Dipp}}) \cdot (\text{toluene})$  ( $\text{R} = \text{H}, \text{Me}$ ) or  $[\text{Co}(\text{Me}_6\text{BDI}^{\text{Dipp}})]_2$  were used, the neutral species  $\{\text{Co}(\text{RBDI}^{\text{R}2})\}_2(\mu, \eta^{4:4}\text{-P}_4)$  ( $\text{R}2 = \text{Dipp}, \text{Dep}$ ) were obtained.<sup>211</sup> In a separate study, the cobaltate anion,  $[(\text{PHDI})\text{Co}(\eta^4\text{-cod})]^-$  ( $\text{PHDI} = (\text{Dipp})_2\text{phenanthrene-9,10-diiimine}$ ) was reacted with  $\text{P}_4$  to generate the *cyclo*-( $\text{P}$ )<sub>4</sub> complex,  $[\text{K}(18\text{-c-6})][(\text{PHDI})\text{Co}\{\eta^4\text{-cyclo}-(\text{P})_4\}]$ .<sup>212</sup> Addition of  $\text{R}_2\text{PCL}$  ( $\text{R} = \text{Cy}, \text{tBu}, \text{pH}, \text{Mes}, \text{NiPr}_2$ ) to this product functionalized the phosphorus ring to give  $(\text{PHDI})\text{Co}(\eta^4\text{-P}_5\text{R}_2)$ , which contains the  $\text{P}_5$ -ring in an envelope conformation.

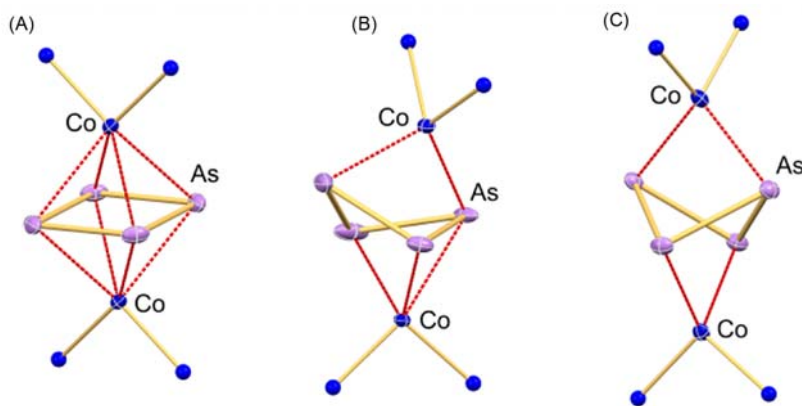
The cobalt complex  $\{\text{Cp}^*\text{Co}\}_2(\mu, \eta^{4:4}\text{-C}_7\text{H}_8)$  was reacted with  $\text{P}_4$  at  $0^\circ\text{C}$  to give the *cyclo*-( $\text{P}$ )<sub>4</sub> complex  $\text{Cp}^*\text{Co}(\eta^4\text{-P}_4)$ .<sup>213</sup> When the reaction mixture was allowed to warm to room temperature, the compound converted to two isomeric species with formula  $\{\text{Cp}^*\text{Co}\}_2(\mu, \eta^{4:2:1}\text{-P}_8)$ , which differ in how the  $\text{P}_5\text{-P}_3$  ring topology binds to the cobalt centers. When the same cobalt complex was reacted with  $\text{As}_4$ , a mixture of arsenic  $\text{As}_n$ -ligands were formed at the metal centers.<sup>214</sup> Structurally characterized examples isolated from the mixture include  $[\text{Cp}^*\text{Co}(\mu, \eta^{2:2}\text{-As}_2)]_2$ ,  $\{\text{Cp}^*\text{Co}\}_4(\mu_4, \eta^{4:4:2:2:1:1}\text{-As}_{10})$  and  $\{\text{Cp}^*\text{Co}\}_3(\mu_3, \eta^{4:4:2:1}\text{-As}_{12})$ , which were all separated from the mixture and fully characterized. The first of these compounds was shown to be a triple decker compound with two  $\text{As}_2$ -units in the middle deck, each with bond lengths consistent with double bonds. The  $\text{As}_{10}$ -unit in the second complex was considered as an 'all arsenic' analogue of dihydrofulvalene consisting of two  $\text{As}_5$ -rings joined by an  $\text{As}-\text{As}$  bond and the last compound from this list was related to the  $\text{As}_{10}$ -complex by replacing one of the ' $\text{As}_5(\text{Cp}^*\text{Co})_2$ ' units with a norbornane-like ' $\text{As}_7(\text{Cp}^*\text{Co})$ ' unit (Scheme 19).



**Scheme 19** Mixture of  $[\text{Cp}^*\text{Co}(\mu, \eta^{2:2}\text{-As}_2)]_2$ ,  $\{\text{Cp}^*\text{Co}\}_4(\mu_4, \eta^{4:4:2:2:1:1}\text{-As}_{10})$  and  $\{\text{Cp}^*\text{Co}\}_3(\mu_3, \eta^{4:4:2:1}\text{-As}_{12})$  generated from the reaction of  $\text{As}_4$  with  $\{\text{Cp}^*\text{Co}\}_2(\mu, \eta^{4:4}\text{-C}_7\text{H}_8)$ .

It was also shown that low-valent cobalt compounds of general formula  $\text{Co}(\text{R}_1\text{BDI}^{\text{R}2})(\text{toluene})$  ( $\text{R}_1 = \text{H}, \text{Me}$ ;  $\text{R}_2 = \text{Dmp}, \text{Dipp}$ ) oxidatively cleave  $\text{As}-\text{As}$  bonds in  $\text{As}_4$ .<sup>215</sup> The BDI-ligand substitution pattern was found to influence the  $\text{Co}_2\text{As}_4$  core of the products (Fig. 32), with *trans*-octahedral (Fig. 32A.  $\text{R}_1 = \text{H}, \text{R}_2 = \text{Dipp}$ ), trigonal prismatic (Fig. 32B.  $\text{R}_1 = \text{Me}, \text{R}_2 = \text{Dmp}$ ) and 'asterane-like' (Fig. 32C.  $\text{R}_1 = \text{Me}, \text{R}_2 = \text{Dipp}$ ) structures reported. Heating the latter compound thermally extruded a single 'As' atom to afford  $\{\text{Co}(\text{Me}_6\text{BDI}^{\text{Dipp}})\}_2(\mu, \eta^{3:3}\text{-As}_3)$ . This study was subsequently extended to the corresponding low-valent iron compounds,  $\text{Fe}(\text{R}_1\text{BDI}^{\text{R}2})(\text{toluene})$ .<sup>216</sup> In this case, the sterically more demanding Dipp-substituted ligands afford bimetallic  $\{\text{Fe}(\text{R}_1\text{BDI}^{\text{Dipp}})\}_2(\mu_2, \eta^{4:4}\text{-As}_4)$  complexes containing the *cyclo*-( $\text{As}$ )<sub>4</sub> group, whereas the sterically less demanding Dmp substituted ligands lead to formation of the realgar-type  $\text{As}_8$  cluster,  $\{\text{Fe}(\text{R}_1\text{BDI}^{\text{Dmp}})\}_4(\mu_4, \eta^{2:2:2:2}\text{-As}_8)$ . A related  $\{\text{Fe}(\text{tBuBDI}^{\text{Dipp}})\}_2(\mu_2, \eta^{2:2}\text{-As}_2)$  compound was accessed from the reaction of  $\text{Fe}(\text{tBuBDI}^{\text{Dipp}})\text{Cl}$  with  $\text{Na}[\text{OCAs}] \cdot (\text{dioxane})_{2.1}$  (a source of the arsaethynolate anion  $[\text{AsCO}]^-$ ).<sup>217</sup> This  $\text{Fe}_2\text{As}_2$ -species was used as a single source precursor to FeAs nanostructured materials.

Reaction of the coordinatively and electronically unsaturated nickel(0) complexes  $\text{Ni}(\text{NHC})_2$  ( $\text{NHC} = {}^{\text{H}}\text{Imes}, {}^{\text{H}}\text{IDipp}$ ) with  $\text{P}_4$  gave a series of  $\text{Ni}_x\text{P}_y$  cluster compounds.<sup>218</sup> For example, reacting  $\text{Ni}({}^{\text{H}}\text{Imes})_2$  with  $\text{P}_4$  in toluene gave  $\text{Ni}_3\text{P}_4({}^{\text{H}}\text{Imes})_3$ , consisting of a  $\text{Ni}_3$  triangle capped on each face by a phosphorus atom, one of which is part of a  $\text{P}_3$ -chain. Repeating the reaction in THF afforded a mixture of  $\text{Ni}_3\text{P}_6({}^{\text{H}}\text{Imes})_3$ , comprised of a distorted trigonal prism of six P-atoms capped on each face by Ni groups, and  $\{\text{Ni}({}^{\text{H}}\text{Imes})\}_2(\mu, \eta^{5:5}\text{-P}_5)$ . Changing to the bulkier  ${}^{\text{H}}\text{IDipp}$  carbene gave  $\text{Ni}_3\text{P}_8({}^{\text{H}}\text{IDipp})_3$  as an eleven-vertex *closo*-cluster. The related Ni(I) complexes  $\text{CpNi}(\text{NHC})$  ( $\text{NHC} = {}^{\text{H}}\text{Imes}, {}^{\text{H}}\text{IDipp}$ ) reacted with  $\text{P}_4$  to give the bicyclo[1.1.0]tetraphosphabutane products,



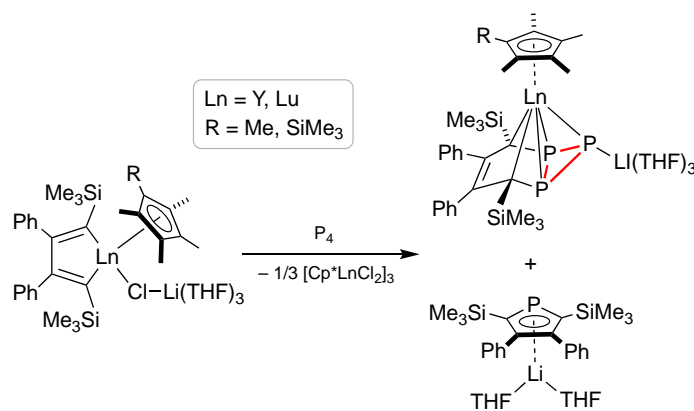
**Fig. 32** Different  $\text{Co}_2\text{As}_4$  core structures in  $(\text{Co}(\text{R}_1\text{BDI}^{\text{R}2}))_2(\mu\text{-}\eta^{\text{x,y}}\text{-As}_4)$ . (A)  $\text{R}_1 = \text{H}$ ,  $\text{R}_2 = \text{Dipp}$ ; (B)  $\text{R}_1 = \text{Me}$ ,  $\text{R}_2 = \text{Dmp}$ ; (C)  $\text{R}_1 = \text{Me}$ ,  $\text{R}_2 = \text{Dipp}$ .

$\{\text{CpNi}(\text{NHC})\}_2(\mu, \eta^{1:1}\text{-P}_4)$ .<sup>219</sup> A reversible insertion reaction was noted when these compounds were exposed to phenylisothiocyanate, affording an unusual bicyclo[3.1.0]-2-thia-1,4,5,6-tetraphosphahexane group.<sup>220</sup>

### 1.19.5.2.3 Activation of $\text{P}_4$ and $\text{As}_4$ with lanthanide and actinide (f-block) reagents

A four-coordinate yttrium complex supported by the  $N,N'$ -Dipp<sub>2</sub>-1,4-diazabutadiene ligand, a 2- $N$ -dimethylbenzyl group (R) and THF was reacted with  $\text{P}_4$  to give the 1,2- $\text{R}_2$ -*cyclo*-( $\text{P}_4$ ) ligand which bridges two metal centers.<sup>221</sup> This species converted into the  $\text{R}_2\text{P}$ -substituted *cyclo*-( $\text{P}_3$ ) complex on heating, and eliminated one equivalent of  $\text{PR}_3$  when  $\text{KR}$  was added to afford the a complex containing the  $(\mu, \eta^{3:3}\text{-P}_3)$ -ligand.

A study examining the reaction of  $\text{P}_4$  with rare-earth metallacyclopentadienes  $[\text{Li}(\text{THF})_3][\text{Cp}^*\text{LnCl}(\text{C}_4\text{Ph}_2\{\text{SiMe}_3\}_2)]$  ( $\text{R} = \text{Me}$ ,  $\text{Ln} = \text{Lu}$  and  $\text{Y}$ ;  $\text{R} = \text{SiMe}_3$ ,  $\text{Ln} = \text{Lu}$ ) showed a related extrusion of 'P' from  $\text{P}_4$  to form a three component mixture (Scheme 20).<sup>222</sup>



**Scheme 20** Reactivity of lanthanide metallacyclopentadienes with  $\text{P}_4$ .

Analysis revealed formation of the phospholyl lithium species  $[\text{Li}(\text{THF})_2][2,5\text{-}(\text{SiMe}_3)_2\text{-}3,4\text{-}(\text{Ph}_2)\text{C}_4\text{P}]$ ,  $[\text{Cp}^*\text{LnCl}_2]_3$  and a new organolanthanide anion in which a  $\text{P}_3$  unit was trapped in a bicyclo[4.1.0]triphosphaheptanide ligand. This unusual bicyclic ligand which binds to the lanthanide metal via 2 carbon atoms and all three phosphorus atoms, with the unique P-atom forming a bond to the  $\text{Li}(\text{THF})_3$  counter-ion.

The bimetallic ferrocene dianionic, diamido ligand  $\text{Fc}\{\text{NSi}t\text{BuMe}\}_2$  ( $\text{NN}_{\text{Fc}}$ ) has been used to support lanthanum and lutetium compounds  $\{(\text{NN}_{\text{Fc}})\text{M}\}_2(\mu\text{-C}_{10}\text{H}_8)$  ( $\text{M} = \text{La}$ ,  $\text{Lu}$ ) that incorporate a bridging naphthalene ligand. These react with  $\text{P}_4$  to give the heptaphosphanortricyclane complex  $\{(\text{NN}_{\text{Fc}})\text{M}\}_3(\text{P}_7)$ , regardless of the stoichiometry of the reaction.<sup>223</sup>

Extending this area of metal activation of  $\text{P}_4$  to the actinide elements, it was shown that uranium is active toward the conversion of  $\text{P}_4$  into  $\text{P}_7$ -cluster species.<sup>224</sup> The 1:1.1 stoichiometry reaction of  $\{\text{U}(\text{Ts}^{\text{Tot}})\}_2(\mu, \eta^{6:6}\text{-C}_7\text{H}_8)$  ( $\text{Ts}^{\text{Tot}} = [\text{HC}(\text{SiMe}_2\text{NAr})_3]^{3-}$ ,  $\text{Ar} = 4\text{-MeC}_6\text{H}_4$ ) with  $\text{P}_4$  afforded the tris-uranium complex  $\{\text{U}(\text{Ts}^{\text{Tot}})\}_3(\mu_3, \eta^{2:2:2}\text{-P}_7)$  (Fig. 33). It was shown that the reaction of this complex with the electrophilic reagents  $\text{Me}_3\text{SiCl}$ ,  $\text{LiCl}$  (in *tmeda*),  $\text{MeI}$  and  $\text{PhI}$  enabled the cage to be isolated as  $\text{P}_7\text{R}_3$  ( $\text{R} = \text{SiMe}_3$ ,  $\text{Li}(\text{tmeda})$ ,  $\text{Me}$  and  $\text{Ph}$ , respectively) species.



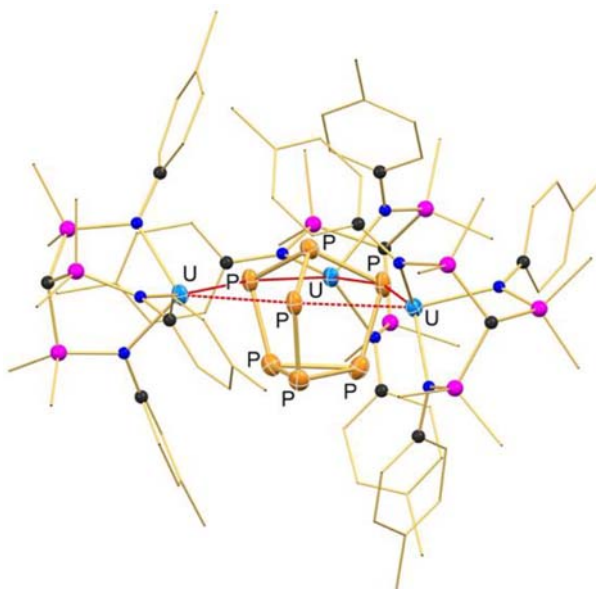


Fig. 33 Molecular structure of  $(U(Ts^{Tol}))_3(\mu_3,\eta^{2:2:2}-P_7)$ .

### 1.19.5.3 Synthesis of polycyclic *catena*-pnictogens from other sources

Although the reactivity of the  $P_4$  allotrope has dominated the molecular chemistry of phosphorus, a report of the generation of soluble polyphosphide anions from polymeric red phosphorus offers possibilities for further chemistry starting from this more stable source of the element. The reaction of commercial red phosphorus with potassium ethoxide gave mixtures of  $[P_5]^-$ ,  $[P_{16}]^{2-}$  and  $[P_{21}]^{3-}$ , with a crystal structure of the  $P_{16}$ -dianion reported as the  $[N(nBu)_4]^+$  salt.<sup>225</sup>

Although the *exo,exo*-derivative of  $Mes^*(P_4)Mes^*$  (containing the bicyclo[1.1.0]tetraphosphabutane arrangement of phosphorus atoms) was reported in 1995,<sup>226</sup> attempts to repeat the preparation afforded a mixture of the *exo,exo*- and *exo,endo*-isomers, allowing the latter to be fully characterized for the first time.<sup>227</sup>

It was shown that the diarsadiazanediyl compound  $[Ter^{Mes}NAS]_2$ , an arsenic centered biradical consisting of  $As_2N_2$  core, reacts with  $PhP=PPh$  (generated in situ from the magnesium reduction of phenyldichlorophosphane) via a [2 + 2] addition to give the [2.2.1]-bicyclic species.<sup>228</sup>

The hexa-*t*Bu-octaphosphane  $[cyclo-(P_4tBu_3)]_2$ , consisting of two four-membered  $P_4$ -rings joined by a P–P bond, was prepared by the reductive coupling of two *cyclo*-( $P_4tBu_3Cl$ ) units.<sup>229</sup> The compound is a versatile ligand with examples of its complexation at  $AuCl$ ,  $RhCl(CO)$ ,  $PdCl_2$ ,  $Co(CO)(NO)$ ,  $CuBr$  (Fig. 34) and  $PdPPh_3$  fragments with a  $\kappa^2P^2,P^{A'}$ -coordination mode.<sup>230</sup> Addition of a second equivalent of  $CuBr$  to the copper complex generated a dinuclear metal complex with a  $\kappa^2P^2,P^{2'},\kappa^2P^4,P^{4'}$ -coordination. When hexa-*t*Bu-octaphosphane was reacted with Lewis acidic metal centers  $MX_2$  ( $M = Mg, Mn, Fe, Co, Zn, Cd, Sn$  and  $X = Cl$ ,

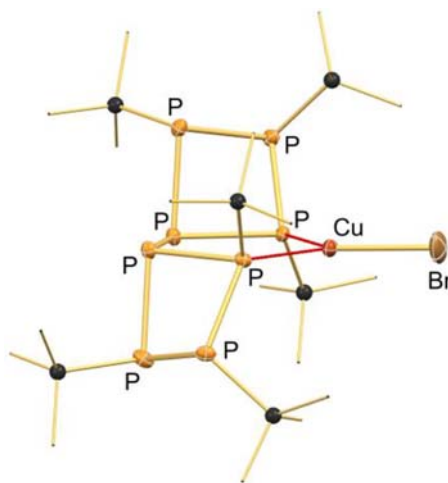


Fig. 34 Molecular structure of copper(I) bromide complex with a  $\kappa^2P^2,P^{A'}$ -(hexa-*t*Bu-octaphosphane) ligand.

Br) an unexpected isomerization was observed to form the constitutional isomer 2,2',2'',2''',3,3'-hexa-*t*Bu-bicyclo[3.3.0]octaphosphane.<sup>231</sup> Once isolated, this new bicyclic octaphosphane was also used as a ligand for 'AuCl' and 'PdCl<sub>2</sub>' groups.

The versatile As(V) reagent Ph<sub>3</sub>As(OTf)<sub>2</sub> facilitates the reductive coupling of PCl<sub>3</sub> to afford the tricationic [P<sub>7</sub>(AsPh<sub>3</sub>)<sub>3</sub>][OTf]<sub>3</sub> salt in a one pot reaction.<sup>232</sup> The molecular structure of the product shows that the three AsPh<sub>3</sub> groups are coordinated to the bridging phosphorus atoms of a heptaphosphanorotricyclane cage. The P–P bond lengths are comparable to other [P<sub>7</sub>R<sub>3</sub>]<sup>3-</sup> clusters suggesting little influence from the AsPh<sub>3</sub> substituents.

Although less well developed than the polycyclic chemistry of the lighter pnictogens, the construction of polybismuthane compounds has been demonstrated by a controlled bond formation approach, giving access to Bi<sub>4</sub> and Bi<sub>8</sub> cluster species.<sup>233</sup> The reaction of Cp\*<sub>2</sub>BiCl with Ga(Me<sub>6</sub>BDI<sup>Dipp</sup>) generated the thermally unstable dibismuthane [(Ga(Me<sub>6</sub>BDI<sup>Dipp</sup>)Cl)Bi]<sub>2</sub>, which formed the tetrabismuthane product {Ga(Me<sub>6</sub>BDI<sup>Dipp</sup>)Cl}<sub>2</sub>(μ,η<sup>1:1</sup>-Bi<sub>4</sub>) with the bicyclo[1.1.0]butane arrangement of bismuth atoms on warming to room temperature. The reaction of tetraphenyldibismuthane with Jones' Mg(I) reducing agents was also studied, affording the tetra-magnesium coordinated Bi<sub>8</sub> cluster, {Mg(Me<sub>6</sub>BDI<sup>Mes</sup>)<sub>4</sub>(μ<sub>4</sub>,η<sup>2:2:2:2</sup>-Bi<sub>8</sub>)} (Fig. 35). The analogous Sb<sub>4</sub>-<sup>234,235</sup> and Sb<sub>8</sub>-clusters<sup>21,236</sup> have also been isolated using similar synthetic strategies, as well as the corresponding {Cp\*<sub>2</sub>Sm}-supported Sb<sub>8</sub>-cluster, which was isolated from heating a mixture of antimony amalgam with Cp\*<sub>2</sub>Sm to 120 °C for 2 days.<sup>237</sup>

During research into the formation of Sb–Bi bonds from the metathesis of 'R<sub>2</sub>SbLi' and R<sub>2</sub>BiCl (R<sub>2</sub> = [Naph(NSiR<sub>3</sub>)<sub>2</sub>]<sup>2-</sup>), (Naph{NSiR<sub>3</sub>})<sub>2</sub>SbCl was reacted *n*BuLi in an attempt to make the stibanide anion. However, the instant formation of an insoluble red product was observed, which was identified crystallographically as the Sb<sub>12</sub> cluster consisting Sb<sub>8</sub>-realgar core supported by four 'Sb(Naph{NSiEt<sub>3</sub>})<sub>2</sub>' groups bonded via additional Sb–Sb bonds.<sup>17</sup>

#### 1.19.5.4 The chemistry of non-metalated polycyclic *catena*-pnictogens

The reaction of the protonated heptaphosphide anion [HP<sub>7</sub>]<sup>2-</sup> with E{N(SiMe<sub>3</sub>)<sub>2</sub>}<sub>2</sub> (E = Ge, Sn, Pb) proceeded via protonolysis of one of the E–N bonds to give the substituted anions, [P<sub>7</sub>(E{N(SiMe<sub>3</sub>)<sub>2</sub>})]<sup>2-</sup>.<sup>238</sup> The tin and lead compounds were stable, but the germanium analogue decomposed at room temperature to give the dimeric anion, [(P<sub>7</sub>Ge)<sub>2</sub>N(SiMe<sub>3</sub>)<sub>2</sub>]<sup>3-</sup>.

The nature of the products of the reaction between the silicon complex (L)Si(η<sup>2</sup>-P<sub>4</sub>)<sup>239</sup> (L = [HC{C(Me)NDipp}{C(CH<sub>2</sub>)NDipp}]<sup>2-</sup>) and the Ni(0) source, Ni(NHC)(vtms)<sub>2</sub> (NHC = <sup>H</sup>IMes, <sup>H</sup>IDipp; vtms = vinyl trimethylsilyl) was found to be temperature dependent.<sup>240</sup> At –50 °C, both derivatives formed the bis-substituted Si complex, {(L)Si(μ,η<sup>2:2</sup>-P<sub>4</sub>)}Ni(NHC), which contains two bridging P<sub>4</sub>-groups that each bind in a side-on mode to the Ni. At room temperature the <sup>H</sup>IDipp derivative formed the mono-adduct {(L)Si(μ,η<sup>2:2</sup>-P<sub>4</sub>)}Ni(<sup>H</sup>IDipp) whilst at 60 °C, an asymmetric Ni<sub>2</sub>Si<sub>2</sub>P<sub>8</sub> cluster was formed.

The neutral trisubstituted cluster P<sub>7</sub>(SiMe<sub>3</sub>)<sub>3</sub> reacted with CuCl(<sup>H</sup>IDipp) to form the η<sup>4</sup>-bonded anion [(<sup>H</sup>IDipp)Cu(P<sub>7</sub>{SiMe<sub>3</sub>})]<sup>-</sup> as the [Cu(<sup>H</sup>IDipp)]<sup>+</sup> salt (Fig. 36).<sup>241</sup> In contrast, the corresponding reaction with AuCl(<sup>H</sup>IDipp) gave the neutral trimetallic compound {Au(<sup>H</sup>IDipp)}<sub>3</sub>(P<sub>7</sub>) containing three linear Au(I) fragments bonded to the cluster.

The [DippP<sub>5</sub>Cl][GaCl<sub>4</sub>] salt (formed from the insertion of [DippPCL]<sup>+</sup> cations into a P–P bond of P<sub>4</sub>)<sup>242</sup> reacted with the chlorinated *N*-heterocyclic carbene (<sup>Cl</sup>IDipp) via a [3 + 2] fragmentation to form P<sub>2</sub> and P<sub>3</sub><sup>+</sup> species, (<sup>Cl</sup>IDipp)P<sub>2</sub>(Dipp)Cl and {(<sup>Cl</sup>IDipp)P<sub>2</sub>}<sub>2</sub>P[GaCl<sub>4</sub>].<sup>243</sup> Related [P<sub>5</sub>R<sub>2</sub>][GaCl<sub>4</sub>] (R = *i*Pr, Mes) salts react with [Cp<sup>bis</sup>Fe(μ-Br)]<sub>2</sub> or K[Cp<sup>bis</sup>] to afford bicyclo[1.1.0]pentaphosphanes with a nonsymmetric substitution pattern.<sup>244</sup> When [Cp<sup>bis</sup>M(μ-Br)]<sub>2</sub> (M = Co, Ni) was used, [Cp<sup>bis</sup>Co(η<sup>4</sup>-P<sub>5</sub>R<sub>2</sub>)]<sup>+</sup> and [{Cp<sup>bis</sup>Ni}<sub>2</sub>(η<sup>3:3</sup>-P<sub>5</sub>R<sub>2</sub>)]<sup>+</sup> were produced.

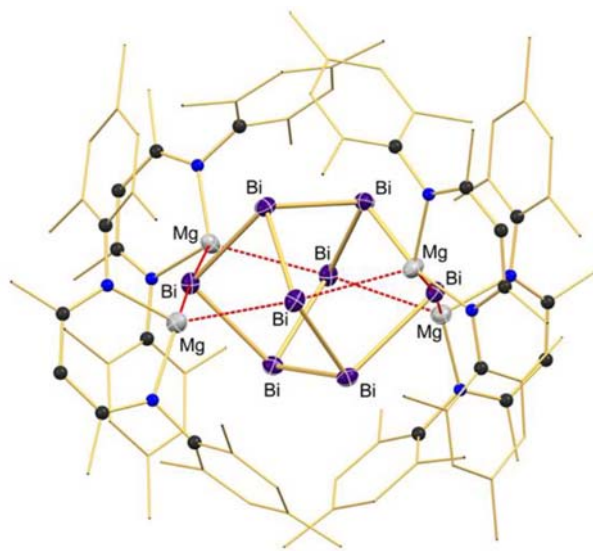
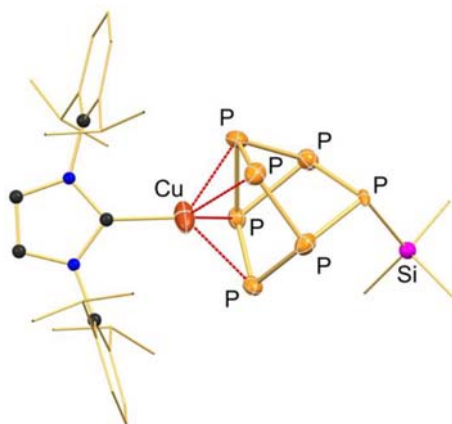


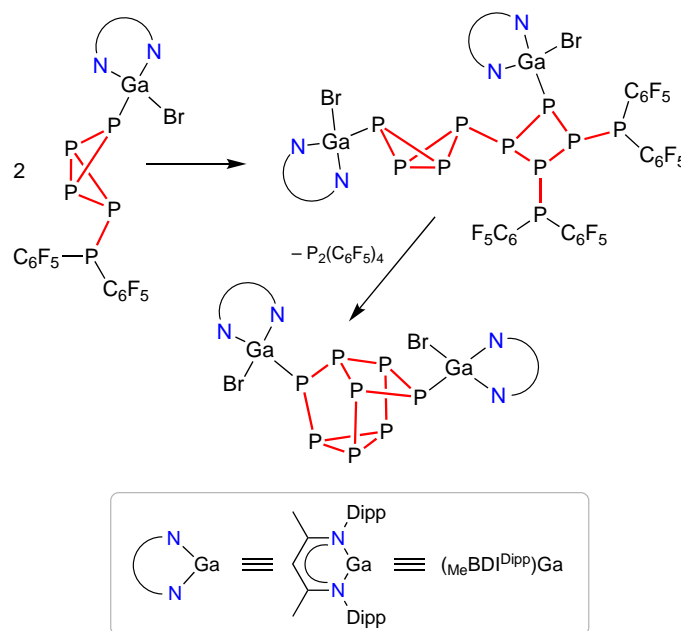
Fig. 35 Molecular structure of {Mg(Me<sub>6</sub>BDI<sup>Mes</sup>)<sub>4</sub>(μ<sub>4</sub>,η<sup>2:2:2:2</sup>-Bi<sub>8</sub>)}.



**Fig. 36**  $\eta^4$ -bonded  $[P_7(SiMe_3)]^{2-}$  at a Cu(I) center in the anion  $[(^H)Dipp)Cu(P_7(SiMe_3))]^-$  ( $[Cu(^H)Dipp]^+$  cation omitted).

### 1.19.5.5 The chemistry of metalated polycyclic *catena*-pnictogens

Reaction of the gallium complex  $\{Ga(Me)BDI^{Dipp}\}(\eta^{1:1}-P_4)$  with  $R_2PX$  ( $R = Ph, Cy, Mes, C_6F_5$ ;  $X = Br, Cl$ ) afforded the *endo,exo*-pentaphosphanes, which isomerized to the corresponding *exo,exo*-isomers.<sup>245</sup> During this study it was found that the pentafluorophenyl product  $\{Ga(Me)BDI^{Dipp}Br\}(\mu, \eta^{1:1}-P_4)\{P(C_6F_5)_2\}$  dimerized to generate a decaphosphane, in which the *exo,exo*[1.1.0]octane bicycle is linked to a *bis*(phosphanyl)-substituted four membered ring, and that this species spontaneously eliminated  $(C_6F_5)_4P_2$  to afford the tetracyclo[3.3.0.0<sup>2,7</sup>.0<sup>4,6</sup>]octaphosphane  $\{Ga(Me)BDI^{Dipp}Br\}_2P_8$  (Scheme 21). It was also shown that



**Scheme 21** Formation of tetracyclo[3.3.0.0<sup>2,7</sup>.0<sup>4,6</sup>]octaphosphane  $\{Ga(Me)BDI^{Dipp}Br\}_2P_8$  via spontaneous loss of  $(C_6F_5)_4P_2$  from an isolable decaphosphane intermediate.

$\{Ga(Me)BDI^{Dipp}\}(\eta^{1:1}-P_4)$  reacted with  $[K(Et_2O)][(^{Mes}BIAN)Co(\eta^4-1,5-cod)]$  to afford  $[K(dme)_2][\{(^{Mes}BIAN)Co\}(\mu, \eta^{4:2}-P_4)\{Ga(Me)BDI^{Dipp}\}]$  containing a non-cyclic  $P_4$ -ligand bridging the two metals.<sup>147</sup> When the anthracene complexes  $[K(18-c-6)(THF)_2][Fe(\eta^4-C_{14}H_{10})_2]$  or  $[K(dme)_2][Co(\eta^4-C_{14}H_{10})_2]$  were used as a source of low-valent transition-metal, analogous  $\mu, \eta^{4:2}-P_4$  chains were formed.<sup>246</sup>

$\{Cp^*Fe(CO)_2\}_2(\mu, \eta^{1:1}-P_4)$  was reacted with different iron complexes to promote rearrangement of the  $P_4$ -ligand.<sup>247</sup> Reaction with  $FeBr_2(dme)$  resulted in coordination of the  $FeBr_2$  fragment to the wing-tip P-atoms in the *tris*-iron complex

$\{\text{Cp}^m\text{Fe}(\text{CO})_2\}_2(\mu_3, \eta^{1:1:2}\text{-P}_4)\{\text{FeBr}_2\}$ , whereas reaction with  $[\text{Fe}(\text{MeCN})_6][\text{PF}_6]_2$  gave the sandwich compound  $[\{(\text{Cp}^m\text{Fe}(\text{CO})_2)_2(\mu_3, \eta^{1:1:4}\text{-P}_4)\}_2\text{Fe}][\text{PF}_6]_2$ , in which the  $\text{P}_4$ -ligand transformed to the  $6\pi$  aromatic  $\text{P}_4\text{R}_2$ -ligand.

The chromium complex  $\{\text{Cp}^*\text{Cr}(\text{CO})_3\}_2(\mu, \eta^{1:1}\text{-P}_4)$  will coordinate a tungsten carbonyl group in the trimetallic  $\{\text{Cp}^*\text{Cr}(\text{CO})_3\}_2(\mu_3, \eta^{1:1:1:1}\text{-P}_4)\{\text{W}(\text{CO})_4\}$ .<sup>248</sup> In contrast, reaction with Cr and Mo carbonyl fragments proceeded to the stepwise formation of  $\{\text{Cp}^*\text{Cr}(\text{CO})_2\}_2(\mu_3, \eta^{3:1:1}\text{-P}_4)\{\text{M}(\text{CO})_5\}$  and  $\{\text{Cp}^*\text{Cr}(\text{CO})_2\}_2(\mu_4, \eta^{3:1:1:1}\text{-P}_4)\{\text{M}(\text{CO})_5\}_2$  containing folded *cyclo*- $\text{P}_4$  units.

An approach to mixed  $\text{P}_n\text{As}_m$  ligands has been successfully developed, based on the reaction of the bimetallic  $\{\text{Cp}^m\text{Fe}(\text{CO})_2\}_2(\mu, \eta^{1:1}\text{-P}_4)$  with  $\text{As}_4$ , which yields  $\{\text{Cp}^m\text{Fe}\}_2(\mu, \eta^{4:4}\text{-P}_n\text{As}_{4-n})$  and  $\text{Cp}^m\text{Fe}(\eta^5\text{-P}_n\text{As}_{5-n})$ .<sup>249</sup> The crystal structures show these to contain mixtures of the  $[\text{P}_3\text{As}]/[\text{P}_2\text{As}_2]$  and  $[\text{P}_4\text{As}]/[\text{P}_3\text{As}_2]/[\text{P}_2\text{As}_3]$  ligands, respectively.

### 1.19.6 Miscellaneous reactions forming *catena*-polypnictogens

The short section collects together reactions that generate a range of *catena*-pnictogen containing molecules that do not fit in well with the previous classifications but are worthy of inclusion in this chapter.

Phosphaalkynes ( $\text{R}-\text{C}\equiv\text{P}$ ) are known to react with themselves under various conditions to generate different oligomers, some of which contain  $\text{P}-\text{P}$  groups. An unusual cascade reaction involving four consecutive  $[4 + 2]/[4 + 2]$  phospho-ene/ $[4 + 2]$  steps was noted when di-2-pyrone was exposed to excess trimethylsilylphosphaalkyne  $\text{Me}_3\text{Si}-\text{C}\equiv\text{P}$ .<sup>250</sup> The polycyclic triphosphatricyclo  $[3.2.1.0^{2,7}]$ oct-3-ene product was formed in high yield, and was applied as a ligand at Au(I) and Cu(I) centers.

The reaction of  $\text{K}_5\text{Bi}_4$  with  $\text{M}(\eta^6\text{-Ar})(\text{CO})_3$  ( $\text{M} = \text{Cr}$ ,  $\text{Ar} = \text{C}_6\text{H}_6$ ;  $\text{M} = \text{Mo}$ ,  $\text{Ar} = \text{C}_7\text{H}_8$ ) and 2.2.2-crypt in liquid ammonia afforded the  $[(\eta^3\text{-Bi}_3)\text{M}(\text{CO})_3]^{3-}$  anions containing the cyclic tribismuthide ion,  $[\text{Bi}_3]^{3-}$ .<sup>251</sup> These compounds complete the series of  $\eta^3\text{-E}_3$  ligands that have previously been reported for  $\text{E} = \text{P}$ ,  $\text{As}$  and  $\text{Sb}$ .

The addition of  $\text{ECl}_3$  ( $\text{E} = \text{As}$ ,  $\text{P}$ ) to  $[\text{NEt}_4]_2[\text{AsH}\{\text{Fe}(\text{CO})_4\}_3]$  generated a mixture of compounds from which the octahedral clusters  $[\text{NEt}_4][\text{Fe}_2(\text{CO})_6(\mu_3\text{-As})\{\mu_3\text{-EFe}(\text{CO})_4\}_2]$  were isolated.<sup>252</sup> Crystallographic analysis revealed a square-based pyramidal core with an  $\text{AsE}_2\text{Fe}$  basal plane and apical  $\text{Fe}(\text{CO})_3$  unit.

The reaction of  $\text{SbCl}_3$  with tin granules in the presence of mercury gave the  $\text{Sb}/\text{Hg}$  amalgam as a grey solid. Powder X-ray diffraction gave peaks that could be assigned to elemental antimony allowing this material to be investigated as a source of  $\text{Sb}(0)$ .<sup>237</sup> The reaction of  $\text{Sb}/\text{Hg}$  with  $\text{Cp}^*_2\text{Sm}$  gave a mixture of products including  $\{\text{Cp}^*_2\text{Sm}\}_2(\mu\text{-}\eta^{2:2}\text{-Sb}_2)$  and the mercury bridged species  $\{(\text{Cp}^*_2\text{Sm})_2\text{Sb}\}_2(\mu\text{-Hg})$ . The product mixture also contained a  $\text{Sb}_8\text{Sm}_6\text{Hg}$  cluster in which two  $\text{Sb}_4$  [1,2]-edge missing tetrahedra are joined bonded to a central  $\mu\text{-Hg}$  atom within an  $\text{Sb}-\text{Hg}-\text{Sb}$  unit (Fig. 37).

The bimetallic  $\text{Bi}_4\{\text{Fe}(\text{CO})_3\}_3$  cluster contains a  $\text{Bi}_4$  core with  $3 \times \text{Fe}(\text{CO})_3$  groups  $\mu_3$ -capping three of the four faces.<sup>253</sup> The compound crystallized as toluene solvate and X-ray analysis showed that in the solid state the  $\text{Bi}_4\text{Fe}_3$  core is encapsulated with toluene solvate molecules that interact via low-valent  $\text{Bi} \cdots \pi(\text{arene})$  contacts.

### 1.19.7 Conclusions

The chemistry of *catena*-pnictogen compounds containing chains, rings and clusters of  $(\text{E})_n$  atoms ( $\text{E} = \text{P}$ ,  $\text{As}$ ,  $\text{Sb}$  and  $\text{Bi}$ ) since the year 2013 has been surveyed. Dipnictogens represent the simplest examples of such compounds, with the addition of further E-atoms either extending the chain or closing the ring in cyclic systems. Both classes of compounds exist as both independent species supported by ancillary ligands, or as a component of a coordination compound at a metal center. More complex three-dimensional structures composed of polycyclic systems are also included, with individual *cyclo*- $(\text{E})_n$  units either linked by additional E-E bonds

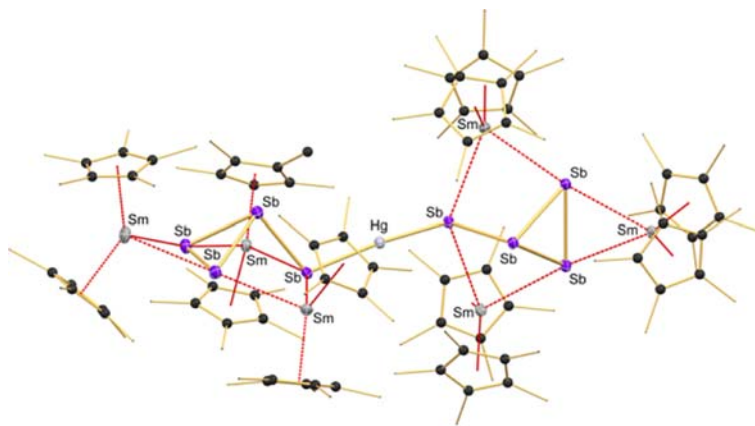


Fig. 37 Molecular structure of  $[(\text{Cp}^*_2\text{Sm})_3(\mu_3, \eta^{2:2}\text{-Sb}_4)]_2(\mu\text{-Hg})$ .

or fused into clusters. The structural aspects of each class of compound have been reported as well as key details of their synthesis and reactivity.

It is this author's opinion that advances in analytical and computational techniques that complement existing knowledge in the field ensure that the area of *catena*-pnictogen chemistry is in a healthy position for its continued growth and development as a research topic. It is anticipated that this will lead to the contribution of many new and unusual compounds containing the pnictogens to the scientific community, advancing the understanding of the fundamental chemistry of these elements.

## References

- Seyferth, D. *Organometallics* **2001**, *20*, 1488–1498.
- Ashe, A. J.; Ludwig, E. G. *Organometallics* **1982**, *1*, 1408.
- Schulz, S.; Heimann, S.; Kuczowski, A.; Bläser, D.; Wölper, C. *Organometallics* **2013**, *32*, 3391–3394.
- Breunig, H. J.; Lork, E.; Moldovan, O.; Rač, C. I. *Z. Naturforsch. B* **2013**, *68*, 87–90.
- Wang, Y.; Xie, Y.; Wei, P.; King, R. B.; Schaefer, H. F.; Schleyer, P. v. R.; Robinson, G. H. *J. Am. Chem. Soc.* **2008**, *130*, 14970–14971.
- Abraham, M. Y.; Wang, Y.; Xie, Y.; Wei, P.; Schaefer, H. F.; Schleyer, P. v. R.; Robinson, G. H. *Chem. A Eur. J.* **2010**, *16*, 432–435.
- Kretschmer, R.; Ruiz, D. A.; Moore, C. E.; Rheingold, A. L.; Bertrand, G. *Angew. Chem. Int. Ed.* **2014**, *53*, 8176–8179.
- Lemp, O.; Balmer, M.; Reiter, K.; Weigend, F.; von Hänisch, C. *Chem. Commun.* **2017**, *53*, 7620–7623.
- Balmer, M.; Gottschling, H.; von Hänisch, C. *Chem. Commun.* **2018**, *54*, 2659–2661.
- Doddi, A.; Bockfeld, D.; Zaretske, M.-K.; Kleeberg, C.; Bannenberg, T.; Tamm, M. *Dalton Trans.* **2017**, *46*, 15859–15864.
- Doddi, A.; Bockfeld, D.; Zaretske, M.-K.; Bannenberg, T.; Tamm, M. *Chem. A Eur. J.* **2019**, *25*, 13119–13123.
- Beil, A.; Gilliard, R. J.; Grützmaier, H. *Dalton Trans.* **2016**, *45*, 2044–2052.
- Kronig, S.; Theuergarten, E.; Daniliuc, C. G.; Jones, P. G.; Tamm, M. *Angew. Chem. Int. Ed.* **2012**, *51*, 3240–3244.
- Ho, L. P.; Zaretske, M.-K.; Bannenberg, T.; Tamm, M. *Chem. Commun.* **2019**, *55*, 10709–10712.
- Marczenko, K. M.; Zurakowski, J. A.; Bamford, K. L.; MacMillan, J. W. M.; Chitnis, S. S. *Angew. Chem. Int. Ed.* **2019**, *58*, 18096–18101.
- Nekouei-shahraki, B.; Samuel, P. P.; Roesky, H. W.; Stern, D.; Matussek, J.; Stalke, D. *Organometallics* **2012**, *31*, 6697–6703.
- Marczenko, K. M.; Chitnis, S. S. *Chem. A Eur. J.* **2019**, *25*, 14183–14191.
- Vránová, I.; Alonso, M.; Jambor, R.; Růžička, A.; Turek, J.; Dostál, L. *Chem. A Eur. J.* **2017**, *23*, 2340–2349.
- Zitz, R.; Gatterer, K.; Reinhold, C. R. W.; Müller, T.; Baumgartner, J.; Marschner, C. *Organometallics* **2015**, *34*, 1419–1430.
- Lee, V. Y.; Ota, K.; Ito, Y.; Gapurenko, O. A.; Sekiguchi, A.; Minyaev, R. M.; Minkin, V. I.; Gornitzka, H. *J. Am. Chem. Soc.* **2017**, *139*, 13897–13902.
- Schwamm, R. J.; Coles, M. P. *Chem. A Eur. J.* **2019**, *25*, 14183–14191.
- Schwamm, R. J.; Lein, M.; Coles, M. P.; Fitchett, C. M. *Angew. Chem. Int. Ed.* **2016**, *55*, 14798–14801.
- Ishida, S.; Hirakawa, F.; Furukawa, K.; Yoza, K.; Iwamoto, T. *Angew. Chem. Int. Ed.* **2014**, *53*, 11172–11176.
- Helling, C.; Wölper, C.; Schulz, S. *Eur. J. Inorg. Chem.* **2020**, *2020*, 4225–4235.
- Ramler, J.; Kruppenacher, I.; Lichtenberg, C. *Chem. A Eur. J.* **2020**, *26*, 14551–14555.
- Schwamm, R. J.; Lein, M.; Coles, M. P.; Fitchett, C. M. *Chem. Commun.* **2018**, *54*, 916–919.
- Hupf, E.; Lork, E.; Mebs, S.; Chęcińska, L.; Beckmann, J. *Organometallics* **2014**, *33*, 7247–7259.
- Nejman, P. S.; Curzon, T. E.; Bühl, M.; McKay, D.; Woollins, J. D.; Ashbrook, S. E.; Cordes, D. B.; Slawin, A. M. Z.; Kilian, P. *Inorg. Chem.* **2020**, *59*, 5616–5625.
- Taylor, L. J.; Bühl, M.; Wawrzyniak, P.; Chalmers, B. A.; Woollins, J. D.; Slawin, A. M. Z.; Fuller, A. L.; Kilian, P. *Eur. J. Inorg. Chem.* **2016**, *2016*, 659–666.
- Surgenor, B. A.; Chalmers, B. A.; Arachchige, K. S. A.; Slawin, A. M. Z.; Woollins, J. D.; Bühl, M.; Kilian, P. *Inorg. Chem.* **2014**, *53*, 6856–6866.
- Taylor, L. J.; Bühl, M.; Chalmers, B. A.; Ray, M. J.; Wawrzyniak, P.; Walton, J. C.; Cordes, D. B.; Slawin, A. M. Z.; Woollins, J. D.; Kilian, P. *J. Am. Chem. Soc.* **2017**, *139*, 18545–18551.
- Chalmers, B. A.; Bühl, M.; Arachchige, K. S. A.; Slawin, A. M. Z.; Kilian, P. *J. Am. Chem. Soc.* **2014**, *136*, 6247–6250.
- Chalmers, B. A.; Bühl, M.; Arachchige, K. S. A.; Slawin, A. M. Z.; Kilian, P. *Chem. A Eur. J.* **2015**, *21*, 7520–7531.
- Brüning, J.; Hupf, E.; Lork, E.; Mebs, S.; Beckmann, J. *Dalton Trans.* **2015**, *44*, 7105–7108.
- Ganesamoorthy, C.; Heimann, S.; Hölscher, S.; Haack, R.; Wölper, C.; Jansen, G.; Schulz, S. *Dalton Trans.* **2017**, *46*, 9227–9234.
- Dzialeski, K.; Gehlhaar, A.; Wölper, C.; Auer, A. A.; Schulz, S. *Organometallics* **2019**, *38*, 2927–2942.
- Clobes, C.; Jerabek, P.; Nußbruch, I.; Frenking, G.; von Hänisch, C. *Eur. J. Inorg. Chem.* **2015**, *2015*, 3264–3273.
- Zhao, M.; Wang, L.; Li, P.; Zhang, X.; Yang, Y.; Zheng, W. *Chem. Commun.* **2015**, *51*, 16184–16187.
- Zhao, M.; Wang, L.; Zhang, X.; Zheng, W. *Dalton Trans.* **2016**, *45*, 10505–10509.
- Zhao, M.-G.; Hao, T.-T.; Zhang, X.; Ma, J.-P.; Su, J.-H.; Zheng, W. *Inorg. Chem.* **2017**, *56*, 12678–12681.
- Zhao, M.-G.; Li, L.; He, R.-R.; Zhang, X.; Ma, J.-P.; Su, J.-H.; Zheng, W. *Dalton Trans.* **2020**, *49*, 15190–15194.
- Imran, M.; Mix, A.; Neumann, B.; Stämmler, H.-G.; Monkowius, U.; Bleckenwegner, P.; Mitzel, N. W. *Dalton Trans.* **2014**, *43*, 14737–14748.
- Sartori, P.; Golloch, A. *Chem. Ber.* **1968**, *101*, 2004–2009.
- Fleischmann, M.; Jones, J. S.; Balázs, G.; Gabbai, F. P.; Scheer, M. *Dalton Trans.* **2016**, *45*, 13742–13749.
- Attenberger, B.; Peresypkina, E. V.; Scheer, M. *Inorg. Chem.* **2015**, *54*, 7021–7029.
- Moussa, M. E.; Fleischmann, M.; Peresypkina, E. V.; Dütsch, L.; Seidl, M.; Balázs, G.; Scheer, M. *Eur. J. Inorg. Chem.* **2017**, *2017*, 3222–3226.
- Moussa, M. E.; Schiller, J.; Peresypkina, E.; Seidl, M.; Balázs, G.; Shelyganov, P.; Scheer, M. *Chem. A Eur. J.* **2020**, *26*, 14315–14319.
- Moussa, M. E.; Schiller, J.; Seidl, M.; Shelyganov, P. A.; Scheer, M. *New J. Chem.* **2021**, *45*, 1800–1804.
- Moussa, M. E.; Attenberger, B.; Peresypkina, E. V.; Fleischmann, M.; Balázs, G.; Scheer, M. *Chem. Commun.* **2016**, *52*, 10004–10007.
- Moussa, M. E.; Seidl, M.; Balázs, G.; Zabel, M.; Virovets, A. V.; Attenberger, B.; Schreiner, A.; Scheer, M. *Chem. A Eur. J.* **2017**, *23*, 16199–16203.
- Moussa, M. E.; Attenberger, B.; Fleischmann, M.; Schreiner, A.; Scheer, M. *Eur. J. Inorg. Chem.* **2016**, *2016*, 4538–4541.
- Moussa, M. E.; Peresypkina, E.; Virovets, A. V.; Venus, D.; Balázs, G.; Scheer, M. *CrystEngComm* **2018**, *20*, 7417–7422.
- Schiller, J.; Schreiner, A.; Seidl, M.; Balázs, G.; Scheer, M. *Chem. A Eur. J.* **2020**, *26*, 14570–14574.
- Fleischmann, M.; Welsch, S.; Peresypkina, E. V.; Virovets, A. V.; Scheer, M. *Chem. A Eur. J.* **2015**, *21*, 14332–14336.
- Moussa, M. E.; Piesch, M.; Fleischmann, M.; Schreiner, A.; Seidl, M.; Scheer, M. *Dalton Trans.* **2018**, *47*, 16031–16035.
- Moussa, M. E.; Attenberger, B.; Seidl, M.; Schreiner, A.; Scheer, M. *Eur. J. Inorg. Chem.* **2017**, *2017*, 5616–5620.
- Fleischmann, M.; Dütsch, L.; Moussa, M. E.; Schindler, A.; Balázs, G.; Lescop, C.; Scheer, M. *Chem. Commun.* **2015**, *51*, 2893–2895.
- Moussa, M. E.; Welsch, S.; Gregoriades, L. J.; Balázs, G.; Seidl, M.; Scheer, M. *Eur. J. Inorg. Chem.* **2018**, *2018*, 1683–1687.
- Moussa, M. E.; Shelyganov, P. A.; Wegley, B.; Seidl, M.; Scheer, M. *Eur. J. Inorg. Chem.* **2019**, *2019*, 4241–4248.



60. Moussa, M. E.; Seidl, M.; Balázs, G.; Hautmann, M.; Scheer, M. *Angew. Chem. Int. Ed.* **2019**, *58*, 12903–12907.
61. Schoo, C.; Köppe, R.; Piesch, M.; Gamer, M. T.; Konchenko, S. N.; Scheer, M.; Roesky, P. W. *Chem. A Eur. J.* **2018**, *24*, 7890–7895.
62. Piesch, M.; GraBl, C.; Scheer, M. *Angew. Chem. Int. Ed.* **2020**, *59*, 7154–7160.
63. Liu, L. L.; Zhou, J.; Kim, Y.; Cao, L. L.; Stephan, D. W. *Dalton Trans.* **2019**, *48*, 14242–14245.
64. Taube, C.; Schwedtmann, K.; Noikham, M.; Somsok, E.; Hennersdorf, F.; Wolf, R.; Weigand, J. J. *Angew. Chem. Int. Ed.* **2020**, *59*, 3585–3591.
65. Matern, E.; Anson, C. E.; Baum, E.; Sattler, E.; Kovács, I. *Eur. J. Inorg. Chem.* **2020**, *2020*, 1311–1318.
66. Becker, G.; Schwarz, W.; Seidler, N.; Westerhausen, M. Z. *Anorg. Allg. Chem.* **1992**, *612*, 72–82.
67. Puschmann, F. F.; Stein, D.; Heift, D.; Hendriksen, C.; Gal, Z. A.; Grützmacher, H.-F.; Grützmacher, H. *Angew. Chem. Int. Ed.* **2011**, *50*, 8420–8423.
68. Tondreau, A. M.; Benkő, Z.; Harmer, J. R.; Grützmacher, H. *Chem. Sci.* **2014**, *5*, 1545–1554.
69. Izod, K.; Evans, P.; Waddell, P. G. *Angew. Chem. Int. Ed.* **2019**, *58*, 11007–11012.
70. Ringler, B.; Müller, M.; von Hänisch, C. *Eur. J. Inorg. Chem.* **2018**, *2018*, 640–646.
71. Ritter, C.; Ringler, B.; Dankert, F.; Conrad, M.; Kraus, F.; von Hänisch, C. *Dalton Trans.* **2019**, *48*, 5253–5262.
72. Dixon, L. S. H.; Allen, L. K.; Less, R. J.; Wright, D. S. *Chem. Commun.* **2014**, *50*, 3007–3009.
73. Hinz, A.; Schulz, A.; Villinger, A. *Chem. A Eur. J.* **2016**, *22*, 12266–12269.
74. Ritter, C.; Weigand, F.; von Hänisch, C. *Chem. A Eur. J.* **2020**, *26*, 8536–8540.
75. Riley, R. D.; Dickie, B.; Land, M. A.; Kemp, R. A.; Macdonald, C. L. B.; Werner-Zwanziger, U.; Robertson, K. N.; Clyburne, J. A. C. *Chem. A Eur. J.* **2020**, *26*, 7711–7719.
76. Mayer, K.; Dums, J. V.; Benda, C. B.; Klein, W.; Fässler, T. F. *Angew. Chem. Int. Ed.* **2020**, *59*, 6800–6805.
77. Emmerling, F.; Längin, N.; Petri, D.; Kroeker, M.; Röhr, C. Z. *Anorg. Allg. Chem.* **2004**, *630*, 171–178.
78. Wiśniewska, A.; Grubba, R.; Ponikiewski, Ł.; Zauliczny, M.; Pikies, J. *Dalton Trans.* **2018**, *47*, 10213–10222.
79. Grubba, R.; Ordyszevska, A.; Kaniewska, K.; Ponikiewski, Ł.; Chojnacki, J.; Gudat, D.; Pikies, J. *Inorg. Chem.* **2015**, *54*, 8380–8387.
80. Grubba, R.; Zauliczny, M.; Ponikiewski, Ł.; Pikies, J. *Dalton Trans.* **2016**, *45*, 4961–4964.
81. Dütsch, L.; Fleischmann, M.; Welsch, S.; Balázs, G.; Kremer, W.; Scheer, M. *Angew. Chem. Int. Ed.* **2018**, *57*, 3256–3261.
82. Li, T.; Arleth, N.; Gamer, M. T.; Köppe, R.; Augenstein, T.; Dielmann, F.; Scheer, M.; Konchenko, S. N.; Roesky, P. W. *Inorg. Chem.* **2013**, *52*, 14231–14236.
83. Seidl, M.; Balázs, G.; Timoshkin, A. Y.; Scheer, M. *Angew. Chem. Int. Ed.* **2016**, *55*, 431–435.
84. Seidl, M.; Stubenhofer, M.; Timoshkin, A. Y.; Scheer, M. *Angew. Chem. Int. Ed.* **2016**, *55*, 14037–14040.
85. Pugh, T.; Chilton, N. F.; Layfield, R. A. *Chem. Sci.* **2017**, *8*, 2073–2080.
86. Bresien, J.; Hering, C.; Schulz, A.; Villinger, A. *Chem. A Eur. J.* **2014**, *20*, 12607–12615.
87. Schumann, A.; Reiß, F.; Jiao, H.; Rabeah, J.; Siewert, J.-E.; Krummenacher, I.; Braunschweig, H.; Hering-Junghans, C. *Chem. Sci.* **2019**, *10*, 7859–7867.
88. Schumann, A.; Bresien, J.; Fischer, M.; Hering-Junghans, C. *Chem. Commun.* **2021**, *57*, 1014–1017.
89. Chitnis, S. S.; Sparkes, H. A.; Annibale, V. T.; Pridmore, N. E.; Oliver, A. M.; Manners, I. *Angew. Chem. Int. Ed.* **2017**, *56*, 9536–9540.
90. Holthausen, M. H.; Knackstedt, D.; Burford, N.; Weigand, J. J. *Aust. J. Chem.* **2013**, *66*, 1155–1162.
91. Robertson, A. P. M.; Dyker, C. A.; Gray, P. A.; Patrick, B. O.; Decken, A.; Burford, N. J. *Am. Chem. Soc.* **2014**, *136*, 14941–14950.
92. Schneider, H.; Schmidt, D.; Radius, U. *Chem. Commun.* **2015**, *51*, 10138–10141.
93. Bresien, J.; Schulz, A.; Villinger, A. *Dalton Trans.* **2016**, *45*, 498–501.
94. Bresien, J.; Faust, K.; Schulz, A.; Villinger, A. *Angew. Chem. Int. Ed.* **2015**, *54*, 6926–6930.
95. Bresien, J.; Schulz, A.; Villinger, A. *Chem. A Eur. J.* **2015**, *21*, 18543–18546.
96. Bresien, J.; Eickhoff, L.; Schulz, A.; Suhrbier, T.; Villinger, A. *Chem. A Eur. J.* **2019**, *25*, 16311–16319.
97. Bresien, J.; Hinz, A.; Schulz, A.; Suhrbier, T.; Thomas, M.; Villinger, A. *Chem. A Eur. J.* **2017**, *23*, 14738–14742.
98. Hinz, A.; Schulz, A.; Villinger, A. *Inorg. Chem.* **2016**, *55*, 3692–3699.
99. Kornev, A. N.; Panova, Y. S.; Sushev, V. V.; Dorado Daza, D. F.; Novikov, A. S.; Cherkasov, A. V.; Fukin, G. K.; Abakumov, G. A. *Inorg. Chem.* **2019**, *58*, 16144–16153.
100. Rottschäfer, D.; Neumann, B.; Stammler, H.-G.; Kishi, R.; Nakano, M.; Ghadwal, R. S. *Chem. A Eur. J.* **2019**, *25*, 3244–3247.
101. Breuers, V.; Lehmann, C. W.; Frank, W. *Chem. A Eur. J.* **2015**, *21*, 4596–4606.
102. Schoemaker, R.; Schwedtmann, K.; Franconetti, A.; Frontera, A.; Hennersdorf, F.; Weigand, J. J. *Chem. Sci.* **2019**, *10*, 11054–11063.
103. Schoemaker, R.; Kossatz, P.; Schwedtmann, K.; Hennersdorf, F.; Weigand, J. J. *Chem. A Eur. J.* **2020**, *26*, 11734–11741.
104. Breen, T. L.; Stephan, D. W. *Organometallics* **1997**, *16*, 365–369.
105. Weigand, J. J.; Burford, N.; Davidson, R. J.; Cameron, T. S.; Seelheim, P. *J. Am. Chem. Soc.* **2009**, *131*, 17943–17953.
106. Su, Y.; Zheng, X.; Wang, X.; Zhang, X.; Sui, Y.; Wang, X. *J. Am. Chem. Soc.* **2014**, *136*, 6251–6254.
107. Jevtovikj, I.; Lönnecke, P.; Hey-Hawkins, E. *Chem. Commun.* **2013**, *49*, 7355–7357.
108. Adhikari, A. K.; Sárosi, M. B.; Grell, T.; Lönnecke, P.; Hey-Hawkins, E. *Chem. A Eur. J.* **2016**, *22*, 15664–15668.
109. Adhikari, A. K.; Grell, T.; Lönnecke, P.; Hey-Hawkins, E. *Eur. J. Inorg. Chem.* **2017**, *2017*, 5329–5333.
110. Schwedtmann, K.; Haberstroh, J.; Roediger, S.; Bauzá, A.; Frontera, A.; Hennersdorf, F.; Weigand, J. J. *Chem. Sci.* **2019**, *10*, 6868–6875.
111. Kekia, O. M.; Jones, R. L.; Rheingold, A. L. *Organometallics* **1996**, *15*, 4104–4106.
112. Green, S. P.; Jones, C.; Stasch, A. *Science* **2007**, *318*, 1754.
113. Ganesamoorthy, C.; Krüger, J.; Wölper, C.; Nizovtsev, A. S.; Schulz, S. *Chem. A Eur. J.* **2017**, *23*, 2461–2468.
114. Chitnis, S. S.; Carpenter, Y.-Y.; Burford, N.; McDonald, R.; Ferguson, M. J. *Angew. Chem. Int. Ed.* **2013**, *52*, 4863–4866.
115. Chitnis, S. S.; Robertson, A. P. M.; Burford, N.; Weigand, J. J.; Fischer, R. *Chem. Sci.* **2015**, *6*, 2559–2574.
116. Chitnis, S. S.; Burford, N.; Weigand, J. J.; McDonald, R. *Angew. Chem. Int. Ed.* **2015**, *54*, 7828–7832.
117. Mehta, M.; McGrady, J. E.; Goicoechea, J. M. *Chem. A Eur. J.* **2019**, *25*, 5445–5450.
118. Borger, J. E.; Le Corre, G.; Mei, Y.; Suter, R.; Schrader, E.; Grützmacher, H. *Chem. A Eur. J.* **2019**, *25*, 3957–3962.
119. Hinz, A.; Hansmann, M. M.; Bertrand, G.; Goicoechea, J. M. *Chem. A Eur. J.* **2018**, *24*, 9514–9519.
120. Liu, L.; Ruiz, D. A.; Munz, D.; Bertrand, G. *Chem* **2016**, *1*, 147–153.
121. Hansmann, M. M.; Jazzar, R.; Bertrand, G. *J. Am. Chem. Soc.* **2016**, *138*, 8356–8359.
122. Yufanyi, D. M.; Grell, T.; Sárosi, M. B.; Lönnecke, P.; Hey-Hawkins, E. *Pure Appl. Chem.* **2019**, *91*, 785–796.
123. Yufanyi, D. M.; Grell, T.; Hey-Hawkins, E. *Eur. J. Inorg. Chem.* **2019**, *2019*, 1557–1561.
124. Nicholson, B. K.; Wilson, P. S.; Nancekivell, A. J. *Organomet. Chem.* **2013**, *745–746*, 80–85.
125. Wiśniewska, A.; Łapczuk-Krygier, A.; Baranowska, K.; Chojnacki, J.; Matern, E.; Pikies, J.; Grubba, R. *Polyhedron* **2013**, *55*, 45–48.
126. Arleth, N.; Gamer, M. T.; Köppe, R.; Pushkarevsky, N. A.; Konchenko, S. N.; Fleischmann, M.; Bodensteiner, M.; Scheer, M.; Roesky, P. W. *Chem. Sci.* **2015**, *6*, 7179–7184.
127. Mädl, E.; Balázs, G.; Peresykina, E. V.; Scheer, M. *Angew. Chem. Int. Ed.* **2016**, *55*, 7702–7707.
128. Piesch, M.; Dielmann, F.; Reichl, S.; Scheer, M. *Chem. A Eur. J.* **2020**, *26*, 1518–1524.
129. Piesch, M.; Seidl, M.; Stubenhofer, M.; Scheer, M. *Chem. A Eur. J.* **2019**, *25*, 6311–6316.
130. Krüger, J.; Ganesamoorthy, C.; John, L.; Wölper, C.; Schulz, S. *Chem. A Eur. J.* **2018**, *24*, 9157–9164.
131. Helling, C.; Wölper, C.; Schulz, S. *J. Am. Chem. Soc.* **2018**, *140*, 5053–5056.
132. Riedlberger, F.; Seidl, M.; Scheer, M. *Chem. Commun.* **2020**, *56*, 13836–13839.

133. Riedlberger, F.; Todisco, S.; Mastroiilli, P.; Timoshkin, A. Y.; Seidl, M.; Scheer, M. *Chem. A Eur. J.* **2020**, *26*, 16251–16255.
134. Piesch, M.; Seidl, M.; Scheer, M. *Chem. Sci.* **2020**, *11*, 6745–6751.
135. Butovskiy, M. V.; Balázs, G.; Bodensteiner, M.; Peresykina, E. V.; Virovets, A. V.; Sutter, J.; Scheer, M. *Angew. Chem. Int. Ed.* **2013**, *52*, 2972–2976.
136. Mädl, E.; Butovskiy, M. V.; Balázs, G.; Peresykina, E. V.; Virovets, A. V.; Seidl, M.; Scheer, M. *Angew. Chem. Int. Ed.* **2014**, *53*, 7643–7646.
137. Brake, H.; Peresykina, E.; Virovets, A. V.; Piesch, M.; Kremer, W.; Zimmermann, L.; Klimas, C.; Scheer, M. *Angew. Chem. Int. Ed.* **2020**, *59*, 16241–16246.
138. Yadav, R.; Simler, T.; Reichl, S.; Goswami, B.; Schoo, C.; Köppe, R.; Scheer, M.; Roesky, P. W. *J. Am. Chem. Soc.* **2020**, *142*, 1190–1195.
139. Yadav, R.; Goswami, B.; Simler, T.; Schoo, C.; Reichl, S.; Scheer, M.; Roesky, P. W. *Chem. Commun.* **2020**, *56*, 10207–10210.
140. Yadav, R.; Simler, T.; Goswami, B.; Schoo, C.; Köppe, R.; Dey, S.; Roesky, P. W. *Angew. Chem. Int. Ed.* **2020**, *59*, 9443–9447.
141. Piesch, M.; Scheer, M. *Organometallics* **2020**, *39*, 4247–4252.
142. Li, T.; Gamer, M. T.; Scheer, M.; Konchenko, S. N.; Roesky, P. W. *Chem. Commun.* **2013**, *49*, 2183–2185.
143. Schoo, C.; Bestgen, S.; Schmidt, M.; Konchenko, S. N.; Scheer, M.; Roesky, P. W. *Chem. Commun.* **2016**, *52*, 13217–13220.
144. Arleth, N.; Gamer, M. T.; Köppe, R.; Konchenko, S. N.; Fleischmann, M.; Scheer, M.; Roesky, P. W. *Angew. Chem. Int. Ed.* **2016**, *55*, 1557–1560.
145. Schmidt, M.; Konieczny, D.; Peresykina, E. V.; Virovets, A. V.; Balázs, G.; Bodensteiner, M.; Riedlberger, F.; Krauss, H.; Scheer, M. *Angew. Chem. Int. Ed.* **2017**, *56*, 7307–7311.
146. Mädl, E.; Peresykina, E.; Timoshkin, A. Y.; Scheer, M. *Chem. Commun.* **2016**, *52*, 12298–12301.
147. Ziegler, C. G. P.; Maier, T. M.; Pelties, S.; Taube, C.; Hennersdorf, F.; Ehlers, A. W.; Weigand, J. J.; Wolf, R. *Chem. Sci.* **2019**, *10*, 1302–1308.
148. Piesch, M.; Reichl, S.; Seidl, M.; Balázs, G.; Scheer, M. *Angew. Chem. Int. Ed.* **2019**, *58*, 16563–16568.
149. Heindl, C.; Peresykina, E. V.; Lüdeker, D.; Brunklaus, G.; Virovets, A. V.; Scheer, M. *Chem. A Eur. J.* **2016**, *22*, 2599–2604.
150. Fleischmann, M.; Dielmann, F.; Gregoriades, L. J.; Peresykina, E. V.; Virovets, A. V.; Huber, S.; Timoshkin, A. Y.; Balázs, G.; Scheer, M. *Angew. Chem. Int. Ed.* **2015**, *54*, 13110–13115.
151. Heindl, C.; Peresykina, E. V.; Virovets, A. V.; Balázs, G.; Scheer, M. *Chem. A Eur. J.* **2016**, *22*, 1944–1948.
152. Turberville, R. S. P.; Jupp, A. R.; McCullough, P. S. B.; Ergöçmen, D.; Goicoechea, J. M. *Organometallics* **2013**, *32*, 2234–2244.
153. Kosnik, S. C.; Nascimento, M. C.; Binder, J. F.; Macdonald, C. L. B. *Dalton Trans.* **2017**, *46*, 17080–17092.
154. Kosnik, S. C.; Bascir, J. F.; Nascimento, M. C.; Swidan, A. A.; Macdonald, C. L. B. *Chem. A Eur. J.* **2019**, *25*, 1208–1211.
155. Kosnik, S. C.; Farrar, G. J.; Norton, E. L.; Cooper, B. F. T.; Ellis, B. D.; Macdonald, C. L. B. *Inorg. Chem.* **2014**, *53*, 13061–13069.
156. Hoidn, C. M.; Scott, D. J.; Wolf, R. *Chem. A Eur. J.* **2021**, *27*, 1886–1902.
157. Borger, J. E.; Ehlers, A. W.; Sloatweg, J. C.; Lammertsma, K. *Chem. A Eur. J.* **2017**, *23*, 11738–11746.
158. Holthausen, M. H.; Weigand, J. J. *Chem. Soc. Rev.* **2014**, *43*, 6639–6657.
159. Seidl, M.; Balázs, G.; Scheer, M. *Chem. Rev.* **2019**, *119*, 8406–8434.
160. Mal, P.; Breiner, B.; Rissanen, K.; Nitschke, J. R. *Science* **2009**, *324*, 1697.
161. Yang, D.; Zhao, J.; Yu, L.; Lin, X.; Zhang, W.; Ma, H.; Gogoll, A.; Zhang, Z.; Wang, Y.; Yang, X.-J.; Wu, B. *J. Am. Chem. Soc.* **2017**, *139*, 5946–5951.
162. Jiao, T.; Chen, L.; Yang, D.; Li, X.; Wu, G.; Zeng, P.; Zhou, A.; Yin, Q.; Pan, Y.; Wu, B.; Hong, X.; Kong, X.; Lynch, V. M.; Sessler, J. L.; Li, H. *Angew. Chem. Int. Ed.* **2017**, *56*, 14545–14550.
163. Schwarzmaier, C.; Schindler, A.; Heindl, C.; Scheuermayer, S.; Peresykina, E. V.; Virovets, A. V.; Neumeier, M.; Gschwind, R.; Scheer, M. *Angew. Chem. Int. Ed.* **2013**, *52*, 10896–10899.
164. Riddlestone, I. M.; Weis, P.; Martens, A.; Schorpp, M.; Scherer, H.; Krossing, I. *Chem. A Eur. J.* **2019**, *25*, 10546–10551.
165. Borger, J. E.; Bakker, M. S.; Ehlers, A. W.; Lutz, M.; Sloatweg, J. C.; Lammertsma, K. *Chem. Commun.* **2016**, *52*, 3284–3287.
166. Forfar, L. C.; Zeng, D.; Green, M.; McGrady, J. E.; Russell, C. A. *Chem. A Eur. J.* **2016**, *22*, 5397–5403.
167. Heindl, C.; Peresykina, E. V.; Timoshkin, A. Y.; Mastroiilli, P.; Gallo, V.; Scheer, M. *Angew. Chem. Int. Ed.* **2013**, *52*, 10887–10891.
168. Hällner, L. J. L.; Mas-Marzá, E.; Cybulski, M. K.; Sanguramath, R. A.; Macgregor, S. A.; Mahon, M. F.; Raynaud, C.; Russell, C. A.; Whittlesey, M. K. *Dalton Trans.* **2017**, *46*, 2861–2873.
169. Schwarzmaier, C.; Sierka, M.; Scheer, M. *Angew. Chem. Int. Ed.* **2013**, *52*, 858–861.
170. Schwarzmaier, C.; Timoshkin, A. Y.; Scheer, M. *Angew. Chem. Int. Ed.* **2013**, *52*, 7600–7603.
171. Spitzer, F.; Sierka, M.; Latronico, M.; Mastroiilli, P.; Virovets, A. V.; Scheer, M. *Angew. Chem. Int. Ed.* **2015**, *54*, 4392–4396.
172. Mirabello, V.; Caporali, M.; Gallo, V.; Gonsalvi, L.; Gudat, D.; Frey, W.; Ienco, A.; Latronico, M.; Mastroiilli, P.; Peruzzini, M. *Chem. A Eur. J.* **2012**, *18*, 11238–11250.
173. Caporali, M.; Calvo, F. D.; Bazzicalupi, C.; Costantini, S. S.; Peruzzini, M. *J. Organomet. Chem.* **2018**, *859*, 68–74.
174. Dorsey, C. L.; Squires, B. M.; Hudnall, T. W. *Angew. Chem. Int. Ed.* **2013**, *52*, 4462–4465.
175. Martin, C. D.; Weinstein, C. M.; Moore, C. E.; Rheingold, A. L.; Bertrand, G. *Chem. Commun.* **2013**, *49*, 4486–4488.
176. Holthausen, M. H.; Hepp, A.; Weigand, J. J. *Chem. A Eur. J.* **2013**, *19*, 9895–9907.
177. Borger, J. E.; Ehlers, A. W.; Lutz, M.; Sloatweg, J. C.; Lammertsma, K. *Angew. Chem. Int. Ed.* **2016**, *55*, 613–617.
178. Borger, J. E.; Ehlers, A. W.; Lutz, M.; Sloatweg, J. C.; Lammertsma, K. *Angew. Chem. Int. Ed.* **2014**, *53*, 12836–12839.
179. Borger, J. E.; Ehlers, A. W.; Lutz, M.; Sloatweg, J. C.; Lammertsma, K. *Angew. Chem. Int. Ed.* **2017**, *56*, 285–290.
180. Xu, L.; Chi, Y.; Du, S.; Zhang, W.-X.; Xi, Z. *Angew. Chem. Int. Ed.* **2016**, *55*, 9187–9190.
181. Du, S.; Hu, J.; Chai, Z.; Zhang, W.-X.; Xi, Z. *Chin. J. Chem.* **2019**, *37*, 71–75.
182. Sängler, I.; Breunig, J.; Schödel, F.; Bolte, M.; Lerner, H.-W. *Z. Naturforsch. B* **2016**, *71*, 135–139.
183. Holthausen, M. H.; Sala, C.; Weigand, J. J. *Inorg. Chem.* **2016**, *2016*, 667–677.
184. Arrowsmith, M.; Hill, M. S.; Johnson, A. L.; Kociok-Köhne, G.; Mahon, M. F. *Angew. Chem. Int. Ed.* **2015**, *54*, 7882–7885.
185. Du, S.; Yang, J.; Hu, J.; Chai, Z.; Luo, G.; Luo, Y.; Zhang, W.-X.; Xi, Z. *J. Am. Chem. Soc.* **2019**, *141*, 6843–6847.
186. Prabusankar, G.; Doddi, A.; Gemel, C.; Winter, M.; Fischer, R. A. *Inorg. Chem.* **2010**, *49*, 7976–7980.
187. Hennersdorf, F.; Frötschel, J.; Weigand, J. J. *J. Am. Chem. Soc.* **2017**, *139*, 14592–14604.
188. Holthausen, M. H.; Weigand, J. J. *Dalton Trans.* **2016**, *45*, 1953–1961.
189. Reiter, D.; Frisch, P.; Wendel, D.; Hörmann, F. M.; Inoue, S. *Dalton Trans.* **2020**, *49*, 7060–7068.
190. Dube, J. W.; Graham, C. M. E.; Macdonald, C. L. B.; Brown, Z. D.; Power, P. P.; Ragogna, P. J. *Chem. A Eur. J.* **2014**, *20*, 6739–6744.
191. Graham, C. M. E.; Macdonald, C. L. B.; Power, P. P.; Brown, Z. D.; Ragogna, P. J. *Inorg. Chem.* **2017**, *56*, 9111–9119.
192. Roy, M. M. D.; Ferguson, M. J.; McDonald, R.; Zhou, Y.; Rivard, E. *Chem. Sci.* **2019**, *10*, 6476–6481.
193. Seitz, A. E.; Eckhardt, M.; Sen, S. S.; Erlebach, A.; Peresykina, E. V.; Roesky, H. W.; Sierka, M.; Scheer, M. *Angew. Chem. Int. Ed.* **2017**, *56*, 6655–6659.
194. Heindl, C.; Balázs, G.; Stauber, A.; Scheer, M. *Angew. Chem. Int. Ed.* **2016**, *55*, 15524–15527.
195. Heindl, C.; Reisinger, S.; Schwarzmaier, C.; Bodensteiner, M.; Scheer, M. *Angew. Chem. Int. Ed.* **2014**, *53*, 7639–7642.
196. Schwamm, R. J.; Harmer, J. R.; Lein, M.; Fitchett, C. M.; Granville, S.; Coles, M. P. *Angew. Chem. Int. Ed.* **2015**, *54*, 10630–10633.
197. Seitz, A. E.; Vogel, U.; Eberl, M.; Eckhardt, M.; Balázs, G.; Peresykina, E. V.; Bodensteiner, M.; Zabel, M.; Scheer, M. *Chem. A Eur. J.* **2017**, *23*, 10319–10327.
198. Schmidt, M.; Seitz, A. E.; Eckhardt, M.; Balázs, G.; Peresykina, E. V.; Virovets, A. V.; Riedlberger, F.; Bodensteiner, M.; Zolnhofer, E. M.; Meyer, K.; Scheer, M. *J. Am. Chem. Soc.* **2017**, *139*, 13981–13984.
199. Borger, J. E.; Jongkind, M. K.; Ehlers, A. W.; Lutz, M.; Sloatweg, J. C.; Lammertsma, K. *ChemistryOpen* **2017**, *6*, 350–353.

200. Schwarzmaier, C.; Timoshkin, A. Y.; Balázs, G.; Scheer, M. *Angew. Chem. Int. Ed.* **2014**, *53*, 9077–9081.
201. Schwarzmaier, C.; Heintl, S.; Balázs, G.; Scheer, M. *Angew. Chem. Int. Ed.* **2015**, *54*, 13116–13121.
202. Grünbauer, R.; Schwarzmaier, C.; Eberl, M.; Balázs, G.; Scheer, M. *Inorg. Chim. Acta* **2021**, *518*, 120234.
203. Chakraborty, U.; Leitt, J.; Mühlhoff, B.; Bodensteiner, M.; Pelties, S.; Wolf, R. *Dalton Trans.* **2018**, *47*, 3693–3697.
204. Heintl, S.; Scheer, M. *Chem. Sci.* **2014**, *5*, 3221–3225.
205. Heintl, S.; Timoshkin, A. Y.; Müller, J.; Scheer, M. *Chem. Commun.* **2018**, *54*, 2244–2247.
206. Spitzer, F.; Graßl, C.; Balázs, G.; Zolnhofer, E. M.; Meyer, K.; Scheer, M. *Angew. Chem. Int. Ed.* **2016**, *55*, 4340–4344.
207. Yao, S.; Szilvási, T.; Lindenmaier, N.; Xiong, Y.; Inoue, S.; Szilvási, T.; Adelhardt, M.; Sutter, J.; Meyer, K.; Driess, M. *Chem. Commun.* **2015**, *51*, 6153–6156.
208. Lohrey, T. D.; Rao, G.; Britt, R. D.; Bergman, R. G.; Arnold, J. *Inorg. Chem.* **2019**, *58*, 13492–13501.
209. Bispinghoff, M.; Benkő, Z.; Grützmacher, H.; Calvo, F. D.; Caporali, M.; Peruzzini, M. *Dalton Trans.* **2019**, *48*, 3593–3600.
210. Spitzer, F.; Graßl, C.; Balázs, G.; Müdl, E.; Keilwerth, M.; Zolnhofer, E. M.; Meyer, K.; Scheer, M. *Chem. A Eur. J.* **2017**, *23*, 2716–2721.
211. Yao, S.; Lindenmaier, N.; Xiong, Y.; Inoue, S.; Szilvási, T.; Adelhardt, M.; Sutter, J.; Meyer, K.; Driess, M. *Angew. Chem. Int. Ed.* **2015**, *54*, 1250–1254.
212. Hoidn, C. M.; Maier, T. M.; Trabitsch, K.; Weigand, J. J.; Wolf, R. *Angew. Chem. Int. Ed.* **2019**, *58*, 18931–18936.
213. Dielmann, F.; Timoshkin, A.; Piesch, M.; Balázs, G.; Scheer, M. *Angew. Chem. Int. Ed.* **2017**, *56*, 1671–1675.
214. Graßl, C.; Bodensteiner, M.; Zabel, M.; Scheer, M. *Chem. Sci.* **2015**, *6*, 1379–1382.
215. Spitzer, F.; Balázs, G.; Graßl, C.; Keilwerth, M.; Meyer, K.; Scheer, M. *Angew. Chem. Int. Ed.* **2018**, *57*, 8760–8764.
216. Spitzer, F.; Balázs, G.; Graßl, C.; Scheer, M. *Chem. Commun.* **2020**, *56*, 13209–13212.
217. Beltrán-Suito, R.; Forstner, V.; Hausmann, J. N.; Mebs, S.; Schmidt, J.; Zaharieva, I.; Laun, K.; Zebger, I.; Dau, H.; Menezes, P. W.; Driess, M. *Chem. Sci.* **2020**, *11*, 11834–11842.
218. Hierlmeier, G.; Coburger, P.; van Leest, N. P.; de Bruin, B.; Wolf, R. *Angew. Chem. Int. Ed.* **2020**, *59*, 14148–14153.
219. Pelties, S.; Herrmann, D.; de Bruin, B.; Hartl, F.; Wolf, R. *Chem. Commun.* **2014**, *50*, 7014–7016.
220. Pelties, S.; Ehlers, A. W.; Wolf, R. *Chem. Commun.* **2016**, *52*, 6601–6604.
221. Zhang, F.; Zhang, J.; Chen, Z.; Weng, L.; Zhou, X. *Inorg. Chem.* **2019**, *58*, 8451–8459.
222. Du, S.; Yin, J.; Chi, Y.; Xu, L.; Zhang, W.-X. *Angew. Chem. Int. Ed.* **2017**, *56*, 15886–15890.
223. Huang, W.; Diaconescu, P. L. *Eur. J. Inorg. Chem.* **2013**, *2013*, 4090–4096.
224. Patel, D.; Tuna, F.; McInnes, E. J. L.; Lewis, W.; Blake, A. J.; Liddle, S. T. *Angew. Chem. Int. Ed.* **2013**, *52*, 13334–13337.
225. Dragulescu-Andrasi, A.; Miller, L. Z.; Chen, B.; McQuade, D. T.; Shatruk, M. *Angew. Chem. Int. Ed.* **2016**, *55*, 3904–3908.
226. Romanenko, V. D.; Rudzevich, V. L.; Rusanov, E. B.; Chernega, A. N.; Senio, A.; Sotiropoulos, J.-M.; Pfister-Guillouzo, G.; Sanchez, M. *J. Chem. Soc. Chem. Commun.* **1995**, (13), 1383–1385.
227. Bresien, J.; Faust, K.; Hering-Junghans, C.; Rothe, J.; Schulz, A.; Villinger, A. *Dalton Trans.* **2016**, *45*, 1998–2007.
228. Bresien, J.; Hinz, A.; Schulz, A.; Villinger, A. *Eur. J. Inorg. Chem.* **2018**, *2018*, 1679–1682.
229. Grell, T.; Hey-Hawkins, E. *Eur. J. Inorg. Chem.* **2020**, *2020*, 732–736.
230. Grell, T.; Hey-Hawkins, E. *Inorg. Chem.* **2020**, *59*, 7487–7503.
231. Grell, T.; Hey-Hawkins, E. *Chem. A Eur. J.* **2020**, *26*, 1008–1012.
232. Donath, M.; Bodensteiner, M.; Weigand, J. J. *Chem. A Eur. J.* **2014**, *20*, 17306–17310.
233. Krüger, J.; Wölper, C.; Schulz, S. *Inorg. Chem.* **2020**, *59*, 11142–11151.
234. Tuscher, L.; Ganesamoorthy, C.; Bläser, D.; Wölper, C.; Schulz, S. *Angew. Chem. Int. Ed.* **2015**, *54*, 10657–10661.
235. Tuscher, L.; Helling, C.; Ganesamoorthy, C.; Krüger, J.; Wölper, C.; Frank, W.; Nizovtsev, A. S.; Schulz, S. *Chem. A Eur. J.* **2017**, *23*, 12297–12304.
236. Ganesamoorthy, C.; Wölper, C.; Nizovtsev, A. S.; Schulz, S. *Angew. Chem. Int. Ed.* **2016**, *55*, 4204–4209.
237. Schöo, C.; Bestgen, S.; Egeberg, A.; Klementyeva, S.; Feldmann, C.; Konchenko, S. N.; Roesky, P. W. *Angew. Chem. Int. Ed.* **2018**, *57*, 5912–5916.
238. Quintero, G. E.; Paterson-Taylor, I.; Rees, N. H.; Goicoechea, J. M. *Dalton Trans.* **2016**, *45*, 1930–1936.
239. Xiong, Y.; Yao, S.; Brym, M.; Driess, M. *Angew. Chem. Int. Ed.* **2007**, *46*, 4511–4513.
240. Ziegler, C. G. P.; Taube, C.; Kelly, J. A.; Hierlmeier, G.; Uttendorfer, M.; Weigand, J. J.; Wolf, R. *Chem. Commun.* **2020**, *56*, 14071–14074.
241. Jo, M.; Li, J.; Dragulescu-Andrasi, A.; Rogachev, A. Y.; Shatruk, M. *Dalton Trans.* **2020**, *49*, 12955–12959.
242. Holthausen, M. H.; Feldmann, K.-O.; Schulz, S.; Hepp, A.; Weigand, J. J. *Inorg. Chem.* **2012**, *51*, 3374–3387.
243. Holthausen, M. H.; Surmiak, S. K.; Jerabek, P.; Frenking, G.; Weigand, J. J. *Angew. Chem. Int. Ed.* **2013**, *52*, 11078–11082.
244. Adhikari, A. K.; Ziegler, C. G. P.; Schwedtmann, K.; Taube, C.; Weigand, J. J.; Wolf, R. *Angew. Chem. Int. Ed.* **2019**, *58*, 18584–18590.
245. Hennersdorf, F.; Weigand, J. J. *Angew. Chem. Int. Ed.* **2017**, *56*, 7858–7862.
246. Ziegler, C. G. P.; Hennersdorf, F.; Weigand, J. J.; Wolf, R. *Z. Anorg. Allg. Chem.* **2020**, *646*, 552–557.
247. Müller, J.; Heintl, S.; Schwarzmaier, C.; Balázs, G.; Keilwerth, M.; Meyer, K.; Scheer, M. *Angew. Chem. Int. Ed.* **2017**, *56*, 7312–7317.
248. Grünbauer, R.; Balázs, G.; Scheer, M. *Chem. A Eur. J.* **2020**, *26*, 11722–11726.
249. Schwarzmaier, C.; Bodensteiner, M.; Timoshkin, A. Y.; Scheer, M. *Angew. Chem. Int. Ed.* **2014**, *53*, 290–293.
250. Giese, S.; Buzsáki, D.; Nyulászi, L.; Müller, C. *Chem. Commun.* **2019**, *55*, 13812–13815.
251. Kaas, M.; Korber, N. Z. *Anorg. Allg. Chem.* **2019**, *645*, 146–148.
252. Schipper, D. E.; Ikhlef, D.; Khalal, S.; Saillard, J.-Y.; Whitmire, K. H. *Inorg. Chem.* **2016**, *55*, 6679–6684.
253. Monakhov, K. Y.; Gourlaouen, C.; Zessin, T.; Linti, G. *Inorg. Chem.* **2013**, *52*, 6782–6784.

## 1.20 Zintl chemistry: From zintl ions to zintl clusters

Lei Qiao<sup>a</sup>, John E. McGrady<sup>b</sup>, and Zhong-Ming Sun<sup>a</sup>, <sup>a</sup>School of Materials Science and Engineering, State Key Laboratory of Elemento-Organic Chemistry, Nankai University, Tianjin, China; and <sup>b</sup>Department of Chemistry, University of Oxford, Oxford, United Kingdom

© 2023 Elsevier Ltd. All rights reserved.

<b>1.20.1</b>	<b>Introduction</b>	<b>903</b>
1.20.1.1	The development of Zintl chemistry	903
1.20.1.2	Definitions	904
<b>1.20.2</b>	<b>New members of main group Zintl polyanions</b>	<b>904</b>
1.20.2.1	Homo-atomic Zintl anions	904
1.20.2.2	Heteroatomic Zintl anions	905
<b>1.20.3</b>	<b>Zintl anions functionalized with organic groups</b>	<b>906</b>
1.20.3.1	Group 14 Zintl anions functionalized with main group elements or organic groups	906
1.20.3.2	Group 15 Zintl anions functionalized with organic groups	907
<b>1.20.4</b>	<b>Inter-metalloid and heterometallic clusters</b>	<b>908</b>
1.20.4.1	Binary inter-metalloid clusters of the group 14 elements	908
1.20.4.1.1	Deltahedral clusters with 9, 10, 11 and 12 vertices	908
1.20.4.1.2	Non-deltahedral cluster with 10 and 12 vertices	910
1.20.4.1.3	Larger intermetalloid clusters of the group 14 elements	911
1.20.4.2	Coordination compounds and heterometallic clusters of the group 14 elements	911
1.20.4.2.1	Coordination compounds of $Tt_4^{4-}$ , $Tt_5^{2-}$ and $Tt_9^{4-}$	911
1.20.4.2.2	Other coordination compounds and heterometallic clusters	913
1.20.4.2.3	Coordination compounds of substituted Zintl anions	915
1.20.4.3	Binary intermetalloid clusters of the group 15 elements	918
1.20.4.4	Coordination compounds and heterometallic clusters of the group 15 elements	919
1.20.4.5	Ternary clusters	922
1.20.4.5.1	Ternary clusters containing the post transition metal atoms	922
1.20.4.5.2	Ternary clusters containing lanthanides, actinides and early transition metal atoms	923
<b>1.20.5</b>	<b>Formation of Zintl clusters in solution</b>	<b>924</b>
1.20.5.1	Oxidation or charge neutralization reactions	925
1.20.5.2	Ligand exchange reactions	925
1.20.5.3	Re-arrangement reactions	925
1.20.5.4	A comprehensive example on the growth of tin cluster	925
<b>1.20.6</b>	<b>Electronic structure and bonding</b>	<b>926</b>
<b>1.20.7</b>	<b>Potential applications of Zintl ions/clusters in materials science and catalysis</b>	<b>927</b>
<b>References</b>		<b>930</b>

### Abstract

Zintl chemistry is an aged and vital research topic in inorganic chemistry and attracts much more attention of inorganic and theoretical chemists as well as materials scientists. Its antiquity lies in durable research interests from 1890s to now; however, the thriving innovative potential in interdiscipline is the embodiment of its vitality. In the past two decades, Zintl chemistry has experienced an unprecedented renaissance as a result of many important breakthroughs in the synthetic methods, characterization techniques and quantum chemical calculations. This chapter will report systematically on the synthesis of related anions or clusters, which includes intermetalloid and heterometallic clusters as well as their derivatives functionalized with organic-group(s). We will also discuss the formation mechanisms of Zintl anions in solution by ex situ investigations (the characterization and even isolation of key intermediates) and quantum chemical investigations. Additionally, the chapter will shed light on the relationships between the electronic structures and topologies by some selected examples. Finally, some recent progress of material science using Zintl cluster as precursor will also be shown in the end of this chapter.

### 1.20.1 Introduction

#### 1.20.1.1 The development of Zintl chemistry

The intrinsic appeal of Zintl chemistry lies in the fact that Zintl anions are building blocks which can, through the judicious use of oxidizing agents, be used to generate higher nuclearity clusters and hybrid materials. Those newly formed materials often exhibit



unprecedented structural motifs and unique modes of bonding, and have, as a result, captured the attention of theoretical chemists as well as materials scientists interested in exploiting their extraordinarily versatile structural chemistry. The field of Zintl chemistry can be traced back to experiments by Joannis performed in 1891, which showed that main group (semi)-metals can react with the liquid ammonia solutions of sodium.<sup>1</sup> Based on electrochemical data, Smyth and Kraus<sup>2–4</sup> subsequently predicted the presence of highly negatively charged poly-anions but it was not until 1931 that Eduard Zintl confirmed the compositions of these solutions using potentiometric titrations.<sup>5</sup> Zintl also noted the similarity between the soluble poly-anions formed by reduction of metals and those obtained from dissolution of the binary alloy  $\text{Na}_4\text{Pb}_9$  in liquid ammonia. Some 10 years later, in recognition of the pioneering work of Zintl, Laves coined the word ‘Zintl phase’ to describe these alloy materials.<sup>6</sup> From that promising beginning, relatively little progress was made until the 1970s, probably due to their extreme air sensitivity and the lack of high-vacuum experimental apparatus. The first characterization of a Zintl anion by X-ray single-crystal diffraction, a *nido*-type  $\text{Sn}_9^{4-}$  anion obtained from dissolution of a Na–Sn alloy in liquid ammonia, was reported by Kummer and Diehl in 1970.<sup>7,8</sup> The advent of cation sequestering agents such as 2,2,2-crypt and 18-crown-6 allowed for a rapid expansion of the field, and the reactions of Zintl anions with transition metal complexes such as  $\text{Pt}(\text{PPh}_3)_4$ <sup>9</sup> and  $\text{Cr}(\text{CO})_3(\text{Mes})$ <sup>10</sup> gave rise to a new class of compounds containing both transition and main-group metals. In more recent times, Zintl chemistry has very much been focused on their unique structural chemistry and chemical bonding patterns, and the emergence of density functional theory as a reliable computational tool has played a significant role in expanding our understanding of increasingly complex structures. More recently, attention has turned to mechanistic questions, relating both to cluster growth and to catalysis of small-molecule activation. The significant recent developments in the field can broadly be grouped into four distinct categories: (1) the synthesis of homoatomic and heteroatomic Zintl anions, organic ligand-protected Zintl anions and Zintl clusters with transition metal atoms; (2) the study of the electronic structure and bonding of Zintl anions; (3) the elucidation of cluster-growth mechanisms for Zintl clusters, an area where quantum chemical calculations have played a particularly prominent role and (4) the incorporation of Zintl phases or clusters into hybrid materials. An 2010 article entitled “Zintl anions” featured in Comprehensive Inorganic Chemistry II, in which Corbett discussed their history, synthetic routes and reactivity. The field has moved on substantially over the past decade, with many new types of cluster anions being formed, and our understanding of their electronic structures and bonding has also evolved through concepts such as superatoms and “aromaticity.” Our purpose in this chapter is to review these advances in the decade since the publication of Comprehensive Inorganic Chemistry II.

### 1.20.1.2 Definitions

The broad subject of Zintl chemistry encompasses studies of Zintl phases as well as of salts containing discrete Zintl polyanions. Zintl phases, typically formed through high-temperature solid-state techniques, contain (semi)-metal polyanions along with alkali/alkaline-earth metals which are directly bound to the clusters whereas Zintl salts are generally based on discrete anions and sequestered or complex cations such as  $[\text{K}(2.2.2\text{-crypt})]^+$ ,  $[\text{Na}(18\text{-crown-6})]^+$  and  $[(\text{C}_4\text{H}_9)_4\text{P}]^+$ . The distinction is, however, not absolutely clear, and there are many examples where both directly-bound and sequestered alkali metal cations are present in the same compound. In this chapter, we focus on the Zintl salts and the related solution-based chemistry. The diverse nature of the field requires a clear frame of reference, and for that purpose we adopt the following conventions: clusters containing only main group (semi)-metal atoms are described as “Zintl anions” or “Zintl polyanions” (e.g.,  $\text{Ge}_9^{4-}$ ,<sup>11</sup>  $\text{Sb}_7^{3-12}$  and  $(\text{Sn}_2\text{Sb}_2)^{2-}$ ).<sup>13</sup> If a structure contains both main group and transition metal elements, the term “Zintl cluster” is more appropriate and more widely used. From a structural perspective, Zintl clusters can be divided into two classes based on the presence or absence of one or more transition metal atoms/ions at the center of the cluster. For the former, we will adopt Fässler’s definition: an inter-metalloid cluster is one where one or more inner (usually transition) metal atoms is encapsulated inside a cluster shell made up of a significantly larger number of (semi) metal atoms.<sup>14</sup> Inter-metalloid clusters of this type can be written as  $[\text{M}_x@E_y]^{q-}$  or  $[\text{M}_x@E_y\text{M}_z]^{q-}$  (M: transition metal, lanthanide, or actinide atoms; E: p-block (semi) metal atoms), where  $x$  is generally much smaller than  $y$  or  $y + z$ . Examples of this kind include  $[\text{Pt}@\text{Pb}_{12}]^{2-15}$  and  $[\text{Zn}@\text{Zn}_5\text{Sn}_3\text{Bi}_8]^{4-}$ .<sup>16</sup> In contrast, clusters such as  $[\text{Bi}_4\text{Ni}_4(\text{CO})_6]^{2-17}$  which lack a transition metal atom/ion at their center will be termed “heterometallic clusters” and designated as  $[E_y\text{M}_z]^{q-}$ .

## 1.20.2 New members of main group Zintl polyanions

Beyond the definitions noted in the previous paragraph, main group Zintl poly-anions can be further divided into homo- and hetero-atomic cases. The utility of Zintl poly-anions as building blocks in the construction of novel Zintl anions or clusters will be documented in Sections 1.20.3 and 1.20.4, so we begin this review with a summary of the many new homo- and hetero-atomic Zintl anions that have emerged in the recent literature.

### 1.20.2.1 Homo-atomic Zintl anions

The *nido*- $\text{Tt}_5^{4-}$  anions of group 14 have been well established for some time, as have the 2-electron oxidized *closo* equivalents,  $\text{Tt}_5^{2-}$  (E = Si, Ge) and also the radical species  $\text{Tt}_5^{3-}$  (E = Si–Pb). Smaller *closo*- $\text{Tt}_5^{2-}$  (E = Si–Pb) and  $\text{Tt}_4^{4-}$  (E = Si–Pb) are known, as are the larger  $\text{Tt}_{10}^{2-}$  (Tt = Ge, Pb). Icosahedral stannaspherene ( $\text{Sn}_{12}^{2-}$ )<sup>18</sup> and plumbaspherene ( $\text{Pb}_{12}^{2-}$ )<sup>19</sup> were detected in the gas phase by Wang and co-workers in 2006, but have still not been isolated from the solution. The square antiprismatic  $\text{Sn}_8^{6-}$  has been observed



in the solid state but has not been isolated from solution.<sup>20</sup> Turning to group 15, nortricyclane-type  $\text{Pn}_7^{3-}$  and ufosane-type  $\text{Pn}_{11}^{3-}$  ( $\text{Pn} = \text{P-Sb}$ ) anions are well known, but the recent synthesis of analogous bismuth poly-anions  $\text{Bi}_7^{3-}$  (Fig. 1A)<sup>21</sup> and  $\text{Bi}_{11}^{3-}$  (Fig. 1B)<sup>22</sup> using pyridine (py) solvent as an oxidizing agent has completed the series of ufosane-type and nortricyclane-type polypnictide anions for the pnictogens P–Bi.

### 1.20.2.2 Heteroatomic Zintl anions

The reactivity of the  $\text{Tt}_4^{4-}$  anions ( $\text{Tt} = \text{Ge-Sn}$ ) is of considerable interest because they are isoelectronic and isostructural with  $\text{P}_4$  and  $\text{As}_4$ , both of which have an extensive coordination chemistry. However, the 4- charge mitigates against solubility, and prevents their isolation from common solvents such as en, py and DMF. One strategy to overcome this problem is to turn instead to binary pseudo-tetrahedral Zintl anions with lower charge such as  $[\text{TrBi}_3]^{2-}$  ( $\text{Tr} = \text{Ga},^{23} \text{In},^{23} \text{Tl}^{24}$ ) or  $[\text{Tt}_2\text{Pn}_2]^{2-}$  ( $\text{Tt/Pn} = \text{Ge/P},^{25} \text{Sn/Sb},^{13,26} \text{Sn/Bi},^{27} \text{Pb/Bi}^{28}$ ), all of which can be extracted from the corresponding ternary Zintl phases. Further oxidation of these anions with solvent or organic or organometallic compounds has opened up pathways to several novel ternary clusters (Section 1.20.4.5) as well as binary Zintl anions such as  $[\text{Tr}_4\text{Bi}_5]^{2-}$ ,<sup>23,29</sup> and  $[\text{Tt}_2\text{Pn}_7]^{2-}$ .<sup>16,25,28,30</sup> For example, the eight-vertex heteroatomic Zintl anion  $[\text{Sn}_5\text{Sb}_3]^{3-}$ ,<sup>31</sup> an *arachno*-type cluster within the Wade-Mingos framework, has been isolated from an en solution of  $\text{K}_2\text{SnSb}$  in the presence of  $[\text{Bu}_4\text{P}]\text{Br}$  (Fig. 2A). The  $[\text{Sn}_5\text{Sb}_3]^{3-}$  anion is found in the ternary cluster dimer  $\{[\text{CuSn}_5\text{Sb}_3]^{2-}\}_2$ <sup>26</sup> while different combinations of tetrel and pnictide elements are found in the family of  $\{[\text{AuTt}_5\text{Pn}_3]^{2-}\}_2$  anions ( $\text{Tt/Pn} = \text{Pb/Sb}; \text{Sn/Sb}; \text{Sn/Bi}$ ).<sup>32</sup> It is possible that the discrete  $[\text{Pn}_5\text{Tt}_3]^{3-}$  anions are active intermediates for the formation of the ternary hetero-metallic clusters. A much larger binary anion,  $[\text{Ge}_4\text{Bi}_{14}]^{4-}$  (Fig. 2B),<sup>33</sup> is obtained by extraction from a ternary Zintl phase with a nominal

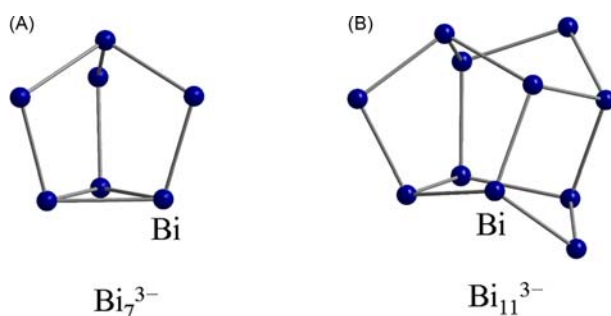


Fig. 1 Molecular structure of new members of homoatomic Zintl anions: (A)  $\text{Bi}_7^{3-}$  and (B)  $\text{Bi}_{11}^{3-}$ .

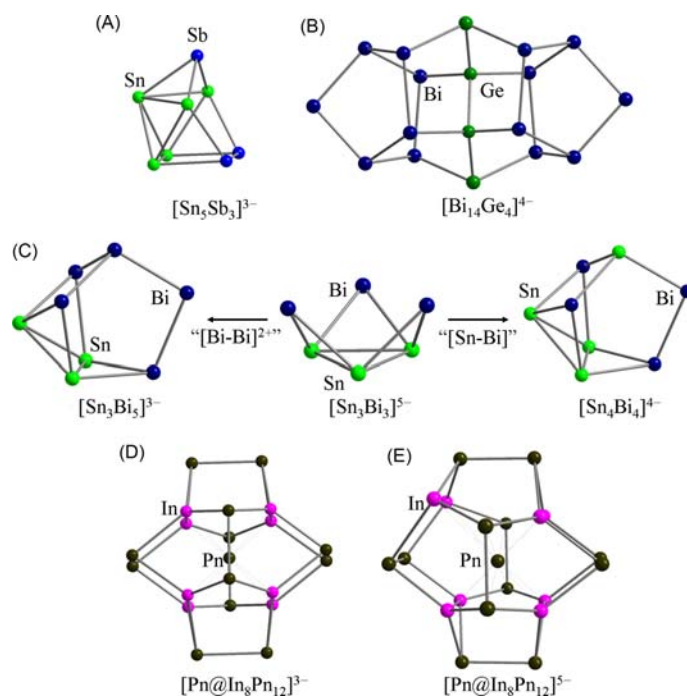


Fig. 2 Molecular structure of new members of heteroatomic Zintl anions: (A)  $[\text{Sn}_5\text{Sb}_3]^{3-}$ , (B)  $[\text{Bi}_{14}\text{Ge}_4]^{4-}$ , (C)  $[\text{Sn}_3\text{Bi}_5]^{3-}$ ,  $[\text{Sn}_3\text{Bi}_3]^{5-}$ ,  $[\text{Sn}_4\text{Bi}_4]^{4-}$ , (D)  $[\text{Pn}@_{\text{In}_8}\text{Pn}_{12}]^{3-}$  ( $\text{Pn} = \text{Sb}, \text{Bi}$ ) and (E)  $[\text{Pn}@_{\text{In}_8}\text{Pn}_{12}]^{5-}$  ( $\text{Pn} = \text{Sb}, \text{Bi}$ ).

composition of "K<sub>2</sub>GeBi." The structure can be described either as two Bi<sub>7</sub> anions connected by a zigzag Ge<sub>4</sub> chain or, alternatively, as a coalescence of Bi<sub>7</sub> and Ge<sub>4</sub>Bi<sub>7</sub> anions. The 4<sup>-</sup> charge is consistent with the pseudo-element concept in the sense that all 18 atomic centers have a stable octet (there are two 3-connected Ge<sup>-</sup> centers, two 2-connected Bi<sup>-</sup> centers, ten 3-connected Bi<sup>0</sup> and two 4-connected Ge<sup>0</sup>). The first *hypho*-type anion with a high negative charge, [Sn<sub>3</sub>Bi<sub>3</sub>]<sup>5-</sup><sup>34</sup> has also been isolated from a liquid ammonia solution of the mixed Zintl precursors RbSn<sub>2</sub>/Rb<sub>3</sub>Bi<sub>2</sub>. This anion may be an intermediate on the pathway to the two 8-vertex anions [Sn<sub>3</sub>Bi<sub>5</sub>]<sup>3-</sup> and [Sn<sub>4</sub>Bi<sub>4</sub>]<sup>4-35</sup> (Fig. 2C).

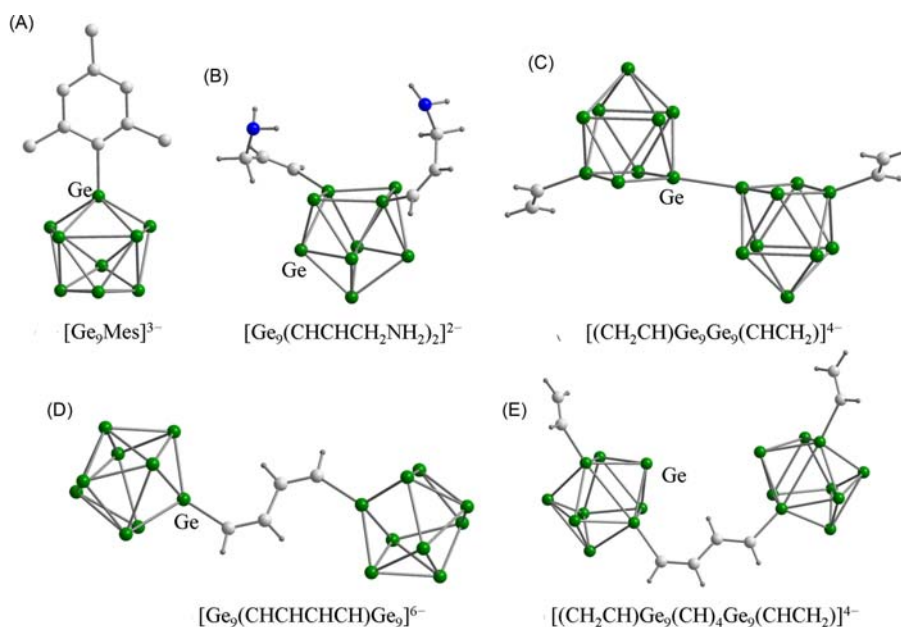
Very recently, two novel binary Zintl anions containing only Group 13 and 15 elements, [Pn@In<sub>8</sub>Pn<sub>12</sub>]<sup>q-</sup> (Pn = Sb or Bi; q = 3 or 5, Fig. 2D and E)<sup>36,37</sup> have been synthesized through wet chemical routes. The Sb compounds was obtained by the reaction of K<sub>5</sub>Sb<sub>4</sub> with In(benzyl)<sub>3</sub> while the Bi analogs were formed from K<sub>5</sub>In<sub>2</sub>Bi<sub>4</sub>/ZnMes<sub>2</sub>. The tri-anions [Pn@In<sub>8</sub>Pn<sub>12</sub>]<sup>3-</sup> are perfectly T<sub>h</sub>-symmetric (the only structurally characterized pure inorganic anions to displaying this unusual point symmetry) and contain an inner [Sb@In<sub>8</sub>]<sup>21+</sup> cube capped by six (Pn<sub>2</sub>)<sup>4-</sup> dimers. The penta-anions, in contrast, have a rather more distorted structure consistent with the reduction of In from In<sup>III</sup>. The electronic structures of these systems will be discussed in detail Section 1.20.6.

### 1.20.3 Zintl anions functionalized with organic groups

#### 1.20.3.1 Group 14 Zintl anions functionalized with main group elements or organic groups

The first example of functionalization of [E<sub>9</sub>] clusters, [Ph<sub>2</sub>Pn-(Ge<sub>9</sub>)-PnPh<sub>2</sub>]<sup>2-</sup><sup>38</sup> came from the treatment of K<sub>4</sub>Ge<sub>9</sub> with the heavier analogs of tri-phenylphosphine, PnPh<sub>3</sub> (Pn = Sb and Bi) and were crystallized from en/tol solutions. These anions can be viewed as two PnPh<sub>2</sub> fragments attached to the open face of a *nido*-type Ge<sub>9</sub> cage by two *exo* bonds and the formation process involves a step-wise nucleophilic attack. Subsequently, the [Ph<sub>2</sub>Sb-Ge<sub>9</sub>-Ge<sub>9</sub>-SbPh<sub>2</sub>]<sup>4-</sup> and [Ph<sub>2</sub>Sb-Ge<sub>9</sub>-Ph]<sup>2-</sup> anions were also obtained from similar reactions,<sup>39</sup> along with [Ge<sub>9</sub>-TtR<sub>3</sub>]<sup>3-</sup>, [R<sub>3</sub>Tt-Ge<sub>9</sub>-TtR<sub>3</sub>]<sup>2-</sup>, [R<sub>3</sub>Tt-Ge<sub>9</sub>-Ge<sub>9</sub>-TtR<sub>3</sub>]<sup>4-</sup> (Tr = Sn, Ge; R = Ph, Me)<sup>40</sup> and [(SbGe<sub>8</sub>)-SbPh<sub>2</sub>]<sup>2-</sup><sup>41</sup> where the PnPh<sub>2</sub><sup>-</sup>, Ph<sup>-</sup> and TtPh<sub>3</sub><sup>-</sup> anions act as nucleophiles. This pattern of reactivity bears close comparison, at least conceptually, with the simpler oxidation reactions wherein the known dimer and trimer of [Ge<sub>9</sub>] can be obtained by the reaction of K<sub>4</sub>Ge<sub>9</sub> with PPh<sub>3</sub> and AsPh<sub>3</sub> in en solution.<sup>42</sup>

In addition to these oxidation reactions with PnPh<sub>3</sub>, alkylation of Ge<sub>9</sub><sup>4-</sup> can also be achieved by reacting with alkyl halides R-Cl to generate structures of the type [R-Ge<sub>9</sub>-R]<sup>2-</sup> and [R-(Ge<sub>9</sub>)<sub>2</sub>-R]<sup>4-</sup> (R = <sup>t</sup>Bu, <sup>n</sup>Bu, <sup>s</sup>Bu, <sup>i</sup>Am, <sup>Pr</sup>Me).<sup>43,44</sup> A radical mechanism has been proposed to rationalize their formation, wherein the LUMO of Ge<sub>9</sub><sup>2-</sup> or the SOMO of Ge<sub>9</sub><sup>3-</sup> provides a low-lying orbital to accommodate the organic radical, forming [R-Ge<sub>9</sub>]<sup>2-</sup> or [R-Ge<sub>9</sub>]<sup>3-</sup> fragments which can then undergo further self-oligomerization or alkylation to afford [R-Ge<sub>9</sub>-R]<sup>2-</sup> and [R-(Ge<sub>9</sub>)<sub>2</sub>-R]<sup>4-</sup>. The Ge<sub>9</sub><sup>4-</sup> anion can also react with AgMes to form [Ge<sub>9</sub>Mes]<sup>3-</sup> via the initial cleavage of the Ag-C bond (Fig. 3A).<sup>45</sup> Interestingly, alkenylation of Ge<sub>9</sub><sup>4-</sup> can also be achieved by treatment with alkynes such as HC≡C-Ph,<sup>46</sup> PhC≡CPh,<sup>46</sup> <sup>t</sup>BuC≡CH,<sup>46</sup> HC≡C-Fc,<sup>46,47</sup> HC≡C-Ph-OMe,<sup>46,47</sup> HC≡C-CH<sub>2</sub>-NH<sub>2</sub>,<sup>48</sup> (Fig. 3B), Me<sub>3</sub>Si-C≡C-SiMe<sub>3</sub> (Fig. 3C),<sup>45,49,50</sup> Me<sub>3</sub>Si-C≡C-Im-CH<sub>3</sub><sup>47</sup> and H<sub>3</sub>C-C≡C-CH<sub>2</sub>-CH<sub>3</sub>,<sup>43</sup> affording mono-, bis- and even tris- vinyl-substituted [Ge<sub>9</sub>] clusters, the vinylization being completed by capture of protons from the en solvent. When 1,4-



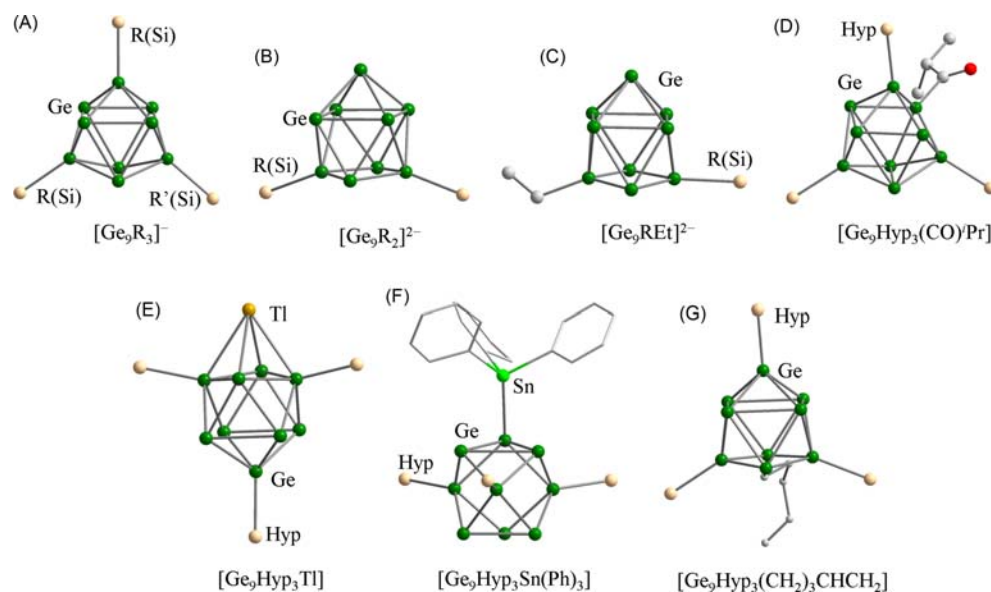
**Fig. 3** Representative examples of Group 14 Zintl anions decorated with organic groups: (A) [Ge<sub>9</sub>Mes]<sup>3-</sup>, (B) [Ge<sub>9</sub>(CHCHCH<sub>2</sub>NH<sub>2</sub>)<sub>2</sub>]<sup>2-</sup>, (C) [(CH<sub>2</sub>CH)Ge<sub>9</sub>Ge<sub>9</sub>(CHCH<sub>2</sub>)]<sup>4-</sup>, (D) [Ge<sub>9</sub>(CHCHCHCH)Ge<sub>9</sub>]<sup>6-</sup>, and (E) [(CH<sub>2</sub>CH)Ge<sub>9</sub>(CH)<sub>4</sub>Ge<sub>9</sub>(CHCH<sub>2</sub>)]<sup>4-</sup>.

bis(trimethylsilyl)butadiyne is allowed to react with  $\text{Ge}_9^{4-}$  in en solution, a remarkable 1,3-butadiene-1,4-diyl-bridged structure,  $[\text{Ge}_9\text{-CH=CH-CH=CH-Ge}_9]^{6-51}$  (Fig. 3D). The two available reaction sites on the  $\text{C}_4$ -linked dimer with can be further functionalized by organic groups, affording extended delocalized systems such as  $[\text{CH}_2=\text{CH-Ge}_9\text{-CH=CH-CH=CH-Ge}_9\text{-CH=CH}_2]^{4-}$  (Fig. 3E)<sup>52</sup> and  $[\text{NH}_2\text{N}(\text{CH}_2)_2=\text{CH-CH=C}(\text{CH}_3)\text{-Ge}_9\text{-CH=CH-CH=CH-Ge}_9\text{-C}(\text{CH}_3)=\text{CH-CH=N}(\text{CH}_2)_2\text{NH}_2]^{4-52}$ .

In an elegant extension of the extensive alkylation and alkenylation chemistry reported in the previous paragraph, the analogous silylation reactions of  $\text{Ge}_9^{4-}$  have also been reported. The hypersilyl (Hyp,  $\text{Si}(\text{SiMe}_3)_3$ ) trisubstituted monoanion  $[\text{Ge}_9\{\text{Si}(\text{SiMe}_3)_3\}_3]^-$  (Fig. 4A) was first synthesized in low yields by the Schnepf group by the disproportionation of  $\text{GeI}$ ,<sup>53</sup> but Sevov subsequently reported its isolation in quantitative yield from the reaction of  $\text{K}_4\text{Ge}_9$  with HypCl in acetonitrile.<sup>54</sup> The monoanion is very soluble in commonly-used organic solvents (acetonitrile, tetrahydrofuran, toluene), which offers opportunities to probe its reactivity toward transition metal organometallics (which will be the subject of Section 1.20.4.2.3) as well as main-group organometallics and organic halides. The reactions with main-group organometallics and their halides, as well as organic halides, afford a range of the tetra-substituted neutral clusters including  $[\text{Ge}_9\{\text{Si}(\text{SiMe}_3)_3\}_3\text{R}]$  ( $\text{R} = \text{SnPh}_3$  (Fig. 4F),<sup>55</sup>  $\text{Sn}^n\text{Bu}_3$ , Et (Fig. 4G),<sup>56</sup> or Tl (Fig. 4E).<sup>56</sup> The alkenyl-functionalized neutral deltahedral  $[\text{Ge}_9]$  anions,  $[\text{Ge}_9\{\text{Si}(\text{SiMe}_3)_3\}_3(\text{CH}_2)_3\text{CH=CH}_2]$  and  $[\text{Ge}_9\{\text{Si}(\text{SiMe}_3)_3\}_3\text{CH}_2\text{CH=CH}_2]$ ,<sup>57</sup> have also been prepared by Fässler and coworkers through the reaction of  $[\text{Ge}_9\{\text{Si}(\text{SiMe}_3)_3\}_3]^-$  with the corresponding organic halides. The corresponding acyl chlorides also react in hexane or toluene to form the family of tetrasubstituted carbonyl-derivatized compounds  $[\{\text{Si}(\text{SiMe}_3)_3\}_3\text{Ge}_9(\text{CO})\text{R}']$  ( $\text{R}' = \text{Me}$ ,  $^t\text{Bu}$ ,  $^i\text{Pr}$  (Fig. 4D), Ph, Bn, phenethyl, 4-vinylphenyl, cyclopropylmethyl).<sup>58</sup> With the exception of the compounds with Ph or Bn substituents, the neutral carbonyl-containing species  $[\text{Ge}_9\{\text{Si}(\text{SiMe}_3)_3\}_3(\text{CO})\text{R}']$  undergo a temperature-dependent decarbonylation process via a radical Norrish-type I  $\alpha$ -bond cleavage, leading to the formation of  $[\text{Ge}_9\{\text{Si}(\text{SiMe}_3)_3\}_3\text{R}']^-$ . Compared with the extensive chemistry of the hypersilyl trisubstituted monoanion  $[\text{Ge}_9\{\text{Si}(\text{SiMe}_3)_3\}_3]^-$ , reports of mono-silylated and bis-silylated analogs are sparse but  $[\text{CH}_3\text{CH}_2\text{Ge}_9\{\text{Si}(\text{SiMe}_3)_3\}_2]^{2-}$  (Fig. 4C)<sup>59</sup>  $[\text{Ge}_9\{\text{Si}(\text{SiMe}_3)_2(\text{SiPh}_3)\}_2]^{2-60}$  and  $[\text{Ge}_9\{\text{Si}^i\text{Bu}\}_2]^{2-61}$  (Fig. 4B) are all known. The functionalization of  $\text{Sn}_9^{4-}$  and the heteroatomic Ge/Sn analogs  $[\text{Ge}_{9-x}\text{Sn}_x]^{4-}$  is relatively uncommon in comparison to  $\text{Ge}_9^{4-}$ , and indeed in the known  $[\text{Ge}_{9-x}\text{Sn}_x(\text{CH=CHR})_n]^{4-n}$  ( $\text{R} = \text{H}$ ,  $^t\text{Pr}$ , Ph)<sup>62</sup> anions, the substituents are invariably attached to the Ge atoms rather than to Sn, just as they are in  $[(\text{SbGe}_8)\text{-CH=CH}_2]^{2-}$ .<sup>41</sup> All of these observations suggest that the incipient inert pair effect in Sn acts as a barrier to bond activation at the heavier tetrel elements.

### 1.20.3.2 Group 15 Zintl anions functionalized with organic groups

In analogous fashion to the group 14 Zintl anions, the functionalization of group 15 Zintl anions with main group elements or organic groups, is mainly the preserve of the lighter members of the group. A very simple example is the common observation of the protonation of  $\text{P}_n^{4-}$  and  $\text{As}_n^{4-}$  anions in mass spectra. In condensed phases, the functionalization of poly-phosphides or poly-arsenides can be achieved by the reduction of the  $\text{P}_4$  or  $\text{As}_4$  or, alternatively, via salt elimination reactions.<sup>63</sup> In the latter class, nucleophilic attack of  $\text{Pn}_7^{3-}$  on R-X generates a series of 7-atom cages through formation of a 2center-2electron *exo*-bond between the cage and the substituents. Only a single non-hydrogen-substituted  $[\text{P}_7\text{R}]^{2-}$  cage has been characterized crystallographically,



**Fig. 4** Representative examples of silylated Group 14 Zintl anions and their organic and main group derivatives (A)  $[\text{Ge}_9\text{R}_3]^-$  ( $\text{R} = \text{R}' = \text{Hyp}$ ,  $\text{Si}^i\text{H}^t\text{Bu}_2$ ,  $\text{Si}(\text{SiMe}_3)_2(\text{Si}^i\text{Pr}_3)$ ;  $\text{R}/\text{R}' = \text{Si}(\text{SiMe}_3)_2(\text{SiPh}_3)/\text{Hyp}$ ), (B)  $[\text{Ge}_9\text{R}_2]^{2-}$  ( $\text{R} = \text{Si}^i\text{Bu}$ ),  $\text{Si}(\text{SiMe}_3)_2(\text{SiPh}_3)$ ), (C)  $[\text{Ge}_9\text{REt}]^{2-}$ , ( $\text{R} = \text{Hyp}$ ) (D)  $[\text{Ge}_9\text{Hyp}_3(\text{CO})\text{C}_2\text{H}_5]$ , (E)  $[\text{Ge}_9\text{Hyp}_3\text{Tl}]$ , (F)  $[\text{Ge}_9\text{Hyp}_3\text{Sn}(\text{Ph})_3]$  and (G)  $[\text{Ge}_9\text{Hyp}_3(\text{CH}_2)_3\text{CH=CH}_2]$ .

that being  $[\text{P}_7\{\text{SiMe}(\text{SiMe}_3)_2\}]^{2-}$  which was synthesized via cleavage of two R groups from neutral  $\text{P}_7\text{R}_3$ .<sup>64</sup> The di-substituted  $[\text{Pn}_7\text{R}_2]^-$  cages (R = Me, Et, Bu,  $\text{PhCH}_2$ ,  $\text{EtOC}(\text{O})\text{CH}_2$ ,  $\text{EtOC}(\text{O})\text{CHMe}$ ; Pn = As; R =  $\text{PhCH}_2$ )<sup>65,66</sup> were also synthesized from the reaction of  $\text{Pn}_7^{3-}$  with  $[\text{RR}'_3\text{N}][\text{X}]$  salts (R = R' = Me, Et, Bu; R =  $\text{PhCH}_2$ ,  $\text{EtOC}(\text{O})\text{CH}_2$ ,  $\text{EtOC}(\text{O})\text{CHMe}$ , R' = Me; X = Cl, Br, I). This reaction involves nucleophilic attack by the 2-connected vertices of  $[\text{Pn}_7]^{3-}$  (those that carry the formal negative charges) at the  $\alpha$ -carbon atom of the ammonium salts. The  $[\text{Pn}_7\text{R}_2]^-$  (R =  $^i\text{Pr}$ ,  $^i\text{Bu}$ ) clusters<sup>67</sup> can also be prepared by the reaction of alkyl tosylates with  $\text{Pn}_7^{3-}$ . Tri-substituted cages with organic, main-group, and transition-metal substituents can also be obtained by salt metathesis reaction with a corresponding halide. Compounds of this type include the alkyl-substituted  $[\text{P}_7\text{R}_3]$  (R = Me, Et,  $^i\text{Pr}$ , Bu,  $^i\text{Bu}$ ),<sup>68–70</sup> main group-decorated  $[\text{Pn}_7\text{R}_3]$  (Pn/R = P/SiH<sub>3</sub>, SiH<sub>2</sub>Me, SiMe<sub>3</sub>, SiMe<sub>2</sub>PEt<sub>2</sub>, SiPh<sub>3</sub>, GeMe<sub>3</sub>, SnMe<sub>3</sub>, P<sup>*t*</sup>Bu<sub>2</sub>, Sb<sup>*t*</sup>Bu<sub>2</sub>; As/SiMe<sub>3</sub>),<sup>69–72</sup> and the hetero-metallic cluster  $[\text{P}_7\{\text{Fe}(\text{Cp})(\text{CO})_2\}_3]$ .<sup>73</sup> Functionalization of group 15 Zintl anions can also be achieved by using the un-catalyzed hydro-pnictionation of the anions  $[\text{HPn}_7]^{2-}$  (E = P, As) with both carbodiimides  $\text{RN}=\text{C}=\text{NR}$  (R = Dipp, Cy,  $^i\text{Pr}$ ) and isocyanates  $\text{RN}=\text{C}=\text{O}$  (R = 1-adamantyl) (Fig. 5A and B).<sup>74–76</sup> The  $[\text{Pn}_7]^{3-}/[\text{HPn}_7]^{2-}$  (Pn = P, As) clusters can also react with diphenylacetylene and phenylacetylene in DMF solution to afford a series of 1,2,3-tripnictolide anions with the general formula  $[\text{Pn}_3\text{C}_2\text{RR}']^-$  (Pn = P, As; R/R' = H/H, Ph/H, Ph/Ph, o-py/H,  $\text{CH}_2\text{NH}_2/\text{H}$ , Fc/H) (Fig. 5C),<sup>77</sup> which can further coordinate to an  $\text{Mo}(\text{CO})_3$  fragment (Fig. 5D).<sup>78,79</sup> When using diphenylacetylene and  $\text{Cs}_3\text{As}_7$  as starting material in liquid ammonia, the dianion (Z)-1,2-diphenylethenyl-heptaarsenide was isolated (Fig. 5F).<sup>80</sup> Using  $\text{Rb}_3\text{As}_{11}$  or  $\text{Cs}_3\text{As}_{11}$  instead of  $\text{Cs}_3\text{As}_7$  generates a diarsabarrelene,  $[\text{As}_2\text{C}_6\text{H}_6]^{2-}$ , which was crystallized as the  $[\text{Cs}(18\text{-crown-6})]^+$  or  $[\text{Rb}(18\text{-crown-6})]^+$  salts from liquid ammonia solution (Fig. 5E).<sup>80</sup>

## 1.20.4 Inter-metalloid and heterometallic clusters

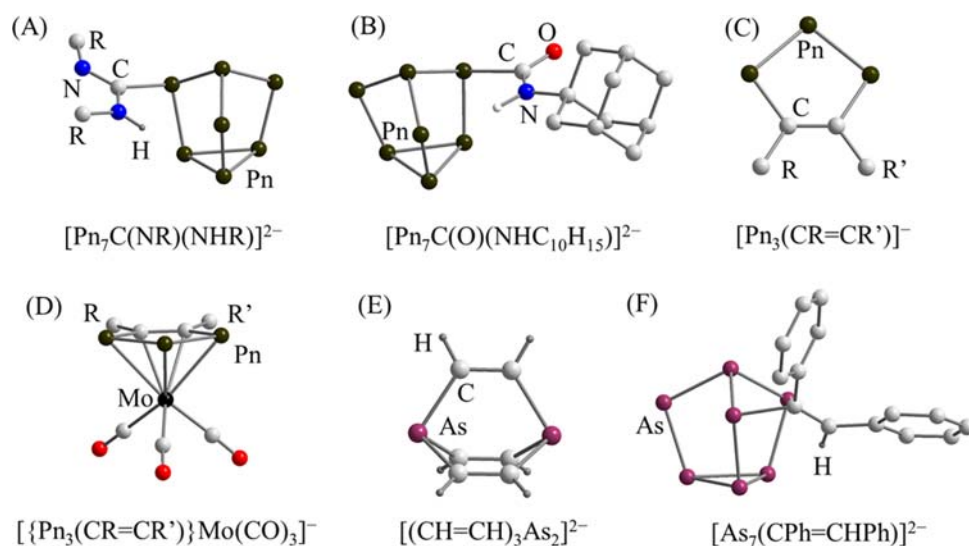
Zintl anions can react with organic halides, d- or f-block organometallic complexes to form oligomers and polymers and organic ligand-protected Zintl anions (Section 1.20.3) as well as the inter-metalloid and heterometallic clusters that are the subject of this section. The expansion of research into inter-metalloid and heterometallic clusters in Zintl chemistry has been driven to a large extent by their unique electronic structures as well as their potential applications. We first introduce binary inter-metalloid and heterometallic clusters before turning to ternary analogs.

### 1.20.4.1 Binary inter-metalloid clusters of the group 14 elements

The general synthetic route to binary inter-metalloid clusters of the tetrel elements containing a single transition metal atom involves treatment of the binary Zintl phase with d- or f-block organometallic complexes in polar solvents. The resulting cluster products can be either deltahedral and non-deltahedral with a range of different vertex counts.

#### 1.20.4.1.1 Deltahedral clusters with 9, 10, 11 and 12 vertices

The isolobality of the tetrel elements with a BH fragment means that the structures of typical binary inter-metalloid clusters are very similar to the isoelectronic boranes, and are generally based on triangular faces. Their electronic structures can be rationalized using



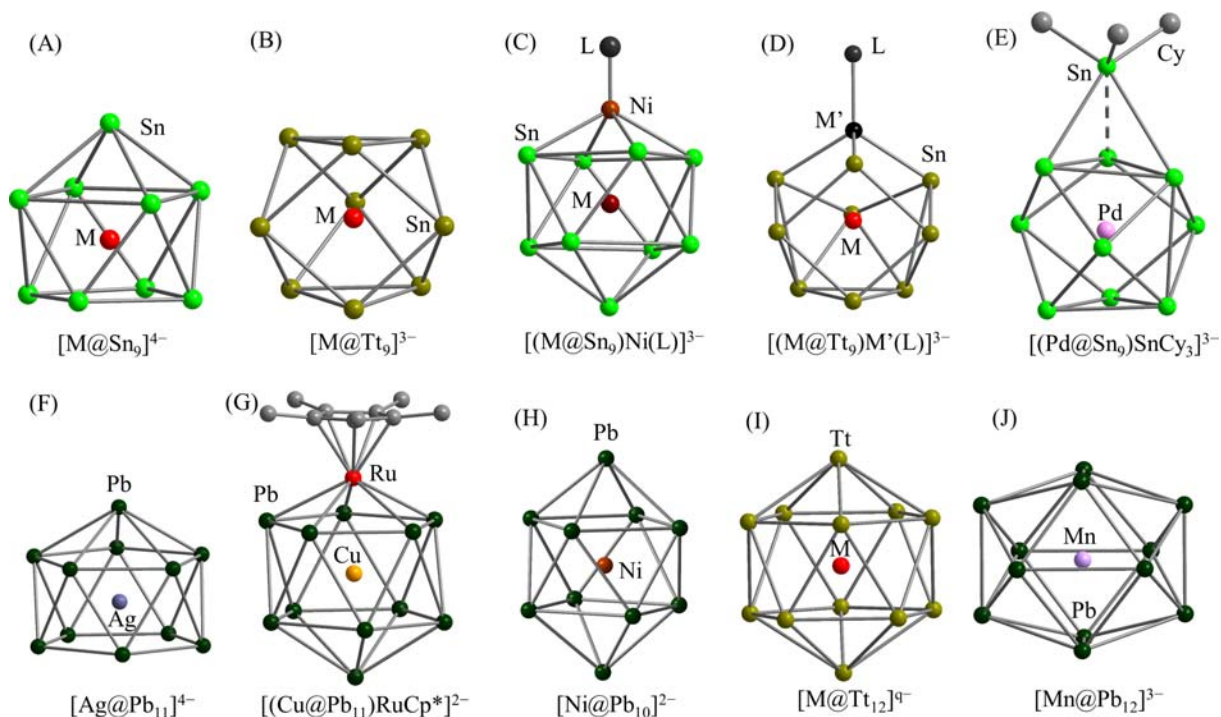
**Fig. 5** Structure of the group 15 Zintl anions functionalized with organic groups (A)  $[\text{Pn}_7\text{C}(\text{NR})(\text{NHR})]^{2-}$  (Pn = P, As, R =  $^i\text{Pr}$ , NCy, Dipp), (B)  $[\text{Pn}_7\text{C}(\text{O})(\text{NHC}_{10}\text{H}_{15})]^{2-}$  (C)  $[\text{Pn}_3(\text{CR}=\text{CR}')^-]$ , (Pn = P, As, R/R' = H/H, Ph/H, Ph/Ph, o-py/H,  $\text{CH}_2\text{NH}_2/\text{H}$ , Fc/H) (D)  $[\{\text{Pn}_3(\text{CR}=\text{CR}')\}\text{Mo}(\text{CO})_3]^-$  (Pn = P, As, R/R' = H/H, Ph/H, Ph/Ph, o-py/H,  $\text{CH}_2\text{NH}_2/\text{H}$ , Fc/H), (E)  $[(\text{CH}=\text{CH})_3\text{As}_2]^{2-}$ , and (F)  $[\text{As}_7(\text{CPh}=\text{CHPh})]^{2-}$ .



the Wade-Mingos rules developed in the context of borane chemistry. Synthetic routes to these deltahedral clusters involve either the reaction of the binary Zintl phases,  $K_4Tt_9$ , with an organometallic complex with labile ligands or extraction from ternary phases that already contain the transition metal atoms. The reported deltahedral structures with different vertex counts for group 14 elements are listed in Fig. 6. Structurally characterized examples of endohedral 9-vertex cages include  $[M@Sn_9]^{4-}$  ( $M = Co, Ni$ ) (Fig. 6A),<sup>81,82</sup>  $[Ni@Tt_9]^{3-}$  ( $Tt = Ge, Sn$ )<sup>83,84</sup> and  $[Cu@Tt_9]^{3-}$  ( $Tt = Sn, Pb$ )<sup>85</sup> (Fig. 6B). The tetra-anionic clusters are obtained by the dissolution of the corresponding ternary K-M-Sn phase from an en solution, and adopt a capped square anti-prismatic shape. The tri-anions, in contrast, are typically isolated from solutions of  $K_4Tt_9$  and low-valence transition metal complexes, and have structures that are close to an ideal tricapped trigonal prism. The absence of a paramagnetic moment in  $[Cu@Tt_9]^{3-}$  indicates the presence of a closed-shell  $d^{10} Cu^+$  ion. It is striking that the  $[Cu@Tt_9]^{3-}$  clusters adopt this tri-capped trigonal prismatic shape rather than the capped square anti-prism which would be more consistent with the *nido* geometry expected for a 22 valence electron count. However,  $^{63}Cu$  and  $^{119}Sn$  NMR studies on  $[Cu@Sn_9]^{3-}$  indicated that the 9-vertex cage is highly fluxional, suggesting the energetic difference between formally *closo* tri-capped trigonal prism and formally *nido* capped square anti-prism is, in this case, marginal.

From a coordination chemistry perspective,  $[M@Tt_9]^{q-}$  can also act as a ligand, binding to a variety of transition metal atoms to form metal fragment-decorated inter-metalloid clusters such as  $[Co@Sn_9Ni(CO)]^{3-}$ ,  $[Co@Sn_9Ni(C_2H_4)]^{3-}$ ,  $[Co@Sn_9AuPh]^{3-}$  and  $[Co@Sn_9Pt(PPh_3)]^{3-}$ ,<sup>86</sup> all of which can be synthesized by reacting  $K_5Co_3Ge_9$  with an appropriate low-valent transition metal complex. The  $[Sn_9]$  cages attached to Ni fragments adopt a  $C_{4v}$ -symmetric mono-capped square anti-prismatic geometry, while the Au and Pt clusters are  $C_{3v}$ -symmetric tricapped trigonal prisms. This again seems to reflect the small energetic differences between the two structural types. Sn clusters containing group 10 elements such as  $[Pt@Sn_9Pt(PPh_3)]^{2-}$  and  $[Pd@Sn_9SnCy_3]^{2-}$ <sup>87,88</sup> (Fig. 6D and E), can also be obtained from  $Sn_9^{4-}$  clusters in one-pot reactions. Germanium analogs such as  $[Ni@Ge_9(NiL)]^{q-}$  ( $L/q = CO/2, PPh_3/2, en/3$ , Fig. 6C) have been synthesized in this way, while  $[Ni@Ge_9Pd(PPh_3)]^{2-}$  has been reached through a two-step process, involving the initial formation of  $[Ge_9Pd(PPh_3)]^{3-}$  followed by insertion of a Ni atom into the cluster framework.<sup>89</sup> The availability of one-pot and step-wise synthetic routes hints at a complex reaction chemistry with multiple pathways leading to the observed products.

In 2020 Sun and co-workers reported the first 11-vertex deltahedral cluster,  $[Ag@Pb_{11}]^{3-}$  (Fig. 6F),<sup>90</sup> formed from the reaction of  $K_4Pb_9$  with  $(AgMes)_4$  in an en solution in the presence of 2.2.2-crypt. This anionic cluster, with a 48 ( $= 4n + 4$ ) valence-electron count (if the  $d^{10}$  core of  $Ag^+$  is ignored) adopts an approximately  $C_{5v}$ -symmetric *nido* structure. The characterization of this  $[Ag@Pb_{11}]^{3-}$  cluster also offers important clues about the mechanism of formation of the larger  $[Au_8Pb_{33}]^{6-}$  and  $[Au_{12}Pb_{44}]^{8-}$  clusters (Fig. 8M and N)<sup>90</sup> reported in the same paper. These two Au/Pb clusters can be considered as the zero-valent  $Au_5$  and  $Au_8$  subunits that are bound to three and four  $[Au@Pb_{11}]^{3-}$  units via the open  $Pb_5$  face of the *nido*  $[Pb_{11}]$  units, respectively.



**Fig. 6** Molecular structures of intermetalloid deltahedral clusters with 9, 10, or 12 vertices and their derivatives for group 14 Zintl clusters (A)  $[M@Sn_9]^{4-}$  ( $M = Co, Ni$ ), (B)  $[M@Tt_9]^{3-}$  ( $M/Tt = Ni/Ge, Ni/Sn, Cu/Sn, Cu/Pb$ ), (C)  $[(M@Sn_9)Ni(L)]^{3-}$  ( $M/L = Co/CO, Co/C_2H_4, Ni/CO$ ), (D)  $[(M@Tt_9)M'(L)]^{3-}$  ( $M(=M')/Tt = Ni/Ge, L/q = PPh_3/2, en/3, CO/2, CPh_3/3$ ;  $Tt = Sn, M(=M')/L/q = Pt/PPh_3/2, M/Tt/M'/L/q = Ni/Ge/Pd/PPh_3/2$ ;  $M = Co, Tt = Sn, q = 3, M'/L = Pt/PPh_3, Au/Ph$ ), (E)  $[(Pd@Sn_9)SnCy_3]^{3-}$ , (F)  $[Ag@Pb_{11}]^{4-}$ , (G)  $[(Cu@Pb_{11})RuCp^*]^{2-}$ , (H)  $[Ni@Pb_{10}]^{2-}$ , (I)  $[M@Tt_{12}]^{q-}$  ( $M/Tt/q = Ni, Pd, Pt/Pb/2, Au, Co, Rh, Ir/Pb/3; Ir/Sn/3$ ), and (J)  $[Mn@Pb_{12}]^{3-}$ .

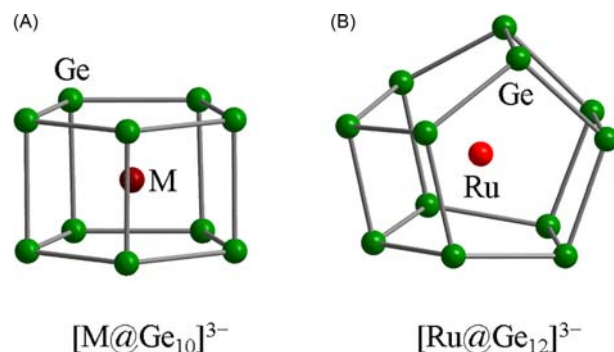


DFT calculations indicated that the secondary interactions between the  $\text{Pb}_{11}$  units and the atoms of the Au cluster play an important stabilizing role, and in fact they contribute more to the integrity of the clusters than direct Au–Au bonding. The role of the  $\text{Pb}_{11}$  units is reminiscent of the ‘divide and protect’ mode of stabilizing  $\text{Au}_x$  core seen in the family of gold thiolate cluster clusters with ‘staple’ ligands,  $[(\text{RS})\text{Au}^+(\text{SR})]^-$  and  $[(\text{RS})\text{Au}^+(\text{SR})\text{Au}^+(\text{SR})]^-$ . A naked  $[\text{Pb}_{11}]$  cage can also act as a ligand to a  $\text{Cp}^*\text{Ru}$  fragment in the presence of 18-crown-6 to form the first non-centered Zintl icosahedron,  $[\text{Cp}^*\text{RuPb}_{11}]^{3-}$  (Fig. 10E) as well as the endohedral  $\text{Cu}^+$  derivative  $[\text{Cu}@\text{Pb}_{11}\text{RuCp}^*]^{2-}$  (Fig. 6G).<sup>91</sup>

The 10- and 12-vertex clusters  $[\text{Ni}@\text{Pb}_{10}]^{2-}$  (Fig. 6H)<sup>92</sup> and  $[\text{M}@\text{Pb}_{12}]^{q-}$  ( $\text{M}/\text{q}=\text{Ni}, \text{Pd}, \text{Pt}/2^{93}; \text{Co}, \text{Rh}, \text{Ir}/3^{94}$ ) (Fig. 6I) can be formed reproducibly from the reaction of naked  $[\text{Tb}_9]^{4-}$  with the appropriate low-valent transition metal complexes, ML (ML =  $\text{Ni}(\text{COD})_2$ ,  $\text{Pd}(\text{PPh}_3)$ ,  $\text{Pt}(\text{PPh}_3)$ ,  $\text{Co}(\text{dppe})\text{Cl}_2$ ,  $\text{Rh}(\text{PPh}_3)_3\text{Cl}$  and  $[\text{Ir}(\text{COD})\text{Cl}]_2$ ). The  $[\text{M}@\text{Pb}_{12}]^{q-}$  clusters share a common 50 ( $= 4n + 2$ ) valence-electron count (if the transition metal is assumed to adopt a  $d^{10}$  configuration) and all adopt almost perfectly icosahedral geometries.<sup>207</sup>  $^{207}\text{Pb}$  NMR spectroscopy of these clusters shows a marked downfield chemical shifts compared to other reported lead clusters, which may be attributed to the  $\sigma$ -aromatic character of the clusters in  $I_h$  point symmetry. The 52-electron  $[\text{Au}@\text{Pb}_{12}]^{3-}$  cluster has also synthesized by the reaction of  $\text{K}_4\text{Pb}_9$  with  $\text{Au}(\text{PPh}_3)\text{Ph}$  in py solution,<sup>95</sup> and while the presence of two additional electrons does not induce a transition to a recognizably *nido* geometry, the  $\text{Pb}_{12}$  unit is markedly elongated along one 3-fold axis, consistent with a strong first order Jahn-Teller distortion in a  $\text{Pb}_{12}^{4-}$  cluster which has a  $g_g^2$  configuration at the icosahedral limit. The  $[\text{Mn}@\text{Pb}_{12}]^{3-}$  (Fig. 6J)<sup>96</sup> is also substantially distorted away from the perfect icosahedron, in this case along a 2-fold axis to generate a  $D_{2h}$ -symmetric structure. EPR spectroscopy and DFT calculations confirm that the ground state is a triplet, and it represents the first inter-metalloid cluster incorporating an open-shell transition metal ion. The total valence electron count, in this case including the metal d electrons, is 58, but the distribution of these electrons between the cluster and transition metal is somewhat ambiguous. The half-filled  $d^5$  configuration at Mn appears to be a significant stabilizing influence, and so to a first approximation the cluster can be viewed as  $[(\text{Mn}^{2+})@(\text{Pb}_{12}^{5-})]$ , the strong distortion along a 2-fold axis arising from a  $g_g^3$  configuration in this case. Distortions were also observed in the approximately icosahedral  $[\text{Co}@\text{Ge}_{12}]^{3-}$ ,<sup>97</sup> which can, in the limit of substantial elongation along one  $C_5$  axis, be viewed approximately as a sandwich cluster with a Co atom flanked by two  $\text{Ge}_6$  ‘hats.’ This cluster is, however, valence isoelectronic with  $[\text{Co}@\text{Pb}_{12}]^{3-}$  which is, as noted above, perfectly icosahedral, as might be expected for a 50-electron count. Quantum chemical calculations indicate that the distortion from  $I_h$  to  $D_{5d}$  topologies stems from size mismatch between the embedded Co atom and the cluster framework rather than any electronic degeneracy.

#### 1.20.4.1.2 Non-deltahedral cluster with 10 and 12 vertices

Inter-metalloid clusters with non-deltahedral geometries are very rare in group 14, the only known examples being  $[\text{M}@\text{Ge}_{10}]^{3-}$  ( $\text{M} = \text{Fe},^{98} \text{Co}^{99}$ ) and  $[\text{Ru}@\text{Ge}_{12}]^{3-}$ .<sup>100</sup> The  $[\text{M}@\text{Ge}_{10}]^{3-}$  clusters, with pseudo  $D_{5h}$  symmetry, were obtained through the reaction of  $\text{K}_4\text{Ge}_9$  with low-valent organometallic precursors  $\text{FeAr}_2$  ( $\text{Ar} = 2,6\text{-Mes}_2\text{C}_6\text{H}_3$ ) and  $[\text{Co}(\text{C}_8\text{H}_{12})(\text{C}_8\text{H}_{13})]$  in en solution, respectively. The Tt–Tt bonds between two five-membered rings are slightly elongated in the pentagonal prismatic cluster (Fig. 7A). DFT studies indicated a substantial charge transfer from the central metal to the  $[\text{Ge}_{10}]$  cage. The  $[\text{Fe}@\text{Sn}_{10}]^{3-}$  anion, valence isoelectronic with  $[\text{Fe}@\text{Ge}_{10}]^{3-}$ , is also known although the structure is highly disordered. DFT calculations revealed that the potential energy surface of  $[\text{Fe}@\text{Sn}_{10}]^{3-}$  is flat, with very little energy separating three pseudo-deltahedral topologies,  $C_{2v}$ ,  $C_{3v}$  and  $D_{4d}$ . Despite the disorder problem, it is clear that  $[\text{Fe}@\text{Sn}_{10}]^{3-}$  is very different, structurally, from its isoelectronic Ge analog, an observation that is reminiscent of the  $[\text{Co}@\text{Ge}_{12}]^{3-}/[\text{Co}@\text{Pb}_{12}]^{3-}$  comparison, and again probably reflects the very small radius of the Ge cage.<sup>101</sup> The non-deltahedral 12-vertex cluster  $[\text{Ru}@\text{Ge}_{12}]^{3-}$  (Fig. 7B) was synthesized by the reaction of  $\text{K}_4\text{Ge}_9$  with  $\text{Ru}(\text{COD})(\text{Me-allyl})_2$ . The anionic cluster with approximate  $D_{2d}$  symmetry can be considered as a fusion of two mutual vertical Dewar benzene-like segments. The 59 valence-electron count is one short of the 60 electrons required for an electron-precise (3-connected) cluster. DFT calculations showed that there is extensive mixing of the Ru 4d orbitals and those of the  $[\text{Ge}_{12}]$  unit, but the unpaired electron occupies an orbital that is localized entirely on the  $\text{Ge}_{12}$  unit, consistent with the Ge hyperfine couplings observed in the EPR spectrum.



**Fig. 7** Molecular structures of inter-metalloid non-deltahedral clusters with 10, or 12 vertices, involving group 14 atoms and transition metal atoms; (A)  $[\text{M}@\text{Ge}_{10}]^{3-}$  ( $\text{M} = \text{Fe}, \text{Co}$ ), (B)  $[\text{Ru}@\text{Ge}_{12}]^{3-}$ .

### 1.20.4.1.3 Larger intermetallic clusters of the group 14 elements

Larger inter-metalloid clusters (defined here as those with more than 12 main-group atoms and more than one interstitial transition metal atom) are generally viewed as fusion products formed by the sharing of vertices, edges and faces of smaller component clusters, and their complex structures present substantial challenges to electron-counting models such as the Wade-Mingos rules. An example is the  $[\text{Co}_2@\text{Ge}_{16}]^-$  cluster which was first observed by mass spectrometry in the reaction of  $\text{K}_4\text{Ge}_9$  with  $\text{Co}(\text{PPhEt}_2)_2(\text{Mes})_2$ ,<sup>102</sup> but the structure of the cluster remained elusive as a result of extensive crystalline disorder. However, high quality crystals were subsequently obtained by using  $[\{(\text{ArN})_2\text{C}^t\text{Bu}\}\text{Co}(\eta\text{-tol})]$  as the Co source in place of  $\text{Co}(\text{PPhEt}_2)_2(\text{Mes})_2$ .<sup>103</sup> The X-ray diffraction experiment showed that the anionic clusters adopt two quite distinct geometries, the so-called  $\alpha$  and  $\beta$  configurations (Fig. 8A and B), which are almost isoenergetic and are connected by several low-lying transition states. The skeleton of the  $\alpha$  isomer, with  $D_{2h}$  symmetry, is approximately 3-connected and can be understood in terms of localized bonds, whereas the more highly connected  $C_{2h}$ -symmetric  $\beta$  configuration is better viewed in the framework of delocalized bonding.

The corresponding chemistry of Sn has generated a diverse range of products, all of which are based on fused deltahedral architectures. The  $[(\text{Co}@\text{Sn}_8)\text{Sn}(\text{Co}@\text{Sn}_8)]^{5-}$  cluster has been obtained by extraction from the ternary phases  $\text{K}_{5-x}\text{Co}_{1-x}\text{Sn}_9$  and  $\text{K}_{4.79}\text{Co}_{0.79}\text{Sn}_9$  in an en solution.<sup>81,104</sup> The structure is based on a fusion of two endohedral  $[\text{Co}@\text{Sn}_9]^{4-}$  through sharing of a Sn vertex, and the odd number of electrons is reflected in the EPR spectroscopy. In contrast, the Ni analog  $[(\text{Ni}@\text{Sn}_8)\text{Sn}(\text{Ni}@\text{Sn}_8)]^{4-}$ ,<sup>105</sup> formed from the reaction of  $\text{K}_4\text{Sn}_9$  with  $[\text{Ni}(\text{COD})_2]$ , is diamagnetic. <sup>119</sup>Sn NMR spectroscopy at  $-64^\circ\text{C}$  shows four different types of Sn atoms in the ratio expected for the equilibrium structure shown in Fig. 8C, confirming the absence of fluxionality on the NMR timescale. The Pt analog  $[\text{Pt}_2\text{Sn}_{17}]^{4-}$ , formed in the reaction of  $\text{K}_4\text{Sn}_9$  with  $\text{Pt}(\text{norbornene})_3$ , adopts a rather different structure with an ellipsoid shape, (Fig. 8G),<sup>106</sup> and is, in contrast, highly fluxional in solution. Changing the organometallic precursor from  $\text{Pt}(\text{norbornene})_3$  to  $\text{Pd}(\text{PPh}_3)_4$ , gives rise to the 18-vertex cluster  $[\text{Pd}_2@\text{Sn}_{18}]^{4-}$  (Fig. 8H)<sup>107,108</sup> where a  $\text{Sn}_6$  hexagon links the two  $\text{M}@\text{Sn}_6$  caps rather than the  $\text{Sn}_5$  pentagon present in  $[\text{Pt}_2@\text{Sn}_{17}]^{4-}$ . The extent to which these differences reflect the different electronic properties of Pd vs Pt rather than subtle differences in reaction conditions remains unclear. Sun and coworkers have recently reported two further 18-vertex clusters with an interstitial  $\text{Cu}_4$  unit,  $[\text{Cu}_4\text{Tt}_{18}]^{4-}$  ( $\text{Tt} = \text{Sn, Pb}$ ).<sup>109</sup> The 18-vertex tin or lead cage is made up of two  $\text{Tt}_{10}$  "sphenocorona" fused along a Tt-Tt edge, giving an approximately  $D_{2h}$ -symmetric structure (Fig. 8I). DFT calculations suggest that the Cu atoms are present as  $\text{Cu}^+$ . The two Cu ions at the foci of the  $\text{Tt}_{10}$  units act as a template to stabilize the  $\text{Tt}_{18}$  skeleton, while the outside Cu ions function as counter ions, similar to the "tightly bound" alkali metal ions in highly charged Zintl anions such as  $\text{K}_{12}[\text{Sn}@\text{Cu}_{12}@\text{Sn}_{20}]^{110}$  and  $[\text{K}_3\text{Rh}_2\text{Sn}_{17}]^{3-}$ .<sup>111</sup>

A striking example of the coalescence of small fragments into large intermetallic clusters comes from the structure of  $[(\text{Ni}@\text{Ge}_9)\text{Ni}(\text{Ni}@\text{Ge}_9)]^{4-}$ ,<sup>112</sup> which can be viewed either as two  $\text{Ni}@\text{Ge}_9\text{Ni}$  sharing a common (Ni) vertex or, alternatively as a  $\text{Ni}_3$  filament inserted into a  $[\text{Ge}_{18}]$  cluster (Fig. 8D). The  $[(\text{Ni}@\text{Ge}_9)\text{Ni}(\text{Ni}@\text{Ge}_9)]^{4-}$  cluster is reminiscent of  $[(\text{Ni}@\text{Ge}_9)\text{Ni}(\text{PPh}_3)]^{2-}$  and  $[(\text{Ni}@\text{Ge}_9)\text{Ni}(\text{en})]^{2-}$ ,<sup>83,113</sup> in which Ni-L fragments are coordinated to the 9-atom cage in an  $\eta^3$  mode. The labile ligands en and  $\text{PPh}_3$  can be replaced by an additional  $[\text{Ni}@\text{Ge}_9]^{4-}$  unit to form the  $[(\text{Ni}@\text{Ge}_9)\text{Ni}(\text{Ni}@\text{Ge}_9)]^{4-}$  cluster. Similar chemistry has been observed in the formation of two isomers of a Ni/Sn/In cluster,  $\{[\eta^3-(\text{Ni}@\text{Sn}_9)]\text{In}[\eta^3-(\text{Ni}@\text{Sn}_9)]\}^{5-}$  and  $\{[\eta^3-(\text{Ni}@\text{Sn}_9)]\text{In}[\eta^4-(\text{Ni}@\text{Sn}_9)]\}^{5-}$  (Fig. 8E and F),<sup>114</sup> which differ only in the identity of the counteranions in the unit cell. The  $\eta^3, \eta^3$  isomer is formed from the reaction of  $[\text{Ni}@\text{Sn}_9]^{3-}$  with  $\text{In}^{3+}$  in DMF in presence of 2.2.2-crypt while  $\eta^3, \eta^4$  form is obtained from the reaction of  $\text{K}_4\text{Sn}_9$  with  $\text{In}(\text{CH}_2\text{Ph})_3$ , followed by insertion of  $\text{Ni}^0$  delivered in the form of  $\text{Ni}(\text{COD})_2$ . The computed energies of the two isomers are very similar, suggesting that the isomerism probably reflect the different packing environments in the two crystals rather than the synthetic route by which they were obtained.

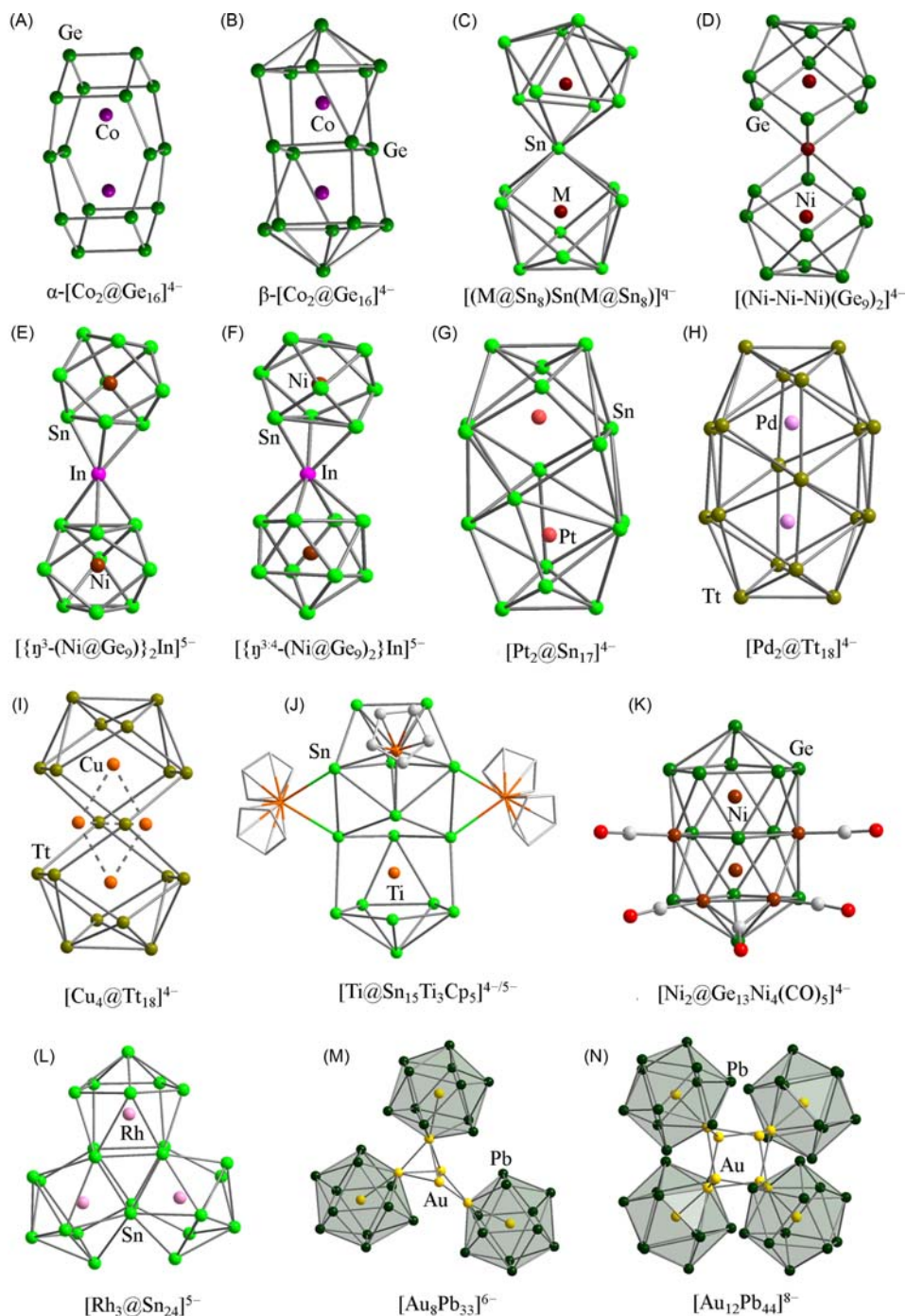
Even larger inter-metalloid clusters can also be prepared by the re-arrangement and fusion of small components such as the  $[\text{M}@\text{Tt}_9]^{4-}$  anion. The first triply-fused stannide  $[\text{Rh}_3@\text{Sn}_{24}]^{5-}$  was isolated from the reaction  $\text{K}_4\text{Sn}_9$  with  $[(\text{COE})_2\text{Rh}(\mu\text{-Cl})_2]_2$ , although a range of other products including  $[\text{Rh}@\text{Sn}_{10}]^{3-}$ ,  $[\text{Rh}@\text{Sn}_{12}]^{3-}$  and  $[\text{Rh}_2@\text{Sn}_{17}]^{6-}$  could also be obtained by subtle changes in the reaction conditions.<sup>111</sup> The approximately  $C_{3v}$ -symmetric geometry of the  $[\text{Rh}_3@\text{Sn}_{24}]^{5-}$  cluster can be viewed as a fusion of three  $[\text{Rh}@\text{Sn}_{10}]^{3-}$  subunits through sharing of rectangular edges (Fig. 8L). The simultaneous observation of  $[\text{Rh}@\text{Sn}_{10}]^{3-}$ ,  $[\text{Rh}@\text{Sn}_{12}]^{3-}$  and  $\{[\text{Rh}_3@\text{Sn}_{24}]^{5-}\}$  in ESI-MS spectroscopy of the reaction mixtures, along with the acquisition of  $[\text{Rh}_3@\text{Sn}_{24}]^{5-}$  via an alternative route of thermolysis of  $[\text{Rh}@\text{Sn}_{10}]^{3-}$ , suggests a very dynamic solution-phase picture, with many different species present in equilibrium. The dominant product obtained will then reflect a balance of intrinsic stability of the anionic cluster and the lattice energy of the resulting solid product.

Some larger inter-metalloid clusters bearing M-L units have also been characterized, including  $[\text{Ni}_2@\text{Ge}_{13}\text{Ni}_4(\text{CO})_5]^{4-}$ <sup>113</sup> and  $[\text{Ti}@\text{Sn}_{15}\text{Ti}_3\text{Cp}_5]^{4/5-}$ .<sup>115</sup> The former was isolated from an en solution of  $\text{K}_4\text{Ge}_9$  and  $[\text{Ni}(\text{CO})_2(\text{PPh}_3)_2]$ , and its 17-atom deltahedral geometry can be viewed as a fusion of two *nido* 11-vertex clusters by sharing a  $\text{Ge}_3\text{Ni}_2$  five-membered ring (Fig. 8K). The  $[\text{Ti}@\text{Sn}_{15}\text{Ti}_3\text{Cp}_5]^{4/5-}$  cluster was obtained from the reaction of  $\text{K}_{12}\text{Sn}_{17}$  with  $\text{TiCp}_2\text{Cl}_2$  in liquid solution. Notably, the oxidation state of this structure is unclear because two independent anionic clusters are balanced by nine counter cations in the asymmetric unit cell, implying the presence of 9 negative charges distributed over the two cluster units. The  $[\text{Ti}@\text{Sn}_{15}\text{Ti}_3\text{Cp}_5]^{4/5-}$  cluster contains two  $\text{TiCp}_2$  groups bridging one  $\text{CpTi}@\text{Sn}_6$  unit and the central three Sn atoms further connected to the other  $\text{Ti}@\text{Sn}_6$  unit (Fig. 8J). It is possible that the  $[\text{CpTi}@\text{Sn}_6]^{3-}$  fragment serves as an intermediate in the growth of these larger intermetallic clusters.

### 1.20.4.2 Coordination compounds and heterometallic clusters of the group 14 elements

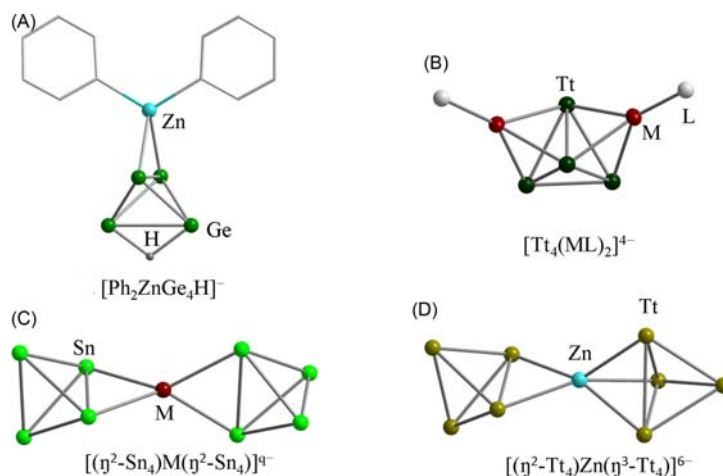
#### 1.20.4.2.1 Coordination compounds of $\text{Tt}_4^{4-}$ , $\text{Tt}_5^{2-}$ and $\text{Tt}_9^{4-}$

The  $\text{Tt}_4^{4-}$  anions, which are isoelectronic and isostructural with the  $\text{P}_4$  and  $\text{As}_4$ , are of particular interest as a result of their flexible coordination modes. The  $\text{Tt}_4^{4-}$  anions are found in the binary Zintl phases  $\text{K}_4\text{Tt}_4$  and also  $\text{K}_{12}\text{Tt}_{17}$ , which contains both  $\text{Tt}_4^{4-}$  and  $\text{Tt}_9^{4-}$  in a 2:1 ratio; both phases are only soluble in liquid ammonia. The homo-atomic tetrahedral anions  $\text{Tt}_4^{4-}$  can replace a ligand



**Fig. 8** Molecular structures of larger inter-metalloid clusters for group 14 elements (A)  $\alpha$ -[Co<sub>2</sub>@Ge<sub>16</sub>]<sup>4-</sup>, (B)  $\beta$ -[Co<sub>2</sub>@Ge<sub>16</sub>]<sup>4-</sup>, (C) [(M@Sn<sub>8</sub>)Sn(M@Sn<sub>8</sub>)]<sup>q-</sup> (M/q = Co/5, Ni/4), (D) [(Ni-Ni-Ni)(Ge<sub>9</sub>)<sub>2</sub>]<sup>4-</sup>, (E) [ $\eta^3$ -(Ni@Ge<sub>9</sub>)<sub>2</sub>In]<sup>5-</sup>, (F) [ $\eta^{3,4}$ -(Ni@Ge<sub>9</sub>)<sub>2</sub>In]<sup>5-</sup>, (G) [Pt<sub>2</sub>@Sn<sub>17</sub>]<sup>4-</sup>, (H) [Pd<sub>2</sub>@Tt<sub>18</sub>]<sup>4-</sup> (Tt = Ge, Sn), (I) [Cu<sub>4</sub>@Tt<sub>18</sub>]<sup>4-</sup> (Tt = Sn, Pb), (J) [Ti@Sn<sub>15</sub>Ti<sub>3</sub>Cp<sub>5</sub>]<sup>4-/5-</sup>, (K) [Ni<sub>2</sub>@Ge<sub>13</sub>Ni<sub>4</sub>(CO)<sub>5</sub>]<sup>4-</sup>, (L) [Rh<sub>3</sub>@Sn<sub>24</sub>]<sup>5-</sup>, (M) [Au<sub>8</sub>Pb<sub>33</sub>]<sup>6-</sup>, (N) [Au<sub>12</sub>Pb<sub>44</sub>]<sup>8-</sup>.

of a transition metal complex, coordinating either via an edge in an  $\eta^2$  fashion, or via a face in an  $\eta^3$  mode. They can also bridge two or more transition metal atom to form dimers or one-dimensional chain structures. The [Si<sub>4</sub>(CuMes)<sub>2</sub>]<sup>4-</sup> and [Si<sub>4-x</sub>Ge<sub>x</sub>(CuMes)<sub>2</sub>]<sup>4-</sup> clusters, obtained by treatment of the Zintl phases K<sub>6</sub>Rb<sub>6</sub>Si<sub>17</sub> and K<sub>12</sub>Si<sub>17-x</sub>Ge<sub>x</sub> with CuMes, have Tt<sub>4</sub><sup>4-</sup> anions decorated with M-L fragments bound in an  $\eta^3$  fashion via triangular faces. A closely related cluster, Sn<sub>4</sub>(ZnEt)<sub>2</sub>, was obtained recently from the reaction of K<sub>12</sub>Sn<sub>17</sub> with ZnEt<sub>2</sub> in liquid ammonia (Fig. 9B).<sup>116-118</sup> The Sn<sub>4</sub> tetrahedron is distorted by a marked elongation of the Sn-Sn edge shared by the two ZnEt fragments. In contrast, the [HGe<sub>4</sub>ZnPh<sub>2</sub>]<sup>3-</sup> cluster,<sup>119</sup> isolated from a liquid ammonia solution, has a tetrahedral Ge<sub>4</sub><sup>4-</sup> anion stabilized by a ZnPh<sub>2</sub> molecule and an H atom bound to opposite edges (Fig. 9A).



**Fig. 9** Structures of coordinated compounds of tetrahedral  $Tt_4^{4-}$  anion. (A)  $[(Ph)_2ZnGe_4H]^{4-}$ , (B)  $[(LMTt_4ML)]$  ( $M/Tt/L = Cu/Ge/Mes, Zn/Ge/Et, Cu/Si/Mes$ ), (C)  $[(\eta^2-Sn_4)M(\eta^2-Sn_4)]^{q-}$  ( $M/q = Zn/6, Au/7$ ), (D)  $[(\eta^2-Tt_4)Zn(\eta^3-Tt_4)]^{6-}$  ( $Tt = Ge, Sn$ ).

Homoleptic complexes where two tetrahedral anions coordinate to a single transition metal atom are also known, examples including  $[(\eta^3-Ge_4)Zn(\eta^3-Ge_4)]^{6-}$ ,<sup>120</sup>  $[(\eta^2-Sn_4)Zn(\eta^2-Sn_4)]^{6-118}$  and  $[(\eta^2-Tt_4)Zn(\eta^3-Tt_4)]^{6-}$  ( $Tt = Ge$ ,<sup>117</sup>  $Sn$ <sup>122</sup>) (Fig. 9C and D). A related cluster  $[(\eta^2-Sn_4)Au(\eta^2-Sn_4)]^{7-}$  was isolated from the reaction of  $K_{12}Sn_{17}$  with  $Au(P^tBu_3)Cl$  in liquid ammonia and can be viewed as an  $Au^+$  ion coordinated to one edge of each  $Tt_4^{4-}$  anion.<sup>123</sup> The uncoordinated edges of the tetrahedra provide further opportunities to form one-dimension infinite chains such as  $Au(\eta^2:\eta^2-Tt_4)$ <sup>124</sup> and  $Au(\eta^2:\eta^2-TlSn_3)$ <sup>125</sup> in the solid phase along with the remarkable  $[M_6Ge_{16}]^{4-}$  ( $M = Zn, Cd$ )<sup>126</sup> clusters that will be discussed in Section 1.20.5.1. Pseudo-tetrahedral Zintl anions  $[Sn_2Sb_2]^{2-}$ ,  $[Ge_3P]^{3-}$  and  $[Ge_3As]^{3-}$  can also act as ligands to transition metals, for example in  $[Au(Sn_2Sb_2)]^{2-}$ ,<sup>127</sup>  $[Cd(Ge_3P)]^{3-25}$  and  $[Au_6(Ge_3As)(Ge_2As_2)_3]^{3-32}$  where the coordination modes are similar to those in homo-atomic anionic  $Tt_4^{4-}$ .

In contrast to the rather extensive coordination chemistry of the  $Tt_4^{4-}$  anions, the corresponding chemistry of  $Tt_5^{5-}$  is rather sparse, with only one well-characterized example,  $[Ge_5Ni_2(CO)_3]^{2-}$ , isolated from the reaction of  $KGe_{1.67}$  with  $[Ni(CO)_2(PPh_3)]$  in en solution in the presence of 2.2.2-crypt.<sup>128</sup> In this hetero-atomic cluster two NiCO fragments bind to adjacent faces of a trigonal bipyramidal  $Ge_5^{5-}$  unit, with a third CO unit bridging the two Ni atoms (Fig. 10A). DFT calculations indicated that the stability of  $[Ge_5Ni_2(CO)_3]^{2-}$  is dominated by four 3c-2e  $Ge_3$   $\sigma$ -delocalized bonds and two 4c-2e delocalized bonds between the Ni atoms and the triangular  $Ge_3$  faces.

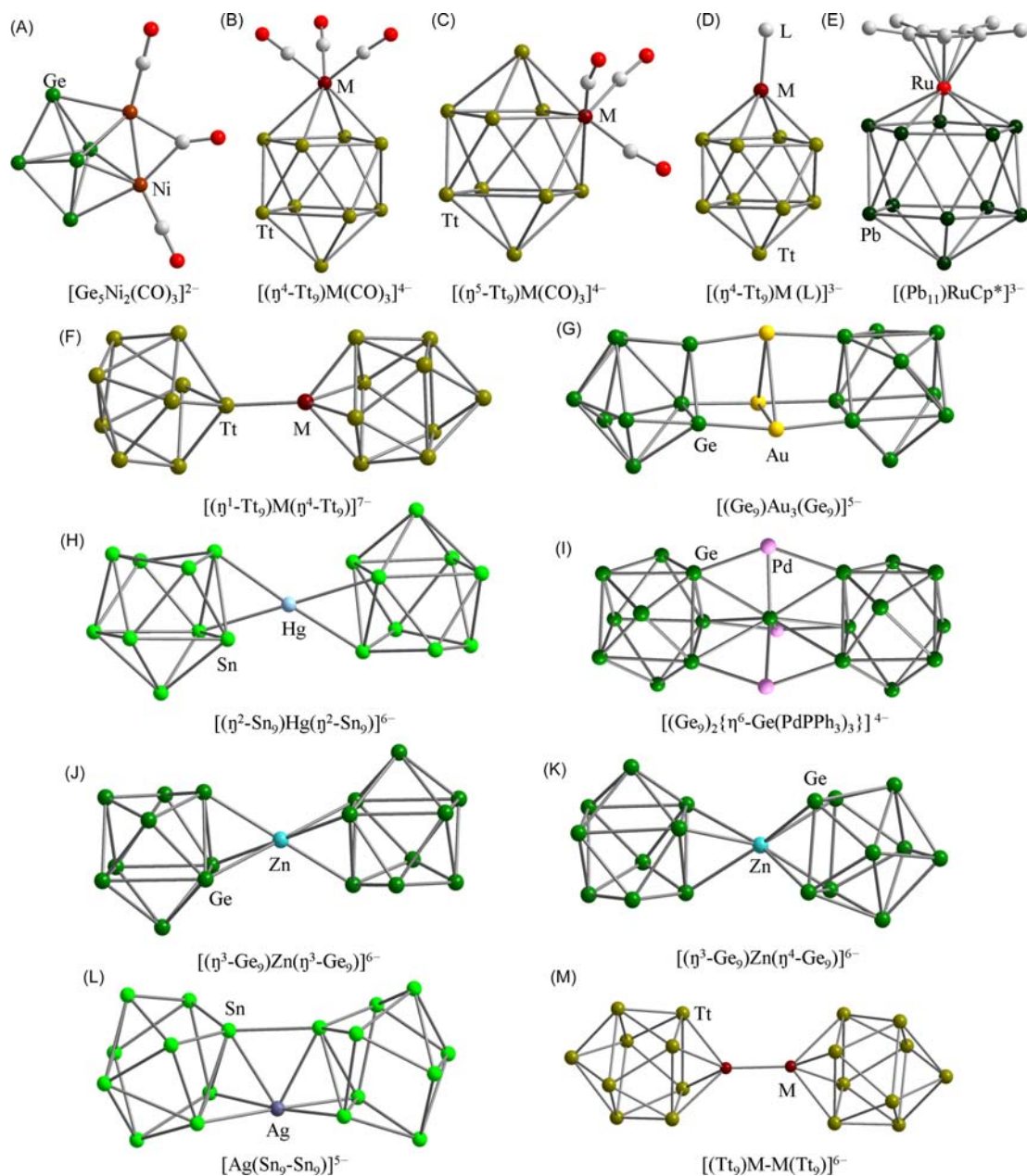
Coordination compounds containing the homo-atomic anions  $Tt_5^{4-}$  are extremely common due to the ready availability of  $Tt_4^{4-}$  in aprotic polar solvents. The hetero-atomic *closo*-10 atom 22-electron cluster,  $[Sn_9Cr(CO)_3]^{4-}$ , was isolated by Eichhorn from the reaction of  $K_4Sn_9$  with  $Cr(CO)_3Mes$ ,<sup>10</sup> and subsequently a series of group 6/group 14 analogs have emerged including  $[\eta^{4/5}-Tt_5M(CO)_3]$  ( $Tt = Sn, Pb; M = Cr, Mo, W$ )<sup>10,129-132</sup> (Fig. 10B and C). In addition to these metal carbonyl complexes, the  $Tt_5^{4-}$  cages have been coordinated to a wide range of different M-L fragments including  $Ir(COD)$ ,<sup>121,133</sup>  $Ni(CO)$ ,<sup>83</sup>  $Pd(PPh_3)$ ,<sup>89</sup>  $CuNHC^{Dipp}$ ,<sup>134</sup>  $CuPR_3$  ( $R = ^iPr_3, PCy_3$ ),<sup>135</sup>  $AgNHC^{Dipp}$ ,<sup>136</sup>  $AuNHC^{Dipp}$ ,<sup>136</sup>  $ZnMes$ ,<sup>137</sup>  $ZnPh$ ,<sup>138</sup>  $Zn^iPr$ <sup>137</sup> and  $CdPh$ <sup>139</sup>) via the open square face of a mono-capped square antiprism (Fig. 10D).

Coordination to naked transition metals leads to the formation of oligomers and polymers with a general formula of  $[Tt_5MT_5]^{q-}$  ( $M =$  transition metal atom or subunit),  $[(Tt_5M)_nT_5]^{q-}$  ( $n = 1, 3$  and  $\infty$ ). There is now an extensive literature covering the properties of "oligomers" such as  $[(\eta^4-Tt_5)M(\eta^1-Tt_5)]^{7-}$  ( $M/Tt = Cu/Ge$ ,<sup>135</sup>  $Ag/Sn$ <sup>136</sup>) (Fig. 10F),  $[(\eta^{3/4}-Ge_5)Zn(\eta^3-Ge_5)]^{6-}$  (Fig. 10J and K),<sup>140</sup>  $[(Tt_5)M-M(Tt_5)]^{6-}$  ( $M/Tt = Zn/Ge$ ,<sup>141</sup>  $Cd/Pb$ <sup>142</sup>) (Fig. 10M),  $[(\eta^2-Sn_5)Hg(\eta^2-Sn_5)]^{6-}$  (Fig. 10H),<sup>143</sup>  $[(Ge_5)Zn(Ge_5)Zn(Ge_5)]^{8-}$ ,<sup>141</sup>  $[(Ge_5)Hg(Ge_5)Hg(Ge_5)Hg(Ge_5)]^{10-144}$  and the polymers  ${}_n[M(Ge_5)]^{2-}$  ( $M = Zn, Hg$ )<sup>141,144-146</sup> (Fig. 11). The  $Tt_5^{4-}$  anions are highly flexible ligands in so much as they can coordinate to transition metals via a vertex, an edge, a triangular face or an open square face ( $\eta^1, \eta^2, \eta^3$  and  $\eta^4$ , respectively). The spherical  $Zn^{2+}$  ion, for example, is known to adopt  $\eta^1, \eta^3$  and  $\eta^4$  modes in  $[(\eta^{3/4}-Ge_5)Zn(\eta^3-Ge_5)]^{6-}$ ,  $[(\eta^4-Ge_5)Zn(\mu_2, \eta^1, \eta^1-Ge_5)Zn(\eta^4-Ge_5)]^{8-}$  and  ${}_n[(\eta^1-Ge_5)Zn(\eta^4-Ge_5)]^{2-}$ .

#### 1.20.4.2.2 Other coordination compounds and heterometallic clusters

The coordination complexes in Section 1.20.4.2.1 were derived from the  $Tt_4^{4-}$ ,  $Tt_5^{2-}$  and  $Tt_9^{q-}$  ( $q = 2, 3$  or  $4$ ) anions through the replacement of ligand(s) of a transition metal complex, usually without any associated oxidation or fragmentation processes. There are also a number of complexes formed from fragmentation and rearrangement products of the precursor anions  $Tt_4^{4-}$ ,  $Tt_5^{2-}$  and  $Tt_9^{q-}$ , although the precise mechanism by which they are formed remains a matter of debate. For example, the cluster anion  $[(CO)_3Mo(Pb_5)Mo(CO)_3]^{4-}$ , which contains a planar five-membered  $Pb_5^{4-}$  ring bridging two zero-valent  $Mo(CO)_3$  fragments in an inverse sandwich structure (Fig. 12A),<sup>147</sup> was isolated from an en solution of  $K_4Pb_9$  with  $Mo(CO)_3Mes$  in the presence of 2.2-crypt. Density functional theory suggests that the  $Pb_5^{4-}$  unit in fact transfers two electrons to the  $Mo(CO)_3$  fragments, resulting in a  $2\pi$  aromatic  $Pb_5^{2-}$ . A highly anionic  $Ge_8^{6-}$  fragment with a distorted square anti-prismatic structure (Fig. 12B),<sup>148</sup> was formed in a reaction of  $K_4Ge_9$  with  $Fe(cot)(CO)_3$  ( $cot =$  cyclooctatetraene) in solution. The  $Ge_8^{6-}$  fragment is isoelectronic with the  $Sn_8^{6-}$  unit

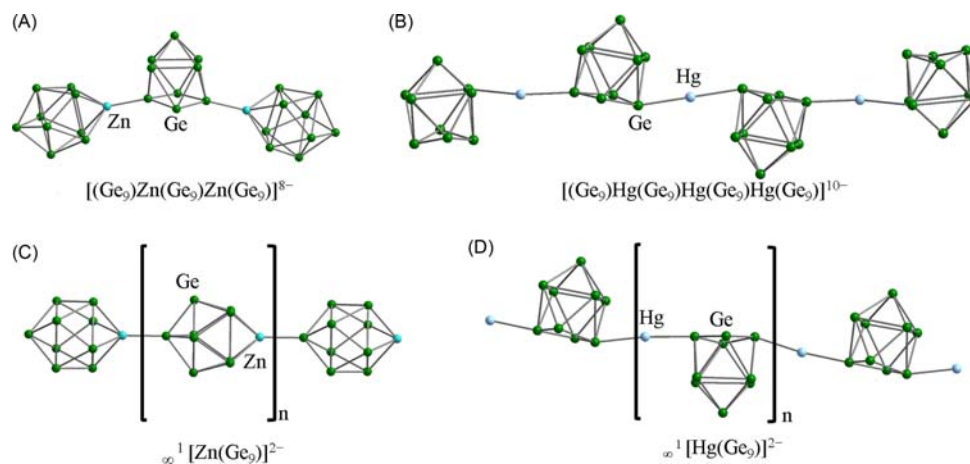




**Fig. 10** Molecular structures of coordinated compounds of  $\text{Tt}_5^{2-}$  and  $\text{Tt}_9^{3-}$  anions. (A)  $[\text{Ge}_5\text{Ni}_2(\text{CO})_3]^{2-}$ , (B)  $[(\eta^4\text{-Tt}_9)\text{M}(\text{CO})_3]^{4-}$  ( $\text{Tt} = \text{Sn, Pb}$ ,  $\text{M} = \text{Cr, Mo, W}$ ), (C)  $[(\eta^5\text{-Tt}_9)\text{M}(\text{CO})_3]^{4-}$  ( $\text{Tt}/\text{M} = \text{Sn}/\text{W, Pb}/\text{Mo}$ ), (D)  $[(\eta^4\text{-Tt}_9)\text{ML}]^{3-}$  ( $\text{Tt}/\text{M}/\text{L} = \text{Si}/\text{Cu}/\text{NHC}^{\text{Dipp}}$ ,  $\text{Si, Ge, Sn, Pb}/\text{Zn}/\text{Ph}$ ,  $\text{Ge, Sn, Pb}/\text{Zn}/\text{Mes, iPr}$ ,  $\text{Sn, Pb}/\text{Cd}/\text{Ph}$ ,  $\text{Ge}/\text{Cu}/\text{P}^i\text{Pr}_3, \text{PCy}_3$ ,  $\text{Sn}/\text{Ag}/\text{NHC}^{\text{Dipp}}$ ,  $\text{Ge}/\text{Ni}/\text{CO}$ ,  $\text{Ge}/\text{Pd}/\text{PPh}_3$ ,  $\text{Sn}/\text{Ir}/\text{COD}$ ,  $\text{Pb}/\text{Ir}/\text{COD}$ ), (E)  $[(\text{Pb}_{11})\text{RuCp}^*]^{3-}$ , (F)  $[(\eta^1\text{-Tt}_9)\text{M}(\eta^4\text{-Tt}_9)]^{7-}$  ( $\text{Tt}/\text{M} = \text{Ge}/\text{Cu, Sn}/\text{Ag}$ ), (G)  $[(\text{Ge}_9)\text{Au}_3(\text{Ge}_9)]^{5-}$ , (H)  $[(\eta^2\text{-Sn}_9)\text{Hg}(\eta^2\text{-Sn}_9)]^{6-}$ , (I)  $[(\text{Ge}_9)_2\{\eta^6\text{-Ge}(\text{PdPPh}_3)_3\}]^{4-}$ , (J)  $[(\eta^3\text{-Ge}_9)\text{Zn}(\eta^3\text{-Ge}_9)]^{6-}$ , (K)  $[(\eta^3\text{-Ge}_9)\text{Zn}(\eta^4\text{-Ge}_9)]^{6-}$ , (L)  $[\text{Ag}(\text{Sn}_9\text{-Sn}_9)]^{5-}$ , (M)  $[(\text{Tt}_9)\text{M-M}(\text{Tt}_9)]^{6-}$  ( $\text{Tt}/\text{M} = \text{Ge}/\text{Zn, Pb}/\text{Cd}$ ).

found in  $\text{A}_4\text{Li}_2\text{Sn}_8$ .<sup>20</sup> EPR spectroscopy confirms that the  $[\text{Ge}_5\text{Fe}(\text{CO})_3]^{3-}$  cluster is paramagnetic with 21 ( $8 \times 2 + 3 + 2$ ) skeletal electrons (the  $\text{Fe}(\text{CO})_3$  fragment is considered as a 2-electron donor), and is isoelectronic and isostructural with the known  $\text{Ge}_5^{3-}$  anion. A further 9-atom cluster,  $[\text{Sn}_8\text{TiCp}]^{3-}$  (Fig. 12C),<sup>115</sup> has been isolated from a liquid ammonia solution of  $\text{K}_4\text{Sn}_9$  and  $[\text{TiCp}_2\text{Cl}_2]$ , and may be an important intermediate in the formation of the larger intermetalloid cluster  $[\text{Ti}@\text{Sn}_{15}\text{Ti}_3\text{Cp}_5]^{4/5-}$ . The long Ti–Sn bonds in this cluster were attributed to the high coordination number of the Ti atom (6 tin and 5 carbon atoms in the  $[\text{Sn}_8\text{TiCp}]^{3-}$  cluster). Similarly, a chair-like 6-membered ring bearing a high formal charge,  $\text{Sn}_6^{12-}$ , was trapped by two formally  $\text{Nb}^{5+}$  fragments in the cluster  $[(\text{tol})\text{Nb}(\eta^3\text{-Sn}_6)\text{Nb}(\text{tol})]^{2-}$  (Fig. 12f).<sup>149</sup> An  $\text{Mo}_2(\text{CO})_6$  fragments with a direct Mo–Mo bond can also be used to cap a  $\text{Ge}_8$  cluster in the bicapped square anti-prismatic  $[\text{Ge}_8\text{Mo}_2(\text{CO})_6]^{4-}$ .<sup>150</sup> The skeletal electron count of 20 in this cluster, 2 fewer than the *closo* count of 22 for a 10-atom cage, may account for its marked distortion.





**Fig. 11** Molecular structures of selected metal bridged Group 14 Zintl clusters. (A)  $[(\text{Ge}_9)\text{Zn}(\text{Ge}_9)\text{Zn}(\text{Ge}_9)]^{8-}$ , (B)  $[(\text{Ge}_9)\text{Hg}(\text{Ge}_9)\text{Hg}(\text{Ge}_9)\text{Hg}(\text{Ge}_9)]^{10-}$ , (C)  $\infty^1 [(\eta^1\text{-Ge}_9)\text{Zn}(\eta^4\text{-Ge}_9)]^{2-}$ , (D)  $\infty^1 [(\text{Ge}_9)\text{Hg}(\text{Ge}_9)]^{2-}$ .

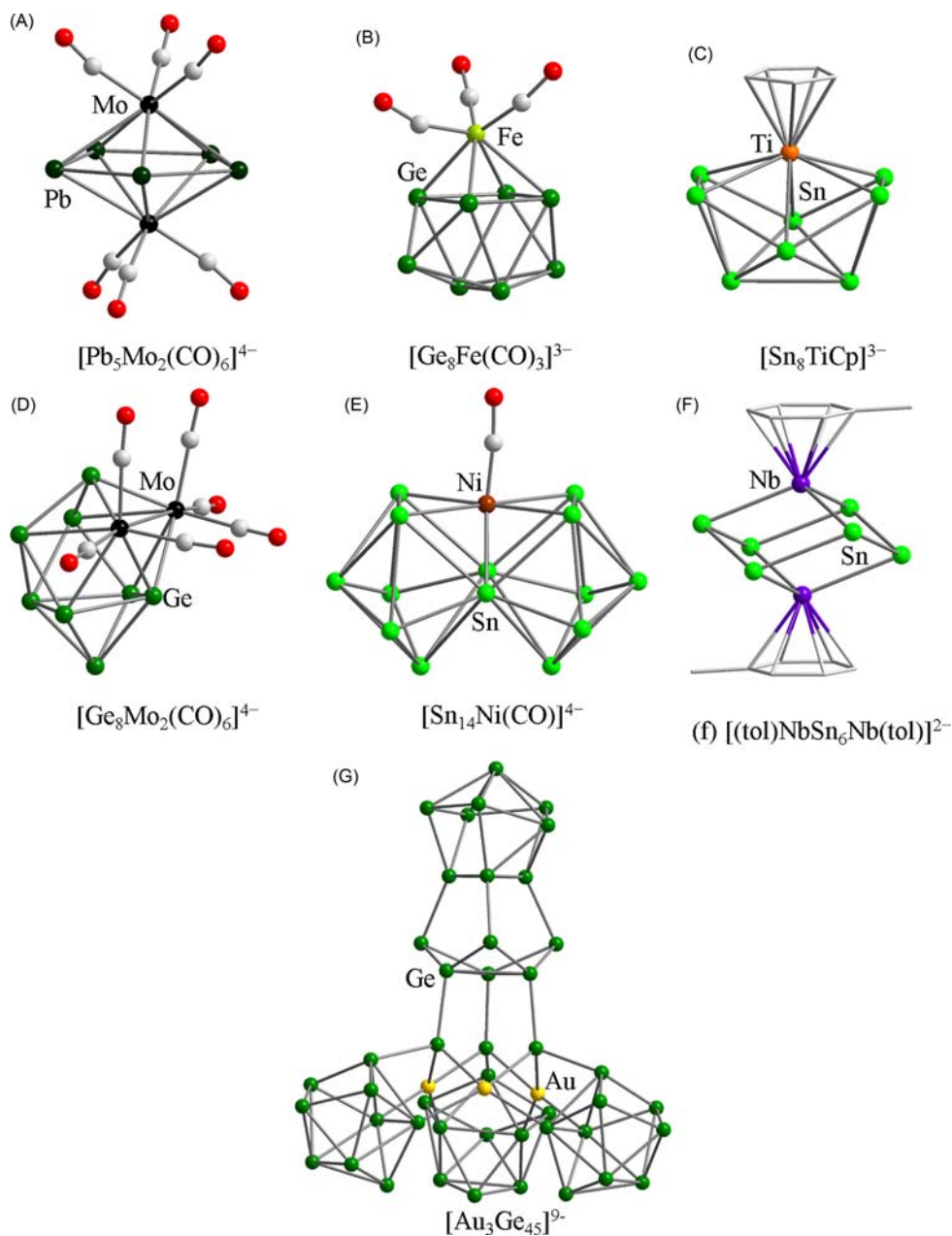
The  $[\text{Ag}(\text{Sn}_9\text{-Sn}_9)]^{5-}$  cluster, where two  $\text{Sn}_9^{4-}$  units are oxidatively coupled, is isolated from the reaction of  $\text{K}_4\text{Sn}_9$  with  $[\text{Ag}_4\text{Mes}_4]$ .<sup>151</sup> The formation of the  $[\text{Ag}(\text{Sn}_9\text{-Sn}_9)]^{5-}$  cluster involves two formal steps: (1) the oxidative coupling of two  $\text{Sn}_9^{4-}$  through formation of an *exo* Sn–Sn bond to generate  $[\text{Sn}_9\text{-Sn}_9]^{6-}$  and (2) the coordination of the newly formed  $[\text{Sn}_9\text{-Sn}_9]^{6-}$  ‘pincer’ ligand to the  $\text{Ag}^+$  ion (Fig. 10L). The related  $[\text{Sn}_{14}\text{Ni}(\text{CO})]^{4-}$  cluster<sup>152</sup> is obtained by heating a DMF solution of the known cluster  $[\text{Ni}@\text{Sn}_9\text{Ni}(\text{CO})]^{3-}$ . Its structure can be viewed as the coordination of a  $\text{Ni}(\text{CO})$  fragment to a  $\text{Sn}_{14}$  unit formed by fusion of two  $[\text{Sn}_8]$  cages via a shared Sn–Sn edge (Fig. 12E). Recently, a sandwich-like structure,  $[(\text{Ge}_9)_2(\eta^6\text{-Ge}(\text{PdPPh}_3)_3)]^{4-}$ , was synthesized by treatment  $\text{K}_4\text{Ge}_9$  with  $\text{Pd}(\text{PPh}_3)_4$ . This novel structure can be considered as a  $\text{Ge}@\text{Pd}_3$  heterometallic sheet sandwiched between the identical  $\text{Ge}_9^{2-}$  anions with  $D_{3h}$  symmetry (Fig. 10I).<sup>153</sup> Quantum chemical investigations suggest a zero-valent central Ge atom in the  $\text{Ge}@\text{Pd}_3$  unit and the cluster is supported by three 2c-2e Pd–Ge  $\sigma$  bonds in  $\text{Ge}@\text{Pd}_3$ , six 2c-2e Pd–Ge  $\sigma$  bonds and two 4c-2e bonds between the  $\text{Ge}@\text{Pd}_3$  sheet and the two nona-germanide caps. The sandwich structure is reminiscent of  $[(\text{Ge}_9)\text{Au}_3(\text{Ge}_9)]^{5-}$ , which contains a triangular  $\text{Au}_3^+$  cluster flanked by one mono-capped square antiprismatic  $\text{Ge}_9^{4-}$  anion and a tricapped trigonal prismatic  $\text{Ge}_9^{2-}$  anion (Fig. 10G).<sup>154</sup> Although the Au–Au contacts are relatively short, in the range of 2.900–3.095 Å, DFT studies reveal only weak Au–Au interactions. The same reaction also yielded a complex cluster,  $[\text{Au}_3\text{Ge}_{45}]^{9-}$ , which contains four polyhedral  $\{\text{Ge}_9\}$  units covalently linked by nine further Ge atoms to form a  $[\text{Ge}_{45}]$  pentamer (Fig. 12G),<sup>155</sup> and three well-separated Au atoms. DFT studies indicated that the Au ions are more highly oxidized in  $[\text{Au}_3\text{Ge}_{45}]^{9-}$  than in  $[\text{Au}_3@\text{Ge}_{18}]^{5-}$ .

#### 1.20.4.2.3 Coordination compounds of substituted Zintl anions

The potential applications of Zintl anions in synthesis and catalysis are understood to be limited by their low solubility and high reactivity. To address this problem, Zintl anions such as  $\text{Ge}_9^{4-}$  and  $\text{Sn}_9^{4-}$  have been decorated with organic ligands to improve both solubility and stability. Alternatively, ligand-protected Zintl clusters can be obtained through the reaction of mono-halides (e.g.,  $\text{GeBr}$ )<sup>53</sup> with an alkali metal silyl compound such as  $\text{LiHyp}$ ;  $\text{Hyp} = \text{Si}(\text{SiMe}_3)_3$ . The tri-silylated mono-anions  $[\text{Ti}_9(\text{SiR}_3)_3]^-$  ( $\text{R} = \text{Et}$ ,  $^i\text{Pr}$ ,  $^t\text{Bu}$ ,  $\text{TMS}$ ) prepared by either of the two methods mentioned above have good solubility in typical organic solvents (e.g.,  $\text{THF}$ ,  $\text{MeCN}$ ).<sup>54,156</sup> The known tri-silylated mono-anions can further react with transition metal complexes to reduce the charge density, a process which further enhances their potential use in applications.<sup>157</sup> The first alkane-soluble Zintl cluster-based homogeneous catalysis  $[\eta^4\text{-Ge}_9(\text{Hyp})_3]\text{Rh}(\text{COD})$ <sup>158</sup> was very recently reported by Goicoechea and co-workers, and will be discussed in detail in Section 1.20.7. The tri-silylated mono-anions  $[\text{Ti}_9(\text{SiR}_3)_3]^-$  coordinate to a  $\text{Rh}(\text{COD})$  fragment via the open square in an  $\eta^4$  mode to form a bi-capped square antiprism (Fig. 13A). The same coordination mode was also observed in  $[\{\text{Ge}_9(\text{SiPh}_3)_2\}\{\text{Cu}(\text{P}^i\text{Pr}_3)\}_2]_2$ <sup>159</sup> where one  $\eta^4\text{-}\{\text{Cu}(\text{P}^i\text{Pr}_3)\}$  moiety caps the open square face of  $\{\text{Ge}_9(\text{SiPh}_3)_2\}$  while the other  $\{\text{Cu}(\text{P}^i\text{Pr}_3)\}$  fragment is bound to two  $\{\text{Ge}_9(\text{SiPh}_3)_2\}$  units in a  $(\mu_2\text{-}\eta^3, \eta^1)$  fashion (Fig. 13B). Another closely-related dimeric cluster is  $[\{\text{Ge}_9\text{Hyp}_2\text{Cu}(\text{P}^t\text{Bu}_2)\}_2]$ , where each  $\{\text{Cu}(\text{P}^t\text{Bu}_2)\}$  fragment acts as a bidentate ligand, with  $\eta^3\text{-Cu}$  and  $\eta^1\text{-P}$  atoms chelating two  $[\text{Ge}_9\text{Hyp}_2]$  clusters (Fig. 13C).<sup>160</sup>

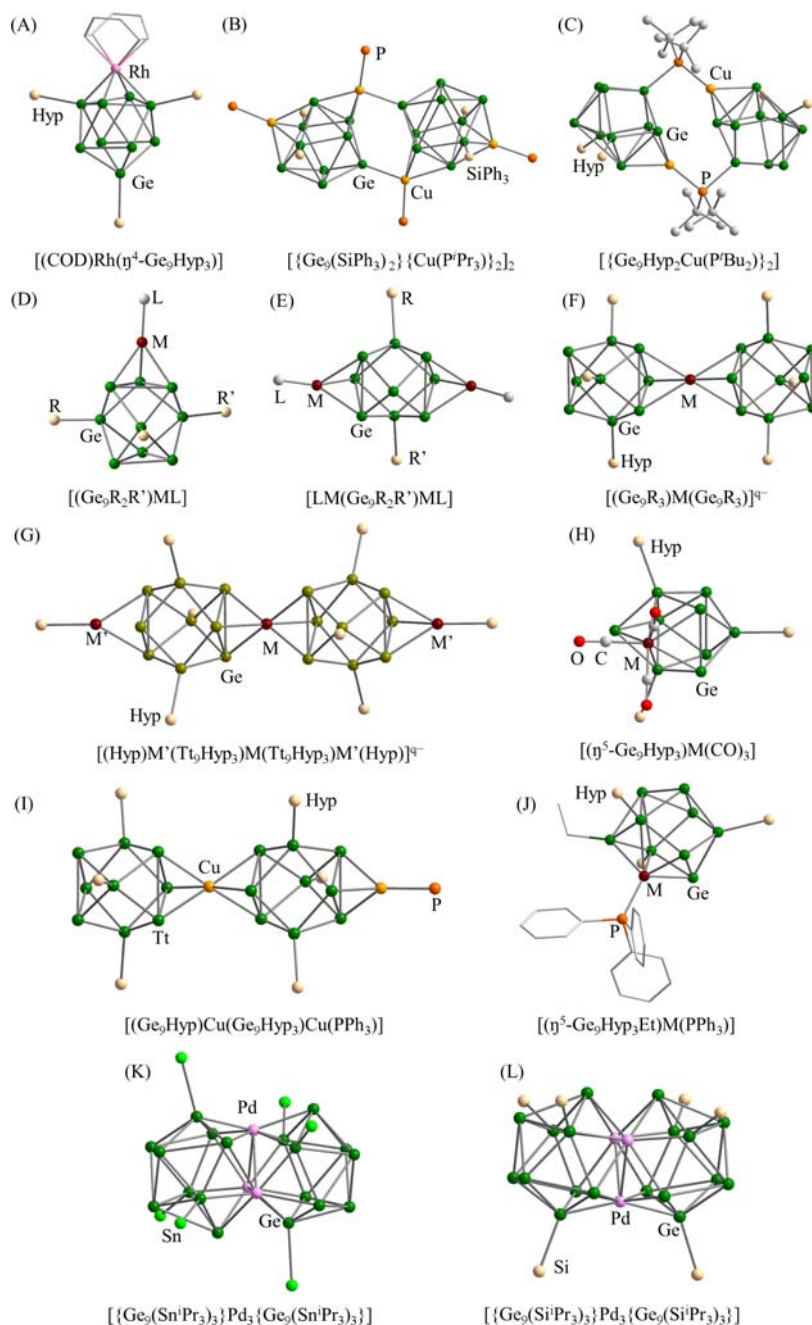
The complex coordination modes in  $[\{\text{Ge}_9(\text{SiPh}_3)_2\}\{\text{Cu}(\text{P}^i\text{Pr}_3)\}_2]_2$  and  $[\{\text{Ge}_9\text{Hyp}_2\text{Cu}(\text{P}^t\text{Bu}_2)\}_2]$  contrast markedly with the  $\eta^3$ -coordination mode found in  $[(\text{Ge}_9\text{R}_2\text{R}')\text{M}(\text{L})]_q$ ,<sup>61,157,159–165</sup>  $[(\text{L})\text{M}(\text{Ge}_9\text{R}_2\text{R}')\text{M}(\text{L})]$ ,<sup>157,160,164,165</sup>  $[(\text{Ge}_9\text{R}_3)\text{M}(\text{Ge}_9\text{R}_3)]$ ,<sup>61,157,161,166,167</sup>  $[(\text{Ge}_9\text{Hyp}_3)\text{Cu}(\text{Ge}_9\text{Hyp}_3)\text{Cu}(\text{PPh}_3)]$ <sup>168</sup> and  $[(\text{Hyp})\text{M}'(\text{Ti}_9\text{Hyp}_3)\text{M}(\text{Ti}_9\text{Hyp}_2)\text{M}'(\text{Hyp})]$ .<sup>169</sup>

The coordination compounds  $[(\text{Ge}_9\text{R}_2\text{R}')\text{M}(\text{L})]$  (Fig. 13D) can be obtained by treatment  $[\text{Ge}_9\text{Hyp}_3]^-$  with a series of transition metal complexes, in which the transition metal fragment was bound to an triangular face of  $[\text{Ge}_9\text{Hyp}_3]^-$  ( $\text{R} = \text{R}' = \text{Hyp}/\text{M}(\text{L}) = \text{Ni}(\text{dppe})$ ,<sup>157</sup>  $\text{Cu}(\text{P}^i\text{Pr}_3)$ ,  $\text{ZnCp}^*$ ,<sup>159</sup>  $(\text{Cu}, \text{Ag}, \text{Au})\text{NHC}^{\text{Dipp}}$ ,<sup>162</sup>  $\text{Cu}(\text{MIC}/\text{CAAC})$ <sup>160</sup>;  $\text{R} = \text{R}' = \text{Si}(\text{Pr})_3$ ,  $\text{Si}(\text{Bu})_3$ ,  $\text{P}(\text{N}^i\text{Pr}_2)_2$ ,  $\text{P}(\text{N}^i\text{Pr}_2)^t\text{Bu}/\text{M}(\text{L}) = \text{CuNHC}^{\text{Dipp}}$ ,<sup>61,164,165</sup>  $\text{R} = \text{Hyp}$ ,  $\text{R}' = \text{P}(\text{Mes})_2/q = 0/\text{M}(\text{L}) = \text{Cu}(\text{NHC}^{\text{Dipp}})$ <sup>163</sup>). Interestingly, the resulting cluster  $[(\text{Ge}_9\text{R}_2\text{R}')\text{M}(\text{L})]$  can be further decorated with the second transition metal fragment. For example, excess  $[\text{Ni}(\text{dppe})_2\text{Cl}_2]$  can further coordinate with a second triangular face of  $[(\text{Ge}_9\text{Hyp}_3)\text{Ni}(\text{dppe})]$  to produce a di-substituted cation  $[(\text{dppe})$



**Fig. 12** Molecular structures of heterometallic clusters involving the group 14 elements and transition metal elements. (A)  $[\text{Pb}_5\text{Mo}_2(\text{CO})_6]^{4-}$ , (B)  $[\text{Ge}_8\text{Fe}(\text{CO})_3]^{3-}$ , (C)  $[\text{Sn}_8\text{TiCp}]^{3-}$ , (D)  $[\text{Ge}_8\text{Mo}_2(\text{CO})_6]^{4-}$ , (E)  $[\text{Sn}_{14}\text{Ni}(\text{CO})_4]^{4-}$ , (F)  $[(\text{tol})\text{NbSn}_6\text{Nb}(\text{tol})]^{2-}$  and (G)  $[\text{Au}_3\text{Ge}_{45}]^{9-}$ .

$\text{Ni}(\text{Ge}_9\text{Hyp}_3)\text{Ni}(\text{dppe})^+$  (Fig. 13E).<sup>157</sup> A similar di-substituted cluster  $[(\text{NHC}^{\text{Dipp}})\text{Cu}(\text{Ge}_9\text{Hyp}_2)\text{Cu}(\text{NHC}^{\text{Dipp}})]^{164}$  was obtained from the acetonitrile solution of  $\text{K}_2(\text{Ge}_9\text{Hyp}_2)$  and  $[\text{Cu}(\text{NHC}^{\text{Dipp}})\text{Cl}]$ . The analogous Ag and Au compounds have also been detected by NMR spectroscopy but have not been structurally characterized.<sup>164</sup> In the case of  $[(\text{Ge}_9\text{R}_3)\text{M}(\text{Ge}_9\text{R}_3)]$  ( $\text{M} = \text{Zn}, \text{Cd}, \text{Hg}, \text{Mn}, \text{Au}, \text{Ag}, \text{Cu}, \text{Pd}$ ), all the ligands of transition metal complexes such as  $\text{M}(\text{L})\text{Cl}$  ( $\text{L} = \text{Cl}, \text{M} = \text{Zn}, \text{Cd}, \text{Hg}$ ,<sup>159,166</sup>  $\text{Mn}$ <sup>157</sup>;  $\text{L} = \text{PPh}_3, \text{M} = \text{Pd}/\text{Au}$ ;  $\text{L} = \text{NHC}^{\text{Dipp}}, \text{M} = \text{Ag}, \text{Cu}\{\text{Al}[\text{OCH}(\text{CF}_3)_2]_4\}_2, \text{Ag}[\text{Al}(\text{OC}_4\text{F}_9)_4]$ , were replaced by  $[(\text{Ge}_9\text{R}_3)]$  to produce “sandwich” clusters (Fig. 13F). The six-coordinate transition metals in these clusters were sandwiched between two  $\text{Ge}_3$  triangles of the tri-substituted  $\text{Ge}_9$  cages in an eclipsed configuration. The  $[(\text{Ge}_9\text{Hyp}_3)\text{Mn}(\text{Ge}_9\text{Hyp}_3)]$  and  $[\text{Mn}@\text{Pb}_{12}]^{3-}$  clusters are both open-shell species whose paramagnetic properties have been confirmed by EPR spectroscopy. The sandwich clusters  $(\text{Ge}_9\text{R}_3)\text{M}(\text{Ge}_9\text{R}_3)$  can also react with transition metal fragments to form oligomeric species or one-dimension chains such as  $[(\text{Ge}_9\text{Hyp}_3)\text{Cu}(\text{Ge}_9\text{Hyp}_3)\text{CuPPh}_3]^{168}$  and  $[\text{HypZn}(\text{Ge}_9\text{Hyp}_3)\text{Pt}(\text{Ge}_9\text{Hyp}_3)\text{ZnHyp}]^{169}$  (Fig. 13I and G), similar to  $[\{\text{Au}(\eta^2: \eta^2\text{-Tt}_4)\}_n]^{3-}$  and  $[\text{M}(\text{Ge}_9)_n]^{2-}$  ( $\text{M} = \text{Zn}, \text{Hg}$ ) noted above. The Cu compound was formed in the reaction of  $\text{K}(\text{Ge}_9\text{Hyp}_3)$  with  $\text{CuPPh}_3\text{Br}$  in acetonitrile, while the Pt/Zn analog, the longest chain in this series, was synthesized in the reaction of  $[\text{ZnGe}_{18}(\text{Hyp})_6]$



**Fig. 13** Molecular structures of coordination compounds of substituted Zintl anions involving the group 14 elements and transition metals. (A)  $[(\text{COD})\text{Rh}(\eta^4\text{-Ge}_9\text{Hyp}_3)]$ , (B)  $[\{\text{Ge}_9(\text{SiPh}_3)_2\}\{\text{Cu}(\text{P}^i\text{Pr}_3)_2\}_2]$ , (C)  $[\{\text{Ge}_9\text{Hyp}_2\text{Cu}(\text{P}^i\text{Bu}_2)_2\}]$ , (D)  $[(\text{Ge}_9\text{R}_2\text{R}')\text{ML}]$  ( $\text{R} = \text{R}' = \text{Hyp}$ ,  $\text{M}(\text{L}) = \text{Ni}(\text{dppe})$ ,  $\text{Cu}(\text{P}^i\text{Pr}_3)$ ,  $\text{ZnCp}^*$ ,  $(\text{Cu}, \text{Ag}, \text{Au})\text{NHC}^{\text{Dipp}}$ ,  $\text{Cu}(\text{MIC}/\text{CAAC})$ ;  $\text{R} = \text{R}' = \text{Si}^i(\text{Pr})_3$ ,  $\text{Si}^i(\text{Bu})_3$ ,  $\text{P}(\text{N}^i\text{Pr}_2)_2$ ,  $\text{P}(\text{N}^i\text{Pr}_2)^i\text{Bu}$ ),  $\text{M}(\text{L}) = \text{CuNHC}^{\text{Dipp}}$ ,  $\text{R} = \text{Hyp}$ ,  $\text{R}' = \text{P}(\text{Mes})_2/q = 0$ ,  $\text{M}(\text{L}) = \text{Cu}(\text{NHC}^{\text{Dipp}})$ , (E)  $[\text{LM}(\text{Ge}_9\text{R}_2\text{R}')\text{ML}]$  ( $\text{R} = \text{R}' = \text{Hyp}$ ,  $\text{M} = \text{Ni}$ ,  $\text{L} = \text{dppe}$ ;  $\text{R} = \text{R}' = \text{Hyp}$ ,  $\text{L} = \text{NHC}^{\text{Dipp}}$ ,  $\text{M} = \text{Cu}$ ,  $\text{Ag}$ ,  $\text{Au}$ ;  $\text{L} = \text{CAAC}$ ,  $\text{M} = \text{Cu}$ ,  $\text{R} = \text{P}(\text{N}^i\text{Pr}_2)_2$ ,  $\text{R}' = \text{Cr}(\text{CO})_5$ ,  $\text{L} = \text{NHC}^{\text{Dipp}}$ ,  $\text{M} = \text{Cu}$ ), (F)  $[(\text{Ge}_9\text{R}_3)\text{M}(\text{Ge}_9\text{R}_3)]^{q-}$ , ( $\text{M}/\text{R}/q = \text{Mn}/\text{TMS}/0$ ,  $\text{Zn}, \text{Cd}, \text{Hg}/\text{TMS}/0$ ,  $\text{Cu}, \text{Ag}, \text{Au}/\text{TMS}/1$ ,  $\text{Au}^i/\text{Bu}/1$ ,  $\text{Pd}/\text{TMS}/2$ ), (G)  $[(\text{Hyp})\text{M}'(\text{Ti}_9\text{Hyp}_3)\text{M}(\text{Ti}_9\text{Hyp}_3)\text{M}'(\text{Hyp})]^{q-}$ , ( $\text{Ti}/\text{M}/q = \text{Ge}/\text{Pt}/\text{Zn}/0$ ,  $\text{Sn}/\text{Au}/\text{Au}/1$ ), (H)  $[(\eta^5\text{-Ge}_9\text{Hyp}_3)\text{M}(\text{CO})_3]$  ( $\text{M} = \text{Cr}, \text{Mo}, \text{W}$ ), (I)  $[(\text{Ge}_9\text{Hyp})\text{Cu}(\text{Ge}_9\text{Hyp}_3)\text{Cu}(\text{PPh}_3)]$ , (J)  $[(\eta^5\text{-Ge}_9\text{Hyp}_3\text{Et})\text{M}(\text{PPh}_3)]$  ( $\text{Ni}, \text{Pd}, \text{Pt}$ ), (K)  $[\{\text{Ge}_9(\text{Sn}^i\text{Pr}_3)_3\}\text{Pd}_3\{\text{Ge}_9(\text{Sn}^i\text{Pr}_3)_3\}]$ , (L)  $[\{\text{Ge}_9(\text{Si}^i\text{Pr}_3)_3\}\text{Pd}_3\{\text{Ge}_9(\text{Si}^i\text{Pr}_3)_3\}]$ .

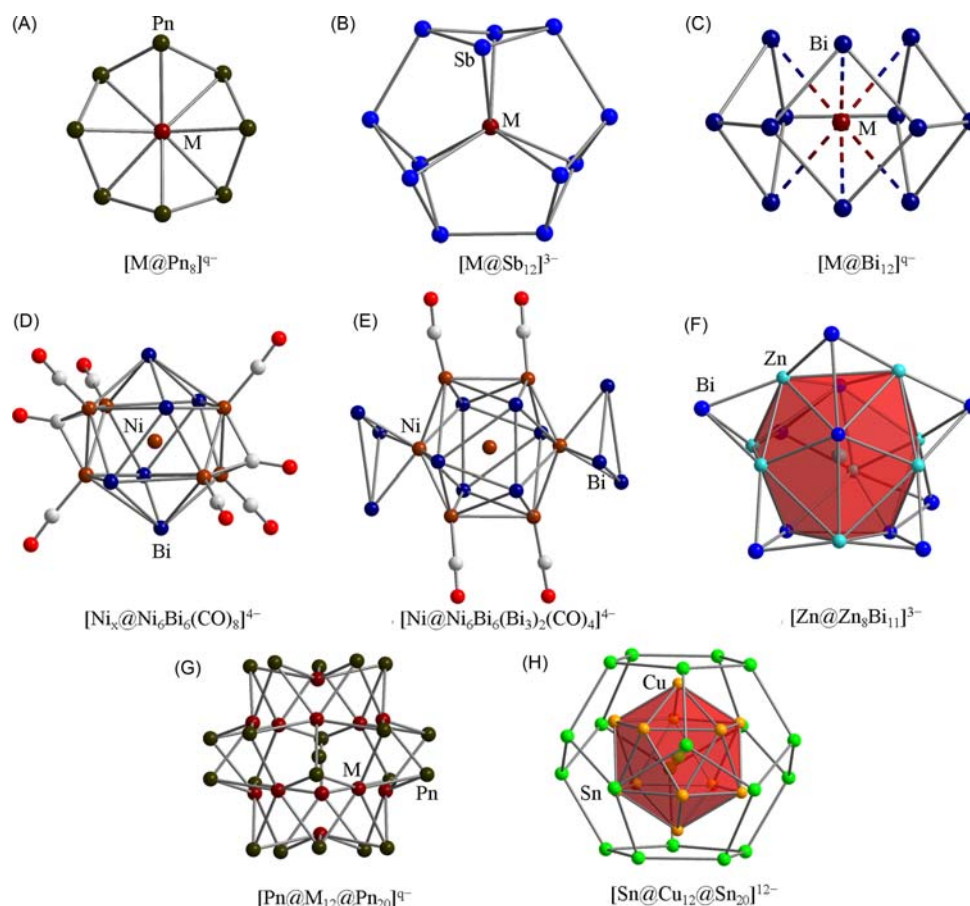
with  $\text{Pt}(\text{PPh}_3)_4$  in THF solution. Only one Sn analog is known,  $[(\text{Hyp})_3\text{Au}(\text{Sn}_9\text{Hyp}_3)\text{Au}(\text{Sn}_9\text{Hyp}_3)\text{Au}(\text{Hyp})_3]^-$ ,<sup>170</sup> which was obtained by reacting  $[\text{Sn}_{10}\text{Hyp}_4]^{2-}$  with  $[\text{Au}(\text{PPh}_3)\text{Hyp}]$  in THF: the starting material  $[\text{Sn}_{10}\text{Hyp}_4]^{2-}$  clearly undergoes re-arrangement while  $[\text{Ge}_9\text{Hyp}_3]^-$  does not. Mono-anionic  $[\text{Ge}_9\text{R}_3]^-$  can also react with  $[\text{M}(\text{CO})_3(\text{NCMe})_3]$  to form a bi-capped square anti-prismatic 10-vertex cage  $\{\eta^5\text{-Ge}_9\text{Hyp}_3\}\text{Mo}(\text{CO})_3$  (Fig. 13H),<sup>171,172</sup> along with gradual release of the NCMe ligand. Quantum chemical investigations, indicate that the  $\text{M}(\text{CO})_3(\text{NCMe})_2$  first coordinates to one Ge atom of the mono-anionic cluster  $[\text{Ge}_9\text{Hyp}_3]^-$ , a proposal that is supported by the reaction of  $[\text{Ge}_9\text{Hyp}_3]^-$  with  $\text{Cr}(\text{CO})_5\text{COE}$  (COE = cyclooctene) which generates

$[\text{Ge}_9\text{R}_3\text{Cr}(\text{CO})_5]^-$ , in which the Cr atom is coordinated to the  $\text{Ge}_9$  cage in an  $\eta^1$  fashion.<sup>171</sup> The intermediate then releases MeCN and undergoes a rearrangement process, resulting in the distorted bicapped square antiprism. A closely-related cluster  $\{[\eta^5\text{-(Ge}_9\text{Hy-p}_3\text{Et)}\}\text{Pd}(\text{PPh}_3)\}$  (Fig. 13J),<sup>173</sup> is the first to contain a penta-functionalized deltahedral Zintl cluster. It was synthesized by the reaction of the tetra-substituted nona-germanium cluster  $[(\text{Me}_3\text{Si})\text{Si}_3\text{EtGe}_9]$  with  $\text{Pd}(\text{PPh}_3)_4$  in toluene solution, and its formation mechanism is thought to be similar to those of the tetra-functionalized anions  $[\text{Ge}_9\text{R}_3\text{M}(\text{CO})_3]^-$ . NMR experiments suggested that the cluster itself is not fluxional in solution, suggesting that the insertion of a  $\{\text{Pd}(\text{PPh}_3)\}$  fragment prevents the rapid exchange of the atoms in this cluster. In contrast, the reaction of  $\text{Pd}(\text{PPh}_3)_4$  with the tri-substituted clusters  $[\text{Ge}_9(\text{E}^i\text{Pr}_3)_3]^-$  produced the fused cluster  $\{[\text{Ge}_9(\text{E}^i\text{Pr}_3)_3]\text{Pd}_3\{[\text{Ge}_9(\text{E}^i\text{Pr}_3)_3]\}^{2-}$ , which can be considered as two  $\{[\text{Ge}_9(\text{E}^i\text{Pr}_3)_3]\text{Pd}_3\}$  icosahedral clusters sharing a  $\text{Pd}_3$  face. The silyl and stannyl groups on the  $\text{Pd}_3\text{Ge}_{18}$  core adopt eclipsed and staggered conformations (Fig. 13K and L),<sup>174,175</sup> respectively, presumably due to the lower steric bulk of the silyl groups. DFT studies confirmed that the conformations of the two clusters are determined by the repulsive interactions between lone-pair electrons on the vicinal Ge atoms.

### 1.20.4.3 Binary intermetallic clusters of the group 15 elements

Binary intermetallic clusters containing group 15 elements are generally prepared by the reaction of binary Zintl phases such as  $\text{K}_5\text{Pn}_4$  ( $\text{Pn} = \text{P-Bi}$ ) and  $\text{K}_3\text{Pn}_7$  ( $\text{Pn} = \text{P-Sb}$ ) with transition metal complexes in polar solvents. Common Zintl anions include  $\text{Pn}_2^{2-}$  ( $\text{Pn} = \text{Sb, Bi}$ ), aromatic  $\text{Pn}_3^-$  ( $\text{Pn} = \text{Sb-Bi}$ ),  $\text{Pn}_4^{2-}$  rings ( $\text{Pn} = \text{P-Bi}$ ) and nortricycane-like  $\text{Pn}_7^{3-}$ . The formation of Zintl clusters of group 15 involves the oxidation and rearrangement of the anions mentioned above. Alternative methods to prepare novel group 15 Zintl clusters include the activation of  $\text{P}_4$  and  $\text{As}_4$  and the reduction of the complexes containing Pn element ( $\text{Sb}_2\text{R}_4$ ,  $[\text{Cp}^*\text{Sb}]_4$ ,  $\text{SbX}_3$ ,  $\text{AsN}$  and  $\text{BiN}$ ). While group 14 clusters tend to adopt delocalized structures based on electron-deficient bonding, the group 15 analogs tend to form 2c-2e localized bonds. The first intermetallic cluster of a group 15 element,  $[\text{Nb}@\text{As}_8]^{3-}$ , was obtained accidentally by extracting the Zintl phase 'RbAs' with en in the presence of 2.2.2-crypt. It contains a *cyclic*- $[\text{As}_8]^{8-}$  unit, isostructural and isoelectronic with  $\text{S}_8$  and  $\text{Se}_8$ , and an endohedral  $\text{Nb}^{5+}$  ion.<sup>176-178</sup> The introduction of the niobium atom resulted from oxidative attack by arsenic on the Nb ampoule at the high temperature prevalent in the reaction. Since that time, a series of  $[\text{M}@\text{Pn}_8]^{q-}$  ( $\text{M/Pn/q} = \text{Nb/As/3, Mo/As/2, Cr/As/3, Nb/Sb/3, Mo/Sb/3}$ )<sup>176-179</sup> where *cyclo*- $\text{Pn}_8^{8-}$  is stabilized by an endohedral high oxidation state transition metal atom (Fig. 14A), have been isolated from the reactions of  $\text{K}_3\text{Pn}_7$  with the corresponding complexes of the group 5 and 6 elements. Quantum chemical calculations indicate that the bonding between *cyclo*- $\text{Pn}_8^{8-}$  and  $\text{M}^{(8-q)}$  is dominated by covalent interactions, and that the low-lying non-bonding orbitals of  $[\text{M}@\text{Pn}_8]^{q-}$  remain available for further reaction. In addition, a series of isomorphous lanthanide ion-centered clusters  $[\text{Ln}@\text{Sb}_{12}]^{3-}$  ( $\text{Ln} = \text{La, Y, Ho, Er, Lu}$ )<sup>180</sup> was recently isolated in the form of  $[\text{K}(2.2.2\text{-crypt})]^+$  salts obtained from pyridine solutions of  $\text{K}_5\text{Sb}_4$  and  $[\text{Ln}(\text{benzyl})_3(\text{THF})_3]$ . The structures feature three slightly distorted  $\text{Sb}_4$  rings surrounding a  $\text{Ln}^{3+}$  ion (Fig. 14B), and quantum chemical calculations indicate that the interactions between the  $\text{Sb}_4$  rings and  $\text{Ln}^{3+}$  ion are delocalized 5c-2e bonds. A heavier analog,  $[\text{U}@\text{Bi}_{12}]^{3-}$ , is also obtained from an en solution of  $[\text{K}(2.2.2\text{-crypt})]_2(\text{GaBi}_3)$  with  $[\text{U}(\text{C}_5\text{Me}_4\text{H})_3]$  or  $[\text{U}(\text{C}_5\text{Me}_4\text{H})_3\text{Cl}]$ ,<sup>24</sup> and contains three distorted  $\text{Bi}_4$  rings, perhaps as a result of the stronger interactions between the  $\text{Bi}_{12}$  unit and the central metal atom. DFT calculations showed that the  $[\text{U}@\text{Bi}_{12}]^{3-}$  cluster was formed from the stepwise replacing the ligands of the U-containing complex by  $\text{Bi}_4^{2-}$  rings (Fig. 14C) the uranium ion acting as a template for the process. The  $[\text{U}@\text{Bi}_{12}]^{3-}$  cluster is formulated as  $\text{Bi}_{12}^{7-}$  rings coordinated to a  $\text{U}^{4+}$  ion, a description consistent with both the magnetic measurements and the quantum chemical investigations. A cluster with the same geometry as  $[\text{U}@\text{Bi}_{12}]^{3-}$ ,  $[\text{Th}@\text{Bi}_{12}]^{4-}$ ,<sup>181</sup> has also been synthesized using the ternary Zintl precursor with  $[\text{Th}(\text{C}_5\text{Me}_4\text{H})_3\text{Cl}]$ . DFT calculations indicated that this cluster can be described as  $\text{Th}^{4+}$  embedded in a  $\text{Bi}_{12}^{8-}$  shell, which is somewhat different from the  $[\text{U}@\text{Bi}_{12}]^{3-}$  analog. Further calculations suggested that the systems are aromatic due to the delocalization of  $2\pi$ -electrons over the ring atoms and the large ring current and the negative NICS value. In contrast to the non-deltahedral clusters  $[\text{Ln}@\text{Sb}_{12}]^{3-}$  and  $[\text{M}@\text{Bi}_{12}]^{q-}$ , intermetallic clusters with triangular faces such as  $[\text{Ni}@\text{Bi}_6\text{Ni}_6(\text{CO})_8]^{4-182}$  and  $[\text{Zn}@\text{Zn}_8\text{Bi}_{11}]^{5-183}$  have also been isolated. The Ni cluster has a pseudo icosahedral topology (Fig. 14D), and can be considered as a chair-like  $\text{Bi}_6$  ring capped by two  $\text{Ni}_3$  triangles on opposite sides. The eight CO units are bound to the six Ni atoms and two  $\text{Ni}_3$ -triangles. There are 26 skeleton electrons, ( $6 \times 3$  from Bi atoms,  $2 \times 2$  from 2  $\text{Ni}(\text{CO})_2$  fragments, 4 from the charge and 0 from 4  $\text{Ni}(\text{CO})$  units) consistent with an icosahedral structure predicted by the Wade-Mingos rules. The cluster anion  $[\text{Ni}@\text{Bi}_6\text{Ni}_6(\text{Bi}_3)_2(\text{CO})_4]^{4-}$  was isolated in a similar way to  $[\text{Ni}@\text{Bi}_6\text{Ni}_6(\text{CO})_8]^{4-}$  although heating was necessary in the presence of 2.2.2-crypt. The cluster adopts the same pseudo-icosahedral structure, although two Ni atoms in the shell are capped by two  $\text{Bi}_3$  rings in an  $\eta^3$  fashion (Fig. 14E). The cluster can therefore be viewed as a fusion of 8 tetrahedra via shared vertices, edges and faces. The second cluster,  $[\text{Zn}@\text{Zn}_8\text{Bi}_{11}]^{5-}$ , with a pseudo-icosahedral core, was synthesized by the reaction of  $\text{K}_5\text{Bi}_4$  with  $\text{ZnPh}_2$  in the presence of 2.2.2-crypt. It contains an endohedral Zn atom and a distorted icosahedral  $[\text{Zn}_8\text{Bi}_4]$  core with seven triangular faces capped by seven  $\eta^3$ -Bi atoms (Fig. 14F). The icosahedral  $[\text{Zn}_8\text{Bi}_4]$  unit is isostructural and isoelectronic with the homoatomic  $\text{Al}_{12}$  and  $\text{Ga}_{12}$  icosahedra. The total valence-electron count of 50 for  $[\text{Zn}@\text{Zn}_8\text{Bi}_{11}]^{5-}$ , made up of 36 from  $\text{Zn}_8\text{Bi}_4$ , 2 from the central zinc atom, 5 from the charge of the cluster and 7 from the seven *exo*-Bi atoms, is consistent with the 12-vertex *closo* icosahedral cluster geometry. Icosahedral symmetry is also found in the so called "onion-type" or "matryoshka-type" structures shown in Fig. 14H, which are formed in the reaction of  $\text{Pn}_7^{3-}$  anions with Ni(0) and Pd(0) complexes, involving an oxidation and re-arrangement. The first example of a cluster of this type,  $[\text{As}@\text{Ni}_{12}@\text{As}_{20}]^{3-}$ ,<sup>184</sup> was isolated from an en solution of  $\text{K}_3\text{As}_7$  and  $\text{Ni}(\text{COD})_2$  in the presence of  $[\text{Bu}_4\text{P}]\text{Br}$ . The cluster can be described as an  $\text{As}_{20}$  dodecahedral cage encapsulating an  $[\text{As}@\text{Ni}_{12}]^{3-}$  icosahedron. Isoelectronic and isostructural  $[\text{Sb}@\text{Pd}_{12}@\text{Sb}_{20}]^{3-}$  was later synthesized by the reaction of  $\text{K}_3\text{Sb}_7$  with  $\text{Pd}(\text{PPh}_3)_4$ , along with small amounts of  $[\text{Sb}@\text{Pd}_{12}@\text{Sb}_{20}]^{4-}$ . The isolation of the cluster in both oxidation states suggests that the 3- and 4- charge states may coexist in solution.<sup>185</sup> The tetra-anion  $[\text{Sb}@\text{Pd}_{12}@\text{Sb}_{20}]^{4-}$  can also be prepared from an





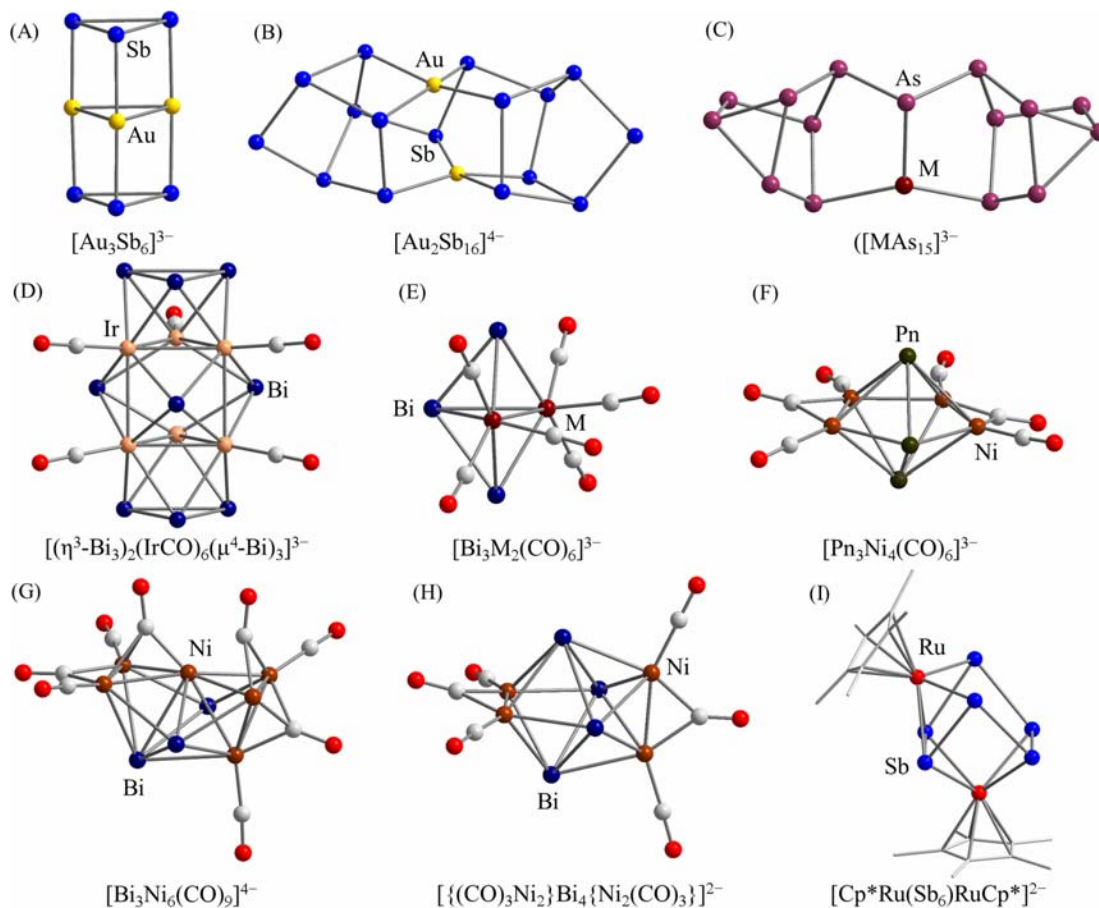
**Fig. 14** Molecular structures of selected coordination compounds and heterometallic cluster of the group 15 elements. (A)  $[M@Pn_8]^{9-}$  ( $M/Pn/q = Nb/As/3, Mo/As/2; Cr/As/3, Nb/Sb/3, Mo/Sb/3$ ) (B)  $[M@Sb_{12}]^{3-}$  ( $M = Y, La, Ho, Er, Lu$ ) (C)  $[M@Bi_{12}]^{9-}$  ( $M/q = U/3, Th/4$ ), (D)  $[Ni_x@Ni_6Bi_6(CO)_8]^{4-}$  ( $x = 0, 1$ ), (E)  $[Ni@Ni_6Bi_6(Bi_3)_2(CO)_4]^{4-}$ , (F)  $[Zn@Zn_8Bi_{11}]^{3-}$ , (G)  $[Pn@M_{12}@Pn_{20}]^{9-}$  ( $Pn/M/q = Ni/As/3; Pd/Sb/3,4$ ), (H)  $[Sn@Cu_{12}@Sn_{20}]^{12-}$ .

en solution of  $K_5Sb_4/Pd(PPh_3)_4/[^{137}Bu_4P]Br$  and its paramagnetic properties were confirmed by EPR measurements. LDI-TOF MS studies of the crystalline samples show signals due to  $[Sb@Pd_{12}@Sb_{20}]^-$  and  $[Sb@Pd_{12}@Sb_{20}]^+$  along with their fragments, indicating the accessibility of multiple oxidation states for this type of cluster. Similar reactions were performed using  $Ni(COD)_2$  instead of  $Pd(PPh_3)_4$ , from which black precipitates instead of crystals corresponding to  $[Sb@Ni_{12}@Sb_{20}]^{n-}$ , corroborated by LDI-TOF MS studies, were obtained. The redox pair  $[Sb@Pd_{12}@Sb_{20}]^{3-/4-}$  can also be isolated separately by varying the cation sequestering agent: 18-crown-6 stabilizes the tetra-anion while 2.2.2-crypt captures the tri-anion.<sup>186</sup> The frontier molecular orbitals and spin densities reveal that the unpaired electron of  $[Sb@Pd_{12}@Sb_{20}]^{4-}$  is located on the outer shell of the cluster, giving rise to a paramagnetic  $\{Sb_{20}\}$  cage (Fig. 14G). A further example of a cluster isostructural with  $[Sb@Pd_{12}@Sb_{20}]^{3-/4-}$  is  $[Sn@Cu_{12}@Sn_{20}]^{12-}$ ,<sup>110</sup> which is found only in the solid state due to its high negative charge. All of these  $[E@M_{12}@E_{20}]^{n-}$  clusters are characterized by strong radial  $M_{12}-E_{20}$  bonding and weak  $M-M$  and  $E-E$  bonding.

#### 1.20.4.4 Coordination compounds and heterometallic clusters of the group 15 elements

The group 15 poly-anions can react with transition metal complexes to yield many novel structures. For example,  $Pn_7^{3-}$  can act as 6e donor or 4e donor in replacing labile ligands of a transition complex, generating  $[(\eta^4-Pn_7)M(CO)_3]^{3-187-189}$  or  $[(\eta^2-Pn_7)M(\eta^2-Pn_7)]^{q-}$  ( $Pn = P, As, Sb, Bi; M = Zn, Cd$ )<sup>190-194</sup> respectively. The  $Pn_7^{3-}$  anion can also coordinate to bimetallic  $M_2$  units (dumbbells) to give  $[Pn_7M_2Pn_7]^{q-}$  ( $M = Pd, Cu, Au, Hg$ ).<sup>190,195-197</sup> The formation of all of these clusters involves coordination without further fragmentation or rearrangement, but such processes are commonly observed in other reactions. The all-metal aromatic sandwich cluster  $[(Sb_3)Au_3(Sb_3)]^{3-}$  (Fig. 15A)<sup>198</sup> with pseudo- $D_{3h}$  symmetry, for example, was synthesized through the reaction of  $K_5Sb_4$  with  $Au(PPh_3)Ph$ , and density functional theory indicates that the  $Sb_3^{3-}$  and  $Au_3^{3+}$  ring were connected by 6 2c-2e bonds and that each  $Sb_3$  ring contains three 3c-2e bonds. When the same reaction is carried out using  $K_3Sb_7$  instead of  $K_5Sb_4$ , the hetero-metallic cluster  $[Au_2Sb_{16}]^{4-199}$  is produced, in which an  $AuSb_2Au$  chain is connected by two  $Sb_7$  cages, a transformation that involved substantial rearrangement of the ligand framework (Fig. 15B). The coordination geometry about the Au centers in



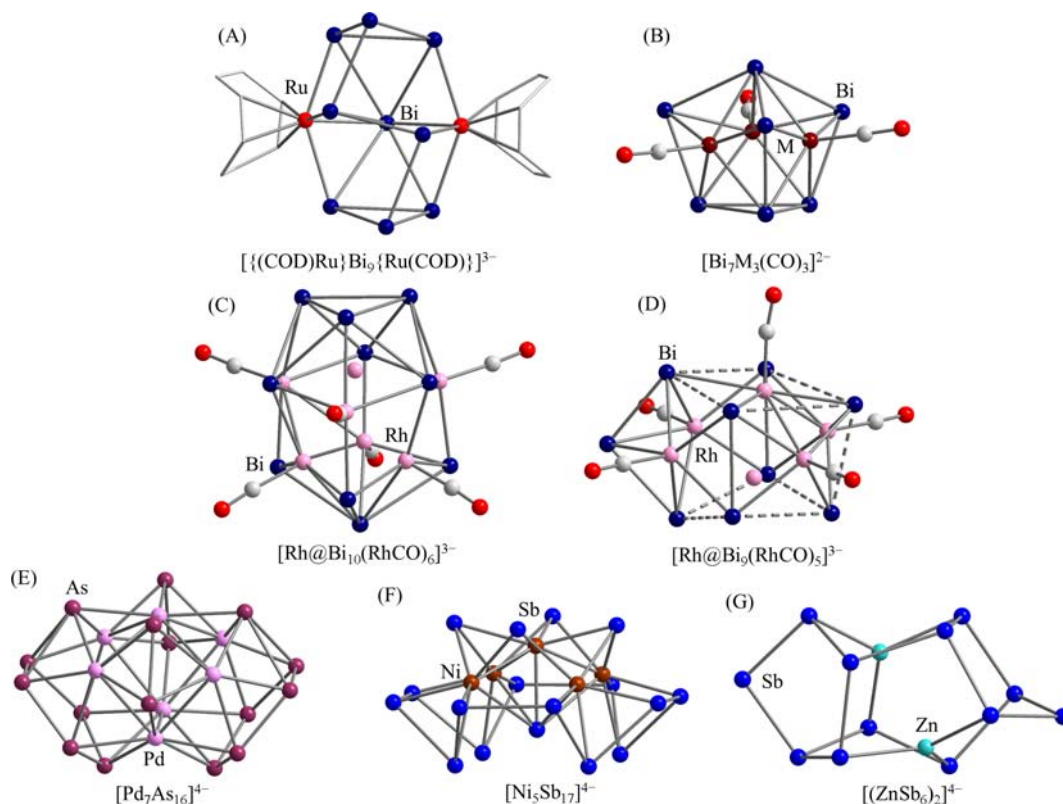


**Fig. 15** Molecular structures of selected coordination compounds and heterometallic cluster of the group 15 elements. (A)  $[\text{Au}_3\text{Sb}_6]^{3-}$ , (B)  $[\text{Au}_2\text{Sb}_{16}]^{4-}$ , (C)  $[\text{As}_{15}\text{M}]^{3-}$  ( $\text{M} = \text{Zn}, \text{Hg}$ ), (D)  $[(\eta^3\text{-Bi}_3)_2(\text{IrCO})_6(\mu^4\text{-Bi})_3]^{3-}$ , (E)  $[\text{Bi}_3\text{M}_2(\text{CO})_6]^{3-}$  ( $\text{M} = \text{Cr}, \text{Mo}$ ) (F)  $[\text{Pn}_3\text{Ni}_4(\text{CO})_6]^{3-}$  ( $\text{Pn} = \text{Sb}, \text{Bi}$ ), (G)  $[\text{Bi}_3\text{Ni}_6(\text{CO})_9]^{4-}$ , (H)  $[(\text{CO})_3\text{Ni}_2]\text{Bi}_4\{\text{Ni}_2(\text{CO})_3\}^{2-}$ , (I)  $[\text{Cp}^*\text{Ru}(\text{Sb}_6)\text{RuCp}^*]^{2-}$ .

$[\text{Au}_2\text{Sb}_{16}]^{4-}$  is approximately square planar with six delocalized  $\sigma$  electrons. This cluster is reminiscent of the  $[(\text{Pn}_7)\text{M}_2(\text{Pn}_7)]^{4-}$  ( $\text{M} = \text{Pd}, \text{Cu}, \text{Au}$  and  $\text{Hg}$ ) and  $[\text{MAS}_{15}]^{3-}$  ( $\text{M} = \text{Zn}$  and  $\text{Hg}$ ),<sup>192,193</sup> which also contain two  $\text{Pn}_7$  cages, bound either to an  $\text{M}_2$  or an  $\text{M-Pn}$  unit (Fig. 15C). A hexa-iridium cluster,  $[(\eta^3\text{-Bi}_3)_2\text{Ir}_6(\text{CO})_6(\mu^4\text{-Bi})_3]^{3-}$ ,<sup>200</sup> was synthesized by the reaction of  $\text{K}_5\text{Bi}_4$  with  $\text{Ir}(\text{CO})_2(\text{acac})$  ( $\text{acac} = \text{acetylacetonate}$ ) in *en* solution. It is composed of two *cyclo*- $\text{Bi}_3^{3-}$  anions and a central  $\text{Ir}_6(\text{CO})_6(\mu^4\text{-Bi})_3$  trigonal prism (Fig. 15D). DFT investigations indicate that the stability of this cluster is a result of the presence of 14 3c-2e bonds localized on two  $\text{Bi}_3$  faces, six  $\text{Bi}_2\text{Ir}$  faces and the six  $\text{Ir}_3$  faces of the trigonal prism.

In contrast to the *cyclo*- $\text{Sb}_3^{3-}$  and  $\text{Bi}_3^{3-}$  units described in the previous paragraph, an ozone-like  $\text{C}_{2v}$ -symmetric  $\text{Bi}_3^{3-}$  cluster is present in the trigonal bi-pyramidal  $[\text{Bi}_3\text{M}_2(\text{CO})_6]^{3-}$  clusters synthesized in the reaction of  $\text{K}_5\text{Bi}_4$  with  $\text{M}(\text{CO})_3\text{L}$  ( $\text{M}/\text{L} = \text{Cr}, \text{W}/\text{Mes}; \text{Mo}/\text{COT}$ ) in *en* solution.<sup>201</sup> The skeletal electron count of 12, 3 from each  $\text{Bi}$  atom and 3 from the charge, is consistent with the *closo* structure according to the Wade-Mingos rules (Fig. 15E). The cluster is isoelectronic and isostructural with the known trigonal bipyramidal  $\text{Tt}_5^{2-}$  anions ( $\text{Tt} = \text{Ge}, \text{Sn}, \text{Pb}$ ) and also the  $\text{Bi}_5^{3+}$  cation. A similar reaction with  $[\text{Ni}(\text{CO})_2(\text{PPh}_3)_2]$  yielded pentagonal bi-pyramidal  $[\text{Bi}_3\text{Ni}_4(\text{CO})_6]^{3-}$  (Fig. 15F)<sup>17</sup> and bis-disphenoidal  $[\text{Bi}_3\text{Ni}_6(\text{CO})_9]^{4-}$  (Fig. 15G).<sup>17</sup> The former has a *closo* 7-atom structure consistent with the presence of 16 skeletal electrons and is isolobal with the binary Zintl anions  $[\text{Tl}_4\text{Bi}_3]^{3-}$ .<sup>202</sup> The lighter analog,  $[\text{Sb}_3\text{Ni}_4(\text{CO})_6]^{3-}$  has also been isolated using  $\text{K}_5\text{Sb}_4$  instead of  $\text{K}_5\text{Bi}_4$ . When a crystalline sample of  $[\text{Bi}_3\text{Ni}_4(\text{CO})_6]^{3-}$  was dissolved in pyridine, an additional  $\text{Bi}$  atom is incorporated into the cluster to form the bis-disphenoidal  $[(\text{CO})_3\text{Ni}_2]\text{Bi}_4\{\text{Ni}_2(\text{CO})_3\}^{2-}$  (Fig. 15H),<sup>17</sup> now with 18 skeletal electrons. The  $[\text{Bi}_3\text{Ni}_6(\text{CO})_9]^{4-}$  cluster can also be isolated from the same reaction, suggesting that it may be an intermediate on the path to the endohedral cluster  $[\text{Ni}@\text{Bi}_6\text{Ni}_6(\text{CO})_8]^{4-}$  which is formed upon further oxidation.<sup>17</sup>

The reaction of  $\text{K}_3\text{Sb}$  with  $\text{Ru}(\text{COD})\text{Cp}^*\text{Cl}$  generates the cluster  $[\text{Cp}^*\text{Ru}(\text{Sb}_6)\text{RuCp}^*]^{2-}$  which contains a chair-like  $\text{Sb}_6$  unit.<sup>203</sup> The  $\text{Sb}_6$  framework can be regarded as a distorted  $\text{Sb}_6^{4-}$  trigonal prism capped by two  $\text{Ru}(\text{Cp}^*)$  fragments (Fig. 15I). The two  $\text{Cp}^*$  groups are symmetry distinct, but  $^1\text{H}$  and  $^{13}\text{C}$  NMR spectroscopies indicate that the cluster is dynamic in solution on the NMR time scale. Another ligand-protected Ru-containing cluster  $[(\text{COD})\text{Ru}(\text{Bi}_9)\text{Ru}(\text{COD})]^{3-}$  was isolated as the  $[\text{K}(2.2.2\text{-crypt})]^+$  salt from an *en* solution of  $[\text{TlBi}_3]^{2-}$  and  $\text{Ru}(\text{COD})(\text{H}_2\text{CC}(\text{Me})\text{CH}_2)_2$ .<sup>29</sup> The  $\{\text{Ru}_2\text{Bi}_9\}$  core can be considered as a  $\text{Bi}_4$  zigzag chain capped by an elongated  $\text{Bi}_5\text{Ru}_2$  hexagonal pyramid (Fig. 16A). DFT studies have identified the presence of localized bonds in the  $\text{Bi}_4$  chain and



**Fig. 16** Molecular structures of selected coordination compounds and heterometallic cluster of the group 15 elements. (A)  $[(\text{COD})\text{Ru}]\text{Bi}_9\{\text{Ru}(\text{COD})\}]^{3-}$ , (B)  $[\text{Bi}_7\text{M}_3(\text{CO})_3]^{2-}$  ( $\text{M} = \text{Co}, \text{Rh}$ ) (C)  $[\text{Rh}@\text{Bi}_{10}(\text{RhCO})_6]^{3-}$ , (D)  $[\text{Rh}@\text{Bi}_9\text{Rh}_5(\text{CO})_5]^{3-}$ , (E)  $[\text{Pd}_7\text{As}_{16}]^{4-}$ , (F)  $[\text{Ni}_5\text{Sb}_{17}]^{4-}$ , (G)  $[(\text{ZnSb}_6)_2]^{4-}$ .

delocalized bonds in  $\text{Ru}_2\text{Bi}_5$  unit. The Ru ions have a  $d^6$  configuration ( $\text{Ru}^{2+}$ ) and attain a closed-shell 18 electron configuration by coordinating to four formally 2-electron donor  $\text{Bi}^-$  ions and one 4-electron donor COD ligand (4e donor). A second product isolated from the same reaction,  $[\text{Ti}_2\text{Bi}_6\{\text{Ru}(\text{cod})\}]^{2-}$ ,<sup>29</sup> will be discussed in detail in Section 1.20.4.5.1.

Two functionalized  $\text{Bi}_7$  clusters  $[\text{Bi}_7\text{M}_3(\text{CO})_3]^{2-}$  ( $\text{M} = \text{Co}, \text{Rh}$ ),<sup>204</sup> were prepared in reactions of  $\text{K}_5\text{Bi}_4$  with the organometallic precursors  $\text{CpCo}(\text{CO})_2/\text{Rh}(\text{CO})_2(\text{acac})$  or  $\text{Rh}_2(\text{CO})_4\text{Cl}_2$ , in en solution in the presence of 2.2.2-crypt. These clusters can be viewed as three  $\text{M}(\text{CO})$  fragments inserted into the  $\text{Bi}_7^{3-}$  cage (Fig. 16B). The formation of  $\text{Bi}_7^{3-}$  with a classic but expanded nortricyclane-type structure results from the oxidation of  $\text{K}_5\text{Bi}_4$  by  $\text{MCO}^+$ . Subsequently, each  $\text{MCO}^+$  unit is coordinated to the resulting  $\text{Bi}_7^{3-}$  in an  $\eta^5$  mode to form the unprecedented 10-vertex deltahedral cluster. Quantum chemical calculations revealed that the cluster is dominated by 9 3c-2e  $\text{RhBi}_2$  delocalized bonds. A second  $\text{Rh}-\text{Bi}$  hybrid,  $[\text{Rh}@\text{Bi}_{10}\text{Rh}_6(\text{CO})_6]^{3-}$ , was also isolated from the same reaction by using the approximately flat sequestering agent,  $[\text{K}(18\text{-crown-6})]^+$  in place of 2.2.2-crypt.<sup>205</sup> This cluster can be considered to contain a  $\text{Bi}_6$  crown and  $\text{Bi}_4$  pyramid stabilized by six  $^+\text{Rh}-\text{CO}$  units (Fig. 16C). Interestingly, on heating, a heterometallic  $[\text{Rh}@\text{Bi}_9\text{Rh}_5(\text{CO})_5]^{3-}$  cluster was also observed in the same reaction.<sup>205</sup> The  $[\text{Rh}@\text{Bi}_9\text{Rh}_5(\text{CO})_5]^{3-}$  cluster contains a  $\text{Bi}_9$  bowl encapsulating a  $\text{Rh}_6$  cluster unit (Fig. 16D). Although the two clusters are not strictly deltahedral, their 36 and 34 skeletal electron counts are consistent with 16-vertex *nido* and 14-vertex *arachno* structures, respectively.

A number of ligand-free hetero-metallic clusters are also accessible from the reaction of  $\text{K}_3\text{Pn}_7$  ( $\text{Pn} = \text{As}, \text{Sb}$ ) with group 10 organometallic compounds. An example is  $[\text{Pd}_7\text{As}_{16}]^{4-}$  which was made in the reaction  $\text{K}_3\text{As}_7$  with  $[\text{Pd}(\text{PCy}_3)_2]$ .<sup>206</sup> This cluster is composed of two planar  $\text{As}_5^-$  units, two  $\text{As}_2^{2-}$  dumbbells, two isolated  $\text{As}^{3-}$  ions and a distorted capped trigonal prismatic  $\text{Pd}_7$  core (Fig. 16E). The  $[(\text{As}_7)\text{Pd}_2(\text{As}_7)]^{4-}$  cluster was also isolated from the same reaction. The two clusters are stabilized primarily by localized 2c-2e bonds. A similar reaction of  $\text{K}_3\text{Sb}_7$  with  $\text{Ni}(\text{COD})_2$  yielded an approximately  $\text{C}_{4v}$ -symmetric heterometallic cluster  $[\text{Ni}_5\text{Sb}_{17}]^{4-}$ <sup>207</sup> which has a  $\text{Sb}_{13}$  bowl encapsulated by a  $\text{Ni}@\text{Ni}_4\text{Sb}_4$  fragment (Fig. 16F), the latter being very similar in structure to the  $\text{Pd}@\text{Pd}_4\text{As}_4$  unit in  $[\text{Pd}_7\text{As}_{16}]^{4-}$ . Although this cluster is necessarily paramagnetic as a result of the total valence-electron count of 139 valence electrons, the EPR spectrum is silent for the  $S = 3/2$  ground state predicted by DFT studies.

A coupled nortricyclane cluster  $[\text{Zn}_2\text{Sb}_{12}]^{4-}$  (Fig. 16G),<sup>208</sup> was obtained from the extraction of the ternary  $\text{K}_6\text{ZnSb}_5$  phase in en solution. This cluster can be considered as a dimer of distorted nortricyclane-like “ $\text{ZnSb}_6$ ” structures, isostructural with  $\text{C}_{14}\text{H}_{16}$  (heptacyclo-[6.6.0.0<sup>2,6</sup>.0<sup>3,13</sup>.0<sup>4,11</sup>.0<sup>5,9</sup>.0<sup>10,14</sup>]-tetra-decane) A DFT study confirms that the bonding is dominated by 2c-2e  $\text{Sb}-\text{Sb}$  and polar covalent  $\text{Zn}-\text{Sb}$  bonds.

### 1.20.4.5 Ternary clusters

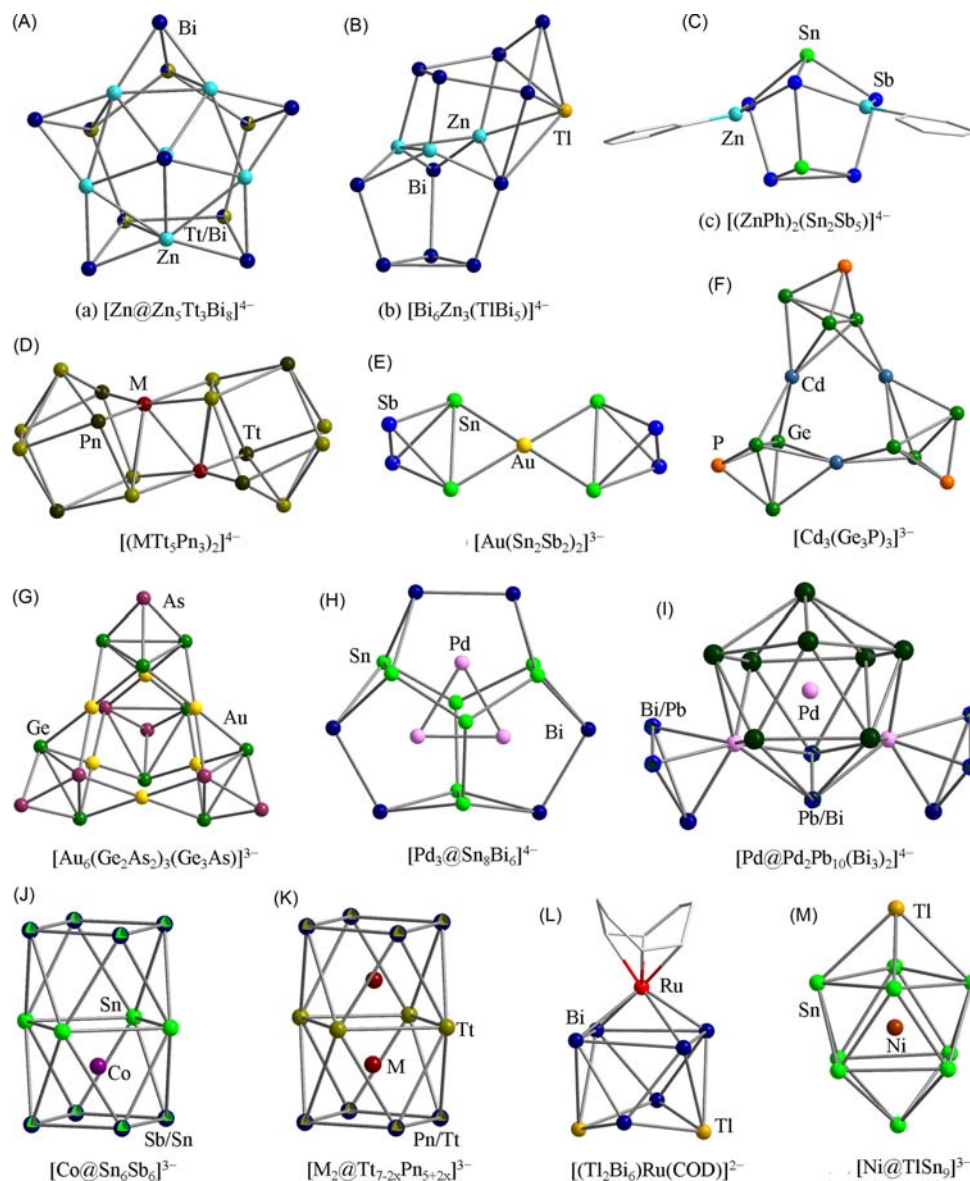
In this subsection, we will introduce ternary clusters, including hetero-metallic and intermetallic examples, which have generally been synthesized either by the extraction of quaternary Zintl phases or by the reaction of the binary Zintl anions  $[\text{TrBi}_3]^{2-}$  ( $\text{Tr} = \text{Ga}, \text{In}, \text{Tl}$ )<sup>23,24</sup> or  $[\text{Tt}_2\text{Pn}_2]^{2-}$  ( $\text{Tt/Pn} = \text{Ge/P}, \text{Sn/Sb}, \text{Sn/Bi}, \text{Pb/Bi}$ ),<sup>13,25–28</sup> with transition metal complexes. The tetrahedral binary Zintl anions  $[\text{TrBi}_3]^{2-}$  and  $[\text{Tt}_2\text{Pn}_2]^{2-}$  can be prepared by dissolving the corresponding ternary Zintl phases in an en solution in the presence of 2.2.2-crypt. These can then be further oxidized by solvents, organic ligands or organometallic compounds to generate 9-atom anions such as  $[\text{Tr}_4\text{Bi}_5]^{2-}$  ( $\text{Tr} = \text{Ga}, \text{In}, \text{Tl}$ ) or  $[\text{Tt}_7\text{Pn}_2]^{2-}$  ( $\text{Tt/Pn} = \text{Ge/P}, \text{Ge/As}, \text{Sn/Bi}, \text{Pb/Bi}$ ),<sup>16,25,28,30</sup> which are isoelectronic and isostructural with  $[\text{Tt}_9]^{4-}$  ( $\text{Tt} = \text{Si}, \text{Ge}, \text{Sn}, \text{Pb}$ ). The reaction chemistry of the 9-vertex binary Zintl anions and also of some of the less common anions such as  $[\text{Sn}_3\text{Bi}_3]^{5-}$ ,<sup>34</sup>  $[\text{Sn}_3\text{Bi}_5]^{3-}$ ,<sup>34</sup>  $[\text{Sn}_4\text{Bi}_4]^{4-35} or  $[\text{Ge}_4\text{Bi}_{14}]^{4-33} has not yet been explored in detail. Occupational disorder is common in their crystal structures, necessitating the combined use of EDX, MS and NMR, along with density functional theory, to confirm the composition and distribution of elements in the clusters.$$

#### 1.20.4.5.1 Ternary clusters containing the post transition metal atoms

We noted in the previous paragraph that the binary Zintl anions are essential starting materials for the synthesis of ternary clusters. The  $[\text{Tt}_2\text{Bi}_2]^{2-}$  anion, for example, reacts with  $\text{Zn}(\text{Ph})_2$  to yield the ternary cluster  $[\text{Zn}@\text{Zn}_5\text{Tt}_3\text{Bi}_8]^{4-}$ ,<sup>16,28</sup> which can be viewed as a *nido* 11-vertex  $[\text{Zn}@\text{Zn}_5\text{Tt}_3\text{Bi}_3]$  core capped by 5 Bi atoms (Fig. 17A). The 48 valence electron count of the  $[\text{Zn}@\text{Zn}_5\text{Tt}_3\text{Bi}_3]$  core (coming from  $2 \times 1$  (the central Zn) +  $5 \times 2 + 3 \times 4 + 3 \times 5 + 4$  (charge) +  $5 \times 1$  (the five external Bi ligands)) is consistent with the Wade-Mingos prediction for an 11-atom *nido*-cluster, and is reminiscent of the icosahedral  $\text{Zn}@\text{Zn}_8\text{Bi}_4$  unit in the  $[\text{Zn}@\text{Zn}_8\text{Bi}_{11}]^{4-}$  cluster.<sup>183</sup> If  $[\text{TlBi}_3]^{2-}$  is used in place of  $[\text{Tt}_2\text{Bi}_2]^{2-}$  in the reaction with  $\text{ZnPh}_2$ , the ternary hetero-metallic cluster  $[(\text{Bi}_6)\text{Zn}_3(\text{TlBi}_5)]^{4-}$  is generated.<sup>194</sup> This cluster contains a five-membered  $\text{Bi}_5$  ring with an envelope conformation, a truncated  $\text{Bi}_4\text{Zn}_3$  fragment and a Tl atom. DFT calculations indicated that the cluster can be described in terms of localized 2c-2e and delocalized multi-center bonds, very similar to the situation in  $[\text{Bi}_9\{\text{Ru}(\text{COD})\}_2]^{3-}$ .<sup>29</sup> Treatment of  $\text{ZnPh}_2$  with the binary anion  $[\text{Sn}_2\text{Sb}_2]^{2-}$  generates the ternary cluster  $[\text{Sn}_2\text{Sb}_5(\text{ZnPh})_2]^{3-}$  (Fig. 17C)<sup>13</sup> where the two  $\text{ZnPh}$  fragments are coordinated to two three-connected Sb atoms of the  $[\text{Sn}_2\text{Sb}_5]^{5-}$  anion (isoelectronic with  $\text{Sb}_7^{3-}$ ) in an  $\eta^{2,2}$  fashion. The  $[\text{Sn}_2\text{Sb}_2]^{2-}$  anion has also found extensive use in reactions with transition metal complexes such as  $[\text{LCu}(\text{NCMe})]$  ( $\text{L} = [\text{N}(\text{C}_6\text{H}_5)_2\text{Pr}_2-2,6]\text{C}(\text{Me})\text{CH}]^-$ ) which yields the ternary dimer  $\{[\text{CuSn}_5\text{Sb}_3]_2\}^{4-}$  as its  $[\text{K}(2.2.2\text{-crypt})]^+$  salt.<sup>26</sup> DFT calculations showed that  $\{[\text{CuSn}_5\text{Sb}_3]_2\}^{4-}$  can be viewed as a dimer of an inhomogeneous superatom (Fig. 17D). A series of analogs of  $\{[\text{CuSn}_5\text{Sb}_3]_2\}^{4-}$ ,  $\{[\text{AuTt}_5\text{Pn}_3]_2\}^{4-}$ ,<sup>32</sup> have also been obtained from the reactions of  $[\text{Au}(\text{PPh}_3)\text{Me}]$  with  $[\text{Tt}_2\text{Pn}_2]^{2-}$  ( $\text{Tt/Pn} = \text{Pb/Sb}, \text{Sn/Bi}, \text{Sn/Sb}$ ). However, reaction of  $[\text{Sn}_2\text{Sb}_2]^{2-}$  with  $[\text{Au}(\text{PPh}_3)\text{Ph}]$  instead of  $[\text{Au}(\text{PPh}_3)\text{Me}]$  led to a different product, the  $[\text{Au}(\eta^2\text{-Sn}_2\text{Sb}_2)_2]^{3-}$  cluster,<sup>127</sup> where two tetrahedral  $[\text{Sn}_2\text{Sb}_2]^{2-}$  anions simply replace the ligands of the  $\text{Au}^+$  precursor (Fig. 17E). The bonding in this cluster is reminiscent of the  $[\text{Au}(\eta^2:\eta^2\text{-TlSn}_3)]^{4-}$  subunits in the solid state  $\text{K}_4\text{AuTlSn}_3$ ,<sup>125</sup> where the two  $[\text{TlSn}_3]^{5-}$  tetrahedra are perpendicular to each other. In contrast to the Au/Sn/Sb system, extensive atom exchange and rearrangement processes were observed in the synthesis of the trimeric  $[\text{Cd}_3(\eta^2:\eta^3\text{-Ge}_3\text{P})_3]^{3-}$  (Fig. 17F)<sup>25</sup> and tetrameric  $[\text{Au}_6(\text{Ge}_3\text{As})(\text{Ge}_2\text{As}_2)_3]^{3-}$  clusters (Fig. 17G).<sup>32</sup> In both cases, the  $[\text{Ge}_2\text{Pn}_2]^{2-}$  ( $\text{Pn} = \text{P}, \text{As}$ ) anions react with transition metal complexes in en, yielding the isoelectronic and isostructural anions of  $[\text{Ge}_2\text{Pn}_2]^{2-}$ ,  $[\text{Ge}_3\text{Pn}]^{3-}$ . In  $[\text{Cd}_3(\eta^2:\eta^3\text{-Ge}_3\text{P})_3]^{3-}$ , each Cd atom is coordinated to the  $\text{Ge}_3$  face of one  $[\text{Ge}_3\text{P}]^{3-}$  and a  $\text{Ge}_2$  edge of the other in a pseudo linear fashion. In  $[\text{Au}_6(\text{Ge}_3\text{As})(\text{Ge}_2\text{As}_2)_3]^{3-}$ , the six  $\text{Au}^+$  ions are coordinated to three  $[\text{Ge}_2\text{As}_2]^{2-}$  and one  $[\text{Ge}_3\text{As}]^{3-}$  units to form the super-tetrahedral Zintl cluster in a planar fashion, isostructural with the  $[\text{M}_6\text{Ge}_{16}]^{4-}$  ( $\text{M} = \text{Zn}, \text{Cd}$ )<sup>126</sup> clusters.

The reactions of these small cluster anions with elements from groups 9 and 10 of the transition metal block have also generated a number of interesting structures. Salt of  $[\text{Sn}_2\text{Bi}_2]^{2-}$  reacts with  $\text{Pd}(\text{dppe})_2$  in en to afford a 14-vertex cluster,  $[\text{Pd}_3@\text{Sn}_8\text{Bi}_6]^{4-}$  (Fig. 17H),<sup>209</sup> in which a  $\text{Pd}_3$  subunit is embedded in a  $[\text{Sn}_8\text{Bi}_6]$  cage. Quantum chemical calculations indicated that the cluster can be formulated as  $[(\text{Pd}_3)^0@(\text{Sn}_8\text{Bi}_6)^{4-}]^{4-}$  and the  $\text{Pd}_3$  cluster has only a weak interaction with the 14-vertex shell. A 12-vertex cluster  $[\text{Pd}@\text{Pd}_2\text{Pb}_{10}(\text{Bi}_3)_2]^{4-}$  isolated from an en solution of  $[\text{Pb}_2\text{Bi}_2]^{2-}$  and  $\text{Pd}(\text{PPh}_3)_4$ <sup>210</sup> can be regarded as a Pd-centered icosahedron  $\text{Pd}@\text{Pd}_2\text{Pb}_{10}$ , with the two skeletal Pd atoms bounded to two *cyclo*- $\text{Bi}_3$  (Fig. 17I), and in that sense is similar to the binary cluster  $[\text{Ni}@\text{Ni}_6\text{Bi}_6(\text{Bi}_3)_2(\text{CO})_4]^{4-}$ . The precise distribution of atoms in this cluster remains a matter of debate because the Pb and Bi elements are indistinguishable by X-ray diffraction. A combination of <sup>119</sup>Pb NMR and DFT calculations suggests that two distributions,  $[\text{Pd}^0@(\text{Pd}_2\text{Pb}_{10})^{6-}(\text{Bi}_3^+)_2]^{4-}$  and  $[\text{Pd}^0@(\text{Pd}_2\text{Pb}_8\text{Bi}_2)^{4-}(\text{PbBi}_2)_2]^{4-}$ , may co-exist. In either scenario, the three-membered rings ( $\text{Bi}_3^+$  or  $\text{PbBi}_2$ ) can act as formal 2-electron donors to the cluster core. A further ternary 12-vertex endohedral anion,  $[\text{Ni}_2@\text{Tt}_7\text{Bi}_5]^{3-}$ , was formed in the reaction of  $[\text{Tt}_2\text{Bi}_2]^{2-}$  with  $\text{Ni}(\text{COD})$  in en.<sup>28,211</sup> The 12-vertex cluster contains two Ni-centered square-antiprisms sharing a  $\text{Tt}_4$  plane (Fig. 17K). There is no Ni–Ni bonding between the two embedded Ni atoms and the 56 valence electrons is not consistent with the Wade-Mingos rules or with an electron-precise cluster. If the reaction of  $[\text{Sn}_2\text{Sb}_2]^{2-}$  with  $[\text{K}(\text{thf})_x][\text{Co}(\text{COD})_2]$  is carried out in DMF at 5 °C, two clusters,  $[\text{Co}@\text{Sn}_6\text{Sb}_6]^{3-}$  and  $[\text{Co}_2@\text{Sn}_5\text{Sb}_7]^{3-}$ , are formed.<sup>212</sup> The presence of either one or two endohedral Co atoms does not appear to perturb the topology of the 12-vertex shell (Fig. 17J). The synthesis of these ternary intermetallic clusters,  $[\text{Co}@\text{Sn}_6\text{Sb}_6]^{3-}$ ,  $[\text{Co}_2@\text{Tt}_5\text{Pn}_7]^{3-}$  and  $[\text{Ni}_2@\text{Tt}_7\text{Pn}_5]^{3-}$  ( $\text{Tt} = \text{Sn}, \text{Pb}$ ;  $\text{Pn} = \text{Sb}, \text{Bi}$ ) is an elegant demonstration of the great potential of binary anions  $[\text{TrBi}_3]^{2-}$  or  $[\text{Tt}_2\text{Pn}_2]^{2-}$  as precursors in the construction of new ternary intermetallic clusters. Moving to group 8, only a single ternary heterometallic cluster,  $[\text{Tl}_2\text{Bi}_6\{\text{Ru}(\text{COD})\}]^{2-}$  (Fig. 17L),<sup>29</sup> has been reported from the reaction of an en solution of  $[\text{TlBi}_3]^{2-}$  with  $[\text{Ru}(\text{COD})(\text{H}_2\text{CC}(\text{Me})\text{CH}_2)_2]$ . This cluster adopts a distorted mono-capped square antiprismatic topology, the *nido* structure being consistent with the 22 skeletal electron count.



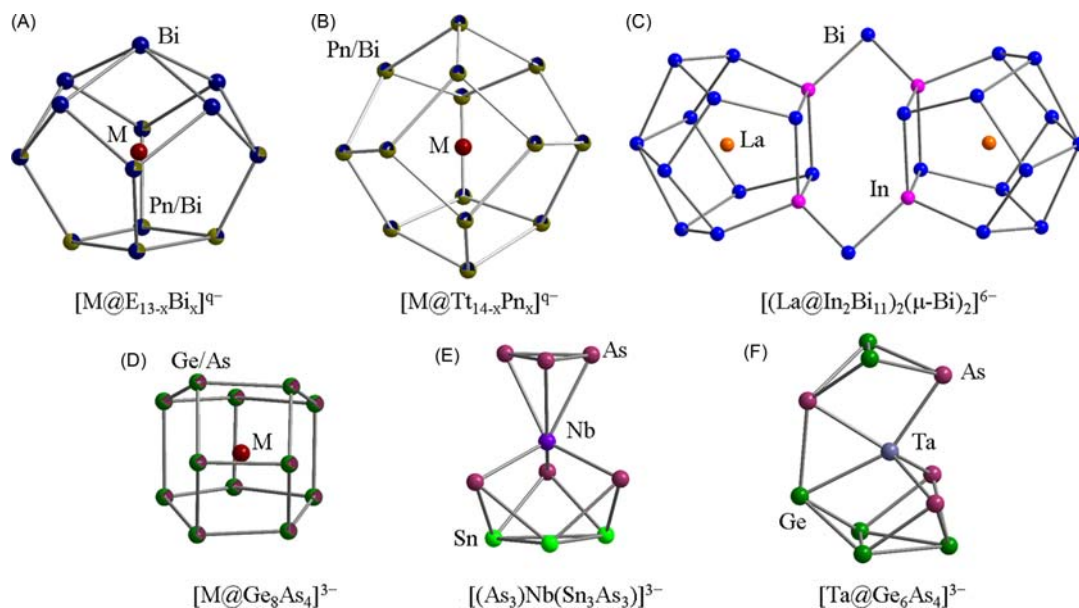


**Fig. 17** Molecular structures of ternary intermetaloid clusters involving electron-rich d-block atoms. Clusters with similar topologies are represented with a model. (A)  $[Zn@Zn_5Tt_3Bi_8]^{4-}$  (Tt = Sn, Pb), (B)  $[Bi_6Zn_3(TlBi_5)]^{4-}$  (C)  $[(ZnPh)_2(Sn_2Sb_5)]^{4-}$ , (D)  $[(MTt_5Pn_3)_2]^{4-}$  (M/Pn/Tt = Cu/Sn/Sb, Au/Sn/Sb, Au/Sn/Sb, Au/Sn/Sb, Au/Sn/Bi), (E)  $[Au(Sn_2Sb_2)_2]^{3-}$ , (F)  $[Cd_3(Ge_3P)_3]^{3-}$ , (G)  $[Au_6(Ge_2As_2)_3(Ge_3As)]^{3-}$ , (H)  $[Pd_3@Sn_8Bi_6]^{4-}$ , (I)  $[Pd@Pd_2Pb_{10}(Bi_3)_2]^{4-}$ , (J)  $[Co@Sn_6Sb_6]^{3-}$ , (K)  $[M_2@Tt_{7-2x}Pn_{5+2x}]^{3-}$  (M/Tt/Pn/x = Ni/Sn/Bi/O, Ni/Pb/Bi/O, Co/Sn/Sb/I), (L)  $[(Tl_2Bi_6)Ru(COD)]^{2-}$ , (M)  $[Ni@TlSn_9]^{3-}$ .

Finally, we note a small number of reports of synthetic routes to ternary clusters that do not involve the 4-atom binary clusters. The *closo*- $[Ni@TlSn_9]^{3-}$  cluster<sup>84</sup> (Fig. 17M) was synthesized by Sevov and co-workers, using the  $[Ni@Sn_9]^{4-}$  precursor in combination with TlCp. The same group reported the  $[(Ni@Sn_8)Ge(Ni@Sn_8)]^{4-}$  anion,<sup>82</sup> made in the reaction of an en solution of  $K_4Ge_{9-x}Sn_x$  with  $Ni(COD)_2$ . This cluster, which is isoelectronic and isostructural with  $[(Ni@Sn_8)Sn(Ni@Sn_8)]^{4-}$ ,<sup>105</sup> can be viewed as the fusion of two  $[Ni@GeSn_8]^{4-}$  units by sharing of a Ge vertex.

#### 1.20.4.5.2 Ternary clusters containing lanthanides, actinides and early transition metal atoms

The binary Zintl anions  $[TrBi_3]^{2-}$  and  $[Tt_2Pn_2]^{2-}$  can also react with lanthanide or actinide complexes to afford 13-<sup>24,213–215</sup> or 14-vertex<sup>24,213,215,216</sup> endohedral Zintl clusters (Fig. 18A and B). The first structure type of note is a 14-atom cage with an embedded  $Ln^{3+}$  ion, adopted by both  $[Ln@Tt_6Bi_8]^{3-}$  and  $[Ln@Tt_7Bi_7]^{3-}$ . The cages are composed of six pentagons and three squares, and the coordination environment of the lanthanide ions is very similar to that in the starting material  $Ln(CpMe_4H)_3$ . These 3-connected electron-precise 14-atom shells with 70 valence electrons conform to the pseudo-element concept, where the group 14 atom can be regarded as a pseudo-pnictogen atom with formal  $-1$  charge. For example,  $[Ln@Tt_6Bi_8]^{3-}$  can be considered as



**Fig. 18** Molecular structures of ternary intermetalloid clusters involving *f*-block atoms or electron-poor *d*-block atoms. Clusters with similar topologies are represented with a model. (A)  $[M@E_{13-x}Bi_x]^{q-}$  ( $M/E/x/q = La, Ce/Sn/9/4; Sm/Ga/9,10/q=3; U/Tl/11/3; U/Pb/9/3$ ), (B)  $[M@Tt_{14-x}Pn_x]^{q-}$  ( $M/Tt/Pn/x/q = Nb, Ta/Ge/As/6/3; Eu/Sn/Bi/8/4; La, Ce/Sn/Bi/7/4; La, Ce, Nd, Sm, Gd, Tb/Pb/Bi/7/4; U/Pb/Bi/7/3$ ), (C)  $[(La@In_2Bi_{11})_2(\mu-Bi)_2]^{6-}$  ( $Tt/M = Sn/W, Pb/Mo$ ), (D)  $[M@Ge_8As_4]^{3-}$  ( $M = V, Ta$ ), (E)  $[(As_3)Nb(Sn_3As_3)]^{3-}$ , (F)  $[Ta@Ge_6As_4]^{3-}$ .

$[Ln^{3+}@Tt_6(Bi^0)_8]^{3-}$ . The 13-vertex analogs  $[Ln@Tt_3Bi_{10}]^{3-}$ ,  $[Ln@Tt_2Bi_{11}]^{4-}$  and  $[Ln@Tt_4Bi_9]^{4-}$ , feature cages made up of five square faces and four pentagons. The bonding and charge distribution in the 13-vertex clusters is less straightforward because both 3- and 4-connected vertices are present. In  $[Sm@Ga_3Bi_{10}]^{3-}$ , where the Ga atoms have a formal  $-2$  charge according to the pseudo-element model,  $^1H$  NMR spectroscopy has confirmed that the high localized charges lead to protonation. Similarly, the In atom in  $[(La@In_2Bi_{11})_2(\mu-Bi)_2]^{6-}$  is a one electron donor (Fig. 18C),<sup>24,217</sup> leading to the formation of four *exo* In–Bi bonds which tightly connect two 13-vertex  $(La@In_2Bi_{11})^{4-}$  cages. The 13- or 14-vertex cages can also encapsulate actinides atoms, and the ternary clusters  $[U@Tl_2Bi_{11}]^{3-}$ ,  $[U@Pb_4Bi_9]^{3-}$  and  $[U@Pb_7Bi_7]^{3-}$  were all obtained from the reactions of  $[TlBi_3]^{2-}$  and  $[Pb_2Bi_2]^{2-}$  with  $U(C_5Me_4H)_3$ .<sup>24</sup> A combination of MS,  $\mu$ -XFS, magnetic susceptibility measurements and X-ray diffraction is indicative of a  $+IV$  oxidation state for the embedded U atom.

Ternary clusters containing the group 5 metal atoms can be synthesized by the extraction of quaternary Zintl phases, some of which have been prepared serendipitously during high-temperature fusion reactions of the corresponding elements sealed in Nb or Ta containers. Elemental arsenic reacts particularly easily with those metals at temperatures above  $650^\circ C$  during the synthesis of the nominal “RbAs” phase (Section 1.20.4.3). A novel heterometallic cluster  $[As_3Nb(As_3Sn_3)]^{3-}$  was made by the extraction of the nominal composition “ $K_8NbSnAs_5$ ” in en solution.<sup>218</sup> In this cluster, a formal  $Nb^{5+}$  ion is coordinated by an  $As_3^{3-}$  ring and an  $As_3Sn_3^{5-}$  bowl (Fig. 18E). DFT calculations showed that the clusters is dominated by localized Nb–As and As–As bonding as well as delocalized 3c-2e Nb–As–Sn and Sn–Sn–Sn bonds.

Ternary intermetalloid clusters can also be synthesized using the methods described in the previous paragraph. For example, extraction of the corresponding quaternary Zintl phase “KMGeAs” ( $M = V, Nb, Ta$ ) in en generated the  $[Ta@Ge_6As_4]^{3-}$  (Fig. 18F),<sup>30</sup>  $[M@Ge_8As_4]^{3-}$  ( $M = V, Ta$ ) (Fig. 18D)<sup>30,219</sup> and  $[M@Ge_8As_6]^{3-}$  ( $M = Nb, Ta$ )<sup>30,219</sup> (Fig. 18B) phases, as well as a tetrahedral  $[Ge_2As_2]^{2-}$  anion (1) and a nine-vertex anion  $[Ge_7As_2]^{2-}$ . The 14-vertex  $[M^{5+}@Ge_8As_6]^{3-}$  anions are isoelectronic and isostructural with the 14-vertex endohedral clusters of lanthanides or uranium atom described previously. The 3-connected 12-atom intermetalloid clusters  $[M@Ge_8As_4]^{3-}$  adopt the same topology as the  $D_{2d}$ -symmetric  $[Ru@Ge_{12}]^{3-}$ .<sup>100</sup> The  $[Ta@Ge_6As_4]^{3-}$  cluster can be regarded as a  $Ta^{5+}$  ion coordinating with an  $Ge_2As_2$  unit and an  $Ge_4As_2$  unit and, with the aid of extensive DFT calculations, this fragmentation pattern was identified as a possible route leading to the coalescence of the complete 12- or 14-atom clusters.

### 1.20.5 Formation of Zintl clusters in solution

The mechanisms that lead to the formation of large Zintl clusters in solution are generally complex and challenging to explore, either experimentally or computationally. In situ analysis techniques such as nuclear magnetic resonance (NMR) spectroscopy, thin-layer chromatography (TLC), or mass spectrometry (MS) often fail to give definitive information due to the transient nature of the intermediates. Ex situ investigations, in contrast, allow for the characterization and even isolation of stable or metastable



species, but their role in the pathway remains uncertain. Experiments are typically complemented with extensive DFT investigations, where the challenges include the sampling of a complex and multi-dimensional potential surface and the treatment of solvation for highly anionic species. In this section, we will approach the question of mechanism from three different perspectives: (1) oxidation or charge neutralization reactions; (2) ligand exchange reactions and (3) re-arrangement reactions.

### 1.20.5.1 Oxidation or charge neutralization reactions

Oxidation reactions are widely used in studies of cluster growth, and are often accompanied by the release of ligands, the formation of radicals or the generation of hydrogen gas. Very recently, Eichhorn and co-workers reported the first non-centered Zintl icosahedron  $[\text{Cp}^*\text{RuPb}_{11}]^{3-}$ ,<sup>91</sup> formed in the reaction of  $\text{Pb}_9^{4-}$  with  $\text{Cp}^*\text{Ru}(\text{COD})\text{Cl}$  in the presence of 18-crown-6. In this reaction, the  $\text{Pb}_9^{4-}$  cage undergoes a complex oxidation and rearrangement reaction which, along with the release of COD from the Ru center, to form a 12-vertex, 26-electron *closo*-cluster. Further reaction with  $\text{Cu}(\text{PPh}_3)\text{Cl}$  led to a Cu-centered icosahedron,  $[\text{Cu}@\text{Cp}^*\text{RuPb}_{11}]^{2-}$ . This final step is reminiscent of the synthetic route leading to  $[\text{Ge}_9(\text{PdPPh}_3)]^{3-}$  and  $[\text{Ni}@\text{Ge}_9(\text{PdPPh}_3)]^{2-}$ , where metal atoms are incorporated into pre-formed *closo* clusters.<sup>89</sup> Treatment of  $\text{K}_4\text{Ge}_9$  with excess  $\text{Cu}_5\text{Mes}_5$  leads to a dimeric Cu/Ge binary cluster anion,  $\{[\text{CuGe}_9\text{Mes}]_2\}^{4-}$  isolated from DMF solution as its  $[\text{K}(2.2.2\text{-crypt})]^+$  salt.<sup>220</sup> The formation of this cluster involves an oxidation from  $\text{Ge}_9^{4-}$  to  $\text{Ge}_9^{2-}$  in the presence of excess  $\text{Cu}_5\text{Mes}_5$ , followed by a nucleophilic substitution of  $\text{Ge}_9^{2-}$  with  $\text{Cu}_5\text{Mes}_5$  to afford  $[\text{Ge}_9\text{Mes}]^{3-}$ . The  $[\text{Ge}_9\text{Mes}]^{3-}$  anion was further oxidized in the presence of  $\text{Cu}^+$  to form the dimeric cluster  $\{[\text{CuGe}_9\text{Mes}]_2\}^{4-}$ .

### 1.20.5.2 Ligand exchange reactions

Ligand exchange reactions with metal halides, phosphine-stabilized halides and Cp or mesitylene complexes also play an important role in the preparation of multi-metallic Zintl clusters. In the formation of the intermetalloid clusters, the ligands of the transition metals are released, at which point the metal(s) insert into the cluster cages via redox or re-arrangement steps. In some cases the ligand exchange reaction occurs without further redox events.

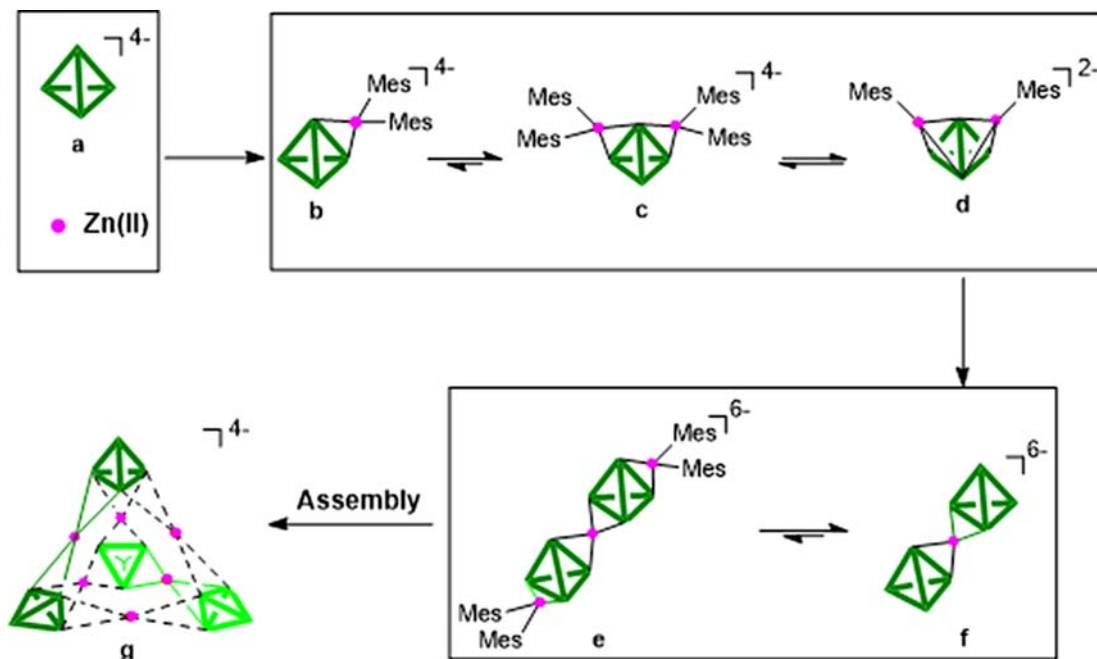
The largest hetero-metallic super-tetrahedral clusters,  $[\text{Zn}_6\text{Ge}_{16}]^{4-}$  and  $[\text{Cd}_6\text{Ge}_{16}]^{4-}$ , were prepared by the reaction of  $\text{K}_{12}\text{Ge}_{17}$  with  $\text{ZnMes}_2/\text{CdMes}_2$  ( $\text{Mes} = 2, 4, 6\text{-Me}_3\text{C}_6\text{H}_2$ ),<sup>126</sup> summarized in Fig. 19. In these reactions, the  $\text{Ge}_4^{4-}$  units interact with  $\text{ZnMes}_2/\text{CdMes}_2$  molecules to form complexes b and c, both of which have been detected by ESI-MS. Stepwise release of the ligands on Zn or Cd leads to intermediates d and f which have also been detected by ESI-MS. The intermediates e found in the gas phase (ESI-MS) can also transform into the species f. The proposed coordination geometries in d and f resemble those in the known clusters  $[\text{Ti}_4(\text{ML})_2]^{4-}$  and  $[(\eta^2\text{-Sn}_4)\text{M}(\eta^2\text{-Sn}_4)]^{4-}$  (Fig. 9B and C). Further assembly leads to the final super-tetrahedral clusters, as shown in Fig. 19G. Overall, the 22 atoms of the cluster define a highly symmetric concave polyhedron containing 24  $\text{Ge}_3$  and  $\text{Ge}_2\text{M}$  triangles and 4 chair-like concave  $\text{M}_3\text{Ge}_3$  hexagons. The assembly of four  $\text{Ge}_4$  units and six  $\text{M}^{2+}$  ions creates a large cavity (diameter 4.6 Å for Zn, 5.0 Å for Cd) at the center of the clusters. This strategy for self-assembly of  $[\text{M}_6\text{Ge}_{16}]^{4-}$  ( $\text{M} = \text{Zn}, \text{Cd}$ ) is potentially extendable to other  $d^{10}$  transition metal ions that can support planar coordination, and so may lead to novel porous inorganic materials.

### 1.20.5.3 Re-arrangement reactions

Re-arrangement processes often accompany redox steps, which are themselves common and complex in Zintl chemistry. An illustrative example is the formation of  $[\text{M}@\text{Ti}_9]^{3-}/\text{Ti}_{10}^{2-}/[\text{M}@\text{Ti}_{10}]^{4-}/[\text{M}@\text{Ti}_{12}]^{4-}$  from  $\text{Ti}_9^{4-}$ .<sup>92,93,136</sup> In contrast, re-arrangement of clusters in the absence of a preceding redox event is relatively uncommon. In 2009, Schnepf discovered that  $[\text{Ge}_9\text{R}_3]^-$  can act as a flexible ligand, forming both 9-atom and 10-atom cages,  $[\text{Ge}_9\text{R}_3\text{Cr}(\text{CO})_5]^-$  and  $[\text{Ge}_9\text{R}_3\text{Cr}(\text{CO})_3]^-$ .<sup>171</sup> The latter reaction involves the insertion of the  $\text{Cr}(\text{CO})_3$  into a triangular face of the tri-substituted  $[\text{Ge}_9\text{R}_3]^-$ , resulting in cluster expansion to form a 10-vertex cage  $\{\eta^5\text{-}[\text{Ge}_9\text{R}_3\text{Cr}(\text{CO})_3]\}^-$ . DFT studies indicated that this re-arrangement step is energetically favorable. A similar phenomenon was also observed in the penta-functionalized deltahedral Zintl cluster  $\text{Ge}_9(\text{TMS})_3\text{Et}(\text{PdPPh}_3)$ ,<sup>173</sup> which was obtained from the reaction of the tetra-substituted nona-germanium cluster  $(\text{TMS})_3\text{EtGe}_9$  with  $\text{Pd}(\text{PPh}_3)_4$ . The  $\text{Pd}(\text{PPh}_3)$  fragment in this case inserts into a triangular face of the  $\text{Ge}_9$  cluster, driving cluster expansion.

### 1.20.5.4 A comprehensive example on the growth of tin cluster

The formation of large clusters inevitably involves rather complex mechanisms with multiple possible intermediates.<sup>136</sup> The previous paragraph highlights the point that nine-atom tetrel cages like  $\text{Sn}_9^{4-}$  are very flexible and this, combined with their ready availability, makes them good candidates for the study of cluster growth. The reaction of Zintl anion  $\text{Sn}_9^{4-}$  with  $\text{Cu}_5\text{Mes}_5$  at room temperature yielded the intermetalloid cluster  $[\text{Cu}@\text{Sn}_9]^{3-}$ , presumably as a result of the rather labile Cu–C bonds. In contrast, the more stable Cu–NHC<sup>Dipp</sup> bond allows for the isolation of the ligand-protected  $\text{Sn}_9$  cluster,  $[\text{NHC}^{\text{Dipp}}\text{M}(\eta^4\text{-Sn}_9)]^{3-}$ , which can, in turn, be regarded as a feasible intermediate in the formation of Cu-filled endohedral stannides by releasing the of NHC<sup>Dipp</sup> ligand and embedding a Cu ion. For the Ag analog  $[\text{NHC}^{\text{Dipp}}\text{Ag}(\eta^4\text{-Sn}_9)]^{3-}$ , further ligand exchange reaction occurred in the presence of excess  $\text{Sn}_9^{4-}$ , resulting in the formation of  $[(\eta^4\text{-Sn}_9)\text{Ag}(\eta^1\text{-Sn}_9)]^{7-}$ . Pre-formed  $[\text{Sn}_9\text{ML}]^{3-}$  ( $\text{M} = \text{Ir}, \text{L} = \text{COD}$ ) can further react with dppp to give an Ir-filled dodecahedral stannide species  $[\text{Ir}@\text{Sn}_{12}]^{3-}$  via a combined oxidation/re-arrangement pathway. A formal



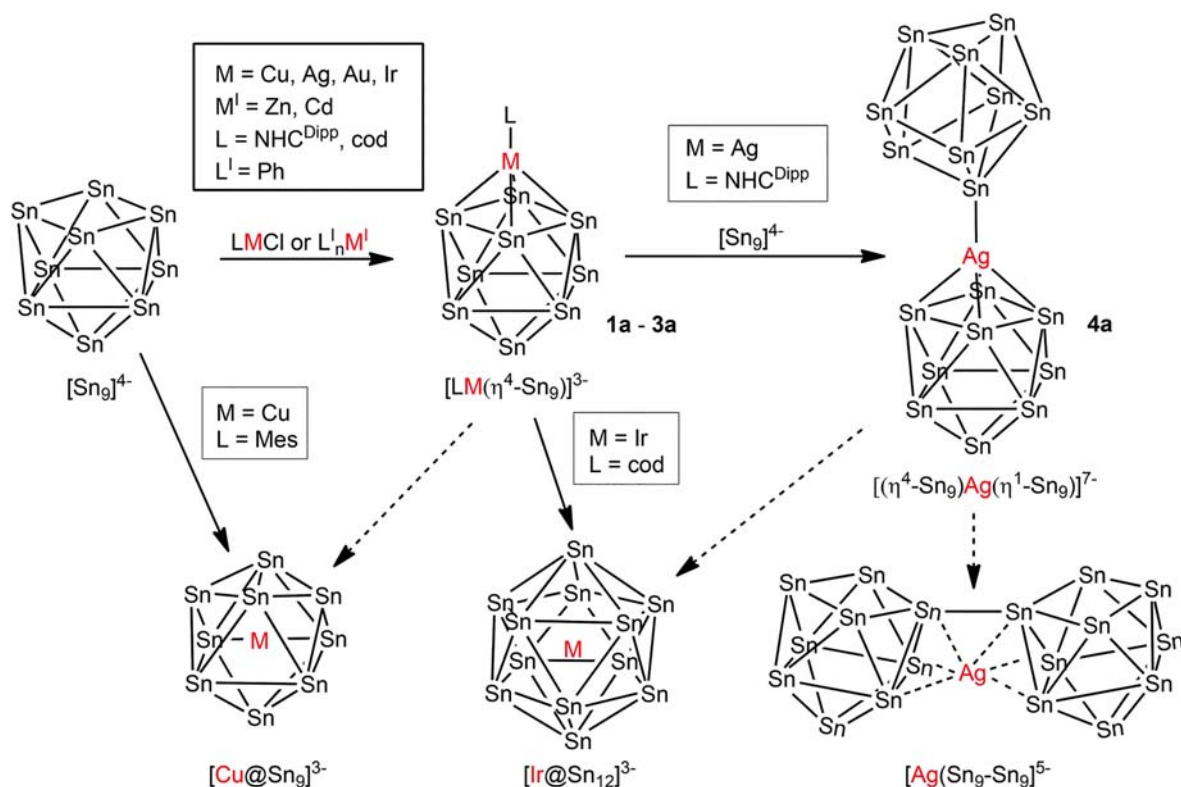
**Fig. 19** The assembly mechanism of tetrahedral cluster  $[Zn_6Ge_{16}]^{4-}$ . Species that have been observed in the mass spectra are boxed (b, c, d, e, f). (Double arrows stands for mutual transformation in those species.)

two-electron oxidation of  $[(\eta^4-Sn_9)Ag(\eta^1-Sn_9)]^{7-}$  leads to  $[Ag(Sn_9-Sn_9)]^{5-}$  where the two  $Sn_9^{3-}$  units are linked by an exo covalent bond, and the whole  $Sn_{18}$  unit bridges the two Ag centers (Fig. 20).<sup>136</sup>

### 1.20.6 Electronic structure and bonding

The relationship between geometry and electron count in clusters of all types has been the subject of many textbooks, and has been reviewed extensively on many occasions, and we only briefly mention the key aspects here. The Wade-Mingos rules are commonly applied to electronic structures of deltahedral clusters, and the hierarchy of *closo*, *nido*, *arachno* structures with their associated skeletal electron counts of  $2n + 2$ ,  $2n + 4$ ,  $2n + 6$  is a well-established paradigm. Among the clusters discussed in this review, the  $I_h$ -symmetric  $[M@Pb_{12}]^{2-}$ ,  $M = Ni, Pd, Pt$ , fit most obviously into the Wade-Mingos structure. If the metal d electrons are considered to be part of the core rather than valence then the cluster has 50 valence electrons in total, and 26 skeletal electrons, corresponding to a  $2n + 2$  count and hence a *closo* structure. The applicability of these rules becomes less obvious when the metal d electrons are higher in energy, and hence less clearly placed in the core set rather than valence. Examples here include the  $[Mn@Pb_{12}]^{3-}$ , which has only 48 valence electrons if the Mn is considered to have a closed  $d^{10}$  shell analogous to  $Ni^0$ . An alternative perspective is to note the stability of the half-filled  $d^5$  shell ( $Mn^{2+}$ ) and hence assign a skeletal electron count of 29 to the  $Pb_{12}^{5-}$  cluster rather than 26. This is consistent with the marked  $D_{2h}$ -symmetric distortion observed in the crystal structure, but the topology is certainly not *nido* or *arachno*, as might be anticipated based on the electron count. The persistence of the approximately icosahedral structure in these circumstances reflects the presence of a cation at the center of the cluster, which naturally favors approximately spherical arrangements of atoms over those where one or more vertex is missing. At its extreme limit, the transfer of electron density from the central metal to the cluster can cause a complete collapse of the deltahedral structure in favor of a more open 3-connected geometry. Examples of this type include pentagonal prismatic  $[Fe@Ge_{10}]^{3-}$  and  $[Co@Ge_{10}]^{3-}$  (51 and 52 valence electrons, respectively) and the 12-vertex clusters  $[Ru@Ge_{12}]^{3-100}$  and  $[Ta@Ge_8As_4]^{3-}$ , with electron counts of 59 and 60, respectively. The 3-connected geometries of the cluster framework in these electron-rich clusters are reminiscent of the structures adopted by neutral and anionic cages of the pnictide elements such as  $Pn_4$  and  $Pn_7^{3-}$ , where the 3-connectivity reflects the need to form 3 single bonds to satisfy the octet rule. This leads to the concept of a 'pseudo-element' alluded to at various points in this review, where  $Pn$ ,  $Tl^-$  and  $Tr^{2-}$  are isolobal and can replace each other while maintaining a constant electron count and hence constant framework structure. The 14-vertex cages  $[Pd_3@Sn_8Sb_6]^{3-209}$  and  $[Eu@Sn_6Bi_8]^{4-216}$  are all composed of three-connected atoms. The electron-precise 70-electron count on the cage is obviously achieved in the latter if the Eu ion is in the 2+ oxidation state, and in the former if the  $Pd_3$  triangle is assumed to donate 5 electrons to the cluster framework.

An alternative perspective on cluster bonding comes from the jellium model, which is based on an approximately spherical potential defined by the positive charged nuclei of the component atoms. By analogy to atoms, this allows orbitals to be characterized by their global nodal properties (labelled S, P, D, F, G) rather than by their local bonding and antibonding character. The rather different nature of the potentials in atoms and clusters means, however, that the traditional Madelung order of levels in atoms is not followed. The jellium model is at its most powerful in clusters that are close to spherically symmetric and where the confining potentials of the atoms are relatively weak. A conspicuous example is the centered icosahedral  $Al_{13}^-$  cluster, the 40



**Fig. 20** The possible pathway of the related tin clusters starts out from the reactions of  $[\text{Sn}_9]^{4-}$  with various organometallic complexes and subsequent reactions, which is involved in the three basic mechanisms mentioned above. From Geitner, F.S.; Kleinb, W.; Fässler, T.F. *Dalton Trans.* **2017**, 46, 5796–5800.

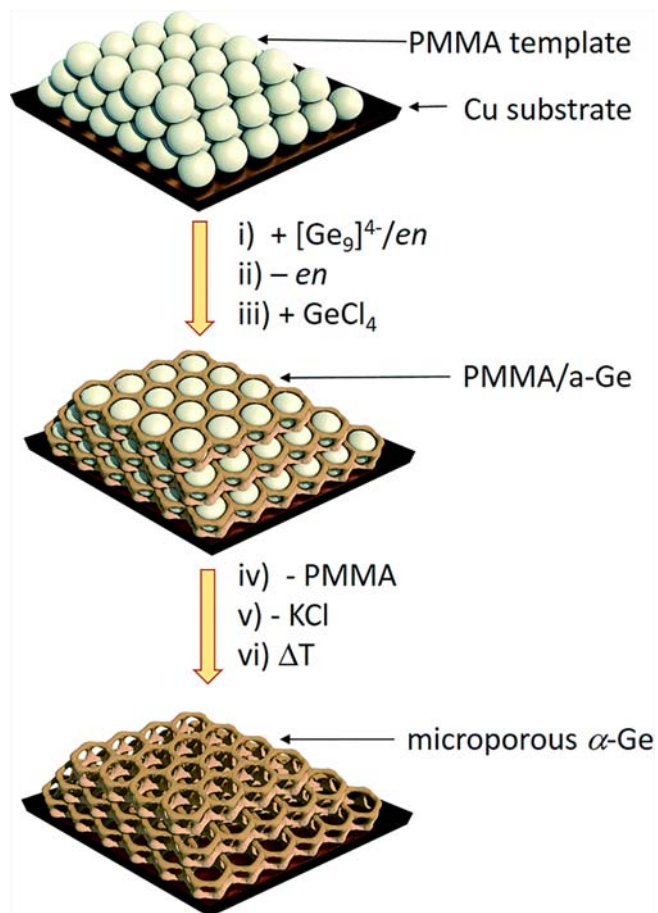
valence electrons of which form a closed-shell  $1\text{S}^21\text{P}^61\text{D}^{10}2\text{S}^21\text{F}^{14}2\text{P}^6$  configuration.<sup>221</sup> The analogy to the closed-shell configuration of the noble gas atoms has led to the concept of a ‘superatom’ – a cluster whose outer electronic configuration mimics the properties of a single atom. The highly symmetric (icosahedral) ‘matryoshka-type’ clusters such as  $[\text{Sn@Cu}_{12}\text{@Sn}_{20}]^{12-}$  alluded to in Section 1.20.4<sup>110</sup> are well described by the superatom model.<sup>222</sup>

Beyond formal electron counting rules, a range of computed physical parameters have been used to explore questions of delocalization and bonding. Prominent among these is the concept of 3-dimensional aromaticity, which is, as the name suggests, analogous to the familiar idea of aromatic character in cyclic 2-dimensional rings. 3-dimensional aromaticity has been invoked widely in anions with closed-shell configurations such as  $\text{Pn}_3^{2-}$ ,  $\text{Pn}_4^{2-}$ ,  $\text{Tt}_5^-$  and  $\text{Tt}_{12}^{2-}$  units.<sup>223</sup> Many clusters with spherical aromaticity have now been isolated from the gas phase, including the empty stannaspherene  $\text{Sn}_{12}^{2-}$  and plumbaspherene  $\text{Pb}_{12}^{2-}$ .<sup>95</sup> A negative value of the Nucleus Independent Chemical Shift (NICS) at the center of the cluster or another point of high symmetry is typically taken as an indicator of aromatic character. As an illustrative example, we take the flower-vase shaped  $[\text{As}_3\text{Nb}(\text{As}_3\text{Sn}_3)]^{3-}$  cluster synthesized by Sun and co-workers in 2016 by extraction of the intermetallic compound  $\text{K}_8\text{NbSnAs}_5$  in en solution.<sup>218</sup> The NICS value of  $-39.55$  ppm at the center of the  $\text{Sn}_3$  ring is indicative of a high degree of aromaticity. A second example comes in the form of two unprecedented all-metal  $T_h$ -symmetric clusters,  $[\text{Pn@In}_8\text{Pn}_{12}]^{3-}$  ( $\text{Pn} = \text{Sb, Bi}$ ),<sup>36,37</sup> also prepared by the Sun group. These clusters can be viewed as a  $\text{Pn@In}_8$  cube capped by six  $\text{Bi}_2^{4-}$  units, and DFT shows that the 92 valence electrons can be sub-divided into 12  $\sigma$ -type lone pairs on the six dimer  $\text{Pn}_2^{4-}$  unit, 24 localized 2c-2e In-Pn bonds between the In cube and the outer 12 Pn atoms and 4 delocalized 9c-2e bonds in  $\text{Pn@In}_8$  core. The presence of 8 delocalized electrons is consistent with the  $2*(N+1)^2$  electron count expected for 3-d aromatic systems, and the NICS value at the center of the cluster is indeed very negative ( $-28.37$  ppm).

### 1.20.7 Potential applications of Zintl ions/clusters in materials science and catalysis

The application of Zintl ions or clusters in materials science has expanded significantly in the past decade. An important example is the use of the  $\text{Ge}_9^{4-}$  anion as a soluble germanium source for lithium ion batteries.<sup>224</sup> The  $\text{Ge}_9^{4-}$  ions are cast on a template made of spherical poly(methyl) methacrylate, and an oxidizer such as  $\text{SiCl}_4$ ,  $\text{GeCl}_4$  or  $\text{PCl}_3$  is then added. The resulting thin film material with an ‘inverse opal’ structure has a high initial capacitance and coulombic efficiency, both of which make it a promising candidate for electrode materials (Fig. 21).<sup>224</sup>

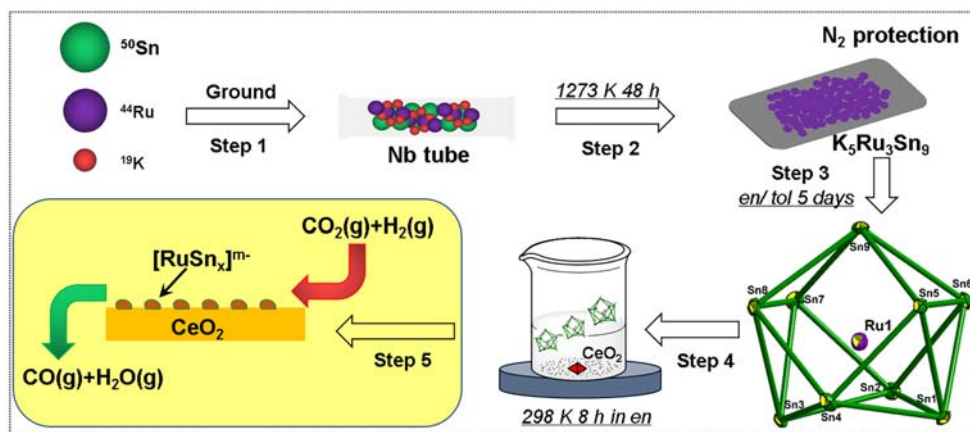
Recently, Sun and co-workers have reported that an isolated  $\text{Ru-SnO}_x$  catalyst can be selectively dispersed onto  $\text{CeO}_2$  via an incipient wetness impregnation method using the Zintl cluster  $[\text{Ru@Sn}_9]^{6-}$  as a precursor. The as-prepared  $\text{Ru-SnO}_x/\text{CeO}_2$  shows



**Fig. 21** Synthesis route to inverse Ge opals using a polymethyl methacrylate (PMMA) template. From Ref. Geier, S.; Jung, R.; Peters, K.; Gasteiger, H.A.; Fattakhova-Rohlfing, D.; Fässler, T.F. *Sustainable Energy Fuels* **2018**, *2*, 85–90.

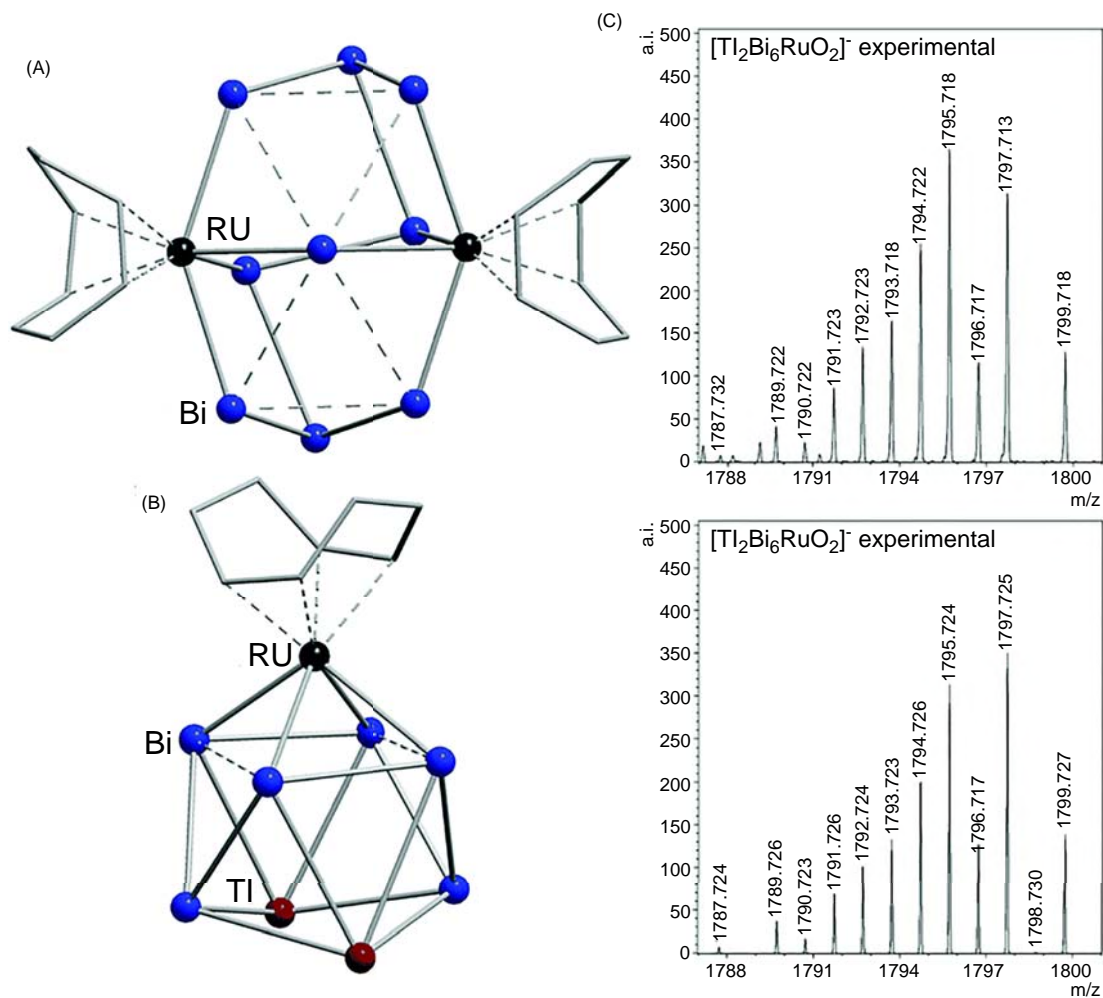
more than 95% CO selectivity in  $\text{CO}_2$  hydrogenation, but this can be switched to  $\sim 100\%$  methanation by simply adding water to the reaction system. This work opens a range of possibilities for monodispersed catalysis using Zintl clusters (Fig. 22).<sup>22,25</sup>

In addition to the examples mentioned above, Zintl clusters have also proven capable of activating small molecules. The heterometallic cluster  $[\text{Bi}_9\{\text{Ru}(\text{cod})\}_2]^{3-}$  obtained from the reaction of  $[\text{TlBi}_3]^{2-}$  with  $[\text{Ru}(\text{cod})(\text{H}_2\text{CC}(\text{Me})\text{CH}_2)_2]^-$  captures an  $\text{O}_2$  molecule in the electrospray mass spectrometry experiment to generate  $[\text{Bi}_9\{\text{Ru}(\text{cod})\}_2\text{O}_2]^-$ . While the binding site of the  $\text{O}_2$  is not clear from the experiment, density functional theory suggests that the ruthenium atom is the most favored site (Fig. 23).<sup>29</sup>



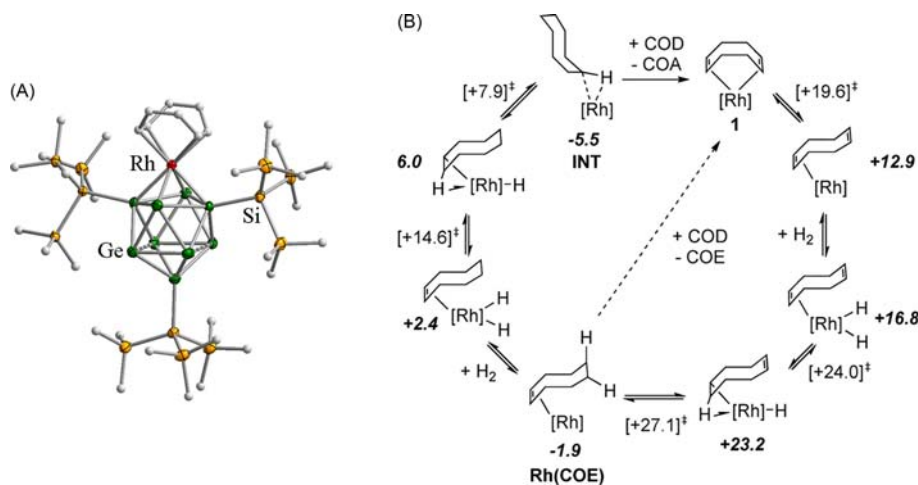
**Fig. 22** Schematic illustration of the  $\text{Ru-SnO}_x/\text{CeO}_2$  preparation process. From Ref. Wang, Y.; Zhang, C.; Wang, X.; Guo, J.; Sun, Z.M.; Zhang, H. *ACS Catal.* **2020**, *10*, 7808–7819.





**Fig. 23** The Zintl clusters  $[\text{Ti}_2\text{Bi}_6(\text{Ru}(\text{cod}))]^{2-}$  (A) and  $[\text{Bi}_9\text{Ru}(\text{cod})_2]^{3-}$  (B). The ESI mass spectra (C) shows the experimental and simulated mass spectrum of  $[\text{Ti}_2\text{Bi}_6\text{RuO}_2]^-$ , in which  $\text{O}_2$  is presumably attached to the ruthenium atom. From Ref. Lichtenberger, N.; Spang, N.; Eichhöfer, A.; Dehnen, S. *Angew. Chem. Int. Ed.* **2017**, *56*, 13253–13258.

Recently, a hetero-metallic cluster  $[\eta^4\text{-Ge}_9(\text{Hyp})_3]\text{Rh}(\text{COD})$  has been used for catalytic hydrogenation of cyclic alkenes. In situ NMR experiments and kinetics tests indicated that the neutral heteroatomic Zintl cluster is competent to transform COD or COE to cyclooctane. Density functional theory calculations were used to probe the possible catalytic mechanism, which is consistent with the experimental observations (Fig. 24).<sup>158</sup>



**Fig. 24** The Zintl cluster  $[\eta^4\text{-Ge}_9(\text{Hyp})_3]\text{Rh}(\text{COD})$  (A) and the Proposed Reaction Mechanism for the Hydrogenation of COD with  $[\eta^4\text{-Ge}_9(\text{Hyp})_3]\text{Rh}(\text{COD})$  (B). All energies are in kcal/mol relative to the Rh–Ge cluster. From Ref. Townrow, O.P.E.; Chung, C.; Macgregor, S.A.; Weller, A.S.; Goicoechea, J.M. *J. Am. Chem. Soc.* **2020**, *142*, 18330.



## References

1. Joannis, M. *Hebd. Seances Acad. Sci.* **1891**, *113*, 795.
2. Kraus, C. A. *J. Am. Chem. Soc.* **1922**, *44*, 1216.
3. Kraus, C. A. *Trans. Am. Electrochem. Soc.* **1924**, *45*, 175.
4. Smyth, F. H. *J. Am. Chem. Soc.* **1917**, *39*, 1299.
5. Zintl, E.; Goubean, J.; Dullenkopf, W. *Z. Phys. Chem. Abt. A* **1931**, *154*, 47.
6. Laves, F. *Naturwissenschaften* **1941**, *29*, 30.
7. Diehl, L.; Khodadadeh, K.; Kummer, D.; Strähle, J. *Chem. Ber.* **1976**, *109*, 3404.
8. Diehl, L.; Khodadadeh, K.; Kummer, D.; Strähle, J. *Z. Naturforsch. B* **1976**, *31*, 522.
9. Teixidor, F.; Luetkens, M. L.; Rudolph, R. W. *J. Am. Chem. Soc.* **1983**, *105*, 149.
10. Eichhorn, B. W.; Haushalter, R. C.; Pennington, W. T. *J. Am. Chem. Soc.* **1988**, *110*, 8704.
11. Von Schnering, H.; Baitinger, M.; Bolle, U.; Carrillo-Cabrera, W.; Curda, J.; Grin, Y.; Heinemann, F.; Llanos, J.; Peters, K.; Schmeding, A.; Somer, M. *Z. Anorg. Allg. Chem.* **1997**, *623*, 1037.
12. Critchlow, S. C.; Corbett, J. D. *Inorg. Chem.* **1984**, *23*, 770.
13. Lips, F.; Schellenberg, I.; Pöttgen, R.; Dehnen, S. *Chem. -Eur. J.* **2009**, *15*, 12968.
14. Fässler, T. F.; Hoffmann, S. D. *Angew. Chem. Int. Ed.* **2004**, *43*, 6242.
15. Esenturk, E. N.; Fettingner, J.; Lam, Y. F.; Eichhorn, B. *Angew. Chem. Int. Ed.* **2004**, *43*, 2132.
16. Lips, F.; Dehnen, S. *Angew. Chem. Int. Ed.* **2009**, *48*, 6435.
17. Goicoechea, J. M.; Hull, M. W.; Sevov, S. C. *J. Am. Chem. Soc.* **2007**, *129*, 7885.
18. Cui, L.-F.; Huang, X.; Wang, L.-M.; Zubarev, D. Y.; Boldyrev, A. I.; Li, J.; Wang, L.-S. *J. Am. Chem. Soc.* **2006**, *128*, 8390.
19. Cui, L.-F.; Huang, X.; Wang, L.-M.; Li, J.; Wang, L.-S. *J. Phys. Chem. A* **2006**, *110*, 10169.
20. Bobev, S.; Sevov, S. C. *Angew. Chem. Int. Ed.* **2000**, *39*, 4108.
21. Perla, L. G.; Oliver, A. G.; Sevov, S. C. *Inorg. Chem.* **2015**, *54*, 872.
22. Weinert, B.; Eulenstein, A. R.; Ababei, R.; Dehnen, S. *Angew. Chem. Int. Ed.* **2014**, *53*, 4704.
23. Xu, L.; Sevov, S. C. *Inorg. Chem.* **2000**, *39*, 5383.
24. Lichtenberger, N.; Wilson, R. J.; Eulenstein, A. R.; Massa, W.; Clerac, R.; Weigend, F.; Dehnen, S. *J. Am. Chem. Soc.* **2016**, *138*, 9033.
25. Mitzinger, S.; Bandemehr, J.; Reiter, K.; Scott McIndoe, J.; Xie, X.; Weigend, F.; Corrigan, J. F.; Dehnen, S. *Chem. Commun.* **2018**, *54*, 1421.
26. Wilson, R. J.; Broeckaert, L.; Spitzer, F.; Weigend, F.; Dehnen, S. *Angew. Chem. Int. Ed.* **2016**, *55*, 11775.
27. Critchlow, S. C.; Corbett, J. D. *Inorg. Chem.* **1982**, *21*, 3286.
28. Ababei, R.; Heine, J.; Holynska, M.; Thiele, G.; Weinert, B.; Xie, X.; Weigend, F.; Dehnen, S. *Chem. Commun.* **2012**, *48*, 11295.
29. Lichtenberger, N.; Spang, N.; Eichhöfer, A.; Dehnen, S. *Angew. Chem. Int. Ed.* **2017**, *56*, 13253.
30. Mitzinger, S.; Broeckaert, L.; Massa, W.; Weigend, F.; Dehnen, S. *Nat. Commun.* **2016**, *7*, 10480.
31. Wilson, R. J.; Weigend, F.; Dehnen, S. *Angew. Chem. Int. Ed.* **2020**, *59*, 14251.
32. Pan, F.; Guggolz, L.; Weigend, F.; Dehnen, S. *Angew. Chem. Int. Ed.* **2020**, *59*, 16638.
33. Wilson, R. J.; Dehnen, S. *Angew. Chem. Int. Ed.* **2017**, *56*, 3098.
34. Friedrich, U.; Korber, N. J. C. *Chemistryopen* **2016**, *5*, 306.
35. Friedrich, U.; Neumeier, M.; Koch, C.; Korber, N. J. *Chem. Commun.* **2012**, *48*, 10544.
36. Liu, C.; Tkachenko, N. V.; Popov, I. A.; Fedik, N.; Min, X.; Xu, C. Q.; Li, J.; McGrady, J. E.; Boldyrev, A. I.; Sun, Z. M. *Angew. Chem. Int. Ed.* **2019**, *58*, 8367.
37. Tkachenko, N. V.; Zhang, X.-W.; Qiao, L.; Shu, C.-C.; Steglenko, D.; Muñoz-Castro, A.; Sun, Z.-M.; Boldyrev, A. I. *Chem. -Eur. J.* **2020**, *26*, 2073.
38. Ugrinov, A.; Sevov, S. C. *J. Am. Chem. Soc.* **2002**, *124*, 2442.
39. Ugrinov, A.; Sevov, S. C. *J. Am. Chem. Soc.* **2003**, *125*, 14059.
40. Ugrinov, A.; Sevov, S. C. *Chem. -Eur. J.* **2004**, *10*, 3727.
41. Gillett-Kunnath, M. M.; Oliver, A. G.; Sevov, S. C. *J. Am. Chem. Soc.* **2011**, *133*, 6560.
42. Ugrinov, A.; Sevov, S. C. *J. Am. Chem. Soc.* **2002**, *124*, 10990.
43. Hull, M. W.; Sevov, S. C. *J. Am. Chem. Soc.* **2009**, *131*, 9026.
44. Hull, M. W.; Ugrinov, A.; Petrov, I.; Sevov, S. C. *Inorg. Chem.* **2007**, *46*, 2704.
45. Benda, C. B.; Wang, J. Q.; Wahl, B.; Fässler, T. F. *Eur. J. Inorg. Chem.* **2011**, *2011*, 4262.
46. Hull, M. W.; Sevov, S. C. *Angew. Chem. Int. Ed.* **2007**, *46*, 6695.
47. Hull, M. W.; Sevov, S. C. *J. Organomet. Chem.* **2012**, *721-722*, 85.
48. Hull, M. W.; Sevov, S. C. *Chem. Commun.* **2012**, *48*, 7720.
49. Hull, M. W.; Sevov, S. C. *Inorg. Chem.* **2007**, *46*, 10953.
50. Benda, C. B.; He, H.; Klein, W.; Somer, M.; Fässler, T. F. *Z. Anorg. Allg. Chem.* **2015**, *641*, 1080.
51. Bentlohner, M. M.; Frischhut, S.; Fässler, T. F. *Chem. -Eur. J.* **2017**, *23*, 17089.
52. Frischhut, S.; Bentlohner, M. M.; Klein, W.; Fässler, T. F. *Inorg. Chem.* **2017**, *56*, 10691.
53. Schnepf, A. *Angew. Chem. Int. Ed.* **2003**, *42*, 2624.
54. Li, F.; Sevov, S. C. *Inorg. Chem.* **2012**, *51*, 2706.
55. Li, F.; Muñoz-Castro, A.; Sevov, S. C. *Angew. Chem. Int. Ed.* **2012**, *51*, 8581.
56. Li, F.; Sevov, S. C. *J. Am. Chem. Soc.* **2014**, *136*, 12056.
57. Frischhut, S.; Fässler, T. F. *Dalton Trans.* **2018**, *47*, 3223.
58. Frischhut, S.; Klein, W.; Drees, M.; Fässler, T. F. *Chem. -Eur. J.* **2018**, *24*, 9009.
59. Frischhut, S.; Klein, W.; Fässler, T. F. *C. R. Chimie* **2018**, *21*, 932.
60. Kysliak, O.; Kunz, T.; Schnepf, A. *Eur. J. Inorg. Chem.* **2017**, *2017*, 805.
61. Schiegerl, L. J.; Geitner, F. S.; Fischer, C.; Klein, W.; Fässler, T. F. *Z. Anorg. Allg. Chem.* **2016**, *642*, 1419.
62. Gillett-Kunnath, M. M.; Petrov, I.; Sevov, S. C. *Inorg. Chem.* **2010**, *49*, 721.
63. Turberville, R. S. P.; Goicoechea, J. M. *Chem. Rev.* **2014**, *114*, 10807.
64. Noblet, P.; Cappello, V.; Tekautz, G.; Baumgartner, J.; Hassler, K. *Eur. J. Inorg. Chem.* **2011**, *2011*, 101.
65. Charles, S.; Fettingner, J. C.; Eichhorn, B. W. *J. Am. Chem. Soc.* **1995**, *117*, 5303.
66. Mattamana, S. P.; Promprai, K.; Fettingner, J. C.; Eichhorn, B. W. *Inorg. Chem.* **1998**, *37*, 6222.
67. Milyukov, V. A.; Kataev, A. V.; Hey-Hawkins, E.; Sinyashin, O. G. *Russ. Chem. Bull. Int. Ed.* **2007**, *56*, 298.
68. Baudler, M.; Faber, W.; Hahn, J. Z. *Z. Anorg. Allg. Chem.* **1980**, *469*, 15.
69. Fritz, G.; Hoppe, K. D.; Höhle, W.; Weber, D.; Mujica, C.; Manriquez, V.; Schnering, H. G. V. *J. Organomet. Chem.* **1983**, *249*, 63.

70. Fritz, H. C. G.; Schneider, H. W. Z. *Z. Anorg. Allg. Chem.* **1990**, *584*, 12.
71. von Schnering, H. G.; Fenske, D.; Hönle, W.; Binnewies, M.; Peters, K. *Angew. Chem. Int. Ed.* **1979**, *18*, 679.
72. Fritz, H. C. G.; Layher, E.; Goesmann, H.; Hanke, D.; Persau, C. Z. *Z. Anorg. Allg. Chem.* **1991**, *594*, 36.
73. Ahlrichs, R.; Fenske, D.; Fromm, K.; Krautscheid, H.; Krautscheid, U.; Treutler, O. *Chem. -Eur. J.* **1996**, *2*, 238.
74. Turbervill, R. S. P.; Goicoechea, J. M. *Organometallics* **2012**, *31*, 2452.
75. Turbervill, R. S. P.; Goicoechea, J. M. *Eur. J. Inorg. Chem.* **2014**, *2014*, 1660.
76. Turbervill, R. S. P.; Goicoechea, J. M. *Chem. Commun.* **2012**, *48*, 1470.
77. Rottschäfer, D.; Blomeyer, S.; Neumann, B.; Stämmler, H.-G.; Ghadwal, R. S. *Chem. Sci.* **2019**, *10*, 11078.
78. Turbervill, R. S. P.; Goicoechea, J. M. *Inorg. Chem.* **2013**, *52*, 5527.
79. Turbervill, R. S. P.; Jupp, A. R.; McCullough, P. S. B.; Ergöçmen, D.; Goicoechea, J. M. *Organometallics* **2013**, *32*, 2234.
80. Grassl, T.; Friedrich, U.; Kaas, M.; Korber, N. Z. *Anorg. Allg. Chem.* **2015**, *641*, 1203.
81. He, H.; Klein, W.; Jantke, L.-A.; Fässler, T. F. *Z. Anorg. Allg. Chem.* **2014**, *640*, 2864.
82. Gillett-Kunnath, M. M.; Paik, J. I.; Jensen, S. M.; Taylor, J. D.; Sevov, S. C. *Inorg. Chem.* **2011**, *50*, 11695.
83. Goicoechea, J. M.; Sevov, S. C. *J. Am. Chem. Soc.* **2006**, *128*, 4155.
84. Rios, D.; Gillett-Kunnath, M. M.; Taylor, J. D.; Oliver, A. G.; Sevov, S. C. *Inorg. Chem.* **2011**, *50*, 2373.
85. Scharfe, S.; Fässler, T. F.; Stegmaier, S.; Hoffmann, S. D.; Ruhland, K. *Chem. -Eur. J.* **2008**, *14*, 4479.
86. Liu, C.; Li, L.-J.; Jin, X.; McGrady, J. E.; Sun, Z.-M. *Inorg. Chem.* **2018**, *57*, 3025.
87. Kesanli, B.; Fettingner, J.; Gardner, D. R.; Eichhorn, B. *J. Am. Chem. Soc.* **2002**, *124*, 4779.
88. Kocak, F. S.; Zavalij, P.; Eichhorn, B. *Chem. -Eur. J.* **2011**, *17*, 4858.
89. Sun, Z.-M.; Zhao, Y.-F.; Li, J.; Wang, L.-S. *J. Clust. Sci.* **2009**, *20*, 601.
90. Shu, C. C.; Morgan, H. W. T.; Qiao, L.; McGrady, J. E.; Sun, Z. M. *Nat. Commun.* **2020**, *11*, 3477.
91. Li, A. M.; Wang, Y.; Zavalij, P. Y.; Chen, F.; Munoz-Castro, A.; Eichhorn, B. W. *Chem. Commun.* **2020**, *56*, 10859.
92. Esenturk, E. N.; Fettingner, J.; Eichhorn, B. *Chem. Commun.* **2005**, 247.
93. Esenturk, E. N.; Fettingner, J.; Eichhorn, B. *J. Am. Chem. Soc.* **2006**, *128*, 9178.
94. Li, A. M.; Wang, Y.; Downing, D. O.; Chen, F.; Zavalij, P.; Munoz-Castro, A.; Eichhorn, B. W. *Chem. -Eur. J.* **2020**, *26*, 5824.
95. Li, L.-J.; Pan, F.-X.; Li, F.-Y.; Chen, Z.-F.; Sun, Z.-M. *Inorg. Chem. Front.* **2017**, *4*, 1393.
96. Zhou, B.; Kramer, T.; Thompson, A. L.; McGrady, J. E.; Goicoechea, J. M. *Inorg. Chem.* **2011**, *50*, 8028.
97. Liu, C.; Li, L.-J.; Popov, I. A.; Wilson, R. J.; Xu, C.-Q.; Li, J.; Boldyrev, A. I.; Sun, Z.-M. *Chinese J. Chem.* **2018**, *36*, 1165.
98. Zhou, B.; Denning, M. S.; Kays, D. L.; Goicoechea, J. M. *J. Am. Chem. Soc.* **2009**, *131*, 2802.
99. Wang, J. Q.; Stegmaier, S.; Fässler, T. F. *Angew. Chem. Int. Ed.* **2009**, *48*, 1998.
100. Espinoza-Quintero, G.; Duckworth, J. C.; Myers, W. K.; McGrady, J. E.; Goicoechea, J. M. *J. Am. Chem. Soc.* **2014**, *136*, 1210.
101. Kramer, T.; Duckworth, J. C.; Ingram, M. D.; Zhou, B.; McGrady, J. E.; Goicoechea, J. M. *Dalton Trans.* **2013**, *42*, 12120.
102. Jin, X.; Espinoza-Quintero, G.; Below, B.; Arcisauskaitė, V.; Goicoechea, J. M.; McGrady, J. E. *J. Organomet. Chem.* **2015**, *792*, 149.
103. Liu, C.; Popov, I. A.; Li, L. J.; Li, N.; Boldyrev, A. I.; Sun, Z. M. *Chem. -Eur. J.* **2018**, *24*, 699.
104. Hluchyy, V.; He, H.; Jantke, L. A.; Fässler, T. F. *Chem. -Eur. J.* **2012**, *18*, 12000.
105. Esenturk, E. N.; Fettingner, J. C.; Eichhorn, B. W. *J. Am. Chem. Soc.* **2006**, *128*, 12.
106. Kesanli, B.; Halsig, J. E.; Zavalij, P.; Fettingner, J. C.; Lam, Y. F.; Eichhorn, B. W. *J. Am. Chem. Soc.* **2007**, *129*, 4567.
107. Goicoechea, J. M.; Sevov, S. C. *J. Am. Chem. Soc.* **2005**, *127*, 7677.
108. Sun, Z.-M.; Xiao, H.; Li, J.; Wang, L.-S. *J. Am. Chem. Soc.* **2007**, *129*, 9560.
109. Qiao, L.; Zhang, C.; Shu, C. C.; Morgan, H. W. T.; McGrady, J. E.; Sun, Z. M. *J. Am. Chem. Soc.* **2020**, *142*, 13288.
110. Stegmaier, S.; Fässler, T. F. *J. Am. Chem. Soc.* **2011**, *133*, 19758.
111. Liu, C.; Jin, X.; Li, L. J.; Xu, J.; McGrady, J. E.; Sun, Z. M. *Chem. Sci.* **2019**, *10*, 4394.
112. Goicoechea, J. M.; Sevov, S. C. *Angew. Chem. Int. Ed.* **2005**, *44*, 4026.
113. Esenturk, E. N.; Fettingner, J.; Eichhorn, B. *Polyhedron* **2006**, *25*, 521.
114. Zhang, C.; Morgan, H. W. T.; Wang, Z. C.; Liu, C.; Sun, Z. M.; McGrady, J. E. *Dalton Trans.* **2019**, *48*, 15888.
115. Benda, C. B.; Waibel, M.; Fässler, T. F. *Angew. Chem. Int. Ed.* **2015**, *54*, 522.
116. Waibel, M.; Kraus, F.; Scharfe, S.; Wahl, B.; Fässler, T. F. *Angew. Chem. Int. Ed.* **2010**, *49*, 6611.
117. Stegmaier, S.; Waibel, M.; Henze, A.; Jantke, L.-A.; Karttunen, A. J.; Fässler, T. F. *J. Am. Chem. Soc.* **2012**, *134*, 14450.
118. Wallach, C.; Mayer, K.; Henneberger, T.; Klein, W.; Fässler, T. F. *Dalton Trans.* **2020**, *49*, 6191.
119. Henneberger, T.; Klein, W.; Dums, J. V.; Fässler, T. F. *Chem. Commun.* **2018**, *54*, 12381.
120. Queneau, V.; Sevov, S. C. *J. Am. Chem. Soc.* **1997**, *119*, 8109.
121. Wang, J. Q.; Stegmaier, S.; Wahl, B.; Fässler, T. F. *Chem. -Eur. J.* **2010**, *16*, 1793.
122. Fendt, F.; Koch, C.; Gartner, S.; Korber, N. *Dalton Trans.* **2013**, *42*, 15548.
123. Benda, C. B.; Waibel, M.; Kochner, T.; Fässler, T. F. *Chem. -Eur. J.* **2014**, *20*, 16738.
124. Zachwieja, U.; Wlodarski, J. Z. *Anorg. Allg. Chem.* **2004**, *630*, 993.
125. Huang, D.; Corbett, J. D. *Inorg. Chem.* **1998**, *37*, 5007.
126. Xu, H. L.; Popov, I. A.; Tkachenko, N. V.; Wang, Z. C.; Munoz-Castro, A.; Boldyrev, A. I.; Sun, Z. M. *Angew. Chem. Int. Ed.* **2020**, *59*, 17286.
127. Pan, X.-F.; Li, L.-J.; Sun, Z.-M. *Chinese J. Struct. Chem.* **2016**, *35*, 1099.
128. Liu, C.; Li, L. J.; Pan, Q. J.; Sun, Z. M. *Chem. Commun.* **2017**, *53*, 6315.
129. Eichhorn, B. W.; Haushalter, R. C. *J. Chem. Soc., Chem. Commun.* **1990**, 937.
130. Campbell, J.; Mercier, H. P. A.; Franke, H.; Santry, D. P.; Dixon, D. A.; Schrobilgen, G. J. *Inorg. Chem.* **2002**, *41*, 86.
131. Kesanli, B.; Fettingner, J.; Eichhorn, B. *Chem. -Eur. J.* **2015**, *7*, 5277.
132. Yong, L.; Hoffmann, S. D.; Fässler, T. F. *Eur. J. Inorg. Chem.* **2005**, *2005*, 3663.
133. Downing, D. O.; Zavalij, P.; Eichhorn, B. W. *Eur. J. Inorg. Chem.* **2010**, *2010*, 890.
134. Geitner, F. S.; Fässler, T. F. *Chem. Commun.* **2017**, *53*, 12974.
135. Scharfe, S.; Fässler, T. F. *Eur. J. Inorg. Chem.* **2010**, *2010*, 1207.
136. Geitner, F. S.; Klein, W.; Fässler, T. F. *Dalton Trans.* **2017**, *46*, 5796.
137. Zhou, B.; Denning, M. S.; Jones, C.; Goicoechea, J. M. *Dalton Trans.* **2009**, 1571.
138. Goicoechea, J. M.; Sevov, S. C. *Organometallics* **2006**, *25*, 4530.
139. Zhou, B.; Denning, M. S.; Chapman, T. A. D.; Goicoechea, J. M. *Inorg. Chem.* **2009**, *48*, 2899.
140. Bentlohner, M. M.; Jantke, L. A.; Henneberger, T.; Fischer, C.; Mayer, K.; Klein, W.; Fässler, T. F. *Chem. -Eur. J.* **2016**, *22*, 13946.
141. Mayer, K.; Jantke, L.-A.; Schul, S.; Fässler, T. F. *Angew. Chem. Int. Ed.* **2017**, *56*, 2350.
142. Zhou, B.; Denning, M. S.; Chapman, T. A.; McGrady, J. E.; Goicoechea, J. M. *Chem. Commun.* **2009**, 7221.

143. Yong, L.; Boeddinghaus, M. B.; Fässler, T. F. *Z. Anorg. Allg. Chem.* **2010**, *636*, 1293.
144. Denning, M. S.; Goicoechea, J. M. *Dalton Trans.* **2008**, 5882.
145. Nienhaus, A.; Hauptmann, R.; Fässler, T. F. *Angew. Chem. Int. Ed.* **2002**, *41*, 3213.
146. Boeddinghaus, M. B.; Hoffmann, S. D.; Fässler, T. F. *Z. Anorg. Allg. Chem.* **2007**, *633*, 2338.
147. Yong, L.; Hoffmann, S. D.; Fässler, T. F.; Riedel, S.; Kaupp, M. *Angew. Chem. Int. Ed.* **2005**, *44*, 2092.
148. Zhou, B.; Goicoechea, J. M. *Chem. -Eur. J.* **2010**, *16*, 11145.
149. Kesanli, B.; Fettinger, J.; Eichhorn, B. *Angew. Chem. Int. Ed.* **2001**, *40*, 2300.
150. Wang, Y.; Qin, Q.; Wang, J.; Sang, R.; Xu, L. *Chem. Commun.* **2014**, *50*, 4181.
151. Wang, J. Q.; Wahl, B.; Fässler, T. F. *Angew. Chem. Int. Ed.* **2010**, *49*, 6592.
152. Perla, L. G.; Sevov, S. C. *Angew. Chem. Int. Ed.* **2016**, *55*, 6721.
153. Xu, H. L.; Tkachenko, N. V.; Wang, Z. C.; Chen, W. X.; Qiao, L.; Munoz-Castro, A.; Boldyrev, A. I.; Sun, Z. M. *Nat. Commun.* **2020**, *11*, 5286.
154. Spiekermann, A.; Hoffmann, S. D.; Kraus, F.; Fässler, T. F. *Angew. Chem. Int. Ed.* **2007**, *46*, 1638.
155. Spiekermann, A.; Hoffmann, S. D.; Fässler, T. F.; Krossing, I.; Preiss, U. *Angew. Chem. Int. Ed.* **2007**, *46*, 5310.
156. Kysliak, O.; Schnepf, A. *Dalton Trans.* **2016**, *45*, 2404.
157. Kysliak, O.; Schrenk, C.; Schnepf, A. *Chem. -Eur. J.* **2016**, *22*, 18787.
158. Townrow, O. P. E.; Chung, C.; Macgregor, S. A.; Weller, A. S.; Goicoechea, J. M. *J. Am. Chem. Soc.* **2020**, *142*, 18330.
159. Mayer, K.; Schiegl, L. J.; Fässler, T. F. *Chem. -Eur. J.* **2016**, *22*, 18794.
160. Schiegl, L. J.; Melaimi, M.; Tolentino, D. R.; Klein, W.; Bertrand, G.; Fässler, T. F. *Inorg. Chem.* **2019**, *58*, 3256.
161. Mayer, K.; Schiegl, L. J.; Fässler, T. F. *Chem. -Eur. J.* **2016**, *22*, 18794.
162. Geitner, F. S.; Fässler, T. F. *Eur. J. Inorg. Chem.* **2016**, *2016*, 2688.
163. Geitner, F. S.; Wallach, C.; Fässler, T. F. *Chem. -Eur. J.* **2018**, *24*, 4103.
164. Geitner, F. S.; Giebel, M. A.; Alexander, P. T.; Fässler, T. F. *Molecules* **2017**, *22*, 1204.
165. Geitner, F. S.; Klein, W.; Fässler, T. F. *Angew. Chem. Int. Ed.* **2018**, *57*, 14509.
166. Henke, F.; Schenk, C.; Schnepf, A. *Dalton Trans.* **2009**, 9141.
167. Schenk, C.; Henke, F.; Santiso-Quiñones, G.; Krossing, I.; Schnepf, A. *Dalton Trans.* **2008**, 4436.
168. Li, F.; Sevov, S. C. *Inorg. Chem.* **2015**, *54*, 8121.
169. Kysliak, O.; Nguyen, D. D.; Clayborne, A. Z.; Schnepf, A. *Inorg. Chem.* **2018**, *57*, 12603.
170. Binder, M.; Schrenk, C.; Block, T.; Pottgen, R.; Schnepf, A. *Chem. Commun.* **2017**, *53*, 11314.
171. Henke, F.; Schenk, C.; Schnepf, A. *Dalton Trans.* **2011**, *40*, 6704.
172. Schenk, C.; Schnepf, A. *Chem. Commun.* **2009**, 3208.
173. Li, F.; Muñoz-Castro, A.; Sevov, S. C. *Angew. Chem. Int. Ed.* **2016**, *55*, 8630.
174. Perla, L. G.; Sevov, S. C. *J. Am. Chem. Soc.* **2016**, *138*, 9795.
175. Perla, L. G.; Muñoz-Castro, A.; Sevov, S. C. *J. Am. Chem. Soc.* **2017**, *139*, 15176.
176. Schnering, H. G. V.; Wolf, J.; Weber, D.; Ramirez, R.; Meyer, T. *Angew. Chem. Int. Ed.* **1986**, *25*, 353.
177. Kesanli, B.; Fettinger, J.; Scott, B.; Eichhorn, B. *Inorg. Chem.* **2004**, *43*, 3840.
178. Kesanli, B.; Fettinger, J.; Eichhorn, B. *J. Am. Chem. Soc.* **2003**, *125*, 7367.
179. Eichhorn, B. W.; Mattamana, S. P.; Gardner, D. R.; Fettinger, J. C. *J. Am. Chem. Soc.* **1998**, *120*, 9708.
180. Min, X.; Popov, I. A.; Pan, F. X.; Li, L. J.; Matito, E.; Sun, Z. M.; Wang, L. S.; Boldyrev, A. I. *Angew. Chem. Int. Ed.* **2016**, *55*, 5531.
181. Eulenstein, A. R.; Franzke, Y. J.; Lichtenberger, N.; Wilson, R. J.; Deubner, H. L.; Kraus, F.; Clerac, R.; Weigend, F.; Dehnen, S. *Nat. Chem.* **2021**, *13*, 149.
182. Perla, L. G.; Sevov, S. C. *Inorg. Chem.* **2015**, *54*, 8401.
183. Goicoechea, J. M.; Sevov, S. C. *Angew. Chem. Int. Ed.* **2006**, *45*, 5147.
184. Moses, M. J.; Fettinger, J. C.; Eichhorn, B. W. *Science* **2003**, *300*, 778.
185. Wang, Y.; Moses-DeBusk, M.; Stevens, L.; Hu, J.; Zavali, P.; Bowen, K.; Dunlap, B. I.; Glaser, E. R.; Eichhorn, B. *J. Am. Chem. Soc.* **2017**, *139*, 619.
186. Li, Z.; Ruan, H.; Wang, L.; Liu, C.; Xu, L. *Dalton Trans.* **2017**, *46*, 3453.
187. Eichhorn, B. W.; Haushalter, R. C.; Huffman, J. C. *Angew. Chem. Int. Ed.* **1989**, *28*, 1032.
188. Charles, S.; Eichhorn, B. W.; Rheingold, A. L.; Bott, S. G. J. *J. Am. Chem. Soc.* **1994**, *116*, 8077.
189. Bolle, U.; Tremel, W. *J. Chem. Soc., Chem. Commun.* **1994**, 217.
190. Knapp, C.; Zhou, B.; Denning, M. S.; Rees, N. H.; Goicoechea, J. M. *Dalton Trans.* **2010**, 426.
191. Qian, M.; Reber, A. C.; Ugrinov, A.; Chaki, N. K.; Mandal, S.; Saavedra, H. M.; Khanna, S. N.; Sen, A.; Weiss, P. S. *ACS Nano* **2010**, *4*, 235.
192. Mandal, S.; Reber, A. C.; Qian, M.; Liu, R.; Saavedra, H. M.; Sen, S.; Weiss, P. S.; Khanna, S. N.; Sen, A. *Dalton Trans.* **2012**, *41*, 12365.
193. Kaas, M.; Korber, N. *Z. Anorg. Allg. Chem.* **2017**, *643*, 1331.
194. Lichtenberger, N.; Massa, W.; Dehnen, S. *Angew. Chem. Int. Ed.* **2019**, *58*, 3222.
195. Knapp, C. M.; Jackson, C. S.; Large, J. S.; Thompson, A. L.; Goicoechea, J. M. *Inorg. Chem.* **2011**, *50*, 4021.
196. Chaki, N. K.; Mandal, S.; Reber, A. C.; Qian, M.; Saavedra, H. M.; Weiss, P. S.; Khanna, S. N.; Sen, A. *ACS Nano* **2010**, *4*, 5813.
197. Mandal, S.; Reber, A. C.; Qian, M.; Liu, R.; Saavedra, H. M.; Sen, S.; Weiss, P. S.; Khanna, S. N.; Sen, A. *Dalton Trans.* **2012**, *41*, 5454.
198. Pan, F. X.; Li, L. J.; Wang, Y. J.; Guo, J. C.; Zhai, H. J.; Xu, L.; Sun, Z. M. *J. Am. Chem. Soc.* **2015**, *137*, 10954.
199. Popo, I. A.; Pan, F. X.; You, X. R.; Li, L. J.; Matito, E.; Liu, C.; Zhai, H. J.; Sun, Z. M.; Boldyrev, A. I. *Angew. Chem. Int. Ed.* **2016**, *55*, 15344.
200. Li, Z.; Liu, C.; Wu, J.; Lin, Z.; Xu, L. *Dalton Trans.* **2019**, *48*, 12013.
201. Xu, L.; Ugrinov, A.; Sevov, S. C. *J. Am. Chem. Soc.* **2001**, *123*, 4091.
202. Lichtenberger, N.; Franzke, Y. J.; Massa, W.; Weigend, F.; Dehnen, S. *Chem. -Eur. J.* **2018**, *24*, 12022.
203. Wang, Y.; Zavali, P.; Eichhorn, B. *Chem. Commun.* **2018**, *54*, 11917.
204. Li, Z.; Ouyang, D.; Xu, L. *Chem. Commun.* **2019**, *55*, 6783.
205. Chen, S.; Li, Z.; Yuan, B.; Lin, L.; Whangbo, M. H.; Xu, L. *Inorg. Chem.* **2020**, *59*, 10628.
206. Moses, M. J.; Fettinger, J.; Eichhorn, B. *J. Am. Chem. Soc.* **2002**, *124*, 5944.
207. Moses, M. J.; Fettinger, J. C.; Eichhorn, B. W. *Inorg. Chem.* **2007**, *46*, 1036.
208. Wang, Y.; Zavali, P.; Eichhorn, B. *Chem. Commun.* **2017**, *53*, 11600.
209. Lips, F.; Clerac, R.; Dehnen, S. *J. Am. Chem. Soc.* **2011**, *133*, 14168.
210. Ababei, R.; Massa, W.; Harms, K.; Xie, X.; Weigend, F.; Dehnen, S. *Angew. Chem. Int. Ed.* **2013**, *52*, 13544.
211. Lips, F.; Dehnen, S. *Angew. Chem. Int. Ed.* **2011**, *50*, 955.
212. Wilson, R. J.; Hastreiter, F.; Reiter, K.; Buschelberger, P.; Wolf, R.; Gschwind, R. M.; Weigend, F.; Dehnen, S. *Angew. Chem. Int. Ed.* **2018**, *57*, 15359.
213. Lips, F.; Holynska, M.; Clerac, R.; Linne, U.; Schellenberg, I.; Pottgen, R.; Weigend, F.; Dehnen, S. *J. Am. Chem. Soc.* **2012**, *134*, 1181.
214. Weinert, B.; Müller, F.; Harms, K.; Clerac, R.; Dehnen, S. *Angew. Chem. Int. Ed.* **2014**, *53*, 11979.
215. Ababei, R.; Massa, W.; Weinert, B.; Pollak, P.; Xie, X.; Clerac, R.; Weigend, F.; Dehnen, S. *Chem. -Eur. J.* **2015**, *21*, 386.

216. Lips, F.; Clerac, R.; Dehnen, S. *Angew. Chem. Int. Ed.* **2011**, *50*, 960.
217. Weinert, B.; Weigend, F.; Dehnen, S. *Chem. -Eur. J.* **2012**, *18*, 13589.
218. Pan, F.-X.; Xu, C.-Q.; Li, L.-J.; Min, X.; Wang, J.-Q.; Li, J.; Zhai, H.-J.; Sun, Z.-M. *Dalton Trans.* **2016**, *45*, 3874.
219. Mitzinger, S.; Broeckaert, L.; Massa, W.; Weigend, F.; Dehnen, S. *Chem. Commun.* **2015**, *51*, 3866.
220. Wang, Z. C.; Tkachenko, N. V.; Qiao, L.; Matito, E.; Munoz-Castro, A.; Boldyrev, A. I.; Sun, Z. M. *Chem. Commun.* **2020**, *56*, 6583.
221. Reber, A. C.; Khanna, S. N.; Castleman, A. W. *J. Am. Chem. Soc.* **2007**, *129* (33), 10189–10194.
222. Rauhalahhti, M.; Muñoz-Castro, A. *RSC Adv.* **2015**, *5*, 18782.
223. Liu, C.; Popov, I. A.; Chen, Z.; Boldyrev, A. I.; Sun, Z. M. *Chem. -Eur. J.* **2018**, *24*, 14583.
224. Geier, S.; Jung, R.; Peters, K.; Gasteiger, H. A.; Fattakhova-Rohlfing, D.; Fässler, T. F. *Sustainable Energy Fuels* **2018**, *2*, 85.
225. Wang, Y.; Zhang, C.; Wang, X.; Guo, J.; Sun, Z.-M.; Zhang, H. *ACS Catal.* **2020**, *10*, 7808.

## 1.21 Polychalcogen molecules, ligands, and ions Part 1: Homo- and heteronuclear chalcogen rings

Risto S. Laitinen<sup>a</sup>, Raija Oilunkaniemi<sup>a</sup>, Liam McGeachie<sup>a</sup>, Paul F. Kelly<sup>b</sup>, and Roberto S.P. King<sup>c</sup>, <sup>a</sup>Laboratory of Inorganic Chemistry, Environmental and Chemical Engineering, University of Oulu, Oulu, Finland; <sup>b</sup>Department of Chemistry, Loughborough University, Leicestershire, United Kingdom; and <sup>c</sup>Foster + Freeman Ltd, Evesham, United Kingdom

© 2023 Elsevier Ltd. All rights reserved.

<b>1.21.1</b>	<b>Introduction</b>	<b>935</b>
<b>1.21.2</b>	<b>Homocyclic chalcogen molecules</b>	<b>935</b>
1.21.2.1	General	935
1.21.2.2	Sulfur	935
1.21.2.2.1	Cyclohexasulfur, S <sub>6</sub>	936
1.21.2.2.2	Cycloheptasulfur, S <sub>7</sub>	937
1.21.2.2.3	Cyclooctasulfur, S <sub>8</sub>	939
1.21.2.2.4	Larger sulfur rings S <sub>9</sub> -S <sub>16</sub> , S <sub>18</sub> , and S <sub>20</sub>	940
1.21.2.3	Selenium and tellurium	941
1.21.2.3.1	Cyclohexaselenium, Se <sub>6</sub>	941
1.21.2.3.2	Cycloheptaselenium, Se <sub>7</sub>	941
1.21.2.3.3	Cyclooctaselenium Se <sub>8</sub>	941
1.21.2.3.4	Homocyclic tellurium molecules	942
1.21.2.4	Homocyclic oxygen molecules	942
<b>1.21.3</b>	<b>Heterocyclic chalcogen molecules</b>	<b>942</b>
1.21.3.1	General	942
1.21.3.2	Selenium sulfides	942
1.21.3.3	Tellurium-containing chalcogen rings	943
<b>1.21.4</b>	<b>Supramolecular chemistry involving chalcogen rings</b>	<b>946</b>
<b>1.21.5</b>	<b>Homocyclic sulfur oxides</b>	<b>947</b>
<b>1.21.6</b>	<b>Chalcogen rings as ligands in metal complexes</b>	<b>948</b>
1.21.6.1	Sulfur	948
1.21.6.2	Selenium	950
1.21.6.3	Tellurium	951
<b>1.21.7</b>	<b>Polyatomic chalcogen cations</b>	<b>952</b>
1.21.7.1	General	952
1.21.7.2	(E <sub>4</sub> ) <sup>2+</sup> (E = S, Se, Te)	952
1.21.7.3	(E <sub>6</sub> ) <sup>n+</sup> (n = 2, 4)	954
1.21.7.4	(E <sub>8</sub> ) <sup>n+</sup> (n = 2, 4)	954
1.21.7.5	(E <sub>n</sub> ) <sup>2+</sup> (n > 8)	957
<b>1.21.8</b>	<b>Cyclic chalcogen-halogen cations</b>	<b>959</b>
1.21.8.1	General	959
1.21.8.2	Sulfur-bromine and selenium-chlorine cations	959
1.21.8.3	Chalcogen-iodine cations	960
<b>1.21.9</b>	<b>Cyclic chalcogen anions</b>	<b>962</b>
1.21.9.1	General	962
1.21.9.2	Discrete anions	963
1.21.9.3	Cyclic radical anions	963
1.21.9.4	Extended polytelluride networks	963
<b>1.21.10</b>	<b>Summary</b>	<b>964</b>
<b>References</b>		<b>965</b>

### Abstract

The present chapter describes the recent developments in the chemistry of homo- and heteroatom chalcogen rings. The emphasis is on the relationships between the structures and bonding in cyclic polychalcogen molecules and ions, as well as on their ligand chemistry. The advent and progress in modern instrumental methods of analysis have shown that the structural features of chalcogen rings show a clear trend from sulfur to tellurium with the heavier elements often differing from sulfur.



### 1.21.1 Introduction

The Group 16 elements sulfur, selenium, and tellurium show propensity to form molecular species containing cumulated homo- and heteronuclear chalcogen-chalcogen bonds leading to rich chemistry, which involves homo- and heteronuclear, both cyclic and acyclic polychalcogen molecules,<sup>1–6</sup> cations,<sup>4–12</sup> anions,<sup>4,5,13–15</sup> main group compounds,<sup>5,16–24</sup> and transition metal complexes<sup>5,25–30</sup> that contain polychalcogen ligands. Illustrative examples of compounds containing cumulated chalcogen-chalcogen bonds are shown in **Table 1**.

The structural chemistry of catenated polysulfur compounds is the most extensive among the three chalcogen elements.<sup>1–4,6–10</sup> The related chemistry of selenium and tellurium species is still simpler, though it is developing very rapidly.<sup>1,5–15</sup> While sulfur, selenium, and tellurium show similarities in their molecular structures, there are also pronounced differences among the three chalcogen elements. For instance, sulfur has a stronger ability to form homocyclic molecules than selenium and tellurium, and the polymeric trigonal chains of selenium and tellurium are thermodynamically the most stable forms of the two elements. By contrast, acyclic polymeric sulfur is unstable. The stable form of sulfur at NTP consists of cyclooctasulfur molecules, but the related cyclic selenium molecules are metastable and cyclooctatellurium has not been isolated as a single species.

Decreasing propensity to form  $\pi$ -bonds,<sup>7,31</sup> hypervalency,<sup>32,33</sup> and the increasing strength of the chalcogen bonding interactions<sup>7,34</sup> when going down Group 16 in Periodic Table play an important role in explaining the structural and chemical differences. It has also been shown that heavier organic chalcogenides show propensity to associate in longer aggregates in solution.<sup>35</sup>

The structural features of cumulated chalcogen-chalcogen bonds can be explained by three types of interactions. Without steric effects, the unstrained chalcogen-chalcogen bond adopts a torsional angle near  $90^\circ$ . This can be explained by the minimized repulsion of  $np$  lone pairs of the adjacent atoms [see **Fig. 1A**]. The second lone pair occupies the valence  $ns$  orbital and has no stereochemical consequences.

The  $np$  lone pairs are often involved in hyperconjugative  $np^2 \rightarrow n\sigma^*$  interactions [see **Fig. 1B**] that explain significant bond length alternations in molecules like  $S_7$  (**Section 1.21.2.2.2**) and can also be utilized to justify the bonding and structures of many ionic and electrically neutral polychalcogen species (see, for instance, **Section 1.21.8**). Partially occupied  $\pi^*$  orbitals of two chalcogen fragments also lead to attractive  $\pi^*-\pi^*$  interactions, as shown in **Fig. 1C**.

Chalcogen bonds are a special case of secondary bonding interactions (SBI) that are mainly due to electrostatic and dispersion effects in which the so called  $\sigma$ -holes and polarizability play important roles [see **Fig. 1D**], though the chalcogen bonds can also be attributed to donor-acceptor interactions  $n^2(E) \rightarrow \sigma^*(E-X)$  in which  $n$  is the lone pair of a chalcogen donor atom in one molecule and  $\sigma^*(E-X)$  the antibonding orbital of the E-X bond in another molecule.<sup>36</sup> This 3c-4e arrangement is of variable strength, from a very weak interaction to that of a hypervalent single bond.<sup>37</sup> Since the energy difference between the bonding  $\sigma(E-X)$  and antibonding  $\sigma^*(E-X)$  orbitals is smaller in case of tellurium than selenium or sulfur, SBIs are stronger for tellurium than for selenium and sulfur.<sup>38</sup> These interactions are illustrated in **Fig. 1E**.

This chapter explores the structural properties of ring and cage compounds involving cyclic chalcogen molecules containing cumulated chalcogen-chalcogen bonds in different chemical environments. The emphasis is on the structures and bonding of the different species in the solid state, but the synthetic aspects will be discussed, where appropriate. Illustrative examples will be provided throughout the chapter.

### 1.21.2 Homocyclic chalcogen molecules

#### 1.21.2.1 General

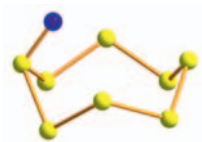
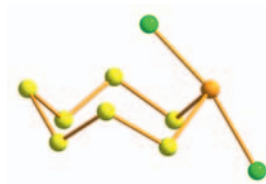
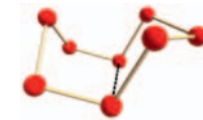
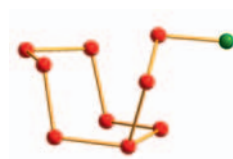
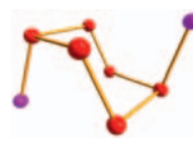
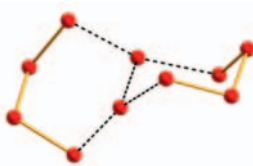
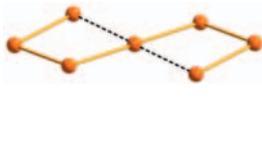
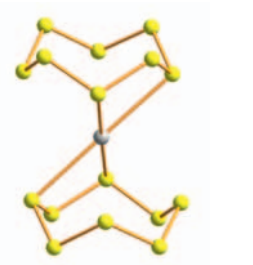
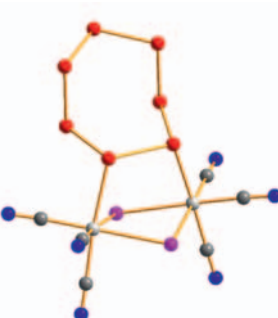
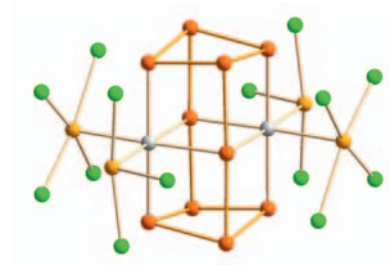
Sulfur is known to exhibit a wide variety of homocyclic molecular forms of different ring sizes.<sup>1–4,6,8</sup> The existence of analogous selenium rings is much sparser being limited to  $Se_8$ ,  $Se_7$ , and  $Se_6$ .<sup>1,5,6,8,9</sup> There are only a few reports on homocyclic tellurium molecules, but they have not been characterized as isolated species.

#### 1.21.2.2 Sulfur

Sulfur occurs in the Earth's crust both as a free element and as sulfide minerals. In addition, crude oil contains organic sulfides and polysulfides, and natural gas may contain significant amounts of hydrogen sulfide. Cyclooctasulfur,  $S_8$ , is the thermodynamically stable form in NTP. While sulfur forms several molecules with other ring sizes, as well as the polymeric form, they all are metastable and eventually revert to  $S_8$ .

The preparation and the determination of the molecular structures of different homocyclic sulfur molecules have been reviewed several times.<sup>1–4,6,8</sup> The synthetic methods have been summarized in **Table 2**.

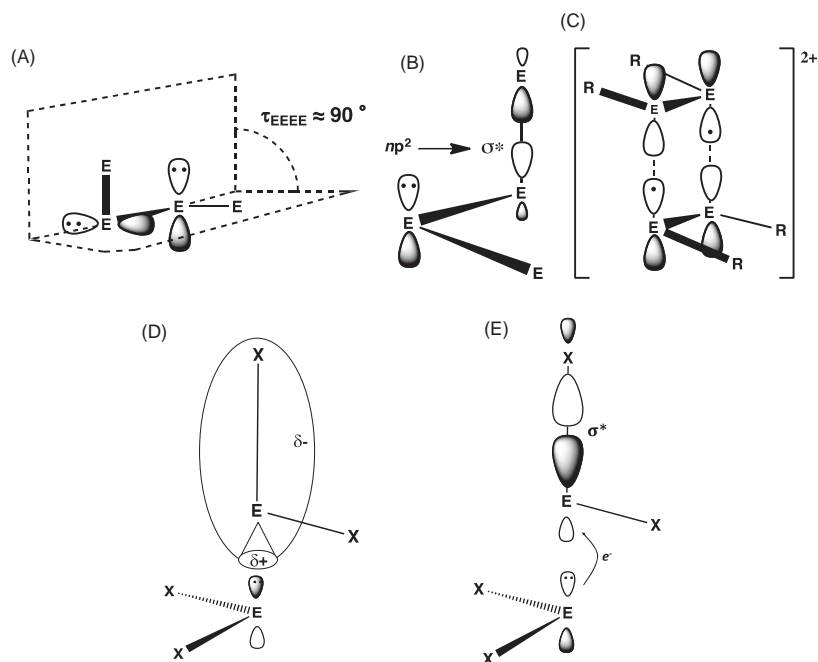
The crystal structures of eleven homocyclic sulfur rings have been determined to date, as shown in **Table 3**. In addition, several polymorphs are known for  $S_7$ ,  $S_8$ , and  $S_9$ .  $S_{18}$  is a special case, since it occurs as two different conformational isomers.  $S_6$  and  $S_{10}$  have been observed to crystallize together.<sup>65</sup> A general characteristic feature of the puckered rings is the consequence of the mutual interactions of the  $p$  lone-pair orbitals of the neighboring sulfur atoms resulting in the observed torsional angle of approximately

**Table 1** Illustrative examples of the cyclic chalcogen species.**Molecular species**
 $S_8, Se_8, Se_nS_{8-n}, Te_nS_{8-n}, Se_nTe_8,$   
 $n, Te_nSe_mS_{8-(n+m)}$ 
 $S_8O$  $S_7TeCl_2$ **Homo- and heterocyclic cations** $(S_8)^{2+}, (Se_8)^{2+}$  $(Te_6)^{4+}$  $(Te_2Se_6)^{2+}$ **Homocyclic cations with exocyclic groups** $(S_7)^+$  $(Se_9Cl)^+$  $(Se_6I_2)^{2+}, (Te_6I_2)^{2+}$ **Homocyclic anions** $(Se_{10})^{2-}$  $(Te_7)^{2-}$  $(Te_5)_n^{2n-}$ **Metal complexes with cyclic homopolychalcogen ligands** $[Ag(S_8)_2]^+$  $[Re_2(CO)_6(\mu-l)_2(Se_7)]$  $[Ir(TeCl_4)(TeCl_3)_2(Te_{10})]$ 

90° (see Refs. 67, 68 for the pioneering discussion of the properties of the SS bonds. The conclusions presented therein are still valid). During the past decades there have been several computational studies at different levels of theory to establish the relative energetics of various conformations of different isomers (see Refs. 1–4, 6, 8, and references therein).

**1.21.2.2.1 Cyclohexasulfur,  $S_6$** 

Cyclohexasulfur has originally been prepared for more than 100 years ago from the acidified aqueous solution of sodium thiosulfate.<sup>63,84</sup> It has later been shown that the elemental sulfur precipitation contains  $S_8$  and  $S_7$  in addition to  $S_6$ .<sup>64</sup> Cyclohexasulfur has more conveniently been prepared from  $[TiCp_2S_5]$  and  $SCl_2$ , which also affords  $S_{12}$ ,<sup>52</sup> as well as by treating the  $CS_2$  solution of  $S_2Cl_2$  with aqueous solution of alkali metal iodide (potassium or sodium).<sup>51</sup>



**Fig. 1** (A) The minimized repulsion of the  $np$  lone pairs of adjacent chalcogen atoms leads to a torsional angle of approximately  $90^\circ$ . (B) The hyperconjugative  $np^2 \rightarrow \sigma^*$  interaction results often in the alternation of chalcogen-chalcogen bond lengths. (C) The  $\pi^*-\pi^*$  interaction between two  $R_2E_2^+$  stabilizes the square-planar  $(RE)_4^{2+}$  cation. (D) Electrostatic attraction due to the presence of a  $\sigma$ -hole. (E) Intermolecular donor-acceptor interaction  $n^2(E) \rightarrow \sigma^*(E-X)$ .

**Table 2** Laboratory preparation of homocyclic sulfur molecules.

Reaction	Isolated product	References
Molten sulfur	$S_n$ ( $n = 6-8, 12, 18, 20$ )	39–45
$S_nCl_2 + H_2S_m$	$S_{m+n}$ ( $S_6, S_{10}, S_{12}, S_{18}, S_{20}$ )	46–50
+ KI	$S_n$ ( $n = 6-$ )	51
+ $[TiCp_2S_5]$	$S_5 + n$ ( $S_6, S_7, S_9, S_{11}, S_{12}, S_{13}$ )	52–56
+ $[TiCp_2(\mu - S_2)_mTiCp_2]$ ( $m = 2, 3$ )	$S_n$ ( $S_6, S_7, S_8, S_{10}, S_{15}, S_{20}$ )	57
+ $[TiCp_2(CO)_2] + S_6$	$S_8 + n$ ( $S_9, S_{11}$ )	58
+ $[TiCp_2(CO)_2] + S_8$	$S_n$	58
$S_8Cl_2 + [Zn(tmeda)S_6]^a$	$S_{14}$	59
$SO_2Cl_2 + [TiCp_2S_5]$	$S_{10}, S_{15}, S_{20}$	52, 60
$S_4(SCN)_2 + [TiCp_2S_5]$	$S_9$	61
Decomposition of $CuSSCOC_2H_5$	$\gamma$ - $S_8$	62
$Na_2S_2O_3(aq) + HCl(aq)$	$S_6, S_7, S_8$	63, 64
$S_6$ or $S_7 + CF_3COOH$	$S_{10}, S_6S_{10}$	65, 66

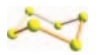

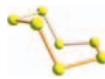
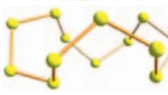
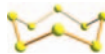
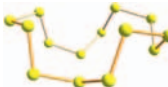
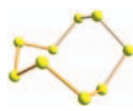
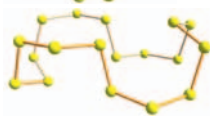
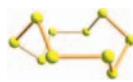
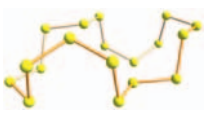
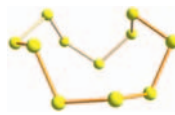
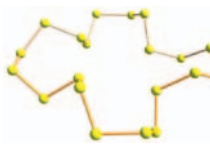
<sup>a</sup>tmeda = tetramethylethylenediamine.

The crystal structure determination<sup>69</sup> has established that the orange-yellow rhombohedral crystals consist of homocyclic six-atomic molecules in the chair conformation (see Table 3). The same molecular conformation for  $S_6$  is found in the solid solution of  $S_6 \cdot S_{10}$ .<sup>66</sup> The bond parameters in the molecule indicate S–S single bonds, but the lattice shows several short intermolecular contacts of 3.4432(12)–3.4713(10) Å, which accounts for the high observed density of the material (Fig. 2).<sup>69</sup>

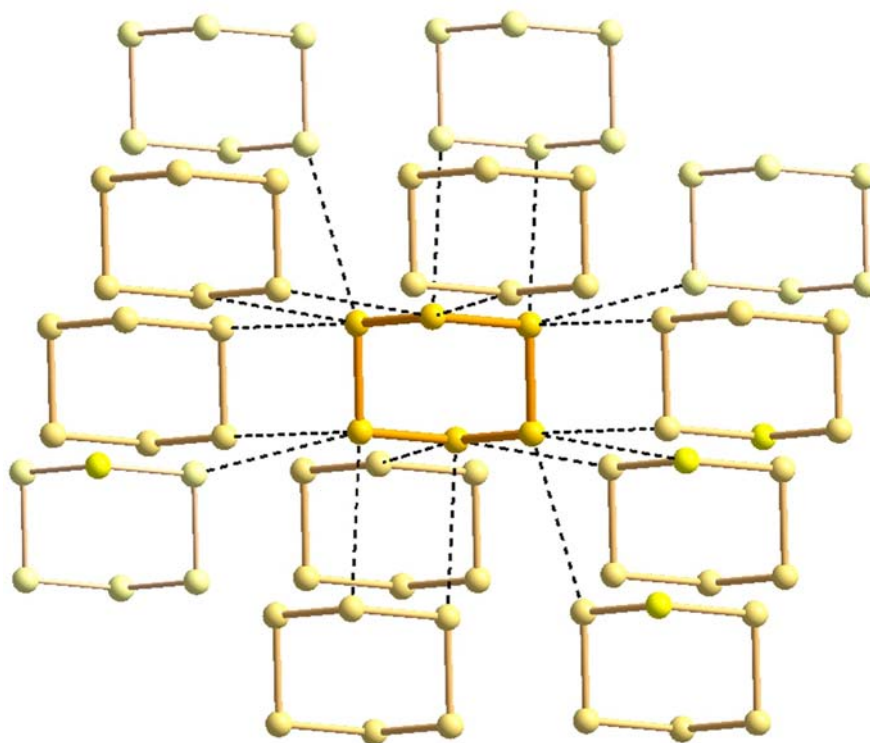
#### 1.21.2.2.2 Cycloheptasulfur, $S_7$

It has been deduced by Raman and IR spectroscopy that  $S_7$  can form four polymorphs denoted  $\alpha$ - $\delta$ .<sup>85</sup> The crystal structures  $\gamma$ - and  $\delta$ - $S_7$  have been determined.<sup>70,71</sup> The molecules in both polymorphs exhibit a planar fragment of four sulfur atoms, which leads to significant bond length alternation (see Table 3), as shown schematically in Fig. 3. This alternation can be rationalized in terms of the mutual 3p lone-pair repulsion of the two central atoms in the planar four-atomic fragment and of the hyperconjugative interactions of these lone-pairs with the  $\sigma^*$  orbitals of the bonds connecting the fragment to the rest of the molecule (see Fig. 3).<sup>70,71</sup> The Raman spectra of the four polymorphs indicate that the molecular conformations are similar also in  $\alpha$ - and  $\beta$ - $S_7$  and the

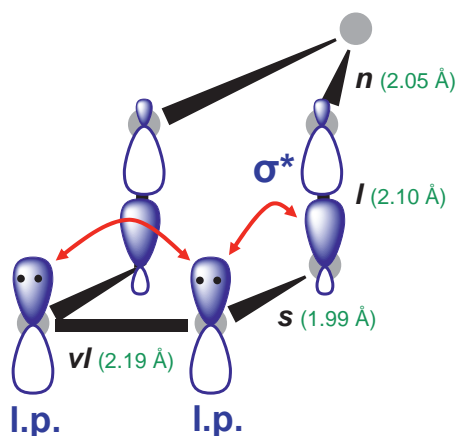
**Table 3** Molecular structures of homocyclic sulfur molecules.

Molecule	Structure	Bond parameters	Motif <sup>a</sup>	References	Molecule	Structure	Bond parameters	Motif <sup>a</sup>	References
S <sub>6</sub>		$r = 2.061(3)–2.068(2) \text{ \AA}$ $\alpha = 102.1(1)–103.1(1)^\circ$ $\tau = 73.5(1)–74.2(1)^\circ$	+ - + - + -	66,69	S <sub>12</sub>		$r = 2.0483(5)–2.572(4) \text{ \AA}$ $\alpha = 105.435(8)–106.953(6)^\circ$ $\tau = 86.006(9)–89.406(9)^\circ$	+ - - + + - - + + - - +	56
S <sub>7</sub>		$r = 1.997(1)–2.182(3) \text{ \AA}$ $\alpha = 101.5(1)–107.5(1)^\circ$ $\tau = 0.3(1)–108.78(6)^\circ$	0 + - + - + -	70,71	S <sub>13</sub>		$r = 1.976(2)–2.0739(17) \text{ \AA}$ $\alpha = 103.27(5)–111.08(5)^\circ$ $\tau = 30.83(7)–116.26(6)^\circ$	- + + - - + + + - - + + -	55
S <sub>8</sub>		$r = 2.035(2)–2.060(2) \text{ \AA}$ $\alpha = 107.1(1)–109.00(3)^\circ$ $\tau = 94.76(3)–101.38(3)^\circ$	+ - + - + - + -	62 72–80	S <sub>14</sub>		$r = 2.0485(10)–2.602(12) \text{ \AA}$ $\alpha = 103.99(3)–109.281(18)^\circ$ $\tau = 72.54(4)–101.68(3)^\circ$	- + + - - + + - + - - + + -	59
S <sub>9</sub>		$r = 2.0389(5)–2.0678(5) \text{ \AA}$ $\alpha = 105.810(8)–109.713(12)^\circ$ $\tau = 60.509(15)–115.574(13)^\circ$	+ + - - + + - + -	61	S <sub>18</sub>		$r = 2.052–2.067 \text{ \AA}$ $\alpha = 104.8–107.9^\circ$ $\tau = 79.4–100.5^\circ$	+ - - + + - + + + - + + - - + - - -	49
S <sub>10</sub>		$r = 2.0328(13)–2.0783(12) \text{ \AA}$ $\alpha = 103.35(3)–110.201(18)^\circ$ $\tau = 75.41(3)–123.73(3)^\circ$	+ - - + - + - - + -	66,81	<i>endo</i> 	$r = 2.054(5)–2.097(4) \text{ \AA}$ $\alpha = 104.24(7)–108.44(7)^\circ$ $\tau = 73.5(1)–74.2(1)^\circ$	+ - - + + + + - - + - - + - + + - -	83	
S <sub>11</sub>		$r = 2.0281(6)–2.1112(6) \text{ \AA}$ $\alpha = 103.656(14)–107.47(3)^\circ$ $\tau = 70.56(4)–117.32(3)(1)^\circ$	+ - - + - + - + - - +	55,82	<i>exo</i> 	$r = 2.023–2.104 \text{ \AA}$ $\alpha = 105.2–107.7^\circ$ $\tau = 30.83–116.26^\circ$	+ + + + - + + + + - + + + + - + + + + -	49	

<sup>a</sup>In the motif, the positive sign of the torsional angle indicates clockwise rotational and the negative sign counterclockwise rotation.



**Fig. 2** The close contacts between  $S_6$  molecules.<sup>69</sup>



**Fig. 3** Lone-pair interactions and hyperconjugation in cycloheptasulfur molecules leading to bond length alternation ( $vl$  = very long,  $l$  = long,  $s$  = short,  $n$  = normal single bond; the approximate bond lengths are taken from the X-ray structures.<sup>70,71</sup> for more detailed discussion, see ref. 85).

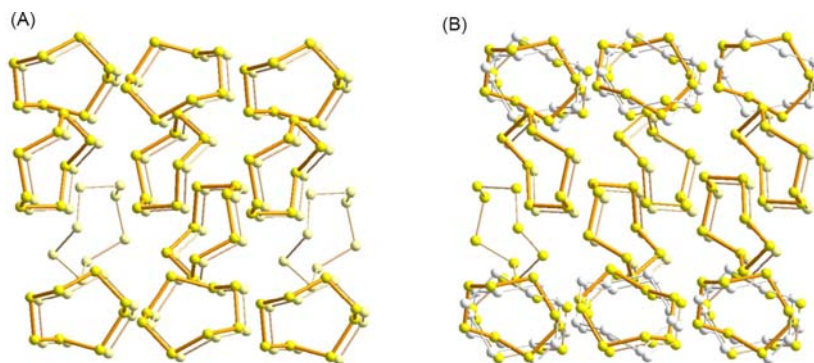
polymorphs differ only in the packing of the molecules. It is the weak S-S bond in the central part of the four-atomic fragment that is considered to be responsible for the low stability of  $S_7$ .

In solution and gaseous state, cycloheptasulfur is fluxional undergoing facile pseudorotation,<sup>86</sup> as judged experimentally by Raman spectroscopy<sup>87</sup> and demonstrated by MO computations at different levels of theory (see reviews in refs 1 and 2). All computations show qualitative agreement. The most reliable barrier to pseudorotation is  $5.6 \text{ kJ mol}^{-1}$ .<sup>88</sup>

### 1.21.2.2.3 Cyclooctasulfur, $S_8$

There are three known polymorphs of cyclooctasulfur molecule  $S_8$ . They all show similar puckered crown-shaped molecules (see Table 3) but differ in their packing in the crystal lattice. Orthorhombic  $\alpha$ - $S_8$  is the thermodynamically stable form at NTP.<sup>1-4</sup> It has long been known that there is a phase transition from orthorhombic  $\alpha$ - $S_8$  to the monoclinic  $\beta$  form at *ca.*  $96^\circ\text{C}$  with this form being stable up to the melting point of sulfur.<sup>89,90</sup>  $\beta$ - $S_8$  is conventionally prepared either by slow solidification of the molten





**Fig. 4** Crystal structure of  $\beta$ -S<sub>8</sub> at (A)  $-153^{\circ}\text{C}$ <sup>91</sup> and (B) at ambient temperature.<sup>75</sup>

element or by crystallization from organic solvent (see, for instance ref. 83). At room temperature, the crystal structure shows orientational disorder.<sup>75–77</sup> The order-disorder transition has been estimated upon cooling the crystals below  $-75^{\circ}\text{C}$  (see Fig. 4) with the ordering enthalpy of  $4.6\text{ kJ mol}^{-1}$ .<sup>76</sup>

The third polymorph of sulfur, monoclinic  $\gamma$ -S<sub>8</sub> has been prepared by the reaction of pyridine with CuSSCOEt.<sup>62</sup> The packing of the S<sub>8</sub> molecules results in the highest-density solid lattice of all sulfur molecular forms.<sup>62,78–80</sup>  $\gamma$ -S<sub>8</sub> is also found in nature as the mineral rosickyite. The presence of rosickyite as a geological material has been shown to be a biosignature. Studies upon evaporite basins in Death Valley have shown that the mineral is constantly replenished by a cycle of microbial attack on gypsum deposits, followed by bacterial re-oxidation of the resulting sulfide to this form of elemental sulfur.<sup>92</sup>

Elemental sulfur can directly be associated with or in microorganisms, as shown in the case of *Thiomargarita namibiensis* which is the largest bacterium thus far discovered (with individual cells up to 0.75 mm in size).<sup>93</sup> XANES (X-ray Near Edge Structure) was employed to show that the sulfur in this bacterium was present as S<sub>8</sub>.<sup>94</sup> Raman spectroscopy has also been employed to identify the form of the element, as demonstrated by the use of Raman spectroscopy on living samples of the nematode *Eubostriechus diana*.<sup>95</sup>

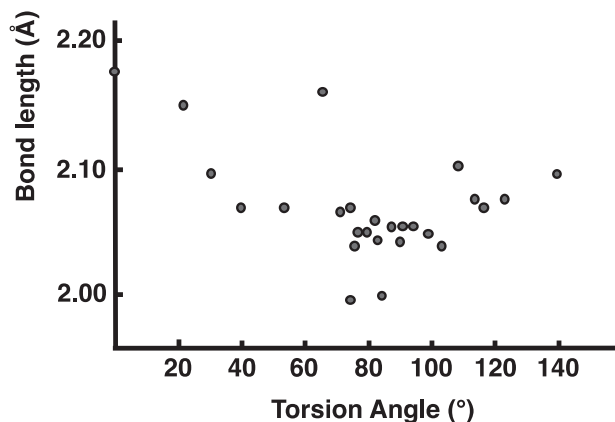
#### 1.21.2.2.4 Larger sulfur rings S<sub>9</sub>–S<sub>16</sub>, S<sub>18</sub>, and S<sub>20</sub>

As shown in Table 2, larger sulfur rings can be prepared in analogous manner to S<sub>6</sub> and S<sub>7</sub>. The most convenient method to prepare rings with odd number of sulfur atoms involves the reaction between [TiCp<sub>2</sub>S<sub>5</sub>] (Cp = dicyclopentadienyl C<sub>5</sub>H<sub>5</sub><sup>−</sup> or its alkylated derivatives) and appropriate chlorosulfanes S<sub>n</sub>Cl<sub>2</sub>. The reaction of sulfanes H<sub>2</sub>S<sub>m</sub> and S<sub>n</sub>Cl<sub>2</sub> mainly afford sulfur rings with even number of atoms. There are also other more specialized reactions to prepare and isolate large sulfur rings (see Table 2).

The crystal structure determinations summarized in Table 3 show that while the puckered conformations in all different rings are rather similar, there is variation both in the bond lengths and torsional angles. The dependence of the bond length on the torsional barriers has been discussed by comparing the metrical values in different homocyclic molecules shown in Table 3. This information has been summarized in Fig. 5.

There are a few interesting special cases that merit comments:

Cyclononasulfur, S<sub>9</sub> crystallizes at least as two distinct polymorphs. The crystal structure of  $\alpha$ -S<sub>9</sub> has been determined, but that of  $\beta$ -S<sub>9</sub> is still unknown.<sup>61</sup> The comparison of the Raman spectra of the  $\alpha$ - and  $\beta$ -forms demonstrates that the molecular conformation in both polymorphs is similar (see Table 3).



**Fig. 5** The dependence of the S–S bond length on the torsion angle in solid homocyclic sulfur molecules.<sup>2</sup> Adapted with permission from Steudel, R.; Eckert, B., *Topics Curr. Chem.* **2003**, *230*, 1–79. Copyright 2003 Springer-Verlag, Heidelberg.

In the course of preparation of cyclodecasulfur,  $S_{10}$  from  $S_6$ , the solid solution of  $S_6 \cdot S_{10}$  was obtained.<sup>65</sup> The crystal structure determination showed that this phase is completely ordered and contain alternating layers of  $S_6$  and  $S_{10}$  homocycles.<sup>66</sup>

Cyclododecasulfur,  $S_{12}$  can be crystallized both without the solvent molecule and containing the  $CS_2$  molecule of crystallization.<sup>56</sup> It was observed that in the case of  $S_{12} \cdot CS_2$  adduct, the intermolecular forces for  $S_{12}$  are smaller than in the case of the  $S_{12}$  lattice, and therefore the molecule in the former case displays the geometry, which is closer to the ideal gas-state symmetry of  $D_{3d}$ .

Whereas cyclopentadecasulfur,  $S_{15}$  has only been obtained as impure lemon-yellow powder containing trace amounts of  $S_{14}$  and  $S_{16}$ ,<sup>96</sup> its crystal structure is not known. The B3PW91/6-311+G(3df) calculations predict that the molecule should have  $C_2$  symmetry.<sup>97</sup> The optimized bond parameters are  $r_{SS} = 2.053\text{--}2.065 \text{ \AA}$ ,  $\alpha_S = 104.9\text{--}109.4^\circ$ , and  $\tau = 77.1\text{--}112.3^\circ$ .

Two conformational isomers have been obtained for cyclooctadecasulfur  $S_{18}$ .<sup>49,83</sup> As seen from Table 3, the metrical values of the bond parameters are very similar in the *endo* and *exo* forms, but the motifs of the torsion angles are different leading to the different conformation.

### 1.21.2.3 Selenium and tellurium

#### 1.21.2.3.1 Cyclohexaselenium, $Se_6$

The first report on cyclohexaselenium involved the crystallization of amorphous selenium from  $CS_2$ , which afforded monoclinic  $\beta$ - $Se_8$  and  $Se_6$  that were separated under microscope.<sup>98</sup>  $Se_6$  can also be obtained by treating  $Se_2Cl_2$  with KI.<sup>99</sup> It has also been shown that  $SeCl_2$  can be stabilized in coordinating solvents long enough to use it as an *in situ* reagent.<sup>100</sup> Its reaction with  $[TiCp_2Se_5]$  also affords  $Se_6$ ,<sup>5</sup> though also in these two latter reactions  $Se_8$  is also formed and the crystalline products need to be separated under microscope.

The crystals of  $Se_6$ <sup>98</sup> are isomorphic with those of  $S_6$ ,<sup>69</sup> and consequently the molecule shows a similar six-atomic ring as  $S_6$  (see Table 3). The bond lengths, the bond angles, and the torsion angles indicate single bonds (see Table 4). There are several intermolecular close contacts of 3.863(3) and 3.964(5)  $\text{\AA}$  in the analogous manner to those in  $S_6$ .<sup>69</sup> The intermolecular interactions in  $Se_6$  appear to be somewhat stronger than in  $S_6$  (the approximate Pauling bond orders based on the internuclear distances are 0.18 and 0.01<sup>101</sup>).

#### 1.21.2.3.2 Cycloheptaselenium, $Se_7$

The reaction of  $[TiCp_2Se_5]$  and  $Se_2Cl_2$  affords cycloheptaselenium  $Se_7$  in good yields.<sup>108</sup> In the  $CS_2$  solution,  $Se_7$  quickly equilibrates to a mixture of  $Se_6$ ,  $Se_7$ , and  $Se_8$ .<sup>109</sup>

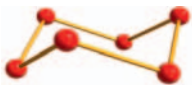


The crystal structure of  $Se_7$  is unknown, but its Raman spectrum<sup>108</sup> is similar to that of  $\gamma$ - and  $\delta$ - $S_7$ <sup>85</sup> indicating a similar structure. The molecular  $Se_7$  ring in two ionic products  $[Na(12\text{-crown-}4)_2(Se_8) \cdot (Se_6, Se_7)]^{103}$  and  $(NET_4)_2(Se_5) \cdot (\frac{1}{2}Se_6 \cdot Se_7)$ ,<sup>102</sup> shows a conformation and bond length alternation similar to those in  $S_7$ <sup>70,71</sup> (see Table 4 and Fig. 3).

In solution  $Se_7$  undergoes similar pseudorotation to  $S_7$ . The <sup>77</sup>Se NMR spectrum shows only one resonance at 996 ppm, though four resonances of with relative intensities of 2:2:2:1 would be expected for the  $C_s$  symmetry in the chair conformation.<sup>110</sup>

#### 1.21.2.3.3 Cyclooctaselenium $Se_8$

Three monoclinic polymorphs are known for  $Se_8$ .<sup>105–107,111,112</sup> They all consist of cyclic puckered crown-shaped  $Se_8$  molecules, which are similar to those of the three known crystallographic modifications of  $S_8$ .<sup>62,72–80</sup> The bond parameters in all three cyclic selenium modifications are near to those expected for single bonds (see Table 4).

**Table 4** Room-temperature crystal structures of homocyclic selenium molecules.

Molecule Structure	$r_{SeSe} (\text{\AA})$	$\alpha_{SeSeSe} (^\circ)$	$\tau_{SeSeSeSe} (^\circ)$	References	
 $Se_6$	$Se_6$	2.356(9)	101.1(3)	76.2(4)	98
	$(NET_4)_2(Se_5) \cdot (\frac{1}{2}Se_6 \cdot Se_7)$	2.319(7)–2.419(7)	97.3(2)–105.8(2)	71.5(3)–77.9(3)	102
 $Se_7$	$[Na(12\text{-crown-}4)_2(Se_8) \cdot (Se_6, Se_7)]$	2.281(6)–2.440(8)	99.6(2)–110.3(3)	1.6(3), 69.9(2)–	103
	$(NET_4)_2(Se_5) \cdot (\frac{1}{2}Se_6 \cdot Se_7)$	2.324(7)–2.409(7)	101.1(2)–108.3(2)	114.0(3)	102
	$[Re_2(\mu\text{-I})_2(\mu\text{-}Se_7)(CO)_6] \cdot \frac{1}{2}C_7H_{16}$	2.309(3)–2.558(3)	99.33(10)–104.28(9)	4.6(3), 73.7(3)–	104
 $Se_8$	$\alpha$ - $Se_8$	2.3268(12)–	103.345(10)–	96.287(13)–	105
	$\beta$ - $Se_8$	2.3456(8)	107.693(11)	106.952(12)	106
	$\gamma$ - $Se_8$	2.30–2.36	104.2–107.1	98.21(6)–104.27(6)	107
		2.325(2)–2.344(2)	103.26(8)–109.08(8)	98.9–103.9	

The structures of monoclinic  $\alpha$ - and  $\beta$ -Se<sub>8</sub> are expectedly dependent on temperature. In both polymorphs, the individual bond lengths in the two low-temperature structures are significantly shorter than the corresponding bonds in the room temperature structures.<sup>111,112</sup> In case of  $\alpha$ -Se<sub>8</sub>, the ring becomes more distorted from the ideal  $D_{4d}$  symmetry, as the temperature is lowered.<sup>111</sup> Similar distortion is not as evident in monoclinic  $\beta$ -Se<sub>8</sub>.<sup>112</sup>

The intermolecular interactions in all three monoclinic polymorphs are stronger than those in S<sub>8</sub>. In monoclinic  $\gamma$ -Se<sub>8</sub>,<sup>107</sup> the shortest intermolecular contact is in fact shorter than in any modifications of S<sub>8</sub>.<sup>62,72–80</sup>

#### 1.21.2.3.4 Homocyclic tellurium molecules

The evidence for tellurium rings is very sparse.<sup>1,5,6,8</sup> The presence of cyclic Te<sub>8</sub> molecule in zeolites has been suggested based on conductivity measurements<sup>113</sup> and Raman spectroscopy.<sup>114</sup> The treatment of [Ti(C<sub>5</sub>H<sub>5</sub>)<sub>2</sub>( $\mu$ -Te<sub>2</sub>)<sub>2</sub>Ti(C<sub>5</sub>H<sub>5</sub>)<sub>2</sub>] with Te<sub>2</sub>Cl<sub>2</sub> in CS<sub>2</sub> results in the observation of a single resonance at 869 ppm in the <sup>125</sup>Te NMR spectrum.<sup>115</sup> This resonance is in the region that could be expected for Te<sub>8</sub> (*c.f.* 611.5 ppm for Se<sub>8</sub><sup>116</sup>).

#### 1.21.2.4 Homocyclic oxygen molecules

Whereas experimental information on electrically neutral homocyclic oxygen molecules O<sub>*n*</sub> (*n* ≥ 6) is virtually non-existent, their potential as high energy-density materials has long encouraged computational approach to understand their geometries and stabilities. Whereas energy minima have been found for O<sub>6</sub>,<sup>117–121</sup> O<sub>8</sub>,<sup>120,121,123–125</sup> and O<sub>12</sub><sup>120,121,126</sup> rings at different levels of Hartree-Fock and MP2 computations, the calculations yield different conformations. The B3LYP and B3PW91 functionals using 6-31G\* and 6-311G(2df) basis sets did not find energy minima on the potential energy surface for any ring conformations of O<sub>6</sub>, O<sub>8</sub>, and O<sub>12</sub>.<sup>120</sup> The highest-level optimizations for the cyclic O<sub>6</sub>, O<sub>8</sub>, and O<sub>12</sub> molecules are CCSD(T,full)/cc-pCVTZ,<sup>122</sup> CCSD/cc-pVTZ,<sup>124</sup> and SCF/DZP,<sup>126</sup> respectively. These molecules show structures, which are analogous to the related S<sub>6</sub>, S<sub>8</sub>, and S<sub>12</sub> molecules (Table 3) as well as to Se<sub>6</sub> and Se<sub>8</sub> (Table 4). The optimized bond parameters for O<sub>6</sub> ( $D_{3d}$ ) are  $r_{OO} = 1.4294 \text{ \AA}$ ,  $\alpha_O = 103.6^\circ$ ,  $\tau = 72.1^\circ$ ,<sup>122</sup> for O<sub>8</sub> ( $D_{4d}$ )  $r_{OO} = 1.404 \text{ \AA}$ ,  $\alpha_O = 107.9^\circ$ ,  $\tau = 98^\circ$ ,<sup>124</sup> and for O<sub>12</sub> ( $D_{3d}$ )  $r_{OO} = 1.358 \text{ \AA}$ ,  $\alpha_O = 108.7\text{--}108.8^\circ$ ,  $\tau = 86.9\text{--}88.0^\circ$ .<sup>126</sup> Interestingly, the MP2/6-311++G\*\* calculations have reported to yield a different optimized structure for O<sub>12</sub>.<sup>121</sup> It consists of two O<sub>6</sub> molecules in the chair-conformation, in which the molecules lie on top of each other and show only weak interactions of 3.37 Å.

Based on the smaller bond energy of OO single bond than that of SS single bond, and the larger bond energy of the O=O double bond than that of the S=S double bond, it was estimated that the decomposition energy for O<sub>*n*</sub> → *n*/2 O<sub>2</sub> should be *ca.* 100 kJ mol<sup>-1</sup> per oxygen atoms.<sup>127</sup> The computed values at different levels of theory are 58–71,<sup>117,118,121</sup> 54–71,<sup>122,123</sup> and 87 kJ mol<sup>-1</sup>,<sup>126</sup> for O<sub>6</sub>, O<sub>8</sub>, and O<sub>12</sub>, respectively.

### 1.21.3 Heterocyclic chalcogen molecules

#### 1.21.3.1 General

The chemical and structural similarity of the three chalcogen elements has led to investigations on the structures and properties of the binary and ternary systems.<sup>1,4</sup> Heterocyclic selenium sulfides form a particularly extensive binary system that bridge the properties of an electrical insulator (sulfur) and a semiconductor (selenium). The heterocyclic tellurium-containing species are much sparser, and therefore very little is known about their properties.

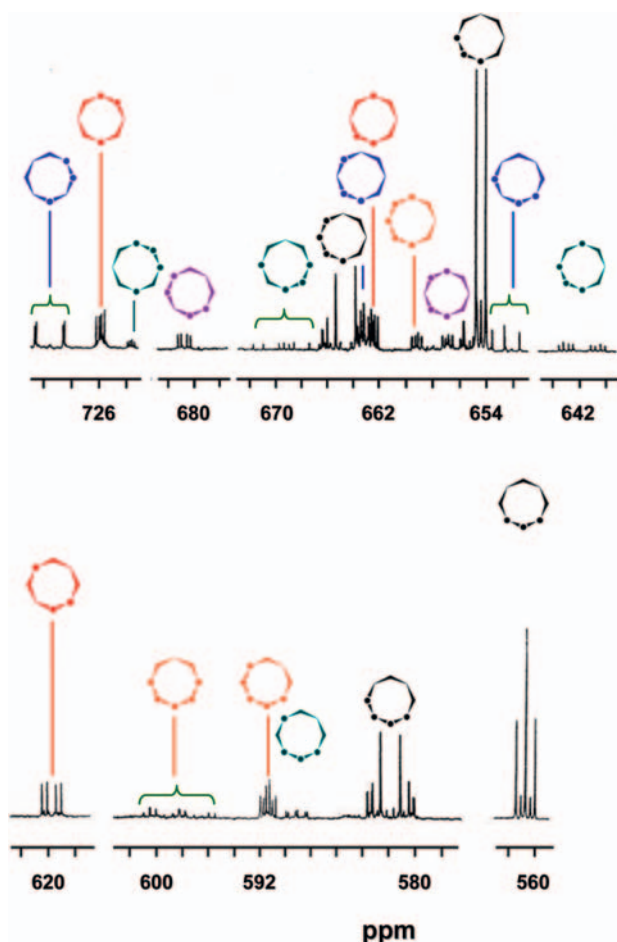
#### 1.21.3.2 Selenium sulfides

The similarity of sulfur and selenium is reflected by a complicated binary system between the two elements. With the exception of the condensation reactions of [TiCp<sub>2</sub>E<sub>5</sub>] or [TiCp<sub>2</sub>( $\mu$ -E<sub>2</sub>)<sub>2</sub>TiCp<sub>2</sub>] (E = S, Se) with sulfur and selenium chlorides, most synthetic routes produce mixtures of various selenium sulfides.<sup>1</sup> The eight-membered Se<sub>*n*</sub>S<sub>8-*n*</sub> species are the most abundant and most stable molecular species, though heterocyclic selenium sulfides of other ring sizes can also be formed.

All known crystal structures of heterocyclic selenium sulfides are disordered.<sup>108,128–134</sup> It has therefore not been possible to calculate accurate bond parameters or identify individual molecular species. Vibrational spectroscopy provided the first indications that selenium sulfides are present in the various mixtures.<sup>135,136</sup> The normal coordinate calculations enabled the assignment of the Raman spectra of 1,2-Se<sub>2</sub>S<sub>5</sub>,<sup>137,138</sup> 1,2,3,4,5-Se<sub>5</sub>S<sub>2</sub>,<sup>108,138</sup> 1,2,3-Se<sub>3</sub>S<sub>5</sub>,<sup>133</sup> 1,2,5,6-Se<sub>4</sub>S<sub>4</sub>,<sup>134</sup> and Se<sub>7</sub>S<sup>128</sup> thereby resulting in the identification of the molecular species.

<sup>77</sup>Se NMR spectroscopy is the most powerful technique to date to identify individual heterocyclic selenium sulfides in mixtures of complicated composition.<sup>116,139,140</sup> The spectral assignment is based on the combined information from the natural-abundance samples and from the samples of the same chemical composition but involving selenium enriched with <sup>77</sup>Se-isotope (enrichment 92%).<sup>116</sup> Due to the low natural abundances of the <sup>77</sup>Se-isotope in the natural-abundance selenium, the coupling can only be observed by the appearance of small satellites that are often lost in the background. Full coupling information is only obtained with the enrichment of the <sup>77</sup>Se-isotope.

The assignment of the <sup>77</sup>Se chemical shifts to individual molecules is exemplified in Fig. 6 by the NMR spectrum of the CS<sub>2</sub> solution that was prepared from the quenched sulfur-selenium melt containing 30 % of <sup>77</sup>Se-enriched selenium (enrichment 92



**Fig. 6**  $^{77}\text{Se}$  NMR spectrum of the  $\text{CS}_2$  solution of quenched sulfur-selenium melt containing 30 mol-% of selenium enriched in  $^{77}\text{Se}$ -isotope (enrichment 92 %).<sup>116</sup> The different  $\text{Se}_n\text{S}_{8-n}$  species have been color-coded. The colored circles indicate selenium atoms and the empty corners sulfur atoms.

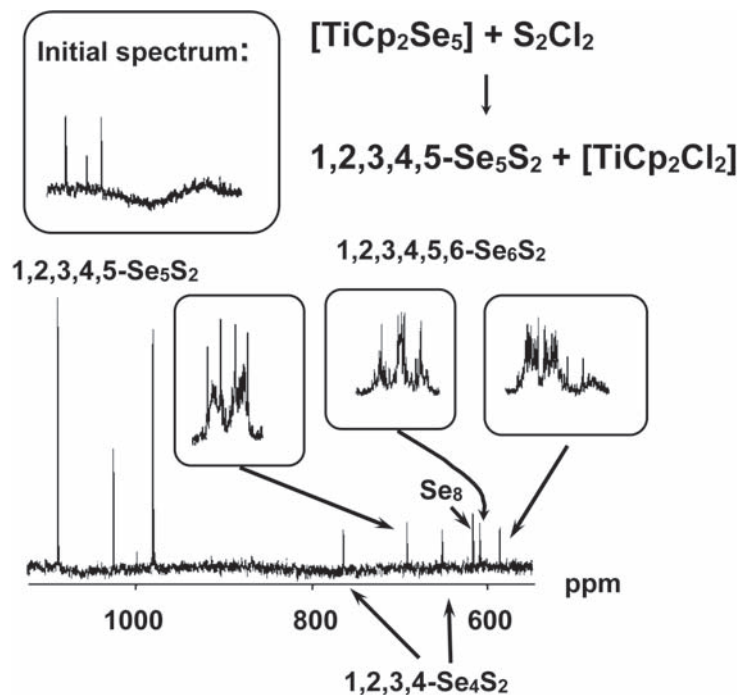
%) and 70 % of sulfur. In addition to the resonances shown in the figure, there are eight resonances in the spectrum, which appear as singlets even in the  $^{77}\text{Se}$ -enriched sample.<sup>116</sup> These singlets were assigned to  $\text{SeS}_7$ , all isomers of  $\text{Se}_2\text{S}_6$ , 1,2,5,6- $\text{Se}_4\text{S}_4$ ,  $\text{Se}_8$ , and  $\text{Se}_6$  on the basis of the trends in the chemical shifts deduced from unambiguously identified molecular species.<sup>116,141</sup> The assignments were later verified by DFT calculations of  $^{77}\text{Se}$  chemical shifts.<sup>142</sup> Sulfur-rich  $\text{SeS}_7$  and 1,2- $\text{Se}_6\text{S}_2$  are the main components in the mixture even, when the initial selenium-content is high. Other major components are 1,2,3- $\text{Se}_3\text{S}_5$ , 1,2,3,4- $\text{Se}_4\text{S}_4$ , 1,2,3,4,5- $\text{Se}_5\text{S}_3$ , 1,2,3,4,5,6- $\text{Se}_6\text{S}_2$ , and  $\text{Se}_8$ <sup>116</sup> in agreement with the deductions from earlier vibrational analysis<sup>135</sup> that the number of homonuclear Se-Se or S-S bonds is maximized in the eight-membered rings.

$^{77}\text{Se}$  NMR spectroscopy can also be utilized to monitor interconversion reactions that take place between the different chalcogen rings in solution. This is exemplified in Fig. 7 for the reaction of  $[\text{TiCp}_2\text{Se}_5]$  and  $\text{S}_2\text{Cl}_2$ .<sup>143</sup> It can be seen that the initial fluxional seven-membered 1,2,3,4,5- $\text{Se}_5\text{S}_2$  ring decomposes into 1,2,3,4- $\text{Se}_4\text{S}_2$  and 1,2,3,4,5,6- $\text{Se}_6\text{S}_2$ . Similar interconversion has been shown to take place between  $\text{Se}_7$ ,  $\text{Se}_6$ , and  $\text{Se}_8$ <sup>109</sup> and 1,2- $\text{Se}_2\text{S}_5$ ,  $\text{SeS}_5$ , and 1,2,3- $\text{Se}_3\text{S}_5$ .<sup>133,137</sup>

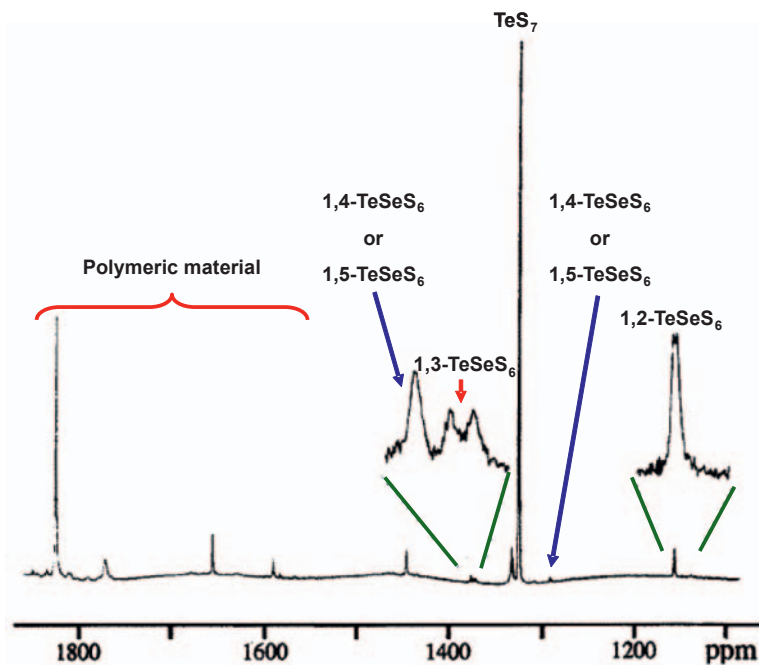
### 1.21.3.3 Tellurium-containing chalcogen rings

The formation of  $\text{Te}_n\text{S}_{8-n}$  rings in sulfur-tellurium melt has been deduced by mass spectrometry,<sup>144</sup> Mössbauer spectrometry,<sup>145</sup> and  $^{125}\text{Te}$  NMR spectroscopy.<sup>146</sup> The disordered crystal structure of the phase prepared from  $\text{H}_2\text{S}$  and  $\text{TeCl}_4$  was deduced to contain a mixture of cyclic molecules  $\text{S}_8$ ,  $\text{TeS}_7$ , and  $\text{Te}_2\text{S}_6$ <sup>147</sup> with a conformation similar to that in  $\text{TeS}_7\text{X}_2$  ( $\text{X} = \text{Cl}, \text{Br}$ ).<sup>148,149</sup> The seven- and eight-membered selenium-rich selenium telluride heterocycles<sup>150,151</sup> have been shown to have similar conformations to those of the analogous sulfur, selenium, and selenium sulfide rings.<sup>62,70–80,102–104,129–134</sup>

$^{125}\text{Te}$  and  $^{77}\text{Se}$  NMR spectroscopic characterization of sulfur-tellurium and sulfur-selenium-tellurium melts at 145 °C using both natural-abundance selenium and tellurium and  $^{77}\text{Se}$ -enriched and  $^{125}\text{Te}$ -enriched isotopes have indicated that the sulfur-rich binary molten mixture contains  $\text{TeS}_7$  and 1,2-, 1,3-, and 1,4-isomers of  $\text{Te}_2\text{S}_6$ .<sup>146</sup> In addition, 1,2-, 1,3-, 1,4-, and 1,5- $\text{TeSe}_6$  rings have been detected in the ternary melt (1.5 mol-% of both tellurium and selenium and 97 mol-% of sulfur; see Fig. 8).<sup>146</sup>



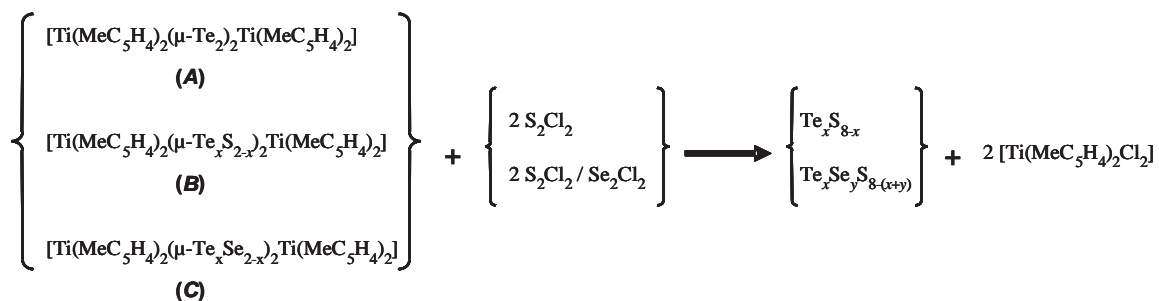
**Fig. 7** The natural-abundance  $^{77}\text{Se}$  NMR spectrum of the reaction mixture of  $[\text{TiCp}_2\text{Se}_5]$  and  $\text{S}_2\text{Cl}_2$  recorded after 1 day of decomposition.<sup>143</sup> The uppermost insert is the spectrum recorded at the beginning of the reaction. The lower inserts are resonances of the  $^{77}\text{Se}$ -enriched 1,2,3,4,5,6-Se<sub>6</sub>S<sub>2</sub> (enrichment 92 %).



**Fig. 8**  $^{125}\text{Te}$  NMR spectrum of ternary sulfur-selenium-tellurium melt containing 1.5 mol % of both  $^{77}\text{Se}$ -enriched selenium and  $^{125}\text{Te}$ -enriched tellurium (enrichment in both cases 92 %) recorded at 145 °C.<sup>146</sup> Adapted with permission from Chivers, T.; Laitinen, R. S.; Schmidt, K. J.; Taavitsainen, J. *Inorg. Chem.* **1993**, 32, 337–340. Copyright 1993 American Chemical Society.

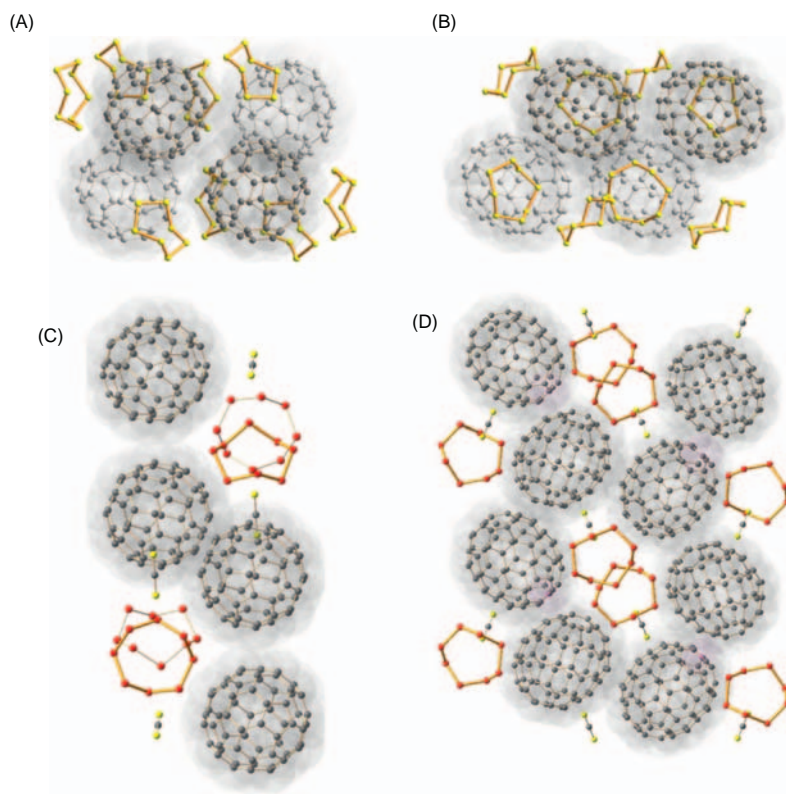
Tellurium containing chalcogen-rings are also formed by following the preparative routes known for other chalcogen rings (see ref. 1 and references therein). The most important processes have been summarized below (Scheme 1).<sup>152</sup>





**Scheme 1** Formation of tellurium-containing heterocyclic chalcogen molecules.<sup>152</sup>

An *ab initio* MO study of eight-membered sulfur-rich tellurium selenium sulfide rings has shown that the most stable species contain Se–Te bonds.<sup>152</sup> 1,2,8-TeSe<sub>2</sub>S<sub>5</sub> was deduced to be the most stable of the isomers. The formation of this species was indeed observed in the reaction of (Me<sub>3</sub>Si)<sub>2</sub>Te with ClSeS<sub>5</sub>SeCl.<sup>152</sup>

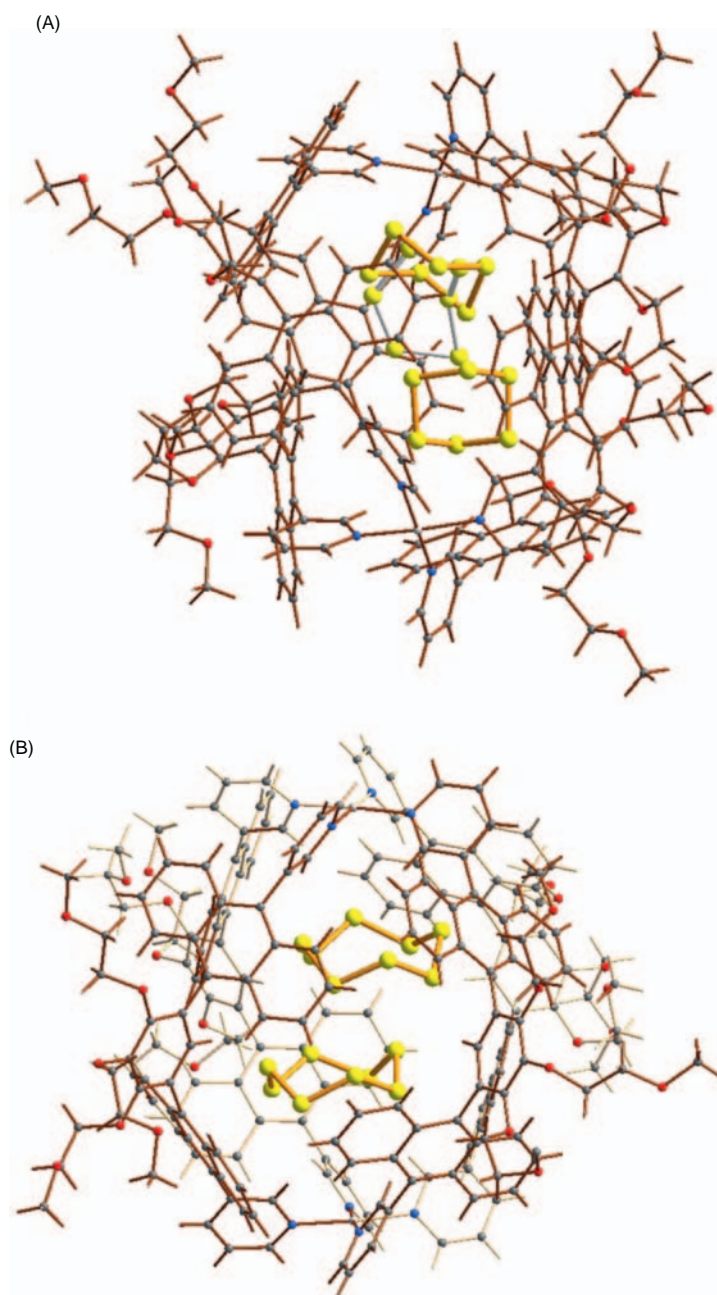


**Fig. 9** Examples of the co-crystals of fullerenes and chalcogen-rings. (A) C<sub>60</sub>·2S<sub>8</sub>,<sup>153</sup> (B) C<sub>70</sub>·2S<sub>8</sub>,<sup>158</sup> (C) C<sub>60</sub>·Se<sub>8</sub>·CS<sub>2</sub>,<sup>159</sup> and (D) C<sub>70</sub>·Se<sub>8</sub>·CS<sub>2</sub>.<sup>160</sup>

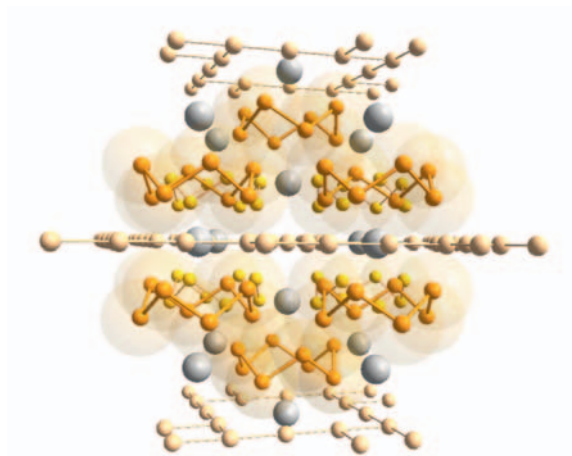
### 1.21.4 Supramolecular chemistry involving chalcogen rings

Cyclooctasulfur molecules have been reported to co-crystallize with a number of main group compounds and transition metal complexes (see ref. 1 for review of early literature). Recent examples involve fullerenes  $C_{60}$ ,<sup>153,154,156</sup>  $C_{70}$ ,<sup>157,158</sup> and  $C_{76}$  (Fig. 9).<sup>155</sup> Related co-crystals have also been reported for  $Se_8$  and  $C_{60}$ <sup>159</sup> and  $C_{70}$ .<sup>160</sup> The  $Gd@C_{2v}(9)-C_{82} \cdot 2.5(S_8) \cdot 0.5(CS_2)$  showed the presence of endohedral  $Gd^{3+}$  ions inside the  $C_{82}^{3-}$  cage.<sup>161</sup> Whereas the  $C_{82}^{3-}$  cage,  $S_8$  molecules, and  $CS_2$  were fully ordered in the crystal structure, multiple disordered sites were identified for  $Gd^{3+}$  ions inside the cage. The DFT optimizations were performed to model the crystal structure and two local energy minima were found for the metal ion, which are closely related to the observed disordered atom sites in the experimental structure. The relative energies of the structures with different  $Gd^{3+}$  sites were rather close to each other thereby rationalizing the observed disorder.<sup>161</sup>

There are solid phases, in which cyclooctasulfur molecules co-crystallize in supramolecular lattices of different metal complexes.<sup>162–175</sup> Some relevant early literature has been reviewed in ref. 176.



**Fig. 10** Encapsulation of (A)  $S_6$  and (B)  $S_8$  in the polyaromatic dinuclear palladium macrocycle.<sup>177</sup>



**Fig. 11** Crystal structure of Cs<sub>3</sub>Te<sub>22</sub> consisting of pucker Te<sub>8</sub> rings between the [Te<sub>4</sub>Te<sub>4/2</sub>]<sub>2</sub><sup>3-</sup> layers (tellurium is depicted in orange and cesium in gray).<sup>179</sup>

S<sub>6</sub>, S<sub>8</sub>, and S<sub>12</sub> have been encapsulated in a polyaromatic dinuclear palladium macrocyclic matrix and characterized using ESI-TOF mass spectrometry and single-crystal X-ray diffraction, as exemplified in Fig. 10.<sup>177</sup>

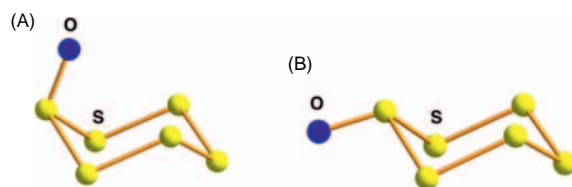
When sodium polyselenide and 12-crown-4 were treated with cerium(III)chloride, [Na(12-crown-4)<sub>2</sub>]<sub>2</sub>(Se<sub>8</sub>)·(Se<sub>6</sub>,Se<sub>7</sub>) was obtained.<sup>103</sup> The lattice contains Se<sub>6</sub> and Se<sub>7</sub> rings in addition to [Na(12-crown-4)<sub>2</sub>]<sup>+</sup> and acyclic Se<sub>8</sub><sup>2-</sup> anions. The structures of these molecules are described in Table 4.

Cs<sub>3</sub>Se<sub>22</sub> has been shown to contain a cyclooctaselenium molecule between the layer anions.<sup>178</sup> The tellurium analog Cs<sub>3</sub>Te<sub>22</sub> has a similar structure and contains the Te<sub>8</sub> ring<sup>179</sup> between the telluride layers (see Fig. 11). The Te-Te distances in the ring are 2.787–2.818 Å, the bond angles 99.32–101.12°, and the torsional angles 106.53–106.95°. Cs<sub>4</sub>Te<sub>28</sub> also contains a Te<sub>8</sub> ring in a related layered two-dimensional polytelluride lattice.<sup>180</sup> These two cesium tellurides are the only known species in which the structural identity of the Te<sub>8</sub> ring has been established.

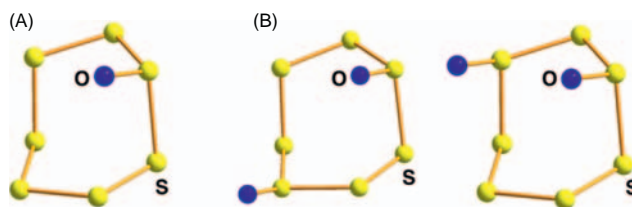
### 1.21.5 Homocyclic sulfur oxides

Reactions of any of the five homocyclic S<sub>*n*</sub> (*x* = 6–10) molecules with CF<sub>3</sub>CO<sub>3</sub>H in CH<sub>2</sub>Cl<sub>2</sub> at low temperature result in the formation of S<sub>*n*</sub>O in which the cyclic structure is retained with one of the sulfur atoms now oxidized via formation of a S=O double bond.<sup>181,182</sup> S<sub>6</sub>O can also be generated *in situ* in CS<sub>2</sub> at low temperature in the absence of light by the reaction of [TiCp<sub>2</sub>S<sub>5</sub>] with SOCl<sub>2</sub>.<sup>183</sup> The thermodynamic instability of the S<sub>*n*</sub>O species has precluded the determination of the crystal structures. X-ray structures have thus far been recorded only for S<sub>7</sub>O<sup>181</sup> and S<sub>8</sub>O.<sup>184,185</sup> The inference of the molecular structures of S<sub>*n*</sub>O (*n* = 6–10) species can be made using Raman spectroscopy, assisted by DFT calculations.<sup>181,186</sup> For example, S<sub>6</sub>O can be crystallized in two forms. Raman spectroscopy indicates that these two forms may represent *endo*- and *exo*-orientations of the S=O bond in the ring (see Fig. 12),<sup>182</sup> though their differing spectral properties may also indicate the presence of two different polymorphs.<sup>181</sup> This has yet to be confirmed by X-ray crystallography. The DFT calculations at G3X(MP2) level of theory<sup>187</sup> have demonstrated that α- and β-S<sub>6</sub>O are the two energetically most favorable isomers (relative Gibbs energies are 1.6 and 0.0 kJ mol<sup>-1</sup>, respectively).<sup>186</sup>

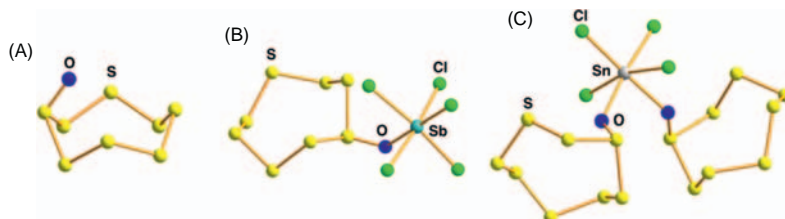
It has been suggested that with the use of an excess of the oxidizing agent CF<sub>3</sub>CO<sub>3</sub>H, the dioxide S<sub>6</sub>O<sub>2</sub> may be formed.<sup>181</sup> The treatment of S<sub>6</sub>O with SbCl<sub>5</sub> affords S<sub>12</sub>O<sub>2</sub>·2SbCl<sub>5</sub>, which consists of a 12-membered sulfur ring coordinated to the two antimony centers *via* the two oxygen atoms.<sup>188</sup> Free S<sub>12</sub>O<sub>2</sub> is not known.



**Fig. 12** The B3LYP/6-31G(2df)-optimized geometries of (A) α-S<sub>6</sub>O (*endo*) and (B) β-S<sub>6</sub>O (*exo*).<sup>186</sup>



**Fig. 13** (A) Crystal structure of  $S_7O$ <sup>189</sup> and (B) the MD DFT optimized structures of the two energetically lowest-lying isomers of  $S_7O_2$ .<sup>191</sup>



**Fig. 14** Molecular structures of (A)  $S_8O$ ,<sup>184,185</sup> (B)  $[SbCl_5(OS_8)]$ ,<sup>192</sup> and (C)  $[SnCl_4(OS_8)_2]$ .<sup>193</sup>

The product from  $S_7O$  shows the expected bond-length alteration [Fig. 13A],<sup>189</sup> which is similar to that observed in  $S_7$ .<sup>70,71</sup>  $S_7O$  can further be oxidized to  $S_7O_2$ . While crystal structure of  $S_7O_2$  is not known, the molecular structure of the isomer has been deduced by Raman spectroscopy [Fig. 13B]<sup>190</sup> and rationalized by use of MD DFT computations.<sup>191</sup>

$S_7O$  is also formed upon oxidation of  $S_8$  with an excess of  $CF_3CO_3H$ , possibly *via* the higher oxide  $S_8O_3$ .<sup>190</sup> The stoichiometric reaction affords  $S_8O$  and this material has been shown to form adducts with antimony pentachloride<sup>192</sup> and tin tetrachloride<sup>193</sup> (Fig. 14).  $[SbCl_5(OS_8)]$  and  $[SnCl_4(OS_8)_2]$  expectedly coordinate to antimony and tin centers through the oxygen atoms.

Cyclic structures have also been postulated for  $S_9O$  and  $S_{10}O$  by Raman spectroscopy, though this has not been confirmed by X-ray work.<sup>181</sup> In terms of reactivity of the oxides, studies beyond the aforementioned acid/base reactions are limited, though the ability of  $S_6O$  to react with alkenes and act as a sulfur source has also been investigated.<sup>183</sup>

As indicated experimentally, DFT computations<sup>186,191,194</sup> have interestingly shown that while sulfur, selenium, and tellurium substitute each other in the ring framework, the formation of exocyclic  $S=O$  bonds is energetically more favorable than substitution of oxygen into the  $S_n$  rings. The relative Gibbs energy difference between the homocyclic sulfur molecule with the exocyclic  $S=O$  bond, which constitutes a global minimum for each molecule, and the heterocyclic sulfur-oxygen ring has been computed to range 24.4–51.8 kJ mol<sup>-1</sup> depending on the ring size.<sup>186</sup>

## 1.21.6 Chalcogen rings as ligands in metal complexes

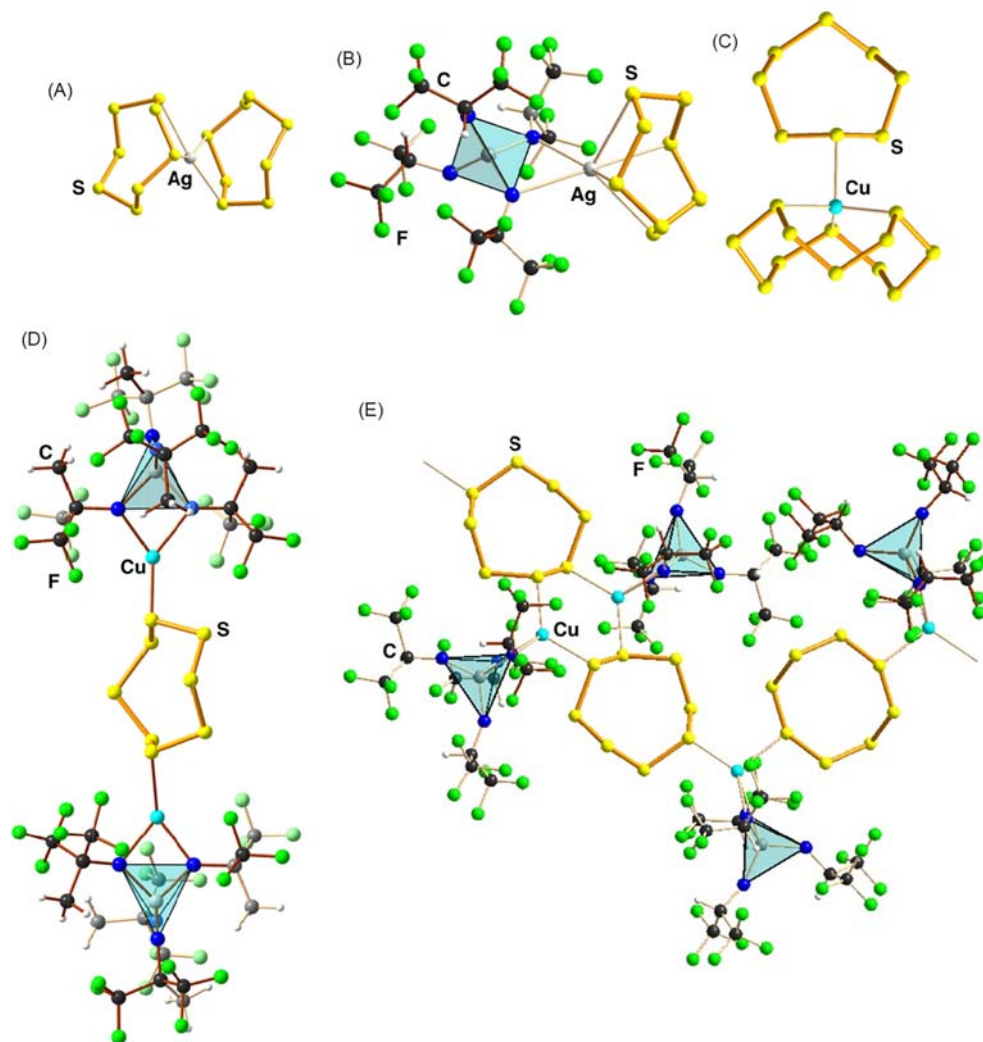
### 1.21.6.1 Sulfur

Catenated polysulfide anions form an abundance of coordination complexes both with main group and transition metals and homocyclic sulfur molecules, in particular  $S_8$ , co-crystallize in various lattices involving different metal complexes (Section 1.21.4). By contrast, ligand chemistry of homocyclic sulfur molecules is very limited comprising only a few structurally characterized complexes. It has been explained to be due to facile redox reactions leading to  $S_n^{2-}$  anions upon the treatment with transition metal cations.<sup>195</sup>

Cyclooctasulfur is a soft Lewis base and accordingly coordinates with some soft transition metals. The reaction of  $Ag[MF_6]$  ( $M = As, Sb$ ) with two equivalents of  $S_8$  in liquid  $SO_2$  affords  $[Ag(S_8)_2][MF_6]$  [Fig. 15A].<sup>196,197</sup> When using  $Ag[Al\{OC(CF_3)_3\}_4]$  or  $Ag[Sb(OTeF_5)_6]$  as starting materials instead of  $Ag[MF_6]$ , the related  $[Ag(S_8)_2]^+$  salts were obtained. The reaction with the  $Ag[Al\{OCH(CF_3)_2\}_4]$  reagent afforded  $[Ag(S_8)][\{Al\{OCH(CF_3)_2\}_4\}]$  [Fig. 15B].<sup>197</sup> The related reactions with  $Cu[Al\{OC(CF_3)_3\}_4]$ ,  $Cu[Al\{OC(CH_3)(CF_3)_2\}_4]$ , and  $Cu[Al\{OCH(CF_3)_2\}_4]$  in  $CH_2Cl_2/CS_2$  afforded  $[Cu(S_{12})(S_8)]^+$  or  $[Cu(S_{12})(Cl_2CH_2)]^+$ ,<sup>198</sup>  $[Cu_2(\mu-1,5-S_8)\{Al\{OC(CH_3)(CF_3)_2\}_4\}_2]$ ,<sup>199</sup> and the 1D-coordination polymer  $[Cu_2(S_8)_2\{Al\{OCH(CF_3)_2\}_4\}_2]_n$ ,<sup>199</sup> respectively [see Figs. 15C–E].

The  $[Ag(S_8)_2]^+$  cation in  $[Ag(S_8)_2][SbF_6]$  shows two short Ag-S contacts in the 1,3-positions with distances of 2.744(1) and 2.792(1) Å.<sup>197</sup> With the two bulkier anions, both  $S_8$  ligands in the two  $[Ag(S_8)_2]^+$  cations have only one short Ag-S contact of 2.68(1)–2.700(5) Å with three other longer but still short distances ranging 2.921(5)–3.354(5) Å. There is some temperature dependence in the structure of the cation.<sup>197</sup> Cu-S bond lengths in  $[Cu(S_{12})(S_8)]^+$  and  $[Cu(S_{12})(Cl_2CH_2)]^+$  range 2.313(2)–2.328(2) Å and 2.277(7)–2.288(4) Å, respectively.<sup>198</sup> The bond parameters of the cyclic  $S_n$  ligands were close to those in corresponding free cyclic sulfur molecules.





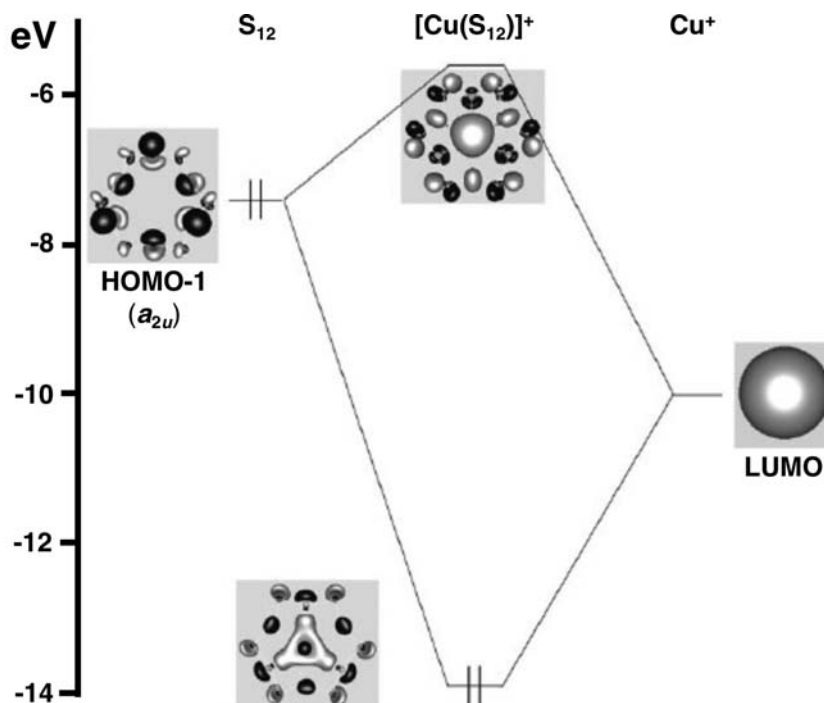
**Fig. 15** The structure of (A)  $[\text{Ag}(\text{S}_8)_2]^+$ ,<sup>196,197</sup> (B)  $[\text{Ag}(\text{S}_8)]\text{Al}[\text{OCH}(\text{CF}_3)_2]_4$ ,<sup>197</sup> (C)  $[\text{Cu}(\text{S}_{12})(\text{S}_8)]^+$ ,<sup>198</sup> (D)  $[\text{Cu}_2(\mu\text{-}1,5\text{-S}_8)\{\text{Al}[\text{O}(\text{C}(\text{H}_3)(\text{CF}_3)_2]_4\}_2]$ ,<sup>199</sup> and (E)  $[\text{Cu}_2(\text{S}_8)_2\{\text{Al}[\text{OCH}(\text{CF}_3)_2]_4\}_2]$ .<sup>199</sup> The  $\text{AlO}_4$  coordination entity is shown as blue-shaded tetrahedra. Any orientational disorder in the sulfur rings is omitted for clarity.

In all these complexes, sulfur rings generally act as polydentate ligands, since the p lone-pair orbitals in each atom can at least in principle be an electron-pair donor. This has been exemplified by the PBE0/TZVPP calculations on the  $[\text{Cu}(\text{S}_{12})]^+$  cation.<sup>199</sup> The main bonding interaction is shown in Fig. 16.

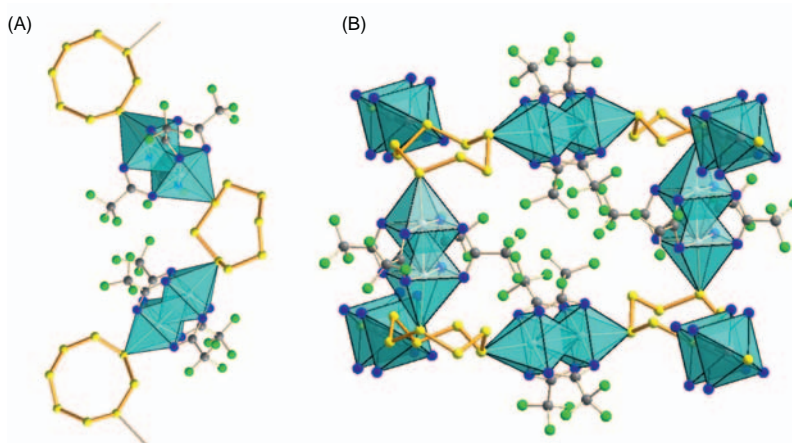
HOMO and HOMO-1 orbitals mainly represent the 3p lone-pair orbitals of sulfur atoms. The HOMO-1 orbital interacts with the 4s orbital of  $\text{Cu}^+$ , which is the LUMO of the interaction. The estimated interaction energy for each three  $\text{S}(3\text{p}^2) \rightarrow \text{Cu}(4\text{s}^0)$  interaction is  $50 \text{ kJ mol}^{-1}$ .<sup>199</sup> It was concluded based on the PBE0/TZVPP studies that  $[\text{Cu}(\text{S}_{12})]^+$  is the most stable complex containing  $\text{Cu}^+$  and cyclic  $\text{S}_n$  both in the gas phase and also in the solid state, when the counter anion is very weakly basic, which mimics the gas-phase conditions.<sup>199</sup> This conclusion finds support from the gas-phase mass-spectrometric study of the reaction of  $\text{Cu}^+$  and  $\text{S}_8$ , which indeed indicated that the main component is  $[\text{Cu}(\text{S}_{12})]^+$  ion.<sup>200</sup>

$[\text{Re}_2\text{X}_2(\text{CO})_6(\text{THF})_2]$  ( $\text{X} = \text{Br}, \text{I}$ ) was found to react with cyclooctasulfur in  $\text{CS}_2$  yielding  $[\text{Re}_2\text{X}_2(\text{CO})_6(\text{S}_8)]$  in 49 % or 61 % yield for  $\text{X} = \text{Br}$  or  $\text{I}$ , respectively.<sup>201</sup> It has been proposed that  $\text{S}_8$  acts as a bridging ligand between two rhenium centers along with the halogenido ligands.<sup>104,201</sup> While no crystal structure has been reported, this inference is based on the elemental analysis, the IR spectrum of the product, and comparison with the known crystal structure of  $[\text{Re}_2\text{I}_2(\text{CO})_6(\text{Se}_7)]$ .<sup>104</sup> The preparation of products and growth of X-ray quality crystals of  $[\text{Rh}_2(\text{O}_2\text{CCF}_3)_4]_n(\text{S}_8)_m$  ( $n:m = 1:1, 3:2$ ) have been carried out by a sublimation and deposition procedure employing dirhodium(II) tetra(trifluoroacetate) in the presence of elemental sulfur vapour.<sup>176</sup>  $\text{S}_8$  acts also in these complexes as a bridging ligand between two dinuclear rhodium clusters (see Fig. 17).





**Fig. 16** The main PBE0/TZVPP bonding interaction in the  $[\text{Cu}(\text{S}_{12})]^+$  cation between the 4s orbital of  $\text{Cu}^+$  and the p orbitals of  $\text{S}_{12}$ .<sup>199</sup> Reproduced with permission from Santiso-Quiñones, G.; Higelin, A.; Schaefer, J.; Brückner, R.; Knapp, C.; Krossing, I., *Chem. Eur. J.* **2009**, *15*, 6663–6677. © 2009 Wiley-VCH Verlag GmbH & Co. KGaA, Weinheim.

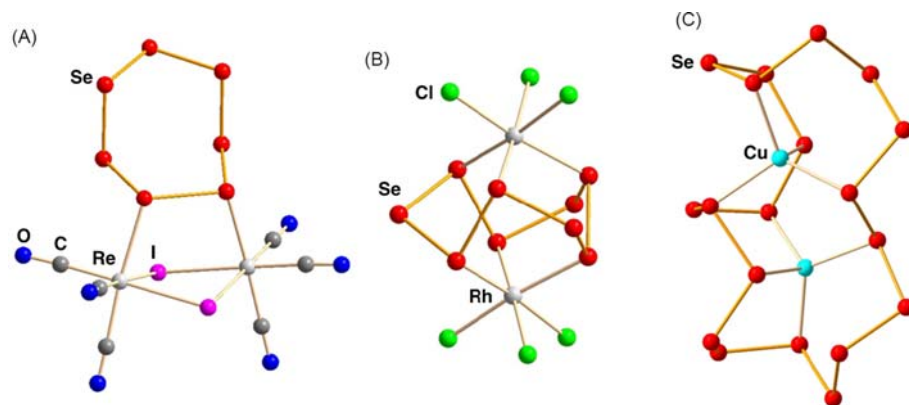


**Fig. 17** Crystal structures of  $[\text{Rh}_2(\text{O}_2\text{CCF}_3)_4]_n(\text{S}_8)_m$ . (A)  $n:m = 1:1$  (B)  $n:m = 3:2$ .<sup>176</sup>

### 1.21.6.2 Selenium

Selenium also forms several complexes, which contain homocyclic molecules as a ligands.<sup>104,202–206</sup> The coordination of  $\text{Se}_6$  ring with  $\text{Ag}^+$  has been demonstrated in  $[(\text{AgI})_2(\text{Se}_6)]^{202}$  and in the formation of isolated  $[\text{Ag}(\text{Se}_6)\text{Ag}]^{2+}$  ions or close packed stacked arrays of  $\text{Se}_6$  molecules with  $\text{Ag}^+$  residing in the octahedral holes depending on the size of the counterion.<sup>206</sup> Solvothermal reactions also lead to solid phases containing  $\text{Se}_6$ <sup>203,207</sup> or  $\text{Se}_8$ <sup>203,208,209</sup> molecules. In addition to X-ray structures these phases have been characterized by vibrational spectroscopy,<sup>203,208</sup> solid state NMR spectroscopy,<sup>207</sup> and thermal analysis.<sup>208</sup>

The homocyclic  $\text{Se}_7$  molecule has been characterized as a bridging ligand in the dinuclear rhenium complex  $[\text{Re}_2(\mu\text{-I})_2(\mu\text{-Se}_7)(\text{CO})_6]$  [Fig. 18A].<sup>104</sup> Despite the coordination to the dinuclear Re center, the molecules shows the four coplanar atoms and the bond length alternation well established for  $\text{S}_7$ .<sup>70,71</sup>  $[\text{Rh}_2(\text{Se}_9)\text{Cl}_6]$  has been prepared from  $\text{RhCl}_3 \cdot 4\text{H}_2\text{O}$  and  $\text{Se}_2\text{Cl}_2$ .<sup>204</sup> It was found to contain the  $\text{Se}_9$  ring as a bridging ligand between two Rh centers [see Fig. 18B]. The heating of metallic iridium,



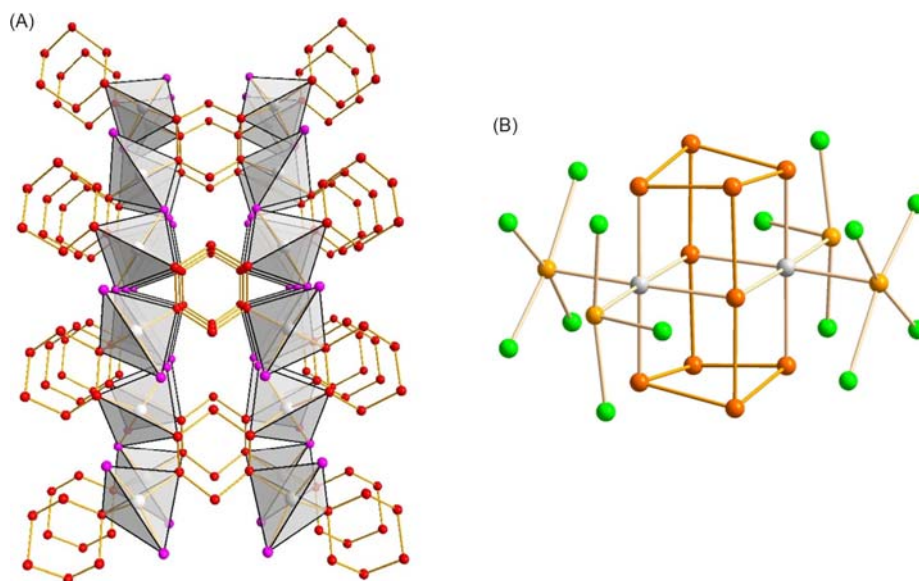
**Fig. 18** Structures of (A)  $[\text{Re}_2(\mu\text{-I})_2(\mu\text{-Se}_7)(\text{CO})_6]$ ,<sup>104</sup> (B)  $[\text{Rh}_2\text{Cl}_6(\text{Se}_9)]$ ,<sup>204</sup> and (C)  $[\text{Cu}_2(\text{Se}_{19})]^{2+}$ .<sup>212</sup>

and selenium tetrachloride or tetrabromide in appropriate molar ratios afforded  $[\text{Ir}_2(\text{Se}_9)\text{X}_6]$  ( $\text{X} = \text{Cl}, \text{Br}$ )<sup>210,211</sup> and  $[\text{Ir}_8\text{Se}_{40}\text{Br}_{40}]$ , respectively.<sup>210</sup> The former complexes are isostructural with  $[\text{Rh}_2(\text{Se}_9)\text{Cl}_6]$  and the latter is a disordered mixed phase containing statistical distribution of  $[(\text{Ir}^{3+})_8(\text{Se}_2^{2-})_6(\text{Se}_4^{2-})_6(\text{Se}_7)_2(\text{Br}^-)_{10}]$  and  $[(\text{Ir}^{3+})_8(\text{Se}_2^{2-})_6(\text{Se}_4^{2-})_6(\text{Se}_6)_2(\text{Br}^-)_{10}]$  clusters (the respective molar ratio is 9:1).

Similarly, homocyclic dodecaselenium molecule was observed as a bridging ligand in the dinuclear  $[\text{Ag}_2(\text{Se}_{12})]^{2+}$  containing a weakly coordinating counteranions  $[\text{Al}\{\text{OC}(\text{CF}_3)_3\}_4]^-$  or  $[\text{AlF}\{\text{OC}(\text{C}_5\text{F}_{10})(\text{C}_6\text{F}_5)\}_3]^-$ .<sup>205</sup> The  $\text{Se}_{12}$  molecule shows a similar conformation and analogous bond parameters to  $\text{S}_{12}$ .<sup>56</sup> A  $\text{Se}_{19}$  homocycle was isolated and characterized as a chelating and bridging ligand involving two copper(I) centers.<sup>212</sup> The ESI-MS studies and DFT calculations at PBE0/def2-TZVPP level of theory facilitated the discussion of the relative stabilities of homocyclic selenium molecules of different ring sizes.

### 1.21.6.3 Tellurium

The  $\text{Te}_6$  ring has been stabilized as  $[(\text{AgI})_2(\text{Te}_6)]$ , which is isomorphic with  $[(\text{AgI})_2(\text{Se}_6)]$  [see Fig. 19A],<sup>202</sup> and  $[\text{Re}_6\text{Te}_{10}\text{Cl}_6(\text{Te}_6)]$ .<sup>213</sup> Despite coordination to the metal they both show bond parameters that are expected for the isolated  $\text{Te}_6$  ring (bond lengths 2.729–2.760 Å<sup>202</sup> and 2.762–2.900 Å<sup>213</sup>; bond angles 95.9–100.2°<sup>202</sup> and 92.2–100.2°<sup>213</sup>; torsion angles 78.5–82.0°<sup>202</sup> and 75.2–87.0°<sup>213</sup>).



**Fig. 19** (A) The  $\text{Te}_6$  molecule stabilized as  $[(\text{AgI})_2(\text{Te}_6)]$ ,<sup>202</sup>  $[(\text{AgI})_2(\text{Se}_6)]$  is isomorphic with the tellurium analog. (B) The novel uncharged  $\text{Te}_{10}$  cage stabilized as  $[(\text{Ir}(\text{TeCl}_4)(\text{TeCl}_3)_2)(\text{Te}_{10})]$ .<sup>214</sup> Tellurium atoms in the  $\text{Te}_{10}$  molecule are depicted in orange, those in the  $\text{TeCl}_4$  and  $\text{TeCl}_3$  fragments in light orange, chlorine atoms in green, and iridium in light gray.

The reaction of elemental tellurium and iridium, and tellurium tetrachloride in a sealed, evacuated ampoule at 250 °C for seven days afforded black crystals of  $[\{\text{Ir}(\text{TeCl}_4)(\text{TeCl}_3)\}_2(\text{Te}_{10})]$  containing a novel type of electrically neutral tellurium cage molecule  $\text{Te}_{10}$  [see Fig. 19B].<sup>214</sup> The molecule consists of two nearly linear 3c-4e bonding arrangements bridging the two four-membered rings. The ten-atomic cage is considered to be formally uncharged  $(\text{Te}^{+0.50})_4(\text{Te}^0)_4(\text{Te}^-)_2$ .<sup>214</sup> The  $\text{Te}_{10}$  unit is also a common motif in many tellurium-rich compounds containing electron-rich transition metals.<sup>215</sup>

The heating of ruthenium, indium, tellurium, and tellurium tetrachloride or ruthenium, tellurium, and tellurium tetrachloride at 300 °C afforded shiny black  $[\text{Ru}(\text{Te}_9)][\text{InCl}_4]_2$  and  $[\text{Ru}(\text{Te}_8)]\text{Cl}_2$ , respectively.<sup>216</sup> A similar reaction involving rhodium or iridium, tellurium, and tellurium tetrahalogenides yielded  $[\text{M}(\text{Te}_6)]\text{X}_3$  ( $\text{M} = \text{Rh}, \text{Ir}; \text{X} = \text{Cl}, \text{Br}, \text{I}$ ), or, in case of ruthenium,  $[\text{Ru}_2(\text{Te}_6)](-\text{TeBr}_3)_4(\text{TeBr}_2)_2$ .<sup>217</sup> All complexes are one-dimensional coordination polymers with the uncharged tellurium rings acting as bridging bis-tridentate ligands.

## 1.21.7 Polyatomic chalcogen cations

### 1.21.7.1 General

It has been known since late 18<sup>th</sup> and beginning of 19<sup>th</sup> century that elemental sulfur, selenium and tellurium can be dissolved in oleum with the formation of intensively colored solutions. With the advent of modern instrumental techniques it is now well established that all three chalcogen elements form homopolyatomic cations with weakly coordinating anions in such strongly oxidizing media.<sup>4-6,8-11</sup> In addition to oleum, the synthetic routes involve super acids, acidic melts, or  $\text{SO}_2$  and related aprotic solvents. Suitable oxidizing agents comprise strong main group Lewis acids like  $\text{AlCl}_3$ ,  $\text{AsF}_5$ ,  $\text{SbCl}_5$ , and  $\text{BiCl}_5$  and transition metal halides such as  $\text{MF}_6$  ( $\text{M} = \text{W}, \text{Re}, \text{Os}, \text{Ir}, \text{Pt}$ ),  $\text{MCl}_6$  ( $\text{M} = \text{V}, \text{W}, \text{Zr}, \text{Hf}, \text{Nb}, \text{Ta}, \text{Re}$ ),  $\text{VOCl}_3$ ,  $\text{NbOCl}_3$ , and  $\text{WOCl}_4$ . The use of chemical vapor transport methods,<sup>9</sup> ionic liquids,<sup>218-220</sup> and electrochemical methods<sup>221</sup> have been suggested for the syntheses of the cations. The known homopolynuclear selenium and tellurium cations are summarized in Table 5.

### 1.21.7.2 $(\text{E}_4)^{2+}$ ( $\text{E} = \text{S}, \text{Se}, \text{Te}$ )

$(\text{S}_4)^{2+}$ ,  $(\text{Se}_4)^{2+}$ , and  $(\text{Te}_4)^{2+}$  are  $6\pi$  electron square-planar dications that can be described as mostly aromatic with the formal bond order of 1.25.<sup>4-6,8-11,222</sup> However, all three cations have been found to show significant singlet diradical character in their electronic structures.<sup>223</sup> The diradical character increases in the order  $(\text{S}_4)^{2+} < (\text{Se}_4)^{2+} < (\text{Te}_4)^{2+}$ . The diradical nature is manifested in the computational prediction of different molecular properties. This is well exemplified by comparing the theoretical computation of <sup>77</sup>Se NMR chemical shifts for different  $(\text{Se}_n\text{S}_{4-n})^{2+}$  ( $n = 1-4$ ) cations<sup>223</sup> for which experimental spectroscopic data and the tentative assignment of the resonances to different species have been reported.<sup>224</sup> Multiconfigurational ab initio methods or pure density functionals are needed to compute the chemical shifts with sufficient accuracy to enable the full verification of the assignment (see Fig. 20).<sup>223</sup>

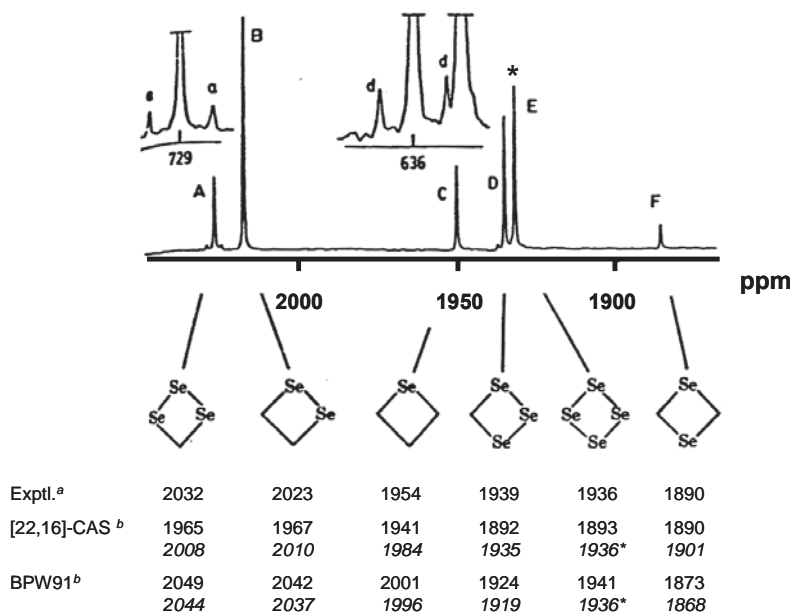
Numerous structures containing different counterions have been determined by X-ray crystallography.<sup>4-6,8-11</sup> The bond lengths in each cation depend on the nature of the counterions. This is exemplified by  $(\text{Te}_4)^{2+}$ , the bond length of which spans a range of 2.660–2.695 Å. The halogen atoms of the counterions bridge the Te-Te edges of the square-planar cation, as illustrated in Fig. 21 by  $(\text{Te}_4)[\text{WCl}_6]_2$ .<sup>225</sup> The bond lengthening is caused by the transfer of electron density from the halogen into the  $\sigma^*$  orbital of the cation, and therefore the more basic anions give rise to longer bonds.<sup>11</sup>

The  $(\text{Te}_4)^{2+}$  polycation in  $(\text{Te}_4)[\text{Ga}_2\text{Cl}_7]_2$  and  $(\text{Te}_4)[\text{Al}_2\text{Cl}_7]_2$  molecular crystals has been shown to be a smart near-infrared emitter with characteristic emission peaks at 1252 and 1258 nm, respectively, resulting from the intrinsic electronic transitions of  $(\text{Te}_4)^{2+}$ .<sup>226</sup> Both emissions strongly depend on the excitation wavelengths, which has been inferred to be due to the co-existence of other Te-related optically active centers.

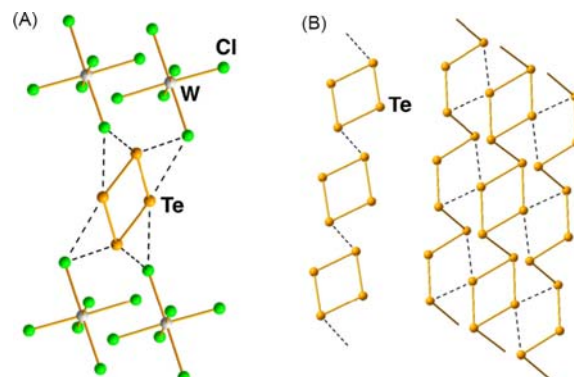
Unlike  $(\text{S}_4)^{2+}$  and  $(\text{Se}_4)^{2+}$ , the  $(\text{Te}_4)^{2+}$  cation shows propensity for extended structures. In  $(\text{Te}_4)(\text{Te}_{10})[\text{Bi}_4\text{Cl}_{16}]$ ,<sup>227</sup> the four-membered rings are linked together through 1,3-positions [see Fig. 21]. The formal  $(\text{Te}_{10})^{2+}$  cation in the structure can be conceived to consist of another stack of polymeric four-membered rings surrounded by two polymeric tellurium helical chains.

**Table 5** Homo- and heteropolynuclear sulfur, selenium, and tellurium cations for which the solid-state structures are known (see refs. 4–6, 8–11 and references therein).

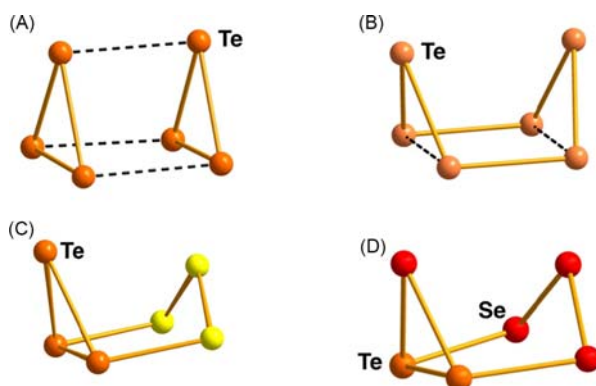
Chalcogen framework	Homopolychalcogen cations	Heteropolychalcogen cations
4	$(\text{S}_4)^{2+}, (\text{Se}_4)^{2+}, (\text{Te}_4)^{2+}, (\text{Te}_4)_n^{2n+}$	$(\text{Se}_x\text{S}_{4-x})^{2+}, (\text{Te}_2\text{S}_2)^{2+}$
6	$(\text{Te}_6)^{2+}, (\text{Te}_6)^{4+}$	$(\text{Te}_3\text{S}_3)^{2+}, (\text{Te}_2\text{Se}_4)^{2+}$
7	$(\text{Te}_7)^{2+}$	$(\text{Te}_3\text{Se}_4)^{2+}$
8	$(\text{S}_8)^{2+}, (\text{Se}_8)^{2+}, (\text{Te}_8)^{2+}, (\text{Te}_8)^{4+}$	$(\text{Te}_2\text{Se}_6)^{2+}, (\text{Te}_x\text{Se}_{8-x})^{2+}$
10	$(\text{Se}_{10})^{2+}, (\text{Te}_{10})_n^{2n+}$	$(\text{Te}_2\text{Se}_8)^{2+}$
17–19	$(\text{S}_{19})^{2+}, (\text{Se}_{17})^{2+}$	
$\infty$	$(\text{Te}_7)_n^{2n+}, (\text{Te}_8)_n^{2n+}$	



**Fig. 20** The  $^{77}\text{Se}$  NMR spectrum of the mixture of  $(\text{Se}_n\text{S}_{4-n})^{2+}$  ions in  $\text{SO}_2$ .<sup>224</sup> <sup>a</sup> The assignment of experimental resonances have tentatively been made by Collins et al.<sup>224</sup> <sup>b</sup> The [22,16]-CAS/cc-pVTZ and BPW91/cc-pVTZ calculations of the  $^{77}\text{Se}$  chemical shifts are according to Tuononen et al.<sup>223</sup> Two sets of chemical shifts are reported for both methods. The upper line in each case represents values referenced with respect to  $\text{Me}_2\text{Se}$ . The lower line of data shown in italics have been referenced with respect to  $(\text{Se}_4)^{2+}$  (marked with \*). All chemical shifts are reported relative to  $\text{Me}_2\text{Se}$ . Reprinted with permission from Collins, M. J.; Gillespie, R. J.; Sawyer, J. F.; Schrobilgen, G. J., *Inorg. Chem.* **1986**, *25*, 2053–2057. Copyright 1986 American Chemical Society.



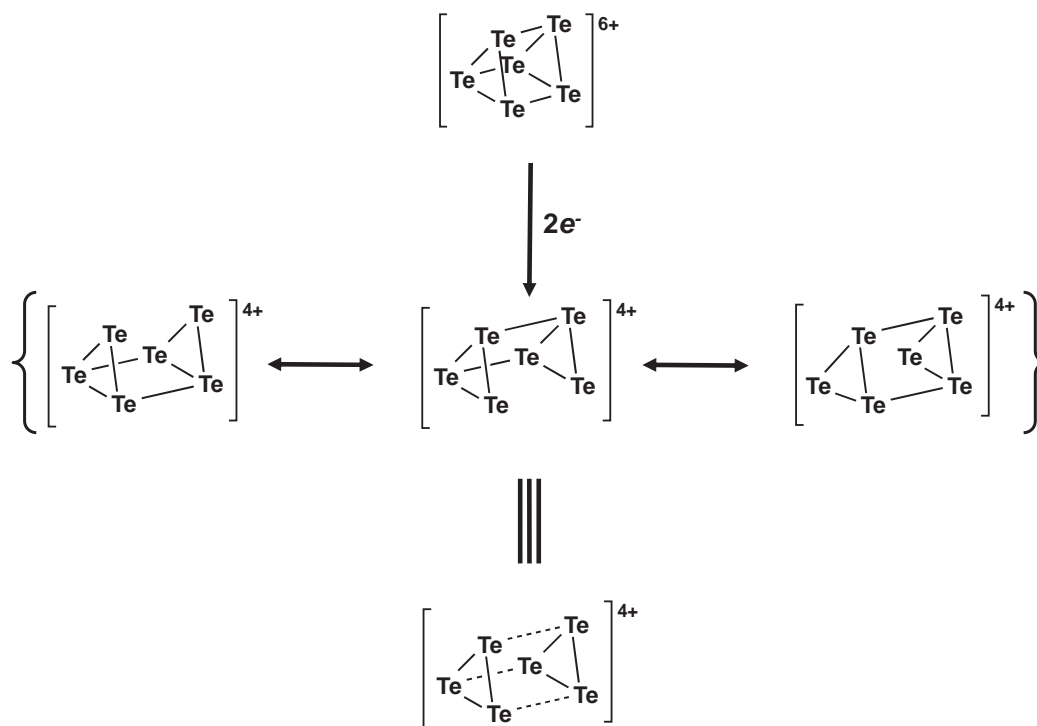
**Fig. 21** (A) The cation-anion interactions in  $(\text{Te}_4)[\text{WCl}_6]_2$ .<sup>225</sup> (B) The structure of the cation in  $(\text{Te}_4)(\text{Te}_{10})[\text{Bi}_4\text{Cl}_{16}]$ .<sup>227</sup> Interatomic contacts  $> 3 \text{ \AA}$  have been shown as black dashed lines.



**Fig. 22** (A) The structure of the  $(\text{Te}_6)^{4+}$  cation.<sup>228,229</sup> (B) The structure of  $(\text{Te}_6)^{2+}$ .<sup>230,231</sup> (C) The structure of  $(\text{Te}_3\text{S}_3)^{2+}$  cation.<sup>232</sup> (D) The structure of  $(\text{Te}_2\text{Se}_4)^{2+}$  cation.<sup>232,233</sup> Tellurium atoms are depicted in orange, selenium in red, and sulfur in yellow.

1.21.7.3  $(E_6)^{n+}$  ( $n = 2, 4$ )

There are four known hexachalcogen cations:  $(Te_6)^{4+}$ ,<sup>228,229</sup>  $(Te_6)^{2+}$ ,<sup>230,231</sup>  $(Te_3S_3)^{2+}$ ,<sup>232</sup> and  $(Te_2Se_4)^{2+}$ .<sup>232,233</sup> Their structures are shown in Fig. 22. They cannot be described in terms of electron precise Lewis structures. The structural relationships, however, can be rationalized by applying the electron accounting principles presented by Gillespie.<sup>234</sup>



**Scheme 2** The addition of two electrons to the classical  $30 e^-$  cluster  $(Te_6)^{6+}$  to form  $(Te_6)^{4+}$ , a  $32 e^-$  elongated trigonal prism.

$(Te_6)^{6+}$  is a hypothetical cation containing 30 valence electrons. It fulfills the relationship  $e = 5n$  in which  $n$  is the number of atoms and  $e$  is the number of valence electrons. According to Gillespie,<sup>234</sup> this species is therefore an electron-precise classical cluster and appears as a trigonal prism in which each framework atom is connected to three other framework atoms with single bonds and in addition contains one lone pair of electrons.

Upon addition of two electrons into  $(Te_6)^{6+}$ , a 32-electron cation,  $(Te_6)^{4+}$  is formed. It is an elongated trigonal prism [Fig. 22A] the structure of which has been established experimentally by X-ray diffraction a long time ago.<sup>228,229</sup> The bonds at the triangular face show approximately single bond lengths (2.662–2.679 Å), but those at the rectangular face are significantly longer (3.062–3.172 Å). According to the electron accounting,<sup>234</sup> it is expected that one bond in  $(Te_6)^{6+}$  would be broken by the addition of two electrons. The observed elongated trigonal prism can be rationalized according to the following resonance (Scheme 2):

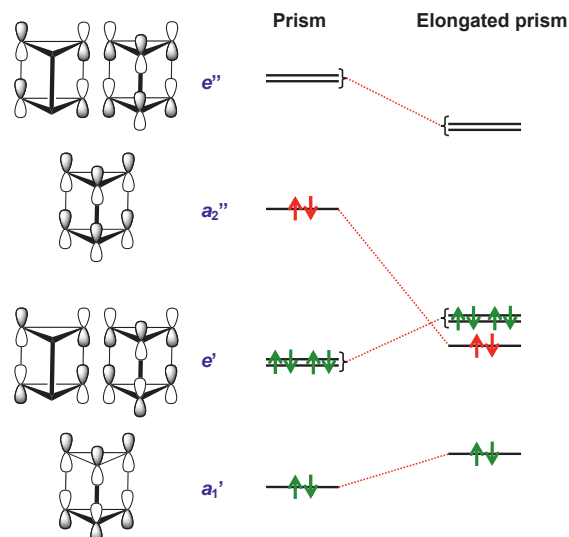
These observations are in accordance with the suggestion that the characteristic features in the bonding of homopolyatomic chalcogen cations involve the delocalization of the positive charge over all atoms, the presence of  $np_\pi - np_\pi$  bonds ( $n > 3$ ) and long intracationic transannular interactions, as well as the  $4c-2e$  or  $6c-2e$  bonds.<sup>235</sup> DFT calculations show that the Te–Te bond lengths in  $(Te_6)^{4+}$  can be explained by the interaction of two  $(Te_3)^{2+}$  fragments through  $6c-2e \pi^* - \pi^*$  bonds, as depicted in Fig. 23.<sup>236</sup> The elongated prism is energetically favored because of the lowering of energy of the occupied  $a_2''$  orbital, which is antibonding with respect to the three bonds parallel to the  $C_3$  axis.

$(E_6)^{2+}$  is a 34 electron cation. The addition of two electron pairs into the classic  $(E_6)^{6+}$  cage should lead to the cleavage of two bonds.<sup>234</sup> The crystal structure determinations of  $(Te_6)^{2+}$ <sup>230,231</sup> show, however, that one bond is delocalized between two different triangular faces [the relevant Te–Te distances are 3.209–3.382 Å<sup>230,231</sup>] and only one bond is completely missing [see Fig. 22B]. The DFT calculations on the MO interactions again support this bonding description.<sup>237</sup> It is only in the case of hybrid  $(Te_3S_3)^{2+}$ <sup>232</sup> and  $(Te_2Se_4)^{2+}$ <sup>233</sup> cations that the expected,<sup>234</sup> more open structure is seen, as shown in Fig. 22C and 22D, respectively.

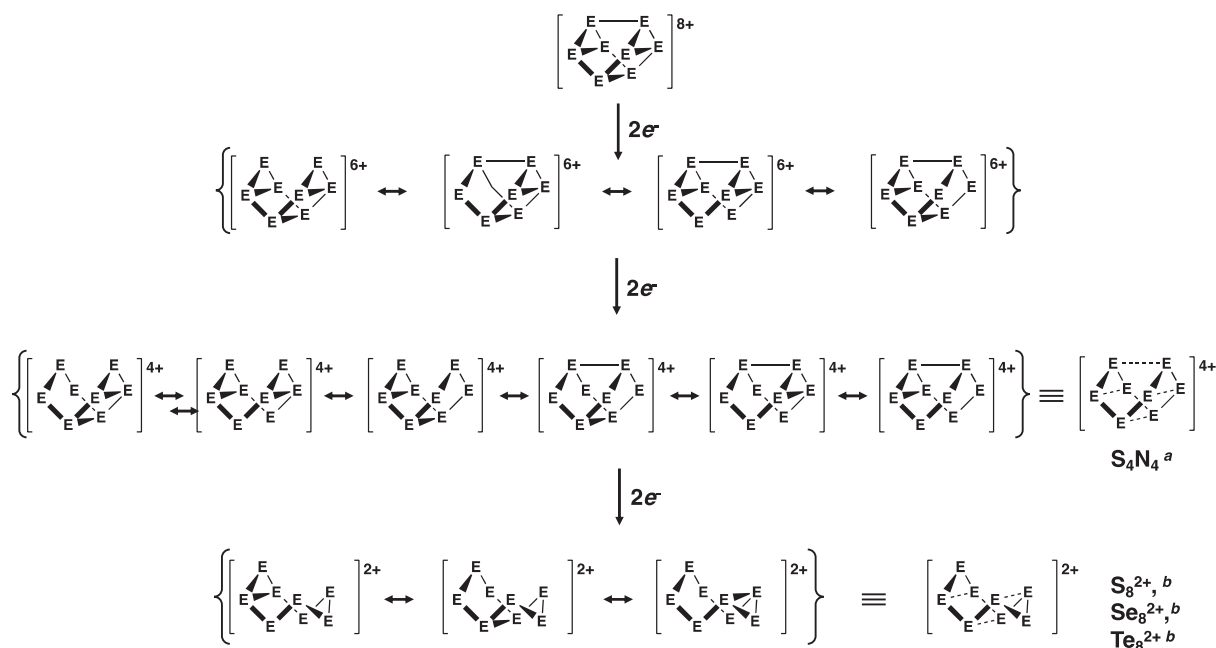
1.21.7.4  $(E_8)^{n+}$  ( $n = 2, 4$ )

$(S_8)^{2+}$ ,  $(Se_8)^{2+}$ , and  $(Te_8)^{2+}$  are mutually isostructural.<sup>4–6,8–11</sup> The solid-state structures show three weak transannular interactions, which can be derived from the classical 40 electron  $(E_8)^{8+}$  cuneane cage,<sup>234</sup> as shown in Scheme 3. Deductions from the DFT study





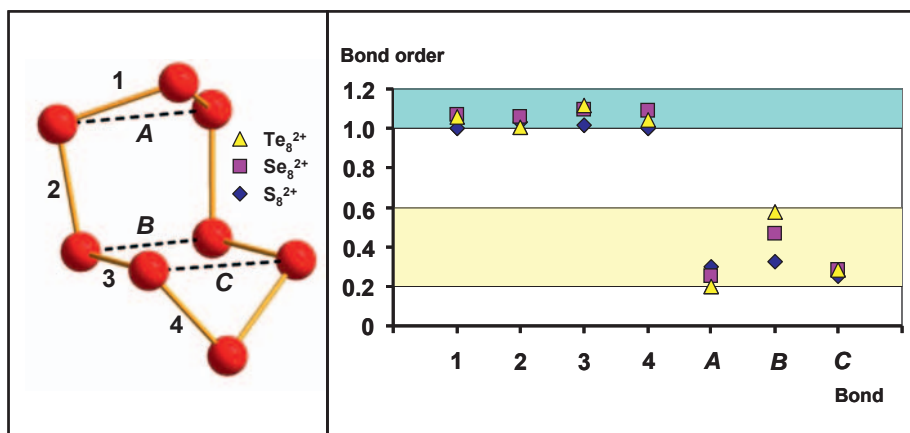
**Fig. 23** BP88/TZ(d,p) molecular orbitals of the intertriangular  $\sigma$ -bonding and antibonding orbitals of the  $(\text{Te}_6)^{4+}$  prism.<sup>236</sup> The electrons depicted in green represent those in the highest occupied molecular orbitals of the electron-precise  $(\text{Te}_6)^{6+}$  prism (30 electrons). The two extra electrons (depicted in red) to form the observed  $(\text{Te}_6)^{4+}$  cation occupy the  $a_2''$  orbital, which is stabilized by the elongation of the prism.



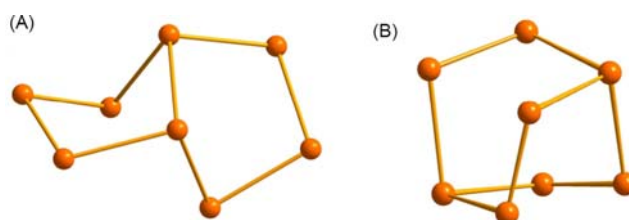
**Scheme 3** Structural relationships between the  $(\text{E}_8)^{8+}$  (40 valence electrons) classical cage and other species derived from it by successive addition of electrons. Illustrative examples: <sup>a</sup> Ref. 240. <sup>b</sup> Refs. 7–11.

of the structures, bonding, and energetics of different  $(\text{E}_8)^{2+}$  ( $\text{E} = \text{S}, \text{Se}, \text{Te}$ ) cations<sup>237</sup> are consistent with the concept of three weak transannular interactions and the observed slight bond length alternation, as shown in Fig. 24. It can be seen from the figure that while the orders of the endocyclic bonds show very little variation around the bond order of one, the strength of the 1,5-transannular interaction increases in the order  $(\text{S}_8)^{2+} < (\text{Se}_8)^{2+} < (\text{Te}_8)^{2+}$  (see interaction marked as *B* in Fig. 24).<sup>4–6,8–11</sup> An even more pronounced bicyclic nature is found in the  $(\text{Te}_8)^{2+}$  cation in  $(\text{Te}_8)[\text{WCl}_6]_2$ <sup>238</sup> [see Fig. 25A]. The transannular bond is only 2.993 Å and approaches the single bond length. The  $(\text{Te}_8)^{2+}$  cation has also been found to show a bicyclo[2,2,2]octane structure<sup>11</sup> similar to that observed in  $(\text{Te}_2\text{Se}_6)^{2+}$ <sup>239</sup> [see Fig. 25B].

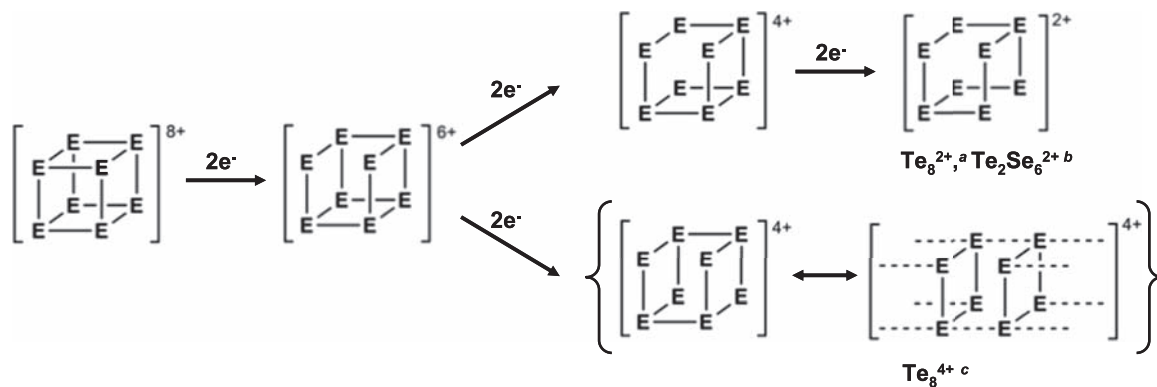
While the structure of the  $(\text{Te}_8)^{2+}$  in  $(\text{Te}_8)[\text{WCl}_6]_2$  can also be derived from the classic 40 electron cuneane cage by adding six electrons and breaking three bonds (see Scheme 3), that in  $(\text{Te}_6)(\text{Te}_8)[\text{WCl}_6]_4$  is derived from the cube that is another classic 40 electron cage (Scheme 4).<sup>234</sup> The  $(\text{Te}_8)^{4+}$  cation in  $(\text{Te}_8)[\text{VOCl}_4]_2$ <sup>242</sup> is another  $(\text{Te}_8)^{n+}$  cation, the structure of which is also based



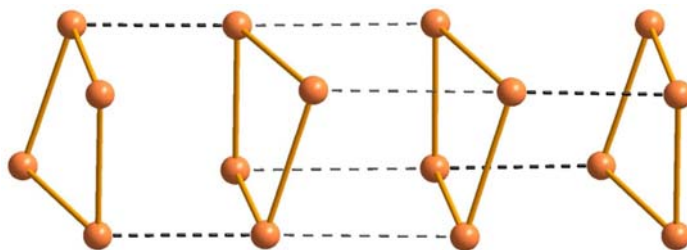
**Fig. 24** Pauling bond orders<sup>142</sup> based on structural data of  $(E_8)^{2+}$  ( $E = S, ^{236}Se, ^{229}Te^{241}$ ).



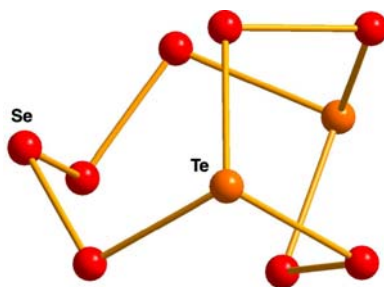
**Fig. 25** The  $(Te_8)^{2+}$  cation in (A)  $(Te_8)[WCl_6]_2$ <sup>238</sup> and (B) the  $(Te_8)^{2+}$  cation in  $(Te_6)(Te_8)[WCl_6]_4$ .<sup>11</sup>



**Scheme 4** Structural relationships between the classic 40 electron cube and cations derived from it. <sup>a</sup> Ref. 11. <sup>b</sup> Ref. 239. <sup>c</sup> Ref. 242.



**Fig. 26** Structure of the  $(Te_8)^{4+}$  cation in  $(Te_8)[VOCl_4]_2$ .<sup>242</sup>

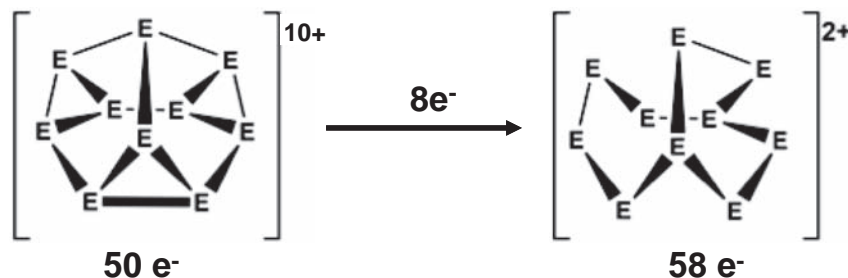


**Fig. 27** The structure of the  $(\text{Te}_2\text{Se}_8)^{2+}$  in  $(\text{Te}_2\text{Se}_8)[\text{AsF}_6]_2\text{SO}_2$ .<sup>248</sup>

on the cube. It can be considered as a dimer of two  $(\text{Te}_4)^{2+}$  cations. In the solid state this  $(\text{Te}_4)_2^{2+}$  dimer shows significant association (see Fig. 26).

The bond lengths of the long bonds within the  $(\text{Te}_4)^{4+}$  dimer are 3.010 Å and the contacts between the dimers are 3.594 Å.<sup>242</sup> Evoking the Pauling equation for the bond orders,<sup>101</sup> it can be concluded that the sum of the bond orders of the weak bonds for one  $(\text{Te}_8)^{4+}$  unit is almost exactly 2 in accordance with the expectations for the 44 electron cage.<sup>234</sup> These weak bonds have been explained in terms of  $5p^2 \rightarrow \sigma^*$  interactions.<sup>222</sup>

The  $(\text{Se}_8)^{2+}$  cation has been characterized by <sup>77</sup>Se NMR spectroscopy in  $\text{SO}_2$  solution using both natural-abundance selenium and <sup>77</sup>Se-isotope enriched selenium in the preparation of the sample and provided for a full <sup>77</sup>Se-<sup>77</sup>Se coupling information.<sup>243,244</sup> The ZORA NMR calculations of the <sup>77</sup>Se chemical shifts using the rPBE GGA functional and a large QZAP basis set and involving explicit solvent molecules<sup>244</sup> agreed with the observed spectroscopic data but led to a slightly modified assignment of the resonances.



**Scheme 5** Derivation of the structure of  $(\text{E}_{10})^{2+}$  from a classical  $(\text{E}_{10})^{10+}$  cluster.

### 1.21.7.5 $(\text{E}_n)^{2+}$ ( $n > 8$ )

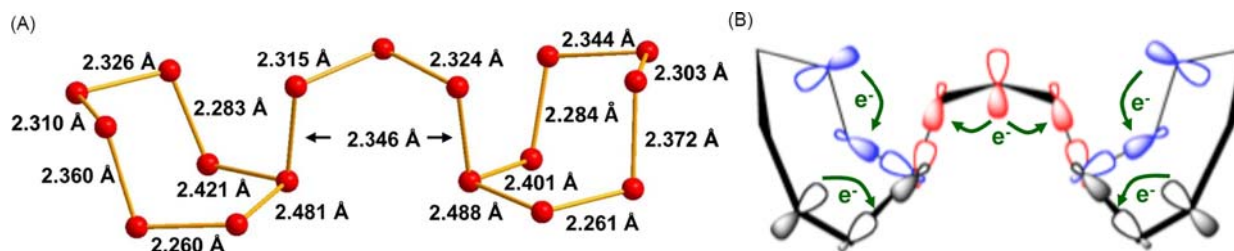
Both selenium and tellurium show a number of higher nuclearity polyatomic cations. The crystal structure of  $(\text{Se}_{10})^{2+}$  has been elucidated from several salts.<sup>245–247</sup> The cation is isostructural with  $(\text{Te}_2\text{Se}_8)^{2+}$ ,<sup>239,248</sup> [see Fig. 27].

The structure of this 58-electron cation can be derived from one of the alternative classical ten-atom 50 electron cages (Scheme 5).<sup>234</sup>

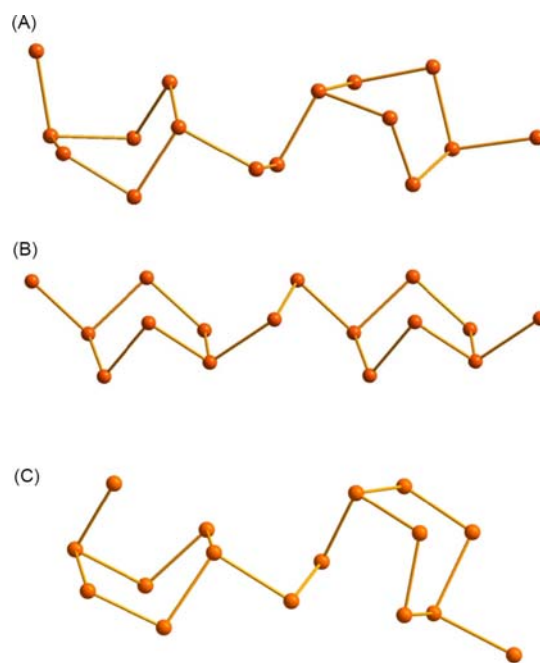
The structure and geometry of  $(\text{Se}_{10})^{2+}$  has been explored by DFT methods involving the PBE0 functional and the cc-pVTZ basis set.<sup>244</sup> The experimental bond parameters could be reproduced well by the computations. The structural features have been discussed in terms of  $4p^2 \rightarrow \sigma^*$  and  $4p^2 \rightarrow 4p^2$  interactions within the cation.<sup>5,7–10</sup>

It has been shown by <sup>77</sup>Se NMR spectroscopy that in  $\text{SO}_2$  solution  $(\text{Se}_{10})^{2+}$  is fluxional undergoing a complicated exchange process even at low temperature.<sup>243</sup> Consequently, only two resonances are observed even using the <sup>77</sup>Se-enriched selenium with relative intensities varying as a function of temperature. It was also concluded on the basis of significant differences between the electronic spectra in the solid  $(\text{Se}_{10})[\text{AsF}_6]_2$  and that recorded for the dissolved material that  $(\text{Se}_{10})^{2+}$  does not retain its solid state structure in solution.<sup>243</sup>

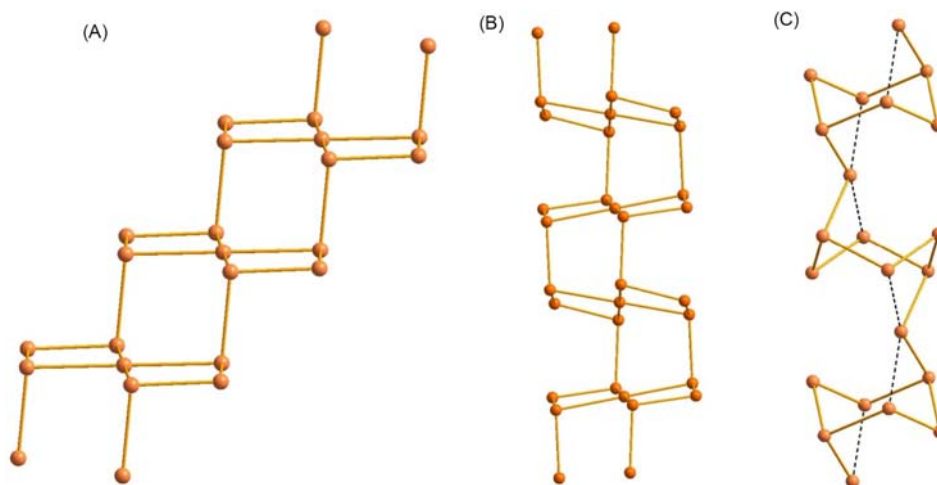
The largest known discrete selenium cation,  $(\text{Se}_{17})^{2+}$ ,<sup>249,250</sup> consists of two seven-membered rings with similar conformations as in  $\text{S}_7$ .<sup>70,71</sup> The ring fragments are linked together by a  $\text{Se}_3$  bridge [see Fig. 28A]. There is expectedly marked bond length alternation in this dication. The bonds from the two three-coordinate selenium atoms are long and the adjacent bonds are short. Normal single bond lengths are observed only for bonds further removed from the three-coordinate selenium. This bond length alternation can again be explained by charge delocalization through the  $4p^2 \rightarrow \sigma^*$  interactions involving the p lone pair of electrons of the selenium atoms bound to the three-coordinate selenium. [see Fig. 28B].



**Fig. 28** (A) The structure of the  $(\text{Se}_{17})^{2+}$  cation in  $(\text{Se}_{17})[\text{WCl}_6]_2$  indicating the Se–Se bond lengths.<sup>249,250</sup> (B)  $4p^2 \rightarrow \sigma^*$  interactions rationalizing the bond length alternations (for more details, see refs. 6, 8–10).



**Fig. 29** The structures of  $(\text{Te}_8)^{2+}$ , in (A)  $(\text{Te}_8)[\text{Bi}_4\text{Cl}_{14}]$ ,<sup>253</sup> (B)  $(\text{Te}_8)[\text{U}_2\text{Br}_{10}]$ ,<sup>254</sup> and (C)  $(\text{Te}_8)_2[\text{Ta}_4\text{O}_4\text{Cl}_{16}]$ .<sup>255</sup>



**Fig. 30** The structure of  $(\text{Te}_7)^{2+}$  in (A)  $(\text{Te}_7)[\text{Be}_2\text{Cl}_6]$ ,<sup>227</sup> (B)  $(\text{Te}_7)[\text{NbOCl}_4]\text{Cl}$ ,<sup>256</sup> and (C)  $(\text{Te}_7)[\text{AsF}_6]_2$ .<sup>257</sup>

The  $(\text{S}_{19})^{2+}$  cation in  $(\text{S}_{19})[\text{MF}_6]_2$ <sup>251,252</sup> shows a similar structure. Two homocyclic seven-membered rings are connected by the  $\text{S}_5$  fragment. The bonding scheme is related to that in  $\text{Se}_7^{2+}$  shown in Fig. 28.

**Table 6** Cyclic polychalcogen-halogen cations that have been structurally characterized by X-ray diffraction.

	Cl	Br	I
S		(S <sub>7</sub> Br) <sup>+</sup>	(S <sub>7</sub> I) <sup>+</sup>
Se	(Se <sub>9</sub> Cl) <sup>+</sup>		(Se <sub>6</sub> I) <sub>n</sub> <sup>n+</sup> , (Se <sub>6</sub> I <sub>2</sub> ) <sup>2+</sup>
Te	(Te <sub>15</sub> Cl <sub>4</sub> ) <sub>n</sub> <sup>2n+</sup>	(Te <sub>15</sub> Br <sub>4</sub> ) <sub>n</sub> <sup>2n+</sup>	(Te <sub>6</sub> I <sub>2</sub> ) <sup>2+</sup>

Two polymeric forms of (Te<sub>8</sub>)<sub>n</sub><sup>2+</sup> have been synthesized and characterized. They both contain six-membered rings in a boat conformation that are linked together by Te<sub>2</sub> fragments in 1,4-positions.<sup>253–255</sup> The main difference between the two isomers is the relative orientations of adjacent ring fragments [see Fig. 29].

Other polymeric homonuclear tellurium cations have also been recently prepared, as shown in Fig. 30. They are all based on repeating (Te<sub>7</sub>)<sub>n</sub><sup>2+</sup> units.

## 1.21.8 Cyclic chalcogen-halogen cations

### 1.21.8.1 General

Recent decades have seen rapid development in the chemistry of sulfur-halogen and selenium-halogen cations<sup>258–260</sup> with much slower progress in that of tellurium-halogen cations. In particular, selenium-iodine cations have grown from non-existence to show a rich variety of species.<sup>244,258</sup> The cyclic polychalcogen-halogen cations for which the structure in the solid state is known are listed in Table 6. Only those cations, which have chalcogen-chalcogen bonds, are shown.

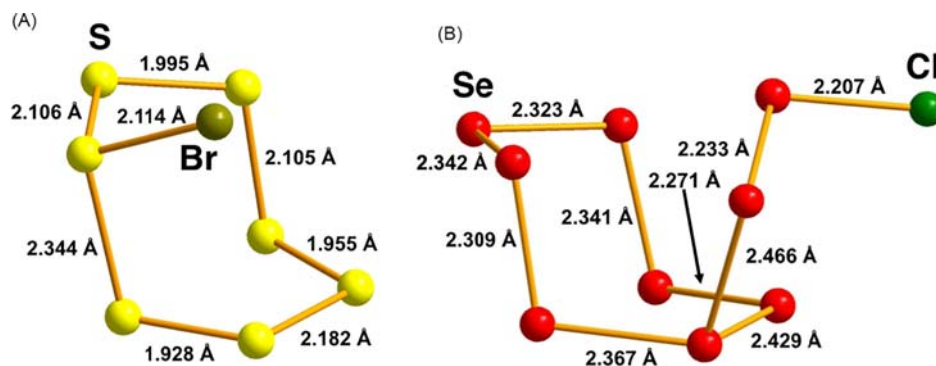
The cyclic chalcogen-halogen cations may generally be prepared by the reaction of elemental chalcogen and halogen in appropriate molar ratios to AsF<sub>5</sub> or other suitable strong Lewis acids in liquid SO<sub>2</sub>.<sup>20,21,244,258,259</sup> In some cases, other synthetic routes have also been successfully realized. (Se<sub>9</sub>Cl)[SbCl<sub>6</sub>] is prepared by the reaction of elemental selenium with (NO)[SbCl<sub>6</sub>] in SO<sub>2</sub>,<sup>260</sup> and (Te<sub>15</sub>X<sub>4</sub>)<sub>n</sub>[MOX<sub>4</sub>]<sub>2n</sub> (M = Mo, W; X = Cl, Br) by the reactions of Te<sub>2</sub>Br with MoOBr<sub>3</sub>, TeCl<sub>4</sub> with MoNCl<sub>3</sub>/MoNCl<sub>2</sub>/MoOCl<sub>3</sub>, and Te with WBr<sub>5</sub>/WOBr.<sup>261</sup>

### 1.21.8.2 Sulfur-bromine and selenium-chlorine cations

The structure of (S<sub>7</sub>Br)<sup>+</sup> is shown in Fig. 31A and that of (Se<sub>9</sub>Cl)<sup>+</sup> in Fig. 31B. Both cations show marked bond length alternation, which has been discussed the bond length alternation in terms of maximized intracationic X⋯Se contacts, charge delocalization, and π bonding.<sup>20,21,258,260,262</sup> The locations of the Se<sub>2</sub>Cl side chain in (Se<sub>9</sub>Cl)<sup>+</sup> and the bromine atom in (Se<sub>7</sub>Br)<sup>+</sup> enhances the charge delocalization.

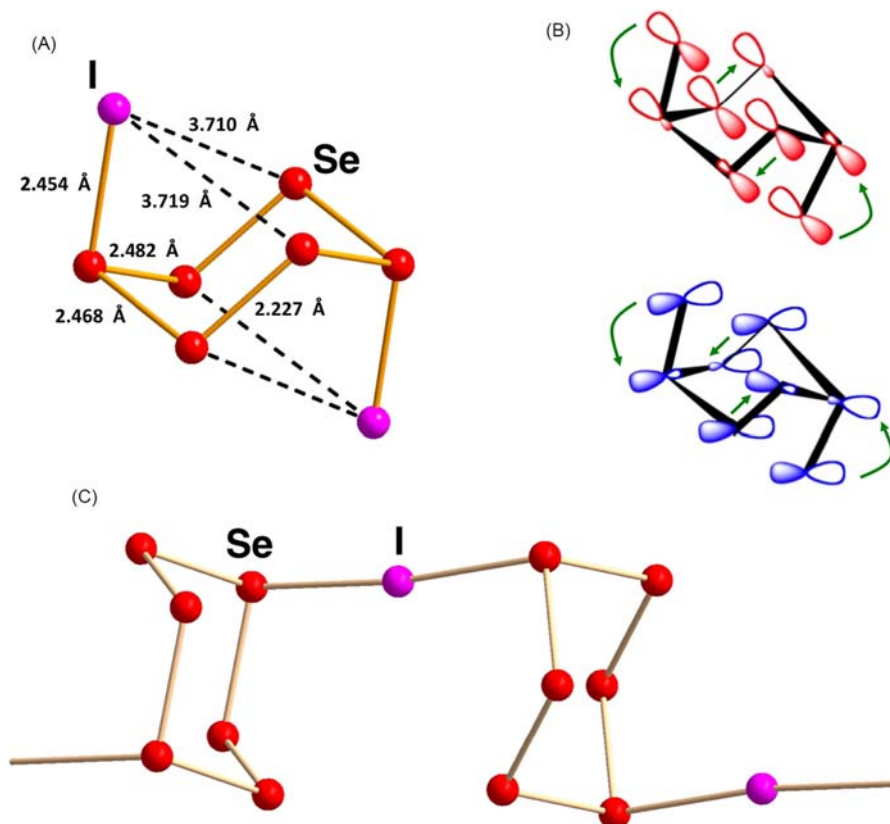
By contrast to the discrete selenium-halogen cations, tellurium-chlorine and tellurium-bromine cations (Te<sub>15</sub>X<sub>4</sub>)<sub>n</sub><sup>n+</sup> show polymeric structures that are related with that of the tellurium subhalide Te<sub>2</sub>Br.<sup>261</sup> The crystal structures, however, are disordered.

A preliminary natural-abundance <sup>77</sup>Se NMR study of the soluble products of the reaction of (Se<sub>4</sub>)[AsF<sub>6</sub>]<sub>2</sub> and bromine in liquid SO<sub>2</sub> exhibited resonances attributable to 1,1,4,4-(Se<sub>4</sub>Br<sub>4</sub>)<sup>2+</sup> and (Se<sub>7</sub>Br)<sup>+</sup>. These assignments are supported by calculated <sup>77</sup>Se chemical shifts.<sup>244</sup>



**Fig. 31** The structures of (A) (S<sub>7</sub>Br)<sup>+</sup> in (S<sub>7</sub>Br)(S<sub>4</sub>)[AsF<sub>6</sub>]<sub>2</sub><sup>262</sup> and (B) (Se<sub>9</sub>Cl)<sup>+</sup> in (Se<sub>9</sub>Cl)[SbCl<sub>6</sub>].<sup>260</sup>





**Fig. 32** (A) The crystal structure of the  $(\text{Se}_6\text{I}_2)^{2+}$  cation in  $(\text{Se}_6\text{I}_2)[\text{AsF}_6]_2 \cdot 2\text{SO}_2$ .<sup>265</sup> The  $(\text{Te}_6\text{I}_2)^{2+}$  cation in  $(\text{Te}_6\text{I}_2)[\text{WCl}_6]_2$ <sup>230</sup> shows a similar conformation and similar bond length alternation. (B) The bond length alternation can be explained by two parallel  $4p^2 \rightarrow \sigma^*$  electron transfers.<sup>244</sup> (C) The polymeric  $(\text{Se}_6\text{I})_n^{n+}$  in  $(\text{Se}_6\text{I})_n[\text{AsF}_6]_n$ .<sup>267</sup>

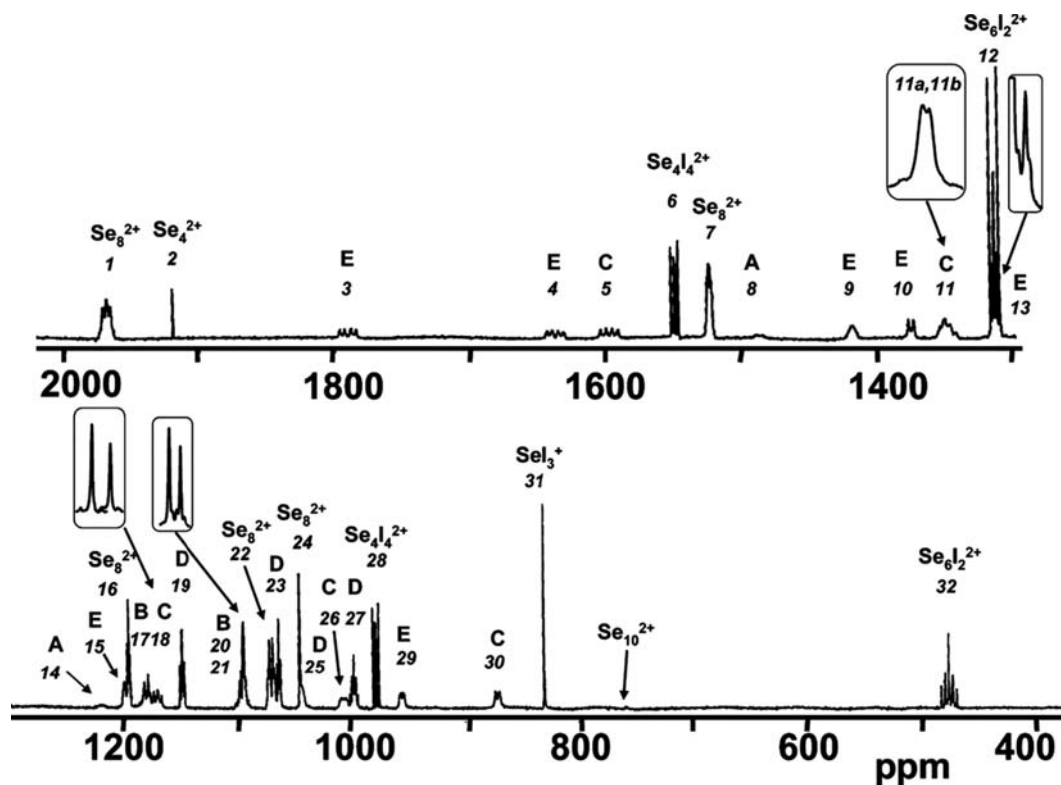
### 1.21.8.3 Chalcogen-iodine cations

The  $(\text{S}_7\text{I})^+$  cation is the longest known and most stable homocyclic sulfur-iodine cation. It has been prepared and structurally characterized with many counteranions.<sup>263</sup> It is isostructural with  $(\text{S}_7\text{Br})^+$  (see Fig. 31).  $(\text{S}_7\text{I})^+$  is also found together with  $(\text{S}_4)^{2+}$  in  $(\text{S}_7\text{I})_4(\text{S}_4)[\text{AsF}_6]_6$ , and in  $[(\text{S}_7\text{I})_2\text{I}][\text{SbF}_6]_3 \cdot 2 \text{AsF}_3$ , there are two  $\text{S}_7\text{I}$  moieties linked by iodine in the  $[(\text{S}_7\text{I})_2\text{I}]^{3+}$  cation.<sup>264</sup>

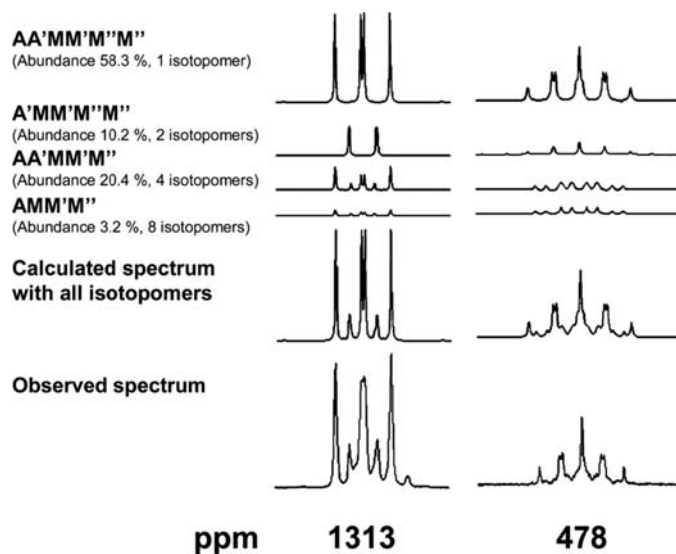
The structures of  $(\text{Se}_6\text{I}_2)^{2+}$  and  $(\text{Te}_6\text{I}_2)^{2+}$  are expectedly similar<sup>230,265</sup> and can be described as distorted cubes [see Fig. 32A]. In a similar fashion to other polychalcogen cations, the positive charge of the three-coordinate chalcogen atom is delocalized and leads to bond length alternation. The relevant orbital interactions are shown in Fig. 32B. A related polymeric cation  $(\text{Se}_6\text{I})_n^{n+}$  has been isolated as hexafluoroarsenate and hexafluoroantimonate salts and its crystal structure has been determined.<sup>266,267</sup> The six-membered  $\text{Se}_6$  ring is in the chair conformation like in  $(\text{Se}_6\text{I}_2)^{2+}$ . Two bridging iodine atoms in 1,4-positions link the rings into a polymeric zig-zag chain [Fig. 32C].

When solid  $(\text{Se}_6\text{I}_2)_2[\text{AsF}_6]_2 \cdot 2\text{SO}_2$  is dissolved into liquid  $\text{SO}_2$ , a complicated equilibrium is set up.<sup>244</sup> The composition of the equilibrium mixture was studied by  $^{77}\text{Se}$  NMR spectroscopy at  $-70^\circ\text{C}$  using both natural-abundance and enriched  $^{77}\text{Se}$ -isotope samples (enrichment 92 %). Some of the resonances in Fig. 33 were due to known species  $[(\text{Se}_6\text{I}_2)^{2+}$ ,  $(\text{Se}_4\text{I}_4)^{2+}$  and  $(\text{SeI}_3)^+$ ,<sup>235,268</sup>  $(\text{Se}_4)^{2+}$ ,<sup>224,269</sup> as well as to  $(\text{Se}_8)^{2+}$  and  $(\text{Se}_{10})^{2+243}$ . The unknown 22 resonances were assigned on the basis of homonuclear  $^{77}\text{Se}$ - $^{77}\text{Se}$  COSY NMR spectrum, selective irradiation experiments, and spectral simulation.<sup>244</sup> Because the  $^{77}\text{Se}$ -enrichment is 92 %, several isotopomers of a given cation have a significant abundance and need to be considered in the simulation. This is exemplified for  $(\text{Se}_6\text{I}_2)^{2+}$  in Fig. 34.

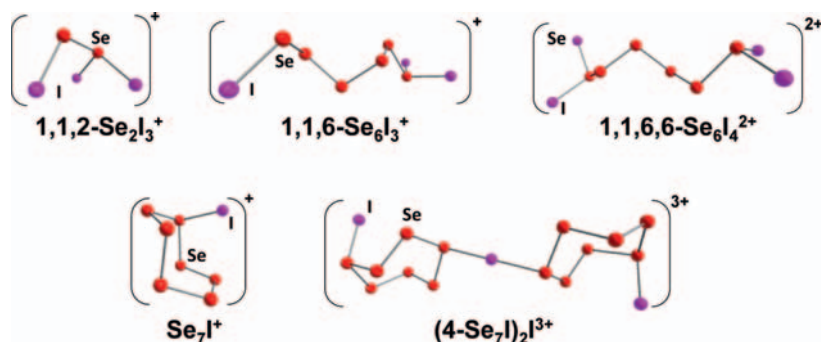
It was inferred that the 22 resonances are due to five cationic species, and the simulations provided for their spin systems. This information was combined with the trends in the chemical shifts, with iodine, selenium, and charge balances, as well as with ZORA chemical shift predictions, which employ the rPBE GGA functional and large QZ4P basis sets, an implicit conductor-like screening model, and a small number of explicit solvent molecules to include solvent effects.<sup>244</sup> All information available is consistent with the assignment of the unknown resonances to acyclic 1,1,2- $(\text{Se}_2\text{I}_3)^+$ , 1,1,6,6- $(\text{Se}_6\text{I}_4)^{2+}$ , and 1,1,6- $(\text{Se}_6\text{I}_3)^+$ , as well as to cyclic  $(\text{Se}_7\text{I})^+$  and  $(4\text{-Se}_7\text{I})_2\text{I}^{3+}$  (see Fig. 35). It is interesting to note that upon evaporation of the  $\text{SO}_2$  from solution, the solid material contains only  $(\text{Se}_6\text{I}_2)[\text{AsF}_6]_2 \cdot 2\text{SO}_2$  indicating that the dissociation of  $(\text{Se}_6\text{I}_2)^{2+}$  is reversible.<sup>244</sup> Volume-based thermodynamics calculations (VBT) show that non-solvated  $(\text{Se}_6\text{I}_2)[\text{AsF}_6]_2$  is not thermodynamically stable disproportionating to  $(\text{Se}_4\text{I}_4)[\text{AsF}_6]_2(\text{s})$  and  $(\text{Se}_8)[\text{AsF}_6]_2(\text{s})$  (estimated  $\Delta G^\circ = -17 \pm 15 \text{ kJ mol}^{-1}$  at 298 K).<sup>244</sup>



**Fig. 33** The  $^{77}\text{Se}$  NMR spectrum of the  $\text{SO}_2(\text{l})$  solution of the dissociation equilibrium of  $(\text{Se}_6\text{I}_2)^{2+}$  at  $-70^\circ\text{C}$  using selenium enriched in the  $^{77}\text{Se}$ -isotope (enrichment 92 %).<sup>244</sup> The inserts represent portions of the spectrum recorded for the natural-abundance sample. Reprinted (adapted) with permission from Brownridge, S.; Calhoun, L.; Jenkins, H. D. B.; Laitinen, R. S.; Murchie, M. P.; Passmore, J.; Pietikäinen, J.; Rautiainen, J. M.; Sanders, J. C. P.; Schrobilgen, G. J.; Suontamo, R. J.; Tuononen, H. M.; Valkonen, J. U.; Wong, C.-M., *Inorg. Chem.* **2009**, *48*, 1938–1959. Copyright 2009 American Chemical Society.



**Fig. 34** The simulated and observed  $^{77}\text{Se}$  NMR chemical shifts of  $(\text{Se}_6\text{I}_2)^{2+}$  using a sample prepared from selenium enriched in the  $^{77}\text{Se}$ -isotope (enrichment 92%).<sup>244</sup> The observed resonance at 1313 ppm overlaps a resonance due to another cationic species. Reprinted (adapted) with permission from Brownridge, S.; Calhoun, L.; Jenkins, H. D. B.; Laitinen, R. S.; Murchie, M. P.; Passmore, J.; Pietikäinen, J.; Rautiainen, J. M.; Sanders, J. C. P.; Schrobilgen, G. J.; Suontamo, R. J.; Tuononen, H. M.; Valkonen, J. U.; Wong, C.-M., *Inorg. Chem.* **2009**, *48*, 1938–1959. Copyright 2009 American Chemical Society.



**Fig. 35** The species assigned to the 22  $^{77}\text{Se}$  NMR resonances observed from dissociation of  $(\text{Se}_6\text{I}_2)^{2+}$  in  $\text{SO}_2(\text{l})$  solution.<sup>244</sup>

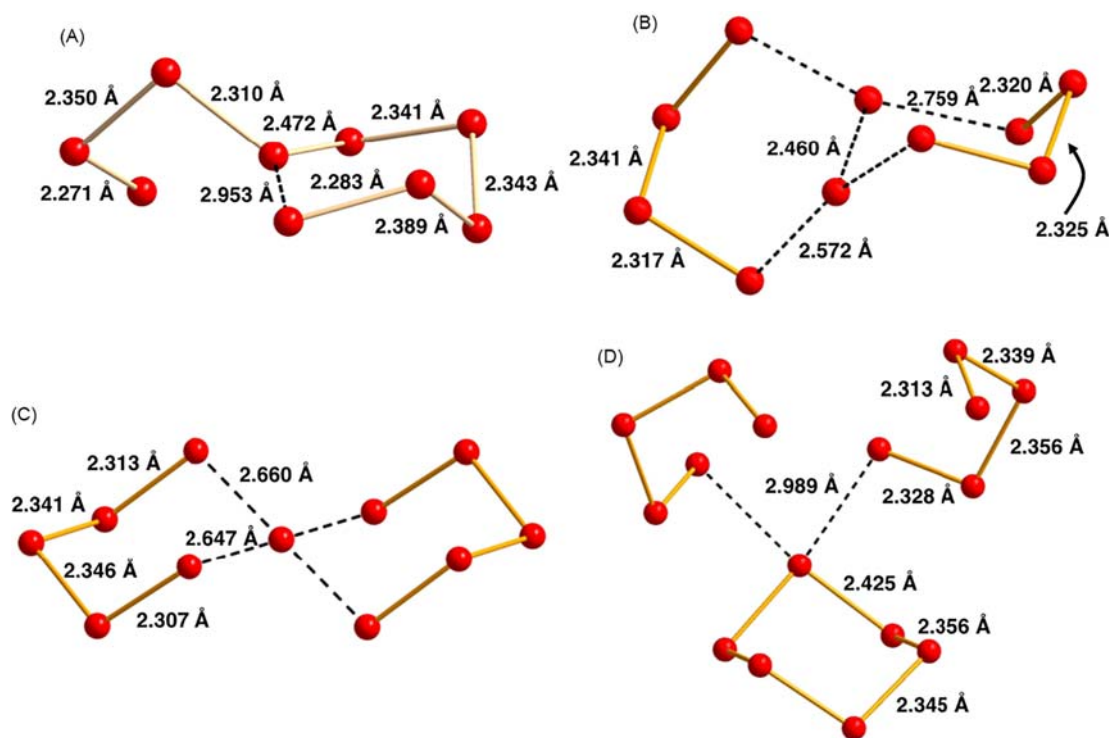
## 1.21.9 Cyclic chalcogen anions

### 1.21.9.1 General

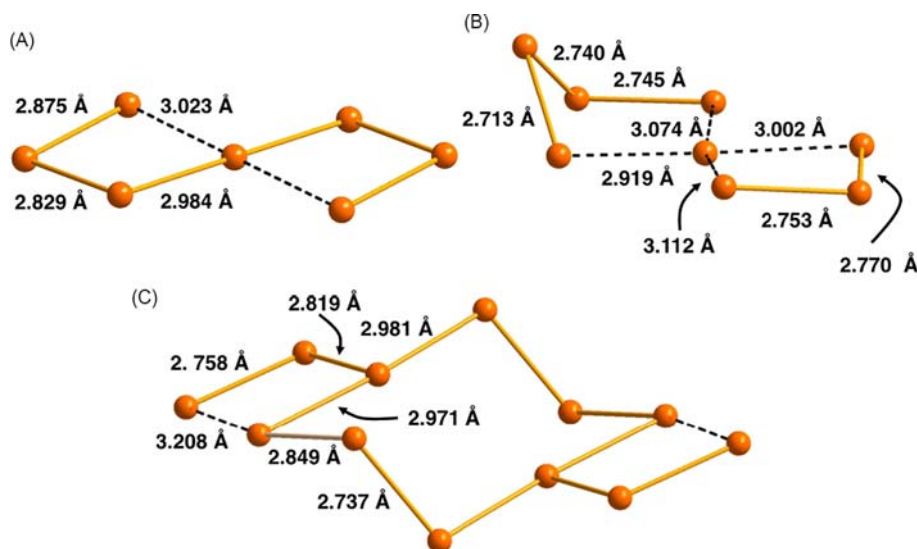
Polychalcogenide anions show a rich and diverse structural chemistry. Whereas polysulfides are solely acyclic, both selenium and tellurium form in addition to the open-chain species also polycyclic anions. Their synthetic and structural chemistry as well as ligand properties and applications have been reviewed several times (for some reviews, see ref. [4,5,13–15,270–272](#)).

The usual preparation of the materials involves direct high-temperature combination of the elements, solution reactions involving chalcogen elements and alkali metal carbonates, solvothermal reactions, or oxidation-reduction reactions with Lewis acids.<sup>273,274</sup> These methods have mostly been applied to alkali metal or alkaline earth metal selenides and tellurides that can then serve as precursors to other chalcogenides. The presence of a large organic cation or an encapsulating agent such as a crown ether complex of an alkali metal leads to the stabilization of otherwise unstable anions.

Tellurium shows more diverse polyanion chemistry than sulfur and selenium due to increasing importance of hyperconjugation and secondary bonding, when going down Group 16 (see Refs. [271](#) and [274](#), and references therein). By contrast to polysulfides and polyselenides, polytelluride anions can exhibit charges that deviate from  $-2$ .



**Fig. 36** (A)  $(\text{Se}_9)^{2-}$  in  $[\text{Sr}(15\text{-crown-5})_2](\text{Se}_9)$ ,<sup>275</sup> (B)  $(\text{Se}_{10})^{2-}$  in  $[(\text{PPh}_3)_2\text{N}]_2(\text{Se}_{10})\text{Me}_2\text{CHO}$ ,<sup>276</sup> (C)  $(\text{Se}_{11})^{2-}$  in  $[(\text{PPh}_3)_2\text{N}]_2(\text{Se}_{11})$ ,<sup>280</sup> (D)  $(\text{Se}_{16})^{4-}$  in  $\text{Cs}_4(\text{Se}_{16})$ .<sup>281</sup>



**Fig. 37** (A)  $(\text{Te}_7)^{2-}$  in  $[\text{Re}_6\text{Te}_8](\text{Te}_7)$ ,<sup>282</sup> (B)  $(\text{Te}_8)^{2-}$  in  $[\text{K}(15\text{-crown-5})_2]_2(\text{Te}_8)$ ,<sup>283</sup> and  $(\text{Te}_{14})^{4-}$  in  $\text{Me}_2\text{N}(\text{CH}_2)_4(\text{Te}_{12})$ .<sup>285</sup>

### 1.21.9.2 Discrete anions

The importance of hypervalent 3c-4e bonding increases when going down the Group 16.<sup>270</sup> While  $(\text{Se}_9)^{2-}$  can be regarded as having an open chain structure [Fig. 36A,<sup>275</sup> it has a short intra-chain contact of 2.953 Å that indicates incipient tendency toward ring formation. A similar, though stronger transannular distance [2.460 Å] is observed in a nominally bicyclic  $(\text{Se}_{10})^{2-276}$  [Fig. 36B]. Other cyclic polyselenide anions comprise  $(\text{Se}_{11})^{2-101,277-280}$  and  $(\text{Se}_{16})^{4-281}$  and are shown in Fig. 36C and D.

Tellurium has also been shown to form two spirocyclic polytellurides.  $(\text{Te}_7)^{2-}$  has been isolated as a  $[\text{Re}_6\text{Te}_8](\text{Te}_7)$  salt [Fig. 37A]<sup>282</sup> and  $(\text{Te}_8)^{2-}$  has been characterized in  $[\text{K}(15\text{-crown-5})_2]_2(\text{Te}_8)$  [Fig. 37B].<sup>283</sup> The tricyclic  $(\text{Te}_{12})^{4-}$  anion has been prepared by the reduction of elemental tellurium with  $\text{Li}_3\text{Sb}$  followed by the crystallization from ethylenediamine in the presence of 12-crown-4.<sup>284</sup> The structure of the  $[\text{Li}(12\text{-crown-4})_2]_4(\text{Te}_{12})$  salt is disordered with the anion assuming two different orientation. The same anion has been produced by the spontaneous decomposition of dimethylpyrrolidinium trimethylsilyltellurate in acetonitrile solution in the presence of traces of silicone grease or air.<sup>285</sup> In this case, there was no disorder in the structure [Fig. 37C].

### 1.21.9.3 Cyclic radical anions

Sodium-sulfur batteries have recently attracted extensive attentions and a large number of research has appeared in recent years (for a review, see ref. 286). Homocyclic radical anions  $(\text{S}_6)^{\cdot-}$  and  $(\text{S}_7)^{\cdot-}$  are thought to play a significant role in the redox reactions in sulfur-based batteries. The G3X(MP2) calculations predict that both these species are homocyclic and exhibit conformations similar to electrically neutral molecules, except that one bond in both radical anions is very long (2.956 and 2.889 Å, for  $(\text{S}_6)^{\cdot-}$  and  $(\text{S}_7)^{\cdot-}$ , respectively).<sup>287</sup>  $\text{S}_8$  and  $(\text{S}_8)^{\cdot-}$  have been shown to exhibit analogous structural relationship.<sup>287</sup> Experimental information has been obtained from the crystal structure of  $(\text{Ph}_4\text{P})(\text{S}_6)$ , which shows two  $\text{S}_3$  fragments connected by two long contacts of 2.633(4) Å.<sup>288</sup>

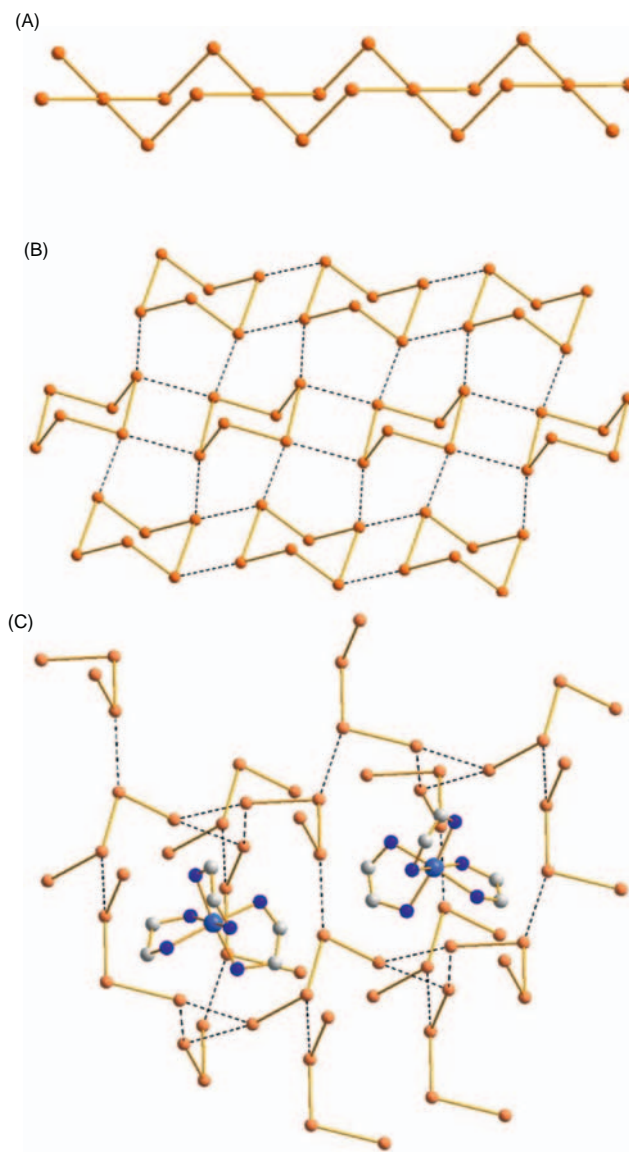
Two  $[\text{Ir}_2\text{Te}_{14}\text{Br}_{12}]_2(\text{InBr}_4)_2$  clusters containing a  $(\text{Te}_{10})^{\cdot-}$  radical anion have recently been prepared and characterized.<sup>289</sup> While the structure of the radical anion is similar to the neutral  $\text{Te}_{10}$ , the strong ESR signal and the DFT computations indicate the presence of a unpaired electron, which is located in the  $\text{Te}_{10}$  cage.

### 1.21.9.4 Extended polytelluride networks

The propensity of polychalcogenide anions to form extended structures increases down Group 16. Polysulfides are discrete acyclic  $(\text{S}_n)^{2-}$  anions,<sup>272</sup> polyselenides show only a few structures with an extended anionic network, as exemplified by  $\text{Cs}_3\text{Se}_{22}$ ,<sup>178</sup> but polytellurides exhibit rich structural variety that obscures the deceptively simple stoichiometry of the polytelluride salts. Sheldrick<sup>270</sup> has summarized the structural and bonding features in polytellurides, which can contain classical bent  $(\text{TeTe}_2)^{2-}$  units, linear  $(\text{TeTe}_2)^{4-}$ , T-shaped  $(\text{TeTe}_3)^{4-}$ , and square-planar  $(\text{TeTe}_4)^{6-}$  unit involving 3c-4e bonds of formal bond order of 0.5. In addition, the fragments can be linked together by weak secondary  $\text{Te}\cdots\text{Te}$  bonds.<sup>34</sup> These interactions result in the formation of 1D, 2D, and 3D networks, as exemplified in Fig. 38.

$\text{Rb}_2\text{Te}_5$  exhibits a continuous spirocyclic chain  $(\text{Te}_5)_n^{2-290}$  that can be thought to consist of square-planar  $\text{TeTe}_4$  units stacked together [see Fig. 38A]. A related extended structure containing a  $(\text{Te}_5)^{6-}$  fragment is observed in  $(\text{Et}_4\text{N})_2[\text{As}_2\text{Te}_5]$ .<sup>291</sup>

The charge of the polytellurides can deviate from -2. This is exemplified by  $\text{RbTe}_6$ <sup>292</sup> that is shown in Fig. 38B. It consists of  $\text{Te}_6$  rings that are linked together into a two-dimensional network by two pairs of  $\text{Te}\cdots\text{Te}$  contacts. Interestingly,  $[\text{Cr}(\text{en})_3]\text{Te}_6$  has been



**Fig. 38** The structures of (A)  $(\text{Te}_5)_n^{2-}$  in  $\text{Rb}_2\text{Te}_5$ ,<sup>290</sup> (B)  $(\text{Te}_6)_n^-$  in  $\text{RbTe}_6$ ,<sup>292</sup> and (C)  $[\text{Cr}(\text{en})_3]_2(\text{Te}_4)_3$ .<sup>293</sup>

reported to contain a polymeric  $(\text{Te}_6)^{3-}$  anion.<sup>293</sup> Considering the Te-Te distances in the 3D network of the anion, the formula of the complex is best described as  $[\text{Cr}(\text{en})_3]_2(\text{Te}_4)_3$  in which case each tetratelluride carries the charge  $-2$  [see Fig. 38C].

Particularly interesting structures of  $\text{Cs}_3\text{Te}_{22}$ <sup>179</sup> and  $\text{Cs}_4\text{Te}_{28}$ <sup>180</sup> have been discussed above (see Section 1.21.4).

### 1.21.10 Summary

Catenation, i.e. the tendency to form compounds containing cumulated chalcogen-chalcogen bonds, is a characteristic feature for Group 16 elements sulfur, selenium, and tellurium. They all exhibit a large number of both cyclic and acyclic homo- and heterochalcogen molecules and ions. The formation, structures, and properties of compounds containing cyclic polychalcogen molecules, ligands and ions have been discussed in this chapter. Part 2 on the catenated compounds with acyclic chalcogen fragments are treated in the next chapter. The structural chemistry of polysulfur rings is particularly extensive, but while information on related polyselenium and -tellurium chemistry is much sparser, recent decades have seen rapid progress also in this area of chemistry.



The bonding, the geometrical features, and the intermolecular interactions can be described in terms of  $np^2$ - $np^2$  interactions, hyperconjugative  $np^2$ - $\sigma^*$  interactions, and  $\pi^*$ - $\pi^*$  interactions. The significance of the latter two interactions increases when going down Group 16, and they play a major role in so-called secondary bonding interactions. They also explain, why the structures and properties of selenium and, in particular, tellurium species differ from those of sulfur.

## References

- Laitinen, R. S.; Pekonen, P.; Suontamo, R. *Coord. Chem. Rev.* **1994**, *130*, 1–62.
- Studel, R.; Eckert, B. *Topics Curr. Chem.* **2003**, *230*, 1–79.
- Eckert, B.; Studel, R. *Topics Curr. Chem.* **2003**, *231*, 31–98.
- Kelly, P. F.; King, R. S. P. In *Comprehensive Inorganic Chemistry II*; Reedijk, J., Poeppelmeier, K., Eds., 2nd ed.; vol. 1; Elsevier: Amsterdam, 2013; pp 179–196.
- Laitinen, R. S.; Oilunkaniemi, R. In *Comprehensive Inorganic Chemistry II*; Reedijk, J., Poeppelmeier, K., Eds., 2nd ed.; vol. 1; Elsevier: Amsterdam, 2013; pp 197–231.
- Krossing, I. In *Handbook of Chalcogen Chemistry*; Devillanova, F. A., Ed., RSC Publishing: Cambridge, 2007; pp 381–416.
- Chivers, T.; Laitinen, R. S. *Chem. Soc. Rev.* **2015**, *44*, 1725–1739.
- Krossing, I. In *Handbook of Chalcogen Chemistry, New Perspectives in Sulfur, Selenium and Tellurium*; Devillanova, F. A., du Mont, W.-W., Eds., 2nd ed.; vol. 1; RSC Publishing: Cambridge, 2013; pp 349–381.
- Brownridge, S.; Krossing, I.; Passmore, J.; Jenkins, H. D. B.; Rootbottom, H. K. *Coord. Chem. Rev.* **2000**, *197*, 397–481.
- Krossing, I. *Top. Curr. Chem.* **2003**, *230*, 135–165.
- Beck, J. *Coord. Chem. Rev.* **1997**, *163*, 55–70.
- Graf, C.; Assoud, A.; Mayasree, O.; Kleinke, H. *Molecules* **2009**, *14*, 3115–3131.
- Sheldrick, W. S. *Z. Anorg. Allg. Chem.* **2012**, *638*, 2401–2424.
- Kanatzidis, M. G. *Comm. Inorg. Chem.* **1990**, *10*, 161–195.
- Drake, G. W.; Kolis, J. W. *Coord. Chem. Rev.* **1994**, *137*, 131–178.
- Okazaki, R. *Phosphorus Sulfur Relat. Elem.* **2001**, *168–169*, 41–50.
- Chivers, T. *A Guide to Chalcogen-Nitrogen Chemistry*, World Scientific Publishing: New Jersey, 2005; p 318.
- Takeda, N.; Tokitoh, N.; Okazaki, R. In *Handbook of Chalcogen Chemistry*; Devillanova, F. A., Ed., RSC Publishing: Cambridge, 2007; pp 195–222.
- Takeda, N.; Tokitoh, N. In *Handbook of Chalcogen Chemistry, New Perspectives in Sulfur, Selenium and Tellurium*; Devillanova, F. A., du Mont, W.-W., Eds., 2nd ed.; vol. 1; RSC Publishing: Cambridge, 2013; pp 160–190.
- Xu, Z. In *Handbook of Chalcogen Chemistry*; Devillanova, F. A., Ed., RSC Publishing: Cambridge, 2007; pp 457–476.
- Wang, J.; Xu, Z. In *Handbook of Chalcogen Chemistry, New Perspectives in Sulfur, Selenium and Tellurium*; Devillanova, F. A., du Mont, W.-W., Eds., 2nd ed.; vol. 1; RSC Publishing: Cambridge, 2013; pp 425–447.
- Potapov, V. A. In *Chemistry of Organic Selenium and Tellurium Compounds*; Patai, S., Rappoport, Z., Eds.; 2013; pp 765–843.
- Nordheider, A.; Woolf, J. D.; Chivers, T. *Chem. Rev.* **2015**, *115*, 10378–10406.
- Chivers, T.; Laitinen, R. S. *Chalcogen-nitrogen Chemistry. From Fundamentals to Applications in Physical, Biologic, and Materials Sciences*, World Scientific Publishing: New Jersey, 2021; p 450.
- Draganjac, M.; Rauchfuss, T. B. *Angew. Chem. Int. Ed. Engl.* **1985**, *24*, 742–757.
- Müller, A.; Diemann, E. *Adv. Inorg. Chem.* **1987**, *31*, 89–122.
- Kolis, J. W. *Coord. Chem. Rev.* **1990**, *105*, 195–219.
- Ansari, M. A.; Ibers, J. A. *Coord. Chem. Rev.* **1990**, *100*, 223–266.
- Roof, L. C.; Kolis, J. W. *Chem. Rev.* **1993**, *93*, 1037–1080.
- Ruck, M.; Locherer, F. *Coord. Chem. Rev.* **2015**, *297–298*, 208–217.
- Chivers, T. *J. Chem. Soc., Dalton Trans.* **1996**, 1185–1194.
- Hayashi, S.; Nakanishi, W. In *Handbook of Chalcogen Chemistry, New Perspectives in Sulfur, Selenium and Tellurium*; Devillanova, F. A., du Mont, W.-W., Eds., 2nd ed.; vol. 2; RSC Publishing: Cambridge, 2013; pp 335–372.
- Crabtree, R. H. *Chem. Soc. Rev.* **2017**, *46*, 1720–1729.
- Alcock, N. W. *Adv. Inorg. Chem. Radiochem.* **1972**, *15*, 1–58.
- Elder, P. J. W.; Vargas-Baca, I. *Phys. Chem. Chem. Phys.* **2016**, *18*, 30740–30747.
- Karjalainen, M. M.; Sanchez-Perez, C.; Rautiainen, M. J.; Oilunkaniemi, R.; Laitinen, R. S. *Cryst. Eng. Commun.* **2016**, *18*, 4538–4545. and references therein.
- Cozzolino, A. F.; Elder, P. J. W.; Vargas-Baca, I. *Coord. Chem. Rev.* **2011**, *255*, 1426–1438.
- Bleiholder, C.; Werz, D. B.; Köppel, H.; Gleiter, R. *J. Am. Chem. Soc.* **2006**, *128*, 2666–2674.
- Meyer, B. *Sulfur, Energy, and Environment*, Elsevier: Amsterdam, 1977; p 448.
- Elkin, E. M. In *Kirk-Othmer Encyclopedia of Chemical Technology*; Grayson, M., Eckroth, D., Eds.; 20; Wiley: New York, 1982; pp 575–601.
- Schmidt, M.; Block, H.-D. *Angew. Chem. Int. Ed. Engl.* **1967**, *6*, 955.
- Studel, R.; Mäusle, H.-J. *Angew. Chem. Int. Ed. Engl.* **1978**, *17*, 56–57.
- Studel, R.; Mäusle, H.-J. *Z. Anorg. Allg. Chem.* **1981**, *478*, 156–176.
- Studel, R.; Mäusle, H.-J. *Angew. Chem. Int. Ed. Engl.* **1979**, *18*, 152–153.
- Studel, R.; Holz, B. *Z. Naturforsch.* **1988**, *43b*, 581–589.
- Schmidt, M.; Wilhelm, E. *Inorg. Nucl. Chem. Lett.* **1965**, *1*, 39–41.
- Schmidt, M.; Wilhelm, E. *Angew. Chem. Int. Ed. Engl.* **1966**, *5*, 964–965.
- Schmidt, M.; Knippschild, G.; Wilhelm, E. *Chem. Ber.* **1968**, *101*, 381–382.
- Schmidt, M.; Wilhelm, E.; Debaerdemaeker, T.; Hellner, E.; Kutoglu, A. *Z. Anorg. Allg. Chem.* **1974**, *405*, 153–162.
- Debaerdemaeker, T.; Hellner, E.; Kutoglu, A.; Schmidt, M.; Wilhelm, E. *Naturwissenschaften* **1973**, *60*, 300.
- Studel, R.; Mäusle, H.-J. *Z. Anorg. Allg. Chem.* **1980**, *463*, 27–31.
- Schmidt, M.; Block, B.; Block, H. D.; Köpf, H.; Wilhelm, E. *Angew. Chem. Int. Ed. Engl.* **1968**, *7*, 632–633.
- Schmidt, M.; Wilhelm, E. *J. Chem. Soc., Chem. Commun.* **1970**, 1111–1112.
- Sandow, T.; Steidel, J.; Studel, R. *Angew. Chem. Int. Ed. Engl.* **1982**, *21*, 794.
- Studel, R.; Steidel, R.; Sandow, T. *Z. Naturforsch.* **1986**, *41b*, 958–970.
- Steidel, J.; Studel, R.; Kutoglu, A. *Z. Anorg. Allg. Chem.* **1981**, *476*, 171–178.
- Studel, R.; Jensen, D.; Papavassiliou, M. *Phosphorus Sulfur Silicon Relat. Elem.* **1989**, *41*, 349–353.

58. Westphal, U.; Steudel, R. *Phosphorus Sulfur Silicon Relat. Elem.* **1992**, *65*, 151–155.
59. Steudel, R.; Schumann, O.; Buschmann, J.; Luger, P. *Angew. Chem. Int. Ed.* **1998**, *37*, 2377–2378.
60. Steudel, R.; Strauss, R. *J. Chem. Soc., Dalton Trans.* **1984**, 1775–1777.
61. Steudel, R.; Bergemann, K.; Buschmann, J.; Luger, P. *Inorg. Chem.* **1996**, *35*, 2184–2188.
62. Watanabe, Y. *Acta Crystallogr. Sect. B* **1974**, *30*, 1396–1401.
63. Aten, A. H. W. *Z. Phys. Chem.* **1914**, *88*, 321–379.
64. Steudel, R.; Mäusle, H.-J. *Z. Anorg. Allg. Chem.* **1979**, *457*, 165–173.
65. Steudel, R.; Steidel, J.; Sandow, T.; Schuster, F. *Z. Naturforsch.* **1978**, *33b*, 1198–1200.
66. Steudel, R.; Steidel, J.; Reinhardt, R. *Z. Naturforsch.* **1983**, *38b*, 1548–1556.
67. Steudel, R. *Angew. Chem. Int. Ed. Engl.* **1975**, *14*, 655–664.
68. Meyer, B. *Chem. Rev.* **1976**, *76*, 367–388.
69. Steidel, J.; Pickardt, J.; Steudel, R. *Z. Naturforsch.* **1978**, *33b*, 1554–1555.
70. Steudel, R.; Reinhardt, R.; Schuster, F. *Angew. Chem. Int. Ed. Engl.* **1977**, *16*, 715.
71. Steudel, R.; Steidel, J.; Pickardt, J.; Schuster, F.; Reinhardt, R. *Z. Naturforsch.* **1980**, *35b*, 1378–1383.
72. Coppens, P.; Yang, Y. W.; Blessing, R. H.; Cooper, W. F.; Larsen, F. K. *J. Am. Chem. Soc.* **1977**, *99*, 760–766.
73. Rettig, S. J.; Trotter, I. *Acta Crystallogr. Sect. C* **1987**, *43*, 2260–2262.
74. Mikuriya, M.; Taniguchi, K.; Koyama, Y.; Watanabe, H.; Yoshioka, D.; Mitsushashi, R.; Asato, E. *X-ray Struct. Anal. Online* **2020**, *36*, 1–2.
75. Templeton, L. K.; Templeton, D. H.; Zalkin, A. *Inorg. Chem.* **1976**, *15*, 1999–2001.
76. Goldsmith, L. M.; Strouse, C. E. *J. Am. Chem. Soc.* **1977**, *99*, 7580–7589.
77. David, W. I. F.; Ibberson, R. M.; Cox, S. F. J.; Wood, P. T. *Acta Crystallogr. Sect. B* **2006**, *62*, 953–959.
78. Gallacher, A. C.; Pinkerton, A. A. *Acta Crystallogr. Sect. C* **1993**, *49*, 125–126.
79. Kräuter, T.; Neumüller, B. *Z. Anorg. Allg. Chem.* **1995**, *621*, 597–606.
80. Veganova, E.; Wachtel, E.; Rozenberg, H.; Khodorkovsky, G. L.; Shimon, R.; Shlomo, Y. *Chem. Mater.* **2004**, *16*, 3976–3979.
81. Reinhardt, R.; Steudel, R.; Schuster, F. *Angew. Chem. Int. Ed. Engl.* **1978**, *17*, 55–56.
82. Steidel, J.; Steudel, R. *J. Chem. Soc., Chem. Commun.* **1982**, 1312–1313.
83. Debaerdemeker, T.; Kutoglu, A. *Cryst. Struct. Commun.* **1974**, *3*, 611–613.
84. Engel, M. *Compt. Rend. Hebd. Scaenc. Acad. Sci.* **1891**, *112*, 866–868.
85. Steudel, R.; Schuster, F. *J. Mol. Struct.* **1978**, *44*, 143–157.
86. Steudel, R. *Z. Naturforsch.* **1983**, *38b*, 543–545.
87. Steudel, R.; Papavassiliou, M.; Jensen, D. *Z. Naturforsch.* **1988**, *43*, 245–246.
88. Wong, M. W.; Steudel, Y.; Steudel, R. *Inorg. Chem.* **2005**, *44*, 8908–8915.
89. MacKnight, W. J.; Tobolsky, A. V. In *Elemental Sulfur*; Meyer, B., Ed.; Interscience: New York, 1965; p 95.
90. Currell, B. R.; Williams, A. J. *Thermochim. Acta* **1974**, *9*, 255–259.
91. Clegg, J. K.; Meng, W.; Nitschke, J. R., Private communication. *CSD Communications* 2012, FURHU10.
92. Douglas, S. *Planet. Space Sci.* **2004**, *52*, 223–227.
93. Schulz, N. H.; Brinkhoff, T.; Ferdelman, T. G.; Hernández Maríné, M.; Teske, A.; Jørgensen, B. B. *Science* **1999**, *284*, 493–495.
94. Prange, A.; Chauvistre, R.; Modrow, H.; Hormes, J.; Truper, H. G.; Dahl, C. *Microbiology* **2002**, *148*, 267–276.
95. Himmel, D.; Maurin, L. C.; Gros, O.; Mansot, J.-L. *Biol. Cell* **2009**, *101*, 43–54.
96. Strauss, R.; Steudel, R. *Z. Naturforsch.* **1988**, *43b*, 1151–1155.
97. Lyle, P. *Phosphorus Sulfur Relat. Elem.* **2001**, *168*, 287–290.
98. Miyamoto, Y. *Jpn. J. Appl. Phys.* **1980**, *19*, 1813–1819.
99. Steudel, R.; Strauss, E.-M. *Adv. Inorg. Chem. Radiochem.* **1984**, *28*, 135–166.
100. Maaninen, A.; Chivers, T.; Parvez, M.; Pietikäinen, J.; Laitinen, R. S. *Inorg. Chem.* **1999**, *38*, 4093–4097.
101. Pauling, L. *The Nature of The Chemical Bond*, 3rd ed.; Cornell University Press: Ithaca, NY, 1960; p 644.
102. Dietz, J.; Müller, U.; Müller, V.; Dehnicke, K. *Z. Naturforsch.* **1991**, *46b*, 1293–1299.
103. Staffel, R.; Müller, U.; Ahle, A.; Dehnicke, K. *Z. Naturforsch.* **1991**, *46b*, 1287–1292.
104. Bacchi, A.; Baratta, W.; Calderazzo, F.; Marchetti, F.; Pelizzi, G. *Angew. Chem. Int. Ed. Engl.* **1994**, *33*, 193–195.
105. Cherin, P.; Unger, P. *Acta Crystallogr. Sect. B* **1972**, *28*, 313–317.
106. Marsch, R. E.; Pauling, L.; McCullough, J. D. *Acta Crystallogr.* **1953**, *6*, 71–75.
107. Foss, O.; Janickis, V. *J. Chem. Soc., Dalton Trans.* **1980**, 624–627.
108. Steudel, R.; Papavassiliou, M.; Strauss, E.-M.; Laitinen, R. *Angew. Chem. Int. Ed. Engl.* **1986**, *25*, 99–101.
109. Steudel, R.; Strauss, E.-M. *Z. Naturforsch.* **1981**, *36b*, 1085–1088.
110. Steudel, R.; Papavassiliou, M.; Krampe, W. *Polyhedron* **1988**, *7*, 581–583.
111. Maaninen, A.; Konu, J.; Laitinen, R. S.; Chivers, T.; Schatte, G.; Pietikäinen, J.; Ahlgrén, M. *Inorg. Chem.* **2001**, *40*, 3539–3543.
112. Maaninen, T.; Konu, J.; Laitinen, R. S. *Acta Crystallogr. Sect. E* **2004**, *60*, o2235–o2237.
113. Bogomolov, V. N.; Zadorozhnyi, A. I.; Petranovskii, V. P.; Fokin, A. V.; Kholodkevich, S. V. *JETP Lett.* **1979**, *29*, 373–375.
114. Bogomolov, V. N.; Zadorozhnyi, A. I.; Pavlova, T. M.; Petranovskii, V. P.; Podkhaluzin, V. P.; Kholkin, A. L. *JETP Lett.* **1980**, *31*, 378–381.
115. Pietikäinen, J.; Laitinen, R. S. *J. Chem. Soc., Chem. Commun.* **1998**, 2381–2382.
116. Laitinen, R. S.; Pakkanen, T. A. *Inorg. Chem.* **1987**, *26*, 2598–2603.
117. Blahous, C. P., III; Schaefer, H. F., III *J. Phys. Chem.* **1988**, *92*, 959–962.
118. Xie, Y.; Schaefer, H. F., III; Jang, J. H.; Mhin, B. J.; Ho, S. K.; Yoon, C. W.; Kim, K. S. *Mol. Phys.* **1992**, *76*, 537–546.
119. Gimarc, B. M.; Zhao, M. *J. Phys. Chem.* **1993**, *98*, 1596–1600.
120. Polizer, P.; Lane, P. *Int. J. Quantum. Chem.* **2000**, *77*, 336–370.
121. Forte, G.; Angiella, G. G. N.; March, N. H.; Pucci, R. *Phys. Lett. A* **2013**, *377*, 801–803.
122. Gadzhiev, O. B.; Ignatov, S. K.; Kulikov, M. Y.; Feigin, A. M.; Razuvaev, A. G.; Sennikov, P. G.; Schrems, O. *J. Chem. Theory Comput.* **2013**, *9*, 247–262.
123. Kim, K. S.; Jang, J. H.; Kim, S.; Mhin, B.-J.; Schaefer, H. F., III *J. Chem. Phys.* **1990**, *92*, 1887–1892.
124. Ochoa-Calle, A. J.; Ramirez-Solis, A. *Chem. Phys. Lett.* **2014**, *592*, 326–329.
125. Jones, R. O.; Hohl, D. *Int. J. Quantum Chem. Quantum Chem. Symp.* **1990**, *24*, 141–151.
126. Kim, K. S.; Kim, H. S.; Kim, S.; Jang, J. H.; Schaefer, H. F. *J. Am. Chem. Soc.* **1989**, *111*, 7746–7749.
127. Seidl, E. T.; Schaefer, H. F., III *J. Chem. Phys.* **1988**, *88*, 7043–7049.
128. Steudel, R.; Papavassiliou, M.; Baumgart, F. *Z. Naturforsch.* **1991**, *46b*, 1674–1678.
129. Laitinen, R.; Niinistö, L.; Steudel, R. *Acta Chem. Scand.* **1979**, *A33*, 737–747.
130. Weiss, J. *Z. Anorg. Allg. Chem.* **1977**, *435*, 113–118.

131. Calvo, C.; Gillespie, R. J.; Vekris, J. E.; Ng, H. N. *Acta Crystallogr. Sect. B* **1978**, *34*, 911–912.
132. Boudreau, R. A.; Haendler, H. M. *J. Solid State Chem.* **1981**, *36*, 289–296.
133. Laitinen, R.; Rautenberg, N.; Steidel, J.; Steudel, R. *Z. Anorg. Allg. Chem.* **1982**, *486*, 116–128.
134. Giolando, D. M.; Papavassiliou, M.; Pickardt, J.; Rauchfuss, T. B.; Steudel, R. *Inorg. Chem.* **1988**, *27*, 2596–2600.
135. Laitinen, R.; Steudel, R. *J. Mol. Struct.* **1980**, *68*, 19–32.
136. Eysel, H. H. *J. Mol. Struct.* **1982**, *78*, 203–213.
137. Steudel, R.; Strauss, E.-M. *Angew. Chem. Int. Ed. Engl.* **1984**, *23*, 362–363.
138. Laitinen, R.; Steudel, R.; Strauss, E.-M. *J. Chem. Soc., Dalton Trans.* **1985**, 1869–1875.
139. Laitinen, R. S.; Pekonen, P.; Hiltunen, Y.; Pakkanen, T. A. *Acta Chem. Scand.* **1989**, *43*, 436–440.
140. Chivers, T.; Laitinen, R. S.; Schmidt, K. J. *Can. J. Chem.* **1992**, *70*, 719–725.
141. Pekonen, P.; Taavitsainen, J.; Laitinen, R. S. *Acta Chem. Scand.* **1998**, *52*, 1188–1193.
142. Komulainen, J.; Laitinen, R. S.; Suontamo, R. J. *Can. J. Chem.* **2002**, *80*, 1435–1443.
143. Pekonen, P.; Hiltunen, Y.; Laitinen, R. S.; Pakkanen, T. A. *Inorg. Chem.* **1991**, *30*, 3679–3682.
144. (a) Cooper, R.; Culka, J. V. *J. Inorg. Nucl. Chem.* **1967**, *29*, 1877–1879; (b) Binnewies, M. *Z. Anorg. Allg. Chem.* **1976**, *422*, 43–46.
145. Jones, C. H. W.; Mauguin, M. *J. Chem. Phys.* **1977**, *67*, 1587–1593.
146. Chivers, T.; Laitinen, R. S.; Schmidt, K. J.; Taavitsainen, J. *Inorg. Chem.* **1993**, *32*, 337–340.
147. Pupp, M.; Weiss, J. *Z. Anorg. Allg. Chem.* **1978**, *440*, 31–36.
148. Weiss, J.; Pupp, M. *Angew. Chem. Int. Ed. Engl.* **1970**, *9*, 463–464.
149. Weiss, J.; Pupp, M. *Acta Crystallogr. Sect. B* **1972**, *28*, 3653–3655.
150. Nagata, K.; Hayashi, H.; Miyamoto, Y. *Fukuoka Univ. Sci. Rep.* **1988**, *18*, 23–33.
151. Nagata, K.; Hayashi, H.; Miyamoto, Y. *Fukuoka Univ. Sci. Rep.* **1988**, *18*, 35–46.
152. Taavitsainen, J.; Laitinen, R. S. *Main Group Chem.* **1999**, *3*, 59–67.
153. Ghiassi, K. B.; Chen, S. Y.; Westcott, J.; Balch, A. L.; Olmstead, M. M. *Cryst. Growth Des.* **2015**, *15*, 404–410. and references therein.
154. Dyachenko, O. A.; Yagubskii, E. B.; Konovalkhin, S. V.; Kusch, N. D.; Shilov, G. V.; Spitsina, N. G. *Mol. Cryst. Liq. Cryst. Sci. Technol. Sect. C* **1994**, *4*, 133–135.
155. Michel, R.; Kappes, M. M.; Adelman, P.; Roth, G. *Angew. Chem. Int. Ed.* **1994**, *33*, 1651–1654.
156. Roth, G.; Adelman, P.; Knitter, R. *Mater. Lett.* **1993**, *16*, 357–363.
157. Bürgi, H. B.; Venugopalan, P.; Schwarzenbach, D.; Diederich, F.; Thilgen, C. *Helv. Chim. Acta* **1993**, *76*, 2155–2159.
158. Takahashi, H.; Matsubara, E.; Shiro, E.; Matsubara, S.; Sato, N.; Muramatsu, A.; Tohji, K. *Fullerenes, Nanotubes, Carbon Nanostruct.* **2002**, *10*, 217–226.
159. Panthofer, M.; Shopova, D.; Jansen, M. *Z. Anorg. Allg. Chem.* **2005**, *631*, 1387–1390.
160. Shopova, D.; Panthofer, M.; Petricek, V.; Jansen, M. *Kristallogr.* **2007**, *222*, 546–550.
161. Li, C.; Gao, X. J.; Yao, H.; Huang, H.; Cui, R.; Guo, X.; Zhang, L.; Liu, B.; Xu, B.; Shi, W.; Dong, J.; Feng, L.; Gao, X.; Sun, B. *Nano Res.* **2018**, *11*, 2277–2284.
162. Beheshti, A.; Nozarian, K.; Mousavifard, E. S.; Abrahams, C. T.; Mayer, P.; Gajda, R.; Wozniak, K.; Motamedi, H. *J. Solid State Chem.* **2021**, *294*, 12874.
163. Hao, M.-T.; Du, C.-F.; Tian, C.-B.; Li, J.-R.; Huang, X.-Y. *Inorg. Chem. Commun.* **2016**, *72*, 128–131.
164. Duang, P.-C.; Wang, Z.-Y.; Chen, J.-H.; Yang, G.; Raptis, R. G. *Dalton Trans.* **2013**, *42*, 14951–14954. and references therein.
165. Poplalkhin, P.; Arman, H. D.; Tiekink, E. R. T. *Z. Kristallogr.* **2012**, *227*, 363–368.
166. Fan, L.-Q. *Z. Kristallogr.* **2012**, *227*, 79–80.
167. Castineiras, A.; Dehnen, S.; Fuchs, A.; Garcia-Santos, I.; Sevillano, P. *Dalton Trans.* **2009**, 2731–2739.
168. Castineiras, A.; Garcia-Santos, I. *Z. Anorg. Allg. Chem.* **2008**, *634*, 2907–2916.
169. Youngme, S.; Wannarit, N.; Pakawatchai, C.; Chaichit, N.; Somsok, E.; Turpeinen, U.; Mutikainen, I. *Polyhedron* **2007**, *26*, 1459–1468. Errata 5191.
170. Lu, C.-Z.; Zhuang, J.-N.; Chi, L.-S.; Wang, Y.-G.; Huang, H.-H.; Zhang, Q.-E. *J. Chem. Crystallogr.* **1999**, *29*, 1019–1022.
171. Noll, A.; Müller, U. *Z. Anorg. Allg. Chem.* **1999**, *625*, 803–805.
172. Andrews, P. C.; Atwood, J. L.; Barbour, L. J.; Croucher, P. D.; Nichols, P. J.; Smith, N. O.; Skelton, B. W.; White, A. H.; Raston, C. L. *J. Chem. Soc., Dalton Trans.* **1999**, 2927–2932.
173. Umakoshi, K.; Sasaki, Y. *Inorg. Chem.* **1997**, *36*, 4296–4297.
174. Li, H.; Sheng, T.; Huang, Q.; Wu, X. *J. Cluster Sci.* **1995**, *6*, 403–410.
175. Baratta, W.; Calderazzo, F.; Daniels, L. M. *Inorg. Chem.* **1994**, *33*, 3842–3844.
176. Cotton, F. A.; Dikarev, E. V.; Petrukina, M. A. *Angew. Chem. Int. Ed.* **2001**, *40*, 1521–1523.
177. Matsuno, S.; Yamashina, M.; Sei, Y.; Akita, M.; Kuzume, A.; Yamamoto, K.; Yoshizawa, M. *Nature Commun.* **2017**, *8*, 749.
178. Kromm, A.; Sheldrick, W. S. *Z. Anorg. Allg. Chem.* **2006**, *632*, 191–194.
179. Sheldrick, W. S.; Wachhold, M. *Angew. Chem., Int. Ed. Engl.* **1995**, *34*, 450–451.
180. Sheldrick, W. S.; Wachhold, M. *J. Chem. Soc., Chem. Commun.* **1996**, *5*, 607–608.
181. Steudel, R. *Topics Curr. Chem.* **2003**, *231*, 203–230. and references therein.
182. Steudel, R.; Steidel, J. *Angew. Chem. Int. Ed. Engl.* **1978**, *17*, 134–135.
183. Ishii, A.; Yamashita, R. *J. Sulfur Chem.* **2008**, *29*, 303–308.
184. Steudel, R.; Luger, P.; Bradaczek, H.; Rebsch, M. *Angew. Chem. Int. Ed. Engl.* **1973**, *12*, 423–424.
185. Luger, P.; Bradaczek, H.; Steudel, R.; Rebsch, M. *Chem. Ber.* **1976**, *109*, 180–184.
186. Wong, M. W.; Steudel, Y.; Steudel, R. *Chem. Eur. J.* **2007**, *13*, 502–514.
187. Curtiss, L. A.; Redfern, P. C.; Raghavachari, K.; Pople, J. A. *J. Chem. Phys.* **2001**, *114*, 108–117.
188. Steudel, R.; Steidel, J.; Pichardt, J. *Angew. Chem. Int. Ed. Engl.* **1980**, *19*, 325–326.
189. Steudel, R.; Reinhardt, R.; Sandow, T. *Angew. Chem. Int. Ed. Engl.* **1977**, *16*, 716.
190. Steudel, R.; Sandow, T. *Angew. Chem. Int. Ed. Engl.* **1978**, *17*, 611–612.
191. Jones, R. O. *Inorg. Chem.* **1994**, *33*, 1340–1343.
192. Steudel, R.; Sandow, T.; Steidel, J. *J. Chem. Soc., Chem. Commun.* **1980**, 180–181.
193. Steudel, R.; Steidel, J.; Sandow, T. *Z. Naturforsch.* **1986**, *41b*, 951–957.
194. Hohl, D.; Jones, R. O.; Car, R.; Parrinello, M. *J. Am. Chem. Soc.* **1989**, *111*, 825–828.
195. Paul, P. P.; Rauchfuss, T. B.; Wilson, S. R. *J. Am. Chem. Soc.* **1993**, *115*, 3316–3317. and references therein.
196. Roesky, H. W.; Thomas, M.; Schimkowiak, J.; Jones, P. G.; Pinkert, W.; Sheldrick, G. M. *J. Chem. Soc., Chem. Commun.* **1982**, 895–896.
197. Cameron, T. S.; Decken, A.; Dionne, I.; Fang, M.; Krossing, I.; Passmore, J. *Chem. Eur. J.* **2002**, *8*, 3386–3401.
198. Santiso-Quiñones, G.; Brückner, R.; Knapp, C.; Dionne, I.; Passmore, J.; Krossing, I. *Angew. Chem. Int. Ed.* **2009**, *48*, 1133–1137.
199. Santiso-Quiñones, G.; Higelin, A.; Schaefer, J.; Brückner, R.; Knapp, C.; Krossing, I. *Chem. Eur. J.* **2009**, *15*, 6663–6677.
200. Dance, I. G.; Fisher, K. J.; Willett, G. D. *Inorg. Chem.* **1996**, *35*, 4177–4184.
201. Baratta, W.; Calderazzo, F. *Organometallics* **1993**, *12*, 1489–1490.
202. Deiseroth, H.-J.; Wagoner, M.; Neumann, E. *Eur. J. Inorg. Chem.* **2004**, 4755–4758.

203. Deiseroth, H.-J.; Reiner, C.; Schlosser, M.; Wang, X.; Ajaz, H.; Kienie, L. *Inorg. Chem.* **2007**, *46*, 8418–8425. and references therein.
204. Demchenko, P. Y.; Gkadyshyevskii, R. E.; Volkov, S. V.; Yanko, O. G.; Kharkova, L. B.; Fokina, Z. A.; Fokin, A. A. *Chem. Commun.* **2010**, *46*, 4520–4522. and references therein.
205. Köchner, T.; Trapp, N.; Engesser, T. A.; Lehner, A. J.; Röhr, C.; Riedel, S.; Knapp, C.; Scherer, H.; Krossing, I. *Angew. Chem. Int. Ed.* **2011**, *50*, 11253–11256. and references therein.
206. Aris, D.; Beck, J.; Decken, A.; Dionne, I.; Schmedt auf der Günne, J.; Hoffbauer, W.; Köchner, T.; Krossing, I.; Passmore, J.; Rivard, E.; Steden, F.; Wang, X. *Dalton Trans.* **2011**, *40*, 5865–5880. and references therein.
207. Dickerson, C. A.; Fisher, M. J.; Sykora, R. E.; Albrecht-Schmitt; Cody, J. A. *Inorg. Chem.* **2002**, *41*, 640–642.
208. Goldbach, A.; Fayon, F.; Vosegaard, T.; Wachhold, M.; Kanatzidis, M. G.; Massiot, D.; Saboungi, M.-L. *Inorg. Chem.* **2003**, *42*, 6996–7000.
209. Wachhold, M.; Kanatzidis, M. G. *J. Am. Chem. Soc.* **1999**, *121*, 4189–4195.
210. Stolze, K.; Ruck, M. Z. *Anorg. Allg. Chem.* **2014**, *640*, 1559–1563.
211. Stolze, K.; Ruck, M. Z. *Anorg. Allg. Chem.* **2015**, *641*, 2005–2008.
212. Schaefer, J.; Steffani, A.; Plattner, D. A.; Krossing, I. *Angew. Chem. Int. Ed.* **2012**, *51*, 6009–6012.
213. Mironov, Y. V.; Pell, M. A.; Ibers, J. A. *Angew. Chem. Int. Ed. Engl.* **1996**, *35*, 2854–2856.
214. Günther, A.; Heise, M.; Wagner, F. R.; Ruck, M. *Angew. Chem. Int. Ed.* **2011**, *50*, 9987–9990.
215. Günther, A.; Isaeva, A.; Ruck, M. Z. *Anorg. Allg. Chem.* **2013**, *639*, 254–260.
216. Günther, A.; Isaeva, A.; Baranov, A. I.; Ruck, M. *Chem. Eur. J.* **2011**, *17*, 6382–6388.
217. Günther, A.; Ruck, M. Z. *Anorg. Allg. Chem.* **2012**, *638*, 317–323.
218. Ahmed, E.; Ruck, M. *Coord. Chem. Rev.* **2011**, *255*, 2892–2903.
219. Groh, M. F.; Müller, U.; Ahmed, E.; Rothenberger, A.; Ruck, M. Z. *Naturforsch.* **2013**, *68b*, 1108–1122.
220. Grasser, M. A.; Pietsch, T.; Blasius, J.; Hollóczki, O.; Brunner, E.; Doert, T.; Ruck, M. *Chem. Eur. J.* **2021**. <https://doi.org/10.1002/chem.202103770>.
221. Schulz, C.; Daniels, J.; Bredow, T.; Beck, J. *Angew. Chem. Int. Ed. Engl.* **2016**, *55*, 1173–1177.
222. Krossing, I.; Passmore, J. *Inorg. Chem.* **1999**, *38*, 5203–5211. and references therein.
223. Tuononen, H. M.; Suontamo, R.; Valkonen, J.; Laitinen, R. S. *J. Phys. Chem. A* **2004**, *108*, 5670–5677.
224. Collins, M. J.; Gillespie, R. J.; Sawyer, J. F.; Schrobilgen, G. J. *Inorg. Chem.* **1986**, *25*, 2053–2057.
225. Beck, J. Z. *Naturforsch.* **1990**, *45b*, 413–416.
226. Sun, H.-T.; Sakka, Y.; Shirahata, N.; Fujii, M.; Yonezawa, T. *J. Mater. Chem.* **2012**, *22*, 24792–24797.
227. Beck, J.; Fischer, A.; Stankowski, A. Z. *Anorg. Allg. Chem.* **2002**, *628*, 2542–2548.
228. (a) Burns, R. C.; Gillespie, R. J.; Luk, W.-C.; Slim, D. R. *Inorg. Chem.* **1979**, *18*, 3086–3094; (b) Beck, J.; Steden, F. *Acta Crystallogr. Sect. E* **2003**, *E59*, i158–i160.
229. Collins, M. J.; Gillespie, R. J.; Sawyer, J. F. *Acta Crystallogr. Sect. C* **1988**, *44*, 405–409.
230. Beck, J. *Chem. Ber.* **1995**, *128*, 23–27.
231. Beck, J.; Bock, G. Z. *Anorg. Allg. Chem.* **1996**, *622*, 823–828.
232. Gillespie, R. J.; Luk, W. C.; Maharajh, E.; Slim, D. R. *Inorg. Chem.* **1977**, *16*, 892–896.
233. Burns, R. C.; Collins, M. J.; Eicher, S. M.; Gillespie, R. J.; Sawyer, J. F. *Inorg. Chem.* **1988**, *27*, 1807–1813.
234. Gillespie, R. J. *Chem. Soc. Rev.* **1979**, *8*, 315–352.
235. Passmore, J. In *Studies in Inorganic Chemistry*; Stuedel, R., Ed.; vol. 14; Elsevier: Amsterdam, 1992; pp 373–406.
236. Lyne, P. D.; Mingos, D. M. P.; Ziegler, T. *J. Chem. Soc., Dalton Trans.* **1992**, 2743–2747.
237. Cameron, T. S.; Deeth, R. J.; Dionne, I.; Du, H.; Jenkins, H. D. B.; Krossing, I.; Passmore, J.; Roobottom, H. K. *Inorg. Chem.* **2000**, *39*, 5614–5631. and references therein.
238. Beck, J. *Angew. Chem. Int. Ed. Engl.* **1990**, *29*, 293–295.
239. Collins, M. J.; Gillespie, R. J.; Sawyer, J. F. *Inorg. Chem.* **1987**, *26*, 1476–1481.
240. DeLucia, M. L.; Coppens, P. *Inorg. Chem.* **1978**, *17*, 2336–2338.
241. Beck, J.; Müller-Buschbaum, K. Z. *Anorg. Allg. Chem.* **1997**, *623*, 409–413.
242. Beck, J.; Bock, G. *Angew. Chem. Int. Ed. Engl.* **1995**, *34*, 2559–2561.
243. Burns, R. C.; Collins, M. J.; Gillespie, R. J.; Schrobilgen, G. J. *Inorg. Chem.* **1986**, *23*, 4465–4469.
244. Brownridge, S.; Calhoun, L.; Jenkins, H. D. B.; Laitinen, R. S.; Murchie, M. P.; Passmore, J.; Pietikäinen, J.; Rautiainen, J. M.; Sanders, J. C. P.; Schrobilgen, G. J.; Suontamo, R. J.; Tuononen, H. M.; Valkonen, J. U.; Wong, C.-M. *Inorg. Chem.* **2009**, *48*, 1938–1959.
245. Burns, R. C.; Chan, W. L.; Gillespie, R. J.; Luk, W. C.; Sawyer, J. F.; Slim, D. R. *Inorg. Chem.* **1980**, *19*, 1432–1439.
246. Collins, M. J.; Gillespie, R. J.; Sawyer, J. F.; Schrobilgen, G. J. *Acta Crystallogr. Sect. C* **1986**, *42*, 13–16.
247. Beck, J.; Hilbert, T. Z. *Anorg. Allg. Chem.* **2000**, *626*, 837–844.
248. Boldrini, P.; Brown, I.; Gillespie, R. J.; Ireland, P. R.; Luk, W. C.; Slim, D. R.; Vekris, J. E. *Inorg. Chem.* **1976**, *15*, 765–770.
249. Beck, J.; Fischer, A. Z. *Anorg. Allg. Chem.* **1997**, *623*, 780–784.
250. Beck, J.; Wetterau, J. *Inorg. Chem.* **1995**, *34*, 6202–6204.
251. Burns, R. C.; Gillespie, R. J.; Sawyer, J. F. *Inorg. Chem.* **1980**, *19*, 1423–1432.
252. Faggiani, R.; Gillespie, R. J.; Sawyer, J. F.; Vekris, J. E. *Acta Crystallogr. Sect. C* **1989**, *C45*, 1847–1853.
253. Beck, J.; Stankowski, A. Z. *Naturforsch.* **2001**, *56b*, 453–457.
254. Beck, J.; Fischer, A. Z. *Anorg. Allg. Chem.* **2002**, *628*, 369–372.
255. Freudenmann, D.; Feldmann, C. Z. *Anorg. Allg. Chem.* **2011**, *637*, 1481–1485.
256. Beck, J.; Bock, G. Z. *Anorg. Allg. Chem.* **1994**, *620*, 1971–1975.
257. Drake, G. W.; Schimek, G. L.; Kolis, J. W. *Inorg. Chem.* **1996**, *35*, 1740–1742.
258. Klapötke, T.; Passmore, J. *Acc. Chem. Res.* **1989**, *22*, 234–240.
259. Brownridge, S.; Cameron, T. S.; Passmore, J.; Schatte, G.; Way, T. C. *J. Chem. Soc., Dalton Trans.* **1996**, 2553–2570.
260. Faggiani, R.; Gillespie, R. J.; Kolis, J. W.; Malhotra, K. C. *J. Chem. Soc., Chem. Commun.* **1987**, 591–592.
261. Beck, J.; Richter, J.; Pell, M. A.; Ibers, J. A. Z. *Anorg. Allg. Chem.* **1996**, *622*, 473–478.
262. Passmore, J.; Sutherland, G.; Whidden, T. K.; White, P. S.; Wong, C.-M. *Can. J. Chem.* **1985**, *63*, 1209–1214.
263. Passmore, J.; Sutherland, G.; Taylor, P.; Whidden, T. K.; White, P. S. *Inorg. Chem.* **1981**, *20*, 3839–3845. and references therein.
264. Passmore, J.; Sutherland, G.; White, P. S. *Inorg. Chem.* **1982**, *21*, 2717–2723. and references therein.
265. Passmore, J.; White, P. S.; Wong, C. M. *J. Chem. Soc., Chem. Commun.* **1985**, 1178–1179.
266. Nandana, W. A. S.; Passmore, J.; White, P. S. *J. Chem. Soc., Chem. Commun.* **1983**, 526–527.
267. Nandana, W. A. S.; Passmore, J.; White, P. S.; Wong, C.-M. *Inorg. Chem.* **1989**, *28*, 3320–3328.
268. Carnell, M. M.; Grein, F.; Murchie, M. P.; Passmore, J.; Wong, C.-M. *J. Chem. Soc., Chem. Commun.* **1986**, 225–227.
269. Schrobilgen, G. J.; Burns, R. C.; Granger, P. *J. Chem. Soc., Chem. Commun.* **1978**, 957–958.
270. Sheldrick, W. S. In *Handbook of Chalcogen Chemistry. New Perspectives in Sulfur, Selenium and Tellurium*; Devillanova, F. A., du Mont, W.-W., Eds., 2nd ed.; vol. 1; RSC Publishing: Cambridge, 2013; pp 514–544. and references therein.

271. Smith, D. M.; Ibers, J. A. *Coord. Chem. Rev.* **2000**, *187*, 200–205.
272. Steudel, R. *Topic Curr. Chem.* **2003**, *231*, 127–152.
273. Kanatzidis, M. G.; Das, B. K. *Comments Inorg. Chem.* **1999**, *21*, 29–51.
274. Kanatzidis, M. G.; Huang, S. P. *Coord. Chem. Rev.* **1994**, *130*, 509–621.
275. Müller, V.; Grebe, C.; Müller, U.; Dehnicke, K. *Z. Anorg. Allg. Chem.* **1993**, *619*, 416–420.
276. Fenske, D.; Krauter, G.; Dehnicke, K. *Angew. Chem. Int. Ed.* **1990**, *29*, 390–391.
277. Kanatzidis, M. G.; Huang, S.-P. *Inorg. Chem.* **1989**, *28*, 4667–4669.
278. Krebs, B.; Lührs, E.; Willmer, R.; Ahlers, F.-P. *Z. Anorg. Allg. Chem.* **1991**, *592*, 17–34.
279. Huang, S.-P.; Dhingra, S.; Kanatzidis, M. G. *Polyhedron* **1992**, *11*, 1869–1875.
280. Liebing, P.; Kuhling, M.; Swanson, C.; Feneberg, M.; Hilfert, L.; Goldhahn, R.; Chivers, T.; Edelmann, F. T. *Chem. Commun.* **2019**, *55*, 14965–14967.
281. Sheldrick, W. S.; Braunbeck, H. G. *Z. Naturforsch.* **1989**, *44b*, 1397–1401.
282. Klaiber, F.; Petter, W.; Hulliger, F. *J. Solid State Chem.* **1983**, *46*, 112–120.
283. Schreiner, B.; Dehnicke, K.; Maczek, K.; Fenske, D. *Z. Anorg. Allg. Chem.* **1993**, *619*, 1414–1418.
284. Feldmann, C.; Okrut, A. *Z. Anorg. Allg. Chem.* **2009**, *635*, 1807–1811.
285. Finger, L. H.; Scheibe, B.; Sundermeyer, J. *Inorg. Chem.* **2015**, *54*, 9568–9575.
286. Steudel, R.; Chivers, T. *Chem. Soc. Rev.* **2019**, *48*, 3279–3319.
287. Steudel, R.; Steudel, Y. *Chem. Eur. J.* **2013**, *19*, 3162–3176.
288. Neumüller, B.; Schmock, F.; Kirmse, R.; Voigt, A.; Diefenbach, A.; Bickelhaupt, F. M.; Dehnicke, K. *Angew. Chem. Int. Ed.* **2000**, *39*, 4580–4582.
289. Günther, A.; Isaeva, A.; Ruck, M. *Z. Anorg. Allg. Chem.* **2012**, *638*, 2521–2525.
290. Boettcher, P.; Kretschmann, U. *J. Less-Common Metals* **1983**, *95*, 81–91.
291. Warren, C. J.; Haushalter, R. C.; Bocarsly, A. B. *Chem. Mater.* **1994**, *6*, 780–783.
292. Sheldrick, W. S.; Schaaf, B. *Z. Naturforsch.* **1994**, *49*, 993–996.
293. Reisner, C.; Tremel, W. *Chem. Commun.* **1997**, 387–388.



## 1.22 Polychalcogen molecules, ligands, and ions Part 2: Catenated acyclic molecules, ions, and p-block element derivatives

Risto S. Laitinen<sup>a</sup>, Raija Oilunkaniemi<sup>a</sup>, Tristram Chivers<sup>b</sup>, Liam McGeachie<sup>a</sup>, Paul F. Kelly<sup>c</sup>, and Roberto S.P. King<sup>d</sup>,

<sup>a</sup>Laboratory of Inorganic Chemistry, Environmental and Chemical Engineering, University of Oulu, Oulu, Finland; <sup>b</sup>Department of Chemistry, University of Calgary, Calgary, AB, Canada; <sup>c</sup>Department of Chemistry, Loughborough University, Loughborough, Leicestershire, United Kingdom; and <sup>d</sup>Foster + Freeman Ltd, Evesham, United Kingdom

© 2023 Elsevier Ltd. All rights reserved.

<b>1.22.1</b>	<b>Introduction</b>	<b>970</b>
<b>1.22.2</b>	<b>Acyclic sulfur, selenium, and tellurium allotropes</b>	<b>971</b>
1.22.2.1	Sulfur	971
1.22.2.2	Selenium and tellurium	971
1.22.2.3	High-pressure allotropes	971
<b>1.22.3</b>	<b>Acyclic polychalcogenide anions</b>	<b>974</b>
1.22.3.1	General	974
1.22.3.2	Preparation	974
1.22.3.3	Structures	974
1.22.3.4	Polysulfide radical anions $S_n^{\cdot-}$ ( $n = 2-9$ )	975
<b>1.22.4</b>	<b>Polychalcogenide derivatives of the p-block elements</b>	<b>976</b>
1.22.4.1	General	976
1.22.4.2	Group 13 complexes	976
1.22.4.3	Group 14 derivatives and complexes	981
1.22.4.3.1	Organic polychalcogenides and related silicon derivatives	981
1.22.4.3.2	Germanium, tin, and lead complexes	987
1.22.4.4	Group 15 derivatives and complexes	988
1.22.4.4.1	Chalcogen-nitrogen compounds	988
1.22.4.4.2	Chalcogen-phosphorus compounds	994
1.22.4.4.3	Chalcogen-arsenic, -antimony, and -bismuth compounds and complexes	998
1.22.4.5	Chalcogen halogenides	1005
1.22.4.5.1	Electrically neutral molecules	1005
1.22.4.5.2	Chalcogen-halogen cations	1010
1.22.4.5.3	Polychalcogen-halogen anions	1013
<b>1.22.5</b>	<b>Summary</b>	<b>1014</b>
<b>References</b>		<b>1015</b>

### Abstract

The present chapter is Part 2 of the treatise about the chemistry of polychalcogen molecules, ligands, and ions and provides an overview of the recent developments in the chemistry of catenated polychalcogen species. Cyclic all-chalcogen species in different chemical environments are covered in Part 1. This review includes acyclic chalcogen allotropes, acyclic polychalcogenide dianions and radical monoanions, as well as representative examples of their derivatives comprising both molecular polychalcogenides and the complexes in which heavy p-block elements act as central atoms. Sulfur has the strongest propensity for catenation and the number of polysulfur species is the highest among the chalcogens. By contrast, selenium and in particular tellurium exhibit structural diversity, which has not been observed for sulfur. This review emphasizes the preparation, structures, and bonding of the polychalcogen derivatives and complexes, but important applications are also described. The main bulk of literature covers the period 1991–2022, but older references have been cited, as appropriate.

### 1.22.1 Introduction

With the exception of carbon due to the discovery of fullerenes and carbon nanotubes, sulfur is known to exhibit the largest number of allotropic forms of all elements because of its strong tendency to catenate, i.e., to form cumulated sulfur-sulfur bonds.<sup>1–6</sup> The two heavier chalcogen elements, selenium and tellurium mirror this propensity, though their allotropy is significantly simpler.<sup>1,4,6</sup> Catenation also leads to a large number of compounds,<sup>7–11</sup> ions,<sup>12–21</sup> and complexes<sup>22–31</sup> that contain polychalcogen moieties.

This article is Part 2 of the discussion of the structural and chemical consequences of chalcogen bond catenation in different environments. Part 1 was concerned with cyclic all-chalcogen molecules, ions, and ligands.<sup>6</sup> In the current treatise, the synthetic, structural, and bonding aspects of catenated acyclic molecules and ions, as well as their main group compounds are discussed. The chemistry of the related transition metal complexes has been reviewed several times during the recent decades<sup>22–31</sup> and will not be considered in this account.

Some illustrative examples of chalcogen species, which are within the scope of this review, are shown in **Table 1**.

The structural features of the chalcogen molecules and ions can be explained in terms of minimized  $np$  lone-pair interactions, the propensity to form  $\pi$ -bonds,<sup>1–6,9</sup> hypervalency,<sup>32,33</sup> hyperconjugative  $np^2 \rightarrow n\sigma^*$  interactions,<sup>9,34</sup> attractive  $\pi^*-\pi^*$  interactions,<sup>35</sup> and secondary bonding interactions (also known as chalcogen bonds).<sup>36–41</sup>

## 1.22.2 Acyclic sulfur, selenium, and tellurium allotropes

### 1.22.2.1 Sulfur

In addition to 11 well-characterized homocyclic molecules,<sup>1–6</sup> sulfur also exhibits several polymeric, acyclic allotropes. Their structural chemistry has been thoroughly reviewed by Steudel and Eckert.<sup>42</sup> Three crystalline forms have been reported at ambient temperature and pressure, two of them are fibrous and the third is laminar. The crystal structure of one fibrous form,  $S_\psi$  is characterized more completely. In addition, there are several incompletely characterized polymeric forms.<sup>42</sup> In most cases, polymeric allotropes and several homocyclic rings are formed as mixtures.

$S_\psi$  is prepared by stretching freshly quenched liquid sulfur, which has been heated above the polymerization threshold.<sup>43–45</sup> The soluble sulfur ring fractions are removed by extracting with  $CS_2$ . The X-ray studies<sup>46–48</sup> reveal that the crystal lattice is composed of both right- and left-handed helical chains, as shown in **Fig. 1**. The S–S bond length is 2.066 Å, the bond angle 106.0°, and the torsional angle 85.3°. These values are close to those in  $S_8$ <sup>1–6</sup> and can be considered to represent the unstrained bonding arrangement.

The composition of molten sulfur has been under extensive investigations over a hundred years (for detailed reviews about the historical development, see Refs. 49,50). While the melting point of monoclinic  $\beta$ - $S_8$  of 120.1 °C<sup>51</sup> is generally considered to be the thermodynamical melting point of sulfur, the liquid freezes at this temperature, only if it is frozen immediately after the melting. Upon prolonged standing at temperatures slightly above 120 °C, the freezing point is lowered to *ca.* 115.2 °C,<sup>51</sup> which has been interpreted to be due to the dissociation of molten  $S_8$  to other molecular forms, called  $S_\pi$ . The equilibrium concentration of  $S_\pi$  was estimated to be *ca.* 4.8% based on Raoult's law.<sup>52</sup>

The molecular composition of  $S_\pi$  was unambiguously determined from melts at different temperatures after they were quenched using liquid nitrogen by using Raman spectroscopy<sup>52</sup> and high-performance liquid chromatography involving the reversed-phase columns.<sup>53</sup> The equilibrium melt consisted of  $S_6$  (0.6%),  $S_7$  (2.8%), and rings larger than  $S_8$  (1.5%) in addition to  $S_8$  (95.1%).

Polymeric sulfur was detected in the melt only above the polymerization threshold of 159 °C. The determination was based on the content of insoluble material in the quenched melt, which was redissolved in  $CS_2$ .<sup>54</sup> It can be seen from **Fig. 2** that the polymerization takes place at the expense of  $S_8$ . The content of other sulfur rings remains relatively constant.

### 1.22.2.2 Selenium and tellurium

Contrasting the behavior of sulfur, polymeric hexagonal  $\alpha$ -selenium and -tellurium are the thermodynamically stable allotropes of the elements. They are mutually isostructural and are composed of a network of trigonal helical chains, as shown in **Fig. 3(a)**. The Se–Se bond length is 2.350 Å<sup>63</sup> and the Te–Te bond length is 2.835 Å<sup>64</sup> both corresponding closely to single bond lengths. The closest interchain distances are 3.463 Å<sup>63</sup> and 3.4912 Å,<sup>64</sup> respectively. As seen from **Fig. 3(a)**, the closest interchain contacts expand the coordination around each atom into a distorted octahedron consistent with the concept of secondary bonding interactions by Alcock.<sup>36</sup> They are expectedly weaker in selenium than in tellurium (the van der Waals' radii of selenium and tellurium are 1.80 and 2.20 Å, respectively).


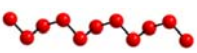
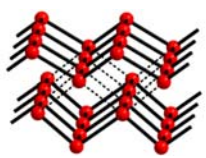
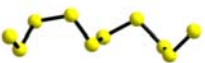
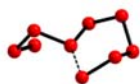

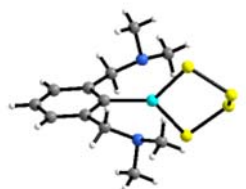
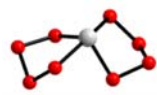
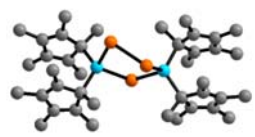
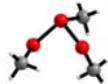
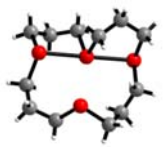
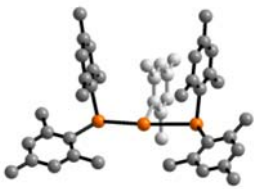
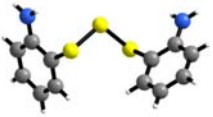
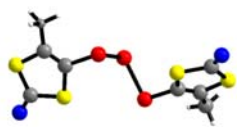
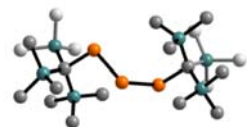
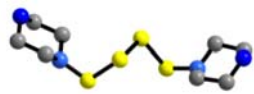
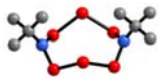
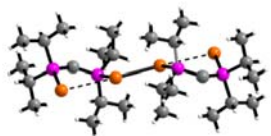
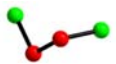
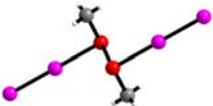
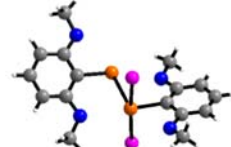
### 1.22.2.3 High-pressure allotropes

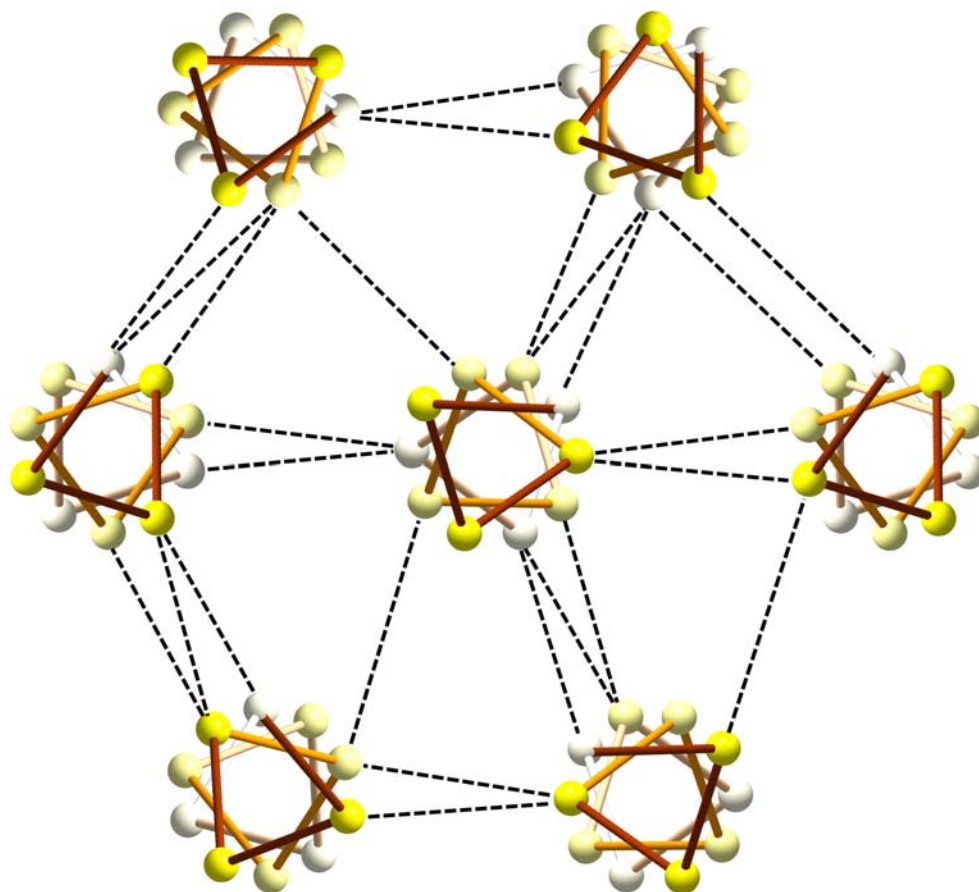
Sulfur, selenium, and tellurium all have several high-pressure allotropes, though complete information on their high-pressure behavior is still rather vague. The comprehensive reviews of the high-pressure forms of sulfur<sup>42,65</sup> indicate often contradictory conclusions, and the situation is not much better in the case of selenium and tellurium.<sup>66</sup> Some high-pressure phases, which have been unambiguously isolated and structurally characterized for sulfur, selenium, and tellurium are shown in **Fig. 3**. At relatively low pressure of 3 GPa, the trigonal helical form of sulfur has been characterized.<sup>55</sup>

Recently, however, even the structures of the two lowest high-pressure forms have been questioned and incommensurate crystal structures have been suggested instead.<sup>67</sup> It can be seen from **Fig. 3(a–d)** that as the pressure increases, the packing becomes more efficient and approaches and finally reaches the *bcc* structure.

The electrical properties of sulfur, selenium, and tellurium are dependent on pressure. Whereas the ambient form of sulfur is an electrical insulator, the trigonal forms of selenium and tellurium are semiconducting. All high-pressure polymorphs exhibit metallic conductivity.<sup>62,68</sup> In addition, both the high-pressure polymorphs of the elements are superconducting.<sup>69,70</sup> The transition

**Table 1** Examples of catenated polychalcogen molecules, ions, compounds, and p-block element derivatives.

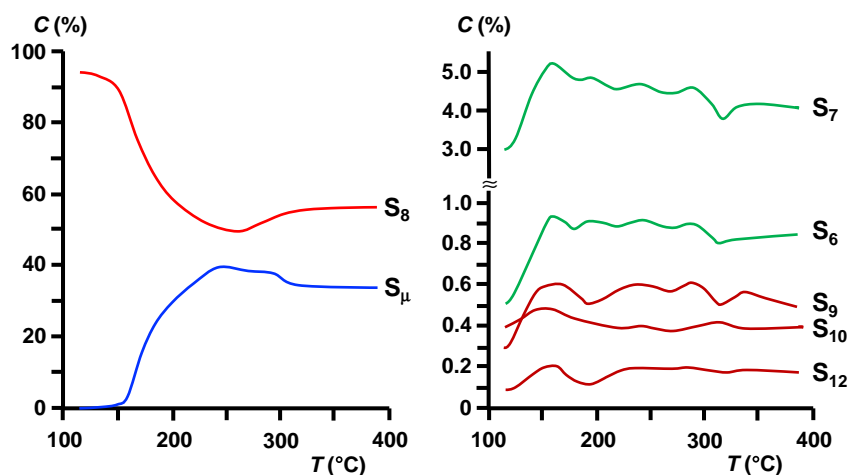
<i>Polymeric chalcogen phases</i>		
		
$S_{\infty}$	$Se_{\infty}, Te_{\infty}$	High-pressure allotope ( <i>bco</i> ) S, Se, Te
<i>Anions</i>		
		
$S_{10}^{2-}$	$Se_9^{2-}$	$Te_{13}^{2-}$
<i>p-Block element derivatives</i>		
		
$[Ga\{(CH_3)_2NCH_2\}_2C_6H_3(S_4)]$	$[Pb(Se_4)_2]^{2-}$	$[\{Si(C_5Me_5)_2\}_2(Te)(Te_2)]$
<i>Cations</i>		
		
$Me_3S_3^+, Me_3Se_3^+$	$[Se_4(CH_2)_{12}]^{2+}$	$(mes)_3Te_3^+$
<i>Organic polychalcogenides</i>		
		
$S_3(C_6H_4NH_2)_2$	$[SC(O)SC(Me)C]_2Se_3$	$E_3[C(SiMe_3)_3]_2$ (E = Se, Te)
<i>Group 15 derivatives</i>		
		
$[O(CH_2)_4N]_2E_4$ (E = S, Se)	$Se_6(N^iBu)_2$	$(TeP^iPr_2Np^iPr_2Te)_2$
<i>Chalcogen halogenides</i>		
		
$E_2X_2$ (E = S, Se, Te; X = F, Cl, Br)	$Me_2Se_2(I_2)_2$	$\{(MeO)_2C_6H_3\}TeI_2Te\{C_6H_3(OMe)_2\}$



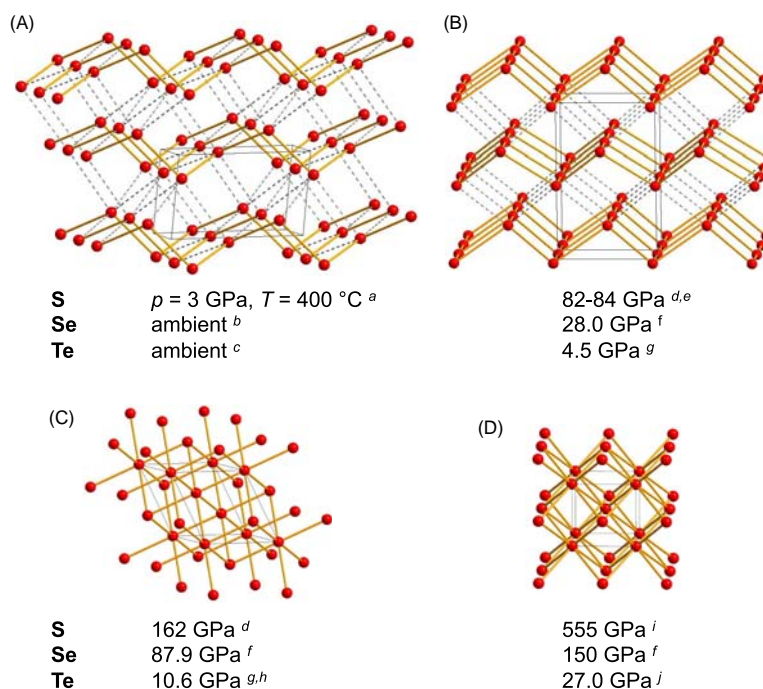
**Fig. 1** The left and right-handed helices in polymeric fibrous sulfur  $S_{\psi}$ . The shortest interhelical distances are in the range 3.33–3.48 Å as indicated by dashed lines.<sup>42,47</sup>

temperature seems to increase as a function of pressure and is in the range of 2.5–4.3 K up to 15 GPa and is *ca.* 6.5 K in the range 15–18 GPa.<sup>71</sup>

The research activity has been boosted by the observation that a mixed selenium-tellurium system shows enhanced conducting and photoconducting properties compared to those of selenium.<sup>72</sup> The indexing of X-ray powder diagrams in terms of a hexagonal unit cell indicates an almost linear variation in the lattice constants as a function of the elemental composition.<sup>73</sup> These results can be interpreted by the statistical distribution tellurium and selenium atoms in the helical chain that is shown in Fig. 3(a).



**Fig. 2** The concentration (%) of sulfur species in liquid sulfur as a function of temperature.<sup>50,54</sup>  $S_{\mu}$  indicates of polymeric sulfur of unspecified chain length. Adapted with permission from Steudel, R. *Topics Curr. Chem.* **2003**, 230, 81–116. © 2003, Springer-Verlag.



**Fig. 3** Well-characterized sulfur, selenium, and tellurium allotropes as a function of pressure. (a) hexagonal polymorph, (b) base-centered orthorhombic polymorph (*bco*), (c) rhombohedral polymorph ( $\beta$ -Po structure), (d) base-centered cubic polymorph (*bcc*). <sup>a</sup> Ref. 55, <sup>b</sup> Ref. 56, <sup>c</sup> Ref. 57, <sup>d</sup> Ref. 56, <sup>e</sup> Ref. 57, <sup>f</sup> Ref. 58, <sup>g</sup> Ref. 59, <sup>h</sup> Ref. 60, <sup>i</sup> Ref. 61, <sup>j</sup> Ref. 62.

### 1.22.3 Acyclic polychalcogenide anions

#### 1.22.3.1 General

Polychalcogenide anions serve as useful nucleophilic reagents in many chemical applications.<sup>74</sup> The wB97XD/6-311++G(d,p)//wB97XD/6-31+G(d) computations of  $\text{H}_2\text{S}_n$ ,  $\text{HS}_n^-$ , and  $\text{S}_n^{2-}$  ( $n \leq 30$ ) including continuum model for the solvation effects of water indicated that for  $n > 4$ , deprotonated  $\text{S}_n^{2-}$  are predominant.<sup>75</sup> It was also reported that polysulfides may serve as reservoirs for sulfane sulfur.

Their synthetic and structural chemistry as well as ligand properties and applications have been reviewed several times.<sup>15–20</sup> Single-chain polysulfides  $\text{S}_n^{2-}$  ( $n = 2–6$ ) are known for alkali metals and related simple univalent cations. With bulkier counterions, anions with up to 12 sulfur atoms have been prepared and characterized.<sup>15,16,76,77</sup> Related polyselenides  $\text{Se}_n^{2-}$  ( $n = 2–11$ ) and  $\text{Te}_n^{2-}$  ( $n = 2–6, 8, 12, 13$ ) have also been reviewed.<sup>18–23</sup> In addition to acyclic polychalcogenides, cyclic anions are known for selenium and tellurium (for the more detailed description of polychalcogenide ring anions, see Ref. 6, and references therein).

#### 1.22.3.2 Preparation

The usual preparation of polychalcogenides involves (a) direct high-temperature combination of the elements, (b) reactions of alkali metals and elemental chalcogens in liquid ammonia, (c) solution reactions involving chalcogen elements and alkali metal carbonates, (d) solvothermal reactions, or (e) oxidation-reduction reactions with Lewis acids.<sup>23,74,75,78,79</sup> These methods have mostly been applied to alkali metal or alkaline earth metal sulfides, selenides, and tellurides that can then serve as precursors to other polychalcogenides. The presence of a large organic cation or the encapsulating agent such as the crown ether complex of an alkali metal leads to the stabilization of otherwise unstable anions.

Tellurium shows more diverse polyanion chemistry than sulfur and selenium due to increasing importance of hyperconjugation and secondary bonding,<sup>34</sup> when going down Group 16 (see Refs. 18,23 and references therein). By contrast to polysulfides and polyselenides, polytelluride anions can exhibit charges that deviate from  $-2$ .

#### 1.22.3.3 Structures

The X-ray structures have been determined for several acyclic polychalcogenides  $\text{E}_n^{2-}$  ( $n = 2–9, 10$ , and 12 for sulfur, 2–9 for selenium, and 2–6, 8, 12, 13, and 15 for tellurium). Shorter polychalcogenides occur as binary alkali metal or alkaline earth metal salts, but longer chains require bulkier counter-ions for stabilization.<sup>15–20</sup> These may comprise alkali or alkaline earth metals



encapsulated with crown-ethers or cryptates, or large non-coordinating monocations such as  $(Et_4N)^+$ ,  $(Ph_4P)^+$ , and  $[Ph_3PNPPh_3]^+$ . Typical structures of the open-chain polychalcogenides are exemplified by  $Se_3^{2-}$ - $Se_9^{2-}$ , and by  $S_{10}^{2-}$  and  $S_{12}^{2-}$ , as shown in Fig. 4.

Since the monoatomic counter-cations have a significant effect on the bond parameters of the polychalcogenides, the examples in Fig. 4 have been selected from salts containing bulky polyatomic cations.

It can also be seen in the examples of Fig. 4 that the counter ions have an impact on the conformations of the polychalcogenide chains. In addition to the changes in the numerical values of torsional angles, there is also a possibility for isomerism in case of  $E_n^{2-}$  chains with  $n \geq 4$  depending on the signs of the torsional angles. Longer polychalcogenides, however, tend to adopt helical conformations that mimic the hexagonal polymeric allotropic forms of the elements.<sup>63,64</sup> In some cases the helical chains can be disordered in the crystalline lattice, as exemplified for  $S_6^{2-}$  in Fig. 5.

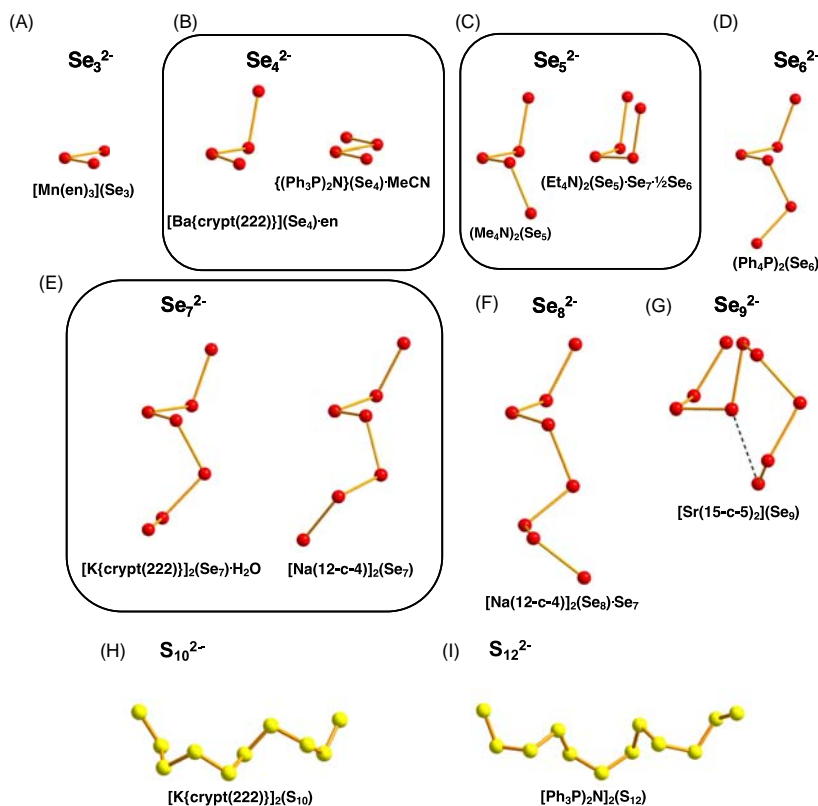
Dodecasulfide  $S_{12}^{2-}$ ,<sup>77</sup> dodecatelluride  $Te_{12}^{2-}$ ,<sup>91</sup> tridecatelluride  $Te_{13}^{2-}$ ,<sup>92</sup> and  $Te_{15}^{4-93}$  anions are the longest reported acyclic polychalcogenides. The structures of latter two dianions are shown in Fig. 6.

#### 1.22.3.4 Polysulfide radical anions $S_n^{\cdot-}$ ( $n = 2-9$ )

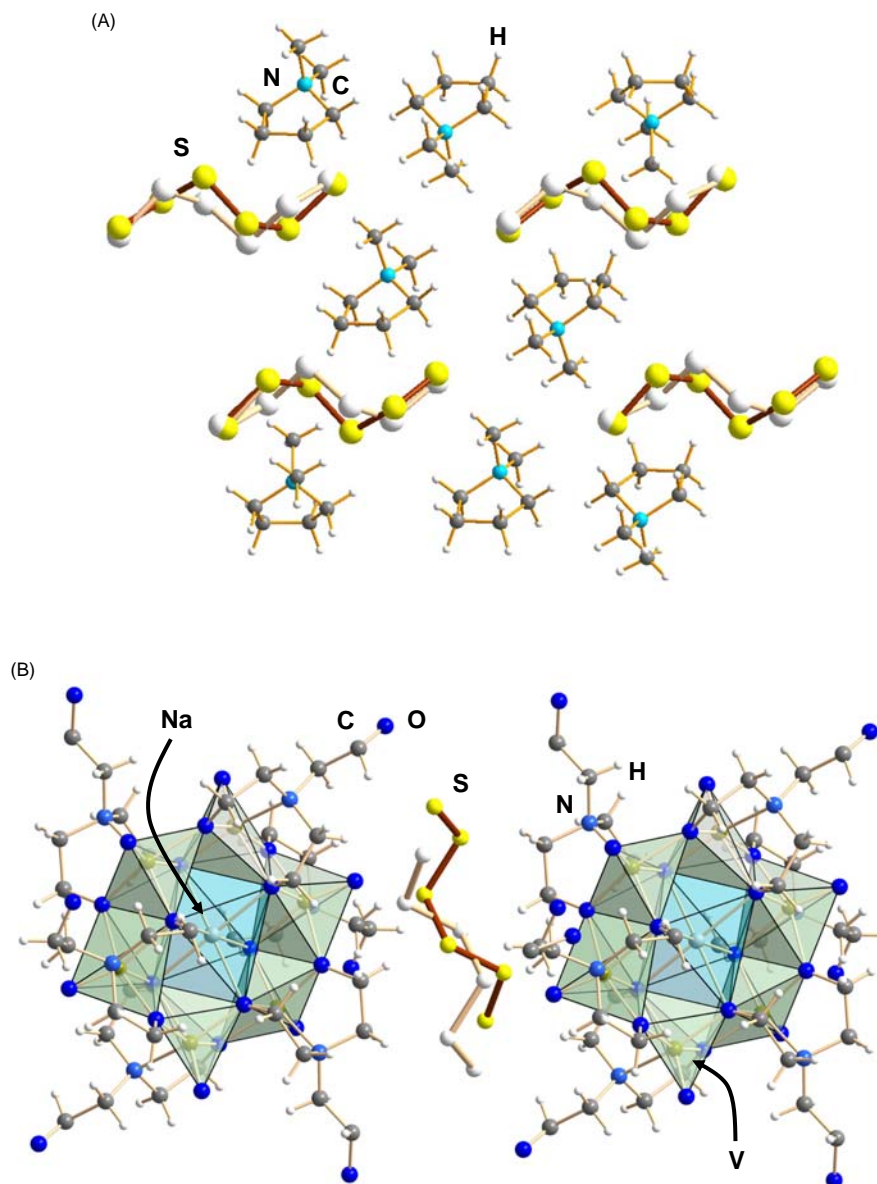
Polysulfide dianions  $S_n^{2-}$  may dissociate or disproportionate in polar solvents to afford radical anions  $S_n^{\cdot-}$ .<sup>15,16</sup> A well-known representative in this series is  $S_3^{\cdot-}$ <sup>94</sup> which is the blue chromophore in ultramarine blue, when trapped in zeolitic aluminosilicate matrix. The identity of the chromophore in ultramarine red is controversial. Recent DFT calculations for  $S_4$  and  $S_4^{\cdot-}$  embedded in a sodalite lattice indicate the red color should be attributed to the neutral allotrope rather than the radical anion.<sup>95</sup>

The occurrence and structures of  $S_n^{\cdot-}$  have been explored by Raman and EPR spectroscopy and augmented by high-level DFT calculations.<sup>15,16,96</sup> Small radical monoanions ( $n = 2-5$ ) lie at the global minima, but the larger species are cyclic, though with at least one very long S...S distance. The optimized structures of  $S_n^{\cdot-}$  ( $n = 3-5$ ) are shown in Fig. 7.

The radical anions  $S_n^{\cdot-}$  have a role in materials science, electrochemistry, organic synthesis, analytical chemistry, and geochemistry.<sup>16</sup> They are also important species in different biological processes and alkali metal-sulfur batteries. The likely reversible redox pathways suggested for the discharge of the batteries indicate that the polysulfide dianions play a significant role in generating the radical anions by dissociation or disproportionation (see Scheme 1). This mechanism has been discussed in detail.<sup>16,95</sup>



**Fig. 4** Structures of selected acyclic polychalcogenides containing weakly coordinating counter-cations. (a)  $[Mn(en)_3](Se_3)$ .<sup>79</sup> (b)  $[Ba\{crypt(222)\}](Se_4) \cdot en$ <sup>80</sup> and  $\{(Ph_3P)_2N\}(Se_4) \cdot MeCN$ .<sup>81</sup> (c)  $(Me_4N)_2(Se_5)$ <sup>82</sup> and  $(NEt_4)_2(Se_5) \cdot (1/2 Se_6 Se_7)$ .<sup>83</sup> (d)  $(Ph_4P)_2(Se_6)$ .<sup>84</sup> (e)  $[K\{crypt(222)\}]_2(Se_7) \cdot H_2O$ <sup>85</sup> and  $[Na(12-crown-4)]_2(Se_7)$ .<sup>86</sup> (f)  $[Na(12-crown-4)]_2(Se_8) \cdot (Se_7)$ .<sup>87</sup> (g)  $[Sr(15-crown-5)]_2(Se_9)$ .<sup>88</sup> (h)  $[K\{crypt(222)\}]_2(S_{10})$ .<sup>76</sup> (i)  $[(Ph_3P)_2N]_2(S_{12})$ .<sup>77</sup>



**Fig. 5** Disordered  $S_6^{2-}$  anion in (a) bis[4,5-dimethyl-1,3-bis(propan-2-yl)-1H-imidazol-3-ium] hexasulfide<sup>89</sup> and (b) bis(hexakis[ $\mu_4$ -bis(2-oxyethyl)(2-hydroxyethyl)amine]-oxo-vanadium(IV)sodium) hexasulfide methanol solvate.<sup>90</sup>

## 1.22.4 Polychalcogenide derivatives of the p-block elements

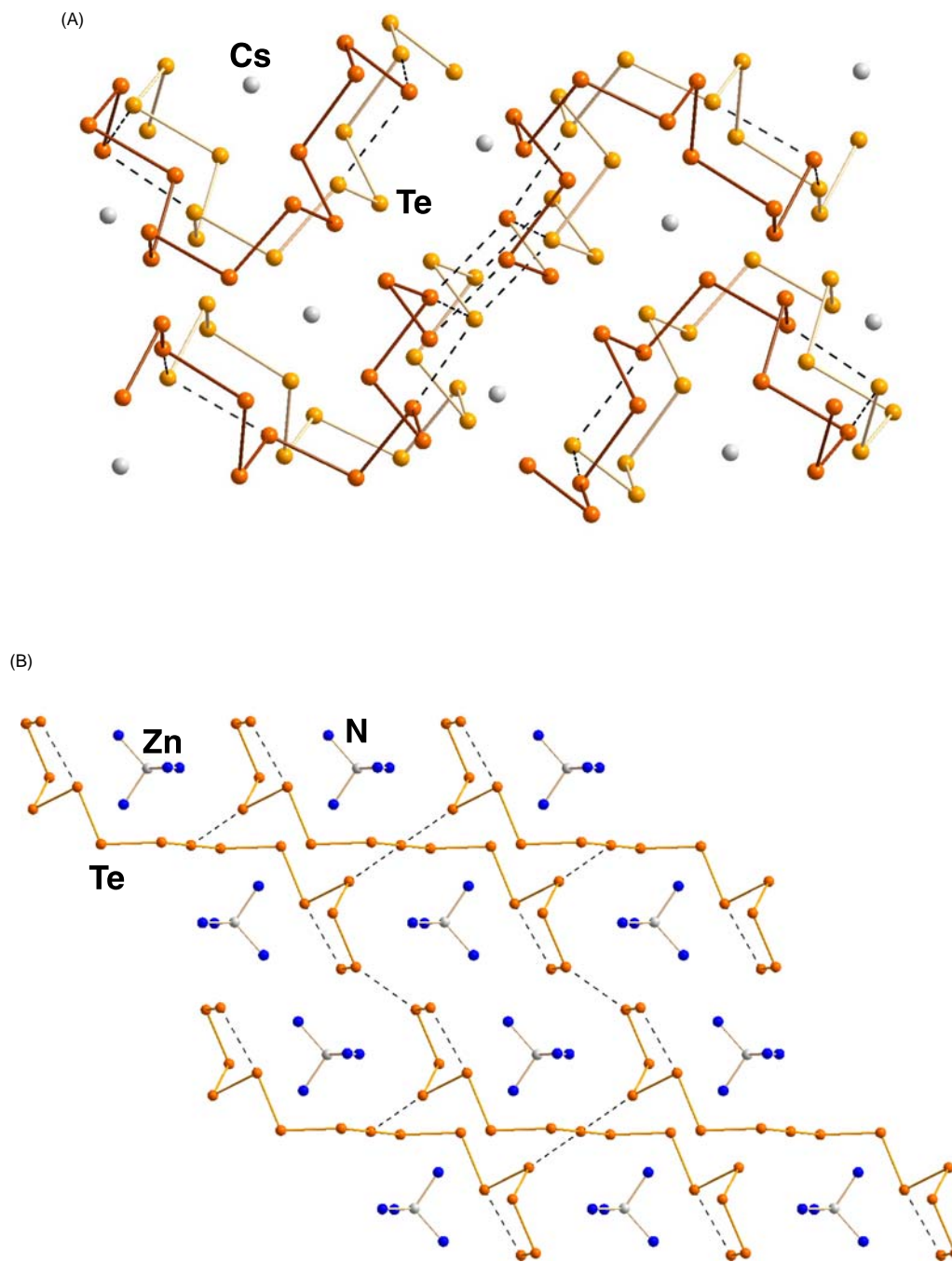
### 1.22.4.1 General

Several main group compounds contain polychalcogen fragments. Both electrically neutral molecules, as well as cationic and anionic species have been prepared and structurally characterized. The most important features of the polychalcogen compounds of the p-block elements groups 13–15, and 17 are discussed below. The chemistry of Group 16 species has been discussed in Ref. 6.

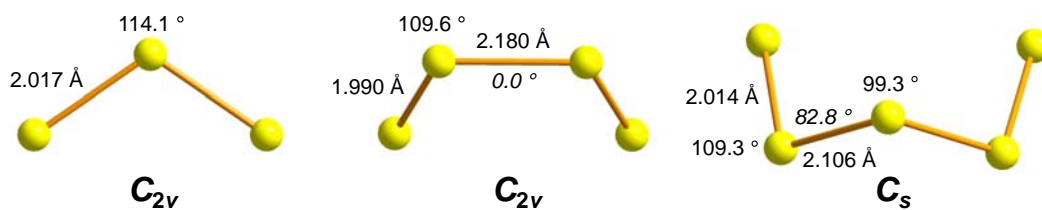
### 1.22.4.2 Group 13 complexes

Aluminum has been reported to form a few complexes containing chelating or bridging  $S_n^{2-}$  ligands (see examples in Fig. 8).<sup>97–100</sup>

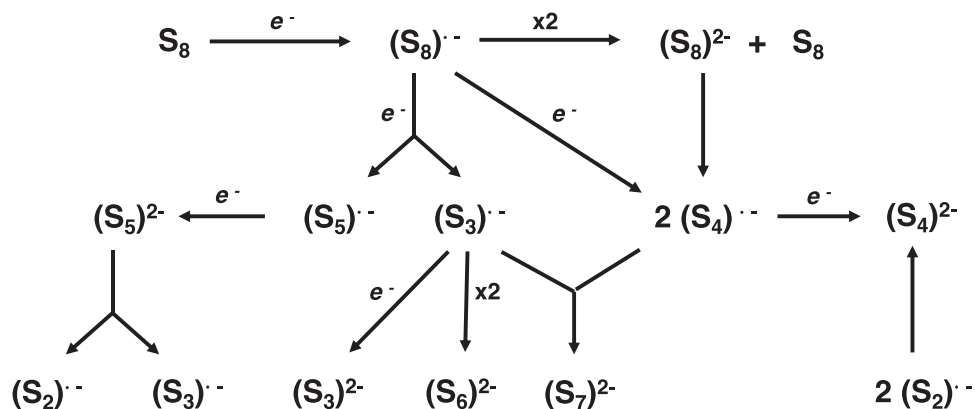
The treatment of  $[Al\{N(iPr_2C_6H_3CMe)_2CH\}(SH)_2]$  with  $(mesAg)_4$  affords  $[Al\{N(iPr_2C_6H_3CMe)_2CH\}(S_6)]$  as a by-product (see Scheme 2).<sup>100</sup> Interestingly, with an excess of  $S_8$ , only  $[Al\{N(iPr_2C_6H_3CMe)_2CH\}(S_4)]$  is formed with no indication of the formation of the hexasulfido complex.



**Fig. 6** Molecular structures of (a)  $\text{Cs}_2(\text{Te}_{13})$ <sup>92</sup> and (b)  $[\text{Zn}(\text{NH}_3)_4]_2(\text{Te}_{15})$ .<sup>93</sup>



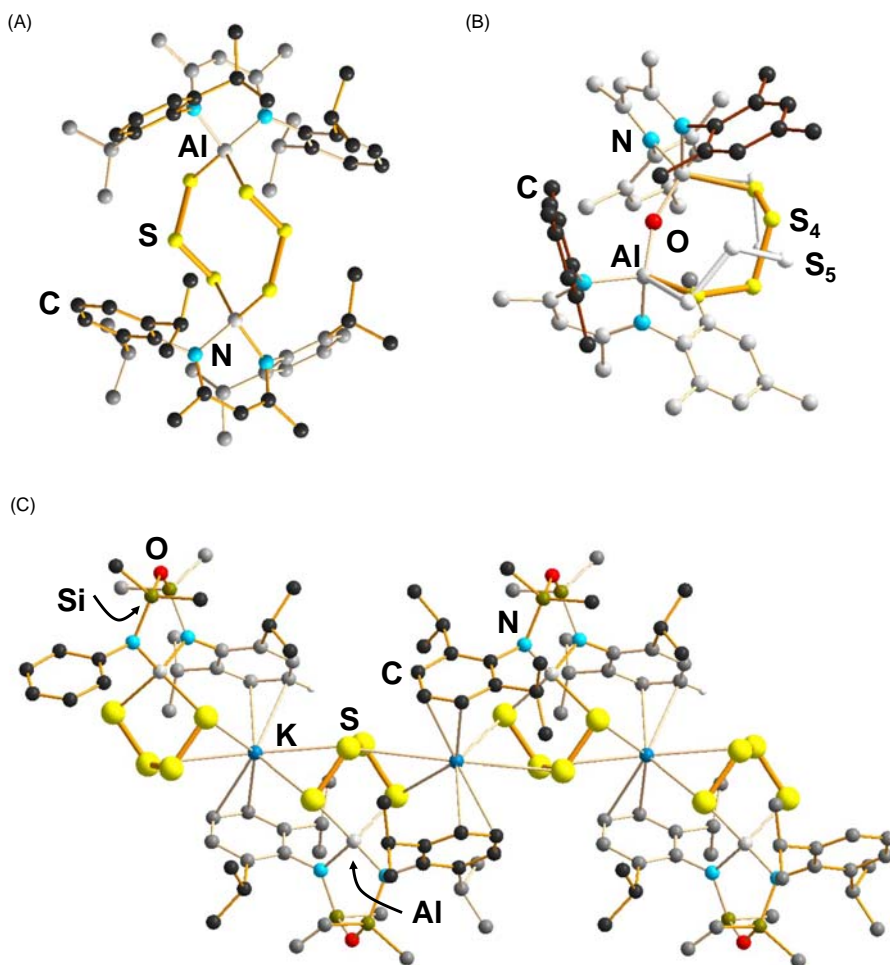
**Fig. 7** B3LYP/6-31 + G(2df,p) optimized geometries of acyclic  $\text{S}_3^{2-}$ ,  $\text{S}_4^{2-}$ , and  $\text{S}_5^{2-}$  in a polar medium with  $\epsilon = 78$ .<sup>95</sup>



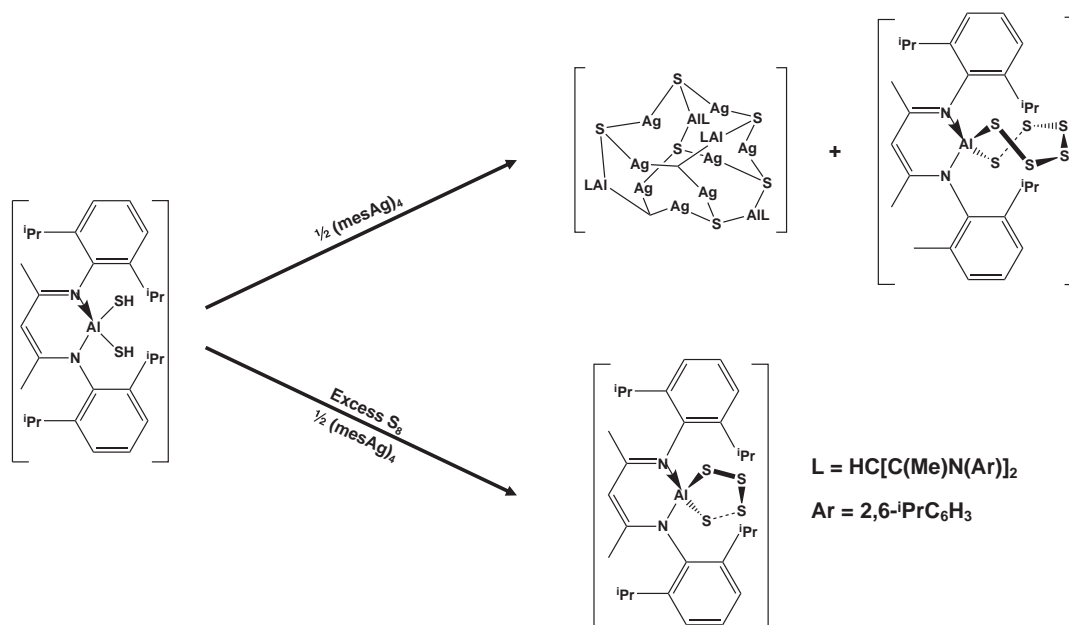
**Scheme 1** Suggested electrochemical reduction processes of  $S_8$  molecules in Li-S batteries on discharging.<sup>95</sup>

$[Al(Ar_1)(Ar_2)(H)_2]$  or  $[Al(Ar_1)(Ar_2)(SH)_2]$   $Ar_1 = 2,6-(2.4.6\text{-}^i\text{-Pr}_3\text{C}_6\text{H}_2)_2\text{C}_6\text{H}_3$ ;  $Ar_2 = 1,3,4,5\text{-tetramethylimidazol-2-ylidene}$ ) have been used to prepare  $[Al(Ar_1)(Ar_2)(S_5)]$ , with the chelating  $S_5^{2-}$  ligand.<sup>101</sup> Upon treatment of the product with  $PPh_3$ , the chain length of the pentasulfido ligand is reduced with the formation of  $[Al(Ar_1)(Ar_2)(S_4)]$  (see **Scheme 3**).

Only three complexes involving chelating or bridging polysulfido ligands are known in the case of gallium.<sup>102–104</sup>  $(C_6H_{17}N_3)_4n(C_6H_{16}N_3)_4n[Ga_{20}S_{38}]_n$ <sup>103</sup> and  $(C_4H_{12}N)_{12n}[Ga_{20}OS_{37}]_n$ <sup>104</sup> are interesting open-framework structures in which  $Ga_{20}S_{16}$  cages are linked together by bridging  $S^{2-}$  and  $S_3^{2-}$  ligands, and in the case of the latter complex also by bridging oxido



**Fig. 8** Structure of (a)  $[Al\{N(^i\text{Pr})_2C_6H_3CMe\}_2CH\}(S_3)]_2$ .<sup>97</sup> (b) Solid solution of  $[Al\{mes\}NCMe\}_2CH\}_2(O)(S_4)] \cdot THF$  (94%) and  $[Al\{mes\}NCMe\}_2CH\}_2(O)(S_5)] \cdot THF$  (6%).<sup>98</sup> (c) Structure of  $K_n[Al\{N(^i\text{Pr})_2C_6H_3SiMe_2\}_2O\}_n(S_4)_n \cdot nTHF$ .<sup>99</sup>

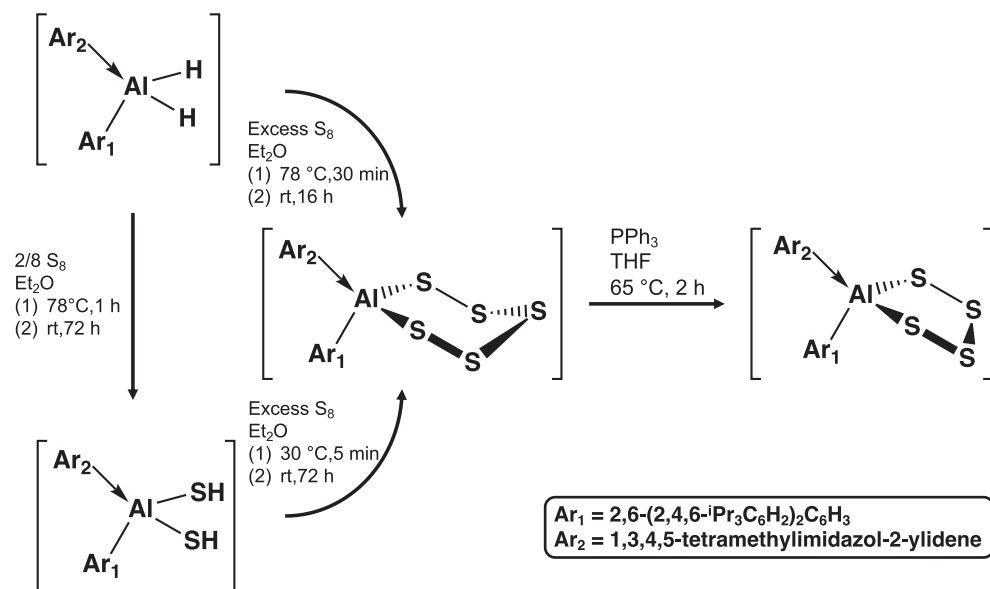


**Scheme 2** Formation of  $[\text{Al}(\text{N}^i\text{Pr}_2\text{C}_6\text{H}_3)\text{CMe}_2\text{CH}(\text{S}_6)]$  and  $[\text{Al}(\text{N}^i\text{Pr}_2\text{C}_6\text{H}_3)\text{CMe}_2\text{CH}(\text{S}_4)]$ .<sup>100</sup>

ligand (see Fig. 9). The Group 13 open-framework chalcogenide phases have seen research interest because they are microporous, exhibit fast ion conductivity and photoluminescence and tunable electronic band gaps.<sup>105</sup>

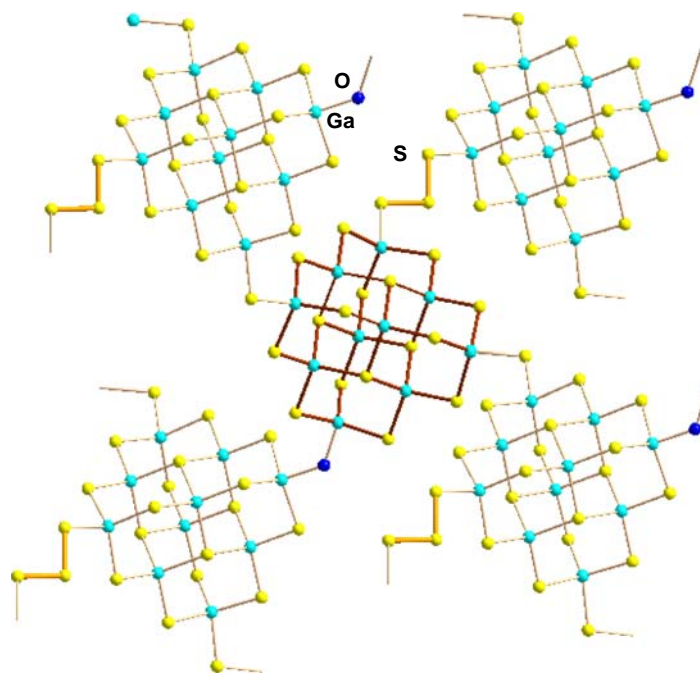
Chelating tetrasulfido ligands<sup>106–110</sup> are common in the case of indium complexes. There are also complexes in which other chelating or bridging polysulfido ligands are coordinated to indium in addition to  $\text{S}_4^{2-}$ .<sup>108,111,112</sup>

The structural chemistry involving Group 13 metal complexes with polyselenido or polytellurido ligands is mainly centered on indium, though some gallium and thallium species have also been reported.<sup>113,114</sup> The reaction of  $\text{Na}_2\text{Se}_5$  and  $\text{InCl}_3$  in DMF in the presence of  $\text{R}_4\text{MX}$  ( $\text{R} = \text{Ph}, \text{Pr}, \text{Et}; \text{M} = \text{P}, \text{N}; \text{X} = \text{Cl}, \text{Br}$ ) affords  $(\text{R}_4\text{M})_4[\text{In}_2(\text{Se}_4)_4(\text{Se}_5)]$  [see Fig. 10(a)] in good yields.<sup>115,116</sup> The hydrothermal reaction of  $\text{InCl}_3$  with  $\text{Na}_2\text{Se}_4$  in the presence of  $\text{R}_4\text{MX}$  and water at  $110^\circ\text{C}$  for 3 days yielded  $(\text{R}_4\text{M})_2[\text{In}(\text{Se}_2)(\text{Se}_4)_2]$  [see Fig. 10(b)]. When the molar ratio of  $\text{InCl}_3$  and  $\text{Na}_2\text{Se}_5$  was changed to 1:2 and the reaction was carried out in acetonitrile in the presence of  $\text{Et}_4\text{NBr}$ ,  $(\text{Et}_4\text{N})_3[\text{In}_3(\text{Se}_4)_3]$  [see Fig. 10(c)] was formed. The reaction with thallium(I) chloride resulted in the formation of the analogous salt.<sup>116</sup>

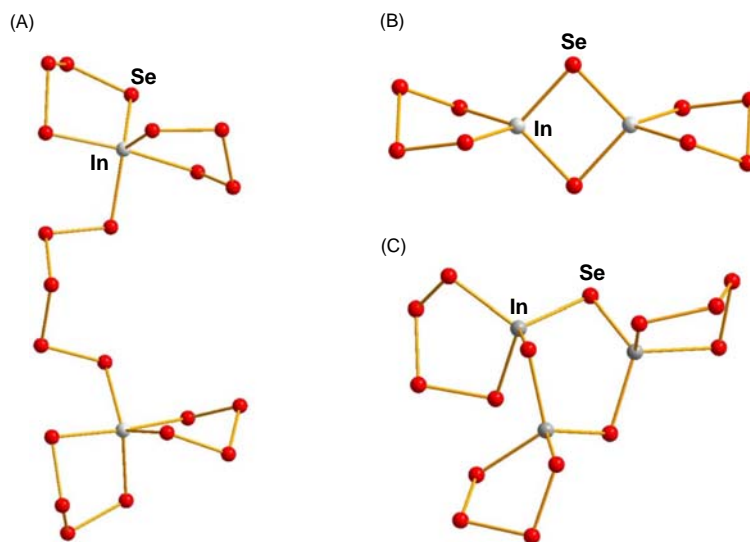


**Scheme 3** Formation of  $[\text{Al}(\text{Ar}_1)(\text{Ar}_2)(\text{S}_5)]$  and  $[\text{Al}(\text{Ar}_1)(\text{Ar}_2)(\text{S}_4)]$ .<sup>101</sup>





**Fig. 9** Crystal structure of  $(C_4H_{12}N)_{12n}(Ga_{20}OS_{37})_n$  indicating the linking of the  $Ga_{10}S_{16}$  cages by  $S_3^{2-}$ ,  $S^{2-}$ , and  $O^{2-}$  bridging ligands.<sup>104</sup>

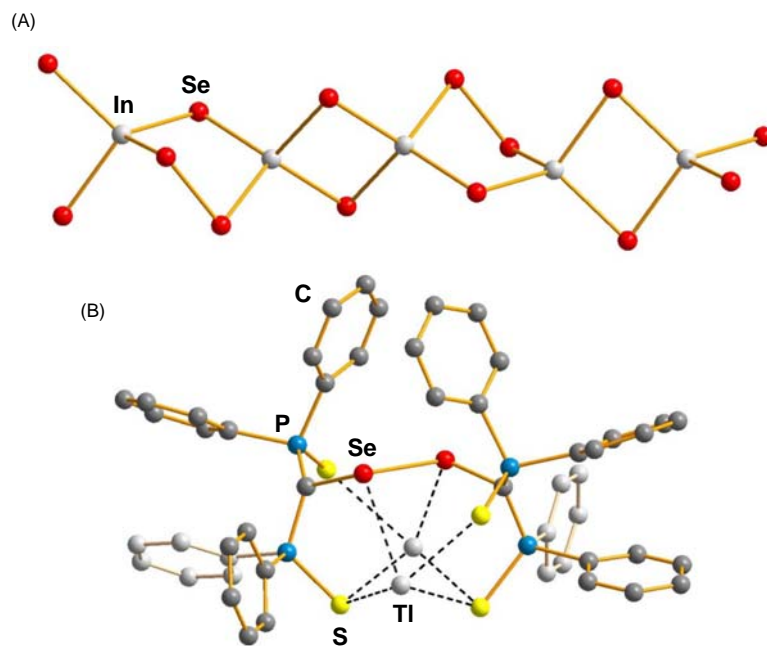


**Fig. 10** The structure of (a)  $[In_2(Se_4)_4(Se_5)]^{4-}$ ,<sup>115,116</sup> (b)  $[In_2(Se)_2(Se_4)_2]^{2-}$ ,<sup>116</sup> and (c)  $[In_3(Se)_3(Se_4)_3]^{3-}$ .<sup>116</sup>

The reaction of elemental gallium, indium, or thallium with  $(Ph_4P)_2Se_5$  and an excess of elemental selenium in a sealed, evacuated Pyrex tube at 200 °C yielded red crystals of  $(Ph_4P)[M(Se_6)_2]$  ( $M = Ga, In, Tl$ ), which exhibit an open layered framework.<sup>117</sup> These compounds have congruent melting points and transform into a glassy state upon cooling. The materials recrystallize, when subsequently reheated. The materials are also capable of ion exchange reactions, which could lead to the possibility for generation of microporous materials.

A hydrothermal reaction involving elemental indium, selenium, and *trans*-1,4-diaminocyclohexane in water at 170 °C for 10 days affords  $(C_6H_{16}N_2)[In_2(Se)_3(Se_2)]$ , which contains polymeric  $[In_2(Se)_3(Se_2)]^{2-}$  chains [see Fig. 11(a)].<sup>118</sup> The optical band gap of  $(C_6H_{16}N_2)[In_2(Se)_3(Se_2)]$  was estimated as 2.23 eV at room temperature.

The metathetical reaction of  $[Li(TMEDA)]_2\{(SPh_2P)_2C\}_2Se_2$  and TIOEt at a low temperature cleanly affords  $Tl_2\{(SPh_2P)_2C\}_2Se_2$  in good yield.<sup>119</sup> The molecular structure is shown in Fig. 11(b). The Se–Se bond length of 2.531 Å is significantly longer than the single bond, but it is near the Se–Se bond of 2.508 Å observed in  $[Li(TMEDA)]_2\{(SPh_2P)_2C\}_2Se_2$ .<sup>120</sup> Their respective Pauling bond orders of 0.76 and 0.79 are close to the value 0.84 calculated for the bond order of the Se–Se bond in



**Fig. 11** (a) The structure of polymeric  $[\text{In}_2(\text{Se})_3(\text{Se}_2)]^{2-}$  anion.<sup>118</sup> (b) The structure of  $\text{Tl}_2\{[(\text{SPh}_2\text{P})_2\text{C}]_2\text{Se}_2\}$ .<sup>119</sup>

$(\text{SePR}_2\text{NPR}_2\text{Se})_2$  with the observed elongation of 6%.<sup>121</sup> This is consistent with the conclusion that the long Se–Se bond is a consequence of the dimerization of the  $(\text{SPh}_2\text{P})_2\text{CSe}^-$  radical anion.<sup>119</sup>

The few known polymeric telluroindates have been prepared by solvothermal reactions.<sup>122–126</sup> The polymeric anions all have a formal composition  $\text{In}_2\text{Te}_6^{2-}$ . They are all composed of similar cyclic six-membered  $\text{TeInTeTeInTe}$  building blocks, but their overall structures differ considerably, as shown in Fig. 12.

The interest in anionic indium or thallium networks comes from their thermal behavior. Thermogravimetry and DSC studies have shown that they may provide a low-temperature route to binary chalcogenides of catalytic and electronic importance and therefore they may prove to be suitable precursors for fabrication of thin films.<sup>117,118</sup>

### 1.22.4.3 Group 14 derivatives and complexes

#### 1.22.4.3.1 Organic polychalcogenides and related silicon derivatives

A large number of organic dichalcogenides are known. The number of crystal structures reported in Cambridge crystallographic database<sup>127</sup> (July 11, 2022) is shown in Table 2.

The number of organic polysulfides is significantly larger than those of polyselenides and polytellurides. While the maximum observed chain length in acyclic organic polysulfides is seven and that in cyclic polysulfides is nine, no structures with longer than three selenium or tellurium atoms in the chains are known with the exception of one acyclic and two cyclic tetraselenides. Examples of acyclic  $\text{R}_2\text{S}_n$  ( $n = 4\text{--}7$ ) are shown in Fig. 13.

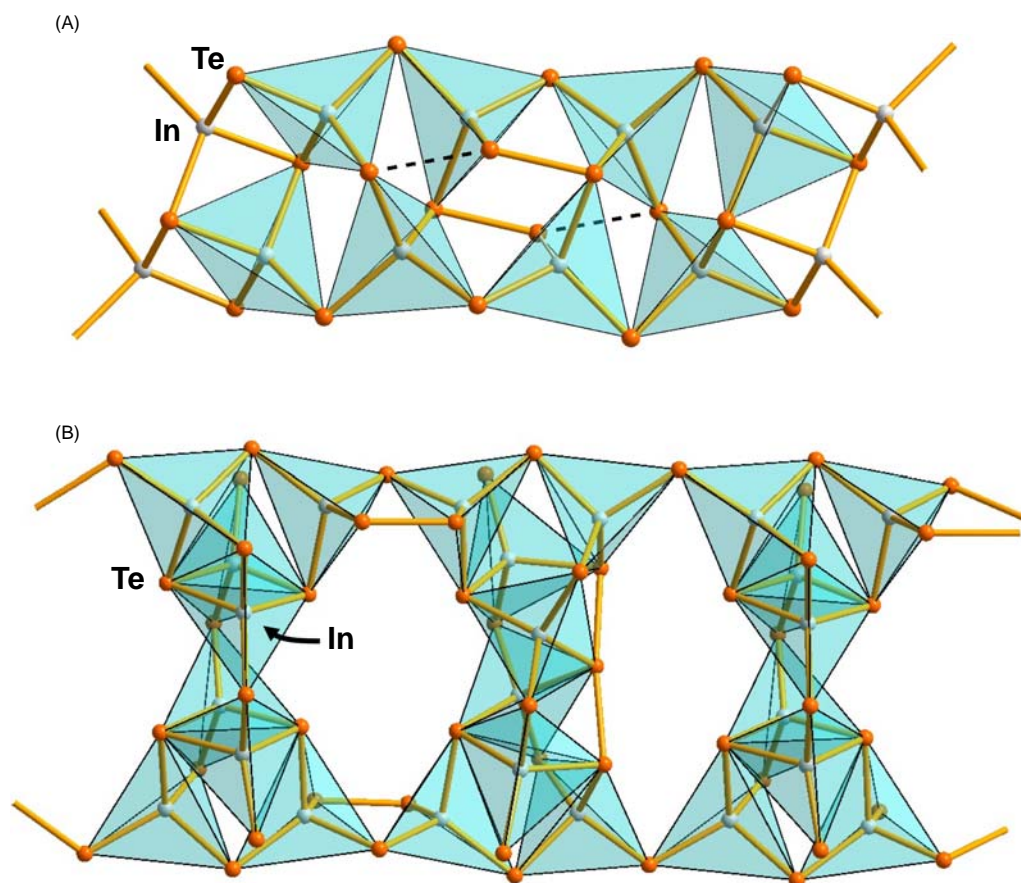
The chalcogen-chalcogen bonds in these species show quite normal single-bond values with the torsional angles near  $90^\circ$ , as exemplified for acyclic trichalcogenides in Fig. 14. The dependence of the chalcogen-chalcogen bond lengths on the p lone-pair interactions of the adjacent chalcogen atoms have been discussed in several reviews.<sup>1,2,7</sup>

While the presence of organic polyselenides  $\text{R}_2\text{Se}_n$  ( $n > 4$ ) has been detected in different mixtures by  $^{77}\text{Se}$  NMR spectroscopy,<sup>132,133</sup> the structural information on the isolated tetraselenides is much sparser than that of di- and triselenides. Crystal structures of bis[2-*N,N'*-dimethyl(amino)phenyl] diselenide,<sup>134</sup> triselenide,<sup>135</sup> and tetraselenide<sup>136</sup> are shown in Fig. 15. The polyselenium chain is stabilized by  $\text{N}\cdots\text{Se}$  secondary bonding interactions.

In addition to acyclic polychalcogenides, also cyclic organic species have been prepared and characterized. Their chalcogen-chalcogen bond parameters are in close agreement with those of dichalcogenides. Some examples are shown in Fig. 16.

The trisulfide-linked oligopyrrolic macrocycle [see Fig. 16(a)] has been prepared by treating 3,4-diethylpyrrole with  $\text{S}_2\text{Cl}_2$  in THF at  $-78^\circ\text{C}$ .<sup>137</sup> It has a bowl-shaped structure with a similar cone conformation to that of calix[4]-pyrroles.  $\text{C}_5\text{H}_5\text{O}(\text{OAc})_3\text{Se}_4$  [see Fig. 16(b)] has been obtained as a main product from mannose by treatment with  $(\text{Et}_4\text{N})_2\text{WSe}_2$ .<sup>138</sup> It is the first tetraselenide in which the  $\text{Se}_4$  fragment forms a cyclic arrangement with the carbon backbone.

The molecular structure of  $\text{Se}_6\{\text{C}=\text{C}(\text{Et}_2\text{N})_2\}_2$ <sup>139</sup> resembles that of 1,5- $\text{Se}_6(\text{N}^t\text{Bu})_2$ ,<sup>141</sup> as shown in Fig. 16(c); for a more detailed discussion on chalcogen imide derivatives, see Section 1.22.4.4.1. The compound is prepared from  $(\text{Et}_2\text{N})_2\text{C}=\text{CHCl}$  by refluxing with gray selenium in benzene for 5 h.  $\text{Se}_6\{\text{C}=\text{C}(\text{Et}_2\text{N})_2\}_2$  was reported to be a convenient reagent for carbenium ions (see Scheme 4).<sup>142</sup>

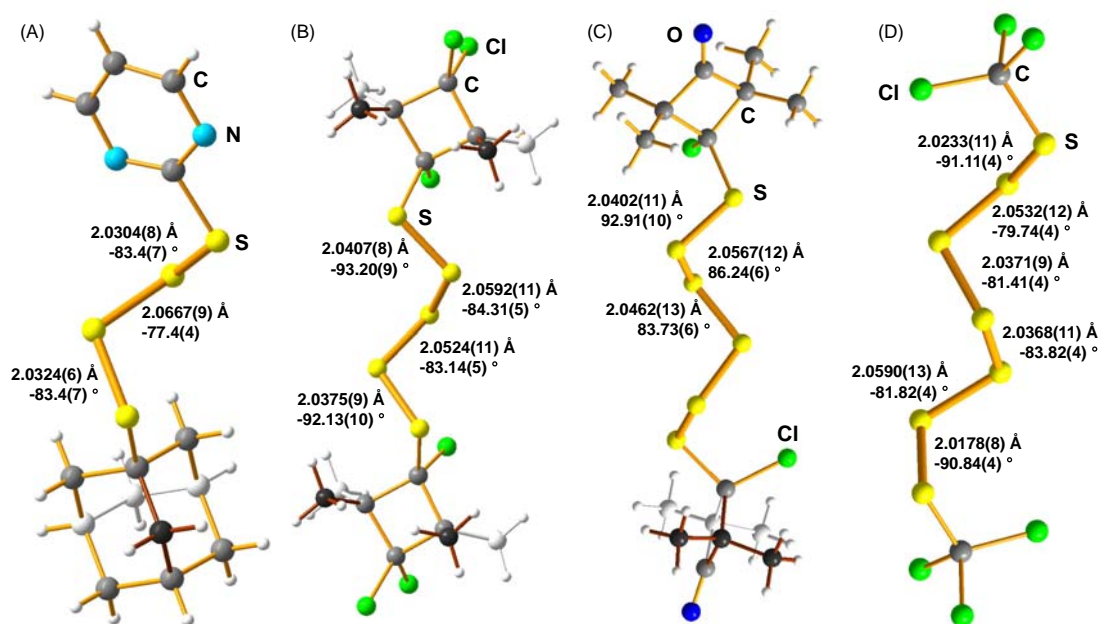


**Fig. 12** Structure of the anionic indium-tellurium framework in (a)  $[\text{HDAP}]_8[\text{In}_{12}\text{Te}_{23}]^{125}$  and (b)  $[\text{Zn}(\text{en})_3]_4[\text{In}_{16}(\text{Te}_2)_4(\text{Te}_3)(\text{Te})_{22}]^{126}$  (en = 1,2-diaminoethane; DAP = 1,3-diaminopropane).

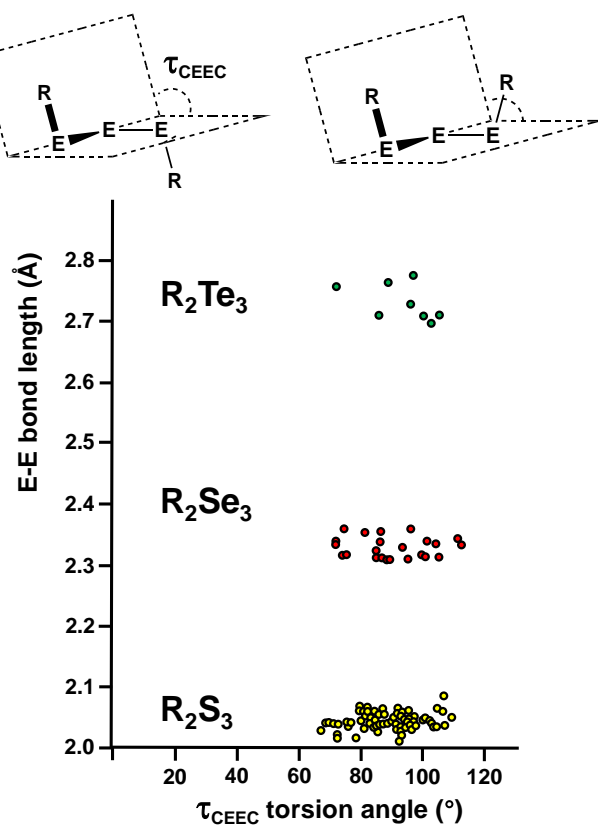
$\{(\text{Ph}_3\text{Te})(\text{TeC}_6\text{H}_4\text{R})\}_2$  (R = Me, OMe) is an ionic salt with triphenyltelluronium cation and 4-methylphenyltelluroate or 4-methoxyphenyltelluroate anion.<sup>140</sup> The products are prepared by adding triphenyltelluronium chloride in methanol to an ethanolic solution of an appropriate sodium aryltelluroate. The orange crystals thus formed are stable below  $-18^\circ\text{C}$  with the methoxyphenyl telluroate slightly more stable than the methylphenyltelluroate. The crystal structure determinations reveal that both products have a cyclic  $(\text{Ph}_3\text{Te})_2(\text{TeC}_6\text{H}_4\text{R})_2$  arrangement with a nearly planar  $\text{Te}_4$  ring. This arrangement with the two  $\text{Ph}_3\text{Te}^+$  cations and  $\text{RTe}^-$  anions is reminiscent of the crystal structure of  $\text{Ph}_3\text{TeCl}$ , which also shows two  $\text{Ph}_3\text{Te}^+$  cations linked by two  $\text{Cl}^-$  bridges into a square-planar arrangement.<sup>143</sup> The  $\text{Te}\cdots\text{Te}$  distances in the two salts range  $3.1507(8)$ – $3.5957(14)$  Å.<sup>140</sup> It can be seen

**Table 2** Number of organic polychalcogenides in Cambridge Crystallographic Database (July 11, 2022).<sup>127</sup>

Species	n	Acyclic poly-chalcogenides	Cyclic poly-chalcogenides
$\text{RS}_n\text{R}$	2	1589	1204
	3	66	65
	4	12	50
	5	3	67
	6	4	4
	7	1	2
	8	–	1
	9	–	1
	$\text{RSe}_n\text{R}$	2	319
3		29	10
4		1	2
$\text{RTe}_n\text{R}$	2	107	41
	3	5	–

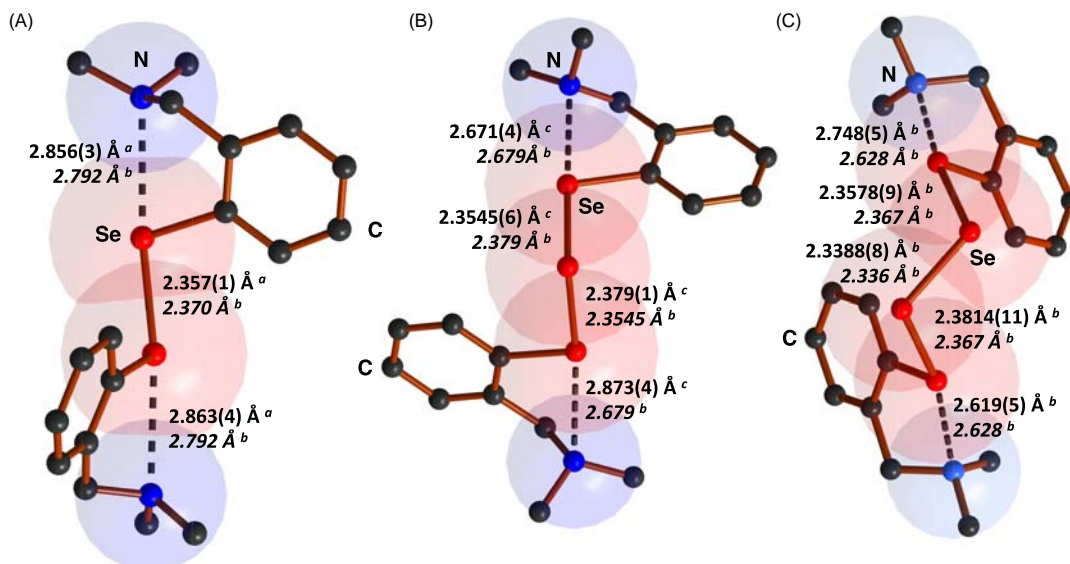


**Fig. 13** Structures of some illustrative examples of  $R_2S_n$  ( $n = 4-7$ ) indicating the SS bond lengths and the corresponding torsional angles. (a) adamantyl pyrimidyl tetrasulfide.<sup>128</sup> (b) 1,5-bis(1,3,3-trichloro-2,2,4,4-tetramethylcyclobutyl)pentasulfide.<sup>129</sup> (c) 1,6-bis(1-chloro-2,2,4,4-tetramethyl-3-oxocyclobutan-1-yl)hexasulfide.<sup>130</sup> (d) 1,7-bis(trichloromethyl)heptasulfide.<sup>131</sup>

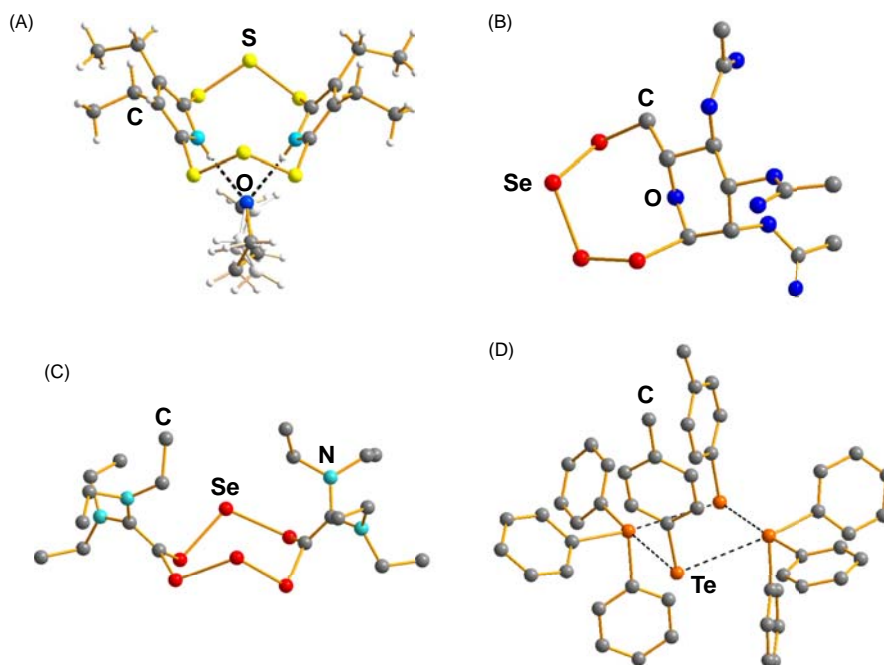


**Fig. 14** The chalcogen-chalcogen bond lengths as a function of the torsional angle in acyclic organic trichalcogenides. Data taken from Cambridge Crystallographic Database on July 11, 2022. ConQuest, Version 2022.1.0. Cambridge Crystallographic Data Center, 2022 (11.7.2022).





**Fig. 15** The structures of (a) bis[2-*N,N*-dimethyl(amino)phenyl] diselenide, triselenide, and tetraselenide. <sup>a</sup> Ref. 134. <sup>b</sup> Ref. 135. <sup>c</sup> Ref. 136.

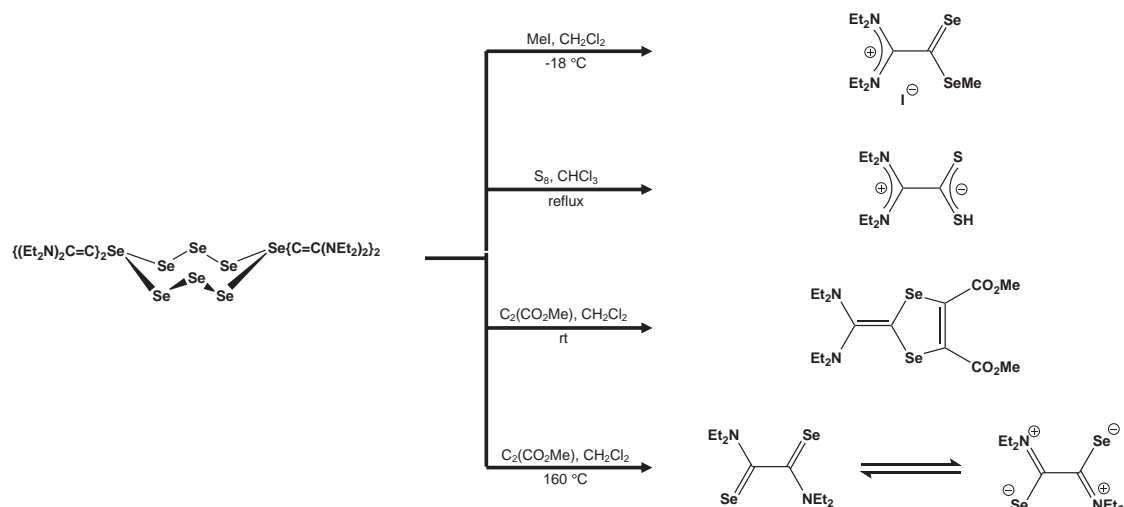


**Fig. 16** Cyclic organic polychalcogenides: (a)  $S_6\{(NC_5Et_2)_2\}_2 \cdot THF$ ,<sup>137</sup> (b)  $C_5H_5O(OAc)_3Se_4$ ,<sup>138</sup> (c)  $Se_6\{C=C(NEt_2)_2\}_2$ ,<sup>139</sup> and (d)  $(Ph_3Te)(TeC_6H_4Me)_2$ .<sup>140</sup>

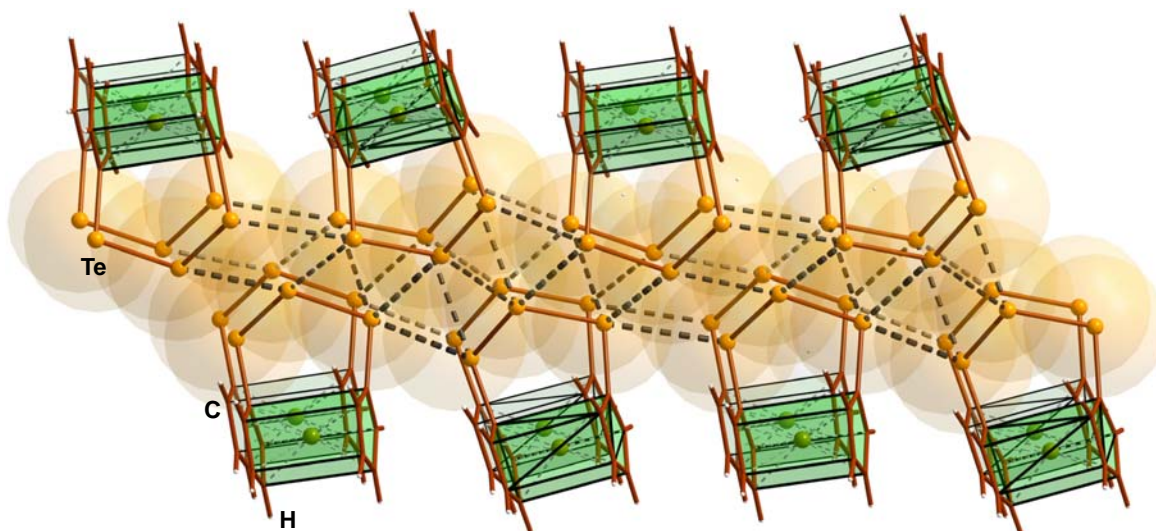
from Fig. 16(d) that the relative orientations of the formal cation and anion are suitable for both  $\sigma$ -hole and  $n(p)^2 \rightarrow \sigma^*$  interactions. The differing charges seem to enhance the electrostatic attraction between the formal cations and anions, as evidenced by the observation that the  $Te \cdots Te$  contacts are somewhat shorter than the intermolecular distances in hexagonal tellurium (see Section 1.22.2.2).

Trichalcogenoferrocenophanes can also be viewed as cyclic trichalcogenides.<sup>38</sup> They serve as useful model compounds to study the trends in secondary bonding interactions. The crystal structures of  $[Fe(C_5H_4E)_2E']$  ( $E, E' = S, Se, Te$ ) have been considered by solid state PBE0/pob-TZVP calculations involving periodic boundary conditions. The intermolecular chalcogen-chalcogen secondary bonding interactions are significant for species containing tellurium. The DFT computations have shown that  $n(p)^2 \rightarrow \sigma^*$  interaction energies of trichalcogenoferrocenophanes are most significant in case of  $[Fe(C_5H_4Te)_2Te]$  resulting in short intermolecular contacts and a continuous quasi 2D structure.<sup>144</sup> These interactions are further enhanced by electrostatic effects between the  $\sigma$ -holes and tellurium lone pairs. The most important intermolecular contacts are shown in Fig. 17. The most





**Scheme 4** Some reactions of  $\text{Se}_6[\text{C}=\text{C}(\text{NEt}_2)_2]_2$ .<sup>139</sup>



**Fig. 17** The main intermolecular contacts in  $[\text{Fe}(\text{C}_5\text{H}_4\text{Te})_2\text{Te}]$ .<sup>144</sup> The transparent spheres indicate van der Waals radii.

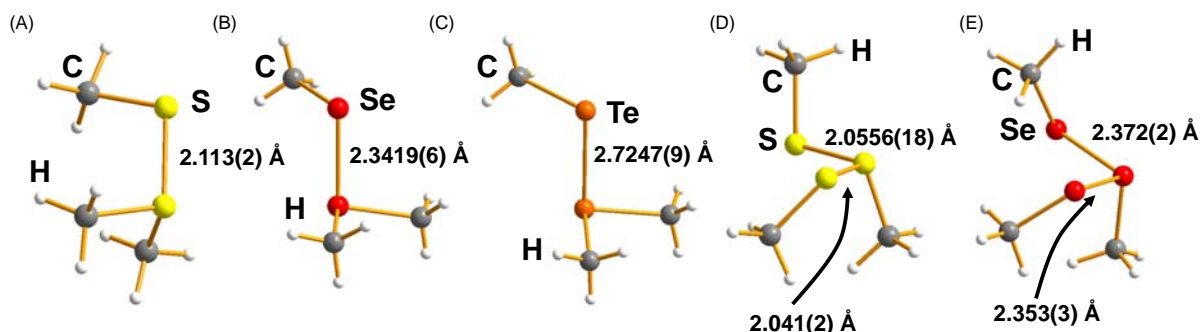
significant contacts range  $3.4552(17)$ – $3.7673(17)$  Å<sup>145</sup> and the corresponding NBO  $n(5p_{\text{Te}})^2 \rightarrow \sigma^*(\text{Te}-\text{Te})$  interaction energies span  $34$ – $94$  kJ mol<sup>-1</sup> at PBE0/pop-TZVP level of theory.<sup>38</sup>

$(\text{Me}_2\text{EEMe})^+$  and  $(\text{MeE})_3^+$  ( $\text{E} = \text{S}, \text{Se}, \text{Te}$ ) cations are powerful sources of  $\text{MeE}^+$  cations in many synthetic applications, such as the preparation of thiirenium, selenirenium, and tellurenium salts.<sup>146</sup> They can be formed by oxidizing methyl dichalcogenides  $\text{MeEEMe}$ , for instance with  $\text{MeSCl}$  and  $\text{BCl}_3$ ,<sup>147</sup>  $\text{SbCl}_5$ ,<sup>148,149</sup> or  $(\text{Me}_2\text{SCL})^+$ .<sup>150</sup> The attempt to utilize the mixture of  $\text{XeF}_2$  and  $\text{BF}_3 \cdot \text{OEt}_2$  in the oxidation of  $\text{Me}_2\text{Se}_2$  to  $(\text{MeSe})_3^+$  resulted in the formation of  $(\text{MeSe})_4^{2+}$ .<sup>151</sup> The structures of some  $(\text{R}_2\text{EER})^+$  and  $(\text{RE})_3^+$  cations are shown in Fig. 18.

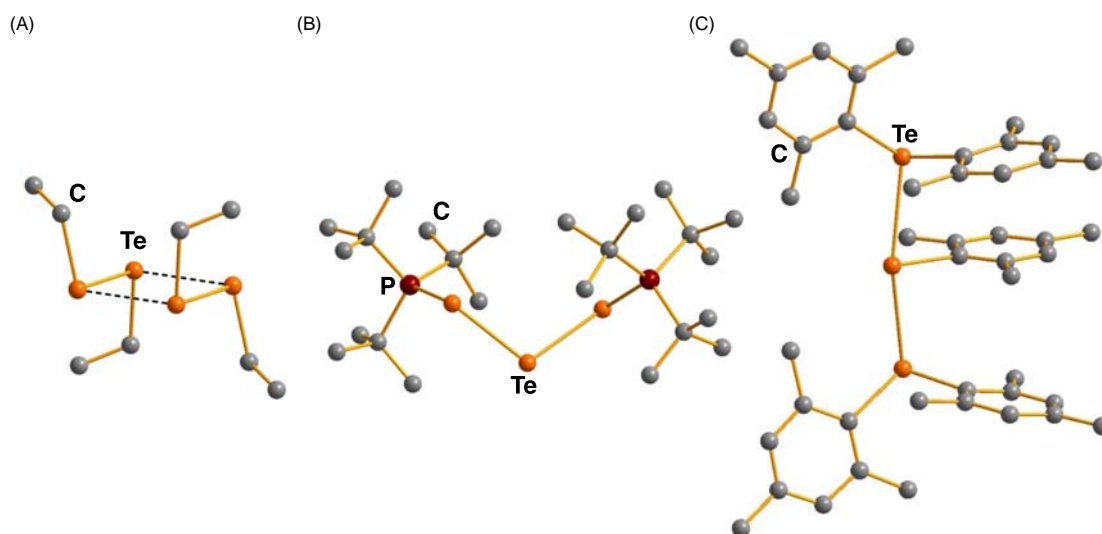
One-electron oxidation of dialkyl ditellurides can be carried out with nitrosyl trifluoromethyl sulfonate  $(\text{NO})(\text{O}_3\text{SCF}_3)$ .<sup>152</sup> The radical  $(\text{RTE})_2^{\cdot+}$  cations thus formed dimerize to form rectangular  $(\text{RTE})_4^{2+}$  [see Fig. 19(a)]. Dialkyl diselenides can also be oxidized in a similar fashion.

The long  $\text{Te} \cdots \text{Te}$  contact of  $3.284$  Å in  $(\text{EtTe})_4^{2+}$  is due to  $\pi^*-\pi^*$  interaction.<sup>152</sup> Consequently, the  $\text{Te}-\text{Te}$  bond of  $2.653$  Å in the  $(\text{RTE})_2^{\cdot+}$  fragment is shorter than the single bond. The  $\text{Te}-\text{Te}$  bond in the  $\{(\text{tBu}_3\text{P})_2\text{Te}_3\}^+$  cation is also slightly shorter than the single bond [see Fig. 19(b)]. By contrast the  $\text{P}-\text{Te}$  bond is weak. Kuhn et al.<sup>153</sup> have deduced that the bonding is best described as tri(*tert*-butyl)phosphane coordinated to a  $\text{Te}_3^{2+}$  cation.

$\{(\text{mes})_2\text{Te}\}_2\text{Te}(\text{mes})$  [see Fig. 19(c)] has been obtained by the reaction of  $[(\text{mes})_2\text{TeTe}(\text{mes})][\text{SbF}_6]$  with  $(\text{mes})_2\text{Te}$  [ $\text{mes} = \text{mesityl}, 2,4,6\text{-Me}_3(\text{C}_6\text{H}_2)$ ].<sup>154</sup> The two elongated  $\text{Te}-\text{Te}$  bonds of  $2.979$  and  $3.049$  Å in the  $\text{R}_2\text{Te}-\text{Te}(\text{R})-\text{TeR}_2^+$  cation can be understood in terms of  $3c-4e$  bonding. Alternatively, the central tellurium of the cation can be considered as a five-electron pair  $\text{AX}_3\text{E}_2$  system with a trigonal bipyramidal arrangement of electron pairs. The two long  $\text{Te}-\text{Te}$  bonds are in the axial positions.



**Fig. 18** Structures of (a)  $(\text{Me}_2\text{SSMe})^+$  in  $(\text{Me}_2\text{SSMe})[\text{SbCl}_6]$ ,<sup>149</sup> (b)  $(\text{Me}_2\text{SeSeMe})^+$  in  $(\text{Me}_2\text{SeSeMe})[\text{BF}_4]$ ,<sup>146</sup> (c)  $(\text{Me}_2\text{TeTeMe})^+$  in  $(\text{Me}_2\text{TeTeMe})[\text{BF}_4]$ ,<sup>146</sup> (d)  $(\text{MeS})_3^+$  in  $(\text{MeS})_3[\text{SbCl}_6]$ ,<sup>149</sup> and (e)  $(\text{MeSe})_3^+$  in  $(\text{MeSe})_3[\text{SbCl}_6]$ .<sup>149</sup>



**Fig. 19** Structure of (a)  $(\text{EtTe})_4^{2+}$  in  $(\text{EtTe})_4(\text{O}_3\text{SCF}_3)$ ,<sup>152</sup> (b)  $(^t\text{Bu}_3\text{P})_2\text{Te}_3^+$  in  $(^t\text{Bu}_3\text{P})_2\text{Te}_3[\text{SbF}_6]$ ,<sup>153</sup> and (c)  $\{[(\text{mes})_2\text{Te}]_2\text{Te}(\text{mes})\}^+$  in  $\{[(\text{mes})_2\text{Te}]_2\text{Te}(\text{mes})\}[\text{SbF}_6] \cdot \text{CH}_2\text{Cl}_2$ .<sup>154</sup>

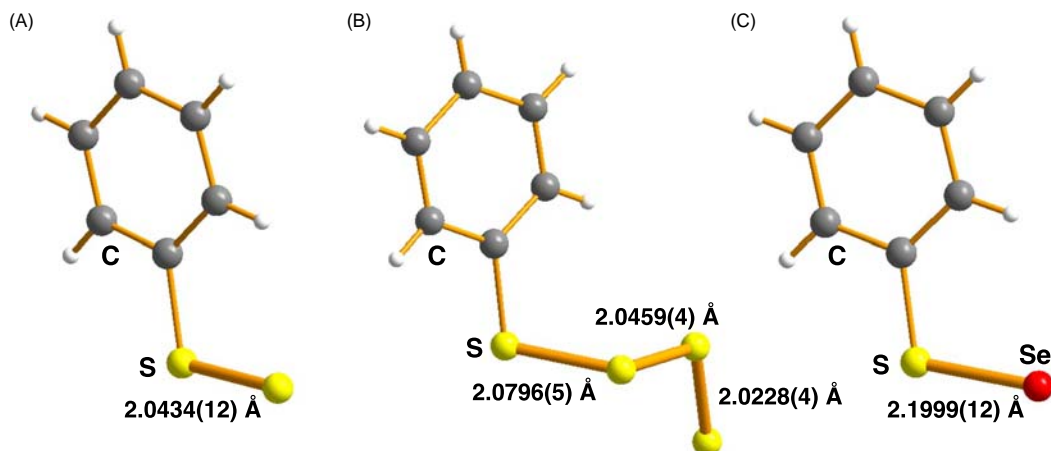
Some anionic polychalcogen species are also known, though their chemistry is not so developed as that of the cations. Unstable organic disulfides  $(\text{RSS})^-$  have been observed as intermediates in different chemical reactions, as well as in biological processes involving enzymes like rhodanese, SoxAX, or MocS3 (for a brief review, see Ref. 155).  $(\text{PPh}_4)(\text{S}_n\text{R})$  ( $n \geq 2$ ) have recently been prepared in a one-step process by stirring sodium phenylthiolate with tetraphenylphosphonium chloride and elemental sulfur in acetonitrile (MeCN) at room temperature (r.t.).<sup>156</sup> While  $(\text{PPh}_4)(\text{S}_2\text{Ph})$  was produced in a stoichiometric reaction, with an excess of sulfur,  $(\text{PPh}_4)_2(\text{S}_7)$  was formed with  $(\text{PPh}_4)(\text{S}_4\text{Ph})$  as a transient intermediate. The corresponding reaction of sodium phenylthiolate, elemental selenium and one equivalent of tetraphenylphosphonium chloride affords known  $(\text{PPh}_4)_2(\text{Se}_5)$  and the orange crystals of air-sensitive  $(\text{PPh}_4)(\text{SeSPh})$ .<sup>155</sup> The crystal structures of  $(\text{PPh}_4)(\text{S}_2\text{Ph})$ ,  $(\text{PPh}_4)(\text{S}_4\text{Ph})$ , and  $(\text{PPh}_4)(\text{SSePh})$  are shown in Fig. 20.

While  $(\text{PPh}_4)(\text{S}_2\text{Ph})$  and  $(\text{PPh}_4)(\text{SSePh})$  are relatively stable in the solid state, they dissociate in solution forming anions of different chalcogen chain lengths,<sup>156</sup> as shown by the ESI-MS spectra in Fig. 21.

The  $[\text{Se}_5\text{C}(\text{Se})(\text{COMe})]^-$  anion in  $[(\text{Ph}_3\text{P})_2\text{N}][\text{Se}_5\text{C}(\text{Se})(\text{COMe})]$  is another of the few discrete anions containing catenated polyselenium anions.<sup>157</sup> It is formed in the reaction of  $\text{K}_2\text{CO}_3$  with red selenium in acetone in the presence of  $[(\text{Ph}_3\text{P})_2\text{N}]\text{Cl}$ . The anion shows two short contacts of 2.942 and 2.955 Å between the exocyclic selenium atom and the geminal endocyclic selenium atoms.

The preparation and crystal structures of several species containing the tritelluride anion  $[\text{RTeTe}(\text{R})\text{TeR}]^-$  have been reported (see Fig. 22).<sup>158–160</sup> Like in the case of the  $[\text{R}_2\text{TeTe}(\text{R})\text{TeR}_2]^+$  cation, the axial Te–Te bonds form a 3c–4e system. Consequently, the axial Te–Te bonds of ca. 3.0 Å are rather long.

The information on polyselenium and polytellurium species with heavier Group 14 elements is much sparser than on those of carbon. Kückmann et al.<sup>161</sup> have reported the preparation and structure of acyclic  $^t\text{Bu}_2\text{RSiE-ESiR}^t\text{Bu}_2$  ( $\text{E} = \text{Se}, \text{Te}$ ;  $\text{R} = ^t\text{Bu}, \text{Ph}$ ) from  $\text{Na}(\text{ESiR}^t\text{Bu}_2)$ . The molecular structures of the four dichalcogenides are analogous to those in organic diselenides and ditellurides. Both the Se–Se and Te–Te bonds show approximate single bond lengths (2.368–2.390 Å and 2.724–2.740 Å, respectively). The torsional angle about the chalcogen-chalcogen bond is 180° in each molecule.



**Fig. 20** Structures of (a)  $(\text{PhSS})^-$  in  $(\text{PPh}_4)(\text{SSPh})$ ,<sup>156</sup> (b)  $(\text{PhSSSS})^-$  in  $(\text{PPh}_4)(\text{S}_4\text{Ph})$ ,<sup>156</sup> and (c)  $(\text{PhSSe})^-$  in  $(\text{PPh}_4)(\text{SeSPh})$ .<sup>155</sup>

### 1.22.4.3.2 Germanium, tin, and lead complexes

Power<sup>162</sup> has discussed that by contrast to light main group elements of the first and second row in the Periodic Table, the heavier elements have different structural, bonding, and chemical properties that resemble those of the transition metals. These trends are clearly demonstrated by the Group 14 elements. Carbon obeys the octet rule and forms molecular compounds containing covalent bonds. The structures and bonding of germanium, tin, and lead compounds can mostly be rationalized in terms of coordination chemistry, and these species can conveniently be considered as complexes. In this section, some recent advances in structural chemistry of polychalcogenido complexes of germanium, tin, and lead are discussed by considering some illustrative examples.

Whereas polychalcogenido complexes of transition metals are well-explored due to their utility in synthetic chemistry, catalysis, and diverse applications in materials science and they have been reviewed for several times,<sup>21–31</sup> the chemistry of coordination complexes of Group 14 with polychalcogen ligands is much less explored.

The stability of the complexes was originally enhanced by the use of bulky organic ligands, such as 2,4,6-tris[bis(trimethylsilyl)methyl]phenyl (Tbt), which enabled the preparation and structural characterization of  $[\text{M}(\text{Tbt})(\text{R})\text{E}_4]$  ( $\text{M} = \text{Si}, \text{Ge}, \text{Sn}, \text{Pb}$ ;  $\text{E} = \text{S}, \text{Se}$ ;  $\text{R} =$  other bulky organic group, such as mesityl or 2,4,6-tris[bis(2-propyl)phenyl]).<sup>163,164</sup> Other bulky ligands have also been utilized in the preparation of Group 14 tetrachalcogenido complexes.<sup>164–169</sup> These complexes have generally been precursors for the preparation of species containing double bonds between Group 14 and chalcogen atoms.<sup>163</sup> Some examples are depicted in Fig. 23.

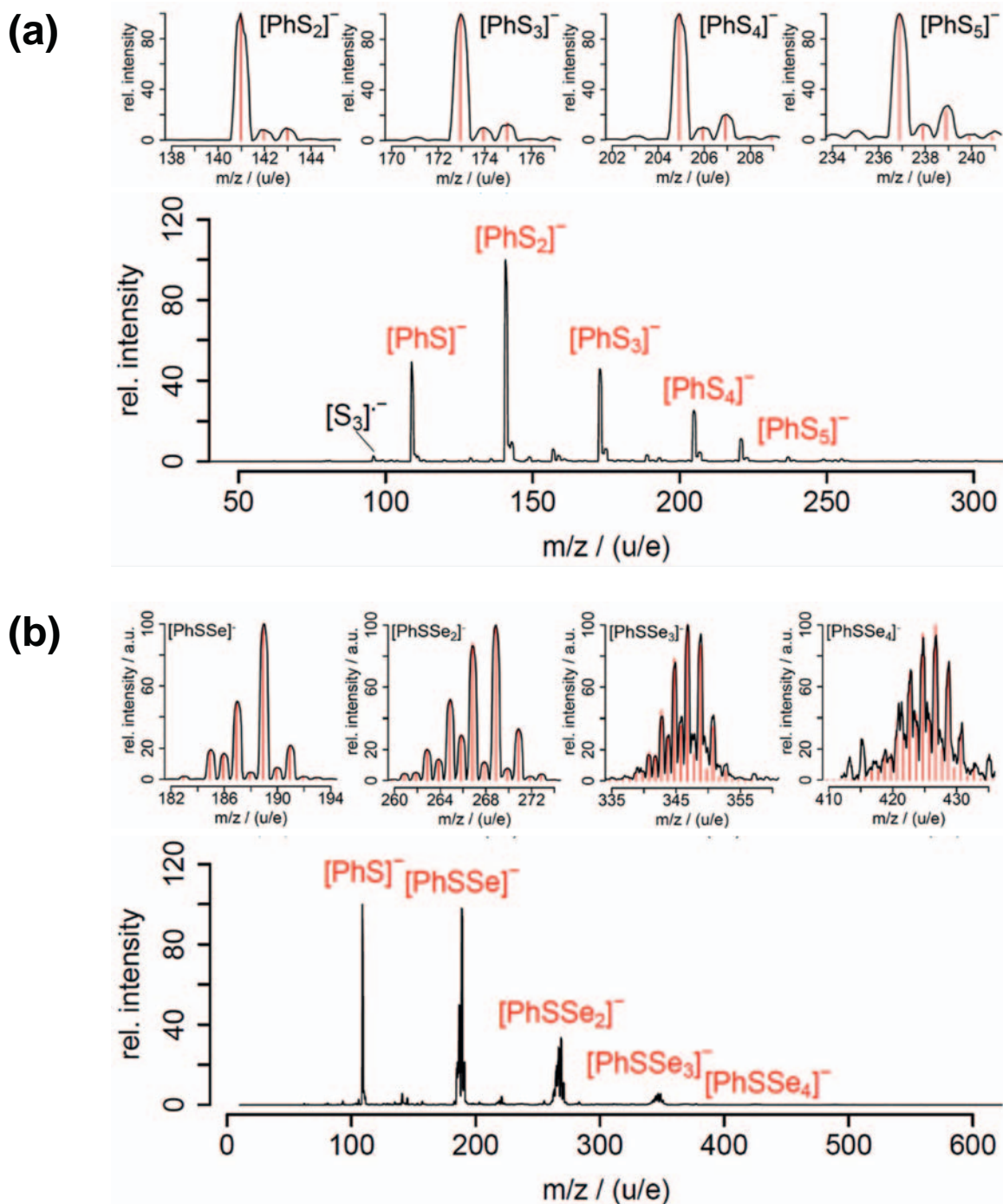
Crystalline phases containing discrete  $[\text{Ge}_2\text{Se}_4(\mu\text{-Se})(\mu\text{-Se}_2)]^{4-}$  have been prepared by solvothermal methods involving transition metal counter cations [see Fig. 24(a)].<sup>145,173,175,176</sup> Dimeric  $[\text{Ge}_2\text{Se}_4(\mu\text{-Se}_2)]^{4-}$  anion in  $\text{M}_4\text{Ge}_4\text{Se}_{12}$  ( $\text{M} = \text{Rb}; \text{Cs}$ ) has recently been shown by DFT calculations to be the source for the large second-harmonic generation (SHG) responses.<sup>174</sup> The predominant contribution to the total SHG effect has been estimated to be due to the lone pair atoms on the terminal selenium atoms to the five  $\sigma^*$  orbitals of the five-membered  $\text{Ge}_2\text{Se}_3$  rings. The crystal structure of  $\text{Rb}_4\text{Ge}_4\text{Se}_{12}$  has been shown in Fig. 24(b).

Tin and lead can also form complexes in which more than one chelating polychalcogen ligand is coordinated to the same central atom [for some examples, see Fig. 25(a–c)]. Complexation with extended anionic networks is also possible. The formation, structures, and utilization of this kind of complexes have been reviewed by Sheldrick and Wachold with a special interest in the design of nanoporous materials with tailored properties.<sup>181</sup> Such extended phases can be exemplified by  $\{[\text{Ga}(\text{en})_3]_2[\text{Ge}_2\text{Te}_{15}]\}_n$  that has recently been prepared by solvothermal methods.<sup>180</sup> The single crystal X-ray structure was interpreted in terms of two interacting polytelluride anions: cross-shaped  $\text{TeTe}_4^{6-}$  anions and  $\text{Te}_8^{4-}$  rings [see Fig. 25(d)]. The material was found to be a p-type semiconductor at room temperature. It switches to a n-type semiconductor at 380 K.

Single crystals of polymer-chalcogenide composites have been prepared by trapping polyethyleneglycol within a selenidostannate matrix under surfactant thermal conditions.<sup>182</sup> Orange crystals of  $(\text{DBNH})_2[\text{Sn}_3\text{Se}_7] \cdot \text{PEG}$  ( $\text{DBN} = 1,5\text{-diazabicyclo-[4.3.0]non-5-ene}$ ;  $\text{PEG} =$  polyethyleneglycol) and black crystals of  $(\text{DBNH})_6[\text{Sn}_8\text{Se}_{30}]$  have been obtained by reacting elemental tin and selenium in the mixed solution of DBN,  $\text{H}_2\text{O}$ , ethylene glycol, and PEG-400 at 120 °C for 6 days. When the reaction temperature was increased to 190 °C, red crystals of  $(\text{DBNH})_6(\text{NH}_4)_2[\text{Sn}_{12}\text{Se}_{28}]$  were obtained in a moderate yield. The network structure built up by the  $[\text{Sn}_8\text{Se}_{30}]^{6-}$  anion is shown in Fig. 26.

A dinuclear tin complex containing a tripodal cryptand-type ligand reacts with elemental sulfur or selenium generating a complex with both bridging pentachalcogenido and monochalcogenido ligands (see Scheme 5).<sup>183</sup> Upon coordination, both Sn(II) centers are oxidized to Sn(IV). The structural characterization of the selenium complex has been determined by single-crystal X-ray diffraction.

When the yellow sulfur complex was dissolved in DMF or DMSO, the color of the solution turned blue-green. Whereas the UV-Vis spectrum of the solution showed two maxima with  $\lambda_{\text{max}}$  at 392 and 617 nm, only one maximum at 392 nm was observed in the diffuse reflectance spectrum in the solid state.<sup>183</sup> The absorption maximum at 617 nm in solution was inferred to be due to  $\text{S}_3^{\cdot -}$  radical anion<sup>16</sup> (see also Section 1.22.3.4).



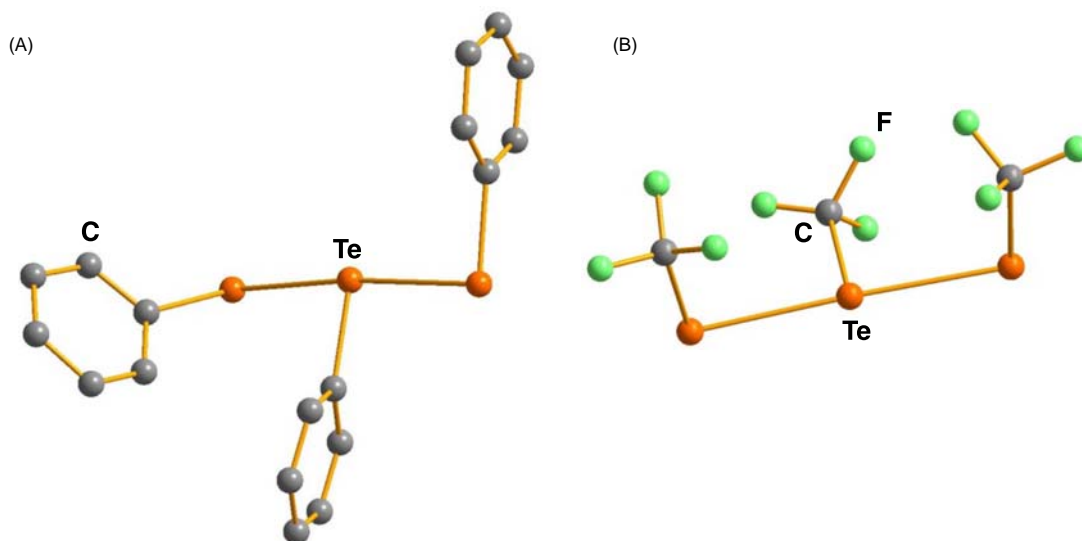
**Fig. 21** Anion ESI-MS spectra of the dissociation equilibria in MeCN of (a)  $(\text{PPh}_4)(\text{SSPh})^{156}$  and (b)  $(\text{PPh}_4)(\text{SeSPh})^{155}$  (a): Reproduced with permission from Jungen, S.; Paenurk, E.; Chen, P. *Inorg. Chem.* **2020**, *59*, 12322–12336. © 2020 ACS. (b): Reproduced with permission from Jungen, S.; Chen, P. *Inorg. Chem.* **2020**, *59*, 13315–13319. © 2020 ACS.

#### 1.22.4.4 Group 15 derivatives and complexes

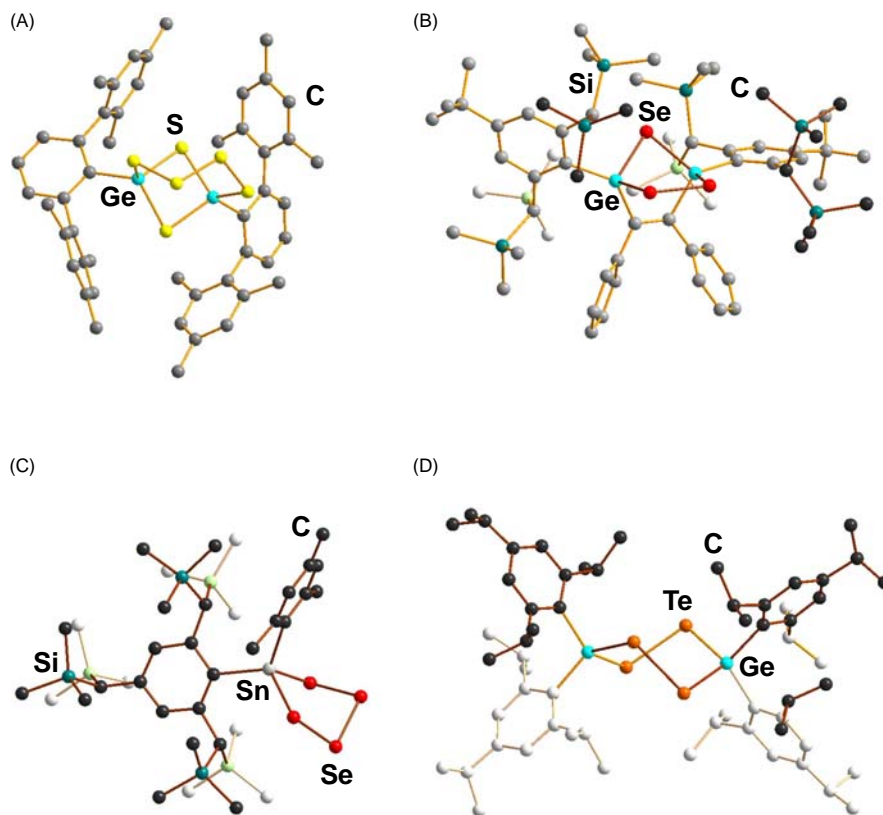
##### 1.22.4.4.1 Chalcogen-nitrogen compounds

Sulfur-nitrogen chemistry is very extensive and has a long history (for early development, see the classic book by Heal<sup>184</sup>). Selenium-nitrogen, and tellurium-nitrogen chemistry has developed very rapidly in recent decades (the different features and the recent progress in this vast field have been described in detail in Ref. 9; see also reviews on various aspects of chalcogen-nitrogen chemistry in Refs. 10, 185–187). The related chalcogen-phosphorus system is also rather versatile.<sup>11,184,188,189</sup> The





**Fig. 22** The structure of (a)  $[(\text{PhTe})_2\text{TePh}]^-$  in  $[\text{Sm}(\text{Tp}^{\text{Me,Me}})_2][(\text{PhTe})_2\text{TePh}]$  [ $\text{Tp}^{\text{Me,Me}}$  = hydrotris(3,5-dimethylpyrazolyl)borate]<sup>[158]</sup> and  $[\text{MPh}_4](\text{Te}_3\text{Ph}_3)$  ( $\text{M} = \text{P}, \text{As}$ ),<sup>[159]</sup> and (b)  $[(\text{CF}_3\text{Te})_2\text{TeCF}_3]^-$  in  $[(\text{Ph}_3\text{P})_2\text{N}][(\text{CF}_3\text{Te})_2\text{TeCF}_3]$ .<sup>[160]</sup>

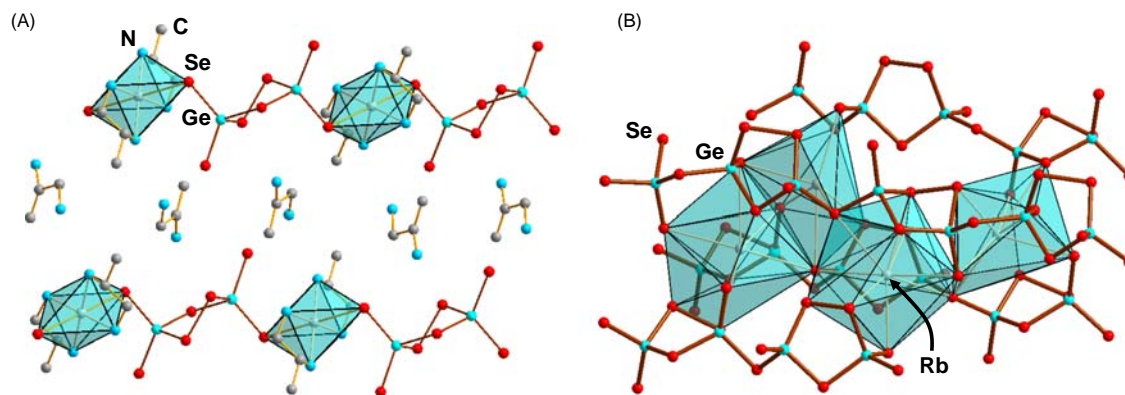


**Fig. 23** Structures of (a)  $[\{\text{Ge}(\text{C}_6\text{H}_3(\text{mes})_2)_2(\mu\text{-S})_2(\mu\text{-S}_4)\}]$  ( $\text{mes}$  = mesityl),<sup>[142]</sup> (b)  $[\{\text{Ge}(\text{C}_6\text{H}_2[\text{CH}(\text{SiMe}_3)_2]_2(\text{tBu}))_2(\mu\text{-C}_2\text{Ph}_2)(\mu\text{-Se})(\mu\text{-Se}_2)\}]$ ,<sup>[170]</sup> (c)  $[\text{Sn}(\text{C}_6\text{H}_2[\text{CH}(\text{SiMe}_3)_2]_3)(\text{C}_6\text{H}_2\text{Me}_3)(\text{Se}_4)]$ ,<sup>[171]</sup> and (d)  $[\{\text{Ge}(\text{C}_6\text{H}_2\text{Pr}^3)_2(\mu\text{-Te})_2\}]$ .<sup>[172]</sup>

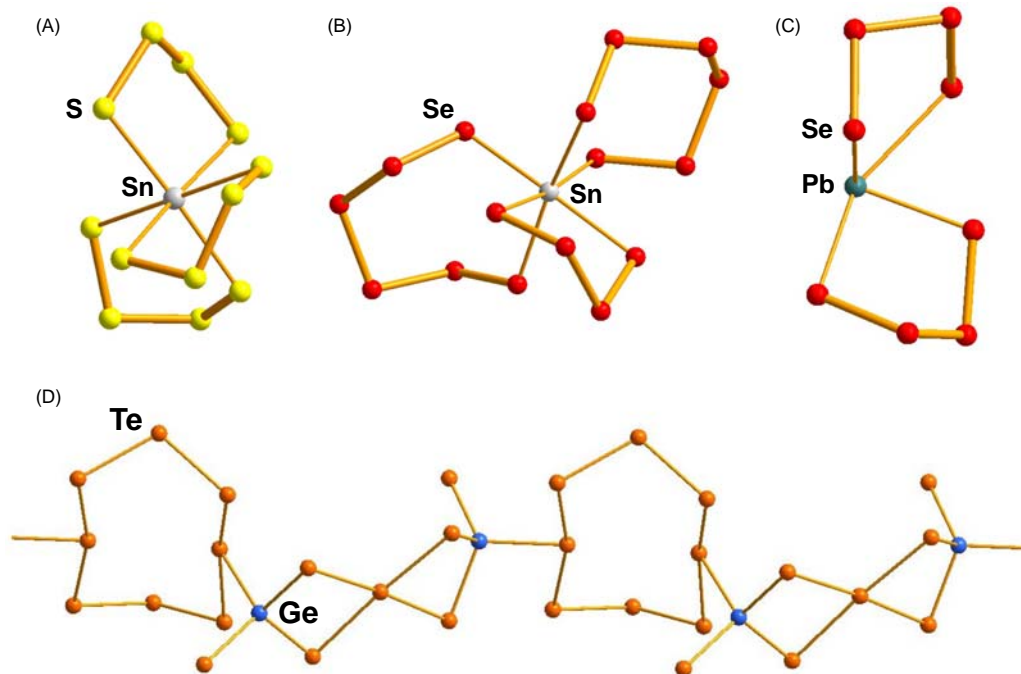
complete review of this material is clearly beyond the scope of the current treatise, but the discussion will concentrate on examples that contain chalcogen-chalcogen bonds.

Cyclic eight-membered sulfur imides have been known for a long time (for early history, see Ref. 184, and for more recent development, see Ref. 9). A mixture of  $\text{S}_{8-n}(\text{NH})_n$  ( $n = 1-3$ ) has traditionally been obtained by treating  $\text{S}_2\text{Cl}_2$  with gaseous ammonia in DMF with subsequent hydrolysis using dilute hydrochloric acid.<sup>[190]</sup>  $\text{S}_7\text{NH}$  is the main product, but the reaction affords also the 1,3-





**Fig. 24** Crystal structure of (a)  $(1,2\text{-dapH})_2[\text{Mn}(1,2\text{-dap})_2(\text{Se}_7\text{Ge}_2)]$  (1,2-dap = 1,2-propanediamine)<sup>173</sup> and (b)  $\text{M}_{4n}[\text{Ge}_4\text{Se}_{12}]_n$  (M = Rb; Cs).<sup>174</sup>



**Fig. 25** Polychalcogenidotin and -lead complexes: (a)  $[\text{Sn}(\text{Se}_4)_3]^{2-}$ ,<sup>177</sup> (b)  $[\text{Sn}(\text{Se}_4)(\text{Se}_6)_2]^{2-}$ ,<sup>178</sup> and (c)  $[\text{Pb}(\text{Se}_4)_2]^{2-}$ .<sup>179</sup> (d) The extended anionic network involving  $\text{GeTe}_2$ ,  $\text{Te}_8^{4-}$ , and  $\text{TeTe}_4^{6-}$ .<sup>180</sup>

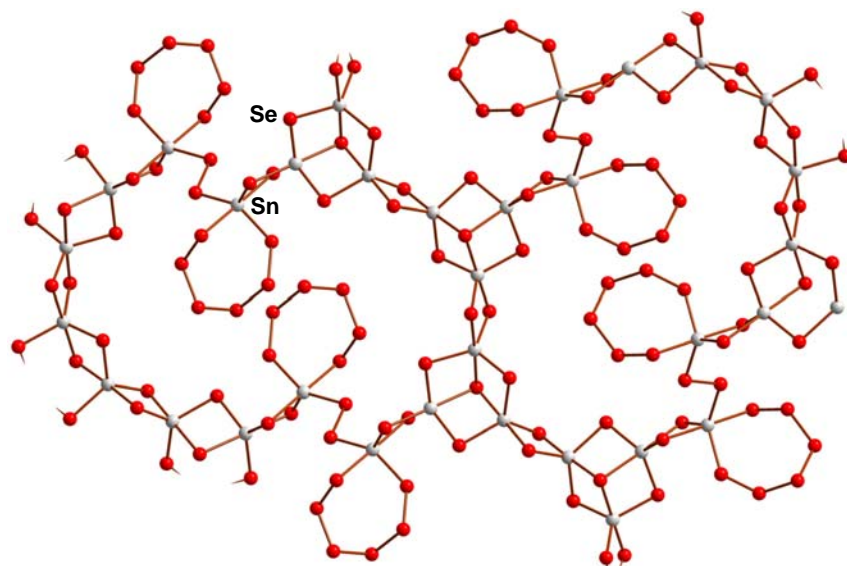
1,4-, and 1,5-isomers of  $\text{S}_6(\text{NH})_2$ , and a very small amount of 1,3,5- $\text{S}_5(\text{NH})_3$ , as could be demonstrated by reversed-phase HPLC.<sup>191</sup> The reaction of sodium azide with elemental sulfur in  $(\text{Me}_3\text{N})_3\text{PO}$  affords  $\text{S}_7\text{NH}$  in a very good yield.<sup>192</sup> This approach is suitable for the preparation of isotopically enriched samples. 1,3,5,7- $\text{S}_4(\text{NH})_4$  can be prepared in a good yield by the reduction of  $\text{S}_4\text{N}_4$  with methanolic  $\text{SnCl}_2 \cdot 2\text{H}_2\text{O}$ .<sup>193</sup>

Cyclic sulfur imides with ring sizes larger than eight have been prepared.  $[\text{TiCp}_2(\text{CO})_2]$  is a convenient reagent for these reactions. The insertion of the  $\text{Cp}_2\text{Ti}$  fragment into the S–S bond of  $\text{S}_7\text{NH}$  affords  $[\text{TiCp}_2(\text{S}_7\text{NH})]$ ,<sup>194</sup> which has been used for the preparation of  $\text{S}_8\text{NH}$  and  $\text{S}_9\text{NH}$  upon the treatment with  $\text{SCl}_2$  and  $\text{S}_2\text{Cl}_2$ , respectively (see Scheme 6).<sup>194,195</sup>

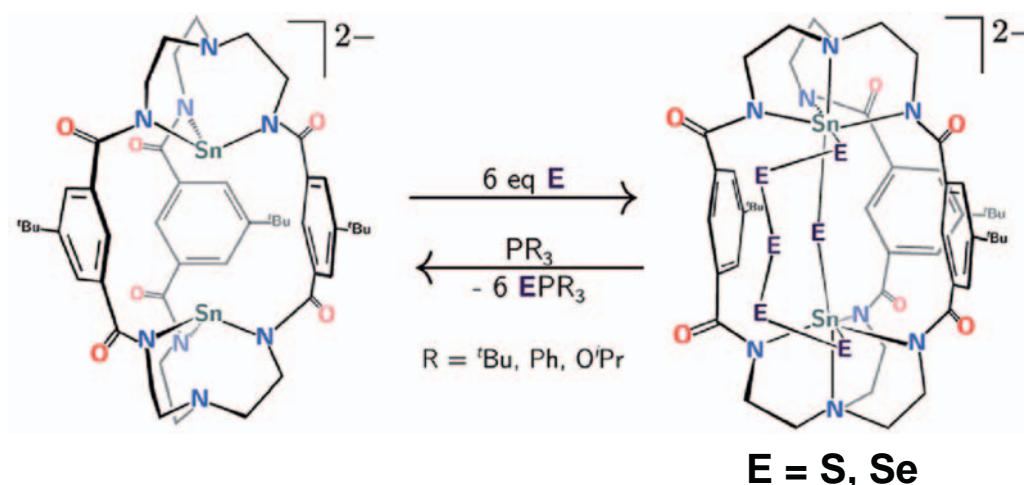
Cyclic sulfur imides can formally be formed by the substitution of one or more sulfur atoms by NH groups leading to a planar trigonal  $\text{S}_2\text{NH}$  fragment. The molecular geometry of the rings therefore resembles that of homocyclic sulfur molecules of the corresponding ring size. Whereas  $\text{S}_6(\text{NH})_2$  and  $\text{S}_5(\text{NH})_3$  show the occurrence of more than one isomer, thus far no species have been detected that contain two adjacent NH groups.

The molecular structures and the bond parameters of different sulfur imide rings, for which the crystal structure is known, are listed in Table 3. In some cases, the crystal structures have been determined several times (see, for instance, Refs. 9,184). The most reliable structural information is given for each molecule in Table 3.

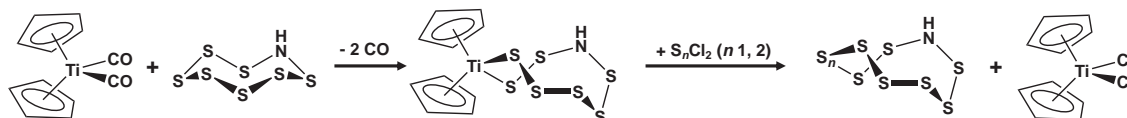
No cyclic imides have been reported for selenium and tellurium. However, several derivatives, in which the hydrogen of the NH group has been substituted by an organic group, are known.<sup>9</sup>



**Fig. 26** The anionic network in  $[\text{Sn}_8\text{Se}_{30}]^{6-}$ .<sup>182</sup>



**Scheme 5** Reaction of a dinuclear tin complex with elemental sulfur or selenium.<sup>183</sup> Reproduced with permission from Stauber, J. M.; Müller, P.; Dai, Y.; Wu, G.; Nocera, D. G.; Cummins, C. C. *Chem. Sci.*, **2016**, 7, 6928–6933. © 2016 RSC.



**Scheme 6** Formation of  $\text{S}_{7+n}\text{NH}$  ( $n = 1, 2$ ) from  $[\text{TiCp}_2(\text{CO})_2]$  and  $\text{S}_7\text{NH}$ .<sup>194,195</sup>

Heterocyclic inorganic compounds can generally be prepared by cyclocondensation.<sup>202</sup> A typical example of such reactions is the formation of cyclophosphazanes from Group 15 trichlorides and primary amines. The suggested reaction steps are shown in Fig. 27<sup>203</sup> together with the application of similar principles to cyclic organic selenium imide derivatives, which will be described in more detail below.

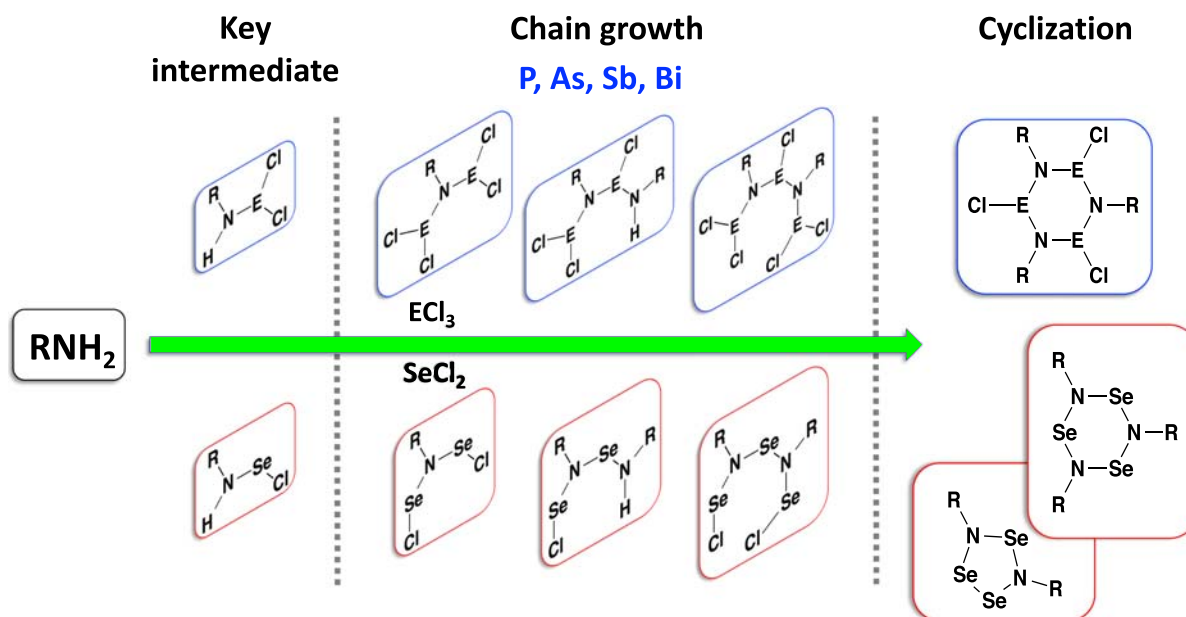
Cyclic organic sulfur imide derivatives have been prepared from primary amines  $\text{RNH}_2$  ( $\text{R}$  = an aliphatic or aromatic substituent) and chlorosulfanes  $\text{S}_n\text{Cl}_2$ .<sup>204</sup> Typical ring sizes are six and eight (for some examples, see Fig. 28).

Cyclic selenium imide derivatives were first prepared from  $(\text{Me}_3\text{Si})(^t\text{Bu})\text{NLi}$ , which reacts with  $\text{Se}_2\text{Cl}_2$  to afford  $1,5\text{-Se}_6(\text{N}^t\text{Bu})_2$  or with  $\text{SeOCl}_2$  to give  $1,3,6,8,11,13\text{-Se}_9(\text{N}^t\text{Bu})_6$ .<sup>141</sup> The yields, however, were very low. The latter species was later prepared in significantly better yield by treatment of  $^t\text{BuNH}_2$  with an equimolar mixture of elemental selenium and selenium tetrachloride.<sup>209</sup> The

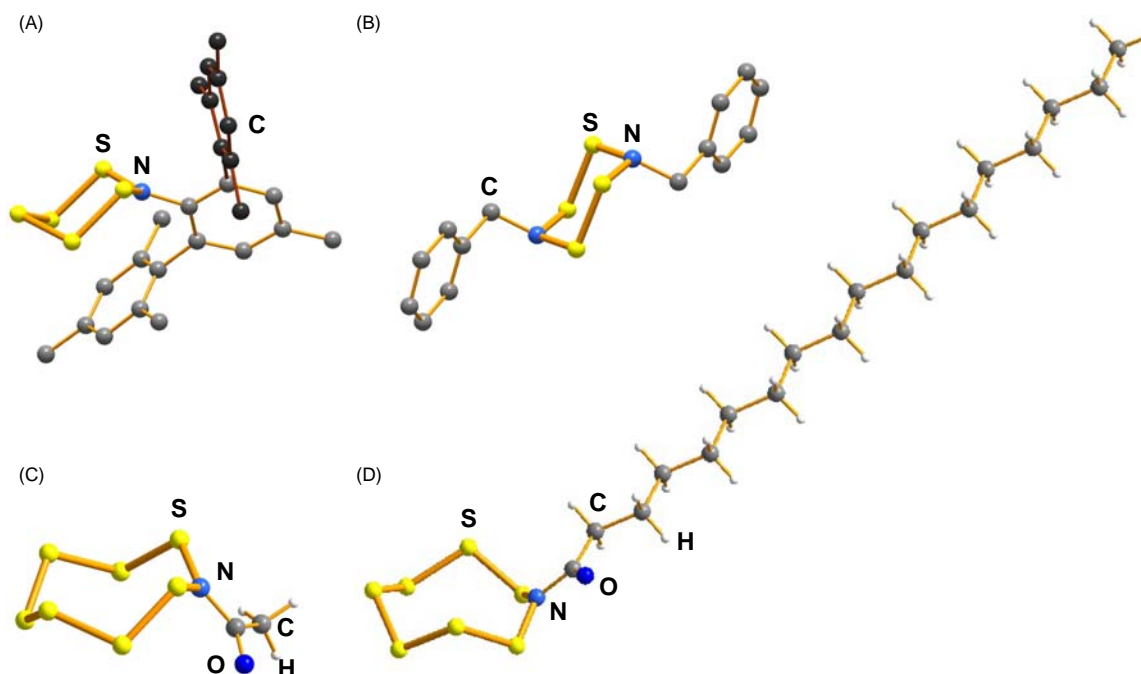
**Table 3** Molecular structures of cyclic sulfur imides.

Molecule	Bond length	Bond angle	Torsion angle	Ref.
S <sub>7</sub> NH <sup>a</sup>	$r_{SS} = 2.0322(3)–2.0541(2) \text{ \AA}$ $r_{SN} = 1.6673(3) \text{ \AA}$	$\alpha_S = 107.579(6)–110.035(8)^\circ$ $\alpha_N = 123.982(8)^\circ$	$\tau_{SS} = 93.286–99.330(8)^\circ$ $\tau_{SN} = 96.44(2)^\circ$	196
1,3-S <sub>6</sub> (NH) <sub>2</sub> <sup>a</sup>	$r_{SS} = 2.0448(2)–2.0624(2) \text{ \AA}$ $r_{SN} = 1.6604(2)–1.6750(1) \text{ \AA}$	$\alpha_S = 105.529(3)–110.052(4)^\circ$ $\alpha_N = 123.140(5)–124.664(4)^\circ$	$\tau_{SS} = 93.286–99.330(8)^\circ$ $\tau_{SN} = 88.961(6)–104.070(5)^\circ$	197
1,4-S <sub>6</sub> (NH) <sub>2</sub> <sup>a</sup>	$r_{SS} = 2.034(3)–2.059(4) \text{ \AA}$ $r_{SN} = 1.692(4)–1.742(4) \text{ \AA}$	$\alpha_S = 107.25(9)–111.19(18)^\circ$ $\alpha_N = 118.2(3)–120.0(2)^\circ$	$\tau_{SS} = 93.286(8)–99.330(8)^\circ$ $\tau_{SN} = 93.1(3)–96.9(3)^\circ$	198
1,5-S <sub>6</sub> (NH) <sub>2</sub> <sup>a</sup>	$r_{SS} = 2.0531(8)–2.0638(8) \text{ \AA}$ $r_{SN} = 1.6767(12)–1.6832(12) \text{ \AA}$	$\alpha_S = 108.82(3)–108.83(3)^\circ$ $\alpha_N = 122.75(3)–122.94(3)^\circ$	$\tau_{SS} = 97.13(8)–97.40(8)^\circ$ $\tau_{SN} = 85.4(3)–87.56(12)^\circ$	199
1,3,5-S <sub>5</sub> (NH) <sub>3</sub> <sup>a</sup>	$r_{SS} = 2.0 \text{ \AA}$ $r_{SN} = 1.9–2.1 \text{ \AA}$	$\alpha_S = 98.9–103.2^\circ$ $\alpha_N = 92.8–99.6^\circ$	$\tau_{SS} = 102.6^\circ$ $\tau_{SN} = 104.1–111.9^\circ$	200
1,3,5,7-S <sub>4</sub> (NH) <sub>4</sub> <sup>a</sup>	$r_{SN} = 1.6697(15)–1.6762(16) \text{ \AA}$	$\alpha_S = 107.579(6)–110.035(8)^\circ$ $\alpha_N = 123.24(3)–124.56(8)^\circ$	$\tau_{SN} = 86.80(14)–88.28(13)^\circ$	201
S <sub>8</sub> NH <sup>b</sup>	$r_{SS} = 2.044(2)–2.067(2) \text{ \AA}$ $r_{SN} = 1.705(5)–1.720(5) \text{ \AA}$	$\alpha_S = 104.1(9)–108.8(2)^\circ$ $\alpha_N = 121.9(2)^\circ$	$\tau_{SS} = 67.96(11)–114.60(9)^\circ$ $\tau_{SN} = 74.5(3)–75.1(3)^\circ$	195
S <sub>9</sub> NH <sup>c</sup>	$r_{SS} = 2.042(3)–2.0074(3) \text{ \AA}$ $r_{SN} = 1.671(5) \text{ \AA}$	$\alpha_S = 103.21(7)–109.27(11)^\circ$ $\alpha_N = 124.00(8)^\circ$	$\tau_{SS} = 81.12(3)–120.85(13)^\circ$ $\tau_{SN} = 85.0(5)^\circ$	195

Motifs clockwise starting from one nitrogen atom: <sup>a</sup> + - + - + - + - . <sup>b</sup> + + - + - + - + - . <sup>c</sup> + + - + - + - + - .



**Fig. 27** The three steps of the cyclocondensation reactions suggested for cyclophosphazanes<sup>203</sup> and applied to cyclic organic selenium imide derivatives.<sup>204</sup> Adapted with permission from Chivers, T.; Laitinen, R. S. *Dalton Trans.* **2017**, *46*, 1357–1367. © 2017 RSC.



**Fig. 28** Molecular structures of (a)  $S_5N(C_6H_2(mes)_2Me-2,6,4)$  (mes = mesityl),<sup>205</sup> (b)  $1,4-S_4\{N(CH_2Ph)\}_2$ ,<sup>206</sup> (c)  $S_7N(C(O)Me)$ ,<sup>207</sup> and (d)  $S_7N(C(O)C_{17}H_{35})$ .<sup>208</sup>

reaction of  $(Me_3Si)^tBuNLi$  and  $SeCl_4$  results in the formation of  $Se_3(N^tBu)_2$ .<sup>210</sup> It was identified only by NMR spectroscopy, but the related  $Se_3(NAd)_2$  (Ad = adamantyl) has been obtained as a crystalline solid by the reaction of  $AdNH_2$  and  $SeCl_2$ , and its crystal structure could be determined.<sup>211</sup> The treatment of  $^tBuNH_2$  with  $SeCl_2$  led to a mixture of several products, which in addition to 1,5- $Se_6(N^tBu)_2$  and 1,3,6,8,11,13- $Se_9(N^tBu)_6$  affords 1,3,5- $Se_3(N^tBu)_3$ .<sup>209</sup> The cyclocondensation reaction of  $SeCl_2$  and  $(Me_3Si)_2NMe$  has yielded 1,3,5,7- $Se_4(NMe)_4$  in excellent yields.<sup>212</sup>

The structural information from the crystal structure determinations for the known cyclic organic selenium imide derivatives is given in **Table 4**. The bond parameters indicate that while the metrical values of the Se–Se bonds are close to that of the single bond, the Se–N bonds seem to be slightly shorter indicating a higher bond order. It has been deduced also for  $S_7NH$  that the bond order of the S–N bond is slightly over 1.<sup>196</sup> This is supported by the observation that the  $E_2NR$  (R = H, C) moiety in most cyclic sulfur imides and their organic derivatives is planar.

The exceptionally long Se–Se bond of 2.4043(9) Å in 1,3- $Se_3(NAd)_2$  (Ad = adamantyl) is a consequence of the rather small torsional angles of 16.1(3)–46.70(19)° and indicates ring strain.<sup>211</sup>

It has been observed that the reaction of  $^tBuNH_2$  and  $SeCl_2$  also affords highly moisture-sensitive imidoselenium chlorides  $ClSe[N(^tBu)Se]_nCl$  ( $n = 1-3$ ).<sup>213,214</sup> They act as reaction intermediates in the formation of cyclic selenium imide derivatives (see **Scheme 7**).

Support for the reaction pathway in **Scheme 7** is found by the reaction of  $ClSe[N(^tBu)Se]_2Cl$  with  $^tBuNH_2$ . This chloride is a bifunctional reagent and affords 1,3- $Se_3(N^tBu)_2$  and 1,3,5- $Se_3(N^tBu)_3$  in almost equimolar amounts.<sup>214</sup> Although the sulfur analogs  $ClS[N(^tBu)S]_nCl$  have not been reported, the formation of 1,3,5,7- $S_4(NMe)_4$ <sup>215</sup> via cyclocondensation of  $MeNH_2$  and  $S_2Cl_2$  indicates that this kind of intermediates may also play a role in the case of sulfur. The DFT calculations also indicate that the formation of  $ClS[N(^tBu)S]_nCl$  ( $n = 1-3$ ) is strongly exergonic and therefore plausible.<sup>204</sup>

The only known cyclic organic tellurium imide derivative is the six-membered ring 1,3,5- $Te_3(N^tBu)_3$ .<sup>216</sup>

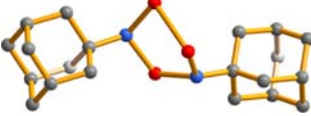

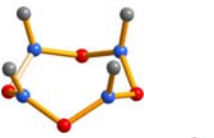

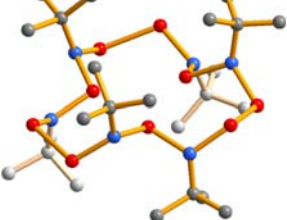
The  $Se_2N_2CH$  dimer has been prepared from 1,3,5-triazine according to **Scheme 8**<sup>217</sup>: In the solid state, the dimer  $(HCN_2Se_2)_2$  is diamagnetic, with a residual spin density of 0.01%. The material exhibits three orders of magnitude higher single-crystal conductivity than the other monofunctional selenium-based radical dimers.<sup>218</sup>

$Se(NSO)_2$  is a versatile reagent for chalcogen-nitrogen species.<sup>219,220</sup> It can be prepared by the reaction of  $Me_3SiNSO$  and  $Se_2Cl_2$ . With the reaction of  $POCl_3$ ,  $Se(NSO)_2$  yields molecular  $SeCl_2(SeNSN)$  [**Fig. 29(a)**]. With  $MF_5$  in  $SO_2(l)$  solution followed by the reaction with  $Cl_2$ , the ionic isomer  $\{SeCl(SeNSN)\}Cl$  is formed [**Fig. 29(b)**].

The reaction of  $\{(Me_3Si)_2N\}_2S$  and  $SeCl_4$  is dependent on the reaction conditions. Whereas in dioxane at 50 °C, the product mixture contains ca. 70%  $[(Se_2SN_2)Cl]_2$  and 30% 1,5- $Se_2S_2N_4$ ,<sup>221</sup> in carbon disulfide at –70 °C only 1,5- $Se_2S_2N_4$  is formed.<sup>222</sup> At ambient temperature either in  $CS_2$  or dichloromethane, the reaction affords ca. 75% 1,5- $Se_2S_2N_4$  and 25%  $[(Se_2SN_2)Cl]_2$ . This is consistent with the proposal of Haas et al.<sup>219</sup> that 1,5- $Se_2S_2N_4$  is an intermediate in the formation of the  $Se_2SN_2$  ring upon treatment of  $Se(NSO)_2$  with Lewis acids. The crystal structure of  $[(Se_2SN_2)Cl]_2$  is shown in **Fig. 29(c)**.



**Table 4** Molecular structures of cyclic selenium imide derivatives.

Molecule	Bond length	Bond angle	Torsion angle	Ref.
1,3-Se <sub>3</sub> (NAd) <sub>2</sub>	 $r_{\text{SeSe}} = 2.4043(9) \text{ \AA}$ $r_{\text{SeN}} = 1.845(4) \text{--} 1.892(4) \text{ \AA}$ $r_{\text{NC}} = 1.507(7) \text{--} 1.516(7) \text{ \AA}$	$\alpha_{\text{Se}} = 92.93(13) \text{--}$ $105.78(19)$ $\alpha_{\text{N}} = 110.5(2) \text{--} 111.3(2)^\circ$ $\alpha_{\text{C}} = 112.8(3) \text{--} 120.0(3)^\circ$	$\tau_{\text{SeSe}} = 46.70(19)^\circ$ $\tau_{\text{SeN}} = 16.1(3) \text{--} 37.6(2)^\circ$	211
1,3,5-Se <sub>3</sub> (N <sup>t</sup> Bu) <sub>3</sub> <sup>b</sup>	 $r_{\text{SeN}} = 1.825(4) \text{--} 1.842(5) \text{ \AA}$ $r_{\text{NC}} = 1.496(7) \text{ \AA}$	$\alpha_{\text{Se}} = 106.61(18)^\circ$ $\alpha_{\text{N}} = 113.33(18)^\circ$ $\alpha_{\text{C}} = 106.61(18) \text{--}$ $119.9(3)^\circ$	$\tau_{\text{SeN}} = 58.7(3) \text{--} 58.9(3)^\circ$	209
1,3,5,7-Se <sub>4</sub> (NMe) <sub>4</sub> <sup>c</sup>	 $r_{\text{SeN}} = 1.818(8) \text{--} 1.872(10) \text{ \AA}$ $r_{\text{NC}} = 1.388(14) \text{--}$ $1.462(12) \text{ \AA}$	$\alpha_{\text{Se}} = 108.4(3)^\circ$ $\alpha_{\text{N}} = 120.6(5) \text{--} 123.0(5)^\circ$ $\alpha_{\text{C}} = 115.8(8) \text{--} 119.5(7)^\circ$	$\tau_{\text{SeN}} = 86.7(6) \text{--} 93.0(5)^\circ$	212
1,5-Se <sub>6</sub> (N <sup>t</sup> Bu) <sub>2</sub> <sup>c</sup>	 $r_{\text{SeSe}} = 2.3327(10) \text{ \AA}$ $r_{\text{SeN}} = 1.830(5) \text{ \AA}$ $r_{\text{NC}} = 1.470(9) \text{ \AA}$	$\alpha_{\text{Se}} = 108.84(3) \text{--}$ $110.00(15)^\circ$ $\alpha_{\text{N}} = 114.8(2)^\circ$ $\alpha_{\text{C}} = 121.9(4)^\circ$	$\tau_{\text{SeSe}} = 99.45(18)^\circ$ $\tau_{\text{SeN}} = 89.9(3)^\circ$	141
1,3,6,8,11,13-Se <sub>9</sub> (N <sup>t</sup> Bu) <sub>6</sub> <sup>d</sup>	 $r_{\text{SeSe}} = 2.331(3) \text{--} 2.345(3) \text{ \AA}$ $r_{\text{SeN}} = 1.801(17) \text{--}$ $1.896(17) \text{ \AA}$ $r_{\text{NC}} = 1.473(3) \text{--} 1.561(3) \text{ \AA}$	$\alpha_{\text{Se}} = 100.8(6) \text{--} 112.6(5)^\circ$ $\alpha_{\text{N}} = 110.8(7) \text{--} 117.0(10)^\circ$ $\alpha_{\text{C}} = 114.9(12) \text{--}$ $121.3(13)^\circ$	$\tau_{\text{SeSe}} = 73.6(9) \text{--} 82.0(8)^\circ$ $\tau_{\text{SeN}} = 68.8(10) \text{--}$ $121.0(10)^\circ$	141

Motifs (+) clockwise, (–) anticlockwise starting from one of the nitrogen atoms: <sup>a</sup> + + + + –. <sup>b</sup> + + + + –. <sup>c</sup> + + + + + + –. <sup>d</sup> + + + + + + + + –.

Catenated tellurium-nitrogen species are very rare. Unlike the corresponding selenium compound TeCl<sub>2</sub>(TeNSN) contains two covalent Te–Cl bonds.<sup>223</sup> It can be converted to a {ClTe(TeNSN)}<sup>+</sup> cation by the reaction with AsF<sub>5</sub> (see Scheme 9). Another example is (Te<sub>2</sub>S<sub>2</sub>N<sub>4</sub>)[AsF<sub>6</sub>] that contains a cyclic cation with a transannular TeTe single bond.<sup>224</sup>

#### 1.22.4.4.2 Chalcogen-phosphorus compounds

Whereas several binary phosphorus chalcogenides are known, only P<sub>2</sub>Se<sub>5</sub> contains chalcogen-chalcogen bonds [see Fig. 30(a)].<sup>225</sup> Catenated phosphoryl polyselenides and tellurides have also been prepared and characterized. The metrical parameters of the chalcogen-chalcogen bonds indicate strainless single bonds [see Fig. 30(b and c)].

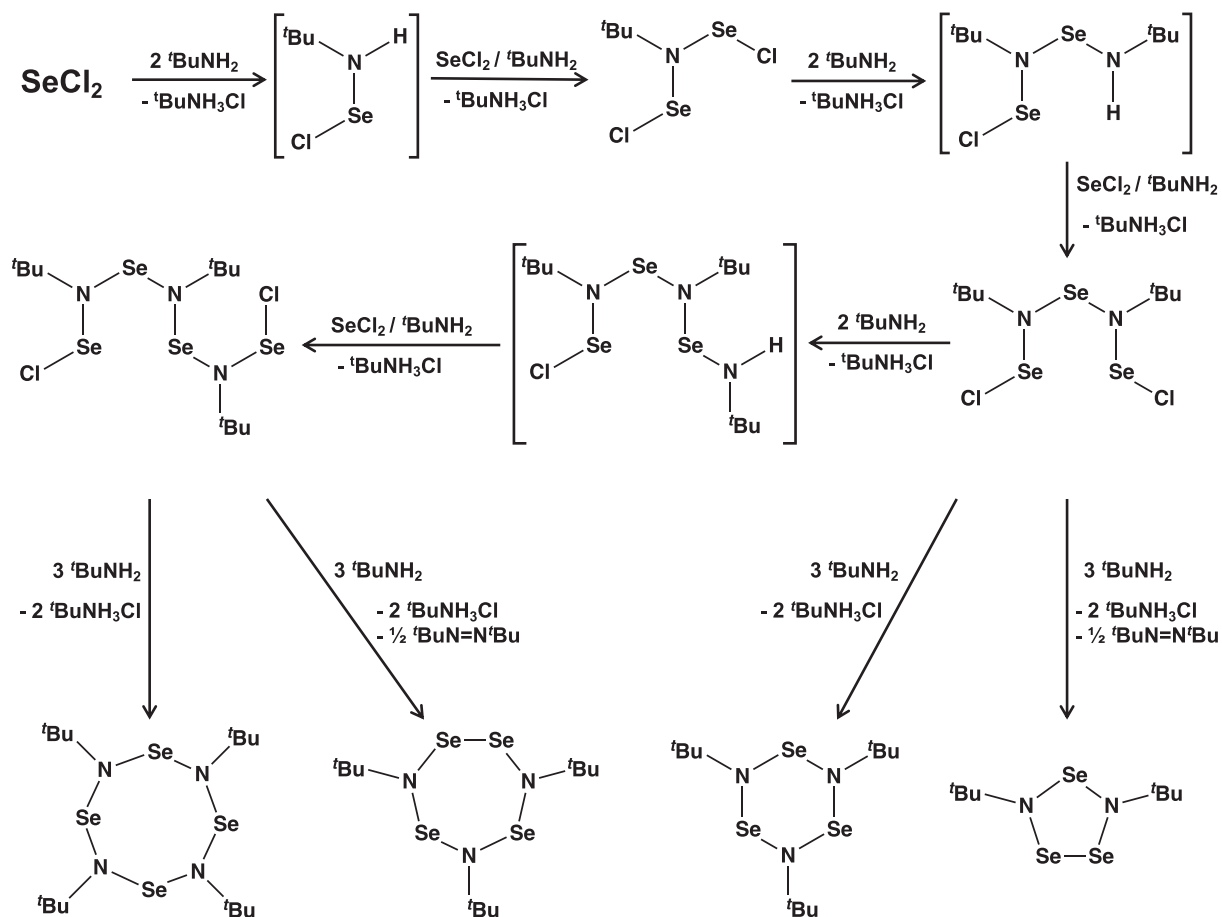
Upmann and Jones<sup>228</sup> demonstrated that the reaction of phosphane selenides RR′PSe (R, R′ = Ph, <sup>t</sup>Bu, <sup>i</sup>Pr) with PhICl<sub>2</sub> in dichloromethane affords RR′PSe<sub>2</sub>Cl<sub>2</sub>. Upon a slow decomposition of <sup>t</sup>Bu<sub>3</sub>PSe<sub>2</sub>Cl<sub>2</sub>, <sup>t</sup>Bu<sub>3</sub>PSe<sub>3</sub>Cl<sub>2</sub> was isolated in the reaction mixture. The propensity for catenation is seen by the formation of dimers due to secondary bonding interactions (see Fig. 31).

(PhPSe)<sub>2</sub>Se<sub>2</sub>, the so-called Woollins reagent (WR),<sup>229</sup> has proven to be a useful synthon in the development of macrocyclic organoselenium chemistry.<sup>230</sup> It is available commercially, but a convenient method for its preparation has also been reported.<sup>231</sup> For example, the treatment of WR with a diol yields bis(diselenophosphonic) acids quantitatively. The reaction with primary alkylamines converts these acids into alkylammonium salts and subsequent oxidation with I<sub>2</sub>/KI affords the macrocyclic diselenides (see Scheme 10 and Fig. 32).

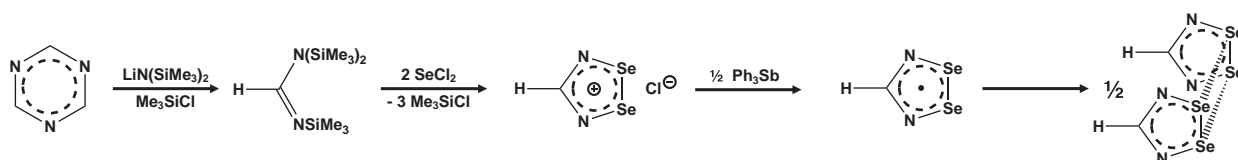
Dichalcogenoimidodiphosphinates (EPR<sub>2</sub>NPR<sub>2</sub>E)<sup>–</sup> (E = S, Se, Te; R = <sup>i</sup>Pr, <sup>t</sup>Bu) are versatile reactants for the preparation of new types of catenated selenium and tellurium species.<sup>121,233</sup> While the sulfur- and selenium-containing anions can be prepared by the deprotonation of EPR<sub>2</sub>N(H)PR<sub>2</sub>E, which is obtained by prolonged reflux of (R<sub>2</sub>P)<sub>2</sub>NH with elemental sulfur or selenium in toluene, the related tellurium-containing anions are best obtained as sodium salts from Na[R<sub>2</sub>PNPR<sub>2</sub>] and elemental tellurium in hot toluene containing TMEDA. This procedure has been extended also for the lighter congeners of tellurium.<sup>121</sup> One-electron oxidation of the sodium salts by iodine in THF affords unprecedented molecular dimers (see Scheme 11):

The molecular structures of (EPR<sub>2</sub>NPR<sub>2</sub>E)<sub>2</sub> (E = S, Se, Te; R = <sup>i</sup>Pr, <sup>t</sup>Bu) dimers are shown in Fig. 33. The formal chalcogen-chalcogen bond between the monomers is elongated from the corresponding single bond in each molecule shown. The elongation increases in the order S–S (2%) < Se–Se (6%) < Te–Te (8%).<sup>121</sup> These elongations correspond to the respective Pauling bond orders





**Scheme 7** Imidoselenium(II) chlorides as reaction intermediates in the formation of cyclic organic selenium imide derivatives from the cyclocondensation reaction of  $t\text{BuNH}_2$  and  $\text{SeCl}_2$ .<sup>214</sup> Reproduced with permission from Karhu, A. J.; Pakkanen, O. J.; Rautiainen, J. M.; Oilunkaniemi, R.; Chivers, T.; Laitinen, R. S. *Dalton Trans.* **2016**, 45, 6210–6221. Copyright 2016 RSC.



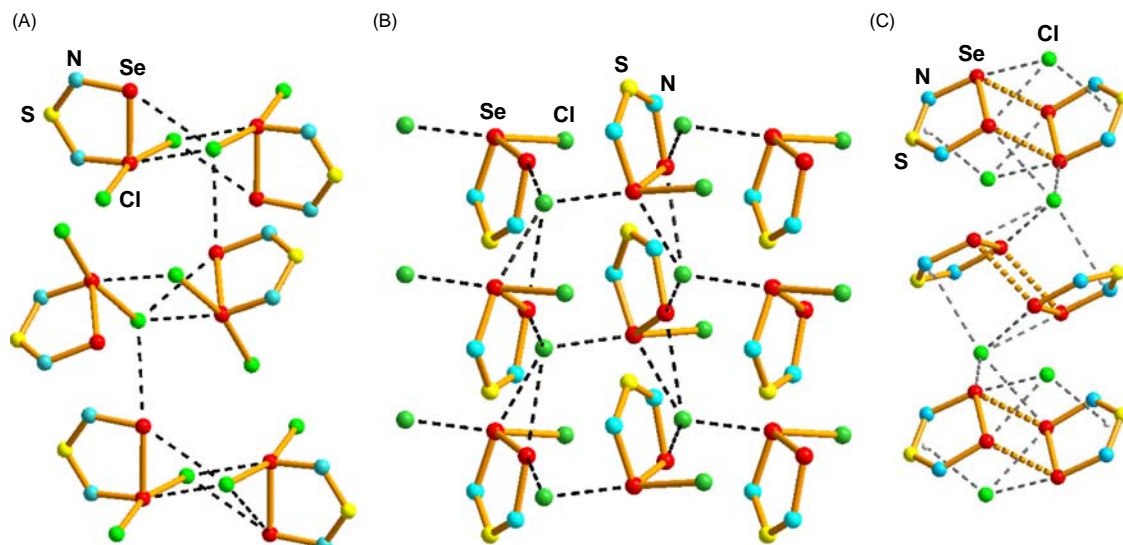
**Scheme 8** The preparation of the  $\text{Se}_2\text{N}_2\text{CH}$  dimer from 1,3,5-triazine.<sup>217</sup>

of 0.97, 0.84, and 0.75. The opposite trend in the interactions between the terminal chalcogen-chalcogen bonds is observed. In case of  $(\text{SP}^t\text{Bu}_2\text{NP}^t\text{Bu}_2\text{S})_2$  [Fig. 33(c)], the terminal  $\text{S}\cdots\text{S}$  distance is  $5.182 \text{ \AA}$ <sup>121</sup> indicating no interaction. The observed bond elongation of the middle  $\text{S}-\text{S}$  bond ( $2.104 \text{ \AA}$ ) is probably only due to the p lone-pair repulsion as a consequence of the PSSP torsional angle of  $180^\circ$ .<sup>235</sup> The selenium and tellurium dimers [Fig. 33(a, b and d)] show the terminal chalcogen-chalcogen contacts of  $3.329$ – $3.355$  and  $3.464 \text{ \AA}$ .<sup>121</sup> In these cases, all three chalcogen-chalcogen distances can be explained by the interaction between two  $(\text{EPR}_2\text{NPR}_2\text{Te})$ -SOMOs, as exemplified in Fig. 34 by the model dimer  $(\text{Te}^i\text{Pr}_2\text{NP}^i\text{Pr}_2\text{Te})_2$ .<sup>234</sup>

The MO formed by the two SOMOs for the four chalcogen fragment is bonding with respect to the middle bond (E-E) but antibonding with respect to the terminal contacts (E-E'). The overlap between the SOMOs is decreased, as the chalcogen atoms become heavier. This is consistent with the observed trend of the increase in the elongation of the central chalcogen-chalcogen bond.

This increasing elongation of the E-E bond may additionally be attributed to the increasing strength of the  $n^2(\text{E}') \rightarrow \sigma^*(\text{E}-\text{E})$  (E, E' = chalcogen atoms) interactions. The trend of decreasing bond orders of the formal E-E bonds calculated by the Pauling relationship<sup>236</sup> correlate well with increasing bond orders calculated for the non-bonded chalcogen distances (E'...E), as shown in Fig. 35.

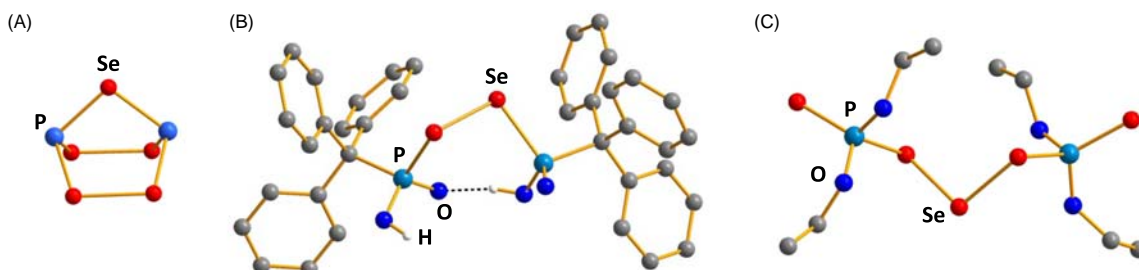
The DFT computations<sup>234</sup> yield a value of  $-80 \text{ kJ mol}^{-1}$  for the energy of dimerization of  $(\text{TeMe}_2\text{PNPMe}_2\text{Te})$ , which is clearly lower than the bond energy of the  $\text{Te}-\text{Te}$  bond of  $138 \text{ kJ mol}^{-1}$ .<sup>239</sup> This is in qualitative agreement with the estimated bond order of 0.75.



**Fig. 29** Crystal structures of (a) molecular  $\text{SeCl}_2(\text{SeNSN})$ ,<sup>219</sup> (b) ionic  $[\text{SeCl}(\text{SeNSN})]\text{Cl}$ ,<sup>219</sup> and ionic of  $[(\text{Se}_2\text{SN}_2)\text{Cl}]_2$ .<sup>221</sup>



**Scheme 9** The conversion of  $\text{TeCl}_2(\text{TeNSN})$  to a  $[\text{TeCl}(\text{TeNSN})]^+$  cation by treatment with  $\text{Ph}_3\text{Sb}$  and  $\text{AsF}_5$ .<sup>224</sup>

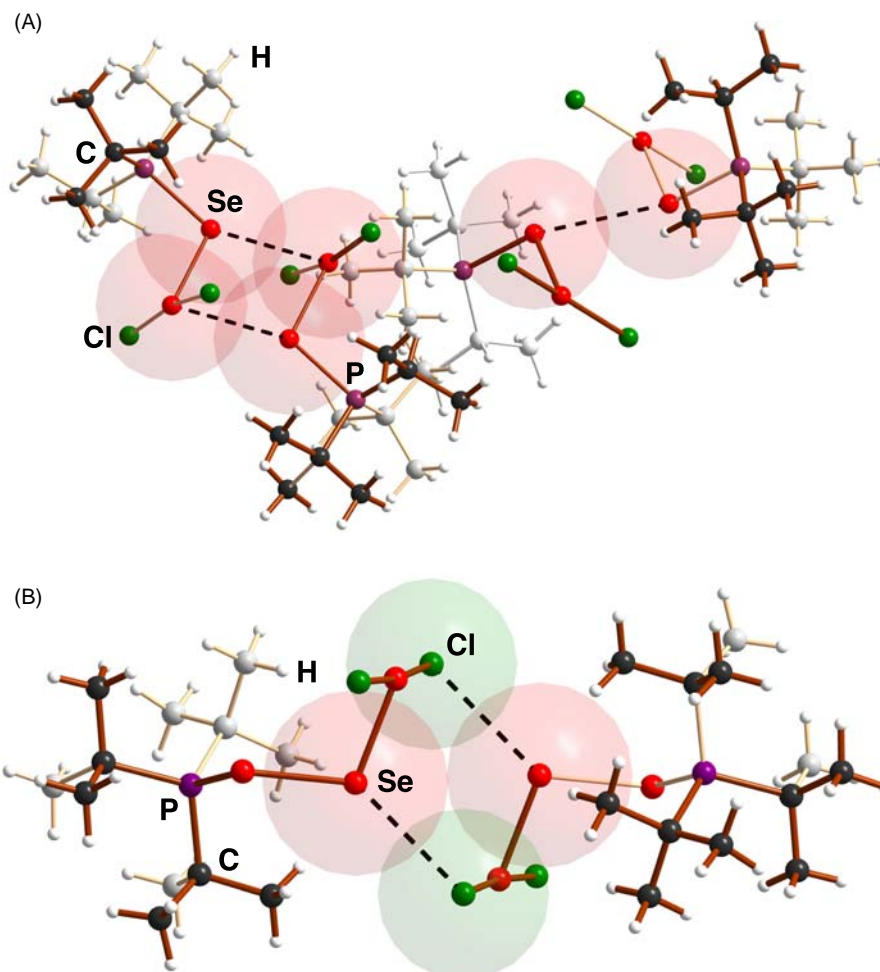


**Fig. 30** Molecular structures of (a)  $\text{P}_2\text{Se}_5$ ,<sup>225</sup> (b)  $\{(\text{Ph}_3\text{C})\text{P}(\text{O})(\text{OH})\}_2\text{Se}_2$ ,<sup>226</sup> and (c)  $\{(\text{EtO})_2\text{P}(\text{Se})\}_2\text{Se}_3$ .<sup>227</sup>

The geometry optimization of  $(\text{TeP}^i\text{Bu}_2\text{NP}^i\text{Bu}_2\text{Te})_2$  predicts the middle Te–Te bond to be longer than in  $(\text{TeP}^i\text{Pr}_2\text{NP}^i\text{Pr}_2\text{Te})_2$ .<sup>234</sup> In agreement with this observation, the repetition of the preparation by using  $\{[(\text{P}^i\text{Bu}_2\text{Te})_2](\text{TMEDA})\text{Na}\}$  instead of the isopropyl analog did not result in the formation of the dimer, but a contact-ion pair involving the  $\{(\text{TeP}^i\text{Bu}_2)_2\text{N}\}^+$  cation and  $\{(\text{TeP}^i\text{Bu}_2)_2\text{N}\}^+$  anion [see Fig. 33(e)].<sup>121</sup> Another route was later designed to prepare similar contact ion salts for other dichalcogenoimidodiphosphinates (see Scheme 12).<sup>237</sup>

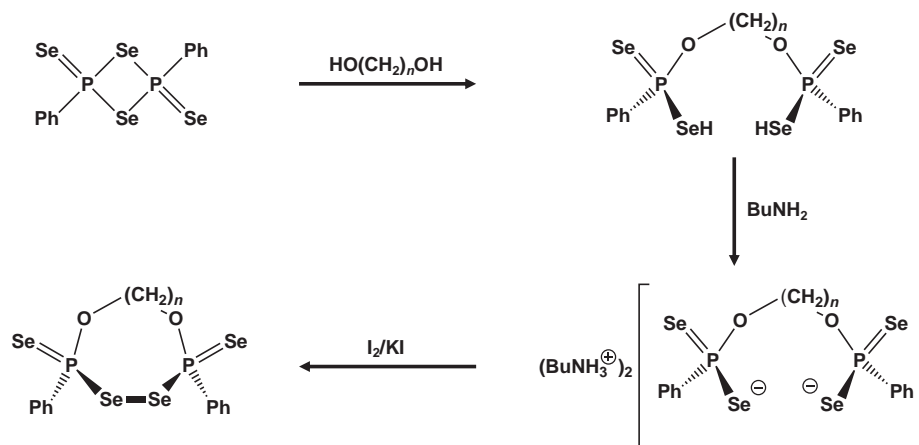
Oxidation of the dianion  $[\text{Se}(\text{tBuN})\text{P}(\mu\text{-N}^i\text{Bu})_2\text{P}(\text{N}^i\text{Bu})\text{Se}]^{2-}$  with  $\text{I}_2$  produces a 15-membered macrocycle in which a planar  $\text{P}_6\text{Se}_6$  motif is stabilized by perpendicular  $\text{P}_2\text{N}_2$  scaffolds (see Scheme 13).<sup>240</sup> The related reaction of  $[\text{Te}(\text{tBuN})\text{P}(\mu\text{-N}^i\text{Bu})_2\text{P}(\text{N}^i\text{Bu})\text{Te}]^{2-}$  produces a cyclic tritelluride via the dimeric intermediate  $[\text{Te}(\text{tBuN})\text{P}(\mu\text{-N}^i\text{Bu})_2\text{P}(\text{N}^i\text{Bu})\text{Te}]_2^{2-}$ .<sup>241</sup> The oxidation of the dilithium salt of  $[\text{Te}(\text{tBuN})\text{P}(\mu\text{-N}^i\text{Bu})_2\text{P}(\text{N}^i\text{Bu})\text{Te}]^{2-}$  with  $\text{Se}_2\text{Cl}_2$  in toluene affords a mixture of cyclic tetrachalcogenides and trichalcogenides with the  $\text{P}_2\text{N}_2\text{Se}_2\text{Te}_2$  and  $\text{P}_2\text{N}_2\text{Te}_2\text{Se}$  motifs (see Scheme 14).<sup>242</sup> This reaction is analogous to that of the sodium salt  $[\text{Se}(\text{tBuN})\text{P}(\mu\text{-N}^i\text{Bu})_2\text{P}(\text{N}^i\text{Bu})\text{Se}]^{2-}$  (see Scheme 13). The oxidation of the heavy alkali metal (K, Rb) salt of  $(\text{R}_2\text{PSe}_2)^-$  [ $\text{R} = \text{Ph}(\text{CH}_2)_2$ ,  $2\text{-Fu}(\text{CH}_2)_2$ ;  $\text{Fu} = \text{furyl } \text{C}_4\text{H}_3\text{O}$ ] with iodine affords  $[\text{R}_2\text{P}(\text{Se})_2\text{Se}_x]$  ( $x = 1$  or  $3$ ).<sup>243</sup>

The  $\{[\text{tBuN}(\text{Te})\text{P}(\text{N}^i\text{Bu})_2\text{P}(\text{Te})\text{N}^i\text{Bu}]_2\text{Te}\}^{2-}$  dianion contains a spirocyclic  $\text{Te}_5$  fragment [see Fig. 36(a)].<sup>239</sup> This dianion was unexpectedly observed as sodium and rhodium complexes. In the sodium complex the anion is  $N, N'$ -coordinated to two sodium cations. In the  $\text{Rh}(\text{C}_5\text{Me}_5)$  complex, it adopts a  $\text{Te}, \text{Te}', \text{Te}''$ -ligating mode [see Fig. 36(b)]. Similar spirocyclic arrangement is found in electrically neutral  $[\text{Ph}_2\text{P}(\text{Te})\text{NP}(\text{Te})\text{Ph}_2]_2\text{Te}$  [see Fig. 36(c)].<sup>244</sup>

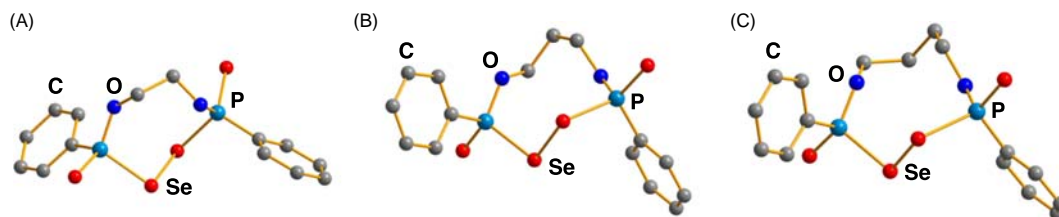


**Fig. 31** The dimer formation of (a)  ${}^1\text{Bu}_2\text{PrPSe}_2\text{Cl}_2$  and (b)  ${}^1\text{Bu}_3\text{PSe}_3\text{Cl}_2$ .<sup>228</sup> The transparent spheres represent the van der Waals radii of selenium and chlorine.

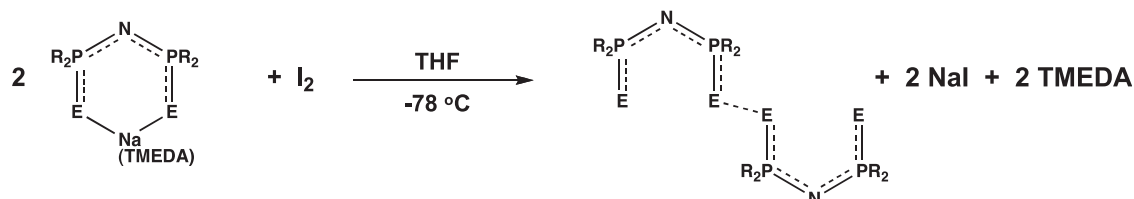
The fusion of stoichiometric amounts of potassium or rubidium selenide with  $\text{Cs}_2\text{Se}_2$ , elemental phosphorus and selenium in evacuated silica tubes afforded both crystalline and amorphous  $\text{MCsP}_2\text{Se}_8$  ( $M = \text{K}, \text{Rb}, \text{Cs}$ ), which contain a cyclic  $[\text{Se}_2\text{P}(\mu\text{-Se}_2)\text{PSe}_2]^{2-}$  dianion,<sup>245</sup> which has a twist conformation in the solid state. In solution it has been inferred by  ${}^{31}\text{P}$  NMR to be fluxional, as shown in Fig. 37.



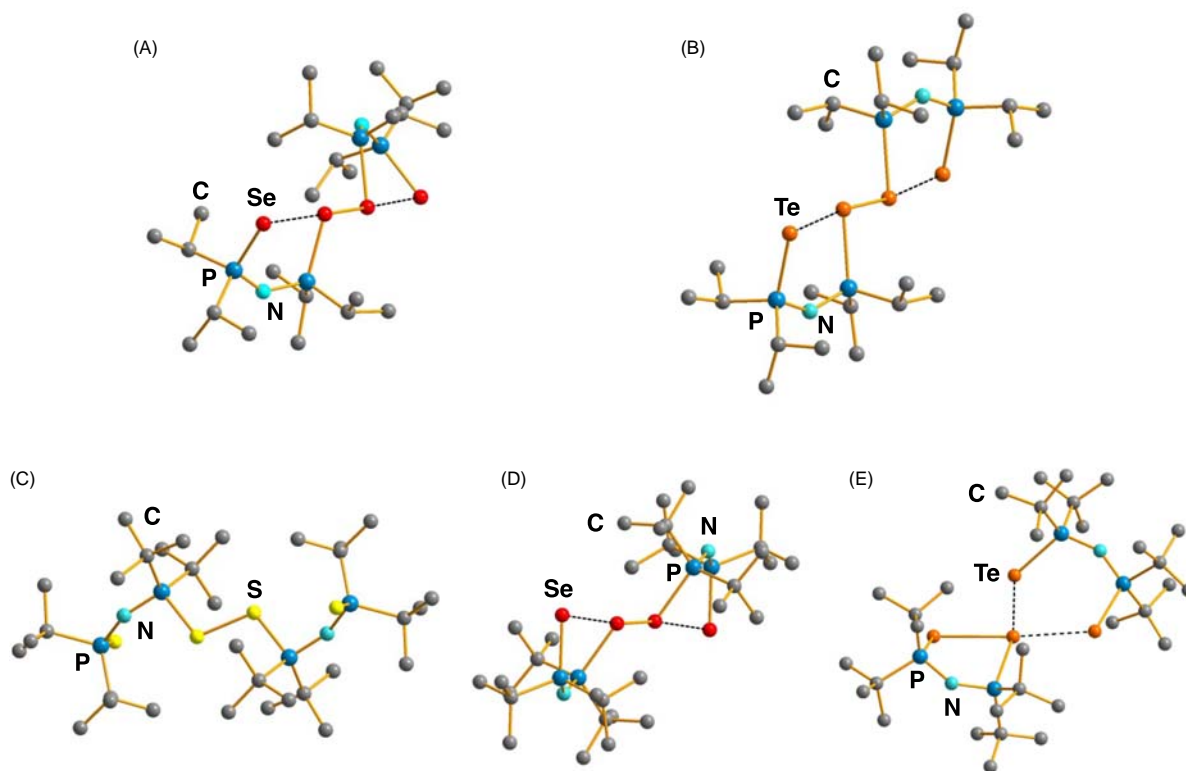
**Scheme 10** Macrocyclic diselenides from Woollins reagent with diols.<sup>232</sup>



**Fig. 32** Molecular structures of  $[\text{Ph}(\text{Se})\text{P}]_2[\mu\text{-O}_2(\text{CH}_2)_n](\mu\text{-Se}_2)$ . (a)  $n = 2$ , (b)  $n = 3$ , and (c)  $n = 4$ .<sup>232</sup>



**Scheme 11** One electron oxidation of  $\text{Na}(\text{TMDEA})(\text{EPR}_2\text{NPR}_2\text{E})$  by iodine to form dimers  $(\text{EPR}_2\text{NPR}_2\text{E})_2$  ( $\text{E} = \text{S}, \text{Se}, \text{Te}$ ).<sup>121</sup>



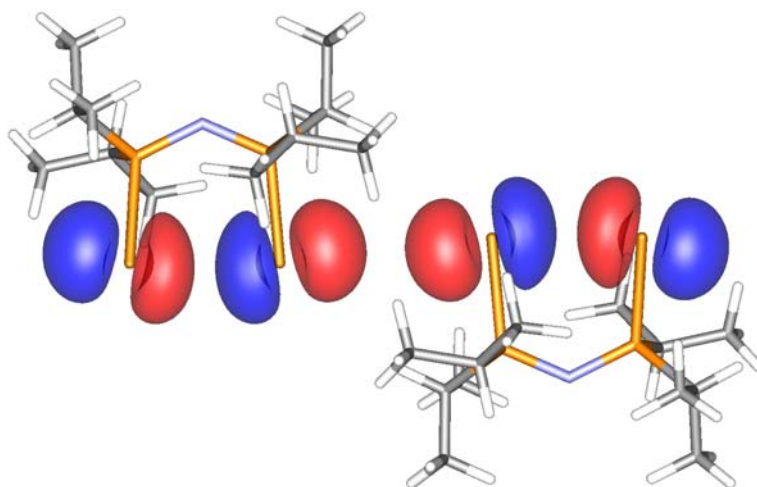
**Fig. 33** Molecular structures of (a)  $(\text{SeP}^i\text{Pr}_2\text{NP}^i\text{Pr}_2\text{Se})_2$ ,<sup>121</sup> (b)  $(\text{TeP}^i\text{Pr}_2\text{NP}^i\text{Pr}_2\text{Te})_2$ ,<sup>234</sup> (c)  $(\text{SP}^i\text{Bu}_2\text{NP}^i\text{Bu}_2\text{S})_2$ ,<sup>121</sup> (d)  $(\text{SeP}^i\text{Bu}_2\text{NP}^i\text{Bu}_2\text{Se})_2$ ,<sup>121</sup> and (e) the contact ion pair  $\{(\text{TeP}^i\text{Bu}_2)_2\text{N}^+\}\{(\text{TeP}^i\text{Bu}_2)_2\text{N}^-\}$ .<sup>121</sup>

Chung et al.<sup>246</sup> have demonstrated that potassium or rubidium polyselenidophosphates  $\text{APSe}_6$  can be processed into smooth amorphous thin films with strong and permanent NLO response. Heating these amorphous films produces crystalline films with increased NLO efficiency.

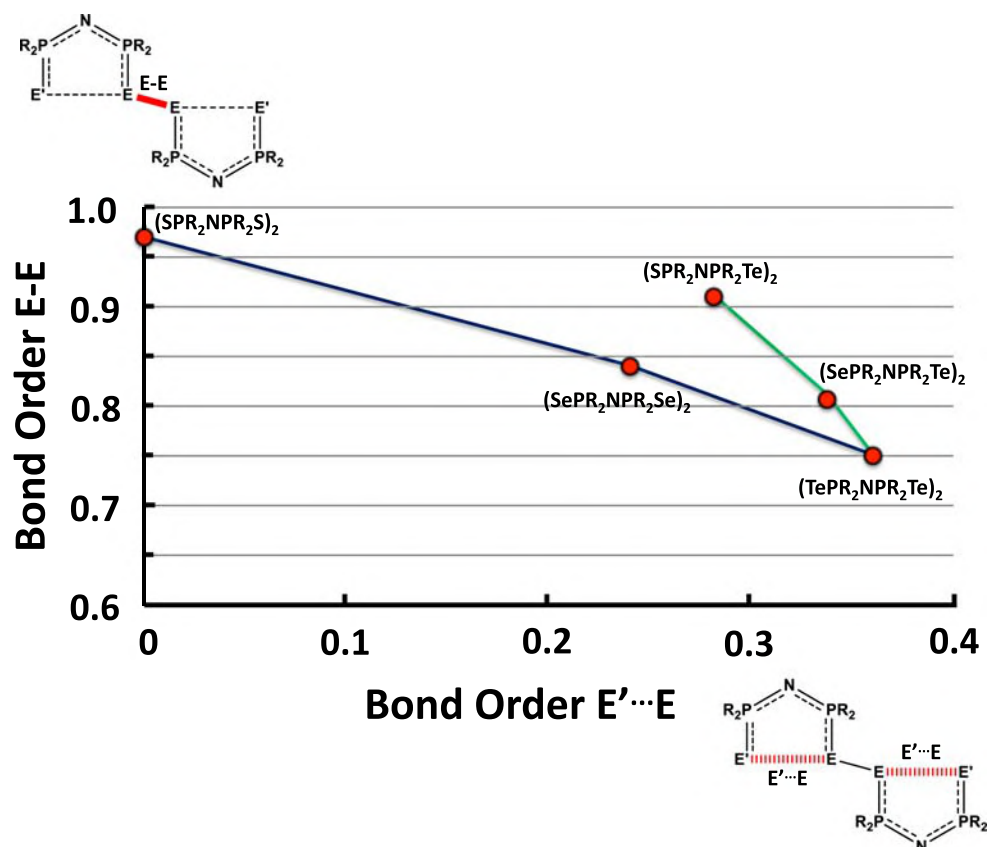
The reactions of  $[\text{FeCp}(\text{CO})_2\text{P}(\text{Se})(\text{O}^i\text{Pr})_2]$  with  $\text{MCl}_3$  ( $\text{M} = \text{Ga}, \text{In}$ ) afford  $[\{\text{FeCp}(\text{CO})_2\text{P}(\text{O}^i\text{Pr})_2\}_2\text{Se}_n][\text{MCl}_4]_2$  ( $n = 2, 3$ ) in good yields (see Scheme 15).<sup>247</sup>

#### 1.22.4.4.3 Chalcogen-arsenic, -antimony, and -bismuth compounds and complexes

Arsenic forms several cyclic molecules and ions with sulfur and selenium.  $\text{ArAs}(\text{SPh})_2$  [ $\text{Ar} = \text{Ph}, 2\text{-(O}_2\text{N)}_2\text{C}_6\text{H}_4$ ] reacts with elemental sulfur in the presence of catalytic amounts of triethylamine to afford  $\text{cyclo}(\text{PhAsS})_4$ , and  $(\text{ArAs})_2\text{S}_3$ .<sup>248</sup> It has also



**Fig. 34** The bonding interaction between two  $\{\text{TeP}^i\text{Pr}_2\text{NP}^i\text{Pr}_2\text{Te}\} \cdot \text{SOMOs}$ .<sup>233,234</sup> Reproduced with permission from Chivers, T.; Konu, J. In *Selenium and Tellurium Chemistry. From Small Molecules to Biomolecules and Materials*, Woollins, J. D.; Laitinen, R. S., Eds.; Springer: Heidelberg, Dordrecht, London, New York, 2011, pp. 79–102. © 2011 Springer.

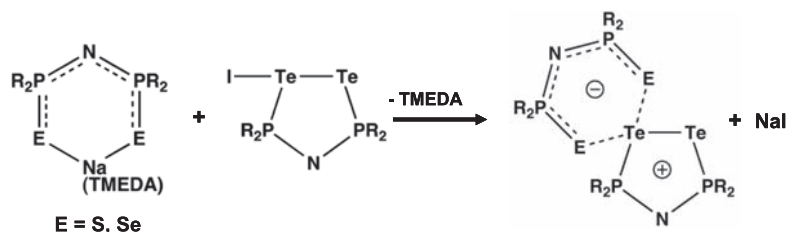


**Fig. 35** The correlation of the bond orders of the chalcogen-chalcogen bonds ( $BO_2$ ) with those of the non-bonded chalcogen-chalcogen contacts ( $BO_1$ ). The bond orders have been calculated from the metrical data in Refs. 121, 234, 237, 238, by utilizing the Pauling relationship.<sup>236</sup>

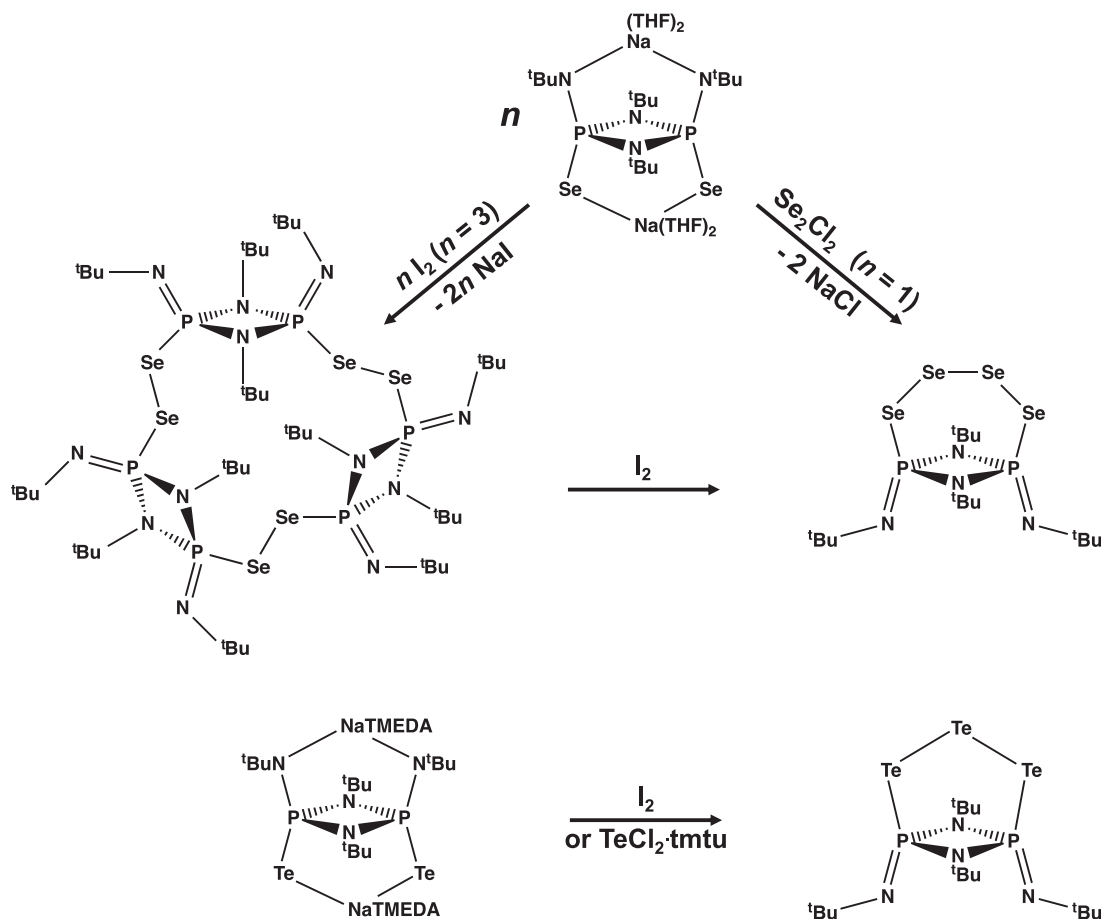
been reported that the reduction of  $(\text{TerNAsCl})_2$  affords a  $(\text{TerNAs})_2$  biradicaloid, which can react with elemental sulfur or selenium to form a tricyclic  $(\text{TerNAs})_2(\text{E}_2)$   $\{\text{E} = \text{S}, \text{Se}; \text{Ter} = \text{bis}[2,6-(2,4,6\text{-trimethyl})]\text{phenyl}\}$  molecule, as shown in **Scheme 16**.<sup>249</sup>

Cations containing Group 15 and Group 16 elements have been reviewed by Eich et al.<sup>250</sup> Cationic species containing chalcogen-chalcogen bonds are extremely rare. Elemental selenium or tellurium and antimony or bismuth react with gallium or aluminum trihalogenide in the presence of a weak pnictogen trihalogenide oxidizing agent to produce a few tetrahalogenidogallate





**Scheme 12** Formation of the contact ion pair for dichalcogenoimidodiphosphinates.<sup>237</sup>

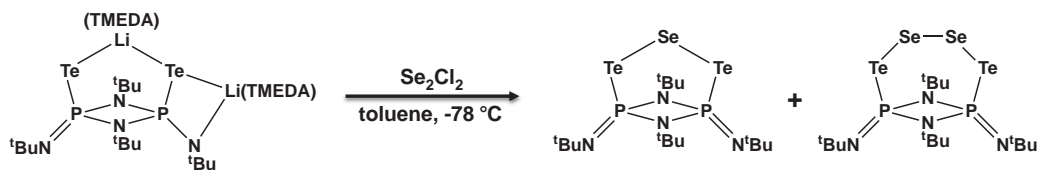


**Scheme 13** The oxidation of  $[Na(THF)_2]_2[E(tBuN)(\mu-N^tBu)_2P(N^tBu)E]^{2-}$  ( $E = Se, Te$ ) by  $I_2$ .<sup>240,241</sup>

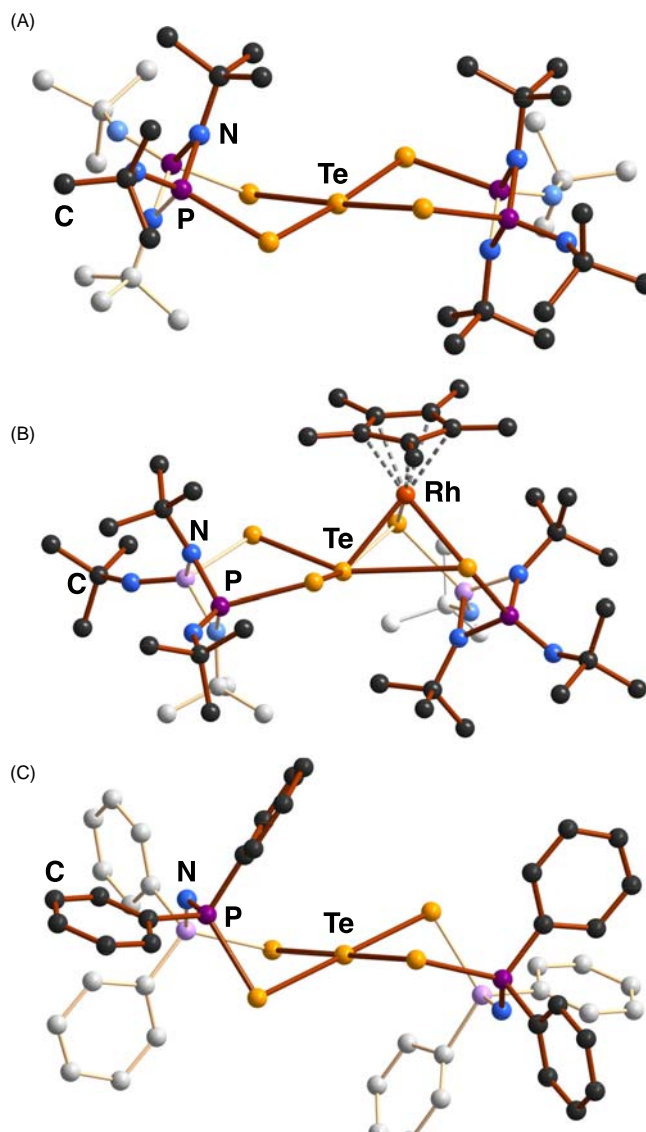
or -aluminate salts containing polyatomic pnictogen-tellurium or pnictogen-selenium cations.<sup>250</sup> The structures of  $(SbTe_4)_n^{n+}$  is composed of fused seven-membered rings containing cumulated Te-Te bonds. The structure can also be understood in terms of a series of two  $Te_4^{2-}$  ligands bridging to  $Sb^{5+}$ -centers (see Fig. 38).

The structural chemistry of the anions is more established. Solvothermal synthesis involving a mixture of elemental indium and sulfur, arsenic sulfide  $As_2S_3$ , and  $NH_4Cl$  afford  $(enH_2)_{4.5}[In(AsS_4)_3][As_2S_2(\mu-S_2)(\mu-S)]Cl$ .<sup>251</sup> The lattice is composed of homoleptic  $[In(S_4As)_4]^{6-}$  and discrete  $[As_2S_2(\mu-S_2)(\mu-S)]^{2-}$  anions, in addition to discrete 1,2-ethylene diammonium and chloride anions. The hydrothermal reaction involving arsenic, sulfur, and manganese carbonate together with 2,2'-bipy (2,2'-bipyridine) and water produces  $\{[Mn(2,2'-bipy)_2](\mu-S_4As)\}(SAsS_5)$ .<sup>252</sup> Other structurally characterized discrete anions, which have been prepared with various counter cations, are exemplified in Fig. 39.

Several reports of the preparation and structural characterization of  $[SeAs(\mu-Se_2)_2AsSe]^{2-}$  anion with different counter cations have been published during the recent decades.<sup>255</sup> Like the conformation of  $(SAsS_7)^-$ , the selenium analog can be conceived to be based on the puckered crown-shaped  $S_8$  ring in which one sulfur atom has been replaced by the  $AsSe^-$  unit. The exocyclic As-Se bond [2.262(3)–2.2983(8) Å,<sup>127</sup> average 2.282(10) Å] is significantly shorter than the endocyclic As-Se bond [2.386(3)–2.571(4) Å,<sup>127</sup> average 2.43(4) Å], and there is some double-bond character in the exocyclic bond (the estimated Pauling bond orders<sup>236</sup> for



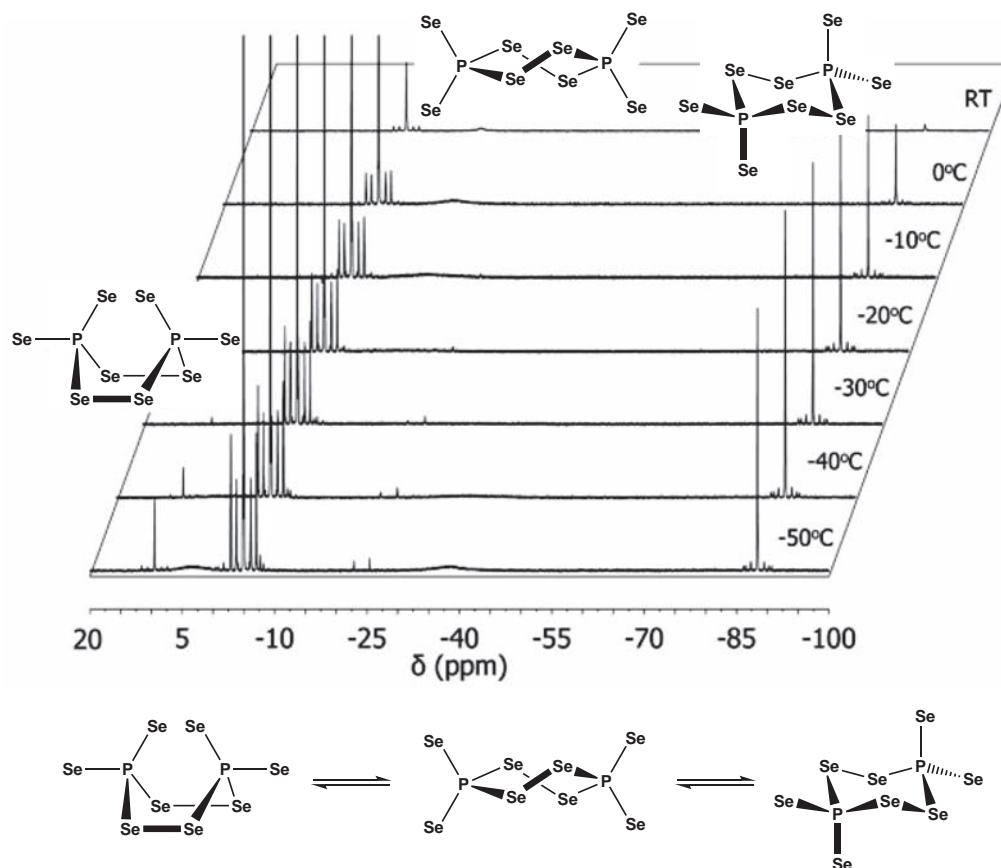
**Scheme 14** The oxidation of  $[\text{Te}(\text{tBuN})\text{P}(\mu\text{-N}^t\text{Bu})_2\text{P}(\text{N}^t\text{Bu})\text{Te}]^{2-}$  by  $\text{Se}_2\text{Cl}_2$ .<sup>242</sup>



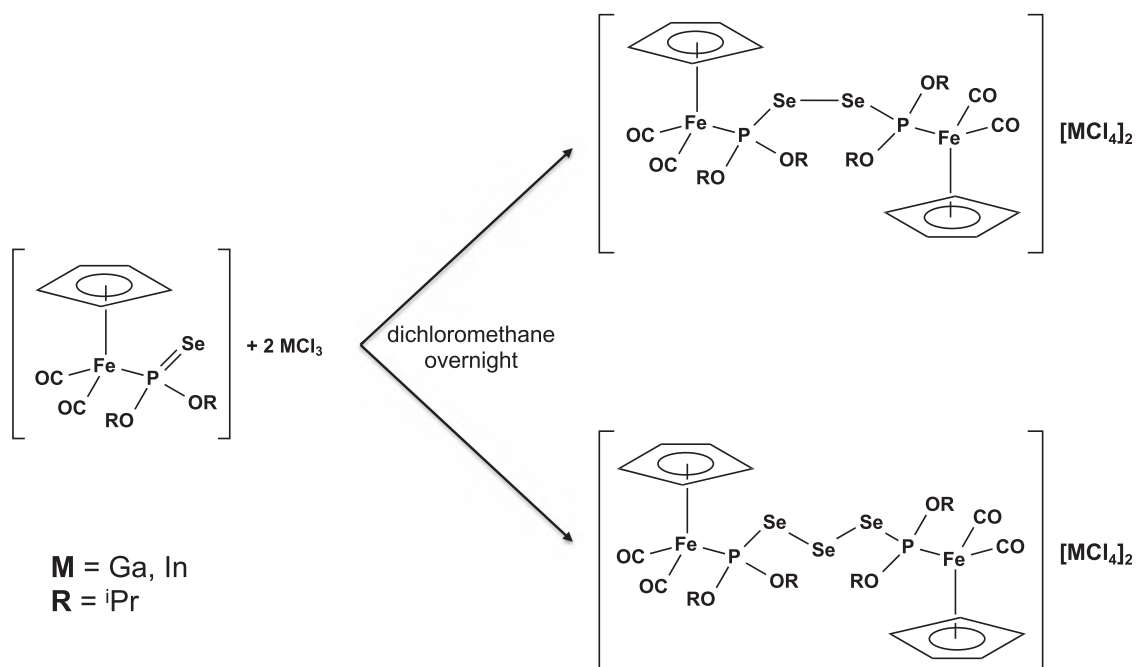
**Fig. 36** The spirocyclic  $\text{TeTe}_4$  arrangement in (a) the  $[\text{tBuN}(\text{Te})\text{P}(\text{N}^t\text{Bu})_2\text{P}(\text{Te})\text{N}^t\text{Bu}]^{2-}$  dianion and (b) its  $\text{Rh}(\text{C}_5\text{H}_5)$  complex,<sup>239</sup> as well as (c) in  $[\text{Ph}_2\text{P}(\text{Te})\text{NP}(\text{Te})\text{Ph}_2]_2\text{Te}$ .<sup>244</sup>

the exocyclic and endocyclic  $\text{As}-\text{Se}$  bonds are 1.25 and 0.75, respectively). The  $\text{Se}-\text{Se}$  bond is close to a standard single bond [2.335(4)–2.3596(13) Å,<sup>127</sup> average 2.350(8) Å].

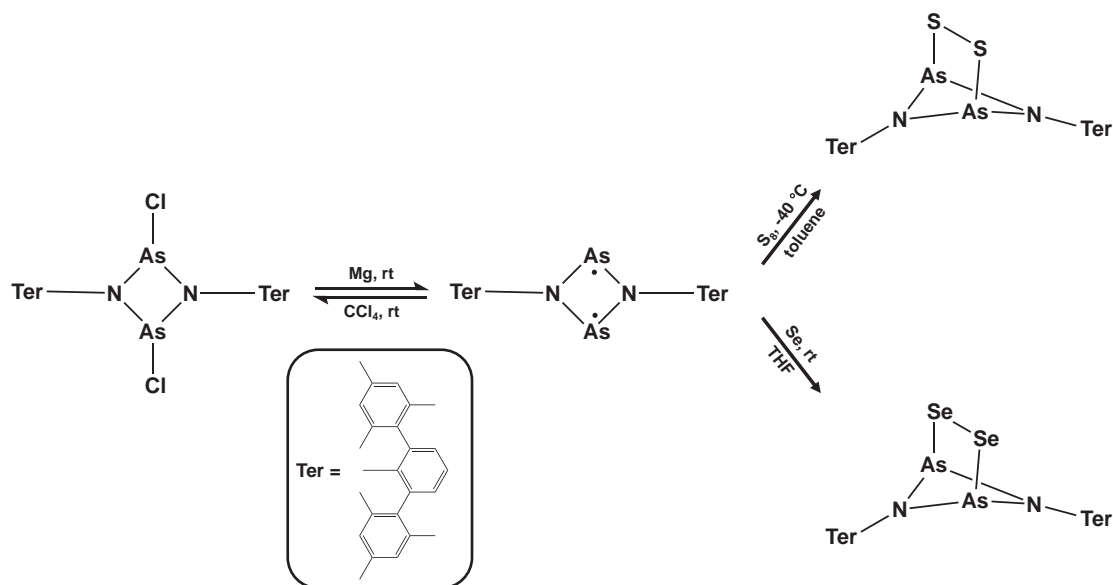
Polysulfido- and polyselenidoarsenate anions can also act as ligands in transition-metal complexes, as exemplified by a few known manganese complexes. The hydrothermal synthesis involving elemental arsenic and sulfur, manganese carbonate, ammonium thiocyanate, and 2,2'-bipyridine resulted in the dinuclear manganese complex  $[\{\text{Mn}(2,2'\text{-bipy})_2(\text{SCN})\}_2\{\mu\text{-S}_2[\text{As}_2(\text{S}_2)_2\}]]$  [see Fig. 40(a)].<sup>256</sup> The related reaction involving arsenic, selenium, and  $[\text{MnCl}_2(\text{tren})]$ , [tren = tris(2-aminoethyl)amine], and  $\text{CsCO}_3$  afforded  $[\{\text{Mn}(\text{tren})\}_2(\mu\text{-As}_2\text{Se}_6)_2]$  [see Fig. 40(b)].<sup>257</sup> The change of the manganese source to  $[\text{MnCl}_2(\text{cyclam})]$  (cyclam = 1,4,8,11-tetraazacyclotetradecane) resulted in the formation of the discrete bridging acyclic  $(\text{As}_2\text{Se}_6)^{4-}$  ligand



**Fig. 37** Interconversion equilibrium of the boat-, twist- and chair-conformations of the  $[\text{Se}_2\text{P}(\mu\text{-Se}_2)\text{PSe}_2]^{2-}$  anion.<sup>245</sup> Reproduced with permission from Haynes, A. S.; Banerjee, A.; Saouma, F. O.; Otieno, C. O.; Jang, J. I.; Kanatzidis, M. G. *Chem. Mater.* **2016**, *28*, 2374–2383. © American Chemical Society.



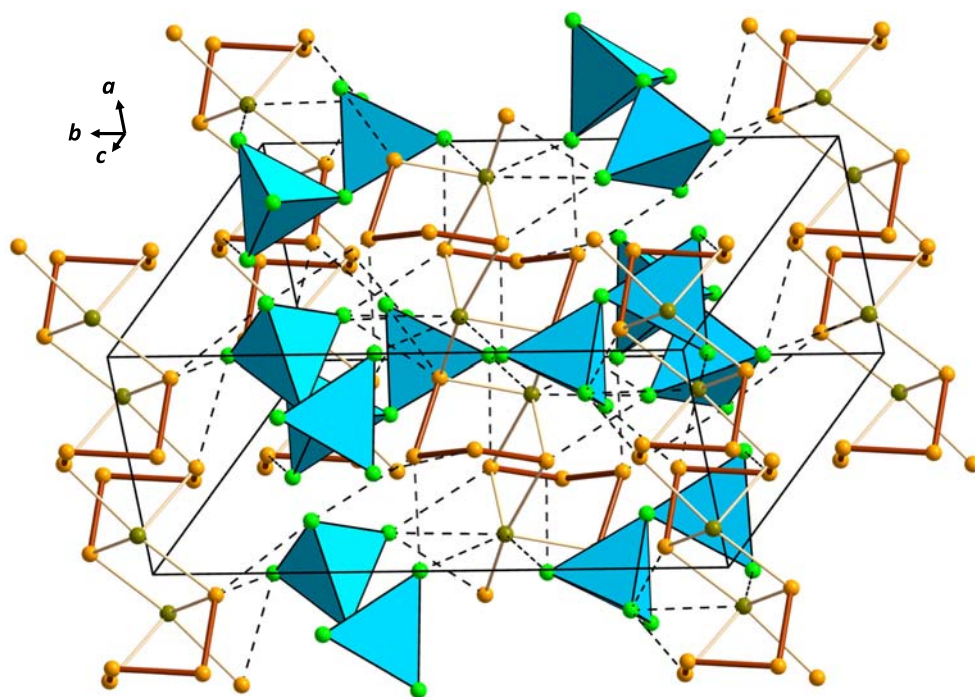
**Scheme 15** One-electron oxidation of the  $[\text{FeCp}(\text{CO})_2(\text{PSe}(\text{OR})_2)]$  by  $\text{MCl}_3$  ( $\text{M} = \text{Ga}, \text{In}$ ).<sup>247</sup>



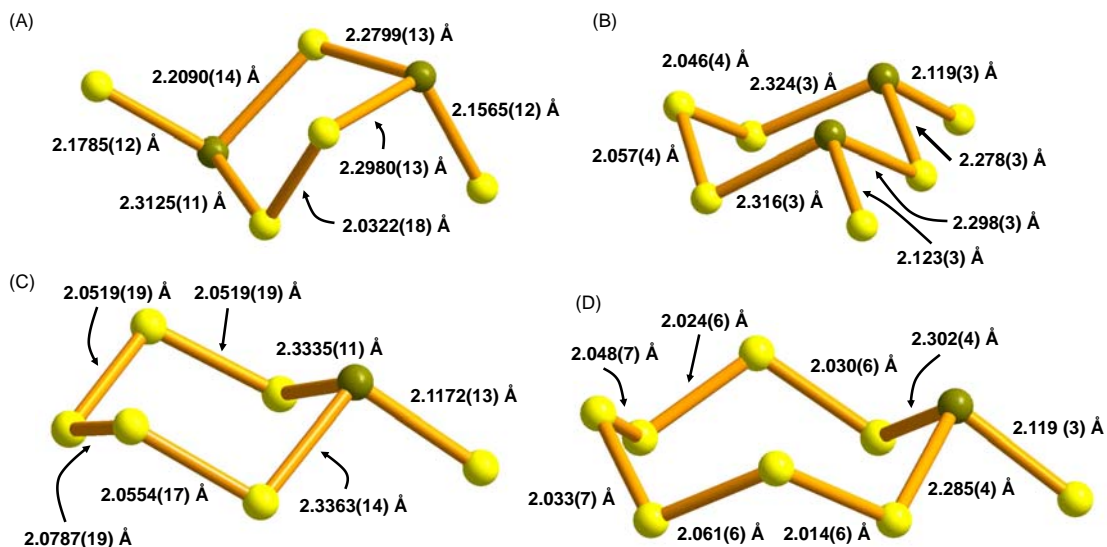
**Scheme 16** The preparation of  $(\text{TerNAs})_2(\text{E})_2$  ( $\text{E} = \text{S}, \text{Se}$ ;  $\text{Ter} = \text{bis}[2,6-(2,4,6\text{-trimethyl})]\text{phenyl}$ ).<sup>249</sup>

[Fig. 40(c), and with  $[\text{MnCl}_2(\text{terpy})]$  [ $\text{terpy} = 2,6\text{-}(2\text{-pyridyl})\text{-pyridyl}$ ] a polymeric  $(\text{As}_2\text{Se}_8)^{6-}$  was obtained [Fig. 40(d)].<sup>258</sup> The hydrothermal reaction of elemental selenium, arsenic, and manganese with 1,10-phenantroline also yields a single-strand polymeric  $[\text{As}_2\text{Se}_2(\mu\text{-Se})(\mu\text{-Se}_2)]^{2-}$  anion coordinated in the regular fashion to the  $[\text{Mn}(\text{phen})_2]^{2+}$  cation through the two terminal selenium atoms [Fig. 40(e)].<sup>259</sup>

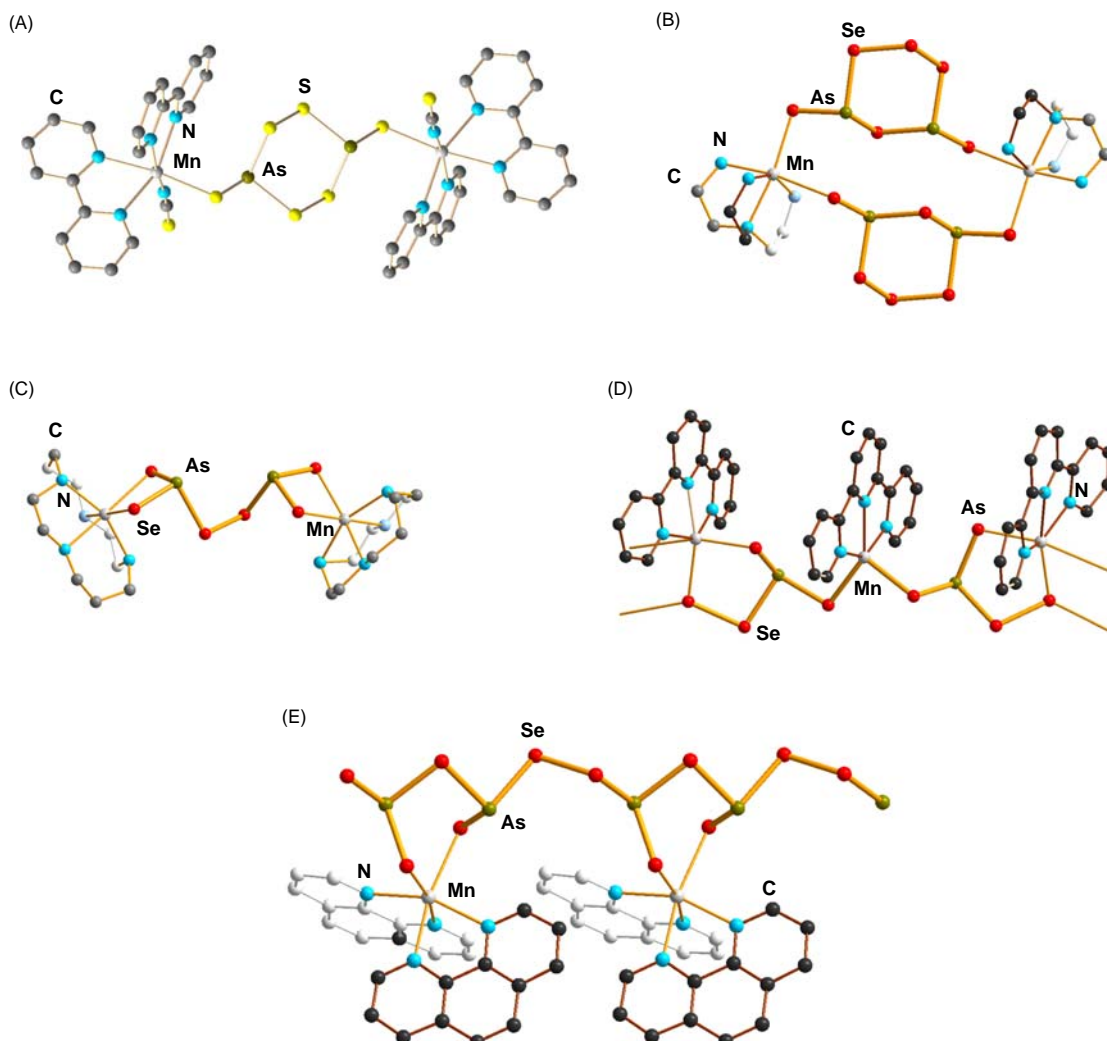
There are very few polychalcogenidoantimonate salts or complexes, which contain chalcogen-chalcogen bonds.<sup>260–265</sup> Nie et al.<sup>261</sup> have reported the synthesis of ultrathin nanosheets of 1D  $(\text{NHMe}_2)[\text{Sb}_4\text{S}_5(\text{S}_3)]$  by a solvothermal method involving  $\text{Sb}_2\text{S}_3$  powder, sulfur, *N,N*-dimethylformamide, hydrazine monohydrate, and octylamine. The authors conclude that the salt could be employed as an anode material for lithium-ion batteries and that this crystalline thioantimonate has potential in applications in high-performance power sources.



**Fig. 38** The crystal structure of  $(\text{SbTe}_4)_n[\text{GaCl}_4]$ . Tellurium atoms are depicted in orange and antimony in olive green. The  $[\text{GaCl}_4]^-$  counterions are displayed as tetrahedra drawn with green chloride ligands.<sup>250</sup>



**Fig. 39** Structures of (a)  $[\text{As}_2\text{S}_2(\mu\text{-S}_2)(\mu\text{-S})]^{2-}$  in  $(\text{enH}_2)_{4,5}[\text{In}(\text{AsS}_4)_3][\text{As}_2\text{S}_2(\mu\text{-S}_2)(\mu\text{-S})]\text{Cl}$ ,<sup>251</sup> (b)  $[\text{As}_2\text{S}_2(\mu\text{-S})(\mu\text{-S}_3)]^{2-}$  in  $(\text{PPh}_4)_2\text{As}_2\text{S}_6$ ,<sup>253</sup> (c)  $(\text{SAsS}_5)^-$  in  $[\text{Mn}(2,2'\text{-bipy})_2(\mu\text{-S}_4\text{As})](\text{SAsS}_5)$ ,<sup>252</sup> (d)  $(\text{SAsS}_7)^-$  in  $(\text{PPh}_4)(\text{SAsS}_7)$ .<sup>254</sup>



**Fig. 40** (a) Structures of  $[\text{Mn}(2,2'\text{-bipy})_2(\text{NCS})_2]_2(\mu\text{-As}_2\text{S}_6)$ ,<sup>256</sup> (b)  $[\text{Mn}(\text{tren})_2(\mu\text{-As}_2\text{Se}_6)]$ ,<sup>257</sup> (c)  $[\text{Mn}(\text{cyclam})_2(\mu\text{-As}_2\text{Se}_6)_2]$ ,<sup>258</sup> (d)  $[\text{Mn}(\text{terpy})_3(\mu\text{-As}_2\text{Se}_8)]$ ,<sup>258</sup> and (e)  $[\text{Mn}(\text{phen})_2(\mu\text{-As}_2\text{Se}_5)]$ .<sup>259</sup>



In 2017, Schwamm et al.<sup>266</sup> reported the first structurally characterized complex of  $S_4^{\cdot-}$  by the reaction of bismuth(II) radicals  $Bi(NON^{Ar^\ddagger})^\cdot$   $\{NON^R = [O(SiMe_2NAr^\ddagger)_2]^{2-}; Ar^\ddagger = 2,6-[(C_6H_5)_2CH]_2-4-C_6H_2^tBu\}$  with cyclo- $S_8$ , which resulted in the formation of yellow crystals of the dimer  $[Bi(NON^{Ar^\ddagger})_2(\mu-S_8)]$ , as shown in **Scheme 17**. The complex is centrosymmetric consisting of two  $Bi(NON^{Ar^\ddagger})(S_4)$  monomeric units. The S–S bond lengths in the  $S_4$  unit are in the range 2.021(3)–2.113(3) Å, and the two  $S_4$  monomer complexes are linked by weak S⋯S interactions of 2.758(4)–3.213(4) Å. Thus, it can formally be considered as the dimer of the bismuth complex of the  $S_4^{\cdot-}$  radical anion, which dimerizes via a  $\pi^*(SOMO)-\pi^*(SOMO)$  interaction (see **Fig. 41**).

The related reactions of  $[Bi(NON^R)]^\cdot$   $\{NON^R = [O(SiMe_2NR)_2]^{2-}\}$  and sulfur afford mixtures of  $[Bi(NON^R)]_2(\mu^2-S_n)$   $\{n = 1$  and 3; R = Dipp, 2,6- $tPr_2C_6H_3$ ,  $tBu$ ;  $n = 5$ , R = Dipp $\}$ .<sup>266</sup>

The information on coordination complexes with Group 15 central atoms is much sparser than that of Groups 13 and 14 and concentrates mainly on antimony and bismuth. Like the polychalcogenido complexes of Groups 13 and 14, those involving Group 15 central atoms can be divided into two structural classes. One class involves mononuclear complexes, which contain one or several  $MS_n$  chelate rings in which the ring size is generally between five and seven (see **Sections 1.22.4.2 and 1.22.4.3**, and Ref. 268, as well as references cited therein). Polynuclear polychalcogenido complexes may be linked by one or two chalcogen bridges. Such species are exemplified by  $[ArQ(E)(E_n)QAr]$   $\{Q = P, Sb, Bi; Ar = 2,6-bis[bis(trimethylsilyl)methyl]-4-[tris(trimethylsilyl)methyl]phenyl\}$ , which can be prepared by treatment of  $ArQ = QAr$  with  $S_8$ ,<sup>268,269</sup> Se,<sup>270</sup> or  $Bu_3P = Te$ <sup>270</sup> in benzene at room temperature (see **Scheme 18**).

The treatment of  $[MCl_3L]$   $[M = Sb, Bi; L = \text{the pincer ligand } 2,6-(CH_2NMe_2)C_6H_3]$  with  $Na_2S$  generates in toluene the dinuclear complex  $[ML(\mu-S)_2ML]$  that upon treatment with  $S_8$  in  $CH_2Cl_2$  leads to the extension of the chain length of the bridging sulfido ligands and the formation of  $[ML(\mu-S_5)_2ML]$ .<sup>268,271</sup> Their molecular structures, which have been shown in **Fig. 42**, are virtually identical. The packing of the antimony and bismuth complexes, however, is different.

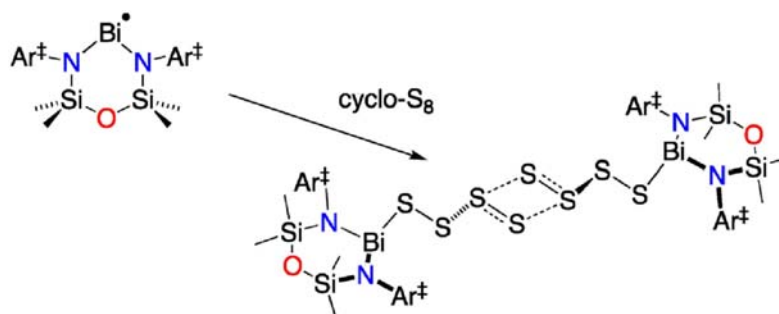
The hydrothermal reactions involving elemental antimony or antimony trichloride, sulfur, and tetraphenylphosphonium bromide in aqueous ammonia afforded dinuclear  $[Sb_2S_x]^{2-}$  anions containing both chelating and bridging sulfido ligands of varying chain length.<sup>272,273</sup>  $\{[SbS_5]_2(\mu-S)(\mu-S_4)\}^{2-}$  has also been prepared from antimony, sulfur, and magnesium in *N*-methylimidazole.<sup>109</sup> Magnesium is considered to assist the dissolution of antimony. Interestingly, this rationale also resulted in the formation of  $\{[Sb(S_5)]_2(\mu-S)(\mu-S_4)\}^{2-}$  from  $Sb_2S_3$ . The crystal structures are exemplified in **Fig. 43**.  $(PPh_4)_3[(Sb_2S_{17})(Sb_2S_{16})_{0.5}]$  shown in **Fig. 43(a)** is a solid solution of the  $[(SbS_5)(\mu-S)(\mu-S_4)(SbS_4)]^{2-}$  and  $[(SbS_5)(\mu-S)(\mu-S_4)(SbS_6)]^{2-}$  anions the latter of which occupies the special position in the lattice.

## 1.22.4.5 Chalcogen halogenides

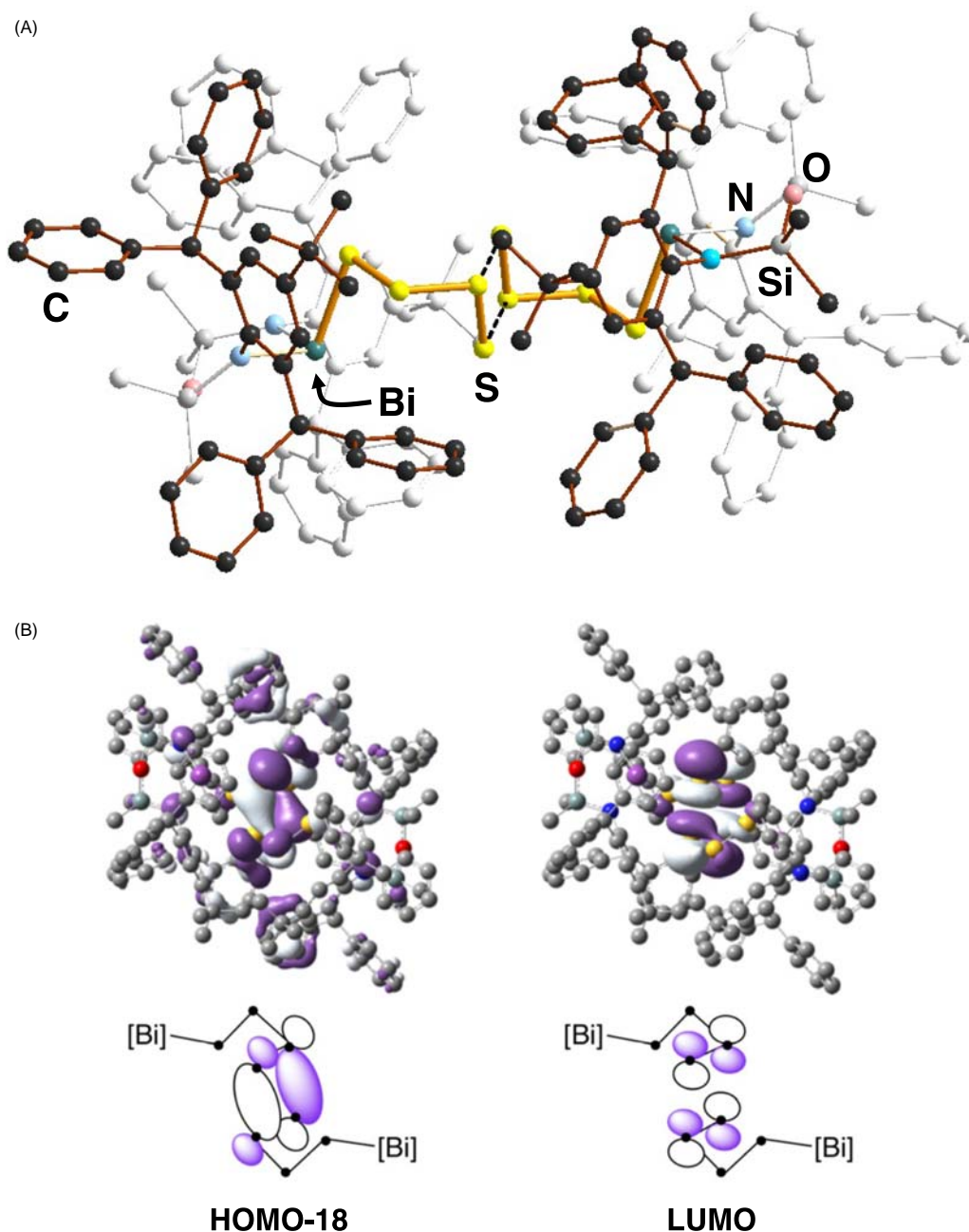
### 1.22.4.5.1 Electrically neutral molecules

Some binary chalcogen halides incorporate chalcogen-chalcogen bonds. For example,  $E_2X_2$  ( $E = S, Se; X = Cl, Br$ ) are a well-characterized, commercially available class of reagents the structures of which have been known for a long time.<sup>8</sup> They are all useful reagents in synthetic applications. They are liquids at room temperature the color of which deepens from yellow to brown and to dark red, as the chalcogen and/or the halogen atoms become heavier. Their low-temperature crystal structures<sup>267,274</sup> show gauche XEE conformations with the torsional angle  $\tau_{XEE}$  spanning a narrow range of 83.9(1)–87.41(5)°. <sup>267,274</sup> While the molecular geometry of each species is similar, the packing of the molecules in the solid lattice shows variation (see **Fig. 44**).  $S_2Br_2$  and the thermodynamically stable form  $\alpha$ - $Se_2Br_2$  are isomorphous.  $Se_2Cl_2$  and the metastable  $\beta$ - $Se_2Br_2$  are also isomorphous. It can also be seen in **Fig. 44** that the  $E\cdots E$ ,  $E\cdots X$ , and  $X\cdots X$  intermolecular interactions become stronger and more numerous, as the chalcogen or the halogen element become heavier. The shortest  $E\cdots X$  contacts are 3.2246(7)–3.2260(8) and 3.415(1) Å for  $S_2Cl_2$  and  $S_2Br_2$ , respectively, and 3.495(1)–3.513(1) and 3.628(1)–3.715(2) Å for the different isomers of  $Se_2Br_2$ , respectively. The chalcogen-chalcogen short contacts of 3.483(6) and 3.4489(14) Å are found in  $S_2Br_2$  and  $Se_2Br_2$ .<sup>267</sup>

Both  $S_2X_2$  and  $Se_2X_2$  have been found to undergo facile disproportionation into  $EX_2$  and  $E_nX_2$ , as exemplified for  $Se_2X_2$ , and the interconversion reaction of a mixture of  $Se_2Cl_2$  and  $Se_2Br_2$  affords  $Se_2ClBr$ .<sup>275</sup> In a similar fashion, a mixture of  $Se_2Cl_2$  and  $S_2Cl_2$  yields an equilibrium mixture containing  $SeS_2Cl_2$ .<sup>276,277</sup>



**Scheme 17** Reaction of  $Bi(NON^{Ar^\ddagger})^\cdot$  with sulfur.<sup>266</sup> Reproduced with permission from Schwamm, R. J.; Lein, M.; Coles, M. P.; Fitchett, C. M. *J. Am. Chem. Soc.* **2017**, *139*, 16490–16493. © 2017 ACS.

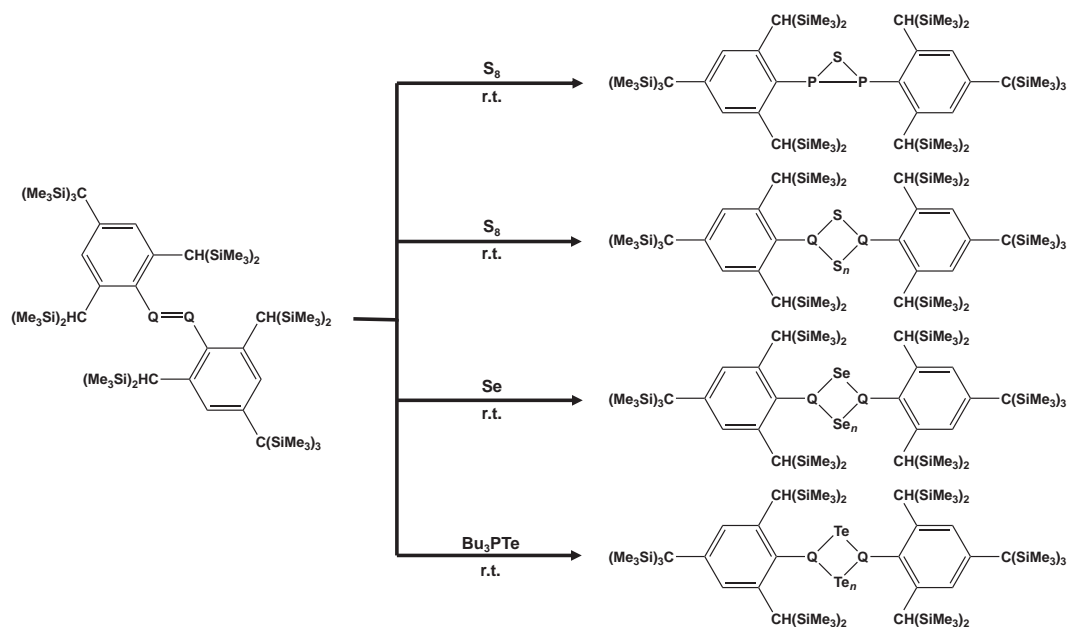


**Fig. 41** (a) Structure of  $[(\text{BINONArf})(\text{S}_4)]_2$  dimer.<sup>266</sup> (b) HOMO-18  $\rightarrow$  HOMO-18  $[\pi^*(\text{SOMO}) \rightarrow \pi^*(\text{SOMO})]$  interaction between the  $\text{S}_4$  radical units and the LUMO-LUMO overlap.<sup>266</sup> Reproduced with permission from Schwamm, R. J.; Lein, M.; Coles, M. P.; Fitchett, C. M. *J. Am. Chem. Soc.* **2017**, *139*, 16490–16493. © 2017 ACS.

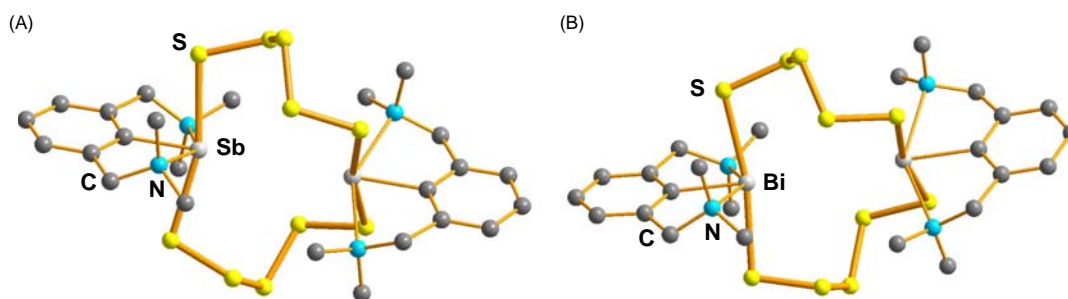
Chlorosulfanes containing longer chalcogen chains have been traditionally prepared by the reaction of  $\text{SCl}_2$  or  $\text{S}_2\text{Cl}_2$  and sulfanes  $\text{H}_2\text{S}_n$ , as exemplified in Ref. 278. The corresponding bromosulfanes can be formed by treatment of chlorosulfanes with  $\text{HBr}$  at room temperature.<sup>279</sup> These reactions generally form mixtures of halosulfanes. The composition of these mixtures with up to the sulfur chain length of 30 has been determined by utilizing reversed-phase HPLC.<sup>280</sup>

Reasonably pure stoichiometric  $\text{S}_4\text{Cl}_2$  and  $\text{S}_6\text{Cl}_2$ ,  $\text{S}_7\text{Cl}_2$ , and  $\text{S}_8\text{Cl}_2$  have been prepared by careful chlorination of cyclo- $\text{S}_6$ ,<sup>281,282</sup> cyclo- $\text{S}_7$ ,<sup>283</sup> and cyclo- $\text{S}_8$ ,<sup>281</sup> respectively. The related reaction with the heterocyclic 1,2- $\text{Se}_2\text{S}_5$  affords  $\text{Se}_2\text{S}_5\text{Cl}_2$ .<sup>284</sup> All these chlorides are useful synthons in the preparation of chalcogen rings.<sup>6</sup> The NMR study of the reactions of  $\text{Se}_2\text{S}_5\text{Cl}_2$  with  $(\text{Me}_3\text{Si})_2\text{E}$  ( $\text{E} = \text{S}, \text{Se}, \text{Te}$ )<sup>285,286</sup> indicated that the chlorination of 1,2- $\text{Se}_2\text{S}_5$  afforded two isomers of the chlorochalcogenane:  $\text{ClSeS}_5\text{SeCl}$  and  $\text{ClSeSeS}_5\text{Cl}$ .

Ditellurium dichloride  $\text{Te}_2\text{Cl}_2$  and dibromide  $\text{Te}_2\text{Br}_2$  can be prepared in moderate yields by reducing elemental tellurium with  $\text{LiBHET}_3$  in THF with a subsequent treatment with  $\text{TeX}_4$  ( $\text{X} = \text{Cl}, \text{Br}$ ).<sup>287</sup> Both are dark brown liquids that decompose rapidly. In  $\text{CS}_2$



**Scheme 18** Preparation of  $\text{ArQ(E)}(\text{E}_n)\text{QAr}$  ( $\text{Q} = \text{P}, \text{Sb}, \text{Bi}$ ;  $\text{Ar} = -\text{C}_6\text{H}_2[\text{CH}(\text{SiMe}_3)_2-2,6]_2[\text{C}(\text{SiMe}_3)_3-4]$ ;  $n = 0-2$ ).<sup>269,270</sup>



**Fig. 42** The structures of (a)  $[\text{SbL}(\mu\text{-S}_5)_2\text{SbL}]$ <sup>268</sup> and (b)  $[\text{BiL}(\mu\text{-S}_5)_2\text{BiL}]$ <sup>271</sup> [ $\text{L} = 2,6\text{-}(\text{CH}_2\text{NMe}_2)_2\text{C}_6\text{H}_3$ ].

solution, however, they are rather stable. The molecular species were identified by EI mass spectroscopy (see Fig. 45). The reactions of  $\text{Te}_2\text{Cl}_2$  and  $[\text{TiCp}_2\text{S}_5]$  or  $[\text{TiCp}_2\text{Se}_5]$  expectedly afford 1,2- $\text{Te}_2\text{S}_5$  and 1,2- $\text{Te}_2\text{Se}_5$ , respectively, which were identified by  $^{77}\text{Se}$  and  $^{125}\text{Te}$  NMR spectroscopy.<sup>287</sup>

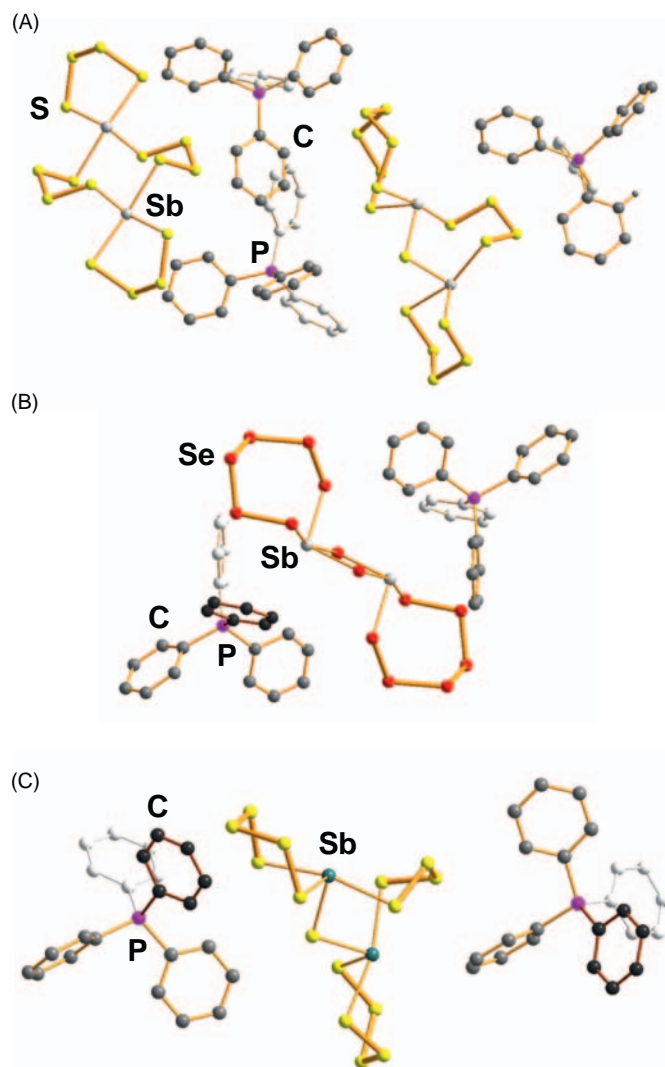
Tellurium forms subhalides that do not find analogs with lighter chalcogen elements.<sup>288,289</sup> The main characterized species are  $\text{Te}_3\text{Cl}_2$ ,  $\text{Te}_2\text{X}$  ( $\text{X} = \text{Cl}, \text{Br}, \text{I}$ ), and two polymorphs of  $\text{TeI}$ . The general method of preparation involves the heating of the elements at 200–300 °C with subsequent homogenization, annealing, quenching, and extraction to remove the excess tellurium tetrahalogenide.<sup>290–294</sup> Single crystals of  $\text{Te}_2\text{I}$ , and  $\alpha$ - and  $\beta$ - $\text{TeI}$  can be produced by hydrothermal methods in concentrated aqueous hydroiodic acid.<sup>292–294</sup> Crystals of stable  $\text{Te}_3\text{Cl}_2$ ,  $\text{Te}_2\text{Br}$ , and  $\alpha$ - $\text{TeI}$  can also be grown from the melt.<sup>289</sup> The reduction of tellurium tetrabromides and tetraiodides by the corresponding tin dihalogenide affords tellurium subbromides and -iodides.<sup>290,292</sup>

There is a structural relationship between all subhalides and hexagonal tellurium.<sup>8,289</sup>  $\text{Te}_3\text{Cl}_2$  contains a continuous twisted tellurium chain with every third tellurium atom bonded to two chlorine atoms in axial positions of the trigonal bipyramidal coordination environment [see Fig. 46(a)].<sup>290</sup> The  $\text{Te}-\text{Te}$  bonds within the chain are approximate single bonds. The chains are connected by secondary  $\text{Te}\cdots\text{Cl}$  contacts.<sup>294</sup>

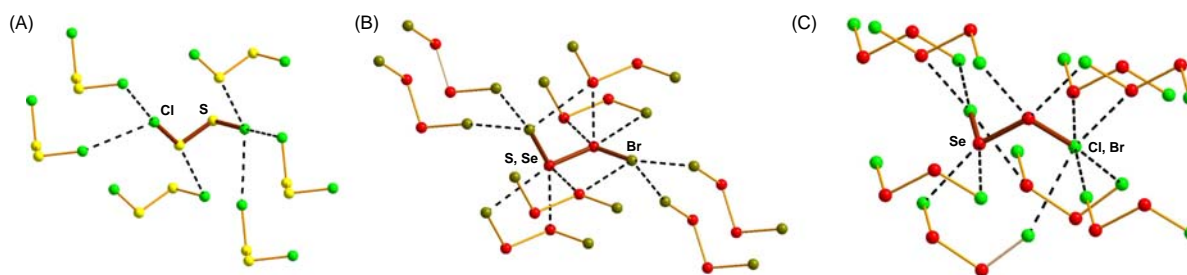
$\text{Te}_2\text{Cl}$ ,  $\text{Te}_2\text{Br}$  and  $\text{Te}_2\text{I}$  show mutually similar structures [see Fig. 46(b)]. The ring fragments are connected together by two halogen bridges in 1- and 4-positions.<sup>290,294</sup> The polymeric chains are linked together by very weak  $\text{Te}\cdots\text{Br}$  and  $\text{Te}\cdots\text{I}$  secondary bonds.

$\text{TeI}$  has two different polymorphs.  $\alpha$ - $\text{TeI}$  is composed of infinite chains of  $\text{Te}(\text{TeI})_2(\text{TeI}_2)$  units containing a slightly puckered four-membered  $\text{Te}_4$  ring [see Fig. 46(c)].<sup>294</sup> One tellurium atom is bound to two iodine atoms that also exhibit the  $\text{Te}\cdots\text{I}$  secondary bonding contacts to the adjacent unit. Other  $\text{Te}\cdots\text{I}$  and  $\text{I}\cdots\text{I}$  secondary bonds also link adjacent  $[\text{Te}(\text{TeI})_2(\text{TeI}_2)]_n$  chains together.

$\beta$ - $\text{TeI}$  is a slightly different polymer the structure of which is related to that of  $\text{Te}_2\text{X}$  [see Fig. 46(d)].<sup>294</sup> It consists of a four-membered spirocyclic  $(\text{Te}_3\text{I}_2)_n$  fragments with one exocyclic and one endocyclic iodine atoms. The polymeric chains are linked together by  $\text{Te}\cdots\text{Te}$  and  $\text{I}\cdots\text{I}$  secondary bonding interactions also in this species.



**Fig. 43** Crystal structures of (a)  $(\text{PPh}_4)_3[(\text{Sb}_2\text{S}_{17})(\text{Sb}_2\text{S}_{16})_{0.5}]$ ,<sup>271</sup> (b)  $(\text{PPh}_4)_2[\text{Sb}_2\text{Se}_{14}]$ ,<sup>273</sup> and (c)  $(\text{Ph}_4\text{P})_2[\text{Sb}_2\text{S}_{15}] \cdot \text{MeC}_6\text{H}_5$ .<sup>109</sup>

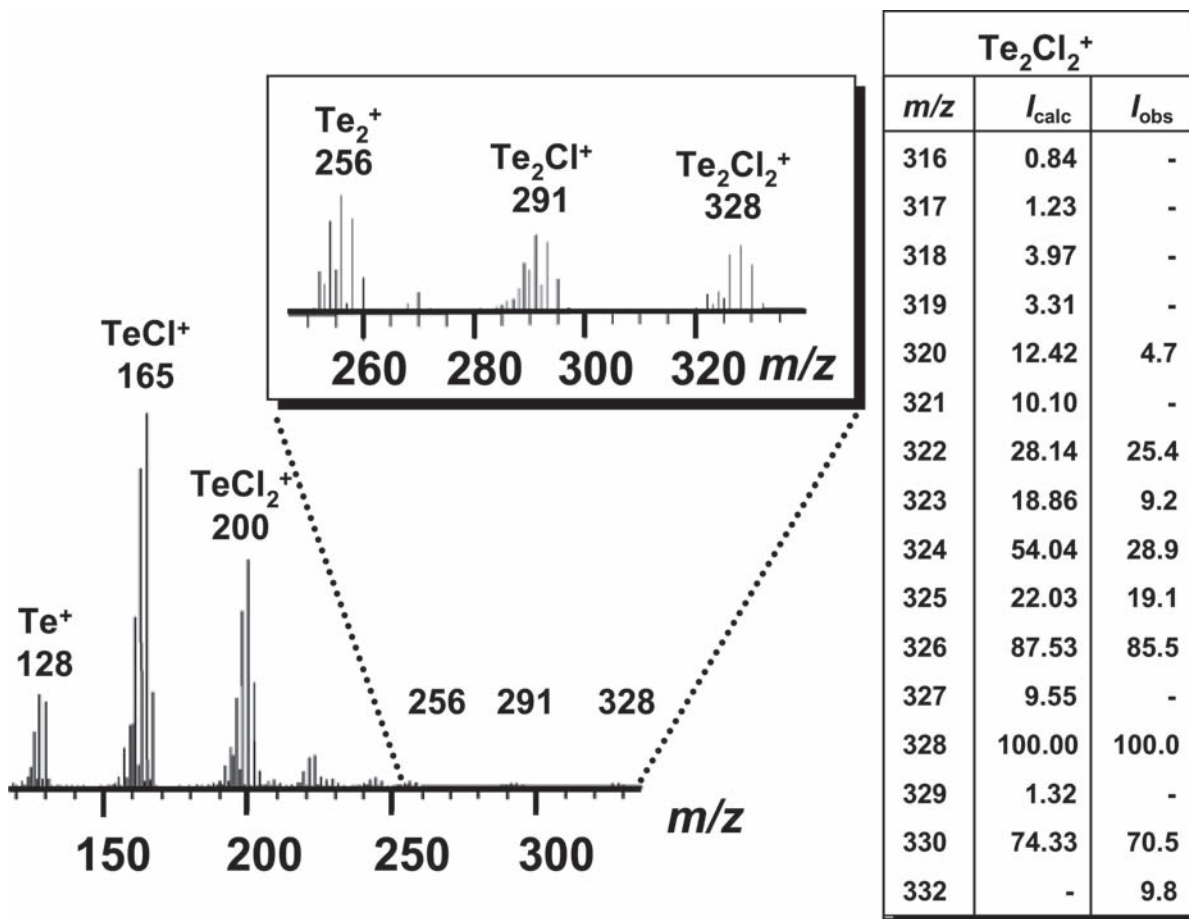


**Fig. 44** Crystal structures of (a)  $\text{S}_2\text{Cl}_2$ , (b)  $\text{S}_2\text{Br}_2$  and  $\alpha\text{-Se}_2\text{Br}_2$ , and (c)  $\text{Se}_2\text{Cl}_2$  and  $\beta\text{-Se}_2\text{Br}_2$ .<sup>267,274</sup>

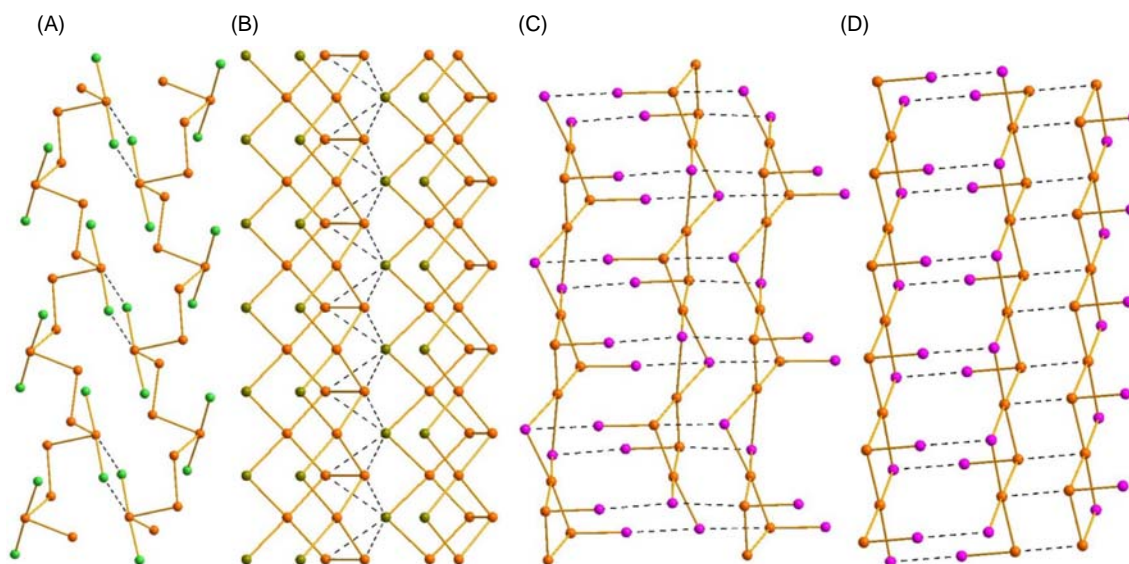
The optical, electrical, and thermodynamic properties of tellurium subhalides have attracted considerable research interest for some time.<sup>291</sup> For instance,  $\alpha\text{-TeI}$  has been suggested to find applications as a solid electrolyte in galvanic cells.

In addition to binary halogenides, sulfur, selenium and tellurium also form catenated compounds, which contain other main group elements in addition to halogens. Some examples of molecular compounds include  $\text{Ph}_3\text{CS}_n\text{Cl}$  ( $n = 1-3$ ),<sup>295</sup>  $(\text{PhEX})_4$  ( $\text{E} = \text{Se}$ ,  $\text{X} = \text{Cl}$ ,  $\text{Br}$ ;  $\text{E} = \text{Te}$ ,  $\text{X} = \text{I}$ ),<sup>296-299</sup> mixed valence aryltellurenyl halogenides,<sup>300,301</sup> as well as thio- and selenourea adducts of  $\text{TeX}_2$  ( $\text{X} = \text{Cl}$ ,  $\text{Br}$ ,  $\text{I}$ ,  $\text{SCN}$ ,  $\text{SeCN}$ ),<sup>302-304</sup> and an adduct of  $(\text{mes})_2\text{Te}$  with two molecules of  $(\text{mes})\text{TeI}$ <sup>305</sup> (see Fig. 47).



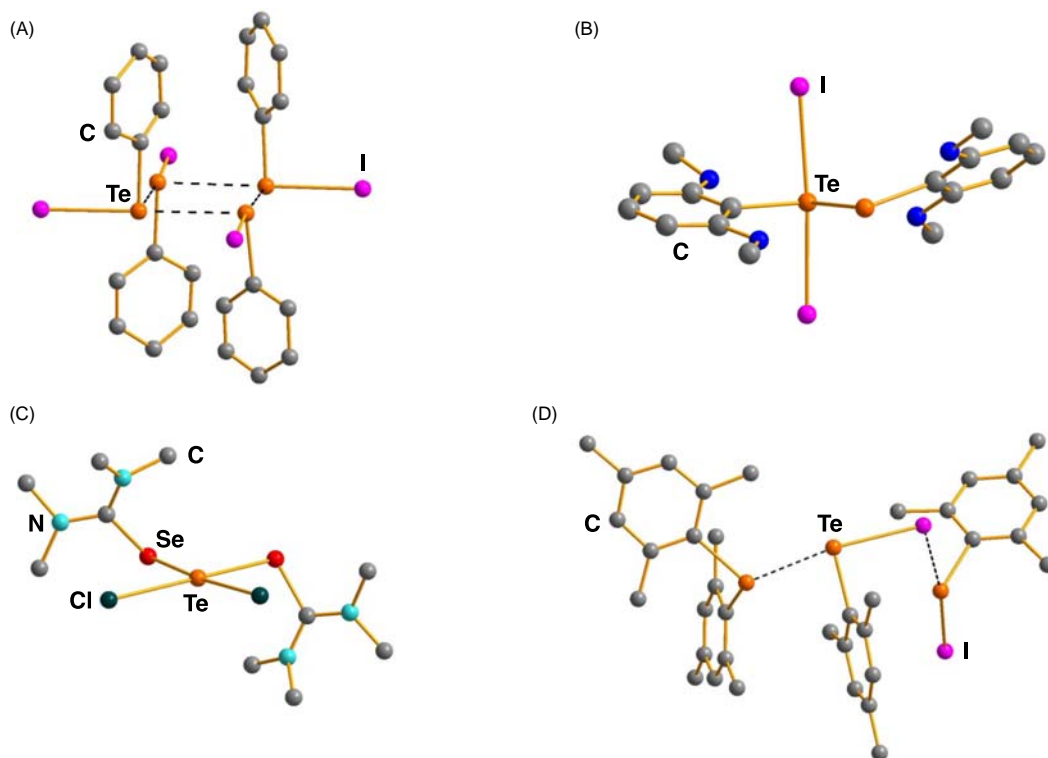


**Fig. 45** EI mass spectrum of Te<sub>2</sub>Cl<sub>2</sub>. The fragmentation and their isotopic distributions indicate the expected composition of the species.<sup>287</sup> Reproduced with permission from Pietikäinen, J.; Laitinen, R.S. *J. Chem. Soc., Chem. Commun.* **1998**, 2381–2382. © RSC 1998.



**Fig. 46** (a) The structure of Te<sub>3</sub>Cl<sub>2</sub>.<sup>293</sup> (b) Te<sub>2</sub>X (X = Cl, Br, I).<sup>290,294</sup> (c) α-Te.<sup>294</sup> and (d) β-Te.<sup>294</sup> Tellurium atoms are depicted in orange, chlorine in bright green, bromine in dark green, and iodine in violet.





**Fig. 47** The structures of (a)  $(\text{PhTeI})_4$ ,<sup>297</sup> (b)  $\{(\text{MeO})_2\text{C}_6\text{H}_3\text{-}2,6\}\text{TeI}_2\text{Te}\{\text{C}_6\text{H}_3(\text{OMe})_2\text{-}2,6\}$ ,<sup>299</sup> (c)  $\{(\text{Me}_2\text{N})_2\text{CSeI}_2\text{TeCl}_2\}$ ,<sup>302</sup> and (d)  $(\text{mes})_2\text{TeTeI}(\text{mes})\text{TeI}(\text{mes})$ .<sup>306</sup>

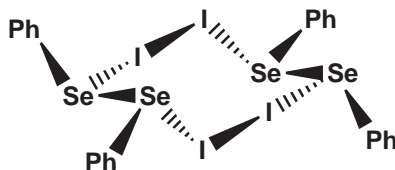
The  $(\text{REX})_4$  ( $\text{E} = \text{Se}, \text{Te}$ ) tetramer, which is exemplified by  $(\text{PhTeI})_4$  in Fig. 47(a), is formed in the halogenation reaction of PhEPh.<sup>296–299</sup> The close  $\text{Se}\cdots\text{Se}$  and  $\text{Te}\cdots\text{Te}$  contacts of the four-membered rings in  $(\text{PhEX})_4$  can be considered to be due to secondary bonding  $p^2 \rightarrow \sigma^*(\text{E}-\text{I})$  interactions. The approximate average bond orders of 0.38 and 0.57 can be estimated for the  $\text{Se}_4$ <sup>296,297</sup> and  $\text{Te}_4$ <sup>298,299</sup> rings, respectively, based on the interatomic distances and Pauling's equation.<sup>236</sup> Interestingly, the reaction of  $\text{PhSeSePh}$  with  $\text{I}_2$  did not afford the  $(\text{PhSeI})_4$  tetramer, but a dimeric charge-transfer complex  $(\text{Ph}_2\text{Se}_2\text{I}_2)_2$  (see Fig. 48).<sup>305</sup>

The high-yield transannular addition of  $\text{SeX}_2$  ( $\text{X} = \text{Cl}, \text{Br}$ ) to cyclooctadiene affords a bicyclic selenoether. The subsequent treatment of this product with selenium dihalogenide produces the 2:1 adduct (see Scheme 19).<sup>307,308</sup> The 2:1 adduct thus formed can be viewed as a coordination compound of a square-planar selenium center with two halogenido and two selenoether ligands. The  $\text{Se}-\text{Se}-\text{Se}$  fragment is linear with the two  $\text{Se}-\text{Se}$  bond lengths of 2.6403(3) and 2.656(3)–2.620(5) Å for  $\text{RSe}-\text{SeCl}_2-\text{SeR}$  and  $\text{RSe}-\text{SeBr}_2-\text{SeR}$ , respectively (see Fig. 49). The coordination environment resembles that of  $\text{SeCl}_2(\text{tht})_2$  ( $\text{tht} = \text{tetrahydrothiophene}$ ).<sup>309</sup>

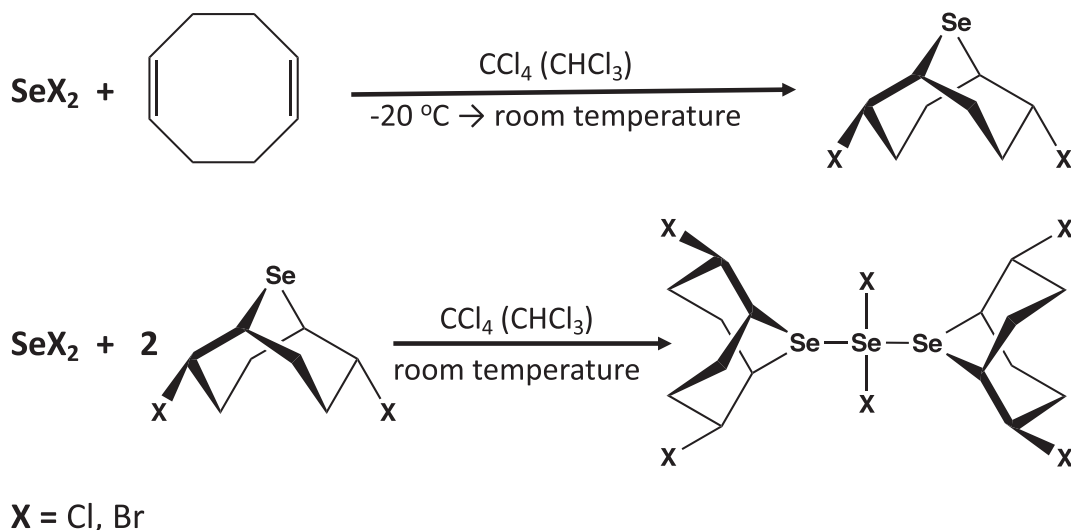
Popov et al.<sup>310</sup> have used high-level DFT calculations to compare the viability to produce  $\text{M}_n\text{F}_{4n+2}$  molecules ( $\text{M} = \text{S}, \text{Se}; n = 2-9$ ) and extended the study to polymeric  $(-\text{MF}_4-\text{MF}_4-)_{\infty}$  chains. Whereas both the sulfur- and selenium-containing molecules are thermodynamically unstable to chain contraction with the production of  $\text{MF}_4$ , they seem to be kinetically inert. The calculations involving periodic boundary conditions indicate that while  $(-\text{SF}_4-\text{SF}_4-)_{\infty}$  is dynamically stable with no imaginary phonon frequency in the whole Brillouin zone, the related  $(-\text{SeF}_4-\text{SeF}_4-)_{\infty}$  is dynamically unstable with several imaginary phonon frequencies.

#### 1.22.4.5.2 Chalcogen-halogen cations

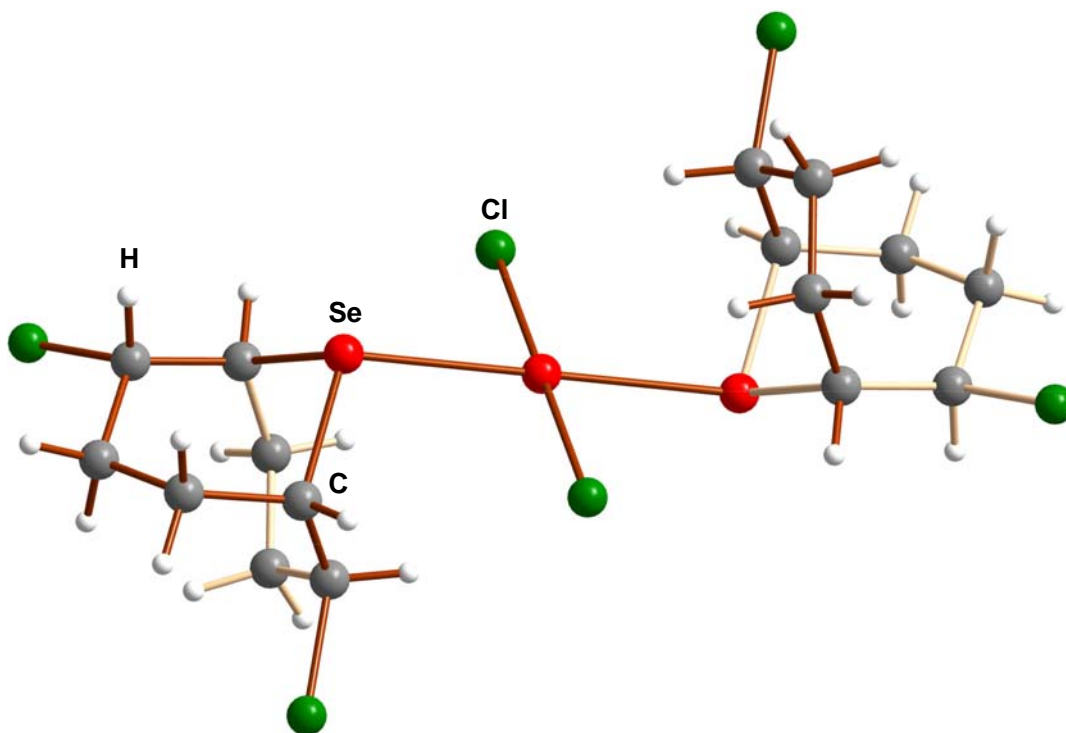
Some chalcogen-halogen cations also exist as catenated species. Both cyclic and acyclic chalcogen-halogen cations may generally be prepared by the oxidation of a combination of elemental chalcogen and halogen with  $\text{AsF}_5$  or another strong Lewis acid in liquid  $\text{SO}_2$  (for reviews, see Refs. 2, 5, 6, 12, 13). There are also special methods to prepare individual salts. For example,  $(\text{Se}_2\text{I}_4)[\text{Sb}_2\text{F}_{11}]$



**Fig. 48** The dimeric charge-transfer complex of  $(\text{Ph}_2\text{Se}_2\text{I}_2)_2$ .<sup>305</sup>



**Scheme 19** Reaction of  $\text{SeX}_2$  with cyclooctadiene.<sup>307</sup>



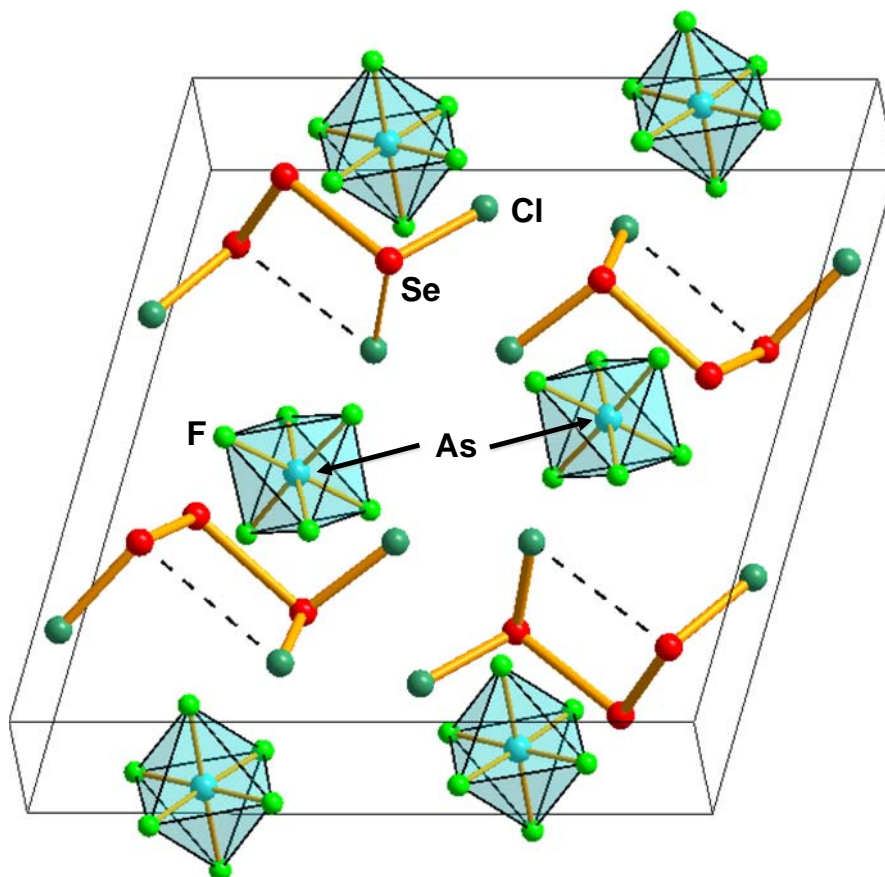
**Fig. 49** Molecular structure of the complex of  $\text{SeCl}_2$  and 2,6-dihalogenido-9-selenabicyclo-[3.3.1]nonane.<sup>307</sup>

was prepared by the treatment of elemental selenium with  $(\text{I}_2)[\text{Sb}_2\text{F}_{11}]$ <sup>311</sup> or the reaction of  $(\text{Se}_3\text{X}_3)[\text{MF}_6]$  ( $M = \text{As, Sb, X} = \text{Cl, Br}$ ) with  $(\text{SeCl}_3)[\text{MF}_6]$ .<sup>312</sup>  $(\text{Se}_4\text{I}_4)[\text{AsF}_6]$  can be made by the reaction of  $(\text{Se}_4)[\text{AsF}_6]$  and iodine.<sup>313</sup>

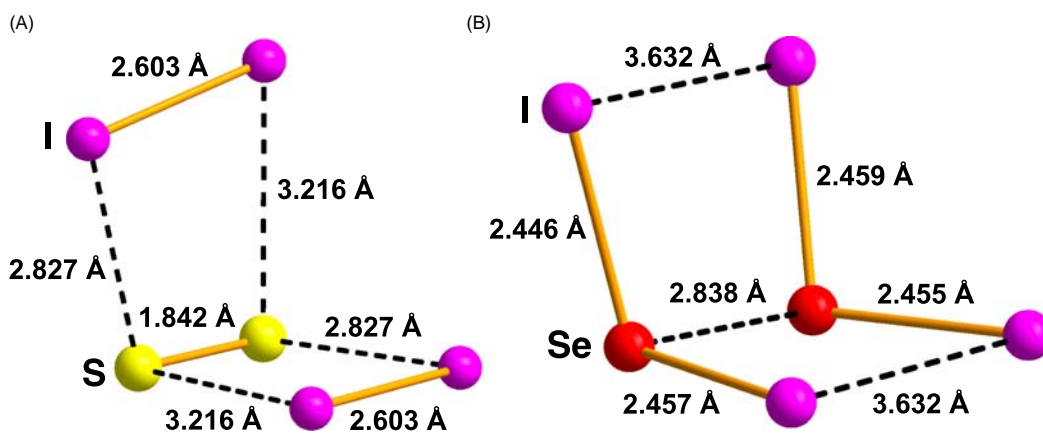
The crystals of  $(\text{Se}_3\text{X}_3)[\text{MF}_6]$  ( $M = \text{As, Sb, X} = \text{Cl, Br}$ ) are isomorphic.<sup>312</sup> Their unit cell contents are exemplified by  $(\text{Se}_3\text{Cl}_3)[\text{AsF}_6]$  in Fig. 50. Both  $\text{Se}_3\text{Cl}_3^{2+}$  and  $\text{Se}_3\text{Br}_3^+$  cations show marked bond length alternation [ $\text{XSe-Se}$ : 2.191(3) and 2.207(6) Å;  $\text{X}_2\text{Se-Se}$  2.551(3) and 2.558(6) Å for  $X = \text{Cl}$  and  $\text{Br}$ , respectively]. The respective long  $\text{Se}\cdots\text{X}$  distances are 3.289(5) and 3.436(7) Å. These distances have been discussed in terms of maximized intracationic  $\text{X}\cdots\text{Se}$  contacts, charge delocalization, and  $\pi$  bonding.<sup>314</sup>

A preliminary natural-abundance  $^{77}\text{Se}$  NMR study of the soluble products of the reaction of  $(\text{Se}_4)[\text{AsF}_6]_2$  and bromine in liquid  $\text{SO}_2$  revealed resonances attributable to  $1,1,4,4\text{-Se}_4\text{Br}_4^{2+}$  and  $\text{Se}_7\text{Br}^+$ . These assignments are supported by calculated  $^{77}\text{Se}$  chemical shifts.<sup>315</sup>

$\text{S}_2\text{I}_4^{2+}$  and  $\text{Se}_2\text{I}_4^{2+}$  form an interesting pair of cations. Their structures and conformations resemble each other, but there are key differences in interatomic distances that also reflect the differences in their bonding (see Fig. 51).



**Fig. 50** The unit cell of  $(\text{Se}_3\text{X}_3)[\text{MF}_6]$  ( $\text{X} = \text{Cl}, \text{Br}$ ;  $\text{M} = \text{As}, \text{Sb}$ ) as exemplified by  $(\text{Se}_3\text{Cl}_3)[\text{AsF}_6]$ .<sup>312</sup>



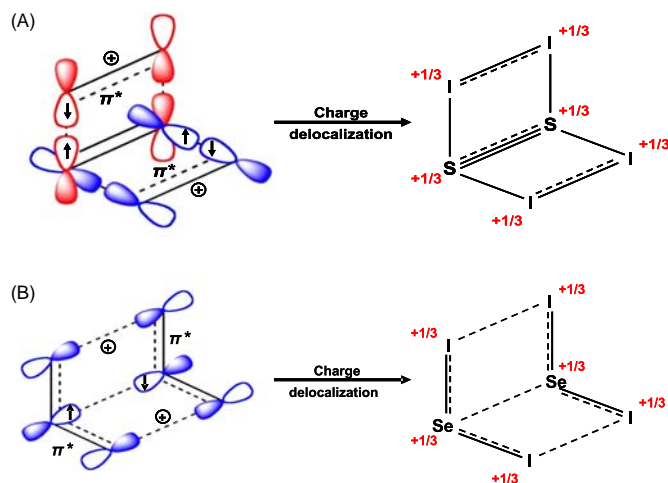
**Fig. 51** The structure of the cation in (a)  $(\text{S}_2\text{I}_4)[\text{AsF}_6]_2$ <sup>316</sup> and (b)  $(\text{Se}_2\text{I}_4)[\text{AsF}_6]_2 \cdot \text{SO}_2$ .<sup>317</sup>

The bonding in  $\text{S}_2\text{I}_4^{2+}$  can be described in terms of mutually perpendicular  $4c-2e \pi^*-\pi^*$  bonds [Fig. 52(a)],<sup>35,318</sup> whereas that in  $\text{Se}_2\text{I}_4^{2+}$  consists of two  $\text{SeI}_2^+$  fragments that are joined by  $6c-2e \pi^*-\pi^*$  bonds [Fig. 52(b)].<sup>35,317</sup>

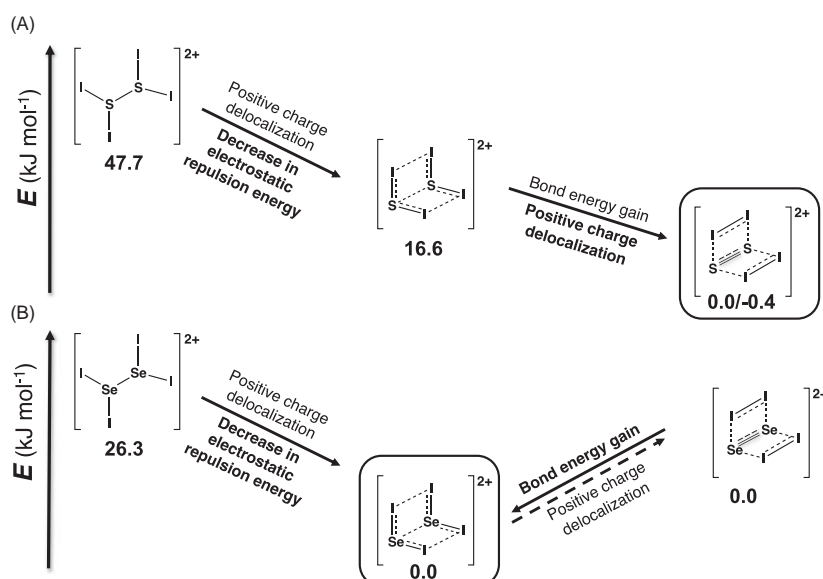
The summary of the detailed analysis to account for the structural differences are presented in Fig. 53.<sup>35</sup> The main factors are related to the strong S–S  $\pi$  bond compared to the weak S–I  $\sigma$  bond and the additional stabilization from increased delocalization of the positive charge in  $\text{S}_2\text{I}_4^{2+}$  that is missing in  $\text{Se}_2\text{I}_4^{2+}$ .

In addition to binary chalcogen-halogen cations, several organic chalcogen-halogen cations are known. Some examples are shown in Fig. 54.

$[\text{MeS}(\text{Cl})\text{SMe}][\text{SbCl}_3]$  was prepared from  $(\text{SCl}_3)[\text{SbCl}_6]$  and MeSH in  $\text{SO}_2(\text{l})$ .<sup>319</sup> The crystals for X-ray structure determination were obtained by fractional crystallization in liquid  $\text{SO}_2$ . The cation shows a relatively short S–S bond length of 2.004(3) Å. The



**Fig. 52** (a)  $S_2I_4^{2+}$ : Interaction of  $\pi^*$  orbitals of  $S_2$  with those of two  $(I_2)^+$  in mutually perpendicular planes with subsequent charge delocalization. The bond orders: S-S 2.33; I-I 1.33.<sup>35,318</sup> (b)  $Se_2I_4^{2+}$ : Interaction of two  $\pi^*$   $Se_2^+$  SOMOs with subsequent charge delocalization. The bond orders: Se-Se  $\ll 1$ , Se-I 1.25.<sup>35,317</sup>

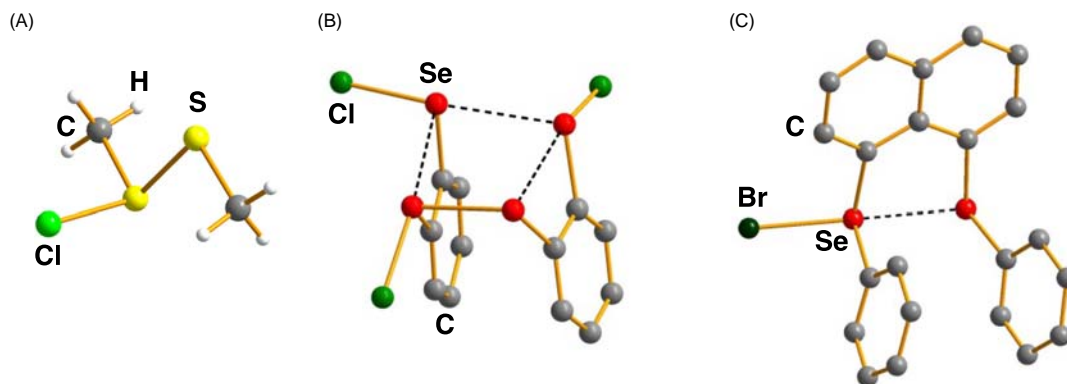


**Fig. 53** Relative CCSD(T)/SDB-cc-pVTZ//PBE0/SDB-ccpVTZ energies (in kJ mol<sup>-1</sup>) of selected isomers of (a)  $S_2I_4^{2+}$  and (b)  $Se_2I_4^{2+}$  and the main factors leading to the adoption of the observed geometries (marked in rounded rectangles).<sup>35</sup> Adapted with permission from Brownridge, S.; Crawford, M. -J.; Du, H.; Harcourt, R. D.; Knapp, C.; Laitinen, R. S.; Passmore, J.; Rautiainen, J. M.; Suontamo, R. J.; Knapp, C.; Valkonen, J. *Inorg. Chem.* **2007**, *46*, 681–699. © 2007 American Chemical Society.

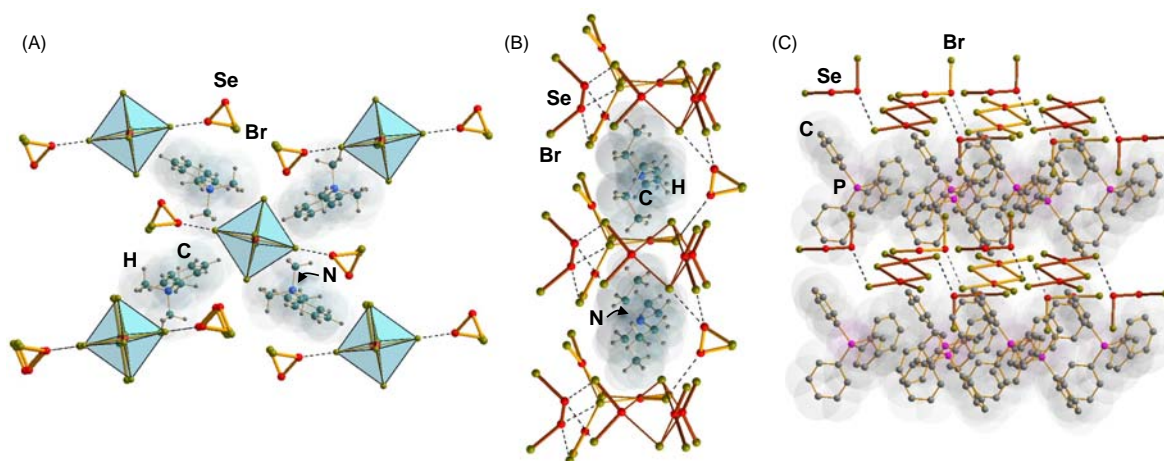
S–Cl bond of 2.040(3) Å and the S–C bonds of 1.812(8) and 1.828(9) Å are close to single-bond lengths. The three-coordinated sulfur atom exhibits pyramidal geometry [ $\alpha_S = 98.6(3)$ – $107.4(1)^\circ$ ].

### 1.22.4.5.3 Polychalcogen-halogen anions

Only a few polychalcogen-halogen anions containing chalcogen-chalcogen bonds are known. The stirring and heating of selenium, phenyltrimethylammonium bromide and bromine in acetonitrile afforded dark red prisms of  $[Me_3PhN]_2[SeBr_6] \cdot 2(Se_2Br_2)$  [see Fig. 55(a)].<sup>322</sup> With tetraethylammonium bromide and the stoichiometry Se:Br<sub>2</sub>:Br<sup>-</sup> = 5:4:1,  $(Et_4N)_2(Se_3Br_8) \cdot (Se_2Br_2)$  was obtained [Fig. 55(b)].<sup>325</sup> When the starting bromide was changed to tetraphenylphosphonium bromide and the stoichiometry was adjusted to Se:Br<sub>2</sub>:Br<sup>-</sup> = 6:4:2,  $(Ph_4P)_2[Se_2Br_6] \cdot 2(Se_2Br_2)$ , was crystallized [Fig. 55(c)].<sup>323</sup> The anionic part of the salts forms an extended framework in which  $Se_2Br_2$  molecules interact with the mono-, di- or trinuclear bromidoselenate anions. The bond parameters of the coordinated  $Se_2Br_2$  molecules [ $r_{SeSe} = 2.272(2)$ – $2.2945(8)$ ,  $r_{SeBr} = 2.247(2)$ – $2.3936(8)$  Å,  $\alpha_{Se} = 102.40(8)$ – $104.22(7)^\circ$ ,  $\tau_{SeSe} = 77.85(2)$ – $97.49(8)^\circ$ ] are in close agreement with those of pure  $\beta$ - $Se_2Br_2$ .<sup>274</sup> The diselenium dibromide molecules are linked to the  $[SeBr_6]^{2-}$ ,<sup>322</sup>  $[Se_3Br_8]^{2-}$ ,<sup>325</sup>  $[Se_2Br_6]^{2-}$ ,<sup>323</sup> and  $[Se_4Br_{10}]^{2-}$ <sup>324</sup> anions via secondary bonding interactions.



**Fig. 54** The structures of the cations in (a)  $[\text{MeS}(\text{Cl})\text{SMe}][\text{SbCl}_6]$ ,<sup>319</sup> (b)  $(\text{C}_6\text{H}_4(\text{SeCl}))_2(\text{Se}_2\text{Cl})[\text{SbCl}_6] \cdot \text{MeCN}$ ,<sup>320</sup> and (c)  $\{(\text{C}_6\text{H}_5)_2(\text{C}_{10}\text{H}_6)\text{Se}_2\text{Br}\}(\text{Br}_3)$ .<sup>321</sup>



**Fig. 55** Crystal structures of (a)  $[\text{Me}_3\text{PhN}]_2[\text{SeBr}_6] \cdot 2(\text{Se}_2\text{Br}_2)$ ,<sup>322</sup> (b)  $(\text{Et}_4\text{N})_2(\text{Se}_3\text{Br}_8) \cdot (\text{Se}_2\text{Br}_2)$ ,<sup>323</sup> and (c)  $(\text{Ph}_4\text{P})_2[\text{Se}_2\text{Br}_6] \cdot 2\text{Se}_2\text{Br}_2$ .<sup>324</sup>

The treatment of  $(\text{Me}_3\text{PhN})\text{Br}$ ,  $(\text{EtPh}_3\text{P})\text{Br}$  or  $(\text{Ph}_4\text{P})\text{Br}$  with elemental selenium, and tellurium tetrabromide in acetonitrile affords  $(\text{Me}_3\text{PhN})_2[\text{TeBr}_6] \cdot 2(\text{Se}_2\text{Br}_2)$ ,<sup>326</sup>  $(\text{EtPh}_3\text{P})_2[\text{TeBr}_6] \cdot 2(\text{Se}_2\text{Br}_2)$ <sup>327</sup> or  $(\text{Ph}_4\text{P})_2[\text{TeBr}_6] \cdot 2(\text{Se}_2\text{Br}_2)$ ,<sup>327</sup> respectively, whereas the use of  $(\text{Et}_3\text{MeN})\text{Br}$  produces polymeric  $\{(\text{NEt}_3\text{Me})_2[\text{TeBr}_6] \cdot 3(\text{Se}_2\text{Br}_2)\}_n$  (see Fig. 55).<sup>328</sup> The adducts  $(\text{Me}_3\text{PhN})_2[\text{EBr}_6] \cdot 2(\text{Se}_2\text{Br}_2)$  ( $\text{E} = \text{Se}, \text{Te}$ )<sup>322,326</sup> are isomorphous and consist of discrete  $[\text{EBr}_6] \cdot 2(\text{Se}_2\text{Br}_2)^{2-}$  anions [see Fig. 55(a)].

In the anions of  $(\text{EtPh}_3\text{P})_2[\text{TeBr}_6] \cdot 2(\text{Se}_2\text{Br}_2)$ <sup>327</sup> and  $(\text{NEt}_3\text{Me})_2[\text{TeBr}_6] \cdot 3(\text{Se}_2\text{Br}_2)$ ,<sup>328</sup> the  $[\text{TeBr}_6]^{2-}$  octahedra are linked into quasi-one-dimensional polymeric chains with two or three bridging  $\text{Se}_2\text{Br}_2$  molecules, respectively (see Fig. 56).

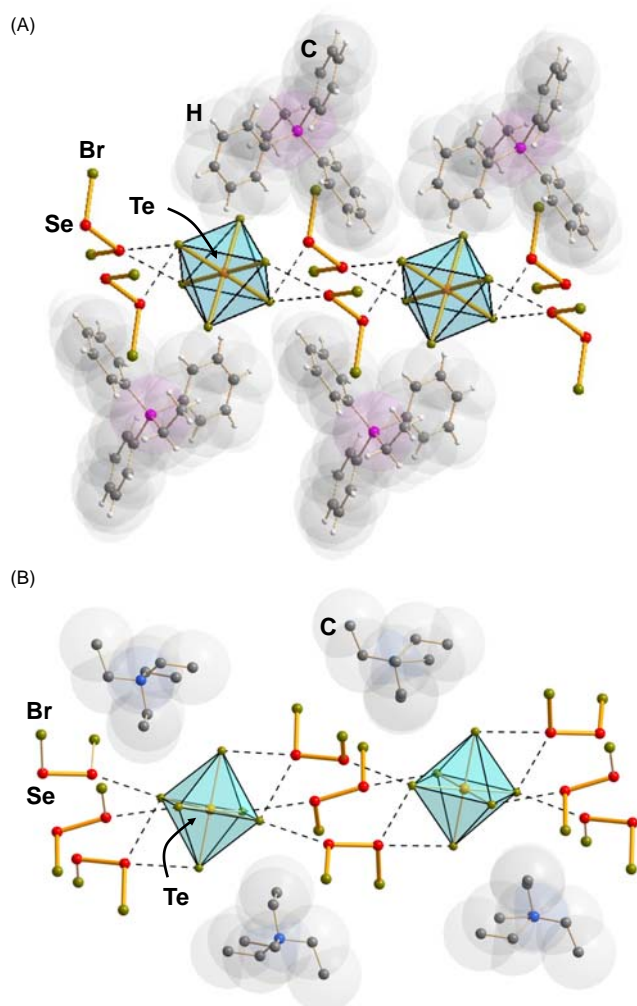
$(\text{Ph}_4\text{P})_2[\text{TeBr}_6] \cdot 2(\text{Se}_2\text{Br}_2)$  exhibits an incommensurately one-dimensionally modulated structure with planar monoclinic super-space group.<sup>327</sup> The  $[\text{TeBr}_6]^{2-}$  octahedron is nearly regular also in this structure. The bromido ligands bound to the selenium atom in  $\text{Se}_2\text{Br}_2$  can be either in trans or cis positions due to the alternations caused by modulation of the crystal structure.

### 1.22.5 Summary

The overarching theme of this chapter has been the synthesis and structure of acyclic chalcogen molecules and ions involving catenation. The treatise begins with a discussion of polymeric forms of the elements. This is followed by a consideration of polysulfide dianions and radical anions. The dianions are frequently obtained as s-block metal salts by direct reaction of alkali or alkaline earth metals with the elemental chalcogens. However, bulky organic cations are often needed to stabilize these anions in the solid state, especially for longer chains. The subsequent sections describe sequentially metal complexes or derivatives of the p-block elements of Groups 13, 14 and 15 in which polychalcogenide dianions function as bridging or chelating ligands or groups. The final section is devoted to the preparation and structural chemistry of neutral, cationic, and anionic chalcogen halide species that exhibit catenation.

The tendency for catenation is most pronounced for sulfur as exemplified by the unbranched structures established for polysulfide dianions, organic polysulfides, and dichlorosulfanes, with chain lengths of up to 12, 9 and 8, respectively. Polyselenides and





**Fig. 56** Crystal structures of (a)  $(\text{EtPh}_3\text{P})_2[\text{TeBr}_6] \cdot 2(\text{Se}_2\text{Br}_2)$ <sup>327</sup> and (b)  $(\text{Et}_3\text{MeN})_2[\text{TeBr}_6] \cdot 3(\text{Se}_2\text{Br}_2)$ <sup>328</sup>.

polytellurides, in particular, exhibit a more diverse range of structures due to the tendency of the heavier chalcogens to engage in hypervalency or secondary bonding. This characteristic is manifested in the unique structures of the tellurium subhalides.

In addition to the important insights into the unusual chemical bonding characteristics of the chalcogens provided by the structural and computational investigations of the class of polychalcogen compounds discussed in this chapter, many of them also have important applications. For example, polychalcogenido complexes of p-block metals such as Sn, Pb, Sb or Bi may serve as precursors of binary metal chalcogenide semiconductors in the form of thin films or nanomaterials. Inorganic polysulfide dianions have an especially broad influence in areas ranging from biological chemistry to alkali metal-sulfur batteries. Finally, the closely related polysulfide radical anions have emerged as important reagents for the synthesis for a variety of organosulfur compounds with known or potential uses as pharmaceuticals or conducting materials.

## References

- Laitinen, R. S.; Pekonen, P.; Suontamo, R. *Coord. Chem. Rev.* **1994**, *130*, 1–62.
- Studel, R., Ed.; *Elemental Sulfur and Sulfur-Rich Compounds I, Topics Current Chemistry*; vol. 230; Springer, 2003, 213 pp.
- Studel, R., Ed.; *Elemental Sulfur and Sulfur-Rich Compounds II, Topics Current Chemistry*; vol. 231; Springer, 2003, 259 pp.
- Krossing, I., Devillanova, F. A., du Mont, W.-W., Eds.; *Handbook of Chalcogen Chemistry, New Perspectives in Sulfur, Selenium and Tellurium*, RSC Publishing: Cambridge, 2013; pp 349–381.
- Kelly, P. F.; King, R. S. P. In *Comprehensive Inorganic Chemistry II*; Reedijk, J., Poeppelemeier, K., Eds., 2nd ed.; vol. 1; Elsevier: Amsterdam, 2013; pp 179–196.
- Laitinen, R. S.; Ollunkaniemi, R.; McGeachie, L.; Kelly, P. F.; King, R. S. P. In *Comprehensive Inorganic Chemistry III*; Reedijk, J., Poeppelemeier, K., Eds., 3rd ed.; vol. 1; Elsevier: Amsterdam, 2022. in press.
- Okazaki, R. *Phosphorus Sulfur Rel. Elem.* **2001**, *168–169*, 41–50.
- Wang, J.; Xu, Z. In *Handbook of Chalcogen Chemistry, New Perspectives in Sulfur, Selenium and Tellurium*; Devillanova, F. A., du Mont, W.-W., Eds., RSC Publishing: Cambridge, 2013; pp 425–447.

9. Chivers, T.; Laitinen, R. S. *Chalcogen-nitrogen Chemistry. From Fundamentals to Applications in Physical, Biological, and Materials Sciences*, World Scientific Publishing: New Jersey, 2021, 450 pp.
10. Martin, C. D.; Ragogna, P. J. *Ann. Rep. Prog. Chem., Sect. A* **2011**, *107*, 110–124.
11. Nordheider, A.; Woolfins, J. D.; Chivers, T. *Chem. Rev.* **2015**, *115*, 10378–10406.
12. Brownridge, S.; Krossing, I.; Passmore, J.; Jenkins, H. D. B.; Rootbottom, H. K. *Coord. Chem. Rev.* **2000**, *197*, 397–481.
13. Beck, J. *Coord. Chem. Rev.* **1997**, *163*, 55–70.
14. Nenajdenko, V. G.; Shevchenko, N. E.; Balenkova, E. S.; Alabugin, I. V. In *Handbook of Chalcogen Chemistry, New Perspectives in Sulfur, Selenium and Tellurium*; Devillanova, F. A., du Mont, W.-W., Eds., RSC Publishing: Cambridge, 2013; pp 382–421.
15. Steudel, R. *Top. Curr. Chem.* **2003**, *231*, 127–152.
16. Steudel, R.; Chivers, T. *Chem. Soc. Rev.* **2019**, *48*, 3279–3319.
17. Ruck, M.; Locherer, F. *Coord. Chem. Rev.* **2015**, *297-298*, 208–217.
18. Sheldrick, W. S. In *Handbook of Chalcogen Chemistry. New Perspectives in Sulfur, Selenium and Tellurium*; Devillanova, F. A., du Mont, W.-W., Eds., RSC Publishing: Cambridge, 2013; pp 514–544. and references therein.
19. Sheldrick, W. S. *Z. Anorg. Allg. Chem.* **2012**, *638*, 2401–2424.
20. Graf, C.; Assoud, A.; Mayasree, O.; Kleinke, H. *Molecules* **2009**, *14*, 3115–3131.
21. Smith, D. M.; Ibers, J. A. *Coord. Chem. Rev.* **2000**, *187*, 200–205.
22. Tremel, W.; Kleinke, H.; Derstroff, V.; Reisner, C. *J. Alloys Compd.* **1995**, 73–75.
23. Kanatzidis, M. G.; Huang, S. P. *Coord. Chem. Rev.* **1994**, *130*, 509–621.
24. Thiele, G.; Vondung, L.; Donsbach, C.; Pulz, S.; Dehnen, S. *Z. Anorg. Allg. Chem.* **2014**, 2684–2700.
25. Drake, G. W.; Kolis, J. W. *Coord. Chem. Rev.* **1994**, *137*, 131–178.
26. Roof, L. C.; Kolis, J. W. *Chem. Rev.* **1993**, *93*, 1037–1080.
27. Kanatzidis, M. G. *Comments Inorg. Chem.* **1990**, *10*, 161–195.
28. Kolis, J. W. *Coord. Chem. Rev.* **1990**, *105*, 195–219.
29. Ansari, M. A.; Ibers, J. A. *Coord. Chem. Rev.* **1990**, *100*, 223–266.
30. Müller, A.; Diemann, E. *Adv. Inorg. Chem.* **1987**, *31*, 89–122.
31. Draganjac, M.; Rauchfuss, T. B. *Angew. Chem. Int. Ed. Eng.* **1985**, *24*, 742–757.
32. Hayashi, S.; Nakanishi, W. In *Handbook of Chalcogen Chemistry, New Perspectives in Sulfur, Selenium and Tellurium*; Devillanova, F. A., du Mont, W.-W., Eds., RSC Publishing: Cambridge, 2013; pp 338–372.
33. Crabtree, R. H. *Chem. Soc. Rev.* **2017**, *46*, 1720–1729.
34. Chivers, T.; Laitinen, R. S. *Chem. Soc. Rev.* **2015**, *44*, 1725–1739. and references therein.
35. Brownridge, S.; Crawford, M.-J.; Du, H.; Harcourt, R. D.; Knapp, C.; Laitinen, R. S.; Passmore, J.; Rautiainen, J. M.; Suontamo, R. J.; Valkonen, J. *Inorg. Chem.* **2007**, *46*, 681–699. and references therein.
36. Alcock, N. W. *Adv. Inorg. Chem. Radiochem.* **1972**, *15*, 1–58.
37. Elder, P. J. W.; Vargas-Baca, I. *Phys. Chem. Chem. Phys.* **2016**, *18*, 30740–30747.
38. Karjalainen, M. M.; Sanchez-Perez, C.; Rautiainen, M. J.; Oilunkaniemi, R.; Laitinen, R. S. *CrystEngComm* **2016**, *18*, 4538–4545. and references therein.
39. Cozzolino, A. F.; Elder, P. J. W.; Vargas-Baca, I. *Coord. Chem. Rev.* **2011**, *255*, 1426–1438.
40. Bleiholder, C.; Werz, D. B.; Köppel, H.; Gleiter, R. *J. Am. Chem. Soc.* **2006**, *128*, 2666–2674.
41. Kolb, S.; Oliver, G. A.; Werz, D. B. *Angew. Chem. Int. Ed.* **2020**, *59*, 22306–22310.
42. Steudel, R.; Eckert, B. *Top. Curr. Chem.* **2003**, *230*, 1–79.
43. Trillat, J.-J.; Forestier, J. *Bull. Soc. Chim. Fr.* **1932**, *51*, 248–253.
44. Prins, J. A.; Schenk, J.; Wachters, L. H. J. *Physica* **1957**, *23*, 746–752.
45. Prins, J. A.; Schenk, J.; Hospel, P. A. M. *Physica* **1956**, *22*, 770–772.
46. Tuinstra, F. *Acta Cryst* **1966**, *20*, 341–349.
47. Lind, M. D.; Geller, S. *J. Chem. Phys.* **1969**, *51*, 348–353.
48. Geller, S.; Lind, M. D. *Acta Crystallogr. Sect. B* **1969**, *25*, 2166–2167.
49. Steudel, R. *Z. Anorg. Allg. Chem.* **1981**, *478*, 139–155.
50. Steudel, R. *Top. Curr. Chem.* **2003**, *230*, 81–116.
51. West, E. D. *J. Am. Chem. Soc.* **1959**, *81*, 29–37.
52. Mäusle, H.-J.; Steudel, R. *Z. Anorg. Allg. Chem.* **1981**, *478*, 177–190.
53. Steudel, R.; Mäusle, H.-J. *Z. Anorg. Allg. Chem.* **1981**, *478*, 156–176.
54. Steudel, R.; Strauss, R.; Koch, L. *Angew. Chem. Int. Ed. Eng.* **1985**, *24*, 59–60.
55. Chrichton, W. A.; Vaughan, G. B. M.; Mezouar, M. Z. *Kristallogr.* **2001**, *216*, 417–419.
56. Luo, H.; Greene, R. G.; Ruoff, A. L. *Phys. Rev. Lett.* **1993**, *71*, 2943–2946.
57. Akahama, Y.; Kobayashi, M.; Kawamura, H. *Phys. Rev. B* **1993**, *48*, 6862–6864.
58. Akahama, Y.; Kobayashi, M.; Kawamura, H. *Phys. Rev. B* **1993**, *47*, 20–26. and references therein.
59. Aoki, K.; Shimomura, O.; Minomura, S. *J. Phys. Soc. Jpn.* **1980**, *48*, 551–556.
60. Jamieson, J. C.; McWhan, D. B. *J. Chem. Phys.* **1965**, *43*, 1149–1152.
61. Zakharov, O.; Cohen, M. L. *Phys. Rev. B* **1995**, *52*, 12572–12578.
62. Parthasarathy, G.; Holzapfel, W. B. *Phys. Rev. B* **1988**, *37*, 8499–8501.
63. Keller, R.; Holzapfel, W. B.; Schulz, H. *Phys. Rev. B* **1977**, *16*, 4404–4412.
64. Adenis, C.; Langer, V.; Lindqvist, O. *Acta Crystallogr.* **1989**, *C45*, 941–942.
65. Shi, K.; Liu, B.; Wu, Y.; Liang, Z.; Wang, X.; Su, L.; Wang, Y.; Zhang, L.; Yang, G.; Zhang, Y.; Xie, C.; Zhao, Z. *J. Chem. Phys. C* **2019**, *123*, 14696–14700. and references therein.
66. Hejny, C.; McMahon, M. I. *Phys. Rev. B* **2004**, *70*, 184109/1–184109/5, and references therein.
67. Hejny, C.; McMahon, M. I. *Phys. Rev. Lett.* **2003**, *91*, 215502/1–215502/4.
68. Bridgman, P. W. *Proc. Am. Acad. Arts Sci.* **1952**, *81*, 165–251.
69. Bundy, F. P.; Dunn, K. J. *J. Chem. Phys.* **1979**, *71*, 1550–1558.
70. Bundy, F. P.; Dunn, K. J. *Phys. Rev. B* **1980**, *22*, 3157–3164.
71. Bundy, F. P.; Dunn, K. J. *Phys. Rev. Lett.* **1980**, *44*, 1623–1626.
72. Misra, R.; Goel, S.; Tripathi, S. K.; Agnihotri, A. K.; Kumar, A. *Physica B* **1990**, *167*, 195–199.
73. Smith, K. W.; Smith, S. D.; Badesha, S. S. *J. Am. Chem. Soc.* **1984**, *106*, 7247–7248.
74. Laitinen, R. S.; Oilunkaniemi, R.; Chivers, T. In *Selenium and Tellurium Reagents*; Laitinen, R. S., Oilunkaniemi, R., Eds., de Gruyter: Berlin, 2019; pp 1–26. and references therein.

75. Song, W.-H.; Hu, C.-H. *Chem. Phys. Lett.* **2020**, *761*, 138069.
76. Mondal, M. K.; Zhang, L.; Feng, Z.; Tang, S.; Feng, R.; Zhao, Y.; Tan, G.; Ruan, H.; Wang, X. *Angew. Chem. Int. Ed.* **2019**, *58*, 15829–15833.
77. Liebing, P.; Kühling, M.; Swanson, C.; Feneberg, M.; Hilfert, L.; Goldhahn, R.; Chivers, T.; Edelman, F. T. *Chem. Commun.* **2019**, *55*, 14965–14967.
78. Kanatzidis, M. G.; Das, B. K. *Comments Inorg. Chem.* **1999**, *21*, 29–51.
79. Wendland, F.; Näther, C.; Bensch, W. *Z. Naturforsch.* **2000**, *55b*, 871–876.
80. König, T.; Eisenmann, B.; Schafer, H. Z. *Anorg. Allg. Chem.* **1983**, *498*, 99–104.
81. Brese, N. E.; Randall, C. R.; Ibers, J. A. *Inorg. Chem.* **1988**, *27*, 940–943.
82. Barrie, P. J.; Clark, R. J. H.; Chung, D.-Y.; Chakrabarty, D.; Kanatzidis, M. G. *Inorg. Chem.* **1995**, *34*, 4299–4304.
83. Dietz, J.; Müller, U.; Müller, V.; Dehnicke, K. *Z. Naturforsch.* **1991**, *46b*, 1293–1299.
84. Fenske, D.; Kraus, C.; Dehnicke, K. *Z. Anorg. Allg. Chem.* **1992**, *607*, 109–112.
85. Müller, V.; Dehnicke, K.; Fenske, D. *Z. Naturforsch.* **1991**, *46b*, 63–67.
86. Müller, V.; Ahle, A.; Frenzen, G.; Neumüller, B.; Dehnicke, K.; Fenske, D. *Z. Anorg. Allg. Chem.* **1993**, *619*, 1247–1256.
87. Staffel, R.; Müller, U.; Ahle, A.; Dehnicke, K. *Z. Naturforsch.* **1991**, *46b*, 1287–1292.
88. Müller, V.; Grebe, C.; Müller, U.; Dehnicke, K. *Z. Anorg. Allg. Chem.* **1993**, *619*, 416–420.
89. Wang, Y.; Xie, Y.; Wei, P.; Blair, S. A.; Cui, D.; Johnson, M. K.; Schaefer, H. F.; Robinson, G. H. *J. Am. Chem. Soc.* **2020**, *142*, 17301–17305.
90. Chen, Y.; Liu, Q.; Deng, Y.; Zhu, H.; Chen, C.; Fan, H.; Liao, D.; Gao, E. *Inorg. Chem.* **2001**, *40*, 3725–3733.
91. Warren, C. J.; Haushalter, R. C.; Bocarsly, A. B. *J. Alloys Compd.* **1996**, *233*, 23–29.
92. Sheldrick, W. S.; Wachhold, M. *Chem. Commun.* **1996**, 607–608.
93. Kysliak, O.; Marcus, M.; Bredow, T.; Beck, J. *Inorg. Chem.* **2013**, *52*, 8327–8333.
94. Chivers, T.; Elder, P. J. W. *Chem. Soc. Rev.* **2013**, *42*, 5996–6005.
95. Steudel, R.; Steudel, Y. *Chem. Eur. J.* **2013**, *19*, 3162–3176.
96. Rejmak, P. *Phys. Chem. Chem. Phys.* **2020**, *22*, 22684–22698.
97. Peng, Y.; Fan, H.; Jancik, V.; Roesky, H. W.; Herbst-Irmer, R. *Angew. Chem. Int. Ed.* **2004**, *43*, 6190–6192.
98. Hidalgo-Bonilla, S.; Peyrot, R.; Jancik, V.; Barroso-Flores, J.; Reyes-Lezama, M.; Moya-Cabrera, M. *Eur. J. Inorg. Chem.* **2013**, 2849–2857.
99. Anker, M. D.; McMullin, C. L.; Rajabi, N. A.; Coles, M. P. *Angew. Chem. Int. Ed.* **2020**, *59*, 12806–12810.
100. Li, B.; Li, J.; Roesky, H. W.; Zhu, H. *J. Am. Chem. Soc.* **2015**, *137*, 162–164.
101. Xu, H.; Weetman, C.; Hanusch, F.; Inoue, S. *Chem. Eur. J.* **2022**, *28*, e202104042.
102. Ricca, T.; Svetlik, T.; Dostal, L.; Ruzicka, A.; Benes, L.; Nemeč, P.; Bouska, M.; Jambor, R. *Chem. Eur. J.* **2016**, *22*, 18817–18823.
103. Zheng, N.; Bu, X.; Feng, P. *J. Am. Chem. Soc.* **2003**, *125*, 1138–1139.
104. Vaquero, P.; Romero, M. L. *J. Phys. Chem. Solids* **2007**, *68*, 1239–1243.
105. Feng, P.; Bu, X.; Zheng, N. *Acc. Chem. Res.* **2005**, *38*, 293–303.
106. Kuchta, M. C.; Parkin, G. *Main Group Chem.* **1996**, *1*, 291–295.
107. Ricca, T.; Milasheuskaya, Y.; Ruzickova, Z.; Nemeč, P.; Svanda, P.; Zmrhalova, Z. O.; Jambor, R.; Bouska, M. *Chem. Asian J.* **2019**, *14*, 4229–4235.
108. Bubenheim, W.; Müller, U. *Z. Anorg. Allg. Chem.* **1994**, *620*, 1607–1612.
109. Paul, P. P.; Rauchfuss, T. B.; Wilson, S. R. *J. Am. Chem. Soc.* **1993**, *115*, 3316–3317.
110. Reger, D. L.; Coan, P. S. *Inorg. Chem.* **1995**, *34*, 6226–6227.
111. Dhingra, S.; Kanatzidis, M. G. *Polyhedron* **1991**, *10*, 1069–1073.
112. Dhingra, S.; Kanatzidis, M. G. *Inorg. Chem.* **1993**, *32*, 3300–3305.
113. Xiong, W.-W.; Li, J.-R.; Feng, M.-L.; Huang, X.-Y. *CryEngComm* **2011**, *13*, 6206–6211.
114. Ricca, T.; Dostal, L.; Ruzickova, Z.; Benes, L.; Nemeč, P.; Bouska, M.; Macak, J. M.; Knotek, P.; Ruleova, P.; Jambor, R. *Chem. Eur. J.* **2018**, *24*, 14470–14476.
115. Kanatzidis, M. G.; Dhingra, S. *Inorg. Chem.* **1989**, *28*, 2024–2026.
116. Dhingra, S. S.; Kanatzidis, M. G. *Inorg. Chem.* **1993**, *32*, 1350–1362.
117. Dhingra, S.; Kanatzidis, M. G. *Science* **1992**, *258*, 1769–1772.
118. Ewing, S. J.; Powell, A. V.; Vaquero, P. *J. Solid State Chem.* **2011**, *184*, 1800–1804.
119. Risto, M.; Chivers, T.; Konu, J. *Dalton Trans.* **2011**, *40*, 8238–8246.
120. Konu, J.; Chivers, T.; Tuononen, H. M. *Chem. Eur. J.* **2010**, *16*, 12977–12987.
121. Ritch, J. S.; Chivers, T.; Eisler, D. J.; Tuononen, H. M. *Chem. Eur. J.* **2007**, *13*, 4643–4653.
122. Wang, C.; Haushalter, R. C. *Inorg. Chem.* **1997**, *36*, 3806–3807.
123. Li, J.; Chen, Z.; Emge, T. J.; Proserpio, D. M. *Inorg. Chem.* **1997**, *36*, 1437–1442.
124. Chen, Z.; Li, J.; Proserpio, D. M.; Huang, Z.-X. *Acta Chim. Sin.* **2000**, *58*, 835–839.
125. Heine, J.; Santner, S.; Dehnen, S. *Inorg. Chem.* **2013**, *52*, 4424–4430.
126. Chen, X.; Huang, X.; Li, J. *Inorg. Chem.* **2001**, *40*, 1341–1346.
127. *ConQuest, Version 2022.1.0*, Cambridge Crystallographic Data Center, 2022 (11.7.2022).
128. Xue, J.; Jiang, X. *Nat. Commun.* **2020**, *11*, 4170.
129. Mloston, G.; Majchrzak, A.; Rutkowska, M.; Woznicka, M.; Linden, A.; Heimgartner, H. *Helv. Chim. Acta* **2005**, *88*, 2624–2636.
130. Linden, A.; Majchrzak, A.; Cavegn, J.; Mloston, G.; Heimgartner, H. *Acta Crystallogr. Sect. C* **2002**, *58*, o480–o484.
131. Steudel, R.; Pridöhl, M.; Buschmann, J.; Luger, P. *Chem. Ber.* **1995**, *128*, 725–728.
132. Eggert, H.; Nielsen, O.; Henriksen, L. *J. Am. Chem. Soc.* **1986**, *108*, 1725–1730.
133. Bates, C. M.; Morley, C. P. *J. Organomet. Chem.* **1997**, *533*, 193–196.
134. Kaur, R.; Singh, H. B.; Patel, R. P. *J. Chem. Soc. Dalton Trans.* **1996**, 2719–2726.
135. Kulcsar, M.; Silvestru, A.; Cziple, F. *Acta Crystallogr. Sect. C* **2007**, *63*, o701–o703.
136. Takaluoma, E. M.; Takaluoma, T. T.; Oilunkaniemi, R.; Laitinen, R. S. *Z. Anorg. Allg. Chem.* **2015**, *641*, 772–779.
137. Danchez-Garcia, D.; Köhler, T.; Seidel, D.; Lynch, V.; Sessler, J. L. *Chem. Commun.* **2005**, 2122–2124.
138. Sivapriya, K.; Suguna, P.; Chandrasekaran, S. *Tetrahedron Lett.* **2007**, *48*, 2091–2095.
139. Nakayama, J.; Akiyama, I.; Sugihara, Y.; Nishio, T. *J. Am. Chem. Soc.* **1998**, *120*, 10027–10031.
140. Jeske, J.; du Mont, W.-W.; Jones, P. G. *Angew. Chem. Int. Ed.* **1996**, *35*, 2653–2655.
141. Roesky, H. W.; Weber, K.-L.; Bats, J. W. *Chem. Ber.* **1984**, *117*, 2686–2692.
142. Matsumoto, T.; Matsui, Y.; Ito, M.; Tatsumi, K. *Chem. Asian J.* **2008**, *3*, 607–613.
143. Ziolo, R. F.; Exline, M. *Inorg. Chem.* **1980**, *19*, 2964–2967.
144. Herberhold, M.; Leitner, P.; Thewalt, U. *Z. Naturforsch. B* **1990**, *45*, 1503–1507.
145. Kromm, A.; Sheldrick, W. S. *Z. Anorg. Allg. Chem.* **2008**, *634*, 1005–1010.
146. Poleschner, H.; Seppelt, K. *Angew. Chem. Int. Ed.* **2008**, *47*, 6461–6464.
147. Destro, R.; Lucchini, V.; Modena, G.; Pasquato, L. *J. Org. Chem.* **2000**, *65*, 3367–3370.

148. Weiss, R.; Schlierf, C.; Weiss, R.; Schlierf, C. *Synthesis* **1976**, 323–324.
149. Laitinen, R.; Steudel, R.; Weiss, R. *J. Chem. Soc. Dalton Trans.* **1986**, 1095–1100.
150. Minkwitz, R.; Prenzel, H. *Z. Naturforsch. B* **1987**, *42*, 750–757.
151. Poleschner, H.; Seppelt, K. *Angew. Chem. Int. Ed.* **2013**, *52*, 12838–12842.
152. Müller, B.; Poleschner, H.; Seppelt, K. *Dalton Trans.* **2008**, 4424–4427.
153. Kuhn, N.; Schumann, H.; Boese, R. *Chem. Commun.* **1987**, 1257–1258.
154. Jeske, J.; du Mont, W.-W.; Jones, P. G. *Angew. Chem. Int. Ed.* **1997**, *36*, 2219–2221.
155. Jungen, S.; Chen, P. *Inorg. Chem.* **2020**, *59*, 13315–13319.
156. Jungen, S.; Paenurk, E.; Chen, P. *Inorg. Chem.* **2020**, *59*, 12322–12336.
157. Chivers, T.; Parvez, M.; Peach, M.; Vollmerhaus, R. *J. Chem. Soc. Chem. Commun.* **1992**, 1539–1540.
158. Hillier, A. C.; Liu, S.-Y.; Sella, A.; Elsegood, M. R. *J. Angew. Chem. Int. Ed.* **1999**, *38*, 2745–2747.
159. Witthaut, D.; Kirschbaum, K.; Conrad, O.; Giolando, D. M. *Organometallics* **2000**, *19*, 5238–5240.
160. Fischer, H. T. M.; Naumann, D.; Tyrna, W. *Chem. Eur. J.* **2006**, *12*, 2515–2519.
161. Kückmann, T. L.; Hermesen, M.; Bolte, M.; Wagner, M.; Lerner, H.-W. *Inorg. Chem.* **2005**, *44*, 3449–3458.
162. Power, P. P. *Nature* **2010**, *463*, 171–177.
163. Tokitoh, N.; Kano, N.; Shibata, K.; Okazaki, R. *Organometallics* **1995**, *14*, 3121–3123. and references therein.
164. Takeda, N.; Tokitoh, N.; Okazaki, R. *Top. Curr. Chem.* **2003**, *231*, 153–202.
165. Fujita, N.; Li, L.; Lentz, N.; Konaka, S.; Kuroda, A.; Ohno, R.; Hayakawa, N.; Tamao, K.; Madec, D.; Kato, T.; Rosas-Sanchez, A.; Hashizume, D.; Matsuo, T. *Chem. Lett.* **2020**, *49*, 141–144. and references therein.
166. Foley, S. R.; Yap, G. P. A.; Richeson, D. S. *Organometallics* **1999**, *18*, 4700–4705.
167. Iwamoto, T.; Sato, K.; Ishida, S.; Kabuto, C.; Kira, M. *J. Am. Chem. Soc.* **2006**, *128*, 16914–16920.
168. Barman, M. K.; Nembenna, S. *RSC Adv.* **2016**, *6*, 338–345.
169. Ahmet, I. Y.; Hill, M. S.; Rathby, P. R.; Johnson, A. L. *Dalton Trans.* **2018**, *47*, 5031–5048.
170. Sugahara, T.; Sasamori, T.; Tokitoh, N. *Chem. Lett.* **2018**, *47*, 719–722; Sasamori, T. *CSD Communication (Private Communication)*, 2018.
171. Matsuhashi, Y.; Tokitoh, N.; Okazaki, R.; Goto, M.; Nagase, S. *Organometallics* **1993**, *12*, 1351–1358.
172. Ramaker, G.; Saak, W.; Haase, D.; Weidenbruch, M. *Organometallics* **2003**, *22*, 5212–5216.
173. Zhang, G.; Li, P.; Ding, J.; Liu, Y.; Xiong, W.-W.; Nie, L.; Wu, T.; Zhao, Y.; Tok, A. I. Y.; Zhang, Q. *Inorg. Chem.* **2014**, *53*, 10248–10256.
174. Liu, B.-W.; Zhang, M.-Y.; Jiang, X.-M.; Li, S.-F.; Zeng, H.-Y.; Wang, G.-Q.; Fan, Y.-H.; Su, Y.-F.; Li, C.; Guo, G. C.; Huang, J.-S. *Chem. Mater.* **2017**, *29*, 9200–9207.
175. van Almsick, T.; Loose, A.; Heldrick, W. S. *Z. Anorg. Allg. Chem.* **2005**, *631*, 21–23.
176. Liu, S.; Sun, P.; Han, J.; Liu, Y.; Shen, Y.; Tang, C.; Sun, H.; Jia, D. *J. Chem. Sci.* **2017**, *129*, 167–175.
177. Bubenheim, W.; Müller, U. *Z. Naturforsch. B* **1995**, *50*, 1135–1612.
178. Lehman, S. E., Jr.; Schimek, G. L.; Cusick, J. M.; Kolis, J. W. *Inorg. Chim. Acta* **1997**, *260*, 173–181.
179. Banda, R. M.; Cusick, J.; Scudder, M. I.; Craig, D. C.; Dance, I. G. *Polyhedron* **1989**, *8*, 1995–1998.
180. Zhang, Q.; Malliakas, C. D.; Kanatzidis, M. G. *Inorg. Chem.* **2009**, *48*, 10910–10912.
181. Sheldrick, W. S.; Wachold, M. *Coord. Chem. Rev.* **1998**, *176*, 211–322.
182. Xiong, W.-W.; Miao, J.; Ye, K.; Wang, Y.; Liu, B.; Zhang, Q. *Angew. Chem. Int. Ed.* **2015**, *54*, 546–550.
183. Stauber, J. M.; Müller, P.; Dai, Y.; Wu, G.; Nocera, D. G.; Cummins, C. C. *Chem. Sci.* **2016**, *7*, 6928–6933.
184. Heal, H. G. *The Inorganic Heterocyclic Chemistry of Sulphur, Nitrogen, and Phosphorus*, Academic Press: London, New York, 1980, 271 pp.
185. Chivers, T.; Laitinen, R. S. In *Handbook of Chalcogen Chemistry*; Devillanova, F. A., Ed., RSC Press: Cambridge, 2007; pp 223–285.
186. Laitinen, R. S.; Oilunkaniemi, R.; Chivers, T. *Selenium and Tellurium Chemistry*. In *From Small Molecules to Biomolecules and Materials*; Woollins, J. D., Laitinen, R. S., Eds., Springer: Heidelberg, 2011; pp 103–122.
187. Chivers, T.; Laitinen, R. S. In *Handbook of Chalcogen Chemistry, New Perspectives in Sulfur, Selenium and Tellurium*; Devillanova, F. A., du Mont, W.-W., Eds., RSC Publishing: Cambridge, 2013; pp 191–237.
188. Chivers, T.; Konu, J. *Selenium and Tellurium Chemistry*. In *From Small Molecules to Biomolecules and Materials*; Woollins, J. D., Laitinen, R. S., Eds., Springer: Heidelberg, 2011; pp 57–102.
189. Davies, R.; Patel, L. In *Handbook of Chalcogen Chemistry, New Perspectives in Sulfur, Selenium and Tellurium*; Devillanova, F. A., du Mont, W.-W., Eds., RSC Publishing: Cambridge, 2013; pp 238–306.
190. Heal, H. G.; Kane, J. *Inorg. Synth.* **1968**, *11*, 184–194.
191. Steudel, R.; Rosenbauer, D. *J. Chromatogr.* **1981**, *216*, 399–401.
192. Bojes, J.; Chivers, T.; Drummond, I. *Inorg. Synth.* **1978**, *18*, 203–206.
193. Brauer, G. *Handbook of Preparative Inorganic Chemistry*, 2nd ed.; vol. 1; Academic Press, 1963; p 411.
194. Bergemann, K.; Kustos, M.; Krüger, P.; Steudel, R. *Angew. Chem. Int. Ed.* **1995**, *34*, 1330–1331.
195. Steudel, R.; Bergemann, K.; Buschmann, J.; Luger, P. *Angew. Chem. Int. Ed.* **1996**, *35*, 2537–2539.
196. Wang, C.-C.; Hong, Y.-Y.; Ueng, C.-H.; Wang, Y. *J. Chem. Soc. Dalton Trans.* **1992**, 3331–3336.
197. Postma, H. J.; van Bolhuis, F.; Vos, A. *Acta Crystallogr. Sect. B* **1971**, *27*, 2480–2486.
198. Van de Grampel, J. C.; Vos, A. *Acta Crystallogr. Sect. B* **1969**, *25*, 611–617.
199. Postma, H. J.; van Bolhuis, F.; Vos, A. *Acta Crystallogr. Sect. B* **1973**, *29*, 915–917.
200. Garcia-Fernandez, H.; Rerat, C. *C. R. Ser. C* **1966**, *262*, 1866–1868.
201. Gregson, D.; Jlebe, G.; Fuess, H. *J. Am. Chem. Soc.* **1988**, *110*, 8488–8493.
202. Chivers, T.; Manners, I. *Inorganic Rings and Polymers of the p-Block Elements: From Fundamentals to Applications*, RSC Publishing: Cambridge, 2009; pp 7–11.
203. Chandrasekhar, V. *Inorganic and Organometallic Polymers*, Springer-Verlag: Berlin, 2005; pp 86–88.
204. Chivers, T.; Laitinen, R. S. *Dalton Trans.* **2017**, *46*, 1357–1367. and references therein.
205. Sasaki, S.; Hatsushiba, H.; Yoshifuji, M. *J. Chem. Soc., Chem. Commun.* **1998**, 2221–2222.
206. Jones, R.; Williams, D. J.; Woollins, J. D. *Angew. Chem. Int. Ed.* **1985**, *24*, 760–761.
207. Vegas, A.; Martinez-Ripoll, M.; Garcia-Blanco, S. *Cryst. Struct. Commun.* **1978**, *7*, 215–218.
208. Bromley, C. J.; Slawin, A. M. Z.; Waddell, P. G.; Woollins, J. D. *Inorg. Chem. Commun.* **2009**, *12*, 804–805.
209. Maaninen, T.; Chivers, T.; Laitinen, R.; Schatte, G.; Nissinen, M. *Inorg. Chem.* **2000**, *39*, 5341–5347.
210. Herberhold, M.; Jellen, W. *Z. Naturforsch.* **1986**, *41b*, 144–148.
211. Maaninen, T.; Tuononen, H. M.; Schatte, G.; Suontamo, R.; Valkonen, J.; Laitinen, R.; Chivers, T. *Inorg. Chem.* **2004**, *43*, 2097–2104.
212. Karhu, A. J.; Pakkanen, O. J.; Rautiainen, J. M.; Oilunkaniemi, R.; Chivers, T.; Laitinen, R. S. *Inorg. Chem.* **2015**, *54*, 4990–4997.
213. Maaninen, T.; Chivers, T.; Laitinen, R.; Wegelius, E. *Chem. Commun.* **2000**, 759–760.
214. Karhu, A. J.; Pakkanen, O. J.; Rautiainen, J. M.; Oilunkaniemi, R.; Chivers, T.; Laitinen, R. S. *Dalton Trans.* **2016**, *45*, 6210–6221.
215. Macdonald, A. L.; Trotter, J. *Can. J. Chem.* **1973**, *51*, 2504–2506.



216. Chivers, T.; Gao, X.; Parvez, M. *J. Am. Chem. Soc.* **1995**, *117*, 2359–2360.
217. Cordes, A. W.; Glarum, S. H.; Haddon, R. C.; Hallford, R.; Hicks, R. G.; Kenepohl, D. K.; Oakley, R. T.; Palstra, T. T. M.; Scott, S. R. *J. Chem. Soc., Chem. Commun.* **1992**, 1265–1266.
218. Cordes, A. W.; Haddon, R. C.; Hicks, R. G.; Oakley, R. T.; Palstra, T. T. M. *Inorg. Chem.* **1992**, *31*, 1802–1808.
219. Haas, A.; Kasprowski, J.; Angermund, K.; Betz, P.; Kruger, C.; Tsay, Y.-H.; Werner, S. *Chem. Ber.* **1991**, *124*, 1895–1906.
220. Haas, A. *J. Organomet. Chem.* **2002**, *646*, 80–93.
221. Maaninen, A.; Konu, J.; Laitinen, R. S.; Chivers, T.; Schatte, G.; Pietikainen, J.; Ahlgren, M. *Inorg. Chem.* **2001**, *40*, 3539–3543.
222. Maaninen, A.; Laitinen, R. S.; Chivers, T.; Pakkanen, T. A. *Inorg. Chem.* **1999**, *38*, 3450–3454.
223. Haas, A.; Kasprowski, J.; Pryka, M. *J. Chem. Soc., Chem. Commun.* **1992**, 1144–1145.
224. Haas, A.; Pryka, M. *J. Chem. Soc., Chem. Commun.* **1994**, 391–392.
225. Blachnik, R.; Lonneck, P.; Boldt, K.; Engelen, B. *Acta Crystallogr. Sect. C* **1994**, *50*, 659–661.
226. Gushwa, A. F.; Belabassi, Y.; Montchamp, J. L.; Richards, A. F. *J. Chem. Crystallogr.* **2009**, *39*, 337.
227. Bureau, V.; Ibers, J. A. *Acta Crystallogr. Sect. C* **2000**, *56*, 584–586.
228. Upmann, D.; Jones, P. G. *Z. Anorg. Allg. Chem.* **2014**, *640*, 2776–2780.
229. Gray, I. P.; Bhattacharyya, P.; Slawin, A. M. Z.; Woollins, J. D. *Chem. Eur. J.* **2005**, *11*, 6221–6227.
230. Hua, G.; Fuller, A. M.; Slawin, A. M. Z.; Woollins, J. D. *Polyhedron* **2011**, *30*, 805–808. and references therein.
231. Hua, G.; Woollins, J. D. *ACS Omega* **2021**, *6*, 31226–31228.
232. Hua, G.; Li, Y.; Slawin, A. M. Z.; Woollins, J. D. *Angew. Chem. Int. Ed.* **2008**, *47*, 2857–2859. and references therein.
233. Chivers, T.; Konu, J. In *Selenium and Tellurium Chemistry. From Small Molecules to Biomolecules and Materials*; Woollins, J. D., Laitinen, R. S., Eds.; Springer: Heidelberg, Dordrecht, London, New York, 2011; pp 79–102.
234. Chivers, T.; Eisler, D. J.; Ritch, J. S.; Tuononen, H. M. *Angew. Chem. Int. Ed.* **2005**, *44*, 4953–4956.
235. Steudel, R. *Z. Naturforsch.* **1983**, *38b*, 543–545.
236. Pauling, L. *The Nature of the Chemical Bond*, 3rd ed.; Cornell University Press: Ithaca, NY, 1960, 644 pp.
237. Robertson, S. D.; Chivers, T.; Tuononen, H. M. *Inorg. Chem.* **2009**, *48*, 6755–6762.
238. Robertson, S. D.; Chivers, T.; Tuononen, H. M. *Inorg. Chem.* **2008**, *47*, 10634–10643.
239. Nordheider, A.; Arachchige, K. S. A.; Slawin, A. M. Z.; Woollins, J. D.; Chivers, T. *Dalton Trans.* **2015**, *44*, 8781–8783.
240. Nordheider, A.; Chivers, T.; Thirumoorthi, R.; Vargas-Baca, I.; Woollins, J. D. *Chem. Commun.* **2012**, *48*, 6346–6348.
241. Nordheider, A.; Chivers, T.; Thirumoorthi, R.; Athukorala Arachchige, K. S.; Slawin, A. M. Z.; Woollins, J. D.; Vargas-Baca, I. *Dalton Trans.* **2013**, *42*, 3291–3294.
242. Nordheider, A.; Hüll, K.; Prentis, J. K. D.; Athukorala Arachchige, K. S.; Slawin, A. M. Z.; Woollins, J. D.; Chivers, T. *Inorg. Chem.* **2015**, *54*, 3043–3054.
243. Artem'ev, A. V.; Malysheva, S. F.; Sukhov, B. G.; Belogorlova, N. A.; Gatilov, Y. V.; Mamatyuk, V. I.; Gusarova, N. K. *Mendeleev Commun.* **2012**, *22*, 18–20.
244. Chivers, T.; Ritch, J. S. *Acta Crystallogr. Sect. C* **2015**, *C71*, 407–409.
245. Haynes, A. S.; Banerjee, A.; Saouma, F. O.; Otieno, C. O.; Jang, J. I.; Kanatsidis, M. G. *Chem. Mater.* **2016**, *28*, 2374–2383.
246. Chung, I.; Kim, M.-G.; Jang, J. I.; He, J.; Ketterson, J. B.; Kanatzidis, M. G. *Angew. Chem. Int. Ed.* **2011**, *50*, 10867–10870.
247. Kuimov, V. A.; Liao, P.-K.; Chiou, L.-S.; You, H.-C.; Fang, C.-S.; Liu, C. W. *Eur. J. Inorg. Chem.* **2013**, 2083–2092.
248. Terzis, A.; Ioannou, P. V. *Z. Anorg. Allg. Chem.* **2004**, *630*, 278–285.
249. Demeshko, S.; Godemann, C.; Kuzova, R.; Schulz, A.; Villinger, A. *Angew. Chem. Int. Ed.* **2013**, *52*, 2105–2108.
250. Eich, A.; Bredow, T.; Beck, J. *Inorg. Chem.* **2015**, *54*, 484–491. and references therein.
251. Du, K. Z.; Feng, M.-L.; Qi, X.-H.; Ma, Z.-J.; Li, L.-H.; Li, J.-R.; Du, C.-F.; Zou, G.-D.; Huang, X.-H. *Dalton Trans.* **2014**, *43*, 2233–2236.
252. Liu, G.-N.; Guo, G.-C.; Chen, F.; Wang, S.-H.; Sun, J.; Huang, J.-S. *Inorg. Chem.* **2012**, *51*, 472–482.
253. Wendel, K.; Müller, U. *Z. Anorg. Allg. Chem.* **1995**, *621*, 979–981.
254. Siewert, B.; Müller, U. *Z. Anorg. Allg. Chem.* **1991**, *595*, 211–215.
255. Chen, R.; Tang, W.; Jiang, W.; Zhang, Y.; Jia, D. *J. Coord. Chem.* **2012**, *65*, 3316–3328. and references therein.
256. Liu, G.-N.; Guo, G.-C.; Wang, M.-S.; Huang, J.-S. *Dalton Trans.* **2014**, *43*, 3931–3938.
257. Kromm, A.; Sheldrick, W. S. *Z. Anorg. Allg. Chem.* **2008**, *634*, 121–124.
258. Kromm, A.; Sheldrick, W. S. *Z. Anorg. Allg. Chem.* **2009**, *635*, 205–207.
259. Jiang, H.; Wang, X.; Sheng, T.-L.; Hu, S.-M.; Fu, R.-B.; Wu, X.-T. *Inorg. Chem. Commun.* **2012**, *17*, 5–8.
260. Puls, A.; Näther, C.; Bensch, W. *Acta Crystallogr., Sect. E* **2006**, *62*, m1045–m1047. and references therein.
261. Nie, L.; Zhang, Y.; Xiong, W.-W.; Lim, T.-T.; Xu, R.; Yan, Q.; Zhang, Q. *Inorg. Chem. Front.* **2016**, *3*, 111–116.
262. Smith, D. M.; Park, C.-W.; Ibers, J. A. *Inorg. Chem.* **1997**, *36*, 3798–3800.
263. Martin, T. M.; Schimek, G. L.; Mlsna, D. A.; Kolis, J. W. *Phosphorus Sulfur Silicon Relat. Elem.* **1994**, *93*, 93–103.
264. Shreeve-Keyer, J. L.; Haushalter, R. C. *Polyhedron* **1996**, *15*, 1213–1215.
265. Dhingra, S. S.; Haushalter, R. C. *J. Am. Chem. Soc.* **1994**, *116*, 3651–3652.
266. Schwamm, R. J.; Lein, M.; Coles, M. P.; Fitchett, C. M. *J. Am. Chem. Soc.* **2017**, *139*, 16490–16493.
267. Kniep, R.; Korte, L.; Mootz, D. *Z. Naturforsch.* **1983**, *38b*, 1–6.
268. Dostal, L.; Jambor, R.; Ruzicka, A.; Jirasko, R.; Lochar, V.; Benes, L.; de Proft, F. *Inorg. Chem.* **2009**, *48*, 10495–10497.
269. Sasamori, T.; Mieda, E.; Takeda, N.; Tokitoh, N. *Chem. Lett.* **2004**, *33*, 104–105.
270. Sasamori, T.; Mieda, E.; Takeda, N.; Tokitoh, N. *Bull. Chem. Soc. Jpn.* **2007**, *80*, 2425–2435.
271. Dostal, L.; Jambor, R.; Erben, M.; Ruzicka, A. *Z. Anorg. Allg. Chem.* **2012**, *638*, 614–616.
272. Schur, M.; Bensch, W. *Z. Anorg. Allg. Chem.* **1998**, *624*, 310–314.
273. Rijnberk, H.; Näther, C.; Schur, M.; Jess, I.; Bensch, W. *Acta Crystallogr. Sect. C* **1998**, *54*, 920–923.
274. Katryniok, D.; Kniep, R. *Angew. Chem. Int. Ed. Eng.* **1980**, *19*, 645.
275. Lamoureux, M.; Milne, J. *Can. J. Chem.* **1989**, *67*, 1936–1941.
276. Milne, J. *J. Chem. Soc. Chem. Commun.* **1991**, 1048–1049.
277. Steudel, R.; Plinke, B.; Jensen, D.; Baumgart, F. *Polyhedron* **1991**, *10*, 1037–1048.
278. Feher, F.; Naused, K.; Weber, H. *Z. Anorg. Allg. Chem.* **1957**, *290*, 303–319.
279. Feher, F.; Ristic, S. *Z. Anorg. Allg. Chem.* **1957**, *293*, 311–313.
280. Steudel, R.; Strauss, R.; Jemsem, D. *Chem. Ztg.* **1985**, *109*, 349–350.
281. Steudel, R.; Steidel, J.; Sandow, T. *Z. Naturforsch. B* **1986**, *41*, 958–970.
282. Steudel, R.; Bergmann, K.; Buschmann, J.; Luger, P. *Inorg. Chem.* **1996**, *35*, 2184–2188.
283. Steudel, R.; Münchow, V.; Pickardt, J. *Z. Anorg. Allg. Chem.* **1996**, *622*, 1594–1600.
284. Priddhi, M.; Steudel, R.; Baumgart, F. *Phosphorus Sulfur Silicon Relat. Elem.* **1992**, *65*, 169–172.
285. Pekonen, P.; Taavitsainen, J.; Laitinen, R. S. *Acta Chem. Scand.* **1998**, *52*, 1188–1193.
286. Taavitsainen, J.; Laitinen, R. S. *Main Group Chem.* **1999**, *3*, 59–67.



287. Pietikäinen, J.; Laitinen, R. S. *J. Chem. Soc. Chem. Commun.* **1998**, 2381–2382.
288. Krebs, B.; Ahlers, F.-P. *Adv. Inorg. Chem.* **1990**, *35*, 235–317.
289. Kniep, R.; Rabenau, A. *Top. Curr. Chem.* **1983**, *111*, 145–192.
290. Kniep, R.; Mootz, D.; Rabenau, A. *Z. Anorg. Allg. Chem.* **1976**, *422*, 17–38.
291. Rabenau, A.; Rau, H. *Z. Anorg. Allg. Chem.* **1973**, *395*, 273–279.
292. Bauhofer, W.; Kniep, R. *Mater. Res. Bull.* **1973**, *8*, 989–995.
293. Rabenau, A.; Rau, H.; Eckerlin, P. *Angew. Chem. Int. Ed. Eng.* **1967**, *6*, 706.
294. Rabenau, A.; Rau, H.; Rosenstein, G. *Angew. Chem. Int. Ed. Eng.* **1970**, *9*, 802–803.
295. Williams, C. R.; Britten, J. F.; Harpp, D. N. *J. Org. Chem.* **1994**, *59*, 806–812.
296. Barnes, N. A.; Godfrey, S. M.; Halton, R. T. A.; Mushtaq, I.; Parsons, S.; Pritchard, R. G.; Sadler, M. *Polyhedron* **2007**, *26*, 1053–1060.
297. Barnes, N. A.; Godfrey, S. M.; Halton, R. T. A.; Mushtaq, I.; Pritchard, R. G.; Sarwar, S. *Dalton Trans.* **2006**, 1517–1523.
298. Lang, E. S.; Fernandez, R. M., Jr.; Silveira, E. T.; Abram, U.; Vazquez-Lopez, E. M. *Z. Anorg. Allg. Chem.* **1999**, *625*, 1401–1404.
299. Boyle, P. D.; Cross, W. I.; Godfrey, S. M.; McAuliffe, C. A.; Pritchard, R. G.; Sarwar, S.; Sheffield, J. M. *Angew. Chem. Int. Ed. Eng.* **2000**, *39*, 1796–1798.
300. de Oliveira, G. M.; Faoro, E.; Lang, E. S. *Inorg. Chem.* **2009**, *48*, 4607–4609.
301. Beckmann, J.; Hesse, M.; Poleschner, H.; Seppelt, K. *Angew. Chem. Int. Ed.* **2007**, *46*, 8277–8280.
302. Eide, J.; Foss, O.; Silvestru, C.; Lippolis, V.; Varga, R. A. *Acta Crystallogr. Sect. C* **2007**, *63*, o528–o529.
303. Foss, O.; Henjum, J.; Maartmann-Moe, K.; Maroy, K. *Acta Chem. Scand.* **1987**, *41A*, 77–86.
304. Foss, O.; Maartmann-Moe, K. *Acta Chem. Scand.* **1987**, *41A*, 121–129.
305. Faggiani, R.; Gillespie, R. J.; Kolis, J. W. *J. Chem. Soc. Chem. Commun.* **1987**, 592–5893.
306. Copolovici, L.; Silvestru, C.; Lippolis, V.; Varga, R. A. *Acta Crystallogr. Sect. C* **2007**, *63*, o528–o529.
307. Potapov, V. A.; Amosova, S. V.; Abramova, E. V.; Musalov, M. V.; Lyssenko, K. A.; Finn, M. G. *New J. Chem.* **2015**, *39*, 8055–8059.
308. Abramova, E. V.; Stekhova, I. V.; Molokoev, M. S.; Potapov, V. A.; Amosova, S. V. *Mendeleev Commun.* **2016**, *26*, 532–534.
309. Maaninen, A.; Chivers, T.; Parvez, M.; Pietikäinen, J.; Laitinen, R. S. *Inorg. Chem.* **1999**, *38*, 4093–4098.
310. Popov, I. A.; Averkiev, B. B.; Starikova, A. A.; Boldyref, A. I.; Minyaev, M.; V. I., *Angew. Chem. Int. Ed.* **2015**, *54*, 1476–1480.
311. Nandana, W. A. S.; Passmore, J.; White, P. S.; Wong, C.-M. *J. Chem. Soc. Chem. Commun.* **1982**, 1098–1099.
312. Brownridge, S.; Cameron, T. S.; Passmore, J.; Schatte, G.; Way, T. C. *J. Chem. Soc., Dalton Trans.* **1996**, 2553–2570.
313. Carnell, M. M.; Grein, F.; Murchie, M. P.; Passmore, J.; Wong, C.-M. *J. Chem. Soc. Chem. Commun.* **1986**, 225–227.
314. Klapötke, T.; Passmore, J. *Acc. Chem. Res.* **1989**, *22*, 234–240.
315. Brownridge, S.; Calhoun, L.; Jenkins, H. D. B.; Laitinen, R. S.; Murchie, M. P.; Passmore, J.; Pietikäinen, J.; Rautiainen, J. M.; Sanders, J. C. P.; Schrobilgen, G. J.; Suontamo, R. J.; Tuononen, H. M.; Valkonen, J. U.; Wong, C.-M. *Inorg. Chem.* **2009**, *48*, 1938–1959.
316. Brownridge, S.; Cameron, T. S.; Du, H.; Knapp, C.; Koeppe, R.; Passmore, J.; Rautiainen, J. M.; Schnoeckel, H. *Inorg. Chem.* **2005**, *44*, 1660–1671.
317. Nandana, W. A. S.; Passmore, J.; White, P. S.; Wong, C.-M. *Inorg. Chem.* **1990**, *29*, 3529–3538.
318. Passmore, J.; Sutherland, G. W.; Whidden, T. K.; White, P. S. *J. Chem. Soc. Chem. Commun.* **1980**, 289–290.
319. Minkwitz, R.; Kornath, A.; Krause, R.; Preut, H. *Z. Naturforsch. B* **1990**, *45*, 1637–1642.
320. Heckmann, G.; Wolmershauser *Chem. Ber.* **1993**, *126*, 1071–1076.
321. Knight, F. R.; Fuller, A. L.; Buhl, M.; Slawin, A. M. Z.; Woollins, J. D. *Inorg. Chem.* **2010**, *49*, 7577–7596.
322. Hauge, S.; Janickis, V.; Marøy, K. *Acta Chem. Scand.* **1998**, *52*, 1104–1109.
323. Janickis, V.; Milius, W.; Törnroos, K. W. *Z. Anorg. Allg. Chem.* **2005**, *631*, 882–886.
324. Janickis, V.; Necas, M. *Z. Anorg. Allg. Chem.* **2010**, *636*, 818–823.
325. Janickis, V.; Necas, M. *Z. Anorg. Allg. Chem.* **2008**, *634*, 905–910.
326. Janickis, V.; Sonstad, J.; Törnroos, K. W. *Chem. Aust.* **2001**, *12*, 93–98.
327. Janickis, V.; Necas, M.; Novosad, J.; Dusek, M.; Petricek, V. *Acta Crystallogr. Sect. B* **2002**, *58*, 977–985.
328. Janickis, V.; Herberhold, M.; Necas, M.; Milius, W. *Z. Anorg. Allg. Chem.* **2003**, *629*, 641–646.

## 1.23 Catenated compounds in group 17—polyhalides<sup>☆</sup>

Lars Kloo, Applied Physical Chemistry, Department of Chemistry, KTH Royal Institute of Technology, Stockholm, Sweden

© 2023 Elsevier Ltd. All rights reserved.

<b>1.23.1</b>	<b>Introduction</b>	<b>1021</b>
<b>1.23.2</b>	<b>The triiodide ion and its lighter congeners</b>	<b>1022</b>
1.23.2.1	The bonding in trihalide ions	1025
1.23.2.2	Bonding trends in trihalides	1025
<b>1.23.3</b>	<b>Polyiodides</b>	<b>1027</b>
<b>1.23.4</b>	<b>Trends in polyiodide chemistry</b>	<b>1030</b>
1.23.4.1	Structural confinement	1030
1.23.4.2	Metal-iodide/iodine compounds	1032
<b>1.23.5</b>	<b>Liquids and solvent effects</b>	<b>1034</b>
<b>1.23.6</b>	<b>Polybromides—An expanding branch of polyhalide chemistry</b>	<b>1036</b>
<b>1.23.7</b>	<b>Other polyhalides</b>	<b>1038</b>
<b>1.23.8</b>	<b>Applications</b>	<b>1040</b>
1.23.8.1	Optical applications	1040
1.23.8.2	X-ray contrast agents	1040
1.23.8.3	Triiodide detection	1041
1.23.8.4	Doping of polymers and carbons	1041
1.23.8.5	Polyhalides for metal extraction	1041
1.23.8.6	Polyhalides in energy applications	1042
<b>References</b>		<b>1044</b>

### Abstract

The present chapter offers an overview of polyanions of the Group 17 as examples of catenation. The main knowledge obtained from the rich literature on polyiodides is summarized, and comparisons are made with other polyhalide systems in order to gain insights into similarities and differences. A strong emerging field is represented by polybromides in the liquid and solid state, as well as novel or rejuvenated areas of application. A detailed analysis of chemical bonding is given, and the special properties of halogen-halogen bonding are highlighted.

### 1.23.1 Introduction

The concept of catenation can be traced to organic chemistry, which essentially is based on the ability of the element carbon to make strong carbon–carbon bonds. Catenation originates from the Greek work for chain, and through its origin from organic chemistry it also implicates that the chains are formed through covalent bonds between the elements involved. This is certainly a characteristic of the organic C–C-chains, but it is not so obvious for polyhalides, as will be discussed later. Although carbon chemistry is the most prolific example, catenation is an inherent property of many of the p-block elements. For instance, the lighter pnictogens form tetrahedral P<sub>4</sub> and As<sub>4</sub> molecules and various polymers, sulfur forms ring-shaped S<sub>8</sub> molecules and polymeric species, the chemistry of selenium and tellurium contains many examples of chain structures etc.<sup>1</sup> Interestingly enough, the tendency to catenation appears to decrease down the Group 14–16, but for the Group 17, the halogens, the tendency is the opposite albeit this conclusion has recently been challenged by the surge in new polychloride, polybromide and polyinterhalide compounds.<sup>2,3</sup> The reasons can be understood on the basis of the different type of chemical bonding involving aspects of both classical coordination chemistry and effects of the halogen  $\sigma$ -hole,<sup>4,5</sup> which changes down the Group 17, and such aspects will be discussed later in this overview.

There are comprehensive reviews on polyiodides in the literature offering a good overview of the chemistry of the Group-17 elements.<sup>6–9</sup> There are also more recent reviews on the exciting and emerging chemistry of the lighter polyhalide compounds offering new insights into the structure and bonding in this class of compounds.<sup>2,3,10</sup> These reviews offer a highly comprehensive overview of the literature and focus on the aspect of structural chemistry. The more recent reviews also highlight new trends, mainly regarding three phenomena. First, quantum-chemical calculations have become a regularly used tool to rationalize structures and

<sup>☆</sup> *Change History:* June 2021. L. Kloo made the changes with respect to the previous version mainly involve an up-date of the literature from about 2010. The new contributions have added to in particular the sections on polychlorides, polybromides and the application of polyhalides in renewable energy fields. The figures 7, 13, 19, 20, 21 are new. The figures 10, 15, 16, 18, 22 have been significantly up-dated. Figure 12 in the previous version has been removed.

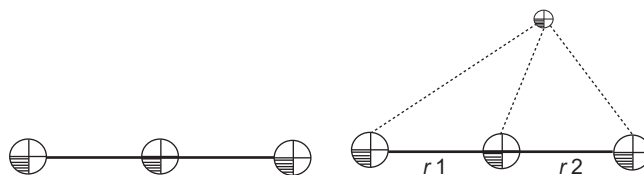
bonding patterns, and to relate solid structures to liquid media through spectroscopic studies. In this aspect, the special usefulness of Raman spectroscopy has become clear. Second, ionic liquids as reaction media for the formation of, much owing to their excellent properties as solvents for both ionic and molecular components, have emerged as the preferred media of synthesis of novel polyhalides. Third, whereas polyiodides expanded significantly from the use of organic salts and involvement of metal iodides came in at a later stage, the role of the structure-directing ability of the cations, including metal complexes, have become much more clear for polychlorides and polybromides making such a distinction less relevant.<sup>11</sup> These insights have also fed back to the field of polyiodides. The objective of the present overview is *not* to “top up” on published work; rather, the objective is to use the vast body of information to highlight the fundamental properties of the expanding field of polyhalides. Special attention will be paid to insights from structural patterns and bonding aspects. It will also aim to identify some recent directions of research and some important applications of polyhalides. In this context, it is notable that the ambition towards a more sustainable society also sets its mark here, where polyhalides have found new applications in the energy and metal recycling fields, typically in the form of polyhalide ionic liquids.<sup>12,13</sup> The polyhalides included in this work are essentially negatively charged. Also positively charged polyhalogen species exist, but that is a much smaller, less active and reviewed area of research.<sup>8</sup> Therefore, such species are not included in this overview.

### 1.23.2 The triiodide ion and its lighter congeners

Formally, the Group 17 concatenation starts with the well-known  $X_2$  molecules, also in the forms of a monocation or monoanion. However, these are thoroughly handled by all textbooks on fundamental, descriptive inorganic chemistry. In a recent review, the start of polyhalogenides was set to the  $X_2^-$  ions,<sup>3</sup> however from a bonding perspective the new and interesting features arise when adding another halogen atom to the fundamental  $X_2$  units, and therefore we will regard the trihalides as the lowest representatives of concatenated polyhalides in this overview. The most extensively studied trihalide is the triiodide ion,  $I_3^-$ . Several hundreds of crystal structures are known. In 2003 we obtained about 500 crystalline triiodide compounds in a search of the Cambridge Structural Database, and since then another 100 or so have been added to the list. There are about 100 compounds that can be characterized as tribromides, and fewer examples of the lighter trihalides. Some new aspects need to be taken into account from the structures of the lighter elements, and these will be included at the end of this section. Regarding the triiodide ions, the most exciting insights and applications emerge from low-dimensional structures of interacting triiodide ion (*vide infra*). Most likely, most of the triiodide compounds have emerged serendipitously, in the line of chemical synthesis of completely different molecular targets, often through reactions involving accidental or intentional oxidation by iodine.

In Fig. 1 the typical structures of a triiodide ion are shown. If interacting weakly with the surrounding ions or molecules, a centrosymmetric structure is normally observed. Upon stronger interaction with cations or, in particular, hydrogen-bonding components of the compounds the triiodide is most commonly linearly distorted. However, a few features of the triiodide structures deserve some attention. For instance, in the structures of tetrahydrothiophene derivatives pairs of triiodides interact at a fairly long distance of 3.79 Å, can be observed.<sup>14</sup> These may be regarded as dimer models of long-chain triiodide structures. Reiss and co-workers isolated two closely placed (at 3.63 Å) triiodide ions in a host-guest structure and asked the question whether they were packed so closely by the host or were directly interacting.<sup>15</sup> Their conclusion was that the triiodide ions indeed are interacting, and at an unusually short inter-molecular distance. Chains of triiodide ions are for instance found in quinoline derivatives with a shortest inter-molecular I–I-distance of 3.80 Å,<sup>16,17</sup> and as a side-product in the chemistry of bispyridyls with a distance of 3.69 Å.<sup>18</sup> Model systems for the very old application of iodine/iodide-containing solutions, starch tinting, still offer new insights. In the isolation of a helical sugar, Saenger and co-workers found triiodides in the channels at as short inter-molecular distances as 3.66 Å.<sup>19</sup> It is also notable that it is not uncommon that double-salts of iodide and triiodides with the same cation are formed.<sup>20–23</sup> Such compounds can be quite stable, and, as will be discussed in the section on applications, can constitute a problem because of low solubility.<sup>24</sup> An interesting case of polymorphism was discussed by Dance and co-workers showing that crystallization from different solvents in a reproducible way may give different crystal forms of a phosphonium triiodide compound.<sup>25</sup>

The chains of triiodide ions may be regarded as a link to applications. Such compounds are special in the sense that they do not fit into the simple coordination chemistry model of iodine solvation of ions described for the polyiodides below. Instead, the triiodide ions tend to interact end-on along chains at fairly long distances; typically around 4 Å. A few examples are given below, and considering the applications noted in the end of this review, it is notable that the stacking, structural confinement, of triiodide ions is a unique and important phenomenon in polyiodide chemistry. Lu and co-workers reported two-dimensional sheets of triiodide



**Fig. 1** A centrosymmetric and a non-centrosymmetric triiodide ion; the latter with a cation coordinated. The figure is taken from Ref. Svensson, P. H.; Kloo, L., *J. Chem. Soc. Dalton Trans.* **2000**, 2000: 2449–2455.

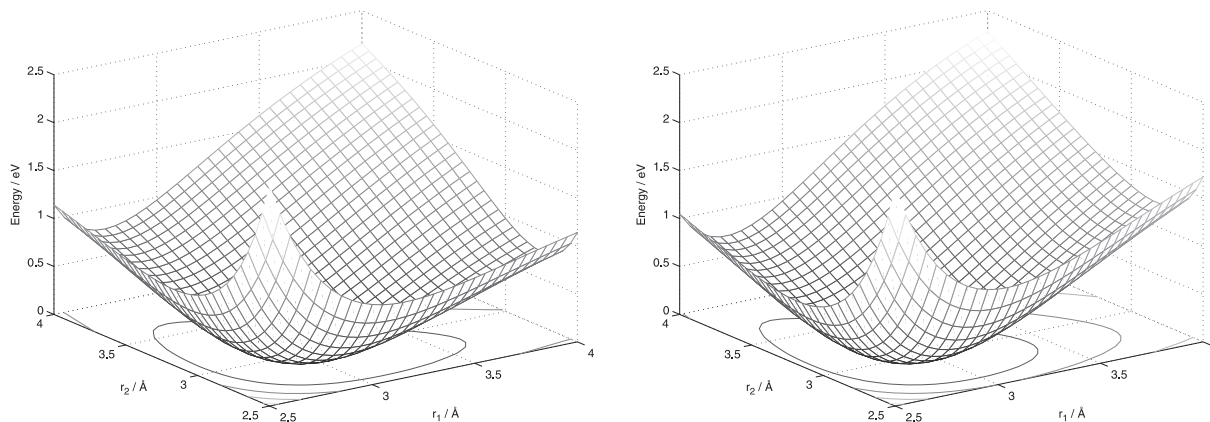
ions, albeit the inter-triiodide distances appear rather long.<sup>26</sup> A crystal engineering approach afforded chains of triiodides using long-chain diammonium cations<sup>27</sup> The inter-triiodide contacts observed are 4.13–4.17 Å. Using a substituted tetrathiafulvalene, an anisotropic organic metal was formed containing both stacked fulvalene molecules and chains of triiodide ions along the plane of stacking.<sup>28</sup> The inter-triiodide distances found are around 3.90 Å.

In the crystalline solids, the triiodide ion most typically exists in two forms; either linear and centrosymmetric, or linear and non-centrosymmetric, Fig. 1. Most commonly, the triiodide ion is slightly linearly distorted. One very important factor controlling the level of distortion is cation coordination. A cation is often found in the position indicated in Fig. 1 (right). The degree of polarization determines the degree of distortion. Also, in solution, most notably for strongly donating solvents, similar effects can be observed; in particular, when the solvent molecules interact with the triiodide ion via hydrogen bonding. The solvation effects in  $I_3^-$  have been monitored by shifts in the electron binding energies and ab initio molecular dynamics in solution.<sup>29,30</sup> The molecular dynamics studies revealed that the asymmetric vibration reached essentially an  $I_2^{\cdot-}I^-$  state moderated by the solvent hydrogen bonding.<sup>31</sup> It has also been noted that the presence of lithium ions can initiate a redox process forming  $I_3^-$  in iodide ionic liquids and mixtures with alcohols.<sup>32</sup> The strongly polarizing hydrogen atom as donor can be regarded as mimicking the effect of a cation. The reason for this facile linear distortion is the extremely low energy required; see Fig. 2, in which the flat one-dimensional, potential-energy surfaces are shown for a centrosymmetric and non-centrosymmetric triiodide ion. In contrast, I–I–I angular distortions are much more rarely observed in solid structures, since the energy required for bending distortions is considerably higher. This difference can be traced to the  $\sigma$ -type of bonding involving the valence p-orbitals, as discussed below.

The extremely low energy required to pull the terminal iodine atom far away from the remaining  $I_2$  unit can directly be connected to the special form of electrical conductivity observed in many polyiodide compounds; the Grotthuss mechanism of conductivity.<sup>33</sup> Initially, the mechanism was used to explain the conductivity properties of water through hopping protons. It is equally well applied to polyiodides, where the hopping units instead are the iodide ions. This phenomenon will be discussed in more detail below in the light of polyiodide bonding. In fact, on the basis of a theoretical study involving the coordination of alkali-metal cations and  $X_3^-$  ions ( $X = Cl, Br$  or  $I$ ), Hoffmann and co-workers question the description of the systems as an  $M^+X_3^-$  ion pair in favor of an  $MX-X_2$  complex.<sup>34,35</sup>

In the ideal case, the linear and centrosymmetric triiodide ion has  $D_{\infty h}$  symmetry. The consequence in terms of group theory is that it exhibits four normal vibration modes; the symmetrical stretch ( $\Sigma_g^+$  symmetry,  $\nu_1$ ), the asymmetrical stretch ( $\Sigma_u^+$  symmetry,  $\nu_3$ ) and the doubly degenerate bending modes ( $\Pi_u$  symmetry,  $\nu_2$ ). The combination of comparatively weak I–I-bonding (bond order of 0.5), extremely flat potential-energy surface of linear distortion and the high atom mass of iodine make the frequencies of the vibration modes quite low.

This of course has some consequences. First, the vibrational modes are not readily observable using a standard experimental set-up for IR spectroscopy with a typical cut-off at about 200 or 400  $cm^{-1}$ . Optics (primarily IR source, beam splitter and detector) are required for far-IR spectroscopy. Second, because of the low energy of vibrational excitation, one should be aware of that all modes typically are highly excited at ambient temperatures. Since excitation of vibrational modes affects the vibrational amplitudes, this again has implications for the shape of the potential energy surface and, as a consequence, also the Grotthuss mechanism of conductivity mentioned above. The technical challenges together with the fact that the triiodide modes of vibration render small changes in the molecular dipole moment typically give rather weak and broad bands in IR-spectra. IR spectroscopy is a feasible but not optimal technique for the study of triiodide and polyiodide compounds. Instead, the large polarizability of the triiodide ion makes it highly suitable for Raman spectroscopic studies. Also the lighter trihalides offer strong Raman bands. Typically, the vibrational bands, allowed by symmetry, come out very strongly and excellent Raman spectra can be obtained even at very low concentrations in solution. However, surface-adsorbed triiodide or polyiodide species still require an extra boost in sensitivity, such as from Raman-enhanced spectroscopy, to be detectable. The characteristics of the triiodide vibrational modes are shown in Table 1.



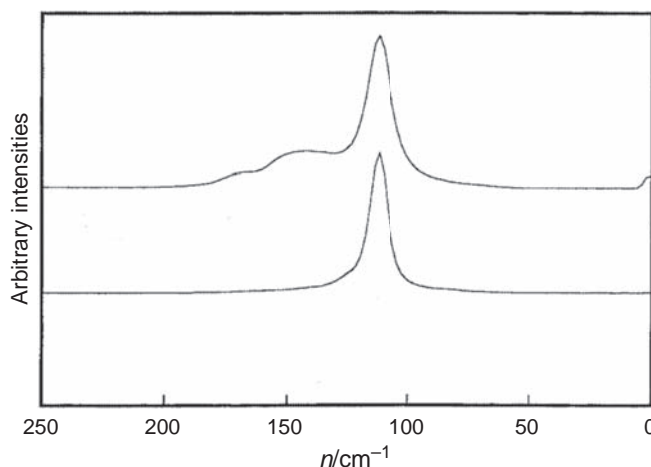
**Fig. 2** Potential energy surfaces of linear distortion of the triiodide ion for the centrosymmetric and non-centrosymmetric configurations. The figures are taken from Ref. Svensson, P. H.; Kloo, L., *J. Chem. Soc. Dalton Trans.* **2000**, 2000: 2449–2455.

**Table 1** Typical vibration characteristics of a centrosymmetric, linear triiodide ion<sup>36</sup>.

Modes of vibration	Typical frequency/cm <sup>-1</sup>	Selection rules
Symmetric stretch ( $\Sigma_g^+$ )	110	Raman active
Asymmetric stretch ( $\Sigma_u^+$ )	145	IR active
Bending ( $\Pi_u$ )	75	IR active

In the ideal state, only the symmetrical stretch mode will be observed in a Raman spectrum of a triiodide compound or solution. The large change in molecular polarizability upon the symmetrical vibration renders extremely strong Raman-spectroscopic signals. However, many factors can disturb the ideal local symmetry. Such factors involve the formation of higher polyiodides in solution, the coordination of cations or solvation by strongly donating solvents. In such cases, also the formally Raman-forbidden vibrational modes will appear in the Raman spectra, sometimes together with extra features from loosely bound I<sub>2</sub>-units. The two types of triiodide Raman spectra are shown in Fig. 3. The very simple and easily interpreted Raman spectra very quickly can become complex and interpretation far from non-ambiguous. Nevertheless, Raman spectroscopy offers beautiful polyiodide spectra and represents one of the most informative experimental techniques available for the study of polyiodide chemistry.

In this context, it is appropriate to mention two other related phenomena concerning triiodide chemistry. As noted above, from the structural and spectroscopic properties, the expected chemical dissociation of a triiodide ion is into I<sup>-</sup> and I<sub>2</sub> fragments. This has one important implication; I<sup>-</sup> as donor to I<sub>2</sub> is readily exposed to competition. Thus, many donors can out-compete I<sup>-</sup> if present in sufficient concentration. Typical competitors involve other halide anions, -N, -P or -S functionalities of various molecules, and chemistry is full of compounds containing -X-I-I-units.<sup>37</sup> A practical example, where this can become a problem, can be taken from the electrolyte chemistry of dye-sensitized solar cells (DSSCs). Part of the reason why an ionic-liquid-based electrolyte requires higher iodine concentration can be traced to an inherent interaction between the ionic-liquid cation and I<sub>2</sub> lowering the effective concentration of triiodide in solution and thus reducing conversion efficiencies.<sup>38</sup> This type of chemistry is not within the scope of the present overview, but represents a characteristic phenomenon of iodine chemistry that should be kept in mind. Consequently, some of the main features of polyiodides can also be observed in related areas of chemistry. The other phenomenon relates to photochemistry. It should be noted that photodissociation of the triiodide ion instead typically renders the ion I<sub>2</sub><sup>-</sup> and the highly reactive radical I<sup>•</sup>.<sup>39</sup> A recent study in gas phase reveals a rather complex, non-adiabatic dissociation with several possible dissociation channels, although the I<sub>2</sub><sup>-</sup> + I<sup>•</sup> ones display the highest yields.<sup>40</sup> It has been shown that the wavelength of the exciting radiation also affects the dissociation channels.<sup>41</sup> Photodissociation of triiodide ionic liquids showed an ultrafast relaxation/recombination of the I<sub>2</sub><sup>-</sup> ions formed.<sup>42</sup> Referring to the section of solvent effects below, hydrogen-bonding solvents are indicated to influence product branching in the dissociation channels. In electrochemical applications, the I<sub>2</sub><sup>-</sup> ion frequently appears as an important intermediate in the redox reactions involving the iodide and triiodide ions.<sup>43–46</sup> Photodissociation studies of the triiodide ion in ionic liquids show effects of bimolecular reactions resulting both in triiodide recombination and inter-I<sub>2</sub><sup>-</sup> reactions depending on the nature of the ionic-liquid system.<sup>47</sup> A K-edge EXAFS analysis of the triiodide ion in various solvents displayed a centrosymmetric triiodide ion with varying I–I bond lengths, albeit it was noted that large vibrational amplitudes blurred the next-neighbor correlations.<sup>48</sup>



**Fig. 3** Raman spectra of a centrosymmetric and a symmetry-broken triiodide ion, as represented by molten (Et<sub>3</sub>S)I<sub>3</sub> (top) and solid (Me<sub>3</sub>S)I<sub>3</sub> (bottom). The figure is taken from Ref. Svensson, P. H.; Kloo, L., *J. Chem. Soc. Dalton Trans.* **2000**, 2000: 2449–2455.



### 1.23.2.1 The bonding in trihalide ions

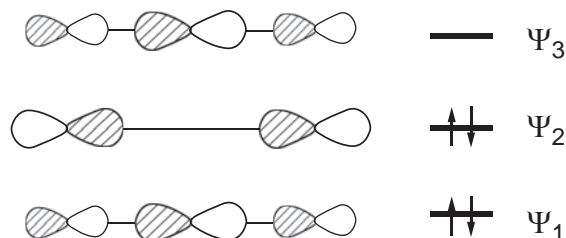
The established scheme of bonding in the triiodide ion was provided by Pimentel and Rundle already in the early 1950s.<sup>49,50</sup> On the basis of molecular-orbital theory involving only the iodine atom 5p-orbitals, three molecular orbitals (MOs) can be derived; see Fig. 4. The bonding formalism is analogous to that of the 1 s-orbitals of the simple  $\text{H}_3^-$  ion, allowing for a bit more complex symmetry consequences when involving the p-orbitals in  $\text{I}_3^-$ . Essentially, the three 5p-orbitals form one bonding, one non-bonding and one anti-bonding MO. The 5p-orbitals are expected to house 4 valence electrons, thus filling the bonding and non-bonding MOs. This simple bonding scheme carries more information than noted at first sight, since it also explains the role of the triiodide ion in donor/acceptor-type of complexes; more about this in the section on polyiodides. As a consequence of the bonding scheme, electrostatically the triiodide ion can be approximated as having  $-1/2$  charge on the terminal iodine atoms and close to zero charge on the central one.

Novoa and co-workers extended the bonding scheme to both the other homoatomic trihalides and later to some interhalogen trihalide species using correlated methods of theory.<sup>51,52</sup> All four trihalide ions,  $\text{F}_3^-$ ,  $\text{Cl}_3^-$ ,  $\text{Br}_3^-$  and  $\text{I}_3^-$ , were found to be stable with respect to dissociation into the  $\text{X}^-$  and  $\text{X}_2$  fragments. The stability was found to increase down the Group 17; in accordance with experiment. Also, the interaction with a cation ( $\text{K}^+$ ) was investigated and the structural consequences in terms of symmetry lowering deduced. The same trend was found for the  $\text{X}_3^-$  series in solution and gas phase with respect to the formation of  $\text{X}^-$  and  $\text{X}_2$ .<sup>53</sup> However, it was also noted that the level of theoretical treatment significantly influence the results. Hoffmann and co-workers have studied both the bonding characteristics of various combinations of trihalides, homogenous and interhalogen ones, and found a similar pattern as Novoa et al. The site preference in interhalogen trihalide ions was also scrutinized and found to be the largest for chlorine.<sup>54</sup> In a later study, the amount of s,p-mixing was investigated in p-block triatomic molecules and ions. Anti-bonding effects from s,p-mixing and electron-pair repulsion tend to be larger further to the left in the P-block.<sup>55</sup> In a calculational study of a large series of interhalogen trihalide ions, Kikuchi et al. found that, in accordance with experiment, the terminal position of the most electronegative (lightest) element in Group 17 promotes stability, whereas polar solvents flatten the potential energy surface enhancing  $\text{X}^- + \text{X}_2$  dissociation.<sup>56</sup> Kloo et al. made a thorough study of the bonding contributions to I–I bonding in the triiodide ion and larger polyiodides. It is clear that the triiodide ion, in addition to covalent interaction, also is stabilized by secondary types of interaction, such as induction, dispersion, as well as ion-quadrupole interaction ( $\text{I}_2$  has a strong quadrupolar moment).<sup>57</sup> It has been argued that a valence-bond (VB) formalism better describes the bonding in trihalide ions, as compared to the established (3c,4e)-MO scheme of Pimentel. The main argument is that dissociation barriers and states are better described by VB theory.<sup>58</sup>

Molecular dynamics and other studies in different solvents show that hydrogen-bonding solvents induce a symmetry breaking for the triiodide ions in solution.<sup>59–63</sup> Such effects must have a consequence for the recorded vibrational spectra, as noted in the experimental studies described above. In additional simulation studies, also solvent-induced shifts of the peak wavenumbers have been determined.<sup>63–65</sup> As previously noted, solvent effects are of importance in the photodissociation of the triiodide ion. The results from high-level multiconfigurational calculations indicate significant effects of solvent interaction on the structure and spectroscopic response of  $\text{I}_3^-$ .<sup>66</sup> One study has suggested that solvent effects give rise to a bent triiodide ion, although such a structural distortion is not necessary to explain the experimentally observed properties.<sup>67</sup>

### 1.23.2.2 Bonding trends in trihalides

The general conclusion from the body of calculational studies on trihalide systems is that the  $\sigma$ -bonded valence p-orbital interaction scheme of Pimentel is a good first approximation for all the  $\text{X}_3^-$  systems in Group 17. Moving down the group, secondary bonding contributions become increasingly important. At the same time, atom-atom distances increase down the group. In view of the coordination chemistry approach described below, the  $\text{X}^- - \text{X}_2$  interaction within the trihalide ions represents a suitable model system for the understanding of the tendency to polyhalide formation, i.e., catenation. In order to get a crude estimate of this tendency, some simple model calculations on the  $\text{X}_3^-$  ion were made using a long-range-corrected B3LYP functional together with the Stuttgart/Dresden/Cologne effective-core potential and triple-zeta valence basis sets to, on a more uniform basis, obtain a few characteristic bonding parameters of the homogenous trihalide ion. The calculational results are collected in Table 2 and are graphically represented in Fig. 5.<sup>68,69</sup>



**Fig. 4** The p-orbital bonding scheme proposed by Pimentel. The figure is taken from Ref. Munzarova, M. L.; Hoffmann, R., *J. Am. Chem. Soc.* **2002**, *124*: 4787–4795.

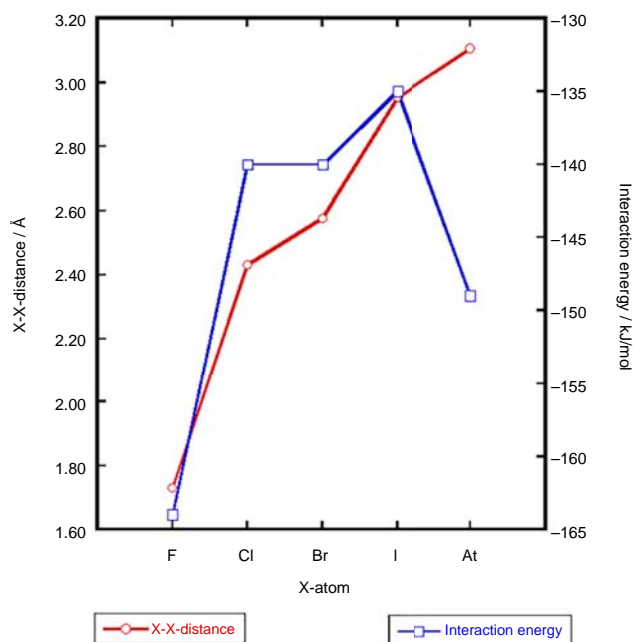
**Table 2** Computational results for the homoatomic trihalide ions of  $D_{\infty h}$  symmetry.

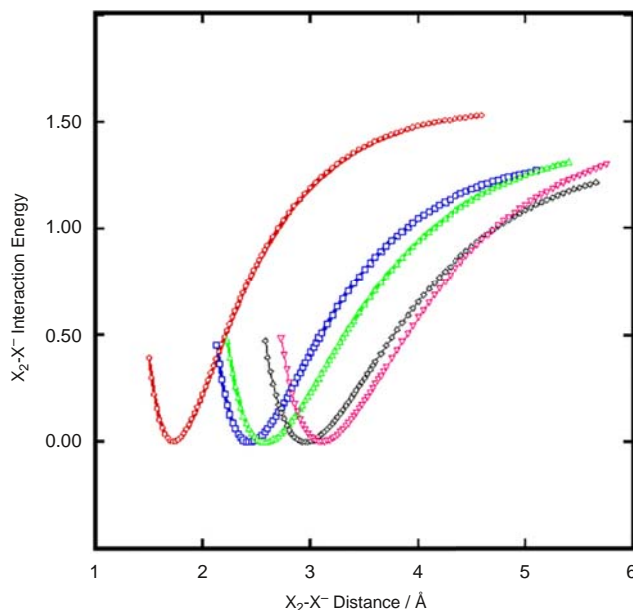
$X_3^-$ ion	X-X distance/Å	Symmetrical stretch vibration/ $\text{cm}^{-1}$	Asymmetrical stretch vibration/ $\text{cm}^{-1}$	$X_2-X^-$ interaction energy/kJ/mol
$F_3^-$	1.729	483	555	-164
$Cl_3^-$	2.431	256	323	-140
$Br_3^-$	2.577	165	182	-140
$I_3^-$	2.952	116	138	-135
$At_3^-$	3.105	84	106	-149

The results are at first sight a bit surprising, since interaction energies alone would suggest that polyfluoride chemistry should be the richest, although the interaction energies between the  $X_2$  and  $X^-$  fragments differ surprisingly little. It is clear that the issue requires a deeper analysis. More insight is obtained from the potential energy surfaces (PES) of the linear  $X_2$  and  $X^-$  interaction.

The PESs of linear distortion shown in Fig. 6 offer a couple of important observations. The widths of the potential energy wells are also numerically specified in Table 3. As expected, the X-X distance increases down the Group 17. However, the increase is non-linear and can be described as periodic. There is a large increase between the F-F and Cl-Cl distances, whereas the Br-Br one is only marginally longer than the Cl-Cl distance. In the same way, there is a fairly large increase in X-X distance between  $Br_3^-$  and  $I_3^-$  but small between  $I_3^-$  and  $At_3^-$ . Going from lighter to heavier systems, one can also note that the PES wells become flatter, more extended, and that the PESs increase less quickly with increasing X-X separation; see also PES well widths given in Table 2. This effect emerges from both more extended covalent interaction and from an increasing influence from inter-molecular interaction; such as induction, dispersion etc. In summary, the interaction between the  $X_2$  and  $X^-$  fragments becomes “stickier” the heavier the element. However, this effect peaks at iodine. In fact, the PES of  $I_3^-$  crosses that of  $At_3^-$  at longer distances (at about 4.7 Å) highlighting some special properties of the element iodine. In this respect, the extensive polyiodide chemistry can be attributed to the strong long-distance attractive forces in iodine; most likely stronger than any of its Group 17 congeners despite the current expansion of the polybromide and polychloride chemistry, rather than the I-I interaction energy *per se*. Thus, the tendency to catenation is expected to be the strongest for iodine; at least at the above level of theory. Explicit spin-orbit coupling was not included in the above calculations, and more advanced calculation may change the order described above. It is clear that proper handling of relativistic effects will be particularly important for the heavy Group-17 elements At and, the late new group member, tennesine (Ts, element no. 117).<sup>70</sup> At the same time, the chemistry of the Period-7 elements may be less predictable because of the close to degenerate valence electrons.<sup>71</sup> And, since the influence of covalent bonding is significant, probably the chains formed should be regarded as a true case of catenation.

In the review by Riedel et al., they include two more bonding concepts to rationalize the structures observed for tri- and polyhalide species.<sup>3</sup> First, they note a halogen bonding effect referring to topological electron-densities.<sup>72,73</sup> Second, and highly related,

**Fig. 5** Graphical representation of the bond distances and interaction energies shown in Table 2.



**Fig. 6** Potential energy curves for linear distortion in the  $X_3^-$  trihalide ions; from  $F_3^-$  furthest to the left to  $At_3^-$  furthest to the right; the conformation with the lowest total energy is set to zero in all systems.

this involves descriptions based on halogen  $\sigma$ -holes. In Fig. 7, the electrostatic potential for the tribromide ion is shown to highlight the expected directionality regarding interactions with surrounding components.

The effects of the  $\sigma$ -holes follow the order  $F < Cl < Br < I$ . This represents a feasible description of the stability order observed above. Polizer and co-workers rationalized the stability of  $XYZ^-$  trihalides in terms of  $\sigma$ -hole effects.<sup>74</sup> However, Mealli and co-workers have noted that the  $\sigma$ -hole effects must be weak in the formation of  $I_3^-$  and  $I_4^{2-}$ .<sup>75</sup> Also, the  $\sigma$ -hole bonding description probably leaves out the polarizing effects of, most relevantly to the topic of this survey, negatively charged anions in the extension of the tribromide bonding direction. The most clear consequence of that are the recent,  $X_2$ -rich polychloride, polybromide and polyinterhalide anions resembling Werner-type coordination compounds. This will be discussed more in detail in the section on polyhalides below.

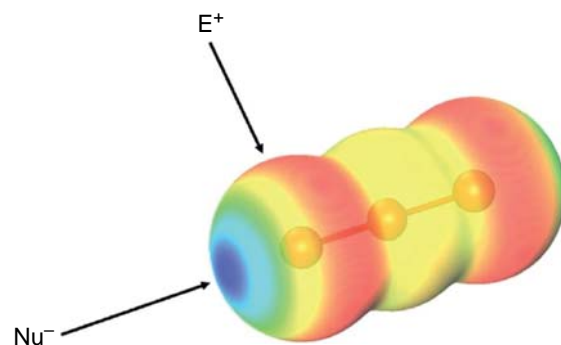
### 1.23.3 Polyiodides

Iodine is unique in the tendency to form extended, catenated structures, so-called polyiodides. Just as for the  $I_3^-$  ion the bonding in the neutral, diatomic  $I_2$  molecule can as a first approximation be described as the result of  $\sigma$ -interaction between the iodine 5p-orbitals forming a single bond. The bonding scheme of  $I_2$  is shown in Fig. 8. This means that the  $\sigma$ -anti-bonding orbital ( $2\sigma_u^*$  MO in Fig. 8) is available for accepting electron density, and thus  $I_2$  readily act as an electron acceptor; a Lewis acid.

In this aspect, it is notable that the polyiodides typically are made from only three fundamental building blocks: the  $I^-$  and  $I_3^-$  ions, and the neutral molecule  $I_2$ . Essentially all polyiodide structures, with very few exceptions, can be rationalized in terms of these three fragments<sup>8</sup> (Fig. 9). Thus, in the polyiodide structures, the ions will act as donors and typically the I–I bond distance in the  $I_2$  fragment is elongated as a consequence of the population of its  $\sigma$ -anti-bonding orbital. In classical coordination chemistry terms, the interaction can be regarded as a simple solvation, where the neutral molecule  $I_2$  solvates the anions  $I^-$  and  $I_3^-$ . This is a useful concept, since it also explains the ready exchange of the anions for others, for instance like in the metal-iodide/iodine systems described later.<sup>76</sup>

**Table 3** Width of the potential energy well of the PES shown in Fig. 6.

$X_3^-$ ion	Well width at 0.026 eV (kT at 298 K)/Å	Well width at 0.4 eV/Å
$F_3^-$	0.14	0.64
$Cl_3^-$	0.19	0.80
$Br_3^-$	0.23	0.98
$I_3^-$	0.24	1.04
$At_3^-$	0.24	0.99

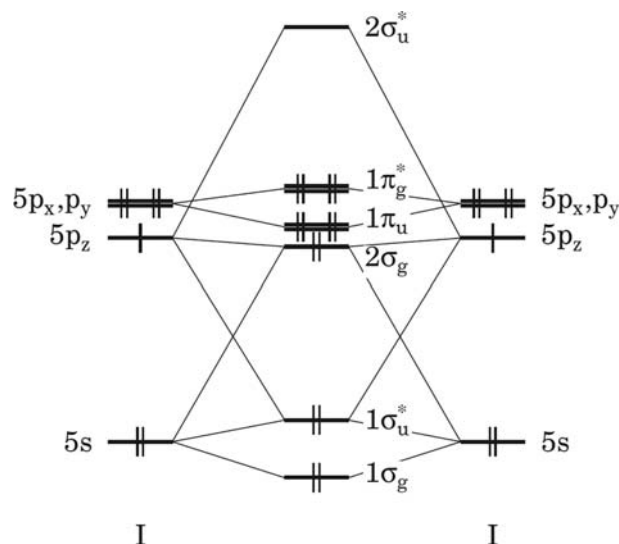


**Fig. 7** Electrostatic potential for the  $\text{Br}_3^-$  ion. Taken from Ref. Sonnenberg, K.; Mann, L.; Redeker, F. A.; Schmidt, B.; Riedel, S., *Angew. Chem. Int. Ed.* **2020**, *59*: 5464–5493.

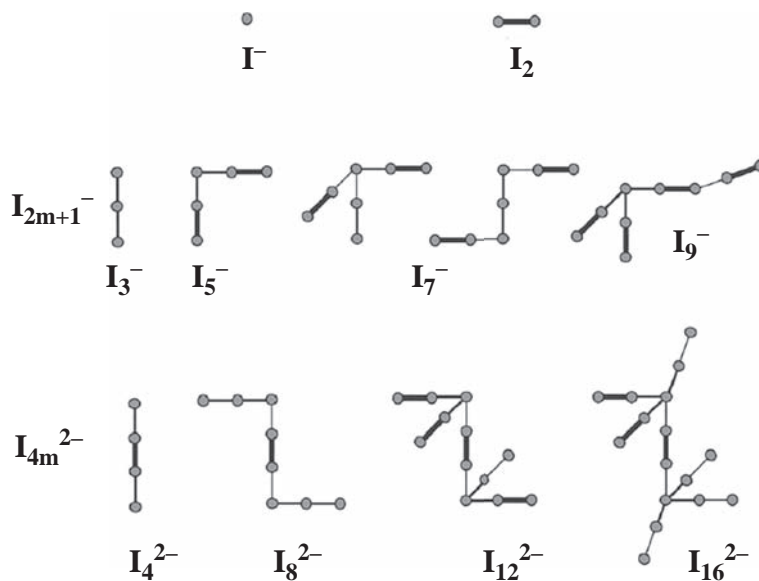
In this perspective, either the solvating power of  $\text{I}_2$  must be unique or the donor capacity of the iodide anion donors exceptional. Judging from the results in **Table 2**, the  $\text{I}_2 \cdots \text{I}^-$  interaction itself does not stand out in strength in comparison with the other halogen-halide interactions. Instead, it is strong attractive interaction at longer ( $> 3 \text{ \AA}$ ) distances that generates the rich polyiodide chemistry (*vide supra*)—a few nice highlights are given in **Fig. 10**.

Nevertheless, the model of solvation justifies the typically used formalism in rationalizing polyiodide structures. For instance, the examples shown in **Fig. 10** can all be broken down into the three fundamental building blocks of polyiodides, in spite of the complexity of indicated by the stoichiometry. A striking feature is the seemingly boundary-less width of the I–I-contact ranging from that in the  $\text{I}_2$  molecule (about  $2.7 \text{ \AA}$ ) up to over  $4 \text{ \AA}$ . A statistical analysis of I–I $\cdots$ I contacts showed a rather continuous distribution;<sup>57</sup> **Fig. 11**. There are clear maxima in I–I $\cdots$ I contacts corresponding to intra-molecular distances ( $\text{I}_2$  and  $\text{I}_3^-$ ) and essentially packing distances ( $> 4 \text{ \AA}$ ). However, all distances in between are also well represented and it is clear that the inter-molecular I–I bond must be very flexible. This phenomenon is also obvious in the attempts to rationalize the polyiodide structures to fit into the simple three-fragment solvation model described above; the assignment of an I $\cdots$ I contact in the range  $3.0\text{--}3.6 \text{ \AA}$  is sometimes far from unambiguous. The distance distributions also have implications for the Grotthuss mechanism of conduction; the transfer of an iodide ion from one polyiodide fragment to another is essentially continuous. The assignment of a specific proton in water to a specific neighboring water molecule oxygen atom can be problematic, just like the assignment of a specific iodide ion to a neighboring iodine molecule. It likely that a proper analysis of the atom probability distributions in many polyiodide structures could challenge the assignments made.

The bonding in polyiodides can be regarded as a logical extension from the bonding scheme in the simple  $\text{I}_3^-$  ion, visualized as a solvated iodide ion of  $\text{I}_2 \cdots \text{I}^-$  type. Consequently, a pentaiodide ion can be regarded as a  $(\text{I}_2)_2 \cdots \text{I}^-$  interaction, a heptaiodide ion as a  $(\text{I}_2)_3 \cdots \text{I}^-$ , etc. In relation to the region of difficult bonding assignment between  $3$  and  $4 \text{ \AA}$ , it is clear that the interaction energy can be partitioned into several different contributions. The partitioned potential-energy surface is shown in **Fig. 12**.



**Fig. 8** The p-orbital bonding scheme of  $\text{I}_2$ . The figure is taken from Ref. Svensson, P. H.; Kloo, L., *Chem. Rev.* **2003**, *103*: 1649–1684.



**Fig. 9** A few polyiodide structures that can be visualized in terms of  $I_2$  solvation of the iodide ions. The figure is taken from Ref. Walbaum, C.; Pantenburg, I.; Meyer, G., *Z. Naturforsch. B* **2010**, *65*, 1077–1083.

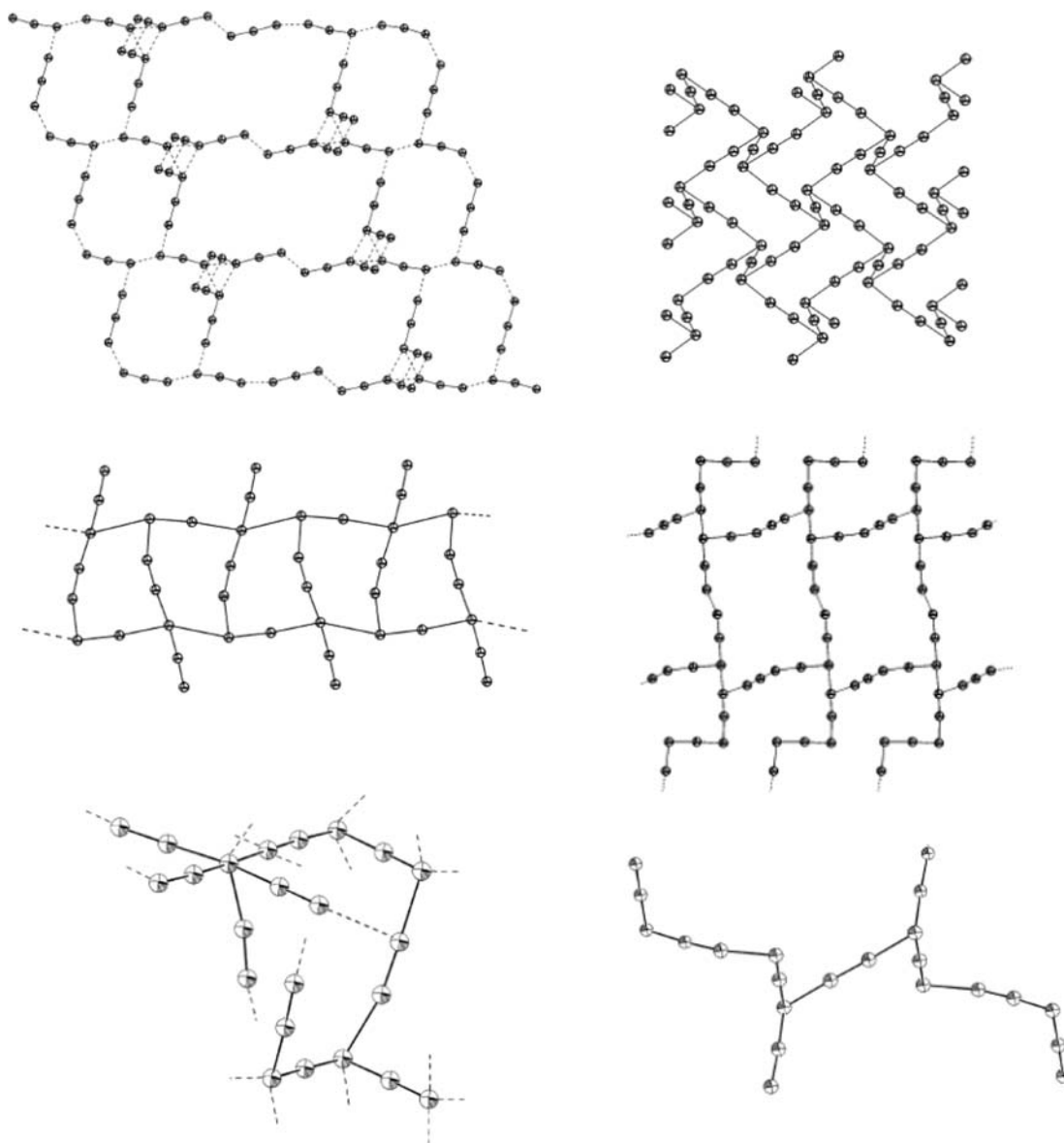
A few characteristics can immediately be noted. First, covalent bonding extends quite far out and is significant out to at least 5 Å. Second, also dispersion, induction and ion-quadrupolar interactions contribute significantly in the 3–4 Å region. For instance, at an I–I distance of 3.5 Å, the attractive contributions, in terms of contribution to the total interaction energy, can be partitioned as follows: 52% covalent, 26% dispersion, 12% induction and 11% ion-quadrupolar interaction. With this in mind, a Grotthuss mechanism of ionic conductivity becomes essentially inevitable. In addition, the reason for the “sticky” character of the long-distance I–I interactions becomes clear. Even the iodide transfer energetics between  $I_3^-$  ions offer indications for facile superionic conductivity.<sup>77</sup>

In a structural analysis of polybromides generating an image similar to that in Fig. 10, it appeared that the polybromides are not characterized by a second long-distance feature in contrast to the polyiodide structures.<sup>78</sup> However, with the current and larger number of structures, in fact the corresponding distance distribution for polybromides highly resembles that of polyiodides, see Fig. 13, with the difference that the region between distances that can be characterized as intra-molecular and inter-molecular seems to be much smaller.

In this context, it is appropriate to discuss the bonding in chains of  $I_3^-$  ions. Although the inter-molecular, attractive forces of iodine-containing species appears to be significant even at the typical  $I_3^- \cdots I_3^-$  distances of about 4 Å, the repulsive force of the negative charges on the terminal iodine atoms are expected to dominate. From an MO perspective, the interaction cannot be explained with a simple donor-acceptor formalism. The chains of triiodides, for instance found in the herapathite compound,<sup>79</sup> are thus not expected to be bound. However, such a view is too simplified in this case. Essentially all known structures of chains of triiodide ions fall into one of two categories; the triiodides are confined into a host structure, where triiodide-host interactions are significant, or they contain bridging cations linking the negatively charged ions together. Consequently, chains of triiodide ions are found in structures, where the surrounding components of the compound place the triiodide ions together at distances balancing the electrostatically repulsive force of the anions. Macroscopically, such an anisotropic molecular arrangement generates anisotropic physical properties. It is notable that dimers or chains of head-on contacting  $I_3^-$  ions are rather frequent in confined structures. A theoretical study of the  $I_3^-$  dimers show, as expected a repulsive potential-energy surface, and it follows that the surrounding cationic environment must have a critical influence of both orientation of the linear ions and their inter-ionic distances.<sup>80,81</sup> And, keeping the  $\sigma$ -hole effects visualized in Fig. 7 in mind, also electron densities may play a role.

In the last 15 years many new polyiodide structures have been published in refereed journals. Many of these repeat known structural features and conform to the expected bonding pattern. However, a few new structures call for special attention and the field as such appears to follow a few new directions, trends, highlighted below. An interesting comparison between polytellurides and polyiodides was recently published by Devillanova et al., in which systematization in terms of few structural building blocks proved more difficult in polytellurides.<sup>82</sup> Lee and colleagues made a very thorough structural and theoretical study on aromatic, organic-polyiodide systems, rating the different types of interactions in such systems.<sup>83</sup> The iodine-iodine interactions were deduced to be the strongest, and thus implicitly the most important structure-directing interaction. Sulfur-containing, organic molecules, or ligands in metal-containing systems, appear as a successful strategy to form new and interesting polyiodide frameworks. Such an example is the quasi-cubic structure using a dipyriddyldisulfide derivative (see Fig. 14),<sup>84</sup> or substituted tetrathiafulvalenes of interesting inherent electrical properties (see more below regarding templating/confinement),<sup>85</sup> or thiacyclonanes as ligands to Group-10 metal ions give rise to a rich structural polyiodide chemistry.<sup>86</sup> Of course, polyiodide structures can be described in different ways, as exemplified by the iodine-rich cryptand compound of Pantenburg and co-workers denoted as a mixed  $I_5^-$  and  $I_8^{2-}$  compound,





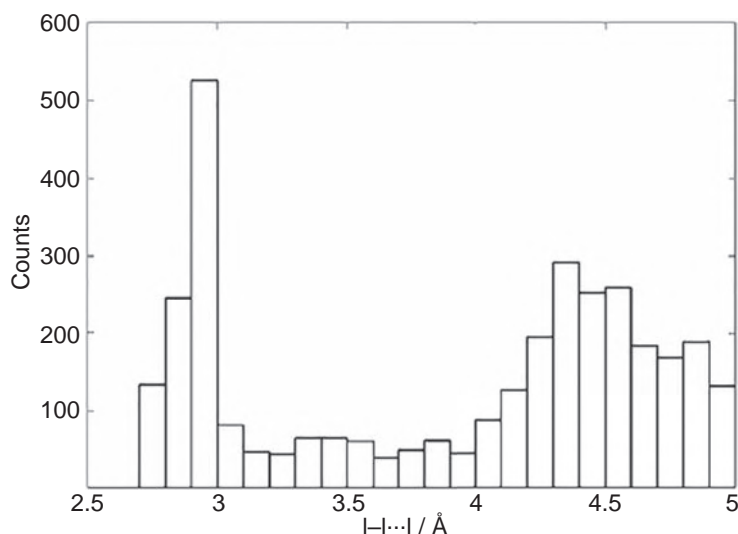
**Fig. 10** Some large polyiodide fragments that can be broken down into the three fundamental building blocks  $I^-$ ,  $I_2$  and  $I_3^-$ , the structures are extracted. From Ref. Svensson, P. H.; Kloo, L., *Chem. Rev.* **2003**, *103*, 1649–1684.

where the anions can be further broken down into the three fundamental building blocks.<sup>87</sup> In another compound, co-habiting  $I_3^-$  and  $I_5^-$  ions were found.<sup>88</sup> Beryllium(II) is a less common cation to be used in coordination chemistry, but in one such compound a mixture between  $I_3^-$  and  $I_4^{2-}$  was determined.<sup>89</sup> In most structures, larger polyiodide fragments tend to be linked into complex structures, and in this aspect the isolated  $I_{12}^{2-}$  ions reported by Lahtinen and co-workers is uncommon.<sup>90</sup> Regarding the structure shown in Fig. 14, in fact novel insights from the structures of the lighter polyhalides provide another way to rationalize the structure; just as for the highly  $X_2$ -rich species  $[(X^-) \bullet 6 X_2]$ ,  $X = Cl$  or  $Br$ ,  $I^-$  can be regarded as surrounded by 6  $I_2$  molecules in a quasi-octahedral configuration with the difference that all  $I_2$  molecules are shared to generate a three-dimensional structure.

### 1.23.4 Trends in polyiodide chemistry

#### 1.23.4.1 Structural confinement

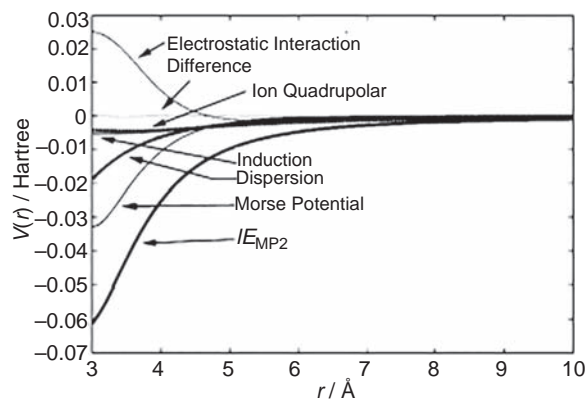
Intercalation of iodide with iodine into a solid zeolite host appears to form various I–I-bonded species, as judged from vibrational spectroscopic and EXAFS data.<sup>91</sup> Yan and co-workers used hydrogen-bonded nucleotide bases to form supramolecular entities with ribbon-like structures; among them a formal  $I_{14}^{2-}$  entity of  $[(I_3^-)_2 \bullet 4I_2]$  type was observed.<sup>92</sup> Lu and Schauss used a metal-organic



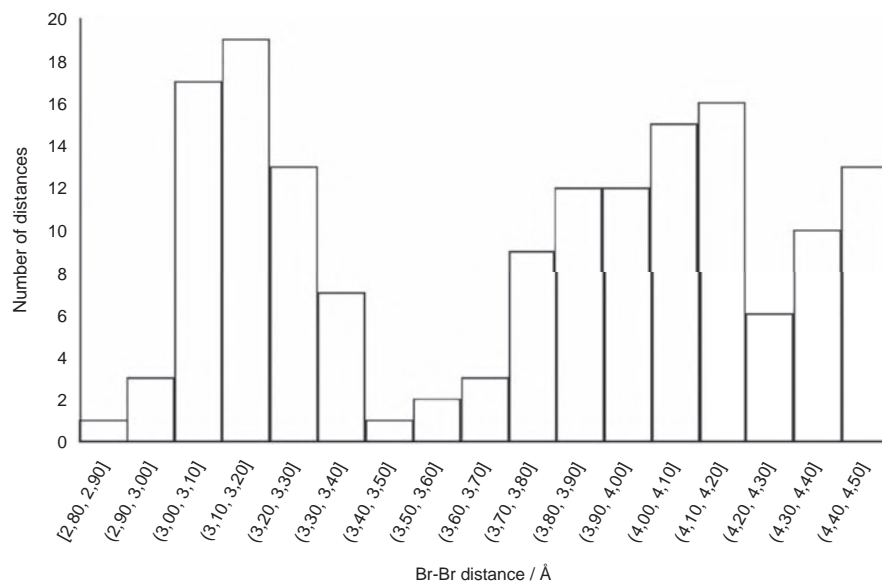
**Fig. 11** Distance distribution of I–I distances in an  $I_3$  unit as derived from the Cambridge Structural Database. The figure is taken from Ref. Kloo, L.; Rosdahl, J.; Svensson, P. H., *Eur. J. Inorg. Chem.* **2002**, 1203–1209.

framework (MOF) to confine pentaiodide ions with inter-molecular contacts of 3.56 Å and of  $[(I^-) \bullet 2I_2]$  type.<sup>93</sup> Since then, several structures including confinement in MOFs have emerged, such as the one by Hou and co-workers containing zigzag-chains of  $I_3^-$  ions,<sup>94</sup> and by others using primarily Raman spectroscopy as analytical tool to identify absorbed iodine in the forms of  $I_3^-$  or larger polyiodides.<sup>95,96</sup> It is clear that this type of confined structures may produce materials with interesting optical properties.<sup>97</sup> Helical, metal-ligand systems were also used by both Dance with co-workers and Schröder et al. to template new polyiodide compounds.<sup>98–100</sup> A similar approach has been used by Devillanova and co-workers isolating a series of polyiodides with high  $I_2$  content.<sup>101</sup> The use of the secondary interactions of cations with long aliphatic chains, self-assembling into low-dimensional structures known from basic colloidal chemistry, is another strategy producing confined polyiodides.<sup>27,102,103</sup> A similar strategy was used by different groups in series of polyiodide compounds and was denoted dimensional caging.<sup>104–106</sup> Templating using cation structures has also been shown successful.<sup>107</sup> A series of substituted tetrathiofulvalenes were used to modulate the dimensionality of the resulting polyiodide networks in charge-transfer systems,<sup>108</sup> and similar approaches based on related and other substituted cation cores have also been reported.<sup>109–111</sup> Recently, also non-halide-containing and cationic metal complexes have been more systematically used to stabilize new polyiodide compounds.<sup>112–114</sup> In this context it can be worth noting that even a simple cation, such as methylammonium, generates a highly complex polyiodide phase diagram.<sup>115</sup> Some beautiful structures of confined polyiodides are shown in Fig. 15.

Of course, this type of structural confinement has strong ties to both the very old application of polyiodide systems to tint starch, but also to other potential applications within mainly optics and electronics. With this in mind, structural confinement based on various carbohydrate systems is rather frequent, using for instance xylan, cyclodextrins and similar molecular systems<sup>116–125</sup>. Also the formation of polyiodides in carbon nanotubes and graphenes have been studied.<sup>126–128</sup> However, most commonly characterization is based on spectroscopic observations and the exact assignment of polyiodide units must in some cases be regarded as



**Fig. 12** Bonding contributions to the I–I bond in  $I_3^-$ . The figure is taken from Ref. Kloo, L.; Rosdahl, J.; Svensson, P. H., *Eur. J. Inorg. Chem.* **2002**, 1203–1209.



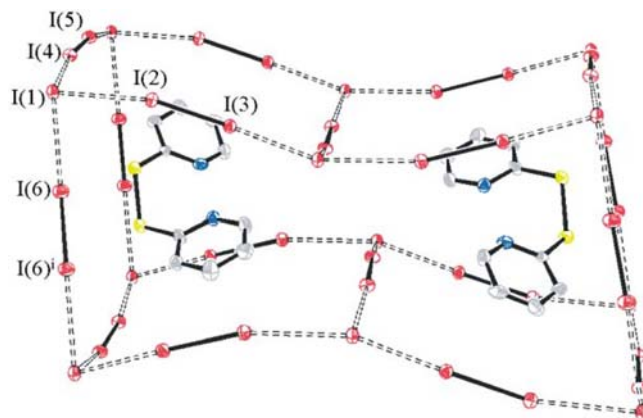
**Fig. 13** Distance distribution of Br–Br distances in a structural Br<sub>3</sub> unit as derived from the Cambridge Structural Database.

models to explain experimental results. Nevertheless, crystal structure data render considerably higher credibility to the models in more disordered systems.<sup>129</sup>

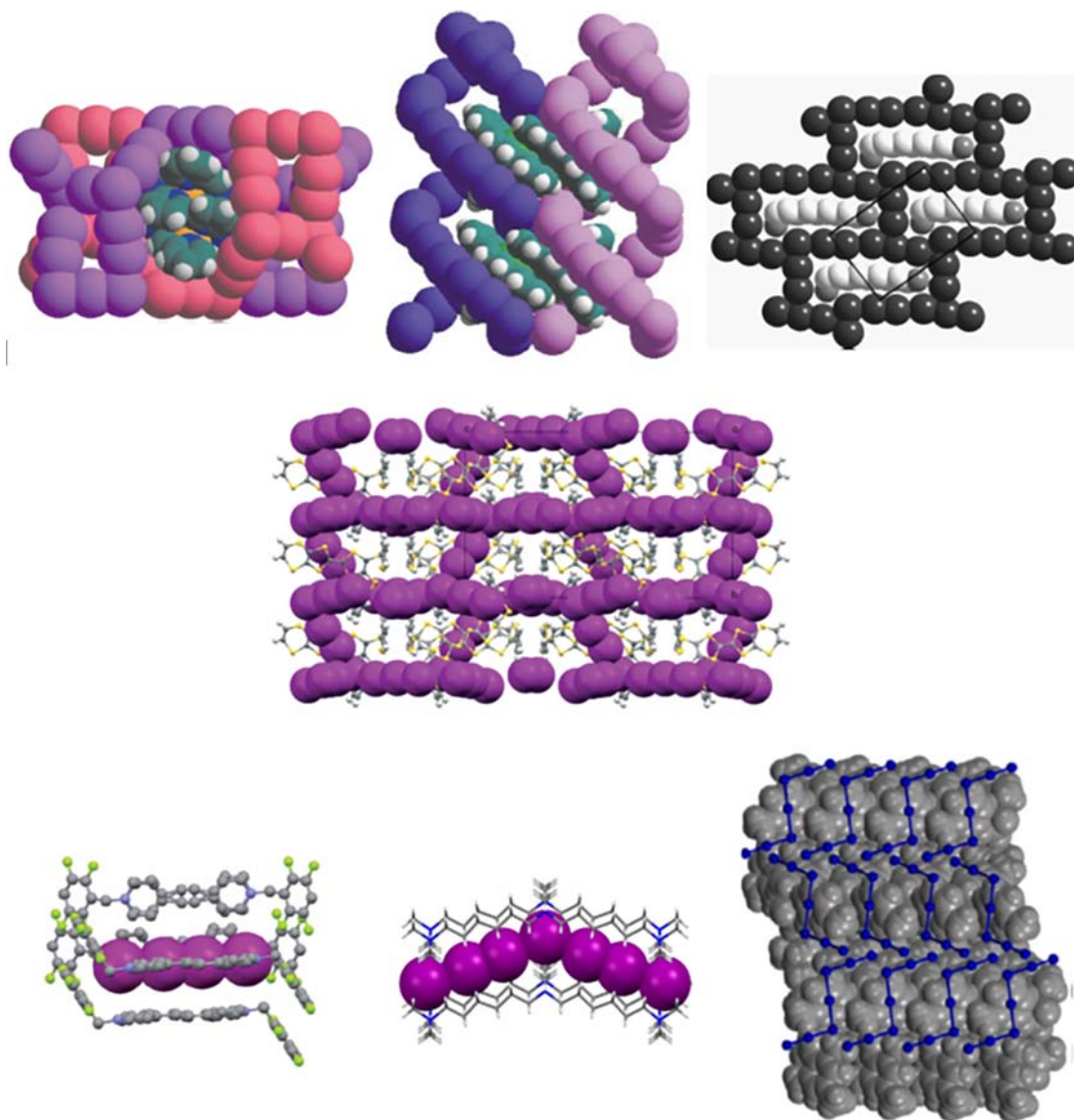
#### 1.23.4.2 Metal-iodide/iodine compounds

As discussed in the section on polyiodides, metal-halide complexes can be regarded as halide donors with respect to the diatomic halogen molecules. Normally, the donation capacity is lower than for a non-coordinated halide ion. The aspect of donor capacity was nicely illustrated in the work by Tsipis and Karipidis, where the donor strength essentially follows that shown in Table 2 for the trihalides; the lighter the element, the larger the electron donation to the X<sub>2</sub> unit.<sup>130</sup> It is pertinent to note that metal-halide/halogen compounds normally are regarded as different from polyhalides with metal-complex cations in that the former type has a halide ion directly coordinated to the metal ion. The metal ion, coordination center, does not necessarily have to be homoleptic, but the interaction with a halogen X<sub>2</sub> molecule or other polyhalide fragment takes place via a coordinated halide ion. As will be highlighted later, this has become a central strategy in the bromide/polybromide systems.

Some early work included complex gold iodides as the iodide/triiodide “substitute.”<sup>131,132</sup> Because of the highly similar coordination chemistry of gold and iodine, this is not unexpected.<sup>8,132</sup> However, there is a quite a number of compounds of this type. Typically, the halide ligands are bridged by I<sub>2</sub> or other halogen/interhalogen molecules (*vide infra*). As compared to the “pure” polyhalides, the weaker metal-halide donor ability tends to give thermally rather unstable compounds. One exception are compounds isolated with a mercury-hexamethylenetetramine complex.<sup>133</sup>



**Fig. 14** The pseudo-cubic structure described by Devillanova et al. The structure is taken from Ref. Aragoni, M. C.; Arca, M.; Devillanova, F. A.; Hursthouse, M. B.; Huth, S. L.; Isaia, F.; Lippolis, V.; Mancini, A., *CrstEngComm* **2004**, *6*, 540–542.



**Fig. 15** Examples of new polyiodide structures in confined environments. In order, taken from Horn, C. J.; Blake, A. J.; Champness, N. R.; Garau, A.; Lippolis, V.; Wilson, C.; Schroder, M., *Chem. Commun.* **2003**, 3, 312–313.; Horn, C. J.; Blake, A. J.; Champness, N. R.; Lippolis, V.; Schroder, M., *Chem. Commun.* 2003, 13, 1488–1489.; Reiss, G. J.; Engel, J. S., *Z. Naturforsch. (B)* **2004**, 59(10), 1114–1117.; Garcia, M. D.; Marti-Rujas, J.; Metrangolo, P.; Peinador, C.; Pilati, T.; Resnati, G.; Terraneo, G.; Ursini, M., *Crystengcomm* **2011**, 13(13), 4411–4416.; Lin, J. X.; Marti-Rujas, J.; Metrangolo, P.; Pilati, T.; Radice, S.; Resnati, G.; Terraneo, G., *Cryst. Growth Des.* **2012**, 12(11), 5757–5762.; Pan, F. F.; Englert, U., *Cryst. Growth Des.* **2014**, 14(3), 1057–1066.; Short, J.; Blundell, T. J.; Yang, S. J.; Sahin, O.; Shakespeare, Y.; Smith, E. L.; Wallis, J. D.; Martin, L., *Crystengcomm* **2020**, 22(40), 6632–6644.

Guloy reported a selection of new gold(I)/gold(III) complex compounds, containing  $I_3^-$  and other halides in layered, perovskite-like structures.<sup>134,135</sup> It is normally rather difficult to isolate the  $I_3^-$  analogue  $AuI_2^-$  from iodine-rich reaction media because of oxidation to gold(III), typically as  $AuI_4^-$ . In these examples the oxidation is only partial, retaining gold in the +I oxidation state. Ligand tuning, *viz.* phosphine-ligand tuning, was used to address this problem by Schmidbauer and co-workers.<sup>136</sup> Several gold(I) compounds were isolated as phosphine gold(I)iodides; some bridged by  $I_2$  at iodide-iodine distances of 3.44–3.65 Å. Also, a triiodide in gold(III) compounds were isolated. Meyer and his co-workers recently reported a series of compounds containing both Au(I) and Au(III) showing that monovalent gold not necessarily is oxidized by an excess of iodine.<sup>73</sup> Iodide-iodine distances range 3.21–3.81 Å in these structures, where shorter distances are correlated with darker colors. This was also verified by the mixed-valence gold-iodide/iodine compound reported by Evans and co-workers.<sup>137</sup> Gold contact material is typically used in perovskite solar cells, described in more detail below under applications, where the formation of this type of compounds has been suggested as a potential degradation mechanism for the devices.<sup>138</sup> Dimeric Pd(II)-halide structures are quite stable, and Pantenburg and Meyer have isolated a compound with an  $I_2$ -bridged  $Pd_2I_6^{2-}$  complex, and with an iodide-iodine distance as short as 3.32 Å.<sup>139</sup> Also

a Pt(IV) iodo complex with bridging  $I_2$  and  $I_3^-$  units has been reported, with iodide-iodine distances in the range of 3.3 Å.<sup>140</sup> By reacting CuI with  $I_2$ , Chen and colleagues obtained a similar  $I_2$ -bridged  $Cu_2I_6^{4-}$  complex.<sup>141</sup> The iodide-iodine distance in this compound is even shorter, 3.02 Å, raising the question whether it should be regarded as a bridging  $I_2$  molecule or rather as a coordinated, asymmetric, triiodide ion. Janiak and co-workers used a copper(I)-iodide-based inorganic starch model to obtain a series of confined polyiodide compounds.<sup>142</sup> Different types of copper complexes coordinated by iodide seem to be suitable templates for iodine bridging,<sup>143,144</sup> also involving MOF systems for iodine capture and sensing.<sup>145</sup> Because of structural disorder, the nature of the encapsulated, linear polyiodide entities is not fully clarified. Relating to the perovskite structures, Mercier et al. isolated a low-dimensional lead-iodide structure, where the metal-iodide ribbons are linked by  $I_2$  molecules at an iodide-iodine distance of 3.51 Å.<sup>146</sup> A similar layered structure with intercalated triiodide ions was described by Chen and co-workers, rendering an optical semiconductor material.<sup>147</sup> In general, the use of bridging iodine or triiodide species has been suggested as a way to close the semi-conducting gap in molecular compounds.<sup>148</sup> Manganese(III) captured in a phthalocyanine ligand was shown to be bridged by  $I_2$  via an asymmetrically bound, terminal iodide ligand.<sup>149</sup> The iodide-iodine bond length is 3.42 Å. As a curiosity, the  $AlI_3$  cluster can be regarded as a superhalide ion forming “polyiodides,” as verified by mass spectrometry and calculations.<sup>150</sup> Not too different in character is the extremely iodine-rich  $W_{15}I_{47}$  compound consisting of  $W_5I_8^{n-}$  (with  $n$  somewhere between 1 and 3) and iodides/triiodides.<sup>151</sup> The tungsten iodide/iodine compounds have proven to be very versatile regarding composition and structure.<sup>151–153</sup> A few examples from these classes of compounds are shown in Fig. 16.

The gold-iodine system was subjected to a high-level calculational study, in which the equatorial interaction of  $I_2$  and  $AuI_2^-$  was deduced to be of predominantly closed-shell type and containing contributions from secondary interactions at long distance, making a direct oxidative addition of  $I_2$  to form gold(III) less plausible.<sup>154</sup> In previous studies, the  $AuI_2^-$  ion was found to be remarkably similar to the  $I_3^-$  ion in terms of internal and external coordination<sup>132</sup>.

As will be discussed in more detail below under the energy applications section, the occurrence of perovskite solar cells based on organic-inorganic hybrid perovskite compounds has generated a new field of materials research.<sup>155</sup> In these studies, the aim has been to use iodine or polyiodides to both structurally and electronically connect low-dimensional entities and as a vehicle to exchange lead for other and environmentally more benign elements. In line with these ambitions, Takaishi and co-workers reported a series of gold-based perovskites also involving the exchange of  $AuI_2^-$  for  $I_3^-$ .<sup>156</sup> Shevelkov and his co-workers have reported a series of such compounds, where iodine or triiodide bridges low-dimensional structural fragments of bismuth(III).<sup>157–159</sup> Chen and co-workers reported a triiodide-bridged low-dimensional structure based on lead complexes,<sup>160</sup> and Svensson et al. isolated a series of iodine/triiodide-bridged low-dimensional lead-based structures with potential application in solar cells.<sup>161</sup>

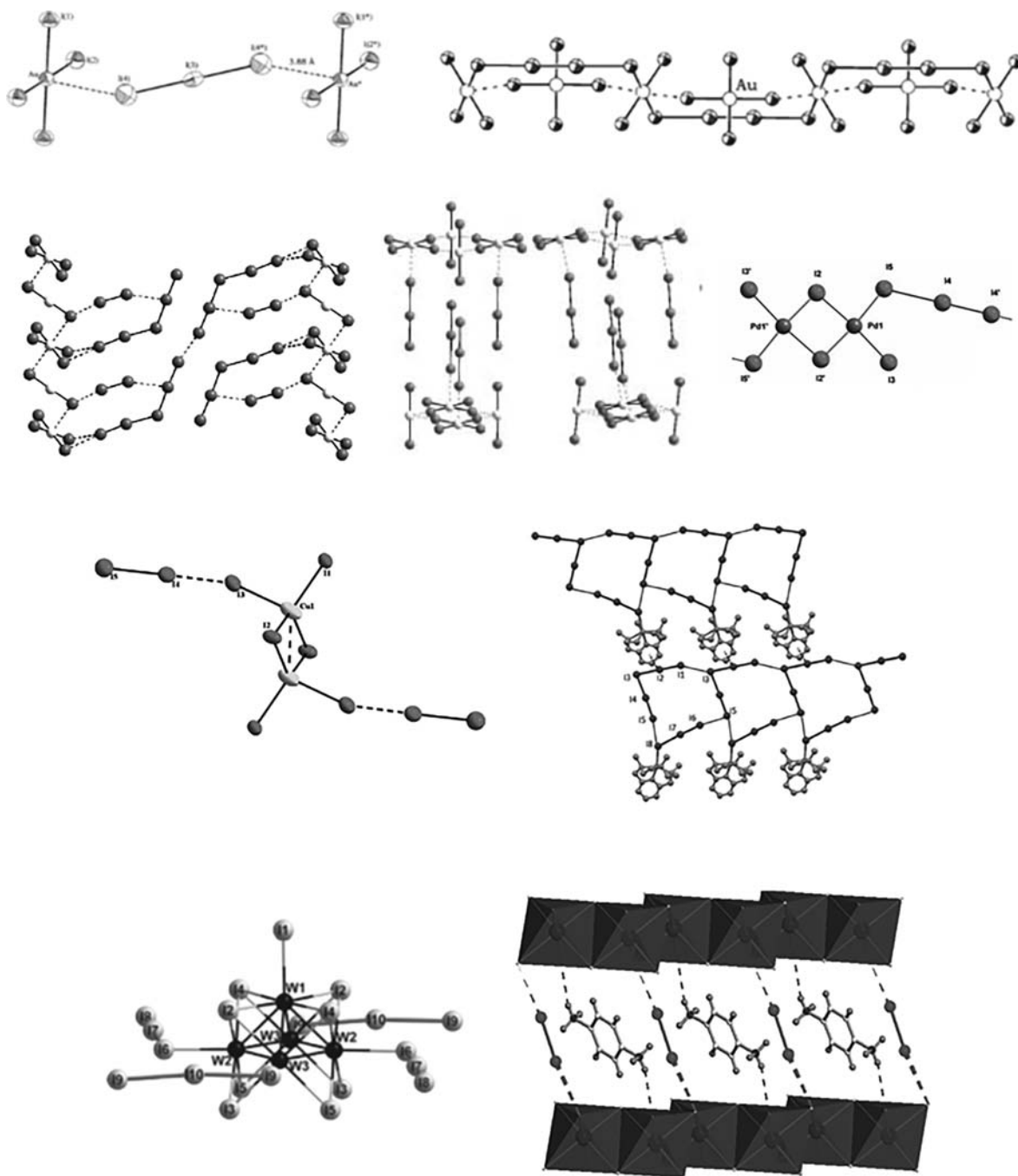
### 1.23.5 Liquids and solvent effects

In an early and thorough study using liquid X-ray scattering and vibrational spectroscopy, Bengtsson et al. showed that sulfonium iodide ionic liquids with added iodine essentially can be described in terms of iodine-solvated triiodide ions.<sup>162</sup> The liquid local structure has resemblance to the known solid polyiodide structures, but even more to the nearest-neighbor structure of solid iodine. When the iodine:iodide ratio is increased, on average the connectivity from the triiodide ions to the solvating iodine increases. This strongly correlates with an increase in conductivity with increasing iodine content.<sup>163</sup>

In the last 15 years a clear increase in polyiodide studies in ionic liquids can be observed. This is to a large extent caused by the use of such electrolyte media in DSSCs,<sup>164</sup> as well as ambitions to recycle metals (see below under the section on energy applications). A few examples of more fundamental character are given in this section, and the DSSCs will be handled more thoroughly in the section on applications. In a comparison of different electrochemical techniques for the determination of triiodide ion-diffusion constants in ionic-liquid mixtures, it was concluded that the transport was non-Stokesian, i.e., of Grotthuss type.<sup>165</sup> A schematic view of the Grotthuss mechanism of conductivity is shown in Fig. 17. Also, microelectrodes appear to give the most accurate and reproducible results; also emphasized by later studies.<sup>166</sup> In ionic-liquid iodides with added iodine, the formation of polyiodides was concluded on the basis of combined electrochemical and vibrational spectroscopic investigations.<sup>167</sup> A related study revealed the formation of polyiodide species in solution as soon as the cation:iodide ratio was increased above 1 by the addition of iodine.<sup>168</sup> The formation of polyiodides was also correlated to an increase in conductivity attributed, once again, to a Grotthuss-type of charge transport. A recent study employing terahertz spectroscopy, also including effects of ion-pairing, concludes that the Grotthuss mechanism can enhance conductivity by as much as 50% in rather viscous ionic-liquid media.<sup>169</sup> Similar results were obtained by Abe et al. on the basis of a combined X-ray diffraction and  $^{127}I$  NMR-spectroscopic study.<sup>170</sup> From a study of a series of liquid and solid polyiodides, Dyson and co-workers attributed the higher conductivity of the higher polyiodide systems to a cation-induced weakening of the I–I interactions in the polyiodide chains formed.<sup>171</sup> In this context it is also interesting to note that the iodine-containing iodide ionic liquids show photoconductivity, and that it increases with iodine content.<sup>172</sup> Photoconductivity has also been manifested in solid polyiodides.<sup>173</sup> Yamada and co-workers recently presented thermocells with high Seebeck coefficients based on choline iodide/triiodide mixtures showing an increase in ionic conduction of four orders of magnitude upon iodine addition.<sup>174</sup>

Reactive molecular dynamics indicated a low barrier of iodide transfer of the same magnitude as in superionic conductors in polyiodide ionic liquids.<sup>175</sup> These results have also been reported using ab initio molecular dynamics identifying extremely low barriers of iodide transfer and  $I_4^{2-}$  and  $I_7^{3-}$  as intermediate structures.<sup>176</sup> Taking on another approach, Thapa and Park instead propose a transfer of  $I_2$  to represent a low-barrier mechanism for exchange in polyiodides.<sup>177</sup> Theoretical studies of the effects of





**Fig. 16** Examples of metal-iodide/iodine structures. In order, taken from Lang, E. S.; Strähle, J., *Z. Anorg. Allg. Chem.* **1996**, 622, 981-984.; Svensson, P. H.; Rosdahl, J.; Kloo, L., *Chem. Eur. J.* **1999**, 5(1), 305-311.; Castro-Castro, L. M.; Guloy, A. M., *Angew. Chem.-Int. Edit.* **2003**, 42(24), 2771-2774.; Castro-Castro, L. M.; Guloy, A. M., *Inorg. Chem.* **2004**, 43(15), 4537-4539.; Walbaum, C.; Pantenburg, I.; Meyer, G., *Cryst. Res. Technol.* **2008**, 43(11), 1183-1186.; Li, H. H.; Chen, Z. R.; Liu, Y.; Liu, J. B.; Guo, L. Q.; Li, J. Q., *J. Mol. Struct.* **2009**, 934(1-3), 112-116.; Martinez-Camarena, A.; Savastano, M.; Linares, J. M.; Verdejo, B.; Bianchi, A.; Garcia-Espana, E.; Bazzicalupi, C., *Inorg. Chem. Front.* **2020**, 7(21), 4239-4255.; Strobele, M.; Meyer, H. J., *Z. Anorg. Allg. Chem.* **2010**, 636(1), 62-66.; Shestimerova, T. A.; Golubev, N. A.; Yelavik, N. A.; Bykov, M. A.; Grigorjeva, A. V.; Wei, Z.; Dikarev, E. V.; Shevelkov, A. V., *Cryst. Growth Des.* **2018**, 18(4), 2572-2578.

pressure on  $\text{CsI}_3$  show an expected pressure-induced dissociation of the triiodide ions into chains of iodine atoms rendering metallic properties and a potential for superconductivity.<sup>178</sup> Pressure has also been shown to influence the conductivity in a penta-iodide system, potentially indicating a use of such materials in pressure sensors,<sup>179</sup> and an iodide ionic liquid was shown to form triiodide species at high pressures.<sup>180</sup> Riedel and co-workers convincingly showed the effects of  $\text{Br}^-$  Grotthuss conduction in  $\text{Br}_3^-$  ionic liquids.<sup>181</sup>

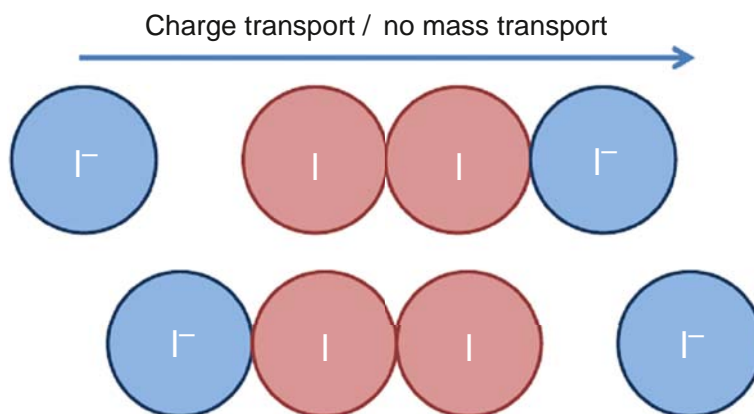


Fig. 17 A schematic view of the Grotthuss mechanism of conduction.

### 1.23.6 Polybromides—An expanding branch of polyhalide chemistry

The chemistry of triiodides in particular and also other polyiodides or iodide-iodine complexes is very extensive. In contrast, the corresponding compounds of the other halides used to be very rare. This situation is under rapid change. There are mainly two factors that need to be considered. First, the knowledge from polyiodide chemistry has been used as a platform, in particular regarding the use of ionic liquids to stabilize the  $\text{Br}_2$ -rich systems. In this context can be noted that there also exist theoretical studies on factors promoting polybromide formation in ionic liquids.<sup>182,183</sup> Second, a similar strategy involves the extensive use of metal-bromide complexes to exploit  $\text{Br}_2$  as bridging units. The latter approach has been so successful in generating new compounds, that it is almost irrelevant to separate “pure” polybromides from metal-bromide-bromine systems, in contrast to the situation (mainly generated because of historical reasons) in polyiodide chemistry, in the overview.

Among tribromides, only a few structures were known experimentally before 2010.<sup>184–188</sup> An outstretched tribromide could be assigned in a complex structure reported by Kornath and Blecher, in which the two  $\text{Br}-\text{Br}$ -distances are about 3.10 and 2.54 Å, respectively.<sup>189</sup> Devillanova et al. isolated a  $\text{Br}_4^{2-}$  bromide of  $[(\text{Br}^-)_2 \bullet \text{Br}_2]$  type.<sup>190</sup> It seems that most knowledge about these compounds is derived from the analogy to triiodide ions together with theoretical comparisons, as described above. However, there is, to say the least, an increasing amount of attention devoted to this type of chemistry. A  $\text{Br}_{10}^{2-}$  unit—in analogy to the polyiodide formalism it can be described as  $[(\text{Br}_3^-)_2 \bullet 2\text{Br}_2]$ —is reported by Cunningham and co-workers.<sup>191</sup> Along with some tribromide structures, Knop and co-workers also revealed the existence of a  $\text{Br}_8^{2-}$  chain of the type  $[(\text{Br}_3^-)_2 \bullet \text{Br}_2]$ .<sup>186</sup> The subsequent theoretical study clearly indicates that the corresponding polybromides are more weakly bound than their polyiodide congeners. A theoretical study at density-functional level showed that  $\text{Br}_3^-$ ,  $\text{Br}_4^{2-}$  and  $\text{Br}_5^-$  all are analogous to their heavier relatives in terms of structural units.<sup>192</sup> Using a dithiolenone compound Devillanova and co-workers isolated a two-dimensional polybromide network of the type  $[(\text{Br}^-)_2 \bullet 3\text{Br}_2]$ .<sup>193</sup> Also more systematic studies of the formation of polybromide species in solution and solid phases have been reported on the basis of spectroscopy and calculations.<sup>194</sup> Just as for polyiodides, Raman spectroscopy is highly informative.<sup>195</sup> Also a three-dimensional network of the type  $[(\text{Br}^-)_2 \bullet 9\text{Br}_2]$  has been reported, where the structure bears strong relations to the later isolated  $\text{Br}_{13}^-$ , see Fig. 18.<sup>196,197</sup>

It is often claimed that the thermal stability of polybromides is lower than that of the corresponding polyiodides, based on the expected lower interaction energy of an ionic unit, such as  $\text{Br}^-$  or  $\text{Br}_3^-$ , with  $\text{Br}_2$ .<sup>186,191</sup> Consequently, it is expected that polybromides much more readily lose  $\text{Br}_2$  and decompose. In this perspective, it is notable that the bromine-rich compound,  $\text{Br}_{20}^{2-}$ <sup>196</sup> clearly exceeds the  $X_2/X^-$ -ratio of the most iodine-rich compound known so far,  $\text{I}_{29}^{3-}$ .<sup>198</sup> And even more bromine-rich compounds have been isolated recently, as discussed below. A general reflection is that  $\text{Br}_2$  appears to be the structure-forming unit rather than polybromide ions; in contrast to the polyiodide structures, where the triiodide ion is much more common in polyiodide structures. This hypothesis gains some support from the very recently published  $\text{Br}_9^-$  compound is of  $[(\text{Br}^-) \bullet 4\text{Br}_2]$  type.<sup>199</sup>

In particular, the group of Riedel and others has extended our knowledge on polybromide systems extensively the last 10 years.<sup>3</sup> Indeed, many polybromide structures can be rationalized in terms of what was learned from polyiodide chemistry, and the early observation that the  $\text{Br}_3^-$  building block may be less frequent no longer seems valid; see Fig. 19. However, and as alluded to in the section above on bonding in the polyhalide systems, polybromides (and polychlorides) and in particular polyinterhalides, show a new feature. Riedel et al. describe the polybromide structures in terms of classical bonding, referring to polyiodide-like,  $X_2$ -bridged, structures, and non-classical bonding, referring to structures centered around an  $X^-$  ion. Of course, the non-classical bonding patterns can be observed also in polyiodide structures, such as  $\text{I}_7^-$  or  $\text{I}_9^-$ , where a central  $\text{I}^-$  can be regarded as being solvated by iodine molecules into the polyiodides observed (three and four iodine molecules, respectively). However, the bromide and chloride ions are much smaller and more polarizing thus offering the possibility to coordinate more  $X_2$  molecules, where the

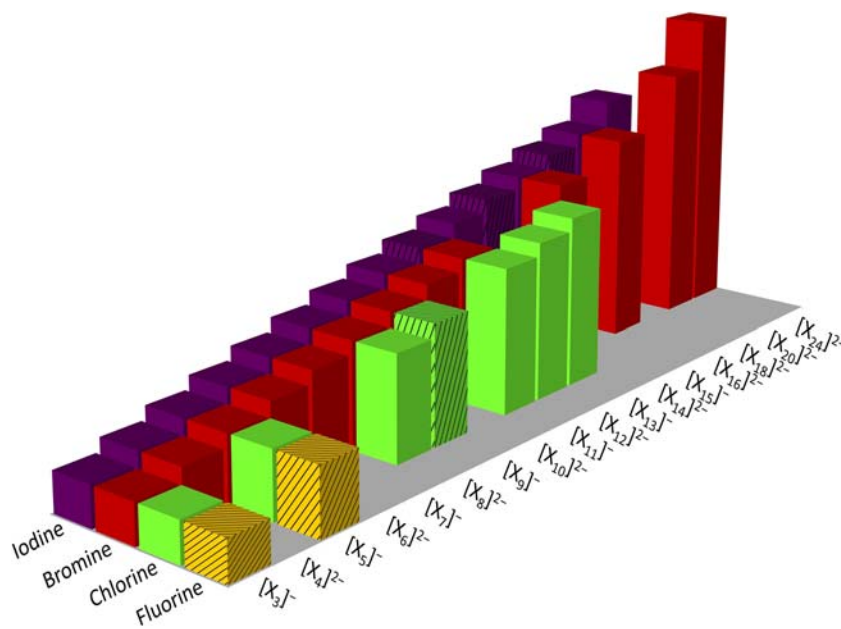


In recent years, the group of Adonin has successfully isolated a large number of what, in analogy to polyiodide chemistry, can be described as metal bromide-bromine compounds.<sup>11,205</sup> In their 2018 review, Adonin et al. give examples from metal-bromide complexes of a large section of the periodic table, although their own main contributions show a center of gravity in the Group 15, viz.  $\text{SbBr}_6^-$ ,  $\text{Bi}_2\text{Br}_9^{3-}$ ,  $\text{BiBr}_6^{3-}$ , etc. The synthesis of these compounds in many cases involves oxidation by bromine. The vast body of the structures reported can be regarded as  $\text{Br}_2$ -bridged complexes forming a formal  $\text{Br}_4^{2-}$  entity in the structures. This is a theme that can be varied extensively.  $\text{Br}_3^-$  entities also appear in the structures reviewed,<sup>206</sup> and those structures mimic observations from polyiodide chemistry, where low-dimensional metal-halide units can be bridged by both  $\text{X}_2$  and  $\text{X}_3^-$  units; sometimes in the same structure. The approach seems to be moving towards the stabilization of larger polybromide species, such as  $\text{Br}_{10}^{2-}$ .<sup>207</sup> The structural chemistry is rich, and this class of compounds is likely to find interesting applications in the future.

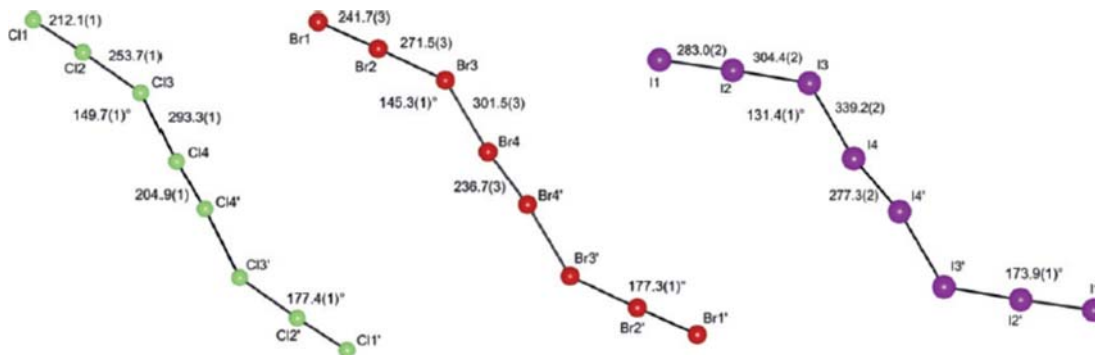
### 1.23.7 Other polyhalides

The existence of polychlorides is more rare than polybromides, although the strategies from the successful work on polybromides have been applied also to the lighter elements of Group 17. And the efforts have turned into a gap-filling game with respect to, in particular, monoanionic species of different size, see Fig. 20. However, as noted in the bonding discussion above, the coordination chemistry-like behavior of the lighter elements give rise to high  $\text{X}_2/\text{X}^-$  ratios.

Rather few trichloride compounds have been isolated in the solid state.<sup>208–210</sup> The crystallographically determined trichloride ions are linear and slightly asymmetric, 2.23 Å and 2.31 Å, and 2.25 Å and 2.34 Å, respectively. The symmetrical stretch vibration is reported to about  $270\text{ cm}^{-1}$ , whereas the data given for asymmetrical stretch vibration differ a bit. However, it appears that the wavenumber is equal or lower than for the symmetrical stretch vibration, which is rather uncommon and different from what is observed for the triiodide ion. It is also different from the calculated results for a centrosymmetric  $\text{Cl}_3^-$ , as reported in Table 2. Matrix-isolation experiments combined with theoretical calculations, similar to those used to isolate trifluoride ion pairs with alkali-metal monocations, identified trichloride ions with the cations in an asymmetric position similar to what is typically observed for triiodide ions.<sup>211</sup> Evans and Lo also suggested the formation of a pentachloride ion on the basis of vibrational spectroscopic data.<sup>208</sup> An NQR spectroscopic study on less well characterized trichloride salts show that they are centrosymmetric and adequately described by the Pimentel bonding scheme proposed for triiodides.<sup>212</sup> This investigation was later followed up by a calculational study.<sup>213</sup> Just as for polyiodides, vibrational spectroscopy is a useful tool for the characterization of trichloride compounds.<sup>214</sup> The formation of trichloride in the gas phase has been proposed.<sup>215</sup> and more or less well defined polychlorides have been used as chlorination agents in organic chemistry.<sup>216</sup> Just as for polybromides, evidence for the formation of polychlorides are mounting. A combined spectroscopic and theoretical study indicated the formation of a series of polychlorides from  $\text{Cl}_3^-$  to  $\text{Cl}_9^-$  in molten chloride/polychloride ionic liquids.<sup>217</sup> A two-dimensional polychloride compound of the composition  $[(\text{Cl}_3^-) \bullet 2\text{ICl}_2]$  has been characterized by Riedel and co-workers.<sup>218</sup> Later, the same group also isolated a dianionic species of  $\text{Cl}_8^{2-}$  composition, resembling the heavier congeners in terms of a  $[2(\text{Cl}_3^-) \bullet \text{ICl}_2]$  composition, see Fig. 21.<sup>219</sup> As noted for the polybromides, also the



**Fig. 20** Crystallographically characterized polyhalides in 2020. From Ref. Sonnenberg, K.; Mann, L.; Redeker, F. A.; Schmidt, B.; Riedel, S., *Angew. Chem. Int. Ed.* **2020**, *59*, 5464–5493.



**Fig. 21** The out-stretched and analogous  $X_8^{2-}$  structure going from Cl to I, to which also the polyinterhalide dianions  $I_2Br_6^{2-}$  and  $I_4Cl_4^{2-}$  be added. From Ref. Sonnenberg, K.; Mann, L.; Redeker, F. A.; Schmidt, B.; Riedel, S., *Angew. Chem. Int. Ed.* **2020**, *59*, 5464–5493.

polychlorides behave in a more coordination chemistry-like way, where the relatively polarizing  $Cl^-$  ion can act as a coordination center for the molecular “solvent” molecules  $Cl_2$ . Presuming rather weak covalent interaction, and thus directionality to be governed by mainly electrostatic ligand–ligand repulsion and the molecular size of the dihalogens, it is logical that a formal octahedral  $[(Cl^-)_6Cl_2]$  species is formed.<sup>220</sup> This allows for quite high  $Cl_2$ -to- $Cl^-$  ratios. The highly successful strategy of using metal-bromide complexes to stabilize  $Br_2$ -linked structures, now also seems to emerge for the chloride systems where  $Cl_2$  bridges  $TeCl_6^{2-}$  in a low-dimensional structure.<sup>221</sup>

The polyfluoride chemistry appears more limited than the polychloride one, maybe because it not yet has received the same attention. Early work involved matrix-isolated trifluorides and theoretical investigations.<sup>222,223</sup> Mass spectrometry has been used to identify  $F_3^-$  in gas phase.<sup>224</sup> Mass spectrometry was also used to determine the dissociation energies of  $F_3^-$  into  $F^- + F_2$  (98 kJ/mol—in close agreement with high-level theory) and  $F + F_2^-$  (27 kJ/mol).<sup>225</sup> The formation of  $F_3^-$  was postulated in crystalline di- and trifluorides doped with rare-earth elements based on X-ray absorption features.<sup>226</sup> Failed reactions aimed at trifluorides in solution have been reported.<sup>227</sup> The symmetrical stretch vibration of  $F_3^-$  is assigned to a peak at about  $460\text{ cm}^{-1}$ . More recent studies on CsF interactions with  $F_2$  in a cryogenic argon matrix offered vibrational spectroscopic assignments of bands at  $461$  and  $550\text{ cm}^{-1}$  to the symmetric and asymmetric stretch vibration modes in  $F_3^-$ .<sup>228,229</sup> Matrix-isolation experiments have also led to the spectroscopic identification of  $F_5^-$ .<sup>230,231</sup> A theoretical study suggests the formation of Cs-polyfluoride crystal structures at high pressures.<sup>232</sup> Some rather early high-level calculations on the  $F_3^-$  ion identified it as a challenging calculational task because of significant multi-configurational character. This has been emphasized also later, in particular regarding the semantics of  $F_3^-$ .<sup>35</sup> A symmetrical stretch frequency, as compared to experiment, was determined by Ault and colleagues, and an F–F bond distance of  $1.74\text{ Å}$  was obtained.<sup>233</sup> Later studies have shown hybrid density-functional methods to give reasonable results for the trifluoride ion in alkali-metal systems.<sup>234</sup> Also for the trifluoride ion, Braida et al. used a VB method to get deeper insight into the bonding properties. Part of the stability of  $F_3^-$  was attributed to a lone-pair stretching instability of the  $F_2$  fragment; a property transferrable also to the heavier analogues.<sup>235</sup> The old low-temperature work of Ault et al. was very recently revisited and combined with calculations at coupled-cluster level. The latter study was extended to tetra- and pentafluoride ions as well, essentially re-discovering the structural pattern known from polyiodide chemistry.<sup>236</sup> However, the main contribution to the  $F_3^-$ – $F_2$  bonding was assigned to electrostatic interaction. Covalent catenation in polyfluoride systems may thus be questioned. High-level calculations were applied to shed light on the coordination and effects of different alkali-metal monocations on the  $M^+$ – $F_3^-$  interaction, and these show a strong dependence on both cation and coordination mode.<sup>237</sup> Density-functional studies of several polyfluorides up to a formal  $F_{29}^-$  showed them energetically feasible but sensitive to a loss of  $F_2$ .<sup>238</sup> In a theoretical study, Hoffmann et al. identified the most stable configuration of a formal Cs $F_5$  system to be an ion pair of more classical Cs $^+$ – $F_5^-$  type.<sup>239</sup>

Astatine is a story of its own—and a very short one. Because of the inherent characteristics of radioactivity and rare appearance, experimental studies are limited. No studies on a triastatide or any polyastatide ions have been found in literature, albeit both the triastatium,  $At_3^+$ , and tritessinium,  $Ts_3^+$ , were theoretically studied at 2-component relativistic level.<sup>240</sup> Strangely enough, the anionic systems do not seem to have been investigated theoretically. A simple presumption regarding a triastatide ion would be that it is even more inclined to polyhalide formation through “sticky” long-range At–At bonding. However, this is not necessarily the case. In the theoretical studies on Period-7 elements in relation to their lighter congeners, a periodic behavior is often identified rather than a monotonous change along a group; a phenomenon attributed to relativistic effects in superheavy elements.<sup>241</sup> The calculational results shown in Table 3 indicate that polyastatides should be stable polyhalide units, and the results in Fig. 6 suggest that the potential-energy surface is more similar to polybromides than to polyiodides.

There is a large plethora of interhalogen compounds. Typically, the most electronegative, i.e., lighter, element takes on the terminal positions, and the heavier Group-17 element can be regarded as the coordination centre.<sup>6</sup> Many of the interhalogen compounds can be described on the basis of classical coordination chemistry, where a central atom is surrounded by ligands in a Werner-type of complex. Also a trihalide, such as  $I_3^-$ , can be visualized in such a way. Of course, quite a number of linear  $XY_2^-$  ions (X and Y being different halogen atoms) have been reported in literature. However, they contribute little new to our previous discussion on trihalide bonding. On the basis of established textbook knowledge, stability increases as the central



atom becomes heavier and the difference in weight between the coordination center and ligand becomes lower. This has also implications for the prospects of forming interhalogen types of polyhalides. The heavier elements are most prone to bind to polyhalide species, and since they typically are buried in the center of interhalogen molecules, they would be expected to show little tendency to form larger entities.<sup>242</sup> Interestingly enough, non-bonded contacts in interhalogen compounds were recently used as an indicator to identify errors in crystal structure data.<sup>243</sup> However, as exemplified below, these expectation have been proven wrong based on another type of coordination chemistry.

A few examples of extended structures exist, and the numbers increase as a consequence of the boost in polybromide and polychloride chemistry. For instance, the rather complex structure of  $I_3Br_4^-$  is pyramidal of the type  $[(Br^-) \bullet 3IBr]$  and with comparably short Br–Br-contacts (3.36 Å) between the molecular units forming a chain-like structure.<sup>244</sup> This polyhalide ion and other interhalogen ions were subjected to a rather thorough diffraction, vibrational spectroscopic and calculational investigation.<sup>245</sup> Parlow and Hartl isolated a series of iodine-bromide interhalogen ions, of which a V-shaped  $I_2Br_3^-$  and a two-dimensional layer of  $I_5Br_2^-$  composition are the most notable.<sup>246</sup> In these structures, the  $I_2Br^-$  ion, linked by  $Br_2$  and  $I_2$  in the structures, respectively, is claimed to be the fundamental structural unit. It is not unexpected that an extended structure is based on the  $I_2$  bridging unit. A V-shaped  $I_2Cl_3^-$ , analogous to a pentaiodide, of the type  $[(Cl^-) \bullet 2ICl]$  has also been reported.<sup>247</sup> In this case, the ionic units are regarded as isolated, since intermolecular Cl–Cl-contact exceed the sum of the van der Waals radii. In a series of amide/thioamide compounds the chlorine-containing  $I_2Cl_2^{2-}$ , analogous to  $I_4^{2-}$ , has been isolated, where the chloride ions take the terminal positions at the ends of the central  $I_2$  unit.<sup>248</sup> In halogenated dithiols,  $IBr$  has been noted as a bridging unit.<sup>249</sup> A similar structure and a  $[2(ICl_2^-) \bullet I_2]$  composition with a classical extended  $X_8^{2-}$  structure was also reported.<sup>250</sup> Using ionic liquids as reaction media, the same authors also isolated highly similar polyinterhalide compounds in the Br–I system.<sup>251</sup> An octahalide dianion of the  $[2(IBr_2^-) \bullet Br_2]$  type and analogous structure has also been reported.<sup>252</sup> A complex and disordered structure of  $I_5Br_7^{2-}$  composition consisting of  $XY_2^-$  and  $X_2$  components has been reported.<sup>253</sup> The complicated structure of  $I_5Br_4^-$  seems best rationalized in polyiodide terms as a pentahalide unit coordinated by two dihalogen molecules,  $[Br(IBr)_2^- \bullet 2IBr]$ .<sup>254</sup> Considering the possibility of the formation of non-classical polyinterhalide units similar to the  $X_2$ -rich polyhalides formed in the polychloride and polybromide systems, it is not surprising that also  $Cl(BrCl)_n^-$  ions of this type have been reported.<sup>255,256</sup> Following the order proposed for  $\sigma$ -hole effects, the BrCl molecules coordinate the central chloride ions via the Br end of the molecules. An interesting, square-planar, representative of this effect is the  $Cl(I_2)_4^-$  ions reported by Meyer and co-workers.<sup>257</sup> In solution, it is clear that mixtures of the halides give rise to an extensive and quite complex situation with many coupled equilibria.<sup>258</sup> This was also a complication in attempts to use interhalogen systems as redox couples in DSSCs, where the complex chemistry raises questions upon the exact nature of the active redox agents in the electrolytes.<sup>259</sup>

### 1.23.8 Applications

Two areas have expanded enormously in terms of published scientific articles, in particular involving iodide or polyiodide ionic liquids: Doping of carbon-based and polymer materials, and halogenation of organic molecules in synthesis. The effects essentially involve a straightforward oxidation and only the former application will be shortly discussed below.

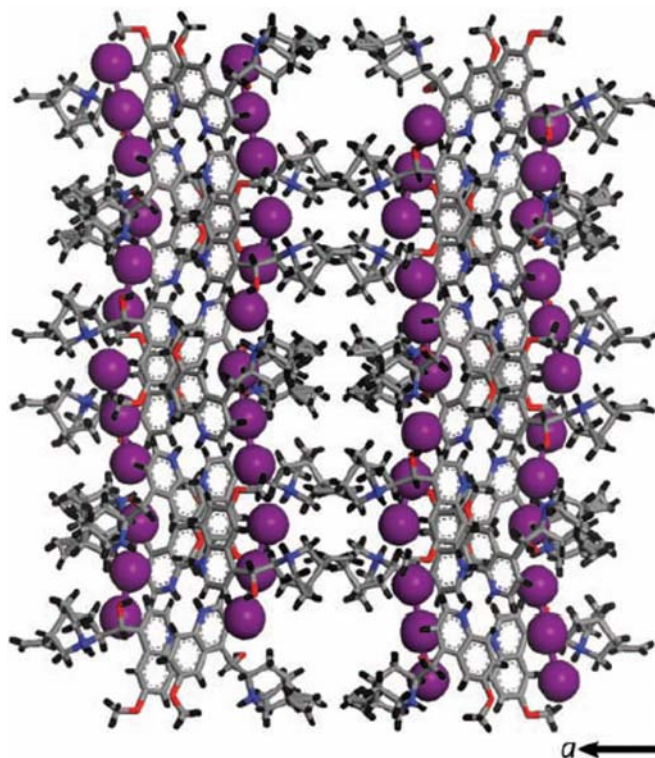
However, the use of polyhalide systems in two other areas have also grown significantly and involve some special properties of polyhalides, and therefore these will be more explicitly discussed below together with some more traditional areas of polyhalide application.

#### 1.23.8.1 Optical applications

One of the oldest applications involving polyiodide chemistry is most likely in quantitative determination of redox-active components in solutions—the iodometric titration. Very strongly associated with this method of analysis is the phenomenon of iodide/iodine-tinting of starch, used as a universal indicator of iodine. Several studies have indicated the presence of polyiodide chains inside the carbohydrate helices as the origin of the intense color observed.<sup>260–263</sup> A rather recent study using L-edge XANES in comparison with model systems of known composition indicated the polyiodide chains in amylose to mainly consist of  $I_5^-$ .<sup>264</sup> It is amazing that the mineral herapathite was successfully used as light-polarizing material for decades until Kahr and co-workers recently determined its structure.<sup>79</sup> The structure of herapathite is shown in Fig. 22. A striking feature of this material is the chains of triiodide ions giving rise to its anisotropic optical properties. The inter-triiodide distances range from 3.74 to 3.81 Å. The remarkable linear dichroism of herapathite is described as originating from molecular transitions in the triiodide ions attributable to the confined linear arrangement.<sup>265</sup> The luminescent properties of metal-organic frameworks was shown to be affected by iodine enrichment, thus attributed to the confined polyiodide formation.<sup>266</sup>

#### 1.23.8.2 X-ray contrast agents

A classical problem in crystallography, in particular for large molecules/unit cells, such as in protein crystallography, is the lack of phase information. One way to facilitate the crystallographic analysis is to introduce a heavy atom—a strong scatterer of X-rays—in



**Fig. 22** The linear triiodide chains in herapathite. The structure is taken from Ref. Kahr, B.; Freudenthal, J.; Phillips, S.; Kaminsky, W., *Science* **2009**, 324, 1407–1407.

a controlled way. Either comparably heavy cations, such as  $\text{Cs}^+$  or  $\text{Gd}^{3+}$ , or anions, such as the heavier halides, or Xe gas have been used. These elements are also known from medical X-ray imaging, where, of course, also biological availability must be taken into account. Recent studies have identified triiodide, for both chemical and physical reasons, to be a good candidate to treat the phasing problem.<sup>267</sup> Both  $\text{I}_3^-$  and  $\text{I}_5^-$  entities were found in the model systems studied.<sup>268</sup>

### 1.23.8.3 Triiodide detection

Important advances in the development of a triiodide-selective electrochemical electrode/sensor have been made. One class of electrodes is based on a PVC membrane incorporating an active, with respect to the triiodide ion, metal-complex or organic species.<sup>269–271</sup> The metal-complex-doped membranes often involve salen-like ligands.<sup>272,273</sup> The chemiluminescence has found an interesting application in the detection of level of NO in human red blood cells.<sup>274</sup>

### 1.23.8.4 Doping of polymers and carbons

As already noted, the tetrathiafulvalene triiodide compound was found to exhibit low-dimensional metallic properties.<sup>28</sup> One example of a iodine-doped superconducting organic system based on a selenium-based tetrathiafulvalene showed the presence of incommensurate  $\text{I}_3^-$  chains and a critical temperature of superconduction at about 8 K.<sup>275,276</sup> This is an interesting model system considering that iodine frequently is used to dope organic polymers in order to enhance hole-conducting properties. The interaction between iodine and carbon materials is also of interest in potential electronic applications. Carbon nanotubes doped with iodine were shown to host polyiodides of  $\text{I}_3^-$  or  $\text{I}_5^-$  type.<sup>277,278</sup> Shi et al. recently showed how hole-doping levels, and thus the conducting character of the nanotubes, could be tuned by iodine and the changes could be correlated with the formation of different polyiodide species inside carbon nanotubes.<sup>279</sup> In a high-pressure study, the confined polyiodide species in the carbon nanotubes displayed an increasing linearization upon increasing pressure.<sup>280</sup> The carbon-iodide/polyiodide interface has a special interest because of, for instance, the development of supercapacitors.<sup>281</sup>

### 1.23.8.5 Polyhalides for metal extraction

One of the most classical extraction processes dating back to the 18th century involves that of gold from suitable ores. The procedure is based on several steps, and one key process is the oxidation of gold in the presence of a suitable complex-forming agent (*viz.* cyanide). The combination of oxidation and complex formation using polyhalides, often in the form of ionic liquids, has recently

emerged to become a highly successful tool both within metallurgy and within sustainable recycling of several different metals of strategic importance or value. In these processes, different halides are exploited as the complex-forming agents and the excess halogen as oxidizing agents.

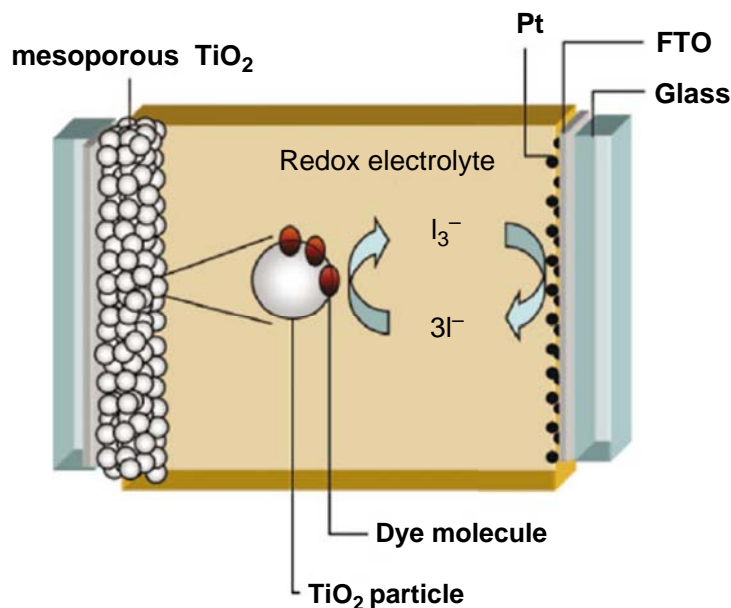
Starting with gold as an example, Altansukh and co-workers have described a process based on polyiodides in aqueous solution for the extraction of gold from electronic circuit boards.<sup>282,283</sup> These processes have also been used for the extraction of other metals, such as Ag, Pd, Cu, Co, etc.<sup>284,285</sup> Considering the increasing strategic value of rare-earth elements also the recovery of such elements are of interest, and polychloride systems have been used for the extraction of samarium from magnets.<sup>286</sup> Depending on the oxidative power and complex-forming properties of the target elements, fine-tuning of the reaction medium may be required, as shown in more fundamental studies by Binnemanns et al.<sup>287,288</sup> These efforts also involve tribromide ionic liquids and other elements of strategic interest in the field of renewable energy, such as gallium and indium.<sup>289</sup> Different polyhalide, including polyinterhalide, ionic liquids were used by Maier and co-workers to dissolve the coinage metals,<sup>290</sup> and by Chu and co-workers for the dissolution of  $\text{UO}_2$ .<sup>291</sup>

### 1.23.8.6 Polyhalides in energy applications

The zinc-bromine (flow) battery receives more and more attention for energy storage of renewable electric energy. The mixture of bromide and bromine in the electrolyte will inevitably lead to the formation of polybromides. Just as in many electrochemical devices, ionic liquids have emerged as attractive electrolyte media. In one such study, in situ IR-spectroscopy identified polybromides at the carbon electrode material and the formation of  $\text{Br}_5^-$  was proposed.<sup>292–294</sup> Also other battery alternatives based on halide/polyhalide systems have entered into focus in the recent years. Other examples involve the polysulfide/polyhalide batteries studied by a few groups,<sup>295,296</sup> aluminium-bromine batteries based on polybromide ionic-liquid electrolytes studied by Krossing and co-workers,<sup>297</sup> an aluminium-iodine battery based on ionic liquids,<sup>298</sup> a zinc-polyiodide battery studied by Wang and co-workers,<sup>299</sup> as well as a more exotic titanium-bromine battery.<sup>300</sup> Mixed trihalides of bromine and iodine have also been used to boost the performance in zinc- and lithium-polyhalide batteries.<sup>301</sup> In general, halogen-based anode systems seem to have obtained a renewed interest in different battery types.<sup>12</sup>

Historically more well-known are the lithium-iodine batteries, which have found special applications, such as in pacemaker batteries, because of their typically very sustainable and stable current output. A recent in situ combined electrochemical and Raman spectroscopic study showed the formation of  $\text{I}_3^-$  and  $\text{I}_5^-$  at the anode.<sup>302</sup> A recent theoretical study suggested quite large polyiodide species to be involved in the electrode processes, such as  $\text{I}_{11}^-$  and  $\text{I}_{13}^-$ .<sup>303</sup> Semi-liquid polyiodide electrolytes have been suggested to reduce dendrite formation in lithium-iodine batteries.<sup>304,305</sup> Also lithium-bromide batteries have been studied involving the redox formation of polybromides.<sup>306</sup> The role of triiodide and tribromide in lithium-air batteries have recently been elucidated.<sup>307</sup>

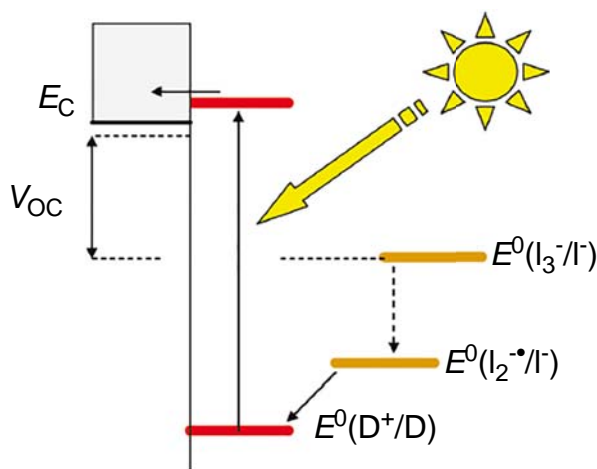
One of the strongest boosts of polyiodide chemistry in relation to redox-active electrolytes can be attributed to the interest in DSSCs. Ever since the remarkable improvement described by Grätzel and O'Regan in 1991,<sup>308,309</sup> redox-active electrolytes based on the iodide/triiodide ( $\text{I}^-/\text{I}_3^-$ ) system have prevailed. The schematic view in Fig. 23 shows the central role of the liquid redox electrolyte in the photoelectrochemical cell. Recent developments strive to avoid iodine in such electrolytes, mainly because of its unwanted photochemistry and corrosive nature setting limits to the DSSC stability<sup>310–312</sup>. Nevertheless, the  $\text{I}^-/\text{I}_3^-$ -system seems to represent a compromise between wanted and unwanted side-reactions that is difficult to out-perform in the ambitions for commercial solar cells. In a simplified view, the redox activity of the iodine-based system undergoes two essential reactions. The triiodide ions are reduced at the DSSC counter electrode forming iodide ions. This is a two-electron process highly facilitated by catalyzing platinum particles adsorbed to the conducting glass substrate constituting the counter electrode. These diffuse to the working electrode (photoanode), where the iodide ions efficiently regenerate the sensitizing dye.<sup>43,45,313</sup> The two-electron process is here divided in space and time, allowing for a quick electron transfer to the dye. This very property of the iodine system also retards one of the most problematic side reactions, the unwanted back transfer of energy-rich photoelectrons from the working electrode to the electrolyte triiodide ions. This process becomes extremely slow, allowing the DSSCs to reach high conversion efficiencies. Yanagida and co-workers have shown indications of efficient Grotthuss-type of conduction in electrolytes based on ionic liquid crystals.<sup>314,315</sup> However, as noted above, double salts of iodide and triiodide appear to be quite stable, and it was shown that an unwanted precipitation in some working DSSCs could be attributed to exactly such a compound involving an additive aimed at blocking the loss of photoelectrons from the working electrode.<sup>24</sup> Solution chemistry sometimes gives unexpected reactions. Another concern regarding losses in conversion efficiencies using the  $\text{I}^-/\text{I}_3^-$ -redox couple is the observed overpotential with respect to dye regeneration. Efficient dye reduction of the system requires about 0.5 V “too” high voltage, of course with a reduction in photovoltage and efficiency as a consequence. However, Boschloo and colleagues recently found that the required overpotential can be traced to the two-electron character of the redox couple, showing that it is instead the  $\text{I}^-/\text{I}_2^-$ -system that constitutes the driving force in dye regeneration, and thus the overpotential is just apparent.<sup>44</sup> Schematically, this is shown in Fig. 24. Privalov and colleagues used density-functional theory to elucidate the electron-transfer mechanism of both organometallic and organic sensitizing dyes, strongly indicating an outer-sphere, two-step mechanism.<sup>45,313</sup> In an experimental study and overview, Meyer and co-workers arrived at a similar two-step mechanism also highlighting the photoinduced formation of I–I-bonds.<sup>316</sup> Ionic-liquid electrolytes have been used successfully in DSSCs, although the main drawback can be attributed to the relatively high viscosity of such solvent media.<sup>164</sup> The high viscosities cause mass-transport problems at higher irradiation. In order to counteract this problem, typically 5–10 times higher concentration of iodine is used in ionic-liquid media as compared to organic solvent ones. This strategy reduces mass-transport limitations but introduces losses because of light absorption by the triiodide/polyiodide



**Fig. 23** A schematic view of the DSSC, including an I<sup>-</sup>/I<sub>3</sub><sup>-</sup>-based electrolyte. The scheme is taken from Ref. Hagfeldt, A.; Boschloo, G.; Sun, L.; Kloo, L.; Pettersson, H., *Chem. Rev.* **2010**, *110*, 6595–6663.

species in solution and higher losses because of recombination with triiodide in the electrolyte.<sup>38</sup> In summary, the polyiodide chemistry in DSSCs offers benefits and drawbacks but certainly calls for an understanding of the polyiodide chemistry. Recently, also ionic-liquid systems extending into the field of liquid crystals have been applied to DSSCs and the structure-directing conduction investigated in detail.<sup>169,317–320</sup> Robertson and Tanaka used similar systems forming solid polyiodide electrolytes relying on the Grotthuss mechanism of conduction.<sup>321</sup> In this context it can be noted that formal Br<sub>20</sub><sup>2-</sup> ionic liquids were recently investigated in p-type DSSCs.<sup>322</sup>

Using the DSSC platform, also a new field in solar cell research has emerged starting with halide perovskite materials. Kanatzidis identified CsSnI<sub>3</sub> as an excellent light-absorbing and conducting material highly suitable as photoabsorber in thin-film solar cells.<sup>155,323</sup> The material was quickly replaced by organic/inorganic lead-iodide perovskite and structurally related compounds.<sup>324</sup> The field also expanded into other areas, such as light-emitting diodes (LEDs),<sup>325</sup> where for instance a nanoring-iodine system emits white light.<sup>326</sup> Although these are iodide (or halide) materials, and not polyiodide (polyhalide) materials, they do involve polyhalides in two aspects: Firstly regarding the synthesis of novel perovskite-like materials, where primarily polyiodides have been exploited.<sup>327–332</sup> As mentioned under the section of metal iodide/iodine compounds above, iodine and polyiodides have been exploited as linkers to generate three-dimensional electronic compounds binding low-dimensional metal-iodide structural units together.<sup>157–159,161</sup> And second, the perovskite-type materials have been shown to be rather unstable, mainly forming Pb(0) and



**Fig. 24** The two-step redox chemistry of dye regeneration in DSSCs. The scheme is taken from Ref. Boschloo, G.; Hagfeldt, A., *Acc. Chem. Res.* **2009**, *42*, 1819–1826.



oxidized iodide products, where polyiodides indeed are formed. Photodegradation and electrochemical experiments indicate the formation of polyiodides.<sup>333,334</sup> Meyer and co-workers could show the I–I bond formation in bismuth-based analogous materials,<sup>335</sup> and theoretical studies by the groups of De Angelis and co-workers suggest the uncommon features of iodine chemistry, involving the formation of triiodide ions, can be the cause for the exceptional defect tolerance shown by the perovskite materials.<sup>336</sup> Further theoretical studies support the formation of triiodide ions during degradation.<sup>337</sup> Regarding bromide-based perovskite materials, polybromides have been suggested to offer a self-healing mechanism.<sup>338</sup> In conclusion, polyhalide species are ominously present also when not desired.

## References

- Beck, J. *Coord. Chem. Rev.* **1997**, *163*, 55–70.
- Haller, H.; Riedel, S. *Z. Anorg. Allg. Chem.* **2014**, *640*, 1281–1291.
- Sonnenberg, K.; Mann, L.; Redeker, F. A.; Schmidt, B.; Riedel, S. *Angew. Chem. Int. Ed.* **2020**, *59*, 5464–5493.
- Brinck, T.; Murray, J. S.; Politzer, P. *Int. J. Quantum Chem.* **1992**, *19*, 57–64.
- Brinck, T.; Murray, J. S.; Politzer, P. *Int. J. Quantum Chem.* **1993**, *48*, 73–88.
- Wiebenga, E. H.; Havinga, E. E.; Boswijk, K. H. *Structures of Interhalogen Compounds and Polyhalides*, vol. 3; Academic Press: New York, 1961; pp 133–169.
- Tebbe, K.-F. *Polyhalogen Cations and Polyhalide Anions*, Elsevier: Amsterdam, 1975; pp 551–615.
- Svensson, P. H.; Kloo, L. *Chem. Rev.* **2003**, *103*, 1649–1684.
- Tebbe, K. F. *Beiträge zur Chemie und Strukturchemie der Polyjodide Komplexer Kationen*, Wilhelms-Universität Münster: Münster, 1975.
- Adonin, S. A.; Bondarenko, M. A.; Abramov, P. A.; Novikov, A. S.; Plyusnin, P. E.; Sokolov, M. N.; Fedin, V. P. *Chem. A Eur. J.* **2018**, *24*, 10165–10170.
- Adonin, S. A.; Sokolov, M. N.; Fedin, V. P. *Coord. Chem. Rev.* **2018**, *367*, 1–17.
- Jameson, A.; Gyenge, E. *Electrochem. Energy Rev.* **2020**, *3*, 431–465.
- Konyratbekova, S. S.; Baikunurova, A.; Akcil, A. *Miner. Process Extr. Metall. Rev.* **2015**, *36*, 198–212.
- Burykin, I. V.; Chernov'yants, M. S.; Aleshina, N. V. *Russ. Chem. Bull.* **2007**, *56*, 1390–1393.
- Meyer, M. K.; Graf, J.; Reiss, G. *J. Naturforsch. B* **2010**, *65*, 1462–1466.
- Kazheva, O. N.; Aleksandrov, G. G.; D'Yachenko, O. A.; Chernov'yants, M. S.; Lykova, E. O.; Tolpygin, I. E.; Raskita, I. M. *Russ. J. Coord. Chem.* **2004**, *30*, 599–603.
- Kazheva, O. N.; Shilov, G. V.; D'Yachenko, O. A.; Chernov'yants, M. S.; Kirsanova, Y. A.; Lykova, E. O.; Tolpygin, I. E. *Russ. J. Inorg. Chem.* **2007**, *52*, 562–566.
- Niu, Y. Y.; Song, Y. L.; Zhang, N.; Hou, H. W.; Che, D. J.; Fan, Y. T.; Zhu, Y.; Duan, C. Y. *Eur. J. Inorg. Chem.* **2006**, 2259–2267.
- Nimz, O.; Gessler, K.; Uson, I.; Laettig, S.; Welfle, H.; Sheldrick, G. M.; Saenger, W. *Carbohydr. Res.* **2003**, *338*, 977–986.
- Chantrapomma, S.; Chanawanno, K.; Fun, H. K. *Acta Crystallogr. Sect. E. Struct. Rep.* **2007**, *63*, 01554–01556.
- Duarte-Ruiz, A.; Nunez-Dallos, N.; Garzon-Tovar, L.; Wurst, K.; Avella-Moreno, E.; Gomez-Baquero, F. *Chem. Commun.* **2011**, *47*, 7110–7112.
- Walbaum, C.; Pantenburg, I.; Meyer, G. Z. *Anorg. Allg. Chem.* **2009**, *635*, 1083–1085.
- Day, E. F.; Dean, N. S.; Franz, A. H. *Acta Crystallogr. Sect. C-Cryst. Struct. Commun.* **2006**, *62*, 0571–0573.
- Fischer, A.; Pettersson, H.; Hagfeldt, A.; Boschloo, G.; Kloo, L.; Gorlov, M. *Sol. Energy Mater. Sol. Cells* **2007**, *91*, 1062–1065.
- Chow, H.; Dean, P. A. W.; Craig, D. C.; Lucas, N. T.; Scudder, M. L.; Dance, I. G. *New J. Chem.* **2003**, *27*, 704–713.
- Lu, J. Y.; Zhang, Y. P.; Cmaidalka, J. E. *CrstEngComm* **2002**, *2002*, 213–214.
- Reiss, G. J.; Engel, J. S. *CrstEngComm* **2002**, *4*, 155–161.
- Bender, K.; Hennig, I.; Schweitzer, D.; Dietz, K.; Endres, H.; Keller, H. J. *Molec. Cryst. Liq. Cryst.* **1984**, *108*, 359–371.
- Eriksson, S. K.; Josefsson, I.; Ottosson, N.; Ohrwall, G.; Bjorneholm, O.; Siegbahn, H.; Hagfeldt, A.; Odelius, M.; Rensmo, H. *J. Phys. Chem. B* **2014**, *118*, 3164–3174.
- Jena, N. K.; Josefsson, I.; Eriksson, S. K.; Hagfeldt, A.; Siegbahn, H.; Bjorneholm, O.; Rensmo, H.; Odelius, M. *Chem.-Eur. J.* **2015**, *21*, 4049–4055.
- Josefsson, I.; Eriksson, S. K.; Ottosson, N.; Ohrwall, G.; Siegbahn, H.; Hagfeldt, A.; Rensmo, H.; Bjorneholm, O.; Odelius, M. *Phys. Chem. Chem. Phys.* **2013**, *15*, 20189–20196.
- Abe, H.; Tokita, T.; Iwata, K.; Ozawa, S. *Spectrosc. Acta Pt. A-Molec. Biomolec. Spectr.* **2019**, *212*, 255–261.
- de Grotthuss, C. J. D. *Ann. Chim.* **1806**, *58*, 54–74.
- Sun, Z.; Moore, K. B.; Hill, J. G.; Peterson, K. A.; Schaefer, H. F.; Hoffmann, R. J. *Phys. Chem. B* **2018**, *122*, 3339–3353.
- Sun, Z.; Schaefer, H. F. *Phys. Chem. Chem. Phys.* **2018**, *20*, 18986–18994.
- Svensson, P. H.; Kloo, L. *J. Chem. Soc. Dalton Trans.* **2000**, *2000*, 2449–2455.
- Pennington, W. T.; Hanks, T. W.; Arman, H. D. *Halogen Bonding: Fundamentals and Applications*, vol. 126; Springer-Verlag Berlin: Berlin, 2008; pp 65–104.
- Yu, Z.; Gorlov, M.; Nissfolk, J.; Boschloo, G.; Kloo, L. *J. Phys. Chem. C* **2010**, *114*, 10612–10620.
- Hoops, A. A.; Gascooke, J. R.; Faulhaber, A. E.; Kautzman, K. E.; Neumark, D. M. *J. Chem. Phys.* **2004**, *120*, 7901–7909.
- Nakanishi, R.; Saitou, N.; Ohno, T.; Kowashi, S.; Yabushita, S.; Nagata, T. *J. Chem. Phys.* **2007**, *126* (204311), 1–17.
- Kim, K. H.; Ki, H.; Oang, K. Y.; Nozawa, S.; Sato, T.; Kim, J.; Kim, T. K.; Kim, J.; Adachi, S.; Ihee, H. *ChemPhysChem* **2013**, *14*, 3687–3697.
- Nishiyama, Y.; Terazima, M.; Kimura, Y. *J. Phys. Chem. B* **2012**, *116*, 9023–9032.
- Farnum, B. H.; Gardner, J. M.; Meyer, G. J. *Inorg. Chem.* **2010**, *49*, 10223–10225.
- Boschloo, G.; Hagfeldt, A. *Acc. Chem. Res.* **2009**, *42*, 1819–1826.
- Privalov, T.; Boschloo, G.; Hagfeldt, A.; Svensson, P. H.; Kloo, L. *J. Phys. Chem. C* **2009**, *113*, 783–790.
- Baratz, A.; Ruhman, S. *Chem. Phys. Lett.* **2008**, *461*, 211–217.
- Nishiyama, Y.; Terazima, M.; Kimura, Y. *Chem. Phys. Lett.* **2010**, *491*, 164–168.
- Sakane, H.; Mitsui, T.; Tanida, H.; Watanabe, I. *J. Synchrotron Radiat.* **2001**, *8*, 674–676.
- Pimentel, C. G. *J. Chem. Phys.* **1951**, *19*, 446–448.
- Hach, R. J.; Rundle, R. E. *J. Am. Chem. Soc.* **1951**, *73*, 4321–4324.
- Novoa, J. J.; Mota, F.; Alvarez, S. *J. Phys. Chem.* **1988**, *92*, 6561–6566.
- Novoa, J. J.; Mota, F.; Whangbo, M. H.; Williams, J. M. *Inorg. Chem.* **1991**, *30*, 54–58.
- Ogawa, Y.; Takahashi, O.; Kikuchi, O. *Theochem.* **1998**, *424*, 285–292.
- Landrum, G. A.; Goldberg, N.; Hoffmann, R. J. *J. Chem. Soc. Dalton Trans.* **1997**, *1997*, 3605–3613.
- Munzarova, M. L.; Hoffmann, R. J. *J. Am. Chem. Soc.* **2002**, *124*, 4787–4795.
- Ogawa, Y.; Takahashi, O.; Kikuchi, O. *Theochem.* **1998**, *429*, 187–196.
- Kloo, L.; Rosdahl, J.; Svensson, P. H. *Eur. J. Inorg. Chem.* **2002**, 1203–1209.
- Braida, B.; Hiberty, P. C. *J. Phys. Chem. A* **2008**, *112*, 13045–13052.



59. Zhang, F. S.; Lynden-Bell, R. M. *Phys. Rev. Lett.* **2003**, *90* (185505), 1–4.
60. Margulis, C. J.; Coker, D. F.; Lynden-Bell, R. M. *J. Chem. Phys.* **2001**, *114*, 367–376.
61. Margulis, C. J.; Coker, D. F.; Lynden-Bell, R. M. *Chem. Phys. Lett.* **2001**, *341*, 557–560.
62. Zhang, F. S.; Lynden-Bell, R. M. *Eur. Phys. J. D* **2005**, *34*, 129–132.
63. Zhang, F. S.; Lynden-Bell, R. M. *Phys. Rev. E* **2005**, *71* (021502), 1–5.
64. Zhang, F. S.; Lynden-Bell, R. M. *Mol. Phys.* **2003**, *101*, 1641–1649.
65. Zhang, F. S.; Lynden-Bell, R. M. *J. Chem. Phys.* **2003**, *119*, 6119–6131.
66. Sato, H.; Hirata, F.; Myers, A. B. *J. Phys. Chem. A* **1998**, *102*, 2065–2071.
67. Koslowski, T.; Vohringer, P. *Chem. Phys. Lett.* **2001**, *342*, 141–147.
68. Frisch, M. J.; Trucks, G. W.; Schlegel, H. B.; Scuseria, G. E.; Robb, M. A.; Cheeseman, J. R.; Scalmani, G.; Barone, V.; Mennucci, B.; Petersson, G. A.; Nakatsuji, H.; Caricato, M.; Li, X.; Hratchian, H. P.; Izmaylov, A. F.; Bloino, J.; Zheng, G.; Sonnenberg, J. L.; Hada, M.; Ehara, M.; Toyota, K.; Fukuda, R.; Hasegawa, J.; Ishida, M.; Nakajima, T.; Honda, Y.; Kitao, O.; Nakai, H.; Vreven, T.; Montgomery, J. J. A.; Peralta, J. E.; Ogliaro, F.; Bearpark, M.; Heyd, J. J.; Brothers, E.; Kudin, K. N.; Staroverov, V. N.; Kobayashi, R.; Normand, J.; Raghavachari, K.; Rendell, A.; Burant, J. C.; Iyengar, S. S.; Tomasi, J.; Cossi, M.; Rega, N.; Millam, N. J.; Klene, M.; Knox, J. E.; Cross, J. B.; Bakken, V.; Adamo, C.; Jaramillo, J.; Gomperts, R.; Stratmann, R. E.; Yazyev, O.; Austin, A. J.; Cammi, R.; Pomelli, C.; Ochterski, J. W.; Martin, R. L.; Morokuma, K.; Zakrzewski, V. G.; Voth, G. A.; Salvador, P.; Dannenberg, J. J.; Dapprich, S.; Daniels, A. D.; Farkas, Ö.; Foresman, J. B.; Ortiz, J. V.; Cioslowski, J.; Fox, D. J. *Gaussian 09, Revision A.1*, Gaussian, Inc.: Wallingford, CT, 2009.
69. Anon (n.d.) *The basis sets were all taken from the compilation of effective-core potentials with associated valence basis sets from the Institut für Theoretische Chemie, Stuttgart* (<http://www.theochem.uni-stuttgart.de/>). The basis sets of Br, I and At were of triple-zeta quality, and slightly less expanded for F and Cl. Short characterization of the basis sets are as follows: F MWB2/(4s5p)/[2s3p]; Cl MWB10/(4s5p)/[2s3p]; Br MDF10/(10s11p9d1f)/[5s4p3d1f]; I MDF28/(12s11p9d1f)/[5s4p3d1f]; At MDF60/(12s11p8d1f)/[5s4p3d1f].
70. Jan-Michael Mewes, O. R. S.; Kresse, G.; Schwerdtfeger, P. *Angew. Chem. Int. Ed.* **2019**, *58*, 17964–17968.
71. Smits, O. R.; Jerabek, P.; Schwerdtfeger, P. *Angew. Chem. Int. Ed.* **2020**, *59*, 23636–23640.
72. Gautam, R.; Desiraju, P. S. H.; Kloo, L.; Legon, A. C.; Marquardt, R.; Metrangolo, P.; Politzer, P.; Resnati, G.; Rissanen, K. *Pure Appl. Chem.* **2013**, *85*, 1711–1713.
73. Rüttgers, E. *Neue Verbindungen des Silbers und Goldes mit organischen Liganden und Halogeniden*, Universität zu Köln: Köln, 2013.
74. Clark, T.; Murray, J. S.; Politzer, P. *ChemPhysChem* **2018**, *19*, 3044–3049.
75. Manca, G.; Ienco, A.; Mealli, C. *Cryst. Growth Des.* **2012**, *12*, 1762–1771.
76. Walbaum, C.; Pantenburg, I.; Meyer, G. *Z. Naturforsch. B* **2010**, *65*, 1077–1083.
77. Grossi, J.; Kohanoff, J. J.; English, N. J.; Bringa, E. M.; Del Popolo, M. G. *J. Phys. Chem. B* **2017**, *121*, 6436–6441.
78. Nemeč, V.; Lisac, K.; Stilić, V.; Cincic, D. *J. Mol. Struct.* **2017**, *1128*, 400–409.
79. Kahr, B.; Freudenthal, J.; Phillips, S.; Kaminsky, W. *Science* **2009**, *324*, 1407.
80. Groenewald, F.; Esterhuysen, C.; Dillen, J. *Theor. Chem. Acc.* **2012**, *131* (1281), 1–12.
81. Groenewald, F.; Esterhuysen, C.; Dillen, J. *Comput. Theor. Chem.* **2016**, *1090*, 225–233.
82. Aragoni, M. C.; Arca, M.; Devillanova, F. A.; Isaia, F.; Lippolis, V. *Phosphorus Sulfur Silicon Relat. Elem.* **2008**, *183*, 1036–1045.
83. Lee, S.; Chen, B. L.; Fredrickson, D. C.; DiSalvo, F. J.; Lobkovsky, E.; Adams, J. A. *Chem. Mater.* **2003**, *15*, 1420–1433.
84. Aragoni, M. C.; Arca, M.; Devillanova, F. A.; Hursthouse, M. B.; Huth, S. L.; Isaia, F.; Lippolis, V.; Mancini, A. *CrstEngComm* **2004**, *6*, 540–542.
85. Dolder, S.; Liu, S. X.; Beurer, E.; Ouahab, L.; Decurtins, S. *Polyhedron* **2006**, *25*, 1514–1518.
86. Blake, A. J.; Li, W. S.; Lippolis, V.; Parsons, S.; Schroder, M. *Acta Crystallogr. Sect. B-Struct. Sci.* **2007**, *63*, 81–92.
87. Link, C.; Pantenburg, I.; Meyer, G. *Z. Anorg. Allg. Chem.* **2008**, *634*, 616–618.
88. Walbaum, C.; Pantenburg, I.; Meyer, G. *Z. Anorg. Allg. Chem.* **2008**, *634*, 1247–1248.
89. Neumüller, B.; Dehnicke, K. *Z. Anorg. Allg. Chem.* **2010**, *636*, 515–517.
90. Peuronen, A.; Rinta, H.; Lahtinen, M. *CrstEngComm* **2015**, *17*, 1736–1740.
91. Basch, A.; Hartl, M.; Behrens, P. *Microporous Mesoporous Mat.* **2007**, *99*, 244–250.
92. Wang, Z. M.; Cheng, Y. J.; Liao, C. S.; Yan, C. H. *CrstEngComm* **2001**, 1–6.
93. Lu, J. Y.; Schauss, V. *Eur. J. Inorg. Chem.* **2002**, 1945–1947.
94. Li, H. J.; Wang, X.; Jia, Y. Y.; Zhao, B.; Ding, R.; Hou, H. W.; Fan, Y. T. *CrstEngComm* **2012**, *14*, 5155–5157.
95. Al Lafi, A. G.; Assfour, B.; Assaad, T. *J. Inorg. Organomet. Polym. Mater.* **2020**, *30*, 1218–1230.
96. Massasso, G.; Rodriguez-Castillo, M.; Long, J.; Grandjean, A.; Onida, B.; Guari, Y.; Guerin, C.; Larionova, J. *J. Mater. Chem. A* **2015**, *3*, 179–188.
97. Yin, Z.; Wang, Q. X.; Zeng, M. H. *J. Am. Chem. Soc.* **2012**, *134*, 4857–4863.
98. Horn, C.; Scudder, M.; Dance, I. *CrstEngComm* **2001**, *1*, 1–8.
99. Horn, C. J.; Blake, A. J.; Champness, N. R.; Garau, A.; Lippolis, V.; Wilson, C.; Schroder, M. *Chem. Commun.* **2003**, 312–313.
100. Horn, C. J.; Blake, A. J.; Champness, N. R.; Lippolis, V.; Schroder, M. *Chem. Commun.* **2003**, 1488–1489.
101. Aragoni, M. C.; Arca, M.; Demartin, F.; Devillanova, F. A.; Garau, A.; Isaia, F.; Lippolis, V.; Rizzato, S.; Verani, G. *Inorg. Chim. Acta* **2004**, *357*, 3803–3809.
102. Reiss, G. J.; Engel, J. S. *Z. Naturforsch. B* **2004**, *59*, 1114–1117.
103. Das, G. C.; Das, B.; Sen Sarma, N.; Medhi, O. K. *Polyhedron* **2012**, *37*, 14–20.
104. Svensson, P. H.; Gorlov, M.; Kloo, L. *Inorg. Chem.* **2008**, *47*, 11464–11466.
105. Abate, A.; Brischetto, M.; Cavallo, G.; Lahtinen, M.; Metrangolo, P.; Pilati, T.; Radice, S.; Resnati, G.; Rissanen, K.; Terraneo, G. *Chem. Commun.* **2010**, *46*, 2724–2726.
106. Garcia, M. D.; Marti-Rujas, J.; Metrangolo, P.; Peinador, C.; Pilati, T.; Resnati, G.; Terraneo, G.; Ursini, M. *CrstEngComm* **2011**, *13*, 4411–4416.
107. Lin, J. X.; Marti-Rujas, J.; Metrangolo, P.; Pilati, T.; Radice, S.; Resnati, G.; Terraneo, G. *Cryst. Growth Des.* **2012**, *12*, 5757–5762.
108. Ma, L. F.; Peng, H. L.; Lu, X. F.; Liu, L.; Shao, X. F. *Chin. J. Chem.* **2018**, *36*, 845–850.
109. Pan, F. F.; Englert, U. *Cryst. Growth Des.* **2014**, *14*, 1057–1066.
110. Pang, X.; Wang, H.; Zhao, X. R.; Jin, W. *J. Dalton Trans.* **2013**, *42*, 8788–8795.
111. Short, J.; Blundell, T. J.; Yang, S. J.; Sahin, O.; Shakespeare, Y.; Smith, E. L.; Wallis, J. D.; Martin, L. *CrstEngComm* **2020**, *22*, 6632–6644.
112. Savinkina, E. V.; Golubev, D. V.; Grigoriev, M. S.; Albov, D. V. *Polyhedron* **2013**, *54*, 140–146.
113. Savinkina, E. V.; Golubev, D. V.; Grigoriev, M. S. *J. Coord. Chem.* **2015**, *68*, 4119–4129.
114. Savinkina, E. V.; Golubev, D. V.; Grigoriev, M. S. *J. Coord. Chem.* **2019**, *72*, 347–357.
115. Petrov, A. A.; Fateev, S. A.; Zubavichus, Y. V.; Dorovatovskii, P. V.; Khrustalev, V. N.; Zvereva, I. A.; Petrov, A. V.; Goodilin, E. A.; Tarasov, A. B. *J. Phys. Chem. Lett.* **2019**, *10*, 5776–5780.
116. Yu, X. C.; Atalla, R. H. *Carbohydr. Res.* **2005**, *340*, 981–988.
117. Papaioannou, J. C.; Ghikas, T. C. *Mol. Phys.* **2003**, *101*, 2601–2608.
118. Papaioannou, J. C. *Mol. Phys.* **2004**, *102*, 95–99.
119. Charalampopoulos, V. G.; Papaioannou, J. C.; Karayianni, H. S. *Solid State Sci.* **2006**, *8*, 97–103.
120. Charalampopoulos, V. G.; Papaioannou, J. C.; Tampouris, K. E. *Solid State Ion.* **2007**, *178*, 793–799.
121. Charalampopoulos, V. G.; Papaioannou, J. C.; Viras, K.; Karayianni, H. S.; Kakali, G. *Supramol. Chem.* **2010**, *22*, 499–510.

122. Charalampopoulos, V. G.; Papaioannou, J. C.; Tsekouras, A. A.; Kakali, G.; Karayianni, H. S. *Spectrosc. Acta Pt. A-Molec. Biomolec. Spectr.* **2011**, *83*, 279–287.
123. Savastano, M.; Bazzicalupi, C.; Gellini, C.; Bianchi, A. *Crystals* **2020**, *10* (387), 1–5.
124. Savastano, M.; Bazzicalupi, C.; Gellini, C.; Bianchi, A. *Chem. Commun.* **2020**, *56*, 551–554.
125. Savastano, M.; Martínez-Camarena, A.; Bazzicalupi, C.; Delgado-Pinar, E.; Linares, J. M.; Mariani, P.; Verdejo, B.; García-España, E.; Bianchi, A. *Inorganics* **2019**, *7* (48), 1–17.
126. Chorro, M.; Kane, G.; Alvarez, L.; Cambedouzou, J.; Paineau, E.; Rossberg, A.; Kociak, M.; Aznar, R.; Pascarelli, S.; Launois, P.; Bantignies, J. L. *Carbon* **2013**, *52*, 100–108.
127. Tristant, D.; Puech, P.; Gerber, I. C. *Phys. Chem. Chem. Phys.* **2015**, *17*, 30045–30051.
128. Yoshida, Y.; Ishii, Y.; Kato, N.; Li, C. H.; Kawasaki, S. *J. Phys. Chem. C* **2016**, *120*, 20454–20461.
129. Charalampopoulos, V. G.; Papaioannou, J. C.; Kakali, G.; Karayianni, H. S. *Carbohydr. Res.* **2008**, *343*, 489–500.
130. Tsiplis, A. C.; Karipidis, P. A. *Polyhedron* **2008**, *27*, 289–298.
131. Lang, E. S.; Strähle, J. Z. *Anorg. Allg. Chem.* **1996**, *622*, 981–984.
132. Svensson, P. H.; Rosdahl, J.; Kloo, L. *Chem. A Eur. J.* **1999**, *5*, 305–311.
133. Svensson, P. H.; Kloo, L. *Inorg. Chem.* **1999**, *38*, 3390–3393.
134. Castro-Castro, L. M.; Guloy, A. M. *Angew. Chem. Int. Ed.* **2003**, *42*, 2771–2774.
135. Castro-Castro, L. M.; Guloy, A. M. *Inorg. Chem.* **2004**, *43*, 4537–4539.
136. Schneider, D.; Schier, A.; Schmidbaur, H. *Dalton Trans.* **2004**, *2004*, 1995–2005.
137. Evans, H. A.; Schueller, E. C.; Smock, S. R.; Wu, G.; Seshadri, R.; Wudl, F. *Inorg. Chim. Acta* **2017**, *468*, 280–284.
138. Shlenskaya, N. N.; Belich, N. A.; Gratzel, M.; Goodilin, E. A.; Tarasov, A. B. *J. Mater. Chem. A* **2018**, *6*, 1780–1786.
139. Walbaum, C.; Pantenburg, I.; Meyer, G. *Cryst. Res. Technol.* **2008**, *43*, 1183–1186.
140. Evans, H. A.; Andrews, J. L.; Fabini, D. H.; Preefer, M. B.; Wu, G.; Cheatham, A. K.; Wudl, F.; Seshadri, R. *Chem. Commun.* **2019**, *55*, 588–591.
141. Li, H. H.; Chen, Z. R.; Liu, Y.; Liu, J. B.; Guo, L. Q.; Li, J. Q. *J. Mol. Struct.* **2009**, *934*, 112–116.
142. Redel, E.; Rohr, C.; Janiak, C. *Chem. Commun.* **2009**, 2103–2105.
143. Hu, J.; Zhou, J.; Cao, S. M. *Dalton Trans.* **2018**, *47*, 17216–17220.
144. Martínez-Camarena, A.; Savastano, M.; Linares, J. M.; Verdejo, B.; Bianchi, A.; García-España, E.; Bazzicalupi, C. *Inorg. Chem. Front.* **2020**, *7*, 4239–4255.
145. Hu, Y. Q.; Li, M. Q.; Wang, Y. Y.; Zhang, T.; Liao, P. Q.; Zheng, Z. P.; Chen, X. M.; Zheng, Y. Z. *Chem.-Eur. J.* **2017**, *23*, 8409–8413.
146. Louvain, N.; Bi, W. H.; Mercier, N.; Buzare, J. Y.; Legein, C.; Corbel, G. *Dalton Trans.* **2007**, *2007*, 965–970.
147. Li, H. H.; Chen, Z. R.; Cheng, L. C.; Liu, J. B.; Chen, X. B.; Li, J. Q. *Cryst. Growth Des.* **2008**, *8*, 4355–4358.
148. He, J.; Cao, P.; Wu, C.; Huang, J. H.; Huang, J. H.; He, Y. H.; Yu, L.; Zeller, M.; Hunter, A. D.; Xu, Z. T. *Inorg. Chem.* **2015**, *54*, 6087–6089.
149. Janczak, J. *Acta Crystallogr. Sect. C-Cryst. Struct. Commun.* **2004**, *60*, M330–M332.
150. Bergeron, D. E.; Roach, P. J.; Castleman, A. W.; Jones, N.; Khanna, S. N. *Science* **2005**, *307*, 231–235.
151. Strobele, M.; Meyer, H. J. Z. *Anorg. Allg. Chem.* **2010**, *636*, 62–66.
152. Strobele, M.; Castro, C.; Fink, R. F.; Meyer, H. J. *Angew. Chem. Int. Ed.* **2016**, *55*, 4814–4817.
153. Strobele, M.; Meyer, H. J. *Dalton Trans.* **2019**, *48*, 1547–1561.
154. Mendizabal, F. *Theochem-J. Mol. Struct.* **2010**, *955*, 71–74.
155. Chung, B. L.; He, J.; Chang, R. P. H.; Kanatzidis, M. G. *Nature* **2012**, *485*, 486–490.
156. Murasugi, H.; Kumagai, S.; Iguchi, H.; Yamashita, M.; Takaishi, S. *Chem. A Eur. J.* **2019**, *25*, 9885–9891.
157. Shestimerova, T. A.; Golubev, N. A.; Yelavik, N. A.; Bykov, M. A.; Grigorieva, A. V.; Wei, Z.; Dikarev, E. V.; Shevelkov, A. V. *Cryst. Growth Des.* **2018**, *18*, 2572–2578.
158. Shestimerova, T. A.; Mironov, A. V.; Bykov, M. A.; Grigorieva, A. V.; Wei, Z.; Dikarev, E. V.; Shevelkov, A. V. *Molecules* **2020**, *25* (2765), 1–15.
159. Shestimerova, T. A.; Yelavik, N. A.; Mironov, A. V.; Kuznetsov, A. N.; Bykov, M. A.; Grigorieva, A. V.; Utochnikova, V. V.; Lepnev, L. S.; Shevelkov, A. V. *Inorg. Chem.* **2018**, *57*, 4077–4087.
160. Zhao, L. M.; Zhang, W. T.; Song, K. Y.; Wu, Q. Q.; Li, Y.; Li, H. H.; Chen, Z. R. *CrstEngComm* **2018**, *20*, 2245–2252.
161. Starkholm, A.; Kloo, L.; Svensson, P. H. *ACS Appl. Energ. Mater.* **2019**, *2*, 477–485.
162. Bengtsson, L. A.; Stegemann, H.; Holmberg, B.; Füllbier, H. *Mol. Phys.* **1991**, *73*, 283–296.
163. Stegemann, H.; Schnitzke, A.; Füllbier, H. *Electrochim. Acta* **1990**, *35*, 355–359.
164. Gorlov, M.; Kloo, L. *Dalton Trans.* **2008**, *2008*, 2655–2666.
165. Zistler, M.; Wachter, P.; Wasserscheid, P.; Gerhard, D.; Hinsch, A.; Sastrawan, R.; Gores, H. J. *Electrochim. Acta* **2006**, *52*, 161–169.
166. Wachter, P.; Schreiner, C.; Zistler, M.; Gerhard, D.; Wasserscheid, P.; Gores, H. J. *Microchim. Acta* **2008**, *160*, 125–133.
167. Jovanovski, V.; Orel, B.; Jerman, I.; Hocevar, S. B.; Ogorevc, B. *Electrochim. Commun.* **2007**, *9*, 2062–2066.
168. Jerman, I.; Jovanovski, V.; Vuk, A. S.; Hocevar, S. B.; Gaberscek, M.; Jesih, A.; Orel, B. *Electrochim. Acta* **2008**, *53*, 2281–2288.
169. Thorsmolle, V. K.; Rothenberger, G.; Topgaard, D.; Brauer, J. C.; Kuang, D. B.; Zakeeruddin, S. M.; Lindman, B.; Gratzel, M.; Moser, J. E. *ChemPhysChem* **2011**, *12*, 145–149.
170. Abe, H.; Aono, M.; Kiyotani, T.; Tsuzuki, S. *Phys. Chem. Chem. Phys.* **2016**, *18*, 32337–32344.
171. Fei, Z. F.; Bobbink, F. D.; Paunescu, E.; Scopelliti, R.; Dyson, P. J. *Inorg. Chem.* **2015**, *54*, 10504–10512.
172. Aono, M.; Miyazaki, H.; Takekiyo, T.; Tsuzuki, S.; Abe, H. *Phys. Chem. Chem. Phys.* **2018**, *20*, 5780–5784.
173. Yu, H. T.; Yan, L. J.; He, Y. W.; Meng, H.; Huang, W. *Chem. Commun.* **2017**, *53*, 432–435.
174. Shimono, T.; Matsuki, M.; Yamada, T.; Morikawa, M.; Yasuda, N.; Fujigaya, T.; Kimizuka, N. *Chem. Lett.* **2018**, *47*, 261–264.
175. Byrne, A.; Bringa, E. M.; Del Popolo, M. G.; Kohanoff, J. J.; Galassi, V.; English, N. J. *Int. J. Mol. Sci.* **2019**, *20* (1123), 1–14.
176. McDaniel, J. G.; Yethiraj, A. *J. Phys. Chem. B* **2018**, *122*, 250–257.
177. Thapa, R.; Park, N. J. *Phys. Chem. Lett.* **2012**, *3*, 3065–3069.
178. Wei, S. B.; Wang, J. Y.; Deng, S. Y.; Zhang, S. T.; Li, Q. *Sci. Rep.* **2015**, *5* (14393), 1–7.
179. Poreba, T.; Ernst, M.; Zimmer, D.; Macchi, P.; Casati, N. *Angew. Chem. Int. Ed.* **2019**, *58*, 6625–6629.
180. Takekiyo, T.; Yoshimura, Y. *J. Phys. Chem. B* **2020**, *124*, 7659–7667.
181. Haller, H.; Hog, M.; Scholz, F.; Scherer, H.; Krossing, I.; Riedel, S. Z. *Naturforsch. B* **2013**, *68*, 1103–1107.
182. Easton, M. E.; Ward, A. J.; Chan, B.; Radom, L.; Masters, A. F.; Maschmeyer, T. *Phys. Chem. Chem. Phys.* **2016**, *18*, 7251–7260.
183. Easton, M. E.; Ward, A. J.; Hudson, T.; Turner, P.; Masters, A. F.; Maschmeyer, T. *Chem. A Eur. J.* **2015**, *21*, 2961–2965.
184. Breneman, G. L.; Willett, R. D. *Acta Crystallogr.* **1967**, *23*, 334.
185. Stroemme, K. O. *Acta Chem. Scand.* **1959**, *13*, 2089–2100.
186. Robertson, K. N.; Bakshi, P. K.; Cameron, T. S.; Knop, O. Z. *Anorg. Allg. Chem.* **1997**, *623*, 104–114.
187. Atwood, J. L.; Junk, P. C.; May, M. T.; Robinson, K. D. *J. Chem. Crystallogr.* **1994**, *24*, 243–245.
188. Chekhlov, A. N. *Russ. J. Inorg. Chem.* **2008**, *53*, 1197–1202.
189. Kornath, A.; Blecher, O. Z. *Anorg. Allg. Chem.* **2002**, *628*, 570–574.
190. Aragoni, M. C.; Arca, M.; Devillanova, F. A.; Hursthouse, M. B.; Huth, S. L.; Isaia, F.; Lippolis, V.; Mancini, A.; Ogilvie, H. *Inorg. Chem. Commun.* **2005**, *8*, 79–82.
191. Cunningham, C. W.; Burns, G. R.; McKee, V. *Inorg. Chim. Acta* **1990**, *167*, 135–137.

192. Schuster, P.; Mikosch, H.; Bauer, G. *J. Chem. Phys.* **1998**, *109*, 1833–1844.
193. Aragoni, M. C.; Arca, M.; Devillanova, F. A.; Isaia, F.; Lippolis, V.; Mancini, A.; Pala, L.; Slawin, A. M. Z.; Woollins, J. D. *Chem. Commun.* **2003**, 2226–2227.
194. Chen, X. Y.; Rickard, R. M. A.; Hull, J. W.; Zheng, C.; Leugers, A.; Simoncic, P. *Inorg. Chem.* **2010**, *49*, 8684–8689.
195. Burns, G. R.; Renner, R. M. *Spectrosc. Acta Pt. A-Molec. Biomolec. Spectr.* **1991**, *47*, 991–999.
196. Wolff, M.; Meyer, J.; Feldmann, C. *Angew. Chem. Int. Ed.* **2011**, *50*, 4970–4973.
197. Wolff, M.; Okrut, A.; Feldmann, C. *Inorg. Chem.* **2011**, *50*, 11683–11694.
198. Tebbe, K.-F.; Buchem, R. *Angew. Chem. Int. Ed. Engl.* **1997**, *36*, 1345–1346.
199. Haller, H.; Ellwanger, M.; Higelin, A.; Riedel, S. *Angew. Chem. Int. Ed.* **2011**, *50*, 11528–11532.
200. Groessel, M.; Fei, Z. F.; Dyson, P. J.; Katsyuba, S. A.; Vikse, K. L.; McIndoe, J. S. *Inorg. Chem.* **2011**, *50*, 9728–9733.
201. Pichièri, F. *Chem. Phys. Lett.* **2011**, *515*, 116–121.
202. Easton, M. E.; Chan, B.; Masters, A. F.; Radom, L.; Maschmeyer, T. *Chem. Asian J.* **2016**, *11*, 682–686.
203. Schneider, D.; Schuster, O.; Schmidbaur, H. *Dalton Trans.* **2005**, 1940–1947.
204. Berkei, M.; Bickley, J. F.; Heaton, B. T.; Steiner, A. *Chem. Commun.* **2002**, 2180–2181.
205. Adonin, S. A.; Gorokh, I. D.; Samsonenko, D. G.; Sokolov, M. N.; Fedin, V. P. *Chem. Commun.* **2016**, *52*, 5061–5063.
206. Adonin, S. A.; Bondarenko, M. A.; Novikov, A. S.; Plyusnin, P. E.; Korolkov, I. V.; Sokolov, M. N.; Fedin, V. P. *Inorg. Chim. Acta* **2020**, *502* (119278), 1–8.
207. Bondarenko, M. A.; Novikov, A. S.; Fedin, V. P.; Sokolov, M. N.; Adonin, S. A.; J. Coord. Chem., 25: 6.
208. Evans, J. C.; Lo, G. Y.-S. *J. Chem. Phys.* **1966**, *44*, 3638–3639.
209. Bogaard, M. P.; Peterson, J.; Rae, A. D. *Acta Crystallogr. Sect. B-Struct. Sci.* **1981**, *37*, 1357–1359.
210. Chivers, T.; Richardson, J. F.; Smith, N. R. M. *Inorg. Chem.* **1985**, *24*, 2453–2458.
211. Redeker, F. A.; Beckers, H.; Riedel, S. *Chem. Commun.* **2017**, *53*, 12958–12961.
212. Riedel, E. F.; Willett, R. D. *J. Am. Chem. Soc.* **1975**, *97*, 701–704.
213. Riedel, E. F.; Willett, R. D. *Theor. Chim. Acta* **1976**, *42*, 237–246.
214. Ault, B. S.; Andrews, L. *J. Chem. Phys.* **1976**, *64*, 4853–4859.
215. Robbiani, R.; Franklin, J. L. *J. Am. Chem. Soc.* **1979**, *101*, 764–765.
216. Zelikman, V. M.; Tyurin, V. S.; Smimov, V. V.; Zyk, N. V. *Russ. Chem. Bull.* **1998**, *47*, 1541–1546.
217. Bruckner, R.; Haller, H.; Ellwanger, M.; Riedel, S. *Chem.-Eur. J.* **2012**, *18*, 5741–5747.
218. Bruckner, R.; Haller, H.; Steinhauer, S.; Muller, C.; Riedel, S. *Angew. Chem. Int. Ed.* **2015**, *54*, 15579–15583.
219. Bruckner, R.; Prohm, P.; Wiesner, A.; Steinhauer, S.; Muller, C.; Riedel, S. *Angew. Chem. Int. Ed.* **2016**, *55*, 10904–10908.
220. Sonnenberg, K.; Prohm, P.; Schwarze, N.; Muller, C.; Beckers, H.; Riedel, S. *Angew. Chem. Int. Ed.* **2018**, *57*, 9136–9140.
221. Usoltsev, A. N.; Adonin, S. A.; Kolesov, B. A.; Novikov, A. S.; Fedin, V. P.; Sokolov, M. N. *Chem. A Eur. J.* **2020**, *26*, 13776–13778.
222. Ault, B. S.; Andrews, L. *J. Am. Chem. Soc.* **1976**, *98*, 1591–1593.
223. Ault, B. S.; Andrews, L. *Inorg. Chem.* **1977**, *16*, 2024–2028.
224. Tuinman, A. A.; Gakh, A. A.; Hinde, R. J.; Compton, R. N. *J. Am. Chem. Soc.* **1999**, *121*, 8397–8398.
225. Artau, A.; Nizzi, K. E.; Hill, B. T.; Sunderlin, L. S.; Wenthold, P. G. *J. Am. Chem. Soc.* **2000**, *122*, 10667–10670.
226. Radzhabov, E. A. *Opt. Spectrosc.* **2016**, *120*, 294–299.
227. Christie, K. O. *J. Fluor. Chem.* **1995**, *71*, 149–150.
228. Andrews, L.; Wang, X. F. *Phys. Chem. Chem. Phys.* **2018**, *20*, 23378–23385.
229. Redeker, F. A.; Beckers, H.; Riedel, S. *RSC Adv.* **2015**, *5*, 106568–106573.
230. Brosi, F.; Vent-Schmidt, T.; Kieninger, S.; Schloder, T.; Beckers, H.; Riedel, S. *Chem. A Eur. J.* **2015**, *21*, 16455–16462.
231. Vent-Schmidt, T.; Brosi, F.; Metzger, J.; Schloder, T.; Wang, X. F.; Andrews, L.; Muller, C.; Beckers, H.; Riedel, S. *Angew. Chem. Int. Ed.* **2015**, *54*, 8279–8283.
232. Zhu, Q.; Oganov, A. R.; Zeng, Q. F. *Sci. Rep.* **2015**, *5* (7875), 1–6.
233. Heard, G. L.; Marsden, C. J.; Scuseria, G. E. *J. Phys. Chem.* **1992**, *96*, 4359–4366.
234. Tozer, D. J.; Sosa, C. P. *Mol. Phys.* **1997**, *90*, 515–524.
235. Braida, B.; Hiberty, P. C. *J. Am. Chem. Soc.* **2004**, *126*, 14890–14898.
236. Riedel, S.; Koechner, T.; Wang, X. F.; Andrews, L. *Inorg. Chem.* **2010**, *49*, 7156–7164.
237. Getmanskii, I. V.; Koval, V. V.; Minyaev, R. M.; Minkin, V. I. *Mendeleev Commun.* **2015**, *25*, 417–419.
238. Gutsev, G. L.; Belay, K. G.; Weatherford, C. A.; Ramachandran, B. R.; Gutsev, L. G.; Jena, P. *J. Phys. Chem. A* **2015**, *119*, 6483–6492.
239. Rogachev, A. Y.; Miao, M. S.; Merino, G.; Hoffmann, R. *Angew. Chem. Int. Ed.* **2015**, *54*, 8275–8278.
240. Ilev, S. I.; Gaul, K.; Chen, M. Y.; Karttunen, A. J.; Berger, R.; Kraus, F. *Chem. A Eur. J.* **2019**, *25*, 5793–5802.
241. Thierfelder, C.; Schwerdtfeger, P.; Koers, A.; Borschevsky, A.; Fricke, B. *Phys. Rev. A* **2009**, *80* (022501), 1–10.
242. Dove, M. F. A. *Coord. Chem. Rev.* **1988**, *85*, 504–522.
243. Serezhkin, V. V.; Prokaeva, M. A.; Pushkin, D. V.; Serezhkina, L. B. *Russ. J. Inorg. Chem.* **2009**, *54*, 1251–1260.
244. Minkwitz, R.; Berkei, M.; Ludwig, R. *Inorg. Chem.* **2001**, *40*, 25–28.
245. Aragoni, M. C.; Arca, M.; Devillanova, F. A.; Hursthouse, M. B.; Huth, S. L.; Isaia, F.; Lippolis, V.; Mancini, A.; Ogilvie, H. R.; Verani, G. *J. Organomet. Chem.* **2005**, *690*, 1923–1934.
246. Parlow, A.; Hartl, H. Z. *Naturforsch., Teil B* **1985**, *35*, 45–52.
247. Parlow, A.; Hartl, H. *Acta Crystallogr., Sect. B* **1979**, *1979*, 1930–1933.
248. Parigoridi, I. E.; Corban, G. J.; Hadjilakou, S. K.; Hadjiliadis, N.; Kourkoumelis, N.; Kostakis, G.; Psycharis, V.; Raptopoulou, C. P.; Kubicki, M. *Dalton Trans.* **2008**, *2008*, 5159–5165.
249. Sakbara, P. J.; Bricklebank, N.; Berridge, R.; Long, S.; Light, M. E.; Coles, S. J.; Hursthouse, M. B. *Dalton Trans.* **2000**, 3235–3236.
250. Abdelbassit, M. S.; Curnow, O. J.; Dixon, M. K.; Waterland, M. R. *Chem. A Eur. J.* **2019**, *25*, 11650–11658.
251. Abdelbassit, M. S.; Curnow, O. J.; Dixon, M. K.; Waterland, M. R. *Chem. A Eur. J.* **2019**, *25*, 11659–11669.
252. Babu, R.; Bhargavi, G.; Rajasekharan, M. V. *Eur. J. Inorg. Chem.* **2015**, 4689–4698.
253. Hausmann, D.; Koppe, R.; Wolf, S.; Roesky, P. W.; Feldmann, C. *Dalton Trans.* **2016**, *45*, 16526–16532.
254. Mann, L.; Vossnacker, P.; Muller, C.; Riedel, S. *Chem. A Eur. J.* **2017**, *23*, 244–249.
255. Schmidt, B.; Ponath, S.; Hannemann, J.; Vossnacker, P.; Sonnenberg, K.; Christmann, M.; Riedel, S. *Chem. A Eur. J.* **2020**, *26*, 15183–15189.
256. Schmidt, B.; Sonnenberg, K.; Beckers, H.; Steinhauer, S.; Riedel, S. *Angew. Chem. Int. Ed.* **2018**, *57*, 9141–9145.
257. Walbaum, C.; Richter, M.; Sachs, U.; Pantenburg, I.; Riedel, S.; Mudring, A. V.; Meyer, G. *Angew. Chem. Int. Ed.* **2013**, *52*, 12732–12735.
258. Olsson, L.-F. *Inorg. Chem.* **1985**, *24*, 1398–1405.
259. Gorlov, M.; Pettersson, H.; Hagfeldt, A.; Kloo, L. *Inorg. Chem.* **2007**, *46*, 3566–3575.
260. Reddy, J. M.; Knox, K.; Robin, M. B. *J. Chem. Phys.* **1964**, *40*, 1082–1089.
261. Teitelbaum, R. C.; Ruby, S. I.; Mrks, T. J. *J. Am. Chem. Soc.* **1980**, *102*, 3322–3328.
262. Robin, M. B. *J. Chem. Phys.* **1964**, *40*, 3369–3377.

263. Teitelbaum, R. C.; Ruby, S. L.; Marks, T. J. *J. Am. Chem. Soc.* **1978**, *100*, 3215–3217.
264. Konishi, T.; Tanaka, W.; Kawai, T.; Fujikawa, T. *J. Synchrotron Radiat.* **2001**, *8*, 737–739.
265. Liang, L.; Rulis, P.; Kahr, B.; Ching, W. Y. *Phys. Rev. B* **2009**, *80* (235132), 1–5.
266. Liu, Q. K.; Ma, J. P.; Dong, Y. B. *Chem. Commun.* **2011**, *47*, 7185–7187.
267. Evans, G.; Bricogne, G. *Acta Crystallogr. Sect. D-Biol. Crystallogr.* **2002**, *58*, 976–991.
268. Evans, G.; Bricogne, G. *Acta Crystallogr. Sect. D-Biol. Crystallogr.* **2003**, *59*, 1923–1929.
269. Ganjali, M. R.; Emami, M.; Javanbakht, M.; Salavati-Niasari, M.; Shamsipur, M.; Yousefi, M. *Sens. Actuator B-Chem.* **2005**, *105*, 127–131.
270. Ganjali, M. R.; Norouzi, P.; Shirvani-Arani, S.; Salavati-Niasari, M. *Bull. Korean Chem. Soc.* **2005**, *26*, 1738–1742.
271. Ganjali, M. R.; Moghaddamb, M. R.; Norouzi, P.; Shirvani-Arani, S.; Daneshgar, P.; Adib, M.; Sobhi, H. R. *Anal. Lett.* **2006**, *39*, 683–695.
272. Sadeghi, S.; Fathi, F.; Ali Esmaeili, A.; Naeimi, H. *Sens. Actuator B-Chem.* **2006**, *114*, 928–935.
273. Sadeghi, S.; Gafarzadeh, A.; Naeimi, H. *J. Anal. Chem.* **2006**, *61*, 677–682.
274. Rogers, S. C.; Khalatbari, A.; Gapper, P. W.; Frenneaux, M. P.; James, P. E. *J. Biol. Chem.* **2005**, *280*, 26720–26728.
275. Kawamoto, T.; Mori, T.; Terashima, T.; Uji, S.; Kitagawa, H.; Takimiya, K.; Takamori, A.; Otsubo, T. *J. Phys. IV* **2004**, *114*, 517–519.
276. Kawamoto, T.; Mori, T.; Uji, S.; Yamaura, J. I.; Kitagawa, H.; Takamori, A.; Takimiya, K.; Otsubo, T. *Phys. Rev. B* **2005**, *71* (172503), 1–4.
277. Zhou, W. Y.; Xie, S. S.; Sun, L. F.; Tang, D. S.; Li, Y. B.; Liu, Z. Q.; Ci, L. J.; Zou, X. P.; Wang, G.; Tan, P.; Dong, X.; Xu, B.; Zhao, B. *Appl. Phys. Lett.* **2002**, *80*, 2553–2555.
278. Jung, Y.; Hwang, S. J.; Kim, S. J. *J. Phys. Chem. C* **2007**, *111*, 10181–10184.
279. Wang, Z. Y.; Wang, L.; Shi, Z. J.; Lu, J.; Gu, Z. N.; Gao, Z. X. *Chem. Commun.* **2008**, 3429–3431.
280. Alvarez, L.; Bantignies, J. L.; Le Parc, R.; Aznar, R.; Sauvajol, J. L.; Merlen, A.; Machon, D.; San Miguel, A. *Phys. Rev. B* **2010**, *82* (205403), 1–7.
281. Lota, G.; Fic, K.; Frackowiak, E. *Electrochem. Commun.* **2011**, *13*, 38–41.
282. Altansukh, B.; Haga, K.; Ariunbolor, N.; Kawamura, S.; Shibayama, A. *Eng. J. Thailand* **2016**, *20*, 29–40.
283. Altansukh, B.; Haga, K.; Huang, H. H.; Shibayama, A. *Mater. Trans.* **2019**, *60*, 287–296.
284. Batnasan, A.; Haga, K.; Shibayama, A. In *Rare Metal Technology 2018*; Kim, H., Wessstrom, B., Alam, S., Ouchi, T., Azimi, G., Neelameggham, N. R., Wang, S., Guan, X., Eds., Springer International Publishing Ag: Cham, 2018; pp 131–142.
285. Cuscusa, M.; Rigoldi, A.; Artizzu, F.; Cammi, F.; Fornasiero, P.; Marchio, L.; Serpe, A. *ACS Sustain. Chem. Eng.* **2017**, *5*, 4359–4370.
286. Li, X. H.; Li, Z.; Orefice, M.; Binnemans, K. *ACS Sustain. Chem. Eng.* **2019**, *7*, 2578–2584.
287. Li, X. H.; Van den Bossche, A.; Vander Hoogerstraete, T.; Binnemans, K. *Chem. Commun.* **2018**, *54*, 475–478.
288. Van den Bossche, A.; De Witte, E.; Dehaen, W.; Binnemans, K. *Green Chem.* **2018**, *20*, 3327–3338.
289. Van den Bossche, A.; Vereycken, W.; Vander Hoogerstraete, T.; Dehaen, W.; Binnemans, K. *ACS Sustain. Chem. Eng.* **2019**, *7*, 14451–14459.
290. May, B.; Lexow, M.; Taccardi, N.; Steinruck, H. P.; Maier, F. *Chem. Open* **2019**, *8*, 15–22.
291. Yao, A. N.; Qu, F.; Liu, Y.; Qu, G. Y.; Lin, H.; Hu, S. W.; Wang, X. Y.; Chu, T. W. *Dalton Trans.* **2019**, *48*, 16249–16257.
292. Kautek, W.; Conradi, A.; Fabjan, C.; Bauer, G. *Electrochim. Acta* **2001**, *47*, 815–823.
293. Bryans, D.; Berlouis, L.; Spicer, M.; McMillan, B. G.; Wark, A. In *Battery Electrolytes*; Wieczorek, W., Johansson, P., Marcinek, M., Lucht, B., DiNoto, V., Eds.; vol. 77; Electrochemical Society Inc.: Pennington, 2017; pp 33–36.
294. Duranti, M.; Macchi, E. G.; Crema, L. *J. Electrochem. Soc.* **2020**, *167* (100523), 1–8.
295. Gross, M. M.; Manthiram, A. *ACS Appl. Energy Mater.* **2019**, *2*, 3445–3451.
296. Su, L.; Badel, A. F.; Cao, C. S.; Hinricher, J. J.; Brushett, F. R. *Ind. Eng. Chem. Res.* **2017**, *56*, 9783–9792.
297. Hog, M.; Burgenmeister, B.; Bromberger, K.; Schuster, M.; Riedel, S.; Krossing, I. *ChemElectroChem* **2017**, *4*, 2934–2942.
298. Tian, H. J.; Zhang, S. L.; Meng, Z.; He, W.; Han, W. Q. *ACS Energy Lett.* **2017**, *2*, 1170–1176.
299. Li, B.; Nie, Z. M.; Vijayakumar, M.; Li, G. S.; Liu, J.; Sprenkle, V.; Wang, W. *Nat. Commun.* **2015**, *6* (6303), 1–8.
300. Li, X. J.; Xie, C. X.; Li, T. Y.; Zhang, Y. H.; Li, X. F. *Adv. Mater.* **2020**, *8* (2005036), 1–8.
301. Weng, G. M.; Li, Z. J.; Cong, G. T.; Zhou, Y. C.; Lu, Y. C. *Energ. Environ. Sci.* **2017**, *10*, 735–741.
302. Weinstein, L.; Yourey, W.; Gural, J.; Amatucci, G. G. *J. Electrochem. Soc.* **2008**, *155*, A590–A598.
303. Liu, Z. X.; Pu, X.; Gao, F.; Hu, W. Y.; Deng, H. Q. *Energy Storage Mater.* **2019**, *17*, 211–219.
304. Ren, Y. X.; Liu, M.; Zhao, T. S.; Zeng, L.; Wu, M. C. *J. Power Sources* **2017**, *342*, 9–16.
305. Ren, Y. X.; Zhao, T. S.; Jiang, H. R.; Wu, M. C.; Liu, M. *J. Power Sources* **2017**, *347*, 136–144.
306. Chang, Z.; Wang, X. J.; Yang, Y. Q.; Gao, J.; Li, M. X.; Liu, L. L.; Wu, Y. P. *J. Mater. Chem. A* **2014**, *2*, 19444–19450.
307. Kim, H.; Kwak, W. J.; Jung, H. G.; Sun, Y. K. *Energy Storage Mater.* **2019**, *19*, 148–153.
308. Hagfeldt, A.; Boschloo, G.; Sun, L.; Kloo, L.; Pettersson, H. *Chem. Rev.* **2010**, *110*, 6595–6663.
309. O'Regan, B.; Grätzel, M. *Nature* **1991**, *353*, 737–740.
310. Feldt, S. M.; Gibson, E. A.; Gabrielson, E.; Sun, L.; Boschloo, G.; Hagfeldt, A. *J. Am. Chem. Soc.* **2010**, *132*, 16714–16724.
311. Wang, M.; Chamberland, N.; Breau, L.; Moser, J.-E.; Humphry-Baker, R.; Marsan, M.; Zakeeruddin, S. M.; Grätzel, M. *Nat. Chem.* **2010**, *2*.
312. Tian, H.; Jiang, X.; Yu, Z.; Kloo, L.; Hagfeldt, A.; Sun, L. *Angew. Chem. Int. Ed.* **2010**, *49*, 7328–7331.
313. Nyhlen, J.; Boschloo, G.; Hagfeldt, A.; Kloo, L.; Privalov, T. *ChemPhysChem* **2010**, *11*, 1858–1862.
314. Yamanaka, N.; Kawano, R.; Kubo, W.; Kitamura, T.; Wada, Y.; Watanabe, M.; Yanagida, S. *Chem. Commun.* **2005**, 740–742.
315. Yamanaka, N.; Kawano, R.; Kubo, W.; Masaki, N.; Kitamura, T.; Wada, Y.; Watanabe, I.; Yanagida, S. *J. Phys. Chem. B* **2007**, *111*, 4763–4769.
316. Rowley, J. G.; Farnum, B. H.; Ardo, S.; Meyer, G. J. *J. Phys. Chem. Lett.* **2010**, *1*, 3132–3140.
317. Thorsmolle, V. K.; Brauer, J. C.; Zakeeruddin, S. M.; Grätzel, M.; Moser, J. E. *J. Phys. Chem. C* **2012**, *116*, 7989–7992.
318. Noriyo Yamanaka, R. K.; Kubo, W.; Kitamura, T.; Wada, Y.; Watanabe, M.; Yanagida, S. *Chem. Commun.* **2005**, 2005, 740–742.
319. Daniel Högberg, B. S.; Uchida, S.; Yoshio, M.; Kloo, L.; Segawa, H.; Kato, T. *Chem. Mater.* **2014**, *26*, 6496–6502.
320. Daniel Högberg, B. S.; Yatagai, R.; Uchida, S.; Yoshio, M.; Kloo, L.; Segawa, H.; Kato, T. *Chem. Mater.* **2016**, *28*, 6493–6500.
321. Tanaka, E.; Robertson, N. *J. Mater. Chem. A* **2020**, *8*, 19991–19999.
322. Luz, A.; Conradi, J.; Wolff, M.; Kalt, H.; Feldmann, C. *Solid State Sci.* **2013**, *19*, 172–177.
323. Chung, J.-H. S.; Jino, I. M.; Androulakis, J.; Malliakas, C. D.; Li, H.; Freeman, A. J.; Kenney, J. T.; Kanatzidis, M. G. *J. Am. Chem. Soc.* **2012**, *134*, 8579–8587.
324. Grätzel, M. *Nat. Mater.* **2014**, *13*, 838–842.
325. Sjoerd, A.; Veldhuis, P. P. B.; Yantara, N.; Li, M.; Sum, T. C.; Mathews, N.; Mhaisalkar, S. G. *Adv. Mater.* **2016**, *28*, 6804–6834.
326. Ozaki, N.; Sakamoto, H.; Nishihara, T.; Fujimori, T.; Hijikata, Y.; Kimura, R.; Irle, S.; Itami, K. *Angew. Chem. Int. Ed.* **2017**, *56*, 11196–11202.
327. Akin, S.; Akman, E.; Sonmezoglu, S. *Adv. Funct. Mater.* **2020**, *30* (2002964), 1–8.
328. Belich, N. A.; Petrov, A. A.; Rudnev, P. O.; Stepanov, N. M.; Turkevych, I.; Gudilin, E. A.; Tarasov, A. B. *ACS Appl. Mater. Interfaces* **2020**, *12*, 20456–20461.
329. Grishko, A. Y.; Petrov, A. A.; Goodilin, E. A.; Tarasov, A. B. *RSC Adv.* **2019**, *9*, 37079–37081.
330. Petrov, A. A.; Belich, N. A.; Grishko, A. Y.; Stepanov, N. M.; Dorofeev, S. G.; Maksimov, E. G.; Shevelkov, A. V.; Zakeeruddin, S. M.; Grätzel, M.; Tarasov, A. B.; Goodilin, E. A. *Mater. Horizons* **2017**, *4*, 625–632.
331. Petrov, A. A.; Tarasov, A. B. *Front. Chem.* **2020**, *8* (418), 1–6.

332. Turkevych, I.; Kazaoui, S.; Belich, N. A.; Grishko, A. Y.; Fateev, S. A.; Petrov, A. A.; Urano, T.; Aramaki, S.; Kosar, S.; Kondo, M.; Goodilin, E. A.; Graetzel, M.; Tarasov, A. B. *Nat. Nanotech.* **2019**, *14*, 57–64.
333. Udalova, N. N.; Tutantsev, A. S.; Chen, Q.; Kraskov, A.; Goodilin, E. A.; Tarasov, A. B. *ACS Appl. Mater. Interfaces* **2020**, *12*, 12755–12762.
334. Yamilova, O. R.; Danilov, A. V.; Mangrulkar, M.; Fedotov, Y. S.; Luchkin, S. Y.; Babenko, S. D.; Bredikhin, S. I.; Aldoshin, S. M.; Stevenson, K. J.; Troshin, P. A. *J. Phys. Chem. Lett.* **2020**, *11*, 221–228.
335. Maurer, A. B.; Hu, K.; Meyer, G. J. *J. Am. Chem. Soc.* **2017**, *139*, 8066–8069.
336. Meggiolaro, D.; Motti, S. G.; Mosconi, E.; Barker, A. J.; Ball, J.; Perini, C. A. R.; Deschler, F.; Petrozza, A.; De Angelis, F. *Energ. Environ. Sci.* **2018**, *11*, 702–713.
337. Zhang, L. H.; Sit, P. H. L. *J. Mater. Chem. A* **2017**, *5*, 23976–23986.
338. Ceratti, D. R.; Rakita, Y.; Cremonesi, L.; Tenne, R.; Kalchenko, V.; Elbaum, M.; Oron, D.; Potenza, M. A. C.; Hodes, G.; Cahen, D. *Adv. Mater.* **2018**, *30* (1706273), 1–7.



## 1.24 Synthesis, carbon-polymetal bonding and applications of organometallic clusters

**Kui Xiao and Liang Zhao**, Key Laboratory of Bioorganic Phosphorus Chemistry and Chemical Biology (Ministry of Education), Department of Chemistry, Tsinghua University, Beijing, China

© 2023 Elsevier Ltd. All rights reserved.

<b>1.24.1</b>	<b>Introduction</b>	<b>1050</b>
<b>1.24.2</b>	<b>Alkynyl ligands and alkenyl ligands</b>	<b>1051</b>
1.24.2.1	Metal alkynyl clusters with $\mu\text{-}\eta^1$ and $\mu\text{-}\eta^1, \eta^2$ modes	1051
1.24.2.2	Alkynyl metal clusters with $\mu_3\text{-}\eta^1$ ; $\mu_3\text{-}\eta^1, \eta^1, \eta^2$ and $\mu_3\text{-}\eta^1, \eta^2, \eta^2$ modes	1053
1.24.2.3	Alkynyl and alkenyl involved metal clusters with $\mu_4\text{-}\eta^1, \mu_4\text{-}\eta^1, \eta^1, \eta^2, \eta^2$ and $\mu_5\text{-}\eta^1, \eta^1, \eta^1, \eta^1, \eta^2$ modes	1060
1.24.2.4	Metal clusters protected by alkynyl ligands in multiple coordination modes	1061
<b>1.24.3</b>	<b>Aryl ligands</b>	<b>1062</b>
1.24.3.1	Aryl bridged <i>gem</i> -dimetal moieties in metal clusters	1062
1.24.3.2	Aryl involved metal clusters with $\mu_3\text{-}\eta^1$ mode	1064
1.24.3.3	Aryl ligands with adjacent two or three coordination sites	1065
<b>1.24.4</b>	<b>Alkyl carbons as coordination sites</b>	<b>1065</b>
1.24.4.1	Alkyl carbon centered metal clusters with $\mu_2\text{-}\eta^1$ and $\mu_3\text{-}\eta^1$ modes	1066
1.24.4.2	Alkyl carbon centered metal clusters with $\mu_4\text{-}\eta^1$ mode	1067
<b>1.24.5</b>	<b>Conclusion</b>	<b>1069</b>
<b>References</b>		<b>1069</b>

### Abstract

Organometallic clusters feature the aggregation of several metal atoms and the multi-centered carbon-metal bonding. Here are various carbon-polymetal bonds and considerable metal-metal interactions within the skeletons. The characteristic multi-bonding nature enables organometallic clusters to feature unique catalytic reactivity and optical properties. To date, a plethora of homo- or hetero- organometallic clusters with variable C–M<sub>n</sub> coordination modes and adjustable nuclear numbers are reported. This chapter summarizes the development of different types of carbon (*sp*<sup>3</sup>, *sp*<sup>2</sup>, *sp*) involved organometallic clusters. Based on the analysis of the well-defined structures and theoretical calculations, organometallic clusters show promising applications in organometallic catalysis and luminescent materials.

### 1.24.1 Introduction

Polynuclear organometallic clusters feature the aggregation of several metal atoms and the involvement of carbon-metal bonds. In typical mononuclear organometallic complexes, the carbon-metal bonding modes are relatively simple and can be divided into  $\sigma$ - or  $\pi$ -type. However, organometallic clusters always contain various carbon-polymetal bonds with mixed  $\sigma$  and  $\pi$ -type carbon-metal bonding and considerable metal-metal bonding. The characteristic multi-bonding nature enables organometallic clusters to feature unique synergistic mechanisms and multiple redox behaviors in catalytic reactions. Till now, organometallic clusters are extensively found as the organometallic reagent, the isolated intermediates of metal-catalyzed organic reaction, and homogeneous or heterogeneous catalysts.

On the other hand, the controllable synthesis of organometallic clusters is still challenging due to the variable coordination modes between different types of carbon (*sp*<sup>3</sup>, *sp*<sup>2</sup>, *sp*) and metal atoms, the complex homo- or hetero-metallic cores with adjustable nuclearity numbers, and the flexible cluster structures in solution. The current investigations on carbon-multimetal bonding and multi-metallic catalysis mainly rely on the structurally well-defined organometallic clusters. The development of X-ray crystallography and theoretical calculations play key roles in the field of organometallic clusters. Thus, this chapter will summarize the structures and reactivity studies of organometallic clusters classified by different organic ligands.

Many monographs and review articles of organometallic clusters have appeared in the preceding two decades.<sup>1</sup> The diverse structures with high nuclearity numbers and the applications concerned catalysis, electronic or optical materials as well as precursors for nanoscale materials are extensively reviewed. The chapter on *Synthesis, Carbon-Polymetal Bonding and Applications of Organometallic Clusters* is the first time summarized in *Comprehensive Inorganic Chemistry*. This chapter focuses on the bonding modes of carbon-polymetal bonds involved in organometallic clusters.

As a developing research field, significant progress has been made along with the development of structural characterization methods in the past few years. The metals treated in this chapter are mainly focus on the late transition metals of groups 8–12 and main group metals like Li, Al. This could be ascribed to the requirements of both stable carbon-metal interactions and metal-metal interactions in the formation of organometallic clusters. Among them, the coinage metals Cu, Ag, Au make up the majority of organometallic cluster compounds. One reason is the Cu(I), Ag(I) and Au(I) cations with a  $d^{10}$  closed-shell electronic configuration tend to aggregate together to form polynuclear cluster structures with high nuclear numbers. The other reason is the C–M bonds of late transition metals are more stable toward moisture and air than those of former ones. Thus, most examples for this chapter come from the organometallic cluster chemistry of Cu, Ag, Au, Fe, Ru, Os, Co, Rh, Ir, Ni, Pd, Li, and Al.

### 1.24.2 Alkynyl ligands and alkenyl ligands

Alkynyl ligands are applied to fabricate a large variety of coordination compounds due to their versatile interactions with transition metal atoms. The negatively charged  $RC\equiv C^-$  terminal of the alkynyl ligands can coordinate to 3–5 ( $\mu_3$ – $\mu_5$ ) metal atoms via both  $\sigma$  and  $\pi$  bonding in many metal clusters. Not only can the geometric structures of the alkynyl-protected clusters be engineered by the multiply coordination motifs, the electronic properties, and catalytic reactivity are also profoundly influenced by the delocalization of the  $\pi$  electrons of alkynyl. As the development of controllable synthetic methods, a series of organometallic alkynyl clusters of Group 8–12 metals with 3 to more than a hundred nuclear numbers were synthesized. Their structures and properties are summarized in the order of coordination modes as below.

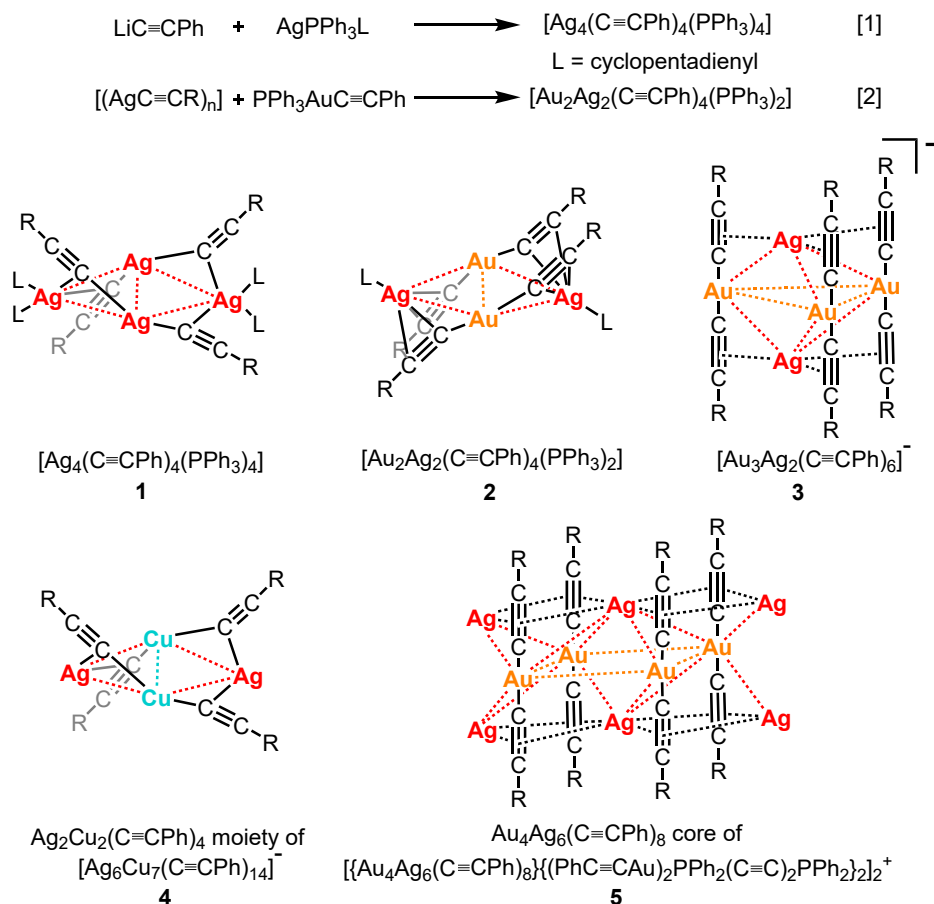
#### 1.24.2.1 Metal alkynyl clusters with $\mu$ - $\eta^1$ and $\mu$ - $\eta^1$ , $\eta^2$ modes

Polymeric coinage metal alkynyl complexes like  $[(AgC\equiv CR)_n]^7$  exhibit low solubility in most organic solvents. A typical strategy to obtain soluble metal alkynyl complexes relies on the employment of strong coordinative ligands like phosphane. In a tetranuclear cluster formulated as  $[M_2M'_2(C\equiv CR)_4(PPh_3)_n]$  ( $M = Ag$ ;  $M' = Ag, Au$ ;  $n = 2, 4$ ), the number of phosphane ligands determines the coordination modes of alkynyl ligands as  $\mu$ - $\eta^1$  or  $\mu$ - $\eta^1$ ,  $\eta^2$ . Using cyclopentadienyl (Cp) as a leaving group,  $[Ag_4(C\equiv CPh)_4(PPh_3)_4]$  (1) (Fig. 1 Eq. [1]) was prepared by adding  $LiC\equiv CPh$  to  $CpAgPPh_3$  in 1:1 M ratio.<sup>2</sup> The structure consists of a tetranuclear “flat-butterfly” silver cluster (Ag–Ag 2.921(1)–3.084(1) Å), with two apical  $Ag(PPh_3)_2$  moieties connected with the other two “hinge” Ag atoms by  $\mu$ - $\eta^1$ -C $\equiv$ CPh. Each “hinge” Ag atom is  $\sigma$ -bonded to two alkynyl ligands with the C–Ag–C angles of 171.6(3)° and 174.6(3)°. Due to the coordination of two  $PPh_3$  ligands, each apical Ag atom is only bonded to the terminal carbon of adjacent alkynyl ligands. Moreover, the addition of one equiv. silver phenylacetylide to a solution of  $PPh_3AuC\equiv CPh$  produced  $[Au_2Ag_2(C\equiv CPh)_4(PPh_3)_2]$  (2) (Fig. 1 Eq. [2]) with a nearly square planar metal tetragon (Au–Ag 2.894–3.028 Å).<sup>3</sup> Each gold atom is  $\sigma$ -bonded to two alkynyl ligands in a nearly linear fashion and each silver atom is coordinated by one  $PPh_3$  then  $\pi$ -bonded to two alkynyl units via a  $\mu$ - $\eta^1$ ,  $\eta^2$  mode. Complex  $[Au_4\{(C\equiv C)_2Fc'\}_2(PPh_3)_2]$  ( $Fc' = Fe(\eta-C_5H_4-)_2$ ) is in the same skeleton with  $[Au_2Ag_2(C\equiv CR)_4(PPh_3)_2]$  but with a tetranuclear gold core with the Au–Au distances in the range of 3.003(1)–3.296(1) Å.<sup>8</sup>

It is noteworthy that  $RC\equiv C^-$  ligands prefer to  $\pi$ -bond to Ag and  $\sigma$ -bond to Au in a  $\mu$ - $\eta^1$ ,  $\eta^2$  coordination mode. More significantly, mixing  $[(AuPR_3)_2\{\mu-Ar(C\equiv C)_{2-1,2}\}]$  with  $AgClO_4$  at a molar ratio of 2:1 generated  $[Ag\{(AuPR_3)_2\{\mu-Ar(C\equiv C)_{2-1,2}\}\}_2]ClO_4$  ( $R = C_6H_4Me-4$ ).<sup>9</sup> The encased Ag ion is  $\pi$ -bonded to four  $C\equiv CAu$  fragments through quadruple  $\mu$ - $\eta^1$  mode. Similarly, two  $\pi$ -bonded Ag atoms could crosslink three collinear  $[RC\equiv CAuC\equiv CR]^-$  moieties via triple  $\mu$ - $\eta^1$ ,  $\eta^2$  coordination to each Ag, finally forming gold-silver pentanuclear cluster  $[Au_3Ag_2(C\equiv CPh)_6]^-$  (3) (Fig. 1).<sup>4</sup> The parallel  $[RC\equiv CAuC\equiv CR]^-$  anions form an equilateral triangle and two Ag atoms are fixed on the 3-fold axis via triple interactions with six carbon atoms. The trigonal-bipyramidal  $Ag_2Au_3$  cluster has six axial-equatorial Ag–Au bonds ranging from 2.854(2) to 3.040(1) Å and three long equatorial-equatorial Au–Au distance at an average of 3.95 Å. However, these pentanuclear clusters reversibly dissociate to the linear and polymeric complexes. In this regard, applying rigid diphosphino-gold cationic species could trap the above-mentioned trigonal-bipyramidal cluster analogs.<sup>6</sup>  $[\{Au_8Ag_{10}(C\equiv CPh)_{16}\}\{(PhC\equiv CAu)_2-PPh_2(C_6H_4)_3PPh_2\}_2]^{2+}$ ,  $[\{Au_4Ag_6(C\equiv CPh)_8\}\{(PhC\equiv CAu)_2PPh_2(C\equiv C)_2PPh_2\}_2]^{2+}$  (5),  $[\{Au_3Ag_2(C\equiv CPh)_6\}_2\{AuPPh_2(CH_2)_4PPh_2\}_6]^{4+}$  (Fig. 1) all demonstrated effective phosphorescence and negligible oxygen quenching, which benefit from the involving  $C\equiv C$  moieties with rich metal–metal contacts in the charge transfer processes and the shielding of the emissive central cluster by the outer shell.

In addition, alkynyl ligands in the  $\mu$ - $\eta^1$  and  $\mu$ - $\eta^1$ ,  $\eta^2$  coordination modes also play an important role in the construction of close-packed clusters. An anionic cluster  $[Ag_6Cu_7(C\equiv CPh)_{14}]^-$  (4) (Fig. 1) was synthesized through mixing  $[RC\equiv CAgC\equiv CR]^-$  with  $[(AgC\equiv CR)_n]$  and  $[(CuC\equiv CR)_n]$ .<sup>5</sup> This bimetallic cluster contains one internal Cu core with two attached alkynyl ligands, 12 circumjacent metal atoms, and 12 attached alkynyl ligands. The peripheral metal atoms are divided into three rectangles with Ag and Cu bonded alternately. In each subcluster  $[Ag_2Cu_2(C\equiv CPh)_4]$ , each Cu atom is  $\sigma$ -bonded by two  $RC\equiv C^-$  in almost linear fashion and the adjacent Ag atoms are  $\pi$ -bonded by two  $RC\equiv C^-$  via a  $\mu$ - $\eta^1$  coordination mode, which is similar with the  $[Au_2Ag_2(C\equiv CR)_4(PPh_3)_2]$  cluster mentioned above.

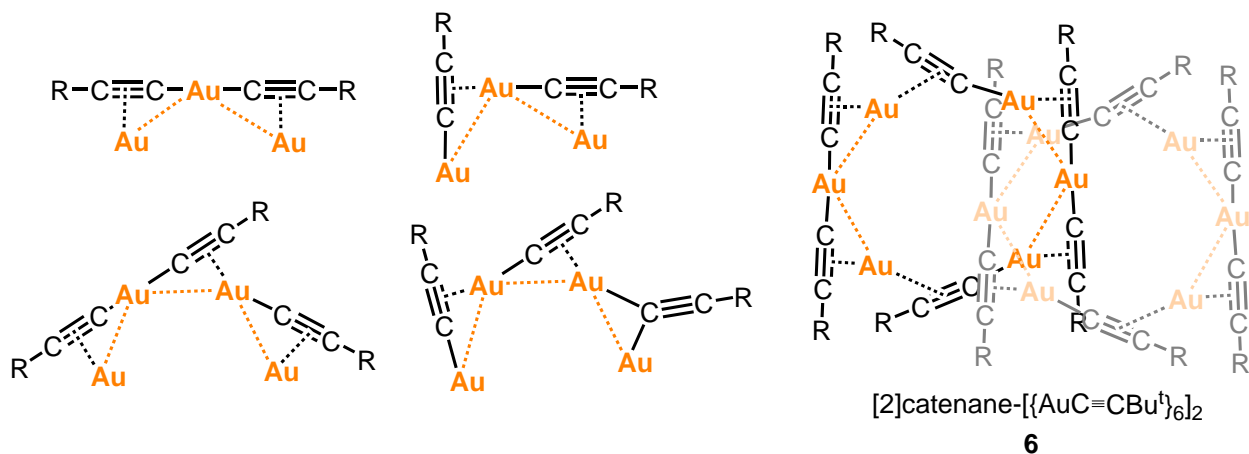
In the surface of alkynyl protected gold nanoclusters with a high nuclearity number, the moieties in  $\mu$ - $\eta^1$ ,  $\eta^2$  coordination mode could share the  $\sigma$ -bonded and  $\pi$ -bonded Au to constitute linear, L-shaped  $RC\equiv C-Au-C\equiv CR$  or V-shaped  $RC\equiv C-Au-C\equiv C(R)-Au-C\equiv CR$  (Fig. 2).<sup>10</sup> In 1995, a [2]catenane- $[\{AuC\equiv CBu^1\}_6]_2$  consisting of two  $Au_6$  rings each linked by six  $\mu$ - $\eta^1$ ,  $\eta^2$  alkynyl ligands (6) (Fig. 2) was reported.<sup>11</sup> This kind of linking arrangement was later found in many peripheral stable motifs of alkynyl protected gold nanoclusters. A series of alkynyl-protected gold nanoclusters were prepared by the direct reduction of  $[AuC\equiv CPh]_n$



**Fig. 1** Examples of  $\mu$ - $\eta^1$  metal alkynyl clusters.  $[\text{Ag}_4(\text{C}\equiv\text{CPh})_4(\text{PPh}_3)_4]$ ,<sup>2</sup>  $[\text{Au}_2\text{Ag}_2(\text{C}\equiv\text{CPh})_4(\text{PPh}_3)_2]$ ,<sup>3</sup>  $[\text{Au}_3\text{Ag}_2(\text{C}\equiv\text{CPh})_6]^-$ ,<sup>4</sup>  $[\text{Ag}_6\text{Cu}_7(\text{C}\equiv\text{CPh})_{14}]^-$ ,<sup>5</sup>  $\{[\text{Au}_4\text{Ag}_6(\text{C}\equiv\text{CPh})_8](\text{PhC}\equiv\text{CAu})_2\text{PPh}_2(\text{C}\equiv\text{C})_2\text{PPh}_2\}_2^{2+}$ .<sup>6</sup>

and other gold salts. The surface binding structures of alkynyl ligands revealed by crystal structure determination showed a typical V-shaped stable motif in  $[\text{Au}_{19}(\text{C}\equiv\text{CPh})_9(\text{Hdppa})_3](\text{SbF}_6)_2$  (Hdppa = *N,N*-bis-(diphenylphosphino)amine)<sup>12</sup> and L-shaped stable motif in  $[\text{Au}_{24}(\text{C}\equiv\text{CPh})_{14}(\text{PPh}_3)_4](\text{SbF}_6)_2$ ,<sup>13</sup> which could be ascribed to the horizontal or perpendicular orientation of alkynyl ligands.

Apart from the construction of diverse stable-protected gold clusters, the electronic perturbation through  $\pi$ -conjugated  $\text{C}\equiv\text{C}$  could modulate the electronic properties of the whole organometallic cluster and then influence their optical absorption,



**Fig. 2** Stable motifs in alkynyl-protected gold nanoclusters and  $[\text{2}]$ catenane- $\{[\text{AuC}\equiv\text{CBu}]_6\}_2$ .<sup>10,11</sup>

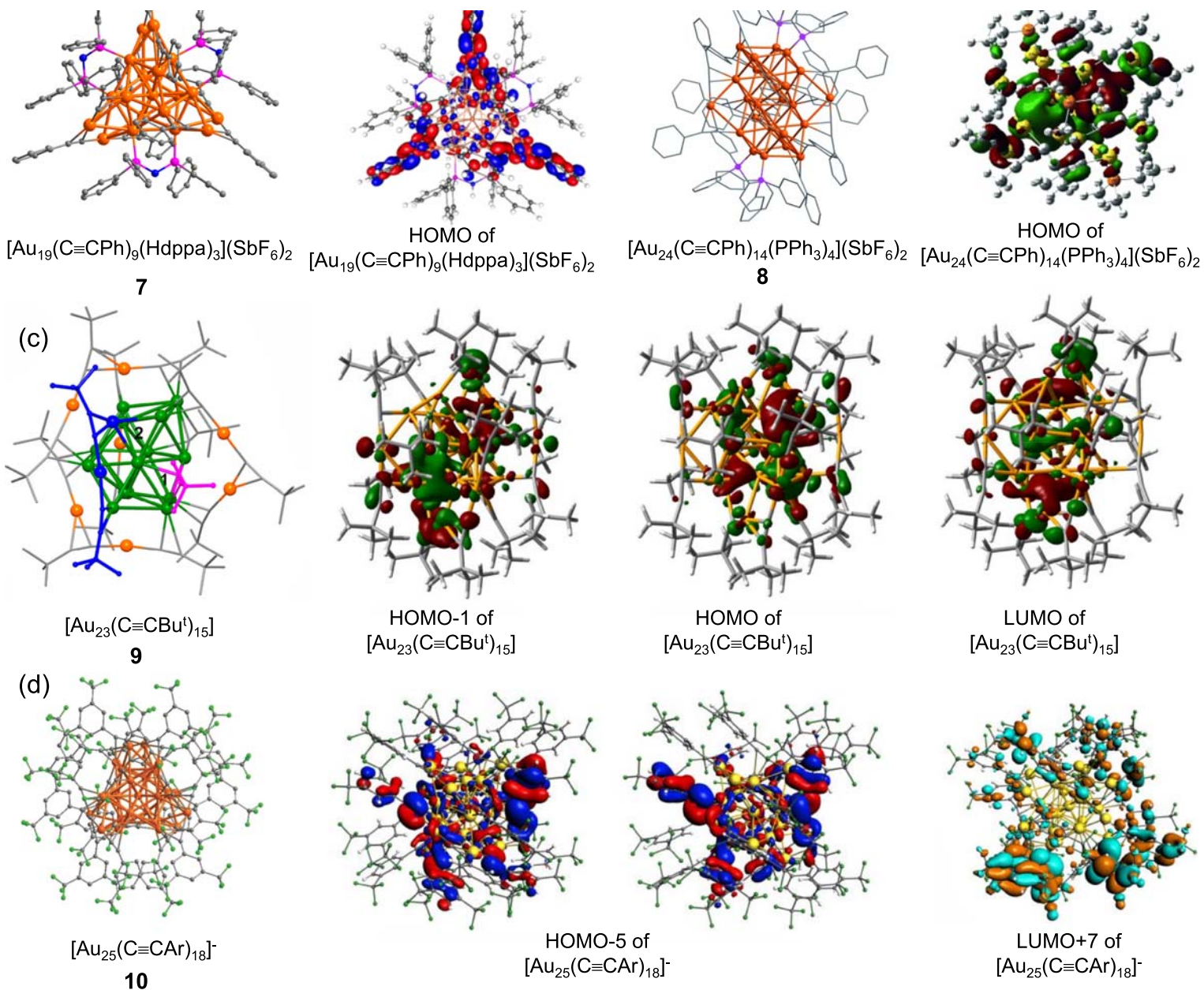
luminescence, and catalysis performance.  $[\text{Au}_{19}(\text{C}\equiv\text{CPh})_9(\text{Hdppa})_3](\text{SbF}_6)_2$  (7) (Fig. 3A and B) comprises a centered icosahedral  $\text{Au}_{13}$  kernel encapsulated by three V-shaped motifs. Orbital analysis revealed that the HOMO-1 (HOMO = highest occupied molecular orbital) spreads on all  $\text{C}\equiv\text{CPh}$  groups, indicating the dominant participation of alkynyl ligands in the frontier orbitals of the whole cluster.<sup>12</sup> A couple of cluster isomers of  $[\text{Au}_{23}(\text{C}\equiv\text{CBu}^t)_{15}]^{14}$  (8) (Fig. 3C and D) both have a  $\text{Au}_{15}$  core and two bridging  $\text{C}\equiv\text{CBu}^t$ , two linear  $\text{Bu}^t\text{C}\equiv\text{C}-\text{Au}-\text{C}\equiv\text{CBu}^t$  and three V-shaped motifs. TDDFT (time-dependent density functional theory) calculations demonstrated that the  $\text{Au}_{15}$  core and V-shaped alkynyl-gold motifs mainly contribute to the HOMO-1, HOMO, and LUMO (lowest unoccupied molecular orbital) orbitals of the  $\text{Au}_{23}$  cluster.  $[\text{Au}_{24}(\text{C}\equiv\text{CPh})_{14}(\text{PPh}_3)_4](\text{SbF}_6)_2$  (9) (Fig. 3E and F) contains a  $\text{Au}_{22}$  kernel two L-shaped alkynyl-gold motifs, and ten simple bridging  $\text{C}\equiv\text{CPh}$  via a  $\mu-\eta^1$ ,  $\eta^2$  coordination mode. Some weak coupling between the s and d orbitals of the gold core and the  $\pi^*$  orbitals of the alkynyl ligands were largely found in the HOMO orbital. Strong near-IR emission ( $\lambda_{\text{ex}} = 380$  nm,  $\lambda_{\text{em}} = 925$  nm, quantum yield = 0.12) originating from the HOMO-LUMO transition was found in this double cuboctahedra-cored  $\text{Au}_{24}$  cluster.<sup>13</sup>  $[\text{Au}_{25}(\text{C}\equiv\text{CAr})_{18}]^-$  (10) (Fig. 3G and H) (Ar = 3,5-bis(trifluoromethyl)-phenyl) is a cluster analogous to  $[\text{Au}_{25}(\text{SR})_{18}]^-$ , which share the same  $\text{Au}_{13}$  kernel but adopt different arrangement of the six peripheral V-shaped stable motifs.<sup>15</sup> The chiral  $[\text{Au}_{25}(\text{C}\equiv\text{CAr})_{18}]^-$  cluster exhibits a  $D_3$  symmetry due to the steric hindrance of the alkynyl ligands while  $[\text{Au}_{25}(\text{SR})_{18}]^-$  is achiral. The steric hindrance also causes higher stability toward  $\text{H}_2\text{O}_2$  for this alkynyl-protected  $\text{Au}_{25}$  cluster than its thiolate-protected analog. As a result of the introduction of a large portion of C(p) character to the HOMO-5 and LUMO+7 orbitals of the cluster, the optical absorption features of  $[\text{Au}_{25}(\text{C}\equiv\text{CAr})_{18}]^-$  display a different profile in comparison with that of  $[\text{Au}_{25}(\text{SR})_{18}]^-$ . Similarly,  $[\text{Au}_{36}(\text{C}\equiv\text{CPh})_{24}]$  and  $[\text{Au}_{44}(\text{C}\equiv\text{CPh})_{28}]$  showed distinctly different UV-Vis spectra with their thiolate-protected analogs  $[\text{Au}_{36}(\text{SR})_{24}]$  and  $[\text{Au}_{44}(\text{SR})_{28}]$  because of the disturbance of their electronic structures by peripheral  $\mu-\eta^1$  and  $\mu-\eta^1$ ,  $\eta^2$  alkynyl ligands.<sup>16</sup>

More significantly, the surface structures especially the metal-ligand interface can influence the catalytic activities of the cluster.  $[\text{Au}_{38}(\text{C}\equiv\text{CPh})_{20}(\text{PPh}_3)_4]^{2+}$  (11) (Fig. 4A) and  $[\text{Au}_{38}(\text{3-methylbenzenethiol})_{20}(\text{PPh}_3)_4]^{2+}$  contain the same fcc-type  $\text{Au}_{34}$  core and four similar L-shaped stable motifs and 12  $\mu-\eta^1$ ,  $\eta^2$  bridging ligands.<sup>17</sup> The two clusters were supported on  $\text{TiO}_2$  to study the catalytic performance in the semihydrogenation transformation of alkynes into alkenes. Although the two  $\text{Au}_{38}$  clusters are isostructural, the conversion of the alkynyl protected  $\text{Au}_{38}$  clusters was larger than 97% (turnover number up to 88,195 within 24 h; Z-alkenes selectivity >93%) while the thiolate protected  $\text{Au}_{38}$  clusters was inactive (conversion <2%). The facts indicate that the alkynyl protected clusters have advantages of promoting the dissociation of  $\text{H}_2$  absorbed on the cluster, which is the key step for the semihydrogenation of both terminal and internal alkynes in this process. Moreover, the alkynyl protected 62-core intermetallic cluster  $[\text{Au}_{34}\text{Ag}_{28}(\text{C}\equiv\text{CPh})_{34}]$  (12) (Fig. 4B) was used to study the hydrolytic oxidation of organosilanes to silanols by using activated carbon as a support.<sup>18</sup> There are 17  $\text{PhC}\equiv\text{C}-\text{Au}-\text{C}\equiv\text{CPh}$  stable motifs in pentagonal stripes at the outermost layer of the cluster and the surface alkynyl ligands are readily removed upon thermal treatment, while the metal framework remains intact. However, the cluster capped with surface ligands has higher catalytic activities than the  $\text{Au}_{34}\text{Ag}_{28}$  kernel without surface ligands, which is usually supposed to have more active sites without blocking ligands. More importantly, re-treating the non-ligand protected cluster with deprotonated terminal alkynes enabled the catalysis to recover. It is evidenced that alkynyl ligands play an important role in improving the catalytic activities of the organometallic clusters.  $[\text{Au}_{144}(\text{C}\equiv\text{CC}_6\text{H}_4\text{F}-2)_{60}]$  is a typical example of  $\mu-\eta^1$ ,  $\eta^2$ - $\text{C}\equiv\text{CR}$  protected gold nanocluster with a very high nuclearity number.<sup>19</sup> The  $\text{A}_{12}@A_{42}@A_{60}$  shell-by-shell arranged  $\text{Au}_{114}$  core is further enwrapped by 30 linear  $\text{RC}\equiv\text{C}-\text{Au}-\text{C}\equiv\text{CR}$  stable motifs. This  $\text{Au}_{144}$  cluster keeps the structure intact in solution under ambient conditions for 6 weeks, implying that the Au-alkynyl stable motifs are also qualified to support large metal nanoclusters.

#### 1.24.2.2 Alkynyl metal clusters with $\mu_3-\eta^1$ ; $\mu_3-\eta^1$ , $\eta^1$ , $\eta^2$ and $\mu_3-\eta^1$ , $\eta^2$ , $\eta^2$ modes

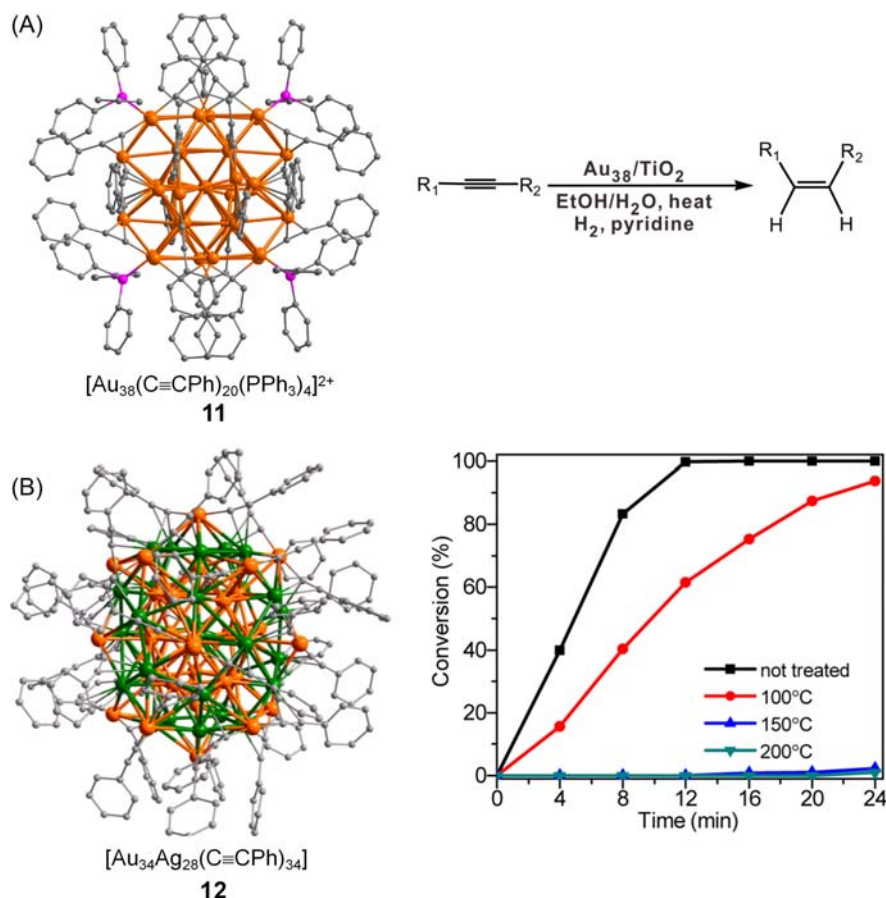
The  $\mu_3$  coordination mode is adopted by a wide variety of trinuclear metal acetylides and trimer metal moieties in alkynyl-protected clusters. A typical example is  $[\text{Cu}_3(\mu\text{-dppm})_3(\mu_3-\eta^1\text{-C}\equiv\text{CPh})](\text{BF}_4)_2$  (dppm =  $\text{PPh}_2\text{CH}_2\text{PPh}_2$ ),<sup>22</sup> a triangular copper cluster with each edge bridged by a dppm ligands and one face capped by a  $\mu_3-\eta^1\text{-C}\equiv\text{CPh}$  ligand. The phenylacetylide ligand shows a bond angle of  $176(2)^\circ$  and the typical  $\text{C}\equiv\text{C}$  distance of  $1.22(2)\text{\AA}$  indicates negligible  $\pi$ -interaction. Notably, the three edges of the triangle  $\text{Cu}_3$  (2.904(3), 2.813(3), 3.274(3) $\text{\AA}$ ) are shorter than those (3.120(2), 3.127(2), 3.322(2) $\text{\AA}$ ) in  $[\text{Cu}_3(\mu\text{-dppm})_3(\mu_3-\eta^1\text{-OH})](\text{BF}_4)_2$  due to the better  $\sigma$ -donation of alkynyl ligands. By capping the other face with a chloride atom,  $[\text{Cu}_3(\mu\text{-dppm})_3(\mu_3-\eta^1\text{-C}\equiv\text{CBu}^t)(\mu_3\text{-Cl})]\text{PF}_6$ <sup>23</sup> contains an isosceles triangular array of  $\text{Cu}_3$  with shorter Cu-Cu edges (2.791(2), 2.927(2), 2.754(2) $\text{\AA}$ ) than  $[\text{Cu}_3(\mu\text{-dppm})_3(\mu_3-\eta^1\text{-C}\equiv\text{CPh})](\text{BF}_4)_2$ . Moreover, the bicapped triangular  $\text{Cu}_3$  cluster  $[\text{Cu}_3(\mu\text{-dppm})_3(\mu_3-\eta^1\text{-C}\equiv\text{CPh})_2]\text{BF}_4$ <sup>20</sup> (13) (Fig. 5A) with a linear  $\mu_3-\eta^1$  fashion was prepared via adding more  $\text{HC}\equiv\text{CPh}$ . The Cu-Cu distances (average 2.594(3) $\text{\AA}$ ) of the bicapped  $\text{Cu}_3\text{C}_2$  system are much shorter than the mono-capped ones. In contrast, the Cu-C bond lengths (2.063(18)-2.342(17) $\text{\AA}$ ) of the bicapped  $\text{Cu}_3\text{C}_2$  system are significantly larger than the mono-capped ones. This suggests that the electrons of the three-center-two-electron ( $3c-2e$ )  $\text{Cu}_3\text{C}_2$  system are more localized at the  $\text{Cu}_3$  center. More importantly, it was found that the  $\sigma$ -donation of the alkynyl ligands could influence the structures, photoluminescence and electrochemistry of these bicapped  $\text{Cu}_3$  clusters.<sup>21</sup> Two mix-capped trinuclear copper acetylide complexes  $[\text{Cu}_3(\mu\text{-dppm})_3(\mu_3-\eta^1\text{-C}\equiv\text{CC}_6\text{H}_4\text{OMe-}p)(\mu_3-\eta^1\text{-C}\equiv\text{CC}_6\text{H}_4\text{OEt-}p)]\text{PF}_6$  and  $[\text{Cu}_3(\mu\text{-dppm})_3(\mu_3-\eta^1\text{-C}\equiv\text{CC}_6\text{H}_4\text{OMe-}p)(\mu_3-\eta^1\text{-C}\equiv\text{CC}_6\text{H}_4\text{NO}_2\text{-}p)]\text{PF}_6$  were synthesized by treating Cu precursors with 1:1 M ratio of mixed ligands. As the result of the nitro electron-withdrawing group, the Cu-Cu distances (average 2.674(1) $\text{\AA}$ ) in the nitro substituted cluster is longer than those (average 2.601(1) $\text{\AA}$ ) of the ethoxyl-substituted cluster. The two mix-capped clusters both show long-lived and intense luminescence in solid state and fluid solutions. However, the nitro-substituted cluster emitted at a much lower energy (671 nm, 0.2  $\mu\text{s}$ , 298 K) than the ethoxyl-substituted cluster (475 nm, 502 nm, 17.6  $\mu\text{s}$ , 298 K) in the solid state. It is conjectured that the electron deficient 4-nitrophenylacetylide changes the lowest lying excited states from ligand-to-metal charge transfer (LMCT) to intraligand  $\pi \rightarrow \pi^*(\text{RC}\equiv\text{C}^-)$  character. The irreversible electrode process upon the oxidation of the nitro-substituted cluster is also in sharp contrast to the quasi-reversible oxidation couple





**Fig. 3** (A), (B) HOMO of  $[\text{Au}_{19}(\text{C}\equiv\text{CPh})_9(\text{Hdppa})_3](\text{SbF}_6)_2$ .<sup>12</sup> Color codes: orange, Au; gray, C; blue, N; pink, P. (C), (D) HOMO-1, HOMO and LUMO of  $[\text{Au}_{23}(\text{C}\equiv\text{CBu}^t)_{15}]$ .<sup>14</sup> Color codes: orange, dark green, Au; gray, C; blue, linear “ $^t\text{Bu}-\text{C}\equiv\text{C}-\text{Au}-\text{C}\equiv\text{C}-\text{Bu}^t$ ” motif; pink, alkynyl bridge. (E), (F) HOMO of  $[\text{Au}_{24}(\text{C}\equiv\text{CPh})_{14}(\text{PPh}_3)_4](\text{SbF}_6)_2$ .<sup>13</sup> Color codes: orange, Au; gray, C; pink, P. (G), (H) HOMO-5 (doubly degenerated) and LUMO + 7 of  $[\text{Au}_{25}(\text{C}\equiv\text{CAr})_{18}]^-$ .<sup>15</sup> Color codes: orange, Au; gray, C; green, F. From Wan, X.-K.; Tang, Q.; Yuan, S.-F.; Jiang, D.-e.; Wang, Q.-M. *J. Am. Chem. Soc.* **2015**, *137*, 652–655; Wan, X. K.; Xu, W. W.; Yuan, S.-F.; Gao, Y.; Zeng, X.-C.; Wang, Q.-M. *Angew. Chem. Int. Ed.* **2015**, *54*, 9683–9686; Guan, Z.-J.; Hu, F.; Li, J.-J.; Wen, Z.-R.; Lin, Y.-M.; Wang, Q.-M. *J. Am. Chem. Soc.* **2020**, *142*, 2995–3001; Li, J.-J.; Guan, Z.-J.; Lei, Z.; Hu, F.; Wang, Q.-M. *Angew. Chem. Int. Ed.* **2019**, *58*, 1083–1087.

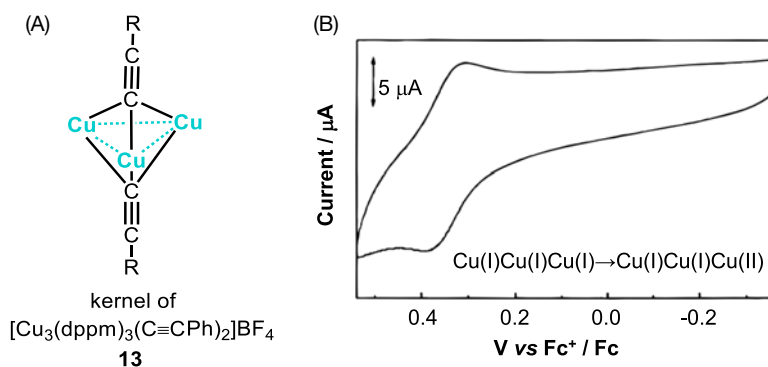




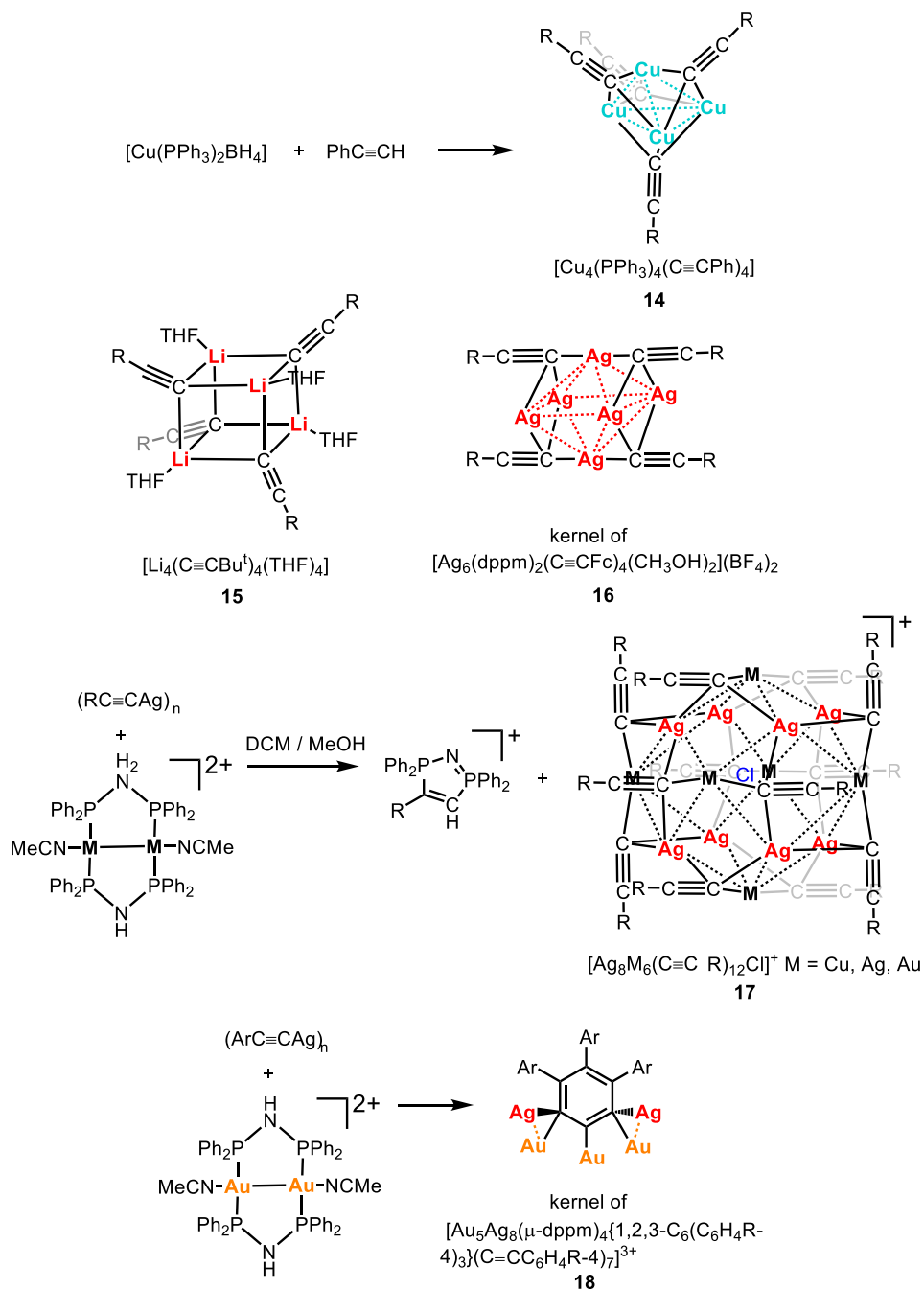
**Fig. 4** (A) catalytic performance of  $[\text{Au}_{38}(\text{C}\equiv\text{CPh})_{20}(\text{PPh}_3)_4]^{2+}$  in the semihydrogenation reactions.<sup>17</sup> Color codes: orange, Au; gray, C; pink, P. (B) catalytic performance of  $[\text{Au}_{34}\text{Ag}_{28}(\text{C}\equiv\text{CPh})_{34}]$  in the hydrolytic oxidation reactions.<sup>18</sup> Color codes: orange, Au; green, Ag; gray, C. From Wan, X.-K.; Wang, J.-Q.; Nan, Z.-A.; Wang, Q.-M. *Sci. Adv.* **2017**, *3*, e1701823; Wang, Y.; Wan, X.-K.; Ren, L.; Su, H.; Li, G.; Malola, S.; Lin, S.; Tang, Z.; Häkkinen, H.; Teo, B. K.; Wang, Q.-M.; Zheng, N. *J. Am. Chem. Soc.* **2016**, *138*, 3278–3281.

of  $\text{Cu(I)Cu(I)Cu(I)} \rightarrow \text{Cu(I)Cu(I)Cu(II)}$  (Fig. 5B) at ca. +0.33 V vs  $\text{Fc}^+/\text{Fc}$  for the ethoxyl-substituted cluster. Clearly, weakening the  $\sigma$ -donation of the alkynyl ligands would significantly reduce the stability of the  $\text{Cu}_3$  clusters toward oxidation. In addition, the bicapped triangular  $\text{Ag}_3$  analog  $[\text{Ag}_3(\mu\text{-dppm})_3(\mu_3\text{-}\eta^1\text{-C}\equiv\text{CPh})_2]\text{Cl}^{24}$  was prepared by the reaction of  $[(\text{AgC}\equiv\text{CR})_n]$  with dppm. At room temperature, this isostructural  $\text{Ag}_3$  cluster only has a solid-state emission at 440 nm with a lifetime of 0.43  $\mu\text{s}$ , which is different with  $[\text{Cu}_3(\mu\text{-dppm})_3(\mu_3\text{-}\eta^1\text{-C}\equiv\text{CPh})_2]\text{PF}_6$  ( $\lambda_{\text{em}} = 494$  nm,  $\tau_0 = 6.5$   $\mu\text{s}$  in solution and  $\lambda_{\text{em}} = 493$  nm,  $\tau_0 = 14$   $\mu\text{s}$  in solid state).

Alkynyl ligands can also protect metal clusters as peripheral ligands via the  $\mu_3\text{-}\eta^1$  coordination modes. The first  $\mu_3\text{-}\eta^1$  bridging alkynyl ligand was reported in 1985. Complex  $[\text{Cu}_4(\text{PPh}_3)_4(\mu_3\text{-}\eta^1\text{-C}\equiv\text{CPh})_4]$  (14) (Fig. 6) was obtained by treatment of



**Fig. 5** (A) Example of  $\mu_3\text{-}\eta^1$  coordination mode in  $\text{Cu}_3$  cluster.<sup>20</sup> (B) Cyclic voltammogram of  $[\text{Cu}_3(\mu\text{-dppm})_3(\mu_3\text{-}\eta^1\text{-C}\equiv\text{CC}_6\text{H}_4\text{OMe-}p)(\mu_3\text{-}\eta^1\text{-C}\equiv\text{CC}_6\text{H}_4\text{OEt-}p)]\text{PF}_6$  in acetonitrile (0.1 M  $n\text{Bu}_4\text{NPF}_6$ ) showing the quasi-reversible oxidation couple. Scan rate: 100 mV/s.<sup>21</sup>



**Fig. 6** Examples of metal alkynyl clusters in the  $\mu_3\text{-}\eta^1$  coordination modes.  $[\text{Cu}_4(\text{PPh}_3)_4(\mu_3\text{-}\eta^1\text{-C}\equiv\text{CPh})_4]$ ,<sup>25</sup>  $[\text{Li}_4(\mu_3\text{-}\eta^1\text{-C}\equiv\text{CBu}^t)_4(\text{THF})_4]$ ,<sup>25</sup>  $[\text{Ag}_6(\mu\text{-dppm})_2(\mu_3\text{-}\eta^1\text{-C}\equiv\text{CFc})_4(\text{CH}_3\text{OH})_2](\text{BF}_4)_2$ ,<sup>25</sup>  $[\text{Ag}_8\text{M}_6(\mu_3\text{-}\eta^1\text{-C}\equiv\text{CFc})_{12}\text{Cl}]\text{BF}_4$  ( $\text{M} = \text{Cu}, \text{Ag}, \text{Au}$ ),<sup>26</sup>  $[\text{Au}_5\text{Ag}_8(\mu\text{-dppm})_4\{1,2,3\text{-C}_6(\text{C}_6\text{H}_4\text{R-4})_3\}(\text{C}\equiv\text{CC}_6\text{H}_4\text{R-4})_7\}]^{3+}$ .<sup>27</sup>

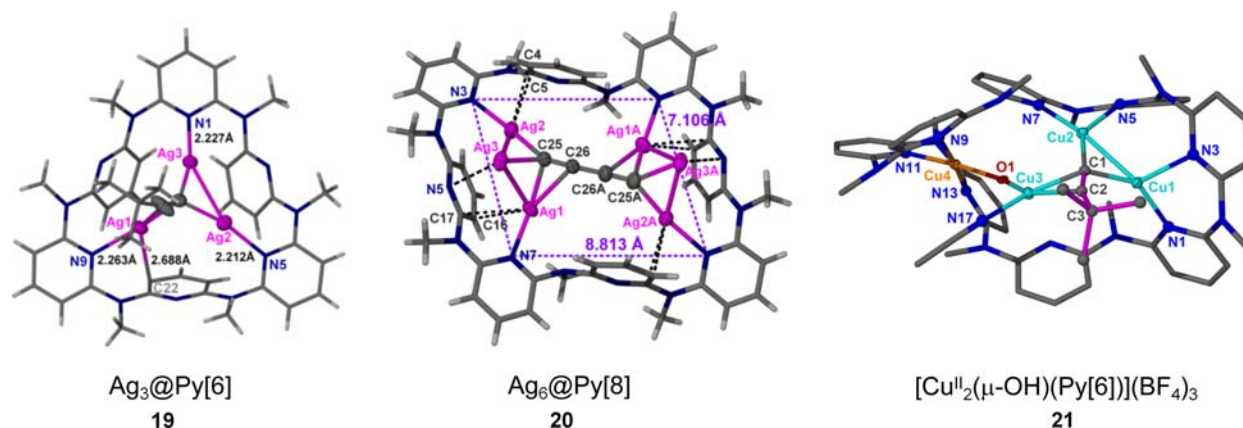
$[\text{Cu}(\text{PPh}_3)_2]\text{BH}_4$  with one equiv. phenylacetylene.<sup>28</sup> This  $\text{Cu}_4$  cluster consists of a tetrahedral metal skeleton bearing four  $\text{PPh}_3$  ligands at each vertex and four  $\mu_3\text{-}\eta^1$  bridging alkynyl ligands capping to each face. The  $\text{Cu}\text{-Cu}$  average distance is 2.603 Å and the  $\text{Cu}\text{-C}$  contacts of the asymmetric  $\mu_3\text{-}\eta^1$  coordination mode are in the range of 2.072(4)–2.380(4) Å. The structure of the  $\text{C}\text{-Cu}_3$  moieties is in line with the trimer ones mentioned above. Two  $\mu_3\text{-}\eta^1\text{-C}\equiv\text{CFc}$  ( $\text{Fc} = \text{ferrocenyl}$ ) capped octahedral hexanuclear clusters  $[\text{Ag}_6(\mu\text{-dppm})_2(\mu_3\text{-}\eta^1\text{-C}\equiv\text{CFc})_4(\text{CH}_3\text{OH})_2](\text{BF}_4)_2$  (**16**) (Fig. 6) and  $[\text{Cu}_6(\mu\text{-dppm})_2(\mu_3\text{-}\eta^1\text{-C}\equiv\text{CFc})_4(\text{ClO}_4)_2]$  were reported.<sup>29</sup> Four of the eight  $\text{M}_3$  ( $\text{M} = \text{Ag}, \text{Cu}$ ) trigonal planes in the octahedral  $\text{M}_6$  cluster are capped by the asymmetric  $\mu_3\text{-}\eta^1$ -bonded acetylides. And the equatorial  $\text{M}_4$  plane is bridged by two  $\text{dppm}$  ligands. The asymmetric  $\mu_3\text{-}\eta^1$ -bonding mode in  $\text{Ag}_6$  cluster has one short  $\text{Ag}\text{-C}$  distance (2.059(9)–2.099(9) Å) and two longer ones (2.304(9)–2.436(9) Å). Similarly, the asymmetric  $\mu_3\text{-}\eta^1$ -bonding mode in  $\text{Cu}_6$  cluster has one short  $\text{Cu}\text{-C}$  distance (1.897(10)–1.898(11) Å) and two longer ones

(2.116(10)–2.230(10)Å). However, no appreciable responses referred to electronic communication between Fc group and the  $M_6$  core are found in the cyclic voltammogram of the  $\mu_3\text{-}\eta^1\text{-C}\equiv\text{CFC}$  capped  $M_6$  clusters, which is in contrast with the obvious responses revealed by the  $\mu_3\text{-}\eta^1\text{-C}\equiv\text{CFC}$  bicapped triangular  $[\text{Cu}_3(\mu\text{-dppm})_3(\mu_3\text{-}\eta^1\text{-C}\equiv\text{CFC})_2]\text{PF}_6$  clusters.<sup>30</sup> This could be ascribed to that the bicapped coordination mode contains more direct electronic interaction. In 2001, it was reported a series of halide anions templated silver-alkynyl cage-type complexes  $[\text{Ag}_{14}(\mu_3\text{-}\eta^1\text{-C}\equiv\text{CBu}^t)_{12}\times\text{Y}]$  ( $\text{X} = \text{F}, \text{Cl}, \text{Br}; \text{Y} = \text{OH}, \text{BF}_4$ ).<sup>31</sup> The authors isolated  $[\text{Ag}_{14}(\mu_3\text{-}\eta^1\text{-C}\equiv\text{CBu}^t)_{12}\text{Cl}]\text{OH}$  when they tried to recrystallize the hard-soluble  $[\text{Ag}(\text{C}\equiv\text{CBu}^t)]_n$  in chloroform. This strategy is proven to be generally applied by adding  $[\text{NBu}_4]\text{Br}$  and  $[\text{NBu}_4]\text{F}$  to the synthesis of  $[\text{Ag}_{14}(\mu_3\text{-}\eta^1\text{-C}\equiv\text{CBu}^t)_{12}\text{Br}]\text{BF}_4$  and  $[\text{Ag}_{14}(\mu_3\text{-}\eta^1\text{-C}\equiv\text{CBu}^t)_{12}\text{F}]\text{BF}_4$  respectively. These molecular  $O_h$  symmetric clusters are composed of a halide anion at the center, a near-regular rhombic dodecahedron shaped  $\text{Ag}_{14}$  cage, and 12 peripheral asymmetric coordinated  $\mu_3\text{-}\eta^1\text{-C}\equiv\text{CBu}^t$  ligands. Later, it was found that  $[\text{Ag}_{14}(\mu_3\text{-}\eta^1\text{-C}\equiv\text{CBu}^t)_{12}](\text{BF}_4)_2$  could also be synthesized without templated halide-anions and the  $\text{Ag}\text{--}\text{Ag}$  distances 2.945(1)Å are equal to the corresponding bonds 2.971(2)Å in the chloride-encapsulated cage.<sup>32</sup> Moreover, a  $[3+2]$  addition product 1,2,5-azadiphospholium  $[\text{Fc}(\text{C}_2\text{HNP}_2)\text{Ph}_4]\text{BF}_4$  in the synthesis process of rhombic dodecahedral  $[\text{Ag}_8\text{M}_6(\mu_3\text{-}\eta^1\text{-C}\equiv\text{CFC})_{12}\text{Cl}]\text{BF}_4$  ( $\text{M} = \text{Cu}, \text{Ag}, \text{Au}$ ) (17) (Fig. 6) was found.<sup>26</sup> The  $[\text{Fc}(\text{C}_2\text{HNP}_2)\text{Ph}_4]\text{BF}_4$  is obtained from the cyclic addition between the  $\text{Ph}_2\text{PNHPh}_2$  in  $[\text{M}_2(\text{Ph}_2\text{PNHPh}_2)_2(\text{MeCN})_2]^{2+}$  ( $\text{M} = \text{Cu}, \text{Ag}, \text{Au}$ ) and the  $\text{HC}\equiv\text{CFC}$ . Subsequently, the  $\text{Cu}(\text{I})$ -catalyzed azide-terminal alkyne cycloaddition reactivity of the  $\text{Bu}^t\text{C}\equiv\text{CCu}\equiv\text{CBu}^t$  moieties on the surface of the  $[\text{Ag}_8\text{Cu}_6(\mu_3\text{-}\eta^1\text{-C}\equiv\text{CBu}^t)_{12}\text{Cl}]\text{BF}_4$  cluster was studied.<sup>33</sup> As expected, 1,4-disubstituted 1,2,3-triazole is isolated in 83% yield after treating the cluster with benzyl azide.

Moreover, the bimetallic  $[\text{Au}_6\text{Ag}_{13}(\mu\text{-dppm})_3(\mu_3\text{-}\eta^1\text{-C}\equiv\text{CC}_6\text{H}_4\text{CH}_3\text{-4})_{14}]^{5+}$  cluster was prepared by the reactions of  $[\text{AgC}\equiv\text{CC}_6\text{H}_4\text{CH}_3\text{-4}]_n$  with  $[\text{Au}_2(\mu\text{-dppm})_2]^{2+}$ .<sup>34</sup> The middle part of the cluster is a triangular prismatic framework composed of six  $\text{Ag}$  atoms with another  $\text{Ag}$  atom lying at the center of the triangular prism. Each of the two triangular  $\text{Ag}_3$  faces is capped by a symmetrically bonded  $\mu_3\text{-}\eta^1$  alkynyl ligand. And six  $\text{RC}\equiv\text{C}\text{--}\text{Au}\text{--}\text{C}\equiv\text{C}\text{--}\text{R}$  ( $\text{R} = \text{--C}_6\text{H}_4\text{CH}_3\text{-4}$ ) moieties in quasi-linear arrangements are adjacent to the  $\text{Ag}\text{--}\text{Ag}$  edges of the triangular prismatic core. Three  $\mu\text{-dppmAg}_2$  motifs are connected by  $\text{RC}\equiv\text{C}\text{--}\text{Au}\text{--}\text{C}\equiv\text{C}\text{--}\text{R}$  motifs forming 12  $\text{RC}\equiv\text{C}\text{--}\text{AuAg}_2$  groups in an asymmetric  $\mu_3\text{-}\eta^1$  mode. Just like the triangular clusters, the  $\text{Au}_6\text{Ag}_{13}$  cluster also shows intense luminescence emission at 560 nm ( $\tau_0 = 5.66 \mu\text{s}$ ,  $\Phi_{\text{em}} = 0.112$ ) in solution. Notably, this light-sensitive  $\text{Au}_6\text{Ag}_{13}$  cluster will photolyze into a more stable  $[\text{Au}_5\text{Au}_8(\mu\text{-dppm})_4\{\mu_5\text{-}1,2,3\text{-C}_6(\text{C}_6\text{H}_4\text{CH}_3\text{-4})_3\}(\text{C}\equiv\text{CC}_6\text{H}_4\text{CH}_3\text{-4})_7]^{3+}$  cluster with a penta-metallized aryl core via a  $\mu_5\text{-C,C,C}\text{-}\eta^2, \eta^1, \eta^2$  mode (18) (Fig. 6). The cyclotrimerization of the arylacetylide  $\text{C}\equiv\text{CC}_6\text{H}_4\text{CH}_3\text{-4}$  in to  $1,2,3\text{-C}_6(\text{C}_6\text{H}_4\text{CH}_3\text{-4})_3^{3-}$  trianions was first found by Chen in early work.<sup>27</sup> This  $\mu_5\text{-C,C,C}\text{-}\eta^2, \eta^1, \eta^2$  coordination mode will be discussed in 1.14.3.3 *vide infra*.

Except for the coinage metals, alkynyl-protected poly-lithium clusters also tend to take the  $\mu_3\text{-}\eta^1$  coordination mode. Two *tert*-butylethynyllithium clusters, (15) (Fig. 6) and  $[\text{Li}_{12}(\mu_3\text{-}\eta^1\text{-C}\equiv\text{CBu}^t)_{12}(\text{THF})_4]$ , are isolated from THF-containing solutions.<sup>25</sup> The tetrameric organolithium complex shows a twisted cubane skeleton of  $\text{Li}_4\text{C}_4$ , in which four vertexes are terminal carbons of the  $\text{Bu}^t\text{C}\equiv\text{C}$  in  $\mu_3\text{-}\eta^1$  coordination modes and the other four vertexes are THF protected  $\text{Li}$  atoms. This tetranuclear  $\text{Li}$  cluster could grow into a dodeca-nuclear one and the two clusters both would effloresce very readily. This  $\text{Li}_{12}$  cluster is composed of linear coupling of three cubane-like  $\text{Li}_4$  subunits, resulting in four  $\mu_3\text{-}\eta^1$  coordinated  $\text{Bu}^t\text{C}\equiv\text{C}$  vertexes and eight  $\mu_4\text{-}\eta^1$  coordinated  $\text{Bu}^t\text{C}\equiv\text{C}$  linkages.

Taking the advantages of flexible conformation, size tunability and cooperative coordination of a class of emerging macrocycles, azacalix[ $n$ ]pyridines (Py[ $n$ ]s), a series of alkynyl centered organometallic clusters with different nuclearity numbers and coordination modes were captured. In this part, Py[6] and Py[8] encapsulated silver and copper alkynyl clusters with the  $\mu_3\text{-}\eta^1, \eta^1, \eta^2$  and  $\mu_3\text{-}\eta^1, \eta^2, \eta^2$  modes will be introduced. In a typical example  $\{(\text{CF}_3\text{SO}_3)_{1.5}\text{Ag}_{3.5}(\mu_3\text{-}\eta^1, \eta^1, \eta^2\text{-C}\equiv\text{CBu}^t)(\text{Py}[6])\}^+$  (19) (Fig. 7),<sup>37</sup> the



**Fig. 7** Py[ $n$ ]s captured Ag and Cu clusters with  $\mu_3$  coordinated alkynyl center.  $\{(\text{CF}_3\text{SO}_3)_{1.5}\text{Ag}_{3.5}(\mu_3\text{-}\eta^1, \eta^1, \eta^2\text{-C}\equiv\text{CBu}^t)(\text{Py}[6])\}^+$ <sup>25</sup>  $\{[\text{Ag}_3\text{C}\equiv\text{CC}\equiv\text{C}\text{Ag}_3] \subset \text{Py}[8]\}^{4+}$ <sup>35</sup>  $\{[\text{Cu}_3\text{Cu}^{\text{II}}(\mu_3\text{-}\eta^1, \eta^1, \eta^2\text{-Bu}^t\text{C}\equiv\text{C})(\mu\text{-OH})(\text{CH}_3\text{CN})] \subset \text{Py}[8]\}^{3+}$ <sup>36</sup> From Gao, C. Y.; Zhao, L.; Wang, M. X. *J. Am. Chem. Soc.* **2012**, *134*, 824–827; Gao, C.-Y.; He, X.; Zhao, L.; Wang, M.-X. *Chem. Commun.* **2012**, *48*, 8368–8370; Zhang, S.; Zhao, L. *Nat. Commun.* **2019**, *10*, 4848.

size of Py[6] is well-matched with a Ag<sub>3</sub>-acetylide moiety, wherein the Ag<sub>3</sub> triangle is situated on the concave surface of the bowl-shaped Py[6]. The pyridines of the polydentate macrocyclic ligands supply flexible coordination to support one Ag atom η<sup>2</sup>-bonded to the Bu<sup>1</sup>C≡C (Ag–C bond lengths: 2.231(6) and 2.372(7)Å) and two Ag atoms σ-bonded to the terminal *sp*-carbon (Ag–C bond lengths: 2.109(6) and 2.126(6)Å; Ag–Ag bond length: 3.019(1)Å). The {[Ag<sub>3</sub>C≡CR] ⊂ Py[6]}<sup>2+</sup> (C represents encirclement) complexes are also applicable to other alkynyls like phenylacetylide.<sup>35</sup> Furthermore, di-acetylide such as 1,3-butadiynediide and 1,4-phenylenediacytylide could bridge two Ag<sub>3</sub> moieties, consequently generating a clamlike {[Ag<sub>3</sub>C≡CC≡CAg<sub>3</sub>] ⊂ (Py[6])<sub>2</sub>}<sup>4+</sup> and a dumbbell-like {[Ag<sub>3</sub>C≡C–C<sub>6</sub>H<sub>4</sub>–C≡CAg<sub>3</sub>] ⊂ (Py[6])<sub>2</sub>}<sup>4+</sup>.<sup>36</sup> Due to the different lengths of the carbon chain adapted to distinct face-to-face conformation of the macrocycles, {[Ag<sub>3</sub>C≡CC≡CAg<sub>3</sub>] ⊂ (Py[6])<sub>2</sub>}<sup>4+</sup> is arranged in a μ<sub>3</sub>-η<sup>1</sup>, η<sup>1</sup>, η<sup>2</sup> coordination mode and {[Ag<sub>3</sub>C≡C–C<sub>6</sub>H<sub>4</sub>–C≡CAg<sub>3</sub>] ⊂ (Py[6])<sub>2</sub>}<sup>4+</sup> is in a μ<sub>3</sub>-η<sup>1</sup>, η<sup>2</sup>, η<sup>2</sup> fashion. Upon the use of a larger macrocycle Py[8], the Ag<sub>3</sub>C≡CC≡CAg<sub>3</sub> aggregate can be encapsulated in one parallelogram conformational Py[8] molecule forming {[Ag<sub>3</sub>C≡CC≡CAg<sub>3</sub>] ⊂ Py[8]}<sup>4+</sup> (**20**) (Fig. 7).<sup>36</sup> And two pile-up Ag<sub>3</sub>C≡C–C<sub>6</sub>H<sub>4</sub>–C≡CAg<sub>3</sub> aggregates are protected by two Py[8] molecules through sharing one silver atom at each side generating {[Ag<sub>5</sub>(C≡C–C<sub>6</sub>H<sub>4</sub>–C≡C)<sub>2</sub>Ag<sub>5</sub>] ⊂ (Py[8])<sub>2</sub>}<sup>6+</sup>. Moreover, by employing Py[8] as a peripheral ligand, a mixed-valence copper acetylide cluster merging with a copper-oxygen moiety, {[Cu<sup>1</sup><sub>3</sub>-Cu<sup>II</sup>(μ<sub>3</sub>-η<sup>1</sup>, η<sup>1</sup>, η<sup>2</sup>-Bu<sup>1</sup>C≡C)(μ-OH)(CH<sub>3</sub>CN)] ⊂ Py[8]}<sup>3+</sup> (**21**) (Fig. 7),<sup>38</sup> is trapped from the Glaser coupling condition. The acetylide-centered trinuclear copper cluster composed of two σ-bonded Cu<sup>I</sup> atoms (Cu–C distances: 1.892(5)–1.973(5)Å) and one π-bonded Cu<sup>I</sup> atom (Cu–C distances: 1.994(5)–2.015(5)Å) while the π-bonded Cu<sup>I</sup> atom is connected with the Cu<sup>II</sup> atom via a μ<sub>2</sub>-hydroxo. Notably, the significant [d<sub>Cu(I)</sub> → π\*(C≡C)] back donation (long C–C distance: 1.241(8)Å and deviated bond angle: 161.0(5)°) enables the π-bonded Cu<sup>I</sup> atom featuring uneven positive charge, resulting in a remarkably strong oxidation capacity (E<sub>1/2</sub> = 0.77 V vs NHE) of (μ<sub>3</sub>-η<sup>1</sup>, η<sup>1</sup>, η<sup>2</sup>-Bu<sup>1</sup>C≡CCu<sup>1</sup>)-(μ<sub>2</sub>-OH)-Cu<sup>I</sup>. Consequently, this bi-cluster exhibits high reactivity in single-electron transfer and hydrogen atom transfer reactions for a broad scope of substrates like alcohol, amine, alkene and even hydrocarbons with C(*sp*<sup>3</sup>)-H bond dissociation energy (BDE) up to 99 kcal mol<sup>-1</sup>.

Trinuclear group 8 metal clusters have rich reactions with alkynes. For example, Bu<sup>1</sup>C≡CH can react with Ru<sub>3</sub>(CO)<sub>12</sub> to generate [HRu<sub>3</sub>(CO)<sub>9</sub>(C≡CBu<sup>1</sup>)] cluster with a μ<sub>3</sub>-η<sup>1</sup>, η<sup>2</sup>, η<sup>2</sup> fashion. And the bridging H atom can be further removed by OH<sup>-</sup> in CO atmosphere to form [Ru<sub>3</sub>(CO)<sub>9</sub>(C≡CBu<sup>1</sup>)]<sup>-</sup> cluster (**22**) (Fig. 8).<sup>39</sup> In the two clusters, the terminal carbon atom of the alkynyl ligand is significantly close to one σ-bonded Ru atom than the other two π-bonded Ru atoms (Ru–C<sub>terminal</sub> distances of the protonated cluster: 1.947(3), 2.207(3), and 2.214(3)Å; Ru–C<sub>terminal</sub> distances of the deprotonated cluster: 1.95(2), 2.18(2), and 2.16(2)Å). And the carbon-carbon bond lengths (1.315(3)Å for the protonated one and 1.27(3)Å for the deprotonated one) are slightly elongated due to the double [d<sub>Ru</sub> → π\*(C≡C)] back donation. The C≡C–C bond angles are also significantly deviated to 141.0(2)° for the protonated one and 141(2)° for the deprotonated one.

At the surface of the coinage metal nanoclusters with high nuclearity numbers, the Au shell is more trend to take the μ<sub>2</sub>-η<sup>1</sup>, η<sup>2</sup> bridged stable motifs as mentioned above, but the Ag and Cu shells are usually composed of the μ<sub>3</sub> coordination modes. Mak and Wang have reported a class of anion-templated high-nuclearity Ag alkynyl clusters with general cage structures. Here are SO<sub>4</sub><sup>2-</sup> templated [Ag<sub>21</sub>(C≡CBu<sup>1</sup>)<sub>18</sub>(SO<sub>4</sub>)<sup>+</sup> (**23**) (Fig. 9), SiF<sub>6</sub><sup>-</sup> templated [Ag<sub>24</sub>(C≡CBu<sup>1</sup>)<sub>20</sub>(SiF<sub>6</sub>)<sup>+</sup>, CrO<sub>4</sub><sup>2-</sup> templated [Ag<sub>22</sub>(C≡CBu<sup>1</sup>)<sub>18</sub>(CrO<sub>4</sub>)<sup>2+</sup> (**24**) (Fig. 9) and [Ag<sub>35</sub>(C≡CPh)<sub>28</sub>(CrO<sub>4</sub>)<sub>2</sub>(TMEDA)<sub>4</sub>]<sup>3+</sup> (TMEDA = *N,N,N',N'*-tetramethylethylenediamine).<sup>40</sup> In these anion-templated silver clusters, the interstitial anions are encapsulated by the peripheral Ag skeletons which are composed of alkynyl ligands bridged Ag<sub>3</sub> triangles. In addition, two Ag nanoclusters [Ag<sub>19</sub>(dppm)<sub>3</sub>(C≡CPh)<sub>14</sub>]<sup>3+</sup> (**25**) (Fig. 9) and [Ag<sub>25</sub>(dpppe)<sub>3</sub>(C≡CPhOMe-4)<sub>20</sub>]<sup>3+</sup> (**26**) (Fig. 9) (dpppe = 1,5-bis(diphenylphosphino)pentane) both feature a centered anticuboctahedral Ag<sub>13</sub> core and peripheral Ag<sub>2</sub> motifs.<sup>41</sup> Two alkynyl ligands cap the top and bottom Ag<sub>3</sub> triangles of the Ag<sub>13</sub> core via a μ<sub>3</sub>-η<sup>1</sup> mode and the other alkynyl ligands link the peripheral Ag<sub>2</sub> units with the Ag<sub>13</sub> core via a μ<sub>3</sub>-η<sup>1</sup>, η<sup>2</sup>, η<sup>2</sup> mode. In a bimetallic Au<sub>19</sub>Cu<sub>30</sub> nanocluster [Au<sub>19</sub>Cu<sub>30</sub>(C≡CR)<sub>22</sub>(PPh<sub>3</sub>P)<sub>6</sub>Cl<sub>2</sub>]<sup>3+</sup> (**27**) (Fig. 9) (R = thiophene-3 or benzene), the alkynyl protected Cu<sub>30</sub>Au<sub>6</sub> shell surrounds a centered icosahedral Au<sub>13</sub> kernel.<sup>42</sup> All the 22 alkynyl ligands function as μ<sub>3</sub>-bridges on the Cu<sub>3</sub> or Cu<sub>2</sub>Au triangles of Cu<sub>30</sub>Au<sub>6</sub> shell via μ<sub>3</sub>-η<sup>1</sup>(Cu), η<sup>1</sup>(Cu), η<sup>1</sup>(Cu); μ<sub>3</sub>-η<sup>1</sup>(Cu), η<sup>1</sup>(Cu), η<sup>2</sup>(Cu); μ<sub>3</sub>-η<sup>1</sup>(Cu), η<sup>2</sup>(Cu), η<sup>2</sup>(Cu) and μ<sub>3</sub>-η<sup>1</sup>(Au), η<sup>2</sup>(Cu), η<sup>2</sup>(Cu) modes. Similarly, in an all-alkynyl protected Ag<sub>74</sub> nanocluster [Ag<sub>74</sub>(C≡CPh)<sub>44</sub>],<sup>43</sup> all 44 phenylethynyl ligands are coordinated with Ag<sub>3</sub> triangles in μ<sub>3</sub>-η<sup>1</sup>, μ<sub>3</sub>-η<sup>1</sup>, η<sup>1</sup>, η<sup>2</sup> and μ<sub>3</sub>-η<sup>1</sup>, η<sup>2</sup>, η<sup>2</sup> modes forming a protective monolayer. The structures demonstrate that both the Cu and Ag surfaces of the coinage nanoclusters prefer the μ<sub>3</sub>-bridge triangle coordination modes instead of the μ-η<sup>1</sup>, η<sup>2</sup> stable motifs at Au surfaces. The difference could be ascribed to the preference for the linear double coordination of gold atoms and the energy privilege of creating gold adatoms on the surface of gold nanoclusters.

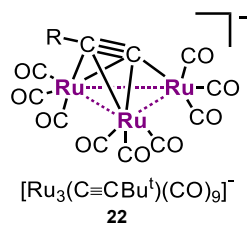
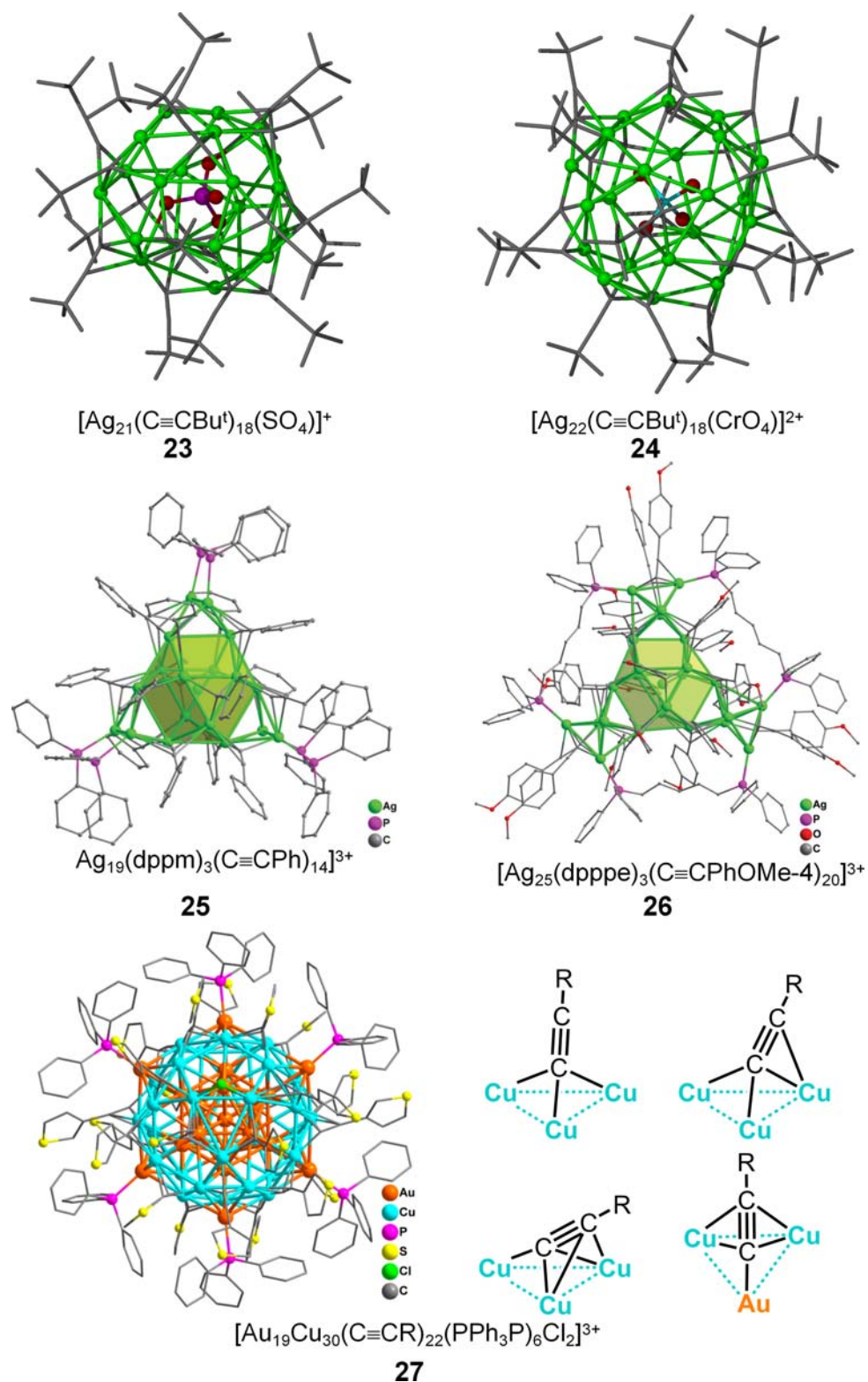


Fig. 8 Example of the μ<sub>3</sub>-η<sup>1</sup>, η<sup>2</sup>, η<sup>2</sup> coordination mode in [Ru<sub>3</sub>(CO)<sub>9</sub>(C≡CBu<sup>1</sup>)]<sup>-</sup> cluster.<sup>39</sup>





**Fig. 9** Examples of multiple  $\mu_3$  coordination modes in Ag and Cu shells of metal clusters.  $[\text{Ag}_{21}(\text{C}\equiv\text{C}^t\text{Bu})_{18}(\text{SO}_4)]^+$  (Color codes: green, Ag; gray, C; red, O; purple, S) and  $[\text{Ag}_{22}(\text{C}\equiv\text{C}^t\text{Bu})_{18}(\text{CrO}_4)]^{2+}$  (Color codes: green, Ag; gray, C; cyan, Cr; red, O),<sup>40</sup>  $[\text{Ag}_{19}(\text{dppm})_3(\text{C}\equiv\text{CPh})_{14}]^{3+}$  and  $[\text{Ag}_{25}(\text{dpppe})_3(\text{C}\equiv\text{CPhOMe-4})_{20}]^{3+}$ ,<sup>41</sup>  $[\text{Au}_{19}\text{Cu}_{30}(\text{C}\equiv\text{CR})_{22}(\text{PPh}_3\text{P})_6\text{Cl}_2]^{3+}$ .<sup>42</sup> From Bian, S.-D.; Wu, H.-B.; Wang, Q.-M. *Angew. Chem. Int. Ed.* **2009**, *48*, 5363–5365; Yuan, S.-F.; Li, P.; Tang, Q.; Wan, X.-K.; Nan, Z.-A.; Jiang, D.-e.; Wang, Q.-M. *Nanoscale* **2017**, *9*, 11405–11409; Wan, X.-K.; Cheng, X.-L.; Tang, Q.; Han, Y.-Z.; Hu, G.; Jiang, D.-e.; Wang, Q.-M. *J. Am. Chem. Soc.* **2017**, *139*, 9451–9454.



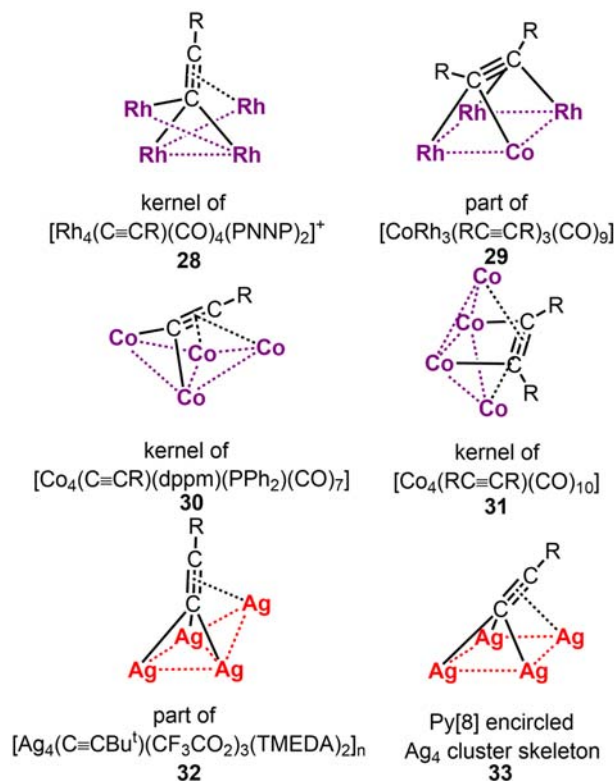
1.24.2.3 Alkynyl and alkenyl involved metal clusters with  $\mu_4\text{-}\eta^1$ ,  $\mu_4\text{-}\eta^1, \eta^1, \eta^2$  and  $\mu_5\text{-}\eta^1, \eta^1, \eta^1, \eta^1, \eta^2$  modes

The alkynyl ligand can also be coordinated to four metal atoms forming the  $\mu_4$  cluster units. For instance, cationic tetranuclear acetylide complex  $[\text{Rh}_4(\text{C}\equiv\text{CR})(\text{CO})_4(\text{PNNP})_2]^+$  (**28**) (Fig. 10) ( $\text{R} = p\text{-tol}$ ; PNNP = 3,5-bis((diphenylphosphino)methyl)pyrazolato) composes of a  $\mu_4\text{-}\eta^1, \eta^1, \eta^1, \eta^2$  coordinated center.<sup>44</sup> Each tetradentate PNNP ligand can protect two Rh atoms and the two parts are connected by a *p*-tolylethynyl. The molecular structure determined by X-ray crystallography shows the four Rh atoms are arranged in a folded Z-shaped linkage and one wingtip Rh atom has a moderate distance of 2.386(5) Å with the  $\text{C}_\beta$  of the  $\text{C}_\alpha\equiv\text{C}_\beta\text{R}$ . Meanwhile, the  $\text{C}_\alpha$  exhibits tetra-fold interactions with all the four Rh atoms (Rh- $\text{C}_\alpha$  distances: 2.151(4), 2.223(4), 2.309(4) and 2.335(4) Å), leading to a  $\mu_4\text{-}\eta^1, \eta^1, \eta^1, \eta^2$  coordination mode.

The  $\mu_4\text{-}\eta^1, \eta^1, \eta^1, \eta^2$  coordination units are also found in some counter-anions linked  $[\text{C}_2\text{Ag}_4]$  aggregates. A kind of  $[\text{Ag}_4\text{C}_4\text{Ag}_4]$  aggregates,  $\text{Ag}_8(\text{C}\equiv\text{C}-\text{C}\equiv\text{C})(\text{NO}_3)_6(\text{H}_2\text{O})_m$  ( $m = 2, 3$ ), is obtained by the reaction of  $[\text{Li}_2(\text{C}\equiv\text{C}-\text{C}\equiv\text{C})]$  with  $\text{AgNO}_3$ .<sup>50</sup> In the crystal structure, each terminal carbon atom of the  $\text{C}_4^{2-}$  anion is capped by a butterfly-like  $\text{Ag}_4$  basket. In each  $\mu_4\text{-}\eta^1, \eta^1, \eta^1, \eta^2$  coordinated  $\text{C}_2\text{Ag}_4$  unit, one Ag atom is  $\pi$ -bonded to the adjacent triple bond of  $\text{C}_\alpha\equiv\text{C}_\beta\text{-C}_\beta\equiv\text{C}_\alpha$  with  $\text{Ag-C}_\beta = 2.633(8)$  Å, longer than the other  $\sigma$ -bonded  $\text{Ag-C}_\alpha$  distances (2.161(8)-2.338(8) Å). The  $[\text{Ag}_4\text{C}_4\text{Ag}_4]$  arrays are linked by nitrate groups into a layer, then further generating a network with the linkage of the remaining nitrate groups. This coordination is stabilized by the inner argentophilic interactions and the outer ionic network. Likewise, the  $[\text{C}_2\text{Ag}_4]$  aggregates,  $[\text{Ag}_4(\text{C}\equiv\text{CBu}^t)(\text{CF}_3\text{CO}_2)_3(\text{TMEDA})_2]_n$  (**32**) (Fig. 8), are butterfly-shaped tetrasilver units bridged by  $\text{C}\equiv\text{CBu}^t$  in a  $\mu_4\text{-}\eta^1, \eta^1, \eta^1, \eta^2$  mode.<sup>48</sup> The tetrasilver units protected by TMEDA could aggregate into a chain structure linked by the  $\text{CF}_3\text{CO}_2^-$  ligands.

Moreover, taking the advantages of the larger cavity and cooperative coordination of azacalix[8]pyridines (Py[8]), a square-planar tetranuclear aggregate with a *tert*-butylacetylide anion center is captured by Py[8] from a suspension of  $[\text{AgC}\equiv\text{CBu}^t]_n$  and silver triflate (**33**) (Fig. 10).<sup>49</sup> The cluster contains a  $\mu_4\text{-}\eta^1, \eta^1, \eta^1, \eta^2$  coordination mode with  $\pi$ -type Ag-C bonding distance at 2.704(16) Å and  $\sigma$ -type Ag-C bonding distances in the range of 2.130(14)-2.430(19) Å. Four-fold argentophilic interactions (Ag-Ag edges: 2.941(1) and 2.997(1) Å) support the  $\text{Ag}_4$  square skeleton. As the alkynyl substrate extended to conjugated 1,3-bis((3-ethynylphenyl)ethynyl)benzene, two encircled  $\text{Ag}_4$  clusters in  $\mu_4\text{-}\eta^1, \eta^1, \eta^1, \eta^2$  mode can be bridged by the two terminal alkynyls with small conformational changes of the Py[8] ligands. The adjustments of the conformation of the macrocycle are essential for the control of the nuclearity number and cluster geometry.

Alkynyl centered organometallic clusters in the  $\mu_4\text{-}\eta^1, \eta^1, \eta^2, \eta^2$  coordination modes involve double  $[\text{d}_M \rightarrow \pi^*(\text{C}\equiv\text{C})]$  back donation like the  $\mu_3\text{-}\eta^1, \eta^2, \eta^2$  coordinated ones. Therefore the  $\text{C}\equiv\text{C}$  bond lengths and  $\text{C}\equiv\text{C}-\text{C}$  bond angles will also be



**Fig. 10** Examples of multiple  $\mu_4$  coordination modes in metal clusters.  $[\text{Rh}_4(\text{C}\equiv\text{CR})(\text{CO})_4(\text{PNNP})_2]^+$ ,<sup>44</sup>  $[\text{CoRh}_3(\text{RC}\equiv\text{CR})_3(\text{CO})_9]$ ,<sup>45</sup>  $[\text{Co}_4(\mu_4\text{-}\eta^1, \eta^1, \eta^2\text{-C}\equiv\text{CCMe}_3)(\text{dppm})(\text{PPh}_2)(\text{CO})_7]$ ,<sup>46</sup>  $[\text{Co}_4(\text{RC}\equiv\text{CR})_3(\text{CO})_{10}]$ ,<sup>47</sup>  $[\text{Ag}_4(\text{C}\equiv\text{CBu}^t)(\text{CF}_3\text{CO}_2)_3(\text{TMEDA})_2]_n$ ,<sup>48</sup>  $[(\text{CF}_3\text{SO}_3)\text{Ag}_4(\text{Bu}^t\text{C}\equiv\text{C})(\text{Py}8)](\text{CF}_3\text{SO}_3)_2$ .<sup>49</sup>

significantly influenced by the double  $\pi$ -type coordination. In a typical complex  $[\text{Co}_4(\mu_4\text{-}\eta^1, \eta^1, \eta^2, \eta^2\text{-C}\equiv\text{CCMe}_3)(\text{dppm})(\text{PPh}_2)(\text{CO})_7]$  (**30**) (Fig. 10),<sup>46</sup> the  $\text{Co}_4$  cluster is butterfly-like with a dihedral angle of  $135.1^\circ$ , wherein two Co atoms are  $\sigma$ -bonded to the  $\text{C}_\alpha$  carbon of the  $\text{C}_\alpha\equiv\text{C}_\beta\text{R}$  (Co–C distances: 1.932(7) and 2.001(8)Å) and other two Co atoms have interactions with both the  $\text{C}_\alpha$  and  $\text{C}_\beta$  (Co–C distances in the range 1.912(9) and 2.306(8)Å). The C–C bond length of the triple bond is elongated to 1.301(11)Å and the  $\text{C}\equiv\text{C}$  bond angle widens to  $138.2(9)^\circ$ . It indicates that the metals of the cluster and the alkynyl ligands can have richer electron communications with more  $\pi$ -type coordination.

The reaction of tetranuclear  $\text{Co}_4$ ,  $\text{RuCo}_3$ ,  $\text{Rh}_2\text{Co}_2$ ,  $\text{Mo}_2\text{Ir}_2$ ,  $\text{W}_2\text{Ir}_2$ , etc. carbonyl clusters with phenylacetylene result in generating the  $\mu_4\text{-}\eta^1, \eta^1, \eta^2, \eta^2$  coordinated butterfly-like clusters (**31**) (Fig. 10).<sup>47</sup> Here are two  $\sigma$ -bonded metal atoms at each side of the carbon-carbon bond and two  $\pi$ -bonded metal atoms at the two “wings” consisting of a butterfly configuration. The centered  $\text{C}\equiv\text{C}$  bonds in the products are elongated to longer than 1.40 Å in most examples and the bond angles with the adjacent carbons are *ca.*  $126^\circ$ . Moreover, the reaction between  $\text{Co}_3\text{Rh}(\text{CO})_{12}$  and excess of dimethyl acetylenedicarboxylate not only gives the  $\mu_4\text{-}\eta^1, \eta^1, \eta^2, \eta^2$  coordinated butterfly-like clusters, but also generates a square-shaped  $\text{CoRh}_3$  cluster  $[\text{CoRh}_3(\text{RC}\equiv\text{CR})_3(\text{CO})_9]$  (**29**) (Fig. 10).<sup>45</sup> There are two carbon-carbon bonds capping the two faces of the planar array via a  $\mu_4\text{-}\eta^1$  mode as well as one another carbon-carbon bond  $\mu_2\text{-}\eta^1$  bridging one of the Rh–Rh edges. The carbon-carbon distances in the  $\mu_4$ -coordinated mode are 1.411(6) and 1.428(6)Å with adjacent bond angles of  $119.8(4)$ – $120.6(4)^\circ$ . The carbon-carbon distance in the  $\mu_2$ -coordinated mode is 1.290(7)Å with adjacent bond angles of  $130.6(4)$  and  $132.5(4)^\circ$ . This  $\mu_4\text{-}\eta^2(\text{C}), \eta^2(\text{C})$  featured tetra-metalated carbon-carbon bond resembles the adjacent double *gem*-dimetalated carbon-carbon bonding of aryls in Section 1.24.3.1.

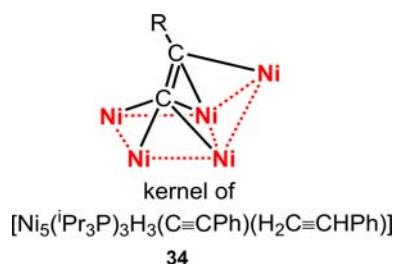
A pentanuclear nickel hydride cluster was applied to selectively cleave the C=C double bonds of ethylene, styrene, and isobutylene, generating a pentanuclear nickel carbide and methane, toluene, and propane respectively.<sup>51</sup> In the isolation of the intermediate in the reactions, the authors find the pentanuclear nickel kernel cooperatively  $\eta^2$  bound to the triple dehydrogenated double bond of  $(\text{pH-C}\equiv\text{C})^{3-}$  and  $\eta^3$  bound to the triple dehydrogenated allyl fragment of  $(\text{CC}(\text{Me})=\text{CH}_2)^{3-}$ . The 1.397(5)Å carbon-carbon bond length of  $\mu_5\text{-}\eta^1, \eta^1, \eta^1, \eta^1, \eta^2\text{-C}\equiv\text{C}$  in  $[\text{Ni}_5(^1\text{Pr}_3\text{P})_3(\mu\text{-H})_3(\text{C}\equiv\text{CPh})(\text{H}_2\text{C}=\text{CHPh})]$  (**34**) (Fig. 11) along with a bent bond angle indicates the maintained double bond character in the reaction intermediates. The multi-activations from the Ni atoms facilitate the C=C bond cleavage under  $\text{H}_2$  atmosphere to give carbide and the consequent alkanes.

#### 1.24.2.4 Metal clusters protected by alkynyl ligands in multiple coordination modes

In some high nuclearity numbered or multifarious ligands (polydentate phosphane ligands, acetate ligands, halides, etc.) co-protected Cu, Ag, and alloy organometallic clusters, the alkynyl ligands will trend to take multiple coordination modes to cater for the structural stability. Copper alkynyl clusters usually feature more sophisticated structures due to richer coordination geometries than Au and Ag. A homoleptic  $[\text{Cu}_{24}(\text{C}\equiv\text{CBu}^t)_{24}]$  cluster with identical numbers of metal and ligands was reported.<sup>52</sup> Here are five types of coordination modes revealed by alkynyl ligands:  $\mu\text{-}\eta^1, \mu\text{-}\eta^1, \eta^2, \mu_3\text{-}\eta^1; \mu_3\text{-}\eta^1, \eta^1, \eta^2$  and  $\mu_4\text{-}\eta^1, \eta^1, \eta^1, \eta^2$ . Later, a  $[\text{Cu}_{20}(\text{C}\equiv\text{CBu}^t)_{20}]$  cluster was reported and the authors believe the architectures of these homoleptic clusters are associated with the  $[(\text{CuC}\equiv\text{CR})_n]$  aggregates.<sup>53</sup> Taking the diverse coordination modes and extensive intermolecular interactions of the homoleptic clusters as an example, the authors determine the polymeric structures of the insoluble  $[(\text{CuC}\equiv\text{CR})_n]$  solid.

A series of Cu–Ag heterometallic alkynyl complexes were prepared with the assistance of Hdppa and dppm ligands.<sup>54</sup> The alkynyl ligands in hexanuclear clusters  $[\text{Ag}_4\text{Cu}_2(\text{Hdppa})_4(\text{C}\equiv\text{CC}_6\text{H}_4\text{R-4})_4](\text{ClO}_4)_2$  (R = H,  $\text{CH}_3$ ) display  $\mu_3\text{-}\eta^1(\text{Ag}), \eta^1(\text{Ag}), \eta^1(\text{Cu})$  and  $\mu_4\text{-}\eta^1(\text{Ag}), \eta^1(\text{Ag}), \eta^1(\text{Cu})$  bonding modes. And three types  $\mu_3\text{-}\eta^1(\text{Ag}), \eta^1(\text{Ag}), \eta^1(\text{Cu}), \mu_3\text{-}\eta^1(\text{Ag}), \eta^1(\text{Cu}), \eta^2(\text{Ag})$  and  $\mu_4\text{-}\eta^1(\text{Ag}), \eta^1(\text{Ag}), \eta^1(\text{Cu}), \eta^1(\text{Cu})$  bonding modes are adopted by the octanuclear clusters  $[\text{Ag}_6\text{Cu}_2(\text{dppm})_3(\text{C}\equiv\text{CC}_6\text{H}_4\text{R-4})_6(\text{MeCN})](\text{ClO}_4)_2$  (R = H,  $\text{CH}_3, \text{OCH}_3, \text{NO}_2, n = 1$ ). All the clusters show intense luminescence with emissive lifetimes in the microsecond scale derived from a  $^3\text{LMCT}$  ( $\text{C}\equiv\text{CC}_6\text{H}_4\text{R-4} \rightarrow \text{Ag}_4\text{Cu}_2$  or  $\text{Ag}_6\text{Cu}_2$ ) transition. With the assistance of bis(2-(diphenylphosphino)ethyl)-phenylphosphane (dpepp) ligands, a  $\text{Ag}_{16}\text{Cu}_9$  heterometallic alkynyl cluster,  $[\text{Ag}_{16}\text{Cu}_9(\text{dpepp})_3(\text{C}\equiv\text{CC}_6\text{H}_4\text{Bu}^t\text{-4})_{20}]^{5+}$  was synthesized. The alkynyl ligands show five types of asymmetric bonding modes, including  $\mu\text{-}\eta^1(\text{Ag}), \eta^1(\text{Ag}), \mu\text{-}\eta^1(\text{Ag}), \eta^2(\text{Cu}), \mu_3\text{-}\eta^1(\text{Ag}), \eta^1(\text{Ag}), \eta^1(\text{Cu}/\text{Ag}), \mu_3\text{-}\eta^1(\text{Ag}), \eta^1(\text{Cu}), \eta^2(\text{Cu})$  and  $\mu_4\text{-}\eta^1(\text{Ag}), \eta^1(\text{Ag}), \eta^1(\text{Ag}), \eta^1(\text{Ag})$ . This  $\text{Ag}_{16}\text{Cu}_9$  cluster is emissive in the visible to near-infrared region (650–812 nm at room temperature) with lifetimes 0.36–0.43  $\mu\text{s}$  derived from the  $^3\text{LMCT}$  ( $\text{C}\equiv\text{CC}_6\text{H}_4\text{Bu}^t\text{-4} \rightarrow \text{Ag}_{16}\text{Cu}_9$ ) transition.

In an alkynyl and acetate ligands consolidated  $\text{Cu}_{20}$  cluster  $[\text{Cu}_{20}(\text{C}\equiv\text{CPh})_{12}(\text{OAc})_6]$ ,<sup>55</sup> there are one alkynyl ligand featuring a  $\mu_4\text{-}\eta^1, \eta^1, \eta^2, \eta^2$  bonding mode, four featuring a  $\mu_3\text{-}\eta^1, \eta^1, \eta^2$  bonding mode and seven featuring a  $\mu_4\text{-}\eta^1, \eta^1, \eta^1, \eta^2$  bonding



**Fig. 11**  $\text{Ni}_5$  cluster with  $\mu_5$  coordinated alkenyl center  $[\text{Ni}_5(^1\text{Pr}_3\text{P})_3(\mu\text{-H})_3(\text{C}\equiv\text{CPh})(\text{H}_2\text{C}=\text{CHPh})]$ .<sup>51</sup>

mode. This Cu<sub>20</sub> cluster could be grafted onto silica by the release of one equiv. of phenylacetylene per cluster, generating immobilized [Cu<sub>20</sub>(C≡CPh)<sub>11</sub>(OAc)<sub>6</sub>(OSiR<sub>3</sub>)] cluster with similar structures. Both clusters are effective catalysts for [3+2] cycloadditions (such as “Click” reaction) between alkynes and azides at room temperature. Notably, the unsupported Cu<sub>20</sub> cluster could act as a precatalyst and dissociate into smaller active species under the reaction conditions. But the immobilized Cu<sub>20</sub> cluster shows minor structural changes during the reaction. Meanwhile, the reaction supernatant undergoes no reactivity toward fresh substrates after removing the supported Cu<sub>20</sub> catalyst, indicating no Cu<sup>+</sup> ions are leached from the immobilized Cu<sub>20</sub> cluster during the reaction process.

The small spherical halides can supply flexible coordination to promote the formation of alkynyl-protected Au/Ag nanoclusters with multiple coordination modes. Two Ag<sub>38</sub> clusters [Ag<sub>38</sub>(C≡CBu<sup>t</sup>)<sub>20</sub>Cl<sub>6</sub>(ClO<sub>4</sub>)<sub>12</sub>] and [Ag<sub>38</sub>(C≡Cchx)<sub>20</sub>Cl<sub>6</sub>(ClO<sub>4</sub>)<sub>10</sub>](ClO<sub>4</sub>)<sub>2</sub> (chx = cyclohexyl) bearing the same Ag<sub>8</sub>Cl<sub>6</sub> kernel and the Ag<sub>30</sub> shell were synthesized from smaller Ag<sub>14</sub> clusters via inner-core transformation.<sup>56</sup> The 20 *tert*-butylethynide ligands can be divided into three types of ligation modes: 10 μ<sub>3</sub>-η<sup>1</sup>, η<sup>1</sup>, η<sup>2</sup>, two μ<sub>3</sub>-η<sup>1</sup>, η<sup>2</sup>, η<sup>2</sup> as well as eight μ<sub>4</sub>-η<sup>1</sup>, η<sup>2</sup>, η<sup>2</sup>, η<sup>2</sup> and the 20 cyclohexylethynide ligands also contain three groups based on the different ligation modes: six μ<sub>3</sub>-η<sup>1</sup>, η<sup>1</sup>, η<sup>2</sup>, six μ<sub>3</sub>-η<sup>1</sup>, η<sup>2</sup>, η<sup>2</sup> as well as eight μ<sub>4</sub>-η<sup>1</sup>, η<sup>2</sup>, η<sup>2</sup>, η<sup>2</sup>. In the larger bimetallic nanoclusters [Au<sub>80</sub>Ag<sub>30</sub>(C≡CPh)<sub>42</sub>X<sub>9</sub>]<sup>+</sup> and [Au<sub>57</sub>Ag<sub>53</sub>(C≡CPh)<sub>40</sub>X<sub>12</sub>] (X = Cl or Br),<sup>57</sup> here are six μ-η<sup>1</sup>(Au), η<sup>1</sup>(Au), 12 μ-η<sup>1</sup>(Au), η<sup>2</sup>(Au), six μ-η<sup>1</sup>(Au), η<sup>2</sup>(Ag) as well as 18 μ<sub>3</sub>-η<sup>1</sup>(Au), η<sup>1</sup>(Ag), η<sup>2</sup>(Ag) in Au<sub>80</sub>Ag<sub>30</sub> clusters and two μ-η<sup>1</sup>(Au), η<sup>1</sup>(Ag), 15 μ-η<sup>1</sup>(Au), η<sup>2</sup>(Ag), three μ<sub>3</sub>-η<sup>1</sup>(Au), η<sup>1</sup>(Ag), η<sup>1</sup>(Ag), 18 μ<sub>3</sub>-η<sup>1</sup>(Au), η<sup>1</sup>(Ag), η<sup>2</sup>(Ag) as well as two μ<sub>3</sub>-η<sup>1</sup>(Au), η<sup>2</sup>(Ag), η<sup>2</sup>(Ag) in Au<sub>57</sub>Ag<sub>53</sub> clusters. In addition, the peripheral alkynyl coordination shell of [Ag<sub>112</sub>(C≡CAr)<sub>51</sub>Cl<sub>6</sub>]<sup>3-</sup> is consisted of four types of alkynyl-silver bonding modes: μ-η<sup>1</sup>, symmetric μ<sub>3</sub>-η<sup>1</sup>, asymmetric μ<sub>3</sub>-η<sup>1</sup> and even μ<sub>5</sub>-η<sup>1</sup>.<sup>58</sup>

### 1.24.3 Aryl ligands

The C=C involved C–M<sub>n</sub> bonds show distinct coordination features from the C≡C triple bonds. For instance, alkenyl bridged *gem*-digold species are extensively detected in gold-catalyzed reactions.<sup>59</sup> The isolated alkenyl bridged diaurated complexes adopt the [Au<sub>2</sub>-μ-η<sup>1</sup>, η<sup>2</sup>-C<sub>β</sub>R=C<sub>α</sub>H<sub>2</sub>]<sup>+</sup> skeleton (35) (Fig. 12), wherein the C<sub>β</sub> of alkenyl usually participate in the coordination. Although the alkenyl ligands centered organometallic clusters are relatively rare and fragile, the coordination modes of alkenyl ligands could give insight into the bonding modes of the *sp*<sup>2</sup> carbons in more abundant aryl ligands centered organometallic clusters.

The *gem*-dimetalated aryl species contain a three-center two-electron moiety with one negatively charged *sp*<sup>2</sup> carbon and two metal cations. With the involvement of π systems, the stable C(aryl)-M<sub>2</sub> groups are extensively found in the di-metal agent (μ-C(aryl)-Al<sub>2</sub>, μ-C(aryl)-Li<sub>2</sub>) (37, 38) (Fig. 12),<sup>60</sup> di-metal catalysts (like μ-aryl dicopper catalyst),<sup>61</sup> intermediates of metal-mediated reaction (such as *gem*-diaurated aryls)<sup>62</sup> and products of organometallic complex transformations (such as μ-C(aryl)-Fe<sub>2</sub>,<sup>63</sup> μ-C(aryl)-Ru<sub>2</sub> and μ-C(aryl)-Os<sub>2</sub><sup>64</sup>). In addition, C(aryl)<sub>x</sub>-M<sub>y</sub> (x = 1–3; y = 2–5) moieties can also make up a broad range of small organometallic clusters with novel structures.

#### 1.24.3.1 Aryl bridged *gem*-dimetal moieties in metal clusters

The *gem*-dimetalated aryl species are building blocks for a class of μ-η<sup>1</sup> aryl connected linear, square, pentagonal, triangular biconical, and cubic metal clusters. Two *gem*-dicopper aryl moieties can form a linear tricopper cluster by sharing one Cu atom. An aryl

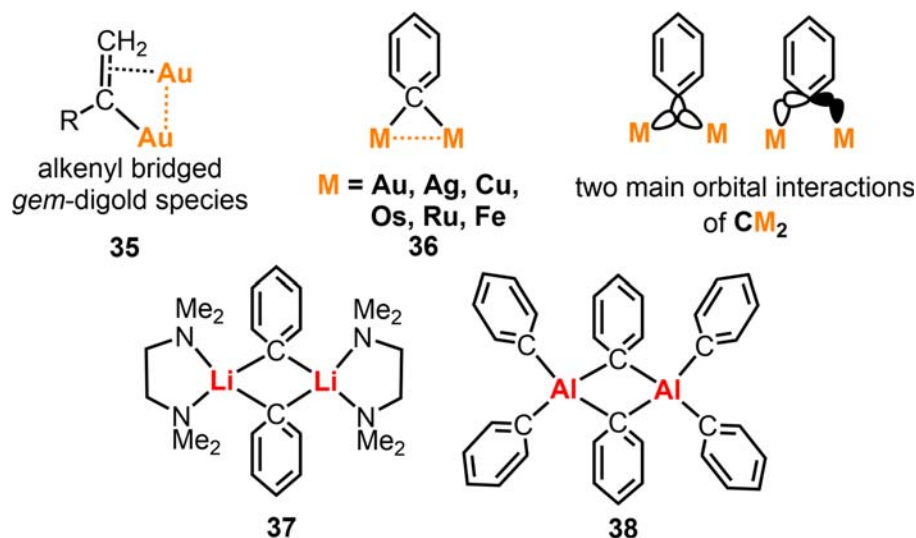
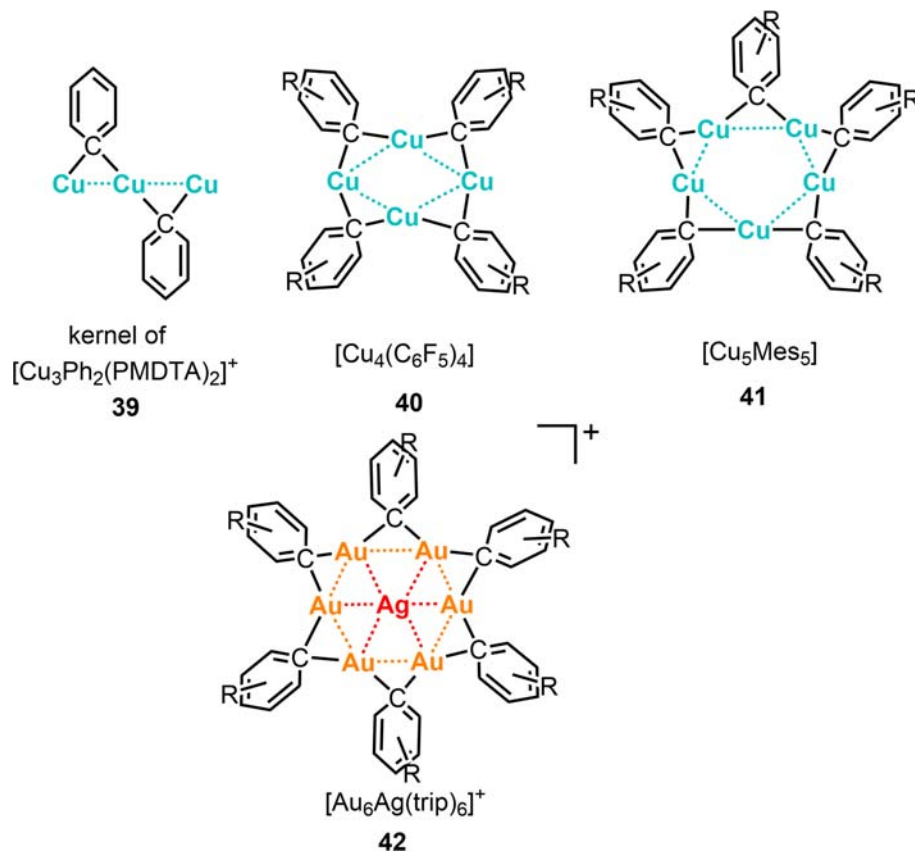


Fig. 12 Alkenyl and aryl bridged *gem*-dimetal species.

bridged organocopper(I) cluster composed of cationic  $[\text{Cu}_3\text{Ph}_2(\text{PMDTA})_2]^+$  (PMDTA = N,N,N',N',N''-pentamethyldiethylenetriamine) (39) (Fig. 13) and anionic  $[\text{Cu}_5\text{Ph}_6]^-$  was found.<sup>65</sup> In the  $\text{Cu}_3$  cations, two phenyls connect three copper atoms  $\text{Cu}(2) - \text{Cu}(1) - \text{Cu}(2a)$  in a linearly fashion. The phenyl rings are oriented almost perpendicular to the  $\text{Cu}(2) - \text{Cu}(1) - \text{Cu}(2a)$  axis ( $86.5^\circ$  and  $83.8^\circ$ ) and the  $\text{Cu}(2) - \text{C} - \text{Cu}(1)$  angles of  $\text{CCu}_2$  moieties are  $75.4(2)^\circ$  and  $72.5(2)^\circ$ . Each of the terminal  $\text{Cu}(2)$  and  $\text{Cu}(2a)$  atoms is protected by one tridentate PMDTA ligand. The triangular biconical  $[\text{Cu}_5\text{Ph}_6]^-$  anion will be introduced *vide infra*. Trinuclear clusters  $[\text{Au}_2\text{Ag}(\text{mes})_2\text{L}_2]^+$  (mes = mesityl; L =  $\text{PPh}_3$  or  $\text{AsPh}_3$ ) in similar skeleton with  $[\text{Cu}_3\text{Ph}_2(\text{PMDTA})_2]^+$  were subsequently reported.<sup>69</sup> In  $[\text{Au}_2\text{Ag}(\text{mes})_2(\text{AsPh}_3)_2]^+$ , the  $\text{Au} - \text{Ag} - \text{Au}$  axis are bridged by two mesityl groups via a  $\mu - \eta^1$  coordination mode. The central Ag atom is linearly coordinated by two carbon atoms and each of the terminal Au atoms is coordinated by one bridged carbon atom and one peripheral  $\text{AsPh}_3$  ligand. The two-electron three-center  $\text{Au} - \text{C}(\text{mesityl}) - \text{Ag}$  bond is air and moisture stable, which may be ascribed to two main orbital interactions. The former shows the involvement of C-M interaction and  $\text{Au} - \text{Ag}$  interaction in the  $3c, 2e^-$  center and the latter is responsible for the perpendicular orientation of the bridging aryl to the metal vector (36) (Fig. 12). Recently, a cationic organo-copper cluster  $[\text{Cu}_4(\text{PCP})_3]^+$  (PCP = 2,6-( $\text{PPh}_2$ ) $_2\text{C}_6\text{H}_3$ ) with bulky tridentate bisphosphane phenyl ligand is reported to feature robust narrow-band green luminescence with a photoluminescent efficiency up to 93%.<sup>70</sup> The rhombic arranged  $\text{Cu}_4$  core involves one rather short  $\text{Cu} - \text{Cu}$  distance, 2.316 Å, which is  $\mu - \eta^1$  bridged by one phenyl carbon atom. Such rigid coordination of the  $\text{Cu}_4$  cluster limits the nonradiative decays and promotes the photoluminescent efficiency.

The tetramer  $[\text{Cu}_4(\text{C}_6\text{H}_3(5\text{-Me})\text{-}2\text{-CH}_2\text{NMe}_2)_4]$  with bridging  $\mu - \eta^1$  phenyl groups is the first reported arylcopper cluster in 1972,<sup>71</sup> in which four Cu atoms are arranged in a butterfly shape with average  $\text{Cu} - \text{Cu}$  distances at 2.38 Å. In each  $\mu - \text{C}(\text{aryl}) - \text{Cu}_2$  moiety, the plane of the phenyl groups is orientated almost perpendicular to the  $\text{Cu} - \text{Cu}$  axis. Later,  $[\text{Cu}_4\text{Mes}_4(\text{C}_4\text{H}_8\text{S})_2]$ ,<sup>67</sup>  $[\text{Cu}_4(2,4,6\text{-}i\text{Pr}_3\text{C}_6\text{H}_2)_4]$ ,<sup>72</sup> and  $[\text{Cu}_4(\text{C}_6\text{F}_5)_4]$ <sup>66</sup> (40) (Fig. 13) with similar structures are also found, indicating the good stability of the phenyl bridged  $\text{Cu}_4$  kernels. Moreover, the structures of the reactive lithium phenylcuprate reagents in the formula of  $[\text{M}_2\text{Li}_2(\text{C}_6\text{H}_5)_4]$  are verified to adopt a  $\mu - \eta^1, \eta^1$  bridging mode in each  $\text{Li} - \text{C}(\text{aryl}) - \text{M}$  fragment. In 1984, the organo-aurates analog of organocuprates,  $[\text{Au}_2\text{Li}_2(\text{C}_6\text{H}_4\text{CH}_2\text{NMe}_2\text{-}2)_4]$ ,<sup>73</sup> was reported. The  $\text{Au}_2\text{Li}_2\text{C}(\text{ipso})_4$  skeleton has a square planar  $\text{Au}_2\text{Li}_2$  arrangement with  $\text{Li} - \text{Au} - \text{Li}$  and  $\text{Au} - \text{Li} - \text{Au}$  angles both close to  $90^\circ$ . Notably, the *gem*-dimetalated aryl moieties take typical asymmetrically coordination modes, wherein the  $\text{C}(\text{ipso})$  of aryl primarily bond to Au ( $\text{Au} - \text{C}$  distances: average 2.06(2) Å) with the near coplanarity of the two phenyl in  $\text{Ph} - \text{Au} - \text{Ph}$  arrangements in contrast to the much longer bond distance of  $\text{C}(\text{ipso}) - \text{Li}$  (average 2.46 Å). Similar asymmetric  $\mu - \eta^1$  coordination modes are also found in organocuprates  $[\text{Cu}_2\text{Li}_2(\text{C}_6\text{H}_5)_4(\text{SMe}_2)_3]$  synthesized.<sup>74</sup>



**Fig. 13** The *gem*-dimetalated aryl species as building blocks for the linear and ring-shaped metal clusters.  $[\text{Cu}_3\text{Ph}_2(\text{PMDTA})_2]^+$ ,<sup>65</sup>  $[\text{Cu}_4(\text{C}_6\text{F}_5)_4]$ ,<sup>66</sup>  $[\text{Cu}_4(\text{C}_6\text{F}_5)_4]$ ,<sup>67</sup>  $[\text{Au}_6\text{Ag}(\text{trip})_6]^+$ .<sup>68</sup>

Each  $\text{CuPh}_2$  unit is bridged by two Li atoms, forming a  $\text{Cu}_2\text{Li}_2$  butterfly center with a fold angle of  $145.9^\circ$ . Moreover, the  $\text{Li}-\text{C}-\text{Cu}$  moieties also take typical asymmetric coordination modes, wherein the dihedral angle between the  $\text{Cu}-\text{C}$  bonds and their adjacent phenyl planes is only  $10.5^\circ$  in contrast to the much larger dihedral angle of  $71.5^\circ$  between the  $\text{Li}-\text{C}$  bonds and their adjacent phenyl planes.

Polymeric phenylcopper(I)  $(\text{CuAr})_n$  is widely applied in organic synthesis as organocuprate reagents.<sup>75</sup> However,  $(\text{CuAr})_n$  is insoluble in common organic solvents due to the high degree of association. Apart from  $[\text{Cu}_4\text{Ar}_4]$  clusters mentioned before, thermally stable and soluble  $[\text{Cu}_5\text{Ar}_5]$  clusters are also isolated.<sup>67</sup> The small cyclic pentameric arylcopper cluster  $[\text{Cu}_5\text{Mes}_5]$  (41) (Fig. 13) shows good solubility in the most common organic solvents. The puckered five-pointed star-shaped ring consists of five Cu atoms and five  $\mu\text{-}\eta^1$  bridged C(aryl) atoms. The mesitylene groups between coppers take  $91.0(5)$ – $105.0(4)^\circ$  dihedral angles with the  $\text{Cu}_5$  plane.  $[\text{Au}_5\text{Mes}_5]$ ,<sup>76</sup> featuring similar 10-membered star-shaped kernels with  $[\text{Cu}_5\text{Mes}_5]$ , is synthesized from the reaction between  $\text{AuCOCl}$  and  $\text{MesMgBr}$ . The dihedral angles between the mesitylene groups and the  $\text{Au}_5$  plane are ranging from  $85.8(5)$ – $89.7(5)^\circ$ .  $[\text{Au}_6\text{Ag}(\text{trip})_6]^+$  ( $\text{trip} = 2,4,6\text{-Triisopropylbenzyl}$ ) (42) (Fig. 13) could be the largest  $\mu\text{-}\eta^1$  aryl bridged cluster ring, in which six gold atoms and six carbon atoms form the rim and the silver atom is located at the center.<sup>68</sup> The  $\text{AgAu}_6$  core is almost planar with  $\text{Ag}-\text{Au}$  distances in the range of  $2.797(1)$ – $2.809(1)\text{\AA}$  and  $\text{Au}-\text{Au}$  distances in the range of  $2.795(1)$ – $2.817(1)\text{\AA}$ . Moreover,  $[\text{Li}(\text{THF})_4][\text{Cu}_5\text{Ph}_6]^-$  (43) (Fig. 14) is isolated from the reaction mixture of phenyllithium and  $\text{CuBr}$  in  $\text{THF}$ .<sup>78</sup> The five copper atoms are shaped in a “squashed” trigonal bipyramid, in which the distances of  $\text{Cu}_{\text{apical}(\text{ap})}-\text{Cu}_{\text{equatorial}(\text{eq})}$  (average  $2.449(9)\text{\AA}$ ) are much shorter than those of the  $\text{Cu}_{\text{eq}}-\text{Cu}_{\text{eq}}$  (average  $3.151(6)\text{\AA}$ ). The distinct  $\text{Cu}-\text{Cu}$  edges can be ascribed to that each of the  $\text{Cu}_{\text{ap}}-\text{Cu}_{\text{eq}}$  edges is  $\mu\text{-}\eta^1$  bridged by one carbon atom of the phenyl groups but none of the  $\text{Cu}_{\text{eq}}-\text{Cu}_{\text{eq}}$  edges is bridged. Similar  $[\text{Li}_2\text{Cu}_3\text{Ph}_6]^-$  organocopper-lithium cluster is further characterized,<sup>79</sup> wherein two axial Cu atoms in  $[\text{Cu}_5\text{Ph}_6]^-$  were replaced by Li atoms. Here are also no significant  $\text{Cu}-\text{Cu}$  interactions between the non-bridged  $\text{Cu}-\text{Cu}$  edges in the  $\text{Cu}_3$  triangle.

Mixed aryl and halide protected copper(I) clusters could be catalytically active species in Ullmann biaryl synthesis, such as an octahedral arranged  $[\text{Cu}_6(2\text{-Me}_2\text{NC}_6\text{H}_4)_4\text{Br}_2]$  cluster.<sup>80</sup> Four triangular faces of the octahedron are spanned by the  $2\text{-Me}_2\text{NC}_6\text{H}_4$  groups by bridging a  $\text{Cu}_{\text{ap}}-\text{Cu}_{\text{eq}}$  edge via a  $\mu\text{-}\eta^1$  carbon and bonding to another  $\text{Cu}_{\text{eq}}$  atom via a nitrogen atom. The other two Br atoms symmetrically bridge two opposite  $\text{Cu}_{\text{eq}}-\text{Cu}_{\text{eq}}$  edges. Here are four types  $\text{Cu}-\text{Cu}$  edges with different distances,  $2.69\text{\AA}$  bromide bridged  $\text{Cu}_{\text{eq}}-\text{Cu}_{\text{eq}}$ ,  $2.52\text{\AA}$  aryl bridged  $\text{Cu}_{\text{ap}}-\text{Cu}_{\text{eq}}$ ,  $2.58\text{\AA}$  and  $2.63\text{\AA}$  unbridged  $\text{Cu}_{\text{ap}}-\text{Cu}_{\text{eq}}$  and  $\text{Cu}_{\text{eq}}-\text{Cu}_{\text{eq}}$ . More importantly, quantitative formation of symmetric coupling product  $\text{N}^2, \text{N}^2, \text{N}^2, \text{N}^2$ -tetramethyl-[1,1'-biphenyl]-2,2'-diamine biaryls is achieved by the reaction of  $[\text{Cu}_6(2\text{-Me}_2\text{NC}_6\text{H}_4)_4\text{Br}_2]$  and  $\text{CuOTf}$ . However, asymmetric coupling product  $\text{RC}\equiv\text{CR}'$  ( $R = 2\text{-Me}_2\text{NC}_6\text{H}_4$ ,  $R' = \text{-C}_6\text{H}_4\text{Me-4}$ ) is selectively and quantitatively generated upon heating  $[\text{Cu}_6\text{R}_4\text{R}'_2]$ , the analog of  $[\text{Cu}_6\text{R}_4\text{Br}_2]$ .  $[\text{Cu}_6(2\text{-Me}_2\text{NC}_6\text{H}_4)_4(4\text{-MeC}_6\text{H}_4\text{C}\equiv\text{C})_2]$  (44) (Fig. 14) is synthesized by ligand substitution of  $[\text{Cu}_6(2\text{-Me}_2\text{NC}_6\text{H}_4)_4\text{Br}_2]$  with  $[\text{Li}(4\text{-MeC}_6\text{H}_4\text{C}\equiv\text{C})]$ .<sup>77</sup> The  $\mu\text{-}\eta^1$  bridged  $\text{C}\equiv\text{C}$  bond is collinear with the central line through the  $\text{Cu}_4(\text{eq})$  plane, thus resulting in the edge bridged by aryl and the edge bridged by ethynyl sharing one  $\text{Cu}_{\text{eq}}$  atom in the triangular face. The author proposes that through the valence disproportionation of  $\text{Cu(I)}$ , the two kinds of organic groups could bond to the shared copper center then occur elimination. In addition, octahedral gold cluster  $[\text{Au}_6(2\text{-Ph}_2\text{PC}_6\text{H}_4)_4]^{2+}$  with a closest  $\text{Au}-\text{Au}$  edge of  $2.71\text{\AA}$  can also be prepared with similar aryl ligands.<sup>81</sup>

### 1.24.3.2 Aryl involved metal clusters with $\mu_3\text{-}\eta^1$ mode

The  $sp^2$  hybridized carbon in aryl ligands can bridge up to three metals in some typical clusters. In the polymeric structures of the mesityl bridged bimetallic Ag and Au clusters, the *ipso* carbon of the aryl ligands can bind one Au center and two Ag atoms at the sides via a  $\mu_3\text{-}\eta^1$  coordination mode (45) (Fig. 15).<sup>82</sup> In each C(*ipso*)-AgAuAg group, here are one short  $\text{Au}-\text{C}$  bond ( $2.045(4)\text{\AA}$ ) and two long  $\text{Ag}-\text{C}$  bonds ( $2.614(4)\text{\AA}$  and  $2.530(4)\text{\AA}$ ). Moreover, in the isolation and structural characterization of dimethyl sulfide solvates of lithium phenylcuprate reagents, apart from the  $[\text{Cu}_4\text{Ph}_4(\text{SMe}_2)_2]$  and  $[\text{Li}_2\text{Cu}_2\text{Ph}_2(\text{SMe}_2)_3]$  mentioned in Section 1.24.3.1, here are two

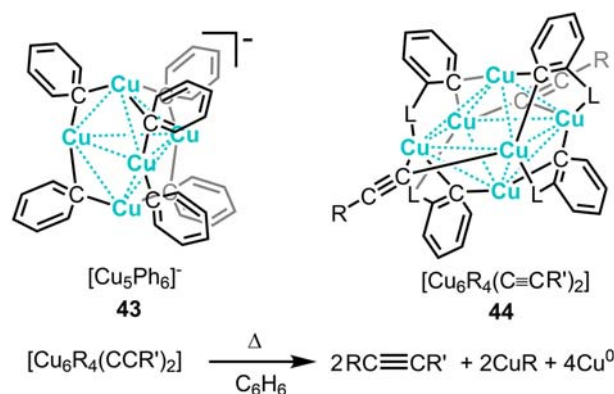
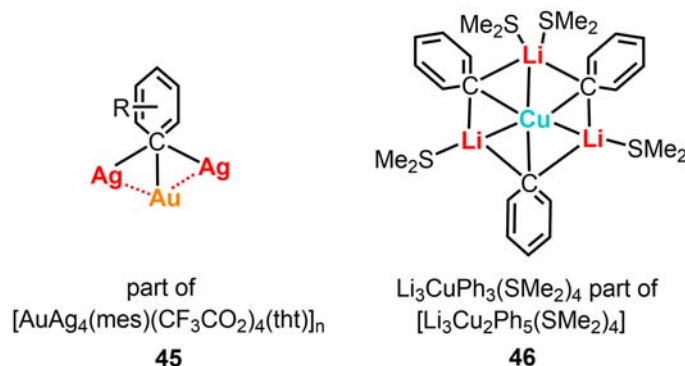


Fig. 14 The *gem*-dimetalated aryl species protected Cu clusters.  $[\text{Cu}_5\text{Ph}_6]^-$ ,<sup>65</sup>  $[\text{Cu}_6(2\text{-Me}_2\text{NC}_6\text{H}_4)_4(4\text{-MeC}_6\text{H}_4\text{C}\equiv\text{C})_2]$ .<sup>77</sup>





**Fig. 15** Aryl ligands in the  $\mu_3\text{-}\eta^1$  bridged coordination modes.  $[\text{AuAg}_4(\text{mes})(\text{CF}_3\text{CO}_2)_4(\text{tht})]_n$ ,<sup>82</sup>  $[\text{Li}_3\text{Cu}_2\text{Ph}_5(\text{SMe}_2)_4]$ .<sup>74</sup>

bimetallic clusters  $[\text{Li}_3\text{Cu}_2\text{Ph}_5(\text{SMe}_2)_4]$  and  $[\text{Li}_5\text{Cu}_4\text{Ph}_9(\text{SMe}_2)_4]$  featuring a  $\mu_3\text{-}\eta^1$  ( $\text{C}_{\text{phenyl}}\text{-LiCuLi}$ ) coordinating mode and one lithium cluster  $[\text{Li}_4\text{Ph}_4(\text{SMe}_2)_4]$  with a  $\mu_3\text{-}\eta^1$  ( $\text{C}_{\text{phenyl}}\text{-Li}_3$ ) moiety.<sup>74</sup> The two bimetallic clusters can be described as  $[\text{Li}_3\text{CuPh}_3(\text{SMe}_2)_4]^+[\text{CuPh}_2]^-$  and  $[\text{Li}_3\text{CuPh}_3(\text{SMe}_2)_4]^+[\text{Li}_2\text{Cu}_3\text{Ph}_6]^-$ , wherein the  $[\text{Li}_3\text{CuPh}_3(\text{SMe}_2)_4]^+$  moiety shares similar skeletons (46) (Fig. 15). There are three  $\text{C}_{\text{phenyl}}$  atoms and three Li atoms making up a distorted six-membered cycle accompanied by a Cu atom approximately locating at the center of the  $\text{C}(\text{ipso})_3$  plane. The three phenyl rings are almost perpendicular to the  $\text{C}(\text{ipso})_3$  plane, each with one Cu atom at the center and two Li atoms at the sides. In the distorted tetrahedral  $\text{Li}_4$  cluster  $[\text{Li}_4\text{Ph}_4(\text{SMe}_2)_4]$ , each of the four faces is  $\mu_3$ -capped by an *ipso*  $\text{C}_{\text{phenyl}}$  atom.

### 1.24.3.3 Aryl ligands with adjacent two or three coordination sites

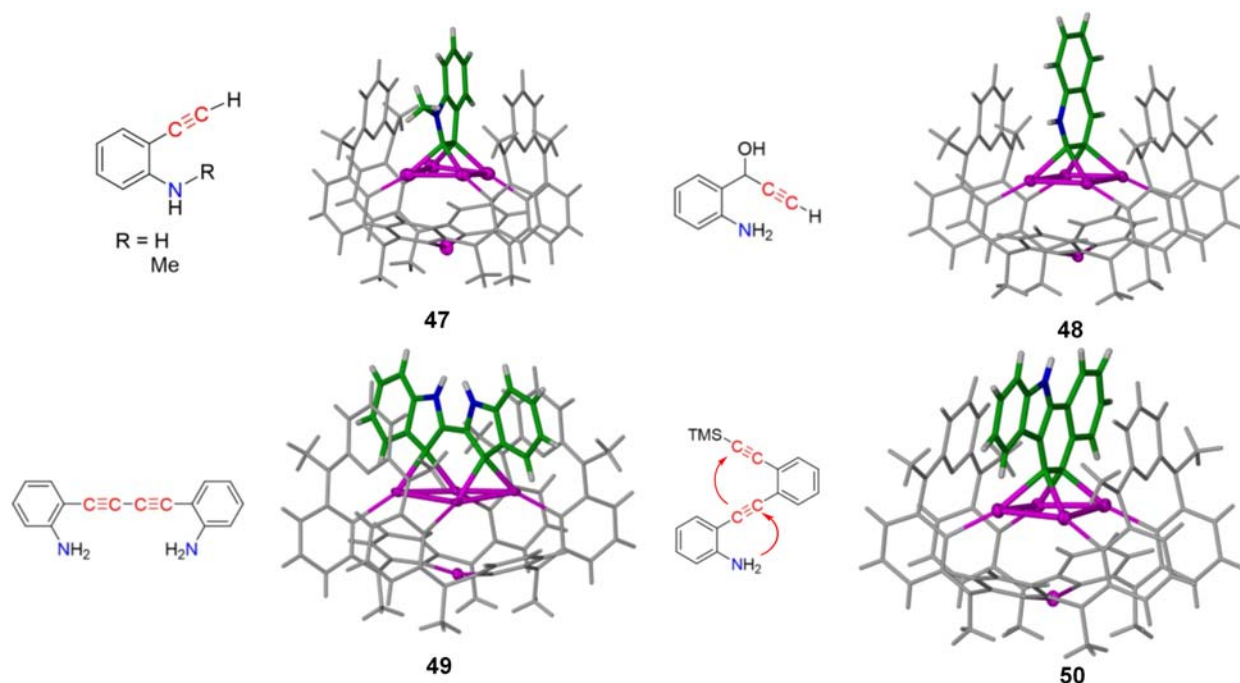
Aryl ligands can supply two or more carbon anions as coordination sites due to the stability from the delocalization in the aromatic rings. The poly-deprotonated aryl ligands centers with adjacent coordination sites in organometallic clusters can be synthesized from the in situ cyclization. Therefore, the isolation of poly-anionic aryl centered metal clusters is usually accompanied by poly-metal promoted organometallic reactions. For example, in the reaction of polymeric  $(\text{AgC}\equiv\text{CC}_6\text{H}_5)_n$  with  $[\text{Au}_2(\text{dppm})_2(\text{MeCN})_2]^{2+}$ , the phenylacetylide cyclotrimerized into  $[1,2,3\text{-C}_6(\text{C}_6\text{H}_5)_3]^{3-}$  trianions, which is  $\mu_5\text{-}\eta^2(\text{C})$ ,  $\eta^1(\text{C})$ ,  $\eta^2(\text{C})$  coordinated by a  $\text{Au}_3\text{Ag}_2$  moiety.<sup>27</sup> The adjacent three  $\text{C}\text{-Au}$  bonds are almost coplanar with the trianions ring of  $[1,2,3\text{-C}_6(\text{C}_6\text{H}_5)_3]^{3-}$  and the other two  $\text{C}\text{-Ag}$  bonds (2.672 Å) are oriented in an anti-conformation.

Taking  $\text{Py}[n]$ s as a molecular flask, polynuclear silver clusters promoted in situ aromatic cyclization were conducted. In a typical example, a  $\text{Py}[8]$  encaged indole dianion-centered  $\text{Ag}_4$  rectangle with a  $\mu_4\text{-}\eta^2(\text{C})$ ,  $\eta^2(\text{C})$  mode is isolated via  $\text{AgOTf}$  mediated 5-*endo-dig* cyclization of *o*-ethynylaniline.<sup>83</sup> The *gem*-disilver coordinated  $\text{C}_{\text{aryl}}$  carbons are adjacent to each other and both show *pseudo*-tetrahedral coordination featuring with a short  $\text{Ag}\text{-Ag}$  edge. Moreover, taking advantage of the flexible conformation of the macrocycle capsule, polynuclear silver clusters mediated 6-*endo-dig* cyclization and cascade cyclization can also be achieved. Therefore, dianionic quinolinium, 2,2'-biindole and benzo[*a*]carbazole centered  $\text{Ag}_4$  clusters in the  $\mu_4\text{-}\eta^2(\text{C})$ ,  $\eta^2(\text{C})$  coordination modes are captured accordingly (47–50) (Fig. 16). It is worth noting that the  $\text{Py}[n]$ s encapsulated polymetalated aromatics show superb stability upon exposed to air and moisture. It could be ascribed to the three-centered bonding nature in the *gem*- $\text{CAg}_2$  moiety, which involves the  $sp^2$  hybrid orbital and  $p_\pi$  orbital of  $\text{C}(\text{ipso})$  atom.

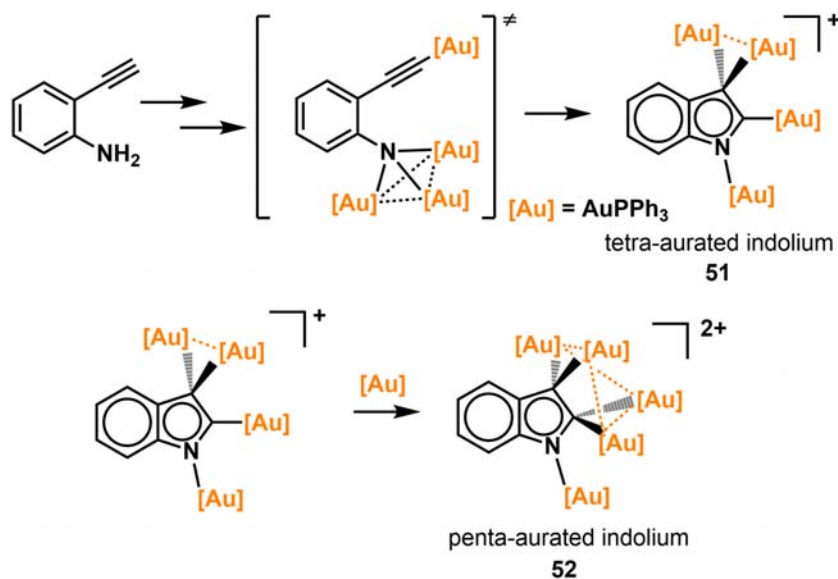
Moreover, using a multi-activation strategy, a series of poly-aurated heteroaromatics with hyperconjugative aromaticity were prepared.<sup>84</sup> The synthesis relies on the intramolecular 5-*endo-dig* cyclization between the nucleophilic tri-aurated imido group and the electrophilic  $\sigma$ ,  $\pi$ -aurated carbon-carbon triple bond. Here is only one *gem*-diaurated carbon moiety in  $\mu_4\text{-}\eta^2(\text{C}1), \eta^1(\text{C}2), \eta_1(\text{N})$  coordinated tetra-aurated indolium, while two folds *gem*- $\text{CAu}_2$  in  $\mu_5\text{-}\eta^2(\text{C}1), \eta^2(\text{C}2), \eta_1(\text{N})$  coordinated penta-aurated indolium (51,52) (Fig. 17). The poly-aurated indoliums show superb stability upon exposure to air and moisture. According to the nucleus-independent chemical shift (NICS) and anisotropy of current-induced density (ACID) calculations, a type of transition metal involved hyperconjugative aromaticity is found in the poly-aurated indoliums. It worth noting that the gold substituents perform better hyperconjugation than the traditional main group substituents. It could be ascribed to the multi-bonding nature of the *gem*-digold groups inducing a more significant hyperconjugative effect between the Au orbitals and the  $\pi$  system. Between the tetra- and the penta-aurated indoliums, the penta-aurated one shows smaller bond length alternations in the five-member ring. This could be ascribed to the double hyperconjugative effect induced better electron delocalization, which consequently causes the reduction of charge distribution on the N atom and the elongation of the  $\text{N}\text{-Au}$  bond (2.052(11) Å in the  $\text{Au}_4$  cluster, 2.062(11) Å in the  $\text{Au}_5$  cluster). Therefore, such difference in aromaticity accounts for the higher protodeauration reactivity of the  $\text{Au}_5$  cluster over the  $\text{Au}_4$  cluster.

### 1.24.4 Alkyl carbons as coordination sites

Double deprotonated methylene  $\text{CH}_2\text{R}_2$  and carbene, as well as triple deprotonated methyl  $\text{CH}_3\text{R}$  and carbyne are capable to coordinate to 2–4 metal atoms by one carbon atom. The adjacent groups of the deprotonated carbon are usually phenyl,  $\text{PR}'_3$ , and  $\text{SOR}'_2$ , electron withdrawing groups like cyanogroup and carbonyl, electron donating groups like trimethylsilyl, and even one



**Fig. 16** Py[n]s engaged indole dianion-centered Ag clusters. Color codes: purple, Ag; gray, green, C; blue, N. From He, X.; Xue, Y.; Li, C.-C.; Wang, Y.; Jiang, H.; Zhao, L. *Chem. Sci.* **2018**, *9*, 1481–1487.

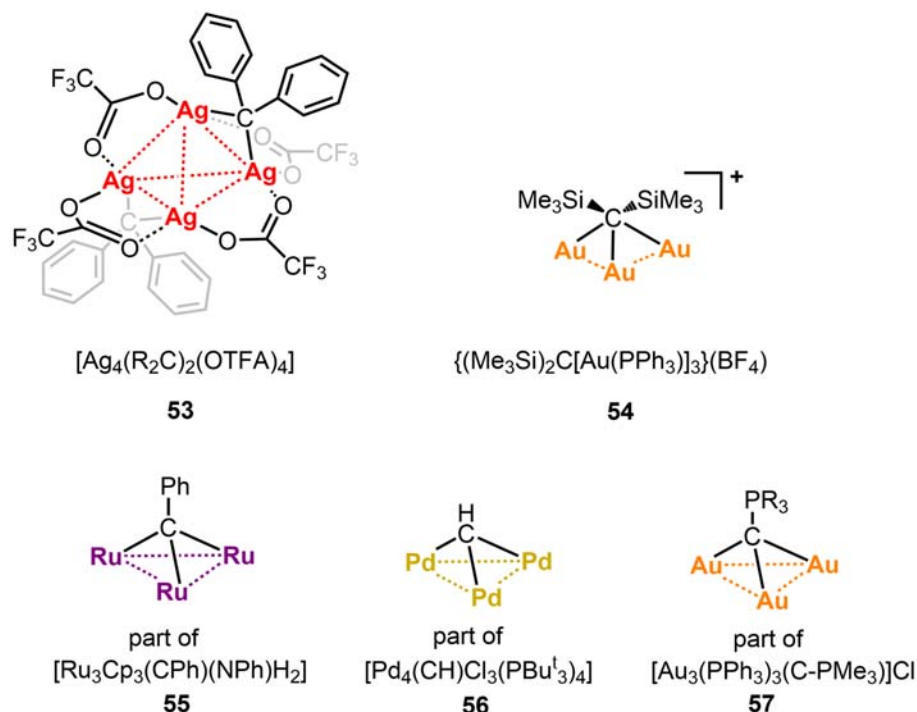


**Fig. 17** Poly-aurated indoliums.<sup>84</sup>

hydrogen atom. The novel structures, promising reactivities and intriguing physicochemical properties of these hypercoordinated carbon centered organometallic clusters enable the studies worthwhile.

#### 1.24.4.1 Alkyl carbon centered metal clusters with $\mu_2\text{-}\eta^1$ and $\mu_3\text{-}\eta^1$ modes

A  $\mu\text{-}\eta^1$ -bridged diphenyl carbene that connects *gem*-disilver moieties of triangular or tetrahedral Ag kernels was reported.<sup>85</sup> The carbene bridged silver clusters  $[\text{Ag}_3(\text{R}_2\text{C})(\text{OTFA})_3]$  and  $[\text{Ag}_4(\text{R}_2\text{C})_2(\text{OTFA})_4]$  (OTFA =  $\text{CF}_3\text{COO}^-$ ; R = NMe<sub>2</sub>-Ph-4) (53) (Fig. 18) are synthesized by the reaction of diaryl diazo derivatives with silver trifluoroacetate at low temperature. In each carbene bridged *gem*-disilver moiety, the carbene acceptor orbital benefits from enhanced back-donation from the two Ag atoms compared to that of the



**Fig. 18** The  $\mu_2$  and  $\mu_3$  coordinated carbene, methyldiene and anionic methyl ligands.  $[Ag_4(R_2C)_2(OTFA)_4]$ ,<sup>85</sup>  $\{(Me_3Si)_2C[Au(PPh_3)]_3\}(BF_4)^+$ ,<sup>86</sup>  $[Ru_3Cp_3(\mu_3-CPh)(\mu_3-NPh)(\mu-H)_2]$ ,<sup>87</sup>  $[Pd_4(\mu_3-CH)(\mu-Cl)_3(PBu^t_3)_4]$ ,<sup>88</sup>  $[Au_3(PPh_3)_3(\mu_3-\eta^1-C-PMe_3)]Cl$ .<sup>89</sup>

traditional terminal carbene. The Ag–C bond lengths are almost equidistant in this three-center four-electron bonding mode. More importantly, the tetra-nuclear Ag cluster could first occur a ligand exchange of OTFA with diaryl diazo,  $PhCH_2NH_2$  or  $PhMgBr$ , then followed by insertion of Ag–C(carbene) bond and oxidation from Ag(I), generating two-electron oxidative coupling organic products and precipitated Ag(0).

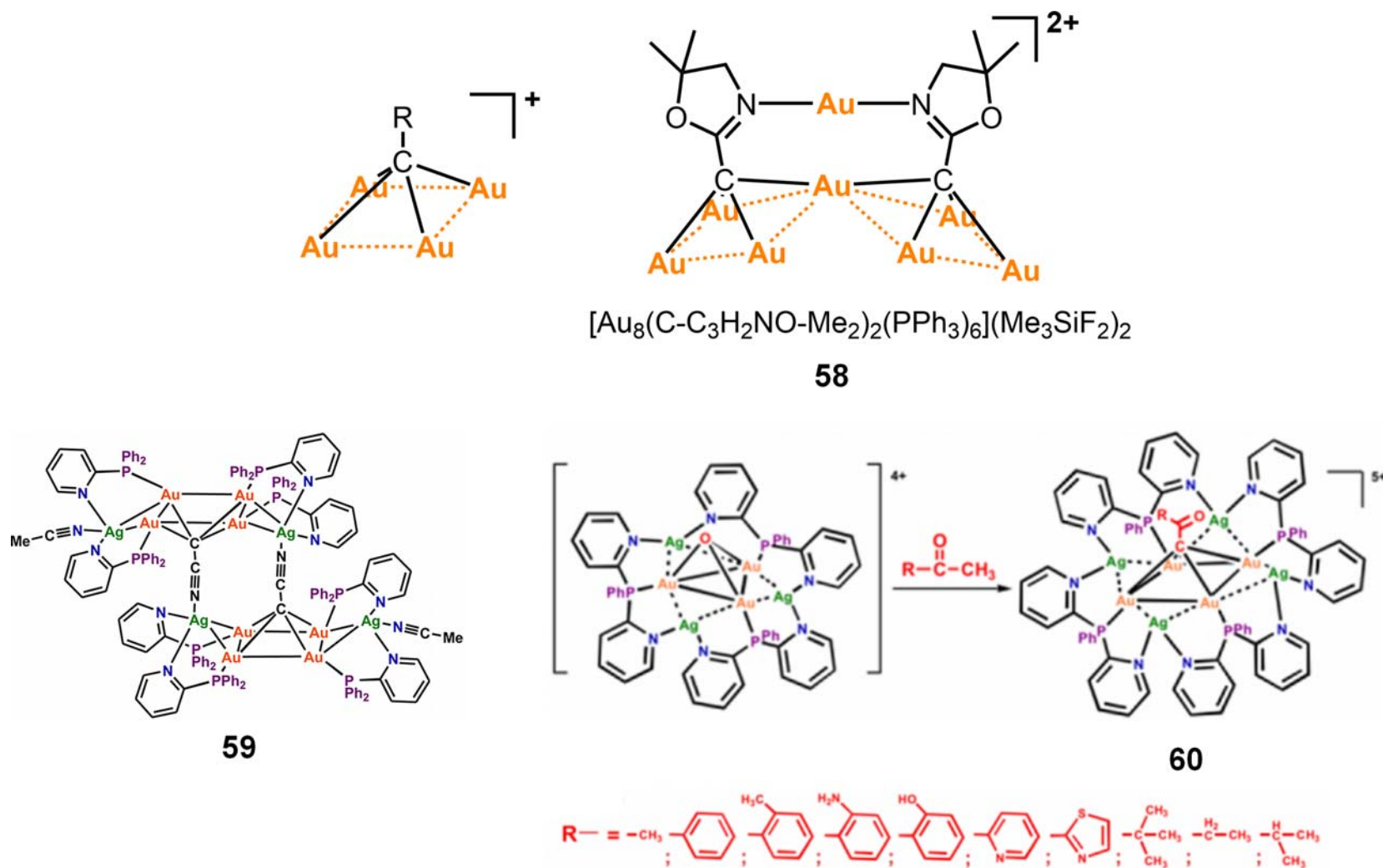
The  $\mu_3$  coordinated methyldiene ligands in many metal hydride clusters are mainly generated from bond cleavage. For example, the reaction of  $[Ru_3Cp_3(\mu-H)_3(\mu_3-H)_2]$  with  $PhCH=NPh$  at  $100^\circ C$  results in the cleavage of the C=N bond and formation of  $\mu_3$ -benzylidene– $\mu_3$ -phenylimido complex  $[Ru_3Cp_3(\mu_3-CPh)(\mu_3-NPh)(\mu-H)_2]$  (55) (Fig. 18).<sup>87</sup> The C–Ru<sub>3</sub>–N moiety is shaped in a trigonal bipyramid with the  $\mu_3$ -C atom and the  $\mu_3$ -N atom capping the two faces of the Ru<sub>3</sub> triangular. Apart from these, the  $\mu_3$ -CH ligand could also be obtained from the reaction of  $[Pd_2(dba)_3]$  (dba = dibenzylideneacetone),  $PBu^t_3$  and 0.5 equiv.  $CHCl_3$  in toluene via triple cleavage of C–Cl bonds.<sup>88</sup> The isolated tetrahedral cluster  $[Pd_4(\mu_3-CH)(\mu-Cl)_3(PBu^t_3)_4]$  (56) (Fig. 18) involves a face capping methyldiene ligand with three Pd–C bonds.

Deprotonated  $sp^3$  carbons show special stability in coordination to poly gold clusters. In 1988, a  $[Au_3(PPh_3)_3(\mu_3-\eta^1-C-PMe_3)]Cl$  (57) (Fig. 18) trimer was prepared by the reaction of  $Me_3P=CHSiMe_3$  trimethylphosphonio(trimethylsilylmethanide) with  $PPh_3AuCl$  in the presence of C–Si bond cleavage agent  $CsF$ .<sup>89</sup> In the ylidic carbon atom bridged four-center six-electron moiety, the three gold atoms are almost equidistant from the center carbon and here are triple Au–Au aurophilic interactions supporting the Au<sub>3</sub> triangular. Trinuclear gold(I) compound  $[(PPh_3Au)_3(\mu-O)](BF_4)$  ( $[Au_3O]$ ) can be regarded as a type of strong base. Treatment of  $[Bis(trimethylsilyl)methyl](triphenylphosphane)gold(I)$  with  $[Au_3O]$  gives a dinuclear compound  $(Me_3Si)_2C[Au(PPh_3)]_2$  and a trinuclear compound  $\{(Me_3Si)_2C[Au(PPh_3)]_3\}(BF_4)$  (54) (Fig. 18).<sup>86</sup> In the penta-coordinated carbon centered trinuclear gold cluster, the center carbon atom of  $\mu_3-\eta^1-R_2C^{2-}$  moiety is coplanar with two Si atoms and one Au atom. The Si–C–Si face is almost vertical to the two Au–Au interactions and three C–Au bonds supported C–(Au)<sub>3</sub> face.

#### 1.24.4.2 Alkyl carbon centered metal clusters with $\mu_4-\eta^1$ mode

Metalated  $\mu_4$  methyl carbons can also be divided into tri-radical carbyne and tri-anions  $R-C^{3-}$  according to different synthetic methods. Using two equiv.  $[Ru_3(CO)_{12}]$  to react with 6,6'-dimethyl-2,2'-bipyridine ( $Me_2bipy$ ) or 2,9-dimethyl-1,10-phenanthroline ( $Me_2phen$ ) will give a carbyne-type carbon atom capped Ru<sub>4</sub> square moiety. Take  $[Ru_6(\mu-CO)_3CO_{13}(\mu_3-H)(\mu_5-Cbi-pyMe)]$  as an example,<sup>90</sup> the  $\mu_4-\eta^1-C-Ru_4$  fragment shows square-pyramidal skeleton with one Ru<sub>4</sub> basal square and one carbon vertex.

Tetra-aurated  $R-C^{3-}$  methyl carbon is a class of extensively existed molecular pattern in small gold organometallic clusters. In 1988, Schmidbaur reported the first tetra-aurated methyl in  $(Me_3SiF_2)_2[Au_8(PPh_3)_6(Me_2C_3H_2ON-C)_2]$  (58) (Fig. 19),<sup>92</sup> wherein takes advantage of the acidity of the R-CH<sub>3</sub> group of 2,4,4-trimethyl-4,5-dihydrooxazole toward  $nBuLi$ . The terminal  $R-C^{3-}$  carbon



**Fig. 19** The  $\mu_4\text{-}\eta^1$  coordination mode with tri-anionic methyl.  $[\text{Au}_4(\text{PPh}_3)_4(\mu_4\text{-}\eta^1\text{-CR})](\text{BF}_4)$ ,<sup>91</sup>  $(\text{Me}_3\text{SiF}_2)_2[\text{Au}_8(\text{PPh}_3)_6(\text{Me}_2\text{C}_3\text{H}_2\text{ON}-\text{C})_2]$ ,<sup>92</sup>  $[\text{Au}_8\text{Ag}_4(\text{PPh}_2\text{py})_8(\text{CH}_3\text{CN})_2(\text{CCN})_2](\text{BF}_4)_6$ ,<sup>93</sup>  $[\text{Au}_4\text{Ag}_4(\text{PPhpy})_4[\mu_4\text{-CC}(\text{O})\text{R}]](\text{BF}_4)_5$ .<sup>94</sup> From Pei, X.-L.; Yang, Y.; Lei, Z.; Wang, Q.-M. *J. Am. Chem. Soc.* **2013**, *135*, 6435–6437; Pei, X.-L.; Yang, Y.; Lei, Z.; Chang, S.-S.; Guan, Z.-J.; Wan, X.-K.; Wen, T.-B.; Wang, Q.-M. *J. Am. Chem. Soc.* **2015**, *137*, 5520–5525.

is coordinated to four gold atoms of the Au<sub>4</sub> plane in roughly equal bond lengths. Later, [Au<sub>4</sub>(PPh<sub>3</sub>)<sub>4</sub>(μ<sub>4</sub>-η<sup>1</sup>-CMe)](BF<sub>4</sub>) and [Au<sub>4</sub>(PPh<sub>3</sub>)<sub>4</sub>(μ<sub>4</sub>-η<sup>1</sup>-CH)](BF<sub>4</sub>) were isolated.<sup>91</sup> The [Au<sub>4</sub>(PPh<sub>3</sub>)<sub>4</sub>(CH)](BF<sub>4</sub>) was synthesized by the reaction of [Au<sub>3</sub>O] with Me<sub>3</sub>SiCHN<sub>2</sub> by the loss of N<sub>2</sub> and desilylation. The C–Au<sub>4</sub> moiety adopts a distorted square-pyramidal structure with the carbon atom as the vertex and quadruple Au–Au interactions as the square plane. Subsequently, tetra-aurated sulfur ylide complex {Au<sub>4</sub>(PPh<sub>3</sub>)<sub>4</sub>(μ<sub>4</sub>-η<sup>1</sup>-C–S(=O)–Me<sub>2</sub>)}(ClO<sub>4</sub>)<sub>2</sub> was reported, which is similar to the tri-aurated phosphorus ylide complex [Au<sub>3</sub>(PPh<sub>3</sub>)(μ<sub>3</sub>-η<sup>1</sup>-C–PMe<sub>3</sub>)]Cl.<sup>95</sup> The identical square-pyramidal coordination is revealed in this tetra-aurated sulfur ylide complex with the carbon atom lying 0.86(1) Å out of the center of the Au<sub>4</sub> basal plane. Apart from the tri-aurated phosphorus ylide complex, tetra-aurated phosphorus ylide complex {Au<sub>8</sub>[CH(NC<sub>8</sub>H<sub>9</sub>)]<sub>4</sub>(μ<sub>4</sub>-η<sup>1</sup>-C–P(Ph<sub>2</sub>)Me)<sub>2</sub>} is also successfully constructed by the reaction of digold amidinate precursors with the neutral ylide CH<sub>2</sub>=P(Ph<sub>2</sub>)Me.<sup>96</sup> In this distorted Au<sub>8</sub> cube, the opposite upper and lower faces are capped by two μ<sub>4</sub>-hypercoordinated ylide carbon atoms which are placed 0.755 Å from the Au<sub>4</sub> basal plane. The successful synthesis of these tetra-aurated methyl mainly relies on the affinity between gold and carbon atoms and the involvement of acid-base reactions. A type of Ag(I) involved oxonium Au(I) cluster [OAu<sub>3</sub>Ag(PPh<sub>2</sub>py)<sub>3</sub>](BF<sub>4</sub>)<sub>2</sub> (PPh<sub>2</sub>py = dihenylphosphino-2-pyridine) was adopted as base to deprotonate the weakly acidic H atoms of acetonitrile in result of generating a Ag-μ<sub>5</sub>-NCC<sup>3-</sup>-Au<sub>4</sub> moiety.<sup>93</sup> The isolated [Au<sub>8</sub>Ag<sub>4</sub>(PPh<sub>2</sub>py)<sub>8</sub>(CH<sub>3</sub>CN)<sub>2</sub>(CCN)<sub>2</sub>](BF<sub>4</sub>)<sub>6</sub> (**59**) (Fig. 19) contains two basic Au<sub>4</sub>Ag<sub>2</sub> units dimerized by double Ag-μ<sub>5</sub>-NCC<sup>3-</sup>-Au<sub>4</sub> fashions. The continuous generation of H<sub>2</sub>O from the reaction of oxo ions and CH<sub>3</sub>CN was verified by <sup>1</sup>H NMR spectra, indicating the basicity of the oxo ions is one of the important driving force in the deprotonation-metalation process. Another driving force for auration can be the strong carbophilicity of gold due to relativistic effects.<sup>97</sup> The carbophilicity of gold is further verified by the selective auration of the –CH<sub>3</sub> rather than the more reactive –NH<sub>2</sub> or –OH with [OAu<sub>3</sub>Ag<sub>3</sub>(PPhpy)<sub>3</sub>](BF<sub>4</sub>)<sub>4</sub>.<sup>94</sup> [OAu<sub>3</sub>Ag<sub>3</sub>(PPh<sub>2</sub>py)<sub>3</sub>](BF<sub>4</sub>)<sub>4</sub> could activate C(sp<sup>3</sup>)–H bonds under mild conditions for a series of methyl ketones, generating μ<sub>4</sub>-C–Au<sub>4</sub> centered {Au<sub>4</sub>Ag<sub>4</sub>(PPhpy)<sub>2</sub>}(μ<sub>4</sub>-CC(O)R)}(BF<sub>4</sub>)<sub>5</sub> (**60**) (Fig. 19) heterometallic clusters. Moreover, the terminal methyl group is auated in preference to the secondary C(sp<sup>3</sup>)–H bonds of 3-methylbutanone, which may be ascribed to the stability of μ<sub>4</sub>-C–Au<sub>4</sub> structures.

### 1.24.5 Conclusion

This chapter provides an account of reported organometallic clusters, mainly with metals of Group 8–12. The transition metals featuring variable orbitals can construct multiple carbon-metal bonds and metal-metal interactions. From the minimal carbon bridged clusters like alkynyl centered trimers and *gem*-dimetallic species to several units composed of ring-shaped, geometry-shaped and high-nuclear numbered organometallic clusters, there are substantial examples with well-defined structures. The isolation of different ligand involved clusters with adjustable nuclear numbers and cluster transformation have been the focus of organometallic clusters studies in the past few years. However, to date applicable multi-metal mediated synthetic strategies are rarely explored. This could be ascribed to several hurdles in the catalytic mechanism studies of multi-metallic catalytic reactions. First, the actual role of the known organometallic clusters in the catalytic cycle, active species or “dead-end,” needs to be classified. Whether the clusters defined by X-ray crystallography will keep their structural integrity in reaction solution should be further monitored by multiple methods. Second, we need deeper comprehension of the bonding modes between the poly-metallic catalytic sites and a substrate. Comparing with the systematic bonding rules of mono-nuclear organometallic species, the bonding nature in the most common carbon-polymetal bonds still lacks comprehensive studies. Third, typical elementary reactions in the polymetallic catalysis need to be established, like the oxidative addition, reductive elimination, and migratory insertion in mononuclear metal-catalyzed reactions. By using instrumental analytical methods like synchrotron radiation and the improvement of theoretical and computational chemistry, researchers are able to study the cluster-involved reaction kinetics within nanoseconds as well as the complex structural changes in the cluster-involved elementary reaction. There is no doubt that the organometallic cluster chemistry will open a promising future for organometallic catalysis and synthetic methodology.

### References

- (a) Richmond, M. G. *Coord. Chem. Rev.* **2005**, *249*, 2763–2786; (b) Keister, J. B. Organometallic clusters. In *Comprehensive Organometallic Chemistry III*; Mingos, D. M. P., Crabtree, R. H., Eds., Elsevier: Amsterdam, 2007; pp 755–780; (c) Low, P. J.; Brown, N. J. *J. Clust. Sci.* **2010**, *21*, 235–278; (d) Xie, Y.-P.; Mak, T. C. W. *J. Clust. Sci.* **2014**, *25*, 189–204; (e) Koutsantonis, G. A. Organo-transition metal cluster complexes. In *Organometallic Chemistry*; Fairlamb, I. J. S., Lynam, J. M., Eds., Royal Society Chemistry: Cambridge, 2014; pp 210–237; (f) Lei, Z.; Wan, X.-K.; Yuan, S.-F.; Guan, Z.-J.; Wang, Q.-M. *Acc. Chem. Res.* **2018**, *51*, 2465–2474; (g) Tang, J.; Zhao, L. *Chem. Commun.* **2020**, *56*, 1915–1925.
- Brasse, C.; Raitby, P. R.; Rennie, M. A.; Russell, C. A.; Steiner, A.; Wright, D. S. *Organometallics* **1996**, *15*, 639–644.
- Abu-Salah, O. M.; Knobler, C. B. *J. Organomet. Chem.* **1986**, *302*, C10.
- (a) Abu-Salah, O. M.; A-Ohaly, A. R.; Mutter, Z. F. *J. Organomet. Chem.* **1990**, *389*, 427–434; (b) Schuster, O.; Monkowius, U.; Schmidbaur, H.; Ray, R. S.; Krüger, S.; Rösch, N. *Organometallics* **2005**, *25*, 1004–1011.
- (a) Abu-Salah, O. M.; Hussain, M. S.; Schlemper, E. O. *J. Chem. Soc. Chem. Commun.* **1988**, 212–213; (b) Abu-Salah, O. M. *Polyhedron* **1992**, *11*, 951–955; (c) Hussain, M. S.; Abu-Salah, O. M. *J. Organomet. Chem.* **1993**, *445*, 295–300.
- (a) Koshevoy, I. O.; Koskinen, L.; Haukka, M.; Yunik, S. P.; Serdobintsev, P. Y.; Melnikov, A. S.; Pakkanen, T. A. *Angew. Chem. Int. Ed.* **2008**, *47*, 3942–3945; (b) Koshevoy, I. O.; Lin, Y.-C.; Karttunen, A. J.; Haukka, M.; Chou, P.-T.; Tunik, S. P.; Pakkanen, T. A. *Chem. Commun.* **2009**, 2860–2862; (c) Koshevoy, I. O.; Lin, Y.-C.; Karttunen, A. J.; Jänis, J.; Haukka, M.; Tunik, S. P.; Chou, P.-T.; Pakkanen, T. A. *Inorg. Chem.* **2011**, *50*, 2395–2403; (d) Koshevoy, I. O.; Karttunen, A. J.; Kritchenkou, I. S.; Krupenya, D. V.; Selivanov, S. I.; Melnikov, A. S.; Yunik, S. P.; Haukka, M.; Pakkanen, T. A. *Inorg. Chem.* **2013**, *52*, 3663–3673.



7. Blake, G. C.; Coates, G. E. *Proc. Chem. Soc.* **1959**, *12*, 396–397.
8. Bruce, M. I.; Jevric, M.; Skelton, B. W.; White, A. H.; Zaitseva, N. N. *J. Organomet. Chem.* **2010**, *695*, 1906–1910.
9. Vicente, J.; Chicote, M.-T.; Alvarez-Falcón, M. M.; Jones, P. G. *Organometallics* **2005**, *24*, 4666–4675.
10. Lei, Z.; Wan, X.-K.; Yuan, S.-F.; Guan, Z.-J.; Wang, Q.-M. *Acc. Chem. Res.* **2018**, *51*, 2465–2474.
11. Mingos, D. M. P.; Yau, J.; Menzer, S.; Williams, D. J. *Angew. Chem. Int. Ed. Engl.* **1995**, *34*, 1894–1895.
12. Wan, X.-K.; Tang, Q.; Yuan, S.-F.; Jiang, D.-E.; Wang, Q.-M. *J. Am. Chem. Soc.* **2015**, *137*, 652–655.
13. Wan, X. K.; Xu, W. W.; Yuan, S.-F.; Gao, Y.; Zeng, X.-C.; Wang, Q.-M. *Angew. Chem. Int. Ed.* **2015**, *54*, 9683–9686.
14. Guan, Z.-J.; Hu, F.; Li, J.-J.; Wen, Z.-R.; Lin, Y.-M.; Wang, Q.-M. *J. Am. Chem. Soc.* **2020**, *142*, 2995–3001.
15. Li, J.-J.; Guan, Z.-J.; Lei, Z.; Hu, F.; Wang, Q.-M. *Angew. Chem. Int. Ed.* **2019**, *58*, 1083–1087.
16. Wan, X.-K.; Guan, Z.-J.; Wang, Q.-M. *Angew. Chem. Int. Ed.* **2017**, *56*, 11494–11497.
17. Wan, X.-K.; Wang, J.-Q.; Nan, Z.-A.; Wang, Q.-M. *Sci. Adv.* **2017**, *3*, e1701823.
18. Wang, Y.; Wan, X.-K.; Ren, L.; Su, H.; Li, G.; Malola, S.; Lin, S.; Tang, Z.; Häkkinen, H.; Teo, B. K.; Wang, Q.-M.; Zheng, N. *J. Am. Chem. Soc.* **2016**, *138*, 3278–3281.
19. Lei, Z.; Li, J.-J.; Wan, X.-K.; Zhang, W.-H.; Wang, Q.-M. *Angew. Chem. Int. Ed.* **2018**, *57*, 8639–8643.
20. Díez, J.; Gamasa, M. P.; Gimeno, J.; Aguirre, A.; García-Granda, S. *Organometallics* **1991**, *10*, 380–382.
21. Yam, V. W.-W.; Wendy, K.-M. F.; Cheung, K.-K. *Organometallics* **1998**, *17*, 3293–3298.
22. Gamasa, M. P.; Gimeno, J.; Lastra, E.; Aguirre, A.; García-Granda, S. *J. Organomet. Chem.* **1989**, *378*, C11–C14.
23. Yam, V. W.-W.; Lee, W.-K.; Lai, T.-F. *Organometallics* **1993**, *12*, 2383–2387.
24. Wang, C. F.; Peng, S. M.; Chan, C. K.; Che, C. M. *Polyhedron* **1996**, *15*, 1853–1858.
25. Geissler, M.; Kopf, J.; Schubert, B.; Weiss, E.; Neugebauer, W.; Schleyer, P. v. R. *Angew. Chem. Int. Ed. Engl.* **1987**, *26*, 587–588.
26. Wei, Q. H.; Yin, G. Q.; Zhang, L. Y.; Chen, Z.-N. *J. Organomet. Chem.* **2006**, *25*, 4941–4944.
27. Wei, Q.-H.; Zhang, L.-Y.; Yin, G.-Q.; Shi, L.-X.; Chen, Z.-N. *J. Am. Chem. Soc.* **2004**, *126*, 9940–9941.
28. Naldini, L.; Demartin, F.; Manassero, M.; Sansoni, M.; Rassu, G.; Zoroddu, M. A. *J. Organomet. Chem.* **1985**, *279*, C42–C44.
29. Wei, Q. H.; Zhang, L. Y.; Shi, L. X.; Chen, Z. N. *Inorg. Chem. Commun.* **2004**, *7*, 286–288.
30. Yip, J. H. K.; Wu, J.; Wong, K. Y.; Yeung, K. W.; Vittal, J. J. *Organometallics* **2002**, *21*, 1612–1621.
31. (a) Rais, D.; Yau, J.; Mingos, D. M. P.; Vilar, R.; White, A. J. P.; Williams, D. J. *Angew. Chem. Int. Ed.* **2001**, *40*, 3464–3467; (b) Rais, D.; Mingos, D. M. P.; Vilar, R.; White, A. J. P.; Williams, D. J. *J. Organomet. Chem.* **2002**, *652*, 87–93.
32. Abu-Salah, O. M.; Ja'far, M. H.; Al-Ohaly, A. R.; Al-Farhan, K. A.; Al-Enzi, H. S.; Dolomanov, O. V.; Howard, J. A. K. *Eur. J. Inorg. Chem.* **2006**, 2353–2356.
33. Connell, T. U.; Sandanayake, S.; Khairallah, G. N.; White, J. M.; O'Hair, R. A. J.; Donnelly, P. S.; Williams, S. J. *Dalton Trans.* **2013**, *42*, 4903–4907.
34. Wei, Q. H.; Zhang, L.-Y.; Yin, G.-Q.; Shi, L.-X.; Chen, Z.-N. *Organometallics* **2005**, *24*, 3818–3820.
35. Guo, H.; He, X.; Wan, C.-Q.; Zhao, L. *Chem. Commun.* **2016**, *52*, 7723–7726.
36. Gao, C.-Y.; He, X.; Zhao, L.; Wang, M.-X. *Chem. Commun.* **2012**, *48*, 8368–8370.
37. Gao, C. Y.; Zhao, L.; Wang, M. X. *J. Am. Chem. Soc.* **2012**, *134*, 824–827.
38. Zhang, S.; Zhao, L. *Nat. Commun.* **2019**, *10*, 4848.
39. (a) Sappa, E.; Gambino, O.; Milone, L.; Cetini, G. *J. Organomet. Chem.* **1972**, *39*, 169–172; (b) Barner-Thorsen, C.; Hardcastle, K. I.; Rosenberg, E.; Siegel, J.; Landfredi, A. M. M.; Tripicchio, A.; Camellini, M. T. *Inorg. Chem.* **1981**, *20*, 4306–4311.
40. (a) Bian, S.-D.; Wu, H.-B.; Wang, Q.-M. *Angew. Chem. Int. Ed.* **2009**, *48*, 5363–5365; (b) Xie, Y.-P.; Al-Thabaiti, S. A.; Mak, T. C. W. *J. Mol. Struct.* **2013**, *1048*, 121–123.
41. Yuan, S.-F.; Li, P.; Tang, Q.; Wan, X.-K.; Nan, Z.-A.; Jiang, D.-E.; Wang, Q.-M. *Nanoscale* **2017**, *9*, 11405–11409.
42. Wan, X.-K.; Cheng, X.-L.; Tang, Q.; Han, Y.-Z.; Hu, G.; Jiang, D.-E.; Wang, Q.-M. *J. Am. Chem. Soc.* **2017**, *139*, 9451–9454.
43. Qu, M.; Li, H.; Xie, L.-H.; Yan, S.-T.; Li, J.-R.; Wang, J.-H.; Wei, C.-Y.; Wu, Y.-W.; Zhang, X.-M. *J. Am. Chem. Soc.* **2017**, *139*, 12346–12349.
44. Tanaka, S.; Dubs, C.; Inagaki, A.; Akita, M. *Organometallics* **2004**, *23*, 317–319.
45. Watson, W. H.; Poola, B.; Richmond, M. G. *Organometallics* **2005**, *24*, 4687–4690.
46. Hong, F.-E.; Lai, Y.-C.; Ho, Y.-J.; Chang, Y.-C. *J. Organomet. Chem.* **2003**, *688*, 161–167.
47. (a) Osella, D.; Ravera, M.; Nervi, C.; Housecroft, C. E.; Ralby, P. R.; Zanello, P.; Laschi, F. *Organometallics* **1991**, *10*, 3253–3259; (b) Choualeb, A.; Braunstein, P.; Rosé, J.; Bouaoud, S.-E.; Welter, R. *Organometallics* **2003**, *22*, 4405–4417; (c) Choualeb, A.; Rosé, J.; Braunstein, P.; Welter, R. *Organometallics* **2003**, *22*, 2688–2693; (d) Zhu, B.-H.; Hu, B.; Zhang, W.-Q.; Zhang, Y.-H.; Yin, Y.-Q.; Sun, J. *J. Organomet. Chem.* **2003**, *681*, 275–279; (e) Lucas, N. T.; Notaras, E. G. A.; Cifuentes, M. P.; Humphrey, M. G. *Organometallics* **2003**, *22*, 284–301; (f) Notaras, E. G. A.; Lucas, N. T.; Humphrey, M. G.; Willis, A. C.; Rae, A. D. *Organometallics* **2003**, *22*, 3659–3670; (g) Lucas, N. T.; Notaras, E. G. A.; Petrie, S.; Stranger, R.; Humphrey, M. G. *Organometallics* **2003**, *22*, 708–721.
48. Bian, S.-D.; Wang, Q.-M. *Chem. Commun.* **2008**, *43*, 5586–5588.
49. Gao, C.-Y.; Zhao, L.; Wang, M.-X. *J. Am. Chem. Soc.* **2011**, *133*, 8448–8451.
50. Zhao, L.; Mak, T. C. W. *J. Am. Chem. Soc.* **2004**, *126*, 6852–6853.
51. Shoshani, M. M.; Johnson, S. A. *Nat. Chem.* **2017**, *9*, 1282–1285.
52. Olbrich, F.; Kopf, J.; Weiss, E. *Angew. Chem. Int. Ed. Engl.* **1993**, *32*, 1077–1079.
53. Chui, S. S. Y.; Ng, M. F. Y.; Che, C.-M. *Chem. Eur. J.* **2005**, *11*, 1739–1749.
54. Chen, Z.-H.; Zhang, L.-Y.; Chen, Z.-N. *Organometallics* **2012**, *31*, 256–260.
55. Cook, A. W.; Jones, Z. R.; Wu, G.; Scott, S. L.; Hayton, T. W. *J. Am. Chem. Soc.* **2018**, *140*, 394–400.
56. Hau, S. C. K.; Cheng, P.-S.; Mak, T. C. W. *J. Am. Chem. Soc.* **2012**, *134*, 2922–2925.
57. (a) Zeng, J.-L.; Guan, Z.-J.; Du, Y.; Nan, Z.-A.; Lin, Y.-M.; Wang, Q.-M. *J. Am. Chem. Soc.* **2016**, *138*, 7848–7851; (b) Guan, Z.-J.; Zeng, J.-L.; Yuan, S.-F.; Hu, F.; Lin, Y.-M.; Wang, Q.-M. *Angew. Chem. Int. Ed.* **2018**, *57*, 5703–5707.
58. Hu, F.; Li, J.-J.; Guan, Z.-J.; Yuan, S.-F.; Wang, Q.-M. *Angew. Chem. Int. Ed.* **2020**, *59*, 5312–5315.
59. (a) Weber, D.; Tarselli, M. A.; Gagné, M. R. *Angew. Chem. Int. Ed.* **2009**, *54*, 5733–5736; (b) Wyss, C. M.; Tate, B. K.; Bacsa, J.; Wieliczko, M.; Sadighi, J. P. *Polyhedron* **2014**, *84*, 87–95; (c) Espada, M. F.; Campos, J.; López-Serrano, J.; Poveda, M. L.; Carmona, E. *Angew. Chem. Int. Ed.* **2015**, *54*, 15379–15384.
60. (a) Thoennes, D.; Weiss, E. *Chem. Ber.* **1978**, *111*, 3157–3161; (b) Malone, J. F.; McDonald, W. S. *J. Chem. Soc., Dalton Trans.* **1972**, 2646–2648.
61. (a) Ziegler, M. S.; Levine, D. S.; Lakshmi, K. V.; Tilley, T. D. *J. Am. Chem. Soc.* **2016**, *138*, 6484–6491; (b) Ziegler, M. S.; Lakshmi, K. V.; Tilley, T. D. *J. Am. Chem. Soc.* **2017**, *139*, 5378–5386; (c) Ziegler, M. S.; Torquato, N. A.; Levine, D. S.; Nicolay, A.; Celik, H.; Tilley, T. D. *Organometallics* **2018**, *37*, 2807–2823.
62. (a) Baukova, T. V.; Kuz'mina, L. A.; Lemenovskii, D. A.; Blumenfeld, A. L. *J. Organomet. Chem.* **1997**, *530*, 27–38; (b) Heckler, J. E.; Zeller, M.; Hunter, A. D.; Gray, T. G. *Angew. Chem. Int. Ed.* **2012**, *51*, 5924–5928; (c) Gómez-Suárez, A.; Dupuy, S.; Slawin, A. M. Z.; Nolan, S. P. *Angew. Chem. Int. Ed.* **2013**, *52*, 938–942; (d) Hashmi, A. S. K.; Braun, I.; Nösel, P.; Schädlich, J.; Wieteck, M.; Rudolph, M.; Rominger, F. *Angew. Chem. Int. Ed.* **2012**, *51*, 4456–4460.
63. (a) Dönnecke, D.; Wunderle, J.; Imhof, W. *J. Organomet. Chem.* **2004**, *689*, 585–594; (b) Majeed, Z.; McWhinnie, W. R.; Paxton, K.; Hamor, T. A. *J. Chem. Soc., Dalton Trans.* **1998**, 3947–3951.
64. (a) Muna, R. A. A.-M.; Lewis, J.; Raithby, P. R. *J. Organomet. Chem.* **1997**, *530*, 247–250; (b) Bohle, D. S.; Vahrenkamp, H. *Angew. Chem. Int. Ed.* **1990**, *29*, 198–199.
65. He, X.; Ruhlandt-Senge, K.; Power, P. P.; Bertz, S. H. *J. Am. Chem. Soc.* **1994**, *116*, 6963–6964.
66. Sundararaman, A.; Lalancette, R. A.; Zakharov, L. N.; Rheingold, A. L.; Jäkle, F. *Organometallics* **2003**, *22*, 3526–3532.
67. Gambarotta, S.; Floriani, C.; Chiesi-Villa, A.; Guastini, C. *J. Chem. Soc., Chem. Commun.* **1983**, 1156–1158.

68. Cerrada, E.; Contel, M.; Valencia, A. D.; Laguna, M.; Gelbrich, T.; Hursthouse, M. B. *Angew. Chem. Int. Ed.* **2000**, *39*, 2353–2356.
69. Contel, M.; Garrido, J.; Gimeno, M. C.; Jones, P. G.; Laguna, A.; Laguna, M. *Organometallics* **1996**, *15*, 4939–4943.
70. Olaru, M.; Rychagova, E.; Ketskova, S.; Shynkarenko, Y.; Yakunin, S.; Kovalenko, M. V.; Yablonskiy, A.; Andreev, B.; Kleemiss, F.; Beckmann, J.; Vogt, M. *J. Am. Chem. Soc.* **2020**, *142*, 373–381.
71. (a) Guss, J. M.; Mason, R.; Søtofte, I.; van Koten, G.; Noltes, J. G. *J. Chem. Soc., Chem. Commun.* **1972**, 446–447; (b) van Koten, G.; Noltes, J. G. *J. Organomet. Chem.* **1975**, *84*, 129–138.
72. Nobel, D.; van Koten, G.; Spek, A. L. *Angew. Chem. Int. Ed. Engl.* **1989**, *28*, 208–210.
73. Van Koten, G.; Jastrzebski, J. T. B. H.; Stam, C. H.; Niemann, N. C. *J. Am. Chem. Soc.* **1984**, *106*, 1880–1881.
74. Olmstead, M. M.; Power, P. P. *J. Am. Chem. Soc.* **1990**, *112*, 8008–8014.
75. Tsuda, T.; Yazawa, T.; Watanabe, K.; Fujii, T.; Saegusa, T. *J. Org. Chem.* **1981**, *46*, 192–194.
76. Gambarotta, S.; Floriani, C.; Chiessi-Villa, A.; Guastini, C. *J. Chem. Soc., Chem. Commun.* **1983**, 1304–1306.
77. Ten Hoedt, R. W. M.; Noltes, J. G.; van Koten, G.; Spek, A. L. *J. Chem. Soc., Dalton Trans.* **1978**, 1800–1806.
78. Edwards, P. G.; Gellert, R. W.; Marks, M. W.; Bau, R. *J. Am. Chem. Soc.* **1982**, *104*, 2072–2073.
79. Hope, H.; Oram, D.; Power, P. P. *J. Am. Chem. Soc.* **1984**, *106*, 1149–1150.
80. Guss, J. M.; Mason, R.; Thomas, J. M.; van Koten, G.; Noltes, J. G. *J. Organomet. Chem.* **1972**, *40*, C79–C80.
81. Smirnova, E. S.; Echavarren, A. M. *Angew. Chem. Int. Ed.* **2013**, *52*, 9023–9026.
82. Fernández, E. J.; Laguna, A.; López-de-luzuriaga, J. M.; Montiel, M.; Olmos, M. E.; Pérez, J.; Puelles, R. C. *Organometallics* **2006**, *25*, 4307–4315.
83. He, X.; Xue, Y.; Li, C.-C.; Wang, Y.; Jiang, H.; Zhao, L. *Chem. Sci.* **2018**, *9*, 1481–1487.
84. (a) Yuan, J.; Sun, T.; He, X.; An, K.; Zhu, J.; Zhao, L. *Nat. Commun.* **2016**, *7*, 11489; (b) Sun, T.; Guo, P.; Xie, Q.; Zhao, L.; Zhu, J. *J. Org. Chem.* **2019**, *84*, 3881–3886; (c) Xiao, K.; Zhao, Y.; Zhu, J.; Zhao, L. *Nat. Commun.* **2019**, *10*, 5639.
85. Tskhovrebov, A. G.; Goddard, R.; Fürstner, A. *Angew. Chem. Int. Ed.* **2018**, *57*, 8089–8094.
86. Dufour, N.; Schier, A.; Schmidbaur, H. *Organometallics* **1993**, *12*, 2408–2410.
87. Kaanda, H.; Kawashima, T.; Takao, T.; Suzuki, H. *Organometallics* **2012**, *31*, 1917–1926.
88. Burrows, A. D.; Mingos, D. M. P.; Menzer, S.; Vilar, R.; Williams, D. J. *J. Chem. Soc., Dalton Trans.* **1995**, 2107–2108.
89. Schmidbaur, H.; Scherbaum, F.; Huber, B.; Müller, G. *Angew. Chem. Int. Ed. Engl.* **1988**, *27*, 419–421.
90. Cabeza, J. A.; del Río, I.; Martínez-Méndez, L.; Miguel, D. *Chem. Eur. J.* **2006**, *12*, 1529–1538.
91. Schmidbaur, H.; Gabba, F. P.; Schier, A.; Riede, J. *Organometallics* **1995**, *14*, 4969–4971.
92. Scherbaum, F.; Huber, B.; Müller, G.; Schmidbaur, H. *Angew. Chem. Int. Ed. Engl.* **1988**, *27*, 1542–1544.
93. Pei, X.-L.; Yang, Y.; Lei, Z.; Wang, Q.-M. *J. Am. Chem. Soc.* **2013**, *135*, 6435–6437.
94. Pei, X.-L.; Yang, Y.; Lei, Z.; Chang, S.-S.; Guan, Z.-J.; Wan, X.-K.; Wen, T.-B.; Wang, Q.-M. *J. Am. Chem. Soc.* **2015**, *137*, 5520–5525.
95. Vicente, J.; Chicote, M. T.; Guerrero, R.; Jones, P. G. *J. Am. Chem. Soc.* **1996**, *118*, 699–700.
96. Melgarejo, D. Y.; Chiarella, G. M.; Mohamed, A. A.; Fackeler, J. J. P. *Z. Naturforsch., B: Chem. Sci.* **2009**, *64*, 1487–1491.
97. Raubenheimer, H.; Schmidbaur, H. *Organometallics* **2012**, *31*, 2507–2522.